arXiv:0906.1746v1 [nucl-ex] 9 Jun 2009

Proc. 25th Winter Workshop on Nuclear Dynamics (2009) 000–000

25th Winter Workshop on Nuclear Dynamics
Big Sky, Montana, USA
February 1–8, 2009

Enhanced Direct Photon Production in Au+Au Collisions at $\sqrt{s_{NN}} = 200$ GeV in PHENIX

S. Bathe[1] for the PHENIX collaboration

[1] RIKEN-BNL Research Center
Brookhaven National Laboratory
Upton NY 11973, USA

Abstract. The production of electron pairs with p_T between 1 and 5 GeV/c and $m < 300$ MeV has been measured at mid-rapidity in $\sqrt{s_{NN}} = 200$ GeV $p+p$ and Au+Au collisions by the PHENIX experiment at RHIC. A significant excess above the hadronic background was observed in both $p+p$ and Au+Au collisions. Treating the excess as internal conversion of direct photons, the direct photon yield in Au+Au was found to be enhanced compared to the binary-scaled $p+p$ yield. The enhancement is consistent with an exponential inverse slope of $221 \pm 23 \pm 18$ MeV and predictions from hydrodynamical models with initial temperature between 300 and 600 MeV at formation times of 0.6–0.15 fm/c.

Keywords: direct photons, nucleus-nucleus collisions, $p+p$ collisions, heavy ion, elactron pair production, PHENIX, RHIC
PACS: 13.85.Qk, 13.20.Fc, 13.20.He, 25.75.Dw

1. Introduction

A multitude of results from the Relativistic Heavy Ion Collider (RHIC) at Brookhaven National Laboratory (BNL) indicates the creation of a high-density, thermalized medium in ultra-relativistic collisions of heavy ions [1]. Such a medium is expected to radiate thermal photons [2], which, once produced, leave the medium unscathed. Thermal photons from the partonic phase of the collision are predicted to dominate the direct photon spectrum in the transverse momentum (p_T) range of 1–3 GeV/c as illustrated in Fig. 1 [2]. However, here direct photons are submerged in a background of hadronic decay photons, mainly from the π^0 and η. This background constitutes a major experimental challenge in the conventional, calorimeter-based measurement. It can be overcome, though, by measuring low-mass electron pairs in a mass range where electron pairs from the π^0 Dalitz decay do not contribute [3].

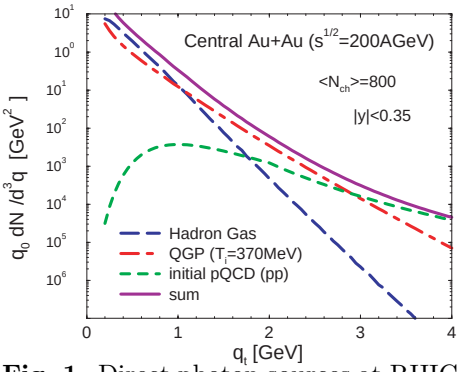

Fig. 1. Direct photon sources at RHIC [2].

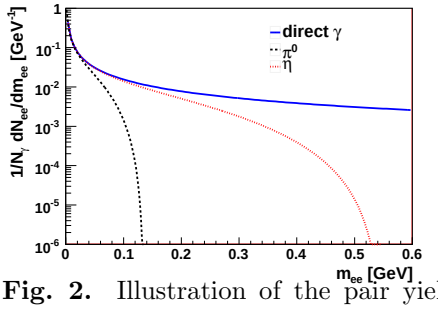

Fig. 2. Illustration of the pair yield mass dependence for direct photons as well as for π^0 and η Dalitz pairs.

The electron-pair yield above the hadronic background can be treated as internal conversion of direct photons [4].

2. Internal Conversion Method

Any source of high-energy photons also emits virtual photons with very low mass [4]. Those virtual photons then convert to low-mass e^+–e^- pairs, which can be measured (*Internal Conversion Method*). The pair yield per direct photon falls with the pair mass as:

$$\frac{d^2n_{ee}}{dm} = \frac{2\alpha}{3\pi}\frac{1}{m}\sqrt{1-\frac{4m_e^2}{m^2}}\left(1+\frac{2m_e^2}{m^2}\right)Sdn_\gamma. \quad (1)$$

Here α is the fine structure constant, m_e and m are the masses of the electron and the e^+–e^- pair, respectively, and S is a process dependent factor that goes to 1 as $m \to 0$ or $m \ll p_T$. Equation 1 also describes the relation between photons from hadron decays (e.g. $\pi^0, \eta \to \gamma\gamma$, and $\omega \to \gamma\pi^0$) and e^+–e^- pairs from Dalitz decays ($\pi^0, \eta \to e^+$–$e^-\gamma$ and $\omega \to e^+$–$e^-\pi^0$). For π^0 and η, the factor S is given by $S = |F(m^2)|^2(1-\frac{m^2}{M_h^2})^3$ [5], where M_h is the meson mass and $F(m^2)$ is the form factor. Figure 2 illustrates the pair yield mass dependence for direct photons as well as for π^0 and η Dalitz pairs. The cut-off of the π^0 pairs at the π^0 mass can be exploited to increase the signal-to-background ratio from 10%, where it is comparable to the systematic uncertainty and therefore not significant, to 50%, making a significant measurement possible. Since the measurement at low p_T is systematics limited, the simultaneous reduction in statistical significance is an acceptable trade-off[1].

[1]There are about 0.001 virtual photons with $m_{ee} > M_{\pi^0}$ for every real photon.

3. Data Set And Backgrounds

The analysis is based on two data sets: Au+Au at $\sqrt{s_{NN}}$ = 200 GeV acquired in 2004 consisting of 0.8 billion minimum bias events (4.9 pb^{-1} $p+p$ equivalent); $p+p$ at the same cms energy acquired in 2005 with 2.25 pb^{-1}. Charged tracks were measured with the Drift Chamber and Pad Chamber of the PHENIX [6] Central Arms covering $|\eta| < 0.35$ and $\Delta\phi = 2 \times \pi/2$ and identified as electrons with the Ring Imaging Čerenkov Detector (RICH) and Electromagnetic Calorimeter (EMCal). Material conversion pairs were removed by a cut on the orientation of the pair plane with respect to the magnetic field. Combinatorial background was removed by an event mixing technique, accurate to 0.25% systematic uncertainty in Au+Au.

There is additional correlated background from two sources: *cross pairs* with one electron/positron from either virtual photon in a double-Dalitz decay; *jet pairs* from two different Dalitz decays within the same jet or from back-to-back jets. These contributions can be well understood in a Monte Carlo calculation and have been subtracted.

4. Signal Extraction

After subtraction of the combinatorial background and the cross and jet pairs, the pair mass spectrum is compared to a "cocktail" of known hadronic sources [7, 8].

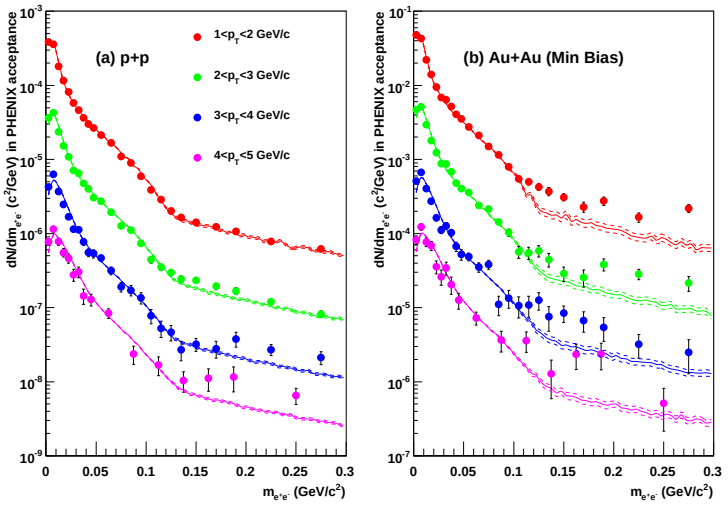

Fig. 3. Pair mass spectra for data (points) and hadronic cocktail (lines) in the PHENIX acceptance for different p_T intervals for $p+p$ (left) and Au+Au (right) [3].

Figure 3 shows this comparison for different p_T intervals for both $p+p$ and Au+Au. The cocktail is normalized to the data for $m < 30$ MeV, where the π^0 Dalitz decay dominates the yield. The "knee" at 100 MeV comes from the π^0 cut-off leading to the 80% background reduction mentioned above.

In $p + p$, the pair yield is consistent with the hadronic background for the lowest p_T interval. At higher p_T a small excess is visible for $m > m_{\pi^0}$. In Au+Au a much larger excess appears at all p_T, indicating an enhanced production of virtual photons[2].

To quantify the direct photon fraction, the mass spectrum is fit with a two-component function $f(m_{ee}) = (1-r)f_c(m_{ee}) + r f_{dir}(m_{ee})$ as illustrated in Fig. 4. Here $f_c(m_{ee})$ is the shape of the cocktail mass distribution (shown in Fig. 3), $f_{dir}(m_{ee})$ is the expected shape of the direct photon internal conversion, and r is the fit parameter. Both $f_c(m_{ee})$ and $f_{dir}(m_{ee})$ are separately normalized to the data for $m_{ee} < 30$ MeV/c^2, where their shapes are nearly identical. This preserves the meaning of r as the *real* direct photon fraction. From the agreement between

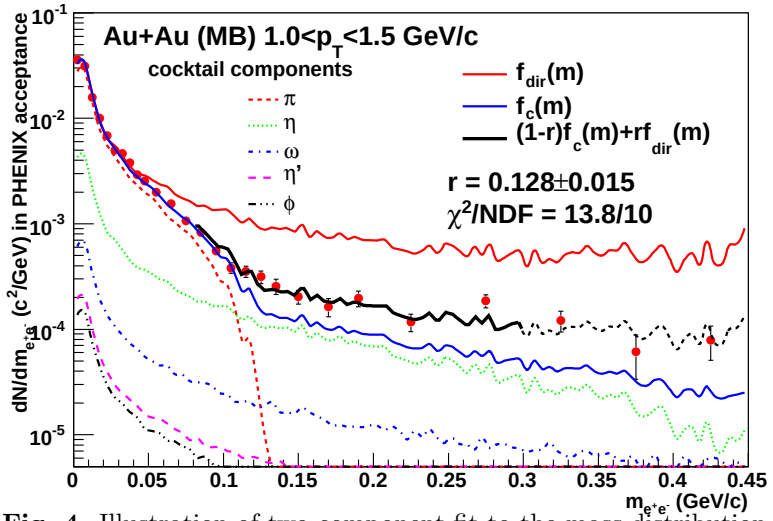

Fig. 4. Illustration of two-component fit to the mass distribution [3].

data and fit it can be concluded that the data matches the expected shape for direct photons.

The so extracted direct photon fraction, r, is plotted as a function of p_T in Fig. 5. While in case of $p + p$ the direct photon fraction is consistent with pQCD, for Au+Au r is enhanced above pQCD.

As this measurement is based on shape differences to extract the direct photon fraction, the η/π^0 ratio is the largest source of systematic uncertainty. This results

[2]This excess is in a different kinematic region (higher p_T, lower mass) than the low-mass enhancement reported in [7], which is expected to be dominated by the hadronic gas phase.

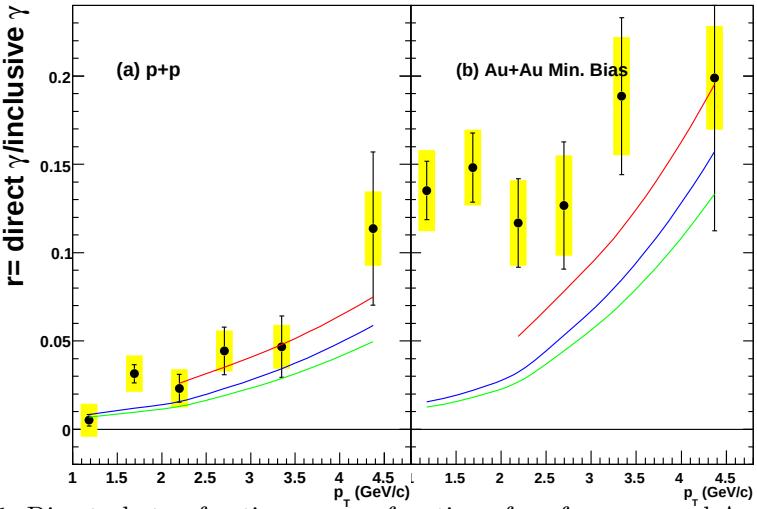

Fig. 5. Direct photon fraction, r, as a function of p_T for $p+p$ and Au+Au events compared to a pQCD calculation for three different scales. In the case of Au+Au the pQCD result is scaled by the nuclear overlap function, T_{AA} [3].

in a 7% uncertainty in $p+p$ and 17% in Au+Au. Other sources contribute only a few percent as the cocktail is normalized to the data and no absolute normalization is required.

In the next step, r is converted into the direct photon yield as $dN^{dir}(p_{\rm T}) = r \times dN^{incl}(p_{\rm T})$. The inclusive photon yield for each $p_{\rm T}$ bin is determined by $dN_\gamma^{incl} = N_{ee}^{data} \times (dN_\gamma^c/N_{ee}^c)$, where N_{ee}^{data} and N_{ee}^c are the measured and the absolutely normalized cocktail e^+–e^- pair yields, respectively, both for $m_{ee} < 30$ MeV/c^2; and dN_γ^c is the yield of photons from the cocktail. Here we use the fact that the ratio of the photon yield to the e^+–e^- pair yield for $m_{ee} < 30$ MeV/c^2 calculated from Eq. 1 is the same within a few percent for any photon source. The systematic uncertainty of γ^{incl} is 14% from the e^+–e^- pair acceptance.

5. Results

Figure 8 shows the invariant yield of direct photons as a function of p_T for $p+p$ and three different centrality classes in Au+Au. The $p+p$ data is again compared to the pQCD calculation. The calculation is consistent with the data for $p_T > 2$ GeV. A modified power law, $A_{pp}(1+p_T^2/b)^{-n}$, fits the data over the entire p_T range.

5.1. Significance of the Modified Power Law

The modified power law appears to yield an at least as good description of the data at low p_T as the pQCD calculation. What is the significance of this observation? It is obvious that the power-law behavior of hard scattering has to break down for $p_T \to 0$. For hadrons, soft production sets in with an exponential slope. This is illustrated in Fig. 6, which shows a parameterization of π^0 production in $p+p$ [

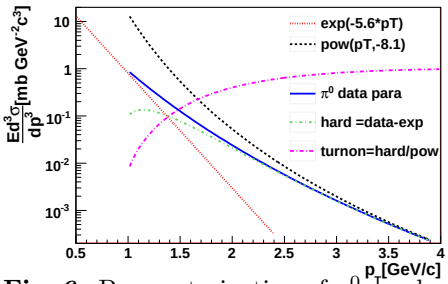

Fig. 6. Parameterization of π^0 production in $p+p$ [9] and its various contributions (for details see text).

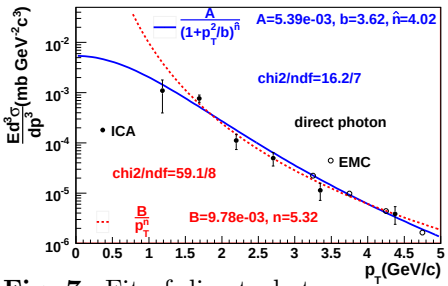

Fig. 7. Fit of direct photon cross section with both a power law and a modified power law.

9]. The parameterization is the sum of a power law and an exponential with a Woods-Saxon transition between the two. The two functions are shown separately. The exponential dies out at high p_T while the power law diverges at low p_T. The hard-scattering contribution can be understood as the difference between the data parameterization and the exponential contribution. One can see that it flattens out towards low p_T, deviating from the power law. This flattening corresponds to an onset of hard scattering as illustrated by the ratio of the hard scattering contribution to the power law.

This onset is not directly observable for hadrons as the production at low p_T is dominated by soft physics. Direct photons, however, are only produced in hard scatterings. This makes the onset of hard scattering at low p_T directly measurable. The onset has also been measured in Drell-Yan production [10].

To evaluate the statistical significance of the onset, the PHENIX data were fitted with both a power law and a modified power law. As shown in Fig. 7, the modified power law yields a smaller reduced χ^2 than the pure power law.

5.2. Au+Au Enhancement

For $1 < p_T < 3$ GeV, the direct photon invariant yield in Au+Au is enhanced above the T_{AA}-scaled modified power law that was fit to the $p+p$ data (Fig. 8). It can be well described, however, if an exponential is added. The resulting fit yields negative inverse exponential slopes of about 220 MeV[3]. If the medium were static, T could

[3]If the $p+p$ data are fit with a pure power law, T increases by 24 MeV in central events.

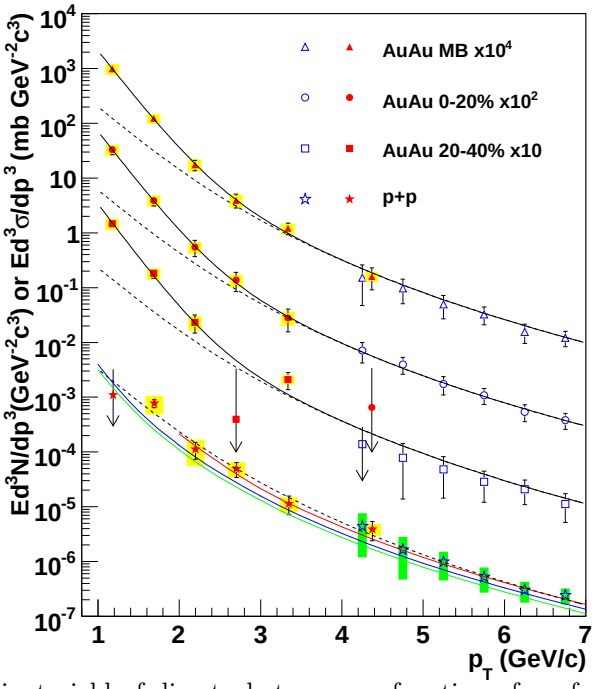

Fig. 8. Invariant yield of direct photons as a function of p_T for $p+p$ and three different centrality classes in Au+Au (solid symbols). The result of an earlier EMCal measurement is also shown (open symbols) [11, 12]. The $p+p$ data is compared to a pQCD calculation shown as three lines for different scales. The dashed line is a fit of a modified power law to the $p+p$ data. The Au+Au data are compared to the T_{AA}-scaled $p+p$ fit (dashed line). The solid line shows the result of a fit where an exponential is added to the T_{AA}-scaled $p+p$ fit [3].

be interpreted as its temperature. For a more realistic temperature estimate, the data is compared to hydrodynamical models. Models that fit the data assume initial temperatures, T_i, between 300 and 600 MeV at formation times, τ_0, between 0.6 and 0.15 fm/c, where the temperature and the formation time are anti-correlated. The $221 \pm 23(\text{stat.}) \pm 18(\text{sys.})$MeV obtained from the data alone serves as a lower limit. Even the lower limit, though, lies above the critical temperature predicted by lattice calculations.

6. Conclusion

An excess of low-mass e^+–e^- pairs above the hadronic background was observed at intermediate p_T (1 GeV $< p_T <$ 5 GeV) for both $p+p$ and Au+Au collisions. The

excess can be understood as the internal conversion of direct photons and shows the expected $1/m$ dependence. In $p+p$, the direct photon yield is consistent with the result of a pQCD calculation. In Au+Au, the yield is much larger. It is enhanced above the binary-scaled $p+p$ yield, represented by a modified power law fit to the $p+p$ data and scaled by T_{AA}. The Au+Au yield can be well described if an exponential is added to the binary-scaled $p+p$ fit. The negative inverse slope of the exponential is 221 $\pm$ 23 (stat.) $\pm$ 18 (sys.) MeV in central Au+Au. For a static medium, this could be interpreted as the temperature. For an expanding medium, it serves as a lower limit of the temperature. It is well above the critical temperature of about 170 MeV. Hydrodynamical models that fit the data assume initial temperatures, T_i, between 300 and 600 MeV at formation times, τ_0, between 0.15 and 0.6 fm/c. Together with the earlier WA98 measurement [13], this result can be interpreted as the first experimental evidence that strongly interacting matter can exceed the Hagedorn temperature of 170 MeV [14].

Acknowledgments

I thank the RIKEN-BNL Research Center for supporting my work and the DOE for operating RHIC and PHENIX.

References

1. K. Adcox et al., *Nucl. Phys.* **A757** (2005) 184.
2. S. Turbide, R. Rapp and C. Gale, *Phys. Rev.* **C69** (2004) 014903.
3. A. Adare et al. ArXiv:0804.4168[nucl-ex] (2008).
4. J. H. Cobb et al., *Phys. Lett.* **B78** (1978) 519.
5. L. G. Landsberg, *Phys. Rept.* **128** (1985) 301.
6. K. Adcox et al., *Nucl. Instrum. Meth.* **A499** (2003) 469.
7. S. Afanasiev et al. ArXiv:0706.3034[nucl-ex] (2007).
8. A. Adare et al., *Phys. Lett.* **B670** (2009) 313.
9. S. S. Adler et al., *Phys. Rev. Lett.* **98** (2007) 172302.
10. A. S. Ito et al., *Phys. Rev.* **D23** (1981) 604.
11. S. S. Adler et al., *Phys. Rev. Lett.* **94** (2005) 232301.
12. S. S. Adler et al., *Phys. Rev. Lett.* **98** (2007) 012002.
13. M. M. Aggarwal et al., *Phys. Rev. Lett.* **85** (2000) 3595.
14. S. C. Frautschi, *Phys. Rev.* **D3** (1971) 2821.

Systematic studies of elliptic flow measurements in Au + Au collisions at $\sqrt{s_{NN}} = 200$ GeV

S. Afanasiev,[17] C. Aidala,[7] N. N. Ajitanand,[44] Y. Akiba,[38,39] J. Alexander,[44] A. Al-Jamel,[34] K. Aoki,[23,38] L. Aphecetche,[46] R. Armendariz,[34] S. H. Aronson,[3] R. Averbeck,[45] T. C. Awes,[35] B. Azmoun,[3] V. Babintsev,[14] A. Baldisseri,[8] K. N. Barish,[4] P. D. Barnes,[26] B. Bassalleck,[33] S. Bathe,[4] S. Batsouli,[7] V. Baublis,[37] F. Bauer,[4] A. Bazilevsky,[3] S. Belikov,[3,16,*] R. Bennett,[45] Y. Berdnikov,[41] M. T. Bjorndal,[7] J. G. Boissevain,[26] H. Borel,[8] K. Boyle,[45] M. L. Brooks,[26] D. S. Brown,[34] D. Bucher,[30] H. Buesching,[3] V. Bumazhnov,[14] G. Bunce,[3,39] J. M. Burward-Hoy,[26] S. Butsyk,[45] S. Campbell,[45] J.-S. Chai,[18] S. Chernichenko,[14] J. Chiba,[19] C. Y. Chi,[7] M. Chiu,[7] I. J. Choi,[53] T. Chujo,[50] V. Cianciolo,[35] C. R. Cleven,[12] Y. Cobigo,[8] B. A. Cole,[7] M. P. Comets,[36] P. Constantin,[16] M. Csanád,[10] T. Csörgő,[20] T. Dahms,[45] K. Das,[11] G. David,[3] H. Delagrange,[46] A. Denisov,[14] D. d'Enterria,[7] A. Deshpande,[39,45] E. J. Desmond,[3] O. Dietzsch,[42] A. Dion,[45] J. L. Drachenberg,[1] O. Drapier,[24] A. Drees,[45] A. K. Dubey,[52] A. Durum,[14] V. Dzhordzhadze,[47] Y. V. Efremenko,[35] J. Egdemir,[45] A. Enokizono,[13] H. En'yo,[38,39] B. Espagnon,[36] S. Esumi,[49] D. E. Fields,[33,39] F. Fleuret,[24] S. L. Fokin,[22] B. Forestier,[27] Z. Fraenkel,[52,*] J. E. Frantz,[7] A. Franz,[3] A. D. Frawley,[11] Y. Fukao,[23,38] S.-Y. Fung,[4] S. Gadrat,[27] F. Gastineau,[46] M. Germain,[46] A. Glenn,[47] M. Gonin,[24] J. Gosset,[8] Y. Goto,[38,39] R. Granier de Cassagnac,[24] N. Grau,[16] S. V. Greene,[50] M. Grosse Perdekamp,[15,39] T. Gunji,[5] H.-Å. Gustafsson,[28] T. Hachiya,[13,38] A. Hadj Henni,[46] J. S. Haggerty,[3] M. N. Hagiwara,[1] H. Hamagaki,[5] H. Harada,[13] E. P. Hartouni,[25] K. Haruna,[13] M. Harvey,[3] E. Haslum,[28] K. Hasuko,[38] R. Hayano,[5] M. Heffner,[25] T. K. Hemmick,[45] J. M. Heuser,[38] X. He,[12] H. Hiejima,[15] J. C. Hill,[16] R. Hobbs,[33] M. Holmes,[50] W. Holzmann,[44] K. Homma,[13] B. Hong,[21] T. Horaguchi,[38,48] M. G. Hur,[18] T. Ichihara,[38,39] K. Imai,[23,38] M. Inaba,[49] D. Isenhower,[1] L. Isenhower,[1] M. Ishihara,[38] T. Isobe,[5] M. Issah,[44] A. Isupov,[17] B. V. Jacak,[45,†] J. Jia,[7] J. Jin,[7] O. Jinnouchi,[39] B. M. Johnson,[3] K. S. Joo,[31] D. Jouan,[36] F. Kajihara,[5,38] S. Kametani,[5,51] N. Kamihara,[38,48] M. Kaneta,[39] J. H. Kang,[53] T. Kawagishi,[49] A. V. Kazantsev,[22] S. Kelly,[6] A. Khanzadeev,[37] D. J. Kim,[53] E. Kim,[43] Y.-S. Kim,[18] E. Kinney,[6] A. Kiss,[10] E. Kistenev,[3] A. Kiyomichi,[38] C. Klein-Boesing,[30] L. Kochenda,[37] V. Kochetkov,[14] B. Komkov,[37] M. Konno,[49] D. Kotchetkov,[4] A. Kozlov,[52] P. J. Kroon,[3] G. J. Kunde,[26] N. Kurihara,[5] K. Kurita,[38,40] M. J. Kweon,[21] Y. Kwon,[53] G. S. Kyle,[34] R. Lacey,[44] J. G. Lajoie,[16] A. Lebedev,[16] Y. Le Bornec,[36] S. Leckey,[45] D. M. Lee,[26] M. K. Lee,[53] M. J. Leitch,[26] M. A. L. Leite,[42] H. Lim,[43] A. Litvinenko,[17] M. X. Liu,[26] X. H. Li,[4] C. F. Maguire,[50] Y. I. Makdisi,[3] A. Malakhov,[17] M. D. Malik,[33] V. I. Manko,[22] H. Masui,[49] F. Matathias,[45] M. C. McCain,[15] P. L. McGaughey,[26] Y. Miake,[49] A. Mignerey,[29] T. E. Miller,[50] A. Milov,[45] S. Mioduszewski,[3] G. C. Mishra,[12] J. T. Mitchell,[3] D. P. Morrison,[3] J. M. Moss,[26] T. V. Moukhanova,[22] D. Mukhopadhyay,[50] J. Murata,[38,40] S. Nagamiya,[19] Y. Nagata,[49] J. L. Nagle,[6] M. Naglis,[52] T. Nakamura,[13] J. Newby,[25] M. Nguyen,[45] B. E. Norman,[26] R. Nouicer,[3] A. S. Nyanin,[22] J. Nystrand,[28] E. O'Brien,[3] C. A. Ogilvie,[16] H. Ohnishi,[38] I. D. Ojha,[50] H. Okada,[23,38] K. Okada,[39] O. O. Omiwade,[1] A. Oskarsson,[28] I. Otterlund,[28] K. Ozawa,[5] R. Pak,[3] D. Pal,[50] A. P. T. Palounek,[26] V. Pantuev,[45] V. Papavassiliou,[34] J. Park,[43] W. J. Park,[21] S. F. Pate,[34] H. Pei,[16] J.-C. Peng,[15] H. Pereira,[8] V. Peresedov,[17] D. Yu. Peressounko,[22] C. Pinkenburg,[3] R. P. Pisani,[3] M. L. Purschke,[3] A. K. Purwar,[45] H. Qu,[12] J. Rak,[16] I. Ravinovich,[52] K. F. Read,[35,47] M. Reuter,[45] K. Reygers,[30] V. Riabov,[37] Y. Riabov,[37] G. Roche,[27] A. Romana,[24,*] M. Rosati,[16] S. S. E. Rosendahl,[28] P. Rosnet,[27] P. Rukoyatkin,[17] V. L. Rykov,[38] S. S. Ryu,[53] B. Sahlmueller,[30] N. Saito,[23,38,39] T. Sakaguchi,[5,51] S. Sakai,[49] V. Samsonov,[37] H. D. Sato,[23,38] S. Sato,[3,19,49] S. Sawada,[19] V. Semenov,[14] R. Seto,[4] D. Sharma,[52] T. K. Shea,[3] I. Shein,[14] T.-A. Shibata,[38,48] K. Shigaki,[13] M. Shimomura,[49] T. Shohjoh,[49] K. Shoji,[23,38] A. Sickles,[45] C. L. Silva,[42] D. Silvermyr,[35] K. S. Sim,[21] C. P. Singh,[2] V. Singh,[2] S. Skutnik,[16] W. C. Smith,[1] A. Soldatov,[14] R. A. Soltz,[25] W. E. Sondheim,[26] S. P. Sorensen,[47] I. V. Sourikova,[3] F. Staley,[8] P. W. Stankus,[35] E. Stenlund,[28] M. Stepanov,[34] A. Ster,[20] S. P. Stoll,[3] T. Sugitate,[13] C. Suire,[36] J. P. Sullivan,[26] J. Sziklai,[20] T. Tabaru,[39] S. Takagi,[49] E. M. Takagui,[42] A. Taketani,[38,39] K. H. Tanaka,[19] Y. Tanaka,[32] K. Tanida,[38,39] M. J. Tannenbaum,[3] A. Taranenko,[44] P. Tarján,[9] T. L. Thomas,[33] M. Togawa,[23,38] J. Tojo,[38] H. Torii,[38] R. S. Towell,[1] V.-N. Tram,[24] I. Tserruya,[52] Y. Tsuchimoto,[13,38] S. K. Tuli,[2] H. Tydesjö,[28] N. Tyurin,[14] C. Vale,[16] H. Valle,[50] H. W. van Hecke,[26] J. Velkovska,[50] R. Vertesi,[9] A. A. Vinogradov,[22] E. Vznuzdaev,[37] M. Wagner,[23,38] X. R. Wang,[34] Y. Watanabe,[38,39] J. Wessels,[30] S. N. White,[3] N. Willis,[36] D. Winter,[7] C. L. Woody,[3] M. Wysocki,[6] W. Xie,[4,39] A. Yanovich,[14] S. Yokkaichi,[38,39] G. R. Young,[35] I. Younus,[33] I. E. Yushmanov,[22] W. A. Zajc,[7] O. Zaudtke,[30] C. Zhang,[7] J. Zimányi,[20,*] and L. Zolin[17]

(PHENIX Collaboration)

[1]*Abilene Christian University, Abilene, Texas 79699, USA*

[2]*Department of Physics, Banaras Hindu University, Varanasi 221005, India*

[3]*Brookhaven National Laboratory, Upton, New York 11973-5000, USA*

[4]*University of California–Riverside, Riverside, California 92521, USA*

[5]*Center for Nuclear Study, Graduate School of Science, University of Tokyo, 7-3-1 Hongo, Bunkyo, Tokyo 113-0033, Japan*

[6]*University of Colorado, Boulder, Colorado 80309, USA*

[7]*Columbia University, New York, New York 10027 and Nevis Laboratories, Irvington, New York 10533, USA*

[8]*Dapnia, CEA Saclay, F-91191, Gif-sur-Yvette, France*

[9]*Debrecen University, H-4010 Debrecen, Egyetem tér 1, Hungary*

[10]*ELTE, Eötvös Loránd University, H-1117 Budapest, Pázmány P.s. 1/A, Hungary*

[11]*Florida State University, Tallahassee, Florida 32306, USA*

[12]*Georgia State University, Atlanta, Georgia 30303, USA*

[13]*Hiroshima University, Kagamiyama, Higashi-Hiroshima 739-8526, Japan*

 ©2009 The American Physical Society

[14]*IHEP Protvino, State Research Center of Russian Federation, Institute for High Energy Physics, Protvino, RU-142281, Russia*
[15]*University of Illinois at Urbana-Champaign, Urbana, Illinois 61801, USA*
[16]*Iowa State University, Ames, Iowa 50011, USA*
[17]*Joint Institute for Nuclear Research, Moscow Region, RU-141980 Dubna, Russia*
[18]*KAERI, Cyclotron Application Laboratory, Seoul, Korea*
[19]*KEK, High Energy Accelerator Research Organization, Tsukuba, Ibaraki 305-0801, Japan*
[20]*KFKI Research Institute for Particle and Nuclear Physics of the Hungarian Academy of Sciences (MTA KFKI RMKI), H-1525 Budapest 114, P. O. Box 49, Budapest, Hungary*
[21]*Korea University, Seoul, 136-701, Korea*
[22]*Russian Research Center "Kurchatov Institute," Moscow, Russia*
[23]*Kyoto University, Kyoto 606-8502, Japan*
[24]*Laboratoire Leprince-Ringuet, Ecole Polytechnique, CNRS-IN2P3, Route de Saclay, F-91128, Palaiseau, France*
[25]*Lawrence Livermore National Laboratory, Livermore, California 94550, USA*
[26]*Los Alamos National Laboratory, Los Alamos, New Mexico 87545, USA*
[27]*LPC, Université Blaise Pascal, CNRS-IN2P3, Clermont-Fd, F-63177 Aubiere Cedex, France*
[28]*Department of Physics, Lund University, Box 118, SE-22100 Lund, Sweden*
[29]*University of Maryland, College Park, Maryland 20742, USA*
[30]*Institut für Kernphysik, University of Muenster, D-48149 Muenster, Germany*
[31]*Myongji University, Yongin, Kyonggido 449-728, Korea*
[32]*Nagasaki Institute of Applied Science, Nagasaki-shi, Nagasaki 851-0193, Japan*
[33]*University of New Mexico, Albuquerque, New Mexico 87131, USA*
[34]*New Mexico State University, Las Cruces, New Mexico 88003, USA*
[35]*Oak Ridge National Laboratory, Oak Ridge, Tennessee 37831, USA*
[36]*IPN-Orsay, Universite Paris Sud, CNRS-IN2P3, BP1, F-91406, Orsay, France*
[37]*PNPI, Petersburg Nuclear Physics Institute, Gatchina, Leningrad region, RU-188300, Russia*
[38]*RIKEN Nishina Center for Accelerator-Based Science, Wako, Saitama 351-0198, Japan*
[39]*RIKEN BNL Research Center, Brookhaven National Laboratory, Upton, New York 11973, USA*
[40]*Physics Department, Rikkyo University, 3-34-1 Nishi-Ikebukuro, Toshima, Tokyo 171-8501, Japan*
[41]*St. Petersburg State Polytechnic University, St. Petersburg, Russia*
[42]*Universidade de São Paulo, Instituto de Física, Caixa Postal 66318, São Paulo CEP05315-970, Brazil*
[43]*System Electronics Laboratory, Seoul National University, Seoul, Korea*
[44]*Chemistry Department, Stony Brook University, SUNY, Stony Brook, New York 11794, USA*
[45]*Department of Physics and Astronomy, Stony Brook University, SUNY, Stony Brook, New York 11794, USA*
[46]*SUBATECH (Ecole des Mines de Nantes, CNRS-IN2P3, Université de Nantes) BP 20722, F-44307, Nantes, France*
[47]*University of Tennessee, Knoxville, Tennessee 37996, USA*
[48]*Department of Physics, Tokyo Institute of Technology, Oh-okayama, Meguro, Tokyo 152-8551, Japan*
[49]*Institute of Physics, University of Tsukuba, Tsukuba, Ibaraki 305, Japan*
[50]*Vanderbilt University, Nashville, Tennessee 37235, USA*
[51]*Waseda University, Advanced Research Institute for Science and Engineering, 17 Kikui-cho, Shinjuku-ku, Tokyo 162-0044, Japan*
[52]*Weizmann Institute, Rehovot 76100, Israel*
[53]*Yonsei University, IPAP, Seoul 120-749, Korea*
(Received 9 May 2009; published 31 August 2009)

We present inclusive charged hadron elliptic flow (v_2) measured over the pseudorapidity range $|\eta| < 0.35$ in Au + Au collisions at $\sqrt{s_{NN}} = 200$ GeV. Results for v_2 are presented over a broad range of transverse momentum ($p_T = 0.2$–8.0 GeV/c) and centrality (0–60%). To study nonflow effects that are correlations other than collective flow, as well as the fluctuations of v_2, we compare two different analysis methods: (1) the event-plane method from two independent subdetectors at forward ($|\eta| = 3.1$–3.9) and beam ($|\eta| > 6.5$) pseudorapidities and (2) the two-particle cumulant method extracted using correlations between particles detected at midrapidity. The two event-plane results are consistent within systematic uncertainties over the measured p_T and in centrality 0–40%. There is at most a 20% difference in the v_2 between the two event-plane methods in peripheral (40–60%) collisions. The comparisons between the two-particle cumulant results and the standard event-plane measurements are discussed.

DOI: 10.1103/PhysRevC.80.024909 PACS number(s): 25.75.Ld

I. INTRODUCTION

Collisions of Au + Au nuclei at the BNL Relativistic Heavy Ion Collider (RHIC) produce matter at very high energy density [1–4]. The dynamical evolution of this hot and dense

*Deceased.
†PHENIX spokesperson: jacak@skipper.physics.sunysb.edu

medium reflects its state and the degrees of freedom that govern the different stages it undergoes [5–7]. Azimuthal anisotropy measurements serve as a probe of the degree of thermalization, transport coefficients, and the equation of state (EOS) [8–10] of the produced medium.

Azimuthal correlations in Au + Au collisions at RHIC have been shown to consist of a mixture of jet and harmonic contributions [11–14]. Jet contributions are found to be relatively small for $p_T \lesssim 2.0$ GeV/c, with away-side jet yields strongly suppressed [13]. Significant modifications to the away-side jet topology have also been reported [15–17]. The harmonic contributions are typically characterized by the Fourier coefficients,

$$v_n = \langle \cos(n[\phi - \Psi_{\mathrm{RP}}]) \rangle \quad (n = 1, 2, \ldots), \tag{1}$$

where ϕ represents the azimuthal emission angle of a charged hadron and Ψ_{RP} is the azimuth of the reaction plane defined as containing both the direction of the impact parameter vector and the beam axis. The brackets denote statistical averaging over particles and events. The first two harmonics v_1 and v_2 are referred to as directed and elliptic flow, respectively.

It has been found that at low p_T ($p_T \lesssim 2.0$ GeV/c), the magnitude and trends of v_2 are underpredicted by hadronic cascade models supplemented with string dynamics [18], but they are well reproduced by models that either incorporate hydrodynamic flow [7,9] with a first-order phase transition and rapid thermalization, $\tau \sim 1$ fm/c [19], or use a quasiparticle ansatz but include more than just 2-to-2 interactions [20].

The mass dependence of v_2 as a function of p_T has been studied using identified baryons and mesons [19,21] and empirical scaling of elliptic flow per constituent quark was observed when the signal and the p_T of the hadron were divided by the number of constituent quarks n_q ($n_q = 2$ for mesons, 3 for baryons). This scaling is most clearly observed by plotting the data as a function of transverse kinetic energy $\mathrm{KE}_T \equiv m_T - m = \sqrt{p_T^2 + m^2} - m$ [22], where m_T and m denote the transverse mass and mass of the particle, respectively. A recent study [23] finds that the constituent quark scaling holds up to $\mathrm{KE}_T \approx 1$ GeV. This indicates partonic, rather than hadronic, flow and suggests that the bulk matter collectivity develops before hadronization takes place [24–26]. Results for the v_2 of the ϕ meson further validate the observation of partonic collectivity. The ϕ is not expected to be affected by hadronic interactions in the late stages of the medium evolution because of to its small interaction cross section with nonstrange hadrons [27].

All of the v_2 measurements referenced above were performed using the event-plane method [28]. In PHENIX studies, the event plane was determined at forward and backward pseudorapidities ($|\eta| = 3.1$–3.9) with the assumption that correlations induced by elliptic flow dominate over all other nonflow correlations [19]. Nonflow correlations are those that are not correlated with the reaction plane. Common sources of nonflow correlations include jets, the near-side ridge, quantum correlations, and resonance decays. Simulation studies [19,29] have shown that the correlations from jets and dijets become negligible when the rapidity separation between the particles and the event plane is greater than three units. Thus we expect that the event plane at forward pseudorapidities $|\eta| = 3.1$–3.9 in the PHENIX experiment would not have significant jet-correlation with particles measured within the PHENIX central arm spectrometer covering the pseudorapidity window $|\eta| < 0.35$. STAR and PHOBOS Collaborations have observed that in central Au + Au collisions, there is a ridge of particles [30,31] that are correlated in azimuthal angle with a high-p_T particle and that this ridge extends to $|\eta| < 4$ (for midrapidity triggers). The ridge could produce a nonflow correlation on which we can provide information by using our v_2 measurements, which are made with different techniques and at different rapidities.

Event-by-event flow fluctuations can also affect the magnitude of the extracted flow signal [32]. This occurs because the event plane at forward pseudorapidities is reconstructed using particles from participant nucleons whose positions fluctuate event-by-event. Assuming that v_2 fluctuates according to a Gaussian distribution, the v_2 fluctuation is proportional to the fluctuation of the initial geometry. This effect scales as $1/N_{\mathrm{part}}$, where N_{part} denotes the number of participant nucleons. The difference between v_2 values obtained from different methods can be quantitatively understood in terms of nonflow and fluctuation effects [33,34].

Hence in this paper we will compare the v_2 results from the event plane determined at two different pseudorapidities with the goal of investigating the sensitivity of v_2 to nonflow and fluctuation effects. Additionally, we will extract the elliptic flow with the two-particle cumulant method, which is expected to have higher sensitivity to nonflow contributions to v_2.

In this paper, we describe the PHENIX measurements of elliptic flow (v_2) at midrapidity ($|\eta| < 0.35$) in Au + Au collisions at $\sqrt{s_{NN}} = 200$ GeV obtained from a cumulant analysis of two-particle azimuthal correlations and the event-plane method over a broad range of p_T ($p_T = 0.2$–8 GeV/c) and centrality (0–60%). Section II describes the PHENIX apparatus, with an emphasis on the detectors relevant to the presented results, as well as the track selections used in the analysis. Section III gives details of the event-plane and cumulant methods as applied in PHENIX, and Sec. IV discusses their systematic uncertainties. The results from the two methods are reported in Sec. V. Section VI presents a comparison of v_2 results across different experiments and a discussion. The v_2 values obtained from the different methods are tabulated in the Appendix.

II. EXPERIMENTAL ANALYSIS

A. The PHENIX detector

The PHENIX detector consists of two central spectrometer arms at midrapidity that are designated East and West for their location relative to the interaction region, and two muon spectrometers at forward rapidity, similarly called North and South. A detailed description of the PHENIX detector can be found in Ref. [35]. The layout of the PHENIX detector during data taking in 2004 is shown in Fig. 1. Each central spectrometer arm covers a pseudorapidity range of $|\eta| < 0.35$ subtending 90° in azimuth and is designed to detect electrons, photons, and charged hadrons. Charged particles are tracked

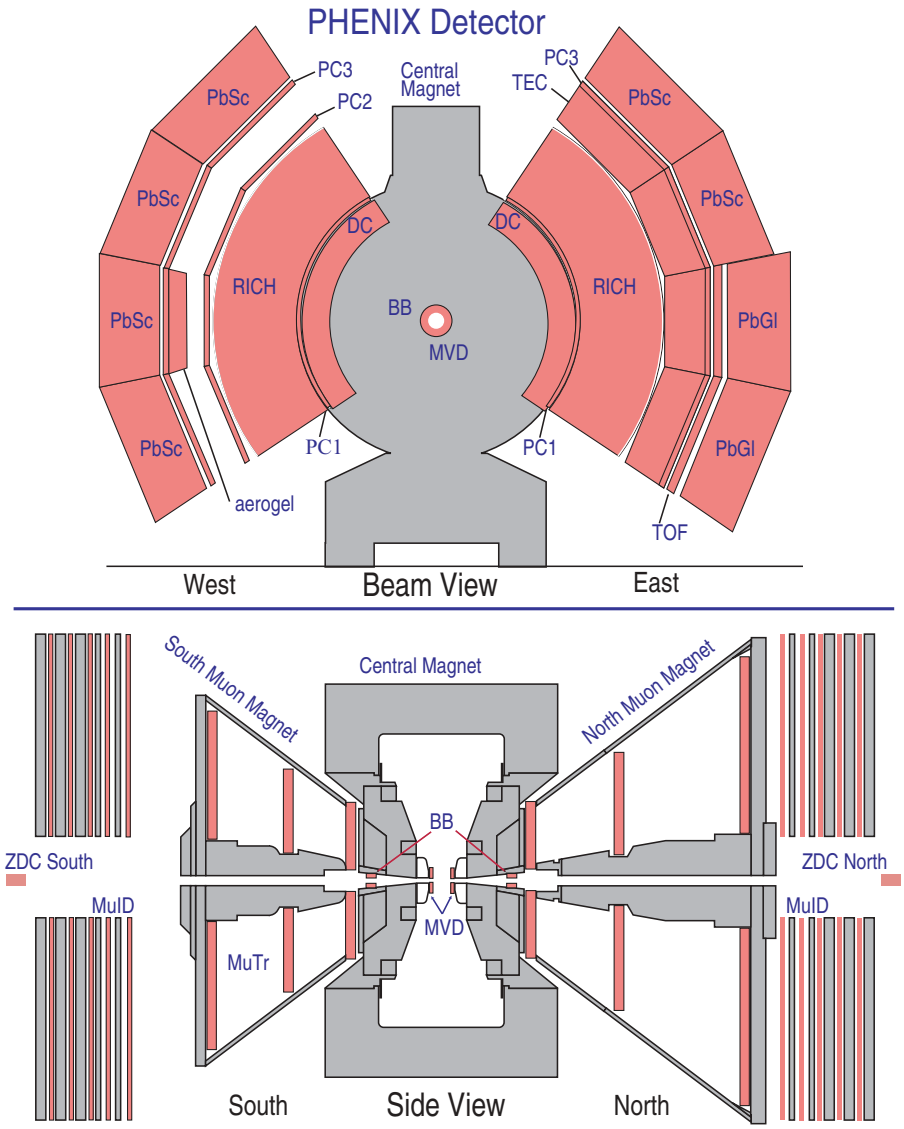

FIG. 1. (Color online) PHENIX experimental layout in 2004. Top: PHENIX central arm spectrometers viewed along the beam axis. Bottom: side view of the PHENIX muon arm spectrometers.

by drift chambers (DCs) positioned between 2.0 and 2.4 m radially outward from the beam axis and layers of multiwire proportional chambers with pad readout (two in the east arm and three in the west arm) PC1, PC2, and PC3 located at a radial distance of 2.4, 4.2, and 5 m, respectively. Particle identification is provided by ring imaging Čerenkov counters (RICHs), a time-of-flight scintillator wall (TOF), and two types of electromagnetic calorimeter (EMCAL), the lead scintillator (PbSc) and lead glass (PbGl).

The detectors used to characterize each event are the beam-beam counters (BBCs) [36] and the zero-degree calorimeters (ZDCs) [37]. These detectors are used to determine the time of the collision, the position of the collision vertex along the beam axis, and the collision centrality and also provide the event trigger. In this analysis the BBCs are also used to determine the event plane. Each BBC is composed of 64 elements, and a single BBC element consists of a 1 in. diameter mesh dynode photomultiplier tube (PMT) mounted on a 3 cm long quartz radiator. The BBCs are installed on the north and south sides of the collision point along the beam axis at a distance of 144 cm from the center of the interaction region and they surround the beam pipe. The BBC acceptance covers the pseudorapidity range $3.1 < |\eta| < 3.9$ and the full range of azimuthal angles.

The ZDCs are hadronic calorimeters located on both sides of the PHENIX detector. Each ZDC is mechanically subdivided into three identical modules of two interaction lengths. They cover a pseudorapidity range of $|\eta| > 6.5$ and measure the energy of the spectator neutrons with a 20 GeV energy resolution [37]. The shower maximum detectors (ZDC-SMDs) are scintillator strip hodoscopes between the first and second ZDC modules. This location approximately corresponds to the maximum of the hadronic shower. The horizontal coordinate is sampled by seven scintillator strips of 15 mm width, while the vertical coordinate is sampled by eight strips of 20 mm width. The active area of a ZDC-SMD is 105 mm $\times$ 110 mm (horizontal $\times$ vertical dimension). Scintillation light is delivered to a multichannel PMT M16 by wavelength-shifter fibers. The ZDC-SMD position resolution depends on the energy deposited in the scintillator. It varies from $<$3 mm, when the number of particles exceeds 100, to 10 mm for a smaller number of particles.

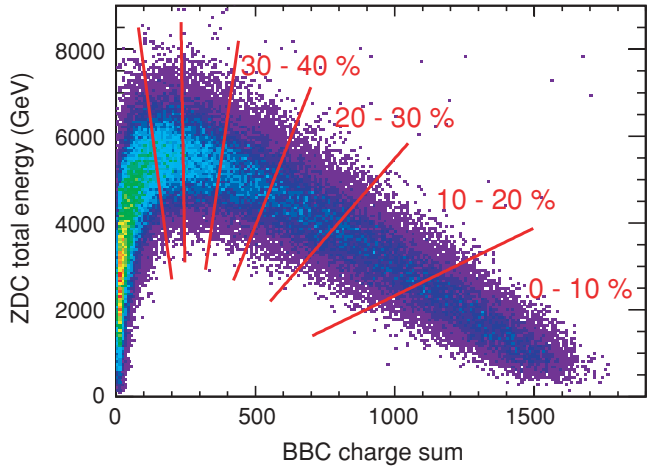

FIG. 2. (Color online) Correlation between ZDC energy and BBC charge sum for Au + Au collisions at $\sqrt{s_{NN}} = 200$ GeV. Solid lines represent the corresponding centrality boundaries up to 60% centrality bin.

B. Event selection

For the analyses presented here, we used approximately 850×10^6 minimum-bias triggered events. The minimum-bias trigger was defined by a coincidence between North and South BBC signals and an energy threshold of one neutron in the ZDCs. The events are selected offline to be within a z vertex of less than 30 cm from the nominal center of the PHENIX spectrometer. This selection corresponds to $92.2^{+2.5}_{-3.0}\%$ of the 6.9 b Au + Au inelastic cross section at $\sqrt{s_{NN}} = 200$ GeV [38]. The event centrality was determined by correlating the charge detected in the BBCs with the energy measured in the ZDCs, as shown in Fig. 2.

A Glauber model Monte Carlo simulation [39–41] that includes the responses of BBC and ZDC gives an estimate of the average number of participating nucleons $\langle N_{\rm part}\rangle$ for each centrality class. The simulation does not include fluctuations in the positions of the nucleons which give rise to eccentricity fluctuations. Table I lists the calculated values of $\langle N_{\rm part}\rangle$ for each centrality class.

TABLE I. Centrality classes and average number of participant nucleons $\langle N_{\rm part}\rangle$ obtained from a Glauber Monte Carlo simulation of the BBC and ZDC responses for Au + Au collision at $\sqrt{s_{NN}} = 200$ GeV. Each centrality class is expressed as a percentage of $\sigma_{\rm AuAu} = 6.9$ b inelastic cross section. Errors denote systematic uncertainties from the Glauber MC simulation.

Centrality	$\langle N_{\rm part}\rangle$
0–10%	325.2 ± 3.3
10–20%	234.6 ± 4.7
20–30%	166.6 ± 5.4
30–40%	114.2 ± 4.4
40–50%	74.4 ± 3.8
50–60%	45.5 ± 3.3

C. Track selection

Charged particle tracks are measured using information from the DC, the PC1 and PC3 detectors, and the z vertex from the BBC. The DC has 12 wire planes, which are spaced at 0.6 cm intervals along the radial direction from the beam axis. Each wire provides a track position measurement, with better than 150 μm spatial resolution in the azimuthal (ϕ) direction. The PC1 provides a space point in the ϕ and beam directions, albeit with lower resolution. This space point and the vertex position help determine the three-dimensional momentum vector by providing the polar angle for charged tracks at the exit of the DC. Trajectories are confirmed by requiring matching hits at PC3 to reduce secondary background. Tracks are then projected back to the collision vertex through the magnetic field to determine the momentum $\vec{p}$ [42]. The momentum resolution is $\delta p/p \simeq 0.7\% \oplus 1.0\% \times p$ (GeV/c). The momentum scale is known to 0.7%, as determined from the reconstructed proton mass using the TOF detector. Further details on track reconstruction and momentum determination can be found in Refs. [41,42].

The tracks reconstructed by the DC that do not originate from the event vertex have been investigated as potential background to the charged particle measurement. The main background sources include secondary particles from decays and e^+e^- pairs from the conversion of photons in the material between the vertex and the DC [41]. Tracks are required to have a hit in the PC3, as well as in the EMCAL, within at most 2σ of the expected hit location in both the azimuthal and beam directions. This cut reduces the background not originating in the direction of the vertex. To reduce the conversion background, we further require tracks to have $E/p_T > 0.2$, where E denotes the energy deposited in the EMCAL and p_T is the transverse momentum of particles measured in the DC. Since most of the electrons from photon conversion are genuine low p_T particles that were reconstructed as high p_T particles, requiring a large deposit of energy in the EMCAL suppresses the electron background [43]. We also require that there are no associated hits in the RICH. The RICH is filled with CO_2 gas at atmospheric pressure and has a charged particle threshold $\gamma_{\rm th} = 35$ to emit Čerenkov photons.

III. METHODS OF AZIMUTHAL ANISOTROPY MEASUREMENT

In this section, we introduce the methods for azimuthal anisotropy measurements as used in the PHENIX experiment. Section III A describes the event-plane method using the BBCs and ZDC-SMDs detectors, and Sec. III B describes the two-particle cumulant method.

A. Event-plane method

The event-plane method [28] uses the azimuthal anisotropy signal to estimate the angle of the reaction plane. The estimated reaction plane is called the "event plane" and is determined for each harmonic of the Fourier expansion of the azimuthal distribution. The event flow vector $\vec{Q}_n = (Q_x, Q_y)$ and azimuth of the event plane Ψ_n for the nth harmonic of the

azimuthal anisotropy can be expressed as

$$Q_x \equiv |\vec{Q}_n| \cos(n\Psi_n) = \sum_i^M w_i \cos(n\phi_i), \tag{2}$$

$$Q_y \equiv |\vec{Q}_n| \sin(n\Psi_n) = \sum_i^M w_i \sin(n\phi_i), \tag{3}$$

$$\Psi_n = \frac{1}{n}\tan^{-1}\left(\frac{Q_y}{Q_x}\right), \tag{4}$$

where M denotes the number of particles used to determine the event plane, ϕ_i is the azimuthal angle of each particle, and w_i is the weight chosen to optimize the event-plane resolution. Once the event plane is determined, the elliptic flow v_2 can be extracted by correlating the azimuthal angle of emitted particles ϕ with the event plane, i.e.,

$$v_2 = \frac{v_2^{\rm obs}}{{\rm Res}\{\Psi_n\}} = \frac{\langle\cos(2[\phi - \Psi_n])\rangle}{\langle\cos(2[\Psi_n - \Psi_{\rm RP}])\rangle}, \tag{5}$$

where ϕ is the azimuthal angle of tracks in the laboratory frame, Ψ_n is the nth-order event plane, and the brackets denote an average over all charged tracks and events. The denominator Res $\{\Psi_n\}$ is the event-plane resolution that corrects for the difference between the estimated event plane Ψ_n and true reaction plane $\Psi_{\rm RP}$.

In this paper, the second-harmonic event planes were independently determined with two BBCs located at the forward (BBC South, referred to as BBCS) and backward (BBC North, referred to as BBCN) pseudorapidities $|\eta| =$ 3.1–3.9 [19]. The difference between the two independent event planes was used to estimate the event-plane resolution. The planes were also combined to determine the event plane for the full event. A large pseudorapidity gap between the charged particles detected in the central arms and the event plane at the BBCs reduces the effect of possible nonflow contributions, especially those from dijets [29]. The measured v_2 of hadrons in the central arms with respect to the combined second-harmonic BBC event plane will be denoted throughout this paper as $v_2\{\text{BBC}\}$.

Two first-harmonic event planes were also determined using spectator neutrons at the two shower maximum detectors (ZDC-SMDs) that are sandwiched between the first and second modules of the ZDCs. Forward (ZDCS) and backward (ZDCN) SMDs which cover pseudorapidity $|\eta| > 6.5$ were used. The measured v_2 of hadrons in the central arms determined with respect to the first-harmonic ZDC-SMD event plane is denoted as $v_2\{\text{ZDC-SMD}\}$.

The pseudorapidity gap between the hadrons measured in the central arms and the ZDC-SMDs is larger than that for the BBCs, which could cause a further reduction of nonflow contributions on $v_2\{\text{ZDC-SMD}\}$. Since the ZDC-SMD measures spectator neutrons, the ZDC-SMD event plane should be insensitive to fluctuations in the participant event plane. Hence fluctuations in $v_2\{\text{ZDC-SMD}\}$ should be suppressed up to fluctuations in the spectator positions.

For completeness, two further event planes are defined: (1) a combined event plane defined by the weighted average of event planes at the forward and backward pseudorapidities for both BBCs and ZDC-SMDs, and (2) an event plane found using tracks in the central arm. The event plane at the central arms (CNT) is only used to estimate the resolution of BBC and ZDC-SMD event planes by using a three-subevent combination of the ZDC-SMD, BBC, and CNT.

1. Event-plane determination

To determine an event plane, the contribution at each azimuthal angle needs to be appropriately weighted depending on the detector used. For the BBC, we chose the weights to be the number of particles detected in each phototube, while for the ZDC-SMD, the weights were based on the energy deposited in each of the SMD strips. For the CNT event plane, the weight was taken to be proportional to p_T up to 2 GeV/c and constant for $p_T > 2$ GeV/c. For the CNT event plane, we also adopted a unit weight ($w_i = 1$) and found that the resulting CNT event-plane resolution extracted by comparing the CNT event plane with the BBC and ZDC-SMD planes was nearly identical when using the p_T-dependent or unit weights.

Corrections were performed to remove possible biases from the finite acceptance of the BBC and ZDC-SMD. In this analysis, we applied two corrections called the recentering and shift methods [28]. In the recentering method, event flow vectors are shifted and normalized by using the mean $\langle Q\rangle$ and width σ of flow vectors, i.e.,

$$Q_x' = \frac{Q_x - \langle Q_x\rangle}{\sigma_x}, \quad Q_y' = \frac{Q_y - \langle Q_y\rangle}{\sigma_y}. \tag{6}$$

This correction reduces the dependence of the event-plane resolution on the laboratory angle. Most acceptance effects were removed by the application of the recentering method. However, remaining small corrections were applied after recentering using the shift method [28], in which the reaction plane is shifted by $\Delta\Psi_n$ defined by

$$n\Delta\Psi_n(\Psi_n) = \sum_{k=1}^{k_{\rm max}} \frac{2}{k}[-\langle\sin(kn\Psi_n)\rangle\cos(kn\Psi_n) + \langle\cos(kn\Psi_n)\rangle\sin(kn\Psi_n)], \tag{7}$$

where $k_{\rm max} = 8$ in this analysis. The shift ensures that $dN/d\Psi_n$ is isotropic. When $k_{\rm max}$ was reduced to $k_{\rm max} = 4$, the difference in the extracted v_2 was negligible, and thus we include no systematic uncertainty due to the choice of $k_{\rm max}$ in our v_2 results.

Independent corrections were applied to each centrality selection in 5% increments and in 20 cm steps in the z vertex to optimize the event-plane resolution. The corrections were also done for each experimental run (the duration of a run is typically 1–3 h) to minimize the possible time-dependent response of detectors.

Figure 3 shows event-plane distributions for a subsample of the entire data set. After all corrections are applied, the event-plane distributions are isotropic.

2. Event-plane resolution

The event-plane resolution for v_2 was evaluated by both the two-subevent and three-subevent methods. In the two-subevent

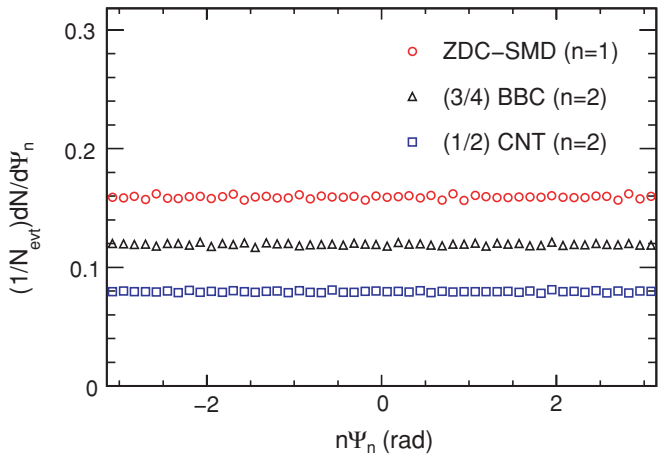

FIG. 3. (Color online) Event-plane distributions after applying all corrections for the ZDC-SMD, BBC, and CNT. The statistical error bars are smaller than the symbols. The distributions for the BBC and CNT event planes are scaled by 3/4 and 1/2 to improve visibility.

method, the event-plane resolution [28] is expressed as

$$\langle \cos\left(kn[\Psi_n - \Psi_{\mathrm{RP}}]\right)\rangle = \frac{\sqrt{\pi}}{2\sqrt{2}}\chi_n e^{-\chi_n^2/4}\left[I_{(k-1)/2}\left(\frac{\chi_n^2}{4}\right) + I_{(k+1)/2}\left(\frac{\chi_n^2}{4}\right)\right], \quad (8)$$

where $\chi_n = v_n\sqrt{2M}$, M is the number of particles used to determine the event plane Ψ_n, I_k is the modified Bessel function of the first kind, and $k = 1$ for the second-harmonic BBC event plane. For the ZDC-SMD event plane, the resolution is estimated with either $k = 1$ or 2 in Eq. (8). We will discuss the difference between these estimates in Sec. IV A.

To determine the event-plane resolution, we need to determine χ_n. Since the North and South BBCs have approximately the same η coverage, the event-plane resolution of each subdetector is expected to be the same. The same is true for the North and South ZDC-SMDs. Thus, the subevent resolution for South and North event planes can be expressed as

$$\left\langle \cos\left(2\left[\Psi_n^{\mathrm{S(N)}} - \Psi_{\mathrm{RP}}\right]\right)\right\rangle = \sqrt{\left\langle \cos\left(2\left[\Psi_n^{\mathrm{S}} - \Psi_n^{\mathrm{N}}\right]\right)\right\rangle}, \quad (9)$$

where $\Psi_n^{\mathrm{S(N)}}$ denotes the event plane determined by the South (North) BBC or ZDC-SMD. Once the subevent resolution is obtained from Eq. (9), one can calculate χ_n^{sub} using Eq. (8). The χ_n for the full event can then be estimated by $\chi_n = \sqrt{2}\chi_n^{\mathrm{sub}}$. This is then substituted into Eq. (8) to give the full-event resolution. Since the multiplicity of the full event is twice as large as that of the subevent, χ_n is proportional to $\sqrt{M}$.

In the three-subevent method, the resolution of each subevent is calculated by adding a reference event plane Ψ_n^{C} in Eq. (9):

$$\mathrm{Res}\{\Psi_l^{\mathrm{A}}\} = \sqrt{\left\langle \cos\left(2\left[\Psi_l^{\mathrm{A}} - \Psi_m^{\mathrm{B}}\right]\right)\right\rangle}\sqrt{\frac{\left\langle \cos\left(2\left[\Psi_n^{\mathrm{C}} - \Psi_l^{\mathrm{A}}\right]\right)\right\rangle}{\left\langle \cos\left(2\left[\Psi_m^{\mathrm{B}} - \Psi_n^{\mathrm{C}}\right]\right)\right\rangle}}, \quad (10)$$

where l, m, n are the harmonics of the event plane for subevents A, B, and C, respectively. The multiplicity of each subevent is not necessarily the same in Eq. (10).

The resolution of each subdetector for the BBC and ZDC-SMD can be evaluated with the three-subevent method. For the BBC event plane, the reference event plane is chosen to be the ZDC-SMD event plane and vice versa. We found that the agreement of the event-plane resolutions for BBCS and BBCN is much better than 1%, while the ZDCS and ZDCN resolutions agree within 2%.

Figure 4 shows the full-event resolution as a function of centrality. The resolution of ZDC-SMD is much smaller than that of BBC because the resolution of the first-harmonic event plane is proportional to $(\chi_1)^2$. The dashed lines are the resolutions obtained from the three-subevent method with the CNT event plane as the reference plane. For example, the BBC event-plane resolution is estimated by substituting $\Psi_l^{\mathrm{A}} \to \Psi_2^{\mathrm{BBC}}$, $\Psi_m^{\mathrm{B}} \to \Psi_2^{\mathrm{CNT}}$, and $\Psi_n^{\mathrm{C}} \to \Psi_1^{\mathrm{ZDC-SMD}}$ in Eq. (10). By including the CNT event plane, the BBC resolution increases by about 3% over that of the two-subevent method. For the ZDC-SMD, we observe the opposite effect, namely, the resolution decreases by about 8%. In Sec. VI, the resulting $v_2\{\mathrm{BBC}\}$ and $v_2\{\mathrm{ZDC\text{-}SMD}\}$, corrected by the resolution obtained using the ZDC-BBC-CNT combination, will be compared against those with the resolution determined from South-North subevents. Table II summarizes the event-plane resolutions.

3. *Correlation of event planes*

Figure 5 shows the correlation of two different event planes as a function of centrality. The first-harmonic event-plane correlation for South-North detector combinations is negative both for the ZDC-SMDs and the BBCs over all centrality bins, as shown in Fig. 5(a). This is because v_1 is an odd function of η. The magnitude of the ZDC-SMD correlation is about a factor of 2 larger than that of the BBCs for midcentral collisions. This indicates that the magnitude of v_1 and the subevent multiplicity

TABLE II. Event-plane resolutions for centrality 0–60% at $\sqrt{s_{NN}} = 200$ GeV. S-N denotes the resolutions estimated from South and North correlation of BBC and ZDC-SMD using Eqs. (8) and (9), and resolutions for ZDC-BBC-CNT are estimated from Eq. (10). The errors are statistical only.

Centrality	S-N	ZDC-BBC-CNT
	$\mathrm{Res}\{\Psi_2^{\mathrm{BBC}}\}$	
0–10%	0.2637 ± 0.0003	0.272 ± 0.003
10–20%	0.3809 ± 0.0002	0.394 ± 0.001
20–30%	0.3990 ± 0.0002	0.4106 ± 0.0008
30–40%	0.3634 ± 0.0002	0.3759 ± 0.0007
40–50%	0.2943 ± 0.0003	0.3067 ± 0.0007
50–60%	0.2106 ± 0.0004	0.2240 ± 0.0009
	$\mathrm{Res}\{\Psi_1^{\mathrm{ZDC-SMD}}\}$	
0–10%	0.02 ± 0.01	0.0223 ± 0.0003
10–20%	0.059 ± 0.003	0.0574 ± 0.0002
20–30%	0.087 ± 0.002	0.0818 ± 0.0002
30–40%	0.100 ± 0.002	0.0928 ± 0.0002
40–50%	0.102 ± 0.002	0.0920 ± 0.0002
50–60%	0.100 ± 0.002	0.0798 ± 0.0003

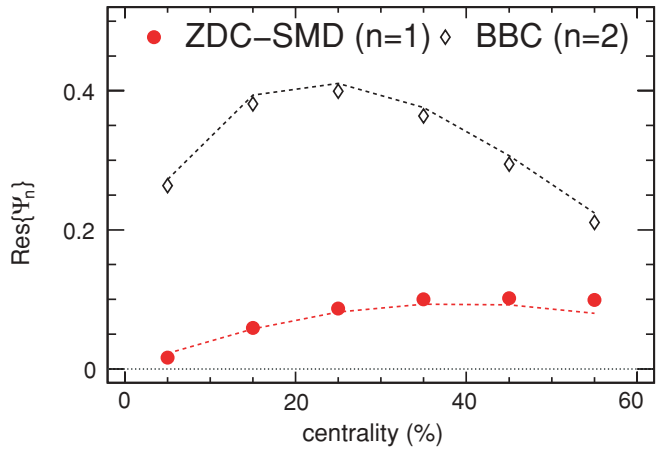

FIG. 4. (Color online) Full-event resolutions for the ZDC-SMD and BBC from the two-subevent method, Eq. (8), as a function of centrality in Au + Au at $\sqrt{s_{NN}} = 200$ GeV. The dashed lines represent resolutions from the three-subevent method with the CNT event plane as a reference. Statistical errors are smaller than the symbols.

at higher pseudorapidities are larger than those at the BBC location, since the magnitude of the correlation is proportional to $v_1^2 M$. Figure 5(b) shows the correlation of the first-harmonic event planes between BBC and ZDC-SMD. The same-side η correlation is negative, while the opposite-side η correlation is positive, which shows that the particles detected at the BBCs (dominantly charged pions emitted from participant nucleons) have the opposite sign of v_1 compared to the spectator neutrons detected at the ZDCs-SMDs.

The correlation of the mixed-harmonic event planes provides the sign of v_2, since the correlation is given by the expression [28]

$$\begin{aligned}\left\langle \cos\left(2\left[\Psi_1^{\mathrm{ZDC-SMD}} - \Psi_2^{\mathrm{BBC}}\right]\right)\right\rangle &\approx \frac{2}{\pi}\left(\mathrm{Res}\left\{\Psi_1^{\mathrm{ZDC-SMD}}\right\}\right)^2 \mathrm{Res}\left\{\Psi_2^{\mathrm{BBC}}\right\} \\ &= \pm 2\sqrt{2}\frac{2}{\pi}\left\langle \cos\left(\Psi_1^{\mathrm{ZDCS}} - \Psi_1^{\mathrm{ZDCN}}\right)\right\rangle \\ &\quad \times \sqrt{\left\langle \cos\left(2\left[\Psi_2^{\mathrm{BBCS}} - \Psi_2^{\mathrm{BBCN}}\right]\right)\right\rangle}. \end{aligned} \tag{11}$$

Three assumptions were made to obtain Eq. (11): (1) the BBC and ZDC-SMD are statistically independent, (2) the weak flow limit ($\chi_n \ll 1$) is applicable [28], and (3) the subevent multiplicity M is equal in the North-South direction for the same detector type. Thus the sign of the correlation of the mixed-harmonic event planes in Eq. (11) is determined by the term $\mathrm{Res}\{\Psi_2^{\mathrm{BBC}}\}$, which in turn determines the sign of v_2 measured at the BBC.

Figure 6 shows the mixed-harmonic correlation of the ZDC-SMD and BBC event planes as a function of centrality. The approximations in Eq. (11) provide a good description of the magnitude of the measured correlation as shown by the dashed line. The correlation is positive over all centrality bins. This result indicates that the sign of v_2 at the BBC is positive.

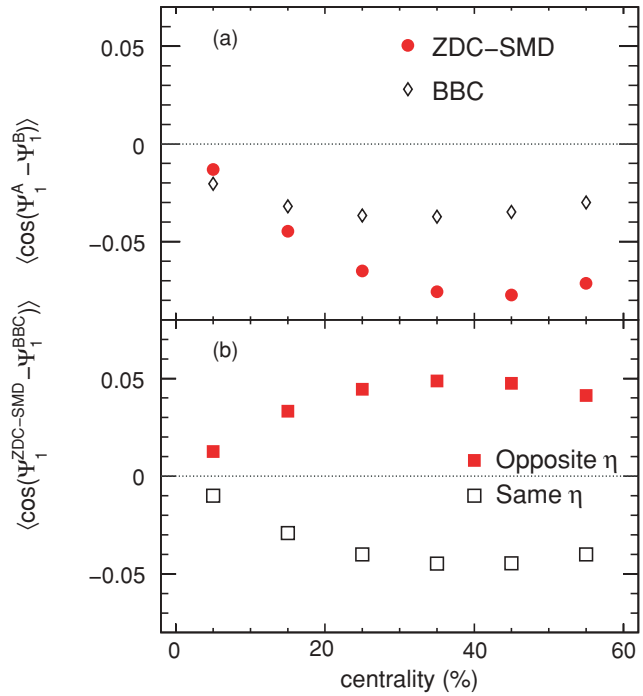

FIG. 5. (Color online) (a) Correlation of first-harmonic event planes between forward and backward ZDC-SMDs and BBCs as a function of centrality. (b) Correlation of first-harmonic event planes between ZDC-SMDs and BBCs as a function of centrality, for correlations of opposite- and same-side η subevents. Statistical errors are smaller than the symbols.

B. Cumulant method

In this section, we present the application of the cumulant method for azimuthal anisotropy measurements in PHENIX. This method uses cumulants of multiparticle correlations [44,45] to extract the azimuthal anisotropy. The cumulant method has been successfully applied in several heavy-ion experiments utilizing detectors with full azimuthal coverage (NA49, STAR) [46,47]. Here, we describe the first application

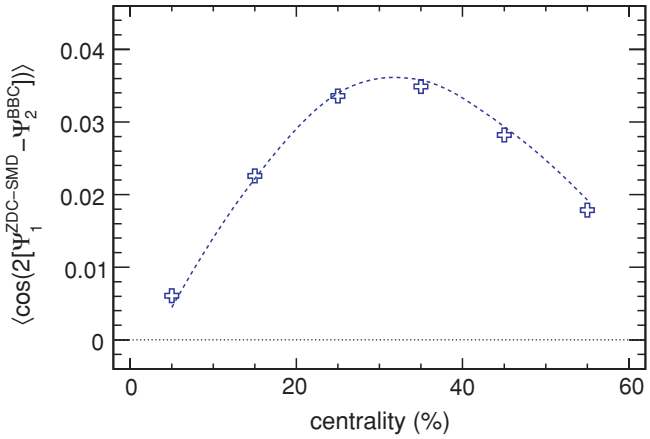

FIG. 6. (Color online) Correlation between the first-harmonic ZDC-SMD and the second-harmonic BBC event planes as a function of centrality. The dashed line shows the result obtained using Eq. (11). Statistical errors are smaller than the data symbols.

of the method for a detector with only partial azimuthal coverage. The cumulant method does not require the measurement of the reaction plane, instead the cumulants of multiparticle azimuthal correlations are related to the flow harmonics v_n, where n is the harmonic being evaluated. The cumulants can be constructed in increasing order according to the number of particles that are correlated with each other. Since PHENIX has partial azimuthal coverage, reliable extraction of azimuthal anisotropy requires the choice of a fixed number of particles from each event to avoid additional numerical errors [44].

Particles in an event are selected over a fixed (p_T,η) range where there is sufficient multiplicity. From this set, particles (called integral particles hereafter) are selected to determine the integrated flow, which is flow measured over a large (p_T,η) bin. This is done by excluding particles within small (p_T,η) bins from all available particles to avoid autocorrelations. The particles within a small (p_T,η) window (called differential particles hereafter) are used to determine the differential flow. For each event, a fixed number M of particles, chosen at random among the integral particles in the event, are used to reconstruct the integrated flow through the generating function $G_2(z)$ defined by

$$G_2(z) = \prod_{j=1}^{M}\left[1 + \frac{w_j}{M}(z^* e^{2i\phi_j} + z e^{-2i\phi_j})\right], \tag{12}$$

where w_j is the weight, chosen to be equal to 1 in our analysis, ϕ_j is the azimuth of the detected particles, and M is the multiplicity chosen for the integrated flow reconstruction. $G_2(z)$ is a real-valued function of the complex variable z. The average of $G_2(z)$ over events is then expanded in a power series to generate multiparticle azimuthal correlations. The generating function of the cumulants, defined by

$$\mathcal{C}_2(z) \equiv M(\langle G_2(z)\rangle^{1/M} - 1), \tag{13}$$

generates cumulants of azimuthal correlations to all orders, the lowest being the second order, as detailed in Sec. II B of Ref. [44]. The formulas used to compute the cumulants from which the v_2 is computed are given in Appendix B of Ref. [44]. In the case of a perfect acceptance, the relations between the anisotropy parameter v_2 and the lowest order cumulants are

$$v_2\{2\}^2 = c_2\{2\}, \tag{14}$$

$$v_2\{4\}^4 = -c_2\{4\}, \tag{15}$$

for the integrated anisotropy. Here $v_2\{2\}$ and $v_2\{4\}$ are the second- and fourth-order v_2, respectively; whereas, $c_2\{2\}$ and $c_2\{4\}$ are the second- and fourth-order cumulants. Because the typical multiplicity of charged hadrons in PHENIX, which is $\approx$40 for midcentral collisions, did not allow a reliable calculation of $v_2\{4\}$, we report here only the $v_2\{2\}$ results.

The remaining differential particles in the same event are selected in different (p_T,η) bins, and the differential cumulants are calculated from the generating function

$$\mathcal{D}_{2/2}(z) \equiv \frac{\langle e^{2i\psi} G_2(z)\rangle}{\langle G_2(z)\rangle}, \tag{16}$$

where $\langle G(z)\rangle$ denotes an average over all events, and ψ is the azimuth of each differential particle. $D_{2/2}$ denotes the second-order differential cumulant computed with respect to the second-order integral cumulant.

The differential $v_{2/2}\{2\}(p_T,\eta)$, the second-order differential v_2 with respect to the second-order integrated v_2, is calculated from the relation

$$v_{2/2}\{2\}(p_T,\eta) = \frac{d_{2/2}\{2\}(p_T,\eta)}{v_2\{2\}}, \tag{17}$$

where $d_{2/2}\{2\}(p_T,\eta)$ is the second-order differential cumulant. These relations have to be modified through acceptance corrections, which are detailed below.

1. Acceptance/efficiency corrections

The central arms detectors in PHENIX have only partial azimuthal coverage, and the implementation of the cumulant method requires an additional acceptance correction. To correct for the influence of the detector acceptance on the raw anisotropy values, we apply a correction factor using the prescription described in Ref. [44]. The acceptance and efficiency of the detector is characterized by a function $A(\phi,p_T,\eta)$, which is expressed in terms of the Fourier series as

$$A(\phi,p_T,\eta) = \sum_{p=-\infty}^{+\infty} a_p(p_T,\eta)e^{ip\phi}. \tag{18}$$

The Fourier coefficients $a_p(p_T,\eta)$ for the detector acceptance were extracted from the fit of the respective azimuthal distributions of integral and differential particles. The coefficients resulting from such fits were then used to calculate the correction factor for the raw values of the v_2 following the procedure detailed in Appendix C of Ref. [44].

Figure 7 shows a typical azimuthal angular distribution of differential particles detected in the PHENIX central arms and the corresponding Fourier fit used to correct for acceptance inhomogeneities. The Fourier fit reproduces well the overall features of the acceptance profile. This produces typical correction factors, which are in the range 1.1–1.2 for the differential flow and depend very little on centrality and p_T, as shown in Fig. 8.

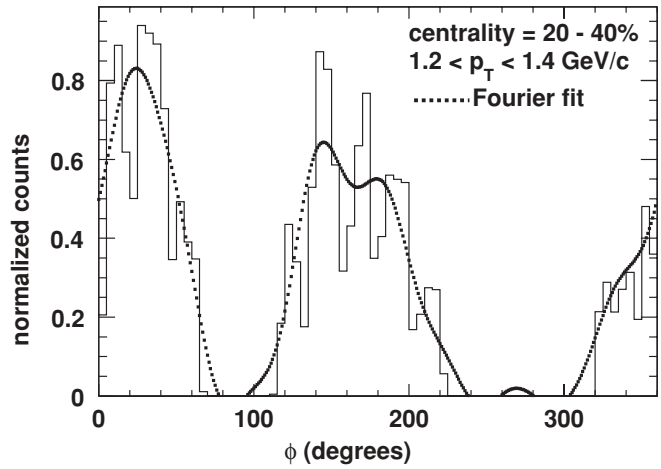

FIG. 7. Azimuthal angular distribution and corresponding Fourier fit for centrality 20–40% and p_T = 1.2–1.4 GeV/c.

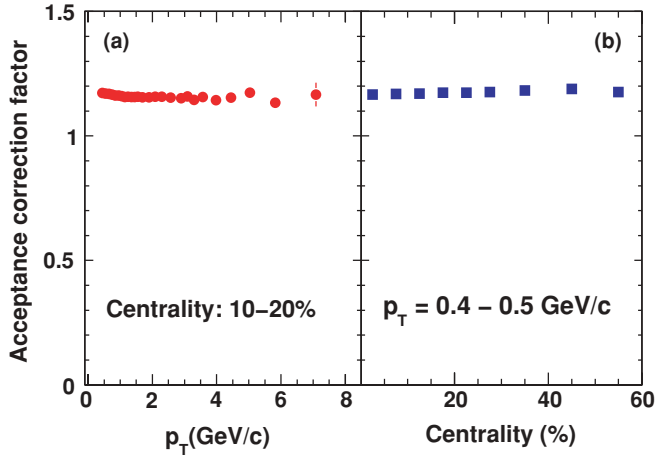

FIG. 8. (Color online) Acceptance correction factor for differential $v_2\{2\}$ as a function of (a) p_T for centrality 10–20% and (b) centrality for p_T range 0.4–0.5 GeV/c in Au + Au collisions at $\sqrt{s_{NN}} = 200$ GeV.

2. *Simulations*

While Fig. 7 shows that the uneven detector acceptance is reproduced by the Fourier fit, a better test of the cumulant method is to use Monte Carlo simulations, as in Ref. [44]. For these tests, events were generated with particles having a distribution of the form $1 + 2v_1 \cos\phi + 2v_2 \cos 2\phi$, with known integrated and differential azimuthal anisotropies. The anisotropy was introduced into the events by way of a Fourier weighted selection of the azimuthal angles followed by a random event rotation designed to simulate the random orientation of the reaction plane. The multiplicity of these events was chosen to reflect the typical multiplicity measured with the PHENIX detector, and the ϕ angles were chosen from a filter that is representative of the PHENIX acceptance. We extracted Fourier components from these simulated results and applied these to extract corrected elliptic flow values.

Figure 9 shows selected results from these simulations. Corrected differential anisotropy values are compared for various input differential v_2 values, with the integrated v_2 kept fixed. The dotted line shows the trend expected if the extracted v_2 is identical to the input value used to generate the events. The good agreement between the input and extracted v_2 attests to the reliability of the analysis method within the acceptance of the PHENIX central arms.

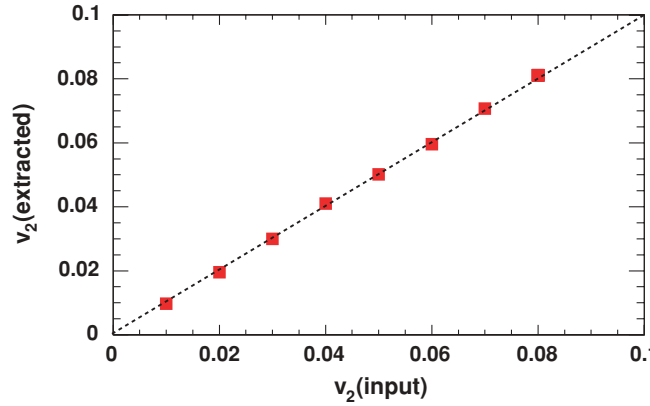

FIG. 9. (Color online) Comparison of input and extracted differential v_2 values for a fixed integrated v_2 of 8%. The dotted line indicates the expectation if input and reconstructed values are the same.

IV. SYSTEMATIC UNCERTAINTIES

In this section, we present the systematic uncertainties on the v_2 from the event-plane method (Sec. IV A) and the two-particle cumulant method (Sec. IV B). Table III lists the different sources of systematic errors for each method. The errors in Table III are categorized by type:

(i) point-to-point error uncorrelated between p_T bins,
(ii) p_T correlated, all points move in the same direction but not by the same factor,
(iii) an overall normalization error in which all points move by the same factor independent of p_T.

TABLE III. Systematic uncertainties given in percent on the $v_2\{\text{ZDC-SMD}\}$, $v_2\{\text{BBC}\}$, and $v_2\{2\}$ measurements. The ranges correspond to different systematic errors for different centrality bins.

Error source	Percentage error		Type
	$v_2\{\text{BBC}\}$	$v_2\{\text{ZDC-SMD}\}$	
Background contribution	<5% in $p_T < 4$ GeV/c		B
	5–30% in $p_T > 4$ GeV/c		B
Event-plane calibration	1–5%		C
Event-plane determination	1–4%	1–16%	C
Acceptance effect on event planes	1%	1–25%	C
	$v_2\{2\}$		
Fixed multiplicity	5%		B
Integrated p_T range	3–8%		B
Background correction	6–10%		B

A. Event-plane method

1. Background contributions

To study the influence of background on our results, we varied one of the track selections while keeping other cuts fixed and investigated the effect on v_2 in the following two cases: (i) the PC3 and EMCAL matching cuts, $\pm 1.5\sigma$ and $\pm 2.5\sigma$ matching cuts, and (ii) $E > 0.15 p_T$ and $E > 0.25 p_T$. For both conditions, we found that the difference of the v_2 is 1–2% for $p_T < 4$ GeV/c, and 5–20% for $p_T > 4$ GeV/c depending on p_T and centrality.

The effect of the RICH veto cut has also been studied. Since the contribution of charged π increases without the RICH veto cut, the p/π ratio decreases at high p_T. Thus, the v_2 for charged hadrons could be modified due to the difference of v_2 between protons and π in the range $4 < p_T < 8$ GeV/c. We found that v_2 is 10–20% different without the RICH veto cut for $p_T > 4$–5 GeV/c, where the charged π starts firing the RICH.

One of the remaining sources of background contribution comes from the random tracks that are accidentally associated with the tracks in PC3. These random tracks have been estimated by swapping the z coordinate of the PC3 hits and then by associating those hits with the real tracks. Figure 10 shows the comparison of the radial PC3 matching distribution between the real and random tracks for $6 < p_T < 8$ GeV/c. The signal-to-background ratio S/B is evaluated in the $\sigma_{\mathrm{PC3}} < 2$ window and is ~52 for $6 < p_T < 8$ GeV/c in centrality 0–60%.

The ratio of real and random tracks with and without the $E/p_T > 0.2$ cut is shown as a function of p_T for centrality 0–60% in Fig. 11. The $E/p_T > 0.2$ cut reduces the random tracks and improves the S/B ratio by a factor of ≈10–24 for $p_T > 4$ GeV/c. Since random tracks are not expected to be correlated with the event plane, we assume that their $v_2 = 0$ and evaluate the systematic uncertainty on v_2 to be less than 2% for $p_T > 4$ GeV/c, increasing to 5% for $p_T < 0.5$ GeV/c.

There is a finite residual background contribution even after the $E/p_T > 0.2$ has been applied, as observed in Fig. 10. The residual backgrounds have been estimated by fitting the σ_{PC3}

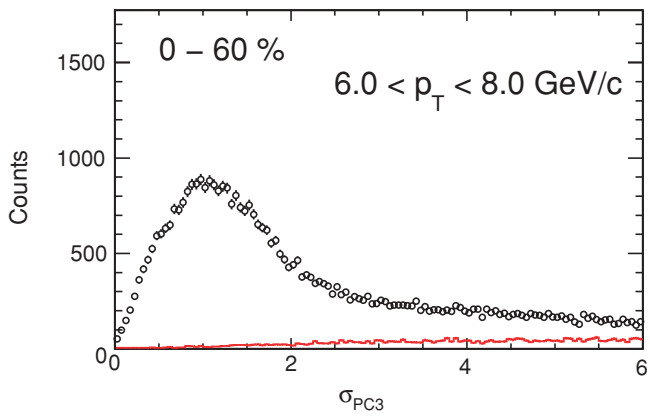

FIG. 10. (Color online) Radial PC3 matching distribution for real (open circles) and random (solid lines) tracks for $6 < p_T < 8$ GeV/c in centrality 0–60%.

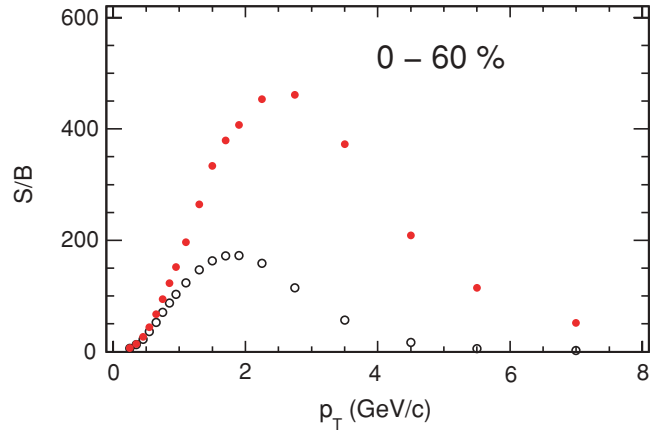

FIG. 11. (Color online) Ratio of real S to random B tracks as a function of p_T in centrality 0–60%. Solid and open circles show the S/B ratio with and without $E/p_T > 0.2$, respectively.

with a double Gaussian while requiring that the signal and residual background σ_{PC3} distribution have the same mean. For the highest p_T bin, we found that the signal-to-background ratio is ~5 for $\sigma_{\mathrm{PC3}} < 2$. The systematic error on v_2 is evaluated by comparing the measured v_2 with that of the signal

$$v_2^S = \left(1 + \frac{B}{S}\right) v_2 - \frac{B}{S} v_2^B, \tag{19}$$

where v_2^S, v_2^B and v_2 are, respectively, v_2 of signal, background estimated for $\sigma_{\mathrm{PC3}} > 3$, and measured within the 2σ matching window. The systematic uncertainties are less than 5% for $p_T < 4$ GeV/c, and ~5–10% for higher p_T. All the above systematic errors are added in quadrature, and the overall systematic error from the background contribution is estimated to vary from <5% for $p_T < 4$ GeV/c to ~30% for higher p_T.

2. Event-plane calibrations

The procedures used in the determination and calibration of event planes are the dominant sources of systematic errors on v_2 and are discussed in the following sections.

Different calibration procedures of the BBC event plane were extensively studied for previous Au + Au data sets [19]. We followed the same procedure to study the systematic errors on the BBC and ZDC-SMD event planes. Systematic uncertainties from the shift methods on $v_2\{\mathrm{BBC}\}$ are ~1–5% depending on the centrality. The systematic errors on the $v_2\{\mathrm{ZDC\text{-}SMD}\}$ are 1–2% larger than those on $v_2\{\mathrm{BBC}\}$ for centrality 10–30% and 50–60%, although those are still less than 5%.

3. Event-plane determination

Figure 12 shows the comparison of $\langle v_2 \rangle$ for different subdetectors with respect to the BBC and ZDC-SMD event planes as a function of centrality. Systematic errors are estimated by taking the maximum difference of the v_2 from the South and North event planes to that from the combined

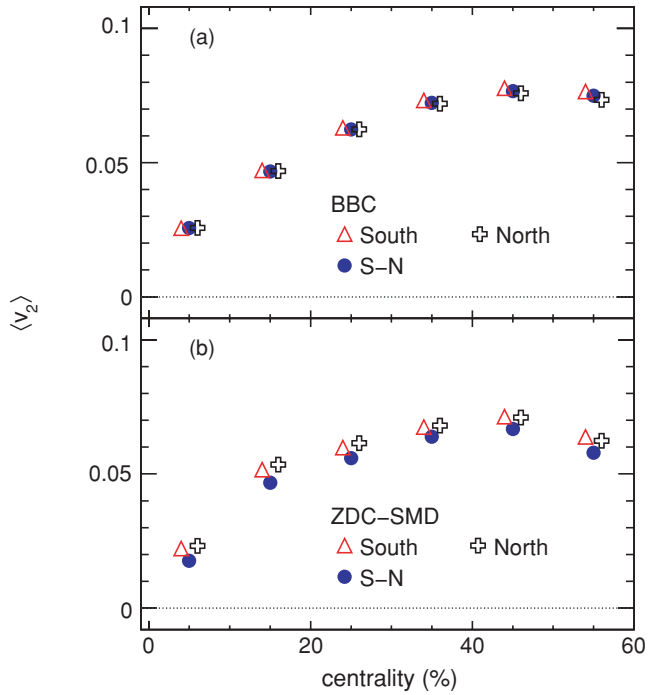

FIG. 12. (Color online) Comparison of $\langle v_2 \rangle$ averaged over $0.2 < p_T < 8$ GeV/c as a function of centrality for the (a) BBC and (b) ZDC-SMD event planes from South and North subdetectors and from combined South-North (S-N) event planes. Results from South and North event planes are shifted in the x direction to improve visibility. Only statistical errors are shown and they are smaller than the symbols.

South-North event plane scaled by $2/\sqrt{12}$ for each centrality. Systematic errors range from 1–4% for the BBC, and 1–16% for the ZDC-SMD event planes depending on the centrality bins.

4. Effect of nonuniform acceptance on v_2

In this subsection, we discuss the effect of nonuniform acceptance on the measured v_2. In practice, the imperfect azimuthal acceptance of the BBC or ZDC-SMD or the central arms could induce an azimuthal-dependent event-plane resolution and/or smear the magnitude of v_2. To study the possible effect of nonuniform acceptance, the measured v_2 is decomposed into X and Y components [48]:

$$v_2^{\mathrm{X}} = \frac{\sqrt{2}}{a_4^+} \frac{\langle \cos(2\phi) \cos\left(2\Psi_n^{\mathrm{A}}\right) \rangle}{\mathrm{Res}\left\{\Psi_n^{\mathrm{A}}; \mathrm{X}\right\}},$$
$$v_2^{\mathrm{Y}} = \frac{\sqrt{2}}{a_4^-} \frac{\langle \sin(2\phi) \sin\left(2\Psi_n^{\mathrm{A}}\right) \rangle}{\mathrm{Res}\left\{\Psi_n^{\mathrm{A}}; \mathrm{Y}\right\}}, \tag{20}$$

where ϕ denotes the azimuthal angle of hadrons measured in the central arms and $a_4^{\pm} = 1 \pm \langle \cos(4\phi) \rangle$ are the acceptance correction factors of the measured v_2 in the central arms. The coefficient $a_4^{\pm}$ should be unity in the case of perfect azimuthal acceptance. $\mathrm{Res}\{\Psi_n^{\mathrm{A}}; \mathrm{X}\}$ and $\mathrm{Res}\{\Psi_n^{\mathrm{A}}; \mathrm{Y}\}$ denote the event-plane resolution for v_2^{X} and v_2^{Y}, respectively, and are expressed as

$$\mathrm{Res}\left\{\Psi_l^{\mathrm{A}}; \mathrm{X}\right\} = \sqrt{\left\langle \cos\left(2\Psi_l^{\mathrm{A}}\right) \cos\left(2\Psi_m^{\mathrm{B}}\right) \right\rangle} \times \sqrt{\frac{\left\langle \cos\left(2\Psi_n^{\mathrm{C}}\right) \cos\left(2\Psi_l^{\mathrm{A}}\right) \right\rangle}{\left\langle \cos\left(2\Psi_m^{\mathrm{B}}\right) \cos\left(2\Psi_n^{\mathrm{C}}\right) \right\rangle}},$$
$$\mathrm{Res}\left\{\Psi_l^{\mathrm{A}}; \mathrm{Y}\right\} = \sqrt{\left\langle \sin\left(2\Psi_l^{\mathrm{A}}\right) \sin\left(2\Psi_m^{\mathrm{B}}\right) \right\rangle} \times \sqrt{\frac{\left\langle \sin\left(2\Psi_n^{\mathrm{C}}\right) \sin\left(2\Psi_l^{\mathrm{A}}\right) \right\rangle}{\left\langle \sin\left(2\Psi_m^{\mathrm{B}}\right) \sin\left(2\Psi_n^{\mathrm{C}}\right) \right\rangle}}, \tag{21}$$

where l, m, n are the harmonics of event planes for subevents A, B, and C, respectively. Another acceptance effect from the difference between $\mathrm{Res}\{\Psi_n^{\mathrm{A}}; \mathrm{X}\}$ and $\mathrm{Res}\{\Psi_n^{\mathrm{A}}; \mathrm{Y}\}$ is discussed below.

Figure 13 shows the acceptance correction factor $a_4^{\pm}$ as a function of p_T in the central arms for centrality 0–60%. The p_T dependence is parametrized by

$$a_4^{\pm}(p_T) = 1 \mp \left(p_0 e^{-p_1 p_T} + \frac{p_2}{1 + e^{(p_T - p_3)/p_4}} + p_5 \right), \tag{22}$$

where $p_n (n = 0, 1, \ldots, 5)$ are free parameters. From the fit, we get $p_0 = 0.131$, $p_1 = 1.203$, $p_2 = 0.029$, $p_3 = 0.640$, $p_4 = 0.096$, and $p_5 = -0.097$. There is no centrality dependence of the acceptance corrections in the measured centrality range, and these same correction factors are applied for all centrality bins.

Figure 14 shows the raw $v_2\{\mathrm{BBC}\}$ as a function of p_T in the 20–60% centrality bin. v_2^{Y} is systematically higher than v_2^{X} for $p_T > 1$ GeV/c as shown in Fig. 14(a). Figure 14(b) shows that v_2^{X} and v_2^{Y} agree with each other after dividing v_2^{obs} by $a_4^{\pm}$, the remaining difference between them being accounted

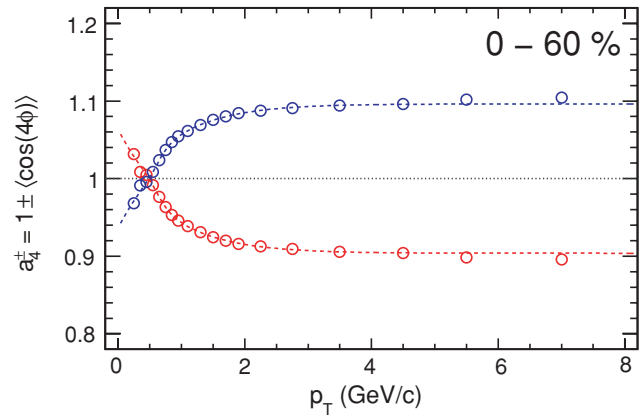

FIG. 13. (Color online) Acceptance correction factors $a_4^{\pm}$ in the central arms as a function of p_T for centrality 0–60%. Correction factors become unity for a perfect azimuthal acceptance. Statistical errors are smaller than the symbols.

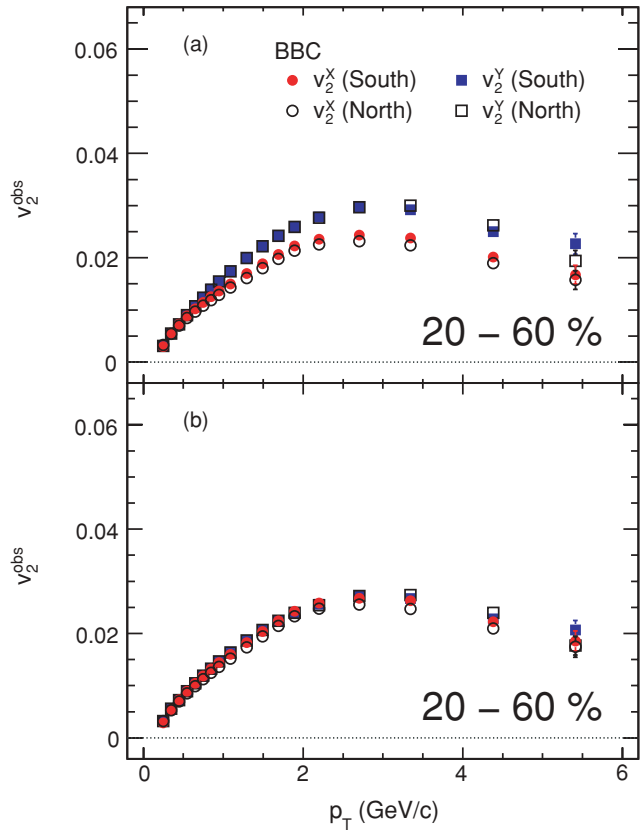

FIG. 14. (Color online) (a) Raw $v_2\{\text{BBC}\}$ without the acceptance correction as a function of p_T in centrality 20–60% for v_2^X and v_2^Y with the South and North BBC event planes. (b) Same comparison, but with the acceptance correction.

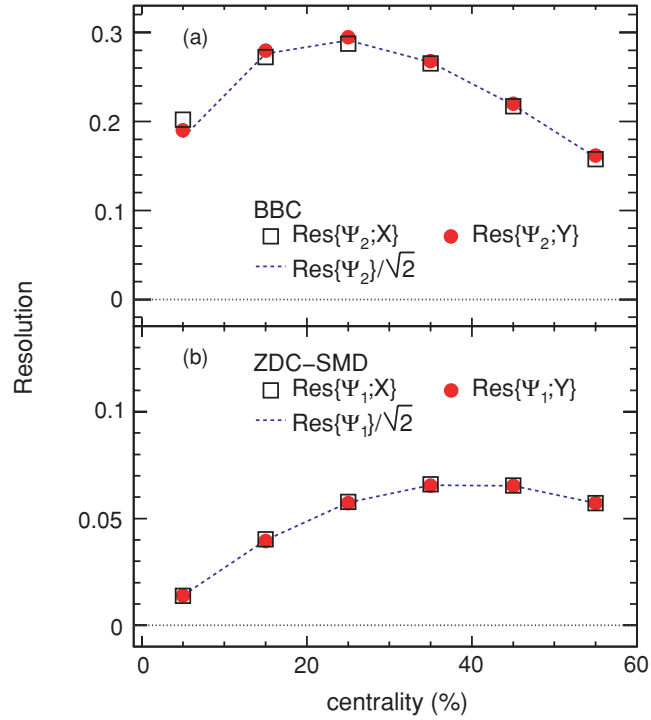

FIG. 15. (Color online) Comparison of $\text{Res}\{\Psi_n;\text{X}\}$ and $\text{Res}\{\Psi_n;\text{Y}\}$ with $\text{Res}\{\Psi_n\}$ for the (a) BBC event plane ($n = 2$) and (b) ZDC-SMD event plane ($n = 1$) as a function of centrality. The resolutions are calculated by using Eq. (21) with the ZDC-SMD, BBC, and CNT event planes. $\text{Res}\{\Psi_n\}$ is divided by $\sqrt{2}$ in order to compare $\text{Res}\{\Psi_n;\text{X}\}$ and $\text{Res}\{\Psi_n;\text{Y}\}$. Only statistical errors are shown and are smaller than symbols.

for as a systematic error. For the ZDC-SMD event plane, we observed a similar trend for v_2^X and v_2^Y.

A possible nonuniform acceptance of the BBC and ZDC-SMD could lead to the difference between $\text{Res}\{\Psi_n;\text{X}\}$ and $\text{Res}\{\Psi_n;\text{Y}\}$. If the azimuthal coverage of both detectors is perfect, $\text{Res}\{\Psi_n;\text{X}\}$ and $\text{Res}\{\Psi_n;\text{Y}\}$ should be identical. Therefore, the effect of the acceptance of the detector on the event-plane resolution can be assessed by comparing $\text{Res}\{\Psi_n;\text{X}\}$ and $\text{Res}\{\Psi_n;\text{Y}\}$.

Figure 15 shows $\text{Res}\{\Psi_n;\text{X}\}$ and $\text{Res}\{\Psi_n;\text{Y}\}$ of the BBC and ZDC-SMD as a function of centrality. The resolutions are calculated by using Eq. (21) with the ZDC-SMD, BBC, and CNT event planes. $\text{Res}\{\Psi_n;\text{X}\}$ was comparable to $\text{Res}\{\Psi_n;\text{Y}\}$ for both the BBC and ZDC-SMD event planes. They also agreed, within statistical errors, with the expected resolution, namely, the full-event resolution scaled by $1/\sqrt{2}$. We also evaluated $\text{Res}\{\Psi_n;\text{X}\}$ and $\text{Res}\{\Psi_n;\text{Y}\}$ of BBC and ZDC-SMD for the two-subevent method. $\text{Res}\{\Psi_2^{\text{BBC}};\text{X}\}$ was consistent with $\text{Res}\{\Psi_2^{\text{BBC}};\text{Y}\}$. However, for the ZDC-SMD event plane, $\text{Res}\{\Psi_1^{\text{ZDC-SMD}};\text{Y}\}$ ($\text{Res}\{\Psi_1^{\text{ZDC-SMD}};\text{X}\}$) was systematically higher (lower) by about 30% than the expected resolution when the resolutions were calculated with $k = 1$ in Eq. (8). The difference between $\text{Res}\{\Psi_1^{\text{ZDC-SMD}};\text{X}\}$ and $\text{Res}\{\Psi_1^{\text{ZDC-SMD}};\text{Y}\}$ for the two-subevent method is attributed to the nonuniform acceptance between horizontal (x) and vertical (y) directions of the ZDC-SMD. Those resolutions of the ZDC-SMD were consistent with each other using $k = 2$. For $k = 2$, the nonuniform acceptance in the azimuthal directions cancels out, since $\text{Res}\{\Psi_1^{\text{ZDC-SMD}};\text{X, Y}\}$ contains both $\langle\cos(\Psi)\rangle$ and $\langle\sin(\Psi)\rangle$ terms. Thus, $\text{Res}\{\Psi_1^{\text{ZDC-SMD}};\text{X, Y}\}$ should be the same and consistent with that from the expected resolution.

The comparison of v_2^X and v_2^Y with v_2 with respect to the BBC and ZDC-SMD event planes is shown in Fig. 16. The maximum difference of v_2^X and v_2^Y relative to $v_2\{\text{BBC}\}$ is about 2% for the centrality range 20–60% and is independent of centrality. Systematic uncertainties are evaluated by scaling the maximum difference by $2/\sqrt{12}$. The same comparison is also made for $v_2\{\text{ZDC-SMD}\}$ as shown in the bottom panel in Fig. 16. The systematic errors range from 1–25% and strongly depend on the centrality, as well as on the corrections by the different event-plane resolutions. v_2^X and v_2^Y are ~10–25% different from $v_2\{\text{ZDC-SMD}\}$ in the 0–20% centrality bin because of the very low resolution. This systematic uncertainty is denoted as "Acceptance effect on event planes" in Table III.

B. Cumulant method

The potential sources of systematic errors on the cumulant measurements are detailed below.

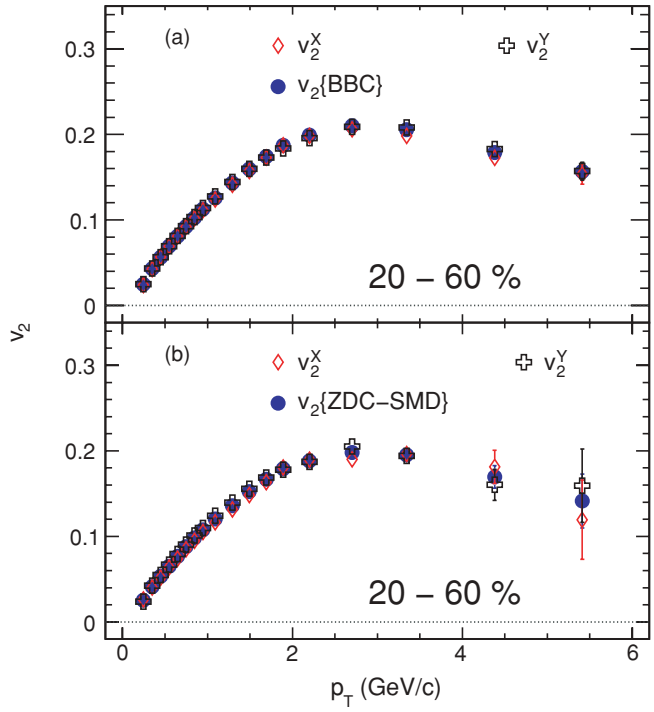

FIG. 16. (Color online) Comparison of v_2^X and v_2^Y with the total v_2 for the (a) BBC and (b) ZDC-SMD event planes as a function of p_T for the centrality bin 20–60%. Res$\{\Psi_n; X\}$ and Res$\{\Psi_n; Y\}$ are calculated by the combination of the ZDC-SMD, BBC, and CNT event planes. Acceptance corrections are included into v_2^X and v_2^Y. Error bars denote statistical errors.

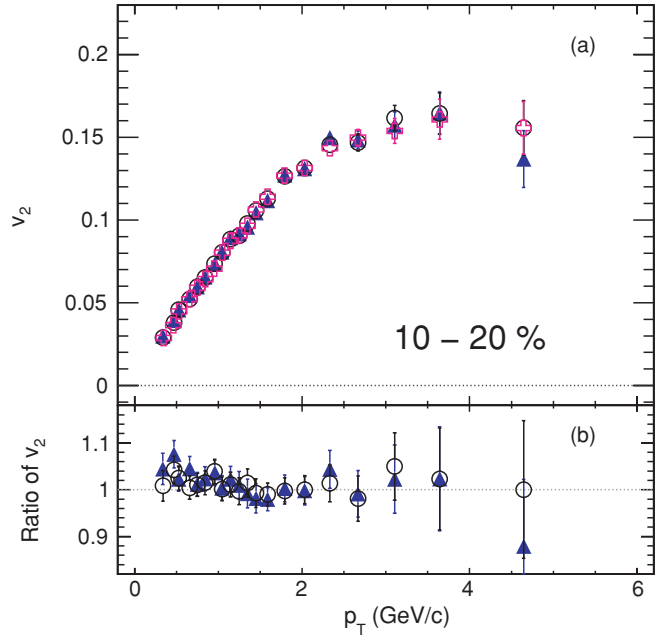

FIG. 17. (Color online) (a) $v_2\{2\}$ as a function of p_T for centrality 10–20% in Au + Au collisions at $\sqrt{s_{NN}} = 200$ GeV for different fixed multiplicity cuts, corresponding to 60% (filled triangles), 70% (open circles), and 80% (open crosses) of the mean multiplicity. (b) Ratio of $v_2(p_T)$ for the two lowest multiplicity cuts to $v_2(p_T)$ for 80% of the mean multiplicity.

1. *Fixed multiplicity cut*

Following Ref. [44], a fixed multiplicity is used to reconstruct the integrated flow to avoid introducing additional errors arising from a fluctuating multiplicity. In our analysis, the systematic errors were estimated by varying the fixed multiplicity cut used for the reconstruction of the integrated flow and studying its effect on the differential flow values.

Figure 17(a) shows the variation of v_2 with p_T for integral multiplicity cuts equal to 60%, 70%, and 80% of the mean multiplicity for the centrality bin 10–20%, which corresponds to 17, 20, and 22 particles, respectively. The ratio of the differential v_2 values, shown in Fig. 17(b), is used to estimate the systematic error on our measurements, which is ∼5%.

2. *p_T range for integrated flow*

To assess the influence of the p_T range used to estimate the integrated flow on the differential flow, we chose different p_T ranges over which the integral particles were selected. Differential v_2 results were obtained for three p_T ranges: 0.25–2.0, 0.25–1.5, and 0.3–1.5 GeV/c. The systematic error from this source is estimated to be 3–8% depending on centrality and p_T.

3. *Background contribution*

The procedures followed for studying the background contribution to $v_2\{2\}$ were the same as for the event-plane method. After background subtraction, the systematic error is calculated by determining the difference between the v_2 obtained from using 2σ and 3σ association cuts. We determined that the overall systematic error due to these differences is 6–10% depending on p_T and centrality.

V. RESULTS

A. p_T dependence of v_2

The p_T dependence of v_2 has been instrumental in revealing the hydrodynamic properties of the matter formed at RHIC [19,21]. In this context, it is important to compare the p_T dependence of v_2 from different methods to establish the robustness of our v_2 measurements. This comparison is displayed in Fig. 18, which shows the differential charged hadron v_2 as a function of p_T from the event-plane and cumulant methods for different centrality bins in the range 0–60% in Au + Au at $\sqrt{s_{NN}} = 200$ GeV. $v_2\{2\}$ increases up to $p_T \approx 3$ GeV/c and saturates at 0.1–0.25, depending on centrality, for higher p_T. On the other hand, $v_2\{\text{BBC}\}$ and $v_2\{\text{ZDC-SMD}\}$ reach their maximum value at $p_T \approx 3$ GeV/c, and decrease for higher p_T.

The differences between $v_2\{\text{BBC}\}$ and $v_2\{\text{ZDC-SMD}\}$ are independent of p_T within systematic errors in the measured centrality range. $v_2\{\text{ZDC-SMD}\}$ is consistent with $v_2\{\text{BBC}\}$ within systematic errors in the 0–40% centrality range,

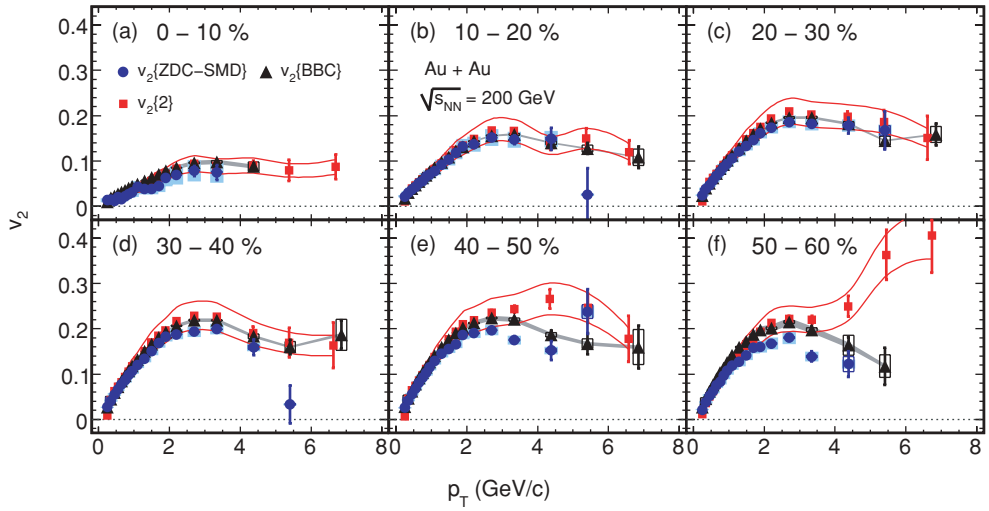

FIG. 18. (Color online) Charged hadron $v_2(p_T)$ in Au + Au collisions at $\sqrt{s_{NN}} = 200$ GeV from the two-particle cumulant method (filled squares), the BBC event plane (filled triangles), and the ZDC-SMD event plane (filled circles) for the indicated centralities. Error bars denote statistical errors. The type B systematic uncertainties are represented by the open boxes for the $v_2\{\text{BBC}\}$ and $v_2\{\text{ZDC-SMD}\}$, and by the solid lines for the $v_2\{2\}$. The gray bands and blue boxes represent the type C systematic uncertainties on the $v_2\{\text{BBC}\}$ and $v_2\{\text{ZDC-SMD}\}$, respectively.

but it is ∼10–20% smaller than $v_2\{\text{BBC}\}$ in the 40–60% centrality range. These results could indicate that the influence of nonflow effects on $v_2\{\text{BBC}\}$ is small and within the systematic errors, because nonflow effects are not expected to influence $v_2\{\text{ZDC-SMD}\}$. The difference between $v_2\{\text{BBC}\}$ and $v_2\{\text{ZDC-SMD}\}$ in peripheral collisions could be attributed to nonflow contributions that might be proportionally larger in more peripheral collisions.

The cumulant and event-plane v_2 agree well within systematic uncertainties in the centrality range 0–40%. In more peripheral collisions, there may be some differences developing above $p_T \simeq 4$ GeV/c. Correlations between particles from jets affect the cumulant results, but have less influence on $v_2\{\text{BBC}\}$, as explained in Ref. [29], where it was shown that the smaller the rapidity gap between the leading particle from a jet and the event plane, the greater the v_2 of the leading particle of the jet.

To illustrate more clearly the differences between the different methods, Fig. 19 shows the ratio of $v_2\{\text{ZDC-SMD}\}$ and $v_2\{2\}$ to $v_2\{\text{BBC}\}$. The results from the three methods are comparable in magnitude within systematic errors, except for the central and peripheral bins where the largest deviations occur. In addition, $v_2\{2\}$ and $v_2\{\text{ZDC-SMD}\}$ show different behaviors at $p_T > 3$ GeV/c, with $v_2\{2\}$ being larger, and $v_2\{\text{ZDC-SMD}\}$, smaller than $v_2\{\text{BBC}\}$.

B. Centrality dependence of v_2

Figure 20 shows the N_{part} dependence of v_2 from different methods for charged hadrons in the range $1.0 < p_T <$

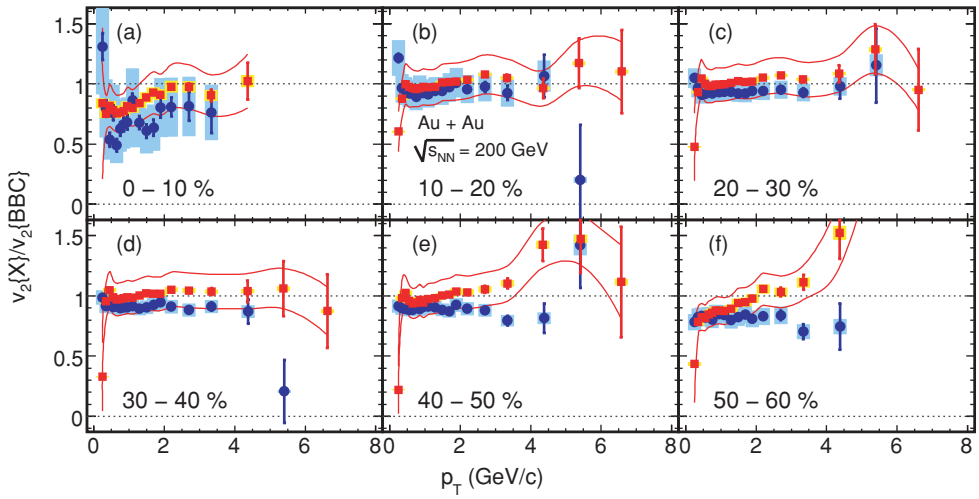

FIG. 19. (Color online) Ratio of v_2 to $v_2\{\text{BBC}\}$ as a function of p_T for six centrality bins over the range 0–60% in Au + Au collisions at $\sqrt{s_{NN}} = 200$ GeV. Data symbols are the same as in the Fig. 18. Error bars denote statistical errors. The solid red lines represent the type B systematic errors on the $v_2\{2\}$. The blue and yellow bands represent type C systematic uncrtainties on $v_2\{\text{ZDC-SMD}\}$ and $v_2\{2\}$.

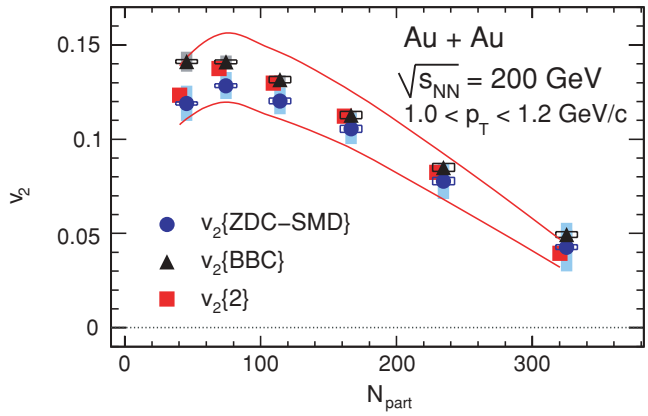

FIG. 20. (Color online) Comparison of charged hadron v_2 at $1 < p_T < 1.2$ GeV/c as a function of N_{part} for $v_2\{\text{BBC}\}$, $v_2\{\text{ZDC-SMD}\}$, and $v_2\{2\}$ in Au + Au at $\sqrt{s_{NN}} = 200$ GeV. The error bars represent statistical errors. The open boxes represent type B systematic uncertainties on $v_2\{\text{BBC}\}$ and $v_2\{\text{ZDC-SMD}\}$. Type B systematic uncertainties on $v_2\{2\}$ are represented by solid red lines. The gray and blue bands represent type C systematic errors on $v_2\{\text{BBC}\}$ and $v_2\{\text{ZDC-SMD}\}$, respectively. $v_2\{2\}$ values are shifted in the x axis to improve the plot.

1.2 GeV/c. v_2 is observed to increase with decreasing N_{part} and then decrease slightly for $N_{\text{part}} \lesssim 75$. Note that v_2 values obtained with the different methods agree well within systematic errors for all centralities. This is p_T dependent, as shown in Fig. 18.

C. Pseudorapidity dependence of v_2

Figure 21 compares the pseudorapidity dependence of the v_2 of charged hadrons within the η range (± 0.35) of the PHENIX central arms for different p_T selections. It can be

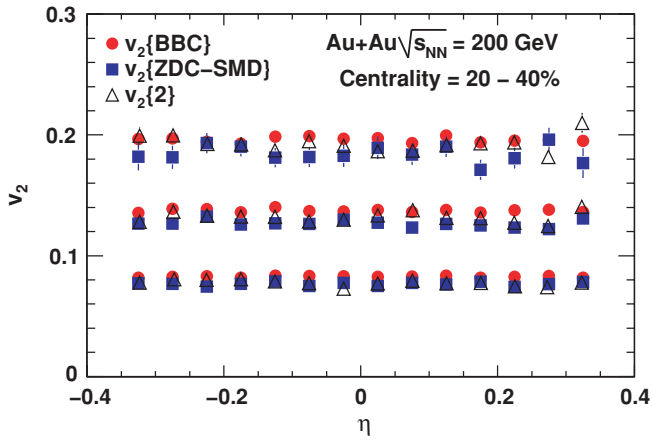

FIG. 21. (Color online) Anisotropy parameter v_2 as a function of pseudorapidity within the PHENIX central arms using event planes from the BBC and ZDC-SMD, and from the two-particle cumulant method for centrality 20–40%. The results are shown for three p_T bins, which are from top to bottom: 2.0–3.0, 1.2–1.4 and 0.6–0.8 GeV/c. Only statistical errors are shown.

observed that v_2 is constant over the η coverage of the PHENIX detector, and the constancy does not depend on p_T. This is not the case when the v_2 is measured far from midrapidity, where the PHOBOS and STAR Collaborations observe a drop in v_2 for $|\eta| > 1.0$ [49,50].

VI. DISCUSSION

A. Effect of CNT event-plane resolution

Figure 22 shows the comparison of $v_2\{\text{ZDC-SMD}\}$ and $v_2\{\text{BBC}\}$ as a function of p_T corrected either by the resolution from South-North correlations from the same detectors or by the resolution from ZDC-SMD-CNT correlations in the 20–60% centrality bin. Figures 22(a) and 22(b) compare the v_2 obtained by using two different corrections from the South-North and ZDC-BBC-CNT subevents for the BBC and ZDC-SMD event planes. The v_2 from the South-North subevent is consistent with that from the ZDC-BBC-CNT subevent, within systematic uncertainties. The small difference between South-North and ZDC-BBC-CNT subevents is attributed to the difference between the event-plane resolution, as shown in Fig. 4. Figures 22(c) and 22(d) compare $v_2\{\text{ZDC-SMD}\}$ with $v_2\{\text{BBC}\}$ for the South-North and ZDC-BBC-CNT subevents. The data points in Figs. 22(c) and 22(d) are the same as in Figs. 22(a) and 22(b). Figure 22(c) shows that $v_2\{\text{ZDC-SMD}\}$ is about 10% smaller than $v_2\{\text{BBC}\}$ for the South-North subevent. The ratio of $v_2\{\text{ZDC-SMD}\}$ to $v_2\{\text{BBC}\}$ is found to be independent of p_T except for $6 < p_T < 8$ GeV/c. If jets are the dominant source of nonflow, one expects its contribution to v_2 to become larger at higher p_T. The constant ratio suggests that the nonflow contribution from jets is small, and v_2 fluctuations may affect $v_2\{\text{BBC}\}$ below $p_T \approx 6$ GeV/c, since the effect of fluctuations is expected to be independent of p_T. $v_2\{\text{ZDC-SMD}\}$ agrees with $v_2\{\text{BBC}\}$ within systematic uncertainties for the ZDC-BBC-CNT subevent, as shown in Fig. 22(d). The event-plane resolution from the ZDC-BBC-CNT subevents includes the effect of nonflow contributions and v_2 fluctuations, since the CNT and BBC event planes are sensitive to both effects, though nonflow effects especially from jets could be negligible in the BBC event plane, as discussed earlier. The consistency between v_2 from the ZDC-SMD and BBC event planes may suggest that $v_2\{\text{ZDC-SMD}\}$ becomes sensitive to v_2 fluctuations when the BBC and CNT event planes are included in the estimation of resolution.

B. Comparison with other experiments

It is instructive to compare measurements made by different experiments at RHIC. Figure 23 shows a comparison of the p_T dependence of charged hadron v_2 in the 20–60% centrality range between PHENIX and STAR experiments [51]. The relative systematic errors on the STAR $v_2\{2\}$ and $v_2\{4\}$ measurements range up to 10% for $p_T < 1$ GeV/c, with the lowest p_T bin having the largest error ~10%, while they are of the order of 1% above 1 GeV/c [51]. The $v_2\{2\}$ from PHENIX is lower than that from STAR, but they are comparable within

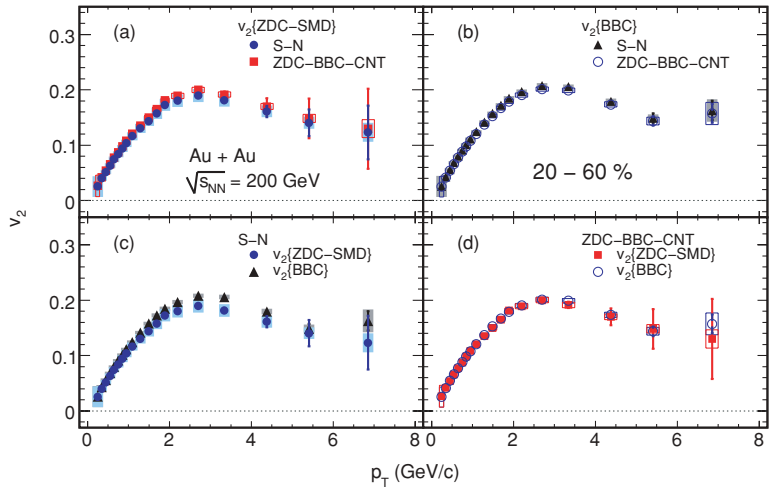

FIG. 22. (Color online) (a) Comparison of the $v_2\{\text{ZDC-SMD}\}$ obtained from the S-N and ZDC-BBC-CNT subevents as a function of p_T in the 20–60% centrality range. (b) Same comparison as (a), but for the $v_2\{\text{BBC}\}$. (c) Comparison of v_2 between BBC and ZDC-SMD event planes from the S-N subevent as a function of p_T in centrality 20–60%. (d) Same comparison as (c), but from the ZDC-BBC-CNT subevent. Error bars denote statistical errors. Open boxes and shaded bands describe the quadratic sum of type B and C systematic uncertainties from the S-N and ZDC-BBC-CNT subevents, respectively.

systematic uncertainties, as shown in Fig. 23(a). Figure 23(b) compares $v_2\{\text{BBC}\}$ and $v_2\{\text{ZDC-SMD}\}$ with $v_2\{4\}$, obtained from four-particle cumulants, as measured in STAR. For

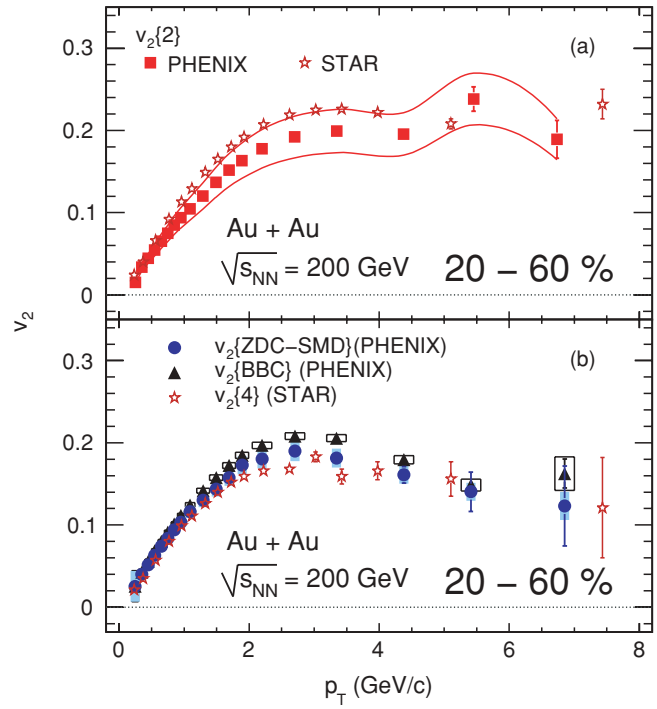

FIG. 23. (Color online) (a) Comparison of charged hadron $v_2\{2\}$ between PHENIX and STAR experiments as a function of p_T in centrality 20–60%. Solid lines represent the quadratic sum of type B and C systematic errors on the PHENIX $v_2\{2\}$. (b) Comparison of charged hadron v_2 from four-particle cumulant $v_2\{4\}$ at STAR with the PHENIX $v_2\{\text{BBC}\}$ and $v_2\{\text{ZDC-SMD}\}$ as a function of p_T in centrality 20–60%. Open boxes and shaded bands represent the quadratic sum of type B and C systematic errors on the $v_2\{\text{BBC}\}$ and $v_2\{\text{ZDC-SMD}\}$, respectively. STAR results are taken from Ref. [51]. Systematic errors on the STAR v_2 are not plotted, see text for more details.

$p_T > 2$ GeV/c, the STAR $v_2\{4\}$ is systematically smaller than the PHENIX event-plane v_2, while $v_2\{\text{ZDC-SMD}\}$ is lower than $v_2\{\text{BBC}\}$. However, the three sets of measurements are consistent within systematic errors. The order of v_2, that is, $v_2\{\text{BBC}\} > v_2\{\text{ZDC-SMD}\} > v_2\{4\}$, could be explained by the effect of flow fluctuations [33,52] if other nonflow contributions are small.

Figure 24 compares our charged hadron v_2 from the BBC and ZDC-SMD event planes to v_2 from a modified event-plane method [49], labeled $v_2\{\text{EP}_2\}$, from the STAR experiment for three centrality bins in the range 10–40%. Particles within $|\Delta\eta| < 0.5$ around the highest p_T particle were excluded for the determination of the modified event plane in order to reduce some of the nonflow effects at high p_T. We find that $v_2\{\text{BBC}\}$ agrees well with $v_2\{\text{EP}_2\}$ over the measured p_T range, whereas $v_2\{\text{ZDC-SMD}\}$ is generally slightly smaller than $v_2\{\text{EP}_2\}$.

VII. SUMMARY

In summary, we have presented PHENIX elliptic flow measurements for unidentified charged hadrons from the event plane and the two-particle cumulant methods as a function of p_T and centrality at midrapidity ($|\eta| < 0.35$) in Au + Au collisions at $\sqrt{s_{NN}} = 200$ GeV. The first-harmonic ZDC-SMD event plane is used to measure v_2 and is compared with v_2 from the second-harmonic BBC event plane in order to understand the possible nonflow contributions as well as the effect of v_2 fluctuations on $v_2\{\text{BBC}\}$.

The comparison between v_2 from two-particle cumulant and event-plane methods shows that they agree within systematic errors. However, nonflow effects from jet correlations begin to contribute to the two-particle cumulant v_2, especially for peripheral collisions and at high p_T.

In contrast, nonflow effects on $v_2\{\text{BBC}\}$ are very small. The measured $v_2\{\text{BBC}\}$ values decrease by about 3% when the central arm event plane is included in the estimate of the BBC reaction plane resolution. This could be due to a

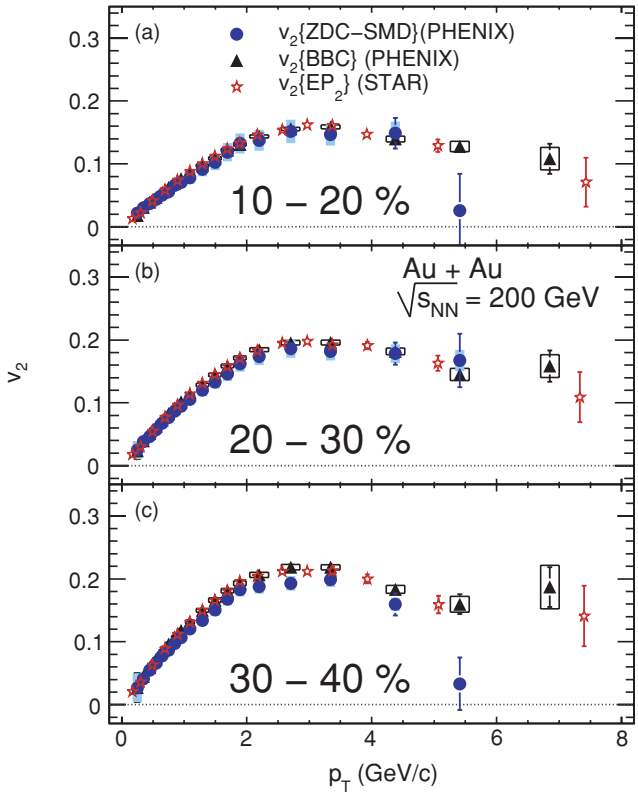

FIG. 24. (Color online) Comparison of the PHENIX $v_2\{\text{BBC}\}$ and $v_2\{\text{ZDC-SMD}\}$ with the STAR v_2 from the modified event-plane method for charged hadrons [49] as a function of p_T in three centralities. Open boxes and shaded bands represent the quadratic sum of type B and C systematic errors on $v_2\{\text{BBC}\}$ and $v_2\{\text{ZDC-SMD}\}$, respectively.

partial compensation of the nonflow effects on the measured v_2, though the results of $v_2\{\text{BBC}\}$ with and without the CNT event-plane resolution are consistent within systematic errors. The strongest evidence that nonflow effects on $v_2\{\text{BBC}\}$ are small comes from the observation that $v_2\{\text{ZDC-SMD}\}$ is comparable to $v_2\{\text{BBC}\}$ within systematic uncertainties in the 0–40% centrality range, and is only ∼5–10% smaller than $v_2\{\text{BBC}\}$ for the 40–60% centrality bin. The magnitude of this difference could indicate the level at which nonflow effects such as jets or the ridge could impact the measured flow. However, the PHOBOS Collaboration has observed the ridge to be strongest in central collisions [31] where we observe that $v_2\{\text{ZDC-SMD}\}$ is comparable with $v_2\{\text{BBC}\}$. For collisions that are more peripheral than 40% centrality, PHOBOS observes no ridge [31], so it is unlikely that our observation that $v_2\{\text{ZDC-SMD}\}$ is ∼5–10% smaller than $v_2\{\text{BBC}\}$ for the 40–60% centrality bin is caused by the ridge. Moreover, the difference between $v_2\{\text{ZDC-SMD}\}$ and $v_2\{\text{BBC}\}$ is independent of p_T in the measured centrality range.

Because of the large pseudorapidity gap between the event plane and the particles detected in the central arms spectrometer, and the first-harmonic event plane from directed flow by spectator neutrons, $v_2\{\text{ZDC-SMD}\}$ is considered to provide an unbiased measure of the elliptic flow. Within systematic uncertainties, the measured $v_2\{\text{ZDC-SMD}\}$ from PHENIX is consistent with v_2 from the four-particle cumulant method measured by the STAR experiment in the 20–60% centrality bin, and it is also consistent with the STAR v_2 from a modified event-plane method in 10–40% centrality bins. These comparisons (1) further demonstrate the validity of the $v_2\{\text{ZDC-SMD}\}$, because both STAR results aim to minimize the nonflow effects, (2) reinforce the robustness of the BBC event-plane method at RHIC, and (3) confirm previous studies of the influence of jets on the measured v_2 for different rapidity gaps. Hence, $v_2\{\text{BBC}\}$ can be used to infer constraints on the hydrodynamic behavior of heavy-ion collisions at RHIC.

ACKNOWLEDGMENTS

We thank the staff of the Collider-Accelerator and Physics Departments at Brookhaven National Laboratory and the staff of the other PHENIX participating institutions for their vital contributions. We acknowledge support from the Office of Nuclear Physics in the Office of Science of the US Department of Energy, the National Science Foundation, Abilene Christian University Research Council, Research Foundation of SUNY, and Dean of the College of Arts and Sciences, Vanderbilt University (USA), Ministry of Education, Culture, Sports, Science, and Technology and the Japan Society for the Promotion of Science (Japan), Conselho Nacional de Desenvolvimento Científico e Tecnológico and Fundação de Amparo à Pesquisa do Estado de São Paulo (Brazil), Natural Science Foundation of China (People's Republic of China), Centre National de la Recherche Scientifique, Commissariat à l'Énergie Atomique, and Institut National de Physique Nucléaire et de Physique des Particules (France), Ministry of Industry, Science and Tekhnologies, Bundesministerium für Bildung und Forschung, Deutscher Akademischer Austausch Dienst, and Alexander von Humboldt Stiftung (Germany), Hungarian National Science Fund, OTKA (Hungary), Department of Atomic Energy (India), Israel Science Foundation (Israel), Korea Research Foundation and Korea Science and Engineering Foundation (Korea), Ministry of Education and Science, Russia Academy of Sciences, Federal Agency of Atomic Energy (Russia), VR and the Wallenberg Foundation (Sweden), the US Civilian Research and Development Foundation for the Independent States of the Former Soviet Union, the US-Hungarian NSF-OTKA-MTA, and the US-Israel Binational Science Foundation.

APPENDIX: DATA TABLES OF v_2

Tables IV–X show numerical data in the same units as plotted in the figures: p_T (GeV/c), v_2, type A statistical error σ_{stat}, type B systematic error σ^B_{syst} and type C systematic error σ^C_{syst}.

TABLE IV. $v_2\{2\}$ as a function of p_T in centralities 0–10%, 10–20%, 20–30%, 30–40%, 40–50%, and 50–60%.

Centrality $v_1\{\}$	p_T (GeV/c)	v_2	σ_{stat}	σ^B_{syst}	σ^C_{syst}	Centrality $v_2\{\}$	p_T (GeV/c)	v_2	σ_{stat}	σ^B_{syst}	σ^C_{syst}
	0.247	0.00859	0.00014	0.00001	0.00000		0.250	0.00898	0.00021	0.00001	0.00000
	0.347	0.01406	0.00019	0.00004	0.00000		0.349	0.04323	0.00030	0.00026	0.00000
	0.450	0.01882	0.00023	0.00007	0.00000		0.448	0.06214	0.00036	0.00053	0.00000
	0.547	0.02140	0.00027	0.00009	0.00000		0.548	0.07193	0.00042	0.00071	0.00000
	0.649	0.02395	0.00031	0.00011	0.00000		0.648	0.08243	0.00048	0.00093	0.00000
	0.748	0.02718	0.00036	0.00014	0.00000		0.748	0.09401	0.00055	0.00121	0.00000
	0.847	0.03087	0.00041	0.00018	0.00000		0.848	0.10533	0.00063	0.00153	0.00000
	0.949	0.03605	0.00047	0.00024	0.00000		0.948	0.11678	0.00071	0.00187	0.00000
	1.090	0.03950	0.00041	0.00029	0.00000		1.092	0.12972	0.00063	0.00231	0.00000
0–10%	1.291	0.04734	0.00053	0.00042	0.00000	30–40%	1.291	0.15059	0.00081	0.00312	0.00000
$v_2\{2\}$	1.490	0.05633	0.00070	0.00059	0.00000	$v_2\{2\}$	1.489	0.16955	0.00107	0.00395	0.00000
	1.689	0.06542	0.00095	0.00080	0.00000		1.689	0.18422	0.00147	0.00467	0.00000
	1.890	0.07148	0.00128	0.00096	0.00000		1.891	0.19625	0.00198	0.00529	0.00000
	2.194	0.08352	0.00128	0.00130	0.00000		2.197	0.21718	0.00196	0.00648	0.00000
	2.698	0.09362	0.00249	0.00164	0.00000		2.702	0.22835	0.00369	0.00717	0.00000
	3.329	0.08866	0.00421	0.00147	0.00000		3.338	0.22623	0.00556	0.00704	0.00000
	4.365	0.08997	0.01134	0.00151	0.00000		4.360	0.19059	0.01496	0.00499	0.00000
	5.376	0.07933	0.02365	0.00118	0.00000		5.379	0.16931	0.03256	0.00394	0.00000
	6.695	0.08701	0.02720	0.00142	0.00000		6.628	0.16346	0.05010	0.00367	0.00000
	0.248	0.01089	0.00013	0.00002	0.00000		0.250	0.00625	0.00032	0.00001	0.00000
	0.348	0.02714	0.00018	0.00011	0.00000		0.349	0.04611	0.00044	0.00028	0.00000
	0.449	0.03914	0.00023	0.00023	0.00000		0.448	0.06387	0.00054	0.00054	0.00000
	0.547	0.04592	0.00027	0.00032	0.00000		0.548	0.07455	0.00062	0.00073	0.00000
	0.649	0.05281	0.00030	0.00042	0.00000		0.648	0.08575	0.00072	0.00097	0.00000
	0.748	0.05977	0.00035	0.00054	0.00000		0.748	0.09774	0.00082	0.00126	0.00000
	0.848	0.06637	0.00040	0.00066	0.00000		0.848	0.11126	0.00094	0.00163	0.00000
	0.948	0.07459	0.00045	0.00083	0.00000		0.948	0.11974	0.00108	0.00189	0.00000
	1.092	0.08249	0.00040	0.00102	0.00000		1.092	0.13745	0.00095	0.00249	0.00000
10–20%	1.291	0.09506	0.00051	0.00136	0.00000	40–50%	1.291	0.15672	0.00123	0.00324	0.00000
$v_2\{2\}$	1.490	0.10997	0.00067	0.00181	0.00000	$v_2\{2\}$	1.489	0.17633	0.00166	0.00410	0.00000
	1.689	0.12394	0.00090	0.00230	0.00000		1.689	0.19315	0.00229	0.00492	0.00000
	1.891	0.13378	0.00121	0.00268	0.00000		1.891	0.20965	0.00309	0.00580	0.00000
	2.196	0.14881	0.00121	0.00332	0.00000		2.199	0.21909	0.00304	0.00633	0.00000
	2.699	0.16781	0.00232	0.00422	0.00000		2.701	0.23572	0.00567	0.00733	0.00000
	3.328	0.16669	0.00382	0.00417	0.00000		3.344	0.24331	0.00808	0.00781	0.00000
	4.357	0.13468	0.01047	0.00272	0.00000		4.346	0.26575	0.02124	0.00932	0.00000
	5.371	0.14951	0.02244	0.00335	0.00000		5.414	0.24613	0.03288	0.00799	0.00000
	6.587	0.11931	0.02641	0.00214	0.00000		6.566	0.17786	0.05097	0.00417	0.00000
	0.249	0.01127	0.00015	0.00002	0.00000		0.251	0.01201	0.00052	0.00002	0.00000
	0.349	0.03713	0.00022	0.00019	0.00000		0.349	0.03575	0.00056	0.00016	0.00000
	0.448	0.05370	0.00028	0.00040	0.00000		0.448	0.05111	0.00063	0.00033	0.00000
	0.548	0.06252	0.00032	0.00054	0.00000		0.548	0.06256	0.00071	0.00050	0.00000
	0.648	0.07147	0.00036	0.00070	0.00000		0.648	0.07591	0.00080	0.00073	0.00000
	0.748	0.08144	0.00041	0.00091	0.00000		0.748	0.08903	0.00091	0.00101	0.00000
	0.848	0.09118	0.00047	0.00114	0.00000		0.848	0.09965	0.00103	0.00126	0.00000
	0.948	0.10071	0.00053	0.00139	0.00000		0.948	0.11124	0.00118	0.00157	0.00000
	1.092	0.11227	0.00047	0.00173	0.00000		1.091	0.12340	0.00103	0.00193	0.00000
20–30%	1.291	0.12982	0.00060	0.00232	0.00000	50–60%	1.290	0.14241	0.00133	0.00257	0.00000
$v_2\{2\}$	1.489	0.14786	0.00079	0.00301	0.00000	$v_2\{2\}$	1.489	0.16236	0.00178	0.00334	0.00000
	1.689	0.16113	0.00107	0.00357	0.00000		1.689	0.17737	0.00248	0.00399	0.00000
	1.891	0.17515	0.00145	0.00422	0.00000		1.890	0.19295	0.00337	0.00472	0.00000
	2.196	0.19364	0.00143	0.00515	0.00000		2.198	0.21282	0.00330	0.00575	0.00000
	2.699	0.20931	0.00271	0.00602	0.00000		2.700	0.22201	0.00623	0.00625	0.00000
	3.333	0.20299	0.00430	0.00567	0.00000		3.348	0.21980	0.00917	0.00613	0.00000
	4.356	0.19729	0.01175	0.00535	0.00000		4.373	0.24935	0.02292	0.00789	0.00000
	5.383	0.18635	0.02567	0.00477	0.00000		5.452	0.36285	0.05515	0.01671	0.00000
	6.611	0.15079	0.04839	0.00313	0.00000		6.734	0.40554	0.08167	0.02087	0.00000

TABLE V. $v_2\{2\}$ as a function of p_T in centrality 20–60%.

Centrality $v_2\{\}$	p_T (GeV/c)	v_2	σ_{stat}	σ^B_{syst}	σ^C_{syst}	p_T (GeV/c)	v_2	σ_{stat}	σ^B_{syst}	σ^C_{syst}
	0.251	0.00778	0.00011	0.00001	0.00000	1.489	0.14884	0.00058	0.00292	0.00000
	0.349	0.03793	0.00016	0.00019	0.00000	1.689	0.16226	0.00080	0.00347	0.00000
	0.448	0.05476	0.00020	0.00040	0.00000	1.890	0.17456	0.00108	0.00402	0.00000
	0.548	0.06374	0.00023	0.00054	0.00000	2.198	0.19027	0.00106	0.00478	0.00000
20–60%	0.648	0.07303	0.00026	0.00070	0.00000	2.700	0.20415	0.00201	0.00550	0.00000
$v_2\{2\}$	0.748	0.08283	0.00030	0.00091	0.00000	3.348	0.21363	0.00304	0.00602	0.00000
	0.848	0.09301	0.00034	0.00114	0.00000	4.373	0.19568	0.00653	0.00505	0.00000
	0.948	0.10247	0.00039	0.00139	0.00000	5.452	0.23823	0.01494	0.00749	0.00000
	1.091	0.11444	0.00034	0.00173	0.00000	6.734	0.18915	0.02297	0.00472	0.00000
	1.290	0.13201	0.00044	0.00230	0.00000					

TABLE VI. $v_2\{\text{BBC}\}$ and $v_2\{\text{ZDC-SMD}\}$ from S-N and ZDC-BBC-CNT subevents as a function of p_T in centrality 20–60%.

Centrality $v_2\{\}$	p_T (GeV/c)	S-N subevents				ZDC-BBC-CNT subevents			
		v_2	σ_{stat}	σ^B_{syst}	σ^C_{syst}	v_2	σ_{stat}	σ^B_{syst}	σ^C_{syst}
	0.247	0.02569	0.00009	0.00049	0.00001	0.02486	0.00009	0.00045	0.00001
	0.348	0.04271	0.00009	0.00016	0.00003	0.04133	0.00010	0.00015	0.00003
	0.448	0.05587	0.00010	0.00014	0.00006	0.05407	0.00012	0.00013	0.00005
	0.548	0.06846	0.00011	0.00015	0.00009	0.06625	0.00013	0.00014	0.00008
	0.648	0.08009	0.00013	0.00015	0.00012	0.07751	0.00015	0.00014	0.00011
	0.748	0.09123	0.00014	0.00016	0.00015	0.08828	0.00017	0.00015	0.00014
	0.848	0.10124	0.00016	0.00019	0.00019	0.09798	0.00019	0.00018	0.00018
	0.948	0.11159	0.00018	0.00017	0.00023	0.10799	0.00021	0.00016	0.00021
20–60%	1.092	0.12439	0.00016	0.00018	0.00029	0.12038	0.00020	0.00017	0.00027
$v_2\{\text{BBC}\}$	1.292	0.14170	0.00020	0.00019	0.00037	0.13713	0.00025	0.00018	0.00035
	1.492	0.15770	0.00027	0.00027	0.00046	0.15261	0.00031	0.00025	0.00043
	1.692	0.17244	0.00037	0.00027	0.00055	0.16688	0.00040	0.00026	0.00051
	1.892	0.18481	0.00050	0.00030	0.00063	0.17885	0.00052	0.00028	0.00059
	2.200	0.19684	0.00049	0.00029	0.00071	0.19049	0.00052	0.00027	0.00067
	2.703	0.20803	0.00092	0.00025	0.00080	0.20132	0.00092	0.00023	0.00075
	3.343	0.20569	0.00141	0.00039	0.00078	0.19905	0.00138	0.00037	0.00073
	4.381	0.17942	0.00371	0.00066	0.00059	0.17363	0.00360	0.00062	0.00056
	5.410	0.14862	0.00877	0.00098	0.00041	0.14382	0.00849	0.00092	0.00038
	6.852	0.16262	0.01770	0.00328	0.00049	0.15738	0.01713	0.00308	0.00046
	0.247	0.02532	0.00025	0.00047	0.00004	0.02661	0.00035	0.00052	0.00002
	0.348	0.04002	0.00029	0.00014	0.00010	0.04188	0.00037	0.00015	0.00004
	0.448	0.05165	0.00032	0.00012	0.00017	0.05395	0.00041	0.00013	0.00007
	0.548	0.06296	0.00036	0.00013	0.00025	0.06567	0.00046	0.00014	0.00010
	0.648	0.07433	0.00041	0.00013	0.00035	0.07746	0.00051	0.00014	0.00014
	0.748	0.08377	0.00046	0.00013	0.00044	0.08730	0.00057	0.00015	0.00017
	0.848	0.09429	0.00052	0.00017	0.00056	0.09827	0.00065	0.00018	0.00022
	0.948	0.10365	0.00059	0.00015	0.00067	0.10808	0.00074	0.00016	0.00027
20–60%	1.092	0.11617	0.00053	0.00016	0.00085	0.12065	0.00063	0.00017	0.00033
$v_2\{\text{ZDC-SMD}\}$	1.292	0.13006	0.00066	0.00016	0.00106	0.13535	0.00081	0.00018	0.00042
	1.492	0.14367	0.00086	0.00023	0.00129	0.14994	0.00109	0.00024	0.00052
	1.692	0.15763	0.00115	0.00023	0.00156	0.16504	0.00150	0.00025	0.00062
	1.892	0.17281	0.00151	0.00026	0.00187	0.18136	0.00203	0.00029	0.00075
	2.200	0.18031	0.00149	0.00024	0.00204	0.18912	0.00200	0.00026	0.00082
	2.703	0.18983	0.00263	0.00021	0.00226	0.19998	0.00375	0.00023	0.00092
	3.343	0.18147	0.00393	0.00030	0.00206	0.19147	0.00576	0.00034	0.00084
	4.381	0.16102	0.01018	0.00053	0.00162	0.17005	0.01517	0.00059	0.00066
	5.410	0.14043	0.02402	0.00088	0.00124	0.14833	0.03585	0.00098	0.00050
	6.852	0.12310	0.04849	0.00188	0.00095	0.13003	0.07240	0.00210	0.00039

TABLE VII. $v_2\{\text{BBC}\}$ from S-N and ZDC-BBC-CNT subevents as a function of p_T in centrality 0–10%, 10–20%, and 20–30%.

Centrality $v_2\{\}$	p_T (GeV/c)	S-N subevents				ZDC-BBC-CNT subevents			
		v_2	σ_{stat}	σ^B_{syst}	σ^C_{syst}	v_2	σ_{stat}	σ^B_{syst}	σ^C_{syst}
0–10% $v_2\{\text{BBC}\}$	0.247	0.01025	0.00012	0.00008	0.00001	0.00966	0.00016	0.00007	0.00000
	0.348	0.01868	0.00014	0.00003	0.00002	0.01762	0.00025	0.00003	0.00002
	0.448	0.02300	0.00016	0.00005	0.00003	0.02169	0.00030	0.00005	0.00002
	0.548	0.02741	0.00018	0.00007	0.00004	0.02586	0.00035	0.00006	0.00003
	0.648	0.03174	0.00020	0.00007	0.00005	0.02993	0.00041	0.00006	0.00005
	0.748	0.03570	0.00023	0.00007	0.00006	0.03367	0.00046	0.00006	0.00006
	0.848	0.03990	0.00026	0.00007	0.00008	0.03763	0.00051	0.00006	0.00007
	0.948	0.04428	0.00029	0.00008	0.00010	0.04176	0.00057	0.00007	0.00009
	1.092	0.04941	0.00025	0.00008	0.00012	0.04660	0.00061	0.00007	0.00011
	1.292	0.05631	0.00032	0.00008	0.00016	0.05310	0.00070	0.00007	0.00014
	1.492	0.06349	0.00042	0.00008	0.00020	0.05988	0.00082	0.00007	0.00018
	1.692	0.07065	0.00058	0.00012	0.00025	0.06663	0.00096	0.00010	0.00022
	1.892	0.07859	0.00078	0.00011	0.00031	0.07412	0.00115	0.00010	0.00028
	2.200	0.08557	0.00078	0.00009	0.00037	0.08070	0.00121	0.00008	0.00033
	2.703	0.09598	0.00151	0.00015	0.00046	0.09052	0.00179	0.00014	0.00041
	3.343	0.09806	0.00245	0.00031	0.00049	0.09249	0.00257	0.00028	0.00043
	4.381	0.08795	0.00699	0.00089	0.00039	0.08295	0.00667	0.00079	0.00035
10–20% $v_2\{\text{BBC}\}$	0.247	0.01804	0.00010	0.00008	0.00000	0.01754	0.00011	0.00007	0.00000
	0.348	0.03095	0.00011	0.00008	0.00001	0.03008	0.00015	0.00008	0.00001
	0.448	0.03927	0.00012	0.00012	0.00002	0.03816	0.00018	0.00011	0.00002
	0.548	0.04714	0.00014	0.00018	0.00003	0.04582	0.00020	0.00017	0.00003
	0.648	0.05480	0.00015	0.00016	0.00004	0.05326	0.00023	0.00015	0.00004
	0.748	0.06236	0.00017	0.00016	0.00006	0.06060	0.00026	0.00015	0.00005
	0.848	0.06895	0.00019	0.00016	0.00007	0.06701	0.00029	0.00015	0.00006
	0.948	0.07647	0.00022	0.00017	0.00008	0.07432	0.00033	0.00016	0.00008
	1.092	0.08498	0.00019	0.00018	0.00010	0.08259	0.00033	0.00017	0.00010
	1.292	0.09731	0.00024	0.00018	0.00014	0.09457	0.00040	0.00017	0.00013
	1.492	0.10883	0.00032	0.00022	0.00017	0.10576	0.00047	0.00021	0.00016
	1.692	0.12204	0.00044	0.00021	0.00021	0.11860	0.00058	0.00020	0.00020
	1.892	0.13129	0.00059	0.00029	0.00025	0.12760	0.00072	0.00027	0.00023
	2.200	0.14375	0.00058	0.00021	0.00030	0.13970	0.00074	0.00020	0.00028
	2.703	0.15569	0.00112	0.00023	0.00035	0.15130	0.00120	0.00022	0.00033
	3.343	0.15885	0.00177	0.00033	0.00037	0.15437	0.00180	0.00031	0.00034
	4.381	0.13970	0.00491	0.00056	0.00028	0.13577	0.00480	0.00053	0.00027
	5.410	0.12763	0.01194	0.00101	0.00024	0.12403	0.01161	0.00095	0.00022
	6.852	0.10820	0.02401	0.00193	0.00017	0.10515	0.02334	0.00183	0.00016
20–30% $v_2\{\text{BBC}\}$	0.247	0.02367	0.00011	0.00032	0.00001	0.02303	0.00012	0.00030	0.00001
	0.348	0.03981	0.00012	0.00014	0.00002	0.03874	0.00015	0.00014	0.00002
	0.448	0.05138	0.00014	0.00016	0.00004	0.04999	0.00017	0.00015	0.00004
	0.548	0.06250	0.00015	0.00019	0.00006	0.06081	0.00020	0.00018	0.00005
	0.648	0.07276	0.00017	0.00020	0.00008	0.07080	0.00023	0.00019	0.00007
	0.748	0.08298	0.00019	0.00018	0.00010	0.08075	0.00026	0.00017	0.00010
	0.848	0.09184	0.00022	0.00020	0.00012	0.08937	0.00029	0.00019	0.00012
	0.948	0.10139	0.00024	0.00020	0.00015	0.09866	0.00032	0.00019	0.00014
	1.092	0.11279	0.00021	0.00022	0.00019	0.10976	0.00032	0.00021	0.00018
	1.292	0.12862	0.00027	0.00023	0.00024	0.12516	0.00038	0.00022	0.00023
	1.492	0.14459	0.00036	0.00029	0.00031	0.14070	0.00046	0.00027	0.00029
	1.692	0.15864	0.00049	0.00030	0.00037	0.15437	0.00058	0.00029	0.00035
	1.892	0.17169	0.00066	0.00032	0.00043	0.16707	0.00074	0.00030	0.00041
	2.200	0.18437	0.00065	0.00032	0.00050	0.17941	0.00075	0.00030	0.00047
	2.703	0.19554	0.00123	0.00042	0.00056	0.19028	0.00127	0.00039	0.00053
	3.343	0.19585	0.00192	0.00048	0.00056	0.19058	0.00192	0.00046	0.00053
	4.381	0.18189	0.00521	0.00088	0.00049	0.17700	0.00509	0.00083	0.00046
	5.410	0.14502	0.01244	0.00138	0.00031	0.14112	0.01211	0.00131	0.00029
	6.852	0.15856	0.02490	0.00286	0.00037	0.15430	0.02423	0.00271	0.00035

TABLE VIII. $v_2\{\text{BBC}\}$ from S-N and ZDC-BBC-CNT subevents as a function of p_T in centrality 30–40%, 40–50%, and 50–60%.

Centrality $v_2\{\}$	p_T (GeV/c)	S-N subevents				ZDC-BBC-CNT subevents			
		v_2	σ_{stat}	σ^B_{syst}	σ^C_{syst}	v_2	σ_{stat}	σ^B_{syst}	σ^C_{syst}
30–40% $v_2\{\text{BBC}\}$	0.247	0.02733	0.00015	0.00064	0.00001	0.02643	0.00016	0.00059	0.00001
	0.348	0.04523	0.00016	0.00017	0.00004	0.04375	0.00018	0.00016	0.00003
	0.448	0.05935	0.00018	0.00017	0.00006	0.05740	0.00021	0.00016	0.00006
	0.548	0.07263	0.00020	0.00016	0.00010	0.07024	0.00024	0.00015	0.00009
	0.648	0.08502	0.00023	0.00015	0.00013	0.08223	0.00028	0.00014	0.00012
	0.748	0.09651	0.00025	0.00020	0.00017	0.09334	0.00031	0.00018	0.00016
	0.848	0.10742	0.00029	0.00019	0.00021	0.10390	0.00035	0.00018	0.00020
	0.948	0.11793	0.00033	0.00018	0.00025	0.11406	0.00039	0.00017	0.00024
	1.092	0.13156	0.00028	0.00022	0.00032	0.12724	0.00038	0.00020	0.00030
	1.292	0.15004	0.00036	0.00019	0.00041	0.14512	0.00046	0.00018	0.00038
	1.492	0.16604	0.00048	0.00030	0.00050	0.16059	0.00057	0.00028	0.00047
	1.692	0.18107	0.00066	0.00029	0.00060	0.17513	0.00073	0.00027	0.00056
	1.892	0.19290	0.00089	0.00034	0.00068	0.18657	0.00094	0.00032	0.00063
	2.200	0.20640	0.00088	0.00035	0.00078	0.19962	0.00094	0.00032	0.00073
	2.703	0.21859	0.00164	0.00042	0.00087	0.21142	0.00164	0.00040	0.00081
	3.343	0.21843	0.00252	0.00037	0.00087	0.21127	0.00247	0.00034	0.00081
	4.381	0.18342	0.00662	0.00101	0.00061	0.17740	0.00641	0.00095	0.00057
	5.410	0.15970	0.01568	0.00197	0.00046	0.15446	0.01517	0.00184	0.00043
	6.852	0.18703	0.03171	0.00640	0.00064	0.18090	0.03067	0.00599	0.00060
40–50% $v_2\{\text{BBC}\}$	0.247	0.02840	0.00024	0.00071	0.00002	0.02735	0.00024	0.00066	0.00002
	0.348	0.04699	0.00025	0.00018	0.00005	0.04524	0.00027	0.00017	0.00005
	0.448	0.06236	0.00028	0.00015	0.00009	0.06005	0.00031	0.00014	0.00009
	0.548	0.07757	0.00031	0.00015	0.00014	0.07469	0.00035	0.00014	0.00013
	0.648	0.09141	0.00035	0.00015	0.00020	0.08802	0.00040	0.00014	0.00018
	0.748	0.10354	0.00039	0.00016	0.00025	0.09969	0.00045	0.00015	0.00024
	0.848	0.11530	0.00044	0.00019	0.00032	0.11102	0.00051	0.00017	0.00029
	0.948	0.12668	0.00050	0.00016	0.00038	0.12198	0.00057	0.00015	0.00035
	1.092	0.14106	0.00044	0.00015	0.00047	0.13583	0.00054	0.00014	0.00044
	1.292	0.15967	0.00056	0.00019	0.00061	0.15374	0.00066	0.00017	0.00056
	1.492	0.17584	0.00075	0.00025	0.00074	0.16932	0.00083	0.00023	0.00068
	1.692	0.19082	0.00104	0.00031	0.00087	0.18373	0.00110	0.00029	0.00080
	1.892	0.20216	0.00141	0.00031	0.00097	0.19466	0.00144	0.00029	0.00090
	2.200	0.21274	0.00138	0.00031	0.00108	0.20485	0.00142	0.00029	0.00100
	2.703	0.22348	0.00256	0.00039	0.00119	0.21518	0.00252	0.00036	0.00110
	3.343	0.22044	0.00387	0.00067	0.00116	0.21226	0.00376	0.00063	0.00107
	4.381	0.18665	0.00994	0.00094	0.00083	0.17973	0.00958	0.00087	0.00077
	5.410	0.16716	0.02325	0.00178	0.00067	0.16095	0.02239	0.00165	0.00062
	6.852	0.15951	0.04732	0.00616	0.00060	0.15359	0.04556	0.00571	0.00056
50–60% $v_2\{\text{BBC}\}$	0.247	0.02767	0.00043	0.00056	0.00003	0.02604	0.00042	0.00050	0.00003
	0.348	0.04569	0.00046	0.00019	0.00008	0.04300	0.00046	0.00017	0.00007
	0.448	0.06193	0.00050	0.00018	0.00014	0.05828	0.00052	0.00016	0.00013
	0.548	0.07654	0.00056	0.00014	0.00022	0.07203	0.00060	0.00013	0.00019
	0.648	0.08963	0.00064	0.00013	0.00030	0.08435	0.00068	0.00012	0.00027
	0.748	0.10358	0.00072	0.00014	0.00040	0.09747	0.00077	0.00012	0.00036
	0.848	0.11362	0.00082	0.00020	0.00048	0.10692	0.00087	0.00018	0.00043
	0.948	0.12637	0.00093	0.00011	0.00060	0.11892	0.00099	0.00010	0.00053
	1.092	0.14117	0.00082	0.00014	0.00075	0.13284	0.00091	0.00012	0.00066
	1.292	0.15953	0.00105	0.00020	0.00095	0.15013	0.00114	0.00017	0.00085
	1.492	0.17233	0.00141	0.00028	0.00111	0.16217	0.00146	0.00024	0.00099
	1.692	0.18714	0.00196	0.00029	0.00131	0.17611	0.00196	0.00026	0.00116
	1.892	0.19757	0.00266	0.00054	0.00146	0.18592	0.00260	0.00047	0.00130
	2.200	0.20146	0.00260	0.00054	0.00152	0.18959	0.00255	0.00048	0.00135
	2.703	0.21521	0.00480	0.00066	0.00174	0.20252	0.00458	0.00059	0.00154
	3.343	0.19757	0.00712	0.00083	0.00146	0.18593	0.00674	0.00074	0.00130
	4.381	0.16368	0.01791	0.00363	0.00100	0.15403	0.01686	0.00321	0.00089
	5.410	0.11745	0.04124	0.00292	0.00052	0.11053	0.03881	0.00259	0.00046

TABLE IX. $v_2\{\text{ZDC-SMD}\}$ from S-N and ZDC-BBC-CNT subevents as a function of p_T in centralities 0–10%, 10–20%, and 20–30%.

Centrality $v_2\{\}$	p_T (GeV/c)	S-N subevents				ZDC-BBC-CNT subevents			
		v_2	σ_{stat}	σ^B_{syst}	σ^C_{syst}	v_2	σ_{stat}	σ^B_{syst}	σ^C_{syst}
0–10% $v_2\{\text{ZDC-SMD}\}$	0.247	0.01342	0.00114	0.00013	0.00005	0.01723	0.00158	0.00022	0.00004
	0.348	0.01488	0.00131	0.00002	0.00007	0.01929	0.00183	0.00003	0.00005
	0.448	0.01231	0.00133	0.00002	0.00005	0.01688	0.00205	0.00003	0.00004
	0.548	0.02085	0.00170	0.00004	0.00013	0.02643	0.00230	0.00006	0.00010
	0.648	0.01557	0.00166	0.00002	0.00007	0.02132	0.00256	0.00003	0.00006
	0.748	0.02236	0.00203	0.00003	0.00015	0.02928	0.00289	0.00005	0.00012
	0.848	0.02656	0.00233	0.00003	0.00021	0.03444	0.00326	0.00005	0.00017
	0.948	0.03014	0.00265	0.00004	0.00027	0.03909	0.00371	0.00006	0.00021
	1.092	0.04275	0.00268	0.00006	0.00055	0.04922	0.00319	0.00008	0.00034
	1.292	0.03826	0.00304	0.00004	0.00044	0.04801	0.00405	0.00006	0.00032
	1.492	0.03859	0.00367	0.00003	0.00045	0.05124	0.00534	0.00005	0.00037
	1.692	0.04492	0.00476	0.00005	0.00061	0.06137	0.00730	0.00009	0.00053
	1.892	0.06318	0.00654	0.00007	0.00120	0.08583	0.00992	0.00014	0.00103
	2.200	0.06910	0.00672	0.00006	0.00143	0.09233	0.00989	0.00011	0.00119
	2.703	0.07798	0.01123	0.00010	0.00182	0.11270	0.01925	0.00021	0.00178
	3.343	0.07481	0.01667	0.00018	0.00168	0.11230	0.03125	0.00041	0.00177
10–20% $v_2\{\text{ZDC-SMD}\}$	0.247	0.02194	0.00061	0.00011	0.00006	0.02145	0.00067	0.00011	0.00003
	0.348	0.02987	0.00070	0.00008	0.00011	0.02924	0.00074	0.00008	0.00005
	0.448	0.03696	0.00078	0.00010	0.00017	0.03621	0.00083	0.00010	0.00008
	0.548	0.04342	0.00088	0.00015	0.00023	0.04255	0.00092	0.00014	0.00011
	0.648	0.05052	0.00098	0.00013	0.00031	0.04951	0.00103	0.00013	0.00016
	0.748	0.05556	0.00110	0.00013	0.00037	0.05445	0.00115	0.00012	0.00019
	0.848	0.06572	0.00125	0.00014	0.00052	0.06442	0.00130	0.00014	0.00026
	0.948	0.07064	0.00141	0.00014	0.00060	0.06923	0.00148	0.00014	0.00030
	1.092	0.07773	0.00122	0.00015	0.00073	0.07626	0.00126	0.00014	0.00037
	1.292	0.09169	0.00155	0.00016	0.00102	0.08993	0.00162	0.00015	0.00051
	1.492	0.10236	0.00204	0.00019	0.00127	0.10031	0.00214	0.00019	0.00064
	1.692	0.11847	0.00275	0.00020	0.00170	0.11598	0.00293	0.00019	0.00085
	1.892	0.13255	0.00365	0.00029	0.00212	0.12960	0.00397	0.00028	0.00107
	2.200	0.13748	0.00363	0.00020	0.00229	0.13446	0.00393	0.00019	0.00115
	2.703	0.15166	0.00640	0.00022	0.00278	0.14772	0.00754	0.00021	0.00139
	3.343	0.14679	0.00945	0.00028	0.00261	0.14255	0.01196	0.00026	0.00129
	4.381	0.14874	0.02444	0.00064	0.00268	0.14410	0.03301	0.00060	0.00132
	5.410	0.02580	0.05846	0.00004	0.00008	0.02498	0.08004	0.00004	0.00004
20–30% $v_2\{\text{ZDC-SMD}\}$	0.247	0.02479	0.00045	0.00035	0.00005	0.02523	0.00056	0.00037	0.00002
	0.348	0.03843	0.00052	0.00013	0.00011	0.03893	0.00061	0.00014	0.00005
	0.448	0.04673	0.00058	0.00013	0.00017	0.04726	0.00067	0.00013	0.00008
	0.548	0.05726	0.00065	0.00016	0.00025	0.05785	0.00075	0.00016	0.00012
	0.648	0.06796	0.00073	0.00017	0.00036	0.06860	0.00084	0.00018	0.00016
	0.748	0.07649	0.00082	0.00015	0.00045	0.07721	0.00094	0.00016	0.00021
	0.848	0.08664	0.00093	0.00018	0.00058	0.08745	0.00106	0.00018	0.00027
	0.948	0.09430	0.00105	0.00018	0.00069	0.09523	0.00120	0.00018	0.00032
	1.092	0.10554	0.00093	0.00019	0.00086	0.10622	0.00103	0.00020	0.00040
	1.292	0.12012	0.00118	0.00020	0.00112	0.12107	0.00132	0.00020	0.00051
	1.492	0.13329	0.00153	0.00025	0.00138	0.13466	0.00176	0.00025	0.00064
	1.692	0.14589	0.00202	0.00026	0.00165	0.14785	0.00242	0.00026	0.00077
	1.892	0.16194	0.00265	0.00028	0.00204	0.16454	0.00327	0.00029	0.00095
	2.200	0.17353	0.00265	0.00028	0.00234	0.17613	0.00322	0.00029	0.00109
	2.703	0.18631	0.00458	0.00038	0.00269	0.19024	0.00610	0.00039	0.00127
	3.343	0.18180	0.00683	0.00042	0.00257	0.18612	0.00952	0.00044	0.00121
	4.381	0.17827	0.01783	0.00084	0.00247	0.18283	0.02570	0.00088	0.00117
	5.410	0.16731	0.04246	0.00184	0.00217	0.17163	0.06153	0.00194	0.00103

TABLE X. $v_2\{\text{ZDC-SMD}\}$ from S-N and ZDC-BBC-CNT subevents as a function of p_T in centralities 30–40%, 40–50%, and 50–60%.

Centrality $v_2\{\}$	p_T (GeV/c)	S-N subevents				ZDC-BBC-CNT subevents			
		v_2	σ_{stat}	σ^B_{syst}	σ^C_{syst}	v_2	σ_{stat}	σ^B_{syst}	σ^C_{syst}
	0.247	0.02694	0.00045	0.00062	0.00004	0.02819	0.00061	0.00068	0.00002
	0.348	0.04133	0.00050	0.00014	0.00010	0.04305	0.00065	0.00015	0.00004
	0.448	0.05500	0.00057	0.00015	0.00018	0.05713	0.00071	0.00016	0.00007
	0.548	0.06605	0.00064	0.00013	0.00026	0.06852	0.00079	0.00014	0.00010
	0.648	0.07744	0.00073	0.00013	0.00035	0.08028	0.00089	0.00014	0.00013
	0.748	0.08648	0.00082	0.00016	0.00044	0.08966	0.00099	0.00017	0.00016
	0.848	0.09719	0.00092	0.00016	0.00055	0.10077	0.00112	0.00017	0.00021
	0.948	0.10647	0.00104	0.00014	0.00066	0.11046	0.00128	0.00016	0.00025
	1.092	0.12033	0.00093	0.00018	0.00085	0.12430	0.00110	0.00020	0.00031
30–40%	1.292	0.13425	0.00117	0.00015	0.00106	0.13898	0.00141	0.00017	0.00039
$v_2\{\text{ZDC-SMD}\}$	1.492	0.15041	0.00152	0.00025	0.00133	0.15615	0.00188	0.00027	0.00050
	1.692	0.16789	0.00203	0.00025	0.00165	0.17486	0.00260	0.00027	0.00062
	1.892	0.18310	0.00266	0.00031	0.00196	0.19124	0.00353	0.00033	0.00074
	2.200	0.18792	0.00263	0.00029	0.00207	0.19616	0.00346	0.00031	0.00078
	2.703	0.19298	0.00458	0.00033	0.00218	0.20250	0.00649	0.00036	0.00083
	3.343	0.19902	0.00685	0.00031	0.00232	0.20918	0.00995	0.00034	0.00089
	4.381	0.15951	0.01765	0.00077	0.00149	0.16787	0.02619	0.00085	0.00057
	5.410	0.03318	0.04176	0.00008	0.00006	0.03492	0.06213	0.00009	0.00002
	0.247	0.02601	0.00054	0.00060	0.00004	0.02771	0.00077	0.00068	0.00001
	0.348	0.04210	0.00060	0.00014	0.00010	0.04474	0.00081	0.00016	0.00003
	0.448	0.05541	0.00067	0.00012	0.00017	0.05880	0.00089	0.00013	0.00005
	0.548	0.06853	0.00076	0.00012	0.00026	0.07264	0.00099	0.00013	0.00008
	0.648	0.08077	0.00086	0.00011	0.00036	0.08558	0.00111	0.00013	0.00012
	0.748	0.09316	0.00097	0.00013	0.00048	0.09868	0.00125	0.00015	0.00015
	0.848	0.10257	0.00110	0.00015	0.00059	0.10868	0.00141	0.00017	0.00019
	0.948	0.11494	0.00125	0.00013	0.00074	0.12181	0.00161	0.00015	0.00023
	1.092	0.12842	0.00112	0.00012	0.00092	0.13572	0.00139	0.00014	0.00029
40–50%	1.292	0.14455	0.00141	0.00015	0.00116	0.15299	0.00179	0.00017	0.00037
$v_2\{\text{ZDC-SMD}\}$	1.492	0.15539	0.00183	0.00020	0.00134	0.16483	0.00240	0.00022	0.00043
	1.692	0.16641	0.00245	0.00023	0.00154	0.17691	0.00333	0.00027	0.00049
	1.892	0.18706	0.00325	0.00027	0.00195	0.19913	0.00453	0.00030	0.00063
	2.200	0.19007	0.00319	0.00025	0.00201	0.20228	0.00443	0.00028	0.00065
	2.703	0.19675	0.00563	0.00030	0.00215	0.20991	0.00824	0.00034	0.00069
	3.343	0.17518	0.00833	0.00043	0.00171	0.18706	0.01244	0.00049	0.00055
	4.381	0.15207	0.02120	0.00062	0.00129	0.16245	0.03198	0.00071	0.00042
	5.410	0.23778	0.04958	0.00360	0.00315	0.25402	0.07485	0.00410	0.00102
	0.247	0.02164	0.00071	0.00034	0.00004	0.02529	0.00114	0.00047	0.00002
	0.348	0.03766	0.00077	0.00013	0.00011	0.04384	0.00120	0.00017	0.00007
	0.448	0.05159	0.00087	0.00013	0.00021	0.05986	0.00132	0.00017	0.00013
	0.548	0.06277	0.00098	0.00010	0.00031	0.07273	0.00148	0.00013	0.00020
	0.648	0.07471	0.00111	0.00009	0.00044	0.08647	0.00166	0.00012	0.00028
	0.748	0.08320	0.00125	0.00009	0.00054	0.09633	0.00188	0.00012	0.00035
	0.848	0.09675	0.00143	0.00015	0.00074	0.11196	0.00214	0.00020	0.00047
	0.948	0.10720	0.00163	0.00008	0.00090	0.12413	0.00244	0.00011	0.00058
	1.092	0.11901	0.00146	0.00010	0.00111	0.13707	0.00212	0.00013	0.00070
50–60%	1.292	0.12717	0.00184	0.00013	0.00127	0.14709	0.00274	0.00017	0.00081
$v_2\{\text{ZDC-SMD}\}$	1.492	0.14188	0.00243	0.00019	0.00158	0.16469	0.00370	0.00025	0.00101
	1.692	0.15811	0.00331	0.00021	0.00196	0.18411	0.00516	0.00028	0.00127
	1.892	0.15997	0.00439	0.00035	0.00201	0.18679	0.00701	0.00048	0.00131
	2.200	0.16724	0.00431	0.00037	0.00220	0.19518	0.00684	0.00051	0.00142
	2.703	0.18027	0.00776	0.00047	0.00255	0.21100	0.01265	0.00064	0.00166
	3.343	0.13888	0.01139	0.00041	0.00152	0.16274	0.01878	0.00056	0.00099
	4.381	0.12204	0.02867	0.00202	0.00117	0.14306	0.04745	0.00277	0.00077

[1] I. Arsene *et al.* (BRAHMS Collaboration), Nucl. Phys. **A757**, 1 (2005).
[2] K. Adcox *et al.* (PHENIX Collaboration), Nucl. Phys. **A757**, 184 (2005).
[3] B. B. Back *et al.* (PHOBOS Collaboration), Nucl. Phys. **A757**, 28 (2005).
[4] J. Adams *et al.* (STAR Collaboration), Nucl. Phys. **A757**, 102 (2005).
[5] M. Gyulassy and L. McLerran, Nucl. Phys. **A750**, 30 (2005).
[6] B. Muller, arXiv:nucl-th/0404015.
[7] E. V. Shuryak, Nucl. Phys. **A750**, 64 (2005).
[8] J.-Y. Ollitrault, Phys. Rev. D **46**, 229 (1992).
[9] P. F. Kolb, U. W. Heinz, P. Huovinen, K. J. Eskola, and K. Tuominen, Nucl. Phys. **A696**, 197 (2001).
[10] T. Hirano and Y. Nara, Nucl. Phys. **A743**, 305 (2004).
[11] N. N. Ajitanand (PHENIX Collaboration), Nucl. Phys. **A715**, 765 (2003).
[12] M. Chiu (PHENIX Collaboration), Nucl. Phys. **A715**, 761 (2003).
[13] C. Adler *et al.* (STAR Collaboration), Phys. Rev. Lett. **90**, 082302 (2003).
[14] S. S. Adler *et al.* (PHENIX Collaboration), Phys. Rev. C **71**, 051902 (2005).
[15] J. Adams *et al.* (STAR Collaboration), Phys. Rev. Lett. **95**, 152301 (2005).
[16] S. S. Adler *et al.* (PHENIX Collaboration), Phys. Rev. Lett. **97**, 052301 (2006).
[17] A. Adare *et al.* (PHENIX Collaboration), Phys. Rev. C **78**, 014901 (2008).
[18] M. Bleicher and H. Stoecker, Phys. Lett. **B526**, 309 (2002).
[19] S. S. Adler *et al.* (PHENIX Collaboration), Phys. Rev. Lett. **91**, 182301 (2003).
[20] Z. Xu, C. Greiner, and H. Stocker, J. Phys. G **35**, 104016 (2008).
[21] J. Adams *et al.* (STAR Collaboration), Phys. Rev. Lett. **92**, 052302 (2004).
[22] A. Adare *et al.* (PHENIX Collaboration), Phys. Rev. Lett. **98**, 162301 (2007).
[23] S. Huang (PHENIX Collaboration), J. Phys. G **35**, 104105 (2008).
[24] D. Molnár and S. A. Voloshin, Phys. Rev. Lett. **91**, 092301 (2003).
[25] R. J. Fries, B. Müller, C. Nonaka, and S. A. Bass, Phys. Rev. C **68**, 044902 (2003).
[26] V. Greco, C. M. Ko, and P. Lévai, Phys. Rev. C **68**, 034904 (2003).
[27] A. Shor, Phys. Rev. Lett. **54**, 1122 (1985).
[28] A. M. Poskanzer and S. A. Voloshin, Phys. Rev. C **58**, 1671 (1998).
[29] J. Jia (PHENIX Collaboration), Nucl. Phys. **A783**, 501 (2007).
[30] J. Putschke, J. Phys. G **34**, S679 (2007).
[31] B. Alver *et al.* (PHOBOS Collaboration), arXiv:0903.2811.
[32] P. Sorensen (STAR Collaboration), J. Phys. G **35**, 104102 (2008).
[33] M. Miller and R. Snellings, arXiv:nucl-ex/0312008.
[34] J.-Y. Ollitrault, A. M. Poskanzer, and S. A. Voloshin, Phys. Rev. C **80**, 014904 (2009).
[35] K. Adcox *et al.* (PHENIX Collaboration), Nucl. Instrum. Methods A **499**, 469 (2003).
[36] M. Allen *et al.* (PHENIX Collaboration), Nucl. Instrum. Methods A **499**, 549 (2003).
[37] C. Adler *et al.*, Nucl. Instrum. Methods A **499**, 433 (2003).
[38] M. L. Miller, K. Reygers, S. J. Sanders, and P. Steinberg, Annu. Rev. Nucl. Part. Sci. **57**, 205 (2007).
[39] R. J. Glauber and G. Matthiae, Nucl. Phys. **B21**, 135 (1970).
[40] K. Adcox *et al.* (PHENIX Collaboration), Phys. Rev. Lett. **86**, 3500 (2001).
[41] S. S. Adler *et al.* (PHENIX Collaboration), Phys. Rev. C **69**, 034910 (2004).
[42] J. T. Mitchell *et al.* (PHENIX Collaboration), Nucl. Instrum. Methods A **482**, 491 (2002).
[43] S. S. Adler *et al.* (PHENIX Collaboration), Phys. Rev. C **73**, 054903 (2006).
[44] N. Borghini, P. M. Dinh, and J.-Y. Ollitrault, Phys. Rev. C **64**, 054901 (2001).
[45] N. Borghini, P. M. Dinh, and J.-Y. Ollitrault, arXiv:nucl-ex/0110016.
[46] C. Alt *et al.* (NA49 Collaboration), Phys. Rev. C **68**, 034903 (2003).
[47] C. Adler *et al.* (STAR Collaboration), Phys. Rev. C **66**, 034904 (2002).
[48] I. Selyuzhenkov and S. Voloshin, Phys. Rev. C **77**, 034904 (2008).
[49] J. Adams *et al.* (STAR Collaboration), Phys. Rev. C **72**, 014904 (2005).
[50] B. Alver *et al.* (PHOBOS Collaboration), Phys. Rev. Lett. **98**, 242302 (2007).
[51] J. Adams *et al.* (STAR Collaboration), Phys. Rev. Lett. **93**, 252301 (2004).
[52] R. S. Bhalerao and J.-Y. Ollitrault, Phys. Lett. **B641**, 260 (2006).

Measurement of Bottom Versus Charm as a Function of Transverse Momentum with Electron-Hadron Correlations in $p + p$ Collisions at $\sqrt{s} = 200$ GeV

A. Adare,[11] S. Afanasiev,[25] C. Aidala,[12,36] N. N. Ajitanand,[53] Y. Akiba,[47,48] H. Al-Bataineh,[42] J. Alexander,[53] K. Aoki,[30,47] L. Aphecetche,[55] R. Armendariz,[42] S. H. Aronson,[6] J. Asai,[47,48] E. T. Atomssa,[31] R. Averbeck,[54] T. C. Awes,[43] B. Azmoun,[6] V. Babintsev,[21] M. Bai,[5] G. Baksay,[17] L. Baksay,[17] A. Baldisseri,[14] K. N. Barish,[7] P. D. Barnes,[33] B. Bassalleck,[41] A. T. Basye,[1] S. Bathe,[7] S. Batsouli,[43] V. Baublis,[46] C. Baumann,[37] A. Bazilevsky,[6] S. Belikov,[6,*] R. Bennett,[54] A. Berdnikov,[50] Y. Berdnikov,[50] A. A. Bickley,[11] J. G. Boissevain,[33] H. Borel,[14] K. Boyle,[54] M. L. Brooks,[33] H. Buesching,[6] V. Bumazhnov,[21] G. Bunce,[6,48] S. Butsyk,[33,54] C. M. Camacho,[33] S. Campbell,[54] B. S. Chang,[62] W. C. Chang,[2] J.-L. Charvet,[14] S. Chernichenko,[21] J. Chiba,[26] C. Y. Chi,[12] M. Chiu,[22] I. J. Choi,[62] R. K. Choudhury,[4] T. Chujo,[58,59] P. Chung,[53] A. Churyn,[21] V. Cianciolo,[43] Z. Citron,[54] C. R. Cleven,[19] B. A. Cole,[12] M. P. Comets,[44] P. Constantin,[33] M. Csanád,[16] T. Csörgő,[27] T. Dahms,[54] S. Dairaku,[30,47] K. Das,[18] G. David,[6] M. B. Deaton,[1] K. Dehmelt,[17] H. Delagrange,[55] A. Denisov,[21] D. d'Enterria,[12,31] A. Deshpande,[48,54] E. J. Desmond,[6] O. Dietzsch,[51] A. Dion,[54] M. Donadelli,[51] O. Drapier,[31] A. Drees,[54] K. A. Drees,[5] A. K. Dubey,[61] A. Durum,[21] D. Dutta,[4] V. Dzhordzhadze,[7] Y. V. Efremenko,[43] J. Egdemir,[54] F. Ellinghaus,[11] W. S. Emam,[7] T. Engelmore,[12] A. Enokizono,[32] H. En'yo,[47,48] S. Esumi,[58] K. O. Eyser,[7] B. Fadem,[38] D. E. Fields,[41,48] M. Finger, Jr.,[8,25] M. Finger,[8,25] F. Fleuret,[31] S. L. Fokin,[29] Z. Fraenkel,[61,*] J. E. Frantz,[54] A. Franz,[6] A. D. Frawley,[18] K. Fujiwara,[47] Y. Fukao,[30,47] T. Fusayasu,[40] S. Gadrat,[34] I. Garishvili,[56] A. Glenn,[11] H. Gong,[54] M. Gonin,[31] J. Gosset,[14] Y. Goto,[47,48] R. Granier de Cassagnac,[31] N. Grau,[12,24] S. V. Greene,[59] M. Grosse Perdekamp,[22,48] T. Gunji,[10] H.-Å. Gustafsson,[35] T. Hachiya,[20] A. Hadj Henni,[55] C. Haegemann,[41] J. S. Haggerty,[6] H. Hamagaki,[10] R. Han,[45] H. Harada,[20] E. P. Hartouni,[32] K. Haruna,[20] E. Haslum,[35] R. Hayano,[10] M. Heffner,[32] T. K. Hemmick,[54] T. Hester,[7] X. He,[19] H. Hiejima,[22] J. C. Hill,[24] R. Hobbs,[41] M. Hohlmann,[17] W. Holzmann,[53] K. Homma,[20] B. Hong,[28] T. Horaguchi,[10,47,57] D. Hornback,[56] S. Huang,[59] T. Ichihara,[47,48] R. Ichimiya,[47] Y. Ikeda,[58] K. Imai,[30,47] J. Imrek,[15] M. Inaba,[58] Y. Inoue,[49,47] D. Isenhower,[1] L. Isenhower,[1] M. Ishihara,[47] T. Isobe,[10] M. Issah,[53] A. Isupov,[25] D. Ivanischev,[46] B. V. Jacak,[54,†] J. Jia,[12] J. Jin,[12] O. Jinnouchi,[48] B. M. Johnson,[6] K. S. Joo,[39] D. Jouan,[44] F. Kajihara,[10] S. Kametani,[10,47,60] N. Kamihara,[47,48] J. Kamin,[54] M. Kaneta,[48] J. H. Kang,[62] H. Kanou,[47,57] J. Kapustinsky,[33] D. Kawall,[36,48] A. V. Kazantsev,[29] T. Kempel,[24] A. Khanzadeev,[46] K. M. Kijima,[20] J. Kikuchi,[60] B. I. Kim,[28] D. H. Kim,[39] D. J. Kim,[62] E. Kim,[52] S. H. Kim,[62] E. Kinney,[11] K. Kiriluk,[11] A. Kiss,[16] E. Kistenev,[6] A. Kiyomichi,[47] J. Klay,[32] C. Klein-Boesing,[37] L. Kochenda,[46] V. Kochetkov,[21] B. Komkov,[46] M. Konno,[58] J. Koster,[22] D. Kotchetkov,[7] A. Kozlov,[61] A. Král,[13] A. Kravitz,[12] J. Kubart,[8,23] G. J. Kunde,[33] N. Kurihara,[10] K. Kurita,[49,47] M. Kurosawa,[47] M. J. Kweon,[28] Y. Kwon,[56,62] G. S. Kyle,[42] R. Lacey,[53] Y.-S. Lai,[12] Y. S. Lai,[12] J. G. Lajoie,[24] D. Layton,[22] A. Lebedev,[24] D. M. Lee,[33] K. B. Lee,[28] M. K. Lee,[62] T. Lee,[52] M. J. Leitch,[33] M. A. L. Leite,[51] B. Lenzi,[51] P. Liebing,[48] T. Liška,[13] A. Litvinenko,[25] H. Liu,[42] M. X. Liu,[33] X. Li,[9] B. Love,[59] D. Lynch,[6] C. F. Maguire,[59] Y. I. Makdisi,[5] A. Malakhov,[25] M. D. Malik,[41] V. I. Manko,[29] E. Mannel,[12] Y. Mao,[45,47] L. Mašek,[8,23] H. Masui,[58] F. Matathias,[12] M. McCumber,[54] P. L. McGaughey,[33] N. Means,[54] B. Meredith,[22] Y. Miake,[58] P. Mikeš,[8,23] K. Miki,[58] T. E. Miller,[59] A. Milov,[6,54] S. Mioduszewski,[6] M. Mishra,[3] J. T. Mitchell,[6] M. Mitrovski,[53] A. K. Mohanty,[4] Y. Morino,[10] A. Morreale,[7] D. P. Morrison,[6] T. V. Moukhanova,[29] D. Mukhopadhyay,[59] J. Murata,[49,47] S. Nagamiya,[26] Y. Nagata,[58] J. L. Nagle,[11] M. Naglis,[61] M. I. Nagy,[16] I. Nakagawa,[47,48] Y. Nakamiya,[20] T. Nakamura,[20] K. Nakano,[47,57] J. Newby,[32] M. Nguyen,[54] T. Niita,[58] B. E. Norman,[33] R. Nouicer,[6] A. S. Nyanin,[29] E. O'Brien,[6] S. X. Oda,[10] C. A. Ogilvie,[24] H. Ohnishi,[47] H. Okada,[30,47] K. Okada,[48] M. Oka,[58] O. O. Omiwade,[1] Y. Onuki,[47] A. Oskarsson,[35] M. Ouchida,[20] K. Ozawa,[10] R. Pak,[6] D. Pal,[59] A. P. T. Palounek,[33] V. Pantuev,[54] V. Papavassiliou,[42] J. Park,[52] W. J. Park,[28] S. F. Pate,[42] H. Pei,[24] J.-C. Peng,[22] H. Pereira,[14] V. Peresedov,[25] D. Yu. Peressounko,[29] C. Pinkenburg,[6] M. L. Purschke,[6] A. K. Purwar,[33] H. Qu,[19] J. Rak,[41] A. Rakotozafindrabe,[31] I. Ravinovich,[61] K. F. Read,[43,56] S. Rembeczki,[17] M. Reuter,[54] K. Reygers,[37] V. Riabov,[46] Y. Riabov,[46] D. Roach,[59] G. Roche,[34] S. D. Rolnick,[7] A. Romana,[31,*] M. Rosati,[24] S. S. E. Rosendahl,[35] P. Rosnet,[34] P. Rukoyatkin,[25] P. Ružička,[23] V. L. Rykov,[47] B. Sahlmueller,[37] N. Saito,[30,47,48] T. Sakaguchi,[6] S. Sakai,[58] K. Sakashita,[47,57] H. Sakata,[20] V. Samsonov,[46] S. Sato,[26] T. Sato,[58] S. Sawada,[26] K. Sedgwick,[7] J. Seele,[11] R. Seidl,[22] A. Yu. Semenov,[24] V. Semenov,[21] R. Seto,[7] D. Sharma,[61] I. Shein,[21] A. Shevel,[46,53] T.-A. Shibata,[47,57] K. Shigaki,[20] M. Shimomura,[58] K. Shoji,[30,47] P. Shukla,[4] A. Sickles,[6,54] C. L. Silva,[51] D. Silvermyr,[43] C. Silvestre,[14] K. S. Sim,[28] B. K. Singh,[3] C. P. Singh,[3] V. Singh,[3] S. Skutnik,[24] M. Slunečka,[8,25] A. Soldatov,[21] R. A. Soltz,[32] W. E. Sondheim,[33] S. P. Sorensen,[56] I. V. Sourikova,[6] F. Staley,[14] P. W. Stankus,[43] E. Stenlund,[35] M. Stepanov,[42] A. Ster,[27] S. P. Stoll,[6] T. Sugitate,[20] C. Suire,[44] A. Sukhanov,[6] J. Sziklai,[27] T. Tabaru,[48] S. Takagi,[58] E. M. Takagui,[51] A. Taketani,[47,48]

 © 2009 The American Physical Society

R. Tanabe,[58] Y. Tanaka,[40] K. Tanida,[47,48] M. J. Tannenbaum,[6] A. Taranenko,[53] P. Tarján,[15] H. Themann,[54] T. L. Thomas,[41] M. Togawa,[30,47] A. Toia,[54] J. Tojo,[47] L. Tomášek,[23] Y. Tomita,[58] H. Torii,[20,47] R. S. Towell,[1] V-N. Tram,[31] I. Tserruya,[61] Y. Tsuchimoto,[20] C. Vale,[24] H. Valle,[59] H. W. van Hecke,[33] A. Veicht,[22] J. Velkovska,[59] R. Vertesi,[15] A. A. Vinogradov,[29] M. Virius,[13] V. Vrba,[23] E. Vznuzdaev,[46] M. Wagner,[30,47] D. Walker,[54] X. R. Wang,[42] Y. Watanabe,[47,48] F. Wei,[24] J. Wessels,[37] S. N. White,[6] D. Winter,[12] C. L. Woody,[6] M. Wysocki,[11] W. Xie,[48] Y. L. Yamaguchi,[60] K. Yamaura,[20] R. Yang,[22] A. Yanovich,[21] Z. Yasin,[7] J. Ying,[19] S. Yokkaichi,[47,48] G. R. Young,[43] I. Younus,[41] I. E. Yushmanov,[29] W. A. Zajc,[12] O. Zaudtke,[37] C. Zhang,[43] S. Zhou,[9] J. Zimányi,[27,*] and L. Zolin[25]

(PHENIX Collaboration)

[1]*Abilene Christian University, Abilene, Texas 79699, USA*
[2]*Institute of Physics, Academia Sinica, Taipei 11529, Taiwan*
[3]*Department of Physics, Banaras Hindu University, Varanasi 221005, India*
[4]*Bhabha Atomic Research Centre, Bombay 400 085, India*
[5]*Collider-Accelerator Department, Brookhaven National Laboratory, Upton, New York 11973-5000, USA*
[6]*Physics Department, Brookhaven National Laboratory, Upton, New York 11973-5000, USA*
[7]*University of California - Riverside, Riverside, California 92521, USA*
[8]*Charles University, Ovocný trh 5, Praha 1, 116 36, Prague, Czech Republic*
[9]*China Institute of Atomic Energy (CIAE), Beijing, People's Republic of China*
[10]*Center for Nuclear Study, Graduate School of Science, University of Tokyo, 7-3-1 Hongo, Bunkyo, Tokyo 113-0033, Japan*
[11]*University of Colorado, Boulder, Colorado 80309, USA*
[12]*Columbia University, New York, New York 10027 and Nevis Laboratories, Irvington, New York 10533, USA*
[13]*Czech Technical University, Zikova 4, 166 36 Prague 6, Czech Republic*
[14]*Dapnia, CEA Saclay, F-91191, Gif-sur-Yvette, France*
[15]*Debrecen University, H-4010 Debrecen, Egyetem tér 1, Hungary*
[16]*ELTE, Eötvös Loránd University, H - 1117 Budapest, Pázmány P. s. 1/A, Hungary*
[17]*Florida Institute of Technology, Melbourne, Florida 32901, USA*
[18]*Florida State University, Tallahassee, Florida 32306, USA*
[19]*Georgia State University, Atlanta, Georgia 30303, USA*
[20]*Hiroshima University, Kagamiyama, Higashi-Hiroshima 739-8526, Japan*
[21]*IHEP Protvino, State Research Center of Russian Federation, Institute for High Energy Physics, Protvino, 142281, Russia*
[22]*University of Illinois at Urbana-Champaign, Urbana, Illinois 61801, USA*
[23]*Institute of Physics, Academy of Sciences of the Czech Republic, Na Slovance 2, 182 21 Prague 8, Czech Republic*
[24]*Iowa State University, Ames, Iowa 50011, USA*
[25]*Joint Institute for Nuclear Research, 141980 Dubna, Moscow Region, Russia*
[26]*KEK, High Energy Accelerator Research Organization, Tsukuba, Ibaraki 305-0801, Japan*
[27]*KFKI Research Institute for Particle and Nuclear Physics of the Hungarian Academy of Sciences (MTA KFKI RMKI), H-1525 Budapest 114, Post Office Box 49, Budapest, Hungary*
[28]*Korea University, Seoul, 136-701, Korea*
[29]*Russian Research Center "Kurchatov Institute", Moscow, Russia*
[30]*Kyoto University, Kyoto 606-8502, Japan*
[31]*Laboratoire Leprince-Ringuet, Ecole Polytechnique, CNRS-IN2P3, Route de Saclay, F-91128, Palaiseau, France*
[32]*Lawrence Livermore National Laboratory, Livermore, California 94550, USA*
[33]*Los Alamos National Laboratory, Los Alamos, New Mexico 87545, USA*
[34]*LPC, Université Blaise Pascal, CNRS-IN2P3, Clermont-Fd, 63177 Aubiere Cedex, France*
[35]*Department of Physics, Lund University, Box 118, SE-221 00 Lund, Sweden*
[36]*Department of Physics, University of Massachusetts, Amherst, Massachusetts 01003-9337, USA*
[37]*Institut für Kernphysik, University of Muenster, D-48149 Muenster, Germany*
[38]*Muhlenberg College, Allentown, Pennsylvania 18104-5586, USA*
[39]*Myongji University, Yongin, Kyonggido 449-728, Korea*
[40]*Nagasaki Institute of Applied Science, Nagasaki-shi, Nagasaki 851-0193, Japan*
[41]*University of New Mexico, Albuquerque, New Mexico 87131, USA*
[42]*New Mexico State University, Las Cruces, New Mexico 88003, USA*
[43]*Oak Ridge National Laboratory, Oak Ridge, Tennessee 37831, USA*
[44]*IPN-Orsay, Universite Paris Sud, CNRS-IN2P3, BP1, F-91406, Orsay, France*
[45]*Peking University, Beijing, People's Republic of China*
[46]*PNPI, Petersburg Nuclear Physics Institute, Gatchina, Leningrad region, 188300, Russia*
[47]*RIKEN Nishina Center for Accelerator-Based Science, Wako, Saitama 351-0198, Japan*
[48]*RIKEN BNL Research Center, Brookhaven National Laboratory, Upton, New York 11973-5000, USA*

[49]Physics Department, Rikkyo University, 3-34-1 Nishi-Ikebukuro, Toshima, Tokyo 171-8501, Japan
[50]Saint Petersburg State Polytechnic University, St. Petersburg, Russia
[51]Universidade de São Paulo, Instituto de Física, Caixa Postal 66318, São Paulo CEP05315-970, Brazil
[52]System Electronics Laboratory, Seoul National University, Seoul, Korea
[53]Chemistry Department, Stony Brook University, Stony Brook, SUNY, New York 11794-3400, USA
[54]Department of Physics and Astronomy, Stony Brook University, SUNY, Stony Brook, New York 11794, USA
[55]SUBATECH (Ecole des Mines de Nantes, CNRS-IN2P3, Université de Nantes) BP 20722 - 44307, Nantes, France
[56]University of Tennessee, Knoxville, Tennessee 37996, USA
[57]Department of Physics, Tokyo Institute of Technology, Oh-okayama, Meguro, Tokyo 152-8551, Japan
[58]Institute of Physics, University of Tsukuba, Tsukuba, Ibaraki 305, Japan
[59]Vanderbilt University, Nashville, Tennessee 37235, USA
[60]Waseda University, Advanced Research Institute for Science and Engineering, 17 Kikui-cho, Shinjuku-ku, Tokyo 162-0044, Japan
[61]Weizmann Institute, Rehovot 76100, Israel
[62]Yonsei University, IPAP, Seoul 120-749, Korea

(Received 29 March 2009; published 18 August 2009)

The momentum distribution of electrons from semileptonic decays of charm and bottom quarks for midrapidity $|y| < 0.35$ in $p + p$ collisions at $\sqrt{s} = 200$ GeV is measured by the PHENIX experiment at the Relativistic Heavy Ion Collider over the transverse momentum range $2 < p_T < 7$ GeV/c. The ratio of the yield of electrons from bottom to that from charm is presented. The ratio is determined using partial $D/\bar{D} \to e^{\pm}K^{\mp}X$ (K unidentified) reconstruction. It is found that the yield of electrons from bottom becomes significant above 4 GeV/c in p_T. A fixed-order-plus-next-to-leading-log perturbative quantum chromodynamics calculation agrees with the data within the theoretical and experimental uncertainties. The extracted total bottom production cross section at this energy is $\sigma_{b\bar{b}} = 3.2^{+1.2}_{-1.1}(\text{stat})^{+1.4}_{-1.3}(\text{syst})\mu b$.

DOI: 10.1103/PhysRevLett.103.082002 PACS numbers: 13.85.Qk, 13.20.Fc, 13.20.He, 25.75.Dw

Measurements of heavy flavor production (charm and bottom) in $p + p$ collisions present stringent tests for perturbative quantum chromodynamics (pQCD) calculations. For instance, while bottom production at the Tevatron is well described by next-to-leading order (NLO) pQCD [1], the cross section for charm production at high p_T, though compatible within the theoretical uncertainties, is higher than the preferred theoretical value by ~50% [2]. Measurement of heavy flavor in $p + p$ collisions also provides an important baseline for study of the medium created in relativistic heavy-ion collisions. The PHENIX experiment at the Relativistic Heavy Ion Collider (RHIC) has measured single electrons from the semileptonic decay of heavy flavor at midrapidity in $p + p$ and Au + Au collisions at $\sqrt{s_{NN}} = 200$ GeV [3,4]. Strong suppression of the single electron yield at high p_T, which includes contributions from both charm and bottom decays, was observed in central Au + Au collisions [4]. This effect is conventionally attributed to energy loss by the parent parton in the medium [5]; one also expects the energy loss suffered by bottom quarks to be significantly less than that suffered by charm quarks due to the difference in their masses [6,7]. Clearly, for both pQCD comparisons and the heavy-ion reference, one wants to disentangle the yields of charm and bottom at RHIC energies.

In this Letter, we present the yield ratio of single electrons from bottom to those from heavy flavor at midrapidity in $p + p$ collisions at $\sqrt{s} = 200$ GeV, using partial $D/\bar{D} \to e^{\pm}K^{\mp}X$ (K unidentified) reconstruction. The data were collected with the PHENIX detector [8] in the 2005 and 2006 RHIC runs using its two central arm spectrometers. Each spectrometer covers $|\eta| < 0.35$ in pseudorapidity and $\Delta\phi = \pi/2$ in azimuth. The arms include drift chambers (DC) and pad chambers (PC1,2,3) for charged particle tracking, a ring imaging Čerenkov detector (RICH) and an electromagnetic calorimeter (EMCal) for electron identification and triggering. Beam-beam counters (BBCs), covering pseudorapidity $3.1 < |\eta| < 3.9$, measure the position of the collision vertex along the beam (z_{vtx}) and provide the interaction trigger. In the 2005 run, helium bags were placed in the space between the beam pipe and DC to reduce photon conversions. The bags were removed in 2006.

Two data sets are used for the analysis: (i) a minimum bias (MB) data set recorded with the BBC trigger, and (ii) an electron enriched sample, recorded with a level-1 "ERT" trigger requiring a combination of EMCal and RICH information in coincidence with the BBC trigger. The BBC trigger cross section is 23.0 ± 2.2 mb [9]. The BBC trigger selects ~53% of inelastic $p + p$ collisions and $(79 \pm 2)\%$ of hard scattering events, such as those with high-p_T particles at midrapidity. The latter efficiency is approximately p_T and particle independent, which was verified by the observed ratio of high-p_T pion and eta yields with and without the BBC trigger, and confirmed with a Monte Carlo simulation [9,10]. After selection of good runs and a vertex cut of $|z_{\text{vtx}}| < 25$ cm, an integrated luminosity ($\int Ldt$) in the ERT data of 1.77 pb^{-1} in the 2005 run and 4.22 pb^{-1} in the 2006 run are used for this analysis.

Charged particle tracks are reconstructed using the DC and PC1. The momentum resolution is ~1% at

$p_T \sim 1$ GeV/c, and the momentum scale is calibrated within 1%. Electron identification (eID) is performed using the RICH and EMCal. The purity of the electron sample is better than 99% for $1 < p_T < 5$ GeV/c [3]. Our previous measurement [3] determined the spectrum of the single electrons from heavy flavor in the 2005 run. Inclusive electron spectra from the 2005 run and the 2006 run are consistent within 5% after taking into account a contribution from the increased photon conversion due to the absence of the helium bags.

The spectrum of the single electrons from heavy flavor is determined using the "cocktail method" [3,4]. The electron spectrum from all known sources except semileptonic decay of heavy flavor is calculated using a Monte Carlo simulation and subtracted from the inclusive spectrum in the cocktail method. The dominant source of background is the π^0 Dalitz decay. The cocktail also includes contributions from quarkonium (J/ψ, Υ) and the Drell-Yan process, which were neglected in our previous measurements [3,4]. These contributions are negligible (smaller than 1% in background) for $p_T < 1$ GeV/c, but become significant at high p_T (above 10% for $p_T > 2.5$ GeV/c) [11]. The signal to background ratio increases with increasing p_T, approaching unity for $p_T \sim 3$ GeV/c [3].

The systematic uncertainties of the inclusive electron spectrum includes the uncertainty in luminosity (9.6%), geometrical acceptance (3%), eID efficiency (2%), and the ERT trigger efficiency (4% at $p_T > 2$ GeV/c). The uncertainty in the cocktail method is p_T dependent (3% at $p_T \sim 2$ GeV/c, increasing to 9% at 9 GeV/c).

The ratio of $(b \to e)$ to $[(c \to e) + (b \to e)]$ is extracted from the correlation between the heavy flavor electrons and associated hadrons [12,13]. The extraction is based on partial reconstruction of the $D/\bar{D} \to e^{\pm}K^{\mp}X$ decay. The invariant mass of unlike charge-sign electron-hadron pairs reveals a correlated signal below the D meson mass of ~ 1.9 GeV/c^2, because of the charge correlation in the D decays. Pairs are formed between a trigger electron ($2.0 < p_T < 7.0$ GeV/c) and an oppositely charged hadron ($0.4 < p_T < 5.0$ GeV/c). The hadron p_T is required to be less than 5 GeV/c, because pions also emit Čerenkov photons in the RICH above 5 GeV/c. The acceptances of positive and negative charged particles are forced to be identical by a geometrical acceptance cut. Since the momentum range of good charged kaon identification is limited, K identification is not performed but the mass of all reconstructed hadrons is set to be that of the K. Most e^+e^- pairs are then removed by an electron veto cut for the hadrons. The reconstructed mass of e^+e^- pairs has a clear peak at low mass. The remaining background e^+e^- pairs are removed by requiring $M_{ee} > 80$ MeV/c^2, where the pair mass is calculated assuming both particles in the pair are electrons.

Depending on the origin of the trigger electrons, the inclusive reconstructed electron-hadron pairs are (i) unlike-sign pairs from charm, (ii) unlike-sign pairs from bottom, (iii) combinatorial background where the electron is a background electron and (iv) background from unlike-sign hadron-hadron pairs due to hadron contamination in the electrons. The main background source is the combinatorial background (iii) and almost all background electrons are from e^+e^- pair creation. Like-sign electron-hadron pairs are used to subtract this background. Since electrons from e^+e^- pair creation and hadrons do not contribute to charge correlated signals, subtraction using like-sign pairs cancels out completely the combinatorial background where the trigger electron is from e^+e^- pair creation (iii). Only the negligibly small (<1%) contribution from K^0_{e3} decay is not canceled out by the subtraction in the background (iii). The contribution from

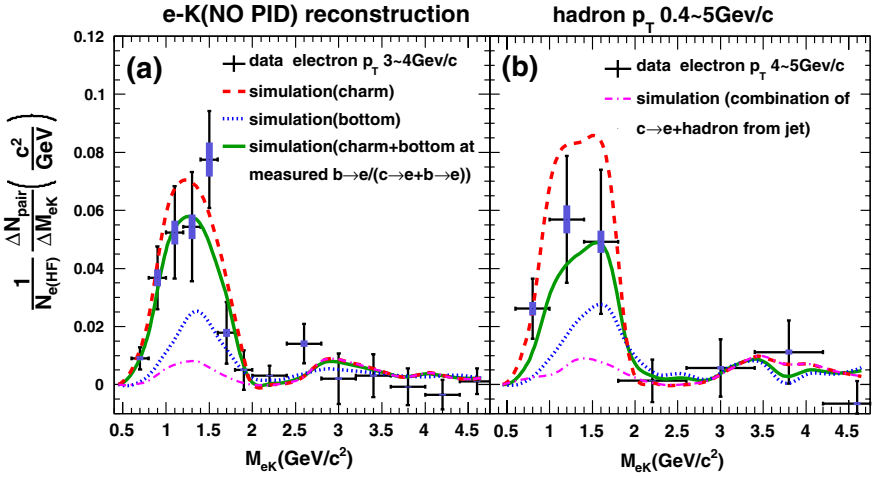

FIG. 1 (color online). Comparison of data to a PYTHIA and EVTGEN [14,15] simulation of the invariant mass distributions in PHENIX acceptance for the reconstructed signal in the 2006 run. The electron p_T range is 3.0–4.0 GeV/c (a) and 4.0–5.0 GeV/c (b). The ratios, $(b \to e)/[(c \to e) + (b \to e)]$, in solid lines are 0.26 (a) and 0.63 (b). Error bars (boxes) indicate statistical (systematic) uncertainties.

hadron contamination (iv) is also less than a 1% effect due to the excellent electron identification. After the subtraction, the reconstructed pairs include a contribution from bottom (ii) due to not identifying K. The contribution from bottom (ii) is much smaller than that from charm (i) due to the bottom decay modes and kinematics. The reconstructed pairs also contain a signal from partial reconstruction of heavy flavor hadrons and a contribution from a combination of heavy flavor electrons and hadrons from jet fragmentation. The ratio of the yield of unlike-sign pairs to that of like-sign pairs is about 1.1 for invariant masses (M_{eK}) below 1.9 GeV/c^2.

The fraction of bottom contribution to the electrons from heavy flavor is obtained as follows:

$$\frac{b \to e}{(c \to e) + (b \to e)} = \frac{\epsilon_c - \epsilon_{\rm data}}{\epsilon_c - \epsilon_b}, \quad (1)$$

where $\epsilon_{\rm data}$ is the tagging efficiency in real data and $\epsilon_{c(b)}$ is the tagging efficiency for charm (bottom) production. These are defined as

$$\epsilon_{\rm data} \equiv \frac{N_{\rm pair}}{N_{e({\rm HF})}} = \frac{N_{c\to{\rm tag}} + N_{b\to{\rm tag}}}{(c \to e) + (b \to e)}, \quad (2)$$

$$\epsilon_c \equiv \frac{N_{c\to{\rm tag}}}{c \to e}, \qquad \epsilon_b \equiv \frac{N_{b\to{\rm tag}}}{b \to e}, \quad (3)$$

where $N_{e({\rm HF})}$ is the number of measured heavy flavor electrons. $N_{\rm pair}$ is the number of background subtracted unlike-sign electron-hadron pairs for invariant mass within $0.4 < M_{eK} < 1.9$ GeV/c^2, which corresponds to the mass range of charmed hadrons. Here, $N_{c(b)\to{\rm tag}}$ is the number of reconstructed signals within $0.4 < M_{eK} < 1.9$ GeV/c^2 for charm (bottom) production.

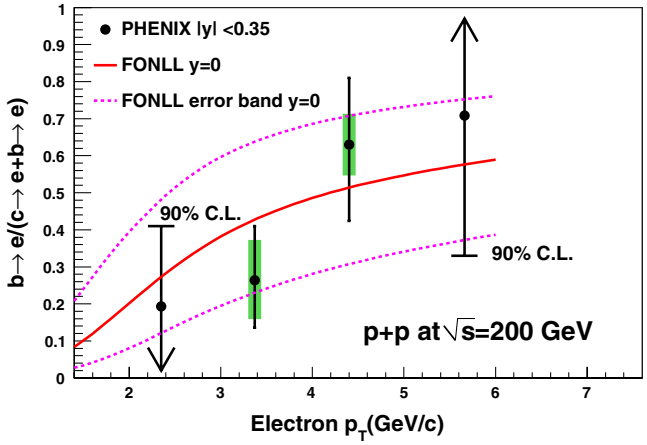

FIG. 2 (color online). $(b \to e)/[(c \to e) + (b \to e)]$ as a function of electron p_T compared to a FONLL calculation [20]. The points show the experimental result. Vertical arrows are used to indicate upper and lower limits. The solid line is a FONLL prediction and the dotted lines represent the uncertainty of this FONLL prediction.

Figure 1 shows the M_{eK} distribution of the reconstructed signals, which is normalized by the yield of heavy flavor electrons ($N_{e({\rm HF})}$) in the range $3 < p_T < 4$ GeV/c [panel (a)] and $4 < p_T < 5$ GeV/c [panel (b)]. The tagging efficiency in real data, $\epsilon_{\rm data}$, is determined by the integration of the M_{eK} distribution in Fig. 1 from $M_{eK} = 0.4$ to 1.9 GeV/c^2 as a function of electron p_T.

The tagging efficiencies for charm and bottom production, ϵ_c and ϵ_b, are calculated with the combination of PYTHIA and EVTGEN [14,15]. PYTHIA is used to simulate charm and bottom production in $p + p$ collisions at $\sqrt{s} =$ 200 GeV and is tuned to reproduce heavy flavor hadron ratios: $D^+/D^0 = 0.45 \pm 0.10$, $D_s/D_0 = 0.25 \pm 0.10$, $\Lambda_c/D^0 = 0.10 \pm 0.05$, $B^+/B^0 = 0.50$, $B_s/B_0 = 0.40 \pm 0.20$, and $B_{\rm baryon}/B^0 = 0.20 \pm 0.15$ [11,16–19]. The Monte Carlo simulation EVTGEN, which is suited for decays of D and B hadrons, is used to simulate the semileptonic decays. The dashed (dotted) lines in Fig. 1 show the M_{eK} distributions of the reconstructed signal for the simulated charm (bottom) production for an electron $3 < p_T < 4$ GeV/c (panel a) and $4 < p_T < 5$ GeV/c [panel (b)]. Some fluctuations in the simulated curves in Fig. 1 come from the limited statistics in the simulation, but the statistical uncertainties in the simulation are negligible compared to that of the data. $\epsilon_{c(b)}$ is determined in the same way as $\epsilon_{\rm data}$ from the M_{eK} distribution for charm (bottom) production. Since about 85% of the extracted

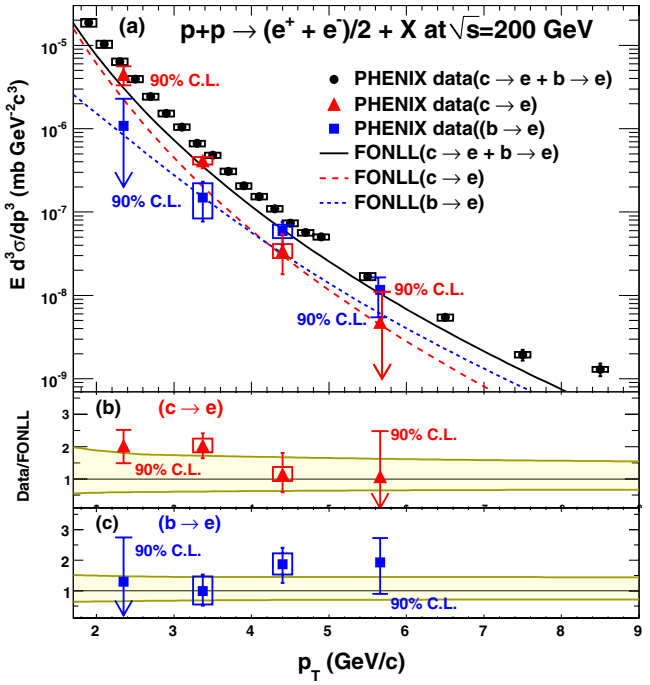

FIG. 3 (color online). (a) Invariant cross sections of electrons from charm and bottom with the FONLL calculation [20]. (b) and (c) The ratios of data points over the FONLL prediction as a function of electron p_T for charm and bottom. The shaded area shows the uncertainty in the FONLL prediction.

signal comes from partial reconstruction of heavy flavor hadrons, the tagging efficiency is determined largely by decay kinematics and $\epsilon_{c(b)}$ can be determined with good precision. The dot-dash lines in Fig. 1 show the contribution from the combination of an electron from charm and hadrons from jet fragmentation for charm production. The solid line in Fig. 1 shows the sum of the M_{eK} distributions for charm and bottom in the simulation with the ratio, $(b \to e)/[(c \to e) + (b \to e)]$, obtained with Eq. (1).

Systematic uncertainties are categorized into two parts related to (i) ϵ_{data} in the real data analysis and (ii) ϵ_c and ϵ_b in the simulation study. The dominant uncertainty in $\epsilon_{\rm data}$ is the uncertainty in the number of heavy flavor electrons (~10%). Uncertainty in $\epsilon_{\rm data}$ also includes a background subtraction uncertainty (1%–10%, p_T dependent). Category (2) includes the uncertainties in geometrical acceptance (3%) and the event generator (~8% for charm and ~9% for bottom). The event generator uncertainty is based on uncertainties, which are known in the production ratios of heavy flavor hadrons (D^+/D^0, D_s/D^0, etc.), known in the branching ratios [16–19], estimated in the momentum distribution of heavy flavor hadrons and estimated in the PYTHIA parameters.

Figure 2 shows the resulting bottom fraction, $(b \to e)/[(c \to e) + (b \to e)]$ as a function of electron p_T compared to a fixed-order-plus-next-to-leading-log perturbative QCD calculation (FONLL) [20]. In this figure, the points show the measured $(b \to e)/[(c \to e) + (b \to e)]$. For the bins with electron p_T ranges $2 < p_T < 3$ and $5 < p_T < 7$ GeV/c, 90% C.L. and mean values are shown. The solid line shows the central value of the FONLL prediction and the dotted lines show its uncertainty.

In Fig. 3, the single electron spectra for charm and bottom are measured from the ratio, $(b \to e)/[(c \to e) + (b \to e)]$, and the spectrum of the electrons from heavy flavor decays. The top panel shows the resulting single electron spectra from charm (triangles) and bottom (squares) compared to the FONLL predictions [20]. The measured spectrum of single electrons (circles) is also shown for reference. The middle (bottom) panel shows the ratio of the measured cross sections to the FONLL calculation for charm (bottom) production. The shaded area shows the uncertainty in the FONLL prediction. The larger mass makes this uncertainty smaller in the case of bottom quarks. These calculations agree with the data for bottom production within the large theoretical and experimental uncertainty. The same is true for charm within the theoretical uncertainty with a ratio of data/FONLL of ~2. A similar tendency was obtained at the Tevatron [1,2].

The electron spectrum from bottom shown in Fig. 3 is integrated from $p_T = 3$ to 5 GeV/c and gives $4.8^{+1.8}_{-1.6}(\text{stat})^{+1.9}_{-1.8}(\text{syst})$ nb. This spectrum is then extrapolated to $p_T = 0$ using the shape predicted by pQCD. PYTHIA with varying intrinsic k_T ($1.5 < k_T < 10$ GeV/c) and FONLL with varying factorization (μ_F) and renormalization (μ_R) scales ($0.5 < \mu_{F,R}/\sqrt{m^2 + p_T^2} < 2$) are used to evaluate the systematic uncertainty (12%) to this extrapolation. The extrapolation results in a bottom cross section at midrapidity of $d\sigma_{b\bar{b}}/dy\,|_{y=0} = 0.92^{+0.34}_{-0.31}(\text{stat})^{+0.39}_{-0.36}(\text{syst})\mu b$, using a $b \to e$ total branching ratio of 10 ± 1%, calculated using the heavy flavor hadron ratios described above. Using HVQMNR [21] with CTEQ5M [22] parton distribution functions (PDF's) to integrate over rapidity, the total bottom cross section is determined to be $\sigma_{b\bar{b}} = 3.2^{+1.2}_{-1.1}(\text{stat})^{+1.4}_{-1.3}(\text{syst})\mu b$. Various PDF's and bottom mass values are used to evaluate the systematic uncertainty (8%) of the rapidity extrapolation. This result is consistent with our result from the dielectron spectrum, which gave $\sigma_{b\bar{b}} = 3.9 \pm 2.5(\text{stat})^{+3}_{-2}(\text{syst})\mu b$ [23]. FONLL predicts $\sigma_{b\bar{b}} = 1.87^{+0.99}_{-0.67}\mu b$, in agreement with both these experimental results.

The fraction of bottom in heavy flavor electrons is found to be larger than 0.33 with 90% confidence level at $p_T > 5$ GeV/c. Furthermore, the assumption of no bottom suppression directly leads to a lower limit on the nuclear modification factor of single electrons, R_{AA}, of greater than 0.33 with the same confidence level. However, according to our measurements, R_{AA} is $\sim 0.25 \pm 0.05(\text{stat}) \pm 0.05(\text{syst})$ at $5 < p_T < 6$ GeV/c [4] in the 0–10% central Au + Au collisions. At the same time the current level of uncertainty in the measurement precludes us from placing significant limits on the possible energy loss of bottom quarks.

In conclusion, the ratio of the yield of electrons from bottom to that from charm has been measured in $p + p$ collisions at $\sqrt{s} = 200$ GeV. The ratio provides the first measurement of the spectrum of electrons from bottom at RHIC. FONLL calculations [20] agree with this result, which provides an important baseline for the study of heavy quark production in the hot and dense matter created in Au + Au collisions.

We thank the staff of the Collider-Accelerator and Physics Departments at BNL for their vital contributions. We acknowledge support from the Office of Nuclear Physics in DOE Office of Science, NSF and a sponsored research grant from Renaissance Technologies (USA), MEXT and JSPS (Japan), CNPq and FAPESP (Brazil), NSFC (China), MSMT (Czech Republic), IN2P3/CNRS, and CEA (France), BMBF, DAAD, and AvH (Germany), OTKA (Hungary), DAE (India), ISF (Israel), KRF and KOSEF (Korea), MES, RAS, and FAAE (Russia), VR and KAW (Sweden), U.S. CRDF for the FSU, US-Hungary Fulbright, and US-Israel BSF.

*Deceased.
†PHENIX spokesperson.
jacak@skipper.physics.sunysb.edu

[1] D. Acosta *et al.*, Phys. Rev. D **71**, 032001 (2005).

[2] D. Acosta *et al.*, Phys. Rev. Lett. **91**, 241804 (2003).
[3] A. Adare *et al.*, Phys. Rev. Lett. **97**, 252002 (2006).
[4] S. S. Adler *et al.*, Phys. Rev. Lett. **98**, 172301 (2007).
[5] M. Gyulassy and M. Plumer, Phys. Lett. B **243**, 432 (1990).
[6] Y. L. Dokshitzer and D. E. Kharzeev, Phys. Lett. B **519**, 199 (2001).
[7] H. van Hees, M. Mannarelli, V. Greco, and R. Rapp, Phys. Rev. Lett. **100**, 192301 (2008).
[8] K. Adcox *et al.*, Nucl. Instrum. Methods Phys. Res., Sect. A **499**, 469 (2003).
[9] S. S. Adler *et al.*, Phys. Rev. C **75**, 024909 (2007).
[10] S. S. Adler *et al.*, Phys. Rev. Lett. **95**, 202001 (2005).
[11] Y. Morino, arXiv:0903.3504.
[12] C. Albajar *et al.*, Phys. Lett. B **186**, 237 (1987).
[13] A. Mischke *et al.*, J. Phys. G **35**, 104117 (2008).
[14] T. Sjostrand, Comput. Phys. Commun. **82**, 74 (1994).
[15] D. Lange, Nucl. Instrum. Methods Phys. Res., Sect. A **462**, 152 (2001).
[16] D. Acosta *et al.*, Phys. Rev. Lett. **91**, 241804 (2003).
[17] L. Gladilin, arXiv:hep-ex/9912064.
[18] G. Alves *et al.*, Phys. Rev. Lett. **77**, 2388 (1996).
[19] W. M. Yao *et al.*, J. Phys. G **33**, 1 (2006).
[20] M. Cacciari, P. Nason, and R. Vogt, Phys. Rev. Lett. **95**, 122001 (2005); (private communication).
[21] M. L. Mangano *et al.*, Nucl. Phys. B **405**, 507 (1993).
[22] H. L. Lai *et al.*, Eur. Phys. J. C **12**, 375 (2000).
[23] A. Adare *et al.*, Phys. Lett. B **670**, 313 (2009).

High-$p_{\rm T}$ π^0 Production with Respect to the Reaction Plane in Au + Au Collisions at $\sqrt{s_{NN}} = 200$ GeV

arXiv:0903.4886v1 [nucl-ex] 27 Mar 2009

S. Afanasiev,[17] C. Aidala,[7] N.N. Ajitanand,[43] Y. Akiba,[37,38] J. Alexander,[43] A. Al-Jamel,[33] K. Aoki,[23,37] L. Aphecetche,[45] R. Armendariz,[33] S.H. Aronson,[3] R. Averbeck,[44] T.C. Awes,[34] B. Azmoun,[3] V. Babintsev,[14] A. Baldisseri,[8] K.N. Barish,[4] P.D. Barnes,[26] B. Bassalleck,[32] S. Bathe,[4] S. Batsouli,[7] V. Baublis,[36] F. Bauer,[4] A. Bazilevsky,[3] S. Belikov,[3,16,*] R. Bennett,[44] Y. Berdnikov,[40] M.T. Bjorndal,[7] J.G. Boissevain,[26] H. Borel,[8] K. Boyle,[44] M.L. Brooks,[26] D.S. Brown,[33] D. Bucher,[29] H. Buesching,[3] V. Bumazhnov,[14] G. Bunce,[3,38] J.M. Burward-Hoy,[26] S. Butsyk,[44] S. Campbell,[44] J.-S. Chai,[18] S. Chernichenko,[14] J. Chiba,[19] C.Y. Chi,[7] M. Chiu,[7] I.J. Choi,[52] T. Chujo,[49] V. Cianciolo,[34] C.R. Cleven,[12] Y. Cobigo,[8] B.A. Cole,[7] M.P. Comets,[35] P. Constantin,[16] M. Csanád,[10] T. Csörgő,[20] T. Dahms,[44] K. Das,[11] G. David,[3] H. Delagrange,[45] A. Denisov,[14] D. d'Enterria,[7] A. Deshpande,[38,44] E.J. Desmond,[3] O. Dietzsch,[41] A. Dion,[44] J.L. Drachenberg,[1] O. Drapier,[24] A. Drees,[44] A.K. Dubey,[51] A. Durum,[14] V. Dzhordzhadze,[46] Y.V. Efremenko,[34] J. Egdemir,[44] A. Enokizono,[13] H. En'yo,[37,38] B. Espagnon,[35] S. Esumi,[48] D.E. Fields,[32,38] F. Fleuret,[24] S.L. Fokin,[22] B. Forestier,[27] Z. Fraenkel,[51,*] J.E. Frantz,[7] A. Franz,[3] A.D. Frawley,[11] Y. Fukao,[23,37] S.-Y. Fung,[4] S. Gadrat,[27] F. Gastineau,[45] M. Germain,[45] A. Glenn,[46] M. Gonin,[24] J. Gosset,[8] Y. Goto,[37,38] R. Granier de Cassagnac,[24] N. Grau,[16] S.V. Greene,[49] M. Grosse Perdekamp,[15,38] T. Gunji,[5] H.-Å. Gustafsson,[28] T. Hachiya,[13,37] A. Hadj Henni,[45] J.S. Haggerty,[3] M.N. Hagiwara,[1] H. Hamagaki,[5] H. Harada,[13] E.P. Hartouni,[25] K. Haruna,[13] M. Harvey,[3] E. Haslum,[28] K. Hasuko,[37] R. Hayano,[5] M. Heffner,[25] T.K. Hemmick,[44] J.M. Heuser,[37] X. He,[12] H. Hiejima,[15] J.C. Hill,[16] R. Hobbs,[32] M. Holmes,[49] W. Holzmann,[43] K. Homma,[13] B. Hong,[21] T. Horaguchi,[37,47] M.G. Hur,[18] T. Ichihara,[37,38] K. Imai,[23,37] M. Inaba,[48] D. Isenhower,[1] L. Isenhower,[1] M. Ishihara,[37] T. Isobe,[5] M. Issah,[43] A. Isupov,[17] B.V. Jacak,[44,†] J. Jia,[7] J. Jin,[7] O. Jinnouchi,[38] B.M. Johnson,[3] K.S. Joo,[30] D. Jouan,[35] F. Kajihara,[5,37] S. Kametani,[5,50] N. Kamihara,[37,47] M. Kaneta,[38] J.H. Kang,[52] T. Kawagishi,[48] A.V. Kazantsev,[22] S. Kelly,[6] A. Khanzadeev,[36] D.J. Kim,[52] E. Kim,[42] Y.-S. Kim,[18] E. Kinney,[6] A. Kiss,[10] E. Kistenev,[3] A. Kiyomichi,[37] C. Klein-Boesing,[29] L. Kochenda,[36] V. Kochetkov,[14] B. Komkov,[36] M. Konno,[48] D. Kotchetkov,[4] A. Kozlov,[51] P.J. Kroon,[3] G.J. Kunde,[26] N. Kurihara,[5] K. Kurita,[39,37] M.J. Kweon,[21] Y. Kwon,[52] G.S. Kyle,[33] R. Lacey,[43] J.G. Lajoie,[16] A. Lebedev,[16] Y. Le Bornec,[35] S. Leckey,[44] D.M. Lee,[26] M.K. Lee,[52] M.J. Leitch,[26] M.A.L. Leite,[41] H. Lim,[42] A. Litvinenko,[17] M.X. Liu,[26] X.H. Li,[4] C.F. Maguire,[49] Y.I. Makdisi,[3] A. Malakhov,[17] M.D. Malik,[32] V.I. Manko,[22] H. Masui,[48] F. Matathias,[44] M.C. McCain,[15] P.L. McGaughey,[26] Y. Miake,[48] T.E. Miller,[49] A. Milov,[44] S. Mioduszewski,[3] G.C. Mishra,[12] J.T. Mitchell,[3] D.P. Morrison,[3] J.M. Moss,[26] T.V. Moukhanova,[22] D. Mukhopadhyay,[49] J. Murata,[39,37] S. Nagamiya,[19] Y. Nagata,[48] J.L. Nagle,[6] M. Naglis,[51] T. Nakamura,[13] J. Newby,[25] M. Nguyen,[44] B.E. Norman,[26] A.S. Nyanin,[22] J. Nystrand,[28] E. O'Brien,[3] C.A. Ogilvie,[16] H. Ohnishi,[37] I.D. Ojha,[49] H. Okada,[23,37] K. Okada,[38] O.O. Omiwade,[1] A. Oskarsson,[28] I. Otterlund,[28] K. Ozawa,[5] D. Pal,[49] A.P.T. Palounek,[26] V. Pantuev,[44] V. Papavassiliou,[33] J. Park,[42] W.J. Park,[21] S.F. Pate,[33] H. Pei,[16] J.-C. Peng,[15] H. Pereira,[8] V. Peresedov,[17] D.Yu. Peressounko,[22] C. Pinkenburg,[3] R.P. Pisani,[3] M.L. Purschke,[3] A.K. Purwar,[44] H. Qu,[12] J. Rak,[16] I. Ravinovich,[51] K.F. Read,[34,46] M. Reuter,[44] K. Reygers,[29] V. Riabov,[36] Y. Riabov,[36] G. Roche,[27] A. Romana,[24,*] M. Rosati,[16] S.S.E. Rosendahl,[28] P. Rosnet,[27] P. Rukoyatkin,[17] V.L. Rykov,[37] S.S. Ryu,[52] B. Sahlmueller,[29] N. Saito,[23,37,38] T. Sakaguchi,[5,50] S. Sakai,[48] V. Samsonov,[36] H.D. Sato,[23,37] S. Sato,[3,19,48] S. Sawada,[19] V. Semenov,[14] R. Seto,[4] D. Sharma,[51] T.K. Shea,[3] I. Shein,[14] T.-A. Shibata,[37,47] K. Shigaki,[13] M. Shimomura,[48] T. Shohjoh,[48] K. Shoji,[23,37] A. Sickles,[44] C.L. Silva,[41] D. Silvermyr,[34] K.S. Sim,[21] C.P. Singh,[2] V. Singh,[2] S. Skutnik,[16] W.C. Smith,[1] A. Soldatov,[14] R.A. Soltz,[25] W.E. Sondheim,[26] S.P. Sorensen,[46] I.V. Sourikova,[3] F. Staley,[8] P.W. Stankus,[34] E. Stenlund,[28] M. Stepanov,[33] A. Ster,[20] S.P. Stoll,[3] T. Sugitate,[13] C. Suire,[35] J.P. Sullivan,[26] J. Sziklai,[20] T. Tabaru,[38] S. Takagi,[48] E.M. Takagui,[41] A. Taketani,[37,38] K.H. Tanaka,[19] Y. Tanaka,[31] K. Tanida,[37,38] M.J. Tannenbaum,[3] A. Taranenko,[43] P. Tarján,[9] T.L. Thomas,[32] M. Togawa,[23,37] J. Tojo,[37] H. Torii,[37] R.S. Towell,[1] V-N. Tram,[24] I. Tserruya,[51] Y. Tsuchimoto,[13,37] S.K. Tuli,[2] H. Tydesjö,[28] N. Tyurin,[14] C. Vale,[16] H. Valle,[49] H.W. van Hecke,[26] J. Velkovska,[49] R. Vertesi,[9] A.A. Vinogradov,[22] E. Vznuzdaev,[36] M. Wagner,[23,37] X.R. Wang,[33] Y. Watanabe,[37,38] J. Wessels,[29] S.N. White,[3] N. Willis,[35] D. Winter,[7] C.L. Woody,[3] M. Wysocki,[6] W. Xie,[4,38] A. Yanovich,[14] S. Yokkaichi,[37,38] G.R. Young,[34] I. Younus,[32] I.E. Yushmanov,[22] W.A. Zajc,[7] O. Zaudtke,[29] C. Zhang,[7] J. Zimányi,[20,*] and L. Zolin[17]

(PHENIX Collaboration)

[1] *Abilene Christian University, Abilene, TX 79699, U.S.*
[2] *Department of Physics, Banaras Hindu University, Varanasi 221005, India*
[3] *Brookhaven National Laboratory, Upton, NY 11973-5000, U.S.*
[4] *University of California - Riverside, Riverside, CA 92521, U.S.*

[5]Center for Nuclear Study, Graduate School of Science, University of Tokyo, 7-3-1 Hongo, Bunkyo, Tokyo 113-0033, Japan
[6]University of Colorado, Boulder, CO 80309, U.S.
[7]Columbia University, New York, NY 10027 and Nevis Laboratories, Irvington, NY 10533, U.S.
[8]Dapnia, CEA Saclay, F-91191, Gif-sur-Yvette, France
[9]Debrecen University, H-4010 Debrecen, Egyetem tér 1, Hungary
[10]ELTE, Eötvös Loránd University, H - 1117 Budapest, Pázmány P. s. 1/A, Hungary
[11]Florida State University, Tallahassee, FL 32306, U.S.
[12]Georgia State University, Atlanta, GA 30303, U.S.
[13]Hiroshima University, Kagamiyama, Higashi-Hiroshima 739-8526, Japan
[14]IHEP Protvino, State Research Center of Russian Federation, Institute for High Energy Physics, Protvino, 142281, Russia
[15]University of Illinois at Urbana-Champaign, Urbana, IL 61801, U.S.
[16]Iowa State University, Ames, IA 50011, U.S.
[17]Joint Institute for Nuclear Research, 141980 Dubna, Moscow Region, Russia
[18]KAERI, Cyclotron Application Laboratory, Seoul, Korea
[19]KEK, High Energy Accelerator Research Organization, Tsukuba, Ibaraki 305-0801, Japan
[20]KFKI Research Institute for Particle and Nuclear Physics of the Hungarian Academy of Sciences (MTA KFKI RMKI), H-1525 Budapest 114, POBox 49, Budapest, Hungary
[21]Korea University, Seoul, 136-701, Korea
[22]Russian Research Center "Kurchatov Institute", Moscow, Russia
[23]Kyoto University, Kyoto 606-8502, Japan
[24]Laboratoire Leprince-Ringuet, Ecole Polytechnique, CNRS-IN2P3, Route de Saclay, F-91128, Palaiseau, France
[25]Lawrence Livermore National Laboratory, Livermore, CA 94550, U.S.
[26]Los Alamos National Laboratory, Los Alamos, NM 87545, U.S.
[27]LPC, Université Blaise Pascal, CNRS-IN2P3, Clermont-Fd, 63177 Aubiere Cedex, France
[28]Department of Physics, Lund University, Box 118, SE-221 00 Lund, Sweden
[29]Institut für Kernphysik, University of Muenster, D-48149 Muenster, Germany
[30]Myongji University, Yongin, Kyonggido 449-728, Korea
[31]Nagasaki Institute of Applied Science, Nagasaki-shi, Nagasaki 851-0193, Japan
[32]University of New Mexico, Albuquerque, NM 87131, U.S.
[33]New Mexico State University, Las Cruces, NM 88003, U.S.
[34]Oak Ridge National Laboratory, Oak Ridge, TN 37831, U.S.
[35]IPN-Orsay, Universite Paris Sud, CNRS-IN2P3, BP1, F-91406, Orsay, France
[36]PNPI, Petersburg Nuclear Physics Institute, Gatchina, Leningrad region, 188300, Russia
[37]RIKEN Nishina Center for Accelerator-Based Science, Wako, Saitama 351-0198, JAPAN
[38]RIKEN BNL Research Center, Brookhaven National Laboratory, Upton, NY 11973-5000, U.S.
[39]Physics Department, Rikkyo University, 3-34-1 Nishi-Ikebukuro, Toshima, Tokyo 171-8501, Japan
[40]Saint Petersburg State Polytechnic University, St. Petersburg, Russia
[41]Universidade de São Paulo, Instituto de Física, Caixa Postal 66318, São Paulo CEP05315-970, Brazil
[42]System Electronics Laboratory, Seoul National University, Seoul, Korea
[43]Chemistry Department, Stony Brook University, Stony Brook, SUNY, NY 11794-3400, U.S.
[44]Department of Physics and Astronomy, Stony Brook University, SUNY, Stony Brook, NY 11794, U.S.
[45]SUBATECH (Ecole des Mines de Nantes, CNRS-IN2P3, Université de Nantes) BP 20722 - 44307, Nantes, France
[46]University of Tennessee, Knoxville, TN 37996, U.S.
[47]Department of Physics, Tokyo Institute of Technology, Oh-okayama, Meguro, Tokyo 152-8551, Japan
[48]Institute of Physics, University of Tsukuba, Tsukuba, Ibaraki 305, Japan
[49]Vanderbilt University, Nashville, TN 37235, U.S.
[50]Waseda University, Advanced Research Institute for Science and Engineering, 17 Kikui-cho, Shinjuku-ku, Tokyo 162-0044, Japan
[51]Weizmann Institute, Rehovot 76100, Israel
[52]Yonsei University, IPAP, Seoul 120-749, Korea

(Dated: March 27, 2009)

Measurements of the azimuthal anisotropy of high-$p_{\rm T}$ neutral pion (π^0) production in Au+Au collisions at $\sqrt{s_{NN}} = 200$ GeV by the PHENIX experiment are presented. The data included in this paper were collected during the 2004 RHIC running period and represent approximately an order of magnitude increase in the number of analyzed events relative to previously published results. Azimuthal angle distributions of π^0s detected in the PHENIX electromagnetic calorimeters are measured relative to the reaction plane determined event-by-event using the forward and backward beam-beam counters. Amplitudes of the second Fourier component (v_2) of the angular distributions are presented as a function of π^0 transverse momentum ($p_{\rm T}$) for different bins in collision centrality. Measured reaction plane dependent π^0 yields are used to determine the azimuthal dependence of the π^0 suppression as a function of $p_{\rm T}$, $R_{\rm AA}(\Delta\phi, p_{\rm T})$. A jet-quenching motivated geometric analysis is presented that attempts to simultaneously describe the centrality dependence and reaction plane angle dependence of the π^0 suppression in terms of the path lengths of hypothetical parent partons

in the medium. This set of results allows for a detailed examination of the influence of geometry in the collision region, and of the interplay between collective flow and jet-quenching effects along the azimuthal axis.

PACS numbers: 21.65.Qr,25.75.-q,25.75.Dw

I. INTRODUCTION

Over the past few years, experiments at the Relativistic Heavy Ion Collider (RHIC) have established that a dense partonic medium is formed in Au + Au collisions at $\sqrt{s_{NN}}$=200 GeV [1, 2, 3, 4]. This medium thermalizes very quickly [1, 5, 6, 7, 8, 9, 10, 11], is extremely opaque to the passage of high-$p_{\rm T}$ particles [12, 13], and the strong coupling of matter in the medium produces a system for which the ratio of shear viscosity to entropy (η/s) approaches zero [14, 15, 16, 17, 18]. Much of the current focus is on the extraction of key transport and thermodynamic characteristics of the matter produced in these collisions. Measurements of high-$p_{\rm T}$ parton propagation in the medium as well as medium-induced modification of the fragmentation parton spectrum and its products provide a critical tool for probing medium properties.

One of the most striking early results from RHIC was the observation of strongly suppressed production of high-$p_{\rm T}$ particles in central Au+Au events compared to appropriately scaled $p + p$ collisions [12, 13]. High-$p_{\rm T}$ partons are formed from hard scattering between the initial colliding partons, and these partons fragment into two or more jets of hadrons. When propagating through a dense volume of deconfined matter, these high-$p_{\rm T}$ partons are expected to scatter from color charges in the medium, losing energy through a combination of gluon bremsstrahlung radiation and collisional energy transfer to partons in the medium. These radiated gluons eventually fragment into hadrons at lower $p_{\rm T}$, resulting in a depletion of the observed yields of hadrons at higher $p_{\rm T}$.

A useful way to quantify the suppression of high-$p_{\rm T}$ hadrons is the nuclear modification factor ($R_{\rm AA}$) where the $p+p$ cross section is scaled by the thickness function $\langle T_{\rm AA}\rangle$ of the two Au nuclei

$$R_{\rm AA}(p_{\rm T}) = \frac{(1/N_{\rm AA}^{\rm evt})d^2N_{\rm AA}^{\pi^0}/dp_{\rm T}dy}{\langle T_{\rm AA}\rangle \times d^2\sigma_{pp}^{\pi^0}/dp_{\rm T}dy}.$$

PHENIX has measured a π^0 $R_{\rm AA}$ close to unity in both peripheral Au + Au collisions and Au+Au collisions [19, 20], consistent with the expectation that these collisions would not produce an extended, dense medium. As the collisions become more central, $R_{\rm AA}$ decreases to about 0.2, indicating a stronger parton energy loss. Furthermore, the measured π^0 $R_{\rm AA}$ is nearly constant as a function of $p_{\rm T}$, for $p_{\rm T} \gtrsim 5$ GeV/c up to the highest currently accessibly $p_{\rm T}$, 20 GeVc [19].

These data can be well reproduced by models that calculate the energy lost by the hard scattered partons as they traverse the dense medium. The amount of energy-loss depends on the density of the medium [21], so measurements of high-$p_{\rm T}$ hadron suppression provide constraints on the transport coefficient $\langle\hat{q}^2\rangle$, a measure of mean transverse momentum squared $\langle k_{\rm T}^2\rangle$ transferred by the medium to a high-energy parton. However, multiple models with different physical assumptions can reproduce the measured $R_{\rm AA}(p_{\rm T})$ [22, 23]. The different models vary widely in how they include the crucial interference terms between multiple-scattering centers as well as the interplay between inelastic, elastic and flavor-changing processes during the parton's passage.

To discriminate between these models we need to increase our experimental control of the path length, since the amount of energy lost by a high-$p_{\rm T}$ parton strongly increases with the distance traveled through the medium. A quadratic dependence on the path length is predicted for a static medium if the dominant energy-loss mechanism is the bremsstrahlung radiation of gluons surviving the destructive interference caused by multiple scattering [22, 23]. For an expanding plasma the quadratic increase should be moderated to a linear dependence [24].

The centrality dependence of $R_{\rm AA}(p_{\rm T})$ offers a probe of the path-length dependence of partonic energy loss. However, we can better test the path-length dependence by studying the azimuthal variation of the high-$p_{\rm T}$ suppression at a fixed centrality. Since the collision zone has a nearly elliptical shape in the transverse plane due to the non-central overlap of the colliding Au nuclei, partons that travel along the short axis of the nuclear overlap region lose less energy and should therefore be less suppressed. The key observable is then the two-dimensional modification factor $R_{\rm AA}(\Delta\phi, p_{\rm T})$, where $\Delta\phi$ is the angle of emission with respect to the event plane. The azimuthal dependence of the spectra can be also parameterized by a Fourier expansion, where up to second order $\frac{dN}{d\Delta\phi} = N_0[1 + 2v_2\cos(2\Delta\phi)]$, with v_2 being called elliptic flow coefficient. While both quantities characterize azimuthal asymmetries, historically and conceptually they have different roots. The notion of elliptic flow is primarily tied to lower $p_{\rm T}$ phenomena ("soft physics"), the domain where particle production is proportional to the number of participating nucleons ($N_{\rm part}$), and positive v_2 arises from the *boost* to the mean $p_{\rm T}$ in the direction where the pressure gradient is highest (along the reaction plane). Conversely, $R_{\rm AA}(p_{\rm T})$ and $R_{\rm AA}(\Delta\phi, p_{\rm T})$ are commonly used to describe high $p_{\rm T}$ behavior (hard scattering, which scales with the number of binary collisions $N_{\rm coll}$). When $R_{\rm AA}$ deviates from unity at high $p_{\rm T}$, it becomes a valuable probe of the *loss* of energy/momentum

*Deceased
†PHENIX Spokesperson: jacak@skipper.physics.sunysb.edu

in a particular direction. However, there is no clear separation between soft and hard regions, and both $R_{\rm AA}$ and v_2 are well-defined in the entire momentum range, so in this sense v_2 is sensitive to differential energy loss at high $p_{\rm T}$.

PHENIX has measured high-$p_{\rm T}$ v_2 for π^0 particles from Au+Au collisions [25]. The energy-loss models that reproduce $R_{\rm AA}(p_{\rm T})$ diverge in their predictions of the azimuthal anisotropy at high $p_{\rm T}$. They generally underpredict the observed azimuthal variation of $R_{\rm AA}(\Delta\phi)$, or equivalently, are unable to describe the $p_{\rm T}$ dependence of v_2 over the full range of $p_{\rm T}$ where one would naively expect them to be applicable [26, 27, 28]. These models include the hydrodynamical evolution of the medium, and therefore the high-$p_{\rm T}$ probe loses energy in a medium that is becoming spatially isotropic with time. Several early papers noticed that the measured v_2 values were larger than what one would expect from a completely opaque almond-shape collision zone [29, 30]. Other early energy-loss calculations came close to reproducing the measured $R_{\rm AA}(\Delta\phi)$ [31, 32], but in these the plasma expansion was not taken into account, which resulted in unrealistically strong azimuthal anisotropy. Another calculation [33] has reproduced $R_{\rm AA}(\Delta\phi)$, but in this model the Au nuclei were parameterized as hard-spheres instead of using a more realistic Woods-Saxon density profile, and this mechanism artificially increases the azimuthal dependence of the energy density.

One potential resolution of the problem with energy loss calculations not reproducing the measured azimuthal dependence of yields is a recent calculation that allowed the high-$p_{\rm T}$ parton to resonantly scatter with the medium [34] (and references therein), increasing the energy lost by a parton at plasma densities that correspond to temperatures near the critical temperature. This produces a sharper dependence of the energy-loss on the spatial variation of the medium's energy density and hence the model is able to simultaneously reproduce both $R_{\rm AA}(p_{\rm T})$ and $R_{\rm AA}(\Delta\phi)$. A critical check will be to examine whether the same parameters work for the full range of collision centralities.

In order to discriminate among all the models that attempt to reproduce $R_{\rm AA}(\Delta\phi, p_{\rm T})$, the experimental challenge is to extend the range and increase the precision of observations which can be used to test different energy-loss models. In this paper we extend the range of published data on $R_{\rm AA}(\Delta\phi)$ [25] by a) reaching higher $p_{\rm T}$, and thereby moving to a $p_{\rm T}$ region that is completely dominated by the fragmentation of hard partons and reducing the possible contribution of particles from recombination [35], b) using finer bins in centrality, thus achieving less averaging of the path length, and c) reducing the statistical and systematic uncertainties to further constrain models. We present in this article measurements using data collected during the 2004 RHIC running period. These data represent a high-statistics sample of Au + Au collisions (approximately 50 times that of the 2002 RHIC running period) and therefore extend our ability to measure $R_{\rm AA}(\Delta\phi)$ and v_2 to much higher $p_{\rm T}$ with better precision.

II. EXPERIMENTAL DETAILS

The data presented in this paper were taken by the PHENIX experiment [36] in 2004 (RHIC Run-4), and represent the analysis of 821M minimum bias Au+Au collisions at $\sqrt{s_{NN}} = 200$ GeV. The detectors involved in this analysis are the beam-beam counters [37] (BBC; triggering, centrality and reaction plane determination), the zero-degree calorimeter [38] (ZDC, centrality determination) and the electromagnetic calorimeter [39] (EMCal, π^0 measurement).

The BBCs are two groups of 64 hexagonal quartz Čerenkov radiator counters with photomultiplier readout surrounding the beampipe 144 cm up- and downstream ("North" and "South") from the center of the nominal collision diamond, covering the $3 < |\eta| < 3.9$ pseudorapidity range and the full azimuth. Coincidence of signals in at least two photomultiplier tubes in both BBCs served as a minimum bias trigger and according to simulations it captured 92% of all inelastic collisions. The size of the total signal in the BBCs increases monotonically with collision centrality at this $\sqrt{s_{NN}}$. The collision vertex z was calculated from the difference between the fastest timing signals in the North and South BBCs, respectively, with $\sigma < 2.0$ cm resolution. Only events with $|z| < 30$ cm were analyzed.

The ZDCs are small tungsten/scintillator hadron calorimeters with quartz fiber lightguides and photomultiplier readout, located between the beampipes at 18 m North and South from the collision point. They measure non-interacting "spectator" neutrons in a cone of about 2 mrad, and their signal is double-valued as a function of centrality (it is low in very central and very peripheral collisions but large at mid-centrality). The correlation of ZDC *vs* BBC signals resolves this ambiguity and allows a precise measurement of the true centrality for all but the most peripheral collisions.

The reaction plane (spanned by the beam direction and the impact vector of the colliding nuclei) is determined event-by-event from the azimuthal charge distribution in the BBCs, after taking into account small nonuniformities (in the response of individual radiators, PMTs, electronics, etc.), using the assumption that over a large number of events the ϕ distribution of per-event reaction planes should be uniform. Due to the large rapidity gap between the central arm ($|\eta| < 0.35$) where π^0s are measured, and the BBCs where the reaction plane is established, we assume that the reaction plane is unbiased and free from auto-correlations. However, the relatively coarse granularity of BBCs affects the resolution. Note that in this analysis precise knowledge of the reaction plane resolution, which depends strongly on centrality, is crucial. This will be discussed in detail in the next Section.

Neutral pions are measured by reconstructing their decay photons ($\pi^0 \rightarrow \gamma\gamma$) in the EMCal. The EMCal consists of 8 sectors at midrapidity ($|\eta| < 0.35$), covering a total of $2 \times 90^\circ$ in azimuth. Six sectors are lead/scintillator (PbSc) sampling calorimeter with photomultiplier readout and 5.5×5.5 cm^2 granularity, two sectors are lead/glass (PbGl) Čerenkov counters with 4×4 cm^2 granularity and photomultiplier readout. The two detectors are $18X_0$ and $16X_0$ radiation lengths deep, respectively, both ensuring essentially full containment of electromagnetic showers in the relevant energy range. The *in situ* energy resolution is well reproduced by simulation both in PbSc and PbGl: the π^0 peak positions and the widths both agree with the data to better than 1 MeV over the entire momentum range. Therefore, the error on the energy (and momentum) scale is less than 1%. Timing resolution σ_t is $\sim$ 450 ps and $\sim$ 650 ps for the PbSc and PbGl, respectively, allowing the rejection of neutrons and antineutrons up to a few GeV/c transverse momentum, which would otherwise be a major source of neutral showers up to a few GeV energy. At sufficiently high transverse momenta, decay photons from a nearly symmetric ($E_{\gamma_1} \approx E_{\gamma_2}$) decay may produce showers in the calorimeter that start to merge into one reconstructed cluster. In the PbSc this effect is first visible around $p_{\rm T} \sim 10$ GeV/c, at the upper end of the $p_{\rm T}$ region considered in this paper. Due to its higher granularity and smaller Molière-radius the PbGl is immune to this "merging" problem up to $p_{\rm T}$ $\sim$15 GeV/c. The hadronic response, timing properties and other sources of systematic errors are very different for the two calorimeter types. Therefore, when extracting the ϕ-integrated $R_{\rm AA}$, which serves as absolute normalization, the PbSc and PbGl were analyzed separately and the results combined to decrease the total systematic uncertainty.

III. DATA ANALYSIS

A. Centrality

As mentioned, the minimum-bias trigger in the Run-4 PHENIX configuration is supplied by the BBCs, and the correlation of the charge deposited in the BBCs with energy deposited in the ZDCs provided a determination of the centrality of the collision. The elliptic flow measurement presented in this paper is measured in seven bins of the centrality range 0-92%, with lowest corresponding to the most central: 0-5%, 5-10%, 10-20%, 20-30%, 30-40%, 40-50%, and 50-60%. In addition, the combined ranges 0-20%, 20-40%, 40-60%, and minimum bias bins are included. For the yields with respect to the reaction plane, the centralities presented are 0-10%, 10-20%, 20-30%, 30-40%, 40-50%, 50-60%. Finally, the $R_{\rm AA}$ versus nuclear path length result excludes the most central bin due to its smaller intrinsic ellipticity (the average path length is insensitive to $\Delta\phi$).

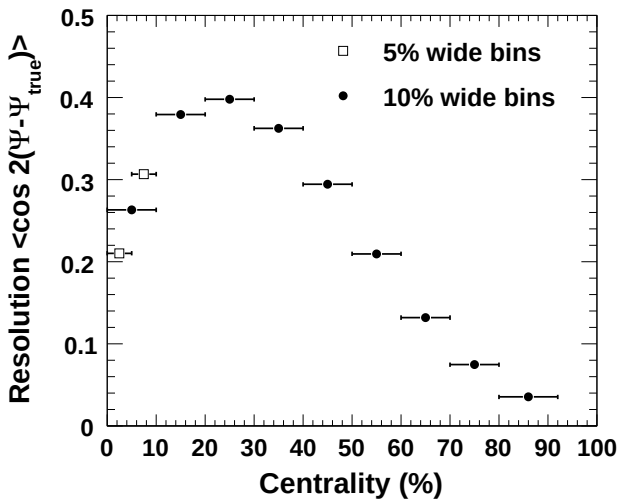

FIG. 1: Reaction plane resolution correction as a function of centrality.

B. Reaction plane determination

The technique used to determine the reaction plane on an event-by-event basis is the same used in previous PHENIX analyses [14, 40, 41]. The quartz radiators of each counter are arranged in approximately concentric circles around the beam axis. The light collected in the photo-multiplier tubes (PMTs) allows for an estimate of the number of charged particles passing through the detector.

The number of charged particles at a given PMT position, N_i, is weighted in a manner to reduce the bias of the inner rings and used to measure the orientation of the reaction plane from the formula

$$\tan(2\Psi) = \frac{\sum_i w_i N_i \sin(2\phi_i) - \langle \sum_i w_i N_i \sin(2\phi_i) \rangle}{\sum_i w_i N_i \cos(2\phi_i) - \langle \sum_i w_i N_i \cos(2\phi_i) \rangle}, \quad (1)$$

where ϕ_i is the nominal azimuth of the radiator. Subtraction of the average centroid removes biases due to various detector effects. A final flattening technique is used to remove the residual non-uniformities in the distribution of angles.

To estimate the resolution of the reaction plane measurement, we use the sub-event technique [42]. The approach consists of dividing the event up into two sub-events roughly equal in size. The two individual BBCs provide a natural sub-event division, so we analyze the distribution of event-by-event differences between the reaction plane angles measured in the north and south counters, $\Delta\Psi = \Psi_N - \Psi_S$. In the presence of pure flow, this distribution takes the form [42]:

$$\frac{dN}{d\Delta\Psi} = \frac{e^{-\chi^2}}{2}\left\{\frac{2}{\pi}(1+\chi^2) + z\left[I_0(z) + \mathrm{L}_0(z)\right] + \chi^2\left[I_1(z) + \mathrm{L}_1(z)\right]\right\}. \quad (2)$$

where $z = \chi^2 \cos(2\Delta\Psi)$ and the functions I_n and $\mathrm{L_n}$ are the modified Bessel functions of the first kind and modified Struve functions, respectively. The parameter χ describes the dispersion of the flow $\vec{Q}$ vector and thus determines the correction required for the reaction plane resolution. Since $\Delta\Psi$ represents the whole-event difference distribution and we are dealing with sub-events with roughly half the multiplicity of the event, we replace $\chi \to \chi/\sqrt{2}$ in Eq. 2 and fit this function to the measured $\Delta\Psi$ distribution to extract χ. The resulting value is then used to evaluate the resolution of the event-plane of n^{th} order [42]:

$$\langle \cos n\left(\Psi - \Psi_{RP}\right)\rangle = \frac{\sqrt{\pi}}{2}\chi e^{-\frac{\chi^2}{2}}\left[I_{\frac{n-1}{2}}\left(\frac{\chi^2}{2}\right) + I_{\frac{n+1}{2}}\left(\frac{\chi^2}{2}\right)\right] \quad (3)$$

where the true reaction plane orientation is denoted by Ψ_{RP} and the observed orientation by Ψ. Figure 1 shows the resolution correction obtained using the above-described procedure as a function of centrality. Both 5% and 10% wide bins are shown for comparison.

Eq. 2 is derived under the assumption that the azimuthal distributions are free of non-flow effects. Due to the large rapidity gap between the BBCs and the central arm region, it is expected that particles observed in the BBCs have no correlation with those measured in the central arm detectors. PYTHIA [43] studies have been used to confirm that jets observed in the central arm have negligible effect on the reaction plane measurement from the BBCs[44].

C. Neutral pion measurement

Measurement of neutral pions has played a critical role in the study of high-p_{T} phenomena at RHIC, and especially by PHENIX [12, 19, 25]. The two-particle decay channel $\pi^0 \to \gamma + \gamma$ provides a clean signal of identified hadrons out to the highest p_{T} regions.

EMCal showers are found by clustering contiguous towers with energy above a threshold energy (10 MeV) and requiring at least 50 MeV in the tower with highest energy deposit. The impact position is calculated from the positions of the participating towers weighted by the logarithm of deposited energy. The energy of the cluster is corrected for non-perpendicular incidence – the angle being derived by assuming a straight path between the actual vertex and the calculated impact point – as well as nonlinearities [25]. In high-multiplicity events such as central Au + Au collisions, there is an increasing probability for clusters to overlap (one tower accumulates energy from more than one particle), which can distort an energy measurement from a simple sum over contiguous towers. To mitigate this effect, the EMCal clustering algorithm also provides a quantity called *ecore*, which is determined by extrapolating the "core" energy represented by the central four or five towers in the cluster, assuming an electromagnetic shower profile. The energy- and impact angle- dependent shower profile is a model developed from and checked against beam test data. In this way, *ecore* provides a more realistic measurement of the shower energy, less prone to contributions from accidental overlaps (particles hitting close enough they deposit energy in the same towers) than a simple energy sum of participating towers would be. We use this *ecore* for the energy of reconstructed clusters in this analysis.

The invariant mass of a photon pair γ_i, γ_j as measured in the EMCal is calculated from the energy of the clusters and their measured position:

$$m_{\gamma_i\gamma_j} = \sqrt{(P^2_{\gamma_i} + P^2_{\gamma_j})} = \sqrt{2E_iE_j\cos(1-\theta_{ij})} \quad (4)$$

where θ_{ij} is the opening angle between the two photons and $m_{\gamma_i\gamma_j}$ is equal to the π^0 mass for photons from the decay of the same π^0. Since the photons from the π^0 are not tagged, such pairs have to be formed from each photon pair in the event where the pair momentum falls in a particular p_{T} bin, and some of these pairs might accidentally reproduce the π^0 mass as well (combinatorial background), particularly at lower p_{T} and higher centralities (multiplicities). Since π^0s cannot be uniquely identified, raw π^0 yields are extracted statistically, by subtracting the combinatorial background from the invariant mass distribution.

A well-known technique to reduce the combinatorial background is to place a cut on the energy asymmetry of the pair, as defined by:

$$\alpha = \frac{|E_1 - E_2|}{E_1 + E_2} = \beta|\cos\theta^*|. \quad (5)$$

Because the angular distribution $d\sigma/d\cos\theta^*$ of the pairs in the rest frame of the π^0 is uniform, the asymmetry distribution should be flat. However, due to the steeply falling photon spectrum, fake (non-correlated) pairs which still give the proper π^0 mass are strongly peaked towards $\alpha = 1$. A pair of clusters in the EMCal is considered a neutral pion candidate only if the pair's

asymmetry is less than 0.8. In addition, the two photons are required to be separated by at least 8 cm for the combination to be considered as a π^0 candidate.

There remains a non-trivial background contribution which passes these cuts: pairs of photons from different π^0s, or, more generally, from pairs of uncorrelated clusters which pass the photon identification cuts and accidentally give an invariant mass near the true π^0 mass. This remaining combinatorial background is estimated and subtracted using the event mixing method. The procedure involves forming pairs from different events, which will by definition be uncorrelated. Each photon candidate is combined with all the photon candidates in previous events stored in memory. In order to replicate the background from uncorrelated pairs within the same event as closely as possible in the mixed events, mixing is performed within bins of centrality, vertex z position, and reaction plane orientation. Since all events analyzed are minimum-bias, no special steps are needed to avoid the distortions of the mixed-event background by the trigger requirement. All cuts applied to the combinations of same event pairs are also applied to mixed-event pairs. The number of events buffered determines the statistics of the event-mixed distributions, chosen as a tradeoff between desired statistical accuracy and computational resources. The data presented in this article are mixed with five previous events (in each centrality, vertex, and reaction plane bin).

For a given $p_{\rm T}$ bin, the mixed-event mass distribution is normalized to the same-event distribution in a region away from the π^0 mass peak. The normalization region is 0.25–0.45 GeV/c^2 for $p_{\rm T} < 6.0$ GeV/c and 0.21–0.45 GeV/c^2 otherwise. Fig. 2 shows an example of this subtraction process for two $p_{\rm T}$ ranges in two centrality bins.

The scaled background distribution is then subtracted from the same-event pair distribution. The subtracted result thus represents a sample of real π^0s. The peak is fit to a Gaussian to determine its width and mean position. The raw yield of π^0s is determined by integrating the counts in a window of $\pm 2\sigma$ around the mean. The width and mean are recorded and parameterized as a function of $p_{\rm T}$ and centrality based upon this ϕ-integrated, large sample. The positions and widths from this parameterization are then used when we extract the (much smaller) raw yields in bins of angle $\Delta\phi$ with respect to the reaction plane. The maximum variation of the yields (multiplicities) with $\Delta\phi$ is only about a factor of 2, and therefore the means and widths are not expected to change substantially. Furthermore, the statistics are much poorer in the $\Delta\phi$ bins, which would make individual π^0 fits unreliable.

There is a residual background in the invariant mass distributions even after the mixed-event distribution has been removed, especially at lower $p_{\rm T}$ (below ~ 2 GeV/c). This is due to correlations that event mixing cannot reproduce, like the "sub-event structure" due to the presence of jets or multiple, close-by showers from an annihilating anti-neutron, or imperfections of the reconstruction algorithm, such as cluster merging, cluster splitting, and a host of other contributions. Much of the residual background is excluded by starting the fit at 0.09 GeV/c. What is left is accounted for by including a first-order polynomial in the fits to the (already background-subtracted) invariant mass distribution, and subtracting its integral from the raw π^0 yield (see Fig. 2). In the more central events, the peak deviates slightly from gaussian on the high mass side, due to overlapping clusters. The use of *ecore* mitigates this effect, and the systematic uncertainty on yield extraction arising from the remaining asymmetry has been estimated to be 3-4% [19].

D. Elliptic flow measurement

To obtain the azimuthal angle dependence of π^0 production, we measure raw π^0 yields in a given $p_{\rm T}$ bin as a function of the π^0 angle with respect to the reaction plane orientation in six equally-spaced bins of $\Delta\phi = \phi(\pi^0) - \Psi_{RP}$ covering the range $0 < \Delta\phi < \pi/2$. The π^0 yields are measured in each $\Delta\phi$ bin using the same procedure described in III C for the reaction-plane inclusive measurement except that the mass fits are not performed in each $\Delta\phi$ bin. Instead, the peak integration window is set $\pm 2\sigma$ around the mean where the width and mean are taken from the inclusive analysis. The resulting raw π^0 angular distribution $dN/d\Delta\phi$ can then be fit to determine the strength of the modulation in the yield. Because the PHENIX BBCs have uniform azimuthal coverage, the π^0 measurements have uniform acceptance in $\Delta\phi$ when averaged over a large event sample, despite the limited azimuthal acceptance of the PHENIX electromagnetic calorimeters.

Assuming elliptic flow is the dominant source of $\Delta\phi$ variation in the π^0 yields, we perform a fit to the angular distributions of the form

$$\frac{dN}{d\Delta\phi} = N_0(1 + 2v_2^{\rm meas}\cos 2\Delta\phi). \qquad (6)$$

We use an analytic linear χ^2 fitting procedure that matches the integral of Eq. 6 over each of the $\Delta\phi$ bins to the measured π^0 yield within the corresponding bin. In the definition of the χ^2 function we account for non-zero covariances between the yields in the different $\Delta\phi$ bins resulting from the limited acceptance of the calorimeters. These covariances have been evaluated separately for each $p_{\rm T}$ and centrality bin. Examples of the raw $dN/d\Delta\phi$ distributions and the results of the χ^2 fits are shown in Fig. 3. The resulting $v_2^{\rm meas}$ values are then corrected upward to account for reaction plane resolution using correction factors described in Section III B.

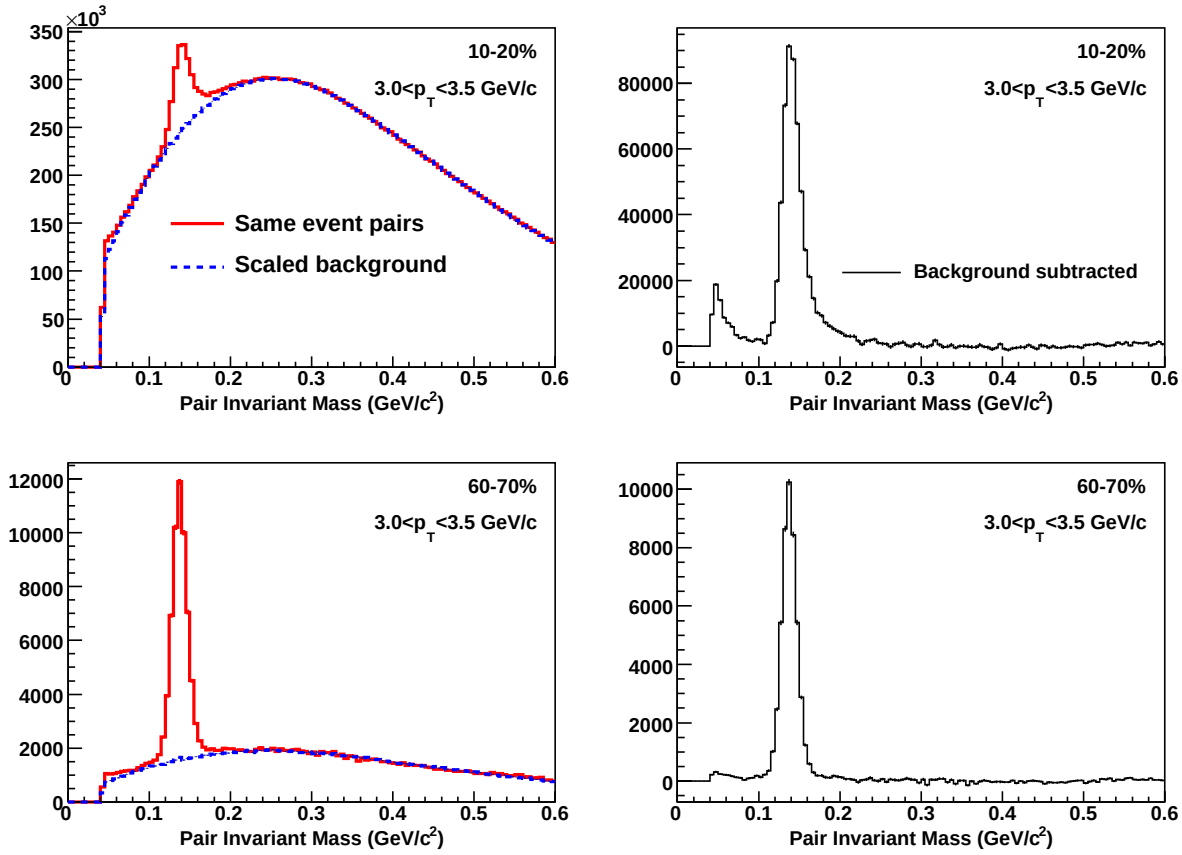

FIG. 2: Invariant mass distributions at moderate $p_{\rm T}$ and two different centralities. Left panels: same event and normalized mixed event distributions. Right panel: the subtracted distributions, which are then fitted with the sum of a first degree polynomial and a Gaussian.

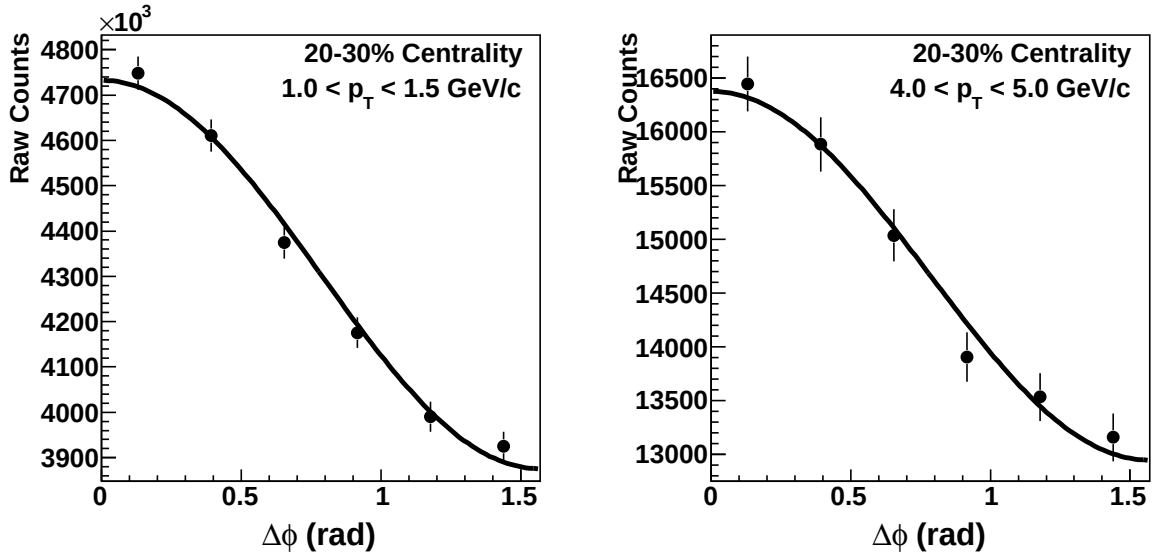

FIG. 3: Example of analytic fitting of raw $dN/d\Delta\phi$ distributions

E. $R_{\rm AA}$ ($\Delta\phi$) measurement

The nuclear modification factor $R_{\rm AA}$ has played a critical role in understanding energy loss mechanisms. $R_{\rm AA}$ is defined as

$$R_{\rm AA}(p_{\rm T}) = \frac{(1/N_{\rm AA}^{\rm evt})d^2N_{\rm AA}^{\pi^0}/dp_{\rm T}dy}{\langle T_{\rm AA}\rangle \times d^2\sigma_{pp}^{\pi^0}/dp_{\rm T}dy} \quad (7)$$

where $\langle T_{\rm AA}\rangle$ is the mean Glauber overlap function for the centrality being analyzed:

$$\langle T_{\rm AA}\rangle \equiv \frac{\int T_{\rm AA}(\mathbf{b})d\mathbf{b}}{\int (1-e^{-\sigma_{pp}^{inel}T_{\rm AA}(\mathbf{b})})d\mathbf{b}}, \quad (8)$$

from which the mean number of binary nucleon-nucleon collisions can be calculated, $\langle N_{\rm coll}\rangle = \sigma_{pp}^{inel}\langle T_{\rm AA}\rangle$.

For each $p_{\rm T}$ bin, we can calculate the ratio

$$R(\Delta\phi_i, p_{\rm T}) = \frac{N(\Delta\phi_i, p_{\rm T})}{\sum_{i=1}^{6} N(\Delta\phi_i, p_{\rm T})} \quad (9)$$

where $N(\Delta\phi_i, p_{\rm T})$ is the number of π^0s observed in the given $(\Delta\phi_i, p_{\rm T})$ bin. Since the BBC is azimuthally symmetric the PHENIX acceptance has no $\Delta\phi$ dependence, there should be no azimuthal dependence to efficiency and acceptance corrections. As a result,

$$R_{\rm AA}(\Delta\phi_i, p_{\rm T}) = R(\Delta\phi_i, p_{\rm T}) \times R_{\rm AA}(p_{\rm T}). \quad (10)$$

Thus, we can use measured inclusive $R_{\rm AA}(p_{\rm T})$ to convert $R(\Delta\phi_i, p_{\rm T})$ to $R_{\rm AA}(\Delta\phi_i, p_{\rm T})$. Since the detector efficiency and acceptance corrections are already contained in $R_{\rm AA}(p_{\rm T})$, there is no need to apply them to $R(\Delta\phi_i, p_{\rm T})$.

Prior to calculating $R_{\rm AA}(\Delta\phi_i, p_{\rm T})$ we correct the ratios $R(\Delta\phi_i, p_{\rm T})$ for the finite reaction plane resolution using an approximate unfolding technique. For a pure flow $\Delta\phi$ distribution, we can express the influence of the resolution broadening on the measured $\Delta\phi$ distribution

$$R^{\rm meas}(\Delta\phi_i, p_{\rm T}) = R^{\rm true}(\Delta\phi_i, p_{\rm T})\left[\frac{1+2v_2^{\rm meas}\cos(2\Delta\phi)}{1+2v_2^{\rm corr}\cos(2\Delta\phi)}\right], \quad (11)$$

where according to the results of Section III B $v_2^{\rm meas} = v_2^{\rm corr}/\langle\cos 2(\Psi-\Psi_{RP})\rangle$. Then, if the measured $\Delta\phi$ distribution resulted from pure elliptic flow, it could be corrected back to the true distribution by

$$R^{\rm corr}(\Delta\phi_i, p_{\rm T}) = R^{\rm meas}(\Delta\phi_i, p_{\rm T})\left[\frac{1+2v_2^{\rm corr}\cos(2\Delta\phi)}{1+2v_2^{\rm meas}\cos(2\Delta\phi)}\right]. \quad (12)$$

As shown above, the general features of the measured π^0 $\Delta\phi$ distributions are well-described by pure $\cos(2\Delta\phi)$ modulation. However, we wish to preserve in our measurements of the azimuthal dependence of the π^0 production the full shape of the measured $\Delta\phi$ distribution, including possible small non-elliptic contributions. For this purpose, the correction described in Eq. 12 applied to the data represents an approximation to a full unfolding procedure that becomes exact when the distribution is purely $\cos(2\Delta\phi)$ in form. We have checked for a few cases that a full unfolding procedure applied to the measured $dN/\Delta\phi$ distributions using singular value decomposition regulation of the response matrix reproduces the correction in Eq. 12. From the corrected ratios, $R^{\rm corr}(\Delta\phi_i, p_{\rm T})$, we use Eq. 10 to obtain $R_{\rm AA}(\Delta\phi_i, p_{\rm T})$.

IV. RESULTS

A. Elliptic flow coefficient

The results of the v_2 measurements using the methods described in Sec. III D are presented in Fig. 4 as a function of $p_{\rm T}$ for different centrality bins. The data points in the figure are plotted at the mean π^0 $p_{\rm T}$ in bins of width $\Delta p_{\rm T} = 0.5$ GeV/c for $p_{\rm T} < 4$ GeV/c and $\Delta p_{\rm T} = 1$ GeV/c for $p_{\rm T} > 4$ GeV/c. The error bars shown on the v_2 data points were obtained by multiplying the raw v_2 fit errors (see Section III D) by the same reaction plane resolution correction factor applied to the v_2 values themselves. The error bars, then, represent uncorrelated statistical errors on the measured v_2 values arising from statistical errors on the $dN/d\Delta\phi$ data points used in the fits (these errors would be categorized as Type A uncertainties in the framework described in [45] or $p_{\rm T}$-uncorrelated). Systematic errors on the v_2 measurements due to the reaction plane determination procedure and from systematic uncertainties in the reaction plane resolution correction are represented in Figs. 4,5 by filled boxes, which for most data points are similar in size or smaller than the data points (these uncertainties are classified as Type B [45] or $p_{\rm T}$-correlated).

Figure 5 shows $v_2(p_{\rm T})$ for four centrality ranges, obtained by combining data from the centrality bins shown in Fig. 4. The corrected $dN/d\Delta\phi$ distributions from individual centrality bins were summed over a given centrality range and then fit to obtain the corrected v_2 values shown in Fig. 5. The reaction plane resolution correction produces correlated errors in the corrected $dN/d\Delta\phi$ distributions for each original centrality bin, and these correlated errors persist in the summed $dN/d\Delta\phi$ distribution. These correlated errors are not included in the statistical errors for the fit to the combined $dN/d\Delta\phi$ distribution, but their impact on the final v_2 value is estimated separately by evaluating the changes in the v_2 fit parameter that result from adding to the summed $dN/d\Delta\phi$ values ±1 σ of the correlated errors. Since this estimated uncertainty results from the statistical uncertainties on the v_2 values for the original centrality bins, we include the 1σ bounds obtained from this procedure in the statistical error on the v_2 values for the combined centrality bins. Systematic errors for the combined bins are plotted similarly to those in Fig. 4.

The results presented here nearly double the $p_{\rm T}$ range of previous PHENIX π^0 v_2 measurements from RHIC

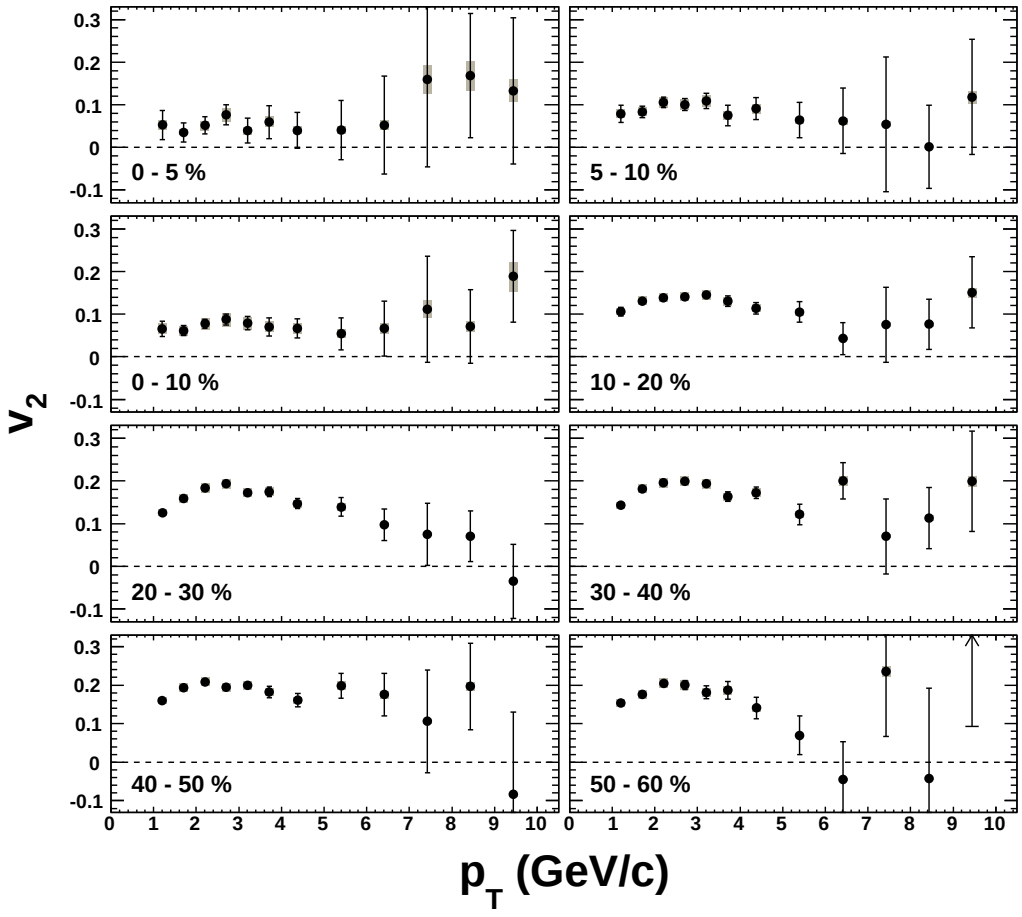

FIG. 4: π^0 v_2 versus $p_{\rm T}$ for centralities 0-5%, 5-10%, 0-10%, 10-20%, 20-30%, 30-40%, 40-50%, and 50-60%. The arrow in the 50-60% panel shows the lower limit of the uncertainty on the data point, which lies outside the bounds of the plot.

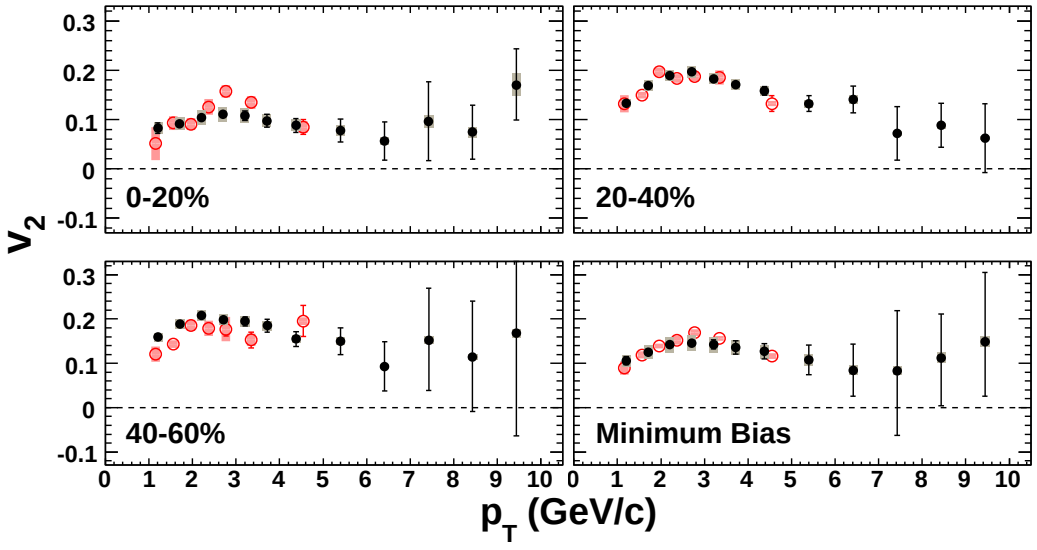

FIG. 5: (Color online) π^0 v_2 versus $p_{\rm T}$ for centralities 0-20%, 20-40%, 40-60%, and minimum bias. The closed (black) circles are data presented in this paper, and the open (red) circles are previously published results [40].

Run-2 [40]. Those measurements are shown for comparison purposes in Fig. 5. Good agreement is seen between the Run-4 measurements presented here and the Run-2 results except in the 40-60% centrality bin where the new v_2 measurements are systematically higher by $\sim 30\%$. This difference is attributed to improved reaction plane resolution corrections for the 40-60% centrality bin resulting from the combining of *corrected* $dN/\Delta\phi$ distributions from smaller centrality bins. This summing procedure better handles the rapid variation of reaction plane resolution with centrality in mid-central to peripheral collisons. Furthermore, we have cross-checked the procedure using 5% bins, verifying the combined result reproduces the data analyzed in wider bins. The previous Run 2 analysis did not have a sufficiently large data sample to allow the use of separate 40-50% and 50-60% bins, and therefore the reaction plane resolution correction was necessarily less accurate. The measured v_2 values presented in Fig. 4 and Fig. 5 are also consistent with previously published PHENIX charged pion v_2 measurements [14, 40].

The results in Figures 4 and 5 show a rapid increase of v_2 with increasing $p_{\rm T}$ at low $p_{\rm T}$, a maximum in the range $2 < p_{\rm T} < 3$ GeV/c, and then at higher $p_{\rm T}$ a decrease of v_2 with increasing $p_{\rm T}$. An increase in v_2 at low $p_{\rm T}$ is well-established [46, 47, 48] and is understood to result from the collective elliptic flow of the medium generated by the initial spatial anisotropy of the collision zone. Hydrodynamical models have been successful in quantitatively describing the pion $v_2(p_{\rm T})$ in the region $p_{\rm T} < 1.5$ GeV/c. However, it has also been well-established that the pion $v_2(p_{\rm T})$ deviates from the hydrodynamic prediction above 1.5 GeV/c, a result that is understood to imply the contribution of hard processes, distortions of the spectrum due to recombination at freeze-out, and/or effects from dispersive hadronic evolution after freeze-out. Thus, a change in the variation of v_2 with $p_{\rm T}$ near $p_{\rm T} \sim 2$ GeV/c is not unexpected. If the large v_2 values at lower $p_{\rm T}$ are interpreted as resulting from soft, collective mechanismsm, then a decrease in v_2 for $p_{\rm T} > 3$ GeV/c suggested by the data in Fig. 4 would naturally reflect an increasing contribution of hard processes with smaller v_2.

To statistically test the significance of the decrease of v_2 with $p_{\rm T}$, we show in Fig. 6 the results of linear fits to the high-$p_{\rm T}$ v_2 values for the 20-30% and 30-40% centralities. The panels on the left-hand side of Fig. 6 display a series of fits beginning at higher $p_{\rm T}$ values, the first fit starting at the $p_{\rm T}$ near the maximum v_2, $p_{\rm T} = 2.5$ GeV/c. The right-hand panels show the 1-σ limits of the functions for the three fits in the series, calculated from the 1-σ variation of the two fit parameters (and including the covariance between them). The results of the fits indicate that the decrease of v_2 with $p_{\rm T}$ at higher $p_{\rm T}$ is statistically significant, though the data points for $p_{\rm T} > 5$ GeV/c are not sufficient by themselves to establish a trend. We can state, however, that the points for $p_{\rm T} > 5$ GeV/c are consistent with the linear decrease obtained including the lower $p_{\rm T}$ points. A question we would like to answer, then, is whether the data show any indications of devation from a monotonic decrease in $v_2(p_{\rm T})$ indicating the transition to a quenching-dominated azimuthal variation.

A complete understanding of $v_2(p_{\rm T})$ over the measured $p_{\rm T}$ range therefore requires the treatment of the transition from soft to hard dominated physics. According to the above discussion, in the $p_{\rm T}$ range where v_2 is maximum, particle production is likely not dominated by hard processes and the reduction of v_2 with increasing $p_{\rm T}$ indicates increasing hard-scattering contributions (or decreasing soft contamination). Motivated by this general argument, we have attempted to describe the results in Figs. 4 and 5 by a functional form

$$v_2(p_{\rm T}) = \left(\frac{(p_{\rm T}/\lambda)^m}{1+(p_{\rm T}/\lambda)^m}\right)\left(a + \frac{1}{p_{\rm T}^n}\right). \qquad (13)$$

The first term is intended to describe a rapidly rising and saturating soft v_2 resulting from collective motion while the second term represents a rapidly falling soft/hard ratio. The additive constant in the second term represents an asymptotic v_2 that could describe a constant or slowly varying azimuthal-dependent quenching. We show in Figs. 7-8 the optimum fits to the full set of $v_2(p_{\rm T})$ values in the different centrality bins and the result of 1σ variation of the fit parameters taking into account the complete covariance matrix from the fits.

The fits to the data show that the measured $p_{\rm T}$ dependence of the π^0 v_2 is qualitatively compatible with a description of the of low and intermediate $p_{\rm T}$ region in terms of a collective flow modulation diluted by a decreasing relative soft contribution with increasing $p_{\rm T}$. Assuming this picture, it is then important to determine at what $p_{\rm T}$ the contamination from the soft production no longer dominates the measured $\Delta\phi$ variation of π^0 yield. For most of the centrality bins, the fits suggest that v_2 decreases over most of the measured $p_{\rm T}$ range albeit with a decreasing slope at higher $p_{\rm T}$. The central bins are compatible with v_2 continuing to decrease beyond the measured $p_{\rm T}$ range although the 1σ uncertainty bands also accommodate v_2 saturating within the measured range. The more peripheral bins (30-40% and 40-50%) suggest that the v_2 has reached a nearly $p_{\rm T}$ independent value by ~ 5 GeV/c. The 50-60% centrality bin has sufficient fluctuations that little can be inferred from the $p_{\rm T}$ dependence of v_2 in that centrality bin. In all of the centrality bins, the data are consistent with a smooth reduction of $v_2(p_{\rm T})$ from a maximum to a nonzero value at high $p_{\rm T}$ with that value increasing in more peripheral collisions as would be expected from quenching in an increasingly anisotropic medium. While the functional form in Eq. 13 can describe the $p_{\rm T}$ variation of v_2 within the range of the current data and within the statistical fluctuations of the data points, it is possible that this description will fail at higher $p_{\rm T}$ with improved statistics. In fact, a statistically significant deviation of $v_2(p_{\rm T})$ from the form in Eq. 13 might provide the most direct evidence of the dominance of quenching effects in

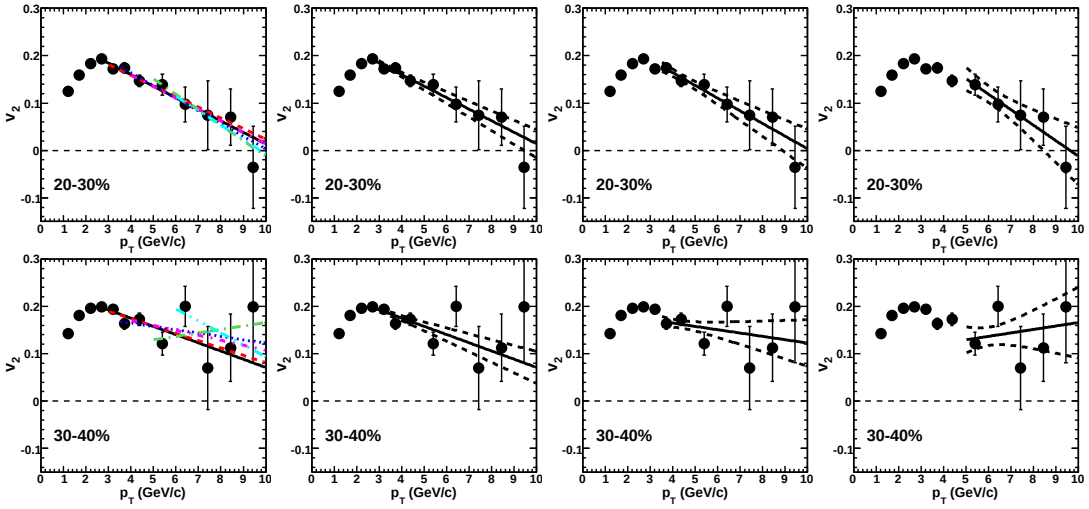

FIG. 6: (Color online) v_2 versus $p_{\rm T}$ for 20-30% and 30-40% centralities, with fits of the high-$p_{\rm T}$ data to a first order polynomial. From right to left, the first panel shows the series of fits, with each fit starting with a successively higher $p_{\rm T}$. The second, third, and fourth panels show selected fits with uncertainty bands based on the 1-σ variation of the fit parameters, including their covariance.

determining v_2.

B. Nuclear modification factor with respect to the reaction plane

The nuclear modification factor as a function of $\Delta\phi$ for six centrality bins is shown in Figs. 9-14. The closed circles represent the $\Delta\phi$-dependent measurements described in this paper while the open circles positioned at $\Delta\phi = \pi/4$ represent the inclusive $R_{\rm AA}$ measurement [19]. In both cases statistical uncertainties (i.e. Type A) are represented by the error bars. For the inclusive $R_{\rm AA}$ measurement, the total systematic uncertainties (or Type C [45]) are shown by the boxes. The upper and lower 1σ ranges of the correlated statistical uncertainties (i.e. Type B) on the $R_{\rm AA}(\Delta\phi)$ measurements resulting from the reaction plane resolution correction are shown by the (blue) solid and (red) dashed lines. For all bins except the 0-10% centrality bin a dotted line is plotted at $R_{\rm AA} = 1$ for reference. We note that by construction, the average $R_{\rm AA}(\Delta\phi)$ from the reaction plane dependent measurements must be equal to the inclusive $R_{\rm AA}$.

The results in the Figs. 9-14 show that the in-plane π^0 suppression is generally weaker and varies more rapidly with $p_{\rm T}$ than the suppression for π^0s produced at larger angles. As the collisions become more peripheral (for example, 50-60%), the small suppression seen in the inclusive $R_{\rm AA}$ almost vanishes for π^0s emitted close to the reaction plane. In a previous analysis [25], it was observed that the in-plane $R_{\rm AA}$ even exceeded unity for peripheral collisions; these data exhibit no such enhancement. However, the results presented in this article agree within systematic errors with previously reported data.

The $R_{\rm AA}(\Delta\phi)$ results are combined in Fig. 15 that shows the $p_{\rm T}$ dependence of the $R_{\rm AA}$ in each of the six $\Delta\phi$ bins included in this analysis. We use a semi-log scale so that the reduction of the $\Delta\phi$-integrated $R_{\rm AA}$ in more

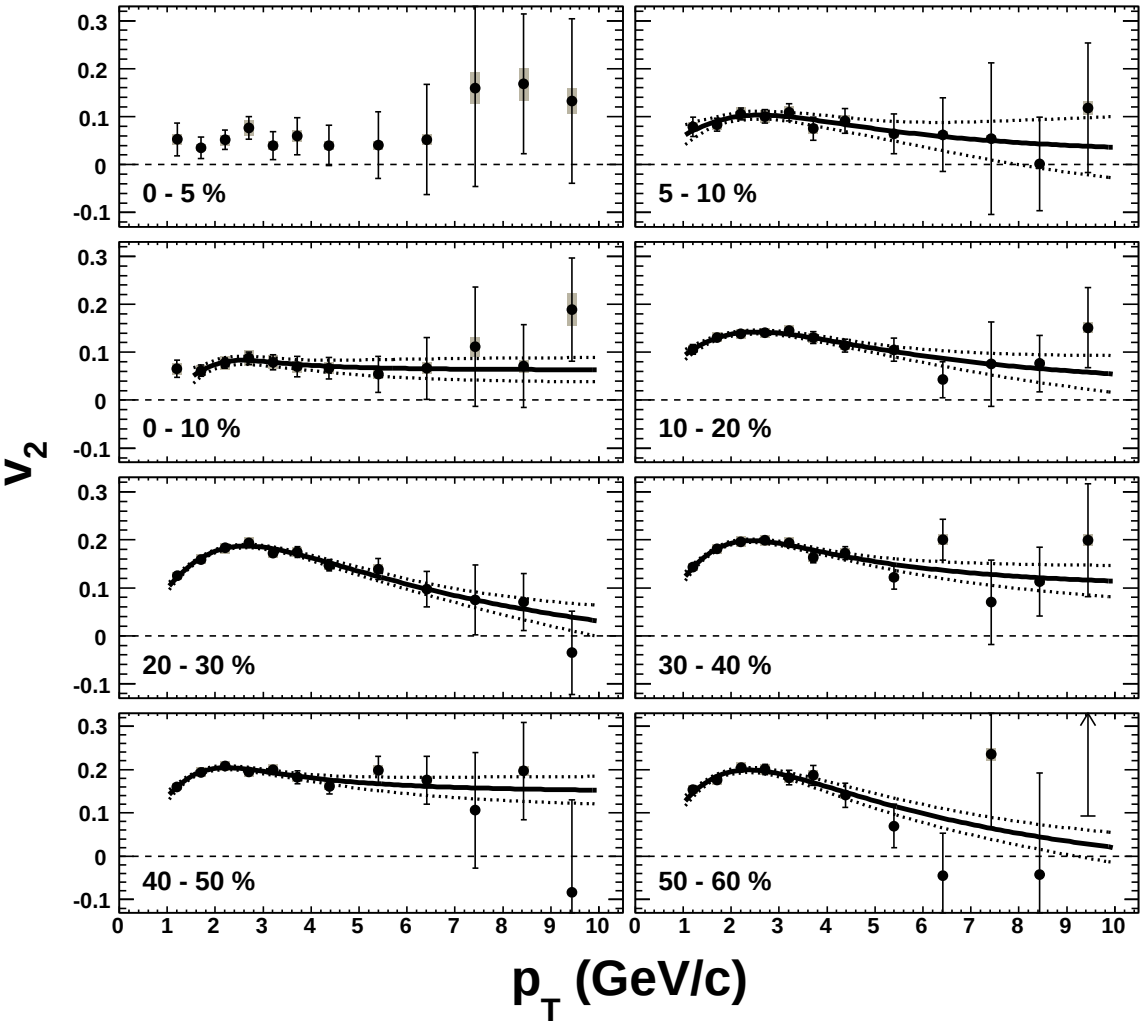

FIG. 7: π^0 v_2 versus $p_{\rm T}$ for centralities 0-5%, 5-10%, 0-10%, 10-20%, 20-30%, 30-40%, 40-50%, and 50-60%. The arrow in the 50-60% panel shows the lower limit of the uncertainty on the data point, which lies outside the bounds of the plot. The solid lines represent the fit to the data, Eq. 13. The dashed lines represent the 1 σ deviations of the fit function. See text for more details.

central collisions does not confuse the interpretation of the results. For clarity, the results from the 20-30%, 30-40%, 40-50%, and 50-60% centrality bins are shown on linear plots in Fig. 16.

The $R_{\rm AA}(p_{\rm T})$ results exhibit a peak near 2 GeV/c, which becomes more prominent for more central collisions. The peak is strongest in the 0-10% bin where there is little modulation of the $\Delta\phi$ distributions at low or high $p_{\rm T}$, so the peak cannot be directly attributed to elliptic flow. The peak in $R_{\rm AA}$ near 2 GeV/c is much weaker in the more peripheral (40-50% and 50-60%) centrality bins, particularly for π^0s produced at larger $\Delta\phi$, and the primary variation seen in these peripheral bins with increasing $\Delta\phi$ is a reduction in $R_{\rm AA}$ that is only weakly $p_{\rm T}$ dependent.

For the intermediate centrality bins (10-20% through 30-40%) the peaking in $R_{\rm AA}$ is seen in all $\Delta\phi$ bins, but is much stronger in the in-plane bins. For these intermediate centralities and for $p_{\rm T}$ values above the peak in $R_{\rm AA}$ ($p_{\rm T} \gtrsim 3$ GeV/c), the $R_{\rm AA}$ for π^0s produced at angles normal to the reaction plane is nearly constant with $p_{\rm T}$ while the $R_{\rm AA}$ for π^0s produced at small angles from the reaction plane decreases rapidly with increasing $p_{\rm T}$. The near constancy of the out-of-plane $R_{\rm AA}$ together with the rapid reduction in in-plane $R_{\rm AA}$ indicates that in the intermediate centrality bins, the v_2 and inclusive $R_{\rm AA}$ decrease simultaneously with increasing $p_{\rm T}$ such that $R_{\rm AA}(\pi/2, p_{\rm T}) = R_{\rm AA}(p_{\rm T})(1 - 2v_2)$ is approximately constant. We will argue below that a correlation between $R_{\rm AA}$ and v_2 may naturally result from the underlying physics responsible for the azimuthal variation of the particle yields. However, we observe that a simultaneous reduction in integrated $R_{\rm AA}$ and v_2 suggested by the more central $R_{\rm AA}(p_{\rm T})$ data would be contrary to

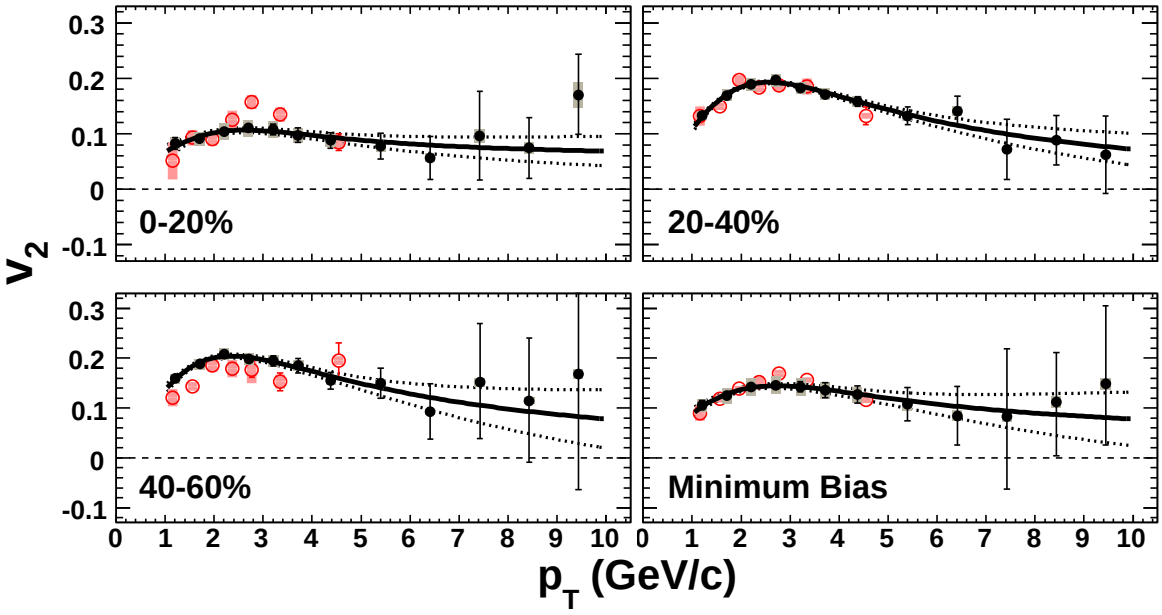

FIG. 8: (Color online) π^0 v_2 versus $p_{\rm T}$ for centralities 0-20%, 20-40%, 40-60%, and minimum bias. The closed (black) circles are data presented in this paper, and the open (red) circles are previously published results [40]. The solid and dashed lines as in Fig. 7.

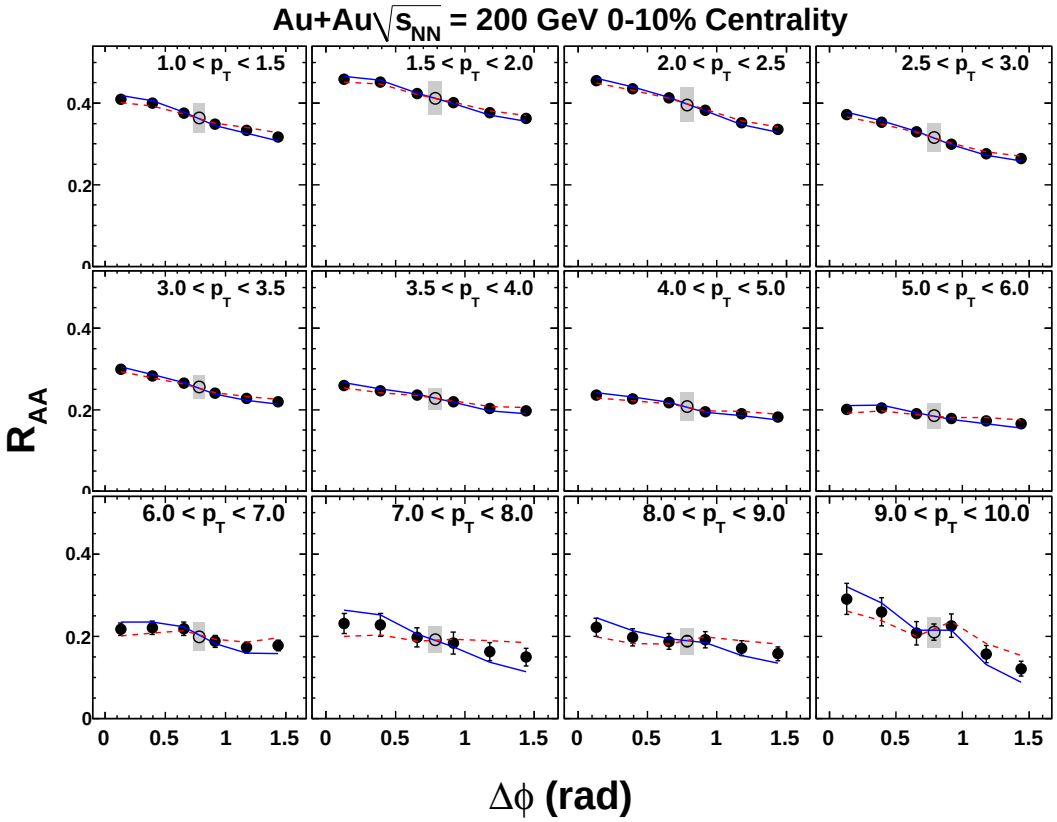

FIG. 9: (Color online) π^0 $R_{\rm AA}$ versus angle of emission with respect to the reaction plane for 0-10% centrality. The error bars denote the statistical errors, while the solid (blue) line and dashed (red) line represent the systematic error due to the resolution correction factor. The inclusive $R_{\rm AA}$ measurement is shown with the open circle, for which the error bar shows the statistical error and the box shows the systematic error.

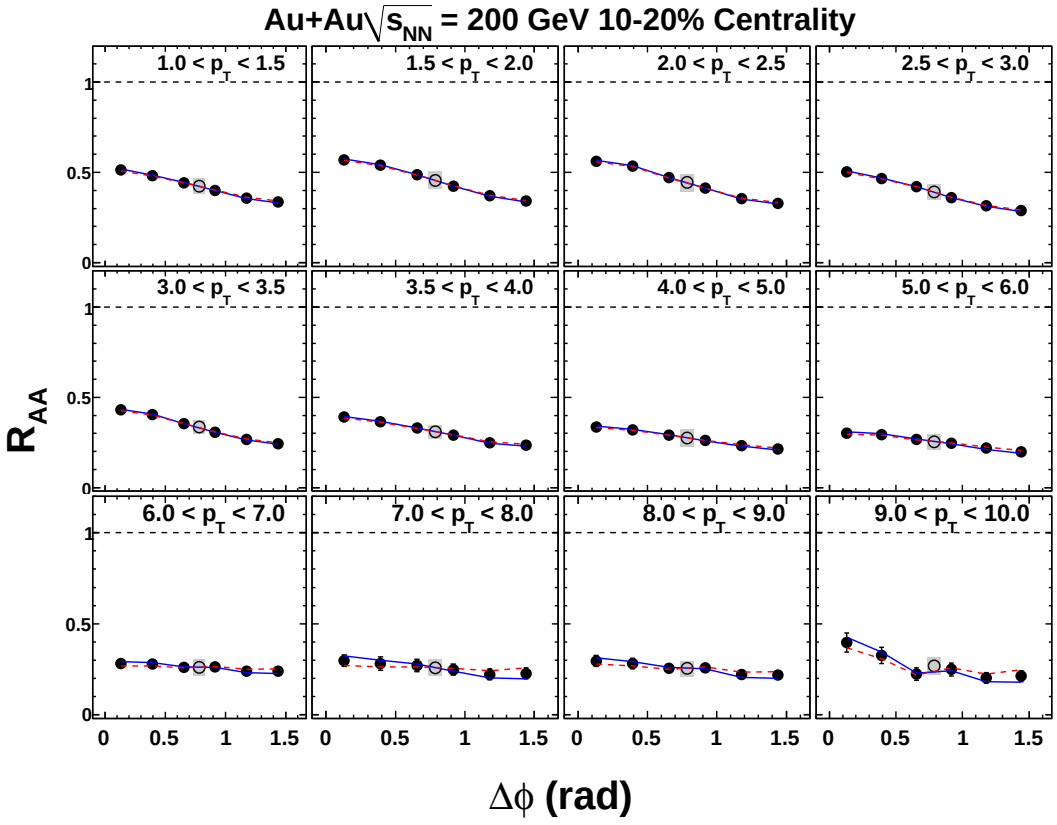

FIG. 10: π^0 $R_{\rm AA}$ versus angle of emission with respect to the reaction plane for 10-20% centrality. Colors/data points as in Fig. 9.

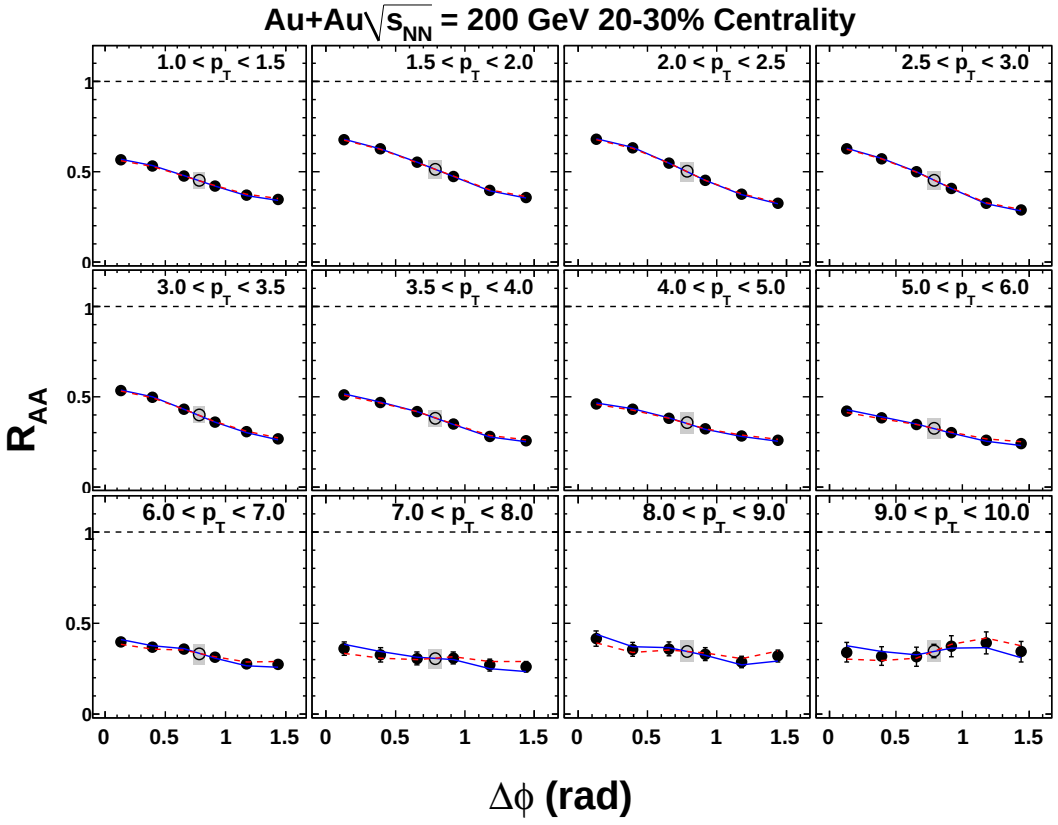

FIG. 11: π^0 $R_{\rm AA}$ versus angle of emission with respect to the reaction plane for 20-30% centrality. Colors/data points as in Fig. 9.

naive energy loss expectations since smaller $R_{\rm AA}$ would imply stronger quenching in the medium which would, in turn, imply larger variation between in-plane and out-of-plane quenching.

A similar implicit correlation between integrated $R_{\rm AA}$ and v_2 is seen in the centrality dependence of the $R_{\rm AA}(\Delta\phi)$ results. These are re-plotted in Fig. 17 as a function of $N_{\rm part}$ for three $\Delta\phi$ bins – the bins closest to and further from the reaction plane and one of the intermediate bins. For $N_{\rm part} > 100$, the out-of-plane $R_{\rm AA}$ values are nearly independent of centrality while the in-plane $R_{\rm AA}$ values decrease rapidly with increasing centrality. This result would have a natural geometric interpretation for π^0 production dominated by hard scattering and jet quenching. The length of the medium normal to the reaction plane varies only slowly with centrality except in the most peripheral collisions. Then, if the π^0 suppression is determined primarily by the path length of its parent parton in the medium, the π^0 $R_{\rm AA}$ would be nearly constant. Following the same argument, the yield for pions in the direction of the reaction plane would be much less suppressed in non-central collisions due to the short path lengths of the parent partons in the medium. However, with increasing centrality and decreasing anisotropy of the collision zone, the in-plane parton path lengths would grow to match those in the out-of-plane direction. Thus, if the π^0 suppression depended primarily on path length, the in-plane $R_{\rm AA}$ would naturally drop to match the out-of-plane values reproducing the behavior of Fig. 17. In order to better see the difference between the in- and out-of-plane behaviors, these data are also plotted on Fig. 18 with a semi-log scale.

One difficulty with this geometric interpretation of the $R_{\rm AA}(\Delta\phi)$ results given above is that the trend in the data that it is supposed to explain persists down to low $p_{\rm T}$, where the v_2 values are too large to be accounted for via perturbative or formation time based energy loss scenarios [26, 27, 28, 29, 30, 49]. That fact coupled with the pronounced peaking in $R_{\rm AA}(\Delta\phi)$ near 2 GeV/c suggests that physics other than hard scattering and jet quenching must be invoked to explain the π^0 yields at intermediate $p_{\rm T}$. However, the fact that the out-of-plane yields show less pronounced peaking near 2 GeV/c, that they vary little as a function of $p_{\rm T}$ above 3 GeV/c, and that they vary little with centrality for $N_{\rm part} > 100$ could be interpreted to imply that the π^0 suppression at angles normal to the reaction plane more directly represents the effects of quenching of hard quarks and gluons while the yield of π^0s produced more closely aligned with the reaction plane is enhanced by the collective motion of the system. That additional enhancement could either be due to soft hadrons being boosted to larger $p_{\rm T}$ values by the collec-

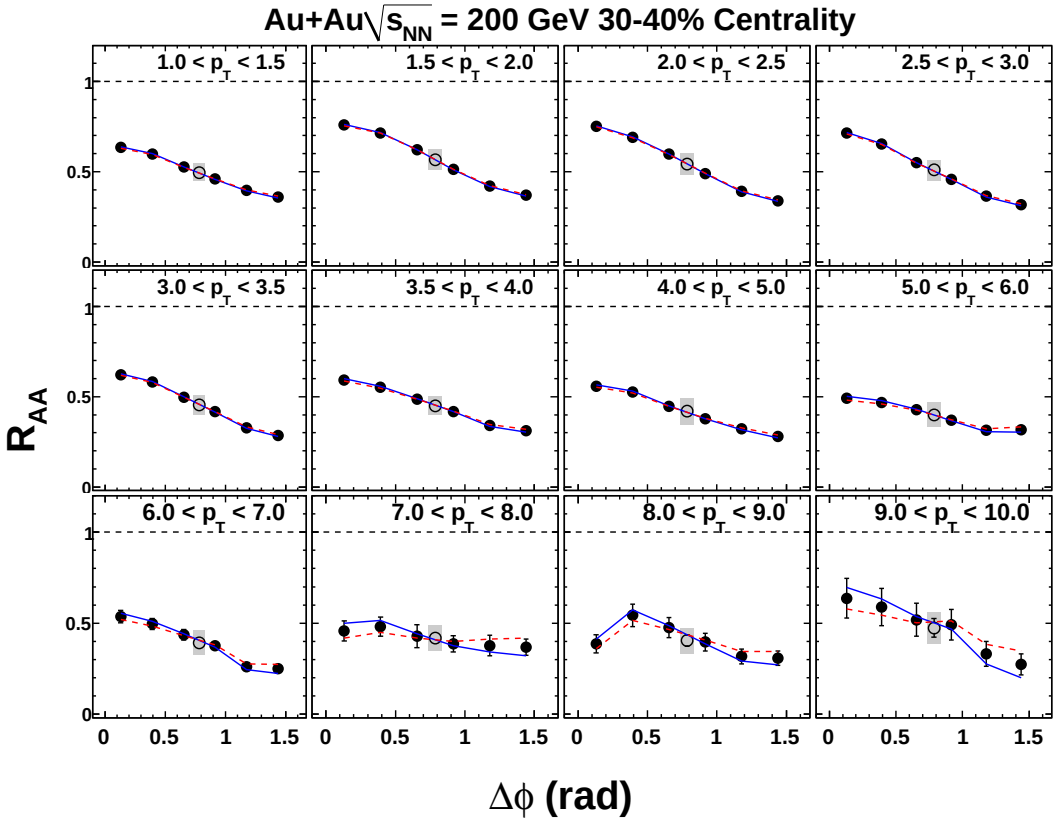

FIG. 12: π^0 $R_{\rm AA}$ versus angle of emission with respect to the reaction plane for 30-40% centrality. Colors/data points as in Fig. 9.

tive elliptic flow or could result from weaker quenching for partons moving in the direction of the flow field [27, 50]. Simultaneous description of the in-plane and out-of-plane behavior is a sensitive test of energy loss models.

The v_2 values presented in Figs. 7-8 also peak near 2 GeV/c, but the locations of the maxima in v_2 are shifted to higher $p_{\rm T}$ than the maxima in $R_{\rm AA}(\Delta\phi)$. This suggests that the two effects may not directly related, but we observe that the maxima in the $R_{\rm AA}(p_{\rm T})$ distributions in Figs. 15-16 shift to larger $p_{\rm T}$ for smaller $\Delta\phi$. To better illustrate the shift of the maxima in $R_{\rm AA}(p_{\rm T})$ we show in Fig. 19 the $R_{\rm AA}(p_{\rm T})$ values for the different $\Delta\phi$ bins and indicate the variation of the peak position obtained using polynomial fits to the first four $p_{\rm T}$ bins. For the 30-40% centrality bin, the maximum in $R_{\rm AA}(p_{\rm T})$ for $\Delta\phi < \pi/12$ is shifted by 0.4 GeV/c relative to the $5\pi/12 < \Delta\phi < \pi/2$ bin. This shift in the peak $R_{\rm AA}(p_{\rm T})$ with $\Delta\phi$ can produce a $v_2(p_{\rm T})$ that peaks higher in $p_{\rm T}$ than the inclusive $R_{\rm AA}$.

The observed shift in the peak of $R_{\rm AA}(p_{\rm T})$ with $\Delta\phi$ illustrates an important property of collective motion of the medium. The collective motion does not simply superimpose azimuthal variation on the particles produced at a given $p_{\rm T}$, it provides a $\Delta\phi$ dependent shift and/or broadening in the transverse momentum spectrum of the produced particles. The resulting distortion will be the smallest for particles produced at angles normal to the reaction plane and will be largest for particles produced in the plane. Any collective shift of soft particles to higher $p_{\rm T}$ will increase the measured $R_{\rm AA}(\Delta\phi, p_{\rm T})$ for small $\Delta\phi$ relative to large $\Delta\phi$ values producing a simultaneous increase in both the $\Delta\phi$-integrated $R_{\rm AA}$ and the v_2. With increasing $p_{\rm T}$, an expected decrease in the soft contamination would naturally explain the simultaneous reduction in v_2 and $\Delta\phi$-integrated $R_{\rm AA}$ evident in the 10-20% and 20-30% bins where the separation between the $R_{\rm AA}(p_{\rm T})$ curves for different $\Delta\phi$ bins decreases while the average $R_{\rm AA}$ also decreases. We will return to investigate this correlation again below.

The 40-50% and 50-60% centrality bins in Fig. 15 show little of the peaking near 2 GeV/c, especially in $\Delta\phi$ bins not aligned with the reaction plane. Nonetheless the v_2 values for the more peripheral bins reach the same large maximum values, $v_2 \sim 0.2$, at intermediate $p_{\rm T}$ as the v_2 values for more central bins where the peak in $R_{\rm AA}(p_{\rm T})$ is more prominent. Thus, while the peaking in $R_{\rm AA}(p_{\rm T})$ is less prominent in the more peripheral bins, the relative difference between the in-plane and out-of-plane π^0 yields in the 40-50% centrality bin is comparable to that in the 20-30% centrality bin. However, it is possible that the large $\Delta\phi$ dependence in the more peripheral bins and the apparent persistence of that variation to high $p_{\rm T}$ in

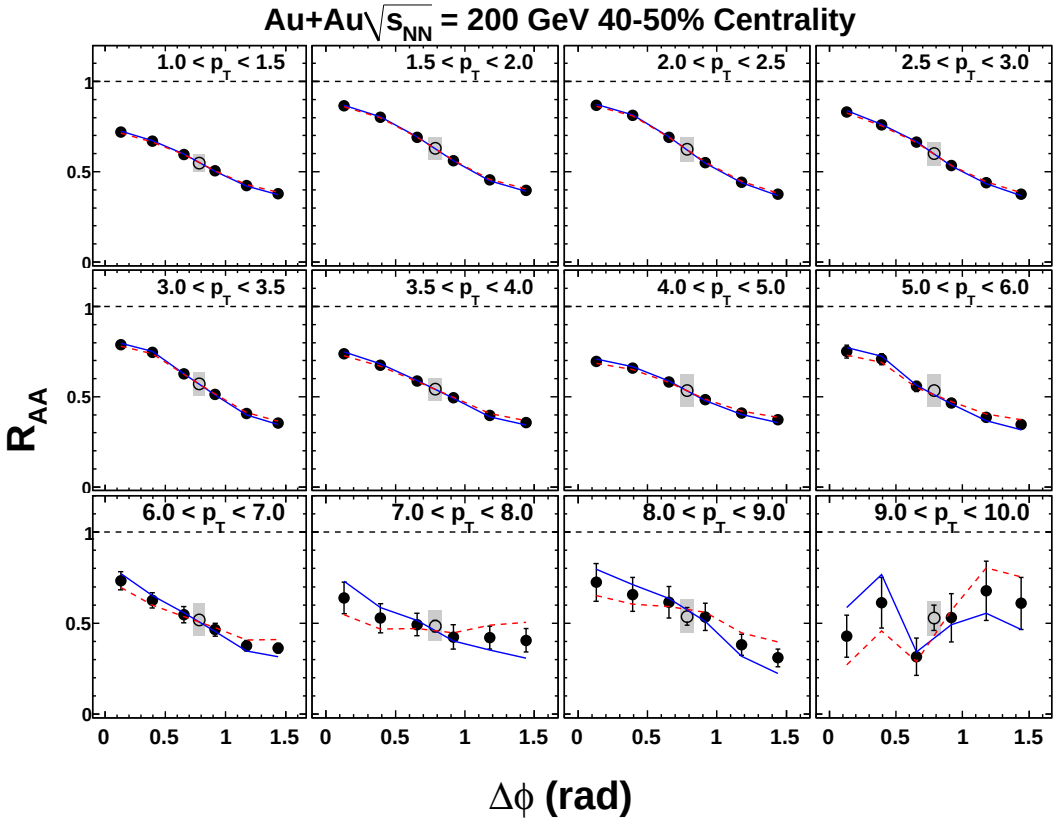

FIG. 13: π^0 $R_{\rm AA}$ versus angle of emission with respect to the reaction plane for 40-50% centrality. Colors/data points as in Fig. 9.

the 40-50% centrality bin more directly reflects the larger spatial anisotropy of the collision zone in more peripheral collisions. The question of whether the π^0 suppression measurements presented here can be understood on the basis of geometry and jet quenching will be more fully explored in the following section.

We have observed above that the $p_{\rm T}$ and centrality dependence of $R_{\rm AA}$ indicate a correlation between inclusive $R_{\rm AA}$ and v_2 such that the out-of-plane π^0 yields vary only slowly with $p_{\rm T}$ or centrality while the in-plane yields approach the out-of-plane yields with increasing $p_{\rm T}$ or increasing $N_{\rm part}$. Such a correlation between these two seemingly unrelated quantities merely indicates that the yields or $R_{\rm AA}$ of π^0's measured in-plane and out-of-plane more directly reflect the underlying physics responsible for the azimuthal variation than the $\Delta\phi$-integrated yield or $R_{\rm AA}$ and the amplitude of the $\Delta\phi$ modulation, v_2. Indeed, we have argued above that at higher $p_{\rm T}$ the centrality dependence of $R_{\rm AA}(\Delta\phi)$ may reflect the geometry of jet quenching. At intermediate $p_{\rm T}$, the $R_{\rm AA}(p_{\rm T})$ results suggest contamination of the in-plane yields by soft production and a simultaneous decrease in $R_{\rm AA}$ and v_2 with increasing $p_{\rm T}$ as the relative contribution of collective soft processes to π^0 production decreases. To more directly demonstrate the correlation that forms the basis of these arguments we show in Fig. 20 a plot of v_2 versus the inclusive $R_{\rm AA}$ for centralities from 0 to 60%. Data are displayed for $p_{\rm T} > 2$ GeV/c. The intermediate centrality bins show a correlated increase of v_2 and $R_{\rm AA}$ consistent with the discussion above and a possible saturation of v_2 for larger $R_{\rm AA}$ values. In fact, the trends for different centrality bins appear to be in general agreement. However, their exact relationship and establishing or excluding a causal connection requires further investigation.

C. Nuclear modification factor dependence on path length

The centrality of a collision fixes the geometry of the overlap region between the nuclei, and fixing the angle of emission of the particles further constrains the path length through the medium. We can use this feature to study the dependence of the nuclear modification factor on the path length traversed by the partons. We investigate the path length dependence by expanding on several methods previously described in [25]. We start with three estimators of the path length that are purely geometric, and one that includes the color density of the medium in its calculation:

1. We start by modeling the overlap region as an el-

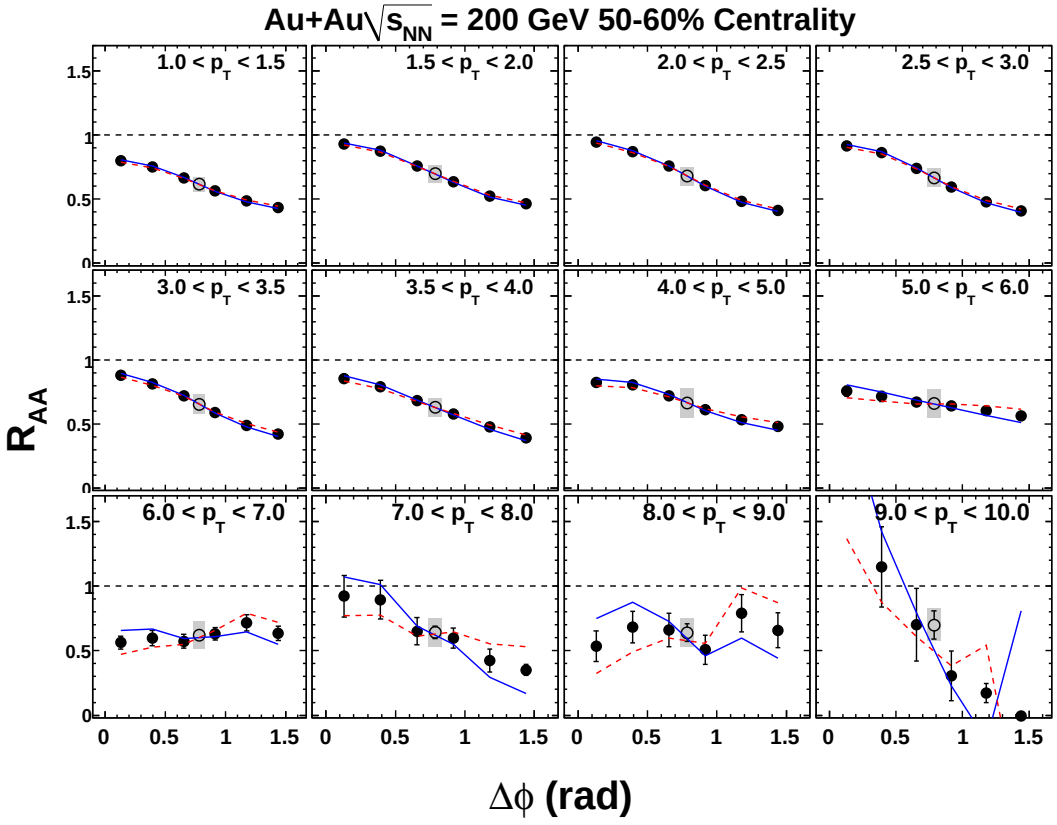

FIG. 14: π^0 $R_{\rm AA}$ versus angle of emission with respect to the reaction plane for 50-60% centrality. Colors/data points as in Fig. 9.

lipse defined by

$$\frac{x^2}{b^2} + \frac{y^2}{a^2} = 1 \tag{14}$$

where the minor axis b is oriented in the x direction and is parallel to the reaction plane. The axes a and b are fixed by the intersection in the transverse plane of two hard spheres with $R = 6.8$ fm. In terms of the spatial eccentricity $\epsilon = \langle y^2 - x^2 \rangle / \langle y^2 + x^2 \rangle$ (often used with Glauber calculations), we can express the distance from the origin to the edge of the ellipse at a given angle:

$$L_\epsilon(\Delta\phi) = \frac{b\sqrt{1+\epsilon}}{\sqrt{1+\epsilon\cos 2\Delta\phi}}. \tag{15}$$

Since this length starts at the origin, and does not take into account color density, the expression provides a very simple estimator with which we can evaluate the dependence of the $R_{\rm AA}$ on path length. We will refer to the hard sphere result as $L_{\epsilon,hs}$.

2. Instead of an ellipse strictly defined by the transverse profile of two hard spheres, we model the collision region as an effective ellipse whose dimensions are determined by equating the RMS radius and eccentricity to the corresponding quantities calculated from the transverse distribution of participant density based on standard Glauber calculations. This length, L_ϵ, is evaluated using the same expression as Eq. 15, with $b = \sqrt{x^2}$. Both quantities are determined using the PHENIX Glauber model [51].

3. For a more realistic approach, we evaluate the distance along the parton's path weighted by the participant density,

$$\rho L_{xy} = \int_0^\infty dl \rho_{\rm part}(x_0 + l\cos\Delta\phi, y_0 + l\sin\Delta\phi), \tag{16}$$

where (x_0, y_0) is the hard-scattering position and $\Delta\phi$ is the angle of the jet with respect to the x axis. The jet production point is sampled from a Monte Carlo using a weighted $T_{\rm AA}(x,y)$ distribution and a uniform $\Delta\phi$ distribution. The participant density, assumed to be proportional to the color density, is calculated from the Glauber model. The $\rho_{\rm part}$ density in Eq. 16 is modeled using a 1D Bjorken expansion,

$$\rho_c(\tau) \propto \left(\frac{\tau^2/\tau_0^2}{1+\tau^2/\tau_0^2}\right)\left(\frac{\tau_0}{\tau}\right).$$

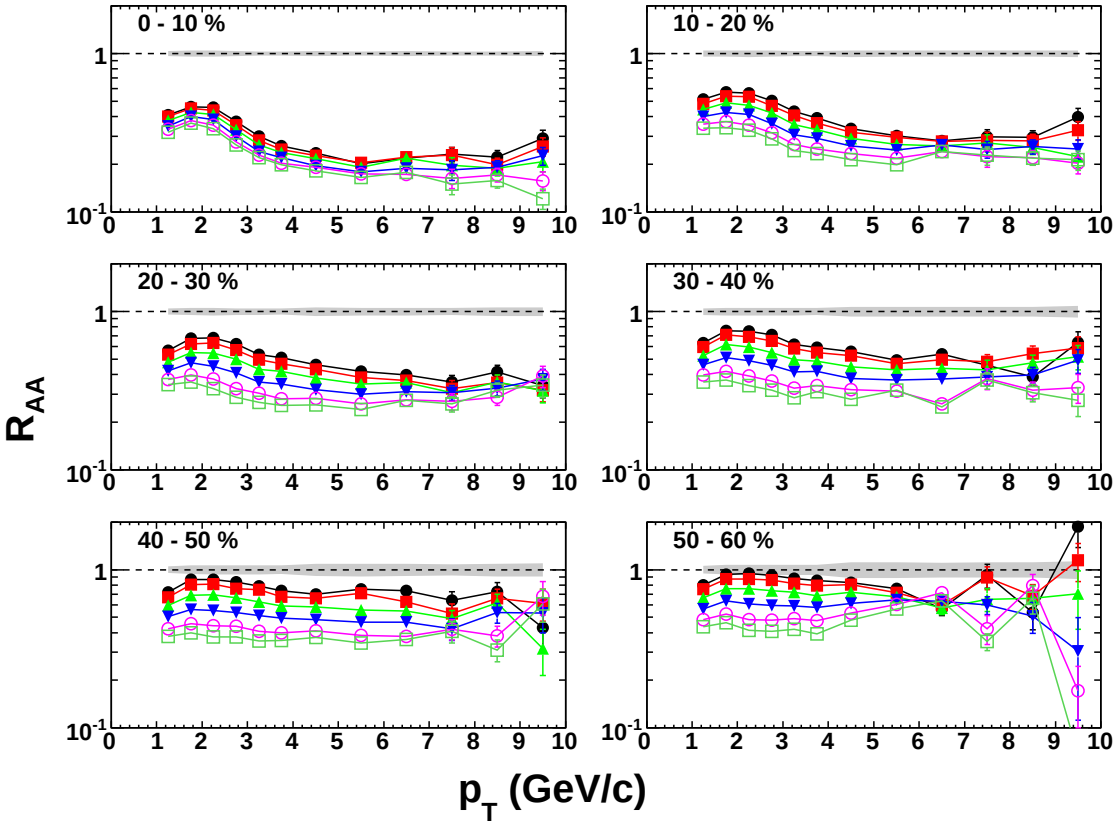

FIG. 15: (Color online) Semi-log plots of $R_{\rm AA}(p_{\rm T})$ for each $\Delta\phi$ bin, in different centrality ranges. The $\Delta\phi$ bins are represented as follows: closed (black) circles, 0-15°; closed (red) squares, 15-30°; closed (light green) triangles, 30-45°; closed inverted (blue) triangles, 45-60°; open (magenta) circles, 60-75°; and open (dark green) squares, 75-90°. The systematic error in the inclusive $R_{\rm AA}$ is represented by the grey bands. Errors due to the correction factor have been omitted for clarity.

Thus ρL_{xy} roughly represents LPM energy loss [52]. Note that ρ_c approaches the same $1/\tau$ dependence as the standard $\rho \propto \tau_0/\tau$ but differs from by a factor of 2 at $\tau = \tau_0$ (additionally this form is regular at $\tau = 0$).

4. Finally, we modify ρL_{xy} by normalizing it by the value of the participant density at the center of the collision region, $\rho_{\rm cent} = \rho_{\rm part}(0,0)$. As a result, $\rho L_{xy}/\rho_{\rm cent}$ is an estimator based on geometry alone, but also accounts for the effect of the density distribution both on the jet production point as well as the path from that point to the edge of the medium.

Figs. 21-24 show the $R_{\rm AA}$ dependence on $L_{\epsilon,hs}$, L_ϵ, ρL_{xy}, and $\rho L_{xy}/\rho_{\rm cent}$ respectively. The results shown in this paper cover the $p_{\rm T}$ range $p_{\rm T}$ = 1-10 GeV/c, not only extending the measurement presented previously but allowing a much finer binning in $p_{\rm T}$. The statistical errors in the $R_{\rm AA}$ measurements are represented by error bars (see Section IV B). The systematic errors shown in these data are on the $R_{\rm AA}$ values only, and are indicated by the filled boxes. The major contribution to the systematic error in the L_ϵ values is the determination of $N_{\rm part}$, and is at the 10-20% level.

Both the $L_{\epsilon,hs}$ and L_ϵ behavior show an interesting degree of scaling. This result is all the more unexpected because of the overly simple geometric picture they represent. Despite the simplistic picture they present, they both exhibit striking universality: the hard sphere $R_{\rm AA}(L_{\epsilon,hs})$ scales well in the low $p_{\rm T}$ region (as high as $p_{\rm T} \approx 4$ GeV/c) while $R_{\rm AA}(L_\epsilon)$ scales well to higher $p_{\rm T}$, at least one bin in $p_{\rm T}$ beyond $L_{\epsilon,hs}$ (though one might argue qualitatively this trend continues even higher when the most peripheral centrality is excluded). The more precise $p_{\rm T}$ dependence available in this data set reveals a slight deviation from the universality with L_ϵ that was previously reported [25].

By contrast, we expect the ρL_{xy} estimator to provide a somewhat more intuitive and concrete picture, as it represents a more realistic approach to the geometry and medium. Since we expect radiative energy loss to play a greater role at high $p_{\rm T}$, this should be the estimator that would provide the best scaling. In fact, at the higher $p_{\rm T}$ range, a universality does emerge, though not until $p_{\rm T} \approx 6$ GeV/c. Below that value, the measured $R_{\rm AA}$

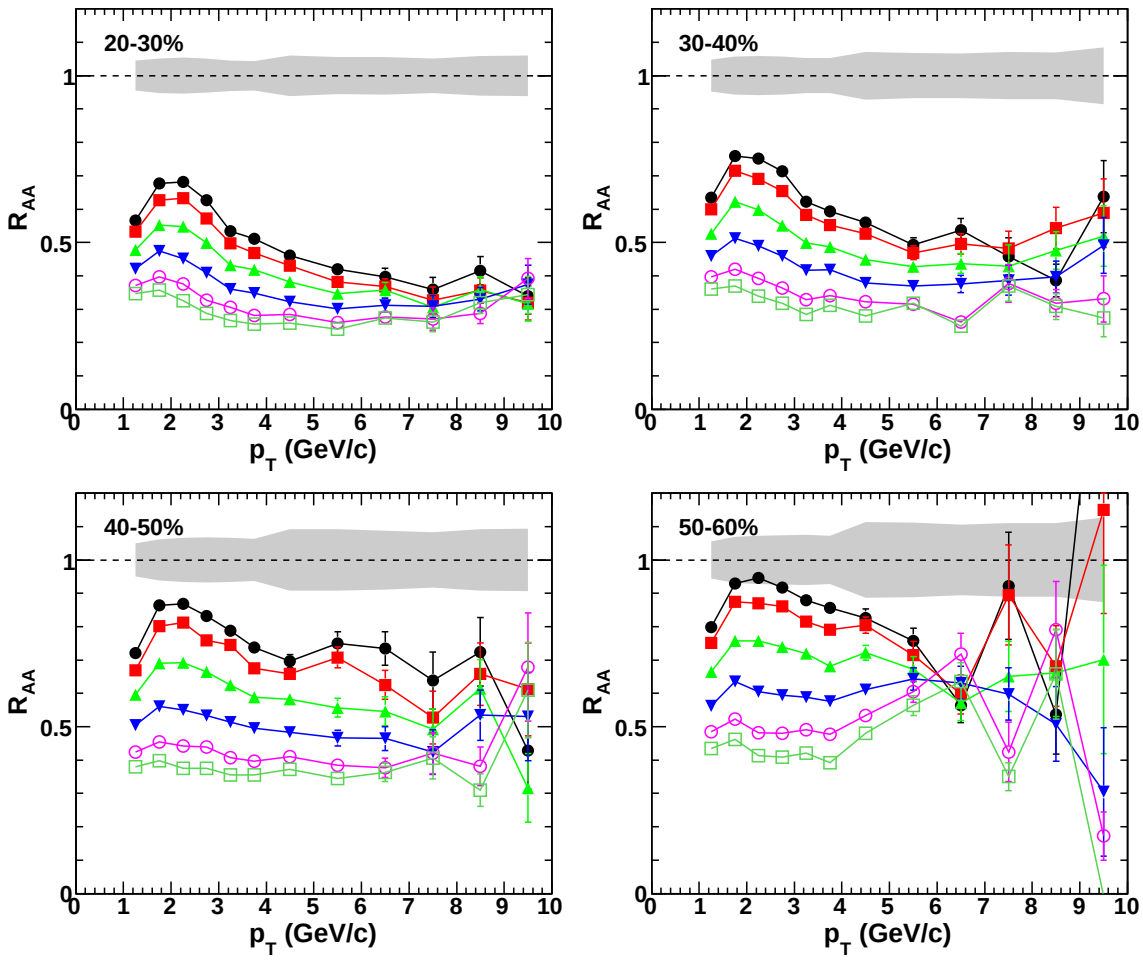

FIG. 16: (Color online) $R_{\rm AA}(p_{\rm T})$ for different $\Delta\phi$ bins in the 20-30%, 30-40%, 40-50%, and 50-60% centrality ranges. Colors/data points as in Fig. 15.

points lie on parallel, but separate, curves. When ρL_{xy} is normalized to the central density, data again exhibit a more universal dependence over a wider $p_{\rm T}$ range than what is seen with ρL_{xy} alone, as shown in Fig. 24.

When considered together these results offer a rich picture. At low to moderate $p_{\rm T}$ simple geometry may play a larger role in determining the final level of $R_{\rm AA}$ than conventionally thought. At higher $p_{\rm T}$ the scaling motivated by energy loss (ρL_{xy}) describes the data well. We note that there are three possible (and not necessarily exclusive) interpretations: 1) at low to moderate $p_{\rm T}$ the combined effects of the boost due to expansion and fragmentation are sensitive primarily to the difference in lengths traveled by the partons, and only weakly dependent on other parameters 2) we need to restrict the analysis of the π^0 $R_{\rm AA}$ to $p_{\rm T} > 5$ GeV/c to be in the range where fragmentation followed by energy loss dominates, or 3) the assumption that energy loss does not depend linearly on color density [34] is incorrect and leads a departure from scaling with ρL_{xy} at low to moderate $p_{\rm T}$.

V. SUMMARY AND CONCLUSIONS

We have presented measurements for the azimuthal anisotropy of neutral pions in Au + Au collisions at $\sqrt{s_{_{NN}}} = 200$ GeV. These measurements include the v_2 and $R_{\rm AA}(\Delta\phi)$ of π^0s as a function of transverse momentum and centrality. The v_2 has been measured from $p_{\rm T} \approx$ 1–10 GeV/c in eight centrality bins and four combined centrality bins. The $R_{\rm AA}$ has been measured in the same $p_{\rm T}$ range in six centrality bins. In addition, the $R_{\rm AA}$ dependence on effective path length through the collision region has been presented for five centralities.

The general trend seen in the $v_2(p_{\rm T})$ data is an initial increase in v_2 with increasing $p_{\rm T}$, peaking of the v_2 in the region of $2 < p_{\rm T} < 3$ GeV/c, followed by a decrease in the v_2. We have argued that such a trend implies a transition from particle production dominated by soft processes to a $p_{\rm T}$ region dominated by hard processes. In order to quantify the $p_{\rm T}$ and centrality evolution of v_2, we have fit its $p_{\rm T}$ dependence to an empirical expression that allows for such a transition. While the statistical precision of the

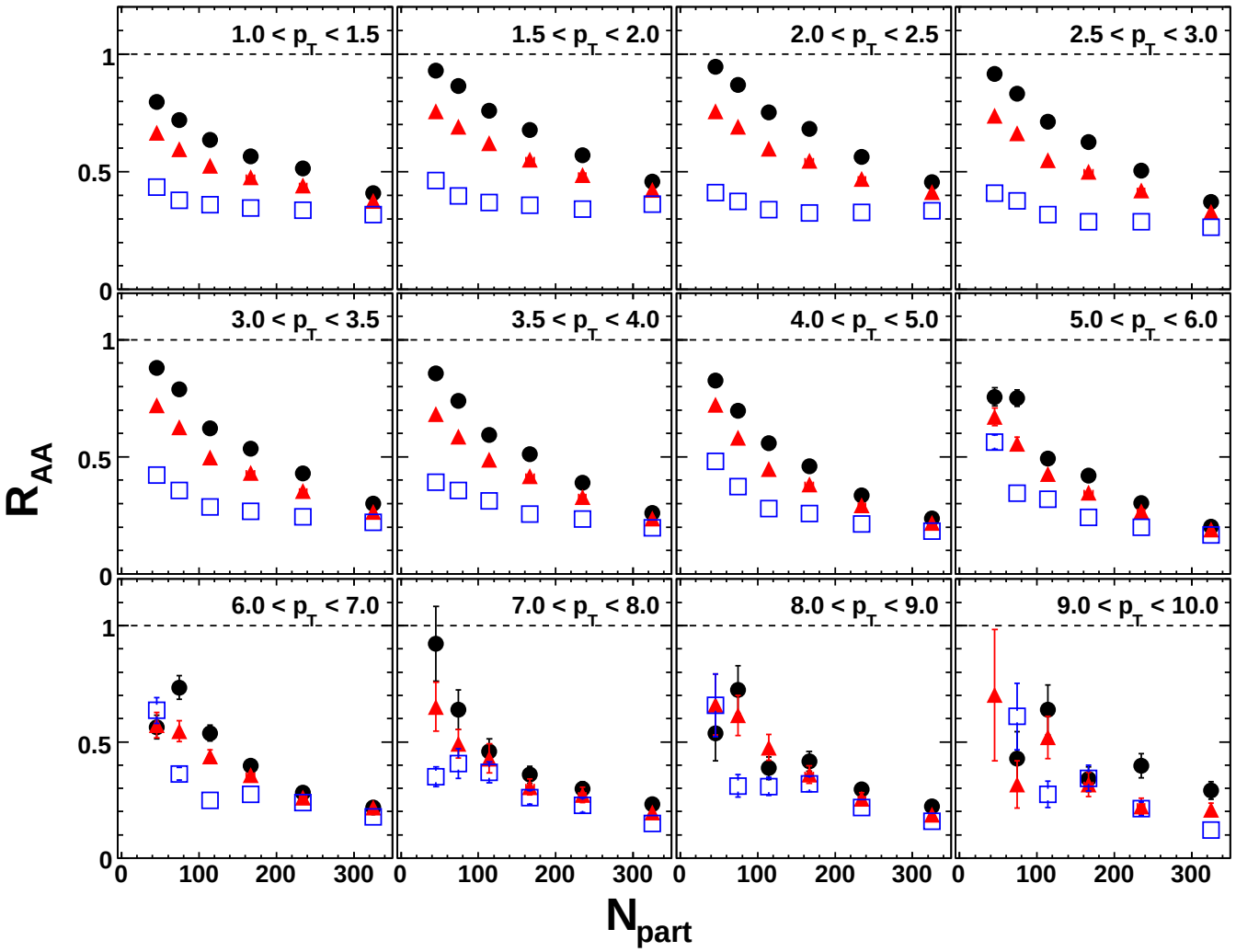

FIG. 17: (Color online) π^0 $R_{\rm AA}(N_{\rm part})$ in reaction-plane bins at fixed $p_{\rm T}$. The three bins are as follows: closed (black) circles are $R_{\rm AA}(0 < \Delta\phi < 15^\circ)$ (in plane), the closed (red) triangles are the $R_{\rm AA}(30 < \Delta\phi < 45^\circ)$, and open (blue) squares are $R_{\rm AA}(85 < \Delta\phi < 90^\circ)$ (out of plane).

high-$p_{\rm T}$ data limits the conclusions we can draw from the fits, it is clear that the data support the assumption of a decreased dominance of soft processes transitioning to an increased dominance of hard process with increasing $p_{\rm T}$. The more peripheral bins suggest that a $p_{\rm T}$-independent v_2 may be reached by $p_{\rm T} \sim 5$ GeV/c.

The differential probes represented by $R_{\rm AA}(\Delta\phi)$ provide a more sophisticated handle on the role of geometry in the collision region. For example, we see that in mid-centrality collisions the suppression of pions out-of-plane is approximately the same as the suppression in more central collisions. The data suggest that the interplay between the two main effects, namely collective flow and jet quenching, may take place not only along the expected transition in $p_{\rm T}$ from soft to hard physics, but perhaps also azimuthally, with the quenching effects being dominant along the direction normal to the reaction plane. To further shed light on the transition from soft to hard $p_{\rm T}$ regions, we have fit the maxima of mid-central $R_{\rm AA}(p_{\rm T})$ in each $\Delta\phi$ range. Between the in and out of plane directions, we observe a shift of 0.4 GeV/c in position of the peak of the spectrum.

In order to further clarify the centrality evolution of the azimuthal dependence of the π^0 suppression, we have presented the $R_{\rm AA}$ as a function of $N_{\rm part}$ in fixed $p_{\rm T}$ bins, for three directions: along the reaction plane, normal to the reaction plane, and midway between. For $N_{\rm part} \gtrsim 100$, the $R_{\rm AA}$ along the normal to the reaction plane is almost constant, a trend seen in most $p_{\rm T}$ bins. By contrast, the $R_{\rm AA}$ nearest to the reaction plane drops by almost a factor of two, converging on the out-of-plane value at the highest $N_{\rm part}$. This important feature may provide the most compelling argument for geometry as the source of suppression. Since the path length in the direction normal to the reaction plane varies slowly with centrality, we would expect the $R_{\rm AA}$ to be nearly flat. Conversely,

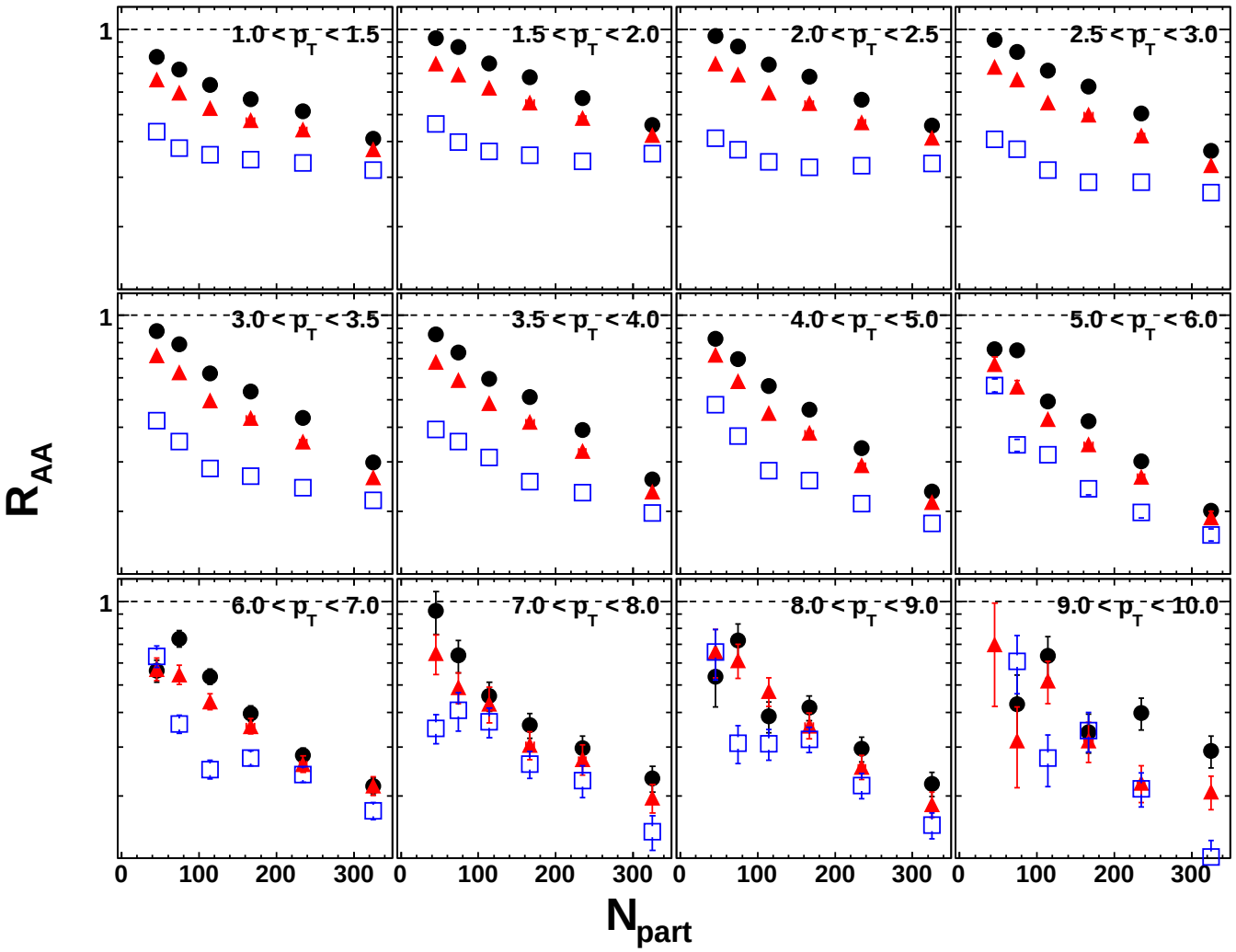

FIG. 18: (Color online) π^0 $R_{\rm AA}(N_{\rm part})$ in reaction-plane bins at fixed $p_{\rm T}$, with log scale on the y axis. Colors/data as in Fig. 17.

the in-plane path length will be sensitive to the degree of overlap and strongly influence the observed $R_{\rm AA}$. Thus it would lead to a small suppression in peripheral collisions while eventually converging on the same value as seen normal to the plane as the anisotropy vanishes in more central collisions. This effect is further borne out in the correlation observed between v_2 and the inclusive $R_{\rm AA}$. However, we have also argued that contamination from soft production could produce a similar behavior and we have no independent indication of how far in $p_{\rm T}$ soft contamination might extend. Nonetheless, under both interpretations we can conclude that the $R_{\rm AA}$ for pions produced along the normal to the reaction plane more directly reflects the physics of quenching. We also conclude that the correlation between $R_{\rm AA}$ and v_2 makes separate treatment of these quantities disadvantageous.

We have examined $R_{\rm AA}$ as function of the average path length of the parent parton through the overlap region in the collision, through the estimators $L_{\epsilon,hs}$, L_{ϵ}, $\rho L_{xy}/\rho_{\rm cent}$, and ρL_{xy}. Each of the first three quantities represents a progressively more sophisticated estimator for the distance traveled by the parton, with ρL_{xy} at the end providing a proxy for LPM energy loss. Comparison of the scaling with these three measures of lengths seems to suggest that the pion suppression at low- to moderate-$p_{\rm T}$ is mostly dependent upon simply the geometric length. The estimator that should in principle be the most realistic one, ρL_{xy}, exhibits good universality at the highest $p_{\rm T}$ values, suggesting that energy loss comparisons should be restricted to the $p_{\rm T}$ range $p_{\rm T} > 5$ GeV/c. The importance of simple geometry at low- to moderate-$p_{\rm T}$ is further supported when ρL_{xy} is normalized by the participant density at the center. This normalization effectively makes ρL_{xy} a length. These geometric descriptions offer a description of the suppression both at low and high $p_{\rm T}$ regions, clearly showing a transition between the ranges. The features seen in the $R_{\rm AA}$ as function of path length tie in consistently with the observations of a transition in the behavior of the measured v_2. These two observables, v_2 and $R_{\rm AA}(\Delta\phi)$, analyzed

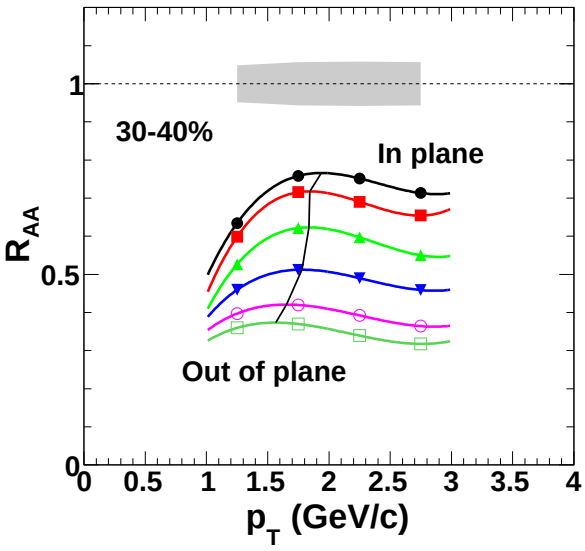

FIG. 19: (Color online) Illustration of the shift in the peak positions in $R_{\rm AA}(p_{\rm T})$ for the 30-40% centrality bin. Colors/data points as in Fig. 15.

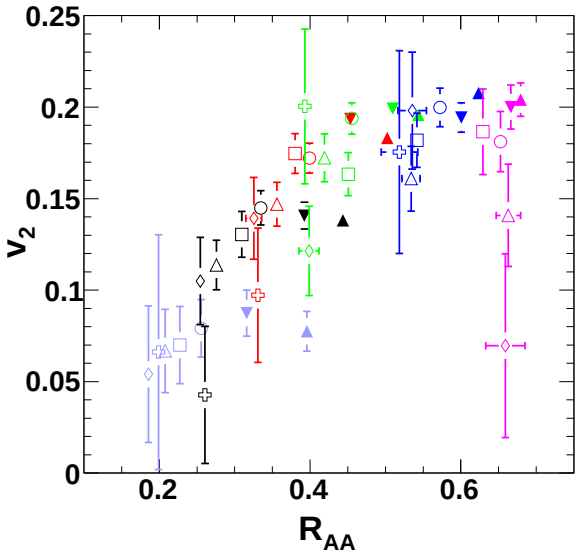

FIG. 20: (Color online) π^0 v_2 vs. inclusive $R_{\rm AA}$. The points denote bins in $p_{\rm T}$ as follows: triangles $2 < p_{\rm T} < 2.5$ GeV/c, inverted triangles $2.5 < p_{\rm T} < 3$ GeV/c, circles, $3 < p_{\rm T} < 3.5$ GeV/c; squares, $3.5 < p_{\rm T} < 4$ GeV/c; open triangles, $4.0 < p_{\rm T} < 4.5$ GeV/c; diamonds, $4.5 < p_{\rm T} < 5$ GeV/c; crosses, $5 < p_{\rm T} < 6$ GeV/c. Centrality bins are indicated by the colors: light blue, 0-10%; black, 10-20%; red, 20-30%; green, 30-40%; blue, 40-50%; magenta 50-60%.

together provide a valuable set of probes for understanding the processes governing the suppression of yields in Au + Au collisions.

Acknowledgments

We thank the staff of the Collider-Accelerator and Physics Departments at Brookhaven National Laboratory and the staff of the other PHENIX participating institutions for their vital contributions. We acknowledge support from the Office of Nuclear Physics in the Office of Science of the Department of Energy, the National Science Foundation, Abilene Christian University Research Council, Research Foundation of SUNY, and Dean of the College of Arts and Sciences, Vanderbilt University (U.S.A), Ministry of Education, Culture, Sports, Science, and Technology and the Japan Society for the Promotion of Science (Japan), Conselho Nacional de Desenvolvimento Científico e Tecnológico and Fundação de Amparo à Pesquisa do Estado de São Paulo (Brazil), Natural Science Foundation of China (People's Republic of China), Centre National de la Recherche Scientifique, Commissariat à l'Énergie Atomique, and Institut National de Physique Nucléaire et de Physique des Particules (France), Ministry of Industry, Science and Tekhnologies, Bundesministerium für Bildung und Forschung, Deutscher Akademischer Austausch Dienst, and Alexander von Humboldt Stiftung (Germany), Hungarian National Science Fund, OTKA (Hungary), Department of Atomic Energy (India), Israel Science Foundation (Israel), Korea Research Foundation and Korea Science and Engineering Foundation (Korea), Ministry of Education and Science, Rassia Academy of Sciences, Federal Agency of Atomic Energy (Russia), VR and the Wallenberg Foundation (Sweden), the U.S. Civilian Research and Development Foundation for the Independent States of the Former Soviet Union, the US-Hungarian NSF-OTKA-MTA, and the US-Israel Binational Science Foundation.

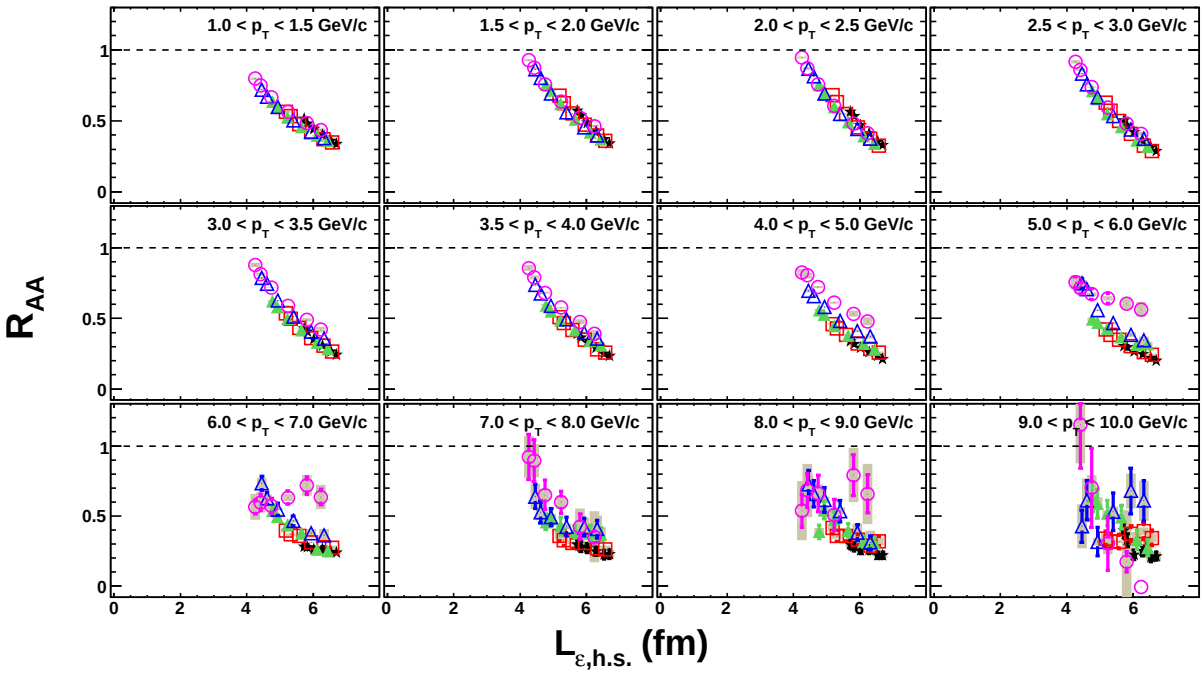

FIG. 21: (Color online) π^0 $R_{\rm AA}$ versus L_ϵ based on the hard sphere calculation. Each panel corresponds to a $p_{\rm T}$ bin. Each data point corresponds to a particular centrality bin and $\Delta\phi$ value. The centralities are represented as follows: (black) stars, 10-20%; open (red) squares, 20-30%; (green) triangles, 30-40%, open (blue) triangles, 40-50%; open (magenta) circles, 50-60%. The height of the boxes represent the systematic errors on $R_{\rm AA}$ for the corresponding L_ϵ.

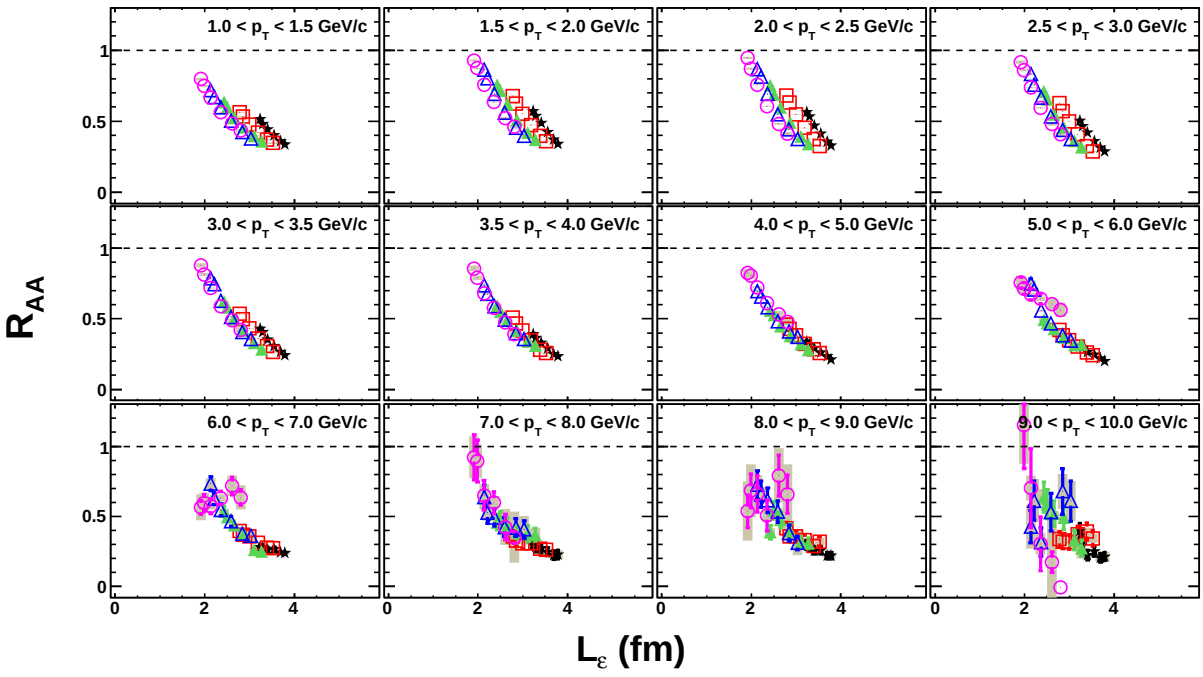

FIG. 22: (Color online) π^0 $R_{\rm AA}$ versus L_ϵ based on the RMS radius. Colors/data points as in Fig. 21.

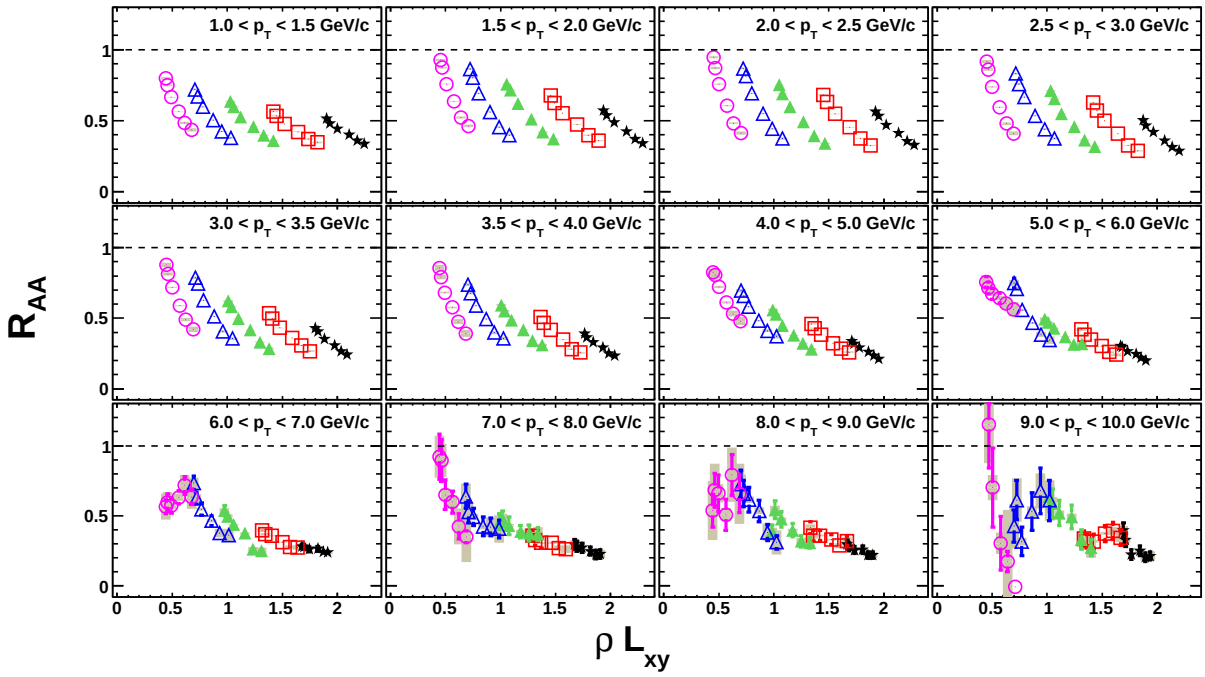

FIG. 23: (Color online) π^0 $R_{\rm AA}$ versus ρL_{xy}. The units of ρL_{xy} are participant $\times$ fm. Colors/data points as in Fig. 21.

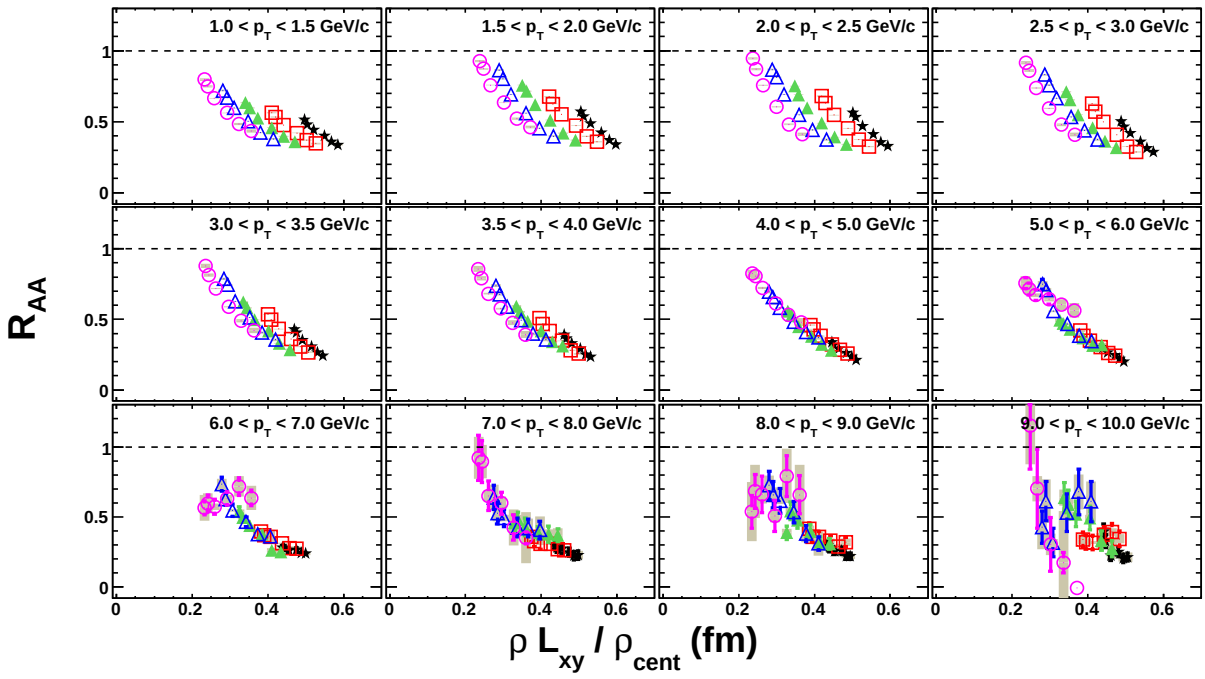

FIG. 24: (Color online) π^0 $R_{\rm AA}$ versus $\rho L_{xy}/\rho_{\rm cent}$. The units of $\rho L_{xy}/\rho_{\rm cent}$ are fm. Colors/data points as in Fig. 21.

APPENDIX A: DATA TABLES

TABLE I: π^0 v_2 for 0–5% and 5–10% centrality. All errors are absolute.

Centrality	$\langle p_T \rangle$ Gev/c	v_2	Stat Err		Syst Err
0–5%	1.21	0.052	+0.034	-0.034	0.011
	1.70	0.035	+0.022	-0.022	0.007
	2.20	0.051	+0.020	-0.020	0.010
	2.70	0.076	+0.023	-0.023	0.016
	3.21	0.039	+0.029	-0.029	0.008
	3.71	0.059	+0.039	-0.039	0.012
	4.37	0.040	+0.042	-0.042	0.008
	5.40	0.040	+0.070	-0.070	0.008
	6.41	0.052	+0.115	-0.115	0.011
	7.43	0.160	+0.206	-0.206	0.033
	8.43	0.168	+0.146	-0.146	0.034
	9.44	0.132	+0.171	-0.171	0.027
5–10%	1.21	0.079	+0.020	-0.020	0.010
	1.71	0.083	+0.013	-0.013	0.010
	2.20	0.106	+0.012	-0.012	0.013
	2.70	0.100	+0.014	-0.014	0.012
	3.21	0.109	+0.018	-0.018	0.014
	3.71	0.075	+0.024	-0.024	0.009
	4.38	0.091	+0.026	-0.026	0.011
	5.40	0.064	+0.041	-0.041	0.008
	6.41	0.062	+0.077	-0.077	0.008
	7.42	0.054	+0.158	-0.158	0.007
	8.43	0.002	+0.097	-0.097	0.0002
	9.44	0.118	+0.136	-0.136	0.015

TABLE II: π^0 v_2 for other centralities. All errors are absolute.

Centrality	$\langle p_T \rangle$ Gev/c	v_2	Stat Err		Syst Err	Centrality	$\langle p_T \rangle$ Gev/c	v_2	Stat Err		Syst Err
	1.20	0.066	+0.018	-0.018	0.012		1.21	0.153	+0.010	-0.010	0.009
	1.71	0.061	+0.012	-0.012	0.011		1.71	0.175	+0.008	-0.008	0.010
	2.20	0.078	+0.011	-0.011	0.014		2.21	0.204	+0.009	-0.009	0.012
	2.70	0.087	+0.013	-0.013	0.016		2.71	0.200	+0.012	-0.012	0.012
	3.21	0.079	+0.016	-0.016	0.014		3.21	0.181	+0.016	-0.016	0.011
	3.71	0.070	+0.021	-0.021	0.013		3.72	0.187	+0.023	-0.023	0.011
0–10%	4.37	0.067	+0.023	-0.023	0.012	50–60%	4.38	0.141	+0.028	-0.028	0.008
	5.40	0.054	+0.037	-0.037	0.010		5.40	0.070	+0.050	-0.050	0.004
	6.41	0.066	+0.064	-0.064	0.012		6.41	-0.044	+0.097	-0.097	0.003
	7.42	0.112	+0.124	-0.124	0.020		7.42	0.235	+0.168	-0.168	0.014
	8.43	0.071	+0.087	-0.087	0.013		8.43	-0.042	+0.234	-0.234	0.002
	9.44	0.189	+0.108	-0.108	0.034		9.44	0.520	+0.428	-0.428	0.031
	1.20	0.106	+0.010	-0.010	0.008		1.20	0.083	+0.011	-0.011	0.011
	1.71	0.131	+0.006	-0.006	0.010		1.71	0.091	+0.007	-0.007	0.012
	2.20	0.138	+0.006	-0.006	0.010		2.20	0.104	+0.007	-0.007	0.014
	2.70	0.141	+0.007	-0.007	0.010		2.70	0.110	+0.008	-0.008	0.015
	3.21	0.145	+0.009	-0.009	0.011		3.21	0.107	+0.010	-0.010	0.015
	3.71	0.130	+0.012	-0.012	0.010		3.71	0.097	+0.013	-0.013	0.013
10–20%	4.37	0.114	+0.014	-0.014	0.008	0–20%	4.37	0.088	+0.014	-0.014	0.012
	5.40	0.105	+0.024	-0.024	0.008		5.40	0.077	+0.023	-0.023	0.010
	6.41	0.043	+0.037	-0.037	0.003		6.41	0.056	+0.039	-0.039	0.007
	7.42	0.075	+0.088	-0.088	0.006		7.42	0.096	+0.081	-0.079	0.013
	8.43	0.076	+0.059	-0.059	0.006		8.43	0.074	+0.055	-0.054	0.010
	9.44	0.151	+0.083	-0.083	0.011		9.44	0.170	+0.074	-0.072	0.023
	1.21	0.125	+0.008	-0.008	0.008		1.21	0.133	+0.005	-0.005	0.008
	1.71	0.159	+0.005	-0.005	0.010		1.71	0.169	+0.004	-0.004	0.010
	2.20	0.183	+0.005	-0.005	0.011		2.20	0.189	+0.004	-0.004	0.011
	2.70	0.193	+0.006	-0.006	0.012		2.71	0.197	+0.005	-0.005	0.012
	3.21	0.172	+0.008	-0.008	0.010		3.21	0.182	+0.006	-0.006	0.011
	3.71	0.175	+0.011	-0.011	0.010		3.71	0.171	+0.008	-0.008	0.010
20–30%	4.38	0.147	+0.012	-0.012	0.009	20–40%	4.38	0.158	+0.009	-0.009	0.009
	5.40	0.139	+0.022	-0.022	0.008		5.40	0.132	+0.016	-0.016	0.008
	6.41	0.097	+0.037	-0.037	0.006		6.41	0.140	+0.027	-0.027	0.008
	7.42	0.074	+0.073	-0.073	0.004		7.42	0.071	+0.055	-0.054	0.004
	8.43	0.070	+0.059	-0.059	0.004		8.43	0.088	+0.045	-0.044	0.005
	9.44	-0.035	+0.087	-0.087	0.002		9.44	0.062	+0.070	-0.069	0.004
	1.21	0.143	+0.007	-0.007	0.008		1.21	0.159	+0.007	-0.007	0.009
	1.71	0.181	+0.005	-0.005	0.010		1.71	0.188	+0.005	-0.005	0.010
	2.20	0.196	+0.005	-0.005	0.011		2.21	0.208	+0.006	-0.006	0.012
	2.71	0.199	+0.007	-0.007	0.011		2.71	0.198	+0.008	-0.008	0.011
	3.21	0.194	+0.009	-0.009	0.011		3.21	0.195	+0.010	-0.010	0.011
	3.71	0.163	+0.012	-0.012	0.009		3.72	0.185	+0.014	-0.014	0.010
30–40%	4.38	0.172	+0.013	-0.013	0.010	40–60%	4.38	0.155	+0.017	-0.017	0.009
	5.40	0.121	+0.024	-0.024	0.007		5.40	0.149	+0.031	-0.030	0.008
	6.41	0.200	+0.042	-0.042	0.011		6.41	0.093	+0.056	-0.055	0.005
	7.43	0.070	+0.088	-0.088	0.004		7.42	0.152	+0.118	-0.113	0.008
	8.43	0.113	+0.071	-0.071	0.006		8.43	0.114	+0.126	-0.124	0.006
	9.44	0.199	+0.118	-0.118	0.011		9.44	0.168	+0.266	-0.231	0.009
	1.20	0.160	+0.008	-0.008	0.009		1.20	0.106	+0.009	-0.009	0.013
	1.71	0.193	+0.006	-0.006	0.010		1.71	0.125	+0.006	-0.006	0.015
	2.21	0.208	+0.006	-0.006	0.011		2.20	0.142	+0.006	-0.006	0.017
	2.71	0.194	+0.008	-0.008	0.010		2.71	0.146	+0.008	-0.008	0.018
	3.21	0.200	+0.011	-0.011	0.011		3.21	0.143	+0.011	-0.011	0.017
	3.72	0.182	+0.015	-0.015	0.010		3.71	0.136	+0.015	-0.015	0.016
40–50%	4.38	0.161	+0.018	-0.018	0.009	0–92%	4.38	0.127	+0.017	-0.017	0.015
	5.40	0.198	+0.032	-0.032	0.011		5.40	0.108	+0.033	-0.033	0.013
	6.41	0.175	+0.055	-0.055	0.009		6.41	0.084	+0.059	-0.059	0.010
	7.42	0.106	+0.133	-0.133	0.006		7.42	0.083	+0.136	-0.145	0.009
	8.43	0.196	+0.112	-0.112	0.011		8.43	0.113	+0.099	-0.109	0.011
	9.44	-0.084	+0.214	-0.214	0.005		9.44	0.149	+0.156	-0.123	0.012

TABLE III: $R_{\rm AA}$ vs. path length for (upper) $1.0 < p_{\rm T} < 1.5$ and (lower) $1.5 < p_{\rm T} < 2.0$ GeV/c.

Centrality	$\Delta\phi$	L_ϵ	ρL_{xy}	$R_{\rm AA}$	Stat Error(abs)	Sys Error(abs)
	0–15	3.23	1.90	0.514	0.009	0.005
	15-30	3.29	1.93	0.481	0.009	0.003
	30–45	3.41	2.00	0.443	0.008	0.001
10–20%	45-60	3.55	2.11	0.400	0.007	0.001
	60–75	3.69	2.18	0.358	0.007	0.004
	75-90	3.78	2.24	0.337	0.006	0.006
	0–15	2.78	1.42	0.565	0.009	0.004
	15-30	2.85	1.45	0.533	0.008	0.003
	30–45	2.99	1.52	0.477	0.008	0.001
20–30%	45-60	3.19	1.64	0.421	0.007	0.001
	60–75	3.39	1.74	0.371	0.006	0.003
	75-90	3.52	1.82	0.346	0.006	0.005
	0–15	2.43	1.03	0.634	0.009	0.004
	15-30	2.50	1.06	0.599	0.009	0.003
	30–45	2.66	1.12	0.526	0.008	0.001
30–40%	45-60	2.87	1.24	0.459	0.007	0.001
	60–75	3.11	1.33	0.397	0.006	0.004
	75-90	3.27	1.42	0.360	0.005	0.005
	0–15	2.14	0.70	0.721	0.009	0.005
	15-30	2.21	0.73	0.669	0.009	0.004
	30–45	2.37	0.78	0.596	0.008	0.002
40–50%	45-60	2.59	0.87	0.505	0.007	0.002
	60–75	2.84	0.95	0.424	0.006	0.005
	75-90	3.03	1.03	0.379	0.005	0.007
	0–15	1.92	0.44	0.798	0.010	0.009
	15-30	1.99	0.46	0.751	0.010	0.007
	30–45	2.14	0.49	0.665	0.008	0.002
50–60%	45-60	2.36	0.56	0.562	0.007	0.003
	60–75	2.61	0.61	0.485	0.006	0.007
	75-90	2.81	0.68	0.435	0.006	0.010
Centrality	$\Delta\phi$	L_ϵ	ρL_{xy}	$R_{\rm AA}$	Stat Error(abs)	Sys Error(abs)
	0–15	3.23	1.94	0.570	0.007	0.003
	15-30	3.29	1.96	0.539	0.007	0.002
	30–45	3.41	2.03	0.486	0.006	0.001
10–20%	45-60	3.55	2.15	0.424	0.009	0.001
	60–75	3.69	2.22	0.370	0.005	0.003
	75-90	3.78	2.29	0.341	0.005	0.004
	0–15	2.78	1.46	0.677	0.008	0.003
	15-30	2.85	1.49	0.626	0.008	0.002
	30–45	2.99	1.57	0.552	0.007	0.001
20–30%	45-60	3.19	1.70	0.475	0.006	0.001
	60–75	3.39	1.80	0.397	0.005	0.002
	75-90	3.52	1.89	0.358	0.004	0.003
	0–15	2.43	1.06	0.758	0.009	0.003
	15-30	2.50	1.09	0.716	0.008	0.002
	30–45	2.66	1.16	0.622	0.007	0.001
30–40%	45-60	2.87	1.28	0.512	0.006	0.001
	60–75	3.11	1.38	0.420	0.005	0.003
	75-90	3.27	1.48	0.370	0.004	0.004
	0–15	2.14	0.72	0.865	0.010	0.004
	15-30	2.21	0.75	0.802	0.009	0.003
	30–45	2.37	0.80	0.691	0.008	0.001
40–50%	45-60	2.59	0.90	0.561	0.006	0.001
	60–75	2.84	0.99	0.455	0.005	0.004
	75-90	3.03	1.08	0.398	0.005	0.006
	0–15	1.92	0.45	0.929	0.010	0.008
	15-30	1.99	0.47	0.874	0.010	0.006
	30–45	2.14	0.51	0.757	0.009	0.002
50–60%	45-60	2.36	0.58	0.635	0.007	0.002
	60–75	2.61	0.64	0.523	0.006	0.007
	75-90	2.81	0.71	0.462	0.005	0.009

TABLE IV: $R_{\rm AA}$ vs. path length for (upper) $2.0 < p_{\rm T} < 2.5$ and (lower) $2.5 < p_{\rm T} < 3.0$ GeV/c.

Centrality	$\Delta\phi$	L_ϵ	ρL_{xy}	$R_{\rm AA}$	Stat Error(abs)	Sys Error(abs)
	0–15	3.23	1.92	0.562	0.007	0.003
	15-30	3.29	1.95	0.534	0.007	0.002
	30–45	3.41	2.02	0.470	0.006	0.001
10–20%	45-60	3.55	2.13	0.413	0.006	0.001
	60–75	3.69	2.21	0.354	0.005	0.003
	75-90	3.78	2.28	0.329	0.004	0.004
	0–15	2.78	1.45	0.681	0.008	0.003
	15-30	2.85	1.48	0.633	0.008	0.002
	30–45	2.99	1.56	0.547	0.007	0.001
20–30%	45-60	3.19	1.69	0.452	0.006	0.001
	60–75	3.39	1.79	0.375	0.005	0.003
	75-90	3.52	1.88	0.325	0.004	0.004
	0–15	2.43	1.05	0.752	0.009	0.003
	15-30	2.50	1.08	0.691	0.008	0.002
	30–45	2.66	1.15	0.597	0.007	0.001
30–40%	45-60	2.87	1.27	0.490	0.006	0.001
	60–75	3.11	1.37	0.392	0.005	0.003
	75-90	3.27	1.46	0.339	0.004	0.004
	0–15	2.14	0.72	0.869	0.010	0.005
	15-30	2.21	0.75	0.813	0.009	0.004
	30–45	2.37	0.80	0.691	0.008	0.001
40–50%	45-60	2.59	0.90	0.550	0.006	0.001
	60–75	2.84	0.99	0.443	0.005	0.004
	75-90	3.03	1.08	0.375	0.004	0.006
	0–15	1.92	0.45	0.946	0.011	0.009
	15-30	1.99	0.47	0.870	0.010	0.007
	30–45	2.14	0.50	0.757	0.009	0.003
50–60%	45-60	2.36	0.57	0.606	0.007	0.003
	60–75	2.61	0.63	0.482	0.006	0.007
	75-90	2.81	0.70	0.413	0.005	0.010
Centrality	$\Delta\phi$	L_ϵ	ρL_{xy}	$R_{\rm AA}$	Stat Error(abs)	Sys Error(abs)
	0–15	3.23	1.87	0.504	0.007	0.003
	15-30	3.29	1.90	0.467	0.007	0.002
	30–45	3.41	1.96	0.421	0.006	0.001
10–20%	45-60	3.55	2.07	0.360	0.005	0.001
	60–75	3.69	2.14	0.315	0.005	0.003
	75-90	3.78	2.20	0.288	0.004	0.004
	0–15	2.78	1.42	0.626	0.009	0.003
	15-30	2.85	1.45	0.573	0.008	0.002
	30–45	2.99	1.52	0.499	0.007	0.001
20–30%	45-60	3.19	1.64	0.409	0.006	0.001
	60–75	3.39	1.74	0.326	0.005	0.003
	75-90	3.52	1.82	0.287	0.004	0.004
	0–15	2.43	1.03	0.713	0.009	0.004
	15-30	2.50	1.07	0.654	0.009	0.003
	30–45	2.66	1.13	0.550	0.007	0.001
30–40%	45-60	2.87	1.25	0.459	0.006	0.001
	60–75	3.11	1.34	0.364	0.005	0.003
	75-90	3.27	1.43	0.318	0.004	0.005
	0–15	2.14	0.72	0.832	0.011	0.006
	15-30	2.21	0.74	0.758	0.010	0.004
	30–45	2.37	0.79	0.665	0.009	0.002
40–50%	45-60	2.59	0.89	0.534	0.007	0.002
	60–75	2.84	0.98	0.439	0.006	0.005
	75-90	3.03	1.07	0.376	0.005	0.007
	0–15	1.92	0.45	0.916	0.012	0.011
	15-30	1.99	0.47	0.861	0.011	0.008
	30–45	2.14	0.50	0.738	0.010	0.003
50–60%	45-60	2.36	0.57	0.594	0.008	0.003
	60–75	2.61	0.63	0.480	0.006	0.010
	75-90	2.81	0.70	0.409	0.006	0.013

TABLE V: $R_{\rm AA}$ vs. path length for (upper) $3.0 < p_{\rm T} < 3.5$ and (lower) $3.5 < p_{\rm T} < 4.0$ GeV/c.

Centrality	$\Delta\phi$	L_ϵ	ρL_{xy}	$R_{\rm AA}$	Stat Error(abs)	Sys Error(abs)
	0–15	3.23	1.80	0.430	0.008	0.003
	15-30	3.29	1.82	0.405	0.007	0.003
	30–45	3.41	1.88	0.355	0.006	0.001
10–20%	45-60	3.55	1.97	0.307	0.006	0.001
	60–75	3.69	2.04	0.266	0.005	0.003
	75-90	3.78	2.09	0.243	0.004	0.004
	0–15	2.78	1.38	0.534	0.009	0.003
	15-30	2.85	1.41	0.497	0.008	0.003
	30–45	2.99	1.48	0.431	0.007	0.001
20–30%	45-60	3.19	1.59	0.360	0.006	0.001
	60–75	3.39	1.67	0.305	0.005	0.003
	75-90	3.52	1.75	0.267	0.005	0.004
	0–15	2.43	1.01	0.622	0.010	0.004
	15-30	2.50	1.04	0.582	0.009	0.003
	30–45	2.66	1.10	0.498	0.008	0.001
30–40%	45-60	2.87	1.21	0.417	0.007	0.001
	60–75	3.11	1.30	0.328	0.005	0.004
	75-90	3.27	1.38	0.285	0.005	0.006
	0–15	2.14	0.71	0.788	0.012	0.007
	15-30	2.21	0.74	0.745	0.012	0.006
	30–45	2.37	0.79	0.625	0.010	0.002
40–50%	45-60	2.59	0.88	0.514	0.008	0.002
	60–75	2.84	0.96	0.407	0.007	0.007
	75-90	3.03	1.05	0.355	0.006	0.009
	0–15	1.92	0.45	0.880	0.015	0.015
	15-30	1.99	0.46	0.814	0.014	0.011
	30–45	2.14	0.50	0.720	0.012	0.004
50–60%	45-60	2.36	0.57	0.589	0.010	0.004
	60–75	2.61	0.63	0.490	0.008	0.013
	75-90	2.81	0.69	0.421	0.007	0.018
Centrality	$\Delta\phi$	L_ϵ	ρL_{xy}	$R_{\rm AA}$	Stat Error(abs)	Sys Error(abs)
	0–15	3.23	1.76	0.390	0.009	0.004
	15-30	3.29	1.78	0.364	0.008	0.003
	30–45	3.41	1.84	0.329	0.007	0.001
10–20%	45-60	3.55	1.93	0.291	0.007	0.001
	60–75	3.69	1.99	0.249	0.006	0.004
	75-90	3.78	2.04	0.234	0.005	0.005
	0–15	2.78	1.36	0.511	0.011	0.004
	15-30	2.85	1.39	0.468	0.010	0.003
	30–45	2.99	1.46	0.418	0.009	0.001
20–30%	45-60	3.19	1.57	0.348	0.007	0.001
	60–75	3.39	1.65	0.281	0.006	0.004
	75-90	3.52	1.72	0.256	0.005	0.006
	0–15	2.43	1.01	0.593	0.012	0.006
	15-30	2.50	1.04	0.552	0.011	0.004
	30–45	2.66	1.10	0.487	0.010	0.002
30–40%	45-60	2.87	1.21	0.418	0.008	0.002
	60–75	3.11	1.29	0.341	0.007	0.005
	75-90	3.27	1.38	0.311	0.007	0.007
	0–15	2.14	0.70	0.738	0.015	0.010
	15-30	2.21	0.73	0.676	0.014	0.007
	30–45	2.37	0.78	0.588	0.012	0.003
40–50%	45-60	2.59	0.87	0.495	0.010	0.003
	60–75	2.84	0.95	0.397	0.008	0.009
	75-90	3.03	1.03	0.356	0.008	0.012
	0–15	1.92	0.44	0.856	0.019	0.021
	15-30	1.99	0.46	0.791	0.017	0.015
	30–45	2.14	0.50	0.682	0.015	0.006
50–60%	45-60	2.36	0.56	0.577	0.013	0.006
	60–75	2.61	0.62	0.477	0.011	0.018
	75-90	2.81	0.68	0.392	0.009	0.023

TABLE VI: $R_{\rm AA}$ vs. path length for (upper) $4.0 < p_{\rm T} < 5.0$ and (lower) $5.0 < p_{\rm T} < 6.0$ GeV/c.

Centrality	$\Delta\phi$	L_ϵ	ρL_{xy}	$R_{\rm AA}$	Stat Error(abs)	Sys Error(abs)
	0–15	3.23	1.71	0.336	0.010	0.004
	15-30	3.29	1.73	0.319	0.009	0.003
	30–45	3.41	1.78	0.292	0.009	0.001
10–20%	45-60	3.55	1.86	0.261	0.008	0.001
	60–75	3.69	1.91	0.234	0.007	0.004
	75-90	3.78	1.95	0.213	0.006	0.005
	0–15	2.78	1.34	0.461	0.012	0.004
	15-30	2.85	1.37	0.430	0.012	0.003
	30–45	2.99	1.43	0.381	0.010	0.001
20–30%	45-60	3.19	1.54	0.322	0.009	0.001
	60–75	3.39	1.61	0.284	0.008	0.004
	75-90	3.52	1.68	0.258	0.007	0.006
	0–15	2.43	0.99	0.559	0.015	0.006
	15-30	2.50	1.02	0.527	0.014	0.005
	30–45	2.66	1.08	0.448	0.012	0.002
30–40%	45-60	2.87	1.18	0.379	0.010	0.002
	60–75	3.11	1.26	0.322	0.009	0.006
	75-90	3.27	1.34	0.279	0.008	0.008
	0–15	2.14	0.70	0.697	0.020	0.012
	15-30	2.21	0.72	0.658	0.019	0.009
	30–45	2.37	0.77	0.583	0.016	0.003
40–50%	45-60	2.59	0.87	0.483	0.014	0.004
	60–75	2.84	0.94	0.411	0.012	0.010
	75-90	3.03	1.02	0.372	0.011	0.014
	0–15	1.92	0.45	0.826	0.026	0.026
	15-30	1.99	0.47	0.804	0.025	0.020
	30–45	2.14	0.50	0.722	0.022	0.008
50–60%	45-60	2.36	0.57	0.611	0.019	0.008
	60–75	2.61	0.63	0.534	0.017	0.022
	75-90	2.81	0.70	0.480	0.0155	0.030
Centrality	$\Delta\phi$	L_ϵ	ρL_{xy}	$R_{\rm AA}$	Stat Error(abs)	Sys Error(abs)
	0–15	3.23	1.67	0.301	0.014	0.007
	15-30	3.29	1.68	0.294	0.013	0.005
	30–45	3.41	1.73	0.267	0.012	0.002
10–20%	45-60	3.55	1.81	0.246	0.011	0.002
	60–75	3.69	1.85	0.218	0.010	0.006
	75-90	3.78	1.90	0.199	0.009	0.008
	0–15	2.78	1.31	0.420	0.018	0.008
	15-30	2.85	1.34	0.382	0.017	0.006
	30–45	2.99	1.40	0.347	0.015	0.002
20–30%	45-60	3.19	1.50	0.301	0.013	0.002
	60–75	3.39	1.56	0.260	0.012	0.007
	75-90	3.52	1.63	0.240	0.011	0.010
	0–15	2.43	0.98	0.492	0.022	0.011
	15-30	2.50	1.01	0.469	0.020	0.008
	30–45	2.66	1.06	0.428	0.019	0.003
30–40%	45-60	2.87	1.17	0.370	0.017	0.003
	60–75	3.11	1.24	0.315	0.015	0.009
	75-90	3.27	1.32	0.318	0.014	0.014
	0–15	2.14	0.70	0.750	0.035	0.021
	15-30	2.21	0.72	0.708	0.032	0.016
	30–45	2.37	0.77	0.557	0.028	0.006
40–50%	45-60	2.59	0.87	0.466	0.023	0.006
	60–75	2.84	0.94	0.385	0.019	0.019
	75-90	3.03	1.02	0.345	0.017	0.027
	0–15	1.92	0.45	0.757	0.039	0.050
	15-30	1.99	0.47	0.715	0.040	0.036
	30–45	2.14	0.50	0.672	0.038	0.013
50–60%	45-60	2.36	0.57	0.642	0.033	0.014
	60–75	2.61	0.63	0.605	0.032	0.038
	75-90	2.81	0.69	0.563	0.030	0.051

TABLE VII: $R_{\rm AA}$ vs. path length for (upper) $6.0 < p_{\rm T} < 7.0$ and (lower) $7.0 < p_{\rm T} < 8.0$ GeV/c.

Centrality	$\Delta\phi$	L_ϵ	ρL_{xy}	$R_{\rm AA}$	Stat Error(abs)	Sys Error(abs)
	0–15	3.23	1.68	0.281	0.017	0.011
	15-30	3.29	1.70	0.278	0.017	0.008
	30–45	3.41	1.75	0.261	0.017	0.003
10–20%	45-60	3.55	1.82	0.264	0.018	0.003
	60–75	3.69	1.87	0.241	0.015	0.009
	75-90	3.78	1.91	0.240	0.015	0.012
	0–15	2.78	1.32	0.396	0.026	0.013
	15-30	2.85	1.34	0.368	0.023	0.010
	30–45	2.99	1.40	0.357	0.023	0.004
20–30%	45-60	3.19	1.50	0.312	0.021	0.004
	60–75	3.39	1.57	0.277	0.018	0.011
	75-90	3.52	1.64	0.274	0.017	0.016
	0–15	2.43	0.98	0.537	0.035	0.018
	15-30	2.50	1.00	0.496	0.030	0.013
	30–45	2.66	1.06	0.437	0.029	0.005
30–40%	45-60	2.87	1.16	0.376	0.026	0.006
	60–75	3.11	1.23	0.261	0.018	0.015
	75-90	3.27	1.31	0.249	0.019	0.025
	0–15	2.14	0.70	0.734	0.050	0.038
	15-30	2.21	0.72	0.625	0.043	0.026
	30–45	2.37	0.77	0.546	0.044	0.010
40–50%	45-60	2.59	0.86	0.465	0.036	0.011
	60–75	2.84	0.93	0.377	0.029	0.030
	75-90	3.03	1.01	0.363	0.027	0.046
	0–15	1.92	0.44	0.564	0.051	0.093
	15-30	1.99	0.46	0.597	0.059	0.070
	30–45	2.14	0.49	0.572	0.054	0.023
50–60%	45-60	2.36	0.56	0.631	0.049	0.024
	60–75	2.61	0.62	0.717	0.063	0.072
	75-90	2.81	0.68	0.635	0.056	0.085
Centrality	$\Delta\phi$	L_ϵ	ρL_{xy}	$R_{\rm AA}$	Stat Error(abs)	Sys Error(abs)
	0–15	3.23	1.67	0.297	0.032	0.026
	15-30	3.29	1.69	0.282	0.037	0.019
	30–45	3.41	1.74	0.272	0.034	0.007
10–20%	45-60	3.55	1.82	0.248	0.030	0.007
	60–75	3.69	1.86	0.222	0.031	0.020
	75-90	3.78	1.91	0.227	0.030	0.030
	0–15	2.78	1.29	0.359	0.037	0.025
	15-30	2.85	1.31	0.327	0.040	0.018
	30–45	2.99	1.37	0.306	0.035	0.007
20–30%	45-60	3.19	1.47	0.308	0.033	0.007
	60–75	3.39	1.53	0.270	0.033	0.020
	75-90	3.52	1.59	0.261	0.029	0.027
	0–15	2.43	0.99	0.458	0.055	0.042
	15-30	2.50	1.02	0.482	0.052	0.033
	30–45	2.66	1.08	0.429	0.063	0.012
30–40%	45-60	2.87	1.18	0.387	0.044	0.012
	60–75	3.11	1.26	0.377	0.057	0.034
	75-90	3.27	1.34	0.369	0.045	0.048
	0–15	2.14	0.69	0.639	0.086	0.091
	15-30	2.21	0.71	0.527	0.079	0.058
	30–45	2.37	0.75	0.492	0.062	0.022
40–50%	45-60	2.59	0.84	0.424	0.066	0.022
	60–75	2.84	0.91	0.420	0.062	0.069
	75-90	3.03	0.99	0.406	0.063	0.099
	0–15	1.92	0.45	0.922	0.161	0.149
	15-30	1.99	0.46	0.895	0.150	0.118
	30–45	2.14	0.50	0.651	0.106	0.039
50–60%	45-60	2.36	0.56	0.598	0.078	0.048
	60–75	2.61	0.62	0.424	0.089	0.128
	75-90	2.81	0.69	0.351	0.042	0.182

TABLE VIII: $R_{\rm AA}$ vs. path length for (upper) $8.0 < p_{\rm T} < 9.0$ and (lower) $9.0 < p_{\rm T} < 10.0$ GeV/c.

Centrality	$\Delta\phi$	L_ϵ	ρL_{xy}	$R_{\rm AA}$	Stat Error(abs)	Sys Error(abs)
	0–15	3.23	1.67	0.296	0.030	0.017
	15-30	3.29	1.68	0.280	0.029	0.013
	30–45	3.41	1.73	0.255	0.026	0.005
10–20%	45-60	3.55	1.81	0.258	0.026	0.005
	60–75	3.69	1.86	0.220	0.023	0.013
	75-90	3.78	1.90	0.219	0.022	0.019
	0–15	2.78	1.33	0.415	0.043	0.024
	15-30	2.85	1.36	0.356	0.038	0.016
	30–45	2.99	1.42	0.359	0.038	0.006
20–30%	45-60	3.19	1.52	0.329	0.035	0.006
	60–75	3.39	1.59	0.288	0.032	0.017
	75-90	3.52	1.66	0.320	0.033	0.027
	0–15	2.43	0.98	0.387	0.049	0.026
	15-30	2.50	1.01	0.543	0.063	0.029
	30–45	2.66	1.07	0.476	0.056	0.010
30–40%	45-60	2.87	1.17	0.396	0.048	0.010
	60–75	3.11	1.25	0.318	0.041	0.026
	75-90	3.27	1.32	0.308	0.039	0.037
	0–15	2.14	0.70	0.724	0.103	0.072
	15-30	2.21	0.73	0.658	0.094	0.053
	30–45	2.37	0.77	0.614	0.087	0.022
40–50%	45-60	2.59	0.87	0.535	0.076	0.025
	60–75	2.84	0.94	0.382	0.058	0.065
	75-90	3.03	1.03	0.310	0.048	0.086
	0–15	1.92	0.45	0.536	0.118	0.212
	15-30	1.99	0.46	0.682	0.121	0.192
	30–45	2.14	0.50	0.661	0.130	0.065
50–60%	45-60	2.36	0.56	0.508	0.112	0.047
	60–75	2.61	0.62	0.791	0.144	0.193
	75-90	2.81	0.69	0.658	0.135	0.215
Centrality	$\Delta\phi$	L_ϵ	ρL_{xy}	$R_{\rm AA}$	Stat Error(abs)	Sys Error(abs)
	0–15	3.23	1.69	0.397	0.051	0.028
	15-30	3.29	1.71	0.327	0.045	0.018
	30–45	3.41	1.76	0.223	0.034	0.005
10–20%	45-60	3.55	1.84	0.249	0.035	0.007
	60–75	3.69	1.89	0.203	0.030	0.021
	75-90	3.78	1.94	0.213	0.030	0.034
	0–15	2.78	1.33	0.340	0.054	0.038
	15-30	2.85	1.36	0.319	0.051	0.025
	30–45	2.99	1.42	0.316	0.052	0.009
20–30%	45-60	3.19	1.53	0.374	0.058	0.010
	60–75	3.39	1.60	0.392	0.061	0.027
	75-90	3.52	1.67	0.343	0.055	0.032
	0–15	2.43	1.02	0.637	0.108	0.059
	15-30	2.50	1.05	0.588	0.103	0.044
	30–45	2.66	1.11	0.519	0.090	0.018
30–40%	45-60	2.87	1.22	0.491	0.084	0.022
	60–75	3.11	1.31	0.331	0.069	0.054
	75-90	3.27	1.40	0.274	0.057	0.075
	0–15	2.14	0.70	0.428	0.115	0.158
	15-30	2.21	0.72	0.612	0.139	0.155
	30–45	2.37	0.77	0.316	0.102	0.026
40–50%	45-60	2.59	0.86	0.530	0.133	0.039
	60–75	2.84	0.94	0.678	0.162	0.125
	75-90	3.03	1.02	0.609	0.143	0.145
	0–15	1.92	0.45	1.866	0.486	0.498
	15-30	1.99	0.47	1.150	0.310	0.273
	30–45	2.14	0.51	0.702	0.282	0.091
50–60%	45-60	2.36	0.58	0.305	0.192	0.077
	60–75	2.61	0.64	0.172	0.073	0.369
	75-90	2.81	0.71	-0.005	-0.002	-0.812

[1] K. Adcox et al. (PHENIX), Nucl. Phys. **A757**, 184 (2005).
[2] J. Adams et al. (STAR), Nucl. Phys. **A757**, 102 (2005).
[3] B. B. Back et al., Nucl. Phys. **A757**, 28 (2005).
[4] I. Arsene et al. (BRAHMS), Nucl. Phys. **A757**, 1 (2005).
[5] S. Mrowczynski, Phys. Lett. **B314**, 118 (1993).
[6] P. Arnold, J. Lenaghan, G. D. Moore, and L. G. Yaffe, Phys. Rev. Lett. **94**, 072302 (2005).
[7] A. Rebhan, P. Romatschke, and M. Strickland, Phys. Rev. Lett. **94**, 102303 (2005).
[8] A. Dumitru and Y. Nara, Phys. Lett. **B621**, 89 (2005).
[9] B. Schenke, M. Strickland, C. Greiner, and M. H. Thoma, Phys. Rev. **D73**, 125004 (2006).
[10] S. Scherer, M. Bleicher, S. Haussler, and H. Stocker, Int. J. Mod. Phys. **E17**, 965 (2008).
[11] Z. Xu, L. Cheng, A. El, K. Gallmeister, and C. Greiner, arXiv: 0812.3839 [hep-ph].
[12] K. Adcox et al. (PHENIX), Phys. Rev. Lett. **88**, 022301 (2002).
[13] C. Adler et al. (STAR), Phys. Rev. Lett. **89**, 202301 (2002).
[14] S. S. Adler et al. (PHENIX), Phys. Rev. Lett. **91**, 182301 (2003).
[15] J. Adams et al. (STAR), Phys. Rev. Lett. **92**, 052302 (2004).
[16] P. Romatschke and U. Romatschke, Phys. Rev. Lett. **99**, 172301 (2007).
[17] K. Dusling and D. Teaney, Phys. Rev. **C77**, 034905 (2008).
[18] H. Song and U. W. Heinz, Phys. Rev. **C77**, 064901 (2008).
[19] A. Adare et al. (PHENIX), Phys. Rev. Lett. **101**, 232301 (2008).
[20] S. S. Adler et al. (PHENIX), Phys. Rev. Lett. **91**, 072303 (2003).
[21] R. Baier, Nucl. Phys. **A715**, 209 (2003).
[22] A. Majumder, J. Phys. **G34**, S377 (2007).
[23] I. Vitev, J. Phys. **G35**, 104011 (2008).
[24] M. Gyulassy, P. Levai, and I. Vitev, Phys. Lett. **B538**, 282 (2002).
[25] S. S. Adler et al. (PHENIX), Phys. Rev. **C76**, 034904 (2007).
[26] T. Hirano and Y. Nara, Phys. Rev. C **69**, 034908 (2004).
[27] T. Renk, J. Ruppert, C. Nonaka, and S. A. Bass, Phys. Rev. **C75**, 031902 (2007).
[28] A. Majumder, C. Nonaka, and S. A. Bass, Phys. Rev. C **76**, 041902 (2007).
[29] E. V. Shuryak, Phys. Rev. **C66**, 027902 (2002).
[30] A. Drees, H. Feng, and J. Jia, Phys. Rev. **C71**, 034909 (2005).
[31] A. Dainese, C. Loizides, and G. Paic, Eur. Phys. J. **C38**, 461 (2005).
[32] B. Cole, Nuclear Physics A **774**, 225 (2006).
[33] H. Zhang, J. F. Owens, E. Wang, and X.-N. Wang, Phys. Rev. Lett. **98**, 212301 (2007).
[34] J. Liao and E. Shuryak (2008), 0810.4116.
[35] R. J. Fries, B. Muller, C. Nonaka, and S. A. Bass, Phys. Rev. **C68**, 044902 (2003).
[36] S. S. Adler et al. (PHENIX), Nucl. Instrum. Meth. **A499**, 560 (2003).
[37] M. Allen et al. (PHENIX), Nucl. Instrum. Meth. **A499**, 549 (2003).
[38] C. Adler et al., Nucl. Instrum. Meth. **A470**, 488 (2001).
[39] L. Aphecetche et al. (PHENIX), Nucl. Instrum. Meth. **A499**, 521 (2003).
[40] S. S. Adler et al. (PHENIX), Phys. Rev. Lett. **96**, 032302 (2006).
[41] S. Afanasiev et al. (PHENIX), Phys. Rev. Lett. **99**, 052301 (2007).
[42] J.-Y. Ollitrault, nucl-ex/9711003.
[43] T. Sjostrand, S. Mrenna, and P. Skands, JHEP **05**, 026 (2006).
[44] A. Adare et al. (PHENIX), Phys. Rev. **C78**, 014901 (2008).
[45] A. Adare et al. (PHENIX), Phys. Rev. **C77**, 064907 (2008).
[46] A. Adare et al. (PHENIX), Phys. Rev. Lett. **98**, 162301 (2007).
[47] J. Adams et al. (STAR), Phys. Rev. **C72**, 014904 (2005).
[48] B. B. Back et al. (PHOBOS), Phys. Rev. **C72**, 051901 (2005).
[49] V. S. Pantuev, JETP Lett. **85**, 104 (2007).
[50] N. Armesto, C. A. Salgado, and U. A. Wiedemann (2004).
[51] M. L. Miller, K. Reygers, S. J. Sanders, and P. Steinberg, Ann. Rev. Nucl. Part. Sci. **57**, 205 (2007), nucl-ex/0701025.
[52] P. Aurenche, F. Gelis, and H. Zaraket, Phys. Rev. **D62**, 096012 (2000).

Kaon interferometric probes of space-time evolution in Au+Au collisions at $\sqrt{s_{\rm NN}} = 200$ GeV

S. Afanasiev,[17] C. Aidala,[7] N.N. Ajitanand,[43] Y. Akiba,[37,38] J. Alexander,[43] A. Al-Jamel,[33] K. Aoki,[23,37] L. Aphecetche,[45] R. Armendariz,[33] S.H. Aronson,[3] R. Averbeck,[44] T.C. Awes,[34] B. Azmoun,[3] V. Babintsev,[14] A. Baldisseri,[8] K.N. Barish,[4] P.D. Barnes,[26] B. Bassalleck,[32] S. Bathe,[4] S. Batsouli,[7] V. Baublis,[36] F. Bauer,[4] A. Bazilevsky,[3] S. Belikov,[3,16,*] R. Bennett,[44] Y. Berdnikov,[40] M.T. Bjorndal,[7] J.G. Boissevain,[26] H. Borel,[8] K. Boyle,[44] M.L. Brooks,[26] D.S. Brown,[33] D. Bucher,[29] H. Buesching,[3] V. Bumazhnov,[14] G. Bunce,[3,38] J.M. Burward-Hoy,[26] S. Butsyk,[44] S. Campbell,[44] J.-S. Chai,[18] S. Chernichenko,[14] J. Chiba,[19] C.Y. Chi,[7] M. Chiu,[7] I.J. Choi,[52] T. Chujo,[49] V. Cianciolo,[34] C.R. Cleven,[12] Y. Cobigo,[8] B.A. Cole,[7] M.P. Comets,[35] P. Constantin,[16] M. Csanád,[10] T. Csörgő,[20] T. Dahms,[44] K. Das,[11] G. David,[3] H. Delagrange,[45] A. Denisov,[14] D. d'Enterria,[7] A. Deshpande,[38,44] E.J. Desmond,[3] O. Dietzsch,[41] A. Dion,[44] J.L. Drachenberg,[1] O. Drapier,[24] A. Drees,[44] A.K. Dubey,[51] A. Durum,[14] V. Dzhordzhadze,[46] Y.V. Efremenko,[34] J. Egdemir,[44] A. Enokizono,[13] H. En'yo,[37,38] B. Espagnon,[35] S. Esumi,[48] D.E. Fields,[32,38] F. Fleuret,[24] S.L. Fokin,[22] B. Forestier,[27] Z. Fraenkel,[51,*] J.E. Frantz,[7] A. Franz,[3] A.D. Frawley,[11] Y. Fukao,[23,37] S.-Y. Fung,[4] S. Gadrat,[27] F. Gastineau,[45] M. Germain,[45] A. Glenn,[46] M. Gonin,[24] J. Gosset,[8] Y. Goto,[37,38] R. Granier de Cassagnac,[24] N. Grau,[16] S.V. Greene,[49] M. Grosse Perdekamp,[15,38] T. Gunji,[5] H.-Å. Gustafsson,[28] T. Hachiya,[13,37] A. Hadj Henni,[45] J.S. Haggerty,[3] M.N. Hagiwara,[1] H. Hamagaki,[5] H. Harada,[13] E.P. Hartouni,[25] K. Haruna,[13] M. Harvey,[3] E. Haslum,[28] K. Hasuko,[37] R. Hayano,[5] M. Heffner,[25] T.K. Hemmick,[44] J.M. Heuser,[37] X. He,[12] H. Hiejima,[15] J.C. Hill,[16] R. Hobbs,[32] M. Holmes,[49] W. Holzmann,[43] K. Homma,[13] B. Hong,[21] T. Horaguchi,[37,47] M.G. Hur,[18] T. Ichihara,[37,38] K. Imai,[23,37] M. Inaba,[48] D. Isenhower,[1] L. Isenhower,[1] M. Ishihara,[37] T. Isobe,[5] M. Issah,[43] A. Isupov,[17] B.V. Jacak,[44,†] J. Jia,[7] J. Jin,[7] O. Jinnouchi,[38] B.M. Johnson,[3] K.S. Joo,[30] D. Jouan,[35] F. Kajihara,[5,37] S. Kametani,[5,50] N. Kamihara,[37,47] M. Kaneta,[38] J.H. Kang,[52] T. Kawagishi,[48] A.V. Kazantsev,[22] S. Kelly,[6] A. Khanzadeev,[36] D.J. Kim,[52] E. Kim,[42] Y.-S. Kim,[18] E. Kinney,[6] A. Kiss,[10] E. Kistenev,[3] A. Kiyomichi,[37] C. Klein-Boesing,[29] L. Kochenda,[36] V. Kochetkov,[14] B. Komkov,[36] M. Konno,[48] D. Kotchetkov,[4] A. Kozlov,[51] P.J. Kroon,[3] G.J. Kunde,[26] N. Kurihara,[5] K. Kurita,[39,37] M.J. Kweon,[21] Y. Kwon,[52] G.S. Kyle,[33] R. Lacey,[43] J.G. Lajoie,[16] A. Lebedev,[16] Y. Le Bornec,[35] S. Leckey,[44] D.M. Lee,[26] M.K. Lee,[52] M.J. Leitch,[26] M.A.L. Leite,[41] H. Lim,[42] A. Litvinenko,[17] M.X. Liu,[26] X.H. Li,[4] C.F. Maguire,[49] Y.I. Makdisi,[3] A. Malakhov,[17] M.D. Malik,[32] V.I. Manko,[22] H. Masui,[48] F. Matathias,[44] M.C. McCain,[15] P.L. McGaughey,[26] Y. Miake,[48] T.E. Miller,[49] A. Milov,[44] S. Mioduszewski,[3] G.C. Mishra,[12] J.T. Mitchell,[3] D.P. Morrison,[3] J.M. Moss,[26] T.V. Moukhanova,[22] D. Mukhopadhyay,[49] J. Murata,[39,37] S. Nagamiya,[19] Y. Nagata,[48] J.L. Nagle,[6] M. Naglis,[51] T. Nakamura,[13] J. Newby,[25] M. Nguyen,[44] B.E. Norman,[26] R. Nouicer,[3] A.S. Nyanin,[22] J. Nystrand,[28] E. O'Brien,[3] C.A. Ogilvie,[16] H. Ohnishi,[37] I.D. Ojha,[49] H. Okada,[23,37] K. Okada,[38] O.O. Omiwade,[1] A. Oskarsson,[28] I. Otterlund,[28] K. Ozawa,[5] D. Pal,[49] A.P.T. Palounek,[26] V. Pantuev,[44] V. Papavassiliou,[33] J. Park,[42] W.J. Park,[21] S.F. Pate,[33] H. Pei,[16] J.-C. Peng,[15] H. Pereira,[8] V. Peresedov,[17] D.Yu. Peressounko,[22] C. Pinkenburg,[3] R.P. Pisani,[3] M.L. Purschke,[3] A.K. Purwar,[44] H. Qu,[12] J. Rak,[16] I. Ravinovich,[51] K.F. Read,[34,46] M. Reuter,[44] K. Reygers,[29] V. Riabov,[36] Y. Riabov,[36] G. Roche,[27] A. Romana,[24,*] M. Rosati,[16] S.S.E. Rosendahl,[28] P. Rosnet,[27] P. Rukoyatkin,[17] V.L. Rykov,[37] S.S. Ryu,[52] B. Sahlmueller,[29] N. Saito,[23,37,38] T. Sakaguchi,[5,50] S. Sakai,[48] V. Samsonov,[36] H.D. Sato,[23,37] S. Sato,[3,19,48] S. Sawada,[19] V. Semenov,[14] R. Seto,[4] D. Sharma,[51] T.K. Shea,[3] I. Shein,[14] T.-A. Shibata,[37,47] K. Shigaki,[13] M. Shimomura,[48] T. Shohjoh,[48] K. Shoji,[23,37] A. Sickles,[44] C.L. Silva,[41] D. Silvermyr,[34] K.S. Sim,[21] C.P. Singh,[2] V. Singh,[2] S. Skutnik,[16] W.C. Smith,[1] A. Soldatov,[14] R.A. Soltz,[25] W.E. Sondheim,[26] S.P. Sorensen,[46] I.V. Sourikova,[3] F. Staley,[8] P.W. Stankus,[34] E. Stenlund,[28] M. Stepanov,[33] A. Ster,[20] S.P. Stoll,[3] T. Sugitate,[13] C. Suire,[35] J.P. Sullivan,[26] J. Sziklai,[20] T. Tabaru,[38] S. Takagi,[48] E.M. Takagui,[41] A. Taketani,[37,38] K.H. Tanaka,[19] Y. Tanaka,[31] K. Tanida,[37,38] M.J. Tannenbaum,[3] A. Taranenko,[43] P. Tarján,[9] T.L. Thomas,[32] M. Togawa,[23,37] J. Tojo,[37] H. Torii,[37] R.S. Towell,[1] V-N. Tram,[24] I. Tserruya,[51] Y. Tsuchimoto,[13,37] S.K. Tuli,[2] H. Tydesjö,[28] N. Tyurin,[14] C. Vale,[16] H. Valle,[49] H.W. van Hecke,[26] J. Velkovska,[49] R. Vertesi,[9] A.A. Vinogradov,[22] E. Vznuzdaev,[36] M. Wagner,[23,37] X.R. Wang,[33] Y. Watanabe,[37,38] J. Wessels,[29] S.N. White,[3] N. Willis,[35] D. Winter,[7] C.L. Woody,[3] M. Wysocki,[6] W. Xie,[4,38] A. Yanovich,[14] S. Yokkaichi,[37,38] G.R. Young,[34] I. Younus,[32] I.E. Yushmanov,[22] W.A. Zajc,[7] O. Zaudtke,[29] C. Zhang,[7] J. Zimányi,[20,*] and L. Zolin[17]

(PHENIX Collaboration)

[1] *Abilene Christian University, Abilene, TX 79699, U.S.*

arXiv:0903.4863v1 [nucl-ex] 27 Mar 2009

[2]Department of Physics, Banaras Hindu University, Varanasi 221005, India
[3]Brookhaven National Laboratory, Upton, NY 11973-5000, U.S.
[4]University of California - Riverside, Riverside, CA 92521, U.S.
[5]Center for Nuclear Study, Graduate School of Science, University of Tokyo, 7-3-1 Hongo, Bunkyo, Tokyo 113-0033, Japan
[6]University of Colorado, Boulder, CO 80309, U.S.
[7]Columbia University, New York, NY 10027 and Nevis Laboratories, Irvington, NY 10533, U.S.
[8]Dapnia, CEA Saclay, F-91191, Gif-sur-Yvette, France
[9]Debrecen University, H-4010 Debrecen, Egyetem tér 1, Hungary
[10]ELTE, Eötvös Loránd University, H - 1117 Budapest, Pázmány P. s. 1/A, Hungary
[11]Florida State University, Tallahassee, FL 32306, U.S.
[12]Georgia State University, Atlanta, GA 30303, U.S.
[13]Hiroshima University, Kagamiyama, Higashi-Hiroshima 739-8526, Japan
[14]IHEP Protvino, State Research Center of Russian Federation, Institute for High Energy Physics, Protvino, 142281, Russia
[15]University of Illinois at Urbana-Champaign, Urbana, IL 61801, U.S.
[16]Iowa State University, Ames, IA 50011, U.S.
[17]Joint Institute for Nuclear Research, 141980 Dubna, Moscow Region, Russia
[18]KAERI, Cyclotron Application Laboratory, Seoul, Korea
[19]KEK, High Energy Accelerator Research Organization, Tsukuba, Ibaraki 305-0801, Japan
[20]KFKI Research Institute for Particle and Nuclear Physics of the Hungarian Academy of Sciences (MTA KFKI RMKI), H-1525 Budapest 114, POBox 49, Budapest, Hungary
[21]Korea University, Seoul, 136-701, Korea
[22]Russian Research Center "Kurchatov Institute", Moscow, Russia
[23]Kyoto University, Kyoto 606-8502, Japan
[24]Laboratoire Leprince-Ringuet, Ecole Polytechnique, CNRS-IN2P3, Route de Saclay, F-91128, Palaiseau, France
[25]Lawrence Livermore National Laboratory, Livermore, CA 94550, U.S.
[26]Los Alamos National Laboratory, Los Alamos, NM 87545, U.S.
[27]LPC, Université Blaise Pascal, CNRS-IN2P3, Clermont-Fd, 63177 Aubiere Cedex, France
[28]Department of Physics, Lund University, Box 118, SE-221 00 Lund, Sweden
[29]Institut für Kernphysik, University of Muenster, D-48149 Muenster, Germany
[30]Myongji University, Yongin, Kyonggido 449-728, Korea
[31]Nagasaki Institute of Applied Science, Nagasaki-shi, Nagasaki 851-0193, Japan
[32]University of New Mexico, Albuquerque, NM 87131, U.S.
[33]New Mexico State University, Las Cruces, NM 88003, U.S.
[34]Oak Ridge National Laboratory, Oak Ridge, TN 37831, U.S.
[35]IPN-Orsay, Universite Paris Sud, CNRS-IN2P3, BP1, F-91406, Orsay, France
[36]PNPI, Petersburg Nuclear Physics Institute, Gatchina, Leningrad region, 188300, Russia
[37]RIKEN Nishina Center for Accelerator-Based Science, Wako, Saitama 351-0198, Japan
[38]RIKEN BNL Research Center, Brookhaven National Laboratory, Upton, NY 11973-5000, U.S.
[39]Physics Department, Rikkyo University, 3-34-1 Nishi-Ikebukuro, Toshima, Tokyo 171-8501, Japan
[40]Saint Petersburg State Polytechnic University, St. Petersburg, Russia
[41]Universidade de São Paulo, Instituto de Física, Caixa Postal 66318, São Paulo CEP05315-970, Brazil
[42]System Electronics Laboratory, Seoul National University, Seoul, Korea
[43]Chemistry Department, Stony Brook University, Stony Brook, SUNY, NY 11794-3400, U.S.
[44]Department of Physics and Astronomy, Stony Brook University, SUNY, Stony Brook, NY 11794, U.S.
[45]SUBATECH (Ecole des Mines de Nantes, CNRS-IN2P3, Université de Nantes) BP 20722 - 44307, Nantes, France
[46]University of Tennessee, Knoxville, TN 37996, U.S.
[47]Department of Physics, Tokyo Institute of Technology, Oh-okayama, Meguro, Tokyo 152-8551, Japan
[48]Institute of Physics, University of Tsukuba, Tsukuba, Ibaraki 305, Japan
[49]Vanderbilt University, Nashville, TN 37235, U.S.
[50]Waseda University, Advanced Research Institute for Science and Engineering, 17 Kikui-cho, Shinjuku-ku, Tokyo 162-0044, Japan
[51]Weizmann Institute, Rehovot 76100, Israel
[52]Yonsei University, IPAP, Seoul 120-749, Korea

(Dated: March 27, 2009)

Bose-Einstein correlations of charged kaons are used to probe Au+Au collisions at $\sqrt{s_{\rm NN}} = 200$ GeV and are compared to charged pion probes, which have a larger hadronic scattering cross section. Three dimensional Gaussian source radii are extracted, along with a one-dimensional kaon emission source function. The centrality dependences of the three Gaussian radii are well described by a single linear function of $N_{\rm part}^{1/3}$ with zero intercept. Imaging analysis shows a deviation from a Gaussian tail at $r \gtrsim 10$ fm, although the bulk emission at lower radius is well-described by a Gaussian. The presence of a non-Gaussian tail in the kaon source reaffirms that the particle emission region in a heavy ion collision is extended, and that similar measurements with pions are not solely due to the decay of long-lived resonances.

PACS numbers: 25.75.Dw

Experiments at the Relativistic Heavy Ion Collider (RHIC) at Brookhaven National Laboratory have revealed that collisions of Au ions at $\sqrt{s_{\rm NN}} = 200$ GeV produce a new form of matter which is opaque to jets and exhibits anisotropic flow consistent with perfect fluid hydrodynamics [1, 2]. Studies of the space-time evolution of the collisions are needed to elucidate the properties of the hot, dense, and strongly interacting matter, probe the time scale and degree of thermalization, and investigate the order of the deconfinement phase transition.

Two-particle interferometry, also known as HBT after the radio astronomers R. Hanbury Brown and R.Q. Twiss [3], is a powerful tool for measuring the space-time extent of particle-emitting sources. In elementary particle and nuclear physics, enhanced production of like-sign pions with small relative momenta was discovered experimentally and explained by the Bose-Einstein symmetrization of identical bosons [4]. Correlations are produced by the combination of quantum mechanical interference of identical particles and strong and/or electromagnetic final state interactions such as Coulomb repulsion for same-sign charged pairs. HBT radii refer to Gaussian measures of source sizes on the femtometer scale.

Although the traditional HBT analyses are constrained by the assumption of a Gaussian distribution of particle emission, recent detailed measurements of pion emission sources using an imaging technique show a non-Gaussian structure for the two-particle source region above ∼20 fm [5], suggesting the possibility that decays of long-lived resonances or a temporal component of the source contribute to the non-Gaussian tail [6]. While charged pions are strongly affected by rescattering among hadrons and decays of hadronic resonances, charged kaons have smaller rescattering cross sections than charged pions ($\sigma_{K-N} < \sigma_{\pi-N}$) and are less affected by resonance decays. Until recently, no full hydrodynamic calculation has accurately predicted particle spectra and HBT radii for pions, and none can simultaneously describe the momentum asymmetry measurements of flow. The measurement of the kaon source describe herein add an important new constraint to address this "HBT puzzle" [7, 8].

An angle-averaged one-dimensional Gaussian measurement of correlations of neutral kaons by STAR [9] suggests that the transverse mass dependence for neutral kaons and charged pions falls on one universal curve. In this paper, 3D Gaussian HBT correlations of like-sign kaons are presented in three transverse momentum bins for $0.3 < p_{\rm T} < 1.5$ GeV/c and three collision centrality bins. The resulting HBT radius parameters for kaons are compared to those of like-sign pion pairs [10]. In addition we present 1D emission source functions for charged kaons in relativistic heavy-ion collisions.

This analysis of 2004 data from the PHENIX detector [11] uses ∼ 600 million minimum bias events, which are triggered by the coincidence of the Beam-Beam Counters (BBC) and Zero-Degree Calorimeters (ZDC) with collision vertex $|z| < 30$ cm. A Monte Carlo Glauber model [12] is used to match the observed BBC and ZDC distributions and to bin the data according to the number of nucleons participating in the collisions, $N_{\rm part}$.

Charged kaons are tracked and identified using the drift chamber (DC), pad chambers (PC1,PC3) and PbSc Electromagnetic Calorimeters (EMCal) to cover pseudorapidity $|\eta| < 0.35$ and azimuthal angle $\Delta\phi = \pi/2$ ($\Delta\phi = \pi/4$) in one (and the other) central arm. A track model provides a 3-dimensional trajectory and momentum vector for charged particles based on DC and PC1 information with a momentum resolution of $\delta p/p \simeq 0.7\% \oplus 1.0\% \times p$ (GeV/c). Backgrounds are reduced by requiring 2 σ position match between track projections and EMCal hits, and 3 σ match for PC3. Kaons are separated from pions up to $p_{\rm T}$ ∼0.9 GeV/c using timing information from BBC and EMC. Particles at higher $p_{\rm T}$ that fall within 2 σ of the ideal mass-squared for kaons but $\geq 3\,\sigma$ away from the peak for pions or (anti-)protons are identified as kaons. The contamination level is ∼4% from pions, and ∼1% from protons at $p_{\rm T} \sim 1.5$ GeV/c.

The correlation function is experimentally measured as $C_2(\mathbf{q}) = A(\mathbf{q})/B(\mathbf{q})$ where $A(\mathbf{q})$ is the relative momentum ($\mathbf{q}$) distribution of actual pairs obtained by all possible combinations of pairs within the same events and $B(\mathbf{q})$ is the background pair distribution from mixed events. Two-track detection inefficiencies for charged kaons that traverse the DC and EMCal in close proximity have been carefully studied with Monte-Carlo detector simulation and the actual pair distribution is corrected by the MC efficiency factors. After pair selection cuts to remove track splitting and merging (see [10] for details), ∼15 million positive kaon pairs and 14 million negative kaon pairs remain.

To measure multi-dimension source sizes, $\mathbf{q}$ is decomposed into standard "side-out-long" axes [13]: for which $q_{\rm long}$ is parallel to the beam axis, $q_{\rm out}$ is parallel to the transverse momentum of the pair ($k_{\rm T} = (p_{1\rm T} + p_{2\rm T})/2$), and $q_{\rm side}$ is orthogonal to both $q_{\rm long}$ and $q_{\rm out}$. This analysis is performed in the Longitudinally Co-Moving System (LCMS) defined as $p_{1\rm Z} = -p_{2\rm Z}$. For the treatment of charged kaons emitted away from the central region (core), we adopt an effective core-halo Coulomb correction, proposed by Bowler and Sinyukov [14], in which the 3D Gaussian fit function is given by

$$C_2 = C_2^{core} + C_2^{halo} = [\lambda(1+G)]\,F_{\rm C} + [1-\lambda]\,, \qquad (1)$$

where the Coulomb correlation function $F_{\rm C}$ is iteratively evaluated from the Coulomb wave function of kaon pairs

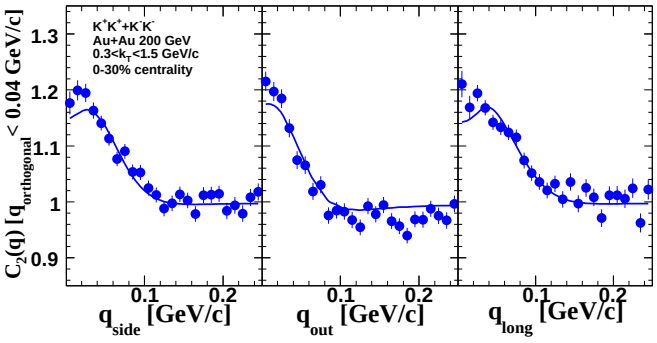

FIG. 1: (color online). 3D correlation function of charged kaon pairs measured for $0.3 < k_{\rm T} < 1.5$ GeV/c at $0-30\%$ centrality in Au+Au collisions at $\sqrt{s_{\rm NN}} = 200$ GeV. The curve is a 3D function is a Coulomb uncorrected fit with Eq. 1 and sliced over the lowest 40 MeV/c in the orthogonal directions.

assuming a spherical Gaussian source. The Gaussian correlation function in the side-out-long decomposition is determined by

$$G = \exp\left(-R^2_{\rm side}q^2_{\rm side} - R^2_{\rm out}q^2_{\rm out} - R^2_{\rm long}q^2_{\rm long}\right). \quad (2)$$

The systematic error estimate incorporates a contribution from the Coulomb interaction of the source halo using a prescription developed by Maj and Mrowczynski [15]. The fitted $R_{\rm side}$ and $R_{\rm long}$ are Gaussian measures of the spatial lengths of homogeneity, where particles of similar momenta are emitted [16], in the transverse and longitudinal directions at freeze-out. $R_{\rm out}$ contains a contribution from the duration of the particle emission in addition to the spatial length [17]. Note that an out-long cross-term vanishes in the expression for G for our $|\eta| < 0.35$ acceptance at midrapidity [18]. The fitted λ is empirically defined and includes contributions from misidentified particles $(1-f)^2$ along with components of the source that are not well resolved by the Gaussian fit.

Figure 1 shows the 3D correlation function of charged kaons without the Coulomb correction measured for $0.3 < k_{\rm T} < 1.5$ GeV/c at $0-30\%$ centrality in Au+Au collisions at $\sqrt{s_{\rm NN}} = 200$ GeV and the fit with Eq. (1). Separate fits to the $2K^+$ and $2K^-$ correlation functions were performed, yielding consistent results for all $k_{\rm T}$ and centrality bins.

Panels (a)-(e) in Fig. 2 show the HBT radius parameters of charged kaons for $0.3 < k_{\rm T} < 1.5$ GeV/c as functions of $N^{1/3}_{\rm part}$, which is proportional to the transverse radius of the initial collision volume. Similar to pions, kaon radii are well described by linear functions of $N^{1/3}_{\rm part}$. Because initial fits yielded slopes that were consistent for all radii and intercepts that were consistent with zero, the all three radii were fit to a single linear function with zero intercept: $R_i = p_1 * N^{1/3}_{\rm part}$, with $p_1 = 0.51 \pm 0.01$ and $\chi^2/{\rm ndf} = 14.6/8$. We note that similar fits to the pion radii yield non-zero intercepts. Although pions and

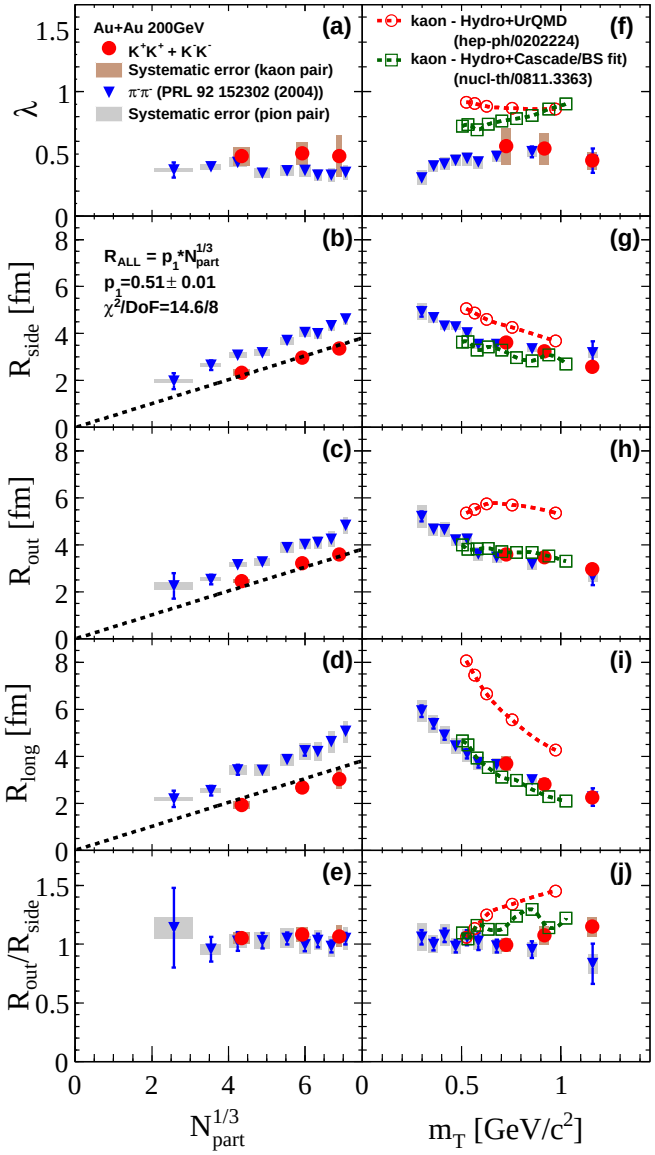

FIG. 2: (color online). 3D Gaussian HBT radius parameters extracted from Eq.(1) for charged kaon pairs as a function of (left) $N^{1/3}_{\rm part}$ measured for $0.3 < k_{\rm T} < 1.5$ GeV/c and (right) $m_{\rm T}$ measured for $0-30\%$ centrality in Au+Au collisions at $\sqrt{s_{\rm NN}} = 200$ GeV. In panels (b)-(d) the dashed line is a fit with $p_1 * N^{1/3}_{\rm part}$.

kaons are measured in a similar $k_{\rm T}$ range ($0.2 < k_{\rm T} < 2.0$ GeV/c for pions), the higher transverse mass ($m_{\rm T} = \sqrt{{k_{\rm T}}^2 + m^2}$) for kaons ($\langle m_{\rm T}\rangle \sim 0.89$ GeV/c^2) than for pions ($\langle m_{\rm T}\rangle \sim 0.47$ GeV/c^2) leads to smaller radii, as expected from $\langle m_{\rm T}\rangle$ scaling [16, 19, 20, 21].

Panels (f)-(j) in Fig. 2 show the $m_{\rm T}$ dependence of the radius parameters for kaons in 3 different $m_{\rm T}$ bins at $0-30\%$ centrality, compared with pions [10]. HBT radii are quite consistent at the same $m_{\rm T}$, clearly indicating that the radii follow $m_{\rm T}$ scaling. The $R_{\rm out}/R_{\rm side}$ ratio

for kaons is ∼1.0-1.2 which is consistent with the value for pions at low $m_{\rm T}$. Kaon HBT results from a 2D+1 hybrid, hydrodynamic + UrQMD calculation (open circles) [22] show slightly larger sidewards radii than the data, and the outwards and longitudinal components are too large by a factor of 2-3. A more recent 1D+1 hybrid calculation [23] for kaons (open squares), which assumes flat rapidity distribution and axial symmetry, compares more favorably, matching all radii to within systematic and statical errors. This calculation incorporates pre-equilibrium flow and a lattice-inspired equation of state, which are two features lacking in earlier calculations of HBT radii. Although promising, these theoretical results remain to be verified with full 3D+1 calculations that can also reproduce the elliptic flow.

Recent femtoscopic measurements [5, 6], which use an imaging technique [24] revealed that the emission source function of charged pions has a non-Gaussian tail which cannot be resolved with traditional Gaussian fitting techniques. In the imaging scheme, the correlation function is expressed by the Koonin-Pratt equation [25, 26]

$$C_2(\mathbf{q}) - 1 = \int d\mathbf{r} K(\mathbf{q},\mathbf{r}) S(\mathbf{r}), \qquad (3)$$

where the kernel $K(\mathbf{q},\mathbf{r})$ is the relative wave function as $|\Phi_{\mathbf{q}}^{(-)}(\mathbf{r})|^2 - 1$ that describes the propagation of pairs emitted with relative separation $\mathbf{r}$ and relative momentum $\mathbf{q}$ in the Pair Center-of-Mass System (PCMS). $S(\mathbf{r})$ is the emission source function of pairs.

The filled squares in Fig. 3 (a) show the 1D kaon correlation as a function of the invariant relative momentum of the pair ($q_{\rm inv} = \sqrt{-(p_1 - p_2)^2}/2$). The 1D source function $S(r)$ imaged from $C_2(q_{\rm inv})$ is shown by filled circles in Fig. 3 (b).

In this analysis, input parameters that govern the imaging procedure [24] were selected to minimize the χ^2 between the data and the restored $C_2(q_{\rm inv})$(χ^2/ndf ∼ 1), shown by open circles in Fig. 3 (a). The solid curve shows the traditional Gaussian source function, obtained by angle-averaging the 3D HBT radius parameters (λ, $R_{\rm side}$, $R_{\rm out}$, $R_{\rm long}$) in the PCMS frame, the same frame in which the imaging is performed.

The imaged $S(r)$ exhibits a non-Gaussian tail at $r \gtrsim 10$ fm. This excess corresponds to the deficit in the $q_{\rm inv} \lesssim 20$ MeV/c region of the angle-averaged Gaussian curve of Fig. 3 (a), and is also visible in the 3D Gaussian slices in Fig. 1. The $S(r)$ for pions in the same $k_{\rm T}$ range shows a similar trend. The deviation from a Gaussian in the shape of the $S(r)$ indicates that the particle emission region is extended, and a similar non-Gaussian tail in the pion source is not solely the result of long lived resonance decays such as the ω, although a less prominent contribution from the K^* is likely. The observation of a more substantial non-Gaussian tail for kaons than for pions is qualitatively consistent with a hadronic resonance

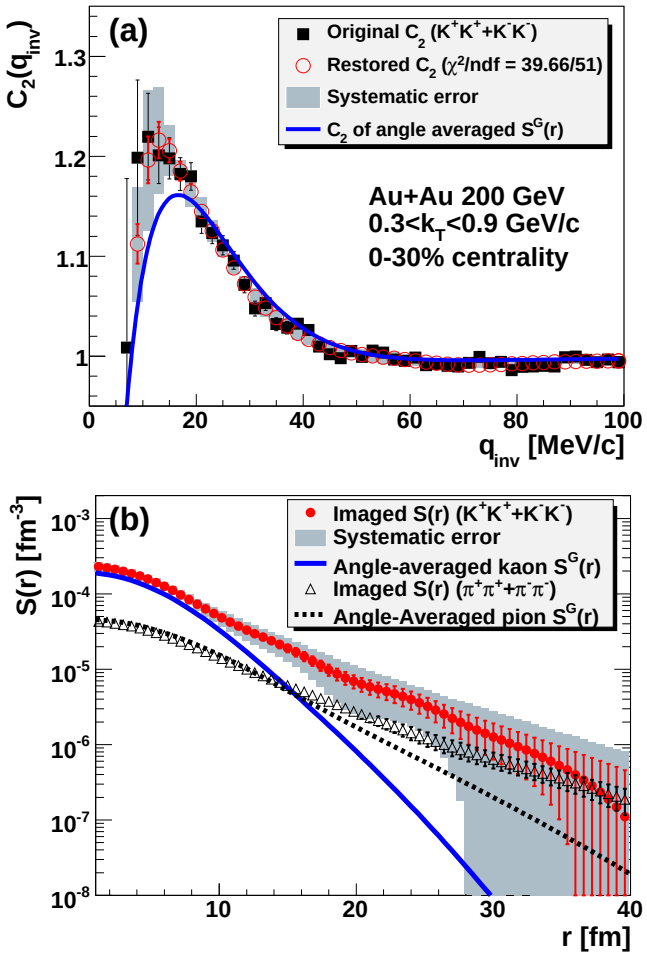

FIG. 3: (color online). (a) (filled squares) measured $C_2(q_{\rm inv})$. (open circles) restored $C_2(q_{\rm inv})$ from imaged $S(r)$, compared with (solid curve) angle-averaged Gaussian $C_2(q_{\rm inv})$ for charged kaon pairs measured for $0.3 < k_{\rm T} < 0.9$ GeV/c at $0-30\%$ central Au+Au collisions at $\sqrt{s_{\rm NN}} = 200$ GeV. (b) (filled circle) Imaged kaon $S(r)$ compared with (solid curve) angle-averaged Gaussian $S(r)$. Error bars are statistical only and boxes indicate the total systematic errors. (open triangle) $S(r)$ for charged pion pairs for the same $k_{\rm T}$ region. For the pion $S(r)$, error bars include both statistical and systematic errors.

cascade model with a time dependent density for an expanding source, in which the larger mean free path for kaons leads to an extended emission region [27, 28]. Detailed measurements with 3D HBT imaging of kaons, or 1D imaging of more species probing different hadronic cross sections will determine contributions from other kinetic effects to $S(r)$.

In summary, we have measured Bose-Einstein correlation functions of charged kaon pairs in Au+Au collisions at $\sqrt{s_{\rm NN}} = 200$ GeV. The 3D HBT radii $R_{\rm side}$ and $R_{\rm long}$ are consistent for pions and kaons at the same $N_{\rm part}$ and $m_{\rm T}$. The 1D emission source function for kaons extracted by imaging shows a non-Gaussian tail at distances greater

than 10 fm. This tail represents a direct measurement of the 1D length of homogeneity of the particle emission source and is not due primarily to resonance decays.

We thank the staff of the Collider-Accelerator and Physics Departments at BNL for their vital contributions. We acknowledge support from the Office of Nuclear Physics in DOE Office of Science and NSF (U.S.A.), MEXT and JSPS (Japan), CNPq and FAPESP (Brazil), NSFC (China), IN2P3/CNRS, and CEA (France), BMBF, DAAD, and AvH (Germany), OTKA (Hungary), DAE (India), ISF (Israel), KRF and KOSEF (Korea), MES, RAS, and FAAE (Russia), VR and KAW (Sweden), U.S. CRDF for the FSU, US-Hungarian NSF-OTKA-MTA, and US-Israel BSF.

* Deceased
† PHENIX Spokesperson: jacak@skipper.physics.sunysb.edu

[1] K. Adcox et al., Nucl. Phys. **A757**, 184 (2005).
[2] T. Hirano and M. Gyulassy, Nucl. Phys. **A769**, 71 (2006).
[3] R. Hanbury Brown and R. Q. Twiss, Phil. Mag. **45**, 663 (1954).
[4] G. Goldhaber, S. Goldhaber, W.-Y. Lee, and A. Pais, Phys. Rev. **120**, 300 (1960).
[5] S. S. Adler et al., Phys. Rev. Lett. **98**, 132301 (2007).
[6] S. Afanasiev et al., Phys. Rev. Lett. **100**, 232301 (2008).
[7] S. Soff, S. A. Bass, D. H. Hardtke, and S. Y. Panitkin, Phys. Rev. Lett. **88**, 072301 (2002).
[8] S. Bernard, D. H. Rischke, J. A. Maruhn, and W. Greiner, Nucl. Phys. **A625**, 473 (1997).
[9] B. I. Abelev et al., Phys. Rev. **C74**, 054902 (2006).
[10] S. S. Adler et al., Phys. Rev. Lett. **93**, 152302 (2004).
[11] K. Adcox et al., Nucl. Instrum. Meth. **A499**, 469 (2003).
[12] R. J. Glauber and G. Matthiae, Nucl. Phys. **B21**, 135 (1970).
[13] S. Pratt, Phys. Rev. Lett. **53**, 1219 (1984).
[14] Y. Sinyukov, R. Lednicky, S. V. Akkelin, J. Pluta, and B. Erazmus, Phys. Lett. **B432**, 248 (1998).
[15] R. Maj and S. Mrowczynski, Int. J. Mod. Phys. **E16**, 3244 (2007).
[16] A. N. Makhlin and Y. M. Sinyukov, Z. Phys. **C39**, 69 (1988).
[17] M. A. Lisa, S. Pratt, R. Soltz, and U. Wiedemann, Ann. Rev. Nucl. Part. Sci. **55**, 357 (2005).
[18] S. Chapman, P. Scotto, and U. W. Heinz, Phys. Rev. Lett. **74**, 4400 (1995).
[19] S. V. Akkelin and Y. M. Sinyukov, Phys. Lett. **B356**, 525 (1995).
[20] I. G. Bearden et al., Phys. Rev. Lett. **78**, 2080 (1997).
[21] M. Csanád and T. Csörgő, Acta Phys. Polon. Supp. **1**, 521 (2008).
[22] S. Soff (2002), [hep-ph/0202240].
[23] S. Pratt (2008), arXiv:0811.3363 [nucl-th].
[24] D. A. Brown and P. Danielewicz, Phys. Lett. **B398**, 252 (1997).
[25] S. E. Koonin, Phys. Lett. **B70**, 43 (1977).
[26] S. Pratt, T. Csörgő, and J. Zimányi, Phys. Rev. **C42**, 2646 (1990).
[27] M. Csanád, T. Csörgő, and M. Nagy, Braz. J. Phys. **37**, 1002 (2007), [hep-ph/0702032].
[28] T. Csörgő, S. Hegyi, T. Novák, and W. A. Zajc, AIP Conf. Proc. **828**, 525 (2006), [nucl-th/0512060].

Photon-hadron jet correlations in $p + p$ and Au + Au collisions at $\sqrt{s_{NN}} = 200$ GeV

A. Adare,[11] S. Afanasiev,[25] C. Aidala,[12,37] N. N. Ajitanand,[54] Y. Akiba,[48,49] H. Al-Bataineh,[43] J. Alexander,[54] A. Al-Jamel,[43] K. Aoki,[31,48] L. Aphecetche,[56] R. Armendariz,[43] S. H. Aronson,[6] J. Asai,[48,49] E. T. Atomssa,[32] R. Averbeck,[55] T. C. Awes,[44] B. Azmoun,[6] V. Babintsev,[21] M. Bai,[5] G. Baksay,[17] L. Baksay,[17] A. Baldisseri,[14] K. N. Barish,[7] P. D. Barnes,[34] B. Bassalleck,[42] A. T. Basye,[1] S. Bathe,[7] S. Batsouli,[12,44] V. Baublis,[47] F. Bauer,[7] C. Baumann,[38] A. Bazilevsky,[6] S. Belikov,[6,24,*] R. Bennett,[55] A. Berdnikov,[51] Y. Berdnikov,[51] A. A. Bickley,[11] M. T. Bjorndal,[12] J. G. Boissevain,[34] H. Borel,[14] K. Boyle,[55] M. L. Brooks,[34] D. S. Brown,[43] D. Bucher,[38] H. Buesching,[6] V. Bumazhnov,[21] G. Bunce,[6,49] J. M. Burward-Hoy,[34] S. Butsyk,[34,55] C. M. Camacho,[34] S. Campbell,[55] J.-S. Chai,[26] B. S. Chang,[63] W. C. Chang,[2] J.-L. Charvet,[14] C.-H. Chen,[55] S. Chernichenko,[21] J. Chiba,[27] C. Y. Chi,[12] M. Chiu,[12,22] I. J. Choi,[63] R. K. Choudhury,[4] T. Chujo,[59,60] P. Chung,[54] A. Churyn,[21] V. Cianciolo,[44] Z. Citron,[55] C. R. Cleven,[19] Y. Cobigo,[14] B. A. Cole,[12] M. P. Comets,[45] M. Connors,[55] P. Constantin,[24,34] M. Csanád,[16] T. Csörgő,[28] T. Dahms,[55] S. Dairaku,[31,48] K. Das,[18] G. David,[6] M. B. Deaton,[1] K. Dehmelt,[17] H. Delagrange,[56] A. Denisov,[21] D. d'Enterria,[12,32] A. Deshpande,[49,55] E. J. Desmond,[6] O. Dietzsch,[52] A. Dion,[55] M. Donadelli,[52] J. L. Drachenberg,[1] O. Drapier,[32] A. Drees,[55] K. A. Drees,[5] A. K. Dubey,[62] A. Durum,[21] D. Dutta,[4] V. Dzhordzhadze,[7,57] Y. V. Efremenko,[44] J. Egdemir,[55] F. Ellinghaus,[11] W. S. Emam,[7] T. Engelmore,[12] A. Enokizono,[20,33] H. En'yo,[48,49] B. Espagnon,[45] S. Esumi,[59] K. O. Eyser,[7] B. Fadem,[39] D. E. Fields,[42,49] M. Finger Jr.,[8,25] M. Finger,[8,25] F. Fleuret,[32] S. L. Fokin,[30] B. Forestier,[35] Z. Fraenkel,[62,*] J. E. Frantz,[12,55] A. Franz,[6] A. D. Frawley,[18] K. Fujiwara,[48] Y. Fukao,[31,48] S.-Y. Fung,[7] T. Fusayasu,[41] S. Gadrat,[35] I. Garishvili,[57] F. Gastineau,[56] M. Germain,[56] A. Glenn,[11,57] H. Gong,[55] M. Gonin,[32] J. Gosset,[14] Y. Goto,[48,49] R. Granier de Cassagnac,[32] N. Grau,[12,24] S. V. Greene,[60] M. Grosse Perdekamp,[22,49] T. Gunji,[10] H.-Å. Gustafsson,[36] T. Hachiya,[20,48] A. Hadj Henni,[56] C. Haegemann,[42] J. S. Haggerty,[6] M. N. Hagiwara,[1] H. Hamagaki,[10] R. Han,[46] H. Harada,[20] E. P. Hartouni,[33] K. Haruna,[20] M. Harvey,[6] E. Haslum,[36] K. Hasuko,[48] R. Hayano,[10] M. Heffner,[33] T. K. Hemmick,[55] T. Hester,[7] J. M. Heuser,[48] X. He,[19] H. Hiejima,[22] J. C. Hill,[24] R. Hobbs,[42] M. Hohlmann,[17] M. Holmes,[60] W. Holzmann,[54] K. Homma,[20] B. Hong,[29] T. Horaguchi,[10,48,58] D. Hornback,[57] S. Huang,[60] M. G. Hur,[26] T. Ichihara,[48,49] R. Ichimiya,[48] Y. Ikeda,[59] K. Imai,[31,48] J. Imrek,[15] M. Inaba,[59] Y. Inoue,[48,50] D. Isenhower,[1] L. Isenhower,[1] M. Ishihara,[48] T. Isobe,[10] M. Issah,[54] A. Isupov,[25] D. Ivanischev,[47] B. V. Jacak,[55,†] J. Jia,[12] J. Jin,[12] O. Jinnouchi,[49] B. M. Johnson,[6] K. S. Joo,[40] D. Jouan,[45] F. Kajihara,[10,48] S. Kametani,[10,48,61] N. Kamihara,[48,49,58] J. Kamin,[55] M. Kaneta,[49] J. H. Kang,[63] H. Kanou,[48,58] J. Kapustinsky,[34] T. Kawagishi,[59] D. Kawall,[37,49] A. V. Kazantsev,[30] S. Kelly,[11] T. Kempel,[24] A. Khanzadeev,[47] K. M. Kijima,[20] J. Kikuchi,[61] B. I. Kim,[29] D. H. Kim,[40] D. J. Kim,[63] E. Kim,[53] S. H. Kim,[63] Y.-S. Kim,[26] E. Kinney,[11] K. Kiriluk,[11] A. Kiss,[16] E. Kistenev,[6] A. Kiyomichi,[48] J. Klay,[33] C. Klein-Boesing,[38] L. Kochenda,[47] V. Kochetkov,[21] B. Komkov,[47] M. Konno,[59] J. Koster,[22] D. Kotchetkov,[7] A. Kozlov,[62] A. Král,[13] A. Kravitz,[12] P. J. Kroon,[6] J. Kubart,[8,23] G. J. Kunde,[34] N. Kurihara,[10] K. Kurita,[48,50] M. Kurosawa,[48] M. J. Kweon,[29] Y. Kwon,[57,63] G. S. Kyle,[43] R. Lacey,[54] Y.-S. Lai,[12] Y. S. Lai,[12] J. G. Lajoie,[24] D. Layton,[22] A. Lebedev,[24] Y. Le Bornec,[45] S. Leckey,[55] D. M. Lee,[34] K. B. Lee,[29] M. K. Lee,[63] T. Lee,[53] M. J. Leitch,[34] M. A. L. Leite,[52] B. Lenzi,[52] P. Liebing,[49] H. Lim,[53] T. Liška,[13] A. Litvinenko,[25] H. Liu,[43] M. X. Liu,[34] X. Li,[9] X. H. Li,[7] B. Love,[60] D. Lynch,[6] C. F. Maguire,[60] Y. I. Makdisi,[5,6] A. Malakhov,[25] M. D. Malik,[42] V. I. Manko,[30] E. Mannel,[12] Y. Mao,[46,48] L. Mašek,[8,23] H. Masui,[59] F. Matathias,[12,55] M. C. McCain,[22] M. McCumber,[55] P. L. McGaughey,[34] N. Means,[55] B. Meredith,[22] Y. Miake,[59] P. Mikeš,[8,23] K. Miki,[59] T. E. Miller,[60] A. Milov,[6,55] S. Mioduszewski,[6] G. C. Mishra,[19] M. Mishra,[3] J. T. Mitchell,[6] M. Mitrovski,[54] A. K. Mohanty,[4] Y. Morino,[10] A. Morreale,[7] D. P. Morrison,[6] J. M. Moss,[34] T. V. Moukhanova,[30] D. Mukhopadhyay,[60] J. Murata,[48,50] S. Nagamiya,[27] Y. Nagata,[59] J. L. Nagle,[11] M. Naglis,[62] M. I. Nagy,[16] I. Nakagawa,[48,49] Y. Nakamiya,[20] T. Nakamura,[20] K. Nakano,[48,58] J. Newby,[33] M. Nguyen,[55] T. Niita,[59] B. E. Norman,[34] R. Nouicer,[6] A. S. Nyanin,[30] J. Nystrand,[36] E. O'Brien,[6] S. X. Oda,[10] C. A. Ogilvie,[24] H. Ohnishi,[48] I. D. Ojha,[60] H. Okada,[31,48] K. Okada,[49] M. Oka,[49] O. O. Omiwade,[1] Y. Onuki,[48] A. Oskarsson,[36] I. Otterlund,[36] M. Ouchida,[20] K. Ozawa,[10] R. Pak,[6] D. Pal,[60] A. P. T. Palounek,[34] V. Pantuev,[55] V. Papavassiliou,[43] J. Park,[53] W. J. Park,[29] S. F. Pate,[43] H. Pei,[24] J.-C. Peng,[22] H. Pereira,[14] V. Peresedov,[25] D.Yu. Peressounko,[30] C. Pinkenburg,[6] R. P. Pisani,[6] M. L. Purschke,[6] A. K. Purwar,[34,55] H. Qu,[19] J. Rak,[24,42] A. Rakotozafindrabe,[32] I. Ravinovich,[62] K. F. Read,[44,57] S. Rembeczki,[17] M. Reuter,[55] K. Reygers,[38] V. Riabov,[47] Y. Riabov,[47] D. Roach,[60] G. Roche,[35] S. D. Rolnick,[7] A. Romana,[32,*] M. Rosati,[24] S. S. E. Rosendahl,[36] P. Rosnet,[35] P. Rukoyatkin,[25] P. Ružička,[23] V. L. Rykov,[48] S. S. Ryu,[63] B. Sahlmueller,[38] N. Saito,[31,48,49] T. Sakaguchi,[6,10,61] S. Sakai,[59] K. Sakashita,[48,58] H. Sakata,[20] V. Samsonov,[47] H. D. Sato,[31,48] S. Sato,[6,27,59] T. Sato,[59] S. Sawada,[27] K. Sedgwick,[7] J. Seele,[11] R. Seidl,[22] A.Yu. Semenov,[24] V. Semenov,[21] R. Seto,[7] D. Sharma,[62] T. K. Shea,[6] I. Shein,[21] A. Shevel,[47,54] T.-A. Shibata,[48,58] K. Shigaki,[20] M. Shimomura,[59] T. Shohjoh,[59] K. Shoji,[31,48] P. Shukla,[4] A. Sickles,[6,55] C. L. Silva,[52] D. Silvermyr,[44] C. Silvestre,[14] K. S. Sim,[29] B. K. Singh,[3] C. P. Singh,[3] V. Singh,[3] S. Skutnik,[24] M. Slunečka,[8,25] W. C. Smith,[1] A. Soldatov,[21] R. A. Soltz,[33] W. E. Sondheim,[34] S. P. Sorensen,[57] I. V. Sourikova,[6] F. Staley,[14] P. W. Stankus,[44] E. Stenlund,[36] M. Stepanov,[43] A. Ster,[28] S. P. Stoll,[6] T. Sugitate,[20] C. Suire,[45] A. Sukhanov,[6] J. P. Sullivan,[34] J. Sziklai,[28] T. Tabaru,[49] S. Takagi,[59] E. M. Takagui,[52] A. Taketani,[48,49] R. Tanabe,[59] K. H. Tanaka,[27] Y. Tanaka,[41] K. Tanida,[48,49] M. J. Tannenbaum,[6] A. Taranenko,[54] P. Tarján,[15] H. Themann,[55] T. L. Thomas,[42] M. Togawa,[31,48] A. Toia,[55] J. Tojo,[48] L. Tomášek,[23] Y. Tomita,[59] H. Torii,[20,48] R. S. Towell,[1] V.-N. Tram,[32] I. Tserruya,[62] Y. Tsuchimoto,[20,48] S. K. Tuli,[3] H. Tydesjö,[36] N. Tyurin,[21] C. Vale,[24] H. Valle,[60] H. W. van Hecke,[34] A. Veicht,[22] J. Velkovska,[60] R. Vertesi,[15] A. A. Vinogradov,[30] M. Virius,[13] V. Vrba,[23] E. Vznuzdaev,[47] M. Wagner,[31,48] D. Walker,[55] X. R. Wang,[43] Y. Watanabe,[48,49] F. Wei,[24] J. Wessels,[38] S. N. White,[6] N. Willis,[45] D. Winter,[12] C. L. Woody,[6] M. Wysocki,[11] W. Xie,[7,49] Y. L. Yamaguchi,[61] K. Yamaura,[20] R. Yang,[22] A. Yanovich,[21]

 ©2009 The American Physical Society

Z. Yasin,[7] J. Ying,[19] S. Yokkaichi,[48,49] G. R. Young,[44] I. Younus,[42] I. E. Yushmanov,[30] W. A. Zajc,[12] O. Zaudtke,[38] C. Zhang,[12,44] S. Zhou,[9] J. Zimányi,[28,*] and L. Zolin[25]
(PHENIX Collaboration)

[1]*Abilene Christian University, Abilene, Texas 79699, USA*
[2]*Institute of Physics, Academia Sinica, Taipei 11529, Taiwan*
[3]*Department of Physics, Banaras Hindu University, Varanasi 221005, India*
[4]*Bhabha Atomic Research Centre, Bombay 400 085, India*
[5]*Collider-Accelerator Department, Brookhaven National Laboratory, Upton, New York 11973-5000, USA*
[6]*Physics Department, Brookhaven National Laboratory, Upton, New York 11973-5000, USA*
[7]*University of California-Riverside, Riverside, California 92521, USA*
[8]*Charles University, Ovocný trh 5, Praha 1, 116 36, Prague, Czech Republic*
[9]*China Institute of Atomic Energy (CIAE), Beijing, People's Republic of China*
[10]*Center for Nuclear Study, Graduate School of Science, University of Tokyo, 7-3-1 Hongo, Bunkyo, Tokyo 113-0033, Japan*
[11]*University of Colorado, Boulder, Colorado 80309, USA*
[12]*Columbia University, New York, NY 10027 and Nevis Laboratories, Irvington, New York 10533, USA*
[13]*Czech Technical University, Zikova 4, 166 36 Prague 6, Czech Republic*
[14]*Dapnia, CEA Saclay, F-91191, Gif-sur-Yvette, France*
[15]*Debrecen University, H-4010 Debrecen, Egyetem tér 1, Hungary*
[16]*ELTE, Eötvös Loránd University, H-1117 Budapest, Pázmány P. s. 1/A, Hungary*
[17]*Florida Institute of Technology, Melbourne, Florida 32901, USA*
[18]*Florida State University, Tallahassee, Florida 32306, USA*
[19]*Georgia State University, Atlanta, Georgia 30303, USA*
[20]*Hiroshima University, Kagamiyama, Higashi-Hiroshima 739-8526, Japan*
[21]*IHEP Protvino, State Research Center of Russian Federation, Institute for High Energy Physics, Protvino, RU-142281, Russia*
[22]*University of Illinois at Urbana-Champaign, Urbana, Illinois 61801, USA*
[23]*Institute of Physics, Academy of Sciences of the Czech Republic, Na Slovance 2, 182 21 Prague 8, Czech Republic*
[24]*Iowa State University, Ames, Iowa 50011, USA*
[25]*Joint Institute for Nuclear Research, RU-141980 Dubna, Moscow Region, Russia*
[26]*KAERI, Cyclotron Application Laboratory, Seoul, Korea*
[27]*KEK, High Energy Accelerator Research Organization, Tsukuba, Ibaraki 305-0801, Japan*
[28]*KFKI Research Institute for Particle and Nuclear Physics of the Hungarian Academy of Sciences (MTA KFKI RMKI), H-1525 Budapest 114, P. O. Box 49, Budapest, Hungary*
[29]*Korea University, Seoul, 136-701, Korea*
[30]*Russian Research Center "Kurchatov Institute," Moscow, Russia*
[31]*Kyoto University, Kyoto 606-8502, Japan*
[32]*Laboratoire Leprince-Ringuet, Ecole Polytechnique, CNRS-IN2P3, Route de Saclay, F-91128, Palaiseau, France*
[33]*Lawrence Livermore National Laboratory, Livermore, California 94550, USA*
[34]*Los Alamos National Laboratory, Los Alamos, New Mexico 87545, USA*
[35]*LPC, Université Blaise Pascal, CNRS-IN2P3, Clermont-Fd, 63177 Aubiere Cedex, France*
[36]*Department of Physics, Lund University, Box 118, SE-221 00 Lund, Sweden*
[37]*Department of Physics, University of Massachusetts, Amherst, Massachusetts 01003-9337, USA*
[38]*Institut für Kernphysik, University of Muenster, D-48149 Muenster, Germany*
[39]*Muhlenberg College, Allentown, Pennsylvania 18104-5586, USA*
[40]*Myongji University, Yongin, Kyonggido 449-728, Korea*
[41]*Nagasaki Institute of Applied Science, Nagasaki-shi, Nagasaki 851-0193, Japan*
[42]*University of New Mexico, Albuquerque, New Mexico 87131, USA*
[43]*New Mexico State University, Las Cruces, New Mexico 88003, USA*
[44]*Oak Ridge National Laboratory, Oak Ridge, Tennessee 37831, USA*
[45]*IPN-Orsay, Universite Paris Sud, CNRS-IN2P3, BP1, F-91406, Orsay, France*
[46]*Peking University, Beijing, People's Republic of China*
[47]*PNPI, Petersburg Nuclear Physics Institute, Gatchina, Leningrad region, RU-188300, Russia*
[48]*RIKEN Nishina Center for Accelerator-Based Science, Wako, Saitama 351-0198, JAPAN*
[49]*RIKEN BNL Research Center, Brookhaven National Laboratory, Upton, New York 11973-5000, USA*
[50]*Physics Department, Rikkyo University, 3-34-1 Nishi-Ikebukuro, Toshima, Tokyo 171-8501, Japan*
[51]*Saint Petersburg State Polytechnic University, St. Petersburg, Russia*
[52]*Universidade de São Paulo, Instituto de Física, Caixa Postal 66318, São Paulo CEP05315-970, Brazil*
[53]*System Electronics Laboratory, Seoul National University, Seoul, Korea*
[54]*Chemistry Department, Stony Brook University, Stony Brook, SUNY, New York 11794-3400, USA*

[55]*Department of Physics and Astronomy, Stony Brook University, SUNY, Stony Brook, New York 11794, USA*
[56]*SUBATECH (Ecole des Mines de Nantes, CNRS-IN2P3, Université de Nantes) BP 20722-44307, Nantes, France*
[57]*University of Tennessee, Knoxville, Tennessee 37996, USA*
[58]*Department of Physics, Tokyo Institute of Technology, Oh-okayama, Meguro, Tokyo 152-8551, Japan*
[59]*Institute of Physics, University of Tsukuba, Tsukuba, Ibaraki 305, Japan*
[60]*Vanderbilt University, Nashville, Tennessee 37235, USA*
[61]*Waseda University, Advanced Research Institute for Science and Engineering, 17 Kikui-cho, Shinjuku-ku, Tokyo 162-0044, Japan*
[62]*Weizmann Institute, Rehovot 76100, Israel*
[63]*Yonsei University, IPAP, Seoul 120-749, Korea*
(Received 20 March 2009; published 31 August 2009)

We report the observation at the Relativistic Heavy Ion Collider of suppression of back-to-back correlations in the direct photon+jet channel in Au + Au relative to $p + p$ collisions. Two-particle correlations of direct photon triggers with associated hadrons are obtained by statistical subtraction of the decay photon-hadron (γ-h) background. The initial momentum of the away-side parton is tightly constrained, because the parton-photon pair exactly balance in momentum at leading order in perturbative quantum chromodynamics, making such correlations a powerful probe of the in-medium parton energy loss. The away-side nuclear suppression factor, $I_{\rm AA}$, in central Au + Au collisions, is $0.32 \pm 0.12^{\rm stat} \pm 0.09^{\rm syst}$ for hadrons of $3 < p_T^h < 5$ in coincidence with photons of $5 < p_T^\gamma < 15$ GeV/c. The suppression is comparable to that observed for high-p_T single hadrons and dihadrons. The direct photon associated yields in $p + p$ collisions scale approximately with the momentum balance, $z_T \equiv p_T^h/p_T^\gamma$, as expected for a measurement of the away-side parton fragmentation function. We compare to Au + Au collisions for which the momentum balance dependence of the nuclear modification should be sensitive to the path-length dependence of parton energy loss.

DOI: 10.1103/PhysRevC.80.024908 PACS number(s): 25.75.Dw, 13.85.Qk, 13.20.Fc, 13.20.He

I. INTRODUCTION

Experimental results from RHIC have established the formation of hot and dense matter of a fundamentally new nature in relativistic heavy-ion collisions at $\sqrt{s_{NN}} = 200$ GeV [1]. Energy loss in this dense nuclear matter by color-charged, hard ($E \gtrsim 2$ GeV) partons, and the jets into which they fragment, is generally accepted to be the mechanism responsible for the suppression of the high-p_T hadron yields observed in central $A + A$ collisions [2,3]. In the large multiplicity environment of heavy-ion collisions, two-particle correlations are often used to study jet modification and to infer properties of the medium. For example, high-p_T azimuthal dihadron correlations demonstrate that the degree of dijet away-side suppression depends on the p_T of the "trigger" and "associated" hadrons. At moderate $p_T (\gtrsim 3$ GeV/$c)$, the jet properties measured through two-particle correlations demonstrate novel features such as shape modifications that are thought to be a manifestation of the response of medium to the energy deposited by the attenuated parton [4].

Dihadron measurements of dijet pairs provide an ambiguous measurement of the energy loss of the away-side parton. The trigger hadron is a product of parton fragmentation and therefore it is not possible to determine, event by event, whether the near-side parton has itself lost energy. Given the steeply falling jet spectrum, the sample of hard scatterings is biased toward configurations in which the parton loses little energy. In particular, it is believed that hadron measurements are subject to a "surface bias" in which the hard scatterings sampled are likely to occur at the periphery of the overlap zone [5,6]. The away-side parton then is more likely to traverse a maximal path-length through the medium. For a sufficiently opaque medium, the attenuation of the parton may be nearly total, in which case the sensitivity to the average path-length is reduced [7]. Back-to-back, high-p_T hadron pairs may originate preferentially from configurations in which the outgoing parton trajectories are tangential to the surface of the overlap zone [8]. However, dihadron pairs may also originate from vertices deep in the collision zone if a parton has a finite probability to "punch-through" or pass through the medium without interaction [9]. Calculations of the relative importance of these two mechanisms depend both on the model of parton energy loss employed and the density profile of the medium [6,10,11].

Direct photon-jet pairs offer two major advantages in studying energy loss as compared to dijets because of the nature of the photon. First, in contrast to partons, photons do not carry color charge and hence do not interact strongly when traversing the medium [12]. The distribution of hard-scattering vertices sampled by direct photon-triggered correlations is thus unbiased by the trigger condition. Suppression of the opposite jet is averaged over all path lengths given by the distribution of hard-scattering vertices. Second, at the Born level, direct photon production in $p + p$ and $A + A$ collisions is dominated by the QCD Compton scattering process, $q + g \rightarrow q + \gamma$, and the photon momentum in the center-of-mass frame is exactly balanced by that of the recoil quark. Higher-order effects and other complications to this idealized picture, such as next-to-leading order (NLO) $2 \rightarrow 3$ bremsstrahlung and other "fragmentation" photons or soft gluon radiation, also do

*Deceased.
†PHENIX spokesperson: jacak@skipper.physics.sunysb.edu

need to be considered. Nonetheless, the level of suppression can then be related directly to the energy loss of a parton of known initial momentum. In this way, the average path length of the away-side parton may then be varied in a well-controlled manner by selecting events of various momentum differences between the γ-h pair.

For this reason, the γ+jet channel has long been considered the "golden channel" for studying parton energy loss [13,14]. Neglecting the above-mentioned complications, specifically effects like transverse momentum broadening (the k_T effect) and parton-to-photon fragmentation, back-to-back γ-h correlations in elementary collisions directly measure the fragmentation function of the recoil jet because $z \equiv p^h/p^{\rm jet} \approx p^h/p^\gamma$. In the standard picture of energy loss, partons are likely to lose some fraction of their energy in the medium but are likely to fragment outside the medium. Hence, the parton energy loss can be considered an effective modification to the fragmentation function. Such a picture may be tested using γ-h correlations in nuclear collisions. Complementary baseline measurements in $p+p$ collisions are used to test the theoretical description of correlations in vacuum and to constrain possible contributions from higher-order processes. Comprehensive reviews of direct photon phenomenology and data from elementary collisions may be found in Refs. [15–17].

II. DETECTOR DESCRIPTION AND PARTICLE IDENTIFICATION

The data were taken with the PHENIX detector [18] using approximately 950 million Au + Au minimum bias events from the 2004 data set and 471 million photon-triggered events from the 2005 and 2006 $p+p$ data sets corresponding to integrated luminosities of 3 (2005) and 10.7 (2006) pb^{-1}. The beam-beam counters (BBC) [19], which are used to trigger the minimum bias data, select 92% of the total inelastic cross section. In Au + Au the BBC and zero-degree calorimeters (ZDC) were used for offline minimum bias event selection and centrality determination. In $p+p$ collisions a high-energy photon trigger, defined by coincidence between the BBC and a high-energy electromagnetic calorimeter (EMCal) tower hit, was used. This EMCal based trigger [20] had an efficiency of >90% for events with photons and π^0 with energies in the range used in the analysis and within the detector's geometric acceptance.

The PHENIX central arms, each covering ± 0.35 units of pseudorapidity around midrapidity and 90° in azimuth, contain charged-particle tracking chambers and electromagnetic calorimeters [21]. The EMCal [22] consists of two types of detectors, six sectors of lead-scintillator (PbSc) sampling calorimeters and two of lead-glass (PbGl) Cerenkov calorimeters measuring EM energy with intrinsic resolution $\sigma_E/E = 8.1\%/\sqrt{E} \oplus 2.1\%$ and $5.9\%/\sqrt{E} \oplus 0.8\%$, respectively. The fine segmentation of the EMCal ($\Delta\eta \times \Delta\phi \sim 0.01 \times 0.01$ for PbSc and $\sim 0.008 \times 0.008$ for PbGl) allows for the reconstruction of π^0 and η mesons in the 2γ decay channel out to p_T of 20 GeV/c. The details of direct photon and π^0 - and η-meson detection and reconstruction within PHENIX have been described previously [12,23,24]. Photon candidates with very high purity (>98% for energies >5 GeV) are selected from EMCal clusters with the use of cluster shower shape and charged particle veto cuts. Two-photon π^0 and η candidates are selected from photon pairs with pair invariant mass in the appropriate π^0 or η mass range. Combinatorial 2γ background is reduced with cuts on energy asymmetry $\alpha_{12} = |E_1 - E_2|/(E_1 + E_2)$, described in detail below. Some fraction of π^0 with p_T starting at ≈13 GeV/c (in the PbSc detector) will appear as a single merged cluster, but with anomalous shower shape, and thus are removed from the analysis. The π^0 and η mesons in the p_T range from about 4 to 17 GeV/c and photons between 5 and 15 GeV/c are used in this analysis. For γp_T between 13 and 15 GeV/c there is a <2% contribution of merged π^0 cluster contamination; however, this together with all sources of nonphoton contamination are found to have a negligible impact on the two-particle correlation analysis of this report. Direct photons and their two-particle correlations are obtained by statistical subtraction of the estimated meson (mainly π^0) decay photon contribution from the inclusive photon and γ-h samples.

Charged hadrons are detected with the PHENIX tracking system [25] that employs a drift chamber in each arm spanning a radial distance of 2.0–2.4 m from the beam axis with a set of pixel pad chambers (PC1) directly behind them. The momentum resolution was determined to be $\delta p/p = 0.7\% \oplus 1.0\% p$, where p is measured in GeV/c. Secondary tracks from decays and conversions are suppressed by matching tracks to hits in a second pad chamber (PC3) at distance of ∼5.0 m. Track projections to the EMCal plane are used to veto photon candidates resulting from charged hadrons that shower in the EMCal.

III. METHOD

A. Two-particle correlations

Two-particle correlations are constructed by measuring the yield of particle pairs as a function of the measured azimuthal angle between photon or parent meson triggers and charged hadron partners. The correlation function, $C(\Delta\phi) \equiv N^{\rm pair}_{\rm real}(\Delta\phi)/N^{\rm pair}_{\rm mixed}(\Delta\phi)$, corrects for the limited acceptance of γ-h or meson-hadron pairs by dividing the distribution in real events $N^{\rm pair}_{\rm real}$ by the mixed event distribution $N^{\rm pair}_{\rm mixed}$. The correlation function is decomposed utilizing a two-source model of pair yields coming from two-particle jet correlations superimposed on a combinatorial background yield from an underlying event. The underlying event in Au + Au is known to have an azimuthal asymmetry of harmonic shape quantified in the elliptic flow parameter v_2 [26,27]. This flow represents a harmonic modulation of the $\Delta\phi$ distribution of this underlying event such that the flow-subtracted jet correlation signal is encoded in the jet pair ratio function, $JPR(\Delta\phi) \equiv C(\Delta\phi) - \xi(1 + 2\langle v_2^\gamma\rangle\langle v_2^h\rangle \cos 2\Delta\phi)$, using the notation of Ref. [4], where $\langle v_2\rangle$ is the average single-particle v_2.

Two methods of determining the background level ξ, known as zero-yield at minimum (ZYAM) and absolute normalization (ABS), respectively, were applied to the Au + Au data. Both methods are described in detail in previous PHENIX publications [4]; see also Refs. [4,28,29] (ABS) and [30]

(ZYAM). ZYAM assigns the level of zero jet yield and hence ξ to the minimum point of the correlation function $C(\Delta\phi)$. The ABS method uses the mean multiplicity of trigger-associated pairs in mixed events and a correction for finite centrality resolution to determine ξ. Where ZYAM statistical precision is reasonable, the direct γ-h extraction of the two methods agree to within much better than the total uncertainties, typically within $\leqslant$20%. The ABS method is chosen for the Au + Au results presented, as this method resulted in a more precise extraction of direct photon-jet pair yields at high trigger p_T where lack of statistics near $\Delta\phi = \pi/2$ severely impairs the ZYAM determination. In the comparatively low multiplicity $p+p$ collisions, the underlying event originates from different physical mechanisms than in Au + Au and is known not to be well described by event mixing. Instead the correlation functions are normalized by fitting to a double Gaussian + constant function, corresponding to the ZYAM method [4].

The results presented here are corrected for the associated charged hadron efficiency ϵ_h such that the quoted yields correspond to a detector with full azimuthal acceptance and $|\eta| < 0.35$ coverage. No correction is applied for the $\Delta\eta$ acceptance of pairs. Final results are presented in terms of the yield Y of jet pairs per trigger, $Y \equiv A \times JPR\,(\Delta\phi)/N_{\text{trigger}}$ with the constant $A = \int N^{\text{pair}}_{\text{mixed}}(\Delta\phi)/(2\pi\epsilon_h)$.

The magnitudes of elliptic flow were determined by measuring the distributions of inclusive photons, neutral pions, and charged hadrons as a function of the angle relative to the reaction plane, which was determined with the BBC's as described in Ref. [31]. The v_2 values measured for this analysis are consistent with previous PHENIX analyses [26,27,32].

At high-p_T ($\geqslant$6 GeV/c) the measured $\pi^0 v_2$ values used in the determination of the decay photon v_2 are fit to a constant function to reduce the effects of large statistical fluctuations. The p_T independence of v_2 of π^0's is motivated by recent preliminary data [33] and by the observed p_T independence of the R_{AA}, because parton energy loss is expected to be the dominant mechanism for azimuthal asymmetry generation at high-p_T [7]. It is also consistent with the findings of Ref. [32] that is direct measurement of $\pi^0 v_2$ for the same data set and is being published concurrently with this measurement. Because, as discussed in that publication, the high-p_T functional behavior for this data set cannot be well constrained, the level of uncertainty we assign to the constant fit assumption increases with p_T. It is further assumed that the v_2 for other mesons that contribute decay photons (e.g., η) are the same as that of the π^0 at high p_T. For the p_T range considered ($\gtrsim$4.5 GeV/c) this assumption is also well motivated under the same expectation of v_2 being due to jet quenching, because R_{AA} suppression is already measured to be the same for a variety of mesons (e.g., η itself [24]). Additionally, other high-p_T v_2 data measurements confirm the expectation [34] for other hadron species.

Table I lists the v_2 values for the inclusive and π^0 decay photons for all p_T ranges used, either the measurements, or for the highest p_T decay v_2 values from the constant fit value. For the fit values the fit errors are listed as statistical error, despite the inherent systematic correlation of the fit value across the p_T bins. The reduction of the statistical error for decay γ v_2 due to fit procedure is clear from comparison to statistical error on the inclusive γ v_2, for which no such fit procedure is used. The assumptions justifying the fit procedure do not apply to the inclusive photons because of their large fraction of direct photons. Direct photon v_2, if present, is not expected to be influenced by the same energy loss mechanisms. The decay photon v_2 is derived from the measured $\pi^0 v_2$ by the same $p_T^{\pi^0} \rightarrow p_T^{\text{decay}\,\gamma}$ mapping procedure applied to the yields, described below, though the difference between π^0 and decay v_2 values are negligible compared to the other uncertainties. Listed v_2 systematic uncertainties come only from reaction plane resolution propagated into each p_T bin [4,31]. This procedure has a component that depends again on the statistics in each bin and thus can fluctuate in relative size. The decay γ values are not corrected for π^0 combinatoric background that is discussed below along with the relevant associated systematic error for the estimated for the final jet yield results.

TABLE I. v_2 values used in the jet function extraction for inclusive and decay photons in Au + Au collisions.

Centrality	p_T^γ	Inclusive γ			Decay γ		
		v_2	Stat.	Sys.	v_2	Stat.	Sys.
0–20%	5–7	0.053	±0.009	±0.011	0.084	±0.009	±0.004
	7–9	0.047	±0.022	±0.015	0.069	±0.018	±0.003
	9–12	0.024	±0.042	±0.017	0.069	±0.020	±0.003
	12–15	0.064	±0.096	±0.094	0.069	±0.023	±0.003
20–40%	5–7	0.096	±0.010	±0.005	0.155	±0.011	±0.036
	7–9	0.079	±0.027	±0.011	0.105	±0.019	±0.025
	9–12	0.025	±0.050	±0.049	0.105	±0.020	±0.025
	12–15	0.287	±0.128	±0.104	0.105	±0.023	±0.024
40–60%	5–7	0.143	±0.023	±0.035	0.136	±0.022	±0.010
	7–9	0.146	±0.064	±0.026	0.126	±0.039	±0.008
	9–12	0.162	±0.126	±0.252	0.126	±0.042	±0.008
	12–15	−0.603	±0.308	±0.191	0.126	±0.046	±0.008

B. Direct γ-hadron correlation subtraction

A direct photon is defined here to be any photon not from a decay process. Direct photons cannot be identified in Au + Au with reasonable purity on an event-by-event basis due to the large background of meson decay in the p_T range of the analysis and the inability to use isolation cuts in the high multiplicity Au + Au environment. Thus both direct γ and γ-h pairs must be determined from the already-mentioned statistical subtraction procedure, which is therefore consistently used in this report for both the $p + p$ and Au + Au.

Single direct photons have previously been measured in PHENIX for Au + Au [12] and $p + p$ [35]. In these analyses, the estimated yield of decay photons $N^{\gamma}_{\rm decay}$ is subtracted from a measured sample of inclusive photons $N^{\gamma}_{\rm inclusive}$ resulting in the direct photon yield. These measurements serve as an input to the current analysis, as they fix the fraction of the photon triggers that are expected to be direct. This fraction is quantified by the fraction $R_\gamma \equiv N^{\gamma}_{\rm inclusive}/N^{\gamma}_{\rm decay}$. The R_γ values used in this analysis are extracted from previous PHENIX measurements, [36,37] by interpolating to obtain the p_T binning used in this analysis. These interpolated values together with the error estimations are tabulated in Table II.

The per-trigger yield of inclusive γ-h pairs $Y_{\rm inclusive}$ is simply the weighted average of the contributions from decay and direct photon triggers,

$$Y_{\rm inclusive} = \frac{N^{\gamma}_{\rm direct} Y_{\rm direct} + N^{\gamma}_{\rm decay} Y_{\rm decay}}{N^{\gamma}_{\rm inclusive}}. \tag{1}$$

Having already determined R_γ, $Y_{\rm direct}$ may then be obtained by simple manipulation of the above terms. This results in a statistical subtraction that involves only per-trigger yields. Solving for $Y_{\rm direct}$ and rewriting in terms of R_γ we obtain the subtraction formula:

$$Y_{\rm direct} = \frac{R_\gamma Y_{\rm inclusive} - Y_{\rm decay}}{R_\gamma - 1}. \tag{2}$$

The direct γ or direct γ-h pair yields do not, by definition, exclude photons from jet fragmentation or medium induced photon production.

TABLE II. Extracted R_γ values used as input to direct γ-h per-trigger yield subtraction [Eq. (2)]. These values are interpolated from previous PHENIX measurements as described in the text.

Centrality	p_T^γ	R_γ	Stat.	Sys.
	5–7	1.77	±0.09	±0.06
	7–9	2.45	±0.09	±0.18
0–20%	9–12	2.99	±0.11	±0.41
	12–15	3.66	±0.24	±0.68
	5–7	1.46	±0.10	±0.04
	7–9	1.85	±0.10	±0.12
20–40%	9–12	2.30	±0.12	±0.28
	12–15	2.35	±0.20	±0.44
	5–7	1.30	±0.09	±0.05
	7–9	1.52	±0.07	±0.13
40–60%	9–12	1.85	±0.10	±0.30
	12–15	1.94	±0.24	±0.36
	5–7	1.18	±0.01	±0.06
	7–9	1.32	±0.01	±0.05
$p + p$	9–12	1.48	±0.03	±0.05
	12–15	1.57	±0.09	±0.07

C. Extraction of decay photon correlations

The decay photon associated yields are estimated from the measured π^0-h and η-h correlations through a calculation that determines the decay correlations statistically from a Monte Carlo (MC) based, pair-by-pair weighting procedure. In this procedure the decay γ-h pair yield $N^{\gamma\text{-}h}_{\rm decay}(p_T^\gamma)$ is constructed by a weighted integral over all π^0-h and η-h pairs. In what follows, we will first describe the procedure schematically, describing the ingredients and how they are obtained. We then give a more exact description and associated formula representing exactly how the weighting was performed in the measurement. Schematically the procedure may be expressed as a convolution of several factors according to the following relation, wherein for simplicity we only consider photons from π^0 decay, although the procedure is also applied to η-decay photons.

$$N^{\gamma\text{-}h}_{\rm decay}(p_T^\gamma) = \int \frac{\epsilon_\gamma(p_T^\gamma, p_T^\pi) \otimes \mathcal{P}(p_T^\gamma, p_T^\pi)}{\epsilon_\pi(p_T^\pi)} \otimes N^{\pi\text{-}h}(p_T^\pi), \tag{3}$$

where ϵ_π and ϵ_γ are the π^0 and single *decay* photon efficiencies, respectively, and $\mathcal{P}$ is the decay probability density, each of which is addressed in turn below.

First, because the starting point is the uncorrected raw meson-h pair yield $N^{\pi\text{-}h}$, a correction for the parent meson reconstruction efficiency, $\epsilon_\pi(p_T^\pi)$, is applied to the raw π^0's as a function of p_T to account for the π^0 daughter photons in the inclusive sample whose sisters lie outside the PHENIX acceptance or are otherwise undetected. Both efficiencies, ϵ_γ and ϵ_π, in Eq. (3) are also evaluated as a function of the position in the calorimeter along the beam direction; however, this dependence mostly cancels in the ratio $\epsilon_\gamma/\epsilon_\pi$ and therefore is suppressed for clarity. The value of $\epsilon_\pi(p_T^\pi)$ is determined by dividing the raw number of π^0's $N^\pi(p_T^\pi)$ obtained in the same data sample by our published π^0 invariant yields [2,24,38] assuming no pseudorapidity dependence over the narrow PHENIX acceptance. The top panel in Fig. 1 illustrates, for the example of central Au + Au events, the π^0 efficiency correction factor $1/\epsilon_\pi(p_T^\pi)$. The correction rises at small p_T due to a p_T-dependent pair energy asymmetry cut designed to reduce combinatorial 2γ pairs reconstructed as real π^0's. This cut, along with the effects of any remaining background, is described below. At large p_T the quantity $1/\epsilon_\pi(p_T^\pi)$ rises again due to losses from cluster merging.

Second, the effect of decay kinematics is evaluated by determining the probability density, $\mathcal{P}(p_T^\gamma, p_T^\pi)$, for the decay of a p_T-independent distribution of π^0's. $\mathcal{P}(p_T^\gamma, p_T^\pi)$ represents the relative probability of a π^0 of $p_T = p_T^\pi$, to decay into a photon of p_T^γ. For a perfect detector, this function is calculable analytically. A simple fast MC generator implements the

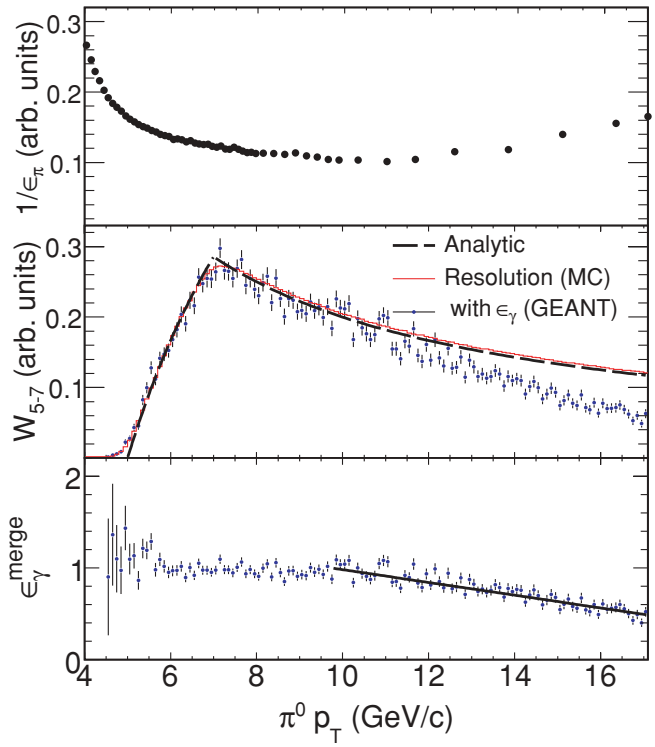

FIG. 1. (Color online) The weight factors used to obtain decay correlations from parent meson correlations. (Top) π^0 reconstruction efficiency correction, $1/\epsilon_\pi$, shown in arbitrary units. (Middle) Decay probability function, W_{ab}, also in arbitrary units, for 5–7 GeV/c decay photons from π^0 derived analytically (black line), using the detector acceptance and resolution smearing (red line) and including the single decay photon efficiency, ϵ_γ, from a GEANT simulation (blue points). (Bottom) $\epsilon_\gamma^{\text{merge}}$ obtained by taking ratio of the blue points to red curve in the previous panel.

PHENIX acceptance and uses Gaussian smearing functions to simulate detector resolution according to the known EMCal energy and position resolution. Occupancy effects give rise to an additional smearing of the π^0 and η invariant masses. This effect is included in the MC by tuning the resolution parameters to match the π^0 peak widths observed in data. False reconstruction of π^0's and η's from combinatorial matches are either subtracted or assigned to the systematic uncertainties as discussed below.

Finally, we wish to estimate the decay photon contribution to the measured raw inclusive photon sample that differs from the true decay photon distribution by the single decay photon efficiency, $\epsilon_\gamma(p_T^\pi)$. At intermediate p_T, $\epsilon_\gamma(p_T^\pi)$ depends only on the photon momentum and is included already implicitly by the fast MC simulation described above to produce $\mathcal{P}(p_T^\gamma, p_T^\pi)$. Thus, it is useful to think of them as a single factor $W(p_T^\gamma, p_T^\pi) \equiv \mathcal{P}(p_T^\gamma, p_T^\pi)\epsilon_\gamma(p_T^\gamma, p_T^\pi)$ At high p_T, however, an efficiency loss is incurred by photons from π^0's whose showers merge into a single cluster in the calorimeter and are rejected by the shower-shape cut. As a consequence, the fraction of photons that are direct is artificially enhanced in the sample of reconstructed photon clusters. The single decay photon efficiency depends on both the parent and daughter p_T and is evaluated in a GEANT simulation. In principle the convolution of both $\mathcal{P}(p_T^\gamma, p_T^\pi)$ and $\epsilon_\gamma(p_T^\gamma, p_T^\pi)$, $W(p_T^\gamma, p_T^\pi)$ could be extracted as one function from the GEANT simulation, but obtaining large-enough MC statistics necessary to properly parametrize the above-mentioned EMCal z position dependence of the $\epsilon_{\pi,\gamma}$ corrections is feasible only with the fast MC. Thus only the efficiency loss by cluster merging for photons $\epsilon_\gamma^{\text{merge}}$ is taken from the GEANT. The bottom panel of Fig. 1 shows $\epsilon_\gamma^{\text{merge}}(p_T^\pi)$ evaluated from the GEANT simulation.

Because we wish to construct per-trigger yields, the same procedure described in Eq. (3) can be applied to find the estimated single decay photon trigger yield from the measured single π^0's, i.e., replacing $N_{\text{decay}}^{\gamma\text{-}h}$ with $N_{\text{decay}}^{\gamma}$ and $N^{\pi\text{-}h}$ with N^π. The exact application of schematic Eq. (3) then takes the form of a sum over all π^0-h pairs and single π^0's found in the data. Each π^0 or π^0-h pair is given a weight that depends on $\pi^0 p_T$. Operationally we now split this weight into two parts: $\epsilon_\pi(p_T^\pi)$ discussed above and a factor $W_{ab}(p_T^\pi)$. The factor W_{ab} is simply the end result of the fast MC-GEANT combined calculation, the convolution of $\mathcal{P}$ and ϵ_γ, including $\epsilon_\gamma^{\text{merge}}$, averaged over a chosen decay photon bin of the range $a < p_T < b$. Thus in terms of the product $W(p_T^\gamma, p_T^\pi)$ then $W_{ab}(p_T^\pi)$ is given by

$$W_{ab}(p_T^\pi) = \int_a^b dp_T^\gamma W(p_T^\pi, p_T^\gamma). \tag{4}$$

The functions $W_{ab}(p_T^\pi)$ are defined for the four photon p_T bins used in the analysis, $[a,b] = [5,7]$, [7,9], [9,12], and [12,15] GeV/c. An example of $W_{ab}(p_T^\pi)$ for the 5- to 7-GeV/c bin is shown in Fig. 1. Procedurally, we construct W_{ab} as product of the fast MC curve shown in the middle panel and the linear fit discussed above to the bottom panel, $\epsilon_\gamma^{\text{merge}}(p_T^\pi)$. Although a decay of $p_T^\pi < a$, the lower limit of the decay p_T bin, is kinematically disallowed, W_{ab} is nonzero below this boundary when resolution effects are considered. For $p_T^\pi > b$, W_{ab} decreases as $\sim 1/p_T^\pi$, slowly enough that π^0's at values of p_T beyond the statistical reach of the data set contribute to the relevant decay photon p_T selections at a non-negligible rate. The π^0 sample is truncated at $p_T = 17$ GeV/c and extrapolated using power-law fits to the single and conditional π^0 spectra to estimate a correction. In the latter case, each associated hadron p_T range is fit independently. The truncation avoids the high-p_T region where cluster merging effects are dominant and the $1/\epsilon^\pi$ correction factor becomes large. Although the truncation corrections for the number of decay photons and decay γ-h pairs are non-negligible, they mostly cancel in the per-trigger yield and are therefore typically <1%, reaching a maximum value of 7% for only the $12 < p_T^\gamma < 15 \otimes 3 < p_T^h < 5$ GeV/c bin.

With the weight functions W_{ab} the entire set of π^0-hadron pairs and single π^0 candidates (within a given range of $\Delta\phi$, $\phi_1 < \Delta\phi < \phi_2$, defining each $\Delta\phi$ bin) are then summed over, once for each decay photon p_T bin, and the per-trigger yield is constructed for each of these decay p_T bins as

$$Y_{\text{decay}}\big|_{a<p_T^\gamma<b}^{\phi_1<\Delta\phi<\phi_2} = \frac{\sum_{i=1-N^{\pi\text{-}h}}^{\phi_1<\Delta\phi_{\pi\text{-}h}<\phi_2} W_{ab}\left(p_{Ti}^{\pi_i}\right)/\epsilon_\pi\left(p_T^{\pi_i}\right)}{\sum_{i=1-N^\pi} W_{ab}\left(p_{Ti}^{\pi_i}\right)/\epsilon_\pi\left(p_T^{\pi_i}\right)}. \tag{5}$$

In this form it is clear that the normalization of the functions $\epsilon_\pi(p_T^\pi)$ and $W_{ab}(p_T^\pi)$ cancel out completely in the per-trigger yield, and therefore only their shapes versus p_T^π are important. Hence in Fig. 1 the curves are shown with arbitrary units. Also, as Eq. (5) implies, the angular deviation between the direction of a decay photon and its parent meson is ignored. The $\Delta\phi$ opening angle of a decay photon and hadron pair is taken to be the same as the $\Delta\phi_{\pi\text{-}h}$ of the parent π^0-h pairs. This approximation is tested in the fast MC and found to be extremely accurate because the distribution of angular deviation between a leading decay photon in a 2γ decay and the parent mesons at these π^0 momenta have an rms around 0 of $\ll$0.01 radians, and the smallest $\Delta\phi$ bins considered in the analysis are typically $\sim$0.1 radians or larger.

D. π^0 and η reconstruction

In $p+p$ collisions $Y_{\rm decay}$ is estimated using both reconstructed π^0 and η mesons in invariant mass windows of 120–160 and 530–580 MeV/c^2, respectively. The total decay per-trigger yield is calculated from

$$Y_{\rm decay} = \left(1-\delta^\gamma_{h/\pi^0}\right)Y^{\pi^0}_{\rm decay} + \delta^\gamma_{h/\pi^0}Y^{\eta}_{\rm decay}, \qquad (6)$$

where δ^γ_{h/π^0} is the ratio of the total number of decay photons to the number of decay photons from π^0. Based on the measurements of η [24] and ω [39], which together with the π^0 account for >99% of decay photons, the value of δ^γ_{h/π^0} is determined to be 1.24 ± 0.05 in the high-p_T region covered by this analysis, independent of collision system and centrality. Note that the per-trigger yields for ω and other heavier meson triggers ($\omega, \eta', \phi, \ldots$) are not measured and are taken to be equivalent to $Y^\eta_{\rm decay}$ in Eq. (6). This assumption was studied in PYTHIA and found to influence $Y_{\rm decay}$ at the level of <2%. In Au + Au collisions correlations using η triggers are not directly measured but rather estimated from the $p+p$ measurement as discussed below.

Figure 2 shows the various components of the decay photon measurement in $p+p$. In $p+p$ collisions the rate of combinatorial background photon pairs is reduced by considering only photons of $p_T > 1$ GeV/c resulting in background levels of <10% for which no correction was applied. The effect of such remaining pairs on $Y^{\pi^0}_{\rm decay}$ was evaluated to be negligible (<2%) compared to the size of other uncertainties on the final $Y_{\rm direct}$ result using a detailed full PYTHIA test of the method that included π^0 reconstruction with combinatorial photon pairs. However, η reconstruction has a much smaller signal-to-background of 1.4–1.6, depending on the p_T selection, even in the low multiplicity $p+p$ environment. In this case, the per-trigger yield of the combinatorial photon pairs is estimated from photon pairs with invariant mass in "sideband" ranges of 400–460 and 640–700 MeV/c^2, beyond 3σ of the η peak. The sideband contribution $Y^{\rm sideband}_{\rm decay}$ is then subtracted using the signal-to-background ratio $f_{\rm bkg}$ evaluated from Gaussian + polynomial background fits to the invariant mass distributions according to $Y^{\rm signal}_{\rm decay} = Y^{\rm raw}_{\rm decay}/(1/f_{\rm bkg}+1) - Y^{\rm sideband}_{\rm decay}/f_{\rm bkg}$. The yield $Y^{\rm sideband}_{\rm decay}$ is generated from the full meson to decay photon weighting function procedure [Eq. (5)]. The subtraction procedure was also tested

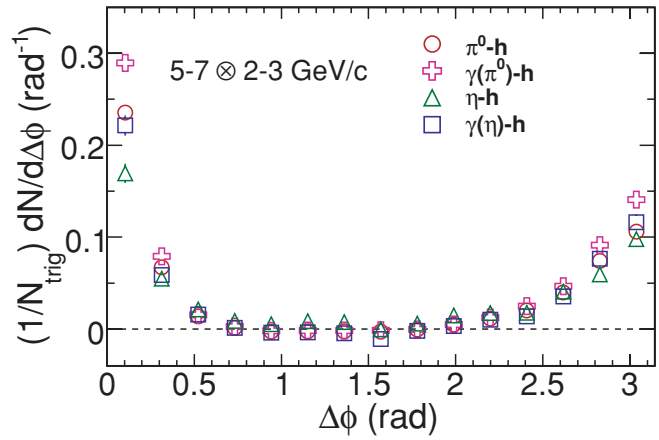

FIG. 2. (Color online) Examples of parent and daughter per-trigger yields for the π^0 and η in $p+p$ collisions for p_T selection $5 < p_T^\gamma < 7$ and $2 < p_T^h < 3$ GeV/c. These ZYAM correlation measurements, fully corrected for acceptance and efficiency (expcept the PHENIX rapidity acceptance), are used to determine the total decay photon per-trigger yield as described in the text.

in PYTHIA and the extracted and input per-trigger yields were found to agree to within 10%.

In Au + Au collisions the combinatorial rate for π^0 reconstruction is substantially larger. Correspondingly, a p_T-dependent cut on the pair energy asymmetry $\alpha_{12} = |E_1 - E_2|/(E_1+E_2)$ [23], visible in Fig. 1 with the smallest allowed asymmetry at the lowest $\pi^0 p_T$ values, is used to reduce this background. With such cuts the signal-to-background in central events varies from 5:1 at its lowest, increasing to about 15:1 for the highest p_T selection. The effect of the combinatorial background is studied through examination of a similar sideband subtraction analysis as in the $p+p\eta-h$ correlation extraction described, this time for π^0-h, using invariant mass ranges just outside the π^0 peak region. However, no clear trend beyond non-negligible statistical limitations is observed, so no correction for the background is applied. Instead the maximum size of the effect (typically $\simeq$7%) is included as source of systematic uncertainty on the decay yields and propagated to the final direct photon per-trigger yields.

In central Au + Au collisions the η meson cannot be reconstructed with sufficient purity to measure its correlations. Instead, a scaling argument is employed. Motivated by the similar high-p_T suppression pattern shown by η and π^0 in Au + Au [24] and corresponding near equality of the $p+p$ and Au + Au η/π^0 ratios, the ratio $Y_{\gamma(\eta)}/Y_{\gamma(\pi^0)}$ is measured in $p+p$ and applied as a correction to the Au + Au $Y_{\gamma(\pi^0)}$. This is justified by the assumption that the jet fragmentation is primarily occurring outside the medium. We do not attribute any additional uncertainty to this scaling beyond the 10% sideband systematic and statistical uncertainties of the η measurement in $p+p$. However, to give an idea of the possible impact of this assumption, the size of the total systematic uncertainty on $Y_{\rm decay}$ from all other sources would be equivalent to a variation of the Au + Au$Y_{\gamma(\eta)}$ by $\sim$50%. Given the similarity of the high-p_T suppression demonstrated

by all light quark bound states measured thus far, this would correspond to a rather large change.

IV. SYSTEMATIC UNCERTAINTIES

There are four main classes of systematic uncertainty in the Au + Au data: elliptic flow, normalization of the underlying event (ABS), R_γ, and the decay per-trigger yield estimate, only the latter two of which are present or non-negligible in the $p+p$ data. Table III lists the fractional contribution of each of these sources to the total systematic uncertainty on the direct photon per-trigger yields in the 20% most central Au + Au and $p+p$ data. In the central Au + Au data the uncertainty at low p_T^h is dominated by the v_2 and correlation function normalization (ABS method) estimation due to large multiplicity of hadrons. At higher p_T^h, but low trigger p_T, p_T^t, the decay error dominates due to the two-photon combinatorial background for π^0 reconstruction. Finally, at large p_T^h and p_T^t the backgrounds responsible for both of these sources of uncertainty decrease and the uncertainty on R_γ, which is relatively constant, dominates. In $p+p$ collisions the decay photon background forms a much larger fraction of the total photon sample. In this case, the decay uncertainty arises from the MC decay photon mapping procedure, the η sideband subtraction and the η/π^0 ratio in approximately equal parts. The yields associated with daughter photons are larger than for the meson parents because of feed-down from larger values of parent p_T, and hence, jet p_T.

The correction for single hadron efficiency $\epsilon_h(p_T^h)$ varies as a function of collision system and centrality. These corrections are obtained by finding the ratio of raw yields of hadrons obtained without the trigger condition in the same analysis (i.e., with the same cuts as in the analysis to the previous PHENIX published measurements of the corresponding charged hadron spectra) [40,41]. As in previous PHENIX two-particle correlation measurements [4,30], this procedure has inherent uncertainties assigned as a p_T-independent 10% uncertainty, on each system and/or centrality.

TABLE III. Fractional contribution to the total systematic uncertainty for each of the main sources of uncertainty in $p+p$ and 0–20% Au + Au collisions. Derived by propagating each uncertainty individually and finding fraction of the total (nonquadrature) sum. For the total systematic uncertainties (see Table IV), sources are added in quadrature as usual.

p_T^γ (GeV)	p_T^h (GeV)	Au + Au, centrality 0–20%				$p+p$	
		R_γ	Decay	v_2	Norm.	R_γ	Decay
5–7	1–2	0.03	0.14	0.50	0.33	0.14	0.86
	2–3	0.02	0.32	0.46	0.20	0.21	0.79
	3–5	0.02	0.71	0.18	0.10	0.05	0.95
7–9	1–2	0.09	0.17	0.45	0.29	0.22	0.78
	2–3	0.10	0.35	0.38	0.17	0.25	0.75
	3–5	0.09	0.61	0.18	0.13	0.21	0.79
9–12	1–2	0.06	0.09	0.53	0.33	0.19	0.81
	2–3	0.26	0.25	0.33	0.16	0.30	0.70
	3–5	0.46	0.30	0.13	0.10	0.35	0.65
12–15	1–2	0.08	0.01	0.63	0.29	0.21	0.79
	2–3	0.21	0.14	0.48	0.17	0.02	0.98
	3–5	0.22	0.14	0.39	0.25	0.10	0.90

V. RESULTS

A. Direct γ-h per-trigger yields

Figure 3 shows examples of direct photon per-trigger yields in $p+p$ and central Au + Au collisions. Also shown are the per-trigger yields for inclusive and decay photon triggers that are the ingredients in the statistical subtraction method as expressed in Eq. (2). A clear away-side correlation is observed ($\Delta\phi \simeq \pi$) for direct photons triggers in $p+p$. In Au + Au collisions the away-side correlation is suppressed for both decay and direct photon triggers. The near-side direct photon associated yields are small relative to that of decay photons, an expected signature of prompt photon production [16].

The away-side yields, integrated over $|\Delta\phi - \pi| < \pi/5$ radians, are shown in Fig. 4 and Table IV for $p+p$ and Au + Au collisions. This range roughly corresponds to the "head region" as defined in Ref. [4] and is chosen primarily to minimize the influence of medium response that is thought to dominate the "shoulder" region further offset from $\Delta\phi = \pi$. Additionally, the acceptance and the signal itself are largest in this range so statistical precision is maximized. It should be noted that the width of the jet correlation is larger than this interval. We do not make a correction for this effect, because we are primarily concerned with the comparison of the yields from $p+p$ and Au + Au collisions. It should be noted, however, that in addition to parton energy loss, any broadening of azimuthal correlations, whether by hot or cold nuclear matter effects, will contribute to a suppression in the yield in the head region. Due to statistical and systematic fluctuations, the subtraction of the decay-photon hadron pairs

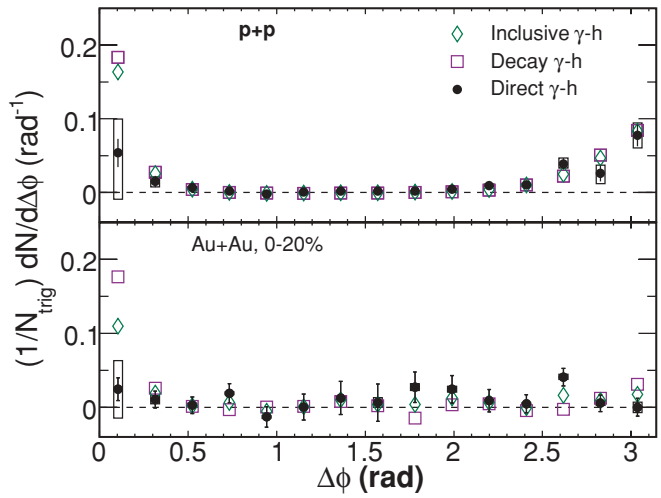

FIG. 3. (Color online) Examples of ZYAM subtracted per-trigger yields, fully corrected for acceptance and efficiency (except rapidity acceptance) used in the direct photon correlation analysis for the $5 < p_T^\gamma < 7$ and $3 < p_T^h < 5$ GeV/c bin. (Top/bottom) Inclusive, decay and direct photon per-trigger yields in $p+p$ (0–20% central Au + Au) collisions.

TABLE IV. Direct γ-h per-trigger yields in 20% most central Au + Au and in $p + p$ collisions. An additional p_T-independent uncertainty of 10% due to the charged hadron efficiency corrections is not shown.

p_T^γ (GeV)	p_T^h (GeV)	$\langle z_T \rangle$	Yield	Stat.	Sys.	Total
			Au + Au, centrality 0–20%			
	1–2	0.23	6.26×10^{-2}	4.72×10^{-2}	4.62×10^{-2}	6.60×10^{-2}
5–7	2–3	0.41	2.68×10^{-2}	1.29×10^{-2}	5.68×10^{-3}	1.41×10^{-2}
	3–5	0.62	4.82×10^{-3}	2.13×10^{-3}	1.96×10^{-3}	2.90×10^{-3}
	1–2	0.17	3.71×10^{-2}	8.48×10^{-2}	5.59×10^{-2}	1.02×10^{-1}
7–9	2–3	0.3	3.45×10^{-2}	2.39×10^{-2}	8.46×10^{-3}	2.53×10^{-2}
	3–5	0.46	9.63×10^{-3}	4.18×10^{-3}	1.96×10^{-3}	4.62×10^{-3}
	1–2	0.13	1.28×10^{-1}	1.34×10^{-1}	6.84×10^{-2}	1.51×10^{-1}
9–12	2–3	0.23	3.94×10^{-2}	3.81×10^{-2}	1.01×10^{-2}	3.94×10^{-2}
	3–5	0.36	-2.16×10^{-3}	6.29×10^{-3}	2.06×10^{-3}	6.62×10^{-3}
	1–2	0.1	5.31×10^{-1}	2.53×10^{-1}	1.49×10^{-1}	2.94×10^{-1}
12–15	2–3	0.18	-6.13×10^{-3}	6.99×10^{-2}	1.80×10^{-2}	7.22×10^{-2}
	3–5	0.28	3.25×10^{-2}	1.60×10^{-2}	2.52×10^{-3}	1.62×10^{-2}
			$p + p$			
	1–2	0.24	1.44×10^{-1}	9.93×10^{-3}	3.42×10^{-2}	3.56×10^{-2}
5–7	2–3	0.43	4.22×10^{-2}	5.47×10^{-3}	1.20×10^{-2}	1.32×10^{-2}
	3–5	0.66	1.55×10^{-2}	2.07×10^{-3}	3.26×10^{-3}	3.86×10^{-3}
	1–2	0.18	1.73×10^{-1}	1.84×10^{-2}	2.88×10^{-2}	3.42×10^{-2}
7–9	2–3	0.31	6.24×10^{-2}	1.11×10^{-2}	1.15×10^{-2}	1.60×10^{-2}
	3–5	0.48	2.26×10^{-2}	4.53×10^{-3}	3.75×10^{-3}	5.88×10^{-3}
	1–2	0.14	2.59×10^{-1}	2.99×10^{-2}	2.50×10^{-2}	3.90×10^{-2}
9–12	2–3	0.24	7.01×10^{-2}	1.73×10^{-2}	1.00×10^{-2}	2.00×10^{-2}
	3–5	0.38	1.94×10^{-2}	7.21×10^{-3}	3.77×10^{-3}	8.14×10^{-3}
	1–2	0.11	1.20×10^{-1}	5.13×10^{-2}	7.22×10^{-2}	8.86×10^{-2}
12–15	2–3	0.19	1.04×10^{-1}	3.11×10^{-2}	2.02×10^{-2}	3.71×10^{-2}
	3–5	0.3	4.26×10^{-2}	1.62×10^{-2}	1.13×10^{-2}	1.97×10^{-2}

from the inclusive γ-h sample can result in a negative yield. In this case 90% confidence-level upper limits are given. In the case that a positive yield is obtained, but the uncertainty is consistent with 0, the lower bound of the error bar is also replaced with an arrow. As noted in the figure caption, a 10% p_T-independent uncertainty due to the charged hadron efficiency corrections is not shown.

B. Suppression factor I_{AA}

Departure from the vacuum QCD processes is quantified by I_{AA}, the ratio of Au + Au to $p + p$ per-trigger yields:

$$I_{AA}\left(p_T^\gamma, p_T^h\right) = \frac{Y^{\text{Au+Au}}\left(p_T^\gamma, p_T^h\right)}{Y^{p+p}\left(p_T^\gamma, p_T^h\right)}. \quad (7)$$

Figure 5 shows the I_{AA} values for all direct photon and associated hadron bins for the most central 0–20% of collisions. The data points for which the subtraction resulted in a negative yield value (the 90% confidence level upper limits) are included with standard 1-σ uncertainties. For the p_T^γ range 5–12 GeV/c, a significant suppression is observed in the $3 < p_T^h < 5$ GeV/c bin in which the highest precision is obtained. At lower p_T^h, where the background subtraction is largest, the data do not have the statistical precision to determine the degree to which the yields are suppressed. I_{AA} for direct photon triggers is consistent to that of charged hadron triggers [4] as shown in the top left panel in which results with similar ranges of $p_{T,t}$ are compared.

Figure 6 shows the I_{AA} for the $p_T^h = 3$–5 GeV/c bin, integrated for all trigger p_T bins ($p_T^\gamma = 5$–15 GeV/c) and for three centrality bins, 0–20%, 20–40%, and 40–60%. For the most central bin, the suppression of the away-side direct photon per-trigger yield is clearly observed, $I_{AA} = 0.32 \pm 0.12^{\text{stat}} \pm 0.09^{\text{syst}}$. Within large uncertainties we see that the γ-jet I_{AA} in this p_T range, dominated by moderate to high values of z ($\equiv p^h/p^{\text{jet}}$), is consistent with the single-particle R_{AA} as a function of centrality, consistent with a scenario in which the geometry of suppression plays an important role as would be expected from a sample dominated by surface emission.

Figure 6 also compares I_{AA} from a measurement of high-p_T dihadron ($h^\pm - h^\pm$) correlations [4] to the γ-jet result for similar $p_{T,t}$ selections. The two results are remarkably similar in the most central bin. This may indicate that surface emission is dominant for both samples in this z region. However it should

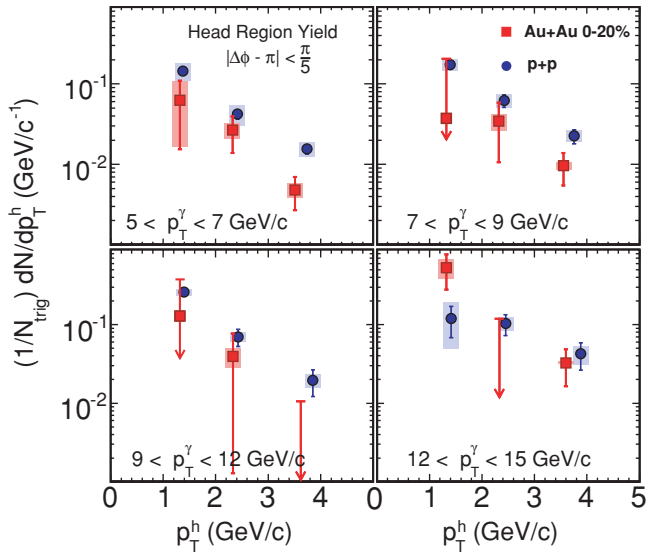

FIG. 4. (Color online) Direct γ-h per-trigger yields for the range $|\Delta\phi - \pi| < \pi/5$ radians vs. associated hadron p_T. Four different direct γp_T ranges (indicated on the figure) are shown in the most central 20% of Au + Au events and $p + p$ events. The upper limits are for 90% confidence levels. A p_T-independent uncertainty of 10% due to the charged hadron efficiency correction is suppressed from the plot.

be noted that the total uncertainties on either measurement are still quite large on a relative scale. Also, because our method does not remove the so-called "fragmentation prompt photon" or NLO direct photon contribution associated with dijet production, a small residual dijet contribution may be present; however, this contribution will be suppressed by R_{AA} relative to that of γ-jet and thus will not affect interpretations

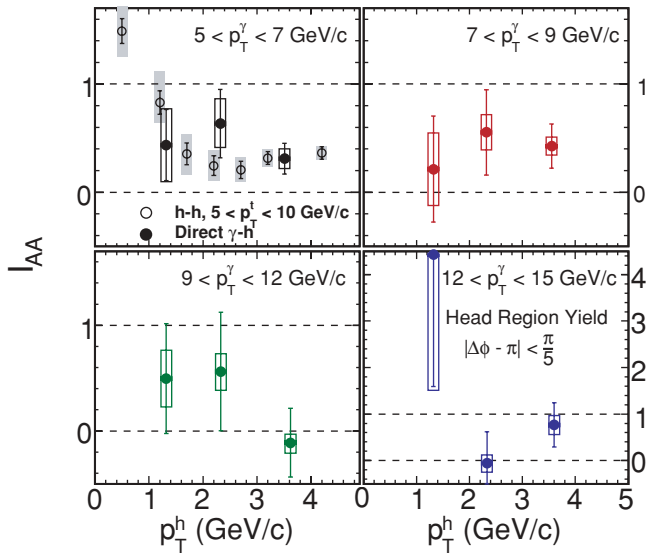

FIG. 5. (Color online) Ratio I_{AA} of the Au + Au to $p + p$ yields shown in Fig. 4. For comparison the first panel shows dihadron correlation data from Ref. [4]. An additional p_T-independent uncertainty of 14% due to the charged hadron efficiency corrections is not shown.

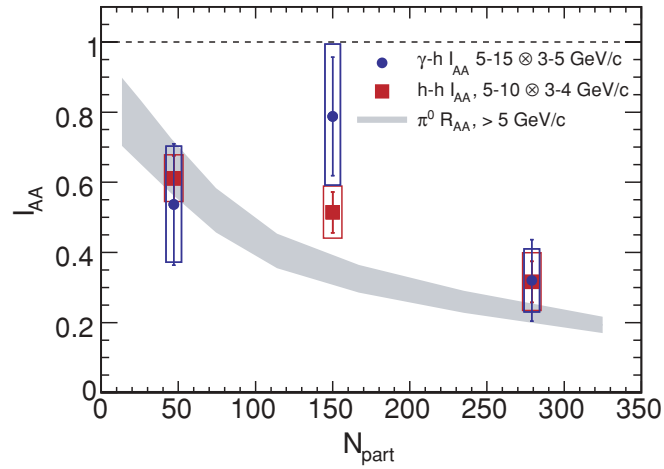

FIG. 6. (Color online) $I_{AA}(p_T^\gamma)$ integrated over the range $5 < p_T^\gamma < 15$ GeV/c for associated hadrons of $3 < p_T^h < 5$ GeV/c vs. centrality compared to single π^0 high-p_T R_{AA} (integrated over $p_T > 5$ GeV/c) [2]. An additional p_T-independent uncertainty of 14% due to the charged hadron efficiency corrections is not shown.

of the data presented here. As explained in the introduction, the dijet and γ-jet measurements should be subject to different geometrical effects. Disentangling such effects through precise comparisons of dihadron and γ-h suppression should be pursued with future measurements with improved statistics.

C. Towards the fragmentation function

Using the distribution of charged hadrons opposite direct γ triggers, parton energy loss may be studied directly as a departure from the (vacuum) fragmentation function. In distinction to π^0-h correlations, where the away-side distribution is sensitive only to the integral of the fragmentation function (the average multiplicity of the away-side jet) [42], the away-side distribution for direct γ-h correlations provides a measurement of the full fragmentation function of the jet from the away-side parton. To the extent that the transverse momentum of the away-side parton and the direct γ are equal and opposite, as in leading order pQCD, the fragmentation function of the jet from the away-parton should be given to a good approximation by the x_E distribution,

$$x_E = \frac{-\vec{p}_T^{\,t} \cdot \vec{p}_T^{\,h}}{\left|\vec{p}_T^{\,t}\right|^2} = \frac{-p_T^h \cos\Delta\phi}{p_T^t}, \tag{8}$$

where the transverse momentum of the trigger $p_T^t = p_T^\gamma$ in the case of γ-h correlations. The reasons why the scaling variable x_E is an approximation to, rather than an exact measure of, the fragmentation variable of the away-side jet with momentum z_a are (i) the away-side parton does not generally balance longitudinal momentum with the trigger γ, although it is restricted by the $\Delta\eta$ acceptance of the detector; (ii) the transverse momenta of the γ and away parton do not exactly balance. The transverse momentum imbalance was discovered at the CERN-ISR using x_E distributions

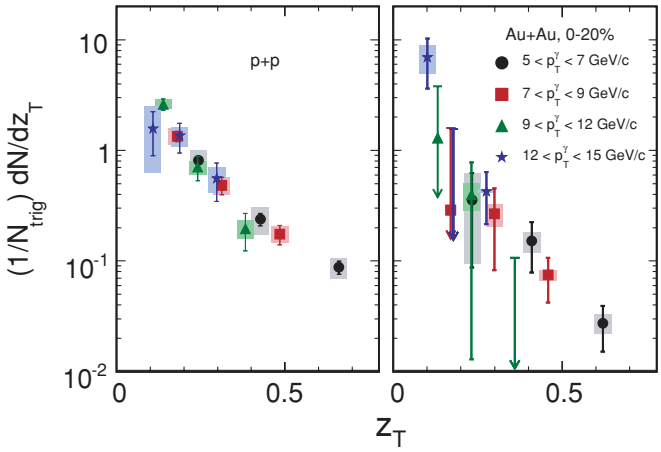

FIG. 7. (Color online) z_T distributions dN/dz_T from the direct photon associated yields in $p + p$ (left) and 0–20% Au + Au (right) collisions.

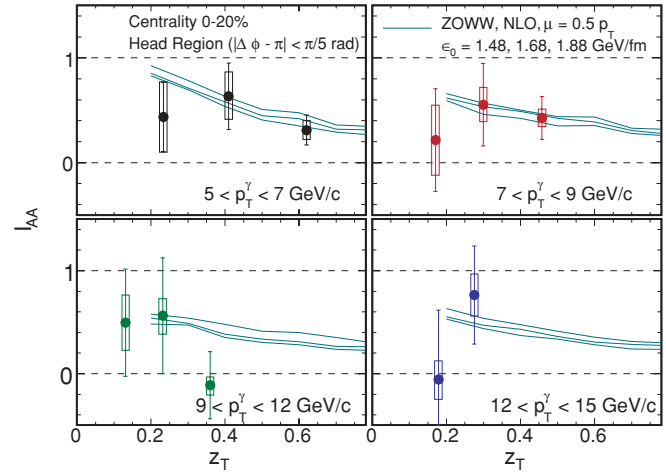

FIG. 8. (Color online) $I_{AA}(z_T)$ for the 20% most central Au + Au data compared to predictions from an energy loss calculation [50]. An additional p_T-independent uncertainty of 14% due to the charged hadron efficiency corrections is not shown.

[43] and originally attributed to an "intrinsic" transverse momentum k_T of each of the initial colliding partons [44], but now understood to be due to "resummation" of soft-gluon effects [45,46].

The validity of the approximation $x_E \approx z_a$ can be tested by observing identical x_E distributions for different values of trigger p_T^γ (x_E scaling), in which case one would accept the x_E distribution in γ-h correlations as the quark fragmentation function from the reaction $q + g \rightarrow q + \gamma$ without need of correction. We approximate x_E by z_T, the ratio of the mean associated p_T^h to mean trigger p_T for each p_T^γ bin.[1] The $\langle p_T^\gamma \rangle$ for the four trigger bins are 5.66, 7.75, 10.07, 13.07 GeV/c, close to the values obtained from a fit to the direct-γ invariant cross section of the form $p_T^{-6.5}$ [35].

Figure 7 shows the z_T distributions for $p + p$ and Au + Au collisions. The $p + p$ data [Fig. 7(a)] exhibit reasonable z_T scaling so that the measured distribution should represent the away-side jet fragmentation function. A fit of this data to a simple exponential (Ne^{-bz_T}) gives an acceptable $\chi^2/\mathrm{DOF} = 12.8/10$ with a value $b = 6.9 \pm 0.8$ that is consistent with the quark fragmentation function, parameterized [42] as a simple exponential with $b = 8.2$ for $0.2 < z < 1.0$, and inconsistent with the gluon fragmentation function value of $b = 11.4$. It should, however, be recalled that the data do not cover the full extent of the away peak, only $|\Delta\phi - \pi| < \pi/5$ radians and that possible variations of the widths of the peaks in both the $p + p$ data and the Au + Au data with p_T^γ and p_T^h have not been taken into account in the present analysis. Additionally a more detailed analysis, differential in trigger p_T, is necessary to study trigger p_T-dependent effects that can influence the fragmentation function fit values [42].

In central Au + Au collisions, the fragmentation function may be modified by the medium[2] so z_T scaling should not hold except in two special cases: (i) pure surface emission or punch-through where the away-side jets are not modified (the z_T distribution will be suppressed, but will have the same shape as in $p + p$ collisions); (ii) constant fractional energy loss of the away jet (the z_T scaling will be preserved in Au + Au collisions but with a steeper slope than in $p + p$ collisions). The Au + Au data [Fig. 7(b)] are consistent with z_T scaling with the same shape as the $p + p$ data, a value of $b = 5.6 \pm 2.2$ and excellent $\chi^2/\mathrm{DOF} = 10.1/10$ for the simple exponential fit. The point at lowest $z_T = 0.11$ for Au + Au is 1.6 standard deviations above the fit, suggesting that improved statistics will permit the observation of any nonsurface emission.

D. Model comparison

Several authors have recently reported predictions for γ-jet in heavy-ion collisions [47–50]. As a demonstration of how such calculations can be compared to the data, the I_{AA} values as a function of z_T are compared to energy loss predictions [50] in Fig. 8. The calculation uses effective fragmentation functions to parametrize the average energy loss of the leading parton by gluon radiation in terms of a parameter ε_0 that is expected to be proportional to the initial gluon density [51]. As in most energy loss calculations, the energy loss of subleading partons and possible medium response effects are neglected. We note that both of these may be important at low values of z. The data are well reproduced by the model over the range of values of ε_0 provided, 1.48–1.88 GeV/fm. This corresponds roughly to the range of ε_0 allowed by comparison to the PHENIX $\pi^0 R_{AA}$ data of $1.9^{+0.2}_{-0.5}$ [52].

[1]The reader is advised to carefully distinguish this variable $z_T = \langle p_T^h \rangle / \langle p_T^t \rangle$ from our previous notation used in Ref. [42] of $z_t = p_T^t / \hat{p}$, which is the fraction of jet momentum $\hat{p}$ contained in the trigger particle.

[2]See Equation 1 in Ref. [51].

It should be noted that the calculation rejects fragmentation photons with an isolation cut. Such a procedure has not yet been demonstrated in central Au + Au data, although doing so would help to eliminate beyond-leading-order effects.

VI. CONCLUSIONS

We have presented the first direct γ-h measurements in Au + Au and $p + p$ collisions at the Relativistic Heavy Ion Collider (RHIC). A significant suppression of $I_{\rm AA} = 0.32 \pm 0.12^{\rm stat} \pm 0.09^{\rm syst}$ for the away-side charged hadron yield in the range $3 < p_T^h < 5$ GeV/c is observed for direct photon triggers in Au + Au as compared to $p + p$. Furthermore, the level of suppression is found to be consistent with the single-particle suppression rate and the importance of energy-loss geometry, notably the expectation of surface emission in the kinematic range sampled. A possible indication that energy-loss geometry may also be important in dijet suppression is that γ-h suppression $I_{\rm AA}$ is also observed to be quite similar to that of dihadron suppression in central events; however, the current precision of the data does not exclude substantial differences. In the $p + p$ data z_T scaling is observed, suggesting that the measured z_T distribution (Fig. 7) is a statistically acceptable representation of the fragmentation function of the quark jet recoiling away from the direct photon. Improvement of the statistical and systematic precision of the measurements should allow further tests of vacuum fragmentation expectations in $p + p$ collisions and insights into details of the medium modification of jet fragmentation in Au + Au. Such studies have begun using subsequently collected larger data sets. The projected order of magnitude increase in RHIC luminosity over the next few years will enable true precision measurements.

ACKNOWLEDGMENTS

We thank the staff of the Collider-Accelerator and Physics Departments at Brookhaven National Laboratory and the staff of the other PHENIX participating institutions for their vital contributions. We acknowledge support from the Office of Nuclear Physics in the Office of Science of the Department of Energy, the National Science Foundation, a sponsored research grant from Renaissance Technologies LLC, Abilene Christian University Research Council, Research Foundation of SUNY, and Dean of the College of Arts and Sciences, Vanderbilt University (USA), Ministry of Education, Culture, Sports, Science, and Technology and the Japan Society for the Promotion of Science (Japan), Conselho Nacional de Desenvolvimento Científico e Tecnológico and Fundação de Amparo à Pesquisa do Estado de São Paulo (Brazil), Natural Science Foundation of China (People's Republic of China), Ministry of Education, Youth and Sports (Czech Republic), Centre National de la Recherche Scientifique, Commissariat à l'Énergie Atomique, and Institut National de Physique Nucléaire et de Physique des Particules (France), Ministry of Industry, Science and Tekhnologies, Bundesministerium für Bildung und Forschung, Deutscher Akademischer Austausch Dienst, and Alexander von Humboldt Stiftung (Germany), Hungarian National Science Fund, OTKA (Hungary), Department of Atomic Energy (India), Israel Science Foundation (Israel), Korea Research Foundation and Korea Science and Engineering Foundation (Korea), Ministry of Education and Science, Russia Academy of Sciences, Federal Agency of Atomic Energy (Russia), VR and the Wallenberg Foundation (Sweden), the US Civilian Research and Development Foundation for the Independent States of the Former Soviet Union, the US-Hungarian Fulbright Foundation for Educational Exchange, and the US-Israel Binational Science Foundation.

[1] K. Adcox *et al.* (PHENIX Collaboration), Nucl. Phys. **A757**, 184 (2005).
[2] A. Adare *et al.* (PHENIX Collaboration), Phys. Rev. Lett. **101**, 232301 (2008).
[3] B. Muller and J. L. Nagle, Annu. Rev. Nucl. Part. Sci. **56**, 93 (2006).
[4] A. Adare *et al.* (PHENIX Collaboration), Phys. Rev. C **78**, 014901 (2008).
[5] B. Muller, Phys. Rev. C **67**, 061901(R) (2003).
[6] T. Renk, Phys. Rev. C **78**, 014903 (2008).
[7] K. J. Eskola, H. Honkanen, C. A. Salgado, and U. A. Wiedemann, Nucl. Phys. **A747**, 511 (2005).
[8] C. Loizides, Eur. Phys. J. C **49**, 339 (2007).
[9] T. Renk and K. J. Eskola, Phys. Rev. C **75**, 054910 (2007).
[10] H.-z. Zhang, J. F. Owens, E. Wang, and X. N. Wang, J. Phys. G **35**, 104067 (2008).
[11] A. Drees, H. Feng, and J. Jia, Phys. Rev. C **71**, 034909 (2005).
[12] S. S. Adler *et al.* (PHENIX Collaboration), Phys. Rev. Lett. **94**, 232301 (2005).
[13] X.-N. Wang and Z. Huang, Phys. Rev. C **55**, 3047 (1997).
[14] X.-N. Wang, Z. Huang, and I. Sarcevic, Phys. Rev. Lett. **77**, 231 (1996).
[15] J. F. Owens, Rev. Mod. Phys. **59**, 465 (1987).
[16] T. Ferbel and W. R. Molzon, Rev. Mod. Phys. **56**, 181 (1984).
[17] W. Vogelsang and M. R. Whalley, J. Phys. G **23**, A1 (1997).
[18] K. Adcox *et al.* (PHENIX Collaboration), Nucl. Instrum. Methods A **499**, 469 (2003).
[19] M. Allen *et al.* (PHENIX Collaboration), Nucl. Instrum. Methods A **499**, 549 (2003).
[20] S. S. Adler *et al.* (PHENIX Collaboration), Phys. Rev. Lett. **91**, 241803 (2003).
[21] K. Adcox *et al.* (PHENIX Collaboration), Nucl. Instrum. Methods A **499**, 489 (2003).
[22] L. Aphecetche *et al.* (PHENIX Collaboration), Nucl. Instrum. Methods A **499**, 521 (2003).
[23] S. S. Adler *et al.* (PHENIX Collaboration), Phys. Rev. C **76**, 034904 (2007).
[24] S. S. Adler *et al.* (PHENIX Collaboration), Phys. Rev. C **75**, 024909 (2007).
[25] K. Adcox *et al.* (PHENIX Collaboration), Nucl. Instrum. Methods A **499**, 489 (2003).
[26] S. Afanasiev *et al.* (PHENIX Collaboration), arXiv:0903.4886 [nucl-ex].
[27] S. S. Adler *et al.* (PHENIX Collaboration), Phys. Rev. Lett. **96**, 032302 (2006).
[28] S. S. Adler *et al.* (PHENIX Collaboration), Phys. Rev. C **71**, 051902 (2005).

[29] M. McCumber and J. Frantz, Acta Phys. Hung. A **27**, 213 (2006).
[30] S. S. Adler *et al.* (PHENIX Collaboration), Phys. Rev. Lett. **97**, 052301 (2006).
[31] S. S. Adler *et al.* (PHENIX Collaboration), Phys. Rev. Lett. **91**, 182301 (2003).
[32] A. Adare *et al.* (PHENIX Collaboration) (to be published).
[33] K. Miki (PHENIX Collaboration), J. Phys. G **35**, 104122 (2008).
[34] S. Huang (PHENIX Collaboration), J. Phys. G **35**, 104105 (2008).
[35] S. S. Adler *et al.* (PHENIX Collaboration), Phys. Rev. Lett. **98**, 012002 (2007).
[36] T. Isobe, Nucl. Phys. **A783**, 569 (2007).
[37] T. Isobe (PHENIX Collaboration), J. Phys. G **34**, S1015 (2007).
[38] A. Adare *et al.* (PHENIX Collaboration), Phys. Rev. D **76**, 051106 (2007).
[39] S. S. Adler *et al.* (PHENIX Collaboration), Phys. Rev. C **77**, 014905 (2008).
[40] S. S. Adler *et al.* (PHENIX Collaboration), Phys. Rev. C **69**, 034910 (2004).
[41] S. S. Adler *et al.* (PHENIX Collaboration), Phys. Rev. Lett. **95**, 202001 (2005).
[42] S. S. Adler *et al.* (PHENIX Collaboration), Phys. Rev. D **74**, 072002 (2006).
[43] M. Della Negra *et al.* (CCHK), Nucl. Phys. **B127**, 1 (1977).
[44] R. P. Feynman, R. D. Field, and G. C. Fox, Nucl. Phys. **B128**, 1 (1977).
[45] A. Kulesza, G. Sterman, and W. Vogelsang, Nucl. Phys. **A721**, 591 (2003).
[46] P. Aurenche, J. P. Guillet, E. Pilon, M. Werlen, and M. Fontannaz, Phys. Rev. D **73**, 094007 (2006).
[47] F. Arleo, J. High Energy Phys. 09 (2006) 015.
[48] T. Renk, Phys. Rev. C **74**, 034906 (2006).
[49] G. Y. Qin, J. Ruppert, C. Gale, S. Jeon, and G. D. Moore, Eur. Phys. J. C **61**, 819 (2009).
[50] H. Zhang, J. F. Owens, E. Wang, and X.-N. Wang, arXiv:0902.4000 [nucl-th] (private communication).
[51] H. Zhang, J. F. Owens, E. Wang, and X.-N. Wang, Phys. Rev. Lett. **98**, 212301 (2007).
[52] A. Adare *et al.* (PHENIX Collaboration), Phys. Rev. C **77**, 064907 (2008).

Physics Letters B 679 (2009) 321–329

Contents lists available at ScienceDirect

Physics Letters B

www.elsevier.com/locate/physletb

Photoproduction of J/ψ and of high mass e^+e^- in ultra-peripheral Au + Au collisions at $\sqrt{s_{NN}} = 200$ GeV

PHENIX Collaboration

S. Afanasiev [q], C. Aidala [g], N.N. Ajitanand [aq], Y. Akiba [ak,al], J. Alexander [aq], A. Al-Jamel [ag], K. Aoki [w,ak], L. Aphecetche [as], R. Armendariz [ag], S.H. Aronson [c], R. Averbeck [ar], T.C. Awes [ah], B. Azmoun [c], V. Babintsev [n], A. Baldisseri [h], K.N. Barish [d], P.D. Barnes [z], B. Bassalleck [af], S. Bathe [d], S. Batsouli [g], V. Baublis [aj], F. Bauer [d], A. Bazilevsky [c], S. Belikov [c,p,1], R. Bennett [ar], Y. Berdnikov [an], M.T. Bjorndal [g], J.G. Boissevain [z], H. Borel [h], K. Boyle [ar], M.L. Brooks [z], D.S. Brown [ag], D. Bucher [ac], H. Buesching [c], V. Bumazhnov [n], G. Bunce [c,al], J.M. Burward-Hoy [z], S. Butsyk [ar], S. Campbell [ar], J.-S. Chai [r], S. Chernichenko [n], J. Chiba [s], C.Y. Chi [g], M. Chiu [g], I.J. Choi [az], T. Chujo [aw], V. Cianciolo [ah], C.R. Cleven [l], Y. Cobigo [h], B.A. Cole [g], M.P. Comets [ai], Z. Conesa del Valle [x], P. Constantin [p], M. Csanád [j], T. Csörgő [t], T. Dahms [ar], K. Das [k], G. David [c], H. Delagrange [as], A. Denisov [n], D. d'Enterria [g], A. Deshpande [al,ar], E.J. Desmond [c], O. Dietzsch [ao], A. Dion [ar], J.L. Drachenberg [a], O. Drapier [x], A. Drees [ar], A.K. Dubey [ay], A. Durum [n], V. Dzhordzhadze [at], Y.V. Efremenko [ah], J. Egdemir [ar], A. Enokizono [m], H. En'yo [ak,al], B. Espagnon [ai], S. Esumi [av], D.E. Fields [af,al], F. Fleuret [x], S.L. Fokin [v], B. Forestier [aa], Z. Fraenkel [ay,1], J.E. Frantz [g], A. Franz [c], A.D. Frawley [k], Y. Fukao [w,ak], S.-Y. Fung [d], S. Gadrat [aa], F. Gastineau [as], M. Germain [as], A. Glenn [at], M. Gonin [x], J. Gosset [h], Y. Goto [ak,al], R. Granier de Cassagnac [x], N. Grau [p], S.V. Greene [aw], M. Grosse Perdekamp [o,al], T. Gunji [e], H.-Å. Gustafsson [ab], T. Hachiya [m,ak], A. Hadj Henni [as], J.S. Haggerty [c], M.N. Hagiwara [a], H. Hamagaki [e], H. Harada [m], E.P. Hartouni [y], K. Haruna [m], M. Harvey [c], E. Haslum [ab], K. Hasuko [ak], R. Hayano [e], M. Heffner [y], T.K. Hemmick [ar], J.M. Heuser [ak], X. He [l], H. Hiejima [o], J.C. Hill [p], R. Hobbs [af], M. Holmes [aw], W. Holzmann [aq], K. Homma [m], B. Hong [u], T. Horaguchi [ak,au], M.G. Hur [r], T. Ichihara [ak,al], K. Imai [w,ak], M. Inaba [av], D. Isenhower [a], L. Isenhower [a], M. Ishihara [ak], T. Isobe [e], M. Issah [aq], A. Isupov [q], B.V. Jacak [ar,2], J. Jia [g], J. Jin [g], O. Jinnouchi [al], B.M. Johnson [c,*], K.S. Joo [ad], D. Jouan [ai], F. Kajihara [e,ak], S. Kametani [e,ax], N. Kamihara [ak,au], M. Kaneta [al], J.H. Kang [az], T. Kawagishi [av], A.V. Kazantsev [v], S. Kelly [f], A. Khanzadeev [aj], D.J. Kim [az], E. Kim [ap], Y.-S. Kim [r], E. Kinney [f], A. Kiss [j], E. Kistenev [c], A. Kiyomichi [ak], C. Klein-Boesing [ac], L. Kochenda [aj], V. Kochetkov [n], B. Komkov [aj], M. Konno [av], D. Kotchetkov [d], A. Kozlov [ay], P.J. Kroon [c], G.J. Kunde [z], N. Kurihara [e], K. Kurita [am,ak], M.J. Kweon [u], Y. Kwon [az], G.S. Kyle [ag], R. Lacey [aq], J.G. Lajoie [p], A. Lebedev [p], Y. Le Bornec [ai], S. Leckey [ar], D.M. Lee [z], M.K. Lee [az], M.J. Leitch [z], M.A.L. Leite [ao], H. Lim [ap], A. Litvinenko [q], M.X. Liu [z], X.H. Li [d], C.F. Maguire [aw], Y.I. Makdisi [c], A. Malakhov [q], M.D. Malik [af], V.I. Manko [v], H. Masui [av], F. Matathias [ar], M.C. McCain [o], P.L. McGaughey [z], Y. Miake [av], T.E. Miller [aw], A. Milov [ar], S. Mioduszewski [c], G.C. Mishra [l], J.T. Mitchell [c], D.P. Morrison [c], J.M. Moss [z], T.V. Moukhanova [v], D. Mukhopadhyay [aw], J. Murata [am,ak], S. Nagamiya [s], Y. Nagata [av], J.L. Nagle [f], M. Naglis [ay], T. Nakamura [m], J. Newby [y], M. Nguyen [ar], B.E. Norman [z], A.S. Nyanin [v], J. Nystrand [ab], E. O'Brien [c], C.A. Ogilvie [p], H. Ohnishi [ak], I.D. Ojha [aw], H. Okada [w,ak], K. Okada [al], O.O. Omiwade [a], A. Oskarsson [ab], I. Otterlund [ab], K. Ozawa [e], D. Pal [aw], A.P.T. Palounek [z], V. Pantuev [ar], V. Papavassiliou [ag], J. Park [ap], W.J. Park [u], S.F. Pate [ag], H. Pei [p], J.-C. Peng [o], H. Pereira [h], V. Peresedov [q], D.Yu. Peressounko [v], C. Pinkenburg [c], R.P. Pisani [c], M.L. Purschke [c], A.K. Purwar [ar], H. Qu [l], J. Rak [p], I. Ravinovich [ay], K.F. Read [ah,at], M. Reuter [ar], K. Reygers [ac], V. Riabov [aj], Y. Riabov [aj], G. Roche [aa], A. Romana [x,1], M. Rosati [p], S.S.E. Rosendahl [ab], P. Rosnet [aa], P. Rukoyatkin [q], V.L. Rykov [ak], S.S. Ryu [az], B. Sahlmueller [ac], N. Saito [w,ak,al], T. Sakaguchi [e,ax], S. Sakai [av], V. Samsonov [aj], H.D. Sato [w,ak], S. Sato [c,s,av], S. Sawada [s], V. Semenov [n], R. Seto [d], D. Sharma [ay], T.K. Shea [c],

0370-2693/$ – see front matter © 2009 Elsevier B.V. All rights reserved.
doi:10.1016/j.physletb.2009.07.061

I. Shein [n], T.-A. Shibata [ak,au], K. Shigaki [m], M. Shimomura [av], T. Shohjoh [av], K. Shoji [w,ak], A. Sickles [ar], C.L. Silva [ao], D. Silvermyr [ah], K.S. Sim [u], C.P. Singh [b], V. Singh [b], S. Skutnik [p], W.C. Smith [a], A. Soldatov [n], R.A. Soltz [y], W.E. Sondheim [z], S.P. Sorensen [at], I.V. Sourikova [c], F. Staley [h], P.W. Stankus [ah], E. Stenlund [ab], M. Stepanov [ag], A. Ster [t], S.P. Stoll [c], T. Sugitate [m], C. Suire [ai], J.P. Sullivan [z], J. Sziklai [t], T. Tabaru [al], S. Takagi [av], E.M. Takagui [ao], A. Taketani [ak,al], K.H. Tanaka [s], Y. Tanaka [ae], K. Tanida [ak,al], M.J. Tannenbaum [c], A. Taranenko [aq], P. Tarján [i], T.L. Thomas [af], M. Togawa [w,ak], J. Tojo [ak], H. Torii [ak], R.S. Towell [a], V.-N. Tram [x], I. Tserruya [ay], Y. Tsuchimoto [m,ak], S.K. Tuli [b], H. Tydesjö [ab], N. Tyurin [n], C. Vale [p], H. Valle [aw], H.W. van Hecke [z], J. Velkovska [aw], R. Vertesi [i], A.A. Vinogradov [v], E. Vznuzdaev [aj], M. Wagner [w,ak], X.R. Wang [ag], Y. Watanabe [ak,al], J. Wessels [ac], S.N. White [c], N. Willis [ai], D. Winter [g], C.L. Woody [c], M. Wysocki [f], W. Xie [d,al], A. Yanovich [n], S. Yokkaichi [ak,al], G.R. Young [ah], I. Younus [af], I.E. Yushmanov [v], W.A. Zajc [g], O. Zaudtke [ac], C. Zhang [g], J. Zimányi [t,1], L. Zolin [q]

[a] *Abilene Christian University, Abilene, TX 79699, United States*
[b] *Department of Physics, Banaras Hindu University, Varanasi 221005, India*
[c] *Brookhaven National Laboratory, Upton, NY 11973-5000, United States*
[d] *University of California – Riverside, Riverside, CA 92521, United States*
[e] *Center for Nuclear Study, Graduate School of Science, University of Tokyo, 7-3-1 Hongo, Bunkyo, Tokyo 113-0033, Japan*
[f] *University of Colorado, Boulder, CO 80309, United States*
[g] *Columbia University, New York, NY 10027 and Nevis Laboratories, Irvington, NY 10533, United States*
[h] *Dapnia, CEA Saclay, F-91191, Gif-sur-Yvette, France*
[i] *Debrecen University, H-4010 Debrecen, Egyetem tér 1, Hungary*
[j] *ELTE, Eötvös Loránd University, H-1117 Budapest, Pázmány P. s. 1/A, Hungary*
[k] *Florida State University, Tallahassee, FL 32306, United States*
[l] *Georgia State University, Atlanta, GA 30303, United States*
[m] *Hiroshima University, Kagamiyama, Higashi-Hiroshima 739-8526, Japan*
[n] *IHEP Protvino, State Research Center of Russian Federation, Institute for High Energy Physics, Protvino 142281, Russia*
[o] *University of Illinois at Urbana-Champaign, Urbana, IL 61801, United States*
[p] *Iowa State University, Ames, IA 50011, United States*
[q] *Joint Institute for Nuclear Research, 141980 Dubna, Moscow Region, Russia*
[r] *KAERI, Cyclotron Application Laboratory, Seoul, Republic of Korea*
[s] *KEK, High Energy Accelerator Research Organization, Tsukuba, Ibaraki 305-0801, Japan*
[t] *KFKI Research Institute for Particle and Nuclear Physics of the Hungarian Academy of Sciences (MTA KFKI RMKI), H-1525 Budapest 114, PO Box 49, Budapest, Hungary*
[u] *Korea University, Seoul, 136-701, Republic of Korea*
[v] *Russian Research Center "Kurchatov Institute", Moscow, Russia*
[w] *Kyoto University, Kyoto 606-8502, Japan*
[x] *Laboratoire Leprince-Ringuet, Ecole Polytechnique, CNRS-IN2P3, Route de Saclay, F-91128, Palaiseau, France*
[y] *Lawrence Livermore National Laboratory, Livermore, CA 94550, United States*
[z] *Los Alamos National Laboratory, Los Alamos, NM 87545, United States*
[aa] *LPC, Université Blaise Pascal, CNRS-IN2P3, Clermont-Fd, 63177 Aubiere Cedex, France*
[ab] *Department of Physics, Lund University, Box 118, SE-221 00 Lund, Sweden*
[ac] *Institut für Kernphysik, University of Muenster, D-48149 Muenster, Germany*
[ad] *Myongji University, Yongin, Kyonggido 449-728, Republic of Korea*
[ae] *Nagasaki Institute of Applied Science, Nagasaki-shi, Nagasaki 851-0193, Japan*
[af] *University of New Mexico, Albuquerque, NM 87131, United States*
[ag] *New Mexico State University, Las Cruces, NM 88003, United States*
[ah] *Oak Ridge National Laboratory, Oak Ridge, TN 37831, United States*
[ai] *IPN-Orsay, Universite Paris Sud, CNRS-IN2P3, BP1, F-91406, Orsay, France*
[aj] *PNPI, Petersburg Nuclear Physics Institute, Gatchina, Leningrad region 188300, Russia*
[ak] *RIKEN Nishina Center for Accelerator-Based Science, Wako, Saitama 351-0198, Japan*
[al] *RIKEN BNL Research Center, Brookhaven National Laboratory, Upton, NY 11973-5000, United States*
[am] *Physics Department, Rikkyo University, 3-34-1 Nishi-Ikebukuro, Toshima, Tokyo 171-8501, Japan*
[an] *Saint Petersburg State Polytechnic University, St. Petersburg, Russia*
[ao] *Universidade de São Paulo, Instituto de Física, Caixa Postal 66318, São Paulo CEP05315-970, Brazil*
[ap] *System Electronics Laboratory, Seoul National University, Seoul, Republic of Korea*
[aq] *Chemistry Department, Stony Brook University, Stony Brook, SUNY, NY 11794-3400, United States*
[ar] *Department of Physics and Astronomy, Stony Brook University, SUNY, Stony Brook, NY 11794, United States*
[as] *SUBATECH (Ecole des Mines de Nantes, CNRS-IN2P3, Université de Nantes) BP 20722-44307, Nantes, France*
[at] *University of Tennessee, Knoxville, TN 37996, United States*
[au] *Department of Physics, Tokyo Institute of Technology, Oh-okayama, Meguro, Tokyo 152-8551, Japan*
[av] *Institute of Physics, University of Tsukuba, Tsukuba, Ibaraki 305, Japan*
[aw] *Vanderbilt University, Nashville, TN 37235, United States*
[ax] *Waseda University, Advanced Research Institute for Science and Engineering, 17 Kikui-cho, Shinjuku-ku, Tokyo 162-0044, Japan*
[ay] *Weizmann Institute, Rehovot 76100, Israel*
[az] *Yonsei University, IPAP, Seoul 120-749, Republic of Korea*

ARTICLE INFO

Article history:
Received 11 March 2009
Received in revised form 9 July 2009
Accepted 29 July 2009
Available online 3 August 2009
Editor: V. Metag

ABSTRACT

We present the first measurement of photoproduction of J/ψ and of two-photon production of high-mass e^+e^- pairs in electromagnetic (or ultra-peripheral) nucleus–nucleus interactions, using Au + Au data at $\sqrt{s_{NN}} = 200$ GeV. The events are tagged with forward neutrons emitted following Coulomb excitation of one or both Au* nuclei. The event sample consists of 28 events with $m_{e^+e^-} > 2$ GeV/c^2 with zero like-sign background. The measured cross sections at midrapidity of $d\sigma/dy\,(J/\psi + Xn, y = 0) =$

PACS:
13.40.-f
13.60.-r
24.85.+p
25.20.-x
25.20.Lj
25.75.-q

$76 \pm 33(\text{stat}) \pm 11(\text{syst})$ μb and $d^2\sigma/dm\,dy\,(e^+e^- + Xn,\, y = 0) = 86 \pm 23(\text{stat}) \pm 16(\text{syst})$ μb/(GeV/c^2) for $m_{e^+e^-} \in [2.0, 2.8]$ GeV/c^2 have been compared and found to be consistent with models for photoproduction of J/ψ and QED based calculations of two-photon production of e^+e^- pairs.

© 2009 Elsevier B.V. All rights reserved.

1. Introduction

The idea to use the strong electromagnetic fields present in high-energy nucleus–nucleus collisions to study photoproduction at hadron colliders has attracted growing interest in recent years, see [1–3] for reviews. Electromagnetic interactions can be studied without background from hadronic processes in ultra-peripheral collisions (UPC) without nuclear overlap, i.e. impact parameters larger than the sum of the nuclear radii. This study focuses on the measurement of exclusively produced high-mass e^+e^- pairs at midrapidity in Au + Au collisions at $\sqrt{s_{NN}} = 200$ GeV, $\text{Au} + \text{Au} \to \text{Au} + \text{Au} + e^+e^-$. The results have been obtained with the PHENIX detector [4] at the BNL Relativistic Heavy Ion Collider (RHIC).

The electromagnetic field of a relativistic particle can be represented by a spectrum of equivalent photons. This is the Weizsäcker–Williams method of virtual quanta [5,6]. The number of photons in the spectrum is proportional to Z^2, where Z is the charge number of the particle, and the equivalent two-photon luminosity is thus proportional to Z^4. The strong dependence on Z favours the use of heavy ions for studying two-photon and photonuclear processes. The virtualities of the equivalent photons when the field couples coherently to the entire nucleus are restricted by the nuclear form factor to $Q^2 = (\omega^2/(c\gamma)^2 + q_\perp^2) \lesssim (\hbar/R_A)^2$. Here, ω and $q_\perp$ are the photon energy and transverse momentum, respectively, R_A is the nuclear radius and γ the Lorentz factor of the beam. At RHIC energies, $\gamma = 108$ and the maximum photon energy in the center-of-mass system is of the order of $\omega_{\max} \sim 3$ GeV corresponding to maximum photon–nucleon and two-photon center-of-mass energies of $W_{\gamma N}^{\max} \sim 34$ GeV and $W_{\gamma\gamma}^{\max} \sim 6$ GeV.

The exclusive production of an e^+e^- pair can proceed either through a purely electromagnetic process (a two-photon interaction to leading order) or through coherent photonuclear production of a vector meson, which decays into an electron pair. Exclusive photoproduction of vector mesons is usually thought of as proceeding via Pomeron-exchange, the perturbative-QCD equivalent of which is the exchange of two gluons or a gluon ladder. The Feynman diagrams for the two leading order processes are shown in Fig. 1. The two-gluon picture is applicable to production of heavy vector mesons, such as the J/ψ, and to production of lighter mesons at high momentum transfers [7]. The J/ψ production cross section is consequently a good probe of the proton [8] and nuclear gluon distribution, $G_A(x, Q^2)$, as well as of vector-meson dynamics in nuclear matter [9,10]. For J/ψ-production, the coverage of the PHENIX central tracking arm, $-0.35 < \eta < 0.35$ corresponds to a range in the photon–nucleon center-of-mass energy between $21 < W_{\gamma N} < 30$ GeV, with a mean $\langle W_{\gamma N} \rangle = 24$ GeV. This corresponds to photon energies in the rest frame of the target nucleus of $240 < E_\gamma < 480$ GeV, with $\langle E_\gamma \rangle = 300$ GeV. Mid-rapidity photoproduction of J/ψ probes nuclear Bjorken-x values of $x = m_{J/\psi}^2/W_{\gamma A}^2 \approx 1.5 \times 10^{-2}$ [10], where the nuclear gluon density is partially depleted by "shadowing" effects [11] compared to the proton.

The strong fields associated with heavy ions at high energies lead to large probabilities for exchanging additional soft photons in the same event. Most of these photons have too low energy to produce particles, but they can excite the interacting nuclei. The dominating excitation is to a Giant-Dipole Resonance (GDR) with energies $\mathcal{O}(10$ MeV), which decays by emitting neutrons at very forward rapidities, providing a very useful means to trigger on UPCs with Zero-Degree Calorimeters (ZDC). The probability for having a Coulomb excitation leading to emission of neutrons in at least one direction in coincidence with coherent J/ψ production is $55\% \pm 6\%$ [12]. The probabilities for exchanging one or several photons factorise, i.e. the Coulomb tagging does not introduce any bias in the extraction of exclusive J/ψ photoproduction cross sections from these events [13]. The soft photons leading to moderate nuclear excitation are indicated to the right of the dashed line in Fig. 1. Incoherent (or quasi-elastic) vector-meson photoproduction can also proceed via the interaction of the exchanged photon with a *single* nucleon in the nucleus. In that case, J/ψ photoproduction is always accompanied by nuclear breakup and emission of nucleons in the forward direction [14].

Photoproduction of vector mesons has been studied with lepton beams first in the 60s [15,16] and more recently at the electron–proton collider HERA [17,18]. Measurements of photonuclear production of ρ mesons [19,20], as well as of two-photon production of *low-mass* e^+e^- pairs [21] in heavy ion interactions have been performed by the STAR Collaboration. The CDF Collaboration has studied two-photon production of e^+e^- pairs [22] and exclusive production of $\mu^+\mu^-$ pairs [23] in $p\bar{p}$ collisions at the Tevatron. The PHENIX analysis presented here is the first on heavy final states in ultra-peripheral nucleus–nucleus collisions. It supersedes a preliminary study presented earlier [24]. The cross section for J/ψ and e^+e^- photoproduction are compared with various theoretical calculations [10,14,25–27].

2. Experimental setup

The data presented here were collected with the PHENIX detector at RHIC during the 2004 high-luminosity Au + Au run at $\sqrt{s_{NN}} = 200$ GeV. The PHENIX detector [4], is a versatile detector designed to study the properties of strongly interacting matter at extreme temperatures and energy densities present in central heavy ion collisions. The current analysis demonstrates its capabilities to also study ultra-peripheral collisions, which have a very different event topology. The PHENIX central tracking system [28] consists of two arms, each covering $|\eta| < 0.35$ and $\Delta\phi = \pi/2$, equipped with multi-layer drift chambers (DC) followed by multi-wire proportional chambers (PC) with pixel-pad readout. The tracking arms also have Ring-Imaging-Čerenkov (RICH, with CO_2 gas radiator) detectors [29] and electromagnetic calorimeters (EMCal) [30] for electron and positron identification. The PHENIX EMCal consists of six sectors of lead-scintillator sandwich calorimeter (PbSc, 15552 individual towers with 5.54 cm × 5.54 cm × 37.5 cm,

* Corresponding author.
E-mail addresses: jacak@skipper.physics.sunysb.edu (B.V. Jacak), brant@bnl.gov (B.M. Johnson).
[1] Deceased.
[2] PHENIX Spokesperson.

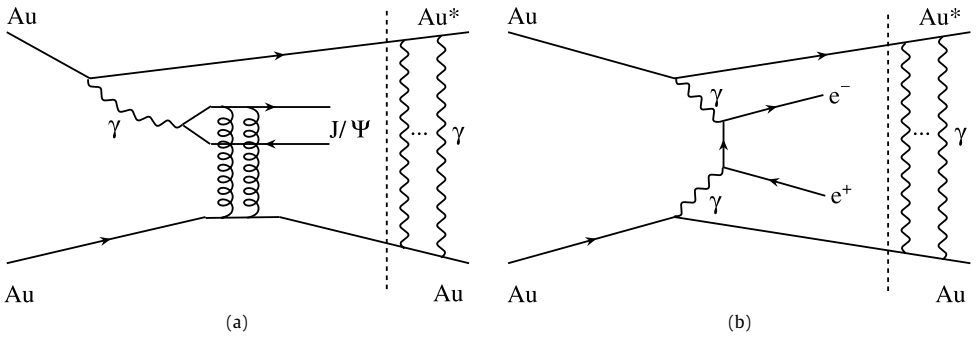

Fig. 1. Lowest order Feynman diagrams for exclusive photoproduction of (a) J/ψ and (b) dielectrons, in ultra-peripheral Au + Au collisions. The photons to the right of the dashed line are soft photons that may excite the nuclei but do not lead to particle production in the central rapidity region. Both diagrams contain at least one photon and occur when the nuclei are separated by impact parameters larger than the sum of the nuclear radii.

$18X_0$) and two sectors of lead-glass Čerenkov calorimeter (PbGl, 9216 modules with 4 cm × 4 cm × 40 cm, $14.4X_0$), at a radial distance of ∼ 5 m from the beam line.

The ultra-peripheral Au + Au events were tagged by neutron detection at small forward angles in the ZDC. The ZDCs [31,32] are hadronic calorimeters placed 18 m up- and down-stream of the interaction point that measure the energy of the neutrons coming from the Au* Coulomb dissociation with ∼ 20% energy resolution and cover $|\theta| < 2$ mrad, which is a very forward region.[3]

The events used in this analysis were collected with the UPC trigger set up for the first time in PHENIX during the 2004 run with the following characteristics:

(1) A veto on coincident signals in both Beam–Beam Counters (BBC, covering $3.0 < |\eta| < 3.9$ and full azimuth) selects exclusive-type events characterised by a large rapidity gap on either side of the central arm.
(2) The EMCal-Trigger (ERT) with a 2×2 tile threshold at 0.8 GeV. The trigger is set if the analog sum of the energy deposit in a 2×2 tile of calorimeter towers is above threshold (0.8 GeV).
(3) At least 30 GeV energy deposited in one or both of the ZDCs is required to select Au + Au events with forward neutron emission (Xn) from the (single or double) Au* decay.

The BBC trigger efficiency for hadronic Au + Au collisions is $92 \pm 3\%$ [33]. A veto on the BBC trigger has an inefficiency of 8%, which implies that the most peripheral nuclear reactions could be a potential background for our UPC measurement if they happen to have an electron pair in the final state. An extrapolation of the measured p–p dielectron rate [34] at $m_{\rm inv} > 2$ GeV/c^2 to the 8% most peripheral interactions – scaled by the corresponding number of nucleon–nucleon collisions (1.6) – results in a negligible contribution (only 0.4 e^+e^- pairs). On the other hand, the ERT trigger requirement (2) has an efficiency of 90 ± 10%, and the requirement (3) of minimum ZDC energy deposit(s) leaves about 55% of the coherent and about 100% of the incoherent J/psi events, as discussed above. All these trigger efficiencies and their uncertainties are used in the final determination of the production cross sections below.

The total number of events collected by the UPC trigger was 8.5 M, of which 6.7 M satisfied standard data quality assurance criteria. The useable event sample corresponds to an integrated luminosity $\mathcal{L}_{\rm int} = 141 \pm 12\ \mu{\rm b}^{-1}$ computed from the minimum bias triggered events.

[3] Much larger than the crossing angle of Au beams at the PHENIX interaction point (0.2 mrad).

3. Data analysis

Charged particle tracking in the PHENIX central arms is based on a combinatorial Hough transform in the track bend plane (perpendicular to the beam direction). The polar angle is determined from the position of the track in the PC outside the DC and the reconstructed position of the collision vertex [35]. For central collisions, the collision vertex is reconstructed from timing information from the BBC and/or ZDC. This does not work for UPC events, which, by definition, do not have BBC coincidences and often do not have ZDC coincidences. The event vertex was instead reconstructed from the position of the PC hits and EMCal clusters associated with the tracks in the event. This gave an event vertex resolution in the longitudinal direction of 1 cm. Track momenta are measured with a resolution $\delta p/p \approx 0.7\% \oplus 1.0\% p[{\rm GeV}/c]$ in minimum bias Au + Au nuclear collisions [36]. Only a negligible reduction in the resolution is expected in this analysis because of the different vertex resolution.

The following global cuts were applied to enhance the sample of genuine γ-induced events:

(1) A standard offline vertex cut $|vtx_z| < 30$ cm was required to select collisions well centered in the fiducial area of the central detectors and to avoid tracks close to the magnet poles.
(2) Only events with two charged particles were analyzed. This is a restrictive criterion imposed to cleanly select "exclusive" processes characterised by only two isolated particles (electrons) in the final state. It allows to suppress the contamination of non-UPC (mainly beam–gas and peripheral nuclear) reactions that fired the UPC trigger, whereas the signal loss is small (less than 5%).

Unlike the $J/\psi \to e^+e^-$ analyses in nuclear Au + Au reactions [36,37] which have to deal with large particle multiplicities, we did not need to apply very strict electron identification cuts in the clean UPC environment. Instead, the following RICH- and EMCal-based offline cuts were used:

(1) RICH multiplicity $n_0 \geqslant 2$ selects $e^\pm$ which fire 2 or more tubes around the track within the nominal ring radius.
(2) Candidate tracks with an associated EMCal cluster with dead or noisy towers within a 2 × 2 tile are excluded.
(3) At least one of the tracks in the pair is required to pass an EMCal cluster energy cut ($E_1 > 1$ GeV ∥ $E_2 > 1$ GeV) to select candidate $e^\pm$ in the plateau region above the turn-on curve of the ERT trigger (which has a 0.8 GeV threshold).

Beyond those global or single-track cuts, an additional "coherent" identification cut was applied by selecting only those e^+e^- candi-

dates detected in opposite arms. Such a cut aims at reducing the high-p_T pairs while improving the detection of the low-p_T pairs expected for $\gamma\gamma$, γA production. Nevertheless, after all the previous cuts were applied the influence of this selection is found to be small; there is only one event in which the e^+ and e^- are in the same arm and have $m_{e^+e^-} > 2$ GeV/c^2.

Finally, J/ψ were reconstructed by invariant mass analysis of the measured e^+e^- pairs. There was no remaining like-sign background after the aforementioned analysis cuts.

The cross sections were obtained after correcting the raw number of signal counts for the geometrical acceptance of our detector system, and the efficiency losses introduced by the previously described analysis cuts. Acceptance and efficiency corrections were obtained using the PHENIX GEANT3 [38] simulation package with input distributions from the STARLIGHT Monte Carlo (MC), based on the models presented in [12,25,39]. The measured $\gamma + p \to V + p$ cross sections from HERA and fixed target experiments with lepton beams are used as input to the models. STARLIGHT well reproduces the existing $d^3N/dy\,d\phi\,dp_T$ distribution of coherent ρ production in UPC Au + Au events measured at RHIC by STAR [19,20]. Helicity conservation is assumed in the model, and the angular distribution of the decay products ($J/\psi \to e^+e^-$) is given by $dN/d\cos(\theta) \propto 1 + \cos^2(\theta)$ in the J/ψ center-of-mass. The angular distribution is different from that for ρ production followed by the decay $\rho \to \pi^+\pi^-$, because of the different spin of the daughters, as well as from the angular distribution in two-photon interactions $\gamma + \gamma \to e^+e^-$. We generated 5×10^4 coherent J/ψ and 8×10^6 coherent high-mass e^+e^- pairs ($m_{e^+e^-} > 1$ GeV/c^2) in Au+Au collisions accompanied by forward neutron emission. The simulated events were passed through the same reconstruction programme as the real data.

Table 1
Coherent J/ψ and e^+e^- (continuum) acceptance and efficiency for $|y_{pair}| < 0.35$ as a function of invariant mass range. The last line shows the trigger efficiency.

$m_{e^+e^-}$ [GeV/c^2]	$Acc \times \varepsilon$
J/ψ	$(2.49 \pm 0.25) \times 10^{-2}$
e^+e^- [2.0, 2.8]	$(2.24 \pm 0.22) \times 10^{-3}$
e^+e^- [2.0, 2.3]	$(2.16 \pm 0.22) \times 10^{-3}$
e^+e^- [2.3, 2.8]	$(2.33 \pm 0.23) \times 10^{-3}$
ϵ_{trigg}	0.9 ± 0.1

Table 1 summarises the J/ψ and dielectron acceptance and efficiency correction factors obtained from our simulation studies. For instance, for J/ψ photoproduction the correction is $1/(2.49 \pm 0.25)$%, of which the experimental acceptance to detect the decay electron pair is about 5% (for J/ψ produced at $|y| < 0.35$). In the $\gamma\gamma \to e^+e^-$ sample, most of the electrons/positrons are emitted at very forward angles. The fraction of events with $|y_{pair}| < 0.35$ and $2.0 < m_{e^+e^-} < 2.8$ GeV/c^2, where both the electron and positron are within $|\eta| < 0.35$ is 1.10%. The corresponding numbers for $2.0 < m_{e^+e^-} < 2.3$ GeV/c^2 and $2.3 < m_{e^+e^-} < 2.8$ GeV/c^2 are 1.11% and 1.08%, respectively. The acceptance and efficiency corrections have a systematic uncertainty of 10% resulting from the accuracy of the simulation to describe the detector, the electron identification parameters, and the event vertex position resolution.

4. Results and discussion

The measured e^+e^- invariant mass distribution for the sample is shown in Fig. 2(a). The amount of background can be estimated from the number of like-sign events (i.e. events where two electrons or two positrons are reconstructed). We find no like-sign pairs for $m_{e^\pm e^\pm} > 2$ GeV/c^2, compared with 28 events with an e^+e^- pair with $m_{e^+e^-} > 2$ GeV/c^2. The shape is consistent with the expected contribution from the two processes in Fig. 1: a continuum distribution corresponding to two-photon production of e^+e^- pairs and a contribution from $J/\psi \to e^+e^-$. Since the offline cuts ($E_1 > 1$ GeV $\parallel$ $E_2 > 1$ GeV) cause a sharp drop in the efficiency for $m_{e^+e^-} < 2$ GeV/c^2, we include only pairs with $m_{e^+e^-} \geqslant 2$ GeV/c^2 in the analysis.

The invariant mass distribution is fitted with a continuum (exponential) curve combined with a Gaussian function at the J/ψ peak, as shown by the solid curve in Fig. 2(a). Simulations based on events generated by the STARLIGHT MC (see last paragraphs of Section 3) processed through GEANT have shown that the shape of the measured continuum contribution is well described by an exponential function $dN/dm_{e^+e^-} = A \cdot e^{cm_{e^+e^-}}$. Those simulations allow us to fix the exponential slope parameter to $c = -1.9 \pm 0.1$ GeV^{-1} c^2. The combined data fit is done with three free parameters: the exponential normalisation (A), the J/ψ yield and the J/ψ peak width (the Gaussian peak position has been fixed at the known J/ψ mass of $m_{J/\psi} = 3.097$ GeV/c^2 [40]). Fig. 2(b) shows the resulting invariant mass distribution obtained by subtracting the fitted exponential curve of the dielectron continuum from the

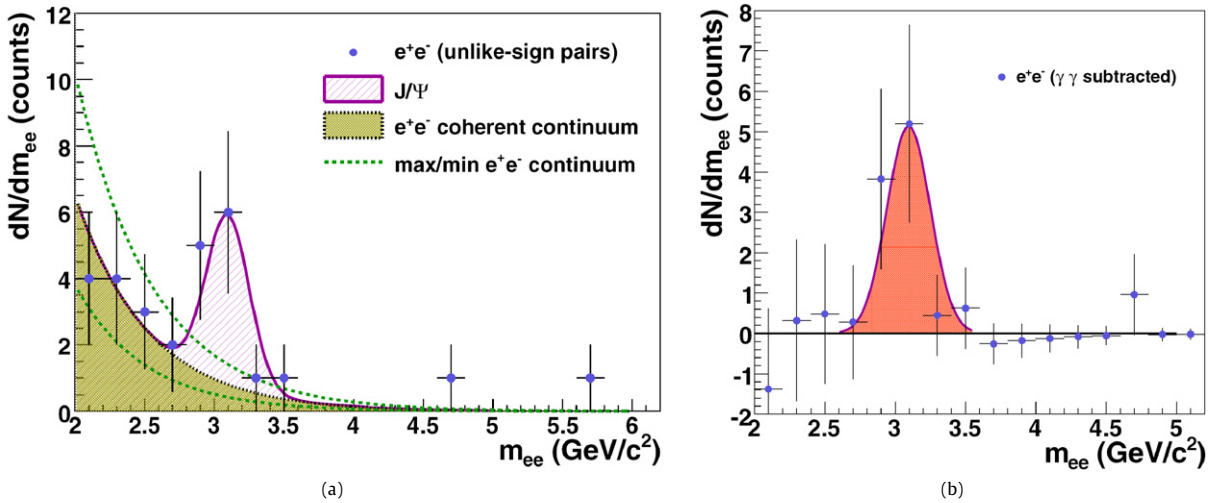

(a) (b)

Fig. 2. Left: (a) Invariant mass distribution of e^+e^- pairs fitted to the combination of (shaded) a dielectron continuum [exponential distribution] and (hatched) a J/ψ [Gaussian] signal. The two additional dashed curves indicate the maximum and minimum continuum contributions considered in this analysis (see text). (b) J/ψ invariant mass distribution after subtracting the fitted dielectron continuum signal in (a).

total experimental e^+e^- pairs distribution. There is a clear J/ψ peak, the width of which ($\sigma_{J/\psi} \sim 155$ MeV/c^2) is consistent with the J/ψ width from our full MC.

The J/ψ and continuum yields and the corresponding statistical errors are calculated from the fit. The dashed curves in Fig. 2(a) show the maximum and minimum e^+e^- continuum contributions considered, including both the statistical and systematical uncertainties. The systematic uncertainties were determined varying the dielectron continuum subtraction method using a power-law form instead of an exponential function and by modifying the corresponding fitted slope parameters by $\pm 3\sigma$. The propagated uncertainty of the extracted yields was estimated to be one count in both cases. The total number of J/ψ's is: $N_{J/\psi} = 9.9 \pm 4.1(\text{stat}) \pm 1.0(\text{syst})$, and the number of e^+e^- continuum pairs for $m_{e^+e^-} \in [2.0, 2.8]$ GeV/c^2 is: $N_{e^+e^-} = 13.7 \pm 3.7(\text{stat}) \pm 1.0(\text{syst})$. Table 2 shows the obtained results per invariant mass range.

Table 2
$J/\psi \to e^+e^-$ and e^+e^- continuum yields obtained from the fit of the data to an exponential plus Gaussian function per invariant mass range. Systematic errors are obtained as described in the text.

$m_{e^+e^-}$ [GeV/c^2]	Yield
J/ψ	$N_{J/\psi} = 9.9 \pm 4.1(\text{stat}) \pm 1.0(\text{syst})$
e^+e^- [2.0, 2.8]	$N_{e^+e^-} = 13.7 \pm 3.7(\text{stat}) \pm 1.0(\text{syst})$
e^+e^- [2.0, 2.3]	$N_{e^+e^-} = 7.4 \pm 2.7(\text{stat}) \pm 1.0(\text{syst})$
e^+e^- [2.3, 2.8]	$N_{e^+e^-} = 6.2 \pm 2.5(\text{stat}) \pm 1.0(\text{syst})$

Fig. 3(a) shows a scatter plot of invariant mass $m_{e^+e^-}$ vs. pair p_T. From the plot, it is clear that most of the pairs outside the J/ψ peak originate in coherent processes with very low pair transverse momenta ($p_T \lesssim 100$ MeV/c), as expected for two-photon interactions. For events with $m_{e^+e^-}$ around the J/ψ mass, however, there are a few counts at larger p_T values which can be ascribed neither to the experimental p_T resolution nor to background events, since there are no like-sign pairs above 2 GeV/c^2. A purely coherent production – corresponding to events where the fields couple coherently to all nucleons and the nucleus remains in its ground state ($\gamma + A \to V + A$) – would yield $p_T \lesssim 200$ MeV/c after reconstruction. On the other hand, incoherent production ($\gamma + A \to V + X$) – dominated by the quasi-elastic vector meson production off one nucleon inside the nucleus, $\gamma + N \to V + N$ – results in much larger p_T for the photoproduced J/ψ [14]. The cross sections for coherent and incoherent J/ψ photoproduction in UPCs at RHIC are expected to be of the same order [14]. We discuss below whether our data confirm such a prediction.

The transverse momentum distribution of the events with $m_{e^+e^-} > 2$ GeV/c^2 is shown in Fig. 3(b). For clarity, only points below $p_T < 1$ GeV/c are drawn. The p_T is here the magnitude of the vector sum of the $\vec{p_T}$ of the electron and positron. One sees a

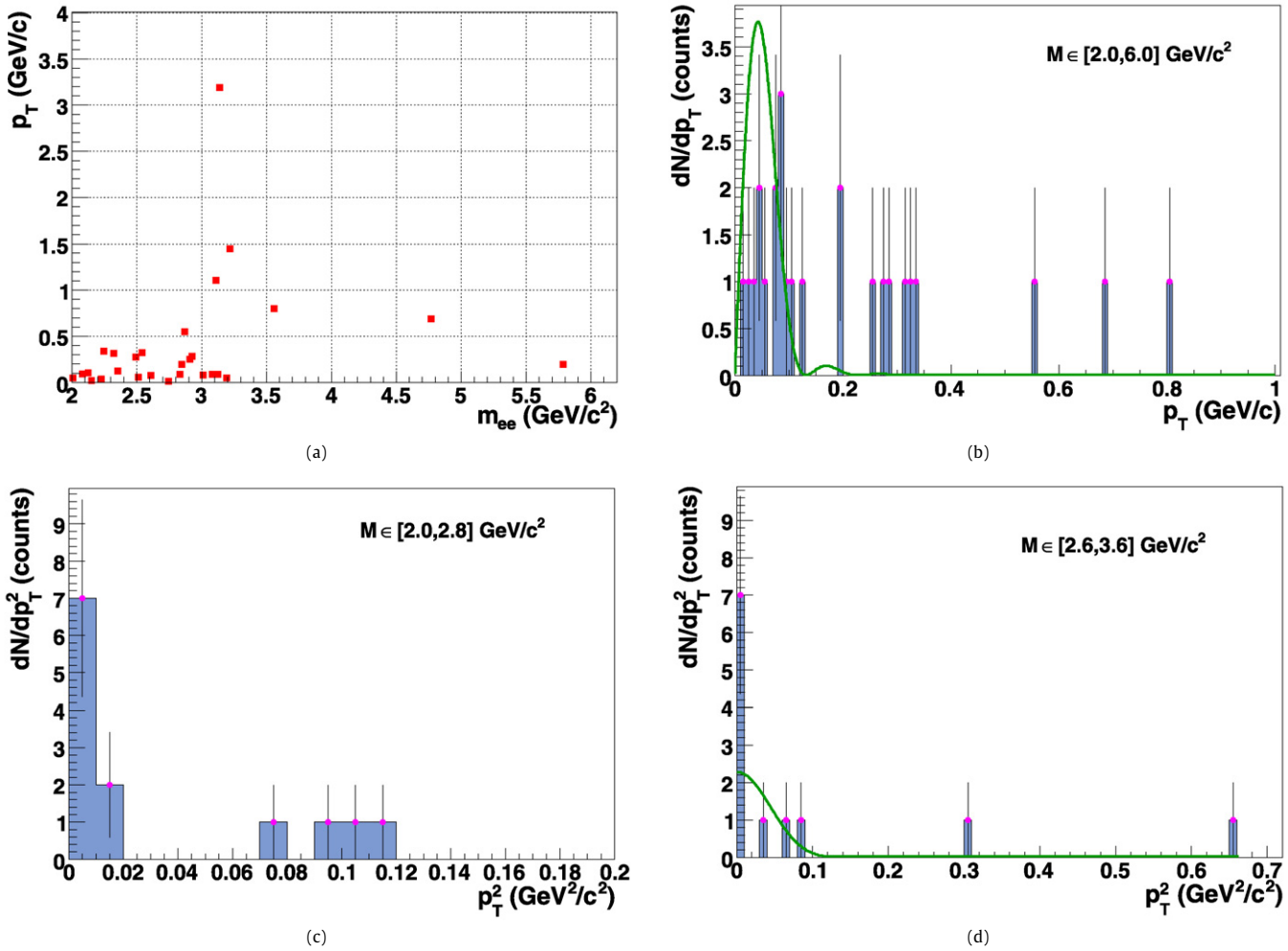

Fig. 3. Top: (a) Scatter plot of $e^+e^- m_{e^+e^-}$ vs. pair p_T. (b) dN/dp_T distribution of the pairs with $m_{e^+e^-} \in [2.0, 6.0]$ GeV/c^2 compared to the Au nuclear form factor, Eq. (1), and for simplicity showing only points with $p_T < 1$ GeV/c. Bottom: dN/dp_T^2 distributions of pairs with (c) $m_{e^+e^-} \in [2.0, 2.8]$ GeV/c^2 and (d) $m_{e^+e^-} \in [2.6, 3.6]$ GeV/c^2 compared to the expected Au nuclear form factor, also for clarity only points with $p_T^2 < 0.7$ GeV^2/c^2 are drawn. Note the difference in scale on the x-axis in the four plots.

Table 3
Measured J/ψ and e^+e^- continuum photoproduction cross sections at midrapidity in ultra-peripheral Au + Au collisions (accompanied with forward neutron emission) at $\sqrt{s_{NN}} = 200$ GeV. The rightmost column in the lower part shows the STARLIGHT predictions [39].

J/ψ	$d\sigma/dy\|_{y=0}$ [μb] $76 \pm 31(\text{stat}) \pm 15(\text{syst})$	
$m_{e^+e^-}$ [GeV/c^2]	$d^2\sigma/dm_{e^+e^-}\,dy\|_{y=0}$ [μb/(GeV/c^2)] data	STARLIGHT
e^+e^- continuum [2.0, 2.8]	$86 \pm 23(\text{stat}) \pm 16(\text{syst})$	90
e^+e^- continuum [2.0, 2.3]	$129 \pm 47(\text{stat}) \pm 28(\text{syst})$	138
e^+e^- continuum [2.3, 2.8]	$60 \pm 24(\text{stat}) \pm 14(\text{syst})$	61

clear enhancement of events with very low transverse momenta, consistent with coherent production. The squared form-factor of a gold nucleus,

$$\left|F_{\text{Au}}\left(p_{\text{T}}^2\right)\right|^2 = \left|3\frac{\sin(Rp_{\text{T}}) - Rp_{\text{T}}\cos(Rp_{\text{T}})}{(Rp_{\text{T}})^3(1+(ap_{\text{T}})^2)}\right|^2, \tag{1}$$

is shown for comparison. Here, $R = 6.7$ fm is the gold radius, and $a = 0.7$ fm represents the diffuseness of the nuclear surface [41]. The magnitude of the form-factor is a free parameter fitted to reproduce the spectra. Fig. 3 also presents the corresponding distribution expressed in terms of the squared momentum transfer from the target nucleus, $p_{\text{T}}^2 \approx -t$, for events with $m_{e^+e^-}$ corresponding to the dielectron continuum $m_{e^+e^-} \in [2.0, 2.8]$ GeV/c^2 (Fig. 3(c) and below the J/ψ-peak, $m_{e^+e^-} \in [2.6, 3.6]$ GeV/c^2 (Fig. 3(d)). The 4 events with $p_T^2 \approx 0.1$ GeV/c^2 in Fig. 3(c) have transverse momenta slightly above what one would expect for two-photon production. They could thus be due to some other, incoherent production process for dielectron pairs. The simulations of the experimental resolution show, however, that a spread in p_T of that magnitude can also be caused by the experimental resolution. We therefore include also these events in the calculation of the continuum cross section.

The extracted yields of J/ψ and e^+e^- are used to calculate the final cross section for photoproduction at midrapidity in ultra-peripheral Au + Au collisions accompanied by forward neutron emission. For dielectrons at midrapidity (y is the rapidity of the pair) the double differential cross section is:

$$\begin{aligned}\frac{d^2\sigma_{e^+e^-+Xn}}{dy\,dm_{e^+e^-}} &= \frac{N_{e^+e^-}}{Acc\cdot\varepsilon\cdot\varepsilon_{\text{trigg}}\cdot\mathcal{L}_{\text{int}}}\cdot\frac{1}{\Delta y}\cdot\frac{1}{\Delta m_{e^+e^-}} \\ &= 86 \pm 23(\text{stat}) \pm 16(\text{syst})\ \mu\text{b}/\left(\text{GeV}/c^2\right) \\ &\quad \text{for } m_{e^+e^-} \in [2.0, 2.8]\ \text{GeV}/c^2 \text{ and } |y| < 0.35. \end{aligned} \tag{2}$$

For J/ψ at midrapidity ($|y| < 0.35$) the differential cross section is:

$$\begin{aligned}\frac{d\sigma_{J/\psi+Xn}}{dy} &= \frac{1}{\text{BR}}\cdot\frac{N_{J/\psi}}{Acc\cdot\varepsilon\cdot\varepsilon_{\text{trigg}}\cdot\mathcal{L}_{\text{int}}}\cdot\frac{1}{\Delta y} \\ &= 76 \pm 31(\text{stat}) \pm 15(\text{syst})\ \mu\text{b}. \end{aligned} \tag{3}$$

The correction factors (and corresponding uncertainties) are quoted in Table 1 as described in previous sections, and BR = 5.94% is the known J/ψ dielectron branching ratio [40]. Table 3 summarises the measured cross sections per invariant mass interval.

The measured dielectron cross sections at midrapidity are in very good agreement with the STARLIGHT predictions for coherent dielectron photoproduction (rightmost column of Table 3) [39]. Exclusive dilepton production in STARLIGHT is calculated combining the two equivalent (Weizsäcker–Williams) photon fluxes from each ion with the Breit–Wheeler formula for $\gamma\gamma \to l^+l^-$. The agreement between STARLIGHT and other leading order calculations [42] is good as long as the pair invariant mass is not too low. A recent calculation has found that higher order terms suppress the e^+e^- cross section by 29% in the invariant mass range $140 < m_{e^+e^-} < 165$ MeV/c^2 [43]. A reduction of the same magnitude in the invariant mass range considered here, $2.0 < m_{e^+e^-} < 2.8$ GeV/c^2, would still be in agreement with our measurement.

The final $J/\psi + Xn$ cross section is compared to the theoretical predictions computed in references [12,14,25,27,39,44] in Fig. 4. The rapidity distributions for the coherent production of Strikman et al. [14] and Ivanov et al. [27] have been scaled down according to [12] to account for the reduction of the yield expected when requiring coincident forward neutron emission (Xn). The scaling has been applied as a function of rapidity with the integrated cross section being 55% of the original one.

The upper limit of the band covered by the Strikman et al. predictions corresponds to calculations in the impulse approximation (no shadowing), and the lower limit corresponds to calculations using the eikonal (Glauber) model with $\sigma(J/\Psi + N) = 3$ mb. The bands for the calculations of Ivanov et al. corresponds to two different parameterisations of the dipole cross section [27]. The predictions by [14] and [27] for the coherent and incoherent photoproduction cross sections are drawn separately in Fig. 4(a) and summed up in Fig. 4(b). STARLIGHT [12,25,39] and Gonçalves–Machado [44] calculations only evaluate the coherent contribution.

As mentioned above, the measured pair p_{T} distributions suggest coherent J/ψ photoproduction ($\gamma + A \to J/\psi + X$) and a possible additional incoherent ($\gamma + N \to J/\psi + X$) contribution at higher p_{T}. To give an indicative estimate of the size of the incoherent contribution, we can assume that it corresponds to the counts in the J/ψ mass window with $p_{\text{T}}^2 > 0.1(0.05)$ GeV$^2/c^2$. This corresponds to about 4(6) counts, which amounts to a contribution of about 40(60)% of the total J/ψ production, compatible with the theoretical calculations [14]. The limited data statistics prevents us from separating in a more quantitative way the two components. Note that although the acceptance correction for the J/ψ was calculated using a Monte Carlo which includes only the coherent component, the obtained correction is also a reasonable approximation for the incoherent component, provided that quasi-elastic scattering on a single nucleon, $\gamma + N \to V + N$, gives the main contribution. The polarisation of the vector meson will then be the same as for coherent production, and the reduction in acceptance because of the different p_{T} range will be of the order of ~ 10–20%. If the incoherent contribution to the total J/ψ photoproduction was 40%, the coherent J/ψ cross section would become ~ 46 μb.

Despite these uncertainties, the final J/ψ cross section is in good agreement, within the (still large) statistical errors, with the theoretical values computed in [12,14,25,27,39,44] as shown in Fig. 4. The current uncertainties unfortunately preclude any more detailed conclusion at this point regarding the two crucial ingredients of the models (nuclear gluon shadowing and J/ψ nuclear absorption cross section). The statistical uncertainties can be improved with significantly higher Au + Au luminosities and a concurrent measurement of the J/ψ in the dimuon decay channel in the more forward acceptances covered by the PHENIX muon spectrometers.

Finally, one can attempt to compare the obtained photonuclear J/ψ cross sections to those from e–p collisions at HERA by dividing the measured differential cross section ($d\sigma/dy$) with the (theoretical) equivalent photon spectrum ($dN_\gamma/d\omega$). At midrapidity: $\sigma_{\gamma A\to J/\psi A} = (d\sigma_{AA\to J/\psi AA}/dy)/(2\,dN_\gamma/d\omega)$, with $2\,dN_\gamma/d\omega = 6.7$ (10.5) for the coherent (incoherent) spectrum at a photon–nucleon center-of-mass energy of $\langle W_{\gamma p}\rangle = 24$ GeV [12]. Assuming, for the sake of simplicity, a 50%–50% contribution from coherent and in-

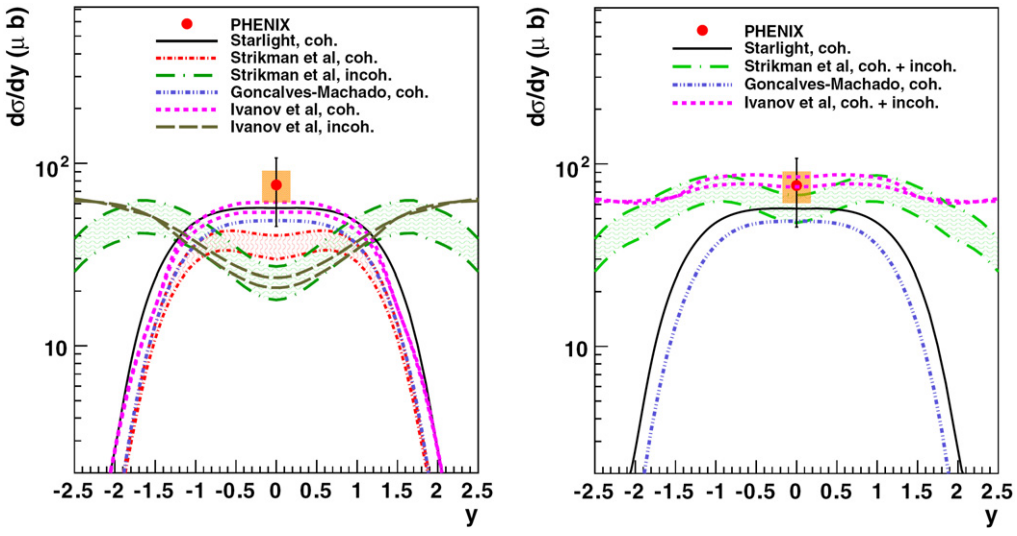

Fig. 4. Measured cross section of $J/\psi + Xn$ production at midrapidity in UPC Au + Au collisions at $\sqrt{s_{NN}} = 200$ GeV. The error bars (boxes) show the statistical (systematical) uncertainties. When available, the theoretical calculations for the coherent and incoherent components are shown separately in (a), and summed up in (b). The theoretical calculations (a) in order from top to bottom near $y = 0$: (short dashed lines) coherent Ivanov et al. [27], (solid line) coherent STARLIGHT [12,25,39], (dashed-double-dotted line) Goncalves–Machado [44], (shaded between short dashed-dotted lines) coherent Strikman et al. [14], (shaded between long dashed-dotted dashed lines) incoherent Strikman et al. [14], and (long dashed lines) coherent Ivanov et al. [27]. And (b) in order from top to bottom near $y = 0$: (short dashed lines) Ivanov et al. [27], (shaded between long dashed-dotted solid lines) Strikman et al. [14], (solid line) STARLIGHT [12,25,39], and (dashed–double-dotted line) Goncalves–Machado [44].

coherent interactions in our total ultra-peripheral J/ψ sample, the extracted photonuclear cross sections are: $\sigma(\gamma + \mathrm{Au} \to J/\psi + \mathrm{Au}) = 5.7 \pm 2.3(\mathrm{stat}) \pm 1.2(\mathrm{syst})$ μb, and $\sigma(\gamma + \mathrm{Au} \to J/\psi + X) = 3.6 \pm 1.4(\mathrm{stat}) \pm 0.7(\mathrm{syst})$ μb, respectively. A fit to the results from the H1 and ZEUS Collaborations [17,18] over their measured energy range gives $\sigma(\gamma + p \to J/\psi + p) = 30.5 \pm 2.7$ nb at $W_{\gamma p} = 24$ GeV. Therefore, the ratios $\sigma(\gamma + \mathrm{Au} \to J/\psi)/\sigma(\gamma + p \to J/\psi) = 186 \pm 88$, 118 ± 54 for the coherent and incoherent components (statistical and systematic errors assumed independent and added in quadrature) are consistent with a scaling of the photonuclear cross section with the number of nucleons in gold ($A = 179$): $\sigma(\gamma + \mathrm{Au} \to J/\psi) = A^{\alpha}\, \sigma(\gamma + p \to J/\psi)$ with $\alpha_{\mathrm{coh}} = 1.01 \pm 0.07$, and $\alpha_{\mathrm{incoh}} = 0.92 \pm 0.08$, respectively.[4]

5. Summary and conclusions

We have presented the first exclusive photoproduction of $J/\psi \to e^+e^-$ and high-mass e^+e^- pairs ever measured in nucleus–nucleus (as well as hadron–hadron) interactions. The measurement has been carried out by the PHENIX experiment in ultra-peripheral Au + Au interactions at $\sqrt{s_{NN}} = 200$ GeV tagged by forward (ZDC) neutron detection from the (single or double) Au* dissociation. Clear signals of J/ψ and high mass dielectron continuum have been found in the data. We have observed 28 e^+e^- pairs in $m_{e^+e^-} \in [2.0, 6.0]$ GeV/c^2 with zero like-sign background. Their p_{T} spectrum is peaked at low $p_{\mathrm{T}} \approx 90$ MeV/c as expected for coherent photoproduction with a realistic Au nuclear form factor.

The measured number of continuum e^+e^- events in the PHENIX acceptance for $m_{e^+e^-} \in [2.0, 2.8]$ GeV/c^2 is: $N(e^+e^-) = 13.7 \pm 3.7(\mathrm{stat}) \pm 1.0(\mathrm{syst})$. After correcting for acceptance and efficiency losses and normalising by the measured luminosity, we obtain a cross section of $d^2\sigma/dm_{e^+e^-}\, dy\, (e^+e^- + Xn)|_{y=0} = 86 \pm 23(\mathrm{stat}) \pm 16(\mathrm{syst})$ μb/(GeV/c^2), which is in good agreement with theoretical expectations for coherent exclusive dielectron production in photon–photon interactions.

The measured invariant mass distribution has a clear peak at the J/ψ mass with an experimental width in good agreement with a full GEANT-based simulation for UPC production and reconstruction in the PHENIX detector. The measured number of J/ψ mesons in the PHENIX acceptance is: $N(J/\psi) = 9.9 \pm 4.1(\mathrm{stat}) \pm 1.0(\mathrm{syst})$. The higher p_{T} distribution suggests an additional incoherent contribution to J/ψ photoproduction in accordance with predictions [14], but statistical limitations prevent a more quantitative estimate. After correcting for acceptance and efficiency losses and normalising by the measured luminosity, the total J/ψ photoproduction cross section is $d\sigma/dy\, (J/\psi + Xn)|_{y=0} = 76 \pm 31(\mathrm{stat}) \pm 15(\mathrm{syst})$ μb, which is consistent (within uncertainties) with theoretical expectations. The low background in the present data sample shows that future higher luminosity runs with reduced experimental uncertainties of the measured cross sections will provide more quantitative information on the nuclear gluon distribution and J/ψ absorption in cold nuclear matter at RHIC energies.

Acknowledgements

We thank the staff of the Collider-Accelerator and Physics Departments at BNL for their vital contributions. We acknowledge support from the Office of Nuclear Physics in DOE Office of Science and NSF (USA), MEXT and JSPS (Japan), CNPq and FAPESP (Brazil), NSFC (China), IN2P3/CNRS, and CEA (France), BMBF, DAAD, and AvH (Germany), OTKA (Hungary), DAE (India), ISF (Israel), KRF and KOSEF (Korea), MES, RAS, and FAAE (Russia), VR and KAW (Sweden), US CRDF for the FSU, US–Hungarian NSF-OTKA-MTA, and US–Israel BSF.

References

[1] G. Baur, K. Hencken, D. Trautmann, S. Sadovsky, Y. Kharlov, Phys. Rep. 364 (2002) 359.
[2] C.A. Bertulani, S.R. Klein, J. Nystrand, Annu. Rev. Nucl. Part. Sci. 55 (2005) 271.
[3] A. Baltz, et al., Phys. Rep. 458 (2008) 1.

[4] Note, for comparison, that repeating the same exercise for the photoproduced ρ in the STAR UPC measurement [20], $\sigma(\gamma + \mathrm{Au} \to \rho + \mathrm{Au}) = 530 \pm 19(\mathrm{stat}) \pm 57(\mathrm{syst})$ μb for $\langle W_{\gamma N} \rangle \sim 12.5$ GeV, and taking the experimentally-derived value $\sigma(\gamma + p \to \rho + p) = 9.88$ μb from [25], yields $\alpha_{\mathrm{coh}} = 0.75 \pm 0.02$ closer to the $A^{2/3}$-scaling expected for soft particle production.

[4] K. Adcox, et al., PHENIX Collaboration, Nucl. Instrum. Methods A 499 (2003) 469.
[5] C.F. von Weizsacker, Z. Phys. 88 (1934) 612.
[6] E.J. Williams, Phys. Rev. 45 (1934) 729.
[7] S. Mohrdieck, et al., H1 Collaboration, hep-ex/0205054, 2002.
[8] M.G. Ryskin, R.G. Roberts, A.D. Martin, E.M. Levin, Z. Phys. C 76 (1997) 231.
[9] L. Frankfurt, W. Koepf, M. Strikman, Phys. Rev. D 54 (1996) 3194.
[10] L. Frankfurt, M. Strikman, M. Zhalov, Phys. Lett. B 540 (2002) 220.
[11] N. Armesto, J. Phys. G 32 (2006) R367.
[12] A.J. Baltz, S.R. Klein, J. Nystrand, Phys. Rev. Lett. 89 (2002) 012301; A.J. Baltz, S.R. Klein, J. Nystrand, private communication.
[13] G. Baur, K. Hencken, A. Aste, D. Trautmann, S.R. Klein, Nucl. Phys. A 729 (2003) 787.
[14] M. Strikman, M. Tverskoy, M. Zhalov, Phys. Lett. B 626 (2005) 72.
[15] L. Lanzerotti, et al., Phys. Rev. Lett. 15 (1965) 210.
[16] T.H. Bauer, R.D. Spital, D.R. Yennie, F.M. Pipkin, Rev. Mod. Phys. 50 (1978) 261.
[17] S. Chekanov, et al., ZEUS Collaboration, Eur. Phys. J. C 24 (2002) 345.
[18] A. Aktas, et al., H1 Collaboration, Eur. Phys. J. C 46 (2006) 585.
[19] C. Adler, et al., STAR Collaboration, Phys. Rev. Lett. 89 (2002) 272302.
[20] B.I. Abelev, et al., STAR Collaboration, Phys. Rev. C 77 (2008) 034910.
[21] J. Adams, et al., STAR Collaboration, Phys. Rev. C 70 (2004) 031902.
[22] A. Abulencia, et al., CDF Collaboration, Phys. Rev. Lett. 98 (2007) 112001.
[23] T. Aaltonen, et al., CDF Collaboration, Phys. Rev. Lett. 102 (2009) 242001.
[24] D. d'Enterria, et al., PHENIX Collaboration, nucl-ex/0601001.
[25] S. Klein, J. Nystrand, Phys. Rev. C 60 (1999) 014903.
[26] V.P. Goncalves, M.V.T. Machado, J. Phys. G 32 (2006) 295.
[27] Y.P. Ivanov, B.Z. Kopeliovich, I. Schmidt, arXiv:0706.1532 [hep-ph]; B. Kopeliovich, private communication.
[28] K. Adcox, et al., PHENIX Collaboration, Nucl. Instrum. Methods A 499 (2003) 489.
[29] M. Aizawa, et al., PHENIX Collaboration, Nucl. Instrum. Methods A 499 (2003) 508.
[30] L. Aphecetche, et al., PHENIX Collaboration, Nucl. Instrum. Methods A 499 (2003) 521.
[31] C. Adler, et al., Nucl. Instrum. Methods A 470 (2001) 488.
[32] M. Chiu, A. Denisov, E. Garcia, J. Katzy, S. White, Phys. Rev. Lett. 89 (2002) 012302.
[33] S.S. Adler, et al., PHENIX Collaboration, Phys. Rev. Lett. 91 (2003) 072301.
[34] A. Adare, et al., PHENIX Collaboration, Phys. Lett. B 670 (2009) 313.
[35] J.T. Mitchell, et al., PHENIX Collaboration, Nucl. Instrum. Methods A 482 (2002) 491.
[36] S.S. Adler, et al., PHENIX Collaboration, Phys. Rev. C 69 (2004) 014901.
[37] A. Adare, et al., PHENIX Collaboration, Phys. Rev. Lett. 98 (2007) 232301.
[38] GEANT 3.2.1, CERN program library (1993).
[39] J. Nystrand, Nucl. Phys. A 752 (2005) 470.
[40] C. Amsler, et al., Phys. Lett. B 667 (2008) 1.
[41] K.T.R. Davies, J.R. Nix, Phys. Rev. C 14 (1976) 1977.
[42] G. Baur, K. Hencken, D. Trautmann, Phys. Rep. 453 (2007) 1.
[43] A.J. Baltz, Phys. Rev. Lett. 100 (2008) 062302.
[44] V.P. Goncalves, M.V.T. Machado, arXiv:0706.2810 [hep-ph].

Gluon-Spin Contribution to the Proton Spin from the Double-Helicity Asymmetry in Inclusive π^0 Production in Polarized $p + p$ Collisions at $\sqrt{s} = 200$ GeV

A. Adare,[12] S. Afanasiev,[26] C. Aidala,[37] N. N. Ajitanand,[54] Y. Akiba,[48,49] H. Al-Bataineh,[43] J. Alexander,[54] K. Aoki,[31,48] L. Aphecetche,[56] J. Asai,[48] E. T. Atomssa,[32] R. Averbeck,[55] T. C. Awes,[44] B. Azmoun,[7] V. Babintsev,[22] M. Bai,[6] G. Baksay,[18] L. Baksay,[18] A. Baldisseri,[15] K. N. Barish,[8] P. D. Barnes,[34] B. Bassalleck,[42] A. T. Basye,[1] S. Bathe,[8] S. Batsouli,[44] V. Baublis,[47] C. Baumann,[38] A. Bazilevsky,[7] S. Belikov,[7,†] R. Bennett,[55] A. Berdnikov,[51] Y. Berdnikov,[51] A. A. Bickley,[12] J. G. Boissevain,[34] H. Borel,[15] K. Boyle,[55] M. L. Brooks,[34] H. Buesching,[7] V. Bumazhnov,[22] G. Bunce,[7,49] S. Butsyk,[34] C. M. Camacho,[34] S. Campbell,[55] P. Chand,[4] B. S. Chang,[63] W. C. Chang,[2] J.-L. Charvet,[15] S. Chernichenko,[22] C. Y. Chi,[13] M. Chiu,[23] I. J. Choi,[63] R. K. Choudhury,[4] T. Chujo,[59] P. Chung,[54] A. Churyn,[22] V. Cianciolo,[44] Z. Citron,[55] B. A. Cole,[13] P. Constantin,[34] M. Csanád,[17] T. Csörgő,[28] T. Dahms,[55] S. Dairaku,[31,48] K. Das,[19] G. David,[7] A. Denisov,[22] D. d'Enterria,[32] A. Deshpande,[49,55] E. J. Desmond,[7] O. Dietzsch,[52] A. Dion,[55] M. Donadelli,[52] O. Drapier,[32] A. Drees,[55] K. A. Drees,[6] A. K. Dubey,[62] A. Durum,[22] D. Dutta,[4] V. Dzhordzhadze,[8] Y. V. Efremenko,[44] J. Egdemir,[55] F. Ellinghaus,[12] T. Engelmore,[13] A. Enokizono,[33] H. En'yo,[48,49] S. Esumi,[59] K. O. Eyser,[8] B. Fadem,[39] D. E. Fields,[42,49] M. Finger,[9] M. Finger, Jr.,[9] F. Fleuret,[32] S. L. Fokin,[30] Z. Fraenkel,[62,†] J. E. Frantz,[55] A. Franz,[7] A. D. Frawley,[19] K. Fujiwara,[48] Y. Fukao,[31,48] T. Fusayasu,[41] I. Garishvili,[57] A. Glenn,[12] H. Gong,[55] M. Gonin,[32] J. Gosset,[15] Y. Goto,[48,49] R. Granier de Cassagnac,[32] N. Grau,[13] S. V. Greene,[60] M. Grosse Perdekamp,[23,49] T. Gunji,[11] H.-Å. Gustafsson,[36] A. Hadj Henni,[56] J. S. Haggerty,[7] H. Hamagaki,[11] R. Han,[46] E. P. Hartouni,[33] K. Haruna,[21] E. Haslum,[36] R. Hayano,[11] M. Heffner,[33] T. K. Hemmick,[55] T. Hester,[8] X. He,[20] J. C. Hill,[25] M. Hohlmann,[18] W. Holzmann,[54] K. Homma,[21] B. Hong,[29] T. Horaguchi,[11,48,58] D. Hornback,[57] S. Huang,[60] T. Ichihara,[48,49] R. Ichimiya,[48] Y. Ikeda,[59] K. Imai,[31,48] J. Imrek,[16] M. Inaba,[59] D. Isenhower,[1] M. Ishihara,[48] T. Isobe,[11] M. Issah,[54] A. Isupov,[26] D. Ivanischev,[47] B. V. Jacak,[55,*] J. Jia,[13] J. Jin,[13] B. M. Johnson,[7] K. S. Joo,[40] D. Jouan,[45] F. Kajihara,[11] S. Kametani,[48] N. Kamihara,[49] J. Kamin,[55] J. H. Kang,[63] J. Kapustinsky,[34] D. Kawall,[37,49] A. V. Kazantsev,[30] T. Kempel,[25] A. Khanzadeev,[47] K. M. Kijima,[21] J. Kikuchi,[61] B. I. Kim,[29] D. H. Kim,[40] D. J. Kim,[63] E. Kim,[53] S. H. Kim,[63] E. Kinney,[12] K. Kiriluk,[12] A. Kiss,[17] E. Kistenev,[7] J. Klay,[33] C. Klein-Boesing,[38] L. Kochenda,[47] V. Kochetkov,[22] B. Komkov,[47] M. Konno,[59] J. Koster,[23] A. Kozlov,[62] A. Král,[14] A. Kravitz,[13] G. J. Kunde,[34] K. Kurita,[50,48] M. Kurosawa,[48] M. J. Kweon,[29] Y. Kwon,[57] G. S. Kyle,[43] R. Lacey,[54] Y. S. Lai,[13] J. G. Lajoie,[25] D. Layton,[23] A. Lebedev,[25] D. M. Lee,[34] K. B. Lee,[29] T. Lee,[53] M. J. Leitch,[34] M. A. L. Leite,[52] B. Lenzi,[52] P. Liebing,[49] T. Liška,[14] A. Litvinenko,[26] H. Liu,[43] M. X. Liu,[34] X. Li,[10] B. Love,[60] D. Lynch,[7] C. F. Maguire,[60] Y. I. Makdisi,[6] A. Malakhov,[26] M. D. Malik,[42] V. I. Manko,[30] E. Mannel,[13] Y. Mao,[46,48] L. Mašek,[9,24] H. Masui,[59] F. Matathias,[13] M. McCumber,[55] P. L. McGaughey,[34] N. Means,[55] B. Meredith,[23] Y. Miake,[59] P. Mikeš,[24] K. Miki,[59] A. Milov,[7] M. Mishra,[3] J. T. Mitchell,[7] A. K. Mohanty,[4] Y. Morino,[11] A. Morreale,[8] D. P. Morrison,[7] T. V. Moukhanova,[30] D. Mukhopadhyay,[60] J. Murata,[50,48] S. Nagamiya,[27] J. L. Nagle,[12] M. Naglis,[62] M. I. Nagy,[17] I. Nakagawa,[48,49] Y. Nakamiya,[21] T. Nakamura,[21] K. Nakano,[48,58] J. Newby,[33] M. Nguyen,[55] T. Niita,[59] R. Nouicer,[5] A. S. Nyanin,[30] E. O'Brien,[7] S. X. Oda,[11] C. A. Ogilvie,[25] H. Okada,[31,48] K. Okada,[49] M. Oka,[59] Y. Onuki,[48] A. Oskarsson,[36] M. Ouchida,[21] K. Ozawa,[11] R. Pak,[5] A. P. T. Palounek,[34] V. Pantuev,[55] V. Papavassiliou,[43] J. Park,[53] W. J. Park,[29] S. F. Pate,[43] H. Pei,[25] J.-C. Peng,[23] H. Pereira,[15] V. Peresedov,[26] D. Yu. Peressounko,[30] C. Pinkenburg,[7] M. L. Purschke,[7] A. K. Purwar,[34] H. Qu,[20] J. Rak,[42] A. Rakotozafindrabe,[32] I. Ravinovich,[62] K. F. Read,[44,57] S. Rembeczki,[18] M. Reuter,[55] K. Reygers,[38] V. Riabov,[47] Y. Riabov,[47] D. Roach,[60] G. Roche,[35] S. D. Rolnick,[8] M. Rosati,[25] S. S. E. Rosendahl,[36] P. Rosnet,[35] P. Rukoyatkin,[26] P. Ružička,[24] V. L. Rykov,[48] B. Sahlmueller,[38] N. Saito,[31,48,49] T. Sakaguchi,[7] S. Sakai,[59] K. Sakashita,[48,58] V. Samsonov,[47] T. Sato,[59] S. Sawada,[27] K. Sedgwick,[8] J. Seele,[12] R. Seidl,[23] A. Yu. Semenov,[25] V. Semenov,[22] R. Seto,[8] D. Sharma,[62] I. Shein,[22] T.-A. Shibata,[48,58] K. Shigaki,[21] M. Shimomura,[59] K. Shoji,[31,48] P. Shukla,[4] A. Sickles,[7] C. L. Silva,[52] D. Silvermyr,[44] C. Silvestre,[15] K. S. Sim,[29] B. K. Singh,[3] C. P. Singh,[3] V. Singh,[3] M. Slunečka,[9] A. Soldatov,[22] R. A. Soltz,[33] W. E. Sondheim,[34] S. P. Sorensen,[57] I. V. Sourikova,[7] F. Staley,[15] P. W. Stankus,[44] E. Stenlund,[36] M. Stepanov,[43] A. Ster,[28] S. P. Stoll,[7] T. Sugitate,[21] C. Suire,[45] A. Sukhanov,[5] J. Sziklai,[28] E. M. Takagui,[52] A. Taketani,[48,49] R. Tanabe,[59] Y. Tanaka,[41] S. Taneja,[55] K. Tanida,[48,49] M. J. Tannenbaum,[7] A. Taranenko,[54] P. Tarján,[16] H. Themann,[55] T. L. Thomas,[42] M. Togawa,[31,48] A. Toia,[55] L. Tomášek,[24] Y. Tomita,[59] H. Torii,[21,48] R. S. Towell,[1] V-N. Tram,[32] I. Tserruya,[62] Y. Tsuchimoto,[21] C. Vale,[25] H. Valle,[60] H. W. van Hecke,[34] A. Veicht,[23] J. Velkovska,[60] R. Vertesi,[16] A. A. Vinogradov,[30] M. Virius,[14] V. Vrba,[24] E. Vznuzdaev,[47] D. Walker,[55] X. R. Wang,[43] Y. Watanabe,[48,49] F. Wei,[25] J. Wessels,[38] S. N. White,[7] S. Williamson,[23] D. Winter,[13] C. L. Woody,[7] M. Wysocki,[12] W. Xie,[49] Y. L. Yamaguchi,[61] K. Yamaura,[21] R. Yang,[23] A. Yanovich,[22] J. Ying,[20] S. Yokkaichi,[48,49]

 © 2009 The American Physical Society

G. R. Young,[44] I. Younus,[42] I. E. Yushmanov,[30] W. A. Zajc,[13] O. Zaudtke,[38] C. Zhang,[44] S. Zhou,[10] and L. Zolin[26]

(PHENIX Collaboration)

[1]*Abilene Christian University, Abilene, Texas 79699, USA*
[2]*Institute of Physics, Academia Sinica, Taipei 11529, Taiwan*
[3]*Department of Physics, Banaras Hindu University, Varanasi 221005, India*
[4]*Bhabha Atomic Research Centre, Bombay 400 085, India*
[5]*Chemistry Department, Brookhaven National Laboratory, Upton, New York 11973-5000, USA*
[6]*Collider-Accelerator Department, Brookhaven National Laboratory, Upton, New York 11973-5000, USA*
[7]*Physics Department, Brookhaven National Laboratory, Upton, New York 11973-5000, USA*
[8]*University of California - Riverside, Riverside, California 92521, USA*
[9]*Charles University, Ovocný trh 5, Praha 1, 116 36, Prague, Czech Republic*
[10]*China Institute of Atomic Energy (CIAE), Beijing, People's Republic of China*
[11]*Center for Nuclear Study, Graduate School of Science, University of Tokyo, 7-3-1 Hongo, Bunkyo, Tokyo 113-0033, Japan*
[12]*University of Colorado, Boulder, Colorado 80309, USA*
[13]*Columbia University, New York, New York 10027 and Nevis Laboratories, Irvington, New York 10533, USA*
[14]*Czech Technical University, Zikova 4, 166 36 Prague 6, Czech Republic*
[15]*Dapnia, CEA Saclay, F-91191, Gif-sur-Yvette, France*
[16]*Debrecen University, H-4010 Debrecen, Egyetem tér 1, Hungary*
[17]*ELTE, Eötvös Loránd University, H - 1117 Budapest, Pázmány P. s. 1/A, Hungary*
[18]*Florida Institute of Technology, Melbourne, Florida 32901, USA*
[19]*Florida State University, Tallahassee, Florida 32306, USA*
[20]*Georgia State University, Atlanta, Georgia 30303, USA*
[21]*Hiroshima University, Kagamiyama, Higashi-Hiroshima 739-8526, Japan*
[22]*IHEP Protvino, State Research Center of Russian Federation, Institute for High Energy Physics, Protvino, 142281, Russia*
[23]*University of Illinois at Urbana-Champaign, Urbana, Illinois 61801, USA*
[24]*Institute of Physics, Academy of Sciences of the Czech Republic, Na Slovance 2, 182 21 Prague 8, Czech Republic*
[25]*Iowa State University, Ames, Iowa 50011, USA*
[26]*Joint Institute for Nuclear Research, 141980 Dubna, Moscow Region, Russia*
[27]*KEK, High Energy Accelerator Research Organization, Tsukuba, Ibaraki 305-0801, Japan*
[28]*KFKI Research Institute for Particle and Nuclear Physics of the Hungarian Academy of Sciences (MTA KFKI RMKI), H-1525 Budapest 114, POBox 49, Budapest, Hungary*
[29]*Korea University, Seoul, 136-701, Korea*
[30]*Russian Research Center "Kurchatov Institute", Moscow, Russia*
[31]*Kyoto University, Kyoto 606-8502, Japan*
[32]*Laboratoire Leprince-Ringuet, Ecole Polytechnique, CNRS-IN2P3, Route de Saclay, F-91128, Palaiseau, France*
[33]*Lawrence Livermore National Laboratory, Livermore, California 94550, USA*
[34]*Los Alamos National Laboratory, Los Alamos, New Mexico 87545, USA*
[35]*LPC, Université Blaise Pascal, CNRS-IN2P3, Clermont-Fd, 63177 Aubiere Cedex, France*
[36]*Department of Physics, Lund University, Box 118, SE-221 00 Lund, Sweden*
[37]*Department of Physics, University of Massachusetts, Amherst, Massachusetts 01003-9337, USA*
[38]*Institut für Kernphysik, University of Muenster, D-48149 Muenster, Germany*
[39]*Muhlenberg College, Allentown, Pennsylvania 18104-5586, USA*
[40]*Myongji University, Yongin, Kyonggido 449-728, Korea*
[41]*Nagasaki Institute of Applied Science, Nagasaki-shi, Nagasaki 851-0193, Japan*
[42]*University of New Mexico, Albuquerque, New Mexico 87131, USA*
[43]*New Mexico State University, Las Cruces, New Mexico 88003, USA*
[44]*Oak Ridge National Laboratory, Oak Ridge, Tennessee 37831, USA*
[45]*IPN-Orsay, Universite Paris Sud, CNRS-IN2P3, BP1, F-91406, Orsay, France*
[46]*Peking University, Beijing, People's Republic of China*
[47]*PNPI, Petersburg Nuclear Physics Institute, Gatchina, Leningrad region, 188300, Russia*
[48]*RIKEN Nishina Center for Accelerator-Based Science, Wako, Saitama 351-0198, JAPAN*
[49]*RIKEN BNL Research Center, Brookhaven National Laboratory, Upton, New York 11973-5000, USA*
[50]*Physics Department, Rikkyo University, 3-34-1 Nishi-Ikebukuro, Toshima, Tokyo 171-8501, Japan*
[51]*Saint Petersburg State Polytechnic University, Saint Petersburg, Russia*
[52]*Universidade de São Paulo, Instituto de Física, Caixa Postal 66318, São Paulo CEP05315-970, Brazil*
[53]*System Electronics Laboratory, Seoul National University, Seoul, Korea*
[54]*Chemistry Department, Stony Brook University, Stony Brook, SUNY, New York 11794-3400, USA*

[55]Department of Physics and Astronomy, Stony Brook University, SUNY, Stony Brook, New York 11794, USA.
[56]SUBATECH (Ecole des Mines de Nantes, CNRS-IN2P3, Université de Nantes) BP 20722 - 44307, Nantes, France
[57]University of Tennessee, Knoxville, Tennessee 37996, USA
[58]Department of Physics, Tokyo Institute of Technology, Oh-okayama, Meguro, Tokyo 152-8551, Japan
[59]Institute of Physics, University of Tsukuba, Tsukuba, Ibaraki 305, Japan
[60]Vanderbilt University, Nashville, Tennessee 37235, USA
[61]Waseda University, Advanced Research Institute for Science and Engineering, 17 Kikui-cho, Shinjuku-ku, Tokyo 162-0044, Japan
[62]Weizmann Institute, Rehovot 76100, Israel
[63]Yonsei University, IPAP, Seoul 120-749, Korea
(Received 6 October 2008; published 1 July 2009)

The double helicity asymmetry in neutral pion production for $p_T = 1$ to 12 GeV/c was measured with the PHENIX experiment to access the gluon-spin contribution, ΔG, to the proton spin. Measured asymmetries are consistent with zero, and at a theory scale of $\mu^2 = 4$ GeV^2 a next to leading order QCD analysis gives $\Delta G^{[0.02,0.3]} = 0.2$, with a constraint of $-0.7 < \Delta G^{[0.02,0.3]} < 0.5$ at $\Delta\chi^2 = 9$ ($\sim 3\sigma$) for the sampled gluon momentum fraction (x) range, 0.02 to 0.3. The results are obtained using predictions for the measured asymmetries generated from four representative fits to polarized deep inelastic scattering data. We also consider the dependence of the ΔG constraint on the choice of the theoretical scale, a dominant uncertainty in these predictions.

DOI: 10.1103/PhysRevLett.103.012003 PACS numbers: 13.88.+e, 13.85.Ni, 21.10.Hw, 25.40.Ep

The originally surprising observations [1–3] that the quark spin contribution to the proton spin is only $\sim 25\%$ indicate that the majority of the proton spin on average comes from the gluon-spin contribution, ΔG, and/or from gluon and quark orbital angular momentum. High energy polarized $p + p$ collisions at the Relativistic Heavy Ion Collider (RHIC) at Brookhaven National Laboratory access ΔG through spin-dependent gluon-gluon (gg) and quark-gluon (qg) scattering.

This Letter presents results from the 2006 RHIC run on ΔG from measurements by the PHENIX experiment of the double-helicity asymmetry ($A_{\rm LL}$) in inclusive midrapidity π^0 production. ΔG can be extracted from $A_{\rm LL}^{\pi^0}$ using next-to-leading order (NLO) perturbative quantum chromodynamics (pQCD) [4], which successfully describes unpolarized cross sections measured at RHIC for many inclusive processes [5–7], including midrapidity π^0 production [8], at $\sqrt{s} = 200$ GeV. These $A_{\rm LL}^{\pi^0}$ data represent a factor of 2 improvement in the statistical uncertainty compared to previous results [8–10]. The data significantly constrain ΔG, as presented in a recent global fit (DSSV) [11] of both RHIC and polarized deep inelastic scattering (pDIS) data, which used a preliminary version of these results. We further present the impact of experimental systematic and two theoretical uncertainties on our determination of ΔG.

We define $\Delta G^{[a,b]}(\mu^2) \equiv \int_a^b dx \Delta g(x, \mu^2)$, with $\Delta g(x, \mu^2)$, the polarized gluon distribution, a function of x, the gluon momentum fraction, and μ^2, the factorization scale. Thus $\Delta G^{[0,1]} \equiv \Delta G$. Figure 1(a) shows the best fit (BF) $\Delta g(x)$ from four NLO pDIS fits (in the $\overline{\rm MS}$ scheme): GRSV-std [12], BB ("ISET-4") [13], LSS [14], and GS-C [15] which assumes a node, or sign change, in $\Delta g(x)$. As the pDIS data have limited sensitivity to ΔG, there remains large uncertainty. Table I lists $\Delta G^{[a,b]}$ for two x ranges.

We define $A_{\rm LL}^{\pi^0} = (\sigma_{++} - \sigma_{+-})/(\sigma_{++} + \sigma_{+-})$, with σ_{++} (σ_{+-}) the beam helicity dependent differential cross sections for inclusive π^0 production from collisions of longitudinally polarized protons with the same (opposite) helicity. The asymmetry is measured using

$$A_{\rm LL}^{\pi^0} = \frac{1}{\langle P_B P_Y \rangle} \frac{N_{++} - R N_{+-}}{N_{++} + R N_{+-}}, \qquad R = \frac{L_{++}}{L_{+-}} \quad (1)$$

where P_B and P_Y are the polarizations of the two RHIC beams, called "blue" and "yellow," and R, the relative luminosity, is the ratio of integrated luminosities (L) for the same and opposite helicity collisions. Here we take N to be the π^0 yield in a transverse momentum (p_T) bin.

Each π^0 p_T bin is sensitive to a broad range in gluon x. Figure 1(b) shows the π^0 yield as a function of gluon x for

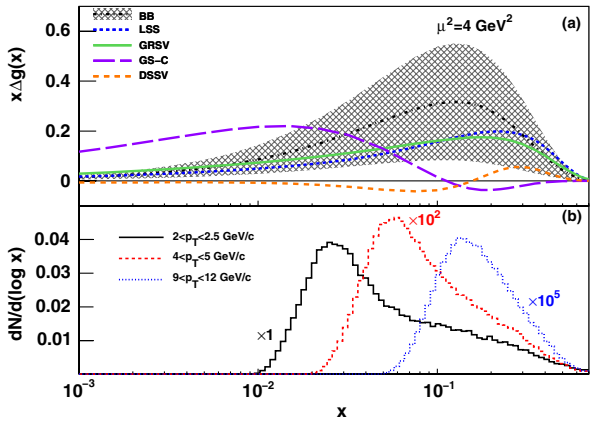

FIG. 1 (color online). (a) The polarized gluon distribution as a function of x for five fits to polarized data. The hatched band is pDIS uncertainty (BB). (b) π^0 yield as a function of gluon x in three π^0 p_T bins from an NLO pQCD simulation.

TABLE I. $\Delta G^{[a,b]}$ at $\mu^2 = 4$ GeV^2 for each group's best fit and the χ^2 when comparing the expected A_{LL} in Fig. 3(a) with the data (8 degrees of freedom). Also shown are the minimum χ^2 and corresponding $\Delta G^{[0.02,0.3]}$ found in Fig. 3(b).

	Published best fit			From Fig. 3(b)	
Group	$\Delta G^{[0,1]}$	$\Delta G^{[0.02,0.3]}$	χ^2	$\Delta G^{[0.02,0.3]}$	χ^2
GS-C	0.95	0.18	8.3	0.1	8.5
DSSV	−0.05	−0.03	7.5	···	···
LSS	0.60	0.37	22.4	0.2	7.0
GRSV	0.67	0.38	14.8	0.2	7.1
BB	0.93	0.67	69.0	0.2	7.2

three $A_{LL}^{\pi^0}$ p_T bins from a NLO pQCD simulation [4,16]. They are peaked at $x_T/0.7$ [17], with $x_T \equiv p_T/(\sqrt{s}/2)$. The x ranges overlap, with the data covering primarily the range $0.02 < x < 0.3$, and so we probe $\Delta G^{[0.02,0.3]}$.

The highly segmented PHENIX electromagnetic calorimeter (EMCal) [18] is used to detect $\pi^0 \to \gamma\gamma$ decays. The EMCal covers a pseudorapidity range of $|\eta| < 0.35$ and azimuthal angle range of $\Delta\phi = \pi$, with segmentation $\Delta\eta \times \Delta\phi = 0.01 \times 0.01$. We required for each of the two decay photons an energy deposition pattern consistent with an electromagnetic shower, no charged track pointing to the location of the deposited energy, and standard quality assurance requirements [9]. Events were obtained from an EMCal based high p_T photon trigger [19] in coincidence with a minimum bias trigger [8] (also used to obtain the relative luminosity). The EMCal based trigger efficiency for π^0 was 5% at $p_T \approx 1$ GeV/c and plateaued at 90% for $p_T > 3.5$ GeV/c. The minimum bias trigger was defined as the coincidence of signals from forward and backward beam-beam counters (BBC) with full azimuthal coverage located at pseudorapidities $\pm(3.0$–$3.9)$ [20]. The analyzed data sample corresponded to an integrated luminosity of 6.5 pb^{-1}.

Each collider ring of RHIC was filled with up to 111 out of a possible 120 bunches, spaced 106 ns apart, with bunch helicities set such that all four beam helicity combinations occurred in sequences of four bunch crossings. The pattern of helicity combinations for each RHIC fill (typically 8 hrs) was cycled between four possibilities to reduce systematic uncertainties that could be correlated to the bunch structure in RHIC [8]. Events were tagged with the bunch crossing number to obtain the beam helicities for the event. The luminosity weighted beam polarization product was $\langle P_B P_Y \rangle = 0.322 \pm 0.027$ (8.3%), with single beam polarizations of 0.560 and 0.575. Small nonzero transverse single spin asymmetries in very forward neutron production [8,21] were measured for each beam. The fill-by-fill ratio of this asymmetry to the beam polarization was constant within statistical uncertainties, confirming the polarization direction stability at PHENIX and the spin sign identification of the recorded collisions. The polarization vector was found to be 99% aligned with the beam (momentum) axis.

As in our previous analyses [8,9], the relative luminosity ratio R was obtained from crossing-by-crossing collected minimum bias (BBC) trigger counts, which measure about half of the $p + p$ inelastic cross section [19]. The uncertainty on R was derived from the comparison with a second trigger based on the zero degree calorimeters [22], which count very forward, energetic neutrals, and so is sensitive to different physics processes with a different angular acceptance than the BBC. It contributed a p_T independent systematic uncertainty to A_{LL} of 7×10^{-4}.

Equation (1) is used to determine, on a fill-by-fill basis, A_{LL} for the yield in the π^0 mass peak (112–162 MeV/c^2) for each p_T bin. The asymmetries were averaged over fills and corrected for the asymmetry in the background contribution (determined from two 50 MeV/c^2 wide sidebands on either side of the π^0 peak) [9], which was consistent with zero.

Figure 2(a) shows the measured $A_{LL}^{\pi^0}$ in comparison with our published data from the 2005 RHIC run [8]. The results are found to be statistically consistent with a 13% confidence level. The inset shows an expanded view of the low p_T region, as well as the relative luminosity uncertainty. Besides this and the scale uncertainty from polarization, other systematic uncertainties that can be found by using a bunch polarization sign randomization technique [9] appear negligible. In addition, the results were robust against variation of the π^0 identification criteria. The parity-violating single helicity asymmetry A_L was measured for each beam, and was consistent with zero within statistical uncertainty for all p_T bins.

Also shown in Fig. 2(a) are NLO pQCD predictions (assuming $\mu = p_T$) of $A_{LL}^{\pi^0}$ [4] based on fits of pDIS data by GRSV with three values for ΔG at the *input* scale of $\mu^2 = 0.4$ GeV^2: (1) "std," their best fit value with $\Delta G = 0.24$, (2) $\Delta G = 0$, and (3) $\Delta G = -1.05$. The results are most consistent with GRSV $\Delta G = 0$. CTEQ6 unpolarized parton distribution functions [23] and DSS fragmentation functions [24] were used in all calculations. Using alternative parton distribution functions [25] or fragmentation functions [26] did not lead to significant differences in the A_{LL} expectations.

A_{LL} expectations were calculated [4] based on refits to the pDIS data with a range of inputs for $\Delta G^{[0,1]}$ at

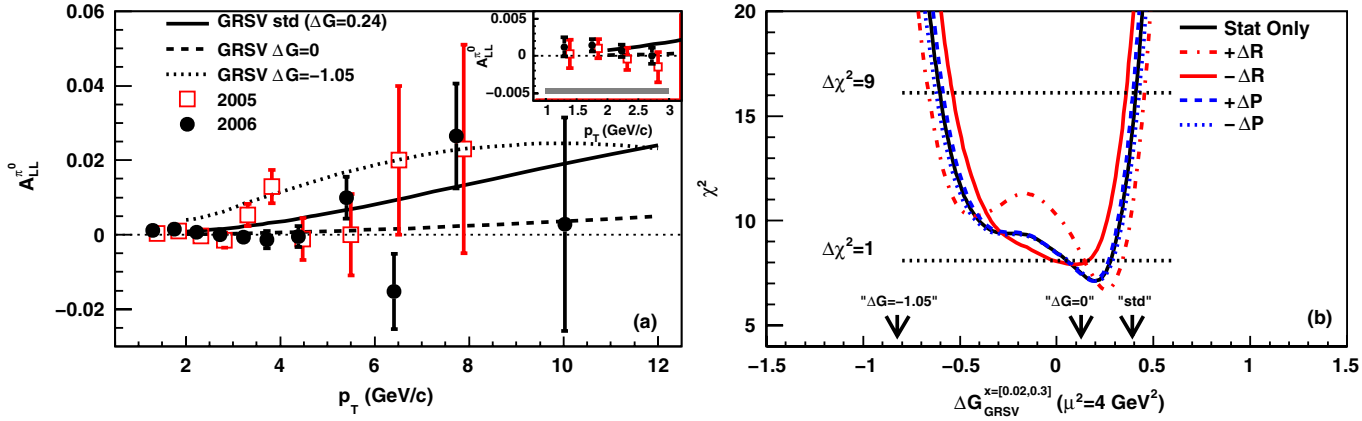

FIG. 2 (color online). (a) Asymmetry in π^0 production as a function of p_T. The error bars are statistical uncertainties. An 8.3% scale uncertainty due to the uncertainty in beam polarization is not shown. The p_T independent uncertainty of 7×10^{-4} due to relative luminosity is shown only in the inset as a shaded bar. For comparison, we also show our 2005 result. NLO pQCD expectations based on several inputs for ΔG in the GRSV parametrization are plotted. (b) The χ^2 profile as a function of $\Delta G^{[0.02,0.3]}_{\mathrm{GRSV}}$ using the combined 2005 and 2006 data considering only statistical uncertainty, or also varying by $\pm 1\sigma$ the two primary experimental systematic uncertainties, from beam polarizations ($\pm\Delta P$) and relative luminosity ($\pm\Delta R$).

$\mu^2 = 0.4$ GeV^2 in the GRSV parametrization. Similar to our previous analysis [8], χ^2 values were calculated using our combined 2005 and 2006 data for these expectations. In Fig. 2(b), these values are plotted as a function of $\Delta G^{[0.02,0.3]}$ evolved to $\mu^2 = 4$ GeV^2. We previously estimated the nonperturbative contribution to be small for $p_T > 2$ GeV$/c$ [8], and so use this as a minimum cutoff in this analysis. The solid curve shows the result considering only statistical uncertainties.

The quadratic ΔG contribution from gg interactions in $p + p$ collisions leads to two minima in Fig. 2(b), while the linear ΔG contribution from qg interactions breaks the symmetry in these minima [4,8]. The χ^2 profile is thus not parabolic, and so we show $\Delta\chi^2 \equiv \chi^2 - \chi^2_{\mathrm{min}} = 1$ and 9 corresponding to "1σ" and "3σ" uncertainties.

The effects of the two largest experimental systematic uncertainties, due to polarization and relative luminosity, are shown in Fig. 2(b). The polarization uncertainty is insignificant when extracting ΔG. However, the uncertainty on relative luminosity, though small, cannot be neglected. Accounting for statistical uncertainty, we find $\Delta G^{[0.02,0.3]}_{\mathrm{GRSV}} = 0.2 \pm 0.1$ (1σ) and $0.2^{+0.2}_{-0.8}$ (3σ) with an additional experimental systematic uncertainty of ± 0.1.

Figure 3(a) shows A_{LL} expectations [4,16] based on the parametrizations discussed above, along with the pDIS uncertainty on $\Delta g(x)$ in BB propagated to A_{LL}. The χ^2 values for comparing each curve with the data are given in Table I. The three fit results without a node in $\Delta g(x)$—LSS, GRSV and BB—have large values of $\Delta G^{[0.02,0.3]}$ which lead to relatively large asymmetries that lie mostly above the data, though they are consistent within the large uncertainty from pDIS. For GS-C and DSSV, which have a node in $\Delta g(x)$ near the center of the sampled x region, a cancellation between the positive and negative contribution in the wide x distribution in each p_T bin leads to a small value of $\Delta G^{[0.02,0.3]}$ and thus small A_{LL}.

To investigate if there is any consistent constraint on $\Delta G^{[0.02,0.3]}$, independent of the parametrization choice, the χ^2 profiles in Fig. 3(b) were calculated based on the pDIS fit results in Fig. 1(a) (excluding DSSV). New polarized gluon distributions were produced using $\Delta g(x) = \lambda \Delta g_{\mathrm{BF}}(x)$ at the input scale, with $\Delta g_{\mathrm{BF}}(x)$ the *best fit* result. For each parametrization, a family of A_{LL} curves were generated by varying λ, i.e., varying $\Delta G^{[0,1]}$ while fixing both the quark helicity distributions and the shape of $\Delta g(x)$ to the best fit values. This approach differs from that of Fig. 2(b), where both the quark helicity distributions and

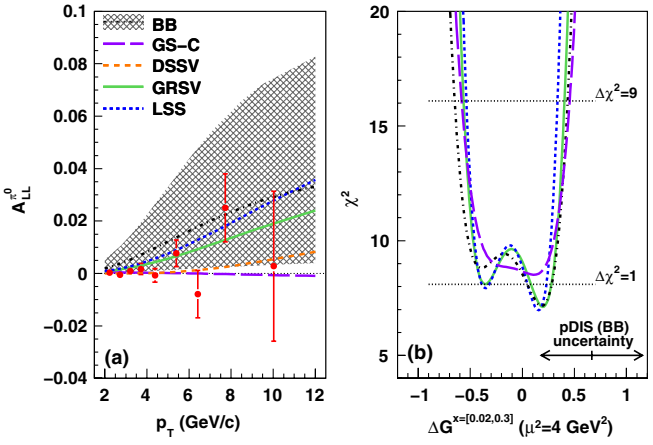

FIG. 3 (color online). (a) π^0 asymmetry expectations for different $\Delta g(x)$ in Fig. 1(b). The hatched band is the pDIS uncertainty (BB). Combined 2005 and 2006 data are also plotted (statistical errors only). (b) The χ^2 profile as a function of $\Delta G^{[0.02,0.3]}$ for the same parametrizations. Arrows indicate uncertainty on the BB best fit. $\Delta\chi^2$ values are shown for GRSV.

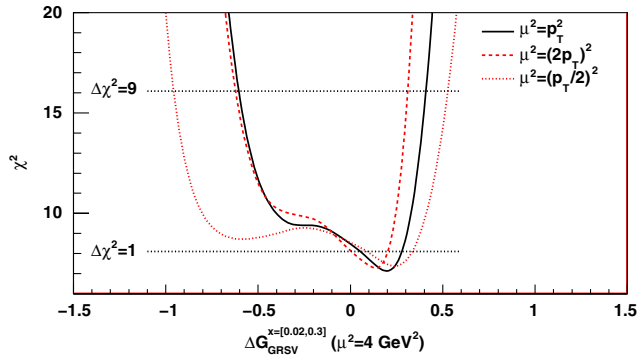

FIG. 4 (color online). χ^2 profile as a function of $\Delta G_{\mathrm{GRSV}}^{[0.02,0.3]}$ when the theoretical scale is set to $\mu = p_T$, $p_T/2$, and $2p_T$.

the shape of $\Delta g(x)$ were also varied. While this results in different GRSV χ^2 profiles, the $\Delta\chi^2 = 1$ and 9 constraints are consistent. The $\Delta G^{[0.02,0.3]}$ values at the χ^2 minimum for each parametrization are between 0.1 and 0.2, and are listed in Table I. At $\Delta\chi^2 = 9$, the profiles of all parametrizations are consistent with $-0.7 < \Delta G^{[0.02,0.3]} < 0.5$, indicating that the data are primarily sensitive to the size of $\Delta G^{[0.02,0.3]}$, while remaining largely insensitive to the shape of $\Delta g(x)$.

The cross section for π^0 production has been presented [8] and compared with NLO pQCD expectations with the theoretical scales (factorization, fragmentation, and renormalization) in the calculation all set equal to $\mu = kp_T$ with $k = 1$. The calculation agreed with the results within the sizable theoretical uncertainties in the choice of scale, which were estimated by varying k up and down by a factor of 2. As we rely on NLO pQCD to extract $\Delta G^{[0.02,0.3]}$ from the measured $A_{\mathrm{LL}}^{\pi^0}$, we must consider the effect of this uncertainty. Figure 4 shows the change in the $\Delta G_{\mathrm{GRSV}}^{[0.02,0.3]}$ constraint when varying k in the A_{LL} calculation in the GRSV parametrization. This variation leads to an additional uncertainty of $\pm 0.1(^{+0.1}_{-0.4})$ at $\Delta\chi^2 = 1$ ($\Delta\chi^2 = 9$). Thus, including these theoretical uncertainties, we find $\Delta G_{\mathrm{GRSV}}^{[0.02,0.3]} = 0.2 \pm 0.1(\mathrm{stat}) \pm 0.1(\mathrm{syst})^{+0.0}_{-0.4} \times (\mathrm{shape}) \pm 0.1(\mathrm{scale})$.

We have presented results for $A_{\mathrm{LL}}^{\pi^0}$ from 2006 which are consistent with zero. We extract $\Delta G^{[0.02,0.3]}$ after combining with the 2005 results [8]. Using four parametrizations of $\Delta g(x)$, we find a shape independent constraint of $-0.7 < \Delta G^{[0.02,0.3]} < 0.5$ at $\Delta\chi^2 = 9$ ($\sim 3\sigma$). The theoretical scale induced uncertainty is small for positive values of $\Delta G_{\mathrm{GRSV}}^{[0.02,0.3]}$, but is sizable for negative values. Future measurements will be required to measure $\Delta g(x)$ for $x < 0.02$ where large uncertainty remains [11] and which may still contribute a significant amount of the proton spin. The quark spin contribution was well constrained by pDIS and our results begin to significantly constrain the gluon-spin contribution.

We thank the staff of the Collider-Accelerator and Physics departments at BNL for their vital contributions, and Marco Stratmann and Werner Vogelsang for communications. We acknowledge support from the Office of Nuclear Physics in the DOE Office of Science; NSF; and a sponsored research grant from Renaissance Technologies (U.S.); MEXT and JSPS (Japan); CNPq and FAPESP (Brazil); NSFC (China); MSMT (Czech Republic); IN2P3/CNRS and CEA (France); BMBF, DAAD, and AvH (Germany); OTKA (Hungary); DAE (India); ISF (Israel); KRF and KOSEF (Korea); MES, RAS, and FAAE (Russia); V.R. and KAW (Sweden); U.S. CRDF for the FSU; U.S.-Hungary Fulbright; U.S.-Israel BSF.

*PHENIX Spokesperson.
jacak@skipper.physics.sunysb.edu
†Deceased.

[1] J. Ashman *et al.*, Nucl. Phys. **B328**, 1 (1989).
[2] A. Airapetian *et al.*, Phys. Rev. D **75**, 012007 (2007).
[3] V. Y. Alexakhin *et al.*, Phys. Lett. B **647**, 8 (2007).
[4] B. Jäger, A. Schäfer, M. Stratmann, and W. Vogelsang, Phys. Rev. D **67**, 054005 (2003).
[5] J. Adams *et al.*, Phys. Rev. Lett. **92**, 171801 (2004).
[6] B. I. Abelev *et al.*, Phys. Rev. Lett. **97**, 252001 (2006).
[7] S. S. Adler *et al.*, Phys. Rev. D **71**, 071102 (2005).
[8] A. Adare *et al.*, Phys. Rev. D **76**, 051106 (2007).
[9] S. S. Adler *et al.*, Phys. Rev. Lett. **93**, 202002 (2004).
[10] S. S. Adler *et al.*, Phys. Rev. D **73**, 091102 (2006).
[11] D. de Florian, R. Sassot, M. Stratmann, and W. Vogelsang, Phys. Rev. Lett. **101**, 072001 (2008).
[12] M. Glück, E. Reya, M. Stratmann, and W. Vogelsang, Phys. Rev. D **63**, 094005 (2001).
[13] J. Bluemlein and H. Bottcher, Nucl. Phys. **B636**, 225 (2002).
[14] E. Leader, A. V. Sidorov, and D. B. Stamenov, Phys. Rev. D **73**, 034023 (2006).
[15] T. Gehrmann and W. J. Stirling, Phys. Rev. D **53**, 6100 (1996).
[16] M. Stratmann (private communication).
[17] S. S. Adler *et al.*, Phys. Rev. D **74**, 072002 (2006).
[18] L. Aphecetche *et al.*, Nucl. Instrum. Methods Phys. Res., Sect. A **499**, 521 (2003).
[19] S. S. Adler *et al.*, Phys. Rev. Lett. **91**, 241803 (2003).
[20] M. Allen *et al.*, Nucl. Instrum. Methods Phys. Res., Sect. A **499**, 549 (2003).
[21] Y. Fukao *et al.*, Phys. Lett. B **650**, 325 (2007).
[22] M. Allen *et al.*, Nucl. Instrum. Methods Phys. Res., Sect. A **470**, 488 (2001).
[23] J. Pumplin *et al.*, J. High Energy Phys. 07 (2002) 012.
[24] D. de Florian, R. Sassot, and M. Stratmann, Phys. Rev. D **75**, 114010 (2007).
[25] A. D. Martin, R. G. Roberts, W. J. Stirling, and R. S. Thorne, Eur. Phys. J. C **28**, 455 (2003).
[26] B. A. Kniehl, G. Kramer, and B. Potter, Nucl. Phys. **B582**, 514 (2000).

Inclusive cross section and double helicity asymmetry for π^0 production in $p + p$ collisions at $\sqrt{s} = 62.4$ GeV

A. Adare,[12] S. Afanasiev,[26] C. Aidala,[37] N. N. Ajitanand,[54] Y. Akiba,[48,49] H. Al-Bataineh,[43] J. Alexander,[54] K. Aoki,[31,48] L. Aphecetche,[56] J. Asai,[48] E. T. Atomssa,[32] R. Averbeck,[55] T. C. Awes,[44] B. Azmoun,[7] V. Babintsev,[22] M. Bai,[6] G. Baksay,[18] L. Baksay,[18] A. Baldisseri,[15] K. N. Barish,[8] P. D. Barnes,[34] B. Bassalleck,[42] A. T. Basye,[1] S. Bathe,[8] S. Batsouli,[44] V. Baublis,[47] C. Baumann,[38] A. Bazilevsky,[7] S. Belikov,[7,*] R. Bennett,[55] A. Berdnikov,[51] Y. Berdnikov,[51] A. A. Bickley,[12] J. G. Boissevain,[34] H. Borel,[15] K. Boyle,[55] M. L. Brooks,[34] H. Buesching,[7] V. Bumazhnov,[22] G. Bunce,[7,49] S. Butsyk,[34] C. M. Camacho,[34] S. Campbell,[55] P. Chand,[4] B. S. Chang,[63] W. C. Chang,[2] J.-L. Charvet,[15] S. Chernichenko,[22] C. Y. Chi,[13] M. Chiu,[23] I. J. Choi,[63] R. K. Choudhury,[4] T. Chujo,[59] P. Chung,[54] A. Churyn,[22] V. Cianciolo,[44] Z. Citron,[55] B. A. Cole,[13] P. Constantin,[34] M. Csanád,[17] T. Csörgő,[28] T. Dahms,[55] S. Dairaku,[31,48] K. Das,[19] G. David,[7] A. Denisov,[22] D. d'Enterria,[32] A. Deshpande,[49,55] E. J. Desmond,[7] O. Dietzsch,[52] A. Dion,[55] M. Donadelli,[52] O. Drapier,[32] A. Drees,[55] K. A. Drees,[6] A. K. Dubey,[62] A. Durum,[22] D. Dutta,[4] V. Dzhordzhadze,[8] Y. V. Efremenko,[44] J. Egdemir,[55] F. Ellinghaus,[12] T. Engelmore,[13] A. Enokizono,[33] H. En'yo,[48,49] S. Esumi,[59] K. O. Eyser,[8] B. Fadem,[39] D. E. Fields,[42,49] M. Finger,[9] M. Finger, Jr.,[9] F. Fleuret,[32] S. L. Fokin,[30] Z. Fraenkel,[62,*] J. E. Frantz,[55] A. Franz,[7] A. D. Frawley,[19] K. Fujiwara,[48] Y. Fukao,[31,48] T. Fusayasu,[41] I. Garishvili,[57] A. Glenn,[12] H. Gong,[55] M. Gonin,[32] J. Gosset,[15] Y. Goto,[48,49] R. Granier de Cassagnac,[32] N. Grau,[13] S. V. Greene,[60] M. Grosse Perdekamp,[23,49] T. Gunji,[11] H.-Å. Gustafsson,[36] A. Hadj Henni,[56] J. S. Haggerty,[7] H. Hamagaki,[11] R. Han,[46] E. P. Hartouni,[33] K. Haruna,[21] E. Haslum,[36] R. Hayano,[11] M. Heffner,[33] T. K. Hemmick,[55] T. Hester,[8] X. He,[20] J. C. Hill,[25] M. Hohlmann,[18] W. Holzmann,[54] K. Homma,[21] B. Hong,[29] T. Horaguchi,[11,48,58] D. Hornback,[57] S. Huang,[60] T. Ichihara,[48,49] R. Ichimiya,[48] Y. Ikeda,[59] K. Imai,[31,48] J. Imrek,[16] M. Inaba,[59] D. Isenhower,[1] M. Ishihara,[48] T. Isobe,[11] M. Issah,[54] A. Isupov,[26] D. Ivanischev,[47] B. V. Jacak,[55,†] J. Jia,[13] J. Jin,[13] B. M. Johnson,[7] K. S. Joo,[40] D. Jouan,[45] F. Kajihara,[11] S. Kametani,[48] N. Kamihara,[49] J. Kamin,[55] J. H. Kang,[63] J. Kapustinsky,[34] D. Kawall,[37,49] A. V. Kazantsev,[30] T. Kempel,[25] A. Khanzadeev,[47] K. M. Kijima,[21] J. Kikuchi,[61] B. I. Kim,[29] D. H. Kim,[40] D. J. Kim,[63] E. Kim,[53] S. H. Kim,[63] E. Kinney,[12] K. Kiriluk,[12] A. Kiss,[17] E. Kistenev,[7] J. Klay,[33] C. Klein-Boesing,[38] L. Kochenda,[47] V. Kochetkov,[22] B. Komkov,[47] M. Konno,[59] J. Koster,[23] A. Kozlov,[62] A. Král,[14] A. Kravitz,[13] G. J. Kunde,[34] K. Kurita,[50,48] M. Kurosawa,[48] M. J. Kweon,[29] Y. Kwon,[57] G. S. Kyle,[43] R. Lacey,[54] Y. S. Lai,[13] J. G. Lajoie,[25] D. Layton,[23] A. Lebedev,[25] D. M. Lee,[34] K. B. Lee,[29] T. Lee,[53] M. J. Leitch,[34] M. A. L. Leite,[52] B. Lenzi,[52] P. Liebing,[49] T. Liška,[14] A. Litvinenko,[26] H. Liu,[43] M. X. Liu,[34] X. Li,[10] B. Love,[60] D. Lynch,[7] C. F. Maguire,[60] Y. I. Makdisi,[6] A. Malakhov,[26] M. D. Malik,[42] V. I. Manko,[30] E. Mannel,[13] Y. Mao,[46,48] L. Mašek,[9,24] H. Masui,[59] F. Matathias,[13] M. McCumber,[55] P. L. McGaughey,[34] N. Means,[55] B. Meredith,[23] Y. Miake,[59] P. Mikeš,[24] K. Miki,[59] A. Milov,[7] M. Mishra,[3] J. T. Mitchell,[7] A. K. Mohanty,[4] Y. Morino,[11] A. Morreale,[8] D. P. Morrison,[7] T. V. Moukhanova,[30] D. Mukhopadhyay,[60] J. Murata,[50,48] S. Nagamiya,[27] J. L. Nagle,[12] M. Naglis,[62] M. I. Nagy,[17] I. Nakagawa,[48,49] Y. Nakamiya,[21] T. Nakamura,[21] K. Nakano,[48,58] J. Newby,[33] M. Nguyen,[55] T. Niita,[59] R. Nouicer,[5] A. S. Nyanin,[30] E. O'Brien,[7] S. X. Oda,[11] C. A. Ogilvie,[25] H. Okada,[31,48] K. Okada,[49] M. Oka,[59] Y. Onuki,[48] A. Oskarsson,[36] M. Ouchida,[21] K. Ozawa,[11] R. Pak,[5] A. P. T. Palounek,[34] V. Pantuev,[55] V. Papavassiliou,[43] J. Park,[53] W. J. Park,[29] S. F. Pate,[43] H. Pei,[25] J.-C. Peng,[23] H. Pereira,[15] V. Peresedov,[26] D. Yu. Peressounko,[30] C. Pinkenburg,[7] M. L. Purschke,[7] A. K. Purwar,[34] H. Qu,[20] J. Rak,[42] A. Rakotozafindrabe,[32] I. Ravinovich,[62] K. F. Read,[44,57] S. Rembeczki,[18] M. Reuter,[55] K. Reygers,[38] V. Riabov,[47] Y. Riabov,[47] D. Roach,[60] G. Roche,[35] S. D. Rolnick,[8] M. Rosati,[25] S. S. E. Rosendahl,[36] P. Rosnet,[35] P. Rukoyatkin,[26] P. Ružička,[24] V. L. Rykov,[48] B. Sahlmueller,[38] N. Saito,[31,48,49] T. Sakaguchi,[7] S. Sakai,[59] K. Sakashita,[48,58] V. Samsonov,[47] T. Sato,[59] S. Sawada,[27] K. Sedgwick,[8] J. Seele,[12] R. Seidl,[23] A. Yu. Semenov,[25] V. Semenov,[22] R. Seto,[8] D. Sharma,[62] I. Shein,[22] T.-A. Shibata,[48,58] K. Shigaki,[21] M. Shimomura,[59] K. Shoji,[31,48] P. Shukla,[4] A. Sickles,[7] C. L. Silva,[52] D. Silvermyr,[44] C. Silvestre,[15] K. S. Sim,[29] B. K. Singh,[3] C. P. Singh,[3] V. Singh,[3] M. Slunečka,[9] A. Soldatov,[22] R. A. Soltz,[33] W. E. Sondheim,[34] S. P. Sorensen,[57] I. V. Sourikova,[7] F. Staley,[15] P. W. Stankus,[44] E. Stenlund,[36] M. Stepanov,[43] A. Ster,[28] S. P. Stoll,[7] T. Sugitate,[21] C. Suire,[45] A. Sukhanov,[5] J. Sziklai,[28] E. M. Takagui,[52] A. Taketani,[48,49] R. Tanabe,[59] Y. Tanaka,[41] K. Tanida,[48,49] M. J. Tannenbaum,[7] A. Taranenko,[54] P. Tarján,[16] H. Themann,[55] T. L. Thomas,[42] M. Togawa,[31,48] A. Toia,[55] L. Tomášek,[24] Y. Tomita,[59] H. Torii,[21,48] R. S. Towell,[1] V-N. Tram,[32] I. Tserruya,[62] Y. Tsuchimoto,[21] C. Vale,[25] H. Valle,[60] H. W. van Hecke,[34] A. Veicht,[23] J. Velkovska,[60] R. Vertesi,[16] A. A. Vinogradov,[30] M. Virius,[14] V. Vrba,[24] E. Vznuzdaev,[47] D. Walker,[55] X. R. Wang,[43] Y. Watanabe,[48,49] F. Wei,[25] J. Wessels,[38] S. N. White,[7] S. Williamson,[23] D. Winter,[13] C. L. Woody,[7] M. Wysocki,[12] W. Xie,[49] Y. L. Yamaguchi,[61] K. Yamaura,[21] R. Yang,[23] A. Yanovich,[22] J. Ying,[20] S. Yokkaichi,[48,49] G. R. Young,[44] I. Younus,[42] I. E. Yushmanov,[30] W. A. Zajc,[13] O. Zaudtke,[38] C. Zhang,[44] S. Zhou,[10] and L. Zolin[26]

 © 2009 The American Physical Society

(PHENIX Collaboration)

[1]*Abilene Christian University, Abilene, Texas 79699, USA*
[2]*Institute of Physics, Academia Sinica, Taipei 11529, Taiwan*
[3]*Department of Physics, Banaras Hindu University, Varanasi 221005, India*
[4]*Bhabha Atomic Research Centre, Bombay 400 085, India*
[5]*Chemistry Department, Brookhaven National Laboratory, Upton, New York 11973-5000, USA*
[6]*Collider-Accelerator Department, Brookhaven National Laboratory, Upton, New York 11973-5000, USA*
[7]*Physics Department, Brookhaven National Laboratory, Upton, New York 11973-5000, USA*
[8]*University of California - Riverside, Riverside, California 92521, USA*
[9]*Charles University, Ovocný trh 5, Praha 1, 116 36, Prague, Czech Republic*
[10]*China Institute of Atomic Energy (CIAE), Beijing, People's Republic of China*
[11]*Center for Nuclear Study, Graduate School of Science, University of Tokyo, 7-3-1 Hongo, Bunkyo, Tokyo 113-0033, Japan*
[12]*University of Colorado, Boulder, Colorado 80309, USA*
[13]*Columbia University, New York, New York 10027 and Nevis Laboratories, Irvington, New York 10533, USA*
[14]*Czech Technical University, Zikova 4, 166 36 Prague 6, Czech Republic*
[15]*Dapnia, CEA Saclay, F-91191, Gif-sur-Yvette, France*
[16]*Debrecen University, H-4010 Debrecen, Egyetem tér 1, Hungary*
[17]*ELTE, Eötvös Loránd University, H-1117 Budapest, Pázmány P. s. 1/A, Hungary*
[18]*Florida Institute of Technology, Melbourne, Florida 32901, USA*
[19]*Florida State University, Tallahassee, Florida 32306, USA*
[20]*Georgia State University, Atlanta, Georgia 30303, USA*
[21]*Hiroshima University, Kagamiyama, Higashi-Hiroshima 739-8526, Japan*
[22]*IHEP Protvino, State Research Center of Russian Federation, Institute for High Energy Physics, Protvino, 142281, Russia*
[23]*University of Illinois at Urbana-Champaign, Urbana, Illinois 61801, USA*
[24]*Institute of Physics, Academy of Sciences of the Czech Republic, Na Slovance 2, 182 21 Prague 8, Czech Republic*
[25]*Iowa State University, Ames, Iowa 50011, USA*
[26]*Joint Institute for Nuclear Research, 141980 Dubna, Moscow Region, Russia*
[27]*KEK, High Energy Accelerator Research Organization, Tsukuba, Ibaraki 305-0801, Japan*
[28]*KFKI Research Institute for Particle and Nuclear Physics of the Hungarian Academy of Sciences (MTA KFKI RMKI), H-1525 Budapest 114, PO Box 49, Budapest, Hungary*
[29]*Korea University, Seoul, 136-701, Korea*
[30]*Russian Research Center "Kurchatov Institute," Moscow, Russia*
[31]*Kyoto University, Kyoto 606-8502, Japan*
[32]*Laboratoire Leprince-Ringuet, Ecole Polytechnique, CNRS-IN2P3, Route de Saclay, F-91128, Palaiseau, France*
[33]*Lawrence Livermore National Laboratory, Livermore, California 94550, USA*
[34]*Los Alamos National Laboratory, Los Alamos, New Mexico 87545, USA*
[35]*LPC, Université Blaise Pascal, CNRS-IN2P3, Clermont-Fd, 63177 Aubiere Cedex, France*
[36]*Department of Physics, Lund University, Box 118, SE-221 00 Lund, Sweden*
[37]*Department of Physics, University of Massachusetts, Amherst, Massachusetts 01003-9337, USA*
[38]*Institut für Kernphysik, University of Muenster, D-48149 Muenster, Germany*
[39]*Muhlenberg College, Allentown, Pennsylvania 18104-5586, USA*
[40]*Myongji University, Yongin, Kyonggido 449-728, Korea*
[41]*Nagasaki Institute of Applied Science, Nagasaki-shi, Nagasaki 851-0193, Japan*
[42]*University of New Mexico, Albuquerque, New Mexico 87131, USA*
[43]*New Mexico State University, Las Cruces, New Mexico 88003, USA*
[44]*Oak Ridge National Laboratory, Oak Ridge, Tennessee 37831, USA*
[45]*IPN-Orsay, Universite Paris Sud, CNRS-IN2P3, BP1, F-91406, Orsay, France*
[46]*Peking University, Beijing, People's Republic of China*
[47]*PNPI, Petersburg Nuclear Physics Institute, Gatchina, Leningrad region, 188300, Russia*
[48]*RIKEN, The Institute of Physical and Chemical Research, Wako, Saitama 351-0198, Japan*
[49]*RIKEN BNL Research Center, Brookhaven National Laboratory, Upton, New York 11973-5000, USA*
[50]*Physics Department, Rikkyo University, 3-34-1 Nishi-Ikebukuro, Toshima, Tokyo 171-8501, Japan*
[51]*Saint Petersburg State Polytechnic University, St. Petersburg, Russia*
[52]*Universidade de São Paulo, Instituto de Física, Caixa Postal 66318, São Paulo CEP05315-970, Brazil*
[53]*System Electronics Laboratory, Seoul National University, Seoul, Korea*
[54]*Chemistry Department, Stony Brook University, Stony Brook, SUNY, New York 11794-3400, USA*
[55]*Department of Physics and Astronomy, Stony Brook University, SUNY, Stony Brook, New York 11794, USA*
[56]*SUBATECH (Ecole des Mines de Nantes, CNRS-IN2P3, Université de Nantes) BP 20722 - 44307, Nantes, France*

[57]University of Tennessee, Knoxville, Tennessee 37996, USA
[58]Department of Physics, Tokyo Institute of Technology, Oh-okayama, Meguro, Tokyo 152-8551, Japan
[59]Institute of Physics, University of Tsukuba, Tsukuba, Ibaraki 305, Japan
[60]Vanderbilt University, Nashville, Tennessee 37235, USA
[61]Waseda University, Advanced Research Institute for Science and Engineering, 17 Kikui-cho, Shinjuku-ku, Tokyo 162-0044, Japan
[62]Weizmann Institute, Rehovot 76100, Israel
[63]Yonsei University, IPAP, Seoul 120-749, Korea
(Received 6 October 2008; published 22 January 2009)

The PHENIX experiment presents results from the RHIC 2006 run with polarized $p + p$ collisions at $\sqrt{s} = 62.4$ GeV, for inclusive π^0 production at midrapidity. Unpolarized cross section results are measured for transverse momenta $p_T = 0.5$ to 7 GeV/c. Next-to-leading order perturbative quantum chromodynamics calculations are compared with the data, and while the calculations are consistent with the measurements, next-to-leading logarithmic corrections improve the agreement. Double helicity asymmetries A_{LL} are presented for $p_T = 1$ to 4 GeV/c and probe the higher range of Bjorken x of the gluon (x_g) with better statistical precision than our previous measurements at $\sqrt{s} = 200$ GeV. These measurements are sensitive to the gluon polarization in the proton for $0.06 < x_g < 0.4$.

DOI: 10.1103/PhysRevD.79.012003 PACS numbers: 13.85.Ni, 13.88.+e, 21.10.Hw, 25.40.Ep

I. INTRODUCTION

Spin is a property of particles as fundamental as charge and mass. The spin of the proton was first determined in the 1920s, yet we still do not have a detailed understanding of what inside the proton makes up the spin of the proton. Polarized lepton-nucleon deep-inelastic scattering (DIS) experiments have revealed that only ~25% of the proton spin can be attributed to the spins of the quarks and antiquarks [1,2] indicating that the proton spin must be largely carried by the spin of the gluons and/or orbital angular momentum of quarks and gluons. Polarized proton-proton collisions at the Relativistic Heavy-Ion Collider (RHIC) provide a laboratory to study the gluon-spin contribution to the proton spin structure, ΔG, with strongly interacting probes via measurements of double helicity asymmetries (A_{LL}) [3].

The A_{LL} of π^0's is defined as

$$A_{LL}^{\pi^0} = \frac{\sigma_{++} - \sigma_{+-}}{\sigma_{++} + \sigma_{+-}}, \tag{1}$$

where $\sigma_{++}(\sigma_{+-})$ represents the π^0 production cross section in polarized $p + p$ collisions with the same (opposite) helicities. In leading order (LO) perturbative Quantum Chromodynamics (pQCD), π^0 production is the sum of all possible subprocesses $ab \to cX$, where a,b represent the initial partons in the protons, c is the final state parton which fragments into a π^0, and X is the unobserved parton. Then A_{LL} is calculated as

$$A_{LL}^{\pi^0} = \frac{\Sigma_{a,b,c} \Delta f_a \Delta f_b \hat{\sigma}^{[ab\to cX]} \hat{a}_{LL}^{[ab\to cX]} D_c^{\pi^0}}{\Sigma_{a,b,c} f_a f_b \hat{\sigma}^{[ab\to cX]} D_c^{\pi^0}}, \tag{2}$$

where $f_{a,b}$ represent unpolarized parton distribution functions (PDFs) of parton a, b and $\Delta f_{a,b}$ represent polarized PDFs, $D_c^{\pi^0}$ is a fragmentation function (FF) of parton c to π^0, $\hat{\sigma}^{[ab\to cX]}$ and $\hat{a}_{LL}^{[ab\to cX]}$ denote, respectively, the cross section and A_{LL} of the subprocess $ab \to cX$. The sum is performed for all possible partons (quarks and gluons). The Bjorken-x dependence of the PDFs, the kinematical dependence of the FFs, and the integral over all possible kinematics are omitted in the equation. The partonic quantities $\hat{\sigma}$ and $\hat{a}_{LL}$ can be calculated in pQCD. Since π^0 production is dominated by gluon-gluon and quark-gluon scattering in the measured p_T range ($p_T < 4$ GeV/c), A_{LL} is directly sensitive to the polarized gluon distribution function in the proton.

Cross-section measurements at RHIC have established the validity of using a next-to-leading order (NLO) pQCD description at $\sqrt{s} = 200$ GeV for inclusive midrapidity π^0 [4,5] and forward π^0 production [6], and for midrapidity jet [7] and direct photon production [8]. However, at lower center of mass energy, NLO pQCD calculations have been less successful in describing the data [9]. The inclusion of "threshold resummation" at next-to-leading logarithmic accuracy (NLL) [10] improves the agreement between theory and data at fixed-target energies. While taking into account threshold logarithms at the fixed-target kinematic region is essential, they may also need to be accounted for at $\sqrt{s} = 62.4$ GeV, but will provide a smaller effect [11].

A precise measurement of the inclusive π^0 production cross section at $\sqrt{s} = 62.4$ GeV is important for the heavy-ion program at RHIC. A new state of dense matter is formed in Au + Au collisions at 200 GeV and parton energy loss in the produced dense medium results in high p_T leading hadron suppression. Measurements of high p_T data at lower energies are of great importance in identifying the energy range at which the suppression sets in. However, they require solid measurements of the cross section in $p + p$ collisions as a baseline for medium effects. At the ISR, inclusive neutral and charged pion

*Deceased
†PHENIX Spokesperson: jacak@skipper.physics.sunysb.edu

cross sections were measured several times at $\sqrt{s} \sim 62$ GeV [12,13], but they have large uncertainties and have a large variation [14]. Having both heavy-ion and baseline $p + p$ measurements with the same experiment is advantageous as it leads to a reduction of the systematic uncertainties and, thus, to a more precise relative comparison of the data.

In this paper, we present results on inclusive neutral pion production at midrapidity from proton-proton collisions at $\sqrt{s} = 62.4$ GeV from data collected during the RHIC 2006 run. A sample of events from longitudinally polarized $p + p$ collisions (about 2/3 of the total data sample) was used for double helicity asymmetry measurements. The other events from the 2006 data sample were from transversely polarized $p + p$ collisions and, along with the longitudinally polarized data, were used for the unpolarized cross section measurements, by averaging over the different initial spin states.

The structure of this paper is as follows. The PHENIX subsystems used in this analysis are briefly introduced in Sec. II. The unpolarized π^0 cross section analysis and the results are discussed in Sec. III. The π^0 A_{LL} analysis and the results follow in Sec. IV, and a summary is given in Sec. V.

II. EXPERIMENT

The PHENIX experiment at RHIC measured π^0's via $\pi^0 \rightarrow \gamma\gamma$ decays using a highly segmented ($\Delta\eta \times \Delta\phi \sim 0.01 \times 0.01$) electromagnetic calorimeter (EMCal) [15], covering a pseudorapidity range of $|\eta| < 0.35$ and azimuthal angle range of $\Delta\phi = \pi$. The EMCal comprises two calorimeter types: 6 sectors of lead scintillator sampling calorimeter (PbSc) and 2 sectors of a lead glass Cherenkov calorimeter (PbGl). Each of the EMCal towers was calibrated by the two-photon invariant mass from π^0 decays and cross checked against the energy deposited by the minimum ionizing particles in the EMCal, and the correlation between the measured momenta of electron and positron tracks and the associated energy deposited in the EMCal. The uncertainty on the absolute energy scale was 1.2%.

The π^0 data in this analysis were collected using two different triggers. One is a beam-beam counter (BBC) trigger which was defined by the coincidence of signals in two BBCs located at pseudorapidities $\pm(3.0$–$3.9)$ with full azimuthal coverage [16]. The time difference between the two BBCs was used to determine the collision vertex along the beam axis, which in this analysis was required to be within 30 cm from the center of the PHENIX interaction region (IR). The other trigger is an EMCal-based high p_T photon trigger, in which threshold discrimination corresponding to a deposited energy of 0.8 GeV was applied independently to sums of analog signals from 2×2 groupings of adjacent EMCal towers [4]. This trigger had limited efficiency for π^0 detection at low p_T (e.g. 50% in 1.0–1.5 GeV/c p_T bin) and close to 100% efficiency at $p_T > 3$ GeV/c.

Beam-beam counters along with zero degree calorimeters (ZDC) [17], which detect neutral particles near the beam axis ($\theta < 2.5$ mrad), were utilized to determine the integrated luminosity for the analyzed data sample needed for the absolute normalization of the measured cross sections. Trigger counts defined with the BBCs and ZDCs were also used for the precise measurements of the relative luminosity between bunches with different spin configuration, and the spin dependence of very forward neutron production [5,18,19], detected by the ZDCs, served for monitoring the orientation of the beam polarization in the PHENIX interaction region (IR) through the run. These are necessary components of the spin asymmetry measurements.

III. THE $pp \rightarrow \pi^0 X$ CROSS SECTION

The unpolarized cross section analysis technique was very similar to our analyses of $\sqrt{s} = 200$ GeV data [4,5] and is briefly discussed in Sec. III A. Cross-section measurements require an absolute determination of luminosity which is described in Sec. III B. The π^0 cross section results are presented and discussed in Sec. III C.

A. π^0 analysis

The π^0 yield in each p_T bin was determined from the two-photon invariant mass spectra. The background contribution under the π^0 peak in the two-photon invariant mass distribution varied from 75% in the lowest 0.5–0.75 GeV/c p_T bin to less than 4% for $p_T > 3$ GeV/c.

One of the main corrections applied to the measured π^0 spectrum is the BBC trigger bias f_{π^0}, which is defined as the fraction of high p_T π^0 events in the midrapidity spectrometer acceptance which fire the BBC trigger. This fraction was determined from the ratio of the number of reconstructed π^0 in the high p_T photon triggered sample with and without the BBC trigger requirement. As shown in Fig. 1, f_{π^0} was about 40% up to $p_T \sim 3$ GeV/c and then monotonically dropped down to 25% at $p_T \sim 7$ GeV/c. The drop can be explained by the fact that most of the energy is used for the production of high-energy jets which contain the measured high p_T π^0 and there is not enough energy left to produce particles in the BBC acceptance $3.0 \leq |\eta| \leq 3.9$, which was optimized for $\sqrt{s} = 200$ GeV (where such a drop was not observed [4]) and was not moved for the present $\sqrt{s} = 62.4$ GeV measurements.

The main contributors to the systematic uncertainties of the measured π^0 spectrum are given in Table I. The ''Energy scale'' uncertainty includes uncertainties due to EMCal energy absolute calibration and nonlinearity. The ''Yield extraction'' uncertainty comes from the background subtraction. The ''Yield correction'' uncertainty comes from the correction for the geometric acceptance,

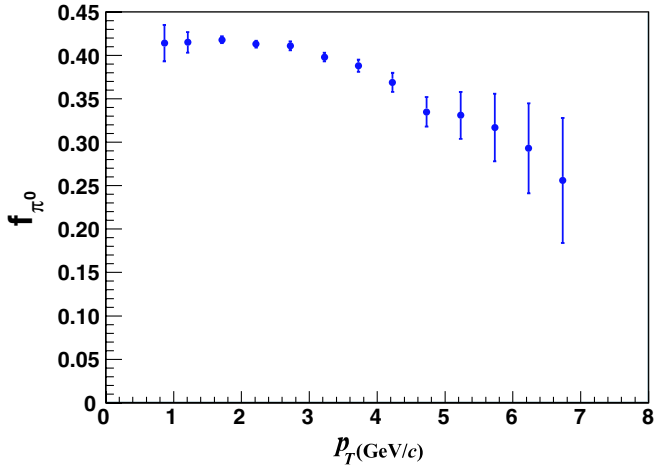

FIG. 1 (color online). The fraction of the inclusive π^0 yield which satisfied the BBC trigger condition.

TABLE I. Main systematic uncertainties in % of the π^0 spectrum from the PbSc for two representative p_T bins (the PbGl uncertainties are similar).

$\langle p_T \rangle$ (GeV/c)	1.2	6.7
Energy scale	3.9	13.1
Yield extraction	3.9	2.0
Yield correction	6.4	6.0

trigger efficiency, reconstruction efficiencies, detector response, and photon conversion. The normalization uncertainty is not included and is discussed in Sec. III B.

The data sets from the two EMCal subsystems, PbSc and PbGl, were analyzed separately and combined for the final results. Results from the two subsystems were consistent within uncertainties. The systematic uncertainty of the combined result is reduced as the major systematic uncertainties in the two EMCal subsystems are not correlated. For final π^0 cross section results, BBC-triggered events were used for $p_T < 3$ GeV/c and high p_T photon triggered events in coincidence with the BBC trigger were used for $p_T > 3$ GeV/c.

B. Vernier scan analysis

The measured π^0 cross section was normalized to the integrated luminosity for the analyzed data sample (L) which was determined from the number of BBC-triggered events using an absolute calibration of the BBC trigger cross section $\sigma_{\rm BBC}$. The value of $\sigma_{\rm BBC}$ is obtained via the van der Meer or Vernier scan technique [20]. This is a crucial part of the absolute cross section analysis and is therefore discussed in detail in this section.

In a scan, the transverse widths of the beam overlap σ_x and σ_y were measured by sweeping one beam across the other in small steps while monitoring the BBC trigger rate. Then the instantaneous machine luminosity of each bunch crossing $L_{\rm machine}$ is computed as

$$L_{\rm machine} = \frac{f_{\rm rev}}{2\pi\sigma_x\sigma_y} \cdot N_B \cdot N_Y, \tag{3}$$

where N_B and N_Y are the bunch intensities of the two beams ($\sim 10^{11}$/bunch), $f_{\rm rev}$ is the revolution frequency (78 kHz). The BBC trigger cross section $\sigma_{\rm BBC}$ is the ratio of the BBC trigger rate when the beams were overlapping maximally ($R_{\rm max}$) to the effective luminosity $L_{\rm eff}$:

$$\sigma_{\rm BBC} = R_{\rm max}/L_{\rm eff}, \tag{4}$$

where

$$L_{\rm eff} = L_{\rm machine} \cdot \epsilon_{\rm vertex}, \tag{5}$$

and $\epsilon_{\rm vertex}$ is the fraction of the number of collisions in the PHENIX interaction region (IR) within the BBC trigger vertex cut (usually $|z| < 30$ cm).

$L_{\rm machine}$ was corrected for the z dependence of the transverse beam sizes caused by the beam focusing in the IR (hourglass effect) and for the beam crossing angle. The value of $\epsilon_{\rm vertex}$ was extracted from the z-vertex distribution of events measured by the BBCs and was corrected for the dependence of the BBC trigger efficiency on the collision vertex position z along the beam axis. These corrections are discussed in more detail below.

In $p + p$ collisions at $\sqrt{s} = 62.4$ GeV, the BBC trigger efficiency vs z shape was estimated from the comparison with a ''detector unbiased'' z-vertex distribution obtained from the convolution of colliding bunch intensity profiles along the z-axis as measured by Wall Current Monitors (WCMs) [21]. The correction factor of 0.83 ± 0.08 for $\epsilon_{\rm vertex}$ in Eq. (5) was obtained, resulting in $\epsilon_{\rm vertex} = 0.37 \pm 10\%$. This approach is confirmed in $p + p$ collisions at $\sqrt{s} = 200$ GeV where the ZDCs have enough efficiency to measure the z vertex distribution. The efficiency of the ZDCs (located at $z = \pm 18$ m) does not depend on collision vertex position in the PHENIX IR, which was distributed with a sigma of 0.5–0.7 m around $z = 0$. The vertex distribution obtained with the WCMs is well reproduced by the measurement with the ZDCs at $\sqrt{s} = 200$ GeV [Fig. 2(a)].

Beam focusing in the IR causes bunch transverse sizes to vary away from the nominal collision point ($z = 0$) as $\sigma^2(z) = \sigma^2(z = 0) \times (1 + z^2/\beta^{*2})$, where β^* is the value of the betatron amplitude function at the interaction point. This is the so-called hourglass effect. The product $\sigma_x\sigma_y$ in Eq. (3) should be replaced by an effective $\langle \sigma_x \cdot \sigma_y \rangle$, which differs from what was measured in a scan (mainly due to the vertex cut implemented in BBC trigger). The correction due to this effect for Vernier scan data at $\sqrt{s} = 62.4$ GeV with a betatron amplitude function at the collision point of $\beta^* = 3$ m was simulated with WCM data and calculated to be 0.93 ± 0.02. The applicability of our calculational technique is illustrated in Fig. 2 with the high statistics Vernier scan data at $\sqrt{s} = 200$ GeV.

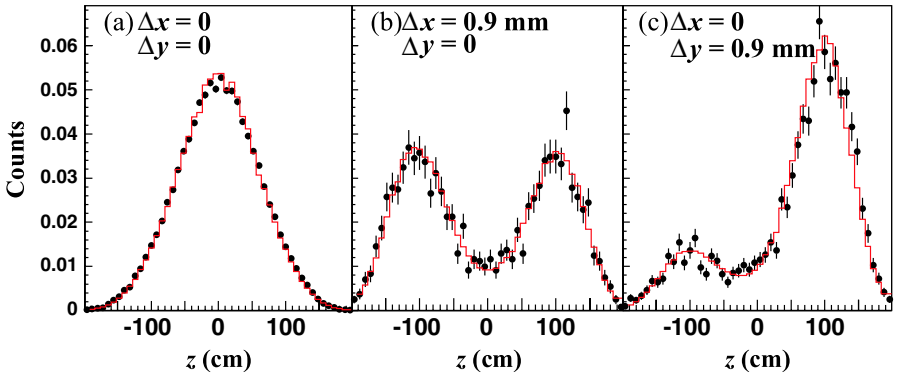

FIG. 2 (color online). Collision z-vertex distribution in the PHENIX IR measured by ZDCs in a Vernier scan at $\sqrt{s} = 200$ GeV (points) and calculations from convolution of colliding bunch intensity profiles along z-axis and including the hourglass effect for $\beta^* = 1$ m, for bunches with typical length of 1 m and transverse size of 0.3 mm (histograms); (a) beams are head-on; (b) one beam is 0.9 mm displaced relative to the other beam in the horizontal direction (illustrates the hourglass effect) and (c) one beam is 0.9 mm displaced relative to the other beam in the vertical direction. The calculations include the bunch crossing angle with a vertical projection of 0.15 mrad.

Figures 2(b) and 2(c) shows the sensitivity of our data for the transversely displaced beams to the hourglass effect and to the crossing angle between the colliding beams, compared with a head-on vertex distribution in Fig. 2(a). The two peaks in Figs. 2(b) and 2(c) caused by the hourglass effect, show an overlap of the diverging colliding beams at large $|z|$ in a particular displaced beam setting from a Vernier scan. The obvious asymmetry in the two peaks in Fig. 2(c) is a result of the nonzero crossing angle between colliding bunches. In all Vernier scan measurements the crossing angle was found to be less than 0.2 mrad, which translates to a negligible correction for L_{machine} at $\sqrt{s} = 62.4$ GeV, with a typical bunch length of $\sim$1 m and bunch transverse size of 1 mm.

After all the corrections discussed above were applied, our BBC trigger cross section in $p + p$ collisions at $\sqrt{s} = 62.4$ GeV was found to be $\sigma_{\text{BBC}} = 13.7$ mb with a systematic uncertainty of ± 1.5 mb ($\pm$ 11%), i.e. $\sim$40% of the world-average value of the inelastic $p + p$ scattering cross section at $\sqrt{s} = 62.4$ GeV[14]. Major contributors to the systematic uncertainty are 4% from the uncertainty in the normalization of bunch intensity measurements and in the calibration of the beam position measurements in the Vernier scan, 10% from the BBC trigger efficiency correction of ϵ_{vertex}, and 2% from the hourglass correction.

C. π^0 cross section results and discussion

Figure 3 presents the inclusive midrapidity π^0 invariant production cross section at $\sqrt{s} = 62.4$ GeV versus p_T, from $p_T = 0.5$ GeV/c to $p_T = 7$ GeV [22]. An overall normalization uncertainty of 11% due to the uncertainty in absolute normalization of the luminosity is not shown. The analyzed data sample with 0.76×10^9 BBC triggers corresponded to about 55 nb^{-1} integrated luminosity. The measurements fall within the large spread of ISR data [12–14].

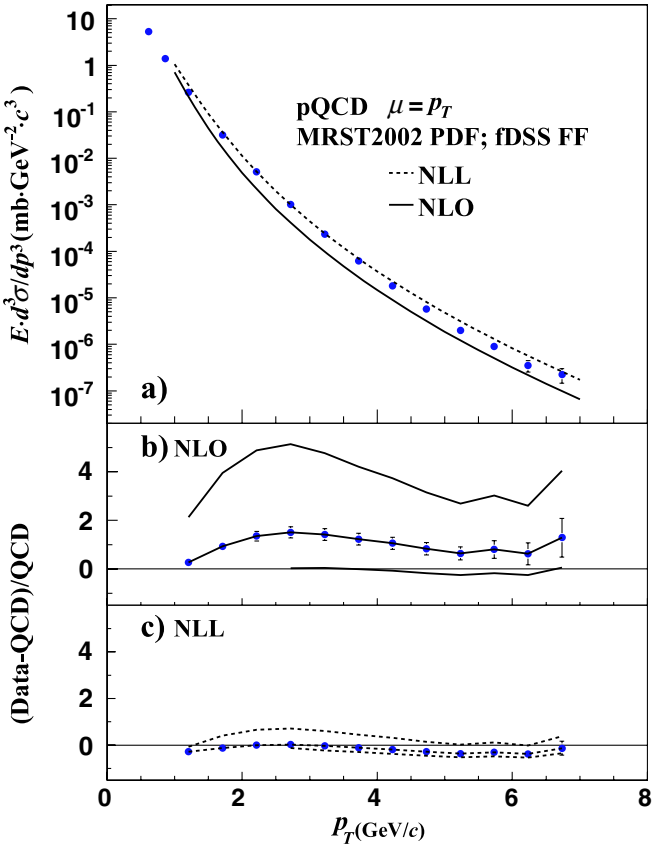

FIG. 3 (color online). (a) The neutral pion production cross section at $\sqrt{s} = 62.4$ GeV as a function of p_T (circles) and the results of NLO (solid) and NLL (dashed) pQCD calculations for the theory scale $\mu = p_T$. (b) The relative difference between the data and NLO pQCD calculations for the three theory scales $\mu = p_T/2$ (upper line), p_T (middle line) and $2p_T$ (lower line); experimental uncertainties (excluding the 11% normalization uncertainty) are shown for the $\mu = p_T$ curve. (c) The same as b) but for NLL pQCD calculations.

The data are compared to NLO and NLL pQCD calculations at a theory scale $\mu = p_T$, where μ represents equal factorization, renormalization, and fragmentation scales [11]. The NLL corrections extend the NLO calculations to include the resummation of extra ''threshold'' logarithmic terms which appear in the perturbative expansion at not very high energies because the initial partons have just enough energy to produce the high p_T parton that fragments into a final pion. The MRST2002 parton distribution functions [23] and the fDSS set of fragmentation functions [24], which are extracted in NLO, are used in both NLO and NLL calculations. We have previously seen that the data are well described by NLO pQCD with a scale of $\mu = p_T$ at $\sqrt{s} = 200$ GeV [4,5]. In contrast, NLO calculations with the same scale underestimate the π^0 cross section at $\sqrt{s} = 62.4$ GeV. At the same time, it is known that NLO calculations are not always successful at describing low-energy fixed-target data [9], while NLL calculations have been successful [10]. The NLL calculations have a smaller scale dependence and describe our data well with $\mu = p_T$; however, as noted in [11], subleading perturbative corrections to the NLL calculation may be significant. The results may indicate that $\sqrt{s} = 62.4$ GeV is at an intermediate energy region where calculations that include threshold logarithm effects may describe the data more accurately. Consequently, we show comparisons below to both NLO and NLL at a scale of $\mu = p_T$.

General principles of hard scattering, including the principle of factorization of the reaction into parton distribution functions for the protons, fragmentation functions for the scattered partons and a short-distance parton-parton hard-scattering cross section, predicted a general x_T-scaling form for the invariant cross section of inclusive particle production near midrapidity [25]:

$$E\frac{d^3\sigma}{dp^3} = \frac{1}{p_T^n}F(x_T) = \frac{1}{\sqrt{s}^n}G(x_T) \tag{6}$$

where $x_T = 2p_T/\sqrt{s}$, and $F(x_T)$ and $G(x_T)$ are universal functions. The parameter n relates to the form of the force-law between constituents. For example for QED or Vector Gluon exchange, $n = 4$ [26]. Because of higher order effects, the running of the coupling constant $\alpha(Q^2)$, the evolution of the parton distribution functions and fragmentation functions, and the initial-state transverse momentum k_T, n is not a constant but is a function of x_T and $\sqrt{s}$: $n(x_T, \sqrt{s})$ [27].

Figure 4(a) shows the inclusive π^0 cross section scaled by $\sqrt{s}^n$ for $\sqrt{s} = 62.4$ GeV and 200 GeV data [5] as a function of x_T, with the parameter $n = 6.38$, which is a weighted average of $n(x_T)$ for $x_T > 0.07$ (corresponding to $p_T > 2$ GeV/c at $\sqrt{s} = 62.4$ GeV). The parameter $n(x_T)$ was calculated as $\ln(\sigma_{62.4}(x_T)/\sigma_{200}(x_T))/\ln(200/62.4)$ for each x_T of $\sqrt{s} = 62.4$ GeV data; $\sigma_{62.4}$ and σ_{200} are invariant differential cross sections at $\sqrt{s} = 62.4$ GeV and $\sqrt{s} = 200$ GeV, respectively. Cross-section values for the corresponding x_T at $\sqrt{s} = 200$ GeV were obtained from parametrization of the measured cross section at $\sqrt{s} = 200$ GeV: $T(p_T)\frac{A}{(1+p_T/p_0)^m} + (1 - T(p_T))\frac{B}{p_T^k}$, $T(p_T) = \frac{1}{1+\exp((p_T-t)/w)}$, where $t = 4.5$ GeV/c, $w = 0.084$ GeV/c, $A = 253.8$ mb $\cdot$ GeV$^{-2} \cdot c^3$, $p_0 = 1.488$ GeV/c, $m = 10.82$, $B = 14.7$ mb $\cdot$ GeV$^{-2+k} \cdot c^{3-k}$, and $k = 8.11$. All $\sqrt{s} = 200$ GeV data points agree with the parametrization curve within uncertainties. The parametrization is shown as the solid curve in Fig. 4(a).

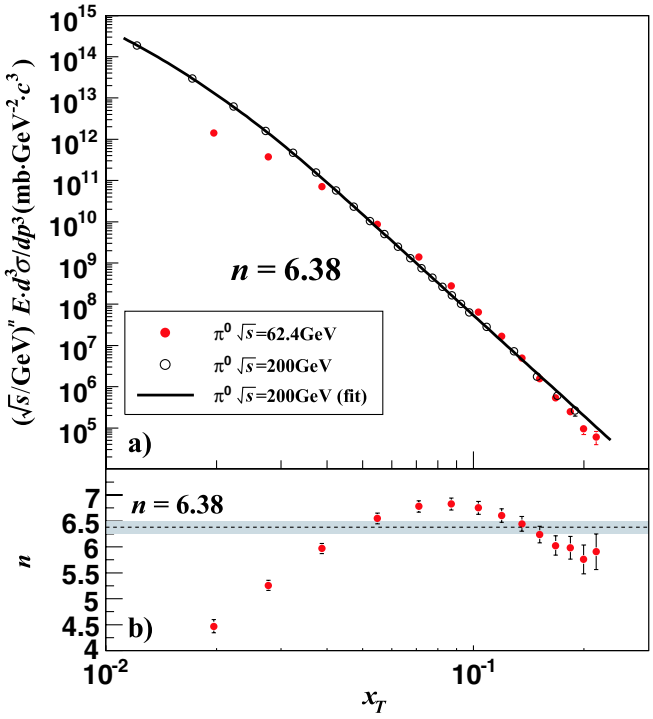

FIG. 4 (color online). (a) The neutral pion production cross section at $\sqrt{s} = 62.4$ GeV and $\sqrt{s} = 200$ GeV as a function of x_T, scaled by $(\sqrt{s}/\text{GeV})^n$ with $n = 6.38$; the solid line is a parametrization of $\sqrt{s} = 200$ GeV data. (b) The parameter n in (6) obtained from the ratio of invariant cross section at $\sqrt{s} = 62.4$ GeV and $\sqrt{s} = 200$ GeV, at each x_T of $\sqrt{s} = 62.4$ GeV data; error bars show the statistical and systematic uncertainties of the $\sqrt{s} = 62.4$ GeV and $\sqrt{s} = 200$ GeV data. The shaded band reflects the 11% $\oplus$ 9.7% normalization uncertainty in the $\sqrt{s} = 62.4$ and 200 GeV cross section measurements, correspondingly.

At low x_T, where soft physics dominates particle production, $n(x_T)$ is supposed to increase with x_T due to the similar exponential shapes of the soft part of the invariant cross section versus p_T at different $\sqrt{s}$ ($\sim e^{-6p_T}$) [26]. In the hard-scattering region $n(x_T)$ is expected to decrease with increasing x_T, due to stronger scale breaking at lower p_T. Such behavior of $n(x_T)$ is demonstrated by our data in Fig. 4(b). A similar drop in the parameter n at $x_T \gtrsim 0.1$ was observed at ISR energies [12]. Figure 4(b) also shows the possible transition from soft- to hard-scattering regions

in π^0 production at $p_T \sim 2$ GeV/c. A similar conclusion was derived from the shape of the π^0 spectrum at $\sqrt{s} = 200$ GeV in [5]. This can serve as a basis for applying the pQCD formalism to the double helicity asymmetry data with $p_T > 2$ GeV/c in order to allow access to ΔG.

IV. INCLUSIVE π^0 DOUBLE HELICITY ASYMMETRY

A. π^0 A_{LL} analysis

For the 2006 run, each of the two independent RHIC collider rings were filled with up to 111 bunches in a 120 bunch pattern, with one of four, fill-by-fill alternating predetermined patterns of polarization sign for the bunches. Bunch polarization signs in each pattern were set in such a way that all four colliding bunch spin combinations occurred in sequences of four bunch crossings. That greatly reduced the systematic effects in spin asymmetry measurements due to variation of detector response versus time and due to possible correlation of detector performance with RHIC bunch structure.

To collect data from collisions of longitudinally polarized protons, the polarization orientation of the beams was rotated from vertical, the stable spin direction in RHIC, to longitudinal at the PHENIX IR and then back to vertical after the IR by spin rotators [28]. PHENIX local polarimeters measured the residual transverse component of the beam polarizations, using the spin dependence of very forward neutron production [5,18,19] observed by the ZDC, and by that means monitored the orientation of the beam polarization in the PHENIX IR throughout the run.

The magnitudes of the beam polarizations at RHIC are measured using fast carbon target polarimeters [29], normalized to absolute polarization measurements by a separate polarized atomic hydrogen jet polarimeter [30]. The luminosity-weighted beam polarizations over 11 RHIC fills used in the A_{LL} analysis were $\langle P \rangle = 0.48$ for both beams, with 0.035 and 0.045 systematic uncertainty for the two RHIC beams, respectively. For the longitudinal polarization run period, the residual transverse polarizations of the beams were $\langle P_T/P \rangle^B = 0.11 \pm 0.15$ and $\langle P_T/P \rangle^Y = 0.11 \pm 0.12$ for ''Blue'' and ''Yellow'' RHIC beams, respectively. The average transverse component of the product was $\langle P_T^B \cdot P_T^Y \rangle / \langle P^B \cdot P^Y \rangle \leq \langle P_T/P \rangle^B \cdot \langle P_T/P \rangle^Y = 0.012 \pm 0.021$; the average of the polarization product over the run was $\langle P^B \cdot P^Y \rangle = 0.23$, with a systematic uncertainty of $\pm 14\%$.

Experimentally, the double helicity asymmetry for π^0 production is determined as

$$A_{LL}^{\pi^0} = \frac{1}{|P^B \cdot P^Y|} \cdot \frac{N_{++} - R \cdot N_{+-}}{N_{++} + R \cdot N_{+-}}; R = \frac{L_{++}}{L_{+-}}, \qquad (7)$$

where N_{++} and N_{+-} are the number of π^0's and R is the relative luminosity between bunches with the same and opposite helicities. The analysis technique for the π^0 A_{LL} measurements is similar to our analyses of $\sqrt{s} = 200$ GeV data [5,18,31].

Double helicity asymmetry results were obtained from longitudinally polarized $p + p$ collisions corresponding to ~ 40 nb^{-1} integrated luminosity. Because of the limited BBC trigger efficiency for high p_T π^0 events, high p_T photon triggered events without the BBC trigger condition requirement were used for the π^0 asymmetry analysis. This led to a slightly increased background in the π^0 reconstruction and additional systematic uncertainty in the measurements of the relative luminosity between bunches with different helicity states.

The background asymmetry under the π^0 peak in the two-photon mass distribution A_{LL}^{BG} was estimated from the counts outside the π^0 peak, from a 177–217 MeV/c^2 range in the two-photon mass distribution. Unlike our $\sqrt{s} = 200$ GeV data analyses, a lower mass range was not used for A_{LL}^{BG} estimations due to cosmic background from noncollision events. This background contribution in the mass ranges of π^0 peak and higher mass was negligible ($< 1\%$), and A_{LL}^{BG} was consistent with zero in all p_T bins.

Similar to our previous analyses, crossing-by-crossing accumulated number of BBC triggers were used for the measurements of the relative luminosity between bunches with different spin configuration. The uncertainty on the relative luminosity measurements δR was derived from the comparison between BBC trigger events and other trigger events, selecting different physics processes in different kinematic ranges. In the $\sqrt{s} = 200$ GeV data analysis the comparison was done to triggers defined by the coincidence of signals from the two ZDCs [5,18,31]. Because of the limited efficiency of the ZDC at $\sqrt{s} = 62.4$ GeV, the comparison in this analysis was performed with the number of events which fired simultaneously either of the two BBCs and either of the two ZDCs. Only 20% of the event statistics in this sample is contributed by BBC-triggered events, so this sample can be considered as essentially independent from the BBC event sample. From this comparison the upper limit of δR was estimated to be 0.6×10^{-3}, which for the average beam polarizations of 0.48 translates to $\delta A_{LL} = 1.4 \times 10^{-3}$, the p_T independent uncertainty of the π^0 double helicity asymmetry results. Single beam background $<0.35\%$, as determined by the trigger counts of noncolliding bunches and pileup probability of $\lesssim 0.002\%$, had negligible impact on the relative luminosity measurements.

A transverse double spin asymmetry A_{TT}, the transverse equivalent to Eqs. (1) and (7), can contribute to A_{LL} through the residual transverse component of the product of the beam polarizations discussed above. Similar to [5], A_{TT} was obtained from the sample with transverse polarization. The maximal possible A_{TT} effect on A_{LL} was determined by $\pm \delta A_{TT}$ from the measured A_{TT}, which was $< 0.15 \cdot \delta A_{LL}$ in all p_T bins.

B. π^0 A_{LL} results and discussion

Figure 5 presents the measured double helicity asymmetry in π^0 production versus p_T [22]. A scale uncertainty of 14% in $A_{LL}^{\pi^0}$ due to the uncertainty in beam polarizations is not shown. The other systematic uncertainties are negligible, as discussed above, and checked using a technique to randomize the sign of bunch polarization and by varying the π^0 identification criteria [18].

Figure 5 also shows a set of A_{LL} curves from pQCD calculations that incorporates different scenarios for gluon polarization within the GRSV parametrization of the polarized parton distribution functions [32]. GRSV-std corresponds to the best fit to inclusive DIS data. The other three scenarios in Fig. 5 (GRSV-max, $\Delta G = 0$, and $\Delta G = -G$) are based on the best fit, but use the functions $\Delta G(x_g) = G(x_g)$, 0, $-G(x_g)$ at the initial scale for parton evolution ($Q^2 = 0.4$ GeV^2), where $G(x_g)$ is the unpolarized gluon distribution, and $\Delta G(x_g)$ is the difference between the distribution of gluons with the same and opposite helicity to the parent proton. In Fig. 5, we compare our asymmetry data with both NLO and NLL calculations. The NLL calculations indicate that we have a reduced sensitivity to positive ΔG, but the effect is far less pronounced than at Fermilab fixed-target energies [11]. Similar to our $\sqrt{s} = 200$ GeV results [5,18], our $\sqrt{s} = 62.4$ GeV A_{LL} data do not support a large gluon polarization scenario, such as GRSV-max.

Figure 6 presents the measured A_{LL} versus x_T in π^0 production overlaid with the results at $\sqrt{s} = 200$ GeV [5]. Clear statistical improvement can be seen at higher x_T. For the measured p_T range 2–4 GeV/c, the range of x_g in each bin is broad and spans the range $x_g = 0.06 - 0.4$, as calculated by NLO pQCD [33]. Thus our data set extends our x_g reach of sensitivity to ΔG and also overlaps previous measurements, providing measurements with the same x_g but at a different Q^2 scale.

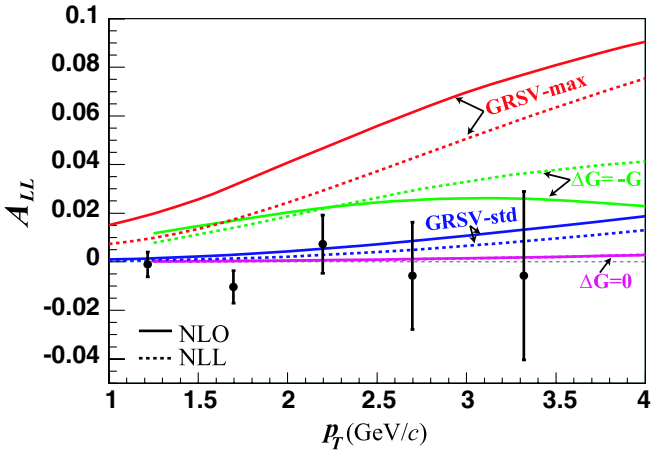

FIG. 5 (color online). The double helicity asymmetry for neutral pion production at $\sqrt{s} = 62.4$ GeV as a function of p_T(GeV/c). Error bars are statistical uncertainties, with the 14% overall polarization uncertainty not shown; other experimental systematic uncertainties are negligible. Four GRSV theoretical calculations based on NLO pQCD (solid curves) and on NLL pQCD (dashed curves) are also shown for comparison with the data (see text for details). Note that the $\Delta G = 0$ curves for NLO and NLL overlap.

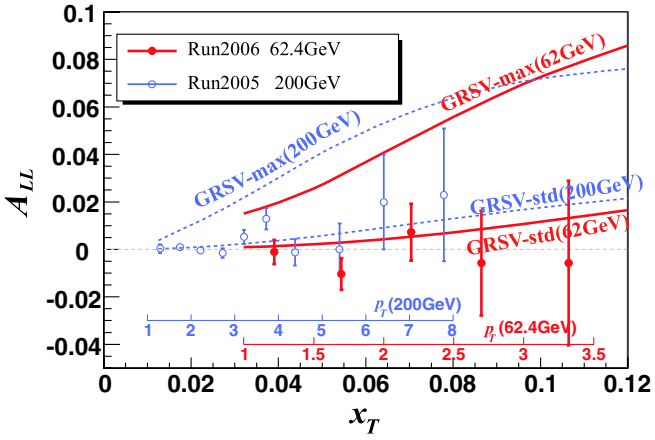

FIG. 6 (color online). The double helicity asymmetry for neutral pion production at $\sqrt{s} = 62.4$ GeV and 200 GeV as a function of x_T. Error bars are statistical uncertainties, with the 14% (9.4%) overall polarization uncertainty for $\sqrt{s} = 62.4$ GeV (200 GeV) data not shown. Two GRSV theoretical calculations based on NLO pQCD are also shown for comparison with the data (see text for details.)

V. SUMMARY

To summarize, we have presented the unpolarized cross section and double helicity asymmetries for π^0 production at midrapidity, for proton-proton collisions at $\sqrt{s} = 62.4$ GeV. The accuracy of the cross section measurements, which fall within the large spread of ISR data, relies on direct π^0 two-photon decay reconstruction, precise calibration of the photon energy measurements, careful study of the trigger performance and accurate control of the integrated luminosity of the analyzed data sample. The results serve as a precise baseline for heavy-ion measurements. Comparisons to NLO and NLL theoretical calculations indicate that including the effects of threshold logarithms may be necessary to more accurately describe the cross section at $\sqrt{s} = 62.4$ GeV. The A_{LL} results extend the sensitivity to the polarized gluon distribution in the proton to higher x_g compared to the previous measurements at $\sqrt{s} = 200$ GeV. A preliminary version of these double helicity asymmetry results was already used in a recent global fit of both RHIC and polarized DIS data to constrain ΔG [34].

ACKNOWLEDGMENTS

We thank the RHIC Polarimeter Group and the staff of the Collider-Accelerator and Physics Departments at

Brookhaven National Laboratory and the staff of the other PHENIX participating institutions for their vital contributions. We thank W. Vogelsang and M. Stratmann for providing the pQCD calculations and for informative discussions. We acknowledge support from the Office of Nuclear Physics in the Office of Science of the Department of Energy, the National Science Foundation, a sponsored research grant from Renaissance Technologies LLC, Abilene Christian University Research Council, Research Foundation of SUNY, and Dean of the College of Arts and Sciences, Vanderbilt University (U.S.A), Ministry of Education, Culture, Sports, Science, and Technology and the Japan Society for the Promotion of Science (Japan), Conselho Nacional de Desenvolvimento Científico e Tecnológico and Fundação de Amparo à Pesquisa do Estado de São Paulo (Brazil), Natural Science Foundation of China (People's Republic of China), Ministry of Education, Youth and Sports (Czech Republic), Centre National de la Recherche Scientifique, Commissariat à l'Énergie Atomique, and Institut National de Physique Nucléaire et de Physique des Particules (France), Ministry of Industry, Science and Tekhnologies, Bundesministerium für Bildung und Forschung, Deutscher Akademischer Austausch Dienst, and Alexander von Humboldt Stiftung (Germany), Hungarian National Science Fund, OTKA (Hungary), Department of Atomic Energy (India), Israel Science Foundation (Israel), Korea Research Foundation and Korea Science and Engineering Foundation (Korea), Ministry of Education and Science, Russian Academy of Sciences, Federal Agency of Atomic Energy (Russia), V. R. and the Wallenberg Foundation (Sweden), the U.S. Civilian Research and Development Foundation for the Independent States of the Former Soviet Union, the U.S.-Hungarian Fulbright Foundation for Educational Exchange, and the U.S.-Israel Binational Science Foundation.

[1] J. Ashman *et al.* (EMC), Phys. Lett. B **206**, 364 (1988); Nucl. Phys. **B328**, 1 (1989).
[2] A. Airapetian *et al.* (HERMES), Phys. Rev. D **75**, 012007 (2007); V. Yu. Alexakhin *et al.* (COMPASS), Phys. Lett. B **647**, 8 (2007).
[3] G. Bunce *et al.*, Annu. Rev. Nucl. Part. Sci. **50**, 525 (2000).
[4] S. S. Adler *et al.* (PHENIX), Phys. Rev. Lett. **91**, 241803 (2003).
[5] A. Adare *et al.* (PHENIX), Phys. Rev. D **76**, 051106(R) (2007).
[6] J. Adams *et al.* (STAR), Phys. Rev. Lett. **92**, 171801 (2004).
[7] B. I. Abelev *et al.* (STAR), Phys. Rev. Lett. **97**, 252001 (2006).
[8] S. S. Adler *et al.* (PHENIX), Phys. Rev. Lett. **98**, 012002 (2007).
[9] P. Aurenche *et al.*, Eur. Phys. J. C **13**, 347 (2000).
[10] D. de Florian, and W. Vogelsang, Phys. Rev. D **71**, 114004 (2005).
[11] D. de Florian, W. Vogelsang, and F. Wagner, Phys. Rev. D **76**, 094021 (2007); D. L. Adams *et al.*, Phys. Lett. B **261**, 197 (1991).
[12] A. L. S. Angelis (CCOR), Phys. Lett. B **79**, 505 (1978); C. Kourkoumelis *et al.* (R-806), Phys. Lett. B **84**, 271 (1979).
[13] A. L. S. Angelis *et al.* (CMOR), Nucl. Phys. **B327**, 541 (1989); T. Akesson *et al.* (AFS), Sov. J. Nucl. Phys. **51**, 836 (1990); C. Kourkoumelis *et al.* (R-806), Z. Phys. C **5**, 95 (1980); A. G. Clark *et al.* (CSZ), Phys. Lett. B **74**, 267 (1978); F. W. Busser *et al.* (CCRS), Nucl. Phys. **B106**, 1 (1976); K. Eggert *et al.* (ACHM), Nucl. Phys. **B98**, 49 (1975); F. W. Busser *et al.* (CCR), Phys. Lett. B **46**, 471 (1973); F. W. Busser *et al.* (CCRS), Phys. Lett. B **55**, 232 (1975); M. Banner *et al.* (Saclay), Nucl. Phys. **B126**, 61 (1977); B. Alper *et al.* (BSC), Nucl. Phys. **B100**, 237 (1975).
[14] D. d'Enterria, J. Phys. G **31**, S491 (2005).
[15] L. Aphecetche *et al.*, Nucl. Instrum. Methods Phys. Res., Sect. A **499**, 521 (2003).
[16] M. Allen *et al.*, Nucl. Instrum. Methods Phys. Res., Sect. A **499**, 549 (2003).
[17] C. Adler *et al.*, Nucl. Instrum. Methods Phys. Res., Sect. A **470**, 488 (2001).
[18] S. S. Adler *et al.* (PHENIX), Phys. Rev. Lett. **93**, 202002 (2004).
[19] Y. Fukao *et al.*, Phys. Lett. B **650**, 325 (2007).
[20] S. van der Meer, ISR-PO/68-31, KEK68-64, available at http://ccdb4fs.kek.jp/cgi-bin/img_index?196800064; A. Drees and Z. Xu, PAC-2001-RPAH116, available at http://accelconf.web.cern.ch/AccelConf/p01/PAPERS/RPAH116.PDF.
[21] P. Cameron *et al.*, *Proceedings of the 1999 Particle Accelerator Conference* (IEEE, New York, 1999), p. 2146.
[22] Tables of data available at http://www.phenix.bnl.gov/phenix/WWW/info/data/ppg087_data.html.
[23] A. D. Martin *et al.*, Eur. Phys. J. C **35**, 325 (2004).
[24] D. de Florian, R. Sassot, and M. Stratmann, Phys. Rev. D **75**, 114010 (2007).
[25] R. Blankenbecler, S. J. Brodsky, and J. F Gunion, Phys. Lett. B **42**, 461 (1972).
[26] S. M. Berman, J. D. Bjorken, and J. B Kogut, Phys. Rev. D **4**, 3388 (1971).
[27] R. F. Cahalan, K. A. Geer, J. B. Kogut, and L. Susskind, Phys. Rev. D **11**, 1199 (1975).
[28] W. W. MacKay *et al.*, *Proceedings of the 2003 Particle Accelerator Conference*, edited by J. Chew, P. Lucas, and S. Webber (IEEE, New York, 2003), p. 1697.
[29] O. Jinnouchi *et al.*, RHIC/CAD Accelerator Physics Note 171 (2004).
[30] H. Okada *et al.*, Phys. Lett. B **638**, 450 (2006).

[31] S. S. Adler *et al.* (PHENIX), Phys. Rev. D **73**, 091102(R) (2006).

[32] B. Jäger, A. Schafer, M. Stratmann, and W. Vogelsang, Phys. Rev. D **67**, 054005 (2003); M. Glück, E. Reya, M. Stratmann, and W. Vogelsang, Phys. Rev. D **63**, 094005 (2001).

[33] M. Stratmann and W. Vogelsang, J. Phys. Conf. Ser. **69**, 012035 (2007); W. Vogelsang (private communication).

[34] D. de Florian, R. Sassot, M. Stratmann, and W. Vogelsang, Phys. Rev. Lett. **101**, 072001 (2008).

Charged hadron multiplicity fluctuations in Au+Au and Cu+Cu collisions from $\sqrt{s_{NN}} = 22.5$ to 200 GeV

A. Adare,[10] S. S. Adler,[5] S. Afanasiev,[24] C. Aidala,[11,39] N. N. Ajitanand,[52] Y. Akiba,[26,46,47] H. Al-Bataineh,[41] J. Alexander,[52] A. Al-Jamel,[41] K. Aoki,[30,46] L. Aphecetche,[54] R. Armendariz,[41] S. H. Aronson,[5] J. Asai,[47] E. T. Atomssa,[31] R. Averbeck,[53] T. C. Awes,[42] B. Azmoun,[5] V. Babintsev,[20] G. Baksay,[16] L. Baksay,[16] A. Baldisseri,[13] K. N. Barish,[6] P. D. Barnes,[33] B. Bassalleck,[40] S. Bathe,[6,36] S. Batsouli,[11,39,42] V. Baublis,[45] F. Bauer,[6] A. Bazilevsky,[5,47] S. Belikov,[5,20,23,*] R. Bennett,[53] Y. Berdnikov,[49] A. A. Bickley,[10] M. T. Bjorndal,[11,39] J. G. Boissevain,[33] H. Borel,[13] K. Boyle,[53] M. L. Brooks,[33] D. S. Brown,[41] N. Bruner,[40] D. Bucher,[36] H. Buesching,[5,36] V. Bumazhnov,[20] G. Bunce,[5,47] J. M. Burward-Hoy,[32,33] S. Butsyk,[33,53] X. Camard,[54] S. Campbell,[53] J.-S. Chai,[25] P. Chand,[4] B. S. Chang,[61] W. C. Chang,[2] J.-L. Charvet,[13] S. Chernichenko,[20] J. Chiba,[26] C. Y. Chi,[11,39] M. Chiu,[11,21,39] I. J. Choi,[61] R. K. Choudhury,[4] T. Chujo,[5,58] P. Chung,[52] A. Churyn,[20] V. Cianciolo,[42] C. R. Cleven,[18] Y. Cobigo,[13] B. A. Cole,[11,39] M. P. Comets,[43] P. Constantin,[23,33] M. Csanád,[15] T. Csörgő,[27] J. P. Cussonneau,[54] T. Dahms,[53] K. Das,[17] G. David,[5] F. Deák,[15] M. B. Deaton,[1] K. Dehmelt,[16] H. Delagrange,[54] A. Denisov,[20] D. d'Enterria,[11,39] A. Deshpande,[47,53] E. J. Desmond,[5] A. Devismes,[53] O. Dietzsch,[50] A. Dion,[53] M. Donadelli,[50] J. L. Drachenberg,[1] O. Drapier,[31] A. Drees,[53] A. K. Dubey,[60] A. Durum,[20] D. Dutta,[4] V. Dzhordzhadze,[6,55] Y. V. Efremenko,[42] J. Egdemir,[53] F. Ellinghaus,[10] W. S. Emam,[6] A. Enokizono,[19,32] H. En'yo,[46,47] B. Espagnon,[43] S. Esumi,[57] K. O. Eyser,[6] D. E. Fields,[40,47] C. Finck,[54] M. Finger Jr.,[7,24] M. Finger,[7,24] F. Fleuret,[31] S. L. Fokin,[29] B. Forestier,[34] B. D. Fox,[47] Z. Fraenkel,[60,*] J. E. Frantz,[11,39,53] A. Franz,[5] A. D. Frawley,[17] K. Fujiwara,[46] Y. Fukao,[30,46,47] S.-Y. Fung,[6] T. Fusayasu,[38] S. Gadrat,[34] I. Garishvili,[55] F. Gastineau,[54] M. Germain,[54] A. Glenn,[10,55] H. Gong,[53] M. Gonin,[31] J. Gosset,[13] Y. Goto,[46,47] R. Granier de Cassagnac,[31] N. Grau,[23] S. V. Greene,[58] M. Grosse Perdekamp,[21,47] T. Gunji,[9] H.-Å. Gustafsson,[35] T. Hachiya,[19,46] A. Hadj Henni,[54] C. Haegemann,[40] J. S. Haggerty,[5] M. N. Hagiwara,[1] H. Hamagaki,[9] R. Han,[44] A. G. Hansen,[33] H. Harada,[19] E. P. Hartouni,[32] K. Haruna,[19] M. Harvey,[5] E. Haslum,[35] K. Hasuko,[46] R. Hayano,[9] M. Heffner,[32] T. K. Hemmick,[53] T. Hester,[6] J. M. Heuser,[46] X. He,[18] P. Hidas,[27] H. Hiejima,[21] J. C. Hill,[23] R. Hobbs,[40] M. Hohlmann,[16] M. Holmes,[58] W. Holzmann,[52] K. Homma,[19] B. Hong,[28] A. Hoover,[41] T. Horaguchi,[46,47,56] D. Hornback,[55] M. G. Hur,[25] T. Ichihara,[46,47] V. V. Ikonnikov,[29] K. Imai,[30,46] M. Inaba,[57] Y. Inoue,[46,48] M. Inuzuka,[9] D. Isenhower,[1] L. Isenhower,[1] M. Ishihara,[46] T. Isobe,[9] M. Issah,[52] A. Isupov,[24] B. V. Jacak,[53,†] J. Jia,[11,39,53] J. Jin,[11,39] O. Jinnouchi,[46,47] B. M. Johnson,[5] S. C. Johnson,[32] K. S. Joo,[37] D. Jouan,[43] F. Kajihara,[9,46] S. Kametani,[9,59] N. Kamihara,[46,56] J. Kamin,[53] M. Kaneta,[47] J. H. Kang,[61] H. Kanou,[46,56] K. Katou,[59] T. Kawabata,[9] T. Kawagishi,[57] D. Kawall,[47] A. V. Kazantsev,[29] S. Kelly,[10,11,39] B. Khachaturov,[60] A. Khanzadeev,[45] J. Kikuchi,[59] D. H. Kim,[37] D. J. Kim,[61] E. Kim,[51] G.-B. Kim,[31] H. J. Kim,[61] Y.-S. Kim,[25] E. Kinney,[10] A. Kiss,[15] E. Kistenev,[5] A. Kiyomichi,[46] J. Klay,[32] C. Klein-Boesing,[36] H. Kobayashi,[47] L. Kochenda,[45] V. Kochetkov,[20] R. Kohara,[19] B. Komkov,[45] M. Konno,[57] D. Kotchetkov,[6] A. Kozlov,[60] A. Král,[12] A. Kravitz,[11,39] P. J. Kroon,[5] J. Kubart,[7,22] C. H. Kuberg,[1,*] G. J. Kunde,[33] N. Kurihara,[9] K. Kurita,[46,48] M. J. Kweon,[28] Y. Kwon,[55,61] G. S. Kyle,[41] R. Lacey,[52] Y.-S. Lai,[11,39] J. G. Lajoie,[23] A. Lebedev,[23,29] Y. Le Bornec,[43] S. Leckey,[53] D. M. Lee,[33] M. K. Lee,[61] T. Lee,[51] M. J. Leitch,[33] M. A. L. Leite,[50] B. Lenzi,[50] H. Lim,[51] T. Liška,[12] A. Litvinenko,[24] M. X. Liu,[33] X. Li,[8] X. H. Li,[6] B. Love,[58] D. Lynch,[5] C. F. Maguire,[58] Y. I. Makdisi,[5] A. Malakhov,[24] M. D. Malik,[40] V. I. Manko,[29] Y. Mao,[44,46] G. Martinez,[54] L. Mašek,[7,22] H. Masui,[57] F. Matathias,[11,39,53] T. Matsumoto,[9,59] M. C. McCain,[1,21] M. McCumber,[53] P. L. McGaughey,[33] Y. Miake,[57] P. Mikeš,[7,22] K. Miki,[57] T. E. Miller,[58] A. Milov,[53] S. Mioduszewski,[5] G. C. Mishra,[18] M. Mishra,[3] J. T. Mitchell,[5] M. Mitrovski,[52] A. K. Mohanty,[4] A. Morreale,[6] D. P. Morrison,[5] J. M. Moss,[33] T. V. Moukhanova,[29] D. Mukhopadhyay,[58,60] M. Muniruzzaman,[6] J. Murata,[46,48] S. Nagamiya,[26] Y. Nagata,[57] J. L. Nagle,[10,11,39] M. Naglis,[60] I. Nakagawa,[46,47] Y. Nakamiya,[19] T. Nakamura,[19] K. Nakano,[46,56] J. Newby,[32,55] M. Nguyen,[53] B. E. Norman,[33] A. S. Nyanin,[29] J. Nystrand,[35] E. O'Brien,[5] S. X. Oda,[9] C. A. Ogilvie,[23] H. Ohnishi,[46] I. D. Ojha,[3,58] H. Okada,[30,46] K. Okada,[46,47] M. Oka,[57] O. O. Omiwade,[1] A. Oskarsson,[35] I. Otterlund,[35] M. Ouchida,[19] K. Oyama,[9] K. Ozawa,[9] R. Pak,[5] D. Pal,[58,60] A. P. T. Palounek,[33] V. Pantuev,[53] V. Papavassiliou,[41] J. Park,[51] W. J. Park,[28] S. F. Pate,[41] H. Pei,[23] V. Penev,[24] J.-C. Peng,[21] H. Pereira,[13] V. Peresedov,[24] D. Yu. Peressounko,[29] A. Pierson,[40] C. Pinkenburg,[5] R. P. Pisani,[5] M. L. Purschke,[5] A. K. Purwar,[33,53] J. M. Qualls,[1] H. Qu,[18] J. Rak,[23,40] A. Rakotozafindrabe,[31] I. Ravinovich,[60] K. F. Read,[42,55] S. Rembeczki,[16] M. Reuter,[53] K. Reygers,[36] V. Riabov,[45] Y. Riabov,[45] G. Roche,[34] A. Romana,[31,*] M. Rosati,[23] S. S. E. Rosendahl,[35] P. Rosnet,[34] P. Rukoyatkin,[24] V. L. Rykov,[46] S. S. Ryu,[61] B. Sahlmueller,[36] N. Saito,[30,46,47] T. Sakaguchi,[5,9,59] S. Sakai,[57] H. Sakata,[19] V. Samsonov,[45] L. Sanfratello,[40] R. Santo,[36] H. D. Sato,[30,46] S. Sato,[5,26,57] S. Sawada,[26] Y. Schutz,[54] J. Seele,[10] R. Seidl,[21] V. Semenov,[20] R. Seto,[6] D. Sharma,[60] T. K. Shea,[5] I. Shein,[20] A. Shevel,[45,52] T.-A. Shibata,[46,56] K. Shigaki,[19] M. Shimomura,[57] T. Shohjoh,[57] K. Shoji,[30,46] A. Sickles,[53] C. L. Silva,[50] D. Silvermyr,[33,42] C. Silvestre,[13] K. S. Sim,[28] C. P. Singh,[3] V. Singh,[3] S. Skutnik,[23] M. Slunečka,[7,24] W. C. Smith,[1] A. Soldatov,[20] R. A. Soltz,[32] W. E. Sondheim,[33] S. P. Sorensen,[55] I. V. Sourikova,[5] F. Staley,[13] P. W. Stankus,[42] E. Stenlund,[35] M. Stepanov,[41] A. Ster,[27] S. P. Stoll,[5] T. Sugitate,[19] C. Suire,[43] J. P. Sullivan,[33] J. Sziklai,[27] T. Tabaru,[47] S. Takagi,[57] E. M. Takagui,[50] A. Taketani,[46,47] K. H. Tanaka,[26] Y. Tanaka,[38] K. Tanida,[46,47] M. J. Tannenbaum,[5] A. Taranenko,[52] P. Tarján,[14] T. L. Thomas,[40] M. Togawa,[30,46] A. Toia,[53] J. Tojo,[46] L. Tomášek,[22] H. Torii,[30,46,47] R. S. Towell,[1] V.-N. Tram,[31] I. Tserruya,[60] Y. Tsuchimoto,[19,46] S. K. Tuli,[3] H. Tydesjö,[35] N. Tyurin,[20] T. J. Uam,[37] C. Vale,[23] H. Valle,[58] H. W. van Hecke,[33] J. Velkovska,[5,58] M. Velkovsky,[53] R. Vertesi,[14] V. Veszprémi,[14] A. A. Vinogradov,[29] M. Virius,[12] M. A. Volkov,[29] V. Vrba,[22] E. Vznuzdaev,[45] M. Wagner,[30,46] D. Walker,[53] X. R. Wang,[18,41] Y. Watanabe,[46,47] J. Wessels,[36] S. N. White,[5] N. Willis,[43] D. Winter,[11,39] F. K. Wohn,[23] C. L. Woody,[5] M. Wysocki,[10] W. Xie,[6,47] Y. L. Yamaguchi,[59] A. Yanovich,[20] Z. Yasin,[6] J. Ying,[18]

 ©2008 The American Physical Society

S. Yokkaichi,[46,47] G. R. Young,[42] I. Younus,[40] I. E. Yushmanov,[29] W. A. Zajc,[11,39] O. Zaudtke,[36] C. Zhang,[11,39,42] S. Zhou,[8] J. Zimányi,[27,*] L. Zolin,[24] and X. Zong[23]
(PHENIX Collaboration)

[1]*Abilene Christian University, Abilene, Texas 79699, USA*
[2]*Institute of Physics, Academia Sinica, Taipei 11529, Taiwan*
[3]*Department of Physics, Banaras Hindu University, Varanasi 221005, India*
[4]*Bhabha Atomic Research Centre, Bombay 400 085, India*
[5]*Brookhaven National Laboratory, Upton, New York 11973-5000, USA*
[6]*University of California-Riverside, Riverside, California 92521, USA*
[7]*Charles University, Ovocný trh 5, Praha 1, CZ-11636, Prague, Czech Republic*
[8]*China Institute of Atomic Energy (CIAE), Beijing, People's Republic of China*
[9]*Center for Nuclear Study, Graduate School of Science, University of Tokyo, 7-3-1 Hongo, Bunkyo, Tokyo 113-0033, Japan*
[10]*University of Colorado, Boulder, Colorado 80309, USA*
[11]*Columbia University, New York, New York 10027, USA*
[12]*Czech Technical University, Zikova 4, CZ-16636, Prague 6, Czech Republic*
[13]*Dapnia, CEA Saclay, F-91191, Gif-sur-Yvette, France*
[14]*Debrecen University, H-4010 Debrecen, Egyetem tér 1, Hungary*
[15]*ELTE, Eötvös Loránd University, H-1117 Budapest, Pázmány P.s. 1/A, Hungary*
[16]*Florida Institute of Technology, Melbourne, Florida 32901, USA*
[17]*Florida State University, Tallahassee, Florida 32306, USA*
[18]*Georgia State University, Atlanta, Georgia 30303, USA*
[19]*Hiroshima University, Kagamiyama, Higashi-Hiroshima 739-8526, Japan*
[20]*IHEP Protvino, State Research Center of Russian Federation, Institute for High Energy Physics, Protvino RU-142281, Russia*
[21]*University of Illinois at Urbana-Champaign, Urbana, Illinois 61801, USA*
[22]*Institute of Physics, Academy of Sciences of the Czech Republic, Na Slovance 2, CZ-18221 Prague 8, Czech Republic*
[23]*Iowa State University, Ames, Iowa 50011, USA*
[24]*Joint Institute for Nuclear Research, RU-141980 Dubna, Moscow Region, Russia*
[25]*KAERI, Cyclotron Application Laboratory, Seoul, Korea*
[26]*KEK, High Energy Accelerator Research Organization, Tsukuba, Ibaraki 305-0801, Japan*
[27]*KFKI Research Institute for Particle and Nuclear Physics of the Hungarian Academy of Sciences (MTA KFKI RMKI), H-1525 Budapest 114, P. O. Box 49, Budapest, Hungary*
[28]*Korea University, Seoul 136-701, Korea*
[29]*Russian Research Center "Kurchatov Institute," Moscow, Russia*
[30]*Kyoto University, Kyoto 606-8502, Japan*
[31]*Laboratoire Leprince-Ringuet, Ecole Polytechnique, CNRS-IN2P3, Route de Saclay, F-91128, Palaiseau, France*
[32]*Lawrence Livermore National Laboratory, Livermore, California 94550, USA*
[33]*Los Alamos National Laboratory, Los Alamos, New Mexico 87545, USA*
[34]*LPC, Université Blaise Pascal, CNRS-IN2P3, Clermont-Fd, F-63177 Aubiere Cedex, France*
[35]*Department of Physics, Lund University, Box 118, SE-221 00 Lund, Sweden*
[36]*Institut für Kernphysik, University of Muenster, D-48149 Muenster, Germany*
[37]*Myongji University, Yongin, Kyonggido 449-728, Korea*
[38]*Nagasaki Institute of Applied Science, Nagasaki-shi, Nagasaki 851-0193, Japan*
[39]*Nevis Laboratories, Irvington, New York 10533, USA*
[40]*University of New Mexico, Albuquerque, New Mexico 87131, USA*
[41]*New Mexico State University, Las Cruces, New Mexico 88003, USA*
[42]*Oak Ridge National Laboratory, Oak Ridge, Tennessee 37831, USA*
[43]*IPN-Orsay, Universite Paris Sud, CNRS-IN2P3, BP1, F-91406, Orsay, France*
[44]*Peking University, Beijing, People's Republic of China*
[45]*PNPI, Petersburg Nuclear Physics Institute, Gatchina, Leningrad Region, RU-188300, Russia*
[46]*RIKEN, Institute of Physical and Chemical Research, Wako, Saitama 351-0198, Japan*
[47]*RIKEN BNL Research Center, Brookhaven National Laboratory, Upton, New York 11973-5000, USA*
[48]*Physics Department, Rikkyo University, 3-34-1 Nishi-Ikebukuro, Toshima, Tokyo 171-8501, Japan*
[49]*St. Petersburg State Polytechnic University, St. Petersburg, Russia*
[50]*Universidade de São Paulo, Instituto de Física, Caixa Postal 66318, São Paulo CEP05315-970, Brazil*
[51]*System Electronics Laboratory, Seoul National University, Seoul, Korea*
[52]*Chemistry Department, Stony Brook University, SUNY, Stony Brook, New York 11794, USA*
[53]*Department of Physics and Astronomy, Stony Brook University, SUNY, Stony Brook, New York 11794, USA*
[54]*SUBATECH (Ecole des Mines de Nantes, CNRS-IN2P3, Université de Nantes) BP 20722-44307, Nantes, France*

[55]*University of Tennessee, Knoxville, Tennessee 37996, USA*
[56]*Department of Physics, Tokyo Institute of Technology, Oh-okayama, Meguro, Tokyo 152-8551, Japan*
[57]*Institute of Physics, University of Tsukuba, Tsukuba, Ibaraki 305, Japan*
[58]*Vanderbilt University, Nashville, Tennessee 37235, USA*
[59]*Waseda University, Advanced Research Institute for Science and Engineering, 17 Kikui-cho, Shinjuku-ku, Tokyo 162-0044, Japan*
[60]*Weizmann Institute, Rehovot 76100, Israel*
[61]*Yonsei University, IPAP, Seoul 120-749, Korea*
(Received 11 May 2008; published 7 October 2008)

A comprehensive survey of event-by-event fluctuations of charged hadron multiplicity in relativistic heavy ions is presented. The survey covers Au+Au collisions at $\sqrt{s_{NN}} = 62.4$ and 200 GeV, and Cu+Cu collisions at $\sqrt{s_{NN}} = 22.5$, 62.4, and 200 GeV. Fluctuations are measured as a function of collision centrality, transverse momentum range, and charge sign. After correcting for nondynamical fluctuations due to fluctuations in the collision geometry within a centrality bin, the remaining dynamical fluctuations expressed as the variance normalized by the mean tend to decrease with increasing centrality. The dynamical fluctuations are consistent with or below the expectation from a superposition of participant nucleon-nucleon collisions based upon $p+p$ data, indicating that this dataset does not exhibit evidence of critical behavior in terms of the compressibility of the system. A comparison of the data with a model where hadrons are independently emitted from a number of hadron clusters suggests that the mean number of hadrons per cluster is small in heavy ion collisions.

DOI: 10.1103/PhysRevC.78.044902 PACS number(s): 25.75.Gz, 25.75.Nq, 21.65.Qr, 25.75.Ag

I. INTRODUCTION

Recent work with lattice gauge theory simulations has attempted to map out the phase diagram of quantum chromodynamics (QCD) in temperature and baryo-chemical potential (μ_B) using finite values of the up and down quark masses. The results of these studies indicate that the QCD phase diagram may contain a first-order transition line between the hadron gas phase and the strongly coupled quark-gluon plasma (sQGP) phase that terminates at a critical point [1]. This property is analogous to that observed in the phase diagram for many common liquids and other substances, including water. However, different model predictions and lattice calculations yield widely varying estimates of the location of the critical point on the QCD phase diagram [2]. Direct experimental observation of critical phenomena in heavy ion collisions would confirm the existence of the critical point, narrow down its location on the QCD phase diagram, and provide an important constraint for the QCD models.

The estimated value of energy densities achieved in heavy ion collisions at the BNL Relativistic Heavy Ion Collider (RHIC) exceeds the threshold for a phase transition from normal hadronic matter to partonic matter. Recent experimental evidence indicates that properties of the matter being produced include strong collective flow and large opacity to scattered quarks and gluons—the matter appears to behave much like a perfect fluid [3]. While measurements suggest the produced matter has properties that differ from normal nuclear matter, unambiguous evidence of the nature and location of any phase transition from normal nuclear matter has been elusive thus far. Described here is a search for direct evidence of a phase transition by measuring the fluctuations of the event-by-event multiplicities of produced charge particles in a variety of collision systems.

To illustrate how the measurement of charged particle multiplicity fluctuations can be sensitive to the presence of a phase transition, the isothermal compressibility of the system can be considered [4]. The isothermal compressibility is defined as

$$k_T = -1/V\,(\delta V/\delta P)_T\,, \tag{1}$$

where V is the volume, T is the temperature, and P is the pressure of the system. To relate the compressibility to measurements of multiplicity fluctuations, we assume that relativistic nucleus-nucleus collisions can be described as a thermal system in the grand canonical ensemble (GCE) [5]. The GCE can be applied to the case of measurements near midrapidity, since energy and conserved quantum numbers in this region can be exchanged with the rest of the system, which serves as a heat bath [6]. Detailed studies of multiplicity fluctuations in the canonical and microcanonical ensembles with the application of conservation laws can be found elsewhere [7,8]. In the GCE, the isothermal compressibility is directly related to the variance of the particle multiplicity as follows:

$$\langle (N - \langle N\rangle)^2\rangle = \mathrm{var}(N) = \frac{k_B T \langle N\rangle^2}{V} k_T, \tag{2}$$

where N is the particle multiplicity, $\langle N\rangle = \mu_N$ is the mean multiplicity, and k_B is the Boltzmann constant [9]. Here, multiplicity fluctuation measurements are presented in terms of the scaled variance, ω_N:

$$\omega_N = \frac{\mathrm{var}(N)}{\mu_N} = k_B T \frac{\mu_N}{V} k_T. \tag{3}$$

In a continuous, or second-order, phase transition, the compressibility diverges to an infinite value at the critical point.

*Deceased
†PHENIX spokesperson: jacak@skipper.physics.sunysb.edu

Near the critical point, this divergence is described by a power law in the variable $\epsilon = (T - T_C)/T_C$, where T_C is the critical temperature. Hence, the relationship between multiplicity fluctuations and the compressibility can be exploited to search for a clear signature of critical behavior by looking for the expected power law scaling of the compressibility,

$$k_T \propto \left(\frac{T - T_C}{T_C}\right)^{-\gamma} \propto \epsilon^{-\gamma}, \tag{4}$$

where γ is the critical exponent for isothermal compressibility [9]. If the QCD phase diagram contains a critical point, systems with a low value of baryo-chemical potential (μ_B) could pass through the cross-over region and undergo a continuous phase transition [2]. Recent estimates [10,11] of the behavior of the quark number susceptibility χ_q, which is proportional to the value of the isothermal compressibility of the system, predict that its value will increase by at least an order of magnitude close to the QCD critical point. Given that the scaled variance is proportional to k_T, measurements of charged particle multiplicity are expected to be a sensitive probe for critical behavior. In addition, within a scenario where droplets of QGP are formed during a first-order phase transition, the scaled variance of the multiplicity could increase by a factor of 10–100 [12].

Experimentally, a search for critical behavior is facilitated by the rich and varied dataset provided by RHIC. It is expected that the trajectory of the colliding system in the QCD phase diagram can be modified by varying the colliding energy [2]. If the system approaches close enough to the critical line for a long enough time period, then critical phenomena could be readily apparent through the measurement of multiplicity fluctuations [13]. It may also be possible to determine the critical exponents of the system. Nature tends to group materials into universality classes whereby all materials in the same universality class share identical values for their set of critical exponents. Although beyond the scope of this analysis, observation of critical behavior in heavy ion collisions and the subsequent measurement of the critical exponents could determine the universality class in which QCD is grouped, providing essential constraints for the models.

Charged particle multiplicity fluctuations have been measured in elementary collisions over a large range of collision energies [14–20]. Initial measurements of multiplicity fluctuations in minimum-bias O+Cu collisions at $\sqrt{s_{NN}} = 4.86$ GeV were made by BNL Experiment E802 [21], minimum-bias O+Au collisions at $\sqrt{s_{NN}} = 17.3$ GeV by CERN Experiment WA80 [22], and minimum-bias S+S, O+Au, and S+Au collisions at $\sqrt{s_{NN}} = 17.3$ GeV by CERN Experiment NA35 [23]. Recently, larger datasets have enabled the measurement of the centrality dependence of multiplicity fluctuations in Pb+Pb collisions at $\sqrt{s_{NN}} = 17.3$ GeV by CERN Experiment WA98 [24] and in Pb+Pb, C+C, and Si+Si collisions at $\sqrt{s_{NN}} = 17.3$ GeV by CERN Experiment NA49 [25]. The PHENIX Experiment at RHIC has performed an analysis of density correlations in longitudinal space with a differential analysis of charged particle multiplicity fluctuations in 200 GeV Au+Au collisions over the entire transverse momentum range [26]. Thus far, the fluctuation measurements in heavy ion collisions do not indicate significant signs of a phase transition. However, the full range of collision energies and species accessible by RHIC are yet to be explored.

Presented here is a comprehensive survey of multiplicity fluctuations of charged hadrons measured by the PHENIX Experiment at RHIC. The survey will cover the following collision systems: $\sqrt{s_{NN}} = 200$ GeV Au+Au, 62.4 GeV Au+Au, 200 GeV Cu+Cu, 62.4 GeV Cu+Cu, and 22.5 GeV Cu+Cu with comparisons to $\sqrt{s} = 200$ GeV $p+p$ collisions, which serve as a baseline measurement. The Au+Au data were taken during RHIC Run-4 (2004), the Cu+Cu data were taken during RHIC Run-5 (2005), and the $p+p$ data were taken during RHIC Run-3 (2003). Multiplicity fluctuations for each collision system with the exception of $p+p$ will also be presented as a function of centrality to help select the system volume. Multiplicity fluctuations will also be presented as a function of transverse momentum range and charge sign.

This paper is organized as follows: Sec. II will discuss the experimental apparatus and details; Sec. III will discuss the methods applied for the measurement of multiplicity fluctuations and the removal of nondynamical fluctuations due to fluctuations of the collision geometry within a centrality bin; Sec. IV will present the results and compare them to those of other models. Sec. V will present a discussion and summary of the results.

II. EXPERIMENTAL SETUP

The PHENIX detector consists of two central spectrometer arms designed for charged particle tracking, designated east and west, and two muon spectrometers designed for muon tracking and identification, designated north and south. The muon spectrometers are not used in this analysis. A comprehensive description of the PHENIX detector is documented elsewhere [27]. The analysis described here utilizes the central spectrometer arms, which consist of a set of tracking detectors [28], particle identification detectors [29], and an electromagnetic calorimeter [30]. The central spectrometer arms cover a rapidity range of $|\eta| < 0.35$, and each arm subtends 90° in azimuth. A detailed description of the algorithms and performance of the central arm track reconstruction and momentum reconstruction can be found in Ref. [31].

There are two detectors that are used for triggering, centrality determination, and event vertex determination. The beam-beam counters (BBCs) consist of 64 individual quartz Cherenkov counters that cover the full azimuthal angle in the pseudorapidity range $3.0 < |\eta| < 3.9$. The zero degree calorimeters (ZDCs) cover the pseudorapidity range $|\eta| > 6$ and measure the energy of spectator neutrons with an energy resolution of approximately 20%. More details about these detectors can be found in Ref. [32]. The collision vertex position is determined using timing information from the BBCs with an r.m.s. resolution for central Au+Au events of 6 mm along the beam axis. The collision vertex is required to be reconstructed within ± 30 cm from the center of the spectrometer. The BBCs also provide a minimum-bias (MB) event trigger.

Because of the large dynamic range in $\sqrt{s_{NN}}$ covered by this analysis, it is necessary to implement algorithms that are dependent on the collision energy for the determination of the centrality of each event. In Au+Au collisions at $\sqrt{s_{NN}} =$ 200 GeV, the centrality of the collision is determined by using correlations of the total energy deposited in the ZDCs with the total charge deposited in the BBCs as described in Ref. [33]. However, in 200 GeV Cu+Cu, 62.4 GeV Cu+Cu, and 62.4 GeV Au+Au collisions, the resolving power of the ZDCs is insufficient to significantly contribute to the centrality definition. Therefore, only the total charge deposited in the BBCs is used to determine centrality in these collision systems, as described in Ref. [33]. Using the 200 GeV Au+Au data, it has been verified that application of the BBC-ZDC correlation for the centrality definition as opposed to the BBC-only definition shows no significant differences in the values of the charged hadron fluctuation quantities presented here as a function of centrality.

The location of the BBCs are fixed for every collision energy. At the lowest collision energy ($\sqrt{s_{NN}} = 22.5$ GeV), it becomes kinematically possible for spectator nucleons to fall within the acceptance of the BBC. This results in a BBC response in its total charge sum that is no longer linear with the number of participating nucleons ($N_{\rm part}$). In this case, it becomes necessary to define the centrality using the total charged particle multiplicity in pad chamber 1 (PC1) [28]. PC1 is chosen because of its fine segmentation, high tracking efficiency, and relative proximity to the event vertex. Details on this procedure are also described in Ref. [33]. For all collision species and energies, the distribution of the number of participants was determined using a Monte Carlo simulation based upon the Glauber model [33,34].

The number of minimum-bias events analyzed for each dataset are 25.6×10^6 events for 200 GeV Au+Au, 24.9×10^6 events for 62.4 GeV Au+Au, 15.0×10^6 events for 200 GeV Cu+Cu, 12.2×10^6 events for 62.4 GeV Cu+Cu, 5.5×10^6 events for 22.5 GeV Cu+Cu, and 2.7×10^6 events for 200 GeV $p+p$. Only a fraction of the complete 200 GeV Au+Au, Cu+Cu, and $p+p$ datasets are analyzed, but this fraction is more than sufficient for this analysis.

The charged particle multiplicity is determined on an event-by-event basis by counting the number of unambiguous reconstructed tracks in the drift chamber originating from the collision vertex that have corresponding hits in PC1 and PC3. Track selection includes cuts on reconstructed tracks in the drift chamber to reduce double-counted ghost tracks to a negligible level. To minimize background originating from the magnets, reconstructed tracks are required to lie within ± 75 cm from the center of the drift chamber along the beam axis. This requirement reduces the pseudorapidity range of reconstructed tracks to $|\eta| < 0.26$. The ring imaging Cherenkov detector (RICH) is utilized to reduce background from electrons resulting from photon conversions.

Although the central arm spectrometer covers a total azimuthal range of π radians, detector and tracking inefficiencies reduce the effective average azimuthal active area to 2.1 radians for the 200 Gev Au+Au and 200 GeV $p+p$ datasets, and 2.0 radians for the other datasets. Fluctuation quantities are quoted for these acceptances separately for each dataset. The differences in acceptance between datasets, which are due to variations in the detector over the three-year period in which the data were collected, result in less than a 1% variation in the fluctuation quantities quoted here.

III. DATA ANALYSIS

Multiplicity fluctuations of charged particles, designated $\omega_{\rm ch}$, can be generally defined [35] as

$$\omega_{\rm ch} = \frac{\langle N_{\rm ch}^2 \rangle - \langle N_{\rm ch} \rangle^2}{\langle N_{\rm ch} \rangle} = \frac{\sigma_{\rm ch}^2}{\mu_{\rm ch}}, \tag{5}$$

where $N_{\rm ch}$ is the charged particle multiplicity. Simply stated, the fluctuations can be quoted as the variance of the multiplicity ($\sigma_{\rm ch}^2$) normalized by the mean ($\mu_{\rm ch} = \langle N_{\rm ch} \rangle$). This is also referred to as the scaled variance [25]. If the multiplicity distribution is Poissonian, the scaled variance is 1.0.

It has been well established that charged particle multiplicity distributions in elementary nucleon-nucleon collisions can be described by the negative binomial distribution (NBD) [17–19]. The NBD also describes well the multiplicity distributions in heavy ion collisions [21,23]. The NBD of an integer n is defined as

$$P(n) = \frac{\Gamma(n + k_{\rm NBD})}{\Gamma(n+1)\Gamma(k_{\rm NBD})} \frac{(\mu_{\rm ch}/k_{\rm NBD})^n}{(1 + \mu_{\rm ch}/k_{\rm NBD})^{n+k_{\rm NBD}}}, \tag{6}$$

where $P(n)$ is normalized to 1.0 over the range $0 \leqslant n \leqslant \infty$, $\mu_{\rm ch} = \langle N_{\rm ch} \rangle = \langle n \rangle$, and $k_{\rm NBD}$ is an additional parameter. The NBD reduces to a Poisson distribution in the limit $k_{\rm NBD} \to \infty$. The NBD variance and mean is related to $k_{\rm NBD}$ as follows:

$$\frac{\sigma_{\rm ch}^2}{\mu_{\rm ch}^2} = \frac{\omega_{\rm ch}}{\mu_{\rm ch}} = \frac{1}{\mu_{\rm ch}} + \frac{1}{k_{\rm NBD}}. \tag{7}$$

Hence, the scaled variance is given by

$$\omega_{\rm ch} = 1 + \frac{\mu_{\rm ch}}{k_{\rm NBD}}. \tag{8}$$

A useful property of the negative binomial distribution concerns its behavior when a population that follows the NBD is subdivided randomly by repeated independent trials with a constant probability onto smaller subsets. This results in a binomial decomposition of the original population into subsets that also follow the NBD with the same value of $k_{\rm NBD}$ [21]. This property can be applied to estimate the behavior of multiplicity fluctuations as a function of acceptance, assuming that there are no significant correlations present over the acceptance range being examined. Starting with an original NBD sample with mean $\mu_{\rm ch}$ and scaled variance $\omega_{\rm ch}$, a sample in a fractional acceptance with mean $\mu_{\rm acc}$ is also described by an NBD distribution. An acceptance fraction can be defined as $f_{\rm acc} = \mu_{\rm acc}/\mu_{\rm ch}$. The scaled variance of the subsample from Eq. (8) is thus

$$\omega_{\rm acc} = 1 + (\mu_{\rm acc}/k_{\rm NBD}) = 1 + (f_{\rm acc}\mu_{\rm ch}/k_{\rm NBD}). \tag{9}$$

Since $k_{\rm NBD}$ is identical for the two samples, $\mu_{\rm ch}/k_{\rm NBD} = \omega_{\rm ch} - 1$ can be substituted, yielding the following relation between

TABLE I. Tabulation of the charged hadron multiplicity data and corrections for $0.2 < p_T < 2.0$ GeV/c. The errors quoted for $\mu_{\rm ch}$ and $\sigma_{\rm ch}$ represent their time-dependent systematic error. The errors quoted for $\omega_{\rm ch,dyn}$ and $1/k_{\rm NBD,dyn}$ represent their total systematic error. For each dataset, the first three columns give the species, collision energy, and geometric correction factor $f_{\rm geo}$, respectively.

Species	$\sqrt{s_{NN}}$ (GeV)	$f_{\rm geo}$	$N_{\rm part}$	$\mu_{\rm ch}$	Raw $\sigma^2_{\rm ch}$	$\omega_{\rm ch,dyn}$	$1/k_{\rm NBD,dyn}$	χ^2/dof
			351	61.0 ± 1.1	75.6 ± 1.9	1.10 ± 0.02	$1.45 \times 10^{-03} \pm 2.2 \times 10^{-04}$	37.1/58
			299	53.1 ± 1.0	71.8 ± 1.8	1.15 ± 0.02	$2.45 \times 10^{-03} \pm 2.7 \times 10^{-04}$	38.6/56
			253	45.8 ± 0.8	65.2 ± 1.5	1.17 ± 0.02	$3.41 \times 10^{-03} \pm 2.9 \times 10^{-04}$	34.0/54
			215	39.1 ± 0.7	57.8 ± 1.6	1.19 ± 0.03	$4.53 \times 10^{-03} \pm 3.6 \times 10^{-04}$	29.1/53
			181	32.6 ± 0.6	49.7 ± 1.3	1.21 ± 0.03	$5.95 \times 10^{-03} \pm 5.1 \times 10^{-04}$	24.5/50
Au+Au	200	0.37 ± 0.027	151	27.4 ± 0.5	41.4 ± 1.0	1.20 ± 0.03	$6.86 \times 10^{-03} \pm 5.5 \times 10^{-04}$	20.7/46
			125	22.3 ± 0.4	33.8 ± 0.9	1.20 ± 0.03	$8.47 \times 10^{-03} \pm 7.1 \times 10^{-04}$	11.9/41
			102	17.8 ± 0.3	26.7 ± 0.6	1.19 ± 0.02	$1.05 \times 10^{-02} \pm 9.0 \times 10^{-04}$	16.6/37
			82	14.2 ± 0.3	20.8 ± 0.6	1.17 ± 0.02	$1.20 \times 10^{-02} \pm 1.0 \times 10^{-03}$	37.8/33
			65	10.8 ± 0.2	16.0 ± 0.4	1.18 ± 0.02	$1.64 \times 10^{-02} \pm 1.3 \times 10^{-03}$	37.8/28
			51	8.3 ± 0.2	12.1 ± 0.3	1.17 ± 0.02	$2.06 \times 10^{-02} \pm 2.0 \times 10^{-03}$	53.8/24
			345	44.0 ± 0.3	53.6 ± 0.5	1.08 ± 0.02	$1.63 \times 10^{-03} \pm 2.0 \times 10^{-04}$	14.6/54
			296	37.3 ± 0.2	48.3 ± 0.3	1.11 ± 0.02	$2.63 \times 10^{-03} \pm 2.6 \times 10^{-04}$	13.8/53
			250	31.0 ± 0.2	39.8 ± 0.4	1.10 ± 0.02	$3.00 \times 10^{-03} \pm 3.0 \times 10^{-04}$	14.0/50
			211	25.4 ± 0.2	33.6 ± 0.5	1.12 ± 0.02	$4.21 \times 10^{-03} \pm 4.4 \times 10^{-04}$	8.36/44
			177	20.8 ± 0.1	27.8 ± 0.2	1.12 ± 0.02	$5.34 \times 10^{-03} \pm 5.5 \times 10^{-04}$	19.2/40
Au+Au	62.4	0.33 ± 0.031	148	16.6 ± 0.1	22.8 ± 0.3	1.13 ± 0.02	$7.43 \times 10^{-03} \pm 7.8 \times 10^{-04}$	25.9/37
			123	13.1 ± 0.1	18.1 ± 0.2	1.13 ± 0.02	$9.61 \times 10^{-03} \pm 9.7 \times 10^{-04}$	34.3/33
			102	10.4 ± 0.1	14.9 ± 0.1	1.15 ± 0.02	$1.38 \times 10^{-02} \pm 1.4 \times 10^{-03}$	44.5/28
			82	7.8 ± 0.1	11.1 ± 0.1	1.14 ± 0.02	$1.76 \times 10^{-02} \pm 1.9 \times 10^{-03}$	50.9/24
			66	5.9 ± 0.04	8.3 ± 0.1	1.14 ± 0.02	$2.37 \times 10^{-02} \pm 3.8 \times 10^{-03}$	45.4/20
			51	4.1 ± 0.03	5.8 ± 0.04	1.13 ± 0.02	$3.08 \times 10^{-02} \pm 9.1 \times 10^{-03}$	36.2/17
			104	19.3 ± 0.3	25.7 ± 0.8	1.14 ± 0.03	$6.93 \times 10^{-03} \pm 1.3 \times 10^{-03}$	24.3/30
			92	16.0 ± 0.2	21.9 ± 0.5	1.15 ± 0.03	$9.26 \times 10^{-03} \pm 1.5 \times 10^{-03}$	21.7/31
			79	13.5 ± 0.2	18.8 ± 0.4	1.16 ± 0.03	$1.15 \times 10^{-02} \pm 2.1 \times 10^{-03}$	19.4/29
Cu+Cu	200	0.40 ± 0.047	67	11.1 ± 0.2	15.3 ± 0.3	1.15 ± 0.03	$1.36 \times 10^{-02} \pm 2.0 \times 10^{-03}$	29.9/26
			57	9.2 ± 0.1	13.0 ± 0.3	1.17 ± 0.03	$1.75 \times 10^{-02} \pm 2.5 \times 10^{-03}$	26.0/25
			48	7.5 ± 0.1	10.5 ± 0.2	1.16 ± 0.03	$2.14 \times 10^{-02} \pm 3.6 \times 10^{-03}$	30.6/22
			40	6.2 ± 0.1	8.7 ± 0.2	1.17 ± 0.03	$2.69 \times 10^{-02} \pm 4.8 \times 10^{-03}$	28.6/20
			33	4.9 ± 0.06	6.8 ± 0.1	1.16 ± 0.03	$3.12 \times 10^{-02} \pm 8.5 \times 10^{-03}$	45.7/18
			104	12.6 ± 0.1	16.7 ± 0.2	1.10 ± 0.03	$8.16 \times 10^{-03} \pm 1.7 \times 10^{-03}$	40.6/31
			92	11.0 ± 0.1	16.2 ± 0.1	1.15 ± 0.04	$1.35 \times 10^{-02} \pm 2.7 \times 10^{-03}$	64.2/30
Cu+Cu	62.4	0.32 ± 0.063	79	9.2 ± 0.1	14.3 ± 0.2	1.18 ± 0.05	$1.92 \times 10^{-02} \pm 3.9 \times 10^{-03}$	37.0/28
			67	7.7 ± 0.1	12.0 ± 0.2	1.18 ± 0.05	$2.29 \times 10^{-02} \pm 4.6 \times 10^{-03}$	32.0/26
			57	6.0 ± 0.1	9.1 ± 0.1	1.17 ± 0.05	$2.85 \times 10^{-02} \pm 5.9 \times 10^{-03}$	32.0/23
			48	5.1 ± 0.1	8.1 ± 0.1	1.19 ± 0.05	$3.66 \times 10^{-02} \pm 8.0 \times 10^{-03}$	29.2/21
			92	9.1 ± 0.04	10.3 ± 0.1	1.04 ± 0.02	$4.31 \times 10^{-03} \pm 9.8 \times 10^{-04}$	7.45/24
Cu+Cu	22.5	0.30 ± 0.064	58	4.9 ± 0.02	5.8 ± 0.04	1.06 ± 0.02	$1.11 \times 10^{-02} \pm 2.9 \times 10^{-03}$	71.1/17

the scaled variances of the original and fractional acceptance samples:

$$\omega_{\rm acc} = 1 + f_{\rm acc}(\omega_{\rm ch} - 1). \quad (10)$$

Thus, the measured scaled variance will decrease as the acceptance is decreased, while $k_{\rm NBD}$ remains constant, if there are no additional correlations present over the given acceptance range.

Figures 1 and 2 show the uncorrected, or raw, multiplicity distributions in the p_T range $0.2 < p_T < 2.0$ GeV for all centralities from each collision system overlaid with fits to negative binomial distributions (dashed lines). For presentation purposes, the data have been normalized on the horizontal axis by the mean of the distribution and scaled on the vertical axis by the successive amounts stated in the legend. The NBD fits describe the data distributions very well for all collision systems, centralities, and p_T ranges. Hence, the mean and variance of the multiplicity distributions presented here are all extracted from NBD fits. The results of each fit for $0.2 < p_T < 2.0$ GeV are compiled in Table I. The mean and standard deviation of each fit for $0.2 < p_T < 2.0$ GeV are plotted in Fig. 3.

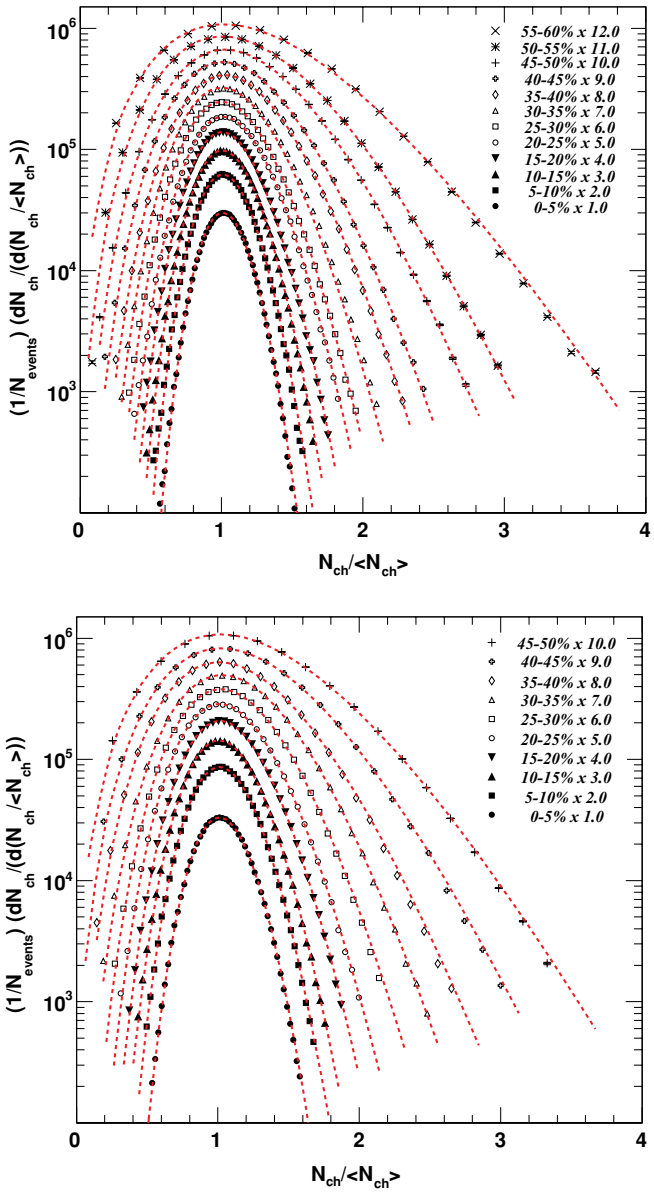

FIG. 1. (Color online) Uncorrected multiplicity distributions of charged hadrons with $0.2 < p_T < 2.0$ GeV/c for 200 (upper) and 62.4 (lower) GeV Au+Au collisions. The dashed lines are fits to the NBD. The data are normalized to the mean and scaled by the amounts in the legend.

Each dataset was taken over spans of several days to several weeks, all spanning three separate RHIC running periods. During these periods, changes in the total acceptance and efficiency of the central arm spectrometers cause the fluctuation measurements to vary, thus introducing an additional systematic error to the results. This systematic error was minimized by requiring that the dataset is stable in quantities that are sensitive to detector variations, including the mean charged particle multiplicity, mean collision vertex position, and mean centrality. A time-dependent systematic error is applied independently to each point by calculating the standard deviation of the scaled variance calculated from subsets of the entire dataset, with each subset containing about 1×10^6

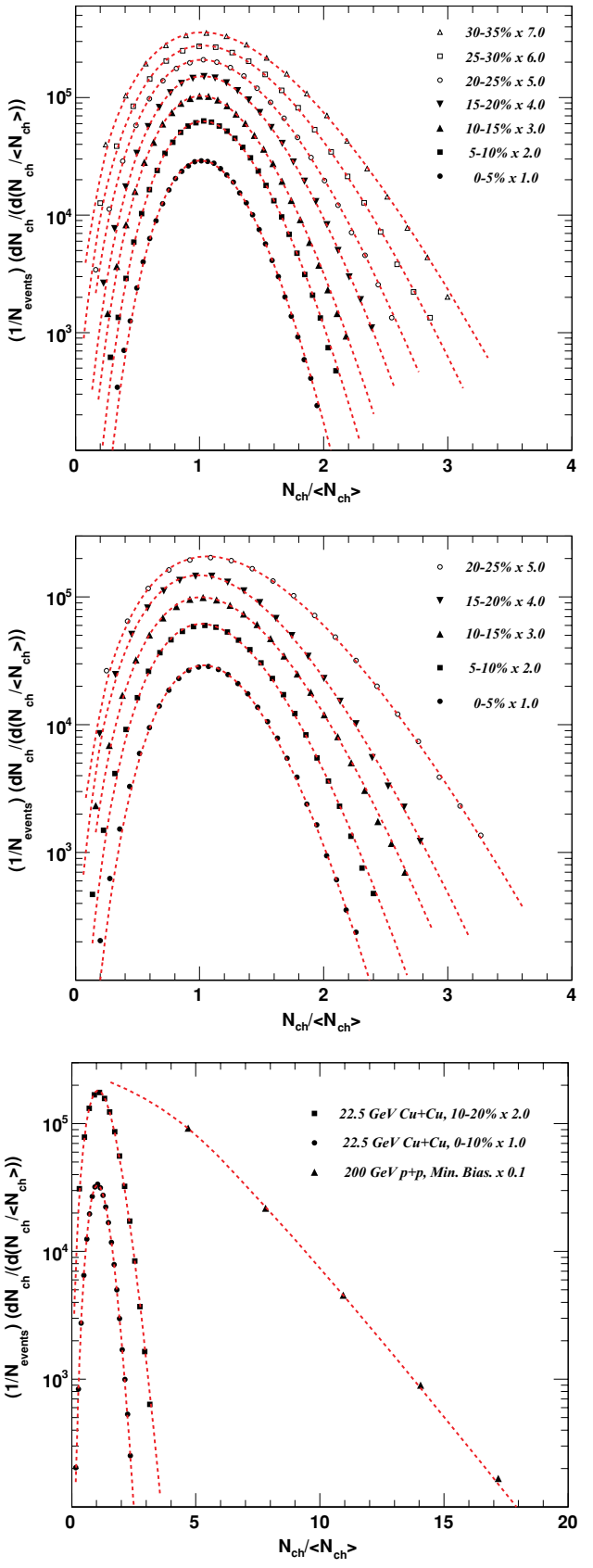

FIG. 2. (Color online) Same as Fig. 1, but for 200 (upper), 62.4 (middle), and 22.5 (lower) GeV Cu+Cu and 200 GeV $p+p$ (lower) collisions.

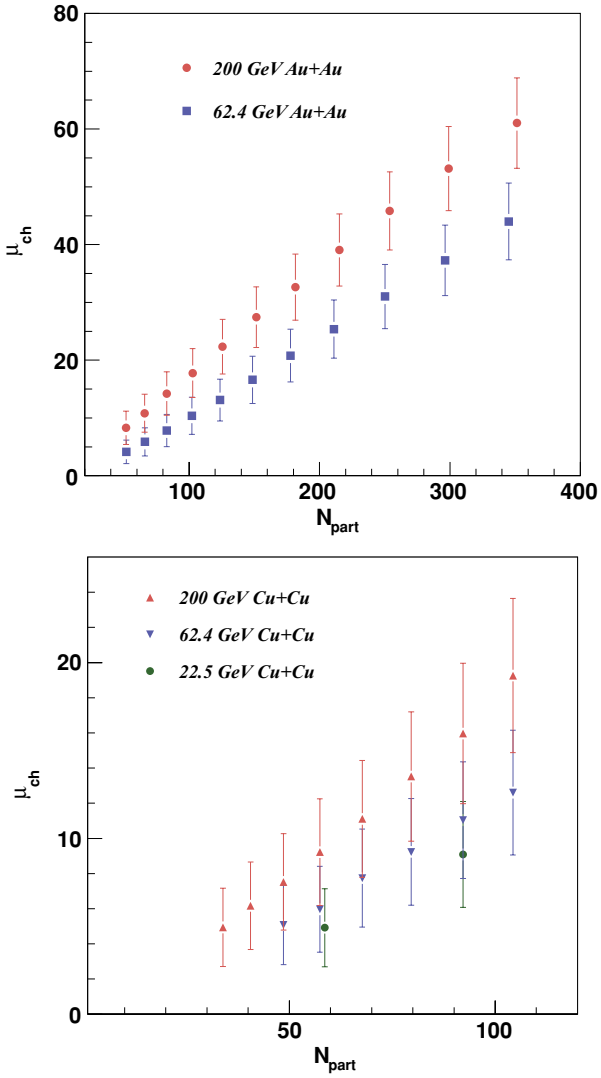

FIG. 3. (Color online) Mean from the NBD fit as a function of N_{part} for Au+Au (upper) and Cu+Cu (lower) collisions over the range $0.2 < p_T < 2.0\,\text{GeV}/c$. The mean shown is within the PHENIX central arm spectrometer acceptance. The error bars represent the standard deviation of the distribution.

events. These systematic errors are applied to all subsequent results.

The tracking efficiency of the PHENIX central arm spectrometer is dependent on centrality, especially in the most central 200 GeV Au+Au collisions [36]. With the assumption that tracking inefficiencies randomly affect the multiplicity distribution on an event-by-event basis, the effect of inefficiencies on the scaled variance can be estimated using Eq. (10), where f_{acc} is replaced by the inverse of the tracking efficiency $1/f_{\text{eff}}$. Tracking efficiency affects the value of the scaled variance by 1.5% at the most. The scaled variance has been corrected for tracking inefficiency as a function of centrality for all species. The uncertainty of the tracking efficiency estimate is typically 2% and has been propagated into the systematic error estimate on a point-by-point basis.

Because of the nonzero width of the centrality bin selection from the data, each centrality bin necessarily selects a range of impact parameters. This introduces a nondynamical fluctuation component to the measured multiplicity fluctuations due to the resulting fluctuations in the geometry of the collisions [26,37]. Therefore, it is necessary to estimate the magnitude of the geometry fluctuation component so that only the interesting dynamical fluctuations remain. The most practical method for estimating the geometry fluctuation component is with a model of heavy ion collisions. The URQMD [38] and HSD [39,40] models have previously been applied for this purpose. Here, the HIJING event generator [41] is chosen for this estimate, because it reproduces well the mean multiplicity in heavy ion collisions [33] as measured by the PHENIX detector. HIJING includes multiple minijet production based upon QCD-inspired models, soft excitation, nuclear shadowing of parton distribution functions, and the interaction of jets in dense nuclear matter. The estimate is performed individually for each centrality bin, collision system, and p_T range using the following procedure. First, HIJING is run with an impact parameter distribution that is sampled from a Gaussian distribution with a mean and standard deviation that, for a given centrality bin, reproduces the distributions of the charge deposited in the BBC and the energy deposited in the ZDC (for 200 GeV Au+Au). Second, HIJING is run at a fixed impact parameter with a value identical to the mean of the Gaussian distribution in the first run. For each centrality bin, 12,000 HIJING events are processed for each impact parameter selection. The scaled variance for each impact parameter selection, ω_{Gauss} and ω_{fixed}, is extracted and the measured scaled variance is corrected as the fractional deviation from a scaled variance of 1.0 of a Poisson distribution as follows:

$$\omega_{\text{ch,dyn}} - 1 = \frac{\omega_{\text{fixed}} - 1}{\omega_{\text{Gauss}} - 1}(\omega_{\text{ch,raw}} - 1) = f_{\text{geo}}(\omega_{\text{ch,raw}} - 1), \tag{11}$$

where $\omega_{\text{ch,dyn}}$ represents the estimate of the remaining dynamical multiplicity fluctuations and $\omega_{\text{ch,raw}}$ represents the uncorrected multiplicity fluctuations. Since the correction f_{geo} is calculated as a ratio of the two running conditions of the simulation, most multiplicity fluctuations intrinsic to the model should be canceled. The correction always reduces the magnitude of the measured scaled variance. Note that the value of f_{geo} is mathematically identical when applied to the inverse of k_{NBD}:

$$k^{-1}_{\text{NBD,dyn}} = f_{\text{geo}} k^{-1}_{\text{NBD}}. \tag{12}$$

The resulting geometrical correction factors for each species are constant as a function of centrality, therefore a single correction factor is calculated for each transverse momentum range by fitting the correction factors as a function of N_{part} to a constant. This behavior is expected, since centrality bins are defined to be constant percentages of the total geometric cross section. The correction factors for each transverse momentum range for a given collision species are consistent with each other, that is, they are independent of transverse momentum. The standard deviation of the individual geometrical correction factors from the linear fits as a function of N_{part} are included in the systematic error of the correction factor estimation and propagated

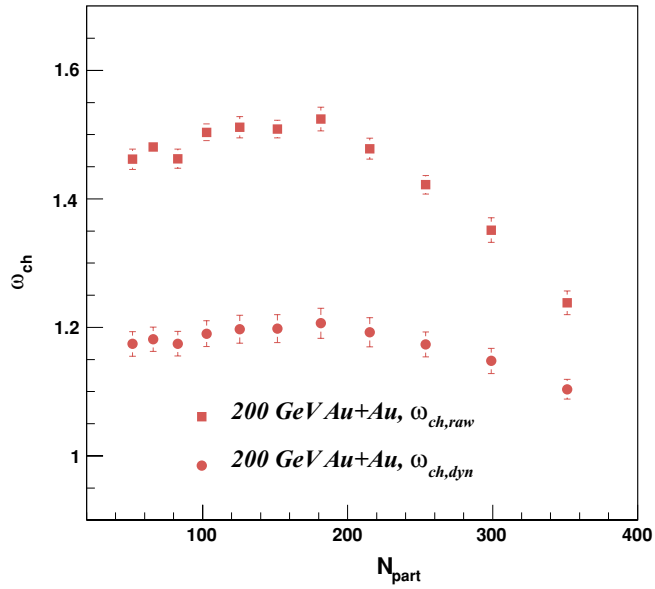

FIG. 4. (Color online) Fluctuations expressed as the scaled variance as a function of centrality for 200 GeV Au+Au collisions in the range $0.2 < p_T < 2.0$ GeV/c. Shown are the uncorrected fluctuations, $\omega_{\mathrm{ch,raw}}$, along with fluctuations after correcting for the estimated contribution from geometry fluctuations using Eq. (11), $\omega_{\mathrm{ch,dyn}}$.

into the total systematic error for each point in $\omega_{\mathrm{ch,dyn}}$ and $k_{\mathrm{NBD,dyn}}$. For $0.2 < p_T < 2.0$ GeV/c, the geometrical correction factors f_{geo} and systematic errors from the fit are 0.37 ± 0.027 for 200 GeV Au+Au, 0.33 ± 0.031 for 62.4 GeV Au+Au, 0.40 ± 0.047 for 200 GeV Cu+Cu, 0.32 ± 0.063 for 62.4 GeV Cu+Cu, and 0.30 ± 0.064 for 22.5 GeV Cu+Cu. The extraction of the geometrical correction factors are inherently model dependent and are also dependent on the accuracy with which the centrality detectors are modeled. The effect of the latter dependence has been studied by also calculating the correction factors using constant but nonoverlapping impact parameter distributions for each centrality bin and comparing them with the correction factors using the Gaussian impact parameter distributions. For all p_T ranges, an additional fraction of the value of $\omega_{\mathrm{ch,dyn}}$ or $k^{-1}_{\mathrm{NBD,dyn}}$ has been included in the final systematic errors for these quantities. The magnitude of this systematic error is 8% for 200 GeV Au+Au, 8% for 62.4 GeV Au+Au, 11% for 200 GeV Cu+Cu, 17% for 62.4 GeV Cu+Cu, and 25% for 22.5 GeV Cu+Cu. A sample comparison of the scaled variance before and after the application of the geometrical correction factor is shown for the 200 GeV Au+Au dataset in Fig. 4.

IV. RESULTS

The scaled variance as a function of the number of participating nucleons N_{part} over the p_T range $0.2 < p_T < 2.0$ GeV/c is shown in Fig. 5. For all centralities, the scaled variance values consistently lie above the Poisson distribution value of 1.0. In all collision systems, the minimum scaled variance occurs in the most central collisions and then begins to increase as the centrality decreases. In 200 GeV Au+Au

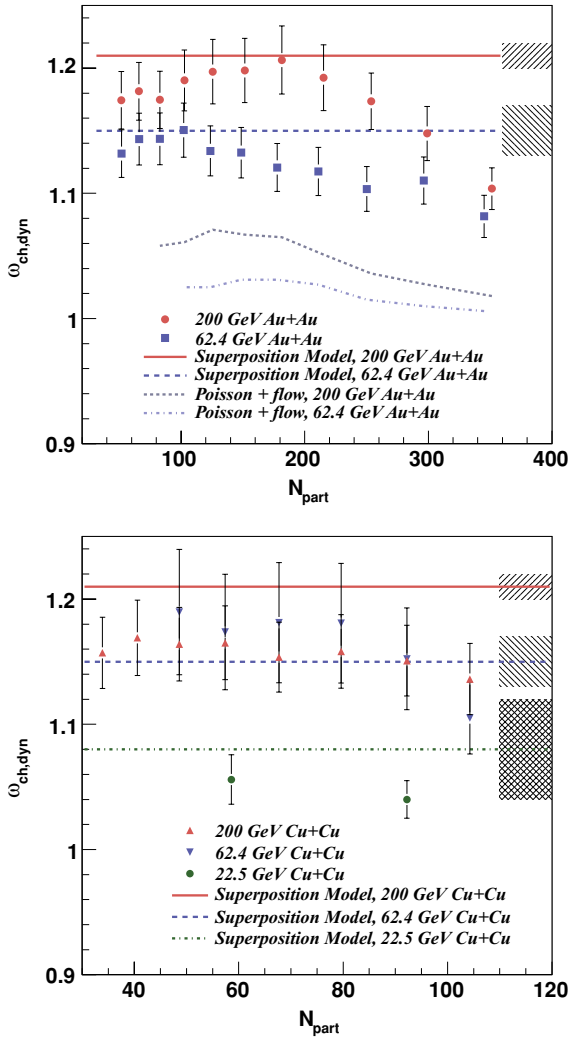

FIG. 5. (Color online) Fluctuations expressed as the scaled variance as a function of N_{part} for Au+Au (upper) and Cu+Cu (lower) collisions for $0.2 < p_T < 2.0$ GeV/c. The estimated contribution from geometry fluctuations has been removed. Results from the superposition model are overlaid with the shaded regions representing a one standard deviation range of the prediction for the fluctuation magnitude derived from $p+p$ collision data. Also shown (upper) is the estimated contribution from noncorrelated particle emission with the Poisson distribution of the scaled variance of 1.0 with the addition of elliptic flow in 200 and 62 GeV Au+Au collisions.

collisions, this increase is only observed for $N_{\mathrm{part}} > 200$. For $N_{\mathrm{part}} < 200$, the magnitude of $\omega_{\mathrm{ch,dyn}}$ suggests a slight decrease but is consistent with a constant value. In 62.4 GeV Au+Au collisions, the increase in $\omega_{\mathrm{ch,dyn}}$ with decreasing centrality is observed only over the range $N_{\mathrm{part}} > 110$. The source of the qualitative differences between the 200 and 62.4 GeV Au+Au collisions are not known, although some of the differences could be explained by the increased contribution from hard scattering processes at 200 GeV compared to 62.4 GeV. Studies performed by varying the centrality selection cuts establish that the differences are not due to the differences in the centrality selection algorithm. A similar centrality-dependent trend of the scaled variance has also been observed at the

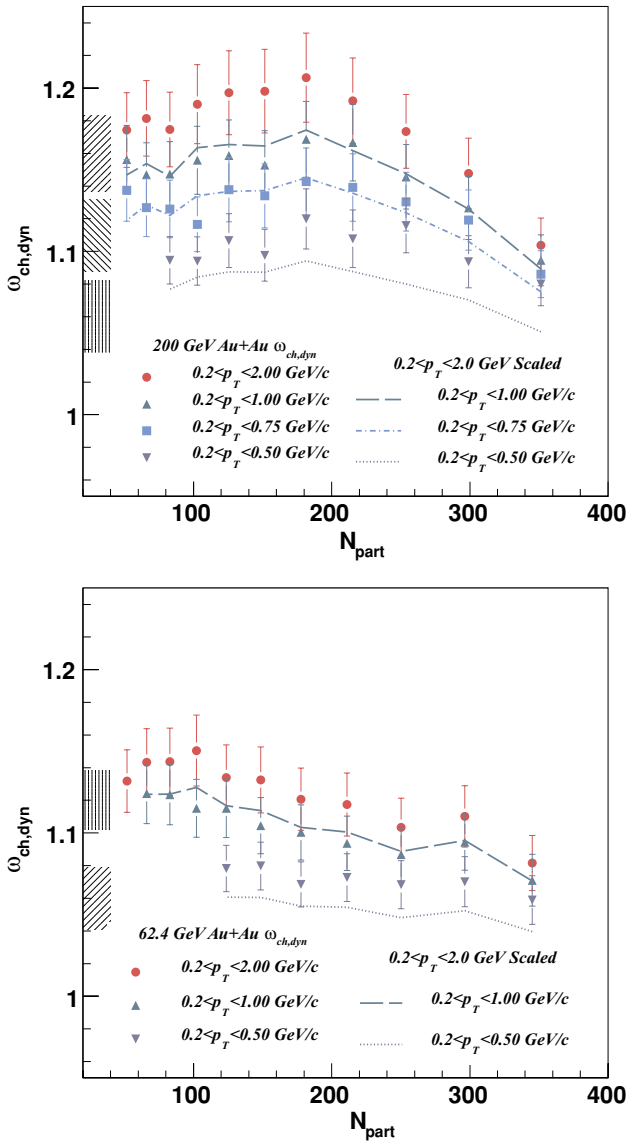

FIG. 6. (Color online) Scaled variance for 200 and 62.4 GeV Au+Au collisions plotted as a function of N_{part} for several p_T ranges. The lines represent the data for the reference range $0.2 < p_T < 2.0$ scaled down using the mean multiplicity in each successive p_T range. The shaded areas represent the systematic errors from the reference range.

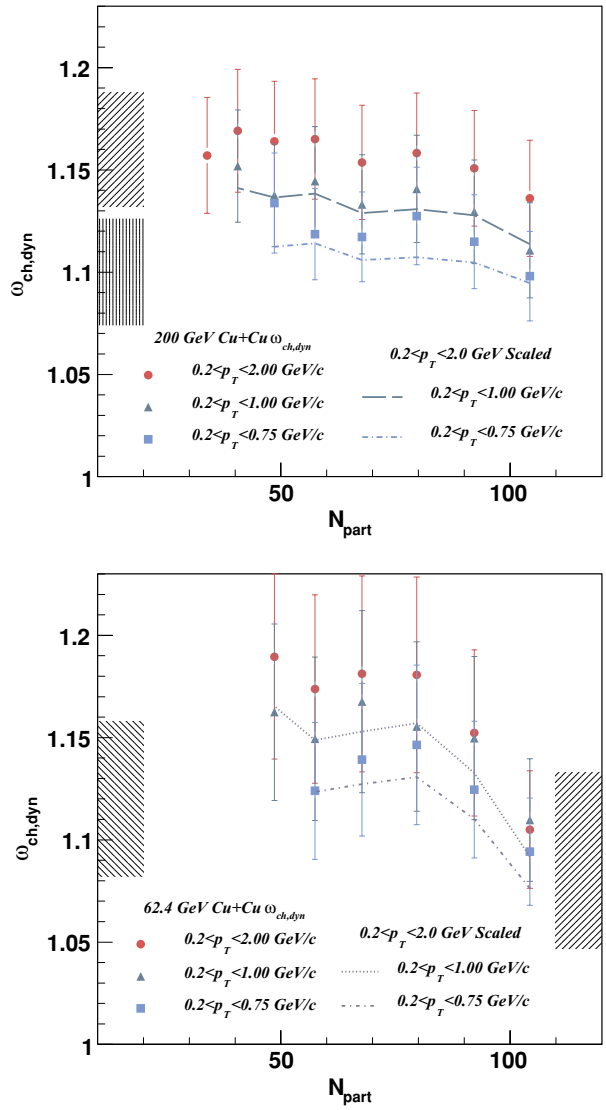

FIG. 7. (Color online) Same as Fig. 6, but for Cu+Cu collisions.

CERN Super Proton Synchrotron (SPS) in low-energy Pb+Pb collisions at $\sqrt{s_{NN}} = 17.3$ GeV and at forward rapidities ($1.1 < y_{\text{c.m.}} < 2.6$), measured by experiment NA49 [25], where the hard scattering contribution is expected to be small. The 200 GeV Cu+Cu data exhibit a weaker decrease in the scaled variance for more central collisions. The 62.4 GeV Cu+Cu scaled variance values are consistently above those from the 200 GeV Cu+Cu dataset, but the two are consistent within the systematic errors for all centralities.

The scaled variance has been studied as a function of the p_T range over which the multiplicity distributions are measured in order to determine if any significant p_T-dependent dynamical fluctuations are present. Results for several p_T ranges from $0.2 < p_T < 2.0$ down to $0.2 < p_T < 0.5$ GeV/c are shown in Figs. 6 and 7. In the absence of p_T-dependent dynamical fluctuations, restricting the p_T range should reduce the scaled variance in the same manner as for a fractional acceptance. Similar to Eq. (10),

$$\omega_{p_T} = 1 + f_{p_T}(\omega_{\text{ref}} - 1), \tag{13}$$

where ω_{p_T} represents the fluctuations in the p_T range of interest, ω_{ref} represents the fluctuations in the reference p_T range, and $f_{p_T} = \mu_{p_T}/\mu_{\text{ref}}$ is the ratio of the mean multiplicity in the two ranges. Also shown are curves representing the expected scaling of the fluctuations using the range $0.2 < p_T < 2.0$ GeV/c as the reference range. The shaded regions reflect the systematic errors of the reference range. For all p_T ranges, the scaled fluctuation curves are consistent with the data, indicating that no significant p_T dependence is observed, although the data in the range $0.2 < p_T < 0.5$ GeV are consistently above the scaled reference curves. The p_T dependence can also be examined more directly with the parameter k_{NBD} from the NBD fits. Substitution of the scaled variance in Eq. (8) into Eq. (13) shows that k_{NBD} should be

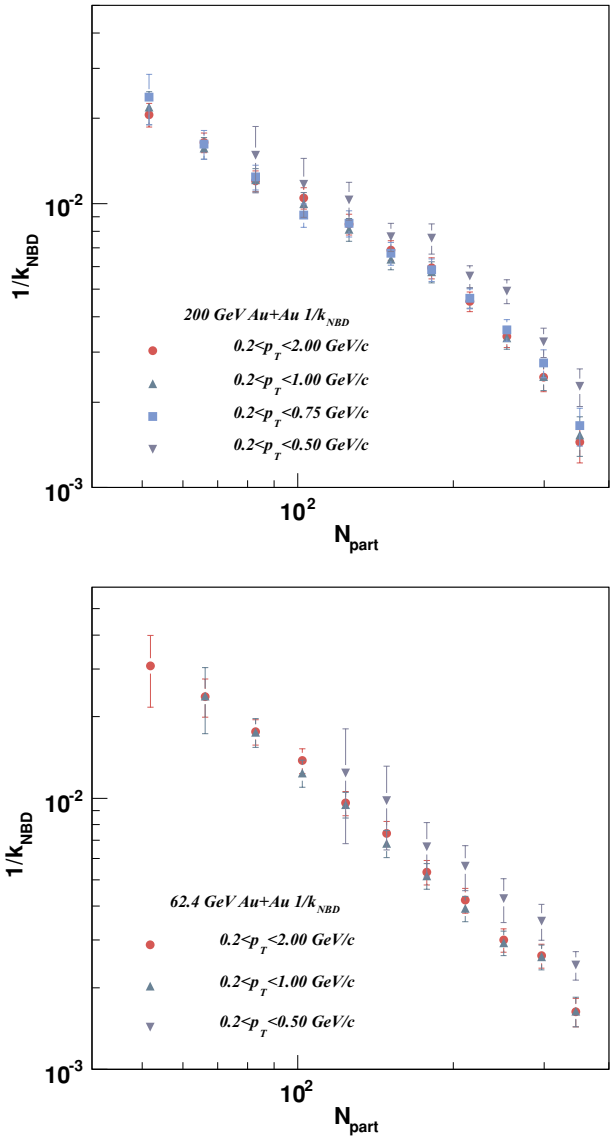

FIG. 8. (Color online) Inverse of the parameter k_{NBD} from the NBD fits for 200 and 62.4 GeV Au+Au collisions. The fluctuations are plotted as a function of N_{part} for several p_T ranges.

independent of p_T in the absence of p_T-dependent dynamical fluctuations. As shown in Figs. 8 and 9, there is no significant p_T-dependence of the observed values of k_{NBD}.

The scaled variance as a function of the charge sign of the charged hadrons is shown in Fig. 10 for 200 GeV Au+Au collisions in the p_T range $0.2 < p_T < 2.0$ GeV/c in order to investigate any Coulomb-based contributions to the fluctuations. In the absence of additional dynamic fluctuations, the scaled variance for positively or negatively charged hadrons should be reduced from the inclusive charged hadron value by

$$\omega_{+-} = 1 + f_{+-}(\omega_{\mathrm{ch}} - 1), \tag{14}$$

where ω_{+-} are the fluctuations for positive or negative particles, ω_{ch} are the fluctuations for inclusive charged hadrons, and $f_{+-} = \mu_{+-}/\mu_{\mathrm{ch}}$ is the ratio of the mean multiplicities. The scaled variance from the positive and negative hadrons

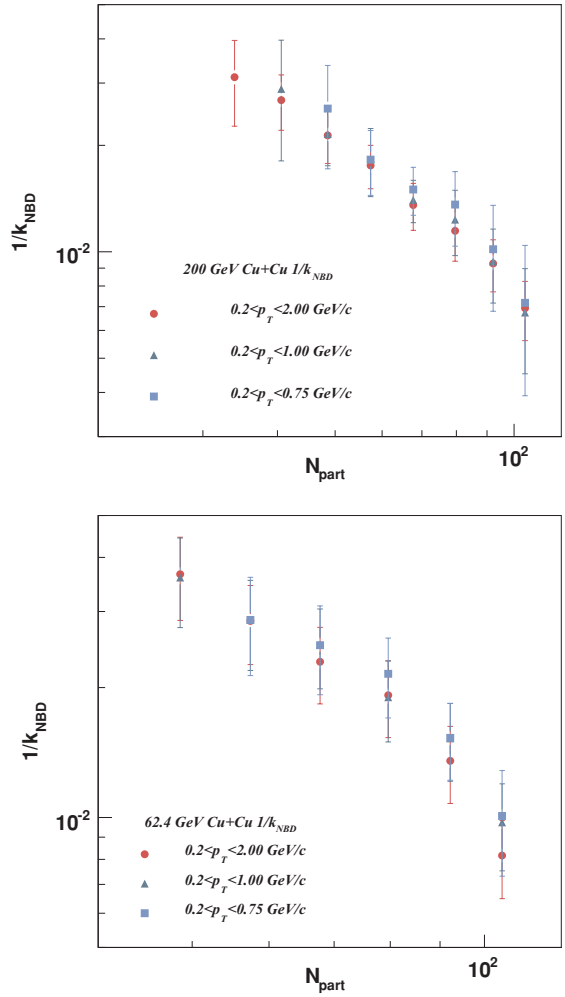

FIG. 9. (Color online) Same as Fig. 8, but for Cu+Cu collisions.

are consistent with each other and with the expected reduction of the inclusive charged hadron fluctuations.

V. DISCUSSION

A. Comparisons with a participant superposition model

It is informative to compare fluctuations in relativistic heavy ion collisions to what can be expected from the superposition of individual participant nucleon-nucleon collisions. For this purpose, PHENIX data will be compared with a participant superposition, or wounded nucleon, model [42] based upon data from elementary collisions. In the participant superposition model, the total multiplicity fluctuations can be expressed in terms of the scaled variance [35],

$$\omega_{\mathrm{N}} = \omega_{\nu} + \mu_{\mathrm{WN}}\omega_{N_{\mathrm{part}}}, \tag{15}$$

where ω_{ν} are the fluctuations from each individual source, e.g., from each elementary collision, $\omega_{N_{\mathrm{part}}}$ are the fluctuations of the number of sources, and μ_{WN} is the mean multiplicity per wounded nucleon. The second term includes nondynamic contributions from geometry fluctuations due to the width of the centrality bin along with additional fluctuations in the number of participants for a fixed impact parameter. Ideally, the second term is nearly nullified after applying the geometry

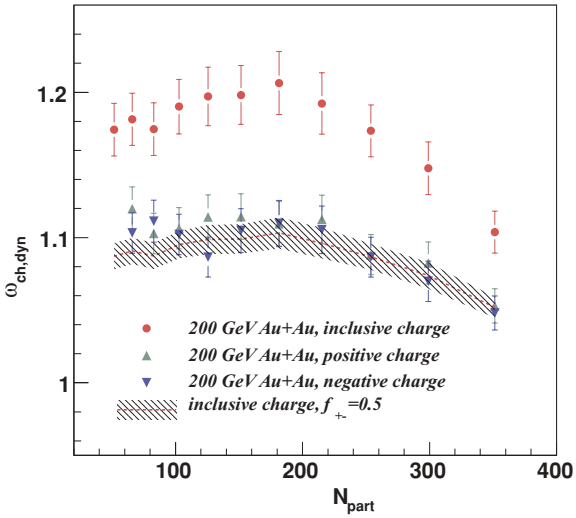

FIG. 10. (Color online) Scaled variance as a function of N_{part} for 200 GeV Au+Au collisions in the range $0.2 < p_T < 2.0$ GeV/c. Shown are measurements for inclusive charged particles, positive particles, and negative particles. The line represents the inclusive data scaled down in acceptance by 50% with the shaded area representing the systematic error.

corrections described previously, so the resulting fluctuations are independent of centrality as well as collision species.

Baseline comparisons are facilitated by PHENIX measurements of charged particle multiplicity fluctuations in minimum-bias 200 GeV $p+p$ collisions. The $p+p$ data and the NBD distribution to the multiplicity distribution are shown in Fig. 2. The NBD fit yields $\mu_{\text{ch}} = 0.32 \pm 0.003$, $\omega_{\text{ch}} = 1.17 \pm 0.01$, and $k_{\text{NBD}} = 1.88 \pm 0.01$. These results are in agreement within errors with previous measurements in the same pseudorapidity range of $k_{\text{NBD}} = 1.9 \pm 0.2 \pm 0.2$ by the UA5 Collaboration [20] in collisions of protons and antiprotons at 200 GeV. Comparisons between the participant superposition model predictions and the 22.5 GeV Cu+Cu data can be made using multiplicity fluctuations measured in 20 GeV $p+p$ collisions by the NA22 Collaboration [19] over the same pseudorapidity range as the PHENIX Cu+Cu measurement. After scaling the NA22 scaled variance to the PHENIX azimuthal acceptance, the participant superposition model scaled variance is expected to be constant as a function of centrality with a value of 1.08 ± 0.04. Lacking multiplicity distribution data from elementary collisions at 62.4 GeV within the PHENIX pseudorapidity acceptance, it is assumed that as a function of collision energy, the scaled variance in the PHENIX pseudorapidity acceptance scales in the same manner as in an acceptance of 4π, which can be parametrized from existing $p+p$ and $p+\bar{p}$ data as follows [17]:

$$\mu_{\text{ch}} \approx -4.2 + 4.69 \left(\frac{s}{\text{GeV}^2} \right)^{0.155}. \tag{16}$$

Given the mean charged particle multiplicity, the scaled variance in $p+p$ and $p+\bar{p}$ can be parametrized as follows [35]:

$$\omega_{\text{ch}} \approx 0.35 \frac{(\mu_{\text{ch}} - 1)^2}{\mu_{\text{ch}}}. \tag{17}$$

Scaling this parametrization to match the values of ω_{ch} at 200 and 22.5 GeV, the estimated value of ω_{ch} at 62.4 GeV is 1.15 ± 0.02.

Comparisons of the data with the predictions of the participant superposition model are shown in Fig. 5 for Au+Au and Cu+Cu collisions. The shaded regions about the participant superposition model lines represent the systematic error of the estimates described above. All of the data points are consistent with or below the participant superposition model estimate. This suggests that the data do not show any indications of the presence of a critical point, where the fluctuations are expected to be much larger than the participant superposition model expectation.

B. Comparisons to the HIJING model

Shown in Fig. 11 are the scaled variance curves from HIJING simulations into the PHENIX acceptance. The HIJING simulations are performed with a fixed impact parameter corresponding to the mean of the impact parameter distribution for each bin as determined by the Glauber model in order to minimize the geometry fluctuation component of the result. The mean and variance of the resulting multiplicity distributions from HIJING are extracted from fits to negative binomial distributions. The HIJING simulation multiplicity fluctuations with the jet production parameter turned on are consistently above the data and increase continuously through the most peripheral collisions. This behavior is not consistent with the data, where the fluctuations do not increase in the most peripheral collisions. Although HIJING reproduces the total charged particle multiplicity well, it consistently overpredicts the amount of fluctuations in multiplicity. When the jet production parameter in HIJING is turned off, the scaled variance as a function of centrality is independent of collision energy, illustrating that jet production accounts for the energy dependence of the HIJING results. Note that the HIJING results with jet production turned off are in better agreement with the data for all collision energies. Together with the observation that the multiplicity fluctuations demonstrate no significant p_T dependence, this may be an indication that correlated emission of particles from jet production do not significantly contribute to the multiplicity fluctuations observed in the data.

C. Comparisons to the clan model

The clan model [43] has been developed to interpret the fact that negative binomial distributions describe charged hadron multiplicity distributions in elementary and heavy ion collisions. In this model, hadron production is modeled as the independent emission of a number of hadronic clusters N_c, each with a mean number of hadrons n_c. The independent emission is described by a Poisson distribution with an average cluster, or clan, multiplicity of $\bar{N}_c$. After the clusters are emitted, they fragment into the final state hadrons. The measured value of the mean multiplicity μ_{ch} is related to the cluster multiplicities by $\mu_{\text{ch}} = \bar{N}_c \bar{n}_c$. In this model, the cluster multiplicity parameters can be simply related to the NBD parameters

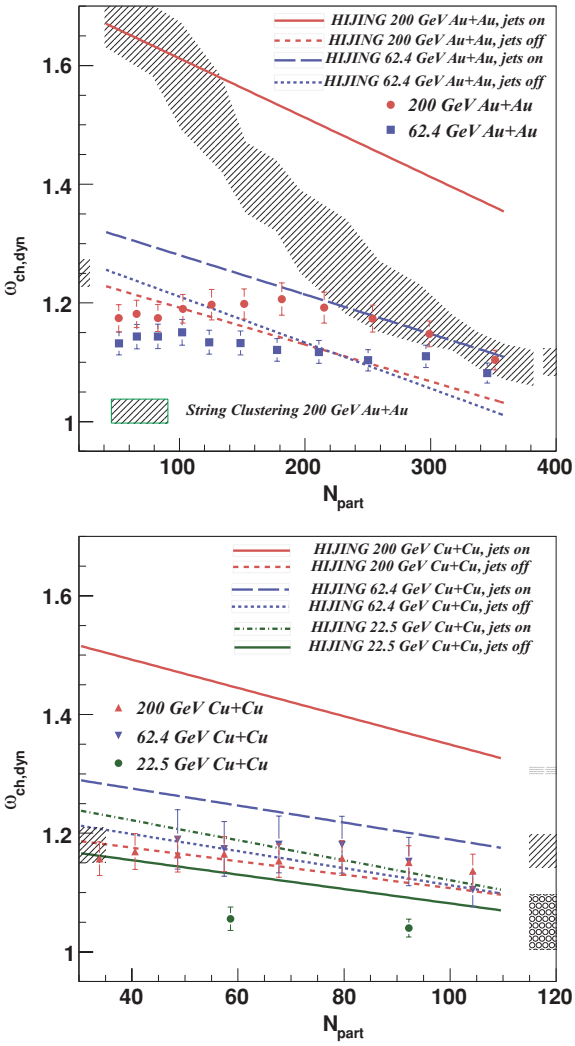

FIG. 11. (Color online) Fluctuations expressed as the scaled variance as a function of N_{part} for Au+Au and Cu+Cu collisions for $0.2 < p_T < 2.0$ GeV/c. The estimated contribution from geometry fluctuations has been removed. Results from the HIJING model code with jets turned on and jets turned off are overlaid with the shaded regions representing the systematic error for each curve.

of the measured multiplicity distribution as follows:

$$\bar{N}_c = k_{\text{NBD}} \ln(1 + \mu_{\text{ch}}/k_{\text{NBD}}), \tag{18}$$

and

$$\bar{n}_c = (\mu_{\text{ch}}/k_{\text{NBD}})/\ln(1 + \mu_{\text{ch}}/k_{\text{NBD}}). \tag{19}$$

The results from the NBD fits to the data are plotted in Fig. 12 for all collision species. Also shown are data from elementary and heavy ion collisions at various collision energies. The individual data points from all but the PHENIX data are taken from multiplicity distributions measured over varying ranges of pseudorapidity, while the PHENIX data are taken as a function of centrality. The characteristics of all of the heavy ion datasets are the same. The value of $\bar{n}_c$ varies little within the range 1.0–1.1. The heavy ion data universally exhibit only weak clustering characteristics as interpreted by the clan model. There is also no significant variation seen with collision energy. However, $\bar{n}_c$ is consistently significantly higher in elementary collisions. In elementary collisions, it is less probable to produce events with a high multiplicity, which can reveal rare sources of clusters such as jet production or multiple parton interactions.

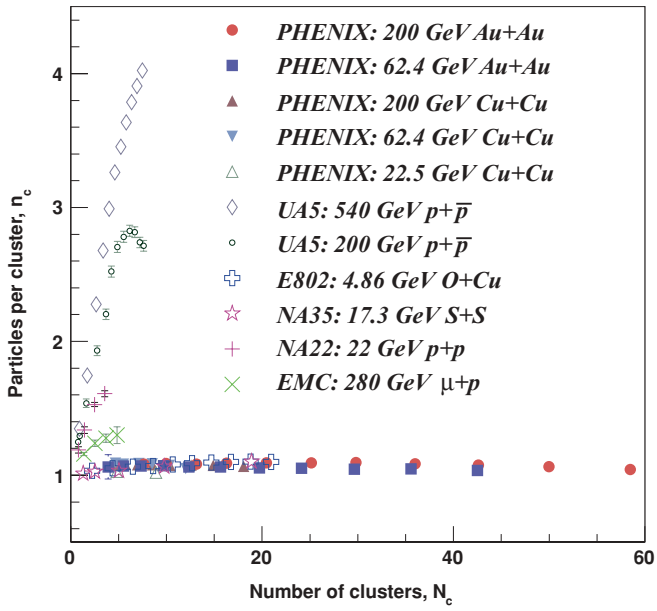

FIG. 12. (Color online) Correlation of the clan model parameters $\bar{n}_c$ and $\bar{N}_c$ for all collision species measured as a function of centrality. Also shown are results from pseudorapidity-dependent studies from elementary collisions (UA5 [17], EMC [18], and NA22 [19]) and heavy ion collisions (E802 [21] and NA35 [23]).

A feature that is especially apparent in the Au+Au data is the fact that the scaled variance decreases with increasing centrality, with the most central point lying below the participant superposition model expectation. The clan model provides one possible explanation for this effect whereby there is a higher probability for contributions from cluster sources such as jet production in the lower multiplicity peripheral events. The cluster sources introduce correlations that can increase the value of $1/k_{\text{NBD}}$ and hence the value of the scaled variance of the multiplicity distribution. Another possible explanation for this feature can be addressed with a string percolation model in heavy ion collisions [44]. In general, percolation theory considers the formation of clusters within a random spatial distribution of individual objects that are allowed to overlap with each other. The clusters are formed by the geometrical connection of one or more of the individual objects. This can be applied to estimate multiplicity fluctuations in heavy ion collisions whereby the objects are the circular cross sections of strings in the transverse plane [45] and the strings form clusters of overlapping strings that then each emit a number of particles related to the number of strings in each cluster. As the centrality increases, the number of individual clusters decreases along with the variance of the number of strings per cluster, which can result in a decrease in the magnitude of the resulting multiplicity fluctuations. The prediction of the scaled variance from the string percolation model for 200 GeV Au+Au collisions scaled down to the PHENIX acceptance in azimuth and pseudorapidity [45] is shown in

Fig. 11. Although percolation describes the trend observed at the four highest centralities very well, the scaled variance from the model continues to increase well above the data as centrality decreases. The implementation of the HIJING model contains merging of strings that are in close spatial proximity, so percolation can explain the trends in the scaled variance from HIJING.

An additional contribution to multiplicity fluctuations within the PHENIX acceptance arises from the presence of elliptic flow. This contribution has been estimated using a simple Monte Carlo simulation. In this simulation, a random reaction plane angle is assigned to each event. The multiplicity distribution due to the elliptic flow component is given by

$$dN/d\phi = C[1 + 2v_2 \cos(2\Delta\phi)], \tag{20}$$

where C is a normalization factor, v_2 is the measured magnitude of the elliptic flow, and $\Delta\phi$ is the difference between the particle emission angle and the reaction plane angle. For each event, this multiplicity distribution function is integrated over the PHENIX azimuthal acceptance and the resulting scaled variance from 1×10^6 events is calculated. The value of v_2 used in the simulation is taken from PHENIX measurements of elliptic flow at the mean transverse momentum of the inclusive charged hadron spectra [46,47]. The estimated contribution from elliptic flow to the observed scaled variance is shown in Fig. 5 for 200 and 62 GeV Au+Au collisions. This flow contribution also exhibits an increasing trend when moving from central to midcentral collisions. The estimated flow contribution increases from 18% of the signal in the most central 200 GeV Au+Au collisions to 35% of the signal at $N_{\text{part}} = 125$. In 62 GeV Au+Au collisions, the estimated flow contribution rises from 8% in the most central collisions to 25% at $N_{\text{part}} = 181$. The presence of elliptic flow can account for the majority of the centrality-dependent shapes observed in the Au+Au data.

VI. SUMMARY

PHENIX has completed a survey of multiplicity fluctuations of charged hadrons in Au+Au and Cu+Cu collisions at three collision energies. The motivation for the analysis is to search for signs of a phase transition or the presence of the predicted critical point on the QCD phase diagram by looking for increased multiplicity fluctuations as a function of system energy and system volume. After correcting for nondynamical fluctuations due to fluctuations of the collision geometry within a centrality bin, the multiplicity fluctuations in 200 and 62.4 GeV Au+Au collisions are consistent with or below the expectation from the superposition model of participant nucleons. The multiplicity fluctuations decrease as the collision centrality increases, dropping below the participant superposition model expectation for the most central Au+Au collisions. Fluctuations from Cu+Cu collisions exhibit a weaker centrality dependence that also is consistent with or below the expectation from the participant superposition model. The absence of large dynamical fluctuations in excess of the participant superposition model expectation indicate that there is no evidence of critical behavior related to the compressibility observable in this dataset. There is also no significant evidence of dynamical fluctuations that are dependent on the transverse momentum or the charge of the particles measured. As interpreted by the clan model, the observed fluctuations demonstrate only weak clustering characteristics for all of the heavy ion collision systems discussed here. The majority of the decreasing scaled variance with increasing centrality trend in Au+Au collisions can be explained by contributions from elliptic flow. Although this analysis does not observe evidence of critical behavior, it does not rule out the existence of a QCD critical point. Further measurements will be possible during the upcoming low-energy scan program at RHIC, allowing a more comprehensive search for critical behavior.

ACKNOWLEDGMENTS

We thank the staff of the Collider-Accelerator and Physics Departments at Brookhaven National Laboratory and the staff of the other PHENIX participating institutions for their vital contributions. We acknowledge support from the Office of Nuclear Physics in the Office of Science of the Department of Energy, the National Science Foundation, Abilene Christian University Research Council, Research Foundation of SUNY, and Dean of the College of Arts and Sciences, Vanderbilt University (U.S.A), Ministry of Education, Culture, Sports, Science, and Technology and the Japan Society for the Promotion of Science (Japan), Conselho Nacional de Desenvolvimento Científico e Tecnológico and Fundação de Amparo à Pesquisa do Estado de São Paulo (Brazil), Natural Science Foundation of China (People's Republic of China), Ministry of Education, Youth and Sports (Czech Republic), Centre National de la Recherche Scientifique, Commissariat à l'Énergie Atomique, and Institut National de Physique Nucléaire et de Physique des Particules (France), Ministry of Industry, Science and Tekhnologies, Bundesministerium für Bildung und Forschung, Deutscher Akademischer Austausch Dienst, and Alexander von Humboldt Stiftung (Germany), Hungarian National Science Fund, OTKA (Hungary), Department of Atomic Energy (India), Israel Science Foundation (Israel), Korea Research Foundation and Korea Science and Engineering Foundation (Korea), Ministry of Education and Science, Russia Academy of Sciences, Federal Agency of Atomic Energy (Russia), VR and the Wallenberg Foundation (Sweden), the US Civilian Research and Development Foundation for the Independent States of the Former Soviet Union, the US.-Hungarian NSF-OTKA-MTA, and the US-Israel Binational Science Foundation.

[1] M. A. Stephanov, K. Rajagopal, and E. V. Shuryak, Phys. Rev. Lett. **81**, 4816 (1998).

[2] M. A. Stephanov, in *LAT2006 Proceedings*, PoS(LAT2006)024 (SISSA, Trieste, Italy, 2006).

[3] K. Adcox *et al*. (PHENIX Collaboration), Nucl. Phys. **A757**, 184 (2005).
[4] S. Mrowczynski, Phys. Lett. **B430**, 9 (1998).
[5] V. V. Begun, M. I. Gorenstein, A. P. Kostyuk, and O. S. Zozulya, Phys. Rev. C **71**, 054904 (2005).
[6] S. Jeon and V. Koch, arXiv:hep-ph/0304012.
[7] V. V. Begun, M. Gazdzicki, M. I. Gorenstein, and O. S. Zozulya, Phys. Rev. C **70**, 034901 (2004).
[8] F. Becattini, A. Keranen, L. Ferroni, and T. Gabbriellini, Phys. Rev. C **72**, 064904 (2005).
[9] H. E. Stanley, *Introduction to Phase Transitions and Critical Phenomena* (Oxford University Press, New York, 1971).
[10] B. J. Schaefer and J. Wambach, Phys. Rev. D **75**, 085015 (2007).
[11] C. Sasaki, B. Friman, and K. Redlich, Phys. Rev. D **75**, 054026 (2007).
[12] I. N. Mishustin, Eur. Phys. J. A **30**, 311 (2006).
[13] M. A. Stephanov, K. Rajagopal, and E. V. Shuryak, Phys. Rev. D **60**, 114028 (1999).
[14] T. Kafka *et al*., Phys. Rev. Lett. **34**, 687 (1975).
[15] W. Thome *et al*. (Aachen-CERN-Heidelberg-Munich Collaboration), Nucl. Phys. **B129**, 365 (1977).
[16] G. J. Alner *et al*. (UA5 Collaboration), Phys. Lett. **B160**, 193 (1985).
[17] G. J. Alner *et al*. (UA5 Collaboration), Phys. Rep. **154**, 247 (1987).
[18] M. Arneodo *et al*. (European Muon Collaboration), Z. Phys. C **35**, 335 (1987) [Erratum-*ibid*. **36**, 512 (1987)].
[19] M. Adamus *et al*. (EHS/NA22 Collaboration), Z. Phys. C **37**, 215 (1988).
[20] R. E. Ansorge *et al*. (UA5 Collaboration), Z. Phys. C **43**, 357 (1989).
[21] T. Abbott *et al*. (E-802 Collaboration), Phys. Rev. C **52**, 2663 (1995).
[22] R. Albrecht *et al*. (WA80 Collaboration), Z. Phys. C **45**, 31 (1989).
[23] J. Bachler *et al*. (NA35 Collaboration), Z. Phys. C **57**, 541 (1993).
[24] M. M. Aggarwal *et al*. (WA98 Collaboration), Phys. Rev. C **65**, 054912 (2002).
[25] C. Alt *et al*. (NA49 Collaboration), Phys. Rev. C **75**, 064904 (2007).
[26] S. S. Adler *et al*. (PHENIX Collaboration), Phys. Rev. C **76**, 034903 (2007).
[27] K. Adcox *et al*. (PHENIX Collaboration), Nucl. Instrum. Methods Phys. Res. A **499**, 469 (2003).
[28] K. Adcox *et al*. (PHENIX Collaboration), Nucl. Instrum. Methods Phys. Res. A **499**, 489 (2003).
[29] M. Aizawa *et al*. (PHENIX Collaboration), Nucl. Instrum. Methods Phys. Res. A **499**, 508 (2003).
[30] L. Aphecetche *et al*. (PHENIX Collaboration), Nucl. Instrum. Methods Phys. Res. A **499**, 521 (2003).
[31] J. T. Mitchell *et al*. (PHENIX Collaboration), Nucl. Instrum. Methods Phys. Res. A **482**, 491 (2002).
[32] M. Allen *et al*. (PHENIX Collaboration), Nucl. Instrum. Methods Phys. Res. A **499**, 549 (2003).
[33] S. S. Adler *et al*. (PHENIX Collaboration), Phys. Rev. C **71**, 034908 (2005); **71**, 049901(E) (2005).
[34] M. L. Miller, K. Reygers, S. J. Sanders, and P. Steinberg, Annu. Rev. Nucl. Part. Sci. **57**, 205 (2007).
[35] H. Heiselberg, Phys. Rep. **351**, 161 (2001).
[36] S. S. Adler *et al*. (PHENIX Collaboration), Phys. Rev. C **69**, 034909 (2004).
[37] V. P. Konchakovski, M. I. Gorenstein, E. L. Bratkovskaya, and H. Stocker, Phys. Rev. C **74**, 064911 (2006).
[38] B. Lungwitz and M. Bleicher, Phys. Rev. C **76**, 044904 (2007).
[39] V. P. Konchakovski, M. I. Gorenstein, and E. L. Bratkovskaya, Phys. Rev. C **76**, 031901(R) (2007).
[40] V. P. Konchakovski, S. Haussler, M. I. Gorenstein, E. L. Bratkovskaya, M. Bleicher, and H. Stocker, Phys. Rev. C **73**, 034902 (2006).
[41] X. N. Wang and M. Gyulassy, Phys. Rev. D **44**, 3501 (1991).
[42] A. Bialas, M. Bleszynski, and W. Czyz, Nucl. Phys. **B111**, 461 (1976).
[43] A. Giovannini and L. Van Hove, Z. Phys. C **30**, 391 (1986).
[44] M. Nardi and H. Satz, Phys. Lett. **B442**, 14 (1998).
[45] L. Cunqueiro, E. G. Ferreiro, F. del Moral, and C. Pajares, Phys. Rev. C **72**, 024907 (2005).
[46] S. S. Adler *et al*. (PHENIX Collaboration), Phys. Rev. Lett. **94**, 232302 (2005).
[47] A. Adare *et al*. (PHENIX Collaboration), Phys. Rev. Lett. **98**, 162301 (2007).

arXiv:0804.4168v1 [nucl-ex] 25 Apr 2008

Enhanced production of direct photons in Au+Au collisions at $\sqrt{s_{NN}}$=200 GeV

A. Adare,[8] S. Afanasiev,[22] C. Aidala,[9] N.N. Ajitanand,[49] Y. Akiba,[43,44] H. Al-Bataineh,[38] J. Alexander,[49] A. Al-Jamel,[38] K. Aoki,[28,43] L. Aphecetche,[51] R. Armendariz,[38] S.H. Aronson,[3] J. Asai,[44] E.T. Atomssa,[29] R. Averbeck,[50] T.C. Awes,[39] B. Azmoun,[3] V. Babintsev,[18] G. Baksay,[14] L. Baksay,[14] A. Baldisseri,[11] K.N. Barish,[4] P.D. Barnes,[31] B. Bassalleck,[37] S. Bathe,[4] S. Batsouli,[9,39] V. Baublis,[42] F. Bauer,[4] A. Bazilevsky,[3] S. Belikov,[3,21,*] R. Bennett,[50] Y. Berdnikov,[46] A.A. Bickley,[8] M.T. Bjorndal,[9] J.G. Boissevain,[31] H. Borel,[11] K. Boyle,[50] M.L. Brooks,[31] D.S. Brown,[38] D. Bucher,[34] H. Buesching,[3] V. Bumazhnov,[18] G. Bunce,[3,44] J.M. Burward-Hoy,[31] S. Butsyk,[31,50] S. Campbell,[50] J.-S. Chai,[23] B.S. Chang,[58] J.-L. Charvet,[11] S. Chernichenko,[18] J. Chiba,[24] C.Y. Chi,[9] M. Chiu,[9,19] I.J. Choi,[58] T. Chujo,[55] P. Chung,[49] A. Churyn,[18] V. Cianciolo,[39] C.R. Cleven,[16] Y. Cobigo,[11] B.A. Cole,[9] M.P. Comets,[40] P. Constantin,[21,31] M. Csanád,[13] T. Csörgő,[25] T. Dahms,[50] K. Das,[15] G. David,[3] M.B. Deaton,[1] K. Dehmelt,[14] H. Delagrange,[51] A. Denisov,[18] D. d'Enterria,[9] A. Deshpande,[44,50] E.J. Desmond,[3] O. Dietzsch,[47] A. Dion,[50] M. Donadelli,[47] J.L. Drachenberg,[1] O. Drapier,[29] A. Drees,[50] A.K. Dubey,[57] A. Durum,[18] V. Dzhordzhadze,[4,52] Y.V. Efremenko,[39] J. Egdemir,[50] F. Ellinghaus,[8] W.S. Emam,[4] A. Enokizono,[17,30] H. En'yo,[43,44] B. Espagnon,[40] S. Esumi,[54] K.O. Eyser,[4] D.E. Fields,[37,44] M. Finger,[5,22] M. Finger, Jr.,[5,22] F. Fleuret,[29] S.L. Fokin,[27] B. Forestier,[32] Z. Fraenkel,[57,*] J.E. Frantz,[9,50] A. Franz,[3] A.D. Frawley,[15] K. Fujiwara,[43] Y. Fukao,[28,43] S.-Y. Fung,[4] T. Fusayasu,[36] S. Gadrat,[32] I. Garishvili,[52] F. Gastineau,[51] M. Germain,[51] A. Glenn,[8,52] H. Gong,[50] M. Gonin,[29] J. Gosset,[11] Y. Goto,[43,44] R. Granier de Cassagnac,[29] N. Grau,[21] S.V. Greene,[55] M. Grosse Perdekamp,[19,44] T. Gunji,[7] H.-Å. Gustafsson,[33] T. Hachiya,[17,43] A. Hadj Henni,[51] C. Haegemann,[37] J.S. Haggerty,[3] M.N. Hagiwara,[1] H. Hamagaki,[7] R. Han,[41] H. Harada,[17] E.P. Hartouni,[30] K. Haruna,[17] M. Harvey,[3] E. Haslum,[33] K. Hasuko,[43] R. Hayano,[7] M. Heffner,[30] T.K. Hemmick,[50] T. Hester,[4] J.M. Heuser,[43] X. He,[16] H. Hiejima,[19] J.C. Hill,[21] R. Hobbs,[37] M. Hohlmann,[14] M. Holmes,[55] W. Holzmann,[49] K. Homma,[17] B. Hong,[26] T. Horaguchi,[43,53] D. Hornback,[52] M.G. Hur,[23] T. Ichihara,[43,44] K. Imai,[28,43] M. Inaba,[54] Y. Inoue,[45,43] D. Isenhower,[1] L. Isenhower,[1] M. Ishihara,[43] T. Isobe,[7] M. Issah,[49] A. Isupov,[22] B.V. Jacak,[50,†] J. Jia,[9] J. Jin,[9] O. Jinnouchi,[44] B.M. Johnson,[3] K.S. Joo,[35] D. Jouan,[40] F. Kajihara,[7,43] S. Kametani,[7,56] N. Kamihara,[43,53] J. Kamin,[50] M. Kaneta,[44] J.H. Kang,[58] H. Kanou,[43,53] T. Kawagishi,[54] D. Kawall,[44] A.V. Kazantsev,[27] S. Kelly,[8] A. Khanzadeev,[42] J. Kikuchi,[56] D.H. Kim,[35] D.J. Kim,[58] E. Kim,[48] Y.-S. Kim,[23] E. Kinney,[8] A. Kiss,[13] E. Kistenev,[3] A. Kiyomichi,[43] J. Klay,[30] C. Klein-Boesing,[34] L. Kochenda,[42] V. Kochetkov,[18] B. Komkov,[42] M. Konno,[54] D. Kotchetkov,[4] A. Kozlov,[57] A. Král,[10] A. Kravitz,[9] P.J. Kroon,[3] J. Kubart,[5,20] G.J. Kunde,[31] N. Kurihara,[7] K. Kurita,[45,43] M.J. Kweon,[26] Y. Kwon,[52,58] G.S. Kyle,[38] R. Lacey,[49] Y.-S. Lai,[9] J.G. Lajoie,[21] A. Lebedev,[21] Y. Le Bornec,[40] S. Leckey,[50] D.M. Lee,[31] M.K. Lee,[58] T. Lee,[48] M.J. Leitch,[31] M.A.L. Leite,[47] B. Lenzi,[47] H. Lim,[48] T. Liška,[10] A. Litvinenko,[22] M.X. Liu,[31] X. Li,[6] X.H. Li,[4] B. Love,[55] D. Lynch,[3] C.F. Maguire,[55] Y.I. Makdisi,[3] A. Malakhov,[22] M.D. Malik,[37] V.I. Manko,[27] Y. Mao,[41,43] L. Mašek,[5,20] H. Masui,[54] F. Matathias,[9,50] M.C. McCain,[19] M. McCumber,[50] P.L. McGaughey,[31] Y. Miake,[54] P. Mikeš,[5,20] K. Miki,[54] T.E. Miller,[55] A. Milov,[50] S. Mioduszewski,[3] G.C. Mishra,[16] M. Mishra,[2] J.T. Mitchell,[3] M. Mitrovski,[49] A. Morreale,[4] D.P. Morrison,[3] J.M. Moss,[31] T.V. Moukhanova,[27] D. Mukhopadhyay,[55] J. Murata,[45,43] S. Nagamiya,[24] Y. Nagata,[54] J.L. Nagle,[8] M. Naglis,[57] I. Nakagawa,[43,44] Y. Nakamiya,[17] T. Nakamura,[17] K. Nakano,[43,53] J. Newby,[30] M. Nguyen,[50] B.E. Norman,[31] A.S. Nyanin,[27] J. Nystrand,[33] E. O'Brien,[3] S.X. Oda,[7] C.A. Ogilvie,[21] H. Ohnishi,[43] I.D. Ojha,[55] H. Okada,[28,43] K. Okada,[44] M. Oka,[54] O.O. Omiwade,[1] A. Oskarsson,[33] I. Otterlund,[33] M. Ouchida,[17] K. Ozawa,[7] R. Pak,[3] D. Pal,[55] A.P.T. Palounek,[31] V. Pantuev,[50] V. Papavassiliou,[38] J. Park,[48] W.J. Park,[26] S.F. Pate,[38] H. Pei,[21] J.-C. Peng,[19] H. Pereira,[11] V. Peresedov,[22] D.Yu. Peressounko,[27] C. Pinkenburg,[3] R.P. Pisani,[3] M.L. Purschke,[3] A.K. Purwar,[31,50] H. Qu,[16] J. Rak,[21,37] A. Rakotozafindrabe,[29] I. Ravinovich,[57] K.F. Read,[39,52] S. Rembeczki,[14] M. Reuter,[50] K. Reygers,[34] V. Riabov,[42] Y. Riabov,[42] G. Roche,[32] A. Romana,[29,*] M. Rosati,[21] S.S.E. Rosendahl,[33] P. Rosnet,[32] P. Rukoyatkin,[22] V.L. Rykov,[43] S.S. Ryu,[58] B. Sahlmueller,[34] N. Saito,[28,43,44] T. Sakaguchi,[3,7,56] S. Sakai,[54] H. Sakata,[17] V. Samsonov,[42] H.D. Sato,[28,43] S. Sato,[3,24,54] S. Sawada,[24] J. Seele,[8] R. Seidl,[19] V. Semenov,[18] R. Seto,[4] D. Sharma,[57] T.K. Shea,[3] I. Shein,[18] A. Shevel,[42,49] T.-A. Shibata,[43,53] K. Shigaki,[17] M. Shimomura,[54] T. Shohjoh,[54] K. Shoji,[28,43] A. Sickles,[50] C.L. Silva,[47] D. Silvermyr,[39] C. Silvestre,[11] K.S. Sim,[26] C.P. Singh,[2] V. Singh,[2] S. Skutnik,[21] M. Slunečka,[5,22] W.C. Smith,[1] A. Soldatov,[18] R.A. Soltz,[30] W.E. Sondheim,[31] S.P. Sorensen,[52] I.V. Sourikova,[3] F. Staley,[11] P.W. Stankus,[39] E. Stenlund,[33] M. Stepanov,[38] A. Ster,[25] S.P. Stoll,[3] T. Sugitate,[17] C. Suire,[40] J.P. Sullivan,[31] J. Sziklai,[25] T. Tabaru,[44] S. Takagi,[54] E.M. Takagui,[47] A. Taketani,[43,44] K.H. Tanaka,[24] Y. Tanaka,[36] K. Tanida,[43,44] M.J. Tannenbaum,[3] A. Taranenko,[49] P. Tarján,[12]

T.L. Thomas,[37] M. Togawa,[28,43] A. Toia,[50] J. Tojo,[43] L. Tomášek,[20] H. Torii,[43] R.S. Towell,[1] V-N. Tram,[29] I. Tserruya,[57] Y. Tsuchimoto,[17,43] S.K. Tuli,[2] H. Tydesjö,[33] N. Tyurin,[18] C. Vale,[21] H. Valle,[55] H.W. van Hecke,[31] J. Velkovska,[55] R. Vertesi,[12] A.A. Vinogradov,[27] M. Virius,[10] V. Vrba,[20] E. Vznuzdaev,[42] M. Wagner,[28,43] D. Walker,[50] X.R. Wang,[38] Y. Watanabe,[43,44] J. Wessels,[34] S.N. White,[3] N. Willis,[40] D. Winter,[9] C.L. Woody,[3] M. Wysocki,[8] W. Xie,[4,44] Y.L. Yamaguchi,[56] A. Yanovich,[18] Z. Yasin,[4] J. Ying,[16] S. Yokkaichi,[43,44] G.R. Young,[39] I. Younus,[37] I.E. Yushmanov,[27] W.A. Zajc,[9] O. Zaudtke,[34] C. Zhang,[9,39] S. Zhou,[6] J. Zimányi,[25,*] and L. Zolin[22]

(PHENIX Collaboration)

[1]*Abilene Christian University, Abilene, TX 79699, USA*
[2]*Department of Physics, Banaras Hindu University, Varanasi 221005, India*
[3]*Brookhaven National Laboratory, Upton, NY 11973-5000, USA*
[4]*University of California - Riverside, Riverside, CA 92521, USA*
[5]*Charles University, Ovocný trh 5, Praha 1, 116 36, Prague, Czech Republic*
[6]*China Institute of Atomic Energy (CIAE), Beijing, People's Republic of China*
[7]*Center for Nuclear Study, Graduate School of Science, University of Tokyo, 7-3-1 Hongo, Bunkyo, Tokyo 113-0033, Japan*
[8]*University of Colorado, Boulder, CO 80309, USA*
[9]*Columbia University, New York, NY 10027 and Nevis Laboratories, Irvington, NY 10533, USA*
[10]*Czech Technical University, Zikova 4, 166 36 Prague 6, Czech Republic*
[11]*Dapnia, CEA Saclay, F-91191, Gif-sur-Yvette, France*
[12]*Debrecen University, H-4010 Debrecen, Egyetem tér 1, Hungary*
[13]*ELTE, Eötvös Loránd University, H - 1117 Budapest, Pázmány P. s. 1/A, Hungary*
[14]*Florida Institute of Technology, Melbourne, FL 32901, USA*
[15]*Florida State University, Tallahassee, FL 32306, USA*
[16]*Georgia State University, Atlanta, GA 30303, USA*
[17]*Hiroshima University, Kagamiyama, Higashi-Hiroshima 739-8526, Japan*
[18]*IHEP Protvino, State Research Center of Russian Federation, Institute for High Energy Physics, Protvino, 142281, Russia*
[19]*University of Illinois at Urbana-Champaign, Urbana, IL 61801, USA*
[20]*Institute of Physics, Academy of Sciences of the Czech Republic, Na Slovance 2, 182 21 Prague 8, Czech Republic*
[21]*Iowa State University, Ames, IA 50011, USA*
[22]*Joint Institute for Nuclear Research, 141980 Dubna, Moscow Region, Russia*
[23]*KAERI, Cyclotron Application Laboratory, Seoul, Korea*
[24]*KEK, High Energy Accelerator Research Organization, Tsukuba, Ibaraki 305-0801, Japan*
[25]*KFKI Research Institute for Particle and Nuclear Physics of the Hungarian Academy of Sciences (MTA KFKI RMKI), H-1525 Budapest 114, POBox 49, Budapest, Hungary*
[26]*Korea University, Seoul, 136-701, Korea*
[27]*Russian Research Center "Kurchatov Institute", Moscow, Russia*
[28]*Kyoto University, Kyoto 606-8502, Japan*
[29]*Laboratoire Leprince-Ringuet, Ecole Polytechnique, CNRS-IN2P3, Route de Saclay, F-91128, Palaiseau, France*
[30]*Lawrence Livermore National Laboratory, Livermore, CA 94550, USA*
[31]*Los Alamos National Laboratory, Los Alamos, NM 87545, USA*
[32]*LPC, Université Blaise Pascal, CNRS-IN2P3, Clermont-Fd, 63177 Aubiere Cedex, France*
[33]*Department of Physics, Lund University, Box 118, SE-221 00 Lund, Sweden*
[34]*Institut für Kernphysik, University of Muenster, D-48149 Muenster, Germany*
[35]*Myongji University, Yongin, Kyonggido 449-728, Korea*
[36]*Nagasaki Institute of Applied Science, Nagasaki-shi, Nagasaki 851-0193, Japan*
[37]*University of New Mexico, Albuquerque, NM 87131, USA*
[38]*New Mexico State University, Las Cruces, NM 88003, USA*
[39]*Oak Ridge National Laboratory, Oak Ridge, TN 37831, USA*
[40]*IPN-Orsay, Universite Paris Sud, CNRS-IN2P3, BP1, F-91406, Orsay, France*
[41]*Peking University, Beijing, People's Republic of China*
[42]*PNPI, Petersburg Nuclear Physics Institute, Gatchina, Leningrad region, 188300, Russia*
[43]*RIKEN, The Institute of Physical and Chemical Research, Wako, Saitama 351-0198, Japan*
[44]*RIKEN BNL Research Center, Brookhaven National Laboratory, Upton, NY 11973-5000, USA*
[45]*Physics Department, Rikkyo University, 3-34-1 Nishi-Ikebukuro, Toshima, Tokyo 171-8501, Japan*
[46]*Saint Petersburg State Polytechnic University, St. Petersburg, Russia*
[47]*Universidade de São Paulo, Instituto de Física, Caixa Postal 66318, São Paulo CEP05315-970, Brazil*
[48]*System Electronics Laboratory, Seoul National University, Seoul, Korea*
[49]*Chemistry Department, Stony Brook University, Stony Brook, SUNY, NY 11794-3400, USA*
[50]*Department of Physics and Astronomy, Stony Brook University, SUNY, Stony Brook, NY 11794, USA*
[51]*SUBATECH (Ecole des Mines de Nantes, CNRS-IN2P3, Université de Nantes) BP 20722 - 44307, Nantes, France*
[52]*University of Tennessee, Knoxville, TN 37996, USA*
[53]*Department of Physics, Tokyo Institute of Technology, Oh-okayama, Meguro, Tokyo 152-8551, Japan*
[54]*Institute of Physics, University of Tsukuba, Tsukuba, Ibaraki 305, Japan*

[55] Vanderbilt University, Nashville, TN 37235, USA
[56] Waseda University, Advanced Research Institute for Science and Engineering, 17 Kikui-cho, Shinjuku-ku, Tokyo 162-0044, Japan
[57] Weizmann Institute, Rehovot 76100, Israel
[58] Yonsei University, IPAP, Seoul 120-749, Korea
(Dated: April 25, 2008)

The production of e^+e^- pairs for $m_{e^+e^-} < 300$ MeV/c^2 and $1 < p_{\rm T} < 5$ GeV/c is measured in $p+p$ and Au+Au collisions at $\sqrt{s_{NN}} = 200$ GeV. Enhanced e^+e^- pair yield above hadronic sources is observed.Treating the excess as photon internal conversion photons, the invariant yield of direct photons is deduced. In central Au+Au collisions, the excess over $p+p$ is exponential in $p_{\rm T}$, with inverse slope $T = 221 \pm 23(\text{stat}) \pm 18(\text{sys})$ MeV. Hydrodynamical models with initial temperatures $T_{init} \approx 300 - 600$ MeV at times of 0.6 - 0.15 fm/c after the collision are in qualitative agreement with the data. Lattice QCD predicts a phase transition at ≈ 170 MeV.

PACS numbers: 13.85.Qk, 13.20.Fc, 13.20.He, 25.75.Dw

Experimental results from the Relativistic Heavy Ion Collider (RHIC) have established the formation of dense partonic matter in Au+Au collisions at $\sqrt{s_{NN}}$=200 GeV [1]. The large energy loss of light quarks and gluons [2] as well as that of heavy quarks [3] indicates that the matter has a very high density. The strong elliptic flow of light [4, 5] and charmed [3] hadrons indicates that the matter thermalizes rapidly. Such a high-density thermalized medium is expected to emit thermal radiation [6]. Thermal photons from the partonic phase are predicted to be the dominant source of direct photons for $1 < p_{\rm T} < 3$ GeV/c in Au+Au collisions at RHIC [7].

The measurement of direct photons for $1 < p_{\rm T} < 3$ GeV/c is notoriously difficult due to a large background from hadronic decay photons. The expected yield is only $\simeq 10$ % of the yield of the background photons [7]. An alternative approach is to measure "quasi-real" virtual photons which appear as low invariant mass e^+e^- pairs. In general, any source of high energy photons can also emit virtual photons which convert to low mass e^+e^- pairs. For example, a direct photon production process, such as gluon Compton scattering ($q + g \rightarrow q + \gamma$) has an associated process that produces low mass e^+e^- pairs through internal conversion ($q+g \rightarrow q+\gamma^* \rightarrow q+e^+e^-$).

The relation between photon production and the associated e^+e^- pair production can be written as

$$\frac{d^2n_{ee}}{dm_{ee}} = \frac{2\alpha}{3\pi}\frac{1}{m_{ee}}\sqrt{1-\frac{4m_e^2}{m_{ee}^2}}\left(1+\frac{2m_e^2}{m_{ee}^2}\right)Sdn_\gamma \qquad (1)$$

Here α is the fine structure constant, m_e and m_{ee} are the masses of the electron and the e^+e^- pair respectively, and S is a process dependent factor that goes to 1 as $m_{ee} \rightarrow 0$ or $m_{ee} \ll p_T$. Eq. (1) also describes the relation between the photons from hadron decays (e.g. $\pi^0, \eta \rightarrow \gamma\gamma$, and $\omega \rightarrow \gamma\pi^0$) and the e^+e^- pairs from Dalitz decays ($\pi^0, \eta \rightarrow e^+e^-\gamma$ and $\omega \rightarrow e^+e^-\pi^0$). For π^0 and η, the factor S is given by $S = |F(m_{ee}^2)|^2(1-\frac{m_{ee}^2}{M_h^2})^3$ [8], where M_h is the meson mass and $F(m_{ee}^2)$ is the form factor.

The factor S for a hadron h is zero for $m_{ee} > M_h$. We exploit this cut-off to separate the direct photon signal from the hadronic background. Since 80% of the hadronic photons are from π^0 decays, the signal to background (S/B) ratio for the direct photon signal improves by a factor of five for $m_{ee} > M_{\pi^0}$=135 MeV/c^2, thereby allowing a direct photon signal that is 10% of the background to be observed as a 50% excess of e^+e^- pairs.

In this Letter we present the analysis of e^+e^- pairs for $m_{ee} < 300$ MeV/c^2 and for $1 < p_{\rm T} < 5$ GeV/c in Au+Au and p+p collisions at $\sqrt{s_{NN}} = 200$ GeV recorded during 2004 and 2005, respectively. The PHENIX detector [9] measures electrons in the two central arms, each covering $|\Delta\eta| \leq 0.35$ in pseudorapidity and $\pi/2$ in azimuthal angle. The Au+Au analysis [10, 11] uses 8×10^8 minimum bias events corresponding to $92.2^{+2.5}_{-3.0}$% of the inelastic Au+Au cross section. The $p+p$ analysis [12] uses 43 nb^{-1} of minimum bias (MB) data recorded using the beam-beam counter trigger (BBC), and 2.25 pb^{-1} of single electron triggered data. Helium bags in both runs reduced the total conversion material, including the beam pipe, to $\sim$0.4% of a radiation length.

All electrons and positrons with $p_{\rm T} > 0.2$ GeV/c are combined into pairs. Pairs from photon conversions in the detector material are removed by a cut on the orientation of the pair in the magnetic field [10]. The combinatorial background is computed with a mixed-event technique and is subtracted [10, 11]. The S/B ratio of the pair signal is typically greater than 1 and is at least 0.1 in the kinematic range of this analysis. There are two sources of correlated background, one originating from two e^+e^- pairs from a meson decay and one from two hadrons decaying into e^+e^- pairs, either within the same jet or in back-to-back jets. The magnitude of the correlated background, about 10% of the signal in $p+p$, is determined from the like-sign pair data and subtracted [12]. The pair signal is corrected for the electron reconstruction efficiency and in p+p also for trigger efficiency, determined as a function of mass and pair $p_{\rm T}$ using a GEANT-based Monte Carlo simulation [13] of the PHENIX detector.

Fig. 1 shows the mass spectra of e^+e^- pairs in $p+p$ and Au+Au collisions for different ranges of pair $p_{\rm T}$,

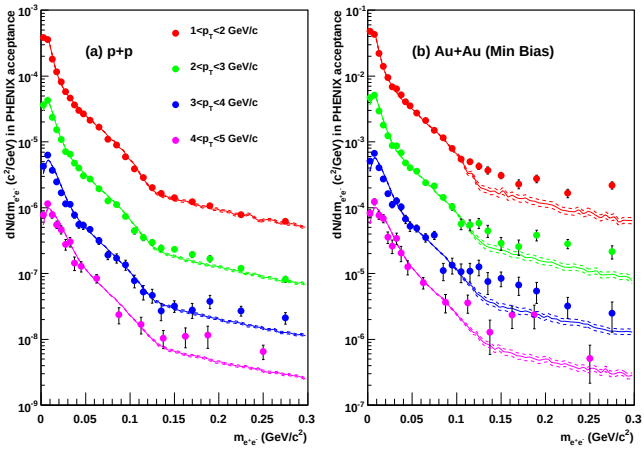

FIG. 1: (color online) The e^+e^- pair invariant mass distributions in (a) $p+p$ and (b) minimum bias Au+Au collisions. The $p_{\rm T}$ ranges are shown in the legend. The solid curves represent an estimate of hadronic sources; the dashed curves represent the uncertainty in the estimate.

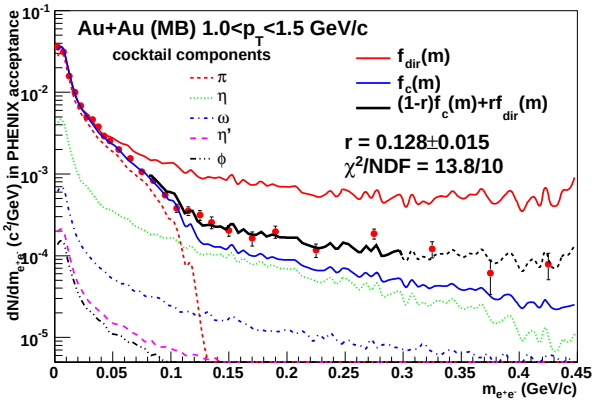

FIG. 2: (color online) Electron pair mass distribution for Au+Au minimum bias events for $1.0 < p_{\rm T} < 1.5$ GeV/c. The two-component fit is explained in the text. The fit range is $80 < m_{ee} < 300$ MeV/c^2. Black dashed curve shows $f(m_{ee})$ outside of the fit range.

comparing them to expected yields from a "cocktail" of hadron decays calculated using a Monte Carlo hadron decay generator based on meson production as measured by PHENIX [11, 12]. Detector resolution effects, which broaden the low mass peak for high $p_{\rm T}$, are included in the cocktail calculation. The open charm contribution, calculated with PYTHIA [14], is included in the cocktail, but is negligible. The cocktail is normalized to the data for $m_{ee} < 30$ MeV/c^2. A cocktail with absolute normalization agrees with the data within a 20% systematic uncertainty [11, 12]. The "knee" beginning at $m_{ee} \simeq 100$ MeV/c^2 corresponds to the π^0 cut-off, leading to an 80% reduction of background above this point. The $p+p$ data are consistent with the background for the lowest $p_{\rm T}$, but reveal a small excess over the background at higher $p_{\rm T}$ for $m_{ee} \geq M_{\pi^0}$. The Au+Au data show a much greater excess for all $p_{\rm T}$, which indicates an enhanced production of virtual photons in Au+Au collisions.

Internal conversion of direct photons is a possible source of the excess. Little contribution from other conventional sources of e^+e^- pairs is expected in this mass region since $\pi^+\pi^- \rightarrow e^+e^-$ can only contribute for $m_{ee} \geq 2M_{\pi}$. PHENIX has observed a strong enhancement of e^+e^- pairs for $150 < m_{ee} < 750$ MeV/c^2 in Au+Au, peaked at low $p_{\rm T}$ [11]. However, as shown in Fig. 2, the shape of the excess is consistent with that expected from internal conversion alone for $m_{ee} < 450$ MeV/c^2 and there is no significant indication of contributions from this "low mass enhancement" to the kinematic region of this analysis. Thus, we treat the excess entirely as internal conversion of photons and deduce the real direct photon yield from the e^+e^- pair using Eq. (1).

In order to quantify the excess, we fit a two-component function, $f(m_{ee}) = (1-r)f_c(m_{ee}) + rf_{dir}(m_{ee})$, to the mass distribution. Here $f_c(m_{ee})$ is the shape of the cocktail mass distribution (shown in Fig. 1), $f_{dir}(m_{ee})$ is the expected shape of the direct photon internal conversion, and r is the fit parameter. Since both $f_c(m_{ee})$ and $f_{dir}(m_{ee})$ are separately normalized to the data for $m_{ee} < 30$ MeV/c^2, where their shapes are nearly identical, this procedure preserves the normalization to the data in this region and determines the direct photon fraction r. We assume that the form factor for direct photons is $F(m_{ee}^2) = 1$, as one would expect from a purely point-like process. For direct photons from parton fragmentation or from hadronic gas, $F(m_{ee}^2)$ may be greater than one. If we arbitrarily set the form factor in $f_{dir}(m_{ee})$ to be the same as that in $f_\eta(m_{ee})$, r would decrease by $\simeq 10\%$.

For each $p_{\rm T}$ bin, $f(m_{ee})$ is fit to the data for several mass ranges $m_{low} < m_{ee} < 300$ MeV/c^2, with r the only fit parameter. Fig. 2 shows $f_{dir}(m_{ee})$ and $f_c(m_{ee})$ together with a fit result for Au+Au MB data for $1.0 < p_{\rm T} < 1.5$ GeV/c. The fit has $\chi^2/DOF = 13.8/10$. We note that the χ^2/DOF of the fit increases to 21.1/10 if $f_\eta(m_{ee})$ is used in place of $f_{dir}(m_{ee})$, demonstrating that the shape of the excess is inconsistent with $f_\eta(m_{ee})$. All fits to the Au+Au data for all centralities and for all $p_{\rm T}$ bins give a similarly good χ^2/DOF for $m_{low} > 80$ MeV/c^2.

This analysis measures the difference in *shape* of the spectra (the data, $f_c(m_{ee})$, and $f_{dir}(m_{ee})$). Therefore, we have focused on the uncertainties which can cause distortions in the mass distribution, namely (i) the particle composition in the hadronic background, (ii) the background (from mixed events and correlated pairs), (iii) the geometric acceptance due to detector active areas, and (iv) the efficiency corrections. These were

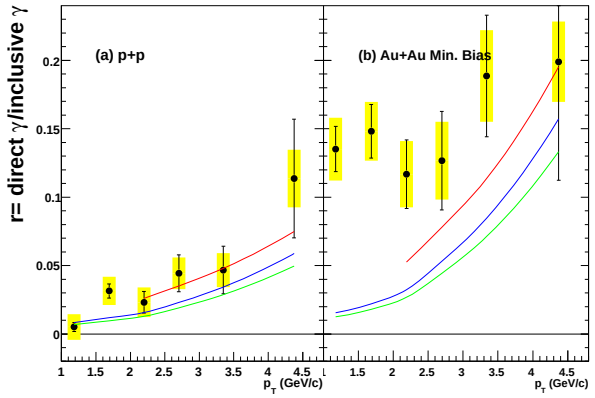

FIG. 3: (color online) The fraction of the direct photon component as a function of $p_{\rm T}$ in (a) $p+p$ and (b) Au+Au (min. bias). The error bars and the error band represent the statistical and systematic uncertainties, respectively. The curves are from a NLO pQCD calculation (see text).

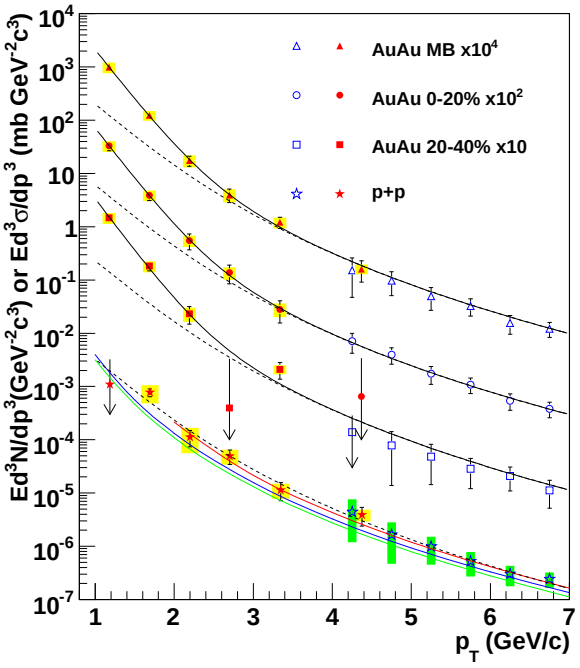

FIG. 4: (color online) Invariant cross section ($p+p$) and invariant yield (Au+Au) of direct photons as a function of $p_{\rm T}$. The filled points are from this analysis and open points are from [17, 18]. The three curves on the $p+p$ data represent NLO pQCD calculations, and the dashed curves show a modified power-law fit to the $p+p$ data, scaled by $T_{\rm AA}$. The black curves are exponential plus the $T_{\rm AA}$ scaled $p+p$ fit.

studied by a Monte Carlo simulation. First, the mass spectrum is distorted within the systematic uncertainties, and the fitting procedure is applied to the distorted spectrum to determine the systematic uncertainties in r. The systematic uncertainty due to the variation of m_{low} from 80 to 120 MeV/c^2 is also included. The largest source of the uncertainty is the particle composition in the hadronic cocktail, namely the η/π^0 ratio which is $0.48 \pm 0.03(0.08)$ at high $p_{\rm T}$ for $p+p$ (Au+Au) based on PHENIX measurements [15]. This corresponds to a $\simeq$ 7% ($\simeq$ 17%) uncertainty in the $p+p$ (Au+Au) cocktail for $100 < m_{ee} < 300$ MeV/c^2. Other sources cause only a few percent uncertainty in the data to cocktail ratio in the mass range once the cocktail is normalized to the data for $m_{ee} < 30$ MeV/c^2. Since the η/π^0 ratio is the largest source of uncertainty, we also studied fits with a three component function, $f_3(m_{ee}) = (1-r-r_\eta)f_c(m_{ee}) + r f_{dir}(m_{ee}) + r_\eta f_\eta(m_{ee})$, with a constraint on r_η such that $\eta/\pi^0 = 0.48 \pm 0.03(0.08)$ for $p+p$ (Au+Au). These alternative fits give consistent results for r within statistical uncertainties.

Figure 3(a) and (b) show the fraction r of the direct photon component determined by the two-component fit in $p+p$ and Au+Au, respectively. The curves represent the expectations from a next-to-leading-order perturbative QCD (NLO pQCD) calculation. For $p+p$, the curves show the ratio $d\sigma_\gamma^{NLO}(p_{\rm T})/d\sigma_\gamma^{incl}(p_{\rm T})$, where $d\sigma_\gamma^{NLO}(p_{\rm T})$ is the direct photon cross section from a NLO pQCD calculation [16] and $d\sigma_\gamma^{incl}(p_{\rm T})$ is the inclusive photon cross section. For Au+Au, the curves represent $T_{\rm AA} d\sigma_\gamma^{NLO}(p_{\rm T})/dN_\gamma^{incl}(p_{\rm T})$, where $T_{\rm AA}$ is the Glauber nuclear overlap function and $dN_\gamma^{incl}(p_{\rm T})$ is the inclusive photon yield. Inclusive spectra $d\sigma_\gamma^{incl}$ and dN_γ^{incl} are determined as described later. The three curves correspond, from top to bottom, to the theory scale $\mu = 0.5\ p_{\rm T}$, $p_{\rm T}$, and $2\ p_{\rm T}$, respectively, showing the scale dependence of the theory. While the fraction r is consistent with the NLO pQCD calculation in $p+p$, it is larger than the calculation in Au+Au for $p_{\rm T} < 3.5$ GeV/c.

The direct photon fraction r in Fig. 3 is converted to the direct photon yield as $dN^{dir}(p_{\rm T}) = r \times dN^{incl}(p_{\rm T})$. The inclusive photon yield for each $p_{\rm T}$ bin is determined by $dN_\gamma^{incl} = N_{ee}^{data} \times (dN_\gamma^c/N_{ee}^c)$, where N_{ee}^{data} and N_{ee}^c are the measured and the absolutely normalized cocktail e^+e^- pair yields, respectively, both for $m_{ee} < 30$ MeV/c^2 and dN_γ^c is the yield of photons from the cocktail. Here we use the fact the ratio of the photon yield to the e^+e^- pair yield for $m_{ee} < 30$ MeV/c^2 calculated from Eq. (1) is the same within a few percent for any photon sources.

In Fig. 4 the direct photon spectra thus obtained are compared with the direct photon data from [17, 18] and NLO pQCD calculations. The systematic uncertainty of the inclusive photon (14% from the uncertainty in the e^+e^- pair acceptance correction[11]) is added in quadrature with the systematic uncertainties of the data. The $p+p$ data are shown as an invariant cross section using $d\sigma = \sigma_{pp}^{inel} dN$. The direct photon data of this analysis are obtained from the yield of e^+e^- pairs using Eq. (1)

under the assumption that other contributions are negligible. In the mass range of the analysis, Eq. (1) implies $\frac{d^2n_{ee}}{dm_{ee}} = \frac{2\alpha}{3\pi}\frac{1}{m_{ee}}dn_\gamma$. Thus the yield of e^+e^- pairs for $100 < m_{ee} < 300$ MeV/c^2 can be obtained by multiplying the photon yield by a factor of $\frac{2\alpha}{3\pi}\log\frac{300}{100} = 1.7\times10^{-3}$.

The pQCD calculation is consistent with the $p+p$ data within the theoretical uncertainties for $p_{\rm T} > 2$ GeV/c. A similarly good agreement is observed for π^0 [19]. The $p+p$ data can be well described by a modified power-law function ($A_{pp}(1+p_{\rm T}^2/b)^{-n}$) as shown by the dashed curve in the figure. The Au+Au data are above the $p+p$ fit curve scaled by $T_{\rm AA}$ for $p_{\rm T} < 2.5$ GeV/c, indicating that the direct photon yield in the low $p_{\rm T}$ range increases faster than the binary-scaled $p+p$ cross section.

We fit an exponential plus the $T_{\rm AA}$-scaled $p+p$ fit function ($Ae^{-p_{\rm T}/T} + T_{\rm AA}\times A_{pp}(1+p_{\rm T}^2/b)^{-n}$) to the Au+Au data. The only free parameters in the fit are A and the inverse slope T of the exponential term. The systematic uncertainties in T are estimated by changing the $p+p$ fit component and the Au+Au data points within the systematic uncertainties. The results of the fits are summarized in Table I, where A is converted to dN/dy for $p_T > 1$GeV/c. For central collisions, $T = 221 \pm 23 \pm 18$ MeV. If a power-law function ($\propto p_T^{-n}$) is used to fit the $p+p$ spectrum, T is higher by 24 MeV. If the direct photons in Au+Au collisions are of thermal origin, the inverse slope T is related to the initial temperature T_{init} of the dense matter. In hydrodynamical models, T_{init} is 1.5 to 3 times T due to the space-time evolution [20]. Several hydrodynamical models can reproduce the central Au+Au data within a factor of two. These assume formation of a hot system with initial temperature ranging from $T_{init} = 300$ MeV at thermalization time $\tau_0 = 0.6$ fm/c to $T_{init} = 600$ MeV at $\tau_0 = 0.15$ fm/c [7, 20].

In conclusion, we have measured e^+e^- pairs with $m_{ee} < 300$ MeV/c^2 and $1 < p_{\rm T} < 5$ GeV/c in $p+p$ and Au+Au collisions. The $p+p$ data show a small excess over the hadronic background while the Au+Au data show a much larger excess. Treating the excess as internal conversion of direct photons, the direct photon yield is deduced. The direct photon yields are consistent with a NLO pQCD calculation in $p+p$. In central Au+Au collisions the shape of the direct photon spectrum above the $T_{\rm AA}$-scaled $p+p$ spectrum is exponential in $p_{\rm T}$, with an inverse slope $T = 221 \pm 23({\rm stat}) \pm 18({\rm sys})$ MeV. Hydrodynamical models with $T_{init} \approx 300 - 600$ MeV at $\tau_0 \approx 0.6 - 0.15$ fm/c are in qualitative agreement with the data. Lattice QCD predicts a phase transition at $\approx$ 170 MeV[1].

TABLE I: Summary of the fits. The first and second errors are statistical and systematical, respectively.

centrality	$dN/dy(p_T > 1{\rm GeV}/c)$	T(MeV)	χ^2/DOF
0-20%	$1.10 \pm 0.20 \pm 0.30$	$221 \pm 23 \pm 18$	3.6/4
20-40%	$0.52 \pm 0.08 \pm 0.14$	$215 \pm 20 \pm 15$	5.2/3
MB	$0.33 \pm 0.04 \pm 0.09$	$224 \pm 16 \pm 19$	0.9/4

We thank the staff of the Collider-Accelerator and Physics Departments at BNL for their vital contributions. We acknowledge support from the Department of Energy and NSF (U.S.A.), MEXT and JSPS (Japan), CNPq and FAPESP (Brazil), NSFC (China), MSMT (Czech Republic), IN2P3/CNRS, and CEA (France), BMBF, DAAD, and AvH (Germany), OTKA (Hungary), DAE (India), ISF (Israel), KRF and KOSEF (Korea), MES, RAS, and FAAE (Russia), VR and KAW (Sweden), U.S. CRDF for the FSU, US-Hungarian NSF-OTKA-MTA, and US-Israel BSF.

* Deceased
† PHENIX Spokesperson: jacak@skipper.physics.sunysb.edu

[1] K. Adcox et al., Nucl. Phys. A **757**, 184 (2005).
[2] K. Adcox et al., Phys. Rev. Lett. **88**, 022301 (2002).
[3] A. Adare et al., Phys. Rev. Lett. **98**, 172301 (2007).
[4] K. H. Ackermann et al., Phys. Rev. Lett. **86**, 402 (2001).
[5] S. S. Adler et al., Phys. Rev. Lett. **91**, 182301 (2003).
[6] P. Stankus, Ann. Rev. Nucl. Part. Sci. **55**, 517 (2005).
[7] S. Turbide et al., Phys. Rev. **C69**, 014903 (2004).
[8] L. G. Landsberg, Phys. Rept. **128**, 301 (1985).
[9] K. Adcox et al., Nucl. Instrum. Meth. **A499**, 469 (2003).
[10] A. Toia, arXiv:0711.2118 [nucl-ex]; Adare et al., in preparation (PPG088).
[11] S. Afanasiev et al. (2007), arXiv:0706.3034 [nucl-ex].
[12] A. Adare et al. (2008), arXiv:0802.0050 [hep-ex].
[13] GEANT3.21 CERN Program Library.
[14] T. Sjöstrand et al., Comp. Phys. Comm. **135**, 238 (2001).
[15] S. S. Adler et al., Phys. Rev. Lett. **96**, 202301 (2006).
[16] L. E. Gordon and W. Vogelsang, Phys. Rev. **D48**, 3136 (1993), and W. Vogelsang, private communication.
[17] S. S. Adler et al., Phys. Rev. Lett. **94**, 232301 (2005).
[18] S. S. Adler et al., Phys. Rev. Lett. **98**, 012002 (2007).
[19] S. S. Adler et al., Phys. Rev. Lett. **91**, 241803 (2003).
[20] D. d'Enterria and D. Peressounko, Eur. Phys. J. **C46**, 451 (2006), and references are therein.

Physics Letters B 670 (2009) 313–320

Contents lists available at ScienceDirect

Physics Letters B

www.elsevier.com/locate/physletb

Dilepton mass spectra in $p+p$ collisions at $\sqrt{s}=200$ GeV and the contribution from open charm

PHENIX Collaboration

A. Adare [h], S. Afanasiev [v], C. Aidala [i], N.N. Ajitanand [av], Y. Akiba [ap,aq], H. Al-Bataineh [ak], J. Alexander [av], K. Aoki [aa,ap], L. Aphecetche [ax], R. Armendariz [ak], S.H. Aronson [c], J. Asai [aq], E.T. Atomssa [ab], R. Averbeck [aw], T.C. Awes [al], B. Azmoun [c], V. Babintsev [r], G. Baksay [n], L. Baksay [n], A. Baldisseri [k], K.N. Barish [d], P.D. Barnes [ad], B. Bassalleck [aj], S. Bathe [d], S. Batsouli [al], V. Baublis [ao], A. Bazilevsky [c], S. Belikov [c,1], R. Bennett [aw], Y. Berdnikov [as], A.A. Bickley [h], J.G. Boissevain [ad], H. Borel [k], K. Boyle [aw], M.L. Brooks [ad], H. Buesching [c], V. Bumazhnov [r], G. Bunce [c,aq], S. Butsyk [ad,aw], S. Campbell [aw], B.S. Chang [be], J.-L. Charvet [k], S. Chernichenko [r], J. Chiba [w], C.Y. Chi [i], M. Chiu [s], I.J. Choi [be], T. Chujo [bb], P. Chung [av], A. Churyn [r], V. Cianciolo [al], C.R. Cleven [p], B.A. Cole [i], M.P. Comets [am], P. Constantin [ad], M. Csanád [m], T. Csörgő [y], T. Dahms [aw], K. Das [o], G. David [c], M.B. Deaton [a], K. Dehmelt [n], H. Delagrange [ax], A. Denisov [r], D. d'Enterria [i], A. Deshpande [aq,aw], E.J. Desmond [c], O. Dietzsch [at], A. Dion [aw], M. Donadelli [at], O. Drapier [ab], A. Drees [aw], A.K. Dubey [bd], A. Durum [r], V. Dzhordzhadze [d], Y.V. Efremenko [al], J. Egdemir [aw], F. Ellinghaus [h], W.S. Emam [d], A. Enokizono [ac], H. En'yo [ap,aq], S. Esumi [ba], K.O. Eyser [d], D.E. Fields [aj,aq], M. Finger [e,v], M. Finger Jr. [e,v], F. Fleuret [ab], S.L. Fokin [z], Z. Fraenkel [bd,1], J.E. Frantz [aw], A. Franz [c], A.D. Frawley [o], K. Fujiwara [ap], Y. Fukao [aa,ap], T. Fusayasu [ai], S. Gadrat [ae], I. Garishvili [ay], A. Glenn [h], H. Gong [aw], M. Gonin [ab], J. Gosset [k], Y. Goto [ap,aq], R. Granier de Cassagnac [ab], N. Grau [u], S.V. Greene [bb], M. Grosse Perdekamp [s,aq], T. Gunji [g], H.-Å. Gustafsson [af], T. Hachiya [q], A. Hadj Henni [ax], C. Haegemann [aj], J.S. Haggerty [c], H. Hamagaki [g], R. Han [an], H. Harada [q], E.P. Hartouni [ac], K. Haruna [q], E. Haslum [af], R. Hayano [g], M. Heffner [ac], T.K. Hemmick [aw], T. Hester [d], X. He [p], H. Hiejima [s], J.C. Hill [u], R. Hobbs [aj], M. Hohlmann [n], W. Holzmann [av], K. Homma [q], B. Hong [y], T. Horaguchi [ap,az], D. Hornback [ay], T. Ichihara [ap,aq], K. Imai [aa,ap], M. Inaba [ba], Y. Inoue [ar,ap], D. Isenhower [a], L. Isenhower [a], M. Ishihara [ap], T. Isobe [g], M. Issah [av], A. Isupov [v], B.V. Jacak [aw,2], J. Jia [i], J. Jin [i], O. Jinnouchi [aq], B.M. Johnson [c,*], K.S. Joo [ah], D. Jouan [am], F. Kajihara [g], S. Kametani [g,bc], N. Kamihara [ap], J. Kamin [aw], M. Kaneta [aq], J.H. Kang [be], H. Kanou [ap,az], D. Kawall [aq], A.V. Kazantsev [z], A. Khanzadeev [ao], J. Kikuchi [bc], D.H. Kim [ah], D.J. Kim [be], E. Kim [au], E. Kinney [h], A. Kiss [m], E. Kistenev [c], A. Kiyomichi [ap], J. Klay [ac], C. Klein-Boesing [ag], L. Kochenda [ao], V. Kochetkov [r], B. Komkov [ao], M. Konno [ba], D. Kotchetkov [d], A. Kozlov [bd], A. Král [j], A. Kravitz [i], J. Kubart [e,t], G.J. Kunde [ad], N. Kurihara [g], K. Kurita [ar,ap], M.J. Kweon [y], Y. Kwon [ay,be], G.S. Kyle [ak], R. Lacey [av], Y.-S. Lai [i], J.G. Lajoie [u], A. Lebedev [u], D.M. Lee [ad], M.K. Lee [be], T. Lee [au], M.J. Leitch [ad], M.A.L. Leite [at], B. Lenzi [at], T. Liška [j], A. Litvinenko [v], M.X. Liu [ad], X. Li [f], B. Love [bb], D. Lynch [c], C.F. Maguire [bb], Y.I. Makdisi [c], A. Malakhov [v], M.D. Malik [aj], V.I. Manko [z], Y. Mao [an,ap], L. Mašek [e,t], H. Masui [ba], F. Matathias [i], M. McCumber [aw], P.L. McGaughey [ad], Y. Miake [ba], P. Mikeš [e,t], K. Miki [ba], T.E. Miller [bb], A. Milov [aw], S. Mioduszewski [c], M. Mishra [b], J.T. Mitchell [c], M. Mitrovski [av], A. Morreale [d], D.P. Morrison [c], T.V. Moukhanova [z], D. Mukhopadhyay [bb], J. Murata [ar,ap], S. Nagamiya [w], Y. Nagata [ba], J.L. Nagle [h], M. Naglis [bd], I. Nakagawa [ap,aq], Y. Nakamiya [q], T. Nakamura [q], K. Nakano [ap,az], J. Newby [ac], M. Nguyen [aw], B.E. Norman [ad], A.S. Nyanin [z], E. O'Brien [c], S.X. Oda [g], C.A. Ogilvie [u], H. Ohnishi [ap], H. Okada [aa,ap], K. Okada [aq], M. Oka [ba], O.O. Omiwade [a], A. Oskarsson [af], M. Ouchida [q], K. Ozawa [g], R. Pak [c], D. Pal [bb], A.P.T. Palounek [ad], V. Pantuev [aw], V. Papavassiliou [ak], J. Park [au], W.J. Park [y], S.F. Pate [ak], H. Pei [u], J.-C. Peng [s], H. Pereira [k], V. Peresedov [v], D.Yu. Peressounko [z], C. Pinkenburg [c], M.L. Purschke [c], A.K. Purwar [ad], H. Qu [p], J. Rak [aj], A. Rakotozafindrabe [ab], I. Ravinovich [bd], K.F. Read [al,ay], S. Rembeczki [n], M. Reuter [aw], K. Reygers [ag], V. Riabov [ao], Y. Riabov [ao], G. Roche [ae], A. Romana [ab,1], M. Rosati [u], S.S.E. Rosendahl [af], P. Rosnet [ae], P. Rukoyatkin [v], V.L. Rykov [ap], B. Sahlmueller [ag], N. Saito [aa,ap,aq], T. Sakaguchi [c], S. Sakai [ba], H. Sakata [q], V. Samsonov [ao], S. Sato [w], S. Sawada [w], J. Seele [h], R. Seidl [s], V. Semenov [r], R. Seto [d], D. Sharma [bd], I. Shein [r], A. Shevel [ao,av], T.-A. Shibata [ap,az], K. Shigaki [q], M. Shimomura [ba], K. Shoji [aa,ap], A. Sickles [aw], C.L. Silva [at], D. Silvermyr [al], C. Silvestre [k], K.S. Sim [y], C.P. Singh [b], V. Singh [b], S. Skutnik [u], M. Slunečka [e,v], A. Soldatov [r],

0370-2693/$ – see front matter © 2008 Elsevier B.V. All rights reserved.
doi:10.1016/j.physletb.2008.10.064

R.A. Soltz [ac], W.E. Sondheim [ad], S.P. Sorensen [ay], I.V. Sourikova [c], F. Staley [k], P.W. Stankus [al], E. Stenlund [af], M. Stepanov [ak], A. Ster [x], S.P. Stoll [c], T. Sugitate [q], C. Suire [am], J. Sziklai [x], T. Tabaru [aq], S. Takagi [ba], E.M. Takagui [at], A. Taketani [ap,aq], Y. Tanaka [ai], K. Tanida [ap,aq], M.J. Tannenbaum [c], A. Taranenko [av], P. Tarján [l], T.L. Thomas [aj], M. Togawa [aa,ap], A. Toia [aw], J. Tojo [ap], L. Tomášek [t], H. Torii [ap], R.S. Towell [a], V.-N. Tram [ab], I. Tserruya [bd], Y. Tsuchimoto [q], C. Vale [u], H. Valle [bb], H.W. van Hecke [ad], J. Velkoška [bb], R. Vertesi [l], A.A. Vinogradov [z], M. Virius [j], V. Vrba [t], E. Vznuzdaev [ao], M. Wagner [aa,ap], D. Walker [aw], X.R. Wang [ak], Y. Watanabe [ap,aq], J. Wessels [ag], S.N. White [c], D. Winter [i], C.L. Woody [c], M. Wysocki [h], W. Xie [aq], Y.L. Yamaguchi [bc], A. Yanovich [r], Z. Yasin [d], J. Ying [p], S. Yokkaichi [ap,aq], G.R. Young [al], I. Younus [aj], I.E. Yushmanov [z], W.A. Zajc [i], O. Zaudtke [ag], C. Zhang [al], S. Zhou [f], J. Zimányi [x,1], L. Zolin [v]

[a] *Abilene Christian University, Abilene, TX 79699, USA*
[b] *Department of Physics, Banaras Hindu University, Varanasi 221005, India*
[c] *Brookhaven National Laboratory, Upton, NY 11973-5000, USA*
[d] *University of California—Riverside, Riverside, CA 92521, USA*
[e] *Charles University, Ovocný trh 5, Praha 1, 116 36, Prague, Czech Republic*
[f] *China Institute of Atomic Energy (CIAE), Beijing, People's Republic of China*
[g] *Center for Nuclear Study, Graduate School of Science, University of Tokyo, 7-3-1 Hongo, Bunkyo, Tokyo 113-0033, Japan*
[h] *University of Colorado, Boulder, CO 80309, USA*
[i] *Columbia University, New York, NY 10027, and Nevis Laboratories, Irvington, NY 10533, USA*
[j] *Czech Technical University, Zikova 4, 166 36 Prague 6, Czech Republic*
[k] *Dapnia, CEA Saclay, F-91191, Gif-sur-Yvette, France*
[l] *Debrecen University, H-4010 Debrecen, Egyetem tér 1, Hungary*
[m] *ELTE, Eötvös Loránd University, H-1117 Budapest, Pázmány P.s. 1/A, Hungary*
[n] *Florida Institute of Technology, Melbourne, FL 32901, USA*
[o] *Florida State University, Tallahassee, FL 32306, USA*
[p] *Georgia State University, Atlanta, GA 30303, USA*
[q] *Hiroshima University, Kagamiyama, Higashi-Hiroshima 739-8526, Japan*
[r] *IHEP Protvino, State Research Center of Russian Federation, Institute for High Energy Physics, Protvino 142281, Russia*
[s] *University of Illinois at Urbana-Champaign, Urbana, IL 61801, USA*
[t] *Institute of Physics, Academy of Sciences of the Czech Republic, Na Slovance 2, 182 21 Prague 8, Czech Republic*
[u] *Iowa State University, Ames, IA 50011, USA*
[v] *Joint Institute for Nuclear Research, 141980 Dubna, Moscow Region, Russia*
[w] *KEK, High Energy Accelerator Research Organization, Tsukuba, Ibaraki 305-0801, Japan*
[x] *KFKI Research Institute for Particle and Nuclear Physics of the Hungarian Academy of Sciences (MTA KFKI RMKI), H-1525 Budapest 114, PO Box 49, Budapest, Hungary*
[y] *Korea University, Seoul 136-701, Republic of Korea*
[z] *Russian Research Center "Kurchatov Institute", Moscow, Russia*
[aa] *Kyoto University, Kyoto 606-8502, Japan*
[ab] *Laboratoire Leprince-Ringuet, Ecole Polytechnique, CNRS-IN2P3, Route de Saclay, F-91128 Palaiseau, France*
[ac] *Lawrence Livermore National Laboratory, Livermore, CA 94550, USA*
[ad] *Los Alamos National Laboratory, Los Alamos, NM 87545, USA*
[ae] *LPC, Université Blaise Pascal, CNRS-IN2P3, Clermont-Fd, 63177 Aubiere Cedex, France*
[af] *Department of Physics, Lund University, Box 118, SE-221 00 Lund, Sweden*
[ag] *Institut für Kernphysik, University of Muenster, D-48149 Muenster, Germany*
[ah] *Myongji University, Yongin, Kyonggido 449-728, Republic of Korea*
[ai] *Nagasaki Institute of Applied Science, Nagasaki-shi, Nagasaki 851-0193, Japan*
[aj] *University of New Mexico, Albuquerque, NM 87131, USA*
[ak] *New Mexico State University, Las Cruces, NM 88003, USA*
[al] *Oak Ridge National Laboratory, Oak Ridge, TN 37831, USA*
[am] *IPN-Orsay, Universite Paris Sud, CNRS-IN2P3, BP1, F-91406 Orsay, France*
[an] *Peking University, Beijing, People's Republic of China*
[ao] *PNPI, Petersburg Nuclear Physics Institute, Gatchina, Leningrad Region 188300, Russia*
[ap] *RIKEN, The Institute of Physical and Chemical Research, Wako, Saitama 351-0198, Japan*
[aq] *RIKEN BNL Research Center, Brookhaven National Laboratory, Upton, NY 11973-5000, USA*
[ar] *Physics Department, Rikkyo University, 3-34-1 Nishi-Ikebukuro, Toshima, Tokyo 171-8501, Japan*
[as] *Saint Petersburg State Polytechnic University, St. Petersburg, Russia*
[at] *Universidade de São Paulo, Instituto de Física, Caixa Postal 66318, São Paulo CEP05315-970, Brazil*
[au] *System Electronics Laboratory, Seoul National University, Seoul, Republic of Korea*
[av] *Chemistry Department, Stony Brook University, Stony Brook, SUNY, NY 11794-3400, USA*
[aw] *Department of Physics and Astronomy, Stony Brook University, SUNY, Stony Brook, NY 11794, USA*
[ax] *SUBATECH (Ecole des Mines de Nantes, CNRS-IN2P3, Université de Nantes), BP 20722-44307, Nantes, France*
[ay] *University of Tennessee, Knoxville, TN 37996, USA*
[az] *Department of Physics, Tokyo Institute of Technology, Oh-okayama, Meguro, Tokyo 152-8551, Japan*
[ba] *Institute of Physics, University of Tsukuba, Tsukuba, Ibaraki 305, Japan*
[bb] *Vanderbilt University, Nashville, TN 37235, USA*
[bc] *Waseda University, Advanced Research Institute for Science and Engineering, 17 Kikui-cho, Shinjuku-ku, Tokyo 162-0044, Japan*
[bd] *Weizmann Institute, Rehovot 76100, Israel*
[be] *Yonsei University, IPAP, Seoul 120-749, Republic of Korea*

ARTICLE INFO

Article history:
Received 5 February 2008
Received in revised form 30 October 2008
Accepted 31 October 2008
Available online 11 November 2008

ABSTRACT

PHENIX has measured the electron–positron pair mass spectrum from 0 to 8 GeV/c^2 in $p+p$ collisions at $\sqrt{s}=200$ GeV. The contributions from light meson decays to e^+e^- pairs have been determined based on measurements of hadron production cross sections by PHENIX. Within the systematic uncertainty of $\sim 20\%$ they account for all e^+e^- pairs in the mass region below ~ 1 GeV/c^2. The e^+e^- pair yield

Editor: V. Metag

remaining after subtracting these contributions is dominated by semileptonic decays of charmed hadrons correlated through flavor conservation. Using the spectral shape predicted by PYTHIA, we estimate the charm production cross section to be $544 \pm 39(\text{stat}) \pm 142(\text{syst}) \pm 200(\text{model})$ μb, which is consistent with QCD calculations and measurements of single leptons by PHENIX.

© 2008 Elsevier B.V. All rights reserved.

Because of the large mass of the charm quark, approximately 1.3 GeV/c^2, it is commonly expected that the charm production cross section can be calculated in quantum chromo-dynamics (QCD) using perturbative methods (pQCD). Comparing such calculations with experimental data serves as a test of pQCD and helps to quantify the importance of higher order terms. Perturbative calculations suggest that charm production at RHIC energies results primarily from gluon fusion, so charm can probe gluonic interactions in the matter formed in heavy ion collisions at RHIC [1]. Medium modifications of heavy quark production and the suppression of bound charmonium states like the J/ψ have received considerable attention and are thought to be keys to better understanding properties of strongly interacting matter. Experiments at RHIC with polarized proton beams will allow the measurement of spin asymmetries in charm production, which gives access to the spin contribution of the gluons to the proton in a new channel [2].

To date, charm production has been calculated in next-to-leading-order (NLO) and fixed-order plus next-to-leading-log approximations (FONLL) [3]. These calculations are consistent with the measured D meson cross sections in 1.96 TeV $p\bar{p}$ collisions published by CDF [4] as well as with single lepton measurements, electrons [5] and muons [6], in 200 GeV $p+p$ collisions from PHENIX. However, the theoretical uncertainties are considerable, at least a factor of two [3] or even larger [7], and the data prefer larger cross sections within these uncertainties.[3] In this Letter we present a different method to determine the charm cross section using electron–positron pairs measured with PHENIX during the RHIC $p+p$ run in 2005.

Electrons are measured in the two PHENIX central arm spectrometers [10], which each cover $|\eta| \leqslant 0.35$ in pseudo-rapidity and $\Delta\phi = \pi/2$ in azimuth in a nearly back-to-back configuration. For charged particles drift chambers (DC) measure the deflection angles in a magnetic field to determine their momenta. Ring imaging Cherenkov counters (RICH) as well as electromagnetic calorimeters (EMCal) distinguish electrons from other particles. The electron analysis is described in detail in [5].

Two data sets are used in the analysis. A reference sample of events was selected with a minimum bias interaction trigger (MB) that was based on beam–beam counters (BBC). The BBC trigger cross section is 23.0 ± 2.2 mb or $55 \pm 5\%$ of the inelastic $p+p$ cross section. Simulations, and data collected without requiring the BBC trigger, indicate that the triggered events include $79 \pm 2\%$ of events with particles in the central arm acceptance. This number coincides with the fraction of non-diffractive events triggered by the BBC from which we conclude that for non-diffractive collisions the BBC trigger can have only little bias towards events with particles produced in the central arms. The bulk of the data sample was recorded requiring a coincidence of the BBC trigger with a single electron trigger (ERT) that matches hits in the RICH to 2×2 trigger tiles in the EMCal with a minimum energy of 400 MeV. In the active area the ERT trigger has a very high efficiency for electrons; around 500 MeV it reaches approximately 50% and then saturates around 1 GeV close to 100%. After applying an interaction-vertex cut of ±30 cm the total integrated luminosities were 43 nb^{-1} and 2.25 pb^{-1} for the MB and ERT trigger, respectively.

All electrons and positrons with $p_T > 200$ MeV/c are combined into like- and unlike-sign pairs. For each pair we check that at least one of the tracks was registered by the ERT trigger. The event is rejected if the two tracks of the pair overlap in any of the detectors; this cut removes 2% of the e^+e^- pairs. This cut is necessary to assure that the combinatorial pair background is reproduced from mixed events. Pairs originating from photon conversions in the detector material are removed by a cut on the orientation of the opening angle of the pairs with respect to the magnetic field; this cut removes 98% of the pairs from photon conversions [11]. Fig. 1 shows the raw yields as a function of pair mass for both like- and unlike-sign pairs. The unlike-sign spectrum measures the signal from hadron decays and open charm plus background, while the like-sign spectrum measures only the background. The PHENIX central arms accept equal number of electrons and positrons, however, because of the two-arm geometry and the magnetic field, the acceptance for electrons and positrons covers a different range in azimuthal angle. Therefore the shape of the mass distribution is different for like- and unlike-sign pairs.

We have developed two independent methods to subtract the background. In the first method we decompose the background into two components: a combinatorial background made of uncorrelated pairs and a background of correlated pairs. The combinatorial background is determined from mixed events using the procedure described in more detail in [11,12] and in Appendix A of [13]. The mixed events are generated from the MB sample. For each pair we check that at least one of the two partners fulfill the ERT trigger condition. The mass distribution for the like-sign mixed event background does not have the same shape as the measured distribution, which indicates the presence of additional correlated background in the data. This can be studied in more detail investigating the pair distributions in mass versus transverse momentum. The biggest differences in shape are at low mass and large p_T as well as at low p_T and large mass, where the data show more yield than the mixed events. We therefore use a region, roughly corresponding to a mass of 300 MeV/c^2, p_T above 400 MeV/c and a transverse mass $m_T = \sqrt{m^2 + (p_T/c)^2}$ below 1.2 GeV/c^2, to normalize the mixed event background to the data.[4] In this region also the shape of the mass distributions are very similar. After normalizing the like-sign mass distribution from mixed events we determine the number of uncorrelated like-sign background pairs N_{++} and N_{--} by integrating the distributions. The normalization of the uncorrelated unlike-sign mixed event background is then given by $2\sqrt{N_{++}N_{--}}$.

The mixed event backgrounds as well as the distributions after subtraction are also shown in Fig. 1. The remaining pairs, like and unlike, are considered correlated pairs, where the like-sign distribution only contains correlated background pairs while the unlike contains also the signal. The correlated background pairs

* Corresponding author.
E-mail addresses: jacak@skipper.physics.sunysb.edu (B.V. Jacak), brant@bnl.gov (B.M. Johnson).

[1] Deceased.

[2] PHENIX Spokesperson.

[3] The STAR Collaboration reports an even larger cross section [8,9], which is about a factor of 2–3 above of what can be accommodated in pQCD calculations.

[4] The exact region used for the normalization is given by the following four conditions $m > 300$ MeV/c^2, $m_T < 1.2$ MeV/c^2, $p_T/c - 1.5m \leqslant 200$ MeV/c^2, and $p_T/c - 0.75m \geqslant -150$ MeV/c^2.

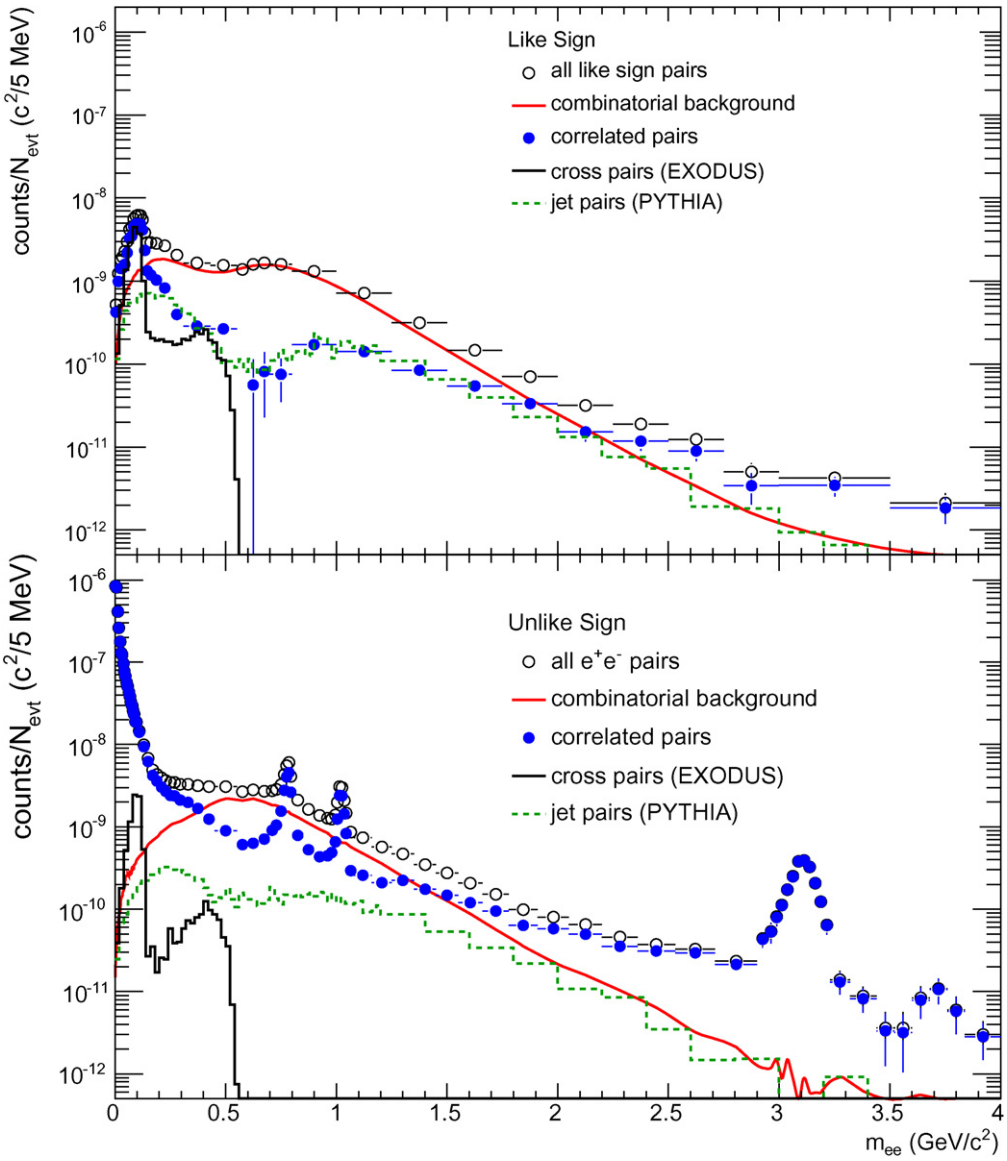

Fig. 1. Raw dielectron spectra. The top panel shows like-sign pairs as measured in the experiment, the combinatorial background from mixed events, the correlated pair background obtained by subtracting the combinatorial background, and the individual contributions from cross and jet pairs to the correlated background (see text). The bottom panel shows the same distributions for unlike-sign pairs.

stem from two sources. "Cross pairs" result from decays of single π^0 or η mesons with two electron pairs in the final state, such as double Dalitz decays, Dalitz decays plus conversion of the accompanying photon, and $\gamma\gamma$ decays where both photons convert. These pairs have a mass lower than the η mass of 548 MeV/c^2. Cross pairs were simulated using our hadron decay generator EXODUS including the PHENIX acceptance.[5] "Jet pairs" are produced by two independent hadron decays yielding electron pairs, either within the same jet or in the back-to-back jets. Jet pairs were simulated using minimum bias events generated with PYTHIA[6] with the branching ratio of the π^0 Dalitz decay set to 100% to enhance the sample of jet pairs per event. We exclude all pairs from single hadron decays so that cross pairs as well as any signal in the unlike-sign pairs are removed. Electrons and positrons from cross and jet pairs are filtered through the PHENIX acceptance and weighted according to the electron identification and ERT trigger efficiency. Pairs from simulated mixed events are subtracted from the like- and unlike-sign pair distributions to find the correlated pair distributions. The mixed event background is normalized by the same method used in the data analysis, described previously. It was found that correlated pairs from the same jet typically have small mass and large p_T while those from back-to-back jets have large mass and smaller p_T.

Correlated background pairs occur in all charge combinations. The simulated correlated like-sign background is then normalized to the measured correlated like-sign background by simultaneously fitting simulated cross and jet pair mass distributions to the measured correlated like-sign pair mass spectrum. Since the Monte Carlo simulation preserves the relative abundance of like- and unlike-sign pairs after filtering them through the

[5] The PHENIX acceptance is parameterized as function of the azimuthal angle ϕ of a track, its p_T, and charge sign q by conditions for the DC and the RICH for each spectrometer arm separately: $\phi_{\min} < \phi + qk_{\rm DC}/p_T < \phi_{\max}$ and $\phi_{\min} < \phi + qk_{\rm RICH}/p_T < \phi_{\max}$. The parameters are $k_{\rm DC} = 0.206$ rad GeV c^{-1}, $k_{\rm RICH} = 0.309$ rad GeV c^{-1}, $\phi_{\min} = -3/16\pi$ to $\phi_{\max} = 5/16\pi$, and $\phi_{\min} = 11/16\pi$ to $\phi_{\max} = 19/16\pi$.

[6] We used PYTHIA 6.319 changing PYTHIA parameters as follows: MSEL = 0 with the following processes switched on MSUB 11, 12, 13, 28, 53, 68, PARP(91) = 1.5 (k_T), MSTP(32) = 4 (Q^2 scale), and CKIN(3) = 2.0 (min. parton p_T).

PHENIX acceptance, we apply the same two normalization factors, one for cross- the other for jet-pairs, to the unlike-sign correlated background. The normalized contributions of both correlated background sources are also shown in Fig. 1. The unlike-sign dilepton signal is extracted by subtracting the simulated unlike-sign correlated backgrounds from the distribution of all correlated pairs.

In our second method to estimate the unlike-sign pair background we make no assumptions about the shape of the correlated background nor about the decomposition of correlated and uncorrelated background (see pp. 85–86 in [13]). We use the measured like-sign distribution which contains only the background, but with a different acceptance than the unlike-sign. We correct for this acceptance difference with the ratio of the mixed event distributions, $N_{+-}/2\sqrt{N_{++}N_{--}}$ as a function of mass and p_T. Projected onto the mass axis the relative acceptance can be estimated by dividing the mixed event background shown in Fig. 1. Since the acceptance for pairs is a function of mass and p_T, we have checked that for different e^+e^- pair sources, which span reasonable variations in mass and p_T shapes of the e^+e^- pairs, the relative acceptance is unchanged. The corrected like-sign distribution is then subtracted from the unlike-sign pairs without further normalization. Up to 3.5 GeV/c^2 the difference between the signal extracted using the two background subtraction techniques agrees to better than ±10%. Above 3.5 GeV/c the difference becomes much larger, which may indicate additional correlated background. In this region we subtract the measured like-sign yield, the larger of our two background estimates, and include the difference of the two methods as asymmetric systematic uncertainty on the signal yield.

In the next step the signal is corrected for electron reconstruction efficiency and trigger efficiency. The electron reconstruction efficiency was determined with a Monte Carlo simulation of the PHENIX detector (similar to [12]). The trigger efficiency for single electrons was measured using the MB sample. For each of the 8 calorimeter sectors we determine the ratio of electrons that fired the ERT trigger to all electrons reconstructed as function of p_T. Pairs from hadron decays simulated with EXODUS are filtered by the acceptance and then folded with the ERT trigger efficiency to extract the pair trigger efficiency as function of mass. At high masses the trigger efficiency saturates at 72%, limited by the active area of the trigger, from 1.5 to 0.5 GeV/c^2 the pair efficiency gradually drops to 32% and remains approximately constant at lower masses. In addition, the yield is divided by $0.79/0.55 = 1.44$ to account for the fraction of the inelastic $p+p$ cross section missed by our interaction trigger. The systematic uncertainties on the fully corrected spectrum shown in Fig. 2 are summarized in Table 1.

We model the e^+e^- pair contributions from hadron decays using the EXODUS decay generator. We follow closely the approach given in [5,14], however, we have updated all input to match the most recent PHENIX data. We assume that all hadrons have a constant rapidity density in the range $|\Delta\eta| \leqslant 0.35$ and a homogeneous distribution in azimuthal angle. Transverse momentum distributions are based on measurements in the same experiment where possible. The key input is the rapidity density $dN/dy = 1.06 \pm 0.11$ of neutral pions, which we determine from a fit to PHENIX data on charged and neutral pions, as shown in Fig. 3. The functional form of the pion transverse momentum distribution is given by:

$$E\frac{d^3\sigma}{dp^3} = A\left(e^{-(ap_T+bp_T^2)} + p_T/p_0\right)^{-n} \quad (1)$$

with $A = 377 \pm 60$ mb GeV$^{-2}\,c^3$, $a = 0.356 \pm 0.014$ (GeV/c)$^{-1}$, $b = 0.068 \pm 0.019$ (GeV/c)$^{-2}$, $p_0 = 0.7 \pm 0.02$ GeV/c and the power $n = 8.25 \pm 0.04$. For all other mesons we assume m_T scaling, replacing p_T by $\sqrt{m^2 - m_\pi^2 + (p_T/c)^2}$, where m is the mass of the meson. For the η, ω, ϕ, and J/ψ we fit a normalization factor to PHENIX data. In Fig. 3 the results are compared to published PHENIX data; excellent agreement with the data is achieved. The η meson is measured only at higher p_T, however, the fit is in good agreement with the p_T distribution of kaons, which have similar mass.

In order to extract the meson yield per inelastic $p+p$ collision we integrate the fits over all p_T. Results, systematic uncertainties, and references to data are given in Table 2. For the ρ meson we assume $\sigma_\rho/\sigma_\omega = 1.15 \pm 0.15$, consistent with values found in jet fragmentation [15]. The η' yield is scaled to be consistent with jet fragmentation $\sigma_{\eta'}/\sigma_\eta = 0.15 \pm 0.15$ [15]. The ψ' is adjusted to the value of $\sigma_{\psi'}/\sigma_{J/\psi} = 0.14 \pm 0.03$ [22]. For the η, ω, ϕ, and J/ψ the quoted uncertainties include those on the data as well as those using different shapes of the p_T distributions to extrapolate to zero p_T. Specifically we have fitted the functional form given in Eq. (1) with all parameters free and also an exponential distribution in m_T. For the ρ, η', and ψ' the uncertainty is given by the uncertainty we assumed for the cross section ratios. We note that the dilepton spectra from meson decays are rather insensitive to the exact shape of the p_T distribution.

Once the meson yields and p_T spectra are known the dilepton spectrum is given by decay kinematics and branching ratios, which are implemented in our decay generator EXODUS following earlier work published in [5,14]. The branching ratios are taken from the compilation of particle properties in [15]. For the Dalitz decays π^0, η, $\eta' \to e^+e^-\gamma$ and the decay $\omega \to e^+e^-\pi^0$ we use the Kroll–Wada expression [23] with electromagnetic transition form factors measured by the Lepton-G Collaboration [24,25]. For the decays of the vector mesons ρ, ω, $\phi \to e^+e^-$ we use the expression derived by Gounaris and Sakurai [26], extending it to 2 GeV/c^2, slightly beyond its validity range. For the J/ψ and $\psi' \to e^+e^-$ we use the same expression modified to include radiative corrections as discussed in [21]. All vector mesons are assumed to be unpolarized. The resulting dilepton spectra are compared to our data in Fig. 2 with the systematic uncertainties shown as a band. They are calculated as a function of mass and are dominated by the uncertainties on the meson yield tabulated in Table 2. The uncertainty from the measured electromagnetic transition form factors, in particular for the $\omega \to e^+e^-\pi^0$ decay, is also included but contributes visibly only in the range around 500 to 600 MeV/c^2. Also shown on Fig. 2 are the contributions from open charm and bottom production, discussed in more detail below, as well as from the Drell–Yan process, which is negligible. The bottom panel shows the ratio of data to the sum of all sources, hadronic cocktail, charm, bottom and Drell–Yan. The data agree very well with the sum of all known sources within the quoted systematic uncertainties.

Except for the vector meson peaks, the dilepton yield in the mass range above 1.1 GeV/c^2 is dominated by semileptonic decays of D and B mesons correlated through flavor conservation. To determine this contribution we subtract the meson decay cocktail from the dilepton data, the resulting mass spectrum is shown in Fig. 4. In the PHENIX acceptance the integrated e^+e^- pair yield per event from heavy flavor decays in the range from 1.1 to 2.5 GeV/c^2 is $4.21 \pm 0.28(\text{stat}) \pm 1.02(\text{syst}) \times 10^{-8}$. The systematic uncertainties are those tabulated in Table 1 plus the uncertainty on the cocktail subtraction. The cocktail subtraction is dominated by the high mass end of the broad ρ resonance. The ρ contribution in this region is not very well known and we therefore assume 100% systematic uncertainty on the ρ contribution. To estimate the rapidity density of $c\bar{c}$ pairs the measured e^+e^- pair yield is corrected for the geometrical acceptance, i.e., corrected from requiring both electron and positron within the PHENIX central arm acceptance to having the electron pair within one unit of rapidity at mid-rapidity. It then is extrapolated to zero e^+e^- pair mass and converted to $c\bar{c}$ using known branching ratios of semileptonic decays [15]. This

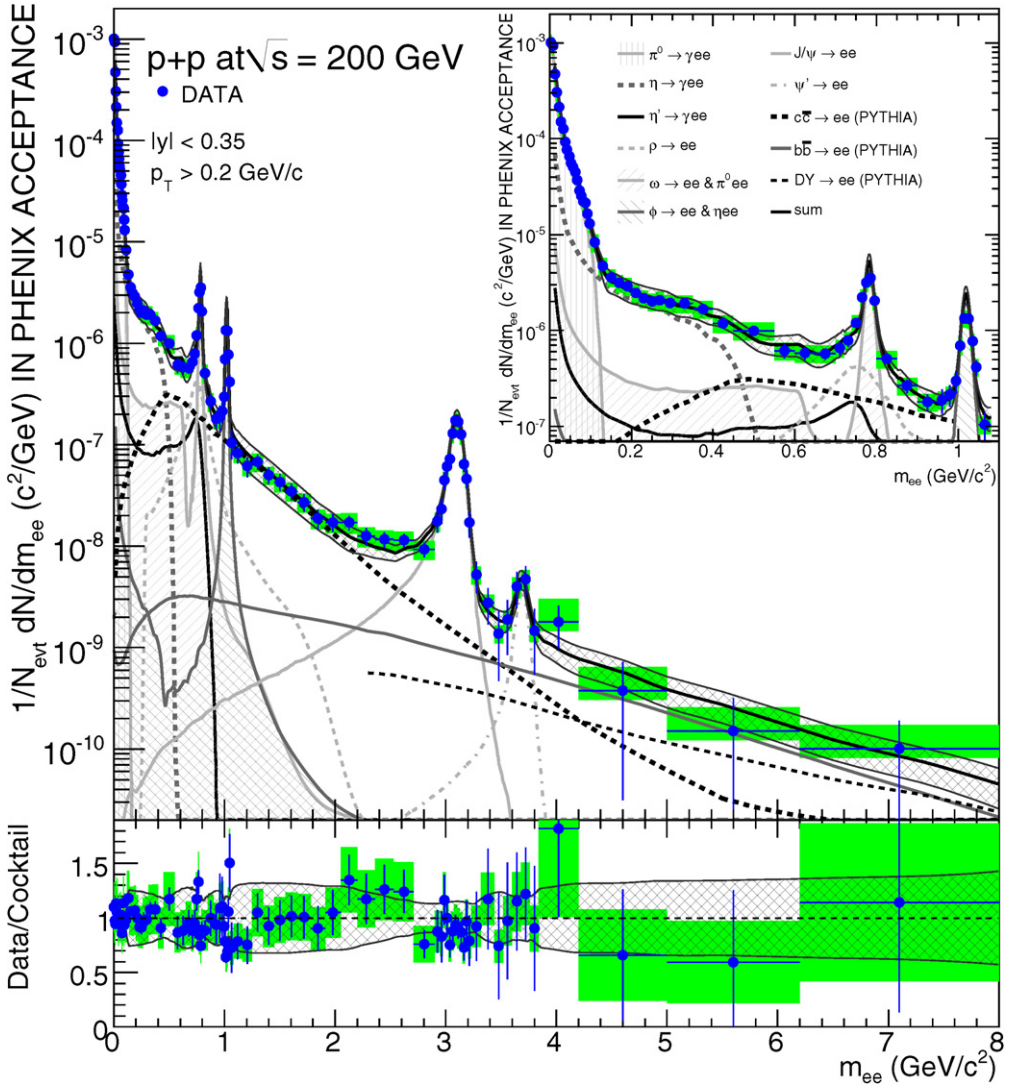

Fig. 2. Electron–positron pair yield per inelastic $p + p$ collision as function of pair mass. Data show statistical (bars) and systematic (shades) errors separately. The yield per event can be converted to a cross section by multiplying with the inelastic $p + p$ cross section of 42.2 mb. The data are compared to a cocktail of known sources. The contribution from hadron decays is independently normalized based on meson measurements in PHENIX, the systematic uncertainties are given by the error band. The contribution from open charm production is scaled to match the data ($\sigma_{c\bar{c}} = 544 \pm 39(\text{stat}) \pm 142(\text{syst}) \pm 200(\text{model})$ μb). The inset shows the same data but focuses on the low mass region. The bottom panel shows the ratio of data to the cocktail of known sources. The systematic uncertainties of the data are shown as boxes, while the uncertainty on the cocktail is shown as band around 1.

Table 1
Systematic uncertainties of the dilepton yield due to different sources and for different mass ranges. The uncertainties vary with mass and the largest uncertainties are quoted for each mass range. The contribution quoted for the jet pair subtraction also accounts for the difference in the signal observed between our two background subtraction techniques.

	< 0.4 GeV/c^2	0.4–1.1 GeV/c^2	1.1–3.5 GeV/c^2	> 3.5 GeV/c^2
Minimum bias trigger	11.3%	11.3%	11.3%	11.3%
ERT trigger efficiency	5%	5%	5%	5%
Conversion rejection	5%	–	–	–
Mixed event background	2%	8%	4%	–
Cross pair subtraction	$< 1\%$	–	–	–
Jet pair subtraction	2%	3%	11%	+70%
Reconstruction efficiency	14.4%	14.4%	14.4%	14.4%
Total	19.8%	20.8%	22.3%	+73%, −19%

correction is model dependent; we used our tuned PYTHIA simulation[7] to directly relate e^+e^- pairs from charm in the PHENIX acceptance and in the mass range from 1.1 to 2.5 GeV/c^2 to the $c\bar{c}$ rapidity density.[8]

[7] We used PYTHIA 6.205 with CTEQ5L parton distribution function [31]. We changed PYTHIA parameters as follows: PARP(91) = 1.5 (k_T), PARP(31) = 3.5 (K factor), MSTP(33) = 1, MSTP(32) = 4 (Q^2 scale) and in addition for charm production we use MSEL = 11 and PMAS(4, 1) = 1.25 (mass), for bottom MSEL = 5 and PMAS(5, 1) = 4.1 (mass), and for Drell–Yan MSEL = 11, PARP(31) = 1.8, and CKIN(3) = 2.0 (min. parton p_T).

[8] It is known that lowest order PYTHIA calculations, as we use, fail to describe single electron production from charmed quarks produced with large p_T. This is

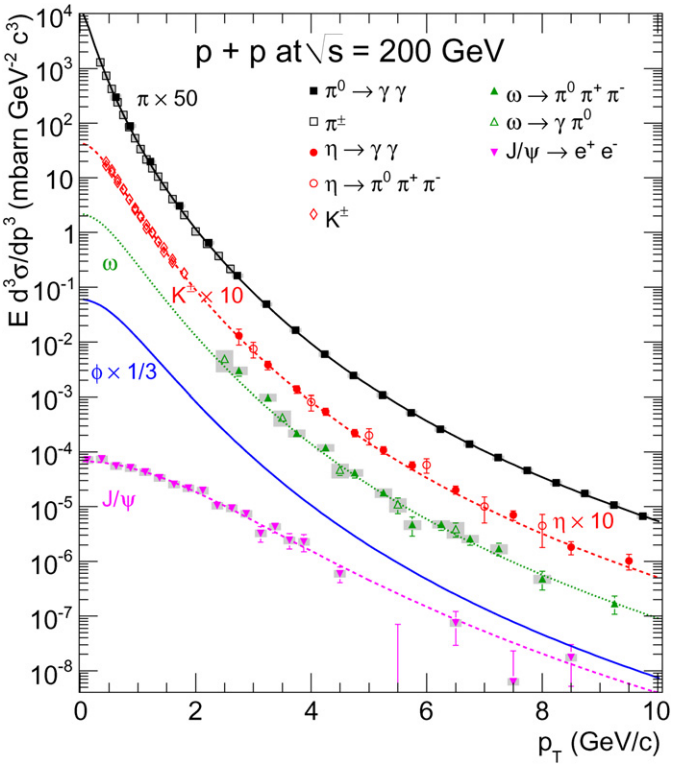

Fig. 3. Compilation of meson production cross sections in $p+p$ collisions at $\sqrt{s}=200$ GeV. Shown are data for neutral [16] and charged pions [17], η [18], kaons [17], ω [19], and J/ψ [21]. The data are compared to the parameterization based on m_T scaling of the measured pion distribution, as used in our hadron decay generator.

Table 2
Hadron rapidity densities used in our hadron decay generator. For the ω and ϕ meson data from this analysis were used together with data from the quoted references.

	$\frac{dN}{dy}\|_{y=0}$	Relative err.	Data used
π^0	1.065 ± 0.11	10%	PHENIX [16,17]
η	0.11 ± 0.03	30%	PHENIX [18]
ρ	0.089 ± 0.025	28%	jet fragmentation [15]
ω	0.078 ± 0.018	23%	PHENIX [19]
ϕ	0.009 ± 0.002	24%	PHENIX [20]
η'	0.016 ± 0.016	100%	jet fragmentation [15]
J/ψ	$(1.77 \pm 0.27) \times 10^{-5}$	15%	PHENIX [21]
ψ'	$(2.5 \pm 0.7) \times 10^{-6}$	27%	world average [22]

For single tracks the acceptance is known to better than 5%. Neglecting correlations between the electron and positron this implies an uncertainty of less than 10% for pairs. However, the fraction of e^+e^- pairs from correlated heavy flavor decays at mid-rapidity depends on the dynamical correlations between the quarks. These are not very accurately known [27], in particular in the azimuthal direction. Therefore additional systematic uncertainties need to be considered. In PYTHIA the intrinsic k_T parameter modifies the azimuthal correlation between c and $\bar{c}$. We have varied k_T between 1 and 3 GeV/c and reevaluate the fraction of e^+e^- pairs at mid-rapidity. A $\pm 20\%$ variation was found. Different choices of parton distribution functions (PDFs) lead to modifications of the longitudinal correlation of the pair, often expressed as the rapidity gap between the c and $\bar{c}$ quarks. We used different

not a concern for our analysis, since the majority of the e^+e^- pairs in our mass spectrum result from $c\bar{c}$ pairs where the c and $\bar{c}$ have low p_T and large opening angle. Future analysis of the pair p_T dependence, however, will need to take this into account.

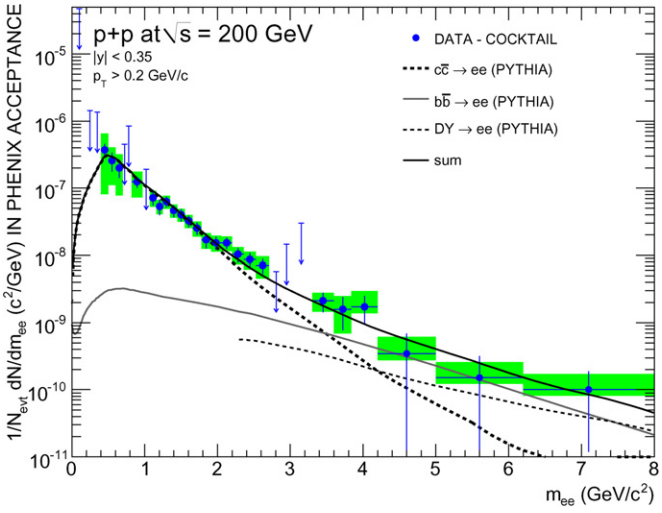

Fig. 4. Electron–positron mass distributions from semileptonic decays of heavy flavor, obtained by subtracting the contribution from π^0, η, ω, ρ, ϕ, η', J/ψ and ψ' mesons from the inclusive e^+e^- pair yield. The arrows indicate upper limits (95% CL) in the mass regions where the charm contribution is smaller or comparable to the systematic uncertainties. For all data points statistical error bars and systematic uncertainty boxes, including data and model contributions, are shown. Also shown is the contribution from charm ($\sigma_{c\bar{c}} = 544 \pm 39(\text{stat}) \pm 142(\text{syst}) \pm 200(\text{model})$ μb), as well as expected contributions from bottom ($\sigma_{b\bar{b}} = 3.7$ μb) and Drell–Yan ($\sigma_{b\bar{b}} = 0.04$ μb).

parton distribution functions available in PYTHIA, specifically we have used CTEQ5L, CTEQ4L, GRV94LO, GRV98LO, and MRST(c-g). We find $\pm 11\%$ deviations for the e^+e^- pair yield in the PHENIX acceptance. When converting the e^+e^- pair yield to $c\bar{c}$ pairs there is also a $\pm 21\%$ uncertainty resulting from uncertainties of relative abundance of charmed hadrons and of the branching ratios to semileptonic decays. We use an effective branching ratio for $c \to e$ of $9.5\% \pm 1\%$, which was calculated from $D^+/D^0 = 0.45 \pm 0.1$, $D_s/D^0 = 0.25 \pm 0.1$, and $\Lambda_c/D^0 = 0.1 \pm 0.05$ and the branching ratios from [15]. The overall uncertainty on the extrapolation is approximately 33%.

We also subtract a 7% contribution from bottom decays and the Drell–Yan mechanism for which we assign a 100% systematic uncertainty. For the bottom cross section we assume 3.7 μb [29], in agreement with our data above 4 GeV/c^2. Though negligible, we have also included the contribution from the Drell–Yan mechanism based on a cross section of 0.04 μb [28]. For the rapidity density of $c\bar{c}$ pairs at mid-rapidity we find:

$$\left.\frac{d\sigma_{c\bar{c}}}{dy}\right|_{y=0} = 118.1 \pm 8.4(\text{stat}) \pm 30.7(\text{syst}) \pm 39.5(\text{model})\ \mu\text{b}. \quad (2)$$

The systematic uncertainties on the data analysis and on the model dependent extrapolation are quoted separately. Using the rapidity distribution from HVQMNR [30] with CTEQ5M [31] PDF as in [5], the total charm cross section is $\sigma_{c\bar{c}} = 544 \pm 39(\text{stat}) \pm 142(\text{syst}) \pm 200(\text{model})$ μb. The extrapolation to 4π adds another 15% systematic uncertainty, which is included in the last term. The charm contribution as shown in Figs. 2 and 4 has been scaled to this result, which is compatible with our previous measurement of single electrons, which gave $\sigma_{c\bar{c}} = 567 \pm 57(\text{stat}) \pm 224(\text{syst})$ μb [5], and with the FONLL prediction of 256^{+400}_{-146} μb [3].

Instead of fixing the bottom cross section, we have tried an alternative approach. We take the shape of the bottom and charm e^+e^- pair distributions from PYTHIA filtered into the PHENIX acceptance and then fit the charm and bottom contribution to the data. For the charm cross section we obtain $\sigma_{c\bar{c}} = 518 \pm 47(\text{stat}) \pm 135(\text{syst}) \pm 190(\text{model})$ μb, consistent with our earlier analysis. The bottom cross section is $\sigma_{b\bar{b}} = 3.9 \pm 2.5(\text{stat})^{+3}_{-2}(\text{syst})$ μb. In addition

to the model dependent systematic uncertainties, which are similar to those on the charm extraction, the subtraction of e^+e^- pairs from the Drell–Yan mechanism contributes an extra 10–20% [32]. We estimate that the combined systematic uncertainty is about 50% and thus similar to the statistical error. The value for the bottom cross section is consistent with our earlier assumption of 3.7 μb as well as with the FONLL prediction of $1.87^{+0.99}_{-0.67}$ μb [3].

In conclusion, we have measured e^+e^- pairs in the mass range from 0 to 8 GeV/c^2 in $p+p$ collisions at $\sqrt{s}=200$ GeV. Within the systematic uncertainties the data can be described by known contributions from light meson decays, mostly measured in the same experiment, as well as from semileptonic decays of mesons carrying heavy flavor. The required charm and bottom production cross sections are consistent with the upper FONLL predictions and with the PHENIX measurement of single electrons.

Acknowledgements

We thank the staff of the Collider-Accelerator and Physics Departments at BNL for their vital contributions. We acknowledge support from the Department of Energy and NSF (USA), MEXT and JSPS (Japan), CNPq and FAPESP (Brazil), NSFC (China), IN2P3/CNRS, and CEA (France), BMBF, DAAD, and AvH (Germany), OTKA (Hungary), DAE (India), ISF (Israel), KRF and KOSEF (Korea), MES, RAS, and FAAE (Russia), VR and KAW (Sweden), US CRDF for the FSU, US–Hungarian NSF-OTKA-MTA, and US–Israel BSF.

References

[1] K. Adcox, et al., Nucl. Phys. A 757 (2005) 184.
[2] C. Aidala, et al., BNL-73798-2005 (2005); available at http://spin.riken.bnl.gov/rsc/report/masterspin.pdf.
[3] M. Cacciari, et al., Phys. Rev. Lett. 95 (2005) 122001.
[4] D. Acosta, et al., CDF Collaboration, Phys. Rev. Lett. 91 (2003) 241804.
[5] A. Adare, et al., PHENIX Collaboration, Phys. Rev. Lett. 97 (2006) 252002.
[6] S.S. Adler, et al., PHENIX Collaboration, Phys. Rev. D 76 (2007) 092002.
[7] R. Vogt, arXiv: 0709.2531 [hep-ph].
[8] B.I. Abelev, et al., STAR Collaboration, Phys. Rev. Lett. 98 (2007) 192301.
[9] J. Adams, et al., STAR Collaboration, Phys. Rev. Lett. 94 (2005) 062301.
[10] K. Adcox, et al., PHENIX Collaboration, Nucl. Instrum. Methods 499 (2003) 469.
[11] A. Toia, et al., PHENIX Collaboration, PoS CPOD07 (2007) 037.
[12] S. Afanasiev, et al., PHENIX Collaboration, arXiv: 0706.3034 [nucl-ex].
[13] T. Dahms, PhD Thesis (2008), Stony Brook University, arXiv: 0810.3040 [nucl-ex].
[14] G. Agakichiev, et al., CERES Collaboration, Eur. Phys. J. C 4 (1998) 231.
[15] W.M. Yao, et al., J. Phys. G 33 (2006) 1.
[16] A. Adare, et al., PHENIX Collaboration, Phys. Rev. D 76 (2007) 051106.
[17] S.S. Adler, et al., PHENIX Collaboration, Phys. Rev. C 74 (2006) 024904.
[18] S.S. Adler, et al., PHENIX Collaboration, Phys. Rev. C 75 (2007) 024909.
[19] S.S. Adler, et al., PHENIX Collaboration, Phys. Rev. C 75 (2007) 051902.
[20] Y. Riabov, et al., PHENIX Collaboration, J. Phys. G 34 (8) (2007) S925.
[21] A. Adare, et al., PHENIX Collaboration, Phys. Rev. Lett. 98 (2007) 232002.
[22] R. Gavai, et al., Int. J. Mod. Phys. A 10 (1995) 3043.
[23] N.M. Kroll, W. Wada, Phys. Rev. 98 (1955) 1355.
[24] R.I. Dzhelyadin, et al., Phys. Lett. B 102 (1981) 296.
[25] L.G. Landsberg, Phys. Rep. 128 (1985) 301.
[26] G.J. Gounaris, J.J. Sakurai, Phys. Rev. Lett. 21 (1968) 244.
[27] E.M. Aitala, et al., E791 Collaboration, Eur. Phys. J. C 1 (1999) 4.
[28] S. Gavin, et al., Int. J. Mod. Phys. A 10 (1995) 2961.
[29] C.H. Jaroschek, Masters Thesis (2001), Stony Brook University; the bottom cross section was obtained by tuning PYTHIA to experimental data and interpolating to $\sqrt{s}=200$ GeV.
[30] M.L. Mangano, P. Nason, G. Ridolfi, Nucl. Phys. B 405 (1993) 507.
[31] H.L. Lai, et al., Eur. Phys. J. C 12 (2000) 375.
[32] W. Vogelsang, private communication.

Onset of π^0 Suppression Studied in Cu + Cu Collisions at $\sqrt{s_{NN}} = 22.4$, 62.4, and 200 GeV

A. Adare,[12] S. Afanasiev,[26] C. Aidala,[13,37] N. N. Ajitanand,[54] Y. Akiba,[48,49] H. Al-Bataineh,[43] J. Alexander,[54] K. Aoki,[31,48] L. Aphecetche,[56] R. Armendariz,[43] S. H. Aronson,[7] J. Asai,[48,49] E. T. Atomssa,[32] R. Averbeck,[55] T. C. Awes,[44] B. Azmoun,[7] V. Babintsev,[22] M. Bai,[6] G. Baksay,[18] L. Baksay,[18] A. Baldisseri,[15] K. N. Barish,[8] P. D. Barnes,[34] B. Bassalleck,[42] A. T. Basye,[1] S. Bathe,[8] S. Batsouli,[44] V. Baublis,[47] C. Baumann,[38] A. Bazilevsky,[7] S. Belikov,[7] R. Bennett,[55] A. Berdnikov,[51] Y. Berdnikov,[51] A. A. Bickley,[12] J. G. Boissevain,[34] H. Borel,[15] K. Boyle,[55] M. L. Brooks,[34] H. Buesching,[7] V. Bumazhnov,[22] G. Bunce,[7,49] S. Butsyk,[34,55] C. M. Camacho,[34] S. Campbell,[55] B. S. Chang,[63] W. C. Chang,[2] J.-L. Charvet,[15] S. Chernichenko,[22] J. Chiba,[27] C. Y. Chi,[13] M. Chiu,[23] I. J. Choi,[63] R. K. Choudhury,[4] T. Chujo,[59,60] P. Chung,[54] A. Churyn,[22] V. Cianciolo,[44] Z. Citron,[55] C. R. Cleven,[20] B. A. Cole,[13] M. P. Comets,[45] P. Constantin,[34] M. Csanád,[17] T. Csörgő,[28] T. Dahms,[55] S. Dairaku,[31,48] K. Das,[19] G. David,[7] M. B. Deaton,[1] K. Dehmelt,[18] H. Delagrange,[56] A. Denisov,[22] D. d'Enterria,[13,32] A. Deshpande,[49,55] E. J. Desmond,[7] O. Dietzsch,[52] A. Dion,[55] M. Donadelli,[52] O. Drapier,[32] A. Drees,[55] K. A. Drees,[6] A. K. Dubey,[62] A. Durum,[22] D. Dutta,[4] V. Dzhordzhadze,[8] Y. V. Efremenko,[44] J. Egdemir,[55] F. Ellinghaus,[12] W. S. Emam,[8] T. Engelmore,[13] A. Enokizono,[33] H. En'yo,[48,49] S. Esumi,[59] K. O. Eyser,[8] B. Fadem,[39] D. E. Fields,[42,49] M. Finger, Jr.,[9,26] M. Finger,[9,26] F. Fleuret,[32] S. L. Fokin,[30] Z. Fraenkel,[62,*] J. E. Frantz,[55] A. Franz,[7] A. D. Frawley,[19] K. Fujiwara,[48] Y. Fukao,[31,48] T. Fusayasu,[41] S. Gadrat,[35] I. Garishvili,[57] A. Glenn,[12] H. Gong,[55] M. Gonin,[32] J. Gosset,[15] Y. Goto,[48,49] R. Granier de Cassagnac,[32] N. Grau,[13,25] S. V. Greene,[60] M. Grosse Perdekamp,[23,49] T. Gunji,[11] H.-Å. Gustafsson,[36] T. Hachiya,[21] A. Hadj Henni,[56] C. Haegemann,[42] J. S. Haggerty,[7] H. Hamagaki,[11] R. Han,[46] H. Harada,[21] E. P. Hartouni,[33] K. Haruna,[21] E. Haslum,[36] R. Hayano,[11] M. Heffner,[33] T. K. Hemmick,[55] T. Hester,[8] X. He,[20] H. Hiejima,[23] J. C. Hill,[25] R. Hobbs,[42] M. Hohlmann,[18] W. Holzmann,[54] K. Homma,[21] B. Hong,[29] T. Horaguchi,[11,48,58] D. Hornback,[57] S. Huang,[60] T. Ichihara,[48,49] R. Ichimiya,[48] Y. Ikeda,[59] K. Imai,[31,48] J. Imrek,[16] M. Inaba,[59] Y. Inoue,[50,48] D. Isenhower,[1] L. Isenhower,[1] M. Ishihara,[48] T. Isobe,[11] M. Issah,[54] A. Isupov,[26] D. Ivanischev,[47] B. V. Jacak,[55,+] J. Jia,[13] J. Jin,[13] O. Jinnouchi,[49] B. M. Johnson,[7] K. S. Joo,[40] D. Jouan,[45] F. Kajihara,[11] S. Kametani,[11,48,61] N. Kamihara,[48,49] J. Kamin,[55] M. Kaneta,[49] J. H. Kang,[63] H. Kanou,[48,58] J. Kapustinsky,[34] D. Kawall,[37,49] A. V. Kazantsev,[30] T. Kempel,[25] A. Khanzadeev,[47] K. M. Kijima,[21] J. Kikuchi,[61] B. I. Kim,[29] D. H. Kim,[40] D. J. Kim,[63] E. Kim,[53] S. H. Kim,[63] E. Kinney,[12] K. Kiriluk,[12] A. Kiss,[17] E. Kistenev,[7] A. Kiyomichi,[48] J. Klay,[33] C. Klein-Boesing,[38] L. Kochenda,[47] V. Kochetkov,[22] B. Komkov,[47] M. Konno,[59] J. Koster,[23] D. Kotchetkov,[8] A. Kozlov,[62] A. Král,[14] A. Kravitz,[13] J. Kubart,[9,24] G. J. Kunde,[34] N. Kurihara,[11] K. Kurita,[50,48] M. Kurosawa,[48] M. J. Kweon,[29] Y. Kwon,[57,63] G. S. Kyle,[43] R. Lacey,[54] Y.-S. Lai,[13] Y. S. Lai,[13] J. G. Lajoie,[25] D. Layton,[23] A. Lebedev,[25] D. M. Lee,[34] K. B. Lee,[29] M. K. Lee,[63] T. Lee,[53] M. J. Leitch,[34] M. A. L. Leite,[52] B. Lenzi,[52] P. Liebing,[49] T. Liška,[14] A. Litvinenko,[26] H. Liu,[43] M. X. Liu,[34] X. Li,[10] B. Love,[60] D. Lynch,[7] C. F. Maguire,[60] Y. I. Makdisi,[6,7] A. Malakhov,[26] M. D. Malik,[42] V. I. Manko,[30] E. Mannel,[13] Y. Mao,[46,48] L. Mašek,[9,24] H. Masui,[59] F. Matathias,[13] M. McCumber,[55] P. L. McGaughey,[34] N. Means,[55] B. Meredith,[23] Y. Miake,[59] P. Mikeš,[9,24] K. Miki,[59] T. E. Miller,[60] A. Milov,[7,55] S. Mioduszewski,[7] M. Mishra,[3] J. T. Mitchell,[7] M. Mitrovski,[54] A. K. Mohanty,[4] Y. Morino,[11] A. Morreale,[8] D. P. Morrison,[7] T. V. Moukhanova,[30] D. Mukhopadhyay,[60] J. Murata,[50,48] S. Nagamiya,[27] Y. Nagata,[59] J. L. Nagle,[12] M. Naglis,[62] M. I. Nagy,[17] I. Nakagawa,[48,49] Y. Nakamiya,[21] T. Nakamura,[21] K. Nakano,[48,58] J. Newby,[33] M. Nguyen,[55] T. Niita,[59] B. E. Norman,[34] R. Nouicer,[5] A. S. Nyanin,[30] E. O'Brien,[7] S. X. Oda,[11] C. A. Ogilvie,[25] H. Ohnishi,[48] H. Okada,[31,48] K. Okada,[49] M. Oka,[59] O. O. Omiwade,[1] Y. Onuki,[48] A. Oskarsson,[36] M. Ouchida,[21] K. Ozawa,[11] R. Pak,[5,7] D. Pal,[60] A. P. T. Palounek,[34] V. Pantuev,[55] V. Papavassiliou,[43] J. Park,[53] W. J. Park,[29] S. F. Pate,[43] H. Pei,[25] J.-C. Peng,[23] H. Pereira,[15] V. Peresedov,[26] D. Yu. Peressounko,[30] C. Pinkenburg,[7] M. L. Purschke,[7] A. K. Purwar,[34] H. Qu,[20] J. Rak,[42] A. Rakotozafindrabe,[32] I. Ravinovich,[62] K. F. Read,[44,57] S. Rembeczki,[18] M. Reuter,[55] K. Reygers,[38] V. Riabov,[47] Y. Riabov,[47] D. Roach,[60] G. Roche,[35] S. D. Rolnick,[8] A. Romana,[32,*] M. Rosati,[25] S. S. E. Rosendahl,[36] P. Rosnet,[35] P. Rukoyatkin,[26] P. Ružička,[24] V. L. Rykov,[48] B. Sahlmueller,[38] N. Saito,[31,48,49] T. Sakaguchi,[7] S. Sakai,[59] K. Sakashita,[48,58] H. Sakata,[21] V. Samsonov,[47] S. Sato,[27] T. Sato,[59] S. Sawada,[27] K. Sedgwick,[8] J. Seele,[12] R. Seidl,[23] A. Yu. Semenov,[25] V. Semenov,[22] R. Seto,[8] D. Sharma,[62] I. Shein,[22] A. Shevel,[47,54] T.-A. Shibata,[48,58] K. Shigaki,[21] M. Shimomura,[59] K. Shoji,[31,48] P. Shukla,[4] A. Sickles,[7,55] C. L. Silva,[52] D. Silvermyr,[44] C. Silvestre,[15] K. S. Sim,[29] B. K. Singh,[3] C. P. Singh,[3] V. Singh,[3] S. Skutnik,[25] M. Slunečka,[9,26] A. Soldatov,[22] R. A. Soltz,[33] W. E. Sondheim,[34] S. P. Sorensen,[57] I. V. Sourikova,[7] F. Staley,[15] P. W. Stankus,[44] E. Stenlund,[36] M. Stepanov,[43] A. Ster,[28] S. P. Stoll,[7] T. Sugitate,[21] C. Suire,[45] A. Sukhanov,[5] J. Sziklai,[28] T. Tabaru,[49] S. Takagi,[59] E. M. Takagui,[52] A. Taketani,[48,49] R. Tanabe,[59] Y. Tanaka,[41] K. Tanida,[48,49] M. J. Tannenbaum,[7] A. Taranenko,[54] P. Tarján,[16] H. Themann,[55] T. L. Thomas,[42]

 © 2008 The American Physical Society

M. Togawa,[31,48] A. Toia,[55] J. Tojo,[48] L. Tomášek,[24] Y. Tomita,[59] H. Torii,[21,48] R. S. Towell,[1] V-N. Tram,[32] I. Tserruya,[62] Y. Tsuchimoto,[21] C. Vale,[25] H. Valle,[60] H. W. vanHecke,[34] A. Veicht,[23] J. Velkovska,[60] R. Vertesi,[16] A. A. Vinogradov,[30] M. Virius,[14] V. Vrba,[24] E. Vznuzdaev,[47] M. Wagner,[31,48] D. Walker,[55] X. R. Wang,[43] Y. Watanabe,[48,49] F. Wei,[25] J. Wessels,[38] S. N. White,[7] D. Winter,[13] C. L. Woody,[7] M. Wysocki,[12] W. Xie,[49] Y. L. Yamaguchi,[61] K. Yamaura,[21] R. Yang,[23] A. Yanovich,[22] Z. Yasin,[8] J. Ying,[20] S. Yokkaichi,[48,49] G. R. Young,[44] I. Younus,[42] I. E. Yushmanov,[30] W. A. Zajc,[13] O. Zaudtke,[38] C. Zhang,[44] S. Zhou,[10] J. Zimányi,[28,*] and L. Zolin[26]

(PHENIX Collaboration)

[1]*Abilene Christian University, Abilene, Texas 79699, USA*
[2]*Institute of Physics, Academia Sinica, Taipei 11529, Taiwan*
[3]*Department of Physics, Banaras Hindu University, Varanasi 221005, India*
[4]*Bhabha Atomic Research Centre, Bombay 400 085, India*
[5]*Chemistry Department, Brookhaven National Laboratory, Upton, New York 11973-5000, USA*
[6]*Collider-Accelerator Department, Brookhaven National Laboratory, Upton, New York 11973-5000, USA*
[7]*Physics Department, Brookhaven National Laboratory, Upton, New York 11973-5000, USA*
[8]*University of California–Riverside, Riverside, California 92521, USA*
[9]*Charles University, Ovocný trh 5, Praha 1, 116 36, Prague, Czech Republic*
[10]*China Institute of Atomic Energy (CIAE), Beijing, People's Republic of China*
[11]*Center for Nuclear Study, Graduate School of Science, University of Tokyo, 7-3-1 Hongo, Bunkyo, Tokyo 113-0033, Japan*
[12]*University of Colorado, Boulder, Colorado 80309, USA*
[13]*Columbia University, New York, New York 10027, USA and Nevis Laboratories, Irvington, New York 10533, USA*
[14]*Czech Technical University, Zikova 4, 166 36 Prague 6, Czech Republic*
[15]*Dapnia, CEA Saclay, F-91191, Gif-sur-Yvette, France*
[16]*Debrecen University, H-4010 Debrecen, Egyetem tér 1, Hungary*
[17]*ELTE, Eötvös Loránd University, H-1117 Budapest, Pázmány P. s. 1/A, Hungary*
[18]*Florida Institute of Technology, Melbourne, Florida 32901, USA*
[19]*Florida State University, Tallahassee, Florida 32306, USA*
[20]*Georgia State University, Atlanta, Georgia 30303, USA*
[21]*Hiroshima University, Kagamiyama, Higashi-Hiroshima 739-8526, Japan*
[22]*IHEP Protvino, State Research Center of Russian Federation, Institute for High Energy Physics, Protvino, 142281, Russia*
[23]*University of Illinois at Urbana-Champaign, Urbana, Illinois 61801, USA*
[24]*Institute of Physics, Academy of Sciences of the Czech Republic, Na Slovance 2, 182 21 Prague 8, Czech Republic*
[25]*Iowa State University, Ames, Iowa 50011, USA*
[26]*Joint Institute for Nuclear Research, 141980 Dubna, Moscow Region, Russia*
[27]*KEK, High Energy Accelerator Research Organization, Tsukuba, Ibaraki 305-0801, Japan*
[28]*KFKI Research Institute for Particle and Nuclear Physics of the Hungarian Academy of Sciences (MTA KFKI RMKI), H-1525 Budapest 114, PO Box 49, Budapest, Hungary*
[29]*Korea University, Seoul, 136-701, Korea*
[30]*Russian Research Center "Kurchatov Institute," Moscow, Russia*
[31]*Kyoto University, Kyoto 606-8502, Japan*
[32]*Laboratoire Leprince-Ringuet, Ecole Polytechnique, CNRS-IN2P3, Route de Saclay, F-91128, Palaiseau, France*
[33]*Lawrence Livermore National Laboratory, Livermore, California 94550, USA*
[34]*Los Alamos National Laboratory, Los Alamos, New Mexico 87545, USA*
[35]*LPC, Université Blaise Pascal, CNRS-IN2P3, Clermont-Fd, 63177 Aubiere Cedex, France*
[36]*Department of Physics, Lund University, Box 118, SE-221 00 Lund, Sweden*
[37]*Department of Physics, University of Massachusetts, Amherst, Massachusetts 01003-9337, USA*
[38]*Institut für Kernphysik, University of Muenster, D-48149 Muenster, Germany*
[39]*Muhlenberg College, Allentown, Pennsylvania 18104-5586, USA*
[40]*Myongji University, Yongin, Kyonggido 449-728, Korea*
[41]*Nagasaki Institute of Applied Science, Nagasaki-shi, Nagasaki 851-0193, Japan*
[42]*University of New Mexico, Albuquerque, New Mexico 87131, USA*
[43]*New Mexico State University, Las Cruces, New Mexico 88003, USA*
[44]*Oak Ridge National Laboratory, Oak Ridge, Tennessee 37831, USA*
[45]*IPN-Orsay, Universite Paris Sud, CNRS-IN2P3, BP1, F-91406, Orsay, France*
[46]*Peking University, Beijing, People's Republic of China*
[47]*PNPI, Petersburg Nuclear Physics Institute, Gatchina, Leningrad region, 188300, Russia*
[48]*RIKEN, The Institute of Physical and Chemical Research, Wako, Saitama 351-0198, Japan*
[49]*RIKEN BNL Research Center, Brookhaven National Laboratory, Upton, New York 11973-5000, USA*

[50]Physics Department, Rikkyo University, 3-34-1 Nishi-Ikebukuro, Toshima, Tokyo 171-8501, Japan
[51]Saint Petersburg State Polytechnic University, St. Petersburg, Russia
[52]Universidade de São Paulo, Instituto de Física, Caixa Postal 66318, São Paulo CEP05315-970, Brazil
[53]System Electronics Laboratory, Seoul National University, Seoul, Korea
[54]Chemistry Department, Stony Brook University, SUNY, Stony Brook, New York 11794-3400, USA
[55]Department of Physics and Astronomy, Stony Brook University, SUNY, Stony Brook, New York 11794, USA
[56]SUBATECH (Ecole des Mines de Nantes, CNRS-IN2P3, Université de Nantes) BP 20722 - 44307, Nantes, France
[57]University of Tennessee, Knoxville, Tennessee 37996, USA
[58]Department of Physics, Tokyo Institute of Technology, Oh-okayama, Meguro, Tokyo 152-8551, Japan
[59]Institute of Physics, University of Tsukuba, Tsukuba, Ibaraki 305, Japan
[60]Vanderbilt University, Nashville, Tennessee 37235, USA
[61]Waseda University, Advanced Research Institute for Science and Engineering, 17 Kikui-cho, Shinjuku-ku, Tokyo 162-0044, Japan
[62]Weizmann Institute, Rehovot 76100, Israel
[63]Yonsei University, IPAP, Seoul 120-749, Korea

(Received 30 January 2008; published 15 October 2008)

Neutral pion transverse momentum (p_T) spectra at midrapidity ($|y| \lesssim 0.35$) were measured in Cu + Cu collisions at $\sqrt{s_{NN}} = 22.4$, 62.4, and 200 GeV. Relative to π^0 yields in $p + p$ collisions scaled by the number of inelastic nucleon-nucleon collisions (N_{coll}) the π^0 yields for $p_T \gtrsim 2$ GeV/c in central Cu + Cu collisions are suppressed at 62.4 and 200 GeV whereas an enhancement is observed at 22.4 GeV. A comparison with a jet-quenching model suggests that final state parton energy loss dominates in central Cu + Cu collisions at 62.4 and 200 GeV, while the enhancement at 22.4 GeV is consistent with nuclear modifications in the initial state alone.

DOI: 10.1103/PhysRevLett.101.162301 PACS numbers: 25.75.Dw

The measurement of particle yields at high transverse momentum ($p_T \gtrsim 2$ GeV/c) has played a key role in characterizing the medium created in nucleus-nucleus collisions at the Relativistic Heavy Ion Collider (RHIC) [1,2]. Hadrons produced at sufficiently high p_T result from the interaction of quarks and gluons with high momentum transfer (''hard scattering'') which can be described by perturbative quantum chromodynamics (pQCD). These hadrons are produced as particle jets in the fragmentation of the scattered partons. A scattered parton propagating through a medium with high color-charge density such as a quark-gluon plasma loses energy (''jet quenching'') resulting in hadron yields at high p_T being suppressed [3]. Such a suppression was indeed observed in central Au + Au collisions at $\sqrt{s_{NN}} = 130$ and 200 GeV at RHIC, providing evidence for large color-charge densities in these systems [4–6]. This Letter presents results on the onset of π^0 suppression in Cu + Cu collisions as a function of $\sqrt{s_{NN}}$.

Characteristic properties of the suppression of hadrons at high p_T, e.g., the dependence on p_T and centrality, were studied in detail in Au + Au collisions at $\sqrt{s_{NN}} =$ 200 GeV [5]. However, the energy dependence of hadron production in $A + A$ collisions as predicted by jet-quenching models [7–9] is not well constrained by measurements. Work in this direction was presented in [10–13]. To study the energy dependence of jet quenching it is desirable to measure identified particles in the same colliding system over a large $\sqrt{s_{NN}}$ range and to compare to $p + p$ reference data measured in the same experimental setup. Identified particles provide an advantage over unidentified hadrons in that the interpretation is not complicated by the different contributions from baryons and mesons. The study of Cu + Cu collisions is particularly useful because hadron suppression in Au + Au collisions is observed for rather peripheral collisions with a number of participating nucleons of $N_{\text{part}} \sim 50$–100 [5]. This N_{part} range can be studied with reduced uncertainties in N_{coll} with the smaller ^{63}Cu nucleus.

A critical parameter in jet-quenching models is the initial color-charge density of the medium. By studying Cu + Cu collisions in the range $\sqrt{s_{NN}} \sim 20$–200 GeV this parameter can be varied with essentially no change in transverse size and shape of the reaction zone. Moreover, the enhancement of hadron yields due to multiple soft scattering of the incoming partons (''nuclear k_T'' or ''Cronin enhancement'') is expected to increase towards smaller $\sqrt{s_{NN}}$ [8], thus the interplay between this enhancement and the suppression due to parton energy loss can be studied.

In this Letter we present π^0 yields for Cu + Cu collisions at $\sqrt{s_{NN}} = 22.4$, 62.4, and 200 GeV. Reference data for $p + p$ collisions at $\sqrt{s} = 62.4$ and 200 GeV were taken with the same experiment [14,15]. At $\sqrt{s_{NN}} = 22.4$ GeV a $p + p$ reference was obtained from a parametrization of the world's data on pion production [16].

Neutral pions were measured via their $\pi^0 \to \gamma\gamma$ decay branch with the electromagnetic calorimeter (EMCal) of the PHENIX experiment [17]. The EMCal comprises two calorimeter types: 6 sectors of a lead scintillator sampling calorimeter (PbSc) and 2 sectors of a lead glass Cherenkov calorimeter (PbGl). Each sector is located ~5 m from the beam line and subtends $|\eta| < 0.35$ in pseudorapidity and

$\Delta\varphi = 22.5°$ in azimuth. Owing to the PbSc (PbGl) granularity of $\Delta\eta \times \Delta\varphi = 0.011 \times 0.011$ (0.008×0.008) the probability that the two photon showers from a π^0 decay result in partially overlapping clusters is negligible up to a π^0 p_T of 12 GeV/c (15 GeV/c). The energy calibration of the EMCal was corroborated by the position of the π^0 invariant mass peak, the energy deposited by minimum ionizing charged particles traversing the EMCal (PbSc), and the correlation between the measured momenta of electron and positron tracks identified by the ring-imaging Cherenkov detector and the associated energy deposited in the EMCal. These studies showed that the accuracy of the energy measurement was better than 1.5%.

The total number of analyzed Cu + Cu events for the three energies is shown in Table I. The minimum bias (MB) trigger for all reaction systems was provided by beam-beam counters (BBCs) located at $3.0 \lesssim |\eta| \lesssim 3.9$. The reaction vertex along the beam axis, determined from the arrival time differences in the BBCs, was required to be in the range $|z| \leq 30$ cm. An additional high-p_T trigger was employed in Cu + Cu at $\sqrt{s_{NN}} = 200$ GeV. This trigger was based on the analog energy signal measured in overlapping 4×4 towers of the EMCal in coincidence with the MB trigger condition. It reached an efficiency plateau for photon energies $E \gtrsim 4$ GeV.

The centrality selection in Cu + Cu at $\sqrt{s_{NN}} = 200$ GeV and $\sqrt{s_{NN}} = 62$ GeV was based on the charge signal of the BBCs which is proportional to the charged-particle multiplicity. The BBC trigger efficiency ($\varepsilon_{\text{trig}}$) for these systems was determined with the aid of the HIJING event generator and a full GEANT simulation of the BBC response (see Table I). At $\sqrt{s_{NN}} = 22.4$ GeV centrality classes were defined based on the charged-particle multiplicity N_{PC1} measured with the pad chamber (PC1) detector ($|\eta| < 0.35$). The measured N_{PC1} distribution was accurately reproduced in a Glauber Monte Carlo calculation [18] and centrality classes were determined by identical cuts on the measured and simulated PC1 multiplicities. In the Glauber calculation N_{PC1} was assumed to scale with N_{part}^{α} and multiplicity fluctuations were described with a negative binomial distribution. Varying α and the negative binomial distribution parameters, the measured N_{PC1} distribution could be reproduced with $\varepsilon_{\text{trig}}$ values between 0.75 and 0.90. Possible autocorrelations between N_{PC1} and the π^0 yield resulting from measuring these quantities in the same pseudorapidity range were studied with HIJING and found to be negligible. Results of the Glauber calculations for $\sqrt{s_{NN}} = 22.4$, 62.4, and 200 GeV are shown in Table II.

Neutral pion yields were measured on a statistical basis by calculating the invariant mass of all photon pairs in a given event and counting those within the π^0 mass range. The background of combinatorial pairs was calculated by pairing photon hits from different events. Only photon pairs with an energy asymmetry $|E_1 - E_2|/(E_1 + E_2) < 0.7$ were accepted. The raw π^0 yields were corrected for the geometrical acceptance and reconstruction efficiency. The latter takes into account the loss of π^0's due to photon identification cuts, the energy asymmetry cut, inactive detector areas, and photon conversions. Moreover, it corrects the distortion of the π^0 spectrum which results from the finite energy resolution in conjunction with the steeply falling spectra and shower overlap effects. The reconstruction efficiency was determined in a Monte Carlo simulation and is typically on the order of $\varepsilon_{\pi^0} \approx 0.7$–$0.8$. For Cu + Cu at $\sqrt{s_{NN}} = 200$ GeV the transition between the minimum bias and the high-p_T sample occurs at $p_T = 8$ GeV/c. The final spectra were calculated as the weighted average of the PbSc and PbGl results, which agree within 15%, a deviation well covered by the uncertainties.

The main systematic uncertainties of the π^0 spectra result from the π^0 peak extraction, the reconstruction efficiency, and the EMCal energy calibration. For $p_T \gtrsim 2$ GeV/c the peak extraction uncertainty is ~4% for all systems, approximately independent of p_T. The uncertainty in the reconstruction efficiency was estimated to be ~15% for the three Cu + Cu analyses. The uncertainty in the EMCal energy scale of 1.5% translates into an uncer-

TABLE I. Cu + Cu data sets presented with the number of analyzed events. For the data taken with the high-p_T trigger, the number of equivalent minimum bias events is given. At 22.4 GeV the given $\varepsilon_{\text{trig}}$ range indicates the uncertainty.

$\sqrt{s_{NN}}$ (GeV)	$\varepsilon_{\text{trig}}$	$N_{\text{evt}}^{\text{MB}}$	$N_{\text{evt}}^{\text{high}-p_T}$ ($N_{\text{evt}}^{\text{sampled}}$)
22.4	75%–90%	5.8×10^6	···
62.4	(88 ± 4)%	192×10^6	···
200	(94 ± 2)%	794×10^6	15.5×10^6 (4720×10^6)

TABLE II. Glauber Monte Carlo calculations for Cu + Cu collisions at 22.4, 62.4, and 200 GeV using inelastic cross sections of 32.3, 35.6, and 42 mb, respectively. The N_{coll} systematic uncertainty at 62.4 and 200 GeV is ~12%, almost independent of N_{coll}. At 22.4 GeV the relative uncertainty of N_{coll} can be parametrized as $0.094 + 0.173e^{-0.0272N_{\text{coll}}}$.

	22.4 GeV		62.4 GeV		200 GeV	
	$\langle N_{\text{part}}\rangle$	$\langle N_{\text{coll}}\rangle$	$\langle N_{\text{part}}\rangle$	$\langle N_{\text{coll}}\rangle$	$\langle N_{\text{part}}\rangle$	$\langle N_{\text{coll}}\rangle$
0%–10%	92.2	140.7	93.3	152.3	98.2	182.7
10%–20%	67.8	93.3	71.1	105.5	73.6	121.1
20%–30%	48.3	59.7	51.3	67.8	53.0	76.1
30%–40%	34.1	38.0	36.2	42.6	37.3	47.1
40%–50%	23.1	22.9	24.9	26.2	25.4	28.1
50%–60%	15.5	13.9	16.1	15.0	16.7	16.2
60%–70%	···	···	···	···	10.4	9.0
70%–80%	···	···	···	···	6.4	4.9
80%–94%	···	···	···	···	3.6	2.4
60%–88%	···	···	7.0	5.5	···	···

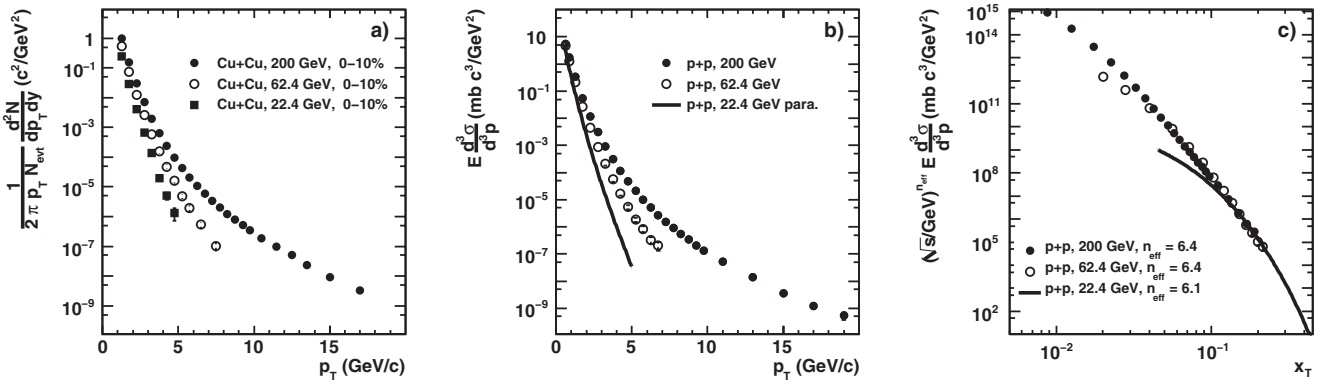

FIG. 1. For $\sqrt{s_{NN}} = 22.4$, 62.4, and 200 GeV are plotted (a) invariant π^0 yields in central Cu + Cu collisions, (b) invariant π^0 cross sections in $p + p$ collisions [14–16], and (c) the $p + p$ data plotted as a function of $x_T = 2p_T/\sqrt{s}$, which exhibit an approximate x_T scaling. The error bars represent the quadratic sum of the statistical and total systematic uncertainties.

tainty in the yields that increases from ~8% at $p_T = 3$ GeV/c to 15% at $p_T = 6$ GeV/c. The part of the spectra in Cu + Cu at 200 GeV measured with the high-p_T trigger is subject to an additional uncertainty of 10% related to the trigger efficiency.

PHENIX has not yet acquired a $p + p$ data set at $\sqrt{s} = 22.4$ GeV. In [16] the world's data on charged and neutral pion production for $21.7 \leq \sqrt{s} \leq 23.8$ GeV were scaled to $\sqrt{s} = 22.4$ GeV and fit with $Ed^3\sigma/d^3p = A(1 + p_T/p_0)^n(1 - 2p_T/\sqrt{s})^m$ where $A = 174.4$ mb GeV$^{-2}c^3$, $p_0 = 2.59$ GeV/c, $n = -17.43$, $m = 6.15$. The scaling correction was determined with a next-to-leading-order pQCD calculation. The correction is largest for $\sqrt{s} = 23.8$ GeV and reduces these spectra by ~30%. The systematic uncertainty of the fit increases from ~12% at $p_T = 1.5$ GeV/c to ~23% at $p_T = 4.0$ GeV/c [16].

The π^0 p_T spectra for $p + p$ and central Cu + Cu collisions (0%–10% of $\sigma_{\text{inel}}^{\text{Cu+Cu}}$) at $\sqrt{s_{NN}} = 22.4, 62.4$ [14], and 200 GeV [6] are shown in Figs. 1(a) and 1(b). At sufficiently high p_T where pion production in $p + p$ collisions is dominated by fragmentation of jets, QCD predicts a scaling law $\sqrt{s}^{n_{\text{eff}}(x_T,\sqrt{s})} Ed^3\sigma/d^3p = G(x_T)$ with a universal function $G(x_T)$ where $x_T = 2p_T/\sqrt{s}$ [19]. Figure 1(c) shows that such a scaling in x_T is indeed observed for $p + p$ collisions at 22.4, 62.4, and 200 GeV, consistent with previous observations [20]. The x_T values at which the universal curve $G(x_T)$ is reached indicate that particle production is dominated by hard processes for $p_T \gtrsim 2$ GeV/c.

Nuclear effects on high-p_T π^0 production can be quantified with the nuclear modification factor

$$R_{AA}(p_T) = \frac{(1/N_{AA}^{\text{evt}})d^2N_{AA}/dp_T dy}{\langle T_{AA}\rangle d^2\sigma_{pp}/dp_T dy}, \qquad (1)$$

where $\langle T_{AA}\rangle = \langle N_{\text{coll}}\rangle/\sigma_{pp}^{\text{inel}}$. Figure 2 shows $R_{AA}(p_T)$ for the 0%–10% most central Cu + Cu collisions. The suppression at 62.4 GeV ($R_{AA} \approx 0.6$ for $p_T \gtrsim 3$ GeV/c) and 200 GeV ($R_{AA} \approx 0.5$–0.6 for $p_T \gtrsim 3$ GeV/c) is consistent with expectations from parton energy loss. The $R_{AA} > 1$ in Cu + Cu at 22.4 GeV is similar to the enhancement by a factor ~1.5 (at $p_T \approx 3$ GeV/c) observed in p + W relative to p + Be collisions at $\sqrt{s_{NN}} = 19.4$ and 23.8 GeV [21]. For similar N_{part} values the R_{AA} in Cu + Cu at 22.4 GeV agrees with the R_{AA} in Pb + Pb collisions at 17.3 GeV [12].

For $p_T \gtrsim 3$ GeV/c the measured R_{AA} values at 62.4 and 200 GeV are consistent with a numerically evaluated parton energy-loss model described in [22,23]; see Fig. 2. This calculation takes into account shadowing from coherent final state interactions in nuclei [24], Cronin enhancement

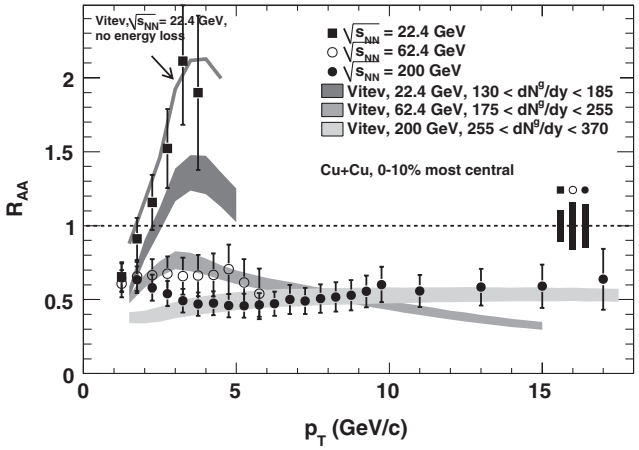

FIG. 2. Measured π^0 R_{AA} are compared to a jet quenching calculation [22,23]. The error bars (here and in Fig. 3) represent the quadratic sum of the statistical and the point-to-point uncorrelated and correlated systematic uncertainties. For $\sqrt{s_{NN}} = 22.4$ GeV the error bars also include the systematic error of the fit of the $p + p$ spectra. The boxes around unity indicate uncertainties related to $\langle N_{\text{coll}}\rangle$ and absolute normalization. The bands for the calculation correspond to the assumed range of the initial gluon density dN^g/dy.

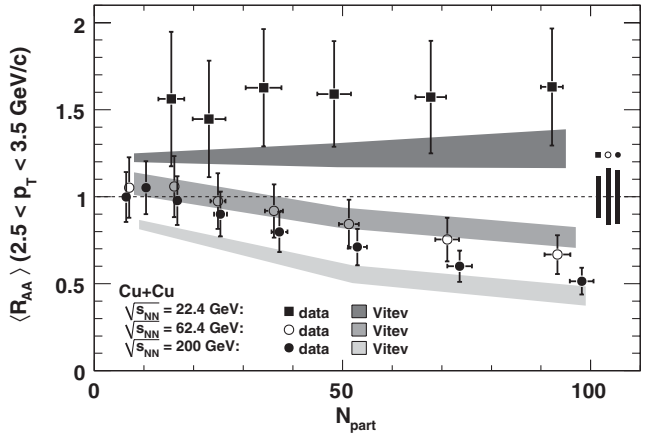

FIG. 3. The average R_{AA} in the interval $2.5 < p_T < 3.5$ GeV/c as a function of centrality for Cu + Cu collisions at $\sqrt{s_{NN}} =$ 22.4, 62.4, and 200 GeV. The shaded bands represent jet-quenching calculations at three discrete centralities ($N_{\text{part}} \sim$ 10, 50, 100) [22,23]. The boxes around unity represent the normalization and $\langle N_{\text{coll}} \rangle$ uncertainties for a typical N_{coll} uncertainty of 12%.

[25], initial state parton energy loss in cold nuclear matter [26], and final state parton energy loss in dense partonic matter [9,22,23]. The Cronin enhancement measured in $p + A$ collisions is described well by this model [25]. The initial gluon rapidity density dN^g/dy which characterizes the medium was not fit to the R_{AA} values, but instead was constrained by measured charged-particle multiplicities and the assumption of parton-hadron duality ($dN^g/dy = \kappa d\eta/dy dN_{ch}/d\eta$ with $\kappa = 3/2 \pm 30\%$ and $d\eta/dy \equiv 1.2$ at all energies) [22,23]. The average fractional energy losses $\Delta E/E$ for a quark (gluon) with $E =$ 6 GeV corresponding to the dN^g/dy ranges in Fig. 2 are 0.13–0.19 (0.29–0.42), 0.16–0.20 (0.35–0.44), 0.20–0.28 (0.44–0.63) in central Cu + Cu collisions at 22.4, 62.4, and 200 GeV, respectively [23]. For Cu + Cu at $\sqrt{s_{NN}} =$ 22.4 GeV the calculation is also shown without final state parton energy loss. The measurement is consistent with this calculation but does not rule out a scenario with parton energy loss.

Figure 3 shows that the π^0 suppression in the range $2.5 < p_T < 3.5$ GeV/c increases towards more central Cu + Cu collisions for $\sqrt{s_{NN}} = 62.4$, 200 GeV. On the other hand, R_{AA} at $\sqrt{s_{NN}} = 22.4$ GeV remains approximately constant as a function of N_{part}, suggesting either that the Cronin enhancement depends only weakly on centrality or that in this energy range parton energy loss is offset by the larger effect of Cronin enhancement.

In conclusion, high-p_T π^0 yields in central Cu + Cu collisions at 62.4 and 200 GeV are suppressed, suggesting that parton energy loss is significant, while at 22.4 GeV the π^0 yields for $p_T \gtrsim 2$ GeV/c are not suppressed. The R_{AA} measured in central Cu + Cu at 22.4 GeV is consistent with Cronin enhancement alone but does not rule out parton energy-loss effects. These measurements provide a unique constraint for jet-quenching models and demonstrate that parton energy loss starts to prevail over the Cronin enhancement between $\sqrt{s_{NN}} = 22.4$ and 62.4 GeV.

We thank the staff of the Collider-Accelerator and Physics Departments at BNL for their vital contributions. We thank Ivan Vitev for providing the jet-quenching calculations. We acknowledge support from the Office of Nuclear Physics in DOE Office of Science, NSF, and a sponsored research grant from Renaissance Technologies (U.S.), MEXT and JSPS (Japan), CNPq and FAPESP (Brazil), NSFC (China), MSMT (Czech Republic), IN2P3/CNRS, and CEA (France), BMBF, DAAD, and AvH (Germany), OTKA (Hungary), DAE (India), ISF (Israel), KRF and KOSEF (Korea), MES, RAS, and FAAE (Russia), VR and KAW (Sweden), U.S. CRDF for the FSU, U.S.-Hungary Fulbright, and U.S.-Israel BSF.

*Deceased.
†PHENIX Spokesperson.
jacak@skipper.physics.sunysb.edu.

[1] K. Adcox *et al.*, Nucl. Phys. **A757**, 184 (2005).
[2] A. Adare *et al.*, Phys. Rev. C **77**, 064907 (2008).
[3] M. Gyulassy and M. Plumer, Phys. Lett. B **243**, 432 (1990).
[4] K. Adcox *et al.*, Phys. Rev. Lett. **88**, 022301 (2001).
[5] S. S. Adler *et al.*, Phys. Rev. Lett. **91**, 072301 (2003).
[6] J. Adams *et al.*, Phys. Rev. Lett. **91**, 172302 (2003).
[7] X.-N. Wang, Phys. Rev. C **61**, 064910 (2000).
[8] I. Vitev and M. Gyulassy, Phys. Rev. Lett. **89**, 252301 (2002).
[9] I. Vitev, Phys. Lett. B **606**, 303 (2005).
[10] B. Alver *et al.*, Phys. Rev. Lett. **96**, 212301 (2006).
[11] B. I. Abelev *et al.*, Phys. Lett. B **655**, 104 (2007).
[12] M. M. Aggarwal *et al.*, Phys. Rev. Lett. **100**, 242301 (2008).
[13] C. Alt *et al.*, Phys. Rev. C **77**, 034906 (2008).
[14] A. Adare *et al.* (to be published).
[15] A. Adare *et al.*, Phys. Rev. D **76**, 051106 (2007).
[16] F. Arleo and D. d'Enterria, arXiv:0807.1252.
[17] L. Aphecetche *et al.*, Nucl. Instrum. Methods Phys. Res., Sect. A **499**, 521 (2003).
[18] M. L. Miller, K. Reygers, S. J. Sanders, and P. Steinberg, Annu. Rev. Nucl. Part. Sci. **57**, 205 (2007).
[19] R. F. Cahalan, K. A. Geer, J. B. Kogut, and L. Susskind, Phys. Rev. D **11**, 1199 (1975).
[20] S. S. Adler *et al.*, Phys. Rev. C **69**, 034910 (2004).
[21] D. Antreasyan *et al.*, Phys. Rev. D **19**, 764 (1979).
[22] I. Vitev, Phys. Lett. B **639**, 38 (2006).
[23] I. Vitev (private communication).
[24] J.-w. Qiu and I. Vitev, Phys. Lett. B **632**, 507 (2006).
[25] I. Vitev, Phys. Lett. B **562**, 36 (2003).
[26] I. Vitev, Phys. Rev. C **75**, 064906 (2007).

Dihadron azimuthal correlations in Au+Au collisions at $\sqrt{s_{NN}} = 200$ GeV

A. Adare,[8] S. Afanasiev,[22] C. Aidala,[9] N. N. Ajitanand,[49] Y. Akiba,[43,44] H. Al-Bataineh,[38] J. Alexander,[49] A. Al-Jamel,[38] K. Aoki,[28,43] L. Aphecetche,[51] R. Armendariz,[38] S. H. Aronson,[3] J. Asai,[44] E. T. Atomssa,[29] R. Averbeck,[50] T. C. Awes,[39] B. Azmoun,[3] V. Babintsev,[18] G. Baksay,[14] L. Baksay,[14] A. Baldisseri,[11] K. N. Barish,[4] P. D. Barnes,[31] B. Bassalleck,[37] S. Bathe,[4] S. Batsouli,[9,39] V. Baublis,[42] F. Bauer,[4] A. Bazilevsky,[3] S. Belikov,[3,21,*] R. Bennett,[50] Y. Berdnikov,[46] A. A. Bickley,[8] M. T. Bjorndal,[9] J. G. Boissevain,[31] H. Borel,[11] K. Boyle,[50] M. L. Brooks,[31] D. S. Brown,[38] D. Bucher,[34] H. Buesching,[3] V. Bumazhnov,[18] G. Bunce,[3,44] J. M. Burward-Hoy,[31] S. Butsyk,[31,50] S. Campbell,[50] J.-S. Chai,[23] B. S. Chang,[58] J.-L. Charvet,[11] S. Chernichenko,[18] J. Chiba,[24] C. Y. Chi,[9] M. Chiu,[9,19] I. J. Choi,[58] T. Chujo,[55] P. Chung,[49] A. Churyn,[18] V. Cianciolo,[39] C. R. Cleven,[16] Y. Cobigo,[11] B. A. Cole,[9] M. P. Comets,[40] P. Constantin,[21,31] M. Csanád,[13] T. Csörgő,[25] T. Dahms,[50] K. Das,[15] G. David,[3] M.B. Deaton,[1] K. Dehmelt,[14] H. Delagrange,[51] A. Denisov,[18] D. d'Enterria,[9] A. Deshpande,[44,50] E. J. Desmond,[3] O. Dietzsch,[47] A. Dion,[50] M. Donadelli,[47] J. L. Drachenberg,[1] O. Drapier,[29] A. Drees,[50] A. K. Dubey,[57] A. Durum,[18] V. Dzhordzhadze,[4,52] Y. V. Efremenko,[39] J. Egdemir,[50] F. Ellinghaus,[8] W. S. Emam,[4] A. Enokizono,[17,30] H. En'yo,[43,44] B. Espagnon,[40] S. Esumi,[54] K. O. Eyser,[4] D. E. Fields,[37,44] M. Finger,[5,22] M. Finger, Jr.,[5,22] F. Fleuret,[29] S. L. Fokin,[27] B. Forestier,[32] Z. Fraenkel,[57] J. E. Frantz,[9,50] A. Franz,[3] A. D. Frawley,[15] K. Fujiwara,[43] Y. Fukao,[28,43] S.-Y. Fung,[4] T. Fusayasu,[36] S. Gadrat,[32] I. Garishvili,[52] F. Gastineau,[51] M. Germain,[51] A. Glenn,[8,52] H. Gong,[50] M. Gonin,[29] J. Gosset,[11] Y. Goto,[43,44] R. Granier de Cassagnac,[29] N. Grau,[21] S. V. Greene,[55] M. Grosse Perdekamp,[19,44] T. Gunji,[7] H.-Å. Gustafsson,[33] T. Hachiya,[17,43] A. Hadj Henni,[51] C. Haegemann,[37] J. S. Haggerty,[3] M. N. Hagiwara,[1] H. Hamagaki,[7] R. Han,[41] H. Harada,[17] E. P. Hartouni,[30] K. Haruna,[17] M. Harvey,[3] E. Haslum,[33] K. Hasuko,[43] R. Hayano,[7] M. Heffner,[30] T. K. Hemmick,[50] T. Hester,[4] J. M. Heuser,[43] X. He,[16] H. Hiejima,[19] J. C. Hill,[21] R. Hobbs,[37] M. Hohlmann,[14] M. Holmes,[55] W. Holzmann,[49] K. Homma,[17] B. Hong,[26] T. Horaguchi,[43,53] D. Hornback,[52] M. G. Hur,[23] T. Ichihara,[43,44] K. Imai,[28,43] M. Inaba,[54] Y. Inoue,[43,45] D. Isenhower,[1] L. Isenhower,[1] M. Ishihara,[43] T. Isobe,[7] M. Issah,[49] A. Isupov,[22] B. V. Jacak,[50,†] J. Jia,[9] J. Jin,[9] O. Jinnouchi,[44] B. M. Johnson,[3] K. S. Joo,[35] D. Jouan,[40] F. Kajihara,[7,43] S. Kametani,[7,56] N. Kamihara,[43,53] J. Kamin,[50] M. Kaneta,[44] J. H. Kang,[58] H. Kanou,[43,53] T. Kawagishi,[54] D. Kawall,[44] A. V. Kazantsev,[27] S. Kelly,[8] A. Khanzadeev,[42] J. Kikuchi,[56] D. H. Kim,[35] D. J. Kim,[58] E. Kim,[48] Y.-S. Kim,[23] E. Kinney,[8] A. Kiss,[13] E. Kistenev,[3] A. Kiyomichi,[43] J. Klay,[30] C. Klein-Boesing,[34] L. Kochenda,[42] V. Kochetkov,[18] B. Komkov,[42] M. Konno,[54] D. Kotchetkov,[4] A. Kozlov,[57] A. Král,[10] A. Kravitz,[9] P. J. Kroon,[3] J. Kubart,[5,20] G. J. Kunde,[31] N. Kurihara,[7] K. Kurita,[43,45] M. J. Kweon,[26] Y. Kwon,[52,58] G. S. Kyle,[38] R. Lacey,[49] Y.-S. Lai,[9] J. G. Lajoie,[21] A. Lebedev,[21] Y. Le Bornec,[40] S. Leckey,[50] D. M. Lee,[31] M. K. Lee,[58] T. Lee,[48] M. J. Leitch,[31] M. A. L. Leite,[47] B. Lenzi,[47] H. Lim,[48] T. Liška,[10] A. Litvinenko,[22] M. X. Liu,[31] X. Li,[6] X. H. Li,[4] B. Love,[55] D. Lynch,[3] C. F. Maguire,[55] Y. I. Makdisi,[3] A. Malakhov,[22] M. D. Malik,[37] V. I. Manko,[27] Y. Mao,[41,43] L. Mašek,[5,20] H. Masui,[54] F. Matathias,[9,50] M. C. McCain,[19] M. McCumber,[50] P. L. McGaughey,[31] Y. Miake,[54] P. Mikeš,[5,20] K. Miki,[54] T. E. Miller,[55] A. Milov,[50] S. Mioduszewski,[3] G. C. Mishra,[16] M. Mishra,[2] J. T. Mitchell,[3] M. Mitrovski,[49] A. Morreale,[4] D. P. Morrison,[3] J. M. Moss,[31] T. V. Moukhanova,[27] D. Mukhopadhyay,[55] J. Murata,[43,45] S. Nagamiya,[24] Y. Nagata,[54] J. L. Nagle,[8] M. Naglis,[57] I. Nakagawa,[43,44] Y. Nakamiya,[17] T. Nakamura,[17] K. Nakano,[43,53] J. Newby,[30] M. Nguyen,[50] B. E. Norman,[31] A. S. Nyanin,[27] J. Nystrand,[33] E. O'Brien,[3] S. X. Oda,[7] C. A. Ogilvie,[21] H. Ohnishi,[43] I. D. Ojha,[55] H. Okada,[28,43] K. Okada,[44] M. Oka,[54] O. O. Omiwade,[1] A. Oskarsson,[33] I. Otterlund,[33] M. Ouchida,[17] K. Ozawa,[7] R. Pak,[3] D. Pal,[55] A. P. T. Palounek.,[31] V. Pantuev,[50] V. Papavassiliou,[38] J. Park,[48] W. J. Park,[26] S. F. Pate,[38] H. Pei,[21] J.-C. Peng,[19] H. Pereira,[11] V. Peresedov,[22] D. Yu. Peressounko,[27] C. Pinkenburg,[3] R. P. Pisani,[3] M. L. Purschke,[3] A. K. Purwar,[31,50] H. Qu,[16] J. Rak,[21,37] A. Rakotozafindrabe,[29] I. Ravinovich,[57] K. F. Read,[39,52] S. Rembeczki,[14] M. Reuter,[50] K. Reygers,[34] V. Riabov,[42] Y. Riabov,[42] G. Roche,[32] A. Romana,[29,*] M. Rosati,[21] S. S. E. Rosendahl,[33] P. Rosnet,[32] P. Rukoyatkin,[22] V. L. Rykov,[43] S. S. Ryu,[58] B. Sahlmueller,[34] N. Saito,[28,43,44] T. Sakaguchi,[3,7,56] S. Sakai,[54] H. Sakata,[17] V. Samsonov,[42] H. D. Sato,[28,43] S. Sato,[3,24,54] S. Sawada,[24] J. Seele,[8] R. Seidl,[19] V. Semenov,[18] R. Seto,[4] D. Sharma,[57] T. K. Shea,[3] I. Shein,[18] A. Shevel,[42,49] T.-A. Shibata,[43,53] K. Shigaki,[17] M. Shimomura,[54] T. Shohjoh,[54] K. Shoji,[28,43] A. Sickles,[50] C. L. Silva,[47] D. Silvermyr,[39] C. Silvestre,[11] K. S. Sim,[26] C. P. Singh,[2] V. Singh,[2] S. Skutnik,[21] M. Slunečka,[5,22] W. C. Smith,[1] A. Soldatov,[18] R. A. Soltz,[30] W. E. Sondheim,[31] S. P. Sorensen,[52] I. V. Sourikova,[3] F. Staley,[11] P. W. Stankus,[39] E. Stenlund,[33] M. Stepanov,[38] A. Ster,[25] S. P. Stoll,[3] T. Sugitate,[17] C. Suire,[40] J. P. Sullivan,[31] J. Sziklai,[25] T. Tabaru,[44] S. Takagi,[54] E. M. Takagui,[47] A. Taketani,[43,44] K. H. Tanaka,[24] Y. Tanaka,[36] K. Tanida,[43,44] M. J. Tannenbaum,[3] A. Taranenko,[49] P. Tarján,[12] T. L. Thomas,[37] M. Togawa,[28,43] A. Toia,[50] J. Tojo,[43] L. Tomášek,[20] H. Torii,[43] R. S. Towell,[1] V.-N. Tram,[29] I. Tserruya,[57] Y. Tsuchimoto,[17,43] S. K. Tuli,[2] H. Tydesjö,[33] N. Tyurin,[18] C. Vale,[21] H. Valle,[55] H. W. van Hecke,[31] J. Velkovska,[55] R. Vertesi,[12] A. A. Vinogradov,[27] M. Virius,[10] V. Vrba,[20] E. Vznuzdaev,[42] M. Wagner,[28,43] D. Walker,[50] X. R. Wang,[38] Y. Watanabe,[43,44] J. Wessels,[34] S. N. White,[3] N. Willis,[40] D. Winter,[9] C. L. Woody,[3] M. Wysocki,[8] W. Xie,[4,44] Y. L. Yamaguchi,[56] A. Yanovich,[18] Z. Yasin,[4] J. Ying,[16] S. Yokkaichi,[43,44] G. R. Young,[39] I. Younus,[37] I. E. Yushmanov,[27] W. A. Zajc,[9] O. Zaudtke,[34] C. Zhang,[9,39] S. Zhou,[6] J. Zimányi,[25,*] and L. Zolin[22]

(PHENIX Collaboration)

[1]*Abilene Christian University, Abilene, Texas 79699, USA*

[2]*Department of Physics, Banaras Hindu University, Varanasi 221005, India*

[3]*Brookhaven National Laboratory, Upton, New York 11973-5000, USA*

[4]*University of California-Riverside, Riverside, California 92521, USA*

 ©2008 The American Physical Society

[5]*Charles University, Ovocný trh 5, Praha 1, 116 36, Prague, Czech Republic*
[6]*China Institute of Atomic Energy (CIAE), Beijing, People's Republic of China*
[7]*Center for Nuclear Study, Graduate School of Science, University of Tokyo, 7-3-1 Hongo, Bunkyo, Tokyo 113-0033, Japan*
[8]*University of Colorado, Boulder, Colorado 80309, USA*
[9]*Columbia University, New York, New York 10027, USA and Nevis Laboratories, Irvington, New York 10533, USA*
[10]*Czech Technical University, Zikova 4, 166 36 Prague 6, Czech Republic*
[11]*Dapnia, CEA Saclay, F-91191, Gif-sur-Yvette, France*
[12]*Debrecen University, H-4010 Debrecen, Egyetem tér 1, Hungary*
[13]*ELTE, Eötvös Loránd University, H-1117 Budapest, Pázmány P. s. 1/A, Hungary*
[14]*Florida Institute of Technology, Melbourne, Florida 32901, USA*
[15]*Florida State University, Tallahassee, Florida 32306, USA*
[16]*Georgia State University, Atlanta, Georgia 30303, USA*
[17]*Hiroshima University, Kagamiyama, Higashi-Hiroshima 739-8526, Japan*
[18]*IHEP Protvino, State Research Center of Russian Federation, Institute for High Energy Physics, Protvino, RU-142281, Russia*
[19]*University of Illinois at Urbana-Champaign, Urbana, Illinois 61801, USA*
[20]*Institute of Physics, Academy of Sciences of the Czech Republic, Na Slovance 2, 182 21 Prague 8, Czech Republic*
[21]*Iowa State University, Ames, Iowa 50011, USA*
[22]*Joint Institute for Nuclear Research, RU-141980 Dubna, Moscow Region, Russia*
[23]*KAERI, Cyclotron Application Laboratory, Seoul, Korea*
[24]*KEK, High Energy Accelerator Research Organization, Tsukuba, Ibaraki 305-0801, Japan*
[25]*KFKI Research Institute for Particle and Nuclear Physics of the Hungarian Academy of Sciences (MTA KFKI RMKI), H-1525 Budapest 114, P.O. Box 49, Budapest, Hungary*
[26]*Korea University, Seoul, 136-701, Korea*
[27]*Russian Research Center "Kurchatov Institute," Moscow, Russia*
[28]*Kyoto University, Kyoto 606-8502, Japan*
[29]*Laboratoire Leprince-Ringuet, Ecole Polytechnique, CNRS-IN2P3, Route de Saclay, F-91128, Palaiseau, France*
[30]*Lawrence Livermore National Laboratory, Livermore, California 94550, USA*
[31]*Los Alamos National Laboratory, Los Alamos, New Mexico 87545, USA*
[32]*LPC, Université Blaise Pascal, CNRS-IN2P3, Clermont-Fd, F-63177 Aubiere Cedex, France*
[33]*Department of Physics, Lund University, Box 118, SE-221 00 Lund, Sweden*
[34]*Institut für Kernphysik, University of Muenster, D-48149 Muenster, Germany*
[35]*Myongji University, Yongin, Kyonggido 449-728, Korea*
[36]*Nagasaki Institute of Applied Science, Nagasaki-shi, Nagasaki 851-0193, Japan*
[37]*University of New Mexico, Albuquerque, New Mexico 87131, USA*
[38]*New Mexico State University, Las Cruces, New Mexico 88003, USA*
[39]*Oak Ridge National Laboratory, Oak Ridge, Tennessee 37831, USA*
[40]*IPN-Orsay, Universite Paris Sud, CNRS-IN2P3, BP1, F-91406, Orsay, France*
[41]*Peking University, Beijing, People's Republic of China*
[42]*PNPI, Petersburg Nuclear Physics Institute, Gatchina, Leningrad region, RU-188300, Russia*
[43]*RIKEN, The Institute of Physical and Chemical Research, Wako, Saitama 351-0198, Japan*
[44]*RIKEN BNL Research Center, Brookhaven National Laboratory, Upton, New York 11973-5000, USA*
[45]*Physics Department, Rikkyo University, 3-34-1 Nishi-Ikebukuro, Toshima, Tokyo 171-8501, Japan*
[46]*St. Petersburg State Polytechnic University, St. Petersburg, Russia*
[47]*Universidade de São Paulo, Instituto de Física, Caixa Postal 66318, São Paulo CEP05315-970, Brazil*
[48]*System Electronics Laboratory, Seoul National University, Seoul, Korea*
[49]*Chemistry Department, Stony Brook University, SUNY, Stony Brook, New York 11794-3400, USA*
[50]*Department of Physics and Astronomy, Stony Brook University, SUNY, Stony Brook, New York 11794, USA*
[51]*SUBATECH (Ecole des Mines de Nantes, CNRS-IN2P3, Université de Nantes) BP 20722 F-44307, Nantes, France*
[52]*University of Tennessee, Knoxville, Tennessee 37996, USA*
[53]*Department of Physics, Tokyo Institute of Technology, Oh-okayama, Meguro, Tokyo 152-8551, Japan*
[54]*Institute of Physics, University of Tsukuba, Tsukuba, Ibaraki 305, Japan*
[55]*Vanderbilt University, Nashville, Tennessee 37235, USA*
[56]*Waseda University, Advanced Research Institute for Science and Engineering, 17 Kikui-cho, Shinjuku-ku, Tokyo 162-0044, Japan*
[57]*Weizmann Institute, Rehovot 76100, Israel*
[58]*Yonsei University, IPAP, Seoul 120-749, Korea*
(Received 30 January 2008; published 2 July 2008)

Azimuthal angle ($\Delta\phi$) correlations are presented for a broad range of transverse momentum ($0.4 < p_T < 10$ GeV/c) and centrality (0–92%) selections for charged hadrons from dijets in Au+Au collisions at $\sqrt{s_{NN}} = 200$ GeV. With increasing p_T, the away-side $\Delta\phi$ distribution evolves from a broad and relatively flat shape to a concave shape, then to a convex shape. Comparisons with $p + p$ data suggest that the away-side distribution can be divided into a partially suppressed "head" region centered at $\Delta\phi \sim \pi$, and an enhanced "shoulder" region centered at $\Delta\phi \sim \pi \pm 1.1$. The p_T spectrum for the associated hadrons in the head region softens toward central collisions. The spectral slope for the shoulder region is independent of centrality and trigger p_T. The properties of the near-side distributions are also modified relative to those in $p + p$ collisions, reflected by the broadening of the jet shape in $\Delta\phi$ and $\Delta\eta$, and an enhancement of the per-trigger yield. However, these modifications seem to be limited to $p_T \lesssim 4$ GeV/c, above which both the hadron pair shape and per-trigger yield become similar to $p + p$ collisions. These observations suggest that both the away- and near-side distributions contain a jet fragmentation component which dominates for $p_T \gtrsim 5$ GeV/c and a medium-induced component which is important for $p_T \lesssim 4$ GeV/c. We also quantify the role of jets at intermediate and low p_T through the yield of jet-induced pairs in comparison with binary scaled $p + p$ pair yield. The yield of jet-induced pairs is suppressed at high pair proxy energy (sum of the p_T magnitudes of the two hadrons) and is enhanced at low pair proxy energy. The former is consistent with jet quenching; the latter is consistent with the enhancement of soft hadron pairs due to transport of lost energy to lower p_T.

DOI: 10.1103/PhysRevC.78.014901 PACS number(s): 25.75.Dw

I. INTRODUCTION

High transverse momentum (p_T) partons are informative probes of the high energy density matter created in nuclear collisions at the BNL Relativistic Heavy-Ion Collider (RHIC). These partons lose a large fraction of their energy in the matter prior to forming final state hadrons. Such an energy loss is predicted to lead to a reduction of both single hadron and correlated dihadron yields at high p_T [1–3], a phenomenon known as jet quenching. Indeed, current results for high p_T have revealed a strong suppression of inclusive hadron yields [4–6], as well as the suppression of correlated away-side hadron pairs [7].

Despite this strong suppression, particle production for $p_T \gtrsim 5$ GeV/c appears to have a significant contribution from in-vacuum jet fragmentation. This is suggested by a p_T-independent suppression factor for single hadrons [4–6,8], which implies a $p + p$-like power law spectral shape in Au+Au collisions, and similar π^0 to η meson [9,10] and proton to pion [6,11] ratios between Au+Au and $p + p$ collisions. More direct evidence has been provided by high-p_T dihadron azimuthal angle ($\Delta\phi$) correlation measurements. In particular, our current measurements, as well as prior ones [12,13], reveal characteristic jet-like peaks for the near-side ($\Delta\phi \sim 0$) and the away-side ($\Delta\phi \sim \pi$) at high p_T.

In most energy loss models, the stopping power of the medium is normally characterized by the transport coefficient $\hat{q}$, defined as the squared average momentum transfer from the medium to the hard parton per unit path length. However, because of the steeply falling parton spectra and strong jet quenching, the observed high-p_T single hadrons and hadron pairs mainly come from (di)jets that suffer minimal interaction with the medium. Thus, the overall suppression factor is sensitive to the full energy loss probability distribution instead of just the average energy loss itself. In fact, simple calculations [14] with different energy loss probability distributions have been shown to match the data quite well. However, the extracted $\langle\hat{q}\rangle$ values are sensitive to the theoretical models and their associated assumptions [15]. Additional experimental constraints on the dynamics of the energy loss processes are clearly needed.

To improve our understanding of the parton-medium interactions, it is important to study the fate of partons that suffer energy loss in the medium. These partons are quenched by the medium and their energy is believed to be transported to lower-p_T hadrons ($p_T \lesssim 4$ GeV/c). Prior measurements [7,16–20] in this p_T region, as well as the present study, indicate strong modifications of the near- and away-side $\Delta\phi$ distributions. The near-side jet-induced pairs peak at $\Delta\phi \sim 0$, but the peak is broadened and enhanced with respect to $p + p$ collisions. The away-side jet-induced pairs are observed to peak at $\Delta\phi \sim \pi \pm 1.1$ [13,18,19] with a local minimum at $\Delta\phi \sim \pi$. These modification patterns reflect characteristics of the energy transport of the quenched partons in both p_T and $\Delta\phi$. Many mechanisms for this energy transport have been proposed for the near-side [21–28] and away-side [23–25,29–36].

Such energy transport is expected to enhance jet contributions to the production of low-p_T hadrons. However, jet-induced hadron pair correlations can be affected by soft processes such as hydrodynamic flow [37] and quark coalescence [38–41], which dominate hadron production in the intermediate-p_T region. The coupling of partons with hydrodynamic flow could modify the jet shape and yield. Similarly, quark coalescence could modify the particle composition in the near- and away-side jets [42,43]. Therefore, detailed correlation studies for $p_T \lesssim 4$ GeV/c can improve our knowledge of the interplay between soft and hard processes for hadron production.

In this paper, we present a detailed survey of the trigger p_T, partner p_T, and centrality dependence of the near- and away-side jet shapes and yields from Au+Au collisions.

*Deceased.
†PHENIX spokesperson: jacak@skipper.physics.sunysb.edu

These measurements provide a comprehensive overview of the different physical features that come into play for different p_T ranges, and provide new insights on the interplay between the processes leading to jet energy loss and the response of the medium to the lost energy. In addition, they allow a detailed study of the similarities and differences between the correlation patterns for the near- and away-side jets. When coupled with inclusive hadron production, these measurements also allow quantification of the role of jets at intermediate p_T, where the particle production is believed to be dominated by the soft processes.

The results reported here comprise significant extensions to results published earlier [13,19]. In Sec. II, we introduce variables used to quantify the jet properties and their in-medium modifications. In Sec. III, we present data analysis details, jet signal extraction and background subtraction, and several sources of systematic errors related to the measurements. The main results are presented in Sec. IV, and model comparisons and discussions are given in Sec. V. Several technical issues related to the correlation analysis are addressed in Appendixes A–C, and tabulated data are given in Appendix A.

II. JET AZIMUTHAL CORRELATIONS

The defining characteristic of a jet is the collimated production of hadrons in the direction of a fragmenting parton. Traditionally, such energetic jets have been identified using standard jet reconstruction algorithms. However, direct jet reconstruction in heavy-ion collisions is difficult because of the large amount of soft background. Measurements in a relatively limited acceptance also pose additional challenges because of possible leakage of the jet fragments outside of the detectors acceptance.

The two-particle (dihadron) relative azimuthal angle ($\Delta\phi$) correlation technique provides an alternative approach for accessing the properties of jets. Two classes of hadrons, trigger hadrons (denoted as type a) and partner hadrons (denoted as type b), typically from different p_T ranges, are correlated with each other. Jet properties are extracted on a statistical basis from the $\Delta\phi$ distribution built of many events. This approach overcomes problems due to background and limited acceptance and allows the study of jets to be extended to low p_T where soft processes dominate.

To leading order in QCD, high-p_T jets are produced back-to-back in azimuth. This back-to-back correlation is, however, smeared by the fragmentation process and initial and final state radiation, to give a characteristic $\Delta\phi$ distribution schematically shown in Fig. 1 [44]. Hadron pairs from the same jet (near-side) dominate at $\Delta\phi = \phi^a - \phi^b \sim 0$, and those from back-to-back dijets (away-side) tend to appear at $\Delta\phi \sim \pi$.

Two observables commonly exploited in dihadron correlation studies are the hadron-pair yield (the rate of jet-induced hadron pairs per event, JPY) and the per-trigger yield (jet-induced hadron-pair yield divided by trigger yield, $Y_{\text{jet_ind}}$) in a given event sample. The former is related to the two-particle cross section for jet production; the latter is related to the ratio

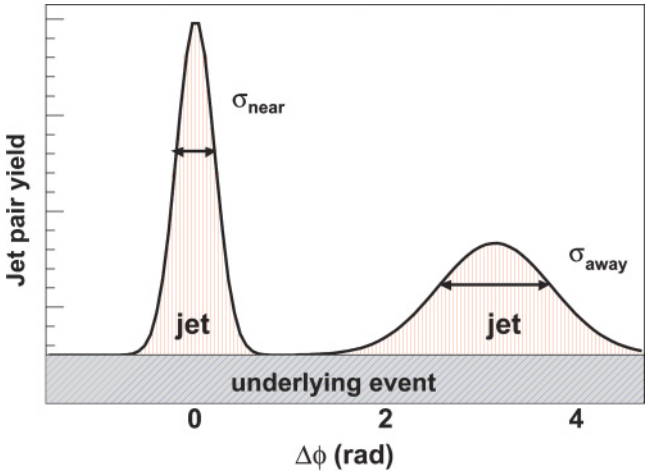

FIG. 1. (Color online) Cartoon of hadron pair distribution in $\Delta\phi$ for $p + p$ collisions. It has two peaks corresponding to near- and away-side jet, and a flat component representing the underlying event pairs.

of the two-particle to single-particle cross sections:

$$\text{JPY}\left(p_T^a, p_T^b, \Delta\phi\right) \equiv \frac{1}{N_{\text{evts}}} \frac{d^3N^{ab}}{dp_T^a dp_T^b d\Delta\phi} = \frac{1}{\sigma_{\text{tot}}} \frac{d^3\sigma_{\text{jet_ind}}}{dp_T^a dp_T^b d\Delta\phi}, \tag{1}$$

$$Y_{\text{jet_ind}}\left(p_T^a, p_T^b, \Delta\phi\right) \equiv \text{JPY}\left(p_T^a, p_T^b, \Delta\phi\right) \Big/ \frac{dN^a}{N_{\text{evts}} dp_T^a} = \frac{d^3\sigma_{\text{jet_ind}}}{dp_T^a dp_T^b d\Delta\phi} \Big/ \frac{d\sigma}{dp_T^a}, \tag{2}$$

where N^{ab} is the number of jet-induced hadron pairs, N_{evts} is the number of events, and σ_{tot} is the semi-inclusive cross section for that event sample. Thus, JPY is simply the product of the per-trigger yield and the number of triggers. To first order, the two-particle cross section for the near-side jet is governed by the dihadron fragmentation function. By contrast, the cross section for the away-side jet is governed by two independent fragmentation functions; i.e., one parton produces a hadron with p_T^a and the other scattered parton produces a hadron with p_T^b.

In $A + A$ collisions, the single-hadron and dihadron cross sections can be modified by the medium. This modification can be quantified by comparing the yield in $A + A$ collisions to that for $p + p$ collisions. Thus, modification to the single-hadron cross section is characterized by the nuclear modification factor R_{AA}

$$R_{AA}(p_T) = \frac{1/\sigma_{A+A}(d\sigma^{A+A}/dp_T)}{\langle N_{\text{coll}}\rangle/\sigma_{p+p}(d\sigma^{p+p}/dp_T)}, \tag{3}$$

where σ_{A+A} and σ_{p+p} are the semi-inclusive cross sections in $A + A$ and $p + p$ collisions, respectively. $\langle N_{\text{coll}}\rangle$ is the average number of binary collisions for a given centrality selection in $A + A$ collisions. Modification of the dihadron cross section

can be characterized by J_{AA}, which is defined as

$$J_{AA}(p_T^a, p_T^b, \Delta\phi) = \frac{\mathrm{JPY}^{A+A}}{\langle N_{\mathrm{coll}}\rangle\, \mathrm{JPY}^{p+p}} = \frac{1}{\sigma_{A+A}} \frac{d^3\sigma_{\mathrm{jet_ind}}^{A+A}}{dp_T^a\, dp_T^b\, d\Delta\phi} \Big/ \times \frac{\langle N_{\mathrm{coll}}\rangle}{\sigma_{p+p}} \frac{d^3\sigma_{\mathrm{jet_ind}}^{p+p}}{dp_T^a\, dp_T^b\, d\Delta\phi}. \quad (4)$$

In the absence of nuclear effects, both the single-hadron and dihadron cross sections from jets are expected to scale with $\langle N_{\mathrm{coll}}\rangle$. Therefore, R_{AA} and J_{AA} should be equal to unity.

The medium modifications of jets are also characterized by the per-trigger yield and its corresponding modification factor I_{AA}, that is,

$$I_{AA}(p_T^a, p_T^b) = \frac{Y_{\mathrm{jet_ind}}^{A+A}(p_T^a, p_T^b)}{Y_{\mathrm{jet_ind}}^{p+p}(p_T^a, p_T^b)}. \quad (5)$$

In general, the value of I_{AA} depends on modifications to both the hadron-pair yield and the trigger yield. For high-p_T correlation measurements, the per-trigger yield is a convenient choice, since each jet typically produces at most one high-p_T trigger. Because of the steeply falling parton spectrum, the probability of having a high-p_T parton that produces multiple trigger hadrons is small. Thus the per-trigger yield effectively represents the per-jet yield in $p + p$ collisions, and I_{AA} represents the modification of the partner yield per-jet. For intermediate and low p_T, however, jet fragmentation is not the only source of triggers, and this can lead to an artificial reduction of the per-trigger yield (see discussion in Sec. IV E). For such situations, J_{AA} is a more robust variable for correlation analysis since it is only sensitive to the modification of jet-induced hadron pairs.

JPY and J_{AA} are symmetric with respect to p_T^a and p_T^b. By contrast, the per-trigger yield and I_{AA} are not because of the appearance of the normalization factor N^a in Eq. (2). This normalization factor is the only distinction between triggers and the partners in this analysis. In addition, JPY can be expressed in terms of the per-trigger yield and the inclusive yield as

$$\mathrm{JPY}(p_T^a, p_T^b) = Y_{\mathrm{jet_ind}}(p_T^a, p_T^b) \frac{dN^a}{N_{\mathrm{evts}} dp_T^a} = Y_{\mathrm{jet_ind}}(p_T^b, p_T^a) \frac{dN^b}{N_{\mathrm{evts}} dp_T^b}. \quad (6)$$

Similarly, J_{AA} can be expressed in terms of R_{AA} and I_{AA} as

$$J_{AA}(p_T^a, p_T^b) = I_{AA}(p_T^a, p_T^b) R_{AA}(p_T^a) = I_{AA}(p_T^b, p_T^a) R_{AA}(p_T^b). \quad (7)$$

Thus, $I_{AA}(p_T^b, p_T^a)$ can be calculated from $I_{AA}(p_T^a, p_T^b)$, $R_{AA}(p_T^a)$, and $R_{AA}(p_T^b)$.

In the current analysis, the in-medium modifications of the jet shape and yield are characterized via comparisons of the per-trigger yield and hadron-pair yield in Au+Au and $p + p$ collisions, i.e., via I_{AA} and J_{AA}. As discussed earlier, these quantities are defined in their differential form in $\Delta\phi$, p_T^a, and p_T^b. Operationally, this means that the hadron-pair yields and the per-trigger yields are measured in a finite p_T range and/or integrated over a limited $\Delta\phi$ range. I_{AA} and J_{AA} are then obtained from these integrated yields.

III. EXPERIMENTAL ANALYSIS

A. Dataset and centrality

The results presented in this article are based on three datasets collected with the PHENIX detector [45] at $\sqrt{s_{NN}} =$ 200 GeV, during the 2004–2005 RHIC running periods. The first is comprised of a minimum-bias (MB) Au+Au dataset triggered by the beam-beam counters (BBCs) and the zero-degree calorimeters (ZDCs) and taken in 2004. The second is a MB $p + p$ dataset triggered by the BBCs and taken in 2005, and the third is a level-1 triggered (LVL1) $p + p$ dataset also obtained in 2005. The level-1 trigger requirement is an energy threshold of 1.4 GeV in 4×4 electromagnetic calorimeter (EMC) towers in coincidence with the BBC trigger [46]. The MB and LVL1 $p + p$ datasets serve as baseline measurements for the Au+Au dataset; they are used to select triggers for $p_T < 5$ and $p_T > 5$ GeV/c, respectively.

The collision vertex along the beam direction, z, was measured by the BBCs. After making an offline vertex cut of $|z| < 30$ cm and selecting good runs, a total of 840 million or 136 $\mu\mathrm{b}^{-1}$ Au+Au events were obtained. This is a 30 times higher than obtained in a previous analysis [18]. The total statistics for MB $p + p$ and LVL1 $p + p$ datasets are equivalent to 73 nb^{-1} and 2.5 pb^{-1} sampled luminosities, respectively.

The event centrality was determined via cuts in the space of BBC charge vs ZDC energy [47]. The efficiency of the MB triggered events is estimated to be $92.2^{+2.5}_{-3.0}$% of the total Au+Au inelastic cross section (6.9 b) [6]. To optimize the p_T reach of our results, relatively *coarse* centrality selections of 0–20%, 20–40%, 40–60%, and 60–92.2% were chosen. However for $p_T < 4$ GeV/c, excellent statistical significance of the measurements allows the results to be presented in *fine* centrality selections of 0–5%, 5–10%, 10–20%, 20–30%, 30–40%, 40–50%, 50–60%, 60–70%, and 70–92.2%.

A Glauber model Monte Carlo simulation [48,49] that includes the responses of the BBCs and ZDCs was used to estimate the average number of binary collisions $\langle N_{\mathrm{coll}}\rangle$ and participating nucleons $\langle N_{\mathrm{part}}\rangle$ for each centrality class. These values are listed in Table I.

B. Tracking and background estimation

Charged hadrons were reconstructed in the two central arms of PHENIX, each covering −0.35 to 0.35 in pseudorapidity and 90° in azimuth. Tracks were measured outside the PHENIX central magnetic field by the drift chambers, located at a radius of 2.0 m from the vertex, and two layers of multiwire proportional chamber (PC1 and PC3), located 2.5 and 5.0 m, respectively, from the vertex [47]. The momentum resolution was determined to be 0.7% ⊕ 1.0% p (GeV/c) [6].

TABLE I. Average number of nucleon-nucleon collisions $\langle N_{\rm coll}\rangle$ and participant nucleons $\langle N_{\rm part}\rangle$ for several centrality classes. $\langle N_{\rm coll}\rangle$ and $\langle N_{\rm part}\rangle$ are obtained from a Glauber Monte Carlo simulation of the response of the BBCs and ZDCs in Au+Au collisions at $\sqrt{s_{NN}} = 200$ GeV. The errors for these centrality classes are correlated.

Centrality	$\langle N_{\rm coll}\rangle$	$\langle N_{\rm part}\rangle$
0–5%	1065 ± 105.5	351.4 ± 2.9
5–10%	854.4 ± 82.1	299 ± 3.8
10–20%	602.6 ± 59.3	234.6 ± 4.7
20–30%	373.8 ± 39.6	166.6 ± 5.4
30–40%	219.8 ± 22.6	114.2 ± 4.4
40–50%	120.3 ± 13.7	74.4 ± 3.8
50–60%	61.0 ± 9.9	45.5 ± 3.3
60–70%	28.5 ± 7.6	25.7 ± 3.8
70–92%	8.3 ± 2.4	9.5 ± 1.9
min. bias	257.8 ± 25.4	109.1 ± 4.1
0–20%	779 ± 75.2	279.9 ± 4.0
20–40%	297 ± 30.8	140.4 ± 4.9
40–60%	90.6 ± 11.8	60 ± 3.5
60–92%	14.5 ± 4	14.5 ± 2.5

To reduce background particles that do not originate from the event vertex, such as weak decays and conversion electrons, tracks were required to have a matching hit within a $\pm 2.3\sigma$ window in PC3. For $p_T > 4$ GeV/c, an additional matching hit at the EMC was required to suppress background tracks that randomly associate with a hit in PC3 [6]. For triggers with $p_T > 5$ GeV/c, a p_T-dependent energy cut in the EMC and a tight $\pm 1.5\sigma$ matching cut at the PC3 were applied to reduce the physical background from post-field photon conversions and weak decays to a level $<10\%$ of real tracks [50]. This energy cut helps to suppress any level-1 bias for the LVL1 $p + p$ dataset. We checked the consistency between the MB and LVL1 $p + p$ datasets for triggers with $p_T > 5$ GeV/c by performing the same analysis separately on the two $p + p$ datasets. Any remaining biases due to level-1 trigger selection were found to be within the quoted errors. With these cuts, the background level for triggers was estimated to be $\lesssim 5\%$ for $p_T \lesssim 3$ GeV/c, and increases to $\sim 10\%$ for $p_T > 4$ GeV/c [6]. A p_T-dependent correction to the per-trigger yield was used to account for this background.

For partner hadrons, the same matching cuts used for trigger hadrons were applied. However, the p_T-dependent energy cut for $5-10$ GeV/c partners was found to be unnecessary. The jet-associated partner charged hadron spectrum is much flatter than that for the trigger hadrons. Thus, the background contamination of partners is much reduced relative to that for the trigger hadrons. In addition, the background tracks contributing to combinatoric pairs do not affect the jet signal and can be subtracted out.

A full GEANT-based simulation of PYTHIA-generated jet events in the PHENIX detector, as detailed in Ref. [50], was used to evaluate the effects of this high-p_T background for partner hadrons. Partner yields were extracted following the same procedures used for the actual data analysis. These were then compared with the input partner hadron spectra. For high-p_T triggered events, the background contributions to the partner hadrons were found to be less than 10% for integrated partner yields in the 5–10 GeV/c cut.

The single particle efficiency for triggers and partners, ϵ^a and ϵ^b in Eqs. (15) and (17), were determined such that the single unidentified hadron p_T spectra reproduce the previously published data for Au+Au [6] and $p + p$ [51]. It includes detector acceptance, reconstruction efficiency, occupancy, and background [6]. The detector acceptance and reconstruction efficiency were estimated with a Monte Carlo simulation in which simulated single tracks were reconstructed in the PHENIX detector, using the same analysis chain employed for the real data. The efficiency loss due to detector occupancy in Au+Au collisions was estimated by reconstructing simulated single tracks embedded into real events. More details can be found in the Au+Au [6] and $p + p$ [51] analyses.

C. Jet signal extraction

The dihadron correlation technique is commonly employed in PHENIX for jet measurements, because it surmounts the challenges posed by the detector's limited azimuthal acceptance for single hadrons. Even so, physical correlations due to anisotropic production of hadrons relative to the reaction plane in Au+Au collisions, i.e., the elliptic flow, need to be distinguished from the jet correlations. In what follows, we lay out the framework for our correlation analysis and an associated decomposition procedure used to separate the elliptic flow and jet correlation contributions. We define the azimuthal correlation function as

$$C(\Delta\phi) \equiv \frac{N^{\rm same}(\Delta\phi)}{N^{\rm mixed}(\Delta\phi)}, \tag{8}$$

where $N^{\rm same}(\Delta\phi)$ and $N^{\rm mixed}(\Delta\phi)$ are pair distributions from the same and mixed events, respectively. Each mixed event is constructed by combining triggers from a real event with partners from a different, randomly selected event with similar centrality and collision vertex as the real event.

The shape of the mixed-event pair distribution reflects the pair $\Delta\phi$ acceptance of the PHENIX detector, but it does not contain physical correlations. The integral of mixed-event pairs reflects the rate of the combinatoric pairs,

$$\int d\Delta\phi N^{\rm mixed}(\Delta\phi) = N_{\rm evts}\langle n^a\rangle\langle n^b\rangle, \tag{9}$$

where $N_{\rm evts}$ is the number of events and $\langle n^a\rangle$, $\langle n^b\rangle$ represent the average number of triggers and partners per event in the PHENIX acceptance. Both $N^{\rm same}(\Delta\phi)$ and $N^{\rm mixed}(\Delta\phi)$ are affected by the pair efficiency, which cancels out in the ratio (see Appendix A). Therefore, the correlation function in Eq. (8) contains only physical correlations.

The elliptic flow correlation leads to a harmonic modulation of the combinatoric pair distribution by a factor that is proportional to $(1 + 2v_2^a v_2^b \cos 2\Delta\phi)$, where v_2^a and v_2^b are the average elliptic flow values for triggers and partners, respectively. To extract the jet-induced pairs, we follow a two-source ansatz in which each particle is assumed to come from a jet-induced source and an underlying event containing

elliptic flow. The pair distribution can be expressed as

$$N^{\text{same}}(\Delta\phi) = \xi\left(1 + 2v_2^a v_2^b \cos 2\Delta\phi\right) N^{\text{mixed}}(\Delta\phi) + \text{Jet}(\Delta\phi) \tag{10}$$

Where the Jet($\Delta\phi$) represents all pairs from (di)jets. The integral of N^{same} can be written as

$$\int d\Delta\phi N^{\text{same}}(\Delta\phi) = N_{\text{evts}}\langle n^a n^b\rangle + \int d\Delta\phi \text{Jet}(\Delta\phi). \tag{11}$$

Comparing to Eq. (9), we obtain

$$\xi = \frac{\langle n^a n^b\rangle}{\langle n^a\rangle\langle n^b\rangle}. \tag{12}$$

Thus, ξ is simply the ratio of the trigger-partner combinatoric rate in the same event to that in mixed events, which can be bigger than unity because of centrality smearing (see discussion in Sec. III E). An alternative approach used to fix ξ is to assume that the jet function has zero yield at its minimum $\Delta\phi_{\text{min}}$ (ZYAM) [18,52].

Finally, the ratio of jet-induced pairs to combinatoric pairs from mixed events, the jet-induced hadron-pair ratio (JPR) is given by

$$\begin{aligned}\text{JPR}(\Delta\phi) &\equiv \frac{\text{Jet}(\Delta\phi)}{N^{\text{mixed}}(\Delta\phi)} \\ &= \frac{N^{\text{same}}(\Delta\phi)}{N^{\text{mixed}}(\Delta\phi)} - \xi\left(1 + 2v_2^a v_2^b \cos 2\Delta\phi\right).\end{aligned} \tag{13}$$

A representative correlation function is given in Fig. 2 for 0–5% Au+Au collisions and for triggers and partners in 2–3 and 1–2 GeV/c, respectively. It shows a peak around $\Delta\phi \sim 0$ and a broad structure around $\Delta\phi \sim \pi$. The dashed line indicates the estimated elliptic flow modulated background via the ZYAM method. The area between the data points and the dashed line reflects the jet-induced pair ratio. It is only a few percent relative to the background level.

We define $\varepsilon^a, \varepsilon^b$ as the single particle efficiency within the PHENIX pseudorapidity acceptance ($|\eta| < 0.35$). The true numbers of triggers and partners are given by

$$\langle n_0^a\rangle = \langle n^{\text{a}}\rangle/\varepsilon^a; \quad \langle n_0^b\rangle = \langle n^b\rangle/\varepsilon^b. \tag{14}$$

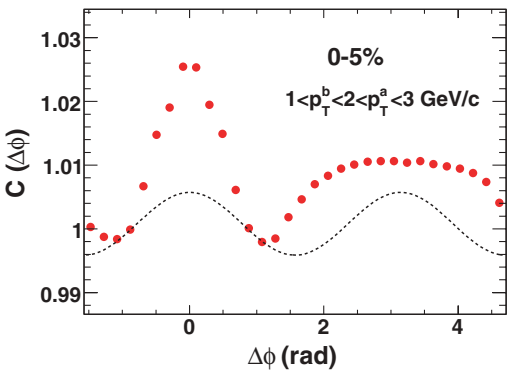

FIG. 2. (Color online) Correlation function for $2 < p_T^a < 3$, $1 < p_T^b < 2$ GeV/c in 0–5% Au+Au collisions. The dashed line represents the estimated elliptic flow modulated combinatoric background using zero yield at minimum (ZYAM) method (see Sec. III E).

For uncorrelated sources, the triggers and partners are uniform in azimuth. Thus the true combinatoric pair distribution for mixed events is flat with $\Delta\phi$ with a density of $\langle n_0^a\rangle\langle n_0^b\rangle/(2\pi)$. The yield of jet-induced pairs per event (JPY) is given as the product of the combinatoric pair rate and the hadron-pair ratio,

$$\begin{aligned}\text{JPY}(\Delta\phi) &= \frac{\langle n_0^a\rangle\langle n_0^b\rangle}{2\pi}\text{JPR}(\Delta\phi) = \frac{\langle n^a\rangle\langle n^{\text{b}}\rangle}{2\pi\,\varepsilon^a\varepsilon^{\text{b}}}\text{JPR}(\Delta\phi) \\ &= \frac{\int d\Delta\phi N^{\text{mixed}}(\Delta\phi)}{2\pi\, N_{\text{evts}}\varepsilon^a\varepsilon^{\text{b}}}\left[\frac{N^{\text{same}}(\Delta\phi)}{N^{\text{mixed}}(\Delta\phi)}\right. \\ &\quad \left. - \xi\left(1 + 2v_2^{\text{a}} v_2^b \cos 2\Delta\phi\right)\right].\end{aligned} \tag{15}$$

Thus far, we have made no distinction between trigger and partner hadrons. As discussed earlier in Sec. II, the correlation function, hadron-pair ratio, and hadron-pair yield are symmetric between the trigger and partner p_T, i.e.,

$$\begin{aligned}C\left(p_T^a, p_T^b\right) &= C\left(p_T^b, p_T^a\right), \\ \text{JPR}\left(p_T^a, p_T^b\right) &= \text{JPR}\left(p_T^b, p_T^a\right), \\ \text{JPY}\left(p_T^a, p_T^b\right) &= \text{JPY}\left(p_T^b, p_T^a\right).\end{aligned} \tag{16}$$

The associated partner yield per trigger, $Y_{\text{jet_ind}}(\Delta\phi)$ is obtained by dividing the hadron-pair yield per event with the number of triggers per event,

$$\begin{aligned}Y_{\text{jet_ind}}(\Delta\phi) &= \frac{\text{JPY}(\Delta\phi)}{n_0^a} = \frac{\int d\Delta\phi N^{\text{mixed}}(\Delta\phi)}{2\pi N^a\varepsilon^b} \\ &\quad \times\left[\frac{N^{\text{same}}(\Delta\phi)}{N^{\text{mixed}}(\Delta\phi)} - \xi\left(1 + 2v_2^a v_2^b \cos 2\Delta\phi\right)\right].\end{aligned} \tag{17}$$

$Y_{\text{jet_ind}}$ is often referred to as the per-trigger yield or conditional yield. It is clearly not invariant to the exchange of trigger and partner p_T.

The analysis proceeds in the following steps. We first measure the correlation function of Eq. (8). We then obtain the efficiency for partner hadrons (ε^b) and the elliptic flow coefficients for the two hadron categories (v_2^a, v_2^b). We then determine the background level (ξ) via the ZYAM background subtraction method (see Sec. III E), followed by a calculation of the per-trigger yield according to Eq. (17). Subsequently, we obtain the hadron-pair yield by multiplying the per-trigger yield with the inclusive charged hadron yield [6] integrated in the corresponding trigger p_T range.

According to Eq. (6), the hadron-pair yields calculated from the per-trigger yields are independent of which hadron, from the pair, is used as trigger. We used this fact to cross-check the efficacy of our analysis. Figure 3 compares the hadron-pair yields obtained when the trigger and partner p_T is exchanged in $p + p$ collisions (in $p_T^a \otimes p_T^b$). The open symbols indicate the results for low-p_T trigger hadrons in association with high-p_T partners. The filled symbols show the converse. A similar comparison for 0–20% Au+Au collisions is shown in Fig. 4. Overall good agreement is indicated by these distributions. It is important to emphasize here that there is no *a priori* reason for these distributions to be identical, since the cuts on trigger and partner hadrons are a little different (cf. Sec. III B) and therefore could lead to somewhat different

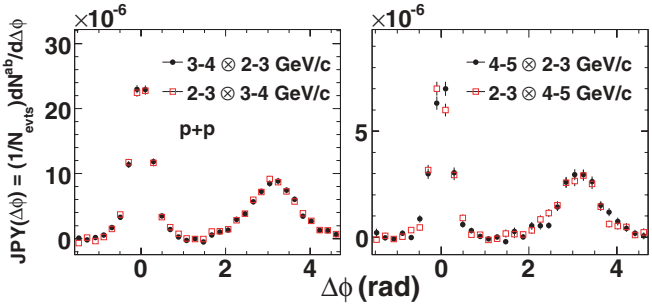

FIG. 3. (Color online) $p+p$ jet-induced hadron-pair yield $\Delta\phi$ distributions calculated from the per-trigger yield using low-p_T hadrons as triggers (solid symbols) and high-p_T hadrons as triggers (open symbols).

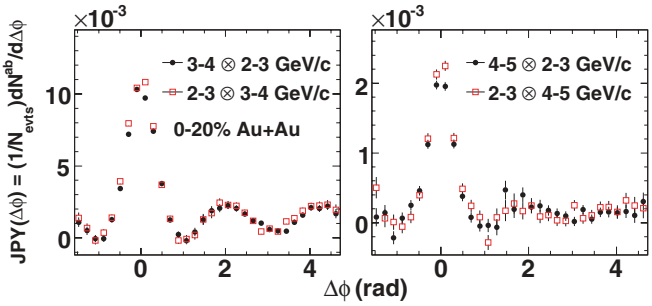

FIG. 4. (Color online) Same as Fig. 3, but for 0–20% Au+Au.

systematic errors for each measurement. We also note that the hadron-pair yield is almost three orders of magnitude stronger in Au+Au collisions than in $p+p$ reactions. This feature reflects the enhanced contributions from the medium response to quenched jets; the hadron-pair yields scale faster than $N_{\rm coll}$ at low $p_T^{a,b}$ (see discussions for Figs. 28–31).

D. Elliptic flow measurement

The differential elliptic flow measurements for charged hadrons were carried out with the reaction plane method [53]. The event plane (EP), which is the experimental estimate of the reaction plane (RP), is determined via the two BBCs positioned symmetrically along the beamline. They cover full azimuth and $3 < |\eta| < 3.9$ in pseudorapidity. The BBCs allow an unbiased measurement of the event plane and ensure that there are no residual distortions on the correlation function that could result from the limited azimuthal coverage of the PHENIX central arms. A detailed analytical proof of this latter point is provided in Appendix B.

We determine the value of elliptic flow v_2 as

$$v_2 = \frac{v_{2,\rm raw}}{c_{v_2}} = \frac{\langle\langle\cos 2(\phi - \Phi_{\rm EP})\rangle\rangle}{\langle\cos 2(\Phi_{\rm EP} - \Phi_{\rm RP})\rangle}, \qquad (18)$$

where $\Phi_{\rm EP}$ is the event plane angle and $\Phi_{\rm RP}$ is the true reaction plane angle, $v_{2,\rm raw} = \langle\langle\cos 2(\phi - \phi_{\rm EP})\rangle\rangle$ is the raw v_2, and $c_{v_2} = \langle\cos 2(\Phi_{\rm EP} - \Phi_{\rm RP})\rangle$ is the estimated reaction plane resolution. The former is obtained by averaging over all tracks and all events; the latter, by averaging over all events. The resolution is estimated from the event plane angle of the north and south BBC as $c_{v_2} = \sqrt{2\langle\cos 2(\Phi_{\rm EP,north} - \Phi_{\rm EP,south})\rangle}$ [54,55]. It is 0.3 for minimum bias events and reaches a maximum of 0.42 in the 20–30% centrality bin. Further details are given in Ref. [55].

Reliable extraction of the jet signal requires accurate determination of v_2^a and v_2^b. To this end, nonflow effects that lead to azimuthal correlations unrelated to the true RP direction need to be studied. These effects include various long- or short-range correlations among clusters of particles, such as momentum conservation effects, resonance decays, Hanbury-Brown–Twiss correlations, and jets [56,57]. While jets potentially bias the v_2 measurement at high p_T, other nonflow effects may be important at low and intermediate p_T. The values of v_2 are also sensitive to event-by-event fluctuations of the collision geometry [58–61] (so-called v_2 fluctuations), which affect all p_T regions.

A bias to v_2 resulting from jets has been reported for high-p_T hadrons [62]. However, the relative significance of other nonflow effects and v_2 fluctuations is still under debate. Recent studies from PHOBOS [63] and STAR [64] suggest that the fluctuations dominate over the nonflow effects for the p_T integral v_2.

Following the two-source assumption in Eq. (11), any correlations other than jets are attributed to the background term, i.e., $1 + 2v_2^a v_2^b \cos 2\Delta\phi$. These naturally include most nonflow correlations and v_2 fluctuations. To estimate the potential biases from jets and dijets, we carried out a detailed study in Appendix C, in which we embedded dijet PYTHIA events into flow-modulated events generated with the HIJING code. Our study shows that the large rapidity separation between the PHENIX BBCs and central arms greatly reduces the influence of jets on our v_2 measurements. Consequently, we use the BBC reaction plane v_2 measurements to evaluate and subtract the elliptic flow modulated background.

E. Combinatoric background subtraction

The background level ξ can be determined precisely if we know the exact functional form for the near- and away-side jets, or if we can independently measure the underlying event rate. However, due to in-medium modifications, the near- and away-side jets are not necessarily Gaussian, especially for $\Delta\phi$ values away from 0 and π. Even in $p+p$ collisions, the underlying event can include contributions from multiple-parton interaction, beam remnants, and initial and final state radiation effects [65], which are related to the hard-scattering but not necessarily correlated in $\Delta\phi$. Such effects have been studied at the Tevatron [65,66] and RHIC [44] energies. For illustration purposes, Fig. 5 shows the dihadron correlation from PYTHIA [67] with and without initial and final state radiation effects. The difference between the two is clearly significant.

Rigorous decomposition of the jet from its underlying event currently requires assumptions about the jet shape or the physics of the underlying event. As discussed earlier, a simple approach to fix ξ is to follow the subtraction procedure outlined in Refs. [18,52]. That is, one assumes that the jet function has zero yield at its minimum $\Delta\phi_{\rm min}$ (ZYAM), after subtraction of

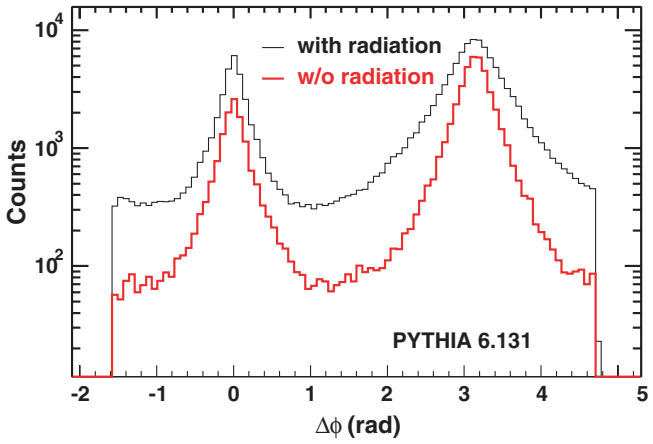

FIG. 5. (Color online) PYTHIA simulation showing jet-induced hadron pair $\Delta\phi$ distribution for $3 < p_T^a, p_T^b < 5$ GeV/c with (top histogram) and without (bottom histogram) initial and final state radiation. The radiation accounts for the increase of the background level.

the underlying event. The uncertainty on ξ from this procedure is related to the statistical accuracy of the data around $\Delta\phi_{\min}$. In the present analysis, this uncertainty is negligible at low p_T, but becomes important for $p_T^{a,b} > 4$ GeV/c in central collisions.

The ZYAM procedure, by definition, provides only a lower limit on the jet yield. To estimate the possible over-subtraction of jet yield at $\Delta\phi_{\min}$, we also made independent estimates of ξ via an absolute combinatoric background subtraction method (ABS) [68] and by a fitting method. In the ABS method, ξ, as defined by Eq. (12), is assumed to reflect only a residual multiplicity smearing effect caused by intrinsic positive correlations between the n_0^a and n_0^b in real events; i.e., a larger n_0^a implies a larger n_0^b and vice versa. Because of this positive correlation, the average of the product can become larger than the product of the average; i.e., $\langle n_0^a n_0^b\rangle > \langle n_0^a\rangle\langle n_0^b\rangle$ or $\xi > 1$.

To estimate ξ, we parametrize the centrality dependence of the trigger and partner rate from the measured single particle spectra in relevant momentum range, as a function of either $N_{\rm part}$ or $N_{\rm coll}$

$$\langle n_0^{a,b}\rangle = f(N_{\rm part}) = g(N_{\rm coll}). \tag{19}$$

We then assume the event-by-event fluctuation of trigger and partner hadrons to follow a Poisson distribution around their mean values,

$$n_0^{a,b} = \text{Poisson}\left(\langle n_0^{a,b}\rangle\right). \tag{20}$$

However, we have verified that that our estimates are not very sensitive to the functional forms of the fluctuations.

For each centrality bin, we determine the distribution of $N_{\rm part}$ and $N_{\rm coll}$ from the standard PHENIX Glauber calculation [48,49]. For each simulated event, we sample randomly from the $N_{\rm part}$ distribution, calculate the corresponding mean value $\langle n_0^{a,b}\rangle$ and then the actual value $n_0^{a,b}$ after taking into account the fluctuation. The same exercise is repeated for the $N_{\rm coll}$ distributions. The final ξ is given by the average of the two, and their difference is taken as the systematic error. The correction modifies the background level by 0.2% in the most central and 25% in the 60–92% centrality bin. The ABS and ZYAM methods give consistent ξ values in central collisions, but the ABS method gives somewhat lower values in peripheral collisions.

TABLE II. Comparison of the ξ values obtained for three different normalization methods for several centrality selections. They are calculated for the $2.5 < p_T^a < 4.0$ and $1.0 < p_T^b < 2.0$ GeV/c bins.

Cent.	ZYAM	ABS	Constrained fit
0–5%	1.0018 ± 0.0004	1.0023 ± 0.0002	0.998 ± 0.002
20–30%	1.015 ± 0.0015	1.012 ± 0.003	1.004 ± 0.006
50–60%	1.076 ± 0.009	1.07 ± 0.02	1.054 ± 0.009

In the fit method, $Y_{\rm jet_ind}(\Delta\phi)$ is fitted with a function comprised of one near- and two symmetric away-side Gaussians, following a procedure similar to that reported in Ref. [19]. One important difference is that a region around $\pi(|\Delta\phi - \pi| < 1)$ is excluded to avoid the punch-through jet contributions (see Fig. 6). Thus, the fit uses the near-side and the falling edge of the away-side to estimate the overlap of the near- and away-side Gaussians at $\Delta\phi_{\min}$. This approach gives systematically lower ξ values than those obtained from the ZYAM and ABS methods.

Table II summarizes the ξ values from the three methods. The results for the ZYAM and ABS methods are close, but the values from the fitting method are systematically lower. This could be due to the correlations between the fitting parameters or a limitation in the Gaussian assumptions for the jet shape. To avoid a possible overestimation of the jet yield in the $\Delta\phi$ region where the near- and away-side Gaussians overlap, we constrain the ξ to be $\geqslant 1$. This is a reasonable assumption in the absence of anticorrelation in trigger and partner hadron multiplicity. We assign the differences with the ZYAM method as a one-sided systematic error on ξ. This error is important in central collisions and for $p_T^{a,b} < 3$ GeV/c.

F. Systematic uncertainties

We classify the systematic errors associated with the jet yield into three main categories: (1) uncertainties in the single particle efficiency correction, ϵ^a and ϵ^b, for Au+Au and $p + p$, (2) statistical and systematic uncertainties associated with the determination of the elliptic flow values, v_2^a and v_2^b, in Au+Au collisions, and (3) uncertainties associated with the determination of the combinatoric background level ξ in both Au+Au and $p + p$ collisions.

The uncertainties associated with the efficiency corrections include contributions from the detector acceptance (5%), matching cuts (4%), and momentum scale and momentum resolution (5%). The background contamination is estimated to be 5% for $p_T < 5$ GeV/c, increasing to 10% for the 5–10 GeV/c bin. This leads to an overall systematic error of ~10% for $p_T < 5$ and 13% for the 5–10 GeV/c bin. For

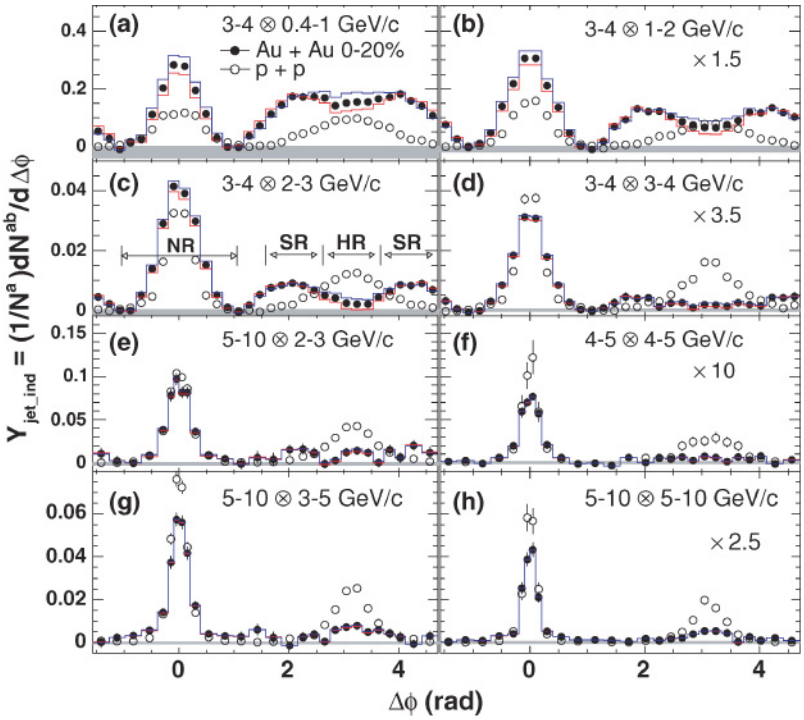

FIG. 6. (Color online) Per-trigger yield vs $\Delta\phi$ for various trigger and partner p_T ($p_T^a \otimes p_T^b$), arranged by increasing pair proxy energy (sum of p_T^a and p_T^b), in $p+p$ and 0–20% Au+Au collisions. The data in several panels are scaled as indicated. Solid histograms (shaded bands) indicate elliptic flow (ZYAM) uncertainties. Arrows in Fig. 6(c) depict the "head" region (HR), the "shoulder" region (SR) and the "near-side" region (NR).

central Au+Au collisions, there is an additional maximally 5%, centrality-dependent uncertainty due to occupancy effect.

The propagation of uncertainties arising from the single particle efficiency are different for different jet variables. For the per-trigger yield, it depends on the errors associated with the efficiency estimated for the partners (ε^b). For the hadron-pair yields, it depends on the errors related to efficiencies for both trigger (ε^a) and partner (ε^b) hadrons. Since the efficiency correction uncertainties are similar for trigger and partner hadrons in both Au+Au and $p+p$ collisions, we can use a single variable ε to represent them. If the uncertainties are independent between Au+Au and $p+p$, the total uncertainty would be $\sim\sqrt{2}\delta\varepsilon/\varepsilon$ for JPY and I_{AA} and $2\delta\varepsilon/\varepsilon$ for J_{AA}. However, some systematic errors partially cancel between Au+Au and $p+p$, especially those for the matching cut, momentum scale, and momentum resolution. The total uncertainties are estimated to be 12% for I_{AA} and JPY and 17% for J_{AA}.

The statistical uncertainties for v_2 are important in the most central and most peripheral centrality bins for $p_T > 4$ GeV/c. The systematic uncertainties are, however, driven by the uncertainty associated with the determination of the reaction plane resolution; they are estimated to be ∼6% for central and midcentral collisions and ∼10% for peripheral collisions [18]. This error is nearly independent of p_T, i.e., $\delta v_2^a/v_2^a \approx \delta v_2^b/v_2^b$, and the resulting error for the hadron-pair ratio is

$$\begin{aligned}\delta\mathrm{JPR}(\Delta\phi) &= 2\xi\left(\delta v_2^a v_2^b + \delta v_2^b v_2^a\right)\cos 2\Delta\phi \\ &\approx (\delta v_2/v_2) 4 v_2^a v_2^b \cos 2\Delta\phi, \end{aligned} \tag{21}$$

where the last approximation takes into account the fact that ξ is close to 1. Additional systematic errors related to v_4 and the factorization assumption that $\langle v_2^a v_2^b\rangle = \langle v_2^a\rangle\langle v_2^b\rangle$ were also estimated and found to be small [19].

The uncertainty due to ξ (ZYAM uncertainty) can be expressed as

$$\delta\mathrm{JPR}(\Delta\phi) = \delta\xi\left(1 + 2v_2^a v_2^b \cos 2\Delta\phi\right) \approx \delta\xi, \tag{22}$$

where we ignored the $\cos 2\Delta\phi$ term, since $2v_2^a v_2^b \ll 1$. The uncertainty of ξ includes both the statistical error of the data points around $\Delta\phi_{\min}$ and the systematic error from the fitting procedure.

Table III summarizes the systematic errors for the jet yield in 0–20% Au+Au collisions due to v_2 and ZYAM subtraction. Errors for several combinations of trigger and partner p_T (in $p_T^a \otimes p_T^b$) are given. The uncertainties are $\Delta\phi$ dependent, so we present them separately for the three regions used in this analysis: a "head" region ($|\Delta\phi - \pi| < \pi/6$, HR), a "shoulder" region ($\pi/6 < |\Delta\phi - \pi| < \pi/2$, SR), and the near-side region ($|\Delta\phi| < \pi/3$, NR). These regions are indicated in Fig. 6(c).

The three types of systematic errors impact the jet shape and jet yield differently. The single particle efficiency correction is a multiplicative factor, so its uncertainty influences the normalization of the jet yield but does not influence its shape. The uncertainties associated with the elliptic flow varies with $\Delta\phi$. It is largest for regions around 0 and π, but reaches a minimum in the shoulder region. The influence of the ξ uncertainty on the jet yield also depends on $\Delta\phi$. It is the dominant uncertainty for the away-side yield at high p_T.

IV. RESULTS

A. Jet-induced dihadron azimuthal ($\Delta\phi$) distributions

Figure 6 shows a representative subset of the per-trigger yield distributions $Y_{\mathrm{jet_ind}}(\Delta\phi)$ for various combinations of

TABLE III. Systematic errors for the per-trigger yield in 0–20% Au+Au collisions for several combinations of trigger and partner p_T (in trigger $p_T \otimes$ partner p_T). The errors are in percentage and are shown separately for near-side ($|\Delta\phi| < \pi/3$), away-side ($|\Delta\phi - \pi| < \pi/2$), away-side head region ($|\Delta\phi - \pi| < \pi/6$), and away-side shoulder region ($\pi/6 < |\Delta\phi - \pi| < \pi/2$).

Errors in %	2–3 ⊗ 0.4–1 GeV/c	2–3 ⊗ 2–3 GeV/c	3–4 ⊗ 3–4 GeV/c	4–5 ⊗ 4–5 GeV/c	5–10 ⊗ 5–10 GeV/c
			Near-side		
v_2 err.	±18	±9.5	±3.8	±1	<1
ZYAM err. stat.	±0.9	±1.1	±4.1	±9	±8
ZYAM over-sub.	+30	+9.5	<1	<1	<1
			Away-side		
v_2 err.	±10	±10	±9.3	±3	±1
ZYAM err. stat.	±0.8	±2	±17	±39	±28
ZYAM over-sub.	+28	+17	<1	<1	<1
			Away-side head region		
v_2 err.	±26	+42–39	+36–34	±5	±1
ZYAM err. stat.	±1	±3	±27	±32	±16
ZYAM over-sub.	+28	+29	<1	<1	<1
			Away-side shoulder region		
v_2 err.	±2.6	±2.3	±2	±1	±1
ZYAM err. stat.	±0.8	±1.6	±15	±43	±45
ZYAM over-sub.	+27	+15	<1	<1	<1

trigger and partner p_T ($p_T^a \otimes p_T^b$) for $p + p$ and 0–20% Au+Au collisions, arranged by increasing pair proxy energy, i.e., by $p_T^{\rm sum} = p_T^a + p_T^b$. The comprehensive array of results, covering the momentum range of 0.4 to 10 GeV/c from which this subset is derived, are summarized in Appendix D (Figs. 36–38). From Eq. (6), one can see that the distributions for $p_T^a \otimes p_T^b$ and $p_T^b \otimes p_T^a$ are related to each other by a normalization factor n_0^a/n_0^b, i.e, the ratio of the number of hadrons in the two p_T ranges. We have checked that these distributions, when rescaled by n_0^a or n_0^b, are consistent with each other. These $\Delta\phi$ distributions not only carry detailed jet shape and yield information but also serve as a basis for our systematic study of the p_T dependence of the contributions from various physical processes.

The results in Fig. 6 constitute one of many possible ways of illustrating the evolution from low p_T to high p_T in the two-dimensional space of p_T^a and p_T^b. It is designed to highlight the main features of an evolution from the soft-process-dominated low-p_T region to the hard-process-dominated high-p_T region. As shown in the figure, the $p + p$ data show essentially Gaussian away-side peaks centered at $\Delta\phi \sim \pi$ for all p_T^a and p_T^b. By contrast, the Au+Au data show substantial modifications relative to those for $p + p$ collisions, and these modifications vary nontrivially with p_T^a and p_T^b. For a fixed value of p_T^a, Figs. 6(a)–6(d) reveal a striking evolution from a broad, roughly flat away-side peak to a local minimum at $\Delta\phi \sim \pi$ with side peaks at $\Delta\phi \sim \pi \pm 1.1$. Interestingly, the location of the side peaks in $\Delta\phi$ is found to be roughly constant with increasing p_T^b (see Fig. 11). Such p_T independence is compatible with an away-side jet modification expected from a medium-induced Mach shock [35] but provides a challenge for models that incorporate large angle gluon radiation [31,32], Cherenkov gluon radiation [34], or deflected jets [23,29].

For relatively large values of $p_T^a \otimes p_T^b$, Figs. 6(e)–6(h) (also Fig. 36) show that the away-side jet shape for Au+Au gradually becomes peaked as for $p + p$, albeit suppressed. This "reappearance" of the away-side peak seems to be due to a reduction of the yield centered at $\Delta\phi \sim \pi \pm 1.1$ relative to that at $\Delta\phi \sim \pi$, rather than a merging of the peaks centered at $\Delta\phi \sim \pi \pm 1.1$. This is consistent with the dominance of dijet fragmentation at large $p_T^a \otimes p_T^b$, possibly due to jets that "punch through" the medium [14] or those emitted tangentially to the medium's surface [69].

The evolution pattern of the away-side jet shape with p_T suggests separate contributions from a medium-induced component at $\Delta\phi \sim \pi \pm 1.1$ and a fragmentation component centered at $\Delta\phi \sim \pi$. A model independent study of these contributions can be made by dividing the away-side jet function into equal-sized "head" ($|\Delta\phi - \pi| < \pi/6$, HR) and "shoulder" ($\pi/6 < |\Delta\phi - \pi| < \pi/2$, SR) regions, as indicated in Fig. 6(c).

TABLE IV. Centrality dependence of $R_{\rm HS}$ for $2 < p_T^a, p_T^b < 3$ GeV/c (Fig. 8).

$\langle N_{\rm part}\rangle$	$R_{\rm HS}$	Stat.	v_2 err.	Norm err.
351.4	0.451	0.030	+0.080–0.087	+0.028–0.021
299.0	0.402	0.024	+0.158–0.175	+0.051–0.019
234.6	0.526	0.018	+0.268–0.308	+0.102–0.011
166.6	0.614	0.021	+0.351–0.402	+0.133–0.009
114.2	0.821	0.030	+0.395–0.477	+0.031–0.006
74.4	1.126	0.045	+0.333–0.394	+0.005–0.022
45.5	1.427	0.060	+0.175–0.215	+0.020–0.018
25.7	2.130	0.125	+0.196–0.267	+0.081–0.110
9.5	2.603	0.164	+0.099–0.158	+0.125–0.124
2.0	2.848	0.090	–	+0.060–0.056

Figure 6 also shows significant modifications of the near-side $\Delta\phi$ distributions. For the $p_T^a \otimes p_T^b$ bins where the away-side has a concave shape, the near-side jet also shows a clear enhancement in the yield and a modification of the width relative to $p+p$. To facilitate a more detailed investigation, we define a near-side region ($|\Delta\phi| < \pi/3$, NR) as indicated in Fig. 6(c). In the following, we focus on the jet-induced pairs in these three $\Delta\phi$ regions, and discuss in detail the p_T and centrality dependence of their shapes and yields.

B. Medium modification of away-side jets

1. Away-side jet shape

We characterize the relative importance of the jet yields in the HR and SR by the ratio $R_{\rm HS}$,

$$R_{\rm HS} = \frac{\int_{\Delta\phi\in{\rm HR}} d\Delta\phi Y_{\rm jet_ind}(\Delta\phi)}{\int_{\Delta\phi\in{\rm HR}} d\Delta\phi} \Big/ \frac{\int_{\Delta\phi\in{\rm SR}} d\Delta\phi Y_{\rm jet_ind}(\Delta\phi)}{\int_{\Delta\phi\in{\rm SR}} d\Delta\phi}, \tag{23}$$

i.e., it is a ratio of area-normalized jet yields in the HR and the SR. This ratio reflects the away-side jet shape and is symmetric with respect to p_T^a and p_T^b, i.e., $R_{\rm HS}(p_T^a, p_T^b) = R_{\rm HS}(p_T^b, p_T^a)$. For concave and convex shapes, one expects $R_{\rm HS} < 1$ and $R_{\rm HS} > 1$, respectively; for a flat distribution, $R_{\rm HS} = 1$.

Figure 7 shows the p_T^b dependence of $R_{\rm HS}$ for both $p+p$ and central Au+Au collisions for four p_T^a bins. The uncertainty for efficiency corrections drops out in the ratio; the v_2 errors (shaded bars) and ZYAM errors (brackets) are correlated in the two regions, thus they partially cancel.

The $R_{\rm HS}$ values for $p+p$ are always above unity and increase with p_T^b. This reflects the narrowing of a peaked away-side jet shape with increasing p_T^b. In contrast, the ratios for Au+Au show a nonmonotonic dependence on $p_T^{a,b}$. They evolve from $R_{\rm HS} \sim 1$ for p_T^a or $p_T^b \lesssim 1$ GeV/c, through $R_{\rm HS} < 1$ for $1 \lesssim p_T^{a,b} \lesssim 4$ GeV/c, followed by $R_{\rm HS} > 1$ for $p_T^{a,b} \gtrsim 5$ GeV/c. These trends reflect the competition between medium-induced modification and jet fragmentation in determining the away-side jet shape, and they suggest that the latter dominates for $p_T^{a,b} \gtrsim 5$ GeV/c.

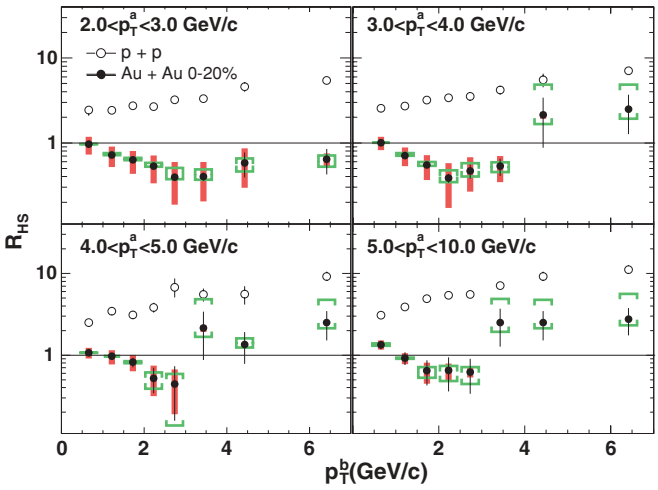

FIG. 7. (Color online) $R_{\rm HS}$ vs p_T^b for $p+p$ (open) and Au+Au (filled) collisions for four trigger selections. Shaded bars (brackets) represent p_T-correlated uncertainties due to elliptic flow (ZYAM procedure).

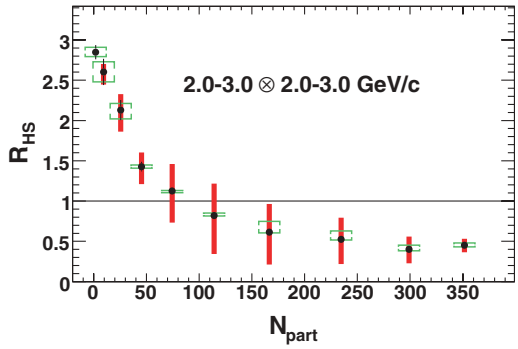

FIG. 8. (Color online) $R_{\rm HS}$ vs $N_{\rm part}$ for 2–3 $\otimes$ 2–3 GeV/c. Shaded bars (brackets) represent p_T-correlated uncertainties due to elliptic flow (ZYAM procedure). The left-most point is from $p+p$.

$R_{\rm HS}$ values for Au+Au are smaller than those for $p+p$ even at the highest p_T. This difference could be due to some medium modification of the punch-through jets. However, the HR yield dominates the SR yield ($R_{\rm HS} \gg 1$) in this p_T region, and the values for $R_{\rm HS}$ become very sensitive to the SR yield. For instance, a small enhancement of the SR yield can significantly reduce the value of $R_{\rm HS}$, without significantly affecting the overall away-side feature.

$R_{\rm HS}$ values reach their minimum around 2–3 GeV/c. Additional information can be obtained from their centrality dependence, as shown in Fig. 8 for the 2–3 $\otimes$ 2–3 GeV/c bin. $R_{\rm HS}$ starts at around 3 for $p+p$ collisions but quickly drops and crosses 1 at $N_{\rm part} \sim 80$. It then slowly decreases with $N_{\rm part}$ to a level of about 0.5 in central collisions. This trend implies a quick change of the HR and/or SR yield in relatively peripheral collisions. The saturation of the $R_{\rm HS}$ for $N_{\rm part} > 200$ may suggest that the HR yield is dominated by the feed-in of the SR yield (see further discussion in Sec. IV B2).

Although the p_T and centrality dependence of $R_{\rm HS}$ suggests that the away-side yield contains separate contributions from a fragmentation component (in the HR) and a medium-induced component (in the SR), $R_{\rm HS}$ does not constrain the shape of the two components directly. An alternative approach for quantifying the away-side shape is to assume a specific functional form for these two components and carry out a model-dependent fit. Such a fit was performed with the following two functional forms:

$$Y^{\rm FIT1}_{\rm jet_ind}(\Delta\phi) = G_1(\Delta\phi) + G_2(\Delta\phi - \pi + D) + G_2(\Delta\phi - \pi - D) + \kappa, \tag{24}$$

$$Y^{\rm FIT2}_{\rm jet_ind}(\Delta\phi) = G_1(\Delta\phi) + G_2(\Delta\phi - \pi + D) + G_2(\Delta\phi - \pi - D) + G_3(\Delta\phi - \pi) + \kappa. \tag{25}$$

The first (FIT1) assumes two Gaussian shoulder components located symmetrically about π, each separated by the distance D from π. The second (FIT2) assumes the same shoulder components but also includes an additional Gaussian component centered at π; the latter represents the

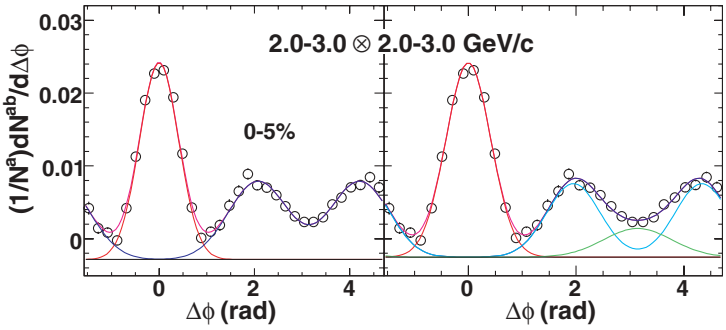

FIG. 9. (Color online) Per-trigger yield $\Delta\phi$ distribution and corresponding fits for 2–3 $\otimes$ 2–3 GeV/c in 0–5% Au+Au collisions. FIT1 (FIT2) is shown in the left panel (right panel). The total fit function and individual components are shown relative to the κ level indicated by the horizontal line.

jet fragmentation contribution and is parametrized to have the same width as that for the $p + p$ away-side jet. FIT1 has six free parameters: background level κ, near-side peak integral and width, and shoulder peak location D, integral, and width. In addition to the parameters of FIT1, FIT2 has a parameter that controls the integral of the fragmentation component.

The separate contributions of FIT1 and FIT2 are illustrated for a typical $p_T^a \otimes p_T^b$ in Fig. 9.

The two fits treat the region around $\Delta\phi = \pi$ differently. FIT2 tends to assign the yield around π to the center Gaussian, while FIT1 tends to split that yield into the two shoulder Gaussians. Note, however, that a single Gaussian centered at π can be treated as two shoulder Gaussians with $D = 0$. Thus FIT1 does a good job at low p_T and high p_T, where the away-side is dominated by shoulder and head components, respectively. It does not work as well for intermediate p_T, where both components are important. The center Gaussian and shoulder Gaussians used in FIT2 are strongly anticorrelated. That is, a small shoulder yield implies a large head yield and vice versa. In addition, the center Gaussian tends to "push" the shoulder Gaussians away from π, and this results in larger D values than obtained with FIT1.

Figure 10(a) shows the D values obtained from the two fitting methods as a function of centrality for the p_T selection 2–3 $\otimes$ 2–3 GeV/c. The systematic errors from v_2 are shown as brackets (shaded bars) for FIT1 (FIT2). The values of D for FIT1 are consistent with zero in peripheral collisions, but grow rapidly to $\sim$1 for $N_{\text{part}} \sim 100$, approaching $\sim$1.05 in the most central collisions. The D values obtained from FIT2 are slightly larger ($\sim$1.2 rad) in the most central collisions. They are also relatively stable to variations of v_2 because most of the yield variation is "absorbed" by the center Gaussian [cf. Fig. 10(b)]. Thus, the associated systematic errors are also smaller than those for FIT1.

For $N_{\text{part}} < 100$, the centrality dependence of D is also quite different for FIT1 and FIT2. As seen in Fig. 10, the D values for FIT2 are above 1. However, the away-side yield in the SR, associated with these D values, are rather small, and the away-side distribution is essentially a single peak centered around π. For such cases, the values of D are prone to fluctuations and non-Gaussian tails. The deviation between the D values obtained with FIT1 and FIT2 for $N_{\text{part}} < 100$ simply reflects the weak constraint of the data on D in peripheral collisions.

Figure 11 shows the p_T dependence of D in 0–20% central Au+Au collisions. The values from FIT2 are basically flat with p_T^b. Those from FIT1 show a small increase with p_T^b, but with a larger systematic error. At low p_T, the values from FIT1 are systematically lower than those from FIT2. However, they approach each other at large $p_T^{a,b}$. From FIT1 and FIT2, it appears that the values of D cover the range 1–1.2 rad for p_T^a, $p_T^b \lesssim 4$ GeV/c. This trend ruled out a Cherenkov gluon radiation model [34] (with only transition from scalar bound states), which predicts decreasing D with increasing momentum.

2. *Away-side jet per-trigger yield*

Relative to $p + p$, the Au+Au yield is suppressed in the HR but is enhanced in the SR (cf. Fig. 6). A more detailed mapping of this modification pattern is obtained by comparing the jet yields in the HR and SR as a function of partner p_T. Such a comparison is given in Fig. 12 for central Au+Au and for $p + p$ collisions. The figure shows that relative to $p + p$,

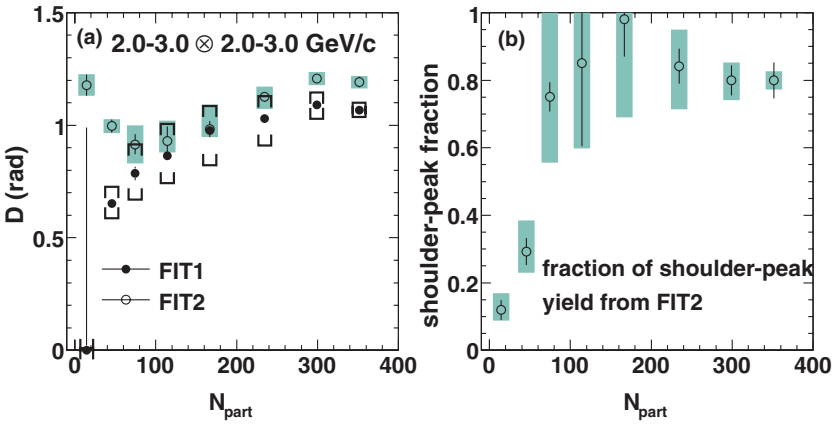

FIG. 10. (Color online) (a) D vs N_{part} from FIT1 (solid circles) and FIT2 (open circles) for 2–3 $\otimes$ 2–3 GeV/c bin. The error bars are the statistical errors; shaded bars and brackets are the systematic errors due to v_2. (b) Fraction of the shoulder Gaussian yield relative to the total away-side yield as function of N_{part} determined from FIT2.

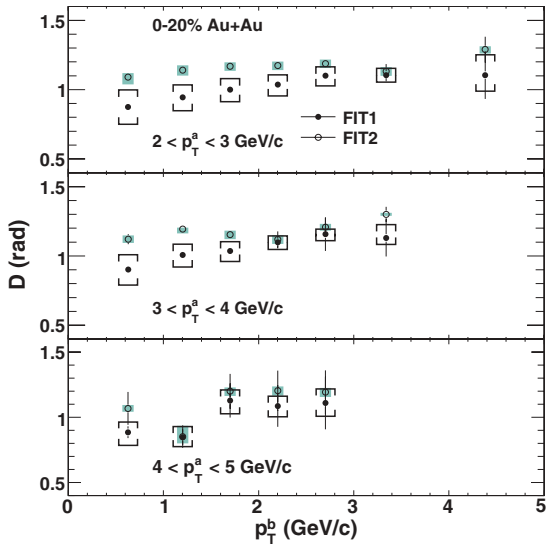

FIG. 11. (Color online) Values of D determined from FIT1 (solid circles) and FIT2 (open circles) as function of partner p_T for three trigger p_T ranges in 0–20% Au+Au collisions. The error bars are the statistical errors. The shaded bars and brackets are the systematic errors due to elliptic flow.

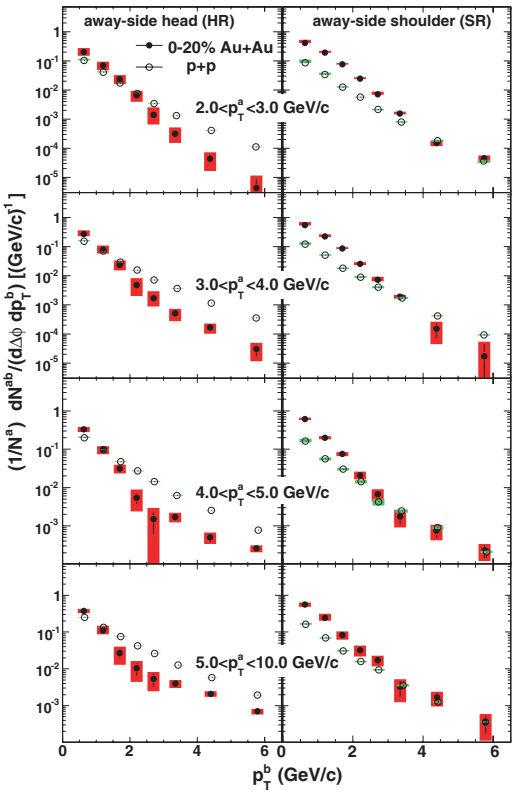

FIG. 12. (Color online) Per-trigger yield as function of partner p_T for the HR (left panels) and the SR region (right panels). Filled (open) circles represent the 0–20% Au+Au ($p + p$) collisions. Results for four trigger p_T in 2–3, 3–4, 4–5, 5–10 GeV/c are shown. The shaded bars represent the total systematic uncertainties.

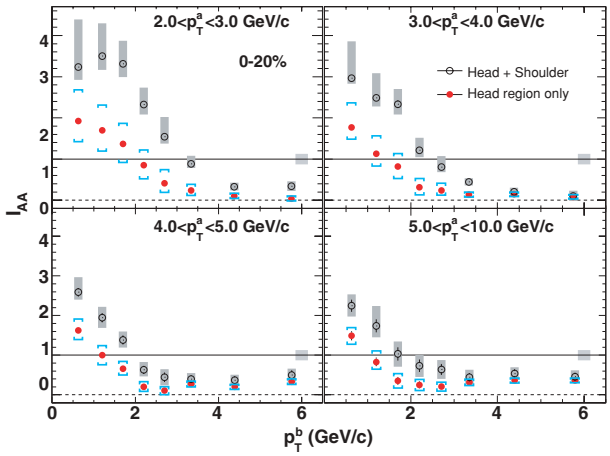

FIG. 13. (Color online) I_{AA} vs p_T^b for four trigger p_T bins in HR+SR ($|\Delta\phi - \pi| < \pi/2$) and HR ($|\Delta\phi - \pi| < \pi/6$) in 0–20% Au+Au collisions. The shaded bars and brackets represent the total systematic errors in the two regions. They are strongly correlated. Grey bands around $I_{AA} = 1$ represent 12% combined uncertainty on the single particle efficiency in Au+Au and $p + p$.

the Au+Au data are enhanced in the SR for low p_T, and suppressed in the HR for high p_T. The shape of the Au+Au spectra in the HR is also quite different from that for $p + p$. For $p_T^{a,b} \lesssim 4$ GeV/c, the spectra for Au+Au are steeper than those for $p + p$. For higher p_T, both spectra have the same shape (parallel to each other), but the yield for Au+Au is clearly suppressed.

To quantify this suppression/enhancement, we use the per-trigger yield ratio I_{AA}, the ratio of per-trigger yield for Au+Au collisions to that for $p + p$ collisions [cf. Eq. (5)]. Such ratios for the HR and the HR+SR are shown as a function of p_T^b for four different p_T^a selections in Fig. 13. For triggers of $2 < p_T^a < 3$ GeV/c, I_{AA} for HR+SR exceeds unity at low p_T^b, but falls with p_T^b and crosses unity around 3.5 GeV/c. A similar trend is observed for the higher p_T triggers, but the enhancement for low p_T^b is smaller, and the suppression for

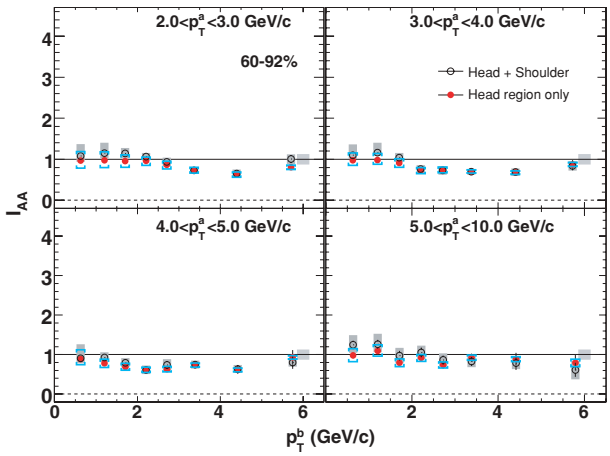

FIG. 14. (Color online) Same as Fig. 13, but for 60–92% Au+Au collisions.

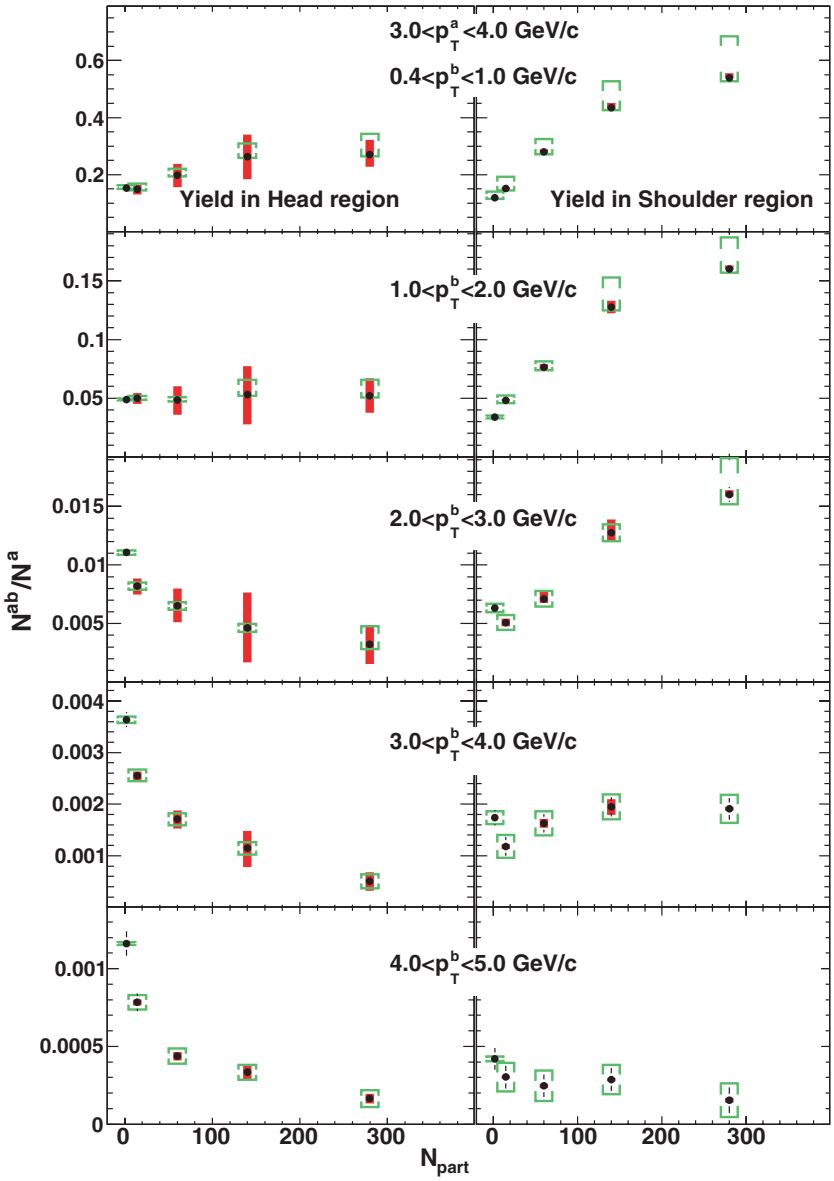

FIG. 15. (Color online) Per-trigger yield vs $N_{\rm part}$ in the HR (left panels) and the SR (right panels) for partner p_T in 0.4–1, 1–2, 2–3, 3–4, 4–5 GeV/c and fixed trigger in 3–4 GeV/c. The left-most points are from $p + p$ collisions. The shaded bars (brackets) represent uncertainties due to elliptic flow (ZYAM procedure).

high p_T^b is stronger. The I_{AA} values in the HR are also lower relative to HR+SR, for all $p_T^{a,b}$. For the low-p_T triggers, the HR suppression sets in for $1 \lesssim p_T^b \lesssim 3$ GeV/c, followed by a fall-off for $p_T^b \gtrsim 4$ GeV/c. For the higher p_T triggers, a constant level ∼0.2–0.3 is observed above ∼2 GeV/c, similar to the suppression level of inclusive hadrons [6].

For comparison, Fig. 14 shows the I_{AA} for peripheral collisions. They indicate that in contrast to the values for central collisions, there is only a small suppression in both the HR and the HR+SR for low-p_T triggers at large p_T^b. Moreover, the overall modifications are much smaller than observed for the more central Au+Au collisions.

A more detailed view of the enhancement/suppression patterns in the SR/HR can be provided by investigating their centrality dependence. Figure 15 shows the per-trigger yield in the SR and HR as a function of $N_{\rm part}$ for trigger p_T of 3–4 GeV/c and five partner p_T bins ranging from 0.4 to 5 GeV/c. With increasing partner p_T, both the SR and HR yields show a characteristic evolution with $N_{\rm part}$. That is, they first show an increase, followed by an essentially flat dependence, followed by a decrease (in the HR only). However, the value of p_T^b at which the centrality dependence becomes flat is quite different for the SR and the HR ($p_T^b \sim 4$ for the SR and $p_T^b \sim$ 1–2 GeV/c for the HR).

Figures 13 and 15 provide clear evidence that in central Au+Au collisions, there is significant yield suppression in the HR and an enhancement in the SR. The suppression for the HR is consistent with a jet-quenching scenario in which the HR yield at high p_T is dominated by radiated gluons and jets which survive passage through the medium. The enhancement for the SR could reflect the dissipative processes that redistribute the energy lost in the medium.

Several previous jet correlation measurements were carried out for an intermediate range of $p_T^a \otimes p_T^b$ [7,17–19,68,70] and/or in a limited away-side integration window roughly equal to the HR [7,12,68,70]. However, Fig. 15 shows that

away-side yield modifications are sensitive to both p_T and the $\Delta\phi$ integration range. By choosing a certain p_T and $\Delta\phi$ range, the combined effect of SR enhancement and HR suppression can result in away-side yields that are almost independent of centrality, while their shapes still vary with centrality. Thus a detailed survey of the jet yield in a broad p_T and a more differential study in $\Delta\phi$ for the away-side are important to obtaining the full picture.

C. Medium modification of near-side jets

In this section, we map out the p_T and centrality dependence of the shape and yields of the near-side jets.

1. Near-side jet shape

We characterize the near-side shape in $\Delta\phi$ by the Gaussian fit functions FIT1 and FIT2 described in Sec. IV B1. The systematic uncertainties include the differences between FIT1 and FIT2 and the uncertainties associated with the elliptic flow subtraction. To account for a possible influence from feed-in of the shoulder component, we also performed fits to the near-side distribution with a single Gaussian function in $\pm 1\sigma$, $\pm 2\sigma$, and $\pm 3\sigma$ windows, where σ is the width of the near-side peak obtained with FIT2. Deviations from σ were added in quadrature to the total systematic errors. For $p + p$, a simple fit with a near- and an away-side Gaussian plus a constant background was used.

Figure 16 compares the near-side Gaussian widths obtained for $p + p$ and 0–20% central Au+Au collisions. The results are shown as a function of partner p_T for four trigger p_T bins as indicated. The $p + p$ widths show the expected decrease with partner p_T for all trigger bins, as expected from a narrowing of the jet cone as p_T^b increases. The Au+Au widths also decrease with partner p_T except at low $p_T^{a,b}$. For low-p_T triggers of

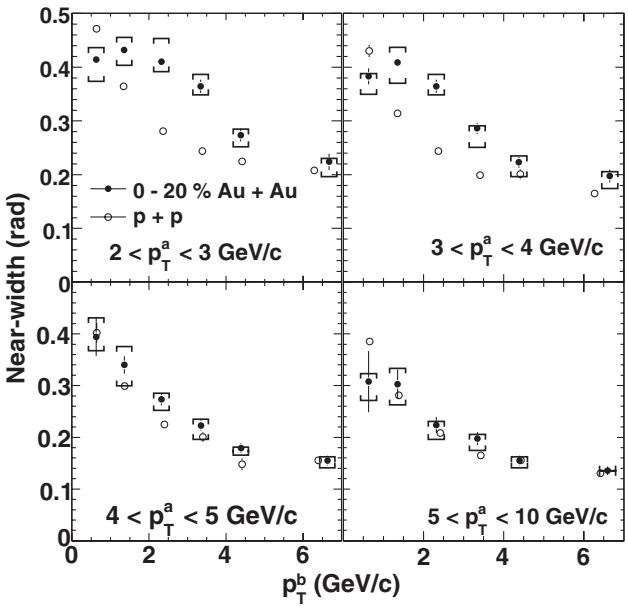

FIG. 16. Near-side Gaussian widths vs partner p_T for four trigger p_T ranges compared between 0–20% Au+Au (solid circles) and $p + p$ (open circles).

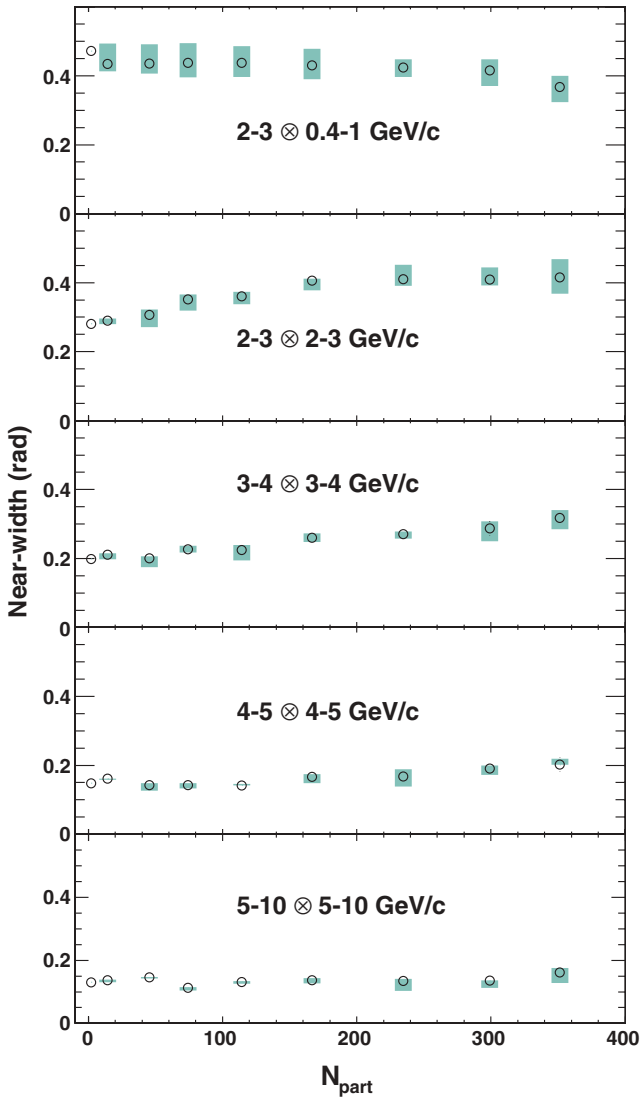

FIG. 17. (Color online) Near-side Gaussian widths vs $N_{\rm part}$ for five successively increasing $p_T^a \otimes p_T^b$. The left-most point in each panel represents the value from $p + p$.

$2 < p_T^a < 3$ and $3 < p_T^a < 4$ GeV/c, the values for the widths are slightly below those for $p + p$ for $p_T^b < 1$ GeV/c; they are, however, significantly broader for $1 \lesssim p_T^b \lesssim 4$ GeV/c. For higher trigger p_T, the extracted widths are similar for Au+Au and $p + p$.

Figure 17 shows the centrality dependence of the near-side widths for successively higher $p_T^a \otimes p_T^b$. For the lowest p_T bin of 2–3 $\otimes$ 0.4–1 GeV/c, the width decreases slightly with $N_{\rm part}$ and approaches a value of 0.4 rad in central collisions. A similar trend has been reported for measurements at low p_T [16]. For the 2–3 $\otimes$ 2–3 GeV/c selection, the near-side width grows with $N_{\rm part}$ and approaches a value about 40% larger than the $p + p$ value for $N_{\rm part} > 200$. For higher $p_T^a \otimes p_T^b$ bins, the near-side widths are narrower, and their centrality dependence is flatter. For the 5–10 $\otimes$ 5–10 GeV/c bin, the near-side widths ($\sim$0.14 rad) are essentially independent of $N_{\rm part}$, as might be expected if the near-side correlations are dominated by jet fragmentation.

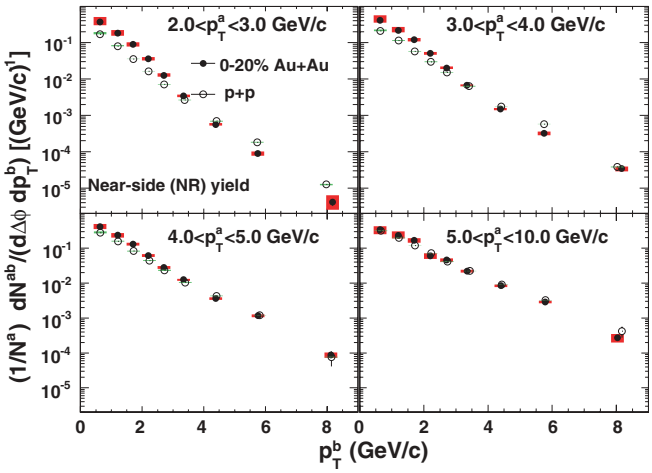

FIG. 18. (Color online) Near-side yield in $|\Delta\phi| < \pi/3$ vs partner p_T for four trigger p_T selections. The filled and open circles are for 0–20% Au+Au and $p + p$, respectively.

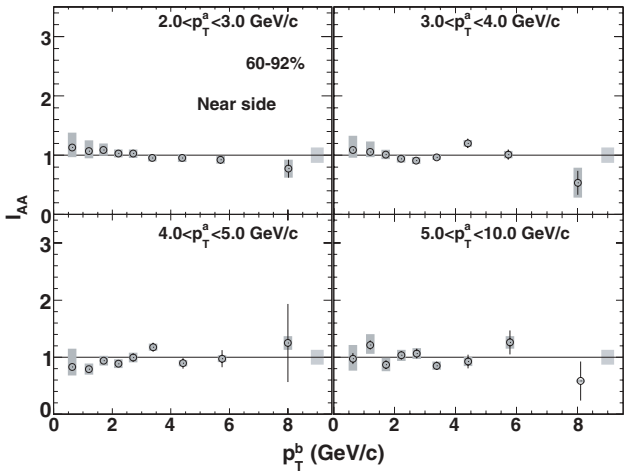

FIG. 20. Near-side I_{AA} in 60–92% Au+Au vs partner p_T for four trigger p_T bins. The shaded bars around the data points are the total systematic errors. Grey bands around $I_{AA} = 1$ represent 12% combined uncertainty on the single particle efficiency in Au+Au and $p + p$.

2. *Near-side jet per-trigger yield*

The near-side yield in $|\Delta\phi| < \pi/3$ (NR) as a function of partner p_T is shown in Fig. 18 for $p + p$ and Au+Au collisions, for four trigger p_T bins. The corresponding results for the modification factor I_{AA} are shown in Fig. 19. For triggers of 2–3 GeV/c, I_{AA} is enhanced by more than a factor of 2 for $p_T^b < 2$ GeV/c, followed by a falloff below unity for $p_T^b \gtrsim 4$ GeV/c. The overall deviation from $I_{AA} = 1$ decreases with increasing trigger p_T. For the highest p_T trigger, the near-side yield is close to that for $p + p$ over the full range of p_T^b. As a comparison, the I_{AA} values for the 60–92% centrality bin, shown in Fig. 20, are close to 1 for all $p_T^{a,b}$, suggesting a rather weak medium modification of the near-side yield in peripheral collisions.

The patterns of the near-side jet shape and yields in Figs. 16–20 suggest an influence from both medium modification and jet fragmentation at intermediate p_T. The influence of the medium has also been linked to a long-range correlation component in $\Delta\eta$ [16,17,20]. This so-called η ridge has been shown to be flat up to $|\Delta\eta| \sim 2$. The PHENIX $\Delta\eta$ acceptance is limited to $|\Delta\eta| < 0.7$. However, if contributions from the ridge are significant, they should show up in $\Delta\eta$ distributions.

The left panel of Fig. 21 shows a two-dimensional $\Delta\eta$-$\Delta\phi$ correlation function for 2–3 $\otimes$ 2–3 GeV/c in 0–20% central Au+Au collisions. The $\Delta\eta$ range is displayed for $|\Delta\eta| < 0.5$ to suppress the relatively large statistical fluctuations at the edge of $\Delta\eta$ acceptance. The correlation function peaks along $\Delta\phi \sim 0$ and π, largely because of the elliptic flow modulation of the combinatoric pairs. To subtract the flow term, we assume that ξ and v_2 are identical to those used in our one-dimensional $\Delta\phi$ correlation analysis and constant for $|\eta| < 0.35$. The distribution after v_2 subtraction is shown in the right panel of Fig. 21. One can clearly see one near-side and two shoulder

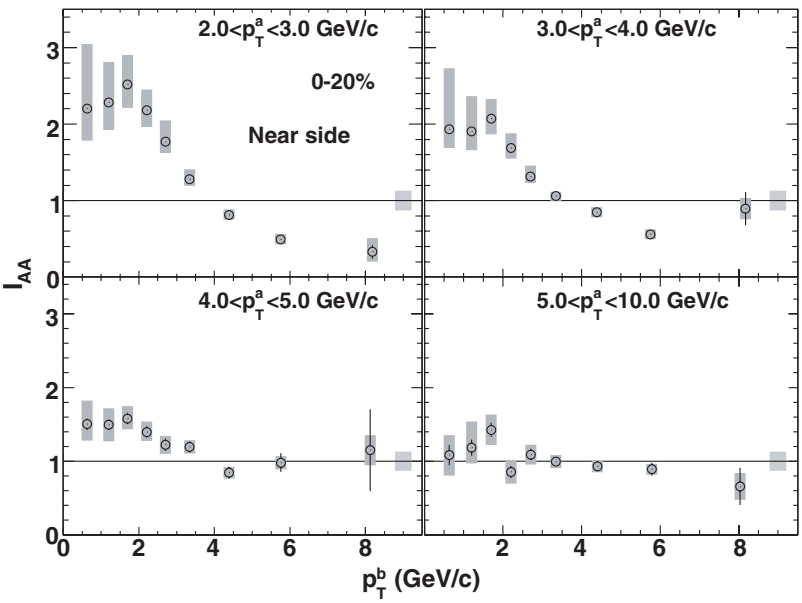

FIG. 19. Near-side I_{AA} in 0–20% Au+Au vs partner p_T for four trigger p_T bins. The shaded bars around the data points are the total systematic errors. Grey bands around $I_{AA} = 1$ represent 12% combined uncertainty on the single particle efficiency in Au+Au and $p + p$.

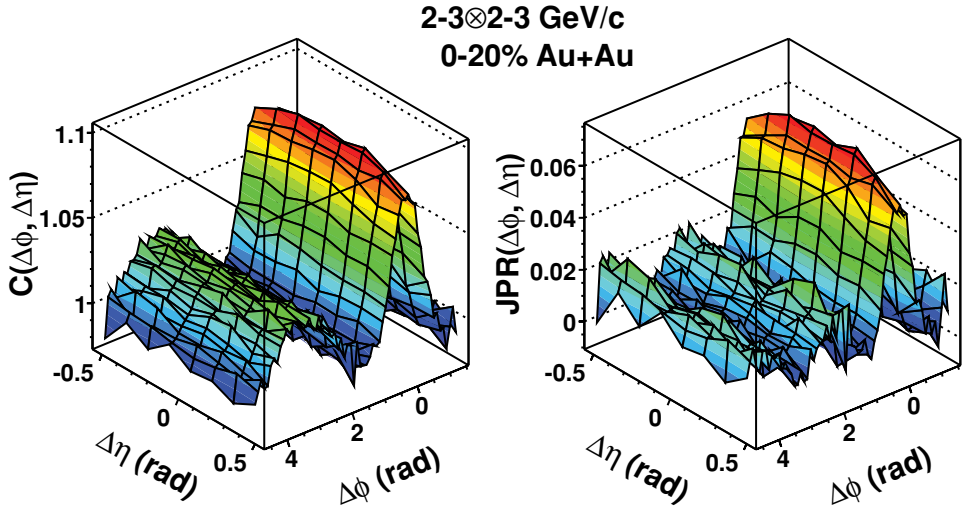

FIG. 21. (Color online) Correlation function [left panel, Eq. (8)] and background subtracted hadron-pair ratio [right panel, Eq. (13)] in $\Delta\eta$ and $\Delta\phi$ space for 2–3 $\otimes$ 2–3 GeV/c in 0–20% Au+Au collisions.

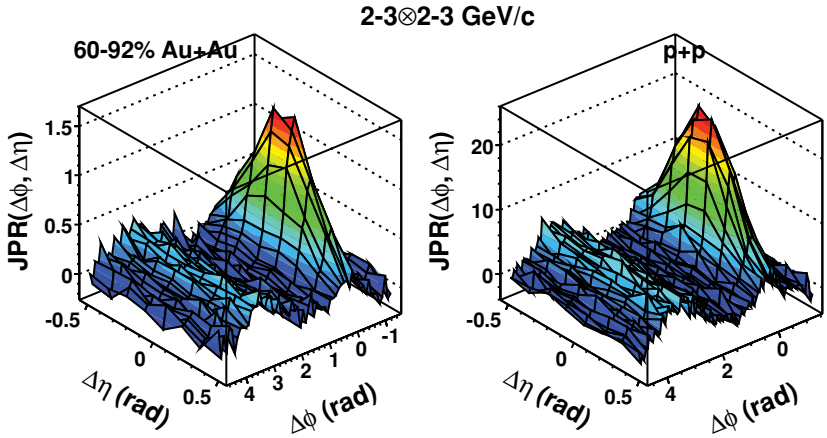

FIG. 22. (Color online) Background subtracted hadron-pair ratio [via Eq. (13)] for 2–3 $\otimes$ 2–3 GeV/c in 60–92% Au+Au (left panel) and $p + p$ (right panel) collisions.

peaks (in $\Delta\phi$), which extend over the full range of $\Delta\eta$. However, both $p + p$ and peripheral Au+Au collisions for the same p_T selections (Fig. 22) show one near-side peak centered around $\Delta\eta \sim 0$ and one away-side peak elongated over $\Delta\eta$. These features are expected for fragmentation of back-to-back dijets in vacuum.

To facilitate further detailed investigation, we focus on a near-side region defined by $|\Delta\phi| < 0.7$ and $|\Delta\eta| < 0.7$ and study the projected distributions in $\Delta\phi$ and $\Delta\eta$. Figure 23 compares the the $\Delta\eta$ distributions for $p + p$ and 0–20% central Au+Au collisions. The $p + p$ data indicate a relatively narrow jet-like peak for all four p_T selections. For the 2–3 $\otimes$ 2–3 GeV/c bin, the Au+Au data are enhanced and broadened relative to $p + p$. However, these differences gradually decrease toward higher p_T and essentially disappear for the 5–10 $\otimes$ 5–10 GeV/c bin. This possibly suggests that the ridge component at high p_T either disappears or becomes overwhelmed by the jet fragmentation component.[1]

Figure 24 compares the projected distributions in $\Delta\eta$ and $\Delta\phi$ for 0–20% central Au+Au collisions. By construction, the integrals of the two distributions are the same. For the 2–3 $\otimes$ 2–3 and 2–3 $\otimes$ 3–4 GeV/c bins, the distributions in $\Delta\eta$ are broader than in $\Delta\phi$. For the 3–4 $\otimes$ 3–5 and 5–10 $\otimes$ 5–10 GeV/c bins, the distributions become similar between $\Delta\phi$ and $\Delta\eta$. These observations suggest that the medium modifications are limited to $p_T^{a,b} \lesssim 4$ GeV/c, a similar p_T range in which the away-side is also strongly modified.

The evolution of the enhancement and broadening with the $p_T^{a,b}$ reflects the competition between contributions from the medium response and jet fragmentation. The former is important at $p_T^{a,b} \lesssim 4$ GeV/c and manifests itself as an enhanced and broadened distribution in $\Delta\eta$ and $\Delta\phi$. The latter dominates at higher p_T, reflected by $I_{AA} \approx 1$ and a near-side width similar to $p + p$. The strong modifications at intermediate p_T may reflect the remnants of those jets that interact with the medium, appearing as low-p_T hadron pairs with modified width and multiplicity. Possible physics mechanisms for this parton-medium interaction include jet interaction with a longitudinal flowing medium [22,23,27], position-momentum correlations induced by radial flow [21], correlation between radial flow boosted beam jet and medium suppressed transverse jet [26], plasma instability [24,25], or

[1]Note that the pseudorapidity coverage of PHENIX is smaller than that used in STAR, thus the amount of ridge yield seen in PHENIX is also smaller. The projected near-side jet shape in $\Delta\phi$ may also depend on the pseudorapidity coverage.

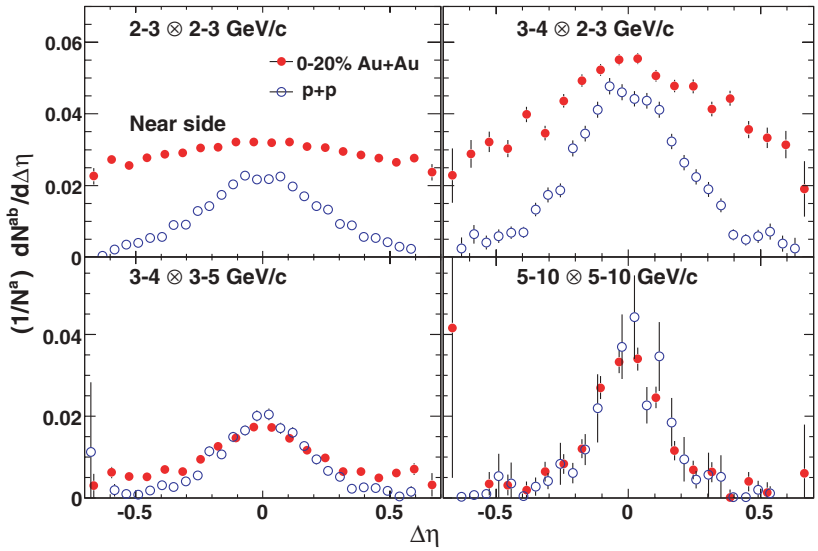

FIG. 23. (Color online) Per-trigger yield vs $\Delta\eta$ for $p + p$ (open symbols) and 0–20% central Au+Au (filled symbols) collisions. Results are shown for four $p_T^a \otimes p_T^b$ selections as indicated.

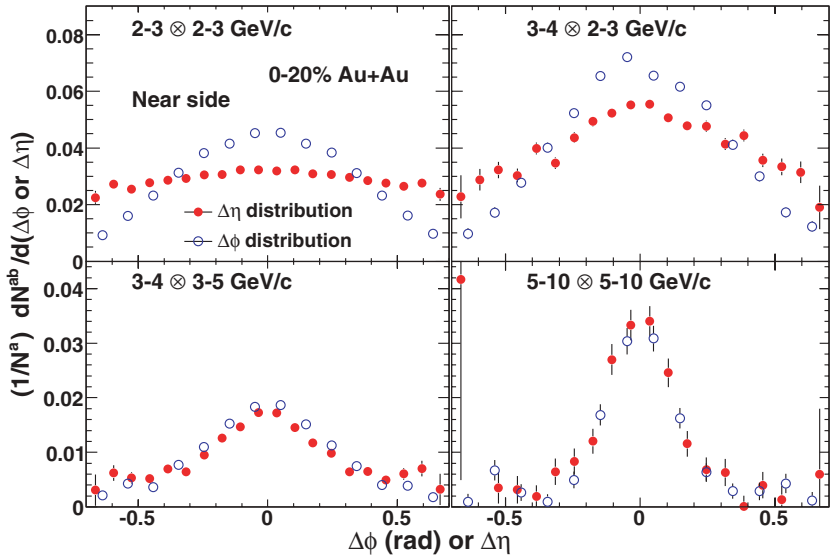

FIG. 24. (Color online) Projection of two-dimensional per-trigger yield in $|\Delta\eta| < 0.7 \otimes |\Delta\phi| < 0.7$ and 0–20% central Au+Au collisions onto $\Delta\phi$ (open symbols) and $\Delta\eta$ (filled symbols) for four $p_T^a \otimes p_T^b$ selections.

back-splash caused by the quenched jets [28]. However, the modification mechanisms for the near- and away-side may be related: both near- and away-side distributions show enhancement and broadening in the lower range $p_T < 4$ GeV/c, above which the jet characteristics qualitatively approach the jet fragmentation.

D. Away- and near-side spectral slopes

To further explore the differences between the NR, HR, and SR, we compare the shapes of the partner p_T spectra in these three $\Delta\phi$ regions. To do this, we characterize the local inverse slope of the spectra via a truncated mean p_T in a given p_T range,

$$\langle p_T' \rangle \equiv \langle p_T^b \rangle_{p_T^{\min} < p_T^b < p_T^{\max}} - p_T^{\min}. \quad (26)$$

where $\langle p_T' \rangle$ is calculated from the jet yields shown in Figs. 12 and 18. For an exponential spectrum with an inverse slope of T and $T \ll p_T^{\max} - p_T^{\min}$, $\langle p_T' \rangle \approx T$.

First, we focus on an intermediate p_T region, $1 < p_T^b < 5$ GeV/c, where the medium-induced contributions are important for the near- and away-side yields. Figure 25 shows values of $\langle p_T' \rangle$ for the HR, SR, and NR as a function of N_{part}. For all trigger p_T bins, the values for the NR drop slightly with centrality to a lower level relative to $p + p$. This can be understood from the shape difference in Fig. 19, where the Au+Au spectra drop faster with increasing p_T^b. For $3 < p_T^a < 4$ GeV/c, a factor of 2 decrease in 1–5 GeV/c amounts to a reduction of ~0.1 GeV/c in $\langle p_T' \rangle$.

Despite the small decrease with N_{part}, the overall average level of $\langle p_T' \rangle$ for the NR for $N_{\text{part}} > 100$ increases with trigger p_T. They are $0.533 + 0.024 - 0.016$, $0.605 + 0.033 - 0.023$, $0.698 + 0.03 - 0.04$, and $0.797 + 0.052 - 0.042$ GeV/c for triggers in 2–3, 3–4, 4–5, and 5–10 GeV/c, respectively. This trend is consistent with the dominance of jet fragmentation on the near-side, i.e., a harder spectrum for partner hadrons is expected for higher p_T trigger hadrons.

Values for the SR also show an almost flat centrality dependence for $N_{\text{part}} \gtrsim 100$. In this case, the values for $\langle p_T' \rangle$

TABLE V. Truncated mean p_T, $\langle p'_T \rangle$, calculated for $1 < p_T^b < 5$ GeV/c and averaged for $N_{\rm part} > 100$ in the NR and SR for various bins of trigger p_T.

p_T^a range (GeV/c)	NR $\langle p'_T \rangle$ (GeV/c)	SR $\langle p'_T \rangle$ (GeV/c)
2–3	0.533+0.024−0.016	0.445+0.013−0.007
3–4	0.605+0.033−0.023	0.443+0.018−0.018
4–5	0.698+0.030−0.040	0.461+0.031−0.051
5–10	0.797+0.052−0.042	0.478+0.079−0.139

are lower (≈0.45 GeV/c, see Table V), and they do not depend on the trigger p_T. They are, however, larger than the values obtained for inclusive charged hadrons (0.36 GeV/c as indicated by the solid lines) [6]. The relatively sharp change in $\langle p'_T \rangle$ for $N_{\rm part} \lesssim 100$ may reflect the dominance of jet fragmentation contribution in peripheral collisions.

The values of $\langle p'_T \rangle$ for the HR show a gradual decrease with $N_{\rm part}$. They start at a level close to the values for the near-side

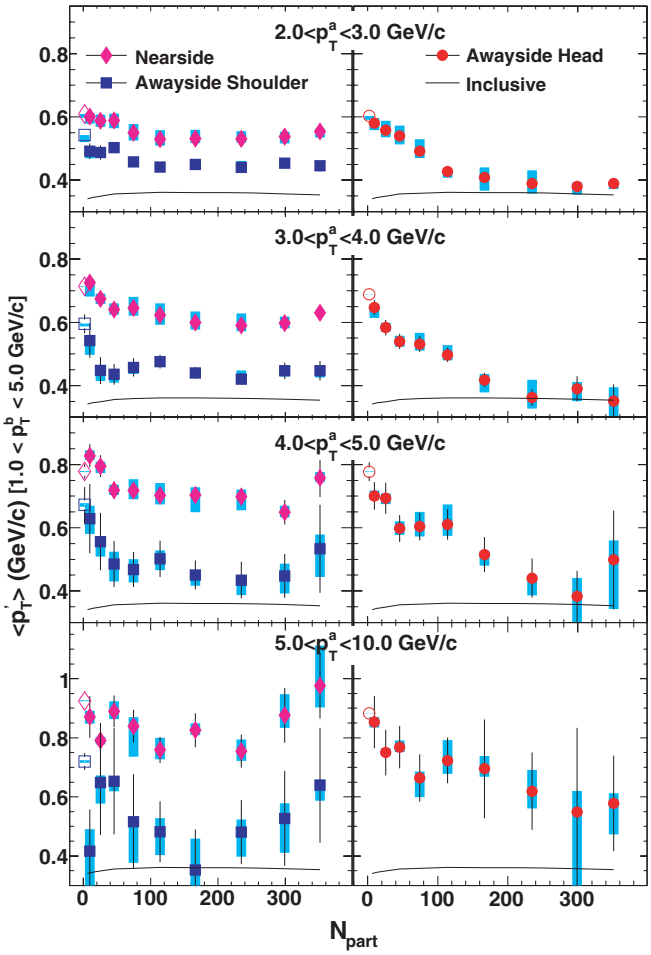

FIG. 25. (Color online) Truncated mean p_T, $\langle p'_T \rangle$, in $1 < p_T^b < 5$ GeV/c vs $N_{\rm part}$ for the near-side (diamonds), away-side shoulder (squares), and head (circles) regions for Au+Au (filled) and $p+p$ (open) for four trigger p_T bins. Solid lines represent values for inclusive charged hadrons (∼0.36 GeV/c) [6]. Error bars represent the statistical errors. Shaded bars represent the sum of $N_{\rm part}$-correlated elliptic flow and ZYAM error.

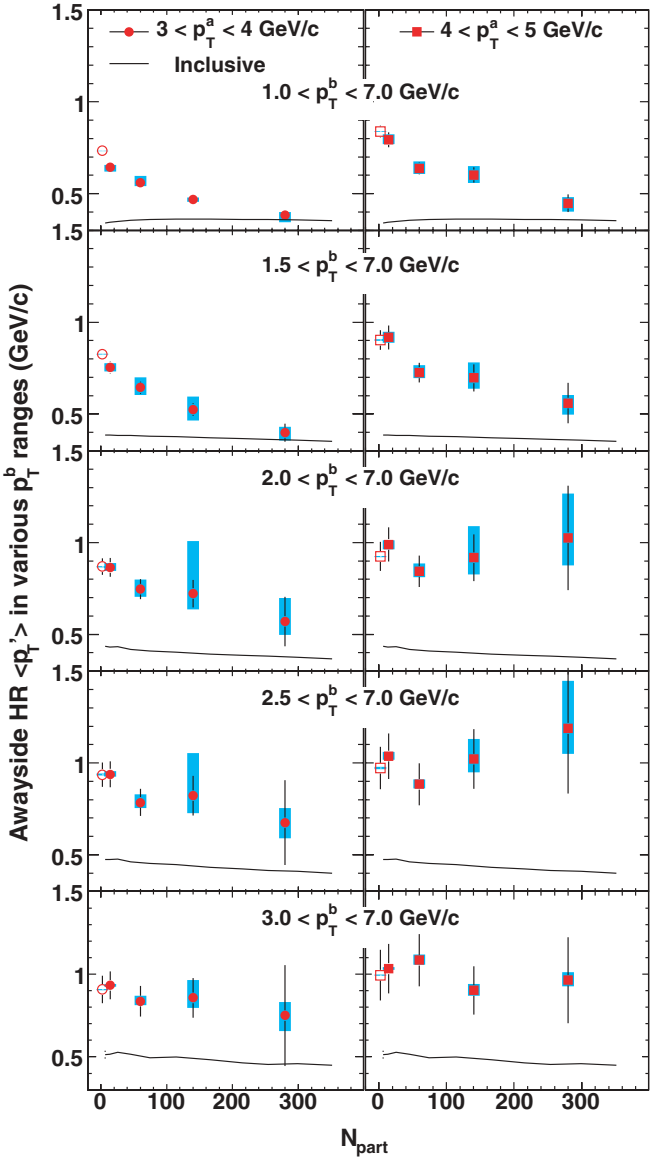

FIG. 26. (Color online) Truncated mean p_T, $\langle p'_T \rangle$, calculated for five partner-p_T ranges (from top to bottom) in the HR. The left panels (right panels) show the results for triggers in 3–4 (4–5) GeV/c. Solid lines represent values for inclusive charged hadrons. Error bars represent the statistical errors. Shaded bars represent the sum of $N_{\rm part}$-correlated elliptic flow and ZYAM error.

and gradually decrease with increasing $N_{\rm part}$, consistent with a softening of the partner spectrum in central collisions. For 2–3 and 3–4 GeV/c trigger bins, the values of $\langle p'_T \rangle$ for $N_{\rm part} \gtrsim 150$ approach those for inclusive spectra. For higher trigger p_T bins, the drop with $N_{\rm part}$ is less dramatic, possibly because of the punch-through jet fragmentation contribution at high p_T.

To further investigate the onset of jet fragmentation in the HR, we study the dependence of $\langle p'_T \rangle$ on partner momentum. Figure 26 shows the centrality dependence of $\langle p'_T \rangle$ calculated in various ranges of p_T^b for triggers in 3–4 GeV/c (left panels) and 4–5 GeV/c (right panels). These results are compared with values for inclusive hadron spectra calculated in the same p_T^b ranges. For $1 < p_T^b < 7$ GeV/c bin, $\langle p'_T \rangle$ decreases with

$N_{\rm part}$. As the p_T^b range shifts upward, the centrality dependence becomes flatter. $\langle p_T' \rangle$ for $3 < p_T^b < 7$ GeV/c is essentially constant with $N_{\rm part}$. The flattening of the spectral slope with $N_{\rm part}$ starts at a lower p_T^b for $4 < p_T^a < 5$ GeV/c than that for $3 < p_T^a < 4$ GeV/c. This implies (1) a similar spectra shape for Au+Au and $p + p$ at high $p_T^{a,b}$, and (2) the jet fragmentation contribution dominates the HR yield at large $p_T^{a,b}$.

The different patterns observed for the yields in the HR and SR suggest a different origin for these yields. The suppression of the HR yield and the softening of its spectrum are consistent with jet quenching. The observed HR yield could be comprised of contributions from punch-through jets, radiated gluons, and feed-in from the SR. By contrast, the enhancement of the SR yield for $p_T^{a,b} \lesssim 4$ GeV/c suggests a remnant of the lost energy from quenched jets. The very weak dependence on p_T and centrality (for $N_{\rm part} \gtrsim 100$) for its peak location and mean p_T may reflect an intrinsic response of the medium to the lost energy. These observations are challenging for simple deflected jet scenarios [23,29], since both the deflection angle and jet spectral slope would depend on p_T^a or p_T^b. On the other hand, they are consistent with expectations for Mach shock in a near-ideal hydrodynamic medium [35,71], and thus they can be used to constrain the medium transport properties such as speed of sound and viscosity-to-entropy ratio within these models.

E. Medium modification of hadron pair yield

In $p + p$ collisions at 200 GeV, it is generally believed that hadrons for $p_T > 2$ GeV/c are dominated by jet fragmentation [72]. By contrast, particle production in heavy-ion collisions is complicated by final state medium effects. Because of strong jet quenching, the jet fragmentation contribution only dominates for $p_T \gtrsim 5$–7 GeV/c [6,11]. The bulk of hadrons, i.e., those at $p_T \lesssim 4$ GeV/c, are dominated by soft processes such as the hydrodynamic flow of locally thermalized partonic medium [37,73,74] which subsequently hadronizes via the coalescence of constituent quarks [38–41]. The p_T of $4 \lesssim p_T \lesssim 7$ GeV/c is a transition region where both soft and hard processes contribute.

Dihadron correlations provide new tools for separating the hard and soft contributions at low and intermediate p_T, albeit for hadron pair production instead of single hadron production. If jets are quenched by the medium, and their energy is transported to lower p_T, a significant fraction of the low- and intermediate-p_T hadron pairs may retain some correlation with the original jet [42]. Consequently, they can contribute to a dihadron correlation analysis. However, such pairs can also be influenced by soft processes which dominate the inclusive hadron production in the same p_T region. For instance, they may couple with hydrodynamic flow at the partonic stage [23] or reflect the effects of the coalescence between shower parton and thermal partons during hadronization [39].

Thus far, we have quantified the jet modifications via per-trigger yields. While sensitive to modifications of jet-induced pairs, these yields are also sensitive to modifications in the number of triggers. For high-p_T triggers, however, the per-trigger yield is roughly equal to the per-jet yield, because most jets fragment into at most one trigger hadron due to the steeply falling jet spectra [44]. For intermediate- and low-p_T triggers, a large fraction of triggers may come from soft processes and hence "dilute" the per-trigger yield.

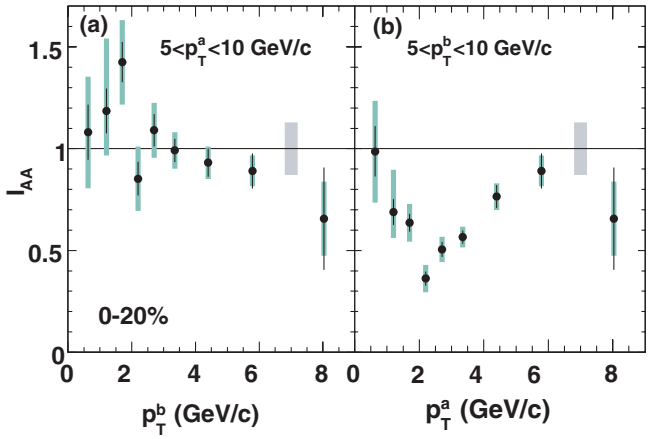

FIG. 27. (Color online) (a) I_{AA} vs partner p_T when 5–10 GeV/c hadrons are designated triggers. (b) I_{AA} vs trigger p_T when 5–10 GeV/c hadrons are used as partners.

To illustrate this dilution effect, we focus on the near-side jet-induced pairs in which the first hadron is fixed in the 5–10 GeV/c p_T range, and the second hadron is varied in p_T from 0.4 to 7 GeV/c. We note here that the requirement of a high-p_T hadron ensures that most of the near-side pairs come from fragmentation of partons. Figure 27(a) shows the per-trigger yield modification factor I_{AA} when hadrons in the 5–10 GeV/c p_T range are designated triggers; Fig. 27(b) shows the corresponding I_{AA} when the lower p_T hadrons are designated as triggers, which is calculated according to Eq. (7).

Figure 27(a) shows that I_{AA} is near unity for all p_T^b for the 5–10 GeV/c hadron triggers. This is consistent with each high-p_T trigger coming from one jet. On the other hand, when low-p_T hadrons are used as triggers, Fig. 27(b) shows that I_{AA} has a nontrivial dependence on p_T^a. That is, there is a strong suppression of I_{AA} in the 2–4 GeV/c p_T range, which reflects an excess of trigger hadrons at low p_T with weaker jet correlation strength. This dilution effect is also reflected in the near-side I_{AA} values in Fig. 19 and for the away-side I_{AA} values in Fig. 13 (also reflected in Fig. 36 for low p_T^a and high p_T^b). The former shows a suppression at large p_T^b for soft triggers ($2 < p_T^a < 3$ and $3 < p_T^a < 4$ GeV/c). The latter shows a stronger suppression for low-p_T triggers ($2 < p_T^a < 3$ and $3 < p_T^a < 4$ GeV/c) than for high-p_T triggers ($4 < p_T^a < 5$ and $5 < p_T^a < 10$ GeV/c). This dilution effect might be the result of the following two scenarios: (1) a large fraction of low-p_T hadrons are from soft processes such as coalescence of flow-boosted thermal quarks related to the anomalous proton/pion ratio [6,11], or (2) jets are quenched, and these hadrons are the remnants of the quenched jets and thus lack associated hadrons at high p_T.

To gain more insight into intermediate-p_T correlations, we focus on the pair suppression factor J_{AA} defined in Eq. (4). We recall here that J_{AA} quantifies the modification of jet-induced

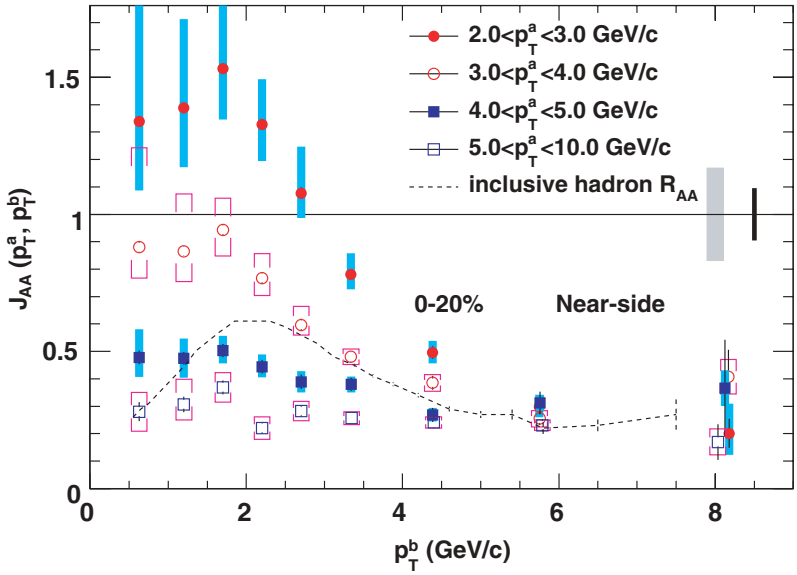

FIG. 28. (Color online) Near-side pair suppression factor J_{AA} in 0–20% Au+Au collisions as function of p_T^b for various ranges of p_T^a. The dashed line indicates the charged hadron R_{AA}. The grey band around unity is the systematic error due to the 20% combined single particle efficiency of the triggers and partners in Au+Au and $p+p$. The dark line around unity indicates the uncertainty on the $N_{\rm coll}$.

pairs in Au+Au relative to that in $p+p$ normalized by $N_{\rm coll}$. It is symmetric with respect to the interchange of p_T^a and p_T^b and equals unity in the absence of medium effects. Figure 28 shows the near-side J_{AA} as function of p_T^b for 0–20% central Au+Au collisions and for four different p_T^a bins. Values of J_{AA} are above unity for $p_T^{a,b} < 2$ GeV/c. However, they decrease with increasing $p_T^{a,b}$ and drop below unity. For high $p_T^{a,b}$, J_{AA} reaches a constant value of ∼0.2–0.3, which is similar to the high-p_T single particle suppression factor R_{AA}.

To interpret these observations, we note that each high-p_T pair at the near-side comes from the same jet. Thus J_{AA} reflects the modification of single jets, which at high p_T should be the same as the leading hadron R_{AA}. Since the values of R_{AA} are constant at high p_T, we expect high-p_T J_{AA} to be constant and equal to R_{AA}.

Furthermore, if each high-p_T near-side pair comes from the same jet, then the sum of their transverse momentum, $p_T^{\rm sum} = p_T^a + p_T^b$, should serve as a better proxy for the original jet energy. With this in mind, we replot in Fig. 29 the near-side J_{AA} values as a function of this "pair proxy energy" $p_T^{\rm sum}$. Interestingly, the pair modification factors roughly follow a single curve in $p_T^{\rm sum}$. It is above unity below 5 GeV/c, followed by a decrease with $p_T^{\rm sum}$, and reaches a constant for $p_T^{\rm sum} >$ 8 GeV/c. The approximate scaling behavior breaks when the p_T of one hadron is $\lesssim$2 GeV/c, where J_{AA} is systematically below the overall trend.

The fact that $J_{AA} > 1$ for $p_T^{\rm sum} < 5$ GeV/c implies that the total jet-induced pair yield is enhanced relative to the $N_{\rm coll}$ scaled $p+p$ collisions. This enhancement may reflect the energy of the quenched jets being transported to low p_T. J_{AA} is almost a factor of 6–7 larger than its high $p_T^{\rm sum}$ limit. By contrast, the enhancement shown for I_{AA} in Fig. 19 is only a factor of 2.5 at low $p_T^{a,b}$. This difference can be attributed to the dilution effect on the triggers. For completeness, Fig. 30 shows the values of J_{AA} vs p_T^b (left panels) and vs $p_T^{\rm sum}$ (right panels) for 20–40%, 40–60%, and 60–92% centrality

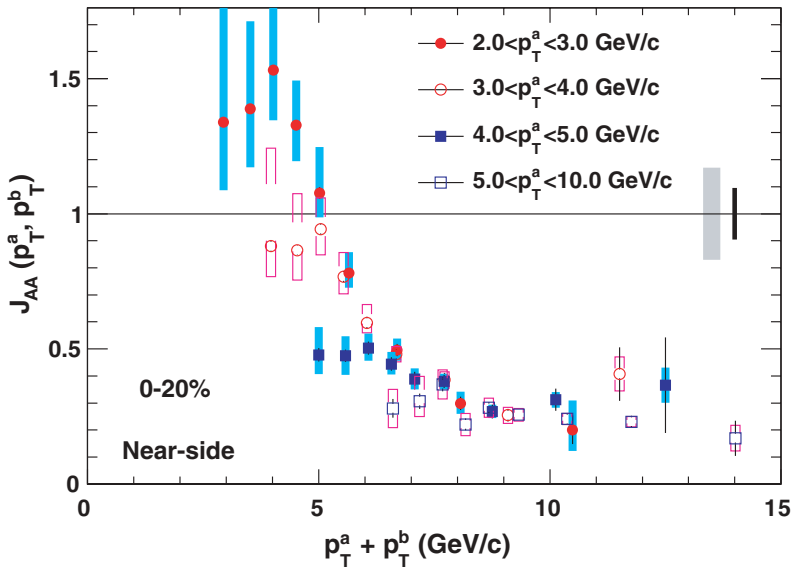

FIG. 29. (Color online) Near-side pair suppression factor J_{AA} as function of pair transverse momentum, $p_T^{\rm sum} = p_T^a + p_T^b$ in 0–20% Au+Au collisions. The grey band around unity is the systematic error due to the 20% combined single particle efficiency of the triggers and partners in Au+Au and $p+p$. The dark line around unity indicates the uncertainty on the $N_{\rm coll}$.

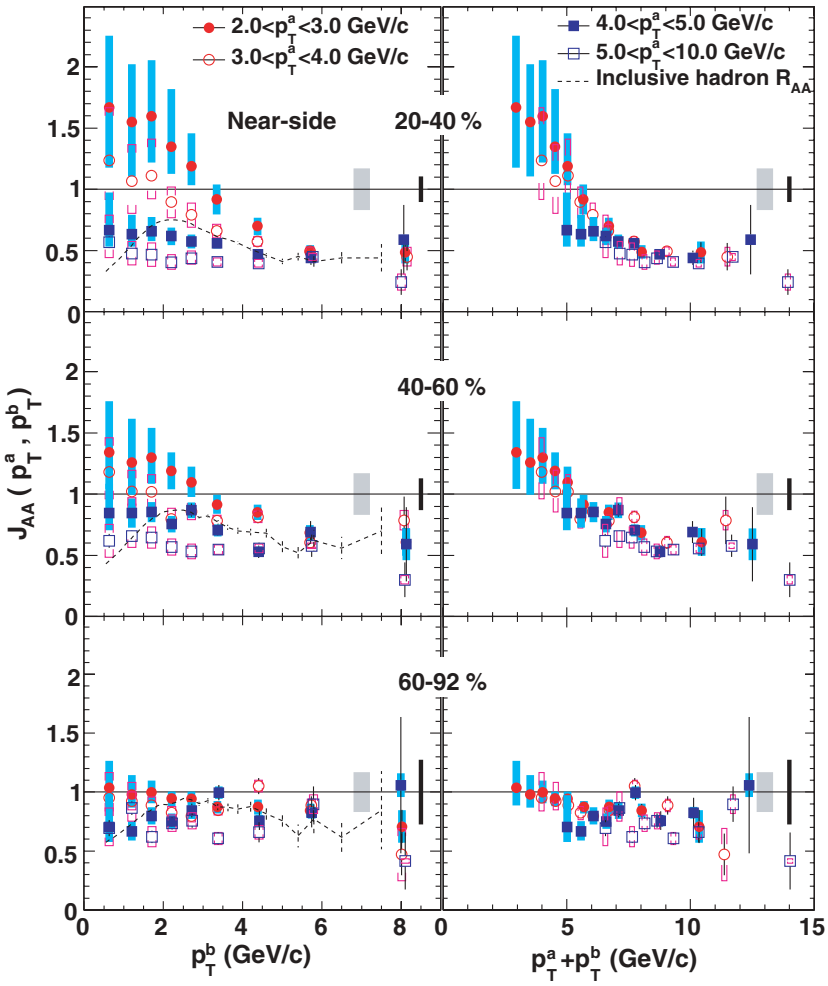

FIG. 30. (Color online) Near-side J_{AA} as function of p_T^b (left panels) and $p_T^{\rm sum}$ (right panels) for four p_T^a bins and three centrality bins. From top to bottom are 20–40%, 40–60%, and 60–92%. The dashed lines in the left panels indicate the charged hadron R_{AA}. The grey bands around unity are the systematic errors due to the 17% combined single particle efficiency of the triggers and partners in Au+Au and $p+p$. The dark lines around unity indicate the uncertainty on the $N_{\rm coll}$.

bins. J_{AA} vs $p_T^{\rm sum}$ shows an approximate scaling behavior for all centralities, i.e, J_{AA} for large $p_T^{\rm sum}$ approaches a constant level roughly equal to that for the high-p_T R_{AA} values.

In Fig. 31, we show the J_{AA} for the away-side HR as a function of p_T^b in various centrality bins. In central collisions, a possible enhancement at low $p_T^{a,b}$ and a strong suppression at large $p_T^{a,b}$ can be seen. This is consistent with the feedback of lost energy to lower p_T on the away-side. The modifications decrease for peripheral collisions, as expected for a weaker medium effect. However, the suppression level seems to approach a constant value for high p_T^b for all centralities. This is expected since $I_{AA} \approx R_{AA}$ at high p_T for the away-side HR. This implies that $J_{AA} = I_{AA} R_{AA} \approx R_{AA}^2$ when one of the hadrons is at high p_T, as indicated by the dashed line.

To quantify this high-p_T scaling behavior, we calculate the ratio $\frac{J_{AA}}{R_{AA}^2}$ for the away-side head region for $4 < p_T^b < 7$ GeV/c and various p_T^a selections. The values for the four centrality ranges used in Fig. 31 are summarized in Table VI. Although the uncertainties are quite substantial, the HR J_{AA} approximately equals R_{AA}^2, suggesting a similar suppression factor for inclusive hadrons and the away-side jet at high p_T. This, as pointed out in Refs. [75,76], could be a canceling effect between a stronger energy loss, which increases the suppression, and harder away-side hadron spectra associated with high-p_T triggers, which decrease the suppression.

V. DISCUSSION

A. Insights from identified particle and energy dependent correlations

To elucidate the underlying physics of the medium-induced component, we focus on intermediate p_T where the SR dominates, and we study the particle composition of the yield in the SR. PHENIX has published results on correlations of a trigger hadron, at intermediate transverse momentum ($2.5 < p_T^a < 4$ GeV/c), with identified partner mesons or baryons at lower p_T [43]. The away-side shape was found to be similar for partner baryons and mesons; namely, the pairs peak at $\Delta\phi \sim \pi \pm 1.1$ with a local minimum at $\Delta\phi \sim \pi$. The particle composition in the away-side jet, as reflected by the baryon-to-meson ratio, was also found to grow with increasing

TABLE VI. Average ratio J_{AA}/R_{AA}^2 for the away-side HR for $4 < p_T^b < 7$ GeV/c (see Fig. 31).

Centrality	J_{AA}/R_{AA}^2 for HR ($\pm$Stat.+Sys.$-$Sys.)
0–20%	$0.81 \pm 0.07 + 0.44 - 0.41$
20–40%	$0.89 \pm 0.05 + 0.37 - 0.35$
40–60%	$0.80 \pm 0.03 + 0.26 - 0.23$
60–92%	$0.90 \pm 0.03 + 0.25 - 0.23$

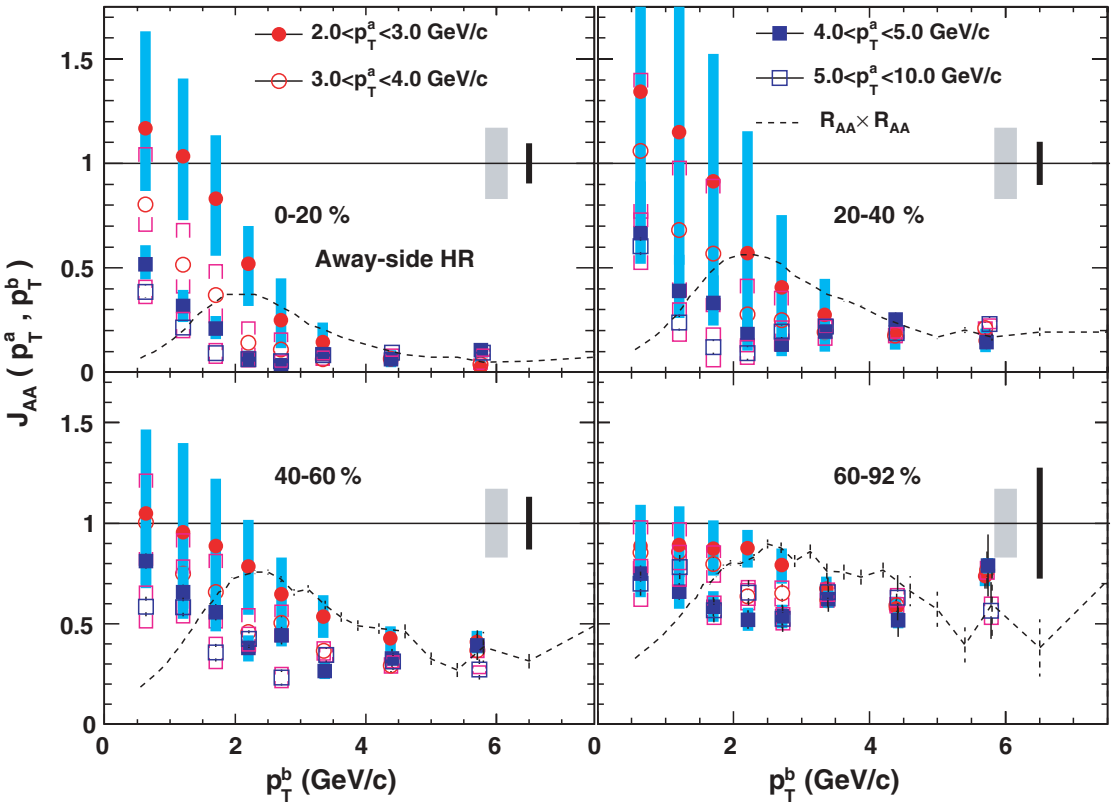

FIG. 31. (Color online) Pair suppression factor J_{AA} for the away-side HR in Au+Au collisions as function of p_T^b for various ranges of p_T^a. The dashed lines indicate the square of the charged hadron R_{AA}. The grey bands around unity are the systematic errors due to the combined single particle efficiency of the two particles in Au+Au and $p+p$. The dark lines around unity indicate the uncertainty on the $N_{\rm coll}$.

partner p_T. The trend is similar to that observed for inclusive hadron production. These observations for intermediate-p_T correlations are consistent with strong parton-medium interactions which induce correlations between soft partons, followed by coalescence at hadronization.

Further insight into the physics underlying the SR yield can be obtained by studying its energy dependence. In particular, it is interesting to see whether the two-component picture applies at much lower collision energy. Figure 32 compares the per-trigger yield at $\sqrt{s_{NN}} = 200$ and 62.4 GeV for $1 < p_T^b < 2.5 < p_T^a < 4$ GeV/c. They are the yields associated with the jet functions previously published in Ref. [19]. The away-side shapes are strongly non-Gaussian in both cases. The 62.4 GeV data seem to be somewhat flatter, however, their relatively large statistical uncertainties do not allow a definite statement to be made.

The CERES Collaboration recently released their high-statistics preliminary results of per-trigger yields in 0–5% and 5–10% Pb+Au collisions for $1 < p_T^b < 2.5 < p_T^a < 4$ GeV/c [77]. This measurement was carried out at $\sqrt{s_{NN}} = 17.2$ GeV at the CERN Super Proton Synchrotron (SPS), for $0.1 < \eta < 0.7$ in the center-of-mass (c.m.) frame. The equivalent pseudorapidity window of 0.6 is close to the PHENIX value of 0.7. Thus, the jet yields from both experiments can be compared after applying the correction of $0.7/0.6 = 1.17$. In contrast to the PHENIX results, the CERES data show an essentially flat away-side jet shape. The maximum of SR is about half that of the PHENIX value, whereas the yield at the HR is close to the PHENIX value. The former might suggest a weaker medium effect at lower energy; the latter could be a combination of a lower jet multiplicity and a weaker jet quenching at SPS energy. However, it is conceivable that other nuclear effects, especially the Cronin effect [78], may also broaden the away-side jet shape. Further detailed

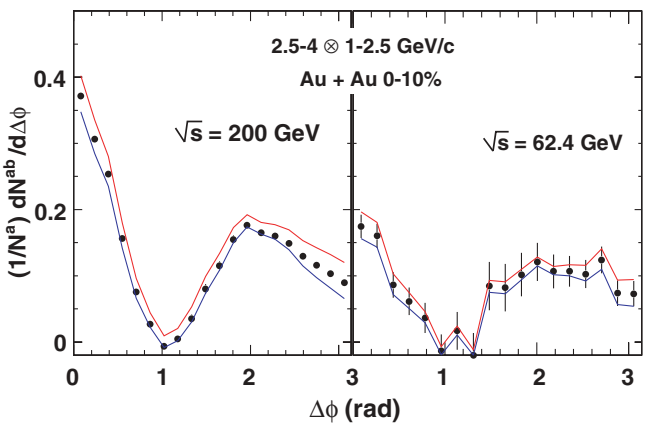

FIG. 32. (Color online) Per-trigger yield in 0–10% central Au+Au collisions from PHENIX at (a) $\sqrt{s_{NN}} = 200$ GeV and (b) $\sqrt{s_{NN}} = 62.4$ GeV. The histograms show the combined uncertainty of the elliptic flow and ZYAM errors.

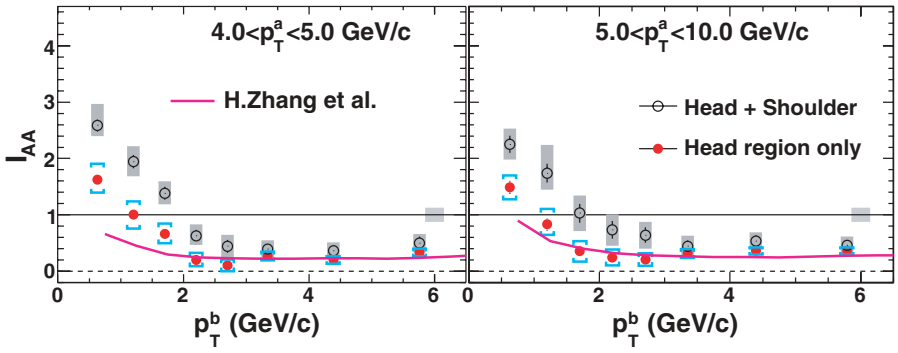

FIG. 33. (Color online) Comparison of I_{AA} with energy loss calculation from Ref. [76].

study of the collision energy dependence of the HR and SR components might elucidate the onset of jet quenching and medium response.

B. Comparison with models

If jets are generated close to the surface, they exit and subsequently fragment outside the medium. Otherwise, they lose energy by radiating gluons. These shower gluons may be emitted at large angles relative to the original partons [31,32] and fragment into hadrons, or they can be deflected to large angles by interactions with medium. Examples of the latter include medium deflection in the azimuthal [23,29] and the beam directions [25] or excitation of collective Mach shock [35,36].

Several calculations for radiative energy loss have been carried out [14,31,76] to describe dihadron production at high p_T. They all describe the data fairly well. As an example, Fig. 33 shows a comparison of data for the 4–5 and 5–10 GeV/c triggers with recent calculations from Ref. [76]. For $p_T^a > 2$ GeV/c, the calculated I_{AA} is approximately constant and agrees well with the data. According to this calculation, both tangential and punch-through jet emission are important, accounting for 3/4 and 1/4 of the away-side high-p_T pairs, respectively.

To extend the calculation to low and intermediate p_T, contributions from radiated gluons have to be taken into account. Early energy loss model calculations suggested that these radiated gluons are almost collinear with the jet axis [79]. However, recent calculations [31] favor large-angle gluon emission due to destructive interference that suppresses collinear emission. By including gluon feedback, the calculation can reproduce away-side per-trigger yields at low partner p_T, but the gluon emission angle is too small to reproduce the away-side jet shape.

In an improved calculation that includes the Sudakov form factors [32], the authors can qualitatively describe the away-side jet shape and its centrality dependence at intermediate p_T, when the leading parton is assumed to split into two semihard gluons which then fragment into hadrons. This model assumes a transport coefficient of $\hat{q} \sim 5$–10 GeV^2/fm. A smaller $\hat{q}$, for instance, would substantially reduce the predicted split angle.

The away-side broadening may also arise from Cherenkov gluon radiation [34]. It could occur when the gluon is scattered by colored bound states in such a way that the permittivity for in-medium gluons becomes space-like. A first calculation that includes only scalar bound states suggests that the peak angle D should gradually decrease to zero with increasing momentum; this trend seems to be ruled out by the present data. More sophisticated calculations including other bound states are needed in future studies.

It has been suggested that shower partons could couple with the longitudinal and transverse flow and are broadened or deflected in $\Delta\eta$ [21–23,27] and/or $\Delta\phi$ [23,29] directions. The longitudinal deflection was argued to be responsible for the $\Delta\eta$ ridge structure at the near-side. The transverse deflection can lead to broadening in $\Delta\phi$. It was argued in Ref. [29] that a random multiple scattering of the leading parton, combined with energy loss, can result in the double peaked structure of the away-side. However, in general, the deflection angle decreases with the hadron momentum. This is not compatible with the observation of p_T-independent D values and universal spectral slopes of the SR.

Finally, it has been proposed that the lost energy can be absorbed by the medium and converted into collective Mach shock [35,36]. In this picture, the fluid elements are boosted along the Mach angle [71] and then hadronize via coalescence. The Mach angle depends only on the sound speed of the medium thus is independent of p_T and consistent with the data. The boost effect also produces a harder slope for the partners, qualitatively consistent with experimental observations. Our results on the PID dependence of the correlation pattern [43] are consistent with the above picture. The propagation of the shock wave requires hydrodynamic behavior of the medium with small viscosity. If the Mach shock is the underlying physics, the observation can be used to constrain the value of η/s.

Many of the models discussed in this section are quite qualitative in nature. These models typically focus on either jet shape or jet yield, near-side or away-side, high p_T or low p_T. The fact that both near- and away-side distributions are enhanced and broadened at low p_T and that the modifications are limited to $p_T \lesssim 4$ GeV/c, above which the jet characteristics qualitatively approach jet fragmentation, may suggest that the modification mechanisms for the near- and away-side are related. A model framework that includes both jet quenching and medium response and can describe the full p_T evolution of the jet shape and yield at both near- and away-side is required to understand the parton-medium interactions. Our data provide valuable guidance for such future model developments.

VI. SUMMARY AND CONCLUSIONS

We have analyzed dihadron azimuthal correlations for $0.4 < p_T < 10$ GeV/c unidentified charged hadrons in Au+Au collisions at $\sqrt{s_{NN}} = 200$ GeV. The results are presented as functions of trigger p_T, partner p_T, and centrality and are compared with correlations of identified hadrons as well as results from lower energies. The evolution of the jet shape and yield with p_T seems to suggest four distinct contributions to jet-induced pairs: (1) a jet fragmentation component around $\Delta\phi \sim 0$, (2) a punch-through jet fragmentation component around $\Delta\phi \sim \pi$, (3) a medium-induced component around $\Delta\phi \sim 0$, and (4) a medium-induced component around $\Delta\phi \sim \pi \pm 1.1$.

The jet fragmentation components arise from jets that suffer small energy loss due to the surface or punch-through jet emissions. They dominate the near- and away-side pairs at large p_T. The near-side pair suppression factor J_{AA} follows an approximate scaling with the pair proxy energy $p_T^{\rm sum}$. It reaches a constant for $p_T^{\rm sum} > 8$ GeV/c, at a level similar to the suppression for single jets at high p_T. In this p_T region, the yield of both the single jets (near-side pairs) and back-to-back jets (away-side pairs) are consistent with energy loss calculations.

By contrast, the enhancement of medium-induced components may reflect a remnant of the lost energy from quenched jets. This enhancement is limited to $p_T^{a,b} \lesssim 4$ GeV/c. The near-side medium-induced component is responsible for broadening in $\Delta\phi$ and significant elongation in $\Delta\eta$, and is related to the ridge structure [16,17,20]. The away-side medium-induced component exhibits p_T- and centrality-independent shape and mean p_T and a bulk medium-like particle composition [43], possibly reflecting an intrinsic property of the medium response to energetic jets.

We have also investigated the contribution of medium-induced components to single particle production at intermediate p_T, where soft processes such as hydrodynamic flow and coalescence are important. The yields of jet-induced hadron pairs (via J_{AA}) are not suppressed at low pair proxy energy $p_T^{\rm sum} = p_T^a + p_T^b$. However, pair yields divided by the yield of soft triggers show an apparent dilution effect at large partner p_T. This suggests that these soft hadrons either come from soft processes such as from coalescence of thermal partons, or they are the remnant of quenched jets, and thus lack high-p_T jet partners.

ACKNOWLEDGMENTS

We thank the staff of the Collider-Accelerator and Physics Departments at Brookhaven National Laboratory and the staff of the other PHENIX participating institutions for their vital contributions. We thank Hanzhong Zhang and XinNian Wang for providing theoretical calculation input. We acknowledge support from the U.S. Department of Energy, Office of Science, Office of Nuclear Physics, the National Science Foundation, Abilene Christian University Research Council, Research Foundation of SUNY, and Dean of the College of Arts and Sciences, Vanderbilt University (U.S.A), Ministry of Education, Culture, Sports, Science, and Technology and the Japan Society for the Promotion of Science (Japan), Conselho Nacional de Desenvolvimento Científico e Tecnológico and Fundação de Amparo à Pesquisa do Estado de São Paulo (Brazil), Natural Science Foundation of China (People's Republic of China), Ministry of Education, Youth and Sports (Czech Republic), Centre National de la Recherche Scientifique, Commissariat à l'Énergie Atomique, and Institut National de Physique Nucléaire et de Physique des Particules (France), Ministry of Industry, Science and Tekhnologies, Bundesministerium für Bildung und Forschung, Deutscher Akademischer Austausch Dienst, and Alexander von Humboldt Stiftung (Germany), Hungarian National Science Fund, OTKA (Hungary), Department of Atomic Energy (India), Israel Science Foundation (Israel), Korea Research Foundation and Korea Science and Engineering Foundation (Korea), Ministry of Education and Science, Russia Academy of Sciences, Federal Agency of Atomic Energy (Russia), VR and the Wallenberg Foundation (Sweden), the U.S. Civilian Research and Development Foundation for the Independent States of the Former Soviet Union, the U.S.-Hungarian NSF-OTKA-MTA, and the U.S.-Israel Binational Science Foundation.

APPENDIX A: DIHADRON CORRELATION METHOD

This section demonstrates that the shape of the $\Delta\phi$ correlation function, constructed as the ratio of same to mixed events, reproduces the shape of the true-pair distribution in $\Delta\phi$. We demonstrate this is generally true for a nonuniform experimental acceptance such as in the PHENIX experiment. Our argument is not original with our analysis but has been used numerous times before in correlation analyses in heavy-ion experiments.

We start by giving notation for the true distributions of type a and type b particles. They are

$$\frac{d^2N_0^{ab}}{d\phi^a d\phi^b}, \quad \frac{dN_0^a}{d\phi^a}, \quad \frac{dN_0^b}{d\phi^b}, \tag{A1}$$

for the true azimuthal distributions for ab pairs and a and b singles produced for PHENIX pseudorapidity acceptance and for events in one centrality bin. We use subscript 0 to indicate the true distributions. The *true* distributions are for particles in PHENIX η range, but with full azimuthal coverage.

The PHENIX beam-beam counter (BBC) and zero-degree calorimeter (ZDC), which trigger on events and determine their centrality, are uniform in azimuth. Therefore the *true* singles distributions are uniform, and the *true* pair distribution depends only on the difference between the two angles:

$$\frac{d^2N_0^{ab}}{d\phi^a\, d\phi^b} = f(\phi^a - \phi^b), \quad \frac{dN_0^a}{d\phi^a} = \text{const}, \quad \frac{dN_0^b}{d\phi^b} = \text{const}. \tag{A2}$$

To study the pair distribution as a function of $\Delta\phi$, we define the difference and average of ϕ^a and ϕ^b as new orthogonal variables:

$$\Delta\phi \equiv \phi^a - \phi^b, \quad \bar{\Phi} \equiv (\phi^a + \phi^b)/2. \tag{A3}$$

We integrate the true pairs over $\bar{\Phi}$ to obtain the projection onto $\Delta\phi$. This is equivalent to binning the data in $\Delta\phi$.

$$\frac{dN_0^{ab}}{d(\Delta\phi)} = \int \frac{d^2N_0^{ab}}{d\phi^a\, d\phi^b}\, d\bar{\Phi} = \int f(\Delta\phi)\, d\bar{\Phi} = f(\Delta\phi) \int d\bar{\Phi} \propto f(\Delta\phi), \tag{A4}$$

The measured distributions (without superscript) are related to the true distributions through the experimental acceptance/efficiency (here just "acceptance" for short):

$$\frac{d^2N^{ab}}{d\phi^a\, d\phi^b} = \varepsilon^{ab}(\phi^a, \phi^b)\, \frac{d^2N_0^{ab}}{d\phi^a\, d\phi^b}, \qquad \frac{dN^a}{d\phi^a} = \varepsilon^a(\phi^a)\, \frac{dN_0^a}{d\phi^a}, \quad \frac{dN^b}{d\phi^b} = \varepsilon^b(\phi^b)\, \frac{dN_0^b}{d\phi^b}, \tag{A5}$$

where ε^{ab}, ε^a, and ε^b describe the experimental acceptances for pairs and singles. The pair acceptance is, to a very good approximation, equal to the product of the singles acceptances:

$$\varepsilon^{ab}(\phi^a, \phi^b) = \varepsilon^a(\phi^a)\, \varepsilon^b(\phi^b), \tag{A6}$$

i.e., the experimental acceptance for a particles is not influenced by the presence or absence of b particles in any particular event, and vice versa.[2]

The numerator of the correlation function is the measured pair distribution projected onto $\Delta\phi$

$$N^{\text{same}}(\Delta\phi) = \int \frac{d^2N_0^{ab}}{d\phi^a\, d\phi^b}\, d\bar{\Phi} = f(\Delta\phi) \int \varepsilon^{ab}(\phi^a, \phi^b)\, d\bar{\Phi}. \tag{A7}$$

Mixed-event pairs are constructed by combining a particle at ϕ^a from one event with particles at ϕ^b from other, unrelated events. The mixed-event pairs over (ϕ^a, ϕ^b) factorize and have the form

$$\frac{d^2N_{\text{mixed}}^{ab}}{d\phi^a\, d\phi^b} \propto \frac{dN^a}{d\phi^a}\frac{dN^b}{d\phi^b}. \tag{A8}$$

The denominator of the correlation function is the projection of the measured mixed-event pairs:

$$N^{\text{mixed}}(\Delta\phi) = \int \frac{d^2N_{\text{mixed}}^{ab}}{d\phi^a\, d\phi^b}\, d\bar{\Phi} \propto \int \frac{dN^a}{d\phi^a}\frac{dN^b}{d\phi^b}\, d\bar{\Phi} \propto \int \varepsilon^a(\phi^a)\varepsilon^b(\phi^b)\, d\bar{\Phi}. \tag{A9}$$

Writing the correlation function with Eqs. (A7) and (A9), and applying Eqs. (A6) and (A4) yields

$$C(\Delta\phi) \equiv \frac{N^{\text{same}}(\Delta\phi)}{N^{\text{mixed}}(\Delta\phi)} \propto \frac{f(\Delta\phi) \int \varepsilon^{ab}(\phi^a, \phi^b)\, d\bar{\Phi}}{\int \varepsilon^a(\phi^a)\varepsilon^b(\phi^b)\, d\bar{\Phi}} \tag{A10}$$

$$\propto f(\Delta\phi) \propto \frac{dN_0^{ab}}{d(\Delta\phi)}. \tag{A11}$$

This shows that the shape of the true-pair distribution is recovered in the correlation function.

APPENDIX B: ROLE OF THE REACTION PLANE

No mention, explicit or implicit, was made of the reaction plane in the preceding proof; this is not surprising, since its validity holds for *any* source of correlation, whether from flow, jets, or other. We show that Eq. (A11) holds for limited detector acceptance with the reaction plane included explicitly.

For events with reaction plane direction Ψ, we define the conditional probabilities of finding an a or b particle, including the effects of acceptance, as

$$P^a(\phi^a|\Psi) = \varepsilon^a(\phi^a)\, \frac{dN^a}{d(\phi^a - \Psi)}, \qquad P^b(\phi^b|\Psi) = \varepsilon^b(\phi^b)\, \frac{dN^b}{d(\phi^b - \Psi)}. \tag{B1}$$

We can write the acceptances, and the *true* singles distributions with respect to Ψ, into their Fourier expansions:

$$\varepsilon^a(\phi) = \sum_{p=-\infty}^{p=+\infty} a_p e^{ip\phi}, \qquad \varepsilon^b(\phi) = \sum_{q=-\infty}^{q=+\infty} b_q e^{iq\phi}, \tag{B2}$$

where $a_{-p} = a_p^*$, $b_{-q} = b_q^*$, and

$$\frac{dN^a}{d(\phi^a - \Psi)} = \frac{1}{2\pi} \sum_{n=-\infty}^{n=+\infty} v_n^a\, e^{in(\phi^a - \Psi)} = \frac{1}{2\pi}\left(1 + \sum_{n=1}^{+\infty} 2v_n^a \cos n(\phi^a - \Psi)\right), \qquad \frac{dN^b}{d(\phi^b - \Psi)} = \frac{1}{2\pi} \sum_{m=-\infty}^{m=+\infty} v_m^b\, e^{im(\phi^b - \Psi)} = \frac{1}{2\pi}\left(1 + \sum_{m=1}^{+\infty} 2v_m^b \cos m(\phi^b - \Psi)\right). \tag{B3}$$

In the case that ab correlations are due to particle correlation with respect to the same reaction plane, as would be true of background pairs, then the *measured* same-event pair

[2] The condition of Eq. (A6) can be violated by some experimental effects, such as ghost-pair tracking artifacts at small angles. We recover the result of Eq. (A6) by applying pair cuts to remove such artifacts identically to same-event and mixed-event pairs. Pair cuts affect the integrands in the numerator and denominator of Eq. (A10) equally and so leave the end result of Eq. (A11) intact.

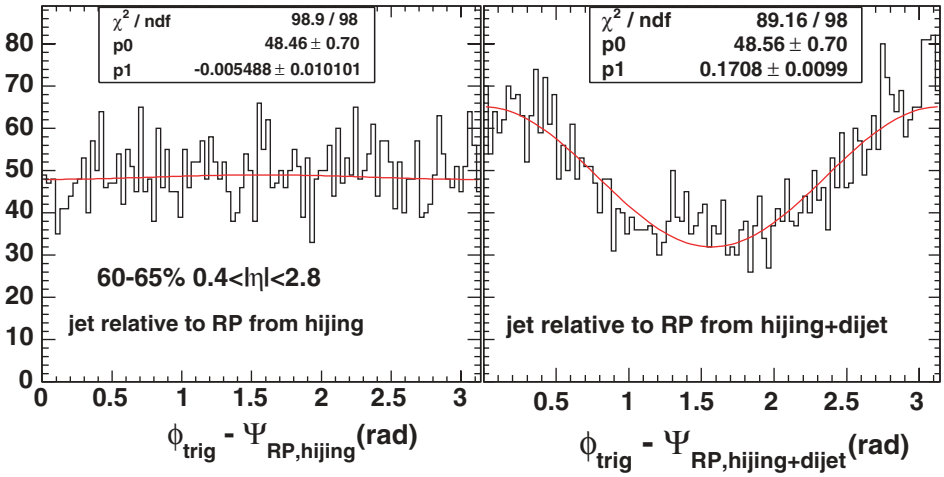

FIG. 34. (Color online) Distribution of the leading particle from the dijets relative to the event plane calculated from HIJING only (left) and event plane from the embedded event (right).

distribution can be written as

$$N^{\text{same}}(\Delta\phi) = \int \frac{d\phi^a}{2\pi}\frac{d\Psi}{2\pi} P^a(\phi^a|\Psi)P^b[(\phi^a - \Delta\phi)|\Psi]$$

$$= \sum_{p=-\infty}^{p=+\infty}\sum_{n=-\infty}^{n=+\infty} a_p\, b_p^*\, v_n^a v_n^b e^{i(p+n)\Delta\phi}. \quad \text{(B4)}$$

Similarly, the *measured* mixed-event pair distribution is

$$N^{\text{mixed}}(\Delta\phi) = \int \frac{d\phi^a d\Psi^a d\Psi^b}{8\pi^3} P^a(\phi^a|\Psi^a)P^b[(\phi^a - \Delta\phi)|\Psi^b]$$

$$= \sum_{p=-\infty}^{p=+\infty} a_p\, b_p^*\, e^{ip\Delta\phi}. \quad \text{(B5)}$$

Using these to construct the correlation function, we find

$$C(\Delta\phi) \equiv \frac{N^{\text{same}}(\Delta\phi)}{N^{\text{mixed}}(\Delta\phi)} = \sum_{n=-\infty}^{n=+\infty} v_n^a v_n^b e^{in\Delta\phi}. \quad \text{(B6)}$$

It is clear that the dependence upon the reaction plane angle is integrated out when forming the correlation function. It is also clear that the quadruple modulation strength of the correlation function $v_2^a v_2^b$ for background pairs is exactly the product of the *true* modulation strengths of the *true* singles distributions v_2^a and v_2^b.

APPENDIX C: SIMULATION STUDY OF THE NONFLOW EFFECT FROM JETS

The elliptic flow of the triggers and partners, which are used to estimate the background contribution in the correlation function of Eq. (15), are provided by the BBC reaction plane method. In this section, we show that the large rapidity separation of $|\Delta\eta| > 2.75$ between the PHENIX BBC and central arm greatly suppresses the bias due to jets and dijets to the reaction plane determination. More details can be also be found in Ref. [80].

The intrajet correlation is typically limited by the size of the jet cone, which is much smaller than the $\Delta\eta$ separation between the BBC and central arm. However, due to their broad distribution of parton x values, the away-side jets have a very broad distribution in $\Delta\eta$. Hence the interjet correlations can potentially bias the BBC reaction plane determination. We study the biases by embedding back-to-back jet pairs into HIJING events. The HIJING events serve as the underlying Au+Au events and were checked to reproduce the charged hadron multiplicity in η from PHOBOS [81]. Elliptic flow is implemented by applying a track-by-track weight in each HIJING event:

$$w(\mathbf{b}, p_T, \eta) = 1 + 2v_2(\mathbf{b}, p_T, \eta)\cos 2(\phi - \Psi),$$

where Ψ is the direction of the impact parameter $\mathbf{b}$. The centrality and p_T dependence of the v_2 is tuned according to the PHENIX measurement [82]. The η dependence of v_2 is obtained from PHOBOS [60] minimum bias events. The v_2 shape vs η is assumed to be independent of centrality selections. This gives an overall $\mathbf{b}$, p_T, and η dependence by a single function,

$$v_2(p_T, \mathbf{b}, \eta) = 0.02834\ \mathbf{b}\ e^{-0.5(\eta/3.92)^2}\left(1 - \frac{2.1}{1 + e^{1.357 p_T}}\right).$$

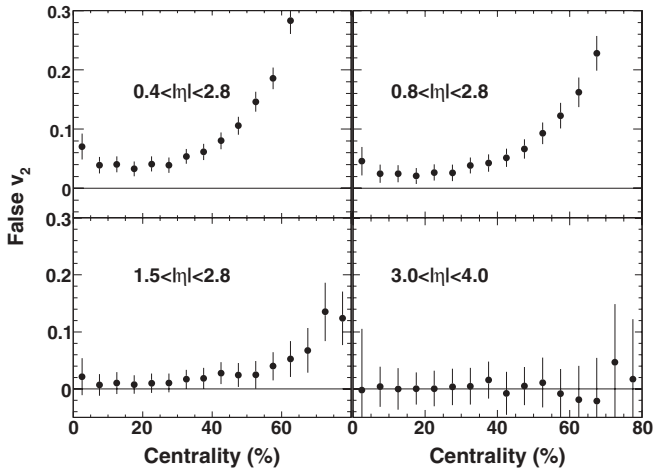

FIG. 35. False reaction plane v_2 of the leading hadron from the embedded dijet as function of centrality. The η range used to determine the event plane is indicated in each panel. The embedded dijet is required to have a trigger hadron above 6 GeV/c with a midrapidity window of $|\eta| < 0.35$.

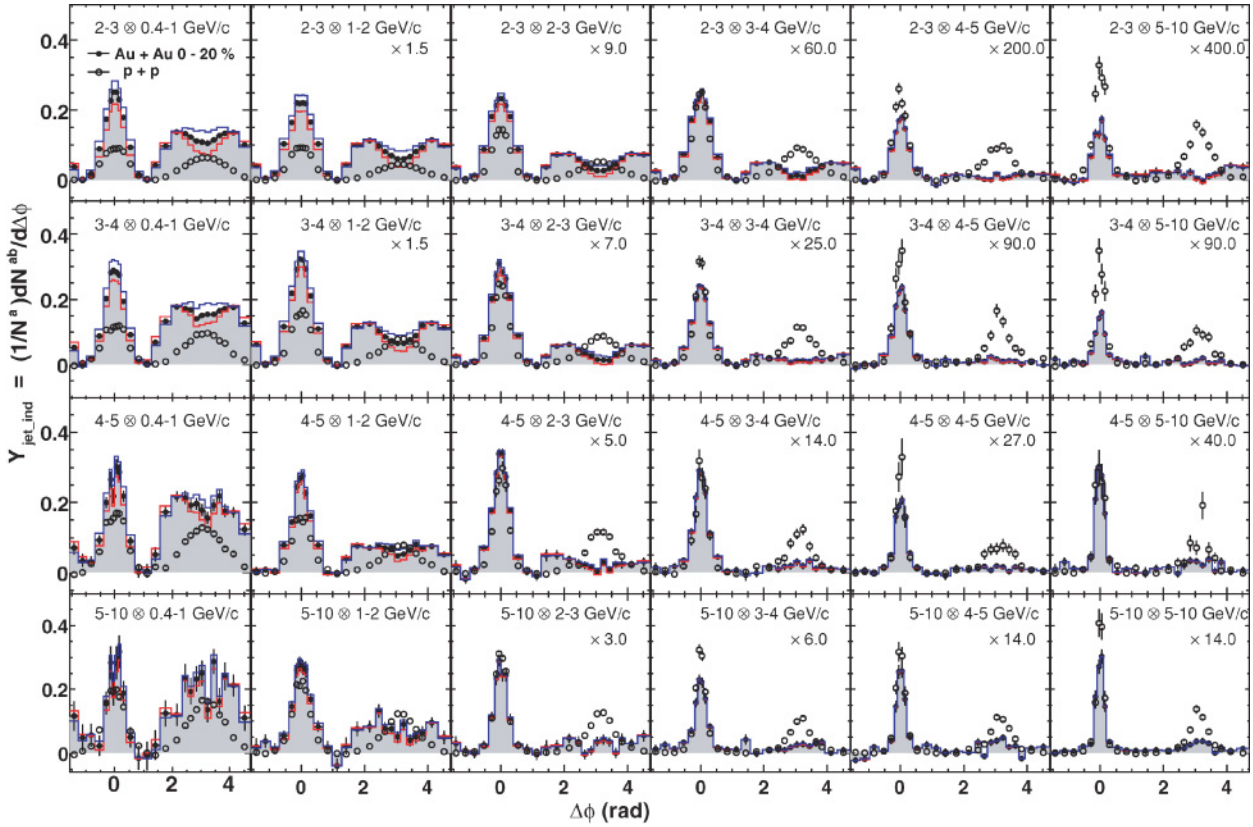

FIG. 36. (Color online) Per-trigger yield vs $\Delta\phi$ for successively increasing trigger and partner p_T ($p_T^a \otimes p_T^b$) in $p + p$ (open circles) and 0–20% Au+Au (filled circles) collisions. Data are scaled to the vertical axes of the four left panels. Histograms indicate elliptic flow uncertainties for Au+Au collisions.

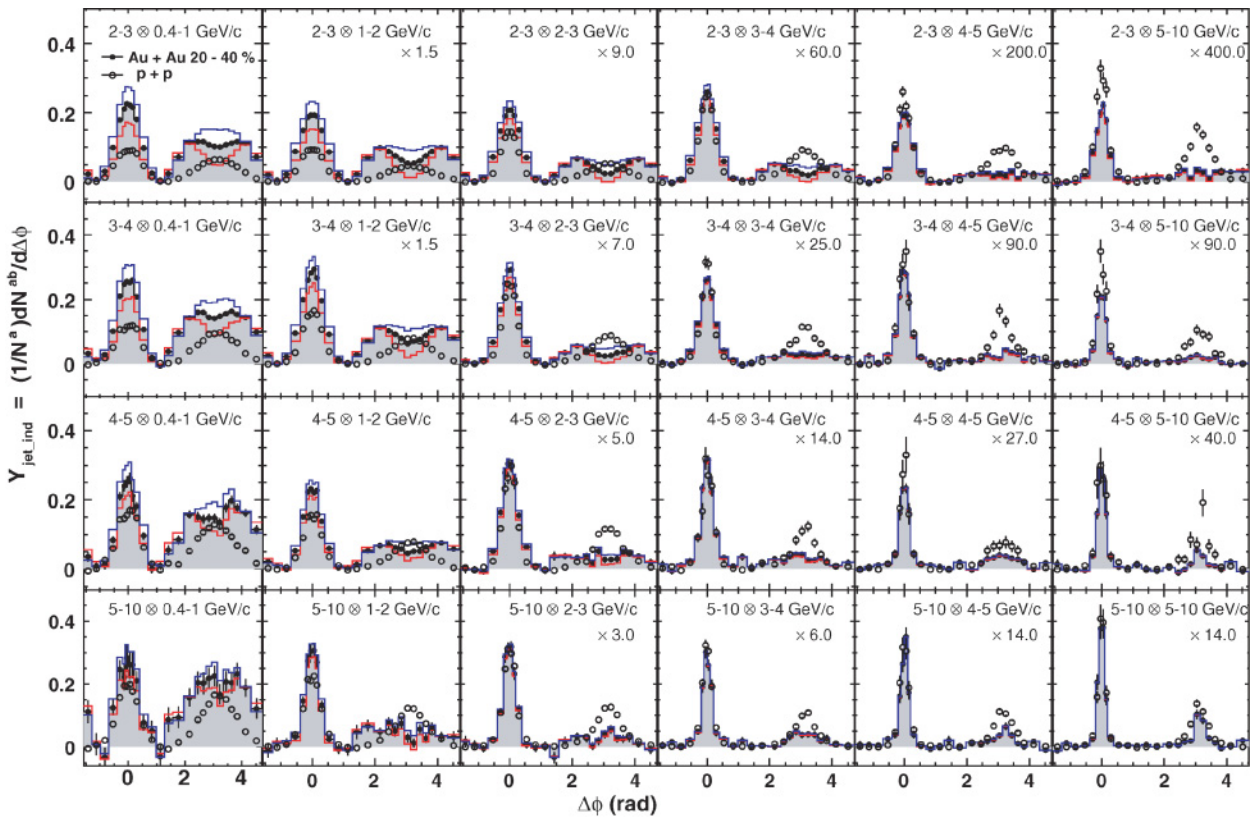

FIG. 37. (Color online) Same as Fig. 36, but for 20–40% Au+Au collisions.

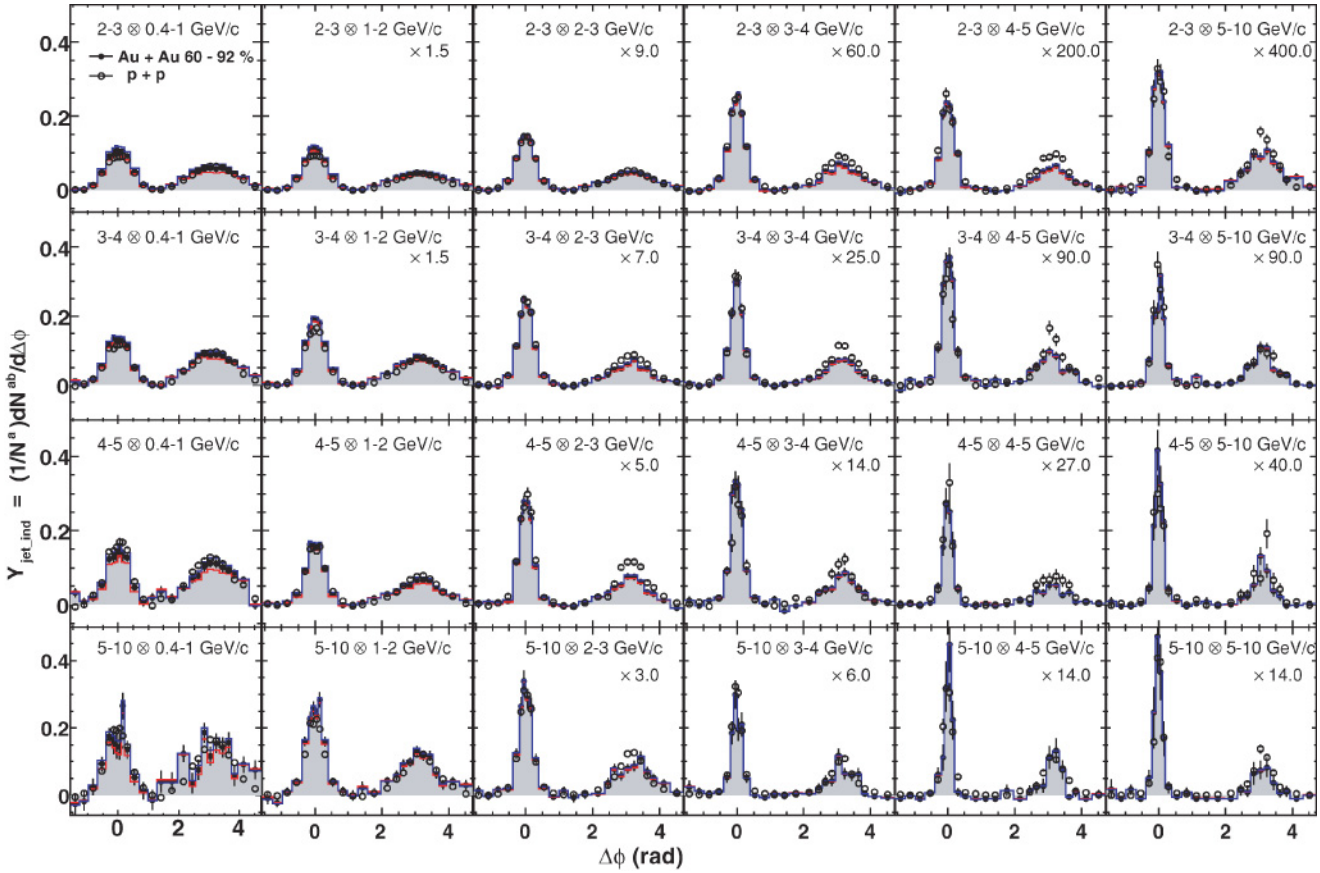

FIG. 38. (Color online) Same as Fig. 36, but for 60–92% Au+Au collisions.

We then generate back-to-back jet pairs from the PYTHIA event generator, requiring a leading particle above 6 GeV/c at midrapidity ($|\eta| < 0.35$). Assuming the fractional momentum of the leading hadron is $\langle z \rangle \approx 0.7$ [44], this corresponds to a typical jet energy of $6/\langle z \rangle \approx 9$ GeV/c.

We evaluate the dijet bias by comparing the event plane before and after the embedding. Dijets tend to bias the event plane toward the dijet direction, resulting in a false v_2 for the jet particles. Figure 34 shows the relative azimuth distribution between the jet leading hadrons and the event plane (EP) from the HIJING event (left panel) or the combined event (right panel). The dijets clearly become correlated with the EP determined from the combined event, leading to a false v_2 for the leading hadrons. However, since we embed one such dijet pair for every event, the bias shown in Fig. 34 should be interpreted as the bias for those events containing a high-p_T dijet. Thus it sets an upper limit for the bias effect.

To understand the impact of the false v_2, we have to determine their magnitudes in the same way as the real data analysis, i.e., according to

$$v_2 = \frac{v_{2,\mathrm{raw}}}{c_{v_2}} = \frac{\langle\langle \cos 2(\phi - \Phi_{\mathrm{EP}})\rangle\rangle}{\langle \cos 2(\Phi_{\mathrm{EP}} - \Phi_{\mathrm{RP}})\rangle}.$$

We obtain the raw v_2 by fitting the embedded trigger distribution (such as in Fig. 34) for each individual centrality bin. The raw v_2 is then divided by the corresponding reaction plane resolution, which can be calculated as $c_{v_2} = \langle \cos 2(\Phi_{\mathrm{EP}} - \Phi_{\mathrm{RP}})\rangle$.

The magnitude of the false v_2 depends on the rapidity separation between the trigger and the subevent used to determine the EP. Because of away-side jet swing, this bias could persist to large rapidity regions. Figure 35 shows the centrality dependence of false trigger v_2 for events containing high-p_T dijets for various rapidity windows used for EP determination. The false v_2 decreases as the subevent used to determine the EP moves toward large η. When the subevent is in the BBC acceptance ($3 < |\eta| < 4$), the false v_2 becomes negligible.

APPENDIX D: COMPREHENSIVE DATA PLOTS AND DATA TABLES

Figures 36–38 show the comprehensive array of results, covering the momentum range of 0.4–10 GeV/c from which the representative subset shown in Fig. 6 was derived. These results are described in Secs. III and IV.

Tables VII to XIX show numerical values of the plotted data. The corresponding figures are indicated in the table captions.

TABLE VII. D from FIT1 and FIT2 vs p_T^b for three p_T^a bins (Fig. 11).

$\langle p_T^b \rangle$ GeV/c	$D\pm$Stat.+Sys.−Sys. FIT1	$D\pm$Stat.+Sys.−Sys. FIT2
	$2 < p_T^a < 3$ GeV/c	
0.6	0.88±0.01+0.12−0.12	1.09±0.01+0.03−0.05
1.2	0.94±0.01+0.09−0.10	1.14±0.01+0.04−0.04
1.7	1.00±0.01+0.08−0.09	1.17±0.01+0.03−0.03
2.2	1.04±0.01+0.07−0.08	1.17±0.01+0.03−0.03
2.7	1.10±0.02+0.06−0.07	1.19±0.02+0.03−0.03
3.3	1.11±0.05+0.05−0.05	1.13±0.05+0.03−0.03
4.4	1.11±0.17+0.15−0.12	1.29±0.09+0.02−0.03
	$3 < p_T^a < 4$ GeV/c	
0.6	0.90±0.01+0.11−0.11	1.12±0.04+0.03−0.03
1.2	1.01±0.01+0.08−0.09	1.19±0.02+0.01−0.03
1.7	1.04±0.02+0.07−0.08	1.15±0.03+0.03−0.03
2.2	1.10±0.04+0.05−0.05	1.12±0.06+0.03−0.03
2.7	1.16±0.12+0.04−0.05	1.21±0.07+0.02−0.03
3.3	1.13±0.13+0.10−0.05	1.30±0.06+0.01−0.01
	$4 < p_T^a < 5$ GeV/c	
0.6	0.89±0.05+0.08−0.10	1.07±0.13+0.03−0.03
1.2	0.85±0.06+0.08−0.07	0.85±0.09+0.08−0.05
1.7	1.13±0.13+0.08−0.10	1.20±0.13+0.03−0.04
2.2	1.09±0.16+0.08−0.08	1.21±0.16+0.03−0.04
2.7	1.11±0.20+0.11−0.10	1.19±0.17+0.03−0.04

TABLE VIII. Near-side jet width for $p + p$ and 0-20% Au+Au for various p_T^a and p_T^b bins (Fig. 16). The width is unchanged by interchanging p_T^a and p_T^b.

Au+Au 0–20%				p+p	
		$2 < p_T^a < 3$ GeV/c			
$\langle p_T^b \rangle$ GeV/c	Width	Stat.	Sys.	Width	Sys.
0.6	0.415	0.002	+0.022–0.041	0.472	0.006
1.4	0.432	0.001	+0.024–0.028	0.364	0.003
2.3	0.410	0.002	+0.043–0.019	0.281	0.003
		$3 < p_T^a < 4$ GeV/c			
0.6	0.383	0.015	+0.006–0.033	0.430	0.012
1.4	0.409	0.004	+0.028–0.039	0.314	0.005
2.3	0.365	0.012	+0.022–0.016	0.244	0.005
3.3	0.286	0.010	+0.005–0.035	0.199	0.007
		$4 < p_T^b < 5$ GeV/c			
0.6	0.394	0.037	+0.036–0.027	0.402	0.018
1.4	0.340	0.017	+0.036–0.040	0.299	0.008
2.3	0.274	0.012	+0.011–0.022	0.225	0.007
3.3	0.223	0.010	+0.012–0.027	0.201	0.010
4.4	0.179	0.009	+0.002–0.013	0.148	0.011
		$5 < p_T^a < 10$ GeV/c			
0.6	0.308	0.059	+0.016–0.036	0.385	0.008
1.4	0.303	0.029	+0.031–0.040	0.281	0.003
2.3	0.224	0.015	+0.007–0.028	0.208	0.003
3.3	0.198	0.012	+0.008–0.023	0.165	0.003
4.4	0.155	0.009	+0.007–0.014	0.155	0.005
6.6	0.135	0.008	+0.001–0.001	0.130	0.004

TABLE IX. Centrality dependence of near-side jet widths for various $p_T^a \otimes p_T^b$ bins (Fig. 17).

	$\langle N_{\rm part}\rangle$	Width	Stat. err.	Sys. err.
2–3 $\otimes$ 0.4–1 GeV/c	351.4	0.367	0.012	+0.032–0.043
	299.0	0.415	0.007	+0.033–0.044
	234.6	0.424	0.002	+0.024–0.027
	166.6	0.431	0.002	+0.048–0.041
	114.2	0.438	0.002	+0.048–0.041
	74.4	0.438	0.003	+0.057–0.043
	45.5	0.436	0.004	+0.055–0.030
	14.5	0.435	0.003	+0.059–0.022
	2.0	0.472	0.006	+0.001–0.001
2–3 $\otimes$ 2–3 GeV/c	351.4	0.415	0.005	+0.054–0.047
	299.0	0.409	0.005	+0.035–0.017
	234.6	0.410	0.003	+0.042–0.019
	166.6	0.406	0.008	+0.006–0.028
	114.2	0.360	0.008	+0.013–0.023
	74.4	0.352	0.008	+0.014–0.033
	45.5	0.307	0.005	+0.015–0.037
	14.5	0.289	0.004	+0.006–0.009
	2.0	0.281	0.003	+0.001–0.001
3–4 $\otimes$ 3–4 GeV/c	351.4	0.318	0.019	+0.023–0.032
	299.0	0.287	0.021	+0.021–0.037
	234.6	0.271	0.010	+0.008–0.013
	166.6	0.260	0.010	+0.012–0.012
	114.2	0.225	0.008	+0.015–0.030
	74.4	0.228	0.008	+0.009–0.011
	45.5	0.201	0.008	+0.005–0.026
	14.5	0.211	0.006	+0.004–0.014
	2.0	0.199	0.007	+0.001–0.001
4–5 $\otimes$ 4–5 GeV/c	351.4	0.202	0.020	+0.017–0.000
	299.0	0.191	0.018	+0.009–0.019
	234.6	0.168	0.013	+0.021–0.029
	166.6	0.167	0.010	+0.008–0.019
	114.2	0.142	0.008	+0.004–0.001
	74.4	0.143	0.009	+0.005–0.010
	45.5	0.143	0.011	+0.005–0.016
	14.5	0.161	0.010	+0.001–0.003
	2.0	0.148	0.011	+0.002–0.002
5–10 $\otimes$ 5–10 GeV/c	351.4	0.162	0.017	+0.014–0.034
	299.0	0.135	0.017	+0.001–0.023
	234.6	0.133	0.011	+0.008–0.031
	166.6	0.136	0.009	+0.007–0.009
	114.2	0.131	0.008	+0.002–0.005
	74.4	0.113	0.015	+0.002–0.008
	45.5	0.146	0.016	+0.001–0.004
	14.5	0.137	0.015	+0.002–0.007
	2.0	0.130	0.004	+0.002–0.002

TABLE X. $R_{\rm HS}$ in $p+p$ and 0–20% Au+Au for various p_T^a and p_T^b bins (Fig. 7).

	Au+Au 0–20%				$p+p$	
$\langle p_T^b\rangle$ GeV/c	$R_{\rm HS}$	Stat.	v_2 err.	ZYAM err.	$R_{\rm HS}$	Total err.
			$2.0 < p_T^a < 3.0$ GeV/c			
0.66	0.965	0.008	+0.211–0.236	+0.007–0.000	2.428	+0.007–0.000
1.22	0.722	0.008	+0.180–0.201	+0.038–0.002	2.419	+0.038–0.002

TABLE X. *(Continued.)*

Au+Au 0–20%					$p+p$	
$\langle p_T^b \rangle$ GeV/c	$R_{\rm HS}$	Stat.	v_2 err.	ZYAM err.	$R_{\rm HS}$	Total err.
1.72	0.628	0.010	+0.176–0.196	+0.040–0.005	2.752	+0.040–0.005
2.23	0.531	0.016	+0.178–0.198	+0.051–0.009	2.673	+0.051–0.009
2.73	0.395	0.027	+0.198–0.208	+0.113–0.021	3.234	+0.113–0.021
3.43	0.402	0.044	+0.192–0.198	+0.083–0.035	3.325	+0.083–0.035
4.43	0.581	0.190	+0.278–0.285	+0.076–0.119	4.590	+0.076–0.119
6.42	0.638	0.213	+0.114–0.111	+0.070–0.114	5.438	+0.070–0.114
			$3.0 < p_T^a < 4.0$ GeV/c			
0.66	1.003	0.021	+0.174–0.183	+0.000–0.001	2.553	+0.000–0.001
1.22	0.711	0.023	+0.169–0.180	+0.048–0.007	2.730	+0.048–0.007
1.72	0.550	0.028	+0.166–0.185	+0.044–0.016	3.199	+0.044–0.016
2.23	0.384	0.046	+0.190–0.213	+0.093–0.039	3.418	+0.093–0.039
2.73	0.467	0.088	+0.208–0.200	+0.109–0.065	3.525	+0.109–0.065
3.43	0.531	0.122	+0.166–0.185	+0.059–0.079	4.184	+0.059–0.079
4.43	2.145	1.271	+0.165–0.216	+2.705–0.472	5.528	+2.705–0.472
6.42	2.488	1.216	+0.042–0.048	+2.378–0.567	7.077	+2.378–0.567
			$4.0 < p_T^a < 5.0$ GeV/c			
0.66	1.069	0.057	+0.157–0.164	+0.004–0.006	2.495	+0.004–0.006
1.22	0.971	0.087	+0.181–0.202	+0.003–0.003	3.464	+0.003–0.003
1.72	0.822	0.112	+0.184–0.185	+0.019–0.024	3.109	+0.019–0.024
2.23	0.520	0.179	+0.223–0.207	+0.093–0.132	3.835	+0.093–0.132
2.73	0.443	0.286	+0.225–0.254	+0.146–0.306	6.726	+0.146–0.306
3.43	2.145	1.271	+0.165–0.216	+2.705–0.472	5.528	+2.705–0.472
4.43	1.344	0.565	+0.056–0.060	+0.265–0.104	5.579	+0.265–0.104
6.42	2.489	0.972	+0.008–0.009	+2.250–0.358	9.191	+2.250–0.358
			$5.0 < p_T^a < 10.0$ GeV/c			
0.66	1.339	0.165	+0.169–0.173	+0.050–0.039	3.073	+0.050–0.039
1.22	0.917	0.162	+0.140–0.144	+0.018–0.016	3.884	+0.018–0.016
1.72	0.645	0.219	+0.167–0.198	+0.071–0.117	4.915	+0.071–0.117
2.23	0.649	0.289	+0.141–0.165	+0.086–0.169	5.372	+0.086–0.169
2.73	0.620	0.283	+0.079–0.087	+0.092–0.178	5.525	+0.092–0.178
3.43	2.488	1.216	+0.042–0.048	+2.378–0.567	7.077	+2.378–0.567
4.43	2.489	0.972	+0.008–0.009	+2.250–0.358	9.191	+2.250–0.358
6.42	2.761	1.015	+0.004–0.004	+2.879–0.437	11.159	+2.879–0.437

TABLE XI. Centrality dependence of D from FIT1 and FIT2 (Fig. 10).

	D from FIT1			D from FIT2			Fraction of shoulder yield (FIT2)		
$\langle N_{\rm part} \rangle$	D	Stat. err.	Sys. err.	D	Stat. err.	Sys. err.	Frac	Stat. err.	Sys. err.
351.4	1.068	0.016	+0.032–0.032	1.192	0.024	+0.028–0.028	0.800	0.053	+0.027–0.028
299.0	1.090	0.013	+0.055–0.062	1.208	0.017	+0.028–0.030	0.800	0.044	+0.053–0.059
234.6	1.030	0.010	+0.100–0.120	1.126	0.022	+0.045–0.054	0.842	0.052	+0.108–0.128
166.6	0.976	0.016	+0.110–0.153	0.983	0.035	+0.103–0.036	0.981	0.111	+0.019–0.291
114.2	0.865	0.018	+0.141–0.123	0.930	0.064	+0.091–0.050	0.851	0.246	+0.149–0.253
74.4	0.786	0.030	+0.129–0.116	0.916	0.045	+0.085–0.085	0.750	0.043	+0.250–0.195
45.5	0.652	0.021	+0.074–0.066	0.996	0.029	+0.030–0.030	0.293	0.040	+0.091–0.064
14.5	0.000	0.989	+0.010–0.000	1.178	0.047	+0.050–0.047	0.120	0.029	+0.049–0.032

TABLE XII. Truncated mean p_T, $\langle p'_T \rangle$, for various $\Delta\phi$ ranges and centrality (Fig. 25).

Near-side (GeV/c)				Away-side shoulder (GeV/c)			Away-side head (GeV/c)		
$\langle N_{\text{part}} \rangle$	$\langle p'_T \rangle$	Stat.	Sys.	$\langle p'_T \rangle$	Stat.	Sys.	$\langle p'_T \rangle$	Stat.	Sys.
				$2.0 < p_T^a < 3.0$ GeV/c					
351.4	0.554	0.008	+0.009–0.019	0.445	0.011	+0.001–0.010	0.388	0.017	+0.006–0.017
299.0	0.538	0.007	+0.015–0.022	0.453	0.009	+0.001–0.011	0.379	0.014	+0.014–0.026
234.6	0.530	0.004	+0.025–0.012	0.439	0.006	+0.020–0.004	0.388	0.008	+0.042–0.032
166.6	0.531	0.004	+0.028–0.015	0.449	0.007	+0.018–0.005	0.407	0.008	+0.033–0.042
114.2	0.529	0.005	+0.028–0.020	0.441	0.008	+0.002–0.007	0.426	0.009	+0.005–0.020
74.4	0.549	0.006	+0.028–0.024	0.457	0.012	+0.005–0.011	0.491	0.012	+0.039–0.021
45.5	0.589	0.007	+0.021–0.025	0.503	0.017	+0.000–0.013	0.540	0.013	+0.032–0.027
25.7	0.587	0.009	+0.020–0.019	0.487	0.022	+0.000–0.014	0.557	0.013	+0.030–0.023
9.5	0.600	0.009	+0.011–0.022	0.491	0.025	+0.003–0.023	0.580	0.013	+0.016–0.023
2.0	0.609	0.005	+0.000–0.012	0.543	0.014	+0.000–0.023	0.603	0.008	+0.000–0.012
				$3.0 < p_T^a < 4.0$ GeV/c					
351.4	0.630	0.020	+0.007–0.007	0.446	0.031	+0.018–0.022	0.349	0.054	+0.044–0.060
299.0	0.598	0.017	+0.021–0.017	0.446	0.026	+0.007–0.018	0.388	0.040	+0.021–0.039
234.6	0.590	0.011	+0.038–0.019	0.420	0.018	+0.028–0.013	0.361	0.027	+0.057–0.035
166.6	0.599	0.011	+0.034–0.022	0.439	0.019	+0.009–0.014	0.416	0.022	+0.019–0.040
114.2	0.623	0.011	+0.036–0.031	0.475	0.022	+0.006–0.014	0.495	0.023	+0.030–0.017
74.4	0.646	0.014	+0.034–0.025	0.457	0.029	+0.014–0.021	0.530	0.025	+0.036–0.021
45.5	0.640	0.015	+0.019–0.016	0.435	0.033	+0.011–0.027	0.539	0.024	+0.018–0.017
25.7	0.674	0.018	+0.016–0.016	0.446	0.042	+0.013–0.033	0.582	0.024	+0.015–0.014
9.5	0.725	0.019	+0.010–0.044	0.542	0.054	+0.002–0.045	0.646	0.024	+0.011–0.033
2.0	0.715	0.012	+0.000–0.002	0.595	0.030	+0.002–0.007	0.689	0.016	+0.000–0.001
				$4.0 < p_T^a < 5.0$ GeV/c					
351.4	0.758	0.060	+0.018–0.013	0.533	0.140	+0.045–0.088	0.495	0.156	+0.064–0.146
299.0	0.649	0.039	+0.020–0.017	0.447	0.070	+0.039–0.055	0.381	0.081	+0.058–0.088
234.6	0.698	0.028	+0.022–0.043	0.433	0.058	+0.008–0.047	0.438	0.062	+0.006–0.054
166.6	0.703	0.026	+0.024–0.055	0.449	0.046	+0.002–0.034	0.513	0.055	+0.011–0.034
114.2	0.702	0.026	+0.039–0.029	0.501	0.058	+0.027–0.036	0.609	0.048	+0.064–0.036
74.4	0.717	0.026	+0.036–0.028	0.468	0.055	+0.033–0.040	0.603	0.043	+0.047–0.032
45.5	0.718	0.028	+0.018–0.015	0.485	0.073	+0.039–0.055	0.597	0.042	+0.022–0.021
25.7	0.795	0.034	+0.014–0.022	0.556	0.091	+0.017–0.047	0.693	0.049	+0.016–0.018
9.5	0.827	0.036	+0.017–0.014	0.627	0.109	+0.042–0.049	0.700	0.043	+0.017–0.013
2.0	0.778	0.022	+0.001–0.001	0.672	0.057	+0.005–0.006	0.777	0.030	+0.001–0.001
				$5.0 < p_T^a < 10.0$ GeV/c					
351.4	0.976	0.110	+0.136–0.074	0.640	0.195	+0.018–0.051	0.577	0.162	+0.035–0.085
299.0	0.876	0.092	+0.071–0.042	0.528	0.161	+0.052–0.116	0.536	0.285	+0.081–0.410
234.6	0.754	0.056	+0.040–0.033	0.481	0.109	+0.043–0.083	0.619	0.131	+0.073–0.058
166.6	0.826	0.057	+0.023–0.016	0.356	0.136	+0.102–0.194	0.695	0.167	+0.045–0.028
114.2	0.758	0.045	+0.041–0.031	0.481	0.103	+0.047–0.076	0.722	0.077	+0.069–0.045
74.4	0.839	0.056	+0.031–0.103	0.516	0.161	+0.006–0.131	0.663	0.080	+0.021–0.064
45.5	0.889	0.054	+0.034–0.026	0.654	0.179	+0.014–0.033	0.768	0.072	+0.022–0.017
25.7	0.791	0.059	+0.012–0.013	0.649	0.177	+0.025–0.071	0.749	0.077	+0.015–0.012
9.5	0.871	0.071	+0.021–0.023	0.419	0.142	+0.073–0.135	0.853	0.088	+0.017–0.018
2.0	0.925	0.013	+0.001–0.001	0.720	0.028	+0.004–0.005	0.883	0.015	+0.001–0.001

TABLE XIII. Truncated mean p_T, $\langle p'_T \rangle$, in HR for various $p_T^a \otimes p_T^b$ bins (Fig. 26).

$3.0 < p_T^a < 4.0$ GeV/c				$4.0 < p_T^a < 5.0$ GeV/c		
$\langle N_{\text{part}} \rangle$	$\langle p'_T \rangle$	Stat.	Sys.	$\langle p'_T \rangle$	Stat.	Sys
			$1.0 < p_T^b < 7.0$ GeV/c			
279.9	0.383	0.020	+0.017–0.039	0.448	0.049	+0.034–0.046
140.4	0.469	0.017	+0.010–0.014	0.602	0.042	+0.047–0.044

TABLE XIII. *(Continued.)*

	$3.0 < p_T^a < 4.0$ GeV/c			$4.0 < p_T^a < 5.0$ GeV/c		
$\langle N_{\rm part}\rangle$	$\langle p_T'\rangle$	Stat.	Sys.	$\langle p_T'\rangle$	Stat.	Sys
60.0	0.560	0.018	+0.037–0.020	0.637	0.032	+0.039–0.030
14.5	0.643	0.018	+0.014–0.024	0.794	0.041	+0.030–0.024
2.0	0.732	0.017	+0.000–0.002	0.838	0.032	+0.002–0.002
			$1.5 < p_T^b < 7.0$ GeV/c			
279.9	0.398	0.049	+0.032–0.042	0.559	0.111	+0.044–0.062
140.4	0.525	0.035	+0.071–0.059	0.697	0.073	+0.084–0.059
60.0	0.643	0.033	+0.057–0.040	0.725	0.054	+0.040–0.029
14.5	0.753	0.032	+0.024–0.021	0.917	0.065	+0.031–0.029
2.0	0.827	0.029	+0.002–0.002	0.903	0.053	+0.003–0.003
			$2.0 < p_T^b < 7.0$ GeV/c			
279.9	0.570	0.135	+0.128–0.072	1.026	0.284	+0.240–0.150
140.4	0.722	0.075	+0.285–0.085	0.918	0.127	+0.171–0.093
60.0	0.747	0.054	+0.052–0.043	0.843	0.086	+0.042–0.033
14.5	0.865	0.051	+0.025–0.020	0.989	0.093	+0.024–0.026
2.0	0.869	0.045	+0.004–0.003	0.924	0.079	+0.004–0.004
			$2.5.0 < p_T^b < 7.0$ GeV/c			
279.9	0.675	0.231	+0.078–0.085	1.188	0.354	+0.259–0.140
140.4	0.822	0.107	+0.231–0.095	1.021	0.162	+0.109–0.073
60.0	0.785	0.074	+0.044–0.030	0.884	0.114	+0.027–0.023
14.5	0.939	0.071	+0.018–0.014	1.037	0.124	+0.023–0.019
2.0	0.936	0.066	+0.006–0.005	0.972	0.116	+0.006–0.006
			$3.0 < p_T^b < 7.0$ GeV/c			
279.9	0.750	0.305	+0.082–0.095	0.963	0.260	+0.047–0.037
140.4	0.857	0.121	+0.107–0.062	0.902	0.147	+0.039–0.032
60.0	0.836	0.092	+0.032–0.023	1.085	0.158	+0.035–0.029
14.5	0.932	0.085	+0.008–0.008	1.033	0.150	+0.009–0.008
2.0	0.906	0.083	+0.004–0.003	0.993	0.153	+0.004–0.004

TABLE XIV. Per-trigger yields in NR, HR, and SR and various p_T^b ranges for $2.0 < p_T^a < 3.0$ GeV/c. Theses yields and those in Tables XV–XVII are the bases for Figs. 12–14 and 18–20. The systematic uncertainties due to the single particle efficiency are not included (∼10%).

	p_T^b (GeV/c)	$\int_{\lvert\Delta\phi\rvert<\pi/3,\rm NR} d\Delta\phi(\frac{1}{N^a}\frac{dN^{ab}}{d\Delta\phi})$ Yield±Stat.+Sys.−Sys.	$\int_{\lvert\Delta\phi-\pi\rvert<\pi/6,\rm HR} d\Delta\phi(\frac{1}{N^a}\frac{dN^{ab}}{d\Delta\phi})$ Yield±Stat.+Sys.−Sys.	$\int_{\pi/6<\lvert\Delta\phi-\pi\rvert<\pi/3,\rm SR} d\Delta\phi(\frac{1}{N^a}\frac{dN^{ab}}{d\Delta\phi})$ Yield± Stat.+Sys.−Sys.
0–20%	0.4–1.0	$(2.24 \pm 0.01 + 0.80 - 0.42) \times 10^{-1}$	$(1.20 \pm 0.01 + 0.45 - 0.31) \times 10^{-1}$	$(2.48 \pm 0.01 + 0.68 - 0.05) \times 10^{-1}$
	1.0–1.5	$(9.14 \pm 0.05 + 2.03 - 1.43) \times 10^{-2}$	$(3.47 \pm 0.03 + 1.23 - 1.02) \times 10^{-2}$	$(9.60 \pm 0.06 + 1.54 - 0.24) \times 10^{-2}$
	1.5–2.0	$(4.48 \pm 0.02 + 0.68 - 0.54) \times 10^{-2}$	$(1.18 \pm 0.02 + 0.43 - 0.39) \times 10^{-2}$	$(3.76 \pm 0.03 + 0.46 - 0.10) \times 10^{-2}$
	2.0–2.5	$(1.79 \pm 0.01 + 0.22 - 0.18) \times 10^{-2}$	$(3.25 \pm 0.08 + 1.40 - 1.27) \times 10^{-3}$	$(1.23 \pm 0.02 + 0.15 - 0.04) \times 10^{-2}$
	2.5–3.0	$(6.26 \pm 0.07 + 0.98 - 0.52) \times 10^{-3}$	$(7.07 \pm 0.44 + 5.60 - 3.80) \times 10^{-4}$	$(3.57 \pm 0.09 + 0.83 - 0.13) \times 10^{-3}$
	3.0–4.0	$(3.38 \pm 0.05 + 0.34 - 0.22) \times 10^{-3}$	$(3.14 \pm 0.31 + 2.04 - 1.61) \times 10^{-4}$	$(1.56 \pm 0.07 + 0.25 - 0.09) \times 10^{-3}$
	4.0–5.0	$(5.65 \pm 0.19 + 0.47 - 0.44) \times 10^{-4}$	$(4.41 \pm 1.24 + 2.86 - 2.72) \times 10^{-5}$	$(1.52 \pm 0.26 + 0.34 - 0.34) \times 10^{-4}$
	5.0–7.0	$(1.78 \pm 0.12 + 0.26 - 0.23) \times 10^{-4}$	$(8.83 \pm 8.19 + 14.41 - 12.59) \times 10^{-6}$	$(9.16 \pm 1.67 + 2.28 - 2.22) \times 10^{-5}$
	7.0–10.0	$(1.24 \pm 0.28 + 0.67 - 0.49) \times 10^{-5}$	–	–
20–40%	0.4–1.0	$(2.27 \pm 0.01 + 0.72 - 0.67) \times 10^{-1}$	$(1.12 \pm 0.01 + 0.49 - 0.48) \times 10^{-1}$	$(1.96 \pm 0.01 + 0.34 - 0.11) \times 10^{-1}$
	1.0–1.5	$(8.28 \pm 0.04 + 2.46 - 2.37) \times 10^{-2}$	$(3.14 \pm 0.03 + 1.70 - 1.73) \times 10^{-2}$	$(7.69 \pm 0.06 + 1.12 - 0.39) \times 10^{-2}$
	1.5–2.0	$(3.79 \pm 0.02 + 1.08 - 0.90) \times 10^{-2}$	$(1.05 \pm 0.01 + 0.70 - 0.66) \times 10^{-2}$	$(2.95 \pm 0.03 + 0.70 - 0.15) \times 10^{-2}$
	2.0–2.5	$(1.47 \pm 0.01 + 0.52 - 0.24) \times 10^{-2}$	$(2.90 \pm 0.08 + 2.97 - 1.90) \times 10^{-3}$	$(9.38 \pm 0.16 + 4.41 - 0.20) \times 10^{-3}$
	2.5–3.0	$(5.60 \pm 0.06 + 1.27 - 0.72) \times 10^{-3}$	$(9.27 \pm 0.42 + 7.91 - 5.83) \times 10^{-4}$	$(3.00 \pm 0.09 + 0.93 - 0.12) \times 10^{-3}$
	3.0–4.0	$(3.23 \pm 0.05 + 0.43 - 0.42) \times 10^{-3}$	$(4.87 \pm 0.30 + 3.04 - 3.11) \times 10^{-4}$	$(1.33 \pm 0.06 + 0.12 - 0.11) \times 10^{-3}$
	4.0–5.0	$(6.46 \pm 0.18 + 0.63 - 0.66) \times 10^{-4}$	$(1.06 \pm 0.12 + 0.43 - 0.46) \times 10^{-4}$	$(2.20 \pm 0.24 + 0.32 - 0.32) \times 10^{-4}$

TABLE XIV. *(Continued.)*

	p_T^b (GeV/c)	$\int_{\lvert\Delta\phi\rvert<\pi/3,\mathrm{NR}} d\Delta\phi(\frac{1}{N^a}\frac{dN^{ab}}{d\Delta\phi})$ Yield±Stat.+Sys.−Sys.	$\int_{\lvert\Delta\phi-\pi\rvert<\pi/6,\mathrm{HR}} d\Delta\phi(\frac{1}{N^a}\frac{dN^{ab}}{d\Delta\phi})$ Yield±Stat.+Sys.−Sys.	$\int_{\pi/6<\lvert\Delta\phi-\pi\rvert<\pi/3,\mathrm{SR}} d\Delta\phi(\frac{1}{N^a}\frac{dN^{ab}}{d\Delta\phi})$ Yield± Stat.+Sys.−Sys.
	5.0–7.0	$(2.37 \pm 0.11 + 0.27 - 0.26) \times 10^{-4}$	$(4.54 \pm 0.76 + 1.68 - 1.67) \times 10^{-5}$	$(7.67 \pm 1.50 + 1.98 - 1.96) \times 10^{-5}$
	7.0–10.0	$(2.43 \pm 0.26 + 0.43 - 0.43) \times 10^{-5}$	–	–
40–60%	0.4–1.0	$(1.57 \pm 0.01 + 0.43 - 0.35) \times 10^{-1}$	$(7.52 \pm 0.07 + 2.84 - 2.55) \times 10^{-2}$	$(1.09 \pm 0.01 + 0.19 - 0.06) \times 10^{-1}$
	1.0–1.5	$(5.78 \pm 0.04 + 1.59 - 1.21) \times 10^{-2}$	$(2.24 \pm 0.03 + 1.03 - 0.89) \times 10^{-2}$	$(4.03 \pm 0.06 + 0.92 - 0.21) \times 10^{-2}$
	1.5–2.0	$(2.66 \pm 0.02 + 0.49 - 0.44) \times 10^{-2}$	$(8.80 \pm 0.15 + 3.32 - 3.26) \times 10^{-3}$	$(1.54 \pm 0.03 + 0.29 - 0.08) \times 10^{-2}$
	2.0–2.5	$(1.12 \pm 0.01 + 0.14 - 0.14) \times 10^{-2}$	$(3.43 \pm 0.08 + 1.02 - 1.04) \times 10^{-3}$	$(5.74 \pm 0.15 + 0.42 - 0.31) \times 10^{-3}$
	2.5–3.0	$(4.45 \pm 0.06 + 0.52 - 0.48) \times 10^{-3}$	$(1.27 \pm 0.04 + 0.36 - 0.35) \times 10^{-3}$	$(1.74 \pm 0.08 + 0.19 - 0.14) \times 10^{-3}$
	3.0–4.0	$(2.77 \pm 0.05 + 0.24 - 0.22) \times 10^{-3}$	$(8.14 \pm 0.31 + 1.64 - 1.60) \times 10^{-4}$	$(9.52 \pm 0.61 + 1.01 - 0.86) \times 10^{-4}$
	4.0–5.0	$(6.79 \pm 0.19 + 0.46 - 0.48) \times 10^{-4}$	$(2.04 \pm 0.13 + 0.29 - 0.30) \times 10^{-4}$	$(2.08 \pm 0.24 + 0.33 - 0.33) \times 10^{-4}$
	5.0–7.0	$(2.86 \pm 0.12 + 0.25 - 0.25) \times 10^{-4}$	$(1.05 \pm 0.08 + 0.14 - 0.15) \times 10^{-4}$	$(6.83 \pm 1.55 + 2.10 - 2.11) \times 10^{-5}$
	7.0–10.0	$(2.62 \pm 0.31 + 0.48 - 0.47) \times 10^{-5}$	–	–
60–92%	0.4–1.0	$(1.15 \pm 0.01 + 0.18 - 0.17) \times 10^{-1}$	$(6.03 \pm 0.07 + 1.17 - 1.15) \times 10^{-2}$	$(6.27 \pm 0.12 + 1.08 - 0.50) \times 10^{-2}$
	1.0–1.5	$(4.28 \pm 0.04 + 0.66 - 0.49) \times 10^{-2}$	$(1.99 \pm 0.03 + 0.40 - 0.36) \times 10^{-2}$	$(2.29 \pm 0.05 + 0.49 - 0.11) \times 10^{-2}$
	1.5–2.0	$(1.94 \pm 0.02 + 0.19 - 0.18) \times 10^{-2}$	$(8.25 \pm 0.15 + 1.31 - 1.28) \times 10^{-3}$	$(8.72 \pm 0.29 + 0.74 - 0.47) \times 10^{-3}$
	2.0–2.5	$(8.45 \pm 0.12 + 0.53 - 0.57) \times 10^{-3}$	$(3.65 \pm 0.08 + 0.37 - 0.41) \times 10^{-3}$	$(3.44 \pm 0.15 + 0.26 - 0.21) \times 10^{-3}$
	2.5–3.0	$(3.63 \pm 0.07 + 0.23 - 0.26) \times 10^{-3}$	$(1.48 \pm 0.04 + 0.15 - 0.17) \times 10^{-3}$	$(1.12 \pm 0.08 + 0.12 - 0.13) \times 10^{-3}$
	3.0–4.0	$(2.52 \pm 0.05 + 0.14 - 0.15) \times 10^{-3}$	$(9.76 \pm 0.35 + 0.87 - 0.97) \times 10^{-4}$	$(5.75 \pm 0.64 + 0.91 - 0.93) \times 10^{-4}$
	4.0–5.0	$(6.63 \pm 0.23 + 0.44 - 0.46) \times 10^{-4}$	$(2.63 \pm 0.16 + 0.25 - 0.28) \times 10^{-4}$	$(1.25 \pm 0.27 + 0.36 - 0.36) \times 10^{-4}$
	5.0–7.0	$(3.35 \pm 0.16 + 0.21 - 0.21) \times 10^{-4}$	$(1.79 \pm 0.11 + 0.11 - 0.11) \times 10^{-4}$	$(1.17 \pm 0.18 + 0.22 - 0.21) \times 10^{-4}$
	7.0–10.0	$(2.90 \pm 0.41 + 0.55 - 0.55) \times 10^{-5}$	–	–
$p+p$	0.4–1.0	$(1.02 \pm 0.01 + 0.15 - 0.01) \times 10^{-1}$	$(6.24 \pm 0.05 + 0.77 - 0.05) \times 10^{-2}$	$(5.14 \pm 0.08 + 1.55 - 0.10) \times 10^{-2}$
	1.0–1.5	$(4.00 \pm 0.03 + 0.28 - 0.04) \times 10^{-2}$	$(2.04 \pm 0.02 + 0.14 - 0.02) \times 10^{-2}$	$(1.69 \pm 0.03 + 0.28 - 0.04) \times 10^{-2}$
	1.5–2.0	$(1.78 \pm 0.02 + 0.04 - 0.02) \times 10^{-2}$	$(8.64 \pm 0.11 + 0.18 - 0.10) \times 10^{-3}$	$(6.28 \pm 0.17 + 0.36 - 0.20) \times 10^{-3}$
	2.0–2.5	$(8.20 \pm 0.09 + 0.10 - 0.10) \times 10^{-3}$	$(3.81 \pm 0.06 + 0.05 - 0.05) \times 10^{-3}$	$(2.85 \pm 0.09 + 0.10 - 0.10) \times 10^{-3}$
	2.5–3.0	$(3.54 \pm 0.06 + 0.06 - 0.06) \times 10^{-3}$	$(1.71 \pm 0.04 + 0.03 - 0.03) \times 10^{-3}$	$(1.06 \pm 0.06 + 0.06 - 0.06) \times 10^{-3}$
	3.0–4.0	$(2.64 \pm 0.05 + 0.04 - 0.04) \times 10^{-3}$	$(1.33 \pm 0.03 + 0.02 - 0.02) \times 10^{-3}$	$(7.99 \pm 0.43 + 0.43 - 0.43) \times 10^{-4}$
	4.0–5.0	$(6.94 \pm 0.22 + 0.17 - 0.17) \times 10^{-4}$	$(4.17 \pm 0.17 + 0.08 - 0.08) \times 10^{-4}$	$(1.81 \pm 0.18 + 0.17 - 0.17) \times 10^{-4}$
	5.0–7.0	$(3.64 \pm 0.16 + 0.10 - 0.10) \times 10^{-4}$	$(2.23 \pm 0.13 + 0.05 - 0.05) \times 10^{-4}$	$(7.22 \pm 1.12 + 0.96 - 0.96) \times 10^{-5}$
	7.0–10.0	$(3.76 \pm 0.52 + 0.17 - 0.17) \times 10^{-5}$	–	–

TABLE XV. Same as Table XIV, but for $3.0 < p_T^a < 4.0$ GeV/c.

	p_T^b (GeV/c)	$\int_{\lvert\Delta\phi\rvert<\pi/3,\mathrm{NR}} d\Delta\phi(\frac{1}{N^a}\frac{dN^{ab}}{d\Delta\phi})$ Yield±Stat.+Sys.−Sys.	$\int_{\lvert\Delta\phi-\pi\rvert<\pi/6,\mathrm{HR}} d\Delta\phi(\frac{1}{N^a}\frac{dN^{ab}}{d\Delta\phi})$ Yield±Stat.+Sys.−Sys.	$\int_{\pi/6<\lvert\Delta\phi-\pi\rvert<\pi/3,\mathrm{SR}} d\Delta\phi(\frac{1}{N^a}\frac{dN^{ab}}{d\Delta\phi})$ Yield±Stat.+Sys.−Sys.
0–20%	0.4–1.0	$(2.45 \pm 0.04 + 0.98 - 0.31) \times 10^{-1}$	$(1.62 \pm 0.02 + 0.54 - 0.26) \times 10^{-1}$	$(3.23 \pm 0.05 + 0.89 - 0.08) \times 10^{-1}$
	1.0–1.5	$(1.09 \pm 0.02 + 0.26 - 0.14) \times 10^{-1}$	$(3.90 \pm 0.10 + 1.51 - 1.02) \times 10^{-2}$	$(1.10 \pm 0.02 + 0.22 - 0.03) \times 10^{-1}$
	1.5–2.0	$(5.98 \pm 0.08 + 0.72 - 0.60) \times 10^{-2}$	$(1.19 \pm 0.05 + 0.46 - 0.42) \times 10^{-2}$	$(4.32 \pm 0.11 + 0.48 - 0.17) \times 10^{-2}$
	2.0–2.5	$(2.52 \pm 0.04 + 0.28 - 0.20) \times 10^{-2}$	$(2.40 \pm 0.27 + 1.68 - 1.40) \times 10^{-3}$	$(1.25 \pm 0.06 + 0.22 - 0.08) \times 10^{-2}$
	2.5–3.0	$(9.96 \pm 0.22 + 1.09 - 0.59) \times 10^{-3}$	$(8.44 \pm 1.43 + 6.18 - 4.04) \times 10^{-4}$	$(3.62 \pm 0.30 + 0.94 - 0.40) \times 10^{-3}$
	3.0–4.0	$(6.71 \pm 0.16 + 0.36 - 0.37) \times 10^{-3}$	$(5.07 \pm 1.02 + 2.20 - 2.29) \times 10^{-4}$	$(1.91 \pm 0.21 + 0.28 - 0.28) \times 10^{-3}$
	4.0–5.0	$(1.49 \pm 0.06 + 0.12 - 0.12) \times 10^{-3}$	$(1.65 \pm 0.40 + 0.62 - 0.63) \times 10^{-4}$	$(1.54 \pm 0.83 + 1.09 - 1.09) \times 10^{-4}$
	5.0–7.0	$(6.45 \pm 0.42 + 0.75 - 0.75) \times 10^{-4}$	$(6.18 \pm 2.70 + 3.82 - 3.85) \times 10^{-5}$	$(3.51 \pm 5.43 + 7.28 - 7.28) \times 10^{-5}$
	7.0–10.0	$(1.03 \pm 0.10 + 0.16 - 0.16) \times 10^{-4}$	–	–
20–40%	0.4–1.0	$(2.53 \pm 0.03 + 0.85 - 0.65) \times 10^{-1}$	$(1.58 \pm 0.02 + 0.54 - 0.48) \times 10^{-1}$	$(2.61 \pm 0.04 + 0.56 - 0.09) \times 10^{-1}$
	1.0–1.5	$(9.94 \pm 0.13 + 2.78 - 2.44) \times 10^{-2}$	$(3.83 \pm 0.09 + 1.84 - 1.78) \times 10^{-2}$	$(8.70 \pm 0.18 + 1.63 - 0.45) \times 10^{-2}$
	1.5–2.0	$(5.19 \pm 0.07 + 1.40 - 0.87) \times 10^{-2}$	$(1.34 \pm 0.05 + 0.84 - 0.65) \times 10^{-2}$	$(3.59 \pm 0.09 + 1.11 - 0.16) \times 10^{-2}$
	2.0–2.5	$(2.17 \pm 0.04 + 0.29 - 0.31) \times 10^{-2}$	$(3.48 \pm 0.24 + 2.09 - 2.25) \times 10^{-3}$	$(1.01 \pm 0.05 + 0.08 - 0.08) \times 10^{-2}$
	2.5–3.0	$(9.74 \pm 0.20 + 1.15 - 1.22) \times 10^{-3}$	$(1.44 \pm 0.13 + 0.78 - 0.84) \times 10^{-3}$	$(3.24 \pm 0.26 + 0.48 - 0.49) \times 10^{-3}$
	3.0–4.0	$(6.81 \pm 0.15 + 0.54 - 0.57) \times 10^{-3}$	$(1.14 \pm 0.09 + 0.36 - 0.38) \times 10^{-3}$	$(1.95 \pm 0.19 + 0.28 - 0.29) \times 10^{-3}$
	4.0–5.0	$(1.64 \pm 0.06 + 0.11 - 0.11) \times 10^{-3}$	$(3.34 \pm 0.38 + 0.63 - 0.65) \times 10^{-4}$	$(2.87 \pm 0.74 + 0.95 - 0.95) \times 10^{-4}$

TABLE XV. *(Continued.)*

	p_T^b (GeV/c)	$\int_{\lvert\Delta\phi\rvert<\pi/3,\mathrm{NR}} d\Delta\phi(\frac{1}{N^a}\frac{dN^{ab}}{d\Delta\phi})$ Yield±Stat.+Sys.−Sys.	$\int_{\lvert\Delta\phi-\pi\rvert<\pi/6,\mathrm{HR}} d\Delta\phi(\frac{1}{N^a}\frac{dN^{ab}}{d\Delta\phi})$ Yield±Stat.+Sys.−Sys.	$\int_{\pi/6<\lvert\Delta\phi-\pi\rvert<\pi/3,\mathrm{SR}} d\Delta\phi(\frac{1}{N^a}\frac{dN^{ab}}{d\Delta\phi})$ Yield±Stat.+Sys.−Sys.
	5.0–7.0	$(9.23 \pm 0.38 + 0.64 - 0.64) \times 10^{-4}$	$(2.46 \pm 0.24 + 0.33 - 0.34) \times 10^{-4}$	$(1.95 \pm 0.46 + 0.60 - 0.60) \times 10^{-4}$
	7.0–10.0	$(8.37 \pm 0.94 + 1.38 - 1.38) \times 10^{-5}$	–	–
40–60%	0.4–1.0	$(1.92 \pm 0.03 + 0.42 - 0.35) \times 10^{-1}$	$(1.19 \pm 0.02 + 0.27 - 0.25) \times 10^{-1}$	$(1.68 \pm 0.04 + 0.27 - 0.07) \times 10^{-1}$
	1.0–1.5	$(7.55 \pm 0.12 + 1.28 - 1.22) \times 10^{-2}$	$(3.33 \pm 0.08 + 0.88 - 0.89) \times 10^{-2}$	$(5.51 \pm 0.16 + 0.65 - 0.29) \times 10^{-2}$
	1.5–2.0	$(3.77 \pm 0.07 + 0.51 - 0.45) \times 10^{-2}$	$(1.23 \pm 0.04 + 0.35 - 0.33) \times 10^{-2}$	$(1.85 \pm 0.09 + 0.23 - 0.13) \times 10^{-2}$
	2.0–2.5	$(1.53 \pm 0.03 + 0.17 - 0.14) \times 10^{-2}$	$(4.58 \pm 0.23 + 1.13 - 1.01) \times 10^{-3}$	$(5.31 \pm 0.45 + 0.75 - 0.59) \times 10^{-3}$
	2.5–3.0	$(8.39 \pm 0.19 + 0.60 - 0.63) \times 10^{-3}$	$(2.29 \pm 0.13 + 0.39 - 0.42) \times 10^{-3}$	$(2.47 \pm 0.25 + 0.35 - 0.36) \times 10^{-3}$
	3.0–4.0	$(6.41 \pm 0.15 + 0.34 - 0.35) \times 10^{-3}$	$(1.71 \pm 0.10 + 0.21 - 0.21) \times 10^{-3}$	$(1.63 \pm 0.18 + 0.25 - 0.25) \times 10^{-3}$
	4.0–5.0	$(1.85 \pm 0.06 + 0.10 - 0.11) \times 10^{-3}$	$(4.38 \pm 0.40 + 0.55 - 0.56) \times 10^{-4}$	$(2.47 \pm 0.73 + 0.98 - 0.98) \times 10^{-4}$
	5.0–7.0	$(8.94 \pm 0.44 + 0.76 - 0.62) \times 10^{-4}$	$(3.37 \pm 0.29 + 0.38 - 0.32) \times 10^{-4}$	$(9.01 \pm 4.82 + 7.43 - 6.20) \times 10^{-5}$
	7.0–10.0	$(1.16 \pm 0.12 + 0.11 - 0.11) \times 10^{-4}$	–	–
60–92%	0.4–1.0	$(1.37 \pm 0.03 + 0.28 - 0.16) \times 10^{-1}$	$(8.92 \pm 0.19 + 1.54 - 1.11) \times 10^{-2}$	$(9.12 \pm 0.36 + 2.42 - 0.53) \times 10^{-2}$
	1.0–1.5	$(6.04 \pm 0.12 + 1.01 - 0.47) \times 10^{-2}$	$(3.38 \pm 0.08 + 0.56 - 0.35) \times 10^{-2}$	$(3.58 \pm 0.16 + 0.91 - 0.20) \times 10^{-2}$
	1.5–2.0	$(2.91 \pm 0.06 + 0.22 - 0.21) \times 10^{-2}$	$(1.32 \pm 0.04 + 0.15 - 0.15) \times 10^{-2}$	$(1.13 \pm 0.08 + 0.13 - 0.11) \times 10^{-2}$
	2.0–2.5	$(1.40 \pm 0.04 + 0.09 - 0.09) \times 10^{-2}$	$(5.61 \pm 0.24 + 0.54 - 0.58) \times 10^{-3}$	$(3.77 \pm 0.44 + 0.60 - 0.59) \times 10^{-3}$
	2.5–3.0	$(6.90 \pm 0.21 + 0.40 - 0.42) \times 10^{-3}$	$(2.63 \pm 0.14 + 0.23 - 0.25) \times 10^{-3}$	$(1.42 \pm 0.25 + 0.32 - 0.33) \times 10^{-3}$
	3.0–4.0	$(6.11 \pm 0.17 + 0.25 - 0.26) \times 10^{-3}$	$(2.56 \pm 0.12 + 0.14 - 0.14) \times 10^{-3}$	$(1.18 \pm 0.18 + 0.23 - 0.23) \times 10^{-3}$
	4.0–5.0	$(2.11 \pm 0.09 + 0.09 - 0.10) \times 10^{-3}$	$(7.84 \pm 0.56 + 0.49 - 0.50) \times 10^{-4}$	$(3.02 \pm 0.74 + 0.92 - 0.92) \times 10^{-4}$
	5.0–7.0	$(1.16 \pm 0.07 + 0.07 - 0.07) \times 10^{-3}$	$(6.24 \pm 0.48 + 0.35 - 0.36) \times 10^{-4}$	$(1.31 \pm 0.50 + 0.69 - 0.69) \times 10^{-4}$
	7.0–10.0	$(6.14 \pm 1.86 + 2.90 - 2.90) \times 10^{-5}$	–	–
$p+p$	0.4–1.0	$(1.26 \pm 0.02 + 0.12 - 0.03) \times 10^{-1}$	$(9.18 \pm 0.14 + 0.61 - 0.14) \times 10^{-2}$	$(7.19 \pm 0.22 + 1.22 - 0.29) \times 10^{-2}$
	1.0–1.5	$(5.74 \pm 0.08 + 0.16 - 0.11) \times 10^{-2}$	$(3.46 \pm 0.06 + 0.08 - 0.05) \times 10^{-2}$	$(2.53 \pm 0.09 + 0.16 - 0.11) \times 10^{-2}$
	1.5–2.0	$(2.88 \pm 0.05 + 0.06 - 0.06) \times 10^{-2}$	$(1.45 \pm 0.04 + 0.03 - 0.03) \times 10^{-2}$	$(9.08 \pm 0.52 + 0.60 - 0.58) \times 10^{-3}$
	2.0–2.5	$(1.49 \pm 0.03 + 0.03 - 0.03) \times 10^{-2}$	$(7.73 \pm 0.24 + 0.16 - 0.16) \times 10^{-3}$	$(4.52 \pm 0.31 + 0.31 - 0.31) \times 10^{-3}$
	2.5–3.0	$(7.59 \pm 0.21 + 0.18 - 0.18) \times 10^{-3}$	$(3.53 \pm 0.15 + 0.09 - 0.09) \times 10^{-3}$	$(2.00 \pm 0.18 + 0.18 - 0.18) \times 10^{-3}$
	3.0–4.0	$(6.35 \pm 0.18 + 0.13 - 0.13) \times 10^{-3}$	$(3.64 \pm 0.14 + 0.06 - 0.06) \times 10^{-3}$	$(1.74 \pm 0.15 + 0.13 - 0.13) \times 10^{-3}$
	4.0–5.0	$(1.76 \pm 0.09 + 0.02 - 0.02) \times 10^{-3}$	$(1.16 \pm 0.08 + 0.01 - 0.01) \times 10^{-3}$	$(4.20 \pm 0.70 + 0.16 - 0.16) \times 10^{-4}$
	5.0–7.0	$(1.15 \pm 0.08 + 0.01 - 0.01) \times 10^{-3}$	$(7.15 \pm 0.65 + 0.05 - 0.05) \times 10^{-4}$	$(1.88 \pm 0.44 + 0.10 - 0.10) \times 10^{-4}$
	7.0–10.0	$(1.15 \pm 0.26 + 0.03 - 0.03) \times 10^{-4}$	–	–

TABLE XVI. Same as Table XIV, but for $4.0 < p_T^a < 5.0$ GeV/c.

	p_T^b (GeV/c)	$\int_{\lvert\Delta\phi\rvert<\pi/3,\mathrm{NR}} d\Delta\phi(\frac{1}{N^a}\frac{dN^{ab}}{d\Delta\phi})$ Yield±Stat.+Sys.−Sys.	$\int_{\lvert\Delta\phi-\pi\rvert<\pi/6,\mathrm{HR}} d\Delta\phi(\frac{1}{N^a}\frac{dN^{ab}}{d\Delta\phi})$ Yield±Stat.+Sys.−Sys.	$\int_{\pi/6<\lvert\Delta\phi-\pi\rvert<\pi/3,\mathrm{SR}} d\Delta\phi(\frac{1}{N^a}\frac{dN^{ab}}{d\Delta\phi})$ Yield±Stat.+Sys.−Sys.
0–20%	0.4–1.0	$(2.50 \pm 0.11 + 0.48 - 0.36) \times 10^{-1}$	$(1.96 \pm 0.07 + 0.32 - 0.27) \times 10^{-1}$	$(3.66 \pm 0.14 + 0.33 - 0.19) \times 10^{-1}$
	1.0–1.5	$(1.19 \pm 0.05 + 0.17 - 0.17) \times 10^{-1}$	$(4.84 \pm 0.31 + 1.14 - 1.17) \times 10^{-2}$	$(9.97 \pm 0.63 + 1.03 - 0.87) \times 10^{-2}$
	1.5–2.0	$(6.58 \pm 0.24 + 0.66 - 0.58) \times 10^{-2}$	$(1.55 \pm 0.16 + 0.43 - 0.38) \times 10^{-2}$	$(3.76 \pm 0.34 + 0.46 - 0.44) \times 10^{-2}$
	2.0–2.5	$(3.09 \pm 0.12 + 0.30 - 0.25) \times 10^{-2}$	$(2.70 \pm 0.81 + 1.76 - 1.51) \times 10^{-3}$	$(1.04 \pm 0.17 + 0.25 - 0.22) \times 10^{-2}$
	2.5–3.0	$(1.42 \pm 0.07 + 0.13 - 0.13) \times 10^{-2}$	$(7.43 \pm 4.34 + 7.21 - 7.37) \times 10^{-4}$	$(3.35 \pm 0.92 + 1.19 - 1.19) \times 10^{-3}$
	3.0–4.0	$(1.25 \pm 0.05 + 0.09 - 0.09) \times 10^{-2}$	$(1.72 \pm 0.31 + 0.47 - 0.48) \times 10^{-3}$	$(1.76 \pm 0.63 + 0.84 - 0.84) \times 10^{-3}$
	4.0–5.0	$(3.63 \pm 0.20 + 0.33 - 0.33) \times 10^{-3}$	$(5.04 \pm 1.24 + 1.65 - 1.65) \times 10^{-4}$	$(7.50 \pm 2.55 + 3.26 - 3.26) \times 10^{-4}$
	5.0–7.0	$(2.35 \pm 0.13 + 0.22 - 0.22) \times 10^{-3}$	$(5.18 \pm 0.85 + 1.09 - 1.09) \times 10^{-4}$	$(4.59 \pm 1.64 + 2.16 - 2.16) \times 10^{-4}$
	7.0–10.0	$(2.63 \pm 0.35 + 0.46 - 0.46) \times 10^{-4}$	–	–
20–40%	0.4–1.0	$(2.27 \pm 0.08 + 1.03 - 0.45) \times 10^{-1}$	$(1.64 \pm 0.06 + 0.60 - 0.36) \times 10^{-1}$	$(2.80 \pm 0.11 + 0.84 - 0.17) \times 10^{-1}$
	1.0–1.5	$(1.03 \pm 0.04 + 0.26 - 0.16) \times 10^{-1}$	$(3.86 \pm 0.24 + 1.70 - 1.29) \times 10^{-2}$	$(9.10 \pm 0.48 + 1.58 - 0.71) \times 10^{-2}$
	1.5–2.0	$(5.59 \pm 0.19 + 0.97 - 0.66) \times 10^{-2}$	$(1.59 \pm 0.13 + 0.63 - 0.51) \times 10^{-2}$	$(3.33 \pm 0.26 + 0.66 - 0.34) \times 10^{-2}$
	2.0–2.5	$(2.80 \pm 0.10 + 0.31 - 0.33) \times 10^{-2}$	$(5.10 \pm 0.65 + 2.08 - 2.21) \times 10^{-3}$	$(1.01 \pm 0.13 + 0.18 - 0.18) \times 10^{-2}$
	2.5–3.0	$(1.36 \pm 0.05 + 0.12 - 0.13) \times 10^{-2}$	$(1.95 \pm 0.35 + 0.77 - 0.80) \times 10^{-3}$	$(3.69 \pm 0.72 + 0.94 - 0.94) \times 10^{-3}$
	3.0–4.0	$(1.20 \pm 0.04 + 0.08 - 0.08) \times 10^{-2}$	$(2.51 \pm 0.26 + 0.47 - 0.48) \times 10^{-3}$	$(2.78 \pm 0.51 + 0.69 - 0.69) \times 10^{-3}$
	4.0–5.0	$(4.12 \pm 0.17 + 0.26 - 0.26) \times 10^{-3}$	$(1.31 \pm 0.11 + 0.14 - 0.14) \times 10^{-3}$	$(9.06 \pm 2.02 + 2.57 - 2.57) \times 10^{-4}$

TABLE XVI. *(Continued.)*

	p_T^b (GeV/c)	$\int_{\lvert\Delta\phi\rvert<\pi/3,\mathrm{NR}} d\Delta\phi(\frac{1}{N^a}\frac{dN^{ab}}{d\Delta\phi})$ Yield±Stat.+Sys.−Sys.	$\int_{\lvert\Delta\phi-\pi\rvert<\pi/6,\mathrm{HR}} d\Delta\phi(\frac{1}{N^a}\frac{dN^{ab}}{d\Delta\phi})$ Yield±Stat.+Sys.−Sys.	$\int_{\pi/6<\lvert\Delta\phi-\pi\rvert<\pi/3,\mathrm{SR}} d\Delta\phi(\frac{1}{N^a}\frac{dN^{ab}}{d\Delta\phi})$ Yield±Stat.+Sys.−Sys.
	5.0–7.0	$(2.16 \pm 0.12 + 0.18 - 0.18) \times 10^{-3}$	$(4.57 \pm 0.75 + 0.91 - 0.91) \times 10^{-4}$	$< 2.4 \times 10^{-4}$
	7.0–10.0	$(2.75 \pm 0.34 + 0.18 - 0.18) \times 10^{-4}$	–	–
40–60%	0.4–1.0	$(2.06 \pm 0.07 + 0.54 - 0.34) \times 10^{-1}$	$(1.43 \pm 0.05 + 0.31 - 0.23) \times 10^{-1}$	$(1.83 \pm 0.09 + 0.46 - 0.13) \times 10^{-1}$
	1.0–1.5	$(9.80 \pm 0.32 + 1.36 - 1.36) \times 10^{-2}$	$(4.63 \pm 0.21 + 0.90 - 0.92) \times 10^{-2}$	$(6.99 \pm 0.42 + 0.68 - 0.65) \times 10^{-2}$
	1.5–2.0	$(5.18 \pm 0.17 + 0.46 - 0.49) \times 10^{-2}$	$(1.90 \pm 0.11 + 0.30 - 0.32) \times 10^{-2}$	$(2.41 \pm 0.22 + 0.30 - 0.30) \times 10^{-2}$
	2.0–2.5	$(2.44 \pm 0.09 + 0.21 - 0.21) \times 10^{-2}$	$(7.52 \pm 0.59 + 1.23 - 1.30) \times 10^{-3}$	$(8.59 \pm 1.17 + 1.56 - 1.57) \times 10^{-3}$
	2.5–3.0	$(1.47 \pm 0.05 + 0.09 - 0.10) \times 10^{-2}$	$(4.59 \pm 0.34 + 0.52 - 0.54) \times 10^{-3}$	$(3.79 \pm 0.64 + 0.83 - 0.83) \times 10^{-3}$
	3.0–4.0	$(1.08 \pm 0.04 + 0.07 - 0.07) \times 10^{-2}$	$(2.43 \pm 0.26 + 0.36 - 0.36) \times 10^{-3}$	$(9.42 \pm 4.72 + 6.40 - 6.41) \times 10^{-4}$
	4.0–5.0	$(3.31 \pm 0.18 + 0.26 - 0.25) \times 10^{-3}$	$(1.21 \pm 0.12 + 0.13 - 0.13) \times 10^{-3}$	$(5.53 \pm 1.90 + 2.62 - 2.52) \times 10^{-4}$
	5.0–7.0	$(2.41 \pm 0.14 + 0.14 - 0.14) \times 10^{-3}$	$(8.88 \pm 0.95 + 0.69 - 0.69) \times 10^{-4}$	$(3.75 \pm 1.33 + 1.36 - 1.36) \times 10^{-4}$
	7.0–10.0	$(1.97 \pm 0.43 + 0.43 - 0.43) \times 10^{-4}$	–	–
60–92%	0.4–1.0	$(1.38 \pm 0.07 + 0.52 - 0.24) \times 10^{-1}$	$(1.06 \pm 0.05 + 0.28 - 0.16) \times 10^{-1}$	$(9.05 \pm 0.89 + 4.79 - 1.23) \times 10^{-2}$
	1.0–1.5	$(6.25 \pm 0.30 + 0.77 - 0.70) \times 10^{-2}$	$(3.76 \pm 0.21 + 0.49 - 0.48) \times 10^{-2}$	$(3.28 \pm 0.39 + 0.60 - 0.51) \times 10^{-2}$
	1.5–2.0	$(3.91 \pm 0.17 + 0.34 - 0.32) \times 10^{-2}$	$(1.61 \pm 0.11 + 0.21 - 0.20) \times 10^{-2}$	$(1.43 \pm 0.21 + 0.28 - 0.27) \times 10^{-2}$
	2.0–2.5	$(1.96 \pm 0.09 + 0.17 - 0.15) \times 10^{-2}$	$(8.35 \pm 0.63 + 0.94 - 0.86) \times 10^{-3}$	$(4.30 \pm 1.10 + 1.43 - 1.40) \times 10^{-3}$
	2.5–3.0	$(1.15 \pm 0.06 + 0.09 - 0.09) \times 10^{-2}$	$(4.51 \pm 0.39 + 0.46 - 0.49) \times 10^{-3}$	$(2.32 \pm 0.65 + 0.82 - 0.82) \times 10^{-3}$
	3.0–4.0	$(1.23 \pm 0.05 + 0.06 - 0.06) \times 10^{-2}$	$(4.62 \pm 0.34 + 0.29 - 0.30) \times 10^{-3}$	$(1.90 \pm 0.45 + 0.55 - 0.55) \times 10^{-3}$
	4.0–5.0	$(3.84 \pm 0.27 + 0.24 - 0.23) \times 10^{-3}$	$(1.54 \pm 0.18 + 0.12 - 0.11) \times 10^{-3}$	$(6.30 \pm 2.14 + 2.36 - 2.28) \times 10^{-4}$
	5.0–7.0	$(2.33 \pm 0.22 + 0.14 - 0.14) \times 10^{-3}$	$(1.44 \pm 0.18 + 0.07 - 0.07) \times 10^{-3}$	$(1.35 \pm 1.32 + 1.37 - 1.37) \times 10^{-4}$
	7.0–10.0	$(2.85 \pm 0.83 + 0.27 - 0.27) \times 10^{-4}$	–	–
$p+p$	0.4–1.0	$(1.67 \pm 0.05 + 0.16 - 0.07) \times 10^{-1}$	$(1.21 \pm 0.03 + 0.08 - 0.03) \times 10^{-1}$	$(9.66 \pm 0.52 + 1.62 - 0.65) \times 10^{-2}$
	1.0–1.5	$(7.94 \pm 0.21 + 0.25 - 0.25) \times 10^{-2}$	$(4.83 \pm 0.16 + 0.12 - 0.12) \times 10^{-2}$	$(2.79 \pm 0.22 + 0.25 - 0.25) \times 10^{-2}$
	1.5–2.0	$(4.16 \pm 0.13 + 0.13 - 0.13) \times 10^{-2}$	$(2.34 \pm 0.10 + 0.06 - 0.06) \times 10^{-2}$	$(1.50 \pm 0.12 + 0.13 - 0.13) \times 10^{-2}$
	2.0–2.5	$(2.21 \pm 0.09 + 0.06 - 0.06) \times 10^{-2}$	$(1.36 \pm 0.07 + 0.03 - 0.03) \times 10^{-2}$	$(7.09 \pm 0.76 + 0.65 - 0.65) \times 10^{-3}$
	2.5–3.0	$(1.16 \pm 0.06 + 0.04 - 0.04) \times 10^{-2}$	$(7.13 \pm 0.48 + 0.21 - 0.21) \times 10^{-3}$	$(2.12 \pm 0.41 + 0.41 - 0.41) \times 10^{-3}$
	3.0–4.0	$(1.05 \pm 0.05 + 0.03 - 0.03) \times 10^{-2}$	$(6.29 \pm 0.44 + 0.13 - 0.13) \times 10^{-3}$	$(2.46 \pm 0.41 + 0.27 - 0.27) \times 10^{-3}$
	4.0–5.0	$(4.30 \pm 0.33 + 0.07 - 0.07) \times 10^{-3}$	$(2.53 \pm 0.27 + 0.04 - 0.04) \times 10^{-3}$	$(9.06 \pm 1.99 + 0.73 - 0.73) \times 10^{-4}$
	5.0–7.0	$(2.39 \pm 0.28 + 0.03 - 0.03) \times 10^{-3}$	$(1.55 \pm 0.24 + 0.01 - 0.01) \times 10^{-3}$	$(4.20 \pm 1.29 + 0.29 - 0.29) \times 10^{-4}$
	7.0–10.0	$(2.29 \pm 1.06 + 0.03 - 0.03) \times 10^{-4}$	–	–

TABLE XVII. Same as Table XIV, but for $5.0 < p_T^a < 10.0$ GeV/c.

	p_T^b (GeV/c)	$\int_{\lvert\Delta\phi\rvert<\pi/3,\mathrm{NR}} d\Delta\phi(\frac{1}{N^a}\frac{dN^{ab}}{d\Delta\phi})$ Yield±Stat.+Sys.−Sys.	$\int_{\lvert\Delta\phi-\pi\rvert<\pi/6,\mathrm{HR}} d\Delta\phi(\frac{1}{N^a}\frac{dN^{ab}}{d\Delta\phi})$ Yield±Stat.+Sys.−Sys.	$\int_{\pi/6<\lvert\Delta\phi-\pi\rvert<\pi/3,\mathrm{SR}} d\Delta\phi(\frac{1}{N^a}\frac{dN^{ab}}{d\Delta\phi})$ Yield±Stat.+Sys.−Sys.
0–20%	0.4–1.0	$(2.04 \pm 0.25 + 0.51 - 0.52) \times 10^{-1}$	$(2.25 \pm 0.17 + 0.31 - 0.32) \times 10^{-1}$	$(3.36 \pm 0.32 + 0.45 - 0.45) \times 10^{-1}$
	1.0–1.5	$(1.17 \pm 0.11 + 0.35 - 0.21) \times 10^{-1}$	$(5.59 \pm 0.72 + 1.85 - 1.24) \times 10^{-2}$	$(1.22 \pm 0.15 + 0.34 - 0.20) \times 10^{-1}$
	1.5–2.0	$(8.45 \pm 0.57 + 1.22 - 1.23) \times 10^{-2}$	$(1.34 \pm 0.38 + 0.68 - 0.69) \times 10^{-2}$	$(4.14 \pm 0.78 + 1.05 - 1.05) \times 10^{-2}$
	2.0–2.5	$(3.05 \pm 0.29 + 0.56 - 0.57) \times 10^{-2}$	$(5.22 \pm 1.93 + 2.97 - 3.02) \times 10^{-3}$	$(1.61 \pm 0.40 + 0.53 - 0.53) \times 10^{-2}$
	2.5–3.0	$(2.27 \pm 0.16 + 0.28 - 0.28) \times 10^{-2}$	$(2.67 \pm 1.02 + 1.42 - 1.43) \times 10^{-3}$	$(8.61 \pm 2.15 + 2.74 - 2.74) \times 10^{-3}$
	3.0–4.0	$(2.22 \pm 0.12 + 0.20 - 0.20) \times 10^{-2}$	$(4.01 \pm 0.74 + 1.01 - 1.01) \times 10^{-3}$	$(3.22 \pm 1.46 + 1.98 - 1.98) \times 10^{-3}$
	4.0–5.0	$(8.47 \pm 0.52 + 0.72 - 0.72) \times 10^{-3}$	$(2.09 \pm 0.32 + 0.36 - 0.36) \times 10^{-3}$	$(1.68 \pm 0.60 + 0.72 - 0.72) \times 10^{-3}$
	5.0–7.0	$(5.76 \pm 0.36 + 0.48 - 0.48) \times 10^{-3}$	$(1.40 \pm 0.22 + 0.24 - 0.24) \times 10^{-3}$	$(7.07 \pm 3.55 + 4.85 - 4.85) \times 10^{-4}$
	7.0–10.0	$(8.24 \pm 1.30 + 2.29 - 2.29) \times 10^{-4}$	–	–
20–40%	0.4–1.0	$(2.53 \pm 0.21 + 0.98 - 0.56) \times 10^{-1}$	$(2.15 \pm 0.14 + 0.57 - 0.39) \times 10^{-1}$	$(3.22 \pm 0.27 + 0.81 - 0.36) \times 10^{-1}$
	1.0–1.5	$(1.11 \pm 0.09 + 0.23 - 0.21) \times 10^{-1}$	$(3.78 \pm 0.60 + 1.52 - 1.41) \times 10^{-2}$	$(9.89 \pm 1.21 + 1.65 - 1.61) \times 10^{-2}$
	1.5–2.0	$(6.54 \pm 0.48 + 1.32 - 1.37) \times 10^{-2}$	$(1.08 \pm 0.32 + 0.80 - 0.84) \times 10^{-2}$	$(9.71 \pm 6.42 + 9.33 - 9.41) \times 10^{-3}$
	2.0–2.5	$(3.40 \pm 0.25 + 0.53 - 0.47) \times 10^{-2}$	$(4.62 \pm 1.66 + 3.02 - 2.66) \times 10^{-3}$	$(6.14 \pm 3.33 + 4.50 - 4.41) \times 10^{-3}$
	2.5–3.0	$(2.14 \pm 0.14 + 0.30 - 0.23) \times 10^{-2}$	$(5.97 \pm 0.93 + 1.53 - 1.18) \times 10^{-3}$	$(5.03 \pm 1.83 + 3.03 - 2.32) \times 10^{-3}$
	3.0–4.0	$(2.14 \pm 0.11 + 0.17 - 0.17) \times 10^{-2}$	$(6.53 \pm 0.72 + 0.88 - 0.89) \times 10^{-3}$	$(3.25 \pm 1.28 + 1.67 - 1.67) \times 10^{-3}$
	4.0–5.0	$(8.49 \pm 0.52 + 0.70 - 0.70) \times 10^{-3}$	$(2.57 \pm 0.33 + 0.35 - 0.35) \times 10^{-3}$	$(8.49 \pm 4.99 + 6.95 - 6.95) \times 10^{-4}$

TABLE XVII. *(Continued.)*

	p_T^b (GeV/c)	$\int_{\lvert\Delta\phi\rvert<\pi/3,\mathrm{NR}} d\Delta\phi(\frac{1}{N^a}\frac{dN^{ab}}{d\Delta\phi})$ Yield±Stat.+Sys.−Sys.	$\int_{\lvert\Delta\phi-\pi\rvert<\pi/6,\mathrm{HR}} d\Delta\phi(\frac{1}{N^a}\frac{dN^{ab}}{d\Delta\phi})$ Yield±Stat.+Sys.−Sys.	$\int_{\pi/6<\lvert\Delta\phi-\pi\rvert<\pi/3,\mathrm{SR}} d\Delta\phi(\frac{1}{N^a}\frac{dN^{ab}}{d\Delta\phi})$ Yield±Stat.+Sys.−Sys.
	5.0–7.0	$(6.82 \pm 0.42 + 0.42 - 0.42) \times 10^{-3}$	$(2.12 \pm 0.25 + 0.21 - 0.21) \times 10^{-3}$	$(6.51 \pm 3.10 + 4.23 - 4.23) \times 10^{-4}$
	7.0–10.0	$(7.18 \pm 1.78 + 1.93 - 1.93) \times 10^{-4}$	–	–
40–60%	0.4–1.0	$(2.07 \pm 0.19 + 0.44 - 0.45) \times 10^{-1}$	$(1.57 \pm 0.13 + 0.27 - 0.28) \times 10^{-1}$	$(1.92 \pm 0.24 + 0.32 - 0.32) \times 10^{-1}$
	1.0–1.5	$(1.15 \pm 0.08 + 0.55 - 0.16) \times 10^{-1}$	$(6.97 \pm 0.55 + 2.79 - 0.94) \times 10^{-2}$	$(6.58 \pm 1.07 + 5.46 - 1.43) \times 10^{-2}$
	1.5–2.0	$(6.80 \pm 0.44 + 0.90 - 0.93) \times 10^{-2}$	$(2.40 \pm 0.29 + 0.51 - 0.53) \times 10^{-2}$	$(1.59 \pm 0.57 + 0.77 - 0.77) \times 10^{-2}$
	2.0–2.5	$(3.61 \pm 0.23 + 0.41 - 0.42) \times 10^{-2}$	$(1.59 \pm 0.16 + 0.22 - 0.22) \times 10^{-2}$	$(1.37 \pm 0.30 + 0.38 - 0.39) \times 10^{-2}$
	2.5–3.0	$(1.96 \pm 0.14 + 0.22 - 0.22) \times 10^{-2}$	$(5.31 \pm 0.89 + 1.14 - 1.15) \times 10^{-3}$	$(1.59 \pm 1.64 + 2.18 - 2.18) \times 10^{-3}$
	3.0–4.0	$(2.18 \pm 0.12 + 0.15 - 0.15) \times 10^{-2}$	$(7.76 \pm 0.79 + 0.78 - 0.78) \times 10^{-3}$	$(3.08 \pm 1.25 + 1.52 - 1.52) \times 10^{-3}$
	4.0–5.0	$(8.98 \pm 0.63 + 0.58 - 0.58) \times 10^{-3}$	$(3.18 \pm 0.41 + 0.29 - 0.29) \times 10^{-3}$	$(1.24 \pm 0.51 + 0.58 - 0.58) \times 10^{-3}$
	5.0–7.0	$(6.63 \pm 0.91 + 0.25 - 0.25) \times 10^{-3}$	$(1.87 \pm 0.32 + 0.13 - 0.13) \times 10^{-3}$	$(7.67 \pm 4.11 + 2.54 - 2.54) \times 10^{-4}$
	7.0–10.0	$(6.68 \pm 2.15 + 0.77 - 0.77) \times 10^{-4}$	–	–
60–92%	0.4–1.0	$(1.84 \pm 0.18 + 0.44 - 0.39) \times 10^{-1}$	$(1.48 \pm 0.13 + 0.25 - 0.24) \times 10^{-1}$	$(1.62 \pm 0.23 + 0.39 - 0.30) \times 10^{-1}$
	1.0–1.5	$(1.20 \pm 0.08 + 0.19 - 0.15) \times 10^{-1}$	$(7.38 \pm 0.55 + 1.02 - 0.90) \times 10^{-2}$	$(5.49 \pm 0.99 + 1.74 - 1.26) \times 10^{-2}$
	1.5–2.0	$(5.16 \pm 0.43 + 0.71 - 0.69) \times 10^{-2}$	$(3.01 \pm 0.31 + 0.38 - 0.37) \times 10^{-2}$	$(2.17 \pm 0.55 + 0.70 - 0.67) \times 10^{-2}$
	2.0–2.5	$(3.69 \pm 0.26 + 0.35 - 0.35) \times 10^{-2}$	$(1.95 \pm 0.18 + 0.18 - 0.19) \times 10^{-2}$	$(1.11 \pm 0.29 + 0.33 - 0.33) \times 10^{-2}$
	2.5–3.0	$(2.21 \pm 0.17 + 0.20 - 0.20) \times 10^{-2}$	$(9.52 \pm 1.14 + 1.00 - 1.01) \times 10^{-3}$	$(5.62 \pm 1.56 + 1.95 - 1.95) \times 10^{-3}$
	3.0–4.0	$(1.91 \pm 0.16 + 0.16 - 0.16) \times 10^{-2}$	$(1.17 \pm 0.12 + 0.08 - 0.08) \times 10^{-2}$	$(1.77 \pm 1.09 + 1.60 - 1.60) \times 10^{-3}$
	4.0–5.0	$(8.40 \pm 1.03 + 0.72 - 0.72) \times 10^{-3}$	$(5.09 \pm 0.88 + 0.36 - 0.36) \times 10^{-3}$	$(4.09 \pm 7.55 + 7.19 - 7.19) \times 10^{-4}$
	5.0–7.0	$(8.14 \pm 1.23 + 0.73 - 0.73) \times 10^{-3}$	$(3.07 \pm 0.73 + 0.36 - 0.36) \times 10^{-3}$	$< 7.3 \times 10^{-4}$
	7.0–10.0	$(7.30 \pm 3.43 + 0.33 - 0.33) \times 10^{-4}$	–	–
$p+p$	0.4–1.0	$(1.89 \pm 0.03 + 0.06 - 0.03) \times 10^{-1}$	$(1.51 \pm 0.02 + 0.03 - 0.02) \times 10^{-1}$	$(9.83 \pm 0.28 + 0.65 - 0.35) \times 10^{-2}$
	1.0–1.5	$(9.88 \pm 0.13 + 0.14 - 0.14) \times 10^{-2}$	$(6.74 \pm 0.10 + 0.07 - 0.07) \times 10^{-2}$	$(3.47 \pm 0.12 + 0.14 - 0.14) \times 10^{-2}$
	1.5–2.0	$(5.93 \pm 0.08 + 0.08 - 0.08) \times 10^{-2}$	$(3.79 \pm 0.07 + 0.04 - 0.04) \times 10^{-2}$	$(1.54 \pm 0.07 + 0.08 - 0.08) \times 10^{-2}$
	2.0–2.5	$(3.58 \pm 0.06 + 0.04 - 0.04) \times 10^{-2}$	$(2.12 \pm 0.05 + 0.02 - 0.02) \times 10^{-2}$	$(7.89 \pm 0.44 + 0.39 - 0.39) \times 10^{-3}$
	2.5–3.0	$(2.08 \pm 0.05 + 0.02 - 0.02) \times 10^{-2}$	$(1.29 \pm 0.04 + 0.01 - 0.01) \times 10^{-2}$	$(4.68 \pm 0.29 + 0.25 - 0.25) \times 10^{-3}$
	3.0–4.0	$(2.24 \pm 0.05 + 0.02 - 0.02) \times 10^{-2}$	$(1.27 \pm 0.04 + 0.01 - 0.01) \times 10^{-2}$	$(3.58 \pm 0.24 + 0.23 - 0.23) \times 10^{-3}$
	4.0–5.0	$(9.09 \pm 0.39 + 0.06 - 0.06) \times 10^{-3}$	$(5.76 \pm 0.28 + 0.03 - 0.03) \times 10^{-3}$	$(1.25 \pm 0.13 + 0.06 - 0.06) \times 10^{-3}$
	5.0–7.0	$(6.47 \pm 0.47 + 0.02 - 0.02) \times 10^{-3}$	$(3.87 \pm 0.29 + 0.01 - 0.01) \times 10^{-3}$	$(7.23 \pm 0.99 + 0.21 - 0.21) \times 10^{-4}$
	7.0–10.0	$(1.25 \pm 0.44 + 0.00 - 0.00) \times 10^{-3}$	–	–

TABLE XVIII. Pair suppression factor J_{AA} in NR and HR for various $p_T^a \otimes p_T^b$ bins. The systematic uncertainties due to the single particle efficiency are not included (∼17%).

	$2.0 < p_T^a < 3.0$ GeV/c			$3.0 < p_T^a < 4.0$ GeV/c		
	$\langle p_T^b \rangle$ GeV/c	$J_{AA}(\lvert\Delta\phi\rvert < \pi/3)$	$J_{AA}(\lvert\Delta\phi - \pi\rvert < \pi/6)$	$\langle p_T^b \rangle$ GeV/c	$J_{AA}(\lvert\Delta\phi\rvert < \pi/3)$	$J_{AA}(\lvert\Delta\phi - \pi\rvert < \pi/6)$
0–20%	0.63	$1.34 \pm 0.01 + 0.52 - 0.25$	$1.17 \pm 0.01 + 0.46 - 0.30$	0.63	$0.88 \pm 0.02 + 0.36 - 0.11$	$0.80 \pm 0.02 + 0.27 - 0.13$
	1.20	$1.39 \pm 0.01 + 0.32 - 0.22$	$1.03 \pm 0.01 + 0.37 - 0.31$	1.20	$0.87 \pm 0.02 + 0.21 - 0.11$	$0.51 \pm 0.02 + 0.20 - 0.13$
	1.70	$1.53 \pm 0.02 + 0.24 - 0.19$	$0.83 \pm 0.02 + 0.30 - 0.27$	1.70	$0.94 \pm 0.02 + 0.12 - 0.10$	$0.37 \pm 0.02 + 0.14 - 0.13$
	2.20	$1.33 \pm 0.02 + 0.17 - 0.13$	$0.52 \pm 0.02 + 0.22 - 0.20$	2.20	$0.77 \pm 0.02 + 0.09 - 0.06$	$0.14 \pm 0.02 + 0.10 - 0.08$
	2.70	$1.08 \pm 0.02 + 0.17 - 0.09$	$0.25 \pm 0.02 + 0.20 - 0.14$	2.70	$0.60 \pm 0.02 + 0.07 - 0.04$	$0.11 \pm 0.02 + 0.08 - 0.05$
	3.34	$0.78 \pm 0.02 + 0.08 - 0.05$	$0.14 \pm 0.01 + 0.09 - 0.07$	3.34	$0.48 \pm 0.02 + 0.03 - 0.03$	$0.06 \pm 0.01 + 0.03 - 0.03$
	4.38	$0.50 \pm 0.02 + 0.04 - 0.04$	$0.06 \pm 0.02 + 0.04 - 0.04$	4.38	$0.39 \pm 0.03 + 0.03 - 0.03$	$0.06 \pm 0.02 + 0.02 - 0.02$
	5.75	$0.30 \pm 0.02 + 0.04 - 0.04$	$0.02 \pm 0.02 + 0.04 - 0.03$	5.75	$0.25 \pm 0.02 + 0.03 - 0.03$	$0.04 \pm 0.02 + 0.02 - 0.02$
	8.18	$0.20 \pm 0.05 + 0.11 - 0.08$	–	8.17	$0.41 \pm 0.10 + 0.06 - 0.06$	–
20–40%	0.63	$1.67 \pm 0.01 + 0.58 - 0.49$	$1.34 \pm 0.01 + 0.61 - 0.58$	0.63	$1.24 \pm 0.02 + 0.43 - 0.32$	$1.06 \pm 0.02 + 0.37 - 0.32$
	1.20	$1.55 \pm 0.01 + 0.47 - 0.44$	$1.15 \pm 0.01 + 0.63 - 0.64$	1.20	$1.07 \pm 0.02 + 0.30 - 0.26$	$0.68 \pm 0.02 + 0.33 - 0.32$
	1.70	$1.60 \pm 0.02 + 0.46 - 0.38$	$0.91 \pm 0.02 + 0.61 - 0.57$	1.70	$1.11 \pm 0.02 + 0.30 - 0.19$	$0.57 \pm 0.02 + 0.36 - 0.28$
	2.20	$1.35 \pm 0.02 + 0.47 - 0.22$	$0.57 \pm 0.02 + 0.58 - 0.37$	2.20	$0.90 \pm 0.02 + 0.12 - 0.13$	$0.28 \pm 0.02 + 0.17 - 0.18$

TABLE XVIII. *(Continued.)*

		$2.0 < p_T^a < 3.0$ GeV/c			$3.0 < p_T^a < 4.0$ GeV/c	
	$\langle p_T^b \rangle$ GeV/c	$J_{AA}(\lvert\Delta\phi\rvert < \pi/3)$	$J_{AA}(\lvert\Delta\phi - \pi\rvert < \pi/6)$	$\langle p_T^b \rangle$ GeV/c	$J_{AA}(\lvert\Delta\phi\rvert < \pi/3)$	$J_{AA}(\lvert\Delta\phi - \pi\rvert < \pi/6)$
	2.70	$1.19 \pm 0.02 + 0.27 - 0.15$	$0.41 \pm 0.02 + 0.35 - 0.26$	2.70	$0.79 \pm 0.03 + 0.09 - 0.10$	$0.25 \pm 0.02 + 0.14 - 0.15$
	3.34	$0.92 \pm 0.02 + 0.12 - 0.12$	$0.27 \pm 0.02 + 0.17 - 0.18$	3.34	$0.66 \pm 0.02 + 0.05 - 0.06$	$0.19 \pm 0.02 + 0.06 - 0.06$
	4.38	$0.70 \pm 0.03 + 0.07 - 0.07$	$0.19 \pm 0.02 + 0.08 - 0.08$	4.38	$0.57 \pm 0.04 + 0.04 - 0.04$	$0.18 \pm 0.02 + 0.03 - 0.03$
	5.70	$0.49 \pm 0.03 + 0.06 - 0.06$	$0.15 \pm 0.03 + 0.06 - 0.06$	5.70	$0.49 \pm 0.04 + 0.03 - 0.03$	$0.21 \pm 0.03 + 0.03 - 0.03$
	8.10	$0.48 \pm 0.08 + 0.09 - 0.09$	–	8.15	$0.45 \pm 0.11 + 0.08 - 0.08$	–
40–60%	0.63	$1.34 \pm 0.01 + 0.42 - 0.30$	$1.05 \pm 0.01 + 0.42 - 0.36$	0.63	$1.18 \pm 0.03 + 0.28 - 0.22$	$1.00 \pm 0.02 + 0.24 - 0.21$
	1.20	$1.26 \pm 0.01 + 0.36 - 0.26$	$0.95 \pm 0.01 + 0.45 - 0.38$	1.20	$1.02 \pm 0.02 + 0.17 - 0.17$	$0.75 \pm 0.02 + 0.20 - 0.20$
	1.70	$1.30 \pm 0.02 + 0.24 - 0.22$	$0.89 \pm 0.02 + 0.33 - 0.33$	1.70	$1.02 \pm 0.03 + 0.14 - 0.12$	$0.66 \pm 0.03 + 0.19 - 0.18$
	2.20	$1.19 \pm 0.02 + 0.15 - 0.15$	$0.78 \pm 0.02 + 0.23 - 0.24$	2.20	$0.80 \pm 0.02 + 0.09 - 0.07$	$0.46 \pm 0.03 + 0.11 - 0.10$
	2.71	$1.10 \pm 0.02 + 0.13 - 0.12$	$0.65 \pm 0.03 + 0.18 - 0.18$	2.71	$0.86 \pm 0.03 + 0.06 - 0.07$	$0.50 \pm 0.04 + 0.09 - 0.09$
	3.35	$0.91 \pm 0.02 + 0.08 - 0.07$	$0.53 \pm 0.02 + 0.11 - 0.10$	3.36	$0.78 \pm 0.03 + 0.04 - 0.05$	$0.36 \pm 0.03 + 0.04 - 0.05$
	4.38	$0.85 \pm 0.04 + 0.06 - 0.06$	$0.43 \pm 0.03 + 0.06 - 0.06$	4.39	$0.81 \pm 0.05 + 0.05 - 0.05$	$0.29 \pm 0.03 + 0.04 - 0.04$
	5.70	$0.68 \pm 0.04 + 0.06 - 0.06$	$0.41 \pm 0.04 + 0.06 - 0.06$	5.70	$0.60 \pm 0.05 + 0.05 - 0.04$	$0.37 \pm 0.05 + 0.04 - 0.03$
	8.12	$0.61 \pm 0.11 + 0.11 - 0.11$	–	8.07	$0.79 \pm 0.19 + 0.08 - 0.08$	–
60–92%	0.63	$1.04 \pm 0.01 + 0.23 - 0.15$	$0.89 \pm 0.01 + 0.20 - 0.17$	0.63	$0.95 \pm 0.02 + 0.21 - 0.11$	$0.85 \pm 0.02 + 0.16 - 0.11$
	1.20	$0.98 \pm 0.01 + 0.17 - 0.11$	$0.89 \pm 0.01 + 0.19 - 0.16$	1.20	$0.92 \pm 0.02 + 0.16 - 0.07$	$0.86 \pm 0.03 + 0.14 - 0.09$
	1.70	$1.00 \pm 0.01 + 0.10 - 0.09$	$0.87 \pm 0.02 + 0.14 - 0.14$	1.71	$0.89 \pm 0.03 + 0.07 - 0.07$	$0.80 \pm 0.03 + 0.09 - 0.09$
	2.21	$0.94 \pm 0.02 + 0.06 - 0.06$	$0.88 \pm 0.02 + 0.09 - 0.10$	2.21	$0.82 \pm 0.03 + 0.05 - 0.06$	$0.64 \pm 0.03 + 0.06 - 0.07$
	2.71	$0.94 \pm 0.02 + 0.06 - 0.07$	$0.79 \pm 0.03 + 0.08 - 0.09$	2.71	$0.80 \pm 0.03 + 0.05 - 0.05$	$0.65 \pm 0.04 + 0.06 - 0.06$
	3.36	$0.87 \pm 0.02 + 0.05 - 0.05$	$0.67 \pm 0.03 + 0.06 - 0.07$	3.38	$0.84 \pm 0.03 + 0.04 - 0.04$	$0.62 \pm 0.04 + 0.03 - 0.04$
	4.39	$0.87 \pm 0.04 + 0.06 - 0.06$	$0.58 \pm 0.04 + 0.06 - 0.06$	4.40	$1.05 \pm 0.07 + 0.05 - 0.05$	$0.59 \pm 0.06 + 0.04 - 0.04$
	5.70	$0.84 \pm 0.05 + 0.06 - 0.06$	$0.74 \pm 0.06 + 0.05 - 0.05$	5.73	$0.89 \pm 0.08 + 0.05 - 0.05$	$0.77 \pm 0.09 + 0.04 - 0.04$
	8.01	$0.71 \pm 0.14 + 0.14 - 0.14$	–	8.01	$0.47 \pm 0.18 + 0.22 - 0.22$	–

TABLE XIX. Pair suppression factor J_{AA} in NR and HR for various $p_T^a \otimes p_T^b$ bins. The systematic uncertainties due to the single particle efficiency are not included (∼17%).

		$4.0 < p_T^a < 5.0$ GeV/c			$5.0 < p_T^a < 10.0$ GeV/c	
	$\langle p_T^b \rangle$ GeV/c	$J_{AA}(\lvert\Delta\phi\rvert < \pi/3)$	$J_{AA}(\lvert\Delta\phi - \pi\rvert < \pi/6)$	$\langle p_T^b \rangle$ GeV/c	$J_{AA}(\lvert\Delta\phi\rvert < \pi/3)$	$J_{AA}(\lvert\Delta\phi - \pi\rvert < \pi/6)$
0–20%	0.63	$0.48 \pm 0.02 + 0.10 - 0.07$	$0.52 \pm 0.02 + 0.09 - 0.07$	0.63	$0.28 \pm 0.04 + 0.07 - 0.07$	$0.39 \pm 0.03 + 0.05 - 0.06$
	1.20	$0.47 \pm 0.02 + 0.07 - 0.07$	$0.32 \pm 0.02 + 0.08 - 0.08$	1.20	$0.31 \pm 0.03 + 0.09 - 0.06$	$0.21 \pm 0.03 + 0.07 - 0.05$
	1.70	$0.50 \pm 0.02 + 0.05 - 0.05$	$0.21 \pm 0.02 + 0.06 - 0.05$	1.70	$0.37 \pm 0.03 + 0.05 - 0.05$	$0.09 \pm 0.03 + 0.05 - 0.05$
	2.20	$0.44 \pm 0.02 + 0.05 - 0.04$	$0.06 \pm 0.02 + 0.04 - 0.04$	2.20	$0.22 \pm 0.02 + 0.04 - 0.04$	$0.06 \pm 0.02 + 0.04 - 0.04$
	2.70	$0.39 \pm 0.03 + 0.04 - 0.04$	$0.03 \pm 0.02 + 0.03 - 0.03$	2.70	$0.28 \pm 0.02 + 0.03 - 0.03$	$0.05 \pm 0.02 + 0.03 - 0.03$
	3.34	$0.38 \pm 0.02 + 0.03 - 0.03$	$0.09 \pm 0.02 + 0.02 - 0.02$	3.35	$0.26 \pm 0.01 + 0.02 - 0.02$	$0.08 \pm 0.02 + 0.02 - 0.02$
	4.38	$0.27 \pm 0.03 + 0.02 - 0.02$	$0.06 \pm 0.02 + 0.02 - 0.02$	4.40	$0.24 \pm 0.02 + 0.02 - 0.02$	$0.09 \pm 0.02 + 0.02 - 0.02$
	5.76	$0.31 \pm 0.04 + 0.03 - 0.03$	$0.11 \pm 0.02 + 0.02 - 0.02$	5.79	$0.23 \pm 0.02 + 0.02 - 0.02$	$0.09 \pm 0.02 + 0.02 - 0.02$
	8.12	$0.37 \pm 0.18 + 0.06 - 0.06$	–	8.03	$0.17 \pm 0.07 + 0.05 - 0.05$	–
20–40%	0.63	$0.67 \pm 0.03 + 0.31 - 0.13$	$0.67 \pm 0.03 + 0.25 - 0.15$	0.63	$0.57 \pm 0.05 + 0.22 - 0.13$	$0.60 \pm 0.04 + 0.16 - 0.11$
	1.20	$0.63 \pm 0.03 + 0.16 - 0.10$	$0.39 \pm 0.03 + 0.17 - 0.13$	1.20	$0.47 \pm 0.04 + 0.10 - 0.09$	$0.24 \pm 0.04 + 0.10 - 0.09$
	1.70	$0.66 \pm 0.03 + 0.12 - 0.08$	$0.33 \pm 0.03 + 0.13 - 0.11$	1.70	$0.47 \pm 0.04 + 0.09 - 0.10$	$0.12 \pm 0.04 + 0.09 - 0.09$
	2.20	$0.62 \pm 0.03 + 0.07 - 0.07$	$0.18 \pm 0.03 + 0.07 - 0.08$	2.20	$0.40 \pm 0.03 + 0.06 - 0.06$	$0.09 \pm 0.03 + 0.06 - 0.05$
	2.71	$0.57 \pm 0.04 + 0.06 - 0.06$	$0.13 \pm 0.03 + 0.05 - 0.06$	2.71	$0.43 \pm 0.03 + 0.06 - 0.05$	$0.20 \pm 0.03 + 0.05 - 0.04$
	3.35	$0.56 \pm 0.03 + 0.04 - 0.04$	$0.19 \pm 0.02 + 0.04 - 0.04$	3.36	$0.40 \pm 0.02 + 0.03 - 0.03$	$0.22 \pm 0.02 + 0.03 - 0.03$
	4.39	$0.47 \pm 0.04 + 0.03 - 0.03$	$0.25 \pm 0.03 + 0.03 - 0.03$	4.40	$0.40 \pm 0.03 + 0.03 - 0.03$	$0.19 \pm 0.03 + 0.03 - 0.03$
	5.72	$0.44 \pm 0.06 + 0.04 - 0.04$	$0.14 \pm 0.03 + 0.03 - 0.03$	5.77	$0.45 \pm 0.04 + 0.03 - 0.03$	$0.23 \pm 0.03 + 0.02 - 0.02$
	8.06	$0.59 \pm 0.28 + 0.04 - 0.04$	–	8.00	$0.24 \pm 0.10 + 0.07 - 0.07$	–

TABLE XIX. *(Continued.)*

		$4.0 < p_T^a < 5.0$ GeV/c		$5.0 < p_T^a < 10.0$ GeV/c		
	$\langle p_T^b \rangle$ GeV/c	$J_{AA}(\lvert\Delta\phi\rvert < \pi/3)$	$J_{AA}(\lvert\Delta\phi - \pi\rvert < \pi/6)$	$\langle p_T^b \rangle$ GeV/c	$J_{AA}(\lvert\Delta\phi\rvert < \pi/3)$	$J_{AA}(\lvert\Delta\phi - \pi\rvert < \pi/6)$
40–60%	0.63	$0.85 \pm 0.04 + 0.24 - 0.14$	$0.81 \pm 0.04 + 0.19 - 0.14$	0.63	$0.62 \pm 0.06 + 0.13 - 0.14$	$0.58 \pm 0.05 + 0.10 - 0.11$
	1.20	$0.85 \pm 0.04 + 0.12 - 0.12$	$0.66 \pm 0.04 + 0.13 - 0.13$	1.20	$0.66 \pm 0.05 + 0.31 - 0.09$	$0.58 \pm 0.05 + 0.23 - 0.08$
	1.70	$0.85 \pm 0.04 + 0.08 - 0.08$	$0.56 \pm 0.04 + 0.09 - 0.10$	1.70	$0.65 \pm 0.04 + 0.09 - 0.09$	$0.36 \pm 0.04 + 0.08 - 0.08$
	2.21	$0.76 \pm 0.04 + 0.07 - 0.07$	$0.38 \pm 0.04 + 0.06 - 0.07$	2.21	$0.57 \pm 0.04 + 0.07 - 0.07$	$0.42 \pm 0.04 + 0.06 - 0.06$
	2.71	$0.87 \pm 0.05 + 0.06 - 0.06$	$0.44 \pm 0.04 + 0.05 - 0.05$	2.71	$0.53 \pm 0.04 + 0.06 - 0.06$	$0.23 \pm 0.04 + 0.05 - 0.05$
	3.37	$0.70 \pm 0.04 + 0.05 - 0.05$	$0.26 \pm 0.03 + 0.04 - 0.04$	3.39	$0.55 \pm 0.03 + 0.04 - 0.04$	$0.35 \pm 0.04 + 0.03 - 0.03$
	4.40	$0.53 \pm 0.05 + 0.04 - 0.04$	$0.33 \pm 0.05 + 0.04 - 0.03$	4.41	$0.56 \pm 0.05 + 0.04 - 0.04$	$0.31 \pm 0.04 + 0.03 - 0.03$
	5.71	$0.69 \pm 0.09 + 0.04 - 0.04$	$0.39 \pm 0.07 + 0.03 - 0.03$	5.74	$0.58 \pm 0.09 + 0.02 - 0.02$	$0.27 \pm 0.05 + 0.02 - 0.02$
	8.13	$0.59 \pm 0.30 + 0.13 - 0.13$	–	8.09	$0.30 \pm 0.14 + 0.03 - 0.03$	–
60–92%	0.63	$0.70 \pm 0.04 + 0.27 - 0.13$	$0.75 \pm 0.04 + 0.20 - 0.12$	0.63	$0.70 \pm 0.07 + 0.17 - 0.15$	$0.70 \pm 0.06 + 0.12 - 0.11$
	1.20	$0.67 \pm 0.04 + 0.08 - 0.08$	$0.66 \pm 0.04 + 0.09 - 0.09$	1.21	$0.86 \pm 0.06 + 0.14 - 0.11$	$0.78 \pm 0.06 + 0.11 - 0.10$
	1.71	$0.80 \pm 0.04 + 0.07 - 0.07$	$0.58 \pm 0.05 + 0.08 - 0.08$	1.71	$0.62 \pm 0.05 + 0.09 - 0.08$	$0.57 \pm 0.06 + 0.07 - 0.07$
	2.21	$0.75 \pm 0.05 + 0.07 - 0.06$	$0.52 \pm 0.05 + 0.06 - 0.05$	2.22	$0.74 \pm 0.05 + 0.07 - 0.07$	$0.65 \pm 0.06 + 0.06 - 0.06$
	2.71	$0.84 \pm 0.06 + 0.07 - 0.07$	$0.54 \pm 0.06 + 0.06 - 0.06$	2.72	$0.76 \pm 0.06 + 0.07 - 0.07$	$0.52 \pm 0.06 + 0.06 - 0.06$
	3.39	$1.00 \pm 0.07 + 0.05 - 0.05$	$0.62 \pm 0.06 + 0.04 - 0.04$	3.38	$0.61 \pm 0.05 + 0.05 - 0.05$	$0.66 \pm 0.07 + 0.05 - 0.05$
	4.42	$0.76 \pm 0.08 + 0.05 - 0.05$	$0.52 \pm 0.08 + 0.04 - 0.04$	4.41	$0.66 \pm 0.09 + 0.06 - 0.06$	$0.63 \pm 0.11 + 0.04 - 0.04$
	5.74	$0.83 \pm 0.13 + 0.05 - 0.05$	$0.79 \pm 0.16 + 0.04 - 0.04$	5.79	$0.90 \pm 0.15 + 0.08 - 0.08$	$0.56 \pm 0.14 + 0.07 - 0.07$
	7.99	$1.06 \pm 0.58 + 0.10 - 0.10$	–	8.10	$0.41 \pm 0.24 + 0.02 - 0.02$	–

[1] R. Baier, Y. L. Dokshitzer, A. H. Mueller, S. Peigne, and D. Schiff, Nucl. Phys. **B484**, 265 (1997).

[2] M. Gyulassy, I. Vitev, X. N. Wang, and B. W. Zhang, in *Quark-Gluon Plasma 3*, edited by R. C. Hwa and X.-N. Wang (World Scientific, Singapore, 2004), nucl-th/0302077.

[3] A. Kovner and U. A. Wiedemann, in *Quark-Gluon Plasma 3*, edited by R. C. Hwa and X.-N. Wang (World Scientific, Singapore, 2004), hep-ph/0304151.

[4] S. S. Adler *et al*. (PHENIX Collaboration), Phys. Rev. Lett. **91**, 072301 (2003).

[5] J. Adams *et al*. (STAR Collaboration), Phys. Rev. Lett. **91**, 172302 (2003).

[6] S. S. Adler *et al*. (PHENIX Collaboration), Phys. Rev. C **69**, 034910 (2004).

[7] C. Adler *et al*. (STAR Collaboration), Phys. Rev. Lett. **90**, 082302 (2003).

[8] K. Adcox *et al*. (PHENIX Collaboration), Phys. Rev. Lett. **88**, 022301 (2002).

[9] S. S. Adler *et al*. (PHENIX Collaboration), Phys. Rev. Lett. **96**, 202301 (2006).

[10] S. S. Adler *et al*. (PHENIX Collaboration), Phys. Rev. C **75**, 024909 (2007).

[11] B. I. Abelev *et al*. (STAR Collaboration), Phys. Rev. Lett. **97**, 152301 (2006).

[12] J. Adams *et al*. (STAR Collaboration), Phys. Rev. Lett. **97**, 162301 (2006).

[13] A. Adare *et al*. (PHENIX Collaboration), Phys. Rev. C **77**, 011901(R) (2008).

[14] T. Renk and K. J. Eskola, Phys. Rev. C **75**, 054910 (2007).

[15] A. Majumder, J. Phys. G **34**, S377 (2007).

[16] J. Adams *et al*. (STAR Collaboration), Phys. Rev. C **73**, 064907 (2006).

[17] J. Adams *et al*. (STAR Collaboration), Phys. Rev. Lett. **95**, 152301 (2005).

[18] S. S. Adler *et al*. (PHENIX Collaboration), Phys. Rev. Lett. **97**, 052301 (2006).

[19] A. Adare *et al*. (PHENIX Collaboration), Phys. Rev. Lett. **98**, 232302 (2007).

[20] J. Adams *et al*. (Star Collaboration), Phys. Rev. C **75**, 034901 (2007).

[21] S. A. Voloshin, Nucl. Phys. **A749**, 287 (2005).

[22] C. B. Chiu and R. C. Hwa, Phys. Rev. C **72**, 034903 (2005).

[23] N. Armesto, C. A. Salgado, and U. A. Wiedemann, Phys. Rev. Lett. **93**, 242301 (2004).

[24] P. Romatschke, Phys. Rev. C **75**, 014901 (2007).

[25] A. Majumder, B. Muller, and S. A. Bass, Phys. Rev. Lett. **99**, 042301 (2007).

[26] E. V. Shuryak, Phys. Rev. C **76**, 047901 (2007).

[27] C. Y. Wong, Phys. Rev. C **76**, 054908 (2007).

[28] V. S. Pantuev, arXiv:0710.1882 [hep-ph].

[29] C. B. Chiu and R. C. Hwa, Phys. Rev. C **74**, 064909 (2006).

[30] N. Armesto, C. A. Salgado, and U. A. Wiedemann, Phys. Rev. C **72**, 064910 (2005).

[31] I. Vitev, Phys. Lett. **B630**, 78 (2005).

[32] A. D. Polosa and C. A. Salgado, Phys. Rev. C **75**, 041901(R) (2007).

[33] I. M. Dremin, JETP Lett. **30**, 140 (1979).

[34] V. Koch, A. Majumder, and X. N. Wang, Phys. Rev. Lett. **96**, 172302 (2006).

[35] J. Casalderrey-Solana, E. V. Shuryak, and D. Teaney, J. Phys. Conf. Ser. **27**, 22 (2005); hep-ph/0602183.

[36] H. Stoecker, Nucl. Phys. **A750**, 121 (2005).
[37] P. F. Kolb and R. Rapp, Phys. Rev. C **67**, 044903 (2003).
[38] D. Molnar and S. A. Voloshin, Phys. Rev. Lett. **91**, 092301 (2003).
[39] R. C. Hwa and C. B. Yang, Phys. Rev. C **70**, 024905 (2004).
[40] R. J. Fries, B. Muller, C. Nonaka, and S. A. Bass, Phys. Rev. C **68**, 044902 (2003).
[41] V. Greco, C. M. Ko, and P. Levai, Phys. Rev. Lett. **90**, 202302 (2003).
[42] R. J. Fries, S. A. Bass, and B. Muller, Phys. Rev. Lett. **94**, 122301 (2005).
[43] S. Afanasiev *et al.* (PHENIX Collaboration), arXiv:0712.3033 [nucl-ex].
[44] S. S. Adler *et al.* (PHENIX Collaboration), Phys. Rev. D **74**, 072002 (2006).
[45] K. Adcox *et al.* (PHENIX Collaboration), Nucl. Instrum. Methods Phys. Res. A **499**, 469 (2003).
[46] A. Adare *et al.* (PHENIX Collaboration), Phys. Rev. Lett. **97**, 252002 (2006).
[47] K. Adcox *et al.* (PHENIX Collaboration), Nucl. Instrum. Methods Phys. Res. A **499**, 489 (2003).
[48] K. Adcox *et al.* (PHENIX Collaboration), Phys. Rev. Lett. **86**, 3500 (2001).
[49] K. Adcox *et al.* (PHENIX Collaboration), Phys. Rev. C **69**, 024904 (2004).
[50] S. S. Adler *et al.* (PHENIX Collaboration), Phys. Rev. C **73**, 054903 (2006).
[51] S. S. Adler *et al.* (PHENIX Collaboration), Phys. Rev. Lett. **95**, 202001 (2005).
[52] N. N. Ajitanand *et al.*, Phys. Rev. C **72**, 011902(R) (2005).
[53] A. M. Poskanzer and S. A. Voloshin, Phys. Rev. C **58**, 1671 (1998).
[54] S. S. Adler *et al.* (PHENIX Collaboration), Phys. Rev. Lett. **91**, 182301 (2003).
[55] S. S. Adler *et al.* (PHENIX Collaboration), Phys. Rev. C **72**, 024901 (2005).
[56] N. Borghini, P. M. Dinh, and J. Y. Ollitrault, Phys. Rev. C **64**, 054901 (2001).
[57] N. Borghini, P. M. Dinh, and J. Y. Ollitrault, Phys. Rev. C **62**, 034902 (2000).
[58] M. Miller and R. Snellings, arXiv:nucl-ex/0312008.
[59] R. S. Bhalerao and J. Y. Ollitrault, Phys. Lett. **B641**, 260 (2006).
[60] S. Manly *et al.* (PHOBOS Collaboration), Nucl. Phys. **A774**, 523 (2006).
[61] X. Zhu, M. Bleicher, and H. Stocker, Phys. Rev. C **72**, 064911 (2005).
[62] J. Adams *et al.* (STAR Collaboration), Phys. Rev. Lett. **93**, 252301 (2004).
[63] B. Alver *et al.* (PHOBOS Collaboration), Int. J. Mod. Phys. E **16**, 3331 (2008).
[64] P. Sorensen (STAR Collaboration), J. Phys. G **34**, S897 (2007).
[65] A. A. Affolder *et al.* (CDF Collaboration), Phys. Rev. D **65**, 092002 (2002).
[66] D. E. Acosta *et al.* (CDF Collaboration), Phys. Rev. D **71**, 052002 (2005).
[67] T. Sjostrand, L. Lonnblad, and S. Mrenna, arXiv:hep-ph/0108264.
[68] S. S. Adler *et al.*, Phys. Rev. C **71**, 051902 (2005).
[69] C. Loizides, Eur. Phys. J. C **49**, 339 (2007).
[70] A. Adare *et al.* (PHENIX Collaboration), Phys. Lett. **B649**, 359 (2007).
[71] T. Renk and J. Ruppert, Phys. Rev. C **73**, 011901(R) (2006).
[72] J. F. Owens, E. Reya, and M. Gluck, Phys. Rev. D **18**, 1501 (1978).
[73] D. Teaney, J. Lauret, and E. V. Shuryak, Phys. Rev. Lett. **86**, 4783 (2001).
[74] P. Huovinen, Nucl. Phys. **A715**, 299 (2003).
[75] J. Jia (PHENIX Collaboration), Int. J. Mod. Phys. E **16**, 2000 (2007).
[76] H. Zhang, J. F. Owens, E. Wang, and X. N. Wang, Phys. Rev. Lett. **98**, 212301 (2007), and private communications with authors.
[77] M. Ploskon (CERES Collaboration), Nucl. Phys. **A783**, 527 (2007).
[78] J. W. Cronin, H. J. Frisch, M. J. Shochet, J. P. Boymond, R. Mermod, P. A. Piroue, and R. L. Sumner, Phys. Rev. D **11**, 3105 (1975).
[79] C. A. Salgado and U. A. Wiedemann, Phys. Rev. Lett. **93**, 042301 (2004).
[80] J. Jia (PHENIX Collaboration), Nucl. Phys. **A783**, 501 (2007).
[81] B. B. Back *et al.*, Phys. Rev. Lett. **91**, 052303 (2003).
[82] A. Adare *et al.* (PHENIX Collaboration), Phys. Rev. Lett. **98**, 162301 (2007)

Suppression Pattern of Neutral Pions at High Transverse Momentum in Au + Au Collisions at $\sqrt{s_{NN}} = 200$ GeV and Constraints on Medium Transport Coefficients

A. Adare,[8] S. Afanasiev,[22] C. Aidala,[9] N. N. Ajitanand,[49] Y. Akiba,[43,44] H. Al-Bataineh,[38] J. Alexander,[49] A. Al-Jamel,[38] K. Aoki,[28,43] L. Aphecetche,[51] R. Armendariz,[38] S. H. Aronson,[3] J. Asai,[44] E. T. Atomssa,[29] R. Averbeck,[50] T. C. Awes,[39] B. Azmoun,[3] V. Babintsev,[18] G. Baksay,[14] L. Baksay,[14] A. Baldisseri,[11] K. N. Barish,[4] P. D. Barnes,[31] B. Bassalleck,[37] S. Bathe,[4] S. Batsouli,[9,39] V. Baublis,[42] F. Bauer,[4] A. Bazilevsky,[3] S. Belikov,[3,21,*] R. Bennett,[50] Y. Berdnikov,[46] A. A. Bickley,[8] M. T. Bjorndal,[9] J. G. Boissevain,[31] H. Borel,[11] K. Boyle,[50] M. L. Brooks,[31] D. S. Brown,[38] D. Bucher,[34] H. Buesching,[3] V. Bumazhnov,[18] G. Bunce,[3,44] J. M. Burward-Hoy,[31] S. Butsyk,[31,50] S. Campbell,[50] J.-S. Chai,[23] B. S. Chang,[58] J.-L. Charvet,[11] S. Chernichenko,[18] J. Chiba,[24] C. Y. Chi,[9] M. Chiu,[9,19] I. J. Choi,[58] T. Chujo,[55] P. Chung,[49] A. Churyn,[18] V. Cianciolo,[39] C. R. Cleven,[16] Y. Cobigo,[11] B. A. Cole,[9] M. P. Comets,[40] P. Constantin,[21,31] M. Csanád,[13] T. Csörgő,[25] T. Dahms,[50] K. Das,[15] G. David,[3] M. B. Deaton,[1] K. Dehmelt,[14] H. Delagrange,[51] A. Denisov,[18] D. d'Enterria,[9] A. Deshpande,[44,50] E. J. Desmond,[3] O. Dietzsch,[47] A. Dion,[50] M. Donadelli,[47] J. L. Drachenberg,[1] O. Drapier,[29] A. Drees,[50] A. K. Dubey,[57] A. Durum,[18] V. Dzhordzhadze,[4,52] Y. V. Efremenko,[39] J. Egdemir,[50] F. Ellinghaus,[8] W. S. Emam,[4] A. Enokizono,[17,30] H. En'yo,[43,44] B. Espagnon,[40] S. Esumi,[54] K. O. Eyser,[4] D. E. Fields,[37,44] M. Finger,[5,22] M. Finger, Jr.,[5,22] F. Fleuret,[29] S. L. Fokin,[27] B. Forestier,[32] Z. Fraenkel,[57,*] J. E. Frantz,[9,50] A. Franz,[3] A. D. Frawley,[15] K. Fujiwara,[43] Y. Fukao,[28,43] S.-Y. Fung,[4] T. Fusayasu,[36] S. Gadrat,[32] I. Garishvili,[52] F. Gastineau,[51] M. Germain,[51] A. Glenn,[8,52] H. Gong,[50] M. Gonin,[29] J. Gosset,[11] Y. Goto,[43,44] R. Granier de Cassagnac,[29] N. Grau,[21] S. V. Greene,[55] M. Grosse Perdekamp,[19,44] T. Gunji,[7] H.-Å. Gustafsson,[33] T. Hachiya,[17,43] A. Hadj Henni,[51] C. Haegemann,[37] J. S. Haggerty,[3] M. N. Hagiwara,[1] H. Hamagaki,[7] R. Han,[41] H. Harada,[17] E. P. Hartouni,[30] K. Haruna,[17] M. Harvey,[3] E. Haslum,[33] K. Hasuko,[43] R. Hayano,[7] M. Heffner,[30] T. K. Hemmick,[50] T. Hester,[4] J. M. Heuser,[43] X. He,[16] H. Hiejima,[19] J. C. Hill,[21] R. Hobbs,[37] M. Hohlmann,[14] M. Holmes,[55] W. Holzmann,[49] K. Homma,[17] B. Hong,[26] T. Horaguchi,[43,53] D. Hornback,[52] M. G. Hur,[23] T. Ichihara,[43,44] K. Imai,[28,43] J. Imrek,[12] M. Inaba,[54] Y. Inoue,[45,43] D. Isenhower,[1] L. Isenhower,[1] M. Ishihara,[43] T. Isobe,[7] M. Issah,[49] A. Isupov,[22] B. V. Jacak,[50,+] J. Jia,[9] J. Jin,[9] O. Jinnouchi,[44] B. M. Johnson,[3] K. S. Joo,[35] D. Jouan,[40] F. Kajihara,[7,43] S. Kametani,[7,56] N. Kamihara,[43,53] J. Kamin,[50] M. Kaneta,[44] J. H. Kang,[58] H. Kanou,[43,53] T. Kawagishi,[54] D. Kawall,[44] A. V. Kazantsev,[27] S. Kelly,[8] A. Khanzadeev,[42] J. Kikuchi,[56] D. H. Kim,[35] D. J. Kim,[58] E. Kim,[48] Y.-S. Kim,[23] E. Kinney,[8] A. Kiss,[13] E. Kistenev,[3] A. Kiyomichi,[43] J. Klay,[30] C. Klein-Boesing,[34] L. Kochenda,[42] V. Kochetkov,[18] B. Komkov,[42] M. Konno,[54] D. Kotchetkov,[4] A. Kozlov,[57] A. Král,[10] A. Kravitz,[9] P. J. Kroon,[3] J. Kubart,[5,20] G. J. Kunde,[31] N. Kurihara,[7] K. Kurita,[45,43] M. J. Kweon,[26] Y. Kwon,[52,58] G. S. Kyle,[38] R. Lacey,[49] Y.-S. Lai,[9] J. G. Lajoie,[21] A. Lebedev,[21] Y. Le Bornec,[40] S. Leckey,[50] D. M. Lee,[31] M. K. Lee,[58] T. Lee,[48] M. J. Leitch,[31] M. A. L. Leite,[47] B. Lenzi,[47] H. Lim,[48] T. Liška,[10] A. Litvinenko,[22] M. X. Liu,[31] X. Li,[6] X. H. Li,[4] B. Love,[55] D. Lynch,[3] C. F. Maguire,[55] Y. I. Makdisi,[3] A. Malakhov,[22] M. D. Malik,[37] V. I. Manko,[27] Y. Mao,[41,43] L. Mašek,[5,20] H. Masui,[54] F. Matathias,[9,50] M. C. McCain,[19] M. McCumber,[50] P. L. McGaughey,[31] Y. Miake,[54] P. Mikeš,[5,20] K. Miki,[54] T. E. Miller,[55] A. Milov,[50] S. Mioduszewski,[3] G. C. Mishra,[16] M. Mishra,[2] J. T. Mitchell,[3] M. Mitrovski,[49] A. Morreale,[4] D. P. Morrison,[3] J. M. Moss,[31] T. V. Moukhanova,[27] D. Mukhopadhyay,[55] J. Murata,[45,43] S. Nagamiya,[24] Y. Nagata,[54] J. L. Nagle,[8] M. Naglis,[57] I. Nakagawa,[43,44] Y. Nakamiya,[17] T. Nakamura,[17] K. Nakano,[43,53] J. Newby,[30] M. Nguyen,[50] B. E. Norman,[31] A. S. Nyanin,[27] J. Nystrand,[33] E. O'Brien,[3] S. X. Oda,[7] C. A. Ogilvie,[21] H. Ohnishi,[43] I. D. Ojha,[55] H. Okada,[28,43] K. Okada,[44] M. Oka,[54] O. O. Omiwade,[1] A. Oskarsson,[33] I. Otterlund,[33] M. Ouchida,[17] K. Ozawa,[7] R. Pak,[3] D. Pal,[55] A. P. T. Palounek,[31] V. Pantuev,[50] V. Papavassiliou,[38] J. Park,[48] W. J. Park,[26] S. F. Pate,[38] H. Pei,[21] J.-C. Peng,[19] H. Pereira,[11] V. Peresedov,[22] D. Yu. Peressounko,[27] C. Pinkenburg,[3] R. P. Pisani,[3] M. L. Purschke,[3] A. K. Purwar,[31,50] H. Qu,[16] J. Rak,[21,37] A. Rakotozafindrabe,[29] I. Ravinovich,[57] K. F. Read,[39,52] S. Rembeczki,[14] M. Reuter,[50] K. Reygers,[34] V. Riabov,[42] Y. Riabov,[42] G. Roche,[32] A. Romana,[29,*] M. Rosati,[21] S. S. E. Rosendahl,[33] P. Rosnet,[32] P. Rukoyatkin,[22] V. L. Rykov,[43] S. S. Ryu,[58] B. Sahlmueller,[34] N. Saito,[28,43,44] T. Sakaguchi,[3,7,56] S. Sakai,[54] H. Sakata,[17] V. Samsonov,[42] H. D. Sato,[28,43] S. Sato,[3,24,54] S. Sawada,[24] J. Seele,[8] R. Seidl,[19] V. Semenov,[18] R. Seto,[4] D. Sharma,[57] T. K. Shea,[3] I. Shein,[18] A. Shevel,[42,49] T.-A. Shibata,[43,53] K. Shigaki,[17] M. Shimomura,[54] T. Shohjoh,[54] K. Shoji,[28,43] A. Sickles,[50] C. L. Silva,[47] D. Silvermyr,[39] C. Silvestre,[11] K. S. Sim,[26] C. P. Singh,[2] V. Singh,[2] S. Skutnik,[21] M. Slunečka,[5,22] W. C. Smith,[1] A. Soldatov,[18] R. A. Soltz,[30] W. E. Sondheim,[31] S. P. Sorensen,[52] I. V. Sourikova,[3] F. Staley,[11] P. W. Stankus,[39] E. Stenlund,[33] M. Stepanov,[38] A. Ster,[25] S. P. Stoll,[3] T. Sugitate,[17] C. Suire,[40] J. P. Sullivan,[31] J. Sziklai,[25] T. Tabaru,[44] S. Takagi,[54] E. M. Takagui,[47] A. Taketani,[43,44] K. H. Tanaka,[24] Y. Tanaka,[36] K. Tanida,[43,44] M. J. Tannenbaum,[3] A. Taranenko,[49] P. Tarján,[12] T. L. Thomas,[37]

 © 2008 The American Physical Society

M. Togawa,[28,43] A. Toia,[50] J. Tojo,[43] L. Tomášek,[20] H. Torii,[43] R. S. Towell,[1] V-N. Tram,[29] I. Tserruya,[57] Y. Tsuchimoto,[17,43] S. K. Tuli,[2] H. Tydesjö,[33] N. Tyurin,[18] C. Vale,[21] H. Valle,[55] H. W. van Hecke,[31] J. Velkovska,[55] R. Vertesi,[12] A. A. Vinogradov,[27] M. Virius,[10] V. Vrba,[20] E. Vznuzdaev,[42] M. Wagner,[28,43] D. Walker,[50] X. R. Wang,[38] Y. Watanabe,[43,44] J. Wessels,[34] S. N. White,[3] N. Willis,[40] D. Winter,[9] C. L. Woody,[3] M. Wysocki,[8] W. Xie,[4,44] Y. L. Yamaguchi,[56] A. Yanovich,[18] Z. Yasin,[4] J. Ying,[16] S. Yokkaichi,[43,44] G. R. Young,[39] I. Younus,[37] I. E. Yushmanov,[27] W. A. Zajc,[9] O. Zaudtke,[34] C. Zhang,[9,39] S. Zhou,[6] J. Zimányi,[25,*] and L. Zolin[22]

(PHENIX Collaboration)

[1]*Abilene Christian University, Abilene, Texas 79699, USA*
[2]*Department of Physics, Banaras Hindu University, Varanasi 221005, India*
[3]*Brookhaven National Laboratory, Upton, New York 11973-5000, USA*
[4]*University of California-Riverside, Riverside, California 92521, USA*
[5]*Charles University, Ovocný trh 5, Praha 1, 116 36, Prague, Czech Republic*
[6]*China Institute of Atomic Energy (CIAE), Beijing, People's Republic of China*
[7]*Center for Nuclear Study, Graduate School of Science, University of Tokyo, 7-3-1 Hongo, Bunkyo, Tokyo 113-0033, Japan*
[8]*University of Colorado, Boulder, Colorado 80309, USA*
[9]*Columbia University, New York, New York 10027 and Nevis Laboratories, Irvington, New York 10533, USA*
[10]*Czech Technical University, Zikova 4, 166 36 Prague 6, Czech Republic*
[11]*Dapnia, CEA Saclay, F-91191, Gif-sur-Yvette, France*
[12]*Debrecen University, H-4010 Debrecen, Egyetem tér 1, Hungary*
[13]*ELTE, Eötvös Loránd University, H-1117 Budapest, Pázmány P. s. 1/A, Hungary*
[14]*Florida Institute of Technology, Melbourne, Florida 32901, USA*
[15]*Florida State University, Tallahassee, Florida 32306, USA*
[16]*Georgia State University, Atlanta, Georgia 30303, USA*
[17]*Hiroshima University, Kagamiyama, Higashi-Hiroshima 739-8526, Japan*
[18]*IHEP Protvino, State Research Center of Russian Federation, Institute for High Energy Physics, Protvino, 142281, Russia*
[19]*University of Illinois at Urbana-Champaign, Urbana, Illinois 61801, USA*
[20]*Institute of Physics, Academy of Sciences of the Czech Republic, Na Slovance 2, 182 21 Prague 8, Czech Republic*
[21]*Iowa State University, Ames, Iowa 50011, USA*
[22]*Joint Institute for Nuclear Research, 141980 Dubna, Moscow Region, Russia*
[23]*KAERI, Cyclotron Application Laboratory, Seoul, Korea*
[24]*KEK, High Energy Accelerator Research Organization, Tsukuba, Ibaraki 305-0801, Japan*
[25]*KFKI Research Institute for Particle and Nuclear Physics of the Hungarian Academy of Sciences (MTA KFKI RMKI), H-1525 Budapest 114, POBox 49, Budapest, Hungary*
[26]*Korea University, Seoul, 136-701, Korea*
[27]*Russian Research Center "Kurchatov Institute", Moscow, Russia*
[28]*Kyoto University, Kyoto 606-8502, Japan*
[29]*Laboratoire Leprince-Ringuet, Ecole Polytechnique, CNRS-IN2P3, Route de Saclay, F-91128, Palaiseau, France*
[30]*Lawrence Livermore National Laboratory, Livermore, California 94550, USA*
[31]*Los Alamos National Laboratory, Los Alamos, New Mexico 87545, USA*
[32]*LPC, Université Blaise Pascal, CNRS-IN2P3, Clermont-Fd, 63177 Aubiere Cedex, France*
[33]*Department of Physics, Lund University, Box 118, SE-221 00 Lund, Sweden*
[34]*Institut für Kernphysik, University of Muenster, D-48149 Muenster, Germany*
[35]*Myongji University, Yongin, Kyonggido 449-728, Korea*
[36]*Nagasaki Institute of Applied Science, Nagasaki-shi, Nagasaki 851-0193, Japan*
[37]*University of New Mexico, Albuquerque, New Mexico 87131, USA*
[38]*New Mexico State University, Las Cruces, New Mexico 88003, USA*
[39]*Oak Ridge National Laboratory, Oak Ridge, Tennessee 37831, USA*
[40]*IPN-Orsay, Universite Paris Sud, CNRS-IN2P3, BP1, F-91406, Orsay, France*
[41]*Peking University, Beijing, People's Republic of China*
[42]*PNPI, Petersburg Nuclear Physics Institute, Gatchina, Leningrad region, 188300, Russia*
[43]*RIKEN, The Institute of Physical and Chemical Research, Wako, Saitama 351-0198, Japan*
[44]*RIKEN BNL Research Center, Brookhaven National Laboratory, Upton, New York 11973-5000, USA*
[45]*Physics Department, Rikkyo University, 3-34-1 Nishi-Ikebukuro, Toshima, Tokyo 171-8501, Japan*
[46]*Saint Petersburg State Polytechnic University, St. Petersburg, Russia*
[47]*Universidade de São Paulo, Instituto de Física, Caixa Postal 66318, São Paulo CEP05315-970, Brazil*
[48]*System Electronics Laboratory, Seoul National University, Seoul, Korea*
[49]*Chemistry Department, Stony Brook University, SUNY, Stony Brook, New York 11794-3400, USA*

[50]Department of Physics and Astronomy, Stony Brook University, SUNY, Stony Brook, New York 11794, USA
[51]SUBATECH (Ecole des Mines de Nantes, CNRS-IN2P3, Université de Nantes) BP 20722-44307, Nantes, France
[52]University of Tennessee, Knoxville, Tennessee 37996, USA
[53]Department of Physics, Tokyo Institute of Technology, Oh-okayama, Meguro, Tokyo 152-8551, Japan
[54]Institute of Physics, University of Tsukuba, Tsukuba, Ibaraki 305, Japan
[55]Vanderbilt University, Nashville, Tennessee 37235, USA
[56]Waseda University, Advanced Research Institute for Science and Engineering, 17 Kikui-cho, Shinjuku-ku, Tokyo 162-0044, Japan
[57]Weizmann Institute, Rehovot 76100, Israel
[58]Yonsei University, IPAP, Seoul 120-749, Korea
(Received 25 January 2008; published 3 December 2008)

For Au + Au collisions at 200 GeV, we measure neutral pion production with good statistics for transverse momentum, p_T, up to 20 GeV/c. A fivefold suppression is found, which is essentially constant for $5 < p_T < 20$ GeV/c. Experimental uncertainties are small enough to constrain any model-dependent parametrization for the transport coefficient of the medium, e.g., $\langle \hat{q} \rangle$ in the parton quenching model. The spectral shape is similar for all collision classes, and the suppression does not saturate in Au + Au collisions.

DOI: 10.1103/PhysRevLett.101.232301 PACS numbers: 25.75.Dw

Large transverse momentum (p_T) hadrons originate primarily from the fragmentation of hard scattered quarks or gluons. In high energy $p + p$ collisions, this is well described in the framework of perturbative QCD [1]. In ultrarelativistic heavy ion collisions, such hard scatterings occur in the early phase of the reaction, and the transiting partons serve as probes of the strongly interacting medium produced in the collisions. Lattice QCD predicts a phase transition to a plasma of deconfined quarks and gluons, which induces gluon radiation from the scattered parton and depletes hadron production at high p_T (''jet quenching'') [2,3]. The measurements in Au + Au collisions at Relativistic Heavy Ion Collider (RHIC) showed suppressed hadron yields in central collisions [4] as predicted [5,6], and motivated advanced theoretical studies of radiative energy loss.

All energy loss models must incorporate the space-time evolution of the medium, as it is not static, and the initial distribution of the partons throughout the medium. Models generally also include an input parameter for the medium density and/or the coupling. Different assumptions in the various models lead to similar descriptions of the π^0 suppression with different model-dependent parameters [7,8]. For instance, the Parton Quenching model (PQM) is a Monte Carlo program using the quenching weights from Baier-Dokshitzer-Mueller-Peigne-Schiff (BDMPS) [5] that combines the coupling strength with the color-charge density to create a single transport coefficient, often referred to as $\langle \hat{q} \rangle$ [9,10], which gives the $\langle p_T^2 \rangle$ transferred from the medium to the parton per mean free path.

Establishing the magnitude, p_T and centrality dependence of the suppression pattern up to the highest possible p_T is crucial to constrain the theoretical models and separate contributions of initial and final state effects from the energy loss mechanism. As neutral pions can be identified up to very high p_T, their suppression and its centrality (average pathlength) dependence puts important constraints on the energy loss. Whereas di-hadron suppression at high p_T may be somewhat more sensitive to medium opacity [11] than single hadron suppression, such improvement is contingent upon theoretical and experimental, statistical and systematic uncertainties.

This Letter reports on the measurement of π^0s up to $p_T = 20$ GeV/c in Au + Au collisions at $\sqrt{s_{NN}} =$ 200 GeV at RHIC, using the high statistics data taken in 2004. The results are used to extract the $\langle \hat{q} \rangle$ parameter of the PQM model for the most central collisions.

The analysis used 1.03×10^9 minimum bias events taken by the PHENIX experiment [12]. Collision centrality was determined from the correlation between the number of charged particles detected in the Beam-Beam Counters (BBC, $3.0 < |\eta| < 3.9$) and the energy measured in the Zero Degree Calorimeters (ZDC). A Glauber model Monte Carlo program with a simulation of the BBC and ZDC responses was used to estimate the average number of participating nucleons ($\langle N_{\mathrm{part}} \rangle$) and binary nucleon-nucleon collisions ($\langle N_{\mathrm{coll}} \rangle$) for each centrality bin [13].

Neutral pions were measured in the $\pi^0 \to \gamma\gamma$ decay channel with the photons reconstructed in the Electromagnetic Calorimeter (EMCal) located in the two central arms of PHENIX ($|\eta| \leq 0.35$). The EMCal [14] consists of two subsystems: six sectors of lead-scintillator sandwich calorimeter (PbSc) and two sectors of lead-glass Čerenkov calorimeter (PbGl) at the radial distance of about 5 m. The fine segmentation of the EMCal ($\delta\phi \times \delta\eta \sim 0.01 \times 0.01$ for PbSc and $\sim 0.008 \times 0.008$ for PbGl) ensures that the two photons from a $\pi^0 \to \gamma\gamma$ decay are well resolved up to $p_T^{\pi^0} \approx 12$ (PbSc) and 16 (PbGl) GeV/c. Data from the two subsystems were analyzed separately, and the fully corrected results were combined.

Details of the analysis including extraction of the raw π^0 yield, correction for acceptance, detector response, reconstruction efficiency have been described elsewhere [15,16]. In this analysis, the higher p_T range required an additional

TABLE I. Summary of the systematic uncertainties on the π^0 yield extracted independently with the PbSc (PbGl) electromagnetic calorimeters. The last row is the total systematic uncertainty on the combined spectra.

p_T (GeV/c)	2	6	10	16
uncertainty source	PbSc (PbGl)			
yield extraction (%)	3.0 (4.1)	3.0 (4.1)	3.0 (4.1)	3.0 (4.1)
PID efficiency (%)	3.5 (3.9)	3.5 (3.5)	3.5 (3.7)	3.5 (3.9)
Energy scale (%)	6.7 (9.0)	8.0 (9.2)	8.0 (8.2)	8.0 (12.3)
Acceptance (%)	1.5 (4.1)	1.5 (4.1)	1.5 (4.1)	1.5 (4.1)
π^0 merging (%)	$\cdots$ ($\cdots$)	$\cdots$ ($\cdots$)	4.4 ($\cdots$)	28 (4.8)
Conversion (%)	3.0 (2.5)	3.0 (2.5)	3.0 (2.5)	3.0 (2.5)
off-vertex π^0 (%)	1.5 (1.5)	1.5 (1.5)	1.5 (1.5)	1.5 (1.5)
Total (%)	8.7 (12)	9.8 (11)	11 (11)	30 (15)
PbSc and PbGl combined: Total (%)	7.0	7.5	7.6	14

correction for losses in the observed (raw) π^0s due to "cluster merging."

With increasing $p_T^{\pi^0}$, the minimum opening angle of the two photons decreases, and eventually they will be reconstructed as a single cluster. Such "merging" reaches 50% of the total raw yield at $p_T = 14$ GeV/c in the PbSc and at $p_T = 18$ GeV/c in the PbGl. Merged clusters were rejected by various shower profile cuts, and the loss was determined by simulated π^0s embedded into real events and analyzed with the same cuts. The systematic uncertainties were estimated by comparing π^0 yields in the PbSc extracted in bins of asymmetry $|E_{\gamma_1} - E_{\gamma_2}|/(E_{\gamma_1} + E_{\gamma_2})$ and also by comparing yields in the PbSc and PbGl.

We considered two sources of π^0s not coming from the vertex (off-vertex π^0): those produced by hadrons interacting with detector material (instrumental background) and feed-down products from weak decay of higher mass hadrons (physics background). Based upon simulations both types of background were found to be negligible ($< 1\%$ at $p_T > 2.0$ GeV/c) except for π^0s from K^0_S decay ($\approx 3\%$ of π^0 yield for $p_T > 1$ GeV/c), which has been subtracted from the data. Finally, the yields were corrected to the center of the p_T bins using the local slope.

The main sources of systematic uncertainties are yield extraction, efficiency corrections, energy scale, and merging, none of which exhibits a significant centrality dependence. The PbSc and PbGl have quite different systematics with all but one of them (off-vertex π^0) uncorrelated. Therefore, when combining their results, the total error is reduced in the weighted average of the two independent measurements. The final systematic uncertainties (1 standard deviation) on the spectra are shown in Table I.

The top panel of Fig. 1 shows the π^0 invariant yield for all centralities and minimum bias, combined from the independent PbSc and PbGl measurements which now extend to $p_T \sim 20$ GeV/c, 6 GeV/c higher than those published earlier [15]. In the overlap region, the results are consistent with the ones in [15] while the errors are reduced by a factor of 2 to 2.5. The bottom panel shows the consistency of the PbSc and PbGl results. The spectra are similar at all centralities: when fitting $p_T > 5$ GeV/c with a power-law function ($\propto p_T^{-n}$), the exponents vary from $n = 8.00 \pm 0.12$ in 0–5% to $n = 8.06 \pm 0.08$ in the 80–92% (most peripheral) bin. Note that $n = 8.22 \pm 0.09$ in $p + p$ collisions. The errors are combined statistical errors and systematic uncertainties.

To quantify the comparison of spectra in heavy ion and $p + p$ collisions, the nuclear modification factor

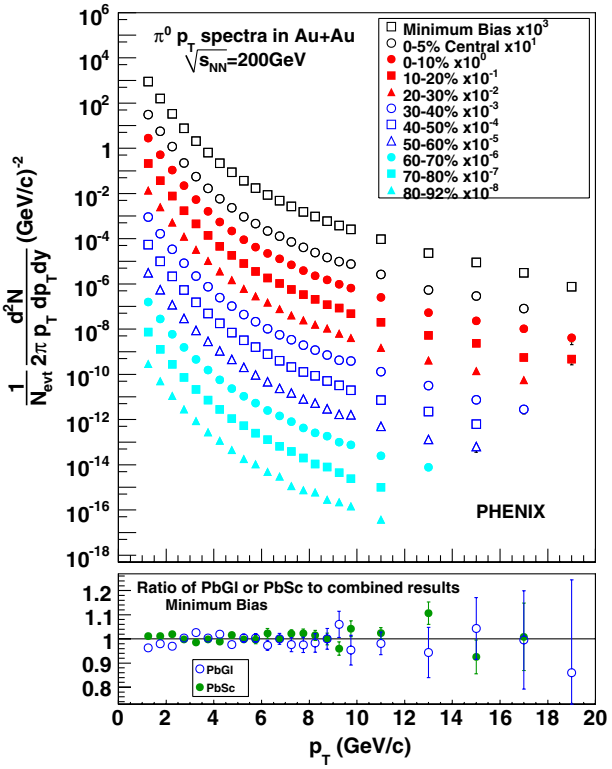

FIG. 1 (color online). Top: π^0 invariant yields for all centralities and minimum bias. Bottom: ratios of the (separately analyzed) PbSc and PbGl yields to the combined minimum bias invariant yield, which is shown in the top panel.

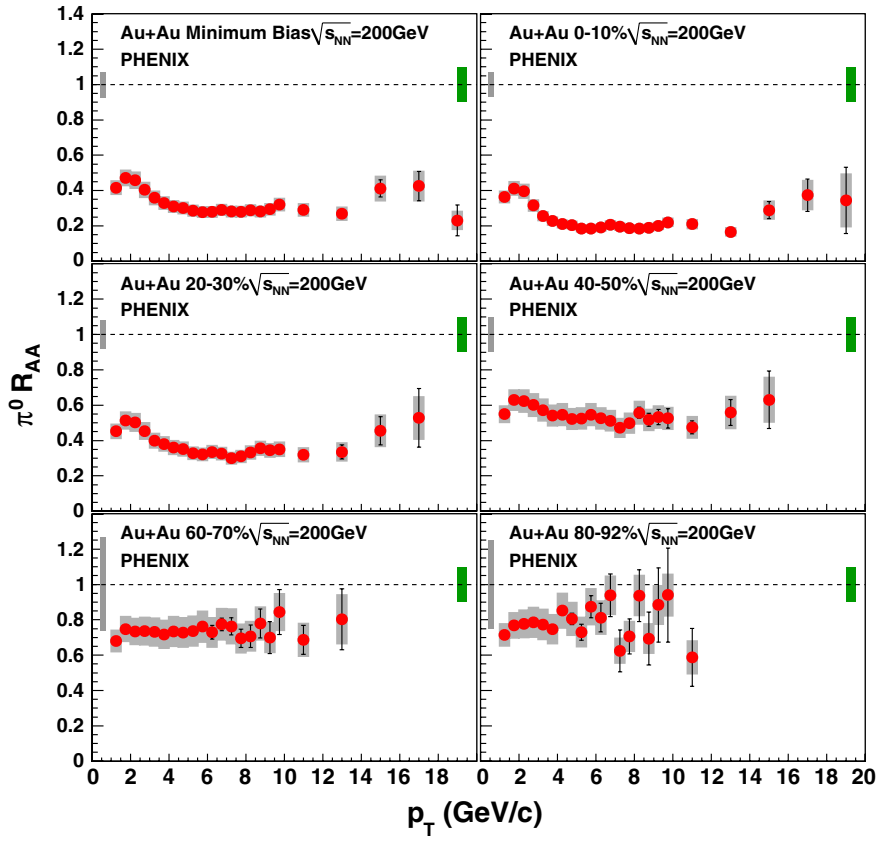

FIG. 2 (color online). Nuclear modification factor (R_{AA}) for π^0s. Error bars are statistical and p_T-uncorrelated errors, boxes around the points indicate p_T-correlated errors. Single box around $R_{AA} = 1$ on the left is the error due to N_{coll}, whereas the single box on the right is the overall normalization error of the $p + p$ reference spectrum.

$$R_{AA} = \frac{1/N_{evt} d^2N/dydp_T}{\langle T_{AB}\rangle d^2\sigma_{pp}/dydp_T} \quad (1)$$

is used, where σ_{pp} is the production cross section of the particle in $p + p$ collisions, and $\langle T_{AB}\rangle$ is the nuclear thickness function averaged over a range of impact parameters for the given centrality, calculated within a Glauber model [13]. Figures 2 and 3 show R_{AA} for π^0 at different centralities. The reference $p + p$ yield was obtained from the 2005 (Run-5) RHIC $p + p$ measurement [17].

R_{AA} reaches ~0.2 in 0–10% centrality at $p_T > 5$ GeV/c with very little (if any) p_T dependence. This trend is compatible with most current energy loss models but not with a semiopaque medium assumption, where R_{AA} would decrease with increasing p_T [7]. While its magnitude changes, the suppression pattern itself is remarkably similar at all centralities suggesting that the bulk R_{AA} (integrated over azimuth) is sensitive only to the N_{part} but not to the specific geometry. Consequently, study of the p_T-integrated R_{AA} vs centrality is instructive.

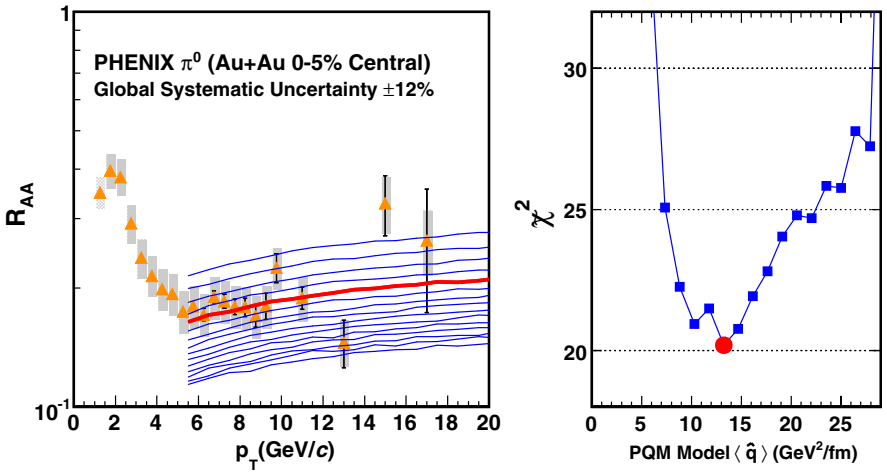

FIG. 3 (color online). Left: π^0 R_{AA} for the most central (0–5%) Au + Au collisions and PQM model calculations for different values of $\langle\hat{q}\rangle$. Right: $\tilde{\chi}^2(\epsilon_b, \epsilon_c, p)$ distribution for the corresponding values of $\langle\hat{q}\rangle$. The bold (red) curve in the left panel and the round (red) point in the right panel are the best fit values.

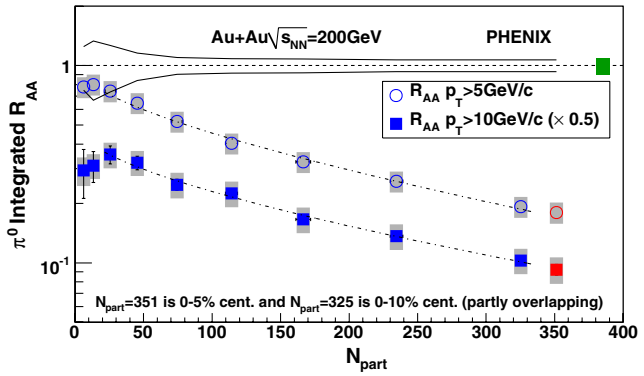

FIG. 4 (color online). Integrated nuclear modification factor (R_{AA}) for π^0 as a function of collision centrality expressed in terms of N_{part}. The error bars/bands are the same as in Fig. 2. The two lines at unity show the errors on $\langle N_{coll}\rangle$. The last two points correspond to partially overlapping centrality bins. The dashed lines show the fit explained in the text.

Figure 4 shows R_{AA} for π^0s integrated above $p_T > 5$ GeV/c, and $p_T > 10$ GeV/c, as a function of centrality. The last two points indicate overlapping 0–10% and 0–5% bins. In both cases, the suppression increases monotonically with N_{part} without any sign of saturation, suggesting that larger colliding systems (such as $U + U$ planned at RHIC) should exhibit even more suppression.

The common power-law behavior ($\propto p_T^{-n}$) in $p + p$ and Au + Au allows the suppression to be reinterpreted as a fractional energy loss $S_{loss} = 1 - R_{AA}^{1/(n-2)}$ where n is the power-law exponent, and we found that $S_{loss} \propto N_{part}^a$ [15,18]. Fitting the integrated R_{AA} with a function $R_{AA} = (1 - S_0 N_{part}^a)^{n-2}$, where n is fixed as 8.1, gives $a = 0.57 \pm 0.13$ for $N_{part} > 20$ for $p_T > 5$ GeV/c, and $a = 0.55 \pm 0.14$ for $p_T > 10$ GeV/c. The fit does not take errors on $p + p$ luminosity into account. The Gyulassy-Levai-Vitev (GLV) [6] and PQM [10] models predict that $a \approx 2/3$, which is consistent with the data. The fitted values of S_0 are $(9.0 \pm 6.1) \times 10^{-3}$ and $(9.4 \pm 7.3) \times 10^{-3}$ for $p_T > 5$ GeV/c and $p_T > 10$ GeV/c, respectively. The fits are shown as dashed lines in Fig. 4.

We use the highest centrality (0–5%) R_{AA} data as shown in Fig. 3 to constrain the PQM model parameter $\langle\hat{q}\rangle$. This must be done with careful consideration of the various, partially coupled error sources, leading to necessary refinement beyond a naive least square analysis. We calculate

$$\tilde{\chi}^2(\epsilon_b, \epsilon_c, p) = \left(\sum_{i=1}^{n} \frac{[y_i + \epsilon_b \sigma_{b_i} + \epsilon_c y_i \sigma_c - \mu_i(p)]^2}{\tilde{\sigma}_i^2}\right) + \epsilon_b^2 + \epsilon_c^2, \quad (2)$$

using theory curves $\mu_i(p)$ with different values of the input parameter p, i.e., $\langle\hat{q}\rangle$ in the PQM model. p_T-uncorrelated, statistical ⊕ systematic errors are σ_i, p_T-correlated errors are σ_{b_i} (boxes on Figs. 2 and 3), while uniform fractional shifts of all points are given by σ_c. All the measured values y_i are allowed to shift by the same fraction, ϵ_b, of their systematic error σ_{b_i} from the nominal values. The ϵ_c is a similar correlated fraction of σ_c, and $\tilde{\sigma}_i = \sigma_i(y_i + \epsilon_b \sigma_{b_i} + \epsilon_c y_i \sigma_c)/y_i$ is the point-to-point random error scaled by the multiplicative shift, so that the fractional error is unchanged by the shift, which is true for the present measurement. The best fit, $\tilde{\chi}^2_{min}$, the minimum of $\tilde{\chi}^2(\epsilon_b, \epsilon_c, p)$ by variation of ϵ_b, ϵ_c, and p, is found by standard methods. Further details are given in [16]. The right panel of Fig. 3 shows the minima of $\tilde{\chi}^2(\epsilon_b, \epsilon_c, p)$ by varying ϵ_b and ϵ_c for a wide range of values of the PQM model transport coefficient, $\langle\hat{q}\rangle$. Our data constrain $\langle\hat{q}\rangle$ as $13.2\ ^{+2.1}_{-3.2}$ and $^{+6.3}_{-5.2}$ GeV^2/fm at the 1 and 2 standard deviation levels. These constraints include only the experimental uncertainties and do not account for the large model-dependent differences in the quenching scenario and description of the medium. Extracting fundamental model-independent properties of the medium from the present data requires resolution of ambiguities and open questions in the models themselves, which also will have to account simultaneously for the p_T and centrality (average path-length) dependence. This work demonstrates the power of data for pion production in constraining the energy loss of partons. The large $\langle\hat{q}\rangle$ suggests that the matter consists of strongly coupled partons.

The $R_{AA}(p_T)$ for 0–5% was fitted with a simple linear function in the entire $p_T > 5$ GeV/c range as well: the slope of the fit is $0.0017\ ^{+0.0035}_{-0.0039}$ and $^{+0.0070}_{-0.0076}$ c/GeV at the 1 and 2 standard deviation levels [16]. The fact that R_{AA} as well as the power (n) for all spectra from $p + p$ to Au + Au are essentially constant proves that the dominant term in energy loss is proportional to p_T.

In summary, PHENIX has measured neutral pions in Au + Au collisions at $\sqrt{s_{NN}} = 200$ GeV at mid rapidity in the transverse momentum range of $1 < p_T < 20$ GeV/c, analyzing high statistics data taken in 2004. The shape of the spectra is similar for all centralities, as is the shape of $R_{AA}(p_T)$ at $p_T > 5$ GeV/c. In central collisions, the yield is suppressed by a factor of ~5 at 5 GeV/c compared to the binary scaled $p + p$ reference, and the suppression prevails with little or no change up to 20 GeV/c. The integrated R_{AA} vs centrality does not saturate at this nuclear size; also, the predicted $S_{loss} \propto N_{part}^{2/3}$ [6,10] is consistent with our data. In this picture, the energy loss increases with p_T. Using the 0–5% (most central) R_{AA}, we find that the transport coefficient $\langle\hat{q}\rangle$ of the PQM model is constrained to $13.2\ ^{+2.1}_{-3.2}$ ($^{+6.3}_{-5.2}$) GeV^2/fm at the one (two) σ level. The experimental evidence for a high transport coefficient, derived with remarkable accuracy due to high quality data and sophisticated new analysis, as presented here and in [16], reveals a totally nontrivial feature of the dense QCD medium created at RHIC. The shape of the spectra and the suppression pattern

indicate that the dominant term in energy loss is proportional to p_T.

We thank the staff of the Collider-Accelerator and Physics Departments at BNL for their vital contributions. We acknowledge support from the Office of Nuclear Physics in DOE Office of Science and NSF (USA), MEXT and JSPS (Japan), CNPq and FAPESP (Brazil), NSFC (China), MSMT (Czech Republic), IN2P3/CNRS, and CEA (France), BMBF, DAAD, and AvH (Germany), OTKA (Hungary), DAE (India), ISF (Israel), KRF and KOSEF (Korea), MES, RAS, and FAAE (Russia), VR and KAW (Sweden), U.S. CRDF for the FSU, US-Hungarian NSF-OTKA-MTA, and US-Israel BSF.

*Deceased

+PHENIX Spokesperson:
jacak@skipper.physics.sunysb.edu

[1] D. de Florian and W. Vogelsang, Phys. Rev. D **71**, 114004 (2005).
[2] M. Gyulassy and M. Plumer, Phys. Lett. B **243**, 432 (1990).
[3] X.-N. Wang and M. Gyulassy, Phys. Rev. Lett. **68**, 1480 (1992).
[4] K. Adcox *et al.*, Phys. Rev. Lett. **88**, 022301 (2001).
[5] R. Baier, Y. L. Dokshitzer, A. H. Mueller, S. Peigne, and D. Schiff, Nucl. Phys. B **484**, 265 (1997).
[6] M. Gyulassy, P. Levai, and I. Vitev, Phys. Rev. Lett. **85**, 5535 (2000).
[7] T. Renk, Phys. Rev. C **74**, 034906 (2006).
[8] R. Baier and D. Schiff, J. High Energy Phys. 09 (2006) 059.
[9] A. Dainese, C. Loizides, and G. Paic, Eur. Phys. J. C **38**, 461 (2005).
[10] C. Loizides, Eur. Phys. J. C **49**, 339 (2007).
[11] H. Zhang, J. F. Owens, E. Wang, and X.-N. Wang, Phys. Rev. Lett. **98**, 212301 (2007).
[12] K. Adcox *et al.*, Nucl. Instrum. Methods Phys. Res., Sect. A **499**, 469 (2003).
[13] M. L. Miller, K. Reygers, S. J. Sanders, and P. Steinberg, Annu. Rev. Nucl. Part. Sci. **57**, 205 (2007).
[14] L. Aphecetche *et al.*, Nucl. Instrum. Methods Phys. Res., Sect. A **499**, 521 (2003).
[15] S. S. Adler *et al.*, Phys. Rev. C **76**, 034904 (2007).
[16] A. Adare *et al.*, Phys. Rev. C **77**, 064907 (2008).
[17] A. Adare, Phys. Rev. D **76**, 051106 (2007).
[18] K. Adcox *et al.* (PHENIX), Nucl. Phys. A **757**, 184 (2005).

Quantitative constraints on the transport properties of hot partonic matter from semi-inclusive single high transverse momentum pion suppression in Au+Au collisions at $\sqrt{s_{NN}} = 200$ GeV

A. Adare,[8] S. Afanasiev,[22] C. Aidala,[9] N. N. Ajitanand,[49] Y. Akiba,[43,44] H. Al-Bataineh,[38] J. Alexander,[49] A. Al-Jamel,[38] K. Aoki,[28,43] L. Aphecetche,[51] R. Armendariz,[38] S. H. Aronson,[3] J. Asai,[44] E. T. Atomssa,[29] R. Averbeck,[50] T. C. Awes,[39] B. Azmoun,[3] V. Babintsev,[18] G. Baksay,[14] L. Baksay,[14] A. Baldisseri,[11] K. N. Barish,[4] P. D. Barnes,[31] B. Bassalleck,[37] S. Bathe,[4] S. Batsouli,[9,39] V. Baublis,[42] F. Bauer,[4] A. Bazilevsky,[3] S. Belikov,[3,21,*] R. Bennett,[50] Y. Berdnikov,[46] A. A. Bickley,[8] M. T. Bjorndal,[9] J. G. Boissevain,[31] H. Borel,[11] K. Boyle,[50] M. L. Brooks,[31] D. S. Brown,[38] D. Bucher,[34] H. Buesching,[3] V. Bumazhnov,[18] G. Bunce,[3,44] J. M. Burward-Hoy,[31] S. Butsyk,[31,50] S. Campbell,[50] J.-S. Chai,[23] B. S. Chang,[58] J.-L. Charvet,[11] S. Chernichenko,[18] J. Chiba,[24] C. Y. Chi,[9] M. Chiu,[9,19] I. J. Choi,[58] T. Chujo,[55] P. Chung,[49] A. Churyn,[18] V. Cianciolo,[39] C. R. Cleven,[16] Y. Cobigo,[11] B. A. Cole,[9] M. P. Comets,[40] P. Constantin,[21,31] M. Csanád,[13] T. Csörgő,[25] T. Dahms,[50] K. Das,[15] G. David,[3] M. B. Deaton,[1] K. Dehmelt,[14] H. Delagrange,[51] A. Denisov,[18] D. d'Enterria,[9] A. Deshpande,[44,50] E. J. Desmond,[3] O. Dietzsch,[47] A. Dion,[50] M. Donadelli,[47] J. L. Drachenberg,[1] O. Drapier,[29] A. Drees,[50] A. K. Dubey,[57] A. Durum,[18] V. Dzhordzhadze,[4,52] Y. V. Efremenko,[39] J. Egdemir,[50] F. Ellinghaus,[8] W. S. Emam,[4] A. Enokizono,[17,30] H. En'yo,[43,44] B. Espagnon,[40] S. Esumi,[54] K. O. Eyser,[4] D. E. Fields,[37,44] M. Finger,[5,22] M. Finger, Jr.,[5,22] F. Fleuret,[29] S. L. Fokin,[27] B. Forestier,[32] Z. Fraenkel,[57,*] J. E. Frantz,[9,50] A. Franz,[3] A. D. Frawley,[15] K. Fujiwara,[43] Y. Fukao,[28,43] S.-Y. Fung,[4] T. Fusayasu,[36] S. Gadrat,[32] I. Garishvili,[52] F. Gastineau,[51] M. Germain,[51] A. Glenn,[8,52] H. Gong,[50] M. Gonin,[29] J. Gosset,[11] Y. Goto,[43,44] R. Greiner de Cassagnac,[29] N. Grau,[21] S. V. Greene,[55] M. Groose Perdekamp,[19,44] T. Gunji,[7] H.-Å. Gustafsson,[33] T. Hachiya,[17,43] A. Hadj Henni,[51] C. Haegemann,[37] J. S. Haggerty,[3] M. N. Hagiwara,[1] H. Hamagaki,[7] R. Han,[41] H. Harada,[17] E. P. Hartouni,[30] K. Haruna,[17] M. Harvey,[3] E. Haslum,[33] K. Hasuko,[43] R. Hayano,[7] M. Heffner,[30] T. K. Hemmick,[50] T. Hester,[4] J. M. Heuser,[43] X. He,[16] H. Hiejima,[19] J. C. Hill,[21] R. Hobbs,[37] M. Hohlmann,[14] M. Holmes,[55] W. Holzmann,[49] K. Homma,[17] B. Hong,[26] T. Horaguchi,[43,53] D. Hornback,[52] M. G. Hur,[23] T. Ichihara,[43,44] K. Imai,[28,43] J. Imrek,[12] M. Inaba,[54] Y. Inoue,[43,45] D. Isenhower,[1] L. Isenhower,[1] M. Ishihara,[43] T. Isobe,[7] M. Issah,[49] A. Isupov,[22] B. V. Jacak,[50,†] J. Jia,[9] J. Jin,[9] O. Jinnouchi,[44] B. M. Johnson,[3] K. S. Joo,[35] D. Jouan,[40] F. Kajihara,[7,43] S. Kametani,[7,56] N. Kamihara,[43,53] J. Kamin,[50] M. Kaneta,[44] J. H. Kang,[58] H. Kanou,[43,53] T. Kawagishi,[54] D. Kawall,[44] A. V. Kazantsev,[27] S. Kelly,[8] A. Khanzadeev,[42] J. Kikuchi,[56] D. H. Kim,[35] D. J. Kim,[58] E. Kim,[48] Y.-S. Kim,[23] E. Kinney,[8] A. Kiss,[13] E. Kistenev,[3] A. Kiyomichi,[43] J. Klay,[30] C. Klein-Boesing,[34] L. Kochenda,[42] V. Kochetkov,[18] B. Komkov,[42] M. Konno,[54] D. Kotchetkov,[4] A. Kozlov,[57] A. Král,[10] A. Kravitz,[9] P. J. Kroon,[3] J. Kubart,[5,20] G. J. Kunde,[31] N. Kurihara,[7] K. Kurita,[45,43] M. J. Kweon,[26] Y. Kwon,[52,58] G. S. Kyle,[38] R. Lacey,[49] Y.-S. Lai,[9] J. G. Lajoie,[21] A. Lebedev,[21] Y. Le Bornec,[40] S. Leckey,[50] D. M. Lee,[31] M. K. Lee,[58] T. Lee,[48] M. J. Leitch,[31] M. A. L. Leite,[47] B. Lenzi,[47] H. Lim,[48] T. Liška,[10] A. Litvinenko,[22] M. X. Liu,[31] X. Li,[6] X. H. Li,[4] B. Love,[55] D. Lynch,[3] C. F. Maguire,[55] Y. I. Makdisi,[3] A. Malakhov,[22] M. D. Malik,[37] V. I. Manko,[27] Y. Mao,[41,43] L. Mašek,[5,20] H. Masui,[54] F. Matathias,[9,50] M. C. McCain,[19] M. McCumber,[50] P. L. McGaughey,[31] Y. Miake,[54] P. Mikeš,[5,20] K. Miki,[54] T. E. Miller,[55] A. Milov,[50] S. Mioduszewski,[3] G. C. Mishra,[16] M. Mishra,[2] J. T. Mitchell,[3] M. Mitrovski,[49] A. Morreale,[4] D. P. Morrison,[3] J. M. Moss,[31] T. V. Moukhanova,[27] D. Mukhopadhyay,[55] J. Murata,[43,45] S. Nagamiya,[24] Y. Nagata,[54] J. L. Nagle,[8] M. Naglis,[57] I. Nakagawa,[43,44] Y. Nakamiya,[17] T. Nakamura,[17] K. Nakano,[43,53] J. Newby,[30] M. Nguyen,[50] B. E. Norman,[31] A. S. Nyanin,[27] J. Nystrand,[33] E. O'Brien,[3] S. X. Oda,[7] C. A. Ogilvie,[21] H. Ohnishi,[43] I. D. Ojha,[55] H. Okada,[28,43] K. Okada,[44] M. Oka,[54] O. O. Omiwade,[1] A. Oskarsson,[33] I. Otterlund,[33] M. Ouchida,[17] K. Ozawa,[7] R. Pak,[3] D. Pal,[55] A. P. T. Palounek,[31] V. Pantuev,[50] V. Papavassiliou,[38] J. Park,[48] W. J. Park,[26] S. F. Pate,[38] H. Pei,[21] J.-C. Peng,[19] H. Pereira,[11] V. Peresedov,[22] D. Yu. Peressounko,[27] C. Pinkenburg,[3] R. P. Pisani,[3] M. L. Purschke,[3] A. K. Purwar,[31,50] H. Qu,[16] J. Rak,[21,37] A. Rakotozafindrabe,[29] I. Ravinovich,[57] K. F. Read,[39,52] S. Rembeczki,[14] M. Reuter,[50] K. Reygers,[34] V. Riabov,[42] Y. Riabov,[42] G. Roche,[32] A. Romana,[29,*] M. Rosati,[21] S. S. E. Rosendahl,[33] P. Rosnet,[32] P. Rukoyatkin,[22] V. L. Rykov,[43] S. S. Ryu,[58] B. Sahlmueller,[34] N. Saito,[28,43,44] T. Sakaguchi,[3,7,56] S. Sakai,[54] H. Sakata,[17] V. Samsonov,[42] H. D. Sato,[28,43] S. Sato,[3,24,54] S. Sawada,[24] J. Seele,[8] R. Seidl,[19] V. Semenov,[18] R. Seto,[4] D. Sharma,[57] T. K. Shea,[3] I. Shein,[18] A. Shevel,[42,49] T.-A. Shibata,[43,53] K. Shigaki,[17] M. Shimomura,[54] T. Shohjoh,[54] K. Shoji,[28,43] A. Sickles,[50] C. L. Silva,[47] D. Silvermyr,[39] C. Silvestre,[11] K. S. Sim,[26] C. P. Singh,[2] V. Singh,[2] S. Skutnik,[21] M. Slunečka,[5,22] W. C. Smith,[1] A. Soldatov,[18] R. A. Soltz,[30] W. E. Sondheim,[31] S. P. Sorensen,[52] I. V. Sourikova,[3] F. Staley,[11] P. W. Stankus,[39] E. Stenlund,[33] M. Stepanov,[38] A. Ster,[25] S. P. Stoll,[3] T. Sugitate,[17] C. Suire,[40] J. P. Sullivan,[31] J. Sziklai,[25] T. Tabaru,[44] S. Takagi,[54] E. M. Takagui,[47] A. Taketani,[43,44] K. H. Tanaka,[24] Y. Tanaka,[36] K. Tanida,[43,44] M. J. Tannenbaum,[3] A. Taranenko,[49] P. Tarján,[12] T. L. Thomas,[37] M. Togawa,[28,43] A. Toia,[50] J. Tojo,[43] L. Tomášek,[20] H. Torii,[43] R. S. Towell,[1] V.-N. Tram,[29] I. Tserruya,[57] Y. Tsuchimoto,[17,43] S. K. Tuli,[2] H. Tydesjö,[33] N. Tyurin,[18] C. Vale,[21] H. Valle,[55] H. W. van Hecke,[31] J. Velkovska,[55] R. Vertesi,[12] A. A. Vinogradov,[27] M. Virius,[10] V. Vrba,[20] E. Vznuzdaev,[42] M. Wagner,[28,43] D. Walker,[50] X. R. Wang,[38] Y. Watanabe,[43,44] J. Wessels,[34] S. N. White,[3] N. Willis,[40] D. Winter,[9] C. L. Woody,[3] M. Wysocki,[8] W. Xie,[4,44] Y. L. Yamaguchi,[56] A. Yanovich,[18] Z. Yasin,[4] J. Ying,[16] S. Yokkaichi,[43,44] G. R. Young,[39] I. Younus,[37] I. E. Yushmanov,[27] W. A. Zajc,[9] O. Zaudtke,[34] C. Zhang,[9,39] S. Zhou,[6] J. Zimányi,[25,*] and L. Zolin[22]

(PHENIX Collaboration)

[1]*Abilene Christian University, Abilene, Texas 79699, USA*

[2]*Department of Physics, Banaras Hindu University, Varanasi 221005, India*

[3]*Brookhaven National Laboratory, Upton, New York 11973-5000, USA*

 ©2008 The American Physical Society

[4]*University of California-Riverside, Riverside, California 92521, USA*
[5]*Charles University, Ovocný trh 5, Praha 1, 116 36, Prague, Czech Republic*
[6]*China Institute of Atomic Energy (CIAE), Beijing, People's Republic of China*
[7]*Center for Nuclear Study, Graduate School of Science, University of Tokyo, 7-3-1 Hongo, Bunkyo, Tokyo 113-0033, Japan*
[8]*University of Colorado, Boulder, Colorado 80309, USA*
[9]*Columbia University, New York, New York 10027 and Nevis Laboratories, Irvington, New York 10533, USA*
[10]*Czech Technical University, Zikova 4, 166 36 Prague 6, Czech Republic*
[11]*Dapnia, CEA Saclay, F-91191, Gif-sur-Yvette, France*
[12]*Debrecen University, H-4010 Debrecen, Egyetem tér 1, Hungary*
[13]*ELTE, Eötvös Loránd University, H-1117 Budapest, Pázmány P. s. 1/A, Hungary*
[14]*Florida Institute of Technology, Melbourne, Florida 32901, USA*
[15]*Florida State University, Tallahassee, Florida 32306, USA*
[16]*Georgia State University, Atlanta, Georgia 30303, USA*
[17]*Hiroshima University, Kagamiyama, Higashi-Hiroshima 739-8526, Japan*
[18]*IHEP Protvino, State Research Center of Russian Federation, Institute for High Energy Physics, Protvino, RU-142281, Russia*
[19]*University of Illinois at Urbana-Champaign, Urbana, Illinois 61801, USA*
[20]*Institute of Physics, Academy of Sciences of the Czech Republic, Na Slovance 2, 182 21 Prague 8, Czech Republic*
[21]*Iowa State University, Ames, Iowa 50011, USA*
[22]*Joint Institute for Nuclear Research, RU-141980 Dubna, Moscow Region, Russia*
[23]*KAERI, Cyclotron Application Laboratory, Seoul, Korea*
[24]*KEK, High Energy Accelerator Research Organization, Tsukuba, Ibaraki 305-0801, Japan*
[25]*KFKI Research Institute for Particle and Nuclear Physics of the Hungarian Academy of Sciences (MTA KFKI RMKI), H-1525 Budapest 114, P. O. Box 49, Budapest, Hungary*
[26]*Korea University, Seoul, 136-701, Korea*
[27]*Russian Research Center "Kurchatov Institute," Moscow, Russia*
[28]*Kyoto University, Kyoto 606-8502, Japan*
[29]*Laboratoire Leprince-Ringuet, Ecole Polytechnique, CNRS-IN2P3, Route de Saclay, F-91128, Palaiseau, France*
[30]*Lawrence Livermore National Laboratory, Livermore, California 94550, USA*
[31]*Los Alamos National Laboratory, Los Alamos, New Mexico 87545, USA*
[32]*LPC, Université Blaise Pascal, CNRS-IN2P3, Clermont-Fd, F-63177 Aubiere Cedex, France*
[33]*Department of Physics, Lund University, Box 118, SE-221 00 Lund, Sweden*
[34]*Institut für Kernphysik, University of Muenster, D-48149 Muenster, Germany*
[35]*Myongji University, Yongin, Kyonggido 449-728, Korea*
[36]*Nagasaki Institute of Applied Science, Nagasaki-shi, Nagasaki 851-0193, Japan*
[37]*University of New Mexico, Albuquerque, New Mexico 87131, USA*
[38]*New Mexico State University, Las Cruces, New Mexico 88003, USA*
[39]*Oak Ridge National Laboratory, Oak Ridge, Tennessee 37831, USA*
[40]*IPN-Orsay, Universite Paris Sud, CNRS-IN2P3, BP1, F-91406, Orsay, France*
[41]*Peking University, Beijing, People's Republic of China*
[42]*PNPI, Petersburg Nuclear Physics Institute, Gatchina, Leningrad region, RU-188300, Russia*
[43]*RIKEN, The Institute of Physical and Chemical Research, Wako, Saitama 351-0198, Japan*
[44]*RIKEN BNL Research Center, Brookhaven National Laboratory, Upton, New York 11973-5000, USA*
[45]*Physics Department, Rikkyo University, 3-34-1 Nishi-Ikebukuro, Toshima, Tokyo 171-8501, Japan*
[46]*Saint Petersburg State Polytechnic University, St. Petersburg, Russia*
[47]*Universidade de São Paulo, Instituto de Física, Caixa Postal 66318, São Paulo CEP05315-970, Brazil*
[48]*System Electronics Laboratory, Seoul National University, Seoul, Korea*
[49]*Chemistry Department, Stony Brook University, Stony Brook, SUNY, New York 11794-3400, USA*
[50]*Department of Physics and Astronomy, Stony Brook University, SUNY, Stony Brook, New York 11794, USA*
[51]*SUBATECH (Ecole des Mines de Nantes, CNRS-IN2P3, Université de Nantes) BP 20722-44307, Nantes, France*
[52]*University of Tennessee, Knoxville, Tennessee 37996, USA*
[53]*Department of Physics, Tokyo Institute of Technology, Oh-okayama, Meguro, Tokyo 152-8551, Japan*
[54]*Institute of Physics, University of Tsukuba, Tsukuba, Ibaraki 305, Japan*
[55]*Vanderbilt University, Nashville, Tennessee 37235, USA*
[56]*Waseda University, Advanced Research Institute for Science and Engineering, 17 Kikui-cho, Shinjuku-ku, Tokyo 162-0044, Japan*
[57]*Weizmann Institute, Rehovot 76100, Israel*
[58]*Yonsei University, IPAP, Seoul 120-749, Korea*
(Received 10 January 2008; published 24 June 2008)

The PHENIX experiment has measured the suppression of semi-inclusive single high-transverse-momentum π^0's in Au+Au collisions at $\sqrt{s_{NN}} = 200$ GeV. The present understanding of this suppression is in terms of energy loss of the parent (fragmenting) parton in a dense color-charge medium. We have performed a quantitative comparison between various parton energy-loss models and our experimental data. The statistical point-to-point uncorrelated as well as correlated systematic uncertainties are taken into account in the comparison. We detail this methodology and the resulting constraint on the model parameters, such as the initial color-charge density dN^g/dy, the medium transport coefficient $\langle\hat{q}\rangle$, or the initial energy-loss parameter ϵ_0. We find that high-transverse-momentum π^0 suppression in Au+Au collisions has sufficient precision to constrain these model-dependent parameters at the ±20–25% (one standard deviation) level. These constraints include only the experimental uncertainties, and further studies are needed to compute the corresponding theoretical uncertainties.

DOI: 10.1103/PhysRevC.77.064907 PACS number(s): 25.75.Dw

I. INTRODUCTION

Heavy-ion collisions at very high energy are of interest due to the formation of a novel partonic medium approximately the size of a large nucleus, but with an energy density exceeding that of normal nuclei by considerably more than an order of magnitude. At such high energy densities, it is believed that quarks and gluons are no longer confined in hadrons but may be constituents of a quark-gluon plasma with characteristics of a near-perfect fluid (for a detailed review see Ref. [1]). Experiments at the Relativistic Heavy Ion Collider (RHIC) have already demonstrated that a very hot and dense, strongly interacting medium is created in Au+Au collisions at $\sqrt{s_{NN}} =$ 200 GeV [2]. The goal is now to quantitatively determine the properties of this medium.

Important properties of the medium include the density of color charges as well as the exchange of transverse momentum between parton probes and the medium. In rare events, in addition to the creation of the medium, there can also be a hard scattering (high-Q^2 process) between the colliding partons that, at leading order, sends two high-energy quark or gluon partons in opposite transverse directions. These high-energy partons can be utilized to probe both the color-charge density of the medium and the coupling strength between the parton and the medium. There are various calculational frameworks for modeling these interactions (for a detailed review see Ref. [3]).

In this article, we consider four specific calculations of parton energy loss (discussed below): the parton quenching model (PQM) [4], the Gyulassy-Levai-Vitev (GLV) model [5], the Wicks-Horowitz-Djordjevic-Gyulassy (WHDG) model [6], and the Zhang-Owens-Wang-Wang (ZOWW) model [7]. We detail a quantitative method of assessing the sensitivity of the latest measurements to the input parameters of these models that characterize the initial parton density or medium transport coefficients.

II. EXPERIMENTAL RESULTS

During the 2004 data-taking period at the Relativistic Heavy Ion Collider, the PHENIX experiment recorded an integrated luminosity of 0.24 nb^{-1} in $\sqrt{s_{NN}} = 200$ GeV Au+Au collisions, which extends the measurement of π^0 to much higher p_T than previous data sets allowed. The results and further details of this measurement are given in Ref. [9]. A brief description is given below.

The PHENIX experiment measures π^0's via the two-photon decay mode with two types of highly segmented ($\Delta\eta \times \Delta\phi \approx 0.01 \times 0.01$) electromagnetic calorimeters (EMCal) located at the radial distance of approximately 5 m from the vertex [8]. One is a lead scintillator sampling calorimeter (PbSc), which covers the geometrical acceptance of $|\eta| < 0.35$ and $\Delta\phi = 3/4\pi$. The other is a lead glass Cerenkov calorimeter (PbGl), whose geometrical coverage is $|\eta| < 0.35$ and $\Delta\phi = \pi/4$. The energy resolution of the PbSc and PbGl calorimeters as determined from test beam measurements are given by $8.1\%/\sqrt{E(\text{GeV})} \oplus 2.1\%$ and $5.9\%/\sqrt{E(\text{GeV})} \oplus 0.8\%$, respectively. The energy calibration of the EMCal modules is based on the measured position of the π^0 mass peak, the deposited energy of minimum ionizing particles that traverse the calorimeter, and the ratio of energy to momentum that is expected to be about 1 for electrons identified by the ring-imaging Cerenkov detector. The systematic uncertainty on the energy scale is ∼1%, which corresponds to ∼7–12% uncertainty on the invariant π^0 yield over the p_T range of the measurement.

Neutral pions were reconstructed in their $\pi^0 \to \gamma\gamma$ decay channel. Photon candidates are identified by applying particle identification cuts based mainly on the shower shape. The invariant mass for all photon-pair combinations within one event that satisfy cuts on the energy asymmetry $|E_{\gamma 1} - E_{\gamma 2}|/|E_{\gamma 1} + E_{\gamma 2}| < 0.8$ were calculated in bins of p_T. The combinatorial background is determined by combining into pairs uncorrelated photons from different events with similar centrality, reaction plane, and vertex location.

The raw π^0 yield was obtained by integrating the mass peak region of the invariant mass distribution after subtracting the combinatorial background. The raw spectra are corrected for the detector response (energy resolution), the reconstruction efficiency, and occupancy effects (e.g., overlapping clusters). These corrections are made by embedding simulated single π^0's from a full GEANT simulation of the PHENIX detector into real events and analyzing the embedded π^0 events with the same analysis cuts as used with real events.

After computing the invariant yields in Au+Au collisions [9], the medium effects are quantified using the nuclear modification factor (R_{AA}). R_{AA} is the ratio between the

*Deceased
†PHENIX Spokesperson: jacak@skipper.physics.sunysb.edu

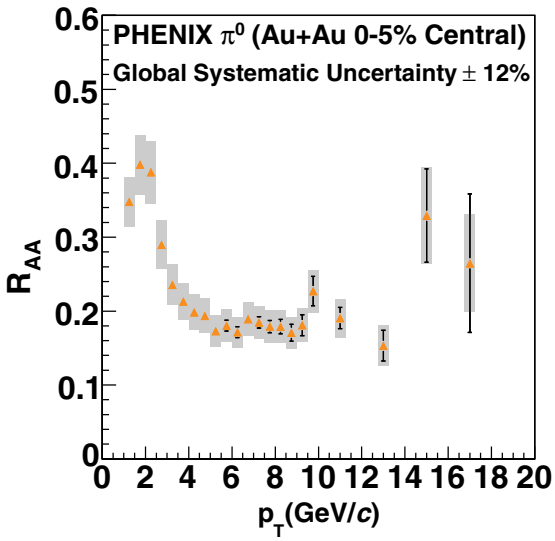

FIG. 1. (Color online) The π^0 nuclear suppression factor $R_{\rm AA}$ as a function of transverse momentum for 0–5% Au+Au collisions at $\sqrt{s_{NN}} = 200$ GeV. Point-to-point uncorrelated statistical and systematic uncertainties are shown as uncertainty bars. Correlated systematic uncertainties are shown as gray boxes around the data points. The global scale factor systematic uncertainty is ±12%.

measured yield and the expected yield for pointlike processes scaled from the $p+p$ result and is defined as:

$$\mathrm{R_{AA}}(p_T) = \frac{\left(1/N_{\rm AA}^{\rm evt}\right) d^2 N_{\rm AA}^{\pi^0}/dp_T dy}{\langle T_{\rm AA}\rangle d^2\sigma_N^{\pi^0}/dp_T dy}, \qquad (1)$$

where $\langle T_{\rm AA}\rangle$ is the average Glauber nuclear overlap function for the Au+Au centrality bin under consideration

$$\langle T_{\rm AA}\rangle \equiv \frac{\int T_{\rm AA}(\mathbf{b}) d\mathbf{b}}{\int \left(1 - e^{-\sigma_{NN}^{\rm inel} T_{\rm AA}(\mathbf{b})}\right) d\mathbf{b}} = \left\langle N_{\rm coll}^{\sigma_{NN}}\right\rangle / \sigma_{NN}^{\rm inel}, \qquad (2)$$

where $\langle N_{\rm coll}^{\sigma_{NN}}\rangle$ is the average number of inelastic nucleon-nucleon collisions for the Au+Au centrality bin under consideration calculated with inelastic nucleon-nucleon cross section $\sigma_{NN}^{\rm inel}$.

The measured nuclear modification factors for 0–5% central Au+Au reactions at $\sqrt{s_{NN}} = 200$ GeV are shown in Fig. 1 and tabulated in Table I with statistical and systematic uncertainties. The systematic uncertainties fall into three categories. We denote type A uncertainties as systematic uncertainties that are uncorrelated from point to point. Type A systematic uncertainties are added in quadrature with statistical uncertainties and are shown as uncertainty bars. Partially correlated point-to-point systematic uncertainties are broken into a 100% correlated component, referred to as type B, and the above mentioned type A. The type B uncertainties are shown as gray boxes. The sources of type B uncertainties are discussed in detail in Ref. [9] and are dominated by energy scale uncertainties but also have contributions from photon shower merging at the highest p_T (≈15–20 GeV/c). There are also global systematic uncertainties, referred to as type C uncertainties, that are globally correlated systematic uncertainties (i.e., where all data points move by the same multiplicative factor). The type C uncertainties are ±12% and derive from uncertainties in the calculated nuclear thickness function and from the $p+p$ absolute normalization.

TABLE I. The π^0 nuclear suppression factor $R_{\rm AA}$ as a function of transverse momentum for 0-5% Au+Au collisions at $\sqrt{s_{NN}} =$ 200 GeV. The type A, B, and C uncertainties are tabulated for each point.

p_T (GeV/c)	$R_{\rm AA}$	Type A uncertainty	Type B uncertainty	Type C uncertainty
1.25	0.347	±0.007	±0.033	±0.041
1.75	0.398	±0.007	±0.040	±0.047
2.25	0.387	±0.007	±0.042	±0.046
2.75	0.289	±0.006	±0.032	±0.034
3.25	0.235	±0.005	±0.027	±0.028
3.75	0.21	±0.005	±0.024	±0.025
4.25	0.198	±0.005	±0.024	±0.023
4.75	0.193	±0.006	±0.023	±0.023
5.25	0.172	±0.006	±0.021	±0.020
5.75	0.180	±0.007	±0.021	±0.021
6.25	0.171	±0.007	±0.020	±0.020
6.75	0.189	±0.007	±0.022	±0.022
7.25	0.184	±0.008	±0.022	±0.022
7.75	0.179	±0.008	±0.021	±0.021
8.25	0.178	±0.010	±0.021	±0.021
8.75	0.170	±0.011	±0.020	±0.020
9.25	0.180	±0.014	±0.022	±0.021
9.75	0.226	±0.019	±0.028	±0.027
11.00	0.190	±0.014	±0.026	±0.022
13.00	0.153	±0.020	±0.027	±0.018
15.00	0.329	±0.063	±0.065	±0.039
17.00	0.264	±0.093	±0.065	±0.031

III. THEORETICAL CALCULATIONS

The parton quenching model (PQM) [4] encodes the dissipative properties of the system in terms of a single transport coefficient, often referred to as $\hat{q}$, obtained as the product of the parton-medium cross section times the color-charge density. The average $\hat{q}$ quantifies the average squared transverse momentum transferred from the medium to the parton per mean free path. The PQM model is a Monte Carlo program constructed using the quenching weights from BDMPS [10,11]. BDMPS is a perturbative calculation explicitly including only coherent radiative energy loss for the parton via gluon bremsstrahlung. The PQM model incorporates a realistic transverse collision geometry, though with a static medium. It is also notable that the PQM model does not include initial state multiple scattering or modified nuclear parton distribution functions (PDF's).

The Gyulassy-Levai-Vitev (GLV) [5] model is a formalism developed to calculate in-medium gluon bremsstrahlung. An analytic expression is derived for the single gluon emission spectrum to all orders in opacity, assuming an infrared cutoff given by the plasmon frequency. Thus, within this framework, one can extract the local color-charge density. The color-charge density is written simply as dN^g/dy, assuming a completely

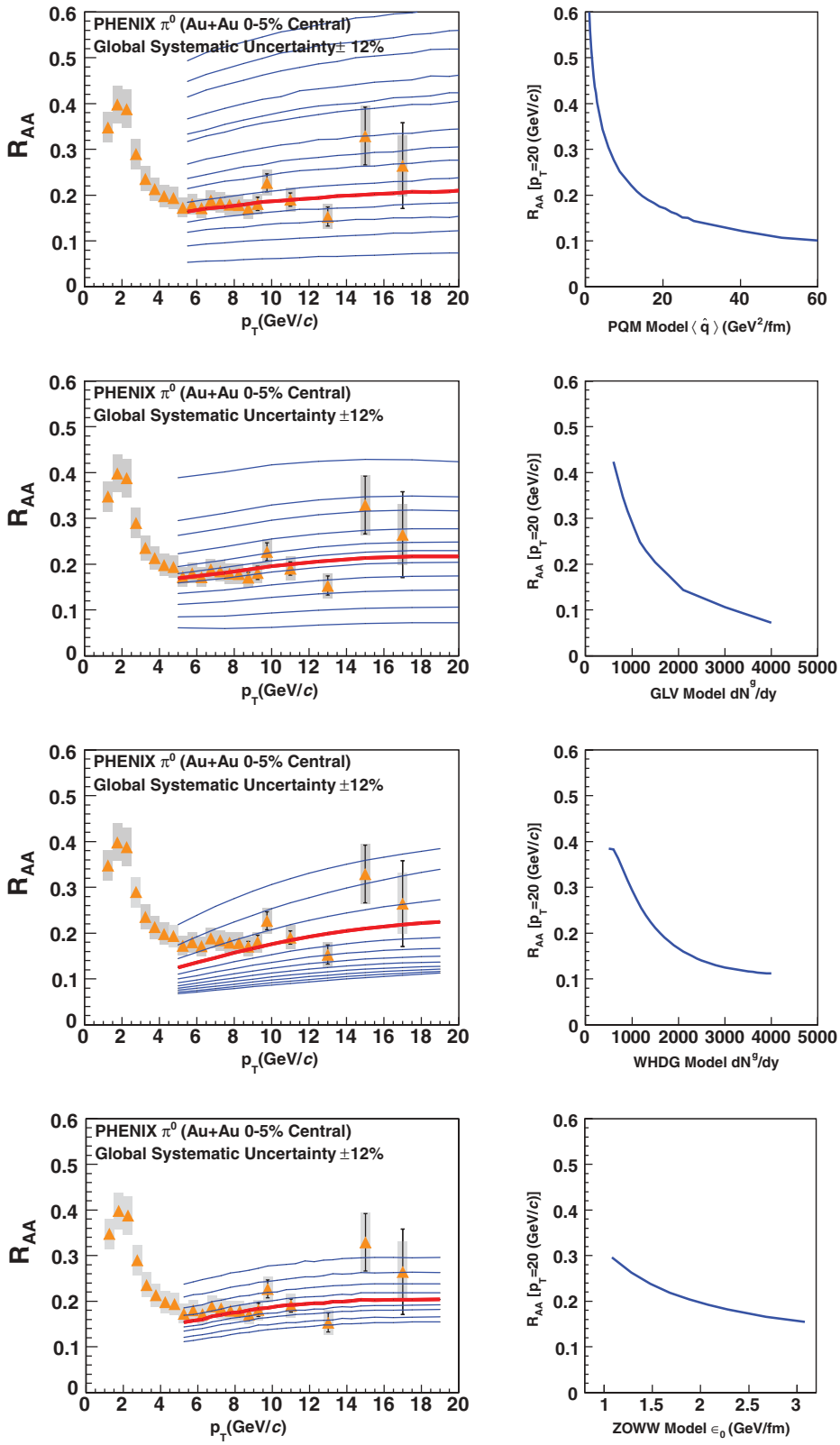

FIG. 2. (Color online) Left panels show π^0 $R_{\rm AA}$ for 0–5% Au+Au collisions at $\sqrt{s_{NN}} = 200$ GeV and predictions from PQM [4], GLV [12], WHDG [6], and ZOWW [7] models with (from top to bottom) $\langle \hat{q} \rangle$ values of 0.3, 0.9, 1.2, 1.5, 2.1, 2.9, 4.4, 5.9, 7.4, 10.3, 13.2, 17.7, 25.0, 40.5, 101.4 GeV^2/fm; dN^g/dy values of 600, 800, 900, 1050, 1175, 1300, 1400, 1500, 1800, 2100, 3000, 4000; dN^g/dy values of 500, 800, 1100, 1400, 1700, 2000, 2300, 2600, 2900, 3200, 3500, 3800; and ϵ_0 values of 1.08, 1.28, 1.48, 1.68, 1.88, 2.08, 2.28, 2.68, 3.08 GeV/fm. Red lines indicate the best fit cases of (top) $\langle \hat{q} \rangle = 13.2$, (upper middle) $dN^g/dy = 1400$, (lower middle) $dN^g/dy = 1400$, and (bottom) $\epsilon_0 = 1.88$ GeV/fm. Right panels show $R_{\rm AA}$ at $p_{\rm T} = 20$ GeV/c.

gluonic medium, or an equivalent $dN^{q,g}/dy$ for a mixture of quarks and gluons. In Ref. [12], using a realistic transverse collision geometry, the authors calculate *a priori*, without energy loss, the single fixed geometrical average path length from the production point to the medium edge, $\langle L \rangle_{\rm prod}$, and use it to calculate the parton energy loss in a Bjorken expanding medium [13]. The calculation also incorporates initial-state multiple scattering effects and modified nuclear PDF's.

The Wicks-Horowitz-Djordjevic-Gyulassy (WHDG) [6] model utilizes the generalized GLV formalism [15] for

radiative energy loss described above. In addition, their calculation includes a convolution of radiative energy loss and collisional energy-loss mechanisms. A realistic transverse collision geometry with a Bjorken time expansion is utilized, and then a full distribution of parton paths through the medium is calculated. The WHDG model does not yet include initial-state multiple scattering or modified PDF's.

The Zhang-Owens-Wang-Wang (ZOWW) [7] calculations incorporate a next-to-leading-order perturbative QCD parton model with modified jet fragmentation functions. The calculation explicitly includes only radiative energy loss. A hard-sphere transverse collision geometry with a one-dimensional expanding medium is utilized. The calculation also incorporates initial-state multiple scattering effects and modified nuclear PDF's.

The top left panel of Fig. 2 shows a comparison of the experimental data with calculated results from the PQM energy-loss model (as described in Ref. [4]) corresponding to different $\langle\hat{q}\rangle$ values [16]. Note that only a subset of all the calculations corresponding to different $\langle\hat{q}\rangle$ values are shown in the figure for clarity. The upper right panel shows the π^0 suppression factor predicted at $p_T = 20$ GeV/c from the PQM model as a function of the $\langle\hat{q}\rangle$ value. One can see that as the $\langle\hat{q}\rangle$ increases, the additional suppression becomes smaller (i.e., saturates). This saturation effect was noted in Ref. [14], and interpreted as a result of the dominance of preferential surface emission.

The other panels of Fig. 2 show similar comparisons of the experimental data with calculated results utilizing the GLV numerical calculation framework (as described in Ref. [12]) corresponding to different dN^g/dy values [17]; the WHDG calculational framework (as described in Ref. [6]) corresponding to different dN^g/dy values [18]; and the ZOWW calculational framework (as detailed in Ref. [7]) corresponding to different ϵ_0 values [19]. Note that all calculations are shown only for $p_T > 5$ GeV/c as that is where the calculations are considered applicable.

In Fig. 3, the same π^0 suppression factor predicted at $p_T = 20$ GeV/c from the PQM model as a function of the $\langle\hat{q}\rangle$ value is shown, but in this case with a log-x and log-y scale. The $R_{\rm AA} \approx 0.75/\sqrt{\langle\hat{q}\rangle}$ with $\langle\hat{q}\rangle$ in units of GeV^2/fm over the range $5 < \langle\hat{q}\rangle < 100$. This means that over this range for a given fractional change in $\langle\hat{q}\rangle$ there is always the same fractional change in $R_{\rm AA}$ (i.e., $\Delta\langle\hat{q}\rangle/\langle\hat{q}\rangle \approx 2.0 \times \Delta R_{\rm AA}/R_{\rm AA}$).

IV. COMBINED RESULTS

The task is now to detail how the experimental uncertainties (statistical and systematic) constrain the model parameters that are reflected in the suppression factors. As described previously, the uncertainties of the measured points are separated into type A (p_T-uncorrelated, statistical $\oplus$ systematic, σ_i), type B (p_T-correlated, σ_{b_i}, boxes on Fig. 1), type C (normalization, uniform fractional shift for all points, σ_c), where the σ's represent the standard deviations of the assumed Gaussian distributed uncertainties. With the predicted theory value $\mu_i(p)$ for each data point calculated for different values of the input parameter p, we perform a least-squares fit the to the theory

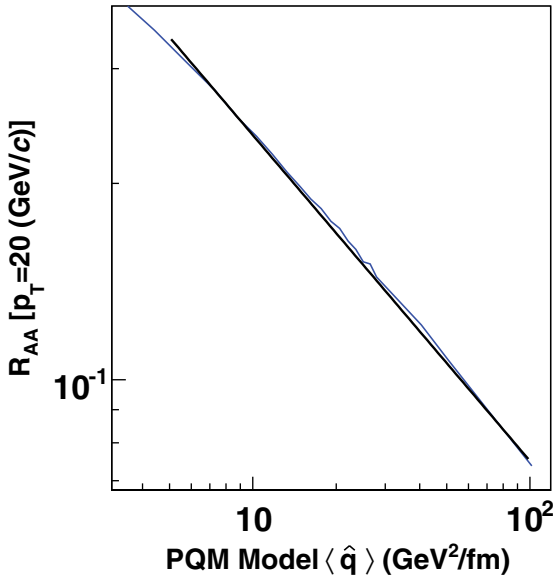

FIG. 3. (Color online) The nuclear suppression factors at $p_T = 20$ GeV/c for PQM as a function of $\langle\hat{q}\rangle$ are shown as a blue line with a log-x and log-y display. Also shown is the functional form $\Delta\langle\hat{q}\rangle/\langle\hat{q}\rangle \approx 2.0 \times \Delta R_{\rm AA}/R_{\rm AA}$) over the range $5 < \langle\hat{q}\rangle < 100$ GeV^2/fm.

by finding the values of $p, \epsilon_b, \epsilon_c$, that minimize:

$$\tilde{\chi}^2(\epsilon_b, \epsilon_c, p) = \left\{ \sum_{i=1}^{n} \frac{[y_i + \epsilon_b \sigma_{b_i} + \epsilon_c y_i \sigma_c - \mu_i(p)]^2}{\tilde{\sigma}_i^2} + \epsilon_b^2 + \epsilon_c^2 \right\}, \quad (3)$$

where ϵ_b and ϵ_c are the fractions of the type B and C systematic uncertainties that all points are displaced together and where $\tilde{\sigma}_i = \sigma_i(y_i + \epsilon_b \sigma_{b_i} + \epsilon_c y_i \sigma_c)/y_i$ is the point-to-point random uncertainty scaled by the multiplicative shift in y_i such that the fractional uncertainty is unchanged under systematic shifts, which is true for the present measurement. For clarity of presentation, the derivation of Eq. (3) (above) is given in Appendix A.

For any fixed values of ϵ_b, ϵ_c, Eq. (3) follows the χ^2 distribution with $n+2$ degrees of freedom, for testing the theoretical predictions $\mu_i(p)$, because it is the sum of $n+2$ Gaussian distributed random variables. The best fit, $\tilde{\chi}^2_{\rm min}$, the minimum of $\tilde{\chi}^2(\epsilon_b, \epsilon_c, p)$ by variation of ϵ_b, ϵ_c, and p, is found by standard methods (for example, using a MINUIT type minimization algorithm) and should follow the χ^2 distribution with $n-1$ degrees of freedom. The correlated uncertainties of the best fit parameters are estimated in the Gaussian approximation by $\tilde{\chi}^2(\epsilon_b, \epsilon_c, p) = \tilde{\chi}^2_{\rm min} + N^2$ for N standard deviation (σ) uncertainties.

The present experimental type B uncertainties have point-to-point correlations whose exact correlation matrix is difficult to evaluate precisely. Thus, we consider two limiting correlation cases. The first is where the type B uncertainties are 100% correlated, i.e., all points move in the same direction by the same fraction of their respective type B uncertainty. The second is where the type B uncertainties are correlated such that the

low p_T and high p_T points may shift with opposite sign (and linearly scaled in between), thus tilting the R_{AA} either upward or downward as a function of p_T. The minimum $\tilde{\chi}^2$ of the two cases is used for each constraint.

We take as a first example the resulting theory predictions from the PQM model. For each calculation characterized by the $\langle\hat{q}\rangle$, we calculate $\tilde{\chi}^2$. We determine this value by varying ϵ_b and ϵ_c (the systematic offsets) until we obtain the minimum $\tilde{\chi}^2$. These values are shown in Fig. 4 in the top panel. One can see that the overall lowest $\tilde{\chi}^2$ value corresponds to $\langle\hat{q}\rangle \approx 13$ GeV^2/fm.

We then calculate the p value for the $\tilde{\chi}^2$ [the minimum of Eq. (3)], where the p value is defined as:

$$p\text{ value} = \int_{\tilde{\chi}^2}^{\infty} \chi^2_{(n_d)}(z)dz, \tag{4}$$

where $\chi^2_{(n_d)}$ is the chi-square distribution with the appropriate number of degrees of freedom, n_d [20]. This calculation is valid because the goodness-of-fit statistic $\tilde{\chi}^2$ follows a standard χ^2 distribution. Note that p value is the probability, under the assumption that the hypothesis is correct, of randomly obtaining data with a worse fit to the hypothesis than the experimental data under test [20]. These p value s are shown in the middle panel of Fig. 4.

We find the overall minimum (or best) $\tilde{\chi}^2$ and then compute which $\langle\hat{q}\rangle$ scenarios are 1 and 2 standard deviations away from this minimum. The PQM transport coefficient $\langle\hat{q}\rangle$ is constrained by the experimental data as $13.2^{+2.1}_{-3.2}$ and $^{+6.3}_{-5.2}$ GeV^2/fm at the 1 and 2 standard deviation levels, respectively. The two standard deviation constraints correspond to the 95% confidence intervals. We note that this range of large $\langle\hat{q}\rangle$ values is currently under intense theoretical debate (see, for example, Ref. [21]). Thus, the quoted $\langle\hat{q}\rangle$ constraint is for the model-dependent parameter of the specific PQM implementation, and relating this parameter to the fundamental value of the mean transverse momentum squared exchange per unit length traversed may substantially lower the value.

We apply the identical procedure to the GLV, WHDG, and ZOWW calculations and show those results in Figs. 5, 6, and 7. For the GLV calculations this results in a constraint of $dN^g/dy = 1400^{+270}_{-150}$ and $^{+510}_{-290}$ at the 1 and 2 standard deviation levels, respectively. All of these constraint results are summarized in Table II. Constraints for the WHDG model are $dN^g/dy = 1400^{+200}_{-375}$ and $^{+600}_{-540}$ at the 1 and 2 standard deviation levels, respectively. Constraints for the ZOWW model are $\epsilon_0 = 1.9^{+0.2}_{-0.5}$ and $^{+0.7}_{-0.6}$ at the 1 and 2 standard deviation levels, respectively.

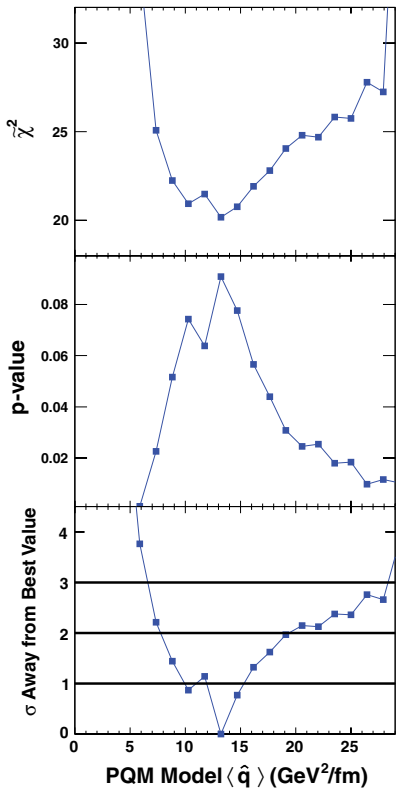

FIG. 4. (Color online) The statistical analysis results from the comparison of the PQM model with the π^0 $R_{AA}(p_T)$ experimental data. The top panel shows the modified $\tilde{\chi}^2$ for different values of the PQM $\langle\hat{q}\rangle$. The middle panel shows the computed p value directly from the modified $\tilde{\chi}^2$ as shown above. The bottom panel shows the number of standard deviations (σ) away from the minimum (best) $\langle\hat{q}\rangle$ parameter value for the PQM model calculations.

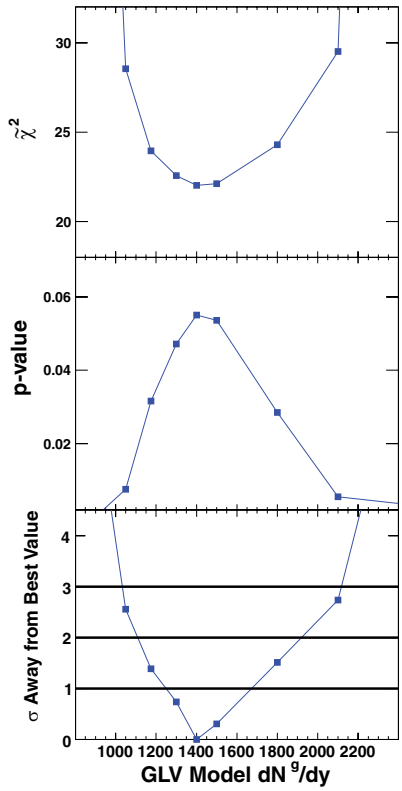

FIG. 5. (Color online) The statistical analysis results from the comparison of the GLV model with the $\pi^0 R_{AA}(p_T)$ experimental data. The top panel shows the modified $\tilde{\chi}^2$ for different values of the GLV dN^g/dy. The middle panel shows the computed p value directly from the modified $\tilde{\chi}^2$ as shown above. The bottom panel shows the number of standard deviations (σ) away from the minimum (best) dN^g/dy parameter value for the GLV model calculations.

TABLE II. Quantitative constraints on the model parameters from the PQM, GLV, WHDG, and ZOWW models and a linear functional form fit.

Model name	Model parameter	1 standard deviation uncertainty	2 standard deviation uncertainty	Maximum p value (%)
PQM	$\langle\hat{q}\rangle = 13.2$ GeV^2/fm	$+2.1 - 3.2$	$+6.3 - 5.2$	9.0
GLV	$dN^g/dy = 1400$	$+270 - 150$	$+510 - 290$	5.5
WHDG	$dN^g/dy = 1400$	$+200 - 375$	$+600 - 540$	1.3
ZOWW	$\epsilon_0 = 1.9$ GeV/fm	$+0.2 - 0.5$	$+0.7 - 0.6$	7.8
Linear	b (intercept) $= 0.168$	$+0.033 - 0.032$	$+0.065 - 0.066$	11.6
	m (slope) $= 0.0017$ (c/GeV)	$+0.0035 - 0.0039$	$+0.0070 - 0.0076$	

For each of the above fits, there is a best fit value of ϵ_b and ϵ_c corresponding to the parameters in Eq. (3). For completeness, these values are for PQM, GLV, WHDG, and ZOWW, $\epsilon_b = 0.6$ and $\epsilon_c = -0.3$, $\epsilon_b = 0.7$ and $\epsilon_c = -0.0$, $\epsilon_b = 2.1$ and $\epsilon_c = -1.5$, and $\epsilon_b = 1.1$ and $\epsilon_c = -0.6$, respectively. All of the models considered here have a steeper p_T dependence of R_{AA} than the experimental data. Thus, the best fit is obtained within the type B uncertainties by tilting the $R_{\rm AA}$.

It is notable that although there is a well-defined overall minimum in the modified $\tilde{\chi}^2$ for all four models, the maximum p value in each case is different. In the PQM, GLV, and ZOWW models the maximum p value s are approximately 9.0%, 5.5%, and 7.8%, respectively. However, in the WHDG model the maximum p value is substantially smaller at 1.3%. This is due to the fact that the WHDG model has a steeper p_T dependence of the nuclear modification factor $R_{\rm AA}$ (regardless of parameter input) than the other models and also steeper than the experimental data points.

The identical best value of dN^g/dy for the GLV and WHDG calculations is interesting, because the inclusion of important collisional energy loss in WHDG leads to the naive expectation that a smaller color-charge density would

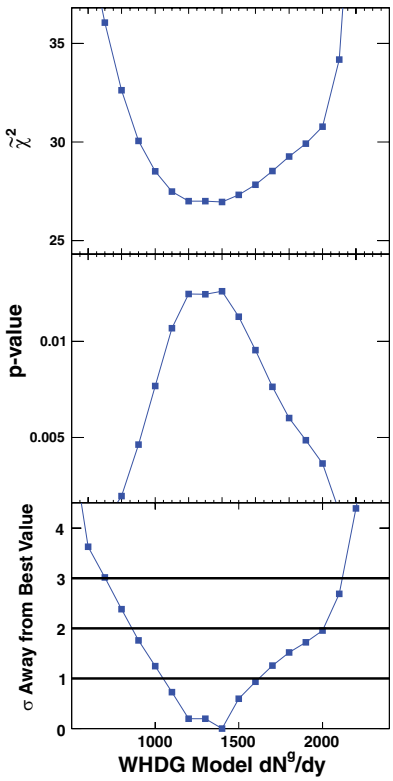

FIG. 6. (Color online) The statistical analysis results from the comparison of the WHDG model with the $\pi^0 R_{\rm AA}(p_T)$ experimental data. The top panel shows the modified $\tilde{\chi}^2$ for different values of the WHDG dN^g/dy. The middle panel shows the computed p value directly from the modified $\tilde{\chi}^2$ as shown above. The bottom panel shows the number of standard deviations (σ) away from the minimum (best) dN^g/dy parameter value for the WHDG model calculations.

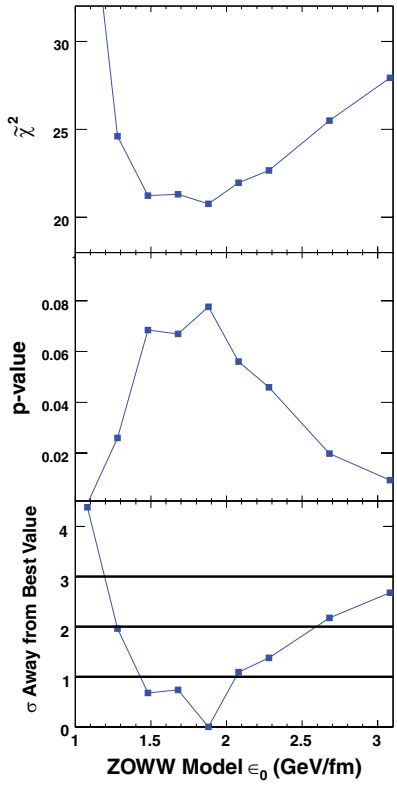

FIG. 7. (Color online) The statistical analysis results from the comparison of the ZOWW model with the $\pi^0 R_{\rm AA}(p_T)$ experimental data. The top panel shows the modified $\tilde{\chi}^2$ for different values of the ZOWW ϵ_0. The middle panel shows the computed p value directly from the modified $\tilde{\chi}^2$ as shown above. The bottom panel shows the number of standard deviations (σ) away from the minimum (best) ϵ_0 parameter value for the ZOWW model calculations.

be needed for a similar suppression. However, the different treatments of the distribution of paths through the medium may be compensating for this effect. Further theoretical studies are needed to disentangle the physics implications of the shape differences and the similar best dN^g/dy from GLV and WHDG. For all the models considered, the relevant parameter constraint is approximately a ±20–25% uncertainty at the 1 standard deviation level.

It is also interesting to inquire what simple linear fit function best describes the experimental data for $p_T >$ 5 GeV/c. The identical procedure to that described above is applied to the function $R_{AA}(p_T) = \mathrm{b} + \mathrm{m} \times p_T$ to determine the best values for the two parameters. The best fit line and the envelope of lines with 1 standard deviation uncertainties are shown in Fig. 8. The results including all types of uncertainties are $b(\text{intercept}) = 0.168^{+0.033}_{-0.032}$ and $\mathrm{m(slope)} = 0.0017^{+0.0035}_{-0.0039}$ (GeV/c). The uncertainties on these parameters are correlated as shown by the 1, 2, and 3 standard deviation contours in Fig. 9.

Thus the data are consistent with a completely flat p_T dependence of R_{AA} for $p_T >$5 GeV/c (i.e., $m = 0$) within 1 standard deviation uncertainties. The maximum p value for this simple linear function fit is 11.6%.

The p value s for all models considered are less than 12%. It is notable that the five highest p_T points ($p_T > 9.5$ GeV/c) contribute over 70% to the total $\tilde{\chi}^2$. As a check on the influence of these points on the extracted parameter values, we have repeated the above procedure to the restricted range $5 < p_T < 9.5$ GeV/c. We find the following new constraints: PQM model

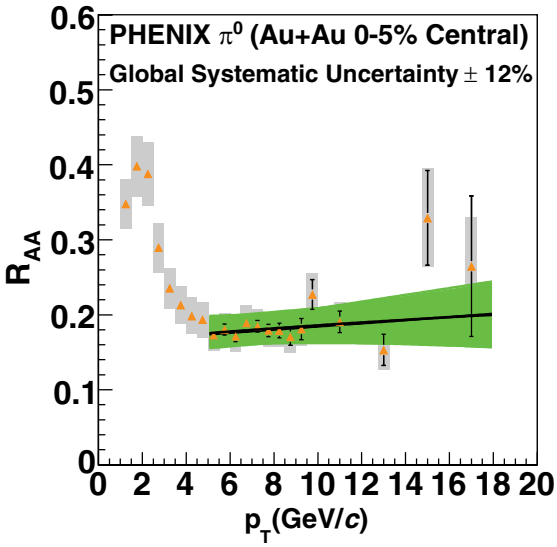

FIG. 8. (Color online) The π^0 nuclear suppression factor R_{AA} as a function of transverse momentum for 0–5% Au+Au collisions at $\sqrt{s_{NN}} = 200$ GeV. Point-to-point uncorrelated statistical and systematic uncertainties are shown as uncertainty bars. Correlated systematic uncertainties are shown as gray boxes around the data points. The global scale factor systematic uncertainty is quoted as text. Also shown are the best fit and the envelope of lines with one standard deviation uncertainty for a simple linear fit function constrained by the statistical and systematic uncertainties.

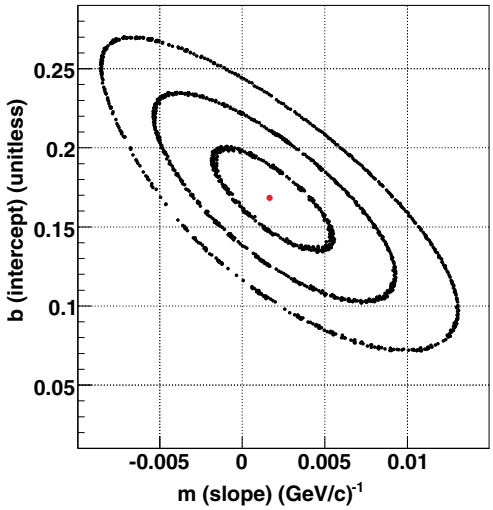

FIG. 9. (Color online) Shown are the best fit values for m(slope) and b(intercept) as constrained by the experimental data. Also shown are the 1, 2, and 3 standard deviation uncertainty contours.

$\langle\hat{q}\rangle = 13.2^{+1.8}_{-4.2}$ GeV^2/fm; GLV model $dN^g/dy = 1400^{+200}_{-210}$; WHDG model $dN^g/dy = 1000^{+300}_{-170}$; ZOWW model $\epsilon_0 = 1.5^{+0.5}_{-0.2}$ GeV/fm; simple linear fit $b(\text{intercept}) = 0.170^{+0.034}_{-0.034}$ and $\mathrm{m(slope)} = 0.0013^{+0.0047}_{-0.0051}$ (GeV/c). We find that the resulting new constraints are within the 1 standard deviation uncertainties of those quoted for the full p_T range. However, with the restricted range, the p value s increase to 55, 36, 17, 62, and 75% for the PQM model, GLV model, WHDG model, ZOWW model, and the simple linear fit, respectively. Improvements in the data for $p_T > 9.5$ GeV/c expected from future measurements will be crucial in determining whether any of the models discussed provide a statistically valid description of the data over the full range $5 \leqslant p_T \leqslant 20$ GeV/c.

V. SUMMARY AND CONCLUSIONS

In this article, we compared model predictions of parton energy loss with experimental data of semi-inclusive single high-transverse-momentum π^0 suppression in central Au+Au reactions at $\sqrt{s_{NN}} = 200$ GeV. In the comparison, statistical and systematic uncertainties were taken into account. We obtained experimental constraints on model parameters of the color-charge density of the medium or its transport coefficient. These values indicate a large medium density. It is crucial to note that the quoted constraints on these parameters do not include any systematic uncertainties in the models but rather give the limits assuming a "perfect theory" with one unknown parameter, for example, the color-charge density, constrained by the measurements, including the experimental statistical and systematic uncertainties. Additional theoretical systematic uncertainties from the time evolution, energy-loss approximations, and calculation details need further investigation.

ACKNOWLEDGMENTS

We thank the staff of the Collider-Accelerator and Physics Departments at Brookhaven National Laboratory and the staff

of the other PHENIX participating institutions for their vital contributions. We thank W. Horowitz, C. Loizides, I. Vitev, and X.-N. Wang for the theoretical calculation input and useful discussions. We acknowledge support from the Office of Nuclear Physics in the Office of Science of the Department of Energy, the National Science Foundation, Abilene Christian University Research Council, Research Foundation of SUNY, and Dean of the College of Arts and Sciences, Vanderbilt University (USA), Ministry of Education, Culture, Sports, Science, and Technology and the Japan Society for the Promotion of Science (Japan), Conselho Nacional de Desenvolvimento Científico e Tecnológico and Fundação de Amparo à Pesquisa do Estado de São Paulo (Brazil), Natural Science Foundation of China (People's Republic of China), Ministry of Education, Youth and Sports (Czech Republic), Centre National de la Recherche Scientifique, Commissariat à l'Énergie Atomique, and Institut National de Physique Nucléaire et de Physique des Particules (France), Ministry of Industry, Science and Tekhnologies, Bundesministerium für Bildung und Forschung, Deutscher Akademischer Austausch Dienst, and Alexander von Humboldt Stiftung (Germany), Hungarian National Science Fund, OTKA (Hungary), Department of Atomic Energy (India), Israel Science Foundation (Israel), Korea Research Foundation and Korea Science and Engineering Foundation (Korea), Ministry of Education and Science, Russian Academy of Sciences, Federal Agency of Atomic Energy (Russia), VR and the Wallenberg Foundation (Sweden), the U.S. Civilian Research and Development Foundation for the Independent States of the Former Soviet Union, the U.S.-Hungarian NSF-OTKA-MTA, and the U.S.-Israel Binational Science Foundation.

APPENDIX: CONSTRAINT FORMALISM

In the case of only point-to-point uncorrelated uncertainties (statistical and/or systematic), if one assumes they are Gaussian distributed and characterized by σ, the root-mean-square (rms), calculating the best-parameter fit is straightforward via a log-likelihood or least-squares χ^2 method [20].

The likelihood function $\mathcal{L}$ is defined as the *a priori* probability of a given outcome. Let $y_1, y_2, \ldots y_n$ be n samples from a population with normalized probability density function $f(y, \vec{p})$, where $\vec{p}$ represents a vector of k parameters. For instance, y_i could represent a measurement of a cross section at transverse momentum $(p_T)_i$, where the probability density of the measurement is Gaussian distributed about the expectation value $\mu = \langle y \rangle$:

$$f(y, \vec{p}) = \frac{1}{\sqrt{2\pi\sigma^2}} \exp - \left[\frac{(y-\mu)^2}{2\sigma^2} \right]. \tag{A1}$$

If the samples are independent, then the likelihood function is:

$$\mathcal{L} = \prod_i f(y_i, \vec{p}) = \frac{1}{\sigma_1 \sigma_2 \ldots \sigma_n} \frac{1}{\sqrt{2\pi}^n} \exp - \left\{ \sum_{i=1}^{n} \frac{[y_i - \mu_i(\vec{p})]^2}{2\sigma_i^2} \right\}. \tag{A2}$$

However, if the samples are correlated, for example, via correlated systematic uncertainties, then the full covariance matrix must be used

$$V_{ij} = \langle [y_i - \mu_i(\vec{p})][y_j - \mu_j(\vec{p})] \rangle. \tag{A3}$$

Then the likelihood function takes the more general form:

$$\mathcal{L} = \frac{1}{\sqrt{|V|}} \frac{1}{\sqrt{2\pi}^n} \exp - \left\{ \sum_{i=1}^{n} \sum_{j=1}^{n} \frac{[y_i - \mu_i(\vec{p})] V_{ij}^{-1} [y_j - \mu_j(\vec{p})]}{2} \right\}, \tag{A4}$$

where $|V|$ is the determinant of the covariance matrix V. Note that Eq. (A4) reduces to Eq. (A2) if the correlations vanish so that the covariances are zero and V_{ij} is diagonal

$$\begin{aligned} V_{ij} &= \langle [y_i - \mu_i(\vec{p})][y_j - \mu_j(\vec{p})] \rangle \\ &= \delta_{ij} \langle [y_i - \mu_i(\vec{p})]^2 \rangle = \delta_{ij} \sigma_i^2. \end{aligned} \tag{A5}$$

Because Gaussian probability distributions are inevitable (as a consequence of the central limit theorem) and because there is also an important theorem regarding likelihood ratios for composite hypotheses, it is convenient to use the logarithm of the likelihood

$$\begin{aligned} -2 \ln \mathcal{L} = \ln |V| + n \log 2\pi \\ + \sum_{i=1}^{n} \sum_{j=1}^{n} [y_i - \mu_i(\vec{p})] V_{ij}^{-1} [y_j - \mu_j(\vec{p})]. \end{aligned} \tag{A6}$$

We separate the uncertainties into four classes: type A (point-to-point uncorrelated systematic uncertainties); type B (correlated systematic uncertainties, for which the point-to-point correlation is 100% by construction, because the uncorrelated part has been separated out and included in uncertainty A); type C [overall systematic uncertainties by

which all the points move by the same fraction (i.e., normalization uncertainties)]; and type D (statistical). Categories A and D are simply added in quadrature and represent the total point-to-point uncorrelated uncertainties, denoted σ_i below.

We model a correlated systematic uncertainty as if there were an underlying uncertainty, e.g., absolute momentum scale, which may cause correlated systematic variations Δy_i of the set of measurements, y_i, around their nominal value, that can be represented as a random variable, z_b. The correlated type B variation of the measurements is represented by the displacement of all points from their nominal values by the correlated amounts

$$\Delta y^b(\mathrm{sys})_i \equiv b_i \Delta z_b \tag{A7}$$

$$\langle \Delta y^b(\mathrm{sys})_i \Delta y^b(\mathrm{sys})_j \rangle = b_i b_j \sigma_b^2 \equiv \sigma_{b_i} \sigma_{b_j}, \tag{A8}$$

where $\Delta z_b \equiv z_b - \langle z_b \rangle = z_b$.

Because $\langle z_b \rangle \equiv 0$, $\langle (\Delta z_b)^2 \rangle = \langle z_b^2 \rangle - \langle z_b \rangle^2 = \sigma_b^2$ and the random variable z_b is the same for all i measurements, whereas b_i is a constant of proportionality that may be different for each i. We define $\sigma_{b_i} \equiv b_i \sigma_b$, where $\pm|\sigma_{b_i}|$ is the systematic uncertainty bar shown on each point (gray box on each data point in Fig. 1) and where b_i may be of either sign, as it is possible that one point could move up while its neighbor moves down. The random variable z_b is assumed to have a Gaussian probability distribution $f(z_b)$, with rms σ_b

$$f(z_b) = \frac{1}{\sigma_b \sqrt{2\pi}} \exp - \left[\frac{(\Delta z_b)^2}{2\sigma_b^2} \right]. \tag{A9}$$

The type C variation is independent of the type B variation. It is similarly assumed to be caused by an underlying random variable z_c that results in a systematic displacement of the measurement by an amount Δy_i^c with

$$\Delta y^c(\mathrm{sys})_i / y_i \equiv \Delta z_c \tag{A10}$$

$$\langle (\Delta y^c(\mathrm{sys})_i / y_i)(\Delta y^c(\mathrm{sys})_j / y_j) \rangle = \sigma_c^2, \tag{A11}$$

where by definition σ_c is the same for all points.

We then assume that the likelihood function factorizes as the product of independent Gaussian probabilities as in Eq. (A2) but that the distributions are correlated through their dependence on the random variables z_b and z_c:

$$\mathcal{L} = \prod_i f(y_i; z_b, z_c, \vec{p}) f(z_b) f(z_c) = \frac{1}{\sigma_1 \sigma_2 \ldots \sigma_n \sigma_b \sigma_c} \frac{1}{\sqrt{2\pi}^{(n+2)}} \exp - \left\{ \sum_{i=1}^{n} \frac{[y_i + b_i \Delta z_b + y_i \Delta z_c - \mu_i(\vec{p})]^2}{2\sigma_i^2} + \frac{(\Delta z_b)^2}{2\sigma_b^2} + \frac{(\Delta z_c)^2}{2\sigma_c^2} \right\}. \tag{A12}$$

To account for the type B systematic uncertainty, we allow any given sample of measurements, y_i, corresponding to theoretical predictions $\mu_i(\vec{p})$ to have a correlated variation from their nominal values by an amount corresponding to a certain fraction ϵ_b of the underlying root-mean-square variation of z_b, i.e., $\Delta z_b = \epsilon_b \sigma_b$, such that each point moves by an amount $\Delta y_i^b = b_i \epsilon_b \sigma_b \equiv \epsilon_b \sigma_{b_i}$, the same fraction ϵ_b of its systematic uncertainty bar, and similarly for the type C uncertainty. Then the likelihood function for any outcome, including the variation of ϵ_b and ϵ_c, would be:

$$\mathcal{L} = \frac{1}{\sigma_1 \sigma_2 \ldots \sigma_n \sigma_b \sigma_c} \frac{1}{\sqrt{2\pi}^{(n+2)}} \exp - \left\{ \sum_{i=1}^{n} \frac{[y_i + \epsilon_b \sigma_{b_i} + \epsilon_c y_i \sigma_c - \mu_i(\vec{p})]^2}{2\sigma_i^2} + \frac{\epsilon_b^2}{2} + \frac{\epsilon_c^2}{2} \right\}, \tag{A13}$$

where the last two terms represent $(\Delta z_b)^2/(2\sigma_b^2) = \epsilon_b^2 \sigma_b^2/(2\sigma_b^2)$ and $(\Delta z_c)^2/(2\sigma_c^2) = \epsilon_c^2 \sigma_c^2/(2\sigma_c^2)$ because we assumed the probability of the systematic displacements $f(z_{b,c})$ to be Gaussian. Other probability distributions for the correlated systematic uncertainty could be used. For instance, if $\pm|\sigma_{b_i}|$ had represented full extent systematic uncertainties, with equal probability for any Δz_b, then the $\epsilon_b^2/2$ term and associated normalization constant $1/\sigma_b\sqrt{2\pi}$ would be absent from Eq. (A13).

Then we use the likelihood ratio test to establish the validity or the confidence interval of the theoretical predictions $\mu_i(\vec{p})$. One can use the modified log likelihood

$$-2 \ln \mathcal{L} = \left\{ \sum_{i=1}^{n} \frac{[y_i + \epsilon_b \sigma_{b_i} + \epsilon_c y_i \sigma_c - \mu_i(\vec{p})]^2}{\sigma_i^2} + \epsilon_b^2 + \epsilon_c^2 \right\} \equiv \chi^2(\epsilon_b, \epsilon_c, \vec{p}) \tag{A14}$$

because we will eventually take the ratio of the likelihood of a given set of parameters $\vec{p}$ to the maximum likelihood when all the parameters ϵ_b, ϵ_c, and $\vec{p}$ are varied [the minimum value of Eq. (A15)] so that the terms preceding the exponential in Eq. (A13) cancel because they are not varied. Equation (A15)

follows the χ^2 distribution with $n+2$ degrees of freedom because it is the sum of $n+2$ independent Gaussian distributed random variables [i.e., in statistical terminology $\chi^2(\epsilon_b, \epsilon_c, \vec{p})$ is $\chi^2_{(n+2)}$]. This establishes Eq. (A15) as the χ^2-distributed quantity that we use for least-squares fit to the theoretical predictions, including the systematic uncertainties. Note that Eq. (A15) agrees with Eq. (8) in Ref. [24] in the discussion of fits with correlated systematics. The specific procedure is described in the next paragraph.

First "fit the theory" to the data by minimizing Eq. (A15) by varying all the parameters to find $\hat{\epsilon}_b, \hat{\epsilon}_c, \hat{\vec{p}}$, the values of the parameters that give the overall minimum $\chi^2_{\rm min}$. If the $\chi^2_{\rm min}$ for this fit is acceptable for the $n+2-(m+2) = n-m$ degrees of freedom, where m are the number of parameters in $\vec{p}$, then the theory is not rejected at this level. A confidence interval is then found for testing any other set of k parameters constrained to specific values, $\vec{p}_0$, by again finding the minimum of Eq. (A15) for the k fixed values of $\vec{p}_0$, by letting all the other parameters, including ϵ_b and ϵ_c, vary. For constant values of σ_i, and large values of n, the "likelihood ratio" $-2\ln[\mathcal{L}(\vec{p}_0)/\mathcal{L}(\hat{\vec{p}})] = -2[\ln\mathcal{L}(\vec{p}_0) - \ln\mathcal{L}(\hat{\vec{p}})]$, i.e., $\chi^2(\vec{p}_0) - \chi^2_{\rm min}$ is χ^2 distributed with k degrees of freedom, from which the confidence interval on the parameters can be evaluated. However, in general, the uncertainty on the parameters is estimated in the Gaussian approximation by $\chi^2(\vec{p}_0) = \chi^2_{\rm min} + N^2$ for N standard deviation uncertainties (for example, using a MINUIT-type fitting algorithm [23]).

For the present data, the statistical and random systematic uncertainties are such that the shift in the measurement y_i due to the correlated systematic uncertainties preserves the fractional uncertainty. In this case the maximum likelihood and least-squares methods no longer coincide and we use a least-squares fit of Eq. (A16) instead of Eq. (A15) to estimate the best fit parameters:

$$\tilde{\chi}^2 = \left\{ \sum_{i=1}^{n} \frac{[y_i + \epsilon_b \sigma_{b_i} + \epsilon_c y_i \sigma_c - \mu_i(\vec{p})]^2}{\tilde{\sigma}_i^2} + \epsilon_b^2 + \epsilon_c^2 \right\}, \tag{A15}$$

where $\tilde{\sigma}_i$ is the uncertainty scaled by the multiplicative shift in y_i such that the fractional uncertainty is unchanged under shifts

$$\tilde{\sigma}_i = \sigma_i \left(\frac{y_i + \epsilon_b \sigma_{b_i} + \epsilon_c y_i \sigma_c}{y_i} \right). \tag{A16}$$

[1] B. Muller and J. L. Nagle, Annu. Rev. Nucl. Part. Sci. **56**, 93 (2006).
[2] I. Arsene *et al.*, Nucl. Phys. **A757**, 1 (2005); K. Adcox *et al.*, *ibid.* **184**; B. B. Back *et al.*, *ibid.* **28**; J. Adams *et al.*, *ibid.* **102**.
[3] M. Gyulassy, I. Vitev, X. N. Wang, and B. W. Zhang, *Quark Gluon Plasma 3*, edited by R. C. Hwa and X. N. Wang (World Scientific, Singapore, 2004).
[4] A. Dainese, C. Loizides, and G. Paic, Eur. Phys. J. C **38**, 461 (2005); C. Loizides, *ibid.* **49**, 339 (2007).
[5] M. Gyulassy, P. Levai, and I. Vitev, Nucl. Phys. **B571**, 197 (2000).
[6] W. A. Horowitz, S. Wicks, M. Djordjevic, and M. Gyulassy, in preparation; S. Wicks, W. Horowitz, M. Djordjevic, and M. Gyulassy, Nucl. Phys. **A783**, 493 (2007); S. Wicks, W. Horowitz, M. Djordjevic, and M. Gyulassy, *ibid.* **A784**, 426 (2007).
[7] H. Zhang, J. F. Owens, E. Wang, and X.-N. Wang, Phys. Rev. Lett. **98**, 212301 (2007).
[8] L. Aphecetche *et al.*, Nucl. Instrum. Methods A **499**, 511 (2003).
[9] A. Adare *et al.*, arXiv:0801.4020v1 [nucl-ex].
[10] R. Baier, Y. L. Dokshitzer, A. H. Mueller, S. Peigne, and D. Schiff, Nucl. Phys. **B484**, 265 (1997); see also Ref. [3].
[11] C. A. Salgado and U. A. Wiedemann, Phys. Rev. D **68**, 014008 (2003).
[12] I. Vitev, Phys. Lett. **B639**, 38 (2006).
[13] J. D. Bjorken, Phys. Rev. D **27**, 140 (1983).
[14] K. J. Eskola, H. Honkanen, C. A. Salgado, and U. A. Wiedemann, Nucl. Phys. **A747**, 511 (2005).
[15] M. Djordjevic and M. Gyulassy, Nucl. Phys. **A733**, 265 (2004).
[16] C. Loizides (private communcation).
[17] I. Vitev (private communication).
[18] W. Horowitz (private communication).
[19] X.-N. Wang (private communication).
[20] W.-M. Yao *et al.* [Particle Data Group], J. Phys. G **33**, 278 (2006).
[21] R. Baier and D. Schiff, J. High Energy Phys. 09 (2006) 059; R. Baier, A. H. Mueller, and D. Schiff, Phys. Lett. **B649**, 147 (2007).
[22] Attributed to S. S. Wilks in S. L. Meyer, *Data Analysis for Scientists and Engineers*, Library Shelf Mark QA 276 MEYE (Peer Management Consultants, Ltd., reprinted 1992).
[23] F. James, MINUIT Reference Manual, CERN Program Library Long Writeup D506, 1994.
[24] J. Heinrich and L. Lyons, Annu. Rev. Nucl. Part. Sci. **57**, 145 (2007).

J/ψ Production in $\sqrt{s_{NN}} = 200$ GeV Cu + Cu Collisions

A. Adare,[8] S. Afanasiev,[22] C. Aidala,[9] N. N. Ajitanand,[48] Y. Akiba,[42,43] H. Al-Bataineh,[37] J. Alexander,[48] K. Aoki,[27,42] L. Aphecetche,[50] R. Armendariz,[37] S. H. Aronson,[3] J. Asai,[43] E. T. Atomssa,[28] R. Averbeck,[49] T. C. Awes,[38] B. Azmoun,[3] V. Babintsev,[18] G. Baksay,[14] L. Baksay,[14] A. Baldisseri,[11] K. N. Barish,[4] P. D. Barnes,[30] B. Bassalleck,[36] S. Bathe,[4] S. Batsouli,[38] V. Baublis,[41] A. Bazilevsky,[3] S. Belikov,[3,*] R. Bennett,[49] Y. Berdnikov,[45] A. A. Bickley,[8] J. G. Boissevain,[30] H. Borel,[11] K. Boyle,[49] M. L. Brooks,[30] H. Buesching,[3] V. Bumazhnov,[18] G. Bunce,[3,43] S. Butsyk,[30,49] S. Campbell,[49] B. S. Chang,[57] J.-L. Charvet,[11] S. Chernichenko,[18] J. Chiba,[23] C. Y. Chi,[9] M. Chiu,[19] I. J. Choi,[57] T. Chujo,[54] P. Chung,[48] A. Churyn,[18] V. Cianciolo,[38] C. R. Cleven,[16] B. A. Cole,[9] M. P. Comets,[39] P. Constantin,[30] M. Csanád,[13] T. Csörgő,[24] T. Dahms,[49] K. Das,[15] G. David,[3] M. B. Deaton,[1] K. Dehmelt,[14] H. Delagrange,[50] A. Denisov,[18] D. d'Enterria,[9] A. Deshpande,[43,49] E. J. Desmond,[3] O. Dietzsch,[46] A. Dion,[49] M. Donadelli,[46] O. Drapier,[28] A. Drees,[49] A. K. Dubey,[56] A. Durum,[18] V. Dzhordzhadze,[4] Y. V. Efremenko,[38] J. Egdemir,[49] F. Ellinghaus,[8] W. S. Emam,[4] A. Enokizono,[29] H. En'yo,[42,43] S. Esumi,[53] K. O. Eyser,[4] D. E. Fields,[36,43] M. Finger,[5,22] M. Finger, Jr.,[5,22] F. Fleuret,[28] S. L. Fokin,[26] Z. Fraenkel,[56,*] J. E. Frantz,[49] A. Franz,[3] A. D. Frawley,[15] K. Fujiwara,[42] Y. Fukao,[27,42] T. Fusayasu,[35] S. Gadrat,[31] I. Garishvili,[51] A. Glenn,[8] H. Gong,[49] M. Gonin,[28] J. Gosset,[11] Y. Goto,[42,43] R. Granier de Cassagnac,[28] N. Grau,[21] S. V. Greene,[54] M. Grosse Perdekamp,[19,43] T. Gunji,[7] H.-Å. Gustafsson,[32] T. Hachiya,[17] A. Hadj Henni,[50] C. Haegemann,[36] J. S. Haggerty,[3] H. Hamagaki,[7] R. Han,[40] H. Harada,[17] E. P. Hartouni,[29] K. Haruna,[17] E. Haslum,[32] R. Hayano,[7] M. Heffner,[29] T. K. Hemmick,[49] T. Hester,[4] X. He,[16] H. Hiejima,[19] J. C. Hill,[21] R. Hobbs,[36] M. Hohlmann,[14] W. Holzmann,[48] K. Homma,[17] B. Hong,[25] T. Horaguchi,[42,52] D. Hornback,[51] T. Ichihara,[42,43] K. Imai,[27,42] M. Inaba,[53] Y. Inoue,[44,42] D. Isenhower,[1] L. Isenhower,[1] M. Ishihara,[42] T. Isobe,[7] M. Issah,[48] A. Isupov,[22] B. V. Jacak,[49,+] J. Jia,[9] J. Jin,[9] O. Jinnouchi,[43] B. M. Johnson,[3] K. S. Joo,[34] D. Jouan,[39] F. Kajihara,[7] S. Kametani,[7,55] N. Kamihara,[42] J. Kamin,[49] M. Kaneta,[43] J. H. Kang,[57] H. Kanou,[42,52] D. Kawall,[43] A. V. Kazantsev,[26] A. Khanzadeev,[41] J. Kikuchi,[55] D. H. Kim,[34] D. J. Kim,[57] E. Kim,[47] E. Kinney,[8] A. Kiss,[13] E. Kistenev,[3] A. Kiyomichi,[42] J. Klay,[29] C. Klein-Boesing,[33] L. Kochenda,[41] V. Kochetkov,[18] B. Komkov,[41] M. Konno,[53] D. Kotchetkov,[4] A. Kozlov,[56] A. Král,[10] A. Kravitz,[9] J. Kubart,[5,20] G. J. Kunde,[30] N. Kurihara,[7] K. Kurita,[44,42] M. J. Kweon,[25] Y. Kwon,[51,57] G. S. Kyle,[37] R. Lacey,[48] Y.-S. Lai,[9] J. G. Lajoie,[21] A. Lebedev,[21] D. M. Lee,[30] M. K. Lee,[57] T. Lee,[47] M. J. Leitch,[30] M. A. L. Leite,[46] B. Lenzi,[46] T. Liška,[10] A. Litvinenko,[22] M. X. Liu,[30] X. Li,[6] B. Love,[54] D. Lynch,[3] C. F. Maguire,[54] Y. I. Makdisi,[3] A. Malakhov,[22] M. D. Malik,[36] V. I. Manko,[26] Y. Mao,[40,42] L. Mašek,[5,20] H. Masui,[53] F. Matathias,[9] M. McCumber,[49] P. L. McGaughey,[30] Y. Miake,[53] P. Mikeš,[5,20] K. Miki,[53] T. E. Miller,[54] A. Milov,[49] S. Mioduszewski,[3] M. Mishra,[2] J. T. Mitchell,[3] M. Mitrovski,[48] A. Morreale,[4] D. P. Morrison,[3] T. V. Moukhanova,[26] D. Mukhopadhyay,[54] J. Murata,[44,42] S. Nagamiya,[23] Y. Nagata,[53] J. L. Nagle,[8] M. Naglis,[56] I. Nakagawa,[42,43] Y. Nakamiya,[17] T. Nakamura,[17] K. Nakano,[42,52] J. Newby,[29] M. Nguyen,[49] B. E. Norman,[30] A. S. Nyanin,[26] E. O'Brien,[3] S. X. Oda,[7] C. A. Ogilvie,[21] H. Ohnishi,[42] H. Okada,[27,42] K. Okada,[43] M. Oka,[53] O. O. Omiwade,[1] A. Oskarsson,[32] M. Ouchida,[17] K. Ozawa,[7] R. Pak,[3] D. Pal,[54] A. P. T. Palounek,[30] V. Pantuev,[49] V. Papavassiliou,[37] J. Park,[47] W. J. Park,[25] S. F. Pate,[37] H. Pei,[21] J.-C. Peng,[19] H. Pereira,[11] V. Peresedov,[22] D. Yu. Peressounko,[26] C. Pinkenburg,[3] M. L. Purschke,[3] A. K. Purwar,[30] H. Qu,[16] J. Rak,[36] A. Rakotozafindrabe,[28] I. Ravinovich,[56] K. F. Read,[38,51] S. Rembeczki,[14] M. Reuter,[49] K. Reygers,[33] V. Riabov,[41] Y. Riabov,[41] G. Roche,[31] A. Romana,[28,*] M. Rosati,[21] S. S. E. Rosendahl,[32] P. Rosnet,[31] P. Rukoyatkin,[22] V. L. Rykov,[42] B. Sahlmueller,[33] N. Saito,[27,42,43] T. Sakaguchi,[3] S. Sakai,[53] H. Sakata,[17] V. Samsonov,[41] S. Sato,[23] S. Sawada,[23] J. Seele,[8] R. Seidl,[19] V. Semenov,[18] R. Seto,[4] D. Sharma,[56] I. Shein,[18] A. Shevel,[41,48] T.-A. Shibata,[42,52] K. Shigaki,[17] M. Shimomura,[53] K. Shoji,[27,42] A. Sickles,[49] C. L. Silva,[46] D. Silvermyr,[38] C. Silvestre,[11] K. S. Sim,[25] C. P. Singh,[2] V. Singh,[2] S. Skutnik,[21] M. Slunečka,[5,22] A. Soldatov,[18] R. A. Soltz,[29] W. E. Sondheim,[30] S. P. Sorensen,[51] I. V. Sourikova,[3] F. Staley,[11] P. W. Stankus,[38] E. Stenlund,[32] M. Stepanov,[37] A. Ster,[24] S. P. Stoll,[3] T. Sugitate,[17] C. Suire,[39] J. Sziklai,[24] T. Tabaru,[43] S. Takagi,[53] E. M. Takagui,[46] A. Taketani,[42,43] Y. Tanaka,[35] K. Tanida,[42,43] M. J. Tannenbaum,[3] A. Taranenko,[48] P. Tarján,[12] T. L. Thomas,[36] M. Togawa,[27,42] A. Toia,[49] J. Tojo,[42] L. Tomášek,[20] H. Torii,[42] R. S. Towell,[1] V-N. Tram,[28] I. Tserruya,[56] Y. Tsuchimoto,[17] C. Vale,[21] H. Valle,[54] H. W. van Hecke,[30] J. Velkovska,[54] R. Vertesi,[12] A. A. Vinogradov,[26] M. Virius,[10] V. Vrba,[20] E. Vznuzdaev,[41] M. Wagner,[27,42] D. Walker,[49] X. R. Wang,[37] Y. Watanabe,[42,43] J. Wessels,[33] S. N. White,[3] D. Winter,[9] C. L. Woody,[3] M. Wysocki,[8] W. Xie,[43] Y. L. Yamaguchi,[55] A. Yanovich,[18] Z. Yasin,[4] J. Ying,[16] S. Yokkaichi,[42,43] G. R. Young,[38] I. Younus,[36] I. E. Yushmanov,[26] W. A. Zajc,[9] O. Zaudtke,[33] C. Zhang,[38] S. Zhou,[6] J. Zimányi,[24,*] and L. Zolin[22]

(PHENIX Collaboration)

 © 2008 The American Physical Society

[1]Abilene Christian University, Abilene, Texas 79699, USA
[2]Department of Physics, Banaras Hindu University, Varanasi 221005, India
[3]Brookhaven National Laboratory, Upton, New York 11973-5000, USA
[4]University of California-Riverside, Riverside, California 92521, USA
[5]Charles University, Ovocný trh 5, Praha 1, 116 36, Prague, Czech Republic
[6]China Institute of Atomic Energy (CIAE), Beijing, People's Republic of China
[7]Center for Nuclear Study, Graduate School of Science, University of Tokyo, 7-3-1 Hongo, Bunkyo, Tokyo 113-0033, Japan
[8]University of Colorado, Boulder, Colorado 80309, USA
[9]Columbia University, New York, New York 10027
and Nevis Laboratories, Irvington, New York 10533, USA
[10]Czech Technical University, Zikova 4, 166 36 Prague 6, Czech Republic
[11]Dapnia, CEA Saclay, F-91191, Gif-sur-Yvette, France
[12]Debrecen University, H-4010 Debrecen, Egyetem tér 1, Hungary
[13]ELTE, Eötvös Loránd University, H-1117 Budapest, Pázmány P. s. 1/A, Hungary
[14]Florida Institute of Technology, Melbourne, Florida 32901, USA
[15]Florida State University, Tallahassee, Florida 32306, USA
[16]Georgia State University, Atlanta, Georgia 30303, USA
[17]Hiroshima University, Kagamiyama, Higashi-Hiroshima 739-8526, Japan
[18]IHEP Protvino, State Research Center of Russian Federation, Institute for High Energy Physics, Protvino, 142281, Russia
[19]University of Illinois at Urbana-Champaign, Urbana, Illinois 61801, USA
[20]Institute of Physics, Academy of Sciences of the Czech Republic, Na Slovance 2, 182 21 Prague 8, Czech Republic
[21]Iowa State University, Ames, Iowa 50011, USA
[22]Joint Institute for Nuclear Research, 141980 Dubna, Moscow Region, Russia
[23]KEK, High Energy Accelerator Research Organization, Tsukuba, Ibaraki 305-0801, Japan
[24]KFKI Research Institute for Particle and Nuclear Physics of the Hungarian Academy of Sciences (MTA KFKI RMKI),
H-1525 Budapest 114, POBox 49, Budapest, Hungary
[25]Korea University, Seoul, 136-701, Korea
[26]Russian Research Center "Kurchatov Institute", Moscow, Russia
[27]Kyoto University, Kyoto 606-8502, Japan
[28]Laboratoire Leprince-Ringuet, Ecole Polytechnique, CNRS-IN2P3, Route de Saclay, F-91128, Palaiseau, France
[29]Lawrence Livermore National Laboratory, Livermore, California 94550, USA
[30]Los Alamos National Laboratory, Los Alamos, New Mexico 87545, USA
[31]LPC, Université Blaise Pascal, CNRS-IN2P3, Clermont-Fd, 63177 Aubiere Cedex, France
[32]Department of Physics, Lund University, Box 118, SE-221 00 Lund, Sweden
[33]Institut für Kernphysik, University of Muenster, D-48149 Muenster, Germany
[34]Myongji University, Yongin, Kyonggido 449-728, Korea
[35]Nagasaki Institute of Applied Science, Nagasaki-shi, Nagasaki 851-0193, Japan
[36]University of New Mexico, Albuquerque, New Mexico 87131, USA
[37]New Mexico State University, Las Cruces, New Mexico 88003, USA
[38]Oak Ridge National Laboratory, Oak Ridge, Tennessee 37831, USA
[39]IPN-Orsay, Universite Paris Sud, CNRS-IN2P3, BP1, F-91406, Orsay, France
[40]Peking University, Beijing, People's Republic of China
[41]PNPI, Petersburg Nuclear Physics Institute, Gatchina, Leningrad region, 188300, Russia
[42]RIKEN, The Institute of Physical and Chemical Research, Wako, Saitama 351-0198, Japan
[43]RIKEN BNL Research Center, Brookhaven National Laboratory, Upton, New York 11973-5000, USA
[44]Physics Department, Rikkyo University, 3-34-1 Nishi-Ikebukuro, Toshima, Tokyo 171-8501, Japan
[45]Saint Petersburg State Polytechnic University, St. Petersburg, Russia
[46]Universidade de São Paulo, Instituto de Física, Caixa Postal 66318, São Paulo CEP05315-970, Brazil
[47]System Electronics Laboratory, Seoul National University, Seoul, Korea
[48]Chemistry Department, Stony Brook University, SUNY, Stony Brook, New York 11794-3400, USA
[49]Department of Physics and Astronomy, Stony Brook University, SUNY, Stony Brook, New York 11794, USA
[50]SUBATECH (Ecole des Mines de Nantes, CNRS-IN2P3, Université de Nantes) BP 20722-44307, Nantes, France
[51]University of Tennessee, Knoxville, Tennessee 37996, USA
[52]Department of Physics, Tokyo Institute of Technology, Oh-okayama, Meguro, Tokyo 152-8551, Japan
[53]Institute of Physics, University of Tsukuba, Tsukuba, Ibaraki 305, Japan
[54]Vanderbilt University, Nashville, Tennessee 37235, USA
[55]Waseda University, Advanced Research Institute for Science and Engineering, 17 Kikui-cho, Shinjuku-ku, Tokyo 162-0044, Japan
[56]Weizmann Institute, Rehovot 76100, Israel
[57]Yonsei University, IPAP, Seoul 120-749, Korea
(Received 31 December 2007; published 18 September 2008)

Yields for J/ψ production in Cu + Cu collisions at $\sqrt{s_{NN}} = 200$ GeV have been measured over the rapidity range $|y| < 2.2$ and compared with results in $p + p$ and Au + Au collisions at the same energy. The Cu + Cu data offer greatly improved precision over existing Au + Au data for J/ψ production in collisions with small to intermediate numbers of participants, in the range where the quark-gluon plasma transition threshold is predicted to lie. Cold nuclear matter estimates based on *ad hoc* fits to d + Au data describe the Cu + Cu data up to $N_{\text{part}} \sim 50$, corresponding to a Bjorken energy density of at least 1.5 GeV/fm^3.

DOI: 10.1103/PhysRevLett.101.122301 PACS numbers: 25.75.Dw

High-energy heavy-ion collisions provide the opportunity to study strongly interacting matter at very high-energy densities where quantum chromodynamics (QCD) predicts a transition from normal nuclear matter to a deconfined system of quarks and gluons, the quark-gluon plasma (QGP) [1]. At the Relativistic Heavy Ion Collider (RHIC) the energy density in central Au + Au collisions is well in excess of the critical energy density expected for this transition [2].

Over the past 20 years, there has been intense theoretical and experimental work on J/ψ production. First predicted by Matsui and Satz [3], suppression of quarkonia production in ultrarelativistic heavy-ion collisions was expected to be an unambiguous signature for the formation of a QGP. It is now recognized that in order to interpret J/ψ production as a QGP probe one has to consider cold nuclear matter effects such as initial state energy loss [4] and shadowing [5], as well as charm quark energy loss [6], comover interactions [7], corrections for feed-down from higher mass charmonium states, and secondary production mechanisms, such as recombination of initially uncorrelated $c\bar{c}$ pairs [8].

Experiment NA50 reported suppression of J/ψ production in Pb + Pb collisions at $\sqrt{s_{NN}} = 17.3$ GeV [9] that exceeds expectations based on their measurements of cold nuclear matter effects in $p + A$ collisions [10]. NA60 observed similar behavior in In + In collisions at the same energy [11]. The PHENIX experiment [12] at RHIC has characterized effects of the nuclear medium on J/ψ production at $\sqrt{s_{NN}} = 200$ GeV. The basic invariant yield reference is obtained from $p + p$ data [13–15]. Cold nuclear matter effects are studied using d + Au data [14,16]. Cold and hot nuclear matter effects are studied for large numbers of participants (N_{part}) using Au + Au data [17,18], and for smaller N_{part} using Cu + Cu data, the subject of this Letter. The results are presented as a nuclear modification factor, R_{AA}, the ratio of the yield in heavy-ion collisions to the yield in $p + p$ collisions scaled by the number of binary nucleon-nucleon collisions (N_{coll}), which is appropriate for pointlike processes.

Lattice QCD calculations [19] indicate that the threshold energy density for QGP formation is of order 1 GeV/fm^3. At $\sqrt{s_{NN}} = 200$ GeV this is expected to occur below $N_{\text{part}} = 100$ [20], in a region where Au + Au data have limited statistical and systematic precision [18]. High statistics measurements with the intermediate sized system Cu + Cu provide crucial information in that important region.

In this Letter we present results obtained by PHENIX during the 2005 RHIC run on the production of J/ψ in Cu + Cu collisions at $\sqrt{s_{NN}} = 200$ GeV. J/ψ invariant yields were studied via $J/\psi \to e^+e^-$ decays measured at midrapidity with the central arm spectrometers ($|y| \leq 0.35$, $\Delta\phi = 2 \times 90°$), and $J/\psi \to \mu^+\mu^-$ decays measured at forward rapidity with the two muon arm spectrometers ($1.2 < |y| < 2.2$, $\Delta\phi = 360°$). Event centrality and the location of the collision vertex along the beam axis (z_{vtx}) are measured with two Beam-Beam Counters (BBC) located at $3.0 < |\eta| < 3.9$. A Glauber model and a simulation of the BBC response was used to determine N_{part} and N_{coll} and their systematic uncertainties for different collision centrality ranges [21].

Data were recorded using lepton triggers in coincidence with a minimum bias trigger which required a coincidence between the BBC detectors and a valid z_{vtx}. After applying a cut of $|z_{vtx}| < 30$ cm and quality assurance criteria, the data correspond to a sampled luminosity of about 2.1 nb^{-1} (1.3 nb^{-1}) in the e^+e^- ($\mu^+\mu^-$) analysis.

Electron detection at midrapidity used the drift chambers for momentum measurement, the pad chambers for pattern recognition and track location, and the ring imaging Cherenkov (RICH) detector plus electromagnetic calorimeter (EMCal) for electron identification. Charged particle tracks were matched with a RICH ring and an EMCal hit to select electron candidates by requiring at least two RICH phototube hits inside an annulus around the projected ring center, ring quality cuts, track or cluster position matching cuts at the EMCal, and a cut on the ratio of EMCal energy to track momentum, $E/p - \langle E/p \rangle > -2\sigma$.

The $J/\psi \to e^+e^-$ trigger required one signal above a certain energy threshold in the EMCal and a matching RICH hit. Two energy thresholds were used during the run, 1.1 and 0.8 GeV, yielding average J/ψ trigger efficiencies of ~65% and 82%, respectively. The $J/\psi \to e^+e^-$ signal extraction method was very similar to the method used in the recent Au + Au [18] and $p + p$ [15] analyses. The like sign invariant mass spectrum was subtracted from the unlike sign spectrum. The remaining yield in the J/ψ mass region ($2.9 \leq M_{\text{inv}} \leq 3.3$ GeV/c^2) was

corrected for pairs lost to the radiative tail and pairs added by the continuum signal under the peak [15]. The total J/ψ count in the e^+e^- channel was ≈ 2050. The signal to background ratio (S/B) was $\approx 1(6)$ for the most central (peripheral) collisions.

Muon detection at forward and backward rapidities used the muon arms, consisting of cathode strip tracking chambers in a magnetic field (MuTr) and Iarocci tube planes interleaved with thick steel absorbers (MuID). Muon candidates were identified by penetration to the last MuID gap, and their momenta were measured by their bend through the MuTr.

The dimuon trigger required two candidate tracks to penetrate the MuID, point back to the event vertex, and pass an opening angle cut ($\theta > 19°$). The dimuon combinatorial background was estimated using the product of the like sign counts, $2\sqrt{N^{++}N^{--}}$, and was subtracted from the unlike sign spectra. The residual background (notably from the open charm pairs and Drell-Yan processes) was evaluated using an exponential form. The $J/\psi \to \mu^+\mu^-$ signal was estimated by direct counting of the remaining pairs above the exponential fit in the mass range $2.6 \leq M_{\rm inv} \leq 3.6$ GeV/c^2 and also by using two fits with different parameterizations (single and double Gaussian) of the J/ψ line shapes, as described in [15,18]. The average of the results gave the signal count and the variation gave the systematic error. The total J/ψ yield was ≈ 9000. The S/B was $\approx 0.3(1.0)$ for the most central(peripheral) collisions.

The J/ψ invariant yield in the appropriate centrality, rapidity, and transverse momentum bin is given by

$$\frac{B_{ll}}{2\pi p_T}\frac{d^2N_{J/\psi}}{dp_T dy} = \frac{1}{2\pi p_T}\frac{N_{J/\psi}}{N_{\rm evt}\Delta y \Delta p_T A\varepsilon}, \qquad (1)$$

with B_{ll} the branching ratio for $J/\psi \to l^+l^-$, $N_{J/\psi}$ the number of observed J/ψ, $N_{\rm evt}$ the number of events; Δy the rapidity range; Δp_T the transverse momentum range, and $A\varepsilon$ the acceptance and efficiency correction (including trigger efficiency).

The determination of $A\varepsilon$ is done with a full GEANT simulation. The method is described in more detail in [15]. $A\varepsilon$ decreases with the collision centrality due to overlapping hits in the RICH and the EMCal in the central arm, and in the MuTr for the forward arms, leading to an increasing fraction of misreconstructed tracks in higher multiplicity events. This effect is evaluated by embedding simulated single J/ψ events in real events. The efficiency loss in the most central collisions is 3% for dielectron measurements and 20% (16%) for dimuon measurements at positive (negative) rapidity.

Systematic uncertainties in the measured J/ψ invariant yield depend on J/ψ rapidity and transverse momentum as well as on event centrality. Systematic uncertainties are grouped into three categories: point to point uncorrelated uncertainties (type A), which can move the points independently of each other, point to point correlated uncertainties (type B), which can move the points coherently, though not necessarily by the same amount, and global systematic uncertainties (type C). In all plots point to point uncorrelated systematic uncertainties and statistical uncertainties are quadratically summed and represented by vertical bars, point to point correlated systematic uncertainties are represented by boxes, and global systematic uncertainties (if any) are quoted.

TABLE I. Systematic error sources, values, and types for $R_{\rm AA}$ vs $N_{\rm part}$ in the two rapidity intervals. Where a range is given, it is from peripheral to central collisions.

Source	$\lvert y\rvert < 0.3$	$\lvert y\rvert \in [1.2, 2.2]$	Type
Signal extraction	6%	5%–6%	A
Detector + trigger efficiency	1.4%–5%	3%	B
Run by run variation	5%	2%	B
Input $y + p_T$ distributions	2%	3%	B
$N_{\rm coll}$	14%–11%	14%–11%	B

Systematic uncertainties of type A and B for $R_{\rm AA}$ vs $N_{\rm part}$ are summarized in Table I. Some uncertainties in the invariant yield, such as that on the acceptance, cancel out for $R_{\rm AA}$ and are not shown. Global systematic uncertainties for $R_{\rm AA}$ vs $N_{\rm part}$ include the $p + p$ J/ψ yield uncertainty and some $p + p$ systematic errors that do not cancel when forming $R_{\rm AA}$.

Results for the two muon arms agree within uncertainties and are combined where appropriate. Figure 1 shows the J/ψ yield vs p_T for different Cu + Cu centrality classes at mid and forward rapidity. As was done previously for the Au + Au case [18], the mean square transverse momentum, $\langle p_T^2\rangle$, was calculated numerically from the data for $p_T < 5$ GeV/c. The Cu + Cu data are plotted vs $N_{\rm part}$ and compared with the corresponding values from

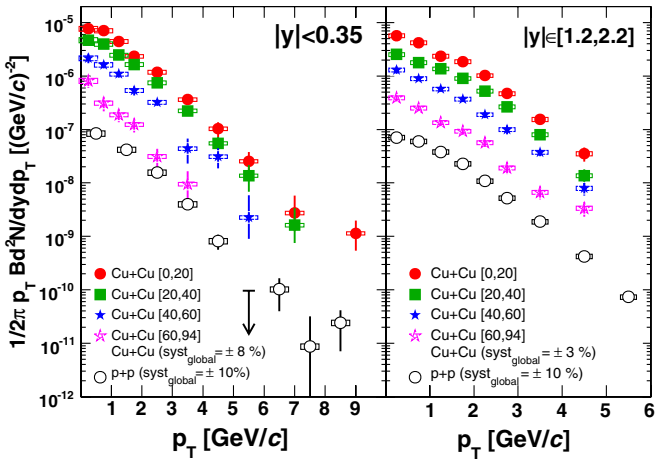

FIG. 1 (color online). J/ψ yield vs p_T at mid (left) and forward (right) rapidity for different Cu + Cu centrality bins and for $p + p$ [15]. Uncertainties are described in the text.

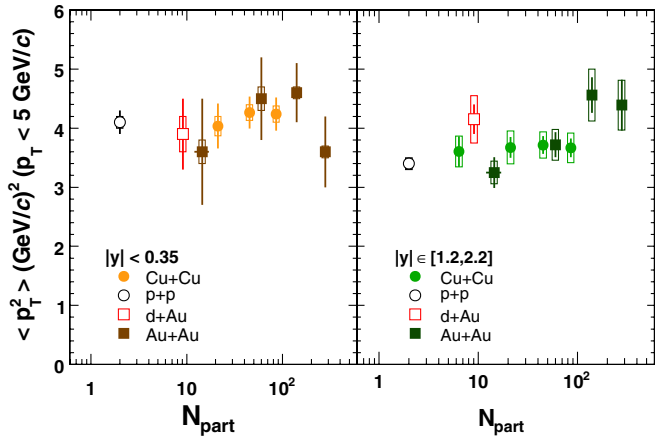

FIG. 2 (color online). The $\langle p_T^2 \rangle$ vs $N_{\rm part}$ for J/ψ production in Cu + Cu, $p + p$ [15], d + Au [16] and Au + Au [18] collisions at mid (left) and forward (right) rapidity.

Au + Au [18], d + Au [16] and $p + p$ [15] collisions in Fig. 2. Within uncertainties, the data for Cu + Cu and Au + Au agree where they overlap in $N_{\rm part}$, and the $\langle p_T^2 \rangle$ for the Cu + Cu data seems independent of $N_{\rm part}$.

The $R_{\rm AA}$ values vs p_T and rapidity are shown in Fig. 3 for the 0–20% most central Cu + Cu collisions. We see similar behavior for mid and forward rapidity, and there appears to be no p_T dependence in all centrality classes. The rms width of the rapidity distribution (evaluated directly from the data) is identical, within ~2–3% uncertainties, in $p + p$ collisions and in all centrality classes for Cu + Cu collisions.

Figures 4(a) and 4(b) show similar behavior within uncertainties for $R_{\rm AA}$ in Cu + Cu and Au + Au [18] collisions at comparable values of $N_{\rm part}$. Theoretical calculations [22] including only modified initial parton distribution functions and an added $J/\psi - N$ breakup cross section were fitted in [16] to d + Au J/ψ $R_{\rm AA}$ data. The EKS98 [23,24] and nDSg [25] shadowing models

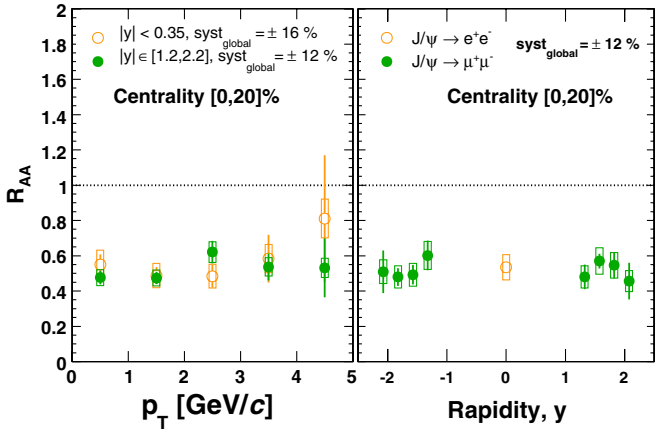

FIG. 3 (color online). $R_{\rm AA}$ vs p_T (left) and y (right) for J/ψ production in the most central Cu + Cu collisions.

were used. The fit was made simultaneously to all rapidities by optimizing the breakup cross section. While consistent with the low statistics d + Au data [16], this method leads to a model dependence of the CNM effects, since the rapidity shape is determined entirely by the shadowing model. In an attempt to reduce this model dependence, we used a data-driven *ad hoc* model to parameterize the d + Au data [16]. The *ad hoc* model uses EKS98 (method 1) and nDSg (method 2) shadowing parameterizations for the relative rapidity dependence within the fitted rapidity ranges, but the breakup cross section is replaced with a quantity, which we call f, that is optimized separately for $y = 0$ and $|y| = 1.7$. The fits using method 1 yielded $f_{dAu} = 2.3 \pm^{2.1}_{1.6}$ mb at $y = 0$ and $3.9 \pm^{1.3}_{1.2}$ mb at $|y| = 1.7$. The method 2 fits yielded $f_{dAu} = 0.9 \pm^{1.9}_{1.8}$ mb at $y = 0$ and $3.3 \pm^{1.3}_{1.2}$ mb at $|y| = 1.7$. The resulting separate parameterizations of the d + Au data vs $N_{\rm coll}$ at mid and forward/backward rapidity can be projected to Cu + Cu and Au + Au using the corresponding parton distribution functions for Cu and Au [22]. The results for method 1 are shown in Fig. 4 as cold nuclear matter baseline $R_{\rm AA}$ curves

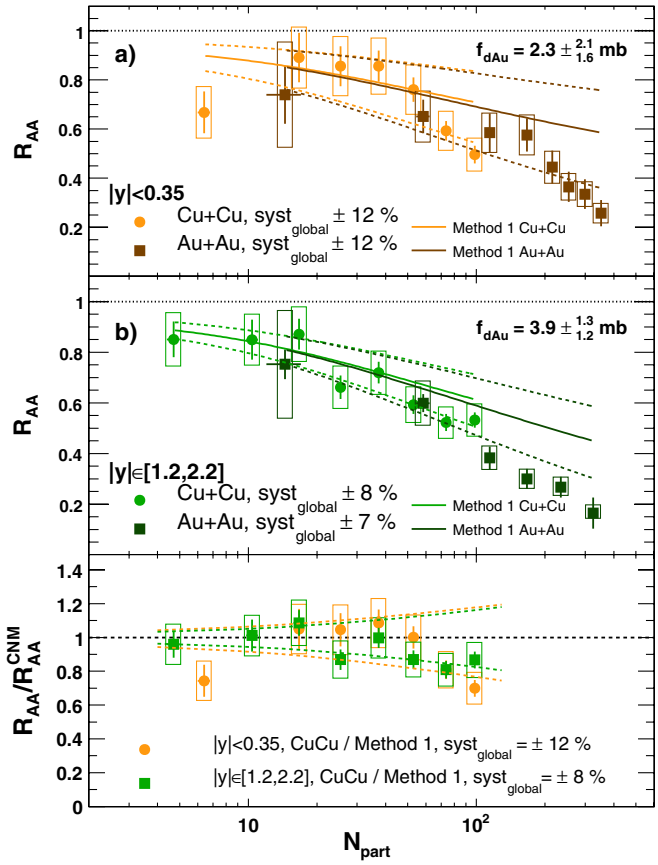

FIG. 4 (color online). (a),(b) $R_{\rm AA}$ vs $N_{\rm part}$ for J/ψ production in Cu + Cu and Au + Au [18] collisions. The curves are predictions from *ad hoc* fits to d + Au data [16] and are discussed in the text. (c) Ratios of the measured $R_{\rm AA}$ values to the predicted cold nuclear matter $R_{\rm AA}$. The dashed lines show the 1σ uncertainties from the d + Au fits.

calculated from the best fit values of f (solid lines) and the 1 standard deviation uncertainty in f (dashed lines). The method 2 heavy-ion calculations are similar to those from method 1, leading to very similar conclusions, and are not shown in Fig. 4. In Fig. 4(c) the measured R_{AA} values for Cu + Cu are shown divided by the method 1 calculations for Cu + Cu. The Cu + Cu R_{AA} is seen to be consistent with the cold nuclear matter projection within about 15% uncertainties up to $N_{part} \sim 50$. Given the uncertainty in the cold nuclear matter reference at larger N_{part} values, we can not currently draw any strong conclusions there. However PHENIX completed in February 2008 a second d + Au run, with approximately 30 times the statistics of the first d + Au run in 2003. With the new reference d + Au data, we expect to be able to identify if and where the measured Cu + Cu R_{AA} departs from the cold nuclear matter baseline.

In summary, we present high statistics J/ψ data from Cu + Cu collisions at RHIC, providing for the first time detailed information on R_{AA} and $\langle p_T^2 \rangle$ for $N_{part} < 100$. The rms values of the rapidity distributions at all centralities are consistent with that for $p + p$, and the measured $\langle p_T^2 \rangle$ for $p_T < 5$ GeV/c is nearly independent of centrality and rapidity. At similar values of N_{part}, R_{AA} and $\langle p_T^2 \rangle$ are found to agree within errors for Cu + Cu and Au + Au collisions. Cold nuclear matter calculations based on *ad hoc* fits to d + Au data reproduce the peripheral Cu + Cu data well up to $N_{part} \sim 50$, corresponding to $\epsilon_{Bjorken}\tau \sim 1.5$ GeV/fm^2/c [20], where $\epsilon_{Bjorken}$ is the Bjorken energy density and τ is the formation time. For an estimate of the thermalized energy density, hydrodynamical models give thermalization times in the range of 0.6 fm/c to 1.0 fm/c [2], which implies that cold nuclear matter effects dominate J/ψ production up to thermalized energy densities of $\sim$1.5 to 2.5 GeV/fm^3.

We thank the staff of the Collider-Accelerator and Physics Departments at BNL for their vital contributions. We acknowledge support from the Office of Nuclear Physics in DOE Office of Science and NSF (U.S.), MEXT and JSPS (Japan), CNPq and FAPESP (Brazil), NSFC (China), MSMT (Czech Republic), IN2P3/CNRS, and CEA (France), BMBF, DAAD, and AvH (Germany), OTKA (Hungary), DAE (India), ISF (Israel), KRF and KOSEF (Korea), MES, RAS, and FAAE (Russia), VR and KAW (Sweden), U.S. CRDF for the FSU, US-Hungarian NSF-OTKA-MTA, and US-Israel BSF.

*Deceased.
+PHENIX Spokesperson:
jacak@skipper.physics.sunysb.edu

[1] J. W. Harris and B. Müller, Annu. Rev. Nucl. Part. Sci. **46**, 71 (1996).
[2] K. Adcox *et al.*, Nucl. Phys. **A757**, 184 (2005).
[3] T. Matsui and H. Satz, Phys. Lett. B **178**, 416 (1986).
[4] M. B. Johnson *et al.*, Phys. Rev. Lett. **86**, 4483 (2001).
[5] V. Guzey, M. Strikman, and W. Vogelsang, Phys. Lett. B **603**, 173 (2004).
[6] R. Baier, D. Schiff, and B. G. Zakharov, Annu. Rev. Nucl. Part. Sci. **50**, 37 (2000).
[7] S. Gavin and R. Vogt, Nucl. Phys. **A610**, 442c (1996).
[8] R. L. Thews and M. L. Mangano, Phys. Rev. C **73**, 014904 (2006).
[9] B. Alessandro *et al.*, Eur. Phys. J. C **39**, 335 (2005).
[10] B. Alessandro *et al.*, Eur. Phys. J. C **48**, 329 (2006).
[11] R. Arnaldi *et al.*, arXiv:0706.4361.
[12] K. Adcox *et al.*, Nucl. Instrum. Methods Phys. Res., Sect. A **499**, 469 (2003).
[13] S. S. Adler *et al.*, Phys. Rev. Lett. **92**, 051802 (2004).
[14] S. S. Adler *et al.*, Phys. Rev. Lett. **96**, 012304 (2006).
[15] A. Adare *et al.*, Phys. Rev. Lett. **98**, 232002 (2007).
[16] A. Adare *et al.*, Phys. Rev. C **77**, 024912 (2008).
[17] S. S. Adler *et al.*, Phys. Rev. C **69**, 014901 (2004).
[18] A. Adare *et al.*, Phys. Rev. Lett. **98**, 232301 (2007).
[19] F. Karsch, Lect. Notes Phys. **583**, 209 (2002).
[20] S. S. Adler *et al.*, Phys. Rev. C **71**, 034908 (2005).
[21] A. Adare *et al.*, arXiv:0801.4555.
[22] R. Vogt, Phys. Rev. C **71**, 054902 (2005).
[23] K. J. Eskola, V. J. Kolhinen, and P. V. Ruuskanen, Nucl. Phys. **B535**, 351 (1998).
[24] K. J. Eskola, V. J. Kolhinen, and C. A. Salgado, Eur. Phys. J. C **9**, 61 (1998).
[25] D. de Florian and R. Sassot, Phys. Rev. D **69**, 074028 (2004).

Source Breakup Dynamics in Au + Au Collisions at $\sqrt{s_{NN}} = 200$ GeV via Three-Dimensional Two-Pion Source Imaging

S. Afanasiev,[17] C. Aidala,[7] N. N. Ajitanand,[43] Y. Akiba,[37,38] J. Alexander,[43] A. Al-Jamel,[33] K. Aoki,[23,37] L. Aphecetche,[45] R. Armendariz,[33] S. H. Aronson,[3] R. Averbeck,[44] T. C. Awes,[34] B. Azmoun,[3] V. Babintsev,[14] A. Baldisseri,[8] K. N. Barish,[4] P. D. Barnes,[26] B. Bassalleck,[32] S. Bathe,[4] S. Batsouli,[7] V. Baublis,[36] F. Bauer,[4] A. Bazilevsky,[3] S. Belikov,[3,16,*] R. Bennett,[44] Y. Berdnikov,[40] M. T. Bjorndal,[7] J. G. Boissevain,[26] H. Borel,[8] K. Boyle,[44] M. L. Brooks,[26] D. S. Brown,[33] D. Bucher,[29] H. Buesching,[3] V. Bumazhnov,[14] G. Bunce,[3,38] J. M. Burward-Hoy,[26] S. Butsyk,[44] S. Campbell,[44] J.-S. Chai,[18] S. Chernichenko,[14] J. Chiba,[19] C. Y. Chi,[7] M. Chiu,[7] I. J. Choi,[52] T. Chujo,[49] P. Chung,[43] V. Cianciolo,[34] C. R. Cleven,[12] Y. Cobigo,[8] B. A. Cole,[7] M. P. Comets,[35] P. Constantin,[16] M. Csanád,[10] T. Csörgő,[20] T. Dahms,[44] K. Das,[11] G. David,[3] H. Delagrange,[45] A. Denisov,[14] D. d'Enterria,[7] A. Deshpande,[38,44] E. J. Desmond,[3] O. Dietzsch,[41] A. Dion,[44] J. L. Drachenberg,[1] O. Drapier,[24] A. Drees,[44] A. K. Dubey,[51] A. Durum,[14] V. Dzhordzhadze,[46] Y. V. Efremenko,[34] J. Egdemir,[44] A. Enokizono,[13] H. En'yo,[37,38] B. Espagnon,[35] S. Esumi,[48] D. E. Fields,[32,38] F. Fleuret,[24] S. L. Fokin,[22] B. Forestier,[27] Z. Fraenkel,[51,*] J. E. Frantz,[7] A. Franz,[3] A. D. Frawley,[11] Y. Fukao,[23,37] S.-Y. Fung,[4] S. Gadrat,[27] F. Gastineau,[45] M. Germain,[45] A. Glenn,[46] M. Gonin,[24] J. Gosset,[8] Y. Goto,[37,38] R. Granier de Cassagnac,[24] N. Grau,[16] S. V. Greene,[49] M. Grosse Perdekamp,[15,38] T. Gunji,[5] H.-Å. Gustafsson,[28] T. Hachiya,[13,37] A. Hadj Henni,[45] J. S. Haggerty,[3] M. N. Hagiwara,[1] H. Hamagaki,[5] H. Harada,[13] E. P. Hartouni,[25] K. Haruna,[13] M. Harvey,[3] E. Haslum,[28] K. Hasuko,[37] R. Hayano,[5] M. Heffner,[25] T. K. Hemmick,[44] J. M. Heuser,[37] X. He,[12] H. Hiejima,[15] J. C. Hill,[16] R. Hobbs,[32] M. Holmes,[49] W. Holzmann,[43] K. Homma,[13] B. Hong,[21] T. Horaguchi,[37,47] M. G. Hur,[18] T. Ichihara,[37,38] K. Imai,[23,37] M. Inaba,[48] D. Isenhower,[1] L. Isenhower,[1] M. Ishihara,[37] T. Isobe,[5] M. Issah,[43] A. Isupov,[17] B. V. Jacak,[44,†] J. Jia,[7] J. Jin,[7] O. Jinnouchi,[38] B. M. Johnson,[3] K. S. Joo,[30] D. Jouan,[35] F. Kajihara,[5,37] S. Kametani,[5,50] N. Kamihara,[37,47] M. Kaneta,[38] J. H. Kang,[52] T. Kawagishi,[48] A. V. Kazantsev,[22] S. Kelly,[6] A. Khanzadeev,[36] D. J. Kim,[52] E. Kim,[42] Y.-S. Kim,[18] E. Kinney,[6] A. Kiss,[10] E. Kistenev,[3] A. Kiyomichi,[37] C. Klein-Boesing,[29] L. Kochenda,[36] V. Kochetkov,[14] B. Komkov,[36] M. Konno,[48] D. Kotchetkov,[4] A. Kozlov,[51] P. J. Kroon,[3] G. J. Kunde,[26] N. Kurihara,[5] K. Kurita,[39,37] M. J. Kweon,[21] Y. Kwon,[52] G. S. Kyle,[33] R. Lacey,[43] J. G. Lajoie,[16] A. Lebedev,[16] Y. Le Bornec,[35] S. Leckey,[44] D. M. Lee,[26] M. K. Lee,[52] M. J. Leitch,[26] M. A. L. Leite,[41] H. Lim,[42] A. Litvinenko,[17] M. X. Liu,[26] X. H. Li,[4] C. F. Maguire,[49] Y. I. Makdisi,[3] A. Malakhov,[17] M. D. Malik,[32] V. I. Manko,[22] H. Masui,[48] F. Matathias,[44] M. C. McCain,[15] P. L. McGaughey,[26] Y. Miake,[48] T. E. Miller,[49] A. Milov,[44] S. Mioduszewski,[3] G. C. Mishra,[12] J. T. Mitchell,[3] D. P. Morrison,[3] J. M. Moss,[26] T. V. Moukhanova,[22] D. Mukhopadhyay,[49] J. Murata,[39,37] S. Nagamiya,[19] Y. Nagata,[48] J. L. Nagle,[6] M. Naglis,[51] T. Nakamura,[13] J. Newby,[25] M. Nguyen,[44] B. E. Norman,[26] A. S. Nyanin,[22] J. Nystrand,[28] E. O'Brien,[3] C. A. Ogilvie,[16] H. Ohnishi,[37] I. D. Ojha,[49] H. Okada,[23,37] K. Okada,[38] O. O. Omiwade,[1] A. Oskarsson,[28] I. Otterlund,[28] K. Ozawa,[5] D. Pal,[49] A. P. T. Palounek,[26] V. Pantuev,[44] V. Papavassiliou,[33] J. Park,[42] W. J. Park,[21] S. F. Pate,[33] H. Pei,[16] J.-C. Peng,[15] H. Pereira,[8] V. Peresedov,[17] D. Yu. Peressounko,[22] C. Pinkenburg,[3] R. P. Pisani,[3] M. L. Purschke,[3] A. K. Purwar,[44] H. Qu,[12] J. Rak,[16] I. Ravinovich,[51] K. F. Read,[34,46] M. Reuter,[44] K. Reygers,[29] V. Riabov,[36] Y. Riabov,[36] G. Roche,[27] A. Romana,[24,*] M. Rosati,[16] S. S. E. Rosendahl,[28] P. Rosnet,[27] P. Rukoyatkin,[17] V. L. Rykov,[37] S. S. Ryu,[52] B. Sahlmueller,[29] N. Saito,[23,37,38] T. Sakaguchi,[5,50] S. Sakai,[48] V. Samsonov,[36] H. D. Sato,[23,37] S. Sato,[3,19,48] S. Sawada,[19] V. Semenov,[14] R. Seto,[4] D. Sharma,[51] T. K. Shea,[3] I. Shein,[14] T.-A. Shibata,[37,47] K. Shigaki,[13] M. Shimomura,[48] T. Shohjoh,[48] K. Shoji,[23,37] A. Sickles,[44] C. L. Silva,[41] D. Silvermyr,[34] K. S. Sim,[21] C. P. Singh,[2] V. Singh,[2] S. Skutnik,[16] W. C. Smith,[1] A. Soldatov,[14] R. A. Soltz,[25] W. E. Sondheim,[26] S. P. Sorensen,[46] I. V. Sourikova,[3] F. Staley,[8] P. W. Stankus,[34] E. Stenlund,[28] M. Stepanov,[33] A. Ster,[20] S. P. Stoll,[3] T. Sugitate,[13] C. Suire,[35] J. P. Sullivan,[26] J. Sziklai,[20] T. Tabaru,[38] S. Takagi,[48] E. M. Takagui,[41] A. Taketani,[37,38] K. H. Tanaka,[19] Y. Tanaka,[31] K. Tanida,[37,38] M. J. Tannenbaum,[3] A. Taranenko,[43] P. Tarján,[9] T. L. Thomas,[32] M. Togawa,[23,37] J. Tojo,[37] H. Torii,[37] R. S. Towell,[1] V-N. Tram,[24] I. Tserruya,[51] Y. Tsuchimoto,[13,37] S. K. Tuli,[2] H. Tydesjö,[28] N. Tyurin,[14] C. Vale,[16] H. Valle,[49] H. W. van Hecke,[26] J. Velkovska,[49] R. Vertesi,[9] A. A. Vinogradov,[22] E. Vznuzdaev,[36] M. Wagner,[23,37] X. R. Wang,[33] Y. Watanabe,[37,38] J. Wessels,[29] S. N. White,[3] N. Willis,[35] D. Winter,[7] C. L. Woody,[3] M. Wysocki,[6] W. Xie,[4,38] A. Yanovich,[14] S. Yokkaichi,[37,38] G. R. Young,[34] I. Younus,[32] I. E. Yushmanov,[22] W. A. Zajc,[7] O. Zaudtke,[29] C. Zhang,[7] J. Zimányi,[20,*] and L. Zolin[17]

(PHENIX Collaboration)

[1]*Abilene Christian University, Abilene, Texas 79699, USA*
[2]*Department of Physics, Banaras Hindu University, Varanasi 221005, India*

 © 2008 The American Physical Society

[3]Brookhaven National Laboratory, Upton, New York 11973-5000, USA
[4]University of California–Riverside, Riverside, California 92521, USA
[5]Center for Nuclear Study, Graduate School of Science, University of Tokyo, 7-3-1 Hongo, Bunkyo, Tokyo 113-0033, Japan
[6]University of Colorado, Boulder, Colorado 80309, USA
[7]Columbia University, New York, New York 10027, USA and Nevis Laboratories, Irvington, New York 10533, USA
[8]Dapnia, CEA Saclay, F-91191, Gif-sur-Yvette, France
[9]Debrecen University, H-4010 Debrecen, Egyetem tér 1, Hungary
[10]ELTE, Eötvös Loránd University, H - 1117 Budapest, Pázmány P. s. 1/A, Hungary
[11]Florida State University, Tallahassee, Florida 32306, USA
[12]Georgia State University, Atlanta, Georgia 30303, USA
[13]Hiroshima University, Kagamiyama, Higashi-Hiroshima 739-8526, Japan
[14]IHEP Protvino, State Research Center of Russian Federation, Institute for High Energy Physics, Protvino, 142281, Russia
[15]University of Illinois at Urbana-Champaign, Urbana, Illinois 61801, USA
[16]Iowa State University, Ames, Iowa 50011, USA
[17]Joint Institute for Nuclear Research, 141980 Dubna, Moscow Region, Russia
[18]KAERI, Cyclotron Application Laboratory, Seoul, Korea
[19]KEK, High Energy Accelerator Research Organization, Tsukuba, Ibaraki 305-0801, Japan
[20]KFKI Research Institute for Particle and Nuclear Physics of the Hungarian Academy of Sciences (MTA KFKI RMKI), H-1525 Budapest 114, PO Box 49, Budapest, Hungary
[21]Korea University, Seoul, 136-701, Korea
[22]Russian Research Center "Kurchatov Institute," Moscow, Russia
[23]Kyoto University, Kyoto 606-8502, Japan
[24]Laboratoire Leprince-Ringuet, Ecole Polytechnique, CNRS-IN2P3, Route de Saclay, F-91128, Palaiseau, France
[25]Lawrence Livermore National Laboratory, Livermore, California 94550, USA
[26]Los Alamos National Laboratory, Los Alamos, New Mexico 87545, USA
[27]LPC, Université Blaise Pascal, CNRS-IN2P3, Clermont-Fd, 63177 Aubiere Cedex, France
[28]Department of Physics, Lund University, Box 118, SE-221 00 Lund, Sweden
[29]Institut für Kernphysik, University of Muenster, D-48149 Muenster, Germany
[30]Myongji University, Yongin, Kyonggido 449-728, Korea
[31]Nagasaki Institute of Applied Science, Nagasaki-shi, Nagasaki 851-0193, Japan
[32]University of New Mexico, Albuquerque, New Mexico 87131, USA
[33]New Mexico State University, Las Cruces, New Mexico 88003, USA
[34]Oak Ridge National Laboratory, Oak Ridge, Tennessee 37831, USA
[35]IPN-Orsay, Universite Paris Sud, CNRS-IN2P3, BP1, F-91406, Orsay, France
[36]PNPI, Petersburg Nuclear Physics Institute, Gatchina, Leningrad region, 188300, Russia
[37]RIKEN, The Institute of Physical and Chemical Research, Wako, Saitama 351-0198, Japan
[38]RIKEN BNL Research Center, Brookhaven National Laboratory, Upton, New York 11973-5000, USA
[39]Physics Department, Rikkyo University, 3-34-1 Nishi-Ikebukuro, Toshima, Tokyo 171-8501, Japan
[40]Saint Petersburg State Polytechnic University, St. Petersburg, Russia
[41]Universidade de São Paulo, Instituto de Física, Caixa Postal 66318, São Paulo CEP05315-970, Brazil
[42]System Electronics Laboratory, Seoul National University, Seoul, Korea
[43]Chemistry Department, Stony Brook University, SUNY, Stony Brook, New York 11794-3400, USA
[44]Department of Physics and Astronomy, Stony Brook University, SUNY, Stony Brook, New York 11794, USA
[45]SUBATECH (Ecole des Mines de Nantes, CNRS-IN2P3, Université de Nantes) BP 20722 - 44307, Nantes, France
[46]University of Tennessee, Knoxville, Tennessee 37996, USA
[47]Department of Physics, Tokyo Institute of Technology, Oh-okayama, Meguro, Tokyo 152-8551, Japan
[48]Institute of Physics, University of Tsukuba, Tsukuba, Ibaraki 305, Japan
[49]Vanderbilt University, Nashville, Tennessee 37235, USA
[50]Waseda University, Advanced Research Institute for Science and Engineering, 17 Kikui-cho, Shinjuku-ku, Tokyo 162-0044, Japan
[51]Weizmann Institute, Rehovot 76100, Israel
[52]Yonsei University, IPAP, Seoul 120-749, Korea

(Received 28 December 2007; published 13 June 2008)

A three-dimensional correlation function obtained from midrapidity, low p_T, pion pairs in central Au + Au collisions at $\sqrt{s_{NN}} = 200$ GeV is studied. The extracted model-independent source function indicates a long range tail in the directions of the pion pair transverse momentum (out) and the beam (long). A proper breakup time $\tau_0 \sim 9$ fm/c and a mean proper emission duration $\Delta\tau \sim 2$ fm/c, leading to sizable emission time differences ($\langle|\Delta t_{\mathrm{LCM}}|\rangle \approx 12$ fm/c), are required to allow models to be successfully matched to these tails. The model comparisons also suggest an outside-in "burning" of the emission source reminiscent of many hydrodynamical models.

DOI: 10.1103/PhysRevLett.100.232301 PACS numbers: 25.75.Ld

Collisions between heavy nuclei at ultrarelativistic energies produce transient systems with energy densities much greater than that required to decompose bulk nuclear matter into quarks and gluons [1]. Such systems were predicted to have long lifetimes if a first order phase transition occurred during their formation or decay [2].

A number of interferometry studies [3] have been made to search for signals of long time delays in emissions from actual reaction sources [4]. For a Gaussian source function, assumed in the traditional Hanbury Brown–Twiss methodology, this would be signaled by an increase in the width R of the emission source function in the out direction of the Berstch-Pratt coordinate system, i.e., $R_{\rm out}/R_{\rm side} \gg 1$. In this system, ''out'' designates the direction of the pair total transverse momentum, ''long'' designates the beam direction, and ''side'' is perpendicular to ''long'' and ''out.'' No such result has been found by these Hanbury Brown–Twiss studies and the reported Gaussian source functions are spheroidal with $R_{\rm out} \approx R_{\rm side}$ in the longitudinally comoving system (LCMS) [4]. However, a recent study with a one-dimensional (1D) source imaging technique [5] has observed a long non-Gaussian tail in the radial source function and attributed it to possible lifetime effects [6,7]. This suggests that further study of the source image may give new insights into the reaction dynamics leading to source breakup.

Here, we extract and perform a detailed study of the 3D two-pion source function using the technique proposed by Danielewicz and Pratt [8,9]. Namely, the 3D correlation function is first decomposed into a basis of Cartesian surface-spherical harmonics to extract the coefficients, also called moments, of the expansion. In turn, they are then imaged or fitted with a trial function to extract the 3D source function, which is then used to probe the emission dynamics of the pion source produced.

Au + Au data (at $\sqrt{s_{NN}} = 200$ GeV) were recorded during 2004 with the PHENIX detector [10] at the Relativistic Heavy Ion Collider (RHIC). The collision vertex z (along the beam axis) was constrained to $|z| < 30$ cm of the nominal crossing point. Charged pions were detected in the east and west central arms of PHENIX, each of which subtends 90° in azimuth ϕ, and ± 0.35 units of pseudorapidity η. Tracking and momentum reconstruction were accomplished with the drift chamber and two layers of multiwire proportional chambers with pad readout (PC1 and PC3). Particle momenta were measured with a resolution $\sigma_p/p = 0.7\% \oplus 1.0\% p$ (GeV/c).

Pion identification was achieved for transverse momentum $p_t \lesssim 2.0$ GeV/c and $p_t \lesssim 1$ GeV/c in the time of flight and electromagnetic calorimeter, respectively. For this analysis, midrapidity ($-0.35 < y < 0.35$, where y is particle rapidity in the nucleus-nucleus center of mass frame) pion pairs were selected with $0.2 < p_T < 0.36$ GeV/c, where p_T is half the pion pair total transverse momentum, from semicentral (0%–20%) Au + Au collisions at $\sqrt{s_{NN}} = 200$ GeV. Track merging and splitting effects were removed by appropriate cuts on both the real and mixed pair distributions [7]. Systematic variations of these cuts were explored to obtain systematic error estimates; on average, they are well within the statistical uncertainty. Hence, the pair cuts do not introduce any significant bias in the correlation function.

The 3D correlation function $C(\mathbf{q}) = N_{\rm fgd}(\mathbf{q})/N_{\rm bkg}(\mathbf{q})$ was constructed as a ratio of 3D relative momentum distribution for $\pi^+\pi^+$ and $\pi^-\pi^-$ pairs in the same event $N_{\rm fgd}(\mathbf{q})$ to that from mixed events $N_{\rm bkg}(\mathbf{q})$. Here, $\mathbf{q} = \frac{(\mathbf{p}_1 - \mathbf{p}_2)}{2}$ where $\mathbf{p}_1$ and $\mathbf{p}_2$ are the momentum 4-vectors in the pair center of mass system (PCMS). The Lorentz transformation of $\mathbf{q}$ from the laboratory frame to the PCMS is made by first transforming to the pair LCMS along the beam direction and then to the PCMS along the pair transverse momentum [11]. $C(\mathbf{q})$ is flat and normalized to unity over $50 < |\mathbf{q}| < 100$ MeV/c.

To obtain the moments, the 3D correlation function $C(\mathbf{q})$ is expanded in a Cartesian harmonic basis [8,9]

$$C(\mathbf{q}) - 1 = R(\mathbf{q}) = \sum_{l,\alpha_1,\ldots,\alpha_l} R^l_{\alpha_1,\ldots,\alpha_l}(q) A^l_{\alpha_1,\ldots,\alpha_l}(\Omega_{\mathbf{q}}) \quad (1)$$

where $l = 0, 1, 2, \ldots$, $\alpha_i = x$, y or z, $A^l_{\alpha_1,\ldots,\alpha_l}(\Omega_{\mathbf{q}})$ are Cartesian harmonic basis elements ($\Omega_{\mathbf{q}}$ is the solid angle in $\mathbf{q}$ space), $R^l_{\alpha_1,\ldots,\alpha_l}(q)$ are Cartesian correlation moments given by Eq. (2), and q is the modulus of $\mathbf{q}$.

$$R^l_{\alpha_1,\ldots,\alpha_l}(q) = \frac{(2l+1)!!}{l!} \int \frac{d\Omega_{\mathbf{q}}}{4\pi} A^l_{\alpha_1,\ldots,\alpha_l}(\Omega_{\mathbf{q}}) R(\mathbf{q}). \quad (2)$$

Here, the coordinate axes are oriented so that z (long) is parallel to the beam direction and x (out) points in the direction of the total transverse momentum of the pair.

Correlation moments can be calculated from the measured 3D correlation function using Eq. (2). In this analysis, Eq. (1) is truncated at $l = 6$ and expressed in terms of independent moments only. As expected from symmetry considerations, odd moments were consistent with zero within statistical uncertainty; higher order moments were negligible [12]. Up to order 6, there are 10 independent moments: R^0, R^2_{x2}, R^2_{y2}, R^4_{x4}, R^4_{y4}, R^4_{x2y2}, R^6_{x6}, R^6_{y6}, R^6_{x4y2}, and R^6_{x2y4} (R^2_{x2} is shorthand for R^2_{xx}, dependent moments are obtained from independent ones [8,9]). These independent moments were extracted as a function of q by fitting the truncated series to the measured 3D correlation function with the moments as the parameters of the fit. The statistical error on the moments reflects the statistical error on the 3D correlation function.

Figure 1 shows the correlation moments $R^l_{\alpha_1,\ldots,\alpha_l}$ up to order $l = 6$. In 1(a), $R^0(q)$ is shown along with $R(q) = C(q) - 1$; both represent angle-averaged correlation functions, but $R^0(q)$ is obtained from the 3D correlation func-

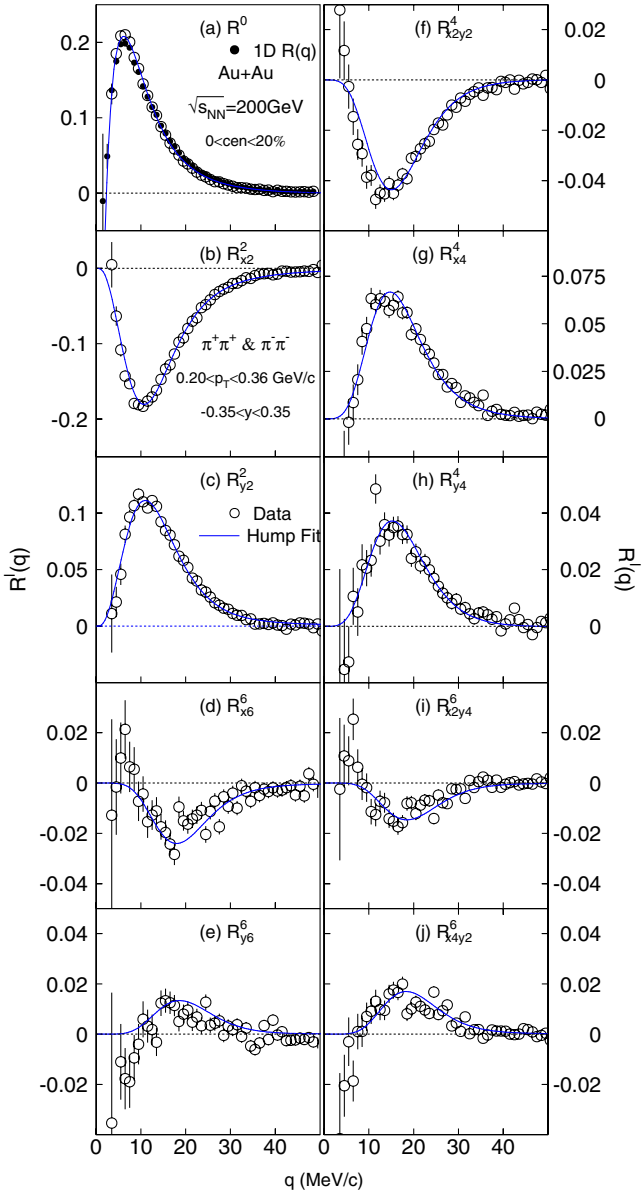

FIG. 1 (color online). Experimental correlation moments $R^l(q)$ for $l = 0, 2, 4, 6$. Panel (a) also shows a comparison between $R^0(q)$ and $R(q)$. Systematic errors are less than the statistical errors. The solid curves indicate the Hump function [Eq. (6)] fit.

tion via Eq. (1) while $R(q)$ is evaluated directly from the 1D correlation function as in Ref. [7].

The very good agreement between $R^0(q)$ and $R(q)$ underlines the absence of any significant angular acceptance issues and attests to the reliability of the moment extraction technique. Figures 1(b)–1(j) show that contributions decrease with increasing l in each direction and are relatively small for $l = 6$ [12]. This justifies truncating Eq. (1) at $l = 6$. The 3D source function $S(\mathbf{r})$ is obtained from these moments via imaging or fitting (see below).

Analogous to Eq. (1), $S(\mathbf{r})$ can be expanded in a Cartesian Surface-spherical harmonic basis [Eq. (3)]

$$S(\mathbf{r}) = \sum_l \sum_{\alpha_1,\ldots,\alpha_l} S^l_{\alpha_1,\ldots,\alpha_l}(r) A^l_{\alpha_1,\ldots,\alpha_l}(\Omega_{\mathbf{r}}). \tag{3}$$

Substitution of the series for $R(\mathbf{q})$ and $S(\mathbf{r})$ into the 3D Koonin-Pratt formalism [Eq. (4)] [3] gives a set of 1D relations [Eq. (5)] [8,9] which connects the correlation moments $R^l_{\alpha_1,\ldots,\alpha_l}(q)$ and source moments $S^l_{\alpha_1,\ldots,\alpha_l}(r)$.

$$C(\mathbf{q}) - 1 = R(\mathbf{q}) = \int d\mathbf{r} K(\mathbf{q}, \mathbf{r}) S(\mathbf{r}) \tag{4}$$

$$R^l_{\alpha_1,\ldots,\alpha_l}(q) = 4\pi \int dr r^2 K_l(q, r) S^l_{\alpha_1,\ldots,\alpha_l}(r). \tag{5}$$

$S(\mathbf{r})$ gives the probability of emitting a pair of particles with a separation vector $\mathbf{r}$ in the PCMS. The 3D kernel, $K(\mathbf{q}, \mathbf{r})$, incorporates Coulomb force and Bose-Einstein symmetrization. Strong interaction is assumed to be negligible for pions. Hence, no correction to the measured correlation function for Coulomb and other final-state interaction effects is required. The 1D imaging code of Brown and Danielewicz [5] was used to numerically invert each correlation moment $R^l_{\alpha_1,\ldots,\alpha_l}(q)$ to extract the corresponding source moment $S^l_{\alpha_1,\ldots,\alpha_l}(r)$; combining the latter as in Eq. (3) yielded the source function.

The 3D source function can also be extracted by directly fitting the 3D correlation function with an assumed functional form for $S(\mathbf{r})$. This corresponds to a simultaneous fit of the ten independent moments. A 4-parameter 3D Gaussian (ellipsoid) fit, using MINUIT minimization, gives a poor result ($\chi^2/\mathrm{ndf} = 3.7$, where ndf is the number of degrees of freedom). The solid curve in Fig. 1 shows the result of a fit to the independent moments with an empirical Hump function given by

$$S^H(r_x, r_y, r_z) = \lambda \exp\Big[-f_s\Big(\frac{x^2}{4r^2_{xs}} + \frac{y^2}{4r^2_{ys}} + \frac{z^2}{4r^2_{zs}}\Big) - f_l\Big(\frac{x^2}{4r^2_{xl}} + \frac{y^2}{4r^2_{yl}} + \frac{z^2}{4r^2_{zl}}\Big)\Big], \tag{6}$$

where λ, r_0, r_{xs}, r_{ys}, r_{zs}, r_{xl}, r_{yl}, r_{zl} are fit parameters and $f_s = 1/[1 + (r/r_0)^2]$, $f_l = 1 - f_s$. This 8-parameter Hump function achieves a better fit to the data ($\chi^2/\mathrm{ndf} = 1.4$). Smearing the track momenta by the measured resolution has a negligible effect on the data points and fits.

Figure 2(a)–2(c) shows a comparison of source function profiles in the x, y, and z directions [$S(r_x)$, $S(r_y)$, and $S(r_z)$] obtained via fitting (line) and source imaging (squares). Source image extraction makes no assumption for the shape of the 3D source function, whereas moment fitting explicitly assumes a shape. Therefore, the good agreement from the two extraction methods confirms the sufficiency of the Hump function but not its uniqueness.

The function $S(r_x)$ is characterized by a long tail, which is resolved up to ~60 fm, in contrast to $S(r_y)$ and $S(r_z)$ which range up to ~25 fm. This difference is also reflected

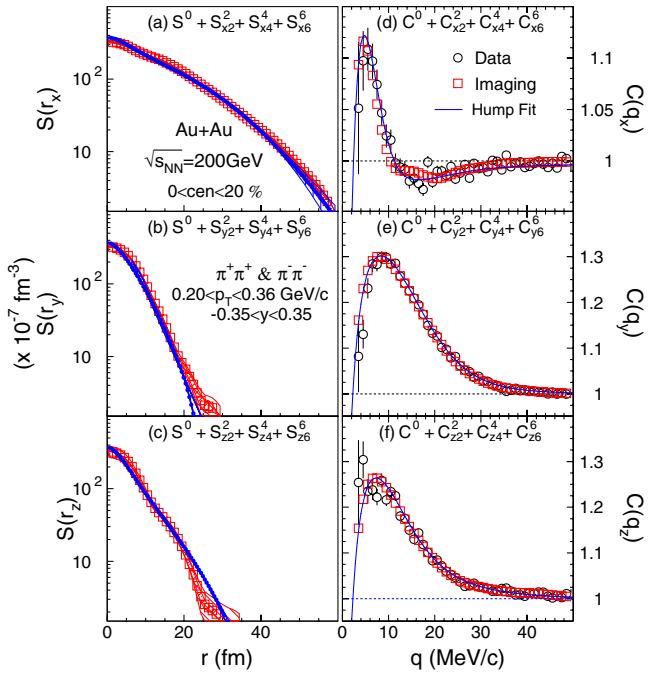

FIG. 2 (color online). Source function profiles $S(r_x)$, $S(r_y)$, and $S(r_z)$ (left panels) and their associated correlation profiles $C(q_x)$, $C(q_y)$, and $C(q_z)$ (right panels) in the PCMS. Symbols are as indicated. The bands indicate statistical and systematic errors.

in the respective correlation profiles [Figs. 2(d)–2(f)] obtained by summation of the data (circle), fit (line), and image (square) moments up to order $l = 6$ (Coulomb effects are not removed). The broader $S(r_x)$ is associated with the narrower $C(q_x)$ [Figs. 2(a) and 2(d)], as expected.

The extended tail lies along the pair total transverse momentum. Thus, the relative emission times between pions, as well as the source geometry, will contribute to $S(r_x)$. The source lifetime contributes to the range of $S(r_z)$, and $S(r_y)$ reflects its mean transverse geometric size. The difference between $S(r_x)$ and $S(r_y)$ is thus driven by the combination of the emission time difference, freeze-out dynamics, and kinematic Lorentz boost.

The event generator THERMINATOR [12,13] can shed more light on the source breakup and emission dynamics. It gives thermal emission from a longitudinally oriented cylinder of radius $\rho_{\max}$, includes all known resonance decays, and assumes Bjorken longitudinal boost invariance. The option for blast-wave transverse expansion was employed with radial velocity v_r semilinear in ρ [14], i.e., $v_r(\rho) = (\rho/\rho_{\max})/(\rho/\rho_{\max} + v_t)$, where $v_t = 1.41$. A differential fluid element is a ring defined by cylindrical coordinates z and ρ; it breaks up at proper time τ in its rest frame or at time t in the lab frame, where $t^2 = \tau^2 + z^2$. The freeze-out hypersurface is given by $\tau = \tau_0 + a\rho$, where τ_0 is the proper breakup time for $\rho = 0$ and a represents the slope of the freeze-out hypersurface in ρ-τ space (it sets the space-time correlation for particle emission: $a > 0$ implies earlier emission of particles at small ρ's, i.e., inside-out "burning" while $a < 0$ implies the reverse, i.e., outside-in "burning"). In blast-wave mode, THERMINATOR sets $a = -0.5$ for source emission from outside in as in many hydrodynamical models.

Using a set of parameters tuned to fit charged pion and kaon spectra [15], midrapidity pion pairs from THERMINATOR were obtained with the effects of all known resonance decay processes on and off. These pairs were then transformed to the PCMS, as in the data analysis, to obtain $S(r_i)$ distributions for comparison with the data.

Figure 3 shows that the 3D source function generated by THERMINATOR calculations (solid triangles) with $\tau_0 = 8.55$ fm/c, $\rho_{\max} = 8.92$ fm, and other previously tuned parameters [15], underestimates $S(r_x)$, $S(r_y)$, and $S(r_z)$. Open triangles (Fig. 3) show that resonance decays reproduce $S(r_y)$ [3(b)] and extend the calculated source function in x [3(a)] as expected, but not enough to account for the long tails in x and z (these are longer than THERMINATOR source profiles with resonance decays alone). This suggests that they have substantial contribution from pion pairs with significantly longer emission time differences. Attempts to fit the distributions by only increasing τ_0 or with $a \geq 0$ failed. The requirement of $a < 0$ in order to reproduce the extracted source function suggests a fireball burning from outside in.

The generated distribution of time differences can also be lengthened by sampling pions from a family of hyper-

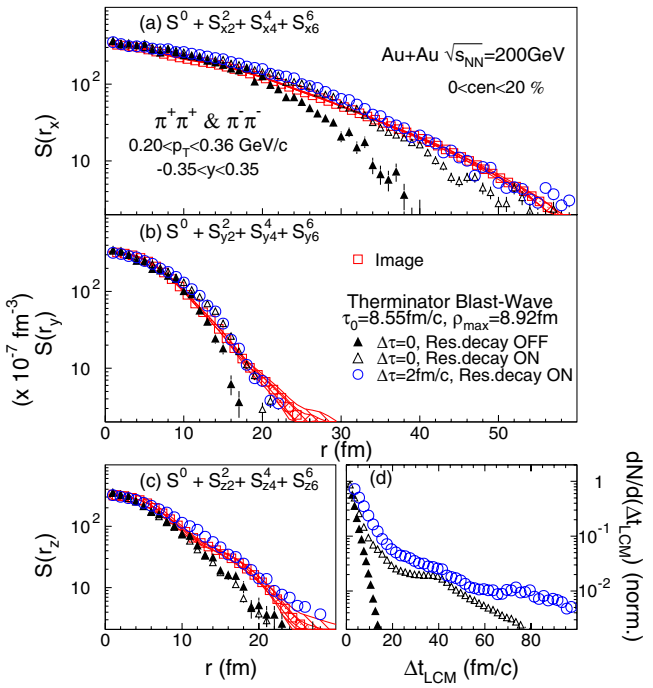

FIG. 3 (color online). Source function comparison between THERMINATOR calculation and image for (a) $S(r_x)$, (b) $S(r_y)$, (c) $S(r_z)$ in PCMS. Panel (d) compares Δt_{LCM} from THERMINATOR events with various assumptions for $\Delta\tau$ and resonance emission.

surfaces defined by a range of values of proper breakup times τ'. One such parametrization consists of replacing τ by τ' chosen from an exponential distribution $dN/d\tau' = \frac{\Theta(\tau'-\tau)}{\Delta\tau}\exp[-(\tau'-\tau)/\Delta\tau]$, where the width of the distribution $\Delta\tau$ represents the mean proper emission duration. Figure 3 shows that this approach, with $\Delta\tau = 2$ fm/c (open circles), leads to a fairly good match to the three observed source profiles. A 10% change in $\Delta\tau$ (with other parameters unchanged) spoils this match.

Figure 3(d) shows the relative emission time distribution in the LCMS, Δt_{LCM}, for pion pairs from events with the parametrizations indicated. For a fixed $\tau_0 = 8.55$ fm/c ($\Delta\tau = 0$) and resonance decays excluded, the distribution Δt_{LCM} is narrow, $\langle|\Delta t_{\mathrm{LCM}}|\rangle = 2.4$ fm/c. The addition of resonance decays adds a long tail and gives $\langle|\Delta t_{\mathrm{LCM}}|\rangle = 8.8$ fm/c. Replacing τ with the exponential distribution τ' with $\Delta\tau = 2$ fm/c results in a Δt_{LCM} distribution which is significantly broadened to give $\langle|\Delta t_{\mathrm{LCM}}|\rangle = 11.8$ fm/c. The wider distribution of time delays is needed to reproduce the source distributions. This implies a finite nonzero proper emission duration in the emission rest frame. Note that this Δt_{LCM} distribution broadening has only a small effect on $S(r_y)$.

The source distensions in Fig. 3 point to substantial time differences Δt_{LCM}; however, the interplay between proper time and breakup dynamics is model dependent. Nevertheless, the picture emerging from the data, in the context of the THERMINATOR model, is consistent with an expanding fireball of proper breakup time $\tau_0 \sim 9$ fm/c which hadronizes and emits particles over a short but nonzero mean proper emission duration $\Delta\tau \sim 2$ fm/c.

In summary, a new model-independent, three-dimensional source imaging technique has been applied to extract the 3D pion emission source function in the PCMS frame from Au + Au collisions at $\sqrt{s_{NN}} = 200$ GeV. The source function has a much greater extent in the out (x) and long (z) than in the side (y) direction. THERMINATOR model comparison indicates a fireball burning from outside in with proper lifetime $\tau_0 \sim 9$ fm/c and a mean proper emission duration $\Delta\tau \sim 2$ fm/c, leading to significant relative emission times ($\langle|\Delta t_{\mathrm{LCM}}|\rangle \approx 12$ fm/c), including those due to resonance decay.

We thank the staff of the Collider-Accelerator and Physics Departments at BNL for their vital contributions. We thank P. Danielewicz, A. Kisiel, and S. Pratt for their interest and input. We acknowledge support from the Office of Nuclear Physics in DOE Office of Science and NSF (U.S.), MEXT and JSPS (Japan), CNPq and FAPESP (Brazil), NSFC (China), IN2P3/CNRS and CEA (France), BMBF, DAAD, and AvH (Germany), OTKA (Hungary), DAE (India), ISF (Israel), KRF and KOSEF (Korea), MES, RAS, and FAAE (Russia), VR and KAW (Sweden), U.S. CRDF for the FSU, US-Hungarian NSF-OTKA-MTA, and US-Israel BSF.

*Deceased.
†PHENIX Spokesperson.
jacak@skipper.physics.sunysb.edu

[1] *Proceedings of Quark Matter 2006*, edited by Y.-G. Ma, E.-K. Wang, X. Cai, H.-Z. Huang, X.-N. Wang, and Z.-Y. Zhu [J. Phys. G: Nucl. Part. Phys. 34, No. 8 (2007)].
[2] S. Pratt, Phys. Rev. Lett. **53**, 1219 (1984).
[3] S. E. Koonin, Phys. Lett. B **70**, 43 (1977).
[4] M. Lisa *et al.*, Annu. Rev. Nucl. Part. Sci. **55**, 357 (2005).
[5] D. A. Brown and P. Danielewicz, Phys. Lett. B **398**, 252 (1997); Phys. Rev. C **57**, 2474 (1998); **64**, 014902 (2001).
[6] P. Chung *et al.*, Nucl. Phys. **A749**, 275c (2005).
[7] S. S. Adler *et al.*, Phys. Rev. Lett. **98**, 132301 (2007).
[8] P. Danielewicz and S. Pratt, Phys. Lett. B **618**, 60 (2005).
[9] P. Danielewicz and S. Pratt, Phys. Rev. C **75**, 034907 (2007).
[10] K. Adcox *et al.*, Nucl. Instrum. Methods Phys. Res., Sect. A **499**, 469 (2003).
[11] R. Lednicky *et al.*, Phys. Part. Nucl. **35**, S50 (2004).
[12] P. Chung, J. Phys. G **35**, 044034 (2008)
[13] A. Kisiel *et al.*, Comput. Phys. Commun. **174**, 669 (2006).
[14] A. Kisiel, Braz. J. Phys. **37**, 917 (2007).
[15] A. Kisiel *et al.*, Phys. Rev. C **73**, 064902 (2006). Values used are $T = 165.6$ MeV for temperature, $\mu_B = 28.5$ MeV, $\mu_S = 6.9$ MeV, $\mu_I = -0.9$ MeV for baryon, strangeness, and isospin chemical potentials.

Particle-Species Dependent Modification of Jet-Induced Correlations in Au + Au Collisions at $\sqrt{s_{NN}} = 200$ GeV

S. Afanasiev,[17] C. Aidala,[7] N. N. Ajitanand,[43] Y. Akiba,[37,38] J. Alexander,[43] A. Al-Jamel,[33] K. Aoki,[23,37] L. Aphecetche,[45] R. Armendariz,[33] S. H. Aronson,[3] R. Averbeck,[44] T. C. Awes,[34] B. Azmoun,[3] V. Babintsev,[14] A. Baldisseri,[8] K. N. Barish,[4] P. D. Barnes,[26] B. Bassalleck,[32] S. Bathe,[4] S. Batsouli,[7] V. Baublis,[36] F. Bauer,[4] A. Bazilevsky,[3] S. Belikov,[3,16] R. Bennett,[44] Y. Berdnikov,[40] M. T. Bjorndal,[7] J. G. Boissevain,[26] H. Borel,[8] K. Boyle,[44] M. L. Brooks,[26] D. S. Brown,[33] D. Bucher,[29] H. Buesching,[3] V. Bumazhnov,[14] G. Bunce,[3,38] J. M. Burward-Hoy,[26] S. Butsyk,[44] S. Campbell,[44] J.-S. Chai,[18] S. Chernichenko,[14] J. Chiba,[19] C. Y. Chi,[7] M. Chiu,[7] I. J. Choi,[52] T. Chujo,[49] V. Cianciolo,[34] C. R. Cleven,[12] Y. Cobigo,[8] B. A. Cole,[7] M. P. Comets,[35] P. Constantin,[16] M. Csanád,[10] T. Csörgő,[20] T. Dahms,[44] K. Das,[11] G. David,[3] H. Delagrange,[45] A. Denisov,[14] D. d'Enterria,[7] A. Deshpande,[38,44] E. J. Desmond,[3] O. Dietzsch,[41] A. Dion,[44] J. L. Drachenberg,[1] O. Drapier,[24] A. Drees,[44] A. K. Dubey,[51] A. Durum,[14] V. Dzhordzhadze,[46] Y. V. Efremenko,[34] J. Egdemir,[44] A. Enokizono,[13] H. En'yo,[37,38] B. Espagnon,[35] S. Esumi,[48] D. E. Fields,[32,38] F. Fleuret,[24] S. L. Fokin,[22] B. Forestier,[27] Z. Fraenkel,[51,*] J. E. Frantz,[7] A. Franz,[3] A. D. Frawley,[11] Y. Fukao,[23,37] S.-Y. Fung,[4] S. Gadrat,[27] F. Gastineau,[45] M. Germain,[45] A. Glenn,[46] M. Gonin,[24] J. Gosset,[8] Y. Goto,[37,38] R. Granier de Cassagnac,[24] N. Grau,[16] S. V. Greene,[49] M. Grosse Perdekamp,[15,38] T. Gunji,[5] H.-Å. Gustafsson,[28] T. Hachiya,[13,37] A. Hadj Henni,[45] J. S. Haggerty,[3] M. N. Hagiwara,[1] H. Hamagaki,[5] H. Harada,[13] E. P. Hartouni,[25] K. Haruna,[13] M. Harvey,[3] E. Haslum,[28] K. Hasuko,[37] R. Hayano,[5] M. Heffner,[25] T. K. Hemmick,[44] J. M. Heuser,[37] X. He,[12] H. Hiejima,[15] J. C. Hill,[16] R. Hobbs,[32] M. Holmes,[49] W. Holzmann,[43] K. Homma,[13] B. Hong,[21] T. Horaguchi,[37,47] M. G. Hur,[18] T. Ichihara,[37,38] K. Imai,[23,37] M. Inaba,[48] D. Isenhower,[1] L. Isenhower,[1] M. Ishihara,[37] T. Isobe,[5] M. Issah,[43] A. Isupov,[17] B. V. Jacak,[44,†] J. Jia,[7] J. Jin,[7] O. Jinnouchi,[38] B. M. Johnson,[3] K. S. Joo,[30] D. Jouan,[35] F. Kajihara,[5,37] S. Kametani,[5,50] N. Kamihara,[37,47] M. Kaneta,[38] J. H. Kang,[52] T. Kawagishi,[48] A. V. Kazantsev,[22] S. Kelly,[6] A. Khanzadeev,[36] D. J. Kim,[52] E. Kim,[42] Y.-S. Kim,[18] E. Kinney,[6] A. Kiss,[10] E. Kistenev,[3] A. Kiyomichi,[37] C. Klein-Boesing,[29] L. Kochenda,[36] V. Kochetkov,[14] B. Komkov,[36] M. Konno,[48] D. Kotchetkov,[4] A. Kozlov,[51] P. J. Kroon,[3] G. J. Kunde,[26] N. Kurihara,[5] K. Kurita,[39,37] M. J. Kweon,[21] Y. Kwon,[52] G. S. Kyle,[33] R. Lacey,[43] J. G. Lajoie,[16] A. Lebedev,[16] Y. Le Bornec,[35] S. Leckey,[44] D. M. Lee,[26] M. K. Lee,[52] M. J. Leitch,[26] M. A. L. Leite,[41] H. Lim,[42] A. Litvinenko,[17] M. X. Liu,[26] X. H. Li,[4] C. F. Maguire,[49] Y. I. Makdisi,[3] A. Malakhov,[17] M. D. Malik,[32] V. I. Manko,[22] H. Masui,[48] F. Matathias,[44] M. C. McCain,[15] P. L. McGaughey,[26] Y. Miake,[48] T. E. Miller,[49] A. Milov,[44] S. Mioduszewski,[3] G. C. Mishra,[12] J. T. Mitchell,[3] D. P. Morrison,[3] J. M. Moss,[26] T. V. Moukhanova,[22] D. Mukhopadhyay,[49] J. Murata,[39,37] S. Nagamiya,[19] Y. Nagata,[48] J. L. Nagle,[6] M. Naglis,[51] T. Nakamura,[13] J. Newby,[25] M. Nguyen,[44] B. E. Norman,[26] A. S. Nyanin,[22] J. Nystrand,[28] E. O'Brien,[3] C. A. Ogilvie,[16] H. Ohnishi,[37] I. D. Ojha,[49] H. Okada,[23,37] K. Okada,[38] O. O. Omiwade,[1] A. Oskarsson,[28] I. Otterlund,[28] K. Ozawa,[5] D. Pal,[49] A. P. T. Palounek,[26] V. Pantuev,[44] V. Papavassiliou,[33] J. Park,[42] W. J. Park,[21] S. F. Pate,[33] H. Pei,[16] J.-C. Peng,[15] H. Pereira,[8] V. Peresedov,[17] D. Yu. Peressounko,[22] C. Pinkenburg,[3] R. P. Pisani,[3] M. L. Purschke,[3] A. K. Purwar,[44] H. Qu,[12] J. Rak,[16] I. Ravinovich,[51] K. F. Read,[34,46] M. Reuter,[44] K. Reygers,[29] V. Riabov,[36] Y. Riabov,[36] G. Roche,[27] A. Romana,[24,*] M. Rosati,[16] S. S. E. Rosendahl,[28] P. Rosnet,[27] P. Rukoyatkin,[17] V. L. Rykov,[37] S. S. Ryu,[52] B. Sahlmueller,[29] N. Saito,[23,37,38] T. Sakaguchi,[5,50] S. Sakai,[48] V. Samsonov,[36] H. D. Sato,[23,37] S. Sato,[3,19,48] S. Sawada,[19] V. Semenov,[14] R. Seto,[4] D. Sharma,[51] T. K. Shea,[3] I. Shein,[14] T.-A. Shibata,[37,47] K. Shigaki,[13] M. Shimomura,[48] T. Shohjoh,[48] K. Shoji,[23,37] A. Sickles,[44] C. L. Silva,[41] D. Silvermyr,[34] K. S. Sim,[21] C. P. Singh,[2] V. Singh,[2] S. Skutnik,[16] W. C. Smith,[1] A. Soldatov,[14] R. A. Soltz,[25] W. E. Sondheim,[26] S. P. Sorensen,[46] I. V. Sourikova,[3] F. Staley,[8] P. W. Stankus,[34] E. Stenlund,[28] M. Stepanov,[33] A. Ster,[20] S. P. Stoll,[3] T. Sugitate,[13] C. Suire,[35] J. P. Sullivan,[26] J. Sziklai,[20] T. Tabaru,[38] S. Takagi,[48] E. M. Takagui,[41] A. Taketani,[37,38] K. H. Tanaka,[19] Y. Tanaka,[31] K. Tanida,[37,38] M. J. Tannenbaum,[3] A. Taranenko,[43] P. Tarján,[9] T. L. Thomas,[32] M. Togawa,[23,37] J. Tojo,[37] H. Torii,[37] R. S. Towell,[1] V-N. Tram,[24] I. Tserruya,[51] Y. Tsuchimoto,[13,37] S. K. Tuli,[2] H. Tydesjö,[28] N. Tyurin,[14] C. Vale,[16] H. Valle,[49] H. W. van Hecke,[26] J. Velkovska,[49] R. Vertesi,[9] A. A. Vinogradov,[22] E. Vznuzdaev,[36] M. Wagner,[23,37] X. R. Wang,[33] Y. Watanabe,[37,38] J. Wessels,[29] S. N. White,[3] N. Willis,[35] D. Winter,[7] C. L. Woody,[3] M. Wysocki,[6] W. Xie,[4,38] A. Yanovich,[14] S. Yokkaichi,[37,38] G. R. Young,[34] I. Younus,[32] I. E. Yushmanov,[22] W. A. Zajc,[7] O. Zaudtke,[29] C. Zhang,[7] J. Zimányi,[20,*] and L. Zolin[17]

(PHENIX Collaboration)

[1]*Abilene Christian University, Abilene, Texas 79699, USA*
[2]*Department of Physics, Banaras Hindu University, Varanasi 221005, India*

 © 2008 The American Physical Society

[3]Brookhaven National Laboratory, Upton, New York 11973-5000, USA
[4]University of California–Riverside, Riverside, California 92521, USA
[5]Center for Nuclear Study, Graduate School of Science, University of Tokyo, 7-3-1 Hongo, Bunkyo, Tokyo 113-0033, Japan
[6]University of Colorado, Boulder, Colorado 80309, USA
[7]Columbia University, New York, New York 10027, USA,
and Nevis Laboratories, Irvington, New York 10533, USA
[8]Dapnia, CEA Saclay, F-91191, Gif-sur-Yvette, France
[9]Debrecen University, H-4010 Debrecen, Egyetem tér 1, Hungary
[10]ELTE, Eötvös Loránd University, H-1117 Budapest, Pázmány P. s. 1/A, Hungary
[11]Florida State University, Tallahassee, Florida 32306, USA
[12]Georgia State University, Atlanta, Georgia 30303, USA
[13]Hiroshima University, Kagamiyama, Higashi-Hiroshima 739-8526, Japan
[14]IHEP Protvino, State Research Center of Russian Federation, Institute for High Energy Physics, Protvino, 142281, Russia
[15]University of Illinois at Urbana-Champaign, Urbana, Illinois 61801, USA
[16]Iowa State University, Ames, Iowa 50011, USA
[17]Joint Institute for Nuclear Research, 141980 Dubna, Moscow Region, Russia
[18]KAERI, Cyclotron Application Laboratory, Seoul, Korea
[19]KEK, High Energy Accelerator Research Organization, Tsukuba, Ibaraki 305-0801, Japan
[20]KFKI Research Institute for Particle and Nuclear Physics of the Hungarian Academy of Sciences (MTA KFKI RMKI),
H-1525 Budapest 114, POBox 49, Budapest, Hungary
[21]Korea University, Seoul, 136-701, Korea
[22]Russian Research Center "Kurchatov Institute," Moscow, Russia
[23]Kyoto University, Kyoto 606-8502, Japan
[24]Laboratoire Leprince-Ringuet, Ecole Polytechnique, CNRS-IN2P3, Route de Saclay, F-91128, Palaiseau, France
[25]Lawrence Livermore National Laboratory, Livermore, California 94550, USA
[26]Los Alamos National Laboratory, Los Alamos, New Mexico 87545, USA
[27]LPC, Université Blaise Pascal, CNRS-IN2P3, Clermont-Fd, 63177 Aubiere Cedex, France
[28]Department of Physics, Lund University, Box 118, SE-221 00 Lund, Sweden
[29]Institut für Kernphysik, University of Muenster, D-48149 Muenster, Germany
[30]Myongji University, Yongin, Kyonggido 449-728, Korea
[31]Nagasaki Institute of Applied Science, Nagasaki-shi, Nagasaki 851-0193, Japan
[32]University of New Mexico, Albuquerque, New Mexico 87131, USA
[33]New Mexico State University, Las Cruces, New Mexico 88003, USA
[34]Oak Ridge National Laboratory, Oak Ridge, Tennessee 37831, USA
[35]IPN-Orsay, Universite Paris Sud, CNRS-IN2P3, BP1, F-91406, Orsay, France
[36]PNPI, Petersburg Nuclear Physics Institute, Gatchina, Leningrad region, 188300, Russia
[37]RIKEN, The Institute of Physical and Chemical Research, Wako, Saitama 351-0198, Japan
[38]RIKEN BNL Research Center, Brookhaven National Laboratory, Upton, New York 11973-5000, USA
[39]Physics Department, Rikkyo University, 3-34-1 Nishi-Ikebukuro, Toshima, Tokyo 171-8501, Japan
[40]Saint Petersburg State Polytechnic University, St. Petersburg, Russia
[41]Instituto de Física, Universidade de São Paulo, Caixa Postal 66318, São Paulo CEP05315-970, Brazil
[42]System Electronics Laboratory, Seoul National University, Seoul, Korea
[43]Chemistry Department, Stony Brook University, SUNY, Stony Brook, New York 11794-3400, USA
[44]Department of Physics and Astronomy, Stony Brook University, SUNY, Stony Brook, New York 11794, USA
[45]SUBATECH (Ecole des Mines de Nantes, CNRS-IN2P3, Université de Nantes) BP 20722-44307, Nantes, France
[46]University of Tennessee, Knoxville, Tennessee 37996, USA
[47]Department of Physics, Tokyo Institute of Technology, Oh-okayama, Meguro, Tokyo 152-8551, Japan
[48]Institute of Physics, University of Tsukuba, Tsukuba, Ibaraki 305, Japan
[49]Vanderbilt University, Nashville, Tennessee 37235, USA
[50]Advanced Research Institute for Science and Engineering, Waseda University, 17 Kikui-cho, Shinjuku-ku, Tokyo 162-0044, Japan
[51]Weizmann Institute, Rehovot 76100, Israel
[52]Yonsei University, IPAP, Seoul 120-749, Korea

(Received 18 December 2007; published 20 August 2008)

Measurements in Au + Au collisions at $\sqrt{s_{NN}} = 200$ GeV of jet correlations for a trigger hadron at intermediate transverse momentum ($p_{T,\mathrm{trig}}$) with associated mesons or baryons at lower $p_{T,\mathrm{assoc}}$ indicate strong modification of the away-side jet. The ratio of jet-associated baryons to mesons increases with centrality and $p_{T,\mathrm{assoc}}$. For the most central collisions, the ratio is similar to that for inclusive measurements. This trend is incompatible with in-vacuum fragmentation but could be due to jetlike contributions from correlated soft partons, which recombine upon hadronization.

DOI: 10.1103/PhysRevLett.101.082301 PACS numbers: 25.75.Ld, 25.75.Gz

Recent measurements at the Relativistic Heavy Ion Collider (RHIC) have indicated the creation of a new state of matter in heavy-ion collisions [1]. The "soft" or small momentum transfer processes leading to the formation of this collision medium are sometimes accompanied by hard parton-parton scatterings. These scattered partons interact strongly with the medium and lose energy as they propagate through it, before fragmenting into jets [2]. This can lead to strong modification of both the yield and the angular correlation patterns of jets [3,4].

Parton energy loss in the nuclear collision medium [2] has been associated with the observation that the single particle yields of mesons (M) are significantly suppressed in Au + Au collisions, when compared to similar yields in $p + p$ collisions scaled by the number of binary nucleon-nucleon collisions [5,6]. This suppression factor $R_{\rm AA}^{M}$ decreases to $\sim$0.2 for transverse momentum $p_T \gtrsim 4$ GeV/c (in the absence of suppression, $R_{\rm AA} = 1.0$). A general pattern of baryon (B) enhancement (for intermediate $p_T \sim$ 2–5 GeV/c) relative to mesons has been observed in central Au + Au collisions at RHIC [7,8]. No suppression is observed for $p_T \sim 1.5$–4 GeV/c [i.e., ($R_{\rm AA}^{B} \sim 1.0$)] [9], and the proton to pion ratio is observed to be about 3 times larger than in $p + p$ collisions [1].

Quark recombination [10–13] has been used to explain the enhancement of baryon emission in the intermediate p_T range. Such models also provide an explanation for the observed dependence of the elliptic flow on hadron species in terms of the "universal" elliptic flow of constituent quarks [14,15]. However, model comparisons to jetlike hadron correlation measurements [16] indicate that jet fragmentation, in concert with the recombination of thermal quarks in a flowing medium, is insufficient to account for the dihadron correlations at intermediate p_T. Thus, the search for a consistent model, which combines fragmentation and recombination dynamics to explain all of the observations in the intermediate p_T range at RHIC, remains open.

Dihadron correlation measurements have indicated suppression of the away-side jet in Au + Au collisions [17]. Recently, modifications to the distributions of the away-side jet partner hadrons measured at lower momentum have also been observed [3,4]. Indeed, these distributions show local minima at $\Delta\phi = \pi$, which contrasts with the characteristic jet peak observed in $p + p$ collisions. This modification has been attributed to strong parton-medium interactions [4,18]. A crucial question is whether or not such interactions could lead to a change in the recombination dynamics and influence the dihadron jet correlations observed at intermediate p_T.

Fries *et al.* [19,20] have argued that such a change in the recombination dynamics is to be expected from the correlations among medium partons and an energetic jet parton, induced by a "wake effect" generated by strong parton-medium interactions. That is, the energy and momentum dissipated by a hard scattered parton are absorbed by the surrounding medium, increasing the temperature by a small amount and setting the medium into motion in the direction of the energetic parton. Thus, dihadron jet correlations could be influenced by correlated medium partons which recombine with each other or with a hard jet parton [21]. The process of recombination would also amplify these jetlike correlations for baryon creation compared to that for mesons and, hence, result in particle ratios different from the in-vacuum fragmentation values [19,21].

To gain more insight into parton-medium interactions and how they might impact recombination, we use measurements of relative azimuthal angle ($\Delta\phi$) correlation functions to make detailed investigations of the distributions and conditional yields of jet-associated baryons and mesons. Our study is made as a function of collision centrality and partner p_T, for the trigger hadron selection $2.5 < p_{T,\rm trig} < 4.0$ GeV/c.

Au + Au data (at $\sqrt{s_{NN}} = 200$ GeV) were recorded during 2004 with the PHENIX detector [22]. Collision centrality was determined with the beam-beam counters (BBCs) and zero degree calorimeters [22]. Charged particle tracking, identification, and momentum reconstruction in the central rapidity region ($|\eta| \leq 0.35$) was provided by two drift chambers, each with an azimuthal coverage $\Delta\varphi = \pi/2$, and two layers of multiwire proportional chambers with pad readout (PC1 and PC3). To reject most background (i.e., conversions, decays, etc.), a confirming hit was required within a 2σ matching window in PC3 [5].

Charged particles were identified via time-of-flight measurement with the time-of-flight (TOF) and lead scintillator (PbSc) detectors. The TOF covers $\Delta\varphi = \pi/4$ with good timing resolution $\simeq$ 120 ps (see Refs. [16,23]); the PbSc as used here covers a larger solid angle ($\Delta\varphi = 3\pi/4$) with a modest timing resolution of 400 ps. The time-of-flight measurements were used in conjunction with the measured momentum and flight-path length to generate a mass-squared (m^2) distribution [24] for charged particle identification. A cut about the baryon ($\bar{p}$, p) peak in the m^2 distribution was used to distinguish baryons and mesons ($\pi^{\pm}$, $K^{\pm}$). The kaon contamination of the baryon sample is $\lesssim 3\%$ for the highest associated p_T bin used ($1.6 < p_{T,\rm assoc}^{M,B} < 2$ GeV/c). We generated area-normalized two-particle correlation functions, in relative azimuthal angle $C(\Delta\phi)$, as the ratio of a signal distribution $N_{\rm cor}(\Delta\phi)$, constructed with correlated particle pairs from the same event, and a background distribution $N_{\rm mix}(\Delta\phi)$, for pairs obtained by mixing particles from different events having similar collision vertex and centrality [3,25]: $C(\Delta\phi) = [N_{\rm cor}(\Delta\phi) \int d\Delta\phi N_{\rm mix}(\Delta\phi)]/[N_{\rm mix}(\Delta\phi) \int d\Delta\phi N_{\rm cor}(\Delta\phi)]$.

Representative examples of the correlation functions $[C(\Delta\phi)]$, so obtained for associated mesons and baryons ($1.3 < p_{T,\rm assoc}^{M,B} < 1.6$ GeV/c) per trigger hadron ($2.5 < p_{T,\rm trig} < 4.0$ GeV/c), are shown for two centrality selections in Fig. 1. They indicate an asymmetry characteristic

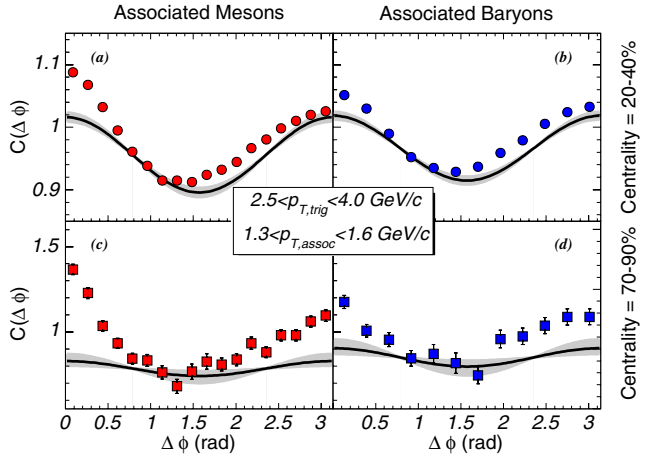

FIG. 1 (color online). Correlation functions for associated partner mesons (a),(c) and baryons (b),(d) for centrality selections of 20%–40% (top panels) and 70%–90% (bottom panels). The curves indicate elliptic flow contributions (see text).

of (di)jet-pair correlations [$J(\Delta\phi)$]and an anisotropy signaling elliptic flow [$H(\Delta\phi) = 1 + 2(v_2^{\rm trig} \times v_2^{B,M}) \times \cos(2\Delta\phi)$]with amplitude $v_2^{\rm trig} \times v_2^{M,B}$ [3]. The correlation functions for associated partner mesons are more asymmetric than those for associated partner baryons, indicating that the jet signal is stronger for hadron-meson correlations. However, clear separation of the jet and flow correlations is required for further study.

To extract $J(\Delta\phi)$ from $C(\Delta\phi)$, a two-source ansatz [25] is used [i.e., $C(\Delta\phi) = b_o H(\Delta\phi) + J(\Delta\phi)$]. Values for $v_2^{\rm trig}$ and $v_2^{M,B}$ were obtained via measurements of the single particle distributions relative to the reaction plane, determined in the BBCs [14,15]. The large (pseudo)rapidity separation ($\Delta|\eta| > 2.75$) between each BBC and the PHENIX central arms minimizes any nonflow contributions to these v_2 values [26].

To fix the value of b_o, we followed the procedure in Refs. [3,25] and assumed that $J(\Delta\phi)$ has zero yield at some minimum $\Delta\phi_{\rm min}$ (ZYAM). That is, the elliptic flow contributions are required to coincide with $C(\Delta\phi)$ at $\Delta\phi_{\rm min}$. Good precision for $\Delta\phi_{\rm min}$ was achieved via a fit to the correlation function; the systematic error on the magnitude of the integrated jet function $J(\Delta\phi)$, due to the ZYAM procedure, is estimated to be $\lesssim 3\%$ from the uncertainty in setting $J(\Delta\phi) = 0$ at $\Delta\phi_{\rm min}$. The solid lines in Fig. 1 show examples of the ZYAM-normalized elliptic flow (v_2) contributions. The gray bands represent systematic errors on the v_2 amplitudes ($\sim$6% for central and midcentral events and $\sim$40% for peripheral events) primarily due to an uncertainty in the reaction plane resolution [3].

The efficiency-corrected associated meson and baryon jet distributions $\frac{1}{N_{\rm trig}} \frac{d^2N}{dp_T d\Delta\phi}$ are shown in Fig. 2 for two associated p_T bins and for the centralities 0–20% and 20%–40%. The shaded error bars and dashed lines indicate the respective systematic error related to v_2 subtraction and fixing b_o. The associated baryon jet-pair distributions are multiplied by the indicated factors to facilitate a shape comparison with the distributions for mesons.

Figure 2 shows that the correlation strength of the near-side jet ($\Delta\phi \leq \Delta\phi_{\rm min}$, NS) is substantially weaker for associated baryons. In contrast, the shapes of the away-side jet distributions ($\Delta\phi \geq \Delta\phi_{\rm min}$, AS) are qualitatively similar for associated mesons and baryons. For the central and midcentral collisions shown, these distributions are also broad and decidedly non-Gaussian, with evidence for local minima at $\Delta\phi = \pi$ [3]. They provide confirmation that the topological signatures for strong jet modification are reflected in the jet-pair distributions for both associated baryons and mesons [27]. The latter finding for baryons and mesons is an important constraint for models of strong jet modification [11,28–30].

For a given centrality and partner p_T, the integral of the extracted $J(\Delta\phi)$ distribution is the fraction of particle pairs associated with the jet, i.e., the jet-pair fraction (JPF): $\mathrm{JPF}_{\rm NS,AS} = \sum_{i\in \rm NS,AS} J(\Delta\phi_i) / \sum_i C(\Delta\phi_i)$ [25]. We use it to determine the conditional yield $\langle N^{M,B}\rangle / \langle N_{\rm trig}\rangle$, or efficiency-corrected pairs per trigger [25],

$$\frac{\langle N^{M,B}\rangle}{\langle N_{\rm trig}\rangle} = \mathrm{JPF} \frac{\langle N_d^{M,B}\rangle}{\langle N_s^{\rm trig}\rangle \times \langle N_s^{M,B}\rangle} \langle N_{\rm eff}^{M,B}\rangle,$$

where $\langle N_d^{M,B}\rangle$ is the average number of detected hadron-meson(baryon) pairs per event, $\langle N_s^{\rm trig}\rangle$ and $\langle N_s^{M,B}\rangle$ are the detected singles rates for hadrons, mesons, and baryons, respectively, and $\langle N_{\rm eff}^{M,B}\rangle$ are the efficiency-corrected singles rates. The systematic error associated with the latter is $\sim$10%. A further division by the p_T bin width gives the conditional yield $CY = \frac{1}{N_{\rm trig}} \frac{dN}{dp_T}$, which is equivalent to an integration of the distributions shown in Fig. 2.

The conditional yields, for near- and away-side associated mesons and baryons, are shown as a function of $p_{T,\rm assoc}^{M,B}$ and collision centrality in Fig. 3. The shaded error bars reflect the combined systematic error associated with

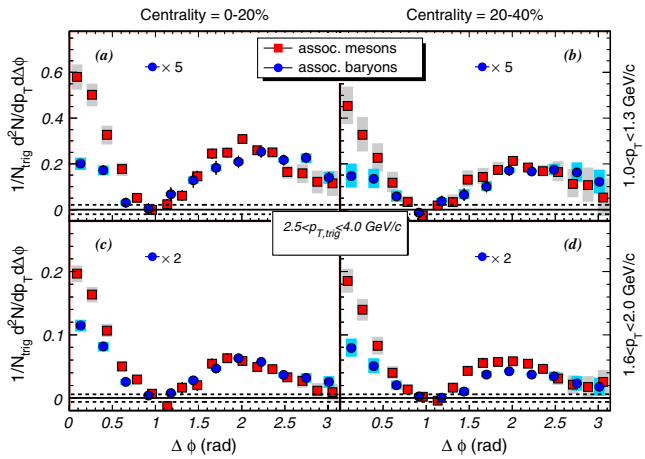

FIG. 2 (color online). Jet-pair distributions for associated mesons (squares) and baryons (circles).

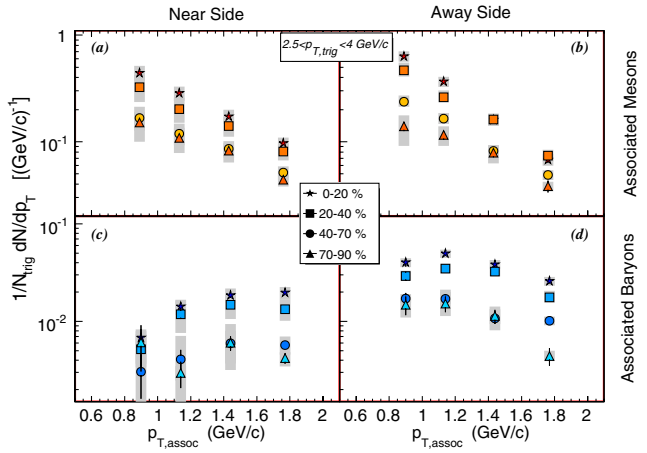

FIG. 3 (color online). Conditional jet yields for associated mesons and baryons for near-side and away-side jets.

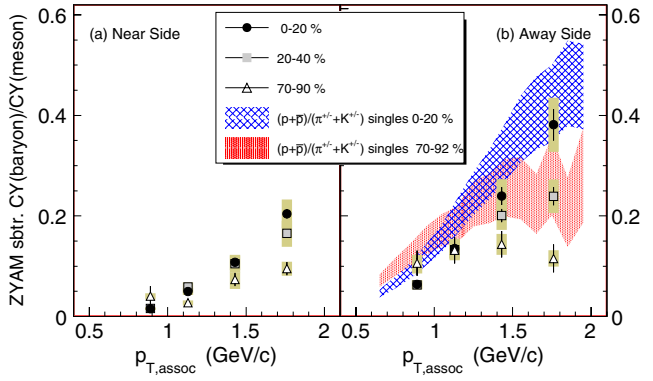

FIG. 4 (color online). Ratio of jet-associated baryons to jet-associated mesons. The hatched bands indicate inclusive B/M ratios (see text).

v_2, b_o, and the efficiency. The yields for associated mesons [Figs. 3(a) and 3(b)] indicate an essentially exponential decrease with increasing $p^M_{T,\mathrm{assoc}}$, for both the near- and away-side jets. An increase in the inverse slope parameter T_{eff} (''temperature'') from central ($T_{\mathrm{eff}} \sim 390$ MeV) to peripheral ($T_{\mathrm{eff}} \sim 700$ MeV) collisions is also apparent for the away-side distributions. For a fixed $p^M_{T,\mathrm{assoc}}$, these yields also show an increase from peripheral to central events, albeit with a stronger dependence for the away-side jet. This trend is incompatible with in-vacuum fragmentation but could be due to jetlike contributions from correlated soft partons which recombine upon hadronization [19,21], softening of the fragmentation function, and fragmentation of radiated gluons, due to energy loss [31].

The conditional yields for associated baryons differ strongly from those for associated mesons [cf. Figs. 3(c) and 3(d)]. That is, they do not show an exponential dependence on p^B_T over the measured range, and the yields for the away-side jet are substantially larger than those for the near-side jet. For a given $p^B_{T,\mathrm{assoc}}$, the near- and away-side conditional yields increase as the collisions become more central; i.e., this trend is similar to that for the associated mesons. The baryon yields show a much stronger increase with centrality [27], as might be expected if correlated soft partons recombine and contribute to the away-side jet correlations [20].

The ratio of associated baryons to associated mesons is shown as a function of associated particle p_T in Fig. 4; the left and right panels show the ratios for the near- and away-side jets, respectively, for three centrality selections as indicated. These ratios clearly increase with p_T and with centrality for $p_T \gtrsim 1.4$ GeV/c. For peripheral collisions, the near-side ratios are qualitatively similar to the p/π ratio for jets produced in $e^+ + e^-$ collisions [32]. For more central collisions, the near- and away-side ratios are much larger, suggesting that the medium influences the relative composition of the associated particles.

The hatched bands in Fig. 4(b) show the inclusive B/M ratios (uncorrected for baryon and meson feeddown) as a function of p_T for the 0–20% and 70%–92% most central Au + Au collisions [24]; an estimate of these ratios after feeddown corrections is within the systematic errors indicated by the bands. These ratios indicate that the trend of the centrality dependent baryon enhancement, apparent in the jetlike associated conditional yields, is similar to that observed for the inclusive particle yields. This suggests that the mechanisms for baryon enhancement in both the inclusive and the current away-side jet measurements have a common origin. Since recombination models can explain the enhancement of inclusive baryon yields, a qualitative explanation is that the away-side correlations result from the recombination of correlated soft partons induced via strong parton-medium interactions.

In summary, we have measured per-trigger yield distributions for jetlike associated mesons and baryons over a wide range of centrality and p_T in Au + Au collisions. The distributions for both species show similar shape modifications for the away-side jet, compatible with several jet-modification models [11,28–30]. The conditional yield distributions for mesons and baryons show different dependencies on collision centrality and associated particle p_T. The ratio of associated baryons to mesons increases with centrality and p_T, similar to the data for inclusive measurements. These results may be qualitatively understood in terms of parton-medium interactions which induce correlations between soft partons, followed by recombination at hadronization [19–21]. The observation that the baryon to meson ratio of the away-side jet approaches the ratio measured for inclusive hadrons in central Au + Au collisions suggests that the increased jetlike associated yield and large baryon to meson ratio have the same origin.

It may therefore be possible to reconcile the observed jetlike structures and the increased baryon/meson ratio at intermediate p_T in a single model for hadron production. Future quantitative model comparisons as well as measurements at higher p_T are required to fully understand the interplay between fragmentation and soft production processes.

We thank the staff of the Collider-Accelerator and Physics Departments at BNL for their vital contributions. We acknowledge support from the Office of Nuclear Physics in DOE Office of Science and NSF (USA), MEXT and JSPS (Japan), CNPq and FAPESP (Brazil), NSFC (China), IN2P3/CNRS and CEA (France), BMBF, DAAD, and AvH (Germany), OTKA (Hungary), DAE (India), ISF (Israel), KRF and KOSEF (Korea), MES, RAS, and FAAE (Russia), VR and KAW (Sweden), U.S. CRDF for the FSU, U.S.–Hungarian NSF-OTKA-MTA, and U.S.–Israel BSF.

*Deceased.
†PHENIX spokesperson.
jacak@skipper.physics.sunysb.edu

[1] K. Adcox *et al.*, Nucl. Phys. **A757**, 184 (2005).
[2] R. Baier *et al.*, Nucl. Phys. **B483**, 291 (1997).
[3] S. S. Adler *et al.*, Phys. Rev. Lett. **97**, 052301 (2006).
[4] A. Adare *et al.*, Phys. Rev. C **77**, 011901 (2008).
[5] K. Adcox *et al.*, Phys. Rev. Lett. **88**, 022301 (2001).
[6] J. Adams *et al.*, Phys. Rev. Lett. **91**, 172302 (2003).
[7] K. Adcox *et al.*, Phys. Rev. Lett. **88**, 242301 (2002).
[8] C. Adler *et al.*, Phys. Rev. Lett. **89**, 092301 (2002).
[9] S. S. Adler *et al.*, Phys. Rev. Lett. **91**, 172301 (2003).
[10] S. A. Voloshin, Nucl. Phys. **A715**, 379 (2003).
[11] V. Greco, C. M. Ko, and P. Levai, Phys. Rev. C **68**, 034904 (2003).
[12] R. C. Hwa and C. B. Yang, Phys. Rev. C **67**, 034902 (2003).
[13] R. J. Fries, B. Muller, C. Nonaka, and S. A. Bass, Phys. Rev. C **68**, 044902 (2003).
[14] A. Adare *et al.*, Phys. Rev. Lett. **98**, 162301 (2007).
[15] R. A. Lacey and A. Taranenko, arXiv:nucl-ex/0610029.
[16] S. S. Adler *et al.*, Phys. Rev. C **71**, 051902 (2005).
[17] C. Adler *et al.*, Phys. Rev. Lett. **90**, 032301 (2003).
[18] A. Adare *et al.*, Phys. Rev. Lett. **98**, 232301 (2007).
[19] R. J. Fries, S. A. Bass, and B. Muller, Phys. Rev. Lett. **94**, 122301 (2005).
[20] R. J. Fries, V. Greco, and P. Sorensen, arXiv:0807.4939.
[21] R. C. Hwa and C. B. Yang, Phys. Rev. C **70**, 024905 (2004).
[22] K. Adcox *et al.*, Nucl. Instrum. Methods Phys. Res., Sect. A **499**, 469 (2003).
[23] A. Adare *et al.*, Phys. Lett. B **649**, 359 (2007).
[24] S. S. Adler *et al.*, Phys. Rev. C **69**, 034909 (2004).
[25] N. N. Ajitanand *et al.*, Phys. Rev. C **72**, 011902(R) (2005).
[26] J. Jia, Nucl. Phys. **A783**, 501 (2007).
[27] The difference between the current conditional yields and those reported in Ref. [23] stem from a difference in integration range for the away-side jet.
[28] N. Armesto, C. A. Salgado, and U. A. Wiedemann, Phys. Rev. Lett. **93**, 242301 (2004).
[29] H. Stoecker, Nucl. Phys. **A750**, 121 (2005).
[30] J. Casalderrey-Solana *et al.*, J. Phys. Conf. Ser. **27**, 22 (2005); Nucl. Phys. **A774**, 577 (2006).
[31] Xin-Nian Wang, Phys. Lett. B **579**, 299 (2004).
[32] P. Abreu *et al.*, Eur. Phys. J. C **17**, 53 (2000).

Cold nuclear matter effects on J/ψ production as constrained by deuteron-gold measurements at $\sqrt{s_{NN}} = 200$ GeV

A. Adare,[10] S. S. Adler,[5] S. Afanasiev,[24] C. Aidala,[11] N. N. Ajitanand,[50] Y. Akiba,[25,44,45] H. Al-Bataineh,[39] J. Alexander,[50] A. Al-Jamel,[39] K. Aoki,[29,44] L. Aphecetche,[52] R. Armendariz,[39] S. H. Aronson,[5] J. Asai,[45] E. T. Atomssa,[30] R. Averbeck,[51] T. C. Awes,[40] B. Azmoun,[5] V. Babintsev,[20] G. Baksay,[16] L. Baksay,[16] A. Baldisseri,[13] K. N. Barish,[6] P. D. Barnes,[32] B. Bassalleck,[38] S. Bathe,[6,35] S. Batsouli,[11,40] V. Baublis,[43] F. Bauer,[6] A. Bazilevsky,[5,45] S. Belikov,[5,*] R. Bennett,[51] Y. Berdnikov,[47] A. A. Bickley,[10] M. T. Bjorndal,[11] J. G. Boissevain,[32] H. Borel,[13] K. Boyle,[51] M. L. Brooks,[32] D. S. Brown,[39] N. Bruner,[38] D. Bucher,[35] H. Buesching,[5,35] V. Bumazhnov,[20] G. Bunce,[5,45] J. M. Burward-Hoy,[31,32] S. Butsyk,[32,51] X. Camard,[52] S. Campbell,[51] P. Chand,[4] B. S. Chang,[59] W. C. Chang,[2] J.-L. Charvet,[13] S. Chernichenko,[20] J. Chiba,[25] C. Y. Chi,[11] M. Chiu,[11,21] I. J. Choi,[59] R. K. Choudhury,[4] T. Chujo,[5,56] P. Chung,[50] A. Churyn,[20] V. Cianciolo,[40] C. R. Cleven,[18] Y. Cobigo,[13] B. A. Cole,[11] M. P. Comets,[41] P. Constantin,[23,32] M. Csanád,[15] T. Csörgő,[26] J. P. Cussonneau,[52] T. Dahms,[51] K. Das,[17] G. David,[5] F. Deák,[15] M. B. Deaton,[1] K. Dehmelt,[16] H. Delagrange,[52] A. Denisov,[20] D. d'Enterria,[11] A. Deshpande,[45,51] E. J. Desmond,[5] A. Devismes,[51] O. Dietzsch,[48] A. Dion,[51] M. Donadelli,[48] J. L. Drachenberg,[1] O. Drapier,[30] A. Drees,[51] A. K. Dubey,[58] A. Durum,[20] D. Dutta,[4] V. Dzhordzhadze,[6,53] Y. V. Efremenko,[40] J. Egdemir,[51] F. Ellinghaus,[10] W. S. Emam,[6] A. Enokizono,[31] H. En'yo,[44,45] B. Espagnon,[41] S. Esumi,[55] K. O. Eyser,[6] D. E. Fields,[38,45] C. Finck,[52] M. Finger Jr.,[7,24] M. Finger,[7,24] F. Fleuret,[30] S. L. Fokin,[28] B. D. Fox,[45] Z. Fraenkel,[58,*] J. E. Frantz,[11,51] A. Franz,[5] A. D. Frawley,[17] K. Fujiwara,[44] Y. Fukao,[29,44,45] S.-Y. Fung,[6] T. Fusayasu,[37] S. Gadrat,[33] I. Garishvili,[53] M. Germain,[52] A. Glenn,[10,53] H. Gong,[51] M. Gonin,[30] J. Gosset,[13] Y. Goto,[44,45] R. Granier de Cassagnac,[30] N. Grau,[23] S. V. Greene,[56] M. Grosse Perdekamp,[21,45] T. Gunji,[9] H.-Å. Gustafsson,[34] T. Hachiya,[19] A. Hadj Henni,[52] C. Haegemann,[38] J. S. Haggerty,[5] H. Hamagaki,[9] R. Han,[42] A. G. Hansen,[32] H. Harada,[19] E. P. Hartouni,[31] K. Haruna,[19] M. Harvey,[5] E. Haslum,[34] K. Hasuko,[44] R. Hayano,[9] M. Heffner,[31] T. K. Hemmick,[51] T. Hester,[6] J. M. Heuser,[44] X. He,[18] P. Hidas,[26] H. Hiejima,[21] J. C. Hill,[23] R. Hobbs,[38] M. Hohlmann,[16] W. Holzmann,[50] K. Homma,[19] B. Hong,[27] A. Hoover,[39] T. Horaguchi,[44,45,54] D. Hornback,[53] T. Ichihara,[44,45] V. V. Ikonnikov,[28] K. Imai,[29,44] M. Inaba,[55] Y. Inoue,[44,46] M. Inuzuka,[9] D. Isenhower,[1] L. Isenhower,[1] M. Ishihara,[44] T. Isobe,[9] M. Issah,[50] A. Isupov,[24] B. V. Jacak,[51,†] J. Jia,[11,51] J. Jin,[11] O. Jinnouchi,[44,45] B. M. Johnson,[5] S. C. Johnson,[31] K. S. Joo,[36] D. Jouan,[41] F. Kajihara,[9] S. Kametani,[9,57] N. Kamihara,[44,54] J. Kamin,[51] M. Kaneta,[45] J. H. Kang,[59] H. Kanou,[44,54] K. Katou,[57] T. Kawabata,[9] D. Kawall,[45] A. V. Kazantsev,[28] S. Kelly,[10,11] B. Khachaturov,[58] A. Khanzadeev,[43] J. Kikuchi,[57] D. H. Kim,[36] D. J. Kim,[59] E. Kim,[49] G.-B. Kim,[30] H. J. Kim,[59] E. Kinney,[10] A. Kiss,[15] E. Kistenev,[5] A. Kiyomichi,[44] J. Klay,[31] C. Klein-Boesing,[35] H. Kobayashi,[45] L. Kochenda,[43] V. Kochetkov,[20] R. Kohara,[19] B. Komkov,[43] M. Konno,[55] D. Kotchetkov,[6] A. Kozlov,[58] A. Král,[12] A. Kravitz,[11] P. J. Kroon,[5] J. Kubart,[7,22] C. H. Kuberg,[1,*] G. J. Kunde,[32] N. Kurihara,[9] K. Kurita,[44,46] M. J. Kweon,[27] Y. Kwon,[53,59] G. S. Kyle,[39] R. Lacey,[50] Y.-S. Lai,[11] J. G. Lajoie,[23] A. Lebedev,[23,28] Y. Le Bornec,[41] S. Leckey,[51] D. M. Lee,[32] M. K. Lee,[59] T. Lee,[49] M. J. Leitch,[32] M. A. L. Leite,[48] B. Lenzi,[48] H. Lim,[49] T. Liška,[12] A. Litvinenko,[24] M. X. Liu,[32] X. Li,[8] X. H. Li,[6] B. Love,[56] D. Lynch,[5] C. F. Maguire,[56] Y. I. Makdisi,[5] A. Malakhov,[24] M. D. Malik,[38] V. I. Manko,[28] Y. Mao,[42,44] G. Martinez,[52] L. Mašek,[7,22] H. Masui,[55] F. Matathias,[11,51] T. Matsumoto,[9,57] M. C. McCain,[1] M. McCumber,[51] P. L. McGaughey,[32] Y. Miake,[55] P. Mikeš,[7,22] K. Miki,[55] T. E. Miller,[56] A. Milov,[51] S. Mioduszewski,[5] G. C. Mishra,[18] M. Mishra,[3] J. T. Mitchell,[5] M. Mitrovski,[50] A. K. Mohanty,[4] A. Morreale,[6] D. P. Morrison,[5] J. M. Moss,[32] T. V. Moukhanova,[28] D. Mukhopadhyay,[56,58] M. Muniruzzaman,[6] J. Murata,[44,46] S. Nagamiya,[25] Y. Nagata,[55] J. L. Nagle,[10,11] M. Naglis,[58] I. Nakagawa,[44,45] Y. Nakamiya,[19] T. Nakamura,[19] K. Nakano,[44,54] J. Newby,[31,53] M. Nguyen,[51] B. E. Norman,[32] A. S. Nyanin,[28] J. Nystrand,[34] E. O'Brien,[5] S. X. Oda,[9] C. A. Ogilvie,[23] H. Ohnishi,[44] I. D. Ojha,[3,56] H. Okada,[29,44] K. Okada,[44,45] M. Oka,[55] O. O. Omiwade,[1] A. Oskarsson,[34] I. Otterlund,[34] M. Ouchida,[19] K. Oyama,[9] K. Ozawa,[9] R. Pak,[5] D. Pal,[56,58] A. P. T. Palounek,[32] V. Pantuev,[51] V. Papavassiliou,[39] J. Park,[49] W. J. Park,[27] S. F. Pate,[39] H. Pei,[23] V. Penev,[24] J.-C. Peng,[21] H. Pereira,[13] V. Peresedov,[24] D. Yu. Peressounko,[28] A. Pierson,[38] C. Pinkenburg,[5] R. P. Pisani,[5] M. L. Purschke,[5] A. K. Purwar,[32,51] J. M. Qualls,[1] H. Qu,[18] J. Rak,[23,38] A. Rakotozafindrabe,[30] I. Ravinovich,[58] K. F. Read,[40,53] S. Rembeczki,[16] M. Reuter,[51] K. Reygers,[35] V. Riabov,[43] Y. Riabov,[43] G. Roche,[33] A. Romana,[30,*] M. Rosati,[23] S. S. E. Rosendahl,[34] P. Rosnet,[33] P. Rukoyatkin,[24] V. L. Rykov,[44] S. S. Ryu,[59] B. Sahlmueller,[35] N. Saito,[29,44,45] T. Sakaguchi,[5,9,57] S. Sakai,[55] H. Sakata,[19] V. Samsonov,[43] L. Sanfratello,[38] R. Santo,[35] H. D. Sato,[29,44] S. Sato,[5,25,55] S. Sawada,[25] Y. Schutz,[52] J. Seele,[10] R. Seidl,[21] V. Semenov,[20] R. Seto,[6] D. Sharma,[58] T. K. Shea,[5] I. Shein,[20] A. Shevel,[43,50] T.-A. Shibata,[44,54] K. Shigaki,[19] M. Shimomura,[55] K. Shoji,[29,44] A. Sickles,[51] C. L. Silva,[48] D. Silvermyr,[32,40] C. Silvestre,[13] K. S. Sim,[27] C. P. Singh,[3] V. Singh,[3] S. Skutnik,[23] M. Slunečka,[7,24] A. Soldatov,[20] R. A. Soltz,[31] W. E. Sondheim,[32] S. P. Sorensen,[53] I. V. Sourikova,[5] F. Staley,[13] P. W. Stankus,[40] E. Stenlund,[34] M. Stepanov,[39] A. Ster,[26] S. P. Stoll,[5] T. Sugitate,[19] C. Suire,[41] J. P. Sullivan,[32] J. Sziklai,[26] T. Tabaru,[45] S. Takagi,[55] E. M. Takagui,[48] A. Taketani,[44,45] K. H. Tanaka,[25] Y. Tanaka,[37] K. Tanida,[44,45] M. J. Tannenbaum,[5] A. Taranenko,[50] P. Tarján,[14] T. L. Thomas,[38] M. Togawa,[29,44] A. Toia,[51] J. Tojo,[44] L. Tomášek,[22] H. Torii,[29,44,45] R. S. Towell,[1] V.-N. Tram,[30] I. Tserruya,[58] Y. Tsuchimoto,[19] H. Tydesjö,[34] N. Tyurin,[20] T. J. Uam,[36] C. Vale,[23] H. Valle,[56] H. W. van Hecke,[32] J. Velkovska,[5,56] M. Velkovsky,[51] R. Vertesi,[14] V. Veszprémi,[14] A. A. Vinogradov,[28] M. Virius,[12] M. A. Volkov,[28] V. Vrba,[22] E. Vznuzdaev,[43] M. Wagner,[29,44] D. Walker,[51] X. R. Wang,[18,39] Y. Watanabe,[44,45] J. Wessels,[35] S. N. White,[5] N. Willis,[41] D. Winter,[11] F. K. Wohn,[23] C. L. Woody,[5]

 ©2008 The American Physical Society

M. Wysocki,[10] W. Xie,[6,45] Y. L. Yamaguchi,[57] A. Yanovich,[20] Z. Yasin,[6] J. Ying,[18] S. Yokkaichi,[44,45] G. R. Young,[40] I. Younus,[38] I. E. Yushmanov,[28] W. A. Zajc,[11] O. Zaudtke,[35] C. Zhang,[11,40] S. Zhou,[8] J. Zimányi,[26,*] L. Zolin,[24] and X. Zong[23]
(PHENIX Collaboration)

[1]*Abilene Christian University, Abilene, Texas 79699, USA*
[2]*Institute of Physics, Academia Sinica, Taipei 11529, Taiwan*
[3]*Department of Physics, Banaras Hindu University, Varanasi 221 005, India*
[4]*Bhabha Atomic Research Centre, Bombay 400 085, India*
[5]*Brookhaven National Laboratory, Upton, New York 11973-5000, USA*
[6]*University of California—Riverside, Riverside, California 92521, USA*
[7]*Charles University, Ovocný trh 5, Praha 1, CZ-116 36 Prague, Czech Republic*
[8]*China Institute of Atomic Energy (CIAE), Beijing, People's Republic of China*
[9]*Center for Nuclear Study, Graduate School of Science, University of Tokyo, 7-3-1 Hongo, Bunkyo, Tokyo 113-0033, Japan*
[10]*University of Colorado, Boulder, Colorado 80309, USA*
[11]*Columbia University, New York 10027, and Nevis Laboratories, Irvington, New York 10533, USA*
[12]*Czech Technical University, Zikova 4, CZ-166 36 Prague 6, Czech Republic*
[13]*Dapnia, CEA Saclay, F-91191 Gif-sur-Yvette, France*
[14]*Debrecen University, Egyetem tér 1, H-4010 Debrecen, Hungary*
[15]*ELTE, Eötvös Loránd University, Pázmány P. s. 1/A, H-1117 Budapest, Hungary*
[16]*Florida Institute of Technology, Melbourne, Florida 32901, USA*
[17]*Florida State University, Tallahassee, Florida 32306, USA*
[18]*Georgia State University, Atlanta, Georgia 30303, USA*
[19]*Hiroshima University, Kagamiyama, Higashi-Hiroshima 739-8526, Japan*
[20]*IHEP Protvino, State Research Center of Russian Federation, Institute for High Energy Physics, Protvino, RU-142281, Russia*
[21]*University of Illinois at Urbana-Champaign, Urbana, Illinois 61801, USA*
[22]*Institute of Physics, Academy of Sciences of the Czech Republic, Na Slovance 2, CZ-182 21 Prague 8, Czech Republic*
[23]*Iowa State University, Ames, Iowa 50011, USA*
[24]*Joint Institute for Nuclear Research, RU-141980 Dubna, Moscow Region, Russia*
[25]*KEK, High Energy Accelerator Research Organization, Tsukuba, Ibaraki 305-0801, Japan*
[26]*KFKI Research Institute for Particle and Nuclear Physics of the Hungarian Academy of Sciences (MTA KFKI RMKI), Post Office Box 49, H-1525 Budapest 114, Hungary*
[27]*Korea University, Seoul, 136-701, Korea*
[28]*Russian Research Center "Kurchatov Institute," Moscow, Russia*
[29]*Kyoto University, Kyoto 606-8502, Japan*
[30]*Laboratoire Leprince-Ringuet, Ecole Polytechnique, CNRS-IN2P3, Route de Saclay, F-91128 Palaiseau, France*
[31]*Lawrence Livermore National Laboratory, Livermore, California 94550, USA*
[32]*Los Alamos National Laboratory, Los Alamos, New Mexico 87545, USA*
[33]*LPC, Université Blaise Pascal, CNRS-IN2P3, Clermont-Fd, F-63177 Aubiere Cedex, France*
[34]*Department of Physics, Lund University, Box 118, SE-221 00 Lund, Sweden*
[35]*Institut für Kernphysik, University of Muenster, D-48149 Muenster, Germany*
[36]*Myongji University, Yongin, Kyonggido 449-728, Korea*
[37]*Nagasaki Institute of Applied Science, Nagasaki-shi, Nagasaki 851-0193, Japan*
[38]*University of New Mexico, Albuquerque, New Mexico 87131, USA*
[39]*New Mexico State University, Las Cruces, New Mexico 88003, USA*
[40]*Oak Ridge National Laboratory, Oak Ridge, Tennessee 37831, USA*
[41]*IPN-Orsay, Universite Paris Sud, CNRS-IN2P3, BP1, F-91406 Orsay, France*
[42]*Peking University, Beijing, People's Republic of China*
[43]*PNPI, Petersburg Nuclear Physics Institute, Gatchina, Leningrad Region, RU-188300, Russia*
[44]*RIKEN, The Institute of Physical and Chemical Research, Wako, Saitama 351-0198, Japan*
[45]*RIKEN BNL Research Center, Brookhaven National Laboratory, Upton, New York 11973-5000, USA*
[46]*Physics Department, Rikkyo University, 3-34-1 Nishi-Ikebukuro, Toshima, Tokyo 171-8501, Japan*
[47]*Saint Petersburg State Polytechnic University, St. Petersburg, Russia*
[48]*Universidade de São Paulo, Instituto de Física, Caixa Postal 66318, São Paulo CEP05315-970, Brazil*
[49]*System Electronics Laboratory, Seoul National University, Seoul, Korea*
[50]*Chemistry Department, Stony Brook University, Stony Brook, SUNY, New York 11794-3400, USA*
[51]*Department of Physics and Astronomy, Stony Brook University, SUNY, Stony Brook, New York 11794, USA*
[52]*SUBATECH (Ecole des Mines de Nantes, CNRS-IN2P3, Université de Nantes) BP 20722, F-44307, Nantes, France*
[53]*University of Tennessee, Knoxville, Tennessee 37996, USA*
[54]*Department of Physics, Tokyo Institute of Technology, Oh-okayama, Meguro, Tokyo 152-8551, Japan*

[55]*Institute of Physics, University of Tsukuba, Tsukuba, Ibaraki 305, Japan*
[56]*Vanderbilt University, Nashville, Tennessee 37235, USA*
[57]*Waseda University, Advanced Research Institute for Science and Engineering, 17 Kikui-cho, Shinjuku-ku, Tokyo 162-0044, Japan*
[58]*Weizmann Institute, Rehovot 76100, Israel*
[59]*Yonsei University, IPAP, Seoul 120-749, Korea*
(Received 26 November 2007; published 28 February 2008)

We present a new analysis of J/ψ production yields in deuteron-gold collisions at $\sqrt{s_{NN}} = 200$ GeV using data taken from the PHENIX experiment in 2003 and previously published in S. S. Adler *et al.* [Phys. Rev. Lett **96**, 012304 (2006)]. The high statistics proton-proton J/ψ data taken in 2005 are used to improve the baseline measurement and thus construct updated cold nuclear matter modification factors ($R_{d\mathrm{Au}}$). A suppression of J/ψ in cold nuclear matter is observed as one goes forward in rapidity (in the deuteron-going direction), corresponding to a region more sensitive to initial-state low-x gluons in the gold nucleus. The measured nuclear modification factors are compared to theoretical calculations of nuclear shadowing to which a J/ψ (or precursor) breakup cross section is added. Breakup cross sections of $\sigma_{\mathrm{breakup}} = 2.8^{+1.7}_{-1.4}$ ($2.2^{+1.6}_{-1.5}$) mb are obtained by fitting these calculations to the data using two different models of nuclear shadowing. These breakup cross-section values are consistent within large uncertainties with the 4.2 ± 0.5 mb determined at lower collision energies. Projecting this range of cold nuclear matter effects to copper-copper and gold-gold collisions reveals that the current constraints are not sufficient to firmly quantify the additional hot nuclear matter effect.

DOI: 10.1103/PhysRevC.77.024912 PACS number(s): 25.75.Dw

I. INTRODUCTION

Understanding the behavior of QCD matter under different conditions of temperature and density is the subject of intense experimental and theoretical work in nuclear physics. The transition from hadronic matter to a quark-gluon plasma at high temperature is expected to be achieved in high-energy heavy-ion collisions. The hadronization of partons in vacuum or cold nuclear matter (i.e., in a nucleus) is also of keen interest and represents a nonperturbative and dynamic QCD process. The formation and interaction of heavy quarkonia (e.g., J/ψ mesons) in vacuum, cold nuclear matter, and hot nuclear matter present an excellent laboratory for gaining insights on these transformations. Recent results from the Relativistic Heavy Ion Collider reveal a significant suppression of the final J/ψ yield in central (small impact parameter) Au + Au reactions at $\sqrt{s_{NN}} = 200$ GeV, relative to expectations scaled from $p + p$ reactions at the same energy [1,2]. A possible source of this suppression is the screening of the attractive interaction between the quark-antiquark pair in the hot nuclear medium, as temperatures are expected to be above the critical temperature for a quark-gluon plasma transition. Larger J/ψ suppression is observed at forward rapidity than at midrapidity, which contradicts models with only color screening of quarkonia proportional to the local energy density.

Produced $c\bar{c}$ pairs must pass through the remaining nuclear material from the incident cold nuclei, in addition to surviving any hot medium environment. The so-called cold nuclear matter effects [3], including modification of initial parton distribution functions (shadowing, gluon saturation, antishadowing, EMC effect, etc.), initial- and final-state partonic multiple scattering, and related initial-state parton energy loss need to be accounted for before firm conclusions can be drawn about the effect of the hot medium thought to be created. In fact, these various cold nuclear matter effects are interesting in their own right, notably in terms of hadronization time scales, parton energy loss in matter, and the various initial-state effects just mentioned.

This paper presents a new analysis of the modification of J/ψ production in deuteron-gold (d + Au) collisions relative to proton-proton ($p + p$) collisions at $\sqrt{s_{NN}} = 200$ GeV and the implications for understanding the Au + Au and Cu + Cu data at the same energy. The PHENIX experiment has previously published a result using $p + p$ and d + Au data taken in 2003 [4]. A modest J/ψ suppression was observed at forward rapidity (i.e., in the deuteron-moving direction), which is a possible indication of shadowing of low-x gluons in the gold nucleus. A substantially larger (more than an order of magnitude) $p + p$ data set was recorded in 2005, with the J/ψ results published in Ref. [2], and has been used as the baseline for recent Au + Au and Cu + Cu nuclear modification factors [1,5]. The same $p + p$ data set is used in the analysis presented here to determine the d + Au nuclear modifications more accurately and in a fully consistent way with those in the Au + Au and Cu + Cu cases. In addition, during the two years between the analyses of the 2003 and 2005 data sets significant improvements in the reconstruction software and signal-extraction method were achieved along with an overall better understanding of the detector performance. These improvements have been included in this analysis, allowing maximal cancellation of systematic errors when using the 2005 $p + p$ data sample to form the J/ψ nuclear modification factor. We first describe the updated analysis, then present the new nuclear modification factors and their implications.

II. EXPERIMENT

The PHENIX apparatus is described in Ref. [6]. It consists of two sets of spectrometers referred to as the central arms,

*Deceased.
†PHENIX Spokesperson; electronic address: jacak@skipper.physics.sunysb.edu

which measure particles emitted at midrapidity ($|y| < 0.35$), and the muon arms, measuring particles emitted at backward and forward rapidity ($-2.2 < y < -1.2$ and $1.2 < y < 2.2$).

At midrapidity, J/ψ particles are measured via their decay into two electrons. Electrons are identified by matching tracks reconstructed with drift chambers (DC) and pad chambers (PC) to clusters in the electromagnetic calorimeters (EMCAL) and hits in the ring imaging Cerenkov counters (RICH). In $d + \mathrm{Au}$ collisions, a charged track is identified as an electron candidate by requiring at least three matching RICH phototube hits within a certain radius with respect to the the center defined by the track projection at the RICH, a position matching of ± 4 standard deviations between the EMCAL cluster and the reconstructed track, and a cut on the ratio of energy to momentum. In $p + p$ collisions the electron identification cuts are the same except that only two matching RICH phototube hits are required.

At forward and backward rapidity, J/ψ particles are measured via their decay into two muons. Muons are identified by matching tracks measured in cathode strip chambers (referred to as the muon tracker, or MuTR) to hits in alternating planes of Iarocci tubes and steel absorbers (referred to as the muon identifier, or MuID). Each muon arm is located behind a thick copper and iron absorber that is meant to absorb most hadrons produced during the collisions, so that the measured muons must penetrate 8 to 11 interaction lengths of material in total.

The $d + \mathrm{Au}$ data used for this analysis were recorded in 2003 using a minimum-bias trigger that required hits in each of the two beam-beam counters (BBCs) located at positive and negative rapidity ($3 < |\eta| < 3.9$) and represent integrated luminosities for the different spectrometers ranging from 1.4 to 1.7 nb^{-1} (or, equivalently, from 2.7 to 3.4 billion interactions). This trigger covers $88\% \pm 4\%$ of the total $d + \mathrm{Au}$ inelastic cross section of 2260 mb [7]. For the electrons, an additional trigger was used that required one hit above threshold in the EMCAL and a matching hit in the RICH. For the muons, two additional triggers were used at different times during the data-taking period. The muon triggers are based on information from the MuID, which has five active detector layers between the steel absorbers. For the first part of the data-taking period, one of the tracks was required to reach the fourth MuID plane, while the other was only required to reach the second MuID plane. For the latter part, the trigger required at least two tracks to reach the fourth MuID plane of Iarocci tubes.

The BBCs are also used to determine the centrality of the $d + \mathrm{Au}$ collisions by measuring the energy deposited in the counters located at negative rapidity (in the gold-going direction). For a given centrality bin, the average number of equivalent nucleon-nucleon collisions (N_{coll}) is derived from this energy by using a Glauber calculation [8] coupled to a simulation of the BBC. The centrality bins used in this analysis and the corresponding number of collisions are listed in Table I. To ensure that the centrality categories are well defined, collisions are required to be within ± 30 cm of the center of the interaction region.

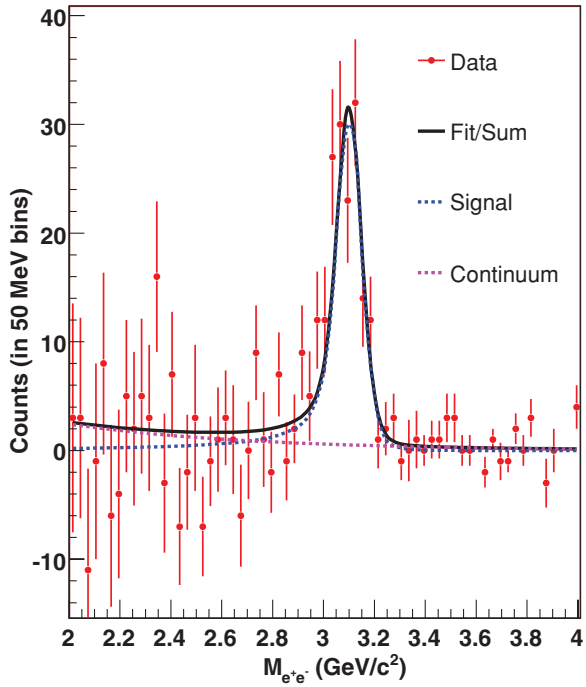

FIG. 1. (Color online) Invariant mass spectra in minimum-bias $d + \mathrm{Au}$ reactions for $J/\psi \longrightarrow e^+e^-$ at $|y| < 0.35$, with the functional forms used to extract the number of reconstructed J/ψ mesons.

III. SIGNAL EXTRACTION

The number of J/ψ particles is determined by using the invariant mass distribution of unlike-sign lepton pairs. At midrapidity, the J/ψ signal count is obtained via counting the number of unlike-sign dielectrons after subtracting the like-sign pairs in a fixed mass window of $2.6 \leqslant M_{e^+e^-} \leqslant 3.6\ \mathrm{GeV}/c^2$ or $2.7 \leqslant M_{e^+e^-} \leqslant 3.5\ \mathrm{GeV}/c^2$, depending on the number of DC hits required for track reconstruction. Figure 1 shows the J/ψ mass spectrum after subtracting the background. The solid

TABLE I. Characterization of the collision centrality for $d + \mathrm{Au}$ collisions. Listed are the centrality bins used in this analysis, the corresponding number of binary collisions, N_{coll}, and the values of $c = \epsilon^{\mathrm{BBC}}_{\mathrm{MB(cent)}}/\epsilon^{\mathrm{BBC}}_{J/\psi}$ for J/ψ mesons emitted in the three rapidity ranges used for this analysis.

Centrality	0–20%	20–40%	40–60%	60–88%	0–100%
N_{coll}	15.4 ± 1.0	10.6 ± 0.7	7.0 ± 0.6	3.1 ± 0.3	7.6 ± 0.3
c ($\lvert y\rvert < 0.35$)	0.95 ± 0.03	0.99 ± 0.01	1.03 ± 0.01	1.04 ± 0.03	0.94 ± 0.02
c ($-2.2 < y < -1.2$)	0.93 ± 0.03	0.99 ± 0.01	1.04 ± 0.01	1.05 ± 0.03	0.94 ± 0.02
c ($1.2 < y < 2.2$)	1.00 ± 0.03	1.00 ± 0.01	1.02 ± 0.01	1.02 ± 0.03	0.94 ± 0.02

black line is the sum of the J/ψ line shape (dashed curve) and an exponential function (dot-dashed curve) describing the continuum component determined from the 2005 $p+p$ data set [2]. The J/ψ line-shape function takes into account the momentum resolution of track reconstruction, internal radiative effects [9], and external radiative effects evaluated by using a GEANT [10] simulation of the PHENIX detector. The number of J/ψ particles in $d+$Au collisions is too small to allow a good fit but a comparison between $d+$Au and $p+p$ J/ψ line shapes shows good agreement. The fraction of J/ψ candidates outside of the mass window owing to the radiative effects is estimated to be $7.2\% \pm 1.0\%$ based on the line-shape functions. The J/ψ signal is also corrected for the dielectron continuum yield, which originates primarily from open charm and Drell-Yan pairs inside the mass window. The estimated contribution is $10\% \pm 5\%$, based on the fitting function and PYTHIA [11] simulations. Approximately 400 J/ψ mesons are obtained.

At backward and forward rapidity an event-mixing technique is now used to estimate the combinatorial background, whereas the like-sign pairs were used in the previous analysis [4]. The previous method suffered from a larger statistical uncertainty for bins where the signal over background is poor. A sample mass distribution after the subtraction of the mixed-event background is shown in Fig. 2. Approximately 500 and 750 J/ψ mesons are obtained for backward and forward rapidity, respectively. The signal counts are determined from this subtracted dimuon invariant mass distribution with a log-likelihood fit and for three different assumed functional forms and parameters. In all three cases, an exponential form is used to account for correlated physical background sources (e.g., Drell-Yan or open charm) and the possible systematic offset in the normalization of the mixed-event background. The number of J/ψ particles is then estimated by direct counting of the remaining number of pairs above the exponential in the mass range $2.6 \leqslant M_{\mu^+\mu^-} \leqslant 3.6$ GeV/c^2, using a Gaussian function with the center fixed to the J/ψ mass and the width and integrated yield left free, or using two Gaussian functions for which both the center and widths are fixed to the values measured in $p+p$ collisions. The two Gaussian functions account for the non-Gaussian tails in the invariant mass distribution. The normalization of the mixed background is varied by a systematic uncertainty of $\pm 2\%$ prior to its subtraction from the mass distribution. This uncertainty is determined by comparing different normalization methods. The corresponding signal variations are included in the systematic uncertainty. Because of the particular fit procedure, for all $p+p$ and $d+$Au cases this normalization uncertainty results in a very small systematic uncertainty on the number of measured J/ψ particles. This entire procedure is identical to the one used in Refs. [1,2].

IV. INVARIANT YIELD

The J/ψ invariant yield in a given centrality, transverse momentum, and rapidity bin is

$$\frac{B_{ll}}{2\pi p_{\mathrm{T}}}\frac{d^2N_{J/\psi}}{dp_T dy} = \frac{1}{2\pi p_T \Delta p_T \Delta y}\frac{N^{J/\psi}_{\mathrm{counts}}}{A\epsilon_{\mathrm{rec}}\epsilon_{\mathrm{trig}}N^{\mathrm{MB}}_{\mathrm{evt}}}\frac{\epsilon^{\mathrm{BBC}}_{\mathrm{MB(cent)}}}{\epsilon^{\mathrm{BBC}}_{J/\psi}}, \quad (1)$$

where B_{ll} is the branching ratio for $J/\psi \to l^+l^-$, $N^{J/\psi}_{\mathrm{counts}}$ is the number of reconstructed J/ψ mesons, $N^{\mathrm{MB}}_{\mathrm{evt}}$ is the number of minimum-bias events sampled, $\epsilon^{\mathrm{BBC}}_{\mathrm{MB(cent)}}$ is the BBC trigger efficiency for minimum-bias events in a given centrality

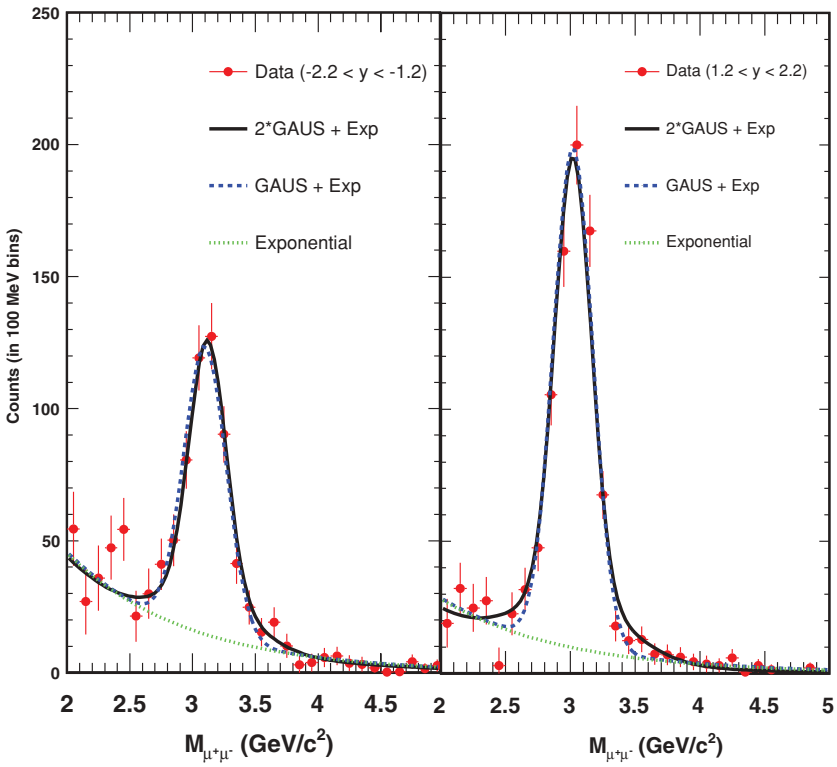

FIG. 2. (Color online) Invariant mass spectra in minimum-bias $d+$Au reactions for (left) $J/\psi \longrightarrow \mu^+\mu^-$ at $-2.2 < y < -1.2$ and (right) $J/\psi \longrightarrow \mu^+\mu^-$ at $1.2 < y < 2.2$, with the functional forms used to extract the number of reconstructed J/ψ mesons.

TABLE II. Statistical and type A systematic uncertainties added in quadrature and type B systematic uncertainties. Type C errors are shown in the relevant figures.

Rapidity	Centrality (%)	p_T (GeV/c)	y	Invariant yield	$R_{d\mathrm{Au}}$
Backward	0–100	All	$[-2.2, -1.2]$	$(4.264 \pm 0.326 \pm 0.923) \times 10^{-6}$	$0.90 \pm 0.08 \pm 0.19$
rapidity results	0–100	All	$[-2.2, -1.7]$	$(3.583 \pm 0.395 \pm 0.775) \times 10^{-6}$	$0.95 \pm 0.12 \pm 0.20$
	0–100	All	$[-1.7, -1.2]$	$(5.292 \pm 0.483 \pm 1.145) \times 10^{-6}$	$0.90 \pm 0.09 \pm 0.19$
	0–100	0–1	$[-2.2, -1.2]$	$(3.040 \pm 0.460 \pm 0.658) \times 10^{-7}$	$0.69 \pm 0.11 \pm 0.15$
	0–100	1–2	$[-2.2, -1.2]$	$(1.782 \pm 0.201 \pm 0.386) \times 10^{-7}$	$0.84 \pm 0.10 \pm 0.18$
	0–100	2–3	$[-2.2, -1.2]$	$(8.141 \pm 0.937 \pm 1.762) \times 10^{-8}$	$1.44 \pm 0.18 \pm 0.31$
	0–100	3–4	$[-2.2, -1.2]$	$(1.789 \pm 0.359 \pm 0.387) \times 10^{-8}$	$1.21 \pm 0.26 \pm 0.26$
	0–100	4–5	$[-2.2, -1.2]$	$(4.016 \pm 1.451 \pm 0.869) \times 10^{-9}$	$1.14 \pm 0.43 \pm 0.24$
	0–20	All	$[-2.2, -1.2]$	$(9.084 \pm 0.922 \pm 1.925) \times 10^{-6}$	$0.94 \pm 0.10 \pm 0.21$
	20–40	All	$[-2.2, -1.2]$	$(3.676 \pm 0.642 \pm 0.770) \times 10^{-6}$	$0.55 \pm 0.10 \pm 0.12$
	40–60	All	$[-2.2, -1.2]$	$(4.013 \pm 0.583 \pm 0.842) \times 10^{-6}$	$0.92 \pm 0.14 \pm 0.21$
	60–88	All	$[-2.2, -1.2]$	$(2.062 \pm 0.312 \pm 0.436) \times 10^{-6}$	$1.07 \pm 0.17 \pm 0.25$
Midrapidity	0–100	All	$[-0.35, 0.35]$	$(6.750 \pm 0.540 \pm 0.950) \times 10^{-6}$	$0.85 \pm 0.07 \pm 0.15$
results	0–100	0–1	$[-0.35, 0.35]$	$(6.700 \pm 0.800 \pm 0.940) \times 10^{-7}$	$1.05 \pm 0.14 \pm 0.21$
	0–100	1–2	$[-0.35, 0.35]$	$(2.400 \pm 0.340 \pm 0.340) \times 10^{-7}$	$0.74 \pm 0.11 \pm 0.15$
	0–100	2–3	$[-0.35, 0.35]$	$(1.200 \pm 0.190 \pm 0.170) \times 10^{-7}$	$0.96 \pm 0.17 \pm 0.19$
	0–100	3–4	$[-0.35, 0.35]$	1.37×10^{-8} (90% CL)	0.41 (90% CL)
	0–100	4–5	$[-0.35, 0.35]$	$(7.500 \pm 3.600 \pm 1.100) \times 10^{-9}$	$1.09 \pm 0.61 \pm 0.22$
	0–20	All	$[-0.35, 0.35]$	$(1.144 \pm 0.160 \pm 0.160) \times 10^{-5}$	$0.71 \pm 0.10 \pm 0.12$
	20–40	All	$[-0.35, 0.35]$	$(7.990 \pm 1.290 \pm 1.120) \times 10^{-6}$	$0.71 \pm 0.12 \pm 0.11$
	40–60	All	$[-0.35, 0.35]$	$(6.800 \pm 1.010 \pm 0.950) \times 10^{-6}$	$0.93 \pm 0.14 \pm 0.14$
	60–88	All	$[-0.35, 0.35]$	$(3.030 \pm 0.500 \pm 0.420) \times 10^{-6}$	$0.94 \pm 0.16 \pm 0.14$
Forward	0–100	All	$[1.2, 2.2]$	$(3.300 \pm 0.242 \pm 0.592) \times 10^{-6}$	$0.63 \pm 0.06 \pm 0.11$
rapidity results	0–100	All	$[1.2, 1.7]$	$(4.522 \pm 0.341 \pm 0.811) \times 10^{-6}$	$0.68 \pm 0.06 \pm 0.11$
	0–100	All	$[1.7, 2.2]$	$(2.406 \pm 0.224 \pm 0.432) \times 10^{-6}$	$0.59 \pm 0.06 \pm 0.10$
	0–100	0–1	$[1.2, 2.2]$	$(2.779 \pm 0.285 \pm 0.498) \times 10^{-7}$	$0.55 \pm 0.06 \pm 0.09$
	0–100	1–2	$[1.2, 2.2]$	$(1.362 \pm 0.115 \pm 0.244) \times 10^{-7}$	$0.60 \pm 0.06 \pm 0.10$
	0–100	2–3	$[1.2, 2.2]$	$(4.667 \pm 0.566 \pm 0.837) \times 10^{-8}$	$0.73 \pm 0.10 \pm 0.12$
	0–100	3–4	$[1.2, 2.2]$	$(1.472 \pm 0.225 \pm 0.264) \times 10^{-8}$	$0.93 \pm 0.16 \pm 0.16$
	0–100	4–5	$[1.2, 2.2]$	$(2.842 \pm 0.756 \pm 0.510) \times 10^{-9}$	$0.84 \pm 0.25 \pm 0.14$
	0–20	All	$[1.2, 2.2]$	$(5.705 \pm 0.501 \pm 0.987) \times 10^{-6}$	$0.54 \pm 0.05 \pm 0.09$
	20–40	All	$[1.2, 2.2]$	$(4.577 \pm 0.474 \pm 0.783) \times 10^{-6}$	$0.62 \pm 0.07 \pm 0.11$
	40–60	All	$[1.2, 2.2]$	$(2.950 \pm 0.347 \pm 0.505) \times 10^{-6}$	$0.62 \pm 0.08 \pm 0.11$
	60–88	All	$[1.2, 2.2]$	$(1.671 \pm 0.195 \pm 0.289) \times 10^{-6}$	$0.79 \pm 0.10 \pm 0.15$

category, Δp_T and Δy are the p_T and y bin widths, A and ϵ_{rec} are the acceptance and reconstruction efficiency corrections, ϵ_{trig} is the additional J/ψ trigger efficiency, and $\epsilon^{\mathrm{BBC}}_{J/\psi}$ is the BBC efficiency for events containing a J/ψ. All invariant yields as a function of p_T and y including statistical and systematic uncertainties are given in Table II.

The experiment measures the number of J/ψ particles per BBC triggered events, which in $d+\mathrm{Au}$ collisions represent only $88\% \pm 4\%$ of the total inelastic cross section. An additional correction is then applied such that the invariant yield represents 100% of the total inelastic cross section (as done in previous PHENIX $d+\mathrm{Au}$ analyses). The correction factor ratio $\epsilon^{\mathrm{BBC}}_{\mathrm{MB(cent)}}/\epsilon^{\mathrm{BBC}}_{J/\psi}$ depends *a priori* on the centrality bin and the rapidity range of the measured J/ψ particles. The values are given in Table I. The same procedure is applied for $p+p$ collisions, so that the yields are normalized to the $p+p$ total inelastic cross section of 42 mb.

The acceptance and efficiency corrections are determined by using a full GEANT simulation [10] of the detector with realistic resolutions and detector plane efficiencies determined from real data. Compared to the original result [4], this simulation benefits from improvements in the understanding of the detector alignment, resolution, and overall performance. It also includes the improvements added to the reconstruction software and used for the recent $p+p$, $\mathrm{Cu}+\mathrm{Cu}$, and

TABLE III. Sources of systematic uncertainties on the J/ψ invariant yield in $d+\mathrm{Au}$ collisions. Columns 2 (3) are the average values at midrapidity (forward rapidity). When two values are given, the first (second) is for peripheral (central) collisions. Uncertainties of type A (type B) are point-to-point uncorrelated (correlated).

Source	$\lvert y\rvert < 0.35$	$\lvert y\rvert \in [1.2, 2.2]$	Type
signal extraction	6%	<10%	A
acceptance	8%	10%	B
efficiency	6%	8–20%	B
run-by-run variation	5%	8%	B
input y, p_{T} distributions	2%	4%	B
embedding	4%	5%	B

Au + Au analyses [1,2,5]. Although the additional underlying hit occupancies per event are modest in $p+p$ and $d+\mathrm{Au}$ collisions, they are accounted for by embedding the simulated J/ψ mesons in real data events. The observed differences (4–5%) between embedded and nonembedded events are not significant given the statistics of the simulations, and therefore they are included only as a contribution to the systematic uncertainty.

The systematic uncertainties in the J/ψ invariant yield (Table III) are grouped into three categories as in the previous analyses: point-to-point uncorrelated (type A), for which the points can move independently from one another; point-to-point correlated (type B), for which the points can move coherently though not necessarily by the same amount; and global uncertainties (type C), for which all points move by the same multiplicative factor. Statistical and uncorrelated systematic uncertainties (type A) are summed in quadrature and represented as vertical bars. Type B uncertainties are represented with boxes. Type C globally correlated systematic uncertainties are quoted directly on the figures.

Figure 3 shows the invariant J/ψ yield as a function of transverse momentum for $d+\mathrm{Au}$ collisions from this new analysis together with the published invariant yield measured in $p+p$ collisions [2]. From these yields, a $\langle p_{\mathrm{T}}^2\rangle$ is calculated

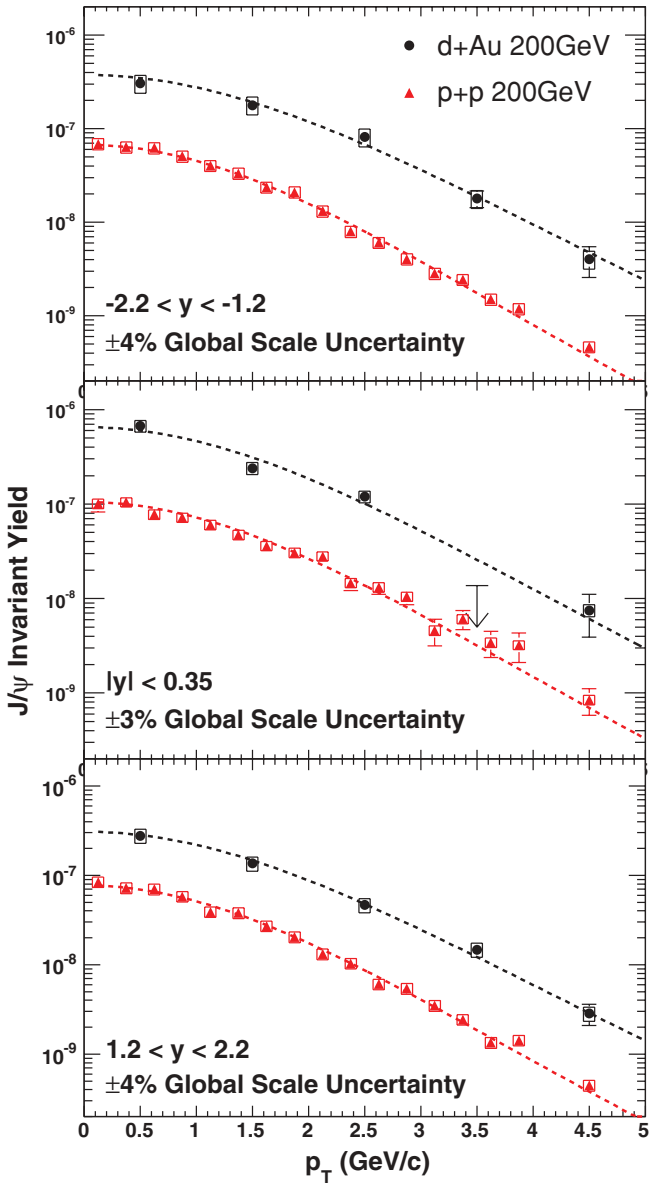

FIG. 3. (Color online) J/ψ invariant yield versus p_{T} in $d+\mathrm{Au}$ collisions and $p+p$ collisions. The three panels are for rapidity selections $-2.2 < y < -1.2$, $|y| < 0.35$, and $1.2 < y < 2.2$ from top to bottom. See text for description of the uncertainties and details of the functional fits.

TABLE IV. $\langle p_{\mathrm{T}}^2\rangle$ calculated from a fit to the data and restricted to the range $0 < p_{\mathrm{T}} < 5$ GeV/c. See text for description of the uncertainties.

Species	Rapidity	$\langle p_{\mathrm{T}}^2\rangle[0,5]$
$d+\mathrm{Au}$	$[-2.2,-1.2]$	$4.3\pm0.3\pm0.4$
$d+\mathrm{Au}$	$[-0.35,0.35]$	$3.9\pm0.3\pm0.3$
$d+\mathrm{Au}$	$[1.2,2.2]$	$4.0\pm0.2\pm0.4$
$p+p$	$[-2.2,-1.2]$	$3.4\pm0.1\pm0.1$
$p+p$	$[-0.35,0.35]$	$4.1\pm0.2\pm0.1$
$p+p$	$[1.2,2.2]$	$3.4\pm0.1\pm0.1$

by using the following generic functional form to fit the data:

$$\frac{d^2N}{p_T dp_T} \sim A[1+(p_{\mathrm{T}}/B)^2]^{-6}. \quad (2)$$

To account for finite p_{T} binning, the fit function is first integrated over each Δp_{T} range and the integral is compared to data in the corresponding bin. The measured $\langle p_{\mathrm{T}}^2\rangle$ values as well as the associated statistical and systematic uncertainties are shown in Table IV.

In previous J/ψ analyses [1,2], it was found that only for the high-statistics $p+p$ data set (where the measurement has good precision out to $p_{\mathrm{T}} \approx 8$ GeV/c) is the functional form of the p_{T} spectrum well constrained. In the Au + Au case,

the functional form is not well constrained and leads to a very large systematic uncertainty on $\langle p_T^2 \rangle$ if integrated from 0 to ∞. The integral was therefore limited to $p_T < 5$ GeV/c, where it is best constrained by the data. The $d + \text{Au}$ data set suffers from the same statistical limitations and the same truncation to $p_T < 5$ GeV/c is applied. Finally, this constraint is also applied to the $p + p$ case to make a direct comparison possible.

Two uncertainties are quoted in Table IV. The first corresponds to the statistical and point-to-point uncorrelated systematic uncertainties (type A) on the measured yields. It is obtained directly from the fit by using the second derivatives of the χ^2 surface at the minimum. The second corresponds to the point-to-point correlated systematic uncertainties (type B). The contribution from type B uncertainty is estimated independently by coherently moving the measured points within the one-standard-deviation limit given by these uncertainties, allowing them to be either correlated or anticorrelated, and then redoing the fit in all cases. The largest difference observed in the values obtained by the fit is used as an upper limit to the one-standard-deviation point-to-point correlated uncertainties on $\langle p_T^2 \rangle$.

In our previous publication [4] values for the fully integrated $\langle p_T^2 \rangle$ in $p + p$ and $d + \text{Au}$ collisions are quoted. However, a significant systematic uncertainty originating from not knowing the functional form to best describe the data was found that was not included in the uncertainty quoted in the paper. In addition, the new analysis revealed a bias in the previous result that increased the signal, particularly in the lowest p_T bin. This bias is now corrected by using the mixed-event background-subtraction technique described here together with the modified log-likelihood fit over a more appropriate range, corresponding to the region where the physical background can accurately be described by a single exponential function. Finally, no separate treatment of the point-to-point correlated systematic uncertainties was performed at that time, because it was assumed that it would move all points in the same direction (positive correlation) and thus have no impact on the measured $\langle p_T^2 \rangle$.

The data, within uncertainties, include the possibility of a modest broadening of the transverse momentum distribution relative to $p + p$ collisions. This is often attributed to initial- and final-state multiple scattering, sometimes referred to as the "Cronin effect." However, in calculating $\Delta\langle p_T^2 \rangle = \langle p_T^2 \rangle_{d\text{Au}} - \langle p_T^2 \rangle_{pp}$ one finds that this effect needs reduced uncertainties from future larger data sets to make any firm conclusions.

Figure 4 shows the J/ψ invariant yield, integrated over all p_T, as a function of rapidity for $d + \text{Au}$ collisions. Shown are the results of the new analysis presented in this paper, as well as the previously published results [4] using the same data set. Overall the agreement of the two analysis results is good. The two sets of points differ in the reconstruction software, analysis cuts, and signal-extraction technique. Thus many of the systematic uncertainties are different, and even the statistical uncertainties are not identical owing to the different analysis cuts and the use of event mixing to estimate the combinatorial background in the new analysis, as opposed to the like-sign mass distribution used in Ref. [4].

Figure 5 shows the J/ψ invariant yield for $p + p$ collisions, from both the published high-statistics result from Run-5 [2], as well as the lower statistics result from Run-3 as published in Ref. [4]. In both cases the points are in good agreement within the systematic uncertainty bands. A new analysis of the Run-3 $p + p$ lower statistics data set was also performed by using the same technique and analysis cuts as for $d + \text{Au}$ collisions. It also shows good agreement with these two sets of measurements, albeit with larger statistical uncertainties.

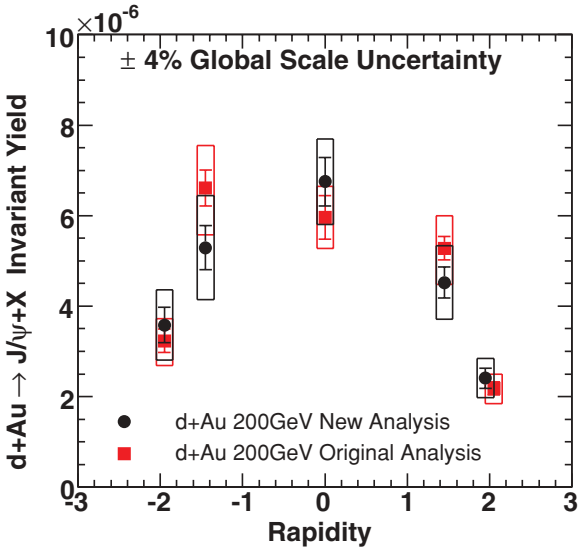

FIG. 4. (Color online) J/ψ invariant yield as a function of rapidity for $d + \text{Au}$ collisions. Shown are the new analysis results from this paper, in addition to the originally published results [4] using the same data. The global systematic uncertainty quoted is for the new analysis.

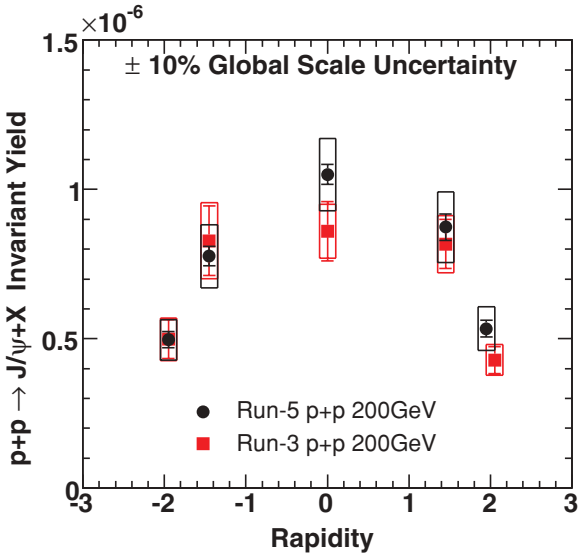

FIG. 5. (Color online) J/ψ invariant yield as a function of rapidity for $p + p$ collisions. Shown are the high statistics results from the 2005 $p + p$ PHENIX data-taking period [2] and the originally published results [4] using the 2003 $p + p$ data set. The global systematic uncertainty quoted is for the new analysis.

In Figs. 4 and 5, the highest rapidity point is not located exactly at the same rapidity position between the original and the new analysis. This is because the positive-rapidity muon arm has a slightly larger rapidity coverage than the negative-rapidity arm. This property was used in the 2003 analysis to include additional J/ψ mesons at forward rapidity to probe a slightly lower region of x. It was found, however, that there were very few counts in this region and that the asymmetric rapidity range created additional difficulties when comparing the results measured at forward and backward rapidity (in case of symmetric collisions) and when comparing the results obtained in $p+p$ collisions to Cu + Cu or Au + Au collisions, for which this extra rapidity coverage was not available (because of high-occupancy limitations at forward rapidity). As a consequence, it was decided for the later analyses to forgo the extra few J/ψ counts at very forward rapidity and use the same-width rapidity bins at both positive and negative rapidity.

V. NUCLEAR MODIFICATION FACTOR

The J/ψ nuclear modification factor in a given centrality and rapidity bin is

$$R_{d\mathrm{Au}} = \frac{1}{\langle N_{\mathrm{coll}} \rangle} \frac{dN_{J/\psi}^{d+\mathrm{Au}}/dy}{dN_{J/\psi}^{p+p}/dy}, \tag{3}$$

where $dN_{J/\psi}^{d\mathrm{Au}}/dy$ is the J/ψ invariant yield measured in $d+$ Au collisions, $dN_{J/\psi}^{pp}/dy$ is the J/ψ invariant yield measured in $p+p$ collisions for the same rapidity bin, and $\langle N_{\mathrm{coll}} \rangle$ is the average number of binary collisions in the centrality bin under consideration, as listed in Table I. All $R_{d\mathrm{Au}}$ values as a function of p_T, y, and centrality including statistical and systematic uncertainties are given in Table II.

Figure 6 shows the nuclear modification factor $R_{d\mathrm{Au}}$ calculated by using the $d+$Au new analysis presented in this paper for the numerator and the 2005 $p+p$ data for the denominator. In contrast to the previous analysis [4], where the $p+p$ results were symmetrized around $y=0$ before calculating $R_{d\mathrm{Au}}$ to compensate for lower J/ψ statistics in the 2003 $p+p$ data set, in this case the $R_{d\mathrm{Au}}$ values are calculated independently at each rapidity.

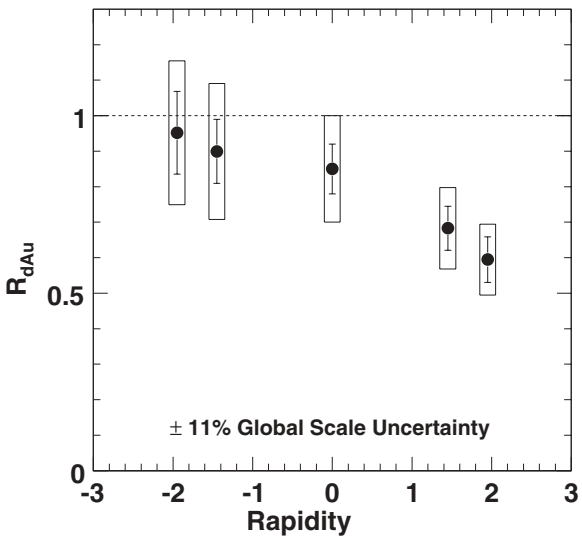

FIG. 6. J/ψ nuclear modification factor $R_{d\mathrm{Au}}$ as a function of rapidity.

The understanding of the detector performance in terms of alignment, resolution, and efficiency has significantly improved between this analysis and previously published PHENIX $d+$Au results [4]. This resulted in changes in the reconstruction software, analysis cuts, signal-extraction technique, and handling of both the physical and combinatorial background in the dilepton invariant mass distribution. Simultaneously, the systematic uncertainties associated with the measurement have also been reevaluated in a way consistent with what was learned for the $p+p$, Cu + Cu, and Au + Au analyses. The new uncertainties are in general larger, although some of them cancel with their $p+p$ counterpart when forming $R_{d\mathrm{Au}}$. This approximately counterbalances the reduction of the statistical uncertainty achieved by using the 2005 $p+p$ data set as a reference. Additionally, the J/ψ production cross sections in $p+p$ collisions measured in 2005 [2] are compatible within uncertainties but higher than the values used in Ref. [4] (based on the 2003 $p+p$ data set) by about 13%. As a consequence, the new nuclear modification factors are systematically lower than the ones previously published by about 5–20% for most points, depending on the p_{T}, y, or centrality bin considered.

Within uncertainties, the nuclear modification factors are consistent with $R_{d\mathrm{Au}} = 1.0$ at negative and midrapidities and are significantly lower than 1.0 at forward rapidity only, that is, in the deuteron-going direction. This trend is similar to that shown in Fig. 1 of Ref. [4], although the new values are systematically smaller for all rapidity bins.

Figure 7 shows the J/ψ nuclear modification factor in $d+$ Au collisions as a function of the number of binary collisions for three rapidity ranges and four centrality classes. Only at forward rapidity is there statistically significant suppression.

VI. DISCUSSION

As stated in the Introduction, the $d+$ Au data are interesting both to fundamentally understand issues of quarkonia and cold nuclear matter and also to separate these effects from hot nuclear matter effects in heavy-ion collisions. To address both issues, we compare the experimental data with two different models including both modification of the initial parton distribution functions (PDFs) and a free parameter to account for the breakup of correlated $c\bar{c}$ pairs that might have otherwise formed J/ψ mesons. Note that, often in the literature, this breakup process in cold nuclear matter is referred to as an absorption cross section of the J/ψ particles on the nucleons in the nucleus. Here we avoid this nomenclature, both because the object that is "absorbed" is generally not a fully formed J/ψ but rather a $c\bar{c}$ pair, and because the actual process is more a breakup of this pair, rather than the absorption of it.

Shown in Fig. 8 is the nuclear modification factor $R_{d\mathrm{Au}}$ as a function of rapidity in comparison to theoretical calculations [3] that include either EKS [12] or NDSG [13] shadowing

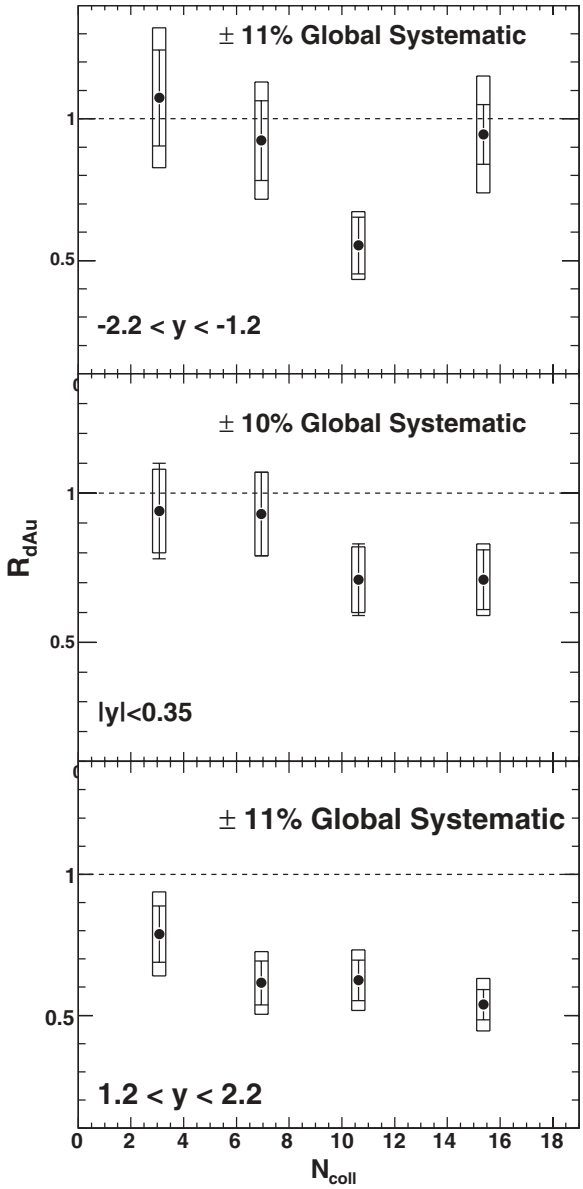

FIG. 7. J/ψ nuclear modification factor $R_{d\mathrm{Au}}$ as a function of N_{coll} for three rapidity ranges.

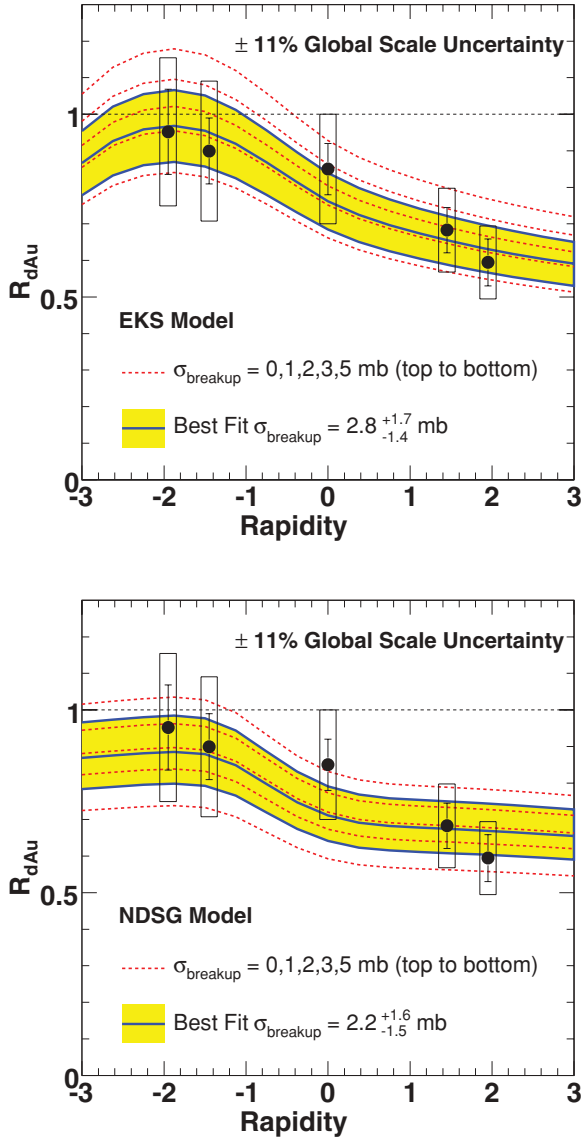

FIG. 8. (Color online) $R_{d\mathrm{Au}}$ data compared to various theoretical curves for different $\sigma_{\mathrm{breakup}}$ values. Also shown as a band are the range of $\sigma_{\mathrm{breakup}}$ values found to be consistent with the data within one standard deviation. The top panel is a comparison for EKS shadowing [12]; the bottom panel is for NDSG shadowing [13].

models for the nuclear PDFs. In each case an additional suppression associated with a $\sigma_{\mathrm{breakup}}$ is also included. Note that there is no *ab initio* calculation of this cross section, and although one might expect a similar value to results at lower energy [14], it need not be identical.

Taking full account of the statistical and systematic uncertainties on the experimental data, we can determine the breakup cross section under certain assumptions. We have followed the statistical procedure detailed in Ref. [15]. If we assume that the EKS-modified nuclear PDFs are exactly correct, and that the only additional suppression is accounted for by $\sigma_{\mathrm{breakup}}$, then the data constrain $\sigma_{\mathrm{breakup}} = 2.8^{+1.7}_{-1.4}$ mb with the uncertainties as one standard deviation. Similarly, if we assume the NDSG-modified nuclear PDFs, then we obtain $\sigma_{\mathrm{breakup}} = 2.2^{+1.6}_{-1.5}$ mb. These breakup cross-section values are consistent (within the large uncertainties) with the 4.2 ± 0.5 mb value determined at lower energies at the CERN-SPS [14]. The extracted breakup cross section at lower energies are found by assuming no contribution from the modification of nuclear PDFs. At the lower energies, J/ψ production is sensitive to higher x partons in the antishadowing regime where the modifications are expected to be smaller and in the opposite direction [16].

The modified nuclear PDFs from EKS and NDSG are constrained from other experimental measurements such as deep inelastic scattering from various nuclear targets and the resulting $F_2(A)$ structure functions. A geometric parametrization of these PDFs based on the path of the parton through the nucleus is described in Refs. [17] and [3]. One can test this geometric dependence by comparison with the $d + \mathrm{Au}$ nuclear modification factors as a function of N_{coll}. Using this

TABLE V. Most probable values and one standard deviations of σ_{breakup} determined by assuming two different shadowing models, from a fit to minimum-bias $R_{d\text{Au}}$ points as a function of rapidity (Fig. 8), and fits to $R_{d\text{Au}}$ as a function of N_{coll} in three separate rapidity bins (Fig. 9).

Fit range in y	EKS (mb)	NDSG (mb)
All	$2.8^{+1.7}_{-1.4}$	$2.2^{+1.6}_{-1.5}$
$[-2.2, -1.2]$	$5.2^{+1.6}_{-1.8}$	$3.3^{+2.0}_{-1.7}$
$[-0.35, 0.35]$	$2.4^{+1.9}_{-1.6}$	$1.0^{+1.8}_{-1.7}$
$[1.2, 2.2]$	$3.2^{+1.6}_{-1.5}$	$3.3^{+1.5}_{-1.5}$

geometric dependence, we can calculate the most probable σ_{breakup} values independently in three rapidity ranges (see Table V). The corresponding nuclear modification values and their one-standard-deviation bands are shown as a function of N_{coll} in Fig. 9. The two calculations with EKS and NDSG nuclear PDFs yield almost identical bands since the same geometric dependence is used in both cases. However, each band represents a different balance of modification owing to the nuclear PDF and the breakup cross section.

For both the EKS and the NDSG PDFs, the values of σ_{breakup} extracted from the overall rapidity dependence of $R_{d\text{Au}}$ and from the N_{coll} dependence of $R_{d\text{Au}}$ within the different rapidity ranges are consistent within the large systematic uncertainties. It should be noted that though the confidence level for the best fit is poor at backward rapidity (as can be seen in Fig. 9), there is still a well-defined maximum in the likelihood function for σ_{breakup}. A future higher precision $R_{d\text{Au}}$ measurement as a function of centrality will be crucial to constrain the exact geometric dependence.

One can also utilize this model to do a consistent calculation of the contribution from cold nuclear matter effects that should be present in Cu + Cu and Au + Au collisions. These contributions, obtained using the best-fit value of σ_{breakup} and their one-standard-deviation values extracted from the data in Fig. 8 for each of the two shadowing models, are shown in Figs. 10 and 11. In the Cu + Cu case, J/ψ production is not suppressed beyond cold nuclear matter effects at midrapidity or at forward rapidity, within the limits of the large error bands, and the midrapidity data in the Au + Au case are similarly inconclusive. However, there is a significant suppression in the data at forward rapidity, beyond the uncertainties in both the data and the projection. It should be noted that the uncertainty bands at forward rapidity and midrapidity are entirely correlated, as they reflect only the uncertainty in σ_{breakup}. There is no systematic uncertainty included for the choice of modified nuclear PDF model, which is the only way to change the relative suppression between forward rapidity and midrapidity within the context of this calculation. The more data-driven calculation described later in this section, however, is performed independently at different rapidities and does not suffer the same stipulation.

It should also be noted that the theoretical calculations yield R_{AA} as a continuous function of the number of participants, whereas the data points are at discrete values

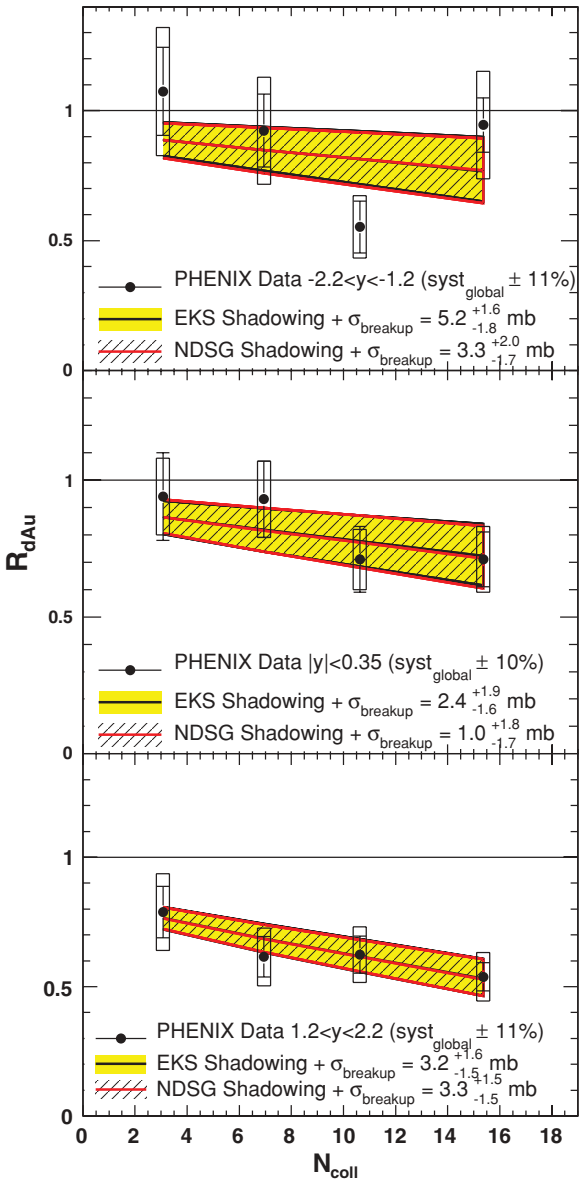

FIG. 9. (Color online) $R_{d\text{Au}}$ data as a function of N_{coll} for three different rapidity ranges. Overlayed are theoretical curves representing the best-fit σ_{breakup} values as determined in each rapidity range separately, utilizing EKS and NDSG nuclear PDFs and a simple geometric dependence. Also shown as bands are the range of σ_{breakup} values found to be consistent with the data within one standard deviation.

representing a convolution of the modification factor with the N_{part} distribution within a particular centrality category. A Glauber simulation combined with a Monte Carlo simulation of the PHENIX experimental trigger and centrality selection is utilized to convert the continuous theory predictions into discrete predictions in the simulated PHENIX centrality categories. Thus, the results shown in the figures are in fact predictions for the matched event selection categories of the experimental data points.

To explore the cold nuclear matter constraints further, an alternative data-driven method proposed in Ref. [18] is

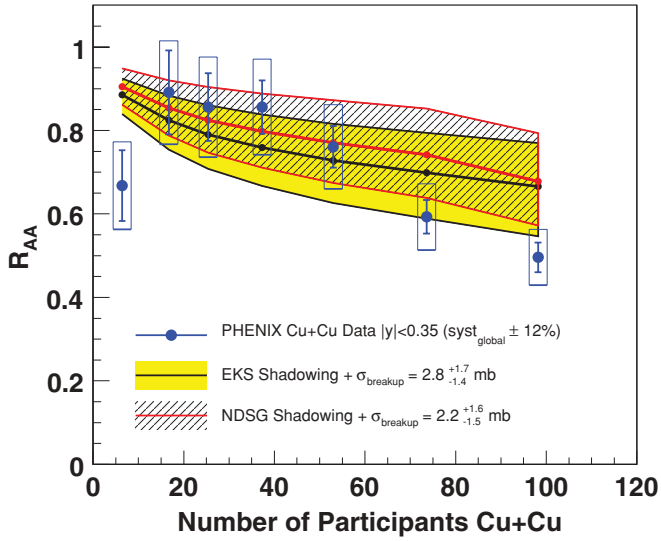

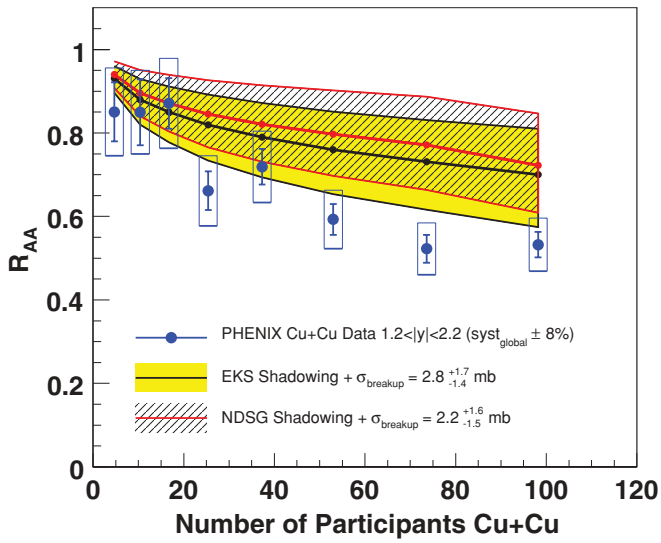

FIG. 10. (Color online) R_{AA} for Cu + Cu [5] collisions compared to a band of theoretical curves for the σ_{breakup} values found to be consistent with the d + Au data as shown in Fig. 8. The top figure includes both EKS shadowing [12] and NDSG shadowing [13] at midrapidity. The bottom figure is the same at forward rapidity.

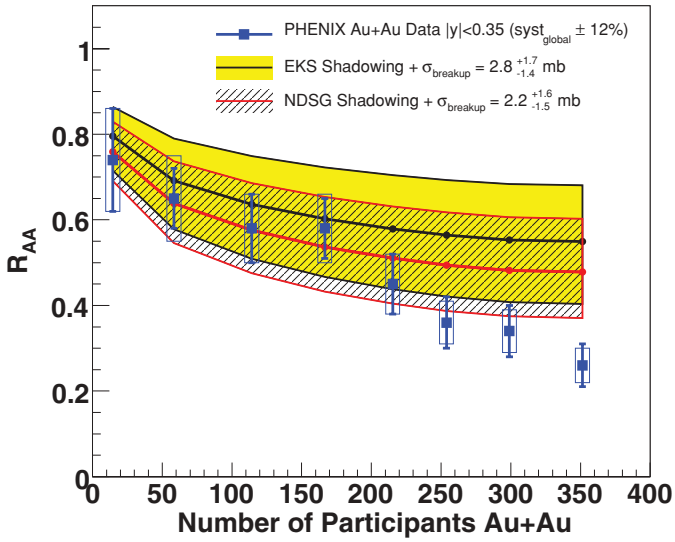

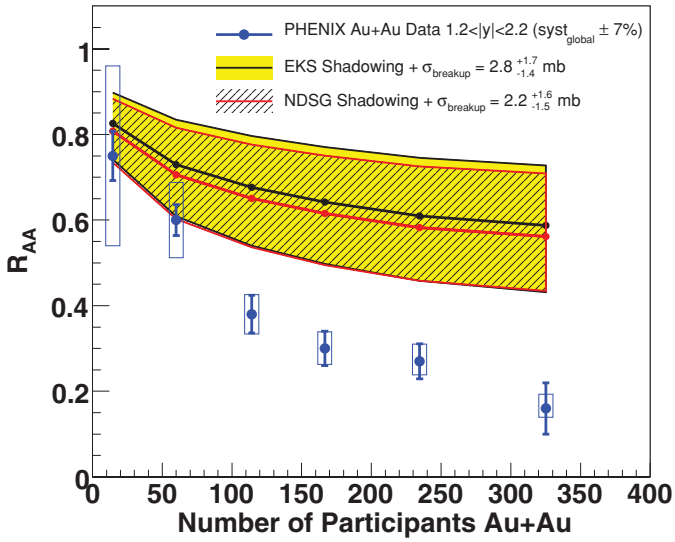

FIG. 11. (Color online) R_{AA} for Au + Au [1] collisions compared to a band of theoretical curves for the σ_{breakup} values found to be consistent with the d + Au data as shown in Fig. 8. The top figure includes both EKS shadowing [12] and NDSG shadowing [13] at midrapidity. The bottom figure is the same at forward rapidity.

used. In this approach it is assumed that there is a single modification factor parametrizing all cold nuclear matter effects that is a simple function of the radial position in the nucleus. This computation has the advantage of our not having to assume a specific shadowing scheme and a specific breakup cross section, but instead relies only on the measured impact parameter dependence. The cold nuclear matter effects suffered by a J/ψ in a Au + Au collision at a given rapidity are assumed to be the product of the modifications measured in d + Au collisions at the same rapidity and the modifications measured at the opposite rapidity (or, equivalently, in a Au + d collision). This assumption holds for the two effects considered so far, namely, shadowing and subsequent breakup. In the computation it is also assumed that the same parton distributions are sampled by the J/ψ particles observed in the (wide) rapidity range in Au + Au and d + Au collisions. Note that since this model implicitly includes any possible modified nuclear PDFs, the modification factors may have an x dependence that is accounted for by considering the backward, mid, and forward rapidity d + Au data. The different rapidity regions are sensitive to the initial-state partons in the gold nucleus in three broad ranges of x, corresponding to $x \approx$ 0.002–0.01, 0.01–0.05, and 0.05–0.2, as determined from PYTHIA.

A Glauber Monte Carlo simulation and a simulation of the BBC detector used for centrality determination and triggering are done. The resulting four centrality categories (0–20%, 20–40%, 40–60%, and 60–88%) in d + Au collisions are characterized by a distribution in the number of binary collisions, as shown in the top panel of Fig. 12. In addition,

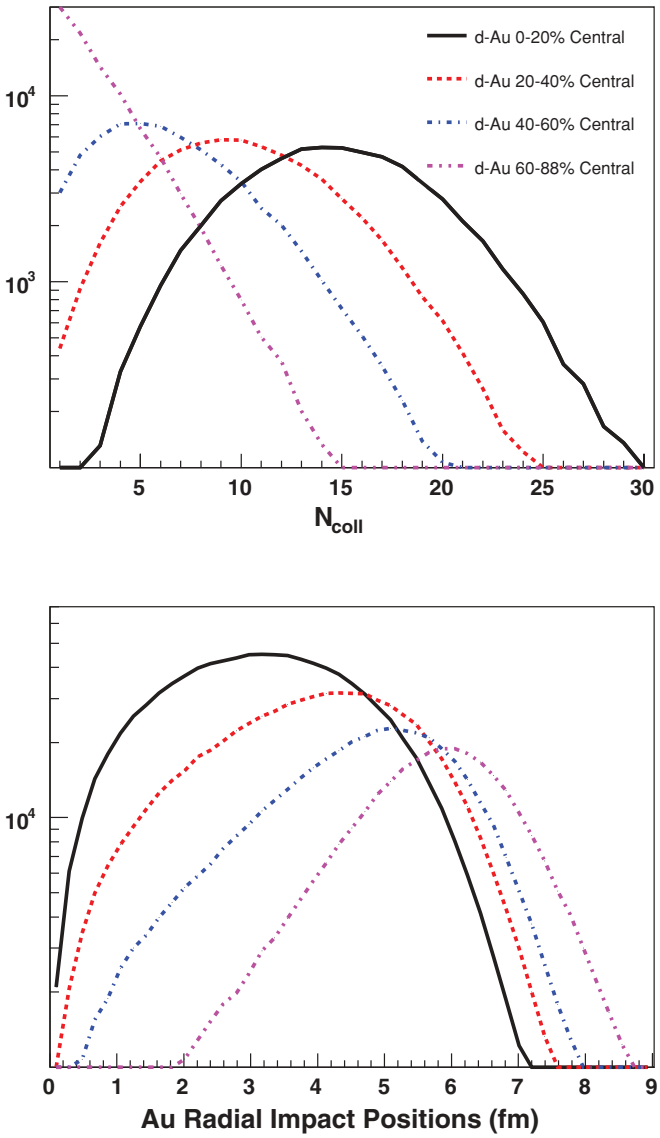

FIG. 12. (Color online) Results from a Glauber model Monte Carlo simulation of the $d + \mathrm{Au}$ centrality selection and triggering based on the PHENIX BBC. The top panel shows the distribution of the number of binary collisions for events in each of the four centrality classes 0–20%, 20–40%, 40–60%, and 60–88%. The distribution for radial impact points in the gold nucleus of binary collisions is shown in the lower panel.

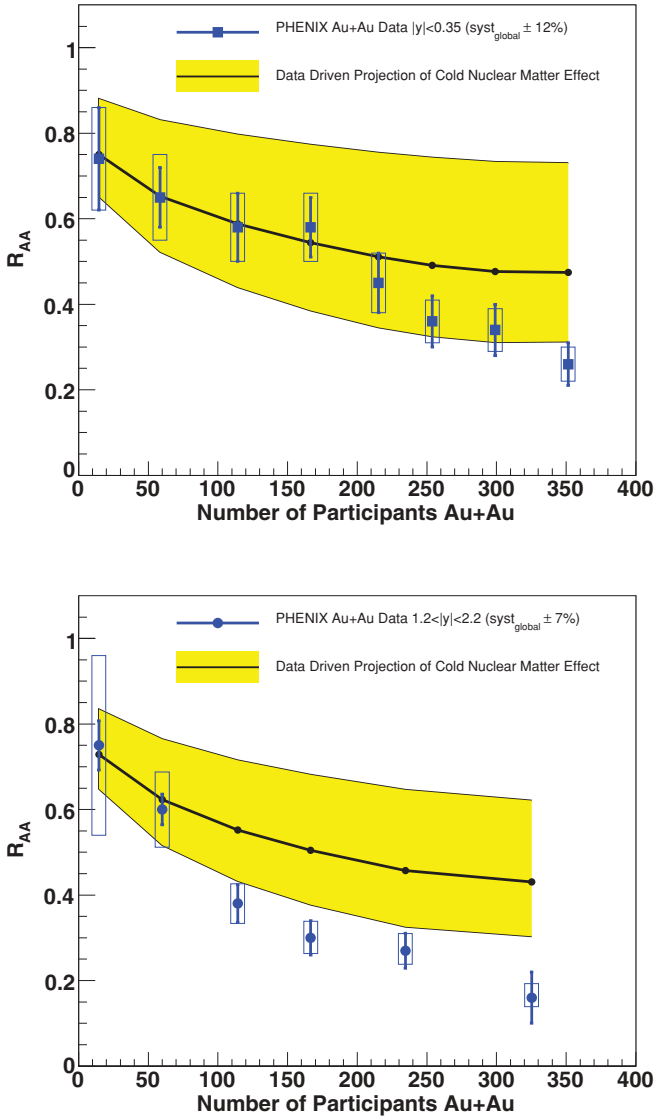

FIG. 13. (Color online) Predictions of the data-driven method [18] constrained by $R_{d\mathrm{Au}}$ as a function of collision centrality for the $\mathrm{Au} + \mathrm{Au}$ R_{AA} for midrapidity (top) and at forward rapidity (bottom).

the distribution of radial positions r in the Au nucleus of binary collisions is calculated and shown in the bottom panel of Fig. 12.

The procedure is to use the forward, mid, and backward rapidity centrality-dependent $R_{d\mathrm{Au}}$ values to constrain the modification factor $\Re(r)$ for three broad regions of initial parton x ($\Re_{\mathrm{low}}$, $\Re_{\mathrm{mid}}$, and $\Re_{\mathrm{high}}$, respectively). Then one can use these parametrizations to project the cold nuclear matter effect in the $\mathrm{Au} + \mathrm{Au}$ case. The current $d + \mathrm{Au}$ data are insufficient to constrain the functional form of $\Re(r)$. As a simplifying case, $\Re(r)$ is assumed to be linear in r and to be fixed at $\Re(r \geqslant 8\,\mathrm{fm}) = 1.0$ at the edge of the gold nucleus. Thus, the only free parameter is the slope (or, equivalently, the magnitude of the modification factor at $r = 0$). Other functions were tried and essentially differ by their extrapolation to lower and higher radial positions, because the data are not precise enough to constrain the shape. This has a particularly strong impact on the most peripheral collisions for which our assumption that $\Re(r \geqslant 8\,\mathrm{fm}) = 1.0$ adds a significant constraint to the shape.

For all possible slope parameters, consistency with the experimental data is checked by using the procedure detailed in Ref. [15], which utilizes the full statistical and systematic uncertainties. The range of parameters within one standard deviation of the uncertainties is determined separately for backward, mid, and forward rapidity. Using this range of parameters, we can project the cold nuclear matter suppression expected in $\mathrm{Au} + \mathrm{Au}$ collisions as a function of collision centrality and for midrapidity and forward rapidity. Note that the forward rapidity $\mathrm{Au} + \mathrm{Au}$ J/ψ production is sensitive to the low-x partons in one gold nucleus and the high-x

partons in the other gold nucleus. Thus, in the Monte Carlo simulation, for every binary collision at r_1 and r_2 (the radii with respect to the center of each nucleus) the expected modification is $\Re_{\rm low}(r_1) \times \Re_{\rm high}(r_2)$. The midrapidity Au + Au J/ψ production is predominantly sensitive to the mid-x partons from both gold nuclei and therefore the expected modification is $\Re_{\rm mid}(r_1) \times \Re_{\rm mid}(r_2)$. The total modification expected is calculated by taking the average over all correlated r_1 and r_2 positions for binary collisions within overall Au + Au collisions in each Au + Au centrality class.

The results of these calculations matched to the experimentally measured Au + Au centrality bins are shown in Fig. 13. It is notable that the midrapidity cold nuclear matter extrapolation agrees within the uncertainty of the experimental data at midrapidity. Thus, it is not possible within the current constraints to determine the potential extent of hot nuclear matter effects. This conclusion is qualitatively similar to that reached from the previous model calculations as shown in Fig. 11. However, at forward rapidity, this method projects a somewhat larger range of possible cold nuclear matter effects than the previous models.

Neither the predictions of cold nuclear matter effects in heavy-ion collisions based on fitting of the d + Au data with theoretical curves (Figs. 10 and 11) nor those obtained directly from the d + Au data points (Fig. 13) are well-enough constrained to permit quantitative conclusions about additional hot nuclear matter effects.

VII. CONCLUSIONS

A new analysis of J/ψ production in d + Au collisions at $\sqrt{s_{NN}} = 200$ GeV has been presented using the PHENIX 2003 d + Au data set. Cuts and analysis techniques that are consistent with the previously published results for $p + p$, Cu + Cu, and Au + Au collisions at the same energy [1,2,5] are used. The new analysis also benefits from the significantly larger $p + p$ data set from Run-5.

A statistical comparison of these new results to theoretical calculations has been performed with a detailed handling of the experimental uncertainties to estimate a J/ψ (or precursor) breakup cross section in cold nuclear matter on top of models for the modifications of the parton distribution functions in the nucleus. Using EKS (NDSG) shadowing, we obtain a breakup cross section of $2.8^{+1.7}_{-1.4}$ ($2.2^{+1.6}_{-1.5}$) mb. These breakup cross-section values are consistent within large uncertainties with the 4.2 ± 0.5 mb determined at lower energies at the CERN-SPS [14]. The measured values are then used to predict the expected cold nuclear matter effects on J/ψ production in Cu + Cu and Au + Au collisions, and these are compared to the measured nuclear modification factors for those systems. These predictions are found to be similar to those from a less model-dependent and more data-driven method based on the variation of the nuclear modification factor measured in d + Au collisions as a function of both rapidity and centrality [18]. It is notable that the latter method yields a somewhat larger possible suppression in the forward rapidity case. In all cases the large error bars associated with the extrapolation prevent us from making firm quantitative statements on any additional J/ψ suppression in Au + Au collisions beyond that expected from cold nuclear matter effects. A d + Au data set with much improved statistical precision is needed to both reduce the statistical uncertainties and permit better control over the systematic uncertainties.

ACKNOWLEDGMENTS

We thank the staff of the Collider-Accelerator and Physics Departments at Brookhaven National Laboratory and the staff of the other PHENIX participating institutions for their vital contributions. We also thank Ramona Vogt for useful discussions and for the calculations used to set the level of the breakup cross sections. We acknowledge support from the Office of Nuclear Physics in the Office of Science of the Department of Energy, the National Science Foundation, Abilene Christian University Research Council, Research Foundation of SUNY, and the Dean of the College of Arts and Sciences, Vanderbilt University (U.S.A.), Ministry of Education, Culture, Sports, Science, and Technology and the Japan Society for the Promotion of Science (Japan), Conselho Nacional de Desenvolvimento Científico e Tecnológico and Fundação de Amparo à Pesquisa do Estado de São Paulo (Brazil), Natural Science Foundation of China (People's Republic of China), Ministry of Education, Youth and Sports (Czech Republic), Centre National de la Recherche Scientifique, Commissariat à l'Énergie Atomique, and Institut National de Physique Nucléaire et de Physique des Particules (France), Ministry of Industry, Science and Tekhnologies, Bundesministerium für Bildung und Forschung, Deutscher Akademischer Austausch Dienst, and Alexander von Humboldt Stiftung (Germany), Hungarian National Science Fund, OTKA (Hungary), Department of Atomic Energy (India), Israel Science Foundation (Israel), Korea Research Foundation and Korea Science and Engineering Foundation (Korea), Ministry of Education and Science, Russia Academy of Sciences, Federal Agency of Atomic Energy (Russia), VR and the Wallenberg Foundation (Sweden), the U.S. Civilian Research and Development Foundation for the Independent States of the Former Soviet Union, the US-Hungarian NSF-OTKA-MTA, and the US-Israel Binational Science Foundation.

[1] A. Adare *et al.*, Phys. Rev. Lett. **98**, 232301 (2007).
[2] A. Adare *et al.*, Phys. Rev. Lett. **98**, 232002 (2007).
[3] R. Vogt, Phys. Rev. C **71**, 054902 (2005).
[4] S. S. Adler *et al.*, Phys. Rev. Lett. **96**, 012304 (2006).
[5] A. Adare *et al.*, arXiv:0801.0220 [nucl-ex].
[6] K. Adcox *et al.*, Nucl. Instrum. Methods A **499**, 469 (2003).
[7] S. N. White, AIP Conf. Proc. **792**, 527 (2005).
[8] M. L. Miller, K. Reygers, S. J. Sanders, and P. Steinberg, Ann. Rev. Nucl. Part. Sci. **57**, 205 (2007).
[9] A. Spiridonov, arXiv:hep-ex/0510076 (2004).
[10] *GEANT 3.2.1 Manual* (CERN, Geneva, 1993); available at http://wwwasdoc.web.cern.ch/wwwasdoc/pdfdir/geant.pdf.

[11] Torbjorn Sjöstrand, Stephen Mrenna, and Peter Skands, PYTHIA 6.4 physics and manual, JHEP 05 (2005) 026 [also hep-ph/0603175].
[12] K. J. Eskola, V. J. Kolhinen, and R. Vogt, Nucl. Phys. **A696**, 729 (2001).
[13] D. deFlorian and R. Sassot, Phys. Rev. D **69**, 074028 (2004).
[14] B. Alessandro *et al*., Eur. Phys. J. C **48**, 329 (2006).
[15] A. Adare *et al*., arXiv:0801.1665 [nucl-ex].
[16] C. Lourenco, Nucl. Phys. **A783**, 451 (2007).
[17] S. R. Klein and R. Vogt, Phys. Rev. Lett. **91**, 142301 (2003).
[18] R. Granier de Cassagnac, J. Phys. G **34**, S955 (2007).

Erratum: Cold nuclear matter effects on J/ψ production as constrained by deuteron-gold measurements at $\sqrt{s_{NN}} = 200$ GeV [Phys. Rev. C 77, 024912 (2008)]

A. Adare, S. S. Adler, S. Afanasiev, C. Aidala, N. N. Ajitanand, Y. Akiba, H. Al-Bataineh, J. Alexander, A. Al-Jamel, K. Aoki, L. Aphecetche, R. Armendariz, S. H. Aronson, J. Asai, E. T. Atomssa, R. Averbeck, T. C. Awes, B. Azmoun, V. Babintsev, G. Baksay, L. Baksay, A. Baldisseri, K. N. Barish, P. D. Barnes, B. Bassalleck, S. Bathe, S. Batsouli, V. Baublis, F. Bauer, A. Bazilevsky, S. Belikov,* R. Bennett, Y. Berdnikov, A. A. Bickley, M. T. Bjorndal, J. G. Boissevain, H. Borel, K. Boyle, M. L. Brooks, D. S. Brown, N. Bruner, D. Bucher, H. Buesching, V. Bumazhnov, G. Bunce, J. M. Burward-Hoy, S. Butsyk, X. Camard, S. Campbell, P. Chand, B. S. Chang, W. C. Chang, J.-L. Charvet, S. Chernichenko, J. Chiba, C. Y. Chi, M. Chiu, I. J. Choi, R. K. Choudhury, T. Chujo, P. Chung, A. Churyn, V. Cianciolo, C. R. Cleven, Y. Cobigo, B. A. Cole, M. P. Comets, P. Constantin, M. Csanád, T. Csörgő, J. P. Cussonneau, T. Dahms, K. Das, G. David, F. Deák, M. B. Deaton, K. Dehmelt, H. Delagrange, A. Denisov, D. d'Enterria, A. Deshpande, E. J. Desmond, A. Devismes, O. Dietzsch, A. Dion, M. Donadelli, J. L. Drachenberg, O. Drapier, A. Drees, A. K. Dubey, A. Durum, D. Dutta, V. Dzhordzhadze, Y. V. Efremenko, J. Egdemir, F. Ellinghaus, W. S. Emam, A. Enokizono, H. En'yo, B. Espagnon, S. Esumi, K. O. Eyser, D. E. Fields, C. Finck, M. Finger, Jr., M. Finger, F. Fleuret, S. L. Fokin, B. D. Fox, Z. Fraenkel,* J. E. Frantz, A. Franz, A. D. Frawley, K. Fujiwara, Y. Fukao, S.-Y. Fung, T. Fusayasu, S. Gadrat, I. Garishvili, M. Germain, A. Glenn, H. Gong, M. Gonin, J. Gosset, Y. Goto, R. Granier de Cassagnac, N. Grau, S. V. Greene, M. Grosse Perdekamp, T. Gunji, H.-Å. Gustafsson, T. Hachiya, A. Hadj Henni, C. Haegemann, J. S. Haggerty, H. Hamagaki, R. Han, A. G. Hansen, H. Harada, E. P. Hartouni, K. Haruna, M. Harvey, E. Haslum, K. Hasuko, R. Hayano, M. Heffner, T. K. Hemmick, T. Hester, J. M. Heuser, X. He, P. Hidas, H. Hiejima, J. C. Hill, R. Hobbs, M. Hohlmann, W. Holzmann, K. Homma, B. Hong, A. Hoover, T. Horaguchi, D. Hornback, T. Ichihara, V. V. Ikonnikov, K. Imai, M. Inaba, Y. Inoue, M. Inuzuka, D. Isenhower, L. Isenhower, M. Ishihara, T. Isobe, M. Issah, A. Isupov, B. V. Jacak,† J. Jia, J. Jin, O. Jinnouchi, B. M. Johnson, S. C. Johnson, K. S. Joo, D. Jouan, F. Kajihara, S. Kametani, N. Kamihara, J. Kamin, M. Kaneta, J. H. Kang, H. Kanou, K. Katou, T. Kawabata, D. Kawall, A. V. Kazantsev, S. Kelly, B. Khachaturov, A. Khanzadeev, J. Kikuchi, D. H. Kim, D. J. Kim, E. Kim, G.-B. Kim, H. J. Kim, E. Kinney, A. Kiss, E. Kistenev, A. Kiyomichi, J. Klay, C. Klein-Boesing, H. Kobayashi, L. Kochenda, V. Kochetkov, R. Kohara, B. Komkov, M. Konno, D. Kotchetkov, A. Kozlov, A. Král, A. Kravitz, P. J. Kroon, J. Kubart, C. H. Kuberg,* G. J. Kunde, N. Kurihara, K. Kurita, M. J. Kweon, Y. Kwon, G. S. Kyle, R. Lacey, Y.-S. Lai, J. G. Lajoie, A. Lebedev, Y. Le Bornec, S. Leckey, D. M. Lee, M. K. Lee, T. Lee, M. J. Leitch, M. A. L. Leite, B. Lenzi, H. Lim, T. Liška, A. Litvinenko, M. X. Liu, X. Li, X. H. Li, B. Love, D. Lynch, C. F. Maguire, Y. I. Makdisi, A. Malakhov, M. D. Malik, V. I. Manko, Y. Mao, G. Martinez, L. Mašek, H. Masui, F. Matathias, T. Matsumoto, M. C. McCain, M. McCumber, P. L. McGaughey, Y. Miake, P. Mikeš, K. Miki, T. E. Miller, A. Milov, S. Mioduszewski, G. C. Mishra, M. Mishra, J. T. Mitchell, M. Mitrovski, A. K. Mohanty, A. Morreale, D. P. Morrison, J. M. Moss, T. V. Moukhanova, D. Mukhopadhyay, M. Muniruzzaman, J. Murata, S. Nagamiya, Y. Nagata, J. L. Nagle, M. Naglis, I. Nakagawa, Y. Nakamiya, T. Nakamura, K. Nakano, J. Newby, M. Nguyen, B. E. Norman, A. S. Nyanin, J. Nystrand, E. O'Brien, S. X. Oda, C. A. Ogilvie, H. Ohnishi, I. D. Ojha, H. Okada, K. Okada, M. Oka, O. O. Omiwade, A. Oskarsson, I. Otterlund, M. Ouchida, K. Oyama, K. Ozawa, R. Pak, D. Pal, A. P. T. Palounek, V. Pantuev, V. Papavassiliou, J. Park, W. J. Park, S. F. Pate, H. Pei, V. Penev, J.-C. Peng, H. Pereira, V. Peresedov, D. Yu. Peressounko, A. Pierson, C. Pinkenburg, R. P. Pisani, M. L. Purschke, A. K. Purwar, J. M. Qualls, H. Qu, J. Rak, A. Rakotozafindrabe, I. Ravinovich, K. F. Read, S. Rembeczki, M. Reuter, K. Reygers, V. Riabov, Y. Riabov, G. Roche, A. Romana,* M. Rosati, S. S. E. Rosendahl, P. Rosnet, P. Rukoyatkin, V. L. Rykov, S. S. Ryu, B. Sahlmueller, N. Saito, T. Sakaguchi, S. Sakai, H. Sakata, V. Samsonov, L. Sanfratello, R. Santo, H. D. Sato, S. Sato, S. Sawada, Y. Schutz, J. Seele, R. Seidl, V. Semenov, R. Seto, D. Sharma, T. K. Shea, I. Shein, A. Shevel, T.-A. Shibata, K. Shigaki, M. Shimomura, K. Shoji, A. Sickles, C. L. Silva, D. Silvermyr, C. Silvestre, K. S. Sim, C. P. Singh, V. Singh, S. Skutnik, M. Slunečka, A. Soldatov, R. A. Soltz, W. E. Sondheim, S. P. Sorensen, I. V. Sourikova, F. Staley, P. W. Stankus, E. Stenlund, M. Stepanov, A. Ster, S. P. Stoll, T. Sugitate, C. Suire, J. P. Sullivan, J. Sziklai, T. Tabaru, S. Takagi, E. M. Takagui, A. Taketani, K. H. Tanaka, Y. Tanaka, K. Tanida, M. J. Tannenbaum, A. Taranenko, P. Tarján, T. L. Thomas, M. Togawa, A. Toia, J. Tojo, L. Tomášek, H. Torii, R. S. Towell, V.-N. Tram, I. Tserruya, Y. Tsuchimoto, H. Tydesjö, N. Tyurin, T. J. Uam, C. Vale, H. Valle, H. W. vanHecke, J. Velkovska, M. Velkovsky, R. Vertesi, V. Veszprémi, A. A. Vinogradov, M. Virius, M. A. Volkov, V. Vrba, E. Vznuzdaev, M. Wagner, D. Walker, X. R. Wang, Y. Watanabe, J. Wessels, S. N. White, N. Willis, D. Winter, F. K. Wohn, C. L. Woody, M. Wysocki, W. Xie, Y. L. Yamaguchi, A. Yanovich, Z. Yasin, J. Ying, S. Yokkaichi, G. R. Young, I. Younus, I. E. Yushmanov, W. A. Zajc, O. Zaudtke, C. Zhang, S. Zhou, J. Zimányi,* L. Zolin, and X. Zong

(PHENIX Collaboration)

(Received 30 March 2009; published 29 May 2009)

DOI: 10.1103/PhysRevC.79.059901 PACS number(s): 25.75.Dw, 99.10.Cd

All of the experimental data points presented in the original paper are correct and unchanged (including statistical and systematic uncertainties). However, herein we correct a comparison between the experimental data and a theoretical picture using a set of shadowing models for the nuclear parton

*Deceased.

†PHENIX spokesperson: jacak@skipper.physics.sunysb.edu

 ©2009 The American Physical Society

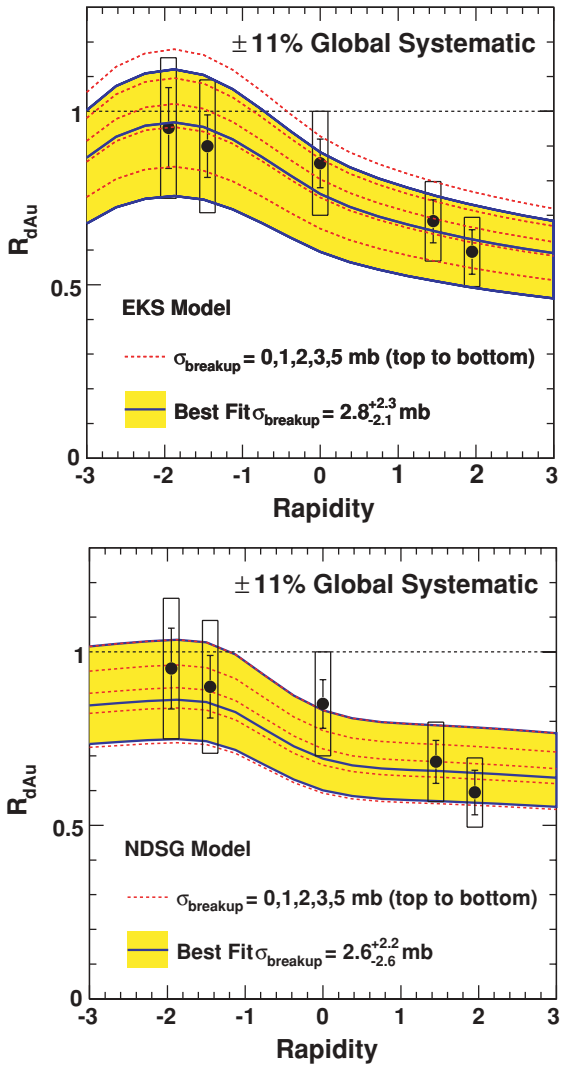

FIG. 1. (Color online) R_{dAu} data compared to various theoretical curves for different $\sigma_{breakup}$ values. Also, shown as a band are the range of $\sigma_{breakup}$ found to be consistent with the data within one standard deviation. The top panel is a comparison for EKS shadowing [1], while the bottom panel is for NDSG shadowing [2].

distribution functions (PDFs) combined with a nuclear breakup cross section ($\sigma_{breakup}$). Under the assumption that a given modified nuclear PDF is correct, we put constraints on the $\sigma_{breakup}$ values as presented in the original paper in Table V,

TABLE I. Most probable values and one standard deviations of $\sigma_{breakup}$ assuming two different shadowing models, from a fit to minimum bias R_{dAu} points as a function of rapidity (Fig. 1), and fits to R_{dAu} as a function of N_{coll} in three separate rapidity bins (Fig. 2).

Fit range in y	EKS (mb)	NDSG (mb)
All	$2.8^{+2.3}_{-2.1}$	$2.6^{+2.2}_{-2.6}$
$[-2.2, -1.2]$	$5.2^{+2.4}_{-2.8}$	$3.3^{+2.9}_{-2.7}$
$[-0.35, 0.35]$	$2.3^{+3.6}_{-1.9}$	$0.8^{+3.6}_{-0.8}$
$[1.2, 2.2]$	$3.4^{+2.0}_{-2.5}$	$3.5^{+2.0}_{-2.7}$

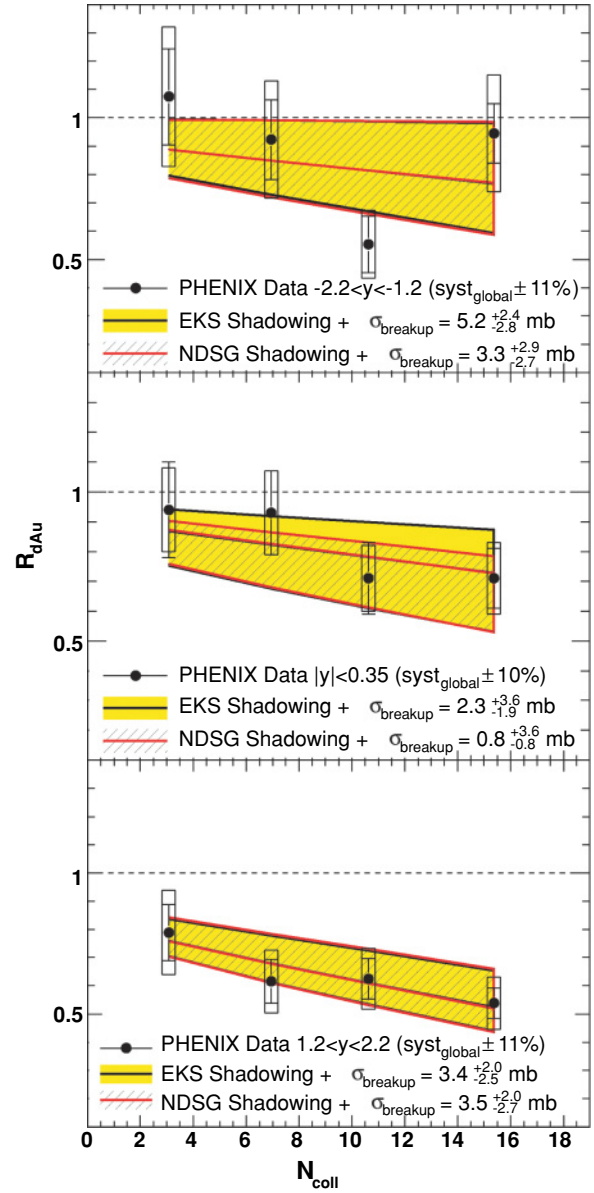

FIG. 2. (Color online) R_{dAu} data as a function of N_{coll} for three different rapidity ranges. Overlayed are theoretical curves representing the best fit $\sigma_{breakup}$ values as determined in each rapidity range separately, utilizing EKS and NDSG nuclear PDFs and a simple geometric dependence. Also, shown as bands are the range of $\sigma_{breakup}$ found to be consistent with the data within one standard deviation.

Sec. VI. In the code that calculated these constrained $\sigma_{breakup}$ values we discovered a mistake, which we now correct. Table I shows the new results, for which all of the most probable $\sigma_{breakup}$ values differ by less than 0.4 mb from those originally presented. However, the one standard deviation uncertainties (that include contributions from both the statistical and systematic uncertainties on the experimental data points) are approximately 30–60% larger than originally reported.

Thus, the one standard deviation uncertainty bands on $\sigma_{breakup}$ in Figs. 8–11 of the original paper need updating with the corrected constraints. Figures 1–4 here show the

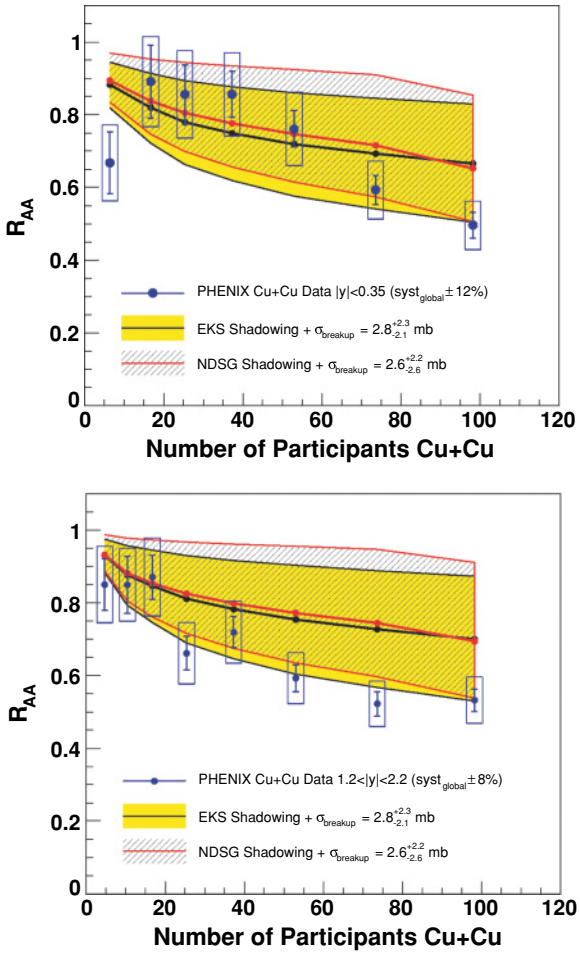

FIG. 3. (Color online) R_{AA} for Cu + Cu [3] collisions compared to a band of theoretical curves for the σ_{breakup} values found to be consistent with the d + Au data as shown in Fig. 1. The top figure includes both EKS shadowing [1] and NDSG shadowing [2] at midrapidity. The bottom figure is the same at forward rapidity.

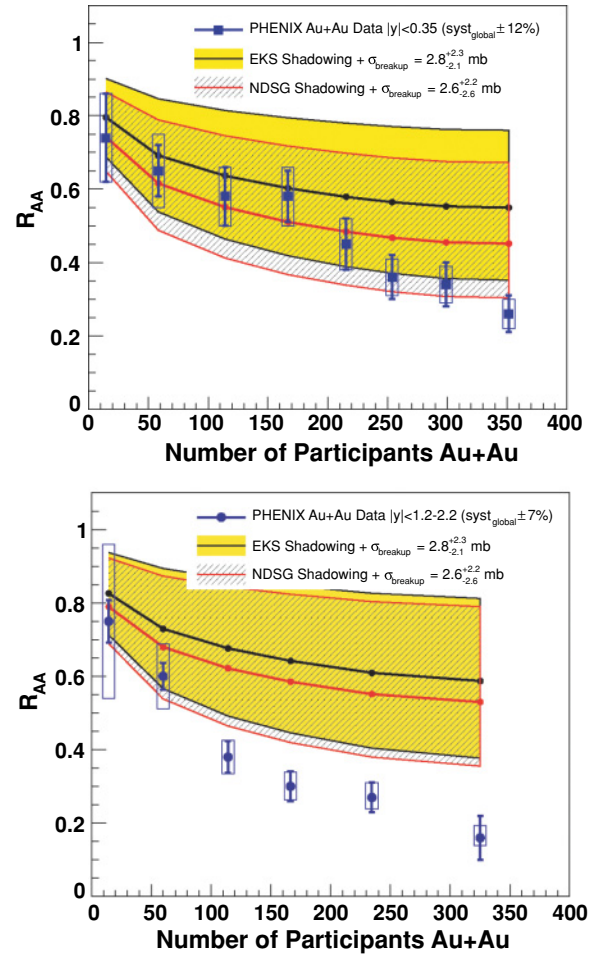

FIG. 4. (Color online) R_{AA} for Au + Au [4] collisions compared to a band of theoretical curves for the σ_{breakup} values found to be consistent with the d + Au data as shown in Fig. 1. The top figure includes both EKS shadowing [1] and NDSG shadowing [2] at midrapidity. The bottom figure is the same at forward rapidity.

corrected constraints. Although the uncertainties are significantly larger with these corrected σ_{breakup} values, there is no qualitative change in the physics conclusions to be drawn from comparisons between these theoretical models (and their extrapolation) and the Au + Au and Cu + Cu measurements. Stronger conclusions can only come from future higher statistics data for d + Au collisions. Note that no correction is needed for results from the data-driven method in Fig. 13 of the original paper.

[1] K. J. Eskola, V. J. Kolhinen, and R. Vogt, Nucl. Phys. **A696**, 729 (2001).
[2] D. deFlorian and R. Sassot, Phys. Rev. D **69**, 074028 (2004).
[3] A. Adare *et al.* (PHENIX Collaboration), Phys. Rev. Lett. **101**, 122301 (2008).
[4] A. Adare *et al.* (PHENIX Collaboration), Phys. Rev. Lett. **98**, 232301 (2007).

EPJ manuscript No.
(will be inserted by the editor)

arXiv:0709.2477v1 [nucl-ex] 16 Sep 2007

Source radii at target rapidity from two-proton and two-deuteron correlations in central Pb+Pb collisions at 158 A GeV

WA98 Collaboration

M.M. Aggarwal[1], Z. Ahammed[2], A.L.S. Angelis[3,*], V. Antonenko[4], V. Arefiev[5], V. Astakhov[5], V. Avdeitchikov[5], T.C. Awes[6], P.V.K.S. Baba[7], S.K. Badyal[7], S. Bathe[8], B. Batiounia[5], T. Bernier[9], K.B. Bhalla[10], V.S. Bhatia[1], C. Blume[8], D. Bucher[8], H. Büsching[8], L. Carlen[11], S. Chattopadhyay[2], M.P. Decowski[12], H. Delagrange[9], P. Donni[3], M.R. Dutta Majumdar[2], K. El Chenawi[11], A.K. Dubey[13], K. Enosawa[14],, S. Fokin[4], V. Frolov[5], M.S. Ganti[2], S. Garpman[11,*], O. Gavrishchuk[5], F.J.M. Geurts[15], T.K. Ghosh[16], R. Glasow[8],, B. Guskov[5], H. Å.Gustafsson[11], H. H.Gutbrod[17],, I. Hrivnacova[18], M. Ippolitov[4], H. Kalechofsky[3], R. Kamermans[15], K. Karadjev[4], K. Karpio[19], B. W. Kolb[17], I. Kosarev[5], I. Koutcheryaev[4], A. Kugler[18], P. Kulinich[12], M. Kurata[14], A. Lebedev[4], H. Liu[19], H. Löhner[16], L. Luquin[9], D.P. Mahapatra[13], V. Manko[4], M. Martin[3], G. Martínez[9], A. Maximov[5]and Y. Miake[14], G.C. Mishra[13], B. Mohanty[13], M.-J. Mora[9], D. Morrison[20], T. Moukhanova[4], D. S. Mukhopadhyay[2], H. Naef[3], B. K. Nandi[13], S. K. Nayak[9], T. K. Nayak[2], A. Nianine[4], V. Nikitine[5], S. Nikolaev[4], P. Nilsson[11], S. Nishimura[14], P. Nomokonov[5], J. Nystrand[11], A. Oskarsson[11], I. Otterlund[11], S. Pavliouk[4], T. Peitzmann[15], D. Peressounko[4], V. Petracek[18],, V. Petracek[13] W. Pinanaud[9], F. Plasil[6], M.L. Purschke[17], J. Rak[18], R. Raniwala[10], S. Raniwala[10], N.K. Rao[7], F. Retiere[9], K. Reygers[8], G. Roland[12], L. Rosselet[3], I. Roufanov[5], C. Roy[9], J.M. Rubio[3], S.S. Sambyal[7], R. Santo[8], S. Sato[14], H. Schlagheck[8], H.-R. Schmidt[17], Y. Schutz[9], G. Shabratova[5], T.H. Shah[7], I. Sibiriak[4], T. Siemiarczuk[19], D. Silvermyr[11], B.C. Sinha[2], N. Slavine[5], K. Söderström[11], G. Sood[1], S.P. Sørensen[20], P. Stankus[6], G. Stefanek[19], P. Steinberg[12], E. Stenlund[11], M. Sumbera[18], T. Svensson[11], A. Tsvetkov[4], L. Tykarski[19], E.C.v.d. Pijll[15], N.v. Eijndhoven[15], G.J.v. Nieuwenhuizen[12], A. Vinogradov[4], Y.P. Viyogi[2], A. Vodopianov[5], S. Vörös[3], B. Wysłouch[12], and G.R. Young[6]

[1] University of Panjab, Chandigarh 160014, India
[2] Variable Energy Cyclotron Centre, Calcutta 700 064, India
[3] University of Geneva, CH-1211 Geneva 4,Switzerland
[4] RRC Kurchatov Institute, RU-123182 Moscow, Russia
[5] Joint Institute for Nuclear Research, RU-141980 Dubna, Russia
[6] Oak Ridge National Laboratory, Oak Ridge, Tennessee 37831-6372, USA
[7] University of Jammu, Jammu 180001, India
[8] University of Münster, D-48149 Münster, Germany
[9] SUBATECH, Ecole des Mines, Nantes, France
[10] University of Rajasthan, Jaipur 302004, Rajasthan, India
[11] Lund University, SE-221 00 Lund, Sweden
[12] MIT Cambridge, MA 02139, USA
[13] Institute of Physics, 751-005 Bhubaneswar, India
[14] University of Tsukuba, Ibaraki 305, Japan
[15] Universiteit Utrecht/NIKHEF, NL-3508 TA Utrecht, The Netherlands
[16] KVI, University of Groningen, NL-9747 AA Groningen, The Netherlands
[17] Gesellschaft für Schwerionenforschung (GSI), D-64220 Darmstadt, Germany
[18] Nuclear Physics Institute, CZ-250 68 Rez, Czech Rep.
[19] Soltan Institute for Nuclear Studies, PL-00-681 Warsaw, Poland
[20] University of Tennessee, Knoxville, Tennessee 37966, USA
[*] Deceased.

Received: date / Revised version: date

Abstract. Two-proton and two-deuteron correlations have been studied in the target fragmentation region of central Pb+Pb collisions at 158 A GeV. Protons and deuterons were measured with the Plastic Ball spectrometer of the WA98 experiment at the CERN SPS. The results of one-dimensional and multi-dimensional analyses using both the Bertsch-Pratt and Yano-Koonin-Podgoretsky parameterizations of the two-particle correlation functions are presented. The proton source exhibits a volume emission, while the deuteron source, with small outward radius, appears opaque. Both proton and deuteron sources have cross-terms R_{ol}^2 and longitudinal velocities β consistent with zero, indicat-

ing a boost-invariant expansion. The invariant radius parameter R follows an approximate $A/\sqrt{m}$ scaling while the longitudinal and transverse radii, R_L and R_T, scale approximately as $A/\sqrt{m_T}$ with $A \approx 3$ fm GeV$^{1/2}$ in both cases.

PACS. 25.75. Gz

1 Introduction

In this paper we report on an analysis of quantum-statistical and final state induced correlations [1] of proton and deuteron pairs emitted from 158 A GeV central Pb+Pb collisions. The study of these two particle species in the same system is of special interest as one would expect that deuterons, due to their loose structure and small binding energy, will survive only in the late, low density environment when scatterings are rare. The generally accepted mechanism of deuteron production is by coalescence of a proton and neutron [2,3,4] at the time of freeze-out. The deuteron measurement thus provides an unique means to measure the geometry of the source in the late time interval of the expansion. Experimental results on Fermi-Dirac correlations for protons are not as abundant as those on Bose-Einstein correlations for mesons, and are very scarce for deuteron correlations. A remarkable feature of the existing proton and deuteron correlation data in hadron-nucleus and nucleus-nucleus collisions, spanning over four orders of magnitude of incident energy from 0.02 to 450 A GeV is the small variation of the extracted source radius parameter [5,6,7,8,9,10,11,12,13,14,15,16,17,18,19,20,21].

2 Experimental setup

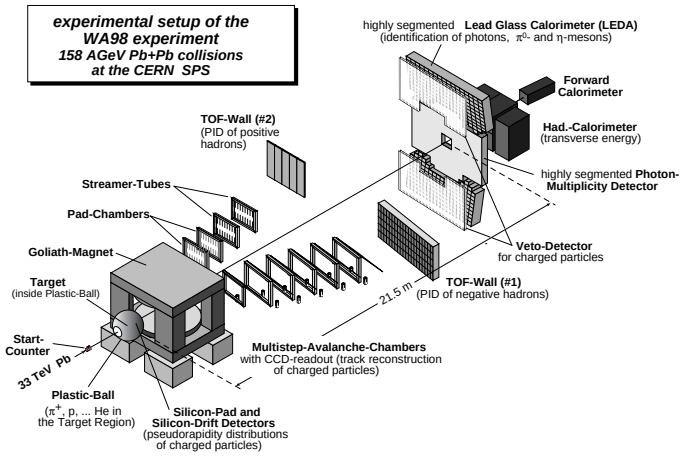

Fig. 1. Experimental setup of the WA98 experiment for the 1996 run.

The CERN SPS experiment WA98 (for details see [22] and references therein) is a general purpose apparatus that consists of large acceptance photon and hadron spectrometers, detectors for charged particle and photon multiplicity measurements, and calorimeters for transverse and forward energy measurements. The layout of the WA98 experimental setup for the 1996 SPS run period is shown in Fig. 1. The results presented in this report were obtained from an analysis of data taken in 1996 with the 158 A GeV ^{208}Pb beam on a 239 mg/cm^2 ^{208}Pb target and made use of the Midrapidity Calorimeter(MIRAC) [23], the Zero Degree Calorimeter(ZDC) [24], and the Plastic Ball spectrometer [25].

The ZDC registers energy emitted along the beam direction in the 3° forward cone. The MIRAC measures the total transverse energy in the pseudorapidity region of $3.5 \leq \eta \leq 5.5$. It is a sampling calorimeter that consists of a lead-scintillator electromagnetic section, followed by an iron-scintillator hadronic section. MIRAC plays the central role in the WA98 minimum bias trigger where the measured transverse energy E_T is required to be above a minimum threshold. MIRAC is used to classify the centrality of each event. The analysis presented here has been performed on the 10% most central events of the measured minimum bias cross section of ≈ 6400 mb. About 3 millions central Pb+Pb events were analyzed with an average of 6.1 identified protons and 2.9 identified deuterons per event.

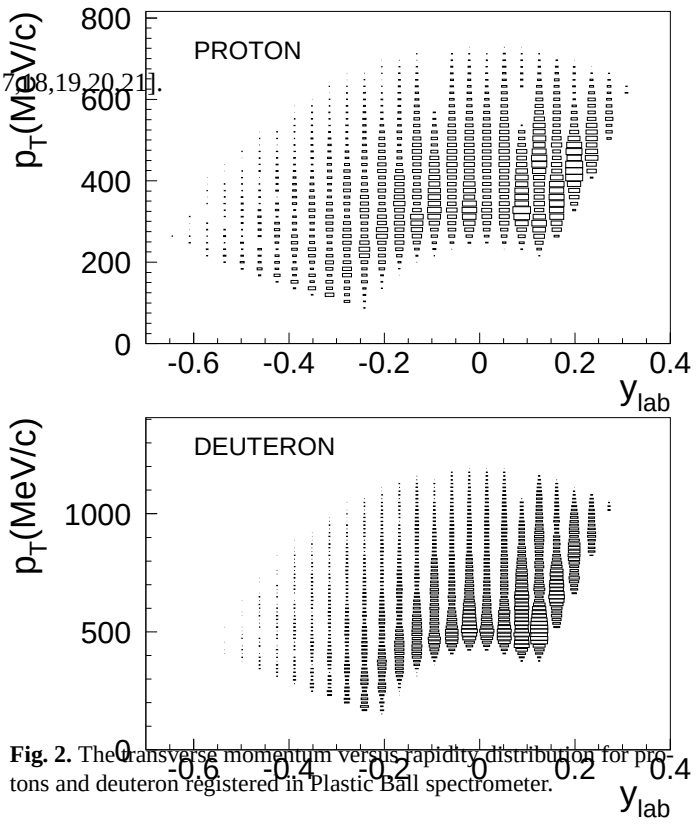

Fig. 2. The transverse momentum versus rapidity distribution for protons and deuteron registered in Plastic Ball spectrometer.

The identification and momentum measurement of protons and deuterons has been made using the Plastic Ball spectrometer [25]. The Plastic Ball consists of 655 detector modules surrounding the target over the range of polar angles ϑ from 30° to 160° with full azimuthal acceptance. Each of the modules consists of a ΔE and E section. The ΔE section is a CaF_2(Eu) crystal scintillator and the E section is a plastic scintillator. The light emission of the plastic scintillator is approximately 100

times faster than that of the CaF_2(Eu), so signals from both scintillators can be read out by a single photomultiplier with subsequent separation of the signals by pulse shape analysis. The $\Delta E-E$ identification technique was used and is capable of identifying pions and charged fragments up to the helium isotopes. Because of the relatively low yield of pions as compared to baryons, an additional positive pion identification is made by means of its sequential decay $\pi^+ \rightarrow \mu^+(\nu_\mu) \rightarrow e^+(\nu_e\bar{\nu_\mu})$. The thickness of the ΔE crystal scintillator was chosen to be 4 mm with 35.6 cm as the length of the E plastic scintillator. This assures that protons up to 200 MeV are fully stopped in the E-counter and provide a complete $\Delta E - E$ signal. Additionally, the mis-identification of punch through deuterons do not disturb the proton spectra below 200 MeV.

The WA98 experimental setup has been implemented in the GEANT Monte Carlo simulation package [26]. This has been used to study the response of the Plastic Ball in order to extract the particle identification efficiency and the kinetic energy resolution for different particle species, as well as two-particle variables and takes into account the granular structure of the Plastic Ball. GEANT transports the particles through the experimental setup taking into account the geometrical material boundaries and particle interactions. The particles are traced through the experimental setup where they may interact with the material they encounter on their way to the detector. When a particle reaches the detector the output signal of the Plastic Ball module is simulated. The particle distributions used as input to the GEANT simulations were adjusted to reproduce the measured momentum and angular distributions of particles. The Plastic Ball acceptance is illustrated in Fig. 2 as the distribution of protons and deuterons that pass the acceptance cuts.

3 One-dimensional analysis

The one-dimensional experimental correlation function was constructed as:

$$C(q) = N\,\frac{Y_{12}(q)}{Y^*_{12}(q)} \tag{1}$$

where $\mathbf{q} = \frac{1}{2}(\mathbf{q_1}-\mathbf{q_2})$ is the two-particle three-momentum difference in the laboratory frame, N is a normalization constant, and the numerator is the coincidence yield while the denominator is the uncorrelated background yield. In this analysis, the event-mixing technique was used to construct the background yields, using the same central event data set as used to construct the numerator. To insure that only particles from comparable events were mixed, the central event sample was further subdivided into 8 subsets according to the measured transverse energy. Particles were picked randomly from different events belonging to the same centrality selection with the additional condition to have the same multiplicities of the studied particle and all particles registered in the Plastic Ball. The number of mixed background pairs was chosen to be 10 times larger than the number of coincident pairs to insure a small statistical error contribution from the background pair yield, Y^*_{12}.

The measurement resolution of the variable q in the Plastic Ball spectrometer had an average value of $\sigma(q) \simeq 10.5$ MeV/c and 12.5 MeV/c for the two-proton and two-deuteron systems, respectively. For small values of q, the resolution was around 7.5 MeV/c for the two-proton system. A bin size of 7.5 MeV/c was chosen for the one-dimensional correlation analyses. It should be noted that the one-dimensional correlation functions presented here have been studied as a function of the momentum difference q rather than the more commonly used invariant four-momentum difference $q_{inv} = \frac{1}{2}\sqrt{-(p^\mu_1 - p^\mu_2)^2}$. The experimental resolution for the pp (dd) system in q_{inv} at 20 (40) MeV/c is about 15 (20) MeV/c. It increases to 20 (27) MeV/c at q_{inv}=100 (200) MeV/c and approximately levels off above that.

3.1 Final state interaction

To calculate the pair-wise final state interaction we used two computer codes for the proton-proton system: (i) the CRAB code written by S.Pratt [27] which includes Coulomb and strong final state interactions, and (ii) the static model developed by A. Deloff [28,29] with both Coulomb and strong S-wave interactions included. The latter incorporates a potential of the delta-shell form

$$2\mu V(r) = -(s/R)\,\delta(r-R), \tag{2}$$

characterized by the range R and the dimensionless parameter s representing the strength of the force (μ is the reduced mass). Only the $^1S_0$ partial wave in the strong interaction was retained. This pp interaction is well known experimentally and the measured phase shifts can be satisfactorily reproduced up to q=150 MeV/c by taking the delta-shell potential parameters as s=0.906 and R=1.84 fm. Both codes gave consistent results for the proton-proton system.

For the deuteron-deuteron case the model by A. Deloff [28] was used in which the strong s-wave interaction in S=0,2 spin states was included together with the Coulomb repulsion between two extended-size deuterons. The Coulomb interaction between two deuterons is different from that between two protons because the deuteron is composite and relatively large. For two extended-size deuterons located at $\mathbf{r}_1$ and $\mathbf{r}_2$, the Coulomb potential can be written as

$$V(|\mathbf{r}_1 - \mathbf{r}_2|) = \alpha \int \mathrm{d}^3\mathbf{x}_1 \mathrm{d}^3\mathbf{x}_2\, \frac{\rho(|\mathbf{x}_1-\mathbf{r}_1|)\rho(|\mathbf{x}_2-\mathbf{r}_2|)}{|\mathbf{x}_1-\mathbf{x}_2|} \tag{3}$$

where $\rho(x)$ is the charge density and α is the fine structure constant. Since the right hand side of Eq. (3) is translationally invariant, the potential $V(r)$ depends only upon the difference $r = |\mathbf{r}_1 - \mathbf{r}_2|$, and for r larger than twice the deuteron radius takes the usual point-like form $V(r) = \alpha/r$. For an assumed uniform charge distribution, this integral can be obtained in analytic form as:

$$V(r) = \begin{cases} \frac{\alpha}{R_c}\,\frac{1}{x}\{1-3(1-x)^4 \\ \quad \times[1-\frac{2}{15}(1-x)(5+x)]\} & 0 \le x \le 1 \\ \frac{\alpha}{r} & x > 1 \end{cases} \tag{4}$$

where $x = r/R_C$ and $R_C = 3.86$ fm is twice the deuteron radius. A comparison of the Coulomb potential for extended-size and point-like deuterons is shown in Fig. 3. The Coulomb repulsion is observed to be substantially reduced when the extended deuteron size is taken into account.

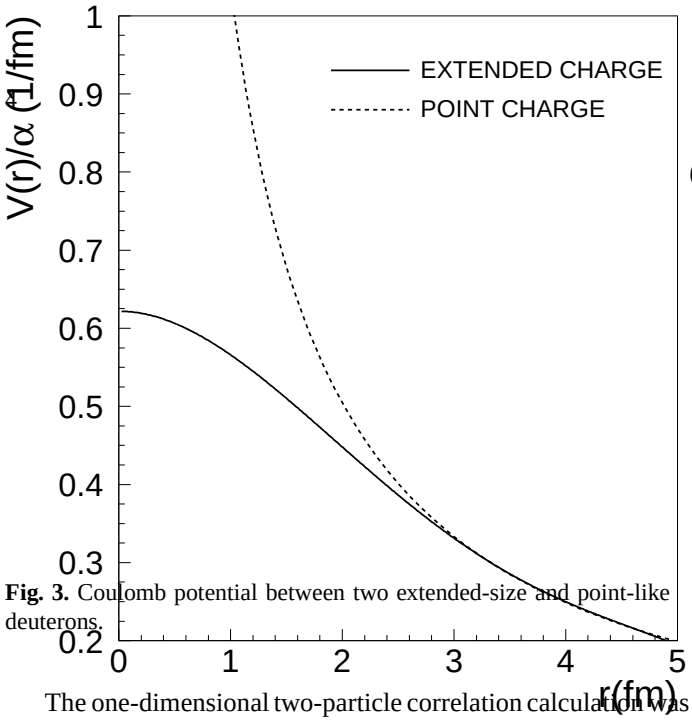

Fig. 3. Coulomb potential between two extended-size and point-like deuterons.

The one-dimensional two-particle correlation calculation was based on a static spherical gaussian shaped source, specified by radius R_0:

$$\rho(x) = (2\pi\, R_0^2)^{-3/2}\, \mathrm{e}^{-x^2/2R_0^2}. \qquad (5)$$

In the case of a non-zero emission lifetime this approach gives an *upper* limit for the spatial extent of the source.

To account for the Plastic Ball resolution all of the calculated correlation functions presented in this paper were calculated as:

$$C(q) = \int r(q,q')C(q')\mathrm{d}q' \qquad (6)$$

with the predicted correlation function $C(q')$ convoluted with the Gaussian resolution function of the Plastic Ball $r(q,q')$.

$$r(q,q') = \frac{1}{(2\pi)^{3/2}}\,\frac{1}{\sigma(q)}\,\mathrm{e}^{-\frac{1}{2}\frac{(q-q')^2}{\sigma(q)^2}}\,\mathrm{d}q' \qquad (7)$$

as determined from the GEANT simulations.

3.2 Systematic errors

The systematic errors have been evaluated by comparison of the results obtained under different conditions. The systematic uncertainties are mainly introduced by the granularity of the detector and, to some extent, by the procedure used to construct the background pair distribution. The following sources of systematic errors have been investigated leading to variations (rms estimates) of the radius parameters given in brackets, with the first and second numbers referring to the pp and dd system, respectively:

(i) Different periods of data taking during the run [0.05, 0.05 fm].
(ii) Different particle identification windows [0.09, 0.12 fm].
(iii) The width of the transverse energy E_T bin used for centrality selection in the background pair distribution calculations: the centrality bin size was halved and the result was compared to the nominal bin size result [0.01, 0.05 fm].
(iv) Non-conservation of momentum in the background pair correlations: local (transverse) momentum conservation in real events, although not expected to be exact, may influence the correlation between real particle pairs due to the fact that a significant fraction, but not all, of the particles in the target rapidity region are measured in the Plastic Ball. To investigate the sensitivity of the fitted parameters to the effect of momentum conservation, in addition to the requirement that the full background event have the same number of particles as the real event detected in the Plastic Ball, it was further required that the background event have a total momentum of all measured particles equal to that of the real event: $P_{Tot}(\mathrm{measured}) = P_{Tot}(\mathrm{reference}) \pm \Delta$, where Δ should be 0 in the ideal case. In practice, Δ was chosen to be 300 MeV/c and 600 MeV/c for the two-proton and two-deuteron background events, respectively [0.07, 0.06 fm].
(v) The granular structure of the Plastic Ball spectrometer: the GEANT program has been used to study the distortion of the correlation function due to the granularity of the Plastic Ball detector [0.15, 0.10 fm].
(vi) The bin width of the correlation function: to examine the dependence of the radius parameters on the q bin width, the analysis was also performed with bin widths of 10 MeV/c and 5 MeV/c [0.06, 0.06 fm].
(vii) Detector variation: the analysis was performed separately in two different azimuthal angle intervals: $0^\circ - 180^\circ$ and $180^\circ - 360^\circ$ [0.01, 0.02 fm].
(viii) The effect of possible mis-identification of protons and deuterons due to the multiple hits to the same Plastic Pall module. Since the multi-hit probability depends very strongly on θ, the analysis was performed with two subsamples with θ intervals of protons and deuterons: $60^\circ - 90^\circ$ and $90^\circ - 160^\circ$. The ratio of contaminations due to multi-hits in these θ intervals is about 10:1. The GEANT simulations also demonstrated that the contamination from spurious protons and deuterons contribute uniformly to their correlation functions. As a result, this background contamination does not affect the shape of the correlation function, leading to the same, within errors, radius parameters [0.15, 0.10 fm].

The total systematic uncertainty was calculated by adding in quadrature the contributions listed above.

3.3 Two-proton system

The measured two-proton correlation function is shown in Fig. 4. The solid line represents the result of the theoretical calculation which gives the best fit to the data using the delta-shell potential. The final state Coulomb and strong interactions, the Fermi-Dirac effect, and the experimental resolution have been implemented in the theoretical calculation. The resulting radius parameter is 3.14$\pm$ 0.03(stat.)$\pm$ 0.21(syst.) fm.

Although the delta-shell potential may not be realistic, its main advantage is that both the phase shift and the enhancement factor can be obtained in an analytic form. Furthermore, it is desirable to use the same model for calculation of both proton and deuteron correlation functions. It was demonstrated in [29] that the calculated pp phase shifts as obtained from both the delta-shell potential and the REID soft core potential [30]

agree well with the experimental data, up to about 150 MeV/c. As a cross check, the REID potential was also used to fit the experimental two-proton correlation function. The resulting correlation function is shown in Fig. 4 as the dashed line. The fitted radius parameter is 3.05 $\pm$ 0.02(stat.)$\pm$ 0.24(syst.) fm which, within errors, is consistent with the delta-shell potential calculation. The calculated two-proton correlation functions without Coulomb interaction and without any final state interactions are also shown in Fig. 4 as the dotted and dot-dashed lines, respectively.

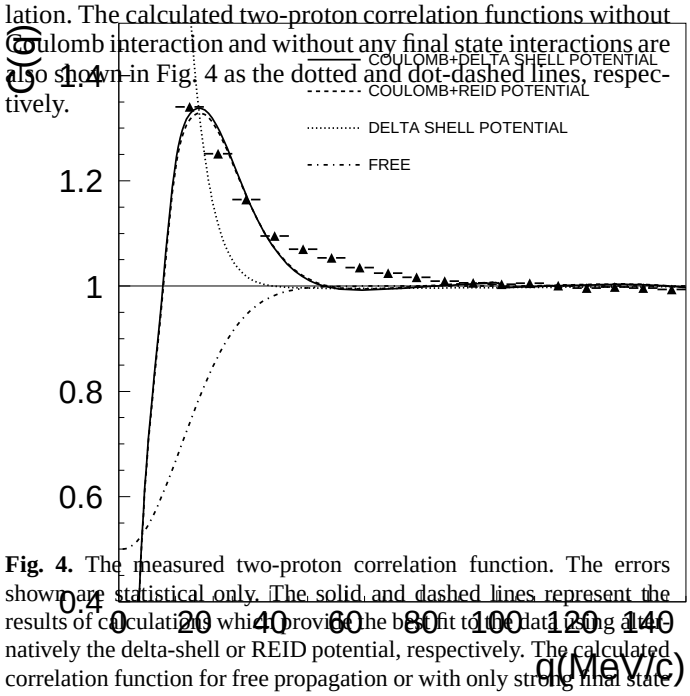

Fig. 4. The measured two-proton correlation function. The errors shown are statistical only. The solid and dashed lines represent the results of calculations which provide the best fit to the data using alternatively the delta-shell or REID potential, respectively. The calculated correlation function for free propagation or with only strong final state interaction included are shown as dot-dashed and dotted lines.

In order to make a direct comparison with other experimental results, the CRAB package [27], provided by Pratt, was also used to extract the radius parameter for the two-proton system. The CRAB calculation takes into account the Coulomb and strong final state interactions. To describe the latter for the two-proton system the REID potential was taken. The measured momentum distribution of protons was used as input to the CRAB calculation. To obtain a radius parameter, the calculation was performed for a set of different radius parameters and then compared to the experimental data by calculating the χ^2 value. This gave a best fit radius parameter of 2.83 ± 0.20 fm, that is consistent, within errors, with the delta-shell model calculation. The CRAB calculation result is shown in Fig. 5. The experimental correlation as a function of q_{inv} is also shown in Fig. 5 with the CRAB calculation. The solid and dashed lines represent the CRAB calculations with and without the experimental resolution effect included, respectively.

The polar angle (or rapidity) dependence of the proton source radius parameter was also investigated. Within errors, the two-proton source radius, R_0 showed no rapidity dependence, as seen from Fig. 6, over the entire polar angle interval.

Two-proton correlations have also been studied in the target fragmentation region at the SPS in the WA80 experiment using the Plastic Ball spectrometer. Measurements were made with 200 A GeV proton, Oxygen, and Sulphur projectiles, on targets of C, Al, Ag, and Au [11]. The source radius extracted from the present analysis of the two-proton correlation for central Pb+Pb collisions at 158 A GeV is compared to the radius

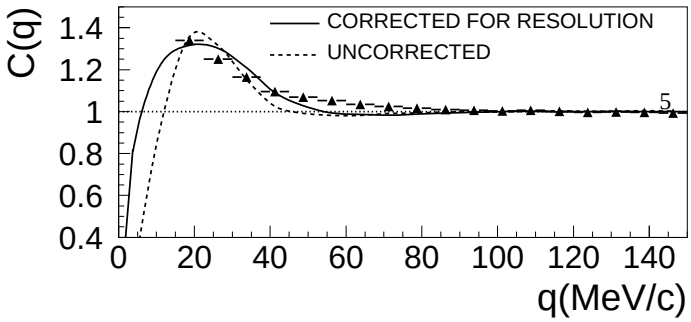

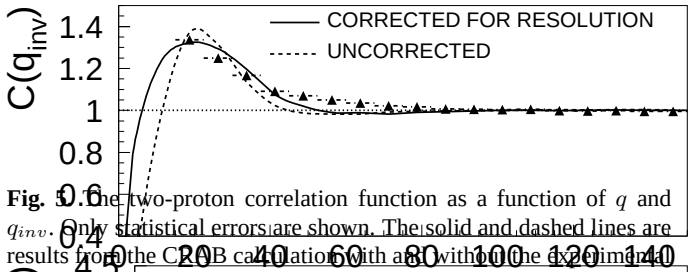

Fig. 5. The two-proton correlation function as a function of q and q_{inv}. Only statistical errors are shown. The solid and dashed lines are results from the CRAB calculation with and without the experimental resolution applied, respectively.

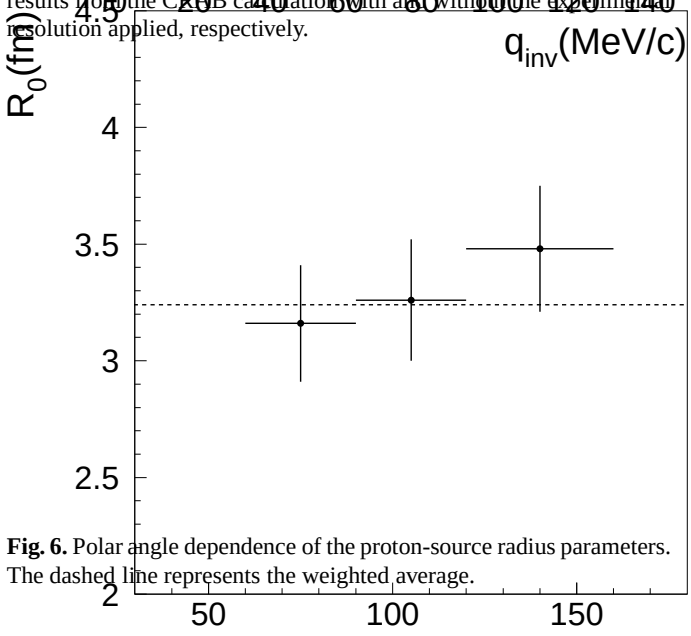

Fig. 6. Polar angle dependence of the proton-source radius parameters. The dashed line represents the weighted average.

parameters extracted in the WA80 experiment in Fig. 7. The radius parameters are plotted as a function of $A^{1/3}_{\rm Target}$. All radii have been converted to root-mean-square radii. Within errors, the radius parameters measured in the WA80 and WA98 experiments at the SPS closely follow the target nuclear radius dependence of $A^{1/3}_{Target}$ with little apparent dependence on the projectile mass. Since the size of the participant overlap region depends on both target and projectile mass, the observation of little projectile mass dependence indicates that the protons detected in the target fragmentation region are emitted from the entire target volume, following substantial rescattering [11].

3.4 Two-deuteron system

Figure 8 shows the measured two-deuteron correlation function and the theoretical calculation which gives the best fit to the data. The solid and dashed line represent the correlation functions calculated with final state interaction taken into account and that for free propagation. The fitted radius parameter is 1.59$\pm$ 0.02(stat.)$\pm$ 0.20(syst.) fm. The range R and the strength s for the delta-shell potential are found to be 0.52 ± 0.01 fm and 1.08 ± 0.01, respectively. The measured two-deuteron

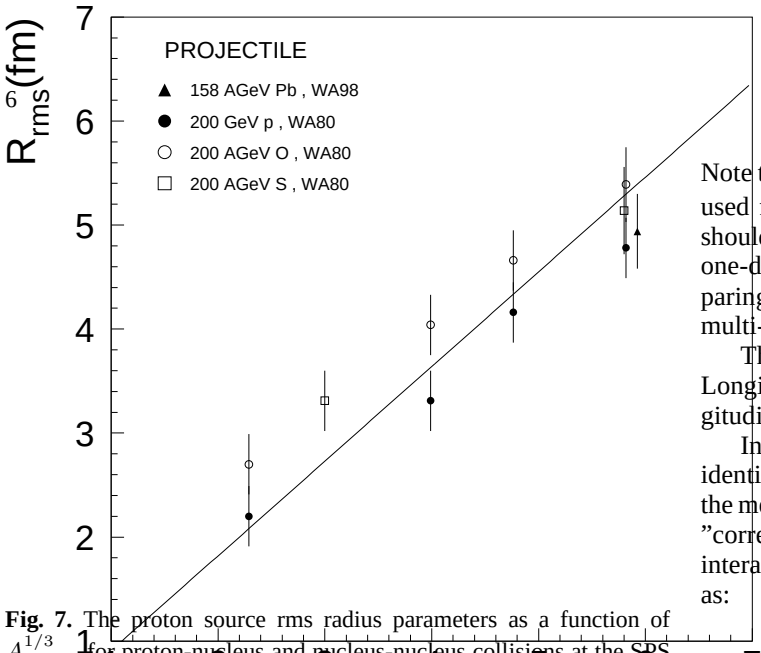

Fig. 7. The proton source rms radius parameters as a function of $A^{1/3}_{\rm Target}$ for proton-nucleus and nucleus-nucleus collisions at the SPS from this measurement and from the WA80 experiment [11]. The protons have been measured in the target fragmentation region with -0.6 $< y <$0.6 and 100 MeV/c $< p_T <$ 650 MeV/c . The symbols are slightly displaced for the Au and Pb target points for clarity. The line represents the fitted function $R_{rms} = aA^{1/3}_{\rm Target}(a = 0.91 \pm 0.02, \chi^2/n = 1.68)$. The WA98 experimental result was obtained using the CRAB code.

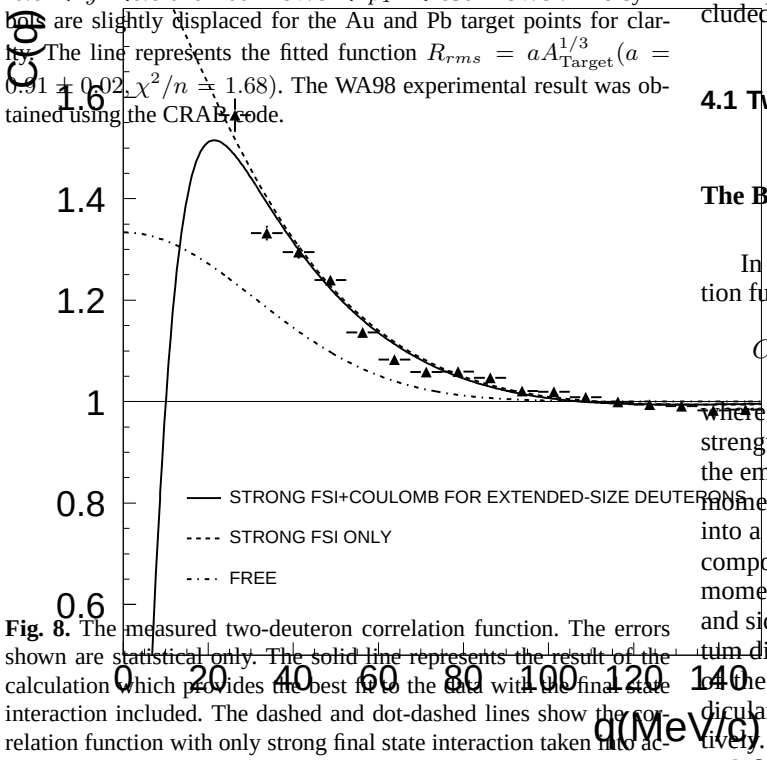

Fig. 8. The measured two-deuteron correlation function. The errors shown are statistical only. The solid line represents the result of the calculation which provides the best fit to the data with the final state interaction included. The dashed and dot-dashed lines show the correlation function with only strong final state interaction taken into account and that for free propagation, respectively.

correlation and extracted radius parameters show no dependence on the polar angle, similar to observations for the two-proton correlation (see Fig. 6).

4 Multi-dimensional analysis

For consistency of notation with previous analyses, the momentum difference $\mathbf{Q} = (\mathbf{p}_1 - \mathbf{p}_2)$ is used in the multi-dimensional analysis. In this case the two-particle correlation $C(Q)$ is given by:

$$C(Q) = 1 + \tilde{\rho}(Q)^2. \quad (8)$$

Note that since the correlation function $C(q) = 1 + \tilde{\rho}(2q)^2$ was used for the calculations presented in section 3, a factor $\sqrt{2}$ should be applied to the radius parameters obtained from the one-dimensional analysis results presented above when comparing with the radius parameters obtained from the following multi-dimensional analysis.

The multi-dimensional analysis has been performed in the Longitudinally CoMoving System (LCMS), in which the longitudinal pair momentum vanishes ($\mathbf{p}_{z1} + \mathbf{p}_{z2} = 0$).

In order to extract that part of the correlation function of identical particles that is due to quantum statistical effects only, the measured multi-dimensional correlation functions have been "corrected" for the effect of the strong and Coulomb final state interactions (FSI). The corrected correlation function is defined as:

$$C(p_1, p_2) = K\, C_{raw}(p_1, p_2) \quad (9)$$

where $K = C_{FREE}(Q)/C_{FSI}(Q)$ is the correction factor, and $C_{FREE}(Q)$ and $C_{FSI}(Q)$ are the calculated correlation functions for free propagation and with final state interactions included, respectively.

4.1 Two-proton system

The Bertsch-Pratt (BP) parametrization

In the Bertsch-Pratt parameterization [31,32], the correlation function for two fermions has the form:

$$C = N\left(1 - \lambda \mathrm{e}^{-Q_l^2 \cdot R_l^2 - Q_s^2 \cdot R_s^2 - Q_o^2 \cdot R_o^2 - 2 \cdot Q_o Q_l \cdot R_{ol}^2}\right) \quad (10)$$

where N is the normalization constant and $0 \leq \lambda \leq 1$ is the strength of the correlation which depends on the chaoticity of the emitter and on the purity of the measured data sample. The momentum difference vector $\mathbf{Q}$ of two particles is decomposed into a longitudinal component along the beam axis (Q_l) and a component transverse to the beam axis (Q_T). The transverse momentum difference is further decomposed into the outward and sideward components. The outward and sideward momentum differences (Q_o) and (Q_s) are defined as the components of the transverse momentum difference parallel and perpendicular to the total transverse momentum of the pair, respectively. The sign convention is that Q_s is always positive, Q_l and Q_o are allowed to be positive or negative. R_{ol}^2 is the "out-longitudinal" cross term [33]. Its value can be either positive or negative. In the LCMS system the average resolutions in the Q_s, Q_l, and Q_o components for the pp system are 20, 23, and 24 MeV/c, respectively.

Figure 9 shows projections of the measured two-proton correlation functions, corrected for final state interactions (Eq. (9)), onto the Q_l, Q_s, and Q_o axes. Also shown are the corresponding projections of the fit of Eq. (10), shown as solid lines. The projected results and the fit results for a given Q component have been integrated up to 75 MeV/c over the other two $|Q|$ components.

The parameters extracted from fits to the data using either the delta-shell corrected and CRAB corrected correlation functions are presented in Table 1. Also listed in this table are the

Table 1. Fitted parameters of the Bertsch-Pratt parametrization of the two-proton correlation function using the delta-shell model or CRAB model final state interaction calculations. Errors are statistical + systematic.

	Delta-shell Model (with cross term)	Delta-shell Model (without cross term)	CRAB Model (with cross term)	CRAB Model (without cross term)
λ	0.76±0.02±0.04	0.76±0.02±0.04	0.78±0.02±0.04	0.79±0.03±0.04
R_l(fm)	4.61±0.06±0.49	4.58±0.06±0.47	4.94±0.07±0.42	4.94±0.08±0.39
R_s(fm)	4.43±0.07±0.45	4.47±0.08±0.44	4.81±0.08±0.41	4.78±0.08±0.44
R_o(fm)	5.46±0.10±0.59	5.48±0.09±0.57	5.64±0.12±0.36	5.70±0.14±0.42
R^2_{ol}(fm^2)	-1.65±0.54±0.52		6.47±0.49±0.64	
χ^2/ndf	1.36	1.36	1.38	1.38

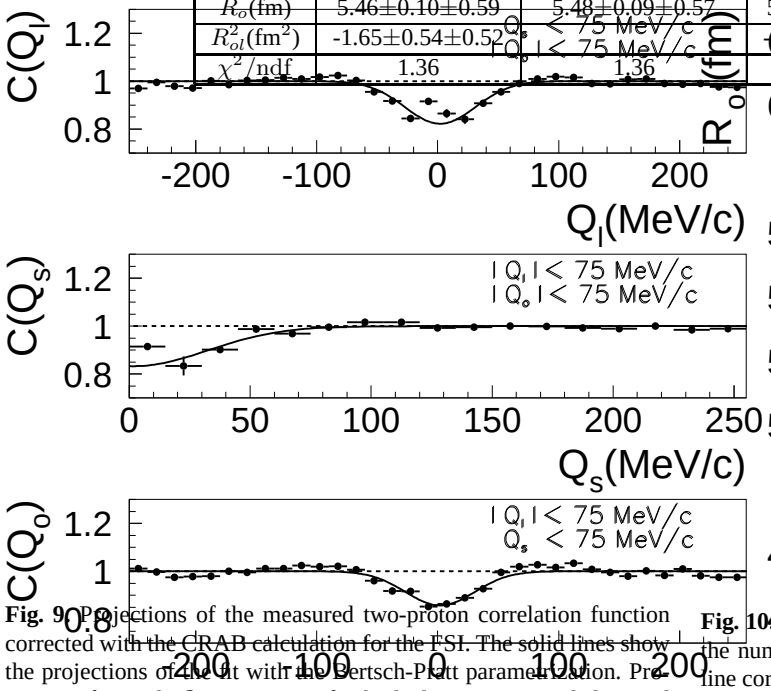

Fig. 9. Projections of the measured two-proton correlation function corrected with the CRAB calculation for the FSI. The solid lines show the projections of the fit with the Bertsch-Pratt parametrization. Projections for each Q component, for both the experimental data and the fit, have been integrated up to 75 MeV/c over the other two $|Q|$ components. The errors shown are statistical only.

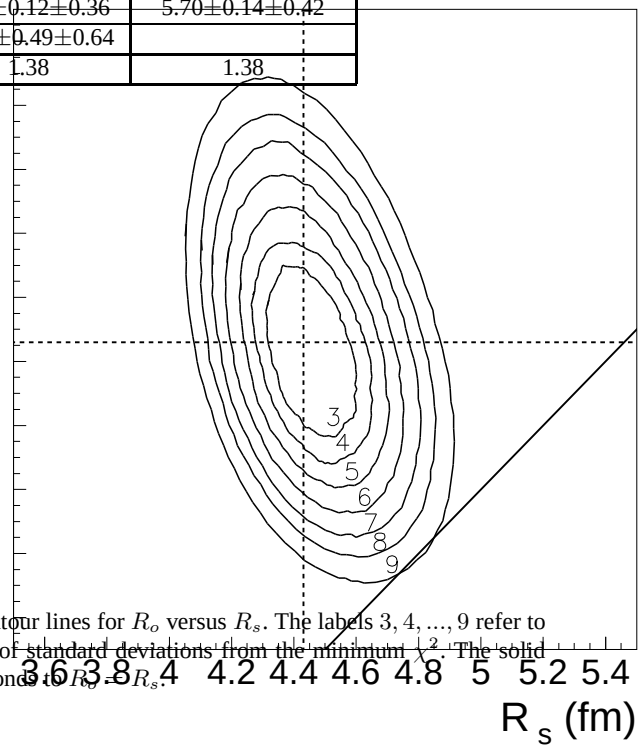

Fig. 10. Contour lines for R_o versus R_s. The labels $3, 4, ..., 9$ refer to the number of standard deviations from the minimum χ^2. The solid line corresponds to $R_o = R_s$.

fitted parameters without the cross term R^2_{ol}. Within errors, the delta-shell and CRAB corrections lead to the same values of fitted parameters. The fitted radius parameters with and without the cross term do not differ within errors. The cross term R_{ol} vanishes in the LCMS frame for longitudinally *boost-invariant* systems. The observation that the cross-term R^2_{ol} is small, indicates that the proton source undergoes an approximate boost invariant expansion.

The statistical significance of the fit is demonstrated in Fig. 10, where contour lines of equal confidence level for R_o versus R_s are plotted. The spacing of contours corresponds to one standard deviation in χ^2 value. The solid line, which represents equal sideward and outward radii, is 9 standard deviations from the minimum χ^2 value.

For transparent sources, where particles are emitted from throughout the entire volume, the longitudinal radius R_l is interpreted to measure the longitudinal size of the system directly, while the sideward radius provides a measurement of the transverse size. The duration of emission $\Delta\tau$ is related [34,35] to the sideward radius R_s and outward radius R_o as:

$$\Delta\tau = \frac{1}{\beta_T}\sqrt{R_o^2 - R_s^2}, \qquad (11)$$

where β_T is the transverse velocity of the particle pair. Notice that Eq. (11) is valid only when opacity effects and transverse flow are ignored. The excess of R_o over R_s is due to the duration of emission from the source in which particles with transverse velocity β_T travel a distance $\beta_T\Delta\tau$ towards the detector, resulting in an apparent extension of the source in that direction. The sideward radius parameter R_s is not affected by the duration of emission since it is perpendicular to β_T.

Within errors, the radius parameters (R_l, R_s, R_o) of the BP fit are quite close to each other (Table 1) which suggests a volume emission of the protons. The extracted R_o and R_s parameters, and the measured average value of $\beta_T = 0.278 \pm 0.09$ for the proton pairs, gives 11.5 ± 2.5 fm/c as an estimate of the emission duration.

In the case of a Bjorken scenario, with longitudinal expansion of the system without transverse flow, the m_T dependence of the longitudinal radius reflects the lifetime of the source[36]:

$$R_l = \tau_f (T_f/m_T)^{1/2}, \qquad (12)$$

where T_f is the freeze-out temperature and $m_T = \sqrt{m^2 + p_T^2}$. Under the assumption that $T_f = 120$ MeV, a source lifetime of about 13 fm/c is obtained.

Strictly speaking, the interpretation of τ_f as the freeze-out time is based on the assumption that the longitudinal boost-invariant velocity profile existed not only at the time of freeze-out but also throughout the dynamical evolution of the reaction

zone. If this were not the case, then τ_f would be larger. Hence, τ_f estimated by Eq. (12) gives a *lower* limit for the lifetime of the source [1].

The Yano-Koonin-Podgoretsky (YKP) parametrization

In the Yano-Koonin-Podgoretsky parameterization[37,38], the two-proton correlation function is defined by the formula:

$$C = N\left(1 - \lambda \mathrm{e}^{-Q_T^2 R_T^2 - (Q_l^2 - Q_0^2) R_l^2 - (Q\cdot U)^2 (R_0^2 + R_l^2)}\right) \quad (13)$$

where $U = \gamma(1, 0, 0, \beta)$ is a 4-velocity with only a longitudinal component, $\gamma = 1/\sqrt{1-\beta^2}$, Q_T and Q_l are the components of the momentum difference projected onto the transverse and longitudinal directions, respectively, Q_0 is the difference in energies. The sign convention is Q_0 is always positive and Q_l can be either positive or negative. This parametrization has an advantage in that the three YKP radius parameters do not depend on the longitudinal velocity of the measurement frame, and the velocity β is closely related to the velocity of the effective particle emitter.

The parameters extracted from YKP fits to the delta-shell corrected or CRAB corrected correlation functions are listed in Table 2. Within errors, the fitted parameters obtained with the two different final state interaction corrections are consistent with each other.

Table 2. Fitted parameters of the YKP parametrization of the two-proton correlation functions using either the delta-shell model or CRAB model FSI corrections. Errors are statistical + systematic.

	Delta-shell Model	CRAB Model
λ	0.75±0.04±0.04	0.77±0.03±0.03
R_l(fm)	4.64±0.16±0.36	4.97±0.08±0.46
R_T(fm)	4.42±0.13±0.40	4.73±0.06±0.46
R_0(fm)	10.54±0.46±1.18	10.58±0.46±1.12
β	0.032±0.023±0.010	0.036±0.014±0.011
χ^2/ndf	1.42	1.47

Since the YKP velocity β is close to 0, it demonstrates that the LCMS frame coincides with the YK frame (the frame for which the YKP velocity parameter β vanishes). For *transparent sources*, and in the absence of flow, the radius parameters in the YK frame have a convenient physical interpretation. R_l and R_T are then interpreted as measures of the longitudinal and transverse size of the source, while R_0 reflects directly the duration of emission from the source.

With similar fitted R_l and R_T parameters, and longitudinal velocity β compatible with 0, the YKP fit indicates a symmetric emission geometry with approximate boost invariant expansion of the source. The emission duration extracted from the YKP or BP fits are in agreement within errors.

The fitted YKP parameters are seen to be consistent with the BP parameters. Since the BP and YKP parametrizations are mathematically equivalent and differ only in the choice of independent components of q, the agreement between the two sets of fitted parameters serves additionally as a consistency check of the fitting procedures.

4.2 Two-deuteron system

The Gaussian parametrization in the LCMS

Fig. 11 shows the experimental one-dimensional two-deuteron correlation function in the LCMS frame, after correction for final state interactions using the delta-shell model described in section 3. The correlation is fitted to the Gaussian correlation function:

$$C(Q) = N\left(1 + \lambda \mathrm{e}^{-Q^2 R^2}\right). \quad (14)$$

The fitted parameters are: $\lambda = 0.43\pm0.03$(stat.)±0.08(syst.), $R = 2.50\pm0.10$(stat.)±0.28(syst.) fm. The radius parameter is in agreement within errors with the radius ($R = 1.59 \times \sqrt{2} = 2.25$ fm) extracted by fit to the one-dimensional correlation function with the full delta-shell model calculation (see Fig. 8).

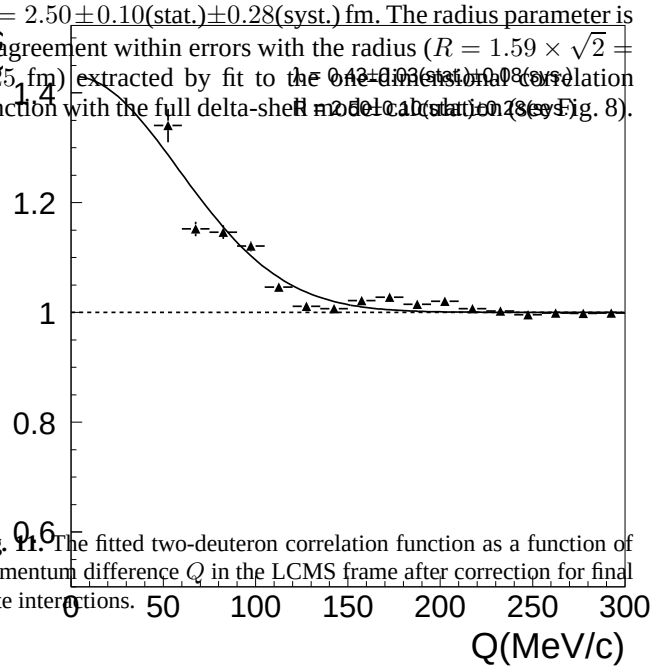

Fig. 11. The fitted two-deuteron correlation function as a function of momentum difference Q in the LCMS frame after correction for final state interactions.

The Bertsch-Pratt parametrization

The two-deuteron correlation function has been corrected by the calculated delta-shell model two-deuteron final state interaction and fitted with the two-boson correlation function using the Bertsch-Pratt parametrization:

$$C = N\left(1 + \lambda \mathrm{e}^{-Q_l^2\cdot R_l^2 - Q_s^2\cdot R_s^2 - Q_o^2\cdot Q_o^2 - 2\cdot Q_o Q_l \cdot R_{ol}^2}\right). \quad (15)$$

Projections of the measured two-deuteron correlation function on the Q_l, Q_s, and Q_o axes are shown in Fig. 12. The measured and fitted projections in a given Q component have been integrated up to 75 MeV/c in the other two $|Q|$ components. All Q components have approximately the same average resolution of 32 MeV/c.

The fitted parameters, with and without the cross term R_{ol}^2, are listed in Table 3. Within errors, the values of parameters extracted from the two different fits are the same. Similar to the result for the proton source, the small cross-term indicates that the deuteron source also experienced an approximate boost invariant expansion.

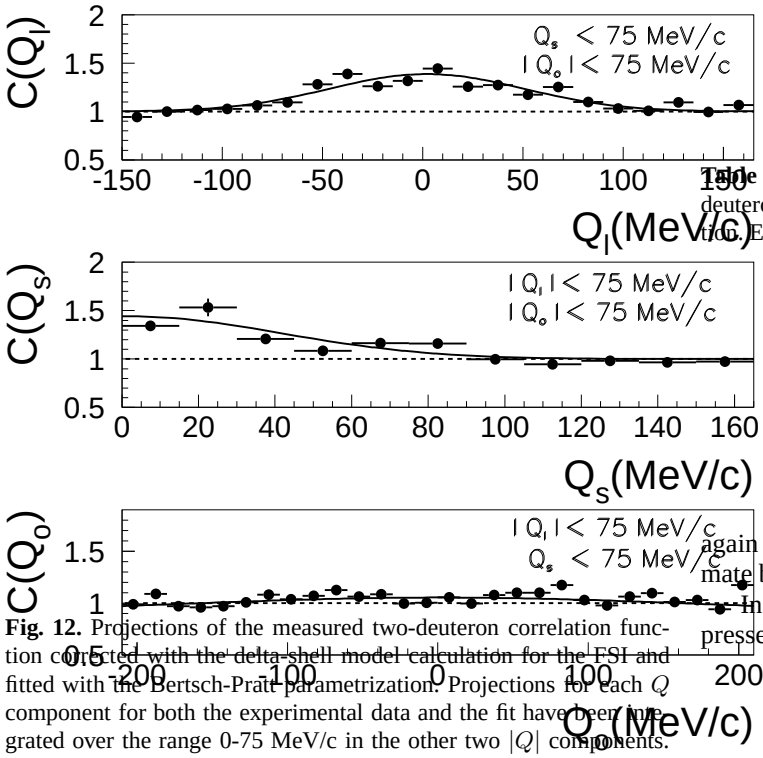

Fig. 12. Projections of the measured two-deuteron correlation function corrected with the delta-shell model calculation for the FSI and fitted with the Bertsch-Pratt parametrization. Projections for each Q component for both the experimental data and the fit have been integrated over the range 0-75 MeV/c in the other two $|Q|$ components. The errors shown are statistical only.

Table 3. Fitted parameters of the Bertsch-Pratt parametrization of the two-deuteron correlation functions using the delta-shell model FSI correction. Errors are statistical + systematic.

	with cross term	without cross term
λ	0.37±0.02±0.19	0.37±0.02±0.19
R_l(fm)	2.17±0.10±0.24	2.13±0.08±0.18
R_s(fm)	3.14±0.11±0.78	3.10±0.10±0.67
R_o(fm)	0.01±0.08±0.02	0.01±0.04±0.03
R^2_{ol}(fm^2)	0.20± 0.08 ±0.69	
χ^2/ndf	1.52	1.52

Within errors, the fitted R_l and R_s parameters are close to the radius value obtained from the one-dimensional fit, while R_o is consistent with 0. For a transparent, azimuthally symmetric emission source, it is expected that R_s and R_o should be similar, except that R_o will be extended by the duration of emission, as discussed with respect to Eq. (11). The observation that $R_o << R_s$ is inconsistent with such a transparent source, but may result naturally from surface emission from an opaque source [39,40]. Since deuterons are relatively large weakly bound objects, it might be expected that only those deuterons produced on the freeze-out surface via coalescence of an emitted proton and neutron survive. This would naturally lead to an opaque emission source, as observed.

The Yano-Koonin-Podgoretsky parametrization

The two-boson correlation function in the Yano-Koonin-Podgoretsky parametrization is given by:

$$C = N\left(1+\lambda \mathrm{e}^{-Q_T^2R_T^2-(Q_l^2-Q_0^2)R_l^2-(Q\cdot U)^2(R_0^2+R_l^2)}\right). \quad (16)$$

The parameters of the YKP fit to the two-deuteron correlation are listed in Table 4. The longitudinal velocity β is close to 0 indicating that the LCMS coincides with the YK frame and again indicates that the deuteron source undergoes an approximate boost invariant expansion.

Table 4. Fitted parameters of the YKP parametrization of the two-deuteron correlation functions using the delta-shell model FSI correction. Errors are statistical + systematic.

λ	0.29±0.02±0.09
R_l(fm)	1.29±0.07±0.42
R_T(fm)	2.35±0.05±0.39
R^2_0(fm^2)	-46.95±1.69±8.82
β	0.020±0.002±0.007
χ^2/ndf	1.42

In the YK frame the YKP radius parameter R_0 can be expressed as [41]:

$$R_0^2 = \frac{1}{\beta_\perp^2}\left(R_o^2 - R_s^2\right), \quad (17)$$

where $\beta_\perp$ is the velocity of the particle pair transverse to the beam direction, and R_o and R_s are the outward and sideward radii of the BP parametrization. The negative value of $R_0^2 \approx -47$ fm^2 obtained from the YKP fit is in agreement with the observation of strong opacity [1,39,42] of the deuteron source made in the previous section.

5 Discussion

Although one does not necessarily expect boost-invariance in the target fragmetnation region at SPS energies, the small values of the cross-term R_{ol} in the BP parametrization as well as the consistency with zero longitudinal velocity β in the YKP parametrization of the correlation functions, indicates that both proton and deuteron sources exhibit boost-invariant expansion.

The measured one-dimensional radius parameter extracted for protons is markedly larger than that for deuterons. Comparison of the present results for protons and deuterons with those for π^+, also measured in the Plastic Ball [43], and π^- measured in the WA98 negative-charged particle spectrometer [44,45], and with K^+ measured in the NA44 experiment [46] for central Pb+Pb collisions at 158 A GeV, reveals that the radii are observed so show a mass ordering with $R_{\pi\pi} > R_{\mathrm{KK}} > R_{\mathrm{pp}} > R_{\mathrm{dd}}$. This observation is in agreement with previous reports [47] that lighter particles tend to give larger radius parameters. It is interesting that a large loosely bound composite object like the deuterons follows the same trend as observed for elementary particles. It has been shown by Alexander [47,48] that the source-size mass dependence of hadrons emerging from Z^0 decays produced in e^+e^- annihilation can be reproduced using the Heisenberg uncertainty relations to derive the relations:

$$R = \frac{A}{\sqrt{m}}, \quad (18)$$

and

$$R_l = \frac{A}{\sqrt{m_T}}, \quad (19)$$

where $A = c\sqrt{\hbar \Delta t}$ is a time scale constant, R_l is the longitudinal radius parameter, and m and m_T are the mass and the mean transverse mass, respectively. An alternative explanation using a QCD derived potential [47] proved to be equally successful. A different approach to explain the R and R_l mass dependence was given by Bialas and Zalewski [49,50,51]. In this description the radius parameter of the source is mass independent and its apparent decrease is a consequence of the momentum-position correlation expressed in the Bjorken-Gottfried condition [52,53]. However, a study of purely kinematical considerations [54] led to the conclusion that this is unlikely to account for the observed $R(m)$ dependence.

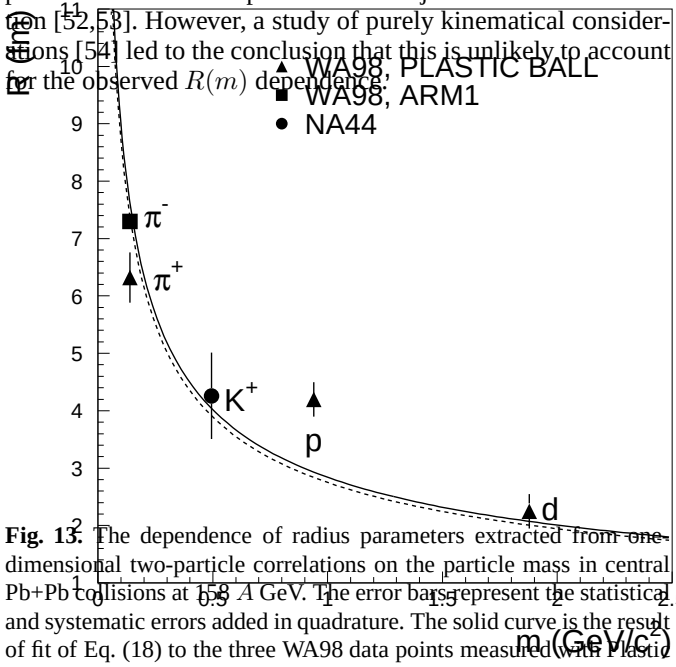

Fig. 13. The dependence of radius parameters extracted from one-dimensional two-particle correlations on the particle mass in central Pb+Pb collisions at 158 A GeV. The error bars represent the statistical and systematic errors added in quadrature. The solid curve is the result of fit of Eq. (18) to the three WA98 data points measured with Plastic Ball spectrometer. The dashed curve includes also the π^- data from WA98 and kaon data from the NA44 experiment.

Radius parameters extracted from one-dimensional two-particle correlation functions for central Pb+Pb collisions at 158 A GeV are shown as a function of the particle mass in Fig. 13. The $\pi^-\pi^-$ radius parameter was measured with the negative-charged particle spectrometer of the WA98 experiment [44,45] and the two-kaon radius parameter was reported by the NA44 Collaboration [46], both measured near mid-rapidity $\langle y \rangle \sim 2.9$. In general, the radii follow the $\sqrt{m}$ dependence expectation of Eq. (18). A fit of Eq. (18) to the π^+ [43], proton, and deuteron radii measured with the WA98 Plastic Ball gives $A = 2.84 \pm 0.13$ fm GeV$^{1/2}$ with χ^2/ndf = 12, as shown by the solid curve. This corresponds to a time scale of $\Delta t = 40.8$ fm/c using the above expression for A, or to a freeze-out lifetime of $\tau_f = 8.2$ fm/c using Eq. (12). A fit to all data points (dashed line) results in $A = 2.75 \pm 0.04$ fm GeV$^{1/2}$ with χ^2/ndf = 7.2.

Previous results on pion and kaon interferometry for S+Pb and Pb+Pb reactions at the SPS have demonstrated scaling of the R_l and R_T radius parameters on the transverse mass, m_T [55,56]. The longitudinal and transverse radius parameters from the multi-dimensional YKP analysis of the two-proton and two-deuteron correlation functions are plotted as a function of the mean transverse mass in Figs. 14 and 15. Also shown are radius parameters for π^+ measured with the Plastic Ball [43]. Radii measured near mid-rapidity for π^- in WA98 [44,45], and for kaons from the NA44 [56] and NA49 [57] experiments are also shown. The

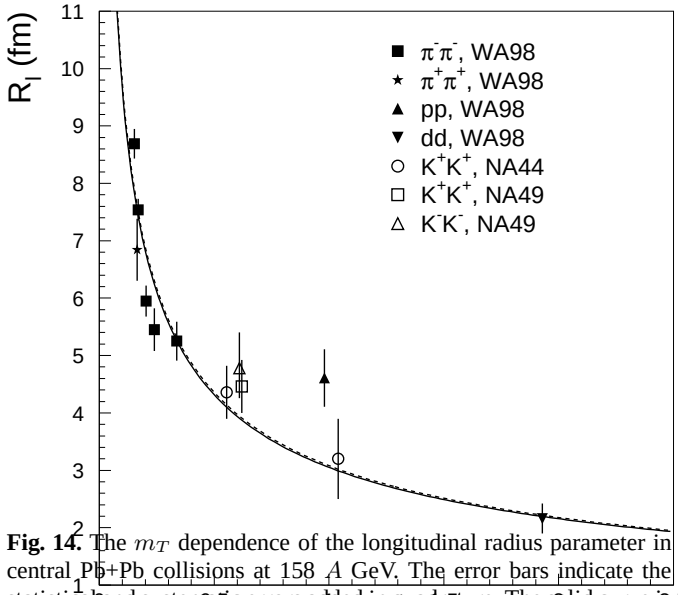

Fig. 14. The m_T dependence of the longitudinal radius parameter in central Pb+Pb collisions at 158 A GeV. The error bars indicate the statistical and systematic errors added in quadrature. The solid curve is the result of a fit of $R = A/\sqrt{m_T}$ to the WA98 data points measured with the Plastic Ball spectrometer, while the dashed curve includes also mid-rapidity π^- data from WA98 and kaon data from the NA44 and NA49 experiments.

data are compared to fits of the form $R_i = A_i/\sqrt{m_T}$, where $i = l, T$. As can be seen from Figs. 14 and 15, within experimental uncertainties, the fitted R_l and R_T radius parameters are consistent with $A/\sqrt{m_T}$ scaling. A fit to the three WA98 data points measured near mid-rapidity with the Plastic Ball spectrometer yields $A_l = 3.05 \pm 0.17$ fm GeV$^{1/2}$ with χ^2/ndf = 3.6. When all data points are included in the fit, the fit yields $A_l = 3.08 \pm 0.05$ fm GeV$^{1/2}$ with χ^2/ndf = 3.4.

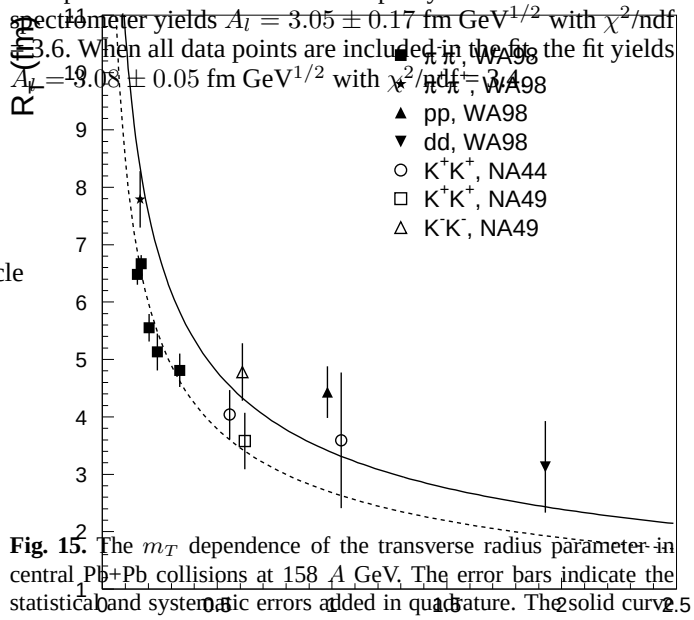

Fig. 15. The m_T dependence of the transverse radius parameter in central Pb+Pb collisions at 158 A GeV. The error bars indicate the statistical and systematic errors added in quadrature. The solid curve is a fit of $R_T = A/\sqrt{m_T}$ to the WA98 data points measured with the Plastic Ball spectrometer only, while the dashed curve includes also mid-rapidity π^- data from WA98 and kaon data from the NA44 and NA49 experiments.

Although there is no theoretical justification to expect an R_T=$A/\sqrt{m_T}$ dependence, the data are seen (Fig. 15) to follow such a dependence, within errors. A fit to the three WA98 data points measured near mid-rapidity with the Plastic Ball spectrometer yields $A_T = 3.38 \pm 0.18$ fm GeV$^{1/2}$ with χ^2/ndf = 2.4 When all data points are included in the fit, the fit yields $A_T = 2.68 \pm 0.04$ fm GeV$^{1/2}$ with χ^2/ndf = 3.3. A fit to the

pion and kaon data from NA44 experiment alone gave $A_T = 3.0 \pm 0.2$ fm GeV$^{1/2}$ [56].

6 Summary

In summary, we have measured two-proton and two-deuteron correlation functions in the target fragmentation region for central Pb+Pb collisions at 158 A GeV.

In the one-dimensional analysis, the radius parameters were extracted from the measured correlations using calculations that assume a static Gaussian-shaped source. The extracted proton source radius parameter is about two times larger than that of the deuteron source. Comparison of the proton and deuteron radius parameters with those extracted from one-dimensional two-pion and two-kaon correlations reveals a common $A/\sqrt{m}$ dependence with $A \approx 3$ fm GeV$^{1/2}$. Such a dependence can be explained as a consequence of the Heisenberg uncertainty relations, under the assumption of a common duration of emission.

The multi-dimensional analysis demonstrates that the proton source exhibits a volume emission with long emission time, whereas the deuteron source is strongly opaque. The cross-term R_{ol}^2 from the Bertsch-Pratt parametrization fit and the longitudinal velocity β from the Yano-Koonin-Podgoretsky parametrization fit are consistent with zero, suggesting that the proton and deuteron sources undergo an approximate longitudinal boost invariant expansion.

The longitudinal and transverse radius parameters, R_l and R_T, extracted from the multi-dimensional correlation analysis follow a common $A/\sqrt{m_T}$ scaling for pions, kaons, protons, and deuterons, with $A \approx 3$ fm GeV$^{1/2}$ in both cases. The existence of a universal function describing the dependence of the radius parameters on the transverse mass for different particle species in the mass interval from pion to deuteron may indicate an approximately simultaneous freeze-out of the studied hadrons.

We wish to express our gratitude to Professor A. Deloff for supplying his codes for the pp and dd FSI calculations, and for his guidance and helpful discussions. We wish to thank the CERN accelerator division for the excellent performance of the SPS accelerator complex. We acknowledge with appreciation the effort of all engineers, technicians, and support staff who have participated in the construction of this experiment. This work was supported jointly by the German BMBF and DFG, the U.S. DOE, the Swedish NFR and FRN, the Dutch Stichting FOM, the Polish MEiN under Contract No. 1P03B02230 and CERN/88/2006 The Grant Agency of the Czech Republic under contract No. 202/95/0217, the Department of Atomic Energy, the Department of Science and Technology, the Council of Scientific and Industrial Research and the University Grants Commission of the Government of India, the Indo-FRG Exchange Program, the PPE division of CERN, the Swiss National Fund, the INTAS under Contract INTAS-97-0158, ORISE, Grant-in-Aid for Scientific Research (Specially Promoted Research & International Scientific Research) of the Ministry of Education, Science and Culture, the University of Tsukuba Special Research Projects, and the JSPS Research Fellowships for Young Scientists. ORNL is managed by UT-Battelle, LLC, for the U.S. DOE under contract DE-AC05-00OR22725. The MIT group has been supported by the U.S. Dept. of Energy under the cooperative agreement DE-FC02- 94ER40818.

References

1. U.A. Wiedemann and U. Heinz, Phys. Rep. **319** (1999) 145 and references therein.
2. L.P. Csernai and J.I. Kapusta, Phys. Rep. **131** (1986) 223.
3. A. Pollieri et al., Phys. Lett. B **419** (1998) 19.
4. A. Pollieri et al., Phys. Lett. B **473** (2000) 193.
5. D. Fox et al., Phys. Rev. C **38** (1988) 146.
6. W.G. Gong et al., Phys. Rev. C **43** (1991) 1804.
7. D.A. Cebra et al., Phys. Lett. B **227** (1989) 336.
8. R. Kotte et al., Z. Phys. A **359** (1997) 47.
9. J. Bartke et al., Z. Phys. A **324** (1986) 471.
10. G.N. Agakishev et al., Z. Phys. A **327** (1987) 443.
11. T.C. Awes et al., Z. Phys. C **65** (1995) 207.
12. H. Boggild et al., Phys. Lett. B **458** (1999) 181.
13. H. Appelshäuser et. al., Phys. Lett. B **467** (1999) 21.
14. H.A. Gustafsson et al., Phys. Rev. Lett. **53** (1984) 544.
15. D.H. Boal et al., Rev. Mod. Phys. **62** (1990) 553.
16. Z. Chen et al., Phys. Rev. C **36** (1987) 2297.
17. J. Pochodzalla et al., Phys. Rev. C **35** (1987) 1695.
18. J. Pochodzalla et al., Phys. Lett. B **175** (1986) 275.
19. W.G. Lynch et al., Phys. Rev. Lett. **51** (1983) 1850.
20. T.C. Awes et al., Phys. Rev. Lett. **61** (1988) 2665.
21. C.B. Chitwood et al., Phys. Rev. Lett. **54** (1985) 302.
22. H. Gutbrod et al., *Proposal for a Large Hadron and Photon Spectrometer*, Report CERN/SPSLC 91-17, SPSLC/P260.
23. T.C. Awes et al., Nucl.Instr.Meth. A **279** (1989) 479.
24. G.R. Young et al., Nucl. Instr. Meth. A **279** (1989) 503.
25. A. Baden et al., Nucl.Instr.Meth. **203** (1982) 189.
26. R. Brun and F. Carminati, *GEANT Detector Description and Simulation Tool*, CERN Program Library, Long Writeup W5013.
27. S. Pratt http://www.nscl.msu.edu/ pratt/freecodes/crab/home.html.
28. A. Deloff (unpublished).
29. A. Deloff, Phys. Rev. C **69** (2004) 035206.
30. B.D. Day, Phys. Rev. C **24** (1981) 1203.
31. S. Pratt , Phys. Rev. Lett. **53** (1984) 1219.
32. G. Bertsch et al., Phys. Rev. C **37** (1988) 1896.
33. S.Chapman et al., Phys. Rev. Lett. **74** (1995) 4400.
34. S. Pratt, Phys. Rev. D **33** (1986) 1314.
35. G. Bertsch and G.E. Brown, Phys. Rev. C **40** (1989) 1830.
36. A. Makhlin and Y.M. Synukov, Z. Phys. C **39** (1988) 69.
37. F. Yano and S. Koonin , Phys. Lett. B **78** (1978) 556.
38. M. Podgoretsky, Sov. J. Nucl. Phys. **37** (1983) 272.
39. H. Heiselberg and A.P. Vischer, Eur. Phys. J. C **1** (1998) 593.
40. S. Padula, Nucl. Phys. A **715** (2003) 637.
41. Y.F. Wu et al., Eur. Phys. J. C **1** (1998) 599.
42. B. Tomasik and U. Heinz, Eur. Phys. J. C **4** (1998) 327.
43. M.M. Aggarwal et al.,WA98 Collaboration, unpublished.
44. M.M. Aggarwal et al., Eur. Phys. J. C **16** (2000) 445.
45. M.M. Aggarwal et al., Phys. Rev. C **67** (2003) 014906.
46. T. Kohama, PhD thesis, Hiroshima University, Jan., 2002.
47. G. Alexander et al., Phys. Lett. B **452** (1999) 159.
48. G. Alexander et al., Phys. Lett. B **506** (2001) 45.
49. A. Bialas and K. Zalewski, Acta Phys. Polon., B **30** (1999) 159.
50. A. Bialas et al., Phys. Rev. D **62** (2000) 114007.
51. A. Bialas et al., Acta Phys. Polon., B **32** (2001) 2901.
52. K. Gottfried, Phys. Rev. Lett. **32** (1974) 957.
53. J. D. Bjorken, Phys. Rev. D **7** (1973) 282.
54. M. Smith, Phys. Lett. B **477** (2000) 141.
55. I.G. Bearden et al., Phys. Rev. C **58** (1998) 1656; Eur. Phys. J. C **18** (2000) 317.
56. I.G. Bearden et al., Phys. Rev. Lett **87** (2001) 112301.
57. S.V. Afanasiev et al., Nucl. Phys. A **715** (2003) 55.

Suppression of High-p_T Neutral Pion Production in Central Pb + Pb Collisions at $\sqrt{s_{NN}} = 17.3$ GeV Relative to p + C and p + Pb Collisions

M. M. Aggarwal,[1] Z. Ahammed,[2] A. L. S. Angelis,[3,*] V. Antonenko,[4] V. Arefiev,[5] V. Astakhov,[5] V. Avdeitchikov,[5] T. C. Awes,[6] P. V. K. S. Baba,[7] S. K. Badyal,[7] S. Bathe,[8] B. Batiounia,[5] C. Baumann,[8] T. Bernier,[9] K. B. Bhalla,[10] V. S. Bhatia,[1] C. Blume,[8] D. Bucher,[8] H. Büsching,[8] L. Carlén,[11] S. Chattopadhyay,[2] M. P. Decowski,[12] H. Delagrange,[9] P. Donni,[3] M. R. Dutta Majumdar,[2] K. El Chenawi,[11] A. K. Dubey,[13] K. Enosawa,[14] S. Fokin,[4] V. Frolov,[5] M. S. Ganti,[2] S. Garpman,[11,*] O. Gavrishchuk,[5] F. J. M. Geurts,[15] T. K. Ghosh,[16] R. Glasow,[8] B. Guskov,[5] H. Å. Gustafsson,[11] H. H. Gutbrod,[17] I. Hrivnacova,[18] M. Ippolitov,[4] H. Kalechofsky,[3] R. Kamermans,[15] K. Karadjev,[4] K. Karpio,[19] B. W. Kolb,[17] I. Kosarev,[5,*] I. Koutcheryaev,[4] A. Kugler,[18] P. Kulinich,[12] M. Kurata,[14] A. Lebedev,[4] H. Löhner,[16] L. Luquin,[9] D. P. Mahapatra,[13] V. Manko,[4] M. Martin,[3] G. Martínez,[9] A. Maximov,[5] Y. Miake,[14] G. C. Mishra,[13] B. Mohanty,[2,13] M.-J. Mora,[9] D. Morrison,[20] T. Mukhanova,[4] D. S. Mukhopadhyay,[2] H. Naef,[3] B. K. Nandi,[13] S. K. Nayak,[7] T. K. Nayak,[2] A. Nianine,[4] V. Nikitine,[5] S. Nikolaev,[5] P. Nilsson,[11] S. Nishimura,[14] P. Nomokonov,[5] J. Nystrand,[11] A. Oskarsson,[11] I. Otterlund,[11] S. Pavliouk,[5] T. Peitzmann,[15] D. Peressounko,[4] V. Petracek,[18] S. C. Phatak,[13] W. Pinganaud,[9] F. Plasil,[6] M. L. Purschke,[17] J. Rak,[18] M. Rammler,[8] R. Raniwala,[10] S. Raniwala,[10] N. K. Rao,[7] F. Retiere,[9] K. Reygers,[16] G. Roland,[12] L. Rosselet,[3] I. Roufanov,[5] C. Roy,[9] J. M. Rubio,[3] S. S. Sambyal,[7] R. Santo,[8] S. Sato,[14] H. Schlagheck,[8] H.-R. Schmidt,[17] Y. Schutz,[9] G. Shabratova,[5] T. H. Shah,[7] I. Sibiriak,[4] T. Siemiarczuk,[19] D. Silvermyr,[11] B. C. Sinha,[2] N. Slavine,[5] K. Söderström,[11] G. Sood,[1] S. P. Sørensen,[20] P. Stankus,[6] G. Stefanek,[19] P. Steinberg,[12] E. Stenlund,[11] M. Sumbera,[18] T. Svensson,[11] A. Tsvetkov,[4] L. Tykarski,[19] E. C. v.d. Pijll,[15] N. v. Eijndhoven,[15] G. J. v. Nieuwenhuizen,[12] A. Vinogradov,[4] Y. P. Viyogi,[2] A. Vodopianov,[5] S. Vörös,[3] B. Wysłouch,[12] and G. R. Young[6]

(WA98 Collaboration)

[1]*University of Panjab, Chandigarh 160014, India*
[2]*Variable Energy Cyclotron Centre, Calcutta 700064, India*
[3]*University of Geneva, CH-1211 Geneva 4,Switzerland*
[4]*RRC "Kurchatov Institute", RU-123182 Moscow*
[5]*Joint Institute for Nuclear Research, RU-141980 Dubna, Russia*
[6]*Oak Ridge National Laboratory, Oak Ridge, Tennessee 37831-6372, USA*
[7]*University of Jammu, Jammu 180001, India*
[8]*University of Münster, D-48149 Münster, Germany*
[9]*SUBATECH, Ecole des Mines, Nantes, France*
[10]*University of Rajasthan, Jaipur 302004, Rajasthan, India*
[11]*University of Lund, SE-221 00 Lund, Sweden*
[12]*MIT Cambridge, Massachusetts 02139, USA*
[13]*Institute of Physics, Bhubaneswar 751005, India*
[14]*University of Tsukuba, Ibaraki 305, Japan*
[15]*Universiteit Utrecht/NIKHEF, NL-3508 TA Utrecht, The Netherlands*
[16]*KVI, University of Groningen, NL-9747 AA Groningen, The Netherlands*
[17]*Gesellschaft für Schwerionenforschung (GSI), D-64220 Darmstadt, Germany*
[18]*Nuclear Physics Institute, CZ-250 68 Rez, Czech Republic*
[19]*Institute for Nuclear Studies, 00-681 Warsaw, Poland*
[20]*University of Tennessee, Knoxville, Tennessee 37966, USA*

(Received 21 August 2007; revised manuscript received 12 May 2008; published 19 June 2008)

Neutral pion transverse momentum spectra were measured in p + C and p + Pb collisions at $\sqrt{s_{NN}} = 17.4$ GeV at midrapidity ($2.3 \lesssim \eta_{\rm lab} \lesssim 3.0$) over the range $0.7 \lesssim p_T \lesssim 3.5$ GeV/c. The spectra are compared to π^0 spectra measured in Pb + Pb collisions at $\sqrt{s_{NN}} = 17.3$ GeV in the same experiment. For a wide range of Pb + Pb centralities ($N_{\rm part} \lesssim 300$), the yield of π^0's with $p_T \gtrsim 2$ GeV/c is larger than or consistent with the p + C or p + Pb yields scaled with the number of nucleon-nucleon collisions ($N_{\rm coll}$), while for central Pb + Pb collisions with $N_{\rm part} \gtrsim 350$, the π^0 yield is suppressed.

DOI: 10.1103/PhysRevLett.100.242301 PACS numbers: 25.75.Dw, 13.87.Ce, 13.87.Fh

 © 2008 The American Physical Society

The study of hadron production at high transverse momentum (p_T) is a sensitive tool to characterize the matter created in ultrarelativistic heavy-ion collisions, and, in particular, to detect the possible formation of a quark-gluon plasma (QGP), i.e., a thermalized phase in which quarks and gluons are the relevant degrees of freedom. Particles at high-p_T result from quark and gluon scatterings with high momentum transfer (''hard scattering'') which can be described by perturbative quantum-chromodynamics (pQCD). The scattered quarks and gluons will traverse the created medium and fragment into the observable hadrons. High-p_T particle production in nucleus-nucleus ($A + A$) collisions was predicted to be suppressed [1] as a consequence of the energy loss of the scattered partons in the dense matter (''jet quenching''). Such suppression was observed by experiments at the Relativistic Heavy Ion Collider (RHIC) in central Au + Au and Cu + Cu collisions at a center-of-mass energy of up to $\sqrt{s_{NN}} = 200$ GeV [2–6]. Within jet-quenching models, the suppression can be related to medium properties, such as the initial gluon density or the transport coefficient [7–9].

A crucial test for the idea of parton energy loss in the hot and dense medium created in $A + A$ collisions is the measurement of the $\sqrt{s_{NN}}$ dependence of high-p_T hadron production [7,8,10–13]. In central Pb + Pb collisions at the CERN SPS energy of $\sqrt{s_{NN}} = 17.3$ GeV ($p_{\mathrm{lab}} = 158A$ GeV/c), the initial energy density, as estimated from the measured transverse energy [14], is above the critical value $\varepsilon_c \approx 1$ GeV/fm^3 [15] for the transition to the QGP. On the other hand, the initial gluon density and the lifetime of a deconfined phase produced at $\sqrt{s_{NN}} = 17.3$ GeV will be significantly reduced as compared to RHIC energies. Results at SPS energies thereby provide a sensitive test of jet-quenching model predictions.

Results on high-p_T particle production in central Pb + Pb collisions at the CERN SPS have already been published [16,17]. However, the interpretation of these data has been complicated by the lack of reference $p + p$ data to allow to quantify nuclear effects. Instead, parameterizations of $p + p$ data have been employed to search for nuclear effects [16,18], but with substantial systematic uncertainties. Moreover, hadron suppression due to parton energy loss might be compensated by an enhancement due to multiple soft scatterings of the incoming partons prior to the hard scattering process (''nuclear k_T-enhancement'' or ''Cronin effect''). Measurements in $p + A$ and $d + A$ collisions at different $\sqrt{s_{NN}}$ suggest that such enhancement is significantly stronger at $\sqrt{s_{NN}} \approx 20$ GeV than at $\sqrt{s_{NN}} = 200$ GeV [11].

In this Letter, π^0 spectra are presented from $p + \mathrm{C}$ and $p + \mathrm{Pb}$ collisions at $\sqrt{s_{NN}} = 17.4$ GeV ($p_{\mathrm{lab}} = 160$ GeV/c) measured in the WA98 experiment. Since the nuclear k_T-enhancement in $p + \mathrm{C}$ is expected to be small [19], this measurement should provide a useful substitute for a $p + p$ reference. Information on the magnitude of the nuclear k_T-enhancement may be obtained by comparison of the $p + \mathrm{Pb}$ and $p + \mathrm{C}$ spectra. The spectra are compared to π^0 spectra measured in Pb + Pb collisions at $\sqrt{s_{NN}} = 17.3$ GeV with the same WA98 experimental setup [16].

In the WA98 experiment, π^0 yields were measured by detection of photons from the $\pi^0 \rightarrow \gamma\gamma$ decay branch with a highly-segmented lead-glass calorimeter. This detector was located 21.5 m downstream from the target and subtended the pseudorapidity range $2.3 \lesssim \eta_{\mathrm{lab}} \lesssim 3.0$. A 400 GeV/$c$ proton beam from the CERN SPS impinged on a beryllium production target to provide a mixed secondary beam selected to have momentum of 160 GeV/c. The secondary beam consisted primarily of protons and pions with roughly equal content. Protons were identified with use of two gas Cherenkov counters located upstream of the 1879 mg/cm^2 ^{12}C (495 mg/cm^2 ^{208}Pb) target. The WA98 minimum bias trigger condition required a minimum amount of transverse energy (E_T) in the region $3.5 \lesssim \eta_{\mathrm{lab}} \lesssim 5.5$, measured with a sampling calorimeter with electromagnetic and hadronic sections. The measured minimum bias cross section σ_{mb} for $p + \mathrm{C}$ ($p + \mathrm{Pb}$) of 193 mb (1422 mb) corresponds to 86% (81%) of the total geometric cross section. The number of analyzed minimum bias events was 1.2×10^6 (1.0×10^6) for $p + \mathrm{C}$ ($p + \mathrm{Pb}$). A high-energy photon (HEP) trigger based on the sum energy signal of overlapping 4×4 groups of towers in the lead-glass calorimeter was used to enhance the sample of high-p_T events. The efficiency of the HEP trigger reached ~100% for photons with $p_T \gtrsim 0.8$ GeV/c. An additional 1.5×10^6 (0.5×10^6) $p + \mathrm{C}$ ($p + \mathrm{Pb}$) HEP events were analyzed which corresponded to 3.9×10^7 (8.2×10^6) sampled minimum bias events.

Neutral pion yields were determined statistically by counting photon pairs with invariant mass in the π^0 mass range after subtraction of the normalized background from uncorrelated pairs. The shape of this background was determined by mixing photons from different events. Only photon pairs with an energy asymmetry $\alpha = |E_1 - E_2|/(E_1 + E_2) < 0.7$ were used in the analysis. A correction for geometrical acceptance and reconstruction efficiency was applied to the raw π^0 yields. The reconstruction efficiency takes into account the loss of π^0's due to the photon identification and energy asymmetry cuts. It also modifies the π^0 yield to account for the p_T shift that results from the finite energy resolution of the lead-glass calorimeter convoluted with the steeply falling π^0 p_T spectrum. Effects of overlapping showers in the calorimeter, which were important in central Pb + Pb collisions, are negligible in $p + \mathrm{C}$ and $p + \mathrm{Pb}$ collisions. The dominant systematic uncertainties are listed in Table I. The systematic uncertainties of the peak extraction, acceptance correction, and efficiency correction are approximately independent of p_T. The energy scale of the calorimeter was confirmed by comparison

TABLE I. Systematic uncertainties (in %) on the π^0 yields in $p + C$ and $p + Pb$ collisions at three p_T values.

p_T (GeV/c)	1	2	3
peak extraction	6	6	6
geometric acceptance	2.5	2.5	2.5
π^0 reconstruction efficiency	11	11	11
energy scale	5	10	20
total	14	16	24

of the measured p_T-dependent π^0 peak positions with GEANT simulations. The estimated uncertainty of 1.5% on the energy scale leads to an uncertainty on the π^0 yields that increases with p_T.

The spectra of the invariant π^0 yields in $p + C$ and $p + Pb$ collisions at $\sqrt{s_{NN}} = 17.4$ GeV are shown in Fig. 1. The transition between the minimum bias and the HEP sample occurs at $p_T = 1.7$ GeV/c. The $p + C$ spectrum is compared to a next-to-leading-order (NLO) pQCD calculation for $p + p$ at the same energy [20]. The calculation was performed with the CTEQ6M [21] parton distribution functions and the "Kniehl-Kramer-Pötter" (KKP) set of fragmentation functions [22] with renormalization and factorization scales set to be the same at $\mu = p_T/2$, p_T, or $2p_T$. For comparison with the $p + C$ data, the pQCD calculations have been scaled by the average number of

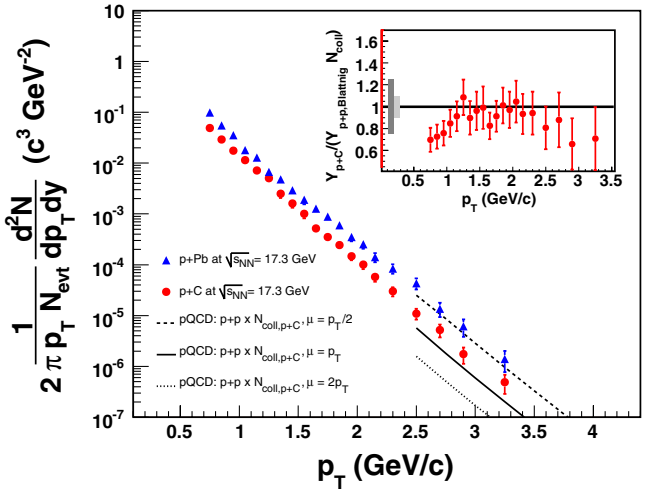

FIG. 1 (color online). Invariant π^0 yields in minimum bias $p + C$ and $p + Pb$ collisions at $\sqrt{s_{NN}} = 17.4$ GeV. The error bars represent the quadratic sum of statistical and systematic uncertainties. The lines represent next-to-leading-order pQCD calculation of the π^0 yield in $\sqrt{s} = 17.4$ GeV $p + p$ collisions for three different scales, scaled by $\langle N_{\rm coll}^{p+C} \rangle = 1.7$. The inset shows a comparison of the $p + C$ spectrum to a parameterization of the yield in $p + p$ collisions at $\sqrt{s} = 17.3$ GeV from [23]. The dark gray box indicates the uncertainty of the parameterization estimated in [18], the light gray box the uncertainty of $\langle N_{\rm coll}^{p+C} \rangle$.

nucleon-nucleon collisions in $p + C$. The pQCD calculation shows a large uncertainty related to the arbitrary choice of scale. It has been suggested that the NLO perturbative expansion is not sufficient at low energies and that threshold resummation corrections must be taken into account [20]. The large theoretical uncertainties demonstrate that pQCD calculations cannot be used as a reliable reference at CERN SPS energies. The inset of Fig. 1 shows that the π^0 yields per nucleon-nucleon collision measured in $p + C$ are in good agreement with a parameterization of π^0 spectra in $p + p$ from Blattnig *et al.* [23] that has been employed to study nuclear effects in Pb + Pb collisions [18].

Nuclear effects in π^0 production can be quantified with the nuclear modification factor defined as

$$R'_{AA} = \frac{\langle N_{\rm coll}^{p+B} \rangle}{\langle N_{\rm coll}^{A+A} \rangle} \frac{dN_{\pi^0}/dp_T|_{A+A}}{dN_{\pi^0}/dp_T|_{p+B}}. \quad (1)$$

In the absence of nuclear effects, R'_{AA} is expected to be unity for $p_T \gtrsim 2$ GeV/c where hard scattering is expected to dominate particle production. $\langle N_{\rm coll} \rangle$ was determined with a Glauber Monte Carlo calculation [24] using an inelastic nucleon-nucleon cross section of $\sigma_{\rm inel}^{NN} = (31.8 \pm 2)$ mb [25]. The same Glauber calculation was used to extract $\langle N_{\rm coll} \rangle$ values in Pb + Pb collisions. In the Glauber calculation, the transverse energy E_T was modeled by sampling a negative binomial distribution to determine the E_T contribution of each participating nucleon [24]. The bias due to the trigger selection on the measured E_T was taken into account. For minimum bias $p + C$ and $p + Pb$ collisions, values of $\langle N_{\rm coll} \rangle_{p+C} = 1.7 \pm 0.2$ and $\langle N_{\rm coll} \rangle_{p+Pb} = 3.8 \pm 0.4$ were obtained.

The $\langle N_{\rm coll} \rangle$ values for Pb + Pb collisions were determined by applying cuts to the simulated E_T that corresponded to the same fraction of $\sigma_{\rm mb}^{\rm Pb+Pb}$ as the cuts applied to the measured E_T. These $\langle N_{\rm coll} \rangle$ values are listed in Table II and agree within systematic uncertainties with those of Ref. [16] that were determined with the VENUS 4.12 event generator in which $\sigma_{\rm inel}^{NN} = 29.6$ mb was used. With the large acceptance of the WA98 E_T measurement, and good description of the E_T distribution, including fluctuations [14], a centrality class corresponding to the 1% most central Pb + Pb collisions could be defined to access very large $\langle N_{\rm coll} \rangle$ values.

The $p + Pb$ π^0 spectrum appears to be flatter than the $p + C$ spectrum (see Fig. 1). The ratio of the $N_{\rm coll}$-normalized $p + Pb$ and $p + C$ spectra is shown in Fig. 2. At low p_T (~1 GeV/c), the ratio is consistent with scaling with the number of participating nucleons ($N_{\rm part} = N_{\rm coll} + 1$ in $p + A$) while scaling with $N_{\rm coll}$ is observed at higher p_T (~2 GeV/c). In fact, for $p_T \gtrsim 2$ GeV/c, the ratio tends to be above unity, consistent with an expected stronger nuclear k_T-enhancement in $p + Pb$ than in $p + C$.

Neutral pion spectra from Pb + Pb collisions at $\sqrt{s_{NN}} = 17.3$ GeV were published by WA98 in [16]. Figure 3 shows

TABLE II. Results of the Glauber calculation for Pb + Pb collisions at $\sqrt{s_{NN}} = 17.3$ GeV ($\sigma_{\text{inel}}^{NN} = 31.8$ mb). Centrality classes are given as a fraction (%) of $\sigma_{\text{mb}}^{\text{Pb+Pb}} \approx 6300$ mb [16]. The systematic uncertainty of $\langle N_{\text{coll}} \rangle$ was parameterized as $\sigma_{N_{\text{coll}}}^2 = 0.1^2 + [0.4 \exp(-N_{\text{coll}}/100)]^2$.

class	1	2	3	4	5	6	7	8	6 − 8
from	82.8	67.0	48.8	25.3	13.0	6.8	1.0	0	0
to	100	82.8	67.0	48.8	25.3	13.0	6.8	1.0	13.0
$\langle N_{\text{part}} \rangle$	8.2	23	54.2	123.2	218.2	289.1	347.8	382.6	322.5
$\langle N_{\text{coll}} \rangle$	6.3	22.1	67.1	202.9	433.1	627.0	803.7	912.0	727.8

the π^0 nuclear modification factor R'_{AA} as defined in Eq. (1) for three Pb + Pb collision centralities. For the 25.3–48.8% (of $\sigma_{\text{mb}}^{\text{Pb+Pb}}$) most central collisions, the data points at high-p_T ($p_T \gtrsim 2$ GeV/c) suggest a stronger nuclear k_T-enhancement than in p + C. On the other hand, for the 0–13% most central Pb + Pb collisions, R'_{AA} is smaller than for the 25.3–48.8% class but still consistent with unity at high-p_T. For the 0–1% most central collisions, the π^0 yield is significantly suppressed compared to either p + Pb or p + C as reference. An apparent suppression of the π^0 yield in very central Pb + Pb collisions compared to peripheral collisions was noted in Ref. [16]. However, the large uncertainty of using the peripheral distribution as a reference did not allow to draw a firm conclusion. The observed suppression is qualitatively consistent with expectations from jet-quenching.

The centrality dependence of the average R'_{AA} for $2 < p_T < 2.5$ GeV/c and $2.5 \leq p_T < 3.0$ GeV/c is shown in Fig. 4. The π^0 yields in Pb + Pb in these p_T ranges are not suppressed for $N_{\text{part}} \lesssim 300$ ($\langle R'_{AA} \rangle \gtrsim 1$). For more central Pb + Pb collisions, $\langle R'_{AA} \rangle$ decreases with centrality indicating significant suppression of the high-p_T π^0 yield. The apparent lack of suppression, or enhancement even, for $N_{\text{part}} \lesssim 300$ may be due to competing effects of suppression due to parton energy loss and nuclear k_T-enhancement.

In summary, π^0 spectra were measured in minimum bias p + C and p + Pb collisions at $\sqrt{s_{NN}} = 17.4$ GeV in the range $0.7 \lesssim p_T \lesssim 3.5$ GeV/c. Based on these spectra, the nuclear modification factors R'_{AA} for Pb + Pb collisions at CERN SPS energies could be determined using a measured $p + A$ reference. In very central Pb + Pb collisions (0–1% of $\sigma_{\text{mb}}^{\text{Pb+Pb}}$), a significant suppression of high-p_T neutral pions was observed ($R'_{AA} \approx 0.5 \pm 0.14$) that is reminiscent of the high-p_T hadron suppression observed in Cu + Cu and Au + Au collisions at RHIC. The pion suppression reported here, together with the results at higher energies from RHIC, constrain jet-quenching models and may help clarify the behavior of the energy loss of partons in strongly interacting matter.

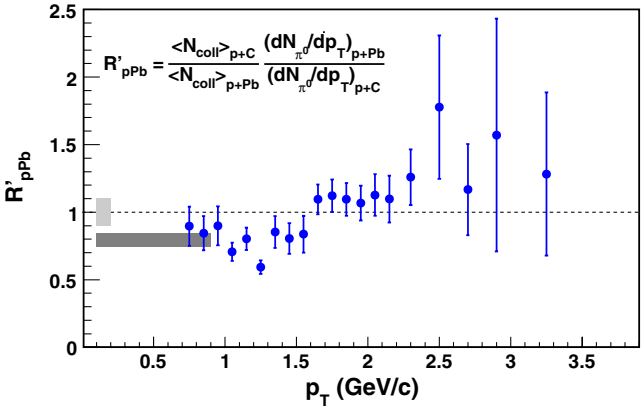

FIG. 2 (color online). The N_{coll}-normalized ratio of π^0 yields in p + Pb and p + C collisions. The box at $R'_{p\text{Pb}} \approx 0.8$ represents the expectation for the case of scaling with N_{part} rather than N_{coll}. The box at unity indicates the N_{coll} systematic uncertainty. The error bars represent the quadratic sum of the statistical and remaining systematic uncertainties. The energy scale uncertainty was assumed to cancel.

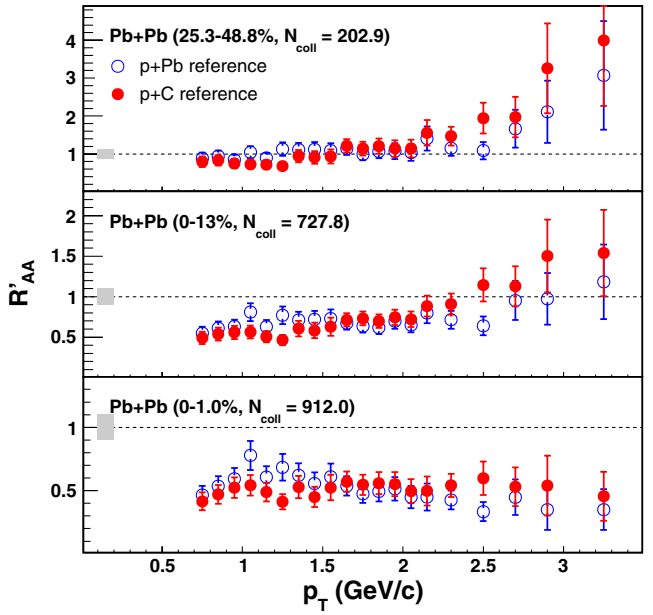

FIG. 3 (color online). π^0 R'_{AA} in Pb + Pb collisions at $\sqrt{s_{NN}} = 17.3$ GeV for three centrality classes using p + C or p + Pb spectra as a reference. The boxes around unity reflect the systematic uncertainties related to $\langle N_{\text{coll}} \rangle$.

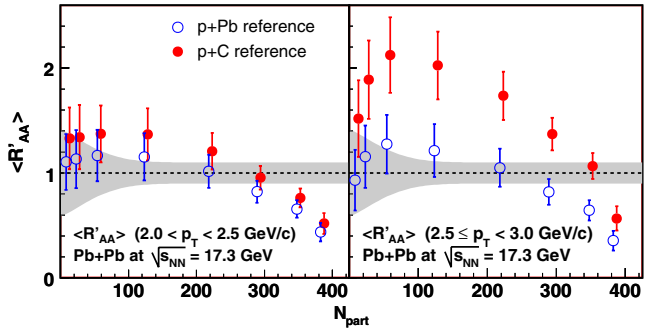

FIG. 4 (color online). Centrality dependence of the average $\langle R'_{AA}\rangle$ for $2 < p_T < 2.5$ GeV/c and $2.5 \leq p_T < 3.0$ GeV/c. The bands around unity indicate the systematic uncertainty of $\langle N_{\rm coll}\rangle$. The error bars represent the quadratic sum of the statistical and systematic uncertainties. The $N_{\rm part}$ values for the full points were shifted by $+5$ for better visibility.

We would like to thank the CERN-SPS accelerator crew for the excellent beam provided and the Laboratoire National Saturne for the loan of the magnet Goliath. We thank W. Vogelsang for providing the QCD calculation shown in this Letter. This work was supported jointly by the German BMBF, DFG, and the Helmholtz-Gemeinschaft (No. VI-VH-146), the U.S. DOE, the Swedish NFR, the Dutch Stichting FOM, the Swiss National Fund, the Humboldt Foundation, the Stiftung für deutsch-polnische Zusammenarbeit, the Department of Atomic Energy, the Department of Science and Technology and the University Grants Commission of the Government of India, the Indo-FRG Exchange Programme, the PPE division of CERN, the INTAS under Contract No. INTAS-97-0158, the Polish KBN under the Grant No. 2P03B16815, the Grant-in-Aid for Scientific Research (Specially Promoted Research & International Scientific Research) of the Ministry of Education, Science, Sports and Culture, JSPS, the University of Tsukuba Special Research Projects, and ORISE. ORNL is managed by UT-Battele, LLC, for the U.S. Department of Energy under Contract No. DE-AC05-00OR22725.

*Deceased

[1] X.-N. Wang and M. Gyulassy, Phys. Rev. Lett. **68**, 1480 (1992).
[2] K. Adcox *et al.* (PHENIX Collaboration), Nucl. Phys. A **757**, 184 (2005).
[3] J. Adams *et al.* (STAR Collaboration), Nucl. Phys. A **757**, 102 (2005).
[4] I. Arsene *et al.* (BRAHMS Collaboration), Nucl. Phys. A **757**, 1 (2005).
[5] B. B. Back *et al.* (PHOBOS Collaboration), Nucl. Phys. A **757**, 28 (2005).
[6] C. Klein-Boesing *et al.* (PHENIX Collaboration), arXiv:nucl-ex/0606013.
[7] I. Vitev and M. Gyulassy, Phys. Rev. Lett. **89**, 252301 (2002).
[8] I. Vitev, Phys. Lett. B **639**, 38 (2006).
[9] A. Kovner and U. A. Wiedemann, arXiv:hep-ph/0304151.
[10] X.-N. Wang, Phys. Rev. Lett. **81**, 2655 (1998).
[11] X.-N. Wang, Phys. Rev. C **61**, 064910 (2000).
[12] Y. Zhang, G. I. Fai, G. Papp, G. G. Barnafoldi, and P. Levai, Phys. Rev. C **65**, 034903 (2002).
[13] A. Adare *et al.* (PHENIX Collaboration), arXiv: 0801.4555.
[14] M. M. Aggarwal *et al.* (WA98 Collaboration), Eur. Phys. J. C **18**, 651 (2001).
[15] M. Cheng *et al.*, Phys. Rev. D **74**, 054507 (2006).
[16] M. M. Aggarwal *et al.* (WA98 Collaboration), Eur. Phys. J. C **23**, 225 (2002).
[17] C. Blume, Nucl. Phys. A **783**, 65 (2007).
[18] D. d'Enterria, Phys. Lett. B **596**, 32 (2004).
[19] G. G. Barnafoldi, G. Papp, P. Levai, and G. I. Fai, arXiv:nucl-th/0307062.
[20] D. de Florian and W. Vogelsang, Phys. Rev. D **71**, 114004 (2005).
[21] J. Pumplin *et al.*, J. High Energy Phys. 07 (2002) 012.
[22] B. A. Kniehl, G. Kramer, and B. Potter, Nucl. Phys. B **597**, 337 (2001).
[23] S. R. Blattnig, S. R. Swaminathan, A. T. Kruger, M. Ngom, and J. W. Norbury, Phys. Rev. D **62**, 094030 (2000).
[24] M. L. Miller, K. Reygers, S. J. Sanders, and P. Steinberg, Annu. Rev. Nucl. Part. Sci. **57**, 205 (2007).
[25] C. Alt *et al.* (NA49 Collaboration), Eur. Phys. J. C **45**, 343 (2006).

Centrality dependence of charged hadron production in deuteron+gold and nucleon+gold collisions at $\sqrt{s_{NN}} = 200$ GeV

S. S. Adler,[5] S. Afanasiev,[20] C. Aidala,[10] N. N. Ajitanand,[44] Y. Akiba,[21,40] A. Al-Jamel,[35] J. Alexander,[44] K. Aoki,[25] L. Aphecetche,[46] R. Armendariz,[35] S. H. Aronson,[5] R. Averbeck,[45] T. C. Awes,[36] V. Babintsev,[17] A. Baldisseri,[11] K. N. Barish,[6] P. D. Barnes,[28] B. Bassalleck,[34] S. Bathe,[6,31] S. Batsouli,[10] V. Baublis,[39] F. Bauer,[6] A. Bazilevsky,[5,41] S. Belikov,[17,19,*] M. T. Bjorndal,[10] J. G. Boissevain,[28] H. Borel,[11] M. L. Brooks,[28] D. S. Brown,[35] N. Bruner,[34] D. Bucher,[31] H. Buesching,[5,31] V. Bumazhnov,[17] G. Bunce,[5,41] J. M. Burward-Hoy,[27,28] S. Butsyk,[45] X. Camard,[46] P. Chand,[4] W. C. Chang,[2] S. Chernichenko,[17] C. Y. Chi,[10] J. Chiba,[21] M. Chiu,[10] I. J. Choi,[53] R. K. Choudhury,[4] T. Chujo,[5] V. Cianciolo,[36] Z. Citron,[45] Y. Cobigo,[11] B. A. Cole,[10] M. P. Comets,[37] P. Constantin,[19] M. Csanád,[13] T. Csörgő,[22] J. P. Cussonneau,[46] D. d'Enterria,[10] K. Das,[14] G. David,[5] F. Deák,[13] H. Delagrange,[46] A. Denisov,[17] A. Deshpande,[41] E. J. Desmond,[5] A. Devismes,[45] O. Dietzsch,[42] J. L. Drachenberg,[1] O. Drapier,[26] A. Drees,[45] A. Durum,[17] D. Dutta,[4] V. Dzhordzhadze,[47] Y. V. Efremenko,[36] H. En'yo,[40,41] B. Espagnon,[37] S. Esumi,[49] D. E. Fields,[34,41] C. Finck,[46] F. Fleuret,[26] S. L. Fokin,[24] B. D. Fox,[41] Z. Fraenkel,[52] J. E. Frantz,[10] A. Franz,[5] A. D. Frawley,[14] Y. Fukao,[25,40,41] S.-Y. Fung,[6] S. Gadrat,[29] M. Germain,[46] A. Glenn,[47] M. Gonin,[26] J. Gosset,[11] Y. Goto,[40,41] R. Granier de Cassagnac,[26] N. Grau,[19] S. V. Greene,[50] M. Grosse Perdekamp,[18,41] H.-Å. Gustafsson,[30] T. Hachiya,[16] J. S. Haggerty,[5] H. Hamagaki,[8] A. G. Hansen,[28] E. P. Hartouni,[27] M. Harvey,[5] K. Hasuko,[40] R. Hayano,[8] X. He,[15] M. Heffner,[27] T. K. Hemmick,[45] J. M. Heuser,[40] P. Hidas,[22] H. Hiejima,[18] J. C. Hill,[19] R. Hobbs,[34] W. Holzmann,[44] K. Homma,[16] B. Hong,[23] A. Hoover,[35] T. Horaguchi,[40,41,48] T. Ichihara,[40,41] V. V. Ikonnikov,[24] K. Imai,[25,40] M. Inaba,[49] M. Inuzuka,[8] D. Isenhower,[1] L. Isenhower,[1] M. Ishihara,[40] M. Issah,[44] A. Isupov,[20] B. V. Jacak,[45,†] J. Jia,[45] O. Jinnouchi,[40,41] B. M. Johnson,[5] S. C. Johnson,[27] K. S. Joo,[32] D. Jouan,[37] F. Kajihara,[8] S. Kametani,[8,51] N. Kamihara,[40,48] M. Kaneta,[41] J. H. Kang,[53] K. Katou,[51] T. Kawabata,[8] A. V. Kazantsev,[24] S. Kelly,[9,10] B. Khachaturov,[52] A. Khanzadeev,[39] J. Kikuchi,[51] D. J. Kim,[53] E. Kim,[43] G.-B. Kim,[26] H. J. Kim,[53] E. Kinney,[9] A. Kiss,[13] E. Kistenev,[5] A. Kiyomichi,[40] C. Klein-Boesing,[31] H. Kobayashi,[41] L. Kochenda,[39] V. Kochetkov,[17] R. Kohara,[16] B. Komkov,[39] M. Konno,[49] D. Kotchetkov,[6] A. Kozlov,[52] P. J. Kroon,[5] C. H. Kuberg,[1,*] G. J. Kunde,[28] K. Kurita,[40] M. J. Kweon,[23] Y. Kwon,[53] G. S. Kyle,[35] R. Lacey,[44] J. G. Lajoie,[19] Y. Le Bornec,[37] A. Lebedev,[19,24] S. Leckey,[45] D. M. Lee,[28] M. J. Leitch,[28] M. A. L. Leite,[42] X. H. Li,[6] H. Lim,[43] A. Litvinenko,[20] M. X. Liu,[28] C. F. Maguire,[50] Y. I. Makdisi,[5] A. Malakhov,[20] V. I. Manko,[24] Y. Mao,[38,40] G. Martinez,[46] H. Masui,[49] F. Matathias,[45] T. Matsumoto,[8,51] M. C. McCain,[1] P. L. McGaughey,[28] Y. Miake,[49] T. E. Miller,[50] A. Milov,[45] S. Mioduszewski,[5] G. C. Mishra,[15] J. T. Mitchell,[5] A. K. Mohanty,[4] D. P. Morrison,[5] J. M. Moss,[28] D. Mukhopadhyay,[52] M. Muniruzzaman,[6] S. Nagamiya,[21] J. L. Nagle,[9,10] T. Nakamura,[16] J. Newby,[47] A. S. Nyanin,[24] J. Nystrand,[30] E. O'Brien,[5] C. A. Ogilvie,[19] H. Ohnishi,[40] I. D. Ojha,[3,50] H. Okada,[25,40] K. Okada,[40,41] A. Oskarsson,[30] I. Otterlund,[30] K. Oyama,[8] K. Ozawa,[8] D. Pal,[52] A. P. T. Palounek,[28] V. Pantuev,[45] V. Papavassiliou,[35] J. Park,[43] W. J. Park,[23] S. F. Pate,[35] H. Pei,[19] V. Penev,[20] J.-C. Peng,[18] H. Pereira,[11] V. Peresedov,[20] A. Pierson,[34] C. Pinkenburg,[5] R. P. Pisani,[5] M. L. Purschke,[5] A. K. Purwar,[45] J. M. Qualls,[1] J. Rak,[19] I. Ravinovich,[52] K. F. Read,[36,47] M. Reuter,[45] K. Reygers,[31] V. Riabov,[39] Y. Riabov,[39] G. Roche,[29] A. Romana,[26,*] M. Rosati,[19] S. S. E. Rosendahl,[30] P. Rosnet,[29] V. L. Rykov,[40] S. S. Ryu,[53] N. Saito,[25,40,41] T. Sakaguchi,[8,51] S. Sakai,[49] V. Samsonov,[39] L. Sanfratello,[34] R. Santo,[31] H. D. Sato,[25,40] S. Sato,[5,49] S. Sawada,[21] Y. Schutz,[46] V. Semenov,[17] R. Seto,[6] T. K. Shea,[5] I. Shein,[17] T.-A. Shibata,[40,48] K. Shigaki,[16] M. Shimomura,[49] A. Sickles,[45] C. L. Silva,[42] D. Silvermyr,[28] K. S. Sim,[23] A. Soldatov,[17] R. A. Soltz,[27] W. E. Sondheim,[28] S. P. Sorensen,[47] I. V. Sourikova,[5] F. Staley,[11] P. W. Stankus,[36] E. Stenlund,[30] M. Stepanov,[35] A. Ster,[22] S. P. Stoll,[5] T. Sugitate,[16] J. P. Sullivan,[28] S. Takagi,[49] E. M. Takagui,[42] A. Taketani,[40,41] K. H. Tanaka,[21] Y. Tanaka,[33] K. Tanida,[40] M. J. Tannenbaum,[5] A. Taranenko,[44] P. Tarján,[12] T. L. Thomas,[34] M. Togawa,[25,40] J. Tojo,[40] H. Torii,[25,41] R. S. Towell,[1] V.-N. Tram,[26] I. Tserruya,[52] Y. Tsuchimoto,[16] H. Tydesjö,[30] N. Tyurin,[17] T. J. Uam,[32] J. Velkovska,[5] M. Velkovsky,[45] V. Veszprémi,[12] A. A. Vinogradov,[24] M. A. Volkov,[24] E. Vznuzdaev,[39] X. R. Wang,[15] Y. Watanabe,[40,41] S. N. White,[5] N. Willis,[37] F. K. Wohn,[19] C. L. Woody,[5] W. Xie,[6] A. Yanovich,[17] S. Yokkaichi,[40,41] G. R. Young,[36] I. E. Yushmanov,[24] W. A. Zajc,[10] C. Zhang,[10] S. Zhou,[7] J. Zimányi,[22,*] L. Zolin,[20] X. Zong,[19] and H. W. vanHecke[28]

(PHENIX Collaboration)

[1]*Abilene Christian University, Abilene, Texas 79699, USA*
[2]*Institute of Physics, Academia Sinica, Taipei 11529, Taiwan*
[3]*Department of Physics, Banaras Hindu University, Varanasi 221 005, India*
[4]*Bhabha Atomic Research Centre, Bombay 400 085, India*
[5]*Brookhaven National Laboratory, Upton, New York 11973-5000, USA*
[6]*University of California - Riverside, Riverside, California 92521, USA*
[7]*China Institute of Atomic Energy (CIAE), Beijing, People's Republic of China*
[8]*Center for Nuclear Study, Graduate School of Science, University of Tokyo, 7-3-1 Hongo, Bunkyo, Tokyo 113-0033, Japan*
[9]*University of Colorado, Boulder, Colorado 80309, USA*
[10]*Columbia University, New York, New York 10027 and Nevis Laboratories, Irvington, New York 10533, USA*
[11]*Dapnia, CEA Saclay, F-91191, Gif-sur-Yvette, France*
[12]*Debrecen University, H-4010 Debrecen, Egyetem tér 1, Hungary*
[13]*ELTE, Eötvös Loránd University, H-1117 Budapest, Pázmány P. s. 1/A, Hungary*

 ©2008 The American Physical Society

[14]*Florida State University, Tallahassee, Florida 32306, USA*
[15]*Georgia State University, Atlanta, Georgia 30303, USA*
[16]*Hiroshima University, Kagamiyama, Higashi-Hiroshima 739-8526, Japan*
[17]*IHEP Protvino, State Research Center of Russian Federation, Institute for High Energy Physics, Protvino, RU-142281, Russia*
[18]*University of Illinois at Urbana-Champaign, Urbana, Illinois 61801, USA*
[19]*Iowa State University, Ames, Iowa 50011, USA*
[20]*Joint Institute for Nuclear Research, RU-141980 Dubna, Moscow Region, Russia*
[21]*KEK, High Energy Accelerator Research Organization, Tsukuba, Ibaraki 305-0801, Japan*
[22]*KFKI Research Institute for Particle and Nuclear Physics of the Hungarian Academy of Sciences (MTA KFKI RMKI), H-1525 Budapest 114, P. O. Box 49, Budapest, Hungary*
[23]*Korea University, Seoul, 136-701, Korea*
[24]*Russian Research Center "Kurchatov Institute," Moscow, Russia*
[25]*Kyoto University, Kyoto 606-8502, Japan*
[26]*Laboratoire Leprince-Ringuet, Ecole Polytechnique, CNRS-IN2P3, Route de Saclay, F-91128, Palaiseau, France*
[27]*Lawrence Livermore National Laboratory, Livermore, California 94550, USA*
[28]*Los Alamos National Laboratory, Los Alamos, New Mexico 87545, USA*
[29]*LPC, Université Blaise Pascal, CNRS-IN2P3, Clermont-Fd, F-63177 Aubiere Cedex, France*
[30]*Department of Physics, Lund University, Box 118, SE-221 00 Lund, Sweden*
[31]*Institut für Kernphysik, University of Muenster, D-48149 Muenster, Germany*
[32]*Myongji University, Yongin, Kyonggido 449-728, Korea*
[33]*Nagasaki Institute of Applied Science, Nagasaki-shi, Nagasaki 851-0193, Japan*
[34]*University of New Mexico, Albuquerque, New Mexico 87131, USA*
[35]*New Mexico State University, Las Cruces, New Mexico 88003, USA*
[36]*Oak Ridge National Laboratory, Oak Ridge, Tennessee 37831, USA*
[37]*IPN-Orsay, Université Paris Sud, CNRS-IN2P3, BP1, F-91406, Orsay, France*
[38]*Peking University, Beijing, People's Republic of China*
[39]*PNPI, Petersburg Nuclear Physics Institute, Gatchina, Leningrad region, RU-188300, Russia*
[40]*RIKEN (The Institute of Physical and Chemical Research), Wako, Saitama 351-0198, Japan*
[41]*RIKEN BNL Research Center, Brookhaven National Laboratory, Upton, New York 11973-5000, USA*
[42]*Universidade de São Paulo, Instituto de Física, Caixa Postal 66318, São Paulo CEP05315-970, Brazil*
[43]*System Electronics Laboratory, Seoul National University, Seoul, South Korea*
[44]*Chemistry Department, Stony Brook University, Stony Brook, SUNY, New York 11794-3400, USA*
[45]*Department of Physics and Astronomy, Stony Brook University, SUNY, Stony Brook, New York 11794, USA*
[46]*SUBATECH (Ecole des Mines de Nantes, CNRS-IN2P3, Université de Nantes) BP 20722-44307, Nantes, France*
[47]*University of Tennessee, Knoxville, Tennessee 37996, USA*
[48]*Department of Physics, Tokyo Institute of Technology, Oh-okayama, Meguro, Tokyo 152-8551, Japan*
[49]*Institute of Physics, University of Tsukuba, Tsukuba, Ibaraki 305, Japan*
[50]*Vanderbilt University, Nashville, Tennessee 37235, USA*
[51]*Waseda University, Advanced Research Institute for Science and Engineering, 17 Kikui-cho, Shinjuku-ku, Tokyo 162-0044, Japan*
[52]*Weizmann Institute, Rehovot 76100, Israel*
[53]*Yonsei University, IPAP, Seoul 120-749, Korea*
(Received 17 August 2007; published 24 January 2008)

We present transverse momentum (p_T) spectra of charged hadrons measured in deuteron-gold and nucleon-gold collisions at $\sqrt{s_{NN}} = 200$ GeV for four centrality classes. Nucleon-gold collisions were selected by tagging events in which a spectator nucleon was observed in one of two forward rapidity detectors. The spectra and yields were investigated as a function of the number of binary nucleon-nucleon collisions, ν, suffered by deuteron nucleons. A comparison of charged particle yields to those in $p+p$ collisions show that yield per nucleon-nucleon collision saturates with ν for high momentum particles. We also present the charged hadron to neutral pion ratios as a function of p_T.

DOI: 10.1103/PhysRevC.77.014905 PACS number(s): 25.75.Dw

I. INTRODUCTION

The measurement of hadron spectra at high transverse momenta (p_T) has been a powerful tool in studying the modification of particle production and propagation in the nuclear medium at the BNL Relativistic Heavy Ion Collider

*Deceased.
†PHENIX spokesperson: jacak@skipper.physics.sunysb.edu

(RHIC). One of the most intriguing results observed so far at RHIC is the strong suppression of the yield of hadrons with p_T above $\sim$2 GeV/c in midcentral and central Au+Au collisions relative to the corresponding yield in $p+p$ collisions scaled by the sum of independent nucleon-nucleon collisions in the Au+Au interaction [1–3]. This is consistent with a picture in which the hard scattered parton loses significant energy when it traverses the medium created during the collision [4]. There is additional evidence for the strong interaction of partons with the final state medium. For example, two particle azimuthal correlations demonstrate significant modifications of jets such as width and particle content [5,6]. In the p_T region, $2 < p_T < 5$ GeV/c, an anomalously large baryon/meson ratio is observed [7]. The coalescence of thermal and shower partons offers a possible explanation of this phenomenon as a final state effect [8].

The hadron spectrum is sensitive to final state effects including jet quenching, parton recombination, and scattering of produced particles, in addition to initial state effects, such as gluon saturation and nuclear shadowing [9], and the Cronin effect [10,11]. If shadowing or gluon saturation are actually responsible for the large suppression seen in Au+Au collisions, these same effects would also produce a suppression of 20–30% in the yield of high p_T [9] hadrons even in d+Au collisions.

To study the role of initial state effects in the high p_T suppression, d+Au collisions at RHIC serve as a control experiment, since no dense matter is expected to be formed in these collisions. Earlier measurements on inclusive hadron production in d+Au collisions show no suppression of high p_T hadrons [12,13]. Rather, there is a small enhancement in the yield of high momentum particles in d+Au collisions. This result implies that the effects seen in central Au+Au collisions are largely due to final state interactions in the dense medium.

In this paper, we extend our investigation of charged hadron production in d+Au collisions at $\sqrt{s_{NN}} = 200$ GeV at midrapidity with detailed centrality selections and with significantly higher statistics. The centrality selection allows one to make quantitative statements about the impact parameter dependence of particle production.

The nuclear modification of high p_T hadron production in proton reactions with heavy nuclei has previously been studied at lower center of mass energies [10,11]. It was found that hadron yield at high p_T in $p+A$ collisions increases faster than the nuclear mass A. This effect, known as the Cronin effect, is conventionally parametrized as A^α. At $\sqrt{s} \sim$ 10–30 GeV, α depends on p_T and is found to be greater than unity for $p_T >$ 2 GeV/c. The exponent α also depends on the particle species; it was found to be larger for baryons than for mesons. The Cronin effect is often attributed to the multiple scattering of projectile partons propagating through the target nucleus [14].

A deuteron projectile has an additional interesting characteristic: since the average separation between the proton and neutron in the deuteron is large, on the order of a few fm, there is a class of events in which only one of the two nucleons participates in the collision. Thus d+Au events can be categorized into "p"+Au or "n"+Au collisions, when only one of the constituent nucleons interacts, and pn+Au, when both nucleons participate in the collision. In such events, the interacting proton or neutron is not a free proton or neutron, so it is not exactly the same as a p+Au or n+Au interaction. For simplicity we will refer to the tagged samples as p+Au and n+Au and collectively N+Au. The selection of p+Au and n+Au collisions in the PHENIX experiment is done by tagging events where the incoming deuteron has a noninteracting neutron or proton. Combined with centrality selection, such event tagging provides better control of the collision geometry and of the number of subsequent inelastic nucleon-nucleon interactions in the gold nucleus.

Very little experimental information has been published about neutron-nucleus collisions at high energy. Tagging allows the direct comparison of pn+Au, p+Au, and n+Au interactions. Results from these collisions are compared with $p+p$ data measured by the PHENIX experiment at the same beam energy to shed light on the Cronin enhancement and other nuclear effects. Further, we have investigated the Cronin effect as a function of the number of collisions per participant nucleon in the deuteron. To estimate the fraction of pions in the charged hadron spectrum, we have looked at hadron to pion ratios as a function of transverse momentum.

The paper is organized as follows. Section II gives a detailed account of the analysis in which we describe the detector, centrality selection, charged particle background rejection, spectra corrections, and systematic errors. In Sec. III, the centrality and p_T dependence of the charged hadron spectra and a comparison with the $p+p$ and the π^0 data are discussed. A summary is given in Sec. IV.

II. EXPERIMENT AND ANALYSIS

A. Detector

The PHENIX detector consists of four spectrometer arms positioned around the vertex of colliding deuteron and gold nuclei—two central arms at midrapidity and two muon arms at forward rapidities—and a set of detectors. A detailed description of the detector can be found elsewhere, see Ref. [15] and references therein. This analysis uses the two central arms and the set of global detectors.

Each central arm covers the pseudorapidity range $|\eta| <$ 0.35, and 90° in azimuth. Charged particles are tracked by drift chambers (DCs) located 2 m from the vertex and layers of pad chambers (PC1 and PC3) positioned at 2.5 and 5 m in the radial direction. The central spectrometer provides axial magnetic fields along the beam pipe. The transverse momentum p_T of each particle is determined by its deflection angle in the azimuthal direction as measured by the DC. The total particle momentum is reconstructed by projecting tracks back to the collision vertex through the magnetic field. The track reconstruction efficiency is approximately 98% and independent of p_T with negligible centrality dependence. The particle momenta are measured with a resolution $\delta p/p = 0.007 \oplus 0.011\,p$, with p in GeV/c. The absolute momentum scale is calibrated to 0.7% from the reconstructed proton mass using the PHENIX time-of-flight system. At high transverse momentum, a substantial background of electrons is produced by photon conversion in the material between the beam pipe and drift chambers. To subtract this background from photon

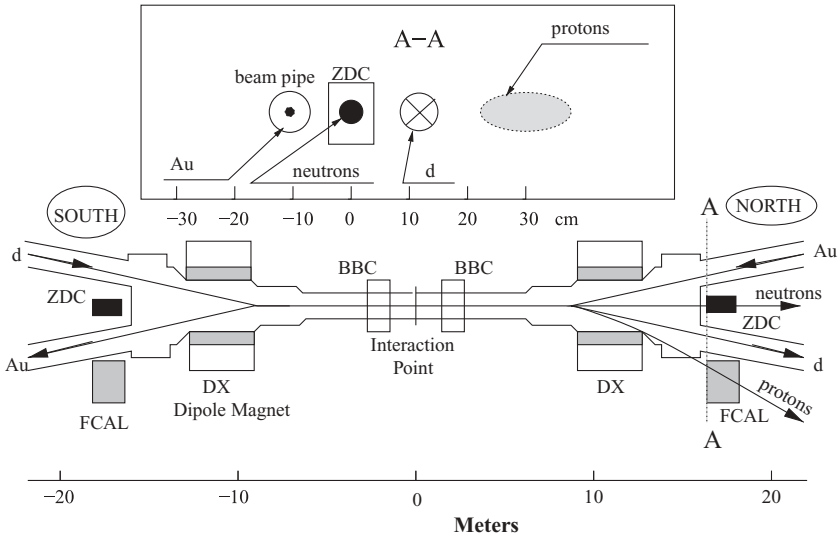

FIG. 1. FCAL, ZDC, and BBC positions relative to the vertex. The vertical scale in the figure is arbitrary. The insert at the top shows the position of primary beam, spectator neutron, and proton spots at the FCAL and ZDC locations; deuteron beam, spectator neutrons, and protons go into the plane, the gold beam is coming out of the plane.

conversion, we use the ring imaging Cherenkov detector (RICH). The RICH is filled with CO_2 gas at atmospheric pressure and has a charged particle threshold $\gamma_{\text{th}} = 35$ for emission of Cherenkov photons.

To characterize the global parameters of the collision and its centrality, the PHENIX experiment uses beam-beam counters (BBCs) covering the pseudorapidity range $3.0 < |\eta| < 3.9$, zero degree calorimeters (ZDCs) and forward calorimeters (FCALs) located at $|\eta| > 6$. The locations of these global detectors are schematically shown in Fig. 1. Each BBC is an array of 64 Cherenkov counters around the beam pipe and is positioned at 1.44 m upstream or downstream of the nominal vertex location. The information from the BBC is used for the event timing, vertex position, and centrality determination. The two ZDCs are hadronic calorimeters which measure spectator neutrons [16]. They are located 18 m from the interaction point. At the top RHIC energy of 100 GeV/nucleon, neutrons evaporated from the spectator remnants of the collision are emitted within 1 mrad from the colliding beam direction. Charged fragments and the noninteracted primary beam are bent by deflecting (DX) magnets to much larger angles. The ZDC measures the total neutron energy within a small cone and with this provides the number of spectator neutrons from the interacting nucleus. The ZDC on the north side measured 100 GeV neutrons from deuteron fragmentation with a resolution of $\sigma = 28$ GeV.

The forward calorimeters were installed before the d+Au run. The FCAL is a hadron calorimeter and consists of lead scintillating fiber modules originally used in BNL Alternating Gradient Synchrotron (AGS) Experiment E864 [17] rearranged into two 9 by 10 arrays. The only difference from the E864 experiment is the readout electronics, which are identical to PHENIX central arm electromagnetic calorimeter electronics. The size of each module is $10 \times 10 \times 117$ cm, the average tower density is 9.6 g/cm^3, and the total length corresponds to 60 nuclear interaction lengths. The two arrays are located 18 m from the interaction point along the beam pipes downstream of the first beam-line deflecting (DX) magnet. The DX magnets work as sweeping magnets for the spectator protons. The FCAL measures the energy of the spectator protons. The resolution of the FCAL on the north side for measuring 100 GeV protons from the deuteron fragmentation was $\sigma = 40$ GeV.

B. Centrality analysis

The present analysis is based on minimum bias events, defined by a coincidence of at least one photomultiplier each in the north and south BBCs. The data were taken for events with vertex position within $|z| < 30$ cm along the beam axis. A total of 6.2×10^7 events were analyzed, which corresponds to 1.6 nb^{-1} of total integrated luminosity. At this vertex cut, the minimum bias trigger cross section measured by BBC is $1.99\,\text{b} \pm 5.2\%$ [18]. Thus at the trigger efficiency [12] of $88.5\% \pm 4\%$ we get the total inelastic d+Au cross section of 2.26 ± 0.1 b. Centrality classes in d+Au events were defined by charged particle multiplicity in the BBC south (BBCS) (the gold fragmentation side). We assume that the number of charged particles firing the BBCS is linearly proportional, on average, to the number of participants from the gold nucleus in the reaction. To check this, the BBCS response was simulated as a superposition of independent N_{targ} nucleon-nucleon type reactions, where N_{targ} is the number of participating nucleons in the struck gold nucleus. As a baseline for the BBCS modeling, we use unbiased data from previous RHIC p+p runs where proton-proton inelastic collisions were selected with a trigger synchronized to fire whenever filled bunches crossed in the PHENIX interaction region. N_{targ} was calculated using a Glauber model [12] with a particular parameter set [19]. The resulting distribution for minimum bias events is plotted in Fig. 2 together with experimental data.

The calculation appears to follow the general features of the data distribution, which supports our assumption that the number of BBCS firings is proportional to N_{targ}. We define four centrality classes for d+Au collisions by slicing the BBCS multiplicity distribution into four regions, A, B, C, and D (Fig. 3). These regions were selected to define in d+Au collisions four centrality classes 0–20%, 20–40%, 40–60%, and 60–88%, respectively. We have taken into account the

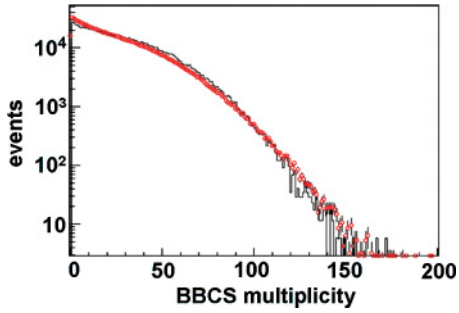

FIG. 2. (Color online) Comparison between the experimental data hit distribution in BBCS in d+Au collisions (open circles) and the calculated BBCS hit distribution (solid line).

limited trigger efficiency for the peripheral collisions. The tagged sample, in which only one nucleon from the deuteron projectile interacts, has a differently shaped BBCS multiplicity distribution than the general data. Nevertheless, for both the tagged sample and the general data, the same BBCS selections were used to define the collision centrality.

In the Glauber model Monte Carlo simulation of d+Au collisions, the deuteron wave function was represented by the Hulthén form [19].[1] The square of this wave function determines the probability distribution for the proton-neutron distance in the deuteron, as shown in Fig. 4. The deuteron is a large system with a mean proton-neutron distance of about 3 fm and a significant probability to be larger. In the left side of Fig. 5, we present the calculated impact parameter distributions of d+Au collisions and the tagged N+Au sample. On the right side of Fig. 5, the corresponding distributions of the number of collisions per participant nucleon from the interacting deuteron, ν, are plotted. The parameter ν is comparable to the number of collisions suffered by the proton in p+A experiments. The impact parameter b is defined as the distance

[1]For the gold nucleus, we use the Woods-Saxon density distribution with radius $R = 6.38$ fm, diffuseness parameter $a = 0.54$ fm, and N-N cross section $\sigma_{NN}^{\text{inel}} = 42$ mb. The deuteron is described by a Hulthén wave function with $\alpha = 0.228\,\text{fm}^{-1}$ and $\beta = 1.18\,\text{fm}^{-1}$, see Ref. [19].

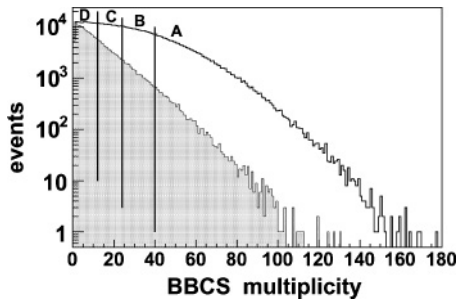

FIG. 3. Multiplicity distribution in BBCS, located on the gold nucleus fragmentation side. Four centrality classes for d+Au collisions are defined by slicing the BBCS distribution, shown with vertical lines. The same multiplicity cuts were used for the tagged sample of p+Au and n+Au events, the summed distribution of which is shown in the lower histogram.

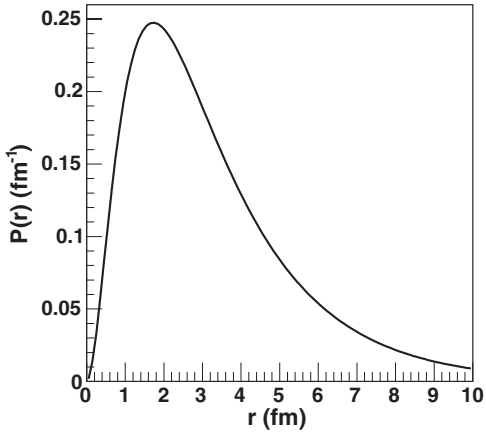

FIG. 4. Probability density distribution for the proton-neutron distance in the deuteron given by the square of the Hulthén wave function [19].

between the centers of the colliding nuclei, Au and d. This means that for the tag sample, the interaction point of participant nucleon from the deuteron is closer to the Au center than the distance b, and the spectator nucleon leaves the interaction region at a distance larger than b. We also did a Monte Carlo simulation with the most recent deuteron wave function parametrization from Ref. [20]. We found that the difference between the calculation with the Hulthén form and the most recent parametrization for the number of nucleon collisions does not exceed 1%.

In Fig. 6, we illustrate our tag selection cuts. A p+Au collision event is tagged by the detection of a spectator neutron in the ZDC north (ZDCN) on the deuteron fragmentation side. Similarly, we use the FCAL north (FCALN) on the deuteron fragmentation side to detect a spectator proton and thereby tag n+Au collision events. The scatter plot in Fig. 6 shows the ZDCN and FCALN signals and has three distinct regions. Region 1 is defined as small or no signal in both the ZDCN and FCALN, which corresponds to the case in which both nucleons from the deuteron interact with the Au nucleus. Region 2 has a small signal in the ZDCN and about 100 GeV amplitude signal in the FCALN. This corresponds to tagged n+Au collisions. Region 3 has a small signal in the FCALN and about 100 GeV energy release in the ZDCN. Events in this region are tagged p+Au events. In Region 3, there is a small (anti) correlation between the ZDCN and FCALN. The reason for this is the close proximity of the FCALN to the ZDCN, see Fig. 1. The ZDCN effectively acts as a secondary target for 100 GeV spectator neutrons. There is some contamination of secondary particles produced in the ZDCN into the large volume FCALN.

The purity of the tag samples from possible background contamination was thoroughly investigated. Figure 7 shows ZDCN and FCALN responses for the most central events. Background may contribute to the tag sample from the left side of the spectrum with low amplitudes. To estimate the background contamination, we fitted the left part of the spectrum using an exponentially falling function and fitted a Gaussian function to the detector response to the spectator nucleon. The thin smooth line in Fig. 7 shows the sum of the

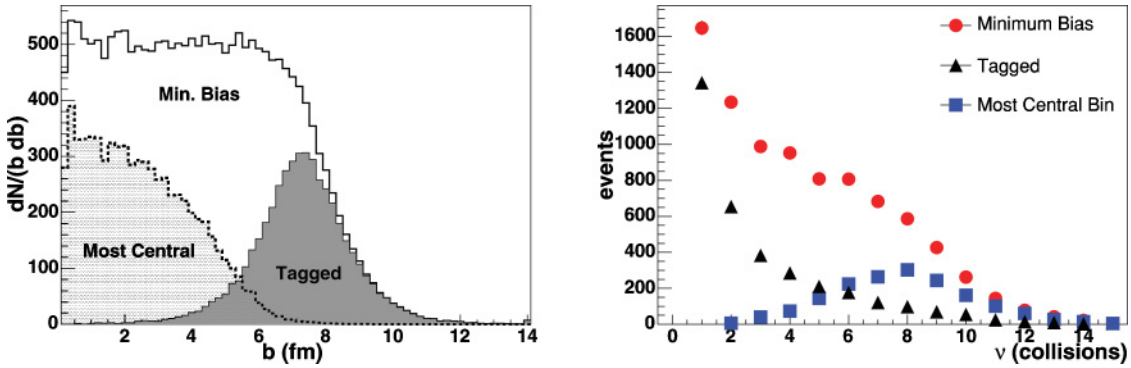

FIG. 5. (Color online) Left: impact parameter distribution for the minimum bias d+Au collisions, for the most central events (centrality bin A), and for the tagged sample. For tagged events, the impact parameter was defined from the center of the deuteron. Right: the corresponding distribution of the number of collisions per participant nucleon from deuteron, ν.

two functions. The background under the Gaussian peak was estimated as the integral of the exponential function above our cut, which is marked by the vertical line and arrow. In central p+Au events, we estimate 2.8% contamination in the ZDCN spectrum. For more peripheral events, this contamination decreases and reaches 1.4% in the most peripheral bin.

The background contamination in the FCALN defined n+Au sample is more complicated. For the most central events, as shown in Fig. 7 on the right, the background contributes 0.4% to the area above our cut. As centrality changes, so too does the shape of the background spectrum. Figure 8 illustrates the problem of background estimation. Attempts to fit the background spectrum with an exponential function, as was done for central events, failed. The sum of the estimated background and the Gauss fit is well above the experimental data, implying that the background spectrum falls much faster than a simple exponential function. However, the relevant question in assessing the background contamination is not its absolute or relative value, but rather how much it could distort our experimental data. The goal of this analysis is to measure the charged hadron spectrum in the PHENIX central arms. Thus, we can estimate the stability of our results measured by the central arms versus different cuts applied to the FCALN. We define the stability of the measurement, S, in a particular FCALN bin (Fig. 9) as the ratio of the number of charged particle tracks per event with $p_T > 0.5\,\mathrm{GeV}/c$ for this cut to a reference cut in which the signal to background ratio is the largest. For the reference cut, we use 100 ± 20 GeV FCALN response (within region 3 as defined above). This is the most probable detector response for a spectator proton, as seen in Fig. 8. We observe that in the region just to the left of our reference cut, where we may expect about equal amount of signal and background events, the parameter S is only 3% smaller than unity, as seen in Fig. 9. Within errors, S does not depend on track momentum. Thus, in the worst case, the background contamination effect is less than 2% for events above our cut in the n+Au tagged sample.

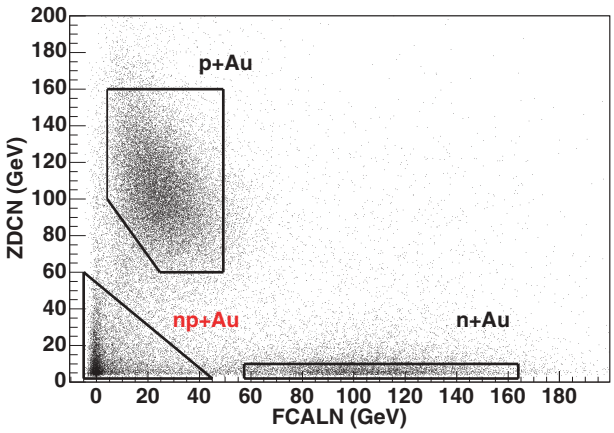

FIG. 6. (Color online) Scatter plot of ZDCN and FCALN signals on the deuteron fragmentation side. Solid lines show cuts which define the p+Au and n+Au collisions.

We do not correct the tagged sample results for any contamination. We average the two tagged samples to form a single nucleon+Au (N+Au) sample.

For each of the four BBCS multiplicity regions shown in Fig. 3, using a Monte Carlo model within the Glauber multiple collision formalism [21], we calculate for the d+Au and the tagged N+Au collisions the average number of participating nucleons N_{part}, the nuclear overlap function T_{AB}, the number of collisions N_{coll}, and number of collisions per participant nucleon from the deuteron ν. The calculated values are presented in Table I. The nuclear overlap function T_{AB} is defined as

$$T_{AB}(b) = \int d^2\,\vec{s}\; T_A(\vec{s})\, T_B(|\vec{b} - \vec{s}|)\,, \tag{1}$$

where the integration is performed over the element of overlapping area $d^2\,\vec{s}$, and $\vec{s} = (x, y)$ is a vector in the transverse plane of interacting nuclei at the impact parameter $\vec{b}$ between the centers of the nuclei. For nucleus A, the nuclear thickness function $T_A(b)$ is defined as

$$T_A(b) = \int dz\, \rho_A(b, z)\,. \tag{2}$$

Normalization of $T_{AB}(b)$ is done by integration over all impact parameters:

$$\int d^2\, b\, T_{AB}(b) = A\, B. \tag{3}$$

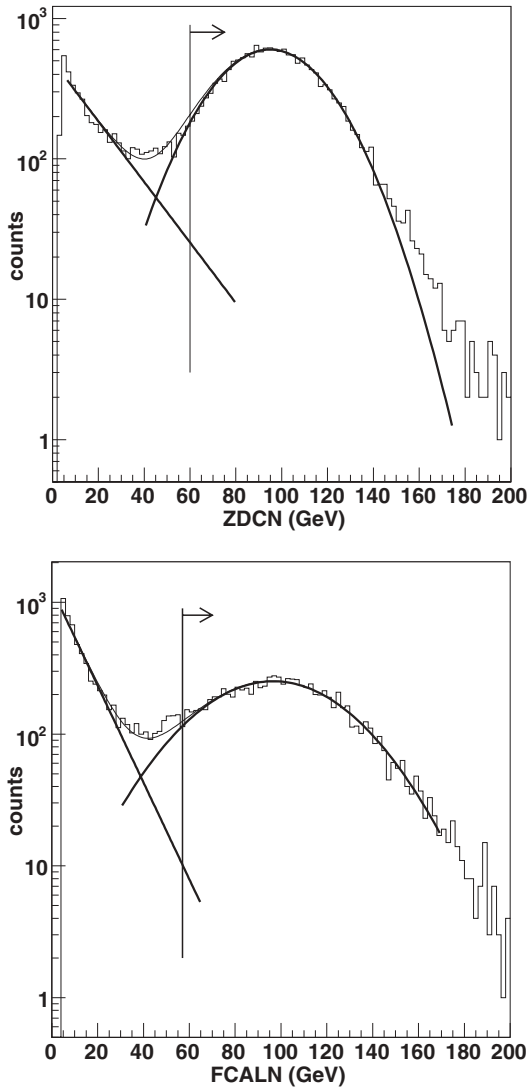

FIG. 7. ZDCN and FCALN spectra for the most central tagged events. Detector response to the spectator nucleon is fit with a Gauss function. Background from the left side of the spectra was fit to an exponential function and extrapolated to the region above our cuts. All events to the right of the cuts, shown by vertical solid lines, were defined as a tag sample.

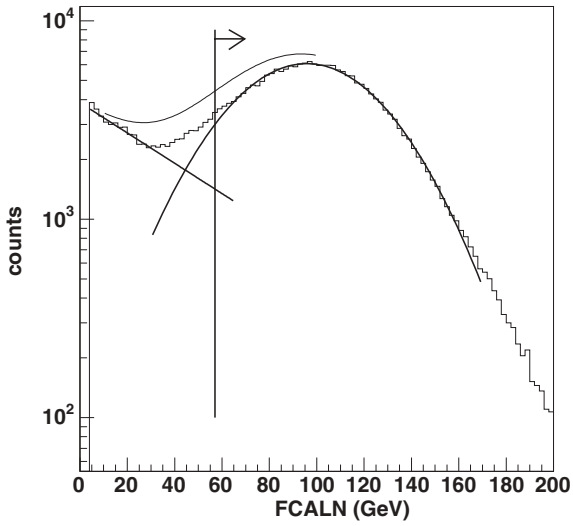

FIG. 8. FCALN spectrum for the most peripheral tagged events, with the same line notation as Fig. 7. The plot illustrates the difficulty of evaluating the background contribution in the most peripheral collisions: background fit with an exponentially falling spectrum significantly overestimates the contribution to the events above our cut.

The average number of binary inelastic nucleon-nucleon collisions at impact parameter b was calculated from $T_{AB}(b)$ as

$$\langle N_{\rm coll}\rangle = \sigma_{NN} T_{AB}(b)\,, \tag{4}$$

where σ_{NN} is the inelastic nucleon-nucleon cross section [19].

An additional multiplicative correction factor, $C_{\rm BBC}$, see Table I, has been applied to the data for different centrality bin selections [22]. This correction addresses two effects, each of which distorts the centrality classification in the opposite direction. Because of natural fluctuations in the number of produced charged particles at a particular impact parameter, the BBCS centrality selections have imperfect resolution. In the case of a steeply falling BBCS multiplicity spectrum, especially for the tagged sample (see Fig. 3), there is a contamination of peripheral collision events into a more central event class. This effectively decreases the actual number of $N_{\rm coll}$ and particle production in the central events. The second

TABLE I. Total number of participants $N_{\rm part}$, number of collisions $N_{\rm coll}$, nuclear overlap function T_{AB}, see Eq. (10), average number of collisions per participant nucleon from deuteron ν, and the BBC bin correction factor for different centrality classes.

Cent. bin	$\langle N_{\rm part}\rangle$	$\langle N_{\rm coll}\rangle$	$\langle T_{AB}\rangle$(mb^{-1})	ν	$C_{\rm BBC}$
A	15.0 ± 1.0	15.4 ± 1.0	0.37 ± 0.02	7.5 ± 0.5	0.95 ± 0.03
B	10.4 ± 0.4	10.6 ± 0.7	0.25 ± 0.02	5.6 ± 0.4	0.99 ± 0.01
C	7.0 ± 0.6	7.0 ± 0.6	0.17 ± 0.01	4.0 ± 0.3	1.03 ± 0.01
D	3.2 ± 0.3	3.1 ± 0.3	0.07 ± 0.01	2.2 ± 0.2	1.04 ± 0.03
tag A	10.6 ± 0.7	9.6 ± 0.7	0.23 ± 0.02	9.6 ± 0.7	0.93 ± 0.03
tag B	8.0 ± 0.6	7.0 ± 0.6	0.17 ± 0.02	7.0 ± 0.6	0.95 ± 0.02
tag C	5.6 ± 0.3	4.6 ± 0.3	0.11 ± 0.01	4.6 ± 0.3	0.95 ± 0.02
tag D	3.1 ± 0.2	2.1 ± 0.2	0.05 ± 0.01	2.1 ± 0.2	0.97 ± 0.04

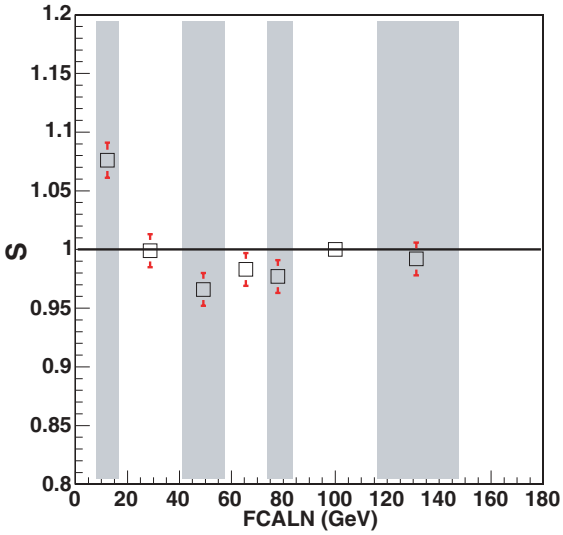

FIG. 9. (Color online) Stability of the results for different FCALN bins, see text for details.

effect is due to the BBC coincidence required for a PHENIX event trigger. In all calculations, we used for the inelastic nucleon-nucleon cross section $\sigma_{NN} = 42$ mb. Actually, this cross section has three components: nondiffractive collisions with 28 mb, single diffractive collisions with 10 mb, and double diffractive collisions with 4 mb cross section [23]. From Monte Carlo simulation of $p+p$ collisions, we found BBC trigger efficiencies of about $(72 \pm 1)\%$, $(7 \pm 1)\%$, and $(32 \pm 1)\%$, for each process, respectively. In the Monte Carlo simulation, we use the PYTHIA 6.2 event generator [23] and the GEANT simulation of the BBC detector. Single and double diffractive collisions produce particles dominantly near the beam rapidity and thus have a small probability for particle production in the BBC acceptance of $3.0 < |\eta| < 3.9$, and an even smaller probability at midrapidity. Therefore, the BBC trigger is biased to the nondiffractive collisions, which have larger particle production at midrapidity. In more central events as the number of nucleon-nucleon collisions increases, the probability that there will be at least one nondiffractive collision approaches 100%; thus the BBC bias becomes negligible in central events.

C. Charged hadron analysis

The present analysis follows the methods of the analysis described in Ref. [3]. The majority of background tracks are particles with low momenta, which in traveling from DC to PC3 undergo multiple scattering and are additionally deflected in the residual magnetic field behind the DC.

To minimize this background, we employ a track matching cut in the PC3 that rejects tracks whose displacement in the ϕ or z direction, D_ϕ and D_z, respectively, is greater than 2.5 standard deviations. In addition, we make a fiducial cut around the z vertex determined by the BBC. Despite these veto cuts, there is still significant background contamination for p_T above $4\,\mathrm{GeV}/c$ which must be subtracted. The main sources of the remaining background are e^+e^- pairs from photon conversions in the material between the collision vertex and the drift chamber, and secondary particles produced by hadron decays.

To distinguish these backgrounds, we use the RICH detector to divide all tracks into two subsets: tracks with an associated RICH signal, N_R, and tracks with no signal in the RICH, N_{NR}. Tracks with at least one hit in the RICH contain high p_T pions and conversion electrons. For reconstructed electrons with momentum above $150\,\mathrm{MeV}/c$, the average number of photomultiplier tube (PMT) hits in the RICH associated with the track is $\langle N_{\mathrm{PMT}} \rangle \approx 4.5$.

The RICH detects more than 99% of all conversion electrons for $N_{\mathrm{PMT}} \geqslant 1$. At this threshold the RICH also detects pions with $p_T \geqslant 4.8\,\mathrm{GeV}/c$, but the number of associated PMTs for pions reaches its asymptotic value well above $10\,\mathrm{GeV}/c$; for a $10\,\mathrm{GeV}/c$ pion $\langle N_{\mathrm{PMT}} \rangle = 3.6$. Therefore we label tracks with $N_{\mathrm{PMT}} \geqslant 5$ as electron tracks, N_e, which compose some fraction, R_e, of conversion electrons. To calculate this fraction, we take advantage of the deflection of conversion electrons in the magnetic field between the DC and PC3. This deflection leads to poor track matching in PC3 which distinguishes electrons from true high p_T pions. We define poor PC3 track matching as a displacement of more than four standard deviations in the ϕ direction. Thus we measure the value of R_e as the fraction of N_R with $4\sigma < |D_\phi| < 10\sigma$. For minimum bias events, we find $R_e = 0.41 \pm 0.01$. The real pion signal S_R in the N_R sample, is calculated for each p_T bin as

$$S_R = N_R - \frac{N_e}{R_e}. \tag{5}$$

The PC3 distribution for the conversion subtraction is shown on the left side of Fig. 10. The conversion subtraction is performed independently in each centrality bin. The definition of N_e (tracks with $N_{\mathrm{PMT}} \geqslant 5$) does not perfectly select electron tracks, as some fraction of pions satisfies the cut. This leads to a fraction of authentic pions, which have $N_{\mathrm{PMT}} \geqslant 5$, being subtracted along with the conversion electrons. This fraction is small below $7\,\mathrm{GeV}/c$, but increases rapidly for higher p_T. We calculate a correction factor to address this over-subtraction, using a Monte Carlo simulation of the detector. The uncertainty associated with this correction, $\delta_{\pi\,\mathrm{loss}}$, is shown later in Table III.

The hadron decay background is of two types: "decay" and "feed down." The decay background is produced by π and K decays far from the source and thus with reconstructed momenta different from their true momenta, whereas the feed-down background is produced by weak decays of short-lived particles, mostly K^0_s and Λ particles near the event vertex with apparent momenta close to their true momenta.

From tracks with no RICH signal, the N_{NR} sample, we define a subsample by selecting tracks with $p_T > 10.5\,\mathrm{GeV}/c$, a p_T region which is almost exclusively background. We expect that its shape in D_ϕ will be the same as the background in the lower p_T region. Within this subsample we calculate the ratio R_{decay} of tracks which pass the PC3 cut ($|D_\phi| < 2.5\sigma$) to those with a poor match ($4\sigma < |D_\phi| < 10\sigma$). For minimum bias events, $R_{\mathrm{decay}} = 0.55 \pm 0.03$. For each momentum bin, the total decay background is then obtained by multiplying

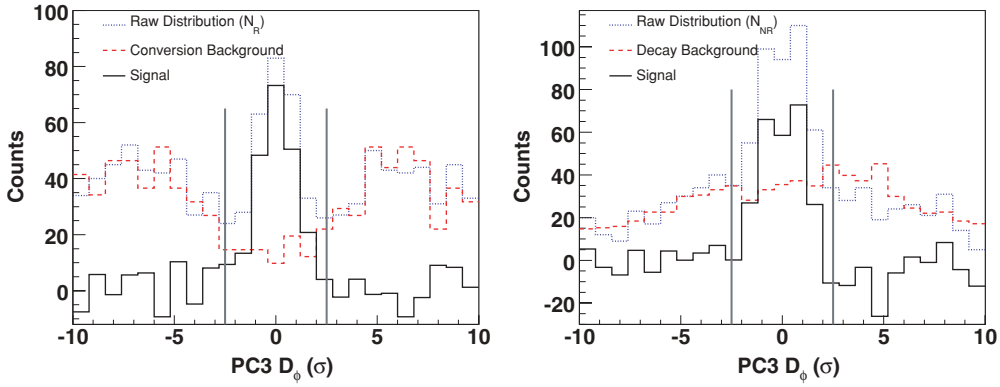

FIG. 10. (Color online) PC3 D_ϕ distributions for the conversion subtraction (left) and the decay subtraction (right) shown for minimum bias with $6 < p_T < 7\,\mathrm{GeV}/c$. The raw distributions, N_R and N_{NR} for conversion and decay, respectively, are shown with dotted lines. The estimated conversion background shown with a dashed line is N_e/R_e. The estimated decay background, shown with a dashed line, was obtained by scaling the PC3 distribution of N_{NR} tracks with $p_T > 10.5\,\mathrm{GeV}/c$ based on the $(4\sigma < |D_\phi| < 10\sigma)$ region. In both plots, the signal is the raw minus the estimated background distributions. The vertical bars show the track matching cuts at $\pm 2.5 D_\phi$.

the N_{NR} tracks with poor PC3 matching $(4\sigma < |D_\phi| < 10\sigma)$ by R_{decay}. The PC3 distribution for the decay subtraction is shown on the right side of Fig. 10. The decay background as a function of p_T is measured and subtracted independently in each centrality bin.

The feed-down subtraction addresses the detected π and p particles that were produced in the decays of K^0_s and Λ particles, so we define the total feed-down contamination as

$$C_{\mathrm{feed}} = \frac{(p+\pi)^{\mathrm{feed}}}{h^{\mathrm{detected}}}, \tag{6}$$

averaging over charged particle and antiparticle yields. For feed-down estimation, we have no statistical recourse and must resort to simulation to find the contamination. We assume that the spectral shapes of the K^0_s and Λ follow the shapes of the charged kaon and proton spectra, respectively. There is good agreement of Monte Carlo simulations in d+Au [24] and minimum bias Au+Au [3] for proton feed down. We therefore use the Au+Au Monte Carlo simulation, which also includes K^0_s to pion processes, to obtain the ratio $(p+\pi)^{\mathrm{feed}}/(p+K)^{\mathrm{detected}} = 0.2$, after the decay background subtraction. To make use of this ratio, we rewrite the contamination as

$$C_{\mathrm{feed}} = \frac{(p+\pi)^{\mathrm{feed}}}{(p+K)^{\mathrm{detected}}} \frac{(p+K)^{\mathrm{detected}}}{h^{\mathrm{detected}}}. \tag{7}$$

To find the contamination, we use the fraction of p+K particles in our measured hadron sample. To do so, for p_T less than $2.5\,\mathrm{GeV}/c$, we use the PHENIX published data on identified hadron production in d+Au [24]. We explicitly calculate the $(p+K)^{\mathrm{detected}}/h^{\mathrm{detected}}$ ratio from those data. At higher p_T assuming π^0 has the same yield as $\pi^\pm$, we subdivide this ratio as

$$\frac{p+K}{h} = \frac{p+K}{\pi}\frac{\pi}{h} = \left(\frac{p}{\pi} + \frac{K}{\pi^0}\right)\frac{\pi^0}{h}, \tag{8}$$

so that the right-hand side consists of all measured quantities. The p/π ratio is taken from STAR measurements [25] scaled to match the PHENIX data [24] in their common p_T region. The K/π^0 ratio is calculated from Refs. [12] and [26]. The ratio of π^0's to hadrons is calculated from the charged hadron measurement of this analysis and π^0 measurements in Ref. [12]. From both the low and high p_T regions, C_{feed} is calculated to be 9.6%. To this factor we assign a 50% systematic uncertainty based on uncertainty of the various particle ratios and the Monte Carlo simulation. C_{feed} is shown in Fig. 11. We correct for the effects of feed-down decay by multiplying the spectra remaining after the conversion and decay subtraction by $1 - C_{\mathrm{feed}}$.

Following the background subtraction, we constructed a single, p_T dependent correction function to correct the hadron spectra for acceptance, decay in flight, reconstruction efficiency, and momentum resolution. The correction is determined by using a Monte Carlo simulation [27] of the PHENIX detector. The correction function is necessarily particle species dependent to take into account multiple

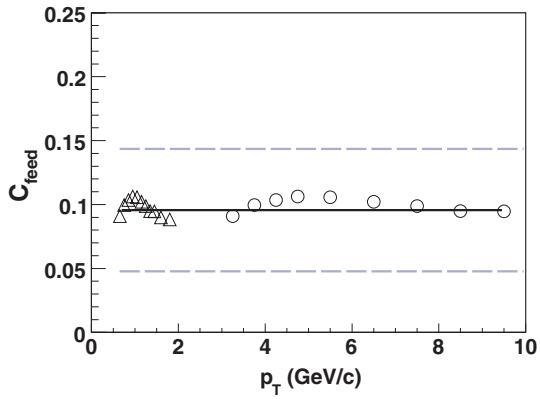

FIG. 11. Feed-down contamination as the ratio of protons and charged pions from feed-down decays to total detected charged hadrons. The low p_T points shown with triangles are calculated using the fraction of p+K particles to hadrons measured in Ref. [24]. The higher p_T points are calculated using the various ratios of Eq. (8). The solid line is a fit to both sets of points and is used as C_{feed}. It is bracketed by dashed lines showing the assigned 50% systematic uncertainty.

scattering and decays, therefore we calculate separate correction functions for $\pi^+, \pi^-, K^+, K^-, p^+$, and p^-. The individual functions are weighted by the particle p_T spectra measured in peripheral Au+Au collisions [28] to form a single correction factor, $C_{\rm MC}(p_T)$, subject to a systematic uncertainty, $\delta_{\rm MC\,weight}$, stemming from uncertainty on the particle mixture [12]. For absolute normalization of the spectra, we match the geometrical acceptance of the Monte Carlo simulation with the actual acceptance of the data. To obtain the charged hadron yield, we multiply the background-subtracted spectra by the correction function. We normalize each centrality bin by dividing by the number of events, and each momentum bin by dividing by its bin width. Each data point is corrected so its value corresponds to the bin center. We define the invariant hadron yield as

$$\frac{1}{N_{\rm evt}}\frac{d^2N}{2\pi p_T\,dp_T\,d\eta} = \left(\frac{d^2N}{2\pi p_T\,dp_T\,d\eta}\right)^{\text{bkg-subtracted}} \times \frac{1}{N_{\rm evt}}(1 - C_{\rm feed})C_{\rm MC}(p_T)C_{\rm BBC}. \quad (9)$$

All of the preceding steps are applied to the tagged N+Au (nucleon+gold) sample as well as to the general d+Au sample.

We further examine the d+Au invariant yields by comparing them with the invariant yield from p+p collisions. Previous experiments have demonstrated the suppression of charged hadron and pion yields in Au+Au collisions [3]; such suppression can be quantified by the nuclear modification factor R_{AB}. For any collision of nuclei A+B, R_{AB} is calculated for each centrality class as the ratio of the yield in A+B collision to the cross section in p+p collisions scaled by the nuclear overlap function $\langle T_{AB}\rangle$, that is,

$$R_{AB}(p_T) = \frac{(1/N_{\rm evt})\,d^2N^{A+B}/dp_T\,d\eta}{\langle T_{AB}\rangle\,d^2\sigma^{p+p}/dp_T\,d\eta}. \quad (10)$$

$\langle T_{AB}\rangle$ is determined by the density distribution in the nuclei A and B and is averaged over the impact parameter range within a particular centrality class. In our case, nucleus A refers to the deuteron (or the single nucleon in tagged events), and nucleus B refers to the gold nucleus. $\langle T_{AB}\rangle$ values are presented in Table I. Using the PHENIX p+p spectra [29], we thus calculate $R_{d\rm Au}$ and $R_{N\rm Au}$.

We estimate systematic uncertainties in the methods and assumptions of our analysis as displayed in Tables II and III. Table II shows uncertainties in the spectra that do not vary with p_T, and Table III shows uncertainties that vary with p_T. All the uncertainties listed in Table II propagate into the R_{AB} and the hadron/π^0 ratio, although the uncertainty from the feed-down correction partially cancels in the R_{AB} because of an analogous uncertainty in the p+p reference spectrum. The background subtraction and momentum scale uncertainties only partially cancel in the R_{AB}; the momentum resolution uncertainty and $\delta_{\pi\,\rm loss}$ fully cancel. The p+p reference spectrum also introduces an uncertainty that ranges from 10.7% in the low p_T bins to 11.3% at $p_T > 2\,{\rm GeV}/c$. The π^0 analysis [13] we used in the hadron/π^0 ratios applies the same BBC bias correction factors as the present analysis, and therefore the uncertainty stemming from this correction factor is canceled.

TABLE II. Systematic uncertainties that are constant for all values of transverse momentum p_T.

Source	Uncertainty (%)
Geometric acceptance correction	2.9
Track matching	2.2
Run-by-run variation	5
Feed-down correction	4.8
$\delta_{\rm MC\,weight}$	3.7
Total	8.7

TABLE III. Systematic uncertainties that vary with p_T. Background subtraction (Bckg. sub.) uncertainties refers to the 0–88% d+Au spectra; the uncertainties are greater in the more peripheral d+Au and more central N+Au spectra.

p_T (GeV/c)	Mom. res. (%)	Mom. scale (%)	Bckg. sub. (%)	$\delta_{\pi\,\rm loss}$ (%)	Total (%)
<4.5	<0.5	<3.2	<0.1	<0.3	<3.3
4.5–5.5	<0.6	3.3	0.5	0.5	3.4
5.5–6.5	0.8	3.5	1.4	1.1	4.0
6.5–7.5	1.0	3.6	2.0	3.6	5.6
7.5–8.5	1.4	3.7	4.9	6.9	9.3
8.5–9.5	1.8	3.8	11.9	13.9	18.8

III. RESULTS

The fully corrected p_T distributions of $(h^+ + h^-)/2$ for d+Au and N+Au collisions for minimum bias and four centrality classes are shown in Fig. 12. The d+Au data are in good agreement with the sum of identified hadrons published in Ref. [24].

The N+Au sample is averaged over p+Au and n+Au events. This is based on the good agreement between the yields of the two tagged samples, as shown in Fig. 13.

Figure 14 shows $R_{d\rm Au}$ and $R_{N\rm Au}$. As expected, in the most peripheral N+Au bin, with $N_{\rm coll} = 2.1$, $R_{N\rm Au}$ is consistent with unity. $R_{d\rm Au}$ and $R_{N\rm Au}$ are in agreement within our uncertainty bounds.

The enhancement of the hadron yield relative to p+p collisions has previously been observed in lower energy p+A collisions [10,11], and is called the Cronin effect. We observe that $R_{d\rm Au}$ and $R_{N\rm Au}$ are systematically larger than unity in the momentum range between 1.5 and 5 GeV/c with maximum amplitude around 1.3.

There are many theoretical models with very different assumptions about initial state effects, which describe the Cronin effect [30–32]. All the models agree that there is at least one additional scattering of the initial nucleon or parton while propagating though the target nucleus. This scattering increases the intrinsic transverse momentum of the colliding parton and leads to a broadening of the parton p_T distribution. We can parametrize the effect of this broadening by writing the mean value of parton intrinsic momentum k_T as

$$\langle k_T^2\rangle_{pA} = \langle k_T^2\rangle_{pp} + \langle k_T^2\rangle_A, \quad (11)$$

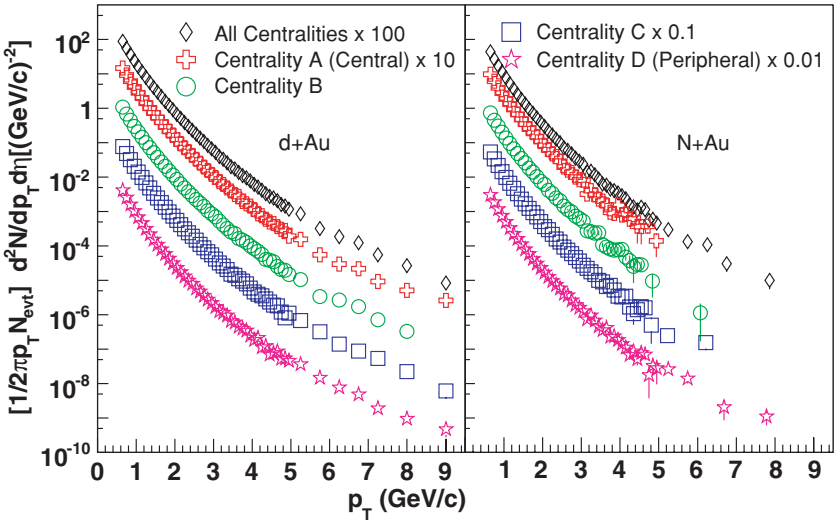

FIG. 12. (Color online) Charged hadron spectra for centrality selected d+Au and N+Au collisions. The error bars represent statistical uncertainties only, although they are generally smaller than the data point symbols. Points from different centrality bins are scaled sequentially by a factor of 10. (See Table I for centrality class definitions.)

where $\langle k_T^2 \rangle_{pp}$ is the square of the initial parton transverse momentum in the proton, $\langle k_T^2 \rangle_A$ is an additional momentum squared after rescattering, and $\langle k_T^2 \rangle_{pA}$ is the final broadened width. Most of the models differ on the assumption they use to describe $\langle k_T^2 \rangle_A$: whether there is a single hard scattering [31] or a sum of small sequential rescatterings [30] that produces the additional k_T.

Common to the models is that $\langle k_T^2 \rangle_A$ is a function of the number of sequential nucleon-nucleon collisions, ν. For impact parameter b, $\langle k_T^2 \rangle_A$ can be written as

$$\langle k_T^2 \rangle_A(b) = H(\nu(b) - 1), \tag{12}$$

where H is the square of the average momentum acquired in $\nu - 1$ rescatterings. For a single hard scattering model, $\langle k_T^2 \rangle_A$ should saturate at $\nu = 2$. We therefore investigate the shape of $R_{d\mathrm{Au}}$ as a function of ν to illuminate the underlying process. The centrality selection of our data and the tagged N+Au sample allow us to investigate precisely the effect of the collision geometry. We use $\nu = \langle N_{\mathrm{coll}}/N_{\mathrm{part}}^{\mathrm{deutron}} \rangle$ (in N+Au collisions, $\nu = \langle N_{\mathrm{coll}} \rangle$) to look explicitly at the impact parameter dependence of the nuclear modification factor.

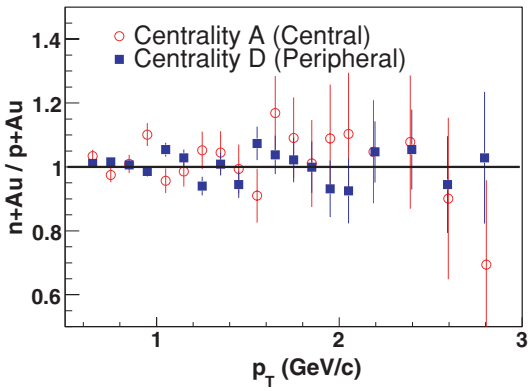

FIG. 13. (Color online) Ratio of n+Au to p+Au invariant yield per event shown in the most central and peripheral bins. The error bars are statistical only, as all systematic uncertainties cancel in the ratio. (See Table I for centrality class definitions.)

In Fig. 15, we plot $R_{d\mathrm{Au}}$ and $R_{N\mathrm{Au}}$ as a function of $(\nu - 1)$. The values of ν are presented in Table I.

Three transverse momentum regions were selected to study the dependence of R_{AB} on ν: $2.8 \leqslant p_T \leqslant 6.0$, $1.5 \leqslant p_T \leqslant 2.7$, and $0.6 \leqslant p_T \leqslant 1.0\,\mathrm{GeV}/c$. In the low p_T region, we expect scaling with the number of participating nucleons rather than with the number of binary collisions; therefore R_{AB} is less than unity. The Cronin effect is observed in the $2.8 \leqslant p_T \leqslant 6.0\,\mathrm{GeV}/c$ region, where within the limits of our uncertainties, it is independent of the number of additional scatterings $(\nu - 1)$. In the intermediate p_T region, the data show little to no Cronin enhancement, thus confirming scaling with the number of binary collisions. Just as $R_{d\mathrm{Au}}(p_T)$ and $R_{N\mathrm{Au}}(p_T)$ matched very closely, so do $R_{d\mathrm{Au}}(\nu)$ and $R_{N\mathrm{Au}}(\nu)$.

As discussed above, previous experiments found a larger Cronin enhancement for protons than pions [11]. Recently the PHENIX Collaboration published identified pion, kaon, and proton production data from $\sqrt{s_{NN}} = 200$ GeV d+Au collisions [24], in which a similar Cronin behavior was observed. $R_{d\mathrm{Au}}$ for protons reaches about 1.8 at $p_T \approx 3\,\mathrm{GeV}/c$, whereas pion $R_{d\mathrm{Au}}$ is measured to be about 1.1 for transverse momentum between 2 and $2.6\,\mathrm{GeV}/c$.

At the time these data were taken, the PHENIX experiment did not have the capability to measure identified charged pions and protons at momenta above 2.6 and $4\,\mathrm{GeV}/c$, respectively. To extend the trends observed in these low momentum regions [24], we calculate the ratio of the charged hadrons measured in the present analysis to the π^0 spectra from Ref. [13], alongside the ratio of $(p^{\pm} + K^{\pm} + \pi^{\pm})/\pi^{\pm}$ from Ref. [24]. These ratios are presented in Fig. 16.

In the transverse momentum region common to the two presented ratios, there is strong agreement between the analyses. The $(h^+ + h^-)/2\pi^0$ ratio is independent of p_T above $2\,\mathrm{GeV}/c$ where the identified particle data end, implying that the $R_{d\mathrm{Au}}$ and particle ratio trends observed at low transverse momentum continue at higher transverse momentum. The average value of 1.58 ± 0.03 of the $(h^+ + h^-)/2\pi^0$ ratio for p_T above $2\,\mathrm{GeV}/c$ in the peripheral D centrality bin agrees well with the value of 1.59 obtained from lower energy collisions in

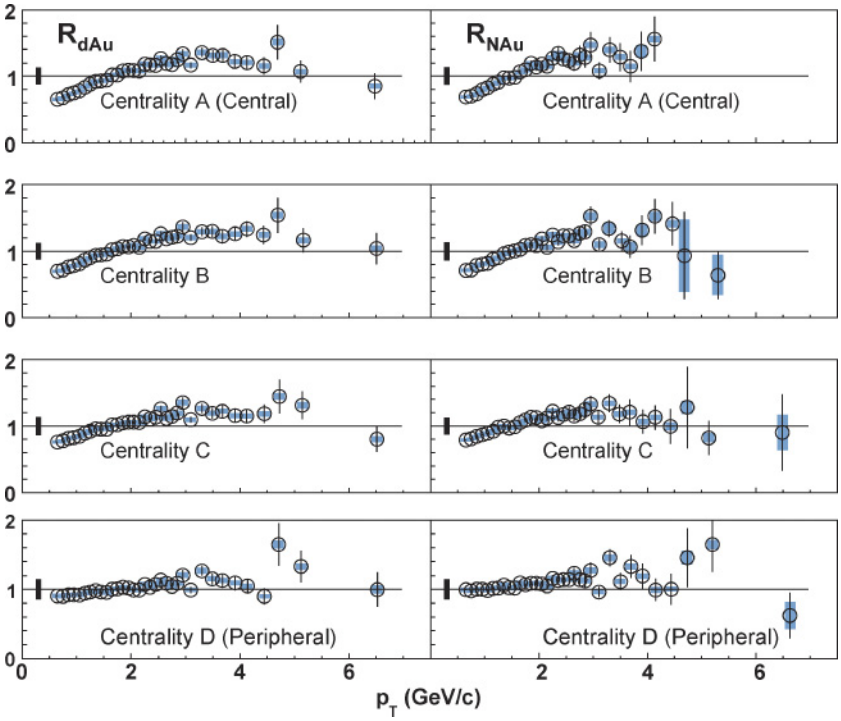

FIG. 14. (Color online) $R_{d\mathrm{Au}}$ and $R_{N\mathrm{Au}}$ as functions of p_T. The bars represent statistical uncertainty (often smaller than the data point symbols), the shaded boxes on each point represent systematic uncertainties that change with p_T, and the black boxes on the left show systematic uncertainties that do not change with p_T. (See Table I for centrality class definitions.)

the CERN Intersecting Storage Rings (ISR) [33]. As found in Ref. [1] for Au+Au collisions, this value rises for more central events: we find average values of 1.78 ± 0.02, 1.77 ± 0.03, and 1.72 ± 0.03 for centrality bins A, B, and C, respectively. There is an additional 11% systematic uncertainty common to all four values. The centrality dependence implies moderate medium modification effects in central $\sqrt{s_{NN}} = 200$ GeV collisions, even in the d+Au system, that increase the production of protons and kaons relative to pions. The PHENIX measurement of particle species dependent $R_{d\mathrm{Au}}$ in Ref. [24] at lower p_T suggests that the increased particle production relative to pions is dominantly proton and not kaon production.

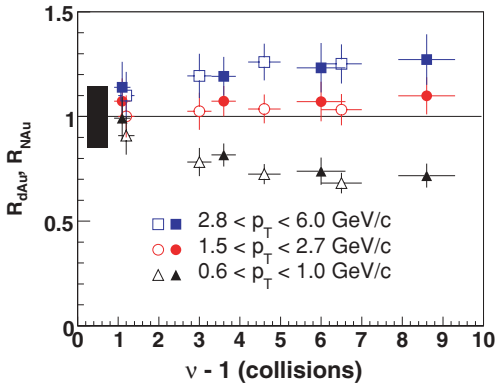

FIG. 15. (Color online) $R_{d\mathrm{Au}}$ (open symbols) and $R_{N\mathrm{Au}}$ (closed symbols) values averaged in three momentum ranges as functions of $\nu - 1$. Point-by-point uncertainty bars show the quadratic sum of the statistical uncertainty in R_{AB} and the systematic uncertainties that change with ν. The box on the far left represents the size of the systematic uncertainty that does not change with ν. Horizontal bars show the uncertainty in the value of ν for each centrality class.

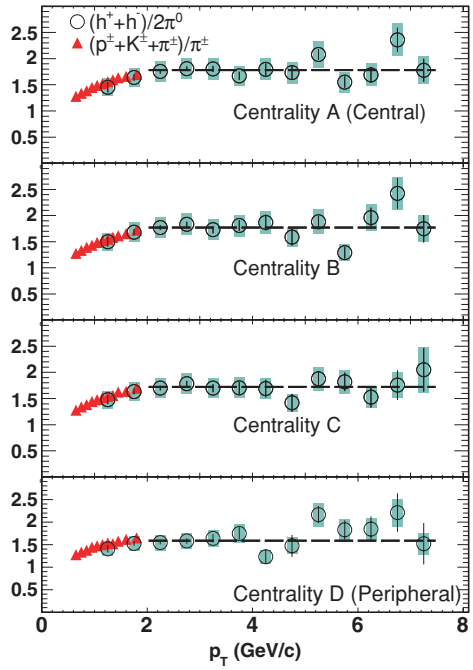

FIG. 16. (Color online) $(h^+ + h^-)/2\pi^0$ ratios as functions of transverse momentum from d+Au collisions in four centrality bins. Open circles are the charged hadron spectra from the present analysis divided by π^0 data from Ref. [13]. Bars indicate statistical uncertainties, and the shaded boxes systematic uncertainties. Triangles are the $(p^{\pm} + K^{\pm} + \pi^{\pm})/\pi^{\pm}$ ratios from Ref. [24], with statistical uncertainties roughly the size of the symbols. (See Table I for centrality class definitions.)

IV. SUMMARY

We have measured the centrality dependence of charged hadron production at midrapidity in d+Au collisions, as well as in p+Au and n+Au collisions that are tagged by a spectator nucleon from the deuteron nucleus. The hadron yields in p+Au and n+Au collisions are identical within our experimental uncertainty. Using the $p+p$ data from same energy, we calculated the nuclear modification factors $R_{d\mathrm{Au}}$ and $R_{N\mathrm{Au}}$ for various centrality selections. Within this analysis and its experimental uncertainty, there is no difference between $R_{d\mathrm{Au}}$ and $R_{N\mathrm{Au}}$. Instead of a strong suppression as predicted by some color glass condensate models [9], an excess of hadron production is seen at $p_T > 2\,\mathrm{GeV}/c$, consistent with enhancement due to the Cronin effect. The magnitude of the Cronin effect is independent of the number of additional scatterings $(\nu - 1)$ within the limits of our uncertainties. We also studied the ratio of charged hadron yield to pion yield. We found that the charged pions account for about 60% of the charged hadrons at $p_T > 3\,\mathrm{GeV}/c$, with a slightly larger value in central d+Au collisions. This implies that $R_{d\mathrm{Au}}$ for protons and kaons remains close to one at higher p_T.

ACKNOWLEDGMENTS

We thank the staff of the Collider-Accelerator and Physics Departments at Brookhaven National Laboratory and the staff of the other PHENIX participating institutions for their vital contributions. We acknowledge support from the Office of Nuclear Physics in the Office of Science of the Department of Energy, the National Science Foundation, Abilene Christian University Research Council, Research Foundation of SUNY, and Dean of the College of Arts and Sciences, Vanderbilt University (U.S.A.); Ministry of Education, Culture, Sports, Science, and Technology and the Japan Society for the Promotion of Science (Japan); Conselho Nacional de Desenvolvimento Científico e Tecnológico and Fundação de Amparo à Pesquisa do Estado de São Paulo (Brazil); Natural Science Foundation of China (People's Republic of China); Centre National de la Recherche Scientifique, Commissariat à l'Énergie Atomique, and Institut National de Physique Nucléaire et de Physique des Particules (France); Ministry of Industry, Science and Tekhnologies, Bundesministerium für Bildung und Forschung, Deutscher Akademischer Austausch Dienst, and Alexander von Humboldt Stiftung (Germany); Hungarian National Science Fund, OTKA (Hungary); Department of Atomic Energy (India); Israel Science Foundation (Israel); Korea Research Foundation and Korea Science and Engineering Foundation (Korea); Ministry of Education and Science, Russia Academy of Sciences, Federal Agency of Atomic Energy (Russia); VR and the Wallenberg Foundation (Sweden); the U.S. Civilian Research and Development Foundation for the Independent States of the Former Soviet Union; the U.S.-Hungarian NSF-OTKA-MTA; and the U.S.-Israel Binational Science Foundation.

[1] K. Adcox *et al.* (PHENIX Collaboration), Phys. Rev. Lett. **88**, 022301 (2002).
[2] S. S. Adler *et al.* (PHENIX Collaboration), Phys. Rev. Lett. **91**, 072301 (2003).
[3] S. S. Adler *et al.* (PHENIX Collaboration), Phys. Rev. C **69**, 034910 (2004).
[4] M. Gyulassy and M. Plumer, Phys. Lett. **B243**, 432 (1990); X. N. Wang and M. Gyulassy, Phys. Rev. Lett. **68**, 1480 (1992).
[5] S. S. Adler *et al.* (PHENIX Collaboration), Phys. Rev. Lett. **97**, 052301 (2006).
[6] S. S. Adler *et al.* (PHENIX Collaboration), Phys. Rev. C **71**, 051902 (2005).
[7] S. S. Adler *et al.* (PHENIX Collaboration), Phys. Rev. Lett. **91**, 172301 (2003).
[8] V. Greco, C. M. Ko, and P. Lévai, Phys. Rev. Lett. **90**, 202302 (2003).
[9] D. Kharzeev, Yu. V. Kovchegov, and K. Tuchin, Phys. Rev. D **68**, 094013 (2003).
[10] J. W. Cronin *et al.*, Phys. Rev. D **11**, 3105 (1975).
[11] P. B. Straub *et al.*, Phys. Rev. Lett. **68**, 452 (1992).
[12] S. S. Adler *et al.* (PHENIX Collaboration), Phys. Rev. Lett. **91**, 072303 (2003).
[13] S. S. Adler *et al.* (PHENIX Collaboration), Phys. Rev. Lett. **98**, 172302 (2007).
[14] M. Lev and B. Peterson, Z. Phys. C **21**, 155 (1983).
[15] K. Adcox *et al.* (PHENIX Collaboration), Nucl. Instrum. Methods A **499**, 469 (2003).
[16] C. Adler *et al.* (STAR Collaboration), Nucl. Instrum. Methods A **499**, 433 (2003).
[17] T. A. Armstrong *et al.*, Nucl. Instrum. Methods A **406**, 227 (1998).
[18] S. White, AIP Conf. Proc. **792**, 527 (2005).
[19] L. Hulthén and M. Sagawara, in *Handbuch der Physik,* edited by S. Flügge (Springer-Verlag, New York, 1957), Vol. 39.
[20] A. F. Krutov and V. E. Troitsky, Phys. Rev. C **76**, 017001 (2007).
[21] R. J. Glauber and G. Matthiae, Nucl. Phys. **B21**, 135 (1970).
[22] S. S. Adler *et al.* (PHENIX Collaboration), Phys. Rev. Lett. **94**, 082302 (2005).
[23] T. Sjöstrand, L. Lönnbland, and S. Mrenna, arXiv:hep-ph/0108264.
[24] S. S. Adler *et al.* (PHENIX Collaboration), Phys. Rev. C **74**, 024904 (2006).
[25] J. Adams *et al.* (STAR Collaboration), Phys. Lett. **B637**, 161 (2006).
[26] V. Ryabov (PHENIX Collaboration), Nucl. Phys. **A774**, 735 (2006).
[27] S. S. Adler *et al.* (PHENIX Collaboration), Nucl. Instrum. Methods A **499**, 593 (2003).
[28] S. S. Adler *et al.* (PHENIX Collaboration), Phys. Rev. C **69**, 034909 (2004).
[29] S. S. Adler *et al.* (PHENIX Collaboration), Phys. Rev. Lett. **95**, 202001 (2005).
[30] X. N. Wang, Phys. Rev. C **61**, 064910 (2000); Y. Zhang *et al.*, *ibid.* **65**, 034903 (2002).
[31] B. Z. Kopeliovich *et al.*, Phys. Rev. Lett. **88**, 232303 (2002); A. Accardi and D. Treleani, Phys. Rev. D **64**, 116004 (2001); I. Vitev and M. Gyulassy, Phys. Rev. Lett. **89**, 252301 (2002).
[32] A. Accardi, arXiv: hep-ph/0212148.
[33] B. Alper *et al.* (British-Scandinavian Collaboration), Nucl. Phys. **B100**, 237 (1975).

Enhancement of the dielectron continuum in Au+Au collisions at $\sqrt{s_{NN}}$=200 GeV

S. Afanasiev,[17] C. Aidala,[7] N.N. Ajitanand,[43] Y. Akiba,[37,38] J. Alexander,[43] A. Al-Jamel,[33] K. Aoki,[23,37] L. Aphecetche,[45] R. Armendariz,[33] S.H. Aronson,[3] R. Averbeck,[44] T.C. Awes,[34] B. Azmoun,[3] V. Babintsev,[14] A. Baldisseri,[8] K.N. Barish,[4] P.D. Barnes,[26] B. Bassalleck,[32] S. Bathe,[4] S. Batsouli,[7] V. Baublis,[36] F. Bauer,[4] A. Bazilevsky,[3] S. Belikov,[3,16] R. Bennett,[44] Y. Berdnikov,[40] M.T. Bjorndal,[7] J.G. Boissevain,[26] H. Borel,[8] K. Boyle,[44] M.L. Brooks,[26] D.S. Brown,[33] D. Bucher,[29] H. Buesching,[3] V. Bumazhnov,[14] G. Bunce,[3,38] J.M. Burward-Hoy,[26] S. Butsyk,[44] S. Campbell,[44] J.-S. Chai,[18] S. Chernichenko,[14] J. Chiba,[19] C.Y. Chi,[7] M. Chiu,[7] I.J. Choi,[52] T. Chujo,[49] V. Cianciolo,[34] C.R. Cleven,[12] Y. Cobigo,[8] B.A. Cole,[7] M.P. Comets,[35] P. Constantin,[16] M. Csanád,[10] T. Csörgő,[20] T. Dahms,[44] K. Das,[11] G. David,[3] H. Delagrange,[45] A. Denisov,[14] D. d'Enterria,[7] A. Deshpande,[38,44] E.J. Desmond,[3] O. Dietzsch,[41] A. Dion,[44] J.L. Drachenberg,[1] O. Drapier,[24] A. Drees,[44] A.K. Dubey,[51] A. Durum,[14] V. Dzhordzhadze,[46] Y.V. Efremenko,[34] J. Egdemir,[44] A. Enokizono,[13] H. En'yo,[37,38] B. Espagnon,[35] S. Esumi,[48] D.E. Fields,[32,38] F. Fleuret,[24] S.L. Fokin,[22] B. Forestier,[27] Z. Fraenkel,[51] J.E. Frantz,[7] A. Franz,[3] A.D. Frawley,[11] Y. Fukao,[23,37] S.-Y. Fung,[4] S. Gadrat,[27] F. Gastineau,[45] M. Germain,[45] A. Glenn,[46] M. Gonin,[24] J. Gosset,[8] Y. Goto,[37,38] R. Granier de Cassagnac,[24] N. Grau,[16] S.V. Greene,[49] M. Grosse Perdekamp,[15,38] T. Gunji,[5] H.-Å. Gustafsson,[28] T. Hachiya,[13,37] A. Hadj Henni,[45] J.S. Haggerty,[3] M.N. Hagiwara,[1] H. Hamagaki,[5] H. Harada,[13] E.P. Hartouni,[25] K. Haruna,[13] M. Harvey,[3] E. Haslum,[28] K. Hasuko,[37] R. Hayano,[5] M. Heffner,[25] T.K. Hemmick,[44] J.M. Heuser,[37] X. He,[12] H. Hiejima,[15] J.C. Hill,[16] R. Hobbs,[32] M. Holmes,[49] W. Holzmann,[43] K. Homma,[13] B. Hong,[21] T. Horaguchi,[37,47] M.G. Hur,[18] T. Ichihara,[37,38] K. Imai,[23,37] M. Inaba,[48] D. Isenhower,[1] L. Isenhower,[1] M. Ishihara,[37] T. Isobe,[5] M. Issah,[43] A. Isupov,[17] B.V. Jacak,[44,*] J. Jia,[7] J. Jin,[7] O. Jinnouchi,[38] B.M. Johnson,[3] K.S. Joo,[30] D. Jouan,[35] F. Kajihara,[5,37] S. Kametani,[5,50] N. Kamihara,[37,47] M. Kaneta,[38] J.H. Kang,[52] T. Kawagishi,[48] A.V. Kazantsev,[22] S. Kelly,[6] A. Khanzadeev,[36] D.J. Kim,[52] E. Kim,[42] Y.-S. Kim,[18] E. Kinney,[6] A. Kiss,[10] E. Kistenev,[3] A. Kiyomichi,[37] C. Klein-Boesing,[29] L. Kochenda,[36] V. Kochetkov,[14] B. Komkov,[36] M. Konno,[48] D. Kotchetkov,[4] A. Kozlov,[51] P.J. Kroon,[3] G.J. Kunde,[26] N. Kurihara,[5] K. Kurita,[39,37] M.J. Kweon,[21] Y. Kwon,[52] G.S. Kyle,[33] R. Lacey,[43] J.G. Lajoie,[16] A. Lebedev,[16] Y. Le Bornec,[35] S. Leckey,[44] D.M. Lee,[26] M.K. Lee,[52] M.J. Leitch,[26] M.A.L. Leite,[41] H. Lim,[42] A. Litvinenko,[17] M.X. Liu,[26] X.H. Li,[4] C.F. Maguire,[49] Y.I. Makdisi,[3] A. Malakhov,[17] M.D. Malik,[32] V.I. Manko,[22] H. Masui,[48] F. Matathias,[44] M.C. McCain,[15] P.L. McGaughey,[26] Y. Miake,[48] T.E. Miller,[49] A. Milov,[44] S. Mioduszewski,[3] G.C. Mishra,[12] J.T. Mitchell,[3] D.P. Morrison,[3] J.M. Moss,[26] T.V. Moukhanova,[22] D. Mukhopadhyay,[49] J. Murata,[39,37] S. Nagamiya,[19] Y. Nagata,[48] J.L. Nagle,[6] M. Naglis,[51] T. Nakamura,[13] J. Newby,[25] M. Nguyen,[44] B.E. Norman,[26] A.S. Nyanin,[22] J. Nystrand,[28] E. O'Brien,[3] C.A. Ogilvie,[16] H. Ohnishi,[37] I.D. Ojha,[49] H. Okada,[23,37] K. Okada,[38] O.O. Omiwade,[1] A. Oskarsson,[28] I. Otterlund,[28] K. Ozawa,[5] D. Pal,[49] A.P.T. Palounek,[26] V. Pantuev,[44] V. Papavassiliou,[33] J. Park,[42] W.J. Park,[21] S.F. Pate,[33] H. Pei,[16] J.-C. Peng,[15] H. Pereira,[8] V. Peresedov,[17] D.Yu. Peressounko,[22] C. Pinkenburg,[3] R.P. Pisani,[3] M.L. Purschke,[3] A.K. Purwar,[44] H. Qu,[12] J. Rak,[16] I. Ravinovich,[51] K.F. Read,[34,46] M. Reuter,[44] K. Reygers,[29] V. Riabov,[36] Y. Riabov,[36] G. Roche,[27] A. Romana,[24,†] M. Rosati,[16] S.S.E. Rosendahl,[28] P. Rosnet,[27] P. Rukoyatkin,[17] V.L. Rykov,[37] S.S. Ryu,[52] B. Sahlmueller,[29] N. Saito,[23,37,38] T. Sakaguchi,[5,50] S. Sakai,[48] V. Samsonov,[36] H.D. Sato,[23,37] S. Sato,[3,19,48] S. Sawada,[19] V. Semenov,[14] R. Seto,[4] D. Sharma,[51] T.K. Shea,[3] I. Shein,[14] T.-A. Shibata,[37,47] K. Shigaki,[13] M. Shimomura,[48] T. Shohjoh,[48] K. Shoji,[23,37] A. Sickles,[44] C.L. Silva,[41] D. Silvermyr,[34] K.S. Sim,[21] C.P. Singh,[2] V. Singh,[2] S. Skutnik,[16] W.C. Smith,[1] A. Soldatov,[14] R.A. Soltz,[25] W.E. Sondheim,[26] S.P. Sorensen,[46] I.V. Sourikova,[3] F. Staley,[8] P.W. Stankus,[34] E. Stenlund,[28] M. Stepanov,[33] A. Ster,[20] S.P. Stoll,[3] T. Sugitate,[13] C. Suire,[35] J.P. Sullivan,[26] J. Sziklai,[20] T. Tabaru,[38] S. Takagi,[48] E.M. Takagui,[41] A. Taketani,[37,38] K.H. Tanaka,[19] Y. Tanaka,[31] K. Tanida,[37,38] M.J. Tannenbaum,[3] A. Taranenko,[43] P. Tarján,[9] T.L. Thomas,[32] M. Togawa,[23,37] A. Toia,[44] J. Tojo,[37] H. Torii,[37] R.S. Towell,[1] V-N. Tram,[24] I. Tserruya,[51] Y. Tsuchimoto,[13,37] S.K. Tuli,[2] H. Tydesjö,[28] N. Tyurin,[14] H. Valle,[49] H.W. vanHecke,[26] J. Velkovska,[49] R. Vertesi,[9] A.A. Vinogradov,[22] E. Vznuzdaev,[36] M. Wagner,[23,37] X.R. Wang,[33] Y. Watanabe,[37,38] J. Wessels,[29] S.N. White,[3] N. Willis,[35] D. Winter,[7] C.L. Woody,[3] M. Wysocki,[6] W. Xie,[4,38] A. Yanovich,[14] S. Yokkaichi,[37,38] G.R. Young,[34] I. Younus,[32] I.E. Yushmanov,[22] W.A. Zajc,[7] O. Zaudtke,[29] C. Zhang,[7] J. Zimányi,[20,†] and L. Zolin[17]

(PHENIX Collaboration)

[1] *Abilene Christian University, Abilene, TX 79699, U.S.*
[2] *Department of Physics, Banaras Hindu University, Varanasi 221005, India*
[3] *Brookhaven National Laboratory, Upton, NY 11973-5000, U.S.*

arXiv:0706.3034v1 [nucl-ex] 20 Jun 2007

[4]University of California - Riverside, Riverside, CA 92521, U.S.
[5]Center for Nuclear Study, Graduate School of Science, University of Tokyo, 7-3-1 Hongo, Bunkyo, Tokyo 113-0033, Japan
[6]University of Colorado, Boulder, CO 80309, U.S.
[7]Columbia University, New York, NY 10027 and Nevis Laboratories, Irvington, NY 10533, U.S.
[8]Dapnia, CEA Saclay, F-91191, Gif-sur-Yvette, France
[9]Debrecen University, H-4010 Debrecen, Egyetem tér 1, Hungary
[10]ELTE, Eötvös Loránd University, H - 1117 Budapest, Pázmány P. s. 1/A, Hungary
[11]Florida State University, Tallahassee, FL 32306, U.S.
[12]Georgia State University, Atlanta, GA 30303, U.S.
[13]Hiroshima University, Kagamiyama, Higashi-Hiroshima 739-8526, Japan
[14]IHEP Protvino, State Research Center of Russian Federation, Institute for High Energy Physics, Protvino, 142281, Russia
[15]University of Illinois at Urbana-Champaign, Urbana, IL 61801, U.S.
[16]Iowa State University, Ames, IA 50011, U.S.
[17]Joint Institute for Nuclear Research, 141980 Dubna, Moscow Region, Russia
[18]KAERI, Cyclotron Application Laboratory, Seoul, South Korea
[19]KEK, High Energy Accelerator Research Organization, Tsukuba, Ibaraki 305-0801, Japan
[20]KFKI Research Institute for Particle and Nuclear Physics of the Hungarian Academy of Sciences (MTA KFKI RMKI), H-1525 Budapest 114, POBox 49, Budapest, Hungary
[21]Korea University, Seoul, 136-701, Korea
[22]Russian Research Center "Kurchatov Institute", Moscow, Russia
[23]Kyoto University, Kyoto 606-8502, Japan
[24]Laboratoire Leprince-Ringuet, Ecole Polytechnique, CNRS-IN2P3, Route de Saclay, F-91128, Palaiseau, France
[25]Lawrence Livermore National Laboratory, Livermore, CA 94550, U.S.
[26]Los Alamos National Laboratory, Los Alamos, NM 87545, U.S.
[27]LPC, Université Blaise Pascal, CNRS-IN2P3, Clermont-Fd, 63177 Aubiere Cedex, France
[28]Department of Physics, Lund University, Box 118, SE-221 00 Lund, Sweden
[29]Institut für Kernphysik, University of Muenster, D-48149 Muenster, Germany
[30]Myongji University, Yongin, Kyonggido 449-728, Korea
[31]Nagasaki Institute of Applied Science, Nagasaki-shi, Nagasaki 851-0193, Japan
[32]University of New Mexico, Albuquerque, NM 87131, U.S.
[33]New Mexico State University, Las Cruces, NM 88003, U.S.
[34]Oak Ridge National Laboratory, Oak Ridge, TN 37831, U.S.
[35]IPN-Orsay, Universite Paris Sud, CNRS-IN2P3, BP1, F-91406, Orsay, France
[36]PNPI, Petersburg Nuclear Physics Institute, Gatchina, Leningrad region, 188300, Russia
[37]RIKEN, The Institute of Physical and Chemical Research, Wako, Saitama 351-0198, Japan
[38]RIKEN BNL Research Center, Brookhaven National Laboratory, Upton, NY 11973-5000, U.S.
[39]Physics Department, Rikkyo University, 3-34-1 Nishi-Ikebukuro, Toshima, Tokyo 171-8501, Japan
[40]Saint Petersburg State Polytechnic University, St. Petersburg, Russia
[41]Universidade de São Paulo, Instituto de Física, Caixa Postal 66318, São Paulo CEP05315-970, Brazil
[42]System Electronics Laboratory, Seoul National University, Seoul, South Korea
[43]Chemistry Department, Stony Brook University, Stony Brook, SUNY, NY 11794-3400, U.S.
[44]Department of Physics and Astronomy, Stony Brook University, SUNY, Stony Brook, NY 11794, U.S.
[45]SUBATECH (Ecole des Mines de Nantes, CNRS-IN2P3, Université de Nantes) BP 20722 - 44307, Nantes, France
[46]University of Tennessee, Knoxville, TN 37996, U.S.
[47]Department of Physics, Tokyo Institute of Technology, Oh-okayama, Meguro, Tokyo 152-8551, Japan
[48]Institute of Physics, University of Tsukuba, Tsukuba, Ibaraki 305, Japan
[49]Vanderbilt University, Nashville, TN 37235, U.S.
[50]Waseda University, Advanced Research Institute for Science and Engineering, 17 Kikui-cho, Shinjuku-ku, Tokyo 162-0044, Japan
[51]Weizmann Institute, Rehovot 76100, Israel
[52]Yonsei University, IPAP, Seoul 120-749, Korea

(Dated: February 1, 2008)

The PHENIX experiment has measured the dielectron continuum in $\sqrt{s_{NN}}$=200 GeV Au+Au collisions. In minimum bias collisions the dielectron yield in the mass range between 150 and 750 MeV/c^2 is enhanced by a factor of 3.4±0.2(stat.)±1.3(syst.)±0.7(model) compared to the expectation from our model of hadron decays. The integrated yield increases faster with the centrality of the collisions than the number of participating nucleons, suggesting emission from scattering processes in the hot and dense medium. The continuum yield between the masses of the ϕ and the J/ψ mesons is consistent with expectations from correlated $c\bar{c}$ production, though other mechanisms are not ruled out.

PACS numbers: 25.75.Dw

Electron-positron pairs, or dileptons in general, have proven to be an excellent tool to study collisions of heavy ions at ultra-relativistic energies. Because leptons do not interact strongly, emission of dileptons from the hot matter created at RHIC should leave an imprint on the observed dilepton distributions. Emission from the hot matter may include thermal radiation and in-medium decays of mesons with short lifetimes, like the ρ meson, while their spectral functions may be strongly modified. However, below the mass of the ϕ meson, these sources compete with a large contribution of e^+e^-–pairs from Dalitz decays of pseudoscalar mesons (π^0, η, η') and decays of vector mesons (ρ, ω, ϕ). Above the ϕ meson mass up to 4.5 GeV/c^2, competing sources are dilepton decays of charmonia ($J/\psi, \psi'$) and semileptonic decays of D and $\bar{D}$ mesons, correlated through flavor conservation, which lead to a continuum of masses. In addition to thermal radiation, energy loss of charm quarks in the medium might modify the continuum yield in this mass region.

The discovery of a large enhancement of the dilepton yield at masses below the ϕ meson mass in ion-ion collisions at the CERN SPS [1] has triggered a broad theoretical investigation of modifications of properties of hadrons in a dense medium and of how these modifications relate to chiral symmetry restoration [2]. These theoretical studies will benefit from the availability of more precise data from CERN [3, 4] and GSI [5]. An enhanced yield was also observed at higher masses, above the ϕ meson mass [6]. Recent NA60 data suggest that the enhancement can not be attributed to decays of D-mesons but may result from prompt production, as expected for thermal radiation [7].

The PHENIX experiment at the Relativistic Heavy Ion Collider (RHIC) extends these measurements in a new energy regime by exploring Au+Au collisions at a center of mass energy of $\sqrt{s_{NN}}$=200 GeV. In this paper we present results from minimum bias data taken in 2004. Collisions were triggered and selected by centrality using beam-beam counters (BBC) and zero degree calorimeters (ZDC). We analyzed a sample of 8×10^8 minimum bias events.

Electrons and positrons are reconstructed in the two central arm spectrometers of PHENIX [8] using Drift Chambers (DC), located outside an axial magnetic field, which measure their momenta with an accuracy of $\sigma_p/p = 0.7\% \oplus 1\% p/(\mathrm{GeV/c})$. They are identified by hits in the Ring Imaging Cherenkov detector (RICH) and by matching the momentum with the energy measured in an electromagnetic calorimeter (EMCal) [9]. Electrons are reconstructed with an efficiency of ∼90%, while a hadron contamination of ∼20% remains.

Each central arm covers $|\Delta\eta| \leq 0.35$ in pseudorapidity and $\pi/2$ in azimuthal angle. Because charged particles are deflected in the azimuthal direction by the magnetic field, the acceptance depends on the momentum and the charge of the particle, and also on the radial location of the detector component (DC, EMCal and RICH). The acceptance for a track with charge q, transverse momentum p_T and azimuthal emission angle ϕ can be described by:

$$\phi_{\min} \leq \phi + q\frac{k_{\mathrm{DC,RICH}}}{p_\mathrm{T}} \leq \phi_{\max} \qquad (1)$$

where k_DC and k_RICH represent the effective azimuthal bend to DC and RICH ($k_{DC} = 0.206$ rad GeV/c and $k_{RICH} = 0.309$ rad GeV/c). One arm has $\phi_{\min} = \frac{-3}{16}\pi$ and $\phi_{\max} = \frac{5}{16}\pi$, the other arm $\phi_{min} = \frac{11}{16}\pi$ and $\phi_{max} = \frac{19}{16}\pi$. Only electrons with $p_\mathrm{T} \geq 200$ MeV/c are used in the analysis. The photon conversion probability was minimized by installing a helium bag between the beam pipe and the DC, reducing the material to ∼0.4% of a radiation length.

In an event the source of any electron or positron is unknown and therefore all electrons and positrons are combined to pairs, like-sign and unlike-sign. This results in a large combinatorial background which must be removed. The background is computed with a mixed event technique, which combines tracks from different events that have similar topology (centrality, collision vertex, reaction plane).

In order to achieve the necessary accuracy, all unphysical correlations that arise from overlapping tracks or hits in the detectors, mostly in the RICH, must be eliminated, because they can not be reproduced by mixed events. If hits of both tracks of a pair overlap in any detector, the event is rejected. About 4% of all pairs are removed by this event rejection. Comparing measured like-sign pairs with the mixed combinatorial background shows that the mixing technique reproduces the shape within the statistical accuracy of the data.

The absolute normalization of the unlike-sign combinatorial background is given by the geometrical mean of the observed positive and negative like-sign pairs $2\sqrt{N_{--}N_{++}}$, where, in principle, N_{--} and N_{++} are the measured number of like-sign pairs. There is a small correlated signal also in the observed like-sign pairs, which can occur if there are two e^+e^-–pairs in the final state of a meson, e.g. double Dalitz decays, Dalitz decays followed by a conversion of the decay photon or two photon decays followed by conversion of both photons. These "cross" pairs have small masses, typically less than the η mass (550 MeV/c^2).

We therefore determine N_{--} and N_{++} by integrating the mixed event distributions after they were normalized to the 7.5×10^6 like-sign pairs measured above 700 MeV/c^2. N_{--} and N_{++} are determined with an accuracy of 0.12%. The normalization is multiplied by 1.004 to account for the fact that the event rejection removes 10% more like-sign than unlike-sign pairs. This correction factor was estimated, using mixed events, with an accuracy better than 50%. Adding the statistical error

and the uncertainty due to the event rejection in quadrature gives an accuracy of 0.25% on the normalization.

After subtraction of the combinatorial background, physical background from photon conversions and cross pairs is removed. Because the tracking assumes that the e^+e^-–pair originates at the collision vertex, pairs from photons that convert in or outside of the beampipe are reconstructed with finite mass and opening angle, which is oriented perpendicular to the magnetic field. A cut on the orientation of the opening angle in the field removes more than 98% of the conversion pairs.

Cross pairs occur as like and unlike-sign pairs. Monte Carlo simulations show that the rate of unlike-sign cross pairs accepted in PHENIX is 44% of the rate for like-sign cross pairs. To deterime the rate of unlike-sign cross pairs, we scale the simulated like-sign cross pair distribution to the observed like-sign signal, obtained by subtraction of the mixed event background normalized above 700 MeV/c^2. We note that the like-sign signal is well described by the Monte Carlo simulation. The simulated unlike-sign cross pair distribution is scaled by the same factor and subtracted from the unlike-sign signal. The uncertainty of this subtraction depends on mass, but is $\leq 9\%$ of the final yield.

Figure 1 shows the mass distribution of e^+e^-–pairs, the normalized mixed event background (B), and the signal yield (S) obtained by subtracting the mixed event background, the cross pairs and the conversion pairs. The insert shows the signal-to-background ratio (S/B). The systematic errors (boxes) reflect the error on the background subtraction, which is given by $\delta_S/S = 0.25\% \cdot B/S$, added in quadrature to the uncertainty due to the cross pair subtraction, assumed to be $9\%S$ below 600 MeV/c^2. Despite the small S/B ratio, the vector meson resonances ω, ϕ and J/ψ which decay directly to e^+e^-, and an e^+e^-–pair continuum is visible up to 4.5 GeV/c^2.

In order to check the background subtraction, a subset of data (5×10^7 events), taken with additional material wrapped around the beam pipe to increase the number of photon conversions [9], was analyzed. In this data set the combinatorial background and the cross pair contribution is larger by a factor of $\sim$2.5. As shown in Fig. 1, the results from both data sets agree well within statistical errors, which are 30% in the range from 150 to 750 MeV/c^2 and much less below. Considering the decreased S/B ratio for the data with the converter we can estimate a 0.1% scale uncertainty of the background normalization, well within the 0.25% systematic uncertainty assigned.

The spectra are corrected to represent the invariant yield of e^+e^-–pairs, with both the e^+ and e^- in the detector acceptance as specified in Eq. 1. The correction is determined using a GEANT simulation [10] of the PHENIX detector that includes the details of the detector response. Simulated e^+e^-–pairs are reconstructed with the same analysis chain and all cuts applied. The correction is determined double differentially in p_T and mass of the e^+e^-–pair. The reduction of the electron reconstruction efficiency (0.92+/-0.03) due to detector occupancy is corrected for. Systematic uncertainties on the correction can be summarized as: (i) 13.4% on di-electron reconstruction, which is twice the uncertainty on the electron reconstruction efficiency [9], (ii) 6% conversion rejection cut, (iii) 5% event rejection and (iv) 3% occupancy. These uncertainties are included in the final systematic error on the invariant e^+e^-–pair yield.

Figure 2 compares the invariant yeild to the expected yield from meson decays and correlated decays of charmed mesons. The cocktail of hadron decay contributions was estimated using PHENIX data for meson production when available. As input distributions we use the measured $\pi, \eta, \phi, J/\psi$ yield and spectra [11, 12, 13, 14, 15]. For other mesons we use the m_T scaling procedure outlined in [9]. The systematic uncertainties depend on mass and range from 10 to 25%.

For the continuum below the J/ψ the dynamic correlation of c and $\bar{c}$ is essential, but unknown. We make two assumptions: (i) the correlation is unchanged by the medium and equal to what is known from p+p collisions. In this case we use PYTHIA [16] scaled from the p+p equivalent $c\bar{c}$ cross section of $567\pm57\pm193$ μbarn [17] to minimum bias Au+Au collisions proportional to the number of binary collisions (258 ± 25) [12]. We note that the p_T distribution for electrons generated by PYTHIA is softer than the spectra measured in p+p data but coincides with those observed in Au+Au [9]. As a second assumption (ii) there is no dynamical correlation, i.e. the direction of c and $\bar{c}$ quarks are uncorrelated. We keep the overall cross section and the p_T distributions fixed to experimental data [9]. Other contributions from bottom and Drell-Yan are expected to be small in the mass region below the J/ψ peak. Each e^+ and e^- must fall in the PHENIX acceptance, given by Eq. 1.

The data below 150 MeV/c^2 are well described by the cocktail of hadronic sources. The vector mesons ω, ϕ and J/ψ are reproduced within the uncertainties. However, the yield is substantially enhanced above the expected yield in the continuum region from 150 to 750 MeV/c^2. The enhancement in this mass range is a factor of 3.4 $\pm$ 0.2(stat.) $\pm$ 1.3(syst.) $\pm$ 0.7(model), where the first error is the statistical error, the second the systematic uncertainty of the data, and the last error is an estimate of the uncertainty of the expected yield. Above the ϕ meson mass the data seem to be well described by the continuum calculation based on PYTHIA. This is somewhat surprising, since single electron distributions from charm show substantial medium modifications [9], and thus it is hard to understand how the dynamic correlation at production of the $c\bar{c}$ remains unaffected by the medium. A complete randomization of that correlation (see Fig.2) leads to a much softer mass spectrum and

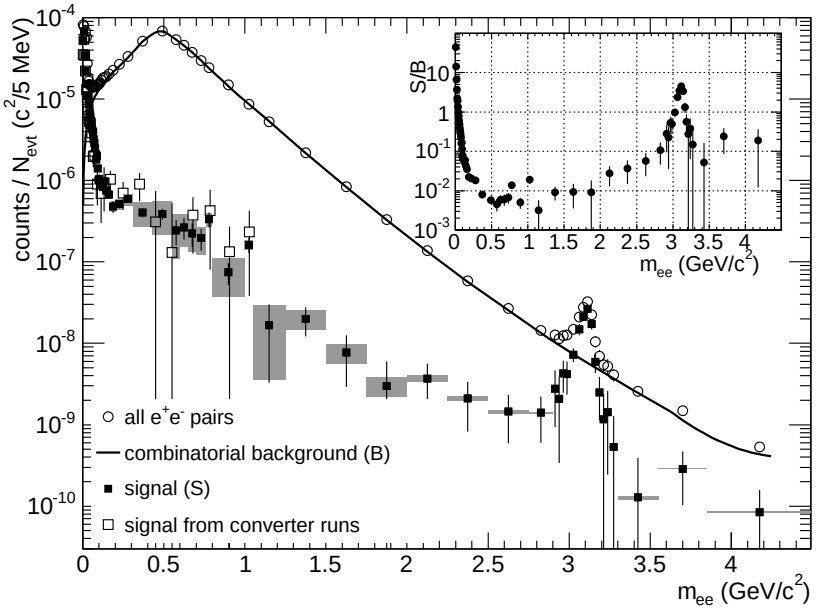

FIG. 1: Uncorrected mass spectra of all e^+e^- pairs, mixed events background (B) and signal (S) with statistical (bars) and systematic (boxes) uncertainties shown separately. The signal from the runs with additional converter is shown with statistical errors only. The insert shows the S/B ratio. The mass range covered by each data point is given by horizontal bars.

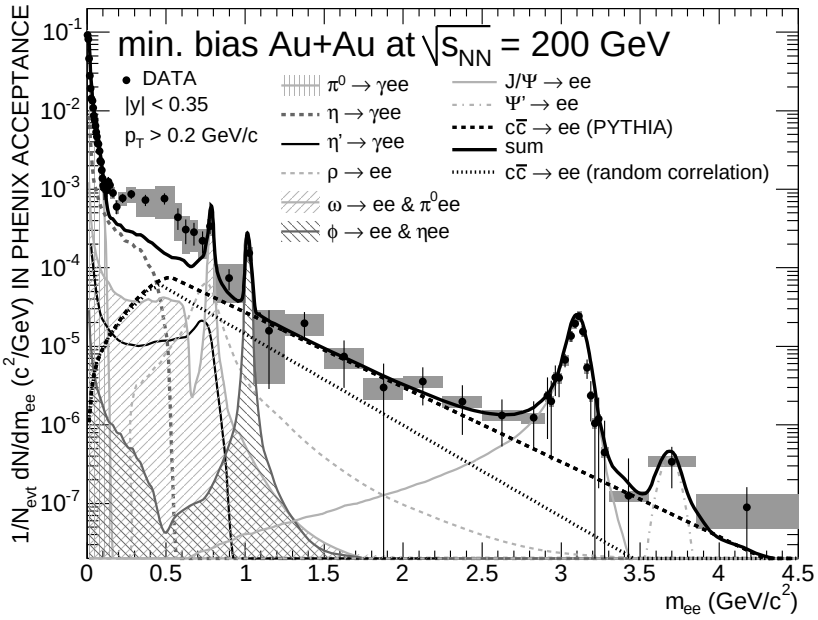

FIG. 2: Invariant e^+e^-–pair yield compared to the yield from the model of hadron decays. The charmed meson decay contribution based on PYTHIA is included in the sum of sources (solid black line). The charm contribution expected if the dynamic correlation of c and $\bar{c}$ is removed is shown separately. Statistical (bars) and systematic (boxes) uncertainties are shown separately; the mass range covered by each data point is given by horizontal bars. The systematic uncertainty on the cocktail is not shown.

would leave significant room for other contributions, e.g. thermal radiation.

To shed more light on the continuum yield we have studied the centrality dependence of the yield in three mass windows, below 100 MeV/c^2, from 150 to 750 MeV/c^2 and 1.2 to 2.8 GeV/c^2. The top panel of Fig. 3 shows the centrality dependence of the yield in the mass region 150–750 MeV/c^2 divided by the number of participating nucleon pairs ($N_{\rm part}/2$). For comparison the yield below 100 MeV/c^2, which is dominated by low p_T

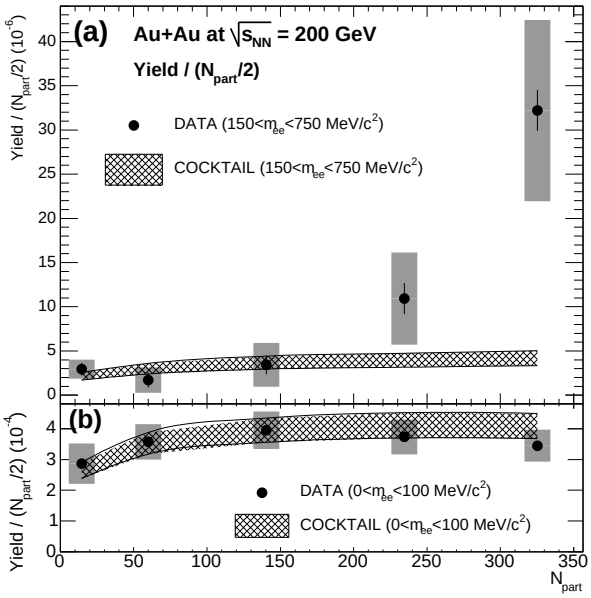

FIG. 3: Dielectron yield per participating nucleon pairs ($N_{\rm part}/2$) as function of N_{part} for two different mass ranges compared to the expected yield from the hadron decay model. The two lines give $\pm 1\sigma$ systematic uncertainty. For the data statistical and systematic uncertainties are shown separately.

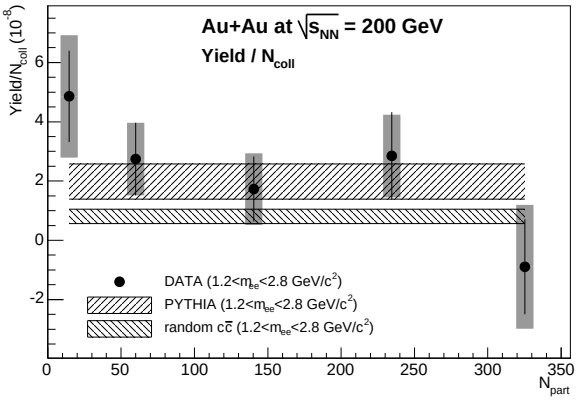

FIG. 4: Dielectron yield per number of collisions N_{coll} in the mass range 1.2 to 2.8 GeV/c^2 as function of $N_{\rm part}$. Statistical and systematic errors are shown separately. Also shown are two bands corresponding to the two different estimates of the contribution from charmed meson decays. The width of the band reflect the uncertainty of the charm cross-section only.

pion decays, is shown in the lower panel. For both intervals the yield is compared to the same yield calculated from the hadron cocktail. In the lower mass range the yield agrees with the expectation, i.e. is proportional to the pion yield. In contrast, in the range from 150 to 750 MeV/c^2, the observed yield rises significantly compared to the expectation, reaching a factor of 7.7 $\pm$ 0.6(stat.) $\pm$ 2.5(syst.) $\pm$ 1.5(model) for most central collisions. The increase is qualitatively consistent with the conjecture that an in-medium enhancement of the dielectron continuum yield arises from scattering processes like $\pi\pi$ or $q\bar{q}$ annihilation, which would result in a yield rising faster than proportional to N_{part}.

We normalize the yield in the mass region 1.2 to 2.8 GeV/c^2 to the number of binary collisions (Fig. 4), which is the correct scaling for pairs from charmed meson decays [9]. The normalized yield shows no significant centrality dependence and is consistent with the expectation based on PYTHIA. It is also likely that a scenario where the correlation between the c and $\bar{c}$ is randomized will require an additional source, e.g. a contribution from thermal radiation. This contribution could increase faster than linear with $N_{\rm part}$ and therefore the apparent scaling with N_{coll} may be a mere coincidence. We note that this coincidence may have been observed in this mass region at the CERN SPS [6], where a major prompt component has now been suggested by NA60 data [7].

In conclusion, measurements of Au+Au collisions at $\sqrt{s_{NN}}$=200 GeV in the mass range 150–750 MeV/c^2 show a significant enhancement of the dielectron continuum and exhibit a clear increase with centrality of the collision. The observed yield between ϕ and J/ψ is consistent with the expectation from correlated $c\bar{c}$ production, but does not exclude other mechanisms.

We thank the staff of the Collider-Accelerator and Physics Departments at BNL for their vital contributions. We acknowledge support from the Office of Nuclear Physics in DOE Office of Science and NSF (U.S.A.), MEXT and JSPS (Japan), CNPq and FAPESP (Brazil), NSFC (China), IN2P3/CNRS, and CEA (France), BMBF, DAAD, and AvH (Germany), OTKA (Hungary), DAE (India), ISF (Israel), KRF and KOSEF (Korea), MES, RAS, and FAAE (Russia), VR and KAW (Sweden), U.S. CRDF for the FSU, US-Hungarian NSF-OTKA-MTA, and US-Israel BSF.

* PHENIX Spokesperson: jacak@skipper.physics.sunysb.edu
† Deceased

[1] G. Agakishiev *et al.*, Phys.Rev.Lett.75 1272 (1995)
[2] R. Rapp, J.Wambach, Adv.Nucl.Phy. 25 1 (2000) and references therein
[3] G.Agakichiev et al., Eur.Phy.J. C 41 475 (2005)
[4] R. Arnaldi *et al.*, Phys. Rev. Lett. **96**, 162302 (2006)
[5] G. Agakishiev, Phys. Rev. Lett. **98**, 052302 (2007)
[6] M.C. Abreu *et al.*, Eur. Phys. J. C **14**, 443 (2000).
[7] R. Shahoian *et al.*, PoS **HEP2005**, 131 (2006).
[8] K. Adcox*et al.*, Nucl. Instr. and Meth. A **A499**, 469 (2003).
[9] A. Adare *et al.*, Phys. Rev. Lett. **98**, 172301 (2007)
[10] GEANT User's Guide, 3.15, CERN Program Library
[11] A. Adare *et al.*, Phys. Rev. Lett. 98, 232301 (2007)
[12] S. S. Adler *et al.*, Phys. Rev. C **69**, 034909 (2004)

[13] S. S. Adler *et al.*, Phys. Rev. Lett. **91**, 072301 (2003)
[14] S. S. Adler *et al.*, Phys. Rev. C **75**, 024909 (2007)
[15] S. S. Adler *et al.*, Phys. Rev. C **72**, 014903 (2005)
[16] We used PYTHIA 6.152 with parameters as in K. Adcox et al., Phys. Rev. Lett. 88,192303 (2002)
[17] A. Adare *et al.* Phys. Rev. Lett. **97**, 252002 (2006)

PHYSICAL REVIEW C **77**, 011901(R) (2008)

Transverse momentum and centrality dependence of dihadron correlations in Au+Au collisions at $\sqrt{s_{NN}} = 200$ GeV: Jet quenching and the response of partonic matter

A. Adare,[8] S. Afanasiev,[22] C. Aidala,[9] N. N. Ajitanand,[49] Y. Akiba,[43,44] H. Al-Bataineh,[38] J. Alexander,[49] A. Al-Jamel,[38] K. Aoki,[28,43] L. Aphecetche,[51] R. Armendariz,[38] S. H. Aronson,[3] J. Asai,[44] E. T. Atomssa,[29] R. Averbeck,[50] T. C. Awes,[39] B. Azmoun,[3] V. Babintsev,[18] G. Baksay,[14] L. Baksay,[14] A. Baldisseri,[11] K. N. Barish,[4] P. D. Barnes,[31] B. Bassalleck,[37] S. Bathe,[4] S. Batsouli,[9,39] V. Baublis,[42] F. Bauer,[4] A. Bazilevsky,[3] S. Belikov,[3,21,*] R. Bennett,[50] Y. Berdnikov,[46] A. A. Bickley,[8] M. T. Bjorndal,[9] J. G. Boissevain,[31] H. Borel,[11] K. Boyle,[50] M. L. Brooks,[31] D. S. Brown,[38] D. Bucher,[34] H. Buesching,[3] V. Bumazhnov,[18] G. Bunce,[3,44] J. M. Burward-Hoy,[31] S. Butsyk,[31,50] S. Campbell,[50] J.-S. Chai,[23] B. S. Chang,[58] J.-L. Charvet,[11] S. Chernichenko,[18] J. Chiba,[24] C. Y. Chi,[9] M. Chiu,[9,19] I. J. Choi,[58] T. Chujo,[55] P. Chung,[49] A. Churyn,[18] V. Cianciolo,[39] C. R. Cleven,[16] Y. Cobigo,[11] B. A. Cole,[9] M. P. Comets,[40] P. Constantin,[21,31] M. Csanád,[13] T. Csörgő,[25] T. Dahms,[50] K. Das,[15] G. David,[3] M. B. Deaton,[1] K. Dehmelt,[14] H. Delagrange,[51] A. Denisov,[18] D. d'Enterria,[9] A. Deshpande,[44,50] E. J. Desmond,[3] O. Dietzsch,[47] A. Dion,[50] M. Donadelli,[47] J. L. Drachenberg,[1] O. Drapier,[29] A. Drees,[50] A. K. Dubey,[57] A. Durum,[18] V. Dzhordzhadze,[4,52] Y. V. Efremenko,[39] J. Egdemir,[50] F. Ellinghaus,[8] W. S. Emam,[4] A. Enokizono,[17,30] H. En'yo,[43,44] B. Espagnon,[40] S. Esumi,[54] K. O. Eyser,[4] D. E. Fields,[37,44] M. Finger,[5,22] M. Finger Jr.,[5,22] F. Fleuret,[29] S. L. Fokin,[27] B. Forestier,[32] Z. Fraenkel,[57] J. E. Frantz,[9,50] A. Franz,[3] A. D. Frawley,[15] K. Fujiwara,[43] Y. Fukao,[28,43] S.-Y. Fung,[4] T. Fusayasu,[36] S. Gadrat,[32] I. Garishvili,[52] F. Gastineau,[51] M. Germain,[51] A. Glenn,[8,52] H. Gong,[50] M. Gonin,[29] J. Gosset,[11] Y. Goto,[43,44] R. Granier de Cassagnac,[29] N. Grau,[21] S. V. Greene,[55] M. Grosse Perdekamp,[19,44] T. Gunji,[7] H.-Å. Gustafsson,[33] T. Hachiya,[17,43] A. Hadj Henni,[51] C. Haegemann,[37] J. S. Haggerty,[3] M. N. Hagiwara,[1] H. Hamagaki,[7] R. Han,[41] H. Harada,[17] E. P. Hartouni,[30] K. Haruna,[17] M. Harvey,[3] E. Haslum,[33] K. Hasuko,[43] R. Hayano,[7] M. Heffner,[30] T. K. Hemmick,[50] T. Hester,[4] J. M. Heuser,[43] X. He,[16] H. Hiejima,[19] J. C. Hill,[21] R. Hobbs,[37] M. Hohlmann,[14] M. Holmes,[55] W. Holzmann,[49] K. Homma,[17] B. Hong,[26] T. Horaguchi,[43,53] D. Hornback,[52] M. G. Hur,[23] T. Ichihara,[43,44] K. Imai,[28,43] M. Inaba,[54] Y. Inoue,[43,45] D. Isenhower,[1] L. Isenhower,[1] M. Ishihara,[43] T. Isobe,[7] M. Issah,[49] A. Isupov,[22] B. V. Jacak,[50,†] J. Jia,[9] J. Jin,[9] O. Jinnouchi,[44] B. M. Johnson,[3] K. S. Joo,[35] D. Jouan,[40] F. Kajihara,[7,43] S. Kametani,[7,56] N. Kamihara,[43,53] J. Kamin,[50] M. Kaneta,[44] J. H. Kang,[58] H. Kanou,[43,53] T. Kawagishi,[54] D. Kawall,[44] A. V. Kazantsev,[27] S. Kelly,[8] A. Khanzadeev,[42] J. Kikuchi,[56] D. H. Kim,[35] D. J. Kim,[58] E. Kim,[48] Y.-S. Kim,[23] E. Kinney,[8] A. Kiss,[13] E. Kistenev,[3] A. Kiyomichi,[43] J. Klay,[30] C. Klein-Boesing,[34] L. Kochenda,[42] V. Kochetkov,[18] B. Komkov,[42] M. Konno,[54] D. Kotchetkov,[4] A. Kozlov,[57] A. Král,[10] A. Kravitz,[9] P. J. Kroon,[3] J. Kubart,[5,20] G. J. Kunde,[31] N. Kurihara,[7] K. Kurita,[43,45] M. J. Kweon,[26] Y. Kwon,[52,58] G. S. Kyle,[38] R. Lacey,[49] Y.-S. Lai,[9] J. G. Lajoie,[21] A. Lebedev,[21] Y. Le Bornec,[40] S. Leckey,[50] D. M. Lee,[31] M. K. Lee,[58] T. Lee,[48] M. J. Leitch,[31] M. A. L. Leite,[47] B. Lenzi,[47] H. Lim,[48] T. Liška,[10] A. Litvinenko,[22] M. X. Liu,[31] X. Li,[6] X. H. Li,[4] B. Love,[55] D. Lynch,[3] C. F. Maguire,[55] Y. I. Makdisi,[3] A. Malakhov,[22] M. D. Malik,[37] V. I. Manko,[27] Y. Mao,[41,43] L. Mašek,[5,20] H. Masui,[54] F. Matathias,[9,50] M. C. McCain,[19] M. McCumber,[50] P. L. McGaughey,[31] Y. Miake,[54] P. Mikeš,[5,20] K. Miki,[54] T. E. Miller,[55] A. Milov,[50] S. Mioduszewski,[3] G. C. Mishra,[16] M. Mishra,[2] J. T. Mitchell,[3] M. Mitrovski,[49] A. Morreale,[4] D. P. Morrison,[3] J. M. Moss,[31] T. V. Moukhanova,[27] D. Mukhopadhyay,[55] J. Murata,[43,45] S. Nagamiya,[24] Y. Nagata,[54] J. L. Nagle,[8] M. Naglis,[57] I. Nakagawa,[43,44] Y. Nakamiya,[17] T. Nakamura,[17] K. Nakano,[43,53] J. Newby,[30] M. Nguyen,[50] B. E. Norman,[31] A. S. Nyanin,[27] J. Nystrand,[33] E. O'Brien,[3] S. X. Oda,[7] C. A. Ogilvie,[21] H. Ohnishi,[43] I. D. Ojha,[55] H. Okada,[28,43] K. Okada,[44] M. Oka,[54] O. O. Omiwade,[1] A. Oskarsson,[33] I. Otterlund,[33] M. Ouchida,[17] K. Ozawa,[7] R. Pak,[3] D. Pal,[55] A. P. T. Palounek,[31] V. Pantuev,[50] V. Papavassiliou,[38] J. Park,[48] W. J. Park,[26] S. F. Pate,[38] H. Pei,[21] J.-C. Peng,[19] H. Pereira,[11] V. Peresedov,[22] D. Yu. Peressounko,[27] C. Pinkenburg,[3] R. P. Pisani,[3] M. L. Purschke,[3] A. K. Purwar,[31,50] H. Qu,[16] J. Rak,[21,37] A. Rakotozafindrabe,[29] I. Ravinovich,[57] K. F. Read,[39,52] S. Rembeczki,[14] M. Reuter,[50] K. Reygers,[34] V. Riabov,[42] Y. Riabov,[42] G. Roche,[32] A. Romana,[29,*] M. Rosati,[21] S. S. E. Rosendahl,[33] P. Rosnet,[32] P. Rukoyatkin,[22] V. L. Rykov,[43] S. S. Ryu,[58] B. Sahlmueller,[34] N. Saito,[28,43,44] T. Sakaguchi,[3,7,56] S. Sakai,[54] H. Sakata,[17] V. Samsonov,[42] H. D. Sato,[28,43] S. Sato,[3,24,54] S. Sawada,[24] J. Seele,[8] R. Seidl,[19] V. Semenov,[18] R. Seto,[4] D. Sharma,[57] T. K. Shea,[3] I. Shein,[18] A. Shevel,[42,49] T.-A. Shibata,[43,53] K. Shigaki,[17] M. Shimomura,[54] T. Shohjoh,[54] K. Shoji,[28,43] A. Sickles,[50] C. L. Silva,[47] D. Silvermyr,[39] C. Silvestre,[11] K. S. Sim,[26] C. P. Singh,[2] V. Singh,[2] S. Skutnik,[21] M. Slunečka,[5,22] W. C. Smith,[1] A. Soldatov,[18] R. A. Soltz,[30] W. E. Sondheim,[31] S. P. Sorensen,[52] I. V. Sourikova,[3] F. Staley,[11] P. W. Stankus,[39] E. Stenlund,[33] M. Stepanov,[38] A. Ster,[25] S. P. Stoll,[3] T. Sugitate,[17] C. Suire,[40] J. P. Sullivan,[31] J. Sziklai,[25] T. Tabaru,[44] S. Takagi,[54] E. M. Takagui,[47] A. Taketani,[43,44] K. H. Tanaka,[24] Y. Tanaka,[36] K. Tanida,[43,44] M. J. Tannenbaum,[3] A. Taranenko,[49] P. Tarján,[12] T. L. Thomas,[37] M. Togawa,[28,43] A. Toia,[50] J. Tojo,[43] L. Tomášek,[20] H. Torii,[43] R. S. Towell,[1] V.-N. Tram,[29] I. Tserruya,[57] Y. Tsuchimoto,[17,43] S. K. Tuli,[2] H. Tydesjö,[33] N. Tyurin,[18] C. Vale,[21] H. Valle,[55] H. W. van Hecke,[31] J. Velkovska,[55] R. Vertesi,[12] A. A. Vinogradov,[27] M. Virius,[10] V. Vrba,[20] E. Vznuzdaev,[42] M. Wagner,[28,43] D. Walker,[50] X. R. Wang,[38] Y. Watanabe,[43,44] J. Wessels,[34] S. N. White,[3] N. Willis,[40] D. Winter,[9] C. L. Woody,[3] M. Wysocki,[8] W. Xie,[4,44] Y. L. Yamaguchi,[56] A. Yanovich,[18] Z. Yasin,[4] J. Ying,[16] S. Yokkaichi,[43,44] G. R. Young,[39] I. Younus,[37] I. E. Yushmanov,[27] W. A. Zajc,[9] O. Zaudtke,[34] C. Zhang,[9,39] S. Zhou,[6] J. Zimányi,[25,*] and L. Zolin[22]

(PHENIX Collaboration)

[1]*Abilene Christian University, Abilene, Texas 79699, USA*

[2]*Department of Physics, Banaras Hindu University, Varanasi 221005, India*

[3]*Brookhaven National Laboratory, Upton, New York 11973-5000, USA*

 ©2008 The American Physical Society

[4]*University of California–Riverside, Riverside, California 92521, USA*
[5]*Charles University, Ovocný trh 5, Praha 1, 116 36 Prague, Czech Republic*
[6]*China Institute of Atomic Energy (CIAE), Beijing, People's Republic of China*
[7]*Center for Nuclear Study, Graduate School of Science, University of Tokyo, 7-3-1 Hongo, Bunkyo, Tokyo 113-0033, Japan*
[8]*University of Colorado, Boulder, Colorado 80309, USA*
[9]*Columbia University, New York, New York 10027 and Nevis Laboratories, Irvington, New York 10533, USA*
[10]*Czech Technical University, Zikova 4, 166 36 Prague 6, Czech Republic*
[11]*Dapnia, CEA Saclay, F-91191, Gif-sur-Yvette, France*
[12]*Debrecen University, H-4010 Debrecen, Egyetem tér 1, Hungary*
[13]*ELTE, Eötvös Loránd University, H-1117 Budapest, Pázmány P. s. 1/A, Hungary*
[14]*Florida Institute of Technology, Melbourne, Florida 32901, USA*
[15]*Florida State University, Tallahassee, Florida 32306, USA*
[16]*Georgia State University, Atlanta, Georgia 30303, USA*
[17]*Hiroshima University, Kagamiyama, Higashi-Hiroshima 739-8526, Japan*
[18]*IHEP Protvino, State Research Center of Russian Federation, Institute for High Energy Physics, Protvino RU-142281, Russia*
[19]*University of Illinois at Urbana-Champaign, Urbana, Illinois 61801, USA*
[20]*Institute of Physics, Academy of Sciences of the Czech Republic, Na Slovance 2, 182 21 Prague 8, Czech Republic*
[21]*Iowa State University, Ames, Iowa 50011, USA*
[22]*Joint Institute for Nuclear Research, Moscow Region, RU-141980 Dubna, Russia*
[23]*KAERI, Cyclotron Application Laboratory, Seoul, Korea*
[24]*KEK, High Energy Accelerator Research Organization, Tsukuba, Ibaraki 305-0801, Japan*
[25]*KFKI Research Institute for Particle and Nuclear Physics of the Hungarian Academy of Sciences (MTA KFKI RMKI), H-1525 Budapest 114, P. O. Box 49, Budapest, Hungary*
[26]*Korea University, Seoul 136-701, Korea*
[27]*Russian Research Center "Kurchatov Institute," Moscow, Russia*
[28]*Kyoto University, Kyoto 606-8502, Japan*
[29]*Laboratoire Leprince-Ringuet, Ecole Polytechnique, CNRS-IN2P3, Route de Saclay, F-91128 Palaiseau, France*
[30]*Lawrence Livermore National Laboratory, Livermore, California 94550, USA*
[31]*Los Alamos National Laboratory, Los Alamos, New Mexico 87545, USA*
[32]*LPC, Université Blaise Pascal, CNRS-IN2P3, Clermont-Fd, F-63177 Aubiere Cedex, France*
[33]*Department of Physics, Lund University, Box 118, SE-221 00 Lund, Sweden*
[34]*Institut für Kernphysik, University of Muenster, D-48149 Muenster, Germany*
[35]*Myongji University, Yongin, Kyonggido 449-728, Korea*
[36]*Nagasaki Institute of Applied Science, Nagasaki-shi, Nagasaki 851-0193, Japan*
[37]*University of New Mexico, Albuquerque, New Mexico 87131, USA*
[38]*New Mexico State University, Las Cruces, New Mexico 88003, USA*
[39]*Oak Ridge National Laboratory, Oak Ridge, Tennessee 37831, USA*
[40]*IPN-Orsay, Universite Paris Sud, CNRS-IN2P3, BP1, F-91406 Orsay, France*
[41]*Peking University, Beijing, People's Republic of China*
[42]*PNPI, Petersburg Nuclear Physics Institute, Gatchina, Leningrad Region RU-188300, Russia*
[43]*RIKEN, The Institute of Physical and Chemical Research, Wako, Saitama 351-0198, Japan*
[44]*RIKEN BNL Research Center, Brookhaven National Laboratory, Upton, New York 11973-5000, USA*
[45]*Physics Department, Rikkyo University, 3-34-1 Nishi-Ikebukuro, Toshima, Tokyo 171-8501, Japan*
[46]*Saint Petersburg State Polytechnic University, Saint Petersburg, Russia*
[47]*Universidade de São Paulo, Instituto de Física, Caixa Postal 66318, São Paulo CEP05315-970, Brazil*
[48]*System Electronics Laboratory, Seoul National University, Seoul, Korea*
[49]*Chemistry Department, Stony Brook University, SUNY, Stony Brook, New York 11794-3400, USA*
[50]*Department of Physics and Astronomy, Stony Brook University, SUNY, Stony Brook, New York 11794, USA*
[51]*SUBATECH (Ecole des Mines de Nantes, CNRS-IN2P3, Université de Nantes), BP 20722-44307, Nantes, France*
[52]*University of Tennessee, Knoxville, Tennessee 37996, USA*
[53]*Department of Physics, Tokyo Institute of Technology, Oh-okayama, Meguro, Tokyo 152-8551, Japan*
[54]*Institute of Physics, University of Tsukuba, Tsukuba, Ibaraki 305, Japan*
[55]*Vanderbilt University, Nashville, Tennessee 37235, USA*
[56]*Waseda University, Advanced Research Institute for Science and Engineering, 17 Kikui-cho, Shinjuku-ku, Tokyo 162-0044, Japan*
[57]*Weizmann Institute, Rehovot 76100, Israel*
[58]*Yonsei University, IPAP, Seoul 120-749, Korea*
(Received 22 May 2007; published 7 January 2008)

Azimuthal angle ($\Delta\phi$) correlations are presented for charged hadrons from dijets for $0.4 < p_T < 10$ GeV/c in Au+Au collisions at $\sqrt{s_{\rm NN}} = 200$ GeV. With increasing p_T, the away-side distribution evolves from a broad and relatively flat shape to a concave shape, then to a convex shape. Comparisons to $p+p$ data suggest that the away-side can be divided into a partially suppressed "head" region centered at $\Delta\phi \sim \pi$ and an enhanced "shoulder" region centered at $\Delta\phi \sim \pi \pm 1.1$. The p_T spectrum for the head region softens toward central collisions, consistent with the onset of jet quenching. The spectral slope for the shoulder region is independent of centrality and trigger p_T, which offers constraints on energy transport mechanisms and suggests that it contains the medium response to energetic jets.

DOI: 10.1103/PhysRevC.77.011901 PACS number(s): 25.75.Dw

High transverse momentum (p_T) partons are valuable probes of the high energy density matter created at the Relativistic Heavy-Ion Collider (RHIC). These partons lose a large fraction of their energy in the matter prior to forming hadrons, a phenomenon known as jet quenching. Such energy loss is predicted to lead to strong suppression of both single and correlated away-side dihadron yields at high p_T [1], consistent with experimental findings [2,3]. The exact mechanism for energy loss is not yet understood. Recent results of dihadron azimuthal angle ($\Delta\phi$) correlations have indicated strong modification of the away-side jet [3–6]. For high p_T hadron pairs, such modification is manifested by a partially suppressed away-side peak at $\Delta\phi \sim \pi$ [3]. This has been interpreted as evidence for the fragmentation of jets that survive their passage through the medium.

For intermediate p_T charged hadron pairs, the away-side jet was observed to peak at $\Delta\phi \sim \pi \pm 1.1$ [4,5], suggesting that the energy lost by high p_T partons is transported to lower p_T hadrons at angles away from $\Delta\phi \sim \pi$. The mechanisms for such energy transport include medium deflection of hard [7] or shower partons [8], large-angle gluon radiation [9], Cherenkov gluon radiation [10], and mach-shock medium excitations [11].

In this brief report we present a detailed "mapping" of the p_T and centrality dependence of away-side jet shapes and yields. These measurements allow a detailed investigation of the jet distributions centered around $\Delta\phi \sim \pi \pm 1.1$ and $\Delta\phi \sim \pi$, provide new insight on the interplay between jet quenching and the response of the medium to the lost energy, and provide new constraints for distinguishing the competing mechanisms for energy transport.

The results presented here are based on minimum-bias (MB) Au+Au and $p+p$ datasets as well as a photon level-1 triggered (PT) $p+p$ dataset collected with the PHENIX detector [12] at $\sqrt{s_{\rm NN}} = 200$ GeV, during the 2004–2005 RHIC run. The PT trigger requires a minimum energy of 1.4 GeV in 4×4 electromagnetic calorimeter (EMC) towers in coincidence with the Beam Beam Counters (BBC) [13]. The event centrality was determined via the method in Ref. [12]. A total of 840 million Au+Au events in the vertex range $|z| < 30$ cm was analyzed. Charged particles were reconstructed in the two central arms of PHENIX, each covering -0.35 to 0.35 in pseudorapidity and 90° in azimuth. The tracking system consisted of the drift chambers and two layers of multiwire proportional chambers with pad readout (PC1 and PC3), achieving a momentum resolution of $0.7\% \bigoplus 1.0\%\ p$ (GeV/c) [2].

Dihadron $\Delta\phi$ correlations were obtained by correlating trigger (type A) hadrons with partner (type B) hadrons. The MB and PT $p+p$ datasets were used for trigger $p_T < 5$GeV/c and $p_T > 5$ GeV/c, respectively. To reduce background from decays and conversions, tracks were required to have a matching hit within a $\pm 2.3\sigma$ window in PC3. For $p_T > 4$GeV/c, an additional matching hit at the EMC was required. For triggers with $p_T > 5$ GeV/c, a p_T dependent energy cut in the EMC and a tight $\pm 1.5\sigma$ matching cut at the PC3 were applied to reduce the background to <10% [14]. This energy cut greatly reduces PT trigger bias effects. The PT $p+p$ results are consistent with the MB $p+p$ data for trigger $p_T > 5$ GeV/c.

The jet associated partner yield per trigger, $Y_{\rm jet}(\Delta\phi)$, is obtained by assuming independent contributions from jets and elliptic flow to the $\Delta\phi$ distribution as [4,14]

$$Y_{\rm jet} = \left[\frac{N^s(\Delta\phi)}{N^m(\Delta\phi)} - b_0\left(1 + 2v_2^A v_2^B \cos 2\Delta\phi\right)\right] \times \frac{\int d\Delta\phi N^m(\Delta\phi)}{2\pi N_A \varepsilon_B}, \quad (1)$$

where N_A is the number of triggers, ε_B is the single-particle efficiency for partners in the full azimuth and $|\eta| < 0.35$; $N^s(\Delta\phi)$ and $N^m(\Delta\phi)$ are pair distributions from the same- and mixed-events, respectively. Mixed-event pairs are obtained by selecting partners from different events with similar centrality and vertex. The ε_B values include detector acceptance and reconstruction efficiency, with an uncertainty of ~10% [2,15]. The harmonic term, $2v_2^A v_2^B \cos 2\Delta\phi$, reflects the elliptic flow modulation of the combinatoric pairs in Au+Au [4], where we have assumed $\langle v_2^A v_2^B\rangle$ is factorizable. v_2^A and v_2^B are measured via the reaction plane method [16] using BBC at $3 < |\eta| < 4$. The large rapidity gap between the BBC and the central arm reduces the nonflow contributions, especially those from dijets [17]. The systematic errors on v_2 are estimated to be ~6% for central and midcentral collisions and ~10% for the peripheral collisions [4].

To fix the value of b_0, we followed the subtraction procedure of Refs. [4] and [18] and assumed that $Y_{\rm jet}$ has zero yield at its minimum $\Delta\phi_{\rm min}$ (ZYAM). To estimate the possible oversubtraction at $\Delta\phi_{\rm min}$, we calculate b_0 values independently by fitting $Y_{\rm jet}(\Delta\phi)$ to a function consisting of one near-side and two symmetric away-side Gaussians. The fitting procedure is similar to that used in Ref. [5], except that $|\Delta\phi - \pi| < 1$ is

*Deceased
†PHENIX Spokesperson: jacak@skipper.physics.sunysb.edu

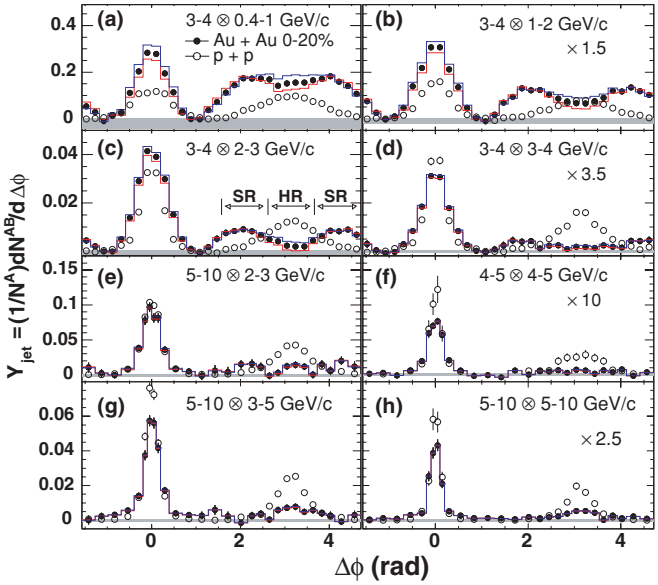

FIG. 1. (Color online) Per-trigger yield versus $\Delta\phi$ for various trigger and partner p_T ($p_T^A \otimes p_T^B$), arranged by increasing pair momentum ($p_T^A + p_T^B$), in $p+p$ and 0–20% Au+Au collisions. The data in some panels are scaled as indicated. Solid histograms (shaded bands) indicate elliptic flow (ZYAM) uncertainties. Arrows in Panel (c) indicate "head" (HR) and "shoulder" (SR) regions. The difference in near-side yield between Au+Au and $p+p$ for Panels (d)–(h) is within the 14% combined uncertainty of the single-particle efficiency.

excluded to avoid punch-through jets around π (see Fig. 1). This fit accounts for the overlap of the near- and away-side Gaussians at $\Delta\phi_{\rm min}$ and thus gives b_0 values systematically lower than that for ZYAM. We assign the differences as one-sided systematic errors on b_0. This oversubtraction error is only significant in central collisions and at $p_{\rm T}^{A,B} < 3$ GeV/c.

The per-trigger yield distributions for $p+p$ and 0–20% central Au+Au collisions are compared in Fig. 1 for various combinations of trigger and partner p_T ranges ($p_T^A \otimes p_T^B$) as indicated. The $p+p$ data show essentially Gaussian away-side peaks centered at $\Delta\phi \sim \pi$ for all p_T^A and p_T^B. In contrast, the Au+Au data show substantial shape modifications dependent on p_T^A and p_T. For a fixed value of p_T^A, Figs. 1(a)–1(d) reveal a striking evolution from a broad, roughly flat peak to a local minimum at $\Delta\phi \sim \pi$ with side peaks at $\Delta\phi \sim \pi \pm 1.1$. Interestingly, the location of the side peaks in $\Delta\phi$ is roughly constant with increasing p_T^B (see also Ref. [5]). Such p_T independence is compatible with the away-side jet modification expected from a medium-induced mach-shock [11] but disfavors models that incorporate large angle gluon radiation [9], Cherenkov gluon radiation [10], or deflected jets [7,8].

For relatively high values of $p_T^A \otimes p_T^B$, Figs. 1(e)–1(h) show that the away-side jet shape for Au+Au gradually becomes peaked as for $p+p$, albeit suppressed. This "reappearance" of the away-side peak seems due to a reduction of the yield centered at $\Delta\phi \sim \pi \pm 1.1$ relative to that at $\Delta\phi \sim \pi$, rather than to a merging of the peaks centered at $\Delta\phi \sim \pi \pm 1.1$. This is consistent with the dominance of dijet fragmentation at large $p_T^A \otimes p_T^B$, possibly due to jets that punch-through the medium [19] or to those emitted tangentially to the medium's surface [20].

The evolution of the away-side jet shape with p_T! (cf. Fig. 1) suggests separate contributions from a medium-induced component centered at $\Delta\phi \sim \pi \pm 1.1$ and a fragmentation component centered at $\Delta\phi \sim \pi$. A model independent study of these contributions can be made by dividing the away-side jet function into equal-sized head ($|\Delta\phi - \pi| < \pi/6$, HR) and shoulder ($\pi/6 < |\Delta\phi - \pi| < \pi/2$, SR) regions, as indicated in Fig. 1(c). We characterize the relative amplitude of these two regions with the ratio, $R_{\rm HS} = \frac{\int_{\Delta\phi\in{\rm HR}} d\Delta\phi Y_{\rm jet}(\Delta\phi)}{\int_{\Delta\phi\in{\rm HR}} d\Delta\phi} / \frac{\int_{\Delta\phi\in{\rm SR}} d\Delta\phi Y_{\rm jet}(\Delta\phi)}{\int_{\Delta\phi\in{\rm SR}} d\Delta\phi}$. Because $N_{\rm A}$ in Eq. (1) cancels in the ratio, $R_{\rm HS}$ is a pure pair variable and is symmetric *w.r.t.* p_T^A and p_T^B: $R_{\rm HS}(p_T^A, p_T^B) = R_{\rm HS}(p_T^B, p_T^A)$. For concave and convex shapes, one expects $R_{\rm HS} < 1$ and $R_{\rm HS} > 1$, respectively.

Figure 2 summarizes the p_T^B dependence of $R_{\rm HS}$ for both $p+p$ and central Au+Au collisions in four p_T^A bins. The ratios for $p+p$ are always above one and increase with p_T^B. This reflects the narrowing of a peaked jet shape with increasing p_T^B [14]. In contrast, the ratios for Au+Au show a nonmonotonic dependence on $p_T^{A,B}$. They evolve from $R_{\rm HS} \sim 1$ for $p_T^{A,B} \lesssim 1$ GeV/c through $R_{\rm HS} < 1$ for $1 \lesssim p_T^{A,B} \lesssim 4$ GeV/c, followed by $R_{\rm HS} > 1$ for $p_T^{A,B} \gtrsim 5$ GeV/c. These trends reflect the competition between medium-induced modification and jet fragmentation and suggest that the latter dominates at $p_T^{A,B} \gtrsim 5$ GeV/c. The results shown in Fig. 1 indicate that, relative to $p+p$, the Au+Au yield is suppressed in the HR but is enhanced in the SR. We quantify this suppression/enhancement via $I_{\rm AA}$, the ratio of jet yield $Y_{\rm jet}$ between Au+Au and $p+p$ collisions over a $\Delta\phi$ region, W, $I_{\rm AA}^W = \int_{\Delta\phi\in W} d\Delta\phi Y_{\rm jet}^{\rm Au+Au} / \int_{\Delta\phi\in W} d\Delta\phi Y_{\rm jet}^{p+p}$.

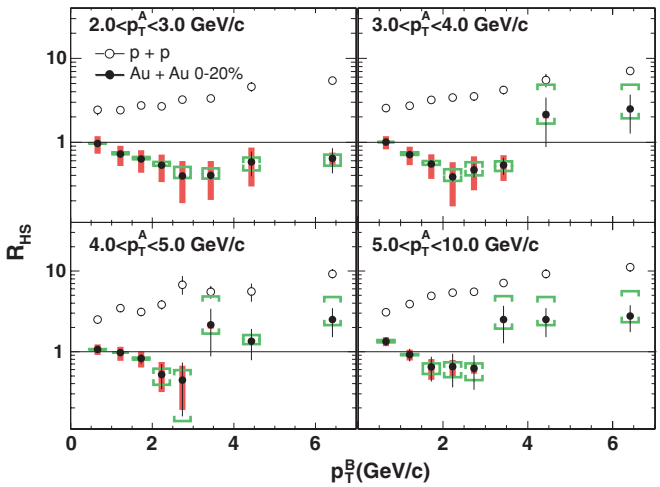

FIG. 2. (Color online) $R_{\rm HS}$ vs p_T^B for $p+p$ (open) and Au+Au (filled) collisions for four trigger selections. Because $R_{\rm HS}$ is purely hadron pair variable, the result is unchanged by swapping p_T^A and p_T^B. Shaded bars (brackets) represent p_T-correlated uncertainties due to elliptic flow (ZYAM procedure).

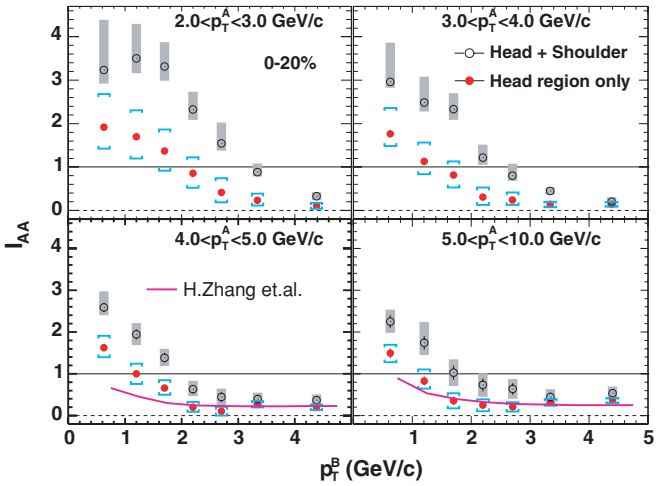

FIG. 3. (Color online) $I_{\rm AA}$ vs p_T^B for four trigger p_T bins in HR+SR ($|\Delta\phi - \pi| < \pi/2$) and HR ($|\Delta\phi - \pi| < \pi/6$). The systematic errors for the two regions, represented by shaded bars and brackets, respectively, include elliptic flow and ZYAM uncertainties and hence are strongly correlated. Grey bands around $I_{\rm AA} = 1$ represent 14% combined uncertainty on the single-particle efficiency in Au+Au and $p+p$. The thick curves are energy loss calculation from Ref. [21] for pairs in $|\Delta\phi - \pi| < 0.64$.

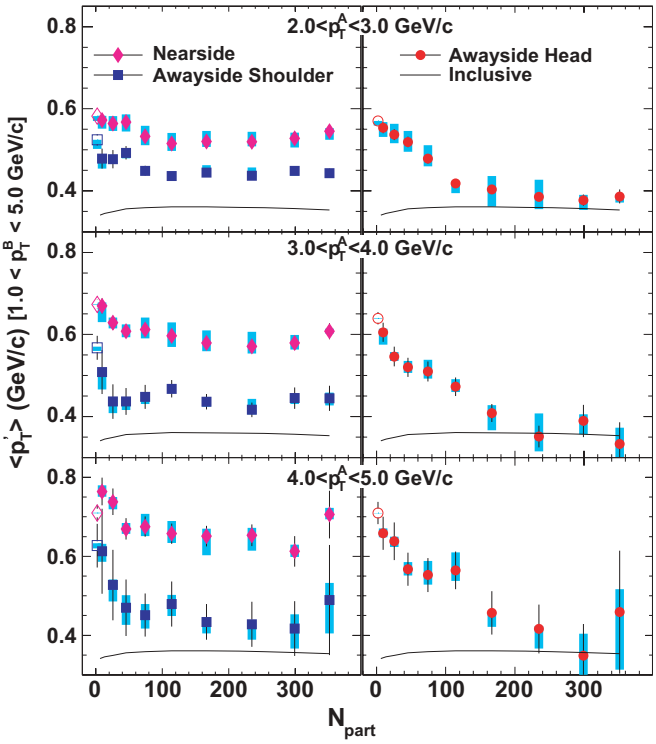

FIG. 4. (Color online) Truncated mean $\langle p'_T \rangle$ in $1 < p_T^B < 5$ GeV/c versus $N_{\rm part}$ for the near-side (diamonds), away-side shoulder (circles), and head (squares) regions for Au+Au (filled) and $p+p$ (open) for three trigger p_T bins. Solid curves represent values for inclusive charged hadrons (~0.36 GeV/c) [2]. Error bars represent the statistical errors. Shaded bars represent the sum of $N_{\rm part}$-correlated elliptic flow and ZYAM error.

Figure 3 shows $I_{\rm AA}$ as a function of p_T^B for the HR and the HR+SR, respectively, in four p_T^A bins. For triggers of $2 < p_{\rm T}^{\rm A} < 3$ GeV/c, $I_{\rm AA}$ for HR+SR exceeds one at low p_T^B, but falls and crosses one at ~3.5 GeV/c. A similar trend is observed for the higher p_T triggers, but the enhancement (at low p_T^B) is smaller and the suppression (at high p_T^B) is stronger. The $I_{\rm AA}$ values in HR are lower relative to HR+SR for all $p_T^{A,B}$. For the low p_T triggers, the suppression sets in around $1 \lesssim p_T^B \lesssim 3$ GeV/c, followed by a fall-off for $p_T^B \gtrsim 4$ GeV/c. For higher p_T triggers, a constant level of ~0.2–0.3 is observed above ~2 GeV/c. The suppression level is similar to the $R_{\rm AA}$ of inclusive hadrons [2] and agrees well with an energy loss model calculation [21] as indicated by the thick solid curves in Fig. 3. These results provide clear evidence for significant yield enhancement in the SR and suppression in the HR. The former reflects the dissipative processes that redistribute the energy lost in the medium, while the latter is consistent with jet quenching. However, we note that the $I_{\rm AA}$ values for the HR are upper limit estimates for the jet fragmentation component. This is because the HR yield includes possible contributions from the tails of the SR, as well as from bremsstrahlung gluon radiations [9].

To further contrast the HR and the SR, we focus on the p_T region of $1 < p_T^B < 5$ GeV/c, where the medium-induced component dominates the away-side. We characterize the inverse local slope of the partner yield in this p_T range via a truncated mean p_T, $\langle p'_T \rangle \equiv \langle p_T^B \rangle|_{1<p_T^B<5{\rm GeV}/c} - 1$ GeV/c. $\langle p'_T \rangle$ is calculated from the jet yields used to make $I_{\rm AA}$ in Fig. 3. Figure 4 shows the $\langle p'_T \rangle$ values for the HR, the SR, and a near-side region ($|\Delta\phi| < \pi/3$, NR) versus the number of participating nucleons, $N_{\rm part}$. The $\langle p'_T \rangle$ values for NR have a weak centrality dependence. Their overall levels for $N_{\rm part} > 100$ are 0.533 ± 0.024, 0.605 ± 0.032, and 0.698 ± 0.040 GeV/c for the p_T^A ranges 2–3, 3–4, and 4–5 GeV/c, respectively [22]. This is consistent with the dominance of jet fragmentation on the near-side, i.e., a harder spectrum for partner hadrons is expected for higher p_T trigger hadrons.

A very weak centrality dependence is observed for the SR for $N_{\rm part} \gtrsim 100$. In this case, the values for $\langle p'_T \rangle$ are lower (≈0.45 GeV/c) and do not depend on p_T^A. They are, however, larger than the values for inclusive charged hadrons [2]. The relatively sharp increase in $\langle p'_T \rangle$ for $N_{\rm part} \lesssim 100$ may reflect a significant jet fragmentation contribution in peripheral collisions. In contrast, the $\langle p'_T \rangle$ values for the HR show a gradual decrease with $N_{\rm part}$, starting close to that for the near-side jet, and approach the value for the inclusive spectrum for $N_{\rm part} \gtrsim 150$.

The different patterns observed for the yields in the HR and SR suggest a different origin for these yields. The suppression of the HR yield and the softening of its spectrum are consistent with a depletion of yield due to jet quenching. Further evidence is given by high p_T pairs, for which the HR yield agrees with energy loss calculations [21] and the HR shape becomes jet like. This suggests that these pairs come mainly from the fragmentation of partons that suffer small energy loss due to tangential or punch-through jet emissions. By contrast, the enhancement of the SR yield reflects a remnant of the lost energy from quenched jets. This enhancement is limited to

$p_T^{A,B} \lesssim 4$ GeV/c, the same p_T region where the soft processes such as hydrodynamical flow and recombination are important. The spectra slope of the SR is almost independent of p_T^A and centrality (for $N_{\rm part} \gtrsim 100$), reflecting an intrinsic property of the response of the medium to the energetic jets. These observations provide separate constraints on geometrical bias at high p_T [19–21] and on the energy transport at low p_T [7–11,23]. However, a model framework including both jet quenching and medium response, which can describe the full p_T evolution of the away-side jet shape and yield, is required to understand the parton-medium interactions.

In conclusion, we have observed strong medium modification of away-side shapes and yields for jet-induced pairs in Au+Au collisions at $\sqrt{s_{\rm NN}} = 200$ GeV. The detailed dependence of these results on p_T and centrality gives strong evidence for two distinct contributions from the regions of $\Delta\phi \sim \pi$ and $\Delta\phi \sim \pi \pm 1.1$. The former shows a strong yield suppression, with a level consistent with a jet quenching calculation at high p_T. The latter exhibits p_T and centrality independent shape and mean p_T, possibly reflecting an intrinsic property of the medium response to energetic jets.

We thank the staff of the Collider-Accelerator and Physics Departments at BNL for their vital contributions. We acknowledge support from the Office of Nuclear Physics in the DOE Office of Science and NSF (USA); MEXT and JSPS (Japan); CNPq and FAPESP (Brazil); NSFC (China); MSMT (Czech Republic); IN2P3/CNRS and CEA (France); BMBF, DAAD, and AvH (Germany); OTKA (Hungary); DAE (India); ISF (Israel); KRF and KOSEF (Korea); MES, RAS, and FAAE (Russia); VR and KAW (Sweden); USA CRDF for the FSU; US-Hungarian NSFOTKA-MTA; and US-Israel BSF.

[1] M. Gyulassy, I. Vitev, X. N. Wang, and B. W. Zhang, in *Quark Gluon Plasma*, edited by R. C.Hwa and X. N. Wang (World Scientific, Singapore, 2003), pp. 123–191; A. Kovner and U. A. Wiedemann, in *Quark Gluon Plasma*, edited by R. C. Hwa and X. N. Wang (World Scientific, Singapore, 2003), pp. 192–248.
[2] S. S. Adler *et al.*, Phys. Rev. C **69**, 034910 (2004).
[3] J. Adams *et al.*, Phys. Rev. Lett. **97**, 162301 (2006).
[4] S. S. Adler *et al.*, Phys. Rev. Lett. **97**, 052301 (2006).
[5] A. Adare *et al.*, Phys. Rev. Lett. **98**, 232302 (2007).
[6] J. Adams *et al.*, Phys. Rev. Lett. **95**, 152301 (2005).
[7] C. B. Chiu and R. C. Hwa, Phys. Rev. C **74**, 064909 (2006).
[8] N. Armesto, C. A. Salgado, and U. A. Wiedemann, Phys. Rev. Lett. **93**, 242301 (2004).
[9] I. Vitev, Phys. Lett. **B630**, 78 (2005); A. D. Polosa and C. A. Salgado, Phys. Rev. C **75**, 041901(R) (2007).
[10] I. M. Dremin, JETP Lett. **30**, 140 (1979); V. Koch, A. Majumder, and X. N. Wang, Phys. Rev. Lett. **96**, 172302 (2006).
[11] J. Casalderrey-Solana, E. V. Shuryak, and D. Teaney, J. Phys. Conf. Ser. **27**, 22 (2005); arXiv:hep-ph/0602183.
[12] K. Adcox *et al.*, Nucl. Instrum. Methods A **499**, 469 (2003).
[13] A. Adare *et al.*, Phys. Rev. Lett. **97**, 252002 (2006).
[14] S. S. Adler *et al.*, Phys. Rev. C **73**, 054903 (2006).
[15] S. S. Adler *et al.*, Phys. Rev. Lett. **95**, 202001 (2005).
[16] S. S. Adler *et al.*, Phys. Rev. Lett. **91**, 182301 (2003).
[17] J. Jia (PHENIX Collaboration), Nucl. Phys. **A783**, 501 (2007).
[18] N. N. Ajitanand *et al.*, Phys. Rev. C **72**, 011902(R) (2005).
[19] T. Renk and K. J. Eskola, Phys. Rev. C **75**, 054910 (2007).
[20] C. Loizides, Eur. Phys. J. C **49**, 339 (2007).
[21] H. Zhang, J. F. Owens, E. Wang, and X. N. Wang, Phys. Rev. Lett. **98**, 212301 (2007), and additional calculations from H. Zhang.
[22] Values at $N_{\rm part} > 100$ are slightly lower than in $p+p$, possibly due to a contribution from a near-side "ridge" [6] in PHENIX η acceptance.
[23] T. Renk and J. Ruppert, Phys. Rev. C **73**, 011901(R) (2006).

PHYSICAL REVIEW D **76,** 051106(R) (2007)

Inclusive cross section and double helicity asymmetry for π^0 production in $p + p$ collisions at $\sqrt{s} = 200$ GeV: Implications for the polarized gluon distribution in the proton

A. Adare,[8] S. Afanasiev,[22] C. Aidala,[9] N. N. Ajitanand,[48] Y. Akiba,[42,43] H. Al-Bataineh,[37] J. Alexander,[48] K. Aoki,[27,42] L. Aphecetche,[50] R. Armendariz,[37] S. H. Aronson,[3] J. Asai,[43] E. T. Atomssa,[28] R. Averbeck,[49] T. C. Awes,[38] B. Azmoun,[3] V. Babintsev,[18] G. Baksay,[14] L. Baksay,[14] A. Baldisseri,[11] K. N. Barish,[4] P. D. Barnes,[30] B. Bassalleck,[36] S. Bathe,[4] S. Batsouli,[38] V. Baublis,[41] A. Bazilevsky,[3] S. Belikov,[3] R. Bennett,[49] Y. Berdnikov,[45] A. A. Bickley,[8] J. G. Boissevain,[30] H. Borel,[11] K. Boyle,[49] M. L. Brooks,[30] H. Buesching,[3] V. Bumazhnov,[18] G. Bunce,[3,43] S. Butsyk,[30,49] S. Campbell,[49] B. S. Chang,[57] J.-L. Charvet,[11] S. Chernichenko,[18] J. Chiba,[23] C. Y. Chi,[9] M. Chiu,[19] I. J. Choi,[57] T. Chujo,[54] P. Chung,[48] A. Churyn,[18] V. Cianciolo,[38] C. R. Cleven,[16] B. A. Cole,[9] M. P. Comets,[39] P. Constantin,[30] M. Csanád,[13] T. Csörgő,[24] T. Dahms,[49] K. Das,[15] G. David,[3] M. B. Deaton,[1] K. Dehmelt,[14] H. Delagrange,[50] A. Denisov,[18] D. d'Enterria,[9] A. Deshpande,[43,49] E. J. Desmond,[3] O. Dietzsch,[46] A. Dion,[49] M. Donadelli,[46] O. Drapier,[28] A. Drees,[49] A. K. Dubey,[56] A. Durum,[18] V. Dzhordzhadze,[4] Y. V. Efremenko,[38] J. Egdemir,[49] F. Ellinghaus,[8] W. S. Emam,[4] A. Enokizono,[29] H. En'yo,[42,43] S. Esumi,[53] K. O. Eyser,[4] D. E. Fields,[36,43] M. Finger,[5,22] M. Finger, Jr.,[5,22] F. Fleuret,[28] S. L. Fokin,[26] Z. Fraenkel,[56] J. E. Frantz,[49] A. Franz,[3] A. D. Frawley,[15] K. Fujiwara,[42] Y. Fukao,[27,42] T. Fusayasu,[35] S. Gadrat,[31] I. Garishvili,[51] A. Glenn,[8] H. Gong,[49] M. Gonin,[28] J. Gosset,[11] Y. Goto,[42,43] R. Granier de Cassagnac,[28] N. Grau,[21] S. V. Greene,[54] M. Grosse Perdekamp,[19,43] T. Gunji,[7] H.-Å. Gustafsson,[32] T. Hachiya,[17] A. Hadj Henni,[50] C. Haegemann,[36] J. S. Haggerty,[3] H. Hamagaki,[7] R. Han,[40] H. Harada,[17] E. P. Hartouni,[29] K. Haruna,[17] E. Haslum,[32] R. Hayano,[7] M. Heffner,[29] T. K. Hemmick,[49] T. Hester,[4] X. He,[16] H. Hiejima,[19] J. C. Hill,[21] R. Hobbs,[36] M. Hohlmann,[14] W. Holzmann,[48] K. Homma,[17] B. Hong,[25] T. Horaguchi,[42,52] D. Hornback,[51] T. Ichihara,[42,43] K. Imai,[27,42] M. Inaba,[53] Y. Inoue,[44,42] D. Isenhower,[1] L. Isenhower,[1] M. Ishihara,[42] T. Isobe,[7] M. Issah,[48] A. Isupov,[22] B. V. Jacak,[49,*] J. Jia,[9] J. Jin,[9] O. Jinnouchi,[43] B. M. Johnson,[3] K. S. Joo,[34] D. Jouan,[39] F. Kajihara,[7] S. Kametani,[7,55] N. Kamihara,[42] J. Kamin,[49] M. Kaneta,[43] J. H. Kang,[57] H. Kanou,[42,52] D. Kawall,[43] A. V. Kazantsev,[26] A. Khanzadeev,[41] J. Kikuchi,[55] D. H. Kim,[34] D. J. Kim,[57] E. Kim,[47] E. Kinney,[8] A. Kiss,[13] E. Kistenev,[3] A. Kiyomichi,[42] J. Klay,[29] C. Klein-Boesing,[33] L. Kochenda,[41] V. Kochetkov,[18] B. Komkov,[41] M. Konno,[53] D. Kotchetkov,[4] A. Kozlov,[56] A. Král,[10] A. Kravitz,[9] J. Kubart,[5,20] G. J. Kunde,[30] N. Kurihara,[7] K. Kurita,[44,42] M. J. Kweon,[25] Y. Kwon,[51,57] G. S. Kyle,[37] R. Lacey,[48] Y.-S. Lai,[9] J. G. Lajoie,[21] A. Lebedev,[21] D. M. Lee,[30] M. K. Lee,[57] T. Lee,[47] M. J. Leitch,[30] M. A. L. Leite,[46] B. Lenzi,[46] T. Liška,[10] A. Litvinenko,[22] M. X. Liu,[30] X. Li,[6] B. Love,[54] D. Lynch,[3] C. F. Maguire,[54] Y. I. Makdisi,[3] A. Malakhov,[22] M. D. Malik,[36] V. I. Manko,[26] Y. Mao,[40,42] L. Mašek,[5,20] H. Masui,[53] F. Matathias,[9] M. McCumber,[49] P. L. McGaughey,[30] Y. Miake,[53] P. Mikeš,[5,20] K. Miki,[53] T. E. Miller,[54] A. Milov,[49] S. Mioduszewski,[3] M. Mishra,[2] J. T. Mitchell,[3] M. Mitrovski,[48] A. Morreale,[4] D. P. Morrison,[3] T. V. Moukhanova,[26] D. Mukhopadhyay,[54] J. Murata,[44,42] S. Nagamiya,[23] Y. Nagata,[53] J. L. Nagle,[8] M. Naglis,[56] I. Nakagawa,[42,43] Y. Nakamiya,[17] T. Nakamura,[17] K. Nakano,[42,52] J. Newby,[29] M. Nguyen,[49] B. E. Norman,[30] A. S. Nyanin,[26] E. O'Brien,[3] S. X. Oda,[7] C. A. Ogilvie,[21] H. Ohnishi,[42] H. Okada,[27,42] K. Okada,[43] M. Oka,[53] O. O. Omiwade,[1] A. Oskarsson,[32] M. Ouchida,[17] K. Ozawa,[7] R. Pak,[3] D. Pal,[54] A. P. T. Palounek,[30] V. Pantuev,[49] V. Papavassiliou,[37] J. Park,[47] W. J. Park,[25] S. F. Pate,[37] H. Pei,[21] J.-C. Peng,[19] H. Pereira,[11] V. Peresedov,[22] D. Yu. Peressounko,[26] C. Pinkenburg,[3] M. L. Purschke,[3] A. K. Purwar,[30] H. Qu,[16] J. Rak,[36] A. Rakotozafindrabe,[28] I. Ravinovich,[56] K. F. Read,[38,51] S. Rembeczki,[14] M. Reuter,[49] K. Reygers,[33] V. Riabov,[41] Y. Riabov,[41] G. Roche,[31] A. Romana,[28,†] M. Rosati,[21] S. S. E. Rosendahl,[32] P. Rosnet,[31] P. Rukoyatkin,[22] V. L. Rykov,[42] B. Sahlmueller,[33] N. Saito,[27,42,43] T. Sakaguchi,[3] S. Sakai,[53] H. Sakata,[17] V. Samsonov,[41] S. Sato,[23] S. Sawada,[23] J. Seele,[8] R. Seidl,[19] V. Semenov,[18] R. Seto,[4] D. Sharma,[56] I. Shein,[18] A. Shevel,[41,48] T.-A. Shibata,[42,52] K. Shigaki,[17] M. Shimomura,[53] K. Shoji,[27,42] A. Sickles,[49] C. L. Silva,[46] D. Silvermyr,[38] C. Silvestre,[11] K. S. Sim,[25] C. P. Singh,[2] V. Singh,[2] S. Skutnik,[21] M. Slunečka,[5,22] A. Soldatov,[18] R. A. Soltz,[29] W. E. Sondheim,[30] S. P. Sorensen,[51] I. V. Sourikova,[3] F. Staley,[11] P. W. Stankus,[38] E. Stenlund,[32] M. Stepanov,[37] A. Ster,[24] S. P. Stoll,[3] T. Sugitate,[17] C. Suire,[39] J. Sziklai,[24] T. Tabaru,[43] S. Takagi,[53] E. M. Takagui,[46] A. Taketani,[42,43] Y. Tanaka,[35] K. Tanida,[42,43] M. J. Tannenbaum,[3] A. Taranenko,[48] P. Tarján,[12] T. L. Thomas,[36] M. Togawa,[27,42] A. Toia,[49] J. Tojo,[42] L. Tomášek,[20] H. Torii,[42] R. S. Towell,[1] V-N. Tram,[28] I. Tserruya,[56] Y. Tsuchimoto,[17] C. Vale,[21] H. Valle,[54] H. W. van Hecke,[30] J. Velkovska,[54] R. Vertesi,[12] A. A. Vinogradov,[26] M. Virius,[10] V. Vrba,[20] E. Vznuzdaev,[41] M. Wagner,[27,42] D. Walker,[49] X. R. Wang,[37] Y. Watanabe,[42,43] J. Wessels,[33] S. N. White,[3] D. Winter,[9] C. L. Woody,[3] M. Wysocki,[8] W. Xie,[43] Y. Yamaguchi,[55] A. Yanovich,[18] Z. Yasin,[4] J. Ying,[16] S. Yokkaichi,[42,43] G. R. Young,[38] I. Younus,[36] I. E. Yushmanov,[26] W. A. Zajc,[9] O. Zaudtke,[33] C. Zhang,[38] S. Zhou,[6] J. Zimányi,[24,†] and L. Zolin[22]

(PHENIX Collaboration)

 © 2007 The American Physical Society

[1]*Abilene Christian University, Abilene, Texas 79699, USA*
[2]*Department of Physics, Banaras Hindu University, Varanasi 221005, India*
[3]*Brookhaven National Laboratory, Upton, New York 11973-5000, USA*
[4]*University of California, Riverside, Riverside, California 92521, USA*
[5]*Charles University, Ovocný trh 5, Praha 1, 116 36 Prague, Czech Republic*
[6]*China Institute of Atomic Energy (CIAE), Beijing, People's Republic of China*
[7]*Center for Nuclear Study, Graduate School of Science, University of Tokyo, 7-3-1 Hongo, Bunkyo, Tokyo 113-0033, Japan*
[8]*University of Colorado, Boulder, Colorado 80309, USA*
[9]*Columbia University, New York, New York 10027, USA, and Nevis Laboratories, Irvington, New York 10533, USA*
[10]*Czech Technical University, Zikova 4, Praha 6, 166 36 Prague, Czech Republic*
[11]*Dapnia, CEA Saclay, F-91191 Gif-sur-Yvette, France*
[12]*Debrecen University, H-4010 Debrecen, Egyetem tér 1, Hungary*
[13]*ELTE, Eötvös Loránd University, H-1117 Budapest, Pázmány P. s. 1/A, Hungary*
[14]*Florida Institute of Technology, Melbourne, Florida 32901, USA*
[15]*Florida State University, Tallahassee, Florida 32306, USA*
[16]*Georgia State University, Atlanta, Georgia 30303, USA*
[17]*Hiroshima University, Kagamiyama, Higashi-Hiroshima 739-8526, Japan*
[18]*IHEP Protvino, State Research Center of Russian Federation, Institute for High Energy Physics, Protvino 142281, Russia*
[19]*University of Illinois at Urbana-Champaign, Urbana, Illinois 61801, USA*
[20]*Institute of Physics, Academy of Sciences of the Czech Republic, Na Slovance 2, Praha 8, 182 21 Prague, Czech Republic*
[21]*Iowa State University, Ames, Iowa 50011, USA*
[22]*Joint Institute for Nuclear Research, 141980 Dubna, Moscow Region, Russia*
[23]*KEK, High Energy Accelerator Research Organization, Tsukuba, Ibaraki 305-0801, Japan*
[24]*KFKI Research Institute for Particle and Nuclear Physics of the Hungarian Academy of Sciences (MTA KFKI RMKI), H-1525 Budapest 114, P.O. Box 49, Budapest, Hungary*
[25]*Korea University, Seoul, 136-701, Korea*
[26]*Russian Research Center Kurchatov Institute, Moscow, Russia*
[27]*Kyoto University, Kyoto 606-8502, Japan*
[28]*Laboratoire Leprince-Ringuet, Ecole Polytechnique (CNRS-IN2P3), Route de Saclay, F-91128 Palaiseau, France*
[29]*Lawrence Livermore National Laboratory, Livermore, California 94550, USA*
[30]*Los Alamos National Laboratory, Los Alamos, New Mexico 87545, USA*
[31]*LPC, Université Blaise Pascal (CNRS-IN2P3), Clermont-Fd, 63177 Aubiere Cedex, France*
[32]*Department of Physics, Lund University, P.O. Box 118, SE-221 00 Lund, Sweden*
[33]*Institut für Kernphysik, University of Muenster, D-48149 Muenster, Germany*
[34]*Myongji University, Yongin, Kyonggido 449-728, Korea*
[35]*Nagasaki Institute of Applied Science, Nagasaki-shi, Nagasaki 851-0193, Japan*
[36]*University of New Mexico, Albuquerque, New Mexico 87131, USA*
[37]*New Mexico State University, Las Cruces, New Mexico 88003, USA*
[38]*Oak Ridge National Laboratory, Oak Ridge, Tennessee 37831, USA*
[39]*IPN-Orsay, Université Paris Sud (CNRS-IN2P3), BP 1, F-91406 Orsay, France*
[40]*Peking University, Beijing, People's Republic of China*
[41] *Petersburg Nuclear Physics Institute (PNPI), Gatchina, Leningrad Region 188300, Russia*
[42] *RIKEN, The Institute of Physical and Chemical Research, Wako, Saitama 351-0198, Japan*
[43]*RIKEN BNL Research Center, Brookhaven National Laboratory, , Upton, New York 11973-5000, USA*
[44]*Physics Department, Rikkyo University, 3-34-1 Nishi-Ikebukuro, Toshima, Tokyo 171-8501, Japan*
[45]*Saint Petersburg State Polytechnic University, St. Petersburg, Russia*
[46]*Universidade de São Paulo, Instituto de Física, Caixa Postal 66318, São Paulo CEP05315-970, Brazil*
[47]*System Electronics Laboratory, Seoul National University, Seoul, South Korea*
[48]*Chemistry Department, Stony Brook University, SUNY, Stony Brook, New York 11794-3400, USA*
[49]*Department of Physics and Astronomy, Stony Brook University, SUNY, Stony Brook, New York 11794-3800, USA*
[50]*SUBATECH Ecole des Mines de Nantes (CNRS-IN2P3), Université de Nantes BP 20722 - 44307 Nantes, France*
[51]*University of Tennessee, Knoxville, Tennessee 37996, USA*
[52]*Department of Physics, Tokyo Institute of Technology, Oh-okayama, Meguro, Tokyo 152-8551, Japan*
[53]*Institute of Physics, University of Tsukuba, Tsukuba, Ibaraki 305, Japan*
[54]*Vanderbilt University, Nashville, Tennessee 37235, USA*
[55]*Waseda University, Advanced Research Institute for Science and Engineering, 17 Kikui-cho, Shinjuku-ku, Tokyo 162-0044, Japan*
[56]*Weizmann Institute, Rehovot 76100, Israel*
[57]*Yonsei University, IPAP, Seoul 120-749, Korea*
(Received 27 April 2007; published 25 September 2007)

[*]PHENIX spokesperson: jacak@skipper.physics.sunysb.edu
[†]Deceased

The PHENIX experiment presents results from the Relativistic Heavy Ion Collider 2005 run with polarized proton collisions at $\sqrt{s} = 200$ GeV, for inclusive π^0 production at midrapidity. Unpolarized cross section results are given for transverse momenta $p_T = 0.5$ to 20 GeV/c, extending the range of published data to both lower and higher p_T. The cross section is described well for $p_T < 1$ GeV/c by an exponential in p_T, and, for $p_T > 2$ GeV/c, by perturbative QCD. Double helicity asymmetries A_{LL} are presented based on a factor of 5 improvement in uncertainties as compared to previously published results, due to both an improved beam polarization of 50%, and to higher integrated luminosity. These measurements are sensitive to the gluon polarization in the proton. Using one representative model of gluon polarization it is demonstrated that the gluon spin contribution to the proton spin is significantly constrained.

DOI: 10.1103/PhysRevD.76.051106 PACS numbers: 13.85.Ni, 13.88.+e, 21.10.Hw, 25.40.Ep

A principal goal of the spin program at the Relativistic Heavy Ion Collider (RHIC) at Brookhaven National Laboratory is to determine the gluon spin contribution to a longitudinally polarized proton (ΔG), taking advantage of the strongly interacting probes available in proton-proton collisions [1]. Previous measurements have established the validity of the perturbative quantum chromodynamics (pQCD) description for inclusive midrapidity π^0 [2] and forward π^0 production [3], and for midrapidity jet [4] and direct photon production [5], at $\sqrt{s} = 200$ GeV. The double helicity asymmetries for the production of these particles involve gluons in the hard scattering processes in this pQCD description, and the first measurements for π^0 [6,7] and for jets [4] have begun to probe ΔG.

The RHIC beam polarization and luminosity have significantly improved [8]. The statistical uncertainty for a double helicity asymmetry measurement is proportional to the inverse of $P^2 \times \sqrt{\mathcal{L}}$ for beam polarizations P and integrated luminosity $\mathcal{L}$, and decreased by a factor of 5 from the previously published data from PHENIX [6,7].

In this paper, we first present the cross section for midrapidity π^0 production for unpolarized proton-proton collisions at $\sqrt{s} = 200$ GeV. These results extend to lower and higher p_T than in previous publications, and we discuss an apparent transition region between soft and hard scattering; the inclusive cross section is dominated by hard scattering, described by pQCD, for $p_T > 2$ GeV/c. We then present the double helicity asymmetry, A_{LL}, for midrapidity π^0 production. We also include measurements of A_{LL} at low p_T, below the hard scattering region. Finally, our results for $p_T > 2$ GeV/c are compared to a pQCD calculation that incorporates a model of gluon polarization. We present the range that we probe in the gluon momentum fraction (x_g) and discuss the constraint from these data on ΔG.

The PHENIX experiment at RHIC measured π^0's via $\pi^0 \rightarrow \gamma\gamma$ decays using a highly segmented ($\Delta\eta \times \Delta\phi \sim 0.01 \times 0.01$) electromagnetic calorimeter (EMCal) [9], covering a pseudorapidity range of $|\eta| < 0.35$ and azimuthal angle range of $\Delta\phi = \pi$. The π^0 data in this analysis were collected using two different trigger conditions. A minimum bias (MB) trigger was defined by the coincidence of signals in two beam-beam counters (BBC) with full azimuthal coverage located at pseudorapidities $\pm(3.0 - 3.9)$ [10]. The cross section for events selected by the MB trigger was 23.0 mb (about half of $\sigma_{pp}^{\text{inel}}$) with a systematic uncertainty of $\pm 9.7\%$, derived from vernier scan results [2] and the variation of MB trigger efficiency for subsequent years. Higher p_T data were collected using the coincidence of the MB trigger and an EMCal-based high p_T photon trigger [2,11], with efficiency $\sim 5\%$ at $p_T(\pi^0) \sim 1$ GeV/c and $\sim 90\%$ for $p_T(\pi^0) > 3.5$ GeV/c. The collision vertex was required to be within $|z| < 30$ cm along the beam axis, based on the time difference between the two BBC detectors. The π^0 acceptance is uniform over this interval. The analyzed data sample of the 2005 run corresponds to an integrated luminosity of 2.5 pb^{-1}.

Details of the unpolarized cross section analysis technique are described in [2,11]. The background contribution under the π^0 peak in the two-photon invariant mass distribution varied from 80% in the lowest 0.5–0.75 GeV/c p_T bin to less than 8% for $p_T > 4$ GeV/c. The π^0 spectrum was corrected for overlapping decay photon showers in the EMCal, based on Monte Carlo simulations confirmed with test beam data [12]. Below a $p_T(\pi^0)$ of 12 GeV/c the correction is less than 4%, and for $p_T(\pi^0) = 20$ GeV/c the correction is $\sim 25\%$ and $\sim 70\%$, for two different EMCal subsystems [9]. The systematic uncertainty of the measurement (excluding the 9.7% uncertainty from the MB trigger cross section) varied from $\sim 7\%$ at $p_T \sim 1$ GeV/c to $\sim 16\%$ for the highest p_T bin.

Figure 1 presents the cross section results for midrapidity π^0 production at $\sqrt{s} = 200$ GeV, versus p_T, from $p_T = 0.5$ GeV/c to $p_T = 20$ GeV [13]. Points are plotted at the average p_T for each bin. The pQCD prediction, at next-to-leading order (NLO), is shown for theory scales $\mu = p_T/2$, p_T and $2p_T$, where μ represents equal factorization, renormalization, and fragmentation scales [14,15]. The Coordinated Theoretical-Experimental Project on QCD (CTEQ6M) parton distribution functions [16] and Kniehl-Kramer-Pötter set of fragmentation functions [17] are used. These data extend the published cross section data at both low and high p_T, and are consistent with previously published results [2,11]. From $p_T = 2$ GeV/c to 20 GeV/c, the NLO pQCD calculation describes the data over a change in cross section of 7 orders of magni-

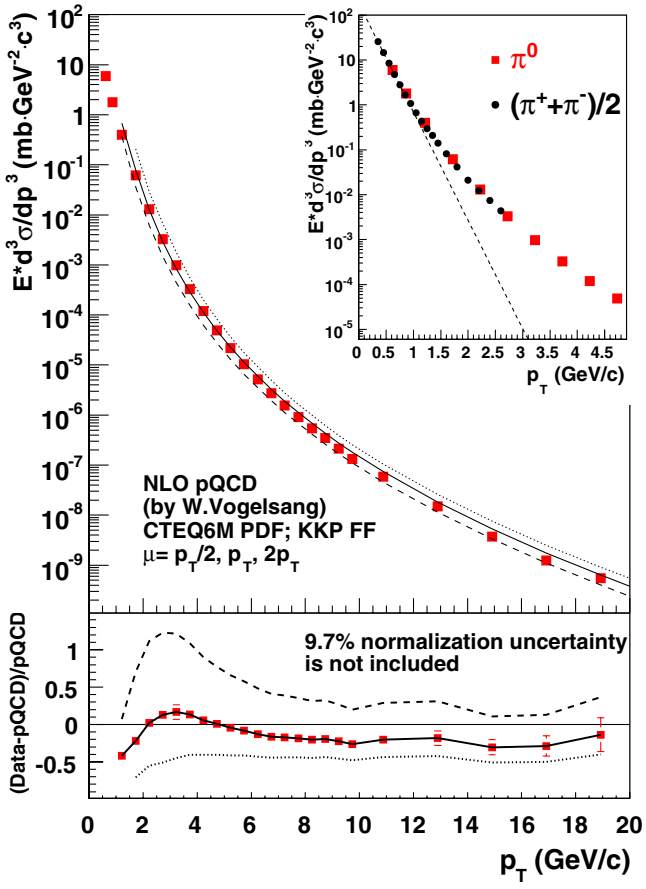

FIG. 1 (color online). The neutral pion production cross section at $\sqrt{s} = 200$ GeV as a function of p_T (squares) and the results of NLO pQCD calculations for theory scales $\mu = p_T/2$ (dotted line), p_T (solid line) and $2p_T$ (dashed line), see text for details; note that the error bars are smaller than the points. The inset shows, in addition to π^0 (squares), data for $(\pi^+ + \pi^-)/2$ (solid circles), and a fit of charged pion data to an exponential function for $p_T < 0.8$ GeV/c (dashed line). The bottom panel shows the relative difference between the data and theory for the three theory scales. Experimental uncertainties (excluding the 9.7% normalization uncertainty) are shown for the $\mu = p_T$ curve.

tude. We note also more recent theoretical work which describes the RHIC midrapidity π^0 data, and which introduces an intrinsic k_T dependence into the parton distribution and fragmentation functions [18], or which includes soft gluon emission in the interaction [19]. Both new approaches improve agreement with data at lower energies and have a smaller effect on the $\sqrt{s} = 200$ GeV midrapidity cross sections.

The inset of Fig. 1 shows the lower p_T region in more detail including high precision data for the charged pion cross section from [20]. The data show a transition in the p_T dependence of the cross section, from exponential to a power law dependence, in the region $p_T \approx 1$–2 GeV/c. In order to estimate possible contamination from nonperturbative physics in the higher p_T data, an exponential function ($\sim e^{-\alpha p_T}$) representing a nonperturbative component is fit to the charged pion spectrum in the region $p_T = 0.3$ to 0.8 GeV/c (only the lowest p_T π^0 data point is in this range) and extrapolated to the higher p_T region. The exponential fit for the low p_T region gives $\alpha = 5.56 \pm 0.02$ $(\mathrm{GeV}/c)^{-1}$, with $\chi^2/NDF = 6.2/3$. Only statistical uncertainties for the charged pion data were used in the fit. The dominant systematic uncertainty for the points in the fitted p_T range is a ~12% normalization uncertainty (excluding the normalization uncertainty from the MB trigger cross section). Beyond about $p_T = 1$ GeV/c, the data lie above this single exponential. The fraction of the exponential contribution to the data for the 2–2.5 GeV/c p_T bin is found to be less than 10%, with a negligible contribution for higher p_T. This is the basis for applying the pQCD formalism to the double helicity asymmetry data with $p_T > 2$ GeV/c.

For the 2005 run, each collider ring of RHIC was filled with up to 111 bunches in a 120 bunch pattern, spaced 106 ns apart, with predetermined patterns of polarization signs for the bunches. Spin rotators, sets of four helical dipole magnets on each side of PHENIX, rotate the polarization orientation from vertical, the stable spin direction in the RHIC arcs, to longitudinal at the interaction point [21]. Beam helicity asymmetries are obtained by tagging the polarization signs of the bunches for each event. The bunches for one beam alternate in polarization sign, and pairs of bunches alternate in sign for the other beam. In this way data for all combinations of beam helicity are collected at the same time, and the possibility of false asymmetries due to changing detector response versus spin state is greatly reduced. Each RHIC fill, typically lasting 8 h, used one of four bunch spin patterns.

The beam polarizations for 2005 were measured using fast carbon target polarimeters [22], normalized by absolute polarization measurements made during 2005 by a separate polarized atomic hydrogen jet polarimeter [23]. The beam polarizations, from luminosity-weighted averages over 104 RHIC fills used in the analysis, were $\langle P^B \rangle = 0.50 \pm 0.002(\mathrm{stat}) \pm 0.025(\mathrm{systB}) \pm 0.015(\mathrm{systG})$ and $\langle P^Y \rangle = 0.49 \pm 0.002(\mathrm{stat}) \pm 0.025(\mathrm{systY}) \pm 0.015(\mathrm{systG})$, for blue ($B$) and yellow ($Y$) RHIC beams, respectively, for the bunches colliding at PHENIX. The systematic uncertainties have been separated into uncorrelated uncertainties for each beam, "systB" and "systY," and a global systematic uncertainty "systG," which is common for both beams and comes from systematic uncertainty in jet polarimeter measurements [24]. For comparison, the polarizations in the 2004 run were $0.44 \pm 0.08(\mathrm{syst})$.

Local polarimeters based on very forward neutron production (production angle 0.3–2.5 mrad) [6,25] were used to set up and monitor the beam polarization orientation at PHENIX. The polarimeters monitor the transverse polarization of each beam at PHENIX, which can be compared to the beam polarization measured by the RHIC polar-

imeters where the polarization direction is vertical. The local polarimeters were calibrated by turning off the spin rotators around PHENIX, and measuring the response of the local polarimeters with the beams vertically polarized. For the longitudinal polarization data, the beams showed a measurable transverse polarization, with $(P_T/P)^B = 0.10 \pm 0.02$ and $(P_T/P)^Y = 0.14 \pm 0.02$, with P_T/P referring to the fraction of transverse polarization of each beam. The polarization directions, as determined by the spin rotator settings and as measured by the local polarimeters, remained constant over the run. The product of the beam polarizations $P^B \cdot P^Y$ is required for the double helicity asymmetry measurement. The average transverse component of the product was $\langle P_T^B \cdot P_T^Y \rangle / \langle P^B \cdot P^Y \rangle < (P_T/P)^B \cdot (P_T/P)^Y = 0.014 \pm 0.003$; the average of the polarization product over the run was $\langle P^B \cdot P^Y \rangle = 0.24$ with a systematic uncertainty of $\pm 9.4\%$.

The double helicity asymmetry A_{LL} is the difference of cross sections for the same versus opposite beam helicities, divided by the sum. Experimentally, for inclusive π^0 production, it can be determined as

$$A_{LL}^{\pi^0} = \frac{1}{|P^B \cdot P^Y|} \cdot \frac{N_{++} - R \cdot N_{+-}}{N_{++} + R \cdot N_{+-}}; \qquad R = \frac{L_{++}}{L_{+-}}, \quad (1)$$

where N is the number of π^0's measured in PHENIX from the colliding bunches with the same $(++)$ and opposite $(+-)$ helicities, and R is the relative luminosity between bunches with the same and opposite helicities. Here we neglect the parity-violating difference in cross section between $(++) \leftrightarrow (--)$ and $(+-) \leftrightarrow (-+)$ beam helicity configurations [26]. A_{LL} was calculated for each fill in order to reduce systematics from variation in beam polarizations and in R for different fills. Even and odd crossings were handled by separate high p_T photon trigger electronics chains. To avoid possible detector bias, A_{LL} was also determined separately for the even and odd crossings. Final asymmetries were averaged, and corrected for the asymmetry of the background under the π^0 peak in the two-photon mass distribution A_{LL}^{BG}, measured from the data outside the π^0 peak region (50 MeV/c^2 wide bands on either side of the π^0 peak) [6]. A_{LL}^{BG} was consistent with zero in all p_T bins.

The relative luminosity ratio R is obtained from the MB triggers discussed above. Scalers keep track of the number of live triggers for each bunch crossing. Single beam background was $<0.05\%$, as measured from noncolliding bunches, and contributes negligible systematic uncertainty to the measured R. We also measured the double helicity asymmetry of the relative luminosity scaler counts, by normalizing using zero degree neutral particle production as measured by zero degree calorimeters (ZDC) [27]. No asymmetry was observed. This gave a limit on an asymmetry bias in the measurement of $\delta A_{LL}^{\pi^0}|_{\text{bias}} < 2 \times 10^{-4}$, and a limit on the systematic uncertainty for the measurement of relative luminosity giving $\delta A_{LL}^{\pi^0}|_R < 2 \times 10^{-4}$. These limits also include the effects from the pileup of two or more collisions in a crossing, calculated at $\lesssim 4\%$ of the crossings. The BBC and ZDC monitors observe the pileup at significantly different rates, and therefore the limits above, from comparing BBC and ZDC counts, include these uncertainties.

A transverse double spin asymmetry A_{TT}, the transverse equivalent to Eq. (1), can contribute to A_{LL} through the 1.4% transverse component of the product of the beam polarizations discussed above. Although A_{TT} has been postulated to be extremely small, $\sim 10^{-4}$ [28], it has not been previously measured. We measured A_{TT} in a short run with transverse polarization. $A_{TT}(p_T)$ was consistent with zero within statistical errors [13]; the errors were 5 times larger than the uncertainties for A_{LL}, $\delta^{\text{stat}} A_{LL}$. Therefore, a limit was determined for the A_{TT} contribution to A_{LL} of $0.07 \cdot \delta^{\text{stat}} A_{LL}$.

Figure 2 presents the measured double helicity asymmetry in π^0 production [13]. A scale uncertainty of 9.4% in $A_{LL}^{\pi^0}$ due to the uncertainty in beam polarization is not shown. The other systematic uncertainties are negligible, as discussed above, and checked using a bunch polarization sign randomization technique, and by varying the π^0 identification criteria [6]. Data for $p_T > 1$ GeV/c were obtained from the high p_T photon triggered sample. For p_T below 1 GeV/c, due to low efficiency for the high p_T photon trigger, we used the MB data sample. In the low p_T region, where the cross section shows an exponential

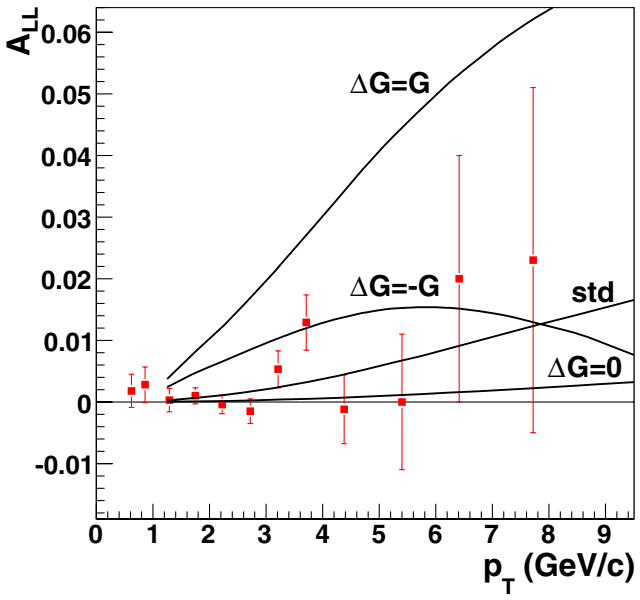

FIG. 2 (color online). The double helicity asymmetry for neutral pion production at $\sqrt{s} = 200$ GeV as a function of p_T (GeV/c). Error bars are statistical uncertainties, with the 9.4% scale uncertainty not shown; other experimental systematic uncertainties are negligible. Four GRSV theoretical calculations based on NLO pQCD are also shown for comparison with the data (see text for details).

behavior, the helicity asymmetry is $A_{LL}^{\pi^0} = 0.002 \pm 0.002$, for the data in the range $p_T = 0.5 - 1$ GeV/c. For the higher p_T region, the four curves in Fig. 2 show calculations of $A_{LL}^{\pi^0}$, using NLO pQCD with $\mu = p_T(\pi^0)$, that reflect the range of gluon polarizations allowed by inclusive deep inelastic scattering (DIS) data. The calculations are based on the Glück-Reya-Stratmann-Vogelsang (GRSV) model, where "standard" (std) was the best fit to inclusive DIS data [29]. For momentum fraction x, $\Delta G(x) = G^+(x) - G^-(x)$ refers to the gluon helicity distribution, and $G^+(x)$ and $G^-(x)$ refer to the gluon densities for + and − helicities in a + helicity proton. The first moment of the gluon helicity distribution, $\int_0^1 \Delta G(x)dx$, for the std parameterization is $\Delta G = 0.4$, at the scale $Q^2 = 1$ GeV^2. The other three curves are calculations based on this best fit, but use at $Q^2 = 0.4$ GeV^2 the function $\Delta G(x) = G(x)$, 0, $-G(x)$, where $G(x)$ is the unpolarized gluon distribution. The gluon distribution at the input scale is evolved to the scale $Q^2 = p_T^2(\pi^0)$.

In order to explore the impact of the new data on the sensitivity to the polarized gluon distribution, we have compared the data with a set of $A_{LL}(p_T)$ curves corresponding to different $\Delta G(x)$ between $\Delta G(x) = -G(x)$ and $\Delta G(x) = G(x)$ at $Q^2 = 0.4$ GeV^2. We used the data for $p_T > 2$ GeV/c, which appear to have little contamination from soft physics as discussed earlier.

Combining the estimate of the soft physics fraction in the $p_T = 2$–2.5 GeV/c bin of $<10\%$, with the soft physics asymmetry as measured for $p_T < 1$ GeV/c, a soft physics contribution to the asymmetry in the $p_T = 2 - 2.5$ GeV/c bin would be $\lesssim 2 \cdot 10^{-4}$, and negligible for higher p_T bins. We note, however, that a parton intrinsic k_T [18] could still affect the lower p_T asymmetries, for $p_T \approx 2$–3 GeV/c, and this is not addressed in the GRSV model.

The most likely x_g for PHENIX π^0 data in each p_T point is $\sim x_T/0.7$ [30], where $x_T = p_T/(\sqrt{s}/2)$. For the measured p_T range 2–9 GeV/c, the range of x_g in each bin is broad, and spans the range $x_g = 0.02$–0.3, as calculated by NLO pQCD [31].

Figure 3 shows the corresponding χ^2 versus $\Delta G_{\rm GRSV}^{x=[0.02\to0.3]}$, where we compare to an integral of ΔG over the probed x_g range. Only experimental statistical uncertainties are used to calculate χ^2, and no theoretical uncertainties are included. It is important to note, that although the range of the first moment explored represents $\sim 60\%$ of the full integral, this reflects using a specific model for the gluon polarization. For example, a gluon polarization model with a crossover from positive to negative gluon polarization within our x_g range would yield a small average asymmetry for each point. Also, other models can generate larger or smaller contributions from the gluon spin in the unmeasured region of x_g.

These data are sensitive to the first moment of the polarized gluon distribution. Using the GRSV model, we find that the gluon polarization contribution to the proton

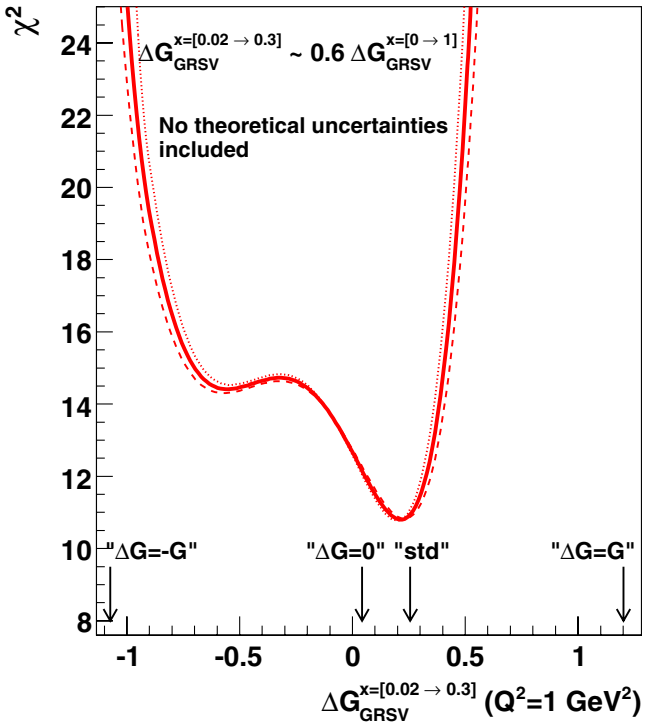

FIG. 3 (color online). The χ^2 distribution of the measured data plotted versus the value of the first moment of the polarized gluon distribution (solid line) in the x_g range from 0.02 to 0.3 corresponding to our π^0 data in p_T bins from 2 to 9 GeV/c. Dashed and dotted lines correspond to -9.4% and $+9.4\%$ variation in A_{LL} normalization related to the beam polarization uncertainty, the dominant systematic uncertainty of our data. Only statistical uncertainties were used for each curve. Arrows indicate ΔG corresponding to the different polarized gluon distributions discussed in the text.

spin (1/2) in the probed x_g range is constrained between -0.9 and $+0.5$, for $\chi^2 - \chi^2_{\rm min} = 9$, representing a "$3\sigma$" limit (a "$1\sigma$" limit would give a constraint between 0.07 and 0.3). The extremes of gluon polarization are ruled out, modulo the above remarks, with the confidence level for "$\Delta G = \pm G$" of less than 10^{-6}. Large positive gluon polarization [32] was proposed shortly after the discovery that the quark contribution to the proton spin was small [33], with the suggestion that such a large gluon polarization would mask a "bare" quark polarization. For std and "$\Delta G = 0$", the confidence levels are 20%–21% and 12%–13%, respectively, for the range of $\pm 9.4\%$ scale uncertainty of the measurement. Semi-inclusive DIS measurements [34] have also presented data on ΔG in a limited x_g range and its comparison with various ΔG scenarios.

The two minima in Fig. 3 reflect the quadratic contribution of the gluon polarization to A_{LL}, from the gluon-gluon scattering subprocess for π^0 production. The symmetry between the two minima is broken by the quark-gluon scattering subprocess, where the gluon polarization contributes linearly to A_{LL}. The quark-gluon subprocess is emphasized at higher p_T, which will become accessible

with additional running at high polarization and luminosity.

To summarize, we have presented the unpolarized cross section and double helicity asymmetries for π^0 production at midrapidity, for proton-proton collisions at $\sqrt{s} = 200$ GeV. We observe an apparent transition region in the cross section, for $p_T \approx 1$ to 2 GeV/c, with the cross section described by an exponential in p_T below $p_T \sim 1$ GeV/c, and with the cross section described by the pQCD prediction for $p_T = 2$ to 20 GeV/c, over 7 orders of magnitude in cross section. The results for A_{LL} in the pQCD region, which we take as $p_T \geq 2$ GeV/c, constrain the gluon polarization in the proton significantly. The range probed is $x_g = 0.02$ to 0.3, for the gluon momentum fraction. Using one representative model for the gluon polarization, GRSV [29], which assumes no crossover in gluon polarization versus x_g, we present a map of χ^2 versus the first moment of the polarized gluon distribution in the measured region. From this study, the present data rule out extreme values of gluon polarization suggested after the surprise of the EMC result that the quarks (and antiquarks) contribute little to the spin of the proton [33], but allow significant contribution from the gluon spin to the proton spin.

We thank the RHIC Polarimeter Group and the staff of the Collider-Accelerator and Physics Departments at BNL for their vital contributions. We thank W. Vogelsang and M. Stratmann for providing the NLO pQCD calculations and for informative discussions. We acknowledge support from the Department of Energy and NSF (USA), MEXT, and JSPS (Japan), CNPq and FAPESP (Brazil), NSFC (China), MSMT (Czech Republic), IN2P3/CNRS, and CEA (France), BMBF, DAAD, and AvH (Germany), OTKA (Hungary), DAE (India), ISF (Israel), KRF and KOSEF (Korea), MES, RAS, and FAAE (Russia), VR and KAW (Sweden), U.S. CRDF for the FSU, USA-Hungarian NSF-OTKA-MTA, and USA-Israel BSF.

[1] G. Bunce *et al.*, Annu. Rev. Nucl. Part. Sci. **50**, 525 (2000).
[2] S. S. Adler *et al.*, Phys. Rev. Lett. **91**, 241803 (2003).
[3] J. Adams *et al.*, Phys. Rev. Lett. **92**, 171801 (2004).
[4] B. I. Abelev *et al.*, Phys. Rev. Lett. **97**, 252001 (2006).
[5] S. S. Adler *et al.*, Phys. Rev. Lett. **98**, 012002 (2007).
[6] S. S. Adler *et al.*, Phys. Rev. Lett. **93**, 202002 (2004).
[7] S. S. Adler *et al.*, Phys. Rev. D **73**, 091102 (2006).
[8] M. Bai *et al.*, *Proceedings of the 2005 Particle Accelerator Conference*, edited by C. Horak (IEEE, New York, 2005), p. 600.
[9] L. Aphecetche *et al.*, Nucl. Instrum. Methods Phys. Res., Sect. A **499**, 521 (2003).
[10] M. Allen *et al.*, Nucl. Instrum. Methods Phys. Res., Sect. A **499**, 549 (2003).
[11] S. S. Adler *et al.*, Phys. Rev. Lett. **98**, 172302 (2007).
[12] G. David *et al.*, IEEE Trans. Nucl. Sci. **47**, 1982 (2000).
[13] Tables of data available at http://www.phenix.bnl.gov / phenix/WWW/info/data/ppg063_data.html
[14] F. Aversa *et al.*, Nucl. Phys. **B327**, 105 (1989).
[15] B. Jäger *et al.*, Phys. Rev. D **67**, 054005 (2003).
[16] J. Pumplin *et al.*, J. High Energy Phys. 07 (2002) 012.
[17] B. A. Kniehl, G. Kramer, and B. Pötter, Nucl. Phys. **B597**, 337 (2001).
[18] U. D'Alesio and F. Murgia, Phys. Rev. D **70**, 074009 (2004).
[19] D. de Florian and W. Vogelsang, Phys. Rev. D **71**, 114004 (2005).
[20] S. S. Adler *et al.*, Phys. Rev. C **74**, 024904 (2006).
[21] W. W. MacKay *et al.*, *Proceedings of the 2003 Particle Accelerator Conference*, edited by J. Chew, P. Lucas, and S. Webber (IEEE, Portland, OR, 2003), p. 1697.
[22] O. Jinnouchi *et al.*, RHIC/CAD Accelerator Physics Note 171, 2004.
[23] H. Okada *et al.*, Phys. Lett. B **638**, 450 (2006).
[24] I. Nakagawa *et al.*, RHIC/CAD Accelerator Physics Note 275, 2007; O. Eyser *et al.*, RHIC/CAD Accelerator Physics Note 274 (2007).
[25] Y. Fukao *et al.*, Phys. Lett. B **650**, 325 (2007).
[26] PHENIX has measured parity-violating single helicity asymmetry A_L for each polarized beam, which was consistent with zero within statistical uncertainty, in all p_T bins [6,13].
[27] C. Adler *et al.*, Nucl. Instrum. Methods Phys. Res., Sect. A **470**, 488 (2001).
[28] A. Mukherjee *et al.*, Phys. Rev. D **72**, 034011 (2005).
[29] B. Jäger, A. Schäfer, M. Stratmann, and W. Vogelsang, Phys. Rev. D **67**, 054005 (2003); M. Glück, E. Reya, M. Stratmann, and W. Vogelsang, Phys. Rev. D **63**, 094005 (2001).
[30] S. S. Adler *et al.*, Phys. Rev. D **74**, 072002 (2006).
[31] M. Stratmann and W. Vogelsang, arXiv:hep-ph/0702083; W. Vogelsang (private communication).
[32] G. Altarelli and G. Ross, Phys. Lett. B **212**, 391 (1988); G. Altarelli and W. J. Stirling, Part. World **1**, 40 (1989); R. D. Carlitz, J. C. Collins, and A. H. Mueller, Phys. Lett. B **214**, 229 (1988).
[33] J. Ashman *et al.* (EMC Collaboration), Phys. Lett. B **206**, 364 (1988); ()Nucl. Phys. **B328**, 1 (1989).
[34] B. Adeva *et al.* (SMC Collaboration), Phys. Rev. D **70**, 012002 (2004); E. S. Ageev *et al.* (COMPASS Colaboration), Phys. Lett. B **633**, 25 (2006); A. Airapetian *et al.* (HERMES Collaboration), Phys. Rev. Lett. **84**, 2584 (2000).

Measurement of density correlations in pseudorapidity via charged particle multiplicity fluctuations in Au+Au collisions at $\sqrt{s_{NN}} = 200$ GeV

S. S. Adler,[5] S. Afanasiev,[17] C. Aidala,[5] N. N. Ajitanand,[43] Y. Akiba,[20,38] J. Alexander,[43] R. Amirikas,[12] L. Aphecetche,[45] S. H. Aronson,[5] R. Averbeck,[44] T. C. Awes,[35] R. Azmoun,[44] V. Babintsev,[15] A. Baldisseri,[10] K. N. Barish,[6] P. D. Barnes,[27] B. Bassalleck,[33] S. Bathe,[30] S. Batsouli,[9] V. Baublis,[37] A. Bazilevsky,[15,39] S. Belikov,[15,16] Y. Berdnikov,[40] S. Bhagavatula,[16] J. G. Boissevain,[27] H. Borel,[10] S. Borenstein,[25] M. L. Brooks,[27] D. S. Brown,[34] N. Bruner,[33] D. Bucher,[30] H. Buesching,[30] V. Bumazhnov,[15] G. Bunce,[5,39] J. M. Burward-Hoy,[26,44] S. Butsyk,[44] X. Camard,[45] J.-S. Chai,[18] P. Chand,[4] W. C. Chang,[2] S. Chernichenko,[15] C. Y. Chi,[9] J. Chiba,[20] M. Chiu,[9] I. J. Choi,[52] J. Choi,[19] R. K. Choudhury,[4] T. Chujo,[5] V. Cianciolo,[35] Y. Cobigo,[10] B. A. Cole,[9] P. Constantin,[16] D. d'Enterria,[45] G. David,[5] H. Delagrange,[45] A. Denisov,[15] A. Deshpande,[39] E. J. Desmond,[5] A. Devismes,[44] O. Dietzsch,[41] O. Drapier,[25] A. Drees,[44] K. A. Drees,[5] A. Durum,[15] D. Dutta,[4] Y. V. Efremenko,[35] K. El Chenawi,[49] A. Enokizono,[14] H. En'yo,[38,39] S. Esumi,[48] L. Ewell,[5] D. E. Fields,[33,39] F. Fleuret,[25] S. L. Fokin,[23] B. D. Fox,[39] Z. Fraenkel,[51] J. E. Frantz,[9] A. Franz,[5] A. D. Frawley,[12] S.-Y. Fung,[6] S. Garpman,[29,*] T. K. Ghosh,[49] A. Glenn,[46] G. Gogiberidze,[46] M. Gonin,[25] J. Gosset,[10] Y. Goto,[39] R. Granier de Cassagnac,[25] N. Grau,[16] S. V. Greene,[49] M. Grosse Perdekamp,[39] W. Guryn,[5] H.-Å. Gustafsson,[29] T. Hachiya,[14] J. S. Haggerty,[5] H. Hamagaki,[8] A. G. Hansen,[27] E. P. Hartouni,[26] M. Harvey,[5] R. Hayano,[8] N. Hayashi,[38] X. He,[13] H. W. van Hecke,[27] M. Heffner,[26] T. K. Hemmick,[44] J. M. Heuser,[44] M. Hibino,[50] J. C. Hill,[16] W. Holzmann,[43] K. Homma,[14] B. Hong,[22] A. Hoover,[34] T. Ichihara,[38,39] V. V. Ikonnikov,[23] K. Imai,[24,38] D. Isenhower,[1] M. Ishihara,[38] M. Issah,[43] A. Isupov,[17] B. V. Jacak,[44,†] W. Y. Jang,[22] Y. Jeong,[19] J. Jia,[44] O. Jinnouchi,[38] B. M. Johnson,[5] S. C. Johnson,[26] K. S. Joo,[31] D. Jouan,[36] S. Kametani,[8,50] N. Kamihara,[38,47] J. H. Kang,[52] S. S. Kapoor,[4] K. Katou,[50] S. Kelly,[9] B. Khachaturov,[51] A. Khanzadeev,[37] J. Kikuchi,[50] D. H. Kim,[31] D. J. Kim,[52] D. W. Kim,[19] E. Kim,[42] G.-B. Kim,[25] H. J. Kim,[52] E. Kistenev,[5] A. Kiyomichi,[48] K. Kiyoyama,[32] C. Klein-Boesing,[30] H. Kobayashi,[38,39] L. Kochenda,[37] V. Kochetkov,[15] D. Koehler,[33] T. Kohama,[14] M. Kopytine,[44] D. Kotchetkov,[6] A. Kozlov,[51] P. J. Kroon,[5] C. H. Kuberg,[1,27,*] K. Kurita,[39] Y. Kuroki,[48] M. J. Kweon,[22] Y. Kwon,[52] G. S. Kyle,[34] R. Lacey,[43] V. Ladygin,[17] J. G. Lajoie,[16] A. Lebedev,[16,23] S. Leckey,[44] D. M. Lee,[27] S. Lee,[19] M. J. Leitch,[27] X. H. Li,[6] H. Lim,[42] A. Litvinenko,[17] M. X. Liu,[27] Y. Liu,[36] C. F. Maguire,[49] Y. I. Makdisi,[5] A. Malakhov,[17] V. I. Manko,[23] Y. Mao,[7,38] G. Martinez,[45] M. D. Marx,[44] H. Masui,[48] F. Matathias,[44] T. Matsumoto,[8,50] P. L. McGaughey,[27] E. Melnikov,[15] F. Messer,[44] Y. Miake,[48] J. Milan,[43] T. E. Miller,[49] A. Milov,[44,51] S. Mioduszewski,[5] R. E. Mischke,[27] G. C. Mishra,[13] J. T. Mitchell,[5] A. K. Mohanty,[4] D. P. Morrison,[5] J. M. Moss,[27] F. Mühlbacher,[44] D. Mukhopadhyay,[51] M. Muniruzzaman,[6] J. Murata,[38,39] S. Nagamiya,[20] J. L. Nagle,[9] T. Nakamura,[14] B. K. Nandi,[6] M. Nara,[48] J. Newby,[46] P. Nilsson,[29] A. S. Nyanin,[23] J. Nystrand,[29] E. O'Brien,[5] C. A. Ogilvie,[16] H. Ohnishi,[5,38] I. D. Ojha,[3,49] K. Okada,[38] M. Ono,[48] V. Onuchin,[15] A. Oskarsson,[29] I. Otterlund,[29] K. Oyama,[8] K. Ozawa,[8] D. Pal,[51] A. P. T. Palounek,[27] V. Pantuev,[44] V. Papavassiliou,[34] J. Park,[42] A. Parmar,[33] S. F. Pate,[34] T. Peitzmann,[30] J.-C. Peng,[27] V. Peresedov,[17] C. Pinkenburg,[5] R. P. Pisani,[5] F. Plasil,[35] M. L. Purschke,[5] A. K. Purwar,[44] J. Rak,[16] I. Ravinovich,[51] K. F. Read,[35,46] M. Reuter,[44] K. Reygers,[30] V. Riabov,[37,40] Y. Riabov,[37] R. du Rietz,[29] G. Roche,[28] A. Romana,[25,*] M. Rosati,[16] P. Rosnet,[28] S. S. Ryu,[52] M. E. Sadler,[1] N. Saito,[38,39] T. Sakaguchi,[8,50] M. Sakai,[32] S. Sakai,[48] V. Samsonov,[37] L. Sanfratello,[33] R. Santo,[30] H. D. Sato,[24,38] S. Sato,[5,48] S. Sawada,[20] Y. Schutz,[45] V. Semenov,[15] R. Seto,[6] M. R. Shaw,[1,27] T. K. Shea,[5] T.-A. Shibata,[38,47] K. Shigaki,[14,20] T. Shiina,[27] C. L. Silva,[41] D. Silvermyr,[27,29] K. S. Sim,[22] C. P. Singh,[3] V. Singh,[3] M. Sivertz,[5] A. Soldatov,[15] R. A. Soltz,[26] W. E. Sondheim,[27] S. P. Sorensen,[46] I. V. Sourikova,[5] F. Staley,[10] P. W. Stankus,[35] E. Stenlund,[29] M. Stepanov,[34] A. Ster,[21] S. P. Stoll,[5] T. Sugitate,[14] J. P. Sullivan,[27] E. M. Takagui,[41] A. Taketani,[38,39] M. Tamai,[50] K. H. Tanaka,[20] Y. Tanaka,[32] K. Tanida,[38] M. J. Tannenbaum,[5] P. Tarján,[11] J. D. Tepe,[1,27] T. L. Thomas,[33] A. Toia,[44] J. Tojo,[24,38] H. Torii,[24,38] R. S. Towell,[1] I. Tserruya,[51] H. Tsuruoka,[48] S. K. Tuli,[3] H. Tydesjö,[29] N. Tyurin,[15] J. Velkovska,[5,44] M. Velkovsky,[44] V. Veszprémi,[11] L. Villatte,[46] A. A. Vinogradov,[23] M. A. Volkov,[23] E. Vznuzdaev,[37] X. R. Wang,[13] Y. Watanabe,[38,39] S. N. White,[5] F. K. Wohn,[16] C. L. Woody,[5] W. Xie,[6] Y. Yang,[7] A. Yanovich,[15] S. Yokkaichi,[38,39] G. R. Young,[35] I. E. Yushmanov,[23] W. A. Zajc,[9] C. Zhang,[9] S. Zhou,[7] S. J. Zhou,[51] and L. Zolin[17]

(PHENIX Collaboration)

[1]*Abilene Christian University, Abilene, Texas 79699, USA*

[2]*Institute of Physics, Academia Sinica, Taipei 11529, Taiwan*

[3]*Department of Physics, Banaras Hindu University, Varanasi 221005, India*

[4]*Bhabha Atomic Research Centre, Bombay 400 085, India*

[5]*Brookhaven National Laboratory, Upton, New York 11973-5000, USA*

[6]*University of California-Riverside, Riverside, California 92521, USA*

[7]*China Institute of Atomic Energy (CIAE), Beijing, People's Republic of China*

[8]*Center for Nuclear Study, Graduate School of Science, University of Tokyo, 7-3-1 Hongo, Bunkyo, Tokyo 113-0033, Japan*

[9]*Columbia University, New York 10027, USA, and Nevis Laboratories, Irvington, New York 10533, USA*

[10]*Dapnia, CEA Saclay, F-91191 Gif-sur-Yvette, France*

[11]*Debrecen University, Egyetem tér 1, H-4010 Debrecen, Hungary*

[12]*Florida State University, Tallahassee, Florida 32306, USA*

[13]*Georgia State University, Atlanta, Georgia 30303, USA*

[14]*Hiroshima University, Kagamiyama, Higashi-Hiroshima 739-8526, Japan*

 ©2007 The American Physical Society

[15]*Institute for High Energy Physics (IHEP), Protvino, Russia*
[16]*Iowa State University, Ames, Iowa 50011, USA*
[17]*Joint Institute for Nuclear Research, RU-141980 Dubna, Moscow Region, Russia*
[18]*KAERI, Cyclotron Application Laboratory, Seoul, South Korea*
[19]*Kangnung National University, Kangnung 210-702, South Korea*
[20]*KEK, High Energy Accelerator Research Organization, Tsukuba-shi, Ibaraki-ken 305-0801, Japan*
[21]*KFKI Research Institute for Particle and Nuclear Physics (RMKI), P. O. Box 49, H-1525 Budapest 114, Hungary*
[22]*Korea University, Seoul, 136-701, Korea*
[23]*Russian Research Center "Kurchatov Institute," Moscow, Russia*
[24]*Kyoto University, Kyoto 606-8502, Japan*
[25]*Laboratoire Leprince-Ringuet, Ecole Polytechnique, CNRS-IN2P3, Route de Saclay, F-91128 Palaiseau, France*
[26]*Lawrence Livermore National Laboratory, Livermore, California 94550, USA*
[27]*Los Alamos National Laboratory, Los Alamos, New Mexico 87545, USA*
[28]*LPC, Université Blaise Pascal, CNRS-IN2P3, Clermont-Fd, F-63177 Aubiere Cedex, France*
[29]*Department of Physics, Lund University, Box 118, SE-221 00 Lund, Sweden*
[30]*Institut für Kernphysik, University of Muenster, D-48149 Muenster, Germany*
[31]*Myongji University, Yongin, Kyonggido 449-728, Korea*
[32]*Nagasaki Institute of Applied Science, Nagasaki-shi, Nagasaki 851-0193, Japan*
[33]*University of New Mexico, Albuquerque, New Mexico 87131, USA*
[34]*New Mexico State University, Las Cruces, New Mexico 88003, USA*
[35]*Oak Ridge National Laboratory, Oak Ridge, Tennessee 37831, USA*
[36]*IPN-Orsay, Université Paris Sud, CNRS-IN2P3, BP1, F-91406 Orsay, France*
[37]*PNPI, Petersburg Nuclear Physics Institute, Gatchina, Russia*
[38]*RIKEN (The Institute of Physical and Chemical Research), Wako, Saitama 351-0198, Japan*
[39]*RIKEN BNL Research Center, Brookhaven National Laboratory, Upton, New York 11973-5000, USA*
[40]*St. Petersburg State Technical University, St. Petersburg, Russia*
[41]*Universidade de São Paulo, Instituto de Física, Caixa Postal 66318, São Paulo CEP05315-970, Brazil*
[42]*System Electronics Laboratory, Seoul National University, Seoul, South Korea*
[43]*Chemistry Department, Stony Brook University, SUNY, Stony Brook, New York 11794-3400, USA*
[44]*Department of Physics and Astronomy, Stony Brook University, SUNY, Stony Brook, New York 11794, USA*
[45]*SUBATECH (Ecole des Mines de Nantes, CNRS-IN2P3, Université de Nantes), Boîte Postal, F-20722-44307, Nantes, France*
[46]*University of Tennessee, Knoxville, Tennessee 37996, USA*
[47]*Department of Physics, Tokyo Institute of Technology, Tokyo, 152-8551, Japan*
[48]*Institute of Physics, University of Tsukuba, Tsukuba, Ibaraki 305, Japan*
[49]*Vanderbilt University, Nashville, Tennessee 37235, USA*
[50]*Waseda University, Advanced Research Institute for Science and Engineering, 17 Kikui-cho, Shinjuku-ku, Tokyo 162-0044, Japan*
[51]*Weizmann Institute, Rehovot 76100, Israel*
[52]*Yonsei University, IPAP, Seoul 120-749, Korea*
(Received 22 April 2007; published 21 September 2007)

Longitudinal density correlations of produced matter in Au+Au collisions at $\sqrt{s_{NN}} = 200$ GeV have been measured from the inclusive charged particle distributions as a function of pseudorapidity window sizes. The extracted $\alpha\xi$ parameter, related to the susceptibility of the density fluctuations in the long-wavelength limit, exhibits a nonmonotonic behavior as a function of the number of participant nucleons, N_{part}. A local maximum is seen at $N_{\text{part}} \sim 90$, with corresponding energy density based on the Bjorken picture of $\epsilon_{\text{Bj}}\tau \sim 2.4$ GeV/(fm$^2 c$) with a transverse area size of 60 fm^2. This behavior may suggest a critical phase boundary based on the Ginzburg-Landau framework.

DOI: 10.1103/PhysRevC.76.034903 PACS number(s): 25.75.Dw

I. INTRODUCTION

Theoretical studies of quantum chromodynamics (QCD) in nonperturbative regimes indicate that QCD matter has a rich phase structure [1]. The phase diagram can be parametrized by temperature T and baryo-chemical potential μ_B. Based on the phase diagram, we can obtain perspectives on how the vacuum structure of the early universe evolved in extremely high temperature states after the Big Bang as well as what happens in extremely high baryon density states such as in the core of neutron stars. Therefore, a comprehensive and quantitative understanding of the QCD phase diagram is one

*Deceased
†PHENIX Spokesperson: jacak@skipper.physics.sunysb.edu

of the most important subjects in modern nuclear physics. At a minimum we expect the phase diagram to exhibit at least two distinct regions: the deconfined phase, where the basic degrees of freedom of QCD, quarks, and gluons emerge, and the hadron phase, where quarks and gluons are confined. There is a first-order phase boundary at $\mu_B > 0$ and $T = 0$ [2–9]. At $\mu_B = 0$ and $T > 0$ a smooth cross-over transition is expected because of finite masses of quarks [10]. Logically, we can then expect that a critical endpoint (CEP) exists at the end of the first-order phase transition line [11]. The location of the CEP would be a landmark in understanding the whole structure of the phase diagram. Although numerical calculations using lattice gauge theory, as well as model calculations, predict the existence of the CEP, none of them have reached a quantitative agreement on the location at present precision [1]. Therefore experimental investigations are indispensable to pin down the location and to establish properties of the phase point based on fundamental observables.

Strongly interacting, high-density matter has been created in nucleus-nucleus collisions at the Relativistic Heavy Ion Collider (RHIC) at Brookhaven National Laboratory (BNL) [12]. Strong suppression of hadrons at high transverse momentum (p_T) observed in central Au+Au collisions at $\sqrt{s_{NN}} =$ 200 GeV at RHIC indicate creation of high-density matter [13,14]. Strong elliptic flow indicates that the matter thermalizes rapidly and behaves like a fluid with very low viscosity [15]. Furthermore, the valence quark number scaling of elliptic flow suggests that quark-like degrees of freedom are pertinent in the evolution of the flow [16]. Those observations naturally lead us to the expectation that the initial thermalized state of matter is at $T > T_c$ in central Au+Au collisions, and possibly at $T < T_c$ in the most peripheral collisions. Therefore a system with initial $T = T_c$ may exist somewhere between peripheral and central collisions.

Since there could be different T_cs depending on order parameters in the cross-over transition [17], it is worth measuring different kinds of order parameters. It is known that density correlations in matter are robust observables for critical temperatures in general [18]. The order parameter we will focus on here is spatial density fluctuations. Following the Ginzburg-Landau (GL) framework [19] we expect a correlation between fluctuations in density at different points, which leads to a two-point correlation function of the form $\alpha e^{-r/\xi}$, where r is the one-dimensional distance, α is the strength of the correlation, and $\xi \propto |T - T_c|^{-1/2}$ is the spatial correlation length. This functional form can be derived from the GL free energy density by expanding it with a scalar order parameter that is small enough (see Appendix A). A large increase of ξ near T_c can be a good indicator of a phase transition. In addition to ξ itself, the product $\alpha\xi$ can also be a good indicator of a phase transition. As shown in Sec. II, $\alpha\xi$ behaves as $|1 - T_c/T|^{-1}$. In the GL framework, this quantity is related to the medium's susceptibility in the long-wavelength limit. (See Appendix A for the derivation.) The matter produced in the collision expands longitudinally from its earliest time, which leads to cooling after the initial thermalization. If the system's evolution takes it near a critical point as it cools, then the large correlated density fluctuations will appear as T approaches T_c from above. If the expansion after that point is rapid enough then these fluctuations can potentially survive into the final state [20].

Experimentally, spatial density fluctuations in longitudinal space z in the early stage of an $A+A$ collision at RHIC can be measured as the density fluctuation in rapidity, or pseudorapidity, space in the final state. The differential length dz between neighboring medium elements at a common proper time $\tau = \sqrt{t^2 - z^2}$ is expressed as $dz = \tau \cosh(y) dy$, where y is rapidity. If we limit the study to only a narrow region around midrapidity, then $dz \sim \tau dy$ is valid with the approximation $\cosh(y) \sim 1$. Therefore we can observe density fluctuation in the z coordinate as being mapped onto density fluctuations in rapidity space. In the region around midrapidity used in this analysis we can approximate rapidity by pseudorapidity (η) for inclusive charged particles, since the mean $\langle p_T \rangle$ ($\langle p_T \rangle = 0.57$ GeV/$c \gg m_\pi$) observed in $\sqrt{s_{NN}} = 200$ GeV collisions at RHIC is so high.

In this paper we measure charged particle density correlations in pseudorapidity space to search for the critical phase boundary in Au+Au collisions at $\sqrt{s_{NN}} = 200$ GeV. The density correlation is extracted from inclusive charged particle multiplicity distributions measured as a function of pseudorapidity window size $\delta\eta$. Negative binomial distributions (NBDs) are fit to the measured multiplicity distributions, and the NBD parameters μ (mean) and k^{-1} (deviation from a Poissonian width) are determined. The product of the correlation strength α and the correlation length ξ is extracted from a known relation between the product of $\alpha\xi$ and the NBD k parameter as a function of $\delta\eta$. We expect a monotonic correspondence between initial temperature and measured energy density based on Bjorken picture [21], which in turn has a monotonic relation with the number of participant nucleons, $N_{\rm part}$, in a collision [22]. Thus the critical behavior of $\alpha\xi$ near T_c can be observed as a nonmonotonic increase as a function of $N_{\rm part}$.

It is worth noting that most experimentally accessible points on the phase diagram are neither phase boundaries nor the endpoint. Therefore, before searching for a special phase point such as CEP based on particular theoretical assumptions, we would rather observe and define phase boundaries by general methods. The application of the GL framework for density correlations far from T_c provides this approach. It is known that the GL framework is not applicable directly at $T = T_c$ because the fluctuations become too large to be described consistently. The correlation length ξ cannot be defined at T_c, where many length scales from small to large emerge. This is the origin of the power-law behavior, or fractal nature of fluctuations at the critical phase boundary. However, in the regions relatively far from T_c, the fluctuations are naturally expected to be small. Therefore the GL approach is suitable in the nuclear collision environment as long as the system approaches a phase boundary from a thermalized state with T well above T_c. As a future prospect, once we define a phase boundary even in the crossover region, we can further investigate the characteristic nature of the phase point, such as critical exponents based on the chiral condensate [23–25] along the phase boundary, to judge whether the point corresponds to a CEP or not.

The organization of this paper is as follows. Section II provides the exact definition of the experimental observables.

Section III describes the PHENIX detector used to make the measurements. Section IV describes the event samples used for this analysis and the method for corrections applied to the measured multiplicity fluctuations. The systematic errors on the measured fluctuations are also explained in this section. In Sec. V, fit results of the NBD parameters in each collision centrality and pseudorapidity window size are presented, and the behaviors of the $\alpha\xi$ product as a function of $N_{\rm part}$ are presented. In Sec. VI, in addition to the discussion on the observed $N_{\rm part}$ dependence of $\alpha\xi$, other possible sources of correlation between inclusive charged particles are discussed. The relation between the measured energy density and $N_{\rm part}$ is discussed to relate $N_{\rm part}$ to the initial temperature. Conclusions are given in Sec. VII. In Appendix A, the density correlation length and susceptibility are exactly defined based on the GL framework. Finally, in Appendix B all measured NBD parameters in all collision centralities are tabulated.

II. EXPERIMENTAL OBSERVABLES

In this analysis the density fluctuation will be discussed via charged particle multiplicity distributions as a function of the pseudorapidity window size for each collision centrality or $N_{\rm part}$ range.

It is known that the charged particle multiplicity distributions are empirically well described by the NBD in $A+A$, $p+p$, and e^+e^- collisions [26]. The distribution is expressed as

$$P_{k,\mu}(n) = \frac{\Gamma(n+k)}{\Gamma(n-1)\Gamma(k)}\left(\frac{\mu/k}{1+\mu/k}\right)\frac{1}{1+\mu/k}, \qquad (1)$$

Here μ is the mean of the distribution and k^{-1} corresponds to the difference between its width and that of a Poisson with that mean. Thus the NBD coincides with the Poisson distribution in the case of $k=\infty$, and with the Bose-Einstein distribution in the case of $k=1$. In this sense, the NBD k directly reflects the degree of correlation between the particles produced into the experimental window.

We can relate the k parameter for the multiplicity distribution within an η window to the correlation between phase-space densities in different η windows. Specifically, k can be mathematically related with the second-order normalized factorial moment F_2 by

$$k^{-1} = F_2 - 1, \qquad (2)$$

where F_2 corresponds to the integrated two-particle correlation function, which can be expressed as [27]

$$F_2(\delta\eta) = \frac{\langle n(n-1)\rangle}{\langle n\rangle^2} = \frac{\int\int^{\delta\eta}\rho_2(\eta_1,\eta_2)d\eta_1 d\eta_2}{\{\int^{\delta\eta}\rho_1(\eta)d\eta\}^2} = \frac{1}{(\delta\eta)^2}\int\int^{\delta\eta}\frac{C_2(\eta_1,\eta_2)}{\bar{\rho_1}^2}d\eta_1 d\eta_2 + 1, \qquad (3)$$

where n is the number of produced particles and $\delta\eta$ is the pseudorapidity window size inside which the multiplicities are measured. In Eq. (3) we introduced one- and two-particle inclusive multiplicity densities ρ_1 and ρ_2 based on the inclusive differential cross section relative to the total inelastic cross section $\sigma_{\rm inel}$ as follows [26]:

$$\frac{1}{\sigma_{\rm inel}}d\sigma = \rho_1(\eta)d\eta, \qquad \frac{1}{\sigma_{\rm inel}}d^2\sigma = \rho_2(\eta_1,\eta_2)d\eta_1 d\eta_2. \qquad (4)$$

Here $\bar{\rho_1}$ is the average density per unit length within $\delta\eta$, which is defined as

$$\bar{\rho_1} = \frac{1}{\delta\eta}\int^{\delta\eta}\rho_1(\eta)d\eta. \qquad (5)$$

With these densities, the two-particle density correlation function is defined as

$$C_2(\eta_1,\eta_2) = \rho_2(\eta_1,\eta_2) - \rho_1(\eta_1)\rho_1(\eta_2). \qquad (6)$$

Instead of measuring C_2 or F_2 directly, in this analysis we extract the NBD k parameter as a measure of particle correlations over η. This is partly for historical reasons [28] but also because, as shown in Sec. IV, we can correct the measurement of k for the detector imperfections in a very robust way by using a statistical property of NBD, whereas the same correction made at the level of F_2 would require additional information on the parent distribution.

The normalized two-particle correlation function C_2 in the experiment can be parametrized as follows, based on the one-dimensional functional form obtained in the GL framework [see Eq. (A8)]:

$$\frac{C_2(\eta_1,\eta_2)}{\bar{\rho_1}^2} = \alpha e^{-|\eta_1-\eta_2|/\xi} + \beta, \qquad (7)$$

where $\bar{\rho_1}$ is proportional to the mean multiplicity in each collision centrality bin, or range of $N_{\rm part}$, and the scale factor α is the strength of the correlations at the zero separation. The constant term β arises from any kind of experimental and physical correlations that are independent of the pseudorapidity separation, such as the residual effect of finite centrality binning.

Further, one has to take into account the fact that the damping behavior in Eq. (A8) is caused only by the spatial inhomogeneity of the system at a fixed temperature. In realistic collisions and event samples there is no single relevant temperature. For instance, finite centrality binning adds together a range of fluctuations originating from collisions with different $N_{\rm part}$. However, in principle these centrality-correlated fluctuations are independent of the thermally induced spatial fluctuations. In addition, although the self-correlation at the zero distance between two subvolumes in Eq. (A6) was excluded, the self-correlation cannot be excluded in the integrated two-particle correlation function contained in Eq. (3). We have tried various functional forms for C_2, which contained power terms and also plural correlation lengths. However, we found empirically that just adding the constant term in Eq. (7) produced the best-fit results to all data points.

Finally, the relation between the NBD k parameter and the pseudorapidity window size $\delta\eta$ can be obtained by the substitution of Eq. (7) into Eq. (3) [28,29]:

$$k^{-1}(\delta\eta) = F_2 - 1 = \frac{2\alpha\xi^2(\delta\eta/\xi - 1 + e^{-\delta\eta/\xi})}{\delta\eta^2} + \beta. \qquad (8)$$

In the limit of $\xi \ll \delta\eta$, which we believe holds in this analysis, Eq. (8) can be approximated as

$$k(\delta\eta) = \frac{1}{2\alpha\xi/\delta\eta + \beta} \quad (\xi \ll \delta\eta), \tag{9}$$

where experimentally we cannot resolve α and ξ separately, but the product $\alpha\xi$ can be directly determined. The product is related to the susceptibility in the long-wavelength limit, $\chi_{\omega=0} \propto |T - T_c|^{-1}$, for a given temperature T based on Eq. (A11). Combined with the parametrization in Eq. (7), the $\alpha\xi$ product should then follow as

$$\alpha\xi \propto \bar{\rho}_1^{-2} \frac{1}{|1 - T_c/T|}. \tag{10}$$

Since we expect that $\bar{\rho}_1$ is a monotonic function of T, in the limit of T far from T_c, $\alpha\xi$ should vary monotonically as a function of T. However, if T approaches T_c, the $\alpha\xi$ product will show a singular behavior. Therefore, any nonmonotonic increase of $\alpha\xi$ could be an indication of $T \sim T_c$ near a critical point. If the experimental bias term β is excluded in Eq. (9), the slope in k versus $\delta\eta$ thus contains crucial information on the phase transition.

It is worth mentioning that in this method, correlations on scales even smaller than the minimum $\delta\eta$ window can be meaningfully discussed based on the differences of the NBD k as a function of $\delta\eta$ window sizes, since the correlations are always integrated from the limit of the detector resolution to $\delta\eta$ window size.

III. PHENIX DETECTOR

PHENIX is one of four experiments operating at RHIC [30]. The PHENIX detector has two central spectrometer arms, denoted East and West. Each central arm covers the pseudorapidity range $|\eta| < 0.35$ and subtends an azimuthal angle range $\Delta\phi$ of $\pi/2$ around the beam axis (z direction). PHENIX includes global detectors that provide information for event triggers as well as measurement of collision points along the beam axis and collision centralities. A detailed description of the PHENIX detector can be found in Ref. [30]. The detector subsystems relevant for this analysis will be briefly explained in the following.

Charged particles are measured by a drift chamber (DC) and two multiwire chambers with pad readout (PC1 and PC3) located at 2.2, 2.5, and 5 m from the beam axis in the East arm, respectively. The collision vertex points were measured using the time difference between two Beam-Beam Counters (BBC) located at $z = +144$ cm (north side) and $z = -144$ cm (south side) from the nominal interaction point (IP) along the beam line, which cover pseudorapidity ranges of $3.0 < \eta < 3.9$ (north) and $-3.9 < \eta < -3.0$ (south), respectively. Each BBC has 64 Čerenkov counter elements with the typical time resolution of 50 ps. Combined with BBC's, two Zero Degree Calorimeters (ZDCs) were further used. The ZDCs are designed to measure energies of spectator neutrons within a cone of 2 mrad around the beam axis. The two ZDC's are located at $z = \pm 18.25$ m from the IP, respectively. The Au+Au minimum bias trigger and collision centralities were provided by combining information from both BBCs and ZDCs.

IV. DATA ANALYSIS

A. Run and event selection

We have used data taken in Au+Au collisions at $\sqrt{s_{NN}} = 200$ GeV with the magnetic field off condition during RHIC Run 2 in 2002, to optimize acceptance for the low-p_T charged particles. The basic trigger required coincident hits in the two BBCs (equal or more than two hit Čerenkov elements in each side) and the two ZDCs (equal or more than one neutron in each side). The efficiency of this minimum-bias trigger is estimated as $92.2^{+2.5}_{-3.0}$% to the total Au+Au inelastic cross section by the Monte Carlo (MC) simulation based on the Glauber model [13]. Events with collision points within ± 5 cm from the nominal IP as measured by the BBC were analyzed. In total, 258,000 events taken by the minimum-bias trigger were used in this analysis. We have rigorously checked the detector stability by looking at multiplicity correlations between the relevant subdetector systems, as well as by monitoring positions of inefficient areas over the span of the analyzed dataset. We allowed 2% fluctuation on the average multiplcity of measured number of charged tracks in the entire analyzed run ranges.

B. Track selection

In this analysis, charged tracks detected in the East arm ($|\eta| < 0.35$, $\Delta\phi < \pi/2$) were used. As charged track selection criteria, we required that each straight-line track reconstructed by a DC hit pattern associated with a PC1 hit be aligned with a PC3 hit and the collision vertex point measured by the BBC. We required associations between DC tracks and PC3 hits to be within 10 cm in the distance of closest approach (DCA), which was determined to minimize the random associations. The DC has six types of wire modules; two of them are used for the track reconstruction for the azimuthal angle and the others are used for the pattern recognition. Selected tracks were reconstructed by using all wire modules of the DC.

In addition to the single track selection, we required a minimum two-track separation to minimize effects from fake tracks and associated secondary particles. When we find tracks within the minimum separation window of $\delta\eta < 0.001$ and $\delta\phi < 0.012$ rad, we count them as one track, independent of the number of reconstructed tracks in the window. These cut values were determined by looking at $\delta\eta$ and $\delta\phi$ distributions on the η-ϕ plane of any two track pairs in the real data sample. The DC track resolution of 2 mm in the z direction at a reference radius of 220 cm from the beam axis corresponds to 1.0×10^{-3} in η. PC1 and PC3, which are used for the track association, have the same solid angle, and these pixel sizes are 8.4 and 14.7 mm, respectively. These pixel sizes are greater than the requirement of two-track separation cuts; however, these resolutions are 1.7 and 3.6 mm for PC1 and PC3, respectively, in the z direction, and these values also corresponds to 1.0×10^{-3} in η. The resolution in ϕ is 1 mrad, but the maximum drift length in the DC corresponds to 0.012 rad. Therefore the two-track separation window size in η and ϕ is consistent with what is expected.

For the normal magnetic field condition at the PHENIX detector, which is used to identify the charged particles, the

threshold transverse momenta p_T correspond to 0.2, 0.4, and 0.6 GeV/c for charged pions $\pi^{\pm}$, charged kaons $K^{\pm}$, and protons p (and antiprotons $\bar{p}$), respectively [31]. Since this analysis used the data taken without magnetic field, the threshold transverse momenta p_T can be lowered to 0.1, 0.25, and 0.35 GeV/c for $\pi^{\pm}$, $K^{\pm}$, and p (and $\bar{p}$), respectively. They were estimated by the GEANT-based MC [32] simulation by requiring the equivalent single-track selection criteria. The average transverse momentum p_T for the detected inclusive charged particles used in this analysis corresponds to 0.57 GeV/c, which was also estimated by using the measured p_T spectra [31] with the MC simulation. Therefore, the difference of the rapidity and pseudorapidity is at most 3% at the edge of the PHENIX acceptance.

C. Centrality definition and the number of participant nucleons

The collision centrality was determined by looking at the correlation between a deposited charge sum in both north and south BBCs and an energy sum in both ZDCs on an event-by-event basis. As shown in Fig. 1, the centrality percentile is defined as the fraction of the number of events in a selected centrality bin on the correlation plot to the total number of minimum-bias events, corrected for the minimum-bias trigger efficiency. Each axis is normalized to its maximum dynamic range. As the standard centrality definition, we adopt a 5% centrality bin width from 0–5% (central) to 60–65% (peripheral) as indicated in the figure. The lower limit of 65% is indicated by the solid line in the figure. In the following analysis, as control samples, we also adopt a 10% bin width by merging two 5% bin width samples from 0–10% to 50–60% and from 5–15% to 55–65%. The latter is referred to as a 5% shifted 10% bin width. It is noteworthy that the change of the centrality bin width shifts the mean values in the charged particle multiplicity distributions, which becomes a strict systematic check on parameter extractions with different event ensembles, even with the same total event sample.

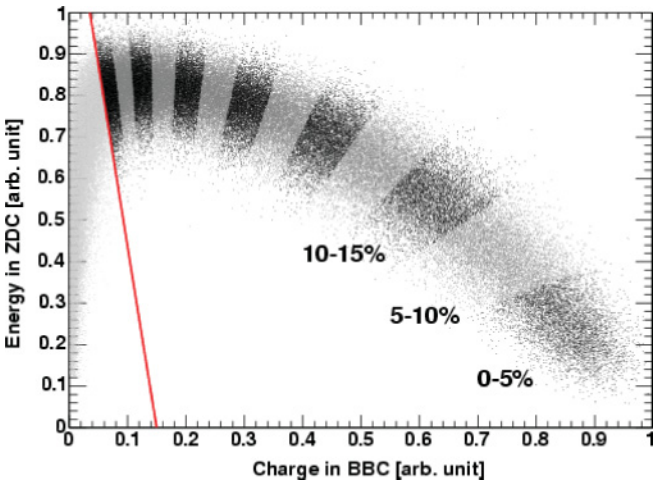

FIG. 1. (Color online) Definition of collision centrality, BBC charges versus ZDC energy. Event samples in 5% bin width are plotted from 0–5% (central) to 60–65% (peripheral). The solid line indicates the limit of the most peripheral sample used for this analysis.

Mapping the centralities to the number of participant nucleons, $N_{\rm part}$, is based on the Glauber model, which is described in detail in Ref. [22]. The quoted mean $N_{\rm part}$ and its error can be obtained from Ref. [31]. Only in the 5% shifted 10% bin width case were the mean $N_{\rm part}$ and its error evaluated by averaging two 5% centrality bins and estimated from its error propagations, respectively.

D. Measurement of multiplicity distributions of charged particles

Multiplicity distributions of charged particles were measured while changing the pseudorapidity window size $\delta\eta$ from 0.066 to 0.7 with a step size of $0.7/2^5 = 0.022$. For a given pseudorapidity window size, the window position in the pseudorapidity axis was shifted by a step of $0.7/2^8 = 0.0027$ as long as the window is fully contained within the PHENIX acceptance of $|\eta| < 0.35$. For each window position NBD fits were performed to the multiplicity distributions. Biases originating from inefficient detector areas were corrected with the procedure explained in Sec. IV E. Since even corrected NBD k parameters are not necessarily equal in the case of extremely inefficient window positions, we have truncated window positions where the reconstruction efficiency is below 50%. This truncation is mainly to exclude biases from the largest hole in the middle of the charged particle detector, as shown in Figs. 2(a) and 2(c). After the truncation, we obtained the weighted mean of corrected NBD parameters ($\langle\mu_c\rangle$, $\langle k_c\rangle$) for a given window size, which are defined as

$$\langle\mu_c\rangle \equiv \sum_{i=1}^{n} \delta\mu_{c_i}^{-2}\mu_{ci} / \sum_{i=1}^{n} \delta\mu_{c_i}^{-2},$$
$$\langle k_c\rangle \equiv \sum_{i=1}^{n} \delta k_{c_i}^{-2} k_{ci} / \sum_{i=1}^{n} \delta k_{c_i}^{-2}, \tag{11}$$

where n is the number of valid window positions after the truncation and δ indicates errors on fitting parameters by the MINUIT program [33] in each window position i. We have performed this procedure in each centrality bin with 5% and 10% centrality bin width, respectively.

The lower limit of 0.066 was determined so that small window sizes, where corrected NBD k was seen to depend heavily on window position, are all excluded. The lower limit is common for all centrality bins.

E. Correction of NBD k and μ

Any dead or inefficient areas in the detector have been identified and the bias on the NBD parameters has been corrected based on a suitable statistical property of NBD. Maps of dead areas were produced from the track projection points onto the η-ϕ plane in the data after the track selections, as shown in Fig. 2(a), where the detector acceptance is divided into $2^8 \times 2^8$ bins in the η-ϕ plane. The accumulated number of hits over the total event sample in each bin is shown by a gray scale reflecting the statistical weights. The scale is normalized to the mean number of hits in the peak position shown in Fig. 2(b). Figure 2(b) shows the number of bins among subdivided $2^8 \times 2^8$ bins as a function of the accumulated

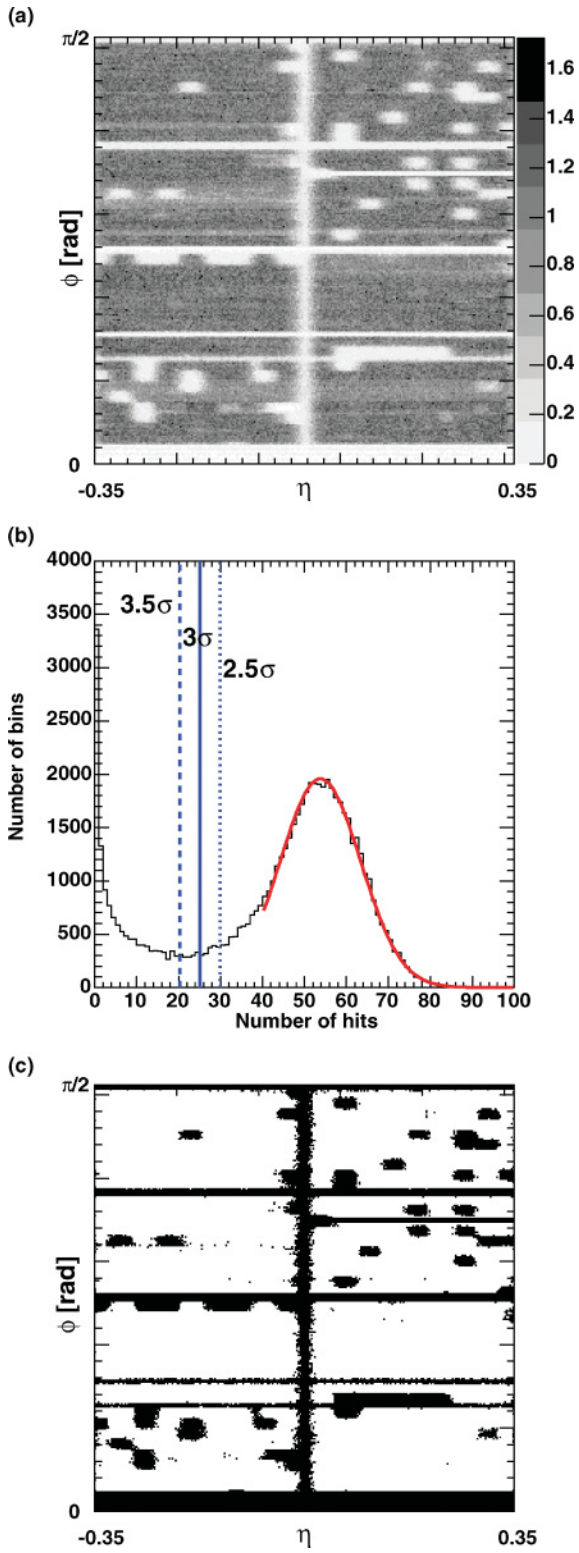

FIG. 2. (Color online) Two-dimensional dead-map definitions. (a) Track projection points onto the η-ϕ plane in the data after all track selections. The scale is normalized to the mean number of hits in the peak position in (b). (b) The number of bins among subdivided $2^8 \times 2^8$ bins as a function of the accumulated number of hits over the total event sample. (c) Definition of the central dead map by excluding the detector region below 3σ, where black parts are identified as dead areas.

number of hits over the total event sample in each $1/2^8 \times 1/2^8$ acceptance. If there were no dead or inefficient area, a binomial distribution is expected with a probability of $1/2^8 \times 1/2^8$ to the total acceptance. For the binomial part, we took a $\pm 3\sigma$ region. However, if there are any dead or inefficient areas they tend to contaminate the lower tail of the binomial distribution. We defined a central dead map by excluding detector region below 3σ, as shown in Fig. 2(c) where black indicates regions that are identified as dead areas. The fraction of good area corresponds to 78% of the total acceptance. This map was used to completely suppress particles that hit the dead areas in the real data.

As long as the baseline distribution is approximated as a NBD, which is certainly true as observed in E802 [28] and in the present analysis, one can estimate the relation between true k values of the NBD and biased k values from dead or inefficient areas based on the convolution theorem of the NBD. For two independent NBDs with (μ_1, k_1) and (μ_2, k_2), it is known that the convolution of the two NBDs is a NBD with (μ_c, k_c) that satisfies the relations

$$\begin{aligned} k_c &= k_1 + k_2, \\ \mu_c &= \mu_1/k_1(k_1 + k_2), \end{aligned} \tag{12}$$

where $\mu_1/k_1 = \mu_2/k_2$ holds [34,35]. Therefore the correction can be applied by multiplying a ratio of the total number of η-ϕ bins in a given η window size to the number of bins excluding dead area, as the geometrical acceptance corrections can be applied.

Strictly speaking, we cannot completely reproduce the original k by this correction, because NBDs in different positions are not completely independent. However, except for the large hole, which is already excluded by the truncation, small holes are scattered rather uniformly in the azimuthal direction for any position of the $\delta\eta$ windows. As the simplest overall correction to each window position, we applied the convolution theorem [34,35] by assuming a collection of independent NBD sources. As long as the correction is applied in the same manner for all the azimuthal holes, it does not greatly affect the differential measurement to the pseudorapidity space. If the correction is accurate enough, we can expect a constancy of the corrected k values that should be independent of the fraction of dead areas. Based on the degree of constancy of corrected k as a function of the fraction of dead areas in each window position for a given $\delta\eta$ window size, the incompleteness of the correction in each window size has been checked. As briefly mentioned in the last paragraph of Sec. IV D, the window sizes to be analyzed were determined so that systematic error bands on $\langle k_c \rangle$ explained in Sec. IV F can contain the most corrected k values, independently of the fraction of dead areas in each window position.

F. Statistical and systematic errors

As a convolution of statistical errors, we adopted errors on weighted mean values $(\delta\langle\mu_c\rangle, \delta\langle k_c\rangle)$ on corrected NBD parameters after the window truncation mentioned in

Sec. IV D, which are defined as

$$\delta\langle\mu_c\rangle^2 \equiv \frac{\delta\bar{\mu}_{ci}{}^2}{n_{\rm ind}},$$
$$\delta\langle k_c\rangle^2 \equiv \frac{\delta\bar{k}_{ci}{}^2}{n_{\rm ind}}, \tag{13}$$

where $\delta\bar{\mu}_{ci}$ and $\delta\bar{k}_{ci}$ are, respectively, defined as $\sum_{i=1}^{n}\delta\mu_c/n$ and $\sum_{i=1}^{n}\delta k_c/n$ with the number of valid window positions n after the truncation and $n_{\rm ind}\equiv 0.75/\delta\eta$ is the number of statistically independent window positions for a given $\delta\eta$ window size. This statistical error on $\delta\langle k_c\rangle$ is referred to as $\delta\langle k_c\rangle$ (stat).

The dominant sources of systematic errors for the correlation length measurement are the correction procedure with dead maps and the two-track separation cuts, since both introduce unphysical correlations. We have allowed 2% fluctuation on the average multiplicity of measured number of charged tracks. This fluctuation is also a result of dead channels in the tracking detectors, as discussed in Sec. IV B. To estimate this, we defined two more patterns of dead maps with the definition of $3\sigma \pm 0.5\sigma$ as indicated in Fig. 2(c). The deviation of $\langle k_c\rangle$ from the central dead-map definition is referred to as $\delta\langle k_c\rangle$ (dead), which corresponds to 3.4% typically.

The two-track separation cut serves mainly to reject fake track effects; these are dominantly observed in the ϕ direction rather than η, since the PC1 hit requirement fixes the z positions along the beam axis. Therefore, the effect of the $\delta\phi$ cut was estimated as ± 0.002 rad around the central cut value of 0.012 rad with a fixed cut value on $\delta\eta$ of 0.001. The deviation of $\langle k_c\rangle$ from the central value reslting from the fake track rejection cut is referred to as $\delta\langle k_c\rangle$ (fake). This systematic error increases at higher centrality bins and is estimated as 5.8% and 0.3% at 0–5% and 60–65% centrality bins, respectively.

The $\langle k_c\rangle$ (stat) is related to agreement between multiplicity distributions and NBDs. The $\langle k_c\rangle$ (dead) and $\langle k_c\rangle$ (fake) depends on the position of the window and the average multiplicity in a selected centrality bin, respectively. By treating these contributions as independent systematic error sources, the total systematic error $\delta\langle k_c\rangle$ (total) on $\langle k_c\rangle$ in each $\delta\eta$ in each centrality was obtained by the quadratic sum over $\delta\langle k_c\rangle$ (stat), $\delta\langle k_c\rangle$ (dead), and $\delta\langle k_c\rangle$ (fake).

V. RESULTS

In this section the results of the NBD fits are first tabulated. Then the measured NBD k as a function of the pseudorapidity window sizes in various centrality bins are shown. Lastly, the $N_{\rm part}$ dependences of extracted $\alpha\xi$ product in Eq. (9) are presented.

A. NBD fit

NBD fit results in all window sizes in all centrality bins are summarized in Tables III–XXVII in Appendix B, where $\langle\mu_c\rangle$ and $\langle\mu\rangle$ are weighted means of corrected and uncorrected μ over all window positions respectively and $\langle k_c\rangle$ and $\langle k\rangle$ are weighted means of corrected and uncorrected k over all window positions, respectively. The $\langle\mu_c\rangle$s are corrected only for the effect of the detector dead areas, as described in Sec. IV E. The mean multiplicities were confirmed to be consistent with the result of the independent analysis by a different method using only PC1 and PC3 [22], after known additional correction factors were taken into account. Statistical errors on weighted means $\delta\langle k_c\rangle$ (stat) are obtained as explained in Sec. IV F. $\langle\chi^2/NDF\rangle$ is the average of reduced χ^2 of NBD fits over all window positions. $\langle NDF\rangle$ is the average of the degree of freedom of NBD fits over all window positions, and the systematic errors $\delta\langle k_c\rangle$ (dead), $\delta\langle k_c\rangle$ (fake), and $\delta\langle k_c\rangle$ (total) are already explained in Sec. IV F.

The mean and r.m.s. values of the reduced χ^2 values in the NBD fit over all window positions and all $\delta\eta$ sizes and all centralities were obtained as 0.75 and 0.33, respectively. The mean value corresponds to typically an 80% confidence level. Therefore, it is good enough to assume NBD as a baseline multiplicity distribution to obtain the integrated correlation function via the k parameter.

As a demonstration to show how well the NBD fits work, Fig. 3 shows the charged particle multiplicity distributions

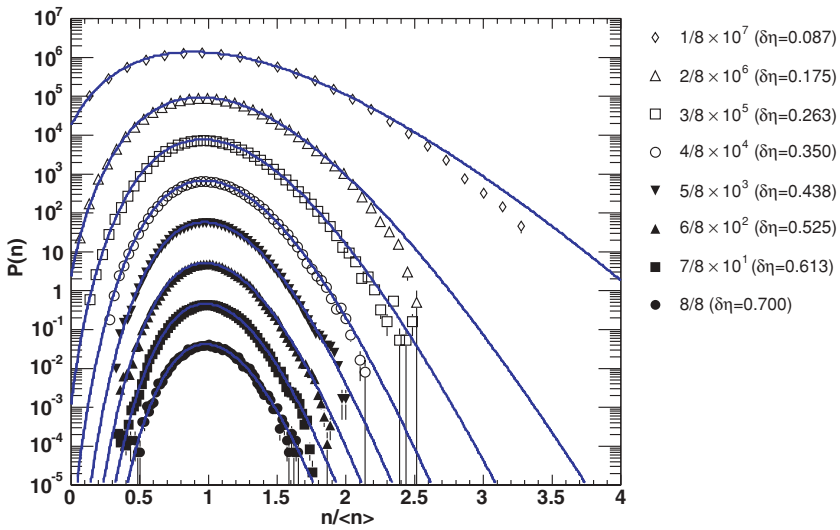

FIG. 3. (Color online) Uncorrected charged particle multiplicity distributions in each pseudorapidity window size, as indicated in the legend, at 0–10% collision centrality. The distributions are shown as a function of the number of tracks n normalized to the mean multiplicity $\langle n\rangle$ in each window. The error bars show the statistical errors. The solid curves are NBD fit results.

in each pseudorapidity window size in 1/8 fractions of the full rapidity coverage of $|\eta| < 0.35$ with 0–10% events in the collision centrality, where the uncorrected multiplicity distributions within the total error bands on $\langle k_c \rangle$ in Table III (Appendix B) are all merged. The distributions are shown as a function of the number of tracks, n, normalized to the mean multiplicity $\langle n \rangle$ in each window. The error bars show the statistical errors on the merged distributions. The solid curves are fit results with the NBD only for demonstration purposes. The fit results in Tables III–XXVII are not obtained from these convoluted distributions, whose accuracies are degraded by the convolutions with different μ values owing to different detector biases depending on the window positions.

B. k versus $\delta\eta$

Figures 4(a) and 4(b) show $\langle k_c \rangle$ as a function of pseudorapidity window size with 10% and 5% centrality bin width, respectively. Centrality classes are indicated inside the figures. The error bars show $\delta\langle k_c \rangle$ (total) defined in Sec. IV F. The solid lines in Fig. 4 indicate the fit results based on Eq. (9). The fits were performed in the $\delta\eta$ region from 0.066 to 0.7 as explained in Sec. IV D.

If we could reliably measure the NBD k parameter for arbitrarily small $\delta\eta \sim 0$ windows, then α and ξ could be treated as independent free parameters for each centrality. In the real experimental situation, there is an anticorrelation between α and ξ because of the lack of reliable data points close to $\delta\eta \sim 0$, if we attempt to fit with Eq. (8). However, at least an upper limit on the absolute scale of ξ was obtained as $\xi < 0.035$ by the free parameter fits based on Eq. (8). It is qualitatively consistent with expectation from numerical calculations [36] that the correlation lengths become smaller in the RHIC energy than for $p+p$ collisions [26] and low-energy $A+A$ collisions [28].

Since the upper limit of ξ is small enough compared to the fitting region of $\delta\eta$ ($\xi \ll \delta\eta$), Eq. (9) can be applied for the fits to the NBD k as a function of $\delta\eta$. In this case, the $\alpha\xi$ product, which is related to the susceptibility in the long-wavelength limit as defined in Eq. (A11), can be obtained by the fits without any physical assumptions. The typical χ^2/NDF in the fit based on Eq. (9) is 0.132, which corresponds to a 99%

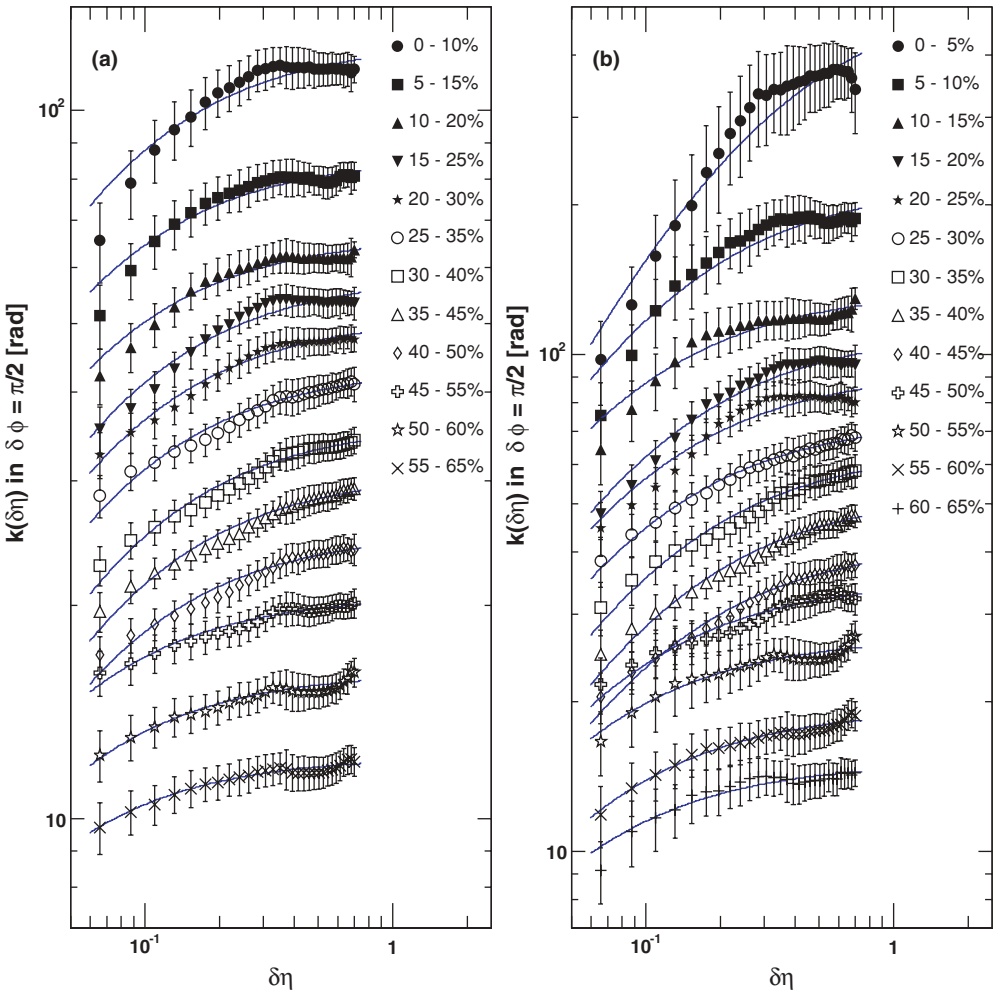

FIG. 4. (Color online) Weighted mean of corrected NBD k, $\langle k_c \rangle$, as a function of pseudorapidity window size with (a) 10% and (b) 5% centrality bin widths. Centrality classes are indicated in the figure legend. The error bars show $\delta\langle k_c \rangle$ (total), as explained in Sec. IV F. The solid lines indicate the fit curves of Eq. (9).

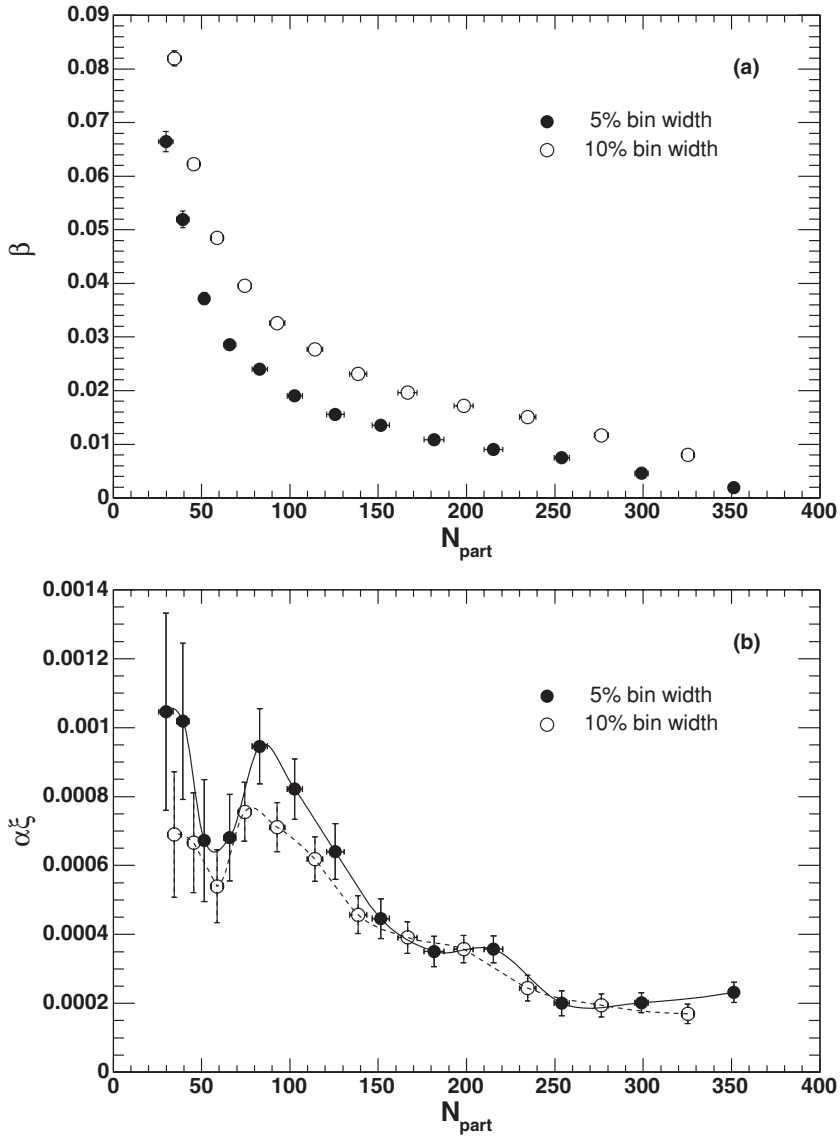

FIG. 5. Fit results based on Eq. (9): (a) β and (b) products of $\alpha\xi$ as a function of N_{part}. The horizontal error bars correspond to ambiguities in the mean value of N_{part} as explained in Sec. IV C. The vertical error bars are obtained from errors on the fitting parameter.

confidence level. Therefore, the small correlation length is confirmed as below the minimum $\delta\eta$ window sizes of 0.066.

As explained in Sec. II for Eq. (9), in the limit of $\beta = 0$, the slopes in k versus $\delta\eta$ have crucial information on the phase transition. In Fig. 4 we can identify different behaviors in slopes around the 40–50% centrality region even without fit curves.

C. $\alpha\xi$ product versus N_{part}

Figures 5(a) and 5(b) show the obtained fit parameters β and $\alpha\xi$ with Eq. (9) as a function of N_{part}, where results for both the 5% and 10% centrality bin width cases are plotted as filled and open circles, respectively. The smooth solid and dotted curves are provided to guide the eye. The horizontal error bars correspond to ambiguities on the mean value of N_{part} as explained in Sec. IV C. The vertical error bars are obtained from errors on the fitting parameter by the MINUIT program [33].

Table I summarizes the fit results where centralities and corresponding $N_{\text{part}}, \alpha\xi, \beta$, and χ^2/NDF obtained by the fit with Eq. (9) are shown for 10% and 5% centrality bin cases, respectively. The β parameter in Eq. (7) can absorb any effects independent of pseudorapidity space correlations, as discussed in Sec. II. For a wider centrality bin, the width of the multiplicity distribution becomes broader, since events with a wider range of centralities are included in the bin. This causes the systematic difference of β in the 5% and 10% centrality datasets as shown in Fig. 5(a). The systematic shift of β parameters to smaller values in the smaller centrality bin width suggests that β dominantly contains fluctuations on N_{part}. The ambiguity of N_{part} measured by PHENIX is not large compared, for example, to NA49, where a nonmonotonic behavior of the scaled variance of multiplicities was seen as a function of the number of projectile participant nucleons [37]. In NA49, only spectators from the projectile nucleus are measurable, causing an increase of scaled variance of multiplicity distributions in peripheral collisions owing to dominantly large N_{part} fluctuations in the target nucleus [38].

TABLE I. The $\alpha\xi$ and β in Eq. (9) obtained by the fits to $\langle k_c \rangle$ versus $\delta\eta$. Upper and lower columns corresponds to 10% and 5% centrality bin width cases, respectively.

Centrality (%)	$\langle N_{\rm part} \rangle$	$\alpha\xi(\propto \chi_{\omega=0})$	β	$\chi^2/NDF(NDF=27)$
0–10	325.2 ± 3.3	$0.17 \times 10^{-3} \pm 0.03 \times 10^{-3}$	$0.80 \times 10^{-2} \pm 0.02 \times 10^{-2}$	0.24
5–15	276.4 ± 4.0	$0.19 \times 10^{-3} \pm 0.03 \times 10^{-3}$	$1.17 \times 10^{-2} \pm 0.02 \times 10^{-2}$	0.16
10–20	234.6 ± 4.7	$0.24 \times 10^{-3} \pm 0.04 \times 10^{-3}$	$1.51 \times 10^{-2} \pm 0.03 \times 10^{-2}$	0.14
15–25	198.4 ± 5.4	$0.36 \times 10^{-3} \pm 0.04 \times 10^{-3}$	$1.72 \times 10^{-2} \pm 0.03 \times 10^{-2}$	0.26
20–30	166.6 ± 5.4	$0.39 \times 10^{-3} \pm 0.05 \times 10^{-3}$	$1.96 \times 10^{-2} \pm 0.03 \times 10^{-2}$	0.09
25–35	138.6 ± 4.9	$0.46 \times 10^{-3} \pm 0.06 \times 10^{-3}$	$2.31 \times 10^{-2} \pm 0.04 \times 10^{-2}$	0.09
30–40	114.2 ± 4.4	$0.62 \times 10^{-3} \pm 0.06 \times 10^{-3}$	$2.77 \times 10^{-2} \pm 0.05 \times 10^{-2}$	0.13
35–45	92.8 ± 4.3	$0.71 \times 10^{-3} \pm 0.07 \times 10^{-3}$	$3.26 \times 10^{-2} \pm 0.05 \times 10^{-2}$	0.14
40–50	74.4 ± 3.8	$0.76 \times 10^{-3} \pm 0.09 \times 10^{-3}$	$3.96 \times 10^{-2} \pm 0.07 \times 10^{-2}$	0.14
45–55	58.8 ± 3.3	$0.54 \times 10^{-3} \pm 0.11 \times 10^{-3}$	$4.85 \times 10^{-2} \pm 0.08 \times 10^{-2}$	0.05
50–60	45.5 ± 3.3	$0.67 \times 10^{-3} \pm 0.14 \times 10^{-3}$	$6.22 \times 10^{-2} \pm 0.11 \times 10^{-2}$	0.11
55–65	34.6 ± 3.8	$0.69 \times 10^{-3} \pm 0.18 \times 10^{-3}$	$8.19 \times 10^{-2} \pm 0.14 \times 10^{-2}$	0.05
0–5	351.4 ± 2.9	$0.23 \times 10^{-3} \pm 0.03 \times 10^{-3}$	$0.19 \times 10^{-2} \pm 0.02 \times 10^{-2}$	0.18
5–10	299.0 ± 3.8	$0.20 \times 10^{-3} \pm 0.03 \times 10^{-3}$	$0.46 \times 10^{-2} \pm 0.02 \times 10^{-2}$	0.27
10–15	253.9 ± 4.3	$0.20 \times 10^{-3} \pm 0.04 \times 10^{-3}$	$0.75 \times 10^{-2} \pm 0.02 \times 10^{-2}$	0.17
15–20	215.3 ± 5.3	$0.36 \times 10^{-3} \pm 0.04 \times 10^{-3}$	$0.90 \times 10^{-2} \pm 0.03 \times 10^{-2}$	0.18
20–25	181.6 ± 5.6	$0.35 \times 10^{-3} \pm 0.04 \times 10^{-3}$	$1.08 \times 10^{-2} \pm 0.03 \times 10^{-2}$	0.32
25–30	151.5 ± 4.9	$0.45 \times 10^{-3} \pm 0.06 \times 10^{-3}$	$1.35 \times 10^{-2} \pm 0.04 \times 10^{-2}$	0.02
30–35	125.7 ± 4.9	$0.64 \times 10^{-3} \pm 0.08 \times 10^{-3}$	$1.55 \times 10^{-2} \pm 0.05 \times 10^{-2}$	0.09
35–40	102.7 ± 4.3	$0.82 \times 10^{-3} \pm 0.09 \times 10^{-3}$	$1.90 \times 10^{-2} \pm 0.05 \times 10^{-2}$	0.08
40–45	82.9 ± 4.3	$0.95 \times 10^{-3} \pm 0.11 \times 10^{-3}$	$2.40 \times 10^{-2} \pm 0.07 \times 10^{-2}$	0.06
45–50	65.9 ± 3.4	$0.68 \times 10^{-3} \pm 0.13 \times 10^{-3}$	$2.86 \times 10^{-2} \pm 0.08 \times 10^{-2}$	0.08
50–55	51.6 ± 3.2	$0.67 \times 10^{-3} \pm 0.18 \times 10^{-3}$	$3.72 \times 10^{-2} \pm 0.11 \times 10^{-2}$	0.11
55–60	39.4 ± 3.5	$1.02 \times 10^{-3} \pm 0.23 \times 10^{-3}$	$5.19 \times 10^{-2} \pm 0.16 \times 10^{-2}$	0.06
60–65	29.8 ± 4.1	$1.05 \times 10^{-3} \pm 0.29 \times 10^{-3}$	$6.64 \times 10^{-2} \pm 0.19 \times 10^{-2}$	0.08

This is due to the partial sampling with respect to the total number of nucleons in two colliding nuclei. Since both projectile and target nuclei on both sides can be measured by BBC and ZDC at PHENIX, such ambiguities of $N_{\rm part}$ are suppressed, even in peripheral collisions. Some $N_{\rm part}$ fluctuations remain, but the β parameter can absorb this kind of fluctuation offset. Consequently, $N_{\rm part}$ fluctuations are not harmful for the measurement of the $\alpha\xi$ products, since they are based on the differential values of fluctuations for a given centrality bin. In addition, β is expected to absorb effects from azimuthal correlations. Because the PHENIX detector does not cover the full azimuthal range, fluctuations of low-p_T particles caused by reaction plane rotations and elliptic flow should contribute to the two-particle correlation function even in the pseudorapidity direction as an offset in principle. Owing to the β parameter, the nonmonotonic behavior of the measured $\alpha\xi$ in the pseudorapidity direction cannot be biased by elliptic flow nor by initial geometrical biases, since the azimuthal correlations are constant over the narrow pseudorapidity window of $|\eta| < 0.35$ [39].

VI. DISCUSSION

A. Other correlation sources

We discuss three other sources of correlation that are not related to the density correlations we are interested in but could affect the measurement of the inclusive charged particle multiplicity fluctuations. The first is charged track pairs from particle decays in flight. The second is background charged track pairs originating from secondary particle interactions in detector materials (i.e., showers and conversion pairs). For these two sources we have estimated the effects of contaminations to the inclusive charged particle multiplicity fluctuations by GEANT-based MC [32] simulations. The third source is the known short-range correlation from the Bose-Einstein correlation of identical particles.

The detectable charged particle compositions in the no-magnetic-field condition with the selection criteria of charged tracks in Sec. IV B are estimated as 94% for charged pions, 4% for charged kaons, and 2% for protons and antiprotons in 0–70% centrality. These are obtained by MC simulations based on identified charged particle spectra measured by PHENIX [31] up to 4 GeV/c of transverse momentum p_T. The statistically dominant weak decay particles that can contribute to the inclusive charged particle multiplicity are $K^0_S \to \pi^+\pi^-$ and $\Lambda(\overline{\Lambda}) \to p(\overline{p})\pi^-(\pi^+)$. The relative invariant yields of those particles to charged pions are 15% and 5% for K^0_S and $\Lambda(\overline{\Lambda})$ [40], respectively. They were calculated by the measured production cross section in Au+Au collisions at $\sqrt{s_{NN}} = 200$ GeV. The production cross section of K^0_S is assumed to be the same as that for charged kaons [31]. The detection efficiency of the charged track pairs from weak decay particles in the one arm acceptance of the PHENIX detector ($|\eta| < 0.35, \Delta\phi < \pi/2$) is obtained by the MC simulation. We estimated it by using the p_T spectra of charged kaons for

K^0_S as the most dominant meson, and by using the p_T spectra of charged pions with transverse mass scaling for $\Lambda(\overline{\Lambda})$ as the most dominant baryon, which contribute to the inclusive charged particle multiplicity fluctuation. As the result, the ratios of charged track pairs originating from those weak decay particles to the number of produced charged pions per event are 0.7% and 0.9% for K^0_S and $\Lambda + \overline{\Lambda}$, respectively. The effects of those correlations on k were estimated as follows. Suppose two independent NBDs in different windows have the same NBD parameters of μ and k for a given window size of $\delta\eta/2$. If there is no correlation between the two windows, NBD in the $\delta\eta$ window size becomes a convoluted distribution between the two NBDs. This is certainly true, since we know the correlation length is well below the minimum size of $\delta\eta$ windows, as already discussed. Based on the NBD convolution theorem, the convoluted NBD parameters $\mu_{\rm conv}$ and $k_{\rm conv}$ are expressed as $\mu_{\rm conv} = 2\mu$ and $k_{\rm conv} = 2k$, respectively, in the case of no correlation. For the case where the correlated pairs are embedded, we define the fraction of the number of correlated pairs with respected to μ as f. Then the mean value before the correlated pairs are embedded is expressed as $\mu(1 - f)$ in the $\delta\eta/2$ window. The effect of the embedded correlation on $k_{\rm conv}$ can be estimated by adding the number of correlated pairs to both windows simultaneously with the fraction of f. With $\mu(1 - f)$ and k, we can generate a NBD with a random number generator in each window of $\delta\eta/2$ and convolute the two NBDs. >From the NBD fit to the convoluted distribution, we can obtain $k_{\rm conv}$ including the effect of the correlated pairs. We define the ratio of the deviation of $k_{\rm conv}$ to the independent case, $\Delta k \equiv (k_{\rm conv} - 2k)/2k$ for K^0_S and $\Lambda + \overline{\Lambda}$, respectively. For all observed $(\langle\mu_c\rangle, \langle k_c\rangle)$ values in all $\delta\eta$ windows in all centralities, we have estimated Δk. The pair fraction f depends on $\delta\eta$ window size, since weak decay particles have their own correlation length owing to the kinematical constraint. The fractions f were obtained based on the two-particle correlation of decayed pairs as a function of $\delta\eta$ window size, which were evaluated from the GEANT-based MC simulation with the actual track-selection criteria. It should be noted that the integrated fractions correspond to the aforementioned fractions, 0.7% and 0.9% for K^0_S and $\Lambda + \overline{\Lambda}$, respectively. As a result, the average values of Δk over all data points were estimated as $+0.27\% \pm 0.35\%$ (standard deviation) and $+0.40\% \pm 0.35\%$ (standard deviation) for K^0_S and $\Lambda + \overline{\Lambda}$ decays, respectively. In contrast, the average value of relative errors, $\delta\langle k_c\rangle(\text{total})/\langle k_c\rangle$, in measured k is $\pm 7.34\% \pm 3.29\%$ (standard deviation). We confirmed that the estimated Δk values are all included within the range of the relative errors on measured k. Therefore, we can conclude that the effect of the statistically dominant weak decay pairs with a few percent level on the $\alpha\xi$ product cannot exceed the full error sizes of the $\alpha\xi$ products in Table I.

The amount of material before the tracking system is 1.3% of a radiation length. It produces electron-positron pairs with 1.0% photon conversion probability. Almost 100% of photons up to 4 GeV/c of p_T are produced by decays from neutral pions. The detection efficiency of electron-positron pairs that survive after the requirement of the charged track associations and two-track separations in Sec. IV B is estimated as 0.22%. It was estimated by the MC simulations with a flat p_T distribution of photons. Since the opening angle of the conversion pairs is very small, these conversion electrons are strongly suppressed by the two-track separation cuts. Consequently, electron-positron pairs of $2.2 \times 10^{-3}\%$ with respect to the produced charged pions per event contribute to the multiplicity fluctuations. The efficiency of charged track pairs, which is produced by the materials from single charged hadrons as knock-on electrons (positrons), is estimated as less than $5.8 \times 10^{-5}\%$. Since the total pair fractions are much smaller than that in weak decays by several orders of magnitude, we can conclude that the effects of those secondary particles on the $\alpha\xi$ products are negligible.

If the observed correlation were to originate only from the Bose-Einstein effect, then we would expect α to be directly related to the chaoticity parameter λ in HBT analysis, which is measured in relative momentum space q. A similar measurement in pseudorapidity space based on Eq. (7) in low-energy $A+A$ collisions [41] indicates the direct relation between λ and α. The observed two-particle correlation strength α in pseudorapidity space is weaker than λ measured in q space and essentially becomes zero for the particle pairs selected in the higher q region where the HBT effect also becomes zero. This indicates that the observed pseudorapidity correlations in the lower energy $A+A$ collisions are essentially explained purely by the HBT effect. In Au+Au collisions at $\sqrt{s_{NN}} = 200$ GeV, the measured λ shows constant behavior as a function of $N_{\rm part}$ within 12% and a monotonic $N_{\rm part}$ dependence of HBT radii has been observed [42,43]. This implies that the nonmonotonic behavior of the $\alpha\xi$ product cannot be explained solely as a result of the known HBT effect, because $\alpha \propto \lambda$ is expected to be constant for any $N_{\rm part}$, and ξ, which would be related to the HBT source radii, is expected to be monotonic, if the known HBT effect is the only source of the correlation.

B. Evaluation of the nonmonotonic behavior of $\alpha\xi$

The $\alpha\xi$ product obtained by Eq. (9) is related to susceptibility in the long-wavelength limit, $\chi_{\omega=0}$, as described in Sec. II. According to Eq. (10), if the system temperature T is far from the critical temperature T_c then $\alpha\xi$ is expected to decrease monotonically with increasing T, which is a monotonic function of $N_{\rm part}$, as will be discussed in Sec. VI C. Therefore, one can assume a monotonically decreasing function as a hypothesis of the baseline in T far from T_c. As baseline functional forms for $\alpha\xi$ versus T we consider the following two cases. The first is a power-law function, which is naturally expected from Eq. (10), and the second is a linear function, the simplest assumption. The power-law baseline and the linear baseline are parametrized as

$$\alpha\xi(N_{\rm part}) = p_1(N_{\rm part})^{p_2} \tag{14}$$

and

$$\alpha\xi(N_{\rm part}) = p_1 + p_2 N_{\rm part} \tag{15}$$

with fit parameter p_1 and p_2, respectively. As a test hypothesis, we assume a local maximum on the monotonic baselines in

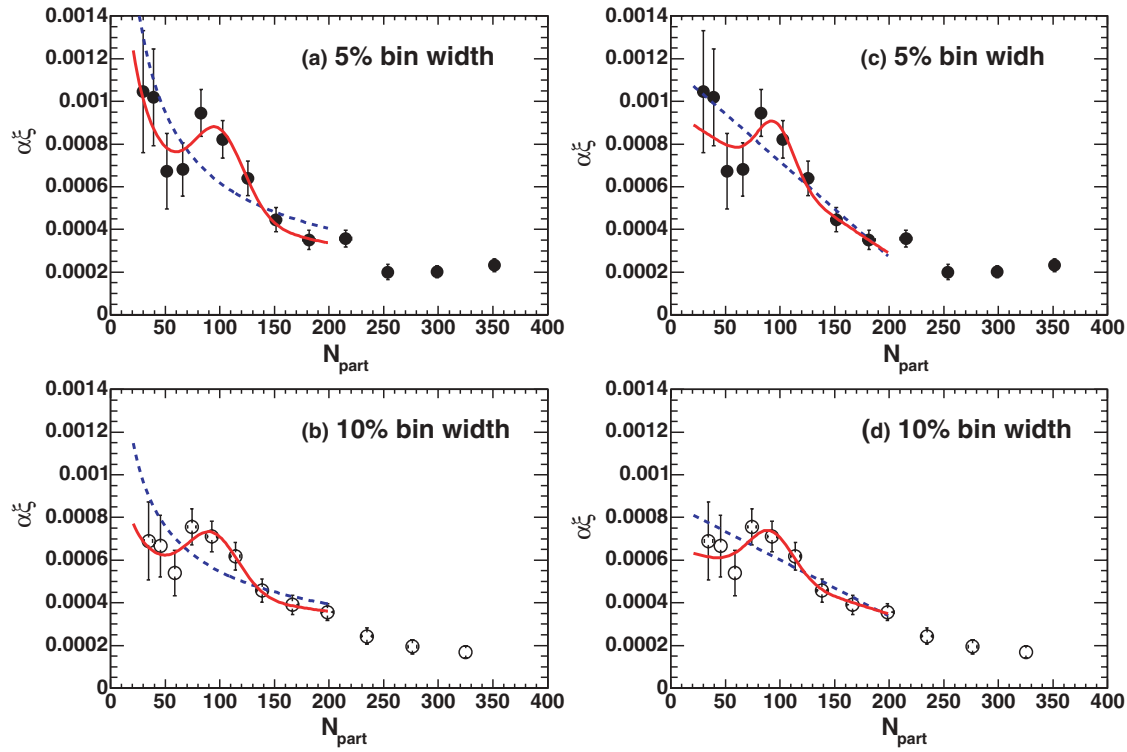

FIG. 6. (Color online) $\alpha\xi$ versus N_{part} in Table I with fit curves. The dashed and solid curves show the fit results with the baseline functions [Eqs. (14) and (15)] and with the composite functions [Eqs. (16) and (17)], respectively. (a) 5% and (b) 10% bin width cases with the power-law baselines. (c) 5% and (d) 10% bin width cases with the linear baselines.

$\alpha\xi$ versus N_{part}. Although the functional form around the local maximum is not known a priori without introducing a physical model, we can at least discuss the significance of the local maximum above the monotonic baseline by introducing a Gaussian distribution. The composite functions are defined as

$$\alpha\xi(N_{\text{part}}) = p_1(N_{\text{part}})^{p_2} + ae^{-\frac{(N_{\text{part}}-m)^2}{2w^2}} \tag{16}$$

and

$$\alpha\xi(N_{\text{part}}) = p_1 + p_2 N_{\text{part}} + ae^{-\frac{(N_{\text{part}}-m)^2}{2w^2}}, \tag{17}$$

where a, m, and w correspond to amplitude, mean, and width of the Gaussian component, respectively. Fits with the four functional forms were performed to $\alpha\xi$ versus N_{part} in the range $20 < N_{\text{part}} < 200$. Figure 6 shows $\alpha\xi$ versus N_{part} from Table I with those fit curves. The dashed and solid curves show the fit results with the baseline functions and with the composite functions. Figures 6(a) and 6(b) correspond to 5% and 10% bin width cases with the power-law baselines. Figures 6(c) and 6(d) correspond to 5% and 10% bin width cases with the linear baselines. Table II summarizes all the fit results from the MINUIT program [33], including functional forms, centrality bin widths, $\chi^2/NDF(NDF)$, the Gaussian amplitude a with its error δa, and the significance of the amplitude defined as $a/\delta a$. Although the significance of the local maximum with the linear baseline is smaller than that with the power-law baseline, this is mainly due to the larger uncertainty on a in Eq. (17) than in Eq. (16). This reflects

TABLE II. The fit parameters in Eqs. (14), (15), (16), and (17).

Functional form	Centrality bin width (%)	$\chi^2/NDF(NDF)$	$a \pm \delta a$	Significance $(a/\delta a)$
Power law in Eq. (14)	5	2.76 (7)		
Power law + Gaussian in Eq. (16)	5	0.60 (4)	$0.37 \times 10^3 \pm 0.09 \times 10^3$	3.98
Linear in Eq. (15)	5	1.23 (7)		
Linear + Gaussian in Eq. (17)	5	0.79 (4)	$0.27 \times 10^3 \pm 0.21 \times 10^3$	1.24
Power law in Eq. (14)	10	2.10 (7)		
Power law + Gaussian in Eq. (16)	10	0.38 (4)	$0.27 \times 10^3 \pm 0.08 \times 10^3$	3.21
Linear in Eq. (15)	10	1.09 (7)		
Linear + Gaussian in Eq. (17)	10	0.43 (4)	$0.22 \times 10^3 \pm 0.13 \times 10^3$	1.69

the fact that the combination of a Gaussian distribution with the linear baseline is not as good a fit as that with the power-law baseline for the given data points. The difference in the significance between 5% and 10% centrality bin width cases is not attributed to the correlations with the β parameter, since β was introduced as a parameter independent of $\delta\eta$. This can, rather, be understood as the smearing effect of a peak-like shape resulting from the difference of centrality bin widths around the mean N_{part}. In all cases in Table II, the χ^2/NDF values indicate that composite functions are favored over monotonic functions. This result supports the nonmonotonicity of $\alpha\xi$ as a function of N_{part}.

Although there is a possibility that more than one correlation length scale is dynamically present, the functional form with one correlation length can reasonably describe the region of $0.066 < \delta\eta < 0.7$ with the average χ^2/NDF of 0.132 over all centralities. We have performed a further check on the N_{part} dependence of the $\alpha\xi$ products by limiting the region of fit to $0.066 < \delta\eta < 0.306$, as shown in Fig. 7. The characteristic behavior of $\alpha\xi$ is still present at around $N_{\text{part}} \sim 90$, though

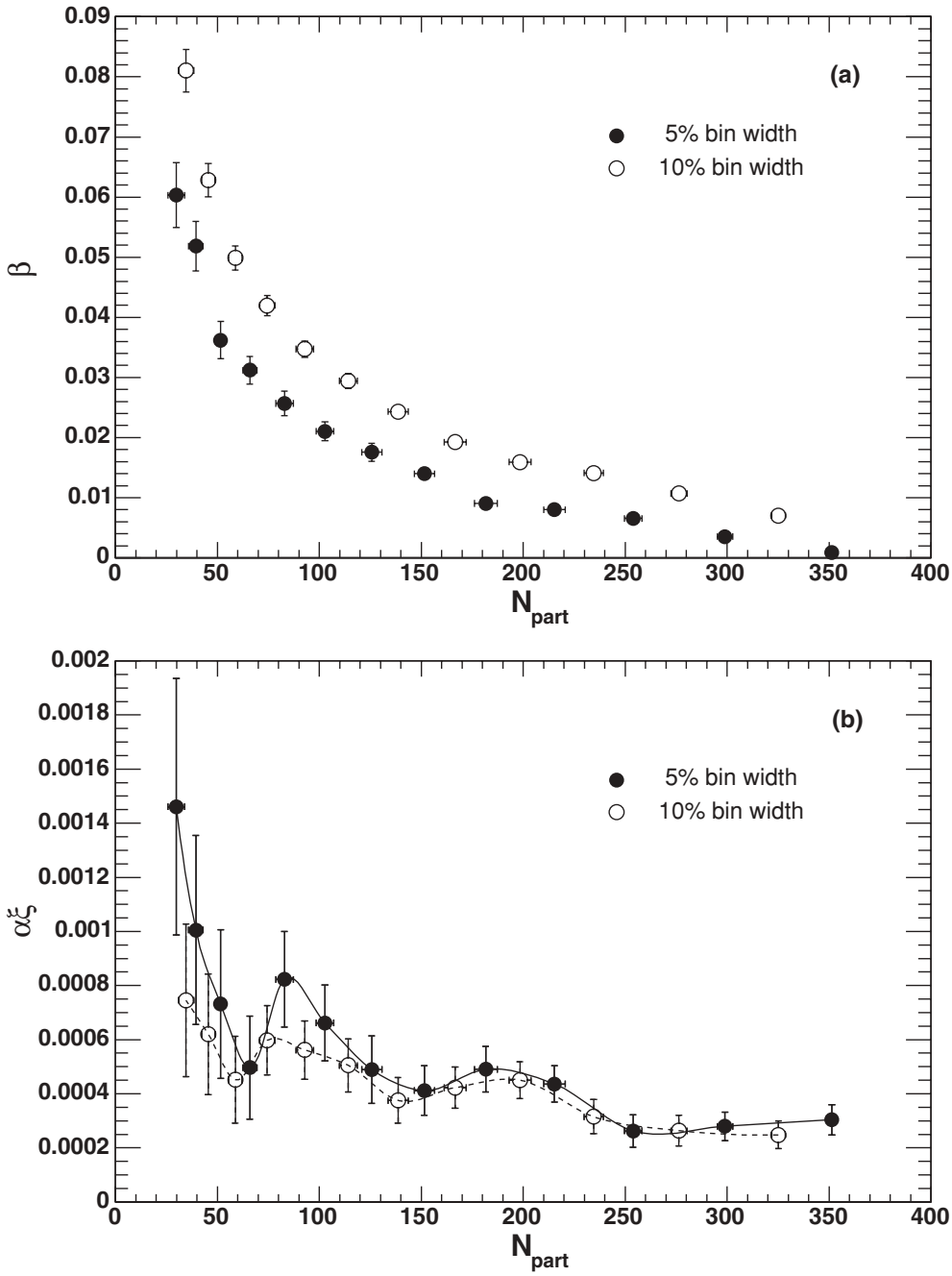

FIG. 7. Fit results based on Eq. (9) by limiting the range of $\delta\eta$ from 0.066 to 0.306: (a) β and (b) products of $\alpha\xi$ as a function of N_{part}. The horizontal error bars correspond to ambiguities in the mean value of N_{part} as explained in Sec. IV C. The vertical error bars are obtained from errors on the fitting parameter.

with smaller levels of significance than those shown in Table II. The same significance value of 1.9 was obtained for both 5% and 10% centrality bin width cases by the fit using Eq. (16) within the range $20 < N_{\rm part} < 160$. Therefore, a possible indication of a local maximum is seen at $N_{\rm part} \sim 90$.

C. Initial temperature and $N_{\rm part}$

The Bjorken energy density [21] derived from the measured $dE_T/d\eta$ in the mid-rapidity region is defined as

$$\epsilon_{\rm Bj} = \frac{1}{c\tau A_T}\frac{dE_T}{dy}, \tag{18}$$

where τ is the formation time and A_T is the nuclei transverse overlap area size. It is well known that the energy density monotonically increases with increasing $N_{\rm part}$ in Au+Au collisions at $\sqrt{s_{NN}} = 200$ GeV [22].

This indicates that the change of $N_{\rm part}$ even at the fixed collision energy can yield a fine scan over the initial temperature. Therefore, the nonmonotonic behavior in the $\alpha\xi$ products could be an indication of the critical initial temperature as defined in Eq. (A11). The Bjorken energy density $\epsilon_{\rm Bj}\tau$ at the local maximum of $\alpha\xi$ seen at $N_{\rm part} \sim 90$ corresponds to $\sim$2.4 GeV/(fm^2c) with $A_T = 60$ fm^2.

VII. CONCLUSIONS

The multiplicity distributions measured in Au+Au collisions at $\sqrt{s_{NN}} = 200$ GeV are found to be well described by negative binomial distributions.

The two-particle density correlations have been measured via the functional form for pseudorapidity density fluctuations derived in the Ginzburg-Landau framework, up to the second-order term in the free energy, with a scalar-order parameter defined as pseudorapidity-dependent multiplicity fluctuations around the mean value. The functional form can reasonably fit k versus $\delta\eta$ in all centralities in the $|\eta| < 0.35$ region with one correlation length assumption and the constant term β, which is independent of $\delta\eta$. We found that β is necessary to absorb residual effects of finite centrality binning.

We found that the absolute scale of the correlation length ξ depends on the magnitude of the correlation strength at zero distance, α, within the range of pseudorapidity window sizes available in this analysis. However, according to the free parameter fit results, the upper limit on $\xi < 0.035$ was obtained, and it was confirmed by the accuracy of the fits with approximated integrated correlation function in the limit of small correlation length ($\xi \ll \delta\eta$).

The $\alpha\xi$ product in the correlation function, which is monotonically related to susceptibility in the long-wavelength limit, $\chi_{\omega=0}$, was seen to exhibit a nonmonotonic behavior as a function of the number of participant nucleons, $N_{\rm part}$. A possible indication of a local maximum is seen at $N_{\rm part} \sim 90$ and the corresponding energy density based on the Bjorken picture is $\epsilon_{\rm Bj}\tau \sim 2.4$ GeV/(fm^2c) with the transverse area size of 60 fm^2.

Trivial particle correlations originating from charged track reconstructions in tracking detectors have been suppressed in this analysis a priori. The ratio of charged particles from statistically dominant weak decays and secondary particles produced in the detector materials, which contribute as correlated pairs, are respectively estimated below $\sim$1% and $\sim 10^{-3}$% with respect to the total number of charged pions in the PHENIX acceptance per event. We have estimated those effects on measured k values and the deviation resulting from the effect is well inside the total error size of observed $\delta\langle k_c\rangle$. Therefore, we conclude that their contributions are almost negligible to the observed behavior of the $\alpha\xi$ products.

The behavior may be explained by the onset of a mixture of different types of particle production mechanisms that are not necessarily related to temperature or density correlations. However, interpreted within the Ginzburg-Landau framework the local maximum of the $\alpha\xi$ product could be an indication of a critical phase boundary.

ACKNOWLEDGMENTS

We thank the staff of the Collider-Accelerator and Physics Departments at Brookhaven National Laboratory and the staff of the other PHENIX participating institutions for their vital contributions. We acknowledge support from the Department of Energy, Office of Science, Nuclear Physics Division, the National Science Foundation, Abilene Christian University Research Council, the Research Foundation of SUNY, and Dean of the College of Arts and Sciences, Vanderbilt University (U.S.A), Ministry of Education, Culture, Sports, Science, and Technology and the Japan Society for the Promotion of Science (Japan), Conselho Nacional de Desenvolvimento Científico e Tecnológico and Fundação de Amparo à Pesquisa do Estado de São Paulo (Brazil), Natural Science Foundation of China (People's Republic of China), Centre National de la Recherche Scientifique, Commissariatà l'Énergie Atomique, Institut National de Physique Nucléaire et de Physique des Particules, and Institut National de Physique Nucléaire et de Physique des Particules (France), Bundesministerium für Bildung und Forschung, Deutscher Akademischer Austausch Dienst, and Alexander von Humboldt Stiftung (Germany), Hungarian National Science Fund, OTKA (Hungary), Department of Atomic Energy and Department of Science and Technology (India), Israel Science Foundation (Israel), Korea Research Foundation and Center for High Energy Physics (Korea), Russian Ministry of Industry, Science and Tekhnologies, Russian Academy of Science, Russian Ministry of Atomic Energy (Russia), VR and the Wallenberg Foundation (Sweden), the U.S. Civilian Research and Development Foundation for the Independent States of the Former Soviet Union, the US–Hungarian NSF-OTKA-MTA, the US–Israel Binational Science Foundation, and the 5th European Union TMR Marie-Curie Programme.

APPENDIX A: DEFINITION OF CORRELATION LENGTH AND SUSCEPTIBILITY IN THE GINZBURG-LANDAU FRAMEWORK

The Ginzburg-Landau (GL) [19] framework with the Ornstein-Zernike picture [18] for a scalar-order parameter is briefly reviewed. The relations with correlation length and susceptibility are explicitly derived in this appendix.

The first attempt to apply free energy discussions to nucleus-nucleus collisions can be found in Ref. [44]; application to the QCD phase transition is in Ref. [25]. The GL framework describes the relation between a free energy density f and an order parameter ϕ as a function of the system temperature T. By adding a spatially inhomogeneous term $A(T)(\nabla\phi)^2$ and an external field h, the general form is described as follows:

$$f(T,\phi,h) = f_0(T) + \tfrac{1}{2}A(T)(\nabla\phi)^2 + \tfrac{1}{2}a(T)\phi^2 + \tfrac{1}{4}b\phi^4 + \cdots - h\phi, \tag{A1}$$

where f_0 is the equilibrium value of the free energy, terms with odd powers are neglected owing to the symmetry of the order parameter, and the sign of b is used to classify the transition orders: $b < 0$ for the first order, $b > 0$ for the second order, and $b = 0$ at the critical point. Since the order parameter should vanish above a critical temperature T_c, it is natural for the coefficient $a(T)$ to be expressed as $a(T) = a_0|T - T_c|$, while b is usually assumed to be constant in the vicinity of T_c. In the following, we neglect higher order terms beyond second order. This approximation corresponds to a picture where a system approaches the phase boundary from afar, since ϕ is close to zero in the regions far from T_c. In this sense, the approximation is insensitive to the details of the phase transition order (i.e., higher order terms), being only sensitive to the behavior near T_c.

We apply this GL framework to density correlations in the longitudinal space coordinate z in heavy-ion collisions. The system of the produced matter dynamically evolves, so we introduce the proper time frame for each subelement. The longitudinal space element becomes $dz = \tau\cosh(y)dy$, at a fixed proper time τ, where y is rapidity, as introduced in Ref. [23]. Since we measure the density fluctuations in the mid-rapidity regions $|\eta| < 0.35$ as described in Sec. III, we use dy in place of dz by the approximation $\cosh(y) \approx 1$ to simplify the form of the correlation function derived from GL free energy.

The order parameter of this analysis corresponds to multiplicity density fluctuations of inclusive charged particles around the mean density. Fluctuations are measured as a function of a one-dimensional pseudorapidity point η, defined as

$$\phi(\eta) = \rho(\eta) - \langle\rho(\eta)\rangle, \tag{A2}$$

where the pair of brackets indicates an operator to take the average. In the rapidity region under consideration, rapidity can be represented by pseudorapidity to a good approximation, as explained in the last paragraph of Sec. IV B.

With the Fourier expansion of the density fluctuation at pseudorapidity point η, $\phi(\eta) = \sum_\omega \phi_\omega e^{i\omega\eta}$, where ω is wave number, one can express the deviation of the free energy density due to spatial fluctuations from the equilibrium value f_0 as

$$\Delta F/Y = \frac{1}{Y}\int (f - f_0)d\eta = \frac{1}{2}\sum_\omega |\phi_\omega|^2[a(T) + A(T)\omega^2], \tag{A3}$$

where Y is the total pseudorapidity range corresponding to a one-dimensional volume. Terms up to the second order are included in the approximation in the vicinity of the critical point in Eq. (A1). Given the free energy deviation, one can obtain the statistical weight w for fluctuation $\phi(\eta)$ to occur in a given temperature T as

$$W[\phi(\eta)] = Ne^{-\Delta F/T}. \tag{A4}$$

Therefore the statistical average of the square of the density fluctuation with the wave number ω is described as

$$\langle|\phi_\omega|^2\rangle = \int_{-\infty}^{+\infty} |\phi_\omega|^2 W\left(\sum_\omega \phi_\omega e^{i\omega\eta}\right) d\phi_\omega = \frac{NT}{Y}\frac{1}{a(T) + A(T)\omega^2}. \tag{A5}$$

An experimentally observable two-point density correlation function can be related to the statistical average of the square of the density fluctuation. With a density $\rho(\eta_i)$ for a given subvolume $d\eta_i$, the two-point density correlation G_2 is expressed in the case of $\langle\rho(\eta_1)\rangle = \langle\rho(\eta_2)\rangle = \langle\rho\rangle$ as

$$G_2(\eta_1,\eta_2) = \langle[\rho(\eta_1) - \langle\rho\rangle][\rho(\eta_2) - \langle\rho\rangle]\rangle, \tag{A6}$$

where case 1 coinciding with case 2 is excluded to simplify the following discussion. Multiplying both sides of Eq. (A6) by $e^{-i\omega\eta} \equiv e^{-i\omega(\eta_2-\eta_1)}$ and integrating over subvolumes $d\eta_1$ and $d\eta_2$ gives

$$Y\int G_2(\eta)e^{-i\omega\eta}d\eta = \langle|\int[\rho(\eta) - \langle\rho\rangle]e^{-i\omega\eta}d\eta|^2\rangle = \langle|\phi_\omega|^2\rangle. \tag{A7}$$

From Eqs. (A5) and (A7), G_2 can be related to the inverse Fourier transformation of the statistical average of $|\phi_\omega|^2$. Therefore in the one-dimensional case G_2 is described as

$$G_2(\eta) = \frac{NT}{2Y^2A(T)}\xi(T)e^{-|\eta|/\xi(T)}, \tag{A8}$$

where the correlation length $\xi(T)$ is introduced, which is defined as

$$\xi(T)^2 = \frac{A(T)}{a_0|T - T_c|}. \tag{A9}$$

In general, a singular behavior of $\xi(T)$ as a function of T indicates the critical temperature of the phase transition.

The wave-number-dependent susceptibility can also be defined from the expansion of the GL free energy based on

Eqs. (A1) and (A3) as follows:

$$\chi_\omega = -\left(\frac{\partial^2 f}{\partial h^2}\right) = \left(\frac{\partial h}{\partial \phi_\omega}\right)^{-1} = \left(\frac{\partial^2(\Delta F/Y)}{\partial \phi_\omega^2}\right)^{-1} = \frac{1}{a_0|T - T_c|[1 + \omega^2 \xi(T)^2]}. \quad \text{(A10)}$$

In the long-wavelength limit of $\omega = 0$, the susceptibility can be expressed as

$$\chi_{\omega=0} = \frac{1}{a_0|T - T_c|} = \frac{2Y^2}{NT}\xi(T)G_2(0). \quad \text{(A11)}$$

In this framework, the ξ and $\chi_{\omega=0}$ diverge at the same temperature.

APPENDIX B: TABLES OF NBD FIT RESULTS

NBD fit results in all window sizes in all centrality bins are shown in Fig. 4. Tables III–XIV and Tables XV–XXVII list results in 10% and 5% bin width cases, respectively. $\langle \mu_c \rangle$ and $\langle \mu \rangle$ are weighted means of corrected and uncorrected μ over all window positions, respectively. $\langle k_c \rangle$ and $\langle k \rangle$ are weighted means of corrected and uncorrected k over all window positions, respectively. Statistical errors on weighted means $\delta\langle k_c \rangle$ (stat) are obtained as explained in Sec. IV F. $\langle \chi^2/NDF \rangle$ is the average of reduced χ^2 of NBD fits over all window positions. $\langle NDF \rangle$ is the average of the degree of freedom of NBD fits over all window positions. Systematic errors $\delta\langle k_c \rangle$ (dead), $\delta\langle k_c \rangle$(fake), and $\delta\langle k_c \rangle$ (total) are explained in Sec. IV F.

TABLE III. NBD fit results in centrality 0–10%.

$\delta\eta$	$\langle \mu_c \rangle(\langle \mu \rangle)$	$\langle k_c \rangle(\langle k \rangle)$	$\langle \chi^2/NDF \rangle(\langle NDF \rangle)$	$\delta\langle k_c \rangle$ (dead)	$\delta\langle k_c \rangle$ (fake)	$\delta\langle k_c \rangle$ (total)
0.700	77.535(60.011) ± 0.108	114.28(88.45) ± 3.21	0.96(71.0)	±2.89	±2.28	±4.89
0.678	75.445(58.445) ± 0.106	113.11(87.62) ± 3.29	0.89(69.7)	±4.92	±3.31	±6.78
0.656	72.977(56.455) ± 0.103	114.40(88.50) ± 3.38	0.95(68.2)	±4.33	±3.04	±6.28
0.634	70.485(54.450) ± 0.101	114.02(88.08) ± 3.42	0.92(66.7)	±4.54	±3.01	±6.43
0.613	67.998(52.489) ± 0.099	114.44(88.33) ± 3.52	0.94(65.3)	±3.79	±2.31	±5.66
0.591	65.530(50.572) ± 0.096	114.28(88.18) ± 3.60	0.95(63.9)	±3.59	±2.62	±5.72
0.569	63.050(48.609) ± 0.094	114.62(88.35) ± 3.71	0.97(62.3)	±3.88	±2.80	±6.05
0.547	60.569(46.624) ± 0.091	114.27(87.94) ± 3.80	0.96(60.8)	±3.61	±2.98	±6.03
0.525	58.100(44.655) ± 0.089	114.38(87.89) ± 3.92	0.95(59.7)	±3.79	±2.87	±6.16
0.503	55.637(42.682) ± 0.086	114.36(87.70) ± 4.03	0.93(57.8)	±3.64	±3.17	±6.29
0.481	53.164(40.688) ± 0.084	114.41(87.54) ± 4.17	0.94(56.3)	±4.24	±3.40	±6.85
0.459	50.682(38.672) ± 0.081	115.19(87.87) ± 4.35	0.98(54.2)	±4.10	±3.14	±6.75
0.438	48.209(36.654) ± 0.079	114.89(87.33) ± 4.51	0.98(52.4)	±4.49	±3.72	±7.37
0.416	45.743(34.645) ± 0.076	115.05(87.11) ± 4.71	0.98(50.3)	±4.79	±3.49	±7.57
0.394	43.283(32.654) ± 0.074	114.86(86.61) ± 4.90	0.97(48.3)	±4.37	±4.15	±7.77
0.372	40.838(30.677) ± 0.071	115.20(86.46) ± 5.17	1.00(46.2)	±4.22	±4.10	±7.83
0.350	38.424(28.782) ± 0.049	115.87(86.69) ± 3.88	1.04(44.5)	±3.81	±4.22	±6.88
0.328	36.034(27.062) ± 0.047	115.35(86.43) ± 4.04	1.04(42.9)	±4.04	±4.58	±7.32
0.306	33.665(25.363) ± 0.045	114.46(86.00) ± 4.21	1.08(41.2)	±4.28	±4.89	±7.74
0.284	31.288(23.638) ± 0.043	113.91(85.92) ± 4.39	1.09(39.9)	±3.60	±5.13	±7.65
0.263	28.916(21.900) ± 0.041	111.53(84.56) ± 4.51	1.10(37.9)	±3.75	±5.29	±7.90
0.241	26.542(20.145) ± 0.039	109.53(83.35) ± 4.67	1.08(36.3)	±3.71	±5.40	±8.04
0.219	24.155(18.360) ± 0.030	107.67(82.28) ± 4.03	1.11(34.4)	±3.66	±5.96	±8.07
0.197	21.758(16.553) ± 0.028	105.84(80.90) ± 4.29	1.15(32.4)	±3.17	±6.12	±8.12
0.175	19.355(14.723) ± 0.023	102.63(78.59) ± 3.96	1.21(30.1)	±3.59	±6.85	±8.69
0.153	16.948(12.880) ± 0.021	97.91(75.16) ± 4.19	1.25(27.6)	±3.83	±6.93	±8.96
0.131	14.536(11.031) ± 0.017	93.93(72.13) ± 4.01	1.34(24.9)	±3.77	±7.03	±8.93
0.109	12.119(9.172) ± 0.014	87.92(66.93) ± 3.81	1.39(21.9)	±3.48	±7.30	±8.94
0.087	9.695(7.305) ± 0.011	78.94(58.95) ± 3.35	1.34(18.7)	±3.48	±7.34	±8.79
0.066	7.308(5.685) ± 0.008	65.53(49.27) ± 2.87	1.09(15.4)	±4.05	±6.83	±8.45

TABLE IV. NBD fit results in centrality 5–15%.

$\delta\eta$	$\langle\mu_c\rangle(\langle\mu\rangle)$	$\langle k_c\rangle(\langle k\rangle)$	$\langle\chi^2/NDF\rangle(\langle NDF\rangle)$	$\delta\langle k_c\rangle$ (dead)	$\delta\langle k_c\rangle$ (fake)	$\delta\langle k_c\rangle$ (total)
0.700	66.445(51.428) ± 0.098	80.80(62.54) ± 1.92	1.20(68.0)	±2.14	±2.17	±3.60
0.678	64.658(50.089) ± 0.097	80.40(62.28) ± 1.95	1.15(66.4)	±3.40	±1.53	±4.21
0.656	62.535(48.377) ± 0.094	81.17(62.79) ± 1.99	1.20(65.0)	±2.28	±1.11	±3.22
0.634	60.379(46.644) ± 0.092	81.10(62.65) ± 2.02	1.23(64.1)	±2.24	±1.57	±3.40
0.613	58.258(44.970) ± 0.090	80.61(62.21) ± 2.06	1.21(62.4)	±2.75	±1.43	±3.72
0.591	56.156(43.337) ± 0.088	79.66(61.47) ± 2.08	1.12(60.6)	±2.85	±1.50	±3.83
0.569	54.043(41.665) ± 0.085	79.26(61.09) ± 2.12	1.07(59.2)	±2.59	±1.88	±3.83
0.547	51.923(39.968) ± 0.083	78.98(60.79) ± 2.17	1.09(57.4)	±2.90	±1.68	±3.99
0.525	49.809(38.283) ± 0.081	79.14(60.81) ± 2.23	1.11(56.2)	±2.83	±1.88	±4.07
0.503	47.691(36.586) ± 0.078	79.62(61.06) ± 2.32	1.13(54.7)	±2.15	±1.91	±3.69
0.481	45.573(34.878) ± 0.076	79.66(60.95) ± 2.39	1.13(53.0)	±2.35	±1.59	±3.71
0.459	43.446(33.150) ± 0.073	80.40(61.33) ± 2.48	1.18(51.3)	±2.25	±1.70	±3.76
0.438	41.327(31.420) ± 0.071	79.99(60.80) ± 2.56	1.15(49.4)	±2.84	±2.29	±4.46
0.416	39.211(29.696) ± 0.069	80.34(60.83) ± 2.67	1.18(47.7)	±2.98	±2.03	±4.49
0.394	37.107(27.993) ± 0.067	80.40(60.62) ± 2.79	1.15(45.9)	±3.24	±2.36	±4.88
0.372	35.007(26.295) ± 0.064	80.45(60.38) ± 2.92	1.18(43.9)	±3.19	±2.29	±4.89
0.350	32.938(24.672) ± 0.044	80.58(60.28) ± 2.17	1.21(42.1)	±3.22	±2.23	±4.48
0.328	30.889(23.196) ± 0.042	80.09(60.08) ± 2.25	1.22(40.3)	±3.29	±2.71	±4.82
0.306	28.861(21.741) ± 0.040	79.49(59.81) ± 2.33	1.22(38.6)	±3.21	±2.56	±4.73
0.284	26.832(20.270) ± 0.038	79.11(59.73) ± 2.44	1.24(37.0)	±2.85	±2.87	±4.72
0.263	24.795(18.778) ± 0.036	78.06(59.22) ± 2.55	1.23(35.3)	±3.01	±3.26	±5.12
0.241	22.758(17.270) ± 0.035	77.16(58.82) ± 2.68	1.22(33.8)	±2.93	±3.39	±5.22
0.219	20.708(15.737) ± 0.026	76.33(58.44) ± 2.32	1.27(32.1)	±2.56	±3.09	±4.64
0.197	18.654(14.187) ± 0.025	75.26(57.80) ± 2.47	1.29(30.2)	±2.84	±3.67	±5.26
0.175	16.591(12.614) ± 0.020	73.89(56.91) ± 2.30	1.36(28.1)	±2.74	±3.58	±5.06
0.153	14.526(11.035) ± 0.019	71.68(55.18) ± 2.44	1.41(25.9)	±2.84	±3.97	±5.46
0.131	12.458(9.451) ± 0.015	69.08(53.03) ± 2.31	1.47(23.1)	±2.81	±4.10	±5.48
0.109	10.385(7.857) ± 0.013	65.32(49.65) ± 2.23	1.46(20.3)	±2.92	±4.28	±5.64
0.087	8.306(6.253) ± 0.010	59.45(44.57) ± 2.03	1.29(17.4)	±2.58	±4.32	±5.43
0.066	6.262(4.870) ± 0.007	51.33(38.86) ± 1.88	0.89(14.4)	±2.75	±4.18	±5.34

TABLE V. NBD fit results in centrality 10–20%.

$\delta\eta$	$\langle\mu_c\rangle(\langle\mu\rangle)$	$\langle k_c\rangle(\langle k\rangle)$	$\langle\chi^2/NDF\rangle(\langle NDF\rangle)$	$\delta\langle k_c\rangle$ (dead)	$\delta\langle k_c\rangle$ (fake)	$\delta\langle k_c\rangle$ (total)
0.700	55.290(42.794) ± 0.090	63.58(49.21) ± 1.47	1.14(64.0)	±0.37	±0.57	±1.62
0.678	53.832(41.701) ± 0.089	62.10(48.11) ± 1.46	0.93(63.1)	±2.48	±2.60	±3.88
0.656	52.092(40.299) ± 0.087	61.78(47.79) ± 1.48	0.88(62.3)	±2.34	±1.54	±3.17
0.634	50.301(38.858) ± 0.085	61.91(47.82) ± 1.51	0.90(60.3)	±2.06	±1.23	±2.83
0.613	48.533(37.463) ± 0.082	61.80(47.70) ± 1.54	0.88(58.5)	±2.10	±1.09	±2.83
0.591	46.769(36.093) ± 0.080	62.00(47.85) ± 1.58	0.90(57.9)	±1.74	±1.21	±2.64
0.569	45.006(34.698) ± 0.078	61.89(47.71) ± 1.61	0.87(56.6)	±1.77	±1.06	±2.62
0.547	43.255(33.296) ± 0.076	61.70(47.49) ± 1.65	0.88(55.1)	±1.80	±1.34	±2.78
0.525	41.499(31.895) ± 0.074	61.86(47.55) ± 1.70	0.89(53.8)	±1.95	±1.21	±2.86
0.503	39.742(30.488) ± 0.072	61.94(47.51) ± 1.75	0.90(52.4)	±1.89	±1.38	±2.92
0.481	37.976(29.063) ± 0.070	61.92(47.38) ± 1.80	0.90(50.8)	±1.84	±1.26	±2.87
0.459	36.206(27.625) ± 0.067	61.91(47.24) ± 1.85	0.91(48.8)	±1.84	±1.46	±2.99
0.438	34.435(26.179) ± 0.065	61.83(47.01) ± 1.91	0.91(47.2)	±1.91	±1.55	±3.12
0.416	32.667(24.739) ± 0.063	62.02(46.98) ± 1.99	0.95(45.6)	±1.96	±1.63	±3.23
0.394	30.908(23.315) ± 0.061	62.18(46.92) ± 2.07	1.00(43.8)	±2.02	±1.58	±3.30
0.372	29.156(21.898) ± 0.059	62.35(46.85) ± 2.16	1.02(42.1)	±2.14	±1.69	±3.48
0.350	27.434(20.547) ± 0.040	62.21(46.61) ± 1.59	1.02(40.4)	±2.30	±1.77	±3.31
0.328	25.727(19.316) ± 0.038	61.90(46.54) ± 1.64	1.06(38.6)	±2.05	±1.66	±3.11
0.306	24.039(18.105) ± 0.037	61.43(46.42) ± 1.71	1.09(36.8)	±2.09	±1.68	±3.17
0.284	22.347(16.876) ± 0.035	60.84(46.18) ± 1.77	1.10(35.1)	±2.30	±1.84	±3.44
0.263	20.653(15.635) ± 0.033	60.20(45.91) ± 1.85	1.12(33.3)	±2.19	±1.93	±3.45

TABLE V. (*Continued*.)

$\delta\eta$	$\langle\mu_c\rangle(\langle\mu\rangle)$	$\langle k_c\rangle(\langle k\rangle)$	$\langle\chi^2/NDF\rangle(\langle NDF\rangle)$	$\delta\langle k_c\rangle$ (dead)	$\delta\langle k_c\rangle$ (fake)	$\delta\langle k_c\rangle$ (total)
0.241	18.956(14.380) ± 0.032	59.81(45.79) ± 1.95	1.19(31.6)	±2.27	±1.91	±3.54
0.219	17.251(13.105) ± 0.024	59.09(45.44) ± 1.68	1.22(29.7)	±2.19	±2.04	±3.43
0.197	15.537(11.813) ± 0.023	58.31(44.99) ± 1.78	1.25(27.6)	±2.23	±2.11	±3.55
0.175	13.816(10.501) ± 0.018	57.38(44.38) ± 1.65	1.31(25.5)	±1.84	±2.17	±3.29
0.153	12.090(9.179) ± 0.017	55.59(43.04) ± 1.75	1.33(23.0)	±1.77	±2.18	±3.31
0.131	10.367(7.858) ± 0.014	52.81(40.76) ± 1.63	1.27(20.6)	±1.83	±2.31	±3.36
0.109	8.639(6.528) ± 0.011	49.83(38.38) ± 1.57	1.14(18.2)	±1.85	±2.55	±3.52
0.087	6.909(5.194) ± 0.009	46.30(35.28) ± 1.45	0.97(15.6)	±1.82	±2.85	±3.68
0.066	5.215(4.052) ± 0.007	42.21(32.18) ± 1.43	0.75(13.0)	±2.04	±2.90	±3.82

TABLE VI. NBD fit results in centrality 15–25%.

$\delta\eta$	$\langle\mu_c\rangle(\langle\mu\rangle)$	$\langle k_c\rangle(\langle k\rangle)$	$\langle\chi^2/NDF\rangle(\langle NDF\rangle)$	$\delta\langle k_c\rangle$ (dead)	$\delta\langle k_c\rangle$ (fake)	$\delta\langle k_c\rangle$ (total)
0.700	45.868(35.502) ± 0.082	53.43(41.35) ± 1.25	1.06(57.0)	±1.83	±1.78	±2.85
0.678	44.657(34.594) ± 0.080	53.48(41.43) ± 1.29	0.95(55.3)	±1.49	±0.53	±2.04
0.656	43.211(33.428) ± 0.078	53.45(41.35) ± 1.31	0.98(54.2)	±1.53	±0.71	±2.14
0.634	41.737(32.242) ± 0.076	53.70(41.48) ± 1.35	0.96(53.0)	±1.43	±0.58	±2.05
0.613	40.288(31.098) ± 0.075	53.41(41.23) ± 1.38	0.92(51.2)	±1.94	±1.12	±2.63
0.591	38.829(29.965) ± 0.073	53.66(41.42) ± 1.42	0.96(50.3)	±1.71	±0.70	±2.33
0.569	37.368(28.808) ± 0.071	53.48(41.23) ± 1.45	0.94(49.0)	±1.76	±0.82	±2.42
0.547	35.911(27.642) ± 0.069	53.32(41.04) ± 1.48	0.91(47.6)	±1.77	±0.88	±2.47
0.525	34.454(26.481) ± 0.067	53.41(41.05) ± 1.52	0.95(46.1)	±1.75	±0.76	±2.44
0.503	32.995(25.311) ± 0.065	53.58(41.11) ± 1.56	1.02(44.9)	±1.50	±0.81	±2.31
0.481	31.532(24.131) ± 0.063	53.73(41.13) ± 1.61	1.02(44.0)	±1.50	±0.66	±2.29
0.459	30.062(22.936) ± 0.061	53.65(40.95) ± 1.65	1.02(42.8)	±1.57	±0.86	±2.44
0.438	28.591(21.736) ± 0.059	53.69(40.84) ± 1.71	1.03(41.4)	±1.70	±0.87	±2.57
0.416	27.125(20.541) ± 0.057	53.76(40.75) ± 1.78	1.04(40.0)	±1.71	±0.84	±2.61
0.394	25.664(19.358) ± 0.055	53.81(40.64) ± 1.84	1.03(38.5)	±1.78	±1.07	±2.78
0.372	24.206(18.179) ± 0.053	54.03(40.64) ± 1.93	1.05(37.1)	±1.71	±1.02	±2.77
0.350	22.778(17.058) ± 0.036	54.05(40.55) ± 1.42	1.09(35.7)	±1.94	±1.07	±2.63
0.328	21.359(16.035) ± 0.035	53.79(40.53) ± 1.48	1.12(34.5)	±1.74	±1.02	±2.50
0.306	19.955(15.027) ± 0.033	53.36(40.43) ± 1.54	1.14(33.2)	±1.74	±1.09	±2.57
0.284	18.552(14.008) ± 0.032	52.52(40.03) ± 1.59	1.16(31.7)	±1.78	±1.17	±2.66
0.263	17.146(12.979) ± 0.030	51.86(39.73) ± 1.66	1.19(29.9)	±1.63	±1.17	±2.60
0.241	15.736(11.936) ± 0.029	51.03(39.31) ± 1.74	1.25(28.0)	±1.53	±1.28	±2.65
0.219	14.320(10.876) ± 0.022	49.80(38.58) ± 1.48	1.26(26.0)	±1.69	±1.32	±2.60
0.197	12.897(9.802) ± 0.021	48.78(37.96) ± 1.57	1.26(24.1)	±1.43	±1.39	±2.53
0.175	11.465(8.711) ± 0.017	47.43(37.04) ± 1.43	1.26(22.3)	±1.39	±1.30	±2.38
0.153	10.030(7.612) ± 0.015	45.48(35.65) ± 1.51	1.21(20.2)	±1.13	±1.41	±2.36
0.131	8.597(6.513) ± 0.013	43.13(33.84) ± 1.41	1.06(18.1)	±1.27	±1.55	±2.45
0.109	7.163(5.409) ± 0.011	40.33(31.64) ± 1.34	0.79(15.9)	±1.21	±1.67	±2.45
0.087	5.730(4.304) ± 0.008	37.88(29.64) ± 1.27	0.64(13.7)	±1.15	±1.77	±2.47
0.066	4.327(3.360) ± 0.006	35.48(27.59) ± 1.28	0.54(11.6)	±1.20	±1.96	±2.63

TABLE VII. NBD fit results in centrality 20–30%.

$\delta\eta$	$\langle\mu_c\rangle(\langle\mu\rangle)$	$\langle k_c\rangle(\langle k\rangle)$	$\langle\chi^2/NDF\rangle(\langle NDF\rangle)$	$\delta\langle k_c\rangle$ (dead)	$\delta\langle k_c\rangle$ (fake)	$\delta\langle k_c\rangle$ (total)
0.700	37.610(29.110) ± 0.073	47.51(36.77) ± 1.17	0.82(53.0)	±1.28	±0.76	±1.89
0.678	36.606(28.358) ± 0.072	47.66(36.92) ± 1.20	0.86(51.7)	±1.61	±0.68	±2.12
0.656	35.403(27.388) ± 0.070	47.76(36.94) ± 1.22	0.83(51.4)	±1.10	±0.43	±1.70
0.634	34.199(26.419) ± 0.069	47.45(36.66) ± 1.24	0.83(50.2)	±1.54	±0.65	±2.08
0.613	33.002(25.474) ± 0.067	47.80(36.90) ± 1.27	0.97(49.3)	±0.99	±0.68	±1.75

TABLE VII. (*Continued*.)

$\delta\eta$	$\langle\mu_c\rangle(\langle\mu\rangle)$	$\langle k_c\rangle(\langle k\rangle)$	$\langle\chi^2/NDF\rangle(\langle NDF\rangle)$	$\delta\langle k_c\rangle$ (dead)	$\delta\langle k_c\rangle$ (fake)	$\delta\langle k_c\rangle$ (total)
0.591	31.812(24.550) ± 0.065	47.37(36.56) ± 1.28	0.96(48.6)	±1.29	±0.62	±1.92
0.569	30.609(23.598) ± 0.063	47.42(36.56) ± 1.31	0.93(47.7)	±1.12	±0.51	±1.80
0.547	29.413(22.641) ± 0.062	47.14(36.29) ± 1.34	0.92(46.0)	±1.26	±0.68	±1.96
0.525	28.218(21.688) ± 0.060	47.13(36.23) ± 1.37	0.94(44.8)	±1.38	±0.66	±2.05
0.503	27.021(20.729) ± 0.058	47.16(36.19) ± 1.41	0.98(43.6)	±1.29	±0.53	±1.98
0.481	25.823(19.762) ± 0.057	47.14(36.08) ± 1.45	0.98(42.2)	±1.40	±0.52	±2.08
0.459	24.623(18.787) ± 0.055	47.14(35.98) ± 1.50	0.98(41.1)	±1.37	±0.57	±2.11
0.438	23.421(17.806) ± 0.053	46.88(35.66) ± 1.54	0.95(39.4)	±1.53	±0.68	±2.28
0.416	22.218(16.826) ± 0.051	47.13(35.72) ± 1.61	1.02(38.0)	±1.42	±0.55	±2.21
0.394	21.024(15.858) ± 0.050	46.86(35.38) ± 1.67	0.99(36.6)	±1.61	±0.68	±2.42
0.372	19.831(14.894) ± 0.048	46.92(35.28) ± 1.74	1.00(35.1)	±1.60	±0.78	±2.49
0.350	18.658(13.973) ± 0.033	46.79(35.08) ± 1.29	1.02(33.7)	±1.63	±0.83	±2.23
0.328	17.499(13.138) ± 0.031	46.40(34.90) ± 1.33	1.02(32.1)	±1.63	±0.79	±2.25
0.306	16.350(12.314) ± 0.030	46.22(34.90) ± 1.40	1.07(30.6)	±1.72	±0.73	±2.33
0.284	15.201(11.480) ± 0.029	45.61(34.60) ± 1.45	1.06(29.0)	±1.56	±0.82	±2.28
0.263	14.048(10.636) ± 0.027	44.99(34.29) ± 1.51	1.06(27.4)	±1.65	±0.90	±2.41
0.241	12.892(9.781) ± 0.026	44.22(33.84) ± 1.58	1.07(25.6)	±1.54	±0.91	±2.39
0.219	11.729(8.913) ± 0.020	43.26(33.22) ± 1.34	1.05(24.0)	±1.36	±0.93	±2.13
0.197	10.561(8.032) ± 0.019	42.28(32.55) ± 1.41	1.05(22.4)	±1.30	±0.95	±2.14
0.175	9.389(7.139) ± 0.015	41.04(31.68) ± 1.29	0.96(20.4)	±1.26	±0.96	±2.04
0.153	8.216(6.239) ± 0.014	39.50(30.60) ± 1.36	0.83(18.6)	±1.18	±1.13	±2.13
0.131	7.045(5.342) ± 0.012	38.08(29.47) ± 1.31	0.68(16.6)	±1.07	±1.20	±2.08
0.109	5.871(4.439) ± 0.009	36.53(28.20) ± 1.30	0.54(14.7)	±1.08	±1.31	±2.14
0.087	4.697(3.532) ± 0.007	35.06(27.06) ± 1.31	0.51(12.4)	±1.03	±1.57	±2.29
0.066	3.547(2.756) ± 0.005	32.64(25.34) ± 1.37	0.46(10.4)	±1.02	±1.72	±2.42

TABLE VIII. NBD fit results in centrality 25–35%.

$\delta\eta$	$\langle\mu_c\rangle(\langle\mu\rangle)$	$\langle k_c\rangle(\langle k\rangle)$	$\langle\chi^2/NDF\rangle(\langle NDF\rangle)$	$\delta\langle k_c\rangle$ (dead)	$\delta\langle k_c\rangle$ (fake)	$\delta\langle k_c\rangle$ (total)
0.700	30.796(23.836) ± 0.065	41.09(31.80) ± 1.05	0.77(48.0)	±1.99	±0.38	±2.28
0.678	29.940(23.193) ± 0.063	41.40(32.07) ± 1.06	0.83(48.9)	±1.53	±0.13	±1.87
0.656	28.970(22.412) ± 0.062	41.18(31.85) ± 1.07	0.81(47.9)	±1.52	±0.55	±1.94
0.634	27.967(21.605) ± 0.060	41.07(31.73) ± 1.09	0.84(46.8)	±1.36	±0.47	±1.81
0.613	26.977(20.823) ± 0.059	40.97(31.62) ± 1.11	0.85(45.4)	±1.15	±0.55	±1.69
0.591	26.003(20.068) ± 0.058	40.72(31.42) ± 1.12	0.88(44.1)	±1.23	±0.36	±1.71
0.569	25.020(19.289) ± 0.056	40.64(31.33) ± 1.15	0.89(42.6)	±1.43	±0.53	±1.91
0.547	24.036(18.502) ± 0.055	40.41(31.11) ± 1.17	0.91(41.1)	±1.35	±0.55	±1.87
0.525	23.058(17.722) ± 0.053	40.37(31.03) ± 1.20	0.91(40.0)	±1.37	±0.44	±1.87
0.503	22.086(16.943) ± 0.052	40.25(30.88) ± 1.23	0.90(38.8)	±1.54	±0.55	±2.05
0.481	21.108(16.155) ± 0.050	40.05(30.66) ± 1.26	0.91(37.2)	±1.56	±0.48	±2.07
0.459	20.126(15.356) ± 0.049	40.00(30.53) ± 1.30	0.92(35.9)	±1.59	±0.39	±2.09
0.438	19.143(14.554) ± 0.047	39.77(30.26) ± 1.34	0.92(34.6)	±1.62	±0.42	±2.15
0.416	18.163(13.755) ± 0.046	39.51(29.96) ± 1.38	0.88(33.3)	±1.70	±0.52	±2.25
0.394	17.184(12.962) ± 0.044	39.36(29.73) ± 1.44	0.91(31.8)	±1.72	±0.50	±2.29
0.372	16.206(12.172) ± 0.043	39.43(29.67) ± 1.50	0.95(30.6)	±1.64	±0.43	±2.27
0.350	15.249(11.420) ± 0.029	39.31(29.50) ± 1.11	0.98(29.2)	±1.63	±0.51	±2.04
0.328	14.299(10.736) ± 0.028	38.92(29.31) ± 1.14	1.00(27.9)	±1.55	±0.53	±2.00
0.306	13.362(10.063) ± 0.027	38.24(28.93) ± 1.18	0.97(26.5)	±1.56	±0.56	±2.04
0.284	12.422(9.381) ± 0.026	37.66(28.62) ± 1.22	0.95(25.2)	±1.48	±0.63	±2.02
0.263	11.476(8.689) ± 0.024	37.27(28.42) ± 1.28	0.97(23.9)	±1.35	±0.59	±1.95
0.241	10.531(7.990) ± 0.023	36.55(27.96) ± 1.33	0.91(22.4)	±1.35	±0.60	±1.99
0.219	9.581(7.281) ± 0.018	35.75(27.42) ± 1.13	0.78(21.0)	±1.21	±0.67	±1.78
0.197	8.626(6.560) ± 0.017	35.01(26.95) ± 1.19	0.73(19.3)	±1.15	±0.74	±1.81
0.175	7.670(5.832) ± 0.013	34.26(26.41) ± 1.09	0.63(17.6)	±1.20	±0.74	±1.78

TABLE VIII. (*Continued*.)

$\delta\eta$	$\langle\mu_c\rangle(\langle\mu\rangle)$	$\langle k_c\rangle(\langle k\rangle)$	$\langle\chi^2/NDF\rangle(\langle NDF\rangle)$	$\delta\langle k_c\rangle$ (dead)	$\delta\langle k_c\rangle$ (fake)	$\delta\langle k_c\rangle$ (total)
0.153	$6.712(5.099)\pm0.013$	$33.65(25.96)\pm1.19$	0.59(16.0)	±1.12	±0.82	±1.82
0.131	$5.756(4.365)\pm0.010$	$32.98(25.42)\pm1.16$	0.53(14.3)	±0.98	±0.85	±1.74
0.109	$4.800(3.629)\pm0.009$	$31.80(24.50)\pm1.17$	0.48(12.4)	±1.01	±0.95	±1.82
0.087	$3.841(2.888)\pm0.006$	$30.92(23.78)\pm1.17$	0.54(10.7)	±0.94	±1.11	±1.87
0.066	$2.902(2.255)\pm0.005$	$28.55(22.23)\pm1.20$	0.47(9.0)	±0.98	±1.24	±1.98

TABLE IX. NBD fit results in centrality 30–40%.

$\delta\eta$	$\langle\mu_c\rangle(\langle\mu\rangle)$	$\langle k_c\rangle(\langle k\rangle)$	$\langle\chi^2/NDF\rangle(\langle NDF\rangle)$	$\delta\langle k_c\rangle$ (dead)	$\delta\langle k_c\rangle$ (fake)	$\delta\langle k_c\rangle$ (total)
0.700	$24.860(19.241)\pm0.058$	$34.21(26.48)\pm0.88$	0.75(47.0)	±1.14	±0.33	±1.47
0.678	$24.177(18.729)\pm0.057$	$34.00(26.34)\pm0.88$	0.77(45.9)	±1.12	±0.30	±1.46
0.656	$23.382(18.088)\pm0.055$	$33.88(26.21)\pm0.90$	0.81(44.2)	±0.91	±0.29	±1.31
0.634	$22.573(17.438)\pm0.054$	$33.73(26.06)\pm0.91$	0.90(42.5)	±1.10	±0.25	±1.45
0.613	$21.776(16.808)\pm0.053$	$33.63(25.96)\pm0.93$	0.94(40.9)	±1.08	±0.27	±1.44
0.591	$20.986(16.195)\pm0.051$	$33.54(25.89)\pm0.94$	0.92(39.8)	±0.97	±0.25	±1.38
0.569	$20.198(15.571)\pm0.050$	$33.46(25.80)\pm0.97$	0.97(38.4)	±1.04	±0.26	±1.44
0.547	$19.406(14.937)\pm0.049$	$33.43(25.74)\pm0.99$	1.01(37.2)	±1.04	±0.24	±1.45
0.525	$18.616(14.307)\pm0.048$	$33.48(25.74)\pm1.02$	1.03(36.0)	±1.04	±0.25	±1.48
0.503	$17.830(13.678)\pm0.046$	$33.37(25.61)\pm1.05$	1.06(34.7)	±1.07	±0.28	±1.52
0.481	$17.040(13.040)\pm0.045$	$33.31(25.51)\pm1.08$	1.03(33.4)	±1.11	±0.28	±1.58
0.459	$16.246(12.395)\pm0.043$	$33.30(25.43)\pm1.12$	1.04(32.2)	±1.03	±0.28	±1.55
0.438	$15.451(11.746)\pm0.042$	$33.14(25.23)\pm1.16$	1.03(31.0)	±1.09	±0.34	±1.63
0.416	$14.662(11.103)\pm0.041$	$32.95(24.99)\pm1.20$	0.97(29.7)	±1.18	±0.38	±1.73
0.394	$13.869(10.461)\pm0.040$	$32.84(24.83)\pm1.25$	0.99(28.4)	±1.21	±0.33	±1.77
0.372	$13.081(9.824)\pm0.038$	$32.69(24.61)\pm1.30$	1.00(26.8)	±1.08	±0.36	±1.73
0.350	$12.306(9.216)\pm0.026$	$32.49(24.40)\pm0.95$	1.00(25.5)	±1.05	±0.35	±1.46
0.328	$11.540(8.663)\pm0.025$	$31.92(24.08)\pm0.98$	0.99(24.2)	±1.05	±0.36	±1.48
0.306	$10.781(8.119)\pm0.024$	$31.35(23.78)\pm1.00$	0.94(23.1)	±1.05	±0.36	±1.49
0.284	$10.020(7.565)\pm0.023$	$30.76(23.49)\pm1.04$	0.91(22.0)	±1.01	±0.35	±1.49
0.263	$9.258(7.008)\pm0.022$	$30.22(23.20)\pm1.07$	0.83(20.8)	±0.93	±0.36	±1.46
0.241	$8.494(6.443)\pm0.021$	$29.75(22.94)\pm1.12$	0.77(19.5)	±0.91	±0.39	±1.49
0.219	$7.727(5.870)\pm0.016$	$29.20(22.62)\pm0.95$	0.70(18.3)	±0.85	±0.37	±1.33
0.197	$6.958(5.290)\pm0.015$	$28.62(22.29)\pm1.01$	0.65(17.0)	±0.76	±0.38	±1.32
0.175	$6.187(4.702)\pm0.012$	$27.94(21.88)\pm0.93$	0.59(15.5)	±0.83	±0.46	±1.33
0.153	$5.416(4.112)\pm0.011$	$27.29(21.40)\pm1.00$	0.50(14.0)	±0.84	±0.56	±1.42
0.131	$4.645(3.520)\pm0.009$	$26.74(20.98)\pm0.99$	0.50(12.5)	±0.81	±0.60	±1.41
0.109	$3.873(2.926)\pm0.008$	$25.80(20.22)\pm1.01$	0.50(10.9)	±0.86	±0.66	±1.48
0.087	$3.098(2.328)\pm0.006$	$24.72(19.40)\pm1.02$	0.54(9.4)	±0.75	±0.74	±1.46
0.066	$2.341(1.819)\pm0.004$	$22.77(17.95)\pm1.02$	0.49(8.0)	±0.64	±0.81	±1.45

TABLE X. NBD fit results in centrality 35–45%.

$\delta\eta$	$\langle\mu_c\rangle(\langle\mu\rangle)$	$\langle k_c\rangle(\langle k\rangle)$	$\langle\chi^2/NDF\rangle(\langle NDF\rangle)$	$\delta\langle k_c\rangle$ (dead)	$\delta\langle k_c\rangle$ (fake)	$\delta\langle k_c\rangle$ (total)
0.700	$19.726(15.268)\pm0.051$	$29.23(22.62)\pm0.80$	1.12(40.0)	±0.69	±0.09	±1.06
0.678	$19.191(14.867)\pm0.050$	$29.24(22.65)\pm0.81$	1.02(39.0)	±0.58	±0.17	±1.01
0.656	$18.568(14.364)\pm0.049$	$29.05(22.47)\pm0.82$	0.98(38.2)	±0.76	±0.16	±1.13
0.634	$17.920(13.844)\pm0.048$	$29.04(22.43)\pm0.83$	1.09(37.1)	±0.73	±0.13	±1.12
0.613	$17.291(13.348)\pm0.046$	$28.91(22.31)\pm0.85$	1.06(36.2)	±0.77	±0.10	±1.15
0.591	$16.672(12.867)\pm0.045$	$28.64(22.10)\pm0.86$	1.04(35.3)	±0.86	±0.20	±1.23
0.569	$16.044(12.369)\pm0.044$	$28.57(22.02)\pm0.88$	1.06(34.2)	±0.79	±0.18	±1.20
0.547	$15.417(11.867)\pm0.043$	$28.48(21.92)\pm0.90$	1.07(33.3)	±0.91	±0.24	±1.30

TABLE X. (*Continued.*)

$\delta\eta$	$\langle\mu_c\rangle(\langle\mu\rangle)$	$\langle k_c\rangle(\langle k\rangle)$	$\langle\chi^2/NDF\rangle(\langle NDF\rangle)$	$\delta\langle k_c\rangle$ (dead)	$\delta\langle k_c\rangle$ (fake)	$\delta\langle k_c\rangle$ (total)
0.525	14.789(11.366) ± 0.042	28.48(21.89) ± 0.92	1.12(32.2)	±0.88	±0.21	±1.29
0.503	14.165(10.866) ± 0.041	28.36(21.76) ± 0.94	1.10(31.2)	±0.82	±0.21	±1.26
0.481	13.537(10.360) ± 0.040	28.27(21.64) ± 0.97	1.11(29.9)	±0.85	±0.20	±1.31
0.459	12.908(9.849) ± 0.039	28.14(21.47) ± 1.00	1.11(28.8)	±0.92	±0.21	±1.38
0.438	12.276(9.334) ± 0.037	28.00(21.28) ± 1.03	1.10(27.7)	±0.88	±0.23	±1.37
0.416	11.648(8.822) ± 0.036	27.82(21.07) ± 1.06	1.08(26.6)	±0.89	±0.23	±1.40
0.394	11.019(8.313) ± 0.035	27.61(20.83) ± 1.09	1.04(25.5)	±0.96	±0.26	±1.47
0.372	10.391(7.805) ± 0.034	27.49(20.65) ± 1.13	0.98(24.5)	±0.85	±0.26	±1.44
0.350	9.774(7.322) ± 0.023	27.32(20.46) ± 0.83	0.92(23.4)	±0.81	±0.21	±1.18
0.328	9.165(6.883) ± 0.022	26.94(20.23) ± 0.85	0.89(22.4)	±0.75	±0.21	±1.15
0.306	8.562(6.451) ± 0.021	26.60(20.05) ± 0.87	0.86(21.4)	±0.72	±0.16	±1.14
0.284	7.959(6.013) ± 0.020	26.19(19.83) ± 0.90	0.82(20.2)	±0.73	±0.21	±1.18
0.263	7.353(5.569) ± 0.019	25.80(19.62) ± 0.93	0.75(19.3)	±0.73	±0.22	±1.21
0.241	6.748(5.122) ± 0.018	25.24(19.28) ± 0.97	0.65(18.3)	±0.80	±0.29	±1.29
0.219	6.138(4.666) ± 0.014	24.84(19.05) ± 0.83	0.63(17.1)	±0.61	±0.29	±1.07
0.197	5.527(4.205) ± 0.013	24.45(18.82) ± 0.88	0.61(15.9)	±0.62	±0.28	±1.11
0.175	4.915(3.739) ± 0.011	24.05(18.53) ± 0.81	0.62(14.7)	±0.55	±0.30	±1.03
0.153	4.303(3.270) ± 0.010	23.55(18.15) ± 0.88	0.57(13.3)	±0.60	±0.37	±1.13
0.131	3.691(2.801) ± 0.008	22.88(17.57) ± 0.85	0.53(11.8)	±0.59	±0.38	±1.11
0.109	3.076(2.328) ± 0.007	22.21(16.99) ± 0.88	0.56(10.4)	±0.51	±0.41	±1.10
0.087	2.461(1.851) ± 0.005	21.27(16.15) ± 0.89	0.61(8.9)	±0.56	±0.47	±1.16
0.066	1.859(1.445) ± 0.004	19.60(14.74) ± 0.92	0.59(7.4)	±0.70	±0.52	±1.27

TABLE XI. NBD fit results in centrality 40–50%.

$\delta\eta$	$\langle\mu_c\rangle(\langle\mu\rangle)$	$\langle k_c\rangle(\langle k\rangle)$	$\langle\chi^2/NDF\rangle(\langle NDF\rangle)$	$\delta\langle k_c\rangle$ (dead)	$\delta\langle k_c\rangle$ (fake)	$\delta\langle k_c\rangle$ (total)
0.700	15.446(11.955) ± 0.044	23.99(18.57) ± 0.65	1.07(36.0)	±1.02	±0.17	±1.22
0.678	15.032(11.644) ± 0.043	23.87(18.49) ± 0.66	1.08(35.1)	±0.64	±0.18	±0.93
0.656	14.534(11.243) ± 0.042	24.03(18.59) ± 0.68	1.24(34.0)	±0.61	±0.06	±0.91
0.634	14.033(10.841) ± 0.041	24.11(18.63) ± 0.69	1.25(33.2)	±0.78	±0.16	±1.06
0.613	13.547(10.457) ± 0.041	23.98(18.51) ± 0.71	1.18(32.4)	±0.77	±0.17	±1.06
0.591	13.055(10.075) ± 0.040	23.97(18.50) ± 0.73	1.15(31.6)	±0.80	±0.16	±1.09
0.569	12.561(9.684) ± 0.038	23.89(18.42) ± 0.74	1.16(30.8)	±0.68	±0.14	±1.02
0.547	12.072(9.293) ± 0.037	23.70(18.24) ± 0.76	1.09(30.2)	±0.74	±0.14	±1.07
0.525	11.583(8.903) ± 0.037	23.65(18.17) ± 0.78	1.02(29.3)	±0.63	±0.12	±1.01
0.503	11.093(8.510) ± 0.036	23.66(18.15) ± 0.81	1.05(28.1)	±0.65	±0.15	±1.05
0.481	10.600(8.112) ± 0.035	23.64(18.09) ± 0.83	1.00(27.3)	±0.66	±0.17	±1.08
0.459	10.106(7.711) ± 0.034	23.56(17.98) ± 0.86	0.95(26.2)	±0.58	±0.16	±1.05
0.438	9.610(7.306) ± 0.033	23.42(17.81) ± 0.89	0.86(25.2)	±0.60	±0.14	±1.08
0.416	9.116(6.904) ± 0.032	23.27(17.62) ± 0.92	0.80(23.9)	±0.67	±0.18	±1.15
0.394	8.620(6.503) ± 0.030	23.36(17.62) ± 0.96	0.81(22.9)	±0.55	±0.17	±1.12
0.372	8.131(6.107) ± 0.029	23.21(17.44) ± 1.00	0.72(22.0)	±0.62	±0.18	±1.19
0.350	7.652(5.731) ± 0.020	22.92(17.18) ± 0.73	0.64(20.9)	±0.77	±0.24	±1.08
0.328	7.176(5.388) ± 0.019	22.61(17.05) ± 0.76	0.63(19.8)	±0.74	±0.21	±1.08
0.306	6.706(5.050) ± 0.018	22.30(16.92) ± 0.78	0.62(18.8)	±0.70	±0.20	±1.07
0.284	6.235(4.708) ± 0.018	22.05(16.82) ± 0.81	0.60(18.0)	±0.65	±0.20	±1.06
0.263	5.762(4.362) ± 0.017	21.72(16.65) ± 0.85	0.59(17.0)	±0.61	±0.22	±1.06
0.241	5.287(4.011) ± 0.016	21.38(16.47) ± 0.89	0.60(16.0)	±0.55	±0.23	±1.07
0.219	4.811(3.656) ± 0.012	20.89(16.16) ± 0.76	0.57(14.9)	±0.58	±0.24	±0.98
0.197	4.333(3.295) ± 0.012	20.52(15.95) ± 0.81	0.53(13.9)	±0.51	±0.25	±0.99
0.175	3.852(2.929) ± 0.009	20.17(15.72) ± 0.76	0.54(12.8)	±0.49	±0.28	±0.94
0.153	3.372(2.561) ± 0.009	19.78(15.44) ± 0.82	0.51(11.6)	±0.45	±0.28	±0.98
0.131	2.891(2.192) ± 0.007	19.34(15.10) ± 0.81	0.49(10.6)	±0.43	±0.28	±0.96
0.109	2.410(1.821) ± 0.006	18.81(14.69) ± 0.85	0.46(9.3)	±0.36	±0.33	±0.98
0.087	1.928(1.449) ± 0.004	18.14(14.19) ± 0.87	0.48(7.9)	±0.38	±0.35	±1.01
0.066	1.456(1.131) ± 0.004	17.03(13.51) ± 0.91	0.48(6.6)	±0.32	±0.35	±1.03

TABLE XII. NBD fit results in centrality 45–55%.

$\delta\eta$	$\langle\mu_c\rangle(\langle\mu\rangle)$	$\langle k_c\rangle(\langle k\rangle)$	$\langle\chi^2/NDF\rangle(\langle NDF\rangle)$	$\delta\langle k_c\rangle$ (dead)	$\delta\langle k_c\rangle$ (fake)	$\delta\langle k_c\rangle$ (total)
0.700	11.838(9.163) ± 0.038	20.15(15.59) ± 0.61	1.14(28.0)	±0.71	±0.06	±0.94
0.678	11.517(8.922) ± 0.037	20.06(15.54) ± 0.61	1.10(27.9)	±0.60	±0.03	±0.86
0.656	11.142(8.620) ± 0.036	19.94(15.43) ± 0.62	1.10(26.6)	±0.48	±0.08	±0.79
0.634	10.759(8.311) ± 0.035	19.94(15.40) ± 0.64	1.08(25.8)	±0.47	±0.11	±0.80
0.613	10.380(8.013) ± 0.035	19.99(15.43) ± 0.65	1.06(24.9)	±0.51	±0.08	±0.83
0.591	10.005(7.721) ± 0.034	19.95(15.39) ± 0.67	1.06(24.1)	±0.41	±0.11	±0.79
0.569	9.629(7.424) ± 0.033	19.85(15.30) ± 0.68	1.05(23.2)	±0.44	±0.10	±0.82
0.547	9.254(7.123) ± 0.032	19.76(15.21) ± 0.70	1.04(22.5)	±0.47	±0.12	±0.85
0.525	8.879(6.824) ± 0.031	19.73(15.16) ± 0.72	1.02(21.8)	±0.42	±0.11	±0.84
0.503	8.505(6.525) ± 0.030	19.69(15.10) ± 0.74	0.96(21.4)	±0.42	±0.13	±0.86
0.481	8.130(6.222) ± 0.030	19.63(15.02) ± 0.76	0.89(20.7)	±0.44	±0.14	±0.89
0.459	7.751(5.915) ± 0.029	19.62(14.97) ± 0.79	0.77(20.1)	±0.49	±0.14	±0.94
0.438	7.370(5.604) ± 0.028	19.66(14.95) ± 0.82	0.66(19.6)	±0.49	±0.14	±0.96
0.416	6.991(5.295) ± 0.027	19.74(14.95) ± 0.85	0.63(18.8)	±0.49	±0.16	±1.00
0.394	6.612(4.988) ± 0.026	19.80(14.94) ± 0.89	0.62(18.1)	±0.55	±0.17	±1.06
0.372	6.236(4.684) ± 0.025	19.79(14.86) ± 0.93	0.58(17.3)	±0.56	±0.17	±1.10
0.350	5.868(4.395) ± 0.017	19.74(14.79) ± 0.69	0.58(16.7)	±0.55	±0.20	±0.91
0.328	5.502(4.131) ± 0.017	19.58(14.75) ± 0.72	0.62(16.1)	±0.52	±0.21	±0.91
0.306	5.141(3.872) ± 0.016	19.30(14.66) ± 0.74	0.62(15.5)	±0.51	±0.19	±0.92
0.284	4.780(3.610) ± 0.015	18.97(14.51) ± 0.78	0.59(14.9)	±0.47	±0.17	±0.93
0.263	4.418(3.345) ± 0.015	18.76(14.44) ± 0.82	0.61(14.2)	±0.48	±0.21	±0.97
0.241	4.056(3.077) ± 0.014	18.53(14.33) ± 0.87	0.59(13.6)	±0.48	±0.19	±1.01
0.219	3.689(2.803) ± 0.011	18.38(14.30) ± 0.76	0.61(13.0)	±0.49	±0.19	±0.93
0.197	3.321(2.526) ± 0.010	18.29(14.30) ± 0.83	0.60(12.2)	±0.44	±0.20	±0.96
0.175	2.953(2.244) ± 0.008	18.03(14.17) ± 0.79	0.56(11.4)	±0.52	±0.20	±0.97
0.153	2.583(1.962) ± 0.007	17.80(14.06) ± 0.89	0.55(10.4)	±0.46	±0.22	±1.02
0.131	2.215(1.678) ± 0.006	17.55(13.94) ± 0.92	0.57(9.3)	±0.34	±0.24	±1.00
0.109	1.846(1.394) ± 0.005	17.10(13.66) ± 0.98	0.56(8.2)	±0.34	±0.29	±1.08
0.087	1.477(1.109) ± 0.004	16.55(13.29) ± 1.05	0.51(7.0)	±0.29	±0.27	±1.12
0.066	1.117(0.875) ± 0.003	16.05(12.98) ± 1.09	0.51(5.8)	±0.26	±0.34	±1.17

TABLE XIII. NBD fit results in centrality 50–60%.

$\delta\eta$	$\langle\mu_c\rangle(\langle\mu\rangle)$	$\langle k_c\rangle(\langle k\rangle)$	$\langle\chi^2/NDF\rangle(\langle NDF\rangle)$	$\delta\langle k_c\rangle$ (dead)	$\delta\langle k_c\rangle$ (fake)	$\delta\langle k_c\rangle$ (total)
0.700	4.508(3.489) ± 0.023	8.89(6.88) ± 0.29	0.90(15.0)	±0.21	±0.01	±0.35
0.678	4.387(3.398) ± 0.022	8.85(6.85) ± 0.29	0.90(14.8)	±0.23	±0.01	±0.37
0.656	4.248(3.286) ± 0.022	8.78(6.79) ± 0.29	0.76(14.2)	±0.25	±0.01	±0.39
0.634	4.102(3.169) ± 0.021	8.74(6.75) ± 0.30	0.76(13.9)	±0.26	±0.01	±0.39
0.613	3.954(3.052) ± 0.021	8.81(6.80) ± 0.31	1.14(13.4)	±0.23	±0.01	±0.38
0.591	3.813(2.942) ± 0.020	8.67(6.69) ± 0.31	0.91(13.1)	±0.24	±0.01	±0.39
0.569	3.666(2.827) ± 0.020	8.66(6.67) ± 0.32	0.96(12.9)	±0.27	±0.02	±0.42
0.547	3.518(2.708) ± 0.019	8.78(6.76) ± 0.33	1.19(12.5)	±0.21	±0.01	±0.40
0.525	3.378(2.596) ± 0.019	8.67(6.66) ± 0.34	0.93(12.0)	±0.21	±0.01	±0.40
0.503	3.236(2.482) ± 0.018	8.67(6.65) ± 0.35	0.86(11.8)	±0.25	±0.01	±0.43
0.481	3.091(2.366) ± 0.018	8.71(6.67) ± 0.36	0.88(11.6)	±0.23	±0.02	±0.43
0.459	2.949(2.250) ± 0.017	8.67(6.62) ± 0.37	0.80(11.1)	±0.20	±0.02	±0.42
0.438	2.806(2.133) ± 0.017	8.63(6.56) ± 0.39	0.76(10.5)	±0.20	±0.03	±0.44
0.416	2.664(2.017) ± 0.017	8.58(6.50) ± 0.40	0.65(9.9)	±0.24	±0.03	±0.47
0.394	2.520(1.901) ± 0.016	8.60(6.49) ± 0.42	0.64(9.5)	±0.23	±0.02	±0.48
0.372	2.376(1.785) ± 0.015	8.69(6.54) ± 0.45	0.75(8.9)	±0.26	±0.02	±0.52
0.350	2.236(1.675) ± 0.011	8.77(6.57) ± 0.34	0.73(8.5)	±0.25	±0.02	±0.43
0.328	2.097(1.575) ± 0.010	8.75(6.58) ± 0.36	0.69(8.1)	±0.25	±0.02	±0.44
0.306	1.960(1.476) ± 0.010	8.74(6.61) ± 0.38	0.74(7.6)	±0.22	±0.03	±0.44
0.284	1.822(1.376) ± 0.009	8.71(6.63) ± 0.41	0.75(7.1)	±0.23	±0.03	±0.47

TABLE XIII. (*Continued*.)

$\delta\eta$	$\langle\mu_c\rangle(\langle\mu\rangle)$	$\langle k_c\rangle(\langle k\rangle)$	$\langle\chi^2/NDF\rangle(\langle NDF\rangle)$	$\delta\langle k_c\rangle$ (dead)	$\delta\langle k_c\rangle$ (fake)	$\delta\langle k_c\rangle$ (total)
0.263	1.683(1.274) ± 0.009	8.70(6.67) ± 0.44	0.78(6.7)	±0.21	±0.03	±0.49
0.241	1.545(1.172) ± 0.008	8.66(6.67) ± 0.47	0.75(6.3)	±0.19	±0.03	±0.51
0.219	1.407(1.069) ± 0.006	8.55(6.62) ± 0.41	0.70(5.9)	±0.18	±0.03	±0.45
0.197	1.267(0.963) ± 0.006	8.45(6.57) ± 0.45	0.59(5.5)	±0.18	±0.03	±0.48
0.175	1.126(0.856) ± 0.005	8.41(6.59) ± 0.44	0.59(5.2)	±0.15	±0.04	±0.47
0.153	0.986(0.749) ± 0.005	8.31(6.54) ± 0.50	0.58(4.8)	±0.14	±0.05	±0.52
0.131	0.846(0.641) ± 0.004	8.07(6.36) ± 0.52	0.52(4.4)	±0.16	±0.06	±0.55
0.109	0.706(0.534) ± 0.003	7.85(6.21) ± 0.54	0.40(3.8)	±0.08	±0.07	±0.55
0.087	0.565(0.424) ± 0.002	7.86(6.23) ± 0.64	0.58(3.3)	±0.06	±0.09	±0.65
0.066	0.428(0.339) ± 0.002	7.22(5.77) ± 0.64	0.44(2.9)	±0.06	±0.07	±0.65

TABLE XIV. NBD fit results in centrality 55–65%.

$\delta\eta$	$\langle\mu_c\rangle(\langle\mu\rangle)$	$\langle k_c\rangle(\langle k\rangle)$	$\langle\chi^2/NDF\rangle(\langle NDF\rangle)$	$\delta\langle k_c\rangle$ (dead)	$\delta\langle k_c\rangle$ (fake)	$\delta\langle k_c\rangle$ (total)
0.700	3.086(2.389) ± 0.019	5.90(4.56) ± 0.20	0.76(13.0)	±0.25	±0.01	±0.32
0.678	3.000(2.324) ± 0.019	5.88(4.56) ± 0.20	0.79(12.7)	±0.13	±0.01	±0.24
0.656	2.902(2.245) ± 0.018	5.85(4.52) ± 0.20	0.76(12.5)	±0.14	±0.02	±0.24
0.634	2.803(2.166) ± 0.018	5.78(4.46) ± 0.20	0.69(12.2)	±0.14	±0.02	±0.25
0.613	2.703(2.086) ± 0.017	5.80(4.48) ± 0.21	0.78(12.1)	±0.07	±0.02	±0.22
0.591	2.607(2.012) ± 0.017	5.76(4.45) ± 0.21	0.70(11.3)	±0.14	±0.02	±0.25
0.569	2.508(1.934) ± 0.017	5.76(4.44) ± 0.22	0.62(10.9)	±0.13	±0.02	±0.25
0.547	2.410(1.855) ± 0.016	5.75(4.43) ± 0.23	0.55(10.3)	±0.12	±0.04	±0.26
0.525	2.313(1.777) ± 0.016	5.75(4.42) ± 0.23	0.50(9.9)	±0.16	±0.04	±0.28
0.503	2.215(1.699) ± 0.015	5.76(4.42) ± 0.24	0.47(9.6)	±0.16	±0.01	±0.29
0.481	2.117(1.620) ± 0.015	5.79(4.43) ± 0.25	0.49(9.2)	±0.16	±0.01	±0.30
0.459	2.018(1.540) ± 0.015	5.78(4.41) ± 0.26	0.49(8.9)	±0.16	±0.01	±0.30
0.438	1.919(1.459) ± 0.014	5.79(4.40) ± 0.27	0.50(8.8)	±0.17	±0.02	±0.32
0.416	1.820(1.378) ± 0.014	5.81(4.40) ± 0.28	0.52(8.6)	±0.20	±0.03	±0.34
0.394	1.721(1.298) ± 0.013	5.84(4.41) ± 0.30	0.53(8.4)	±0.15	±0.02	±0.34
0.372	1.623(1.219) ± 0.013	5.84(4.39) ± 0.32	0.54(7.8)	±0.18	±0.01	±0.36
0.350	1.527(1.144) ± 0.009	5.87(4.41) ± 0.24	0.52(7.6)	±0.21	±0.01	±0.32
0.328	1.432(1.075) ± 0.008	5.86(4.42) ± 0.25	0.49(7.4)	±0.24	±0.02	±0.34
0.306	1.339(1.008) ± 0.008	5.85(4.43) ± 0.27	0.48(7.2)	±0.21	±0.02	±0.34
0.284	1.244(0.940) ± 0.008	5.85(4.45) ± 0.28	0.52(6.9)	±0.21	±0.02	±0.35
0.263	1.150(0.871) ± 0.007	5.85(4.48) ± 0.31	0.59(6.5)	±0.14	±0.02	±0.34
0.241	1.056(0.801) ± 0.007	5.83(4.49) ± 0.33	0.59(6.2)	±0.11	±0.02	±0.35
0.219	0.961(0.730) ± 0.005	5.81(4.50) ± 0.29	0.62(5.9)	±0.10	±0.03	±0.31
0.197	0.866(0.658) ± 0.005	5.73(4.46) ± 0.32	0.57(5.5)	±0.10	±0.03	±0.34
0.175	0.770(0.585) ± 0.004	5.72(4.46) ± 0.32	0.54(5.2)	±0.10	±0.04	±0.33
0.153	0.674(0.511) ± 0.004	5.67(4.44) ± 0.36	0.53(4.8)	±0.09	±0.06	±0.38
0.131	0.578(0.438) ± 0.003	5.50(4.32) ± 0.36	0.40(4.5)	±0.05	±0.07	±0.37
0.109	0.482(0.364) ± 0.003	5.31(4.18) ± 0.39	0.51(4.0)	±0.05	±0.10	±0.41
0.087	0.386(0.292) ± 0.002	4.90(3.89) ± 0.43	0.54(3.6)	±0.05	±0.02	±0.43
0.066	0.292(0.232) ± 0.002	4.56(3.63) ± 0.44	0.57(3.1)	±0.05	±0.05	±0.45

TABLE XV. NBD fit results in centrality 0–5%.

$\delta\eta$	$\langle\mu_c\rangle(\langle\mu\rangle)$	$\langle k_c\rangle(\langle k\rangle)$	$\langle\chi^2/NDF\rangle(\langle NDF\rangle)$	$\delta\langle k_c\rangle$ (dead)	$\delta\langle k_c\rangle$ (fake)	$\delta\langle k_c\rangle$ (total)
0.700	84.371(65.303) ± 0.148	341.22(264.10) ± 31.75	0.54(58.0)	±54.10	±6.72	±63.09
0.678	82.149(63.638) ± 0.144	359.73(278.66) ± 35.51	0.58(57.8)	±29.67	±26.46	±53.31
0.656	79.451(61.463) ± 0.141	369.96(286.25) ± 37.82	0.66(56.4)	±13.85	±14.18	±42.69
0.634	76.740(59.282) ± 0.138	370.46(286.18) ± 38.62	0.63(55.4)	±19.09	±14.98	±45.61
0.613	74.027(57.142) ± 0.135	372.37(287.35) ± 40.79	0.62(54.7)	±13.54	±15.22	±45.60
0.591	71.331(55.050) ± 0.133	374.07(288.55) ± 42.84	0.64(53.6)	±13.41	±17.15	±48.06

TABLE XV. (*Continued*.)

$\delta\eta$	$\langle\mu_c\rangle(\langle\mu\rangle)$	$\langle k_c\rangle(\langle k\rangle)$	$\langle\chi^2/NDF\rangle(\langle NDF\rangle)$	$\delta\langle k_c\rangle$ (dead)	$\delta\langle k_c\rangle$ (fake)	$\delta\langle k_c\rangle$ (total)
0.569	68.629(52.910) ± 0.130	374.10(288.36) ± 44.31	0.64(52.7)	±18.44	±19.49	±51.80
0.547	65.925(50.747) ± 0.127	367.65(282.90) ± 44.42	0.64(52.2)	±16.76	±24.95	±53.63
0.525	63.249(48.612) ± 0.124	368.12(282.88) ± 46.12	0.68(51.2)	±16.19	±24.02	±54.46
0.503	60.566(46.465) ± 0.121	364.03(279.07) ± 46.64	0.65(50.2)	±15.42	±23.48	±54.45
0.481	57.877(44.295) ± 0.118	362.25(277.19) ± 48.15	0.65(49.0)	±12.93	±24.16	±55.40
0.459	55.171(42.098) ± 0.115	363.40(277.12) ± 50.80	0.66(47.9)	±13.82	±20.65	±56.55
0.438	52.479(39.900) ± 0.112	355.07(269.86) ± 51.95	0.64(46.5)	±9.95	±25.57	±58.75
0.416	49.791(37.710) ± 0.109	352.80(267.18) ± 54.68	0.66(45.2)	±14.68	±26.89	±62.68
0.394	47.118(35.547) ± 0.106	349.73(263.69) ± 57.42	0.64(43.6)	±13.29	±32.16	±67.14
0.372	44.456(33.395) ± 0.103	347.01(260.24) ± 64.15	0.65(42.1)	±3.82	±30.09	±70.96
0.350	41.832(31.335) ± 0.070	340.53(254.77) ± 52.65	0.67(40.6)	±11.74	±34.67	±64.13
0.328	39.229(29.465) ± 0.068	340.79(254.20) ± 55.01	0.65(39.4)	±2.10	±27.89	±61.72
0.306	36.653(27.626) ± 0.065	332.14(246.66) ± 60.16	0.68(37.9)	±12.90	±31.13	±68.95
0.284	34.073(25.755) ± 0.062	333.98(247.30) ± 64.64	0.69(37.0)	±1.38	±33.33	±72.74
0.263	31.493(23.870) ± 0.060	313.43(230.73) ± 62.92	0.69(35.2)	±1.26	±26.90	±68.44
0.241	28.903(21.959) ± 0.057	294.86(214.95) ± 59.84	0.68(33.5)	±2.22	±32.24	±68.01
0.219	26.305(20.020) ± 0.044	278.11(200.81) ± 51.12	0.69(31.9)	±3.21	±29.02	±58.87
0.197	23.677(18.009) ± 0.042	253.36(181.02) ± 56.29	0.71(30.2)	±6.54	±23.20	±61.24
0.175	21.066(16.025) ± 0.034	232.35(165.72) ± 50.48	0.73(28.3)	±3.92	±24.00	±56.04
0.153	18.425(13.948) ± 0.032	199.21(140.84) ± 48.99	0.75(26.2)	±8.99	±17.20	±52.70
0.131	15.807(11.964) ± 0.026	181.55(126.91) ± 37.35	0.80(24.2)	±10.43	±17.64	±42.61
0.109	13.174(9.949) ± 0.022	157.69(108.85) ± 28.73	0.83(21.4)	±3.79	±14.86	±32.57
0.087	10.522(7.808) ± 0.017	125.65(86.76) ± 21.21	0.80(18.2)	±3.14	±11.02	±24.10
0.066	7.947(6.122) ± 0.013	97.74(67.60) ± 13.55	0.73(15.1)	±8.30	±9.98	±18.77

TABLE XVI. NBD fit results in centrality 5–10%.

$\delta\eta$	$\langle\mu_c\rangle(\langle\mu\rangle)$	$\langle k_c\rangle(\langle k\rangle)$	$\langle\chi^2/NDF\rangle(\langle NDF\rangle)$	$\delta\langle k_c\rangle$ (dead)	$\delta\langle k_c\rangle$ (fake)	$\delta\langle k_c\rangle$ (total)
0.700	72.246(55.918) ± 0.126	187.62(145.22) ± 10.56	0.80(61.0)	±1.88	±9.61	±14.40
0.678	70.291(54.452) ± 0.124	185.02(143.32) ± 10.61	0.68(61.3)	±10.46	±6.69	±16.33
0.656	67.996(52.602) ± 0.121	188.09(145.50) ± 11.00	0.71(59.8)	±4.99	±4.56	±12.91
0.634	65.656(50.720) ± 0.119	188.72(145.76) ± 11.29	0.76(59.0)	±2.81	±6.48	±13.32
0.613	63.346(48.897) ± 0.116	186.50(143.95) ± 11.39	0.79(57.0)	±4.55	±6.31	±13.79
0.591	61.055(47.118) ± 0.114	185.01(142.75) ± 11.53	0.76(55.6)	±6.00	±5.32	±14.04
0.569	58.752(45.296) ± 0.111	184.61(142.29) ± 11.90	0.76(54.0)	±4.96	±7.98	±15.16
0.547	56.443(43.447) ± 0.108	183.38(141.14) ± 12.28	0.78(52.2)	±5.40	±8.57	±15.92
0.525	54.144(41.614) ± 0.106	183.73(141.18) ± 12.87	0.78(51.2)	±5.90	±8.41	±16.47
0.503	51.839(39.768) ± 0.103	186.84(143.32) ± 13.65	0.81(49.4)	±3.47	±7.23	±15.83
0.481	49.534(37.909) ± 0.100	187.11(143.19) ± 14.16	0.84(47.9)	±3.90	±7.38	±16.44
0.459	47.220(36.030) ± 0.097	189.72(144.71) ± 15.07	0.88(46.3)	±2.39	±7.36	±16.94
0.438	44.921(34.153) ± 0.095	187.66(142.61) ± 15.56	0.85(44.6)	±8.12	±10.08	±20.24
0.416	42.618(32.277) ± 0.092	188.72(142.85) ± 16.50	0.86(43.1)	±7.80	±7.74	±19.83
0.394	40.328(30.425) ± 0.089	186.94(140.87) ± 17.11	0.82(41.6)	±5.86	±9.43	±20.40
0.372	38.053(28.585) ± 0.086	186.28(139.66) ± 18.10	0.85(39.9)	±7.17	±9.93	±21.86
0.350	35.798(26.815) ± 0.059	187.25(139.96) ± 13.64	0.89(38.5)	±5.58	±9.02	±17.28
0.328	33.572(25.212) ± 0.057	184.92(138.46) ± 14.19	0.89(37.3)	±5.46	±12.28	±19.55
0.306	31.368(23.631) ± 0.055	182.12(136.56) ± 14.59	0.91(36.0)	±5.25	±11.88	±19.53
0.284	29.158(22.030) ± 0.052	178.29(134.27) ± 14.70	0.89(34.6)	±4.86	±13.82	±20.75
0.263	26.943(20.408) ± 0.050	173.07(131.50) ± 15.26	0.91(33.1)	±5.84	±15.75	±22.69
0.241	24.731(18.770) ± 0.048	169.01(129.45) ± 15.73	0.88(32.1)	±6.53	±15.73	±23.19
0.219	22.501(17.102) ± 0.037	167.76(129.28) ± 13.97	0.94(30.7)	±3.27	±12.91	±19.31
0.197	20.271(15.421) ± 0.035	160.25(123.65) ± 14.29	0.94(29.1)	±5.43	±15.13	±21.52
0.175	18.030(13.713) ± 0.028	152.49(118.31) ± 13.95	0.99(27.4)	±5.87	±13.32	±20.16

TABLE XVI. (*Continued*.)

$\delta\eta$	$\langle\mu_c\rangle(\langle\mu\rangle)$	$\langle k_c\rangle(\langle k\rangle)$	$\langle\chi^2/NDF\rangle(\langle NDF\rangle)$	$\delta\langle k_c\rangle$ (dead)	$\delta\langle k_c\rangle$ (fake)	$\delta\langle k_c\rangle$ (total)
0.153	15.787(11.998) ± 0.026	144.71(112.06) ± 13.58	1.00(25.4)	±5.81	±15.35	±21.30
0.131	13.540(10.276) ± 0.022	137.12(106.29) ± 12.40	1.05(22.9)	±5.42	±14.45	±19.80
0.109	11.289(8.548) ± 0.018	122.24(92.30) ± 10.92	1.09(20.3)	±6.77	±14.31	±19.23
0.087	9.029(6.805) ± 0.014	99.52(72.96) ± 9.30	1.03(17.2)	±5.46	±10.51	±15.06
0.066	6.807(5.296) ± 0.011	75.37(54.94) ± 6.89	0.81(14.2)	±6.29	±8.08	±12.34

TABLE XVII. NBD fit results in centrality 10–15%.

$\delta\eta$	$\langle\mu_c\rangle(\langle\mu\rangle)$	$\langle k_c\rangle(\langle k\rangle)$	$\langle\chi^2/NDF\rangle(\langle NDF\rangle)$	$\delta\langle k_c\rangle$ (dead)	$\delta\langle k_c\rangle$ (fake)	$\delta\langle k_c\rangle$ (total)
0.700	60.607(46.909) ± 0.119	129.59(100.31) ± 6.29	0.80(58.0)	±1.29	±1.51	±6.60
0.678	59.026(45.725) ± 0.118	123.34(95.54) ± 6.09	0.76(56.6)	±4.71	±9.77	±12.44
0.656	57.108(44.179) ± 0.116	121.44(93.94) ± 6.08	0.70(55.3)	±5.55	±4.90	±9.58
0.634	55.139(42.596) ± 0.113	121.88(94.14) ± 6.24	0.70(54.2)	±4.92	±3.01	±8.50
0.613	53.198(41.064) ± 0.111	120.98(93.37) ± 6.33	0.69(52.9)	±5.23	±2.63	±8.62
0.591	51.256(39.556) ± 0.108	120.49(92.96) ± 6.46	0.71(52.2)	±3.80	±3.87	±8.44
0.569	49.321(38.025) ± 0.106	119.78(92.31) ± 6.58	0.70(51.3)	±3.61	±2.65	±7.95
0.547	47.393(36.482) ± 0.103	117.86(90.68) ± 6.62	0.71(50.1)	±3.12	±3.60	±8.15
0.525	45.463(34.943) ± 0.101	117.65(90.38) ± 6.79	0.71(49.2)	±3.77	±3.44	±8.49
0.503	43.535(33.398) ± 0.098	117.79(90.32) ± 7.03	0.71(48.2)	±3.47	±4.14	±8.87
0.481	41.602(31.839) ± 0.095	118.04(90.30) ± 7.29	0.71(46.9)	±3.18	±3.55	±8.71
0.459	39.668(30.267) ± 0.092	118.96(90.76) ± 7.64	0.73(45.2)	±3.46	±4.65	±9.59
0.438	37.729(28.684) ± 0.090	118.41(90.03) ± 7.87	0.72(44.0)	±3.52	±4.95	±9.94
0.416	35.787(27.104) ± 0.087	118.19(89.52) ± 8.24	0.74(42.5)	±4.23	±5.06	±10.56
0.394	33.864(25.547) ± 0.084	118.35(89.25) ± 8.67	0.76(41.1)	±4.60	±4.92	±10.98
0.372	31.943(23.994) ± 0.082	118.19(88.71) ± 9.20	0.75(39.6)	±4.92	±5.31	±11.70
0.350	30.061(22.517) ± 0.056	117.56(87.92) ± 6.85	0.75(38.1)	±4.91	±5.85	±10.26
0.328	28.191(21.172) ± 0.053	117.37(87.84) ± 7.21	0.78(36.3)	±5.14	±5.41	±10.38
0.306	26.340(19.845) ± 0.051	117.25(87.95) ± 7.59	0.78(34.7)	±4.90	±5.07	±10.36
0.284	24.493(18.509) ± 0.049	117.01(87.82) ± 8.16	0.82(33.5)	±4.41	±5.83	±10.96
0.263	22.636(17.150) ± 0.047	114.86(86.40) ± 8.44	0.80(31.8)	±5.74	±5.96	±11.82
0.241	20.776(15.774) ± 0.044	114.37(86.11) ± 8.95	0.82(30.3)	±5.34	±6.20	±12.13
0.219	18.905(14.375) ± 0.034	112.39(84.83) ± 7.68	0.82(28.8)	±5.37	±7.32	±11.89
0.197	17.029(12.958) ± 0.033	111.32(84.34) ± 8.15	0.83(26.9)	±6.15	±7.47	±12.66
0.175	15.142(11.519) ± 0.026	109.44(83.15) ± 7.72	0.88(25.1)	±5.22	±7.32	±11.85
0.153	13.253(10.073) ± 0.024	106.03(80.26) ± 8.35	0.94(23.0)	±4.18	±6.94	±11.64
0.131	11.367(8.626) ± 0.020	96.68(72.34) ± 7.60	0.94(20.5)	±4.30	±7.09	±11.25
0.109	9.474(7.170) ± 0.017	88.58(65.38) ± 7.20	0.87(18.1)	±3.97	±8.10	±11.54
0.087	7.575(5.704) ± 0.013	77.55(55.69) ± 6.79	0.81(15.6)	±3.54	±7.64	±10.82
0.066	5.714(4.443) ± 0.010	64.41(47.02) ± 6.22	0.63(12.8)	±4.49	±6.13	±9.82

TABLE XVIII. NBD fit results in centrality 15–20%.

$\delta\eta$	$\langle\mu_c\rangle(\langle\mu\rangle)$	$\langle k_c\rangle(\langle k\rangle)$	$\langle\chi^2/NDF\rangle(\langle NDF\rangle)$	$\delta\langle k_c\rangle$ (dead)	$\delta\langle k_c\rangle$ (fake)	$\delta\langle k_c\rangle$ (total)
0.700	50.243(38.888) ± 0.109	95.08(73.59) ± 4.42	0.79(53.0)	±4.84	±6.50	±9.23
0.678	48.892(37.875) ± 0.106	95.76(74.18) ± 4.54	0.67(52.4)	±3.20	±1.41	±5.73
0.656	47.301(36.592) ± 0.104	95.63(73.98) ± 4.65	0.75(51.2)	±2.80	±1.66	±5.68
0.634	45.685(35.292) ± 0.102	95.70(73.94) ± 4.78	0.71(49.2)	±2.09	±1.96	±5.57
0.613	44.087(34.031) ± 0.100	94.78(73.17) ± 4.87	0.71(47.7)	±3.79	±3.17	±6.94
0.591	42.483(32.785) ± 0.097	95.97(74.07) ± 5.05	0.70(47.1)	±2.95	±1.99	±6.18
0.569	40.884(31.519) ± 0.095	96.10(74.10) ± 5.22	0.69(46.1)	±2.66	±2.10	±6.22
0.547	39.301(30.251) ± 0.092	95.92(73.85) ± 5.36	0.70(44.8)	±3.31	±2.60	±6.82

TABLE XVIII. (*Continued*.)

$\delta\eta$	$\langle\mu_c\rangle(\langle\mu\rangle)$	$\langle k_c\rangle(\langle k\rangle)$	$\langle\chi^2/NDF\rangle(\langle NDF\rangle)$	$\delta\langle k_c\rangle$ (dead)	$\delta\langle k_c\rangle$ (fake)	$\delta\langle k_c\rangle$ (total)
0.525	37.708(28.981) ± 0.090	96.52(74.20) ± 5.57	0.71(43.6)	±3.47	±1.98	±6.85
0.503	36.108(27.700) ± 0.088	96.81(74.28) ± 5.77	0.75(42.5)	±2.84	±2.39	±6.86
0.481	34.505(26.406) ± 0.085	96.51(73.88) ± 5.92	0.73(41.4)	±2.38	±1.88	±6.65
0.459	32.897(25.100) ± 0.083	95.50(72.89) ± 6.03	0.73(40.1)	±2.67	±2.54	±7.07
0.438	31.285(23.784) ± 0.081	95.28(72.47) ± 6.24	0.77(38.6)	±2.78	±2.27	±7.19
0.416	29.677(22.474) ± 0.078	95.11(72.09) ± 6.45	0.78(37.3)	±3.02	±2.26	±7.47
0.394	28.079(21.180) ± 0.076	94.76(71.57) ± 6.69	0.78(35.9)	±2.98	±3.07	±7.94
0.372	26.483(19.889) ± 0.073	95.08(71.55) ± 7.04	0.81(34.6)	±2.59	±2.66	±7.96
0.350	24.918(18.661) ± 0.050	94.28(70.78) ± 5.11	0.80(33.3)	±3.11	±2.66	±6.55
0.328	23.365(17.541) ± 0.048	92.98(70.16) ± 5.28	0.82(32.3)	±2.56	±2.78	±6.50
0.306	21.831(16.441) ± 0.046	91.68(69.59) ± 5.47	0.84(31.2)	±2.32	±3.06	±6.69
0.284	20.294(15.325) ± 0.044	89.06(68.15) ± 5.60	0.85(29.8)	±2.62	±3.13	±6.93
0.263	18.754(14.199) ± 0.042	87.46(67.23) ± 5.76	0.85(28.5)	±2.47	±2.87	±6.90
0.241	17.215(13.060) ± 0.040	86.16(66.47) ± 6.04	0.88(27.0)	±2.30	±3.25	±7.23
0.219	15.665(11.902) ± 0.031	83.50(64.86) ± 5.15	0.90(25.4)	±3.27	±3.46	±7.01
0.197	14.110(10.728) ± 0.029	81.20(63.31) ± 5.36	0.88(23.7)	±2.47	±3.88	±7.06
0.175	12.547(9.540) ± 0.024	79.16(61.58) ± 4.86	0.93(21.9)	±2.06	±3.41	±6.28
0.153	10.977(8.337) ± 0.022	73.67(57.42) ± 4.99	0.91(19.8)	±1.63	±3.89	±6.53
0.131	9.409(7.133) ± 0.018	67.77(52.73) ± 4.44	0.83(17.8)	±2.00	±3.98	±6.29
0.109	7.840(5.924) ± 0.015	61.02(47.54) ± 4.01	0.74(15.6)	±1.99	±4.09	±6.06
0.087	6.271(4.713) ± 0.012	54.47(42.05) ± 3.54	0.63(13.4)	±1.64	±3.81	±5.46
0.066	4.734(3.678) ± 0.009	47.73(35.64) ± 3.59	0.58(11.3)	±2.06	±3.33	±5.31

TABLE XIX. NBD fit results in centrality 20–25%.

$\delta\eta$	$\langle\mu_c\rangle(\langle\mu\rangle)$	$\langle k_c\rangle(\langle k\rangle)$	$\langle\chi^2/NDF\rangle(\langle NDF\rangle)$	$\delta\langle k_c\rangle$ (dead)	$\delta\langle k_c\rangle$ (fake)	$\delta\langle k_c\rangle$ (total)
0.700	41.340(31.997) ± 0.101	80.17(62.05) ± 3.85	0.71(48.0)	±1.34	±1.27	±4.27
0.678	40.233(31.167) ± 0.099	80.14(62.08) ± 3.92	0.67(47.2)	±3.19	±1.69	±5.33
0.656	38.920(30.109) ± 0.096	81.43(63.00) ± 4.07	0.68(46.9)	±1.52	±0.92	±4.44
0.634	37.606(29.051) ± 0.094	81.18(62.71) ± 4.17	0.68(45.8)	±3.68	±1.51	±5.76
0.613	36.282(28.006) ± 0.092	82.48(63.67) ± 4.38	0.78(44.7)	±1.90	±1.68	±5.07
0.591	34.986(27.000) ± 0.090	81.78(63.12) ± 4.43	0.76(44.2)	±2.76	±1.37	±5.39
0.569	33.656(25.947) ± 0.088	81.76(63.04) ± 4.53	0.75(43.4)	±1.38	±1.07	±4.86
0.547	32.342(24.895) ± 0.086	81.09(62.42) ± 4.60	0.68(42.5)	±1.91	±1.56	±5.22
0.525	31.029(23.848) ± 0.083	81.53(62.67) ± 4.76	0.72(41.5)	±1.98	±1.63	±5.40
0.503	29.714(22.794) ± 0.081	81.92(62.85) ± 4.93	0.77(40.5)	±1.94	±1.10	±5.41
0.481	28.395(21.731) ± 0.079	82.20(62.93) ± 5.11	0.77(39.3)	±2.21	±1.08	±5.67
0.459	27.071(20.654) ± 0.077	82.39(62.89) ± 5.33	0.79(38.3)	±2.25	±1.31	±5.93
0.438	25.754(19.579) ± 0.074	81.71(62.18) ± 5.47	0.78(37.1)	±2.79	±1.73	±6.38
0.416	24.428(18.499) ± 0.072	82.61(62.66) ± 5.83	0.82(35.8)	±2.05	±1.10	±6.28
0.394	23.116(17.436) ± 0.070	81.91(61.93) ± 6.04	0.78(34.6)	±2.84	±1.75	±6.90
0.372	21.803(16.374) ± 0.068	82.06(61.77) ± 6.34	0.78(33.3)	±2.84	±1.94	±7.21
0.350	20.516(15.364) ± 0.046	82.29(61.74) ± 4.77	0.82(32.1)	±3.10	±2.13	±6.08
0.328	19.244(14.448) ± 0.044	81.98(61.71) ± 4.99	0.82(30.8)	±2.85	±2.02	±6.09
0.306	17.979(13.542) ± 0.043	81.64(61.65) ± 5.26	0.82(29.7)	±3.02	±1.98	±6.38
0.284	16.715(12.625) ± 0.041	80.08(60.81) ± 5.43	0.83(28.4)	±2.99	±2.30	±6.61
0.263	15.448(11.697) ± 0.039	78.84(60.25) ± 5.73	0.84(26.9)	±3.19	±2.34	±6.96
0.241	14.177(10.756) ± 0.037	77.06(59.22) ± 5.98	0.86(25.2)	±2.73	±2.06	±6.89
0.219	12.899(9.802) ± 0.029	74.63(57.61) ± 5.08	0.88(23.8)	±2.84	±2.57	±6.36
0.197	11.616(8.833) ± 0.027	72.40(56.12) ± 5.38	0.92(22.1)	±2.12	±2.05	±6.13
0.175	10.327(7.850) ± 0.022	68.48(53.34) ± 4.75	0.88(20.2)	±2.15	±2.18	±5.65
0.153	9.035(6.859) ± 0.021	62.87(49.41) ± 4.84	0.82(18.3)	±2.09	±2.55	±5.85
0.131	7.744(5.870) ± 0.017	58.29(45.68) ± 4.29	0.71(16.3)	±2.05	±2.65	±5.45
0.109	6.452(4.877) ± 0.014	54.02(41.89) ± 4.10	0.58(14.5)	±1.91	±2.54	±5.19
0.087	5.160(3.881) ± 0.011	49.72(38.24) ± 4.19	0.49(12.2)	±1.74	±2.92	±5.40
0.066	3.895(3.027) ± 0.008	44.74(34.54) ± 4.38	0.49(10.2)	±1.45	±3.09	±5.55

TABLE XX. NBD fit results in centrality 25–30%.

$\delta\eta$	$\langle\mu_c\rangle(\langle\mu\rangle)$	$\langle k_c\rangle(\langle k\rangle)$	$\langle\chi^2/NDF\rangle(\langle NDF\rangle)$	$\delta\langle k_c\rangle$ (dead)	$\delta\langle k_c\rangle$ (fake)	$\delta\langle k_c\rangle$ (total)
0.700	33.991(26.309) ± 0.090	67.99(52.63) ± 3.18	0.56(44.0)	±2.58	±0.80	±4.17
0.678	33.067(25.615) ± 0.088	68.77(53.27) ± 3.29	0.61(44.0)	±2.56	±0.05	±4.17
0.656	31.992(24.750) ± 0.086	67.53(52.23) ± 3.30	0.56(43.6)	±3.20	±1.31	±4.78
0.634	30.890(23.863) ± 0.084	67.26(51.95) ± 3.34	0.58(42.8)	±2.31	±1.01	±4.19
0.613	29.811(23.012) ± 0.082	67.40(52.02) ± 3.41	0.64(41.9)	±1.64	±1.27	±3.99
0.591	28.732(22.173) ± 0.081	66.18(51.07) ± 3.41	0.65(41.3)	±2.18	±0.79	±4.12
0.569	27.643(21.312) ± 0.079	66.17(51.01) ± 3.50	0.62(40.2)	±2.87	±1.24	±4.69
0.547	26.558(20.443) ± 0.077	65.89(50.72) ± 3.57	0.65(38.9)	±2.32	±1.30	±4.45
0.525	25.479(19.583) ± 0.075	65.64(50.44) ± 3.66	0.66(37.9)	±2.53	±0.86	±4.53
0.503	24.403(18.721) ± 0.073	65.21(50.01) ± 3.75	0.66(37.1)	±3.12	±1.03	±4.99
0.481	23.325(17.852) ± 0.071	64.30(49.19) ± 3.80	0.64(35.9)	±3.10	±0.97	±5.00
0.459	22.243(16.972) ± 0.069	64.65(49.31) ± 3.94	0.67(35.0)	±2.62	±0.71	±4.78
0.438	21.155(16.084) ± 0.067	63.75(48.45) ± 4.03	0.68(33.4)	±2.73	±0.89	±4.95
0.416	20.074(15.204) ± 0.065	63.34(47.95) ± 4.15	0.70(32.4)	±2.72	±1.01	±5.06
0.394	18.991(14.327) ± 0.063	62.47(47.09) ± 4.26	0.69(31.0)	±2.95	±1.01	±5.28
0.372	17.912(13.455) ± 0.061	62.61(47.00) ± 4.49	0.71(29.9)	±2.80	±0.83	±5.35
0.350	16.855(12.625) ± 0.042	62.05(46.45) ± 3.30	0.72(28.7)	±2.34	±0.81	±4.12
0.328	15.805(11.868) ± 0.040	61.38(46.04) ± 3.39	0.72(27.5)	±2.67	±1.02	±4.43
0.306	14.769(11.126) ± 0.038	60.26(45.34) ± 3.48	0.72(26.3)	±2.88	±1.01	±4.63
0.284	13.731(10.376) ± 0.037	59.70(44.97) ± 3.62	0.71(25.1)	±2.44	±1.21	±4.54
0.263	12.685(9.610) ± 0.035	59.20(44.67) ± 3.84	0.74(23.7)	±2.61	±1.06	±4.76
0.241	11.640(8.838) ± 0.033	57.91(43.73) ± 4.00	0.71(22.3)	±2.54	±1.09	±4.86
0.219	10.591(8.054) ± 0.026	56.00(42.22) ± 3.34	0.64(21.0)	±2.38	±1.26	±4.29
0.197	9.535(7.258) ± 0.024	54.60(41.11) ± 3.51	0.67(19.3)	±2.10	±1.43	±4.33
0.175	8.479(6.455) ± 0.020	52.59(39.35) ± 3.21	0.64(17.6)	±2.49	±1.42	±4.30
0.153	7.420(5.643) ± 0.018	51.06(38.08) ± 3.48	0.62(16.0)	±1.76	±1.53	±4.19
0.131	6.363(4.832) ± 0.015	49.16(36.41) ± 3.38	0.56(14.3)	±1.61	±1.59	±4.07
0.109	5.306(4.017) ± 0.013	45.94(33.94) ± 3.32	0.49(12.3)	±1.57	±1.75	±4.07
0.087	4.245(3.196) ± 0.010	43.38(31.95) ± 3.30	0.49(10.5)	±1.68	±2.00	±4.21
0.066	3.205(2.492) ± 0.007	38.41(28.81) ± 3.58	0.47(8.8)	±1.46	±2.20	±4.45

TABLE XXI. NBD fit results in centrality 30–35%.

$\delta\eta$	$\langle\mu_c\rangle(\langle\mu\rangle)$	$\langle k_c\rangle(\langle k\rangle)$	$\langle\chi^2/NDF\rangle(\langle NDF\rangle)$	$\delta\langle k_c\rangle$ (dead)	$\delta\langle k_c\rangle$ (fake)	$\delta\langle k_c\rangle$ (total)
0.700	27.652(21.402) ± 0.079	58.33(45.15) ± 2.86	0.67(41.0)	±3.24	±0.86	±4.41
0.678	26.900(20.838) ± 0.078	57.89(44.85) ± 2.86	0.60(40.9)	±2.95	±0.85	±4.20
0.656	26.016(20.126) ± 0.076	57.99(44.86) ± 2.94	0.63(39.6)	±2.17	±0.88	±3.75
0.634	25.115(19.401) ± 0.074	57.51(44.43) ± 2.98	0.66(38.4)	±2.60	±0.72	±4.02
0.613	24.225(18.699) ± 0.073	56.95(43.97) ± 3.03	0.67(37.0)	±2.60	±0.86	±4.09
0.591	23.345(18.015) ± 0.071	56.94(43.95) ± 3.10	0.70(36.3)	±2.27	±0.77	±3.92
0.569	22.464(17.318) ± 0.070	56.67(43.71) ± 3.17	0.74(35.0)	±1.78	±0.77	±3.72
0.547	21.583(16.613) ± 0.068	55.99(43.12) ± 3.22	0.71(33.9)	±2.04	±0.69	±3.87
0.525	20.702(15.911) ± 0.066	56.01(43.07) ± 3.34	0.73(33.0)	±2.00	±0.70	±3.96
0.503	19.828(15.210) ± 0.065	55.63(42.71) ± 3.44	0.76(31.8)	±1.94	±0.84	±4.03
0.481	18.948(14.500) ± 0.063	55.29(42.37) ± 3.57	0.72(30.9)	±2.25	±0.85	±4.30
0.459	18.064(13.781) ± 0.061	55.70(42.57) ± 3.73	0.77(30.1)	±1.76	±0.78	±4.20
0.438	17.181(13.060) ± 0.059	54.86(41.80) ± 3.89	0.79(29.1)	±2.03	±1.04	±4.51
0.416	16.302(12.344) ± 0.058	53.65(40.75) ± 3.97	0.68(28.0)	±2.50	±1.08	±4.82
0.394	15.419(11.629) ± 0.056	53.33(40.40) ± 4.19	0.74(26.8)	±2.48	±0.99	±4.97
0.372	14.543(10.920) ± 0.054	52.71(39.80) ± 4.38	0.75(25.4)	±2.14	±0.93	±4.96
0.350	13.684(10.246) ± 0.037	52.57(39.60) ± 3.27	0.78(24.3)	±2.15	±0.93	±4.02
0.328	12.833(9.633) ± 0.035	51.53(38.93) ± 3.35	0.81(23.0)	±2.25	±0.95	±4.14
0.306	11.991(9.029) ± 0.034	49.87(37.95) ± 3.43	0.77(22.0)	±2.29	±0.94	±4.23
0.284	11.146(8.415) ± 0.033	48.20(36.98) ± 3.59	0.76(20.9)	±2.06	±0.89	±4.23

TABLE XXI. (*Continued*.)

$\delta\eta$	$\langle\mu_c\rangle(\langle\mu\rangle)$	$\langle k_c\rangle(\langle k\rangle)$	$\langle\chi^2/NDF\rangle(\langle NDF\rangle)$	$\delta\langle k_c\rangle$ (dead)	$\delta\langle k_c\rangle$ (fake)	$\delta\langle k_c\rangle$ (total)
0.263	10.299(7.796) ± 0.031	47.05(36.22) ± 3.67	0.71(19.7)	±1.60	±0.93	±4.11
0.241	9.450(7.169) ± 0.030	45.91(35.45) ± 3.79	0.69(18.6)	±1.51	±0.93	±4.18
0.219	8.597(6.532) ± 0.023	44.64(34.66) ± 3.18	0.62(17.5)	±1.43	±1.00	±3.62
0.197	7.740(5.885) ± 0.022	43.61(34.05) ± 3.30	0.57(16.3)	±1.22	±1.01	±3.66
0.175	6.881(5.231) ± 0.018	42.44(33.32) ± 3.04	0.50(14.9)	±1.36	±1.10	±3.51
0.153	6.023(4.574) ± 0.016	41.28(32.47) ± 3.26	0.45(13.6)	±1.39	±1.27	±3.76
0.131	5.165(3.914) ± 0.013	40.29(31.79) ± 3.21	0.45(12.2)	±1.33	±1.30	±3.71
0.109	4.306(3.253) ± 0.011	38.26(30.17) ± 3.27	0.46(10.7)	±1.62	±1.28	±3.87
0.087	3.445(2.587) ± 0.009	35.11(27.79) ± 3.39	0.51(9.2)	±1.18	±1.41	±3.86
0.066	2.606(2.037) ± 0.006	30.96(24.26) ± 3.44	0.54(7.9)	±1.25	±1.14	±3.83

TABLE XXII. NBD fit results in centrality 35–40%.

$\delta\eta$	$\langle\mu_c\rangle(\langle\mu\rangle)$	$\langle k_c\rangle(\langle k\rangle)$	$\langle\chi^2/NDF\rangle(\langle NDF\rangle)$	$\delta\langle k_c\rangle$ (dead)	$\delta\langle k_c\rangle$ (fake)	$\delta\langle k_c\rangle$ (total)
0.700	21.970(17.005) ± 0.071	47.25(36.57) ± 2.31	0.79(38.0)	±0.68	±0.60	±2.48
0.678	21.372(16.556) ± 0.070	47.47(36.77) ± 2.32	0.69(37.7)	±0.44	±0.02	±2.36
0.656	20.684(16.001) ± 0.068	46.97(36.33) ± 2.33	0.71(37.1)	±0.92	±0.23	±2.51
0.634	19.964(15.423) ± 0.067	46.50(35.92) ± 2.35	0.79(36.0)	±0.86	±0.30	±2.52
0.613	19.253(14.862) ± 0.065	46.36(35.78) ± 2.40	0.86(34.6)	±0.91	±0.15	±2.57
0.591	18.572(14.333) ± 0.064	45.46(35.08) ± 2.41	0.82(33.4)	±1.16	±0.36	±2.70
0.569	17.877(13.783) ± 0.063	45.55(35.11) ± 2.48	0.83(32.5)	±1.22	±0.37	±2.79
0.547	17.176(13.221) ± 0.061	45.52(35.05) ± 2.54	0.83(31.7)	±1.26	±0.44	±2.87
0.525	16.475(12.662) ± 0.059	45.45(34.94) ± 2.63	0.87(30.7)	±1.09	±0.34	±2.87
0.503	15.778(12.104) ± 0.058	45.41(34.85) ± 2.70	0.87(29.8)	±0.92	±0.22	±2.86
0.481	15.082(11.542) ± 0.057	44.90(34.38) ± 2.77	0.84(28.6)	±1.02	±0.36	±2.97
0.459	14.380(10.972) ± 0.055	44.50(33.97) ± 2.83	0.81(27.6)	±1.03	±0.31	±3.03
0.438	13.678(10.399) ± 0.053	43.95(33.42) ± 2.91	0.82(26.3)	±1.15	±0.39	±3.15
0.416	12.978(9.829) ± 0.052	43.68(33.09) ± 2.99	0.81(25.4)	±1.16	±0.33	±3.22
0.394	12.280(9.264) ± 0.050	43.03(32.45) ± 3.06	0.79(24.2)	±1.23	±0.41	±3.32
0.372	11.582(8.700) ± 0.049	42.60(31.98) ± 3.17	0.77(23.1)	±1.08	±0.45	±3.38
0.350	10.894(8.161) ± 0.033	42.04(31.45) ± 2.30	0.74(22.0)	±1.00	±0.34	±2.53
0.328	10.213(7.670) ± 0.032	41.13(30.87) ± 2.34	0.72(21.0)	±0.90	±0.35	±2.54
0.306	9.540(7.188) ± 0.031	40.19(30.29) ± 2.39	0.70(20.0)	±0.86	±0.19	±2.55
0.284	8.867(6.699) ± 0.029	39.08(29.61) ± 2.46	0.69(18.9)	±0.92	±0.28	±2.64
0.263	8.191(6.204) ± 0.028	38.50(29.35) ± 2.57	0.67(18.0)	±0.97	±0.34	±2.77
0.241	7.517(5.707) ± 0.027	37.29(28.54) ± 2.64	0.57(17.1)	±1.25	±0.50	±2.97
0.219	6.837(5.198) ± 0.021	36.65(28.17) ± 2.29	0.55(16.1)	±0.92	±0.47	±2.51
0.197	6.155(4.685) ± 0.019	35.93(27.66) ± 2.40	0.55(15.0)	±0.77	±0.51	±2.58
0.175	5.474(4.166) ± 0.016	34.69(26.74) ± 2.20	0.52(13.7)	±0.77	±0.65	±2.43
0.153	4.792(3.644) ± 0.015	33.23(25.56) ± 2.37	0.50(12.4)	±0.86	±0.72	±2.62
0.131	4.111(3.122) ± 0.012	31.76(24.13) ± 2.33	0.48(11.1)	±0.88	±0.72	±2.59
0.109	3.426(2.594) ± 0.010	30.11(22.76) ± 2.52	0.54(9.8)	±0.65	±0.72	±2.69
0.087	2.742(2.069) ± 0.008	28.05(20.82) ± 2.59	0.55(8.3)	±0.86	±0.84	±2.85
0.066	2.070(1.609) ± 0.006	24.89(18.20) ± 2.64	0.54(7.0)	±0.94	±0.95	±2.96

TABLE XXIII. NBD fit results in centrality 40–45%.

$\delta\eta$	$\langle\mu_c\rangle(\langle\mu\rangle)$	$\langle k_c\rangle(\langle k\rangle)$	$\langle\chi^2/NDF\rangle(\langle NDF\rangle)$	$\delta\langle k_c\rangle$ (dead)	$\delta\langle k_c\rangle$ (fake)	$\delta\langle k_c\rangle$ (total)
0.700	17.453(13.508) ± 0.063	37.64(29.13) ± 1.83	0.74(35.0)	±0.40	±0.98	±2.12
0.678	16.988(13.160) ± 0.062	37.36(28.94) ± 1.85	0.74(34.1)	±1.08	±0.27	±2.16
0.656	16.429(12.709) ± 0.061	37.57(29.06) ± 1.91	0.83(33.0)	±0.91	±0.00	±2.12
0.634	15.863(12.255) ± 0.059	37.55(29.01) ± 1.96	0.82(32.2)	±1.54	±0.31	±2.51
0.613	15.315(11.822) ± 0.058	36.88(28.47) ± 1.96	0.76(31.4)	±1.75	±0.34	±2.65

TABLE XXIII. (*Continued*.)

$\delta\eta$	$\langle\mu_c\rangle(\langle\mu\rangle)$	$\langle k_c\rangle(\langle k\rangle)$	$\langle\chi^2/NDF\rangle(\langle NDF\rangle)$	$\delta\langle k_c\rangle$ (dead)	$\delta\langle k_c\rangle$ (fake)	$\delta\langle k_c\rangle$ (total)
0.591	14.758(11.389) ± 0.057	36.84(28.43) ± 2.00	0.83(30.6)	±1.76	±0.32	±2.68
0.569	14.201(10.948) ± 0.056	36.74(28.32) ± 2.04	0.88(29.8)	±1.32	±0.26	±2.45
0.547	13.652(10.508) ± 0.054	36.19(27.85) ± 2.07	0.85(29.2)	±1.54	±0.32	±2.60
0.525	13.096(10.065) ± 0.053	36.01(27.67) ± 2.12	0.83(28.3)	±1.30	±0.22	±2.50
0.503	12.537(9.618) ± 0.051	36.07(27.66) ± 2.21	0.89(27.1)	±1.25	±0.28	±2.55
0.481	11.980(9.169) ± 0.050	35.96(27.51) ± 2.28	0.91(26.3)	±1.27	±0.33	±2.63
0.459	11.422(8.715) ± 0.049	35.74(27.26) ± 2.36	0.91(25.2)	±1.12	±0.33	±2.63
0.438	10.861(8.258) ± 0.048	35.46(26.95) ± 2.43	0.87(24.2)	±1.08	±0.28	±2.67
0.416	10.302(7.803) ± 0.046	35.19(26.64) ± 2.51	0.89(22.9)	±1.10	±0.38	±2.77
0.394	9.742(7.349) ± 0.045	35.42(26.71) ± 2.63	0.92(22.0)	±0.69	±0.34	±2.74
0.372	9.189(6.902) ± 0.043	35.02(26.31) ± 2.70	0.83(21.1)	±0.86	±0.36	±2.86
0.350	8.649(6.478) ± 0.030	34.15(25.59) ± 1.94	0.73(19.9)	±1.22	±0.51	±2.35
0.328	8.110(6.090) ± 0.029	33.55(25.21) ± 1.99	0.71(19.0)	±1.19	±0.45	±2.36
0.306	7.578(5.708) ± 0.027	33.04(24.89) ± 2.06	0.70(18.0)	±1.22	±0.41	±2.43
0.284	7.044(5.321) ± 0.026	32.48(24.52) ± 2.12	0.67(17.0)	±1.18	±0.43	±2.47
0.263	6.509(4.930) ± 0.025	31.66(23.97) ± 2.17	0.63(16.1)	±1.12	±0.45	±2.48
0.241	5.973(4.533) ± 0.024	30.82(23.44) ± 2.22	0.61(15.1)	±1.00	±0.46	±2.48
0.219	5.435(4.131) ± 0.018	29.59(22.59) ± 1.88	0.58(14.0)	±1.09	±0.45	±2.23
0.197	4.894(3.723) ± 0.017	28.75(22.00) ± 2.00	0.54(13.1)	±0.83	±0.49	±2.22
0.175	4.353(3.311) ± 0.014	28.04(21.41) ± 1.89	0.56(12.1)	±0.90	±0.54	±2.16
0.153	3.811(2.896) ± 0.013	26.88(20.50) ± 2.02	0.50(10.9)	±0.74	±0.51	±2.21
0.131	3.267(2.478) ± 0.011	25.91(19.73) ± 2.01	0.52(9.9)	±0.63	±0.54	±2.18
0.109	2.724(2.060) ± 0.009	24.44(18.61) ± 2.05	0.47(8.7)	±0.38	±0.61	±2.18
0.087	2.179(1.639) ± 0.007	22.93(17.48) ± 2.12	0.55(7.4)	±0.38	±0.55	±2.22
0.066	1.646(1.279) ± 0.005	20.46(15.59) ± 2.26	0.54(6.3)	±0.59	±0.51	±2.39

TABLE XXIV. NBD fit results in centrality 45–50%.

$\delta\eta$	$\langle\mu_c\rangle(\langle\mu\rangle)$	$\langle k_c\rangle(\langle k\rangle)$	$\langle\chi^2/NDF\rangle(\langle NDF\rangle)$	$\delta\langle k_c\rangle$ (dead)	$\delta\langle k_c\rangle$ (fake)	$\delta\langle k_c\rangle$ (total)
0.700	13.493(10.444) ± 0.054	32.22(24.94) ± 1.72	0.77(27.0)	±1.57	±0.13	±2.34
0.678	13.123(10.166) ± 0.053	32.44(25.13) ± 1.74	0.79(26.9)	±1.12	±0.09	±2.07
0.656	12.698(9.823) ± 0.052	32.30(24.99) ± 1.77	0.81(25.6)	±0.70	±0.22	±1.92
0.634	12.261(9.472) ± 0.051	32.54(25.14) ± 1.85	0.89(24.6)	±0.78	±0.32	±2.04
0.613	11.829(9.131) ± 0.050	32.98(25.46) ± 1.94	0.89(23.9)	±0.81	±0.20	±2.11
0.591	11.403(8.800) ± 0.049	33.01(25.47) ± 2.00	0.88(23.1)	±0.56	±0.28	±2.10
0.569	10.976(8.462) ± 0.048	32.73(25.23) ± 2.04	0.84(22.3)	±0.56	±0.24	±2.13
0.547	10.547(8.119) ± 0.046	32.55(25.05) ± 2.09	0.84(21.7)	±0.52	±0.29	±2.18
0.525	10.120(7.778) ± 0.045	32.54(25.00) ± 2.16	0.80(21.0)	±0.30	±0.28	±2.20
0.503	9.694(7.437) ± 0.044	32.48(24.91) ± 2.23	0.76(20.5)	±0.39	±0.31	±2.28
0.481	9.267(7.093) ± 0.043	32.14(24.60) ± 2.28	0.67(19.8)	±0.44	±0.30	±2.34
0.459	8.836(6.742) ± 0.042	31.98(24.40) ± 2.37	0.60(19.1)	±0.57	±0.34	±2.46
0.438	8.403(6.389) ± 0.041	31.90(24.26) ± 2.46	0.55(18.5)	±0.56	±0.36	±2.54
0.416	7.970(6.037) ± 0.039	31.80(24.10) ± 2.56	0.52(17.7)	±0.58	±0.38	±2.65
0.394	7.537(5.686) ± 0.038	31.73(23.97) ± 2.67	0.54(17.1)	±0.79	±0.42	±2.82
0.372	7.108(5.339) ± 0.037	31.47(23.68) ± 2.78	0.53(16.4)	±0.83	±0.37	±2.92
0.350	6.688(5.009) ± 0.025	31.14(23.38) ± 2.05	0.54(15.6)	±0.84	±0.38	±2.25
0.328	6.271(4.709) ± 0.024	30.59(23.16) ± 2.12	0.55(15.0)	±0.77	±0.37	±2.29
0.306	5.860(4.413) ± 0.023	29.82(22.83) ± 2.20	0.55(14.4)	±0.72	±0.35	±2.34
0.284	5.450(4.115) ± 0.022	29.04(22.41) ± 2.27	0.54(13.7)	±0.57	±0.36	±2.37
0.263	5.037(3.813) ± 0.021	28.60(22.23) ± 2.41	0.57(13.1)	±0.44	±0.43	±2.49
0.241	4.623(3.508) ± 0.020	28.11(21.89) ± 2.48	0.55(12.4)	±0.47	±0.42	±2.56
0.219	4.205(3.196) ± 0.016	27.55(21.51) ± 2.15	0.55(11.8)	±0.45	±0.38	±2.23
0.197	3.785(2.879) ± 0.015	27.20(21.34) ± 2.35	0.56(11.0)	±0.42	±0.41	±2.42

TABLE XXIV. (*Continued.*)

$\delta\eta$	$\langle\mu_c\rangle(\langle\mu\rangle)$	$\langle k_c\rangle(\langle k\rangle)$	$\langle\chi^2/NDF\rangle(\langle NDF\rangle)$	$\delta\langle k_c\rangle$ (dead)	$\delta\langle k_c\rangle$ (fake)	$\delta\langle k_c\rangle$ (total)
0.175	3.364(2.558) ± 0.012	26.76(21.15) ± 2.25	0.58(10.3)	±0.45	±0.40	±2.33
0.153	2.943(2.236) ± 0.011	26.24(20.74) ± 2.47	0.57(9.4)	±0.16	±0.40	±2.50
0.131	2.523(1.913) ± 0.009	25.81(20.49) ± 2.54	0.53(8.5)	±0.12	±0.42	±2.57
0.109	2.104(1.592) ± 0.008	25.12(19.94) ± 2.71	0.48(7.6)	±0.09	±0.52	±2.76
0.087	1.692(1.306) ± 0.006	23.73(18.71) ± 2.55	0.45(6.6)	±0.14	±0.38	±2.58
0.066	1.277(1.014) ± 0.004	21.69(16.94) ± 2.72	0.49(5.4)	±0.51	±0.45	±2.80

TABLE XXV. NBD fit results in centrality 50–55%.

$\delta\eta$	$\langle\mu_c\rangle(\langle\mu\rangle)$	$\langle k_c\rangle(\langle k\rangle)$	$\langle\chi^2/NDF\rangle(\langle NDF\rangle)$	$\delta\langle k_c\rangle$ (dead)	$\delta\langle k_c\rangle$ (fake)	$\delta\langle k_c\rangle$ (total)
0.700	10.177(7.877) ± 0.046	27.08(20.96) ± 1.52	1.18(24.0)	±1.23	±0.17	±1.96
0.678	9.898(7.667) ± 0.045	26.98(20.90) ± 1.53	1.14(23.0)	±0.62	±0.26	±1.67
0.656	9.584(7.414) ± 0.044	26.02(20.12) ± 1.50	1.07(21.9)	±0.94	±0.23	±1.79
0.634	9.257(7.151) ± 0.044	25.65(19.81) ± 1.51	0.97(21.2)	±0.43	±0.21	±1.58
0.613	8.935(6.897) ± 0.043	25.16(19.42) ± 1.52	0.85(20.8)	±0.63	±0.16	±1.66
0.591	8.613(6.647) ± 0.042	24.75(19.10) ± 1.53	0.82(20.0)	±0.77	±0.21	±1.73
0.569	8.287(6.389) ± 0.041	24.69(19.03) ± 1.58	0.80(19.6)	±0.54	±0.10	±1.68
0.547	7.964(6.130) ± 0.040	24.46(18.82) ± 1.62	0.79(19.1)	±0.70	±0.22	±1.77
0.525	7.640(5.872) ± 0.039	24.42(18.76) ± 1.67	0.79(18.5)	±0.67	±0.28	±1.81
0.503	7.318(5.614) ± 0.038	24.25(18.59) ± 1.72	0.74(18.0)	±0.67	±0.25	±1.86
0.481	6.991(5.351) ± 0.037	24.35(18.62) ± 1.80	0.74(17.5)	±0.57	±0.26	±1.91
0.459	6.664(5.085) ± 0.036	24.37(18.58) ± 1.89	0.70(16.9)	±0.79	±0.24	±2.06
0.438	6.338(4.818) ± 0.035	24.32(18.48) ± 1.96	0.61(16.3)	±0.93	±0.26	±2.19
0.416	6.013(4.554) ± 0.034	24.34(18.42) ± 2.05	0.55(15.7)	±0.93	±0.39	±2.28
0.394	5.689(4.292) ± 0.033	24.43(18.41) ± 2.14	0.52(15.0)	±1.01	±0.22	±2.38
0.372	5.365(4.031) ± 0.032	24.59(18.43) ± 2.28	0.52(14.3)	±0.85	±0.35	±2.46
0.350	5.047(3.781) ± 0.022	24.82(18.54) ± 1.71	0.54(13.8)	±0.85	±0.37	±1.94
0.328	4.731(3.554) ± 0.021	24.90(18.65) ± 1.81	0.62(13.4)	±0.58	±0.26	±1.92
0.306	4.421(3.331) ± 0.020	24.53(18.49) ± 1.90	0.62(12.9)	±0.47	±0.35	±1.99
0.284	4.110(3.106) ± 0.019	24.09(18.29) ± 2.00	0.58(12.3)	±0.62	±0.20	±2.10
0.263	3.798(2.877) ± 0.018	23.76(18.20) ± 2.19	0.61(11.6)	±0.57	±0.11	±2.27
0.241	3.487(2.646) ± 0.018	23.58(18.20) ± 2.34	0.59(11.1)	±0.59	±0.23	±2.43
0.219	3.173(2.412) ± 0.013	23.10(17.98) ± 2.13	0.56(10.5)	±0.77	±0.24	±2.28
0.197	2.858(2.174) ± 0.013	22.73(17.85) ± 2.36	0.53(9.8)	±0.74	±0.25	±2.49
0.175	2.541(1.932) ± 0.010	22.47(17.74) ± 2.36	0.54(9.0)	±0.95	±0.27	±2.56
0.153	2.224(1.691) ± 0.010	22.22(17.61) ± 2.64	0.57(8.2)	±0.89	±0.29	±2.80
0.131	1.906(1.447) ± 0.008	21.76(17.39) ± 2.93	0.64(7.4)	±0.75	±0.36	±3.05
0.109	1.593(1.215) ± 0.006	20.48(16.47) ± 3.02	0.59(6.6)	±0.69	±0.35	±3.11
0.087	1.279(0.982) ± 0.005	19.00(15.26) ± 2.67	0.54(5.5)	±0.67	±0.47	±2.80
0.066	0.969(0.770) ± 0.004	16.64(13.48) ± 2.31	0.52(4.5)	±0.59	±0.54	±2.45

TABLE XXVI. NBD fit results in centrality 55–60%.

$\delta\eta$	$\langle\mu_c\rangle(\langle\mu\rangle)$	$\langle k_c\rangle(\langle k\rangle)$	$\langle\chi^2/NDF\rangle(\langle NDF\rangle)$	$\delta\langle k_c\rangle$ (dead)	$\delta\langle k_c\rangle$ (fake)	$\delta\langle k_c\rangle$ (total)
0.700	7.465(5.778) ± 0.041	18.75(14.52) ± 1.12	0.71(16.0)	±0.59	±0.13	±1.27
0.678	7.258(5.622) ± 0.040	19.02(14.74) ± 1.14	0.76(16.0)	±0.60	±0.08	±1.29
0.656	7.021(5.431) ± 0.039	18.80(14.54) ± 1.14	0.73(15.8)	±0.61	±0.09	±1.29
0.634	6.781(5.238) ± 0.038	18.41(14.22) ± 1.14	0.57(15.4)	±0.57	±0.09	±1.28
0.613	6.547(5.054) ± 0.038	18.01(13.89) ± 1.13	0.51(14.7)	±0.70	±0.07	±1.33
0.591	6.307(4.867) ± 0.037	17.98(13.87) ± 1.15	0.56(14.4)	±0.70	±0.07	±1.34
0.569	6.070(4.680) ± 0.036	17.84(13.75) ± 1.15	0.51(14.1)	±0.69	±0.07	±1.35
0.547	5.833(4.490) ± 0.035	17.66(13.59) ± 1.17	0.47(13.7)	±0.63	±0.07	±1.33
0.525	5.596(4.301) ± 0.034	17.52(13.46) ± 1.19	0.44(13.4)	±0.60	±0.08	±1.34

TABLE XXVI. (*Continued*.)

$\delta\eta$	$\langle\mu_c\rangle(\langle\mu\rangle)$	$\langle k_c\rangle(\langle k\rangle)$	$\langle\chi^2/NDF\rangle(\langle NDF\rangle)$	$\delta\langle k_c\rangle$ (dead)	$\delta\langle k_c\rangle$ (fake)	$\delta\langle k_c\rangle$ (total)
0.503	5.360(4.112) ± 0.033	17.52(13.43) ± 1.22	0.43(13.2)	±0.67	±0.09	±1.40
0.481	5.122(3.920) ± 0.033	17.49(13.38) ± 1.26	0.47(13.1)	±0.66	±0.09	±1.43
0.459	4.885(3.728) ± 0.032	17.37(13.24) ± 1.30	0.49(12.6)	±0.69	±0.09	±1.47
0.438	4.648(3.534) ± 0.031	17.22(13.08) ± 1.33	0.51(12.1)	±0.74	±0.10	±1.53
0.416	4.411(3.340) ± 0.030	17.20(13.01) ± 1.39	0.58(11.5)	±0.62	±0.10	±1.52
0.394	4.173(3.148) ± 0.029	17.18(12.95) ± 1.44	0.62(10.9)	±0.78	±0.12	±1.64
0.372	3.935(2.955) ± 0.028	17.34(13.00) ± 1.54	0.63(10.4)	±0.84	±0.13	±1.76
0.350	3.701(2.772) ± 0.019	17.31(12.94) ± 1.15	0.65(9.9)	±0.67	±0.08	±1.33
0.328	3.472(2.607) ± 0.018	17.17(12.87) ± 1.19	0.66(9.5)	±0.71	±0.10	±1.39
0.306	3.244(2.444) ± 0.018	17.09(12.85) ± 1.25	0.68(9.2)	±0.64	±0.09	±1.41
0.284	3.016(2.279) ± 0.017	16.91(12.74) ± 1.32	0.67(8.6)	±0.53	±0.08	±1.42
0.263	2.787(2.111) ± 0.016	16.61(12.58) ± 1.40	0.62(8.1)	±0.56	±0.09	±1.51
0.241	2.558(1.942) ± 0.015	16.53(12.57) ± 1.50	0.61(7.6)	±0.52	±0.11	±1.59
0.219	2.326(1.769) ± 0.012	16.34(12.46) ± 1.35	0.66(7.1)	±0.49	±0.10	±1.44
0.197	2.095(1.595) ± 0.011	16.13(12.30) ± 1.44	0.62(6.7)	±0.48	±0.11	±1.52
0.175	1.861(1.417) ± 0.009	16.07(12.24) ± 1.45	0.72(6.3)	±0.34	±0.12	±1.49
0.153	1.630(1.240) ± 0.009	15.67(11.91) ± 1.54	0.59(5.7)	±0.17	±0.13	±1.56
0.131	1.399(1.062) ± 0.007	14.90(11.39) ± 1.50	0.47(5.1)	±0.35	±0.15	±1.54
0.109	1.166(0.882) ± 0.006	14.25(10.82) ± 1.56	0.42(4.5)	±0.37	±0.17	±1.61
0.087	0.935(0.714) ± 0.004	13.41(10.20) ± 1.63	0.46(4.0)	±0.30	±0.15	±1.66
0.066	0.703(0.548) ± 0.003	11.85(9.19) ± 1.63	0.53(3.3)	±0.35	±0.17	±1.67

TABLE XXVII. NBD fit results in centrality 60–65%.

$\delta\eta$	$\langle\mu_c\rangle(\langle\mu\rangle)$	$\langle k_c\rangle(\langle k\rangle)$	$\langle\chi^2/NDF\rangle(\langle NDF\rangle)$	$\delta\langle k_c\rangle$ (dead)	$\delta\langle k_c\rangle$ (fake)	$\delta\langle k_c\rangle$ (total)
0.700	5.337(4.131) ± 0.033	14.40(11.14) ± 0.81	0.79(15.0)	±0.33	±0.04	±0.88
0.678	5.197(4.026) ± 0.033	14.25(11.04) ± 0.82	0.77(14.8)	±0.45	±0.04	±0.94
0.656	5.031(3.892) ± 0.032	14.37(11.12) ± 0.86	0.61(14.2)	±0.46	±0.03	±0.97
0.634	4.861(3.755) ± 0.032	14.35(11.09) ± 0.88	0.53(13.8)	±0.47	±0.04	±0.99
0.613	4.686(3.617) ± 0.031	14.41(11.13) ± 0.93	0.78(13.1)	±0.44	±0.04	±1.03
0.591	4.519(3.487) ± 0.030	13.99(10.80) ± 0.90	0.63(12.9)	±0.53	±0.04	±1.05
0.569	4.344(3.349) ± 0.029	14.01(10.80) ± 0.92	0.73(12.7)	±0.51	±0.05	±1.06
0.547	4.169(3.209) ± 0.029	14.23(10.96) ± 0.97	0.82(12.5)	±0.41	±0.04	±1.05
0.525	4.003(3.077) ± 0.028	13.97(10.74) ± 0.97	0.64(12.0)	±0.41	±0.04	±1.06
0.503	3.835(2.942) ± 0.027	13.88(10.65) ± 1.00	0.59(11.8)	±0.45	±0.04	±1.10
0.481	3.665(2.805) ± 0.027	13.89(10.63) ± 1.04	0.60(11.6)	±0.43	±0.04	±1.12
0.459	3.495(2.667) ± 0.026	13.85(10.57) ± 1.07	0.59(11.1)	±0.34	±0.05	±1.12
0.438	3.326(2.529) ± 0.025	13.78(10.48) ± 1.11	0.56(10.5)	±0.33	±0.06	±1.16
0.416	3.159(2.393) ± 0.025	13.65(10.35) ± 1.15	0.48(9.9)	±0.38	±0.06	±1.22
0.394	2.989(2.255) ± 0.024	13.71(10.35) ± 1.23	0.46(9.5)	±0.37	±0.05	±1.28
0.372	2.818(2.117) ± 0.023	13.95(10.48) ± 1.33	0.52(8.9)	±0.40	±0.05	±1.39
0.350	2.652(1.986) ± 0.016	14.10(10.57) ± 1.00	0.54(8.5)	±0.41	±0.06	±1.09
0.328	2.487(1.867) ± 0.015	14.06(10.58) ± 1.06	0.56(8.1)	±0.41	±0.06	±1.15
0.306	2.324(1.750) ± 0.015	14.16(10.71) ± 1.14	0.66(7.6)	±0.34	±0.06	±1.19
0.284	2.160(1.631) ± 0.014	14.12(10.76) ± 1.22	0.66(7.1)	±0.38	±0.06	±1.28
0.263	1.996(1.511) ± 0.013	14.01(10.76) ± 1.31	0.63(6.6)	±0.36	±0.06	±1.36
0.241	1.832(1.390) ± 0.013	13.79(10.64) ± 1.39	0.53(6.3)	±0.40	±0.06	±1.45
0.219	1.667(1.267) ± 0.010	13.49(10.50) ± 1.24	0.51(5.9)	±0.40	±0.07	±1.30
0.197	1.502(1.143) ± 0.009	13.23(10.37) ± 1.35	0.47(5.5)	±0.46	±0.07	±1.43
0.175	1.335(1.015) ± 0.007	13.17(10.38) ± 1.32	0.50(5.1)	±0.47	±0.08	±1.40
0.153	1.168(0.888) ± 0.007	12.96(10.25) ± 1.55	0.56(4.7)	±0.38	±0.10	±1.60
0.131	1.005(0.768) ± 0.006	12.13(9.56) ± 1.46	0.45(4.3)	±0.29	±0.10	±1.50
0.109	0.838(0.639) ± 0.005	11.68(9.21) ± 1.66	0.44(3.8)	±0.15	±0.12	±1.67
0.087	0.673(0.524) ± 0.004	10.96(8.64) ± 1.65	0.54(3.3)	±0.14	±0.14	±1.66
0.066	0.507(0.405) ± 0.003	9.15(7.32) ± 1.29	0.41(2.7)	±0.16	±0.09	±1.31

[1] M. A. Stephanov, Prog. Theor. Phys. Suppl. **153**, 139 (2004); Int. J. Mod. Phys. A **20**, 4387 (2005).
[2] M. Asakawa and K. Yazaki, Nucl. Phys. **A504**, 668 (1989).
[3] A. Barducci, R. Casalbuoni, S. De Curtis, R. Gatto, and G. Pettini, Phys. Lett. **B231**, 463 (1989); Phys. Rev. D **41**, 1610 (1990).
[4] A. Barducci, R. Casalbuoni, G. Pettini, and R. Gatto, Phys. Rev. D **49**, 426 (1994).
[5] J. Berges and K. Rajagopal, Nucl. Phys. **B538**, 215 (1999).
[6] M. A. Halasz, A. D. Jackson, R. E. Shrock, M. A. Stephanov, and J. J. M. Verbaarschot, Phys. Rev. D **58**, 096007 (1998).
[7] O. Scavenius, A. Mocsy, I. N. Mishustin, and D. H. Rischke, Phys. Rev. C **64**, 045202 (2001).
[8] N. G. Antoniou and A. S. Kapoyannis, Phys. Lett. **B563**, 165 (2003).
[9] Y. Hatta and T. Ikeda, Phys. Rev. D **67**, 014028 (2003).
[10] F. R. Brown *et al.*, Phys. Rev. Lett. **65**, 2491 (1990).
[11] M. A. Stephanov, K. Rajagopal, and E. V. Shuryak, Phys. Rev. Lett. **81**, 4816 (1998).
[12] K. Adcox *et al.* (PHENIX Collaboration), Nucl. Phys. **A757**, 184 (2005).
[13] S. S. Adler *et al.* (PHENIX Collaboration), Phys. Rev. Lett. **91**, 072301 (2003).
[14] S. S. Adler *et al.* (PHENIX Collaboration), Phys. Rev. C **69**, 034910 (2004).
[15] A. Adare *et al.* (PHENIX Collaboration), Phys. Rev. Lett. **98**, 172301 (2007).
[16] A. Adare *et al.* (PHENIX Collaboration), Phys. Rev. Lett. **98**, 162301 (2007).
[17] Y. Aoki, Z. Fodor, S. D. Katz, and K. K. Szabo, Phys. Lett. **B643**, 46 (2006).
[18] L. S. Ornstein and F. Zernike, Proc. Sec. Sci. K. Med. Akad. Wet. **17**, 793 (1914).
[19] V. L. Ginzburg and L. D. Landau, Zh. Eksp. Teor. Fiz. **20**, 1064 (1950).
[20] N. Sasaki, O. Miyamura, S. Muroya, and C. Nonaka, Europhys. Lett. **54**, 38 (2001).
[21] J. D. Bjorken, Phys. Rev. D **27**, 140 (1983).
[22] S. S. Adler *et al.* (PHENIX Collaboration), Phys. Rev. C **71**, 034908 (2005).
[23] N. G. Antoniou, C. N. Ktorides, I. S. Mistakidis, and F. K. Diakonos, Eur. Phys. J. C **4**, 513 (1998).
[24] N. G. Antoniou, F. K. Diakonos, A. S. Kapoyannis, and K. S. Kousouris, Phys. Rev. Lett. **97**, 032002 (2006).
[25] N. G. Antoniou, Y. F. Contoyiannis, F. K. Diakonos, A. I. Karanikas, and C. N. Ktorides, Nucl. Phys. **A693**, 799 (2001).
[26] E. A. De Wolf, I. M. Dremin, and W. Kittel, Phys. Rep. **270**, 1 (1996).
[27] A. Bialas and R. Peschanski, Nucl. Phys. **B273**, 703 (1986); **B308**, 857 (1988).
[28] T. Abbott *et al.* (E-802 Collaboration), Phys. Rev. C **52**, 2663 (1995).
[29] H. Nakamura and R. Seki, Phys. Rev. C **66**, 024902 (2002).
[30] K. Adcox *et al.* (PHENIX Collaboration), Nucl. Instrum. Methods A **499**, 469 (2003).
[31] S. S. Adler *et al.* (PHENIX Collaboration), Phys. Rev. C **69**, 034909 (2004).
[32] Computer code GEANT 3.21, CERN, Geneva, 1993.
[33] F. James and M. Roos, Comput. Phys. Commun. **10**, 343 (1975).
[34] P. Carruthers and C. C. Shih, Phys. Lett. **B165**, 209 (1985).
[35] M. J. Tannenbaum, E802 Internal Report No. E-802-MEM-58, 1993.
[36] G. Baym, B. Blattel, L. L. Frankfurt, H. Heiselberg, and M. Strikman, Phys. Rev. C **52**, 1604 (1995).
[37] M. Rybczynski *et al.* (NA49 Collaboration), J. Phys. Conf. Ser. **5**, 74 (2005).
[38] V. P. Konchakovski, S. Haussler, M. I. Gorenstein, E. L. Bratkovskaya, M. Bleicher, and H. Stocker, Phys. Rev. C **73**, 034902 (2006).
[39] B. B. Back *et al.* (PHOBOS Collaboration), Phys. Rev. C **72**, 051901 (2005); E. B. Johnson, AIP Conf. Proc. **842**, 137 (2006).
[40] J. Adams *et al.* (STAR Collaboration), Phys. Rev. Lett. **98**, 062301 (2007); nucl-ex/0601042, Phys. Rev. C (to be published).
[41] Y. Akiba *et al.* (E-802 Collaboration), Phys. Rev. C **56**, 1544 (1997).
[42] S. S. Adler *et al.* (PHENIX Collaboration), Phys. Rev. Lett. **93**, 152302 (2004).
[43] A. Enokizono, Ph.D. thesis, Department of Physical Science, Hiroshima University, 2004.
[44] D. J. Scalapino and R. L. Sugar, Phys. Rev. D **8**, 2284 (1973).

Elliptic Flow for ϕ Mesons and (Anti)deuterons in Au + Au Collisions at $\sqrt{s_{NN}} = 200$ GeV

S. Afanasiev,[17] C. Aidala,[7] N. N. Ajitanand,[43] Y. Akiba,[37,38] J. Alexander,[43] A. Al-Jamel,[33] K. Aoki,[23,37] L. Aphecetche,[45] R. Armendariz,[33] S. H. Aronson,[3] R. Averbeck,[44] T. C. Awes,[34] B. Azmoun,[3] V. Babintsev,[14] A. Baldisseri,[8] K. N. Barish,[4] P. D. Barnes,[26] B. Bassalleck,[32] S. Bathe,[4] S. Batsouli,[7] V. Baublis,[36] F. Bauer,[4] A. Bazilevsky,[3] S. Belikov,[3,16] R. Bennett,[44] Y. Berdnikov,[40] M. T. Bjorndal,[7] J. G. Boissevain,[26] H. Borel,[8] K. Boyle,[44] M. L. Brooks,[26] D. S. Brown,[33] D. Bucher,[29] H. Buesching,[3] V. Bumazhnov,[14] G. Bunce,[3,38] J. M. Burward-Hoy,[26] S. Butsyk,[44] S. Campbell,[44] J.-S. Chai,[18] S. Chernichenko,[14] J. Chiba,[19] C. Y. Chi,[7] M. Chiu,[7] I. J. Choi,[52] T. Chujo,[49] V. Cianciolo,[34] C. R. Cleven,[12] Y. Cobigo,[8] B. A. Cole,[7] M. P. Comets,[35] P. Constantin,[16] M. Csanád,[10] T. Csörgő,[20] T. Dahms,[44] K. Das,[11] G. David,[3] H. Delagrange,[45] A. Denisov,[14] D. d'Enterria,[7] A. Deshpande,[38,44] E. J. Desmond,[3] O. Dietzsch,[41] A. Dion,[44] J. L. Drachenberg,[1] O. Drapier,[24] A. Drees,[44] A. K. Dubey,[51] A. Durum,[14] V. Dzhordzhadze,[46] Y. V. Efremenko,[34] J. Egdemir,[44] A. Enokizono,[13] H. En'yo,[37,38] B. Espagnon,[35] S. Esumi,[48] D. E. Fields,[32,38] F. Fleuret,[24] S. L. Fokin,[22] B. Forestier,[27] Z. Fraenkel,[51] J. E. Frantz,[7] A. Franz,[3] A. D. Frawley,[11] Y. Fukao,[23,37] S.-Y. Fung,[4] S. Gadrat,[27] F. Gastineau,[45] M. Germain,[45] A. Glenn,[46] M. Gonin,[24] J. Gosset,[8] Y. Goto,[37,38] R. Granier de Cassagnac,[24] N. Grau,[16] S. V. Greene,[49] M. Grosse Perdekamp,[15,38] T. Gunji,[5] H.-Å. Gustafsson,[28] T. Hachiya,[13,37] A. Hadj Henni,[45] J. S. Haggerty,[3] M. N. Hagiwara,[1] H. Hamagaki,[5] H. Harada,[13] E. P. Hartouni,[25] K. Haruna,[13] M. Harvey,[3] E. Haslum,[28] K. Hasuko,[37] R. Hayano,[5] M. Heffner,[25] T. K. Hemmick,[44] J. M. Heuser,[37] X. He,[12] H. Hiejima,[15] J. C. Hill,[16] R. Hobbs,[32] M. Holmes,[49] W. Holzmann,[43] K. Homma,[13] B. Hong,[21] T. Horaguchi,[37,47] M. G. Hur,[18] T. Ichihara,[37,38] K. Imai,[23,37] M. Inaba,[48] D. Isenhower,[1] L. Isenhower,[1] M. Ishihara,[37] T. Isobe,[5] M. Issah,[43] A. Isupov,[17] B. V. Jacak,[44,*] J. Jia,[7] J. Jin,[7] O. Jinnouchi,[38] B. M. Johnson,[3] K. S. Joo,[30] D. Jouan,[35] F. Kajihara,[5,37] S. Kametani,[5,50] N. Kamihara,[37,47] M. Kaneta,[38] J. H. Kang,[52] T. Kawagishi,[48] A. V. Kazantsev,[22] S. Kelly,[6] A. Khanzadeev,[36] D. J. Kim,[52] E. Kim,[42] Y.-S. Kim,[18] E. Kinney,[6] A. Kiss,[10] E. Kistenev,[3] A. Kiyomichi,[37] C. Klein-Boesing,[29] L. Kochenda,[36] V. Kochetkov,[14] B. Komkov,[36] M. Konno,[48] D. Kotchetkov,[4] A. Kozlov,[51] P. J. Kroon,[3] G. J. Kunde,[26] N. Kurihara,[5] K. Kurita,[39,37] M. J. Kweon,[21] Y. Kwon,[52] G. S. Kyle,[33] R. Lacey,[43] J. G. Lajoie,[16] A. Lebedev,[16] Y. Le Bornec,[35] S. Leckey,[44] D. M. Lee,[26] M. K. Lee,[52] M. J. Leitch,[26] M. A. L. Leite,[41] H. Lim,[42] A. Litvinenko,[17] M. X. Liu,[26] X. H. Li,[4] C. F. Maguire,[49] Y. I. Makdisi,[3] A. Malakhov,[17] M. D. Malik,[32] V. I. Manko,[22] H. Masui,[48] F. Matathias,[44] M. C. McCain,[15] P. L. McGaughey,[26] Y. Miake,[48] T. E. Miller,[49] A. Milov,[44] S. Mioduszewski,[3] G. C. Mishra,[12] J. T. Mitchell,[3] D. P. Morrison,[3] J. M. Moss,[26] T. V. Moukhanova,[22] D. Mukhopadhyay,[49] J. Murata,[39,37] S. Nagamiya,[19] Y. Nagata,[48] J. L. Nagle,[6] M. Naglis,[51] T. Nakamura,[13] J. Newby,[25] M. Nguyen,[44] B. E. Norman,[26] A. S. Nyanin,[22] J. Nystrand,[28] E. O'Brien,[3] C. A. Ogilvie,[16] H. Ohnishi,[37] I. D. Ojha,[49] H. Okada,[23,37] K. Okada,[38] O. O. Omiwade,[1] A. Oskarsson,[28] I. Otterlund,[28] K. Ozawa,[5] D. Pal,[49] A. P. T. Palounek,[26] V. Pantuev,[44] V. Papavassiliou,[33] J. Park,[42] W. J. Park,[21] S. F. Pate,[33] H. Pei,[16] J.-C. Peng,[15] H. Pereira,[8] V. Peresedov,[17] D. Yu. Peressounko,[22] C. Pinkenburg,[3] R. P. Pisani,[3] M. L. Purschke,[3] A. K. Purwar,[44] H. Qu,[12] J. Rak,[16] I. Ravinovich,[51] K. F. Read,[34,46] M. Reuter,[44] K. Reygers,[29] V. Riabov,[36] Y. Riabov,[36] G. Roche,[27] A. Romana,[24,†] M. Rosati,[16] S. S. E. Rosendahl,[28] P. Rosnet,[27] P. Rukoyatkin,[17] V. L. Rykov,[37] S. S. Ryu,[52] B. Sahlmueller,[29] N. Saito,[23,37,38] T. Sakaguchi,[5,50] S. Sakai,[48] V. Samsonov,[36] H. D. Sato,[23,37] S. Sato,[3,19,48] S. Sawada,[19] V. Semenov,[14] R. Seto,[4] D. Sharma,[51] T. K. Shea,[3] I. Shein,[14] T.-A. Shibata,[37,47] K. Shigaki,[13] M. Shimomura,[48] T. Shohjoh,[48] K. Shoji,[23,37] A. Sickles,[44] C. L. Silva,[41] D. Silvermyr,[34] K. S. Sim,[21] C. P. Singh,[2] V. Singh,[2] S. Skutnik,[16] W. C. Smith,[1] A. Soldatov,[14] R. A. Soltz,[25] W. E. Sondheim,[26] S. P. Sorensen,[46] I. V. Sourikova,[3] F. Staley,[8] P. W. Stankus,[34] E. Stenlund,[28] M. Stepanov,[33] A. Ster,[20] S. P. Stoll,[3] T. Sugitate,[13] C. Suire,[35] J. P. Sullivan,[26] J. Sziklai,[20] T. Tabaru,[38] S. Takagi,[48] E. M. Takagui,[41] A. Taketani,[37,38] K. H. Tanaka,[19] Y. Tanaka,[31] K. Tanida,[37,38] M. J. Tannenbaum,[3] A. Taranenko,[43] P. Tarján,[9] T. L. Thomas,[32] M. Togawa,[23,37] J. Tojo,[37] H. Torii,[37] R. S. Towell,[1] V-N. Tram,[24] I. Tserruya,[51] Y. Tsuchimoto,[13,37] S. K. Tuli,[2] H. Tydesjö,[28] N. Tyurin,[14] C. Vale,[16] H. Valle,[49] H. W. vanHecke,[26] J. Velkovska,[49] R. Vertesi,[9] A. A. Vinogradov,[22] E. Vznuzdaev,[36] M. Wagner,[23,37] X. R. Wang,[33] Y. Watanabe,[37,38] J. Wessels,[29] S. N. White,[3] N. Willis,[35] D. Winter,[7] C. L. Woody,[3] M. Wysocki,[6] W. Xie,[4,38] A. Yanovich,[14] S. Yokkaichi,[37,38] G. R. Young,[34] I. Younus,[32] I. E. Yushmanov,[22] W. A. Zajc,[7] O. Zaudtke,[29] C. Zhang,[7] J. Zimányi,[20,†] and L. Zolin[17]

(PHENIX Collaboration)

[1]*Abilene Christian University, Abilene, Texas 79699, USA*
[2]*Department of Physics, Banaras Hindu University, Varanasi 221005, India*
[3]*Brookhaven National Laboratory, Upton, New York 11973-5000, USA*

 © 2007 The American Physical Society

[4]University of California-Riverside, Riverside, California 92521, USA
[5]Center for Nuclear Study, Graduate School of Science, University of Tokyo, 7-3-1 Hongo, Bunkyo, Tokyo 113-0033, Japan
[6]University of Colorado, Boulder, Colorado 80309, USA
[7]Columbia University, New York, New York 10027, USA
and Nevis Laboratories, Irvington, New York 10533, USA
[8]Dapnia, CEA Saclay, F-91191, Gif-sur-Yvette, France
[9]Debrecen University, H-4010 Debrecen, Egyetem tér 1, Hungary
[10]ELTE, Eötvös Loránd University, H-1117 Budapest, Pázmány P. s. 1/A, Hungary
[11]Florida State University, Tallahassee, Florida 32306, USA
[12]Georgia State University, Atlanta, Georgia 30303, USA
[13]Hiroshima University, Kagamiyama, Higashi-Hiroshima 739-8526, Japan
[14]IHEP Protvino, State Research Center of Russian Federation, Institute for High Energy Physics, Protvino, 142281, Russia
[15]University of Illinois at Urbana-Champaign, Urbana, Illinois 61801, USA
[16]Iowa State University, Ames, Iowa 50011, USA
[17]Joint Institute for Nuclear Research, 141980 Dubna, Moscow Region, Russia
[18]KAERI, Cyclotron Application Laboratory, Seoul, South Korea
[19]KEK, High Energy Accelerator Research Organization, Tsukuba, Ibaraki 305-0801, Japan
[20]KFKI Research Institute for Particle and Nuclear Physics of the Hungarian Academy of Sciences (MTA KFKI RMKI),
H-1525 Budapest 114, P.O. Box 49, Budapest, Hungary
[21]Korea University, Seoul, 136-701, Korea
[22]Russian Research Center "Kurchatov Institute," Moscow, Russia
[23]Kyoto University, Kyoto 606-8502, Japan
[24]Laboratoire Leprince-Ringuet, Ecole Polytechnique, CNRS-IN2P3, Route de Saclay, F-91128, Palaiseau, France
[25]Lawrence Livermore National Laboratory, Livermore, California 94550, USA
[26]Los Alamos National Laboratory, Los Alamos, New Mexico 87545, USA
[27]LPC, Université Blaise Pascal, CNRS-IN2P3, Clermont-Fd, 63177 Aubiere Cedex, France
[28]Department of Physics, Lund University, Box 118, SE-221 00 Lund, Sweden
[29]Institut für Kernphysik, University of Muenster, D-48149 Muenster, Germany
[30]Myongji University, Yongin, Kyonggido 449-728, Korea
[31]Nagasaki Institute of Applied Science, Nagasaki-shi, Nagasaki 851-0193, Japan
[32]University of New Mexico, Albuquerque, New Mexico 87131, USA
[33]New Mexico State University, Las Cruces, New Mexico 88003, USA
[34]Oak Ridge National Laboratory, Oak Ridge, Tennessee 37831, USA
[35]IPN-Orsay, Universite Paris Sud, CNRS-IN2P3, BP1, F-91406, Orsay, France
[36]PNPI, Petersburg Nuclear Physics Institute, Gatchina, Leningrad region, 188300, Russia
[37]RIKEN, The Institute of Physical and Chemical Research, Wako, Saitama 351-0198, Japan
[38]RIKEN BNL Research Center, Brookhaven National Laboratory, Upton, New York 11973-5000, USA
[39]Physics Department, Rikkyo University, 3-34-1 Nishi-Ikebukuro, Toshima, Tokyo 171-8501, Japan
[40]Saint Petersburg State Polytechnic University, St. Petersburg, Russia
[41]Universidade de São Paulo, Instituto de Física, Caixa Postal 66318, São Paulo CEP05315-970, Brazil
[42]System Electronics Laboratory, Seoul National University, Seoul, South Korea
[43]Chemistry Department, Stony Brook University, Stony Brook, SUNY, New York 11794-3400, USA
[44]Department of Physics and Astronomy, Stony Brook University, SUNY, Stony Brook, New York 11794, USA
[45]SUBATECH (Ecole des Mines de Nantes, CNRS-IN2P3, Université de Nantes) BP 20722-44307, Nantes, France
[46]University of Tennessee, Knoxville, Tennessee 37996, USA
[47]Department of Physics, Tokyo Institute of Technology, Oh-okayama, Meguro, Tokyo 152-8551, Japan
[48]Institute of Physics, University of Tsukuba, Tsukuba, Ibaraki 305, Japan
[49]Vanderbilt University, Nashville, Tennessee 37235, USA
[50]Waseda University, Advanced Research Institute for Science and Engineering, 17 Kikui-cho, Shinjuku-ku, Tokyo 162-0044, Japan
[51]Weizmann Institute, Rehovot 76100, Israel
[52]Yonsei University, IPAP, Seoul 120-749, Korea
(Received 14 March 2007; published 31 July 2007)

Differential elliptic flow (v_2) for ϕ mesons and (anti)deuterons $(\bar{d})d$ is measured for Au + Au collisions at $\sqrt{s_{NN}} = 200$ GeV. The v_2 for ϕ mesons follows the trend of lighter $\pi^{\pm}$ and $K^{\pm}$ mesons, suggesting that ordinary hadrons interacting with standard hadronic cross sections are not the primary driver for elliptic flow development. The v_2 values for $(\bar{d})d$ suggest that elliptic flow is additive for composite particles. This further validation of the universal scaling of v_2 per constituent quark for baryons and mesons suggests that partonic collectivity dominates the transverse expansion dynamics.

DOI: 10.1103/PhysRevLett.99.052301 PACS numbers: 25.75.Ld, 25.75.Dw

An important goal of current ultrarelativistic heavy ion research is to map out the accessible regions of the quantum chromodynamics phase diagram. Central to this goal is the creation and study of a new phase of nuclear matter—the quark gluon plasma (QGP). Thermalization and deconfinement are important properties of this matter, believed to be produced in heavy ion collisions at the Relativistic Heavy Ion Collider (RHIC) [1–3].

Detailed elliptic flow measurements provide indispensable information about this high energy density matter [4–8]. Such measurements are characterized by the magnitude of the second-harmonic coefficient $v_2 = \langle e^{i2(\varphi_p - \Phi_{\mathrm{RP}})} \rangle$, of the Fourier expansion of the azimuthal distribution of emitted particles. Here, φ_p represents the azimuthal emission angle of a particle, Φ_{RP} is the azimuthal angle of the reaction plane, and the brackets denote statistical averaging over particles and events [9,10].

At RHIC energies, there is now significant evidence that elliptic flow, in noncentral collisions, results from hydrodynamic pressure gradients developed in a locally thermalized ''almond-shaped'' collision zone. That is, the initial transverse coordinate-space anisotropy of this zone is converted, via particle interactions, into an azimuthal momentum-space anisotropy. Indeed, when plotted as a function of the transverse kinetic energy, $\mathrm{KE}_T \equiv m_T - m$, divided by the number of valence quarks n_q of a given hadron ($n_q = 2$ for mesons and $n_q = 3$ for baryons), v_2/n_q shows universal scaling for a broad range of particle species [11–14] (m_T is the transverse mass). This has been interpreted as evidence that hydrodynamic expansion of the QGP occurs during a phase characterized by (i) a rather low viscosity to entropy ratio η/s [2,3,13,15,16] and (ii) independent quasiparticles which exhibit the quantum numbers of quarks [13,17–21]. A consensus on the detailed dynamical evolution of the QGP has not been reached [3,16].

Elliptic flow measurements for heavy, strange, and multistrange hadrons [22,23] can lend unique insight on reaction dynamics. Here, we use differential v_2 measurements for the ϕ meson and the deuteron to address the important question of how the existence of a hadronic phase affects v_2: Is elliptic flow development dominantly pre- or posthadronization?

The ϕ meson is comprised of a strange (s) and an antistrange ($\bar{s}$) quark, and its interaction with hadrons is suppressed according to the Okubo-Zweig-Izuka (OZI) rules [24]. One consequence of this is that the ϕ meson is expected to have a rather small hadronic cross section with nonstrange hadrons (~ 9 mb) [25–27]. Such a cross section leads to a relatively large mean free path λ_ϕ, when compared to the transverse size of the emitting system. Thus, if elliptic flow was established in a phase involving hadrons interacting with their standard hadronic cross sections (posthadronization), one would expect v_2 for the ϕ meson to be significantly smaller than that for other hadrons (e.g., p and π). A recent measurement [28] has ruled out the possibility of ϕ meson production via K^+K^- coalescence. If v_2 is established in the phase prior to hadronization, the ϕ meson provides an important benchmark test for universal scaling in that its mass is similar to that of the proton and the Λ baryon, but its v_2 should be additive with respect to the v_2 of its two constituent quarks (i.e., $n_q = 2$). This scenario also provides an important constraint for hydrodynamical models which predict a $v_2(p_T)$ ordering pattern based on the mass of different particle species. Therefore, a detailed comparison of the v_2 values for the ϕ meson with those for other particle species, comprised of the lighter u and d quarks or the heavier charm quark c, can provide unique insight on whether or not partonic collectivity plays a central role in reaction dynamics at RHIC [20,29,30].

The deuteron is a very shallow composite $p + n$ bound state, whose binding energy (~ 2.24 MeV) is much less than the hadronization temperature. Thus, it is likely that it would suffer from medium induced breakup in the hadronic phase, even if it was produced at hadronization. In fact, recent investigations [31,32] suggest that $(\bar{p}\,\bar{n})pn$ coalescence dominates the (anti)deuteron $(\bar{d})d$ yield in Au + Au collisions. Thus, v_2 measurements for $(\bar{d})d$ also provide an important test for the universal scaling of elliptic flow [29] in that its v_2 should be additive, first, with respect to the v_2 of its constituent hadrons and, second, with respect to the v_2 of the constituent quarks of these hadrons (i.e., $n_q = 2 \times 3$).

In the 2004 running period the PHENIX detector [33] recorded $\approx 6.5 \times 10^8$ minimum-bias events for Au + Au collisions at $\sqrt{s_{NN}} = 200$ GeV. The collision vertex z (along beam axis) was constrained to $|z| < 30$ cm of the nominal crossing point. The event centrality was determined via cuts in the space of beam-beam counter (BBC) charge versus zero degree calorimeter energy [34]. In the central rapidity region ($|\eta| \leq 0.35$) the drift chambers, each with an azimuthal coverage $\Delta\varphi = \pi/2$, and two layers of multiwire proportional chambers with pad readout (PC1 and PC3) were used for charged particle tracking and momentum reconstruction. The time-of-flight (TOF) and lead scintillator (PbSc) detectors were used for charged particle identification [6,7].

Time-of-flight measurements from the TOF and PbSc were used in conjunction with the measured momentum and flight-path length to generate a mass-squared (m^2) distribution [35]. A track confirmation hit within a 2.5σ matching window in PC3 or TOF/PbSc served to eliminate most albedo, conversions, and resonance decays. A momentum dependent $\pm 2\sigma$ cut about each peak in the m^2 distribution was used to identify pions ($\pi^\pm$), kaons ($K^\pm$), (anti)protons [$(\bar{p})p$], and (anti)deuterons [$(\bar{d})d$] in the range $0.2 < p_T < 2.5$ GeV/c, $0.3 < p_T < 2.5$ GeV/c, $0.5 < p_T < 4.5$ GeV/c, and $1.1 < p_T < 4.5$ GeV/c, respectively, in the TOF, and to identify $K^\pm$ in the range

$0.3 < p_T < 1.5$ GeV/c in the PbSc. This gave $\sim 59\,000 \bar{d} + d$. An invariant mass analysis of the $\phi \rightarrow K^+K^-$ decay channel yielded $\sim 340\,000 \phi$ mesons with relatively good signal to background (14%–42% for the mass window $|m_{\rm inv}| = 5$ MeV/c^2 about the ϕ meson peak) over the range $1.0 < p_T < 5.5$ GeV/c for K^+K^- pairs.

The reaction plane method [6] was used to correlate the azimuthal angles of charged tracks with the azimuth of the event plane Φ_2, determined via hits in the two BBCs covering the pseudorapidity range $3.0 < |\eta| < 3.9$. The large pseudorapidity gap $\Delta\eta > 2.75$ between the central arms and the particles used for reaction plane determination reduces the influence of possible nonflow contributions, especially those from dijets [36]. Charge averaged values of $v_2 = \langle \cos(2(\varphi_p - \Phi_2))\rangle / \langle \cos(2(\Phi_2 - \Phi_{\rm RP}))\rangle$ were evaluated for $\pi^\pm$, $K^\pm$, $(\bar{p})p$, and $(\bar{d})d$. Here, the denominator represents a resolution factor to correct for the difference between the estimated Φ_2 and the true azimuth $\Phi_{\rm RP}$ of the reaction plane [6,37]. The estimated resolution factor of the combined reaction plane from both BBCs has an average of 0.33 over centrality, with a maximum of about 0.42 in midcentral collisions [6,12]. The associated systematic error is estimated to be $\sim 5\%$ for $\pi^\pm$, $K^\pm$, and $(\bar{p})p$. A p_T dependent correction factor ($\sim 5\%$–11%) was applied to the v_2 values for $(\bar{d})d$, to account for background contributions to the (anti)deuteron peak (signal) in the m^2 distributions (dash-dotted curve in Fig. 1(a):

$$v_2^{(\bar{d})d}(p_T) = [v_2^{s+bg}(p_T) - (1 - R)v_2^{bg}(p_T)]/R, \qquad (1)$$

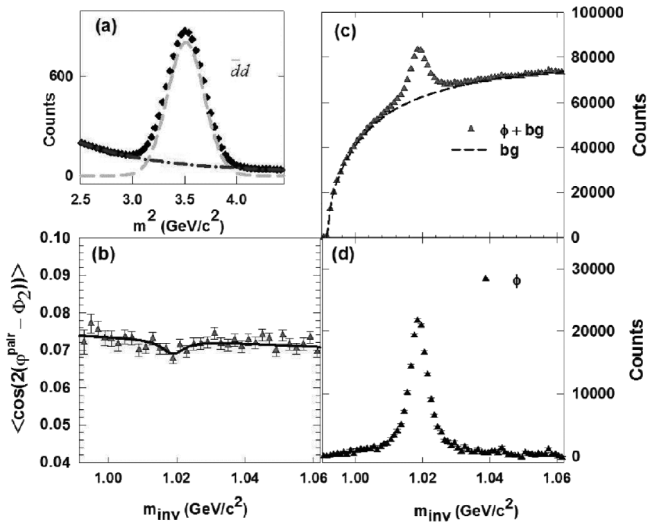

FIG. 1. (a) m^2 distribution for $\bar{d}$, d for $p_T = 1.6$–2.9 GeV/c, (b) $\langle\cos(2(\varphi^{\rm pair} - \Phi_2))\rangle$ versus $m_{\rm inv}$; the solid line is a fit to the data with Eq. (2). (c) $m_{\rm inv}$ distributions for foreground (points) and background (dashed line) K^+K^- pairs ($p_T^{\rm pair} = 1.6$–2.7 GeV/c) for 20%–60% central Au + Au collisions. (d) $m_{\rm inv}$ distribution after subtraction of the background.

where $v_2^{s+bg}(p_T)$ is the measured v_2 for $(\bar{d})d+$ background at a given p_T, R is the ratio signal/(signal + background) at that p_T, and $v_2^{bg}(p_T)$ is the elliptic flow of the background evaluated for m^2 values outside of the $(\bar{d})d$ peaks.

Extraction of the elliptic flow values for the ϕ meson (v_2^ϕ) followed the invariant mass ($m_{\rm inv}$) method [38]. For each event, $m_{\rm inv}$, $p_T^{\rm pair}$, and $\varphi^{\rm pair}$ for each K^+K^- pair were evaluated. Then, for each $p_T^{\rm pair}$ bin, $v_2^{\rm pair} = \langle\cos(2(\varphi^{\rm pair} - \Phi_2))\rangle$ was evaluated as a function of $m_{\rm inv}$ as shown in Fig. 1(b). The value $v_2^\phi(p_T)$ was then obtained from $v_2^{\rm pair}(m_{\rm inv})$ via an expression similar to Eq. (1):

$$v_2^{\rm pair}(m_{\rm inv}) = v_2^\phi R(m_{\rm inv}) + v_2^{\rm bg}(m_{\rm inv})[1 - R(m_{\rm inv})], \qquad (2)$$

where $R(m_{\rm inv}) = N_\phi(m_{\rm inv})/[N_\phi(m_{\rm inv}) + N_{\rm bg}(m_{\rm inv})]$ and $N_\phi(m_{\rm inv})$ and $N_{\rm bg}(m_{\rm inv})$ are distributions for the ϕ meson and the combinatoric background, respectively, $N_\phi(m_{\rm inv})$ is obtained from the distribution $N_{\rm pair}(m_{\rm inv})$ of K^+K^- pairs from the same event (foreground); $N_{\rm bg}(m_{\rm inv})$ is the distribution of pairs obtained from different events with similar centrality, vertex, and event plane orientation [39]. Figure 1(c) shows a representative example of the latter distributions for $1.6 \le p_T^{\rm pair} \le 2.7$ GeV/c and reaction centrality 20%–60%. A clear peak signaling the ϕ meson is apparent in the foreground distribution for $m_{\rm inv} \sim 1.02$ GeV/c^2. The background distribution was normalized to that for the foreground in the region $1.04 < m_{\rm inv} < 1.2$ GeV/c^2 and subtracted to obtain the $N_\phi(m_{\rm inv})$ distribution shown in Fig. 1(d); a relatively narrow ϕ meson peak is apparent.

Determination of the ratio $R(m_{\rm inv})$ was facilitated by fitting this distribution with a Breit-Wigner function plus a linear function, as shown by the solid curve in Fig. 1(c). To ensure robust v_2^ϕ extraction, the combinatorial background was constructed such that $v_{2(\rm mix)}^{\rm bg}(m_{\rm inv})$ gave the same value as $v_2^{\rm pair}(m_{\rm inv})$ for $m_{\rm inv}$ values not associated

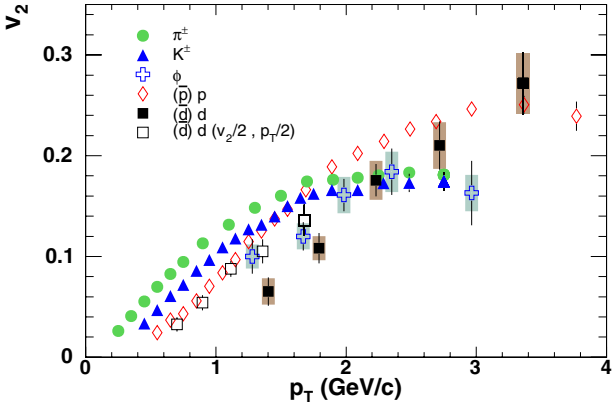

FIG. 2 (color online). Comparison of differential $v_2(p_T)$ for ϕ mesons, $(\bar{d})d$, $\pi^\pm$, $K^\pm$, and $(\bar{p})p$ (as indicated). Results are shown for 20%–60% central Au + Au collisions.

with the ϕ meson peak. Values for v_2^{ϕ} were extracted via direct fits to the $v_2^{\text{pair}}(m_{\text{inv}})$ distribution for each p_T^{pair} selection [cf. Eq. (2)]. That is, $v_2^{\text{bg}}(m_{\text{inv}})$ was parametrized as a linear or quadratic function of m_{inv} (depending on the p_T^{pair} bin) and v_2^{ϕ} was taken as a fit parameter.

The accuracy of the extraction procedure was verified by checking that the m_{inv} dependence of the sine coefficients, $v_{s,2}^{\text{pair}}(m_{\text{inv}}) = \langle \sin(2(\varphi^{\text{pair}} - \Phi_2)) \rangle$, were all zero within statistical errors. An alternative "subtraction method" [40,41], in which the raw ϕ meson yield distribution $dN/d(\varphi_\phi - \Phi_2)$ was extracted and fitted with the function $N\{1 + 2v_2^{\phi} \cos[2(\varphi_\phi - \Phi_2)]\}$, also showed good agreement, albeit with larger error bars; N is an arbitrary normalization constant.

The differential $v_2(p_T)$ obtained for $(\bar{d})d$ and the ϕ meson, for centrality 20%–60%, are compared to those for $\pi^{\pm}$, $K^{\pm}$, and $(\bar{p})p$ in Fig. 2. This centrality selection was so chosen to (i) maximize the ϕ meson signal to background ratio over the full range of p_T bins and (ii) enhance the distinction between baryon and meson v_2 in the intermediate p_T range. The shaded bands for $(\bar{d})d$ and the ϕ meson indicate systematic errors (~6%–15%), primarily associated with the determination of R and $R(m_{\text{inv}})$, v_2^{bg} and $v_2^{\text{bg}}(m_{\text{inv}})$ [cf. Eqs. (1) and (2)], and fitting.

The values for $v_2^{(\bar{d})d}$ shown in Fig. 2 are as much as a factor ≈ 2.5 lower than those for $\pi^{\pm}$ at low p_T. This mass ordering pattern reflects the detailed expansion dynamics of the created matter. As a first test of whether or not v_2 for $(\bar{d})d$ is additive with respect to its constituent hadrons, $v_2^{(\bar{d})d}/2$ versus $p_T/2$ is compared to $v_2^{(\bar{p})p}$ versus p_T. Within errors, they show good agreement as would be expected if $v_2^{(\bar{d})d}$ is additive. The large magnitude of v_2 for the ϕ meson gives an initial indication that significant flow development occurs prior to hadronization.

The left and right panels of Fig. 3 compare the unscaled and scaled results (respectively) for v_2 versus KE_T for $\pi^{\pm}$, $K^{\pm}$, $(\bar{p})p$, $(\bar{d})d$, and the ϕ meson, in 20%–60% central Au + Au collisions. The left panel clearly shows that, despite its mass which is comparable to that for the proton, $v_2(\text{KE}_T)$ for the ϕ meson follows the flow pattern of the other lighter mesons (π and K), whose cross sections are not OZI suppressed. A similar pattern is also observed for the $v_2(\text{KE}_T)$ values inferred for D mesons (comprised of charmed quarks) from nonphotonic electron measurements [13,23,42]. These observations indicate that, when elliptic flow develops, the constituents of the flowing medium are not ordinary hadrons interacting with their standard hadronic cross sections. Instead, partonic collectivity appears to dominate the transverse expansion dynamics of light, strange, and charmed quarks via a common velocity field.

Interestingly, the $v_2(\text{KE}_T)$ results shown for the $(\bar{d})d$ and the ϕ meson are essentially identical at low KE_T ($\text{KE}_T \lesssim 1$ GeV), and are in good agreement with those for other

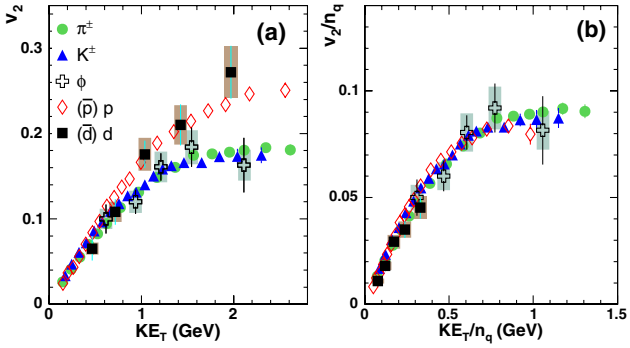

FIG. 3 (color online). (a) v_2 vs KE_T for several identified particle species obtained in midcentral (20%–60%) Au + Au collisions. (b) v_2/n_q vs KE_T/n_q for the same particle species shown in (a). The shaded bands indicate systematic error estimates for $(\bar{d})d$ and ϕ mesons (see text).

charged hadrons, including the pion with a mass ~13 times smaller than the deuteron. This strengthens the earlier finding that, for low KE_T, all particle species exhibit the same v_2 irrespective of their mass [11–13]. The expected difference between $(\bar{d})d$ and $(\bar{p})p$ for $\text{KE}_T \gtrsim 1$ GeV is not tested in Fig. 3, due to the limited KE_T range of the $(\bar{d})d$ data.

The right panel of Fig. 3 shows the results for a validation test of universal scaling for $v_2(\text{KE}_T)$ of baryons and mesons [11–13]. The value $n_q = 2 \times 3$ is used for $(\bar{d})d$ to account for its composite $(p + n)$ nature. The scaled results shown in Fig. 3(b) clearly serve as further validation for the experimentally observed universal scaling of v_2 for baryons and mesons [11–13]. This finding lends strong support to the notion that the high energy density matter, created in RHIC collisions, comprise a prehadronization state that contains the prerequisite quantum numbers of the hadrons to be formed. Thus, it appears that partonic collectivity dominates the expansion dynamics of these collisions. The special role of KE_T as a scaling variable is not fully understood.

We have presented differential v_2 measurements for the ϕ meson and deuteron. For a broad range of KE_T values, the differential $v_2(\text{KE}_T)$ for the ϕ meson follows the flow pattern for other light mesons whose cross sections are not OZI suppressed. The composites $(\bar{d})d$ follow the flow pattern for baryons with additive v_2 values. When v_2/n_q is plotted as a function of the transverse kinetic energy scaled by the number of valence quarks (i.e., KE_T/n_q), universal scaling results for all particle species measured. These observations suggest that the transverse expansion dynamics leading to elliptic flow development cannot be understood in terms of ordinary hadrons interacting with their standard hadronic cross sections, but rather in terms of a prehadronization state in which the flowing medium reflects quark degrees of freedom.

We thank the staff of the Collider-Accelerator and Physics Departments at BNL for their vital contributions. We acknowledge support from the Office of NP in DOE Office of Science and NSF (U.S.A.), MEXT and JSPS (Japan), CNPq and FAPESP (Brazil), NSFC (China), IN2P3/CNRS, and CEA (France), BMBF, DAAD, and AvH (Germany), OTKA (Hungary), DAE (India), ISF (Israel), KRF and KOSEF (Korea), MES, RAS, and FAAE (Russia), VR and KAW (Sweden), U.S. CRDF for the FSU, US-Hungarian NSF-OTKA-MTA, and U.S.-Israel BSF.

*PHENIX Spokesperson.
jacak@skipper.physics.sunysb.edu
†Deceased.

[1] K. Adcox *et al.*, Nucl. Phys. **A757**, 184 (2005).
[2] M. Gyulassy and L. McLerran, Nucl. Phys. **A750**, 30 (2005).
[3] E. V. Shuryak, Nucl. Phys. **A750**, 64 (2005).
[4] K. H. Ackermann *et al.*, Phys. Rev. Lett. **86**, 402 (2001).
[5] K. Adcox *et al.*, Phys. Rev. Lett. **89**, 212301 (2002).
[6] S. S. Adler *et al.*, Phys. Rev. Lett. **91**, 182301 (2003).
[7] S. S. Adler *et al.*, Phys. Rev. Lett. **94**, 232302 (2005).
[8] R. A. Lacey, Nucl. Phys. **A774**, 199 (2006).
[9] M. Demoulins *et al.*, Phys. Lett. B **241**, 476 (1990).
[10] S. Voloshin and Y. Zhang, Z. Phys. C **70**, 665 (1996).
[11] M. Issah and A. Taranenko, arXiv:nucl-ex/0604011.
[12] A. Adare *et al.*, Phys. Rev. Lett. **98**, 162301 (2007).
[13] R. A. Lacey and A. Taranenko, arXiv:nucl-ex/0610029.
[14] J. Jia and C. Zhang, Phys. Rev. C **75**, 031901(R) (2007).
[15] U. W. Heinz and P. F. Kolb, Nucl. Phys. **A702**, 269 (2002).
[16] M. Asakawa, S. A. Bass, and B. Muller, Phys. Rev. Lett. **96**, 252301 (2006).
[17] S. A. Voloshin, Nucl. Phys. **A715**, 379 (2003).
[18] R. J. Fries, B. Muller, C. Nonaka, and S. A. Bass, Phys. Rev. C **68**, 044902 (2003).
[19] V. Greco, C. M. Ko, and P. Levai, Phys. Rev. C **68**, 034904 (2003).
[20] N. Xu, Nucl. Phys. **A751**, 109 (2005).
[21] B. Müller and J. L. Nagle, Annu. Rev. Nucl. Part. Sci. **56**, 93 (2006).
[22] M. Oldenburg, J. Phys. G **32**, S563 (2006).
[23] A. Adare *et al.*, Phys. Rev. Lett. **98**, 172301 (2007).
[24] S. Okubo, Phys. Lett. **5**, 165 (1963).
[25] A. Shor, Phys. Rev. Lett. **54**, 1122 (1985).
[26] C. M. Ko and D. Seibert, Phys. Rev. C **49**, 2198 (1994).
[27] K. Haglin, Nucl. Phys. **A584**, 719 (1995).
[28] J. Adams *et al.* (STAR Collaboration), Phys. Lett. B **612**, 181 (2005).
[29] C. Nonaka *et al.*, Phys. Rev. C **69**, 031902 (2004).
[30] J. H. Chen *et al.*, Phys. Rev. C **74**, 064902 (2006).
[31] C. Adler *et al.*, Phys. Rev. Lett. **87**, 262301 (2001).
[32] S. S. Adler *et al.*, Phys. Rev. Lett. **94**, 122302 (2005).
[33] K. Adcox *et al.*, Nucl. Instrum. Methods Phys. Res., Sect. A **499**, 469 (2003).
[34] K. Adcox *et al.*, Phys. Rev. C **69**, 024904 (2004).
[35] S. S. Adler *et al.*, Phys. Rev. C **69**, 034909 (2004).
[36] J. Jia (PHENIX Collaboration), Nucl. Phys. **A783**, 501 (2007).
[37] A. M. Poskanzer and S. A. Voloshin, Phys. Rev. C **58**, 1671 (1998).
[38] N. Borghini and J. Y. Ollitrault, Phys. Rev. C **70**, 064905 (2004).
[39] S. S. Adler *et al.*, Phys. Rev. C **72**, 014903 (2005).
[40] D. Pal, Nucl. Phys. **A774**, 489 (2006).
[41] S. S. Adler *et al.*, Phys. Rev. Lett. **96**, 032302 (2006).
[42] V. Greco, C. M. Ko, and R. Rapp, Phys. Lett. B **595**, 202 (2004).

PHYSICAL REVIEW C **75**, 051902(R) (2007)

Production of ω mesons at large transverse momenta in $p+p$ and $d+$Au collisions at $\sqrt{s_{NN}} = 200$ GeV

S. S. Adler,[5] S. Afanasiev,[20] C. Aidala,[10] N. N. Ajitanand,[44] Y. Akiba,[21,40] A. Al-Jamel,[35] J. Alexander,[44] K. Aoki,[25] L. Aphecetche,[46] R. Armendariz,[35] S. H. Aronson,[5] R. Averbeck,[45] T. C. Awes,[36] V. Babintsev,[17] A. Baldisseri,[11] K. N. Barish,[6] P. D. Barnes,[28] B. Bassalleck,[34] S. Bathe,[6,31] S. Batsouli,[10] V. Baublis,[39] F. Bauer,[6] A. Bazilevsky,[5,41] S. Belikov,[17,19] M. T. Bjorndal,[10] J. G. Boissevain,[28] H. Borel,[11] M. L. Brooks,[28] D. S. Brown,[35] N. Bruner,[34] D. Bucher,[31] H. Buesching,[5,31] V. Bumazhnov,[17] G. Bunce,[5,41] J. M. Burward-Hoy,[27,28] S. Butsyk,[45] X. Camard,[46] P. Chand,[4] W. C. Chang,[2] S. Chernichenko,[17] C. Y. Chi,[10] J. Chiba,[21] M. Chiu,[10] I. J. Choi,[53] R. K. Choudhury,[4] T. Chujo,[5] V. Cianciolo,[36] Y. Cobigo,[11] B. A. Cole,[10] M. P. Comets,[37] P. Constantin,[19] M. Csanád,[13] T. Csörgő,[22] J. P. Cussonneau,[46] D. d'Enterria,[10] K. Das,[14] G. David,[5] F. Deák,[13] H. Delagrange,[46] A. Denisov,[17] A. Deshpande,[41] E. J. Desmond,[5] A. Devismes,[45] O. Dietzsch,[42] J. L. Drachenberg,[1] O. Drapier,[26] A. Drees,[45] A. Durum,[17] D. Dutta,[4] V. Dzhordzhadze,[47] Y. V. Efremenko,[36] H. En'yo,[40,41] B. Espagnon,[37] S. Esumi,[49] D. E. Fields,[34,41] C. Finck,[46] F. Fleuret,[26] S. L. Fokin,[24] B. D. Fox,[41] Z. Fraenkel,[52] J. E. Frantz,[10] A. Franz,[5] A. D. Frawley,[14] Y. Fukao,[25,40,41] S.-Y. Fung,[6] S. Gadrat,[29] M. Germain,[46] A. Glenn,[47] M. Gonin,[26] J. Gosset,[11] Y. Goto,[40,41] R. Granier de Cassagnac,[26] N. Grau,[19] S. V. Greene,[50] M. Gross Perdekamp,[18,41] H.-Å. Gustafsson,[30] T. Hachiya,[16] J. S. Haggerty,[5] H. Hamagaki,[8] A. G. Hansen,[28] E. P. Hartouni,[27] M. Harvey,[5] K. Hasuko,[40] R. Hayano,[8] X. He,[15] M. Heffner,[27] T. K. Hemmick,[45] J. M. Heuser,[40] P. Hidas,[22] H. Hiejima,[18] J. C. Hill,[19] R. Hobbs,[34] W. Holzmann,[44] K. Homma,[16] B. Hong,[23] A. Hoover,[35] T. Horaguchi,[40,41,48] T. Ichihara,[40,41] V. V. Ikonnikov,[24] K. Imai,[25,40] M. Inaba,[49] M. Inuzuka,[8] D. Isenhower,[1] L. Isenhower,[1] M. Ishihara,[40] M. Issah,[44] A. Isupov,[20] B. V. Jacak,[45] J. Jia,[45] O. Jinnouchi,[40,41] B. M. Johnson,[5] S. C. Johnson,[27] K. S. Joo,[32] D. Jouan,[37] F. Kajihara,[8] S. Kametani,[8,51] N. Kamihara,[40,48] M. Kaneta,[41] J. H. Kang,[53] K. Katou,[51] T. Kawabata,[8] A. V. Kazantsev,[24] S. Kelly,[9,10] B. Khachaturov,[52] A. Khanzadeev,[39] J. Kikuchi,[51] D. J. Kim,[53] E. Kim,[43] G.-B. Kim,[26] H. J. Kim,[53] E. Kinney,[9] A. Kiss,[13] E. Kistenev,[5] A. Kiyomichi,[40] C. Klein-Boesing,[31] H. Kobayashi,[41] L. Kochenda,[39] V. Kochetkov,[17] R. Kohara,[16] B. Komkov,[39] M. Konno,[49] D. Kotchetkov,[6] A. Kozlov,[52] P. J. Kroon,[5] C. H. Kuberg,[1,*] G. J. Kunde,[28] K. Kurita,[40] M. J. Kweon,[23] Y. Kwon,[53] G. S. Kyle,[35] R. Lacey,[44] J. G. Lajoie,[19] Y. Le Bornec,[37] A. Lebedev,[19,24] S. Leckey,[45] D. M. Lee,[28] M. J. Leitch,[28] M. A. L. Leite,[42] X. H. Li,[6] H. Lim,[43] A. Litvinenko,[20] M. X. Liu,[28] C. F. Maguire,[50] Y. I. Makdisi,[5] A. Malakhov,[20] V. I. Manko,[24] Y. Mao,[38,40] G. Martinez,[46] H. Masui,[49] F. Matathias,[45] T. Matsumoto,[8,51] M. C. McCain,[1] P. L. McGaughey,[28] Y. Miake,[49] T. E. Miller,[50] A. Milov,[45] S. Mioduszewski,[5] G. C. Mishra,[15] J. T. Mitchell,[5] A. K. Mohanty,[4] D. P. Morrison,[5] J. M. Moss,[28] D. Mukhopadhyay,[52] M. Muniruzzaman,[6] S. Nagamiya,[21] J. L. Nagle,[9,10] T. Nakamura,[16] J. Newby,[47] A. S. Nyanin,[24] J. Nystrand,[30] E. O'Brien,[5] C. A. Ogilvie,[19] H. Ohnishi,[40] I. D. Ojha,[3,50] H. Okada,[25,40] K. Okada,[40,41] A. Oskarsson,[30] I. Otterlund,[30] K. Oyama,[8] K. Ozawa,[8] D. Pal,[52] A. P. T. Palounek,[28] V. Pantuev,[45] V. Papavassiliou,[35] J. Park,[43] W. J. Park,[23] S. F. Pate,[35] H. Pei,[19] V. Penev,[20] J.-C. Peng,[18] H. Pereira,[11] V. Peresedov,[20] A. Pierson,[34] C. Pinkenburg,[5] R. P. Pisani,[5] M. L. Purschke,[5] A. K. Purwar,[45] J. M. Qualls,[1] J. Rak,[19] I. Ravinovich,[52] K. F. Read,[36,47] M. Reuter,[45] K. Reygers,[31] V. Riabov,[39] Y. Riabov,[39] G. Roche,[29] A. Romana,[26,*] M. Rosati,[19] S. S. E. Rosendahl,[30] P. Rosnet,[29] V. L. Rykov,[40] S. S. Ryu,[53] N. Saito,[25,40,41] T. Sakaguchi,[8,51] S. Sakai,[49] V. Samsonov,[39] L. Sanfratello,[34] R. Santo,[31] H. D. Sato,[25,40] S. Sato,[5,49] S. Sawada,[21] Y. Schutz,[46] V. Semenov,[17] R. Seto,[6] T. K. Shea,[5] I. Shein,[17] T.-A. Shibata,[40,48] K. Shigaki,[16] M. Shimomura,[49] A. Sickles,[45] C. L. Silva,[42] D. Silvermyr,[28] K. S. Sim,[23] A. Soldatov,[17] R. A. Soltz,[27] W. E. Sondheim,[28] S. P. Sorensen,[47] I. V. Sourikova,[5] F. Staley,[11] P. W. Stankus,[36] E. Stenlund,[30] M. Stepanov,[35] A. Ster,[22] S. P. Stoll,[5] T. Sugitate,[16] J. P. Sullivan,[28] S. Takagi,[49] E. M. Takagui,[42] A. Taketani,[40,41] K. H. Tanaka,[21] Y. Tanaka,[33] K. Tanida,[40] M. J. Tannenbaum,[5] A. Taranenko,[44] P. Tarján,[12] T. L. Thomas,[34] M. Togawa,[25,40] J. Tojo,[40] H. Torii,[25,41] R. S. Towell,[1] V.-N. Tram,[26] I. Tserruya,[52] Y. Tsuchimoto,[16] H. Tydesjö,[30] N. Tyurin,[17] T. J. Uam,[32] J. Velkovska,[5] M. Velkovsky,[45] V. Veszprémi,[12] A. A. Vinogradov,[24] M. A. Volkov,[24] E. Vznuzdaev,[39] X. R. Wang,[15] Y. Watanabe,[40,41] S. N. White,[5] N. Willis,[37] F. K. Wohn,[19] C. L. Woody,[5] W. Xie,[6] A. Yanovich,[17] S. Yokkaichi,[40,41] G. R. Young,[36] I. E. Yushmanov,[24] W. A. Zajc,[10,†] C. Zhang,[10] S. Zhou,[7] J. Zimányi,[22,*] L. Zolin,[20] X. Zong,[19] and H. W. vanHecke[28]

(PHENIX Collaboration)

[1]*Abilene Christian University, Abilene, Texas 79699, USA*

[2]*Institute of Physics, Academia Sinica, Taipei 11529, Taiwan*

[3]*Department of Physics, Banaras Hindu University, Varanasi 221005, India*

[4]*Bhabha Atomic Research Centre, Bombay 400 085, India*

[5]*Brookhaven National Laboratory, Upton, New York 11973-5000, USA*

[6]*University of California-Riverside, Riverside, California 92521, USA*

[7]*China Institute of Atomic Energy (CIAE), Beijing, People's Republic of China*

[8]*Center for Nuclear Study, Graduate School of Science, University of Tokyo, 7-3-1 Hongo, Bunkyo, Tokyo 113-0033, Japan*

[9]*University of Colorado, Boulder, Colorado 80309, USA*

[10]*Columbia University, New York, New York 10027 and Nevis Laboratories, Irvington, New York 10533, USA*

[11]*Dapnia, CEA Saclay, F-91191, Gif-sur-Yvette, France*

 ©2007 The American Physical Society

[12]*Debrecen University, H-4010 Debrecen, Egyetem tér 1, Hungary*
[13]*ELTE, Eötvös Loránd University, H-1117 Budapest, Pázmány P. s. 1/A, Hungary*
[14]*Florida State University, Tallahassee, Florida 32306, USA*
[15]*Georgia State University, Atlanta, Georgia 30303, USA*
[16]*Hiroshima University, Kagamiyama, Higashi-Hiroshima 739-8526, Japan*
[17]*IHEP Protvino, State Research Center of Russian Federation, Institute for High Energy Physics, Protvino, RU-142281, Russia*
[18]*University of Illinois at Urbana-Champaign, Urbana, Illinois 61801, USA*
[19]*Iowa State University, Ames, Illinois 50011, USA*
[20]*Joint Institute for Nuclear Research, RU-141980 Dubna, Moscow Region, Russia*
[21]*KEK, High Energy Accelerator Research Organization, Tsukuba, Ibaraki 305-0801, Japan*
[22]*KFKI Research Institute for Particle and Nuclear Physics of the Hungarian Academy of Sciences (MTA KFKI RMKI), H-1525 Budapest 114, P.O. Box 49, Budapest, Hungary*
[23]*Korea University, Seoul, 136-701, Korea*
[24]*Russian Research Center "Kurchatov Institute," Moscow, Russia*
[25]*Kyoto University, Kyoto 606-8502, Japan*
[26]*Laboratoire Leprince-Ringuet, Ecole Polytechnique, CNRS-IN2P3, Route de Saclay, F-91128, Palaiseau, France*
[27]*Lawrence Livermore National Laboratory, Livermore, California 94550, USA*
[28]*Los Alamos National Laboratory, Los Alamos, New Mexico 87545, USA*
[29]*LPC, Université Blaise Pascal, CNRS-IN2P3, Clermont-Fd, F-63177 Aubiere Cedex, France*
[30]*Department of Physics, Lund University, Box 118, SE-221 00 Lund, Sweden*
[31]*Institut für Kernphysik, University of Muenster, D-48149 Muenster, Germany*
[32]*Myongji University, Yongin, Kyonggido 449-728, Korea*
[33]*Nagasaki Institute of Applied Science, Nagasaki-shi, Nagasaki 851-0193, Japan*
[34]*University of New Mexico, Albuquerque, New Mexico 87131, USA*
[35]*New Mexico State University, Las Cruces, New Mexico 88003, USA*
[36]*Oak Ridge National Laboratory, Oak Ridge, Tennessee 37831, USA*
[37]*IPN-Orsay, Universite Paris Sud, CNRS-IN2P3, BP1, F-91406, Orsay, France*
[38]*Peking University, Beijing, People's Republic of China*
[39]*PNPI, Petersburg Nuclear Physics Institute, Gatchina, Leningrad region, RU-188300, Russia*
[40]*RIKEN (The Institute of Physical and Chemical Research), Wako, Saitama 351-0198, Japan*
[41]*RIKEN BNL Research Center, Brookhaven National Laboratory, Upton, New York 11973-5000, USA*
[42]*Universidade de São Paulo, Instituto de Física, Caixa Postal 66318, São Paulo CEP05315-970, Brazil*
[43]*System Electronics Laboratory, Seoul National University, Seoul, South Korea*
[44]*Chemistry Department, Stony Brook University, Stony Brook, SUNY, New York 11794-3400, USA*
[45]*Department of Physics and Astronomy, Stony Brook University, SUNY, Stony Brook, New York 11794, USA*
[46]*SUBATECH (Ecole des Mines de Nantes, CNRS-IN2P3, Université de Nantes) BP 20722-44307, Nantes, France*
[47]*University of Tennessee, Knoxville, Tennessee 37996, USA*
[48]*Department of Physics, Tokyo Institute of Technology, Oh-okayama, Meguro, Tokyo 152-8551, Japan*
[49]*Institute of Physics, University of Tsukuba, Tsukuba, Ibaraki 305, Japan*
[50]*Vanderbilt University, Nashville, Tennessee 37235, USA*
[51]*Waseda University, Advanced Research Institute for Science and Engineering, 17 Kikui-cho, Shinjuku-ku, Tokyo 162-0044, Japan*
[52]*Weizmann Institute, Rehovot 76100, Israel*
[53]*Yonsei University, IPAP, Seoul 120-749, Korea*
(Received 18 November 2006; published 9 May 2007)

The PHENIX experiment at RHIC has measured the invariant cross section for ω-meson production at midrapidity in the transverse momentum range $2.5 < p_T < 9.25$ GeV/c in $p+p$ and d+Au collisions at $\sqrt{s_{NN}} = 200$ GeV. Measurements in two decay channels ($\omega \to \pi^0\pi^+\pi^-$ and $\omega \to \pi^0\gamma$) yield consistent results, and the reconstructed ω mass agrees with the accepted value within the p_T range of the measurements. The ω/π^0 ratio is found to be $0.85 \pm 0.05^{\text{stat}} \pm 0.09^{\text{sys}}$ in $p+p$ and $0.94 \pm 0.08^{\text{stat}} \pm 0.12^{\text{sys}}$ in d+Au collisions, independent of p_T. The nuclear modification factor $R_{d\text{A}}^{\omega}$ is $1.03 \pm 0.12^{\text{stat}} \pm 0.21^{\text{sys}}$ and $0.83 \pm 0.21^{\text{stat}} \pm 0.17^{\text{sys}}$ in minimum bias and central (0–20%) d+Au collisions, respectively.

DOI: 10.1103/PhysRevC.75.051902 PACS number(s): 25.75.Dw

*Deceased.
†PHENIX Spokesperson: zajc@nevis.columbia.edu

Cross sections at large transverse momentum (p_T) for products of "hard" pointlike processes (e.g., inclusive hadrons, jets, direct γ's, and heavy flavor) in high-energy hadron collisions are well described in perturbative quantum chromodynamics (pQCD) [1]. As a result they are considered to be well-calibrated probes of small-distance QCD phenomena. When going from $p+p$ to p(or d)$+A$ and $A+A$ collisions, deviations from cross-section scaling with respect to the number of binary $N+N$ collisions provide information on cold nuclear matter effects such as initial state energy loss [2], shadowing [3] and hot nuclear matter effects such as in-medium energy loss [4], increasing importance of production via recombination [5], and modifications to the QCD vacuum [6].

Production of ω mesons at high-p_T is especially interesting. The ω and π^0 are vector and pseudoscalar mesons, respectively. The ω/π^0 ratio carries information about probabilities of corresponding spin states to be produced in hadronization. Furthermore, ω mesons can be used as a probe of the nuclear medium since a significant fraction of them produced in $A+A$ or $p(d)+A$ collisions will decay inside the produced medium ($c\tau = 23.8$ fm) possibly leading to changes of the mass and/or width of the ω with respect to their values in vacuum.

The PHENIX [7] experiment at RHIC has a unique capability to measure both neutral and charged products of $A+A$ and $p+p$ collisions at very high event rates. The two central arm spectrometers each cover 90° in azimuth and ± 0.35 in pseudorapidity. The electromagnetic calorimeter (EMCal), with energy resolution $\sigma/E = 8.1\%/\sqrt{E(\mathrm{GeV})} \oplus 2.1\%$, is used to reconstruct γ's and π^0's. For charged-particle reconstruction two layers of pad chambers provide 3D pattern recognition and fake track rejection, and a drift chamber gives momentum resolution $\sigma/p_\mathrm{T} = 0.7\%\sqrt{p_\mathrm{T}(\mathrm{GeV}/c)} \oplus 1.1\%$. Beam-beam counters (BBC) are used to provide minimum bias trigger and to determine the collision vertex. The minimum bias trigger cross sections measured by the BBC are 23.0 ± 2.2 mb in $p+p$ [8] and 1.99 ± 0.10 b in $d+$Au [9] collisions. In $d+$Au collisions the BBC are also used to separate events into centrality classes as explained in Ref. [10]. High p_T online triggers are implemented by adding together amplitudes in 4×4 adjacent EMCal towers and comparing them to a threshold of 1.4 GeV in $p+p$ and 2.4 GeV in $d+$Au. The trigger could be fired by one or more photons coming from ω-decay final states, including 3γ or $2\pi 2\gamma$.

The data was collected by the PHENIX experiment during RHIC Run3. After selecting good runs and cutting on the collision vertex ($|z| < 30$ cm) we analyzed approximately 4.6×10^7 and 2.1×10^7 high p_T trigger events, corresponding to a total integrated luminosity of 0.22 pb^{-1} and 1.5 nb^{-1} in the $p+p$ and $d+$Au collision systems, respectively.

Although ω mesons are relatively abundant in high-energy hadronic collisions ($\omega/\pi^0 \approx 1$ at high p_T), their measurement is challenging due to the multiparticle final states of the main decay channels and the combinatorial background associated with their reconstruction.

The procedure used to measure $\omega \to \pi^0\pi^+\pi^-$ is the same as used to measure $\eta \to \pi^0\pi^+\pi^-$ [10]. In case of ω one needs to account for a wider peak and different phase-space density of the three-body decay [11,12]. The analysis procedure for the photonic decay mode, $\omega \to \pi^0\gamma \to 3\gamma$, is very similar to earlier PHENIX measurements of other mesons with photonic decay modes, $\pi^0, \eta \to 2\gamma$ [8,13,14]. For both ω-decay modes studied the first step is to reconstruct π^0 candidates by combining photon pairs and applying a p_T-dependent cut around the mass of the π^0. The root-mean-square of the π^0 peak varies with p_T from 8 to 13 MeV/c^2. Candidates (which include combinatorial background) are combined with a third photon for $\omega \to \pi^0\gamma$ or with two unidentified charged tracks (assumed to be π mesons) for $\omega \to \pi^0\pi^+\pi^-$. Raw yields are extracted by fitting the p_T slices of the invariant mass distribution as in the insert panel in Fig. 1. The signal to background ratio (S/B) of $\pi^0\pi^+\pi^-$ decay channel is 1:7 at low p_T and grows with p_T to 1:1 in $p+p$ collisions. In $d+$Au collisions it starts at 1:20 and grows with p_T to 1:2. For the $\pi^0\gamma$ channel S/B is 1.5–2 times worse. Corrections for acceptance, trigger efficiency, and analysis cuts are described in detail in Ref. [10]. Further details about the analysis procedures can be found in Ref. [15].

We classify systematic error sources as type A (point-to-point uncorrelated, which can move each point independently), type B (point-to-point correlated, which can move points coherently, but potentially by different relative amounts), and type C (global, which move all points by the same relative amount). These errors are summarized in Table I for the different decay modes and collision systems. Major contributors include signal extraction (type A), online high-p_T trigger efficiency (type B) and the total cross-section measurement (type C). The uncertainty on the signal extraction, which is the dominant source of systematic error, is relatively large due to the fact that correlations in the triggered sample rendered background subtraction via event mixing impossible, and therefore the unknown shape of the underlying background had to be accounted for in the peak fit. This error is estimated based on variation of analysis cuts and fitting procedures [10].

Figure 1 shows the invariant cross sections for ω production in $p+p$, minimum bias $d+$Au, and central (0–20%) $d+$Au collisions at $\sqrt{s_{NN}} = 200$ GeV, as a function of p_T. The p_T range ($2.5 < p_T < 9.25$ GeV/c) is limited by statistics at high p_T and by decreasing detector acceptance and trigger efficiency at low p_T. The results for the two decay modes, which involve different kinematics, detector acceptance, and efficiency corrections, agree very well.

Figure 2 shows the results for the ratio of vector to pseudoscalar meson production (ω/π^0) in $d+$Au and $p+p$ collisions at $\sqrt{s_{NN}} = 200$ GeV. For the denominator we

TABLE I. Systematic errors for the ω production cross section for the two decay channels and the two collision systems analyzed. Error types are described in the text. Values with a range indicate variation of the systematic error over the p_T range of the measurement.

Type	$\omega \to \pi^0\pi^+\pi^-$		$\omega \to \pi^0\gamma$	
	$p+p$	$d+$Au	$p+p$	$d+$Au
A	7–20%	10–15%	25–40%	10%
B	8–10%	11–14%	5.8–9.2%	7.4–11%
C	11%	9.4%	13%	11%

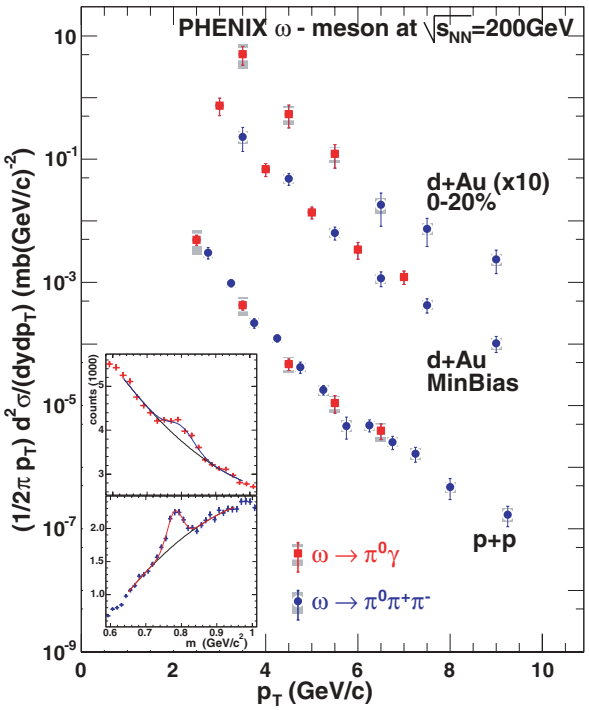

FIG. 1. (Color online) Invariant cross section of ω production in $p+p$ and $d+$Au collisions at $\sqrt{s_{NN}} = 200$ GeV measured in $\omega \to \pi^0\pi^+\pi^-$ and $\omega \to \pi^0\gamma$ decay channels. Bars and boxes represent statistical and systematic errors, respectively. Fits to invariant mass distributions of (top) $\pi^0\gamma$ and (bottom) $\pi^0\pi^+\pi^-$ are shown in the insert.

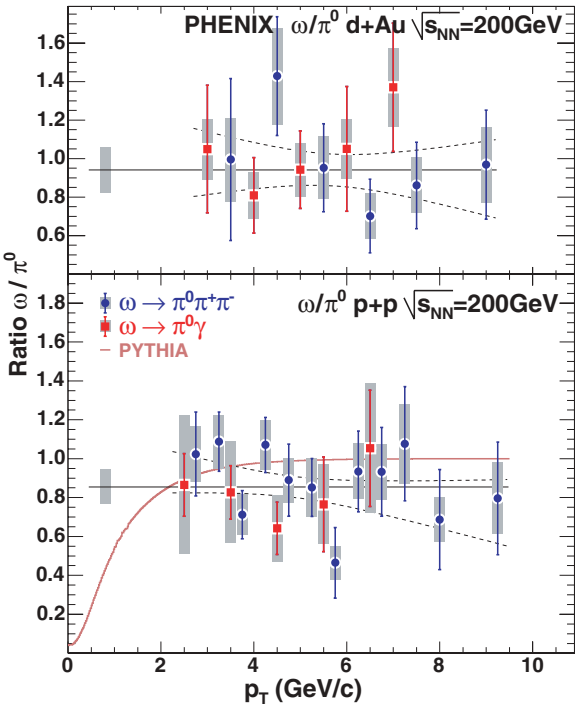

FIG. 2. (Color online) Measured ω/π^0 vs p_T in (upper panel) $d+$Au and (lower panel) $p+p$ collisions at $\sqrt{s_{NN}} = 200$ GeV. Straight lines show fits to a constant for each collision system. The boxes at the left edge of the constant fit lines show the systematic error on the data averaged over p_T. Dashed lines show values within 1σ of the best linear fits to the data. The PYTHIA prediction [17] for $p+p$ collisions at $\sqrt{s} = 200$ GeV is shown with a solid curve in the bottom panel.

use inclusive π^0 yields measured by PHENIX [8,16]. The ratios in both systems are consistent with no p_T dependence over the measured range. Fits to a constant yield $\omega/\pi^0 = 0.85 \pm 0.05^{\text{stat}} \pm 0.09^{\text{sys}}$ and $0.94 \pm 0.08^{\text{stat}} \pm 0.12^{\text{sys}}$, in $p+p$ and $d+$Au collisions, respectively. Fits assuming linear p_T dependence have slopes consistent with zero. Figure 2 also shows that for $p_T > 3$ GeV/c PYTHIA [17] predicts constant behavior for the ω/π^0 ratio.

The R-806 experiment measured ω/π^0 in $p+p$ collisions at $\sqrt{s} = 62$ GeV [18] and found this ratio to be 0.87 ± 0.17 over $3.5 < p_T < 7$ GeV/c. The E706 experiment measured ω/π^0 in π^-+Be collisions at $\sqrt{s_{\pi N}} = 31$ GeV [19] and found values consistent with the results presented in this Rapid Communication. The ω/π^0 ratios measured in hadronic interactions by three experiments at three different energies between 31 and 200 GeV, are the same within the errors.

Several LEP experiments [20–22] have measured ω production in $e^+ + e^-$ collisions at $\sqrt{s} = 91.2$ GeV and presented results as a function of $x_p = 2p_\omega/\sqrt{s}$. This is not a well-defined quantity in hadronic interactions. However, one can compare the ω/π^0 ratio at large values of p_T and x_p. Following the procedure for handling LEP data described in Ref. [10] one finds that for $x_p > 0.5$, the largest value for which statistically significant LEP data is available, the ratio has grown to approximately 0.7, close to the measurements in hadronic interactions.

Figure 3 shows the nuclear modification factor R_{dA}^{ω}, defined as the ratio between the ω meson yields in $d+$Au and $p+p$ interactions scaled by the number of binary collisions in $d+$Au, for minimum bias and central (0–20%) $d+$Au events. The precise definition of R_{dA} and the procedure to determine centrality in $d+$Au is given in sections IV.B and III.C in Ref. [10]. We find R_{dA}^{ω} to be $1.03 \pm 0.12^{\text{stat}} \pm 0.21^{\text{sys}}$ for minimum bias and $0.83 \pm 0.21^{\text{stat}} \pm 0.17^{\text{sys}}$ for central events, independent of p_T. R_{dA} values for two other neutral mesons (π^0 and η) measured by PHENIX [10,16] are also shown in Fig. 3. In all cases PHENIX observes that R_{dA} is close to one for $p_T > 2$ GeV/c and flat out to the highest p_T. Similar behavior is seen in preliminary analyses of K and ϕ mesons [15,23].

Recent publications suggest that modifications to the ω mass can be observed even in cold matter by studying not only the electron decay channel [24,25], but also hadronic channels [26]. For the hadronic decay modes presented here PHENIX lacks acceptance at low p_T where the effect is expected to be the most prominent. However, we have excellent mass resolution (20–25 MeV/c^2) for the mixed neutral-charged particle decay mode. Figure 4 shows extracted values for the ω mass as a function of p_T. In the p_T range of the measurement we observe no modification of the ω mass in either collision system we measure. For $p_T > 3$ GeV/c the mass of the ω meson in $p+p$ collisions at $\sqrt{s_{NN}} = 200$ GeV is consistent with the PDG [27] value within 7 MeV/c^2 at the 95% confidence level.

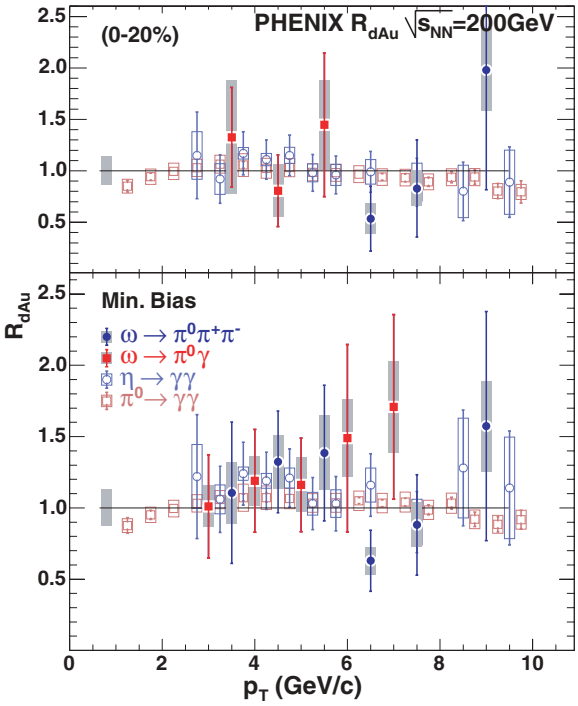

FIG. 3. (Color online) Measured R_{dA} vs p_T for neutral mesons in d+Au collisions at $\sqrt{s_{NN}} = 200$ GeV for (upper panel) 0–20% central and (lower panel) minimum bias. Values for π^0's and η's are from [10,16]. For reference a line is plotted at $R_{dA} = 1$. The scaling systematic error is shown as a box on the left.

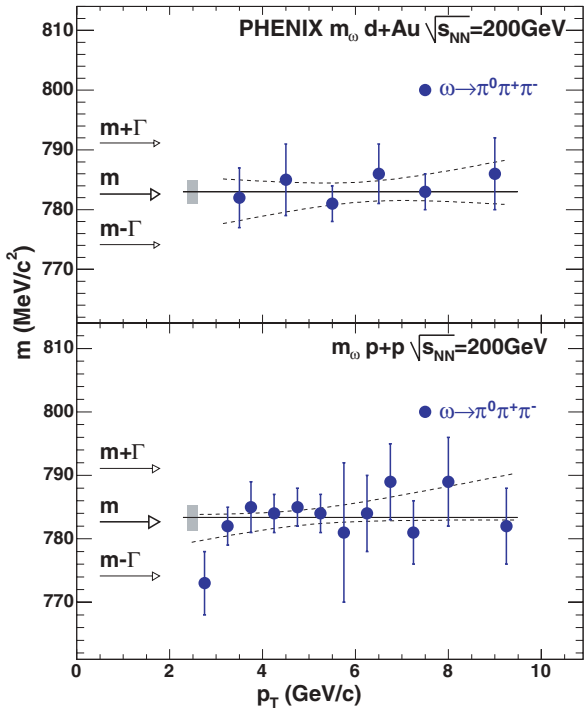

FIG. 4. (Color online) Reconstructed ω mass measured in the $\pi^0\pi^+\pi^-$ decay channel vs p_T in d+Au (upper panel) and p+p (lower panel) collisions at $\sqrt{s_{NN}} = 200$ GeV. Error bars show statistical errors. Straight lines show fits of the data to a constant. Dashed lines show values within 1σ of the best linear fit to the data. The systematic error on the fit values are shown with boxes on the left. PDG values for ω meson mass (m) and width (Γ) are shown with arrows on the left [27].

In summary we have presented the first measurement of ω production in p+p and d+Au collisions at $\sqrt{s_{NN}} = 200$ GeV. The production cross section is measured in two different decay modes with consistent results. The ω/π^0 ratio in p+p collisions is found to be $0.85 \pm 0.05^{\text{stat}} \pm 0.09^{\text{sys}}$ and $0.94 \pm 0.08^{\text{stat}} \pm 0.12^{\text{sys}}$ in d+Au over the measured p_T range. This agrees with previous measurements in hadronic collisions at lower $\sqrt{s}$. The nuclear modification factor for ω production in d+Au collisions is consistent with 1 and p_T independent for $p_T > 2$ GeV/c, consistent with other meson measurements. No modifications to the ω mass were observed in p+p or d+Au collisions. In p+p collisions the mass is consistent with the PDG [27] value within 7 MeV/c^2 at the 95% confidence level. The ω meson is also interesting as a probe of the hot nuclear medium created in A+A collisions. This measurement will serve as an excellent baseline for measurements of ω production in A+A in various decay channels.

We thank the staff of the Collider-Accelerator and Physics Departments at Brookhaven National Laboratory for their vital contributions. We acknowledge support from the Department of Energy and NSF (United States); MEXT and JSPS (Japan); CNPq and FAPESP (Brazil); NSFC (China); IN2P3/CNRS, CEA, and ARMINES (France); BMBF, DAAD, and AvH (Germany); OTKA (Hungary); DAE and DST (India); ISF (Israel); KRF and KOSEF (Korea); RMIST, RAS, and RMAE (Russia); VR and KAW (Sweden); U.S. CRDF for the FSU, U.S.-Hungarian NSF-OTKA-MTA, and U.S.-Israel BSF.

[1] J. F. Owens, Rev. Mod. Phys. **59**, 465 (1987).
[2] I. Vitev, Phys. Lett. **B562**, 36 (2003).
[3] V. Guzey, M. Strikman, and W. Vogelsang, Phys. Lett. **B603**, 173 (2004).
[4] R. Baier, D. Schiff, and B. Zakharov, Annu. Rev. Nucl. Part. Sci. **50**, 37 (2000).
[5] R. J. Fries, J. Phys. G **30**, S853 (2004).
[6] R. Rapp and J. Wambach, Adv. Nucl. Phys. **25**, 1 (2000).
[7] K. Adcox *et al.* (PHENIX Collaboration), Nucl. Instrum. Methods A **499**, 469 (2003).
[8] S. S. Adler *et al.* (PHENIX Collaboration), Phys. Rev. Lett. **91**, 182301 (2003).
[9] S. White, AIP Conf. Proc. **792**, 527 (2005).
[10] S. S. Adler *et al.*, (PHENIX Collaboration), Phys. Rev. C **75**, 024909 (2007).
[11] C. Alff *et al.*, Phys. Rev. Lett. **9**, 325 (1962).
[12] M. L. Stevenson, Phys. Rev. **125**, 687 (1962).
[13] S. S. Adler *et al.* (PHENIX Collaboration), Phys. Rev. Lett. **91**, 072301 (2003).
[14] S. S. Adler *et al.* (PHENIX Collaboration), Phys. Rev. Lett. **96**, 202301 (2006).

[15] V. Riabov (for the PHENIX Collaboration), Nucl. Phys. **A774**, 735 (2006).
[16] S. S. Adler *et al.* (PHENIX Collaboration), Phys. Rev. Lett. **91**, 072303 (2003).
[17] PYTHIA 6.206, T. Sjostrand *et al.*, arXiv:hep-ph/0108264 used with default parameters.
[18] M. Diakonou *et al.*, Phys. Lett. **B89**, 432 (1980).
[19] L. Apanasevich, arXiv:hep-ex/0004012.
[20] M. Acciarri *et al.* (L3 Collaboration), Phys. Lett. **B393**, 465 (1997).
[21] R. Barate *et al.* (ALEPH Collaboration), Phys. Rep. **294**, 1 (1998).
[22] K. Ackerstaff *et al.* (OPAL Collaboration), Eur. Phys. J. C **5**, 411 (1998).
[23] X. Cai (for the STAR Collaboration), Nucl. Phys. **A774**, 485 (2006).
[24] M. Naruki *et al.*, Phys. Rev. Lett. **96**, 092301 (2006).
[25] J. Adams *et al.* (STAR Collaboration), Phys. Rev. Lett. **92**, 092301 (2004).
[26] D. Trnka *et al.*, Phys. Rev. Lett. **94**, 192303 (2005).
[27] Particle Data Group. S. Edelman *et al.*, Phys. Lett. **B592**, 1 (2004).

J/ψ Production versus Centrality, Transverse Momentum, and Rapidity in Au + Au Collisions at $\sqrt{s_{NN}} = 200$ GeV

A. Adare,[8] S. Afanasiev,[22] C. Aidala,[9] N. N. Ajitanand,[49] Y. Akiba,[43,44] H. Al-Bataineh,[38] J. Alexander,[49] A. Al-Jamel,[38] K. Aoki,[28,43] L. Aphecetche,[51] R. Armendariz,[38] S. H. Aronson,[3] J. Asai,[44] E. T. Atomssa,[29] R. Averbeck,[50] T. C. Awes,[39] B. Azmoun,[3] V. Babintsev,[18] G. Baksay,[14] L. Baksay,[14] A. Baldisseri,[11] K. N. Barish,[4] P. D. Barnes,[31] B. Bassalleck,[37] S. Bathe,[4] S. Batsouli,[9,39] V. Baublis,[42] F. Bauer,[4] A. Bazilevsky,[3] S. Belikov,[3,21] R. Bennett,[50] Y. Berdnikov,[46] A. A. Bickley,[8] M. T. Bjorndal,[9] J. G. Boissevain,[31] H. Borel,[11] K. Boyle,[50] M. L. Brooks,[31] D. S. Brown,[38] D. Bucher,[34] H. Buesching,[3] V. Bumazhnov,[18] G. Bunce,[3,44] J. M. Burward-Hoy,[31] S. Butsyk,[31,50] S. Campbell,[50] J.-S. Chai,[23] B. S. Chang,[58] J.-L. Charvet,[11] S. Chernichenko,[18] J. Chiba,[24] C. Y. Chi,[9] M. Chiu,[9,19] I. J. Choi,[58] T. Chujo,[55] P. Chung,[49] A. Churyn,[18] V. Cianciolo,[39] C. R. Cleven,[16] Y. Cobigo,[11] B. A. Cole,[9] M. P. Comets,[40] P. Constantin,[21,31] M. Csanád,[13] T. Csörgő,[25] T. Dahms,[50] K. Das,[15] G. David,[3] M. B. Deaton,[1] K. Dehmelt,[14] H. Delagrange,[51] A. Denisov,[18] D. d'Enterria,[9] A. Deshpande,[44,50] E. J. Desmond,[3] O. Dietzsch,[47] A. Dion,[50] M. Donadelli,[47] J. L. Drachenberg,[1] O. Drapier,[29] A. Drees,[50] A. K. Dubey,[57] A. Durum,[18] V. Dzhordzhadze,[4,52] Y. V. Efremenko,[39] J. Egdemir,[50] F. Ellinghaus,[8] W. S. Emam,[4] A. Enokizono,[17,30] H. En'yo,[43,44] B. Espagnon,[40] S. Esumi,[54] K. O. Eyser,[4] D. E. Fields,[37,44] M. Finger,[5,22] F. Fleuret,[29] S. L. Fokin,[27] B. Forestier,[32] Z. Fraenkel,[57] J. E. Frantz,[9,50] A. Franz,[3] A. D. Frawley,[15] K. Fujiwara,[43] Y. Fukao,[28,43] S.-Y. Fung,[4] T. Fusayasu,[36] S. Gadrat,[32] I. Garishvili,[52] F. Gastineau,[51] M. Germain,[51] A. Glenn,[8,52] H. Gong,[50] M. Gonin,[29] J. Gosset,[11] Y. Goto,[43,44] R. Granier de Cassagnac,[29] N. Grau,[21] S. V. Greene,[55] M. Grosse Perdekamp,[19,44] T. Gunji,[7] H.-Å. Gustafsson,[33] T. Hachiya,[17,43] A. Hadj Henni,[51] C. Haegemann,[37] J. S. Haggerty,[3] M. N. Hagiwara,[1] H. Hamagaki,[7] R. Han,[41] H. Harada,[17] E. P. Hartouni,[30] K. Haruna,[17] M. Harvey,[3] E. Haslum,[33] K. Hasuko,[43] R. Hayano,[7] M. Heffner,[30] T. K. Hemmick,[50] T. Hester,[4] J. M. Heuser,[43] X. He,[16] H. Hiejima,[19] J. C. Hill,[21] R. Hobbs,[37] M. Hohlmann,[14] M. Holmes,[55] W. Holzmann,[49] K. Homma,[17] B. Hong,[26] T. Horaguchi,[43,53] D. Hornback,[52] M. G. Hur,[23] T. Ichihara,[43,44] K. Imai,[28,43] M. Inaba,[54] Y. Inoue,[45,43] D. Isenhower,[1] L. Isenhower,[1] M. Ishihara,[43] T. Isobe,[7] M. Issah,[49] A. Isupov,[22] B. V. Jacak,[50] J. Jia,[9] J. Jin,[9] O. Jinnouchi,[44] B. M. Johnson,[3] K. S. Joo,[35] D. Jouan,[40] F. Kajihara,[7,43] S. Kametani,[7,56] N. Kamihara,[43,53] J. Kamin,[50] M. Kaneta,[44] J. H. Kang,[58] H. Kanou,[43,53] T. Kawagishi,[54] D. Kawall,[44] A. V. Kazantsev,[27] S. Kelly,[8] A. Khanzadeev,[42] J. Kikuchi,[56] D. H. Kim,[35] D. J. Kim,[58] E. Kim,[48] Y.-S. Kim,[23] E. Kinney,[8] A. Kiss,[13] E. Kistenev,[3] A. Kiyomichi,[43] J. Klay,[30] C. Klein-Boesing,[34] L. Kochenda,[42] V. Kochetkov,[18] B. Komkov,[42] M. Konno,[54] D. Kotchetkov,[4] A. Kozlov,[57] A. Král,[10] A. Kravitz,[9] P. J. Kroon,[3] J. Kubart,[5,20] G. J. Kunde,[31] N. Kurihara,[7] K. Kurita,[45,43] M. J. Kweon,[26] Y. Kwon,[52,58] G. S. Kyle,[38] R. Lacey,[49] Y.-S. Lai,[9] J. G. Lajoie,[21] A. Lebedev,[21] Y. Le Bornec,[40] S. Leckey,[50] D. M. Lee,[31] M. K. Lee,[58] T. Lee,[48] M. J. Leitch,[31] M. A. L. Leite,[47] B. Lenzi,[47] H. Lim,[48] T. Liška,[10] A. Litvinenko,[22] M. X. Liu,[31] X. Li,[6] X. H. Li,[4] B. Love,[55] D. Lynch,[3] C. F. Maguire,[55] Y. I. Makdisi,[3] A. Malakhov,[22] M. D. Malik,[37] V. I. Manko,[27] Y. Mao,[41,43] L. Mašek,[5,20] H. Masui,[54] F. Matathias,[9,50] M. C. McCain,[19] M. McCumber,[50] P. L. McGaughey,[31] Y. Miake,[54] P. Mikeš,[5,20] K. Miki,[54] T. E. Miller,[55] A. Milov,[50] S. Mioduszewski,[3] G. C. Mishra,[16] M. Mishra,[2] J. T. Mitchell,[3] M. Mitrovski,[49] A. Morreale,[4] D. P. Morrison,[3] J. M. Moss,[31] T. V. Moukhanova,[27] D. Mukhopadhyay,[55] J. Murata,[45,43] S. Nagamiya,[24] Y. Nagata,[54] J. L. Nagle,[8] M. Naglis,[57] I. Nakagawa,[43,44] Y. Nakamiya,[17] T. Nakamura,[17] K. Nakano,[43,53] J. Newby,[30] M. Nguyen,[50] B. E. Norman,[31] A. S. Nyanin,[27] J. Nystrand,[33] E. O'Brien,[3] S. X. Oda,[7] C. A. Ogilvie,[21] H. Ohnishi,[43] I. D. Ojha,[55] H. Okada,[28,43] K. Okada,[44] M. Oka,[54] O. O. Omiwade,[1] A. Oskarsson,[33] I. Otterlund,[33] M. Ouchida,[17] K. Ozawa,[7] R. Pak,[3] D. Pal,[55] A. P. T. Palounek,[31] V. Pantuev,[50] V. Papavassiliou,[38] J. Park,[48] W. J. Park,[26] S. F. Pate,[38] H. Pei,[21] J.-C. Peng,[19] H. Pereira,[11] V. Peresedov,[22] D. Yu. Peressounko,[27] C. Pinkenburg,[3] R. P. Pisani,[3] M. L. Purschke,[3] A. K. Purwar,[31,50] H. Qu,[16] J. Rak,[21,37] A. Rakotozafindrabe,[29] I. Ravinovich,[57] K. F. Read,[39,52] S. Rembeczki,[14] M. Reuter,[50] K. Reygers,[34] V. Riabov,[42] Y. Riabov,[42] G. Roche,[32] A. Romana,[29,*] M. Rosati,[21] S. S. E. Rosendahl,[33] P. Rosnet,[32] P. Rukoyatkin,[22] V. L. Rykov,[43] S. S. Ryu,[58] B. Sahlmueller,[34] N. Saito,[28,43,44] T. Sakaguchi,[3,7,56] S. Sakai,[54] H. Sakata,[17] V. Samsonov,[42] H. D. Sato,[28,43] S. Sato,[3,24,54] S. Sawada,[24] J. Seele,[8] R. Seidl,[19] V. Semenov,[18] R. Seto,[4] D. Sharma,[57] T. K. Shea,[3] I. Shein,[18] A. Shevel,[42,49] T.-A. Shibata,[43,53] K. Shigaki,[17] M. Shimomura,[54] T. Shohjoh,[54] K. Shoji,[28,43] A. Sickles,[50] C. L. Silva,[47] D. Silvermyr,[39] C. Silvestre,[11] K. S. Sim,[26] C. P. Singh,[2] V. Singh,[2] S. Skutnik,[21] M. Slunečka,[5,22] W. C. Smith,[1] A. Soldatov,[18] R. A. Soltz,[30] W. E. Sondheim,[31] S. P. Sorensen,[52] I. V. Sourikova,[3] F. Staley,[11] P. W. Stankus,[39] E. Stenlund,[33] M. Stepanov,[38] A. Ster,[25] S. P. Stoll,[3] T. Sugitate,[17] C. Suire,[40] J. P. Sullivan,[31] J. Sziklai,[25] T. Tabaru,[44] S. Takagi,[54] E. M. Takagui,[47] A. Taketani,[43,44] K. H. Tanaka,[24] Y. Tanaka,[36] K. Tanida,[43,44] M. J. Tannenbaum,[3] A. Taranenko,[49] P. Tarján,[12] T. L. Thomas,[37] M. Togawa,[28,43] A. Toia,[50] J. Tojo,[43] L. Tomášek,[20]

 © 2007 The American Physical Society

H. Torii,[43] R. S. Towell,[1] V-N. Tram,[29] I. Tserruya,[57] Y. Tsuchimoto,[17,43] S. K. Tuli,[2] H. Tydesjö,[33] N. Tyurin,[18] C. Vale,[21] H. Valle,[55] H. W. van Hecke,[31] J. Velkovska,[55] R. Vertesi,[12] A. A. Vinogradov,[27] M. Virius,[10] V. Vrba,[20] E. Vznuzdaev,[42] M. Wagner,[28,43] D. Walker,[50] X. R. Wang,[38] Y. Watanabe,[43,44] J. Wessels,[34] S. N. White,[3] N. Willis,[40] D. Winter,[9] C. L. Woody,[3] M. Wysocki,[8] W. Xie,[4,44] Y. Yamaguchi,[56] A. Yanovich,[18] Z. Yasin,[4] J. Ying,[16] S. Yokkaichi,[43,44] G. R. Young,[39] I. Younus,[37] I. E. Yushmanov,[27] W. A. Zajc,[9,†] O. Zaudtke,[34] C. Zhang,[9,39] S. Zhou,[6] J. Zimányi,[25,*] and L. Zolin[22]

(PHENIX Collaboration)

[1]*Abilene Christian University, Abilene, Texas 79699, USA*
[2]*Department of Physics, Banaras Hindu University, Varanasi 221005, India*
[3]*Brookhaven National Laboratory, Upton, New York 11973-5000, USA*
[4]*University of California–Riverside, Riverside, California 92521, USA*
[5]*Charles University, Ovocný trh 5, Praha 1, 116 36 Prague, Czech Republic*
[6]*China Institute of Atomic Energy (CIAE), Beijing, People's Republic of China*
[7]*Center for Nuclear Study, Graduate School of Science, University of Tokyo, 7-3-1 Hongo, Bunkyo, Tokyo 113-0033, Japan*
[8]*University of Colorado, Boulder, Colorado 80309, USA*
[9]*Columbia University, New York, New York 10027, USA, and Nevis Laboratories, Irvington, New York 10533, USA*
[10]*Czech Technical University, Zikova 4, 166 36 Prague 6, Czech Republic*
[11]*Dapnia, CEA Saclay, F-91191 Gif-sur-Yvette, France*
[12]*Debrecen University, H-4010 Debrecen, Egyetem tér 1, Hungary*
[13]*ELTE, Eötvös Loránd University, H - 1117 Budapest, Pázmány P. s. 1/A, Hungary*
[14]*Florida Institute of Technology, Melbourne, Florida 32901, USA*
[15]*Florida State University, Tallahassee, Florida 32306, USA*
[16]*Georgia State University, Atlanta, Georgia 30303, USA*
[17]*Hiroshima University, Kagamiyama, Higashi-Hiroshima 739-8526, Japan*
[18]*IHEP Protvino, State Research Center of Russian Federation, Institute for High Energy Physics, Protvino 142281, Russia*
[19]*University of Illinois at Urbana-Champaign, Urbana, Illinois 61801, USA*
[20]*Institute of Physics, Academy of Sciences of the Czech Republic, Na Slovance 2, 182 21 Prague 8, Czech Republic*
[21]*Iowa State University, Ames, Iowa 50011, USA*
[22]*Joint Institute for Nuclear Research, 141980 Dubna, Moscow Region, Russia*
[23]*KAERI, Cyclotron Application Laboratory, Seoul, South Korea*
[24]*KEK, High Energy Accelerator Research Organization, Tsukuba, Ibaraki 305-0801, Japan*
[25]*KFKI Research Institute for Particle and Nuclear Physics of the Hungarian Academy of Sciences (MTA KFKI RMKI), H-1525 Budapest 114, P.O. Box 49, Budapest, Hungary*
[26]*Korea University, Seoul 136-701, Korea*
[27]*Russian Research Center "Kurchatov Institute," Moscow, Russia*
[28]*Kyoto University, Kyoto 606-8502, Japan*
[29]*Laboratoire Leprince-Ringuet, Ecole Polytechnique, CNRS-IN2P3, Route de Saclay, F-91128 Palaiseau, France*
[30]*Lawrence Livermore National Laboratory, Livermore, California 94550, USA*
[31]*Los Alamos National Laboratory, Los Alamos, New Mexico 87545, USA*
[32]*LPC, Université Blaise Pascal, CNRS-IN2P3, Clermont-Fd, 63177 Aubiere Cedex, France*
[33]*Department of Physics, Lund University, Box 118, SE-221 00 Lund, Sweden*
[34]*Institut für Kernphysik, University of Muenster, D-48149 Muenster, Germany*
[35]*Myongji University, Yongin, Kyonggido 449-728, Korea*
[36]*Nagasaki Institute of Applied Science, Nagasaki-shi, Nagasaki 851-0193, Japan*
[37]*University of New Mexico, Albuquerque, New Mexico 87131, USA*
[38]*New Mexico State University, Las Cruces, New Mexico 88003, USA*
[39]*Oak Ridge National Laboratory, Oak Ridge, Tennessee 37831, USA*
[40]*IPN-Orsay, Universite Paris Sud, CNRS-IN2P3, BP 1, F-91406 Orsay, France*
[41]*Peking University, Beijing, People's Republic of China*
[42]*PNPI, Petersburg Nuclear Physics Institute, Gatchina, Leningrad region, 188300, Russia*
[43]*RIKEN, The Institute of Physical and Chemical Research, Wako, Saitama 351-0198, Japan*
[44]*RIKEN BNL Research Center, Brookhaven National Laboratory, Upton, New York 11973-5000, USA*
[45]*Physics Department, Rikkyo University, 3-34-1 Nishi-Ikebukuro, Toshima, Tokyo 171-8501, Japan*
[46]*Saint Petersburg State Polytechnic University, St. Petersburg, Russia*
[47]*Universidade de São Paulo, Instituto de Física, Caixa Postal 66318, São Paulo CEP05315-970, Brazil*
[48]*System Electronics Laboratory, Seoul National University, Seoul, South Korea*

[49]Chemistry Department, Stony Brook University, Stony Brook, SUNY, New York 11794-3400, USA
[50]Department of Physics and Astronomy, Stony Brook University, SUNY, Stony Brook, New York 11794, USA
[51]SUBATECH (Ecole des Mines de Nantes, CNRS-IN2P3, Université de Nantes) BP 20722, 44307 Nantes, France
[52]University of Tennessee, Knoxville, Tennessee 37996, USA
[53]Department of Physics, Tokyo Institute of Technology, Oh-okayama, Meguro, Tokyo 152-8551, Japan
[54]Institute of Physics, University of Tsukuba, Tsukuba, Ibaraki 305, Japan
[55]Vanderbilt University, Nashville, Tennessee 37235, USA
[56]Waseda University, Advanced Research Institute for Science and Engineering, 17 Kikui-cho, Shinjuku-ku, Tokyo 162-0044, Japan
[57]Weizmann Institute, Rehovot 76100, Israel
[58]Yonsei University, IPAP, Seoul 120-749, Korea

(Received 12 November 2006; published 4 June 2007; corrected 7 June 2007)

The PHENIX experiment at the BNL Relativistic Heavy Ion Collider (RHIC) has measured J/ψ production for rapidities $-2.2 < y < 2.2$ in Au + Au collisions at $\sqrt{s_{NN}} = 200$ GeV. The J/ψ invariant yield and nuclear modification factor R_{AA} as a function of centrality, transverse momentum, and rapidity are reported. A suppression of J/ψ relative to binary collision scaling of proton-proton reaction yields is observed. Models which describe the lower energy J/ψ data at the CERN Super Proton Synchrotron invoking only J/ψ destruction based on the local medium density predict a significantly larger suppression at RHIC and more suppression at midrapidity than at forward rapidity. Both trends are contradicted by our data.

DOI: 10.1103/PhysRevLett.98.232301 PACS numbers: 25.75.Dw

The quark-gluon plasma (QGP) is a state of deconfined quarks and gluons which is predicted by lattice quantum chromodynamics (QCD) calculations to be formed above a temperature T_c of the order of 175–192 MeV for a baryon chemical potential $\mu_b = 0$ [1,2]. Heavy quarkonia (J/ψ, ψ', χ_c, and Υ) have long been considered a promising probe to study the formation and properties of the QGP. In the deconfined state, the attraction between heavy quarks and antiquarks is predicted to be reduced due to dynamic screening effects, leading to the suppression of heavy quarkonia yield. The strength of the suppression depends on the binding energies of the quarkonia and the temperature of the surrounding system [3]. Recent lattice QCD calculations suggest that the J/ψ may not dissociate until well above T_c [4–6]. On the other hand, χ_c and ψ', which contribute to the total J/ψ yield via decay, are expected to dissolve at lower temperatures due to smaller binding energies.

A J/ψ suppression was observed at lower energies by the NA50 experiment at the CERN Super Proton Synchrotron (SPS) [7,8] that could be reproduced by various theoretical calculations [9–13]. Models that invoke the formation of a QGP predict a larger suppression at the BNL Relativistic Heavy Ion Collider (RHIC) than SPS due to the larger energy density of the medium created. On the other hand, several models also predict that the J/ψ yield will result from a balance between destruction due to thermal gluons and enhancement due to coalescence of uncorrelated $c\bar{c}$ pairs [9,14], which are produced abundantly at RHIC energy [15,16]. Cold nuclear matter (CNM) effects such as nuclear absorption, shadowing, and antishadowing are also expected to modify the J/ψ yield. PHENIX d + Au data show that CNM effects are smaller at RHIC than those observed at a lower energy [17] and can be reproduced by a nuclear absorption cross section of up to 3 mb plus nuclear shadowing [18].

We report results on J/ψ production measured by the PHENIX Collaboration at midrapidity ($|y| < 0.35$) via e^+e^- decay and at forward rapidity ($|y| \in [1.2, 2.2]$) via $\mu^+\mu^-$ decay in Au + Au collisions at $\sqrt{s_{NN}} = 200$ GeV. These results do not separate primordial J/ψ and J/ψ from χ_c, ψ', or B decay. The J/ψ invariant yields as a function of centrality, rapidity (y), and transverse momentum (p_T) are shown. They are combined with the yield measured in p + p collisions [19] to form the J/ψ nuclear modification factor R_{AA}.

The PHENIX apparatus is described in Ref. [20]. At midrapidity, electrons are measured with two spectrometers consisting of drift chambers (DC), pad chambers (PC), ring-imaging Cerenkov counters (RICH), and electromagnetic calorimeters (EMCal). They are identified by matching tracks reconstructed with the DC and PC to EMCal clusters and RICH hits. The energy-momentum matching requirement is $(E/p - 1) \geq -2.5$ standard deviations (σ). The position matching between the track and the EMCAL cluster is $\leq 2.5\sigma$ (4σ) in azimuth and along the beam axis, for central (peripheral) collisions. For the RICH, at least 4 (2) matching hits are required. Muons are measured with two spectrometers consisting of a front absorber to stop most hadrons produced in the collision, cathode strip chambers (MuTr), which provide momentum information, and a muon identifier (MuID), which uses alternating layers of steel absorber and Iarocci tubes. Charged particle trajectories are first reconstructed in the MuID and then in the MuTr. They must reach the last plane of the MuID and have a good geometrical match between the MuID and the MuTr to be identified as muons. The matching is $<9°$ for the slope and <15 (20) cm for the position in the first layer of the MuID at positive (negative) rapidity.

The data used for this analysis were collected during the 2004 run at RHIC using a minimum bias trigger (a coincidence of the two beam-beam counters), which covers

$92 \pm 3\%$ of the Au + Au inelastic cross section. After quality assurance and vertex cut ($|z| \leq 30$ cm), 9.9×10^8 (1.1×10^9) events were analyzed for mid (forward) rapidity, corresponding to an integrated luminosity of 157 μb^{-1} (174 μb^{-1}).

The J/ψ yield is obtained from the unlike-sign dilepton invariant mass distribution [21] after subtracting the combinatorial background using an event-mixing technique. The background is normalized to the real data by equating $2\sqrt{N^{++}N^{--}}$, with N^{++} (N^{--}) being the number of positive (negative) dilepton pairs. The accuracy of the normalization is estimated to be 2% and is accounted for in the systematic errors. At midrapidity, the J/ψ mass resolution is ~ 35 MeV/c^2. The number of J/ψ is determined by counting the remaining unlike-sign pairs in the mass range $2.9 \leq M \leq 3.3$ GeV/c^2. This number is corrected by the estimated contribution of the dielectron continuum and the loss due to the radiative tail. A total of $\sim 1000 J/\psi$ are obtained, and the signal to background (S/B) varies from 0.5 for central collisions to 15 for peripheral collisions. At forward rapidity, the J/ψ mass resolution varies from 150 to 200 MeV/c^2 and is larger than at midrapidity primarily because of the multiple scattering and energy loss straggling in the front absorber. The residual background (notably, open charm pairs and Drell-Yan processes) in the unlike-sign invariant mass distribution is evaluated using an exponential form. The J/ψ signal is estimated by counting the remaining pairs in the mass range $2.6 \leq M \leq 3.6$ GeV/c^2 and using a fit with different line shapes. The average of the resulting values is used as the number of J/ψ, and their dispersion is included in the systematic error. A total of $\sim 4500 J/\psi$ are obtained, and S/B varies from 0.2 for central collisions to 3 for peripheral collisions.

The J/ψ invariant yield in a given centrality, p_T, and y bin is

$$\frac{B_{ll}}{2\pi p_T}\frac{d^2N_{J/\psi}}{dp_T dy} = \frac{1}{2\pi p_T}\frac{N_{J/\psi}}{N_{\rm evt}\Delta y \Delta p_T A\varepsilon}, \qquad (1)$$

with B_{ll} being the branching ratio for $J/\psi \to l^+l^-$, $N_{J/\psi}$ the number of J/ψ measured in the bin, $N_{\rm evt}$ the corresponding number of events, and $A\varepsilon$ the acceptance and efficiency correction for J/ψ. $A\epsilon$ is determined by full GEANT simulation. It decreases with the collision centrality due to overlapping hits in the RICH, EMCal, and MuTr, leading to an increasing number of misreconstructed tracks, which are then rejected by the analysis cuts. This effect is evaluated by embedding simulated J/ψ in real events. For the most central collisions, the efficiency loss is 20% at midrapidity and 75% (50%) at positive (negative) rapidity.

The nuclear modification factor in a given centrality, p_T, and y bin is

$$R_{AA} = \frac{d^2N^{AA}_{J/\psi}/dp_T dy}{N_{\rm coll} d^2N^{pp}_{J/\psi}/dp_T dy}, \qquad (2)$$

TABLE I. Sources of systematic errors on the J/ψ invariant yield. When two values are given, the first (second) is for peripheral (central) collisions. Errors of type A (type B) are point-to-point uncorrelated (correlated).

Source	$\lvert y\rvert < 0.35$	$\lvert y\rvert \in [1.2, 2.2]$	Type
Signal extraction	6.5%–9%	4%–24%	A
Acceptance	6%	10%	B
Efficiency	4.5%–8%	4%–16%	B
Run by run variation	4%	5%	B
Input y, p_T distributions	2%	4%	B

with $d^2N^{AA}_{J/\psi}/dp_T dy$ being the J/ψ yield in Au + Au collisions, $N_{\rm coll}$ the mean number of binary collisions in the centrality bin, and $d^2N^{pp}_{J/\psi}/dp_T dy$ the J/ψ yield in $p + p$ inelastic collisions.

The systematic errors on the J/ψ invariant yield (Table I) are grouped into three categories: point-to-point uncorrelated (type A), for which the points can move independently one from the other; point-to-point correlated (type B), for which the points can move coherently, though not necessarily by the same amount; and global errors, for which all points move by the same relative amount. Statistical and type A errors are summed in quadrature and represented with vertical bars; type B errors are represented with boxes, and different colors or symbols are used for forward and midrapidity because they are independent; global systematic errors are quoted in the figures. For R_{AA}, additional errors are associated with uncertainties in the calculation of $N_{\rm coll}$ (10%–28%) and the J/ψ yield in $p + p$ (12% and 7% at mid and forward rapidity, respec-

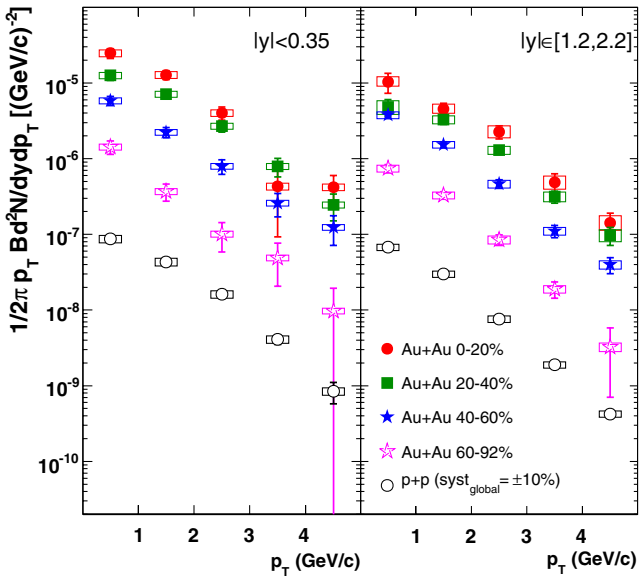

FIG. 1 (color online). J/ψ invariant yield versus p_T for different centrality bins in Au + Au collisions and in $p + p$ collisions [19]. The left (right) panel corresponds to mid (forward) rapidity. See text for description of the errors and Ref. [21] for data tables.

TABLE II. Characterization of the J/ψ, p_T, and y distributions. Column 3 (4): J/ψ $\langle p_T^2 \rangle$ calculated for $p_T \leq 5$ GeV/c at mid (forward) rapidity for different centrality bins in Au + Au collisions and in $p + p$ collisions. The first error corresponds to statistical and type A. The second error is type B.

Percent (%)	N_{part}	$\langle p_T^2 \rangle$ (GeV/c)^2 $\lvert y \rvert < 0.35$	$\langle p_T^2 \rangle$ (GeV/c)^2 $1.2 < \lvert y \rvert < 2.2$	y rms
0–20	280	$3.6 \pm 0.6 \pm 0.1$	$4.4 \pm 0.4 \pm 0.4$	1.32 ± 0.06
20–40	140	$4.6 \pm 0.5 \pm 0.1$	$4.6 \pm 0.3 \pm 0.4$	1.30 ± 0.05
40–60	60	$4.5 \pm 0.7 \pm 0.2$	$3.7 \pm 0.2 \pm 0.3$	1.40 ± 0.04
60–92	14	$3.6 \pm 0.9 \pm 0.2$	$3.3 \pm 0.3 \pm 0.2$	1.43 ± 0.04
$p + p$	2	$4.1 \pm 0.2 \pm 0.1$	$3.4 \pm 0.1 \pm 0.1$	1.41 ± 0.03

tively). On the other hand, some errors that are common to Au + Au and $p + p$ cancel.

Figure 1 shows the J/ψ yield versus p_T for different centrality bins (see Table II for the corresponding number of participants N_{part}). Data from the two muon spectrometers are combined to obtain the forward rapidity points. In each centrality bin, the J/ψ mean square transverse momentum $\langle p_T^2 \rangle$ is numerically calculated for $p_T \leq 5$ GeV/c and is shown in Table II. At midrapidity, the $\langle p_T^2 \rangle$ shows no variation versus centrality within errors. It increases slightly with N_{part} at forward rapidity.

Figure 2 shows the J/ψ yield versus y for different centrality bins. The root mean square (rms) of each distribution is shown in Table II. For the two most peripheral bins, the rms is compatible with that measured in $p + p$ collisions. For the most central bins, the rms is smaller by about 2σ.

Figures 3 and 4 show the J/ψ R_{AA} versus p_T and y, respectively, for different centrality bins. Figure 5(a) shows the p_T integrated R_{AA} versus N_{part} at mid and forward rapidity, respectively. For each rapidity, R_{AA} decreases with increasing N_{part}. For the most central collisions, R_{AA} is below 0.3 (0.2) at mid (forward) rapidity. Figure 5(b) shows the ratio of forward or midrapidity R_{AA} versus N_{part}. The ratio first decreases and then reaches a plateau of about 0.6 for $N_{\text{part}} > 100$.

In summary, a significant J/ψ suppression relative to the binary scaling of proton-proton collisions is observed for central Au + Au collisions at RHIC. Its magnitude is greater than that expected by extrapolating the CNM effects measured in d + Au collisions [17,18,22]. At midrapidity, the suppression is similar to that observed at the SPS [8], whereas at forward rapidity it is significantly larger. Models of quarkonia suppression driven by the local energy density of the medium predict a greater suppression at RHIC than SPS and less suppression at forward rapidity than at midrapidity [9,10]. Both trends are contradicted by

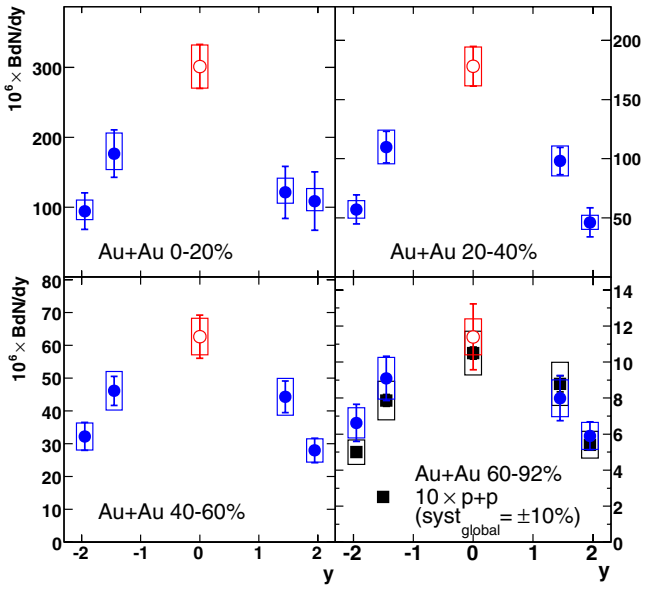

FIG. 2 (color online). J/ψ invariant yield versus y for different centrality bins in Au + Au collisions and for $p + p$ collisions. Open (solid) circles are for mid (forward) rapidity Au + Au data. Black squares are for $p + p$ data [19]. See text for description of the errors and Ref. [21] for data tables.

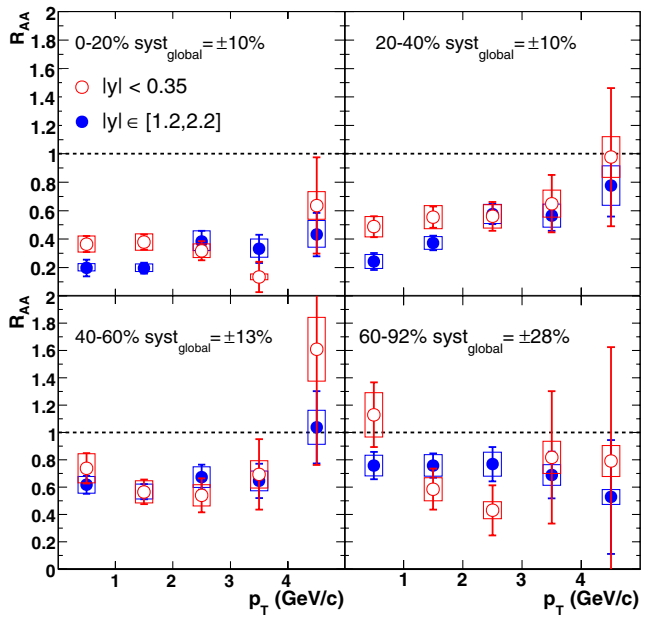

FIG. 3 (color online). J/ψ R_{AA} versus p_T for several centrality bins in Au + Au collisions. Mid (forward) rapidity data are shown with open (solid) circles. See text for description of the errors and Ref. [21] for data tables.

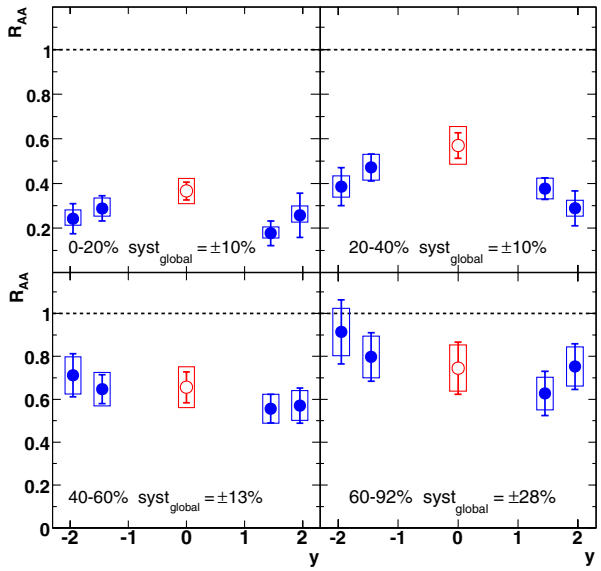

FIG. 4 (color online). J/ψ R_{AA} versus y for different centrality bins. Open (solid) circles are for mid (forward) rapidity. See text for description of the errors and Ref. [21] for data tables.

our data. Additionally, the J/ψ mean square transverse momentum, restricted to $p_T \leq 5$ GeV/c, shows little dependence on centrality. Various models of J/ψ production and suppression, which predict different transverse momentum and rapidity dependencies, can be significantly constrained by the data presented here and recent results on the open charm [16].

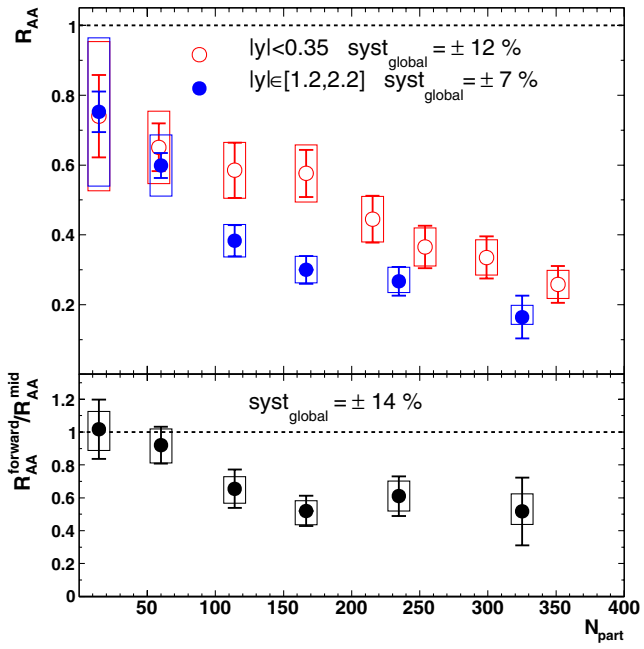

FIG. 5 (color online). (a) J/ψ R_{AA} versus $N_{\rm part}$ for Au + Au collisions. Mid (forward) rapidity data are shown with open (solid) circles. (b) Ratio of forward or midrapidity J/ψ R_{AA} versus $N_{\rm part}$. For the two most central bins, midrapidity points have been combined to form the ratio with the forward rapidity points. See text for description of the errors and Ref. [21] for data tables.

We thank the staff of the Collider-Accelerator and Physics Departments at BNL for their vital contributions. We acknowledge support from the Office of NP in DOE Office of Science and NSF (USA), MEXT and JSPS (Japan), CNPq and FAPESP (Brazil), NSFC (China), MSMT (Czech Republic), IN2P3/CNRS and CEA (France), BMBF, DAAD, and AvH (Germany), OTKA (Hungary), DAE (India), ISF (Israel), KRF and KOSEF (Korea), MES, RAS, and FAAE (Russia), VR and KAW (Sweden), U.S. CRDF for the FSU, U.S.–Hungarian NSF-OTKA-MTA, and U.S.–Israel BSF.

*Deceased.
†PHENIX Spokesperson.
Electronic address: zajc@nevis.columbia.edu

[1] Y. Aoki, Z. Fodor, S. D. Katz, and K. K. Szabo, Phys. Lett. B **643**, 46 (2006).
[2] M. Cheng *et al.*, Phys. Rev. D **74**, 054507 (2006).
[3] T. Matsui and H. Satz, Phys. Lett. B **178**, 416 (1986).
[4] S. Datta, F. Karsch, P. Petreczky, and I. Wetzorke, Phys. Rev. D **69**, 094507 (2004).
[5] M. Asakawa and T. Hatsuda, Phys. Rev. Lett. **92**, 012001 (2004).
[6] T. Umeda, K. Nomura, and H. Matsufuru, Eur. Phys. J. C **39S1**, 9 (2005).
[7] M. C. Abreu *et al.*, Phys. Lett. B **410**, 337 (1997).
[8] B. Alessandro *et al.*, Eur. Phys. J. C **39**, 335 (2005).
[9] L. Grandchamp, R. Rapp, and G. E. Brown, Phys. Rev. Lett. **92**, 212301 (2004).
[10] A. Capella and E. G. Ferreiro, Eur. Phys. J. C **42**, 419 (2005).
[11] X.-l. Zhu, P.-f. Zhuang, and N. Xu, Phys. Lett. B **607**, 107 (2005).
[12] E. L. Bratkovskaya, A. P. Kostyuk, W. Cassing, and H. Stocker, Phys. Rev. C **69**, 054903 (2004).
[13] A. Andronic, P. Braun-Munzinger, K. Redlich, and J. Stachel, Phys. Lett. B **571**, 36 (2003).
[14] R. L. Thews and M. L. Mangano, Phys. Rev. C **73**, 014904 (2006).
[15] S. S. Adler *et al.*, Phys. Rev. Lett. **96**, 032301 (2006).
[16] A. Adare *et al.*, Phys. Rev. Lett. **97**, 252002 (2006).
[17] S. S. Adler *et al.*, Phys. Rev. Lett. **96**, 012304 (2006).
[18] R. Vogt, Acta Phys. Hung. **A25**, 97 (2006).
[19] A. Adare *et al.*, preceding Letter, Phys. Rev. Lett. **98**, 232002 (2007).
[20] K. Adcox *et al.*, Nucl. Instrum. Methods Phys. Res., Sect. A **499**, 469 (2003).
[21] See EPAPS Document No. E-PRLTAO-98-009723 for plain text data files for all of the plotted data points, plots from the figures but with the PHENIX logo for presentations, and mass spectra plots. For more information on EPAPS, see http://www.aip.org/pubservs/epaps.html.
[22] R. Granier de Cassagnac, arXiv:hep-ph/0701222.

J/ψ Production versus Transverse Momentum and Rapidity in $p + p$ Collisions at $\sqrt{s} = 200$ GeV

A. Adare,[8] S. Afanasiev,[22] C. Aidala,[9] N. N. Ajitanand,[48] Y. Akiba,[42,43] H. Al-Bataineh,[37] J. Alexander,[48] K. Aoki,[27,42] L. Aphecetche,[50] R. Armendariz,[37] S. H. Aronson,[3] J. Asai,[43] E. T. Atomssa,[28] R. Averbeck,[49] T. C. Awes,[38] B. Azmoun,[3] V. Babintsev,[18] G. Baksay,[14] L. Baksay,[14] A. Baldisseri,[11] K. N. Barish,[4] P. D. Barnes,[30] B. Bassalleck,[36] S. Bathe,[4] S. Batsouli,[38] V. Baublis,[41] A. Bazilevsky,[3] S. Belikov,[3] R. Bennett,[49] Y. Berdnikov,[45] A. A. Bickley,[8] J. G. Boissevain,[30] H. Borel,[11] K. Boyle,[49] M. L. Brooks,[30] H. Buesching,[3] V. Bumazhnov,[18] G. Bunce,[3,43] S. Butsyk,[30,49] S. Campbell,[49] B. S. Chang,[57] J.-L. Charvet,[11] S. Chernichenko,[18] J. Chiba,[23] C. Y. Chi,[9] M. Chiu,[19] I. J. Choi,[57] T. Chujo,[54] P. Chung,[48] A. Churyn,[18] V. Cianciolo,[38] C. R. Cleven,[16] B. A. Cole,[9] M. P. Comets,[39] P. Constantin,[30] M. Csanád,[13] T. Csörgő,[24] T. Dahms,[49] K. Das,[15] G. David,[3] M. B. Deaton,[1] K. Dehmelt,[14] H. Delagrange,[50] A. Denisov,[18] D. d'Enterria,[9] A. Deshpande,[43,49] E. J. Desmond,[3] O. Dietzsch,[46] A. Dion,[49] M. Donadelli,[46] O. Drapier,[28] A. Drees,[49] A. K. Dubey,[56] A. Durum,[18] V. Dzhordzhadze,[4] Y. V. Efremenko,[38] J. Egdemir,[49] F. Ellinghaus,[8] W. S. Emam,[4] A. Enokizono,[29] H. En'yo,[42,43] S. Esumi,[53] K. O. Eyser,[4] D. E. Fields,[36,43] M. Finger,[5,22] M. Finger, Jr.,[5,22] F. Fleuret,[28] S. L. Fokin,[26] Z. Fraenkel,[56] J. E. Frantz,[49] A. Franz,[3] A. D. Frawley,[15] K. Fujiwara,[42] Y. Fukao,[27,42] T. Fusayasu,[35] S. Gadrat,[31] I. Garishvili,[51] A. Glenn,[8] H. Gong,[49] M. Gonin,[28] J. Gosset,[11] Y. Goto,[42,43] R. Granier de Cassagnac,[28] N. Grau,[21] S. V. Greene,[54] M. Grosse Perdekamp,[19,43] T. Gunji,[7] H.-Å. Gustafsson,[32] T. Hachiya,[17] A. Hadj Henni,[50] C. Haegemann,[36] J. S. Haggerty,[3] H. Hamagaki,[7] R. Han,[40] H. Harada,[17] E. P. Hartouni,[29] K. Haruna,[17] E. Haslum,[32] R. Hayano,[7] M. Heffner,[29] T. K. Hemmick,[49] T. Hester,[4] X. He,[16] H. Hiejima,[19] J. C. Hill,[21] R. Hobbs,[36] M. Hohlmann,[14] W. Holzmann,[48] K. Homma,[17] B. Hong,[25] T. Horaguchi,[42,52] D. Hornback,[51] T. Ichihara,[42,43] K. Imai,[27,42] M. Inaba,[53] Y. Inoue,[44,42] D. Isenhower,[1] L. Isenhower,[1] M. Ishihara,[42] T. Isobe,[7] M. Issah,[48] A. Isupov,[22] B. V. Jacak,[49] J. Jia,[9] J. Jin,[9] O. Jinnouchi,[43] B. M. Johnson,[3] K. S. Joo,[34] D. Jouan,[39] F. Kajihara,[7] S. Kametani,[7,55] N. Kamihara,[42] J. Kamin,[49] M. Kaneta,[43] J. H. Kang,[57] H. Kanou,[42,52] D. Kawall,[43] A. V. Kazantsev,[26] A. Khanzadeev,[41] J. Kikuchi,[55] D. H. Kim,[34] D. J. Kim,[57] E. Kim,[47] E. Kinney,[8] A. Kiss,[13] E. Kistenev,[3] A. Kiyomichi,[42] J. Klay,[29] C. Klein-Boesing,[33] L. Kochenda,[41] V. Kochetkov,[18] B. Komkov,[41] M. Konno,[53] D. Kotchetkov,[4] A. Kozlov,[56] A. Král,[10] A. Kravitz,[9] J. Kubart,[5,20] G. J. Kunde,[30] N. Kurihara,[7] K. Kurita,[44,42] M. J. Kweon,[25] Y. Kwon,[51,57] G. S. Kyle,[37] R. Lacey,[48] Y.-S. Lai,[9] J. G. Lajoie,[21] A. Lebedev,[21] D. M. Lee,[30] M. K. Lee,[57] T. Lee,[47] M. J. Leitch,[30] M. A. L. Leite,[46] B. Lenzi,[46] T. Liška,[10] A. Litvinenko,[22] M. X. Liu,[30] X. Li,[6] B. Love,[54] D. Lynch,[3] C. F. Maguire,[54] Y. I. Makdisi,[3] A. Malakhov,[22] M. D. Malik,[36] V. I. Manko,[26] Y. Mao,[40,42] L. Mašek,[5,20] H. Masui,[53] F. Matathias,[9] M. McCumber,[49] P. L. McGaughey,[30] Y. Miake,[53] P. Mikeš,[5,20] K. Miki,[53] T. E. Miller,[54] A. Milov,[49] S. Mioduszewski,[3] M. Mishra,[2] J. T. Mitchell,[3] M. Mitrovski,[48] A. Morreale,[4] D. P. Morrison,[3] T. V. Moukhanova,[26] D. Mukhopadhyay,[54] J. Murata,[44,42] S. Nagamiya,[23] Y. Nagata,[53] J. L. Nagle,[8] M. Naglis,[56] I. Nakagawa,[42,43] Y. Nakamiya,[17] T. Nakamura,[17] K. Nakano,[42,52] J. Newby,[29] M. Nguyen,[49] B. E. Norman,[30] A. S. Nyanin,[26] E. O'Brien,[3] S. X. Oda,[7] C. A. Ogilvie,[21] H. Ohnishi,[42] H. Okada,[27,42] K. Okada,[43] M. Oka,[53] O. O. Omiwade,[1] A. Oskarsson,[32] M. Ouchida,[17] K. Ozawa,[7] R. Pak,[3] D. Pal,[54] A. P. T. Palounek,[30] V. Pantuev,[49] V. Papavassiliou,[37] J. Park,[47] W. J. Park,[25] S. F. Pate,[37] H. Pei,[21] J.-C. Peng,[19] H. Pereira,[11] V. Peresedov,[22] D. Yu. Peressounko,[26] C. Pinkenburg,[3] M. L. Purschke,[3] A. K. Purwar,[30] H. Qu,[16] J. Rak,[36] A. Rakotozafindrabe,[28] I. Ravinovich,[56] K. F. Read,[38,51] S. Rembeczki,[14] M. Reuter,[49] K. Reygers,[33] V. Riabov,[41] Y. Riabov,[41] G. Roche,[31] A. Romana,[28,*] M. Rosati,[21] S. S. E. Rosendahl,[32] P. Rosnet,[31] P. Rukoyatkin,[22] V. L. Rykov,[42] B. Sahlmueller,[33] N. Saito,[27,42,43] T. Sakaguchi,[3] S. Sakai,[53] H. Sakata,[17] V. Samsonov,[41] S. Sato,[23] S. Sawada,[23] J. Seele,[8] R. Seidl,[19] V. Semenov,[18] R. Seto,[4] D. Sharma,[56] I. Shein,[18] A. Shevel,[41,48] T.-A. Shibata,[42,52] K. Shigaki,[17] M. Shimomura,[53] K. Shoji,[27,42] A. Sickles,[49] C. L. Silva,[46] D. Silvermyr,[38] C. Silvestre,[11] K. S. Sim,[25] C. P. Singh,[2] V. Singh,[2] S. Skutnik,[21] M. Slunečka,[5,22] A. Soldatov,[18] R. A. Soltz,[29] W. E. Sondheim,[30] S. P. Sorensen,[51] I. V. Sourikova,[3] F. Staley,[11] P. W. Stankus,[38] E. Stenlund,[32] M. Stepanov,[37] A. Ster,[24] S. P. Stoll,[3] T. Sugitate,[17] C. Suire,[39] J. Sziklai,[24] T. Tabaru,[43] S. Takagi,[53] E. M. Takagui,[46] A. Taketani,[42,43] Y. Tanaka,[35] K. Tanida,[42,43] M. J. Tannenbaum,[3] A. Taranenko,[48] P. Tarján,[12] T. L. Thomas,[36] M. Togawa,[27,42] A. Toia,[49] J. Tojo,[42] L. Tomášek,[20] H. Torii,[42] R. S. Towell,[1] V-N. Tram,[28] I. Tserruya,[56] Y. Tsuchimoto,[17] C. Vale,[21] H. Valle,[54] H. W. van Hecke,[30] J. Velkovska,[54] R. Vertesi,[12] A. A. Vinogradov,[26] M. Virius,[10] V. Vrba,[20] E. Vznuzdaev,[41] M. Wagner,[27,42] D. Walker,[49] X. R. Wang,[37] Y. Watanabe,[42,43] J. Wessels,[33] S. N. White,[3] D. Winter,[9] C. L. Woody,[3] M. Wysocki,[8] W. Xie,[43] Y. Yamaguchi,[55] A. Yanovich,[18] Z. Yasin,[4] J. Ying,[16] S. Yokkaichi,[42,43] G. R. Young,[38] I. Younus,[36] I. E. Yushmanov,[26] W. A. Zajc,[9,†] O. Zaudtke,[33] C. Zhang,[38] S. Zhou,[6] J. Zimányi,[24,*] and L. Zolin[22]

 © 2007 The American Physical Society

(PHENIX Collaboration)

[1]*Abilene Christian University, Abilene, Texas 79699, USA*
[2]*Department of Physics, Banaras Hindu University, Varanasi 221005, India*
[3]*Brookhaven National Laboratory, Upton, New York 11973-5000, USA*
[4]*University of California–Riverside, Riverside, California 92521, USA*
[5]*Charles University, Ovocný trh 5, Praha 1, 116 36 Prague, Czech Republic*
[6]*China Institute of Atomic Energy (CIAE), Beijing, People's Republic of China*
[7]*Center for Nuclear Study, Graduate School of Science, University of Tokyo, 7-3-1 Hongo, Bunkyo, Tokyo 113-0033, Japan*
[8]*University of Colorado, Boulder, Colorado 80309, USA*
[9]*Columbia University, New York, New York 10027, USA,*
and Nevis Laboratories, Irvington, New York 10533, USA
[10]*Czech Technical University, Zikova 4, 166 36 Prague 6, Czech Republic*
[11]*Dapnia, CEA Saclay, F-91191 Gif-sur-Yvette, France*
[12]*Debrecen University, H-4010 Debrecen, Egyetem tér 1, Hungary*
[13]*ELTE, Eötvös Loránd University, H - 1117 Budapest, Pázmány P. s. 1/A, Hungary*
[14]*Florida Institute of Technology, Melbourne, Florida 32901, USA*
[15]*Florida State University, Tallahassee, Florida 32306, USA*
[16]*Georgia State University, Atlanta, Georgia 30303, USA*
[17]*Hiroshima University, Kagamiyama, Higashi-Hiroshima 739-8526, Japan*
[18]*IHEP Protvino, State Research Center of Russian Federation, Institute for High Energy Physics, Protvino 142281, Russia*
[19]*University of Illinois at Urbana-Champaign, Urbana, Illinois 61801, USA*
[20]*Institute of Physics, Academy of Sciences of the Czech Republic, Na Slovance 2, 182 21 Prague 8, Czech Republic*
[21]*Iowa State University, Ames, Iowa 50011, USA*
[22]*Joint Institute for Nuclear Research, 141980 Dubna, Moscow Region, Russia*
[23]*KEK, High Energy Accelerator Research Organization, Tsukuba, Ibaraki 305-0801, Japan*
[24]*KFKI Research Institute for Particle and Nuclear Physics of the Hungarian Academy of Sciences (MTA KFKI RMKI),*
H-1525 Budapest 114, P.O. Box 49, Budapest, Hungary
[25]*Korea University, Seoul, 136-701, Korea*
[26]*Russian Research Center "Kurchatov Institute," Moscow, Russia*
[27]*Kyoto University, Kyoto 606-8502, Japan*
[28]*Laboratoire Leprince-Ringuet, Ecole Polytechnique, CNRS-IN2P3, Route de Saclay, F-91128 Palaiseau, France*
[29]*Lawrence Livermore National Laboratory, Livermore, California 94550, USA*
[30]*Los Alamos National Laboratory, Los Alamos, New Mexico 87545, USA*
[31]*LPC, Université Blaise Pascal, CNRS-IN2P3, Clermont-Fd, 63177 Aubiere Cedex, France*
[32]*Department of Physics, Lund University, Box 118, SE-221 00 Lund, Sweden*
[33]*Institut für Kernphysik, University of Muenster, D-48149 Muenster, Germany*
[34]*Myongji University, Yongin, Kyonggido 449-728, Korea*
[35]*Nagasaki Institute of Applied Science, Nagasaki-shi, Nagasaki 851-0193, Japan*
[36]*University of New Mexico, Albuquerque, New Mexico 87131, USA*
[37]*New Mexico State University, Las Cruces, New Mexico 88003, USA*
[38]*Oak Ridge National Laboratory, Oak Ridge, Tennessee 37831, USA*
[39]*IPN-Orsay, Universite Paris Sud, CNRS-IN2P3, BP 1, F-91406 Orsay, France*
[40]*Peking University, Beijing, People's Republic of China*
[41]*PNPI, Petersburg Nuclear Physics Institute, Gatchina, Leningrad region, 188300, Russia*
[42]*RIKEN, The Institute of Physical and Chemical Research, Wako, Saitama 351-0198, Japan*
[43]*RIKEN BNL Research Center, Brookhaven National Laboratory, Upton, New York 11973-5000, USA*
[44]*Physics Department, Rikkyo University, 3-34-1 Nishi-Ikebukuro, Toshima, Tokyo 171-8501, Japan*
[45]*Saint Petersburg State Polytechnic University, St. Petersburg, Russia*
[46]*Universidade de São Paulo, Instituto de Física, Caixa Postal 66318, São Paulo CEP05315-970, Brazil*
[47]*System Electronics Laboratory, Seoul National University, Seoul, South Korea*
[48]*Chemistry Department, Stony Brook University, Stony Brook, SUNY, New York 11794-3400, USA*
[49]*Department of Physics and Astronomy, Stony Brook University, SUNY, Stony Brook, New York 11794, USA*
[50]*SUBATECH (Ecole des Mines de Nantes, CNRS-IN2P3, Université de Nantes) BP 20722, 44307 Nantes, France*
[51]*University of Tennessee, Knoxville, Tennessee 37996, USA*
[52]*Department of Physics, Tokyo Institute of Technology, Oh-okayama, Meguro, Tokyo 152-8551, Japan*
[53]*Institute of Physics, University of Tsukuba, Tsukuba, Ibaraki 305, Japan*
[54]*Vanderbilt University, Nashville, Tennessee 37235, USA*
[55]*Waseda University, Advanced Research Institute for Science and Engineering, 17 Kikui-cho, Shinjuku-ku, Tokyo 162-0044, Japan*

[56]Weizmann Institute, Rehovot 76100, Israel
[57]Yonsei University, IPAP, Seoul 120-749, Korea
(Received 12 November 2006; published 8 June 2007)

J/ψ production in $p + p$ collisions at $\sqrt{s} = 200$ GeV has been measured by the PHENIX experiment at the BNL Relativistic Heavy Ion Collider over a rapidity range of $-2.2 < y < 2.2$ and a transverse momentum range of $0 < p_T < 9$ GeV/c. The size of the present data set allows a detailed measurement of both the p_T and the rapidity distributions and is sufficient to constrain production models. The total cross section times the branching ratio is $B_{ll}\sigma_{pp}^{J/\psi} = 178 \pm 3^{\text{stat}} \pm 53^{\text{sys}} \pm 18^{\text{norm}}$ nb.

DOI: 10.1103/PhysRevLett.98.232002 PACS numbers: 13.85.Ni, 13.20.Fc, 14.40.Gx, 25.75.Dw

J/ψ mesons are produced in hadronic collisions involving hard processes that proceed primarily through diagrams involving gluons, such as gluon-gluon fusion. Once the $c\bar{c}$ pair is produced, it must evolve through a hadronization process to form a physical J/ψ meson. While this production has been extensively studied, the details of the production mechanism and hadronization remain an open question. Attempts at a consistent theoretical description of J/ψ meson production have been made, but it has proven difficult to reproduce both the observed cross sections and the polarization [1–4]. An additional complication is that nearly 30%–40% of the measured J/ψ meson yield results from feeddown of higher mass states (ψ', χ_c) [5] which reduces the observed polarization with respect to that expected from directly produced J/ψ mesons.

The color-singlet model [6], which generates a color-singlet $c\bar{c}$ pair in the same quantum state as the J/ψ meson, underpredicts the measured J/ψ cross section by approximately an order of magnitude [2]. Alternatively, the color-octet model includes color-octet $c\bar{c}$ pairs that radiate soft gluons during J/ψ meson formation [7]. However, the predicted transverse J/ψ polarization at high p_T is not seen in the data [2,4], and the color-octet matrix elements are not universal [8]. The color evaporation model, a more phenomenological approach, forms the different charmonium states in proportions determined from experimental data for any $c\bar{c}$ pair with a mass below the $D\bar{D}$ threshold and predicts no polarization. Finally, a recent perturbative QCD calculation including 3-gluon diagrams is able to successfully reproduce both the observed cross section and the polarization results [9].

A fundamental understanding of the J/ψ production process is also critical for defining the configuration of the produced $c\bar{c}$ state. This will have direct implications on the interaction of this state both with cold nuclear matter in proton or deuteron-nucleus collisions and with the high-density partonic matter observed in high-energy heavy-ion collisions. High quality experimental results over a wide kinematic range and collision energies are required to constrain models and to provide an improved understanding of J/ψ (and other heavy quarkonia) production.

In this Letter, J/ψ production in $p + p$ collisions at $\sqrt{s} = 200$ GeV measured by the PHENIX experiment at the BNL Relativistic Heavy Ion Collider (RHIC) is reported. The J/ψ cross section and transverse momentum distributions are studied in the mid ($|y| \leq 0.35$) and forward ($1.2 < |y| < 2.2$) rapidity regions. The data presented were collected during the 2005 RHIC run and exceed by more than 1 order of magnitude the previously reported number of J/ψ mesons [10,11].

At midrapidity, the PHENIX [12] drift chambers (DC), ring imaging Čerenkov detectors (RICH), and electromagnetic calorimeters (EMCal) are used to detect $J/\psi \rightarrow e^+e^-$ decays in two arms, each covering $\Delta\phi = 90°$ in azimuth. The muon detectors, consisting of cathode strip tracking chambers in a magnetic field (MuTr) and alternating layers of steel absorber and Iarocci tube planes (MuID), are used to measure $J/\psi \rightarrow \mu^+\mu^-$ at forward and backward rapidities over $\Delta\phi = 360°$.

The data were recorded using a minimum bias trigger that requires at least one hit in each of the beam-beam counters (BBCs) at forward and backward rapidities, $3.0 < |\eta| < 3.9$. Dielectron events must pass an additional trigger that consists of a logical OR between the level-1 electron and photon triggers. This trigger requires matching hits between the EMCal and RICH in a small angular area with a minimum energy deposition of 0.4 GeV in any 2×2 patch of EMCal towers. The photon trigger requires a minimum energy deposition of 1.4 GeV in any 4×4 set of overlapping EMCal towers. A trigger efficiency of 96% was achieved within the collision vertex range $|z_{\text{vtx}}| < 30$ cm for J/ψ candidates. Dimuon triggered events were selected using an online level-1 trigger that requires at least two particles penetrate the MuID. One particle must penetrate the entire MuID, while the second has a minimum penetration depth of 3 out of the 5 pairs of detector and absorber planes. Approximately 92% of the J/ψ mesons in events that satisfy the $|z_{\text{vtx}}| < 30$ cm cut fulfill this requirement. As part of the reconstruction chain, a level-2 filter is applied, consisting of a fast reconstruction of the particle trajectory in the MuTr and MuID. Events are accepted by this filter when at least two particles penetrate the entire MuID and have a reconstructed invariant mass ≥ 2.0 GeV/c^2. After applying cuts on the collision vertex position and quality assurance criteria, the sampled statistics corresponds to 2.6 pb^{-1} in the dielectron analysis, 2.7 pb^{-1} in the muon arm covering $1.2 < y < 2.2$, and 3.5 pb^{-1} in the muon arm covering $-2.2 < y < -1.2$.

At midrapidity, electron candidates are charged tracks associated with at least two hit phototubes in the RICH and one EMCal hit with a position matching of ± 4 standard

deviations (σ). The energy-momentum matching requirement is $(E/p - 1) \geq -4.0\sigma$. The number of J/ψ candidates is obtained by counting the unlike-sign dielectron pairs in a fixed mass window after subtracting the like-sign pairs. Figure 1(a) shows the invariant mass spectrum for dielectron pairs after subtracting the like-sign background. The mass window for counting the J/ψ signal is 2.7–3.5 or 2.6–3.6 GeV/c^2 depending on the number of DC hits used to reconstruct each track. The solid line in the figure is the sum of the J/ψ line shape (dashed curve) and an exponential function (dotted-dashed curve) describing the continuum component. The J/ψ line shape function accounts for detector resolution, internal radiative effects [13], and external radiative effects evaluated using a GEANT [14] simulation of the PHENIX detector. The J/ψ counts are corrected for the continuum yield, which originates primarily from open charm pairs and Drell-Yan processes inside the mass window (10% ± 5%), and the fraction of J/ψ candidates outside of the mass window (7.2% ± 1.0%). Approximately 1500 $J/\psi \rightarrow e^+e^-$ are obtained.

Muon track candidates are selected based upon their penetration depth in the MuID and the reconstructed track quality within the MuID and MuTr. The particle trajectory must contain at least 8 of 10 possible hits in the MuID, and the position matching between the MuID and MuTr must be within 15 (20) cm at positive (negative) rapidity. The J/ψ yield is obtained from the unlike-sign dimuon invariant mass distribution by subtracting the combinatorial background estimated using an event mixing technique. Three methods, shown in Fig. 1(b), are used to extract the J/ψ yield. Single Gaussian + exponential and double Gaussian + exponential functions are used to fit the J/ψ peak, while the contribution from the physical continuum and background is estimated using an exponential fit. The reported number of J/ψ mesons represents the average of the fit values. A total of 8000 $J/\psi \rightarrow \mu^+\mu^-$ are obtained.

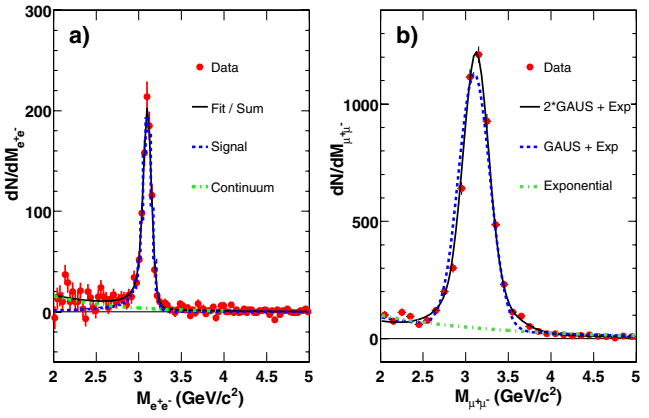

FIG. 1 (color online). Invariant mass spectra for (a) $J/\psi \rightarrow e^+e^-$ at $|y| < 0.35$ and (b) $J/\psi \rightarrow \mu^+\mu^-$ at $1.2 < |y| < 2.2$ with the functional forms used to extract the number of reconstructed J/ψ mesons.

The systematic uncertainty associated with the signal extraction is estimated from the variation between the fits.

The J/ψ cross section in a given rapidity and transverse momentum bin is calculated according to

$$\frac{B_{ll}}{2\pi p_T}\frac{d^2\sigma_{J/\psi}}{dydp_T} = \frac{1}{2\pi p_T \Delta p_T \Delta y}\frac{N_{J/\psi}}{\mathcal{L} A\epsilon_{\rm rec}\epsilon_{\rm trig}\epsilon^{\rm BBC}_{J/\psi}},$$

where B_{ll} is the J/ψ dilepton branching ratio, $N_{J/\psi}$ is the measured J/ψ yield, $\mathcal{L}$ is the integrated luminosity recorded by the minimum bias trigger, $A\epsilon_{\rm rec}$ represents the geometric acceptance and reconstruction efficiency, and $\epsilon_{\rm trig}$ is the trigger efficiency. $\epsilon^{\rm BBC}_{J/\psi}$ is the minimum bias trigger efficiency for events containing a J/ψ meson and was determined to be 0.79 ± 0.02 [10]. The cross section sampled by the BBC trigger, $\sigma^{pp}_{\rm tot} \times \epsilon^{\rm BBC}_{\rm MB} = 23.0 \pm 2.2$ mb, was used to determine the integrated luminosity.

The $A\epsilon_{\rm rec}$ and $\epsilon_{\rm trig}$ terms are determined individually for the central arm and each muon arm based upon the detection of simulated J/ψ mesons processed using the real data analysis chain. Decay events are generated and propagated through a full GEANT simulation of the detector, which includes the specific details of the detector performance including the MuTr and MuID alignment, disabled anodes, and MuID efficiency. Corrections were determined from the single electron yields for the dielectron analysis to account for the detector dead channel map, energy calibration, and run-to-run variations in the detector active area. The J/ψ trigger efficiency is incorporated via a level-1 trigger emulator tuned to describe the experimental trigger response. For the dimuon analysis, the level-2 filtering algorithms are applied to the simulated events. After reconstruction, the number of detected J/ψ mesons is compared to the number of simulated J/ψ mesons in a given rapidity and transverse momentum bin to determine the appropriate correction factors.

The systematic uncertainty associated with the measurement of the J/ψ cross section can be divided into three categories based upon the effect each source has on the measured results. All uncertainties are reported as standard deviations. Point-to-point uncorrelated uncertainties allow the data points to move independently with respect to one another. These include the signal extraction systematic, which is bin-dependent with typical values of 4% (5%) in the dimuon (dielectron) data, and the 1.5% J/ψ momentum smearing effect in the dielectron acceptance measurement. Point-to-point correlated uncertainties allow the data points to move coherently within the quoted value. Their values amount to 10% (8%) for the detector acceptance, 8% (4%) for the run-to-run variation in the detector efficiency, 4% (2.5%) for the J/ψ meson transverse momentum and vertex distributions, and 2% (2%) for the hardware efficiency of the detector. Finally, the global systematic uncertainty allows the data points to move together. The dominant source of this uncertainty originates from the estimation of the BBC triggering efficiency

for minimum bias events 9.7%, with an additional contribution from the uncertainty in the estimation of the number of sampled minimum bias events 1% and $\epsilon_{J/\psi}^{\mathrm{BBC}}$ 2.5%.

Figure 2(a) shows the transverse momentum spectra at both mid and forward rapidities, which are fit with the function $A \times [1 + (p_T/B)^2]^{-6}$ [15] to extract the value of the $\langle p_T^2 \rangle$. At midrapidity, the $\langle p_T^2 \rangle$ is $4.14 \pm 0.18 \pm^{0.30}_{0.20}$ $(\mathrm{GeV}/c)^2$, and the χ^2 per degree of freedom (χ^2/ndf) is 23/19. At forward rapidity, the $\langle p_T^2 \rangle$ is $3.59 \pm 0.06 \pm 0.16$ $(\mathrm{GeV}/c)^2$, and the χ^2/ndf is 28/17. The first error is statistical, and the second includes the systematic uncertainty from the maximum shape deviation permitted by the point-to-point correlated errors and from allowing the exponent of the fit function to be a free parameter. The statistical precision of the data is sufficient to allow the $\langle p_T^2 \rangle$ to be calculated directly from the numerical integration of the data. This calculation results in a $\langle p_T^2 \rangle$ of $4.25 \pm 0.24 \pm 0.14$ $(\mathrm{GeV}/c)^2$ at midrapidity and $3.57 \pm 0.06 \pm 0.15$ $(\mathrm{GeV}/c)^2$ at forward rapidity. Although good agreement is found with the rapidity distribution and total cross section, previously published results [11] yielded a significantly lower $\langle p_T^2 \rangle$ at forward rapidity than found here, even accounting for the quoted statistical and systematic uncertainties. The increased sample size of the present data set allows for an improved understanding of the shape of the p_T spectrum at forward rapidity due to the extended range in p_T and the finer binning at low p_T. The previous results have been revisited, and it was found that the systematic uncertainty was underestimated.

Figure 2(b) shows the ratio of the differential cross section times dilepton branching ratio at forward and midrapidity. The ratio falls with p_T and reaches a minimum of 0.5 above a p_T of 2 GeV/c. Although the present data are limited by significant systematic uncertainties, the data suggest that the forward rapidity p_T distribution is softer than at midrapidity. Such behavior could be attributed to an increase in the longitudinal momentum at forward rapidity leaving less energy available in the transverse direction.

The observed p_T distributions are substantially harder than those for lower energy $p + p$ and $p + A$ collisions as expected from the increased phase space at higher energy. Figure 3 shows the energy dependence of the average $\langle p_T^2 \rangle$ including points from the CERN Super Proton Synchrotron, Fermilab fixed target, and Tevatron measurements. A linear fit versus the log of the center of mass energy describes the general trend, although some variation is expected due to the differing rapidity ranges of the measurements and the use of $p + A$ data for some of the points.

Figure 4 shows the J/ψ differential cross section versus rapidity. The statistical precision of these results is sufficient to allow the data to be divided into 11 rapidity bins compared to the 5 bins used in the previous measurement [11]. Also shown are several models fit to the data. The dashed curve is a nonrelativistic QCD calculation [16]. The dotted-dashed curve is a pQCD calculation that includes diagrams describing a third gluon [9]. This model fails to reproduce the steeply falling cross section observed in the present data at large rapidity. An empirical double Gaussian fit (dotted-dotted curve) is able to reproduce the data best but has no theoretical foundation. The data slightly favor a flatter distribution over the rapidity range $|y| < 1.5$ than most models, but since the systematic error on the mid and forward rapidity points are independent, a narrower distribution is not excluded.

To determine the total cross section, the rapidity distribution was fit with many theoretical and phenomenological shapes including those shown in Fig. 4. A total cross section times the branching ratio of $B_{ll}\sigma_{pp}^{J/\psi} = 178 \pm 3^{\mathrm{stat}} \pm 53^{\mathrm{sys}} \pm 18^{\mathrm{norm}}$ nb is obtained from the fit that pro-

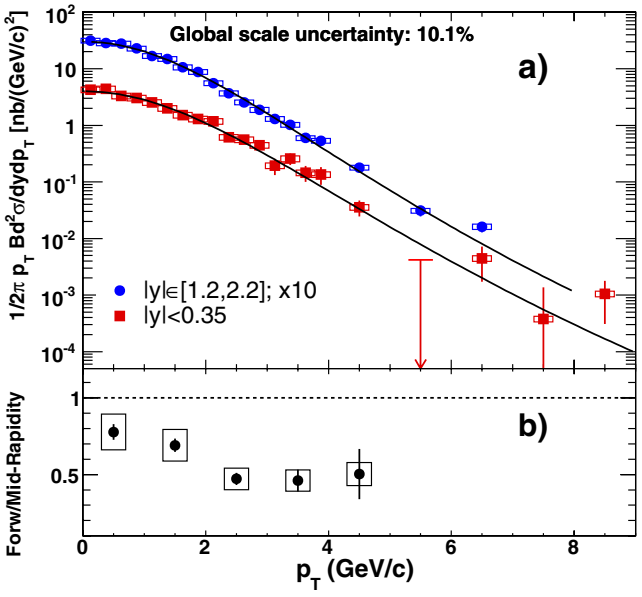

FIG. 2 (color online). (a) The forward rapidity (circles) and midrapidity (squares) J/ψ meson differential cross section times the dilepton branching ratio versus p_T and (b) the ratio of the forward and midrapidity p_T spectra.

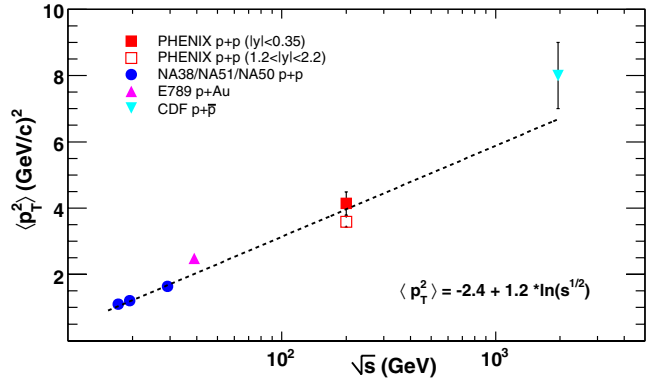

FIG. 3 (color online). PHENIX $\langle p_T^2 \rangle$ measurements compared to measurements at other energies [2,4,19] as a function of collision energy for J/ψ meson production in $p + p$ or $p + A$ collisions.

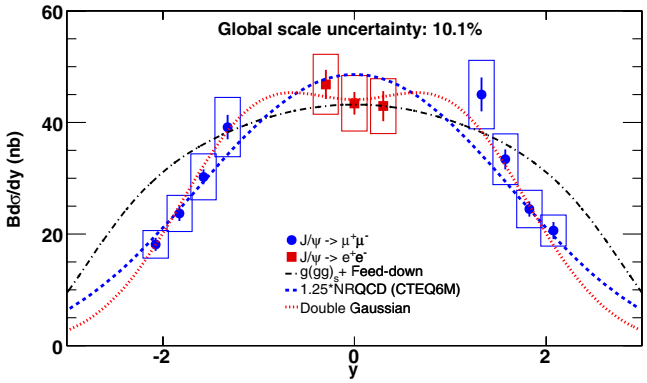

FIG. 4 (color online). The J/ψ differential cross section times the dilepton branching ratio plotted versus rapidity.

vides the best χ^2/ndf, double Gaussian. The absolute normalization error (norm) represents the uncertainty in the BBC trigger cross section. The systematic uncertainty (sys) is estimated by refitting the data with the same theoretical and phenomenological curves while simultaneously allowing the maximum variation in the shape of the distribution by shifting the mid and forward rapidity data independently by their point-to-point correlated systematic errors. Using the double Gaussian fit, the acceptance of the PHENIX data covers 92.1% of the integrated cross section. This result is consistent with our previous measurement [11].

We have presented J/ψ results for $p + p$ collisions at $\sqrt{s} = 200$ GeV that extend the reach in transverse momentum to 9 GeV/c. The measured p_T spectrum is harder than that observed at lower energies. The rapidity shape falls steeply at forward rapidity and cannot be reproduced by the pQCD calculation in Ref. [9]. Futhermore, the data slightly favor a flatter rapidity distribution than most models, but a narrower distribution is not excluded. These data not only constrain production models for heavy quarkonia but also provide a critical baseline for similar studies in deuteron-nucleus and heavy-ion collisions [11,17,18].

We thank the staff of the Collider-Accelerator and Physics Departments at BNL for their vital contributions. We acknowledge support from the Office of NP in DOE Office of Science and NSF (USA), MEXT and JSPS (Japan), CNPq and FAPESP (Brazil), NSFC (China), MSMT (Czech Republic), IN2P3/CNRS and CEA (France), BMBF, DAAD, and AvH (Germany), OTKA (Hungary), DAE (India), ISF (Israel), KRF and KOSEF (Korea), MES, RAS, and FAAE (Russia), VR and KAW (Sweden), U.S. CRDF for the FSU, U.S.–Hungarian NSF-OTKA-MTA, and U.S.–Israel BSF.

*Deceased.
†PHENIX Spokesperson.
Electronic address: zajc@nevis.columbia.edu

[1] M. Beneke, arXiv:hep-ph/9703429.
[2] F. Abe *et al.*, Phys. Rev. Lett. **69**, 3704 (1992); S. Abachi *et al.*, Phys. Lett. B **370**, 239 (1996); B. Abbot *et al.*, Phys. Rev. Lett. **82**, 35 (1999); F. Abe *et al.*, Phys. Rev. D **66**, 092001 (2002); D. Acosta *et al.*, Phys. Rev. D **71**, 032001 (2005). The $\langle p_T^2 \rangle$ was extracted using a fit of the form $A \times [1 + (p_T/B)^2]^{-6}$.
[3] R. Vogt, Phys. Rep. **310**, 197 (1999).
[4] M. H. Schub *et al.*, Phys. Rev. D **52**, 1307 (1995).
[5] I. Abt *et al.*, Phys. Lett. B **561**, 61 (2003).
[6] E. L. Berger and D. Jones, Phys. Rev. D **23**, 1521 (1981); R. Baier *et al.*, Phys. Lett. **102B**, 364 (1981).
[7] G. T. Bodwin, E. Braaten, and G. P. Lepage, Phys. Rev. D **51**, 1125 (1995); **55**, 5853(E) (1997).
[8] J. K. Mizukoshi, arXiv:hep-ph/9911384.
[9] V. A. Khoze *et al.*, Eur. Phys. J. C **39**, 163 (2005); (private communication).
[10] S. S. Adler *et al.*, Phys. Rev. Lett. **92**, 051802 (2004).
[11] S. S. Adler *et al.*, Phys. Rev. Lett. **96**, 012304 (2006).
[12] K. Adcox *et al.*, Nucl. Instrum. Methods Phys. Res., Sect. A **499**, 469 (2003).
[13] A. Spiridonov, arXiv:hep-ex/0510076.
[14] GEANT 3.2.1, CERN Computing Library, http://wwwasd.web.cern.ch/wwwasd/geant/index.html.
[15] J. K. Yoh *et al.*, Phys. Rev. Lett. **41**, 684 (1978); (private communication).
[16] F. Cooper, M. X. Liu, and G. C. Nayak, Phys. Rev. Lett. **93**, 171801 (2004); (private communication).
[17] A. Adare *et al.*, following Letter, Phys. Rev. Lett. **98**, 232301 (2007).
[18] A. Adare *et al.* (to be published).
[19] O. Drapier, Thèse d'habilitation thesis, Université Claude Bernard-Lyon, 1998, http://na50.web.cern.ch/NA50/theses.html.

System Size and Energy Dependence of Jet-Induced Hadron Pair Correlation Shapes in Cu + Cu and Au + Au Collisions at $\sqrt{s_{NN}} = 200$ and 62.4 GeV

A. Adare,[10] S. S. Adler,[5] S. Afanasiev,[24] C. Aidala,[11] N. N. Ajitanand,[51] Y. Akiba,[26,45,46] H. Al-Bataineh,[40] J. Alexander,[51] A. Al-Jamel,[40] K. Aoki,[30,45] L. Aphecetche,[53] R. Armendariz,[40] S. H. Aronson,[5] J. Asai,[46] E. T. Atomssa,[31] R. Averbeck,[52] T. C. Awes,[41] B. Azmoun,[5] V. Babintsev,[20] G. Baksay,[16] L. Baksay,[16] A. Baldisseri,[13] K. N. Barish,[6] P. D. Barnes,[33] B. Bassalleck,[39] S. Bathe,[6,36] S. Batsouli,[11,41] V. Baublis,[44] F. Bauer,[6] A. Bazilevsky,[5,46] S. Belikov,[5,20,23] R. Bennett,[52] Y. Berdnikov,[48] A. A. Bickley,[10] M. T. Bjorndal,[11] J. G. Boissevain,[33] H. Borel,[13] K. Boyle,[52] M. L. Brooks,[33] D. S. Brown,[40] N. Bruner,[39] D. Bucher,[36] H. Buesching,[5,36] V. Bumazhnov,[20] G. Bunce,[5,46] J. M. Burward-Hoy,[32,33] S. Butsyk,[33,52] X. Camard,[53] S. Campbell,[52] J.-S. Chai,[25] P. Chand,[4] B. S. Chang,[60] W. C. Chang,[2] J.-L. Charvet,[13] S. Chernichenko,[20] J. Chiba,[26] C. Y. Chi,[11] M. Chiu,[11,21] I. J. Choi,[60] R. K. Choudhury,[4] T. Chujo,[5,57] P. Chung,[51] A. Churyn,[20] V. Cianciolo,[41] C. R. Cleven,[18] Y. Cobigo,[13] B. A. Cole,[11] M. P. Comets,[42] P. Constantin,[23,33] M. Csanád,[15] T. Csörgő,[27] J. P. Cussonneau,[53] T. Dahms,[52] K. Das,[17] G. David,[5] F. Deák,[15] M. B. Deaton,[1] K. Dehmelt,[16] H. Delagrange,[53] A. Denisov,[20] D. d'Enterria,[11] A. Deshpande,[46,52] E. J. Desmond,[5] A. Devismes,[52] O. Dietzsch,[49] A. Dion,[52] M. Donadelli,[49] J. L. Drachenberg,[1] O. Drapier,[31] A. Drees,[52] A. K. Dubey,[59] A. Durum,[20] D. Dutta,[4] V. Dzhordzhadze,[6,54] Y. V. Efremenko,[41] J. Egdemir,[52] F. Ellinghaus,[10] W. S. Emam,[6] A. Enokizono,[19,32] H. En'yo,[45,46] B. Espagnon,[42] S. Esumi,[56] K. O. Eyser,[6] D. E. Fields,[39,46] C. Finck,[53] M. Finger, Jr.,[7,24] M. Finger,[7,24] F. Fleuret,[31] S. L. Fokin,[29] B. Forestier,[34] B. D. Fox,[46] Z. Fraenkel,[59] J. E. Frantz,[11,52] A. Franz,[5] A. D. Frawley,[17] K. Fujiwara,[45] Y. Fukao,[30,45,46] S.-Y. Fung,[6] T. Fusayasu,[38] S. Gadrat,[34] I. Garishvili,[54] F. Gastineau,[53] M. Germain,[53] A. Glenn,[10,54] H. Gong,[52] M. Gonin,[31] J. Gosset,[13] Y. Goto,[45,46] R. Granier de Cassagnac,[31] N. Grau,[23] S. V. Greene,[57] M. Grosse Perdekamp,[21,46] T. Gunji,[9] H.-Å. Gustafsson,[35] T. Hachiya,[19,45] A. Hadj Henni,[53] C. Haegemann,[39] J. S. Haggerty,[5] M. N. Hagiwara,[1] H. Hamagaki,[9] R. Han,[43] A. G. Hansen,[33] H. Harada,[19] E. P. Hartouni,[32] K. Haruna,[19] M. Harvey,[5] E. Haslum,[35] K. Hasuko,[45] R. Hayano,[9] M. Heffner,[32] T. K. Hemmick,[52] T. Hester,[6] J. M. Heuser,[45] X. He,[18] P. Hidas,[27] H. Hiejima,[21] J. C. Hill,[23] R. Hobbs,[39] M. Hohlmann,[16] M. Holmes,[57] W. Holzmann,[51] K. Homma,[19] B. Hong,[28] A. Hoover,[40] T. Horaguchi,[45,46,55] D. Hornback,[54] M. G. Hur,[25] T. Ichihara,[45,46] V. V. Ikonnikov,[29] K. Imai,[30,45] M. Inaba,[56] Y. Inoue,[47,45] M. Inuzuka,[9] D. Isenhower,[1] L. Isenhower,[1] M. Ishihara,[45] T. Isobe,[9] M. Issah,[51] A. Isupov,[24] B. V. Jacak,[52] J. Jia,[11,52] J. Jin,[11] O. Jinnouchi,[45,46] B. M. Johnson,[5] S. C. Johnson,[32] K. S. Joo,[37] D. Jouan,[42] F. Kajihara,[9,45] S. Kametani,[9,58] N. Kamihara,[45,55] J. Kamin,[52] M. Kaneta,[46] J. H. Kang,[60] H. Kanou,[45,55] K. Katou,[58] T. Kawabata,[9] T. Kawagishi,[56] D. Kawall,[46] A. V. Kazantsev,[29] S. Kelly,[10,11] B. Khachaturov,[59] A. Khanzadeev,[44] J. Kikuchi,[58] D. H. Kim,[37] D. J. Kim,[60] E. Kim,[50] G.-B. Kim,[31] H. J. Kim,[60] Y.-S. Kim,[25] E. Kinney,[10] A. Kiss,[15] E. Kistenev,[5] A. Kiyomichi,[45] J. Klay,[32] C. Klein-Boesing,[36] H. Kobayashi,[46] L. Kochenda,[44] V. Kochetkov,[20] R. Kohara,[19] B. Komkov,[44] M. Konno,[56] D. Kotchetkov,[6] A. Kozlov,[59] A. Král,[12] A. Kravitz,[11] P. J. Kroon,[5] J. Kubart,[7,22] C. H. Kuberg,[1,*] G. J. Kunde,[33] N. Kurihara,[9] K. Kurita,[45,47] M. J. Kweon,[28] Y. Kwon,[54,60] G. S. Kyle,[40] R. Lacey,[51] Y.-S. Lai,[11] J. G. Lajoie,[23] A. Lebedev,[23,29] Y. Le Bornec,[42] S. Leckey,[52] D. M. Lee,[33] M. K. Lee,[60] T. Lee,[50] M. J. Leitch,[33] M. A. L. Leite,[49] B. Lenzi,[49] H. Lim,[50] T. Liška,[12] A. Litvinenko,[24] M. X. Liu,[33] X. Li,[8] X. H. Li,[6] B. Love,[57] D. Lynch,[5] C. F. Maguire,[57] Y. I. Makdisi,[5] A. Malakhov,[24] M. D. Malik,[39] V. I. Manko,[29] Y. Mao,[43,45] G. Martinez,[53] L. Mašek,[7,22] H. Masui,[56] F. Matathias,[11,52] T. Matsumoto,[9,58] M. C. McCain,[1,21] M. McCumber,[52] P. L. McGaughey,[33] Y. Miake,[56] P. Mikeš,[7,22] K. Miki,[56] T. E. Miller,[57] A. Milov,[52] S. Mioduszewski,[5] G. C. Mishra,[18] M. Mishra,[3] J. T. Mitchell,[5] M. Mitrovski,[51] A. K. Mohanty,[4] A. Morreale,[6] D. P. Morrison,[5] J. M. Moss,[33] T. V. Moukhanova,[29] D. Mukhopadhyay,[57,59] M. Muniruzzaman,[6] J. Murata,[47,45] S. Nagamiya,[26] Y. Nagata,[56] J. L. Nagle,[10,11] M. Naglis,[59] I. Nakagawa,[45,46] Y. Nakamiya,[19] T. Nakamura,[19] K. Nakano,[45,55] J. Newby,[32,54] M. Nguyen,[52] B. E. Norman,[33] A. S. Nyanin,[29] J. Nystrand,[35] E. O'Brien,[5] S. X. Oda,[9] C. A. Ogilvie,[23] H. Ohnishi,[45] I. D. Ojha,[3,57] H. Okada,[30,45] K. Okada,[45,46] M. Oka,[56] O. O. Omiwade,[1] A. Oskarsson,[35] I. Otterlund,[35] M. Ouchida,[19] K. Oyama,[9] K. Ozawa,[9] R. Pak,[5] D. Pal,[57,59] A. P. T. Palounek,[33] V. Pantuev,[52] V. Papavassiliou,[40] J. Park,[50] W. J. Park,[28] S. F. Pate,[40] H. Pei,[23] V. Penev,[24] J.-C. Peng,[21] H. Pereira,[13] V. Peresedov,[24] D. Yu. Peressounko,[29] A. Pierson,[39] C. Pinkenburg,[5] R. P. Pisani,[5] M. L. Purschke,[5] A. K. Purwar,[33,52] J. M. Qualls,[1] H. Qu,[18] J. Rak,[23,39] A. Rakotozafindrabe,[31] I. Ravinovich,[59] K. F. Read,[41,54] S. Rembeczki,[16] M. Reuter,[52] K. Reygers,[36] V. Riabov,[44] Y. Riabov,[44] G. Roche,[34] A. Romana,[31,*] M. Rosati,[23] S. S. E. Rosendahl,[35] P. Rosnet,[34] P. Rukoyatkin,[24] V. L. Rykov,[45] S. S. Ryu,[60] B. Sahlmueller,[36] N. Saito,[30,45,46] T. Sakaguchi,[5,9,58] S. Sakai,[56] H. Sakata,[19] V. Samsonov,[44] L. Sanfratello,[39] R. Santo,[36] H. D. Sato,[30,45] S. Sato,[5,26,56] S. Sawada,[26] Y. Schutz,[53] J. Seele,[10] R. Seidl,[21] V. Semenov,[20] R. Seto,[6] D. Sharma,[59] T. K. Shea,[5] I. Shein,[20]

 © 2007 The American Physical Society

A. Shevel,[44,51] T.-A. Shibata,[45,55] K. Shigaki,[19] M. Shimomura,[56] T. Shohjoh,[56] K. Shoji,[30,45] A. Sickles,[52] C. L. Silva,[49] D. Silvermyr,[33,41] C. Silvestre,[13] K. S. Sim,[28] C. P. Singh,[3] V. Singh,[3] S. Skutnik,[23] M. Slunečka,[7,24] W. C. Smith,[1] A. Soldatov,[20] R. A. Soltz,[32] W. E. Sondheim,[33] S. P. Sorensen,[54] I. V. Sourikova,[5] F. Staley,[13] P. W. Stankus,[41] E. Stenlund,[35] M. Stepanov,[40] A. Ster,[27] S. P. Stoll,[5] T. Sugitate,[19] C. Suire,[42] J. P. Sullivan,[33] J. Sziklai,[27] T. Tabaru,[46] S. Takagi,[56] E. M. Takagui,[49] A. Taketani,[45,46] K. H. Tanaka,[26] Y. Tanaka,[38] K. Tanida,[45,46] M. J. Tannenbaum,[5] A. Taranenko,[51] P. Tarján,[14] T. L. Thomas,[39] M. Togawa,[30,45] A. Toia,[52] J. Tojo,[45] L. Tomášek,[22] H. Torii,[30,45,46] R. S. Towell,[1] V-N. Tram,[31] I. Tserruya,[59] Y. Tsuchimoto,[19,45] S. K. Tuli,[3] H. Tydesjö,[35] N. Tyurin,[20] T. J. Uam,[37] C. Vale,[23] H. Valle,[57] H. W. vanHecke,[33] J. Velkovska,[5,57] M. Velkovsky,[52] R. Vertesi,[14] V. Veszprémi,[14] A. A. Vinogradov,[29] M. Virius,[12] M. A. Volkov,[29] V. Vrba,[22] E. Vznuzdaev,[44] M. Wagner,[30,45] D. Walker,[52] X. R. Wang,[18,40] Y. Watanabe,[45,46] J. Wessels,[36] S. N. White,[5] N. Willis,[42] D. Winter,[11] F. K. Wohn,[23] C. L. Woody,[5] M. Wysocki,[10] W. Xie,[6,46] Y. L. Yamaguchi,[58] A. Yanovich,[20] Z. Yasin,[6] J. Ying,[18] S. Yokkaichi,[45,46] G. R. Young,[41] I. Younus,[39] I. E. Yushmanov,[29] W. A. Zajc,[11,†] O. Zaudtke,[36] C. Zhang,[11,41] S. Zhou,[8] J. Zimányi,[27,*] L. Zolin,[24] and X. Zong[23]

(PHENIX Collaboration)

[1]*Abilene Christian University, Abilene, Texas 79699, USA*
[2]*Institute of Physics, Academia Sinica, Taipei 11529, Taiwan*
[3]*Department of Physics, Banaras Hindu University, Varanasi 221005, India*
[4]*Bhabha Atomic Research Centre, Bombay 400 085, India*
[5]*Brookhaven National Laboratory, Upton, New York 11973-5000, USA*
[6]*University of California—Riverside, Riverside, California 92521, USA*
[7]*Charles University, Ovocný trh 5, Praha 1, 116 36, Prague, Czech Republic*
[8]*China Institute of Atomic Energy (CIAE), Beijing, People's Republic of China*
[9]*Center for Nuclear Study, Graduate School of Science, University of Tokyo, 7-3-1 Hongo, Bunkyo, Tokyo 113-0033, Japan*
[10]*University of Colorado, Boulder, Colorado 80309, USA*
[11]*Columbia University, New York, New York 10027 and Nevis Laboratories, Irvington, New York 10533, USA*
[12]*Czech Technical University, Zikova 4, 166 36 Prague 6, Czech Republic*
[13]*Dapnia, CEA Saclay, F-91191, Gif-sur-Yvette, France*
[14]*Debrecen University, H-4010 Debrecen, Egyetem tér 1, Hungary*
[15]*ELTE, Eötvös Loránd University, H—1117 Budapest, Pázmány P. s. 1/A, Hungary*
[16]*Florida Institute of Technology, Melbourne, Florida 32901, USA*
[17]*Florida State University, Tallahassee, Florida 32306, USA*
[18]*Georgia State University, Atlanta, Georgia 30303, USA*
[19]*Hiroshima University, Kagamiyama, Higashi-Hiroshima 739-8526, Japan*
[20]*IHEP Protvino, State Research Center of Russian Federation, Institute for High Energy Physics, Protvino, 142281, Russia*
[21]*University of Illinois at Urbana-Champaign, Urbana, Illinois 61801, USA*
[22]*Institute of Physics, Academy of Sciences of the Czech Republic, Na Slovance 2, 182 21 Prague 8, Czech Republic*
[23]*Iowa State University, Ames, Iowa 50011, USA*
[24]*Joint Institute for Nuclear Research, 141980 Dubna, Moscow Region, Russia*
[25]*KAERI, Cyclotron Application Laboratory, Seoul, South Korea*
[26]*KEK, High Energy Accelerator Research Organization, Tsukuba, Ibaraki 305-0801, Japan*
[27]*KFKI Research Institute for Particle and Nuclear Physics, Hungarian Academy of Sciences (MTA KFKI RMKI), H-1525 Budapest 114, POBox 49, Budapest, Hungary*
[28]*Korea University, Seoul, 136-701, Korea*
[29]*Russian Research Center, Kurchatov Institute, Moscow, Russia*
[30]*Kyoto University, Kyoto 606-8502, Japan*
[31]*Laboratoire Leprince-Ringuet, Ecole Polytechnique, CNRS-IN2P3, Route de Saclay, F-91128, Palaiseau, France*
[32]*Lawrence Livermore National Laboratory, Livermore, California 94550, USA*
[33]*Los Alamos National Laboratory, Los Alamos, New Mexico 87545, USA*
[34]*LPC, Université Blaise Pascal, CNRS-IN2P3, Clermont-Fd, 63177 Aubiere Cedex, France*
[35]*Department of Physics, Lund University, Box 118, SE-221 00 Lund, Sweden*
[36]*Institut für Kernphysik, University of Muenster, D-48149 Muenster, Germany*
[37]*Myongji University, Yongin, Kyonggido 449-728, Korea*
[38]*Nagasaki Institute of Applied Science, Nagasaki-shi, Nagasaki 851-0193, Japan*
[39]*University of New Mexico, Albuquerque, New Mexico 87131, USA*
[40]*New Mexico State University, Las Cruces, New Mexico 88003, USA*
[41]*Oak Ridge National Laboratory, Oak Ridge, Tennessee 37831, USA*
[42]*IPN-Orsay, Universite Paris Sud, CNRS-IN2P3, BP1, F-91406, Orsay, France*

[43]Peking University, Beijing, People's Republic of China
[44]PNPI, Petersburg Nuclear Physics Institute, Gatchina, Leningrad region, 188300, Russia
[45]RIKEN, The Institute of Physical and Chemical Research, Wako, Saitama 351-0198, Japan
[46]RIKEN BNL Research Center, Brookhaven National Laboratory, Upton, New York 11973-5000, USA
[47]Physics Department, Rikkyo University, 3-34-1 Nishi-Ikebukuro, Toshima, Tokyo 171-8501, Japan
[48]Saint Petersburg State Polytechnic University, St. Petersburg, Russia
[49]Universidade de São Paulo, Instituto de Física, Caixa Postal 66318, São Paulo CEP05315-970, Brazil
[50]System Electronics Laboratory, Seoul National University, Seoul, South Korea
[51]Chemistry Department, Stony Brook University, Stony Brook, SUNY, New York 11794-3400, USA
[52]Department of Physics and Astronomy, Stony Brook University, SUNY, Stony Brook, New York 11794, USA
[53]SUBATECH (Ecole des Mines de Nantes, CNRS-IN2P3, Université de Nantes) BP 20722—44307, Nantes, France
[54]University of Tennessee, Knoxville, Tennessee 37996, USA
[55]Department of Physics, Tokyo Institute of Technology, Oh-okayama, Meguro, Tokyo 152-8551, Japan
[56]Institute of Physics, University of Tsukuba, Tsukuba, Ibaraki 305, Japan
[57]Vanderbilt University, Nashville, Tennessee 37235, USA
[58]Waseda University, Advanced Research Institute for Science and Engineering, 17 Kikui-cho, Shinjuku-ku, Tokyo 162-0044, Japan
[59]Weizmann Institute, Rehovot 76100, Israel
[60]Yonsei University, IPAP, Seoul 120-749, Korea

(Received 12 November 2006; published 4 June 2007)

We present azimuthal angle correlations of intermediate transverse momentum (1–4 GeV/c) hadrons from dijets in Cu + Cu and Au + Au collisions at $\sqrt{s_{NN}} = 62.4$ and 200 GeV. The away-side dijet induced azimuthal correlation is broadened, non-Gaussian, and peaked away from $\Delta\phi = \pi$ in central and semicentral collisions in all the systems. The broadening and peak location are found to depend upon the number of participants in the collision, but not on the collision energy or beam nuclei. These results are consistent with sound or shock wave models, but pose challenges to Cherenkov gluon radiation models.

DOI: 10.1103/PhysRevLett.98.232302 PACS numbers: 25.75.Dw

Heavy ion collisions at the Relativistic Heavy Ion Collider (RHIC) produce QCD matter at enormous energy density [1], exceeding that required for a phase transition to partonic, rather than hadronic, matter. The produced matter exhibits collective motion [2] and is opaque to scattered quarks and gluons. The opacity is observed via suppression of high momentum hadrons and intermediate energy dijets [3], and provides clear evidence of large energy loss by partons (quarks or gluons) traversing the medium. A key question is how the hot, dense medium transports the deposited energy.

As partons fragment into back-to-back jets of hadrons, angular correlations of the hadrons are used to study medium effects upon hard scattered parton pairs. Hadron pairs from the same parton appear at $\Delta\phi \sim 0$ (the near side), while those with one hadron from each parton in the hard scattered pair appear at $\Delta\phi \sim \pi$ (the away side). For brevity, we refer to these dijet induced dihadron azimuthal correlations as "dijet correlations."

Of great interest are intermediate transverse momentum (p_T) hadrons, as they can arise from intermediate energy jets or involve partons from the medium [4,5]. Their correlations can provide information about energy loss mechanisms, dissipation of the radiated energy in the medium, and collective modes induced by the deposited energy. Theoretical ideas include Mach cones from density waves induced by supersonic partons [4], comoving radiated gluons producing "wakes" in the medium [5], ultrarelativistic partons creating Cherenkov gluon radiation [6], and medium-induced gluon radiation at large emission angles [7,8]. They all imply significant modifications of dijet correlations in the away side, when the parton path through the medium is long. In particular, some of these theoretical models [4,6,7] imply a transition from the peaked distribution at $\Delta\phi \sim \pi$ characteristic of $p + p$ and $p + A$ collisions to a distribution with a peak away from $\Delta\phi \sim \pi$ in head-on Au + Au collisions.

Low p_T ($\geq$0.15 GeV/c) hadrons associated with high p_T hadrons ($\geq$4 GeV/c) have modified away-side dijet correlations and softened p_T distributions relative to those in $p + p$ collisions, suggesting that at least some of the lost energy is thermalized in the medium [9]. At intermediate p_T, a strong non-Gaussian shape modification of the dijet away-side correlation [10] indicates the possible existence of a local minimum at $\Delta\phi = \pi$. This Letter shows how the away-side jet modification depends on the size of the produced medium, and not on the collision energy or beam species. We report dijet correlations measured by the PHENIX experiment at RHIC.

The data were collected in the years 2005 (Cu + Cu at $\sqrt{s_{NN}} = 200$ and 62.4 GeV), 2004 (Au + Au at $\sqrt{s_{NN}} =$ 200 and 62.4 GeV), and 2003 (d + Au at $\sqrt{s_{NN}} =$ 200 GeV). Charged hadrons are tracked using the drift chambers and pad chambers of the PHENIX central arm spectrometers at midrapidity in the same way as described in [10]. The number of events in the Au + Au data at 200 GeV used here is 30 times higher than that in [10]. Collision centrality and number of participant nucleons

($N_{\rm part}$) are determined using the beam-beam counters (BBCs) and zero degree calorimeters [11].

Relative azimuthal distributions $Y_{\rm same}(\Delta\phi)$ between "trigger" hadrons with $2.5 < p_T < 4$ GeV/c and "associated" hadrons with $1 < p_T < 2.5$ GeV/c are formed. We correct for the nonuniform azimuthal acceptance of the PHENIX central arms by using the mixed event pairs $Y_{\rm mixed}(\Delta\phi)$ from the same data sample [10]:

$$C(\Delta\phi) \equiv \frac{Y_{\rm same}(\Delta\phi)}{Y_{\rm mixed}(\Delta\phi)} \frac{\int Y_{\rm mixed}(\Delta\phi)d\Delta\phi}{\int Y_{\rm same}(\Delta\phi)d\Delta\phi}. \quad (1)$$

Extensive Monte Carlo simulations were performed to ensure that the true pair distribution shape is recovered.

In Au + Au and Cu + Cu collisions, hadrons have an azimuthal correlation with the reaction plane orientation $\Phi_{\rm RP}$ which is proportional to $1 + 2v_2\cos[2(\phi - \Phi_{\rm RP})]$. This generates a significant correlated background to our dijet source $J(\Delta\phi)$ of azimuthal correlations:

$$C(\Delta\phi) = b_0[1 + 2\langle v_2^{\rm assoc}\rangle\langle v_2^{\rm trigg}\rangle\cos(2\Delta\phi)] + J(\Delta\phi). \quad (2)$$

The charged hadron $\langle v_2\rangle$ at midrapidity ($|\eta| < 0.35$), where "$\langle\,\rangle$" signifies an event average, was measured through a reaction plane analysis using the BBCs ($3 < |\eta| < 4$) [10,12]. The large rapidity gap between the BBCs and the central arms substantially reduces nonflow contributions to $\langle v_2\rangle$, in particular, dijet induced.

There also exists a much smaller fourth order azimuthal correlation with the reaction plane orientation. Its effect was studied with the Au + Au data at 200 GeV by including the corresponding $2\langle v_4^{\rm assoc}\rangle\langle v_4^{\rm trigg}\rangle\cos(4\Delta\phi)$ term in Eq. (2), where $\langle v_4\rangle$ has also been measured by the reaction plane analysis [12]. No significant v_4 systematic effects on the shape of the dijet correlations were found.

The background subtraction generates point-by-point ($\Delta\phi$ dependent) systematic errors from $\langle v_2^{\rm assoc}\rangle\langle v_2^{\rm trigg}\rangle$ uncertainty and an overall ($\Delta\phi$ independent) systematic error from b_0 uncertainty. The sources of $\langle v_2^{\rm assoc}\rangle\langle v_2^{\rm trigg}\rangle$ uncertainty are the $\langle v_2\rangle$ systematic error [10], dominated by the reaction plane resolution uncertainty, the $\langle v_2\rangle$ statistical error, and the systematic error from the $\langle v_2^{\rm assoc}v_2^{\rm trigg}\rangle \approx \langle v_2^{\rm assoc}\rangle\langle v_2^{\rm trigg}\rangle$ factorization approximation made in Eq. (2). The latter is estimated to be 5% of the $\langle v_2\rangle$ product for the most central events, where it is the largest.

The b_0 uncertainty is estimated by using three independent methods to calculate b_0. The first method is independent of the measured $C(\Delta\phi)$. We calculate $b_0 = \xi\kappa\langle n_{\rm trigg}\rangle\langle n_{\rm assoc}\rangle/\langle n_{\rm same}\rangle$ with hadron production rates measured from all events within each centrality class and scaled by the same-event pair rate $\langle n_{\rm same}\rangle$. The pair-cut correction κ lowers the combinatoric pair multiplicity for pair loss due to proximity cuts in tracking detectors. A residual multiplicity correlation factor, $\xi = \langle n_{\rm trigg}n_{\rm assoc}\rangle/\langle n_{\rm trigg}\rangle\langle n_{\rm assoc}\rangle$, corrects for averaging production rates over events of different multiplicity within the same centrality class, estimated from Glauber $N_{\rm part}$ and $N_{\rm coll}$ distributions [11,13]. In the second method a functional form for $J(\Delta\phi)$ is added to the background, and the sum fitted to the measured correlation with b_0 as a free parameter. Motivated by the theoretical ideas discussed above, we use a function with a near-side Gaussian, and two symmetric away-side Gaussians:

$$J(\Delta\phi) = G(\Delta\phi) + G(\Delta\phi - \pi - D) + G(\Delta\phi - \pi + D). \quad (3)$$

While the choice of this functional form is not unique, it does provide a reasonable fit to the measured correlations, as shown by the dotted line in Fig. 1. The parameter D, or peak angle, is motivated by an attempt to describe the away-side dijet correlation in terms of its symmetry around $\Delta\phi \sim \pi$. We note that it also tends to absorb any non-Gaussian character of the dijet correlation. The third method, called zero yield at minimum (ZYAM), assumes that there is a region in $\Delta\phi$ where the dijet source of particle pairs is negligible. b_0 is varied until the background component in Eq. (2) matches the measured correlation $C(\Delta\phi)$ at some value of $\Delta\phi$.

As shown in Table I for the Au + Au data at 200 GeV, there are slight b_0 variations depending on which method is used to extract its value. However, the dijet correlation shape is essentially independent of these variations.

Figure 1 summarizes the ZYAM extraction of the dijet correlations using the central (0%–5%) Au + Au data at 200 GeV: the measured correlation is shown with squares, the background term with a full line, and the background subtracted dijet correlation with circles for values and boxes for the point-by-point systematic errors. The systematic errors are correlated since they depend on the same parameter—the $\langle v_2\rangle$ uncertainty. For clarity, $J(\Delta\phi)$ is

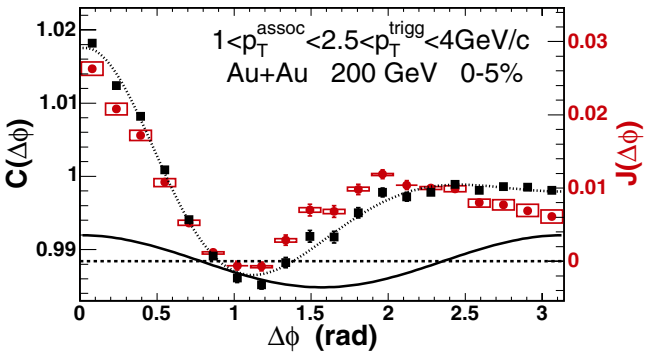

FIG. 1 (color online). The measured correlation $C(\Delta\phi)$ (squares) and the dijet correlation $J(\Delta\phi)$ (circles with boxes for point-to-point systematic errors) in central Au + Au collisions at $\sqrt{s_{NN}} = 200$ GeV. The full line shows the background term and the dotted line shows a $C(\Delta\phi)$ fit with Eqs. (2) and (3). The left axis shows the measured correlation amplitude and the right axis shows the dijet correlation amplitude.

TABLE I. b_0 values in Au + Au data at $\sqrt{s_{NN}} = 200$ GeV: ZYAM values (first row), variation of fit values from the ZYAM values (second row), variation of combinatorial (Comb.) values from the ZYAM values (third row).

Centrality	60%–90%	40%–60%	20%–40%	10%–20%	5%–10%	0%–5%
ZYAM b_0	0.861	0.942	0.960	0.971	0.982	0.988
Fit δb_0	−0.003	−0.003	−0.006	−0.028	−0.035	−0.022
Comb. δb_0	−0.086	−0.013	−0.004	+0.002	+0.001	+0.001

shifted up by b_0, shown with dashed line, and its amplitude is shown on the right axis. We note that, in this case, the measured correlation is flat near $\Delta\phi \sim \pi$, even before any background subtraction. Because of the cosine modulation of the background, a local minimum develops at $\Delta\phi \sim \pi$ in the dijet away-side correlation.

Figure 2 shows a central and a peripheral dijet correlation for each colliding system and energy. A remarkable away-side feature in central and semicentral collisions (<40%) is the peak location away from $\Delta\phi = \pi$, and the appearance of a local minimum at $\Delta\phi = \pi$. To quantify the significance of this minimum in the Au + Au data at 200 GeV, we have studied how much $\langle v_2^{\rm assoc}\rangle\langle v_2^{\rm trig}\rangle$ would need to change for the away side to be flat. For the four most central bins (0%–5%, 5%–10%, 10%–20%, and 20%–40%) it would have to decrease by 85%(5.1σ), 41%(4.2σ), 20%(2.3σ), and 23%(2.7σ), respectively, where σ is the total $\langle v_2^{\rm assoc}\rangle\langle v_2^{\rm trig}\rangle$ uncertainty.

We quantify the away-side shape change and deviation from a Gaussian distribution by extracting the second and fourth central moments around $\Delta\phi \sim \pi$ ($\mu_n \equiv \langle(\Delta\phi - \pi)^n\rangle$, $n = 2, 4$), in the standard form of the following statistical quantities: the root mean square $\equiv \sqrt{\mu_2}$ and the kurtosis $\equiv \mu_4/\mu_2^2$. The away side is defined here as all $\Delta\phi$ values above the dijet function $J(\Delta\phi)$ minimum, typically 1 rad. We extract these statistics on only the away-side jet peaks in $J(\Delta\phi)$; possible jet-associated flat underlying distributions, which are highly sensitive to the uncertainty in b_0 and precluded by the ZYAM assumption, are not included.

The rms and kurtosis centrality dependence is shown in Fig. 3(a). The rms increases with centrality, indicating broadening of the away-side dijet correlation, while the kurtosis decreases from the value characteristic of a Gaussian shape (three), demonstrating a flattening of its shape beyond an increase in the Gaussian width.

The peak angle D centrality dependence, extracted by fitting dijet correlations with Eq. (3), is shown in Fig. 3(b). It is consistent with zero radians in d + Au and peripheral collisions, but rapidly grows to a value around 1 rad in central collisions. Some deviation from zero radians may be due to slight non-Gaussian shapes of the dijet correlations even without medium modification. This is seen in

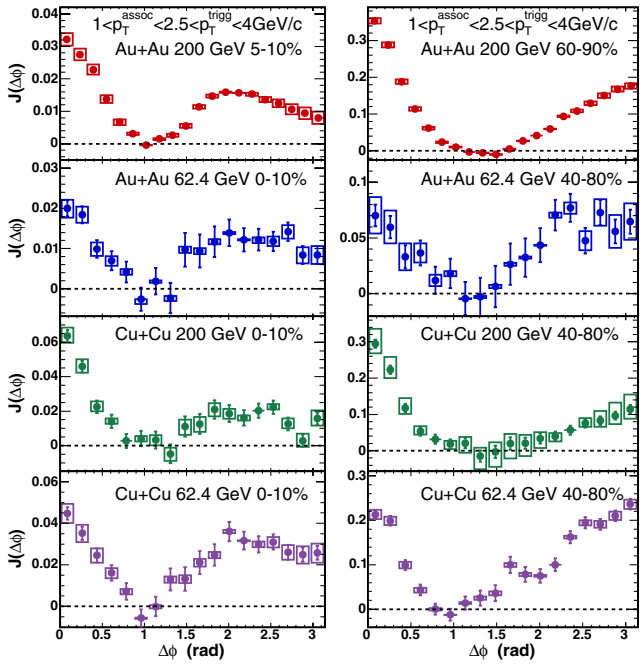

FIG. 2 (color online). Dijet correlations (circles with boxes for point-to-point systematic errors) in Au + Au and Cu + Cu collisions at $\sqrt{s_{NN}} = 62.4$ and 200 GeV. Left panels show central collisions, while right panels show peripheral collisions.

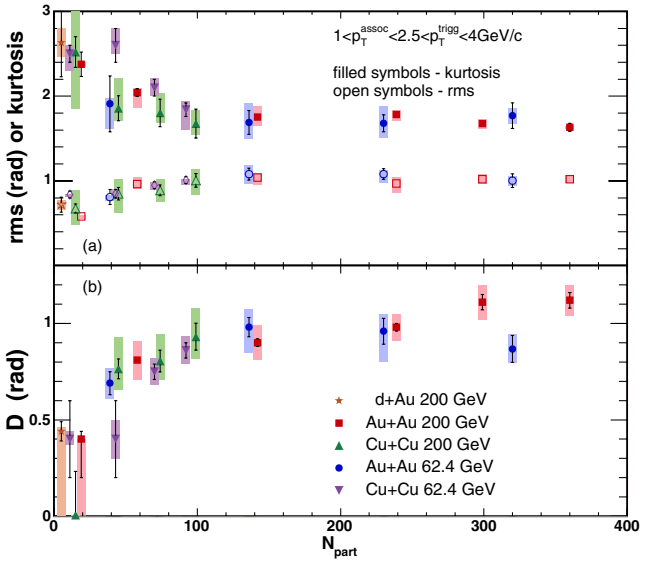

FIG. 3 (color online). Collision centrality, energy, and system size dependence of shape parameters: (a) kurtosis (filled symbols) and rms (open symbols); (b) peak angle D. Bars show statistical errors, shaded bands systematic errors.

TABLE II. Dependence of away-side shape parameters on associated hadron p_T in central (0%–20%) Au + Au collisions at $\sqrt{s_{NN}} = 200$ GeV for $3 < p_T^{\text{trigg}} < 5$ GeV/c. First error is statistical and second error is systematic.

p_T^{assoc}	D (rad)	rms (rad)	Kurtosis
1–1.5	$1.04 \pm 0.03 \pm 0.03$	$1.02 \pm 0.02 \pm 0.05$	$1.68 \pm 0.04 \pm 0.10$
1.5–2	$1.07 \pm 0.04 \pm 0.04$	$1.06 \pm 0.02 \pm 0.05$	$1.58 \pm 0.05 \pm 0.10$
2–2.5	$1.05 \pm 0.03 \pm 0.06$	$1.08 \pm 0.04 \pm 0.08$	$1.38 \pm 0.11 \pm 0.12$
2.5–3	$1.07 \pm 0.06 \pm 0.06$	$1.09 \pm 0.07 \pm 0.07$	$1.35 \pm 0.17 \pm 0.12$
3–5	$0.88 \pm 0.13 \pm 0.16$	$1.01 \pm 0.11 \pm 0.14$	$1.31 \pm 0.23 \pm 0.25$

the kurtosis values for d + Au and peripheral collisions, which have values somewhat lower than three. The systematic errors in Fig. 3 come primarily from the v_2 uncertainty for Cu + Cu and Au + Au and from the $J(\Delta\phi)$ minimum determination for d + Au.

No dependence of rms, kurtosis, or peak angle D on collision energy or species is observed, the away-side dijet shape exhibiting an N_{part} scaling also observed in the suppression of single hadron spectra [14].

Table II shows the dependence of the away-side shape parameters on the associated hadron p_T in the Au + Au data at 200 GeV for a 0%–20% centrality bin, $3 < p_T^{\text{trigg}} < 5$ GeV/c, and the following p_T^{assoc} bins: 1–1.5, 1.5–2, 2–2.5, 2.5–3, and 3–5 GeV/c. The peak angle D and the rms have no p_T dependence, while the kurtosis is consistent with a slow decrease with p_T.

Several phenomenological models for modification of the away-side jet have been proposed; all involve a strong response of the medium to the traversing jet. Bow shocks propagating as sound, or density, waves in the medium produce a peak located away from $\Delta\phi = \pi$ [4,15]. If the peak indeed arises from a sound wave, its location at 1 rad away from the nominal jet direction implies a speed of sound intermediate between that expected in a hadron gas and quark-gluon plasma [4]. A first order phase transition would cause a region with speed of sound identically zero. This region was postulated [4] to reflect sound waves and cause a second away-side peak located at about $\Delta\phi = 1.4$ rad. No clear evidence for a distinct peak is seen in our data.

If the coupling among partons in the medium is strong, then the high momentum parton may induce non-sound-wave collective plasma excitations [5]. In the strong coupling limit the anti–de Sitter/conformal field theory (AdS/CFT) correspondence was applied to calculate the wake of directional emission from a heavy quark traversing the medium, where a peak angle is found at values slightly larger than in these data [16].

The peak may also arise from Cherenkov gluon radiation [6]. Such a mechanism should disappear for high energy gluons, implying that the peak angle D should gradually approach zero with increasing momentum of associated hadrons. Table II shows that this is not supported by the data. The medium may induce gluon radiation at large angles by mechanisms other than Cherenkov radiation [7,8]. Such models can reproduce the observed peak if the density of scattering centers is large and the gluon splitting sufficiently asymmetric [7]. However, the predicted radiation is very sensitive to the treatment of geometry, expansion, and radiative energy loss framework used. Our detailed measurements constrain the options.

An important issue is whether the density wave correlations survive the underlying medium expansion [4,17]. It was shown that the interplay of the longitudinal expansion and limited experimental η acceptance preserves, and even amplifies, the signal of directed collective excitations [15]. The creation of a shock wave consistent with our data requires that 75%–90% of the parton's lost energy be transferred to the collective mode [15].

We have presented azimuthal angle correlations of intermediate transverse momentum hadrons from dijets in Cu + Cu and Au + Au collisions at $\sqrt{s_{NN}} = 62.4$ and 200 GeV. The away-side dijet correlation is seen to be broadened, non-Gaussian, and peaked away from $\Delta\phi = \pi$ in central and semicentral collisions. The away-side shape depends on the number of participants in the collision, and not on the beam nuclei or energy. The general features of the observed shape can be qualitatively accounted for by a number of phenomenological models, all having in common a strong medium response to the energy deposited by the traversing parton. The systematic data presented here provide quantitative tests that could discriminate between these models.

We thank the staff of the Collider-Accelerator and Physics Departments at BNL for their vital contributions. We acknowledge support from the Office of NP in DOE Office of Science and NSF (U.S.), MEXT and JSPS (Japan), CNPq and FAPESP (Brazil), NSFC (China), MSMT (Czech Republic), IN2P3/CNRS and CEA (France), BMBF, DAAD, and AvH (Germany), OTKA (Hungary), DAE (India), ISF (Israel), KRF and KOSEF (Korea), MES, RAS, and FAAE (Russia), VR and KAW (Sweden), U.S. CRDF for the FSU, US-Hungarian NSF-OTKA-MTA, and US-Israel BSF.

*Deceased.
†PHENIX spokesperson.
Electronic address: zajc@nevis.columbia.edu

[1] K. Adcox *et al.*, Nucl. Phys. **A757**, 184 (2005).
[2] S. S. Adler *et al.*, Phys. Rev. Lett. **91**, 182301 (2003).
[3] S. S. Adler *et al.*, Phys. Rev. Lett. **91**, 072301 (2003); Phys. Rev. C **69**, 034910 (2004).
[4] J. Casalderrey-Solana, E. V. Shuryak, and D. Teaney, Nucl. Phys. **A774**, 577 (2006).
[5] J. Ruppert and B. Mueller, Phys. Lett. B **618**, 123 (2005).
[6] V. Koch, A. Majumder, and X.-N. Wang, Phys. Rev. Lett. **96**, 172302 (2006).
[7] A. D. Polosa and C. A. Salgado, Phys. Rev. C **75**, 041901 (2007).
[8] I. Vitev, Phys. Lett. B **630**, 78 (2005).
[9] J. Adams *et al.*, Phys. Rev. Lett. **95**, 152301 (2005).
[10] S. S. Adler *et al.*, Phys. Rev. Lett. **97**, 052301 (2006).
[11] K. Adcox *et al.*, Phys. Rev. C **69**, 024904 (2004).
[12] H. Masui, Nucl. Phys. **A774**, 511 (2006); M. D. Oldenburg, J. Phys. G **31**, S437 (2005).
[13] S. S. Adler *et al.*, Phys. Rev. C **71**, 051902 (2005).
[14] B. Alver *et al.*, Phys. Rev. Lett. **96**, 212301 (2006).
[15] T. Renk and J. Ruppert, Phys. Lett. B **646**, 19 (2007).
[16] J. J. Friess, S. S. Gubser, G. Michalogiorgakis, and S. S. Pufu, arXiv:hep-th/0607022 [Phys. Rev. D (to be published)].
[17] A. K. Chaudhuri and U. Heinz, Phys. Rev. Lett. **97**, 062301 (2006).

Energy Loss and Flow of Heavy Quarks in Au + Au Collisions at $\sqrt{s_{NN}} = 200$ GeV

A. Adare,[8] S. Afanasiev,[22] C. Aidala,[9] N. N. Ajitanand,[49] Y. Akiba,[43,44] H. Al-Bataineh,[38] J. Alexander,[49] A. Al-Jamel,[38] K. Aoki,[28,43] L. Aphecetche,[51] R. Armendariz,[38] S. H. Aronson,[3] J. Asai,[44] E. T. Atomssa,[29] R. Averbeck,[50] T. C. Awes,[39] B. Azmoun,[3] V. Babintsev,[18] G. Baksay,[14] L. Baksay,[14] A. Baldisseri,[11] K. N. Barish,[4] P. D. Barnes,[31] B. Bassalleck,[37] S. Bathe,[4] S. Batsouli,[9,39] V. Baublis,[42] F. Bauer,[4] A. Bazilevsky,[3] S. Belikov,[3,21] R. Bennett,[50] Y. Berdnikov,[46] A. A. Bickley,[8] M. T. Bjorndal,[9] J. G. Boissevain,[31] H. Borel,[11] K. Boyle,[50] M. L. Brooks,[31] D. S. Brown,[38] D. Bucher,[34] H. Buesching,[3] V. Bumazhnov,[18] G. Bunce,[3,44] J. M. Burward-Hoy,[31] S. Butsyk,[31,50] S. Campbell,[50] J.-S. Chai,[23] B. S. Chang,[58] J.-L. Charvet,[11] S. Chernichenko,[18] J. Chiba,[24] C. Y. Chi,[9] M. Chiu,[9,19] I. J. Choi,[58] T. Chujo,[55] P. Chung,[49] A. Churyn,[18] V. Cianciolo,[39] C. R. Cleven,[16] Y. Cobigo,[11] B. A. Cole,[9] M. P. Comets,[40] P. Constantin,[21,31] M. Csanád,[13] T. Csörgő,[25] T. Dahms,[50] K. Das,[15] G. David,[3] M. B. Deaton,[1] K. Dehmelt,[14] H. Delagrange,[51] A. Denisov,[18] D. d'Enterria,[9] A. Deshpande,[44,50] E. J. Desmond,[3] O. Dietzsch,[47] A. Dion,[50] M. Donadelli,[47] J. L. Drachenberg,[1] O. Drapier,[29] A. Drees,[50] A. K. Dubey,[57] A. Durum,[18] V. Dzhordzhadze,[4,52] Y. V. Efremenko,[39] J. Egdemir,[50] F. Ellinghaus,[8] W. S. Emam,[4] A. Enokizono,[17,30] H. En'yo,[43,44] B. Espagnon,[40] S. Esumi,[54] K. O. Eyser,[4] D. E. Fields,[37,44] M. Finger,[5,22] F. Fleuret,[29] S. L. Fokin,[27] B. Forestier,[32] Z. Fraenkel,[57] J. E. Frantz,[9,50] A. Franz,[3] A. D. Frawley,[15] K. Fujiwara,[43] Y. Fukao,[28,43] S.-Y. Fung,[4] T. Fusayasu,[36] S. Gadrat,[32] I. Garishvili,[52] F. Gastineau,[51] M. Germain,[51] A. Glenn,[8,52] H. Gong,[50] M. Gonin,[29] J. Gosset,[11] Y. Goto,[43,44] R. Granier de Cassagnac,[29] N. Grau,[21] S. V. Greene,[55] M. Grosse Perdekamp,[19,44] T. Gunji,[7] H.-Å. Gustafsson,[33] T. Hachiya,[17,43] A. Hadj Henni,[51] C. Haegemann,[37] J. S. Haggerty,[3] M. N. Hagiwara,[1] H. Hamagaki,[7] R. Han,[41] H. Harada,[17] E. P. Hartouni,[30] K. Haruna,[17] M. Harvey,[3] E. Haslum,[33] K. Hasuko,[43] R. Hayano,[7] M. Heffner,[30] T. K. Hemmick,[50] T. Hester,[4] J. M. Heuser,[43] X. He,[16] H. Hiejima,[19] J. C. Hill,[21] R. Hobbs,[37] M. Hohlmann,[14] M. Holmes,[55] W. Holzmann,[49] K. Homma,[17] B. Hong,[26] T. Horaguchi,[43,53] D. Hornback,[52] M. G. Hur,[23] T. Ichihara,[43,44] K. Imai,[28,43] M. Inaba,[54] Y. Inoue,[45,43] D. Isenhower,[1] L. Isenhower,[1] M. Ishihara,[43] T. Isobe,[7] M. Issah,[49] A. Isupov,[22] B. V. Jacak,[50] J. Jia,[9] J. Jin,[9] O. Jinnouchi,[44] B. M. Johnson,[3] K. S. Joo,[35] D. Jouan,[40] F. Kajihara,[7,43] S. Kametani,[7,56] N. Kamihara,[43,53] J. Kamin,[50] M. Kaneta,[44] J. H. Kang,[58] H. Kano,[43] H. Kanou,[43,53] T. Kawagishi,[54] D. Kawall,[44] A. V. Kazantsev,[27] S. Kelly,[8] A. Khanzadeev,[42] J. Kikuchi,[56] D. H. Kim,[35] D. J. Kim,[58] E. Kim,[48] Y.-S. Kim,[23] E. Kinney,[8] A. Kiss,[13] E. Kistenev,[3] A. Kiyomichi,[43] J. Klay,[30] C. Klein-Boesing,[34] L. Kochenda,[42] V. Kochetkov,[18] B. Komkov,[42] M. Konno,[54] D. Kotchetkov,[4] A. Kozlov,[57] A. Král,[10] A. Kravitz,[9] P. J. Kroon,[3] J. Kubart,[5,20] G. J. Kunde,[31] N. Kurihara,[7] K. Kurita,[45,43] M. J. Kweon,[26] Y. Kwon,[52,58] G. S. Kyle,[38] R. Lacey,[49] Y.-S. Lai,[9] J. G. Lajoie,[21] A. Lebedev,[21] Y. Le Bornec,[40] S. Leckey,[50] D. M. Lee,[31] M. K. Lee,[58] T. Lee,[48] M. J. Leitch,[31] M. A. L. Leite,[47] B. Lenzi,[47] H. Lim,[48] T. Liška,[10] A. Litvinenko,[22] M. X. Liu,[31] X. Li,[6] X. H. Li,[4] B. Love,[55] D. Lynch,[3] C. F. Maguire,[55] Y. I. Makdisi,[3] A. Malakhov,[22] M. D. Malik,[37] V. I. Manko,[27] Y. Mao,[41,43] L. Mašek,[5,20] H. Masui,[54] F. Matathias,[9,50] M. C. McCain,[19] M. McCumber,[50] P. L. McGaughey,[31] Y. Miake,[54] P. Mikeš,[5,20] K. Miki,[54] T. E. Miller,[55] A. Milov,[50] S. Mioduszewski,[3] G. C. Mishra,[16] M. Mishra,[2] J. T. Mitchell,[3] M. Mitrovski,[49] A. Morreale,[4] D. P. Morrison,[3] J. M. Moss,[31] T. V. Moukhanova,[27] D. Mukhopadhyay,[55] J. Murata,[45,43] S. Nagamiya,[24] Y. Nagata,[54] J. L. Nagle,[8] M. Naglis,[57] I. Nakagawa,[43,44] Y. Nakamiya,[17] T. Nakamura,[17] K. Nakano,[43,53] J. Newby,[30] M. Nguyen,[50] B. E. Norman,[31] A. S. Nyanin,[27] J. Nystrand,[33] E. O'Brien,[3] S. X. Oda,[7] C. A. Ogilvie,[21] H. Ohnishi,[43] I. D. Ojha,[55] H. Okada,[28,43] K. Okada,[44] M. Oka,[54] O. O. Omiwade,[1] A. Oskarsson,[33] I. Otterlund,[33] M. Ouchida,[17] K. Ozawa,[7] R. Pak,[3] D. Pal,[55] A. P. T. Palounek,[31] V. Pantuev,[50] V. Papavassiliou,[38] J. Park,[48] W. J. Park,[26] S. F. Pate,[38] H. Pei,[21] J.-C. Peng,[19] H. Pereira,[11] V. Peresedov,[22] D. Yu. Peressounko,[27] C. Pinkenburg,[3] R. P. Pisani,[3] M. L. Purschke,[3] A. K. Purwar,[31,50] H. Qu,[16] J. Rak,[21,37] A. Rakotozafindrabe,[29] I. Ravinovich,[57] K. F. Read,[39,52] S. Rembeczki,[14] M. Reuter,[50] K. Reygers,[34] V. Riabov,[42] Y. Riabov,[42] G. Roche,[32] A. Romana,[29,*] M. Rosati,[21] S. S. E. Rosendahl,[33] P. Rosnet,[32] P. Rukoyatkin,[22] V. L. Rykov,[43] S. S. Ryu,[58] B. Sahlmueller,[34] N. Saito,[28,43,44] T. Sakaguchi,[3,7,56] S. Sakai,[54] H. Sakata,[17] V. Samsonov,[42] H. D. Sato,[28,43] S. Sato,[3,24,54] S. Sawada,[24] J. Seele,[8] R. Seidl,[19] V. Semenov,[18] R. Seto,[4] D. Sharma,[57] T. K. Shea,[3] I. Shein,[18] A. Shevel,[42,49] T.-A. Shibata,[43,53] K. Shigaki,[17] M. Shimomura,[54] T. Shohjoh,[54] K. Shoji,[28,43] A. Sickles,[50] C. L. Silva,[47] D. Silvermyr,[39] C. Silvestre,[11] K. S. Sim,[26] C. P. Singh,[2] V. Singh,[2] S. Skutnik,[21] M. Slunečka,[5,22] W. C. Smith,[1] A. Soldatov,[18] R. A. Soltz,[30] W. E. Sondheim,[31] S. P. Sorensen,[52] I. V. Sourikova,[3] F. Staley,[11] P. W. Stankus,[39] E. Stenlund,[33] M. Stepanov,[38] A. Ster,[25] S. P. Stoll,[3] T. Sugitate,[17] C. Suire,[40] J. P. Sullivan,[31] J. Sziklai,[25] T. Tabaru,[44] S. Takagi,[54] E. M. Takagui,[47] A. Taketani,[43,44] K. H. Tanaka,[24] Y. Tanaka,[36] K. Tanida,[43,44] M. J. Tannenbaum,[3] A. Taranenko,[49] P. Tarján,[12] T. L. Thomas,[37] M. Togawa,[28,43] A. Toia,[50] J. Tojo,[43] L. Tomášek,[20] H. Torii,[43] R. S. Towell,[1] V-N. Tram,[29] I. Tserruya,[57] Y. Tsuchimoto,[17,43] S. K. Tuli,[2] H. Tydesjö,[33] N. Tyurin,[18] C. Vale,[21]

 © 2007 The American Physical Society

H. Valle,[55] H. W. van Hecke,[31] J. Velkovska,[55] R. Vertesi,[12] A. A. Vinogradov,[27] M. Virius,[10] V. Vrba,[20] E. Vznuzdaev,[42] M. Wagner,[28,43] D. Walker,[50] X. R. Wang,[38] Y. Watanabe,[43,44] J. Wessels,[34] S. N. White,[3] N. Willis,[40] D. Winter,[9] C. L. Woody,[3] M. Wysocki,[8] W. Xie,[4,44] Y. Yamaguchi,[56] A. Yanovich,[18] Z. Yasin,[4] J. Ying,[16] S. Yokkaichi,[43,44] G. R. Young,[39] I. Younus,[37] I. E. Yushmanov,[27] W. A. Zajc,[9,†] O. Zaudtke,[34] C. Zhang,[9,39] S. Zhou,[6] J. Zimányi,[25,*] and L. Zolin[22]

(PHENIX Collaboration)

[1]*Abilene Christian University, Abilene, Texas 79699, USA*
[2]*Department of Physics, Banaras Hindu University, Varanasi 221005, India*
[3]*Brookhaven National Laboratory, Upton, New York 11973-5000, USA*
[4]*University of California, Riverside, Riverside, California 92521, USA*
[5]*Charles University, Ovocný trh 5, Praha 1, 116 36, Prague, Czech Republic*
[6]*China Institute of Atomic Energy (CIAE), Beijing, People's Republic of China*
[7]*Center for Nuclear Study, Graduate School of Science, University of Tokyo, 7-3-1 Hongo, Bunkyo, Tokyo 113-0033, Japan*
[8]*University of Colorado, Boulder, Colorado 80309, USA*
[9]*Columbia University, New York, New York 10027, USA*
and Nevis Laboratories, Irvington, New York 10533, USA
[10]*Czech Technical University, Zikova 4, 166 36 Prague 6, Czech Republic*
[11]*Dapnia, CEA Saclay, F-91191, Gif-sur-Yvette, France*
[12]*Debrecen University, H-4010 Debrecen, Egyetem tér 1, Hungary*
[13]*ELTE, Eötvös Loránd University, H-1117 Budapest, Pázmány P. s. 1/A, Hungary*
[14]*Florida Institute of Technology, Melbourne, Florida 32901, USA*
[15]*Florida State University, Tallahassee, Florida 32306, USA*
[16]*Georgia State University, Atlanta, Georgia 30303, USA*
[17]*Hiroshima University, Kagamiyama, Higashi-Hiroshima 739-8526, Japan*
[18]*IHEP Protvino, State Research Center of Russian Federation, Institute for High Energy Physics, Protvino, 142281, Russia*
[19]*University of Illinois at Urbana-Champaign, Urbana, Illinois 61801, USA*
[20]*Institute of Physics, Academy of Sciences of the Czech Republic, Na Slovance 2, 182 21 Prague 8, Czech Republic*
[21]*Iowa State University, Ames, Iowa 50011, USA*
[22]*Joint Institute for Nuclear Research, 141980 Dubna, Moscow Region, Russia*
[23]*Cyclotron Application Laboratory, KAERI, Seoul, South Korea*
[24]*High Energy Accelerator Research Organization, KEK, Tsukuba, Ibaraki 305-0801, Japan*
[25]*KFKI Research Institute for Particle and Nuclear Physics of the Hungarian Academy of Sciences (MTA KFKI RMKI), H-1525 Budapest 114, P.O. Box 49, Budapest, Hungary*
[26]*Korea University, Seoul, 136-701, Korea*
[27]*Russian Research Center "Kurchatov Institute," Moscow, Russia*
[28]*Kyoto University, Kyoto 606-8502, Japan*
[29]*Laboratoire Leprince-Ringuet, Ecole Polytechnique, CNRS-IN2P3, Route de Saclay, F-91128, Palaiseau, France*
[30]*Lawrence Livermore National Laboratory, Livermore, California 94550, USA*
[31]*Los Alamos National Laboratory, Los Alamos, New Mexico 87545, USA*
[32]*LPC, Université Blaise Pascal, CNRS-IN2P3, Clermont-Fd, 63177 Aubiere Cedex, France*
[33]*Department of Physics, Lund University, Box 118, SE-221 00 Lund, Sweden*
[34]*Institut für Kernphysik, University of Muenster, D-48149 Muenster, Germany*
[35]*Myongji University, Yongin, Kyonggido 449-728, Korea*
[36]*Nagasaki Institute of Applied Science, Nagasaki-shi, Nagasaki 851-0193, Japan*
[37]*University of New Mexico, Albuquerque, New Mexico 87131, USA*
[38]*New Mexico State University, Las Cruces, New Mexico 88003, USA*
[39]*Oak Ridge National Laboratory, Oak Ridge, Tennessee 37831, USA*
[40]*IPN-Orsay, Universite Paris Sud, CNRS-IN2P3, BP1, F-91406, Orsay, France*
[41]*Peking University, Beijing, People's Republic of China*
[42]*PNPI, Petersburg Nuclear Physics Institute, Gatchina, Leningrad region, 188300, Russia*
[43]*RIKEN, The Institute of Physical and Chemical Research, Wako, Saitama 351-0198, Japan*
[44]*RIKEN BNL Research Center, Brookhaven National Laboratory, Upton, New York 11973-5000, USA*
[45]*Physics Department, Rikkyo University, 3-34-1 Nishi-Ikebukuro, Toshima, Tokyo 171-8501, Japan*
[46]*Saint Petersburg State Polytechnic University, St. Petersburg, Russia*
[47]*Instituto de Física, Universidade de São Paulo, Caixa Postal 66318, São Paulo CEP05315-970, Brazil*
[48]*System Electronics Laboratory, Seoul National University, Seoul, South Korea*
[49]*Chemistry Department, Stony Brook University, Stony Brook, SUNY, New York 11794-3400, USA*

[50]Department of Physics and Astronomy, Stony Brook University, Stony Brook, New York 11794, USA
[51]SUBATECH (Ecole des Mines de Nantes, CNRS-IN2P3, Université de Nantes) BP 20722 - 44307, Nantes, France
[52]University of Tennessee, Knoxville, Tennessee 37996, USA
[53]Department of Physics, Tokyo Institute of Technology, Oh-okayama, Meguro, Tokyo 152-8551, Japan
[54]Institute of Physics, University of Tsukuba, Tsukuba, Ibaraki 305, Japan
[55]Vanderbilt University, Nashville, Tennessee 37235, USA
[56]Advanced Research Institute for Science and Engineering, Waseda University, 17 Kikui-cho, Shinjuku-ku, Tokyo 162-0044, Japan
[57]Weizmann Institute, Rehovot 76100, Israel
[58]Yonsei University, IPAP, Seoul 120-749, Korea
(Received 11 November 2006; published 24 April 2007)

The PHENIX experiment at the BNL Relativistic Heavy Ion Collider (RHIC) has measured electrons with $0.3 < p_T < 9$ GeV/c at midrapidity ($|y| < 0.35$) from heavy-flavor (charm and bottom) decays in Au + Au collisions at $\sqrt{s_{\rm NN}} = 200$ GeV. The nuclear modification factor $R_{\rm AA}$ relative to $p + p$ collisions shows a strong suppression in central Au + Au collisions, indicating substantial energy loss of heavy quarks in the medium produced at RHIC energies. A large azimuthal anisotropy v_2 with respect to the reaction plane is observed for $0.5 < p_T < 5$ GeV/c indicating substantial heavy-flavor elliptic flow. Both $R_{\rm AA}$ and v_2 show a p_T dependence different from those of neutral pions. A comparison to transport models which simultaneously describe $R_{\rm AA}(p_T)$ and $v_2(p_T)$ suggests that the viscosity to entropy density ratio is close to the conjectured quantum lower bound, i.e., near a perfect fluid.

DOI: 10.1103/PhysRevLett.98.172301 PACS numbers: 25.75.Dw

Experimental results from the Relativistic Heavy Ion Collider (RHIC) have established that dense partonic matter is formed in Au + Au collisions at RHIC [1–4]. Strong suppression observed for π^0 and other light hadrons at high transverse momentum (p_T) [5–8] indicates partonic energy loss in the produced medium. The azimuthal anisotropy $v_2(p_T)$ [9,10] provides evidence that collective motion develops in a very early stage of the collision ($\tau \lesssim 5$ fm/c), in accordance with hydrodynamical calculations [11,12]. The comparison of v_2 with several such models suggests [13–15] that the matter formed at RHIC is a near-perfect fluid with viscosity to entropy density ratio η/s close to the conjectured quantum lower bound [16]. Energy loss and flow are related to the transport properties of the medium at temperature T, in particular, the diffusion coefficient $D \propto \eta/(sT)$.

Further insight into properties of the medium can be gained from the production and propagation of particles carrying heavy quarks (charm or bottom). A fixed-order-plus-next-to-leading-log (FONLL) perturbative QCD (pQCD) calculation [17] describes the cross sections of heavy-flavor decay electrons in $p + p$ collisions at $\sqrt{s} = 200$ GeV within theoretical uncertainties [18]. In Au + Au collisions the total yield of such electrons was found to scale with the number of nucleon-nucleon collisions as expected for pointlike processes [19]. Energy loss via gluon radiation is expected to be reduced for heavy quarks due to suppression of forward radiation, thus increasing their expected thermalization time [20–22]. Consequently, a decrease of high p_T suppression and of v_2 is expected from light to charm to bottom quarks, with the absolute values and their p_T dependence sensitive to the properties of the medium. In contrast to these expectations, a strong suppression of heavy-flavor decay electrons was discovered for $2 < p_T < 5$ GeV/c [23,24], together with nonzero electron v_2 for $p_T < 2$ GeV/c [25].

This Letter presents p_T spectra and the elliptic flow amplitude $v_2^{\rm HF}$ of electrons, $(e^+ + e^-)/2$, from heavy-flavor decays at midrapidity in Au + Au collisions at $\sqrt{s_{\rm NN}} = 200$ GeV. An increase in statistics by more than a factor of 10 and reduced systematic uncertainties compared to earlier data [19,23,25] greatly extend the p_T range both for the determination of the centrality dependence of $R_{\rm AA}$ and for the measurement of $v_2^{\rm HF}$.

The data were collected by the PHENIX detector [26] in the 2004 RHIC run. The minimum bias trigger and the collision centrality were obtained from the beam-beam counters (BBC) and zero degree calorimeters [1]. After selecting good runs, data samples of 8.1 and 7.0×10^8 minimum bias events in the vertex range $|z_{\rm vtx}| < 20$ cm are used for the spectra and v_2 analyses, respectively.

Charged particle tracks are reconstructed with the two PHENIX central arm spectrometers, each covering $\Delta\phi = \pi/2$ in azimuth and $|\eta| < 0.35$ in pseudorapidity [26]. Tracks are confirmed by matching showers in the electromagnetic calorimeter (EMC) within 2σ in position. Electron candidates have at least three associated hits in the ring imaging Čerenkov detectors (RICH) and fulfill a shower shape cut in the EMC, where they deposit an energy E, consistent with the momentum ($E/p - 1 > -2\sigma$). Below the Čerenkov threshold for pions ($p_T < 5$ GeV/c) electron misidentification is only due to random coincidences between hadron tracks and hits in the RICH. This small background (<20% at low p_T in central collisions, less toward high p_T and peripheral events) is subtracted statistically using an event mixing technique. Requiring at least five hits in the RICH and tightening the shower shape cut extends the electron measurement to 9 GeV/c in p_T, with negligible hadron background for $p_T < 8$ GeV/c and a hadron contamination of 20% for $8 < p_T < 9$ GeV/c. The raw spectra are corrected for geometrical acceptance and reconstruction efficiency de-

termined by a GEANT simulation. The centrality dependent efficiency loss $<2\%$ ($\approx 23\%$) for peripheral (central) events is evaluated by reconstructing simulated electrons embedded into real events.

The inclusive electron spectra consist of (i) ''nonphotonic'' electrons from heavy-flavor decays, (ii) ''photonic'' background from Dalitz decays and photon conversions (mainly in the beam pipe), and (iii) nonphotonic background from $K \rightarrow e\pi\nu$ (K_{e3}) and dielectron decays of vector mesons. Contribution (iii) is small ($<10\%$ for $p_T < 0.5$ GeV/c, $<2\%$ for $p_T > 2$ GeV/c) compared to (ii). The heavy-flavor signal and the ratio of nonphotonic to photonic electrons, $R_{\rm NP}$, are determined via two independent and complementary methods described in detail in [18], where the identical detector configuration was used. At low p_T ($p_T < 1.6$ GeV/c), where the heavy-flavor signal to background ratio is small ($S/B < 1$), the ''converter subtraction'' method is used, which employs a photon converter of 1.67% radiation length (X_0) installed around the beam pipe for part of the run. The converter multiplies the photonic background by a known, nearly p_T independent factor $R_\gamma \sim 2.3$. The photonic background can then be determined by comparing the inclusive electron yield with and without the converter. For higher p_T, where S/B is large, the ''cocktail subtraction'' method [23] is used. Here the background is calculated with a Monte Carlo hadron decay generator and subtracted from the data. At low p_T the dominant background source is the π^0 Dalitz decay, which is calculated for each centrality using measured pion spectra [6,27] as input. In good agreement with measured data [8], the spectral shapes of other light hadrons h (η, ρ, ω, ϕ, η') are derived from the pion spectrum assuming a universal shape in $m_T = \sqrt{p_T^2 + m_h^2}$ with a fixed constant ratio at high p_T. Photon conversions in the beam pipe, air, and helium bags (total $0.4\%X_0$) are also included, along with background from K_{e3} decays and both external and internal conversions of direct photons which are important for $p_T > 4$ GeV/c. The agreement within the systematic uncertainties in the overlap region $0.3 < p_T < 4$ GeV/c of these two methods demonstrates that the absolute value of photonic backgrounds in the PHENIX aperture is well understood.

The v_2 of inclusive electrons, $v_2^{\rm inc}$, is measured as $v_2^{\rm inc} = \langle\cos(2(\phi - \Phi_R))\rangle/\sigma_R$ [28], where Φ_R is the azimuthal orientation of the reaction plane measured with the resolution σ_R using the BBC [9]. Since σ_R is centrality dependent, v_2 is determined for narrow centrality bins (10%) and then averaged to calculate v_2 for minimum bias events. The v_2 of random hadronic background is subtracted statistically as described in [25].

The $v_2^{\rm non\text{-}\gamma}$ of nonphotonic electrons is obtained by subtracting the photonic electron v_2^γ as $v_2^{\rm non\text{-}\gamma} = [(1 + R_{\rm NP})v_2^{\rm inc} - v_2^\gamma]/R_{\rm NP}$. Here v_2^γ is calculated via a Monte Carlo generator that includes π^0, η, and direct photons. The measured $v_2(p_T)$ of $\pi^\pm$, π^0, and $K^\pm$ [9,29] is used as input, assuming $v_2^{\pi^\pm} = v_2^{\pi^0}$, $v_2^\eta = v_2^{K^\pm}$, and $v_2^{\rm direct\ \gamma} = 0$. A direct measurement of v_2^γ using the converter subtraction method confirms the calculation within statistical uncertainties. The resulting $v_2^{\rm non\text{-}\gamma}$ has a small contribution from K_{e3} background which is simulated and subtracted to obtain $v_2^{\rm HF}$ of heavy-flavor decay electrons.

Three independent categories of systematic uncertainties are considered. (a) The inclusive electron spectra include uncertainties in the geometrical acceptance (5%), the reconstruction efficiency (3%), and the embedding correction ($\leq 4\%$). (b) Uncertainties in the converter subtraction are mainly given by the uncertainty in R_γ (2.7%) and in the relative acceptance of runs with and without the converter being installed (1%). (c) Uncertainties in the cocktail subtraction rise from 8% at $p_T = 0.3$ GeV/c to 13% at 9 GeV/c, dominated by systematic errors in the pion input and, at high p_T, the direct photon spectrum. The v_2 measurement includes a systematic uncertainty of 5% due to the reaction plane uncertainty.

Figure 1 shows the invariant p_T spectra of electrons from heavy-flavor decay for minimum bias events and in five centrality classes. The curves overlayed are the fit to the corresponding data from $p + p$ collisions [18] with the spectral shape taken from a FONLL calculation [17] and scaled by the nuclear overlap integral $\langle T_{\rm AA}\rangle$ for each centrality class [6]. The inset of Fig. 1 shows the ratio of electrons from heavy-flavor decays to background. It increases rapidly with p_T, exceeding unity for $p_T > 1.8$ GeV/c, reflecting the small amount of material in the detector acceptance which makes the accurate measurement of heavy-flavor electron spectra and $v_2^{\rm HF}$ possible.

For all centralities, the Au + Au spectra agree well with the $p + p$ reference at low p_T, but a suppression with respect to $p + p$ develops toward high p_T. This is quantified by the nuclear modification factor $R_{\rm AA} = dN_{\rm Au+Au}/(\langle T_{\rm AA}\rangle d\sigma_{p+p})$, where $dN_{\rm Au+Au}$ is the differential yield in Au + Au and $d\sigma_{p+p}$ is the differential cross section in $p + p$ in a given p_T bin. For $p_T < 1.6$ GeV/c, $d\sigma_{p+p}$ is taken bin-by-bin from [18], whereas a fit to the same data (curves in Fig. 1) is used at higher p_T, taking systematic uncertainties in $d\sigma_{p+p}$ and $T_{\rm AA}$ into account.

Figure 2 shows $R_{\rm AA}$ for electrons from heavy-flavor decays for two different p_T ranges as a function of the number of participant nucleons $N_{\rm part}$. For the integration interval $p_T > 0.3$ GeV/c containing more than half of the heavy-flavor decay electrons [18], $R_{\rm AA}$ is consistent with unity for all $N_{\rm part}$ in accordance with the binary scaling of the total heavy-flavor yield [19]. For $p_T > 3$ GeV/c, the heavy-flavor electron $R_{\rm AA}$ decreases systematically with centrality, while larger than $R_{\rm AA}$ of π^0 with $p_T > 4$ GeV/c [6]. Since above 3 GeV/c electrons from charm decays originate mainly from D mesons with p_T above 4 GeV/c this comparison indicates a smaller suppression of heavy-flavor mesons than observed for light mesons in this intermediate p_T range.

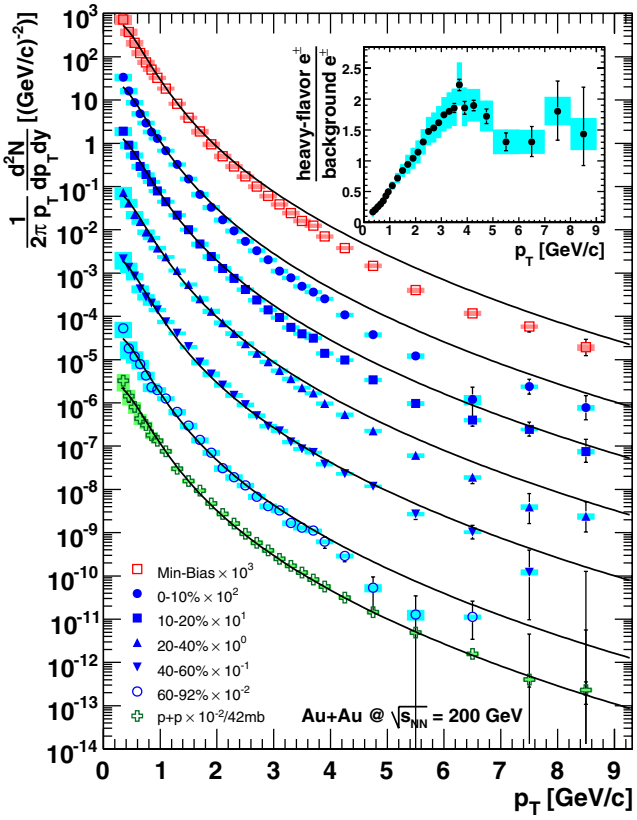

FIG. 1 (color online). Invariant yields of electrons from heavy-flavor decays for different Au + Au centrality classes and for $p + p$ collisions, scaled by powers of 10 for clarity. The solid lines are the result of a FONLL calculation normalized to the $p + p$ data [18] and scaled with $\langle T_{AA}\rangle$ for each Au + Au centrality class. The inset shows the ratio of heavy-flavor to background electrons for minimum bias Au + Au collisions. Error bars (boxes) depict statistical (systematic) uncertainties.

Figure 3 shows the measured R_{AA} and v_2^{HF} of heavy-flavor electrons in 0%–10% central and minimum bias collisions, and our corresponding π^0 data [6,29]. The data indicate strong coupling of heavy quarks to the medium. While at low p_T the suppression is smaller than that of π^0, R_{AA} of heavy-flavor decay electrons approaches the π^0 value for $p_T > 4$ GeV/c although a significant contribution from bottom decays is expected at high p_T. The large v_2^{HF} indicates that the charm relaxation time is comparable to the short time scale of flow development in the produced medium. It should be noted that much reduced uncertainties and the extended p_T range of the present data permit the comparisons of R_{AA} and v_2 of the heavy and light flavors.

More quantitative statements require theoretical guidance. Figure 3 compares the R_{AA} and v_2 of heavy-flavor electrons with models calculating both quantities simultaneously. A pQCD calculation with radiative energy loss (curves I) [30] describes the measured R_{AA} reasonably well using a large transport coefficient $\hat{q} = 14$ GeV^2/fm, which also provides a consistent description of light hadron

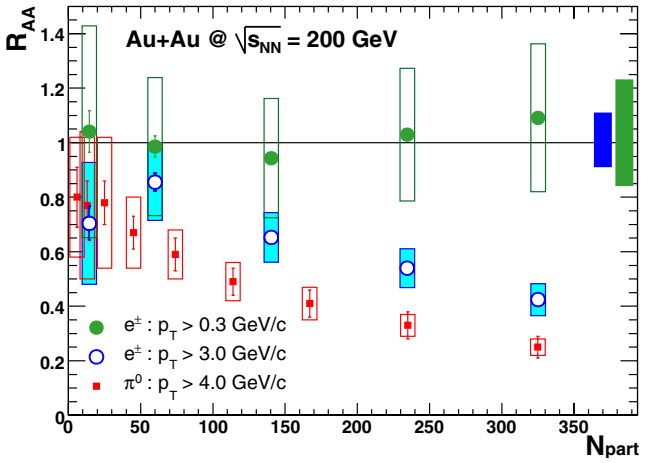

FIG. 2 (color online). R_{AA} of heavy-flavor electrons with p_T above 0.3 and 3 GeV/c and of π^0 with $p_T > 4$ GeV/c as function of centrality given by N_{part}. Error bars (boxes) depict statistical (point-by-point systematic) uncertainties. The right (left) box at $R_{AA} = 1$ shows the relative uncertainty from the $p + p$ reference common to all points for $p_T > 0.3(3)$ GeV/c.

suppression. This value of $\hat{q}$ would imply a strongly coupled medium. In this model the azimuthal anisotropy is only due to the path length dependence of energy loss, and the data clearly favor larger v_2^{HF} than predicted from this effect alone.

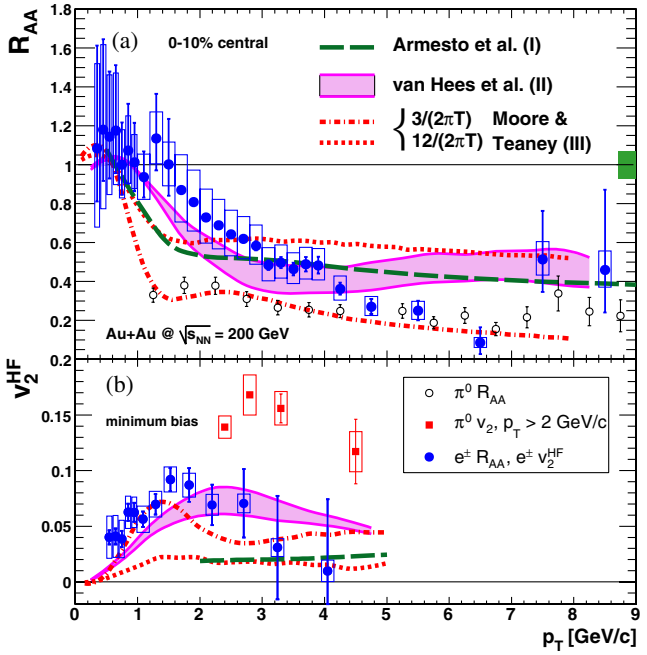

FIG. 3 (color online). (a) R_{AA} of heavy-flavor electrons in 0%–10% central collisions compared with π^0 data [6] and model calculations (curves I [30], II [31], and III [32]). The box at $R_{AA} = 1$ shows the uncertainty in T_{AA}. (b) v_2^{HF} of heavy-flavor electrons in minimum bias collisions compared with π^0 data [29] and the same models. Errors are shown as in Fig. 2.

Figure 3 also shows that the large v_2^{HF} is better reproduced in Langevin-based heavy quark transport calculations [31,32]. A calculation which includes elastic scattering mediated by resonance excitation (curves II) [31] is in good agreement with both the measured R_{AA} and v_2. This is achieved with a small heavy quark relaxation time τ which translates into a diffusion coefficient $D_{\mathrm{HQ}} \times (2\pi T) = 4$–$6$ in this model [31]. Energy loss and flow are also calculated in [32] in terms of D_{HQ} (curves III). While this model fails to simultaneously describe the measured R_{AA} and v_2 with one value for D_{HQ}, the range for D_{HQ} leading to reasonable agreement with R_{AA} or v_2 is similar to that from [31], again implying that small τ and/or $D_{\mathrm{HQ}} \times (2\pi T)$ are required to reproduce the data. Note that D_{HQ} provides an upper bound for the bulk matter's diffusion coefficient D. Using the observation [32] that $D \approx 6 \times \eta/(\epsilon + p)$ with $\epsilon + p = Ts$ at $\mu_B = 0$ provides an estimate for the viscosity to entropy ratio $\eta/s \approx (\frac{4}{3} - 2)/4\pi$, intriguingly close to the conjectured quantum lower bound $1/4\pi$ [33]. This result is consistent with estimates obtained in the light quark sector from elliptic flow [34] and fluctuation analyses [35].

The conjecture of a bound on η/s [16] was obtained using the anti–de Sitter-space/conformal-field-theory correspondence [36,37], which exploits a duality between strongly coupled gauge theories and semiclassical gravitational physics. Recently, such methods were applied to estimate $\hat{q}$ [38] and D_{HQ} in a thermalized plasma [39–41]. These authors also find a small diffusion coefficient $D_{\mathrm{HQ}} \times (2\pi T) \sim 1$.

In conclusion, we have observed large energy loss and flow of heavy quarks in Au + Au collisions at $\sqrt{s_{\mathrm{NN}}} = 200$ GeV. The data provide strong evidence for the coupling of heavy quarks to the produced medium. A short relaxation time of heavy quarks and/or a small diffusion coefficient are required by the data. A model comparison suggests a viscosity to entropy ratio of the medium close to the quantum lower bound, i.e., near a perfect fluid.

We thank the staff of the Collider-Accelerator and Physics Departments at BNL for their vital contributions. We acknowledge support from the Department of Energy and NSF (U.S.A.), MEXT and JSPS (Japan), CNPq and FAPESP (Brazil), NSFC (China), MSMT (Czech Republic), IN2P3/CNRS and CEA (France), BMBF, DAAD, and AvH (Germany), OTKA (Hungary), DAE (India), ISF (Israel), KRF and KOSEF (Korea), MES, RAS, and FAAE (Russia), VR and KAW (Sweden), U.S. CRDF for the FSU, US-Hungarian NSF-OTKA-MTA, and U.S.-Israel BSF.

*Deceased.
†PHENIX spokesperson.
Electronic address: zajc@nevis.columbia.edu

[1] K. Adcox *et al.*, Nucl. Phys. **A757**, 184 (2005).
[2] I. Arsene *et al.*, Nucl. Phys. **A757**, 1 (2005).
[3] B. B. Back *et al.*, Nucl. Phys. **A757**, 28 (2005).
[4] J. Adams *et al.*, Nucl. Phys. **A757**, 102 (2005).
[5] K. Adcox *et al.*, Phys. Rev. Lett. **88**, 022301 (2001).
[6] S. S. Adler *et al.*, Phys. Rev. Lett. **91**, 072301 (2003).
[7] J. Adams *et al.*, Phys. Rev. Lett. **91**, 172302 (2003).
[8] S. S. Adler *et al.*, Phys. Rev. Lett. **96**, 202301 (2006).
[9] S. S. Adler *et al.*, Phys. Rev. Lett. **91**, 182301 (2003).
[10] J. Adams *et al.*, Phys. Rev. Lett. **92**, 052302 (2004).
[11] P. Huovinen *et al.*, Phys. Lett. B **503**, 58 (2001).
[12] T. Hirano and M. Gyulassy, Nucl. Phys. **A769**, 71 (2006).
[13] E. Shuryak, Prog. Part. Nucl. Phys. **53**, 273 (2004).
[14] M. Gyulassy and L. McLerran, Nucl. Phys. **A750**, 30 (2005).
[15] P. F. Kolb and U. W. Heinz, nucl-th/0305084.
[16] P. K. Kovtun, D. T. Son, and A. O. Starinets, Phys. Rev. Lett. **94**, 111601 (2005).
[17] M. Cacciari, P. Nason, and R. Vogt, Phys. Rev. Lett. **95**, 122001 (2005).
[18] A. Adare *et al.*, Phys. Rev. Lett. **97**, 252002 (2006).
[19] S. S. Adler *et al.*, Phys. Rev. Lett. **94**, 082301 (2005).
[20] Y. L. Dokshitzer and D. E. Kharzeev, Phys. Lett. B **519**, 199 (2001).
[21] S. Wicks *et al.*, nucl-th/0512076.
[22] N. Armesto *et al.*, Phys. Rev. D **71**, 054027 (2005).
[23] S. S. Adler *et al.*, Phys. Rev. Lett. **96**, 032301 (2006).
[24] Other measurements for $p + p$ and Au + Au collisions were reported in B. I. Abelev *et al.*, nucl-ex/0607012.
[25] S. S. Adler *et al.*, Phys. Rev. C **72**, 024901 (2005).
[26] K. Adcox *et al.*, Nucl. Instrum. Methods Phys. Res., Sect. A **499**, 469 (2003).
[27] S. S. Adler *et al.*, Phys. Rev. C **69**, 034909 (2004).
[28] A. M. Poskanzer and S. A. Voloshin, Phys. Rev. C **58**, 1671 (1998).
[29] S. S. Adler *et al.*, Phys. Rev. Lett. **96**, 032302 (2006).
[30] N. Armesto *et al.*, Phys. Lett. B **637**, 362 (2006).
[31] H. van Hees, V. Greco, and R. Rapp, Phys. Rev. C **73**, 034913 (2006); (private communication).
[32] G. D. Moore and D. Teaney, Phys. Rev. C **71**, 064904 (2005); (private communication).
[33] Similar estimates of D may be found in J. Casalderrey-Solana and D. Teaney, Phys. Rev. D **74**, 085012 (2006); E. Shuryak, Nucl. Phys. **A783**, 39 (2007).
[34] R. A. Lacey *et al.*, Phys. Rev. Lett. **98**, 092301 (2007).
[35] S. Gavin and M. Abdel-Aziz, Phys. Rev. Lett. **97**, 162302 (2006).
[36] J. M. Maldacena, Adv. Theor. Math. Phys. **2**, 231 (1998).
[37] E. Witten, Adv. Theor. Math. Phys. **2**, 505 (1998).
[38] H. Liu, K. Rajagopal, and U. Wiedemann, Phys. Rev. Lett. **97**, 182301 (2006).
[39] C. P. Herzog *et al.*, J. High Energy Phys. 07 (2006) 013.
[40] S. S. Gubser, Phys. Rev. D **74**, 126005 (2006).
[41] J. J. Friess, S. S. Gubser, and G. Michalogiorgakis, J. High Energy Phys. 09 (2006) 072.

Available online at www.sciencedirect.com
ScienceDirect
Physics Letters B 649 (2007) 359–369
PHYSICS LETTERS B
www.elsevier.com/locate/physletb

Correlated production of p and $\bar{p}$ in Au + Au collisions at $\sqrt{s_{NN}} = 200$ GeV

PHENIX Collaboration

A. Adare [h], S. Afanasiev [v], C. Aidala [i], N.N. Ajitanand [aw], Y. Akiba [aq,ar], H. Al-Bataineh [al], J. Alexander [aw], A. Al-Jamel [al], K. Aoki [ab,aq], L. Aphecetche [ay], R. Armendariz [al], S.H. Aronson [c], J. Asai [ar], E.T. Atomssa [ac], R. Averbeck [ax], T.C. Awes [am], B. Azmoun [c], V. Babintsev [r], G. Baksay [n], L. Baksay [n], A. Baldisseri [k], K.N. Barish [d], P.D. Barnes [ae], B. Bassalleck [ak], S. Bathe [d], S. Batsouli [i,am], V. Baublis [ap], F. Bauer [d], A. Bazilevsky [c], S. Belikov [c,u], R. Bennett [ax], Y. Berdnikov [at], A.A. Bickley [h], M.T. Bjorndal [i], J.G. Boissevain [ae], H. Borel [k], K. Boyle [ax], M.L. Brooks [ae], D.S. Brown [al], D. Bucher [ah], H. Buesching [c], V. Bumazhnov [r], G. Bunce [c,ar], J.M. Burward-Hoy [ae], S. Butsyk [ae,ax], S. Campbell [ax], J.-S. Chai [w], B.S. Chang [bf], J.-L. Charvet [k], S. Chernichenko [r], J. Chiba [x], C.Y. Chi [i], M. Chiu [i,s], I.J. Choi [bf], T. Chujo [bc], P. Chung [aw], A. Churyn [r], V. Cianciolo [am], C.R. Cleven [p], Y. Cobigo [k], B.A. Cole [i], M.P. Comets [an], P. Constantin [u,ae], M. Csanád [m], T. Csörgő [y], T. Dahms [ax], K. Das [o], G. David [c], M.B. Deaton [a], K. Dehmelt [n], H. Delagrange [ay], A. Denisov [r], D. d'Enterria [i], A. Deshpande [ar,ax], E.J. Desmond [c], O. Dietzsch [au], A. Dion [ax], M. Donadelli [au], J.L. Drachenberg [a], O. Drapier [ac], A. Drees [ax], A.K. Dubey [be], A. Durum [r], V. Dzhordzhadze [d,az], Y.V. Efremenko [am], J. Egdemir [ax], F. Ellinghaus [h], W.S. Emam [d], A. Enokizono [q,ad], H. En'yo [aq,ar], B. Espagnon [an], S. Esumi [bb], K.O. Eyser [d], D.E. Fields [ak,ar], M. Finger [e,v], F. Fleuret [ac], S.L. Fokin [aa], B. Forestier [af], Z. Fraenkel [be], J.E. Frantz [i,ax], A. Franz [c], A.D. Frawley [o], K. Fujiwara [aq], Y. Fukao [ab,aq], S.-Y. Fung [d], T. Fusayasu [aj], S. Gadrat [af], I. Garishvili [az], F. Gastineau [ay], M. Germain [ay], A. Glenn [h,az], H. Gong [ax], M. Gonin [ac], J. Gosset [k], Y. Goto [aq,ar], R. Granier de Cassagnac [ac], N. Grau [u], S.V. Greene [bc], M. Grosse Perdekamp [s,ar], T. Gunji [g], H.Å. Gustafsson [ag], T. Hachiya [q,aq], A. Hadj Henni [ay], C. Haegemann [ak], J.S. Haggerty [c], M.N. Hagiwara [a], H. Hamagaki [g], R. Han [ao], H. Harada [q], E.P. Hartouni [ad], K. Haruna [q], M. Harvey [c], E. Haslum [ag], K. Hasuko [aq], R. Hayano [g], M. Heffner [ad], T.K. Hemmick [ax], T. Hester [d], J.M. Heuser [aq], X. He [p], H. Hiejima [s], J.C. Hill [u], R. Hobbs [ak], M. Hohlmann [n], M. Holmes [bc], W. Holzmann [aw], K. Homma [q], B. Hong [z], T. Horaguchi [aq,ba], D. Hornback [az], M.G. Hur [w], T. Ichihara [aq,ar], K. Imai [ab,aq], M. Inaba [bb], Y. Inoue [as,aq], D. Isenhower [a], L. Isenhower [a], M. Ishihara [aq], T. Isobe [g], M. Issah [aw], A. Isupov [v], B.V. Jacak [ax], J. Jia [i], J. Jin [i], O. Jinnouchi [ar], B.M. Johnson [c,*], K.S. Joo [ai], D. Jouan [an], F. Kajihara [g,aq], S. Kametani [g,bd], N. Kamihara [aq,ba], J. Kamin [ax], M. Kaneta [ar], J.H. Kang [bf], H. Kanou [aq,ba], T. Kawagishi [bb], D. Kawall [ar], A.V. Kazantsev [aa], S. Kelly [h], A. Khanzadeev [ap], J. Kikuchi [bd], D.H. Kim [ai], D.J. Kim [bf], E. Kim [av], Y.-S. Kim [w], E. Kinney [h], A. Kiss [m], E. Kistenev [c], A. Kiyomichi [aq], J. Klay [ad], C. Klein-Boesing [ah], L. Kochenda [ap], V. Kochetkov [r], B. Komkov [ap], M. Konno [bb], D. Kotchetkov [d], A. Kozlov [be], A. Král [j], A. Kravitz [i], P.J. Kroon [c], J. Kubart [e,t], G.J. Kunde [ae], N. Kurihara [g], K. Kurita [as,aq], M.J. Kweon [z], Y. Kwon [az,bf], G.S. Kyle [al], R. Lacey [aw], Y.-S. Lai [i], J.G. Lajoie [u], A. Lebedev [u], Y. Le Bornec [an], S. Leckey [ax], D.M. Lee [ae], M.K. Lee [bf], T. Lee [av], M.J. Leitch [ae], M.A.L. Leite [au], B. Lenzi [au], H. Lim [av],

0370-2693/$ – see front matter © 2007 Elsevier B.V. All rights reserved.
doi:10.1016/j.physletb.2007.04.029

T. Liška [j], A. Litvinenko [v], M.X. Liu [ae], X. Li [f], X.H. Li [d], B. Love [bc], D. Lynch [c], C.F. Maguire [bc], Y.I. Makdisi [c], A. Malakhov [v], M.D. Malik [ak], V.I. Manko [aa], Y. Mao [ao,aq], L. Mašek [e,t], H. Masui [bb], F. Matathias [i,ax], M.C. McCain [s], M. McCumber [ax], P.L. McGaughey [ae], Y. Miake [bb], P. Mikeš [e,t], K. Miki [bb], T.E. Miller [bc], A. Milov [ax], S. Mioduszewski [c], G.C. Mishra [p], M. Mishra [b], J.T. Mitchell [c], M. Mitrovski [aw], A. Morreale [d], D.P. Morrison [c], J.M. Moss [ae], T.V. Moukhanova [aa], D. Mukhopadhyay [bc], J. Murata [as,aq], S. Nagamiya [x], Y. Nagata [bb], J.L. Nagle [h], M. Naglis [be], I. Nakagawa [aq,ar], Y. Nakamiya [q], T. Nakamura [q], K. Nakano [aq,ba], J. Newby [ad], M. Nguyen [ax], B.E. Norman [ae], A.S. Nyanin [aa], J. Nystrand [ag], E. O'Brien [c], S.X. Oda [g], C.A. Ogilvie [u], H. Ohnishi [aq], I.D. Ojha [bc], H. Okada [ab,aq], K. Okada [ar], M. Oka [bb], O.O. Omiwade [a], A. Oskarsson [ag], I. Otterlund [ag], M. Ouchida [q], K. Ozawa [g], R. Pak [c], D. Pal [bc], A.P.T. Palounek [ae], V. Pantuev [ax], V. Papavassiliou [al], J. Park [av], W.J. Park [z], S.F. Pate [al], H. Pei [u], J.-C. Peng [s], H. Pereira [k], V. Peresedov [v], D.Yu. Peressounko [aa], C. Pinkenburg [c], R.P. Pisani [c], M.L. Purschke [c], A.K. Purwar [ae,ax], H. Qu [p], J. Rak [u,ak], A. Rakotozafindrabe [ac], I. Ravinovich [be], K.F. Read [am,az], S. Rembeczki [n], M. Reuter [ax], K. Reygers [ah], V. Riabov [ap], Y. Riabov [ap], G. Roche [af], A. Romana [ac,✠], M. Rosati [u], S.S.E. Rosendahl [ag], P. Rosnet [af], P. Rukoyatkin [v], V.L. Rykov [aq], S.S. Ryu [bf], B. Sahlmueller [ah], N. Saito [ab,aq,ar], T. Sakaguchi [c,g,bd], S. Sakai [bb], H. Sakata [q], V. Samsonov [ap], H.D. Sato [ab,aq], S. Sato [c,x,bb], S. Sawada [x], J. Seele [h], R. Seidl [s], V. Semenov [r], R. Seto [d], D. Sharma [be], T.K. Shea [c], I. Shein [r], A. Shevel [ap,aw], T.-A. Shibata [aq,ba], K. Shigaki [q], M. Shimomura [bb], T. Shohjoh [bb], K. Shoji [ab,aq], A. Sickles [ax], C.L. Silva [au], D. Silvermyr [am], C. Silvestre [k], K.S. Sim [z], C.P. Singh [b], V. Singh [b], S. Skutnik [u], M. Slunečka [e,v], W.C. Smith [a], A. Soldatov [r], R.A. Soltz [ad], W.E. Sondheim [ae], S.P. Sorensen [az], I.V. Sourikova [c], F. Staley [k], P.W. Stankus [am], E. Stenlund [ag], M. Stepanov [al], A. Ster [y], S.P. Stoll [c], T. Sugitate [q], C. Suire [an], J.P. Sullivan [ae], J. Sziklai [y], T. Tabaru [ar], S. Takagi [bb], E.M. Takagui [au], A. Taketani [aq,ar], K.H. Tanaka [x], Y. Tanaka [aj], K. Tanida [aq,ar], M.J. Tannenbaum [c], A. Taranenko [aw], P. Tarján [l], T.L. Thomas [ak], M. Togawa [ab,aq], A. Toia [ax], J. Tojo [aq], L. Tomášek [t], H. Torii [aq], R.S. Towell [a], V.-N. Tram [ac], I. Tserruya [be], Y. Tsuchimoto [q,aq], S.K. Tuli [b], H. Tydesjö [ag], N. Tyurin [r], C. Vale [u], H. Valle [bc], H.W. van Hecke [ae], J. Velkovska [bc], R. Vertesi [l], A.A. Vinogradov [aa], M. Virius [j], V. Vrba [t], E. Vznuzdaev [ap], M. Wagner [ab,aq], D. Walker [ax], X.R. Wang [al], Y. Watanabe [aq,ar], J. Wessels [ah], S.N. White [c], N. Willis [an], D. Winter [i], C.L. Woody [c], M. Wysocki [h], W. Xie [d,ar], Y. Yamaguchi [bd], A. Yanovich [r], Z. Yasin [d], J. Ying [p], S. Yokkaichi [aq,ar], G.R. Young [am], I. Younus [ak], I.E. Yushmanov [aa], W.A. Zajc, [i,*] O. Zaudtke [ah], C. Zhang [i,am], S. Zhou [f], J. Zimányi, [y,✠], L. Zolin [v]

[a] *Abilene Christian University, Abilene, TX 79699, USA*
[b] *Department of Physics, Banaras Hindu University, Varanasi 221005, India*
[c] *Brookhaven National Laboratory, Upton, NY 11973-5000, USA*
[d] *University of California–Riverside, Riverside, CA 92521, USA*
[e] *Charles University, Ovocný trh 5, Praha 1, 116 36 Prague, Czech Republic*
[f] *China Institute of Atomic Energy (CIAE), Beijing, People's Republic of China*
[g] *Center for Nuclear Study, Graduate School of Science, University of Tokyo, 7-3-1 Hongo, Bunkyo, Tokyo 113-0033, Japan*
[h] *University of Colorado, Boulder, CO 80309, USA*
[i] *Columbia University, New York, NY 10027*
and Nevis Laboratories, Irvington, NY 10533, USA
[j] *Czech Technical University, Zikova 4, 166 36 Prague 6, Czech Republic*
[k] *Dapnia, CEA Saclay, F-91191 Gif-sur-Yvette, France*
[l] *Debrecen University, Egyetem tér 1, H-4010 Debrecen, Hungary*
[m] *ELTE, Eötvös Loránd University, Pázmány P. s. 1/A, H-1117 Budapest, Hungary*
[n] *Florida Institute of Technology, Melbourne, FL 32901, USA*
[o] *Florida State University, Tallahassee, FL 32306, USA*
[p] *Georgia State University, Atlanta, GA 30303, USA*
[q] *Hiroshima University, Kagamiyama, Higashi-Hiroshima 739-8526, Japan*
[r] *IHEP Protvino, State Research Center of Russian Federation, Institute for High Energy Physics, Protvino 142281, Russia*
[s] *University of Illinois at Urbana-Champaign, Urbana, IL 61801, USA*
[t] *Institute of Physics, Academy of Sciences of the Czech Republic, Na Slovance 2, 182 21 Prague 8, Czech Republic*
[u] *Iowa State University, Ames, IA 50011, USA*

[v] Joint Institute for Nuclear Research, 141980 Dubna, Moscow Region, Russia
[w] KAERI, Cyclotron Application Laboratory, Seoul, South Korea
[x] KEK, High Energy Accelerator Research Organization, Tsukuba, Ibaraki 305-0801, Japan
[y] KFKI Research Institute for Particle and Nuclear Physics of the Hungarian Academy of Sciences (MTA KFKI RMKI), H-1525 Budapest 114, PO Box 49, Budapest, Hungary
[z] Korea University, Seoul 136-701, South Korea
[aa] Russian Research Center "Kurchatov Institute", Moscow, Russia
[ab] Kyoto University, Kyoto 606-8502, Japan
[ac] Laboratoire Leprince-Ringuet, Ecole Polytechnique, CNRS-IN2P3, Route de Saclay, F-91128 Palaiseau, France
[ad] Lawrence Livermore National Laboratory, Livermore, CA 94550, USA
[ae] Los Alamos National Laboratory, Los Alamos, NM 87545, USA
[af] LPC, Université Blaise Pascal, CNRS-IN2P3, Clermont-Fd, 63177 Aubiere Cedex, France
[ag] Department of Physics, Lund University, Box 118, SE-221 00 Lund, Sweden
[ah] Institut für Kernphysik, University of Muenster, D-48149 Muenster, Germany
[ai] Myongji University, Yongin, Kyonggido 449-728, Korea
[aj] Nagasaki Institute of Applied Science, Nagasaki-shi, Nagasaki 851-0193, Japan
[ak] University of New Mexico, Albuquerque, NM 87131, USA
[al] New Mexico State University, Las Cruces, NM 88003, USA
[am] Oak Ridge National Laboratory, Oak Ridge, TN 37831, USA
[an] IPN-Orsay, Universite Paris Sud, CNRS-IN2P3, BP1, F-91406 Orsay, France
[ao] Peking University, Beijing, People's Republic of China
[ap] PNPI, Petersburg Nuclear Physics Institute, Gatchina, Leningrad region 188300, Russia
[aq] RIKEN, The Institute of Physical and Chemical Research, Wako, Saitama 351-0198, Japan
[ar] RIKEN BNL Research Center, Brookhaven National Laboratory, Upton, NY 11973-5000, USA
[as] Physics Department, Rikkyo University, 3-34-1 Nishi-Ikebukuro, Toshima, Tokyo 171-8501, Japan
[at] Saint Petersburg State Polytechnic University, St. Petersburg, Russia
[au] Universidade de São Paulo, Instituto de Física, Caixa Postal 66318, São Paulo CEP05315-970, Brazil
[av] System Electronics Laboratory, Seoul National University, Seoul, South Korea
[aw] Chemistry Department, Stony Brook University, Stony Brook, SUNY, NY 11794-3400, USA
[ax] Department of Physics and Astronomy, Stony Brook University, SUNY, Stony Brook, NY 11794, USA
[ay] SUBATECH (Ecole des Mines de Nantes, CNRS-IN2P3, Université de Nantes) BP 20722-44307, Nantes, France
[az] University of Tennessee, Knoxville, TN 37996, USA
[ba] Department of Physics, Tokyo Institute of Technology, Oh-okayama, Meguro, Tokyo 152-8551, Japan
[bb] Institute of Physics, University of Tsukuba, Tsukuba, Ibaraki 305, Japan
[bc] Vanderbilt University, Nashville, TN 37235, USA
[bd] Waseda University, Advanced Research Institute for Science and Engineering, 17 Kikui-cho, Shinjuku-ku, Tokyo 162-0044, Japan
[be] Weizmann Institute, Rehovot 76100, Israel
[bf] Yonsei University, IPAP, Seoul 120-749, South Korea

Received 21 November 2006; received in revised form 4 April 2007; accepted 10 April 2007

Available online 19 April 2007

Editor: V. Metag

Abstract

Correlations between p and $\bar{p}$ at transverse momenta typical of enhanced baryon production in Au + Au collisions are reported. The PHENIX experiment has measured same and opposite sign baryon pairs in Au + Au collisions at $\sqrt{s_{NN}} = 200$ GeV. Correlated production of p and $\bar{p}$ with the trigger particle from the range $2.5 < p_T < 4.0$ GeV/c and the associated particle with $1.8 < p_T < 2.5$ GeV/c is observed to be nearly independent of the centrality of the collisions. Same sign pairs show no correlation at any centrality. The conditional yield of mesons triggered by baryons (and anti-baryons) and mesons in the same p_T range rises with increasing centrality, except for the most central collisions, where baryons show a significantly smaller number of associated mesons. These data are consistent with a picture in which hard scattered partons produce correlated p and $\bar{p}$ in the p_T region of the baryon excess.
© 2007 Elsevier B.V. All rights reserved.

1. Introduction

A remarkable feature of relativistic heavy ion collisions at RHIC energies is the enhanced production of baryons and anti-baryons relative to mesons at intermediate transverse momenta ($2 < p_T < 5$ GeV/c) [1,2]. In central Au + Au collisions at

* Corresponding authors.
E-mail addresses: brant@bnl.gov (B.M. Johnson), zajc@nevis.columbia.edu (W.A. Zajc).
✠ Deceased.

$\sqrt{s_{NN}} = 200$ GeV the baryon/meson ratio is a factor of three higher than in $p + p$ collisions, while in peripheral Au + Au collisions and in d + Au collisions [3] at the same energy only a small increase ($< 20\%$) is observed. The production of protons and anti-protons at intermediate p_T in Au + Au collisions scales with the number of binary nucleon-nucleon collisions [1], contrary to the suppression of pion production [4]. Similar behavior has been observed for strange baryons (Λ and $\bar{\Lambda}$) and mesons (K^0_S) [5].

In this same momentum range and center of mass energy in $p + p$ collisions the dominant production mechanism shifts from soft processes characterized by non-perturbative low momentum transfer scattering to hard scattering processes characterized by large momentum transfer parton–parton scattering followed by fragmentation of the scattered partons into final state hadrons. Pion production in $\sqrt{s_{NN}} = 200$ GeV $p + p$ collisions is reasonably well described by perturbative QCD (pQCD) down to $p_T \approx 2$ GeV [6]. There are large variations in the p and $\bar{p}$ yield among various fragmentation functions, which make it difficult to establish a definite pQCD expectation for the p and $\bar{p}$ spectra in $p + p$ collisions [7]. Another estimate of the transition from hard to soft physics can be obtained from the $x_T = 2p_T/\sqrt{s}$ scaling of the single particle cross sections. The cross section can be written as [8,9]:

$$E\frac{d^3\sigma}{dp^3} = \frac{1}{\sqrt{s}^{n(\sqrt{s},x_T)}} G(x_T). \tag{1}$$

At high x_T the value of n is found to be independent of both $\sqrt{s}$ and x_T. Since the power of n is related to the quantum exchanged and the number of point-like scatterers, the x_T region corresponding to the asymptotic n value is understood to be the region where particle production is dominated by hard scattering. Recent measurements of the p and $\bar{p}$ and $\pi^{\pm}$ spectra show the cross section can be described by consistent values of n for $p_T > 2$ GeV/c for both the $\pi^{\pm}$ ($n = 6.8 \pm 0.5$) and p and $\bar{p}$ ($n = 6.5 \pm 1.0$) [7] indicating, together with the agreement between the data and pQCD calculations at high p_T [6,7], that at $\sqrt{s} = 200$ GeV the transition from hard to soft particle production happens at $p_T \approx 2$ GeV/c. Since the fragmentation process is believed to be independent of center of mass energy or collision system, baryon and anti-baryon production in central Au + Au collisions appears inconsistent with hard-scattering followed by a universal fragmentation.

The theoretical models that are successful in reproducing the measured single particle spectra, baryon/meson ratios and the nuclear modification factors usually invoke some mechanism to extend the range of soft particle production for baryons to higher p_T than that for mesons. This is either done based on the particle mass (in hydrodynamics models [10,11]) or on the quark content (quark recombination models [12–14]). An alternative approach, which involves production of baryons through gluon junctions, has also been shown to reproduce the data [15]. In this Letter we study two-particle angular correlations involving p, $\bar{p}$, and mesons ($\pi^{\pm}$, $K^{\pm}$). This approach gives information about the hadron production in hard-scattering processes, which is inaccessible from single particle measurements.

Previous studies [16–18] in Au + Au collisions show that at intermediate p_T particles are correlated in azimuthal angle in a manner consistent with jet fragmentation. Namely, particles are emitted close together when they come from fragmentation of the same jet (near side correlations) or approximately back-to-back when they come from the fragmentation of the associated di-jet (away side correlations). Strong modifications of the yields, shapes and particle composition of these correlations are seen from peripheral to central Au + Au collisions. The yields are quantified by the number of associated particles per trigger (conditional yield) after the combinatorial background from the underlying event has been subtracted. The conditional yield is measured separately for the near and away side correlations. The near side conditional yield increases [16–18] with centrality and the away side shape has a peak at $\Delta\phi \approx 2$ rad and no peak at $\Delta\phi \approx \pi$ rad. Correlations between identified baryons (p, $\bar{p}$) and charged hadrons [17] rule out baryon production from $2.5 < p_T < 4.0$ GeV/c as coming dominantly from a thermal parton source with no correlations [17,19]. Moreover, the magnitude of baryon and meson triggered correlations with other charged hadrons in the same event is similar, suggesting that the baryon excess in the intermediate p_T range is associated with hard parton–parton scattering [17].

There are two main recombination models which have attempted to address the connection between hard scattering and recombination. The model of Hwa and Yang [14] has calculated that fragmenting partons from hard scattering process have a high probability to recombine with thermal quarks from the medium. The model of Fries et al. [19] finds these effects to be unimportant, but has correlations from fast partons losing energy in the medium creating a region around the parton trajectory with a slightly increased temperature and with additional momentum in the direction of the energetic parton. Partons from this region then recombine into hadrons, which are correlated with the fast parton direction and with each other.

In order to further explore the jet-like structure of the baryon excess, here we present results on the angular correlations between two identified particles. The baryon production mechanism is studied via correlations between two charge separated p and $\bar{p}$. The trigger particles are taken to be all p or $\bar{p}$ measured within the given p_T window, regardless of whether the event has any associated particles. Thus, an increasing fraction of uncorrelated trigger particles will result in a dilution of the conditional yield. However, if the main source of the baryon excess is jets that fragment outside the medium, the charge dependence of correlations between p and $\bar{p}$ should be the same from peripheral collisions, where baryon production at intermediate p_T is nearly unmodified from $p + p$ collisions, to central collisions. A centrality dependence of the charge combinations of p and $\bar{p}$ correlations would provide evidence for novel baryon production scenarios in central Au + Au collisions.

Correlations between baryon and meson triggers with associated mesons are studied as well. Meson trigger-associated mesons (meson–meson) correlations provide a baseline for jet fragmentation in Au + Au collisions. Separating the baryon–hadron correlations from [17] into baryon–meson and baryon–baryon correlations allows greater sensitivity to possible recom-

bination effects. The recombination model of Fries et al. [19] predicts a greater amplification of baryon–baryon correlations relative to baryon–meson correlations on the near side because of the larger number of possible correlations between the valence quarks.

Near side correlations from jets in $p+p$ collisions are observed to be balanced by away side correlations from the associated di-jet [20]. The away side correlations at intermediate p_T in Au + Au collisions have been shown to have a modified shape in Au + Au collisions [18]. Here we measure the away side correlations with both particles identified in order to see if the dependence on the trigger and associated particle type changes with centrality. If the baryon and meson triggers are from hard scattering with approximately the same momentum transfer, we expect the away side correlations to be independent of the trigger particle type.

The Letter is organized as follows: Section 2 describes the experimental method and setup, the results are presented in Section 3, and Section 4 is devoted to discussion.

2. Experimental procedure and setup

Two particle correlations have been widely used to study jets in heavy ion collisions [16–18,21,22] where, due to the high multiplicity and moderate jet energy the direct reconstruction of jets by standard algorithms, utilizing hadronic calorimetry and cluster algorithms, is not yet possible. In this approach particles are divided into two classes, *triggers* and *associated particles*. We classify the triggers and associated particles by their p_T, particle type and charge. The triggers have $2.5 < p_T < 4.0$ GeV/c and the associated particles have $1.8 < p_T < 2.5$ GeV/c. Thus both particles originate from a region in p_T that is consistent with hard scattering in $p+p$ collisions and shows an excess of baryons relative to mesons in Au + Au collisions. A distribution of the azimuthal angular difference $\Delta\phi$ between trigger-associated particle pairs is constructed and normalized by the number of triggers.

The data presented here are based on an analysis of 600M Au + Au events collected by the PHENIX experiment in 2004 with a minimum bias trigger. Charged particles are reconstructed in the central arms of PHENIX using a combination of drift chambers and one layer of multi-wire proportional chamber with pad readout (PC1) [23], each covering $\Delta\phi = \pi/2$ in azimuthal angle and $|\eta| < 0.35$ in pseudorapity. The pattern recognition is based on a combinatorial Hough transform in the track bend plane. The polar angle is determined from the hit position in PC1 and the collision vertex along the beam axis measured by the Beam–Beam Counters (BBC). The BBC are positioned at $|\eta| = 3$–4. Particles are identified by their mass calculated from the measured momentum and time-of-flight information. The global start time is provided by BBC, while the stop time is measured by the PHENIX high resolution time of flight detector (TOF) or the lead-scintillator electromagnetic calorimeter (EMCal), which provide a 4σ K/p separation up to $p_T \approx 4.0$ GeV/c and $p_T \approx 2.5$ GeV/c, respectively. The trigger particles are identified in the TOF, which covers a portion of the PHENIX East arm ($\Delta\phi = \pi/4$). The associated particles are identified in either the EMCal or the TOF, which together cover the entire PHENIX azimuthal acceptance. For both triggers and associated particles a 2σ spatial match is required between the track projection and the hit position in the particle identification detector. Monte Carlo studies have shown that, due to the decay kinematics in the trigger and partner p_T range used here, the contribution from $\Lambda \to p\pi^-$ and $\bar{\Lambda} \to \bar{p}\pi^+$ resonance decays, which could produce correlations mimicking the jet signal, is negligible.

We perform a correction for the non-uniform pair acceptance in $\Delta\phi$ in PHENIX. This correction is constructed by measuring the $\Delta\phi$ distribution from trigger-associated particle pairs where each particle comes from a different event. Dividing the same-event by the mixed-event distribution removes the effects of the PHENIX acceptance and leaves only the true correlations. The multiplicity of the combinatorial background of the underlying event is determined absolutely by the convolution of the measured trigger and associated particle single particle rates with an additional correction for centrality correlations [17], which raises the combinatorial background level by $\approx 0.2\%$ in the most central collisions and $\approx 25\%$ in peripheral collisions. A correction for the associated particle reconstruction efficiency and acceptance is applied by matching the observed rates for the corresponding single particle spectra measured in [2]. No correction has been made for p and $\bar{p}$ originating from weak decays of Λ and $\bar{\Lambda}$; approximately 30% of the measured p and $\bar{p}$ are from these decays [2]. The PHENIX η acceptance is narrow compared to the width of the typical jet cone in $p+p$ collisions [20], so we do not measure the entire conditional yield associated with the trigger particle in the associated particle p_T range. The results are reported for both trigger and associated particles within $|\eta| < 0.35$ without extrapolating in pseudorapidity. The centrality dependence of the conditional yields allows us to quantify changes in the jet-like correlations as a function of centrality and particle type, despite the limited acceptance.

Elliptic flow is an azimuthal correlation between particles due to the anisotropy in the initial collision geometry. This angular correlation is unrelated to jet fragmentation and thus produces a background for this measurement. The correlations due to elliptic flow are removed by modulating the azimuthally uniform combinatorial background by $1 + 2v_2^{\text{trig}} v_2^{\text{part}} \cos(\Delta\phi)$ where v_2^{trig} and v_2^{part} represent the strength of the elliptic flow signal for the trigger and associated particle, respectively. The v_2 parameter is defined by the 2nd harmonic of the azimuthal anisotropy, $v_2 = \langle \cos[2(\phi - \Psi)] \rangle$, where ϕ is the azimuthal angle of emitted particle, Ψ is the azimuthal angle of event plane in a given collision, and the bracket denotes the average over all particles and events [24]. We measure v_2 of charged baryons and mesons at mid-rapidity, $|\eta| < 0.35$, for each centrality and p_T bin through the event plane method [24]. The azimuthal angle of the event plane is determined by the BBC using the elliptic moment definition [25]. The large rapidity difference, $|\Delta\eta| \sim 3$, between the central arms and the BBCs helps to reduce the non-flow contributions to the measured v_2, especially those arising from di-jets. The systematic errors on the v_2 value are dominated by the uncertainty in the correction for the event

Table 1
The v_2 values and statistical and systematic errors for the centrality and p_T bins used in this analysis

Centrality	v_2 Values ± Statistical Error ± Systematic Error		
	Triggers	Associated particles	
	$2.5 < p_T < 4.0$ GeV/c	$1.8 < p_T < 2.0$ GeV/c	$2.0 < p_T < 2.5$ GeV/c
Baryons			
0–5%	$0.083 \pm 0.006 \pm 0.017$	$0.064 \pm 0.004 \pm 0.013$	$0.068 \pm 0.004 \pm 0.014$
5–10%	$0.126 \pm 0.005 \pm 0.016$	$0.089 \pm 0.003 \pm 0.011$	$0.108 \pm 0.003 \pm 0.013$
10–20%	$0.176 \pm 0.003 \pm 0.013$	$0.134 \pm 0.002 \pm 0.010$	$0.154 \pm 0.002 \pm 0.011$
20–40%	$0.234 \pm 0.003 \pm 0.014$	$0.182 \pm 0.002 \pm 0.011$	$0.203 \pm 0.002 \pm 0.012$
40–60%	$0.264 \pm 0.006 \pm 0.015$	$0.211 \pm 0.004 \pm 0.012$	$0.235 \pm 0.004 \pm 0.013$
60–90%	$0.276 \pm 0.033 \pm 0.044$	$0.158 \pm 0.023 \pm 0.025$	$0.179 \pm 0.021 \pm 0.029$
Mesons			
0–5%	$0.072 \pm 0.007 \pm 0.015$	$0.067 \pm 0.003 \pm 0.014$	$0.078 \pm 0.003 \pm 0.016$
5–10%	$0.109 \pm 0.005 \pm 0.014$	$0.102 \pm 0.002 \pm 0.013$	$0.103 \pm 0.002 \pm 0.013$
10–20%	$0.142 \pm 0.003 \pm 0.011$	$0.133 \pm 0.001 \pm 0.010$	$0.140 \pm 0.001 \pm 0.010$
20–40%	$0.185 \pm 0.003 \pm 0.011$	$0.172 \pm 0.001 \pm 0.010$	$0.180 \pm 0.001 \pm 0.011$
40–60%	$0.186 \pm 0.006 \pm 0.010$	$0.188 \pm 0.003 \pm 0.011$	$0.191 \pm 0.003 \pm 0.011$
60–90%	$0.178 \pm 0.027 \pm 0.029$	$0.173 \pm 0.013 \pm 0.028$	$0.172 \pm 0.014 \pm 0.28$

plane resolution [25]. The v_2 values used in this analysis are shown in Table 1. They are consistent with prior PHENIX v_2 measurements [25] in the common centrality bins. The analysis has been performed separately for associated particles in two transverse momentum ranges: $1.8 < p_T < 2.0$ GeV/c and $2.0 < p_T < 2.5$ GeV/c. This minimizes effects due to the variation of v_2 over the width of the associated particle p_T bin. In order to minimize the statistical errors, the results shown here are a sum of the two bins.

The systematic errors on the conditional yields are due to the systematic and statistical uncertainties on the v_2 values, the uncertainty in the corrections for the centrality correlations in the combinatorial background and in the centrality dependence of the efficiency corrections. The systematic error on the centrality dependence of the efficiency corrections is 6% for meson associated particles and 5% for inclusive p, $\bar{p}$ and baryon (p and $\bar{p}$ combined) associated particles independent of centrality. The size of the systematic error on the conditional yield attributed to a systematic uncertainty in the elliptic flow determination is largest in the most central collisions. The systematic error on the centrality correlations is $\approx 60\%$ of the correction in central collisions and $\approx 5\%$ of the correction in peripheral collisions. There are additional systematic errors (not shown in Section 3 plots) that come from the centrality independent normalization of the efficiency corrections and move all points with the same associated particle type together. These are 8.9% for p and $\bar{p}$ associated particles, 11.4% for baryon (p and $\bar{p}$) associated particles, and 13.6% for meson associated particles.

3. Results

Our goal is to study the jet contribution to baryon and anti-baryon production at intermediate p_T where an excess of baryons over mesons is observed. Thus we choose trigger baryons from the range $2.5 < p_T < 4.0$ GeV/c and associated particles in the range $1.8 < p_T < 2.5$ GeV/c and construct two-particle azimuthal correlation distributions. With the larger data sample obtained in 2004 we are able to extend our previous measurements [17] by studying the proton and anti-proton triggers, as well as identifying the associated particles. Several combinations of trigger-associated particle types are presented below.

We first study baryon–baryon correlation, where both trigger and associated particles are identified as either p or $\bar{p}$. The left panel of Fig. 1 shows the azimuthal angular difference, $\Delta\phi$, between charge inclusive p and $\bar{p}$ measured in six centrality classes. The solid lines show the combinatorial background level modulated by the expected correlation due to elliptic flow, $B(1 + 2v_2^{\text{trig}} v_2^{\text{assoc}} \cos(2\Delta\phi))$. The excess is attributed to jet correlations, $J(\Delta\phi)$. The azimuthal angular difference distributions are then described by:

$$\frac{1}{N_{\text{trig}}} \frac{dN}{d\Delta\phi} = B\left(1 + 2v_2^{\text{trig}} v_2^{\text{assoc}} \cos(2\Delta\phi)\right) + J(\Delta\phi). \qquad (2)$$

The region around $\Delta\phi = \pi/2$ has very limited acceptance for pairs due to the requirement that the trigger particle be measured in the TOF detector. The right panels of Fig. 1 show the $J(\Delta\phi)$ for three centralities after the combinatorial background subtraction. There is a pronounced jet peak at small relative angles (near side), however, there is no visible structure on the away side, where the yields are slightly above or at the level of the combinatorial background.

To further explore the observed structures, in Figs. 2 and 3 we perform the analysis separately for each charge combination. The correlations were measured in the same p_T range as in Fig. 1. A near side excess can be seen over the combinatorial background for opposite sign pairs (left panel of Fig. 2 and right panel of Fig. 3) while no significant excess is seen for the same sign pairs (right panel of Fig. 2 and left panel of Fig. 3).

The correlations involving mesons as associated particles provide a comparison baseline for the baryon–baryon correlations. We study both baryon and meson triggers associated with mesons. The left panel of Fig. 4 shows the baryon–meson and meson–meson correlations. The right panels of Fig. 4 show

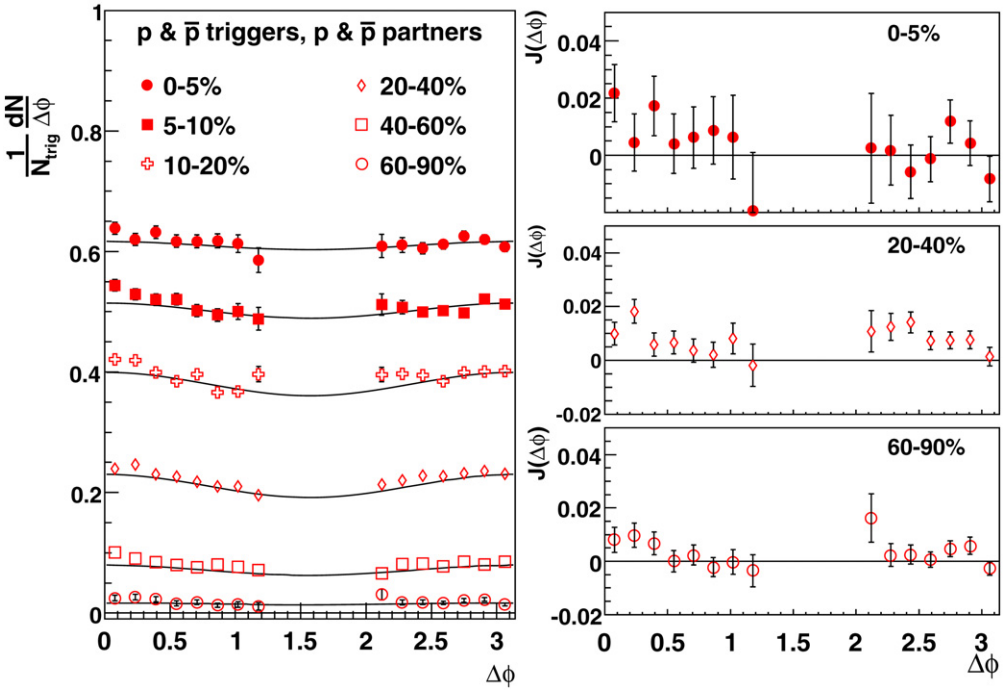

Fig. 1. Left: $\frac{1}{N_{\text{trig}}}\frac{dN}{d\Delta\phi}$ distributions for charge-inclusive baryon triggers and associated particles for six centrality bins. Triggers have $2.5 < p_T < 4.0$ GeV/c and associated particles have $1.8 < p_T < 2.5$ GeV/c. The solid lines indicate the combinatorial background modulated by elliptic flow. Right: Jet distributions, $J(\Delta\phi)$, after combinatorial background and elliptic flow subtraction for 0–5% (top), 20–40% (middle) and 60–90% (bottom) centralities. In all panels, only the statistical errors are shown.

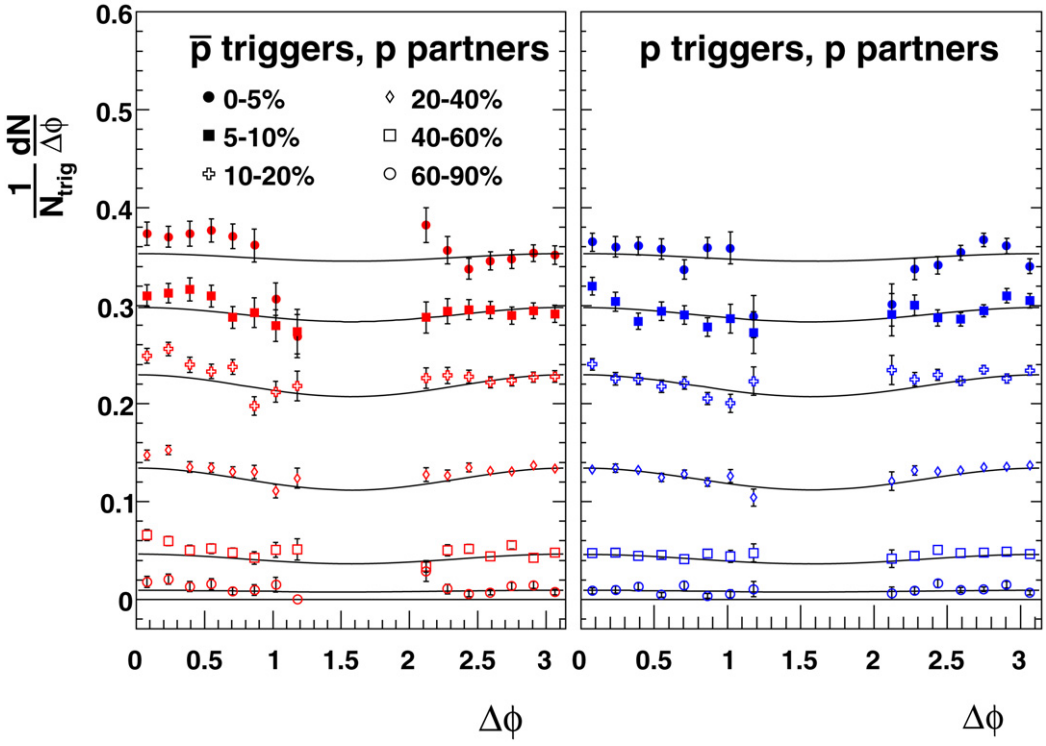

Fig. 2. $\frac{1}{N_{\text{trig}}}\frac{dN}{d\Delta\phi}$ distributions for charge selected $\bar{p}$ (left) and p (right) triggers both with associated p for six centrality bins. Triggers have $2.5 < p_T < 4.0$ GeV/c and associated particles have $1.8 < p_T < 2.5$ GeV/c. The solid lines indicate the combinatorial background modulated by elliptic flow. Only the statistical errors are shown.

$J(\Delta\phi)$ for the 0–5%, 20–40% and 60–90% centrality classes. While in the mid-central collisions the meson and baryon triggered distributions agree well, the baryon triggered distributions in the most central collisions lie systematically below the meson triggered points both before and after the combinatorial background subtraction on the near side.

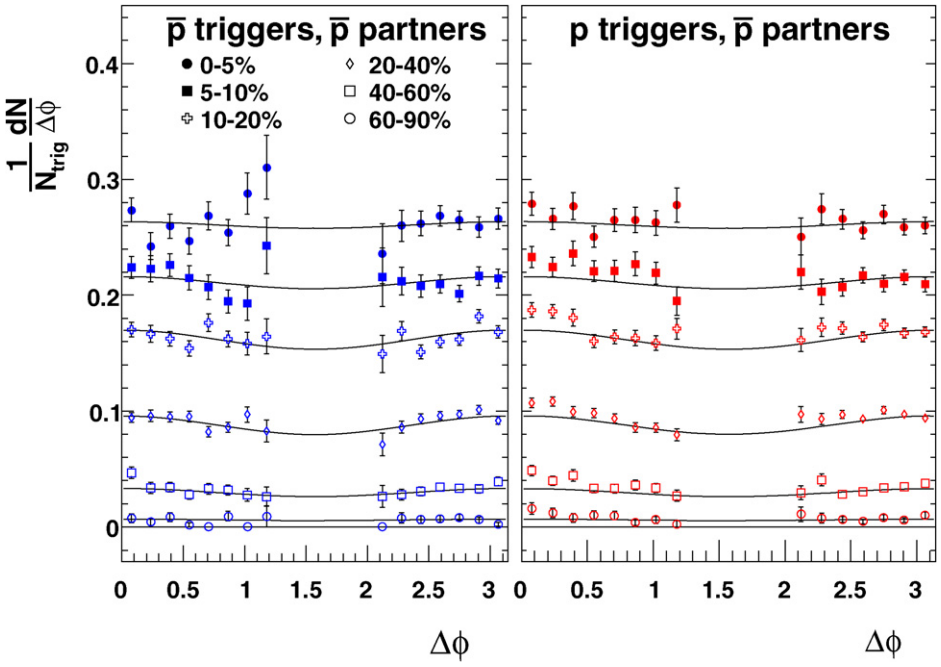

Fig. 3. $\frac{1}{N_{\text{trig}}}\frac{dN}{d\Delta\phi}$ distributions for charge selected $\bar{p}$ (left) and p (right) triggers both with associated $\bar{p}$ for six centrality bins. Triggers have $2.5 < p_T < 4.0$ GeV/c and associated particles have $1.8 < p_T < 2.5$ GeV/c. The solid lines indicate the combinatorial background modulated by elliptic flow. Only the statistical errors are shown.

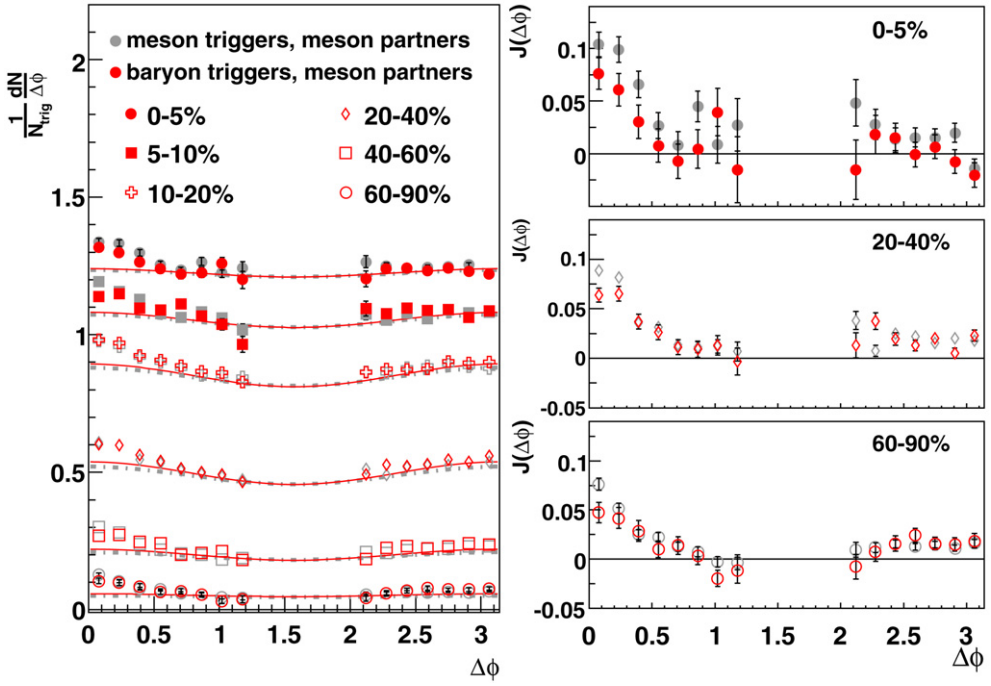

Fig. 4. Left: $\frac{1}{N_{\text{trig}}}\frac{dN}{d\Delta\phi}$ distributions for charge-inclusive baryon and meson triggers and associated mesons for six centrality bins. Triggers have $2.5 < p_T < 4.0$ GeV/c and associated particles have $1.8 < p_T < 2.5$ GeV/c. The solid (dashed) lines indicate the combinatorial background modulated by elliptic flow for baryon (meson) triggers. Right: Jet distributions, $J(\Delta\phi)$, after combinatorial background and elliptic flow subtraction for 0–5% (top), 20–40% (middle) and 60–90% (bottom) centralities. In all panels, only the statistical errors are shown.

To quantify the observed differences in the various trigger-associated particle combinations, we integrate the $J(\Delta\phi)$ distributions in the regions $0.0 < \Delta\phi < 0.94$ rad and $\pi - 0.94 < \Delta\phi < \pi$ rad to obtain the near-side and the away-side conditional yields, respectively. Figs. 5 and 6 show the conditional yield per trigger as a function of the number participating nucleons (N_{part}). The results were obtained from the data in Figs. 2 and 3 (solid points) and Fig. 1 (open points) by integrating the $J(\Delta\phi)$ in the $\Delta\phi$ ranges specified above. This integration range excludes a large part of the away side shape modifica-

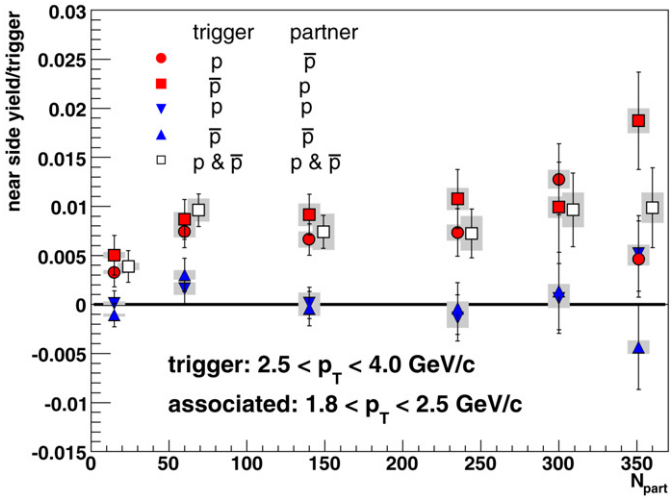

Fig. 5. Conditional yields per trigger on the near side for charge selected (solid points) and charge selected (hollow points) p and $\bar{p}$ correlations. Triggers have $2.5 < p_T < 4.0$ GeV/c and associated particles have $1.8 < p_T < 2.5$ GeV/c. The error bars are the statistical errors and the boxes show the systematic errors. There is an 11.4% additional normalization error on baryon associated particle points and 8.9% each on the p and $\bar{p}$ associated particle points.

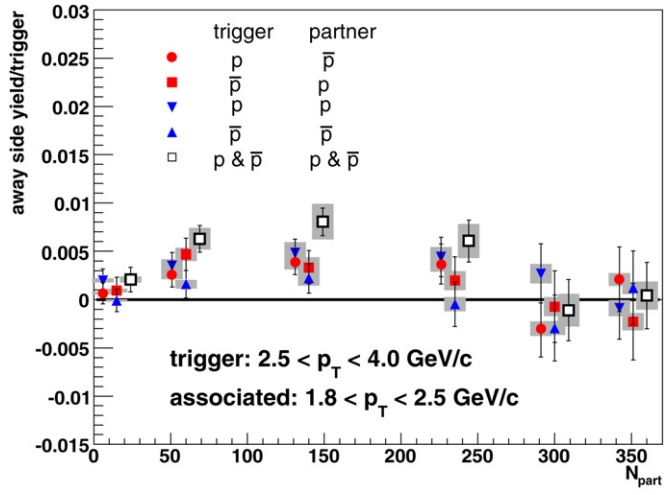

Fig. 6. Conditional yields per trigger on the away side for charge selected (solid points) and charge selected (hollow points) p and $\bar{p}$ correlations. Triggers have $2.5 < p_T < 4.0$ GeV/c and associated particles have $1.8 < p_T < 2.5$ GeV/c. The error bars are the statistical errors and the boxes show the systematic errors. The additional normalization error is the same as in Fig. 5.

tions observed in [18]. The small integration range is used in this analysis only because of the limited acceptance around $\Delta\phi = \pi/2$ due to the requirement to measure the trigger particle in the TOF. These results quantify the centrality and particle type dependence of the jet-like correlations. Fig. 5 shows that the correlations between opposite sign baryon pairs produce a significant non-zero conditional yield that is nearly independent of centrality and that there is no significant yield associated with same sign pairs. The open points in Fig. 5 are from the charge inclusive analysis and show that the conditional yield does come mainly from opposite sign pairs. For all but the most peripheral point, no centrality dependence is observed in the charge inclusive analysis. The most peripheral point sits 2.5σ

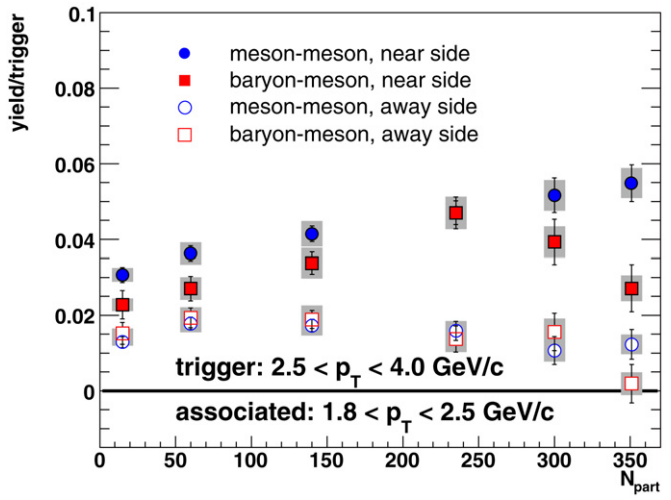

Fig. 7. Conditional yields per trigger for baryon (squares) and meson (circles) triggers with associated mesons. Triggers have $2.5 < p_T < 4.0$ GeV/c and associated particles have $1.8 < p_T < 2.5$ GeV/c. The error bars are the statistical errors and the boxes show the systematic errors. There is an additional 13.6% normalization error.

below the average conditional yield for the other centrality bins. The charge inclusive data are also consistent with a linear increase with N_{part} (χ^2/d.o.f. $= 5.5/4$).

The systematic errors on these distributions are highly correlated since the v_2 values and centrality correlation corrections are the same for all yields at a given centrality. There is an 8.6% systematic error on the relative normalizations of the associated particle p and $\bar{p}$ points, which is not shown. Fig. 6 shows the same correlations as Fig. 5 for the away side region. Here the charge inclusive yields lie above the charge selected yields for peripheral and mid-central collisions because both same and opposite charge pairs have non-zero conditional yield. The conditional yield rises from peripheral to mid-central collisions. In the most central collisions both the charge inclusive and charge selected yields are consistent with zero.

Fig. 7 shows both the near and away side conditional yield for baryon triggers and associated mesons and meson triggers with associated mesons. The meson trigger-associated mesons conditional yield on the near side rises smoothly with centrality. The baryon triggered yields are systematically lower than the meson triggered yields, but also rise linearly with N_{part} for $N_{\text{part}} < 250$. In central collisions the baryon triggered yields are lower than the linear N_{part} dependence observed in the meson–meson points for all N_{part} and the baryon–meson points for $N_{\text{part}} < 250$. The statistical errors on baryon–meson conditional yields exclude a linear increase with N_{part} on the 2.6σ level. The systematic errors on the v_2 values and the centrality correlation correction are correlated with centrality. The most central baryon triggered point is consistent with the most peripheral baryon triggered point. The most central meson–meson conditional yield is $70\% \pm 20\%$ greater than in peripheral collisions. On the away side, no significant dependence on trigger type is observed.

4. Discussion

The observed x_T scaling and pQCD calculations suggest hard scattering is the dominant mechanism for particle production for $p_T > 2$ GeV/c at $\sqrt{s} = 200$ GeV in $p + p$ collisions [7]. Neutral pion production in Au + Au collisions at $\sqrt{s_{NN}} = 200$ GeV follows x_T scaling [26] and is well described by perturbative theories, which include radiative energy loss by hard partons traversing the medium [27–29] at p_T as low as 2 GeV/c. Models describing the excess of baryons relative to mesons [1] typically do so by some mechanism that extends the p_T range of soft physics. Here, we have used two particle azimuthal correlations to study the particle type dependence of jet-like correlations in Au + Au collisions in the region of the baryon excess. Since jets in $e^+ + e^-$ collisions fragment dominantly into mesons [30], we take meson–meson correlations as a baseline for jet fragmentation in Au + Au collisions. The increase in meson–meson near side conditional yield with centrality seen in Fig. 7 has also been observed in meson–hadron correlations [17] and hadron–hadron correlations [16, 18] and is not yet quantitatively understood. Here we are interested primarily in jet correlations of baryons so meson–meson correlations provide a useful reference. The yield of associated mesons per trigger baryon is systematically lower than the yield of associated mesons per trigger meson, but baryon–meson correlations on the near side increase as meson–meson correlations for all centralities except for the most central.

On the away side there is no significant dependence on the trigger type for associated mesons, as is expected if baryon and meson triggers come from jets of approximately the same energy and if the di-jets fragment independently of the trigger jet. The yield of associated baryons per baryon trigger on the near side is observed to be nearly constant with centrality, except for the most peripheral point, which is significantly lower than the others. The data are also consistent with a linear increase in the conditional yield as a function of $N_{\rm part}$. The small yield of associated baryons per baryon trigger does not imply that baryon number is not conserved within the near side jet since the p_T range of the measured associated particles is narrow, and the PHENIX η acceptance does not contain all of the associated particles.

The data presented here are qualitatively consistent with baryons at $2.5 < p_T < 4.0$ GeV/c arising predominately from hard scattering processes. First, the yield of mesons associated with baryon triggers has the same centrality dependence as associated mesons per meson trigger for $N_{\rm part} < 250$ despite a change in the $\bar{p}/\pi^-$ ratio by a factor of three from peripheral collisions. Since the yields are normalized by the number of observed trigger particles, an increasing fraction of uncorrelated baryon triggers would lead to a dilution of the yield. Second, the away side yield into 0.94 rad is independent of the trigger type, consistent with the away side jet fragmenting independently of the trigger jet. Lastly, the charge dependence of p and $\bar{p}$ correlations show that small angle p–$\bar{p}$ and $\bar{p}$–p pairs are correlated beyond the expected correlations from elliptic flow, and that small angle p–p and $\bar{p}$–$\bar{p}$ pairs are not. This is true in peripheral collisions where the $\bar{p}/\pi^-$ ratio is close to the value from $p + p$ collisions [3] and also in central collisions where the ratio is more than a factor of three larger. The weak centrality dependence of opposite sign pair conditional yields shows the number of correlated pairs increase with centrality at approximately the same rate as the number of triggers. However, quantitative understanding of the baryon production mechanism and the fragmentation process will rely on model calculations that are able to explain the single particle yields, elliptic flow, and correlation results.

The results for near side conditional yields presented here disagree with the recombination model calculation in [31], which predicts a very weak centrality dependence for meson–meson and baryon–meson conditional yields and nearly the same magnitude for baryon–meson and baryon–baryon near side conditional yields. In contrast, the data show the conditional yield of associated mesons with baryon triggers to be a factor of two to five times larger than the conditional yield of baryons associated with baryon triggers, depending on centrality.

The results presented here also appear to exclude baryon production via higher twist mechanisms [32], which would produce isolated p and $\bar{p}$. No correlation calculations are available from the gluon junction model [15], so a comparison beyond the successfully described single particle data could not be done at this point.

We have systematically explored the particle type dependence of jet fragmentation at intermediate p_T in Au + Au collisions at $\sqrt{s_{NN}} = 200$ GeV. The new data disagree with calculations from the recombination model presented in [19, 31]. Given the success of recombination models in reproducing elliptic flow and hadron spectra data it would be interesting to see if other recombination calculations are able to describe the data presented here. We find that near side correlations between meson triggers and associated mesons increase with centrality. Near side correlations between baryon triggers and associated mesons show the same centrality dependence except for the most central collisions where there is a significant decrease. The first measurements of baryon pairs on the near side are found to be largely due to opposite charge p–$\bar{p}$ pairs. Under the assumption that the above centrality dependencies of particle pairs and single particles are not coincidental, one can explain the observed baryon excess at intermediate p_T in Au + Au collisions via jet induced production of baryon–antibaryon pairs.

Acknowledgements

We thank the staff of the Collider-Accelerator and Physics Departments at BNL for their vital contributions. We acknowledge support from the Department of Energy and NSF (USA), MEXT and JSPS (Japan), CNPq and FAPESP (Brazil), NSFC (China), MSMT (Czech Republic), IN2P3/CNRS, and CEA (France), BMBF, DAAD, and AvH (Germany), OTKA (Hungary), DAE (India), ISF (Israel), KRF and KOSEF (Korea), MES, RAS, and FAAE (Russia), VR and KAW (Sweden), US CRDF for the FSU, US-Hungarian NSF-OTKA-MTA, and US-Israel BSF.

References

[1] S.S. Adler, et al., Phys. Rev. Lett. 91 (2003) 172301.
[2] S.S. Adler, et al., Phys. Rev. C 69 (2004) 034909.
[3] S.S. Adler, et al., Phys. Rev. C 74 (2006) 024904.
[4] S.S. Adler, et al., Phys. Rev. Lett. 91 (2003) 072301.
[5] J. Adams, et al., Phys. Rev. Lett. 92 (2004) 052302.
[6] S.S. Adler, et al., Phys. Rev. Lett. 91 (2003) 241803.
[7] J. Adams, et al., Phys. Lett. B 637 (2006) 161.
[8] S. Berman, J. Bjorken, J. Kogut, Phys. Rev. D 4 (1971) 3388.
[9] R. Blankenbecler, S. Brodsky, J. Gunion, Phys. Lett. B 42 (1972) 461.
[10] D. Teaney, J. Lauret, E.V. Shuryak, nucl-th/0110037.
[11] T. Hirano, Y. Nara, Phys. Rev. C 69 (2004) 034908.
[12] V. Greco, et al., Phys. Rev. C 68 (2003) 034904.
[13] R.J. Fries, et al., Phys. Rev. C 68 (2003) 044902.
[14] R. Hwa, C.B. Yang, Phys. Rev. C 70 (2004) 024904.
[15] V. Topor Pop, M. Gyulassy, J. Barrette, C. Gale, Phys. Rev. C 72 (2005) 054901.
[16] C. Adler, et al., Phys. Rev. Lett. 90 (2003) 082302.
[17] S.S. Adler, et al., Phys. Rev. C 71 (2005) 051902(R) .
[18] S.S. Adler, et al., Phys. Rev. Lett. 97 (2006) 052301.
[19] R.J. Fries, et al., Phys. Rev. Lett. 94 (2005) 122301.
[20] S.S. Adler, et al., Phys. Rev. D 74 (2006) 072002.
[21] C. Adler, et al., Phys. Rev. Lett. 95 (2005) 152301.
[22] C. Adler, et al., Phys. Rev. Lett. 97 (2006) 162301.
[23] K. Adcox, et al., Nucl. Instrum. Methods A 499 (2003) 489.
[24] A. Poskanzer, S. Voloshin, Phys. Rev. C 58 (1998) 1671.
[25] S.S. Adler, et al., Phys. Rev. Lett. 91 (2003) 182301.
[26] S.S. Adler, et al., Phys. Rev. C 69 (2004) 034910.
[27] I. Vitev, M. Gyulassy, Phys. Rev. Lett. 89 (2002) 232301.
[28] E. Wang, X. Wang, Phys. Rev. Lett. 89 (2002) 162301.
[29] H. Eskola, H. Honkanen, C. Salgado, U. Wiedermann, Nucl. Phys. A 747 (2005) 511.
[30] P. Abreu, et al., Eur. Phys. J. C 17 (2000) 207.
[31] R.J. Fries, J. Phys. Conf. Ser. 27 (2005) 70.
[32] S. Brodsky, H. Pirner, J. Raufeisen, Phys. Lett. B 637 (2006) 58.

Detailed study of high-p_T neutral pion suppression and azimuthal anisotropy in Au+Au collisions at $\sqrt{s_{NN}} = 200$ GeV

S. S. Adler,[5] S. Afanasiev,[17] C. Aidala,[5] N. N. Ajitanand,[43] Y. Akiba,[20,38] J. Alexander,[43] R. Amirikas,[12] L. Aphecetche,[45] S. H. Aronson,[5] R. Averbeck,[44] T. C. Awes,[35] R. Azmoun,[44] V. Babintsev,[15] A. Baldisseri,[10] K. N. Barish,[6] P. D. Barnes,[27] B. Bassalleck,[33] S. Bathe,[30] S. Batsouli,[9] V. Baublis,[37] A. Bazilevsky,[39,15] S. Belikov,[16,15] Y. Berndnikov ,[40] S. Bhagavatula,[16] J. G. Boissevain,[27] H. Borel,[10] S. Borenstein,[25] M. L. Brooks,[27] D. S. Brown,[34] N. Bruner,[33] D. Bucher,[30] H. Buesching,[30] V. Bumazhnov,[15] G. Bunce,[5,39] J. M. Burward-Hoy,[26,44] S. Butsyk,[44] X. Camard,[45] J.-S. Chai,[18] P. Chand,[4] W. C. Chang,[2] S. Chernichenko,[15] C. Y. Chi,[9] J. Chiba,[20] M. Chiu,[9] I. J. Choi,[52] J. Choi,[19] R. K. Choudhury,[4] T. Chujo,[5] V. Cianciolo,[35] Y. Cobigo,[10] B. A. Cole,[9] P. Constantin,[16] D. d'Enterria,[45] G. David,[5] H. Delagrange,[45] A. Denisov,[15] A. Deshpande,[39] E. J. Desmond,[5] A. Devismes,[44] O. Dietzsch,[41] O. Drapier,[25] A. Drees,[44] K. A. Drees,[5] R. du Rietz,[29] A. Durum,[15] D. Dutta,[4] Y. V. Efremenko,[35] K. El Chenawi,[49] A. Enokizono,[14] H. En'yo,[38,39] S. Esumi,[48] L. Ewell,[5] D. E. Fields,[33,39] F. Fleuret,[25] S. L. Fokin,[23] B. D. Fox,[39] Z. Fraenkel,[51] J. E. Frantz,[9] A. Franz,[5] A. D. Frawley,[12] S.-Y. Fung,[6] S. Garpman,[29,*] T. K. Ghosh,[49] A. Glenn,[46] G. Gogiberidze,[46] M. Gonin,[25] J. Gosset,[10] Y. Goto,[39] R. Granier de Cassagnac,[25] N. Grau,[16] S. V. Greene,[49] M. Grosse Perdekamp,[39] W. Guryn,[5] H.-Å. Gustafsson,[29] T. Hachiya,[14] J. S. Haggerty,[5] H. Hamagaki,[8] A. G. Hansen,[27] E. P. Hartouni,[26] M. Harvey,[5] R. Hayano,[8] N. Hayashi,[38] X. He,[13] M. Heffner,[26] T. K. Hemmick,[44] J. M. Heuser,[44] M. Hibino,[50] J. C. Hill,[16] W. Holzmann,[43] K. Homma,[14] B. Hong,[22] A. Hoover,[34] T. Ichihara,[38,39] V. V. Ikonnikov,[23] K. Imai,[24,38] D. Isenhower,[1] M. Ishihara,[38] M. Issah,[43] A. Isupov,[17] B. V. Jacak,[44] W. Y. Jang,[22] Y. Jeong,[19] J. Jia,[44] O. Jinnouchi,[38] B. M. Johnson,[5] S. C. Johnson,[26] K. S. Joo,[31] D. Jouan,[36] S. Kametani,[8,50] N. Kamihara,[47,38] J. H. Kang,[52] S. S. Kapoor,[4] K. Katou,[50] S. Kelly,[9] B. Khachaturov,[51] A. Khanzadeev,[37] J. Kikuchi,[50] D. H. Kim,[31] D. J. Kim,[52] D. W. Kim,[19] E. Kim,[42] G.-B. Kim,[25] H. J. Kim,[52] E. Kistenev,[5] A. Kiyomichi,[48] K. Kiyoyama,[32] C. Klein-Boesing,[30] H. Kobayashi,[38,39] L. Kochenda,[37] V. Kochetkov,[15] D. Koehler,[33] T. Kohama,[14] M. Kopytine,[44] D. Kotchetkov,[6] A. Kozlov,[51] P. J. Kroon,[5] C. H. Kuberg,[1,27,*] K. Kurita,[39] Y. Kuroki,[48] M. J. Kweon,[22] Y. Kwon,[52] G. S. Kyle,[34] R. Lacey,[43] V. Ladygin,[17] J. G. Lajoie,[16] A. Lebedev,[16,23] S. Leckey,[44] D. M. Lee,[27] S. Lee,[19] M. J. Leitch,[27] X. H. Li,[6] H. Lim,[42] A. Litvinenko,[17] M. X. Liu,[27] Y. Liu,[36] C. F. Maguire,[49] Y. I. Makdisi,[5] A. Malakhov,[17] V. I. Manko,[23] Y. Mao,[7,38] G. Martinez,[45] M. D. Marx,[44] H. Masui,[48] F. Matathias,[44] T. Matsumoto,[8,50] P. L. McGaughey,[27] E. Melnikov,[15] F. Messer,[44] Y. Miake,[48] J. Milan,[43] T. E. Miller,[49] A. Milov,[44,51] S. Mioduszewski,[5] R. E. Mischke,[27] G. C. Mishra,[13] J. T. Mitchell,[5] A. K. Mohanty,[4] D. P. Morrison,[5] J. M. Moss,[27] F. Mühlbacher,[44] D. Mukhopadhyay,[51] M. Muniruzzaman,[6] J. Murata,[38,39] S. Nagamiya,[20] J. L. Nagle,[9] T. Nakamura,[14] B. K. Nandi,[6] M. Nara,[48] J. Newby,[46] P. Nilsson,[29] A. S. Nyanin,[23] J. Nystrand,[29] E. O'Brien,[5] C. A. Ogilvie,[16] H. Ohnishi,[5,38] I. D. Ojha,[49,3] K. Okada,[38] M. Ono,[48] V. Onuchin,[15] A. Oskarsson,[29] I. Otterlund,[29] K. Oyama,[8] K. Ozawa,[8] D. Pal,[51] A. P. T. Palounek,[27] V. Pantuev,[44] V. Papavassiliou,[34] J. Park,[42] A. Parmar,[33] S. F. Pate,[34] T. Peitzmann,[30] J.-C. Peng,[27] V. Peresedov,[17] C. Pinkenburg,[5] R. P. Pisani,[5] F. Plasil,[35] M. L. Purschke,[5] A. K. Purwar,[44] J. Rak,[16] I. Ravinovich,[51] K. F. Read,[35,46] M. Reuter,[44] K. Reygers,[30] V. Riabov,[37,40] Y. Riabov,[37] G. Roche,[28] A. Romana,[25,*] M. Rosati,[16] P. Rosnet,[28] S. S. Ryu,[52] M. E. Sadler,[1] N. Saito,[38,39] T. Sakaguchi,[8,50] M. Sakai,[32] S. Sakai,[48] V. Samsonov,[37] L. Sanfratello,[33] R. Santo,[30] H. D. Sato,[24,38] S. Sato,[5,48] S. Sawada,[20] Y. Schutz,[45] V. Semenov,[15] R. Seto,[6] M. R. Shaw,[1,27] T. K. Shea,[5] T.-A. Shibata,[47,38] K. Shigaki,[14,20] T. Shiina,[27] C. L. Silva,[41] D. Silvermyr,[27,29] K. S. Sim,[22] C. P. Singh,[3] V. Singh,[3] M. Sivertz,[5] A. Soldatov,[15] R. A. Soltz,[26] W. E. Sondheim,[27] S. P. Sorensen,[46] I. V. Sourikova,[5] F. Staley,[10] P. W. Stankus,[35] E. Stenlund,[29] M. Stepanov,[34] A. Ster,[21] S. P. Stoll,[5] T. Sugitate,[14] J. P. Sullivan,[27] E. M. Takagui,[41] A. Taketani,[38,39] M. Tamai,[50] K. H. Tanaka,[20] Y. Tanaka,[32] K. Tanida,[38] M. J. Tannenbaum,[5] P. Tarján,[11] J. D. Tepe,[1,27] T. L. Thomas,[33] J. Tojo,[24,38] H. Torii,[24,38] R. S. Towell,[1] I. Tserruya,[51] H. Tsuruoka,[48] S. K. Tuli,[3] H. Tydesjö,[29] N. Tyurin,[15] H. W. van Hecke,[27] J. Velkovska,[5,44] M. Velkovsky,[44] V. Veszprémi,[11] L. Villatte,[46] A. A. Vinogradov,[23] M. A. Volkov,[23] E. Vznuzdaev,[37] X. R. Wang,[13] Y. Watanabe,[38,39] S. N. White,[5] F. K. Wohn,[16] C. L. Woody,[5] W. Xie,[6] Y. Yang,[7] A. Yanovich,[15] S. Yokkaichi,[38,39] G. R. Young,[35] I. E. Yushmanov,[23] W. A. Zajc,[9,†] C. Zhang,[9] S. Zhou,[7] S. J. Zhou,[51] and L. Zolin[17]

(PHENIX Collaboration)

[1]*Abilene Christian University, Abilene, Texas 79699, USA*

[2]*Institute of Physics, Academia Sinica, Taipei 11529, Taiwan*

[3]*Department of Physics, Banaras Hindu University, Varanasi 221005, India*

[4]*Bhabha Atomic Research Centre, Bombay 400 085, India*

[5]*Brookhaven National Laboratory, Upton, New York 11973-5000, USA*

[6]*University of California - Riverside, Riverside, California 92521, USA*

[7]*China Institute of Atomic Energy (CIAE), Beijing, People's Republic of China*

[8]*Center for Nuclear Study, Graduate School of Science, University of Tokyo, 7-3-1 Hongo, Bunkyo, Tokyo 113-0033, Japan*

[9]*Columbia University, New York, New York 10027 and Nevis Laboratories, Irvington, New York 10533, USA*

[10]*Dapnia, CEA Saclay, F-91191, Gif-sur-Yvette, France*

[11]*Debrecen University, H-4010 Debrecen, Egyetem tér 1, Hungary*

[12]*Florida State University, Tallahassee, Florida 32306, USA*

[13]*Georgia State University, Atlanta, Georgia 30303, USA*

[14]*Hiroshima University, Kagamiyama, Higashi-Hiroshima 739-8526, Japan*

 ©2007 The American Physical Society

[15]*Institute for High Energy Physics (IHEP), Protvino, Russia*
[16]*Iowa State University, Ames, Iowa 50011, USA*
[17]*Joint Institute for Nuclear Research, 141980 Dubna, Moscow Region, Russia*
[18]*KAERI, Cyclotron Application Laboratory, Seoul, South Korea*
[19]*Kangnung National University, Kangnung 210-702, South Korea*
[20]*KEK, High Energy Accelerator Research Organization, Tsukuba-shi, Ibaraki-ken 305-0801, Japan*
[21]*KFKI Research Institute for Particle and Nuclear Physics (RMKI), H-1525 Budapest 114, POBox 49, Hungary*
[22]*Korea University, Seoul, 136-701, Korea*
[23]*Russian Research Center "Kurchatov Institute," Moscow, Russia*
[24]*Kyoto University, Kyoto 606-8502, Japan*
[25]*Laboratoire Leprince-Ringuet, Ecole Polytechnique, CNRS-IN2P3, Route de Saclay, F-91128, Palaiseau, France*
[26]*Lawrence Livermore National Laboratory, Livermore, California 94550, USA*
[27]*Los Alamos National Laboratory, Los Alamos, New Mexico 87545, USA*
[28]*LPC, Université Blaise Pascal, CNRS-IN2P3, Clermont-Fd, 63177 Aubiere Cedex, France*
[29]*Department of Physics, Lund University, Box 118, SE-221 00 Lund, Sweden*
[30]*Institut für Kernphysik, University of Muenster, D-48149 Muenster, Germany*
[31]*Myongji University, Yongin, Kyonggido 449-728, Korea*
[32]*Nagasaki Institute of Applied Science, Nagasaki-shi, Nagasaki 851-0193, Japan*
[33]*University of New Mexico, Albuquerque, New Mexico 87131, USA*
[34]*New Mexico State University, Las Cruces, New Mexico 88003, USA*
[35]*Oak Ridge National Laboratory, Oak Ridge, Tennessee 37831, USA*
[36]*IPN-Orsay, Universite Paris Sud, CNRS-IN2P3, BP1, F-91406, Orsay, France*
[37]*PNPI, Petersburg Nuclear Physics Institute, Gatchina, Russia*
[38]*RIKEN (The Institute of Physical and Chemical Research), Wako, Saitama 351-0198, JAPAN*
[39]*RIKEN BNL Research Center, Brookhaven National Laboratory, Upton, New York 11973-5000, USA*
[40]*St. Petersburg State Technical University, St. Petersburg, Russia*
[41]*Universidade de São Paulo, Instituto de Física, Caixa Postal 66318, São Paulo CEP05315-970, Brazil*
[42]*System Electronics Laboratory, Seoul National University, Seoul, South Korea*
[43]*Chemistry Department, Stony Brook University, SUNY, Stony Brook, New York 11794-3400, USA*
[44]*Department of Physics and Astronomy, Stony Brook University, SUNY, Stony Brook, New York 11794, USA*
[45]*SUBATECH (Ecole des Mines de Nantes, CNRS-IN2P3, Université de Nantes) BP 20722 - 44307, Nantes, France*
[46]*University of Tennessee, Knoxville, Tennessee 37996, USA*
[47]*Department of Physics, Tokyo Institute of Technology, Tokyo, 152-8551, Japan*
[48]*Institute of Physics, University of Tsukuba, Tsukuba, Ibaraki 305, Japan*
[49]*Vanderbilt University, Nashville, Tennessee 37235, USA*
[50]*Waseda University, Advanced Research Institute for Science and Engineering, 17 Kikui-cho, Shinjuku-ku, Tokyo 162-0044, Japan*
[51]*Weizmann Institute, Rehovot 76100, Israel*
[52]*Yonsei University, IPAP, Seoul 120-749, Korea*
(Received 7 November 2006; published 25 September 2007)

Measurements of neutral pion (π^0) production at midrapidity in $\sqrt{s_{NN}} = 200$ GeV Au+Au collisions as a function of transverse momentum, p_T, collision centrality, and angle with respect to reaction plane are presented. The data represent the final π^0 results from the PHENIX experiment for the first RHIC Au+Au run at design center-of-mass energy. They include additional data obtained using the PHENIX Level-2 trigger with more than a factor of 3 increase in statistics over previously published results for $p_T > 6$ GeV/c. We evaluate the suppression in the yield of high-p_T π^0's relative to pointlike scaling expectations using the nuclear modification factor $R_{\rm AA}$. We present the p_T dependence of $R_{\rm AA}$ for nine bins in collision centrality. We separately integrate $R_{\rm AA}$ over larger p_T bins to show more precisely the centrality dependence of the high-p_T suppression. We then evaluate the dependence of the high-p_T suppression on the emission angle $\Delta\phi$ of the pions with respect to event reaction plane for seven bins in collision centrality. We show that the yields of high-p_T π^0's vary strongly with $\Delta\phi$, consistent with prior measurements [1,2]. We show that this variation persists in the most peripheral bin accessible in this analysis. For the peripheral bins we observe no suppression for neutral pions produced aligned with the reaction plane, whereas the yield of π^0's produced perpendicular to the reaction plane is suppressed by a factor of $\sim$2. We analyze the combined centrality and $\Delta\phi$ dependence of the π^0 suppression in different p_T bins using different possible descriptions of parton energy loss dependence on jet path-length averages to determine whether a single geometric picture can explain the observed suppression pattern.

DOI: 10.1103/PhysRevC.76.034904 PACS number(s): 25.75.Dw

I. INTRODUCTION

High transverse momentum particles resulting from hard scatterings between incident partons have become one of the most effective tools for probing the properties of the medium created in ultra-relativistic heavy ion collisions at RHIC. Data from the four RHIC experiments have unequivocally established the phenomenon of high transverse momentum hadron suppression in Au+Au compared to (appropriately scaled) $p+p$ collisions [3–9], whereas the lack of similar suppression in d+Au collisions [9–12] provides strong evidence that the suppression is not due to modification of parton distributions in the incident nuclei. This suppression has been observed for a large variety of hadron species, at highest p_T for π^0 and most recently η [13], supporting further the notion that energy loss occurs at the parton level. Conversely, direct photon measurements by the PHENIX collaboration show that the yield of hard photons in Au+Au collisions is consistent with $p+p$ expectations scaled by the number of incoherent nucleon-nucleon collisions [14] and, thus, provide final confirmation that hard scattering processes occur at rates expected from pointlike processes. This observation makes definitive the conclusion that the suppression of high-p_T hadron production in Au+Au collisions is a final-state effect. Measurements of azimuthal angle correlations between hadron pairs resulting from fragmentation of hard-scattered partons into jets have provided additional confirmation of final-state medium effects on these partons [15].

Predictions of high-p_T suppression were made before the start of RHIC operation [16,17] and confirmation of these predictions may be considered one of the key successes of the RHIC program so far. The suppression of high-p_T single hadrons was predicted to result from the energy loss of hard-scattered quarks and gluons in the hot and dense quantum chromodynamics (QCD) medium created in ultrarelativistic heavy-ion collisions (see Refs. [18,19] and references therein). In the canonical models, medium-induced gluon bremsstrahlung is expected to dominate the energy loss process [16], and calculations of the high-p_T suppression factor incorporating this effect have been able to successfully describe the experimental measurements [20–22]; however, recent measurements of heavy quark suppression pose some questions to this canonical view. Nonetheless, from comparisons of the energy loss calculations with the experimental data, estimates of the initial net color charge density that is usually expressed in terms of a gluon rapidity density, dN_g/dy, have been obtained yielding $dN_g/dy \approx 1000$ and, assuming thermalization, estimates of the initial energy density have produced values in excess of $10\,\mathrm{GeV/fm}^3$ [23,24].

However, in spite of this success, there are still a number of outstanding issues with the interpretation of the Au+Au high-p_T single-hadron suppression. Because the properties of the medium created in heavy-ion collisions are not *a priori* known, the energy-loss calculations necessarily use the observed suppression to infer initial parton densities, usually through an intermediate parameter that appears in the energy loss calculations. Although the initial parton density obtained by such "tomographic" studies has to be consistent with the final (measured) total particle multiplicity, it is fair to acknowledge that the p_T dependence of the suppression (rather than its absolute magnitude) is a more discriminating observable to test the various energy loss models. For π^0 spectra, the suppression in central Au+Au collisions at $\sqrt{s_{NN}} = 200$ GeV is found to be approximately constant with p_T over the range, $3 < p_T < 10$ GeV/c. Although the different energy loss calculations can reproduce this p_T-independent suppression, the detailed explanation of the constancy is different in each model. The effects invoked to explain the p_T dependence of the observed Au+Au high-p_T suppression include finite-energy effects, absorption of energy from the medium, evolution from incoherent (Bethe-Heitler) to coherent (Landau-Pomeranchuk-Migdal or LPM) radiation with increasing parton energy [25], the p_T-dependent mixture of quark and gluon contributions to the hard-scattered parton spectrum, the increasingly larger exponent of the underlying (power-law) parton p_T spectra [22], and shadowing/EMC effect [26]. Although most calculations of the high-p_T suppression in Au+Au collisions account for shadowing/EMC modifications of the nuclear parton distributions and for the relative mixture of quarks and gluons in the hard-scattered parton spectra, finite-energy corrections, absorption of energy from the medium, and the description of the energy loss process itself differs from calculation to calculation. Clearly the central Au+Au single-particle spectra are not sufficient, by themselves, to validate or exclude any of the different energy loss models; we must use more "differential" probes of medium-induced energy loss to better understand the phenomenon.

A robust prediction of non-Abelian parton energy loss calculations is that the average energy loss as a function of the in-medium path length L shows a quadratic dependence $\propto L^2$ [27]. Such a behavior predicted for a *static* QCD medium turns into an effective $\propto L$ dependence in an expanding quark-gluon plasma (QGP) [28]. In principle, the centrality dependence of the high-p_T suppression [5,6,8] provides an effective test of energy-loss calculations because the length of the path of the partons in the medium will change between peripheral and central collisions. However, the energy loss calculations also have to account for changes in the initial properties of the medium with centrality and the extra flexibility in the description of the initial conditions means that the measured centrality dependence of the high-p_T suppression also does not stringently constrain energy loss models [29]. However, the path length of the parton in the medium can also be controlled by selecting high-p_T hadrons in different bins of azimuthal angle difference from the event-by-event determined reaction plane. Indeed, shortly after experimental observations of azimuthal anisotropy were reported [1,15], arguments were made that the high-p_T anisotropy in noncentral collisions was due to the spatial asymmetry of the medium and the resulting $\Delta\phi$ dependence of parton path lengths [30,31]. However, recent analyses have argued that the large azimuthal anisotropies at high p_T cannot be accounted for by energy loss alone—at least when realistic nuclear geometry is used to

*Deceased.
†PHENIX Spokesperson: zajc@nevis.columbia.edu

describe the spatial asymmetry of the initial state [29,32,33]. Some of these analyses were based on a picture of the energy loss process in which quarks or gluons that have emitted radiation effectively disappear from the steeply falling high-p_T spectrum because they are overwhelmed by partons of lower energy that escape from the medium losing little or no energy. In this picture, the medium effectively attenuates the high-p_T quarks and gluons and the high-p_T spectrum is dominated by partons originating near the surface—i.e., partons originating in the "corona" [29,32,33]. Then, the azimuthal anisotropy could be largely determined by the shape of the surface [32]. However, it has been separately argued that fluctuations in the number of emitted gluons may be large and such fluctuations may weaken the corona effect [28].

In this article we present measurements of π^0 production in $\sqrt{s_{NN}} = 200$ GeV Au+Au collisions from the PHENIX experiment at RHIC. These data, obtained during Run-2 operation of RHIC in 2002, include additional data obtained with the PHENIX Level-2 trigger, which improved the total statistics by a factor of $\sim$3 compared to the prior analysis in Ref. [6]. The analyses presented here have also benefited from advanced electromagnetic calorimeter calibrations and from improved understanding of the systematic errors in the π^0 measurement in course of the direct photon analysis presented in Ref. [14], where the π^0 decay photons provide the main source of background. With the improved statistics, the p_T reach of the data is extended to higher p_T, allowing us to test whether the suppression starts to diminish above 10 GeV/c in p_T. In addition, we extend the measurement of the centrality dependence of the suppression up to 8 GeV/c.

We present measurements of the dependence of the π^0 yield as a function of the angle $\Delta\phi$ of the π^0 with respect to the event reaction plane. By measuring the high-p_T hadron suppression as a function of $\Delta\phi$, for a given centrality bin, we can keep the properties of the medium fixed and vary only the average geometry of the jet propagation in the medium. By comparing different centrality bins we can, in principle, test how the initial properties of the medium affect the induced energy loss. Traditionally, measurements of the $\Delta\phi$ dependence of hadron yields have been analyzed in terms of the azimuthal asymmetry parameter, v_2, and we note that the data presented here were used to obtain measurements of π^0 v_2 for comparison to inclusive photon v_2 [34]. However, in this publication we focus not on v_2, but explicitly on the suppression as a function of $\Delta\phi$, expressed in terms of the $\Delta\phi$-dependent nuclear modification factor $R_{\rm AA}(\Delta\phi)$. Although the data presented this way contain, in principle, the same information as the combination of $\Delta\phi$-averaged $R_{\rm AA}$ and v_2, $R_{\rm AA}(\Delta\phi)$ provides a useful alternative way to evaluate the dependence of high-p_T suppression on geometry because it effectively combines $R_{\rm AA}(p_T)$ and v_2 into a single set of data. We analyze the combined $\Delta\phi$ and centrality dependence of the high-p_T suppression in the context of different path-length and density dependencies of the parton energy loss process to evaluate whether any geometric picture can simultaneously describe the centrality and $\Delta\phi$ dependence of the observed high p_T deficit.

II. EXPERIMENTAL DETAILS

The data presented in this article were obtained during Run-2 operation of the PHENIX experiment [35] at the Relativistic Heavy Ion Collider facility at Brookhaven National Laboratory [36]. The primary detectors used to obtain the presented results were the PHENIX central arm spectrometers, particularly the electromagnetic calorimeters [37], and the two beam-beam counters (BBC's) [38]. In addition, the PHENIX zero-degree calorimeters [39] were used for triggering and centrality determination.

Two-photon decays of neutral pions were measured in the PHENIX electromagnetic calorimeter, located at a radial distance of $\sim$5.1 m from the beam-line, which has a pseudo-rapidity acceptance of $-0.35 < \eta < 0.35$ and covers π radians in azimuth. The electromagnetic calorimeter is divided into eight sectors, with each sector covering the full pseudo-rapidity range and $\pi/8$ in azimuth. The calorimeter consists of two distinct parts using different technologies. A lead-scintillator sandwich calorimeter (PbSc) with 5 cm $\times$ 5 cm towers covers 3/4 (6 sectors) of the central arm acceptance. A lead-glass Čerenkov calorimeter (PbGl) with 4 cm $\times$ 4 cm towers covers the remaining 1/4 (2 sectors) of the central arm acceptance. The corresponding $\Delta\eta \times \Delta\phi$ acceptance of a single tower at $\eta = 0$ is 0.011^2 and 0.0075^2 for the PbSc and PbGl calorimeters, respectively.

The event reaction plane in Au+Au collisions was measured in the two BBC's. Each BBC consists of 64 hexagonal, quartz Čerenkov radiators closely packed around the beam pipe, in an approximately azimuthally symmetric configuration. The beam-beam counters, located 144 cm in each direction from the nominal center of the interaction diamond, are used to count charged particles produced in the pseudorapidity range $3.0 < |\eta| < 3.9$. The distribution of particles over the individual channels of the BBC's allows measurement of the azimuthal distribution, $dN_{\rm ch}/d\phi$, of charged particles within this pseudorapidity acceptance. The BBC's also provide measurement of the collision vertex position along the interaction diamond with a resolution of 0.6 cm [38].

The data presented here were obtained using the PHENIX minimum-bias Level-1 trigger, based on the BBC's and the PHENIX zero-degree calorimeters, that selects $92.2^{+2.5}_{-3.0}\%$ of the total Au+Au hadronic interaction cross section of 6.9 b [6]. For a subset of the data, events selected by the Level-1 trigger were subjected to software Level-2 trigger filtering after full assembly of events in the PHENIX event builder [40]. A software algorithm performed a crude reconstruction of electromagnetic clusters by summing the pedestal-subtracted and gain-calibrated energies of "tiles" made of adjacent 4 $\times$ 4 calorimeter towers groups. The tiles are allowed to overlap such that every possible such tile that can be constructed in each calorimeter is tested. One of the Level-2 triggers (LVL2A) selected events in which at least one cluster (tile) had energy >3.5 GeV. Another Level-2 trigger (LVL2B) selected events in the 50–92% centrality range (50% most peripheral events) with at least one cluster having energy >1.5 GeV.

The measurements presented in this article were obtained from 31.4 M minimum bias triggers and approximately

1.7 M Level-2 trigger selected events. Of the Level-2 triggered events, 743 K events were selected by the higher energy LVL2A trigger and the remainder were selected by the peripheral, lower-energy LVL2B trigger. Taking into account their rejection factors, the two triggers sampled the equivalent of 44.4×10^6 LVL2A and 28.7×10^6 LVL2B minimum-bias triggers. The difference is due to different online trigger pre-scale factors. Thus, the combined event sample contains approximately a factor of 2.5–3 (considering both triggers over all centralities) more π^0's above 6 GeV/c than previously published Run-2 π^0 measurements [6].

III. DATA ANALYSIS

A. Event selection and centrality

In the offline analysis, the timing difference measured between the two PHENIX BBC's is used to determine the position of the collision vertex along the beam axis and to select events with vertex position within 30 cm of the nominal center of the detector for subsequent analysis. The energies measured in the zero-degree calorimeters and the charged-particle multiplicity measured in the BBC's are used to determine the collision centrality [41]. For the π^0 spectrum measurements presented here the total measured centrality range (0–92.2%) is subdivided into nine bins: 0–10, 10–20, 20–30, 30–40, 40–50, 60–70, 70–80, 80–92.2%. For the reaction plane-dependent analysis, the most central and two most peripheral bins are excluded, the peripheral due to their large uncertainty in the reaction plane resolution, and the 0–10% bin simply because of its smaller intrinsic eccentricity. Additionally, we present also combined 0–20%, 20–60%, and 60–92% data sets for comparison with other PHENIX analyses of high p_T hadron production that use such centralities.

B. Reaction plane measurement

PHENIX has previously published measurements of elliptic flow using an event-by-event measured reaction plane [34,42,43], and the same technique is used for the analysis presented here. Each BBC detector consists of 128 quartz radiators placed in hexagonal, roughly concentric rings whose light is individually collected by photomultiplier tubes (PMT's). The calibrated charge from each radiator is converted into an estimate for the number of charged particles within the acceptance of each detector, N_i, using the measured single-particle peak centroid.

For the reaction plane measurement the measured N_i values are corrected such that the weight of the inner rings that have the fewest radiators covering the full azimuthal angle range is reduced. Then, in terms of the corrected N_i values, N_i^{adj}, the angle of the reaction plane Ψ is obtained from the formula

$$\tan(2\Psi) = \frac{\sum_i N_i^{\mathrm{adj}} \sin(2\phi_i) - \left\langle \sum_i N_i^{\mathrm{adj}} \sin(2\phi_i) \right\rangle}{\sum_i N_i^{\mathrm{adj}} \cos(2\phi_i) - \left\langle \sum_i N_i^{\mathrm{adj}} \cos(2\phi_i) \right\rangle}, \quad (1)$$

where ϕ_i represents the azimuthal angle of the center of a given radiator i. The subtraction of the average centroid position in Eq. (1) removes the bias in the reaction plane measurement resulting from nonzero angle of the colliding beams, nonuniformities in detector acceptance, and other similar effects. The average is taken over many events localized in time with the event in question. A final correction is applied to remove nonuniformities at the 20% level in the Ψ distribution.

TABLE I. Relative systematic uncertainty of the reaction plane resolution for the centrality bins shown in Fig. 1.

Centrality	Syst. error
0–10%	20.3%
10–20%	5.1%
20–30%	3.9%
30–40%	3.8%
40–50%	4.1%
50–60%	4.6%
60–70%	22.5%

Because the above-described procedure can also be applied individually to each BBC, we have a redundant measurement of the reaction plane in the north and in the south, and we exploit this to determine the resolution of the full reaction plane measurement using standard procedures [44]. The resolution of the reaction plane is directly measured from the quantity $\langle \cos 2(\Psi_1 - \Psi_2) \rangle$ where Ψ_1 and Ψ_2 are the reaction plane angles measured in each of the two beam-beam counters individually and the average is taken over events. Figure 1 and Table I show the variation of the resolution, usually determined as $\langle \cos 2(\Psi_{\mathrm{meas}} - \Psi_{\mathrm{true}}) \rangle = \sqrt{(2\langle \cos 2(\Psi_1 - \Psi_2) \rangle}$. The needed correction factors can be derived from this using Eq. (11) in Sec. III F, where the reaction plane corrections are described in more detail.

The systematic errors associated with the measurement of the reaction plane come dominantly from how well the resolution is known. The uncertainty on this quantity is also shown with Fig. 1 for all but the most peripheral centralities. This error is determined by observing comparison of the

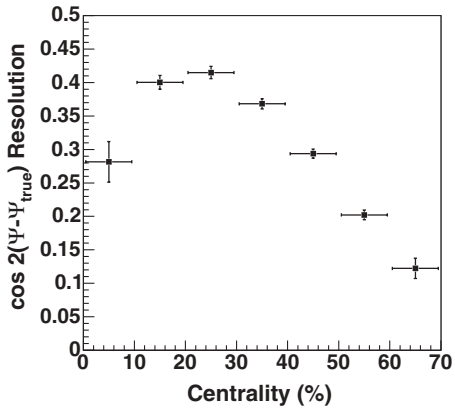

FIG. 1. Resolution of the reaction plane determined in the BBC versus centrality. As usual, the resolution is defined as the unitless quantity $\langle \cos 2(\Psi_{\mathrm{meas}} - \Psi_{\mathrm{true}}) \rangle$, equal to the inverse of the v_2 correction factor.

similarly calculated quantity $\langle \sin 2(\Psi_1 - \Psi_2)\rangle$ which should by definition be equal to zero. The value of $\langle \sin 2(\Psi_1 - \Psi_2)\rangle$ is found to be consistent with 0 for all centralities. The mean size of its fluctuations around 0 are compared to the size of the $\langle \cos 2(\Psi_1 - \Psi_2)\rangle$ to derive the systematic errors in the table. Because the value of $\langle \cos 2(\Psi_1 - \Psi_2)\rangle$ decreases dramatically in the lower multiplicity peripheral events, the relative size of the error increases. The size of this relative error is also cross checked by comparing it to the relative error on elliptic flow (v_2) measurements which is directly comparable since, as discussed in Sec. III F, the resolution correction for v_2 is a plain multiplicative factor. For the cross check, the v_2 error is derived by taking the difference of v_2 made with reaction planes from the BBC North and BBC South separately.

Because of the large rapidity gap between the PHENIX BBC's and the PHENIX Central Arm ($\Delta\eta > 2.7 - 4.0$), the measurements made in the BBC's are assumed to have no correlations (except collision geometry) with processes detected in the central arm that would affect the results presented in Sec. III F. Specifically, PYTHIA studies [45] indicate that any large rapidity-gap production correlated with jets (and thus the hard π^0's we study) detected in the central arm have a negligible effect on reaction plane determination even for the most peripheral events considered in this article. Further, we average both the North and South BBC, which are separated by $\Delta\eta > 6.0$, making potential effects of this nature especially unlikely.

C. Neutral pion detection

The detection of neutral pions is one of the major sources of information on identified particle production at high p_T at RHIC, and PHENIX has already published the results of a number of π^0 measurements in different colliding systems [3,6,10,46,47]. Here we will describe the technique for obtaining π^0 yields as a function of p_T and centrality, which is now well established within PHENIX.

Neutral pions are detected via their $\pi^0 \to \gamma + \gamma$ decay channel. Due to the relatively short mean lifetime of neutral pions of about 10^{-16} s, typical of electromagnetic decays, the pions decay close to the interaction point ($c\tau \approx 25$ nm). This makes the decay vertex well known and the pions can be reconstructed via an invariant mass analysis of photon pairs measured by the EMCal.

In the EMCal, hits or clusters are reconstructed by finding contiguous calorimeter towers with pulse heights above the ADC pedestal value. In order to obtain a cleaner sample of electromagnetic hits shower shape cuts are applied to select candidate photons and time-of-flight cuts are applied to reject slow hadrons. For the PbSc we require measured cluster times to be $t_{\rm clust} < L/c \pm 1.2$ ns, where L is the straight-line path from the collision vertex to the reconstructed cluster centroid. For the PbGl we require reconstructed clusters to have times, $t_{\rm clust} < L/c \pm 2$ ns; the difference is due to the intrinsic timing resolutions of the two calorimeter technologies.

The energy of each EMCal cluster is corrected for angular dependence and nonlinearity based on test beam results and simulation. The linearity corrections for both detector types are different with the PbGl showing a stronger dependence on the energy. The correction factors for a photon with a detected energy of 1 GeV (10 GeV) are 1 (0.95) for the PbSc and 1.05 (0.975) for the PbGl, respectively. The PbGl calorimeter also shows a stronger variation of the measured photon energy with the angle of incidence on the detector surface, at 20° the measured energy is reduced by 5% compared to perpendicular incidence (0°), whereas in the PbSc the effect is only of the order of 2%.

In a typical Au+Au central event the EMCal detects $\gtrsim$300 clusters corresponding to an occupancy of $\sim$10% and therefore a non-negligible probability of cluster overlaps. To minimize the effects of cluster overlaps in high multiplicity events, the energy of each cluster in the PbSc calorimeter is determined not only from the sum of all contiguous towers with deposited energy above a given threshold (15 MeV was our default value) but also, alternatively, "extrapolating" the measured "core energy" of the four to five central towers assuming a standard electromagnetic shower profile in an event with zero background. For this latter case, the *ecore* energy was computed from the experimentally measured center of gravity, central shower energy, and impact angle in the calorimeter using a parameterized shower profile function obtained from electromagnetic showers measured in the beam tests. Such an *ecore* energy represented an estimate of the true energy of a photon impinging on the PbSc unbiased by background contributions from other particles produced in the same event and depositing energy in the neighborhood of a given cluster. The use of *ecore* instead of the total cluster energy for photon reconstruction, helped to reduce considerably the effects of cluster overlaps in central Au+Au collisions.

For a photon pair originating from a π^0 decay the invariant mass

$$m_{\gamma\gamma} = \sqrt{\left(P_{\gamma_1} + P_{\gamma_2}\right)^2} = \sqrt{2E_1 \cdot E_2 \cdot (1 - \cos\theta_{12})} \qquad (2)$$

is identical to the π^0 rest mass. However, due to the finite energy and position resolution in the detection of the photon pair, the actual reconstructed value is smeared around a mean value, which can deviate from the nominal value. The reconstructed peak position is also influenced by the high multiplicity in a heavy-ion collision, where overlapping clusters can shift the measured energy of each photon.

With the invariant mass analysis, π^0's cannot be identified uniquely because all possible photon-photon combinations have to be considered. This leads to a large combinatorial background, which increases quadratically with the multiplicity. The π^0 yield is instead determined on a statistical basis, with the background contribution established via a *mixed event* technique as described below.

One possibility to reduce the combinatorial background is to make use of the phase-space distribution of the photons in a π^0 decay. For the $\pi^0 \to \gamma + \gamma$ decay, the two photons have minimum opening angle

$$\tan\theta_{12}/2 = \frac{m}{p}, \qquad (3)$$

where m is the π^0 mass and p its momentum, with $p \simeq p_T$ in the PHENIX central spectrometer. The angular distribution of

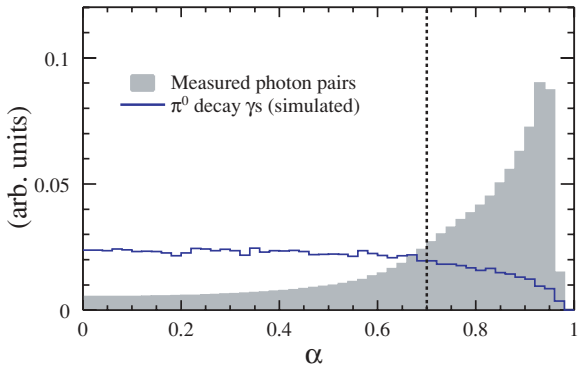

FIG. 2. (Color online) Asymmetry of photon pairs with $3\,\mathrm{GeV}/c \leqslant p_T < 5\,\mathrm{GeV}/c$ within the acceptance of one PbGl sector, for simulated single π^0s and measured within minimum bias events. An asymmetry cut used during the analysis is also shown. (Due to the limited acceptance of the detector, the distribution of the energy asymmetry shows a slight decrease toward $\alpha = 1$.)

the γ pair in the π^0 rest frame, $d\sigma/d\cos\theta^*$, is constant, which leads to a flat distribution in the measured energy asymmetry of the two photons from π^0 decay:

$$\alpha = \frac{|E_1 - E_2|}{E_1 + E_2} = \beta|\cos\theta^*|, \tag{4}$$

where $\beta = p/E \sim 1$ is the velocity of the π^0. However, high p_T combinatorial pairs are strongly peaked near $\alpha = 1$ because of the steeply falling spectrum of single photon candidates. This is illustrated in Fig. 2, where the asymmetry distribution for photons from π^0s in a simulation is compared to the measured asymmetry for photon candidate pairs in real Au+Au collisions. In two independent analyses, asymmetry cuts of $\alpha < 0.7$ and $\alpha < 0.8$ were employed, other values were used as a cross-check and to verify the energy scale (see below).

Pairs of candidate photon clusters within the PbGl and the PbSc calorimeter that satisfy the asymmetry cut are considered candidate π^0's. Figure 3 shows example invariant mass distributions for π^0 candidates with $3.0 < p_T < 3.5$ GeV/c in Au+Au collisions for two different bins of collision centrality. The background under the clear π^0 mass peak in these figures is due to combinatorial mixing of photons from two different decaying π^0's or from pairs containing one or two nonphoton clusters that nonetheless pass the above-described cuts.

Such a combinatorial background can be determined by a so-called *mixed event* technique. It is a widely used method to determine the combinatorial background of combined particle properties, e.g., the invariant mass of a photon pair. The basic idea is to compare the result obtained by combining particles within one event to the result for particle combinations from different events, which are *a priori* not correlated.

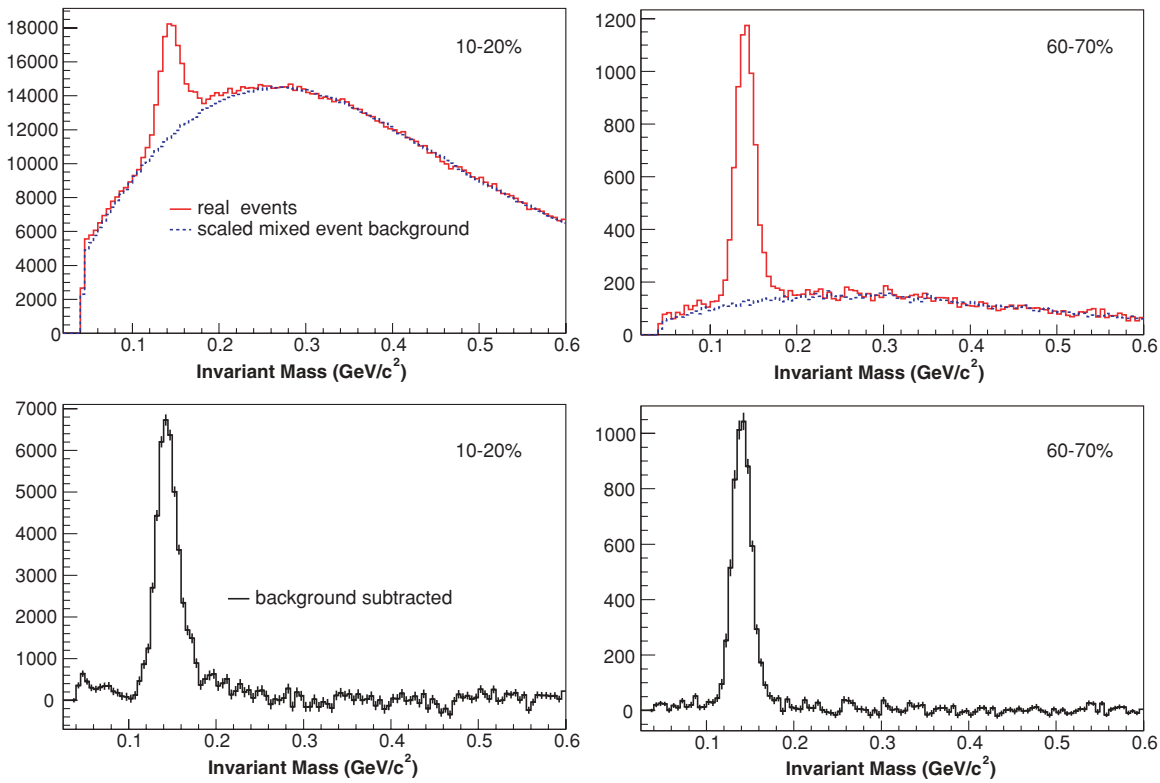

FIG. 3. (Color online) Invariant mass distributions of pairs of electromagnetic clusters passing photon selection cuts for pair transverse momenta satisfying $3.0 < p_T < 3.5$ GeV/c. (Top panels) $m_{\gamma\gamma}$ distributions in Au+Au events compared to a normalized mixed-event sample representing the combinatoric background. (Bottom panels) The $m_{\gamma\gamma}$ distributions after subtraction of the combinatoric background. (Left) 10–20% centrality bin; (right) 60–70% centrality bin.

In the case of the π^0 invariant mass, the mixed event distribution is determined by combining one photon candidate from the current event with all photon candidates from previous events stored in a buffer. The number of previous events used for the pair combinations determines the statistical error of the background, which can be made small by increasing the buffer size. In this analysis, the buffer is varied from ~3 to 10 previous events depending on centrality due to the centrality-dependent multiplicity.

To describe the combinatorial background correctly it is essential that the events used for mixing have similar properties as the real event. Different event classes for collision vertex, centrality, and reaction plane are employed. Also events are chosen for mixing so that they are not biased toward a certain reaction. This is because triggered samples, even from the high-p_T photon trigger, contain biases, e.g., in momenta and centrality distributions, which do not accurately represent the dominant uncorrelated background. For this reason only minimum bias events are used for mixing with both the trigger and minimum bias data sets.

For the photons used in the event mixing the same criteria are applied as for the pair combinations from one event, such as PID cuts, cuts on bad modules, and the asymmetry cut. Other properties valid *a priori* for the real photon pairs, e.g., a minimum distance that allows to distinguish them, have to be considered in addition. In the analysis a minimum distance cut of a least 8 cm is required for each photon pair combination, within one event and for mixed events, respectively.

For a given p_T bin the mixed-event background is normalized to the same-event invariant mass distribution outside the range of the π^0 peak by scaling the mixed-event background with a function $f(m_{\text{inv}})$. This scaling function is determined by fitting the ratio of the same-event and mixed-event invariant mass distribution for p_T bins up to 3 GeV/c with a linear function. This is needed because at low p_T correlations in the real-event background due to overlapping clusters cannot be reproduced by the mixed-event technique. For the p_T bins above 3 GeV/c, a constant is used. To cross-check the result, the linear and the constant scaling function are also determined over the complete invariant mass region, including the π^0 peak, which is taken into account by an additional Gaussian in the fit function (e.g., a linear plus a Gaussian function).

The determination of the scaling function for large pair-p_T is limited by statistics in the real event sample and does not lead to stable results. Instead a constant scaling factor is used if the ratio of the invariant mass distribution shows bins with zero entries in the fit region. The scaling factor is determined by integrating the real and the mixed invariant mass distributions in the range with the peak region excluded.

The scaled mixed-event background is subtracted from the same-event distribution to produce a statistical measure of the true π^0 yield. The result of such a subtraction procedure is shown in the bottom plots of Fig. 3. The raw π^0 yield is obtained in each p_T bin by integrating the subtracted invariant mass distribution in a range around the peak mean (m_{π^0}) of ± 3 times the Gaussian width (σ_{π^0}) of the π^0 peak. Values of the mean and σ_{π^0}, can be seen in Fig. 4. Varying the size

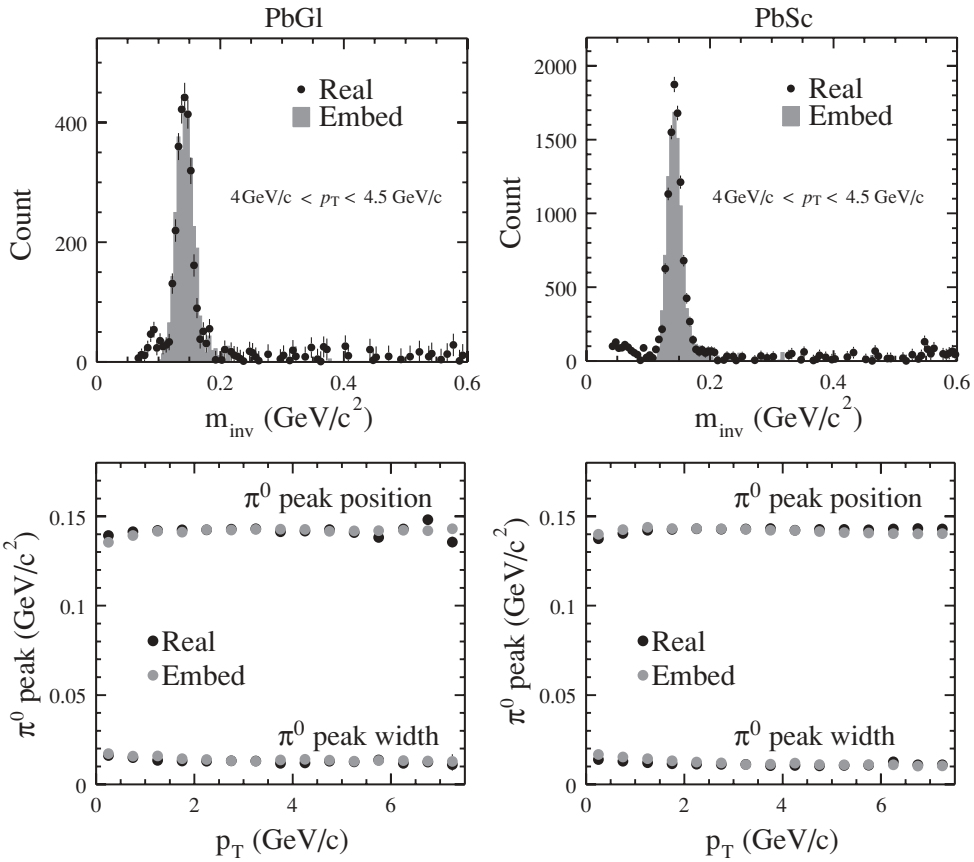

FIG. 4. Comparison of the π^0 peak position in real events (MB) measured with the PbGl and the PbSc with the results obtained for embedded π^0s. The p_T dependence of the peak position and width is due to calorimeter energy resolution as discussed in the text.

of the integration window results in slightly different results, which contributes to the overall systematic uncertainty of the measurement, discussed in Sec. III D4.

Residual differences between the mixed background and the foreground are still apparent in some p_T bins, especially below $\sim$2 GeV/c. Cluster merging, cluster splitting (fluctuations in the two-dimensional $\phi - z$ energy profile cause multiple local maxima that are incorrectly separated into distinct clusters), antineutron annihilation, and even second-order residual physics correlations such as three and multibody decays, flow, HBT, etc., can all cause such differences. These remaining differences are compensated by the shape of the scaling function. In addition, as a systematic check, the shape of the remaining background after subtraction is also fit with various low order polynomial functions and potential contributions to the peak yield are considered in the determination of the total systematic error from the peak extraction procedure.

The values of the peak width and mean are extracted in one initial analysis of the invariant mass distribution in which a p_T-dependent parameterization is determined for different centralities. The use of predefined values for the position and spread of the π^0 peak has the advantage that even in p_T regions where no fit to the subtracted invariant mass distribution is possible, the integration region is well defined just by extrapolation from low p_T.

D. π^0 spectrum measurement

For the reaction-plane independent π^0 spectrum measurement in a given centrality class *cent*, the aforementioned analysis is applied in $\Delta p_T = 0.5$ GeV/c bins for $p_T >$ 1 GeV/c. We cease attempting to extract π^0 yields at high p_T when the number of pairs within the selected (background-subtracted) π^0 mass window falls below 4 counts. We then correct the resulting raw π^0 spectrum for the geometric acceptance $a_{\Delta y}(p_T)$, the overall detection efficiency $\varepsilon_{\rm cent}(p_T)$, which accounts for the cluster cut efficiency, the π^0 mass cut efficiency, for losses due to cluster overlaps in high multiplicity events, for cuts on bad modules and for the calorimeter energy and position resolution. In addition a correction for conversion losses ($c_{\rm conv}$) in the material of the PHENIX central arms and for the branching ratio of the two photon decay ($c_{\gamma\gamma}$) is applied:

$$\frac{1}{2\pi p_T}\frac{d^2N^{\pi^0}_{\rm cent}}{dp_T\,dy} \equiv \frac{1}{2\pi p_T N^{\rm event}_{\rm cent}} \times \frac{1}{a_{\Delta y}(p_T)\varepsilon_{\rm cent}(p_T)c_{\rm conv}c_{\gamma\gamma}} \times \frac{N^{\pi^0}_{\rm cent}(\Delta p_T)}{\Delta p_T \Delta y}. \quad (5)$$

1. Acceptance and detector efficiency

The geometric acceptance of the EMCal for the $\pi^0 \to \gamma\gamma$ decay is evaluated using a Monte Carlo (MC) program that generates π^0s in a rapidity interval Δy with the same vertex distribution and rapidity distribution as observed in real events and contains the complete geometry information of the EMCal. The π^0 decay is calculated via JETSET routines that are part of the PYTHIA event generator [48]. For each π^0 it is verified that both decay photons hit the detector. The resulting p_T distribution of accepted π^0s is divided by the transverse-momentum distribution of the generated π^0s and provides the geometrical acceptance of the PbSc and PbGl, respectively.

The detection efficiency is determined using GEANT to simulate the complete response of the calorimeter to single π^0 decays. The data from each simulated π^0 is then embedded into real Au+Au events by adding the EMCal tower information of the simulated π^0 to the tower information of the real event and recalculating the EMCal clusters. The efficiency for detecting the embedded π^0 is then again determined by comparing the input p_T spectrum to the reconstructed p_T spectrum of the embedded π^0's. Using this technique we determine "efficiency" corrections that account for the energy resolution and position resolution of the calorimeter, as well as for the losses due to overlapping clusters in a real event environment. In addition, the embedding allows for a precise determination of the effect of edge cuts and bad modules. Though these effects can be in principle considered as acceptance corrections, they depend not only on the geometry but also on the energy deposition of an electromagnetic shower in the different calorimeter towers.

In the embedding procedure the effects of photon conversions are also included, as the GEANT simulation considers the material budget in front of the EMCal and the information for decay-photon conversions is retained. The final conversion correction, which is factorized from the rest of the efficiency for book-keeping purposes, is evaluated by comparing the π^0 yield with and without including conversions in the simulation. The final conversion correction, constant with p_T depends on the photon PID cuts and material in front of each individual sector and ranges from 6 to 8% in PbGl and 9 to 10% in PbSc. Comparing this to the sheer probability of a π^0 having at least one photon which converts, 21% PbGl and 14% PbSc, we see that a large portion of these π^0 are still reconstructable.

For the embedding, the input π^0 spectrum is weighted to match a fit function (see below, at the end of Sec. III D3) which is fit to the measured π^0 spectrum so that the correct folding of the π^0 spectrum with the resolution is obtained. This procedure is iterated, with the fit of the p_T dependence of the input weights adjusted as the estimate of the efficiency correction improves, until the procedure converges within the nearly p_T-independent statistical error of the embedded sample, approximately 3%.

Figure 4 compares the invariant-mass peak after background subtraction in the real data and the invariant mass peak of the embedded π^0 for the two different detector types in minimum bias events. The measured π^0 peak position is shifted from the nominal value of approximately 134.98 MeV due to the finite energy resolution of the detector in combination with the steeply falling spectrum and due to the additional effect of overlapping clusters. As illustrated the effects are well reproduced by the embedded π^0's.

2. Trigger efficiency

The efficiency of the Level-2 trigger is separately evaluated by processing recorded minimum-bias events with the Level-2

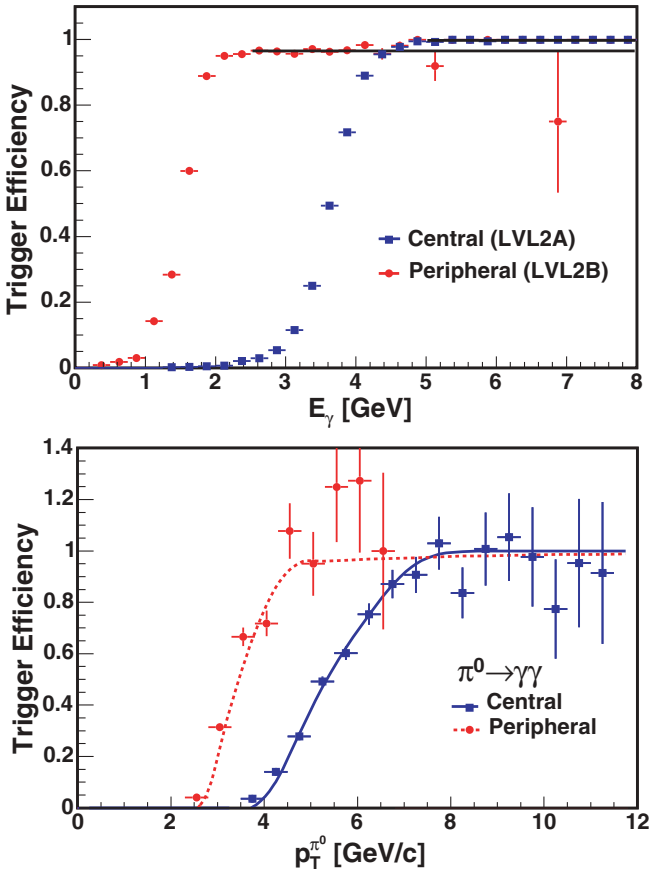

FIG. 5. (Color online) (Upper) Measured efficiency of single clusters of LVL2A (blue) and LVL2B (red) triggers as discussed in the text. The black lines are constant value fits to the plateau efficiency, greater than 99.7 (95%) for LVL2A (LVL2B). (Lower) Efficiency for neutral pion detection of the triggers as a function of π^0 p_T, calculated (solid curves) based on the efficiencies in (upper) and, as a cross-check (data points), compared to ratio of per equivalent minimum-bias event yields in the full trigger sample with the same in the true minimum bias sample. Because the latter is the ratio of two separate data samples, independent statistical fluctuations, as well as ∼8% systematic effects in the yield extraction (discussed Sec. III D4) in either sample can cause this measured ratio to be greater than 100%.

trigger and evaluating the efficiency for the trigger to select events containing a high p_T cluster. This analysis shows complete (100%) efficiency for the LVL2A trigger at momenta well above the trigger threshold of 3.5 GeV/c (95% above 1.5 GeV/c for LVL2B) for obtaining clusters that also pass all offline cluster cuts. This is demonstrated in Fig. 5 (upper). The "plateau" values are determined from fitting the region above the turn-on also shown.

The related trigger efficiency of reconstructed π^0's is calculated from a fast MC simulation based on these measured single cluster efficiencies. The calculation is performed both by using a integrated Gaussian fit to the single cluster efficiency and by directly using the finely binned histogram and constant plateau fit. Both methods give consistent results. The result for the latter method is shown in Fig. 5 (lower), solid curves. The calculation is cross-checked, as demonstrated by the data

TABLE II. Corrections in the PbGl and PbSc to the raw π^0 yield in central collisions (0–10%) and with TOF and shower shape cut applied. The main part of the efficiency loss in PbGl is due to the effect of bad module and edge cuts which is approximately 40% at high p_T for the PbGl and 20% for the PbSc, respectively.

p_T	PbGl		PbSc	
	3.25 GeV/c	8.5 GeV/c	3.25 GeV/c	8.5 GeV/c
$a_{\Delta y}$	0.068	0.080	0.216	0.246
ε	0.351	0.358	0.455	0.515
c_{conv}	0.93	0.93	0.90	0.90
$c_{\gamma\gamma}$	0.98798			

points in Fig. 5 (lower), which show the ratio of the yield from the two Level-2 trigger samples per *equivalent* number of minimum bias events to the same from the true minimum bias sample itself. We combine the yields obtained in the minimum bias event sample and the LVL2A (LVL2B) trigger sample above a cutoff of 6.5 GeV/c (3.5 GeV/c) where the trigger reaches efficiencies greater than 0.4 such that the correction factor is not allowed to be large. A conservative error of 3% is assigned to the efficiency calculations, resulting in a total error of ∼3–5%, based on the three studies: (1) comparisons of the data shown in Fig. 5, (2) comparisons of the two calculational methods, and (3) a study of the yields in the subsample of minimum bias events that also fired the triggers, similar to (1).

3. Other corrections

The calculated corrections are applied to the raw π^0 yield as given by Eq. (5). Table II shows the corrections in central collisions for two different bins in transverse momentum and for the PbGl and PbSc, respectively. As discussed above the effect of the cut on bad modules is included in the efficiency correction, due to its dependence on the depth of the electromagnetic shower.

Following the usual PHENIX procedure of modifying the quoted yield values for each finite sized p_T bin such that the measurement corresponds to p_T value at the bin center instead of the average p_T of the bin [49] (thereby facilitating taking ratios of spectra from different collision systems), a final correction is applied to the *yield* of each data point. Using a continuous function that is fit to the data points, values for the invariant yields at the centers of the chosen p_T bins are scaled by the ratio of the fit value at the fit's average p_T to the fit value at the bin center. This is an iterative procedure similar to the final efficiency correction described in Sec. III D1 above, with a smaller convergence criteria of <0.1% of the previous correction. The fit function is empirically determined and several functional forms were found to give similar performance (e.g., see Fig. 6 below) and negligible differences in the resulting corrections. All the functional forms either explicitly contain or implicitly converge quickly to, a pure power law form (const/p_T^n) above $p_T \sim 4$ GeV/c.

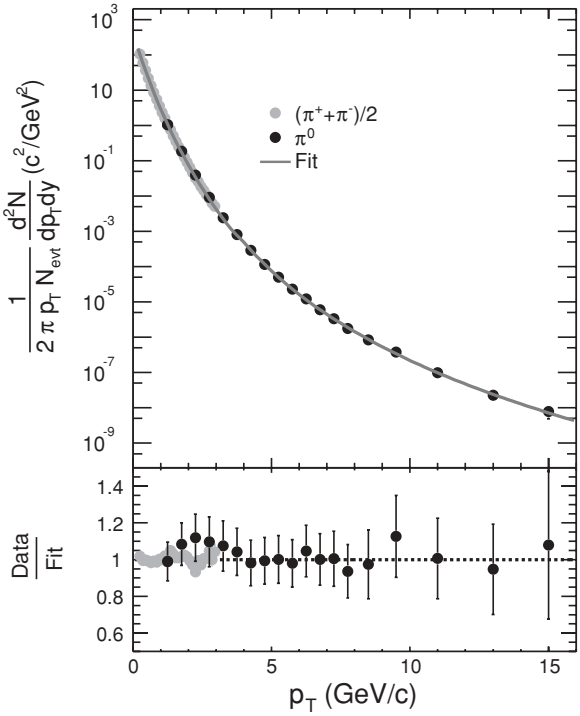

FIG. 6. Comparison of the combined π^0 result to the measurement of charged pions within the PHENIX experiment in minimum bias events. The fit (see previous Sec. III D3) considers the averaged result of the π^+ and π^- measurement [7] below $p_T = 3\,\mathrm{GeV}/c$ and the π^0 data above.

The spectral shape is discussed further under Secs. IV A and IV B.

4. Systematic errors

Each correction of the raw yield following Eq. (5) is afflicted with its own uncertainty, but already the determination of the π^0 raw yield itself is sensitive to the method of extraction. In particular it is sensitive to the choice of the fit function for the background scaling and the extraction window. In principle, both should be taken into account by the detector efficiency, but in the efficiency calculation no background subtraction is necessary. For this reason the systematic error of the peak extraction method is determined in two steps: first via the comparison of the raw yield obtained with two different fits for the background scaling, and second through the comparison of the fully corrected spectra for different sizes of the extraction window, for the real data as well as for the efficiency calculation.

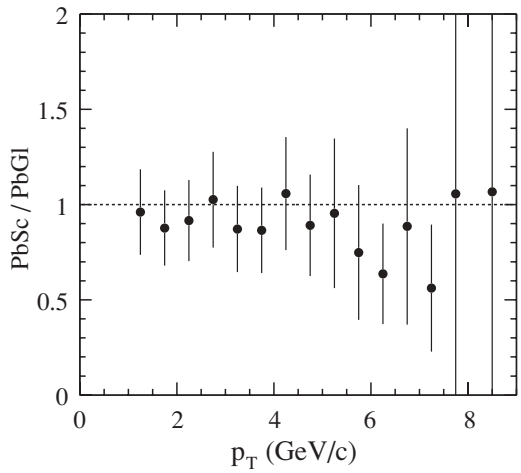

FIG. 7. Comparison of fully corrected spectra for the PbGl and the PbSc for peripheral events. Similar consistency is observed for all centralities. The error bars represent the statistical and systematic uncertainties.

The systematic error introduced by the efficiency calculation is estimated by comparing the fully corrected spectra for different PID criteria as well as for different additional smearing. The smearing (or energy resolution in the simulation) is changed in a way that a clear disagreement between the measured π^0 peak width and the peak width from the embedding is observed.

Apart from the uncertainty of the efficiency, the main contribution to the systematic error is the determination of the absolute energy scale. Based on the comparison of the π^0 peak positions in the data to the expectation from simulation the energy scale can only be determined or confirmed with limited accuracy, $\Delta(E)/E = 1.6\%$ in the PbSc and, because of the smaller acceptance, $\Delta(E)/E = 2\%$ in the PbGl.

The additional contributions to the systematic error that have not been discussed in detail involve the uncertainty of the conversion correction (2.9%) and of the acceptance calculation (2.5%) both due to small uncertainties in detector material and alignment. Table III provides a final overview of the various contributions to the total error of the π^0 measurement in the PbSc and the PbGl, respectively.

The most important cross-check of the final result is the comparison of the result for the two different detector types PbGl and PbSc, which is shown for peripheral events in Fig. 7. A good agreement within the errors is seen and similar consistency is found in all centralities. Because they represent essentially independent measurements, the two

TABLE III. Summary of the dominant sources of systematic errors on the π^0 yields extracted independently with the PbGl and PbSc electromagnetic calorimeters in central events for different p_T. For comparison the statistical uncertainty is also shown.

p_T (GeV/c)	PbGl		PbSc	
	3.25	8.5	3.25	8.5
Yield extraction	8.7%	6.%	9.8%	7.3%
Efficiency	11.4%	11.4%	11.4%	11.4%
Acceptance	2.5%	2.5%	2.5%	2.5%
Conversions	2.9%	2.9%	2.9%	2.9%
Level-2 data	—	—	—	3%
Energy scale	13.8%	14.1%	10.5%	11.2%
Total syst.	20.5%	19.3%	18.8%	18.7%
Statistical	10.6%	50%	8.1%	26.6%

results are averaged and the total error of the combined result is reduced using a standard weighted least-squares method also described in Ref. [50]. An additional cross-check of the final result based on isospin symmetry is provided by the measurement of charged pions in the central arm [7], this is shown for minimum-bias collisions in Fig. 6. The neutral pion measurement smoothly extends the result for charged pions to larger transverse momenta.

E. $R_{AA}(p_T)$ measurement

Using the invariant yields obtained from the above-described analysis and the separately measured invariant cross section for π^0 production in $p+p$ collisions [46], we calculate the nuclear modification factor, R_{AA}, according to

$$R_{AA}(p_T) = \frac{\left(1/N_{AA}^{evt}\right) d^2N_{AA}^{\pi^0}/dp_T\,dy}{\langle T_{AA}\rangle \times d^2\sigma_{pp}^{\pi^0}/dp_T\,dy}, \tag{6}$$

where $\langle T_{AA}\rangle$ is the average Glauber nuclear overlap function for the centrality bin under consideration

$$\langle T_{AA}\rangle \equiv \frac{\int T_{AA}(\mathbf{b})\,d\mathbf{b}}{\int \left(1 - e^{-\sigma_{pp}^{inel} T_{AA}(\mathbf{b})}\right) d\mathbf{b}}, \tag{7}$$

from which the corresponding average number of nucleon-nucleon collisions, $\langle N_{coll}\rangle = \sigma_{pp}^{inel}\langle T_{AA}\rangle$, can be easily obtained [51].

F. $R_{AA}(\Delta\phi)$ measurement

The measurement of the raw π^0 yield with respect to the event reaction plane, $\Delta\phi = \phi(\pi^0) - \Psi$, proceeds as described in Sec. III D for the p_T spectrum except that we measure the yields as a simultaneous function of both p_T and $\Delta\phi$. Because the beam-beam counters have 2π acceptance, PHENIX can measure the π^0 yields with uniform acceptance over $0 < \Delta\phi < 2\pi$ even though the electromagnetic calorimeters have only 1π nominal azimuthal acceptance. Because the measurement of Ψ is ambiguous with respect to a 180° rotation of the reaction plane, and because we expect the π^0 yields to be symmetric with respect to reflection around $\Delta\phi = 0$, we measure the π^0 yields in six bins of $|\Delta\phi|$ over the range $0 < |\Delta\phi| < \pi/2$. For each p_T bin we evaluate the ratio,

$$R(\Delta\phi_i, p_T) = \frac{\Delta N(\Delta\phi_i, p_T)}{\sum_{i=1}^{6} \Delta N(\Delta\phi_i, p_T)}, \tag{8}$$

where $N(\Delta\phi_i, p_T)$ is the measured number of π^0's in a given $(\Delta\phi, p_T)$ bin, $\Delta\phi_i$ representing one orientation of $\Delta\phi$. Because the PHENIX central arm acceptance is effectively constant as a function of $\Delta\phi$ and we do not expect any azimuthal dependence of our π^0 efficiency corrections, $R(\Delta\phi_i, p_T)$ can be written as:

$$R(\Delta\phi_i, p_T) = R_{AA}(\Delta\phi_i, p_T)/R_{AA}(p_T). \tag{9}$$

Using the measured $R_{AA}(p_T)$ values we can directly convert the $R(\Delta\phi, p_T)$ to $R_{AA}(\Delta\phi, p_T)$ without having to apply acceptance and efficiency corrections to the reaction-plane dependent yields. These corrections are already included in the $R_{AA}(p_T)$ values as described above.

However, before applying this procedure we must first correct the $R(\Delta\phi, p_T)$ values for the finite resolution of the reaction plane measurement. One goal of our measurement is to determine $R_{AA}(\Delta\phi, p_T)$ without assuming any particular functional dependence on $\Delta\phi$. For purposes of correcting for reaction plane resolution, we take advantage of the fact that the observed π^0 yields and hence the nuclear modification vary with $\Delta\phi$ to first order as

$$R^{raw}(\Delta\phi, p_T) \approx R_0\left[1 + 2v_2^{raw}\cos(2\Delta\phi)\right], \tag{10}$$

ignoring the much smaller higher-order harmonics such as v_4 terms. The superscript "raw" denotes the values not corrected for the reaction plane resolution. This resolution reduces v_2 by the factor $\sqrt{2\langle\cos 2(\Psi_1 - \Psi_2)\rangle}$ [44], which is given by the independent measurement of Ψ in the two BBC's shown previously in Fig 1. For each p_T bin in a given centrality class we fit the $R(\Delta\phi, p_T)$ values to the functional form in Eq. (10) and then correct each measured $R(\Delta\phi, p_T)$ value according to

$$R^{corr}(\Delta\phi, p_T) = R^{raw}(\Delta\phi, p_T)\left[\frac{1 + v_2^{corr}\cos(2\Delta\phi)}{1 + v_2^{raw}\cos(2\Delta\phi)}\right], \tag{11}$$

with $v_2^{corr} = v_2^{raw}/\sqrt{2\langle\cos 2(\Psi_1 - \Psi_2)\rangle}$. We estimate the systematic error in the reaction plane resolution correction by propagating the centrality dependent uncertainties in $\sqrt{2\langle\cos 2(\Psi_1 - \Psi_2)\rangle} = \langle\cos 2(\Psi_{meas} - \Psi_{true})\rangle$ from Table I. Of course, the above-described correction only strictly applies if $R_{AA}(\Delta\phi)$ is well described by the functional form in Eq. (10). Although we do observe some departure from this harmonic form in the data, the differences are typically below 5% so our correction will not introduce a large error.

IV. RESULTS

A. π^0 transverse-momentum spectra and nuclear modification factors

The π^0 invariant yields obtained using the procedure described in Sec. III D are presented in Fig. 8 as a function of p_T for the nine chosen centrality bins. With the increased statistics included in this analysis, we have extended the p_T range of the previous PHENIX measurement by at least 2 GeV/c for all centrality bins. The p_T range of the central bin has been extended from 10 to 14 GeV/c. Where the spectra overlap, the results shown here are consistent with the previously published results within systematic errors. The errors shown on the points in Fig. 8 include statistical errors and point-to-point varying systematic errors. The appendix tabulates the π^0 spectra plotted in Fig. 8 (centralities: 0–10, 10–20, ... , 70–80, 80–92%) plus the combined spectra for centralities 0–20, 20–60, and 60–92%, which are used for

comparison to other neutral meson measurements [13]. The spectra in Fig. 8 depart from the exponential-like shape above 3 GeV/c, which is consistent with the expectation that high-p_T hadron production is dominated by hard-scattering processes that produce a power-law p_T spectrum [52] for hadrons resulting from quark and gluon fragmentation.

In previous publications, we have established the suppression of high-p_T π^0 production in Au+Au collisions [3,6]. This suppression cannot be easily seen given the large range of invariant yield covered by Fig. 8.

To evaluate the suppression of high-p_T π^0's, we show in Fig. 9 the p_T dependence of the π^0 nuclear modification factor, $R_{\rm AA}(p_T)$, for the nine individual bins of collision centrality and for the full minimum-bias centrality range 0–92.2%. We make use of the PHENIX Run3 $p+p$ baseline π^0 data. [47]. The error bars on the data in Fig. 9 include contributions from statistical errors in the Au+Au and $p+p$ measurements and from the systematic errors that do not cancel between the measurements. The separate band shown in each panel indicates p_T-independent errors on the $R_{\rm AA}$ measurement resulting from uncertainties in estimating $T_{\rm AA}(x, y)$ and systematic errors on the normalization of the Au+Au and $p+p$ measurements that do not cancel. As in previously published articles (e.g., Refs. [4,5,7]), a factor of ∼5 high p_T π^0 suppression in the most central Au+Au collisions, $R_{\rm AA} \approx 0.2$, is observed, with the suppression approximately p_T independent for $p_T > 5$ GeV/c. The suppression at high p_T decreases in more peripheral collisions such that the two most peripheral bins have $R_{\rm AA}$ values consistent with unity for $p_T > 3$ GeV/c.

B. Suppression via spectrum shift

The suppression of high-p_T particles as shown above was determined by comparison of the semi-inclusive measured yields as a function of centrality in Au+Au collisions at $\sqrt{s_{NN}} = 200$ GeV to the $\langle T_{\rm AA}\rangle$ scaled p_T spectrum from $p+p$ collisions [53]. A direct comparison of the 0–10% centrality Au+Au spectrum to the scaled $p+p$ spectrum is shown in Fig. 10 as a log-log plot to emphasize the pure power law

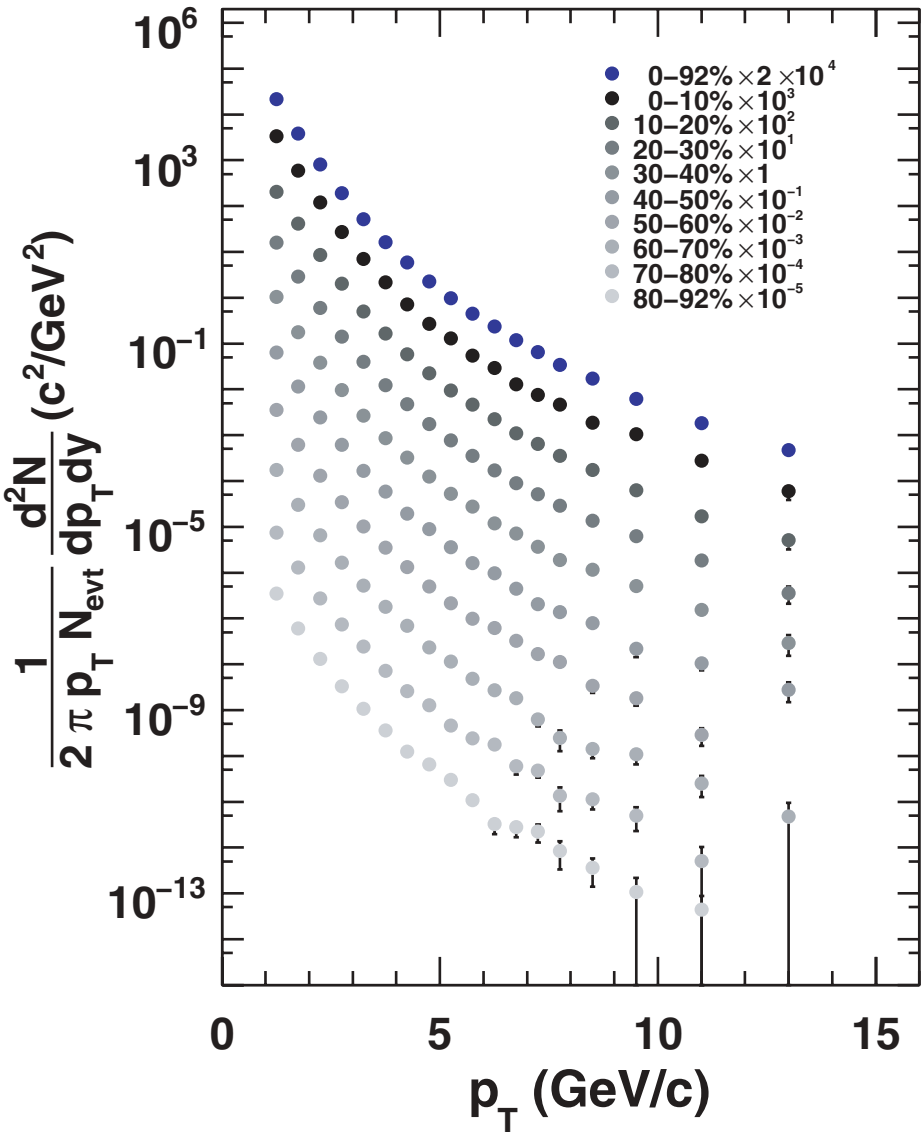

FIG. 8. (Color online) Neutral pion invariant yields as a function of p_T measured in minimum bias and nine centrality classes in Au+Au collisions at $\sqrt{s_{NN}} = 200$ GeV. Spectra for different centralities are scaled for clarity. Errors are total errors, full systematic, and statistical added in quadrature.

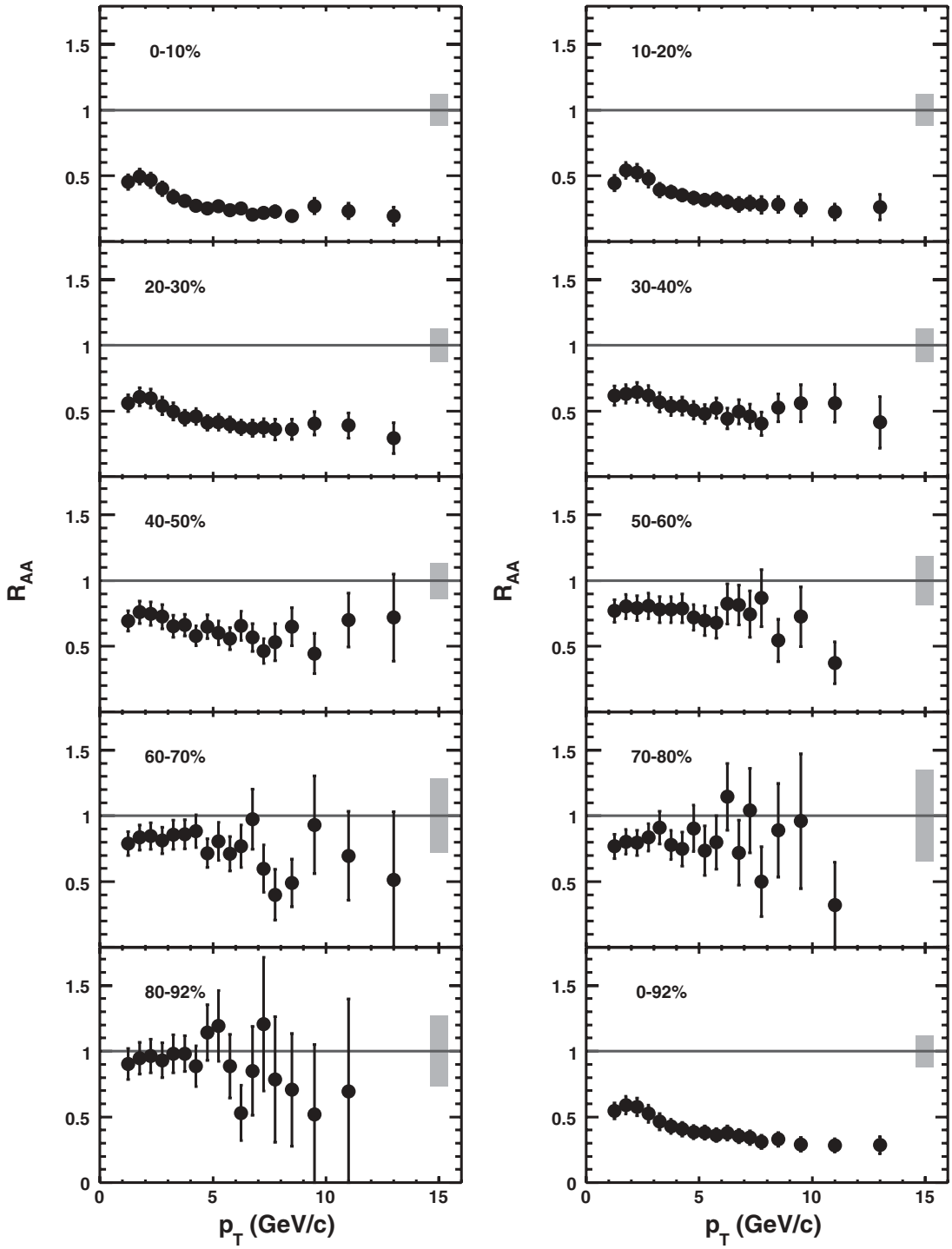

FIG. 9. Nuclear modification factor R_{AA} for neutral pions as a function of p_T for different centralities. The shaded error band around unity indicates the uncertainty in scaling factor T_{AA} and an overall scale uncertainty in the $p+p$ reference.

dependence of the data for $p_T > 3$ GeV/c. The suppression is commonly expressed by taking R_{AA} the ratio of the point-like scaled semi-inclusive yield to the reference distribution [Eq. (6)].

As illustrated in Fig. 10, instead of viewing the suppression in the nuclear modification factor as "vertical" reduction of the Au + Au yields, it can equally well be taken as a "horizontal" shift in the $\langle T_{\mathrm{AA}}\rangle$ scaled Au+Au spectrum, such that

$$\frac{\left(1/N_{\mathrm{AA}}^{\mathrm{evt}}\right)d^2N_{\mathrm{AA}}(p_T)/dp_Tdy}{\langle T_{\mathrm{AA}}\rangle} = \frac{d^2\sigma_{pp}[p'_T{=}p_T{+}S(p_T)]}{dp'_Tdy} \times [1 + dS(p_T)/dp_T], \quad (12)$$

where the last term in parenthesis is the Jacobian, dp'_T/dp_T.

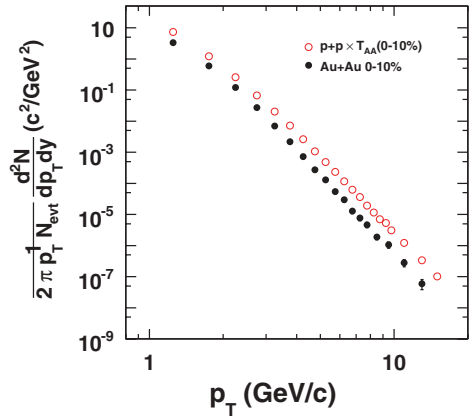

FIG. 10. (Color online) Log-log plot of central Au+Au and scaled $p+p$ π^0 p_T distributions.

Furthermore, owing to the pure power law of the $p+p$ reference spectrum, $Ed^3\sigma/dp^3 \propto p_T^{-n}$ with $n = 8.10 \pm 0.05$ above $p_T \approx 4$ GeV/c, the relative shift of the spectra—assumed to be the result of energy loss for the Au+Au spectrum—is easily related to the equivalent ratio, $R_{\rm AA}(p_T)$:

$$R_{\rm AA}(p_T) = \frac{[p_T + S(p_T)]^{-n+1}}{{p_T}^{-n+1}}[1 + dS(p_T)/dp_T] \qquad (13)$$

$$= [1 + S(p_T)/p_T]^{-n+1}[1 + dS(p_T)/dp_T]$$

where the exponent is $n-1$ because the relevant shift is in the $d\sigma/dp_T$ spectrum rather than in $d\sigma/p_T\,dp_T$. The fact that the Au+Au and reference $p+p$ p_T spectra are parallel in Fig. 10 provides a graphical illustration that the fractional p_T shift in the spectrum, $S(p_T)/pt = S_0$, is a constant for all $p_T > 3$ GeV/c, which also results in a constant ratio of the spectra, $R_{\rm AA}(p_T)$. For the constant fractional shift, the Jacobian is simply $dS(p_T)/dp_T = S_0$ and Eq. (13) becomes:

$$R_{\rm AA}(p_T) = (1 + S_0)^{-n+2}, \qquad (14)$$

$$R_{\rm AA}(p_T)^{1/(n-2)} = \frac{1}{1 + S_0}. \qquad (15)$$

The effective fractional energy loss, $S_{\rm loss}$, is related to the fractional shift in the measured spectrum, S_0. The hadrons that would have been produced in the reference $p+p$ spectrum at transverse momentum $p_T + S(p_T) = (1 + S_0)p_T$, were detected with transverse momentum, p_T, implying a fractional energy loss:

$$S_{\rm loss} = 1 - 1/(1 + S_0) = 1 - R_{\rm AA}(p_T)^{1/(n-2)}. \qquad (16)$$

The fractional energy loss $S_{\rm loss}$ as a function of centrality expressed as $N_{\rm part}$ is shown in Fig. 11 for two different p_T ranges, $3 < p_T < 5$ GeV/c and $5 < p_T < 7$ GeV/c. There appears to be a small decrease of $S_{\rm loss}$ with increasing p_T, but the main observation from Fig. 11 is that $S_{\rm loss}$ increases approximately like $N_{\rm part}^{2/3}$, as suggested by GLV [54] and PQM [55].

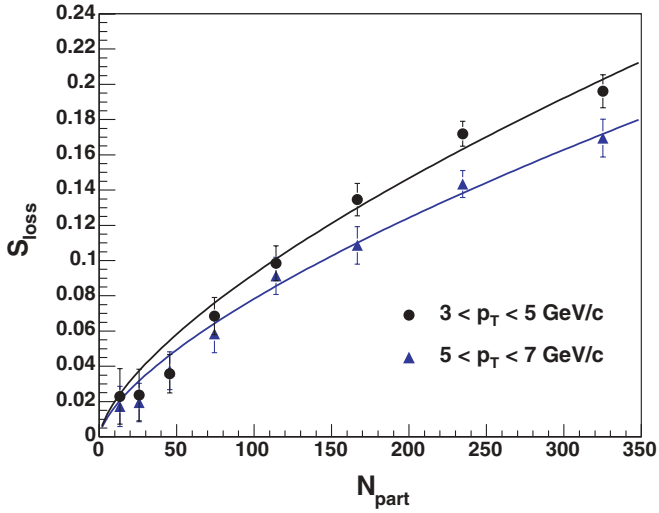

FIG. 11. (Color online) Fractional energy loss $S_{\rm loss}$ obtained from Eq. (16) versus centrality given by $N_{\rm part}$. The lines are fits of the form $\propto N_{\rm part}^{2/3}$ for each p_T range.

It is important to realize that the effective fractional energy loss, $S_{\rm loss}$ estimated from the shift in the p_T spectrum, is actually less than the real average energy loss at a given p_T, i.e., the observed particles have p_T closer to the original value than to the average. The effect is similar to that of "trigger bias" [56] where, due to the steeply falling spectrum, the $\langle z \rangle$ of detected single inclusive particles is much larger than the $\langle z \rangle$ of jet fragmentation, where $z = \vec{p}_{\pi^0} \cdot \vec{p}_{\rm jet}/p_{\rm jet}^2$. Similarly for a given observed p_T, the events at larger p_T' with larger energy loss are lost under the events with smaller p_T' with smaller energy loss.

It should be noted that fluctuations due to the variation of the path length and densities traversed by different partons also contribute to the difference between the true $S_{\rm loss}$ ($S_{\rm loss}^{\rm true}$) and that which is observed ($S_{\rm loss}^{\rm obs}$). However, as long as the dependencies of the induced energy loss on path length and parton energy approximately factorize, these fluctuations will also produce a p_T-independent reduction in $S_{\rm loss}^{\rm obs}$ compared to $S_{\rm loss}^{\rm true}$.

C. Angle dependence of high p_T suppression

To try to separate the effects of the density of the medium and path length traversed, we study the dependence of the π^0 yield with respect to the reaction plane. For a given centrality, variation of $\Delta\phi$ gives a variation of the path length traversed for fixed initial conditions, whereas varying the centrality allows determination of the effect of varying the initial conditions.

Figures 12 and 13 show the nuclear modification factor $R_{\rm AA}$ as a function of $\Delta\phi$ integrated over $3\,{\rm GeV}/c < p_T < 5\,{\rm GeV}/c$ and $5\,{\rm GeV}/c < p_T < 8\,{\rm GeV}/c$, respectively. For all centralities (eccentricities) considered, there is almost a factor of 2 more suppression out-of-plane ($\Delta\phi = \pi/2$) than in-plane ($\Delta\phi = 0$), something that is immediately apparent in viewing the data in this fashion—explicitly displaying information that is implicit only in $R_{\rm AA}$, v_2, or the combination thereof.

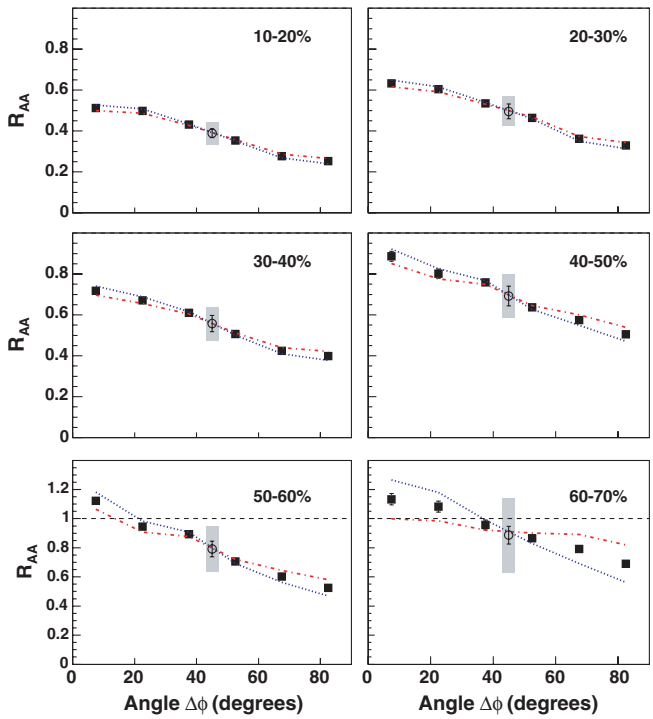

FIG. 12. (Color online) R_{AA} versus $\Delta\phi$ for π^0 yields integrated over $3 < p_T < 5$ GeV/c. Most statistical errors are smaller than the size of the points. The lines following the data points show the bin-to-bin errors resulting from the uncertainty in the reaction plane resolution correction (Fig. 1) and from bin-to-bin uncertainties in the R_{AA} values. The shaded band indicates the overall R_{AA} uncertainty.

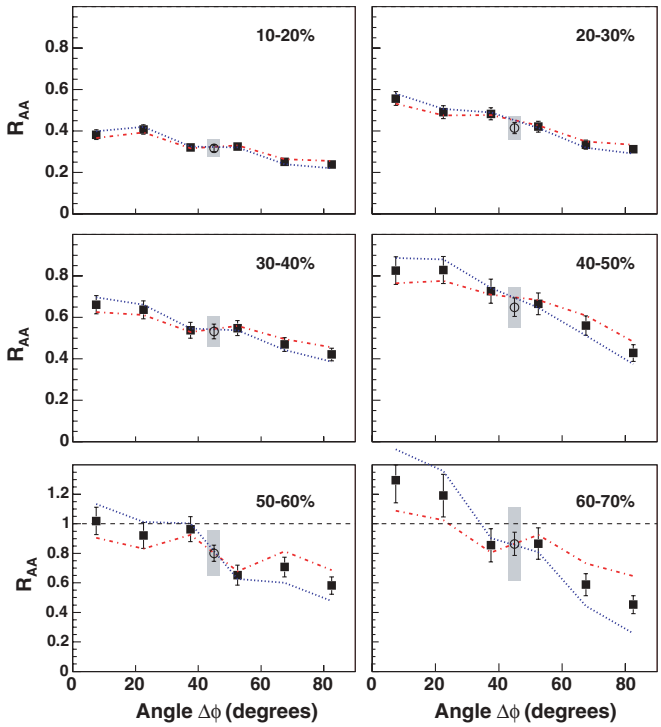

FIG. 13. (Color online) R_{AA} versus $\Delta\phi$ for π^0 yields integrated over $5 < p_T < 8$ GeV/c. The error lines and band are the same as in Fig. 12.

Strikingly, in contradiction to the data the variation in R_{AA} with respect to the reaction plane expected by parton energy loss models [29,57] should be much smaller for the more peripheral bins than for the central bins. As a result, the suppression vanishes (and perhaps an enhancement is observed) for smaller $\Delta\phi$ in the peripheral bins, corresponding to small path length traversed in the medium. Although collective elliptic flow effects, usually not included in those models, are known to boost in-plane (compared to out-of-plane) particle production [2,42], it is unclear how such collective effects can still play such an important role at the high-p_T bins considered. This may point to the possible need for a formation time before suppression can occur [58] and which could also explain why attempts to describe the azimuthal asymmetry v_2 solely in terms of purely geometrical energy loss have failed. Figures 14 and 15 give the angular dependence in terms of the fractional energy loss $S_{\rm loss}$, and provide essentially the same information as shown in the plots of $R_{AA}(\Delta\phi)$ in Figs. 12 and 13. Once again we see a large variation in energy loss as a function of angle. All the measurements of R_{AA} or equivalently $S_{\rm loss}$ vs. reaction plane and centrality, provide new constraints to models of jet quenching. To better understand the implications of the results shown in these figures, we will attempt in the next section to find a common geometric description of the angle and centrality dependences in terms of an estimated path length of the parton in the medium.

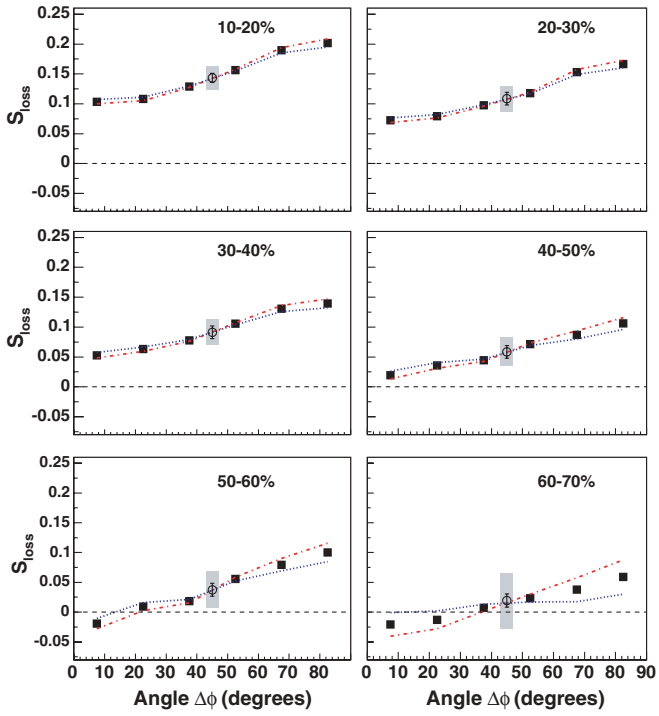

FIG. 14. (Color online) $S_{\rm loss}$ versus $\Delta\phi$ for π^0 yields integrated over $3 < p_T < 5$ GeV/c. The statistical errors are smaller than the size of the points. The lines following the data points show the bin-to-bin errors resulting from the uncertainty in the reaction plane resolution correction (Fig. 1) and from bin-to-bin uncertainties in the $S_{\rm loss}$ values. The shaded band indicates the overall $S_{\rm loss}$ uncertainty.

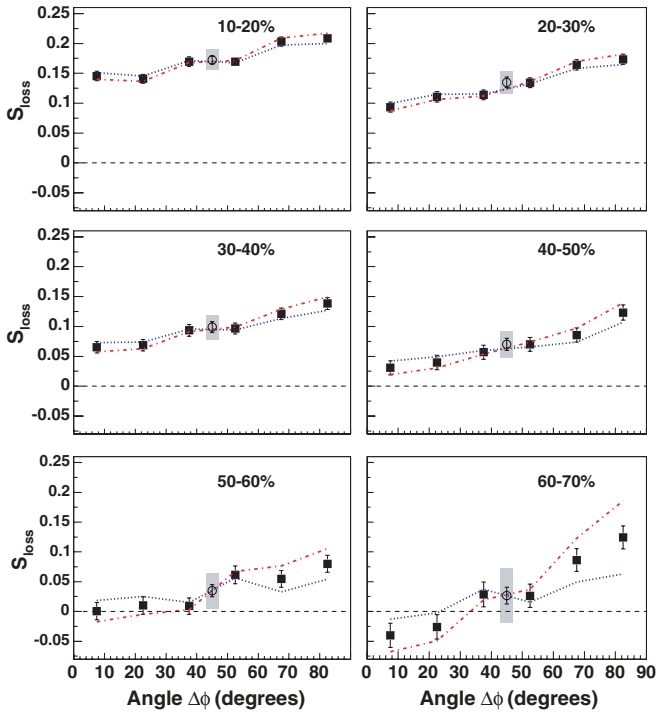

FIG. 15. (Color online) $S_{\rm loss}$ versus $\Delta\phi$ for π^0 yields integrated over $5 < p_T < 8$ GeV/c. The error lines and band are the same as in Fig. 14.

D. Path-length dependence of energy loss

To analyze the path-length dependence of parton energy loss using the data presented here we will use different methods for estimating the path lengths of partons in the medium as a function of centrality and $\Delta\phi$. The "standard" approach would be to evaluate a length-weighted integral of the participant charge density in the medium along the parton path. We will adopt such an approach, described by the parameter L_{xy} defined below, but we will also consider two other simplified approaches that may help indicate which physics is most relevant in determining the observed suppression. We first consider, simply, L_ε, the distance from the edge to the center of the elliptical overlap zone of the Au+Au collision to represent the average path length of a parton in the medium. Then we try to weight the path length (or length-squared) traversed by a parton from the center of the ellipse by the participant density in the transverse plane: $\rho L(\Delta\phi)$ [$\rho L^2(\Delta\phi)$]. Finally, we do the same path-length weighting for partons produced across the overlap ellipse, with hard-scattering production points weighted by $T_{\rm AA}(x, y)$: ρL_{xy} (ρL_{xy}^2). It is obvious that such a $\Delta\phi$-dependent analysis is not possible from just a simple combination of $R_{\rm AA}$ and v_2.

In detail, the three approaches considered here are as follows:

(i) The simplest picture for the angular dependence of the energy loss in noncentral collisions is that it is due to the asymmetric shape of the overlap region of the colliding nuclei. Taking this idea to its extreme, only the simplest length scale, the length of the overlap region in a particular direction, matters.

To evaluate this length, we first estimated the root-mean-square radius and eccentricity of an ellipse approximating the shape of the overlap region from the transverse distribution of the participant density calculated using standard Glauber Monte Carlo techniques in which all variations of impact parameter, etc., for a given centrality class are taken account in the quoted errors of the geometrical quanties [51]. Only the errors on the averages are considered; for instance, the fluctuations in the event-by-event participant eccentricity are taken into account in the quoted error of the centrality averaged ε. We then estimated the path length, L_ε, of partons emitted at a given angle $\Delta\phi$ by evaluating the distance from the center of ellipse to the edge. For each centrality, the value of L_ε is calculated as a function of $\Delta\phi$:

$$L_\varepsilon = \frac{b\sqrt{1+\varepsilon}}{\sqrt{1+\varepsilon\cos(2\Delta\phi)}}, \tag{17}$$

where $b = \sqrt{\langle x^2\rangle}$, the root-mean-square semiminor axis (conventionally taken in the x direction) and $\varepsilon = (\langle y^2\rangle - \langle x^2\rangle)/(\langle y^2\rangle + \langle x^2\rangle)$ are taken from the Monte Carlo Glauber calculation. The errors on b and ε are propagated through Eq. (17) for the error on L_ε. A plot of L_ε as a function of centrality and $\Delta\phi$ is shown in Fig. 16.

As described previously in Section III F, the effect and associated uncertainties of reaction plane resolution are

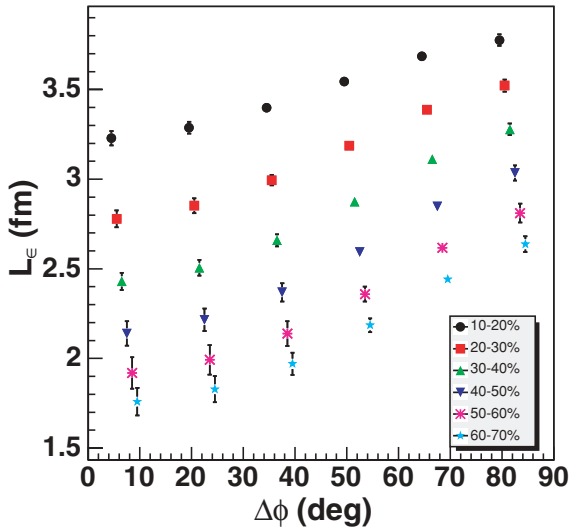

FIG. 16. (Color online) Simple geometrical length estimator L_ε with uncertainties plotted *vs.* angle with respect to reaction plane, plotted for the six centralities considered as indicated in the legend. The angle with respect to reaction plane, $\Delta\phi$, is for the center of the bins (7.5°, 22.5°, 37.5°, 52.5°, 67.5°, and 82.5°), the same for all centralities. For visual clarity a centrality dependent offset is introduced.

taken into account (i.e., corrected for) in the values and quoted errors of $R_{AA}(\Delta\phi)$. Thus detector effects of reaction plane resolution should not be considered in the evaluation of L_ε.

(ii) Although the participant density is used to evaluate the dimensions of the ellipse, the above analysis ignores the dependence of participant density on position in the transverse plane. Thus as a natural extension of the simple length scale in (i), for another analysis of the dependence of energy loss on $\Delta\phi$, we assume that the color-charge density in the medium is proportional to participant density (see Refs. [29,59]) and evaluate ρL, the integral of this density along the path length of the particle. This quantity is proportional to the opacity of the medium ($n = L/\lambda$) divided by some undetermined cross section. Although the integral in principle extends to infinity the participant density naturally cuts off the integral outside the collision zone.

$$\rho L = \int_0^\infty dr\ \rho_{\text{part}}(r, \Delta\phi). \tag{18}$$

To account for the possible role of LPM coherence in the energy loss process, we evaluate a similar quantity, including an extra factor of r in the integrand.

$$\rho L^2 = \int_0^\infty dr\ r\rho_{\text{part}}(r, \Delta\phi). \tag{19}$$

We note that a Bjorken $1/\tau$ expansion of the medium would approximately cancel one power of r in the above expressions. Then, ρL, might represent LPM energy

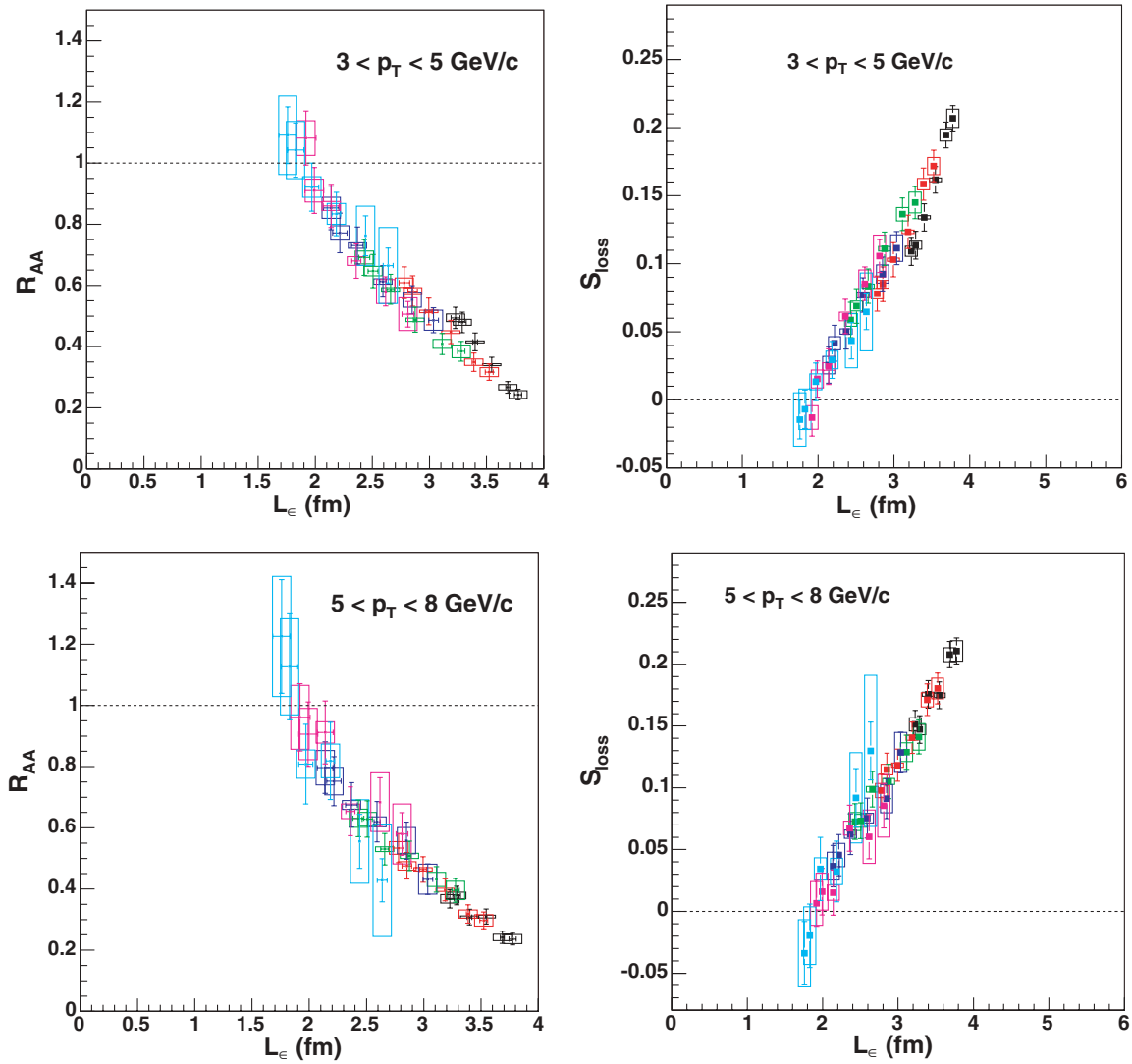

FIG. 17. (Color online) R_{AA} and S_{loss} versus L_ε whose definition is explained in the text. Each data point represents a centrality bin and $\Delta\phi$ (azimuth defined *w.r.t.* the reaction plane) bin combination. The six centrality bins are denoted by different colors as follows: cyan, 60–70%; mauve, 50–60%; blue, 40–50%; green, 30–40%; red, 20–30%; black, 0–10%. Within each centrality group, the six different data points correspond to the same $\Delta\phi$ bins as in Figs. 12–15. The height of the bars around each data point represent the systematic error in $R_{AA}(\Delta\phi)$ (S_{loss}) corresponding to L_ε.

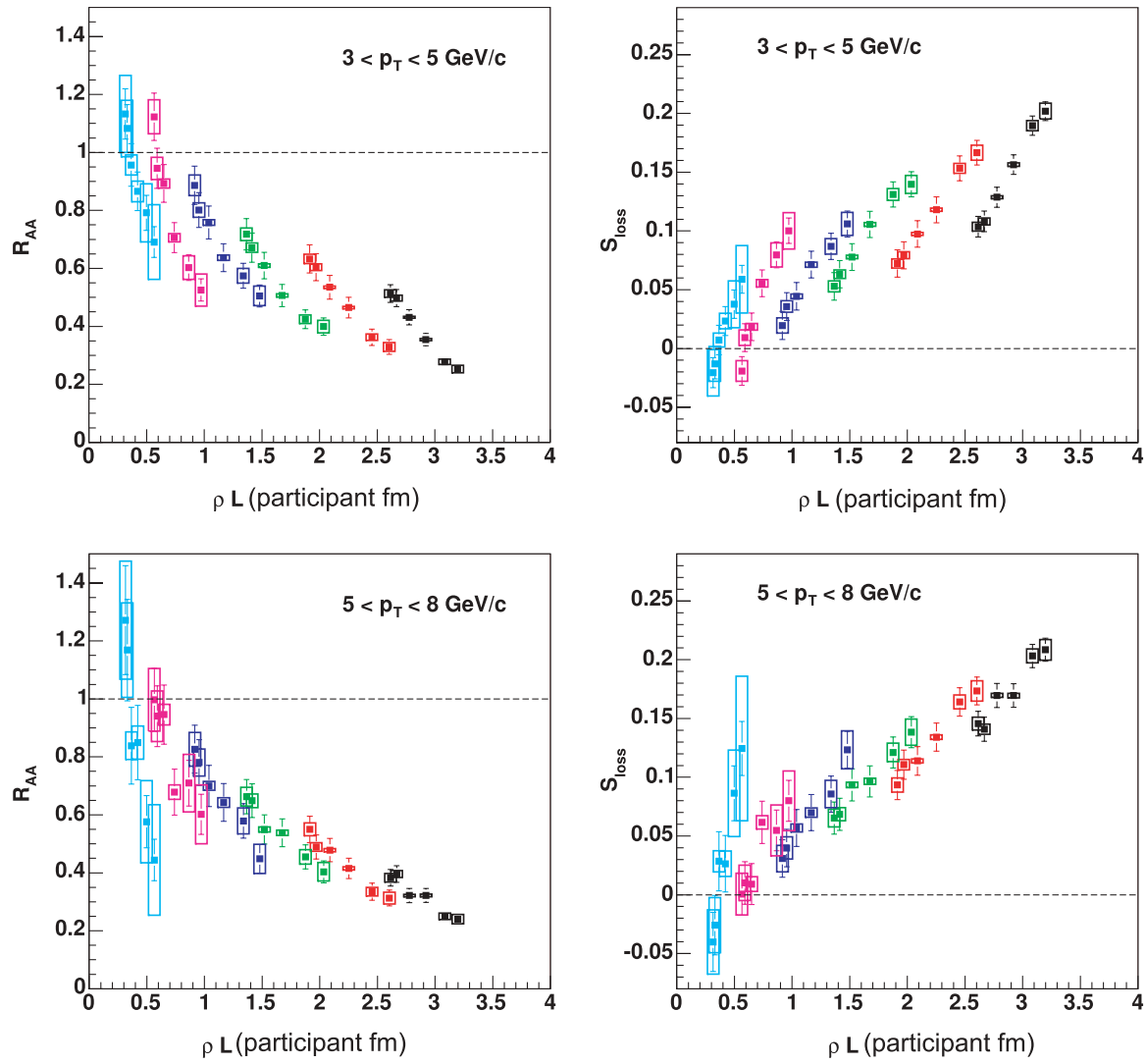

FIG. 18. (Color online) R_{AA} and S_{loss} versus ρL, the participant density-weighted path length. The units of ρL are (nucleon) participants times fm. Colors/data points as in Fig. 17.

loss in the presence of one-dimensional expansion. In the above integrals we assume all jets originate at the center of the collision region similar to our assumption for L_ε.

(iii) A final refinement on our geometrical calculation evaluates integrals like those in Eq. (18) for jet production points distributed over the collision region to better account for geometric fluctuations. We are using a Monte Carlo algorithm to sample jet production points (x_0, y_0) according to $T_{AA}(x, y)$ weighting and $\Delta\phi$ angles from a uniform distribution. For each jet, we evaluate the integral of the color-charge density (assumed $\propto$ participant density as above) along the path of the parton out of the medium,

$$\rho L_{xy} = \int_0^\infty dl\ \rho_{\text{part}}(x_0 + l\cos\Delta\phi,\ y_0 + l\sin\Delta\phi). \tag{20}$$

The above Monte Carlo sampling yields a distribution of ρL_{xy} values for each centrality. The larger values of ρL_{xy} correspond to larger energy loss, which means these jets will have smaller contribution to the observed yield. To take this into account, a weighting factor is applied when evaluating $\langle \rho L_{xy} \rangle$. We assume that the energy loss can be represented by our empirical energy loss, S_{loss} which we take to be proportional to ρL_{xy} but with an undetermined multiplicative constant, κ. We determine this constant in each centrality bin by relating S_{loss} to R_{AA} using Eq. (16) and then evaluating the survival probability of each jet through

$$P_{\text{surv}}(\rho L_{xy}) = 1 - (\kappa \rho L_{xy})^{(n-2)} \tag{21}$$

and requiring that the resulting suppression summed over all sampled jets agrees with the measured $\Delta\phi$-integrated R_{AA} for that centrality bin. This determines the constant $\kappa(N_{\text{part}})$ and allows us to

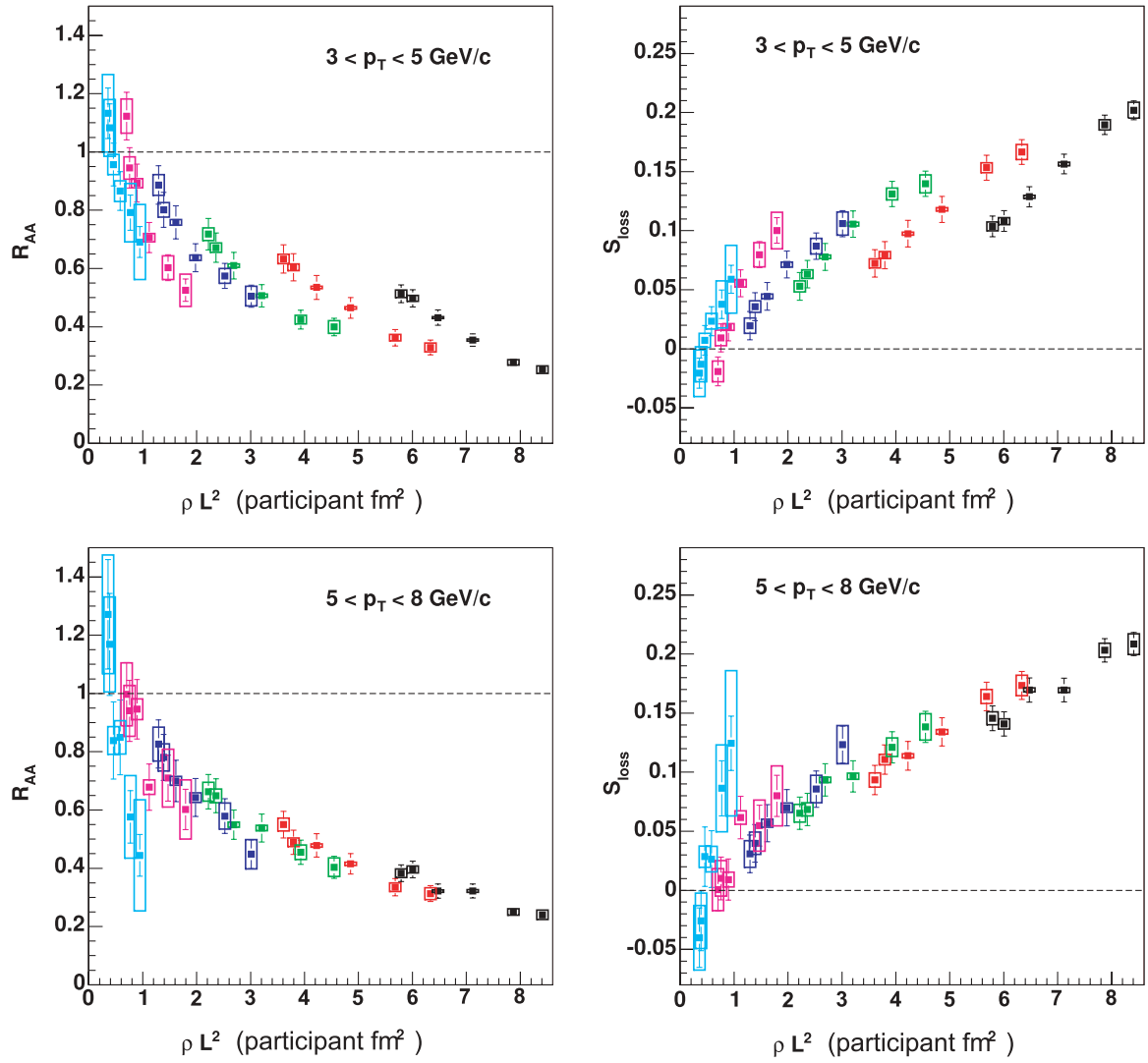

FIG. 19. (Color online) R_{AA} and S_{loss} versus ρL^2, the density-weighted path length squared. The units of ρL^2 are (nucleon) participants times fm squared. Colors/data points as in Fig. 17.

evaluate a survival probability weighted average for ρL_{xy}.

We now evaluate how well the three above-described treatments of the geometry of the parton propagation in the medium perform in providing a consistent description of the $\Delta\phi$ *and* centrality dependence of π^0 suppression.

The plots shown in Figs. 17–21 illustrate the path-length and path-density line-integral dependence of suppression using our empirical estimators. The integral of the ρ_{part} density (i.e., its normalization) is commonly called the "number of participants" N_{part}. The systematic error, mostly from N_{part}, in the estimators due to the uncertainty of the overlap geometry parameter in a centrality class is approximately 10–20%, decreasing with centrality and is not included in the figures. This uncertainty is derived by propagating the impact parameter and eccentricity uncertainties from the PHENIX Glauber MC itself [1,41].

From Figs. 17–21 it is evident that the individual centrality bins exhibit roughly parallel linear dependencies of the variables vs ρL_{xy}, etc. For the $3 < p_T < 5$ GeV/c bin these slopes are such that the curves are disjoint due to the steeper value of the slopes in each centrality group (each color in the plots) compared to the bin-to-bin trend. For the higher $5 < p_T < 8$ GeV/c bin, the slopes in the individual centralities flatten such that they follow the bin-to-bin trend much better. These are meant to be qualitative statements. We defer further quantitative tests, e.g., statistical tests, to subsequent data sets (e.g., the larger PHENIX 2004–2005 Run4 data set) with which we can improve statistical precision.

In this spirit, we note several other interesting qualitative dependencies:

(i) R_{AA} is universal as a function of L_ε for all centrality classes and both p_T ranges.

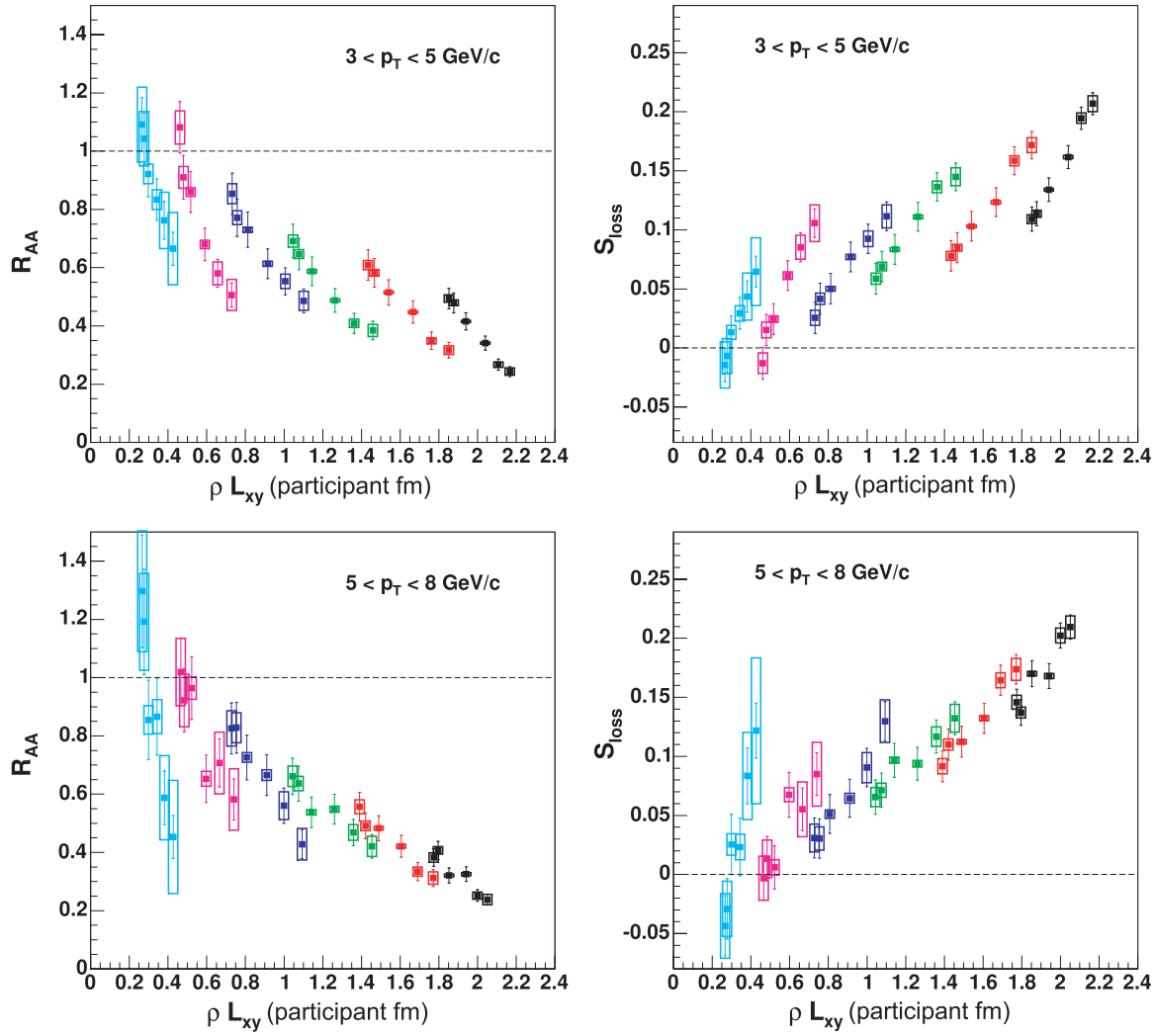

FIG. 20. (Color online) $R_{\rm AA}$ and $S_{\rm loss}$ versus ρL_{xy} whose definition is explained in the text. The units of ρL_{xy} are (nucleon) participants times fm. Colors/data points as in Fig. 17.

(ii) $S_{\rm loss}$ is universal and is a linear function of L_ε for all centrality classes and both p_T ranges.

(iii) Within our errors, we see no suppression $R_{\rm AA} \approx 1$, hence no apparent fractional energy loss $S_{\rm loss}$ for $L_\varepsilon \leqslant 2$ fm.

(iv) Neither $R_{\rm AA}$ nor $S_{\rm loss}$ is universal as a function of ρL, ρL^2, or ρL_{xy} for $3 < p_T < 5$ GeV/c.

(v) For the higher $5 < p_T < 8$ GeV/c p_T bin, $S_{\rm loss}$ ($R_{\rm AA}$) approaches universality as a function of ρL^2, ρL, and ρL_{xy} (possibly to a lesser extent for the latter two) but does not achieve the level of universality found for L_ε. The largest deviations from universality in these quantities are toward the longer axis (perpendicular to the event plane) in the more peripheral events. The dependence of $S_{\rm loss}$ is reasonably linear as a function of ρL but tends to level off at larger values of ρL^2.

(vi) When ρL is normalized by the central density $\rho_{\rm part}(0, 0) = \rho_{\rm cent}$, then $S_{\rm loss}$ ($R_{\rm AA}$) become universal in the quantities $\rho L/\rho_{\rm cent}$ for both p_T ranges with a linear dependence. The universality appears to become more exact in the higher p_T range. A similar improvement (not shown) of the qualitative universality for ρL^2 and ρL_{xy} is also observed when these quantities are scaled in the same way by $\rho_{\rm cent}$. The fact that scaling by $\rho_{\rm cent}$ improves the universality suggests that simple geometry may be more important than the details of the participant density.

The most important of these observations is the absence of suppression for the same value of $L_\varepsilon \leqslant 2$ fm for both p_T ranges, $3 \leqslant p_T \leqslant 5$ GeV/c and $5 \leqslant p_T \leqslant 8$ GeV/c. This may suggest a "formation time effect" (see Ref. [58], also considering mechanisms suggested in Ref. [60]) or some other type of emission zone which has generally not been taken into account in parton energy-loss models. The level of universal scaling with this simple geometric quantity is surprising.

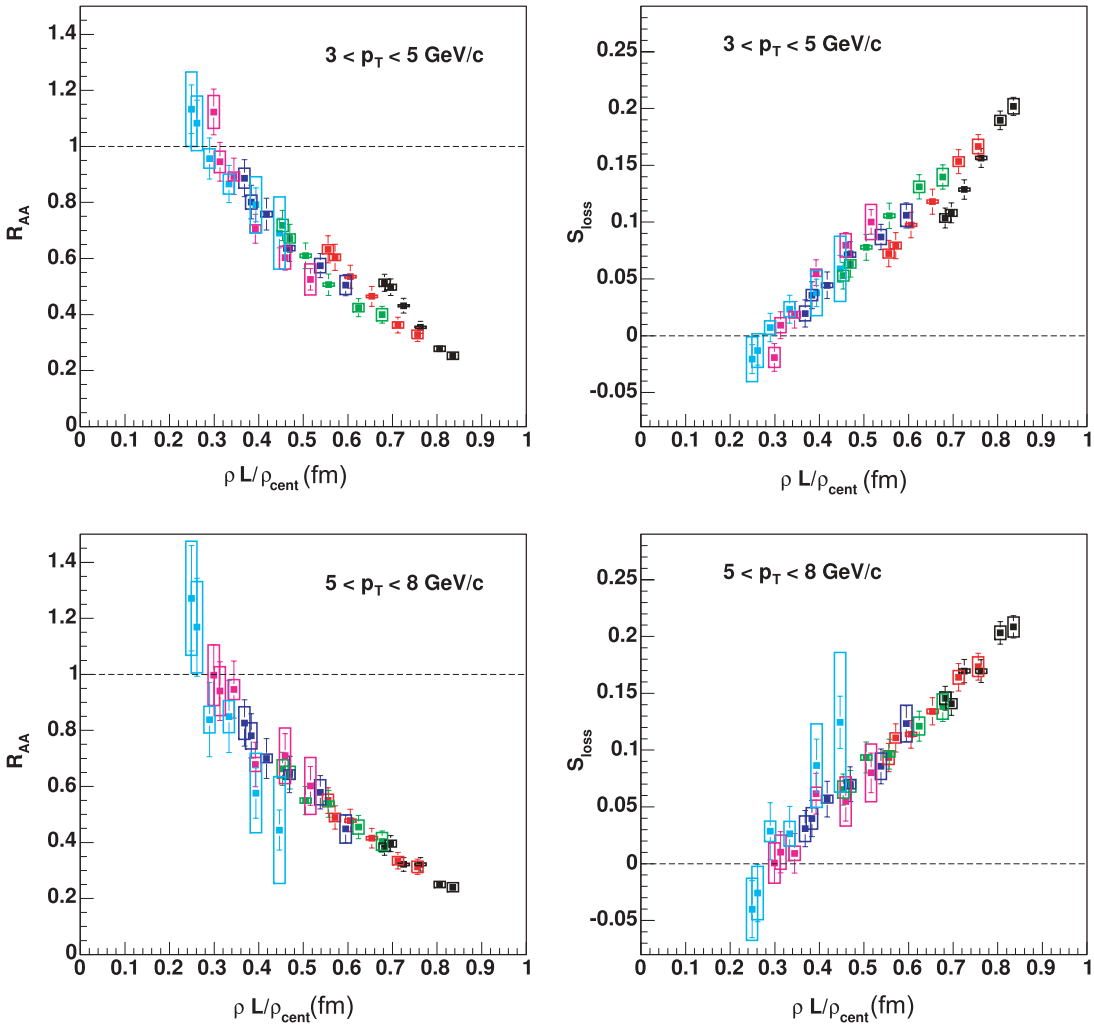

FIG. 21. (Color online) R_{AA} and S_{loss} versus ρL normalized by the most central ($b_x = b_y = 0$) density ρ_{cent}. Colors/data points as in Fig. 17.

V. SUMMARY AND CONCLUSIONS

We have presented a detailed analysis of high-p_T neutral pion suppression as a function of transverse momentum, centrality, and angle with respect to reaction plane in Au+Au collisions at $\sqrt{s_{NN}} = 200$ GeV. The π^0 yields have been measured in the range $p_T \approx 1$–$14\,\mathrm{GeV}/c$ in nine centrality bins and compared to the π^0 differential cross sections measured in $p+p$. The ratio of Au+Au over $p+p$ spectra (scaled by the number of equivalent nucleon-nucleon scatterings) is reduced more and more for larger centralities. The resulting suppression factor is, however, independent of p_T above $p_T \approx 4$ GeV/c for all centralities. This observation can be interpreted as an indication of a constant effective fractional energy loss, fixed S_{loss} "p_T shift," in the Au+Au compared to the $p+p$ yields. The dependence of S_{loss} in the centrality as given by the number of participating nucleons N_{part} follows an approximately $N_{\mathrm{part}}^{2/3}$ law as predicted by parton energy loss models.

To constrain the "jet quenching" models with more differential observables, we have experimentally tested the path-length (L) dependence of the energy loss by exploiting the spatial azimuthal asymmetry of the system produced in noncentral nuclear collisions. Due to the characteristic almondlike shape of the overlapping matter produced in $A+A$ reactions with finite impact parameter, partons traversing the produced medium along the direction perpendicular to the reaction plane ("out-of-plane") will comparatively go through more matter than those going parallel to it ("in-plane") and therefore are expected to lose more energy.

We have studied the suppression pattern along different $\Delta\phi$ trajectories with respect to the reaction plane determined with the beam-beam counters at high rapidities. The measured $R_{\mathrm{AA}}(\Delta\phi)$ curves show clearly a factor of $\sim$2 more suppression out-of-plane ($\Delta\phi = \pi/2$) than in-plane ($\Delta\phi = 0$) for all the centralities (eccentricities) considered. Theoretical calculations of parton energy loss in an azimuthally asymmetric medium predict a significantly smaller difference between the suppression patterns for partons emitted at $\Delta\phi = 0$ and $\Delta\phi = \pi/2$ [29,32,33]. The discrepancy is stronger for more peripheral centralities (with correspondingly larger eccentricities) and challenges the underlying in-medium path-length

dependence of non-Abelian parton energy loss. Although elliptic flow effects are responsible for extra boost of in-plane (compared to out-of-plane) pions, it is unclear how such collective effects persist up to p_T values as high as $\sim$8 GeV/c. We have analyzed the observed reaction-plane and centrality dependence of the nuclear modification factor with three different versions of a Monte Carlo model with an increasing level of refinement in the description of the azimuthal propagation of the parton in the medium. For all three approaches we observe that the π^0 suppression tends to vanish for values of the path-length $L \approx 2$ fm in the two p_T ranges considered, $3 \leqslant p_T \leqslant 5$ GeV/c and $5 \leqslant p_T \leqslant 8$ GeV/c. Such a result suggests either a formation time effect or a surface emission zone that results in a p_T-independent suppression and puts additional constraints to parton energy-loss models.

ACKNOWLEDGMENTS

We thank the staff of the Collider-Accelerator and Physics Departments at Brookhaven National Laboratory and the staff of the other PHENIX participating institutions for their vital contributions. We acknowledge support from the Department of Energy, Office of Science, Nuclear Physics Division, the National Science Foundation, Abilene Christian University Research Council, Research Foundation of SUNY, and Dean of the College of Arts and Sciences, Vanderbilt University (U.S.A), Ministry of Education, Culture, Sports, Science, and Technology and the Japan Society for the Promotion of Science (Japan), Conselho Nacional de Desenvolvimento Científico e Tecnológico and Fundação de Amparo à Pesquisa do Estado de S̃ao Paulo (Brazil), Natural Science Foundation of China (People's Republic of China), Centre National de la Recherche Scientifique, Commissariat à l'Énergie Atomique, and Institut National de Physique Nucléaire et de Physique des Particules, (France), Bundesministerium für Bildung und Forschung, Deutscher Akademischer Austausch Dienst, and Alexander von Humboldt Stiftung (Germany), Hungarian National Science Fund, OTKA (Hungary), Department of Atomic Energy and Department of Science and Technology (India), Israel Science Foundation (Israel), Korea Research Foundation and Korea Science and Engineering Foundation (Korea), Russian Ministry of Industry, Science and Tekhnologies, Russian Academy of Science, Russian Ministry of Atomic Energy (Russia), VR and the Wallenberg Foundation (Sweden), the U.S. Civilian Research and Development Foundation for the Independent States of the Former Soviet Union, the US-Hungarian NSF-OTKA-MTA, the US-Israel Binational Science Foundation, and the 5th European Union TMR Marie-Curie Programme.

APPENDIX: DATA TABLES OF AU + AU $\rightarrow \pi^0 + X$ p_T SPECTRA

Tables IV–XVI show numerical data in the same units as plotted in the figures: p_T (GeV/c) and invariant yield (c^2/GeV^2).

TABLE IV. Final combined PbSc+PbGl π^0 invariant yields vs. p_T for centrality 0–10%.

p_T	Yield	Stat. error	%	Sys. error	%
1.25	3.314	2.518×10^{-2}	0.76	4.026×10^{-1}	12.15
1.75	5.981×10^{-1}	4.946×10^{-3}	0.83	6.784×10^{-2}	11.34
2.25	1.208×10^{-1}	1.253×10^{-3}	1.04	1.447×10^{-2}	11.98
2.75	2.718×10^{-2}	3.744×10^{-4}	1.38	3.521×10^{-3}	12.96
3.25	6.970×10^{-3}	1.270×10^{-4}	1.82	9.751×10^{-4}	13.99
3.75	2.158×10^{-3}	4.713×10^{-5}	2.18	2.686×10^{-4}	12.44
4.25	7.185×10^{-4}	2.133×10^{-5}	2.97	9.349×10^{-5}	13.01
4.75	2.715×10^{-4}	1.063×10^{-5}	3.92	3.575×10^{-5}	13.17
5.25	1.288×10^{-4}	5.931×10^{-6}	4.61	1.702×10^{-5}	13.21
5.75	5.417×10^{-5}	2.606×10^{-6}	4.81	7.731×10^{-6}	14.27
6.25	2.940×10^{-5}	1.560×10^{-6}	5.31	4.106×10^{-6}	13.97
6.75	1.280×10^{-5}	9.501×10^{-7}	7.43	1.922×10^{-6}	15.02
7.25	7.641×10^{-6}	6.459×10^{-7}	8.45	1.241×10^{-6}	16.24
7.75	4.630×10^{-6}	4.668×10^{-7}	10.08	7.508×10^{-7}	16.22
8.50	1.883×10^{-6}	1.809×10^{-7}	9.61	3.033×10^{-7}	16.11
9.50	1.057×10^{-6}	1.276×10^{-7}	12.07	1.952×10^{-7}	18.47
11.00	2.777×10^{-7}	4.274×10^{-8}	15.39	5.664×10^{-8}	20.39
13.00	5.941×10^{-8}	1.704×10^{-8}	28.87	1.222×10^{-8}	20.57

TABLE V. Final combined PbSc+PbGl π^0 invariant yields vs. p_T for centrality 10–20%.

p_T	Yield	Stat. error	%	Sys. error	%
1.25	2.054	1.461×10^{-2}	0.71	2.655×10^{-1}	12.93
1.75	4.137×10^{-1}	2.933×10^{-3}	0.71	4.616×10^{-2}	11.16
2.25	8.576×10^{-2}	7.654×10^{-4}	0.89	1.039×10^{-2}	12.11
2.75	2.028×10^{-2}	2.305×10^{-4}	1.14	2.612×10^{-3}	12.88
3.25	5.057×10^{-3}	7.980×10^{-5}	1.58	6.778×10^{-4}	13.40
3.75	1.665×10^{-3}	3.170×10^{-5}	1.90	1.995×10^{-4}	11.98
4.25	5.859×10^{-4}	1.511×10^{-5}	2.58	7.301×10^{-5}	12.46
4.75	2.253×10^{-4}	7.948×10^{-6}	3.53	3.003×10^{-5}	13.33
5.25	9.486×10^{-5}	4.369×10^{-6}	4.61	1.246×10^{-5}	13.14
5.75	4.651×10^{-5}	2.087×10^{-6}	4.49	6.696×10^{-6}	14.40
6.25	2.224×10^{-5}	1.249×10^{-6}	5.62	3.252×10^{-6}	14.62
6.75	1.109×10^{-5}	8.621×10^{-7}	7.78	1.899×10^{-6}	17.13
7.25	6.455×10^{-6}	5.485×10^{-7}	8.50	1.091×10^{-6}	16.90
7.75	3.568×10^{-6}	3.999×10^{-7}	11.21	7.173×10^{-7}	20.10
8.50	1.724×10^{-6}	1.718×10^{-7}	9.96	3.279×10^{-7}	19.01
9.50	6.318×10^{-7}	9.789×10^{-8}	15.49	1.144×10^{-7}	18.11
11.00	1.701×10^{-7}	3.347×10^{-8}	19.68	3.147×10^{-8}	18.51
13.00	5.093×10^{-8}	1.610×10^{-8}	31.62	9.747×10^{-9}	19.14

TABLE VI. Final combined PbSc+PbGl π^0 invariant yields vs. p_T for centrality 20–30%.

p_T	Yield	Stat. error	%	Sys. error	%
1.25	1.601	9.668×10^{-3}	0.60	1.852×10^{-1}	11.57
1.75	2.879×10^{-1}	1.911×10^{-3}	0.66	3.260×10^{-2}	11.32
2.25	6.045×10^{-2}	5.117×10^{-4}	0.85	7.416×10^{-3}	12.27
2.75	1.429×10^{-2}	1.537×10^{-4}	1.08	1.761×10^{-3}	12.32
3.25	3.983×10^{-3}	5.534×10^{-5}	1.39	5.192×10^{-4}	13.04
3.75	1.233×10^{-3}	2.340×10^{-5}	1.90	1.546×10^{-4}	12.53
4.25	4.749×10^{-4}	1.158×10^{-5}	2.44	6.115×10^{-5}	12.88
4.75	1.732×10^{-4}	5.898×10^{-6}	3.41	2.258×10^{-5}	13.04
5.25	7.761×10^{-5}	3.503×10^{-6}	4.51	1.074×10^{-5}	13.84
5.75	3.573×10^{-5}	1.627×10^{-6}	4.55	4.870×10^{-6}	13.63
6.25	1.714×10^{-5}	9.568×10^{-7}	5.58	2.389×10^{-6}	13.94
6.75	9.015×10^{-6}	6.625×10^{-7}	7.35	1.384×10^{-6}	15.36
7.25	5.146×10^{-6}	4.423×10^{-7}	8.59	8.214×10^{-7}	15.96
7.75	2.878×10^{-6}	3.267×10^{-7}	11.35	5.465×10^{-7}	18.99
8.50	1.363×10^{-6}	1.452×10^{-7}	10.65	2.517×10^{-7}	18.46
9.50	6.216×10^{-7}	8.347×10^{-8}	13.43	1.088×10^{-7}	17.50
11.00	1.825×10^{-7}	2.972×10^{-8}	16.28	3.299×10^{-8}	18.08
13.00	3.552×10^{-8}	1.267×10^{-8}	35.68	6.852×10^{-9}	19.29

TABLE VII. Final combined PbSc+PbGl π^0 invariant yields vs. p_T for centrality 30–40%.

p_T	Yield	Stat. error	%	Sys. error	%
1.25	1.040	5.648×10^{-3}	0.54	1.244×10^{-1}	11.96
1.75	1.754×10^{-1}	1.100×10^{-3}	0.63	2.001×10^{-2}	11.41
2.25	3.833×10^{-2}	3.102×10^{-4}	0.81	4.567×10^{-3}	11.91
2.75	9.610×10^{-3}	9.930×10^{-5}	1.03	1.175×10^{-3}	12.23
3.25	2.670×10^{-3}	3.764×10^{-5}	1.41	3.512×10^{-4}	13.15
3.75	8.612×10^{-4}	1.667×10^{-5}	1.94	1.097×10^{-4}	12.74
4.25	3.270×10^{-4}	8.158×10^{-6}	2.49	4.185×10^{-5}	12.80
4.75	1.252×10^{-4}	4.421×10^{-6}	3.53	1.619×10^{-5}	12.94
5.25	5.266×10^{-5}	2.822×10^{-6}	5.36	7.394×10^{-6}	14.04
5.75	2.761×10^{-5}	1.348×10^{-6}	4.88	3.839×10^{-6}	13.90
6.25	1.189×10^{-5}	8.138×10^{-7}	6.85	1.949×10^{-6}	16.39
6.75	7.115×10^{-6}	5.804×10^{-7}	8.16	1.198×10^{-6}	16.84
7.25	3.705×10^{-6}	3.972×10^{-7}	10.72	6.264×10^{-7}	16.91
7.75	1.898×10^{-6}	2.549×10^{-7}	13.42	3.307×10^{-7}	17.42
8.50	1.168×10^{-6}	1.301×10^{-7}	11.13	1.967×10^{-7}	16.83
9.50	5.043×10^{-7}	8.312×10^{-8}	16.48	9.634×10^{-8}	19.10
11.00	1.541×10^{-7}	2.748×10^{-8}	17.83	2.910×10^{-8}	18.89
13.00	2.941×10^{-8}	1.278×10^{-8}	33.46	5.621×10^{-9}	19.11

TABLE VIII. Final combined PbSc+PbGl π^0 invariant yields vs. p_T for centrality 40–50%.

p_T	Yield	Stat. error	%	Sys. error	%
1.25	6.389×10^{-1}	3.367×10^{-3}	0.53	7.216×10^{-2}	11.29
1.75	1.156×10^{-1}	6.789×10^{-4}	0.59	1.315×10^{-2}	11.37
2.25	2.442×10^{-2}	1.926×10^{-4}	0.79	2.911×10^{-3}	11.92
2.75	6.172×10^{-3}	6.521×10^{-5}	1.06	7.890×10^{-4}	12.78
3.25	1.682×10^{-3}	2.455×10^{-5}	1.46	2.194×10^{-4}	13.04
3.75	5.822×10^{-4}	1.161×10^{-5}	1.99	7.179×10^{-5}	12.33
4.25	1.927×10^{-4}	6.113×10^{-6}	3.17	2.480×10^{-5}	12.87
4.75	8.818×10^{-5}	3.476×10^{-6}	3.94	1.169×10^{-5}	13.26
5.25	3.627×10^{-5}	2.166×10^{-6}	5.97	4.995×10^{-6}	13.77
5.75	1.611×10^{-5}	9.656×10^{-7}	5.99	2.261×10^{-6}	14.04
6.25	9.635×10^{-6}	6.880×10^{-7}	7.14	1.490×10^{-6}	15.47
6.75	4.467×10^{-6}	4.278×10^{-7}	9.58	7.232×10^{-7}	16.19
7.25	2.044×10^{-6}	2.585×10^{-7}	12.65	3.197×10^{-7}	15.64
7.75	1.363×10^{-6}	2.198×10^{-7}	16.13	2.882×10^{-7}	21.15
8.50	7.878×10^{-7}	1.056×10^{-7}	13.41	1.409×10^{-7}	17.88
9.50	2.197×10^{-7}	5.630×10^{-8}	25.62	4.969×10^{-8}	22.61
11.00	1.053×10^{-7}	2.280×10^{-8}	21.66	2.116×10^{-8}	20.10
13.00	2.792×10^{-8}	1.140×10^{-8}	40.82	6.121×10^{-9}	21.92

TABLE IX. Final combined PbSc+PbGl π^0 invariant yields vs. p_T for centrality 50–60%. For points with no errors given, data value represents 90% confidence level upper limit.

p_T	Yield	Stat. error	%	Sys. error	%
1.25	3.593×10^{-1}	1.941×10^{-3}	0.54	4.022×10^{-2}	11.19
1.75	6.197×10^{-2}	4.018×10^{-4}	0.65	7.069×10^{-3}	11.41
2.25	1.309×10^{-2}	1.175×10^{-4}	0.90	1.553×10^{-3}	11.87
2.75	3.479×10^{-3}	4.211×10^{-5}	1.21	4.205×10^{-4}	12.09
3.25	1.019×10^{-3}	1.695×10^{-5}	1.66	1.291×10^{-4}	12.67
3.75	3.480×10^{-4}	8.518×10^{-6}	2.45	4.380×10^{-5}	12.59
4.25	1.329×10^{-4}	4.558×10^{-6}	3.43	1.763×10^{-5}	13.26
4.75	4.959×10^{-5}	2.434×10^{-6}	4.91	6.310×10^{-6}	12.73
5.25	2.125×10^{-5}	1.585×10^{-6}	7.46	3.032×10^{-6}	14.27
5.75	9.917×10^{-6}	7.569×10^{-7}	7.63	1.540×10^{-6}	15.52
6.25	6.127×10^{-6}	5.471×10^{-7}	8.93	9.978×10^{-7}	16.29
6.75	3.246×10^{-6}	3.392×10^{-7}	10.45	4.965×10^{-7}	15.30
7.25	1.664×10^{-6}	2.449×10^{-7}	14.72	3.102×10^{-7}	18.65
7.75	1.129×10^{-6}	1.886×10^{-7}	16.70	2.114×10^{-7}	18.72
8.50	3.362×10^{-7}	7.419×10^{-8}	22.07	6.694×10^{-8}	19.91
9.50	1.817×10^{-7}	4.619×10^{-8}	25.42	3.329×10^{-8}	18.32
11.00	2.858×10^{-8}	1.112×10^{-8}	38.89	4.803×10^{-9}	16.81
13.00	2.311×10^{-8}	—	—	—	—

TABLE X. Final combined PbSc+PbGl π^0 invariant yields vs. p_T for centrality 60–70%.

p_T	Yield	Stat. error	%	Sys. error	%
1.25	1.731×10^{-1}	1.121×10^{-3}	0.65	1.985×10^{-2}	11.47
1.75	3.022×10^{-2}	2.288×10^{-4}	0.76	3.425×10^{-3}	11.33
2.25	6.567×10^{-3}	7.011×10^{-5}	1.07	7.773×10^{-4}	11.84
2.75	1.644×10^{-3}	2.565×10^{-5}	1.56	2.057×10^{-4}	12.51
3.25	5.255×10^{-4}	1.158×10^{-5}	2.20	6.682×10^{-5}	12.72
3.75	1.801×10^{-4}	6.044×10^{-6}	3.36	2.259×10^{-5}	12.54
4.25	6.986×10^{-5}	3.184×10^{-6}	4.56	9.254×10^{-6}	13.25
4.75	2.312×10^{-5}	1.631×10^{-6}	7.06	3.101×10^{-6}	13.41
5.25	1.156×10^{-5}	1.145×10^{-6}	9.90	1.720×10^{-6}	14.87
5.75	4.884×10^{-6}	5.045×10^{-7}	10.33	7.560×10^{-7}	15.48
6.25	2.690×10^{-6}	3.650×10^{-7}	13.57	4.303×10^{-7}	16.00
6.75	1.822×10^{-6}	2.658×10^{-7}	14.58	3.369×10^{-7}	18.48
7.25	6.281×10^{-7}	1.480×10^{-7}	23.57	1.178×10^{-7}	18.76
7.75	2.446×10^{-7}	1.082×10^{-7}	44.22	4.632×10^{-8}	18.94
8.50	1.417×10^{-7}	4.482×10^{-8}	31.62	2.707×10^{-8}	19.10
9.50	1.094×10^{-7}	3.843×10^{-8}	35.14	2.106×10^{-8}	19.26
11.00	2.492×10^{-8}	1.114×10^{-8}	44.72	4.816×10^{-9}	19.33
13.00	4.728×10^{-9}	4.728×10^{-9}	100.00	9.226×10^{-10}	19.51

TABLE XI. Final combined PbSc+PbGl π^0 invariant yields vs. p_T for centrality 70–80%.

p_T	Yield	Stat. error	%	Sys. error	%
1.25	7.416×10^{-2}	5.166×10^{-4}	0.70	8.842×10^{-3}	11.92
1.75	1.282×10^{-2}	1.189×10^{-4}	0.93	1.496×10^{-3}	11.67
2.25	2.721×10^{-3}	3.774×10^{-5}	1.39	3.245×10^{-4}	11.92
2.75	7.455×10^{-4}	1.514×10^{-5}	2.03	9.131×10^{-5}	12.25
3.25	2.461×10^{-4}	7.508×10^{-6}	3.05	3.248×10^{-5}	13.20
3.75	7.200×10^{-5}	3.689×10^{-6}	5.12	9.687×10^{-6}	13.46
4.25	2.609×10^{-5}	2.071×10^{-6}	7.94	4.034×10^{-6}	15.46
4.75	1.288×10^{-5}	1.308×10^{-6}	10.15	2.161×10^{-6}	16.78
5.25	4.650×10^{-6}	7.727×10^{-7}	16.62	9.050×10^{-7}	19.46
5.75	2.416×10^{-6}	3.897×10^{-7}	16.13	4.736×10^{-7}	19.60
6.25	1.763×10^{-6}	2.713×10^{-7}	15.39	2.795×10^{-7}	15.85
6.75	5.945×10^{-7}	1.651×10^{-7}	27.77	1.221×10^{-7}	20.53
7.25	4.817×10^{-7}	1.245×10^{-7}	25.84	8.088×10^{-8}	16.79
7.75	1.344×10^{-7}	6.718×10^{-8}	50.00	2.545×10^{-8}	18.94
8.50	1.135×10^{-7}	4.012×10^{-8}	35.36	2.167×10^{-8}	19.10
9.50	4.968×10^{-8}	2.484×10^{-8}	50.00	9.568×10^{-9}	19.26
11.00	5.060×10^{-9}	5.060×10^{-9}	100.00	9.778×10^{-10}	19.33

TABLE XII. Final combined PbSc+PbGl π^0 invariant yields vs. p_T for centrality 80–92%.

p_T	Yield	Stat. error	%	Sys. error	%
1.25	3.494×10^{-2}	6.093×10^{-4}	1.74	4.504×10^{-3}	12.89
1.75	6.037×10^{-3}	1.291×10^{-4}	2.14	7.607×10^{-4}	12.60
2.25	1.319×10^{-3}	3.628×10^{-5}	2.75	1.701×10^{-4}	12.89
2.75	3.321×10^{-4}	1.243×10^{-5}	3.74	4.570×10^{-5}	13.76
3.25	1.059×10^{-4}	5.281×10^{-6}	4.99	1.483×10^{-5}	14.01
3.75	3.625×10^{-5}	2.408×10^{-6}	6.64	4.455×10^{-6}	12.29
4.25	1.233×10^{-5}	1.293×10^{-6}	10.48	1.730×10^{-6}	14.03
4.75	6.501×10^{-6}	7.988×10^{-7}	12.29	9.044×10^{-7}	13.91
5.25	3.018×10^{-6}	5.360×10^{-7}	17.76	4.224×10^{-7}	13.99
5.75	1.072×10^{-6}	2.315×10^{-7}	21.60	1.815×10^{-7}	16.94
6.25	3.265×10^{-7}	1.154×10^{-7}	35.36	5.945×10^{-8}	18.21
6.75	2.805×10^{-7}	9.918×10^{-8}	35.36	5.185×10^{-8}	18.48
7.25	2.231×10^{-7}	8.434×10^{-8}	37.80	4.187×10^{-8}	18.76
7.75	8.467×10^{-8}	4.888×10^{-8}	57.74	1.604×10^{-8}	18.94
8.50	3.602×10^{-8}	2.080×10^{-8}	57.74	6.880×10^{-9}	19.10
9.50	1.077×10^{-8}	1.077×10^{-8}	100.00	2.074×10^{-9}	19.26
11.00	4.375×10^{-9}	4.375×10^{-9}	100.00	8.455×10^{-10}	19.32

TABLE XIII. Final combined PbSc+PbGl π^0 invariant yields vs. p_T for centrality 0–92%.

p_T	Yield	Stat. error	%	Sys. error	%
1.25	1.078	3.333×10^{-3}	0.31	1.205×10^{-1}	11.17
1.75	1.928×10^{-1}	6.847×10^{-4}	0.36	2.171×10^{-2}	11.26
2.25	4.038×10^{-2}	1.742×10^{-4}	0.43	4.822×10^{-3}	11.94
2.75	9.578×10^{-3}	5.293×10^{-5}	0.55	1.202×10^{-3}	12.55
3.25	2.564×10^{-3}	1.858×10^{-5}	0.72	3.375×10^{-4}	13.17
3.75	8.115×10^{-4}	7.353×10^{-6}	0.91	1.013×10^{-4}	12.48
4.25	2.906×10^{-4}	3.475×10^{-6}	1.20	3.729×10^{-5}	12.84
4.75	1.121×10^{-4}	1.806×10^{-6}	1.61	1.466×10^{-5}	13.08
5.25	4.924×10^{-5}	1.031×10^{-6}	2.09	6.494×10^{-6}	13.19
5.75	2.240×10^{-5}	4.723×10^{-7}	2.11	3.012×10^{-6}	13.45
6.25	1.190×10^{-5}	2.909×10^{-7}	2.44	1.647×10^{-6}	13.83
6.75	5.970×10^{-6}	1.943×10^{-7}	3.25	8.494×10^{-7}	14.23
7.25	3.246×10^{-6}	1.273×10^{-7}	3.92	4.758×10^{-7}	14.65
7.75	1.715×10^{-6}	9.049×10^{-8}	5.28	2.658×10^{-7}	15.49
8.50	8.583×10^{-7}	3.892×10^{-8}	4.53	1.285×10^{-7}	14.98
9.50	3.078×10^{-7}	2.351×10^{-8}	7.64	5.041×10^{-8}	16.38
11.00	9.178×10^{-8}	7.770×10^{-9}	8.47	1.417×10^{-8}	15.44
13.00	2.380×10^{-8}	3.856×10^{-9}	16.20	3.816×10^{-9}	16.03

TABLE XIV. π^0 spectrum for combined centralities: 0–20%

p_T	Yield	Stat. error	%	Sys. error	%
1.25	2.684	1.455×10^{-2}	0.54	3.106×10^{-1}	11.58
1.75	5.059×10^{-1}	2.875×10^{-3}	0.57	5.131×10^{-2}	10.14
2.25	1.033×10^{-1}	7.343×10^{-4}	0.71	1.137×10^{-2}	11.01
2.75	2.373×10^{-2}	2.198×10^{-4}	0.93	2.837×10^{-3}	11.96
3.25	6.014×10^{-3}	7.501×10^{-5}	1.25	7.693×10^{-4}	12.79
3.75	1.912×10^{-3}	2.840×10^{-5}	1.49	2.137×10^{-4}	11.18
4.25	6.522×10^{-4}	1.307×10^{-5}	2.00	7.660×10^{-5}	11.74
4.75	2.484×10^{-4}	6.637×10^{-6}	2.67	3.055×10^{-5}	12.30
5.25	1.118×10^{-4}	3.683×10^{-6}	3.29	1.368×10^{-5}	12.23
5.75	5.034×10^{-5}	1.670×10^{-6}	3.32	6.775×10^{-6}	13.46
6.25	2.582×10^{-5}	9.994×10^{-7}	3.87	3.466×10^{-6}	13.43
6.75	1.194×10^{-5}	6.415×10^{-7}	5.37	1.825×10^{-6}	15.29
7.25	7.048×10^{-6}	4.237×10^{-7}	6.01	1.115×10^{-6}	15.82
7.75	4.099×10^{-6}	3.073×10^{-7}	7.50	7.159×10^{-7}	17.46
8.50	1.804×10^{-6}	1.247×10^{-7}	6.92	3.037×10^{-7}	16.84
9.50	8.445×10^{-7}	8.042×10^{-8}	9.52	1.491×10^{-7}	17.65
11.00	2.239×10^{-7}	2.714×10^{-8}	12.12	4.219×10^{-8}	18.84
13.00	5.517×10^{-8}	1.011×10^{-8}	18.32	1.044×10^{-8}	18.93

TABLE XV. π^0 spectrum for combined centralities: 20–60%

p_T	Yield	Stat. error	%	Sys. error	%
1.25	9.097×10^{-1}	2.963×10^{-3}	0.33	9.041×10^{-2}	9.94
1.75	1.602×10^{-1}	5.854×10^{-4}	0.37	1.570×10^{-2}	9.80
2.25	3.407×10^{-2}	1.599×10^{-4}	0.47	3.579×10^{-3}	10.51
2.75	8.386×10^{-3}	4.969×10^{-5}	0.59	9.138×10^{-4}	10.90
3.25	2.339×10^{-3}	1.832×10^{-5}	0.78	2.711×10^{-4}	11.59
3.75	7.562×10^{-4}	8.034×10^{-6}	1.06	8.387×10^{-5}	11.09
4.25	2.819×10^{-4}	4.021×10^{-6}	1.43	3.259×10^{-5}	11.56
4.75	1.090×10^{-4}	2.126×10^{-6}	1.95	1.263×10^{-5}	11.58
5.25	4.695×10^{-5}	1.310×10^{-6}	2.79	5.959×10^{-6}	12.69
5.75	2.234×10^{-5}	6.107×10^{-7}	2.73	2.907×10^{-6}	13.01
6.25	1.120×10^{-5}	3.833×10^{-7}	3.42	1.605×10^{-6}	14.33
6.75	5.961×10^{-6}	2.591×10^{-7}	4.35	8.809×10^{-7}	14.78
7.25	3.140×10^{-6}	1.732×10^{-7}	5.52	4.937×10^{-7}	15.73
7.75	1.817×10^{-6}	1.264×10^{-7}	6.96	3.292×10^{-7}	18.12
8.50	9.139×10^{-7}	5.846×10^{-8}	6.40	1.581×10^{-7}	17.30
9.50	3.818×10^{-7}	3.462×10^{-8}	9.07	7.055×10^{-8}	18.48
11.00	1.176×10^{-7}	1.194×10^{-8}	10.15	2.061×10^{-8}	17.52
13.00	2.899×10^{-8}	6.031×10^{-9}	20.80	4.497×10^{-9}	15.51

TABLE XVI. π^0 spectrum for combined centralities: 60–92%

p_T	Yield	Stat. error	%	Sys. error	%
1.25	9.037×10^{-2}	4.484×10^{-4}	0.50	9.891×10^{-3}	10.94
1.75	1.571×10^{-2}	9.400×10^{-5}	0.60	1.680×10^{-3}	10.69
2.25	3.397×10^{-3}	2.836×10^{-5}	0.83	3.765×10^{-4}	11.08
2.75	8.712×10^{-4}	1.041×10^{-5}	1.19	1.025×10^{-4}	11.76
3.25	2.808×10^{-4}	4.746×10^{-6}	1.69	3.442×10^{-5}	12.26
3.75	9.236×10^{-5}	2.390×10^{-6}	2.59	1.073×10^{-5}	11.61
4.25	3.461×10^{-5}	1.282×10^{-6}	3.70	4.593×10^{-6}	13.27
4.75	1.369×10^{-5}	7.188×10^{-7}	5.25	1.857×10^{-6}	13.57
5.25	6.198×10^{-6}	4.761×10^{-7}	7.68	9.308×10^{-7}	15.02
5.75	2.683×10^{-6}	2.173×10^{-7}	8.10	4.415×10^{-7}	16.46
6.25	1.514×10^{-6}	1.486×10^{-7}	9.81	2.414×10^{-7}	15.94
6.75	8.605×10^{-7}	1.046×10^{-7}	12.16	1.589×10^{-7}	18.46
7.25	4.305×10^{-7}	6.822×10^{-8}	15.85	7.426×10^{-8}	17.25
7.75	1.502×10^{-7}	4.381×10^{-8}	29.17	2.719×10^{-8}	18.10
8.50	9.326×10^{-8}	2.035×10^{-8}	21.82	1.706×10^{-8}	18.29
9.50	5.374×10^{-8}	1.486×10^{-8}	27.65	9.997×10^{-9}	18.60
11.00	1.101×10^{-8}	4.162×10^{-9}	37.80	2.062×10^{-9}	18.73
13.00	1.478×10^{-9}	1.478×10^{-9}	100.00	2.883×10^{-10}	19.51

[1] K. Adcox *et al.* (PHENIX), Phys. Rev. Lett. **89**, 212301 (2002).
[2] K. H. Ackermann *et al.* (STAR), Phys. Rev. Lett. **86**, 402 (2001).
[3] K. Adcox *et al.* (PHENIX), Phys. Rev. Lett. **88**, 022301 (2002).
[4] K. Adcox *et al.* (PHENIX), Phys. Lett. **B561**, 82 (2003).
[5] J. Adams *et al.* (STAR), Phys. Rev. Lett. **91**, 172302 (2003).
[6] S. S. Adler *et al.* (PHENIX), Phys. Rev. Lett. **91**, 072301 (2003).
[7] S. S. Adler *et al.* (PHENIX), Phys. Rev. C **69**, 034910 (2004).
[8] B. B. Back *et al.* (PHOBOS), Phys. Lett. **B578**, 297 (2004).
[9] I. Arsene *et al.* (BRAHMS), Phys. Rev. Lett. **91**, 072305 (2003).
[10] S. S. Adler *et al.* (PHENIX), Phys. Rev. Lett. **91**, 072303 (2003).
[11] J. Adams *et al.* (STAR), Phys. Rev. Lett. **91**, 072304 (2003).
[12] B. B. Back *et al.* (PHOBOS), Phys. Rev. Lett. **91**, 072302 (2003).
[13] S. S. Adler *et al.* (PHENIX), Phys. Rev. Lett. **96**, 202301 (2006).
[14] S. S. Adler *et al.* (PHENIX), Phys. Rev. Lett. **94**, 232301 (2005).
[15] C. Adler *et al.* (STAR), Phys. Rev. Lett. **90**, 032301 (2003).
[16] X.-N. Wang and M. Gyulassy, Phys. Rev. Lett. **68**, 1480 (1992).
[17] S. A. Bass *et al.*, Nucl. Phys. **A661**, 205 (1999).
[18] M. Gyulassy, I. Vitev, X.-N. Wang, and B.-W. Zhang, *Quark Gluon Plasma*, Vol. 3 (World Scientific, Singapore, 2003).
[19] A. Kovner and U. A. Wiedemann, *Quark Gluon Plasma*, Vol. 3 (World Scientific, Singapore, 2003).
[20] I. Vitev and M. Gyulassy, Phys. Rev. Lett. **89**, 252301 (2002).
[21] E. Wang and X.-N. Wang, Phys. Rev. Lett. **89**, 162301 (2002).
[22] K. J. Eskola, H. Honkanen, C. A. Salgado, and U. A. Wiedemann, Nucl. Phys. **A747**, 511 (2005).
[23] M. Gyulassy and L. McLerran, Nucl. Phys. **A750**, 30 (2005).
[24] X.-N. Wang, Nucl. Phys. **A750**, 98 (2005).
[25] P. Aurenche, F. Gelis, and H. Zaraket, Phys. Rev. D **62**, 096012 (2000).
[26] M. Arneodo, Phys. Rep. **240**, 301 (1994).
[27] R. Baier, D. Schiff, and B. G. Zakharov, Annu. Rev. Nucl. Part. Sci. **50**, 37 (2000).
[28] M. Gyulassy, P. Levai, and I. Vitev, Phys. Lett. **B538**, 282 (2002).
[29] A. Drees, H. Feng, and J. Jia, Phys. Rev. C **71**, 034909 (2005).
[30] M. Gyulassy, I. Vitev, and X. N. Wang, Phys. Rev. Lett. **86**, 2537 (2001).
[31] M. Gyulassy, I. Vitev, X.-N. Wang, and P. Huovinen, Phys. Lett. **B526**, 301 (2002).

[32] E. V. Shuryak, Phys. Rev. C **66**, 027902 (2002).
[33] B. Muller, Phys. Rev. C **67**, 061901(R) (2003).
[34] S. S. Adler *et al*. (PHENIX), Phys. Rev. Lett. **96**, 032302 (2006).
[35] K. Adcox *et al*. (PHENIX), Nucl. Instrum. Methods A **499**, 469 (2003).
[36] H. Hahn *et al*., Nucl. Instrum. Methods A **499**, 245 (2003).
[37] L. Aphecetche *et al*. (PHENIX), Nucl. Instrum. Methods A **499**, 521 (2003).
[38] M. Allen *et al*. (PHENIX), Nucl. Instrum. Methods A **499**, 549 (2003).
[39] C. Adler *et al*., Nucl. Instrum. Methods A **470**, 488 (2001).
[40] S. S. Adler *et al*. (PHENIX), Nucl. Instrum. Methods A **499**, 560 (2003).
[41] K. Adcox *et al*. (PHENIX), Phys. Rev. Lett. **86**, 3500 (2001).
[42] S. S. Adler *et al*. (PHENIX), Phys. Rev. Lett. **91**, 182301 (2003).
[43] S. S. Adler *et al*. (PHENIX), Phys. Rev. C **72**, 024901 (2005).
[44] A. M. Poskanzer and S. A. Voloshin, Phys. Rev. C **58**, 1671 (1998).
[45] J. Jia *et al*. (PHENIX), Nucl. Phys. **A783**, 501c (2007).
[46] S. S. Adler *et al*. (PHENIX), Phys. Rev. Lett. **91**, 241803 (2003).
[47] S. S. Adler *et al*. (PHENIX), Phys. Rev. Lett. **93**, 202002 (2004).
[48] T. Sjostrand *et al*., Comput. Phys. Commun. **135**, 238 (2001).
[49] G. D. Lafferty and T. R. Wyatt, Nucl. Instrum. Methods A **355**, 541 (1995).
[50] S. Eidelman *et al*. (Particle Data Group), Phys. Lett. **B592**, 1 (2004).
[51] M. L. Miller, K. Reygers, S. J. Sanders, and P. Steinberg, to appear in Annu. Rev. Nucl. Part. Sci. **57**, 205 (2007).
[52] K. Adcox *et al*. (PHENIX Collaboration), Nucl. Phys. **A757**, 184 (2005).
[53] S. S. Adler *et al*. (PHENIX), Phys. Rev. Lett. **98**, 172302 (2007).
[54] I. Vitev, Phys. Lett. **B639**, 38 (2006).
[55] A. Dainese, C. Loizides, and G. Paic, Acta Phys. Hung. **A27**, 245 (2006).
[56] M. Jacob and P. V. Landshoff, Phys. Rep. **48**, 285 (1978).
[57] A. Dainese, C. Loizides, and G. Paic, Eur. Phys. J. C **38**, 461 (2005).
[58] V. S. Pantuev, JETP Lett. **85**, 104 (2005).
[59] A. Adil and M. Gyulassy, Phys. Rev. C **72**, 034907 (2005).
[60] E. V. Shuryak and I. Zahed, Phys. Rev. C **70**, 021901(R) (2004).

High transverse momentum η meson production in $p+p$, $d+$Au, and Au+Au collisions at $\sqrt{s_{NN}} = 200$ GeV

S. S. Adler,[5] S. Afanasiev,[20] C. Aidala,[5,10] N. N. Ajitanand,[47] Y. Akiba,[23,42] J. Alexander,[47] A. Al-Jamel,[37] R. Amirikas,[14] K. Aoki,[27] L. Aphecetche,[49] R. Armendariz,[37] S. H. Aronson,[5] R. Averbeck,[48] T. C. Awes,[38] R. Azmoun,[48] V. Babintsev,[17] A. Baldisseri,[11] K. N. Barish,[6] P. D. Barnes,[30] B. Bassalleck,[36] S. Bathe,[6,33] S. Batsouli,[10] V. Baublis,[41] F. Bauer,[6] A. Bazilevsky,[5,17,43] S. Belikov,[17,19] Y. Berdnikov,[44] S. Bhagavatula,[19] M. T. Bjorndal,[10] J. G. Boissevain,[30] H. Borel,[11] S. Borenstein,[28] M. L. Brooks,[30] D. S. Brown,[37] N. Bruner,[36] D. Bucher,[33] H. Buesching,[5,33] V. Bumazhnov,[17] G. Bunce,[5,43] J. M. Burward-Hoy,[29,30,48] S. Butsyk,[48] X. Camard,[49] J.-S. Chai,[21] P. Chand,[4] W. C. Chang,[2] S. Chernichenko,[17] J. Chiba,[23] C. Y. Chi,[10] M. Chiu,[10] I. J. Choi,[56] J. Choi,[22] R. K. Choudhury,[4] T. Chujo,[5] V. Cianciolo,[38] Y. Cobigo,[11] B. A. Cole,[10] M. P. Comets,[39] P. Constantin,[19] M. Csanád,[13] T. Csörgő,[24] J. P. Cussonneau,[49] K. Das,[14] G. David,[5] F. Deák,[13] H. Delagrange,[49] A. Denisov,[17] D. d'Enterria,[10,49] A. Deshpande,[43] E. J. Desmond,[5] A. Devismes,[48] O. Dietzsch,[45] J. L. Drachenberg,[1] O. Drapier,[28] A. Drees,[48] K. A. Drees,[5] R. duRietz,[32] A. Durum,[17] D. Dutta,[4] V. Dzhordzhadze,[50] Y. V. Efremenko,[38] K. El Chenawi,[53] A. Enokizono,[16] H. En'yo,[42,43] B. Espagnon,[39] S. Esumi,[52] L. Ewell,[5] D. E. Fields,[36,43] C. Finck,[49] F. Fleuret,[28] S. L. Fokin,[26] B. D. Fox,[43] Z. Fraenkel,[55] J. E. Frantz,[10] A. Franz,[5] A. D. Frawley,[14] Y. Fukao,[27,42,43] S.-Y. Fung,[6] S. Gadrat,[31] S. Garpman,[32,*] M. Germain,[49] T. K. Ghosh,[53] A. Glenn,[50] G. Gogiberidze,[50] M. Gonin,[28] J. Gosset,[11] Y. Goto,[42,43] R. Granier de Cassagnac,[28] N. Grau,[19] S. V. Greene,[53] M. Grosse Perdekamp,[18,43] W. Guryn,[5] H.-Å. Gustafsson,[32] T. Hachiya,[16] J. S. Haggerty,[5] H. Hamagaki,[8] A. G. Hansen,[30] E. P. Hartouni,[29] M. Harvey,[5] K. Hasuko,[42] R. Hayano,[8] N. Hayashi,[42] M. Heffner,[29] T. K. Hemmick,[48] J. M. Heuser,[42,48] X. He,[15] M. Hibino,[54] P. Hidas,[24] H. Hiejima,[18] J. C. Hill,[19] R. Hobbs,[36] W. Holzmann,[47] K. Homma,[16] B. Hong,[25] A. Hoover,[37] T. Horaguchi,[42,43,51] T. Ichihara,[42,43] V. V. Ikonnikov,[26] K. Imai,[27,42] M. Inaba,[52] M. Inuzuka,[8] D. Isenhower,[1] L. Isenhower,[1] M. Ishihara,[42] M. Issah,[47] A. Isupov,[20] B. V. Jacak,[48] W. Y. Jang,[25] Y. Jeong,[22] J. Jia,[48] O. Jinnouchi,[42,43] B. M. Johnson,[5] S. C. Johnson,[29] K. S. Joo,[34] D. Jouan,[39] F. Kajihara,[8] S. Kametani,[8,54] N. Kamihara,[42,51] M. Kaneta,[43] J. H. Kang,[56] S. S. Kapoor,[4] K. Katou,[54] M. Kaufman,[10] T. Kawabata,[8] A. V. Kazantsev,[26] S. Kelly,[9,10] B. Khachaturov,[55] A. Khanzadeev,[41] J. Kikuchi,[54] D. H. Kim,[34] D. J. Kim,[56] D. W. Kim,[22] E. Kim,[46] G.-B. Kim,[28] H. J. Kim,[56] E. Kinney,[9] A. Kiss,[13] E. Kistenev,[5] A. Kiyomichi,[42,52] K. Kiyoyama,[35] C. Klein-Boesing,[33] H. Kobayashi,[42,43] L. Kochenda,[41] V. Kochetkov,[17] D. Koehler,[36] T. Kohama,[16] R. Kohara,[16] B. Komkov,[41] M. Konno,[52] M. Kopytine,[48] D. Kotchetkov,[6] A. Kozlov,[55] P. J. Kroon,[5] C. H. Kuberg,[1,*] G. J. Kunde,[30] K. Kurita,[42,43] Y. Kuroki,[52] M. J. Kweon,[25] Y. Kwon,[56] G. S. Kyle,[37] R. Lacey,[47] V. Ladygin,[20] J. G. Lajoie,[19] A. Lebedev,[19,26] Y. Le Bornec,[39] S. Leckey,[48] D. M. Lee,[30] S. Lee,[22] M. J. Leitch,[30] M. A. L. Leite,[45] H. Lim,[46] A. Litvinenko,[20] M. X. Liu,[30] Y. Liu,[39] X. H. Li,[6] C. F. Maguire,[53] Y. I. Makdisi,[5] A. Malakhov,[20] V. I. Manko,[26] Y. Mao,[7,40,42] G. Martinez,[49] M. D. Marx,[48] H. Masui,[52] F. Matathias,[48] T. Matsumoto,[8,54] M. C. McCain,[1] P. L. McGaughey,[30] E. Melnikov,[17] F. Messer,[48] Y. Miake,[52] J. Milan,[47] T. E. Miller,[53] A. Milov,[48,55] S. Mioduszewski,[5] R. E. Mischke,[30] G. C. Mishra,[15] J. T. Mitchell,[5] A. K. Mohanty,[4] D. P. Morrison,[5] J. M. Moss,[30] F. Mühlbacher,[48] D. Mukhopadhyay,[55] M. Muniruzzaman,[6] J. Murata,[42,43] S. Nagamiya,[23] J. L. Nagle,[9,10] T. Nakamura,[16] B. K. Nandi,[6] M. Nara,[52] J. Newby,[50] P. Nilsson,[32] A. S. Nyanin,[26] J. Nystrand,[32] E. O'Brien,[5] C. A. Ogilvie,[19] H. Ohnishi,[5,42] I. D. Ojha,[3,53] H. Okada,[27,42] K. Okada,[42,43] M. Ono,[52] V. Onuchin,[17] A. Oskarsson,[32] I. Otterlund,[32] K. Oyama,[8] K. Ozawa,[8] D. Pal,[55] A. P. T. Palounek,[30] V. Pantuev,[48] V. Papavassiliou,[37] J. Park,[46] W. J. Park,[25] A. Parmar,[36] S. F. Pate,[37] H. Pei,[19] T. Peitzmann,[33] V. Penev,[20] J.-C. Peng,[18,30] H. Pereira,[11] V. Peresedov,[20] A. Pierson,[36] C. Pinkenburg,[5] R. P. Pisani,[5] F. Plasil,[38] M. L. Purschke,[5] A. K. Purwar,[48] J. M. Qualls,[1] J. Rak,[19] I. Ravinovich,[55] K. F. Read,[38,50] M. Reuter,[48] K. Reygers,[33] V. Riabov,[41,44] Y. Riabov,[41] G. Roche,[31] A. Romana,[28,*] M. Rosati,[19] S. S. E. Rosendahl,[32] P. Rosnet,[31] V. L. Rykov,[42] S. S. Ryu,[56] M. E. Sadler,[1] B. Sahlmueller,[33] N. Saito,[27,42,43] T. Sakaguchi,[8,54] M. Sakai,[35] S. Sakai,[52] V. Samsonov,[41] L. Sanfratello,[36] R. Santo,[33] H. D. Sato,[27,42] S. Sato,[5,52] S. Sawada,[23] Y. Schutz,[49] V. Semenov,[17] R. Seto,[6] M. R. Shaw,[1,30] T. K. Shea,[5] I. Shein,[17] T.-A. Shibata,[42,51] K. Shigaki,[16,23] T. Shiina,[30] M. Shimomura,[52] A. Sickles,[48] C. L. Silva,[45] D. Silvermyr,[30,32] K. S. Sim,[25] C. P. Singh,[3] V. Singh,[3] M. Sivertz,[5] A. Soldatov,[17] R. A. Soltz,[29] W. E. Sondheim,[30] S. P. Sorensen,[50] I. V. Sourikova,[5] F. Staley,[11] P. W. Stankus,[38] E. Stenlund,[32] M. Stepanov,[37] A. Ster,[24] S. P. Stoll,[5] T. Sugitate,[16] J. P. Sullivan,[30] S. Takagi,[52] E. M. Takagui,[45] A. Taketani,[42,43] M. Tamai,[54] K. H. Tanaka,[23] Y. Tanaka,[35] K. Tanida,[42] M. J. Tannenbaum,[5] A. Taranenko,[47] P. Tarján,[12] J. D. Tepe,[1,30] T. L. Thomas,[36] M. Togawa,[27,42] J. Tojo,[27,42] H. Torii,[27,42,43] R. S. Towell,[1] V.-N. Tram,[28] I. Tserruya,[55] Y. Tsuchimoto,[16] H. Tsuruoka,[52] S. K. Tuli,[3] H. Tydesjö,[32] N. Tyurin,[17] T. J. Uam,[34] H. W. van Hecke,[30] J. Velkovska,[5,48] M. Velkovsky,[48] V. Veszprémi,[12] L. Villatte,[50] A. A. Vinogradov,[26] M. A. Volkov,[26] E. Vznuzdaev,[41] X. R. Wang,[15] Y. Watanabe,[42,43] S. N. White,[5] N. Willis,[39] F. K. Wohn,[19] C. L. Woody,[5] W. Xie,[6] Y. Yang,[7] A. Yanovich,[17] S. Yokkaichi,[42,43] G. R. Young,[38] I. E. Yushmanov,[26] W. A. Zajc,[10,†] C. Zhang,[10] S. Zhou,[7] S. J. Zhou,[55] J. Zimányi,[24,*] L. Zolin,[20] and X. Zong[19]

(PHENIX Collaboration)

[1]*Abilene Christian University, Abilene, Texas 79699, USA*

[2]*Institute of Physics, Academia Sinica, Taipei 11529, Taiwan*

[3]*Department of Physics, Banaras Hindu University, Varanasi 221005, India*

[4]*Bhabha Atomic Research Centre, Bombay 400 085, India*

[5]*Brookhaven National Laboratory, Upton, New York 11973-5000, USA*

[6]*University of California-Riverside, Riverside, California 92521, USA*

 ©2007 The American Physical Society

[7]*China Institute of Atomic Energy (CIAE), Beijing, People's Republic of China*
[8]*Center for Nuclear Study, Graduate School of Science, University of Tokyo, 7-3-1 Hongo, Bunkyo, Tokyo 113-0033, Japan*
[9]*University of Colorado, Boulder, Colorado 80309, USA*
[10]*Columbia University, New York, NY 10027 and Nevis Laboratories, Irvington, New York 10533, USA*
[11]*Dapnia, CEA Saclay, F-91191, Gif-sur-Yvette, France*
[12]*Debrecen University, H-4010 Debrecen, Egyetem tér 1, Hungary*
[13]*ELTE, Eötvös Loránd University, H-1117 Budapest, Pázmány P. s. 1/A, Hungary*
[14]*Florida State University, Tallahassee, Florida 32306, USA*
[15]*Georgia State University, Atlanta, Georgia 30303, USA*
[16]*Hiroshima University, Kagamiyama, Higashi-Hiroshima 739-8526, Japan*
[17]*IHEP Protvino, State Research Center of Russian Federation, Institute for High Energy Physics, Protvino, RU-142281, Russia*
[18]*University of Illinois at Urbana-Champaign, Urbana, IL 61801, USA*
[19]*Iowa State University, Ames, Iowa 50011, USA*
[20]*Joint Institute for Nuclear Research, RU-141980 Dubna, Moscow Region, Russia*
[21]*KAERI, Cyclotron Application Laboratory, Seoul, South Korea*
[22]*Kangnung National University, Kangnung 210-702, South Korea*
[23]*KEK, High Energy Accelerator Research Organization, Tsukuba, Ibaraki 305-0801, Japan*
[24]*KFKI Research Institute for Particle and Nuclear Physics of the Hungarian Academy of Sciences (MTA KFKI RMKI), H-1525 Budapest 114, P. O. Box 49, Budapest, Hungary*
[25]*Korea University, Seoul, 136-701, Korea*
[26]*Russian Research Center "Kurchatov Institute," Moscow, Russia*
[27]*Kyoto University, Kyoto 606-8502, Japan*
[28]*Laboratoire Leprince-Ringuet, Ecole Polytechnique, CNRS-IN2P3, Route de Saclay, F-91128, Palaiseau, France*
[29]*Lawrence Livermore National Laboratory, Livermore, California 94550, USA*
[30]*Los Alamos National Laboratory, Los Alamos, New Mexico 87545, USA*
[31]*LPC, Université Blaise Pascal, CNRS-IN2P3, Clermont-Fd, F-63177 Aubiere Cedex, France*
[32]*Department of Physics, Lund University, Box 118, SE-221 00 Lund, Sweden*
[33]*Institut für Kernphysik, University of Muenster, D-48149 Muenster, Germany*
[34]*Myongji University, Yongin, Kyonggido 449-728, Korea*
[35]*Nagasaki Institute of Applied Science, Nagasaki-shi, Nagasaki 851-0193, Japan*
[36]*University of New Mexico, Albuquerque, New Mexico 87131, USA*
[37]*New Mexico State University, Las Cruces, New Mexico 88003, USA*
[38]*Oak Ridge National Laboratory, Oak Ridge, Tennessee 37831, USA*
[39]*IPN-Orsay, Universite Paris Sud, CNRS-IN2P3, BP1, F-91406, Orsay, France*
[40]*Peking University, Beijing, People's Republic of China*
[41]*PNPI, Petersburg Nuclear Physics Institute, Gatchina, Leningrad region, RU-188300, Russia*
[42]*RIKEN (The Institute of Physical and Chemical Research), Wako, Saitama 351-0198, JAPAN*
[43]*RIKEN BNL Research Center, Brookhaven National Laboratory, Upton, New York 11973-5000, USA*
[44]*Saint Petersburg State Polytechnic University, St. Petersburg, Russia*
[45]*Universidade de São Paulo, Instituto de Física, Caixa Postal 66318, São Paulo CEP05315-970, Brazil*
[46]*System Electronics Laboratory, Seoul National University, Seoul, South Korea*
[47]*Chemistry Department, Stony Brook University, Stony Brook, SUNY, New York 11794-3400, USA*
[48]*Department of Physics and Astronomy, Stony Brook University, SUNY, Stony Brook, New York 11794, USA*
[49]*SUBATECH (Ecole des Mines de Nantes, CNRS-IN2P3, Université de Nantes) BP 20722, F-44307, Nantes, France*
[50]*University of Tennessee, Knoxville, Tennesee 37996, USA*
[51]*Department of Physics, Tokyo Institute of Technology, Oh-okayama, Meguro, Tokyo 152-8551, Japan*
[52]*Institute of Physics, University of Tsukuba, Tsukuba, Ibaraki 305, Japan*
[53]*Vanderbilt University, Nashville, Tennessee 37235, USA*
[54]*Waseda University, Advanced Research Institute for Science and Engineering, 17 Kikui-cho, Shinjuku-ku, Tokyo 162-0044, Japan*
[55]*Weizmann Institute, Rehovot 76100, Israel*
[56]*Yonsei University, IPAP, Seoul 120-749, Korea*
(Received 6 November 2006; published 27 February 2007)

Inclusive transverse momentum spectra of η mesons in the range $p_T \approx 2$–12 GeV/c have been measured at midrapidity ($|\eta| < 0.35$) by the PHENIX experiment at RHIC in $p+p$, d+Au, and Au+Au collisions at $\sqrt{s_{NN}} = 200$ GeV. The η mesons are reconstructed through their $\eta \to \gamma\,\gamma$ channel for the three colliding systems as well as through the $\eta \to \pi^0\pi^+\pi^-$ decay mode in $p+p$ and d+Au collisions. The nuclear modification factor in d+Au collisions, $R_{d\mathrm{Au}}(p_T) \approx 1.0$–1.1, suggests at most only modest p_T broadening ("Cronin enhancement").

In central Au+Au reactions, the η yields are significantly suppressed, with $R_{\mathrm{AuAu}}(p_T) \approx 0.2$. The ratio of η to π^0 yields is approximately constant as a function of p_T for the three colliding systems in agreement with the high-p_T world average of $R_{\eta/\pi^0} \approx 0.5$ in hadron-hadron, hadron-nucleus, and nucleus-nucleus collisions for a wide range of center-of-mass energies ($\sqrt{s_{NN}} \approx$ 3–1800 GeV) as well as, for high scaled momentum x_p, in e^+e^- annihilations at $\sqrt{s} = 91.2$ GeV. These results are consistent with a scenario where high-p_T η production in nuclear collisions at the Relativistic Heavy Ion Collider is largely unaffected by initial-state effects but where light-quark mesons (π^0, η) are equally suppressed due to final-state interactions of the parent partons in the dense medium produced in Au+Au reactions.

DOI: 10.1103/PhysRevC.75.024909 PACS number(s): 25.75.−q, 12.38.Mh, 13.85.−t, 13.87.Fh

I. INTRODUCTION

Single-hadron production at large transverse momenta ($p_T \gtrsim 2$ GeV/c) in high-energy hadronic and nuclear collisions results from the fragmentation of quarks and gluons issuing from parton-parton scatterings with large momentum transfer Q^2. Because the cross sections for such hard processes can be calculated perturbatively within quantum chromodynamics (QCD) [1], inclusive high-p_T hadrons (as well as jets, real and virtual direct photons, and heavy quarks) have long been considered sensitive, well-calibrated probes of the small-distance QCD processes. The study of inclusive hadron production at large p_T in proton-proton interactions provides valuable information about perturbative QCD (pQCD), parton distribution functions (PDF) in the proton, and fragmentation functions (FF) of the partons [2]. Furthermore, the use of polarized beams ($\vec{p} + \vec{p}$) allows one to investigate the spin structure of the proton [3]. High-energy collisions of protons or deuterons on nuclear targets (p, d+A) also provide interesting insights on initial- and final-state QCD effects such as modifications of the nuclear PDFs [4,5] and parton rescattering in the cold nuclear medium [6]. Both effects are sensitive to physics such as parton structure and evolution at small values of fractional momentum x in the hadronic wave functions [7] and the dynamics of hadronization in cold nuclei [8,9]. Last, high-p_T hadron production in nucleus-nucleus (A+A) reactions is a sensitive probe of the properties of the strongly interacting QCD matter produced in the collision. Indeed, because perturbative processes happen at time scales $\tau \approx 1/p_T \lesssim 0.1$ fm/c, the hard-scattered partons traverse and are potentially modified by the bulk matter formed shortly after the collision. In this context, the suppression of leading hadrons has been postulated [10] as a signal of "jet quenching" in a quark-gluon-plasma (QGP) due to medium-induced energy-loss of the parent parton [11–13].

All the aforementioned research topics have been addressed in detail by the rich physics program carried out at the Relativistic Heavy Ion Collider (RHIC) at Brookhaven National Laboratory (BNL) during its first 6 years of operation (2000–2006). For example, the study of inclusive high-p_T neutral pion production at midrapidity in $p+p$ [14], $\vec{p} + \vec{p}$ [15], d+Au [16,17], and Au+Au [18–21] collisions at $\sqrt{s_{NN}} =$ 200 GeV has provided valuable information respectively on (i) the gluon-to-pion FF [14,22], (ii) the gluon contribution to the proton spin [23–25], (iii) initial-state effects in cold nuclear matter such as shadowing of the nuclear PDFs [26–29], Cronin broadening [30–32], and gluon saturation [33–35], and (iv) the thermodynamical and microscopic properties of hot and dense QCD matter [36], such as the initial gluon rapidity density dN^g/dy [37] and the transport coefficient $\langle \hat{q} \rangle$ [38,39] of the produced medium; and the mechanism of hadronization in a dense parton medium [40].

In this article, we extend previous PHENIX analyses of high-p_T hadron production in $p+p$ [14,15], d+Au [16], and Au+Au [19–21,41] collisions at $\sqrt{s_{NN}} = 200$ GeV to include an additional identified particle, the η meson, measured in the range $p_T =$ 2–12 GeV/c. The spectra presented here are the hardest (i.e., have the highest p_T) ever measured for the η meson[1] in $p+p$, p+A, and A+A collisions. The high p_T reach of the η helps to characterize the mechanisms of truly perturbative parton-parton scatterings and parton fragmentation in different QCD environments ($p+p, d$+A, and Au+Au). The η data from $p+p$ collisions are presented here as a baseline for medium effects in d+Au and Au+Au. Once a parametrization of the η FF in e^+e^- is performed (see Sec. IV E2), the observed $p+p$ cross section will additionally allow a test of pQCD predictions. Such a FF parametrization would be useful in particular in the light of upcoming high-p_T η asymmetry data obtained with polarized beams of relevance for the proton spin program [44].

For d+Au and Au+Au reactions, we present the single η spectra, the η nuclear modification factors, and the η-to-π^0 ratio measured as a function of p_T in different centralities. Within uncertainties, the d+Au spectra for all centralities are consistent with the $p+p$ yields scaled by the corresponding number of incoherent nucleon-nucleon (NN) collisions. The maximum amount of p_T broadening seen in the η data is 10%, $R_{dAu}(p_T) \approx$ 1.0–1.1. Such a result confirms the limited influence of cold nuclear matter effects, such as shadowing, Cronin broadening or recombination, on high-p_T meson production at midrapidity at RHIC [16,17]. However, the factor of ∼5 deficit of inclusive η yields observed above $p_T \approx$ 4 GeV/c in central Au+Au compared to binary-scaled $p+p$ collisions, $R_{\mathrm{AuAu}}(p_T) \approx 0.2$, is the same as that found for

*Deceased.
†Electronic address: zajc@nevis.columbia.edu.

[1]Before this measurement, only the ISR AFS Collaboration $p+p \to \eta$+X measurement for $p_T =$ 3–11 GeV/c at $\sqrt{s} =$ 62.4 GeV [42] and the single CDF η/π^0 point measured at $p_T =$ 12 GeV/c in $\bar{p}+p$ collisions at $\sqrt{s} = 1800$ GeV [43] had comparable maximum p_T values.

high-p_T π^0 [19,21] and for inclusive charged hadrons [41,45]. Such a common suppression pattern for π^0, η and $h^{\pm}$ is expected if the energy loss takes place at the parton level in the dense medium formed in the reaction *prior* to its fragmentation into a given hadron in the vacuum. Indeed, in this case the high-p_T deficit will just depend on the energy lost by the parent light-quark or gluon (i.e., on the initial density of scatterers in the produced medium) and not on the nature of the final leading hadron whose production will be described by the same *universal* probabilities (fragmentation functions) that govern vacuum hadron production in more elementary systems. Such an interpretation is supported by the fact that the ratio of p_T-differential cross sections of η mesons with respect to π^0 in Au+Au, d+Au, and p+p collisions is approximately constant, $R_{\eta/\pi^0} \approx 0.40$–$0.48$, which is consistent with the world average measured: (i) in hadron-hadron, hadron-nucleus, and nucleus-nucleus collisions above $p_T \approx 3$ GeV/c; as well as (ii) in electron-positron annihilations at the Z pole ($\sqrt{s} = 91.2$ GeV) for *energetic* η and π^0 with scaled momenta $x_p = p_{\text{hadron}}/p_{\text{beam}} \gtrsim 0.35$. Comparison of our data to a world compilation of η/π^0 ratios is done in the last section of the article.

In addition to their interest as a *signal* in their own right, reliable knowledge of the production of η mesons in p+p, d+Au, and Au+Au reactions is also required to determine and statistically remove the *background* of secondary $e^{\pm}$ and γ for other measurements such as single electrons (from heavy-quark decays) [46,47], dielectrons [47], and direct photons [48,49]. Indeed, η mesons constitute the second most important source after the π^0 of decay electrons (Dalitz and conversion) and photons contributing to these backgrounds.

The article is organized as follows. Section II presents a description of the experimental setup and detector systems used in this work. Section III provides an explanation of the analysis methods employed to obtain the η data. Section IV presents and compares the η results (p_T spectra, nuclear modification factors, and η/π^0 ratios) measured in p+p, d+Au, and Au+Au at $\sqrt{s_{NN}} = 200$ GeV and discusses the relative role of cold nuclear (d+Au) and hot and dense medium (Au+Au) effects on high-p_T meson production. In particular, Sec. IV E discusses the measured η-to-π^0 ratios in the context of different phenomenological models of high-p_T hadron production as well as in comparison to other experimental results measured in high-energy particle collisions at different center-of-mass energies. A less detailed presentation of a subset of these η results has already been published in [20].

II. EXPERIMENTAL SETUP

The PHENIX experiment at the RHIC facility [50] at BNL is specifically designed to measure hard QCD probes such as high-p_T hadrons, direct photons, leptons, and heavy flavor production. PHENIX achieves good mass and particle identification (PID) resolutions as well as small granularity by combining 13 detector subsystems (~350,000 channels) divided into (i) two central arm spectrometers for electron, photon, and hadron measurements at midrapidity ($|\eta| < 0.35$, $\Delta\phi = \pi$); (ii) two forward-backward ($|\eta| = 1.2$–2.2, $\Delta\phi = 2\pi$) spectrometers for muon detection; and (iii) two global (inner) detectors for trigger and centrality selection. A detailed description of the complete detector can be found elsewhere [51]. The data presented in this article were obtained during the Run-2 (2001–2002, Au+Au) and Run-3 (2003, d+Au, p+p) operations at RHIC. The layout of the PHENIX detector during these run periods is shown in Fig. 1. The primary detectors used to obtain the present results are the PHENIX central arm spectrometers, particularly the electromagnetic calorimeters (EMCal) [52] and the charged-particle tracking devices [the drift chamber (DC) [53] and pad chambers (PC) [54]]. In addition, the beam-beam counters (BBC) [55] and the zero-degree calorimeters (ZDC) [56] are used for triggering, event characterization and (Au+Au and d+Au) centrality determination.

A. Electromagnetic calorimeter (EMCal)

The η mesons are detected in PHENIX via their $\gamma\gamma$ (branching ratio BR = 39.43%) and $\pi^0\pi^+\pi^-$ (BR = 22.6%) decays [57]. Photons from the direct $\gamma\gamma$ channel as well as from the secondary (daughter) π^0 decays are measured in the PHENIX EMCal, which has a pseudorapidity acceptance of $-0.35 < \eta < 0.35$ and covers π radians in azimuth. The electromagnetic calorimeter is divided into eight sectors with two distinct detection technologies (see Fig. 1). A lead-scintillator calorimeter (PbSc) consists of 15,552 individual lead-scintillator sandwich modules ($5.54 \times 5.54 \times 37.5$ cm, $18X_0$), grouped in six sectors located at a radial distance of 5.1 m from the beam line, covering a total solid angle of $\Delta\eta \approx 0.7$ and $\Delta\phi \approx 3\pi/4$. A lead-glass Čerenkov calorimeter (PbGl) comprising two sectors, with a total of 9,216 modules ($4 \times 4 \times 40$ cm, $14.4X_0$), is located at a radial distance of ~5 m from the beam pipe and covers a total solid angle at midrapidity of $\Delta\eta \approx 0.7$ and $\Delta\phi = \pi/4$. The corresponding $\Delta\eta \times \Delta\phi$ acceptance of a single tower at $\eta = 0$ is 0.011×0.011 and 0.0075×0.0075 for the PbSc and PbGl calorimeters, respectively. The chosen transverse size of the towers is not much larger than their corresponding Molière radius ($\rho_M = 3.0$ cm and 3.7 cm for PbSc and PbGl, respectively) so that most of the electromagnetic showers extend over several modules, resulting in an improved position resolution based on a "center of gravity" reconstruction of the impact point of the photon clusters.

The energy calibration of the PbSc modules was obtained from the original beam-test values and redundantly confirmed with (i) the position of the reconstructed π^0 mass peak, (ii) the energy deposit from minimum-ionizing charged particles traversing the calorimeter, as well as with (iii) the expected $E_{\text{PbSc}}/p_{\text{tracking}} \sim 1$ value measured for electrons and positrons identified in the Ring-Imaging Čerenkov (RICH) detector and whose momentum was measured in the tracking detectors. In the PbGl modules, the reference energy calibration from the original beam-test values is corrected with the time-dependent gain corrections obtained with a light-emission-diode (LED) system for the lead-glass calorimeter. The LEDs emit light with known intensity, so gain fluctuations can be detected. The final

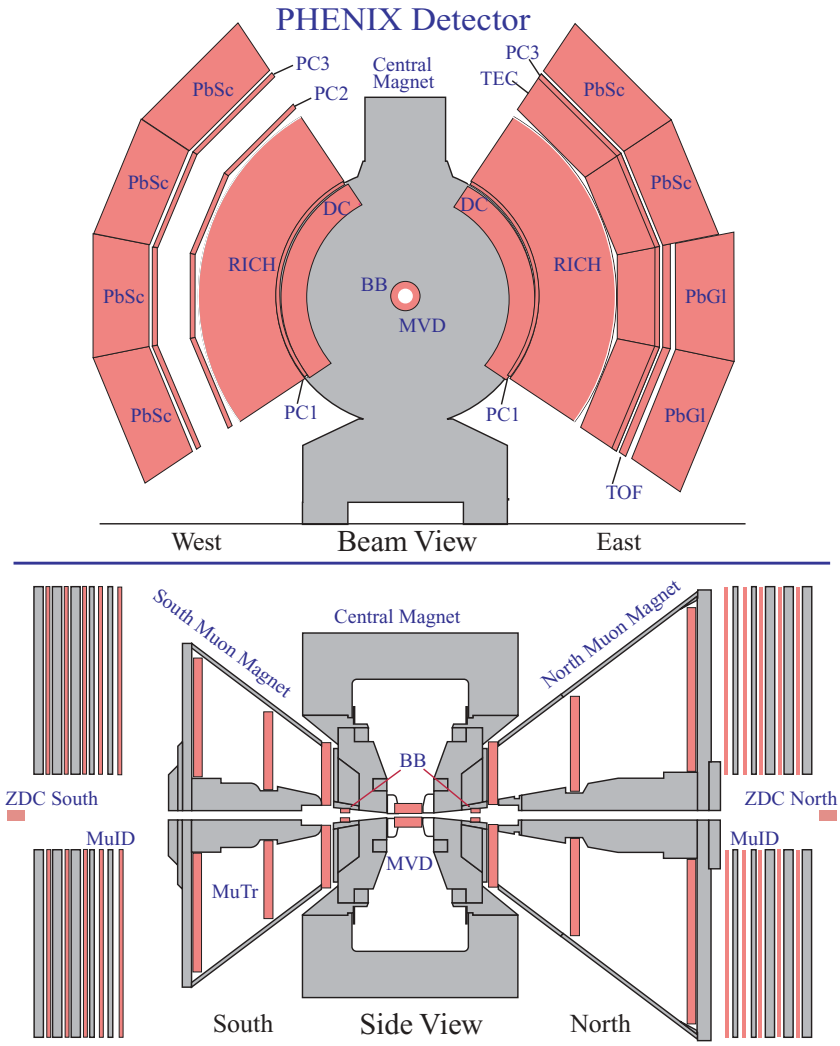

FIG. 1. (Color online) The PHENIX experimental setup during Run-2 and Run-3 at RHIC. The detectors used in the present analysis are the 8 EMCal (PbSc, PbGl) sectors for photon detection ($\eta \to \gamma\,\gamma$), the drift chamber (DC), and two layers of multiwire proportional chambers with pad readout (PC) for charged pion detection ($\eta \to \pi^0\pi^+\pi^-$); as well as the two beam-beam counters (BBC) and the two zero-degree calorimeters (ZDC) for global event characterization.

PbGl calibration is obtained by comparing the measured π^0 peak position to its nominal value.

B. Central arm tracking

Charged pions are measured with the PHENIX central tracking system combining information from the drift and pad chambers. The momenta of the $\pi^{\pm}$ are measured at a radius of 2.0 m from the event vertex by the DC. The DC, located outside the field of PHENIX central magnets, uses several layers of wires to reconstruct the angle of the track, which is inversely proportional to its momentum. The DC momentum resolution is determined to be $0.7 \oplus 1.1\% p_T$ (GeV/c). The polar angle of the track is measured by pad chamber 1 (PC1), a multiwire proportional chamber located just beyond the DC. The last pad-chamber layer, PC3, at a radius of 5.0 m and directly in front of the EMCal, is used in this analysis for two purposes: to confirm the track by matching to a PC3 hit, as well as to veto an EMCal cluster produced by a charged particle track.

The DC momentum scale is checked by the reconstruction of the correct mass of (i) $\pi^{\pm}$, $K^{\pm}$, p, $\bar{p}$ identified with the time-of-flight (TOF) system [58] and (ii) ω, ϕ, J/Ψ mesons decaying into the e^+e^- channel identified with the RICH and EMCal. The momentum scale is thus known with an accuracy better than 0.2%. Because at low p_T, the momentum resolution is better when measured with the tracking system than that using the energy measured via calorimetry, and given that the momentum range of the three η decay products has a relatively low p_T, the uncertainties in the tracking system calibration are less important in the $\pi^0\pi^+\pi^-$ measurement than in the $\gamma\gamma$ decay channel. As a result, the tracking devices provide better accuracy for the η mass reconstruction than the EMCal.

C. Global detectors

Triggering and global event characterization is achieved using the BBC and the ZDC. The two BBC are placed around the beam pipe 1.44 m in each direction from the nominal interaction point. Each BBC consists of 64 hexagonal quartz Čerenkov radiators closely packed in an approximately azimuthally symmetric configuration. The BBC are used to count the charged particle multiplicity in the pseudo-rapidity range $3.0 < |\eta| < 3.9$, to provide the start time for TOF

TABLE I. Events sampled and integrated luminosity (after vertex cuts) in the η analyses for $p+p$, d+Au, and Au+Au collisions. The equivalent $p+p$ luminosities in d+Au (Au+Au) have been obtained normalizing their corresponding luminosities by 2 A (A^2) factors as expected for hard cross-section scaling.

Collision system	Events sampled		Total integrated luminosities		BBC attributes	
	MB (LVL1) trigger	High-p_T (γ) trigger	Absolute	Equivalent $p+p$	Cross section	Efficiency
$p+p$	25.2×10^6	49.3×10^8	216 nb^{-1}	216 nb^{-1}	23.0 mb $\pm$ 9.7%	(55 $\pm$ 5)%
d+Au	58.3×10^6	29.2×10^8	1.5 nb^{-1}	590 nb^{-1}	1.99 b $\pm$ 5.2%	(88 $\pm$ 4)%
Au+Au	34×10^6	30×10^6	9 μb^{-1}	230 nb^{-1}	6.315 b $\pm$ 8.4%	(92 $\pm$ 3)%

measurement, and to give the collision vertex position along the interaction diamond with a typical resolution of 0.6 (2) cm in Au+Au ($p+p$) collisions [55]. In d+Au collisions, the centrality of the collision is determined by measuring the charge deposited in the BBC in the *Au* beam direction [59]; whereas in Au+Au reactions, the correlation between the BBC charge sum and the ZDC total energy is used for centrality determination [60] (see the next section). The ZDC are small hadronic calorimeters that measure the energy carried by spectator neutrons at very forward angles. They are placed 18 m up- and downstream of the interaction point along the beam line ($|\theta| < 2$ mrad). Each ZDC consists of three modules with a depth of 2 hadronic interaction lengths read out by a single photomultiplier tube (PMT). Both time and amplitude are digitized for each PMT along with the analog sum of the three PMT signals for each ZDC.

III. DATA ANALYSIS

In this section, we describe the event selection criteria, the reaction centrality determination in d+Au and Au+Au collisions, the η identification and reconstruction procedures in the $\eta \to \gamma\gamma$ and $\eta \to \pi^0\pi^+\pi^-$ channels and the various corrections (geometrical acceptance, reconstruction efficiency, trigger, absolute cross-section normalization) applied to the raw data. The systematic uncertainties of the measurements are discussed at the end of the section.

A. Event selection

The data presented in this article were collected under two general trigger conditions. The first sample, consisting of minimum-bias (MB) events with vertex position along the beam axis $|z| < 30$ cm, was conditioned on a local-level-1 (LVL1) trigger generated by coincidences between the two BBC (in the case of $p+p$ and d+Au) or by coincidences between the BBC and ZDC detectors (in the case of Au+Au). The MB trigger cross sections measured by the BBC in $p+p$ and d+Au collisions are, respectively, 23.0 mb $\pm$ 9.7% mb and 1.99 b $\pm$ 5.2% [61], whereas the Run-2 Au+Au minimum bias trigger has some inefficiency for the most peripheral interactions and records only $92.2^{+2.5}_{-3.0}$% of $\sigma_{\mathrm{Au\ Au}}$ [19]. In other words, the LVL1 triggers accept, respectively, (55$\pm$5)%, (88$\pm$4)%, and (92$\pm$3)% of the total inelastic cross sections: $\sigma_{pp}^{\mathrm{inel}} = 42 \pm 3$ mb, $\sigma_{dAu}^{\mathrm{inel}} = 2260 \pm 100$ mb, and $\sigma_{\mathrm{Au\ Au}}^{\mathrm{inel}} = 6850 \pm 540$ mb. A second "photon-triggered" sample, requiring electromagnetic showers above a given threshold in the EMCal (with or without the MB BBC requirement), has been used to extend the η measurements to higher p_T. The details of this level-2 (LVL2) software trigger are described in Ref. [21]. The total number of events collected in the MB and photon-triggered samples (after vertex cuts) as well as the integrated luminosities for each collision system are listed in Table I.

B. Centrality determination (d+Au, Au+Au)

The events in d+Au collisions are classified into four different centrality classes given in percentiles of the total cross section: 0–20%, 20–40%, 40–60% and 60–88%, with the latter being the most peripheral. The reaction centrality is related to the number of hits in the south beam-beam counter (BBCS), which is proportional to the number of participant nucleons in the gold nucleus [59]. The distribution of the normalized charge in the BBCS and the classification into different centrality classes is shown in Fig. 2. To obtain reasonably large

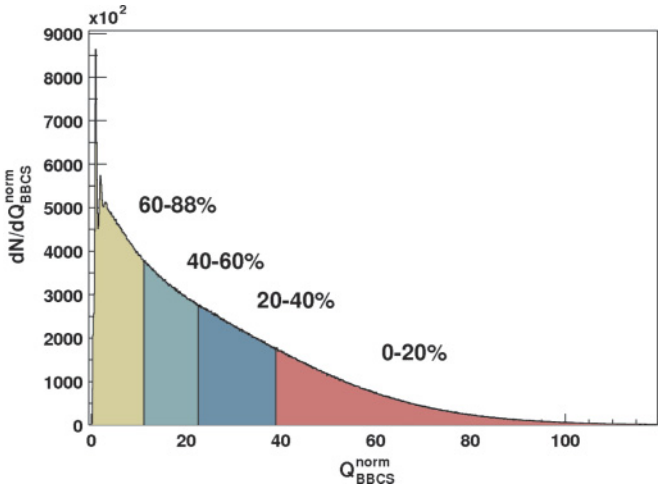

FIG. 2. (Color online) Distribution of the normalized charge in the south beam-beam counter (BBCS) in d+Au collisions at $\sqrt{s_{NN}} =$ 200 GeV. The normalization is done such that the normalized charge corresponds to the number of hits.

TABLE II. Values of the average nuclear overlap function $\langle T_{dA}\rangle$ and $\langle T_{AA}\rangle$ for the different centralities considered in d+Au and Au+Au reactions, respectively.

Centrality bin	$\langle T_{dA}\rangle$ (mb^{-1})	$\langle T_{AA}\rangle$ (mb^{-1})
Min bias	0.20 ± 0.01	6.14 ± 0.45
0–20%	0.36 ± 0.02	18.5 ± 1.3
20–40%	0.25 ± 0.017	—
20–60%	—	4.6 ± 0.4
40–60%	0.17 ± 0.014	—
60–88%	0.073 ± 0.007	—
60–92%	—	0.3 ± 0.1

statistics in each Au+Au centrality class, three centralities are used in the current Au+Au analysis: 0–20% (central), 20–60% (semicentral), and 60–92% (peripheral), determined by cuts in the correlated distribution of the charge detected in the BBC and the energy measured in the ZDC [60]. A Glauber Monte Carlo model combined with a simulation of the BBC (plus ZDC) response allows determination of the mean value of the associated nuclear overlap function $\langle T_{dA}\rangle$ ($\langle T_{AA}\rangle$) for each d+Au (Au+Au) centrality bin. Table II lists the mean value of the nuclear overlap function for different centralities in both systems.

C. $\eta \to \gamma\,\gamma$ Reconstruction

The main mode of η-meson reconstruction in PHENIX is via the electromagnetic channel $\eta \to \gamma\,\gamma$. PHENIX has published the results of a number of $\pi^0 \to \gamma\,\gamma$ measurements in the EMCal for different colliding systems [14–21]. The technique for identifying the photons and reconstructing the π^0 yields as a function of p_T and centrality is now well established and is exactly the same one used here to obtain the corresponding η yields. Although the reconstruction methods are identical, the p+p and d+Au analyses do not suffer from the large particle multiplicity background that the Au+Au η reconstruction faces, and there are a few differences between Au+Au and the other studies. In the Au+Au case, the applied analysis cuts (photon identification, invariant mass reconstruction, and other cuts) are tighter than in the p+p and d+Au cases. Additionally, to deal with cluster overlap effects appropriately, the Au+Au analysis uses a full GEANT [62] Monte Carlo (MC) simulation, in which the simulated single η are embedded into real events rather than a tuned fast MC simulation without embedding. These differences are explained in separate subsections below.

1. Photon reconstruction in EMCal

Electromagnetic clusters are reconstructed in the EMCal sectors by finding contiguous calorimeter towers with pulse heights above the ADC pedestal value. The energy of each EMCal cluster is corrected for angular dependence and nonlinearity based on test-beam results and simulation. The linearity correction for the two detector types is different, with the PbGl having a stronger dependence on the energy. The correction factors for a photon with a detected energy of 1 GeV (10 GeV) are 1.00 (0.95) for the PbSc and 1.05 (0.975) for the PbGl, respectively. The PbGl calorimeter also shows a stronger variation of the measured photon energy with the angle of incidence on the detector surface: at 20° the measured energy is reduced by 5% compared to perpendicular incidence (0°), whereas in the PbSc this reduction is only of the order of 2%.

Because we are interested in high-p_T η production, only EMCal clusters with energy above 1 GeV are selected for further analysis. In addition, fiducial cuts excluding the edges of each EMCal sector, as well as an area of 3×3 towers around the towers that have been determined to be hot or dead, were applied to exclude clusters with incorrectly reconstructed energies. Among the clusters passing the cuts, photon candidates are identified by applying standard particle identification (PID) cuts based on TOF and shower profile. Both cuts are applied to reject slower and broader showers that are mostly of hadronic origin. For the PbSc we require the measured cluster TOF to be $t_{\rm clust} < L/c \pm 1.2$ ns where L is the straight-line path from the collision vertex to the reconstructed cluster centroid. For the PbGl we require reconstructed clusters to have times, $t_{\rm clust} < L/c \pm 2$ ns; the difference is due to the difference in intrinsic timing resolution of the two calorimeter technologies. Shower profile cuts are based on rejecting those clusters whose energy deposition among the modules, and in particular in the most central tower of the cluster, is not consistent, within a given χ^2-test limit, with the shower shape expected for electromagnetic showers as parametrized from test-beam data [52].

In the most central Au+Au events, the EMCal typically detects $\gtrsim$300 clusters, corresponding to a detector occupancy of $\sim$10% in terms of hit towers, resulting in a non-negligible probability of particles making clusters which overlap. To minimize the effects of cluster overlaps due to high multiplicity, two methods are used to determine the cluster energy. First the energy of each cluster in the PbSc calorimeter is determined from the sum of all contiguous towers with deposited energy above a given threshold ($E_{\rm tower} = 15$ MeV, typically). Alternatively, an extrapolation (using a standard electromagnetic shower profile for an event with zero background) from the measured core energy (*ecore*) in the four central towers to the full cluster energy is used. For the latter case, the *ecore* energy was computed from the experimentally measured center of gravity, central shower energy, and impact angle in the calorimeter using a parametrized shower profile function obtained from electromagnetic showers measured in the beam tests. Such an *ecore* energy represents an estimate of the true energy of a photon impinging on the PbSc unbiased by background contributions from other particles produced in the same event and depositing energy in the neighborhood of a given cluster. The use of *ecore* instead of the total cluster energy for photon reconstruction helped considerably to minimize the effects of cluster overlaps in central Au+Au collisions.

2. Raw η yield extraction (p+p and d+Au)

The η yields are obtained by an invariant mass analysis of photon candidate pairs having asymmetries $\alpha = |E_{\gamma_1} -$

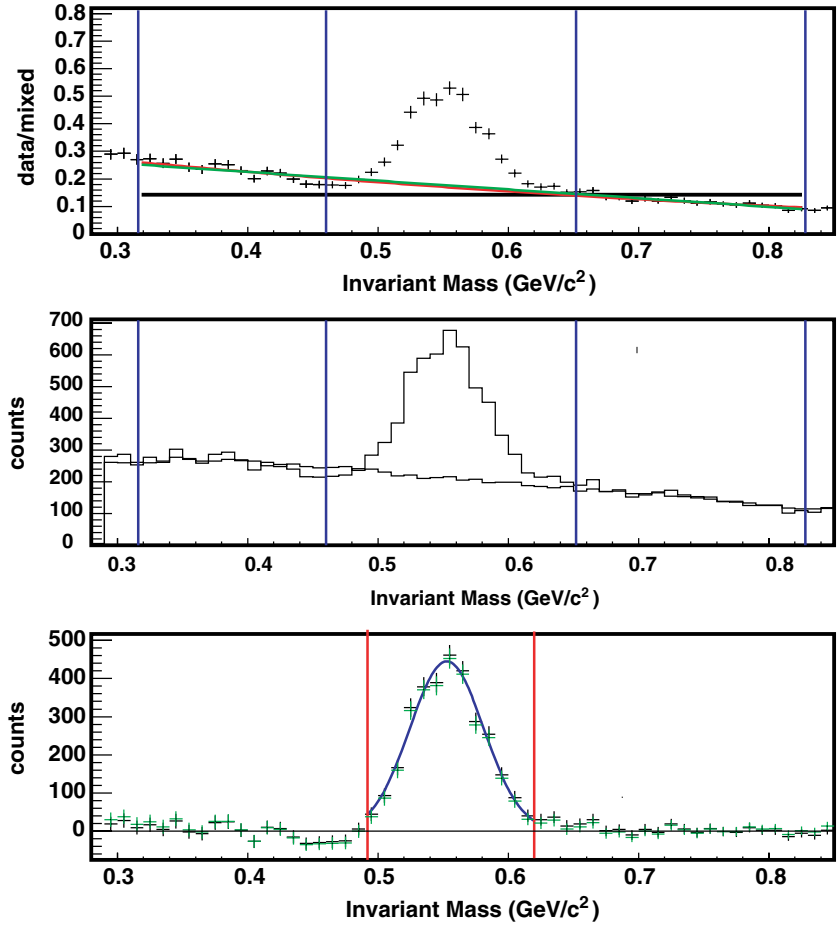

FIG. 3. (Color online) Invariant mass distribution of photon candidate pairs measured in $p+p$ collisions for the default PID cuts with pair transverse momenta 4.0 GeV/c < p_T < 4.5 GeV/c. (Top) Ratio of real and mixed event distributions, and background fits. The red fit is used for the background parametrization and the green fit for estimating the systematic uncertainty. (Middle) Real invariant mass spectrum and scaled background. (Bottom) Final distribution with the scaled background subtracted from the real event distribution (black entries); the green entries result from the background fit for estimating the systematic error. Additionally, the peak is fitted with a Gaussian to get its mean and σ.

$E_{\gamma_2}|/(E_{\gamma_1} + E_{\gamma_2}) < 0.7$. The cut on the asymmetry α reduces the background because high-p_T combinatorial pairs are strongly peaked near $\alpha = 1$ due to the steeply falling spectrum of single-photon candidates. The resulting invariant mass spectra obtained for proton-proton and deuteron-gold collisions are shown in Figs. 3 and 4, respectively, for two typical p_T bins. A peak is seen at about 550 MeV/c^2, the expected mass of the η meson. The measured peak position is modified by detector effects that lead to energy smearing. The combined effects of the energy resolution of the detector, the steeply falling single-photon spectrum, and the finite size of the energy bins lead to a smearing of the measured photon energies that widens the η signal. As a result the average peak position in the invariant mass spectra is about 9 MeV/c^2 larger than the nominal mass of the η meson, an effect that is well reproduced by the simulation.

The combinatorial background below the peak signal is estimated with the event mixing method in which clusters from different events with similar event vertex (and centrality class in d+Au) are combined to produce a "background" invariant mass distribution. This background is normalized to the real invariant mass spectrum and then subtracted from the invariant mass spectrum of the real events. To estimate the normalization of the background, the distribution of the real events is first divided by the mixed event distribution. This ratio is shown in the upper panel of Figs. 3 and 4. The normalization function is estimated by a fit in the region outside the peak. The spectrum, fitted to a second-degree polynomial, is shown in the region denoted by the vertical lines in the upper and the middle panels of Figs. 3 and 4. The final real event mass distribution after the background subtraction is shown in the lower panel of Figs. 3 and 4.

The interval over which the background is adjusted is limited by two considerations: the expected η peak position m and width σ. Both were estimated in a first analysis of the spectra and set to $m = 556$ MeV/c^2 and $\sigma = 32$ MeV/c^2. The background interval includes the region between $m - 7.5\sigma$ and $m + 8.5\sigma$ (320 and 830 MeV/c^2) excluding the peak region $m \pm 3\sigma$ (460 MeV/c^2 < m_{inv} < 650 MeV/c^2). For higher transverse momenta, the background almost vanishes and thus the estimation of the normalization by a fit leads to large errors. Hence an alternative method is used where the fit function is replaced by the ratio of the number of photon pairs in the normalization region in the real and the mixed event distributions.

Finally, the total number of η in a given p_T bin is obtained by integration of the invariant mass distribution within 3σ around the η peak position. The statistical error of the peak extraction is estimated as done for the π^0 and described in Ref. [21]. The uncertainty of the background parametrization is estimated by calculating the error on the ratio of the integrals of the real and the mixed event distributions in the region of the background fit. Above $p_T = 10$ GeV/c in $p+p$ collisions, the mixed event background does not work as expected as there

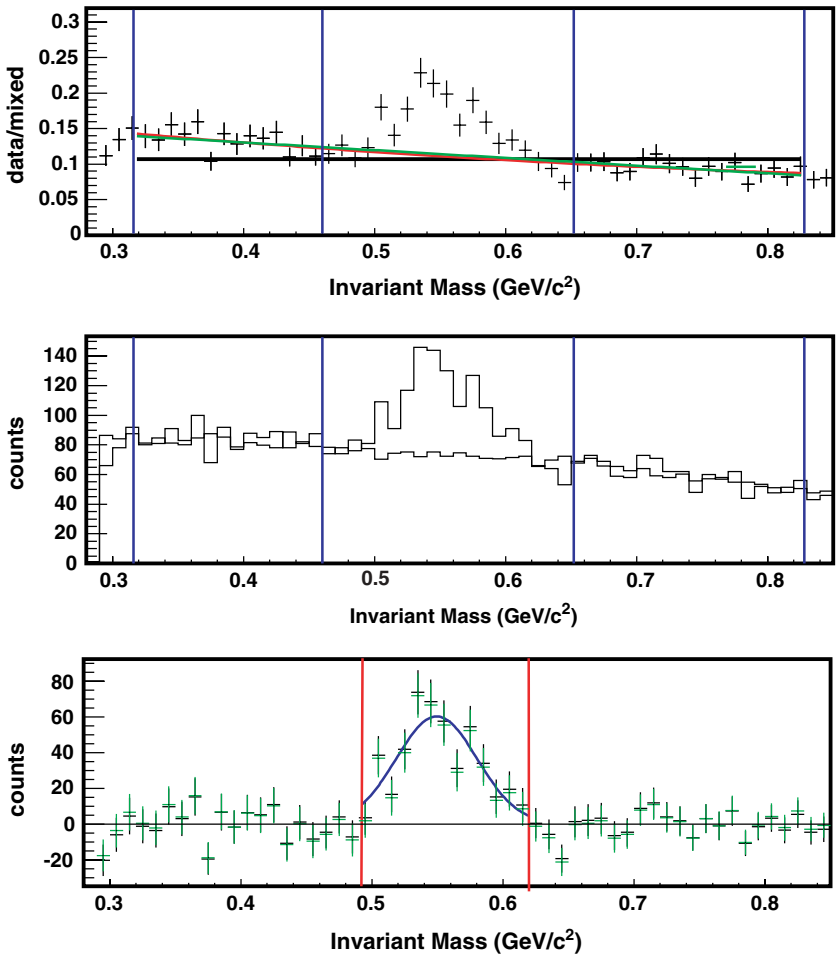

FIG. 4. (Color online) Invariant mass distribution of photon candidate pairs measured in minimum bias d+Au collisions for the default PID cuts with pair transverse momenta 3.5 GeV/c < p_T < 4.0 GeV/c. (Top) Ratio of real and mixed event distribution and background fits (the red fit is used for the background parametrization, the green fit for estimating the systematic uncertainty). (Middle) Real invariant mass spectrum and scaled background. (Bottom) Final distribution with the scaled background subtracted from the real event distribution (black entries). The green entries result from the background fit for estimating the systematic error. Additionally, the peak is fitted with a Gaussian to get its mean and sigma.

are some entries in the mixed event background but not in the η region. For these cases, the background was estimated by integrating the real event distribution outside the peak (in the fit region mentioned above) and scaling this to the η integration region. This background is then subtracted from the real event distribution to get the number of η. The error in this case is estimated with $\sigma^2_{\mathrm{Sig}} = S + 2B$, S being the η signal and B being the background. The integral of the invariant mass distribution after the background subtraction is calculated in a reduced interval $m - 2\sigma; m + 2\sigma$ (492–620 MeV/c^2).

3. *Raw η yield extraction (Au+Au)*

The η yields for Au+Au are determined by calculating the invariant mass of photon pairs with asymmetries $\alpha = |E_{\gamma 1} - E_{\gamma 2}|/(E_{\gamma 1} + E_{\gamma 2}) < 0.5$, a value tighter than that used for the p+p and d+Au cases to reduce the larger uncorrelated background in Au+Au collisions, and binned in p_T. The η yield in each p_T bin is determined by integrating the background-subtracted $\gamma\,\gamma$ invariant mass distribution around the η peak. The combinatorial background is obtained by combining uncorrelated photon pairs from different events with similar centrality and vertex and normalizing the distribution in a region below ($m_{\mathrm{inv}} = 400$–450 MeV/c^2) and above ($m_{\mathrm{inv}} = 750$–1000 MeV/c^2) the η mass peak (Fig. 5 top). After the mixed background subtraction, the resulting distribution is fitted to a Gaussian plus an exponential (or linear, see below) function to account for the residual background—more important at low p_T—not completely removed by the event-mixing technique. The bottom plot in Fig. 5 depicts the η signal after mixed (and residual) background subtraction. To estimate the uncertainty in the subtraction of the residual background, different pair asymmetries and an alternative linear parametrization were used (see Sec. III F). The signal-to-background (S/B) ratio in peripheral (central) Au+Au collisions is approximately 1.3 (1.5) and 0.05 (0.002) for the highest and lowest p_T, respectively. The signal-to-background ratio is comparable for central and peripheral collisions at the highest p_T because the spectrum in the central data extends to higher p_T than that in the peripheral.

The scaled mixed-event distribution is subtracted from the real-event distribution to produce a statistical measure of the true η yield. The result of such a subtraction procedure is shown in the bottom plot of Fig. 5. The raw η yield is obtained by integrating the subtracted invariant mass distribution in a range determined by the mean and the width of the η peak and given by $m_{\mathrm{inv}} \in [m_\eta - 2\sigma_\eta, m_\eta + 2\sigma_\eta]$. The analysis described above is applied in bins of $\Delta p_T = 1$ GeV/c for p_T = 2–4 GeV/c and $\Delta p_T = 2$ GeV/c above. We cease attempting to extract η yields at high p_T when the number of pairs within the

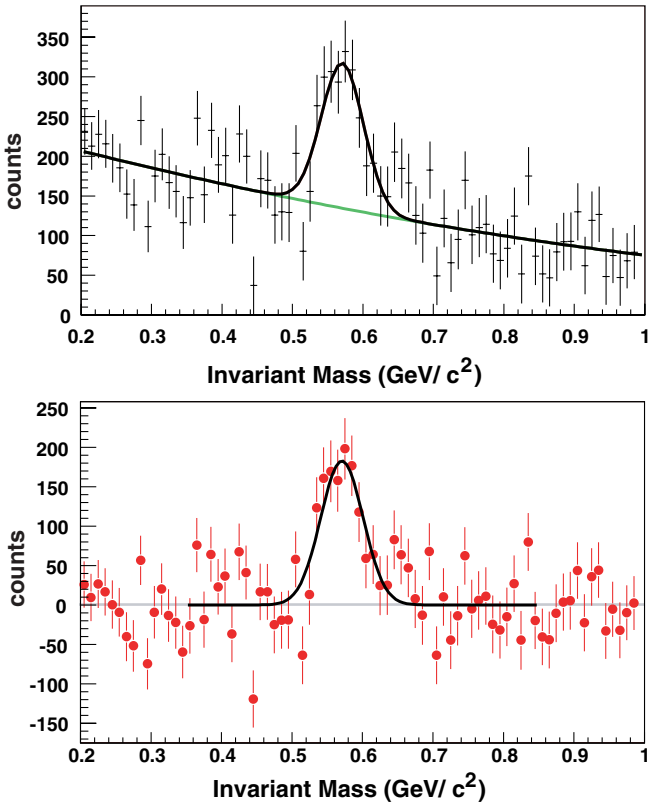

FIG. 5. (Color online) (Top) Invariant mass distribution of pairs of photon candidates measured in minimum bias Au+Au with pair momenta $p_T = 3.5$–4.5 GeV/c around the η mass fitted to a Gaussian plus exponential. (Bottom) Final η signal after mixed-event (and residual) background subtraction.

selected (background-subtracted) η mass window falls below 4 counts.

4. Acceptance correction

The geometric acceptance is evaluated using a fast Monte Carlo (fastMC) program based on routines from the JETSET library [64] to simulate the $\eta \to \gamma\gamma$ decays and determine the geometric acceptance of the calorimeter for the decaying photons. The acceptance correction accounts for the fraction of produced η mesons whose decay photons will not actually hit the detector due to the finite solid angle covered by the detector. A decay photon will be accepted by the EMCal in the fastMC when it hits the active surface of the detector covering the pseudorapidity range $-0.35 < \eta < 0.35$ (computed using a realistic distribution of event vertices within $|z| < 30$ cm) and $2 \times 90^\circ$ in azimuth. The acceptance shows a strong dependence on the transverse momentum because the opening angle of the decay photons decreases with increasing p_T. Thus, the probability that both decay photons hit the detector decreases for small values of p_T. The acceptance for $p+p$ and $d+$Au collisions is shown in Fig. 6. The acceptance is influenced by the geometry of the whole detector as well as by dead and hot modules in the $p+p$ and $d+$Au cases (for Au+Au the efficiency losses due to dead and hot modules are computed from the full GEANT3 simulation plus "embedding" and

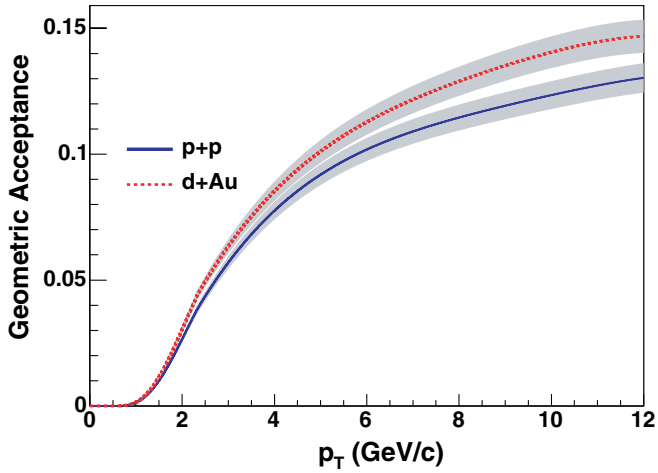

FIG. 6. (Color online) Geometric acceptance (including dead channels) for the η meson as a function of p_T measured in the EMCal in both $d+$Au (dashed curve) and $p+p$ (solid curve) collisions at PHENIX in Run-3.

are accounted for in the *efficiency* loss correction). Due to a different number of masked out modules, the acceptance is not exactly the same in $p+p$ and $d+$Au collisions.

5. Efficiency corrections of the raw η yields ($p+p$, $d+$Au)

a. Reconstruction efficiency correction. The reconstruction efficiency takes into account that the measured η spectrum in the detector is different from the real physical spectrum, i.e., the reconstruction efficiency is defined as the ratio between the output and the input η spectra:

$$\varepsilon(p_T) = \frac{dN_\eta/dp_T|_{\text{output}}}{dN_\eta/dp_T|_{\text{input}}} \tag{1}$$

as obtained using the fastMC, which parametrizes all the detector effects on the input spectrum (EMCal energy and position resolution, efficiency losses due to γ identification cuts and $\gamma\gamma$ reconstruction procedure, etc.). A realistic input η spectrum $dN/dp_T|_{\text{input}}$ is used as an initial spectrum for the efficiency calculation and an iterative procedure is performed, in which the corrected output spectrum is used as the input spectrum of the next iteration. To simulate detector effects, the smeared energies and hit positions of the decay photons are parametrized in the fastMC. The energy smearing has a constant and an energy-dependent term and follows the functional form

$$\sigma_E/E = \frac{A}{\sqrt{E/\text{GeV}}} \oplus B\,. \tag{2}$$

The parameters for Eq. (2) are given in Table III for the different collision systems and the two EMCal detector types. The initial values have been taken from the detector response obtained in the beam tests [52] and retuned for real run conditions in previous π^0 analyses [14,15]. During the cross-checks between simulated and real data it was found that the energy scale of the EMCal was slightly shifted compared to the parametrized results. Because the energy

TABLE III. Parameters for energy smearing, Eq. (2), as used in the fastMC for the different EMCal detector types and the different collision systems.

Collision system	Detector type	Energy-dependent term (A)	Constant term (B)
$p+p$	PbGl	0.085	0.059
$p+p$	PbSc	0.082	0.050
d+Au	PbGl	0.085	0.059
d+Au	PbSc	0.082	0.050

scale is estimated experimentally by fitting the location of the π^0 peak, and the position of the peak is also affected by reconstructed secondary neutral pions from K_s^0 decays that themselves decay off vertex, an additional correction is applied in the fastMC shifting the energy scale by 0.7%. After this correction, the position and the width of the simulated η peaks are confirmed to be consistent with the position and the width measured in the data for all p_T bins.

The efficiency correction also takes into account the different cuts used for particle identification. The simulation must consider the loss of photons and thus of η due to the applied shower shape (or "dispersion") and energy threshold cuts. The effect of the dispersion cut is estimated by a comparison of uncorrected spectra without a PID cut with the spectra obtained with the different PID cuts. The spectra are obtained with a sharp asymmetry (α) cut and as a function of $(E_1 + E_2)/2$. The resulting loss of η is translated into a photon loss probability, which is then used in the simulation. The energy cut is reproduced by rejecting photon hits according to an energy-dependent survival probability in the simulation. Finally, the simulation reconstructs the invariant mass and the transverse momentum of the η from the reconstructed (smeared) information. Only particles inside the interval used for the integration of the real peak are accepted. The overall η efficiency losses obtained by this method are of the order of $\varepsilon_{\eta\to\gamma\gamma} = 76\% \pm 3\%$ (dominated by the asymmetry cut and the invariant mass yield extraction procedure) and are flat within 1–2% in the whole p_T range measured for both ($p+p$ and d+Au) colliding systems.

b. Photon conversion correction. Some of the produced η are not reconstructed due to conversions of one or both decay photons in the inner regions of the PHENIX detector. Such an effect is not included in the fastMC and is computed independently using a full simulation of the detector including a realistic description of the material in front of the EMCal. The correction factors obtained from this analysis are 1.067 ± 0.003 for PbSc West, 1.052 ± 0.004 for PbSc East, and 1.076 ± 0.005 for PbGl, as the material between the collision vertex and the EMCal is different in the east and the west arm and between PbGl and PbSc.

6. *Efficiency corrections of the raw η yields (Au+Au)*

In the Au+Au case, the detection efficiency is determined using a full PISA (PHENIX Integrated Simulation Application) GEANT3-based Monte Carlo (MC) program of the PHENIX detector to simulate the complete response of the calorimeter to single η decays. The nominal energy resolution was adjusted in the simulation by adding an additional p_T-independent energy smearing of ~3% for each PbSc tower. The shape, position, and width of the η peak measured for all p_T and centralities were thus well reproduced by the simulated data. The data from each simulated η is embedded into real Au+Au events and the efficiency for detecting the embedded η is evaluated analyzing the merged events with the same analysis cuts used to obtain the real yields. Using this technique we determine efficiency corrections that account not only for the energy resolution and position resolution of the calorimeter but also for the losses due to overlapping clusters in a real Au+Au event environment. The embedding also permits a precise determination of the effect of edge cuts and bad modules. Though these effects can in principle be considered as geometric acceptance corrections (as done in the $p+p$ and d+Au analyses), they depend not only on the geometry but also on the energy deposition of an electromagnetic shower in the different calorimeter towers. Last, in the full-simulation plus embedding procedure we additionally have control over the effects of photon conversions, as the GEANT simulation considers the material in front of the EMCal and the information whether a decay-photon converts is kept for evaluation in the efficiency determination.

The input η spectrum embedded in real events is weighted to match a functional form fit to the measured η spectrum so that the correct folding of the η spectrum with the resolution is obtained. This procedure is iterated, with the fit of the p_T dependence of the input weights adjusted as the estimate of the efficiency correction improves, until the procedure converges within the nearly p_T-independent statistical error of the embedded sample, approximately 3%. The final overall η yield reconstruction efficiency correction factor was ~3 with a centrality dependence of $\lesssim$20%. The losses were dominated by fiducial and asymmetry cuts.

D. $\eta \to \pi^0\pi^+\pi^-$ Reconstruction

1. *Raw η yield extraction*

The second mode of η-meson reconstruction in PHENIX is via the three-body decay channel $\eta \to \pi^0\pi^+\pi^-$ with branching ratio BR = 22.6% ± 0.4%. This mode has been used for the $p+p$ and d+Au data but not for the Au+Au where the large detector occupancy makes the signal very difficult to extract. Reconstruction starts with identifying the π^0 candidates among the pairs of EMCal γ clusters with energy $E_\gamma > 0.2$ GeV in the same way described in the previous section for the direct $\eta \to \gamma\gamma$ channel. The mass of a candidate is required to be within two standard deviations from the peak position of π^0. The peak position and its width are determined by the π^0 decay kinematics and EMCal resolution for each of the clusters and its position. These parameters were found to be consistent with the expected values. Selected π^0 candidates with transverse momentum $p_T > 1.0$ GeV/c are assigned the exact mass of the meson and measured p_T of the pair. These candidates are further combined into triplets with

positive and negative particle tracks measured by DC and PC1 to have momentum in the range $0.2\ \text{GeV}/c < p_T < 4.0\ \text{GeV}/c$. No particle identification was used on the charged tracks.

To extract the raw η yields the mixed-event subtraction technique was not used in this case because it does not adequately reproduce the shape of the background in the real events. The most important physical reason for this is that there are a significant number of correlated tracks among the $\pi^+\pi^-$ pairs coming from various heavier particle decays. The yield extraction was done by simultaneous fitting of the peak and the background in the adjacent region. The characteristic peak in the three-particle mass distribution is shown in the top panel of Fig. 7. The position of the peak is consistent with the nominal mass of the η meson within the statistical error of the fit shown in the figure. The measured 8 MeV/c^2 width of the peak is narrower than in the $\eta \to \gamma\,\gamma$ decay channel. Unlike the $\gamma\,\gamma$ channel, where the full width of the peak is defined

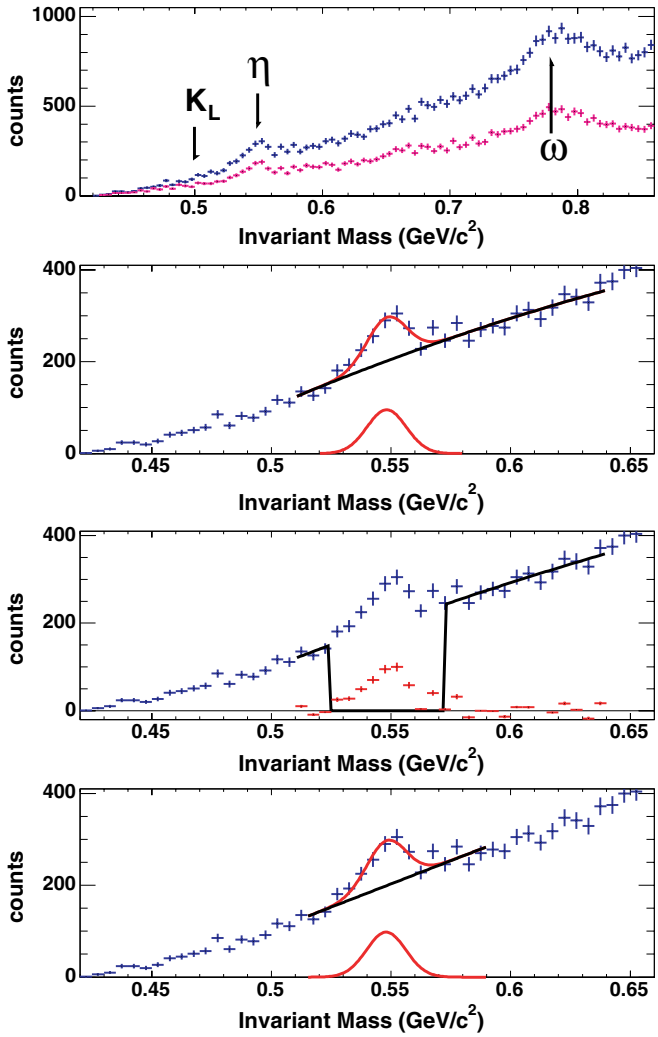

FIG. 7. (Color online) Invariant mass distribution of pion triplets ($\pi^0\pi^+\pi^-$) measured in $p+p$ collisions at $\sqrt{s} = 200$ GeV in the range $m_{\text{inv}} = 0$–0.9 GeV/c^2 (top panel) showing η- and ω-meson peaks. Lower panels showing η-mass region $m_{\text{inv}} = 0.42$–0.66 GeV/c^2 demonstrate three different methods of the extraction of the raw yields. See text for a detailed explanation of each method.

by the EMCal resolution alone, in $\pi^0\pi^+\pi^-$ only 1/4 of the measured mass is derived from an EMCal-based measurement. Given the relatively low p_T of the decay products, tracking has better resolution than the calorimeter. These two effects result in higher accuracy of the mass measurement and smaller width of the peak compared to the $\eta \to \gamma\,\gamma$ analyses.

The raw yield numbers were extracted by simultaneously fitting the signal with a Gaussian function and the background to a quadratic function. The fit was limited to the mass window of 510 MeV/$c^2 < m_{3\pi} <$ 640 MeV/c^2. The lower limit is chosen to avoid the region where the $K^0_L \to \pi^0\pi^+\pi^-$ decay (branching ratio BR = 13%) yields an additional signal at and above $m_{K^0_L} = 498$ MeV/c^2. The upper limit is chosen at a safe distance from the $\omega \to \pi^0\pi^+\pi^-$ (BR = 89.1%) peak at 782 MeV/c^2 with a width of 20–25 MeV/c^2. An example of the fit is shown in the second panel in Fig. 7. We also compared the result of such a combined signal+background fit with separate fitting of the background. For that, the region under the peak, 530 MeV/$c^2 < m_{3\pi} <$ 570 MeV/c^2, was rejected from the fit and the background was approximated by the quadratic function. The function was interpolated and subtracted from the histogram in Fig. 7 (third panel). The histogram counts in the region initially rejected were summed up to calculate the yield.

In addition, simultaneous fitting was done in the restricted window below $m_{3\pi} <$ 580 MeV/c^2, with the background approximated by a linear function. The same three fits were repeated applying an additional condition in the analysis. Each charged track was required to match a hit in PC3 or in the EMCal in case a track missed the active area of PC3. The resultant invariant mass spectrum is shown by the lower curve in the top panel of Fig. 7. The amplitude of the signal is reduced by about a factor of 2 because many tracks fall outside the acceptance of these two detectors, but the background is also reduced and, more importantly, modified in its shape. The overall significance of the results with and without matching is approximately the same. Signal loss due to matching can be corrected with the simulation with small systematic uncertainty and the results can be compared to deduce the accuracy of the yield extraction procedure. Thus, for each p_T point we obtain six statistically correlated measurements of the raw yields. The first measurement with its statistical error is used in further analysis and the variance of the six measurements provides the estimate of the systematic errors of the yield extraction.

2. *Acceptance and efficiency corrections of the raw η yields*

Similar corrections as described for the $\gamma\,\gamma$ decay channel need to be applied to the $\eta \to \pi^0\pi^+\pi^-$ raw yields. However, for the three-pion analysis, we use the full detector simulation and both corrections, namely the acceptance and the efficiency corrections, are computed at the same time. A MC hadron decay generator was used to produce initial η mesons with a p_T distribution providing satisfactory statistical significance in all bins after acceptance and trigger losses. The full GEANT-based PISA simulation was updated with the three-body decay of the η meson and used to decay η mesons. PISA also performs the full simulation of the PHENIX detector and generates the response of all its subsystems up to the electronics-signal

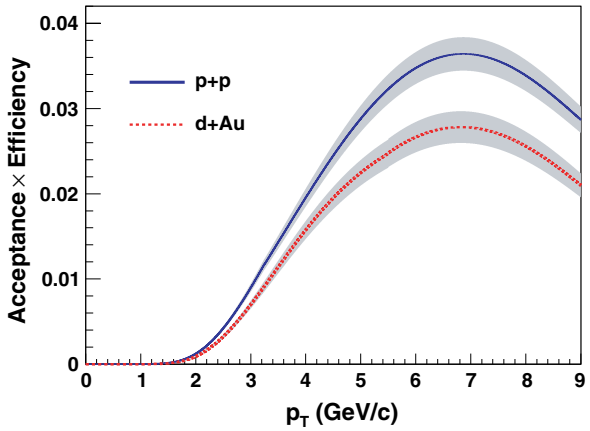

FIG. 8. (Color online) Acceptance×efficiency for the $\eta \to \pi^0\pi^+\pi^-$ as a function of p_T in both d+Au (dashed curve) and p+p (solid curve) collisions at PHENIX in Run-3.

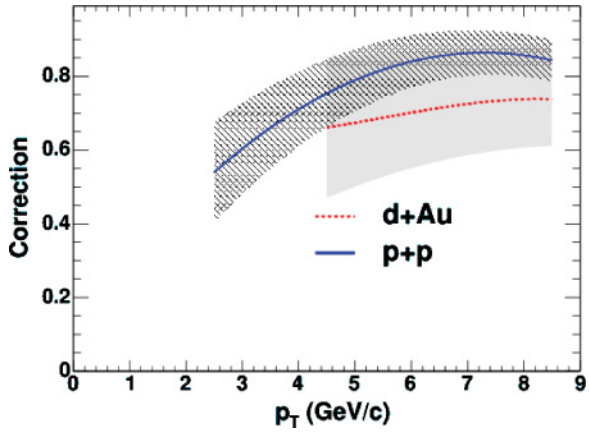

FIG. 10. (Color online) Phase-space density correction for p+p (solid curve) and d+Au (dashed curve) event samples as a function of p_T.

level, which was then processed by standard PHENIX reconstruction software. Special attention was paid to verify that the simulation code represented the real configuration of the detector, and that the π^0 peak parameters in the real data and simulation were consistent with each other. The reconstruction of the simulated data was carried out using the same steps and tools as the real data.

Figure 8 shows the combined efficiency×acceptance as a function of p_T for the three-pion decay analysis. To compare this with the $\gamma\,\gamma$ decay channel reconstruction efficiency one needs to multiply the acceptance curve shown in Fig. 6 with the obtained $\varepsilon_{\eta\to\gamma\,\gamma} = 76\% \pm 3\%$ overall efficiency loss. The three-body decay combined acceptance is significantly lower than the acceptance of the $\gamma\,\gamma$ decay channel. With comparable branching ratios of the two modes the resulting statistics in the three-body decay mode is expected to be smaller. The decrease of the efficiency at high p_T is due to the momentum cut on the $\pi^{\pm}$ to be below 4.0 GeV/c. Above that threshold the track sample is contaminated by products of in-flight decays of long-lived particles with mismeasured momentum.

3. *Phase-space density correction*

The $\eta \to \pi^0\pi^+\pi^-$ decay channel required an additional correction to take into account the uneven distribution of the momenta of the three pions within the kinematically allowed region. Such a distribution, taken from Refs. [65–67], is shown in the left panel of Fig. 9. The vertical axis is the fraction of kinetic energy carried by the π^0 in the η-meson rest frame. The horizontal axis shows the difference between kinetic energies of π^- and π^+ divided by the total in the same system. The left plot of Fig. 9 shows that on average the π^0 meson carries less kinetic energy, and thus momentum, than the two charged π mesons. The right panel shows the PHENIX reconstruction efficiency including geometrical acceptance, high-p_T trigger efficiency (see the next section), and analysis cuts. The latter two effectively select higher momentum π^0 and lower momentum $\pi^{\pm}$ in the lab frame. In the η-meson rest frame these translate into the effect opposite of what is shown in the left panel. To correct for that we used the following approach. The uniform distribution of the phase-space density produced by the simulated event generator was weighted according to the known probabilities of the π-meson momenta to be observed in the η-meson decay. The corresponding correction was deduced by comparing the reconstruction efficiencies with and without applying weights. The systematic uncertainties associated with the measurement of the phase-space density accuracy were thus obtained. This correction is shown in Fig. 10. The correction factor is calculated in the range where data is available.

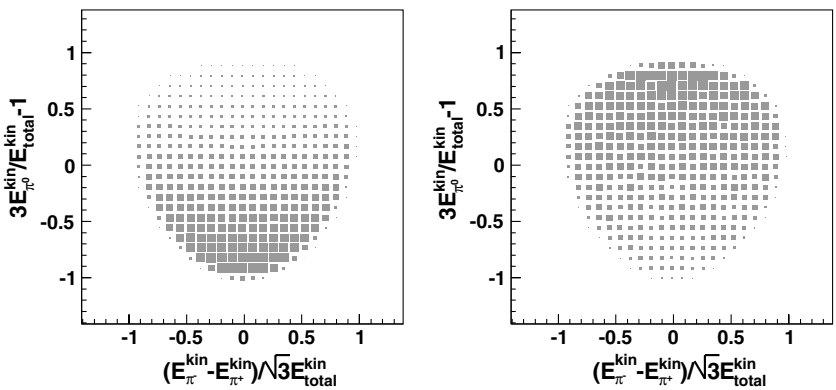

FIG. 9. The phase-space density of the $\eta \to \pi^0\pi^+\pi^-$ decay [65–67] (left panel). PHENIX reconstruction and trigger efficiencies in p+p for the $\eta \to \pi^0\pi^+\pi^-$ decay (right panel).

TABLE IV. Correction factors ($\varepsilon_{\rm trig}/\varepsilon_\eta$), due to the efficiency of the MB trigger for different d+Au centralities [59].

Collision system	Correction factor
d+Au 0–20% central	0.95
d+Au 20–40% semicentral	0.99
d+Au 40–60% semiperipheral	1.03
d+Au 60–88% peripheral	1.04

E. Trigger corrections and absolute cross-section normalization

1. Minimum-bias trigger efficiency

The minimum bias trigger does not detect every collision; only a certain fraction $\varepsilon_{\rm trig}$ of the inelastic collisions and a fraction ε_η of the η mesons can be observed. The spectra have to be corrected for both of these effects. The correction factors $\varepsilon_{\rm trig}/\varepsilon_\eta$, determined in Ref. [59] for d+Au collisions, are shown in Table IV. In the case of p+p collisions, as well as in MB d+Au collisions, one can directly determine the inelastic η cross section. Therefore, one does not apply the correction factors mentioned above but rather multiplies the spectra by the total cross section observed by the BBC, found to be 23.0 mb ± 9.7% in Run-3 p+p collisions and 1.99 b ± 0.10 b in Run-3 d+Au collisions [63]. An additional correction has to be applied for the bias of the BBC to high-p_T η. It is found to be 0.79 for p+p [17] and 0.94 for d+Au [63] collisions.

2. High-p_T γ-trigger efficiency

The efficiency of the high-p_T trigger has to be studied as well to get η spectra for the γ-triggered data at high transverse momenta, as previously performed for PHENIX π^0 analyses [14,21]. The γ triggers in PHENIX are implemented by adding together amplitudes in 4×4 adjacent EMCal towers during data taking and comparing them to a preset threshold. In the case of p+p the threshold was set to correspond to $E_\gamma = 1.5$ GeV, whereas for d+Au it was set at $E_\gamma = 3.5$ GeV. In the case of Au+Au, triggering was performed by a LVL2 software algorithm run over the MB-triggered events during data taking, such that the number of rejected minimum bias events were recorded. This allowed two different threshold triggers to be employed based on event centrality in Au+Au: $E_\gamma = 1.5$ GeV for the 60–92% peripheral sample and $E_\gamma = 3.5$ GeV for the more central event selections.

The trigger efficiency curves versus the energy of a single photon for two different threshold settings used in p+p and d+Au collisions are shown in the top panel of Fig. 11. Based on these curves, the 2-γ efficiency is calculated as for the previous π^0 analyses [14,21] using the fastMC calculation. For this calculation, the single-photon trigger turn-on curve is represented by an integrated Gaussian for the d+Au analysis and by the integrated sum of two Gaussians for the p+p analysis. In the case of the Au+Au LVL2 triggers, the high-statistics measurement of the single-photon efficiency, which

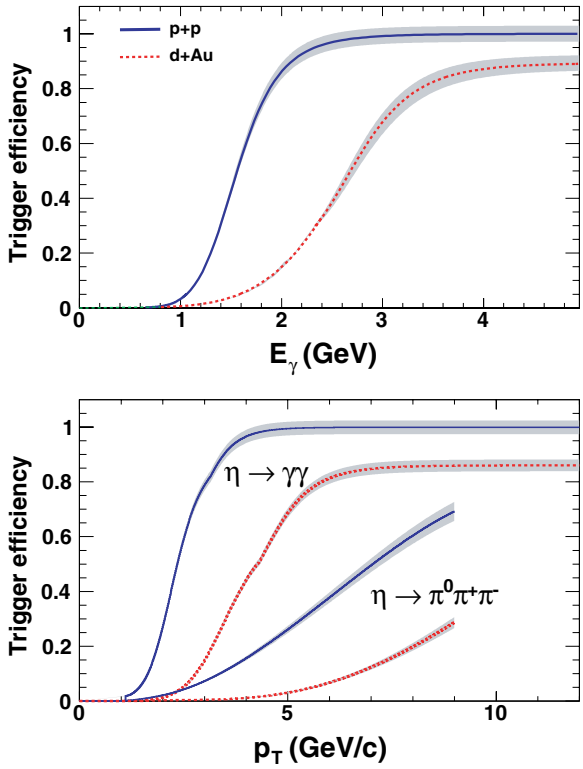

FIG. 11. (Color online) Simulation result for the efficiency of the γ trigger in d+Au collisions. The γ trigger efficiency for a single γ is shown in the top panel for p+p (solid curve) and d+Au (dashed curve). The gray band is the error of the measurement. The lower panel shows the recalculated trigger efficiency for $\gamma\,\gamma$ and $\pi^0\pi^+\pi^-$ channels for both collision systems.

for the central trigger reaches ∼100% above threshold, is used itself as shown in the top panel of Fig. 12. The derived π^0 efficiency is checked by comparing the ratio of the number of π^0 in MB events that carry the trigger flag to the number of π^0 in all MB events. In this way the normalization of the LVL2 data sample relative to the MB data sample is confirmed to be accurate to 2%.

In the same way we determine the $\eta \to \gamma\gamma$ trigger efficiency, which is shown in the lower panels of Figs. 11 and 12. In the $\eta \to \pi^0\pi^+\pi^-$ decay channel where the statistics is very limited, we use the measured single-photon trigger efficiency curves shown in the top panel and full detector MC to determine the efficiency of the trigger. The derived curves for p+p and d+Au are also shown in the lower panel of Fig. 11. One can see that the trigger efficiency plateaus at a p_T of the η about twice the energy of the threshold in the case of the $\gamma\gamma$ decay channel, but in the three-body decay mode where the trigger can only be fired by one of the γ from $\pi^0 \to \gamma\gamma$, it requires the p_T of the η to be approximately four times the threshold. In central Au+Au the η efficiency reaches 50% (∼100%) for η above $p_T = 5$ (7–8) GeV/c, as shown in Fig. 12 (bottom panel). The LVL2 data were used only for p_T regions where the trigger had better than ∼50% η efficiency: $p_T > 5$ GeV/c for the central trigger and $p_T > 2$ GeV/c for peripheral.

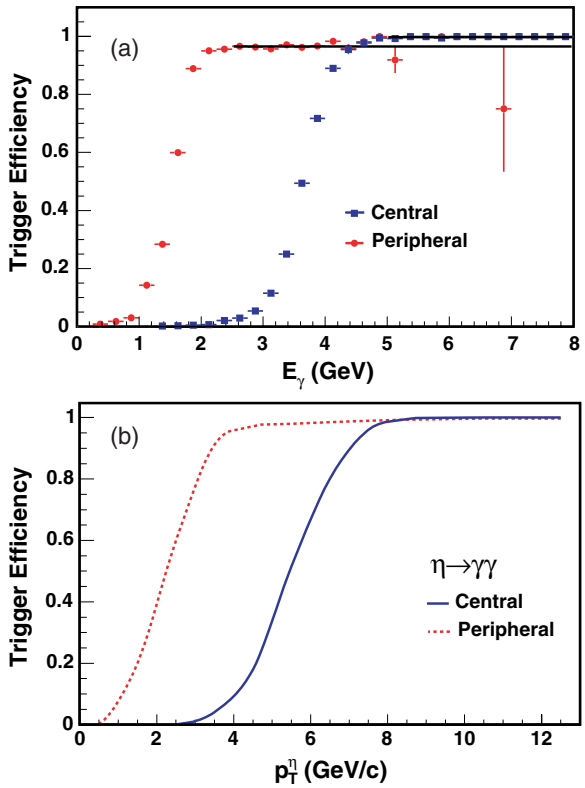

FIG. 12. (Color online) Level-2 trigger photon (top) and η (bottom) efficiencies for central Au+Au ($E_\gamma = 3.5$ GeV threshold) and peripheral Au+Au ($E_\gamma = 1.5$ GeV) collisions as in Fig. 11. For deriving the η efficiencies, the histograms in the top panel were directly used, with the black lines denoting constant fits to the above-threshold asymptotic value, at >99.7% for the central trigger. The central (peripheral) LVL2 η sample was used only above $p_T >$ 5 (2) GeV/c.

3. *Cross-section normalization*

The invariant cross sections for η production as a function of p_T in MB $p+p$ and $d+$Au collisions are obtained from the measured number of counts in each p_T bin via

$$E\frac{d^3\sigma}{d^3p} \equiv \frac{1}{2\pi\, p_T N_{\rm evt}} \frac{1}{\mathcal{L}} \frac{1}{BR} \frac{1}{Acc(p_T)\varepsilon(p_T)\varepsilon_{\rm trig}(p_T)} \frac{N(\Delta p_T)}{\Delta p_T \Delta y}, \tag{3}$$

where Acc, ε, and $\varepsilon_{\rm trig}$ are the acceptance, reconstruction efficiency, and trigger efficiency, respectively, determined in the previous section; $BR = 0.3943 \pm 0.0026$ is the known $\gamma\gamma$ decay branching ratio of the η meson, and $\mathcal{L}$ is the integrated luminosity obtained using the absolute inelastic cross-section normalization (see Sec. III A). The invariant *yields* as a function of p_T for a given bin in collision centrality in $d+$Au and Au+Au collisions are obtained via

$$\frac{1}{2\pi\, p_T}\frac{d^2N_{\rm cent}}{dp_T dy} \equiv \frac{1}{2\pi\, p_T N_{\rm cent}^{\rm event}} \frac{1}{BR} \times \frac{1}{Acc(p_T)\varepsilon(p_T, {\rm cent})\varepsilon_{\rm trig}(p_T)} \frac{N(\Delta p_T, {\rm cent})}{\Delta p_T \Delta y}. \tag{4}$$

A final bin-shift correction is needed to take into account the fact that the data points of the η spectra are plotted at the center of each given p_T interval (bins whose width is as large as $\Delta p_T = 2$ GeV/c), which, due to the exponentially falling spectrum, does not represent the true physical value of the yield in the interval [68]. Usually, either the correction is applied displacing the x values horizontally (i.e., the center of the p_T bin is decreased) keeping their y value, or the y values are moved vertically (i.e., the yields are decreased) keeping the p_T values at the center of the bin. The second method (yield correction) is preferred here because it facilitates taking bin-to-bin p_T ratios of spectra (with slightly different shapes) from different collisions systems. The net effect of this recipe is a small (few %) shift downwards of the invariant η yields in each p_T bin.

F. Systematic uncertainties

1. $\eta \to \gamma\,\gamma$ *analysis (p+p and d+Au)*

All systematic errors for the $p+p$ and the $d+$Au analysis are summarized in Table V. Hereafter, the errors are categorized by type:

(i) (**A**) point-to-point error uncorrelated between p_T bins,
(ii) (**B**) p_T correlated, all points move in the same direction but not by the same factor,
(iii) (**C**) an overall normalization error in which all points move by the same factor independent of p_T.

The cross-section measurement of the MB trigger has a type-C uncertainty of 9.7% in $p+p$ and 5.2% in $d+$Au. All other systematic errors are of type B, i.e. they are p_T correlated.

The error of the raw yield (peak) extraction was estimated, as described in Ref. [21], calculating the error of the ratio of the integrals of the real and the mixed event distributions in the region of the background fit. The systematic error in peak extraction differs from the systematic error estimated for neutral pions in Ref. [21] because the background in the η region cannot be estimated as well as the background in the π^0 region. This type-B error, estimated to be 4% higher than for pions, becomes dominant at very low transverse momenta due to the small S/B ratio. The error on the acceptance correction includes fiducial cuts on the edges of the EMCal sector as well as cuts around towers that have been determined to be hot or dead. The uncertainty in the MC (GEANT) description of the detector geometry is estimated varying these cuts slightly in the fastMC and in the embedded events (Au+Au). Those variations are found to result in differences in the yields of less than 5%. Different combinations of particle ID cuts were used in the analysis to estimate the uncertainty related to the photon identification. The differences among the various samples are less than 4% for all the different PID cuts for $p+p$ as well as for $d+$Au reactions. The error in the reconstruction efficiency contains this difference. The most important source of uncertainty at high p_T is related to the energy scale. The η peak positions and widths observed in the data are not reproduced to better than 1.5%. An error in the energy scale of 1.5% leads to an error of 4% in the yield at $p_T = 2$ GeV/c

TABLE V. Systematic errors of the η measurement in $p+p$ and $d+$Au (Run-3) for different p_T bins. The error of the peak extraction has a very steep slope at low p_T.

Error source	p_T independent	3 GeV/c	5 GeV/c	10 GeV/c	type
Peak extraction		14.5% ($p+p$), 9.5% ($d+$Au)	6%	6%	B
Geometric acceptance		4.5%	4.5%	4.5%	B
η reconstruction efficiency		1.3%	2.3%	3.6%	B
Global energy scale		5.5%	7.0%	8.4%	B
Energy scale linearity		1.5%	0.4%	4.3%	B
γ-trigger efficiency		9% ($p+p$), - ($d+$Au)	0% ($p+p$), 2.5% ($d+$Au)	0%	B
Conversion correction	2.0%				B
Absolute cross-section normalization	9.7% ($p+p$), 5.2% ($d+$Au)				C

and of 8% at $p_T = 10$ GeV/c. The error of the high-p_T trigger efficiency in $p+p$ is different from in $d+$Au: it amounts to 7.5% at $p_T = 3.5$ GeV/c and becomes negligible at $p_T = 5$ GeV/c (see Sec. III E2).

2. $\eta \to \gamma\gamma$ analysis (Au+Au)

The sources of systematic errors in the Au+Au analysis are listed in Table VI. The main sources of systematic errors in the η measurement are the uncertainties in the yield extraction (10–30%), the yield correction (∼10%), and the energy scale (a maximum of ∼8%). The energy scale uncertainty is basically the same as discussed before for the $p+p$ and $d+$Au analyses. The uncertainty on the raw yield extraction was studied by varying the normalization region of the mixed event background and by comparing yields extracted from 2σ and 3σ integration windows. The yields were found to vary within 10% of the expectation for all centralities. The final results obtained with different PID cut combinations are found to be consistent within ∼8%, and this was the assigned systematic uncertainty for the photon identification procedure. The final combined systematic errors on the spectra are at the level of ∼10–15% (type-A, point to point) and ∼10–15% (type-B, p_T correlated).

TABLE VI. List of systematic uncertainties in the PbSc η measurement in Au+Au collisions (Run-2). Ranges generally correspond to uncertainties from the lower p_T to the higher p_T values of the measurement.

Error source	Percentage error	Type
Raw yield (peak) extraction (point to point)	0–31%	A
Raw yield (peak) extraction (p_T correlated)	10–20%	B
Energy scale	3–8%	B
PID cuts	8%	A
Geometric acceptance	4–2%	B
Trigger efficiency	5–2%	B
Reconstruction efficiency	2%	A

3. $\eta \to \pi^0\pi^+\pi^-$ analysis ($p+p$ and $d+$Au)

Systematic errors for the $\pi^0\pi^+\pi^-$ channel are summarized in Table VII. The $p+p$ and $d+$Au data samples have different systematic errors which are usually larger in $d+$Au. This is due to the larger high-p_T trigger threshold set during $d+$Au data taking. The PC3-EMCal matching uncertainty is used to evaluate peak extraction uncertainty. The dominant systematic uncertainties in the $p+p$ ($d+$Au) measurement are in the yield extraction and the phase-space corrections, with uncertainties of 10–30% (10–30%) and ∼10% (∼25%), respectively. The final combined systematic errors on the spectra are at the level of ∼30% ($p+p$) and ∼40% ($d+$Au).

IV. RESULTS AND DISCUSSION

In this section, the fully corrected spectra for η production differential in p_T in $p+p$, $d+$Au and Au+Au are presented, as well as the nuclear modification factors for $d+$Au and Au+Au collisions. The measured η/π^0 ratio as a function of p_T for the three colliding systems is presented and discussed in comparison with a compilation of world data for hadron-hadron, hadron-nucleus, nucleus-nucleus, and e^+e^- collisions and to phenomenological (PYTHIA and "m_T-scaling") expectations.

A. Transverse momentum spectra ($p+p$, $d+$Au, Au+Au)

The fully corrected spectra for the η meson are shown in Fig. 13 for MB events in proton-proton and deuteron-gold collisions at $\sqrt{s_{NN}} = 200$ GeV. The figure shows the spectra obtained in both the $\eta \to \gamma\gamma$ and $\eta \to \pi^0\pi^+\pi^-$ decay channels. For the $\gamma\gamma$ result, the error bars represent the total error, given by the quadratic sum of the statistical and the systematic uncertainties. For the pion-triplet spectra, the error bars (bands) represent the statistical (systematic) uncertainties. These results agree well in spite of very different analysis approaches and sources of systematic uncertainties. Due to higher acceptance and lower trigger threshold (see Figs. 6, 8, and 11), the $\gamma\gamma$ channel has superior statistics and therefore these results alone are used henceforth.

The invariant yields measured in four different centrality classes in $d+$Au collisions at $\sqrt{s_{NN}} = 200$ GeV are shown

TABLE VII. Systematic errors of the $\eta \to \pi^0\pi^+\pi^-$ measurement in $p+p$ and $d+$Au collisions (Run-3). The first number corresponds to the $p+p$ data and the number in parentheses to $d+$Au in cases where it is different from $p+p$.

Error source	p_T independent	3 GeV/c	4 GeV/c	5 GeV/c	6 GeV/c	7 GeV/c	8 GeV/c	Type
EMCal geometrical acceptance	4% (4%)							C
DC-PC1 acceptance	2% (2%)							B
Acceptance variation	0.5% (3%)							B
PC3-EMCal matching	2% (2%)							B
π^0 selection		3%	3%	3% (3%)	3% (3.5%)	3% (4%)	3% (4%)	B
Conversion uncertainty	3% (3%)							C
EMCal energy resolution		2%	2.5%	3% (5%)	4% (5%)	5% (5%)	5% (5%)	B
EMCal energy scale		3%	3%	3% (4%)	3.5% (4%)	4% (4%)	5% (4.5%)	B
γ-trigger efficiency		5%	5%	5% (5%)	5% (5%)	5% (5%)	4% (4.5%)	B
γ-trigger run-by-run variation	4% (4%)							B
Peak extraction in data (fit)		10%	13%	20% (30%)	13% (20%)	23% (20%)	30% (15%)	A
Peak extraction in data (width)		10%	10%	10% (15%)	10% (15%)	10% (10%)	12% (20%)	A
Peak extraction in simulation	3% (5%)							B
Branching ratio uncertainty	1.8% (1.8%)							C
Phase-space corrections		20%	15%	11% (27%)	8% (24%)	7% (20%)	7% (19%)	B
MB trigger	9.7% (5.2%)							C
Trigger bias	2.5% (1%)							C
Total		28%	26%	29% (45%)	24% (38%)	30% (33%)	36% (35%)	

in Fig. 14. In Fig. 15 the fully corrected invariant spectra for MB and three different centrality classes in Au+Au collisions at $\sqrt{s_{NN}} = 200$ GeV are shown. The error bars represent the quadratic sum of the statistical and the point-to-point systematic uncertainties.

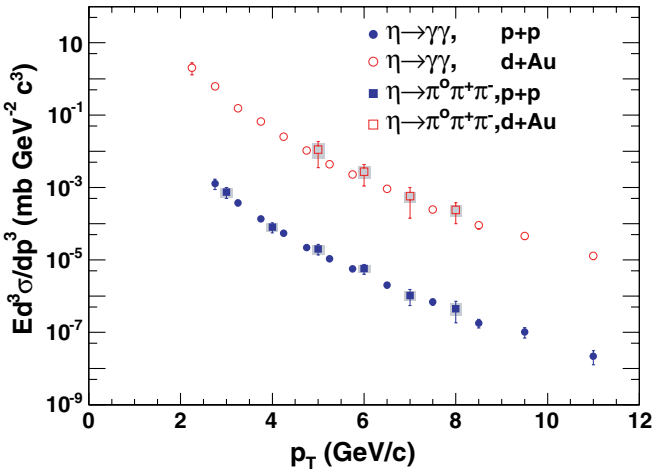

FIG. 13. (Color online) Invariant η cross section as a function of transverse momentum in $p+p$ and $d+$Au collisions at $\sqrt{s_{NN}} = 200$ GeV measured in the $\eta \to \gamma\gamma$ (circles) and $\eta \to \pi^0\pi^+\pi^-$ (squares) decay channels. The error bars of the $\eta \to \gamma\gamma$ are the quadratic sum of statistical and systematic uncertainties. The error bars (bands) of the $\pi^0\pi^+\pi^-$ spectra represent the statistical (systematic) uncertainties of the measurement.

B. Nuclear modification factor in $d+$Au, $R_{d\mathrm{Au}}(p_T)$

Medium effects in $d+$A collisions are quantitatively determined using the *nuclear modification factor* given as the ratio of the measured $d+$A invariant yields, d^2N_{dA}/dp_Tdy, over the measured $p+p$ cross sections, $d^2\sigma_{pp}/dp_Tdy$, scaled by the nuclear thickness function $\langle T_{dA}\rangle$ in the centrality bin under

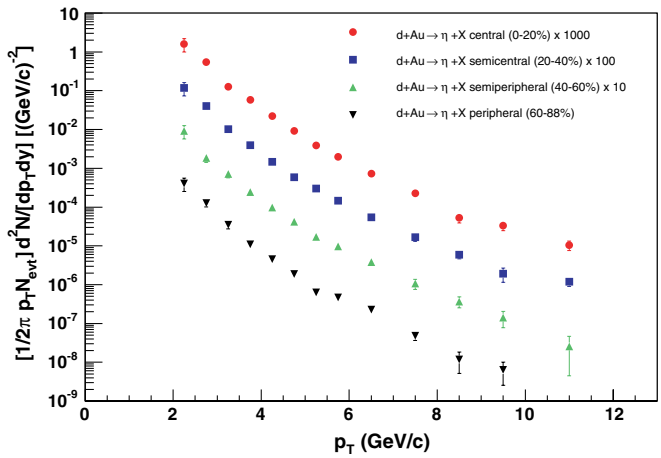

FIG. 14. (Color online) Invariant η yields as a function of transverse momentum in $d+$Au collisions at $\sqrt{s_{NN}} = 200$ GeV in four different centralities (0–20, 20–40, 40–60, 60–88%). The error bars are the quadratic sum of statistical and all systematic uncertainties. For clarity, the data points are scaled vertically as noted in the figure.

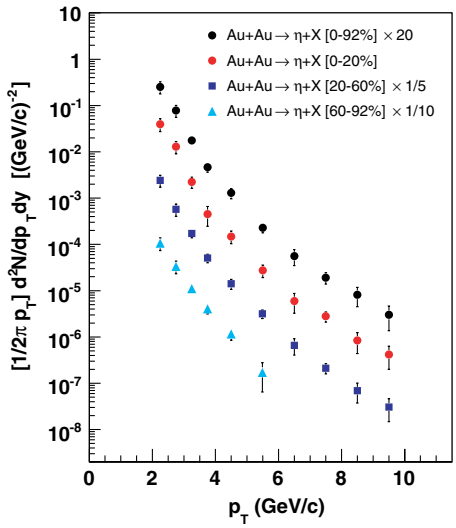

FIG. 15. (Color online) Invariant η yields as a function of transverse momentum in Au+Au collisions at $\sqrt{s_{NN}} = 200$ GeV for MB and three centralities (0–20, 20–60, 60–92%). The error bars are the quadratic sum of statistical and point-to-point systematic uncertainties. For clarity, the data points are scaled vertically as noted in the figure.

consideration:

$$R_{dA}(p_T) = \frac{d^2N_{dA}/dy\,dp_T}{\langle T_{dA}\rangle \cdot d^2\sigma_{pp}/dy\,dp_T}. \tag{5}$$

Deviations from $R_{dA}(p_T) = 1$ quantify the degree of departure of the hard d+A yields from an incoherent superposition of *NN* collisions. The values of the nuclear thickness function for different centralities are obtained in a Glauber MC calculation and tabulated in Table II. The resulting $R_{dA}(p_T)$ for η mesons in d+Au collisions is plotted for different centralities in Fig. 16.

The data points at lower transverse momenta have large statistical errors. This is caused by the poor S/B ratio of the η peak in the sample that is not triggered with the γ trigger. The systematic uncertainties shown in the plot are computed propagating the experimental uncertainties in the p+p and d+Au measurements described in Sec. III F. Some of these uncertainties cancel out when calculating the nuclear modification factor [Eq. (5)]. The error due to the η reconstruction efficiency as well as the error due to uncertainties in the energy scale are very similar for the measurement of η mesons in p+p and d+Au collisions as the measured data have been taken in the same experimental run, and they cancel almost completely in the ratio.

In the case of *minimum bias* d+Au collisions, the nuclear modification factor, shown in Fig. 17, is more simply defined as the ratio of d+Au over p+p *cross sections* normalized by the total number of nucleons ($2 \cdot A$ for a d+A collision) with $A = 197$ for a gold nucleus:

$$R_{dA}(p_T) = \frac{d\sigma_{dA}}{2 \cdot A \cdot d\sigma_{pp}}. \tag{6}$$

All the d+Au nuclear modification factors shown in Figs. 16 and 17 are approximately 1 and show a very weak p_T and/or centrality dependence. Similar trends have been observed for π^0 production [17]. As shown in the comparison plot of Fig. 18, the π^0 nuclear modification factors indicate

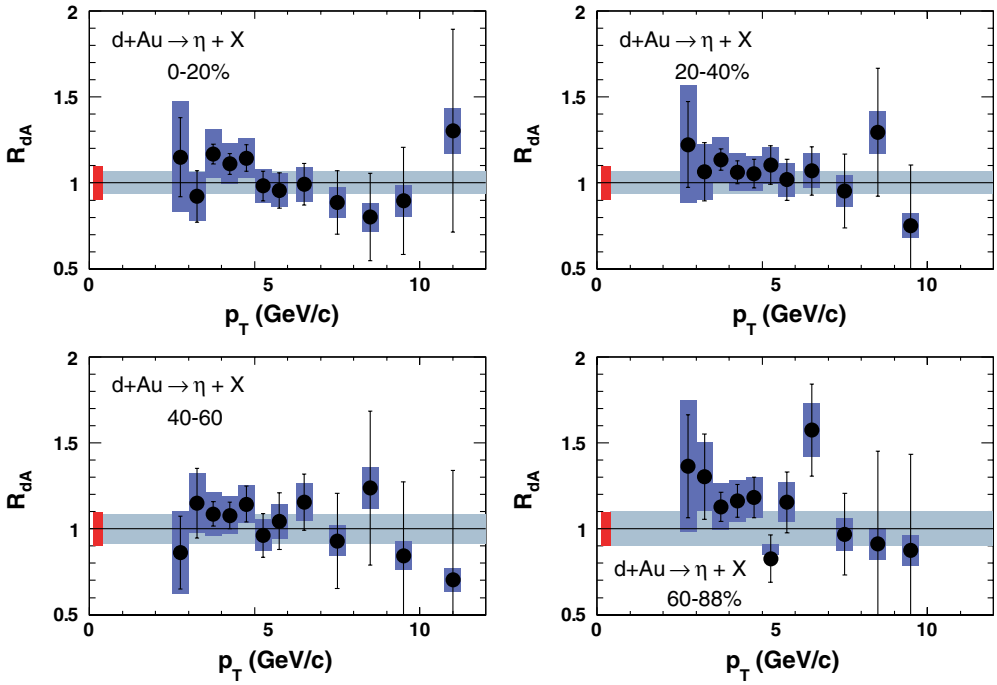

FIG. 16. (Color online) Nuclear modification factors for η production for four d+Au centralities: 0–20, 20–40, 40–60, 60–88%. The error bars (bands) around each point are the statistical (type-B systematic) uncertainties. The error band at $R_{dA} = 1$ indicates the uncertainty in $\langle T_{dA}\rangle$ for each centrality. The error box at $R_{dA} = 1$ indicates the p+p cross-section uncertainty of 9.7%.

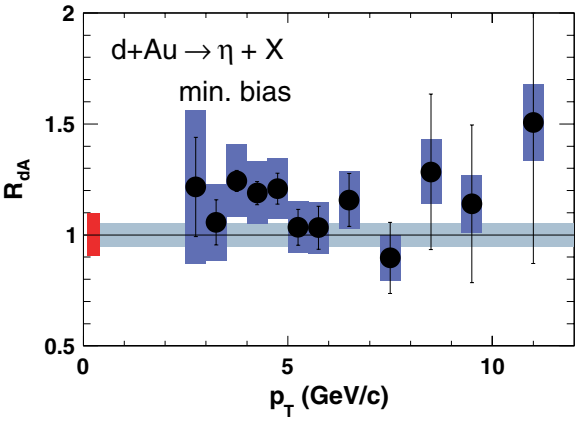

FIG. 17. (Color online) Nuclear modification factor R_{dA} for η mesons as a function of p_T for minimum-bias $\sqrt{s_{NN}} = 200$ GeV d+Au collisions. The uncertainties are the same described in Fig. 16.

small shape modifications with centrality, with a possible Cronin enhancement on the level of 10% around 4 GeV/c disappearing for $p_T > 10$ GeV/c. At high p_T the π^0 MB result can be described well by next-to-leading-order pQCD calculations [27,69] without implementation of the Cronin effect. The contribution of (anti-)shadowing effects [26,27] in the η or π^0 production is very small, as expected for this kinematical region with $x_T = 2p_T/\sqrt{s} \approx 0.02$–$0.2$.

The small role of initial-state cold nuclear effects observed in the midrapidity spectra of neutral mesons at high p_T is also consistent with other similar observations in d+Au reactions at $\sqrt{s_{NN}} = 200$ GeV such as (i) the absence of significant nuclear modifications in the yields of J/Ψ compared to p+p collisions [63] and (ii) the very similar characteristics of near-side and away-side jetlike correlations in p+p and d+Au [70]. Those results indicate that the nuclear medium has little influence on the hard processes in d+Au collisions at top RHIC energies and $y = 0$.

C. Nuclear modification factor in Au+Au, $R_{AA}(p_T)$

The nuclear modification factor, $R_{AA}(p_T)$, for η production in each centrality class in Au+Au collisions is computed using the standard formula:

$$R_{AA}(p_T) = \frac{d^2N_{AA}/dydp_T}{\langle T_{AA}\rangle \cdot d^2\sigma_{pp}/dydp_T}, \qquad (7)$$

where (i) the Au+Au spectra $d^2N/dydp_T$ are used in the numerator (Fig. 15), (ii) the p+p invariant spectrum $d^2\sigma/dydp_T$ (Fig. 13) is used in the denominator, and (iii) $\langle T_{AA}\rangle$ are the values of the average Glauber overlap function for each Au+Au centrality (Table II). The $R_{AA}(p_T)$ is computed taking the bin-to-bin ratio of Au+Au and p+p spectra and propagating the corresponding uncertainties. Only the acceptance uncertainty (~5%) cancels in the Au+Au/p+p ratio of spectra. Figure 19 compares the nuclear modification factor for η measured in central (0–20%), semicentral (20–60%) and peripheral (60–92%) Au+Au collisions. The error bars are the total point-to-point errors (including type-**A** systematic and statistical uncertainties) of the Au+Au and p+p measurements. The error bands on the left are the uncertainties in $\langle T_{AuAu}\rangle$ for each centrality class. The error box on the right is the Run-3 p+p cross-section uncertainty of 9.7%. As observed for high-p_T π^0 [19,21], the Au+Au η yields are consistent with the expectation of independent NN scatterings in peripheral reactions ($R_{AA} \approx 1$) but they are increasingly depleted with respect to this expectation for more central collisions. There is no p_T dependence of R_{AA}, as seen also for neutral pions.

Figure 20 contrasts the nuclear modification factors measured in central Au+Au at $\sqrt{s_{NN}} = 200$ GeV for η, π^0 [19,21], and γ [48]. Whereas direct photons are unsuppressed compared to the scaled reference given by a NLO pQCD calculation [48,71] that reproduces the PHENIX p+p γ results well [49], neutral pions and η are suppressed by a similar factor of ~5 compared to the corresponding cross sections measured in p+p. Within the current uncertainties, light-quark neutral mesons at RHIC show a flat suppression in the range $p_T \approx 4$–15 GeV/c, independent of their mass (note that the η is ~4 times heavier than the π^0). Those results are in agreement with parton energy loss calculations in a system with initial effective gluon densities of the order $dN^g/dy \sim 1000$ (solid curve in the figure) [37]. The equal suppression of η and π^0 mesons and the agreement with parton energy loss calculations suggest that the final fragmentation of the quenched parton into a leading meson occurs in the vacuum according to the same probabilities (fragmentation functions) that govern high-p_T hadroproduction in more elementary systems (p+p, e^+e^-). This conclusion is examined in more detail in the next two sections.

D. Ratio of η to π^0 (p+p, d+Au, Au+Au)

A useful way to determine possible differences in the suppression pattern of π^0 and η is to study the centrality dependence of the η/π^0 ratio, $R_{\eta/\pi^0}(p_T)$, in d+Au and Au+Au reactions and compare it with the values measured in more elementary systems (p+p, e^+e^-). The "world" η/π^0 ratio in hadronic and proton-nucleus collisions increases rapidly with p_T and flattens out above $p_T \approx 2.5$ GeV/c at values R_{η/π^0} ~0.40–0.50 (see Sec. IV E1). Likewise, in electron-positron annihilations at the Z pole ($\sqrt{s} = 91.2$ GeV), $R_{\eta/\pi^0} \sim 0.5$ for *energetic* η and π^0 (with $x_p = p_{\rm hadron}/p_{\rm beam} > 0.4$, consistent with the range of scaled momenta $\langle z\rangle = p_{\rm hadron}/p_{\rm jet}$ considered here), as discussed in Sec. IV E2. It is interesting to test if this ratio is modified in any way by initial- and/or final-state effects in d+Au and Au+Au collisions at RHIC energies.

The production ratio of η and π^0 mesons is shown in Fig. 21 for p+p and in Fig. 22 for d+Au (MB and four centrality classes). The ratio is calculated point by point for the d+Au measurements, propagating the corresponding errors. In the p+p case, a fit to the π^0 spectrum [21] was used. All the ratios are consistent with the PYTHIA [72] curve for p+p at $\sqrt{s} = 200$ GeV (dashed line, see discussion in Sec. IV E1) with an asymptotic $R^{\infty}_{\eta/\pi^0} = 0.5$ value.

Figure 23 shows the $R_{\eta/\pi^0}(p_T)$ ratio for MB and three Au+Au centralities, obtained using the latest PHENIX π^0 spectra [21] and removing those systematic uncertainties that

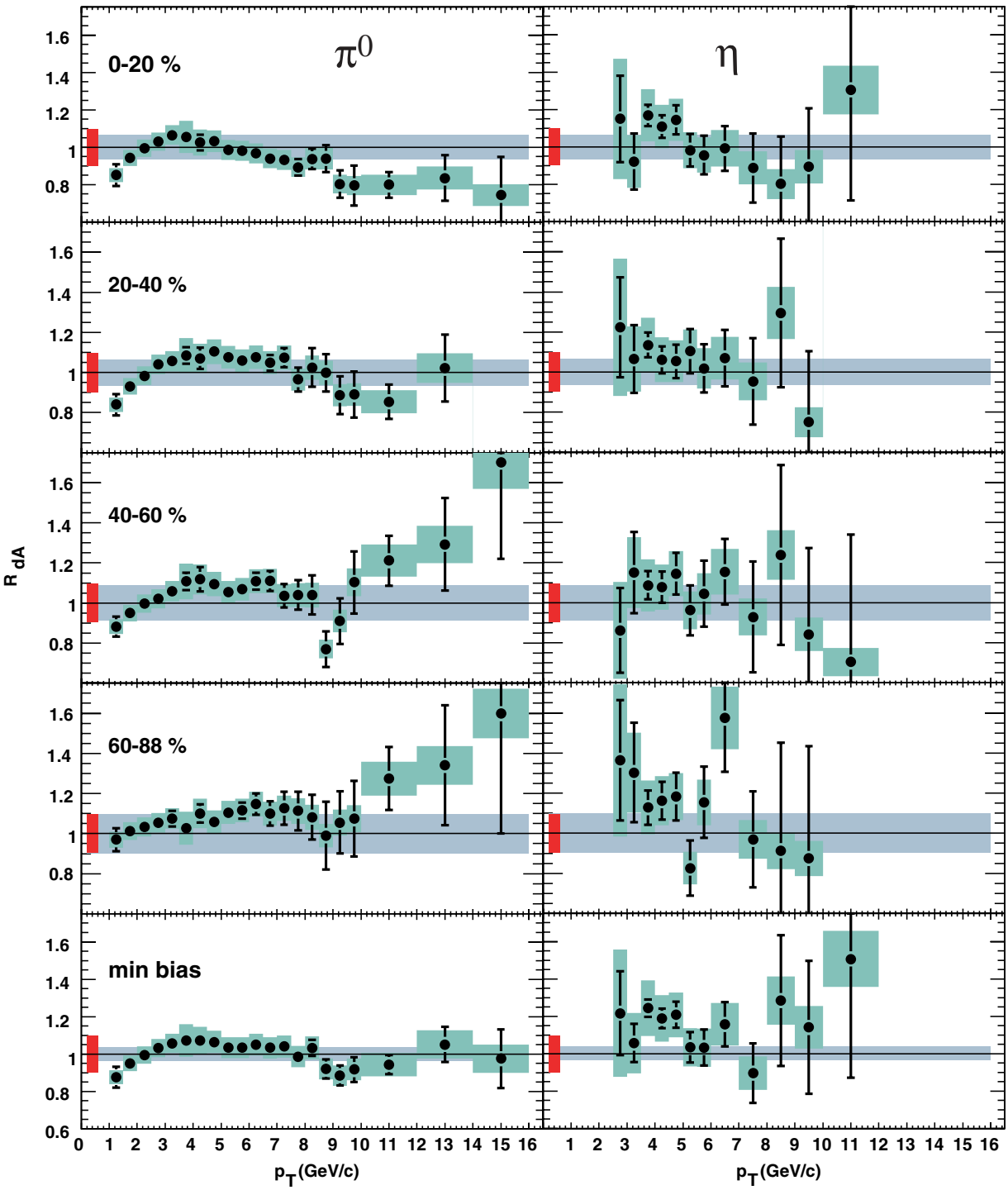

FIG. 18. (Color online) Nuclear modification factor $R_{\rm dA}(p_T)$ for π^0 (left) and η (right) production in different centrality selections and MB d+Au data. The bands around the data points show systematic uncertainties which can vary with p_T (type-B errors). The shaded band around unity indicates the $\langle T_{dA}\rangle$ uncertainty and the small box on the left side of the data points indicates the normalization uncertainty of the p+p total inelastic cross section.

cancel in the ratio. The $R_{\eta/\pi^0}(p_T)$ data for Au+Au is compared to a PYTHIA [72] calculation that reproduces the hadronic collision data well (see the next section). Within uncertainties, all the ratios are consistent with $R_{\eta/\pi^0} \approx 0.5$ (dashed line) and show no collision system, centrality, or p_T dependence. A simple fit to a constant above $p_T = 2$ GeV/c yields the following ratios:

(i) R_{η/π^0} (Au+Au cent) $= 0.40 \pm 0.04$ (stat) ± 0.02 (syst), χ^2/ndf $= 0.48$

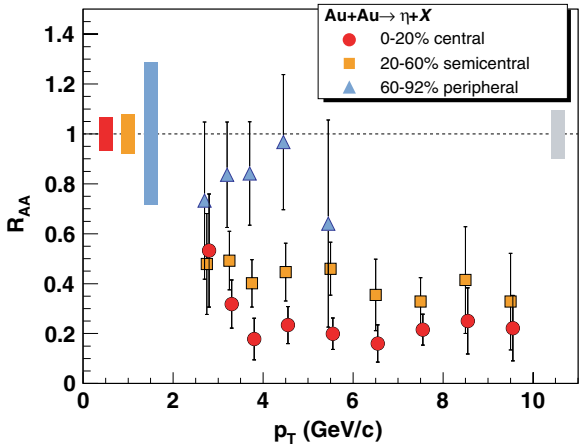

FIG. 19. (Color online) Nuclear modification factors for η in three Au+Au centralities (0–20, 20–60, 60–92%). The errors bars are point-to-point uncertainties. The absolute normalization error bands at $R_{AA} = 1$ are (i) the uncertainties in $\langle T_{AA} \rangle$ for each centrality (left side) and (ii) the p+p cross-section normalization uncertainty of 9.7% (right side). The $R_{AA}(p_T)$ for peripheral/central Au+Au have been slightly displaced to the left/right (±50 MeV/c) along the p_T axis to improve the clarity of the plot.

(ii) R_{η/π^0} (Au+Au semicent) = 0.39 ± 0.03 (stat) ± 0.02 (syst), χ^2/ndf = 0.26

(iii) R_{η/π^0} (Au+Au periph) = 0.40 ± 0.04 (stat) ± 0.02 (syst), χ^2/ndf = 0.42

(iv) R_{η/π^0} (p+p)= 0.48 ± 0.02 (stat) ± 0.02 (syst), χ^2/ndf = 0.89

(v) R_{η/π^0} (d+Au)= 0.47 ± 0.02 (stat) ± 0.02 (syst), χ^2/ndf = 0.84.

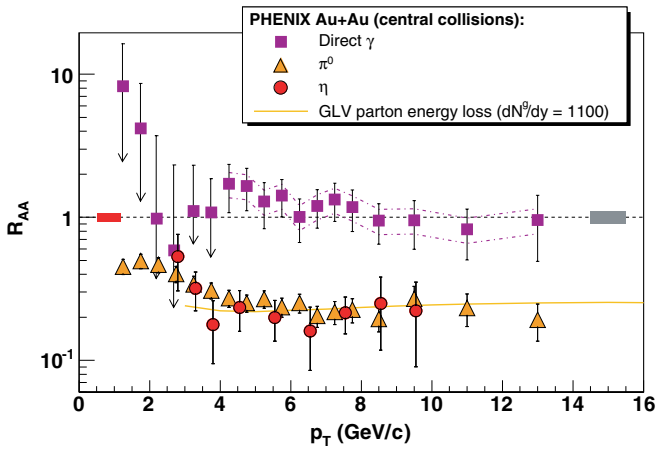

FIG. 20. (Color online) $R_{AA}(p_T)$ measured in central Au+Au at $\sqrt{s_{NN}} = 200$ GeV for η, π^0 [19,21], and for direct γ [48]. The error bars include all point-to-point uncertainties. The error bands at $R_{AA} = 1$ have the same meaning as in Fig. 19. The baseline p+$p \rightarrow \gamma + X$ reference used is a NLO pQCD calculation [48,71] that reproduces our own data well [49], with theoretical (scale) uncertainties indicated by the dash-dotted lines around the points. The solid yellow curve is a parton energy loss prediction for the suppression factor of leading pions in a medium with initial gluon density $dN^g/dy = 1100$ [37].

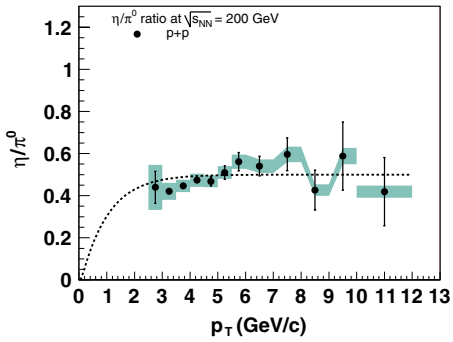

FIG. 21. (Color online) Ratio η/π^0 measured in p+p collisions at $\sqrt{s} = 200$ GeV. The error bars represent the point-to-point errors; the boxes represent the systematic uncertainties. The dashed line is the prediction of PYTHIA [72] for p+p at this center-of-mass energy.

E. World data on the η/π^0 ratio in high-energy particle collisions

In this last section of the article, we present a compilation of experimental η/π^0 ratios as a function of transverse momentum, $R_{\eta/\pi^0}(p_T)$, measured in different hadronic and nuclear colliding systems in a wide range of center-of-mass energies ($\sqrt{s_{NN}} \approx$ 3–1800 GeV). The collected world data on η/π^0 ratios includes (i) hadron-hadron collisions (26 p+p, p+$\bar{p}$, $\pi^{\pm}$+p data sets), (ii) hadron-nucleus collisions (17 $p, \pi^{\pm}$+A sets), and (iii) nucleus-nucleus collisions (7 A+A data sets).

In addition, we present also the $R_{\eta/\pi^0}(x_p)$ ratio obtained from inclusive π^0 and η cross sections in e^+e^- as a function of scaled momentum $x_p = 2\, p_{\rm had}/\sqrt{s}$ measured by the four LEP experiments at the Z pole ($\sqrt{s} = 91.2$ GeV). In all cases, the ratio R_{η/π^0} increases rapidly with p_T (or x_p) and saturates at $R_{\eta/\pi^0} \approx 0.4$–$0.5$ above $p_T \approx 3$ GeV/c ($x_p \approx 0.3$). The experimental $R_{\eta/\pi^0}(p_T)$ ratios are also compared to PYTHIA and to m_T-scaling expectations. PHENIX p+p, d+Au, and

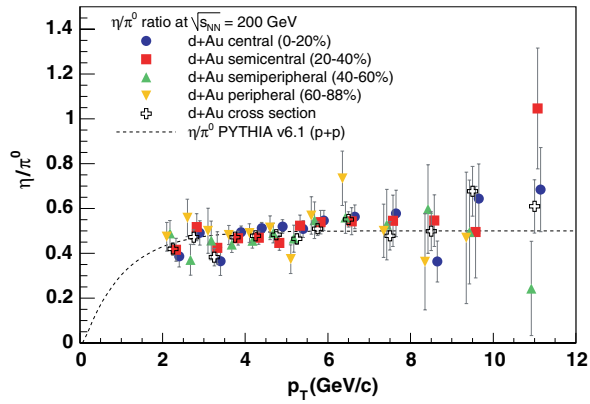

FIG. 22. (Color online) Ratio η/π^0 measured in different centralities in d+Au collisions at $\sqrt{s_{NN}} = 200$ GeV. The error bars represent all point-to-point uncertainties. The dashed line is the prediction of PYTHIA [72] for p+p at this center-of-mass energy. A few $R_{\eta/\pi^0}(p_T)$ ratios have been slightly displaced to the left or right (±<150 MeV/c) along the p_T axis to improve the clarity of the plot.

TABLE VIII. Hadron-hadron collisions with a published η/π^0 ratio and/or η and π^0 spectra. For each reaction we quote: the center-of-mass energy $\sqrt{s}$ (and $p_{\rm lab}$ for fixed-target experiments), the p_T and $x_T = 2p_T/\sqrt{s}$ ranges of the measurement (the x_T values are not quoted for "soft" spectra below $p_T = 1$ GeV/c), and the average η/π^0 ratio above $p_T = 2$ GeV/c obtained by fitting $R_{\eta/\pi^0}(p_T > 2\ \text{GeV}/c)$ to a constant.

System	$\sqrt{s}$ (GeV)	$p_{\rm lab}$ (GeV/c)	p_T range (GeV/c)	x_T range	$R_{\eta/\pi^0}(p_T > 2\ \text{GeV}/c)$	Authors	Collab./Exp.	Ref.
$p+p$	13.8	100	1.6–2.4	0.3–0.4	0.52 ± 0.13	Donaldson 78	FNAL M2	[79]
π^++p	13.8	100	1.6–3.0	0.3–0.4	0.49 ± 0.10	Donaldson 78	FNAL M2	[79]
π^-+p	13.8	100	2.0–3.0	0.3–0.4	0.41 ± 0.13	Donaldson 78	FNAL M2	[79]
π^++p	19.4	200	2.0–3.5	0.2–0.4	0.40 ± 0.07	Donaldson 78	FNAL M2	[79]
π^-+p	19.4	200	1.5–4.0	0.2–0.4	0.43 ± 0.04	Donaldson 78	FNAL M2	[79]
$p+p$	19.4	200	2.0–3.5	0.2–0.4	0.42 ± 0.04	Donaldson 78	FNAL M2	[79]
$p+p$	23.0	280	4.0–5.5	0.2–0.4	0.60 ± 0.04	Bonesini 88	CERN WA70	[80]
π^++p	23.0	280	4.0–5.5	0.2–0.4	0.43 ± 0.05	Bonesini 88	CERN WA70	[80]
π^-+p	23.0	280	4.0–5.5	0.2–0.4	0.57 ± 0.06	Bonesini 88	CERN WA70	[80]
$p+p$	24.3		2.5–4.0	0.2–0.3	0.45 ± 0.06	Antille 87	CERN UA6	[81]
$\bar{p}$+p	24.3		2.5–4.0	0.2–0.3	0.48 ± 0.04	Antille 87	CERN UA6	[81]
$p+p$	27.5	400	0.2–1.6	—	—	Aguilar 91	NA 27	[82]
$p+p$	30.6		0.8–3.0	~0.1–0.2	0.55 ± 0.04	Amaldi 79	ISR	[83]
$p+p$	30.6		3.0–4.0	0.2–0.3	0.54 ± 0.05	Kourkoumelis 79	ISR	[42]
$p+p$	31.6	530	3.0–8.0	0.2–0.5	0.41 ± 0.03	Apanasevich 02	FNAL 706	[84]
$p+p$	38.8	800	3.0–8.0	0.1–0.4	0.44 ± 0.03	Apanasevich 02	FNAL 706	[84]
$p+p$	52.7		3.0–6.0	0.1–0.3	0.58 ± 0.03	Kourkoumelis 79	ISR	[42]
$\bar{p}$+p	53.0		2.5–4.0	0.1–0.2	0.53 ± 0.03	Akesson 85	ISR AFS	[85]
$p+p$	53.0		2.5–4.0	0.1–0.2	0.55 ± 0.02	Akesson 85	ISR AFS	[85]
$p+p$	53.2		3.0–6.0	0.1–0.2	0.54 ± 0.03	Amaldi 79	ISR	[83]
$p+p$	62.4		3.0–11.0	0.2–0.4	0.55 ± 0.03	Kourkoumelis 79	ISR AFS	[42]
$p+p$	63.0		0.2–1.5	—	(0.07 ± 0.055)	Akesson 86	ISR AFS	[86]
$p+p$	63.0		2.0–4.0	0.06–0.13	0.47 ± 0.01	Akesson 83	ISR AFS	[87]
$p+p$	200		2.0–12.0	0.02–0.12	0.48 ± 0.03	S. S. Adler 07	PHENIX	This work
$\bar{p}$+p	540		3.0–6.0	0.01–0.02	0.60 ± 0.04 (stat) $\pm$ 0.15 (syst)	Banner 85	CERN UA2	[88]
$\bar{p}$+p	1800		12.0	0.01	1.02 ± 0.15 (stat) $\pm$ 0.23 (syst)	Abe 93	CDF	[43]

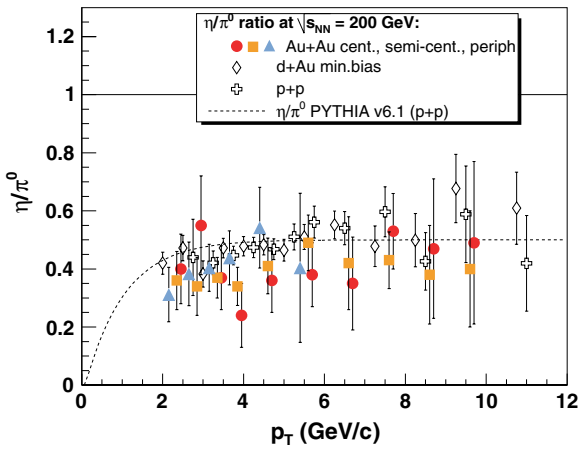

FIG. 23. (Color online) Au+Au R_{η/π^0} ratio in MB and three centrality classes (0–20, 20–60, 60–92%) as a function of p_T compared to the ratio in d+Au and $p+p$ collisions. The error bars include all point-to-point errors. The dashed line is the prediction of PYTHIA [72] for $p+p$ at this center-of-mass energy. A few $R_{\eta/\pi^0}(p_T)$ ratios have been slightly displaced to the left or right ($\pm$50 MeV/c) along the p_T axis to improve the clarity of the plot.

Au+Au η/π^0 ratios at $\sqrt{s} = 200$ GeV are found to be consistent with the obtained world data on R_{η/π^0}.

1. η/π^0 ratio in hadron-hadron, hadron-nucleus, and nuclear collisions ($\sqrt{s} \approx$ 3–1800 GeV)

In Tables VIII, IX, and X we list all data sets with published η and π^0 spectra and/or published $R_{\eta/\pi^0}(p_T)$ ratios in hadron-hadron, hadron-nucleus, and nucleus-nucleus collisions that we have found in the literature. Most of those measurements are performed around midrapidity. Roughly half of the $R_{\eta/\pi^0}(p_T)$ listed have been directly taken from the original works whose references are provided in the data tables. A few others have been constructed by taking the ratio of the published π^0 and η invariant cross-section spectra measured at the same $\sqrt{s}$. In the latter case, the error in the ratio has been computed by adding statistical and systematic uncertainties quadratically. There were a few cases where the p_T binning of the η spectrum did not match that of the π^0. In these cases, the π^0 spectrum was fitted with a functional form that reproduced the data well (usually a modified power law of

TABLE IX. Hadron-nucleus collisions with a published η/π^0 ratio and/or η and π^0 spectra. For each reaction we quote: the center-of-mass energy $\sqrt{s_{NN}}$ (and $p_{\rm lab}$ for fixed-target experiments), the p_T and $x_T = 2p_T/\sqrt{s}$ ranges of the measurement (the x_T values are not quoted for "soft" spectra below $p_T = 1$ GeV/c), and the average η/π^0 ratio above $p_T = 2$ GeV/c obtained by fitting $R_{\eta/\pi^0}(p_T > 2\ \text{GeV}/c)$ to a constant.

System	$\sqrt{s_{NN}}$ (GeV)	$p_{\rm lab}$ (GeV/c)	p_T range (GeV/c)	x_T range	$R_{\eta/\pi^0}(p_T >$ 2 GeV/c)	Authors	Collab./Exp.	Ref.
p+Be	19.4	200	2.5–4.0	0.2–0.4	0.28 ± 0.15	Povlis 83	FNAL E629	[89]
p+C	19.4	200	2.0–5.0	0.2–0.5	0.58 ± 0.05	Povlis 83	FNAL E629	[89]
p+Al	19.4	200	2.0–3.0	0.2–0.3	0.40 ± 0.18	Povlis 83	FNAL E629	[89]
π^-+C	19.4	200	2.0–4.0	0.2–0.5	0.32 ± 0.11	Povlis 83	FNAL E629	[89]
p+Be	23.8	300	2.5–5.0	0.2–0.4	0.47 ± 0.03	Deschamps 85	FNAL E515	[90]
p+Be	29.1	450	0.1–1.0	—	—	Agakichiev 98	TAPS/CERES	[91]
p+Au	29.1	450	0.1–1.2	—	—	Agakichiev 98	TAPS/CERES	[91]
p+Be	29.1	450	0.2–1.6	—	—	Tikhomirov 95	HELIOS	[92]
p+Be	30.7	500	4.0–7.0	0.3–0.5	0.40 ± 0.06	Alverson 93	FNAL E706	[93]
π^-+Be	30.7	500	4.0–8.0	0.2–0.5	0.43 ± 0.05	Alverson 93	FNAL E706	[93]
π^-+p	31.1	515	3.0–8.0	0.1–0.5	0.41 ± 0.05	Apanasevich 03	FNAL 706	[94]
π^-+Be	31.1	515	3.0–8.0	0.1–0.5	0.48 ± 0.01	Apanasevich 03	FNAL 706	[94]
π^-+Cu	31.1	515	3.0–8.0	0.1–0.5	0.50 ± 0.02	Apanasevich 03	FNAL 706	[94]
p+Be	31.6	530	3.0–8.0	0.1–0.5	0.42 ± 0.01	Apanasevich 03	FNAL 706	[94]
p+Cu	31.6	530	3.0–8.0	0.1–0.5	0.42 ± 0.02	Apanasevich 03	FNAL 706	[94]
p+Be	38.8	800	3.0–8.0	0.1–0.4	0.42 ± 0.01	Apanasevich 03	FNAL 706	[94]
p+Cu	38.8	800	3.0–8.0	0.1–0.4	0.45 ± 0.03	Apanasevich 03	FNAL 706	[94]
d+Au	200		2.0–12.0	0.02–0.1	0.47 ± 0.03	S. S. Adler 07	PHENIX	This work

the form discussed in Ref. [73]) and the η/π^0 ratio was then obtained by dividing the η spectrum data points by the values of the π^0 function at each point. In this case, the error was computed by dividing the quoted η error by the function value at that point. The uncertainty arising from the π^0 spectrum fit was obtained by computing the minimum and maximum ratio values at each point. Both errors were then added in quadrature.

In Tables VIII, IX and X, together with the general info on the collected data sets, we indicate for each measurement the approximate p_T and $x_T = 2p_T/\sqrt{s}$ ranges, as well as the average value of R_{η/π^0} at high p_T, obtained by fitting the data to a constant above $p_T = 2$ GeV/c. With the exception of the higher energy data ($\sqrt{s_{NN}} \gtrsim 100$ GeV), most of the experimental ratios have been measured in a fractional momentum range $x_T \approx 0.1$–0.3 where the parton distribution functions are dominated by valence quarks (rather than gluons) and, hence, the produced high-p_T π^0 and η mesons come largely from $q, \bar{q}$ fragmentation. Figures 24, 25, and 26 show the corresponding $R_{\eta/\pi^0}(p_T)$ ratios for each type of colliding system. All the ratios show a rapid increase with p_T and level off at $R_{\eta/\pi^0} \approx 0.4$–$0.5$ above $p_T \approx 3$ GeV/c. No difference is observed for different colliding systems. The PHENIX $p+p$, d+Au, and Au+Au high-p_T data presented in the previous section are consistent with those ratios. A fit of the PHENIX ratios to a constant gives $R_{\eta/\pi^0} = 0.47 \pm 0.03$ for both $p+p$ and d+Au and, slightly lower but still consistent, $R_{\eta/\pi^0} = 0.40 \pm 0.04$ for Au+Au. Together with the data points in Figs. 24–26, we also plot two phenomenological curves with PYTHIA 6.131 [72] based on the Lund fragmentation model [74,75], and on $m_{\rm T}$-scaling expectations for the η/π^0 ratio in $p+p$ collisions at $\sqrt{s} =$ 200 GeV.

a. Lund string fragmentation. The fragmentation mechanism in PYTHIA is based on the phenomenological Lund string

TABLE X. Nucleus-nucleus collisions with a published η/π^0 ratio and/or η and π^0 spectra. For each reaction we quote: the center-of-mass energy $\sqrt{s_{NN}}$ (and $p_{\rm lab}$ for fixed-target experiments), the p_T and $x_T = 2p_T/\sqrt{s_{NN}}$ ranges of the measurement (the x_T values are not quoted for "soft" spectra below $p_T = 1$ GeV/c), and the average η/π^0 ratio above $p_T = 2$ GeV/c obtained by fitting $R_{\eta/\pi^0}(p_T > 2\ \text{GeV}/c)$ to a constant.

System	$\sqrt{s_{NN}}$ (GeV)	$p_{\rm lab}$ (GeV/c)	p_T range (GeV/c)	x_T range	$R_{\eta/\pi^0}(p_T > 2$ GeV/c)	Authors	Collab./Exp.	Ref.
C+C	2.7	2.0	0.0–0.8	—	—	Averbeck 97	GSI TAPS	[95]
Ca+Ca	2.7	2.0	0.0–0.7	—	—	Averbeck 03	GSI TAPS	[96]
Ni+Ni	2.7	1.9	0.0–0.7	—	—	Averbeck 03	GSI TAPS	[96]
Pb+Pb	17.3	158	0.6–2.6	$\sim$0.1–0.3	0.53 ± 0.21	Aggarwal 00	CERN WA98	[97]
S+S	19.4	200	0.5–1.5	0.1–0.2	0.21 ± 0.06	Albrecht 95	CERN WA80	[98]
S+Au	19.4	200	0.5–3.5	0.1–0.3	0.61 ± 0.14	Albrecht 95	CERN WA80	[98]
Au+Au	200		2.0–10.0	0.02–0.1	0.40 ± 0.04	S. S. Adler 07	PHENIX	This work

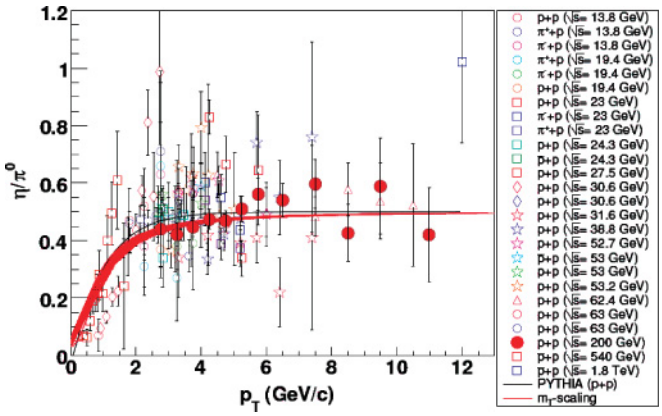

FIG. 24. (Color online) Values of the R_{η/π^0} ratios as a function of p_T measured in the hadron-hadron collisions reported in Table VIII. The black curve is the prediction of PYTHIA [72] for the ratio in $p+p$ at $\sqrt{s} = 200$ GeV, and the red shaded area indicates the empirical m_T-scaling prescription Eq. (10) with fixed $a = 1.2$, power-law exponent $n = 10$–14, and an asymptotic $R^{\infty}_{\eta/\pi^0} = 0.5$ ratio.

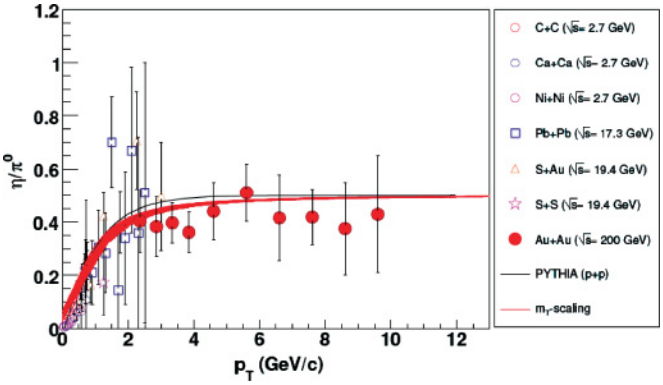

FIG. 26. (Color online) Values of the R_{η/π^0} ratios as a function of p_T measured in the nucleus-nucleus collisions reported in Table X. The black curve is the prediction of PYTHIA [72] for the ratio in $p+p$ at $\sqrt{s} = 200$ GeV, and the red shaded area indicates the empirical m_T-scaling prescription Eq. (10) with fixed $a = 1.2$, power-law exponent $n = 10$–14, and an asymptotic $R^{\infty}_{\eta/\pi^0} = 0.5$ ratio.

scheme [74,75] that considers the color field between the partons to be the fragmenting entity rather than the quarks and gluons themselves. The string is viewed as a color flux tube formed by gluon self-interaction between the partons. As the partons move apart the potential energy stored in the string increases. At some point the string breaks via the production of new $q\bar{q}$ pairs according to the probability of a quantum-mechanical tunneling process, $\exp(-\pi\, m^2_{\mathrm{q,T}}/\kappa)$, which depends on the transverse mass squared ($m^2_{\mathrm{q,T}} = m^2 + {p_T}^2$) and the string tension $\kappa \approx 1$ GeV/fm ≈ 0.2 GeV^2. The string breakup process proceeds repeatedly into color singlet systems as long as the invariant mass of the string pieces exceeds the on-shell mass of a hadron (each hadron corresponding to a small piece of string with a quark at one end and an antiquark at the other). At each branching,

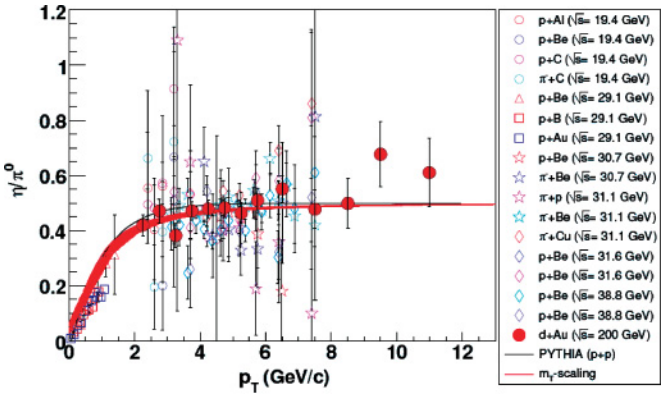

FIG. 25. (Color online) Values of the R_{η/π^0} ratios as a function of p_T measured in the hadron-nucleus collisions reported in Table IX. The black curve is the prediction of PYTHIA [72] for the ratio in $p+p$ at $\sqrt{s} = 200$ GeV, and the red shaded area indicates the empirical m_T-scaling prescription Eq. (10) with fixed $a = 1.2$, power-law exponent $n = 10$–14, and an asymptotic $R^{\infty}_{\eta/\pi^0} = 0.5$ ratio.

probabilistic rules are given for the production of flavors ($u\bar{u} : d\bar{d} : s\bar{s} = 1 : 1 : 0.3$ in the default settings), spin (e.g., a 3:1 mixture between the lowest lying vector and pseudoscalar multiplets is used, suggested by spin counting arguments), and for the sharing of energy and momentum among the products. Regarding the latter, the probability that a hadron picks a fraction z of $E + p_z$ out of the available $E + p$ (p_z is the momentum of the formed hadron along the direction of the quark q) is given by the "Lund symmetric fragmentation function:"

$$f(z) \propto z^{-1}(1-z)^a \exp(-b\, {m_T}^2/z), \tag{8}$$

where a and b are free parameters adjusted to bring the fragmentation into accordance with measured LEP data, e.g., $a = 0.3$ and $b = 0.58$ GeV^{-2} are the current default values for PYTHIA 6.3 [76]. In addition, for the flavor-diagonal meson states $u\bar{u} : d\bar{d} : s\bar{s}$, PYTHIA also includes mixing into the physical mesons. This is done according to a parametrization, based on the mixing angles given in the *Review of Particle Properties* [57]. In particular, the default choices correspond to $\eta = 1/2(u\bar{u} + d\bar{d}) - 1/\sqrt{2}(s\bar{s})$ and $\eta' = 1/2(u\bar{u} + d\bar{d}) + 1/\sqrt{2}(s\bar{s})$. Thus, in the $\pi^0 - \eta - \eta'$ system, no account is taken of the difference in masses, an approximation that seems to lead to an overestimate of η' rates in e^+e^- annihilation [103]. PYTHIA includes therefore parameters to allow an additional "tunable" suppression of η and η' states.

The PYTHIA Monte Carlo simulations of π^0 and η p_T-differential cross sections were carried out with the default settings. In particular, no ad hoc suppression of η was selected. Any uncertainty related to the choice of any (flavor-independent) settings should in principle cancel in the ratio of both p_T spectra. As seen in Figs. 24–26, within the (relatively large in some cases) experimental uncertainties, good agreement between the $R_{\eta/\pi^0}(p_T)$ data and the model prediction is found for all the colliding systems and p_T ranges, despite being at very different center-of-mass energies. We have also run PYTHIA at $\sqrt{s} = 30$ GeV as a reference for lower

energy results, but the resulting η/π^0 curve, though slightly lower at high-p_T ($R_{\eta/\pi^0} \approx 0.44$), is still relatively close to the one obtained at $\sqrt{s} = 200$ GeV. This is an indication that the p_T dependence of the production mechanisms for both neutral mesons is very similar for all systems and center-of-mass energies and, correspondingly, the ratio of p_T-differential cross sections is basically independent of the characteristics of the initial collision process but dominated by the ratio of η and π^0 (vacuum) FF, which is relatively constant in this kinematic range (see discussion in Sec. IV E2).

b. m_T scaling. The red shaded curve shown in Figs. 24, 25, and 26 corresponds to an empirical m_T-scaling observation [77] that assumes that the hadron differential cross sections, plotted as a function of the transverse mass of the produced particle $m_T = \sqrt{m_h^2 + {p_T}^2}$, all have the same shape, $f(m_T)$, with an absolute normalization factor C_h that can vary but is found to be the same for many species:

$$E\frac{d^3\sigma_h}{d^3p} = C_h \cdot f(m_T). \tag{9}$$

Assuming isospin symmetry for pion production, we have combined the measured PHENIX charged $(\pi^+ + \pi^-)/2$ (measured in the range $p_T = 0.2$–2.6 GeV/c) [78] and neutral ($p_T = 1$–14 GeV/c) [17] pion differential m_T cross sections in $p+p$ collisions and fitted them with a modified power-law functional form[2] that reproduces the full spectra well in the range $m_T \approx 0.2$–14 GeV/c^2:

$$f(m_T) = (m_T + a)^{-n}, \quad \text{with } a = 1.2 \quad \text{and } n = 10. \tag{10}$$

If one assumes that m_T scaling holds for η, then its $m_T = \sqrt{m_\eta^2 + {p_T}^2}$ spectrum can also be represented by Eqs. (9) and (10) (with, in principle, a different C_h) and, therefore, the η/π^0 ratio as a function of p_T should follow:

$$R_{\eta/\pi^0}(p_T) = R^{\infty}_{\eta/\pi^0} \cdot \left[\frac{a + \sqrt{m_\eta^2 + {p_T}^2}}{a + \sqrt{m_{\pi^0}^2 + {p_T}^2}}\right]^n, \tag{11}$$

where $R^{\infty}_{\eta/\pi^0} = C_\eta/C_{\pi^0}$ is the asymptotic value of the ratio of η over π^0 for large p_T. Note that because the assumption of m_T scaling is that both m_T-differential cross sections have the same shape, the same parameters $a = 1.2$ and $n = 10$ are valid for both spectra as well as for the ratio [Eq. (11)]. In all figures, the plotted m_T-scaling curve with an asymptotic value of $R^{\infty}_{\eta/\pi^0} = 0.5$ is found to be in good agreement with both the data and the PYTHIA predictions. We note that the agreement between PYTHIA and m_T-scaling is not unexpected in as much as the Lund "fragmentation function," Eq. (8), depends explicitly on the m_T of the produced hadron. The upper red curve shown in all plots is that with the a and n parameters of Eq. (11) that reproduce the power-law shape of the meson spectra at $\sqrt{s} = 200$ GeV. At lower $\sqrt{s}$, the spectra get increasingly steeper and a and n change accordingly [a and n are correlated with $\langle m_T \rangle$ which itself is a logarithmically increasing function of $\sqrt{s}$, i.e., $\langle m_T \rangle = f(\sqrt{s})$]. For illustrative purposes, we have (arbitrarily) fixed the parameter a to the value $a = 1.2$ and refitted the π^0 spectra measured at different center-of-mass energies with n as a free exponent. With fixed a the corresponding values of the power-law exponent increase with decreasing $\sqrt{s}$ as $n \approx 10$, 11.5, 13.5, and 14.0 at $\sqrt{s} = 200$, 63, 27, and 13 GeV, respectively. The shaded red area indicates the range of expected m_T-scaling ratios for power-law exponents $n = 10.$–14. The differences are negligible at large p_T—where the η and π^0 masses are much smaller than their p_T and the ratio Eq. (11) $R_{\eta/\pi^0}(p_T) \approx R^{\infty}_{\eta/\pi^0}$ is independent of n but increases at lower p_T ($p_T \lesssim 3$ GeV/c). Furthermore, it is worth noting that in the low-p_T region below 1 GeV/c, the agreement between the data and the m_T-scaling curve is not always perfect for all data sets, even taking into account different power-law exponents. This is due to the fact that at very low $m_T \approx 0.0$–0.4 GeV/c^2, the pion yield rises due to contributions from multiple resonance decays and the formula [Eq. (10)] does not reproduce the spectral shape of the data anymore. Instead, an exponential behavior of the form $Ed^3\sigma/d^3p = B \cdot \exp(-b\, m_T)$ [99] extrapolates the spectra better in the soft regime all the way down to $m_T = 0$ GeV/c^2. However, for all practical purposes in this analysis focused on high-p_T production, we consider Eq. (10) [(and correspondingly Eq. (11)] to be a good enough approximation.

Last we want to mention that in the case of nucleus-nucleus collisions the existence of a strong collective radial flow ($\beta_{\rm coll} \approx 0.6$ at RHIC [100]), absent in $p+p$ collisions, changes the spectral shape of different hadrons produced at low transverse momenta ($p_T \lesssim 2$ GeV/c) and should result in a violation of the m_T-scaling behavior [101]. Because hydrodynamical flow results in a larger boost for the (heavier) η than for π^0, one expects a comparatively larger $R_{\eta/\pi^0}(p_T)$ ratio in Au+Au than in $p+p$ collisions below $p_T \approx 2$ GeV/c. Unfortunately, we cannot test this assertion with RHIC data since our lowest p_T value ($p_T \approx 2$ GeV/c) is just in the range where radial flow effects start to die out. The same holds true also for the recent proposal [102] to study the η/π^0 ratio as a tool to test different parton recombination scenarios in hadron production in nucleus-nucleus collisions. Lower-p_T η measurements, which are intrinsically more difficult due to the reduced PHENIX acceptance and the larger $\gamma\gamma$ combinatorial background, would be needed to better address the role of collective flow and/or parton recombination effects on the spectral shape and yields of light neutral mesons in Au+Au collisions at RHIC.

2. η/π^0 ratio in e^+e^- collisions at the Z pole ($\sqrt{s} = 91.2$ GeV)

In this last section we are interested in determining the η/π^0 ratio in an elementary colliding system such as e^+e^- and comparing it to the corresponding ratios obtained in hadronic and nuclear collisions. In e^+e^- the dominant high-momentum hadron production mechanism is $q, \bar{q}$ fragmentation because gluon production (and subsequent fragmentation) occurs with a probability that is suppressed by a factor α_S and therefore plays a comparatively less significant role than in the (highest energy) hadronic and nuclear collisions discussed in the

[2]Note that the a and n parameters of Eq. (10) are not independent but strongly correlated. They are actually related to the mean transverse mass of the spectrum via $\langle m_T \rangle = 2a/(n-3)$.

TABLE XI. Experimental measurements at LEP of η, π^0 spectra in e^+e^- collisions at $\sqrt{s} = 91.2$ GeV.

Collaboration/Year	Particle	Authors [Ref.]
ALEPH 92	η	Buskulic *et al.* [103]
ALEPH 96a	π^0	Barate *et al.* [104]
ALEPH 96b	π^0, η	Barate *et al.* [105]
ALEPH 99	π^0, η	Barate *et al.* [106]
ALEPH 01	η	Heister *et al.* [107]
DELPHI 95	π^0	Adam *et al.* [108]
L3 91	π^0	Adeva *et al.* [109]
L3 92	η	Adriani *et al.* [110]
L3 94a	π^0, η	Acciarri*et al.* [111]
OPAL 98	π^0, η	Ackerstaff *et al.* [112]
OPAL 00	π^0, η	Abbiendi *et al.* [113]

previous section. Some of the experimental interest in the study of η production in e^+e^- collisions was in fact triggered by theoretical expectations that the isoscalar mesons contained a significant $g\,g$ component, and thus that gluon jets should exhibit an anomalously large tendency to fragment into η and $\eta'(958)$ mesons [120–122]. However, this hypothesis was not confirmed by a detailed analysis of the ALEPH e^+e^- gluon fragmentation data [106]. Table XI lists all the existing measurements of inclusive π^0 and η production in e^+e^- collisions at LEP at energies around the Z pole. At lower energies, there are several results on inclusive π^0 production in e^+e^- but few η measurements exist ($\sqrt{s} = 29$ and 35 GeV at SLAC PEP [114,115] and SLC [116–119], respectively), and we could not determine the corresponding ratios.

Figures 27 and 28 show the combined inclusive η and π^0 invariant cross sections measured as a function of the scaled particle momentum $x_p = 2\,p_{\rm had}/\sqrt{s}$. Note that the overall η and π^0 spectra have been measured in x_p ranges which

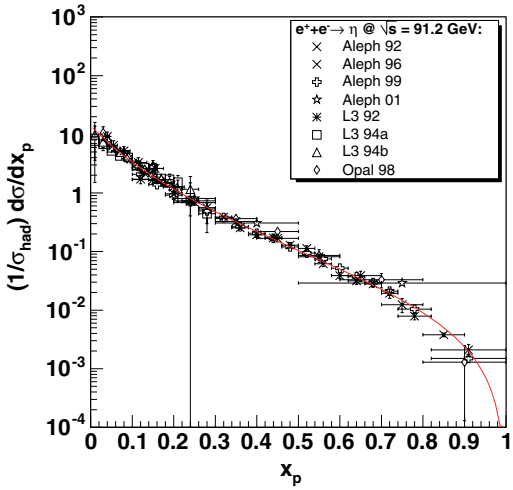

FIG. 27. (Color online) Differential inclusive η cross section as a function of the scaled momentum $x_p = 2\,p_{\rm had}/\sqrt{s}$ measured at the Z pole by the three LEP experiments listed in Table XI, fitted to Eq. (13) (solid curve).

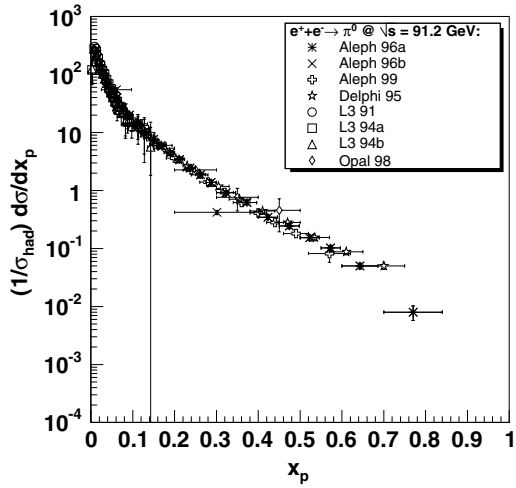

FIG. 28. Differential inclusive π^0 cross section as a function of the scaled momentum $x_p = 2\,p_{\rm had}/\sqrt{s}$ measured at the Z pole by the four LEP experiments listed in Table XI.

are not completely overlapping. There are more experimental measurements on inclusive η (π^0) production at large (small) $x_p \gtrsim 0.7 (x_p \lesssim 0.1)$. For this reason, to obtain the ratio of η over π^0 cross sections, we have parametrized the η cross section as

$$\frac{1}{\sigma_{\rm had}}\frac{d\sigma_\eta}{dx_p} = A \cdot (x_p + b)^n \cdot (1 - x_p)^m \qquad (12)$$

and taken the ratio of the individual π^0 data points over the resulting fit. We note that there is currently no η FF available in the standard FF sets at hand in the literature (BKK [123], KKP [124], Kretzer [125], BFGW [126]). Namely, the LEP data compiled in Fig. 27 have not been fitted and coded so far into any usable format that can be handled within a QCD collinear factorization approach. We are aware of only

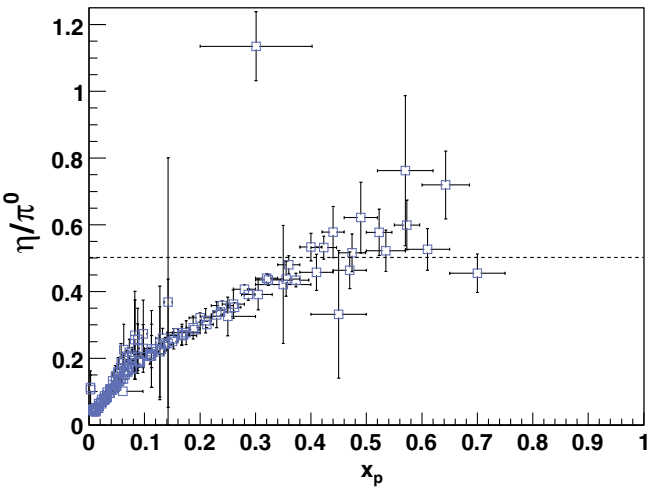

FIG. 29. (Color online) Ratio η/π^0 versus scaled momentum $x_p = 2\,p_{\rm had}/\sqrt{s}$ measured in e^+e^- collisions at LEP energies (Table XI), obtained from the π^0 results of Fig. 28 and the η fit, Eq. (13). The dashed line is the asymptotic $R_{\eta/\pi^0} = 0.5$ measured in hadronic and nuclear collisions.

TABLE XII. Invariant production cross section of η mesons in $p+p$ at $\sqrt{s} = 200$ GeV.

p_T (GeV/c)	$E\,d^3\sigma/d^3p$ (mb/GeV$^{-2}c^3$)	Tot. err.	Stat. err.	Sys. err.	ErrorA	Error B	Error C
			$\eta \to \gamma\gamma$				
2.75	1.30×10^{-3}	4.20×10^{-4}	2.25×10^{-4}	7.91×10^{-6}	0	3.34×10^{-4}	1.20×10^{-4}
3.25	3.78×10^{-4}	6.81×10^{-5}	8.09×10^{-6}	1.37×10^{-6}	0	5.79×10^{-5}	3.48×10^{-5}
3.75	1.37×10^{-4}	2.15×10^{-5}	3.53×10^{-6}	4.03×10^{-7}	0	1.70×10^{-5}	1.26×10^{-5}
4.25	5.49×10^{-5}	8.20×10^{-6}	1.81×10^{-6}	1.47×10^{-7}	0	6.20×10^{-6}	5.05×10^{-6}
4.75	2.22×10^{-5}	3.34×10^{-6}	1.03×10^{-6}	5.76×10^{-8}	0	2.43×10^{-6}	2.04×10^{-6}
5.25	1.08×10^{-5}	1.70×10^{-6}	6.82×10^{-7}	2.83×10^{-8}	0	1.20×10^{-6}	9.90×10^{-7}
5.75	5.66×10^{-6}	9.36×10^{-7}	4.39×10^{-7}	1.52×10^{-8}	0	6.42×10^{-7}	5.21×10^{-7}
6.5	2.02×10^{-6}	3.47×10^{-7}	1.75×10^{-7}	5.58×10^{-9}	0	2.36×10^{-7}	1.86×10^{-7}
7.5	6.99×10^{-7}	1.40×10^{-7}	9.14×10^{-8}	2.00×10^{-9}	0	8.45×10^{-8}	6.43×10^{-8}
8.5	1.81×10^{-7}	4.92×10^{-8}	4.04×10^{-8}	5.35×10^{-10}	0	2.26×10^{-8}	1.67×10^{-8}
9.5	1.02×10^{-7}	3.22×10^{-8}	2.80×10^{-8}	3.08×10^{-10}	0	1.30×10^{-8}	9.34×10^{-9}
11	2.21×10^{-8}	9.24×10^{-9}	8.52×10^{-9}	1.35×10^{-10}	0	2.94×10^{-9}	2.03×10^{-9}
			$\eta \to \pi^0\pi^+\pi^-$				
3.0	7.5×10^{-4}	2.4×10^{-4}	1.3×10^{-4}	2.1×10^{-4}	1.1×10^{-4}	1.6×10^{-4}	8.5×10^{-5}
4.0	8.1×10^{-5}	2.5×10^{-5}	1.4×10^{-5}	2.1×10^{-5}	1.3×10^{-5}	1.4×10^{-5}	9.1×10^{-6}
5.0	2.0×10^{-5}	6.6×10^{-6}	3.3×10^{-6}	5.8×10^{-6}	4.5×10^{-6}	2.9×10^{-6}	2.3×10^{-6}
6.0	5.8×10^{-6}	1.7×10^{-6}	1.1×10^{-6}	1.4×10^{-6}	9.5×10^{-7}	7.2×10^{-7}	6.5×10^{-7}
7.0	1.0×10^{-6}	5.0×10^{-7}	3.9×10^{-7}	3.2×10^{-7}	2.6×10^{-7}	1.3×10^{-7}	1.2×10^{-7}
8.0	4.5×10^{-7}	2.7×10^{-7}	2.1×10^{-7}	1.6×10^{-7}	1.5×10^{-7}	5.6×10^{-8}	5.1×10^{-8}

two works (Rolli *et al.* at NLO [127] and Indumathi and collaborators at LO [128]) that have tried to parametrize the η FF from these data. An updated version of the η FF would be useful as input to a NLO pQCD cross-section calculation for comparison to the results presented here and especially in the light of upcoming high-p_T η asymmetry results using polarized beams of relevance for the proton spin program at RHIC [44]. Fitting all the available η data with Eq. (12), we obtain the following empirical parametrization:

$$\frac{1}{\sigma_{\text{had}}}\frac{d\sigma_\eta}{dx_p} = 0.0975 \cdot (x_p + 0.186)^{-2.953} \cdot (1 - x_p)^{1.507}, \qquad \chi^2/\text{ndf} = 0.37. \tag{13}$$

TABLE XIII. Invariant production cross section of η mesons in d+Au at $\sqrt{s_{NN}} = 200$ GeV.

p_T (GeV/c)	$E\,d^3\sigma/d^3p$ (mb/GeV$^{-2}c^3$)	Tot. err.	Stat. err.	Sys. err.	Error A	Error B	Error C
			$\eta \to \gamma\gamma$				
2.25	2.06	7.49×10^{-1}	1.30×10^{-1}	3.37×10^{-4}	0	7.30×10^{-1}	1.08×10^{-1}
2.75	6.25×10^{-1}	1.09×10^{-1}	4.06×10^{-2}	4.41×10^{-5}	0	9.55×10^{-2}	3.28×10^{-2}
3.25	1.58×10^{-1}	2.40×10^{-2}	1.48×10^{-2}	7.84×10^{-6}	0	1.70×10^{-2}	8.27×10^{-3}
3.75	6.72×10^{-2}	8.21×10^{-3}	1.86×10^{-3}	3.31×10^{-6}	0	7.18×10^{-3}	3.53×10^{-3}
4.25	2.57×10^{-2}	3.18×10^{-3}	7.56×10^{-4}	1.28×10^{-6}	0	2.78×10^{-3}	1.35×10^{-3}
4.75	1.06×10^{-2}	1.34×10^{-3}	3.64×10^{-4}	5.39×10^{-7}	0	1.17×10^{-3}	5.55×10^{-4}
5.25	4.38×10^{-3}	5.65×10^{-4}	1.96×10^{-4}	2.20×10^{-7}	0	4.77×10^{-4}	2.30×10^{-4}
5.75	2.30×10^{-3}	3.08×10^{-4}	1.22×10^{-4}	1.18×10^{-7}	0	2.56×10^{-4}	1.21×10^{-4}
6.5	9.20×10^{-4}	1.27×10^{-4}	5.11×10^{-5}	4.86×10^{-8}	0	1.05×10^{-4}	4.83×10^{-5}
7.5	2.47×10^{-4}	4.39×10^{-5}	3.00×10^{-5}	1.35×10^{-8}	0	2.93×10^{-5}	1.30×10^{-5}
8.5	9.17×10^{-5}	1.89×10^{-5}	1.44×10^{-5}	5.18×10^{-9}	0	1.12×10^{-5}	4.82×10^{-6}
9.5	4.56×10^{-5}	9.14×10^{-6}	6.69×10^{-6}	2.65×10^{-9}	0	5.75×10^{-6}	2.40×10^{-6}
11	1.31×10^{-5}	2.88×10^{-6}	2.21×10^{-6}	7.92×10^{-10}	0	1.72×10^{-6}	6.88×10^{-7}
			$\eta \to \pi^0\pi^+\pi^-$				
5.0	1.1×10^{-2}	7.6×10^{-3}	5.7×10^{-3}	5.1×10^{-3}	3.7×10^{-3}	3.2×10^{-3}	9.9×10^{-4}
6.0	2.7×10^{-3}	1.6×10^{-3}	1.2×10^{-3}	1.0×10^{-3}	6.9×10^{-4}	7.3×10^{-4}	2.4×10^{-4}
7.0	5.8×10^{-4}	4.4×10^{-4}	3.9×10^{-4}	1.9×10^{-4}	1.3×10^{-4}	1.3×10^{-4}	5.1×10^{-5}
8.0	2.4×10^{-4}	1.4×10^{-4}	1.1×10^{-4}	8.4×10^{-5}	6.1×10^{-5}	5.4×10^{-5}	2.1×10^{-5}

TABLE XIV. Invariant yields, $(1/2\pi\, p_T)(d^2N_{\rm cent}/d\,p_T dy)$, measured in d+Au for different centrality classes from most central (0–20%) to most peripheral (60–88%).

p_T (GeV/c)	Inv. yield	Tot. err.	Stat. err.	Sys. err.	Error A	Error B	Error C
			0–20%				
2.25	1.59×10^{-3}	5.96×10^{-4}	1.85×10^{-4}	5.67×10^{-4}	0	5.67×10^{-4}	0
2.75	5.46×10^{-4}	1.02×10^{-4}	5.65×10^{-5}	8.49×10^{-5}	0	8.49×10^{-5}	0
3.25	1.27×10^{-4}	2.49×10^{-5}	2.05×10^{-5}	1.42×10^{-5}	0	1.42×10^{-5}	0
3.75	5.84×10^{-5}	6.89×10^{-6}	2.43×10^{-6}	6.45×10^{-6}	0	6.45×10^{-6}	0
4.25	2.22×10^{-5}	2.66×10^{-6}	9.62×10^{-7}	2.48×10^{-6}	0	2.48×10^{-6}	0
4.75	9.26×10^{-6}	1.15×10^{-6}	4.61×10^{-7}	1.06×10^{-6}	0	1.06×10^{-6}	0
5.25	3.85×10^{-6}	4.92×10^{-7}	2.36×10^{-7}	4.32×10^{-7}	0	4.32×10^{-7}	0
5.75	1.97×10^{-6}	2.70×10^{-7}	1.47×10^{-7}	2.26×10^{-7}	0	2.26×10^{-7}	0
6.5	7.29×10^{-7}	1.06×10^{-7}	6.15×10^{-8}	8.60×10^{-8}	0	8.60×10^{-8}	0
7.5	2.26×10^{-7}	4.57×10^{-8}	3.64×10^{-8}	2.76×10^{-8}	0	2.76×10^{-8}	0
8.5	5.29×10^{-8}	1.36×10^{-8}	1.19×10^{-8}	6.65×10^{-9}	0	6.65×10^{-9}	0
9.5	3.31×10^{-8}	8.26×10^{-9}	7.06×10^{-9}	4.27×10^{-9}	0	4.27×10^{-9}	0
11	1.05×10^{-8}	2.84×10^{-9}	2.47×10^{-9}	1.41×10^{-9}	0	1.41×10^{-9}	0
			20–40%				
2.25	1.18×10^{-3}	4.38×10^{-4}	1.37×10^{-4}	4.16×10^{-4}	0	4.16×10^{-4}	0
2.75	4.02×10^{-4}	7.52×10^{-5}	4.36×10^{-5}	6.13×10^{-5}	0	6.13×10^{-5}	0
3.25	1.02×10^{-4}	1.93×10^{-5}	1.59×10^{-5}	1.09×10^{-5}	0	1.09×10^{-5}	0
3.75	3.92×10^{-5}	4.60×10^{-6}	1.90×10^{-6}	4.18×10^{-6}	0	4.18×10^{-6}	0
4.25	1.47×10^{-5}	1.77×10^{-6}	7.97×10^{-7}	1.59×10^{-6}	0	1.59×10^{-6}	0
4.75	5.89×10^{-6}	7.53×10^{-7}	3.79×10^{-7}	6.50×10^{-7}	0	6.50×10^{-7}	0
5.25	2.99×10^{-6}	4.01×10^{-7}	2.35×10^{-7}	3.25×10^{-7}	0	3.25×10^{-7}	0
5.75	1.45×10^{-6}	2.06×10^{-7}	1.28×10^{-7}	1.61×10^{-7}	0	1.61×10^{-7}	0
6.5	5.44×10^{-7}	8.24×10^{-8}	5.41×10^{-8}	6.22×10^{-8}	0	6.22×10^{-8}	0
7.5	1.68×10^{-7}	3.69×10^{-8}	3.11×10^{-8}	1.99×10^{-8}	0	1.99×10^{-8}	0
8.5	5.91×10^{-8}	1.29×10^{-8}	1.07×10^{-8}	7.23×10^{-9}	0	7.23×10^{-9}	0
9.5	1.92×10^{-8}	7.74×10^{-9}	7.35×10^{-9}	2.42×10^{-9}	0	2.42×10^{-9}	0
11	1.19×10^{-8}	2.90×10^{-9}	2.45×10^{-9}	1.55×10^{-9}	0	1.55×10^{-9}	0
			40–60%				
2.25	9.14×10^{-4}	3.40×10^{-4}	1.03×10^{-4}	3.24×10^{-4}	0	3.24×10^{-4}	0
2.75	1.85×10^{-4}	4.31×10^{-5}	3.25×10^{-5}	2.83×10^{-5}	0	2.83×10^{-5}	0
3.25	7.17×10^{-5}	1.47×10^{-5}	1.25×10^{-5}	7.73×10^{-6}	0	7.73×10^{-6}	0
3.75	2.46×10^{-5}	3.01×10^{-6}	1.47×10^{-6}	2.62×10^{-6}	0	2.62×10^{-6}	0
4.25	9.73×10^{-6}	1.22×10^{-6}	6.23×10^{-7}	1.05×10^{-6}	0	1.05×10^{-6}	0
4.75	4.19×10^{-6}	5.67×10^{-7}	3.27×10^{-7}	4.63×10^{-7}	0	4.63×10^{-7}	0
5.25	1.71×10^{-6}	2.69×10^{-7}	1.95×10^{-7}	1.85×10^{-7}	0	1.85×10^{-7}	0
5.75	9.73×10^{-7}	1.71×10^{-7}	1.33×10^{-7}	1.08×10^{-7}	0	1.08×10^{-7}	0
6.5	3.84×10^{-7}	6.14×10^{-8}	4.29×10^{-8}	4.39×10^{-8}	0	4.39×10^{-8}	0
7.5	1.07×10^{-7}	3.14×10^{-8}	2.87×10^{-8}	1.27×10^{-8}	0	1.27×10^{-8}	0
8.5	3.69×10^{-8}	1.15×10^{-8}	1.06×10^{-8}	4.52×10^{-9}	0	4.52×10^{-9}	0
9.5	1.41×10^{-8}	6.31×10^{-9}	6.06×10^{-9}	1.77×10^{-9}	0	1.77×10^{-9}	0
11	2.56×10^{-9}	2.11×10^{-9}	2.09×10^{-9}	3.35×10^{-10}	0	3.35×10^{-10}	0
			60–88%				
2.25	4.07×10^{-4}	1.54×10^{-4}	5.17×10^{-5}	1.45×10^{-4}	0	1.45×10^{-4}	0
2.75	1.27×10^{-4}	2.64×10^{-5}	1.75×10^{-5}	1.97×10^{-5}	0	1.97×10^{-5}	0
3.25	3.52×10^{-5}	7.72×10^{-6}	6.66×10^{-6}	3.90×10^{-6}	0	3.90×10^{-6}	0
3.75	1.11×10^{-5}	1.45×10^{-6}	7.84×10^{-7}	1.22×10^{-6}	0	1.22×10^{-6}	0
4.25	4.55×10^{-6}	6.09×10^{-7}	3.40×10^{-7}	5.06×10^{-7}	0	5.06×10^{-7}	0
4.75	1.88×10^{-6}	2.71×10^{-7}	1.68×10^{-7}	2.13×10^{-7}	0	2.13×10^{-7}	0
5.25	6.34×10^{-7}	1.21×10^{-7}	9.76×10^{-8}	7.10×10^{-8}	0	7.10×10^{-8}	0
5.75	4.65×10^{-7}	8.14×10^{-8}	6.17×10^{-8}	5.31×10^{-8}	0	5.31×10^{-8}	0
6.5	2.27×10^{-7}	4.27×10^{-8}	3.34×10^{-8}	2.66×10^{-8}	0	2.66×10^{-8}	0
7.5	4.83×10^{-8}	1.17×10^{-8}	1.01×10^{-8}	5.87×10^{-9}	0	5.87×10^{-9}	0
8.5	1.18×10^{-8}	6.61×10^{-9}	6.44×10^{-9}	1.48×10^{-9}	0	1.48×10^{-9}	0
9.5	6.33×10^{-9}	3.76×10^{-9}	3.67×10^{-9}	8.15×10^{-10}	0	8.15×10^{-10}	0

TABLE XV. Invariant yields measured, $(1/2\pi\, p_T)(d^2N_{\rm cent}/d\,p_T dy)$, in Au+Au for different centrality classes, including minimum bias (0–92%) and three centrality classes (0–20, 20–60, 60–92%).

p_T (GeV/c)	Inv. yield	Tot. err.	Sys. err.	Stat. err. + error A	Error B	Error C
			0–92% (MB)			
2.25	1.26×10^{-2}	3.66×10^{-3}	1.84×10^{-3}	3.16×10^{-3}	1.48×10^{-3}	0
2.75	3.90×10^{-3}	1.12×10^{-3}	5.78×10^{-4}	9.61×10^{-4}	4.66×10^{-4}	0
3.25	8.79×10^{-4}	1.70×10^{-4}	1.32×10^{-4}	1.08×10^{-4}	1.07×10^{-4}	0
3.75	2.33×10^{-4}	5.13×10^{-5}	3.53×10^{-5}	3.72×10^{-5}	2.88×10^{-5}	0
4.50	6.44×10^{-5}	1.60×10^{-5}	9.97×10^{-6}	1.25×10^{-5}	8.22×10^{-6}	0
5.50	1.14×10^{-5}	2.57×10^{-6}	1.82×10^{-6}	1.81×10^{-6}	1.52×10^{-6}	0
6.50	2.80×10^{-6}	1.05×10^{-6}	4.59×10^{-7}	9.48×10^{-7}	3.87×10^{-7}	0
7.50	9.60×10^{-7}	2.63×10^{-7}	1.62×10^{-7}	2.07×10^{-7}	1.38×10^{-7}	0
8.50	4.09×10^{-7}	1.84×10^{-7}	7.07×10^{-8}	1.70×10^{-7}	6.09×10^{-8}	0
9.50	1.51×10^{-7}	8.25×10^{-8}	2.67×10^{-8}	7.81×10^{-8}	2.32×10^{-8}	0
			0–20%			
2.25	3.95×10^{-2}	1.24×10^{-2}	5.80×10^{-3}	1.09×10^{-2}	4.65×10^{-3}	0
2.75	1.29×10^{-2}	3.86×10^{-3}	1.91×10^{-3}	3.36×10^{-3}	1.54×10^{-3}	0
3.25	2.23×10^{-3}	5.99×10^{-4}	3.34×10^{-4}	4.97×10^{-4}	2.71×10^{-4}	0
3.75	4.53×10^{-4}	2.07×10^{-4}	6.88×10^{-5}	1.95×10^{-4}	5.61×10^{-5}	0
4.50	1.49×10^{-4}	4.55×10^{-5}	2.30×10^{-5}	3.93×10^{-5}	1.90×10^{-5}	0
5.50	2.74×10^{-5}	8.33×10^{-6}	4.37×10^{-6}	7.09×10^{-6}	3.65×10^{-6}	0
6.50	5.99×10^{-6}	2.73×10^{-6}	9.83×10^{-7}	2.55×10^{-6}	8.30×10^{-7}	0
7.50	2.79×10^{-6}	6.99×10^{-7}	4.71×10^{-7}	5.17×10^{-7}	4.02×10^{-7}	0
8.50	8.42×10^{-7}	4.02×10^{-7}	1.46×10^{-7}	3.75×10^{-7}	1.25×10^{-7}	0
9.50	4.18×10^{-7}	2.18×10^{-7}	7.40×10^{-8}	2.05×10^{-7}	6.43×10^{-8}	0
			20–60%			
2.25	1.21×10^{-2}	3.51×10^{-3}	1.78×10^{-3}	3.03×10^{-3}	1.42×10^{-3}	0
2.75	2.88×10^{-3}	8.52×10^{-4}	4.26×10^{-4}	7.38×10^{-4}	3.43×10^{-4}	0
3.25	8.58×10^{-4}	1.66×10^{-4}	1.29×10^{-4}	1.06×10^{-4}	1.04×10^{-4}	0
3.75	2.54×10^{-4}	5.40×10^{-5}	3.85×10^{-5}	3.78×10^{-5}	3.14×10^{-5}	0
4.50	7.05×10^{-5}	1.74×10^{-5}	1.09×10^{-5}	1.36×10^{-5}	8.99×10^{-6}	0
5.50	1.57×10^{-5}	3.36×10^{-6}	2.51×10^{-6}	2.24×10^{-6}	2.09×10^{-6}	0
6.50	3.30×10^{-6}	1.28×10^{-6}	5.42×10^{-7}	1.16×10^{-6}	4.58×10^{-7}	0
7.50	1.06×10^{-6}	2.65×10^{-7}	1.79×10^{-7}	1.96×10^{-7}	1.53×10^{-7}	0
8.50	3.46×10^{-7}	1.60×10^{-7}	5.99×10^{-8}	1.48×10^{-7}	5.16×10^{-8}	0
9.50	1.54×10^{-7}	7.97×10^{-8}	2.72×10^{-8}	7.49×10^{-8}	2.36×10^{-8}	0
			60–92%			
2.25	1.06×10^{-3}	3.27×10^{-4}	2.41×10^{-4}	2.21×10^{-4}	2.22×10^{-4}	0
2.75	3.34×10^{-4}	1.02×10^{-4}	7.61×10^{-5}	6.83×10^{-5}	7.03×10^{-5}	0
3.25	1.11×10^{-4}	2.34×10^{-5}	1.66×10^{-5}	1.65×10^{-5}	1.34×10^{-5}	0
3.75	4.04×10^{-5}	9.05×10^{-6}	6.13×10^{-6}	6.66×10^{-6}	5.00×10^{-6}	0
4.50	1.16×10^{-5}	3.11×10^{-6}	1.80×10^{-6}	2.54×10^{-6}	1.48×10^{-6}	0
5.50	1.67×10^{-6}	1.07×10^{-6}	2.65×10^{-7}	1.04×10^{-6}	2.22×10^{-7}	0

Using the fit [Eq. (13)] and the π^0 data plotted in Fig. 28 we have obtained the $R_{\eta/\pi^0}(x_p)$ ratio shown in Fig. 29. As seen for the corresponding η/π^0 ratios in hadronic and nuclear collisions, at low values of (scaled) momentum the π^0 production overwhelms that of η (a significant fraction of low-energy pions issues from decay contributions of heavier hadrons), but the ratio increases with x_p. From $x_p \approx 0.35$–0.7, the ratio is consistent with the asymptotic ratio of 0.5 found in hadron and nuclear collisions (dashed curve). This x_p range corresponds to the values of fractional momenta $\langle z \rangle \gtrsim 0.3$–$0.7$ typically carried by the leading high-p_T hadrons produced in high-energy h+p, h+A, and A+A collisions [129,130]. New results on inclusive η and π^0 production above $x_p = 0.6$ in e^+e^- collisions at the B-factories (BELLE and BaBar) would be useful to determine whether the value of the ratio indeed saturates at $R_{\eta/\pi^0} = 0.5$ or keeps increasing with x_p as suggested by Fig. 29.

F. Summary of experimental results

The studies presented here on high-p_T π^0 and η production in the three colliding systems (p+p, d+Au, Au+Au) provide interesting insights on initial- and final-state QCD effects in

TABLE XVI. Nuclear modification factor R_{dA} for η in d+Au collisions for different centrality classes, including minimum bias (0–88%) and four centralities (0–20, 20–40, 40–60, 60–88%).

p_T (GeV/c)	R_{dA}	Tot. err.	Stat. err. + error A	Error B	Error C
		0–88% (MB)			
2.75	1.22	0.435	0.224	0.340	0.134
3.25	1.06	0.233	0.102	0.162	0.117
3.75	1.24	0.220	0.047	0.148	0.137
4.25	1.19	0.201	0.052	0.125	0.131
4.75	1.21	0.205	0.070	0.119	0.133
5.25	1.03	0.183	0.080	0.102	0.114
5.75	1.03	0.191	0.097	0.102	0.114
6.5	1.16	0.220	0.119	0.115	0.128
7.5	0.896	0.215	0.160	0.089	0.099
8.5	1.28	0.406	0.350	0.128	0.142
9.5	1.14	0.400	0.356	0.114	0.126
11	1.51	0.680	0.635	0.151	0.166
		0–20%			
2.75	1.15	0.421	0.231	0.322	0.130
3.25	0.922	0.236	0.150	0.141	0.104
3.75	1.17	0.210	0.057	0.140	0.132
4.25	1.11	0.191	0.060	0.116	0.126
4.75	1.15	0.198	0.078	0.113	0.130
5.25	0.982	0.179	0.087	0.097	0.111
5.75	0.956	0.184	0.103	0.094	0.108
6.5	0.992	0.199	0.120	0.098	0.112
7.5	0.887	0.232	0.184	0.088	0.101
8.5	0.802	0.285	0.254	0.080	0.091
9.5	0.894	0.343	0.312	0.089	0.101
11	1.30	0.626	0.590	0.131	0.148
		20–40%			
2.75	1.22	0.450	0.249	0.342	0.139
3.25	1.07	0.270	0.169	0.163	0.121
3.75	1.14	0.206	0.062	0.136	0.129
4.25	1.06	0.186	0.067	0.111	0.120
4.75	1.05	0.188	0.084	0.104	0.120
5.25	1.10	0.208	0.112	0.109	0.125
5.75	1.02	0.201	0.120	0.100	0.116
6.5	1.07	0.222	0.141	0.106	0.121
7.5	0.953	0.264	0.216	0.095	0.108
8.5	1.30	0.425	0.371	0.129	0.147
9.5	0.750	0.374	0.354	0.075	0.085
11	2.13	0.995	0.934	0.214	0.242
		40–60%			
2.75	0.86	0.338	0.212	0.241	0.102
3.25	1.15	0.305	0.202	0.176	0.136
3.75	1.09	0.201	0.071	0.130	0.128
4.25	1.08	0.192	0.078	0.113	0.127
4.75	1.14	0.210	0.104	0.113	0.135
5.25	0.962	0.198	0.126	0.095	0.114
5.75	1.04	0.234	0.164	0.103	0.123
6.5	1.15	0.246	0.163	0.114	0.136
7.5	0.929	0.314	0.277	0.092	0.110
8.5	1.24	0.490	0.449	0.123	0.146
9.5	0.842	0.451	0.430	0.084	0.099
11	0.704	0.645	0.636	0.071	0.083

TABLE XVI. *(Continued.)*

p_T (GeV/c)	R_{dA}	Tot. err.	Stat. err. + error A	Error B	Error C
			60–88%		
2.75	1.36	0.515	0.301	0.381	0.165
3.25	1.30	0.358	0.248	0.200	0.158
3.75	1.13	0.213	0.085	0.135	0.137
4.25	1.16	0.212	0.095	0.122	0.141
4.75	1.18	0.223	0.119	0.117	0.143
5.25	0.826	0.190	0.138	0.081	0.010
5.75	1.15	0.255	0.177	0.114	0.140
6.5	1.57	0.368	0.269	0.156	0.191
7.5	0.969	0.285	0.239	0.096	0.117
8.5	0.913	0.558	0.538	0.091	0.111
9.5	0.874	0.578	0.561	0.087	0.106

cold nuclear matter (d+Au) and on the properties of the hot and dense medium produced in central Au+Au collisions. The absence of any strong deviation from the pointlike scaling expectations for the p_T-differential π^0 and η yields measured in d+Au relative to $p+p$ (Fig. 18) indicates that the amount of nuclear shadowing and initial-state p_T broadening is a small effect (at the 10% level) at midrapidity at RHIC energies. This is in contrast with results at lower energies that showed a larger Cronin enhancement for high-p_T mesons than observed here. One reason for the difference is likely due to the fact that hadron spectra at lower $\sqrt{s_{NN}}$ have steeper slopes and thus initial-state k_T "kicks" produce a relatively larger net effect than on the harder spectra at RHIC energies. The unsuppressed d+Au yields combined with the observation of strongly depleted yields of η and π^0 in central Au+Au compared to binary-scaled $p+p$ collisions (Fig. 19) indicate that the suppression is a final-state effect in the hot and dense matter produced in the central Au+Au reactions. The consistent values of the η/π^0 ratios measured at high p_T in nuclear (Figs. 25 and 26) as well as in more elementary $p+p$ (Fig. 24) and e^+e^- (Fig. 29) collisions clearly supports the idea that the suppression occurs at the parton level before the fragmentation of the parent quarks and gluons into a given leading meson. In particular, the overall agreement of the η/π^0 ratio measured in Au+Au and e^+e^- collisions suggests that although the fast parent partons lose energy while traversing the system produced in central Au+Au collisions, their relative probability to fragment into a given meson, given by universal fragmentation functions, is preserved as expected for final hadron formation in the vacuum.

V. SUMMARY

In summary, the transverse momentum spectra of η mesons in the range $p_T = 2$–12 GeV/c have been measured at midrapidity by the PHENIX experiment at RHIC in $p+p$, d+Au, and Au+Au collisions at $\sqrt{s_{NN}} = 200$ GeV. The η mesons are reconstructed through their $\eta \to \gamma\gamma$ channel in the three colliding systems, as well as through the $\eta \to \pi^0\pi^+\pi^-$ decay mode in $p+p$ and d+Au collisions. These data provide additional characterization of high-p_T hadroproduction in hadronic and nuclear collisions at RHIC energies. The d+Au yields are largely consistent with the $p+p$ differential cross sections scaled by the number of incoherent nucleon-nucleon collisions ($R_{dA} \approx 1$). No p_T or centrality dependence is observed in the nuclear modification factor within uncertainties. Such an observation indicates a null or very weak p_T

TABLE XVII. Nuclear modification factor $R_{AA}(p_T)$ for η in Au+Au collisions for different centrality classes from most central (0–20%) to most peripheral (60–92%). Note that there is an additional 9.7% normalization uncertainty (Run-3 $p+p$ BBC error, gray box in Fig. 19) not quoted.

p_T (GeV/c)	R_{AA}	Tot. err.	Error C
		0–20%	
2.75	0.532	0.227 (42.6%)	0.036 (6.8%)
3.25	0.318	0.096 (30.2%)	0.022 (6.8%)
3.75	0.178	0.084 (46.9%)	0.012 (6.8%)
4.50	0.234	0.074 (31.7%)	0.016 (6.8%)
5.50	0.199	0.063 (31.6%)	0.014 (6.8%)
6.50	0.160	0.075 (46.9%)	0.011 (6.8%)
7.50	0.215	0.062 (28.9%)	0.015 (6.8%)
8.50	0.250	0.133 (53.0%)	0.017 (6.8%)
9.50	0.222	0.131 (59.3%)	0.015 (6.8%)
		20–60%	
2.75	0.479	0.202 (42.3%)	0.037 (7.8%)
3.25	0.492	0.117 (23.8%)	0.038 (7.8%)
3.75	0.401	0.095 (23.6%)	0.031 (7.8%)
4.50	0.446	0.116 (26.0%)	0.035 (7.8%)
5.50	0.460	0.106 (23.1%)	0.036 (7.8%)
6.50	0.355	0.143 (40.3%)	0.028 (7.8%)
7.50	0.329	0.095 (28.9%)	0.026 (7.8%)
8.50	0.414	0.214 (51.6%)	0.032 (7.8%)
9.50	0.328	0.193 (58.9%)	0.026 (7.8%)
		60–92%	
2.75	0.733	0.315 (43.0%)	0.209 (28.6%)
3.25	0.837	0.211 (25.3%)	0.239 (28.6%)
3.75	0.841	0.208 (24.7%)	0.240 (28.6%)
4.50	0.967	0.271 (28.0%)	0.276 (28.6%)
5.50	0.641	0.415 (64.8%)	0.183 (28.6%)

TABLE XVIII. Ratio of η and π^0 for $p+p$ collisions at $\sqrt{s} =$ 200 GeV.

p_T (GeV/c)	η/π^0	Tot. err.	Stat. err.	Error A	Error B	Error C
2.75	0.440	0.131	0.076	0	0.107	0
3.25	0.421	0.041	0.009	0	0.040	0
3.75	0.446	0.032	0.012	0	0.030	0
4.25	0.473	0.035	0.016	0	0.031	0
4.75	0.468	0.036	0.022	0	0.029	0
5.25	0.510	0.045	0.032	0	0.031	0
5.75	0.561	0.055	0.044	0	0.034	0
6.5	0.540	0.057	0.047	0	0.033	0
7.5	0.596	0.086	0.078	0	0.037	0
8.5	0.426	0.099	0.095	0	0.027	0
9.5	0.588	0.166	0.162	0	0.039	0
11	0.419	0.164	0.162	0	0.029	0

broadening and, in general, a very modest influence of cold nuclear matter effects, such as shadowing of parton distribution functions, Cronin broadening, and/or hadronization by parton recombination, on high-p_T meson production at midrapidity at top RHIC energies. In contrast, the invariant yields measured in Au+Au are increasingly depleted with centrality compared to expectations from binary-scaled $p+p$ collisions, up to a maximum factor of $\sim$5 suppression in central collisions. The magnitude, p_T and centrality dependence of the Au+Au suppression is the same for η mesons and neutral pions. The measured η/π^0 ratio in $p+p$, d+Au, and Au+Au is nearly flat over $p_T = 2$–12 GeV/c and is independent of the reaction centrality. A fit to a constant yields $R_{\eta/\pi^0}(p_T) = 0.4$–0.5, in agreement with the experimental world values at high p_T collected here for hadron-hadron, hadron-nucleus, and nucleus-nucleus collisions in a wide range of center-of-mass energies ($\sqrt{s} \approx 3$–1800 GeV), as well as at high x_p ($x_p \gtrsim 0.35$) in electron-positron annihilations measured at $\sqrt{s} = 91.2$ GeV at LEP. These results indicate that any initial- and/or final-state nuclear effects influence the production of light neutral mesons at large p_T in the same way. The similar suppression pattern of η and π^0 mesons is consistent with the expectations of final-state parton energy loss in the dense medium formed in Au+Au reactions. The approximately constant $\eta/\pi^0 = 0.40 \pm 0.04$ ratio measured in central Au+Au collisions indicates that the attenuated parent partons fragment into leading mesons (η, π^0) in the vacuum according to the same probabilities that govern high-p_T hadron production in more elementary (e^+e^-, $p+p$) collisions.

ACKNOWLEDGMENTS

We thank the staff of the Collider-Accelerator and Physics Departments at Brookhaven National Laboratory and the staff of the other PHENIX participating institutions for their vital contributions. We acknowledge support from the Department of Energy, Office of Science, Office of Nuclear Physics, the National Science Foundation, Abilene Christian University Research Council, Research Foundation of SUNY, and Dean

TABLE XIX. Ratio of η and π^0 for d+Au collisions for different centrality classes, including minimum bias (0–88%), most central (0–20%), and most peripheral (60–88%).

p_T (GeV/c)	η/π^0	Tot. err.	Stat. err. + error A	Error B	Error C
		0–88% (MB)			
2.25	0.420	0.038	0.028	0.025	0
2.75	0.472	0.044	0.033	0.028	0
3.25	0.383	0.045	0.039	0.023	0
3.75	0.472	0.034	0.018	0.028	0
4.25	0.478	0.033	0.017	0.029	0
4.75	0.483	0.035	0.020	0.029	0
5.25	0.465	0.037	0.025	0.028	0
5.75	0.510	0.043	0.030	0.031	0
6.5	0.552	0.048	0.034	0.033	0
7.5	0.478	0.070	0.064	0.029	0
8.5	0.499	0.092	0.087	0.030	0
9.5	0.677	0.118	0.111	0.041	0
11	0.609	0.124	0.119	0.037	0
		0–20%			
2.25	0.386	0.052	0.047	0.023	0
2.75	0.491	0.062	0.054	0.029	0
3.25	0.364	0.066	0.063	0.022	0
3.75	0.494	0.041	0.028	0.030	0
4.25	0.512	0.040	0.026	0.031	0
4.75	0.520	0.043	0.030	0.031	0
5.25	0.508	0.048	0.037	0.030	0
5.75	0.547	0.056	0.045	0.033	0
6.5	0.563	0.063	0.053	0.034	0
7.5	0.579	0.109	0.104	0.035	0
8.5	0.363	0.094	0.091	0.022	0
9.5	0.644	0.159	0.154	0.039	0
11	0.684	0.193	0.188	0.041	0
		20–40%			
2.25	0.416	0.057	0.051	0.025	0
2.75	0.517	0.068	0.060	0.031	0
3.25	0.425	0.077	0.072	0.025	0
3.75	0.467	0.042	0.031	0.028	0
4.25	0.470	0.041	0.029	0.028	0
4.75	0.447	0.043	0.033	0.027	0
5.25	0.524	0.057	0.048	0.031	0
5.75	0.539	0.062	0.053	0.032	0
6.5	0.543	0.069	0.060	0.033	0
7.5	0.545	0.119	0.114	0.033	0
8.5	0.546	0.119	0.115	0.033	0
9.5	0.495	0.206	0.204	0.030	0
11	1.046	0.277	0.269	0.063	0
		40–60%			
2.25	0.489	0.065	0.058	0.029	0
2.75	0.372	0.072	0.069	0.022	0
3.25	0.457	0.091	0.086	0.027	0
3.75	0.439	0.044	0.035	0.026	0
4.25	0.456	0.043	0.033	0.027	0
4.75	0.490	0.053	0.044	0.029	0
5.25	0.466	0.066	0.060	0.028	0
5.75	0.547	0.088	0.082	0.033	0
6.5	0.560	0.078	0.070	0.034	0

TABLE XIX. *(Continued.)*

p_T (GeV/c)	η/π^0	Tot. err.	Stat. err. + error A	Error B	Error C
7.5	0.528	0.160	0.157	0.032	0
8.5	0.598	0.200	0.197	0.036	0
9.5	0.495	0.234	0.232	0.030	0
11	0.243	0.211	0.210	0.015	0
		60–88%			
2.25	0.474	0.070	0.064	0.028	0
2.75	0.558	0.090	0.083	0.033	0
3.25	0.500	0.105	0.101	0.030	0
3.75	0.482	0.051	0.042	0.029	0
4.25	0.490	0.051	0.042	0.029	0
4.75	0.514	0.062	0.053	0.031	0
5.25	0.374	0.068	0.064	0.022	0
5.75	0.569	0.090	0.083	0.034	0
6.5	0.734	0.129	0.121	0.044	0
7.5	0.501	0.123	0.119	0.030	0
8.5	0.362	0.216	0.215	0.022	0
9.5	0.469	0.294	0.293	0.028	0

of the College of Arts and Sciences, Vanderbilt University (USA), Ministry of Education, Culture, Sports, Science, and Technology and the Japan Society for the Promotion of Science (Japan), Conselho Nacional de Desenvolvimento Científico e Tecnológico and Fundação de Amparo à Pesquisa do Estado de São Paulo (Brazil), Natural Science Foundation of China (People's Republic of China), Centre National de la Recherche Scientifique, Commissariat à l'Énergie Atomique, and Institut National de Physique Nucléaire et de Physique des Particules (France), Ministry of Industry, Science and Tekhnologies, Bundesministerium für Bildung und Forschung, Deutscher Akademischer Austausch Dienst, and Alexander von Humboldt Stiftung (Germany), Hungarian National Science Fund, OTKA (Hungary), Department of Atomic Energy (India), Israel Science Foundation (Israel), Korea Research Foundation and Korea Science and Engineering Foundation (Korea), Ministry of Education and Science, Rassia Academy of Sciences, Federal Agency of Atomic Energy (Russia), VR and the Wallenberg Foundation (Sweden), the US Civilian Research and Development Foundation for the Independent States of the Former Soviet Union, the US–Hungarian NSF-OTKA-MTA, and the US–Israel Binational Science Foundation.

TABLE XX. Ratio of η and π^0 in Au+Au collisions for different centrality classes, including minimum bias (0–92%), most central (0–20%), and most peripheral (60–92%).

p_T (GeV/c)	η/π^0	Tot. err.
	0–92% (MB)	
2.25	0.320	0.090 (28.1%)
2.75	0.410	0.120 (29.3%)
3.25	0.340	0.060 (17.6%)
3.75	0.290	0.058 (20.0%)
4.50	0.350	0.083 (23.7%)
5.50	0.350	0.072 (20.6%)
6.50	0.350	0.130 (37.1%)
7.50	0.560	0.100 (17.9%)
8.50	0.480	0.210 (43.8%)
9.50	0.490	0.250 (51.0%)
	0–20%	
2.25	0.400	0.120 (30.0%)
2.75	0.550	0.170 (30.9%)
3.25	0.370	0.110 (29.7%)
3.75	0.240	0.110 (45.8%)
4.50	0.360	0.110 (30.6%)
5.50	0.380	0.110 (28.9%)
6.50	0.350	0.160 (45.7%)
7.50	0.530	0.130 (24.5%)
8.50	0.470	0.240 (51.1%)
9.50	0.490	0.280 (57.1%)
	20–60%	
2.25	0.360	0.100 (27.8%)
2.75	0.340	0.100 (29.4%)
3.25	0.370	0.070 (18.9%)
3.75	0.340	0.066 (19.4%)
4.50	0.410	0.096 (23.4%)
5.50	0.490	0.096 (19.6%)
6.50	0.420	0.160 (38.1%)
7.50	0.430	0.098 (22.8%)
8.50	0.380	0.170 (44.7%)
9.50	0.400	0.200 (50.0%)
	60–92%	
2.25	0.312	0.094 (30.1%)
2.75	0.383	0.110 (28.7%)
3.25	0.404	0.081 (20.0%)
3.75	0.438	0.093 (21.2%)
4.50	0.542	0.139 (25.6%)
5.50	0.404	0.257 (63.6%)

APPENDIX: DATA TABLES

A. Invariant η cross sections ($p+p$, d+Au) and yields (Au+Au)

This appendix collects the data tables of the p_T spectra of η mesons measured at midrapidity in $p+p$, d+Au, and Au+Au collisions at $\sqrt{s_{NN}} = 200$ GeV. The invariant cross sections for η production in MB $p+p$ and d+Au collisions are tabulated in Tables XII and XIII, respectively. The invariant d+Au yields measured in centralities 0–20, 20–40, 40–60, and 60–88% are tabulated in Table XIV. Finally, the invariant yields in Au+Au reactions (MB and centralities 0–20, 20–60, and 60–92%) are presented in Tables XV. The quoted errors are categorized by type:

(i) (**A**) is a point-to-point error uncorrelated between p_T bins,
(ii) (**B**) is p_T correlated, all points move in the same direction but not by the same factor,
(iii) (**C**) is a normalization error in which all points move by the same factor independent of p_T.

B. Nuclear modification factors (d+Au, Au+Au)

We report in Tables XVI and XVII the $R_{AA}(p_T)$ η data tables for various centralities in d+Au and Au+Au collisions. The errors quoted are the point-to-point and absolute normalization ones. Note that there is an additional 9.7% overall normalization uncertainty (Run-3 $p+p$ BBC error, gray box in Fig. 19) not tabulated.

C. η/π^0 ratios ($p+p$, d+Au, Au+Au)

The ratio of η to π^0 invariant yields in $p+p$, d+Au, and Au+Au collisions at $\sqrt{s_{NN}} = 200$ GeV at midrapidity are tabulated in Tables XVIII, XIX, and XX. The data presented here are for minimum bias events and various centrality bins in d+Au and Au+Au collisions.

[1] See, e.g., G. Sterman *et al.* (CTEQ Collaboration), Rev. Mod. Phys. **67**, 157 (1995).
[2] W. M. Geist, D. Drijard, A. Putzer, R. Sosnowski, and D. Wegener, Phys. Rep. **197**, 263 (1990).
[3] G. Bunce, N. Saito, J. Soffer, and W. Vogelsang, Annu. Rev. Nucl. Part. Sci. **50**, 525 (2000).
[4] M. Arneodo, Phys. Rep. **240**, 301 (1994).
[5] N. Armesto, J. Phys. G **32**, R367 (2006).
[6] J. W. Cronin *et al.*, Phys. Rev. D **11**, 3105 (1975); D. Antreasyan, J. W. Cronin, H. J. Frisch, M. J. Shochet, L. Kluberg, P. A. Piroue, and R. L. Sumner, Phys. Rev. D **19**, 764 (1979).
[7] See, e.g., E. Iancu and R. Venugopalan, in *Quark-Gluon Plasma 3*, edited by R. C. Hwa and X. N. Wang (World Scientific, Singapore, 2004).
[8] B. Z. Kopeliovich, J. Nemchik, E. Predazzi, and A. Hayashigaki, Nucl. Phys. **A740**, 211 (2004).
[9] R. C. Hwa and C. B. Yang, Phys. Rev. C **70**, 024905 (2004).
[10] M. Gyulassy and M. Plümer, Phys. Lett. **B243**, 432 (1990); X. N. Wang and M. Gyulassy, Phys. Rev. Lett. **68**, 1480 (1992).
[11] R. Baier, Y. L. Dokshitzer, A. H. Mueller, S. Peigné, and D. Schiff, Nucl. Phys. **B484**, 265 (1997); R. Baier, D. Schiff, B. G. Zakharov, Annu. Rev. Nucl. Part. Sci. **50**, 37 (2000).
[12] M. Gyulassy, P. Lévai, and I. Vitev, Phys. Rev. Lett. **85**, 5535 (2000); Nucl. Phys. **B594**, 371 (2001).
[13] U. A. Wiedemann, Nucl. Phys. **B588**, 30 (2000); C. A. Salgado and U. A. Wiedemann, Phys. Rev. D **68**, 014008 (2003).
[14] S. S. Adler *et al.* (PHENIX Collaboration), Phys. Rev. Lett. **91**, 241803 (2003).
[15] S. S. Adler *et al.* (PHENIX Collaboration), Phys. Rev. Lett. **93**, 202002 (2004); Phys. Rev. Lett. **95**, 202001 (2005).
[16] S. S. Adler *et al.* (PHENIX Collaboration), Phys. Rev. Lett. **91**, 072303 (2003).
[17] S. S. Adler *et al.* (PHENIX Collaboration), nucl-ex/0610036.
[18] K. Adcox *et al.* (PHENIX Collaboration), Phys. Rev. Lett. **88**, 022301 (2002).
[19] S. S. Adler *et al.* (PHENIX Collaboration), Phys. Rev. Lett. **91**, 072301 (2003).
[20] S. S. Adler *et al.* (PHENIX Collaboration), Phys. Rev. Lett. **96**, 202301 (2006).
[21] S. S. Adler *et al.* (PHENIX Collaboration), Phys. Rev. C submitted; nucl-ex/0611007.
[22] S. Albino, B. A. Kniehl, and G. Kramer, Nucl. Phys. **B725**, 181 (2005).
[23] B. Jäger, A. Schäfer, M. Stratmann, and W. Vogelsang, Phys. Rev. D **67**, 054005 (2003); B. Jäger, M. Stratmann, S. Kretzer, and W. Vogelsang, Phys. Rev. Lett. **92**, 121803 (2004); A. Mukherjee, M. Stratmann, and W. Vogelsang, Phys. Rev. D **72**, 034011 (2005).
[24] C. Bourrely and J. Soffer, Eur. Phys. J. C **36**, 371 (2004).
[25] M. Anselmino, M. Boglione, U. D'Alesio, E. Leader, and F. Murgia, Phys. Rev. D **71**, 014002 (2005).
[26] K. J. Eskola, V. J. Kolhinen, and C. A. Salgado, Eur. Phys. J. C **9**, 61 (1999).
[27] D. de Florian and R. Sassot, Phys. Rev. D **69**, 074028 (2004).
[28] B. Z. Kopeliovich, Phys. Rev. C **68**, 044906 (2003).
[29] R. Vogt, Phys. Rev. C **70**, 064902 (2004).
[30] A. Accardi and M. Gyulassy, J. Phys. G **30**, S969 (2004); Phys. Lett. **B586**, 244 (2004).
[31] E. Cattaruzza and D. Treleani, Phys. Rev. D **69**, 094006 (2004).
[32] G. G. Barnaföldi, G. Papp, P. Lévai, and G. Fai, J. Phys. G **30**, S1125 (2004).
[33] J. L. Albacete, N. Armesto, A. Kovner, C. A. Salgado, and U. A. Wiedemann, Phys. Rev. Lett. **92**, 082001 (2004).
[34] E. Iancu, K. Itakura, and D. N. Triantafyllopoulos, Nucl. Phys. **A742**, 182 (2004).
[35] J. Jalilian-Marian and Y. V. Kovchegov, Prog. Part. Nucl. Phys. **56**, 104 (2006).
[36] See, e.g., D. d'Enterria, AIP Conf. Proc. **806**, 252 (2006).
[37] I. Vitev and M. Gyulassy, Phys. Rev. Lett. **89**, 252301 (2002); I. Vitev I, J. Phys. G **30**, S791 (2004).
[38] K. J. Eskola, H. Honkanen, C. A. Salgado, and U. A. Wiedemann, Nucl. Phys. **A747**, 511 (2005).
[39] A. Dainese, C. Loizides, and G. Paic, Eur. Phys. J. C **38**, 461 (2005).
[40] R. C. Hwa and C. B. Yang, Phys. Rev. C **67**, 034902 (2003); R. J. Fries, B. Müller, C. Nonaka, and S. A. Bass, Phys. Rev. Lett. **90**, 202303 (2003); V. Greco, C. M. Ko, and P. Lévai, Phys. Rev. Lett. **90**, 202302 (2003).
[41] S. S. Adler *et al.* (PHENIX Collaboration), Phys. Rev. C **69**, 034910 (2004).
[42] C. Kourkoumelis *et al.* (AFS Collaboration), Phys. Lett. **B84**, 271 (1979); Phys. Lett. **B84**, 277 (1979).
[43] F. Abe *et al.* (CDF Collaboration), Phys. Rev. D **48**, 2998 (1993).
[44] F. Ellinghaus and J. Seele (PHENIX Collaboration), RIKEN Accel. Prog. Rep. 39 (2006); F. Ellinghaus (PHENIX Collaboration), hep-ex/0612031 (to appear in the proceedings of the 17th International Spin Physics Symposium, SPIN 2006).
[45] J. Adams *et al.* (STAR Collaboration), Phys. Rev. Lett. **91**, 172302 (2003).
[46] K. Adcox *et al.* (PHENIX Collaboration), Phys. Rev. Lett. **88**, 192303 (2002); S. S. Adler *et al.* (PHENIX Collaboration), Phys. Rev. C **72**, 024901 (2005); S. S. Adler *et al.* (PHENIX Collaboration), Phys. Rev. Lett. **96**, 032301 (2006); A. Adare *et al.* (PHENIX Collaboration), nucl-ex/0611018.
[47] A. Toia (PHENIX Collaboration), Nucl. Phys. **A774**, 743 (2006).

[48] S. S. Adler *et al.* (PHENIX Collaboration), Phys. Rev. Lett. **94**, 232301 (2005).
[49] S. S. Adler *et al.* (PHENIX Collaboration), Phys. Rev. D **71**, 071102 (2005); S. S. Adler *et al.* (PHENIX Collaboration), Phys. Rev. Lett. **98**, 012002 (2007).
[50] H. Hahn *et al.*, Nucl. Instrum. Methods A **499**, 245 (2003).
[51] K. Adcox *et al.* (PHENIX Collaboration), Nucl. Instrum. Methods A **499**, 469 (2003).
[52] L. Aphecetche *et al.* (PHENIX Collaboration), Nucl. Instrum. Methods A **499**, 521 (2003).
[53] K. Adcox *et al.* (PHENIX Collaboration), Nucl. Instrum. Methods A **499**, 489 (2003).
[54] K. Adcox *et al.*, Nucl. Instrum. Methods A **497**, 263 (2003).
[55] M. Allen *et al.* (PHENIX Collaboration), Nucl. Instrum. Methods A **499**, 549 (2003).
[56] C. Adler *et al.*, Nucl. Instrum. Methods A **470**, 488 (2001).
[57] S. Eidelman *et al.* (Particle Data Group), Phys. Lett. **B592**, 1 (2004).
[58] M. Aizawa *et al.*, Nucl. Instrum. Methods A **499**, 508 (2003).
[59] S. S. Adler *et al.* (PHENIX Collaboration), Phys. Rev. Lett. **94**, 082302 (2005).
[60] K. Adcox *et al.* (PHENIX Collaboration), Phys. Rev. Lett. **86**, 3500 (2001).
[61] S. White, AIP Conf. Proc. **792**, 527 (2005).
[62] F. Carminati *et al.*, GEANT 3.21: Detector Description and Simulation Tool, CERN Program Library Long Writeup W5013, 1993.
[63] S. S. Adler *et al.* (PHENIX Collaboration), Phys. Rev. Lett. **96**, 012304 (2006).
[64] T. Sjöstrand, Comput. Phys. Commun. **82**, 74 (1994).
[65] C. Alff *et al.*, Phys. Rev. Lett. **9**, 325 (1962).
[66] J. S. Danburg *et al.*, Phys. Rev. D **2**, 2564 (1970).
[67] S. Giovanella (KLOE Collaboration), *Proceedings of "La Thuile 2005, Results and perspectives in particle Physics," pp. 241–248, 2005*; hep-ex/0505074.
[68] G. D. Lafferty and T. R. Wyatt, Nucl. Instrum. Methods A **355**, 541 (1995).
[69] V. Guzey, M. Strikman, and W. Vogelsang, Phys. Lett. **B603**, 173 (2004).
[70] S. S. Adler *et al.* (PHENIX Collaboration), Phys. Rev. C **73**, 054903 (2006).
[71] L. E. Gordon and W. Vogelsang, Phys. Rev. D **48**, 3136 (1993); Phys. Rev. D **50**, 1901 (1994); P. Aurenche *et al.*, Phys. Lett. **B140**, 87 (1984); Nucl. Phys. **B297**, 661 (1988).
[72] T. Sjöstrand, P. Eden, C. Friberg, L. Lonnblad, G. Miu, S. Mrenna, and E. Norrbin, Comput. Phys. Commun. **135**, 238 (2001).
[73] D. d'Enterria, J. Phys. G **31**, S491 (2005).
[74] B. Andersson, G. Gustafson, G. Ingelman, and T. Sjöstrand, Phys. Rep. **97**, 31 (1983).
[75] B. Andersson, *The Lund Model* (Cambridge University Press, 1997), p. 1.
[76] T. Sjöstrand, L. Lonnblad, S. Mrenna, and P. Skands, hep-ph/0308153.
[77] M. Bourquin and J.-M. Gaillard, Nucl. Phys. **B114**, 334 (1976).
[78] S. S. Adler *et al.* (PHENIX Collaboration), Phys. Rev. C **74**, 024904 (2006).
[79] G. J. Donaldson *et al.*, Phys. Rev. Lett. **40**, 684 (1978).
[80] M. Bonesini *et al.* (WA70 Collaboration), Z. Phys. C **42**, 527 (1989).
[81] J. Antille *et al.* (UA6 Collaboration), Phys. Lett. **B194**, 568 (1987).
[82] M. Aguilar-Benitez *et al.* (NA27 Collaboration), Z. Phys. C **50**, 405 (1991).
[83] E. Amaldi *et al.*, Nucl. Phys. **B158**, 1 (1979).
[84] L. Apanasevich *et al.* (Fermilab E706 Collaboration), Phys. Rev. D **68**, 052001 (2003).
[85] T. Akesson *et al.* (AFS Collaboration), Phys. Lett. **B158**, 282 (1985).
[86] T. Akesson *et al.* (AFS Collaboration), Phys. Lett. **B178**, 447 (1986).
[87] T. Akesson *et al.* (AFS Collaboration), Z. Phys. C **18**, 5 (1983).
[88] M. Banner *et al.* (UA2 Collaboration), Z. Phys. C **27**, 329 (1985).
[89] J. Povlis *et al.* (Fermilab E629 Collaboration), Phys. Rev. Lett. **51**, 967 (1983).
[90] S. W. Delchamps, FERMILAB-THESIS-1985-35 (1985).
[91] G. Agakishiev *et al.* (TAPS/CERES Collaboration), Eur. Phys. J. C **4**, 249 (1998).
[92] V. Tikhomirov (HELIOS Collaboration), HADRON 95, Proceedings of the 6th International Conference on Hadron Spectroscopy, Manchester, England, 10–14 Jul 1995 (World Scientific Publishing, Singapore, 1995).
[93] G. Alverson *et al.* (Fermilab E706 Collaboration), Phys. Rev. D **48**, 5 (1993).
[94] L. Apanasevich *et al.* (Fermilab E706 Collaboration), Phys. Rev. D **69**, 032003 (2004).
[95] R. Averbeck *et al.* (TAPS Collaboration), Z. Phys. A **359**, 65 (1997).
[96] R. Averbeck, R. Holzmann, V. Metag, and R. S. Simon, Phys. Rev. C **67**, 024903 (2003).
[97] M. M. Aggarwal *et al.* (WA98 Collaboration), nucl-ex/0006007.
[98] R. Albrecht *et al.* (WA80 Collaboration.), Phys. Lett. **B361**, 14 (1995).
[99] R. Hagedorn, Riv. Nuovo Cimento **6N10**, 1 (1984).
[100] K. Adcox *et al.* (PHENIX Collaboration), Nucl. Phys. **A757**, 184 (2005).
[101] R. Witt (STAR Collaboration), nucl-ex/0403021.
[102] T. Peitzmann, nucl-th/0511022.
[103] D. Buskulic *et al.* (ALEPH Collaboration), Phys. Lett. **B292**, 210 (1992).
[104] R. Barate *et al.* (ALEPH Collaboration), Z. Phys. C **74**, 451 (1997).
[105] R. Barate *et al.* (ALEPH Collaboration), Phys. Rep. **294**, 1 (1998).
[106] R. Barate *et al.* (ALEPH Collaboration), Eur. Phys. J. C **16**, 613 (2000).
[107] A. Heister *et al.* (ALEPH Collaboration), Phys. Lett. **B528**, 19 (2002).
[108] W. Adam *et al.* (DELPHI Collaboration), Z. Phys. C **69**, 561 (1996).
[109] B. Adeva *et al.* (L3 Collaboration), Phys. Lett. **B259**, 199 (1991).
[110] O. Adriani *et al.* (L3 Collaboration), Phys. Lett. **B286**, 403 (1992).
[111] M. Acciarri *et al.* (L3 Collaboration), Phys. Lett. **B328**, 223 (1994).
[112] K. Ackerstaff *et al.* (OPAL Collaboration), Eur. Phys. J. C **5**, 411 (1998).

[113] G. Abbiendi *et al*. (OPAL Collaboration), Eur. Phys. J. C **17**, 373 (2000).
[114] G. Wormser *et al*., Phys. Rev. Lett. **61**, 1057 (1988).
[115] S. Abachi *et al*. (HRS Collaboration), Phys. Lett. **B205**, 111 (1988).
[116] W. Bartel *et al*. (JADE Collaboration), Phys. Lett. **B130**, 454 (1983).
[117] W. Bartel *et al*. (JADE Collaboration), Z. Phys. C **28**, 343 (1985).
[118] D. Pitzl *et al*. (JADE Collaboration), Z. Phys. C **46**, 1 (1990); [Erratum-*ibid*. **47**, 676 (1990)].
[119] H. J. Behrend *et al*. (CELLO Collaboration), Z. Phys. C **47**, 1 (1990).
[120] C. Peterson and T. F. Walsh, Phys. Lett. **B91**, 455 (1980).
[121] P. Ball, J. M. Frere, and M. Tytgat, Phys. Lett. **B365**, 367 (1996).
[122] H. Fritzsch, Phys. Lett. **B415**, 83 (1997).
[123] J. Binnewies, B. A. Kniehl, and G. Kramer, Phys. Rev. D **52**, 4947 (1995).
[124] B. A. Kniehl, G. Kramer, and B. Pötter, Nucl. Phys. **B582**, 514 (2000).
[125] S. Kretzer, Phys. Rev. D **62**, 054001 (2000).
[126] L. Bourhis, M. Fontannaz, J. P. Guillet, and M. Werlen, Eur. Phys. J. C **19**, 89 (2001).
[127] M. Greco and S. Rolli, Z. Phys. C **60**, 169 (1993); M. Greco, S. Rolli, and A. Vicini, Z. Phys. C **65**, 277 (1995); S. Rolli, *Proceedings of 31st Rencontres de Moriond: QCD and High-Energy Hadronic Interactions, Les Arcs, France, 23–30 March 1996*; hep-ph/9607480.
[128] D. Indumathi, H. S. Mani, and A. Rastogi, Phys. Rev. D **58**, 094014 (1998). Note that in the second case, the η FF is not explicitly given, but within the framework it could be derived from the FF parameters for other octet mesons.
[129] S. S. Adler (PHENIX Collaboration), Phys. Rev. D **74**, 072002 (2006).
[130] S. Kretzer, Acta Phys. Polon. B **36**, 179 (2005).

Centrality Dependence of π^0 and η Production at Large Transverse Momentum in $\sqrt{s_{NN}} = 200$ GeV d + Au Collisions

S. S. Adler,[5] S. Afanasiev,[20] C. Aidala,[10] N. N. Ajitanand,[44] Y. Akiba,[21,40] A. Al-Jamel,[35] J. Alexander,[44] K. Aoki,[25] L. Aphecetche,[46] R. Armendariz,[35] S. H. Aronson,[5] R. Averbeck,[45] T. C. Awes,[36] V. Babintsev,[17] A. Baldisseri,[11] K. N. Barish,[6] P. D. Barnes,[28] B. Bassalleck,[34] S. Bathe,[6,31] S. Batsouli,[10] V. Baublis,[39] F. Bauer,[6] A. Bazilevsky,[5,41] S. Belikov,[19,17] M. T. Bjorndal,[10] J. G. Boissevain,[28] H. Borel,[11] M. L. Brooks,[28] D. S. Brown,[35] N. Bruner,[34] D. Bucher,[31] H. Buesching,[5,31] V. Bumazhnov,[17] G. Bunce,[5,41] J. M. Burward-Hoy,[28,27] S. Butsyk,[45] X. Camard,[46] P. Chand,[4] W. C. Chang,[2] S. Chernichenko,[17] C. Y. Chi,[10] J. Chiba,[21] M. Chiu,[10] I. J. Choi,[53] R. K. Choudhury,[4] T. Chujo,[5] V. Cianciolo,[36] Y. Cobigo,[11] B. A. Cole,[10] M. P. Comets,[37] P. Constantin,[19] M. Csanád,[13] T. Csörgő,[22] J. P. Cussonneau,[46] D. d'Enterria,[10] K. Das,[14] G. David,[5] F. Deák,[13] H. Delagrange,[46] A. Denisov,[17] A. Deshpande,[41] E. J. Desmond,[5] A. Devismes,[45] O. Dietzsch,[42] J. L. Drachenberg,[1] O. Drapier,[26] A. Drees,[45] A. Durum,[17] D. Dutta,[4] V. Dzhordzhadze,[47] Y. V. Efremenko,[36] H. En'yo,[40,41] B. Espagnon,[37] S. Esumi,[49] D. E. Fields,[34,41] C. Finck,[46] F. Fleuret,[26] S. L. Fokin,[24] B. D. Fox,[41] Z. Fraenkel,[52] J. E. Frantz,[10] A. Franz,[5] A. D. Frawley,[14] Y. Fukao,[25,40,41] S.-Y. Fung,[6] S. Gadrat,[29] M. Germain,[46] A. Glenn,[47] M. Gonin,[26] J. Gosset,[11] Y. Goto,[40,41] R. Granier de Cassagnac,[26] N. Grau,[19] S. V. Greene,[50] M. Grosse Perdekamp,[18,41] H.-Å. Gustafsson,[30] T. Hachiya,[16] J. S. Haggerty,[5] H. Hamagaki,[8] A. G. Hansen,[28] E. P. Hartouni,[27] M. Harvey,[5] K. Hasuko,[40] R. Hayano,[8] X. He,[15] M. Heffner,[27] T. K. Hemmick,[45] J. M. Heuser,[40] P. Hidas,[22] H. Hiejima,[18] J. C. Hill,[19] R. Hobbs,[34] W. Holzmann,[44] K. Homma,[16] B. Hong,[23] A. Hoover,[35] T. Horaguchi,[40,41,48] T. Ichihara,[40,41] V. V. Ikonnikov,[24] K. Imai,[25,40] M. Inaba,[49] M. Inuzuka,[8] D. Isenhower,[1] L. Isenhower,[1] M. Ishihara,[40] M. Issah,[44] A. Isupov,[20] B. V. Jacak,[45] J. Jia,[45] O. Jinnouchi,[40,41] B. M. Johnson,[5] S. C. Johnson,[27] K. S. Joo,[32] D. Jouan,[37] F. Kajihara,[8] S. Kametani,[8,51] N. Kamihara,[40,48] M. Kaneta,[41] J. H. Kang,[53] K. Katou,[51] T. Kawabata,[8] A. V. Kazantsev,[24] S. Kelly,[9,10] B. Khachaturov,[52] A. Khanzadeev,[39] J. Kikuchi,[51] D. J. Kim,[53] E. Kim,[43] G.-B. Kim,[26] H. J. Kim,[53] E. Kinney,[9] A. Kiss,[13] E. Kistenev,[5] A. Kiyomichi,[40] C. Klein-Boesing,[31] H. Kobayashi,[41] L. Kochenda,[39] V. Kochetkov,[17] R. Kohara,[16] B. Komkov,[39] M. Konno,[49] D. Kotchetkov,[6] A. Kozlov,[52] P. J. Kroon,[5] C. H. Kuberg,[1,*] G. J. Kunde,[28] K. Kurita,[40] M. J. Kweon,[23] Y. Kwon,[53] G. S. Kyle,[35] R. Lacey,[44] J. G. Lajoie,[19] Y. Le Bornec,[37] A. Lebedev,[19,24] S. Leckey,[45] D. M. Lee,[28] M. J. Leitch,[28] M. A. L. Leite,[42] X. H. Li,[6] H. Lim,[43] A. Litvinenko,[20] M. X. Liu,[28] C. F. Maguire,[50] Y. I. Makdisi,[5] A. Malakhov,[20] V. I. Manko,[24] Y. Mao,[38,40] G. Martinez,[46] H. Masui,[49] F. Matathias,[45] T. Matsumoto,[8,51] M. C. McCain,[1] P. L. McGaughey,[28] Y. Miake,[49] T. E. Miller,[50] A. Milov,[45] S. Mioduszewski,[5] G. C. Mishra,[15] J. T. Mitchell,[5] A. K. Mohanty,[4] D. P. Morrison,[5] J. M. Moss,[28] D. Mukhopadhyay,[52] M. Muniruzzaman,[6] S. Nagamiya,[21] J. L. Nagle,[9,10] T. Nakamura,[16] J. Newby,[47] A. S. Nyanin,[24] J. Nystrand,[30] E. O'Brien,[5] C. A. Ogilvie,[19] H. Ohnishi,[40] I. D. Ojha,[3,50] H. Okada,[25,40] K. Okada,[40,41] A. Oskarsson,[30] I. Otterlund,[30] K. Oyama,[8] K. Ozawa,[8] D. Pal,[52] A. P. T. Palounek,[28] V. Pantuev,[45] V. Papavassiliou,[35] J. Park,[43] W. J. Park,[23] S. F. Pate,[35] H. Pei,[19] V. Penev,[20] J.-C. Peng,[18] H. Pereira,[11] V. Peresedov,[20] A. Pierson,[34] C. Pinkenburg,[5] R. P. Pisani,[5] M. L. Purschke,[5] A. K. Purwar,[45] J. M. Qualls,[1] J. Rak,[19] I. Ravinovich,[52] K. F. Read,[36,47] M. Reuter,[45] K. Reygers,[31] V. Riabov,[39] Y. Riabov,[39] G. Roche,[29] A. Romana,[26,*] M. Rosati,[19] S. S. E. Rosendahl,[30] P. Rosnet,[29] V. L. Rykov,[40] S. S. Ryu,[53] B. Sahlmueller,[31] N. Saito,[25,40,41] T. Sakaguchi,[8,51] S. Sakai,[49] V. Samsonov,[39] L. Sanfratello,[34] R. Santo,[31] H. D. Sato,[25,40] S. Sato,[5,49] S. Sawada,[21] Y. Schutz,[46] V. Semenov,[17] R. Seto,[6] T. K. Shea,[5] I. Shein,[17] T.-A. Shibata,[40,48] K. Shigaki,[16] M. Shimomura,[49] A. Sickles,[45] C. L. Silva,[42] D. Silvermyr,[28] K. S. Sim,[23] A. Soldatov,[17] R. A. Soltz,[27] W. E. Sondheim,[28] S. P. Sorensen,[47] I. V. Sourikova,[5] F. Staley,[11] P. W. Stankus,[36] E. Stenlund,[30] M. Stepanov,[35] A. Ster,[22] S. P. Stoll,[5] T. Sugitate,[16] J. P. Sullivan,[28] S. Takagi,[49] E. M. Takagui,[42] A. Taketani,[40,41] K. H. Tanaka,[21] Y. Tanaka,[33] K. Tanida,[40] M. J. Tannenbaum,[5] A. Taranenko,[44] P. Tarján,[12] T. L. Thomas,[34] M. Togawa,[25,40] J. Tojo,[40] H. Torii,[25,41] R. S. Towell,[1] V-N. Tram,[26] I. Tserruya,[52] Y. Tsuchimoto,[16] H. Tydesjö,[30] N. Tyurin,[17] T. J. Uam,[32] J. Velkovska,[5] M. Velkovsky,[45] V. Veszprémi,[12] A. A. Vinogradov,[24] M. A. Volkov,[24] E. Vznuzdaev,[39] X. R. Wang,[15] Y. Watanabe,[40,41] S. N. White,[5] N. Willis,[37] F. K. Wohn,[19] C. L. Woody,[5] W. Xie,[6] A. Yanovich,[17] S. Yokkaichi,[40,41] G. R. Young,[36] I. E. Yushmanov,[24] W. A. Zajc,[10,†] O. Zaudtke,[31] C. Zhang,[10] S. Zhou,[7] J. Zimányi,[22,*] L. Zolin,[20] X. Zong,[19] and H. W. vanHecke[28]

(PHENIX Collaboration)

[1]*Abilene Christian University, Abilene, Texas 79699, USA*
[2]*Institute of Physics, Academia Sinica, Taipei 11529, Taiwan*

 © 2007 The American Physical Society

[3]Department of Physics, Banaras Hindu University, Varanasi 221005, India
[4]Bhabha Atomic Research Centre, Bombay 400 085, India
[5]Brookhaven National Laboratory, Upton, New York 11973-5000, USA
[6]University of California-Riverside, Riverside, California 92521, USA
[7]China Institute of Atomic Energy (CIAE), Beijing, People's Republic of China
[8]Center for Nuclear Study, Graduate School of Science, University of Tokyo, 7-3-1 Hongo, Bunkyo, Tokyo 113-0033, Japan
[9]University of Colorado, Boulder, Colorado 80309, USA
[10]Columbia University, New York, New York 10027 and Nevis Laboratories, Irvington, New York 10533, USA
[11]Dapnia, CEA Saclay, F-91191, Gif-sur-Yvette, France
[12]Debrecen University, H-4010 Debrecen, Egyetem tér 1, Hungary
[13]ELTE, Eötvös Loránd University, H-1117 Budapest, Pázmány P. s. 1/A, Hungary
[14]Florida State University, Tallahassee, Florida 32306, USA
[15]Georgia State University, Atlanta, Georgia 30303, USA
[16]Hiroshima University, Kagamiyama, Higashi-Hiroshima 739-8526, Japan
[17]IHEP Protvino, State Research Center of Russian Federation, Institute for High Energy Physics, Protvino, 142281, Russia
[18]University of Illinois at Urbana-Champaign, Urbana, Illinois 61801, USA
[19]Iowa State University, Ames, Iowa 50011, USA
[20]Joint Institute for Nuclear Research, 141980 Dubna, Moscow Region, Russia
[21]KEK, High Energy Accelerator Research Organization, Tsukuba, Ibaraki 305-0801, Japan
[22]KFKI Research Institute for Particle and Nuclear Physics of the Hungarian Academy of Sciences (MTA KFKI RMKI), H-1525 Budapest 114, POBox 49, Budapest, Hungary
[23]Korea University, Seoul, 136-701, Korea
[24]Russian Research Center "Kurchatov Institute", Moscow, Russia
[25]Kyoto University, Kyoto 606-8502, Japan
[26]Laboratoire Leprince-Ringuet, Ecole Polytechnique, CNRS-IN2P3, Route de Saclay, F-91128, Palaiseau, France
[27]Lawrence Livermore National Laboratory, Livermore, California 94550, USA
[28]Los Alamos National Laboratory, Los Alamos, New Mexico 87545, USA
[29]LPC, Université Blaise Pascal, CNRS-IN2P3, Clermont-Fd, 63177 Aubiere Cedex, France
[30]Department of Physics, Lund University, Box 118, SE-221 00 Lund, Sweden
[31]Institut für Kernphysik, University of Muenster, D-48149 Muenster, Germany
[32]Myongji University, Yongin, Kyonggido 449-728, Korea
[33]Nagasaki Institute of Applied Science, Nagasaki-shi, Nagasaki 851-0193, Japan
[34]University of New Mexico, Albuquerque, New Mexico 87131, USA
[35]New Mexico State University, Las Cruces, New Mexico 88003, USA
[36]Oak Ridge National Laboratory, Oak Ridge, Tennessee 37831, USA
[37]IPN-Orsay, Universite Paris Sud, CNRS-IN2P3, BP1, F-91406, Orsay, France
[38]Peking University, Beijing, People's Republic of China
[39]PNPI, Petersburg Nuclear Physics Institute, Gatchina, Leningrad region, 188300, Russia
[40]RIKEN (The Institute of Physical and Chemical Research), Wako, Saitama 351-0198, JAPAN
[41]RIKEN BNL Research Center, Brookhaven National Laboratory, Upton, New York 11973-5000, USA
[42]Universidade de São Paulo, Instituto de Física, Caixa Postal 66318, São Paulo CEP05315-970, Brazil
[43]System Electronics Laboratory, Seoul National University, Seoul, South Korea
[44]Chemistry Department, Stony Brook University, Stony Brook, SUNY, New York 11794-3400, USA
[45]Department of Physics and Astronomy, Stony Brook University, SUNY, Stony Brook, New York 11794, USA
[46]SUBATECH (Ecole des Mines de Nantes, CNRS-IN2P3, Université de Nantes) BP 20722-44307, Nantes, France
[47]University of Tennessee, Knoxville, Tennessee 37996, USA
[48]Department of Physics, Tokyo Institute of Technology, Oh-okayama, Meguro, Tokyo 152-8551, Japan
[49]Institute of Physics, University of Tsukuba, Tsukuba, Ibaraki 305, Japan
[50]Vanderbilt University, Nashville, Tennessee 37235, USA
[51]Waseda University, Advanced Research Institute for Science and Engineering, 17 Kikui-cho, Shinjuku-ku, Tokyo 162-0044, Japan
[52]Weizmann Institute, Rehovot 76100, Israel
[53]Yonsei University, IPAP, Seoul 120-749, Korea

(Received 23 October 2006; published 24 April 2007)

The dependence of transverse momentum spectra of neutral pions and η mesons with $p_T < 16$ GeV/c and $p_T < 12$ GeV/c, respectively, on the centrality of the collision has been measured at midrapidity by the PHENIX experiment at the BNL Relativistic Heavy Ion Collider (RHIC) in d + Au collisions at $\sqrt{s_{NN}} = 200$ GeV. The measured yields are compared to those in $p + p$ collisions at the same $\sqrt{s_{NN}}$ scaled by the number of underlying nucleon-nucleon collisions in d + Au. At all centralities, the yield ratios show no suppression, in contrast to the strong suppression seen for central Au + Au collisions at RHIC. Only a weak p_T and centrality dependence can be observed.

DOI: 10.1103/PhysRevLett.98.172302 PACS numbers: 25.75.Dw

High-energy nucleus-nucleus collisions provide the opportunity to study strongly interacting matter at very high energy densities where Quantum Chromodynamics (QCD) predicts a transition from normal nuclear matter to a deconfined system of quarks and gluons, the Quark-Gluon Plasma (QGP) [1]. At the Relativistic Heavy Ion Collider (RHIC), the energy density is well in excess of the critical energy density that is expected for this transition [2]. One of the most intriguing results observed at RHIC so far is the suppression of hadrons with high transverse momentum (p_T) in central (head-on) Au + Au collisions. The hadron yield at high p_T is a factor of 5 less than expected from $p + p$ collisions scaled by the number of corresponding nucleon-nucleon collisions [3]. Such suppression was predicted as an effect of parton energy loss in the medium generated in the collisions [4,5]. A control experiment of d + Au collisions, where no medium is produced in the final state of the collision, showed no indication of hadron suppression at midrapidity [6], ruling out strong initial-state effects (final-state energy loss in the cold nucleus is generally expected to be small) as the cause for the suppression in Au + Au. For a better understanding of the medium effects at work in Au + Au, however, it is crucial to explore the exact role initial-state effects play in the modification of high-p_T particle production at RHIC.

Initial-state nuclear effects include p_T broadening, shadowing, and gluon saturation. The p_T broadening, often called Cronin effect [7], is an enhancement of the particle yield at intermediate p_T, which is often attributed to multiple soft parton scatterings before a hard interaction of the parton [8,9]. Shadowing is an apparent depletion of the structure function in the nucleus at small Bjorken x ($x \leq 10^{-2}$) [10] with (in some models) a corresponding enhancement at intermediate x ($x \sim 5 \times 10^{-2}$) called antishadowing. This is not well understood, but usually attributed to coherence effects or to gluon saturation. Gluon saturation refers to the nonlinear dynamics of gluons at small x where, due to the large densities, they tend to fuse rather than split. The Color Glass Condensate (CGC) model is a classical description of this saturation effect. In this picture, particle production at moderate p_T originally was predicted to be suppressed in central d + Au collisions at RHIC [11]. In recent CGC models, a Cronin enhancement can also be reproduced with a suitable choice of initial-state parameters [12].

One established way to test the contribution of different initial- and final-state nuclear effects is the study of the centrality dependence of particle production at high p_T. Initial state and medium effects are strongest in central collisions. In Au + Au collisions, a strong dependence of the suppression of high-p_T hadrons on the centrality of the collision has been observed [13–15]; the suppression weakens going to peripheral collisions and finally disappears. This can be compared to the centrality dependence of (initial-state) hadron production in d + Au. The yield of nonidentified charged hadrons in d + Au collisions with $p_T < 6$ GeV/c was found to be increasingly enhanced going from peripheral to central collisions [16], mainly attributed to the influence of (anti)protons [17]. At high p_T, the baryon contribution to the yield of unidentified charged hadrons is expected to become small, and instead the yield is dominated by charged pions [2]. All this sparks paramount interest in the centrality dependence of neutral pion (π^0) production especially as it can be measured up to very high p_T where particle production is truly perturbative. Furthermore, the high-p_T measurement of an additional identified particle like the eta meson (η), with 4 times the mass of the pion, may shed light on the question to what extent the particle-species dependence of the suppression (enhancement) observed in Au + Au (d + Au) depends on the number of constituent quarks rather than on the mass of the particle [18,19].

In this Letter, we present measurements by the PHENIX experiment [20] on the production of π^0 and η in $p + p$ and d + Au collisions at $\sqrt{s_{NN}} = 200$ GeV. The data provide the first measurement of neutral mesons in d + Au collisions at midrapidity as a function of the centrality of the collision. The π^0 measurements described in this Letter are similar to the analysis of minimum bias d + Au data in [6] but are based on an improved data set that allows the study of the particle production for different selections of the centrality of the collision. A more detailed description of the η analysis can be found in [21].

π^0 and η are measured by the PHENIX electromagnetic calorimeter (EMCal) via the $\pi^0 \rightarrow \gamma\gamma$ and $\eta \rightarrow \gamma\gamma$ decay. The EMCal consists of six lead scintillator (PbSc) and two lead glass (PbGl) sectors, each located at a radial distance of ~5 m from the beam axis. The detector covers a pseudorapidity range of $|\eta| \leq 0.35$ and an azimuthal angle of $\Delta\phi = \pi$. The EMCal granularity is $\Delta\eta \times \Delta\phi \approx 0.011 \times 0.011$ for the PbSc and 0.008×0.008 for the PbGl. The data sets from PbSc and PbGl are analyzed separately and combined for the final results. The energy calibration for the EMCal is obtained from beam tests, cosmic rays, and minimum ionizing energy peaks of charged hadrons. In a recent improvement of the calibration, the EMCal is calibrated by the invariant mass distribution of neutral pions for each of the 24768 readout channels separately. The uncertainty on the energy scale is 1.2%.

The data used in this analysis were recorded in 2002-2003 (RHIC Run-3) under two different trigger conditions. 25.2×10^6 and 58.3×10^6 minimum bias events were analyzed for $p + p$ and d + Au collisions, respectively. Minimum bias (MB) events are triggered by the Beam-Beam Counters (BBC) [20] ($|\eta| = 3.0$–3.9) and require a vertex position along the beam axis within $|z| < 30$ cm.

The minimum bias trigger accepts $(88 \pm 4)\%$ of all inelastic $d + \mathrm{Au}$ collisions that satisfy the vertex condition. This corresponds to 1.99 b $\pm 5.2\%$, the measured fraction of the total $d + \mathrm{Au}$ inelastic cross section, determined using photo-dissociation of the deuteron [22]. In $p + p$, this trigger measures 23.0 mb $\pm 9.7\%$ of the $p + p$ inelastic cross section. The measured particle yields are corrected for the $p + p$ MB trigger bias [23]: the MB trigger measures only $(79 \pm 2)\%$ of high-p_T particles. In $d + \mathrm{Au}$ collisions, this fraction varies from 85% to 100% from peripheral to central collisions; here the uncertainty is $\sim 3\%$. The second data sample was collected with a high-p_T photon trigger in the EMCal in addition to the MB trigger requirement in order to extend the measurement to higher p_T. This trigger requires a photon of $p_T > 1.4(1.4)$ GeV and $p_T > 2.5(3.5)$ GeV for PbSc (PbGl) and for $p + p$ and $d + \mathrm{Au}$ collisions, respectively. We analyzed 45.1×10^6 (19.5×10^6) events in $p + p$ ($d + \mathrm{Au}$) under this trigger condition. The sampled integrated luminosity was 216 nb^{-1} for $p + p$ and 1.5 nb^{-1} for $d + \mathrm{Au}$. (In $d + \mathrm{Au}$, that corresponds to an integrated nucleon-nucleon luminosity of 590 nb^{-1}).

The division of $d + \mathrm{Au}$ collisions in different centrality classes is based on the charge deposited in the backward BBC ($-3.9 < \eta < -3.0$), i.e., in the Au beam direction. For each centrality class, the corresponding average nuclear overlap function $\langle T_{AB} \rangle$ (compare Eq. (1)) is calculated using a Glauber Monte Carlo model and simulations of the BBC, taking into account its limited efficiency for peripheral collisions. For the four centrality classes (0–20%, 20–40%, 40–60%, and 60–88%) used in this analysis, the $\langle T_{AB} \rangle$ values are (0.365 ± 0.024), (0.252 ± 0.017), (0.165 ± 0.014), and (0.073 ± 0.007) mb^{-1}. The corresponding number of collisions can be calculated as $\langle N_{\mathrm{coll}} \rangle = \sigma_{\mathrm{inel}}^{pp} \times \langle T_{AB} \rangle$ with $\sigma_{\mathrm{inel}}^{\mathrm{pp}} = 42.2$ mb.

Photon candidates in the EMCal are selected by applying particle identification (PID) cuts based on the shower profile in the detector. To determine the yields of π^0 and η, the invariant mass of all photon pairs with an energy asymmetry $|E_1 - E_2|/(E_1 + E_2) < 0.7$ in a given p_T bin is calculated. After subtraction of the combinatorial background, the invariant mass distribution is integrated around the particle mass peak [13]; the integration window reflects thereby the p_T dependence of the mass peak position and width. The combinatorial background is determined by pairing photons from different events with similar centrality (for $d + \mathrm{Au}$) and vertex. In this analysis, the signal-to-background ratio for high-p_T π^0 is about 25 and 13 at $p_T = 4$ GeV/c in $p + p$ and central $d + \mathrm{Au}$ collisions, respectively. It decreases to 7 and 2 at $p_T = 2$ GeV/c. For η, this ratio is about 2 at $p_T = 8$ GeV/c, decreasing to 0.3 ($p + p$) and 0.2 (central $d + \mathrm{Au}$) at $p_T = 3$ GeV/c. The raw spectra are corrected for trigger efficiency, acceptance, and reconstruction efficiency. This includes dead areas, the influence of energy resolution, analysis cuts, the peak extraction window, and photon conversion. The corrections are determined using Monte Carlo simulations. Because of the fine granularity of the calorimeter, occupancy effects are negligible. Furthermore, the π^0 spectra are corrected at $p_T > 10$ GeV/c (15 GeV/c) for two-photon merging effects in the PbSc (PbGl), studied in Monte Carlo simulations and confirmed with test beam data [24]. Finally, a correction in the π^0 and η yields to account for the true mean value of each p_T bin is applied to the steeply falling spectra. For $p_T < 3.5(3.0)$ GeV/c, the $p + p$ π^0 (η) spectrum is calculated from the minimum bias data sample; above this threshold, the high-p_T triggered sample is used. In $d + \mathrm{Au}$, this transition is made at $p_T = 4.5$ and 3.5 GeV/c for π^0 and η, respectively.

The main contributions to the systematic uncertainty on the $p + p$ and $d + \mathrm{Au}$ spectra are given in Table I for π^0 and η. Most uncertainties are identical for $p + p$ and $d + \mathrm{Au}$; only the uncertainty on the peak extraction is slightly larger in $d + \mathrm{Au}$. Category (d) includes uncertainties on the EMCal global energy scale and nonlinearity. The uncertainties in (d) and (e) are partially correlated. All others are uncorrelated and added in quadrature to get the total uncertainty.

The fully corrected p_T distributions of π^0 and η are shown in Fig. 1. The top panels show the invariant yield in $d + \mathrm{Au}$ collisions for four centrality bins scaled for clarity by the factors indicated. The bottom panels show the

TABLE I. Main systematic uncertainties in % on π^0 and η spectra. The uncertainties are given for PbSc (PbGl). The normalization uncertainties of 9.7% for the $p + p$ and 5.2% for the $d + \mathrm{Au}$ cross section as well as the MB-trigger-bias uncertainty of $\sim 3\%$ for the centrality-selected yields are not listed.

meson [p_T (GeV/c)]	π^0 [2]	π^0 [15]	η [3]	η [10]
(a) peak extraction	2.7(2.7)	2.0(2.0)	14(14)	6.0(6.0)
(b) geom. accept.	3.5(3.5)	3.5(3.5)	4.5(4.5)	4.5(4.5)
(c) π^0 reconstr. eff.	0.7(0.7)	4.0(4.0)	0.7(0.7)	3.6(3.6)
(d) energy scale	5.0(5.0)	11.4(11.4)	5.0(5.0)	9.4(9.4)
(e) merging corr.	⋯	5.9(2.1)	⋯	⋯
Total	6.7(6.7)	17.0(12.9)	15.5(15.5)	12.6(12.6)

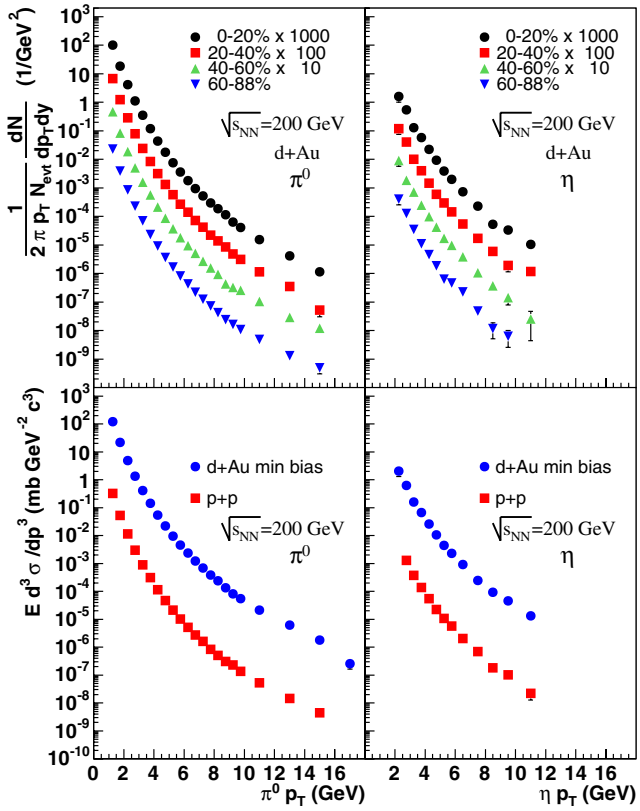

FIG. 1 (color online). Top: invariant yields at midrapidity for π^0 (left) and η (right) in $d + \mathrm{Au}$ collisions as a function of p_T for different selections of the centrality of the collision. Bottom: invariant cross section at midrapidity for π^0 (left) and η (right) in $p + p$ and $d + \mathrm{Au}$ collisions as a function of p_T.

invariant cross section in $p + p$ and $d + \mathrm{Au}$ collisions. The improved data set allows the study of π^0 (η) production up to 18(12) GeV/c, the highest p_T values measured for identified particles in $p + A$ ($d + A$) collisions. For the first time, the invariant cross section for π^0 and η in $d + \mathrm{Au}$ collisions has been measured at this energy. The π^0 result in $p + p$ agrees with the previous measurement at $\sqrt{s_{NN}} = 200$ GeV [23] within statistical uncertainties, and confirms the agreement with pQCD within the uncertainty of the calculation. Therefore, the $p + p$ cross section can be used as a well-understood reference for the production in $d + A$ and Au + Au collisions.

To quantify nuclear medium effects at high p_T, it is customary to use the *nuclear modification factor* which is given by the ratio of the invariant $d + \mathrm{Au}$ yield to the invariant $p + p$ cross section [13] scaled by $\langle T_{AB} \rangle$:

$$R_{AB}(p_T) = \frac{d^2 N_{AB}^{\pi^0}/dy dp_T}{\langle T_{AB} \rangle d^2 \sigma_{pp}^{\pi^0}/dy dp_T}. \quad (1)$$

The average nuclear overlap function $\langle T_{AB} \rangle$, averaged over the respective impact parameter range, is determined solely by the density distribution of the nucleons in the nuclei A and B and the impact parameter.

Figure 2 shows the nuclear modification factor $R_{dA}(p_T)$ for π^0 and η in $d + \mathrm{Au}$ collisions at $\sqrt{s_{NN}} = 200$ GeV for four different centrality selections and for minimum bias events. As the $p + p$ and $d + \mathrm{Au}$ measurements are both made in the same year, many of the systematic errors associated with detector performance are nearly identical, and the corresponding systematic errors in the comparison are negligible. Within systematic errors, $R_{dA}(p_T)$ for π^0 and η is ≈ 1 in all centrality bins, and only a weak p_T dependence can be seen. In order to check the absolute normalization systematics, we can also calculate $R_{dA}(p_T)$ using the inelastic cross section measured through photodissociation of the deuteron. This constitutes an important cross check. It replaces the systematic uncertainties of the BBC efficiency and $\langle T_{AB} \rangle$, which are determined by model calculations, by the uncertainty of the cross section measurement of similar size. The resulting $R_{dA}(p_T)$ is 9.8% larger than that obtained from the minimum bias yield, consistent within 1.5 σ.

Though very different in mass, η and π^0 show a similar, weak centrality dependence of $R_{dA}(p_T)$ over the measured p_T range. These results do not show the significant enhancement seen for protons where the proton R_{AA} is substantially larger than that of pions in the intermediate p_T (2 GeV/c $< p_T <$ 4 GeV/c) region [17]. The π^0 data exhibit small shape variations with centrality that may be due to initial-state effects including shadowing and multiple scattering. Possible Cronin enhancements in the intermediate p_T region due to initial-state multiple scattering or antishadowing are not more than 10% around 4 GeV/c. At low p_T ($p_T < 3$ GeV/c), the drop towards smaller R_{dA} is consistent with analogous measurements for charged pions [17] and is usually attributed to a change to a regime of soft physics (N_{part} scaling) at the smallest p_T values. At the largest p_T values measured ($p_T > 9$ GeV/c), the most central π^0 result hints at a small suppression, though this is only a ~1.7 sigma effect.

In conclusion, we have presented the first study of the centrality dependence of π^0 and η production at midrapidity in $d + \mathrm{Au}$ collisions at $\sqrt{s_{NN}} = 200$ GeV. Transverse momentum spectra up to $p_T = 18$ and 12 GeV/c have been measured for π^0 and η, respectively. The invariant yield per nucleon-nucleon collision is compared to that in $p + p$ collisions measured at the same $\sqrt{s_{NN}}$. The strong suppression observed for π^0 production at high p_T in central Au-Au collisions is not seen for $d + \mathrm{Au}$ in any centrality: Within systematic errors, $R_{dA}(p_T)$ is ≈ 1 in all centrality bins. A weak centrality dependence of the shape of R_{dA} versus p_T is seen, presumably due to initial-state effects. A possible Cronin enhancement is substantially smaller than the $R_{dA} \gtrsim 1.9$ that corresponds to results from lower energy measurements [7,25]. Within systematic errors, R_{dA} for π^0 and η agree well, giving no indication for cold nuclear matter effects having a mass dependence. Since nuclear modifications in $d + \mathrm{Au}$ are

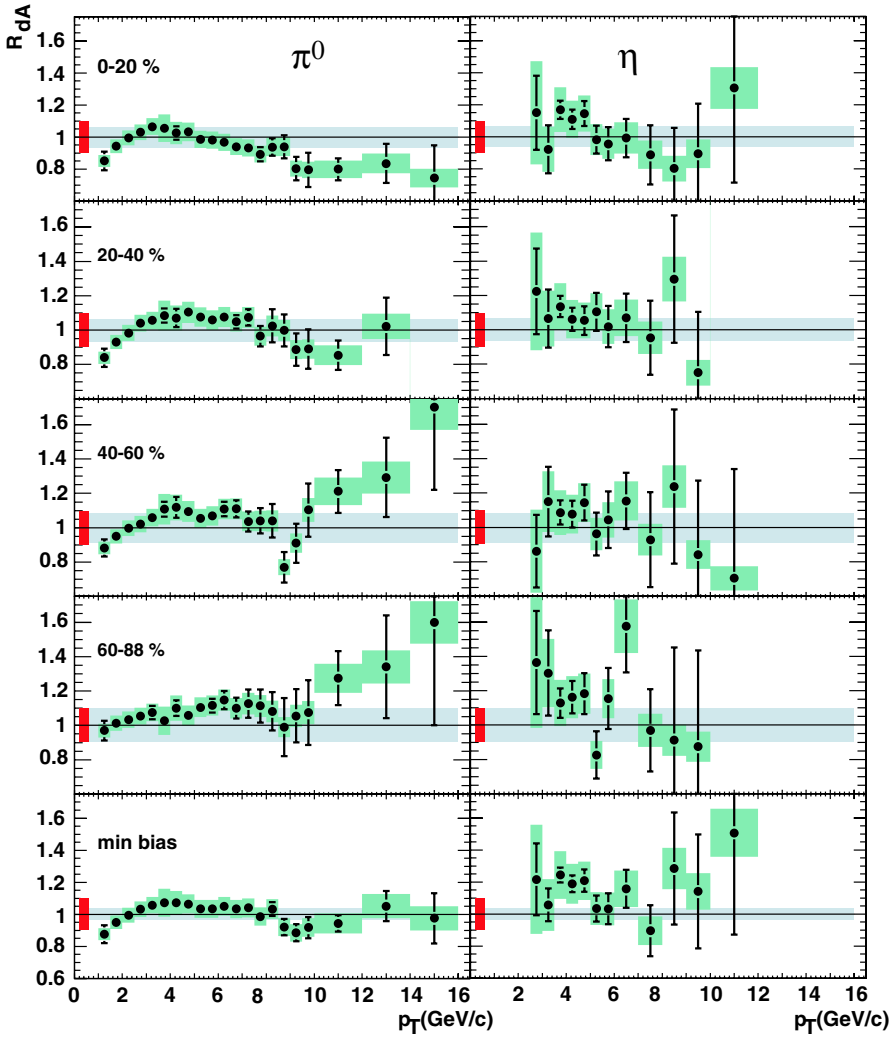

FIG. 2 (color online). Nuclear modification factor R_{dA} for π^0 and η in different centrality selections and min. bias data at midrapidity. The bands around the data points show systematic errors which can vary with p_T. The shaded bands around unity indicate the $\langle T_{AB} \rangle$ uncertainty, and the small bands on the left side of the data points indicate the normalization uncertainty due to the $p + p$ reference.

small even in the most central collisions where initial-state effects are expected to be largest, we conclude that initial-state effects in Au + Au must be small as well, and therefore the large suppression seen in Au + Au must be mostly due to medium effects.

We thank the staff of the Collider-Accelerator and Physics Departments at BNL for their vital contributions. We acknowledge support from the Department of Energy and NSF (U.S.A.), MEXT and JSPS (Japan), CNPq and FAPESP (Brazil), NSFC (China), IN2P3/CNRS, CEA, and ARMINES (France), BMBF, DAAD, and AvH (Germany), OTKA (Hungary), DAE and DST (India), ISF (Israel), KRF and KOSEF (Korea), RMIST, RAS, and RMAE (Russia), VR and KAW (Sweden), U.S. CRDF for the FSU, US-Hungarian NSF-OTKA-MTA, and US-Israel BSF.

*Deceased
†PHENIX Spokesperson: zajc@nevis.columbia.edu

[1] J. W. Harris and B. Müller, Annu. Rev. Nucl. Part. Sci. **46**, 71 (1996).
[2] K. Adcox *et al.* (PHENIX), Nucl. Phys. A **757**, 184 (2005).
[3] K. Adcox *et al.* (PHENIX), Phys. Rev. Lett. **88**, 022301 (2001).
[4] J. D. Bjorken, Fermilab, Report No. FERMILAB-PUB-82-059-THY, 1982.
[5] R. Baier, D. Schiff, and B. G. Zakharov, Ann. Rev. Nucl. Part. Sci. **50**, 37 (2000).
[6] S. S. Adler *et al.* (PHENIX), Phys. Rev. Lett. **91**, 072303 (2003).
[7] J. W. Cronin *et al.*, Phys. Rev. D **11**, 3105 (1975).
[8] I. Vitev, Phys. Lett. B **562**, 36 (2003).
[9] A. Accardi and M. Gyulassy, Phys. Lett. B **586**, 244 (2004).
[10] M. Arneodo, Phys. Rep. **240**, 301 (1994).
[11] D. Kharzeev, E. Levin, and L. McLerran, Phys. Lett. B **561**, 93 (2003).
[12] D. Kharzeev, Y. V. Kovchegov, and K. Tuchin, Phys. Rev. D **68**, 094013 (2003).
[13] S. S. Adler *et al.* (PHENIX), Phys. Rev. Lett. **91**, 072301 (2003).

[14] S. S. Adler *et al.* (PHENIX), Phys. Rev. C **69**, 034910 (2004).
[15] J. Adams *et al.* (STAR), Phys. Rev. Lett. **91**, 172302 (2003).
[16] S. S. Adler *et al.* (PHENIX), High p_T charged centrality dependence and h/π^0 ratio in $d + \mathrm{Au}$ collisions (to be published).
[17] S. S. Adler *et al.* (PHENIX), Phys. Rev. C **74**, 024904 (2006).
[18] S. S. Adler *et al.* (PHENIX), Phys. Rev. C **72**, 014903 (2005).
[19] R. C. Hwa and C. B. Yang, Phys. Rev. Lett. **93**, 082302 (2004).
[20] K. Adcox *et al.* (PHENIX), Nucl. Instrum. Methods Phys. Res., Sect. A **499**, 469 (2003).
[21] S. S. Adler (PHENIX), Phys. Rev. C **75**, 024909 (2007).
[22] S. N. White, AIP Conf. Proc. **792**, 527 (2005).
[23] S. S. Adler *et al.* (PHENIX), Phys. Rev. Lett. **91**, 241803 (2003).
[24] G. David *et al.*, IEEE Trans. Nucl. Sci. **47**, 1982 (2000).
[25] A. L. S. Angelis *et al.* (BCMOR), Phys. Lett. B **185**, 213 (1987).

Eur. Phys. J. C 49, 225–229 (2007)
DOI 10.1140/epjc/s10052-006-0084-7

THE EUROPEAN PHYSICAL JOURNAL C

Regular Article – Experimental Physics

Direct photons measured by the PHENIX experiment at RHIC

S. Bathe[a] for the PHENIX Collaboration

University of California, 900 University Avenue, Riverside, CA 92521, USA

Received: 22 August 2006 /
Published online: 9 December 2006 – © Springer-Verlag / Società Italiana di Fisica 2006

Abstract. Results from the PHENIX experiment at RHIC on direct photon production in $p+p$, $d+\mathrm{Au}$, and $\mathrm{Au}+\mathrm{Au}$ collisions at $\sqrt{s_{NN}} = 200\,\mathrm{GeV}$ are presented. In $p+p$ collisions, direct photon production at high p_T behaves as expected from perturbative QCD calculations. The $p+p$ measurement serves as a baseline for direct photon production in $\mathrm{Au}+\mathrm{Au}$ collisions. In $d+\mathrm{Au}$ collisions, no effects of cold nuclear matter are found within the large uncertainty of the measurement. In $\mathrm{Au}+\mathrm{Au}$ collisions, the production of high p_T direct photons scales as expected for particle production in hard scatterings. This supports jet quenching models, which attribute the suppression of high p_T hadrons to the energy loss of fast partons in the medium produced in the collision. Low p_T direct photons, measured via e^+e^- pairs with small invariant mass, are possibly related to the production of thermal direct photons.

1 Introduction

Depending on their transverse momentum, direct photons convey information about different aspects of ultra-relativistic nucleus–nucleus ($A+A$) collisions. High transverse momentum (p_T) direct photons are produced in early, hard parton–parton scatterings by processes like quark–gluon Compton scattering ($q+g \longrightarrow q+\gamma$). Unlike scattered quarks or gluons, direct photons do not interact strongly with the medium subsequently produced in the collision. High p_T direct photons ($p_\mathrm{T} \gtrsim 6\,\mathrm{GeV}/c$) therefore provide a baseline for measuring medium modifications of high p_T hadron production.

A significant fraction of low p_T direct photons ($1 \leq p_\mathrm{T} \leq 3\,\mathrm{GeV}/c$ in central $\mathrm{Au}+\mathrm{Au}$ collisions at $\sqrt{s_{NN}} = 200\,\mathrm{GeV}$) is expected to come from a thermalized medium of deconfined quarks and gluons, the quark–gluon plasma (QGP), possibly created in $A+A$ collisions [1]. These thermal photons carry information about the initial temperature of the QGP. Thermal photons are produced in the QGP as well as in the hadronic gas over the entire life time of the collision. The initial temperature can be extracted comparing measurements to models which convolute the production rate with the space-time evolution of the collision.

At low and intermediate p_T ($p_\mathrm{T} \leq 6\,\mathrm{GeV}/c$ in central $\mathrm{Au}+\mathrm{Au}$ collisions at $\sqrt{s_{NN}} = 200\,\mathrm{GeV}$) another significant source of direct photons might be the interaction of fast partons from jets with thermal partons in the QGP [2] like $q_\mathrm{hard} + g_\mathrm{QGP} \longrightarrow q+\gamma$.

[a] e-mail: bathe@bnl.gov
Present Address: Brookhaven National Lab, Bldg. 510 C, Upton, NY 11973, USA

Possible modifications of direct photon production from cold nuclear matter effects can be measured in $d+\mathrm{Au}$ collisions where no medium is created. Direct photon measurements in $p+p$ collisions are a superb test of QCD. They constrain the gluon distribution function since the gluon is a direct participant of the partonic scattering. Furthermore, they provide a baseline for understanding direct photon production in $A+A$ collisions.

2 High p_T direct photons

2.1 Measurement

Experimentally, the measurement of direct photons is challenging due to a large background from hadron decays like $\pi^0 \longrightarrow \gamma\gamma$ and $\eta \longrightarrow \gamma\gamma$. PHENIX measures all those photon sources. Photons are measured with the electromagnetic calorimeter (EMCal). Neutral pions and η mesons are measured through their two-photon decay branch [3, 4]. The EMCal [5] consists of six sectors of a lead scintillator and two sectors of a lead glass calorimeter centered at midrapidity ($\eta < 0.35$) and covering 1/4 of the azimuthal angle.

The direct photon spectrum is obtained by subtracting the decay photon spectrum from the inclusive photon spectrum. This is gained from photon-like showers in the EMCal corrected for contaminations from charged hadrons and neutrons. The decay photon spectrum is calculated from the measured π^0 and η spectrum, taking into account minor contributions from other hadrons that decay into photons.

If the detector occupancy is low as in $p+p$ or $d+\mathrm{Au}$ collisions, the signal-to-background ratio can be improved

by event by event tagging of photons that have a matching partner as decay photons.

2.2 Results

2.2.1 $p+p$ collisions

The preliminary direct photon cross section for $p+p$ collisions at $\sqrt{s} = 200\,\mathrm{GeV}$ is shown in Fig. 1 [6]. It is based on an integrated luminosity of $266\,\mathrm{nb}^{-1}$ collected in RHIC Run-3. For the whole p_T range of 5 to 16 GeV/c the observed cross section is consistent with a next-to-leading-order perturbative-QCD (NLO pQCD) calculation [7]. This measurement establishes a reference for direct photon production in $A+A$. In RHIC Run-5, PHENIX took a $p+p$ data set with ten times the Run-3 statistics.

2.2.2 Au + Au collisions

The high p_T direct photon yield in $A+A$ collisions relative to $p+p$ is expected to scale with the parton luminosity in the overlap region of the two nuclei. The parton luminosity is quantified by the nuclear overlap function, T_{AA}. In the absence of nuclear effects the nuclear modification factor

$$R_{AA}(p_\mathrm{T}) = \frac{\mathrm{d}N/\mathrm{d}p_\mathrm{T}|_{A+A}}{\langle T_{AA}\rangle_f \, \mathrm{d}\sigma/\mathrm{d}p_\mathrm{T}|_{p+p}} \qquad (1)$$

is unity for particle production from hard scattering.

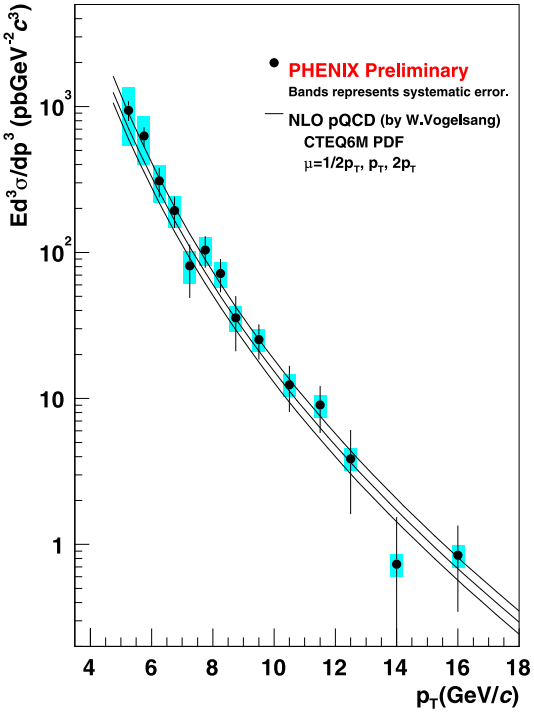

Fig. 1. Preliminary direct photon cross section as a function of p_T for $p+p$ collisions at $\sqrt{s} = 200$ GeV [6]. The *solid curves* are pQCD predictions [7] for three different scales, which represent the uncertainty on the calculation

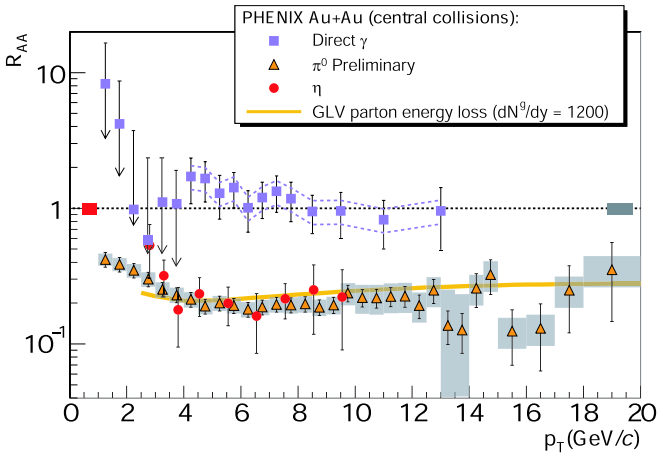

Fig. 2. Nuclear modification factor for direct photon, π^0, and η production in central Au + Au collisions at $\sqrt{s_{NN}} = 200$ GeV. For direct photons, a pQCD calculation is used as the reference

As shown by PHENIX in RHIC Run-2 [8], at high p_T direct photon production is consistent with the T_{AA}-scaled pQCD expectation also in Au + Au collisions. Figure 2 compares the nuclear modification factor for direct photon, π^0, and η production in central Au + Au collisions at $\sqrt{s_{NN}} = 200\,\mathrm{GeV}$. For direct photons, the pQCD calculation is used as a reference. The suppression for π^0 and η, supported by the non-suppression of photons, can be described with energy loss of partons in the produced medium.

While high p_T direct photon production is consistent with the pQCD expectation, one should keep in mind that there are a number of medium effects that might alter direct photon production. On the one hand, a significant fraction of direct photons is expected to stem from the fragmentation of hard-scattered partons into jets. As those partons lose energy in the medium, also the fragmentation photons should be suppressed. On the other hand, as partons lose energy through gluon bremsstrahlung, they should also generate photon bremsstrahlung, enhancing the direct photon yield. It would be a coincidence if these counterbalancing effects exactly canceled.

Experimentally, contributions from these effects can be quantified by studying the azimuthal distribution of direct photon production with respect to the reaction plane. If fragmentation photons are suppressed, less direct photons are expected to be emitted outside of the reaction plane. If bremsstrahlung is enhanced, more direct photons will be found outside of the reaction plane.

2.2.3 d + Au collisions

The preliminary direct photon yield for minimum-bias d + Au collisions at $\sqrt{s_{NN}} = 200\,\mathrm{GeV}$ is shown in the upper panel of Fig. 3 along with the yield in $p+p$ collisions. The d + Au analysis is based on ≈ 3 billion events sampled in RHIC Run-3. The lower panel shows the ratio to the

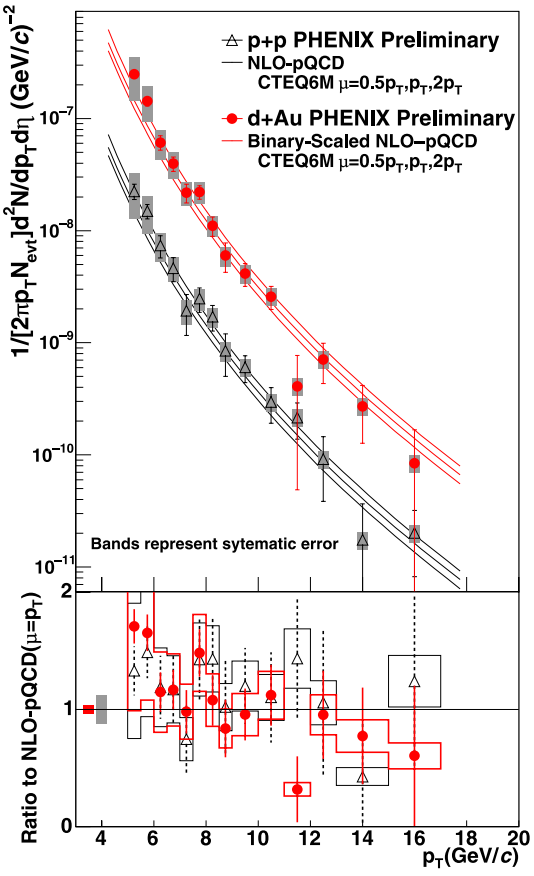

Fig. 3. Preliminary direct photon invariant yield as a function of p_{T} for $p+p$ [6] and minimum-bias $d+\mathrm{Au}$ collisions at $\sqrt{s_{NN}} = 200$ GeV. The *solid curves* are pQCD predictions [7] for three different scales, which represent the uncertainty on the calculation

T_{AA}-scaled NLO pQCD calculation. The ratio is consistent with unity over the entire p_{T} range, showing no indication of cold nuclear matter effects. However, the uncertainty of the measurement is large. A high statistics $d+\mathrm{Au}$ run is planned.

3 Low p_{T} direct photons

3.1 Measurement

The EMCal measurement at low p_{T} suffers from a large background from decay photons. Also, the relative energy resolution of the EMCal becomes worse at low energy. Therefore, a new method [9, 10] to measure direct photons at low p_{T} has been employed. It has been carried out in heavy ion experiments for the first time. The method is based on the measurement of pairs of e^+e^-, which are identified with the PHENIX Ring Imaging Cherenkov Detector (RICH). The basic idea is that any source of real photons also produces virtual photons that decay into e^+e^- with small invariant mass. An example is the π^0 Dalitz decay ($\pi^0 \longrightarrow \gamma e^+e^-$). This internal conversion method is

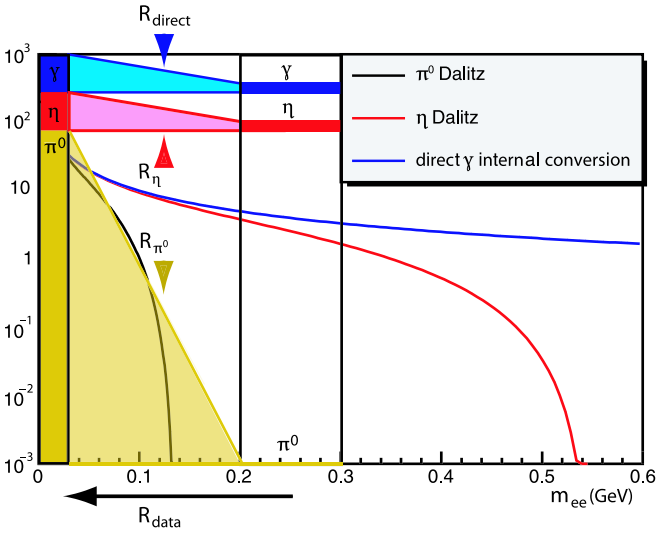

Fig. 4. Invariant-mass distribution of virtual photons from the π^0 and η Dalitz decay as well as from direct photons according to (2). It is illustrated how the various contributions decrease to a fraction R when going to higher invariant mass with the π^0 contribution exhausting

based on two assumptions: first, the ratio of direct-to-all photons is the same for real and virtual photons at small invariant mass close to zero ($m_\gamma < 30$ MeV): $\gamma^\star_{\mathrm{direct}}/\gamma^\star_{\mathrm{incl.}} = \gamma_{\mathrm{direct}}/\gamma_{\mathrm{incl.}}$. Second, the mass distribution can be described by the Kroll–Wada formula [11], which has been established to describe the Dalitz decay[1]:

$$\frac{1}{N_\gamma}\frac{\mathrm{d}N_{ee}}{\mathrm{d}m_{ee}} = \frac{2\alpha}{3\pi}\sqrt{1-\frac{4m_e^2}{m_{ee}^2}}\left(1+\frac{2m_e^2}{m_{ee}^2}\right) \times \frac{1}{m_{ee}}\left|F\left(m_{ee}^2\right)\right|^2\left(1-\frac{m_{ee}^2}{M^2}\right)^3, \qquad (2)$$

The mass distribution according to (2) is depicted in Fig. 4. For e^+e^- pairs from π^0 and η Dalitz decays the yield is suppressed towards higher m_{ee} due to the mass, M, of the parent meson in the phase space factor $(1-m_{ee}^2/M^2)^3$ whereas no suppression takes place for e^+e^- pairs from virtual direct photons as long as $m_{ee} \ll p_{\mathrm{T}}^{ee}$. For the small invariant masses considered here the form factor $\left|F\left(m_{ee}^2\right)\right|$ is assumed to be unity in all cases.

The key advantage of this method is the greatly improved signal-to-background ratio, which is achieved by eliminating the contribution from π^0 Dalitz decays when the invariant mass is increased. In addition, the electron measurement through charged particle tracking provides a better energy resolution at low p_{T} than the EMCal photon measurement. This excellent energy resolution at low p_{T} combined with little material upstream of the detector,

[1] Since the virtual photons decay in the medium, this relation might be slightly modified. This would not affect the significance of the observed excess of direct photons, only its translation into an absolute yield of real direct photons.

where photons could convert generating background e^+e^- pairs, makes this measurement feasible in PHENIX.

The experimentally observed quantity is the ratio of e^+e^- pairs in an invariant mass bin where the π^0 Dalitz decay is largely suppressed to the yield at an invariant mass close to zero: $R_{\rm data} = N_{ee}^{90-300\ {\rm MeV}}/N_{ee}^{<30\ {\rm MeV}}$. If there is no direct photon signal, $R_{\rm data} = R_{\rm hadron}^{\rm calc}$, *i.e.* $R_{\rm data}$ can be calculated[2] from (2) based on the known ratio $\eta/\pi^0 = 0.45 \pm 0.1$. An excess $R_{\rm data} > R_{\rm hadron}^{\rm calc}$ translates into the fraction of virtual direct photons at close to zero invariant mass according to:

$$\frac{\gamma^\star_{\rm direct}}{\gamma^\star_{\rm incl.}} = \frac{R_{\rm data} - R_{\rm hadron}^{\rm calc}}{R_{{\rm direct}\ \gamma}^{\rm calc} - R_{\rm hadron}^{\rm calc}}\,. \tag{3}$$

This can be derived starting from

$$R_{\rm data} = N_{ee}^{90-300\ {\rm MeV}}/N_{ee}^{<30\ {\rm MeV}} \tag{4}$$

with

$$N_{ee} = N_{\rm hadron} + N_{{\rm direct}\ \gamma}: \tag{5}$$

$$R_{\rm data} = \frac{R_{\rm hadron}^{\rm calc} N_{\rm hadron}^{<30\ {\rm MeV}} + R_{{\rm direct}\ \gamma}^{\rm calc} N_{{\rm direct}\ \gamma}^{<30\ {\rm MeV}}}{N_{\rm hadron}^{<30\ {\rm MeV}} + N_{{\rm direct}\ \gamma}^{<30\ {\rm MeV}}} \tag{6}$$

$$= R_{\rm hadron}^{\rm calc} + (R_{{\rm direct}\ \gamma}^{\rm calc} - R_{\rm hadron}^{\rm calc}) \frac{N_{{\rm direct}\ \gamma}^{<30\ {\rm MeV}}}{N_{ee}^{<30\ {\rm MeV}}}\,. \tag{7}$$

The direct photon spectrum is then obtained by multiplying $\gamma^\star_{\rm direct}/\gamma^\star_{\rm incl.}$ by the inclusive photon spectrum measured with the EMCal.

The full 2004 data set of about 900 million minimum bias events is analyzed. Events and centrality are selected as described in [12]. Electrons in the central arms are identified by matching charged particle tracks to clusters in the EMCal and to rings in the RICH detector. To obtain a clean invariant-mass distribution of e^+e^- pairs, pairs originating from photon conversions in the beam pipe or detector material are rejected based on their orientation with respect to the magnetic field. The combinatorial background is removed by an event-mixing technique. The uncertainty of the η-to-π^0 ratio of about 20% [13] is the main source of uncertainty, translating into an uncertainty of 20% of the measured direct photon yield. Other sources are the EMCal-measured inclusive photon yield (10%) and the e^+e^--pair acceptance (5%). The total systematic uncertainty is 25%.

3.2 Results

Figure 5a shows the direct photon signal for central Au + Au collisions at $\sqrt{s_{NN}} = 200\,{\rm GeV}$ in terms of the double ratio $\left(\gamma/\pi^0|_{\rm meas.}\right) / \left(\gamma/\pi^0|_{\rm bckgrd.}\right)$. This ratio indicates a direct photon excess above the decay photon contribution as an enhancement above 1. In this figure, two measurements are compared: the result from the internal conversion method as described above [14] and a preliminary analysis of the conventional EMCal measurement based on a subset of the RHIC Run-4 data set [14]. [3] While the internal conversion measurement results in a significant direct photon signal of about 10% above the decay photon background for $1 < p_{\rm T} < 5\,{\rm GeV}/c$, the EMCal measurement does not yield a significant direct photon signal below $p_{\rm T} = 3\,{\rm GeV}/c$, but agrees with the internal conversion measurement within the uncertainties over the entire range.

Figure 5b shows the direct photon invariant yield from the internal conversion measurement [14] and compares it to theoretical calculations. With large significance, a direct photon spectrum is obtained for $1 < p_{\rm T} < 5\,{\rm GeV}/c$. The spectrum lies significantly above a T_{AA}-scaled NLO pQCD calculation [7] for $p_{\rm T} \lesssim 3\,{\rm GeV}/c$. The pQCD calculation indicates the contribution from hard scatterings. The lines show the scale uncertainty of the calculation. However, it is not clear how meaningful the comparison is down to this low $p_{\rm T}$ where the pQCD calculation reaches its limit of applicability. It is planned to replace the pQCD calculation by a reference measurement of direct photon production in $p+p$ collisions with the same method as in Au + Au.

The excess of the measured direct photon spectrum above the pQCD calculation can be described by models that allow for a significant contribution of thermal photons. In order to describe thermal photon production in $A+A$ collisions, the entire space-time evolution has to be accounted for including the hadronic phase. This is done in hydrodynamical models, which assume local thermal equilibrium. An important free parameter in such models is the initial temperature of the fireball. Figure 5b compares the measured direct photon spectrum to a $2+1$ hydrodynamical model [15] for thermal-photon emission with an average initial temperature of $T_0^{\rm ave} = 360\,{\rm MeV}$ ($T_0^{\rm max} = 570\,{\rm MeV}$) and a formation time of $\tau_0 = 0.15\,{\rm fm}/c$. The model underpredicts the data for $p_{\rm T} \gtrsim 3\,{\rm GeV}/c$. The data can be described when both sources, thermal and pQCD, are combined. Various other calculations come to similar descriptions with initial temperatures in the range $370 < T_{\rm i} < 570\,{\rm MeV}$ [2, 16, 17]. The temperatures are significantly above the critical temperature for the QGP phase transition of $T_{\rm c} = 170\,{\rm MeV}$. However, the obtained temperature is only meaningful if the excess above pQCD is of thermal origin. Besides hard photons, also jet-plasma interactions may play a significant role [2].

4 Conclusions

The direct photon cross section in $p+p$ collisions at $\sqrt{s} = 200\,{\rm GeV}$ is found to be consistent with a NLO pQCD cal-

[2] Besides π^0 and η, decay photons from a cocktail of hadrons are considered here.

[3] The preliminary result from the measurement of virtual photons is presented in the same figure in terms of $\gamma_{\rm direct}/\gamma_{\rm incl.} + 1$, which also indicates a direct photon excess as an enhancement above 1. Note that the two quantities are not exactly equivalent.

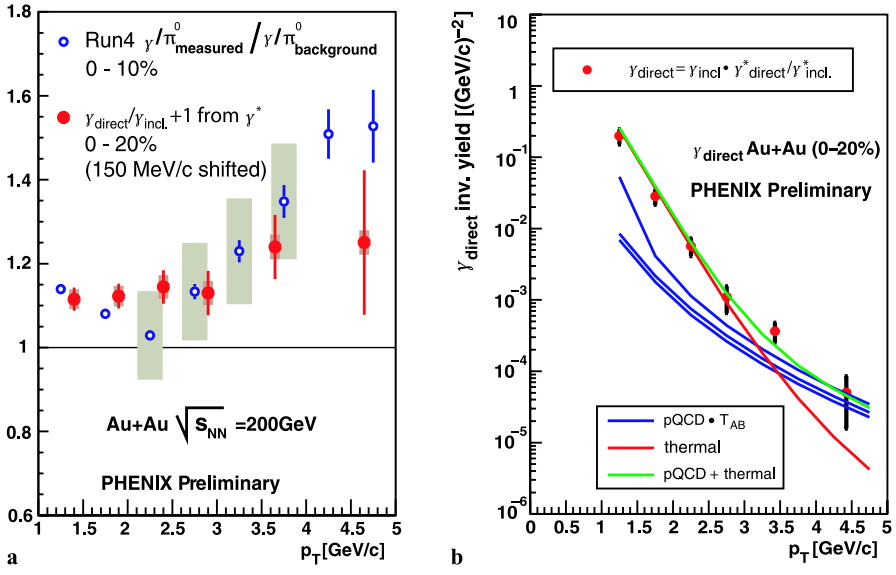

Fig. 5. **a** Direct photon excess for the conventional and the internal-conversion measurement in central Au + Au collisions [14]; **b** direct photon spectrum from the latter [14] compared to pQCD [7], thermal-photon [15], and the sum of both calculations

culation over the entire range of the measurement from 5 GeV $\leq p_{\mathrm{T}} \leq$ 16 GeV/c. In d + Au collisions, no indications for cold nuclear matter effects are found within the large uncertainties of the measurement. A high statistics d + Au run is planned. High p_{T} direct photon production in Au + Au collisions is found to scale with the nuclear overlap function T_{AA}, establishing medium effects as the cause for the hadron suppression observed in central Au + Au collisions.

At low p_{T} ($1 \leq p_{\mathrm{T}} \leq 5$ GeV/c) a significant direct photon excess above the decay photon background is observed employing a new method in heavy ion collisions, which measures low invariant mass e^+e^- pairs from direct photon internal conversions. The signal appears to be above pQCD calculations for $p_{\mathrm{T}} \leq 3$ GeV/c, whose applicability is questionable, however, at this low p_{T}. If a thermal photon source modeled by hydrodynamical calculations is added to the pQCD calculation, the data can be described over the entire p_{T} range. Other direct photon sources like jet-plasma interactions might play a significant role as well.

References

1. S. Turbide, R. Rapp, C. Gale, Phys. Rev. C **69**, 014903 (2004)
2. C. Gale, Nucl. Phys. A **774**, 335 (2006)
3. S.S. Adler et al., Phys. Rev. Lett. **91**, 072301 (2003)
4. S.S. Adler et al., Phys. Rev. Lett. **96**, 202301 (2006)
5. L. Aphecetche et al., Nucl. Instrum. Methods A **499**, 521 (2003)
6. K. Okada, hep-ex/0501066 (2005)
7. L.E. Gordon, W. Vogelsang, Phys. Rev. D **48**, 3136 (1993)
8. S.S. Adler et al., Phys. Rev. Lett. **94**, 232301 (2005)
9. J.H. Cobb et al., Phys. Lett. B **78**, 519 (1978)
10. C. Albajar, et al., Phys. Lett. B **209**, 397 (1988)
11. N.M. Kroll, W. Wada, Phys. Rev. **98**, 1355 (1955)
12. K. Adcox et al., Phys. Rev. C **69**, 024904 (2004)
13. S.S. Adler, et al., Phys. Rev. Lett. **94**, 082301 (2005)
14. S. Bathe, Nucl. Phys. A **774**, 731 (2006)
15. D. d'Enterria, D. Peressounko, nucl-th/0503054 (2005)
16. J. Alam, J.K. Nayak, P. Roy, A.K. Dutt-Mazumder, B. Sinha, nucl-th/0508043 (2005)
17. A.K. Chaudhuri, nucl-th/0512032 (2005)

Measurement of single muons at forward rapidity in $p + p$ collisions at $\sqrt{s} = 200$ GeV and implications for charm production

S. S. Adler,[5] S. Afanasiev,[17] C. Aidala,[5] N. N. Ajitanand,[43] Y. Akiba,[20,38] J. Alexander,[43] R. Amirikas,[12] L. Aphecetche,[45] S. H. Aronson,[5] R. Averbeck,[44] T. C. Awes,[35] R. Azmoun,[44] V. Babintsev,[15] A. Baldisseri,[10] K. N. Barish,[6] P. D. Barnes,[27] B. Bassalleck,[33] S. Bathe,[30] S. Batsouli,[9] V. Baublis,[37] A. Bazilevsky,[39,15] S. Belikov,[16,15,*] Y. Berdnikov,[40] S. Bhagavatula,[16] J. G. Boissevain,[27] H. Borel,[10] S. Borenstein,[25] M. L. Brooks,[27] D. S. Brown,[34] N. Bruner,[33] D. Bucher,[30] H. Buesching,[30] V. Bumazhnov,[15] G. Bunce,[5,39] J. M. Burward-Hoy,[26,44] S. Butsyk,[44] X. Camard,[45] J.-S. Chai,[18] P. Chand,[4] W. C. Chang,[2] S. Chernichenko,[15] C. Y. Chi,[9] J. Chiba,[20] M. Chiu,[9] I. J. Choi,[52] J. Choi,[19] R. K. Choudhury,[4] T. Chujo,[5] V. Cianciolo,[35] Y. Cobigo,[10] B. A. Cole,[9] P. Constantin,[16] D. d'Enterria,[45] G. David,[5] H. Delagrange,[45] A. Denisov,[15] A. Deshpande,[39] E. J. Desmond,[5] A. Devismes,[44] O. Dietzsch,[41] O. Drapier,[25] A. Drees,[44] K. A. Drees,[5] R. du Rietz,[29] A. Durum,[15] D. Dutta,[4] Y. V. Efremenko,[35] K. El Chenawi,[49] A. Enokizono,[14] H. En'yo,[38,39] S. Esumi,[48] L. Ewell,[5] D. E. Fields,[33,39] F. Fleuret,[25] S. L. Fokin,[23] B. D. Fox,[39] Z. Fraenkel,[51] J. E. Frantz,[9] A. Franz,[5] A. D. Frawley,[12] S.-Y. Fung,[6] S. Garpman,[29,*] T. K. Ghosh,[49] A. Glenn,[46] G. Gogiberidze,[46] M. Gonin,[25] J. Gosset,[10] Y. Goto,[39] R. Granier de Cassagnac,[25] N. Grau,[16] S. V. Greene,[49] M. Grosse Perdekamp,[39] W. Guryn,[5] H.-Å. Gustafsson,[29] T. Hachiya,[14] J. S. Haggerty,[5] H. Hamagaki,[8] A. G. Hansen,[27] E. P. Hartouni,[26] M. Harvey,[5] R. Hayano,[8] N. Hayashi,[38] X. He,[13] M. Heffner,[26] T. K. Hemmick,[44] J. M. Heuser,[44] M. Hibino,[50] J. C. Hill,[16] W. Holzmann,[43] K. Homma,[14] B. Hong,[22] A. Hoover,[34] D. Hornback,[46] T. Ichihara,[38,39] V. V. Ikonnikov,[23] K. Imai,[24,38] D. Isenhower,[1] M. Ishihara,[38] M. Issah,[43] A. Isupov,[17] B. V. Jacak,[44] W. Y. Jang,[22] Y. Jeong,[19] J. Jia,[44] O. Jinnouchi,[38] B. M. Johnson,[5] S. C. Johnson,[26] K. S. Joo,[31] D. Jouan,[36] S. Kametani,[8,50] N. Kamihara,[38,47] J. H. Kang,[52] S. S. Kapoor,[4] K. Katou,[50] S. Kelly,[9] B. Khachaturov,[51] A. Khanzadeev,[37] J. Kikuchi,[50] D. H. Kim,[31] D. J. Kim,[52] D. W. Kim,[19] E. Kim,[42] G.-B. Kim,[25] H. J. Kim,[52] E. Kistenev,[5] A. Kiyomichi,[48] K. Kiyoyama,[32] C. Klein-Boesing,[30] H. Kobayashi,[38,39] L. Kochenda,[37] V. Kochetkov,[15] D. Koehler,[33] T. Kohama,[14] M. Kopytine,[44] D. Kotchetkov,[6] A. Kozlov,[51] P. J. Kroon,[5] C. H. Kuberg,[1,27,*] K. Kurita,[39] Y. Kuroki,[48] M. J. Kweon,[22] Y. Kwon,[52] G. S. Kyle,[34] R. Lacey,[43] V. Ladygin,[17] J. G. Lajoie,[16] A. Lebedev,[16,23] S. Leckey,[44] D. M. Lee,[27] S. Lee,[19] M. J. Leitch,[27] X. H. Li,[6] H. Lim,[42] A. Litvinenko,[17] M. X. Liu,[27] Y. Liu,[36] C. F. Maguire,[49] Y. I. Makdisi,[5] A. Malakhov,[17] V. I. Manko,[23] Y. Mao,[7,38] G. Martinez,[45] M. D. Marx,[44] H. Masui,[48] F. Matathias,[44] T. Matsumoto,[8,50] P. L. McGaughey,[27] E. Melnikov,[15] F. Messer,[44] Y. Miake,[48] J. Milan,[43] T. E. Miller,[49] A. Milov,[44,51] S. Mioduszewski,[5] R. E. Mischke,[27] G. C. Mishra,[13] J. T. Mitchell,[5] A. K. Mohanty,[4] D. P. Morrison,[5] J. M. Moss,[27] F. Mühlbacher,[44] D. Mukhopadhyay,[51] M. Muniruzzaman,[6] J. Murata,[38,39] S. Nagamiya,[20] J. L. Nagle,[9] T. Nakamura,[14] B. K. Nandi,[6] M. Nara,[48] J. Newby,[46] P. Nilsson,[29] A. S. Nyanin,[23] J. Nystrand,[29] E. O'Brien,[5] C. A. Ogilvie,[16] H. Ohnishi,[5,38] I. D. Ojha,[3,49] K. Okada,[38] M. Ono,[48] V. Onuchin,[15] A. Oskarsson,[29] I. Otterlund,[29] K. Oyama,[8] K. Ozawa,[8] D. Pal,[51] A. P. T. Palounek,[27] V. Pantuev,[44] V. Papavassiliou,[34] J. Park,[42] A. Parmar,[33] S. F. Pate,[34] T. Peitzmann,[30] J.-C. Peng,[27] V. Peresedov,[17] C. Pinkenburg,[5] R. P. Pisani,[5] F. Plasil,[35] M. L. Purschke,[5] A. K. Purwar,[44] J. Rak,[16] I. Ravinovich,[51] K. F. Read,[35,46] M. Reuter,[44] K. Reygers,[30] V. Riabov,[37,40] Y. Riabov,[37] G. Roche,[28] A. Romana,[25,*] M. Rosati,[16] P. Rosnet,[28] S. S. Ryu,[52] M. E. Sadler,[1] N. Saito,[38,39] T. Sakaguchi,[8,50] M. Sakai,[32] S. Sakai,[48] V. Samsonov,[37] L. Sanfratello,[33] R. Santo,[30] H. D. Sato,[24,38] S. Sato,[5,48] S. Sawada,[20] Y. Schutz,[45] V. Semenov,[15] R. Seto,[6] M. R. Shaw,[1,27] T. K. Shea,[5] T.-A. Shibata,[38,47] K. Shigaki,[14,20] T. Shiina,[27] C. L. Silva,[41] D. Silvermyr,[27,29] K. S. Sim,[22] C. P. Singh,[3] V. Singh,[3] M. Sivertz,[5] A. Soldatov,[15] R. A. Soltz,[26] W. E. Sondheim,[27] S. P. Sorensen,[46] I. V. Sourikova,[5] F. Staley,[10] P. W. Stankus,[35] E. Stenlund,[29] M. Stepanov,[34] A. Ster,[21] S. P. Stoll,[5] T. Sugitate,[14] J. P. Sullivan,[27] E. M. Takagui,[41] A. Taketani,[38,39] M. Tamai,[50] K. H. Tanaka,[20] Y. Tanaka,[32] K. Tanida,[38] M. J. Tannenbaum,[5] P. Tarján,[11] J. D. Tepe,[1,27] T. L. Thomas,[33] J. Tojo,[24,38] H. Torii,[24,38] R. S. Towell,[1] I. Tserruya,[51] H. Tsuruoka,[48] S. K. Tuli,[3] H. Tydesjö,[29] N. Tyurin,[15] H. W. van Hecke,[27] J. Velkovska,[5,44] M. Velkovsky,[44] V. Veszprémi,[11] L. Villatte,[46] A. A. Vinogradov,[23] M. A. Volkov,[23] E. Vznuzdaev,[37] X. R. Wang,[13] Y. Watanabe,[38,39] S. N. White,[5] F. K. Wohn,[16] C. L. Woody,[5] W. Xie,[6] Y. Yang,[7] A. Yanovich,[15] S. Yokkaichi,[38,39] G. R. Young,[35] I. E. Yushmanov,[23] W. A. Zajc,[9,†] C. Zhang,[9] S. Zhou,[7] S. J. Zhou,[51] and L. Zolin[17]

(PHENIX Collaboration)

[1]*Abilene Christian University, Abilene, Texas 79699, USA*
[2]*Institute of Physics, Academia Sinica, Taipei 11529, Taiwan*
[3]*Department of Physics, Banaras Hindu University, Varanasi 221005, India*
[4]*Bhabha Atomic Research Centre, Bombay 400 085, India*

 © 2007 The American Physical Society

[5]*Brookhaven National Laboratory, Upton, New York 11973-5000, USA*
[6]*University of California-Riverside, Riverside, California 92521, USA*
[7]*China Institute of Atomic Energy (CIAE), Beijing, People's Republic of China*
[8]*Center for Nuclear Study, Graduate School of Science, University of Tokyo, 7-3-1 Hongo, Bunkyo, Tokyo 113-0033, Japan*
[9]*Columbia University, New York, New York 10027*
and Nevis Laboratories, Irvington, New York 10533, USA
[10]*Dapnia, CEA Saclay, F-91191, Gif-sur-Yvette, France*
[11]*Debrecen University, H-4010 Debrecen, Egyetem tér 1, Hungary*
[12]*Florida State University, Tallahassee, Florida 32306, USA*
[13]*Georgia State University, Atlanta, Georgia 30303, USA*
[14]*Hiroshima University, Kagamiyama, Higashi-Hiroshima 739-8526, Japan*
[15]*Institute for High Energy Physics (IHEP), Protvino, Russia*
[16]*Iowa State University, Ames, Iowa 50011, USA*
[17]*Joint Institute for Nuclear Research, 141980 Dubna, Moscow Region, Russia*
[18]*KAERI, Cyclotron Application Laboratory, Seoul, South Korea*
[19]*Kangnung National University, Kangnung 210-702, South Korea*
[20]*KEK, High Energy Accelerator Research Organization, Tsukuba-shi, Ibaraki-ken 305-0801, Japan*
[21]*KFKI Research Institute for Particle and Nuclear Physics (RMKI), H-1525 Budapest 114, POBox 49, Hungary*
[22]*Korea University, Seoul, 136-701, Korea*
[23]*Russian Research Center "Kurchatov Institute", Moscow, Russia*
[24]*Kyoto University, Kyoto 606-8502, Japan*
[25]*Laboratoire Leprince-Ringuet, Ecole Polytechnique, CNRS-IN2P3, Route de Saclay, F-91128, Palaiseau, France*
[26]*Lawrence Livermore National Laboratory, Livermore, California 94550, USA*
[27]*Los Alamos National Laboratory, Los Alamos, New Mexico 87545, USA*
[28]*LPC, Université Blaise Pascal, CNRS-IN2P3, Clermont-Fd, 63177 Aubiere Cedex, France*
[29]*Department of Physics, Lund University, Box 118, SE-221 00 Lund, Sweden*
[30]*Institut für Kernphysik, University of Muenster, D-48149 Muenster, Germany*
[31]*Myongji University, Yongin, Kyonggido 449-728, Korea*
[32]*Nagasaki Institute of Applied Science, Nagasaki-shi, Nagasaki 851-0193, Japan*
[33]*University of New Mexico, Albuquerque, New Mexico 87131, USA*
[34]*New Mexico State University, Las Cruces, New Mexico 88003, USA*
[35]*Oak Ridge National Laboratory, Oak Ridge, Tennessee 37831, USA*
[36]*IPN-Orsay, Universite Paris Sud, CNRS-IN2P3, BP1, F-91406, Orsay, France*
[37]*PNPI, Petersburg Nuclear Physics Institute, Gatchina, Russia*
[38]*RIKEN (The Institute of Physical and Chemical Research), Wako, Saitama 351-0198, Japan*
[39]*RIKEN BNL Research Center, Brookhaven National Laboratory, Upton, New York 11973-5000, USA*
[40]*St. Petersburg State Technical University, St. Petersburg, Russia*
[41]*Universidade de São Paulo, Instituto de Física, Caixa Postal 66318, São Paulo CEP05315-970, Brazil*
[42]*System Electronics Laboratory, Seoul National University, Seoul, South Korea*
[43]*Chemistry Department, Stony Brook University, SUNY, Stony Brook, New York 11794-3400, USA*
[44]*Department of Physics and Astronomy, Stony Brook University, SUNY, Stony Brook, New York 11794, USA*
[45]*SUBATECH (Ecole des Mines de Nantes, CNRS-IN2P3, Université de Nantes) BP 20722 - 44307, Nantes, France*
[46]*University of Tennessee, Knoxville, Tennessee 37996, USA*
[47]*Department of Physics, Tokyo Institute of Technology, Tokyo, 152-8551, Japan*
[48]*Institute of Physics, University of Tsukuba, Tsukuba, Ibaraki 305, Japan*
[49]*Vanderbilt University, Nashville, Tennessee 37235, USA*
[50]*Waseda University, Advanced Research Institute for Science and Engineering, 17 Kikui-cho, Shinjuku-ku, Tokyo 162-0044, Japan*
[51]*Weizmann Institute, Rehovot 76100, Israel*
[52]*Yonsei University, IPAP, Seoul 120-749, Korea*

(Received 18 September 2006; revised manuscript received 21 May 2007; published 13 November 2007)

Muon production at forward rapidity ($1.5 \leq |\eta| \leq 1.8$) has been measured by the PHENIX experiment over the transverse momentum range $1 \leq p_T \leq 3$ GeV/c in $\sqrt{s} = 200$ GeV $p + p$ collisions at the Relativistic Heavy Ion Collider. After statistically subtracting contributions from light hadron decays an excess remains which is attributed to the semileptonic decays of hadrons carrying heavy flavor, i.e. charm quarks or, at high p_T, bottom quarks. The resulting muon spectrum from heavy flavor decays is compared to PYTHIA and a next-to-leading-order perturbative QCD calculation. PYTHIA is used to determine the

[*]Deceased.
[†]PHENIX Spokesperson; zajc@nevis.columbia.edu

charm quark spectrum that would produce the observed muon excess. The corresponding differential cross section for charm quark production at forward rapidity is determined to be $d\sigma_{c\bar{c}}/dy|_{y=1.6} = 0.243 \pm 0.013(\text{stat.}) \pm 0.105(\text{data syst.}) \,^{+0.049}_{-0.087}\,(\text{PYTHIA syst.})$ mb.

DOI: 10.1103/PhysRevD.76.092002 PACS numbers: 13.85.Qk, 13.20.Fc, 13.20.He, 25.75.Dw

I. INTRODUCTION

Measurements of heavy quark production in proton-proton ($p + p$) interactions at collider energies serve as important tests for perturbative quantum chromodynamics (pQCD). Bottom production at the Tevatron collider ($\sqrt{s} =$ 1.8 and 1.96 TeV) [1,2] is reasonably well described by a recent fixed order next-to-leading logarithm (FONLL) calculation [3–5]. Charm production at FNAL, which has only been measured at relatively high p_T (> 5 GeV/c), is $\approx 50\%$ higher than the FONLL prediction [6]. However, theoretical and experimental uncertainties are large, such that significant disagreement between theory and data cannot be claimed.

Measurements at Brookhaven National Laboratory's Relativistic Heavy Ion Collider (RHIC), by both the PHENIX and STAR experiments, have provided a wealth of information on midrapidity open charm production in collisions at $\sqrt{s_{NN}} = 130$ GeV ($p + p$) and $\sqrt{s_{NN}} =$ 200 GeV ($p + p$, $d + Au$, and $Au + Au$) down to $p_T \approx$ 0.5 GeV/c. Semileptonic decay of produced charm quarks is the primary source of high p_T leptons after contributions from known (light hadron) sources are subtracted. Both PHENIX [7–16] and STAR [17,18] have made statistical measurements of charm production via single-electron spectra. STAR has also made a direct measurement of charm production through reconstruction of hadronic decay modes of D mesons [17]. In $p + p$ collisions at $\sqrt{s_{NN}} = 200$ GeV PHENIX finds $d\sigma_{c\bar{c}}/dy|_{y=0} = 0.123 \pm 0.012(\text{stat.}) \pm 0.045(\text{syst.})$ mb [13]. STAR finds a somewhat higher central value, $d\sigma_{c\bar{c}}/dy|_{y=0} = 0.30 \pm 0.04(\text{stat.}) \pm 0.09(\text{syst.})$ mb [17], but the two measurements are consistent within the stated uncertainties. Both measurements are noticeably (2–4 $\times$) higher than PYTHIA (a leading order pQCD event generator) [19] [see experimental references for specific parameter sets] and FONLL [20]. Again, quantitative disagreement cannot be established with current experimental and theoretical uncertainties. However, we note that there is some debate about whether charm quarks are heavy enough to be reliably treated by pQCD [21].

Such measurements also serve as an important baseline for charm production in proton-nucleus or deuteron-nucleus ($p + A$ or $d + A$), and nucleus-nucleus ($A + B$) collisions [22–25]. In the absence of any nuclear effects, charm production (since it is a pointlike process) is expected to scale with the number of binary nucleon-nucleon collisions (N_{coll}), which depends on the impact parameter of the nuclear collision and can be obtained from a Glauber calculation [26]. The degree of scaling for any given centrality bin is quantified by the nuclear modification factor:

$$R_{AB} = \frac{1}{N^{AB}_{\text{coll}}} \times \frac{dN^{AB}/dy}{dN^{pp}/dy}. \quad (1)$$

Deviations from this scaling ($R_{AB} \neq 1$) in $p + A$ or $d + A$ collisions quantify cold nuclear matter effects (such as initial state energy loss [27–32], and shadowing [33–37]). Any such deviation must be understood so that in $A + B$ collisions contributions to $R_{AB} \neq 1$ from hot nuclear matter effects (such as in-medium energy loss [[38] and references therein] and cold nuclear matter effects can be disentangled. In $d + Au$ collisions both PHENIX and STAR find little or no effect of cold nuclear matter on charm production ($R_{dAu} \approx 1$ over the measured lepton p_T [10,17]). This contrasts with measurements of open charm in $Au + Au$ collisions: although the *total* charm production appears to scale with N_{coll} [8], there is a strong suppression of lepton spectra for $p_T > 2$ GeV/c that increases with centrality [11,12,18]. Furthermore the elliptical flow of nonphotonic single electrons, as measured by PHENIX in $Au + Au$ collisions [14–16], implies that the charm quarks interact strongly with the created medium.

Finally, since the initial formation of open and closed charm are both sensitive to initial gluon densities [39,40], open charm production serves as an appropriate normalization for J/ψ production. The production of J/ψ mesons is expected to be sensitive to the production of a quark gluon plasma (QGP), should one be formed in $A + B$ collisions [41–46]. In order to understand J/ψ production differences in $A + B$ collisions compared to $p + p$ and $p + A$ collisions it is important to take into account any differences in the charm quark production in each of the different systems.

Until now, open charm measurements at RHIC have been limited to midrapidity. Measurements at forward rapidity are interesting for a variety of reasons. First is the need to constrain theoretical calculations over a wide kinematic range. The importance of this is demonstrated by the D0 measurement of bottom production at large rapidity ($\sqrt{s} = 1.8$ TeV, $p_T > 5$ GeV/c, $2.4 < y_\mu < 3.2$), as deduced from the production of high p_T muons [1]. Significant theoretical improvements resulted from the effort to reduce what was, initially, a discrepancy between theory and experiment that increased with increasing rapidity [5]. Second, significant cold nuclear effects have been seen in RHIC collisions at forward rapidity. PHENIX [47], BRAHMS [48,49], and STAR [50] have all measured light hadron production in $d + Au$ collisions at forward

rapidity and have found significant deviations from $R_{dAu} = 1$. It will be interesting to see whether charm production follows a similar pattern. Finally, open charm production at forward rapidity needs to be understood to fully interpret PHENIX J/ψ measurements at forward rapidity [24,25,51–53].

In this paper we report on the measurement of muon production at forward rapidity ($1.5 \leq |\eta| \leq 1.8$), in the range $1 < p_T < 3$ GeV/c, in $\sqrt{s} = 200$ GeV $p + p$ collisions by the PHENIX experiment. The upper limit of the p_T range is determined by available statistics. The vertex-independent muon yield is statistically extracted by calculating and subtracting contributions from light mesons (π's and K's) which decay into a muon, and hadrons which penetrate through the muon arm absorber material. In the absence of new physics, and in the p_T range measured in this analysis, such muons come dominantly from the decay of hadrons containing a charm quark (with small contributions from decays of hadrons containing a bottom quark and decays of light-vector mesons). PYTHIA is used to determine the charm quark spectrum that would produce the observed vertex-independent muon spectrum, and from this we obtain the differential cross section of charm quark production at forward rapidity. Although the statistical and systematic errors in this analysis preclude strong conclusions about the details of charm production, this paper establishes a method to extract this information from future PHENIX data sets.

The remainder of this paper is organized as follows: In Sec. II we describe the PHENIX experimental apparatus, with special emphasis on the muon arm detectors. In Sec. III we describe the methodology used to extract the vertex-independent muon signal. This section includes details on the run, event, and track selection criteria; values obtained for contributions to the muon yield from abundant light hadrons, which are subtracted to obtain the vertex-independent muon yield; and details on the systematic error analysis. In Sec. IV we extract the differential cross section for charm production at $y = 1.6$, integrated over p_T. Finally, in Sec. V we compare to other measurements, draw conclusions, and discuss the prospects for such measurements with improved data sets currently under analysis.

II. THE PHENIX EXPERIMENT

The PHENIX experiment [54], shown in Fig. 1, is a large multipurpose set of detectors optimized for measuring relatively rare electromagnetic probes (photons, muons, and electrons) of the spin structure of the proton and of the hot dense matter created in ultrarelativistic heavy ion collisions. The data acquisition system and multilevel triggers are designed to handle the very different challenges presented by $p + p$ collisions (relatively small events at very high rates) and $Au + Au$ collisions (very large events at relatively low rates) with little or no dead time [55,56].

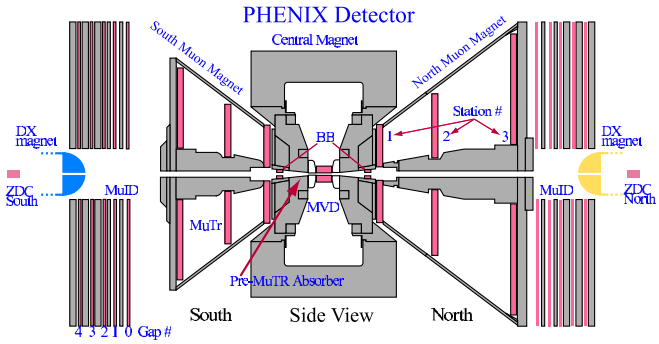

FIG. 1 (color online). Elevation view of the PHENIX experimental layout during the 2001/2 run period.

Event characterization devices, such as the beam-beam counters (BBCs) [57] used in this analysis, provide information on the vertex position, start time, and centrality of the collision. The two muon arms cover $1.2 < |\eta| < 2.4$ in pseudorapidity and $\delta\phi = 2\pi$ in azimuth. The two central arms, which each cover $|\eta| < 0.35$ and $\delta\phi = \pi/2$, are not used in this analysis.

The BBCs [57] each consist of 64 quartz radiators instrumented with mesh dynode photomultiplier tubes (PMTs) and arranged in a cylinder coaxial with the beam. The BBCs are placed on either side of the collision vertex and cover $3.0 < |\eta| < 3.9$. Each channel has a dynamic range extending to 30 times the average energy deposit of a minimum ionizing particle. The BBCs measure the arrival times of particles on both sides of the collision vertex, t_S and t_N. From the average of these times we determine the event start time. From their difference we obtain the position of the vertex along the beam direction, z_{vtx}. The BBCs also provide the minimum bias interaction trigger, which requires that there be at least one hit in each BBC and that $|z_{vtx}| < 38$ cm.

The muon arms [58] are coaxial with the beam on opposite sides of the collision vertex. By convention the arm on the south (north) end of the interaction region is assigned negative (positive) z coordinates and rapidity. For the 2001/2 run period, in which the data for this paper were collected, only the south muon arm was operational. Each muon arm is comprised of a muon tracker (MuTR) and a muon identifier (MuID). The MuTR makes an accurate measurement of particle momenta. The MuID allows coarse resolution track reconstruction through a significant amount of steel absorber. Together the muon arm detectors provide significant pion rejection (> 250:1, increasing with decreasing momentum) through a momentum/penetration-depth match.

Before ever reaching the MuTR detectors a particle must pass through the pre-MuTR absorber: 20 cm of copper (the nosecone) plus 60 cm of iron (part of the MuTR magnet). The nominal nuclear interaction lengths of iron and copper are $\lambda_I^{\mathrm{Fe}} = 16.7$ cm and $\lambda_I^{\mathrm{Cu}} = 15.3$ cm (although this varies with particle species and energy, see Sec. III F).

Therefore the pre-MuTR absorber presents a total thickness of $4.9\lambda_I/\cos\theta$, where θ is the polar angle of a particle's trajectory. This absorber greatly reduces the MuTR occupancy and provides the first level of pion rejection.

Each MuTR arm consists of three stations of cathode strip chambers installed in an eight-sided conical magnet [59]. The radial magnetic field ($\int \mathbf{B} \cdot \mathbf{dl} = 0.72$ T $\cdot$ m at 15 degrees, $B(\theta) \approx B(15°)\tan(\theta)/\tan(15°)$) bends particles in the azimuthal direction. Each station occupies a plane perpendicular to the beam axis and consists of multiple ionization gaps (3 gaps for the two stations closest to the collision vertex, 2 gaps for the last station) which have their charge imaged on two cathode strip planes oriented with a small stereo angle to provide two-dimensional information. An ionizing particle typically fires three adjacent strips in each orientation. A fit to the charge distribution on adjacent strips provides a position measurement with a resolution of $\sigma \approx 100$ μm in the bend direction. The MuTR achieves a momentum resolution of $\sigma_p/p \approx 5\%$, nearly independent of momentum over the analyzed kinematic range. The momentum independence is due to the significant contribution from energy-loss fluctuations in the pre-MuTR absorber, which falls as $1/p$, and which counters the more familiar linear momentum dependence seen for particles tracked through a ''thin'' detector.

Each MuID arm consists of five steel absorber plates interleaved with Iarocci tubes (operated in proportional mode) and specialized shielding to reduce backgrounds not originating from the collision vertex. Gaps are labeled 0–4 proceeding downstream from the collision point.

The Iarocci tubes, which are between 2.5 and 5 m in length, have eight 1 cm^2 square cells, each consisting of a three-sided ground electrode and an anode wire, mounted inside a polyvinyl chloride (PVC) gas enclosure. A readout channel (''two-pack'') is formed by wire-ORing the 16 anode wires of two tubes which are mounted in planes perpendicular to the beam axis and staggered by half of a cell width (0.5 cm). This provides redundancy, eliminates geometric inefficiency due to the cell walls, and reduces the maximum drift time for charge collection. Discriminator outputs from the two-pack signals provide a coarse one-dimensional hit position ($\sigma = 9$ cm$/\sqrt{12} = 2.6$ cm). The tubes in each gap are mounted in six individual panels, each of which contains two layers of two-packs (horizontally and vertically oriented), thus providing two-dimensional information.

The first MuID absorber plate (thickness = 20 cm—south; 30 cm—north) also serves as the return yoke of the MuTR magnet. Successive plates (identical for the two arms) are 10, 10, 20, and 20 cm thick, thus totaling $4.8\lambda_I/\cos\theta$ ($5.4\lambda_I/\cos\theta$) for the south (north) arm. Because of ionization energy loss a particle must have a momentum at the vertex which exceeds $2.31\cos\theta$ GeV$/c$ ($2.45\cos\theta$ GeV$/c$) to penetrate to the most downstream MuID gap of the south (north) arm.

Steel plates surrounding the beam pipe guard against backgrounds caused by low-angle beam-beam collision products which scrape the beam pipe near the MuID z-location (7–9 m) or shine off the RHIC dipole steering magnets immediately downstream of each MuID arm. Steel blocks in the RHIC tunnels guard against penetrating radiation generated by the incoming beams scraping against beamline components, primarily the final focusing quadrupole magnets.

The MuID also contributes information to the first-level trigger decision. For the 2001/2 run, during which the data for this analysis were collected, a relatively coarse trigger was implemented using memory lookup units (MLUs). Each gap was divided into quadrants with a horizontal and vertical split going through the beam axis. Signals from tubes in an individual gap/orientation (layer) and quadrant were logically combined. Only gaps 0, 2, 3, and 4 were used in the trigger due to the 16-bit input limitation of the MLUs. The penetration depth required for the trigger to fire was programmable. The *M1D* trigger fired if more than 6 out of 8 layers in a particular quadrant were hit (indicating the possibility that the event contained a particle penetrating to MuID gap 4). The *M1S* trigger fired if 3 of the 4 most shallow layers (horizontal and vertical layers in gaps 0 and 2) were hit for a particular quadrant. Both triggers required a coincidence with the BBC minimum bias trigger.

III. METHOD FOR EXTRACTION OF MUONS FROM CHARM DECAY

Inclusive muon candidates, N_I, are those particles which are successfully reconstructed to the last MuID gap (gap 4). These consist of four components:

(1) ''free-decay muons,'' N_D, which result from the decay of light hadrons (π and K mesons) before reaching the pre-MuTR absorber.
(2) ''punchthrough hadrons,'' N_P, which penetrate the entire detector and are thus misidentified as muons.
(3) ''background tracks,'' N_B, which in $p + p$ collisions are dominated by hadrons which decay into a muon after reaching the MuTR.
(4) ''vertex-independent muons,'' N_μ, which are primarily due to the decay of heavy flavor mesons.

Figure 2 shows a schematic depiction of the relative yield per event of these different contributions as a function of flightpath into the muon arms, as described below.

The number of hadrons is large and essentially independent of flightpath until the first absorber layer is reached. In each absorber layer these hadrons undergo strong interactions with a probability $\mathcal{P} \approx 1 - \exp(-L/\lambda)$, where L is the length of absorber material traversed, and λ is the species and p_T-dependent nuclear interaction length determined in Sec. III F. The punchthrough hadrons are that small fraction of hadrons ($< 0.4\%$) which penetrate to the last MuID gap and are indistinguishable from muons.

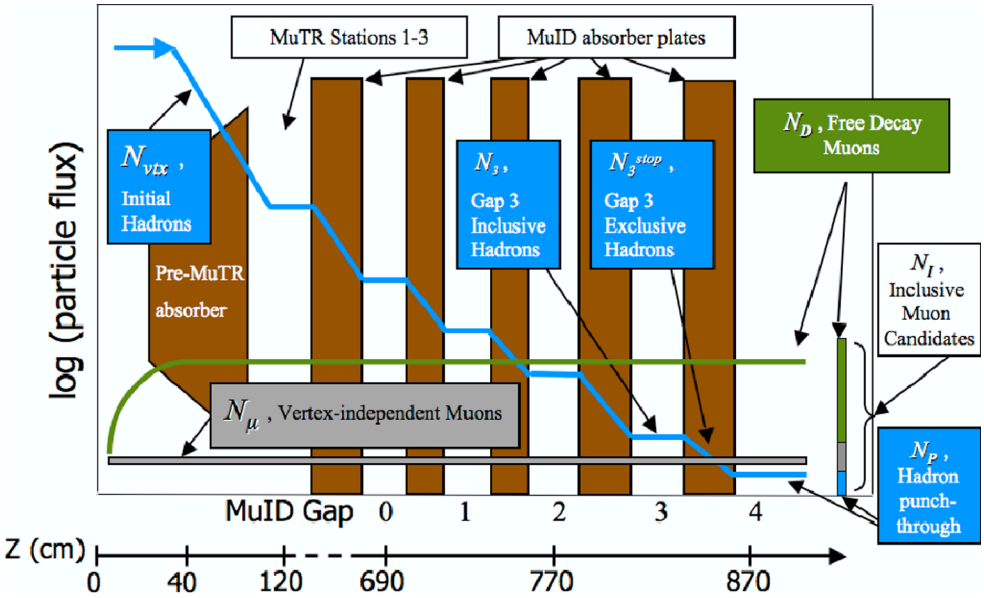

FIG. 2 (color online). Schematic depiction of the relative flux of different components of the inclusive muon candidate yield as a function of flightpath into the muon arm absorber (the nominal event vertex is at $z = 0$). See text for details.

The decay lengths for π's ($c\tau = 780$ cm) and K's ($c\tau = 371$ cm) are long compared to the flightpath from the vertex to the absorber. Therefore, the fraction of decay muons from these sources is relatively small, but increases linearly with the flightpath until the first absorber layer is reached. A hadron which decays prior to the pre-MuTR absorber into a muon that is inside the detector acceptance is indistinguishable from a muon originating at the vertex. After the first absorber layer the number of these free-decay muons remains constant by definition.

Hadrons which decay in the MuTR volume are a relatively small contribution for several reasons: most are absorbed prior to reaching the MuTR; the Lorentz-dilated decay lengths are long compared to the length of the MuTR volume (south ≈ 280 cm, north ≈ 420 cm); and a particle which decays in the MuTR is less likely to be reconstructed. Such tracks are partially accounted for in the calculation of punchthrough hadrons (see Sec. III F) and the remaining fraction falls under the category of background tracks (Sec. III G). This small contribution is not shown in Fig. 2.

Without a high-resolution vertex detector muons from various sources (the decay of open heavy flavor hadrons, the decay of quarkonia, the decay of light-vector mesons, and Drell-Yan production) originate indistinguishably close to the collision vertex. Thus their yield is independent of the flightpath and independent of the vertex position. Since inclusive muon candidates, by definition, penetrate to MuID gap 4, we measure the combined yield at $z \approx 870$ cm.

Figure 3 shows a sample distribution of the inclusive muon candidate yield as a function of collision vertex (z_{vtx}), and its decomposition into the four different contributions. The yield of free-decay muons is seen to have a linear dependence that is set to 0 at $z_{vtx} = z_{abs} - \lambda_D$. Here $z_{abs} = -40$ cm is the upstream face of the pre-MuTR absorber (indicated by the thick solid line), and λ_D is the effective absorption length, beyond which there are no free-decay muons. λ_D was found to be within a few mm of the species and p_T-dependent nuclear interaction lengths determined in Sec. III F. Muons originating from meson decays downstream of this location have no z_{vtx}

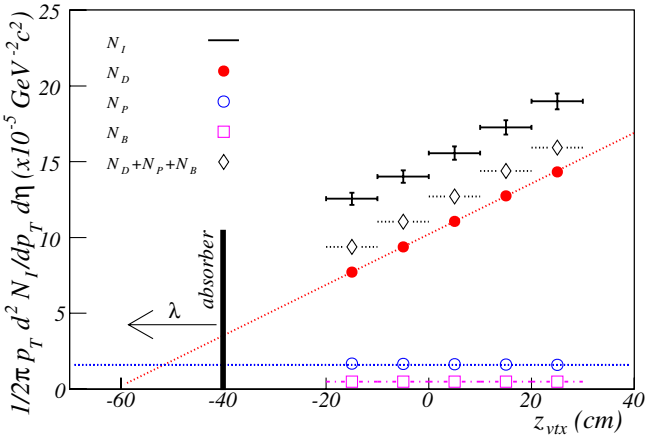

FIG. 3 (color online). Sample z_{vtx} distribution of different components of the inclusive muon candidate yield (measured data for both charge signs over the range $1.0 < p_T < 1.2$ GeV/c). Crosses show inclusive muon candidates, filled circles show free-decay muons, open circles show punchthrough hadrons, open squares show background tracks, and open diamonds show the sum of these three hadronic sources. The vertex-independent muon yield is obtained from the difference between the yield of inclusive muon candidates and the yield of light-hadronic sources.

dependence. The fraction not accounted for in the calculation of the punchthrough hadron yield forms the small contribution from background tracks. The yield of punchthrough hadrons and vertex-independent muons also have no z_{vtx} dependence. Note that the ratio of different contributions to the inclusive muon candidate spectrum is p_T dependent.

In order to extract the cross section for charm production we first need to determine the yield of vertex-independent muons, $N_\mu(p_T)$, the amount beyond that which is due to light hadrons and fake backgrounds. As described in Sec. III A, we select good runs, events, and tracks, and restrict our acceptance to regions where the detector was fully active, and the acceptance variation versus z_{vtx} was negligible. Next, as described in Secs. III B and III C, we obtain the yield of inclusive muon candidates vs p_T and z_{vtx}, corrected for acceptance and efficiency: $N_I(p_T, z_{vtx})$. In Sec. III D we describe a data-driven hadron generator. This generator is used in Sec. III E, in which we describe how the vertex dependence of the inclusive muon candidate yield allows us to obtain the yield of muons from light-meson decay before the pre-MuTR absorber, similarly corrected and binned: $N_D(p_T, z_{vtx})$. This generator is also used in Sec. III F, in which we describe how we use hadrons which stop in MuID gap 3 (the penultimate gap), together with simulations of hadron penetration in the MuID absorber, to obtain the yield of punchthrough hadrons in MuID gap 4: $N_P(p_T, z_{vtx})$. The yield of fake tracks, $N_B(p_T, z_{vtx})$, determined from simulations described in Sec. III G, is found to be small.

The yield of vertex-independent muons is determined by subtracting the contributions from light hadrons and fake backgrounds and averaging over z_{vtx} bins:

$$N_\mu(p_T) = \frac{1}{N_{z_{vtx}}} \sum_{j=1}^{N_{z_{vtx}}} N_I(p_T, z^j_{vtx}) - N_D(p_T, z^j_{vtx}) - N_P(p_T, z^j_{vtx}) - N_B(p_T, z^j_{vtx}), \quad (2)$$

where $d^2/2\pi p_T dp_T d\eta$ is implicit in all terms of the equation.

We convert this into a cross section via

$$\frac{d^2\sigma_\mu(p_T)}{2\pi p_T dp_T dy} = \frac{\sigma^{pp}_{BBC}}{\varepsilon^{c,\bar{c}\to\mu}_{BBC}} \frac{d^2N_\mu(p_T)}{2\pi p_T dp_T d\eta}. \quad (3)$$

Here σ^{pp}_{BBC} is the cross section of the BBC trigger for $p + p$ interactions and $\varepsilon^{c,\bar{c}\to\mu}_{BBC}$ is the efficiency of the BBC trigger for events in which a charm quark is created and decays into a muon. Substituting $\eta \to y$ introduces negligible error due to the small mass of the muon, the only component left after the subtraction. As described in Sec. III I, systematic errors are determined for each component and combined into a term that applies to the overall normalization and a term that applies to the p_T dependence of the spectrum.

We use PYTHIA to derive the p_T-dependent differential cross section for the production of charm quarks responsible for the vertex-independent muon yield. This procedure is very similar to that in Refs. [7–13], and is described in detail, along with the associated systematic error analysis, in Sec. IV.

A. Data reduction

1. Data sets and triggering

Runs were selected for this analysis based on stable detector operation using the same criteria as an earlier analysis of J/ψ production [51]. Further runs were eliminated due to the presence of large beam-related backgrounds entering the *back* of the detector.

We select only those events in the vertex range $-20 < z_{vtx} < 30$ cm. This minimizes the z_{vtx} dependence of the detector acceptance ($< 1\%$ over the entire z_{vtx} range, see Table II) and allows us to treat the amount of absorber material as a simple function of polar angle, ignoring complications in the pre-MuTR absorber near the beam pipe.

The decision to collect an event was made by the Local Level-1 Trigger [55] within 4μs of the collision. Input to the trigger decision was given by the BBC (collision with a valid event vertex) and the MuID (reconstructed penetrating track). Each trigger could be independently scaled down, so that it occupied a predetermined fraction of the available bandwidth, by selecting every N_i^{th} instance, where N_i is the scaledown factor for the i^{th} trigger. Three different data sets were selected from the good runs for different aspects of the data analysis:

(i) *BBC*: To extract N_D the z_{vtx} dependence of N_I is needed. The unbiased collision vertex distribution is obtained from a set of events collected with this trigger, which required at least one hit in each BBC counter and a vertex position, $|z_{vtx}| < 38$ cm. σ^{pp}_{BBC} was found to be 21.8 ± 2.1 mb using a van der Meer scan [60]. This uncertainty is included in the systematic error on the derived cross section, see Table VIII. There were 1.72×10^7 *BBC* triggered events passing offline vertex selection criteria in this data set ($-20 < z_{vtx} < 30$ cm), corresponding to a sampled luminosity of $\int Ldt = 0.79$ nb^{-1}.

(ii) *M1D*: In order to extract N_I, N_D, and N_B we used events selected with this trigger, which enriched the sample of events with tracks penetrating to MuID gap 4. For the *M1D* and *BBC* data sets we used identical run selection criteria. The total number of sampled *BBC* triggers for this data set was 5.77×10^8, corresponding to a sampled luminosity of $\int Ldt = 26.5$ nb^{-1}.

(iii) *M1S*: In order to extract N_P a data set which provides an unbiased measurement of the number of particles which penetrate to MuID gap 3 is needed. Since the *M1D* trigger required tracks to

penetrate to MuID gap 4 it could not be used. This trigger, which only used information from MuID gaps 0–2, is suitable. We used a subset of runs for which the scaledown factor for this trigger was only 10, corresponding to a sampled luminosity of $\int Ldt = 1.72\ \mathrm{nb}^{-1}$.

2. Track selection

The muon arm reconstruction algorithm starts by finding "roads" (collections of hits in the MuID which form straight, two-dimensional lines) and then combining them with hits in the MuTR to form "tracks." We apply strict cuts on both road and track parameters in order to reduce backgrounds, (see Table I).

The resulting purity of the selected tracks is demonstrated in Fig. 4. This figure shows $p\delta\theta$, the angular deviation through the pre-MuTR absorber, scaled by the particle momentum to give a quantity which should be momentum independent, for different p_T bins. As shown in Fig. 5, $\delta\theta$ is the angular difference between the reconstructed particle trajectory at the collision vertex ($x = 0$, $y = 0$, $z = z_{vtx}$) and at MuTR station 1. A GEANT [61] simulation of the PHENIX detector showed that tracks which do not suffer a strong interaction in the pre-MuTR absorber undergo angular deviations consistent with expectations based on standard multiple scattering: $\sigma_{\delta\theta} \propto \sqrt{x/X_0}/p$. The curves in each panel are fits to $Cp\delta\theta \exp(-(p\delta\theta)^2/2(p\sigma_{\delta\theta})^2)$, in which the normalization constant is allowed to float, and $p\sigma_{\delta\theta} = 130\ \mathrm{rad}\cdot\mathrm{MeV}/c$ is given by GEANT and is consistent with a simple estimate based on the radiation length of the pre-MuTR absorber and the standard multiple scattering formula [62–64] ($x/X_0 \approx 48 \rightarrow p\theta^{rms}_{\mathrm{space}} \approx (\sqrt{2}) \times (13.6\ \mathrm{MeV}/c)(\sqrt{48})\ \mathrm{rad} = 133\ \mathrm{rad}\cdot\mathrm{MeV}/c$). The integral beyond $3p\sigma_{\delta\theta}$ is $\approx 5\%$ and is largely due to hadrons which have a strong interaction in the pre-MuTR absorber and are still reconstructed as a muon candidate. Such tracks are accounted for in the calculation of the punchthrough hadron yield, as described below.

TABLE I. Road and track cuts. Here D_p is the penetration depth, defined to be the most downstream MuID gap with at least one hit (from the horizontal or vertical layer) associated with the track; z is the coordinate along the beam; x and y are transverse to each other and to the beam axis; the vertex cut refers to the transverse position of the MuID road projected to the xy plane at $z = 0$; and the slope cut refers to the direction cosine of the road in each transverse direction.

Road cuts:
· # Associated MuID hits >6 (out of a possible $2 \times D_p$)
· Vertex cut, $\sqrt{x^2 + y^2} < 100$ cm at $z = 0$
· Slope cut, $\sqrt{(\frac{dx}{dz})^2 + (\frac{dy}{dz})^2} > 0.25$
· ≥ 1 associated hit in MuID gap 4
Track cuts:
· Track fit quality, $\chi^2/\mathrm{dof} \leq 10$
· # Associated MuTR hits >12 (out of a possible 16)

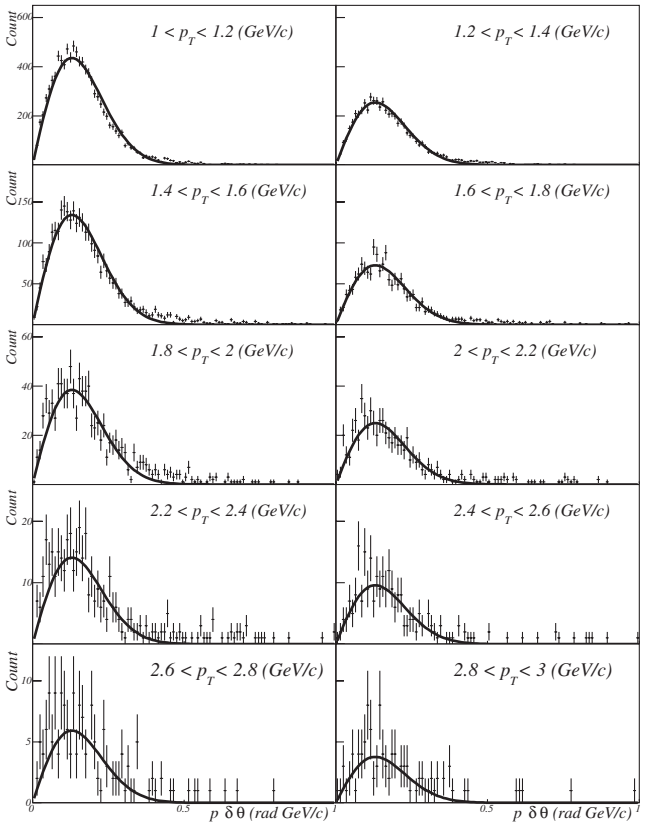

FIG. 4. The scaled angular deflection is the difference in a particle's polar angle caused by passage through the pre-MuTR absorber scaled by the particle's momentum, $p\delta\theta$. For muons (and hadrons not undergoing a strong interaction in the pre-MuTR absorber) one expects the distribution of this quantity to be well described by the standard multiple scattering formula. The different panels show $p\delta\theta$ for different p_T bins with fits (normalization only) to the expected distribution.

3. Acceptance restriction

We further restricted the acceptance of muon candidates for this analysis in two ways:

(1) Tracks were required to pass through regions of the detector that were fully active.
(2) Tracks were required to lie within a pseudorapidity range, $1.5 < |\eta| < 1.8$, in which the acceptance depends negligibly on the collision z_{vtx} location. As shown in Table II the variation is <1% over the entire z_{vtx} range.

B. Acceptance and efficiency

We evaluated four ratios to obtain the acceptance and efficiency for reconstructing tracks penetrating to a particular MuID gap, i:

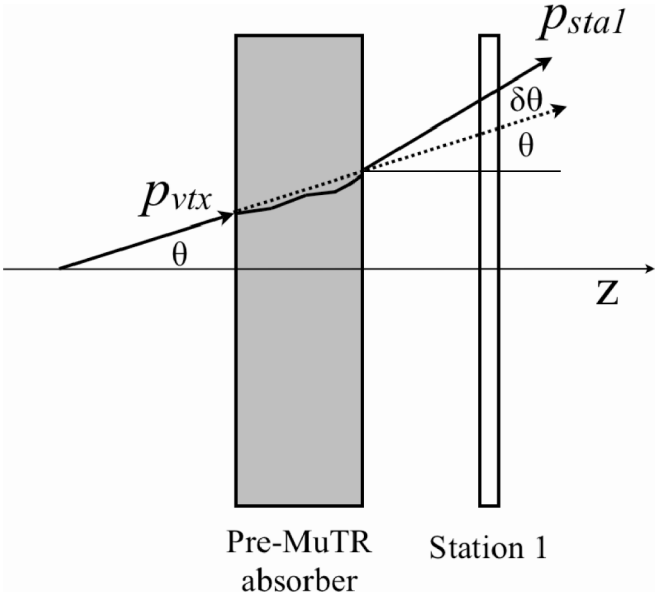

FIG. 5. The angular deflection $\delta\theta$ is the angular difference between the reconstructed particle trajectory at the collision vertex and at MuTR station 1. The momentum used to scale $\delta\theta$ is the average of the momentum reconstructed inside the MuTR magnet ($p_{\rm sta1}$) and the momentum extrapolated to the vertex (p_{vtx}).

(1) $\varepsilon^i_{\rm acc}$: the fraction of particles thrown in $2\pi\delta\eta$ ($\delta\eta = 0.3$) which penetrate to MuID gap 4, pass through active areas in every detector plane, and which pass the acceptance restrictions described above. This quantity ($\approx 50\%$) accounts for nonsensitive structural members in between the cathode strip chambers and chamber regions removed from consideration for the entirety of this analysis.

(2) $\varepsilon^i_{\rm rec}$: the fraction of particles within the accepted region, defined in the previous step, that are reconstructed. This quantity is somewhat low (64%) due to detector problems in this first physics run that have been subsequently resolved.

(3) $\varepsilon^i_{\rm user}$: the fraction of reconstructed tracks that pass the cuts listed in Table I.

(4) $\varepsilon^i_{\rm trig}$: the fraction of selected tracks that fire the MuID trigger.

The overall acceptance and efficiency is the product of these ratios. Note that by construction these ratios factorize since the denominator of each successive ratio is the numerator of the previous ratio.

$\varepsilon^i_{\rm acc}$, $\varepsilon^i_{\rm rec}$, and $\varepsilon^i_{\rm user}$ were evaluated with a GEANT simulation using single muons thrown with a realistic p_T spectrum into the muon arms. The applied detector response incorporated measured detector performance. Reductions in efficiency due to occupancy are negligible in $p + p$ collisions. Run-to-run variations were ignored since we selected runs in which the detector performance was similar and stable. For cuts used in this analysis the acceptance and efficiency are the same for different components of the inclusive muon candidate yield. Efficiency values for tracks penetrating to MuID gap 4 were parametrized in terms of z_{vtx} and p_T and are listed in Table II. There are minor differences in these parametrizations for particles with different charge sign. Fit errors on these parametrizations are included in the systematic uncertainty, as shown in Table V.

We also determined the efficiencies for tracks which only penetrate to MuID gap 3, since these are needed to obtain the yield of punchthrough hadrons. These were found to scale from the efficiencies for tracks penetrating to MuID gap 4: $\varepsilon^3_{\rm acc}\varepsilon^3_{\rm rec}\varepsilon^3_{\rm user} = \varepsilon^3_{\rm scale} \times \varepsilon^4_{\rm acc}\varepsilon^4_{\rm rec}\varepsilon^4_{\rm user}$, where $\varepsilon^3_{\rm scale} = 0.66$. $\varepsilon^3_{\rm scale}$ is less than one because the MuID and the road reconstruction algorithm are optimized for deeply penetrating particles. Particles which do not penetrate to the last gap have poorer resolution matching to MuTR tracks (due to reduced lever arm and smaller number of hits) and are also more susceptible to MuID inefficiencies. There is considerable ambiguity in determining which particles *should* have been reconstructed. Different definitions, together with statistical uncertainties, combined to give a systematic error of 23%, as shown in Table VII.

Trigger efficiencies, $\varepsilon^3_{\rm trig}$ and $\varepsilon^4_{\rm trig}$, are also listed in Table II. These were evaluated using the *BBC* data set, which did not require the MuID trigger to fire.

$$\varepsilon^4_{\rm trig} = \frac{(N_4|M1D) \times S_{M1D}}{(N_4|BBC) \times S_{BBC}}, \tag{4}$$

where $N_4|M1D$ is the number of selected tracks penetrating to MuID gap 4 for events in which the *M1D* trigger fired, S_{M1D} is the scaledown factor applied to the *M1D* trigger, and similarly for $M1D \rightarrow BBC$. $\varepsilon^3_{\rm trig}$ was also evaluated according to Eq. (4), but with $N_4 \rightarrow N_3$, and $M1D \rightarrow M1S$. Different procedures for calculating $\varepsilon^3_{\rm trig}$ gave slightly different answers, resulting in the assignment of a 4.7% systematic error, as shown in Table V.

TABLE II. Trigger, acceptance, track reconstruction, and track selection efficiencies. In the formulae below, the units for p_T are GeV/c and the units for z_{vtx} are cm. Systematic errors for these quantities are given in Tables V and VII.

Quantity	Value
$\varepsilon^{4,+}_{\rm acc}$	$0.51 \times (1 - 114\exp(-5.9p_T)) \times (1 + 0.0015z_{vtx})$
$\varepsilon^{4,-}_{\rm acc}$	$0.50 \times (1 - 531\exp(-7.5p_T)) \times (1 + 0.0013z_{vtx})$
$\varepsilon^{4}_{\rm rec}$	0.64
$\varepsilon^{4,+}_{\rm user}$	$0.74 \times (1 - 0.0019z_{vtx})$
$\varepsilon^{4,-}_{\rm user}$	$0.74 \times (1 - 0.0009z_{vtx})$
$\varepsilon^{3}_{\rm scale}$	0.66
$\varepsilon^{4}_{\rm trig}$	0.86
$\varepsilon^{3}_{\rm trig}$	0.97
$\varepsilon^{c,\bar{c}\rightarrow\mu}_{\rm BBC}$	0.75

Since both the *M1D* and *M1S* triggers required a coincidence with the *BBC* trigger we must also account for the *BBC* trigger efficiency for events in which a reconstructed muon is created via charm quark decay: $\varepsilon_{BBC}^{c,\bar{c}\to\mu}$. The BBC efficiency was evaluated for events in which a J/ψ was produced in the muon arm acceptance using PYTHIA + GEANT simulations [51]. The BBC efficiency was also evaluated for events in which π^0's were produced in the central arm acceptance [60] using data triggered without a BBC requirement. The BBC efficiency under both conditions was found to have a similar value that we therefore adopt: $\varepsilon_{BBC}^{c,\bar{c}\to\mu} = 0.75 \pm 0.04$. This uncertainty is included in the systematic error on the derived cross section (Table VIII).

C. Inclusive muon candidates

We first form two sets of collision vertex (z_{vtx}) histograms with 10 cm bins: one histogram for all interactions selected with the *BBC* trigger, and a series of histograms for interactions selected with the *M1D* trigger and having a good muon candidate within a p_T bin ($1 < p_T < 3$ GeV/c, 200 MeV/c bins). The muon candidate histograms are formed separately for each charge sign. Entries into each histogram are scaled by the appropriate trigger scaledown factor. The muon candidate histograms are divided by the minimum bias histogram to give $N_I(p_T, z_{vtx})$, as shown in Fig. 6. Systematic errors shown in this figure are discussed in Sec. III I and listed in Table V.

In Fig. 6 one can clearly see the linear dependence in the yield of inclusive muon candidates vs z_{vtx} at low transverse momentum ($p_T < 2$ GeV/c). This dependence is due to muons from the decay of abundant light hadrons (π's and K's) prior to the pre-MuTR absorber material at $z_{abs} = -40$ cm. One also observes a charge asymmetry, with the yield of positives significantly exceeding that of negatives. This is due to the substantial charge asymmetry in the kaon nuclear interaction length—positive kaons are much more likely to punch through the muon arm absorber than any other species. This effect is discussed in Sec. III F.

D. Hadron generator

The background components of the inclusive muon candidate yield (free-decay muons (Sec. III E), and punch-through hadrons (Sec. III F)) arise from charged hadrons,

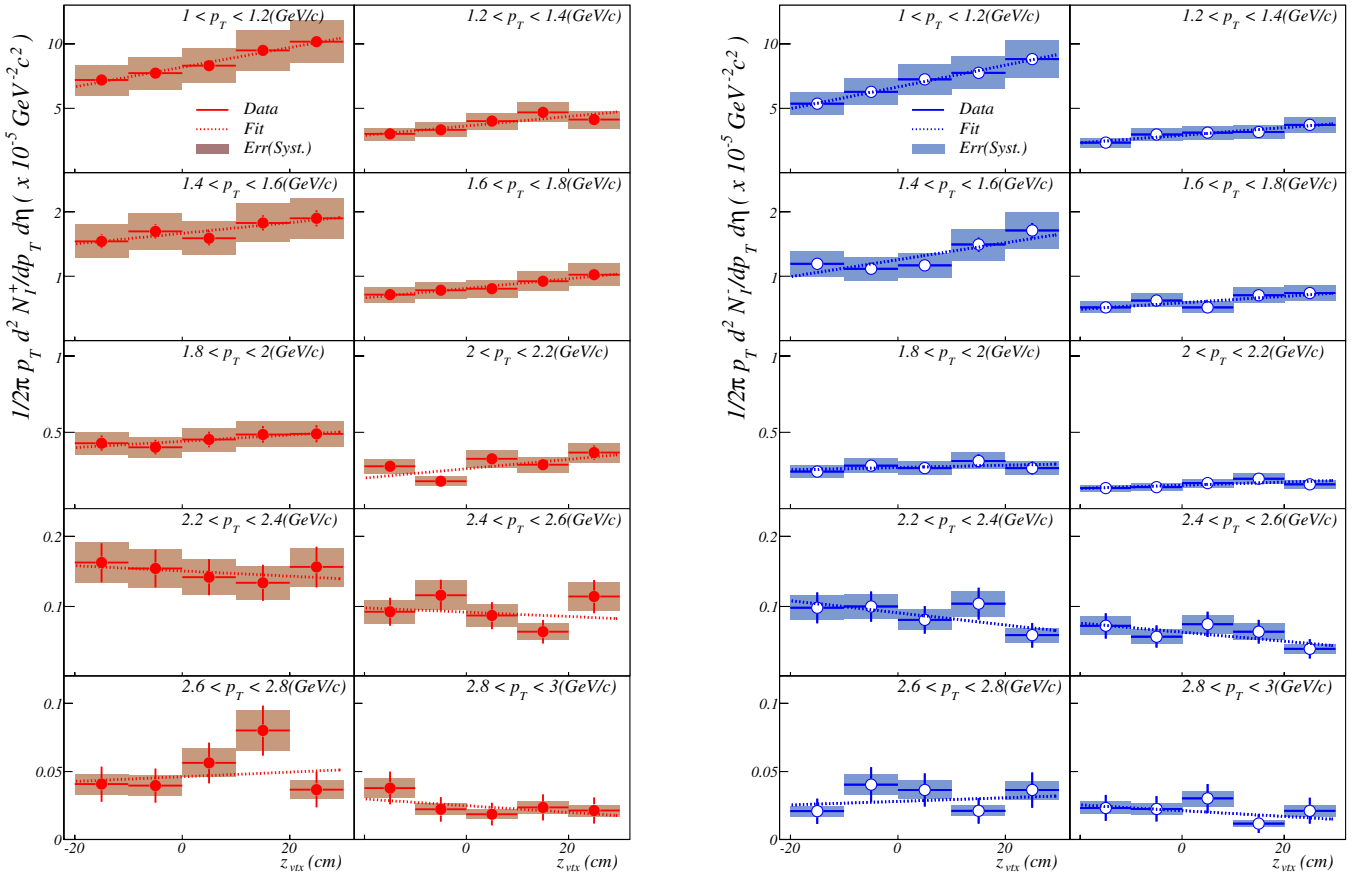

FIG. 6 (color online). Yield of (left) positively and (right) negatively charged inclusive muon candidates vs z_{vtx} for different p_T bins. Fits shown use the functional form $a + bz_{vtx}$ to extract the contribution from hadron decay, as discussed in Sec. III E. Error bars show statistical errors. Shaded bands show systematic errors, as discussed in Sec. III I and listed in Table V. The substantial charge asymmetry is due to the relatively long nuclear interaction length for positive kaons, as discussed in Sec. III F.

primarily pions and kaons, produced in the kinematic range of our measurement. There are no measurements of hadron production in this kinematic range and model predictions have substantial disagreement. This disagreement would lead to unacceptable systematic uncertainty in the extraction of the heavy flavor muon component. In order to reduce this uncertainty we developed a data-driven hadron generator that is based on PHENIX midrapidity measurements and then constrained by the z_{vtx} dependence of the inclusive muon candidate yield presented in this analysis.

The input for this generator is obtained from PHENIX measurements in $\sqrt{s} = 200$ GeV $p + p$ collisions at $y = 0$ [65,66] using the following procedure:

(1) π^+ and π^- spectra at $y = 0$ ($0 < p_T < 3.5$ GeV/c) are fit to a power law and then scaled assuming a Gaussian rapidity dependence ($\sigma_y = 2.5$) and $y - p_T$ factorization:

$$N^{\pi^\pm}_{y=1.65}(p_T) = N^{\pi^\pm}_{y=0}(p_T)\exp(-(1.65^2/2\sigma_y^2)).$$

This rapidity dependence and factorization is observed both in PYTHIA and in BRAHMS [49] data measured at $y = 1$ and $y = 2.2$.

(2) A similar procedure is used to obtain the charged kaon yield at $y = 1.65$.
First the charged kaon yield at $y = 0$ is extrapolated beyond the current measurement limit ($p_T < 2$ GeV/c). To do this we form the isospin averaged K/π ratio vs p_T at $y = 0$. We use charged particles, $(K^+ + K^-)/(\pi^+ + \pi^-)$, for $p_T < 2$ GeV/c [65] and neutral particles, K^0/π^0, for $2 < p_T < 6.5$ GeV/c [66]. This combined ratio is then fit to $f(p_T) = A(1 - B\exp(-Cp_T))$. This function is then normalized separately to the K^+/π^+ and K^-/π^- ratios for $p_T < 2$ GeV/c and multiplied by the corresponding charged pion spectrum to obtain $N^{K^\pm}_{y=0}(p_T)$, our parametrization of the midrapidity charged kaon p_T spectra extending out to 3.5 GeV/c.
As with pions, we need to extrapolate this parametrization of the yield at $y = 0$ to obtain the yield at $y = 1.65$. One possibility is to assume boost invariance of the K/π ratio. However, PYTHIA gives a slightly narrower rapidity distribution for kaons than for pions, resulting in a kaon yield at $y = 1.65$ that is only 85% of that predicted with the boost invariance assumption. We split the difference between these two assumptions:

$$N^{K^\pm}_{y=1.65}(p_T) = 92.5\% N^{K^\pm}_{y=0}(p_T) \times \exp(-(1.65^2/2\sigma_y^2)),$$

where, again, $\sigma_y = 2.5$.

(3) The p and $\bar{p}$ spectra are assumed to have the same shape as the pion spectra with normalization factors set to the measured values at $y = 0$, $p_T = 3$ GeV/c (0.4 for p/π^+, 0.24 for $\bar{p}/\pi^-$) [65]. The exact form used for the p, $\bar{p}$ spectra is unimportant. They obviously do not contribute to the yield of decay muons and their contribution to the yield of punchthrough hadrons is greatly suppressed due to their relatively short nuclear interaction length.

E. Free-decay muons

We fit the histograms shown in Fig. 6 with the function $a + bz_{vtx}$. After multiplying by $dz/dl_{fp} = \cos(\langle\theta\rangle) = 0.947$ the slope, b, and its fit error give, respectively, the yield *per unit length of decay flightpath* of muons from hadron decay, $dN_D(p_T)/dl_{fp}$, and the statistical error on this quantity. We do not allow a to vary in the fit, but we perform the fits for different values of a to account for uncertainty in that quantity. We also allow the z_{vtx} fit range to vary from $|z_{vtx}| < 20$ cm to $|z_{vtx}| < 40$ cm. The resulting variations in N_D (5% and 3.3%, respectively) are incorporated into the systematic error, as shown in Table VI. Results are shown in Fig. 7.

This procedure does not provide a quantitative measure of the decay muon spectrum above $p_T \sim 2$ GeV/c, even though a substantial fraction of the inclusive muons are decay muons up to significantly higher p_T. This is due to the fact that at high p_T the decay slopes decrease (Lorentz time dilation) as do the statistics, both of which make it more difficult to quantify the decay component directly.

In order to extend our estimate of decay muons to higher p_T we simulate charged hadron spectra using the hadron generator described in Sec. III D. These hadrons are allowed to decay into the muon arms, resulting in a predicted p_T spectra (per unit length) of muons from hadron decay separately for each charge sign. We then normalize these predicted spectra to the measured spectra. The normalized predicted spectra are shown as the dashed lines in Fig. 7. The predicted spectral shape agrees with the data where we have a statistically significant measurement. The absolute normalization of the prediction is within 7% of the measured value, easily consistent within errors. This difference, and the effects of reasonable variations on the input spectral shapes, are incorporated into the systematic uncertainty on N_D, as listed in Table VI.

We obtain $N_D(p_T, z_{vtx})$ from the product of $dN_D(p_T)/dl_{fp}$ and the average value of the decay flightpath, $l_{fp} = \lambda_D + |z_{vtx} - z_{abs}|/\cos(\theta)$, for each z_{vtx} bin.

F. Punchthrough hadrons

A reconstructed hadron that penetrates to MuID gap 4 is impossible to distinguish from a muon. The straightforward technique to calculate the contribution of this background component would be to use the PHENIX GEANT-based Monte Carlo program to simulate the response to hadrons sampled from the hadron generator spectra. However, this approach suffers from unacceptable systematic uncertainty due to differences in the predictions for

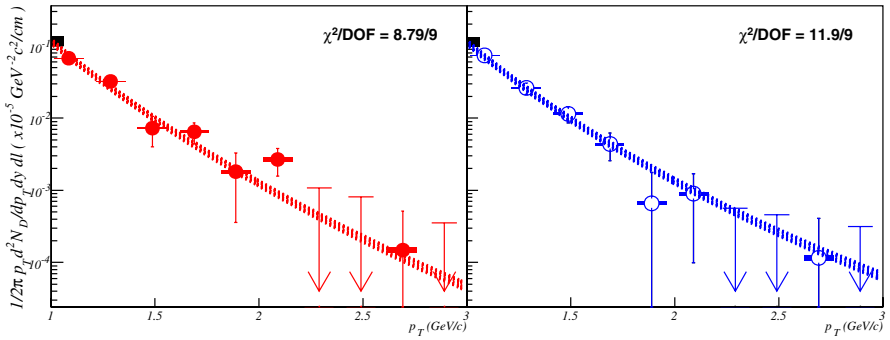

FIG. 7 (color online). Yield per unit length of (left) positively and (right) negatively charged free-decay muons. Points are the measured values determined by linear fits to the inclusive muon candidate yield (Fig. 6). Error bars indicate statistical errors for those fits. p_T bins with a negative (nonphysical) slope in those fits are shown with a line at the 90% C.L. upper limit (statistical errors only) and an arrow pointing down. See Sec. III E for details. Dashed lines are the predictions for each sign from the data-driven hadron generator with the normalization fit to the measured points. See Sec. III D for details. The χ^2/dof for these fits are indicated. The width of the lines corresponds to σ_{R_D} (Table VI), the error on the ratio of free-decay muons to inclusive muon candidates. Black bands at the left edge of each panel show the p_T-independent systematic error on the inclusive muon candidate yield. Shaded bands on each point show the systematic errors that affect the p_T shape of the inclusive muon candidate spectrum. These last two systematic errors (Table V) need to be included in the total error budget for the yield of free-decay muons, σ_{N_D}/N_D (Table VI), but are displayed separately since they are common to all components of the inclusive muon candidate yield. See Eqs. (12) and (13). Systematic errors are discussed in Sec. III I.

different hadronic interaction packages implemented in GEANT. To avoid this limitation we developed a procedure in which we cleanly identify hadrons in shallow gaps and then extrapolate their yield to obtain the yield of punchthrough hadrons in MuID gap 4.

Figure 8 shows the longitudinal momentum (p_z, the momentum projected onto the beam axis) distribution of particles that *stop* in MuID gap 3. The sharp peak at $p_z \approx 2.2$ GeV/c corresponds to charged particles which stopped because they ranged out in the absorber plate between gaps 3 and 4 (this includes both muons and also hadrons which only suffered ionization energy loss.) The width of this peak is due to the 20 cm (11.4 X_0) absorber thickness between MuID gaps 3 and 4, and energy-loss fluctuations in all the preceding absorber layers. Particles at momenta beyond the peak ($p_z > 3$ GeV/c) form a relatively pure sample of hadrons, with only a negligible contamination due to inefficiencies in MuID gap 4 and particles with misreconstructed momentum values. After correcting for acceptance and efficiency these particles are used to obtain the p_T spectrum for the "gap 3 exclusive yield," as shown in Fig. 9. We use data from the *M1S* trigger sample since the *M1D* sample required a hit in MuID gap 4, which would bias this measurement.

In order to extrapolate this measured spectrum for hadrons stopping in MuID gap 3 to the spectrum of punchthrough hadrons which penetrate to MuID gap 4, we start by assuming exponential absorption of hadrons entering the muon arm absorber material. With this assumption we obtain an expression for the "gap 3 inclusive yield," those hadrons that reach *at least* MuID gap 3:

$$N_3^i(p_T, \theta) = N_{vtx}^i(p_T, \theta) \exp(-L_3(\theta)/\lambda^i(p_T)), \quad (5)$$

where i indicates the contributing hadron species ($\pi^{\pm}$, $K^{\pm}$, p, $\bar{p}$), $N_{vtx}^i(p_T, \theta)$ is the yield at the vertex of the i^{th} species, $L_3(\theta)$ is the amount of absorber material traversed to reach MuID gap 3, and $\lambda^i(p_T, \theta)$ is the p_T-dependent nuclear interaction length of the i^{th} species. We can write a similar expression for the punchthrough hadron yield:

$$N_P^i(p_T, \theta) = N_{vtx}^i(p_T, \theta) \exp(-L_4(\theta)/\lambda^i(p_T)), \quad (6)$$

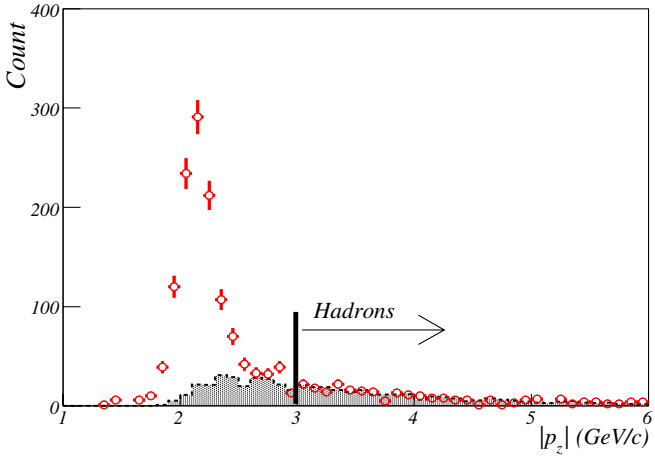

FIG. 8 (color online). Points (measured data) show the longitudinal momentum, measured at the vertex (p_z^{vtx}), of particles that stop in MuID gap 3. The sharp peak is due to muons which range out in the absorber plate between gaps 3 and 4. The histogram (Monte Carlo) shows the longitudinal momentum of all particles that stop in MuID gap 3 and do not decay before the pre-MuTR absorber. The Monte Carlo is normalized to the data for $p_z^{vtx} > 3$ GeV/c. Particles beyond the peak form a relatively pure sample of hadrons.

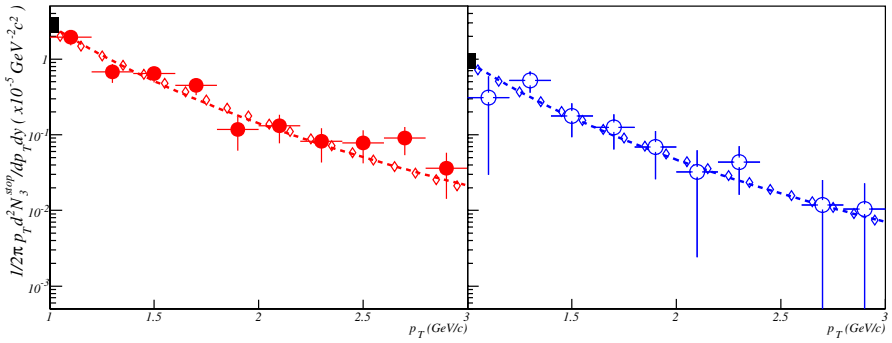

FIG. 9 (color online). Points show the p_T spectrum of (left) positively and (right) negatively charged hadrons stopping in MuID gap 3 (''gap 3 exclusive yield'') with statistical errors. Open diamonds show a power-law fit to the data, effectively a smoothed version of the data. Dashed lines are fits to the smoothed data using the hadron generator (normalized by the measured free-decay spectrum, as shown in Fig. 7) and Eqs. (8) and (9) to obtain values for the species-dependent nuclear interaction lengths, $\lambda^i(p_T)$.

where $L_4(\theta)$ is the amount of absorber material traversed to reach MuID gap 4.

By taking the difference between these two equations we obtain an expression for the gap 3 exclusive yield:

$$\begin{aligned} N_3^{i,\mathrm{stop}}(p_T,\theta) &= N_3^i(p_T,\theta) - N_P^i(p_T,\theta) \\ &= N_{vtx}^i(p_T,\theta)\exp(-L_3(\theta)/\lambda^i(p_T)) \\ &\quad\times(1-\exp((L_3(\theta)-L_4(\theta))/\lambda^i(p_T))). \end{aligned} \quad (7)$$

The species comprising the gap 3 exclusive yield are not determined, but their charge sign is. As a result, Eq. (7) can be rewritten as two equations with six unknowns for each p_T bin:

$$\begin{aligned} N_3^{+,\mathrm{stop}}(p_T,\theta) &= N_3^+(p_T,\theta) - N_P^+(p_T,\theta) \\ &= \sum_{i=\pi^+,K^+,p} N_{vtx}^i(p_T,\theta)\exp(-L_3(\theta)/\lambda^i(p_T)) \\ &\quad\times(1-\exp((L_3(\theta)-L_4(\theta))/\lambda^i(p_T))), \end{aligned} \quad (8)$$

$$\begin{aligned} N_3^{-,\mathrm{stop}}(p_T,\theta) &= N_3^-(p_T,\theta) - N_P^-(p_T,\theta) \\ &= \sum_{i=\pi^-,K^-,\bar{p}} N_{vtx}^i(p_T,\theta)\exp(-L_3(\theta)/\lambda^i(p_T)) \\ &\quad\times(1-\exp((L_3(\theta)-L_4(\theta))/\lambda^i(p_T))). \end{aligned} \quad (9)$$

Based on measured cross sections for various species [67], the number of unknowns is reduced with the following assumption:

$$\begin{aligned} \lambda^{K^+} &= \lambda^{\mathrm{long}}, \\ \lambda^p = \lambda^{\pi^+} = \lambda^{\pi^-} = \lambda^{K^-} &= \lambda^{\mathrm{short}}, \\ \lambda^{\bar{p}} &= 0. \end{aligned}$$

We further assume that λ^{short} and λ^{long} have the form $a + b(p_T[\mathrm{GeV}/c] - 1)$.

We effectively smoothed the gap 3 exclusive yield for each sign by fitting the measured values to a power law. Using $N_{vtx}^i(p_T,\theta)$ from the hadron generator (normalized to the free-decay muon spectrum, as described in Sec. III E) and known values for $L_{3,4}(\theta)$, we fit Eqs. (8) and (9) to the smoothed gap 3 exclusive yield for each sign to obtain:

$$\lambda^{\mathrm{short}} = 19.0 + 2.2(p_T[\mathrm{GeV}/c] - 1)\ \mathrm{cm}, \quad \text{and}$$
$$\lambda^{\mathrm{long}} = 25.9 + 4.4(p_T[\mathrm{GeV}/c] - 1)\ \mathrm{cm}.$$

Results of these fits are shown in Fig. 9. The fit error on the normalization (10%) is incorporated into the systematic error, as listed in Table VII.

With these values for $\lambda^i(p_T)$ and the hadron generator input spectra, we could directly apply Eq. (6) to obtain the final punchthrough spectra. However, we made one further correction, described below, after finding that our assumption of exponential absorption does not hold when applied to GEANT simulations of the punchthrough process.

Using our GEANT-based PHENIX simulation program, we generated data sets with both the FLUKA [68] and GHEISHA [69] hadronic interaction packages. Input spectra for these data sets were given by our decay hadron generator. We selected all particles which did not decay before the pre-MuTR absorber. ''Truth'' values for the punchthrough and gap 3 exclusive yields were obtained by splitting those particles based on the absence (gap 3 exclusive) or presence (punchthrough) of associated charged particles with $E_4 > 100$ MeV in MuID gap 4. We varied E_4 from 50–300 MeV and saw no significant change in the results.

Using the known input spectra, known values for $L_{3,4}(\theta)$, and truth values for the gap 3 exclusive yield, we applied Eq. (7) to the Monte Carlo data sets to obtain $\lambda^i(p_T)$. Because of statistical limitations we integrated our results over θ and into two p_T bins: $1 < p_T < 2$ GeV/c and $p_T > 2$ GeV/c. Values extracted for $\lambda^i(p_T)$ for the different hadronic interaction packages are listed in Table III.

TABLE III. Nuclear interaction lengths, $\lambda^i(p_T)$, for different particle species and p_T bins (in GeV/c) for FLUKA and GHEISHA. Statistical errors on these values are ≈ 2 mm.

	FLUKA $\lambda^i(p_T)$ [cm]		GHEISHA $\lambda^i(p_T)$ [cm]	
Species	$1 < p_T < 2$	$p_T > 2$	$1 < p_T < 2$	$p_T > 2$
π^+	19.6	24.5	16.0	21.1
π^-	19.4	24.8	15.0	19.3
K^+	24.4	29.6	24.9	30.8
K^-	20.5	24.2	17.2	21.2

These values are consistent with those found for our measured data, listed above.

Inserting these values for $\lambda^i(p_T)$ into Eq. (6) we obtained a prediction for $N_P^i(p_T, \theta)$. Ratios of the truth values and predicted values for the punchthrough yield ($R_{N_P^i(p_T)}$) for the different hadronic interaction packages are listed in Table IV. The limitation of the simple exponential absorption model is illustrated by the fact that these ratios deviate significantly from unity. Furthermore, the two hadronic interaction packages disagree on the direction of the deviation: the exponential absorption model tends to overpredict the punchthrough yield for FLUKA and underpredict it for GHEISHA.

TABLE IV. Ratios, $R_{N_P^i(p_T)}$, of truth values for the punchthrough hadron yield to those predicted assuming exponential hadron absorption for different particle species and p_T bins (in GeV/c), for FLUKA and GHEISHA. Average values of the ratios for the two different hadronic interaction packages, $\langle R\rangle^i \times (p_T)$, are smoothed across the p_T bin at 2 GeV/c to obtain correction factors for the exponential absorption model. Statistical errors on these quantities are $\approx 10\%$. The maximum fractional difference in the ratios for the two different packages (32%) is incorporated into the systematic error estimate, as shown in Table VII.

Species	$1 < p_T < 2$	$p_T > 2$	Description
π^+	0.76	0.86	$R^{\mathrm{FLUKA}}_{N_P^i(p_T)}$
π^-	0.91	0.75	
K^+	0.91	1.00	
K^-	1.17	1.06	
π^+	1.48	1.04	$R^{\mathrm{GHEISHA}}_{N_P^i(p_T)}$
π^-	1.47	1.09	
K^+	1.31	1.07	
K^-	2.21	1.69	
π^+	1.12	0.95	$\langle R\rangle^i(p_T)$
π^-	1.19	0.92	
K^+	1.11	1.04	
K^-	1.67	1.38	
π^+	32%	10%	$\delta R_{N_P^i(p_T)}/C^i(p_T)$
π^-	24%	18%	
K^+	18%	3%	
K^-	32%	22%	

Relatively little data exist in the relevant momentum range that would allow us to conclude which, if either, hadronic interaction package is correct. Measurements by RD10 and RD45 [70] of the penetration depth of identified hadrons found that GHEISHA did well for protons and FLUKA did not. But neither did well for pions and no data exist for kaons. Furthermore, the results are sensitive to the definition of a penetrating particle. For RD10/45 an incoming particle with any associated charged particles in the 120×120 cm^2 detector area at a particular depth was defined to have penetrated to that depth. In our measurement we reconstruct particle trajectories, and MuID hits are not associated with a road unless they are within a narrow search window surrounding the projected trajectory. Thus we are relatively insensitive to the leakage of a showering hadron.

As a result of these uncertainties on the applicability of our exponential absorption model we incorporate a species and p_T-dependent correction factor to Eq. (6):

$$N_P^i(p_T, \theta) = C^i(p_T) N_{vtx}^i(p_T, \theta) \exp(-L_4(\theta)/\lambda^i(p_T)). \tag{10}$$

The correction factors for pions and kaons are obtained from the average of the values of $R_{N_P^i(p_T)}$ for the two packages, $\langle R\rangle^i(p_T) = (R^{\mathrm{FLUKA}}_{N_P^i(p_T)} + R^{\mathrm{GHEISHA}}_{N_P^i(p_T)})/2$, which are listed in Table IV. We incorporate the maximum fractional difference in the ratios for the two packages (32%) into our systematic error estimate, as listed in Table VII. The values of $\langle R\rangle^i(p_T)$ for a given species are not the same for the different p_T bins. Therefore we assume the values are valid at the average p_T of each bin ($p_T = 1.25$ GeV/c and 2.31 GeV/c, respectively) and use a linear extrapolation in p_T to obtain the final correction factors:

$$C^i(p_T) = \langle R\rangle^i_{\mathrm{low}\ p_t} + (\langle R\rangle^i_{\mathrm{high}\ p_t} - \langle R\rangle^i_{\mathrm{low}\ p_t}) \times \frac{p_T[\mathrm{GeV}/c] - 1.25}{2.31 - 1.25}. \tag{11}$$

We assume that p's and $\bar{p}$'s have the same correction factors as the corresponding sign pions. Since p's and $\bar{p}$'s make only small contributions to the punchthrough hadrons this simplifying assumption has little consequence. We incorporate a conservative 10% systematic error on N_P to cover extreme possibilities for the p and $\bar{p}$ nuclear interaction lengths, as shown in Table VII.

We use Eq. (10), with the tabulated correction factors, particle yields at the vertex given by our normalized hadron generator, the known value of $L_4(\theta)$, and the values for $\lambda^i(p_T)$ determined from the measured gap 3 exclusive yield, to obtain the p_T spectrum of punchthrough hadrons, $N_P(p_T)$, as shown in Fig. 10. Systematic errors shown in this figure are discussed in Sec. III I and listed in Table VII. We multiply $N_P(p_T)$ by the fraction of the accepted z_{vtx}

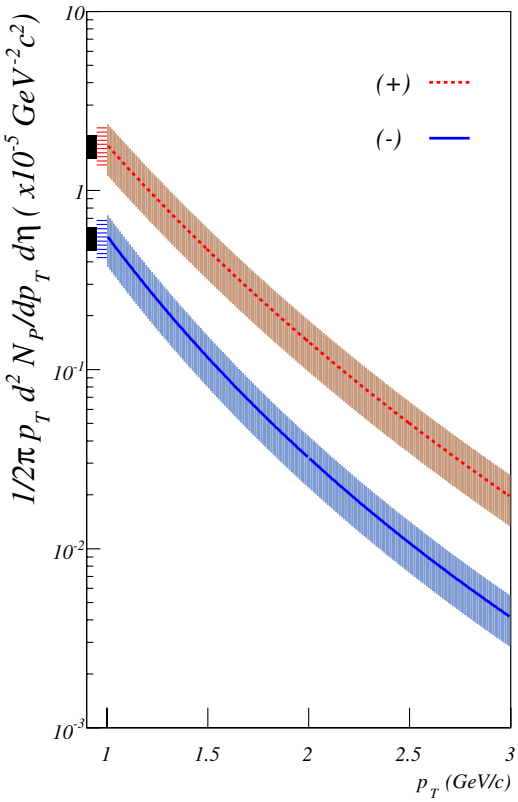

FIG. 10 (color online). Yield of positively (dotted line) and negatively (solid line) charged hadrons which penetrate to MuID gap 4. The curves are obtained from Eq. (10), as described above. Solid bands on the y-axis show the relative normalization uncertainty on the inclusive muon candidate yield, $\sigma^{\mathrm{norm}}_{N_I}/N_I$ (Table V). This needs to be included in the total error budget for the yield of punchthrough hadrons, σ_{N_P}/N_P (Table VII), but is displayed separately since it is common to all components of the inclusive muon candidate yield (see Eqs. (12) and (13)). Hatched bands on the y-axis show $\sigma^{\mathrm{norm}}_{R_P}$ (Table VII), the normalization uncertainty on the ratio of punchthrough hadrons to inclusive muon candidates. The relative fraction of positive and negative punch through hadrons can move up and down together by this amount. Shaded bands around the extracted punchthrough hadron yield show the systematic errors on $\sigma^{p_T}_{R_P}$ which can affect the p_T shape of the relative fraction of positive and negative punch through hadrons (positives and negatives can move independently). These are dominated by differences in the applicability of the simple exponential absorption model observed for FLUKA and GHEISHA. Systematic errors are listed in Tables V and VII and discussed in Sec. III I.

range represented by each z_{vtx} bin to finally obtain $N_P(p_T, z_{vtx})$.

The charge asymmetry in Fig. 10 is substantial, a result of the relatively long nuclear absorption length for positive kaons. As a result of the difference (λ^{K^+} is 19%–66% less than λ^{K^-}, λ^{π^+}, or λ^{π^-} based on GHEISHA and FLUKA values shown in Table III) the PHENIX muon arm steel presents 1.1–4.5 fewer interaction lengths to positive kaons than other hadron species.

G. Background tracks

The main source of tracks which are not accounted for in the yield of punchthrough hadrons and free-decay muons, and which are not due to vertex-independent muons, are light hadrons which penetrate through the pre-MuTR absorber, decay into a muon, and are still reconstructed as a valid track.

A simulation of single pions thrown into the muon arm acceptance shows that the number of hadrons which decay after the pre-MuTR absorber and penetrate to MuID gap 4 is only 5%–10% (increasing with increasing p_T) of the z_{vtx}-averaged number of free-decay muons, $N_D(p_T, z_{vtx} = 0)$. This ratio will be suppressed by the fact that tracks which decay are less likely to be reconstructed successfully. It is further suppressed by our punchthrough calculation procedure: the number of such tracks which stop in MuID gap 3 is roughly half the number that penetrate to gap 4; these will be counted in our calculation of the punchthrough hadron yield.

We express our estimate for the yield of background tracks not otherwise accounted for as $N_B(p_T) = 5\% \times N_D(p_T, z_{vtx} = 0)$. The systematic uncertainty assigned to this quantity, $\sigma_{R_B} = 5\% \times N_D(p_T, z_{vtx} = 0)$, covers the extreme possibilities that the N_B/N_D is unsuppressed or fully suppressed by reconstruction and punchthrough procedures, as described above (see Table VIII).

This estimate was verified in a simulation of π^-'s and K^-'s which were thrown into the muon arm acceptance and fully reconstructed. The reconstructed track information, together with the Monte Carlo truth information, allows us to eliminate uncertainties due to misreconstruction of the track p_T and due to determination of whether a track which penetrated to the last gap did so in a reconstructible fashion.

H. Vertex-independent muons

Figure 11 shows the yield of inclusive muon candidates, $N_I(p_T, z_{vtx})$, with contributions from individual components (free-decay muons, punchthrough hadrons, and background tracks) shown as well as their sum. The vertex-independent muons can be seen as the clear excess above the calculated background sources. The systematic error bands shown on the component sums are discussed in Sec. III I and listed in Tables VI and VII.

We obtain the yield of vertex-independent muons by applying Eq. (2) in each p_T bin, subtracting the hadronic contributions from the inclusive muon candidate yield, and averaging over z_{vtx} bins. This yield is shown, before averaging over z_{vtx} to demonstrate the expected vertex independence, in Fig. 12.

We make one final correction for momentum scale. The observed mass of the J/ψ, reconstructed with the same code and in the same data set, is higher than the nominal value by ≈ 100 MeV(3%) [51]. However, in a higher

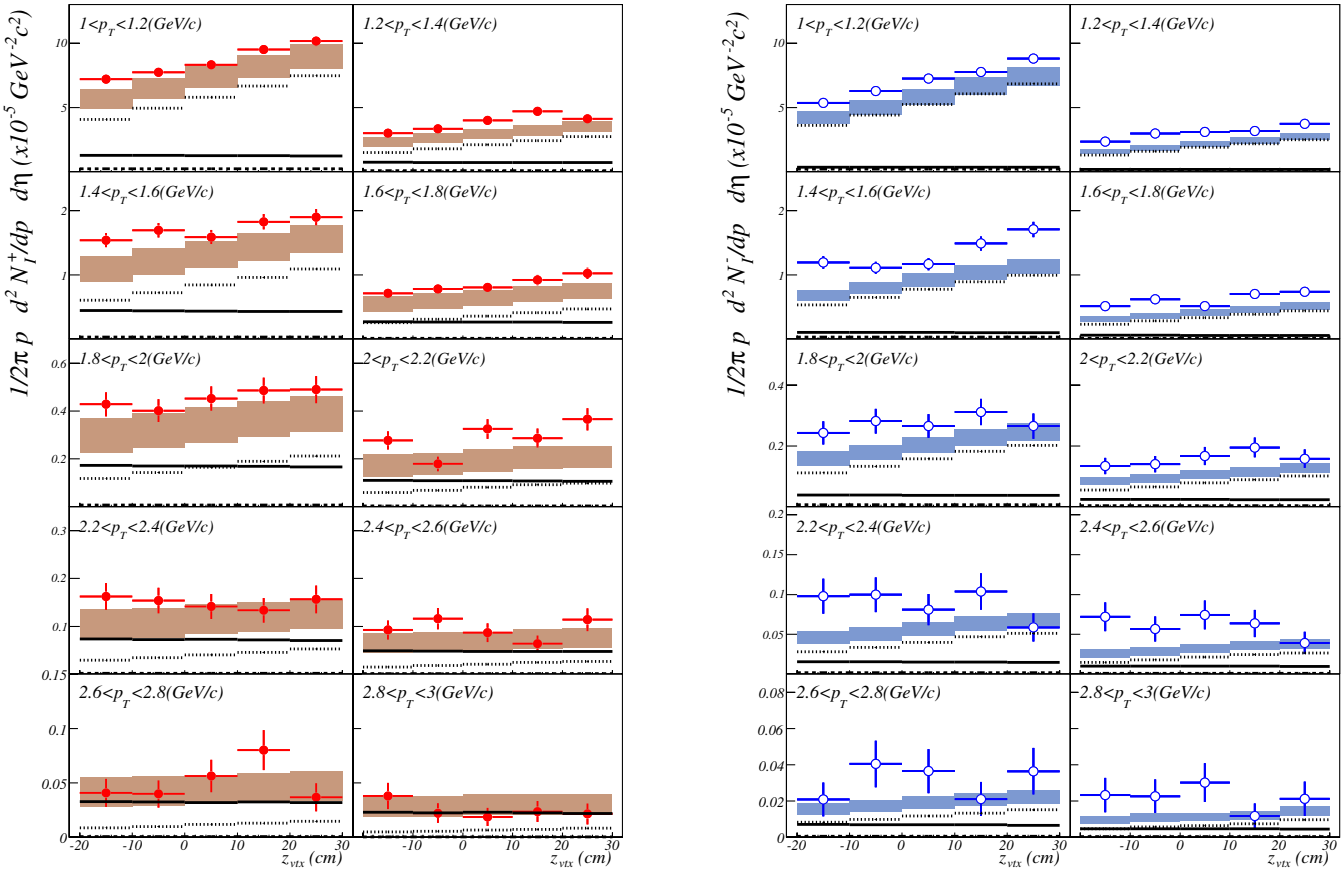

FIG. 11 (color online). Points show the yield of (left) positively and (right) negatively charged inclusive muon candidates vs z_{vtx} for different p_T bins with statistical errors. Dotted, solid, and dashed lines show contributions from decay muons, punchthrough hadrons, and background tracks, respectively. Shaded bands show the systematic error around the sum of these components, as listed in Tables V, VI, and VII and discussed in Sec. III I. The larger systematic uncertainties for positive particles are due to the larger fractional contribution of punchthrough background, which in turn is due to the relatively long nuclear interaction cross section for positive kaons.

statistics data set the momentum scale accuracy is verified to within 1% by our observation of the accepted value for the mass of the J/ψ [52]. Also, the peak observed in the longitudinal momentum distribution of particles stopping in MuID gap 3 (see Fig. 8) is within 0.5% of the predicted value. We therefore assume that the momentum scale is high by 1.5% (splitting the difference between 0 and 3%). This results in a momentum scale correction factor to the prompt muon yield of $0.94 + 0.987 \times (p_T[\mathrm{GeV}/c] - 1)$. We assume a 100% systematic error on this correction factor, as shown in Table V.

Finite momentum resolution can cause a similar effect. Contributions from energy-loss fluctuations, multiple scattering, and chamber resolution combine to give $\delta p/p \approx 5\%$ for the momentum range used in this analysis. Finite resolution, combined with an exponentially falling spectrum, artificially hardens the measured spectrum. For $1 < p_T < 3$ GeV/c this hardening increases the normalization of the yield by 3.7%. However, this is accounted for in our efficiency determination since we use a realistic p_T spectrum as input. Therefore, we apply no explicit correction and no additional systematic uncertainty for this effect.

The final values for the vertex-independent muon cross section, obtained from Eq. (3), are shown in Fig. 13. Points in this figure have been placed at the average p_T value of the bin contents to account for bin shifting in the steeply falling distributions. Systematic errors shown in this figure are discussed in Sec. III I and listed in Tables V, VI, and VII.

I. Systematic errors

Many sources of systematic error on the yield of vertex-independent muons, N_μ, are common to the different components of the inclusive muon candidate yield. In order to account for this we rewrite Eq. (2) (making the p_T and z_{vtx} dependencies implicit) as:

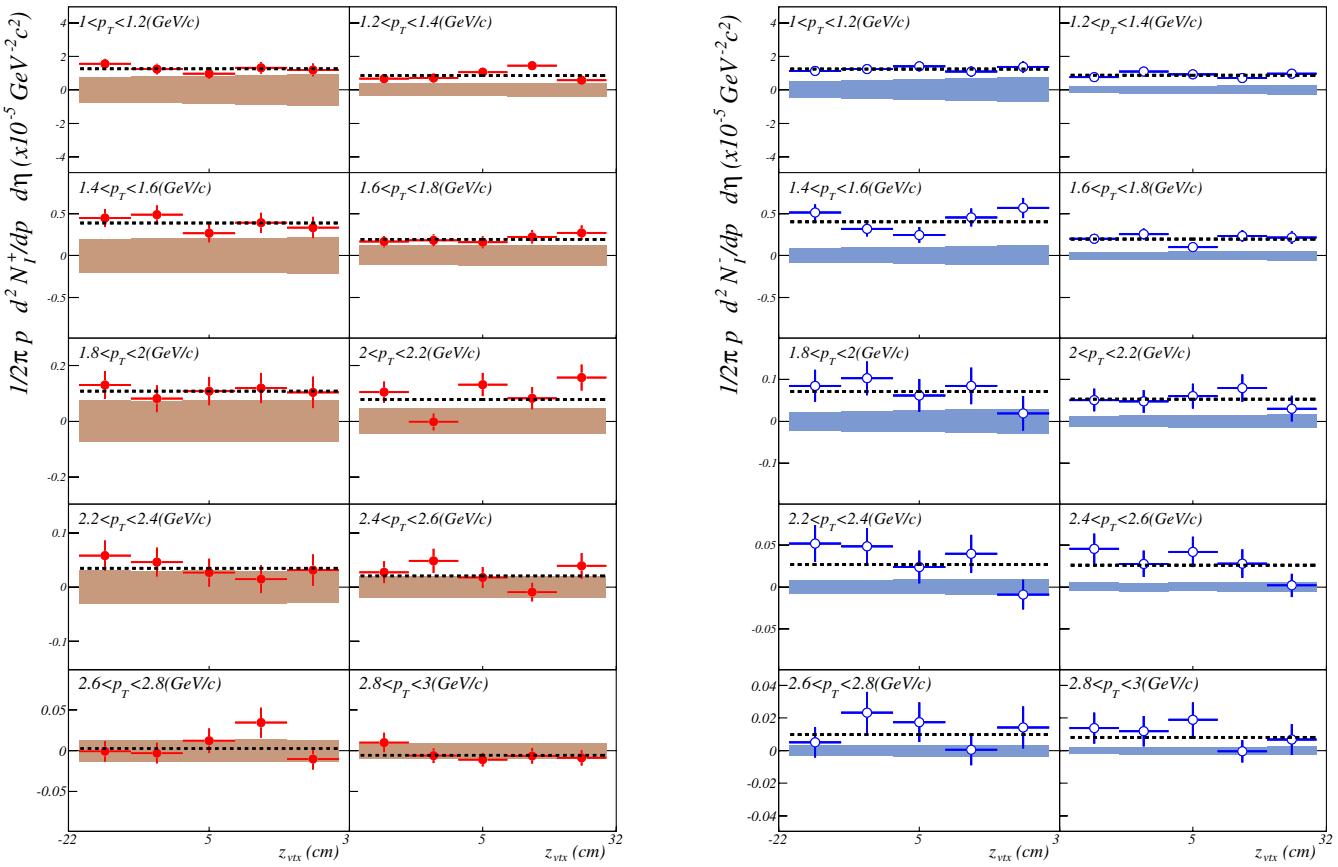

FIG. 12 (color online). Points show the yield of (left) positively and (right) negatively charged vertex-independent muons vs z_{vtx} for different p_T bins with statistical errors. The dashed lines show the yield for each p_T bin, averaged over z_{vtx}. The shaded bands around 0 show the systematic error on the sum of the contributions to the inclusive muon candidate yield from light-hadronic sources, as listed in Tables V, VI, and VII and discussed in Sec. III I. The larger systematic uncertainties for positive particles are due to the larger fractional contribution of punchthrough background, which in turn is due to the relatively long nuclear interaction cross section for positive kaons.

$$\begin{aligned} N_\mu &= N_I \times (N_\mu/N_I) \\ &= N_I \times ((N_I - N_D - N_P - N_B)/N_I) \\ &= N_I \times (1 - R_D - R_P - R_B), \end{aligned} \tag{12}$$

where $R_j = N_j/N_I$ is the fraction of the inclusive muon candidate yield attributed to the j^{th} component. We can now write the systematic error on N_μ as:

$$\sigma_{N_\mu} = \sqrt{(\sigma_{N_I}/N_I)^2 N_\mu^2 + (\sigma_{R_D}^2 + \sigma_{R_P}^2 + \sigma_{R_B}^2) N_I^2} \tag{13}$$

σ_{N_μ}, as determined below, is displayed in Figs. 11 and 12.

Note that the uncertainties for positive particles are significantly larger than for negative particles. This is due to the fact that the fraction of the inclusive muon candidate yield from punchthrough background is significantly larger for positive particles than for negative particles, as shown in Fig. 10. As discussed above, this is due to the relatively long nuclear interaction cross section for positive kaons.

Uncertainties contributing to σ_{N_I} are listed in Table V. Uncertainties contributing to σ_{N_D} and σ_{R_D} are listed in Table VI. Uncertainties contributing to σ_{N_P} and σ_{R_P} are listed in Table VII. Note that in these tables we separately list uncertainties that affect the overall normalization (σ/N^{norm}) and the shape of the p_T spectrum (σ/N^{p_T}).

TABLE V. Sources of systematic error on the calculation of N_I, the yield of inclusive muon candidates. σ_{N_I}/N_I is obtained by adding the different contributions in quadrature.

Error source	σ/N^{norm}	σ/N^{p_T}
Momentum scale	6.0%	$(p_T[\text{GeV}/c] - 1) \times 1.3\%$
ε_{acc}	10%	$(p_T[\text{GeV}/c] - 1) \times 1.5\%$
ε_{rec}	9.0%	0
$\varepsilon_{\text{user}}$	5.0%	$(p_T[\text{GeV}/c] - 1) \times 5.0\%$
$\varepsilon_{\text{trig}}$	4.7%	0
σ_{N_I}/N_I	16.3%	$(p_T[\text{GeV}/c] - 1) \times 5.4\%$

TABLE VI. Sources of systematic error on R_D, the ratio of free-decay muons to inclusive muon candidates, and N_D, the absolute yield of free-decay muons. σ_{R_D} is obtained by adding the different contributions in quadrature. σ_{N_D}/N_D is obtained by adding σ_{R_D} and σ_{N_I}/N_I in quadrature.

Error source	σ/N^{norm}	σ/N^{p_T}
Decay flight path	5%	0
z_{vtx} fit range	3.3%	0
Input hadron spectrum	0	$(p_T[\text{GeV}/c]-1)\times 5.0\%$
Decay normalization	7%	0
σ_{R_D}	9.2%	$(p_T[\text{GeV}/c]-1)\times 5.0\%$
σ_{N_D}/N_D	18.7%	$(p_T[\text{GeV}/c]-1)\times 7.4\%$

TABLE VII. Sources of systematic error on R_P, the ratio of punchthrough hadrons to inclusive muon candidates, and N_P, the absolute yield of punchthrough hadrons. σ_{R_P} is obtained by adding the different contributions in quadrature. σ_{N_P}/N_P is obtained by adding σ_{R_P} and σ_{N_I}/N_I in quadrature.

Error source	σ/N^{norm}	σ/N^{p_T}
$\varepsilon^3_{\text{scale}}$	23%	0
Exponential absorption model	0	32%
p and $\bar{p}$ contributions	10%	0
N_3^{stop} normalization	10%	0
σ_{R_P}	27%	32%
σ_{N_P}/N_P	31.5%	$\approx 32\%$

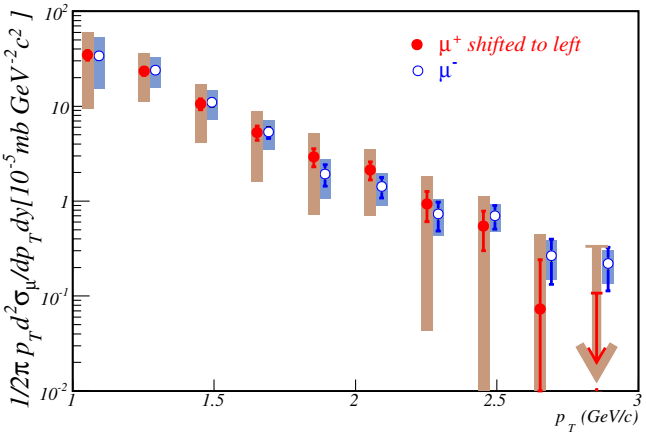

FIG. 13 (color online). p_T spectrum of vertex-independent muons. Error bars indicate statistical errors. One point with unphysical (less than zero) extracted yield is shown as an arrow pointing down from the 90% C.L. upper limit Shaded bands indicate systematic errors, as listed in Tables V, VI, and VII and discussed in Sec. III I. The larger systematic uncertainties for positive particles is due to the larger fractional contribution of punchthrough background, which in turn is due to the relatively long nuclear interaction cross section for positive kaons.

TABLE VIII. Other sources of systematic uncertainty. σ_{R_B} is incorporated into the systematic uncertainty on the vertex-independent muon yield, as shown in Eq. (13). Errors on σ^{pp}_{BBC} and $\varepsilon^{c,\bar{c}\to\mu}_{\text{BBC}}$ are added in quadrature along with the total uncertainty on the vertex-independent muon yield, σ_{N_μ}/N_μ to get the uncertainty on the vertex-independent muon cross section.

Error source	σ/N^{norm}	σ/N^{p_T}
σ_{R_B}	0	$5\%\times N_D(p_T, z_{vtx}=0)$
$\sigma_{\sigma^{pp}_{\text{BBC}}}$	9.6%	0
$\sigma_{\varepsilon^{c,\bar{c}\to\mu}_{\text{BBC}}}$	5%	0

Values for σ_{N_I}/N_I are displayed in Fig. 6. Values for σ_{R_D} and σ_{R_P} are displayed in Figs. 7 and 10 respectively. We insert σ_{N_I}/N_I, σ_{R_D}, σ_{R_P}, and σ_{R_B} into Eq. (13) as part of the final systematic error on N_μ.

To get the vertex-independent muon cross section, as defined in Eq. (3) and displayed in Figs. 13 and 16, we need to add in quadrature the errors on N_μ, σ^{pp}_{BBC}, $\varepsilon^{c,\bar{c}\to\mu}_{BBC}$. The error on N_μ is obtained from the components above according to Eq. (13). Errors on σ^{pp}_{BBC} and $\varepsilon^{c,\bar{c}\to\mu}_{BBC}$ are listed in Table VIII.

IV. CHARM CROSS SECTION

The charm production cross section obtained from the yield of vertex-independent muons (or from the yield of nonphotonic electrons, or D mesons) is necessarily model dependent since we do not measure the charm quarks directly. We use PYTHIA to convert our measurement of the vertex-independent muon yield into an estimate of the differential charm production cross section at forward rapidity, $d\sigma_{c\bar{c}}/dy|_{y=1.6}$, in a procedure very similar to that used in PHENIX measurements of charm production at $y=0$ [7–13]. We use PYTHIA version 6.205 with parameters tuned to reproduce charm production data at SPS and FNAL [71] and single-electron data at the ISR [72–74]. Tuned parameters are listed in Table VIII. The meaning of each parameter is more thoroughly defined in the PYTHIA manual [75].

Vertex-independent muon sources, predicted by a PYTHIA simulation using the same parameters (except that MSEL is set to 2 to generate unbiased collisions), are listed in Table X. These sources include decays of hadrons containing a heavy quark, and light-vector mesons with a decay length too short to be measured with the existing experimental apparatus (ρ, ω, ϕ). Their p_T spectra are shown in Fig. 14. Contributions from quarkonium decays, Drell-Yan, and τ lepton decays are negligible. This shows that vertex-independent muon production in our acceptance is dominated by muons from decay of charm hadrons, although for $p_T > 2.5$ GeV/c the contribution from decays of hadrons containing a bottom quark is starting to become significant.

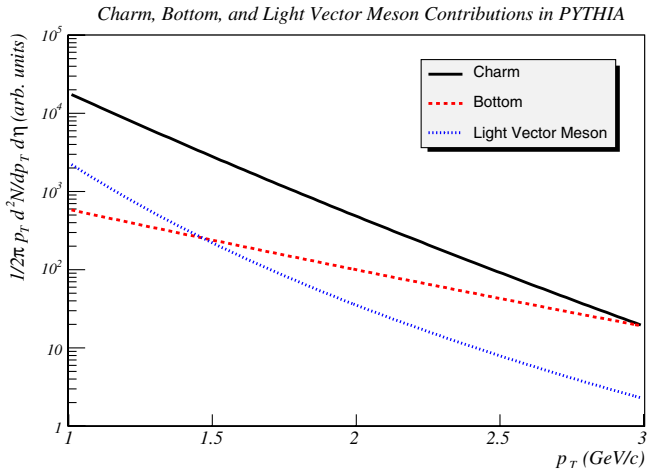

FIG. 14 (color online). PYTHIA calculation showing the major contributions to the vertex-independent muon p_T spectrum. Solid, dashed, and dotted lines show the yield from charm, bottom, and light vector mesons (ρ, ω, ϕ), respectively.

This simulation also gives the distribution of charm quarks (p_T vs y) that produce a muon in our acceptance, as shown in Fig. 15. This demonstrates that the vertex-independent muons we measure sample charm quarks down to $p_T \approx 1$ GeV/c, over a narrow rapidity slice centered at $y = 1.6$.

Figure 16 shows a comparison of the measured vertex-independent negative muon spectrum (from Fig. 13) to the prediction of this default PYTHIA simulation and to a FONLL calculation [20,77]. Note, larger systematic errors for the positive muon spectrum preclude a significant measurement for that charge sign. One can see that the measured values significantly exceed both predictions. The spectrum also appears to be somewhat harder than the PYTHIA spectrum with the parameters listed in Table IX.

We scale the charm (only) contribution to the PYTHIA vertex-independent muon p_T spectrum such that the total

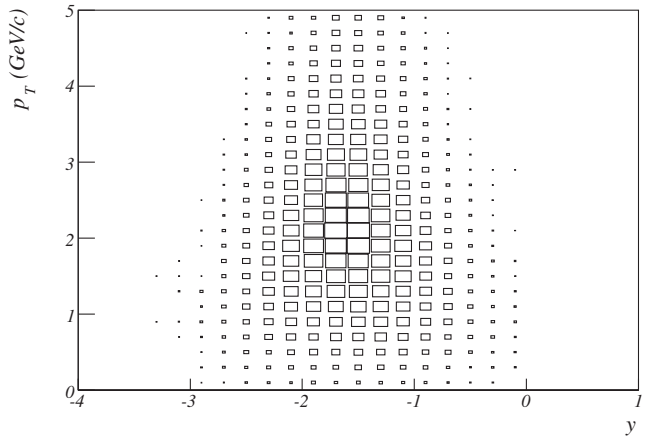

FIG. 15. PYTHIA results for the p_T vs y distribution (linear z-scale) of charm quarks that produce a muon in the PHENIX acceptance.

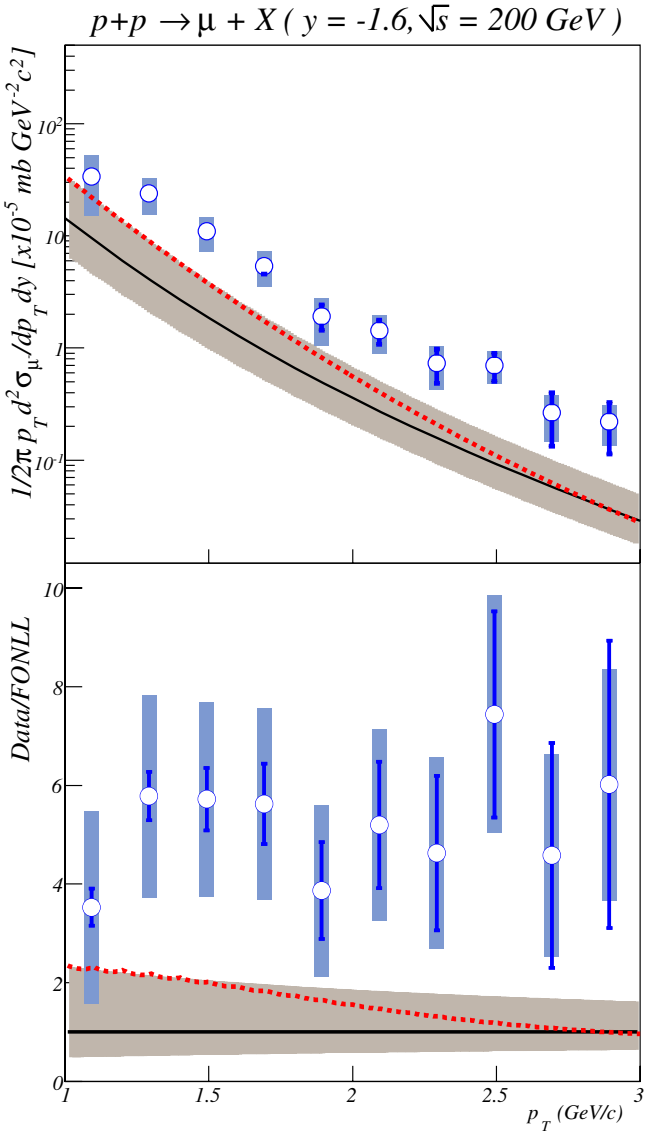

FIG. 16 (color online). The top panel shows the measured p_T spectrum of vertex-independent negative muons from Fig. 13, the PYTHIA prediction using settings listed in Table IX without scaling the charm contribution (dotted line), and a FONLL calculation (solid line with systematic error band) [20,77]. The bottom panel shows the ratio of the measured spectrum to the FONLL calculation with statistical (error bars) and systematic (bands) uncertainties on the data, as well as the theoretical uncertainty (shaded band around 1). The dashed line shows the PYTHIA/FONLL ratio.

spectrum (including the small contributions from open bottom and vector mesons) matches the central values of the measured vertex-independent negative muon spectrum. Only statistical errors are used in the fit. We multiply the scale factor from the fit (2.27) by the PYTHIA value for the charm production cross section, $d\sigma_{c\bar{c}}/dy|^{\mathrm{PYTHIA}}_{y=1.6}$ (0.107 mb), to obtain $d\sigma_{c\bar{c}}/dy|^{\mathrm{PHENIX}}_{y=1.6} = 0.243 \pm 0.013(\mathrm{stat.})$ mb.

TABLE IX. Tuned PYTHIA parameters (default settings for this analysis) for determination of charm production cross section central value.

Parameter	Value	Meaning
MSEL	4	Heavy quark production every event (gluon fusion + $q/\bar{q}$ annihilation).
MSTP (32)	4	Hard scattering scale, $Q^2 = \hat{s}$.
MSTP (33)	1	Use K-factor.
MSTP (52)	2	Use PDF libraries.
MSTP (51)	4046	Select CTEQ5L PDF libraries [76].
MSTP (91)	1	Use Gaussian distribution for intrinsic k_T.
PARP (31)	3.5	K-factor.
PARP (91)	1.5	$\langle k_T \rangle$ (GeV/c).
PARP (93)	5.0	Maximum k_T (GeV/c).
PMAS (4, 1)	1.25	m_c (GeV/c).
D^+/D^0	0.32	Default charm chemistry ratio.

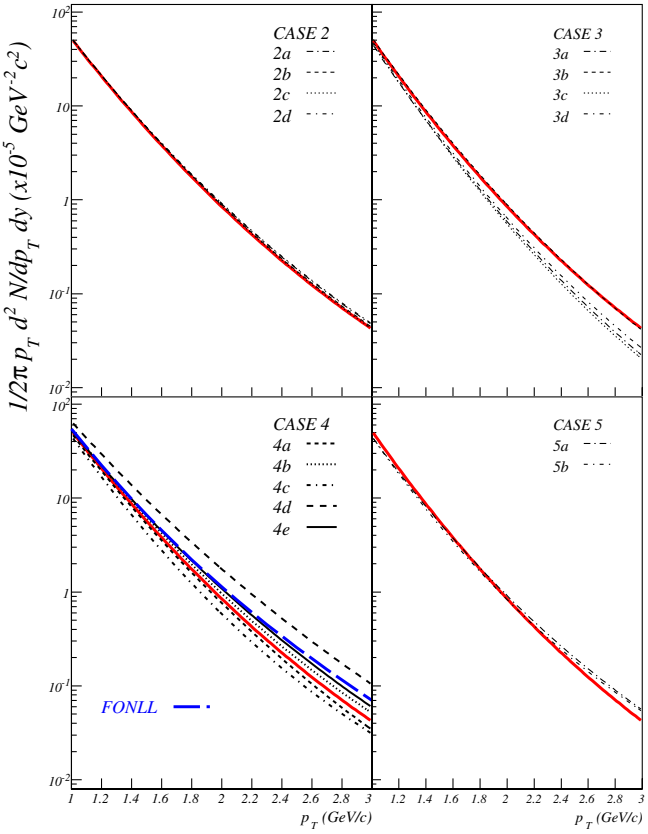

FIG. 17 (color online). PYTHIA results with different parameter sets for the negative vertex-independent muon p_T spectrum per event in which a $c\bar{c}$ pair is created. The solid line in each panel shows the result when using default settings listed in Table IX. Legends indicate the correspondence between line style and the simulation case label. Parameter sets for each case label are given in Table XI.

TABLE X. Percentage contribution of different sources of vertex-independent muons within our acceptance ($1 < p_T < 3$ GeV/c and $1.5 < |\eta| < 1.8$), from PYTHIA, with parameters listed in Table IX (except that MSEL = 2 to generate minimum bias collisions).

Source	Contribution
Open charm	84.6%
Open bottom	6.9%
ρ, ω, ϕ	8.1%
Quarkonia	<0.1%
Drell-Yan	<0.1%
τ leptons	0.4%

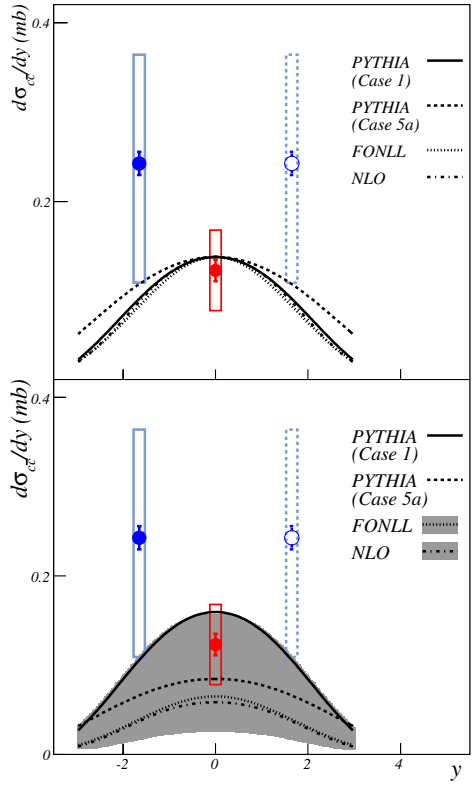

FIG. 18 (color online). Comparisons of measured charm rapidity distributions, $d\sigma_{c\bar{c}}/dy$ vs y, to theoretical predictions. Data points at $y = \pm 1.6$ are from this analysis (the point at $y = 1.6$ is reflected through $y = 0$). The point at $y = 0$ is the PHENIX measurement of charm through semileptonic decay to electrons [13]. Error bars on the data points indicate statistical uncertainties and boxes indicate systematic uncertainties. The top panel shows rapidity spectra from two PYTHIA parameter sets (see Table XI for details), FONLL [20,77], and a NLO calculation [83]. The PYTHIA curve with the default parameter set (case 1) was fit to the two PHENIX data points with statistical and systematic errors added in quadrature. All other theory curves were normalized so that they are equal at $y = 0$ to allow shape comparisons. The bottom panel shows the theory curves without normalization. Theoretical uncertainties associated with the FONLL and NLO calculations are indicated with shaded bands.

TABLE XI. Results for PYTHIA simulations with different parameter sets used to explore the systematic error on the charm cross section due to model uncertainties. The top of the table details the different parameter sets tested. Unless otherwise noted, parameters are the same as those listed in Table IX. The bottom of the table gives the results for different simulations: The first column identifies the simulation; the second column gives the total charm production cross section given the chosen PYTHIA parameter set; the third column gives the differential charm production cross section at $y = 1.6$; the fourth column gives the normalization factor needed to fit the PHENIX data; the fifth column gives the differential charm production cross section at $y = 1.6$ for PHENIX data (the product of the third and fourth columns); the sixth column gives the fractional difference between the results for each simulation compared to the simulation with the default PYTHIA parameter set; the last column gives the ratio $d\sigma_{c\bar{c}}/dy|^{\mathrm{PYTHIA}}_{y=1.6}/d\sigma_{c\bar{c}}/dy|^{\mathrm{PYTHIA}}_{y=0}$.

Case	PYTHIA Settings
1	Default settings, see Table IX.
2a	MSTP(51) = 4032, CTEQ4L PDF libraries [78].
2b	MSTP(51) = 5005, GRV94LO PDF libraries [79].
2c	MSTP(51) = 5012, GRV98LO PDF libraries [80].
2d	MSTP(51) = 3072, MRST (c−g) PDF libraries [81].
3a	MSTP(32) = 1, $Q^2 = 2\hat{s}\,\hat{t}\,\hat{u}/(\hat{s}^2 + \hat{t}^2 + \hat{u}^2)$.
3b	MSTP(32) = 2, $Q^2 = p_T^2 + (m_3^2 + m_4^2)/2$.
3c	MSTP(32) = 3, $Q^2 = \min(-\hat{t}, -\hat{u})$.
3d	MSTP(32) = 5, $Q^2 = -\hat{t}$.
4a	PMAS(4, 1) = $m_c = 1.15$ GeV/c.
4b	PMAS(4, 1) = $m_c = 1.35$ GeV/c.
4c	PARP(91) = $\langle k_T \rangle = 0.3$ GeV/c.
4d	PARP(91) = $\langle k_T \rangle = 3.0$ GeV/c.
4e	MSTP(68) = 2, Maximum virtuality scale and matrix element matching scheme. PARP(67) = 4, Multiplicative factor applied to hard scattering scale.
5a	PARP(31) = K-factor = 1, MSEL = 1, Hard scattering enabled.
5b	PARP(31) = K-factor = 1, MSEL = 1, Hard scattering enabled, All other parameters untuned.
6	$D^+/D^0 = 0.45$ [82].
7	Open bottom and vector mesons scale with charm.

Case	$\sigma_{c\bar{c}}^{\mathrm{PYTHIA}}$ (mb)	$d\sigma_{c\bar{c}}/dy\|^{\mathrm{PYTHIA}}_{y=1.6}$ (mb)	Normalization to Data	$d\sigma_{c\bar{c}}/dy\|^{\mathrm{PHENIX}}_{y=1.6}$ (mb)	$\Delta d\sigma_{c\bar{c}}/dy\|^{\mathrm{PHENIX}}_{y=1.6}$ (%)	$d\sigma_{c\bar{c}}/dy\|^{\mathrm{PYTHIA}}_{y=1.6}/d\sigma_{c\bar{c}}/dy\|^{\mathrm{PYTHIA}}_{y=0}$
1	0.658	0.107	2.27	0.243	—	0.67
2a	0.691	0.111	2.10	0.232	−4.5	0.69
2b	0.698	0.112	2.09	0.233	−3.9	0.71
2c	0.669	0.109	2.18	0.238	−1.7	0.73
2d	0.551	0.088	2.67	0.236	−2.9	0.71
3a	1.520	0.243	1.12	0.271	11.8	0.84
3b	0.863	0.139	1.63	0.226	−6.7	0.71
3c	1.501	0.242	1.11	0.267	10.2	0.84
3d	1.104	0.178	1.45	0.258	6.4	0.78
4a	0.905	0.145	1.73	0.252	3.7	0.67
4b	0.487	0.078	2.91	0.226	−6.7	0.64
4c	0.658	0.104	2.81	0.292	20.4	0.66
4d	0.658	0.104	1.50	0.156	−35.8	0.63
4e	0.658	0.106	2.09	0.220	−9.2	0.63
5a	0.435	0.068	3.91	0.266	9.4	0.80
5b	0.385	0.058	4.67	0.271	11.7	0.79
6	0.658	0.107	2.38	0.255	5.0	0.67
7	0.658	0.107	2.20	0.236	−2.9	0.67

We distinguish between two different sources of systematic uncertainty on the extraction of the charm cross section: (1) uncertainty in the PYTHIA calculation and (2) uncertainty in the data, which is largely independent of PYTHIA.

We determined the uncertainty in the data ($\pm$ 43%) by refitting PYTHIA to the data at the minimum and maximum of the 1σ systematic error band.

We determined the uncertainty in the PYTHIA calculation with a systematic study in which we varied simulation parameters, extracted the new simulated vertex-independent negative muon spectrum, normalized to the measured spectrum, and extracted $d\sigma_{c\bar{c}}/dy|_{y=1.6}^{\mathrm{PHENIX}}$ for the modified parameter sets. We varied PDF libraries, the hard scattering scale, the charm quark mass, the intrinsic k_T value, the D^+/D^0 ratio, charm production mechanism selections, and open bottom and vector meson scaling assumptions. The parameter sets used and the results of this study are summarized in Table XI.

The PYTHIA charm cross section varies substantially ($\Delta(d\sigma_{c\bar{c}}/dy)|_{y=1.6}^{\mathrm{PYTHIA}}) \approx 4$) for the chosen parameter sets. However, the extracted experimental charm cross section is relatively stable ($\Delta(d\sigma_{c\bar{c}}/dy)|_{y=1.6}^{\mathrm{PHENIX}} < 0.36$). This is due to the fact that the parameter set changes have relatively minor effects on the shape of the predicted vertex-independent muon p_T spectrum, and we obtain the experimental charm cross section by normalizing the PYTHIA charm cross section by the ratio of the measured and predicted muon p_T spectra.

One way to visualize this is to plot (see Fig. 17) the vertex-independent muon yield in our acceptance per event in which a $c\bar{c}$ pair is created for the different PYTHIA parameter sets. Because of our procedure, parameter sets which give similar vertex-independent muon yields per $c\bar{c}$ event in the low p_T region (which dominates the fit) will necessarily give similar values for $d\sigma_{c\bar{c}}/dy|_{y=1.6}^{\mathrm{PHENIX}}$, whatever the PYTHIA charm cross section is.

The largest variation in the predicted muon yield at $p_T = 1$ GeV/c per $c\bar{c}$ event is seen for simulations in which the intrinsic k_T is varied from its default value ($\langle k_T \rangle = 1.5$ GeV/c) to the value expected from arguments based on Fermi momentum (case 4c, $\langle k_T \rangle = 0.3$ GeV/c), or to a value which best reproduces the measured spectrum at higher p_T (case 4d, $\langle k_T \rangle = 3.0$ GeV/c). These parameter sets also result in the largest variation in $d\sigma_{c\bar{c}}/dy|_{y=1.6}^{\mathrm{PHENIX}}$, as shown in Table X. We use the cross section values obtained in this pair of simulations to define the systematic uncertainty in our measurement due to the uncertainty in our PYTHIA calculation. This gives us our final answer: $d\sigma_{c\bar{c}}/dy|_{y=1.6} = 0.243 \pm 0.013(\mathrm{stat.}) \pm 0.105(\mathrm{datasyst.})^{+0.049}_{-0.087}(\mathrm{PYTHIAsyst.})$ mb. As shown in the lower-left panel of Fig. 17, the FONLL prediction of the muon yield per $c\bar{c}$ collision lies well within the extreme cases defining the systematic error resulting from the necessary model dependence of our charm extraction. Therefore, using FONLL instead of PYTHIA for the charm extraction would yield consistent results.

Figure 18 shows the PHENIX charm rapidity spectrum. The result of this analysis (mirrored about $y = 0$ since this is a symmetric collision system) is plotted along with the result for $d\sigma_{c\bar{c}}/dy|_{y=0}$ [13]. In order to compare with the data at $y = 0$ the systematic uncertainty on the data from this analysis is shown as the quadrature sum of the two sources of systematic uncertainty described above (data and PYTHIA). Theoretical curves from PYTHIA (case 1 and case 5a), FONLL [20,77], and a NLO calculation from Vogt [83] are also displayed.

In the top panel of the figure PYTHIA with the default parameter set (case 1) is fit to the two PHENIX points with statistical and systematic errors added in quadrature. Other theory curves are normalized so that they are equal at $y = 0$ in order to allow shape comparisons. As shown in Table XI, different PYTHIA parameter sets differ in the predicted ratio $d\sigma_{c\bar{c}}/dy|_{y=1.6}^{\mathrm{PYTHIA}}/d\sigma_{c\bar{c}}/dy|_{y=0}^{\mathrm{PYTHIA}}$ by $>30\%$. Unfortunately, current systematic error bars preclude any conclusions about the charm production rapidity shape.

In the bottom panel of the figure the theory curves are without normalization to allow an absolute comparison. The quoted theoretical uncertainty bands for the FONLL and NLO calculations are also shown. We note that, although our data are above the FONLL prediction, the error bars touch. This is in contrast to the situation for the vertex-independent muon cross section, shown in Fig. 16, where the data are significantly above the prediction. The larger disagreement in the vertex-independent muon cross section is presumably due to different treatment of the fragmentation process in PYTHIA and FONLL [20,77,83].

V. CONCLUSION AND OUTLOOK

We have measured muon production at forward rapidity ($1.5 \leq |\eta| \leq 1.8$), in the range $1 < p_T < 3$ GeV/c, in $\sqrt{s} = 200$ GeV $p + p$ collisions at RHIC. We determined and subtracted the contribution from light hadron sources (π, K, p) to obtain the vertex-independent muon yield which, for the p_T range measured in this analysis, and in the absence of new physics, arises dominantly from the decay of D mesons. We normalized the PYTHIA muon spectrum resulting from the production of charm quarks to obtain the differential cross section for charm production at forward rapidity: $d\sigma_{c\bar{c}}/dy|_{y=1.6} = 0.243 \pm 0.013(\mathrm{stat.}) \pm 0.105(\mathrm{datasyst.})^{+0.049}_{-0.087}(\mathrm{PYTHIAsyst.})$ mb. This is compatible with PHENIX charm measurement at $y = 0$, although even further above predictions from PYTHIA and FONLL. Large systematic uncertainties in the current measurement preclude statements about the rapidity dependence of the charm cross section.

The systematic uncertainty in the data is dominated by uncertainty on the determination of the fractional contribution of decay muons. This will be improved with higher

statistics data sets (already collected) which will allow better measurements of the z_{vtx} dependence of particle production. Final results for identified particle p_T distributions in $p + p$ collisions by BRAHMS will also be invaluable for improving the input to our hadron generator. The systematic uncertainty in PYTHIA is dominated by differences observed when the intrinsic $\langle k_T \rangle$ is varied. In order to reduce this uncertainty we need to reduce the allowed parameter space by improving the measurement of the high p_T portion of the vertex-independent muon spectrum, where the error is dominated by the uncertainty in the yield of punchthrough hadrons. Data sets (already collected) with higher statistics, and with hadrons stopping in MuID gap 2, will allow a completely data-driven approach to the calculation of the punchthrough yield. This will eliminate the reliance on hadronic interaction simulation packages, differences in which are the largest source of systematic error at high p_T. Analogous measurements are also being carried out for $d + Au$, $Cu + Cu$, and $Au + Au$ [84] collisions at $\sqrt{s_{NN}} = 200$ GeV. These will allow determination of the magnitude of nuclear modification effects on charm production at forward rapidity.

ACKNOWLEDGMENTS

We thank the staff of the Collider-Accelerator and Physics Departments at Brookhaven National Laboratory and the staff of the other PHENIX participating institutions for their vital contributions. We acknowledge support from the Department of Energy, Office of Science, Nuclear Physics Division, the National Science Foundation, Abilene Christian University Research Council, Research Foundation of SUNY, and Dean of the College of Arts and Sciences, Vanderbilt University (USA), Ministry of Education, Culture, Sports, Science, and Technology and the Japan Society for the Promotion of Science (Japan), Conselho Nacional de Desenvolvimento Científico e Tecnológico and Fundação de Amparo à Pesquisa do Estado de São Paulo (Brazil), Natural Science Foundation of China (People's Republic of China), Centre National de la Recherche Scientifique, Commissariat à l'Énergie Atomique, Institut National de Physique Nucléaire et de Physique des Particules, and Institut National de Physique Nucléaire et de Physique des Particules (France), Bundesministerium für Bildung und Forschung, Deutscher Akademischer Austausch Dienst, and Alexander von Humboldt Stiftung (Germany), Hungarian National Science Fund, OTKA (Hungary), Department of Atomic Energy and Department of Science and Technology (India), Israel Science Foundation (Israel), Korea Research Foundation and Korea Science and Engineering Foundation (Korea), Russian Ministry of Industry, Science and Tekhnologies, Russian Academy of Science, Russian Ministry of Atomic Energy (Russia), V. R. and the Wallenberg Foundation (Sweden), the U.S. Civilian Research and Development Foundation for the Independent States of the Former Soviet Union, the US-Hungarian NSF-OTKA-MTA, the US-Israel Binational Science Foundation, and the 5th European Union TMR Marie-Curie Programme.

[1] B. Abbott *et al.* (D0 Collaboration), Phys. Rev. Lett. **84**, 5478 (2000).
[2] D. Acosta *et al.* (CDF Collaboration), Phys. Rev. D **71**, 032001 (2005).
[3] M. Cacciari, arXiv:hep-ph/0407187.
[4] M. Cacciari, M. Greco, and P. Nason, J. High Energy Phys. 05 (1998) 007.
[5] M. L. Mangano, AIP Conf. Proc. **753**, 247 (2005).
[6] D. Acosta *et al.* (CDF Collaboration), Phys. Rev. Lett. **91**, 241804 (2003).
[7] K. Adcox *et al.* (PHENIX Collaboration), Phys. Rev. Lett. **88**, 192303 (2002).
[8] S. S. Adler *et al.* (PHENIX Collaboration), Phys. Rev. Lett. **94**, 082301 (2005).
[9] S. S. Adler *et al.* (PHENIX Collaboration), Phys. Rev. Lett. **96**, 032001 (2006).
[10] S. Kelly (PHENIX Collaboration), J. Phys. G **30**, S1189 (2004).
[11] S. S. Adler *et al.* (PHENIX Collaboration), Phys. Rev. Lett. **96**, 032301 (2006).
[12] S. Butsyk (PHENIX Collaboration), Nucl. Phys. **A774**, 669 (2006).
[13] A. Adare *et al.* (PHENIX Collaboration), Phys. Rev. Lett. **97**, 252002 (2006).
[14] S. S. Adler *et al.* (PHENIX Collaboration), Phys. Rev. C **72**, 024901 (2005).
[15] S. Sakai (PHENIX Collaboration), J. Phys. G **32**, S551 (2006).
[16] A. Adare *et al.* (PHENIX Collaboration), to be published.
[17] J. Adams *et al.* (STAR Collaboration), Phys. Rev. Lett. **94**, 062301 (2005).
[18] B. I. Abelev *et al.* (STAR Collaboration), Phys. Rev. Lett. **98**, 192301 (2007).
[19] T. Sjöstrand *et al.*, Comput. Phys. Commun. **135**, 238 (2001).
[20] M. Cacciari, P. Nason, and R. Vogt, Phys. Rev. Lett. **95**, 122001 (2005).
[21] M. L. Mangano, Nucl. Phys. **B405**, 507 (1993).
[22] R. Vogt, arXiv:hep-ph/0203151.
[23] R. Vogt, Int. J. Mod. Phys. E **12**, 211 (2003).
[24] W. Cassing, E. Bratkovskaya, and A. Sibirtsev, Nucl. Phys. **A691**, 753 (2001).
[25] E. L. Bratkovskaya, W. Cassing, and H. Stöcker, Phys. Rev. C **67**, 054905 (2003).

[26] C.-Y. Wong, *Introduction to High-Energy Heavy-Ion Collisions* (World Scientific, Singapore, 1994), p. 251.
[27] M. B. Johnson *et al.* (E772 Collaboration), Phys. Rev. Lett. **86**, 4483 (2001).
[28] G. T. Bodwin, S. J. Brodsky, and G. P. Lepage, Phys. Rev. Lett. **47**, 1799 (1981).
[29] G. T. Bodwin, Phys. Rev. D **31**, 2616 (1985).
[30] G. T. Bodwin, S. J. Brodsky, and G. P. Lepage, Phys. Rev. D **39**, 3287 (1989).
[31] B. Z. Kopeliovich and F. Niedermayer, Tech. Rep. E2-84-834, Dubna 1984; http://ccdb3fs.kek.jp/cgi-bin/img/allpdf?198504113.
[32] S. Gavin and J. Milana, Phys. Rev. Lett. **68**, 1834 (1992).
[33] V. Guzey, M. Strikman, and W. Vogelsang, Phys. Lett. B **603**, 173 (2004).
[34] Y. L. Dokshitzer and D. E. Kharzeev, Phys. Lett. B **519**, 199 (2001).
[35] L. McLerran and R. Venugopalan, Phys. Rev. D **49**, 2233 (1994).
[36] L. McLerran and R. Venugopalan, Phys. Rev. D **49**, 3352 (1994).
[37] J. Ashman *et al.* (EMC Collaboration), Phys. Lett. B **202**, 603 (1988).
[38] R. Baier, D. Schiff, and B. Zakharov, Annu. Rev. Nucl. Part. Sci. **50**, 37 (2000).
[39] J. A. Appel, Annu. Rev. Nucl. Part. Sci. **42**, 367 (1992).
[40] B. Müller and X. N. Wang, Phys. Rev. Lett. **68**, 2437 (1992).
[41] T. Matsui and H. Satz, Phys. Lett. B **178**, 416 (1986).
[42] H. Satz, J. Phys. G **32**, R25 (2006).
[43] R. L. Thews and M. L. Mangano, Phys. Rev. C **73**, 014904 (2006).
[44] L. Grandchamp, R. Rapp, and G. E. Brown, Phys. Rev. Lett. **92**, 212301 (2004).
[45] A. Andronic *et al.*, Phys. Lett. B **571**, 36 (2003).
[46] A. P. Kostyuk *et al.*, Phys. Rev. C **68**, 041902(R) (2003).
[47] S. S. Adler *et al.* (PHENIX Collaboration), Phys. Rev. Lett. **94**, 082302 (2005).
[48] I. Arsene *et al.* (BRAHMS Collaboration), Phys. Rev. Lett. **94**, 032301 (2005).
[49] I. Arsene *et al.* (BRAHMS Collaboration), Phys. Rev. Lett. **93**, 242303 (2004).
[50] J. Adams *et al.* (STAR Collaboration), Phys. Rev. Lett. **97**, 152302 (2006).
[51] S. S. Adler *et al.* (PHENIX Collaboration), Phys. Rev. Lett. **92**, 051802 (2004).
[52] S. S. Adler *et al.* (PHENIX Collaboration), Phys. Rev. Lett. **96**, 012304 (2006).
[53] H. Pereira Da Costa (PHENIX Collaboration), Nucl. Phys. **A774**, 747 (2006).
[54] K. Adcox *et al.* (PHENIX Collaboration), Nucl. Instrum. Methods Phys. Res., Sect. A **499**, 469 (2003).
[55] S. S. Adler *et al.* (PHENIX Collaboration), Nucl. Instrum. Methods Phys. Res., Sect. A **499**, 560 (2003).
[56] S. S. Adler *et al.* (PHENIX Collaboration), Nucl. Instrum. Methods Phys. Res., Sect. A **499**, 593 (2003).
[57] M. Allen *et al.* (PHENIX Collaboration), Nucl. Instrum. Methods Phys. Res., Sect. A **499**, 549 (2003).
[58] H. Akikawa *et al.* (PHENIX Collaboration), Nucl. Instrum. Methods Phys. Res., Sect. A **499**, 537 (2003).
[59] S. H. Aronson *et al.* (PHENIX Collaboration), Nucl. Instrum. Methods Phys. Res., Sect. A **499**, 480 (2003).
[60] S. S. Adler *et al.* (PHENIX Collaboration), Phys. Rev. Lett. **91**, 241803 (2003).
[61] GEANT 3.2.1 Manual, CERN W5013 1994; http://wwwasdoc.web.cern.ch/wwwasdoc/pdfdir/geant.pdf.
[62] V. L. Highland, Nucl. Instrum. Methods **129**, 497 (1975).
[63] V. L. Highland, Nucl. Instrum. Methods **161**, 171 (1979).
[64] G. R. Lynch and O. I. Dahl, Nucl. Instrum. Methods Phys. Res., Sect. B **58**, 6 (1991).
[65] S. S. Adler *et al.* (PHENIX Collaboration), Phys. Rev. D (unpublished).
[66] V. Ryabov (PHENIX Collaboration), Nucl. Phys. **A774**, 735 (2006).
[67] S. Eidelman *et al.*, Phys. Lett. B **592**, 1 (2004).
[68] A. Fassò *et al.*, in *Proceedings of the Monte Carlo 2000 Conference, Lisbon, 2000*, edited by A. Kling *et al.* (Springer-Verlag, Berlin, 2001), p. 955; http://www.fluka.org.
[69] H. S. Fesefeldt, Aachen Report No. PITHA 85/02, 1985.
[70] E. W. Cornell *et al.*, Nucl. Instrum. Methods Phys. Res., Sect. A **350**, 150 (1994).
[71] G. A. Alves *et al.* (E769 Collaboration), Phys. Rev. Lett. **77**, 2388 (1996).
[72] F. W. Büsser *et al.*, Nucl. Phys. **B113**, 189 (1976).
[73] P. Perez *et al.*, Phys. Lett. B **112**, 260 (1982).
[74] M. Basile *et al.*, Nuovo Cimento Soc. Ital. Fis. A **65**, 421 (1981).
[75] T. Sjöstrand *et al.*, arXiv:hep-ph/0108264.
[76] H. L. Lai *et al.* (CTEQ Collaboration), Eur. Phys. J. C **12**, 375 (2000).
[77] M. Cacciari (private communication).
[78] H. L. Lai *et al.* (CTEQ Collaboration), Phys. Rev. D **55**, 1280 (1997).
[79] M. Gluck, E. Reya, and A. Vogt, Z. Phys. C **67**, 433 (1995).
[80] M. Gluck, E. Reya, and A. Vogt, Eur. Phys. J. C **5**, 461 (1998).
[81] A. D. Martin *et al.*, Eur. Phys. J. C **23**, 73 (2002).
[82] A. Tai (STAR Collaboration), J. Phys. G **30**, S809 (2004).
[83] R. Vogt (private communication).
[84] X. R. Wang (PHENIX Collaboration), AIP Conf. Proc. **842**, 68 (2006).

Measurement of Direct Photon Production in $p + p$ Collisions at $\sqrt{s} = 200$ GeV

S. S. Adler,[5] S. Afanasiev,[20] C. Aidala,[10] N. N. Ajitanand,[44] Y. Akiba,[21,40] A. Al-Jamel,[35] J. Alexander,[44] K. Aoki,[25] L. Aphecetche,[46] R. Armendariz,[35] S. H. Aronson,[5] R. Averbeck,[45] T. C. Awes,[36] V. Babintsev,[17] A. Baldisseri,[11] K. N. Barish,[6] P. D. Barnes,[28] B. Bassalleck,[34] S. Bathe,[6,31] S. Batsouli,[10] V. Baublis,[39] F. Bauer,[6] A. Bazilevsky,[5,41] S. Belikov,[19,17] M. T. Bjorndal,[10] J. G. Boissevain,[28] H. Borel,[11] M. L. Brooks,[28] D. S. Brown,[35] N. Bruner,[34] D. Bucher,[31] H. Buesching,[5,31] V. Bumazhnov,[17] G. Bunce,[5,41] J. M. Burward-Hoy,[28,27] S. Butsyk,[45] X. Camard,[46] P. Chand,[4] W. C. Chang,[2] S. Chernichenko,[17] C. Y. Chi,[10] J. Chiba,[21] M. Chiu,[10] I. J. Choi,[53] R. K. Choudhury,[4] T. Chujo,[5] V. Cianciolo,[36] Y. Cobigo,[11] B. A. Cole,[10] M. P. Comets,[37] P. Constantin,[19] M. Csanád,[13] T. Csörgő,[22] J. P. Cussonneau,[46] D. d'Enterria,[10] K. Das,[14] G. David,[5] F. Deák,[13] H. Delagrange,[46] A. Denisov,[17] A. Deshpande,[41] E. J. Desmond,[5] A. Devismes,[45] O. Dietzsch,[42] J. L. Drachenberg,[1] O. Drapier,[26] A. Drees,[45] A. Durum,[17] D. Dutta,[4] V. Dzhordzhadze,[47] Y. V. Efremenko,[36] H. En'yo,[40,41] B. Espagnon,[37] S. Esumi,[49] D. E. Fields,[34,41] C. Finck,[46] F. Fleuret,[26] S. L. Fokin,[24] B. D. Fox,[41] Z. Fraenkel,[52] J. E. Frantz,[10] A. Franz,[5] A. D. Frawley,[14] Y. Fukao,[25,40,41] S.-Y. Fung,[6] S. Gadrat,[29] M. Germain,[46] A. Glenn,[47] M. Gonin,[26] J. Gosset,[11] Y. Goto,[40,41] R. Granier de Cassagnac,[26] N. Grau,[19] S. V. Greene,[50] M. Grosse Perdekamp,[18,41] H.-Å. Gustafsson,[30] T. Hachiya,[16] J. S. Haggerty,[5] H. Hamagaki,[8] A. G. Hansen,[28] E. P. Hartouni,[27] M. Harvey,[5] K. Hasuko,[40] R. Hayano,[8] X. He,[15] M. Heffner,[27] T. K. Hemmick,[45] J. M. Heuser,[40] P. Hidas,[22] H. Hiejima,[18] J. C. Hill,[19] R. Hobbs,[34] W. Holzmann,[44] K. Homma,[16] B. Hong,[23] A. Hoover,[35] T. Horaguchi,[40,41,48] T. Ichihara,[40,41] V. V. Ikonnikov,[24] K. Imai,[25,40] M. Inaba,[49] M. Inuzuka,[8] D. Isenhower,[1] L. Isenhower,[1] M. Ishihara,[40] M. Issah,[44] A. Isupov,[20] B. V. Jacak,[45] J. Jia,[45] O. Jinnouchi,[40,41] B. M. Johnson,[5] S. C. Johnson,[27] K. S. Joo,[32] D. Jouan,[37] F. Kajihara,[8] S. Kametani,[8,51] N. Kamihara,[40,48] M. Kaneta,[41] J. H. Kang,[53] K. Katou,[51] T. Kawabata,[8] A. V. Kazantsev,[24] S. Kelly,[9,10] B. Khachaturov,[52] A. Khanzadeev,[39] J. Kikuchi,[51] D. J. Kim,[53] E. Kim,[43] G.-B. Kim,[26] H. J. Kim,[53] E. Kinney,[9] A. Kiss,[13] E. Kistenev,[5] A. Kiyomichi,[40] C. Klein-Boesing,[31] H. Kobayashi,[41] L. Kochenda,[39] V. Kochetkov,[17] R. Kohara,[16] B. Komkov,[39] M. Konno,[49] D. Kotchetkov,[6] A. Kozlov,[52] P. J. Kroon,[5] C. H. Kuberg,[1,*] G. J. Kunde,[28] K. Kurita,[40] M. J. Kweon,[23] Y. Kwon,[53] G. S. Kyle,[35] R. Lacey,[44] J. G. Lajoie,[19] Y. Le Bornec,[37] A. Lebedev,[19,24] S. Leckey,[45] D. M. Lee,[28] M. J. Leitch,[28] M. A. L. Leite,[42] X. H. Li,[6] H. Lim,[43] A. Litvinenko,[20] M. X. Liu,[28] C. F. Maguire,[50] Y. I. Makdisi,[5] A. Malakhov,[20] V. I. Manko,[24] Y. Mao,[38,40] G. Martinez,[46] H. Masui,[49] F. Matathias,[45] T. Matsumoto,[8,51] M. C. McCain,[1] P. L. McGaughey,[28] Y. Miake,[49] T. E. Miller,[50] A. Milov,[45] S. Mioduszewski,[5] G. C. Mishra,[15] J. T. Mitchell,[5] A. K. Mohanty,[4] D. P. Morrison,[5] J. M. Moss,[28] D. Mukhopadhyay,[52] M. Muniruzzaman,[6] S. Nagamiya,[21] J. L. Nagle,[9,10] T. Nakamura,[16] J. Newby,[47] A. S. Nyanin,[24] J. Nystrand,[30] E. O'Brien,[5] C. A. Ogilvie,[19] H. Ohnishi,[40] I. D. Ojha,[3,50] H. Okada,[25,40] K. Okada,[40,41] A. Oskarsson,[30] I. Otterlund,[30] K. Oyama,[8] K. Ozawa,[8] D. Pal,[52] A. P. T. Palounek,[28] V. Pantuev,[45] V. Papavassiliou,[35] J. Park,[43] W. J. Park,[23] S. F. Pate,[35] H. Pei,[19] V. Penev,[20] J.-C. Peng,[18] H. Pereira,[11] V. Peresedov,[20] A. Pierson,[34] C. Pinkenburg,[5] R. P. Pisani,[5] M. L. Purschke,[5] A. K. Purwar,[45] J. M. Qualls,[1] J. Rak,[19] I. Ravinovich,[52] K. F. Read,[36,47] M. Reuter,[45] K. Reygers,[31] V. Riabov,[39] Y. Riabov,[39] G. Roche,[29] A. Romana,[26,*] M. Rosati,[19] S. S. E. Rosendahl,[30] P. Rosnet,[29] V. L. Rykov,[40] S. S. Ryu,[53] N. Saito,[25,40,41] T. Sakaguchi,[8,51] S. Sakai,[49] V. Samsonov,[39] L. Sanfratello,[34] R. Santo,[31] H. D. Sato,[25,40] S. Sato,[5,49] S. Sawada,[21] Y. Schutz,[46] V. Semenov,[17] R. Seto,[6] T. K. Shea,[5] I. Shein,[17] T.-A. Shibata,[40,48] K. Shigaki,[16] M. Shimomura,[49] A. Sickles,[45] C. L. Silva,[42] D. Silvermyr,[28] K. S. Sim,[23] A. Soldatov,[17] R. A. Soltz,[27] W. E. Sondheim,[28] S. P. Sorensen,[47] I. V. Sourikova,[5] F. Staley,[11] P. W. Stankus,[36] E. Stenlund,[30] M. Stepanov,[35] A. Ster,[22] S. P. Stoll,[5] T. Sugitate,[16] J. P. Sullivan,[28] S. Takagi,[49] E. M. Takagui,[42] A. Taketani,[40,41] K. H. Tanaka,[21] Y. Tanaka,[33] K. Tanida,[40] M. J. Tannenbaum,[5] A. Taranenko,[44] P. Tarján,[12] T. L. Thomas,[34] M. Togawa,[25,40] J. Tojo,[40] H. Torii,[25,41] R. S. Towell,[1] V-N. Tram,[26] I. Tserruya,[52] Y. Tsuchimoto,[16] H. Tydesjö,[30] N. Tyurin,[17] T. J. Uam,[32] J. Velkovska,[5] M. Velkovsky,[45] V. Veszprémi,[12] A. A. Vinogradov,[24] M. A. Volkov,[24] E. Vznuzdaev,[39] X. R. Wang,[15] Y. Watanabe,[40,41] S. N. White,[5] N. Willis,[37] F. K. Wohn,[19] C. L. Woody,[5] W. Xie,[6] A. Yanovich,[17] S. Yokkaichi,[40,41] G. R. Young,[36] I. E. Yushmanov,[24] W. A. Zajc,[10,†] O. Zaudtke,[31] C. Zhang,[10] S. Zhou,[7] J. Zimányi,[22,*] L. Zolin,[20] X. Zong,[19] and H. W. vanHecke[28]

(PHENIX Collaboration)

[1]*Abilene Christian University, Abilene, Texas 79699, USA*
[2]*Institute of Physics, Academia Sinica, Taipei 11529, Taiwan*
[3]*Department of Physics, Banaras Hindu University, Varanasi 221005, India*

 © 2007 The American Physical Society

[4]Bhabha Atomic Research Centre, Bombay 400 085, India
[5]Brookhaven National Laboratory, Upton, New York 11973-5000, USA
[6]University of California—Riverside, Riverside, California 92521, USA
[7]China Institute of Atomic Energy (CIAE), Beijing, People's Republic of China
[8]Center for Nuclear Study, Graduate School of Science, University of Tokyo, 7-3-1 Hongo, Bunkyo, Tokyo 113-0033, Japan
[9]University of Colorado, Boulder, Colorado 80309, USA
[10]Columbia University, New York, New York 10027, USA,
and Nevis Laboratories, Irvington, New York 10533, USA
[11]Dapnia, CEA Saclay, F-91191, Gif-sur-Yvette, France
[12]Debrecen University, H-4010 Debrecen, Egyetem tér 1, Hungary
[13]ELTE, Eötvös Loránd University, H-1117 Budapest, Pázmány P. s. 1/A, Hungary
[14]Florida State University, Tallahassee, Florida 32306, USA
[15]Georgia State University, Atlanta, Georgia 30303, USA
[16]Hiroshima University, Kagamiyama, Higashi-Hiroshima 739-8526, Japan
[17]IHEP Protvino, State Research Center of Russian Federation, Institute for High Energy Physics, Protvino 142281, Russia
[18]University of Illinois at Urbana—Champaign, Urbana, Illinois 61801, USA
[19]Iowa State University, Ames, Iowa 50011, USA
[20]Joint Institute for Nuclear Research, 141980 Dubna, Moscow Region, Russia
[21]KEK, High Energy Accelerator Research Organization, Tsukuba, Ibaraki 305-0801, Japan
[22]KFKI Research Institute for Particle and Nuclear Physics of the Hungarian Academy of Sciences (MTA KFKI RMKI), H-1525
Budapest 114, P.O. Box 49, Budapest, Hungary
[23]Korea University, Seoul 136-701, Korea
[24]Russian Research Center "Kurchatov Institute," Moscow, Russia
[25]Kyoto University, Kyoto 606-8502, Japan
[26]Laboratoire Leprince-Ringuet, Ecole Polytechnique, CNRS-IN2P3, Route de Saclay, F-91128 Palaiseau, France
[27]Lawrence Livermore National Laboratory, Livermore, California 94550, USA
[28]Los Alamos National Laboratory, Los Alamos, New Mexico 87545, USA
[29]LPC, Université Blaise Pascal, CNRS-IN2P3, Clermont-Fd, 63177 Aubiere Cedex, France
[30]Department of Physics, Lund University, Box 118, SE-221 00 Lund, Sweden
[31]Institut für Kernphysik, University of Muenster, D-48149 Muenster, Germany
[32]Myongji University, Yongin, Kyonggido 449-728, Korea
[33]Nagasaki Institute of Applied Science, Nagasaki-shi, Nagasaki 851-0193, Japan
[34]University of New Mexico, Albuquerque, New Mexico 87131, USA
[35]New Mexico State University, Las Cruces, New Mexico 88003, USA
[36]Oak Ridge National Laboratory, Oak Ridge, Tennessee 37831, USA
[37]IPN-Orsay, Universite Paris Sud, CNRS-IN2P3, BP1, F-91406 Orsay, France
[38]Peking University, Beijing, People's Republic of China
[39]PNPI, Petersburg Nuclear Physics Institute, Gatchina, Leningrad Region 188300, Russia
[40]RIKEN (The Institute of Physical and Chemical Research), Wako, Saitama 351-0198, Japan
[41]RIKEN BNL Research Center, Brookhaven National Laboratory, Upton, New York 11973-5000, USA
[42]Instituto de Física, Universidade de São Paulo, Caixa Postal 66318, São Paulo CEP05315-970, Brazil
[43]System Electronics Laboratory, Seoul National University, Seoul, Korea
[44]Chemistry Department, Stony Brook University, Stony Brook, SUNY, New York 11794-3400, USA
[45]Department of Physics and Astronomy, Stony Brook University, SUNY, Stony Brook, New York 11794, USA
[46]SUBATECH (Ecole des Mines de Nantes, CNRS-IN2P3, Université de Nantes), BP 20722-44307, Nantes, France
[47]University of Tennessee, Knoxville, Tennessee 37996, USA
[48]Department of Physics, Tokyo Institute of Technology, Oh-okayama, Meguro, Tokyo 152-8551, Japan
[49]Institute of Physics, University of Tsukuba, Tsukuba, Ibaraki 305, Japan
[50]Vanderbilt University, Nashville, Tennessee 37235, USA
[51]Advanced Research Institute for Science and Engineering, Waseda University, 17 Kikui-cho, Shinjuku-ku, Tokyo 162-0044, Japan
[52]Weizmann Institute, Rehovot 76100, Israel
[53]Yonsei University, IPAP, Seoul 120-749, Korea
(Received 18 September 2006; published 5 January 2007)

Cross sections for midrapidity production of direct photons in $p + p$ collisions at the Relativistic Heavy Ion Collider (RHIC) are reported for transverse momenta of $3 < p_T < 16$ GeV/c. Next-to-leading order perturbative QCD (pQCD) describes the data well for $p_T > 5$ GeV/c, where the uncertainties of the measurement and theory are comparable. We also report on the effect of requiring the photons to be isolated from parton jet energy. The observed fraction of isolated photons is well described by pQCD for $p_T > 7$ GeV/c.

DOI: 10.1103/PhysRevLett.98.012002 PACS numbers: 13.85.Qk, 25.75.Dw

The production of direct photons, i.e., photons not from hadronic decays, in hadron-hadron collisions has been recognized as providing direct access to the gluon distributions in the hadron, both unpolarized and polarized [1,2]. The process of direct-photon production is described, at high energy and high momentum transfer, by perturbative quantum chromodynamics (pQCD). Three parton-parton subprocesses dominate at lowest order: Compton scattering $g + q \rightarrow \gamma + q$, annihilation $q + \bar{q} \rightarrow \gamma + g$, and parton-parton hard scattering with the scattered quark or gluon fragmenting to a photon, where g (q) represent gluon (quark) states. At next-to-leading order (NLO), bremsstrahlung emission of photons from the quarks undergoing hard scattering also contributes to the direct-photon signal. The annihilation process is suppressed for $p + p$ collisions, due to the lower probability density of $\bar{q}$ vs g in the proton. In general, the fragmentation and bremsstrahlung processes will produce photons in the vicinity of parton jets. Therefore, a requirement that the photon be isolated from parton jet activity can emphasize the Compton graph. Here, only the gluon distribution is unknown, particularly for the polarized case, and direct-photon production therefore provides direct access to this (polarized) gluon distribution.

Comparisons of data to theory test our understanding of direct-photon production in hadron-hadron collisions. Previous experiments have shown significant disagreement between data and theory at fixed target energy, $\sqrt{s} <$ 40 GeV, and good agreement at collider energy, $\sqrt{s} >$ 60 GeV [3,4]. Results from the Relativistic Heavy Ion Collider (RHIC) for $p + p$ collisions cover intermediate energy and momentum transfer, overlapping CERN Intersecting Storage Rings, and Super anti-Proton Proton Synchrotron collider kinematics, and address the robustness of the pQCD prediction for direct-photon production. In addition, the comparison of the direct-photon rate using no isolation requirement, to the rate of observed photons that are isolated from parton jets, tests our understanding of the processes of parton fragmentation to photons and of the bremsstrahlung emission of photons from quarks in hard scattering.

Furthermore, direct-photon production in $p + p$ collisions provides a valuable baseline for the interpretation of direct-photon data from heavy ion ($A + A$) collisions. Jet-quenching models attribute the strong suppression of high-p_T hadrons in central $A + A$ collisions to energy loss of scattered quarks and gluons in the hot and dense medium created in these collisions [5]. Since photons interact with the medium only electromagnetically, they provide a monitor of the initial parton flux and therefore test a crucial assumption of these models.

In this Letter, we present cross sections for direct-photon production in $p + p$ collisions at $\sqrt{s} = 200$ GeV, from the 2003 run of RHIC, at midrapidity for $3 < p_T < 16$ GeV/c. An earlier measurement [6] from the 2002 run of RHIC covered a much smaller region of p_T. Unpolarized cross sections are reported, obtained by averaging over the spin states of the beams, with $<1\%$ residual polarization.

The data were collected by the PHENIX detector [7]. The primary detector for this measurement is an electromagnetic calorimeter (EMCal), consisting of two subsystems, a six sector lead-scintillator (PbSc), and a two sector lead glass (PbGl) detector, each located 5 m radially from the beam line. Each sector covers a range of $|\eta| < 0.35$ in pseudorapidity and 22.5° in azimuth. The EMCal has fine granularity. Each calorimeter tower covers $\Delta\eta \times \Delta\phi \sim 0.01 \times 0.01$, and a tower contains $\sim$80% of the photon energy hitting the center of the tower. Two photons from $\pi^0 \rightarrow \gamma\gamma$ decays are clearly resolved up to a π^0 p_T of 12 GeV/c, and a shower profile analysis extends the γ/π^0 discrimination to beyond 20 GeV/c. The energy calibration of each tower is obtained from minimum-ionizing tracks and from the reconstructed π^0 mass. The uncertainty on the energy scale is less than 1.5%.

Beam-beam counters (BBC) positioned at pseudorapidities $3.1 < |\eta| < 3.9$ provide a minimum bias (MB) trigger. Events with high p_T photons are selected by a level-1 trigger that requires a minimum energy deposit of 1.4 GeV in an overlapping tile of 4×4 towers of the EMCal in coincidence with the MB trigger. The MB trigger cross section is $\sigma_{\mathrm{BBC}} = (23.0 \pm 2.2)$ mb, about 50% of $\sigma_{\mathrm{inel}}^{pp}$. The efficiency bias due to the MB trigger in the 2003 run, $\epsilon_{\mathrm{bias}} = 0.79 \pm 0.02$, is determined from the ratio of the yield of high $p_T \pi^0$ with and without the MB trigger. An integrated luminosity ($\mathcal{L}$) of 240 nb^{-1} after a vertex cut of ± 30 cm is used in this analysis.

The first step in the analysis is to cluster the hit towers. If there are two tower energy maxima and at least one lower-energy tower between them, the cluster is split into two, with the energy of each tower divided between the two clusters according to electromagnetic shower profiles associated with the clusters. Photons are identified by a shower profile cut that was calibrated using test beam data, identified electrons, and decay photons from identified π^0. The cut rejects $\sim$50% of hadrons depositing $E >$ 3 GeV in the EMCal and accepts $\sim$98% of real photons. The charged particle veto of the photon sample is based on tracks in drift chambers 2 m from the beam line, and hits in the pad chamber (PC3) immediately in front of the EMCal. Loss of photons from conversions in material before the EMCal is estimated using a GEANT [8] simulation and confirmed by the observed fraction of identified π^0 photons vetoed. The conversion correction is 3% for the drift chamber veto and $\sim$8% for the PC3 veto. Remaining nonphoton background, including converting neutral had-

rons and albedo from the magnet yokes, is also estimated from the GEANT simulation at ~1%.

The experimental challenge in direct-photon measurements is the large photon background from decays of hadrons, primarily from $\pi^0 \to \gamma\gamma$ (~ 80% of the decays) and $\eta \to \gamma\gamma$ (~15%). We use two techniques described below to subtract the decay background: a π^0-tagging method and a cocktail subtraction method.

In the π^0-tagging method, a candidate photon is tagged as a π^0 decay photon if it forms a pair with another photon in the mass range $105 < M_{\gamma\gamma} < 165$ MeV ($M_{\pi^0} \pm 3\sigma$), with $E_\gamma > 150$ MeV. A fiducial region for direct-photon candidates excludes 10 towers (0.1 rad) from the edges of the EMCal, while partner photons are accepted over the entire detector, to improve the probability of observing both decay photons from the π^0.

This method overestimates the yield of photons from π^0 decays, γ_{π^0}, due to combinatorial background. A p_T dependent correction (~10%) is estimated from a fit to the π^0 sidebands, with ±3% uncertainty. The yield of direct photons, $\gamma_{\rm dir}$, is obtained from the inclusive photon yield, $\gamma_{\rm incl}$, using the equation

$$\gamma_{\rm dir} = \gamma_{\rm incl} - (1 + \delta^{\gamma}_{h/\pi^0})(1 + R^{\rm miss}_{\pi^0})\gamma_{\pi^0}, \qquad (1)$$

where $R^{\rm miss}_{\pi^0}$ is the correction for missing photon partners to π^0; $(1 + R^{\rm miss}_{\pi^0})\gamma_{\pi^0}$ represents the total contribution of photons from π^0 decays in each p_T^γ bin, and $\delta^{\gamma}_{h/\pi^0}$ is the fraction of photons from hadrons other than π^0.

To estimate $R^{\rm miss}_{\pi^0}$, a Monte Carlo simulation is used that includes the acceptance, energy resolution, and our measured π^0 spectrum [9] as input. Figure 1 shows $R^{\rm miss}_{\pi^0}$ from the simulation. The largest uncertainty is from the calibration of the EMCal at low energy. $\delta^{\gamma}_{h/\pi^0}$ is estimated by a

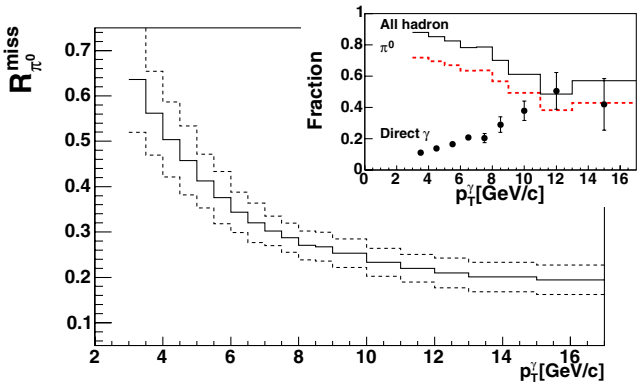

FIG. 1 (color online). Correction for missing photon partners to the π^0 ($R^{\rm miss}_{\pi^0}$) vs p_T^γ. Dashed lines show the systematic uncertainty. Inset: Different contributions to the inclusive photon spectrum. Solid (dashed) lines represent all hadronic (π^0) decay contributions. The data points show the remaining photon contributions.

simulation of hadron decays based on the η/π^0 [10] and ω/π^0 [11] ratios from our measurements: $\delta^{\gamma}_{h/\pi^0} \approx 0.24$, with $\delta^{\gamma}_{\eta/\pi^0} = 0.19$ and $\delta^{\gamma}_{\omega/\pi^0} = 0.05$. The contribution from other hadrons is less than 0.01. A small p_T dependence is assumed to follow m_T scaling [12]. The inset of Fig. 1 shows the fraction of photons from h, π^0, and $\gamma_{\rm dir}$ to $\gamma_{\rm incl}$. The direct-photon fraction ranges from 10% at low p_T^γ to 50% for $p_T^\gamma > 10$ GeV.

In the cocktail method [6,13], the spectrum of decay photons is simulated utilizing our measured π^0 spectrum and applying m_T scaling in order to account for other hadronic contributions. The effect of shower merging is also taken into account in the simulation. A double ratio $R_\gamma = (\gamma/\pi^0)^{\rm data}/(\gamma/\pi^0)^{\rm sim}$ is calculated for each p_T bin. $R_\gamma > 1$ indicates a direct-photon signal. The direct-photon yield is extracted as $\gamma_{\rm dir} = (1 - R_\gamma^{-1})\gamma_{\rm incl}$. Using the γ/π^0 ratio has the advantage that some systematic uncertainties cancel.

A summary of the systematic uncertainties is presented in Table I. Uncertainties of similar contributions are grouped together: global quantities (a), the inclusive photon yield (b), and the direct-photon background (c)–(e). The categories (a)–(d) apply to both analysis methods. Category (a) includes the uncertainties of the energy scale, luminosity, and geometrical acceptance. The main contribution to category (b) is the uncertainty of the nonphoton background estimation. The uncertainty of the charged particle veto is based on a study of the cluster vs track matching in the EMCal and the tracking detectors. The uncertainty in the neutral hadron contamination is estimated from identified charged hadrons. We assign the estimate of the albedo contribution as its uncertainty. Category (c) includes uncertainties of the correction for combinatorial background as estimated by different parametrizations of the background shape and the uncertainties of the π^0 reconstruction efficiency. Category (d) refers to the uncertainty of contributions from hadronic decays other than π^0's, derived from our measurement of the hadron production ratios. Finally, category (e) combines all remaining uncertainties separately for the two analysis

TABLE I. Relative systematic uncertainties of the direct-photon spectra.

p_T [GeV/c]	4.5–5	7.5–8	10–12
Signal fraction	9%	27%	49%
(a) Global	16.8%	14.9%	14.9%
(b) Inclusive photons	12.3%	4.7%	3.1%
(c) Photons from π^0	30.1%	10.7%	6.5%
(d) Other hadrons	21.4%	6.7%	3.8%
(e) Nonlinearity (+ remaining)			
(e_1) π^0 tagging	42.7%	6.8%	5.4%
(e_2) cocktail	69.5%	20.4%	13.4%
Total	71.6%	25.2%	19.8%

methods. Nonlinearity effects in the energy calibration affect the minimum energy cut in the π^0-tagging method (e_1) and distort the π^0 spectra in the cocktail method (e_2). After the individual calibration, a difference in the γ/π^0 ratio of PbGl and PbSc remains (5%–7%). This is used to assign a systematic uncertainty of the nonlinear part of the energy scale. Because of the small signal fraction at low p_T, this translates into the large relative uncertainty in the direct-photon spectra in Table I. In addition, the uncertainty of the shower profile analysis of the γ/π^0 discrimination at high p_T is included in this category. The two uncertainties (e_1, e_2) are combined by averaging the squared uncertainties, and then all uncertainties were added in quadrature.

The results from the π^0-tagging and cocktail method, obtained from independent analyses, agree within systematic uncertainties. We report an average of the results and uncertainties of the two methods giving equal weight to the two analysis methods.

The invariant cross section of direct-photon production is calculated by the following formula:

$$E\frac{d^3\sigma}{dp^3} = \frac{1}{\mathcal{L}}\frac{1}{2\pi p_T}\frac{\gamma_{\rm dir}}{\Delta p_T \Delta y}\frac{1}{\epsilon}\frac{1}{\epsilon_{\rm bias}}, \qquad (2)$$

where ϵ includes geometrical acceptance and the smearing effect from the energy resolution. The data points are plotted at the bin centers, with a correction to take into account the effect of finite bin sizes. The uncertainty of this correction is small compared to other systematic uncertainties.

Figure 2(a) shows the measured invariant cross section for midrapidity direct-photon production at $\sqrt{s} =$ 200 GeV. In addition, a NLO pQCD prediction [14–19], using CTEQ 6M parton distribution functions (PDF) [20] and the BFGII parton to photon fragmentation function (FF) [21], is shown with three theory scales (μ) as indicated. Figure 2(b) shows the fractional difference between the data and this calculation. The results are well described by pQCD.

The direct-photon sample includes photons from the Compton and annihilation subprocesses, which are expected to be isolated from parton jet activity. To measure the fraction of isolated photons, we apply an isolation requirement in the π^0-tagging method. Isolated photons are selected with less than 10% additional energy within a cone of radius $\Delta r = \sqrt{(\Delta\eta)^2 + (\Delta\phi)^2} = 0.5$ around the candidate photon direction. The cone energy is the sum of track momenta in the drift chamber and EMCal energy. In most cases the cone is larger than the PHENIX acceptance, and this is corrected for with a 0.08 increase in the photon isolation fraction in the theory predictions below [22].

Figure 3 presents the results of the isolation cut for photons from the π^0-tagging method. Solid circles show the fraction of isolated direct photons to all direct photons.

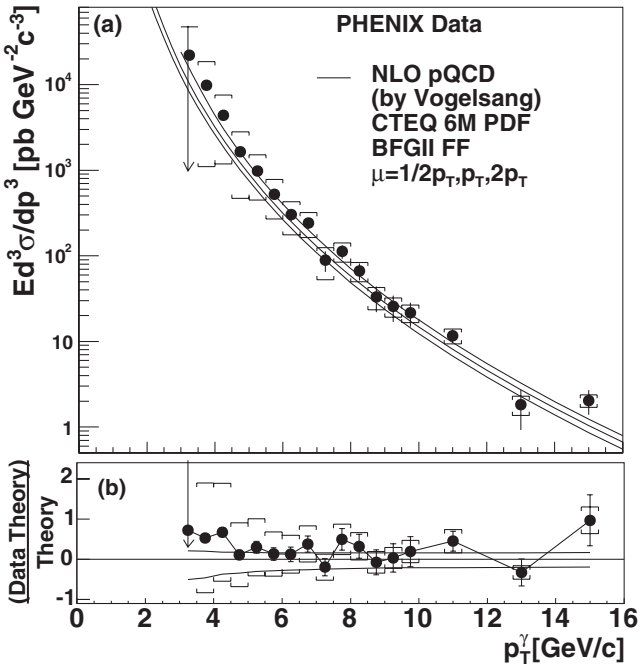

FIG. 2. (a) Direct-photon spectra with NLO pQCD calculations for three theory scales, μ. Brackets around data points show systematic errors. (b) Comparison to the NLO pQCD calculation for $\mu = p_T$, with upper and lower curves for $\mu = p_T/2$ and $2p_T$.

The curves are predictions from NLO pQCD, for the parton distribution and fragmentation functions as in Fig. 2, and for an additional parton to photon fragmentation function. The observed ratio is ~90% for $p_T^\gamma > 7$ GeV/c, and it is well described by pQCD. An additional loss of ~15%

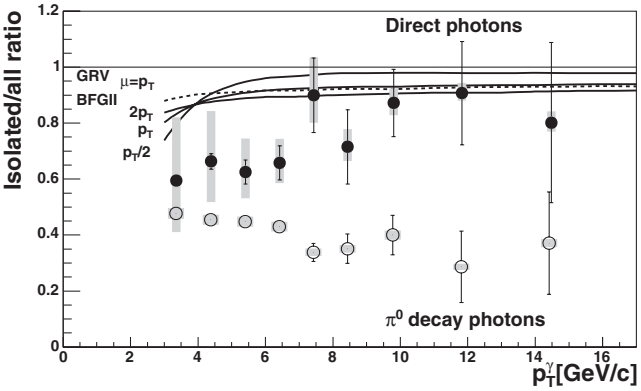

FIG. 3. Solid circles: Ratio of isolated direct photons to all direct photons from the π^0-tagging method. The statistical uncertainties are shown as black error bars and the systematic uncertainties are plotted as shaded bars. The solid and dashed curves are NLO pQCD calculations with three theory scales for BFGII [21] and one scale for GRV [25] parton to photon fragmentation functions. Open circles: Ratio of isolated photons from π^0 decays to all photons from π^0 decays.

($p_T^\gamma = 3$ GeV/c) to less than 5% (for $p_T^\gamma > 10$ GeV/c) due to the underlying event is estimated by a PYTHIA [23] simulation. Finally, for comparison, the open circles show the ratio of isolated photons from π^0 decays to all photons from π^0 decays. This indicates significantly less isolation than in the direct-photon sample.

In summary, invariant cross sections for direct-photon production at midrapidity have been measured up to $p_T = 16$ GeV/c in $\sqrt{s} = 200$ GeV $p + p$ collisions. The data are well described by NLO pQCD predictions for $p_T > 5$ GeV/c where the uncertainties of the measurement and theory are comparable. When these data are combined with fixed target and Tevatron collider data, these measurements demonstrate the robustness of the pQCD description of direct-photon production [24]. In addition, the ratio of isolated photons to all nonhadronic decay photons is well described by pQCD for $p_T > 7$ GeV/c.

Based on the comparison of high p_T direct-photon data from Au + Au collisions at RHIC with a $p + p$ reference from NLO pQCD, the origin of the observed suppression of high-p_T hadrons in central Au + Au collisions can be attributed to properties of the hot and dense matter created in the Au + Au collision [13]. The measurements presented here confirm this conclusion and put it on a firm experimental basis. Furthermore, the successful description of direct-photon production at RHIC is a necessary test for the extraction of the gluon polarization from direct-photon production in collisions of longitudinally polarized protons.

We thank the staff of the Collider-Accelerator and Physics Departments at BNL for their vital contributions. We thank Michel Fontannaz, Werner Vogelsang, and Monique Werlen for their interest and input. We acknowledge support from the Department of Energy and NSF (USA), MEXT and JSPS (Japan), CNPq and FAPESP (Brazil), NSFC (China), IN2P3/CNRS, CEA, and ARMINES (France), BMBF, DAAD, and AvH (Germany), OTKA (Hungary), DAE and DST (India), ISF (Israel), KRF and CHEP (Korea), RMIST, RAS, and RMAE (Russia), VR and KAW (Sweden), U.S. CRDF for the FSU, U.S.-Hungarian NSF-OTKA-MTA, and U.S.-Israel BSF.

*Deceased.
†PHENIX Spokesperson.
Electronic address: zajc@nevis.columbia.edu

[1] C. Papavasiliou, N. Mobed, and M. Svec, Phys. Rev. D **26**, 3284 (1982).
[2] E. L. Berger and J. Qiu, Phys. Rev. D **40**, 3128 (1989).
[3] W. Vogelsang and M. R. Whalley, J. Phys. G **23**, A1 (1997).
[4] P. Aurenche *et al.*, Eur. Phys. J. C **9**, 107 (1999).
[5] K. Adcox *et al.* (PHENIX Collaboration), Nucl. Phys. **A757**, 184 (2005).
[6] S. S. Adler *et al.* (PHENIX Collaboration), Phys. Rev. D **71**, 071102 (2005).
[7] K. Adcox *et al.* (PHENIX Collaboration), Nucl. Instrum. Methods Phys. Res., Sect. A **499**, 469 (2003).
[8] R. Brun *et al.*, GEANT 3.2.1, CERN Program Library Long Writeup (1994), http://wwwasdoc.web.cern.ch/wwwasdoc/pdfdir/geant.pdf.
[9] S. S. Adler *et al.* (PHENIX Collaboration), Phys. Rev. Lett. **91**, 241803 (2003).
[10] S. S. Adler *et al.* (PHENIX Collaboration), Phys. Rev. Lett. **96**, 202301 (2006).
[11] V. Ryabov *et al.* (PHENIX Collaboration), Nucl. Phys. **A774**, 735 (2006).
[12] K. Adcox *et al.* (PHENIX Collaboration), Phys. Rev. Lett. **88**, 192303 (2002).
[13] S. S. Adler *et al.* (PHENIX Collaboration), Phys. Rev. Lett. **94**, 232301 (2005).
[14] L. E. Gordon and W. Vogelsang, Phys. Rev. D **48**, 3136 (1993).
[15] L. E. Gordon and W. Vogelsang, Phys. Rev. D **50**, 1901 (1994).
[16] P. Aurenche *et al.*, Phys. Lett. **140B**, 87 (1984).
[17] P. Aurenche *et al.*, Nucl. Phys. **B297**, 661 (1988).
[18] H. Baer, J. Ohnemus, and J. F. Owens, Phys. Rev. D **42**, 61 (1990).
[19] H. Baer *et al.*, Phys. Lett. B **234**, 127 (1990).
[20] J. Pumplin *et al.*, J. High Energy Phys. 07 (2002) 012.
[21] L. Bourhis, M. Fontannaz, and J. P. Guillet, Eur. Phys. J. C **2**, 529 (1998).
[22] W. Vogelsang (private communication).
[23] T. Sjöstrand *et al.*, hep-ph/0308153 (Rick Field's tune A has been used).
[24] P. Aurenche, J. P. Guillet, E. Pilon, M. Werlen, and M. Fontannaz, Phys. Rev. D **73**, 094007 (2006).
[25] M. Gluck, E. Reya, and A. Vogt, Phys. Rev. D **48**, 116 (1993); **51**, 1427(E) (1995).

Measurement of High-p_T Single Electrons from Heavy-Flavor Decays in $p + p$ Collisions at $\sqrt{s} = 200$ GeV

A. Adare,[8] S. Afanasiev,[22] C. Aidala,[9] N. N. Ajitanand,[48] Y. Akiba,[42,43] H. Al-Bataineh,[37] J. Alexander,[48] K. Aoki,[27,42] L. Aphecetche,[50] R. Armendariz,[37] S. H. Aronson,[3] J. Asai,[43] E. T. Atomssa,[28] R. Averbeck,[49] T. C. Awes,[38] B. Azmoun,[3] V. Babintsev,[18] G. Baksay,[14] L. Baksay,[14] A. Baldisseri,[11] K. N. Barish,[4] P. D. Barnes,[30] B. Bassalleck,[36] S. Bathe,[4] S. Batsouli,[38] V. Baublis,[41] A. Bazilevsky,[3] S. Belikov,[3] R. Bennett,[49] Y. Berdnikov,[45] A. A. Bickley,[8] J. G. Boissevain,[30] H. Borel,[11] K. Boyle,[49] M. L. Brooks,[30] H. Buesching,[3] V. Bumazhnov,[18] G. Bunce,[3,43] S. Butsyk,[30,49] S. Campbell,[49] B. S. Chang,[57] J.-L. Charvet,[11] S. Chernichenko,[18] J. Chiba,[23] C. Y. Chi,[9] M. Chiu,[19] I. J. Choi,[57] T. Chujo,[54] P. Chung,[48] A. Churyn,[18] V. Cianciolo,[38] C. R. Cleven,[16] B. A. Cole,[9] M. P. Comets,[39] P. Constantin,[30] M. Csanád,[13] T. Csörgő,[24] T. Dahms,[49] K. Das,[15] G. David,[3] M. B. Deaton,[1] K. Dehmelt,[14] H. Delagrange,[50] A. Denisov,[18] D. d'Enterria,[9] A. Deshpande,[43,49] E. J. Desmond,[3] O. Dietzsch,[46] A. Dion,[49] M. Donadelli,[46] O. Drapier,[28] A. Drees,[49] A. K. Dubey,[56] A. Durum,[18] V. Dzhordzhadze,[4] Y. V. Efremenko,[38] J. Egdemir,[49] F. Ellinghaus,[8] W. S. Emam,[4] A. Enokizono,[29] H. En'yo,[42,43] S. Esumi,[53] K. O. Eyser,[4] D. E. Fields,[36,43] M. Finger, Jr.,[5,22] F. Fleuret,[28] S. L. Fokin,[26] Z. Fraenkel,[56] A. Franz,[3] J. Frantz,[49] A. D. Frawley,[15] K. Fujiwara,[42] Y. Fukao,[27,42] T. Fusayasu,[35] S. Gadrat,[31] I. Garishvili,[51] A. Glenn,[8] H. Gong,[49] M. Gonin,[28] J. Gosset,[11] Y. Goto,[42,43] R. Granier de Cassagnac,[28] N. Grau,[21] S. V. Greene,[54] M. Grosse Perdekamp,[19,43] T. Gunji,[7] H.-Å. Gustafsson,[32] T. Hachiya,[17] A. Hadj Henni,[50] C. Haegemann,[36] J. S. Haggerty,[3] H. Hamagaki,[7] R. Han,[40] H. Harada,[17] E. P. Hartouni,[29] K. Haruna,[17] E. Haslum,[32] R. Hayano,[7] M. Heffner,[29] T. K. Hemmick,[49] T. Hester,[4] X. He,[16] H. Hiejima,[19] J. C. Hill,[21] R. Hobbs,[36] M. Hohlmann,[14] W. Holzmann,[48] K. Homma,[17] B. Hong,[25] T. Horaguchi,[42,52] D. Hornback,[51] T. Ichihara,[42,43] K. Imai,[27,42] M. Inaba,[53] Y. Inoue,[44,42] D. Isenhower,[1] L. Isenhower,[1] M. Ishihara,[42] T. Isobe,[7] M. Issah,[48] A. Isupov,[22] B. V. Jacak,[49] J. Jia,[9] J. Jin,[9] O. Jinnouchi,[43] B. M. Johnson,[3] K. S. Joo,[34] D. Jouan,[39] F. Kajihara,[7] S. Kametani,[7,55] N. Kamihara,[42] J. Kamin,[49] M. Kaneta,[43] J. H. Kang,[57] H. Kanou,[42,52] H. Kano,[42] D. Kawall,[43] A. V. Kazantsev,[26] A. Khanzadeev,[41] J. Kikuchi,[55] D. H. Kim,[34] D. J. Kim,[57] E. Kim,[47] E. Kinney,[8] A. Kiss,[13] E. Kistenev,[3] A. Kiyomichi,[42] J. Klay,[29] C. Klein-Boesing,[33] L. Kochenda,[41] V. Kochetkov,[18] B. Komkov,[41] M. Konno,[53] D. Kotchetkov,[4] A. Kozlov,[56] A. Král,[10] A. Kravitz,[9] J. Kubart,[5,20] G. J. Kunde,[30] N. Kurihara,[7] K. Kurita,[44,42] M. J. Kweon,[25] Y. Kwon,[51,57] G. S. Kyle,[37] R. Lacey,[48] Y.-S. Lai,[9] J. G. Lajoie,[21] A. Lebedev,[21] D. M. Lee,[30] M. K. Lee,[57] T. Lee,[47] M. J. Leitch,[30] M. A. L. Leite,[46] B. Lenzi,[46] T. Liška,[10] A. Litvinenko,[22] M. X. Liu,[30] X. Li,[6] B. Love,[54] D. Lynch,[3] C. F. Maguire,[54] Y. I. Makdisi,[3] A. Malakhov,[22] M. D. Malik,[36] V. I. Manko,[26] Y. Mao,[40,42] L. Mašek,[5,20] H. Masui,[53] F. Matathias,[9] M. McCumber,[49] P. L. McGaughey,[30] Y. Miake,[53] P. Mikeš,[5,20] K. Miki,[53] T. E. Miller,[54] A. Milov,[49] S. Mioduszewski,[3] M. Mishra,[2] J. T. Mitchell,[3] M. Mitrovski,[48] A. Morreale,[4] D. P. Morrison,[3] T. V. Moukhanova,[26] D. Mukhopadhyay,[54] J. Murata,[44,42] S. Nagamiya,[23] Y. Nagata,[53] J. L. Nagle,[8] M. Naglis,[56] I. Nakagawa,[42,43] Y. Nakamiya,[17] T. Nakamura,[17] K. Nakano,[42,52] J. Newby,[29] M. Nguyen,[49] B. E. Norman,[30] A. S. Nyanin,[26] E. O'Brien,[3] S. X. Oda,[7] C. A. Ogilvie,[21] H. Ohnishi,[42] H. Okada,[27,42] K. Okada,[43] M. Oka,[53] O. O. Omiwade,[1] A. Oskarsson,[32] M. Ouchida,[17] K. Ozawa,[7] R. Pak,[3] D. Pal,[54] A. P. T. Palounek,[30] V. Pantuev,[49] V. Papavassiliou,[37] J. Park,[47] W. J. Park,[25] S. F. Pate,[37] H. Pei,[21] J.-C. Peng,[19] H. Pereira,[11] V. Peresedov,[22] D. Yu. Peressounko,[26] C. Pinkenburg,[3] M. L. Purschke,[3] A. K. Purwar,[30] H. Qu,[16] J. Rak,[36] A. Rakotozafindrabe,[28] I. Ravinovich,[56] K. F. Read,[38,51] S. Rembeczki,[14] M. Reuter,[49] K. Reygers,[33] V. Riabov,[41] Y. Riabov,[41] G. Roche,[31] A. Romana,[28,*] M. Rosati,[21] S. S. E. Rosendahl,[32] P. Rosnet,[31] P. Rukoyatkin,[22] V. L. Rykov,[42] B. Sahlmueller,[33] N. Saito,[27,42,43] T. Sakaguchi,[3] S. Sakai,[53] H. Sakata,[17] V. Samsonov,[41] S. Sato,[23] S. Sawada,[23] J. Seele,[8] R. Seidl,[19] V. Semenov,[18] R. Seto,[4] D. Sharma,[56] I. Shein,[18] A. Shevel,[41,48] T.-A. Shibata,[42,52] K. Shigaki,[17] M. Shimomura,[53] K. Shoji,[27,42] A. Sickles,[49] C. L. Silva,[46] D. Silvermyr,[38] C. Silvestre,[11] K. S. Sim,[25] C. P. Singh,[2] V. Singh,[2] S. Skutnik,[21] M. Slunečka,[5,22] A. Soldatov,[18] R. A. Soltz,[29] W. E. Sondheim,[30] S. P. Sorensen,[51] I. V. Sourikova,[3] F. Staley,[11] P. W. Stankus,[38] E. Stenlund,[32] M. Stepanov,[37] A. Ster,[24] S. P. Stoll,[3] T. Sugitate,[17] C. Suire,[39] J. Sziklai,[24] T. Tabaru,[43] S. Takagi,[53] E. M. Takagui,[46] A. Taketani,[42,43] Y. Tanaka,[35] K. Tanida,[42,43] M. J. Tannenbaum,[3] A. Taranenko,[48] P. Tarján,[12] T. L. Thomas,[36] M. Togawa,[27,42] A. Toia,[49] J. Tojo,[42] L. Tomášek,[20] H. Torii,[42] R. S. Towell,[1] V-N. Tram,[28] I. Tserruya,[56] Y. Tsuchimoto,[17] C. Vale,[21] H. Valle,[54] H. W. van Hecke,[30] J. Velkovska,[54] R. Vertesi,[12] A. A. Vinogradov,[26] M. Virius,[10] V. Vrba,[20] E. Vznuzdaev,[41] M. Wagner,[27,42] D. Walker,[49] X. R. Wang,[37] Y. Watanabe,[42,43] J. Wessels,[33] S. N. White,[3] D. Winter,[9] C. L. Woody,[3] M. Wysocki,[8] W. Xie,[43] Y. Yamaguchi,[55] A. Yanovich,[18] Z. Yasin,[4] J. Ying,[16] S. Yokkaichi,[42,43] G. R. Young,[38] I. Younus,[36] I. E. Yushmanov,[26] W. A. Zajc,[9,†] O. Zaudtke,[33] C. Zhang,[38] S. Zhou,[6] J. Zimányi,[24] and L. Zolin[22]

 © 2006 The American Physical Society

(PHENIX Collaboration)

[1]*Abilene Christian University, Abilene, Texas 79699, USA*
[2]*Department of Physics, Banaras Hindu University, Varanasi 221005, India*
[3]*Brookhaven National Laboratory, Upton, New York 11973-5000, USA*
[4]*University of California - Riverside, Riverside, California 92521, USA*
[5]*Charles University, Ovocný trh 5, Praha 1, 116 36, Prague, Czech Republic*
[6]*China Institute of Atomic Energy (CIAE), Beijing, People's Republic of China*
[7]*Center for Nuclear Study, Graduate School of Science, University of Tokyo, 7-3-1 Hongo, Bunkyo, Tokyo 113-0033, Japan*
[8]*University of Colorado, Boulder, Colorado 80309, USA*
[9]*Columbia University, New York, New York 10027, USA and Nevis Laboratories, Irvington, New York 10533, USA*
[10]*Czech Technical University, Zikova 4, 166 36 Prague 6, Czech Republic*
[11]*Dapnia, CEA Saclay, F-91191, Gif-sur-Yvette, France*
[12]*Debrecen University, H-4010 Debrecen, Egyetem tér 1, Hungary*
[13]*ELTE, Eötvös Loránd University, H - 1117 Budapest, Pázmány P. s. 1/A, Hungary*
[14]*Florida Institute of Technology, Melbourne, Florida 32901, USA*
[15]*Florida State University, Tallahassee, Florida 32306, USA*
[16]*Georgia State University, Atlanta, Georgia 30303, USA*
[17]*Hiroshima University, Kagamiyama, Higashi-Hiroshima 739-8526, Japan*
[18]*IHEP Protvino, State Research Center of Russian Federation, Institute for High Energy Physics, Protvino, 142281, Russia*
[19]*University of Illinois at Urbana-Champaign, Urbana, Illinois 61801, USA*
[20]*Institute of Physics, Academy of Sciences of the Czech Republic, Na Slovance 2, 182 21 Prague 8, Czech Republic*
[21]*Iowa State University, Ames, Iowa 50011, USA*
[22]*Joint Institute for Nuclear Research, 141980 Dubna, Moscow Region, Russia*
[23]*KEK, High Energy Accelerator Research Organization, Tsukuba, Ibaraki 305-0801, Japan*
[24]*KFKI Research Institute for Particle and Nuclear Physics of the Hungarian Academy of Sciences (MTA KFKI RMKI), H-1525 Budapest 114, PO Box 49, Budapest, Hungary*
[25]*Korea University, Seoul, 136-701, Korea*
[26]*Russian Research Center, "Kurchatov Institute", Moscow, Russia*
[27]*Kyoto University, Kyoto 606-8502, Japan*
[28]*Laboratoire Leprince-Ringuet, Ecole Polytechnique, CNRS-IN2P3, Route de Saclay, F-91128, Palaiseau, France*
[29]*Lawrence Livermore National Laboratory, Livermore, California 94550, USA*
[30]*Los Alamos National Laboratory, Los Alamos, New Mexico 87545, USA*
[31]*LPC, Université Blaise Pascal, CNRS-IN2P3, Clermont-Fd, 63177 Aubiere Cedex, France*
[32]*Department of Physics, Lund University, Box 118, SE-221 00 Lund, Sweden*
[33]*Institut für Kernphysik, University of Muenster, D-48149 Muenster, Germany*
[34]*Myongji University, Yongin, Kyonggido 449-728, Korea*
[35]*Nagasaki Institute of Applied Science, Nagasaki-shi, Nagasaki 851-0193, Japan*
[36]*University of New Mexico, Albuquerque, New Mexico 87131, USA*
[37]*New Mexico State University, Las Cruces, New Mexico 88003, USA*
[38]*Oak Ridge National Laboratory, Oak Ridge, Tennessee 37831, USA*
[39]*IPN-Orsay, Universite Paris Sud, CNRS-IN2P3, BP1, F-91406, Orsay, France*
[40]*Peking University, Beijing, People's Republic of China*
[41]*PNPI, Petersburg Nuclear Physics Institute, Gatchina, Leningrad Region, 188300, Russia*
[42]*RIKEN, The Institute of Physical and Chemical Research, Wako, Saitama 351-0198, Japan*
[43]*RIKEN BNL Research Center, Brookhaven National Laboratory, Upton, New York 11973-5000, USA*
[44]*Physics Department, Rikkyo University, 3-34-1 Nishi-Ikebukuro, Toshima, Tokyo 171-8501, Japan*
[45]*Saint Petersburg State Polytechnic University, St. Petersburg, Russia*
[46]*Instituto de Física, Universidade de São Paulo, Caixa Postal 66318, São Paulo CEP05315-970, Brazil*
[47]*System Electronics Laboratory, Seoul National University, Seoul, South Korea*
[48]*Chemistry Department, Stony Brook University, Stony Brook, SUNY, New York 11794-3400, USA*
[49]*Department of Physics and Astronomy, Stony Brook University, SUNY, Stony Brook, New York 11794, USA*
[50]*SUBATECH (Ecole des Mines de Nantes, CNRS-IN2P3, Université de Nantes), BP 20722 - 44307, Nantes, France*
[51]*University of Tennessee, Knoxville, Tennessee 37996, USA*
[52]*Department of Physics, Tokyo Institute of Technology, Oh-okayama, Meguro, Tokyo 152-8551, Japan*
[53]*Institute of Physics, University of Tsukuba, Tsukuba, Ibaraki 305, Japan*
[54]*Vanderbilt University, Nashville, Tennessee 37235, USA*
[55]*Advanced Research Institute for Science and Engineering, Waseda University, 17 Kikui-cho, Shinjuku-ku, Tokyo 162-0044, Japan*
[56]*Weizmann Institute, Rehovot 76100, Israel*

[57]Yonsei University, IPAP, Seoul 120-749, Korea
(Received 6 September 2006; published 21 December 2006)

The momentum distribution of electrons from decays of heavy flavor (charm and bottom) for midrapidity $|y| < 0.35$ in $p + p$ collisions at $\sqrt{s} = 200$ GeV has been measured by the PHENIX experiment at the BNL Relativistic Heavy Ion Collider over the transverse momentum range $0.3 < p_T < 9$ GeV/c. Two independent methods have been used to determine the heavy-flavor yields, and the results are in good agreement with each other. A fixed-order-plus-next-to-leading-log perturbative QCD calculation agrees with the data within the theoretical and experimental uncertainties, with the data/theory ratio of $1.71 \pm 0.02^{\text{stat}} \pm 0.18^{\text{sys}}$ for $0.3 < p_T < 9$ GeV/c. The total charm production cross section at this energy has also been deduced to be $\sigma_{c\bar{c}} = 567 \pm 57^{\text{stat}} \pm 193^{\text{sys}}$ μb.

DOI: 10.1103/PhysRevLett.97.252002 PACS numbers: 13.85.Qk, 13.20.Fc, 13.20.He, 25.75.Dw

Heavy-flavor (charm and bottom) production serves as a testing ground of QCD. Because of the large quark mass, it is expected that next-to-leading order perturbative QCD (NLO pQCD) can describe the production cross section of charm and bottom at high energy, particularly at high p_T. At the Tevatron, bottom production is well described by NLO pQCD [1]. Charm production cross sections at high p_T are found to be higher than the theory by $\approx 50\%$, but are compatible within the theoretical uncertainties [2]. Since heavy-flavor production at Relativistic Heavy Ion Collider (RHIC) energies is dominated by gluon-gluon fusion, its production in polarized $p + p$ collisions probes the gluon distribution $G(x)$ and the gluon polarization $\Delta G(x)$. A good understanding of the reaction mechanism for heavy-flavor production is crucial for reliably extracting these distributions. Furthermore, in Au + Au collisions at RHIC strong suppression of single electrons from heavy-flavor decays has been observed [3]. Measurements of heavy-flavor production in $p + p$ collisions provide a baseline for studying hot and dense matter effects in heavy ion reactions. Earlier measurements at RHIC [4,5] have a limited p_T range with substantial experimental uncertainties, so an improved measurement is crucial.

We report the production cross section of electrons, $(e^+ + e^-)/2$, at midrapidity in $p + p$ collisions at $\sqrt{s} = 200$ GeV for $0.3 < p_T < 9$ GeV/c measured by the PHENIX experiment. Contributions from semileptonic decays of heavy flavor are determined using two independent methods. This measurement has over 2 orders of magnitude larger statistics with much reduced systematic uncertainties compared to our previous measurement [4].

The data were collected by the PHENIX detector [6] during the 2005 RHIC run using the two central arm spectrometers. Each spectrometer covers $|\eta| < 0.35$ in pseudorapidity and $\Delta\phi = \pi/2$ in azimuth. It includes a drift chamber (DC) and pad chambers (PC1) for charged particle tracking, a ring imaging Čerenkov detector (RICH) for electron identification, and an electromagnetic calorimeter (EMCal) for electron identification and trigger. Beam-beam counters (BBCs), positioned at pseudorapidities $3.1 < |\eta| < 3.9$, measure the position of the collision vertex along the beam (z_{vtx}) and provide the interaction trigger. In this run, helium bags, one for each arm, were placed in the space between the beam pipe and DC to reduce multiple scattering and photon conversion.

Two data sets are used for the analysis: (1) the minimum bias (MB) data set recorded by the BBC trigger, and (2) a "photon" trigger (PH) data set triggered at level-1 requiring a minimum energy deposit of 1.4 GeV in an overlapping tile of 4×4 EMCal towers in coincidence with the BBC trigger. The PH trigger has $\simeq 100\%$ efficiency for high p_T electrons above 2 GeV/c in the active trigger tiles. The BBC trigger cross section is 23.0 ± 2.2 mb. Since only $\simeq 50\%$ of inelastic $p + p$ collisions satisfy the BBC trigger condition, only a fraction of the inclusive electron production events is triggered. This p_T and process independent fraction is determined to be $\epsilon_{\text{bias}} = 0.79 \pm 0.02$ from the yield ratio of high p_T π^0's with and without the BBC trigger. After selection of good runs and a vertex cut of $|z_{\text{vtx}}| < 20$ cm, an integrated luminosity ($\mathcal{L}$) of 45 nb^{-1} in the MB data set and 1.57 pb^{-1} in the PH data set are used for the analysis.

Charged particle tracks are reconstructed using DC and PC1 and confirmed by a hit in the EMCal within 4σ in position. The momentum resolution is $\sigma_p/p \simeq 0.7\% \oplus 0.9\% p$ (GeV/c), and the momentum scale is calibrated within 1% using the reconstructed mass of $J/\psi \to e^+e^-$.

Electron identification (eID) requires at least two associated hits in the RICH, a shower shape cut in the EMCal, and a cut in the ratio E/p where E is energy measured in the EMCal. We require $0.7 < E/p < 1.3$ for $0.8 < p_T < 5$ GeV/c. For lower p_T, the minimum value of E/p decreases with decreasing p_T to 0.55 at $p_T = 0.3$ GeV/c. The E/p cut removes background electrons from photon conversions and semileptonic decay of kaons ($K \to e\nu\pi(K_{e3})$) that occur far from the vertex, and most of the remaining hadron background. The hadron contamination after the E/p cut is 3% at $p_T = 0.3$ GeV/c and less than 1% for $0.8 < p_T < 5$ GeV/c with eID efficiency of approximately 90%.

For $p_T > 5$ GeV/c, where pions also emit Čerenkov photons in the RICH, tighter electron identification cuts are applied. We require at least 5 associated hits in the RICH, a tighter shower shape cut in the EMCal, and $0.8 < E/p < 1.3$. With these cuts, the electron measurement is extended to 9 GeV/c in p_T. The eID efficiency of the

tighter cuts is p_T independent, and is determined to be 57% of that for $p_T < 5$ GeV/c by applying the same tighter cuts for $p_T < 5$ GeV/c. With the tighter cuts, hadron contamination is negligible for $p_T < 7$ GeV/c. For $7 < p_T < 8 (8 < p_T < 9)$ GeV/c, a 20% (40%) hadron contamination is determined and subtracted using a Gaussian plus exponential fit to E/p distribution.

The invariant cross section for electron production is calculated using the following formula,

$$E\frac{d^3\sigma}{dp^3} = \frac{1}{\mathcal{L}}\frac{1}{2\pi p_T}\frac{N_e}{\Delta p_T \Delta y}\frac{1}{\epsilon_{\rm rec}}\frac{1}{\epsilon_{\rm bias}}, \quad (1)$$

where N_e is the measured electron yield; $\epsilon_{\rm rec}$, calculated using a full GEANT [7] simulation, includes the geometrical acceptance, track reconstruction and eID efficiency, and the smearing effect due to finite momentum resolution. For the PH data set, $\epsilon_{\rm rec}$ also includes the PH trigger efficiency. The cross sections from the MB and the PH data sets are consistent with each other for the overlapped p_T region.

The inclusive electron yield consists of three components: (1) electrons from heavy-flavor decay, (2) "photonic" background electrons from Dalitz decays of light mesons and photon conversions primarily in the beam pipe, and (3) "nonphotonic" background electrons from the remaining K_{e3} decays and dielectron decays of vector mesons. The photonic background is much larger than the nonphotonic background. We determined the spectrum of electrons from heavy-flavor decay by subtracting the background components from the inclusive spectrum using the following two independent methods.

In the "cocktail subtraction" method [3,4,8] a cocktail of electron spectra from various background sources is calculated using a Monte Carlo event generator of hadron decays. The most important background is the π^0 Dalitz decay, so we use our measured π^0 and $\pi^\pm$ spectra as input to the generator. The spectral shapes of other light hadrons h are obtained from the pion spectra by m_T scaling ($p_T \rightarrow \sqrt{p_T^2 + M_h^2 - M_\pi^2}$). Within this approach the ratios h/π^0 are constant at high p_T. For the relative normalization, we use the following ratios: $\eta/\pi^0 = 0.48 \pm 0.03$ [9], $\rho^0/\pi^0 = 1.0 \pm 0.3$, $\omega/\pi^0 = 0.90 \pm 0.06$ [10], $\eta'/\pi^0 = 0.40 \pm 0.12$, $\phi/\pi^0 = 0.25 \pm 0.08$. For $p_T > 2$ GeV/c, contributions from η and all other hadrons combined are approximately 20% and 10% of π^0, respectively. Another major background electron source is conversions of photons in the beam pipe [0.29% of a radiation length (X_0)] as well as in the air and the helium bags (0.1% X_0). The conversion electron spectrum is very similar to that of Dalitz decays. Using a detailed GEANT simulation of the PHENIX detector, the ratio of electrons from conversions to Dalitz decays, $R_{\rm CD}$, is determined to be 0.40 ± 0.04 for π^0, essentially p_T independent. $R_{\rm CD}$ is approximately half of that in [4] since the helium bags eliminated most of the conversions outside of the beam pipe. The conversion spectra are calculated by scaling the Dalitz decay spectra by $R_{\rm CD}$, with small corrections to account for the species dependence of the relative branching ratio of Dalitz decay to photon decay [$(h \rightarrow ee\gamma)/(h \rightarrow \gamma\gamma)$]. The internal and external conversions of direct photons are also included in the cocktail, using our measured direct photon spectrum [11] as input. The direct photon contribution is comparable to or greater than that from the η for $p_T > 5$ GeV/c. Nonphotonic backgrounds are also included in the cocktail. Since the K_{e3} background depends on the analysis cuts, it is evaluated by a full GEANT simulation.

In the "converter subtraction" method [12], we introduce an additional photon converter (a thin brass sheet of 1.67% X_0) around the beam pipe for part of the run. The converter multiplies the photonic electron background by a fixed factor, $R_\gamma \simeq 2.3$, which is determined precisely via GEANT simulation. R_γ is larger than in [12] since we have less conversion material in the 2005 run. The photonic background N_e^γ is determined as $N_e^\gamma = [N_e^C - (1-\epsilon)N_e^{\rm NC}]/(R_\gamma - 1 + \epsilon)$, where N_e^C and $N_e^{\rm NC}$ are electron yield with and without the converter, respectively, and ϵ (2.1%) represents a small loss of electrons due to the converter. The nonphotonic component is then determined as $N_e^{\rm non\text{-}\gamma} = N_e^{\rm NC} - N_e^\gamma$. Small remaining nonphotonic backgrounds, such as K_{e3} and hadron contamination, are subtracted.

These two methods are complementary to each other. The converter method is more accurate, and it allows us to extract a heavy-flavor signal down to $p_T = 0.3$ GeV/c where the signal is only $\approx 10\%$ of inclusive electrons. In addition, the measured photonic background N_e^γ is used to confirm and to calibrate the normalization of the calculated cocktail yields. A drawback of the method is statistical precision: the converter run contains only a small fraction ($\simeq$7% in the 2005 run) of the data. The cocktail method can use the full statistics at high p_T, where the photonic background becomes a small fraction of inclusive electrons.

Systematic uncertainties are categorized into (a) inclusive electron spectra, (b) cocktail subtraction, and (c) converter subtraction. Category (a) is common to both analyses, and includes the uncertainties in luminosity (9.6%), geometrical acceptance (4%), eID efficiency (3%), and the PH trigger efficiency (3% at the plateau). Uncertainties in cocktail subtraction [category (b)] include the normalization (8%) and p_T dependent shape uncertainty (2% at $p_T \simeq 2$ GeV/c, increasing to 6% at 9 GeV/c). In the converter analysis [category (c)] the dominant uncertainties are in R_γ (2.7%) and in the relative acceptance in the converter and the normal runs (1.0%). These uncertainties are propagated into the uncertainties in the heavy-flavor electron yields and added in quadrature.

Figure 1 shows the ratio of the measured N_e^γ to the cocktail calculation as a function of p_T. The ratio is consistent with unity within the uncertainties of the cocktail. At high p_T (>1.8 GeV/c), the ratio is $0.94 \pm 0.02^{\rm stat}$ on average. Since this is within the uncertainty of the cocktail

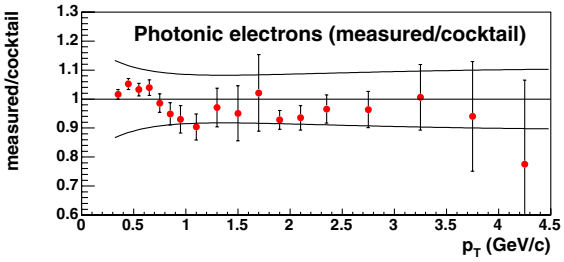

FIG. 1 (color online). Ratio of photonic electrons measured by the converter method to the cocktail calculation. Data from the MB (PH) data set are shown below (above) 1.8 GeV/c. The upper and lower curves show the systematic error of the cocktail. Error bars are statistical only.

normalization, we rescale the cocktail yields by this factor. This removes the 8% normalization uncertainty in the cocktail.

In Fig. 2, filled circles (squares) show the ratio of nonphotonic electrons relative to photonic background determined by the converter (cocktail) method. The nonphotonic electrons are dominantly heavy-flavor decay signals. The remaining nonphotonic background contributions have been calculated and are shown in Fig. 2. The two methods are consistent with each other. The ratio monotonically increases with increasing p_T, becoming greater than unity for $p_T > 2.4$ GeV/c, and saturates at $\simeq 3$ for $p_T > 5$ GeV/c. The large signal-to-background ratio is due to the small amount of conversion material in the spectrometer acceptance.

Figure 3(a) shows the invariant differential cross section of electrons from heavy-flavor decays. All background has been subtracted, including the nonphotonic components shown in Fig. 2. The data from the two analysis methods

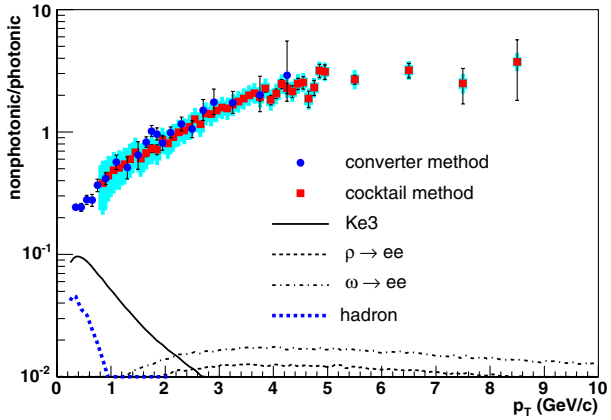

FIG. 2 (color online). Ratio of nonphotonic electrons to photonic background. Error bars are statistical errors and the error bands show the cocktail systematic errors. The solid, dashed, dot-dashed, and dot curve are the remaining nonphotonic backgrounds from K_{e3}, $\rho \rightarrow ee$, $\omega \rightarrow ee$, and hadron contamination, respectively.

are combined: at low p_T ($p_T < 1.6$ GeV/c) the converter subtraction method on the MB data set is used; at intermediate p_T ($1.6 < p_T < 2.6$ GeV/c) the converter method on the PH data set is used; and at high p_T ($p_T > 2.6$ GeV/c) the cocktail method on the PH data set is used.

The data are compared with a fixed-order-plus-next-to-leading-log (FONLL) pQCD calculation [13,14]. The top curve in Fig. 3 shows the central values of the FONLL calculation. The contributions of charm and bottom are also shown. For $p_T > 4$ GeV/c, the bottom contribution becomes dominant. In Fig. 3(b), the ratio of the data to the FONLL calculation is shown. The ratio is nearly p_T independent over the entire p_T range. Fitting to a constant for $0.3 < p_T < 9.0$ GeV/c yields a ratio of $1.71 \pm 0.02^{\text{stat}} \pm 0.18^{\text{sys}}$. Similar ratios are observed in charm production at high p_T at the Tevatron [2]. The upper limit of the FONLL calculation is compatible with the data. Recently STAR also reported nonphotonic electron production in $p + p$ at $\sqrt{s} = 200$ GeV [15].

The total charm cross section is derived by integrating the heavy-flavor electron cross section for $p_T > 0.4$ GeV/c: $d\sigma_e(p_T > 0.4)/dy = 5.95 \pm 0.59^{\text{stat}} \pm 2.0^{\text{sys}}$ μb. The systematic error is obtained by integrating the upper and lower systematic error limits of the differential cross sections, since the systematic errors are essentially coherent. The cross section is then extrapolated to

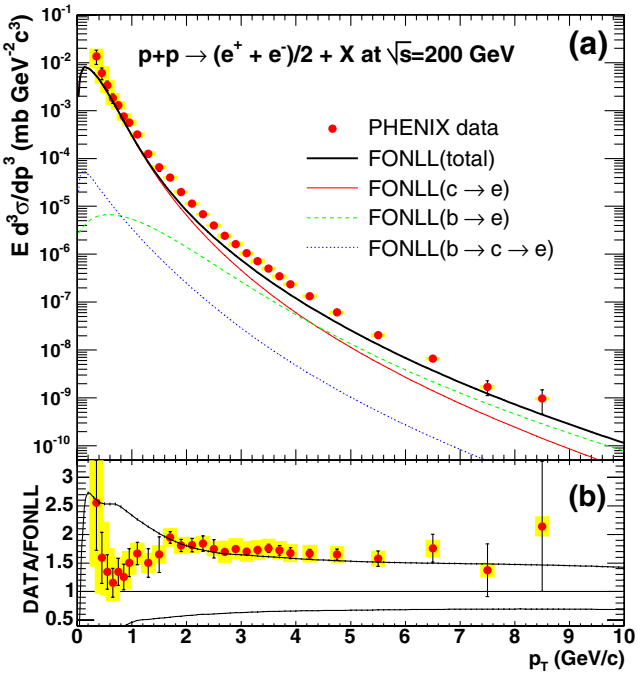

FIG. 3 (color online). (a) Invariant differential cross sections of electrons from heavy-flavor decays. The error bars (bands) represent the statistical (systematic) errors. The curves are the FONLL calculations (see text). (b) Ratio of the data and the FONLL calculation. The upper (lower) curve shows the theoretical upper (lower) limit of the FONLL calculation. In both panels a 10% normalization uncertainty is not shown.

$p_T = 0$ using the spectrum shape predicted by FONLL: $d\sigma_e(p_T > 0)/dy = 10.9 \pm 1.1^{\text{stat}} \pm 3.1^{\text{sys}}$ μb. We have assigned 10% to the systematic uncertainty of the extrapolation, and have subtracted contribution from bottom and bottom cascade decays (0.1 μb). We determine the charm production cross section, $d\sigma_{c\bar{c}}/dy = 123 \pm 12^{\text{stat}} \pm 37^{\text{sys}}$ μb, by using a $c \rightarrow e$ total branching ratio of $9.5 \pm 1.0\%$, calculated using the following charmed hadron ratios: $D^+/D^0 = 0.45 \pm 0.1$, $D_s/D^0 = 0.25 \pm 0.1$, and $\Lambda_c/D^0 = 0.1 \pm 0.05$. The rapidity distribution of electrons is broader than that of D mesons due to decay kinematics. A correction to this effect (7%) has been applied. Using the rapidity distribution from HVQMNR [16] with CTEQ5M [17] PDF, the total charm cross section is determined to be $\sigma_{c\bar{c}} = 567 \pm 57^{\text{stat}} \pm 193^{\text{sys}}$ μb. We have assigned 15% systematic error to the extrapolation. This result is compatible with our previous measurement [4] ($920 \pm 150^{\text{stat}} \pm 540^{\text{sys}}$ μb) and the value derived from Au + Au collisions [12] ($622 \pm 57^{\text{stat}} \pm 160^{\text{sys}}$ μb per NN collision). The FONLL cross section (256^{+400}_{-146} μb) is compatible with the data within its uncertainty. STAR has reported a somewhat larger value in d + Au [5] ($1.3 \pm 0.2^{\text{stat}} \pm 0.4^{\text{sys}}$ mb per NN collisions). Although the data extend to high p_T where the bottom contribution is expected to be dominant, the present analysis does not separate charm and bottom contributions. The bottom cross section predicted by FONLL is $1.87^{+0.99}_{-0.67}$ μb, and the upper FONLL curve is consistent with the data.

In conclusion, we have measured single electrons from heavy-flavor decays in $p + p$ collisions at $\sqrt{s} = 200$ GeV. The new data reported here provide a crucial baseline for the study of heavy quark production in hot and dense matter created in Au + Au collisions. The agreement between the data and the FONLL pQCD calculation within the theoretical and the experimental uncertainties suggests that a reliable extraction of gluon polarization from heavy-flavor production in polarized $p + p$ collisions is attainable.

We thank the staff of the Collider-Accelerator and Physics Departments at BNL for their vital contributions. We acknowledge support from the Department of Energy and NSF (USA), MEXT and JSPS (Japan), CNPq and FAPESP (Brazil), NSFC (China), MSMT (Czech Republic), IN2P3/CNRS, and CEA (France), BMBF, DAAD, and AvH (Germany), OTKA (Hungary), DAE (India), ISF (Israel), KRF and KOSEF (Korea), MES, RAS, and FAAE (Russia), VR and KAW (Sweden), US CRDF for the FSU, US-Hungarian NSF-OTKA-MTA, and US-Israel BSF.

*Deceased.
†PHENIX Spokesperson.
Email address: zajc@nevis.columbia.edu

[1] M. Cacciari, hep-ph/0407187.
[2] D. Acosta *et al.*, Phys. Rev. Lett. **91**, 241804 (2003).
[3] S. S. Adler *et al.*, Phys. Rev. Lett. **96**, 032301 (2006).
[4] S. S. Adler *et al.*, Phys. Rev. Lett. **96**, 032001 (2006).
[5] J. Adams *et al.*, Phys. Rev. Lett. **94**, 062301 (2005).
[6] K. Adcox *et al.*, Nucl. Instrum. Methods Phys. Res., Sect. A **499**, 469 (2003).
[7] F. Carminati *et al.*, *GEANT 3.21: Detector Description and Simulation Tool*, CERN Program Library Long Writeup W5013, 1993.
[8] K. Adcox *et al.*, Phys. Rev. Lett. **88**, 192303 (2002).
[9] S. S. Adler *et al.*, Phys. Rev. Lett. **96**, 202301 (2006).
[10] V. Ryabov *et al.*, Nucl. Phys. **A774**, 735 (2006).
[11] S. S. Adler *et al.*, hep-ex/0609031 [Phys. Rev. Lett. (to be published)].
[12] S. S. Adler *et al.*, Phys. Rev. Lett. **94**, 082301 (2005).
[13] M. Cacciari, P. Nason, and R. Vogt, Phys. Rev. Lett. **95**, 122001 (2005).
[14] M. Cacciari (private communication).
[15] B. I. Abelev *et al.* (STAR Collaboration), nucl-ex/0607012.
[16] M. L. Mangano, P. Nason, and G. Ridolfi, Nucl. Phys. **B405**, 507 (1993).
[17] H. L. Lai *et al.*, Eur. Phys. J. C **12**, 375 (2000).

Scaling Properties of Azimuthal Anisotropy in Au + Au and Cu + Cu Collisions at $\sqrt{s_{NN}} = 200$ GeV

A. Adare,[8] S. Afanasiev,[22] C. Aidala,[9] N. N. Ajitanand,[49] Y. Akiba,[43,44] H. Al-Bataineh,[38] J. Alexander,[49] A. Al-Jamel,[38] K. Aoki,[28,43] L. Aphecetche,[51] R. Armendariz,[38] S. H. Aronson,[3] J. Asai,[44] E. T. Atomssa,[29] R. Averbeck,[50] T. C. Awes,[39] B. Azmoun,[3] V. Babintsev,[18] G. Baksay,[14] L. Baksay,[14] A. Baldisseri,[11] K. N. Barish,[4] P. D. Barnes,[31] B. Bassalleck,[37] S. Bathe,[4] S. Batsouli,[9,39] V. Baublis,[42] F. Bauer,[4] A. Bazilevsky,[3] S. Belikov,[3,21] R. Bennett,[50] Y. Berdnikov,[46] A. A. Bickley,[8] M. T. Bjorndal,[9] J. G. Boissevain,[31] H. Borel,[11] K. Boyle,[50] M. L. Brooks,[31] D. S. Brown,[38] D. Bucher,[34] H. Buesching,[3] V. Bumazhnov,[18] G. Bunce,[3,44] J. M. Burward-Hoy,[31] S. Butsyk,[31,50] S. Campbell,[50] J.-S. Chai,[23] B. S. Chang,[58] J.-L. Charvet,[11] S. Chernichenko,[18] J. Chiba,[24] C. Y. Chi,[9] M. Chiu,[9,19] I. J. Choi,[58] T. Chujo,[55] P. Chung,[49] A. Churyn,[18] V. Cianciolo,[39] C. R. Cleven,[16] Y. Cobigo,[11] B. A. Cole,[9] M. P. Comets,[40] P. Constantin,[21,31] M. Csanád,[13] T. Csörgő,[25] T. Dahms,[50] K. Das,[15] G. David,[3] M. B. Deaton,[1] K. Dehmelt,[14] H. Delagrange,[51] A. Denisov,[18] D. d'Enterria,[9] A. Deshpande,[44,50] E. J. Desmond,[3] O. Dietzsch,[47] A. Dion,[50] M. Donadelli,[47] J. L. Drachenberg,[1] O. Drapier,[29] A. Drees,[50] A. K. Dubey,[57] A. Durum,[18] V. Dzhordzhadze,[4,52] Y. V. Efremenko,[39] J. Egdemir,[50] F. Ellinghaus,[8] W. S. Emam,[4] A. Enokizono,[17,30] H. En'yo,[43,44] B. Espagnon,[40] S. Esumi,[54] K. O. Eyser,[4] D. E. Fields,[37,44] M. Finger,[5,22] M. Finger, Jr.,[5,22] F. Fleuret,[29] S. L. Fokin,[27] B. Forestier,[32] Z. Fraenkel,[57] J. E. Frantz,[9,50] A. Franz,[3] A. D. Frawley,[15] K. Fujiwara,[43] Y. Fukao,[28,43] S.-Y. Fung,[4] T. Fusayasu,[36] S. Gadrat,[32] I. Garishvili,[52] F. Gastineau,[51] M. Germain,[51] A. Glenn,[8,52] H. Gong,[50] M. Gonin,[29] J. Gosset,[11] Y. Goto,[43,44] R. Granier de Cassagnac,[29] N. Grau,[21] S. V. Greene,[55] M. Grosse Perdekamp,[19,44] T. Gunji,[7] H.-Å. Gustafsson,[33] T. Hachiya,[17,43] A. Hadj Henni,[51] C. Haegemann,[37] J. S. Haggerty,[3] M. N. Hagiwara,[1] H. Hamagaki,[7] R. Han,[41] H. Harada,[17] E. P. Hartouni,[30] K. Haruna,[17] M. Harvey,[3] E. Haslum,[33] K. Hasuko,[43] R. Hayano,[7] M. Heffner,[30] T. K. Hemmick,[50] T. Hester,[4] J. M. Heuser,[43] X. He,[16] H. Hiejima,[19] J. C. Hill,[21] R. Hobbs,[37] M. Hohlmann,[14] M. Holmes,[55] W. Holzmann,[49] K. Homma,[17] B. Hong,[26] T. Horaguchi,[43,53] D. Hornback,[52] M. G. Hur,[23] T. Ichihara,[43,44] K. Imai,[28,43] M. Inaba,[54] Y. Inoue,[45,43] D. Isenhower,[1] L. Isenhower,[1] M. Ishihara,[43] T. Isobe,[7] M. Issah,[49] A. Isupov,[22] B. V. Jacak,[50] J. Jia,[9] J. Jin,[9] O. Jinnouchi,[44] B. M. Johnson,[3] K. S. Joo,[35] D. Jouan,[40] F. Kajihara,[7,43] S. Kametani,[7,56] N. Kamihara,[43,53] J. Kamin,[50] M. Kaneta,[44] J. H. Kang,[58] H. Kano,[43] H. Kanou,[43,53] T. Kawagishi,[54] D. Kawall,[44] A. V. Kazantsev,[27] S. Kelly,[8] A. Khanzadeev,[42] J. Kikuchi,[56] D. H. Kim,[35] D. J. Kim,[58] E. Kim,[48] Y.-S. Kim,[23] E. Kinney,[8] A. Kiss,[13] E. Kistenev,[3] A. Kiyomichi,[43] J. Klay,[30] C. Klein-Boesing,[34] L. Kochenda,[42] V. Kochetkov,[18] B. Komkov,[42] M. Konno,[54] D. Kotchetkov,[4] A. Kozlov,[57] A. Král,[10] A. Kravitz,[9] P. J. Kroon,[3] J. Kubart,[5,20] G. J. Kunde,[31] N. Kurihara,[7] K. Kurita,[45,43] M. J. Kweon,[26] Y. Kwon,[52,58] G. S. Kyle,[38] R. Lacey,[49] Y.-S. Lai,[9] J. G. Lajoie,[21] A. Lebedev,[21] Y. Le Bornec,[40] S. Leckey,[50] D. M. Lee,[31] M. K. Lee,[58] T. Lee,[48] M. J. Leitch,[31] M. A. L. Leite,[47] B. Lenzi,[47] H. Lim,[48] T. Liška,[10] A. Litvinenko,[22] M. X. Liu,[31] X. Li,[6] X. H. Li,[4] B. Love,[55] D. Lynch,[3] C. F. Maguire,[55] Y. I. Makdisi,[3] A. Malakhov,[22] M. D. Malik,[37] V. I. Manko,[27] Y. Mao,[41,43] L. Mašek,[5,20] H. Masui,[54] F. Matathias,[9,50] M. C. McCain,[19] M. McCumber,[50] P. L. McGaughey,[31] Y. Miake,[54] P. Mikeš,[5,20] K. Miki,[54] T. E. Miller,[55] A. Milov,[50] S. Mioduszewski,[3] G. C. Mishra,[16] M. Mishra,[2] J. T. Mitchell,[3] M. Mitrovski,[49] A. Morreale,[4] D. P. Morrison,[3] J. M. Moss,[31] T. V. Moukhanova,[27] D. Mukhopadhyay,[55] J. Murata,[45,43] S. Nagamiya,[24] Y. Nagata,[54] J. L. Nagle,[8] M. Naglis,[57] I. Nakagawa,[43,44] Y. Nakamiya,[17] T. Nakamura,[17] K. Nakano,[43,53] J. Newby,[30] M. Nguyen,[50] B. E. Norman,[31] A. S. Nyanin,[27] J. Nystrand,[33] E. O'Brien,[3] S. X. Oda,[7] C. A. Ogilvie,[21] H. Ohnishi,[43] I. D. Ojha,[55] H. Okada,[28,43] K. Okada,[44] M. Oka,[54] O. O. Omiwade,[1] A. Oskarsson,[33] I. Otterlund,[33] M. Ouchida,[17] K. Ozawa,[7] R. Pak,[3] D. Pal,[55] A. P. T. Palounek,[31] V. Pantuev,[50] V. Papavassiliou,[38] J. Park,[48] W. J. Park,[26] S. F. Pate,[38] H. Pei,[21] J.-C. Peng,[19] H. Pereira,[11] V. Peresedov,[22] D. Yu. Peressounko,[27] C. Pinkenburg,[3] R. P. Pisani,[3] M. L. Purschke,[3] A. K. Purwar,[31,50] H. Qu,[16] J. Rak,[21,37] A. Rakotozafindrabe,[29] I. Ravinovich,[57] K. F. Read,[39,52] S. Rembeczki,[14] M. Reuter,[50] K. Reygers,[34] V. Riabov,[42] Y. Riabov,[42] G. Roche,[32] A. Romana,[29,*] M. Rosati,[21] S. S. E. Rosendahl,[33] P. Rosnet,[32] P. Rukoyatkin,[22] V. L. Rykov,[43] S. S. Ryu,[58] B. Sahlmueller,[34] N. Saito,[28,43,44] T. Sakaguchi,[3,7,56] S. Sakai,[54] H. Sakata,[17] V. Samsonov,[42] H. D. Sato,[28,43] S. Sato,[3,24,54] S. Sawada,[24] J. Seele,[8] R. Seidl,[19] V. Semenov,[18] R. Seto,[4] D. Sharma,[57] T. K. Shea,[3] I. Shein,[18] A. Shevel,[42,49] T.-A. Shibata,[43,53] K. Shigaki,[17] M. Shimomura,[54] T. Shohjoh,[54] K. Shoji,[28,43] A. Sickles,[50] C. L. Silva,[47] D. Silvermyr,[39] C. Silvestre,[11] K. S. Sim,[26] C. P. Singh,[2] V. Singh,[2] S. Skutnik,[21] M. Slunečka,[5,22] W. C. Smith,[1] A. Soldatov,[18] R. A. Soltz,[30] W. E. Sondheim,[31] S. P. Sorensen,[52] I. V. Sourikova,[3] F. Staley,[11] P. W. Stankus,[39] E. Stenlund,[33] M. Stepanov,[38] A. Ster,[25] S. P. Stoll,[3] T. Sugitate,[17] C. Suire,[40] J. P. Sullivan,[31] J. Sziklai,[25] T. Tabaru,[44] S. Takagi,[54] E. M. Takagui,[47] A. Taketani,[43,44] K. H. Tanaka,[24] Y. Tanaka,[36] K. Tanida,[43,44] M. J. Tannenbaum,[3] A. Taranenko,[49] P. Tarján,[12] T. L. Thomas,[37]

 © 2007 The American Physical Society

M. Togawa,[28,43] A. Toia,[50] J. Tojo,[43] L. Tomášek,[20] H. Torii,[43] R. S. Towell,[1] V-N. Tram,[29] I. Tserruya,[57] Y. Tsuchimoto,[17,43] S. K. Tuli,[2] H. Tydesjö,[33] N. Tyurin,[18] C. Vale,[21] H. Valle,[55] H. W. van Hecke,[31] J. Velkovska,[55] R. Vertesi,[12] A. A. Vinogradov,[27] M. Virius,[10] V. Vrba,[20] E. Vznuzdaev,[42] M. Wagner,[28,43] D. Walker,[50] X. R. Wang,[38] Y. Watanabe,[43,44] J. Wessels,[34] S. N. White,[3] N. Willis,[40] D. Winter,[9] C. L. Woody,[3] M. Wysocki,[8] W. Xie,[4,44] Y. L. Yamaguchi,[56] A. Yanovich,[18] Z. Yasin,[4] J. Ying,[16] S. Yokkaichi,[43,44] G. R. Young,[39] I. Younus,[37] I. E. Yushmanov,[27] W. A. Zajc,[9,†] O. Zaudtke,[34] C. Zhang,[9,39] S. Zhou,[6] J. Zimányi,[25,*] and L. Zolin[22]

(PHENIX Collaboration)

[1]*Abilene Christian University, Abilene, Texas 79699, USA*
[2]*Department of Physics, Banaras Hindu University, Varanasi 221005, India*
[3]*Brookhaven National Laboratory, Upton, New York 11973-5000, USA*
[4]*University of California–Riverside, Riverside, California 92521, USA*
[5]*Charles University, Ovocný trh 5, Praha 1, 116 36, Prague, Czech Republic*
[6]*China Institute of Atomic Energy (CIAE), Beijing, People's Republic of China*
[7]*Center for Nuclear Study, Graduate School of Science, University of Tokyo, 7-3-1 Hongo, Bunkyo, Tokyo 113-0033, Japan*
[8]*University of Colorado, Boulder, Colorado 80309, USA*
[9]*Columbia University, New York, New York 10027, USA, and Nevis Laboratories, Irvington, New York 10533, USA*
[10]*Czech Technical University, Zikova 4, 166 36 Prague 6, Czech Republic*
[11]*Dapnia, CEA Saclay, F-91191, Gif-sur-Yvette, France*
[12]*Debrecen University, H-4010 Debrecen, Egyetem tér 1, Hungary*
[13]*ELTE, Eötvös Loránd University, H - 1117 Budapest, Pázmány P. s. 1/A, Hungary*
[14]*Florida Institute of Technology, Melbourne, Florida 32901, USA*
[15]*Florida State University, Tallahassee, Florida 32306, USA*
[16]*Georgia State University, Atlanta, Georgia 30303, USA*
[17]*Hiroshima University, Kagamiyama, Higashi-Hiroshima 739-8526, Japan*
[18]*IHEP Protvino, State Research Center of Russian Federation, Institute for High Energy Physics, Protvino, 142281, Russia*
[19]*University of Illinois at Urbana-Champaign, Urbana, Illinois 61801, USA*
[20]*Institute of Physics, Academy of Sciences of the Czech Republic, Na Slovance 2, 182 21 Prague 8, Czech Republic*
[21]*Iowa State University, Ames, Iowa 50011, USA*
[22]*Joint Institute for Nuclear Research, 141980 Dubna, Moscow Region, Russia*
[23]*KAERI, Cyclotron Application Laboratory, Seoul, South Korea*
[24]*KEK, High Energy Accelerator Research Organization, Tsukuba, Ibaraki 305-0801, Japan*
[25]*KFKI Research Institute for Particle and Nuclear Physics of the Hungarian Academy of Sciences (MTA KFKI RMKI), H-1525 Budapest 114, P.O. Box 49, Budapest, Hungary*
[26]*Korea University, Seoul, 136-701, Korea*
[27]*Russian Research Center "Kurchatov Institute," Moscow, Russia*
[28]*Kyoto University, Kyoto 606-8502, Japan*
[29]*Laboratoire Leprince-Ringuet, Ecole Polytechnique, CNRS-IN2P3, Route de Saclay, F-91128, Palaiseau, France*
[30]*Lawrence Livermore National Laboratory, Livermore, California 94550, USA*
[31]*Los Alamos National Laboratory, Los Alamos, New Mexico 87545, USA*
[32]*LPC, Université Blaise Pascal, CNRS-IN2P3, Clermont-Fd, 63177 Aubiere Cedex, France*
[33]*Department of Physics, Lund University, Box 118, SE-221 00 Lund, Sweden*
[34]*Institut für Kernphysik, University of Muenster, D-48149 Muenster, Germany*
[35]*Myongji University, Yongin, Kyonggido 449-728, Korea*
[36]*Nagasaki Institute of Applied Science, Nagasaki-shi, Nagasaki 851-0193, Japan*
[37]*University of New Mexico, Albuquerque, New Mexico 87131, USA*
[38]*New Mexico State University, Las Cruces, New Mexico 88003, USA*
[39]*Oak Ridge National Laboratory, Oak Ridge, Tennessee 37831, USA*
[40]*IPN-Orsay, Universite Paris Sud, CNRS-IN2P3, BP1, F-91406, Orsay, France*
[41]*Peking University, Beijing, People's Republic of China*
[42]*PNPI, Petersburg Nuclear Physics Institute, Gatchina, Leningrad region, 188300, Russia*
[43]*RIKEN, The Institute of Physical and Chemical Research, Wako, Saitama 351-0198, Japan*
[44]*RIKEN BNL Research Center, Brookhaven National Laboratory, Upton, New York 11973-5000, USA*
[45]*Physics Department, Rikkyo University, 3-34-1 Nishi-Ikebukuro, Toshima, Tokyo 171-8501, Japan*
[46]*Saint Petersburg State Polytechnic University, St. Petersburg, Russia*
[47]*Universidade de São Paulo, Instituto de Física, Caixa Postal 66318, São Paulo CEP05315-970, Brazil*
[48]*System Electronics Laboratory, Seoul National University, Seoul, South Korea*
[49]*Chemistry Department, Stony Brook University, SUNY, Stony Brook, New York 11794-3400, USA*

[50]Department of Physics and Astronomy, Stony Brook University, SUNY, Stony Brook, New York 11794, USA
[51]SUBATECH (Ecole des Mines de Nantes, CNRS-IN2P3, Université de Nantes) BP 20722–44307, Nantes, France
[52]University of Tennessee, Knoxville, Tennessee 37996, USA
[53]Department of Physics, Tokyo Institute of Technology, Oh-okayama, Meguro, Tokyo 152-8551, Japan
[54]Institute of Physics, University of Tsukuba, Tsukuba, Ibaraki 305, Japan
[55]Vanderbilt University, Nashville, Tennessee 37235, USA
[56]Waseda University, Advanced Research Institute for Science and Engineering, 17 Kikui-cho, Shinjuku-ku, Tokyo 162-0044, Japan
[57]Weizmann Institute, Rehovot 76100, Israel
[58]Yonsei University, IPAP, Seoul 120-749, Korea
(Received 16 August 2006; published 16 April 2007)

Differential measurements of elliptic flow (v_2) for Au + Au and Cu + Cu collisions at $\sqrt{s_{\mathrm{NN}}} = 200$ GeV are used to test and validate predictions from perfect fluid hydrodynamics for scaling of v_2 with eccentricity, system size, and transverse kinetic energy (KE_T). For $\mathrm{KE}_T \equiv m_T - m$ up to ~1 GeV the scaling is compatible with hydrodynamic expansion of a thermalized fluid. For large values of KE_T mesons and baryons scale separately. Quark number scaling reveals a universal scaling of v_2 for both mesons and baryons over the full KE_T range for Au + Au. For Au + Au and Cu + Cu the scaling is more pronounced in terms of KE_T, rather than transverse momentum.

DOI: 10.1103/PhysRevLett.98.162301 PACS numbers: 25.75.Dw

Quantum chromodynamics calculations performed on the lattice indicate a transition from a low-temperature phase of nuclear matter, dominated by hadrons, into a high-temperature plasma phase of quarks and gluons (QGP) [1]. For matter with zero net baryon density, this phase transition has been predicted to occur at an energy density of ~1 GeV/fm^3 or for a critical temperature $T_c \sim 170$ MeV [2]. Recent estimates from transverse energy (E_T) measurements at the relativistic heavy ion collider (RHIC) have indicated energy densities of at least 5.4 GeV/fm^3 in central Au + Au collisions [3]. Thus, an important prerequisite for QGP production is readily fulfilled at RHIC. Indeed, there is much evidence that thermalized nuclear matter has been created at unprecedented energy densities in collisions at RHIC [3–10].

Hydrodynamics provides a link between the fundamental properties of this matter (its equation of state (EOS) and transport coefficients) and the flow patterns evidenced in the measured hadron spectra and azimuthal anisotropy [11–15]. Experimentally, such a momentum anisotropy is commonly characterized at midrapidity, by the even order Fourier coefficients [16,17], $v_n = \langle e^{in(\phi_p - \Phi_{\mathrm{RP}})} \rangle$, $n = 2, 4, \ldots$, where ϕ_p is the azimuthal emission angle of a particle, Φ_{RP} is the azimuth of the reaction plane, and the brackets denote statistical averaging over particles and events.

At low transverse momentum ($p_T \lesssim 2.0$ GeV/c) the magnitude and trends of elliptic flow, measured by the second Fourier coefficient v_2, is found to be underpredicted by a hadronic cascade model [18]. By contrast, a broad selection of the data showed good quantitative agreement with perfect fluid (very low ratio of viscosity to entropy) hydrodynamics [9,10,12,15] and a transport model calculation which incorporates extremely large opacities [19]. For higher p_T, quark coalescence from a thermalized state of flowing partonic matter [20–22] has been found to be consistent with the data [23,24]. These results provide evidence for the production of a strongly interacting QGP whose subsequent evolution is similar to that of a "perfect" fluid [7–10].

Systematic theoretical and experimental studies of the influence of model parameters are now required to gain more quantitative insight on the transport coefficients and the EOS for this strongly interacting matter. The range of validity of perfect fluid hydrodynamics is affected by the degree of thermalization [25] and the onset of dissipative effects [25–27]. These questions can be addressed by investigating several scaling predictions of perfect fluid hydrodynamics [15,25,28–30].

In the hydrodynamic model, elliptic flow can result from pressure gradients due to the initial spatial asymmetry or eccentricity $\epsilon = (\langle y^2 - x^2 \rangle)/(\langle y^2 + x^2 \rangle)$, of the high energy density matter in the collision zone. The initial entropy density $S(x, y)$, can be used to average over the x and y coordinates in the plane perpendicular to the collision axis, where x points along the impact vector and y is orthogonal. For a system of transverse size $\bar{R}$ ($1/\bar{R} = \sqrt{1/\langle x^2 \rangle + 1/\langle y^2 \rangle}$), this flow develops over a time scale $\sim \bar{R}/\langle c_s \rangle$, where c_s is the speed of sound. Thus, the initial energy density controls how much flow develops globally, while the detailed development of the flow patterns are largely controlled by ϵ and c_s.

An important prediction of perfect fluid hydrodynamics is that the relatively "complicated" dependence of azimuthal anisotropy on centrality, transverse momentum, rapidity, particle type, higher harmonics, etc., can be scaled to a single function [15,31]. Immediate consequences of this [15,25,28,31] are that: (i) v_2 scaling should hold for a broad range of impact parameters for which the eccentricity varies, i.e., $v_2(p_T)/\epsilon$ should be independent of centrality; (ii) $v_2(p_T)$ should be independent of colliding system size for a given eccentricity; and (iii) for different particle species, $v_2(\mathrm{KE}_T)$ at midrapidity should scale with the

transverse kinetic energy $KE_T = m_T - m$ [15], where m_T is the transverse mass.

We use high statistics v_2 data to test these scaling predictions and explore constraints for the range of validity of perfect fluid hydrodynamics. The measurements were made at $\sqrt{s_{NN}} = 200$ GeV with the PHENIX detector [32] at RHIC. Approximately 6.5×10^8 Au + Au and 8.0×10^7 Cu + Cu minimum-bias collisions were analyzed from the 2004 and 2005 running periods, respectively. The collision vertex z, along the beam direction was constrained to be within $|z| < 30$ cm. The event centrality for Au + Au collisions was determined via cuts in the space of beam-beam counter (BBC) versus zero degree calorimeter analog response [33]. For Cu + Cu only the amplitude of the BBC analog response was used. Charged hadrons were detected in the two central arms ($|\eta| \leq 0.35$). Track reconstruction used the drift chambers and two layers of multiwire proportional chambers with pad readout (PC1 and PC3) located at radii of 2m, 2.5, and 5 m, respectively [32].

The time-of-flight (TOF) detector positioned at a radial distance of 5.06 m, was used to identify pions ($\pi^{\pm}$), kaons ($K^{\pm}$), and (anti)protons ($\bar{p}$)p. The BBCs and TOF scintillators provided the global start and stop signals. These measurements were used in conjunction with the measured momentum and flight-path length to generate a mass-squared distribution [34]. A momentum dependent $\pm 2\sigma$ cut about each peak in this distribution was used to identify $\pi^{\pm}$, $K^{\pm}$ and ($\bar{p}$)p in the range $0.2 < p_T < 2.5$ GeV/c, $0.2 < p_T < 2.5$ GeV/c, and $0.5 < p_T < 4.5$ GeV/c, respectively. A track confirmation hit within a 2.5σ matching window in PC3/TOF served to eliminate most albedo, conversions, and resonance decays.

The differential elliptic flow measurements for charged hadrons and identified particles were obtained with the reaction plane method. This technique correlates the azimuthal angles of charged tracks with the azimuth of the event plane Φ_2, determined via hits in the two BBCs positioned symmetrically along the beam line, covering the pseudorapidity range $3 < |\eta| < 3.9$ [23]. A large η gap between the central arms and the particles used for reaction plane determination reduces the influence of possible nonflow contributions, especially those from dijets [35]. Values of v_2 were calculated via the expression $v_2 = \langle \cos[2(\phi_p - \Phi_2)] \rangle / \langle \cos[2(\Phi_2 - \Phi_{RP})] \rangle$, where the denominator is a resolution factor that corrects for the difference between the estimated Φ_2 and the true azimuth Φ_{RP} of the reaction plane [23,36]. The estimated resolution factor of the combined reaction plane from both BBCs [23] has an average of 0.33 (0.16) over centrality with a maximum of about 0.42 (0.19) for Au + Au (Cu + Cu). The estimated correction factor for the v_2 measurements (i.e., the inverse of the resolution factor) ranges from 2.4 (5.5) to 5.0 (13), for which relative systematic errors are estimated to be ~5% and ~10% for Au + Au and Cu + Cu, respectively.

Figure 1 shows the differential $v_2(p_T)$ for charged hadrons obtained in Au + Au and Cu + Cu collisions. The $v_2(p_T)$ results exhibit the familiar increase as collisions become more peripheral and the p_T increase [3–5]. We test these data for eccentricity scaling by dividing the differential values shown in Fig. 1 by the v_2 integrated over the p_T range 0.3–2.5 GeV/c for each of the indicated centrality selections. The hydrodynamic model predicts that this ratio is constant with centrality and independent of colliding system because ϵ is proportional to the p_T-integrated v_2 values (i.e., $\epsilon = k \times v_2$). The latter proportionality has been observed for Au + Au collisions [37,38]. A Glauber model estimate of ϵ [38] gives $k = 3.1 \pm 0.2$ for the cuts employed in this analysis. This method of scaling leads to a scale invariant variable and cancels the systematic errors associated with estimates of the reaction plane resolution and the eccentricity. It contrasts the methodologies of Refs. [39,40] which calculate ϵ directly for different model assumptions.

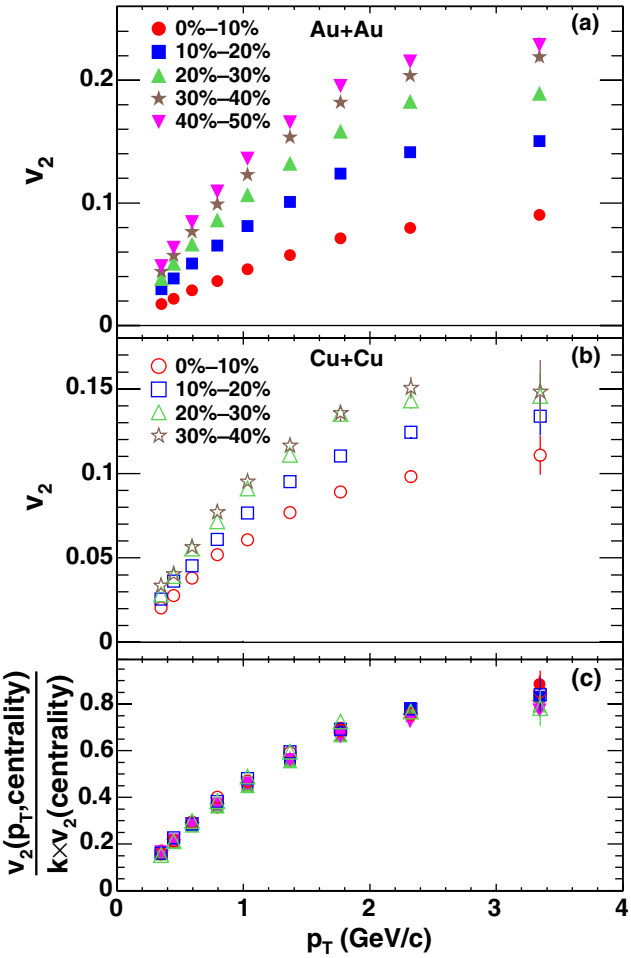

FIG. 1 (color online). v_2 vs p_T for charged hadrons obtained in (a) Au + Au and (b) Cu + Cu collisions for the centralities indicated. (c) v_2(centrality, p_T) divided by $k = 3.1$ (see text) times the p_T-integrated value v_2(centrality) for Au + Au and Cu + Cu.

The resulting scaled $v_2(p_T)$ values for Cu + Cu and Au + Au collisions, are shown in Fig. 1(c). To facilitate later comparisons with the model calculations of Ref. [25], they are divided by $k = 3.1$. These scaled values are clearly independent of the colliding system size and show essentially perfect scaling for the full range of centralities (or ϵ) and p_T selections presented [41]. The scaled v_2 are also in accord with the scale invariance of perfect fluid hydrodynamics [25,29], which suggests that rapid local thermalization [9,10] is achieved. It is noteworthy that similarly robust scaling for the p_T-integrated v_2 is not observed [39,40]. This is probably due to methodological differences in the evaluation of ϵ.

The magnitude of v_2/ϵ depends on c_s [25]. As a reasonable first approximation we compare our measured v_2/ϵ at an integrated $\langle p_T \rangle = 0.45$ GeV/c and the results of Fig. 2 of [25] to obtain $c_s \sim 0.35 \pm 0.05$. Note that this $\langle p_T \rangle$ value accounts for p_T threshold differences and the calculations are done at fixed $b = 8$ fm and constant c_s. Thus, since we expect the speed of sound to vary as a function of time, one might view this c_s value as the approximate average value over the time period $2\,\bar{R}/c_s$, the time over which the flow develops. This value suggests an effective EOS, which is softer than that for the high-temperature QGP [42], but does not reflect a very strong first order phase transition in which matter-flow is significantly slowed or stalled.

Figures 2 and 3 show that the distinctive features of the v_2 for identified particles provide another detailed set of scaling tests. Figure 2(a) shows a comparison of the measured differential anisotropy $v_2(p_T)$, for several particle species obtained in minimum-bias Au + Au collisions at $\sqrt{s_{\rm NN}} = 200$ GeV. The results are in good agreement (better than 3%) with those of our previous measurements [23]. The values for neutral kaons (K^0_s), lambdas (Λ), and the cascades (Ξ) show results from the STAR Collaboration [24,43]. The STAR v_2 values were multiplied by the factor 1.1 to account for a small difference between the average centralities for minimum-bias events from the two experiments. PHENIX and STAR $v_2(p_T)$ results [for $\pi^{\pm}$, $p(\bar{p})$ and K] for 10% centrality bins are essentially identical.

The comparison in Fig. 2(a) shows the well-known particle identification (PID) ordering of $v_2(p_T)$ at both low and high p_T values. At low p_T ($p_T \lesssim 2$ GeV/c), one can see rather clear evidence for mass ordering. If this aspect of v_2 is driven by a hydrodynamic pressure gradient, the prediction is that the differential v_2 values observed for each particle species should scale with KE_T. The pressure gradient that drives elliptic flow is directly linked to the collective kinetic energy of the emitted particles. For higher values of p_T ($p_T \sim 2$–4 GeV/c), Fig. 2(a) indicates that mass ordering is broken and v_2 is more strongly dependent on the quark composition of the particles than on their mass, which has been attributed to the dominance of the quark coalescence mechanism for $p_T \sim 2-4$ GeV/c [22–24].

Figure 2(b) shows the same v_2 data presented in Fig. 2(a) plotted as a function of KE_T. Note that KE_T is a robust scaling variable because it takes into account relativistic effects, which are especially important for the lightest particles. In contrast to the PID ordering observed in Fig. 2(a), all particle species scale to a common set of elliptic flow values for $\mathrm{KE}_T \lesssim 1$ GeV, confirming the strong influence of hydrodynamic pressure gradients. For $\mathrm{KE}_T \gtrsim 1$ GeV, this particle mass scaling (observed for all particle species) gives way to a clear splitting into a meson branch (lower v_2) and a baryon branch (higher v_2). Since both of these branches show rather good scaling separately, we interpret this as an initial hint for the degrees of freedom in the flowing matter at an early stage.

Figure 3 shows the results obtained after quark number scaling of the v_2 values shown in Fig. 2. That is, v_2, p_T, and KE_T are divided by the number of constituent quarks n_q for

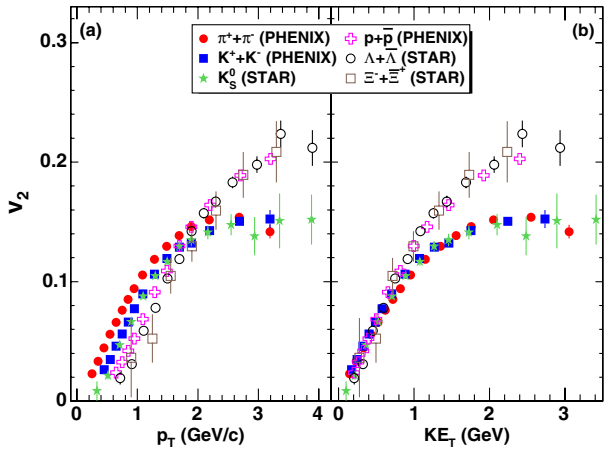

FIG. 2 (color online). (a) v_2 vs p_T and (b) v_2 vs KE_T for identified particle species obtained in minimum-bias Au + Au collisions. The STAR data are from Refs. [24,43].

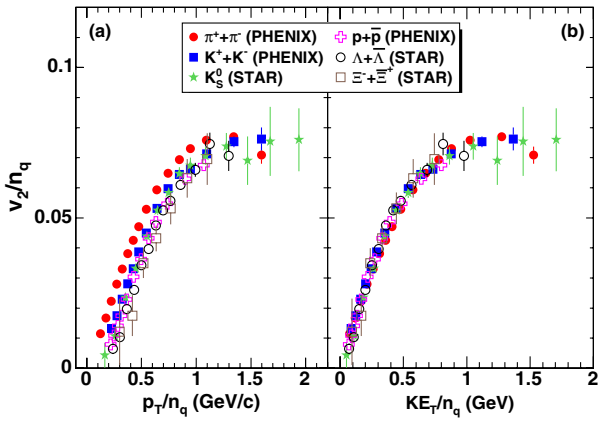

FIG. 3 (color online). (a) v_2/n_q vs p_T/n_q and (b) v_2/n_q vs KE_T/n_q for identified particle species obtained in minimum-bias Au + Au collisions. The STAR data are from Refs. [24,43].

mesons ($n_q = 2$) and baryons ($n_q = 3$). Figure 3(a) indicates rather poor scaling for $p_T/n_q \lesssim 1$ GeV/c and much better scaling for $p_T/n_q \gtrsim 1.3$ GeV/c, albeit with large error bars. The relatively large scaling violation observed for pions indicate that this particle species does not fit the simple quark coalescence picture of Refs. [22–24]. In contrast, Fig. 3(b) shows excellent scaling over the full range of KE_T/n_q values. We interpret this as an indication of the inherent quarklike degrees of freedom in the flowing matter. These degrees of freedom are gradually revealed as KE_T increases above ~1 GeV [cf. Fig. 2(b)] and are apparently hidden by the strong hydrodynamic mass scaling, which predominates at low KE_T. The fact that v_2/n_q shows such good scaling over the entire range of KE_T/n_q and does not for p_T/n_q, serves to highlight the fact that hydrodynamic mass scaling is preserved over the domain of the linear increase in KE_T. Figure 3(b) should serve to distinguish between different quark coalescence models.

In summary, we have presented the results from detailed tests of hydrodynamic scaling of azimuthal anisotropy in Au + Au and Cu + Cu collisions at $\sqrt{s_{\mathrm{NN}}} = 200$ GeV. For a broad range of centralities, eccentricity scaling is observed for charged hadrons for both the Cu + Cu and Au + Au systems. For a given eccentricity, v_2 is also found to be independent of colliding system size. The observed scaling for identified particles in Au + Au collisions, coupled with ϵ scaling, gives strong evidence for hydrodynamic scaling of v_2 over a broad selection of the elliptic flow data. For $\mathrm{KE}_T \sim 1$–4 GeV universal hydrodynamic scaling is violated, but baryons and mesons are found to scale separately. Quark number scaling (v_2/n_q vs KE_T/n_q) in this domain leads to comprehensive overall scaling of the data, with substantially better scaling behavior than that found for v_2/n_q vs p_T/n_q. The scaling with valence quark number may indicate a requirement of a minimum number of objects in a localized space that contain the prerequisite quantum numbers of the hadron to be formed. Whether the scaling further indicates these degrees of freedom are present at the earliest time is in need of more detailed theoretical investigation.

We thank the staff of the Collider-Accelerator and Physics Departments at BNL for their vital contributions. We acknowledge support from the Department of Energy and NSF (U.S), MEXT and JSPS (Japan), CNPq and FAPESP (Brazil), NSFC (China), MSMT (Czech Republic), IN2P3/CNRS, and CEA (France), BMBF, DAAD, and AvH (Germany), OTKA (Hungary), DAE (India), ISF (Israel), KRF and KOSEF (Korea), MES, RAS, and FAAE (Russia), VR and KAW (Sweden) CRDF for the FSU, U.S.-Hungarian NSF-OTKA-MTA, and U.S.-Israel BSF.

*Deceased.
†PHENIX Spokesperson.
Electronic address: zajc@nevis.columbia.edu

[1] F. Karsch, Nucl. Phys. **A698**, 199 (2002).
[2] F. Karsch, E. Laermann, and A. Peikert, Phys. Lett. B **478**, 447 (2000).
[3] K. Adcox *et al.*, Nucl. Phys. **A757**, 184 (2005).
[4] J. Adams *et al.*, Nucl. Phys. **A757**, 102 (2005).
[5] B. B. Back *et al.*, Nucl. Phys. **A757**, 28 (2005).
[6] I. Arsene *et al.*, Nucl. Phys. **A757**, 1 (2005).
[7] M. Gyulassy and L. McLerran, Nucl. Phys. **A750**, 30 (2005).
[8] B. Müller, nucl-th/0404015.
[9] E. Shuryak, Nucl. Phys. **A750**, 64 (2005).
[10] U. Heinz and P. Kolb, Nucl. Phys. **A702**, 269 (2002).
[11] D. Teaney, J. Lauret, and E. V. Shuryak, nucl-th/0110037.
[12] P. Huovinen *et al.*, Phys. Lett. B **503**, 58 (2001).
[13] T. Hirano and Y. Nara, Nucl. Phys. **A743**, 305 (2004).
[14] T. Csörgo and B. Lörstad, Phys. Rev. C **54**, 1390 (1996).
[15] M. Csanád *et al.*, nucl-th/0512078.
[16] M. Demoulins *et al.*, Phys. Lett. B **241**, 476 (1990).
[17] S. Voloshin and Y. Zhang, Z. Phys. C **70**, 665 (1996).
[18] M. Bleicher and H. Stoecker, Phys. Lett. B **526**, 309 (2002).
[19] D. Molnár and M. Gyulassy, Nucl. Phys. **A697**, 495 (2002).
[20] S. A. Voloshin, Nucl. Phys. **A715**, 379 (2003).
[21] V. Greco, C. M. Ko, and P. Levai, Phys. Rev. C **68**, 034904 (2003).
[22] R. J. Fries *et al.*, Phys. Rev. C **68**, 044902 (2003).
[23] S. S. Adler *et al.*, Phys. Rev. Lett. **91**, 182301 (2003).
[24] J. Adams *et al.*, Phys. Rev. Lett. **92**, 052302 (2004).
[25] R. S. Bhalerao *et al.*, Phys. Lett. B **627**, 49 (2005).
[26] T. Hirano and M. Gyulassy Nucl. Phys. **A769**, 71 (2006).
[27] T. Hirano *et al.*, Phys. Lett. B **636**, 299 (2006).
[28] N. Borghini and J.-Y. Ollitrault Phys. Lett. B **642**, 227 (2006).
[29] R. Lacey, Nucl. Phys. **A774**, 199 (2006).
[30] R. Fries *et al.*, Phys. Rev. Lett. **90**, 202303 (2003).
[31] M. Csanad *et al.*, nucl-th/0605044.
[32] K. Adcox *et al.*, Nucl. Instrum. Methods Phys. Res., Sect. A **499**, 469 (2003).
[33] K. Adcox *et al.*, Phys. Rev. C **69**, 024904 (2004).
[34] S. S. Adler *et al.*, Phys. Rev. C **69**, 034909 (2004).
[35] J. Jia Nucl. Phys. **A783**, 501 (2007).
[36] C. Adler *et al.*, Phys. Rev. Lett. **87**, 182301 (2001).
[37] K. H. Ackermann *et al.*, Phys. Rev. Lett. **86**, 402 (2001).
[38] K. Adcox *et al.*, Phys. Rev. Lett. **89**, 212301 (2002).
[39] B. Alver *et al.*, nucl-ex/0610037.
[40] S. Voloshin, AIP Conf. Proc. **870**, 691 (2006).
[41] An apparent difference between these scaled results and those in [38] reflects the fact that eccentricity fluctuations are now taken into account.
[42] F. Karsch, hep-lat/0601013.
[43] J. Adams *et al.*, Phys. Rev. Lett. **95**, 122301 (2005).

Eur. Phys. J. C 48, 343–352 (2006)
DOI 10.1140/epjc/s10052-006-0081-x

THE EUROPEAN PHYSICAL JOURNAL C

Regular Article – Experimental Physics

Pion freeze-out time in Pb + Pb collisions at 158 AGeV/c studied via π^-/π^+ and K^-/K^+ ratios

The WA98 Collaboration

M.M. Aggarwal[1], Z. Ahammed[2], A.L.S. Angelis[3,†], V. Antonenko[4], V. Arefiev[5], V. Astakhov[5], V. Avdeitchikov[5], T.C. Awes[6,a], P.V.K.S. Baba[7], S.K. Badyal[7], S. Bathe[8], B. Batiounia[5], T. Bernier[9], K.B. Bhalla[10], V.S. Bhatia[1], C. Blume[8], D. Bucher[8], H. Büsching[8], L. Carlen[11], S. Chattopadhyay[2], M.P. Decowski[12], H. Delagrange[9], P. Donni[3], M.R. Dutta Majumdar[2], K. El Chenawi[11], A.K. Dubey[13], K. Enosawa[14], S. Fokin[4], V. Frolov[5], M.S. Ganti[2], S. Garpman[11,†], O. Gavrishchuk[5], F.J.M. Geurts[15], T.K. Ghosh[16], R. Glasow[8], B. Guskov[5], H. Å.Gustafsson[11], H.H. Gutbrod[17], I. Hrivnacova[18], M. Ippolitov[4], H. Kalechofsky[3], R. Kamermans[15], K. Karadjev[4], K. Karpio[19], B.W. Kolb[17], I. Kosarev[5,†], I. Koutcheryaev[4], A. Kugler[18], P. Kulinich[12], M. Kurata[14], A. Lebedev[4], H. Löhner[16], L. Luquin[9], D.P. Mahapatra[13], V. Manko[4], M. Martin[3], G. Martínez[9], A. Maximov[5], Y. Miake[14], G.C. Mishra[13], B. Mohanty[13], M.-J. Mora[9], D. Morrison[20], T. Mukhanova[4], D.S. Mukhopadhyay[2], H. Naef[3], B.K. Nandi[13], S.K. Nayak[9], T.K. Nayak[2], A. Nianine[4], V. Nikitine[5], S. Nikolaev[4], P. Nilsson[11], S. Nishimura[14], P. Nomokonov[5], J. Nystrand[11], A. Oskarsson[11], I. Otterlund[11], S. Pavliouk[5], T. Peitzmann[15], D. Peressounko[4], V. Petracek[18], S.C. Phatak[13], W. Pinganaud[9], F. Plasil[6], M.L. Purschke[17], J. Rak[18], R. Raniwala[10], S. Raniwala[10], N.K. Rao[7], F. Retiere[9], K. Reygers[8], G. Roland[12], L. Rosselet[3], I. Roufanov[5], C. Roy[9], J.M. Rubio[3], S.S. Sambyal[7], R. Santo[8], S. Sato[14], H. Schlagheck[8], H.-R. Schmidt[17], Y. Schutz[9], G. Shabratova[5], T.H. Shah[7], I. Sibiriak[4], T. Siemiarczuk[19], D. Silvermyr[11], B.C. Sinha[2], N. Slavine[5], K. Söderström[11], G. Sood[1], S.P. Sørensen[20], P. Stankus[6], G. Stefanek[19], P. Steinberg[12], E. Stenlund[11], M. Sumbera[18], T. Svensson[11], A. Tsvetkov[4], L. Tykarski[19], E.C. v. d. Pijll[15], N. v. Eijndhoven[15], G.J. v. Nieuwenhuizen[12], A. Vinogradov[4], Y.P. Viyogi[2], A. Vodopianov[5], S. Vörös[3], B. Wysłouch[12], G.R. Young[6]

[1] University of Panjab, Chandigarh 160014, India
[2] Variable Energy Cyclotron Centre, Calcutta 700064, India
[3] University of Geneva, 1211 Geneva 4, Switzerland
[4] RRC Kurchatov Institute, 123182 Moscow, Russia
[5] Joint Institute for Nuclear Research, 141980 Dubna, Russia
[6] Oak Ridge National Laboratory, Oak Ridge, Tennessee 37831-6372, USA
[7] University of Jammu, Jammu 180001, India
[8] University of Münster, 48149 Münster, Germany
[9] SUBATECH, Ecole des Mines, Nantes, France
[10] University of Rajasthan, Jaipur 302004, Rajasthan, India
[11] Lund University, 22100 Lund, Sweden
[12] MIT, Cambridge, MA 02139, USA
[13] Institute of Physics, 751-005 Bhubaneswar, India
[14] University of Tsukuba, Ibaraki 305, Japan
[15] Universiteit Utrecht/NIKHEF, 3508 TA Utrecht, The Netherlands
[16] KVI, University of Groningen, 9747 AA Groningen, The Netherlands
[17] Gesellschaft für Schwerionenforschung (GSI), 64220 Darmstadt, Germany
[18] Nuclear Physics Institute, 250 68 Rez, Czech Republic
[19] Institute for Nuclear Studies, 00-681 Warsaw, Poland
[20] University of Tennessee, Knoxville, Tennessee 37966, USA

[†] deceased

Received: 16 July 2006 / Revised version: 1 September 2006 /
Published online: 7 November 2006 – © Springer-Verlag / Società Italiana di Fisica 2006

Abstract. The effect of the final state Coulomb interaction on particles produced in Pb + Pb collisions at 158 AGeV/c has been investigated in the WA98 experiment through the study of the π^-/π^+ and K^-/K^+ ratios measured as a function of $m_{\rm T} - m_0$. While the ratio for kaons shows no significant $m_{\rm T}$ dependence, the π^-/π^+ ratio is enhanced at small $m_{\rm T} - m_0$ values with an enhancement that increases with centrality. A silicon pad detector located near the target is used to estimate the contribution of hyperon decays to the π^-/π^+ ratio. The comparison of results with predictions of the RQMD model in which the Coulomb interaction has been incorporated allows to place constraints on the time of the pion freeze-out.

1 Introduction

The distributions of negatively and positively charged pions produced in heavy ion collisions exhibit significant differences at low transverse kinetic energy (or transverse mass), $m_{\rm T} - m_\pi = \sqrt{p_{\rm T}^2 + m_\pi^2} - m_\pi$. These differences are evident in the behaviour of the ratio of their yields $R_\pi = \pi^-/\pi^+$. The study of charged particle production in Au + Au collisions at SIS (1 AGeV) [1] and AGS (10.8 AGeV) [2–4] shows that for central collisions R_π rises at low $m_{\rm T}$ at both collision energies. At the same time, for peripheral collisions at the AGS, R_π does not depend on $m_{\rm T}$. At 1 AGeV R_π is about 2.9 for $m_{\rm T} - m_\pi$ near zero and its integrated value is $R_\pi = 1.9 \pm 0.1$. The large integrated value at 1 AGeV can be explained by isobar decays and reflects the N/Z asymmetry of the colliding system. The very sharp rise at low $m_{\rm T}$ on the other hand points toward significant Coulomb interactions between charged pions and the remaining nuclear charge distribution (acceleration of π^+ and deceleration of π^-). At 10.8 AGeV and higher energy the isobar contribution to R_π becomes insignificant and it is expected that mainly the Coulomb interaction distorts the R_π ratio. The NA44 experiment has published data on R_π measured in central Pb + Pb collisions at 158 AGeV [5]. A prominent enhancement of R_π at small $m_{\rm T}$ was observed. NA44 has also measured R_π in S + S and S + Pb collisions at 200 AGeV/c, where the ratio remains constant at $m_{\rm T} - m_\pi < 0.5\,{\rm GeV}/c^2$ [5]. At high energies (AGS and SPS) the contribution from strange particle decay can significantly affect the measured pion distribution. The hyperon contribution is influenced by the detector acceptance and the pion vertex reconstruction properties. The excess of hyperon over anti-hyperon yield in heavy ion collisions also leads to an enhancement of R_π at low transverse kinetic energy.

Several dedicated models [6–11] describe the pion ratio detected by the NA44 collaboration in Pb + Pb collisions through the electromagnetic interaction induced by the large amount of charge of the participating protons. The authors of the dynamical model of [6] argue that the R_π enhancement at small momenta depends mainly on the time of freeze-out and extract a freeze-out time of about 7 fm/c. They also predict the corresponding ratio for kaons, $R_K = K^-/K^+$, to be smaller by a factor of m_K/m_π. However, this overestimates the NA44 kaon measurement. This discrepancy is explained as due to the much larger absorption of K^- on nucleons ($K^- + N \to \Lambda + \pi$) than for K^+. For a detector located at mid-rapidity this model predicts a small reduction of the R_π enhancement with respect to the NA44 result measured near rapidity $y_{\rm CMS} = 1$ in the center of mass system. On the other hand, in another model [11] the enhancement of the ratio strongly increases towards mid-rapidity, reaching the value of 2.5. In [9] it is concluded that the influence of the Coulomb force should be computed within an event simulator which takes into account a more accurate description of the space-time evolution of the collision.

Initial results from the SPS experiment WA98 on the measurement of the π^-/π^+ ratio in central Pb + Pb collisions were reported in [12]. The enhancement of R_π at $m_{\rm T} - m_\pi < 50\,{\rm MeV}/c^2$ measured with the two independent tracking arms of WA98 located nearer to mid-rapidity than the NA44 spectrometer was reported to be significantly smaller than that measured by NA44 [5].

In this paper we present the π^-/π^+ ratio as a function of centrality for 158 AGeV/c Pb + Pb collisions. The background pion contribution from hyperon decays is determined and removed by use of vertex information from a silicon detector located near to the target to obtain the ratio of pions that originate in the target. The yields of electrons and positrons are analysed at low momentum where they can be clearly identified through time-of-flight. Their yields provide a check of the normalization of the opposite sign yields at the lowest transverse momenta. They also confirm the validity of estimates of the electron and positron contaminations to the measured pion distributions at higher momenta. The K^-/K^+ratio is also presented for central collisions. The results are compared with predictions of the RQMD 2.4 model [13] in which final state Coulomb interactions have been added. Within the uncertainties of the hyperon decay contribution the results are found to be compatible with predictions of the RQMD model in which the average pion freeze-out time is 15 fm/c for central collisions. Possible modifications of the final state predicted by RQMD, necessary to improve agreement with the measured π^-/π^+ ratios, are investigated and discussed.

2 Experimental setup and data analysis

The CERN SPS experiment WA98 [14] combined photon and hadron spectrometers with other large acceptance detectors that measured a number of global variables on an event-by-event basis. Figure 1 shows the experimental layout during the 158 AGeV ^{208}Pb beam run period in 1996 with a 0.239 g/cm^2 Pb target.

The Mid-Rapidity Calorimeter, MIRAC [15], measured the collision transverse energy ($E_{\rm T}$) in the pseudorapidity

[a] awes@mail.phy.ornl.gov

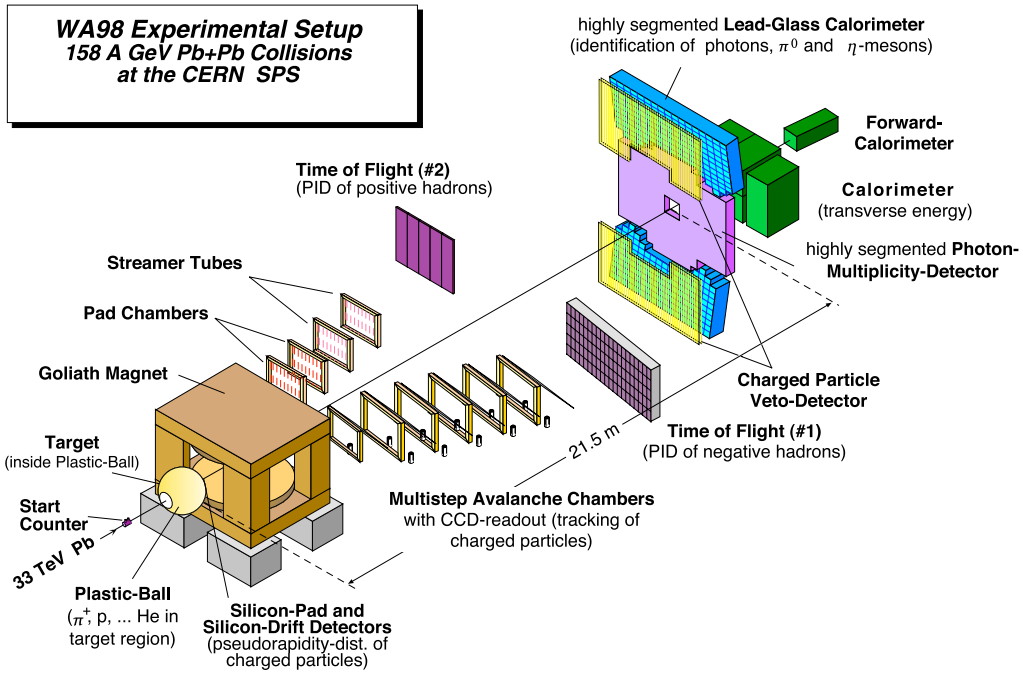

Fig. 1. The WA98 experimental setup

interval $3.5 < \eta < 5.5$. The minimum bias trigger required $E_{\mathrm{T}} \gtrsim 5$ GeV and a valid signal from the beam counters. The measured $\mathrm{d}\sigma/\mathrm{d}E_{\mathrm{T}}$ distribution is used for the calculation of the collision centrality. The minimum bias cross section for the run period used in this analysis is $\sigma_{\mathrm{mb}} = 6451$ mb with an overall systematic error of less than 10%.

Two thin circular silicon wafer detectors were positioned at small distance downstream from the target, where charged particle trajectories were not affected by the magnetic field. A silicon pad multiplicity detector, SPMD [16], was located at a downstream distance of 32.85 cm. It was segmented into 184 azimuthal sectors and 22 pseudorapidity rings in the range $2.35 < \eta < 3.75$, and maintained pad occupancy below 20%. The SPMD measured the energy deposited in each pad. A silicon drift detector, SDD [17], was located at a distances of 12.5 cm from the target. Its position resolution was 25 and 35 μm in the azimuthal and radial coordinates, respectively. The acceptance of the two detectors overlapped in the pseudorapidity interval $2.35 < \eta < 3.4$. The two detectors were used for precise reconstruction of the vertex position of the Pb + Pb primary collision. For that purpose straight lines going through each pair of hits in the SDD and SPMD were projected onto the target plane. The one dimensional spatial resolution was found to be better than 0.3 mm perpendicular to the beam line.

The WA98 experiment comprised two charged particle spectrometer arms located on the right (first arm) and the left (second arm, not used in the present analysis) facing downstream from the target, beyond a dipole magnet (Goliath) with 1.6 Tm bending power in the horizontal plane. The first tracking arm consisted of six Multistep Avalanche Chambers, MSAC, read out by CCD cameras equipped with two image intensifiers [18–20]. Each pixel of a CCD viewed a $3.1 \times 3.1\,\mathrm{mm}^2$ area of a chamber. In addition, a $4 \times 1.9\,\mathrm{m}^2$ time-of-flight wall positioned behind the chambers at a distance of 16.5 m from the target allowed for particle identification with a time resolution better than 120 ps. The TOF detector consisted of 480 scintillator counters with area $3.3 \times 48.5\,\mathrm{cm}^2$ and thickness 2 cm arranged in four rows [21]. Each counter was equipped with two PMTs, one at each end. The position of a hit along a scintillator bar was evaluated using two methods: the first used the time difference of signals obtained from the two ends of the scintillator bar, and the second used the ratio of their amplitudes. Both methods provide a spatial resolution of the order of 2.5 cm.

Tracks were selected which traverse all six MSAC chambers, have detected hits in at least four of them, and were associated with a TOF hit within a $6 \times 6\,\mathrm{cm}^2$ window. An additional momentum dependent time of flight cut was used to exclude misidentified pion, kaon, and proton tracks at a level better than 1%. The $(m_{\mathrm{T}} - m_{\pi})$-rapidity acceptance for pions generated by Monte Carlo is shown in Fig. 2.

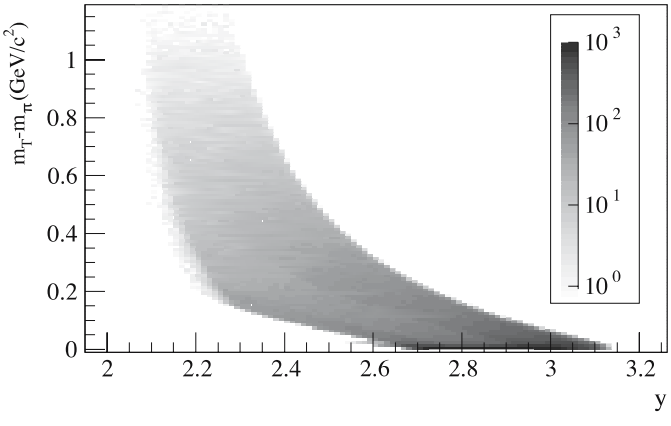

Fig. 2. Acceptance of the first tracking arm in the $(m_{\mathrm{T}} - m_{\pi}, y)$ plane for pions

The center of mass system rapidity is 2.9. The momentum resolution of the spectrometer was $\Delta p/p = 0.005$ at $p = 1.5\,\mathrm{GeV}/c$.

Positive and negative particles were detected in two sets of runs with opposite direction of the magnetic field. Data samples consisting of 0.58×10^6 π^- and 0.22×10^6 π^+ tracks satisfying all quality requirements were used for the ratio measurement.

Efficiency matrices were measured for a grid of 8×8 cells across each MSAC chamber and for several run periods. The overall tracking arm efficiency measured for negative particles was 2% less than that for positive particles due to chamber instabilities, however, there was no significant difference in the m_T dependence of the efficiencies. The detailed analysis of the π^- and K^- measurement in the first tracking arm has been presented in a separate paper [22].

3 Method of simulation

Simulations have been used in this analysis to estimate the different contributions to the measured R_π and R_K ratios, and to compare with the measured results. A detailed description of the primary collisions, of the Coulomb final state interactions, and of the particle propagation through the experimental setup has been simulated.

The primary Pb + Pb collisions were simulated with the RQMD 2.4 model [13] event generator which reproduces well the light strange baryon yield measured by the WA97 experiment [23], but does not include Coulomb interactions. In RQMD the particles are treated semiclassically over the complete evolution of the system. This allows the calculation of the Coulomb forces between each particle pair as an "afterburner" applied to the RQMD output. The electromagnetic interaction of a particle i with another charged particle j was calculated as described in [24] by

$$m_i \frac{\mathrm{d}u_i^\mu}{\mathrm{d}\tau} = \sum_{j \neq i} \frac{e_i}{c} F_{ij}^{\mu\nu} u_i^\nu \,, \tag{1}$$

where j runs over all charged particles of the system. Here particle i has mass m_i, charge e_i and 4-velocity $u_i = (1, \mathbf{v})/\sqrt{1-\mathbf{v}^2}$. The tensor $F_{ij}^{\mu\nu}$ is given by

$$F_{ij}^{\mu\nu} = \frac{e_j}{c} \frac{X^\mu u_j^\nu - X^\nu u_j^\mu}{\left(\frac{1}{c^2} \left(u_j^\lambda X^\lambda \right)^2 - X_\lambda X^\lambda \right)^{3/2}} \,, \tag{2}$$

where X^λ is the relative 4-distance between particles i and j. The forces are calculated at each time step of the system evolution and the positions and momenta of the particles are updated with the effect of the Coulomb forces only for those particles which have undergone their last collision. RQMD events with Coulomb interactions added were used as input to the detector simulation. Delta electrons produced by Pb ions in the target material before the collision were also simulated through the detector response.

The GEANT 3.21 program [25] was used for the detector simulation. The target, beam line, Goliath magnet, SDD and SPMD detectors, and tracking arm have been described in detail. For the track reconstruction the same procedure as used in the treatment of real data was employed. For every hit in the tracking arm all information on the particle and all its predecessors was stored for further analysis so that the history of every track could be traced back to the moment of the primary collision.

4 Experimental results

4.1 Centrality selection

The R_π ratio was studied for six centrality intervals defined by the transverse energy E_T measured with the MIRAC. The value of b may be estimated from the measured E_T according to the equation

$$\pi b^2 = \int_{E_\mathrm{T}}^{\infty} (\mathrm{d}\sigma/\mathrm{d}E_\mathrm{T})\,\mathrm{d}E_\mathrm{T} \,, \tag{3}$$

where $\mathrm{d}\sigma/\mathrm{d}E_\mathrm{T}$ is the experimentally measured distribution. Systematic comparisons of $\mathrm{d}\sigma/\mathrm{d}E_\mathrm{T}$ with predictions of VENUS 4.12 [26] and extraction of the number of participating nucleons or number of binary collisions are given in [27]. Table 1 lists the centrality intervals used in this analysis.

4.2 Particle ratios

The two tracking arms of WA98 provide two independent measurements of the pion ratio and have been shown to be consistent [12]. This study focuses on an analysis of the data obtained by the first tracking arm, whose acceptance for pions is shifted by about 0.5 of a unit of rapidity closer to the target fragmentation region relative to the acceptance of the second arm. This provides more favourable conditions for π/K separation in the region of large transverse mass where the normalization of the ratios is performed. At

Table 1. Centrality intervals defined according to the amount of E_T measured in MIRAC. The number of participants was calculated with VENUS 4.12

Centrality interval number	E_T (GeV)	$\sigma/\sigma_\mathrm{mb}$ (%)	Impact parameter (fm)	Number of participants
1	34.5–130	36.8–70.2	8.6–12.0	34–136
2	130–180	28.0–36.8	7.5–8.6	136–179
3	180–240	19.6–28.0	6.3–7.5	179–231
4	240–325	10.1–19.6	4.5–6.3	231–306
5	325–400	3.58–10.1	2.7–4.5	306–364
6	> 400	< 3.58	< 2.7	> 364

low p_T it allows better rejection of electrons through time-of-flight and a significantly larger number of tracks pass through the active area of the SPMD than is the case for the second arm. Figure 3 shows the R_π ratio normalized at transverse kinetic energy between 0.3 and 0.76 GeV/c^2 for the six centrality selections of Table 1. It should be noted that the Coulomb interaction effect on the ratio is strongly reduced and the contribution from hyperon decays is absent in the normalization region.

The e^-/e^+ ratio can be used as a check of the absolute normalization of the R_π ratio. For $0.8 < p < 1.2$ GeV/c electron and positron tracks are well identified through time-of-flight. As imposed by the tracking arm acceptance these tracks have transverse momenta below 50 MeV/c. Since both electrons and positrons originate mainly from photon conversions in the target material their yields should be identical, except for a small additional electron contribution from the production of delta electrons. These purely electromagnetic processes are well understood, so that the ratio e^-/e^+ is expected to be reproduced in simulation with an accuracy of order 1%. The e^-/e^+ ratio is presented in Fig. 4 as a function of centrality and compared to predictions. For each centrality the e^-/e^+ ratio is normalized with the same normalization used for the corresponding π^-/π^+ ratio in Fig. 3. Any difference between data and simulation is a measure of the systematic error in the normalization of the measured R_π distributions of Fig. 3. Summed over all centrality bins the difference between data and simulation of the e^-/e^+ ratio is $-0.8 \pm 1.2\%$, consistent with the expected accuracy of the comparison. This result indicates that the systematic error on the absolute normalization of R_π introduced by normalization of the ratio in the region $0.3 < m_T - m_\pi < 0.76$ GeV/c^2 is small, and that the normalization error is dominated by the statistical error of the data used for the normalization (shown by the dotted lines in Fig. 3).

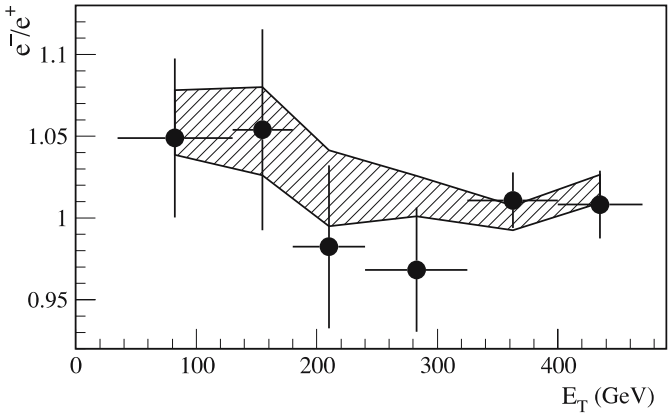

Fig. 4. MIRAC E_T dependence of the e^-/e^+ ratio. The normalization is the same as for the π^-/π^+ ratio. Data are shown by *filled circles*. The *hatched band* indicates the statistical uncertainty (Mean ± RMS) of the RQMD prediction

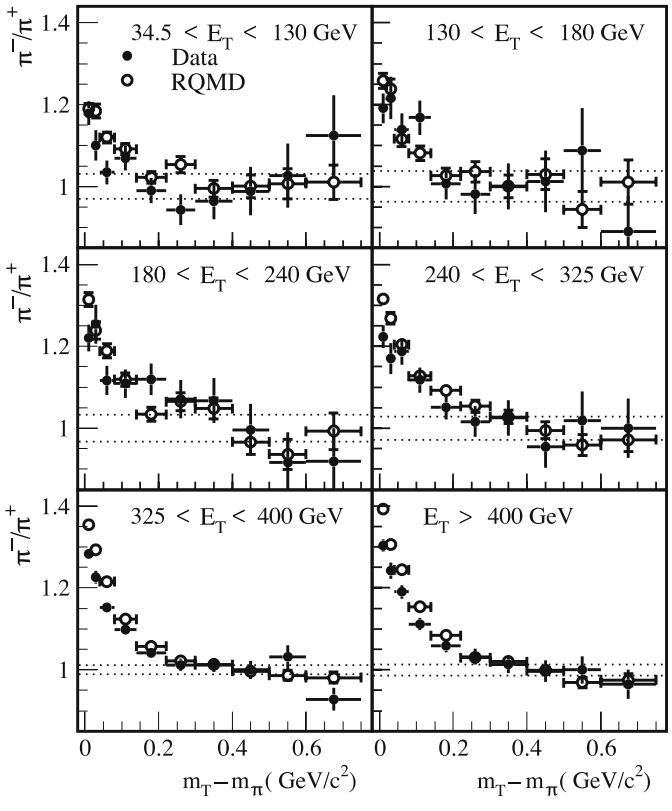

Fig. 3. The ratio R_π vs. $m_T - m_\pi$ for several Pb + Pb collision centrality intervals defined by E_T measured in the MIRAC. Data (*filled circles*) compared with predictions from RQMD including the Coulomb interaction (*open circles*). The ratios are arbitrarily normalized to 1.0 in the region $0.3 < m_T - m_\pi < 0.76$ GeV/c^2. The statistical errors are shown by the *error bars* on the *points*. The *dotted lines* indicate the statistical error on the normalization of the data. The RQMD normalization errors are about half as large

The ratio for kaons R_K measured under the same experimental conditions is presented in Fig. 5 for the 10% most central collisions. The kaon ratio shows no signifi-

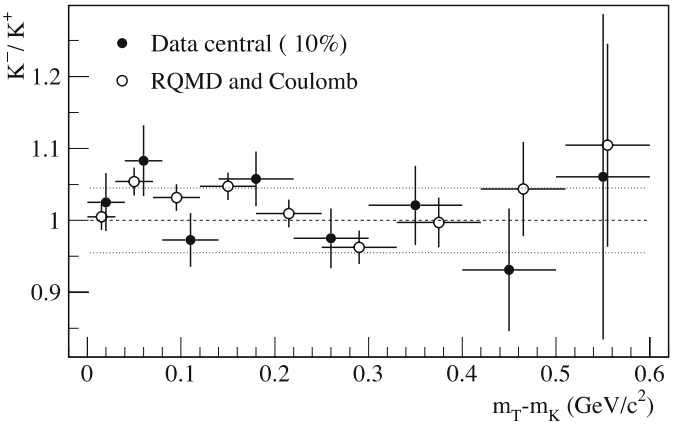

Fig. 5. The kaon ratio for the 10% most central Pb + Pb collisions. Data (*filled circles*) are compared with predictions from the RQMD model with Coulomb interactions included (*open circles*). The ratios are arbitrarily normalized to 1.0 in the region $0.3 < m_T - m_K < 0.6$ GeV/c^2. Errors are as described for Fig. 3

cant dependence on transverse kinetic energy. The lack of enhancement at low transverse mass is consistent with RQMD simulations with Coulomb final state interactions. The acceptance for the lowest transverse mass is located near kaon rapidity $y = 1.8$ in the laboratory system. For $m_{\mathrm{T}} - m_K > 0.2\,\mathrm{GeV}/c^2$ the average rapidity is about $y = 2.15$.

4.3 Hyperon contribution

Pions from hyperon decays have a much steeper transverse momentum spectrum than directly produced pions. Since strange hyperons are more abundantly produced than anti-strange hyperons, the π^-/π^+ ratio will be enhanced at low m_{T} due to this difference. In order to study the Coulomb effect on the directly produced pions, it is necessary to estimate and remove the hyperon contributions.

The silicon pad multiplicity detector has been used to estimate the yield of identified tracks that do not track back to the target vertex, and thus may be attributed to products of strange or anti-strange hadron decays. All pads of the SPMD that overlap with a $4 \times 4\,\mathrm{mm}^2$ window, centered at the point where the extrapolation of the track towards the target intersects the SPMD plane, were selected. The summed energy loss in the pad window is denoted as S, and given in units of the energy loss of a minimum ionizing particle in the silicon wafer of the SPMD. S therefore gives an estimate of the number of minimum ionizing particles traversing the SPMD within the pad window. Simulation indicates that the mean value over a large set of tracks for pion tracks originating in the target is $\langle S \rangle = 0.89$, while for tracks from hyperon and K^0_S decays $\langle S \rangle = 0.17$ and 0.20, respectively. This is because tracks that originate from hyperon or K^0_S decays either traverse the SPMD far from the pad indicated by the extrapolation, or do not traverse it at all (produced downstream of the SPMD). Thus, tracks from hyperon decays will be suppressed by roughly a factor of $0.89/0.17 \approx 5$ with the SPMD hit requirement.

In the case of high pad occupancy the energy loss S_1 measured in the SPMD window associated with the track contains a significant contribution S_2 from spurious tracks. The value of S_2 is estimated by the measured energy loss in a window of the same size centered at a location far from the extrapolated track location (in particular, at a location rotated by 12° in azimuth). The RQMD simulation indicates that $\langle S' \rangle = \langle S_1 - S_2 \rangle$ provides a good estimate of $\langle S \rangle$ for each kind of track.

According to RQMD predictions, in the region of transverse kinetic energy above $0.3\,\mathrm{GeV}/c^2$ the contribution of hyperon decays to the pion yield is expected to be below 1%, due to the hyperon decay kinematics. In this region, most of the tracks originate from the target, with less than 8% contribution from K_S decays. Therefore, we may consider these tracks a relatively clean selection of directly produced pions and use them to estimate the quality of the description of the SPMD response in the simulation. As shown in Fig. 6, the extracted number of particles traversing the SPMD $\langle S_1 - S_2 \rangle$ coincides with simulation within errors while the SPMD occupancy varies by more than a factor of 5 between the most peripheral and most central bins. Mean values of $\langle S_1 - S_2 \rangle = 86.7 \pm 1.4\%$ and $\langle S_1 - S_2 \rangle = 85.4 \pm 0.9\%$ are extracted for positiviely and negatively charged pions, respectively.

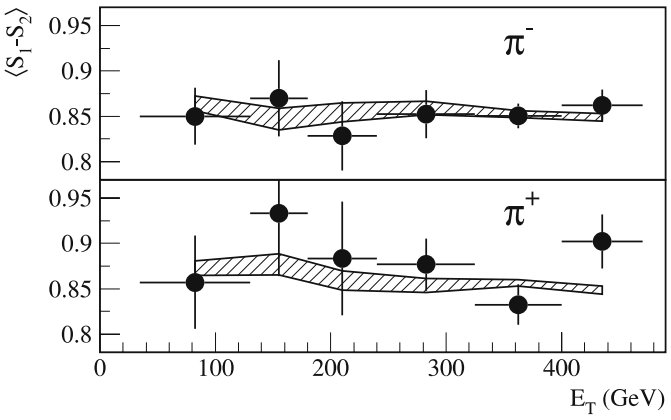

Fig. 6. The corrected average number of minimum ionizing particles, $\langle S' \rangle = \langle S_1 - S_2 \rangle$, as a function of centrality, in the associated SPMD region for negative and positive pions with $m_{\mathrm{T}} - m_\pi > 0.3\,\mathrm{GeV}/c^2$. The results are compared to simulations shown by the *hatched regions*

For tracks whose extrapolation traverses the SPMD the quantities $R_{\mathrm{g}} = \pi^-/\pi^+$ and $R_{\mathrm{SPMD}} = S'^-/S'^+$ are defined, where S'^- and S'^+ are sums of $S_1 - S_2$ values for negative and positive pion tracks identified by the tracking arm. In the case of equal hyperon fractions of the pion yield for both charges one expects $R_{\mathrm{SPMD}} \approx R_{\mathrm{g}}$. The behaviour of R_{g} and R_{SPMD} as a function of transverse kinetic energy for the 10% most central collisions is shown in Fig. 7. Both distributions have the same normalization chosen to give $R_{\mathrm{g}} = 1$ at $m_{\mathrm{T}} - m_\pi > 0.3\,\mathrm{GeV}/c^2$.

Since the contribution to S from hyperon decay tracks is smaller than for tracks originating in the target, a deviation of R_{SPMD} from R_{g} is an indication of different hyperon fractions in the two charge samples. The observed lower

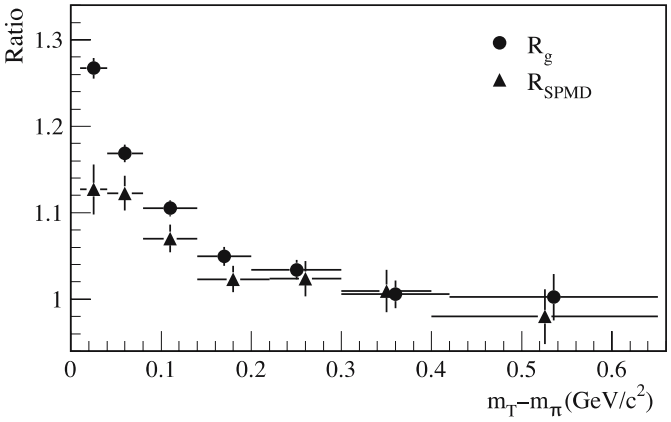

Fig. 7. R_{SPMD} (*triangles*) and R_{g} (*circles*) for the 10% most central events. See text for definitions of R_{SPMD} and R_{g}. Both distributions are normalized to 1.0 for R_{g} at $m_{\mathrm{T}} - m_\pi > 0.3\,\mathrm{GeV}/c^2$

value of R_{SPMD} in comparison to R_{g} for small m_{T} indicates a larger fraction of tracks from hyperon decays in the measured π^- distribution relative to the π^+ distribution. To quantify this difference the quantity $(R_{\mathrm{g}} - R_{\mathrm{SPMD}})/R_{\mathrm{g}}$ is extracted and compared with RQMD simulation as a function of $m_{\mathrm{T}} - m_{\pi}$ in Fig. 8 and as a function of collision centrality in Fig. 9 for $m_{\mathrm{T}} - m_{\pi} < 140\,\mathrm{MeV}/c^2$, where the excess becomes significant. Within errors it is seen that the RQMD simulation provides a good description of the contribution of strange baryon decays to the pion ratio.

The yield distributions of light strange and anti-strange baryons have been reported by the WA97 collaboration [24] and also shown to be successfully reproduced by RQMD calculations. Based on this fact, and on the comparisons of Figs. 8 and 9, the RQMD simulation results have been used to correct the measured pion ratios R_{π} shown in Fig. 3 for the hyperon decay contributions to obtain the corrected ratios R'_{π} of pions originating in the target. For this purpose, for each of the π^- and π^+ yields, the fraction of the pion yield from strange hadron decays has been estimated from RQMD simulation and removed from the total yield. Figure Fig. 10 shows the corrected pion ratios $R'_{\pi} = \pi^-/\pi^+$.

At low momenta the e^- and e^+ tracks have been separated from pions through time-of-flight and their abundances are found to be in agreement with simulation. At high momenta e^- and e^+ tracks cannot be separated from pions and their relative yields have been estimated from simulation. The ratio R'_{π} of pions originating from the target has also been corrected for e^- and e^+ misidentified as pions at high momenta. According to simulation this e^- and e^+ contamination weakens the enhancement of the pion ratio by about 2% for the lowest m_{T}. The corrected ratios R'_{π} shown in Fig. 10 can be used for comparison of the π^-/π^+ ratio with predictions from models including the decay of the η and other short lived resonances.

In Fig. 11 the dependence of the corrected pion ratio R'_{π} on the collision centrality is shown for two intervals of pion transverse kinetic energy: below $40\,\mathrm{MeV}/c^2$ and between 40 and $140\,\mathrm{MeV}/c^2$. The error due to normalization is included in the error bars. Predictions from RQMD calculations with Coulomb interactions included are also shown. Both the measured results and the RQMD predic-

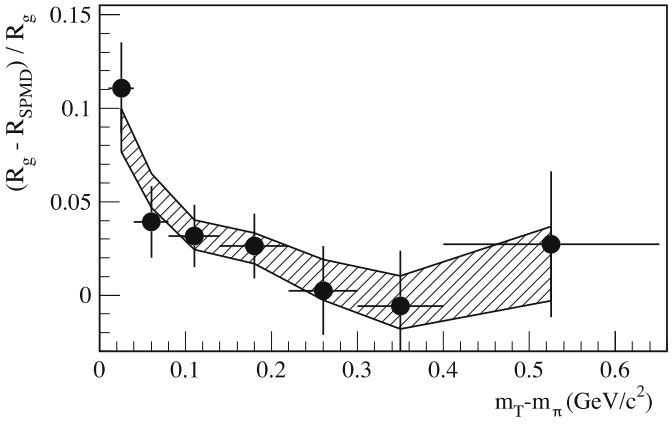

Fig. 8. $(R_{\mathrm{SPMD}} - R_{\mathrm{g}})/R_{\mathrm{g}}$ for the 10% most central events. Data are shown by *filled circles*. See text for definitions of R_{SPMD} and R_{g}. The *hatched band* indicates the statistical uncertainty (Mean ± RMS) of the RQMD prediction

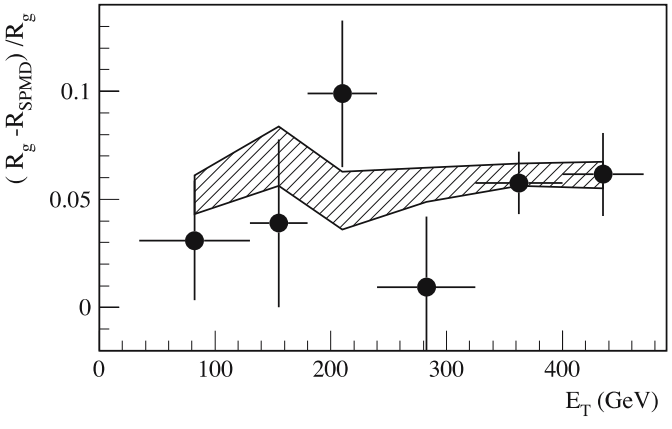

Fig. 9. Centrality dependence of $(R_{\mathrm{SPMD}} - R_{\mathrm{g}})/R_{\mathrm{g}}$ for $m_{\mathrm{T}} - m_{\pi} < 140\,\mathrm{MeV}/c^2$. Data are shown by *filled circles*. The *hatched band* indicates the statistical uncertainty (Mean ± RMS) of the RQMD prediction

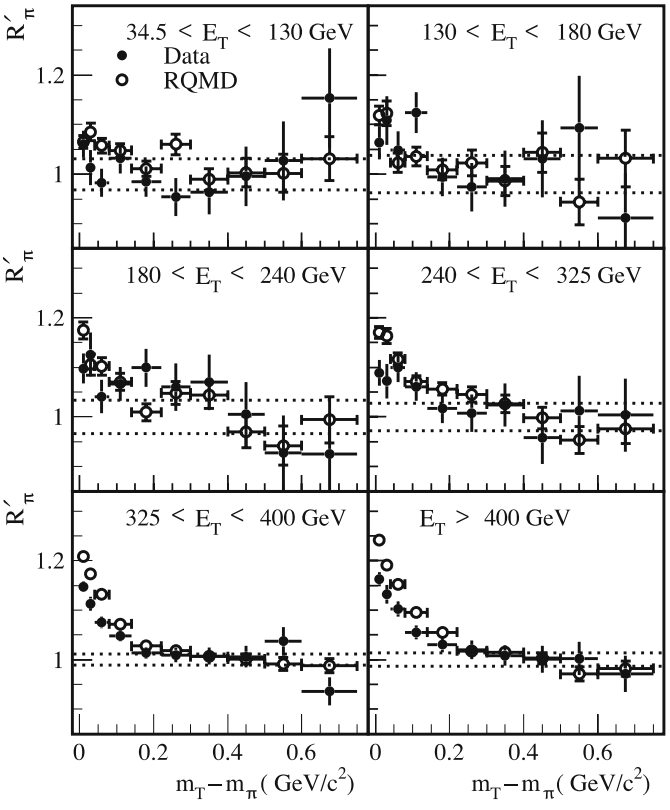

Fig. 10. The corrected charged pion ratio $R'_{\pi} = \pi^-/\pi^+$ for pions originating from the target, after removal of the hyperon decay and electron contamination contributions. Data (*filled circles*) are compared with predictions from RQMD including the Coulomb interaction (*open circles*). The ratios are arbitrarily normalized to 1.0 in the region $0.3 < m_{\mathrm{T}} - m_{\pi} < 0.76\,\mathrm{GeV}/c^2$. Errors are as described for Fig. 3

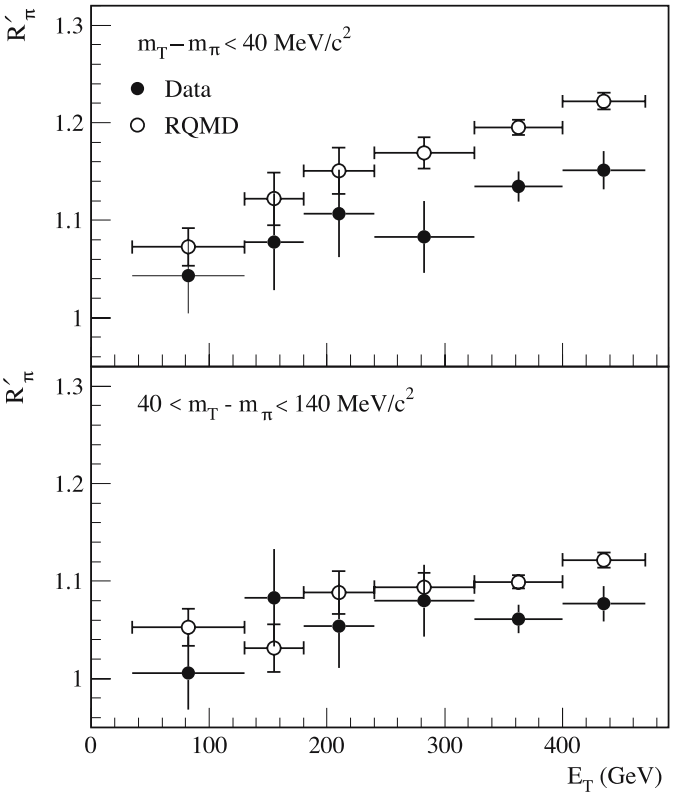

Fig. 11. Centrality dependence of the corrected charged pion ratio for pions originating from the target for $m_{\mathrm{T}} - m_{\pi} < 40\,\mathrm{MeV}/c^2$ and $40 < m_{\mathrm{T}} - m_{\pi} < 140\,\mathrm{MeV}/c^2$. Data (*filled circles*) are compared with predictions from RQMD calculations (*open circles*)

tions show a smooth increase of the pion ratio with increasing centrality. As expected, the ratio tends to a value of unity for peripheral collisions. However, RQMD is seen to overpredict the measured pion ratio with a discrepancy that grows with decreasing transverse mass.

5 Modified Coulomb calculations

Several parameters of the collision, such as the total participant charge at central rapidity, its transverse expansion velocity, and the freeze-out time, affect the π^-/π^+ ratio [6]. In order to investigate the sensitivity of the pion ratio to the collision parameters, the Coulomb calculations were repeated under alternative scenarios following minor modifications of the RQMD output. For this study RQMD events from central Pb + Pb collisions with impact parameter $b < 4.5$ fm were used.

In the first modification, the RQMD baryon rapidity density was adjusted. Since the value of $\mathrm{d}N/\mathrm{d}y$ for protons around mid-rapidity for central Pb + Pb collisions as measured by the NA44 [28] and NA49 [29] experiments is lower than the RQMD prediction by about 30%, the RQMD Coulomb interaction from baryons should be reduced accordingly. The corresponding reduction of the baryon Coulomb source was implemented in the calculation by weighting the Coulomb charge of all baryons during all stages of the collision by the ratio of measured to predicted proton $\mathrm{d}N/\mathrm{d}y$ distributions. This baryon rapidity density correction (BRDC) reduces the ratio at the lowest $m_{\mathrm{T}} - m_{\pi}$ bin by 3% (Fig. 12). Since this correction is based on a discrepancy between RQMD and experimental measurements, further calculations use this modified baryon Coulomb charge rapidity density.

To estimate the sensitivity of the pion ratio to the freeze-out time the application of the Coulomb interaction was simply delayed. The mean time of pion freeze-out at $|y_{\mathrm{CMS}}| < 1$ in the central Pb + Pb RQMD events is 15 fm/c. For demonstration, a 2 fm/c delay was added during which time the particles move freely after freeze-out on their final RQMD trajectories. After propagating freely for 2 fm/c the pions are then subjected to the Coulomb interactions. At $m_{\mathrm{T}} - m_{\pi} < 40\,\mathrm{MeV}/c^2$ the resulting ratio shown in Fig. 12 by triangles is reduced with respect to the unmodified RQMD result by 5%. This total reduction of the ratio is similar in magnitude to the difference between the data and the unmodified RQMD simulation results of Fig. 11. Alternatively, increased collective flow in RQMD would result in a larger freeze-out volume and a reduced Coulomb interaction, with a similarly improved agreement with the measurements.

In Fig. 13 the pion ratio measured in this experiment for the 10% most central Pb + Pb collisions is compared with that reported by the NA44 collaboration [5]. Neither RQMD calculations, nor the previously mentioned models [6, 11], predict the observed difference in the two measurements. This could indicate an earlier pion freeze-out in the center of mass rapidity region near $y = 1$ (NA44) relative to that near $y = 0$ (WA98).

The measured K^-/K^+ ratio (Fig. 5) does not show any significant m_{T} dependence. This is consistent with the data of the NA44 collaboration and with RQMD predictions. The kaon ratio enhancement induced through the

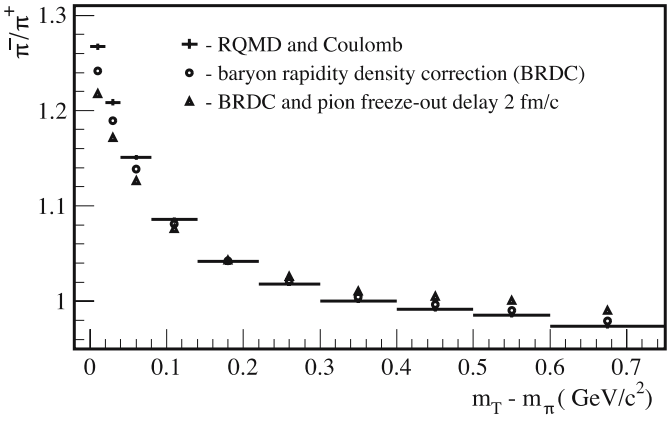

Fig. 12. The pion yield ratio π^-/π^+ at mid-rapidity ($1 < |y_{\mathrm{CMS}}|$). Predictions from RQMD with final state Coulomb interaction unmodified (*crosses*), with BRDC (*circles*), and with BRDC and pion freeze-out delayed an additional 2 fm/c (*triangles*)

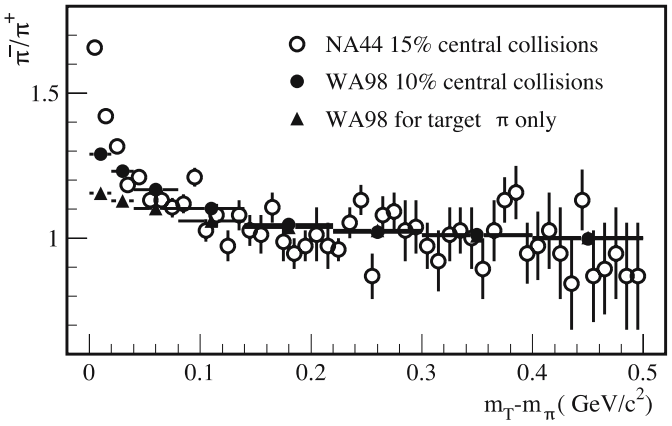

Fig. 13. Comparison of NA44 data (*open circles*) and WA98 data (*filled circles*) for the 10% most central collisions. The ratio for pions originating in the target is also shown (*triangles*)

Coulomb interaction is expected to be less than that for pions by a factor equal to their mass ratio m_π/m_K [7]. However, according to RQMD predictions without Coulomb correction, the kaon ratio has a $\sim 6\%$ drop at low transverse kinetic energy as a result of the greater amount of absorption of K^- than K^+. This large absorption effect must be taken into account when investigating Coulomb effects in the analysis of the kaon ratio data.

6 Discussion and conclusions

The π^-/π^+ ratio has been measured as a function of transverse mass and centrality in Pb + Pb collisions at 158 AGeV/c. The hyperon decay contribution has been deduced and shown to result in an increase of the pion ratio at low m_T that is responsible for about half of the enhancement of π^- relative to π^+ in central collisions, and an even larger fraction of the enhancement in peripheral collisions. The RQMD model was shown to agree with the measured hyperon decay contributions. The hyperon decay contributions have been removed from the measured ratios to extract the ratios for directly emitted pions.

The low m_T enhancement of the π^-/π^+ ratio, after removal of the hyperon decay contribution, increases with collision centrality and tends to zero for the most peripheral events (see Fig. 10). This observation is consistent with the hypothesis that the enhancement is due to the Coulomb interaction induced by the net positive charge of the participant protons. The same behaviour is observed in the framework of RQMD model simulations that include final state Coulomb interactions. However, the RQMD simulation overpredicts the observed enhancement in the ratio by a factor of about 1.5.

Investigations of the RQMD model predictions suggest that rather small modifications of the properties of the participant fireball are necessary to obtain good agreement with the data. For example, good agreement can be achieved after reduction of the baryon rapidity charge density predicted by RQMD according to the NA44 and NA49 proton measurements, together with a small increase of the mean pion freeze-out time (such as an increase from an average of 15 fm/c to 17 fm/c). According to RQMD predictions, the transverse flow velocities of heavy particles are less than those of pions [30]. A slight increase of the baryon transverse flow velocity would have a similar effect as the delay of the freeze-out time. In both cases, the system disperses over a larger volume before freeze-out, which reduces the Coulomb field and, therefore, the π^-/π^+ ratio. Based on comparisons with the RQMD model calculations, the results suggest a relatively large value of the mean freeze-out time for pions (~ 15 fm/c) in central Pb + Pb collisions.

Acknowledgements. We would like to thank the CERN-SPS accelerator crew for the excellent lead beam provided and the Laboratoire National Saturne for the loan of the magnet Goliath. This work was supported jointly by the German BMBF and DFG, the U.S. DOE, the Swedish NFR, the Dutch Stichting FOM, the Swiss National Fund, the Humboldt Foundation, the Stiftung für deutsch-polnische Zusammenarbeit, the Department of Atomic Energy, the Department of Science and Technology and the University Grants Commission of the Government of India, the Indo-FRG Exchange Programme, the PPE division of CERN, the INTAS under contract INTAS-97-0158, the Polish KBN under the grant 2P03B16815, the Grant-in-Aid for Scientific Research (Specially Promoted Research and International Scientific Research) of the Ministry of Edication, Science, Sports and Culture, JSPS Research Fellowships for Young Scientists, the University of Tsukuba Special Research Projects, and ORISE. ORNL is managed by UT-Battele, LLC, for the U.S. Department of Energy under contract DE-AC05-00OR22725.

References

1. D. Pelte et al., Z. Phys. A **357**, 215 (1997)
2. L. Ahle et al., Nucl. Phys. A **610**, 139 (1996)
3. L. Ahle et al., Phys. Rev. C **57**, R466 (1998)
4. C. Müntz, Acta. Phys. Polon. B **29**, 3253 (1998)
5. H. Bøggild et al., Phys. Lett. B **372**, 343 (1996)
6. H.W. Barz et al., Phys. Rev. C **56**, 1553 (1997)
7. H.W. Barz et al., Phys. Rev. C **57**, 2536 (1998)
8. H. Heiselberg, Nucl. Phys. A **638**, 479 (1998)
9. A. Ayala et al., Phys. Rev. C **59**, 3324 (1999)
10. T. Osada et al., Phys. Rev. C **55**, 2615 (1997)
11. T. Osada, Y. Hama, Phys. Rev. C **60**, 034 904 (1999)
12. F. Retiere et al., Nucl. Phys. A **681**, 149 (2001)
13. H. Sorge, Phys. Rev. C **52**, 3291 (1995)
14. WA98 Collaboration, Preprint CERN/SPSLC 91-17, SPSLC/P260 (1991)
15. T.C. Awes et al., Nucl. Instrum. Methods A **279**, 479 (1989)
16. W.T. Lin et al., Nucl. Instrum. Methods A **389**, 415 (1997)
17. E. Gatti, P. Rehak, Nucl. Instrum. Methods A **225**, 608 (1984)
18. J.M. Rubio et al., Nucl. Instrum. Methods A **367**, 358 (1995)
19. A.L.S. Angelis et al., Nucl. Phys. A **566**, 605 (1994)
20. M. Iżycki et al., Nucl. Instrum. Methods A **310**, 98 (1991)

21. V.V. Avdeichikov et al., JINR **8**, 23c (1997)
22. M.M. Aggarwal et al., Phys. Rev. C **67**, 014 906 (2003)
23. F. Antinori et al., Eur. Phys. J. C **11**, 79 (1999)
24. F. Gastineau, J. Aichelin., Phys. Rev. C **65**, 014 901 (2002)
25. R. Brun et al., GEANT3, CERN/DD/cc/84-1
26. K. Werner, Phys. Rep. **232**, 87 (1993)
27. M.M. Aggarwal et al., Eur. Phys. J. C **18**, 651 (2001)
28. I.G. Bearden et al., Phys. Lett. B **388**, 431 (1996)
29. S.V. Afanasiev et al., Nucl. Phys. A **160**, 76 (1996)
30. H. Sorge, Phys. Lett. B **373**, 16 (1996)

Evidence for a Long-Range Component in the Pion Emission Source in Au + Au Collisions at $\sqrt{s_{NN}} = 200$ GeV

S. S. Adler,[5] S. Afanasiev,[18] C. Aidala,[5] N. N. Ajitanand,[44] Y. Akiba,[21,39] J. Alexander,[44] R. Amirikas,[13] L. Aphecetche,[46] S. H. Aronson,[5] R. Averbeck,[45] T. C. Awes,[36] R. Azmoun,[45] V. Babintsev,[16] A. Baldisseri,[10] K. N. Barish,[6] P. D. Barnes,[28] B. Bassalleck,[34] S. Bathe,[31] S. Batsouli,[9] V. Baublis,[38] A. Bazilevsky,[40,16] S. Belikov,[17,16] Y. Berdnikov,[41] S. Bhagavatula,[17] J. G. Boissevain,[28] H. Borel,[10] S. Borenstein,[26] M. L. Brooks,[28] D. S. Brown,[35] N. Bruner,[34] D. Bucher,[31] H. Buesching,[31] V. Bumazhnov,[16] G. Bunce,[5,40] J. M. Burward-Hoy,[27,45] S. Butsyk,[45] X. Camard,[46] J.-S. Chai,[19] P. Chand,[4] W. C. Chang,[2] S. Chernichenko,[16] C. Y. Chi,[9] J. Chiba,[21] M. Chiu,[9] I. J. Choi,[53] J. Choi,[20] R. K. Choudhury,[4] T. Chujo,[5] P. Chung,[44] V. Cianciolo,[36] Y. Cobigo,[10] B. A. Cole,[9] P. Constantin,[17] M. Csanád,[12] T. Csörgő,[22] D. d'Enterria,[46] G. David,[5] H. Delagrange,[46] A. Denisov,[16] A. Deshpande,[40] E. J. Desmond,[5] A. Devismes,[45] O. Dietzsch,[42] O. Drapier,[26] A. Drees,[45] R. du Rietz,[30] A. Durum,[16] D. Dutta,[4] Y. V. Efremenko,[36] K. El Chenawi,[50] A. Enokizono,[15] H. En'yo,[39,40] S. Esumi,[49] L. Ewell,[5] D. E. Fields,[34,40] F. Fleuret,[26] S. L. Fokin,[24] B. D. Fox,[40] Z. Fraenkel,[52] J. E. Frantz,[9] A. Franz,[5] A. D. Frawley,[13] S.-Y. Fung,[6] S. Garpman,[30,*] T. K. Ghosh,[50] A. Glenn,[47] G. Gogiberidze,[47] M. Gonin,[26] J. Gosset,[10] Y. Goto,[40] R. Granier de Cassagnac,[26] N. Grau,[17] S. V. Greene,[50] M. Grosse Perdekamp,[40] W. Guryn,[5] H.-Å. Gustafsson,[30] T. Hachiya,[15] J. S. Haggerty,[5] H. Hamagaki,[8] A. G. Hansen,[28] E. P. Hartouni,[27] M. Harvey,[5] R. Hayano,[8] N. Hayashi,[39] X. He,[14] M. Heffner,[27] T. K. Hemmick,[45] J. M. Heuser,[45] M. Hibino,[51] J. C. Hill,[17] W. Holzmann,[44] K. Homma,[15] B. Hong,[23] A. Hoover,[35] T. Ichihara,[39,40] V. V. Ikonnikov,[24] K. Imai,[25,39] D. Isenhower,[1] M. Ishihara,[39] M. Issah,[44] A. Isupov,[18] B. V. Jacak,[45] W. Y. Jang,[23] Y. Jeong,[20] J. Jia,[45] O. Jinnouchi,[39] B. M. Johnson,[5] S. C. Johnson,[27] K. S. Joo,[32] D. Jouan,[37] S. Kametani,[8,51] N. Kamihara,[48,39] J. H. Kang,[53] S. S. Kapoor,[4] K. Katou,[51] S. Kelly,[9] B. Khachaturov,[52] A. Khanzadeev,[38] J. Kikuchi,[51] D. H. Kim,[32] D. J. Kim,[53] D. W. Kim,[20] E. Kim,[43] G.-B. Kim,[26] H. J. Kim,[53] E. Kistenev,[5] A. Kiyomichi,[49] K. Kiyoyama,[33] C. Klein-Boesing,[31] H. Kobayashi,[39,40] L. Kochenda,[38] V. Kochetkov,[16] D. Koehler,[34] T. Kohama,[15] M. Kopytine,[45] D. Kotchetkov,[6] A. Kozlov,[52] P. J. Kroon,[5] C. H. Kuberg,[1,28,*] K. Kurita,[40] Y. Kuroki,[49] M. J. Kweon,[23] Y. Kwon,[53] G. S. Kyle,[35] R. Lacey,[44] V. Ladygin,[18] J. G. Lajoie,[17] A. Lebedev,[17,24] S. Leckey,[45] D. M. Lee,[28] S. Lee,[20] M. J. Leitch,[28] X. H. Li,[6] H. Lim,[43] A. Litvinenko,[18] M. X. Liu,[28] Y. Liu,[37] C. F. Maguire,[50] Y. I. Makdisi,[5] A. Malakhov,[18] V. I. Manko,[24] Y. Mao,[7,39] G. Martinez,[46] M. D. Marx,[45] H. Masui,[49] F. Matathias,[45] T. Matsumoto,[8,51] P. L. McGaughey,[28] E. Melnikov,[16] F. Messer,[45] Y. Miake,[49] J. Milan,[44] T. E. Miller,[50] A. Milov,[45,52] S. Mioduszewski,[5] R. E. Mischke,[28] G. C. Mishra,[14] J. T. Mitchell,[5] A. K. Mohanty,[4] D. P. Morrison,[5] J. M. Moss,[28] F. Mühlbacher,[45] D. Mukhopadhyay,[52] M. Muniruzzaman,[6] J. Murata,[39,40] S. Nagamiya,[21] J. L. Nagle,[9] M. Nagy,[12] T. Nakamura,[15] B. K. Nandi,[6] M. Nara,[49] J. Newby,[47] P. Nilsson,[30] A. S. Nyanin,[24] J. Nystrand,[30] E. O'Brien,[5] C. A. Ogilvie,[17] H. Ohnishi,[5,39] I. D. Ojha,[50,3] K. Okada,[39] M. Ono,[49] V. Onuchin,[16] A. Oskarsson,[30] I. Otterlund,[30] K. Oyama,[8] K. Ozawa,[8] D. Pal,[52] A. P. T. Palounek,[28] V. Pantuev,[45] V. Papavassiliou,[35] J. Park,[43] A. Parmar,[34] S. F. Pate,[35] T. Peitzmann,[31] J.-C. Peng,[28] V. Peresedov,[18] C. Pinkenburg,[5] R. P. Pisani,[5] F. Plasil,[36] M. L. Purschke,[5] A. K. Purwar,[45] J. Rak,[17] I. Ravinovich,[52] K. F. Read,[36,47] M. Reuter,[45] K. Reygers,[31] V. Riabov,[38,41] Y. Riabov,[38] G. Roche,[29] A. Romana,[26,*] M. Rosati,[17] P. Rosnet,[29] S. S. Ryu,[53] M. E. Sadler,[1] N. Saito,[39,40] T. Sakaguchi,[8,51] M. Sakai,[33] S. Sakai,[49] V. Samsonov,[38] L. Sanfratello,[34] R. Santo,[31] H. D. Sato,[25,39] S. Sato,[5,49] S. Sawada,[21] Y. Schutz,[46] V. Semenov,[16] R. Seto,[6] M. R. Shaw,[1,28] T. K. Shea,[5] T.-A. Shibata,[48,39] K. Shigaki,[15,21] T. Shiina,[28] C. L. Silva,[42] D. Silvermyr,[28,30] K. S. Sim,[23] C. P. Singh,[3] V. Singh,[3] M. Sivertz,[5] A. Soldatov,[16] R. A. Soltz,[27] W. E. Sondheim,[28] S. P. Sorensen,[47] I. V. Sourikova,[5] F. Staley,[10] P. W. Stankus,[36] E. Stenlund,[30] M. Stepanov,[35] A. Ster,[22] S. P. Stoll,[5] T. Sugitate,[15] J. P. Sullivan,[28] E. M. Takagui,[42] A. Taketani,[39,40] M. Tamai,[51] K. H. Tanaka,[21] Y. Tanaka,[33] K. Tanida,[39] M. J. Tannenbaum,[5] A. Taranenko,[44] P. Tarján,[11] J. D. Tepe,[1,28] T. L. Thomas,[34] J. Tojo,[25,39] H. Torii,[25,39] R. S. Towell,[1] I. Tserruya,[52] H. Tsuruoka,[49] S. K. Tuli,[3] H. Tydesjö,[30] N. Tyurin,[16] H. W. van Hecke,[28] J. Velkovska,[5,45] M. Velkovsky,[45] V. Veszprémi,[11] L. Villatte,[47] A. A. Vinogradov,[24] M. A. Volkov,[24] E. Vznuzdaev,[38] X. R. Wang,[14] Y. Watanabe,[39,40] S. N. White,[5] F. K. Wohn,[17] C. L. Woody,[5] W. Xie,[6] Y. Yang,[7] A. Yanovich,[16] S. Yokkaichi,[39,40] G. R. Young,[36] I. E. Yushmanov,[24] W. A. Zajc,[9,†] C. Zhang,[9] S. Zhou,[7] S. J. Zhou,[52] and L. Zolin[18]

(PHENIX Collaboration)

[1]*Abilene Christian University, Abilene, Texas 79699, USA*
[2]*Institute of Physics, Academia Sinica, Taipei 11529, Taiwan*
[3]*Department of Physics, Banaras Hindu University, Varanasi 221005, India*

 © 2007 The American Physical Society

[4]Bhabha Atomic Research Centre, Bombay 400 085, India
[5]Brookhaven National Laboratory, Upton, New York 11973-5000, USA
[6]University of California - Riverside, Riverside, California 92521, USA
[7]China Institute of Atomic Energy (CIAE), Beijing, People's Republic of China
[8]Center for Nuclear Study, Graduate School of Science, University of Tokyo, 7-3-1 Hongo, Bunkyo, Tokyo 113-0033, Japan
[9]Columbia University, New York, New York 10027, USA
and Nevis Laboratories, Irvington, New York 10533, USA
[10]Dapnia, CEA Saclay, F-91191, Gif-sur-Yvette, France
[11]Debrecen University, H-4010 Debrecen, Egyetem tér 1, Hungary
[12]ELTE, Eötvös Loránd University, H - 1117 Budapest, Pázmány P. s. 1/A, Hungary
[13]Florida State University, Tallahassee, Florida 32306, USA
[14]Georgia State University, Atlanta, Georgia 30303, USA
[15]Hiroshima University, Kagamiyama, Higashi-Hiroshima 739-8526, Japan
[16]IHEP Protvino, State Research Center of Russian Federation, Institute for High Energy Physics, Protvino, 142281, Russia
[17]Iowa State University, Ames, Iowa 50011, USA
[18]Joint Institute for Nuclear Research, 141980 Dubna, Moscow Region, Russia
[19]KAERI, Cyclotron Application Laboratory, Seoul, South Korea
[20]Kangnung National University, Kangnung 210-702, South Korea
[21]KEK, High Energy Accelerator Research Organization, Tsukuba, Ibaraki 305-0801, Japan
[22]KFKI Research Institute for Particle and Nuclear Physics of the Hungarian Academy of Sciences (MTA KFKI RMKI),
H-1525 Budapest 114, POBox 49, Budapest, Hungary
[23]Korea University, Seoul, 136-701, Korea
[24]Russian Research Center "Kurchatov Institute", Moscow, Russia
[25]Kyoto University, Kyoto 606-8502, Japan
[26]Laboratoire Leprince-Ringuet, Ecole Polytechnique, CNRS-IN2P3, Route de Saclay, F-91128, Palaiseau, France
[27]Lawrence Livermore National Laboratory, Livermore, California 94550, USA
[28]Los Alamos National Laboratory, Los Alamos, New Mexico 87545, USA
[29]LPC, Université Blaise Pascal, CNRS-IN2P3, Clermont-Fd, 63177 Aubiere Cedex, France
[30]Department of Physics, Lund University, Box 118, SE-221 00 Lund, Sweden
[31]Institut für Kernphysik, University of Muenster, D-48149 Muenster, Germany
[32]Myongji University, Yongin, Kyonggido 449-728, Korea
[33]Nagasaki Institute of Applied Science, Nagasaki-shi, Nagasaki 851-0193, Japan
[34]University of New Mexico, Albuquerque, New Mexico 87131, USA
[35]New Mexico State University, Las Cruces, New Mexico 88003, USA
[36]Oak Ridge National Laboratory, Oak Ridge, Tennessee 37831, USA
[37]IPN-Orsay, Universite Paris Sud, CNRS-IN2P3, BP1, F-91406, Orsay, France
[38]PNPI, Petersburg Nuclear Physics Institute, Gatchina, Leningrad Region, 188300, Russia
[39]RIKEN, The Institute of Physical and Chemical Research, Wako, Saitama 351-0198, Japan
[40]RIKEN BNL Research Center, Brookhaven National Laboratory, Upton, New York 11973-5000, USA
[41]Saint Petersburg State Polytechnic University, St. Petersburg, Russia
[42]Instituto de Física, Universidade de São Paulo, Caixa Postal 66318, São Paulo CEP05315-970, Brazil
[43]System Electronics Laboratory, Seoul National University, Seoul, South Korea
[44]Chemistry Department, Stony Brook University, SUNY, Stony Brook, New York 11794-3400, USA
[45]Department of Physics and Astronomy, Stony Brook University, SUNY, Stony Brook, New York 11794, USA
[46]SUBATECH (Ecole des Mines de Nantes, CNRS-IN2P3, Université de Nantes) BP 20722 - 44307, Nantes, France
[47]University of Tennessee, Knoxville, Tennessee 37996, USA
[48]Department of Physics, Tokyo Institute of Technology, Oh-okayama, Meguro, Tokyo, 152-8551, Japan
[49]Institute of Physics, University of Tsukuba, Tsukuba, Ibaraki 305, Japan
[50]Vanderbilt University, Nashville, Tennessee 37235, USA
[51]Advanced Research Institute for Science and Engineering, Waseda University, 17 Kikui-cho, Shinjuku-ku, Tokyo 162-0044, Japan
[52]Weizmann Institute, Rehovot 76100, Israel
[53]Yonsei University, IPAP, Seoul 120-749, Korea
(Received 26 May 2006; published 26 March 2007)

Emission source functions are extracted from correlation functions constructed from charged pions produced at midrapidity in Au + Au collisions at $\sqrt{s_{NN}} = 200$ GeV. The source parameters extracted from these functions at low k_T give first indications of a long tail for the pion emission source. The source extension cannot be explained solely by simple kinematic considerations. The possible role of a halo of secondary pions from resonance emissions is explored.

DOI: 10.1103/PhysRevLett.98.132301 PACS numbers: 25.75.Ld, 25.75.Dw

Collisions between ultrarelativistic heavy ions can lead to extremely high energy-density nuclear matter [1]. The decay dynamics of this matter is strongly influenced by the nuclear equation of state (EOS) and possibly by a deconfined phase [2]. An emitting system which undergoes a strong first order phase transition is expected to show a much larger space-time extent than would be expected if the system remained in the hadronic phase throughout the collision process [3]. Indeed, several hydrodynamical calculations show such an increase for particle emission sources [3,4], provided hadronization does not occur via a supercooled state [5]. It has also been suggested that the shape of the emission source function can provide signals for a second order phase transition and whether or not particle emission occurs near to the critical end point in the QCD phase diagram [6].

Interferometry studies provide important information on the emission source function for particles produced in nuclear reactions ranging from elementary collisions [e^+e^- and $(\bar{p})pp$] to those involving very heavy ions [7–9]. Recent studies span the beam energies $\sqrt{s_{NN}} \sim$ 2–200 GeV [10–13]. A common theme for these papers is the extraction of the widths of emission source functions which are assumed to be Gaussian. Also, Coulomb effects on the correlation function are usually assumed to be separable [14]. Such an approach was followed earlier in an analysis which used the Bowler-Sinyukov 3D Hanbury Brown and Twiss (HBT) method to probe for a possible long-lived source [15]. The rms widths so obtained for each dimension of the source $R_{\rm long}$, $R_{\rm side}$, and $R_{\rm out}$ gave no evidence for such emissions, suggesting that the sound speed is not zero during an extended hadronization period.

In this Letter we exploit the model-independent imaging technique of Brown and Danielewicz [16,17] to make a more detailed study of both the shape and the space-time characteristics of the pion emission source function. The method uses a numerical calculation of the two particle wave function, which includes final-state interactions (FSI), to produce an inversion matrix that operates on the correlation function to produce the corresponding source function. The technique has been used to address only a few data sets [18,19] at relativistic beam energies.

Measurements were made with the PHENIX detector [20] at the Relativistic Heavy Ion Collider (RHIC). Charged pions were detected in the two central arms ($|\eta| \leq 0.35$). Track reconstruction was accomplished via pattern recognition using the drift chamber (DC) followed by two layers of multiwire proportional chambers with pad readout located at radii of 2, 2.5, and 5 m [20]. Particle momenta were measured with the resolution $\delta p/p = 0.7\% \oplus 1.0\% p$ (GeV/c). Very good pion identification (PID) was achieved with a 2σ cut about the pion peak in the squared-mass distribution for $p_T \lesssim 2.0$ GeV/c and $p_T \lesssim 1$ GeV/c in the time of flight (TOF) and the electromagnetic calorimeter (EMC), respectively. The event centrality was determined using the PHENIX beam-beam counter and the zero degree calorimeter [21]. Approximately 22×10^6 Au + Au events were analyzed to study several centrality and p_T selections.

Two-pion interferometry correlations were obtained via the correlation function $C(q) = N_{\rm cor}(q)/N_{\rm mix}(q)$, where the numerator is the relative momentum distribution of particle pairs from the same event (foreground pairs) and the denominator is the relative momentum distribution of particle pairs obtained from mixed events (background pairs). Here, $q = \frac{1}{2}\sqrt{-(p_1 - p_2)^2}$ is half of the relative momentum between the two particles in the pair c.m. frame (PCMS). p_1 and p_2 are the momentum 4-vectors of each particle in the pair and $C(q) \equiv 1$ for large q values where final-state interactions are negligible. Track-pair cuts similar to those of Ref. [12] were applied to foreground and background pairs, respectively. That is, pairs

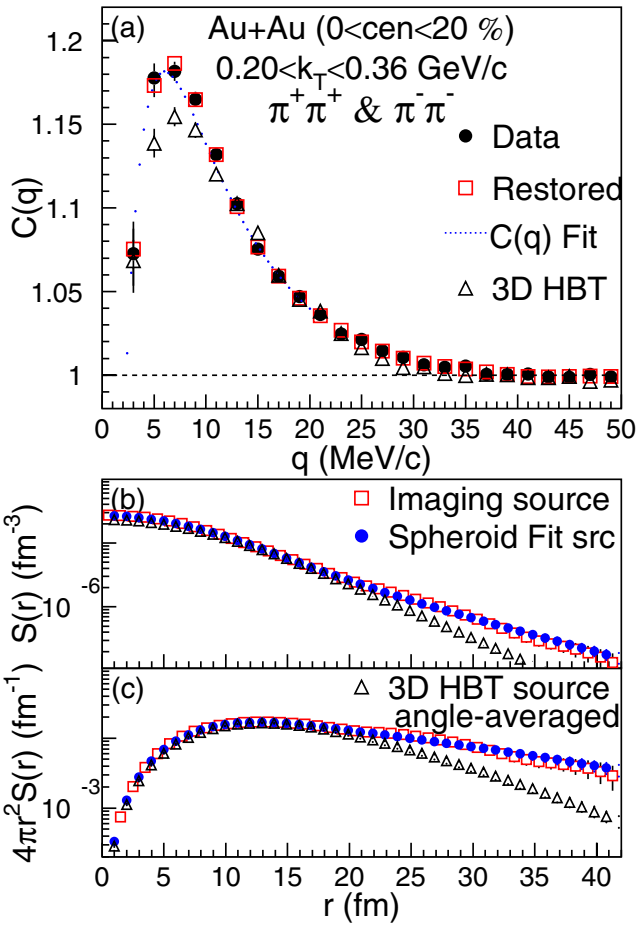

FIG. 1 (color online). [(upper, (a)] (●) Correlation function, $C(q)$, for $\pi^+\pi^+$ and $\pi^-\pi^-$ pairs; (□) restored correlation from imaging technique; (dotted line) direct correlation fitting; (△) 1D angle-averaged correlation of 3D correlation function. (lower) 1D source function (b) $S(r)$ and (c) $4\pi r^2 S(r)$: (□) imaging; (●) spheroid fit to correlation function; (△) angle-averaging of 3D-Gaussian source function. Systematic errors are less than size of data points.

within 5 cm in the beam direction ($\Delta Z_{\rm DC}$) and 0.02 radians in azimuthal angle ($\Delta\phi_{\rm DC}$) in the DC were eliminated from the pair sample to remove ghost tracks, and pairs within $0.0 < \Delta\phi_{\rm DC} < 0.1$ radians for $\Delta Z_{\rm DC} > 5$ cm were removed to avoid an inefficient region. The latter set of cuts were supplemented with the removal of pairs having a separation $\Delta R \leq 14$ cm and ≤ 16 cm in the TOF and EMC, respectively. Systematic variations of all of these cuts were explored to determine systematic error estimates; very little influence on the extracted correlation functions was found. Careful studies of the influence of momentum resolution on the correlation function were also made, as in [22]. The maximum effect was found to be $\sim$0.4% change in the correlation function at low q values, so it was neglected.

The filled circles in Fig. 1(a) show the one-dimensional (1D) correlation function $C(q)$, for a centrality of 0%–20% and for $0.20 < k_T = \frac{1}{2}(p_{T,1} + p_{T,2}) < 0.36$ GeV/c. The characteristic enhancement for $q \lesssim 25$ MeV/c reflects a combination of Bose-Einstein statistics and the FSI between pion pairs. The correlation function is not Coulomb corrected because the FSI (including Coulomb but no strong interaction) is included in the imaging and fitting procedure as described below.

The 1D correlation function and source function $S(r)$ (the probability of emitting a pair of particles at a separation r in the PCMS frame) are related via the 1D Koonin-Pratt equation [23]:

$$C(q) - 1 = 4\pi \int dr r^2 K_0(q, r) S(r). \quad (1)$$

The angle-averaged kernel $K_0(q, r)$ encodes the FSI and is given in terms of the final-state wave function $\Phi_{\mathbf{q}}(\mathbf{r})$, as $K_0(q, r) = \frac{1}{2}\int d[\cos(\theta_{\mathbf{q},\mathbf{r}})][|\Phi_{\mathbf{q}}(\mathbf{r})|^2 - 1]$, where $\theta_{\mathbf{q},\mathbf{r}}$ is the angle between $\mathbf{q}$ and $\mathbf{r}$ [17]. The procedure for the inversion of Eq. (1) to obtain $S(r)$ is also given in Ref. [17].

The open squares in Fig. 1(b) show the source function obtained from the correlation function presented in Fig. 1(a). As a cross-check of the imaging procedure, a restored correlation function was generated via Eq. (1) with the extracted source function as input. The open squares and filled circles in Fig. 1(a) indicate excellent consistency between the measured and restored correlation functions. The 1D source function, cf. Fig. 1(b), points to a Gaussian-like pattern at small r and a previously unresolved "tail" at large r. The robustness of this tail was established via an extensive array of tests including its dependence on pair and PID cuts, and on momentum resolution; no variation outside of the stated error bars was found.

This new observation of a tail is made more transparent via a comparison with the source function constructed from the parameters ($R_{\rm long}$, $R_{\rm side}$, $R_{\rm out}$, and λ), obtained in an earlier 3D HBT analysis [15]. The procedures outlined in Ref. [17] were employed to construct this source function (see Fig. 1). The measured and 3D angle-averaged correlation functions differ for $q \lesssim 15$ MeV/c as do the respective source functions for $r \gtrsim 17$ fm. The imaged source function exhibits a more prominent tail than the angle-averaged 3D HBT source function. This difference could stem from the Gaussian shape assumption employed in the 3D HBT analysis. The 3D Gaussian fitting procedure by construction is sensitive only to the main component of $S(r)$, and thus would not be capable of resolving fine structure at small-q/large-r. Given the fact that the volume element increases quadratically with pair separation, this difference is considerable as shown in Fig. 1(c), where the radial probabilities $[4\pi r^2 S(r)]$ are compared. The open triangles in Fig. 1(a) clearly indicate that the differences in the source functions reflect an important disparity in the corresponding correlation functions for $q \lesssim 10$–15 MeV.

Parameters of the source function for different assumed shapes were extracted via direct fits to the correlation function. Filled circles in Figs. 1(b) and 1(c) show the source function obtained from such a fit for a spheroidal shape [17],

$$S(r) = \frac{\lambda R_{\rm eff} \times e^{-(r^2/4R_T^2)} \mathrm{erfi}\left(\frac{r}{2R_{\rm eff}}\right)}{(8\pi R_T^2 R_0 r)}, \quad \text{for } R_0 > R_T, \quad (2)$$

where $R_{\rm eff} = 1/\sqrt{(1/R_T^2 - 1/R_0^2)}$, R_T is the radius of the spheroid in two perpendicular spatial dimensions and $R_0 = a \times R_T$ is the radius in the third spatial dimension; a is a scale factor. The long axis of the spheroid is assumed to be oriented in the out direction of the Bertsch-Pratt coordinate system. The fraction of pion pairs which contribute to the source λ is given by the integral of the normalized source function over the full range of r.

The procedure for making a direct fit to the correlation function involves the determination of a set of values for the spheroid parameters of Eq. (2), which reproduce the observed correlation function when the resulting source function is inserted into Eq. (1). The minimization package MINUIT was used to minimize the χ^2 between the observed and calculated correlation function. The χ^2/ndf value so obtained was $\sim$1. The dotted curve in Fig. 1(a) shows the fit to the data. The resulting source function shown in Figs. 1(b) and 1(c) indicates very good agreement with that obtained via the imaging technique. This shape parametrization is not unique; an essentially indistinguishable source was also obtained for a fit performed with a Gaussian plus modified exponential [24] shape. The simpler spheroid parametrization was chosen for the discussion below.

The spheroidal source function [Eq. (2)] can be approximated by a short-range Gaussian source $S_{\rm sr}(r)$;

$$S_{\rm sr}(r) \sim \lambda e^{-r^2[(1/6R_T^2)+(1/12R_0^2)]}/(8\pi\sqrt{\pi}R_T^2 R_0), \quad (3)$$

for small r, and a long-range source $S_{\rm lr}(r)$ for

$r \gg 2R_T R_0/\sqrt{R_0^2 - R_T^2}$ given by

$$S_{\rm lr}(r) \sim \lambda R_0 e^{-r^2/4R_0^2}/[4\pi\sqrt{\pi}(R_0^2 - R_T^2)r^2]. \quad (4)$$

Thus, the emission source shown in Figs. 1(b) and 1(c) can be interpreted to reflect a short-range Gaussian source of radius $R_{\rm sr} = \sqrt{3R_T^2R_0^2/(2R_0^2 + R_T^2)} = R_T\sqrt{3a^2/(2a^2 + 1)}$ and a long-range tail of extended space-time extent $R_{\rm lr} = R_0$. The fraction of pairs associated with these sources $\lambda_{\rm sr} = \lambda a^2[3/(2a^2 + 1)]^{3/2}$ and $\lambda_{\rm lr} = (\lambda - \lambda_{\rm sr})$ are obtained from Eq. (3) and the conservation of pairs, respectively.

Source functions were extracted via imaging and spheroid fits for several k_T and centrality selections, in order to map the regions in k_T and centrality where the long-range tail is prominent. Representative results are shown in Fig. 2 for the indicated cuts. The experimental and restored correlation functions, compared in Figs. 2(a) and 2(b), indicate good agreement within the statistics, as do the corresponding source functions shown in Figs. 2(c) and 2(d).

Figure 3 gives a more complete summary of the extracted source parameters. Systematic errors obtained via variations of pair cuts in the analysis are 0.12 fm, 1.0 fm, 0.35, and 0.03 for $R_{\rm sr}$, $R_{\rm lr}$, a, and λ, respectively. The centrality and k_T dependence of the rms radius of the short-range source $R_{\rm sr}$ is similar (within 10%) to that obtained for $R_{\rm long}$ and $R_{\rm side}$ in an earlier analysis [15], cf. Figs. 3(a) and 3(d). The long-range source shows an effective radius $R_{\rm lr} = a \times R_T$, which is ~2–3.5 times $R_{\rm sr}$. The ratio $R_{\rm lr}/R_{\rm sr}$ is also maximal for low k_T and the most central collisions. The fraction of pairs exhibiting these characteristics is given by the λ values shown in Figs. 3(c) and 3(f); for central collisions, maximum prominence is shown for low k_T pairs.

A central question is the origin of the long-range contribution to the emitting source. Instantaneous freeze-out of a source with $R_{\rm out}/R_{\rm side} \sim 1$ in the longitudinal comoving system (LCMS) would give a maximum kinematic boost so that $R_{\rm lr} = R_{\rm out} = \gamma \times R_T$ in the PCMS. Thus, the values for a and γ, shown in Fig. 3(b), can be directly compared. At low k_T, γ is seen to be significantly less than a. Thus, a simple kinematic transformation from the LCMS to PCMS cannot account for the observed source parameters at this k_T.

Could a composite particle emission source comprised of a central core and a halo of long-lived resonances account for the observations? For such emissions, the pairing between pions from the core and secondary pions from the halo is expected to dominate the long-range emissions [25]. If it is assumed that this halo includes only ω decay ($c\tau \sim 24$ fm), one may compare the ω yield with a simple estimate of the fraction of pion pairs associated with the short- and long-range sources. Using the a and γ values in Fig. 3(b), $\lambda_{\rm sr} \sim 0.22$–$0.32$,

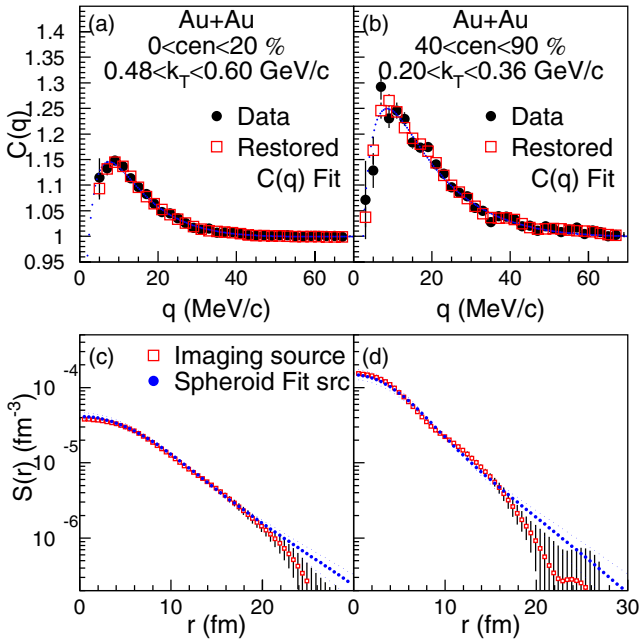

FIG. 2 (color online). (upper) Correlation functions, $C(q)$, for $\pi^+\pi^+$ and $\pi^-\pi^-$ pairs and (lower) corresponding source functions, $S(r)$ for (a), (c) high k_T most central collisions; (b), (d) low k_T peripheral collisions. Error bars indicate statistical errors with symbols as in Fig. 1.

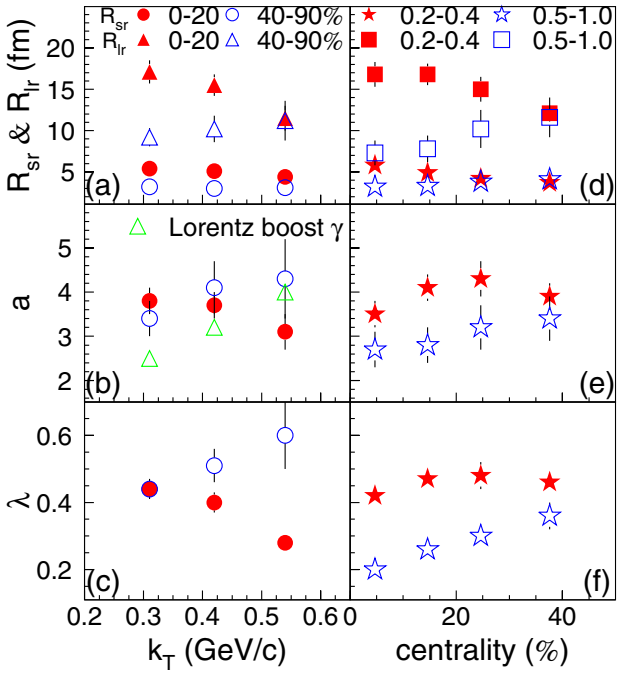

FIG. 3 (color online). (left) k_T dependence of extracted spheroidal source parameters for pion source functions (a) $R_{\rm sr}$, $R_{\rm lr}$, (b) a, and (c) λ for (filled symbols) most central collisions; (open symbols) peripheral collisions. (right) Centrality dependence of same parameters for (★) low k_T (0.2–0.4 GeV/c); (☆) high k_T (0.5–1.0 GeV/c).

$\lambda_{\rm lr} \sim 0.23$–$0.13$, and $\lambda_{\rm lr}/\lambda_{\rm sr} \sim 0.4$–$1.0$ for the lowest k_T. The preliminary values for $\omega/\pi^- = 0.1$ from Ref. [26] give an estimate for $\lambda_{\rm lr}/\lambda_{\rm sr} \sim 2 \times 0.1/\sqrt{\lambda_{\rm sr}} \sim 0.35$–$0.43$ which lies at the lower end of the estimates obtained from the source parameters. (A significant change in the value for ω/π^- would alter this conclusion.) Therefore, it is plausible that a maximal kinematic boost combined with a halo of ωs could account for $\lambda_{\rm lr}/\lambda_{\rm sr}$. However, the steep centrality dependence of the radius of the long-range source inferred from Figs. 3(d) and 3(e) is not compatible with an essentially flat dependence expected for significant ω resonance contribution.

In summary, we have made the first extraction of the full 1D emission source function for pions in Au + Au collisions at RHIC ($\sqrt{s_{NN}} = 200$ GeV). This source function points to separate but prominent contributions from short-range emissions and a long-range tail of larger space-time extent than has been previously observed. This tail cannot be explained solely by simple kinematic considerations associated with a frame transformation from the LCMS to the PCMS. Further studies are required to determine the origin of this tail and whether or not it is related to a phase transition.

We thank the staff of the Collider-Accelerator and Physics Departments at BNL for their vital contributions. We thank S. Pratt and P. Danielewicz for their interest and input. We acknowledge support from the Department of Energy and NSF (USA), MEXT and JSPS (Japan), CNPq and FAPESP (Brazil), NSFC (China), CNRS-IN2P3 and CEA (France), BMBF, DAAD, and AvH (Germany), OTKA (Hungary), DAE and DST (India), ISF (Israel), KRF and KOSEF (Korea), RMIST, RAS, and RMAE (Russia), VR and KAW (Sweden), US CRDF for the FSU, US-Hungarian NSF-OTKA-MTA, and US-Israel BSF.

*Deceased.
†PHENIX Spokesperson.
Email address: zajc@nevis.columbia.edu

[1] K. Adcox *et al.*, Nucl. Phys. **A757**, 184 (2005).
[2] E. V. Shuryak, Nucl. Phys. A **750**, 64 (2005).
[3] S. Pratt, Phys. Rev. Lett. **53**, 1219 (1984).
[4] D. Teaney, J. Lauret, and E. V. Shuryak, Phys. Rev. Lett. **86**, 4783 (2001).
[5] T. Csorgo *et al.*, Phys. Lett. B **333**, 494 (1994).
[6] T. Csorgo, S. Hegyi, T. Novak, and W. A. Zajc, nucl-th/0512060.
[7] E. V. Shuryak, Phys. Lett. **44B**, 387 (1973).
[8] U. Heinz *et al.*, Annu. Rev. Nucl. Part. Sci. **49**, 529 (1999).
[9] T. Csorgo, Heavy Ion Physics **15**, 1 (2002).
[10] M. A. Lisa *et al.*, Annu. Rev. Nucl. Part. Sci. **55**, 357 (2005).
[11] C. Adler *et al.*, Phys. Rev. Lett. **87**, 082301 (2001).
[12] K. Adcox *et al.*, Phys. Rev. Lett. **88**, 192302 (2002).
[13] J. Adams *et al.*, Phys. Rev. Lett. **91**, 262301 (2003).
[14] Y. Sinyukov *et al.*, Phys. Lett. B **432**, 248 (1998).
[15] S. S. Adler *et al.*, Phys. Rev. Lett. **93**, 152302 (2004).
[16] D. A. Brown *et al.*, Phys. Lett. B **398**, 252 (1997).
[17] D. A. Brown and P. Danielewicz, Phys. Rev. C **64**, 014902 (2001).
[18] S. Y. Panitkin *et al.*, Phys. Rev. Lett. **87**, 112304 (2001).
[19] P. Chung *et al.*, Phys. Rev. Lett. **91**, 162301 (2003).
[20] K. Adcox *et al.*, Nucl. Instrum. Methods Phys. Res., Sect. A **499**, 469 (2003).
[21] K. Adcox *et al.*, Phys. Rev. C **69**, 024904 (2004).
[22] M. D. Baker *et al.* (E802 Collaboration), Nucl. Phys. **A610**, 213c (1996).
[23] S. E. Koonin, Phys. Lett. **70B**, 43 (1977).
[24] P. Chung *et al.*, Nucl. Phys. **A749**, 275 (2005).
[25] S. Nickerson, T. Csorgo, and D. Kiang, Phys. Rev. C **57**, 3251 (1998).
[26] W. Broniowski *et al.*, Acta Phys. Hung. A **22**, 159 (2005).

Jet properties from dihadron correlations in $p + p$ collisions at $\sqrt{s} = 200$ GeV

S. S. Adler,[5] S. Afanasiev,[20] C. Aidala,[10] N. N. Ajitanand,[44] Y. Akiba,[21,40] A. Al-Jamel,[35] J. Alexander,[44] K. Aoki,[25] L. Aphecetche,[46] R. Armendariz,[35] S. H. Aronson,[5] R. Averbeck,[45] T. C. Awes,[36] V. Babintsev,[17] A. Baldisseri,[11] K. N. Barish,[6] P. D. Barnes,[28] B. Bassalleck,[34] S. Bathe,[6,31] S. Batsouli,[10] V. Baublis,[39] F. Bauer,[6] A. Bazilevsky,[5,41] S. Belikov,[19,17] M. T. Bjorndal,[10] J. G. Boissevain,[28] H. Borel,[11] M. L. Brooks,[28] D. S. Brown,[35] N. Bruner,[34] D. Bucher,[31] H. Buesching,[5,31] V. Bumazhnov,[17] G. Bunce,[5,41] J. M. Burward-Hoy,[28,27] S. Butsyk,[45] X. Camard,[46] P. Chand,[4] W. C. Chang,[2] S. Chernichenko,[17] C. Y. Chi,[10] J. Chiba,[21] M. Chiu,[10] I. J. Choi,[53] R. K. Choudhury,[4] T. Chujo,[5] V. Cianciolo,[36] Y. Cobigo,[11] B. A. Cole,[10] M. P. Comets,[37] P. Constantin,[19] M. Csanád,[13] T. Csörgő,[22] J. P. Cussonneau,[46] D. d'Enterria,[10] K. Das,[14] G. David,[5] F. Deák,[13] H. Delagrange,[46] A. Denisov,[17] A. Deshpande,[41] E. J. Desmond,[5] A. Devismes,[45] O. Dietzsch,[42] J. L. Drachenberg,[1] O. Drapier,[26] A. Drees,[45] A. Durum,[17] D. Dutta,[4] V. Dzhordzhadze,[47] Y. V. Efremenko,[36] H. En'yo,[40,41] B. Espagnon,[37] S. Esumi,[49] D. E. Fields,[34,41] C. Finck,[46] F. Fleuret,[26] S. L. Fokin,[24] B. D. Fox,[41] Z. Fraenkel,[52] J. E. Frantz,[10] A. Franz,[5] A. D. Frawley,[14] Y. Fukao,[25,40,41] S.-Y. Fung,[6] S. Gadrat,[29] M. Germain,[46] A. Glenn,[47] M. Gonin,[26] J. Gosset,[11] Y. Goto,[40,41] R. Granier de Cassagnac,[26] N. Grau,[19] S. V. Greene,[50] M. Grosse Perdekamp,[18,41] H.-Å. Gustafsson,[30] T. Hachiya,[16] J. S. Haggerty,[5] H. Hamagaki,[8] A. G. Hansen,[28] E. P. Hartouni,[27] M. Harvey,[5] K. Hasuko,[40] R. Hayano,[8] X. He,[15] M. Heffner,[27] T. K. Hemmick,[45] J. M. Heuser,[40] P. Hidas,[22] H. Hiejima,[18] J. C. Hill,[19] R. Hobbs,[34] W. Holzmann,[44] K. Homma,[16] B. Hong,[23] A. Hoover,[35] T. Horaguchi,[40,41,48] T. Ichihara,[40,41] V. V. Ikonnikov,[24] K. Imai,[25,40] M. Inaba,[49] M. Inuzuka,[8] D. Isenhower,[1] L. Isenhower,[1] M. Ishihara,[40] M. Issah,[44] A. Isupov,[20] B. V. Jacak,[45] J. Jia,[45] O. Jinnouchi,[40,41] B. M. Johnson,[5] S. C. Johnson,[27] K. S. Joo,[32] D. Jouan,[37] F. Kajihara,[8] S. Kametani,[8,51] N. Kamihara,[40,48] M. Kaneta,[41] J. H. Kang,[53] K. Katou,[51] T. Kawabata,[8] A. V. Kazantsev,[24] S. Kelly,[9,10] B. Khachaturov,[52] A. Khanzadeev,[39] J. Kikuchi,[51] D. J. Kim,[53] E. Kim,[43] G.-B. Kim,[26] H. J. Kim,[53] E. Kinney,[9] A. Kiss,[13] E. Kistenev,[5] A. Kiyomichi,[40] C. Klein-Boesing,[31] H. Kobayashi,[41] L. Kochenda,[39] V. Kochetkov,[17] R. Kohara,[16] B. Komkov,[39] M. Konno,[49] D. Kotchetkov,[6] A. Kozlov,[52] P. J. Kroon,[5] C. H. Kuberg,[1,*] G. J. Kunde,[28] K. Kurita,[40] M. J. Kweon,[23] Y. Kwon,[53] G. S. Kyle,[35] R. Lacey,[44] J. G. Lajoie,[19] Y. Le Bornec,[37] A. Lebedev,[19,24] S. Leckey,[45] D. M. Lee,[28] M. J. Leitch,[28] M. A. L. Leite,[42] X. H. Li,[6] H. Lim,[43] A. Litvinenko,[20] M. X. Liu,[28] C. F. Maguire,[50] Y. I. Makdisi,[5] A. Malakhov,[20] V. I. Manko,[24] Y. Mao,[38,40] G. Martinez,[46] H. Masui,[49] F. Matathias,[45] T. Matsumoto,[8,51] M. C. McCain,[1] P. L. McGaughey,[28] Y. Miake,[49] T. E. Miller,[50] A. Milov,[45] S. Mioduszewski,[5] G. C. Mishra,[15] J. T. Mitchell,[5] A. K. Mohanty,[4] D. P. Morrison,[5] J. M. Moss,[28] D. Mukhopadhyay,[52] M. Muniruzzaman,[6] S. Nagamiya,[21] J. L. Nagle,[9,10] T. Nakamura,[16] J. Newby,[47] A. S. Nyanin,[24] J. Nystrand,[30] E. O'Brien,[5] C. A. Ogilvie,[19] H. Ohnishi,[40] I. D. Ojha,[3,50] H. Okada,[25,40] K. Okada,[40,41] A. Oskarsson,[30] I. Otterlund,[30] K. Oyama,[8] K. Ozawa,[8] D. Pal,[52] A. P. T. Palounek,[28] V. Pantuev,[45] V. Papavassiliou,[35] J. Park,[43] W. J. Park,[23] S. F. Pate,[35] H. Pei,[19] V. Penev,[20] J.-C. Peng,[18] H. Pereira,[11] V. Peresedov,[20] A. Pierson,[34] C. Pinkenburg,[5] R. P. Pisani,[5] M. L. Purschke,[5] A. K. Purwar,[45] J. M. Qualls,[1] J. Rak,[19] I. Ravinovich,[52] K. F. Read,[36,47] M. Reuter,[45] K. Reygers,[31] V. Riabov,[39] Y. Riabov,[39] G. Roche,[29] A. Romana,[26,*] M. Rosati,[19] S. S. E. Rosendahl,[30] P. Rosnet,[29] V. L. Rykov,[40] S. S. Ryu,[53] N. Saito,[25,40,41] T. Sakaguchi,[8,51] S. Sakai,[49] V. Samsonov,[39] L. Sanfratello,[34] R. Santo,[31] H. D. Sato,[25,40] S. Sato,[5,49] S. Sawada,[21] Y. Schutz,[46] V. Semenov,[17] R. Seto,[6] T. K. Shea,[5] I. Shein,[17] T.-A. Shibata,[40,48] K. Shigaki,[16] M. Shimomura,[49] A. Sickles,[45] C. L. Silva,[42] D. Silvermyr,[28] K. S. Sim,[23] A. Soldatov,[17] R. A. Soltz,[27] W. E. Sondheim,[28] S. P. Sorensen,[47] I. V. Sourikova,[5] F. Staley,[11] P. W. Stankus,[36] E. Stenlund,[30] M. Stepanov,[35] A. Ster,[22] S. P. Stoll,[5] T. Sugitate,[16] J. P. Sullivan,[28] S. Takagi,[49] E. M. Takagui,[42] A. Taketani,[40,41] K. H. Tanaka,[21] Y. Tanaka,[33] K. Tanida,[40] M. J. Tannenbaum,[5] A. Taranenko,[44] P. Tarján,[12] T. L. Thomas,[34] M. Togawa,[25,40] J. Tojo,[40] H. Torii,[25,41] R. S. Towell,[1] V-N. Tram,[26] I. Tserruya,[52] Y. Tsuchimoto,[16] H. Tydesjö,[30] N. Tyurin,[17] T. J. Uam,[32] H. W. van Hecke,[28] J. Velkovska,[5] M. Velkovsky,[45] V. Veszprémi,[12] A. A. Vinogradov,[24] M. A. Volkov,[24] E. Vznuzdaev,[39] X. R. Wang,[15] Y. Watanabe,[40,41] S. N. White,[5] N. Willis,[37] F. K. Wohn,[19] C. L. Woody,[5] W. Xie,[6] A. Yanovich,[17] S. Yokkaichi,[40,41] G. R. Young,[36] I. E. Yushmanov,[24] W. A. Zajc,[10,†] C. Zhang,[10] S. Zhou,[7] J. Zimányi,[22] L. Zolin,[20] and X. Zong[19]

(PHENIX Collaboration)

[1]*Abilene Christian University, Abilene, Texas 79699, USA*
[2]*Institute of Physics, Academia Sinica, Taipei 11529, Taiwan*
[3]*Department of Physics, Banaras Hindu University, Varanasi 221005, India*
[4]*Bhabha Atomic Research Centre, Bombay 400 085, India*

 © 2006 The American Physical Society

[5]*Brookhaven National Laboratory, Upton, New York 11973-5000, USA*
[6]*University of California - Riverside, Riverside, California 92521, USA*
[7]*China Institute of Atomic Energy (CIAE), Beijing, People's Republic of China*
[8]*Center for Nuclear Study, Graduate School of Science, University of Tokyo, 7-3-1 Hongo, Bunkyo, Tokyo 113-0033, Japan*
[9]*University of Colorado, Boulder, Colorado 80309, USA*
[10]*Columbia University, New York, New York 10027 and Nevis Laboratories, Irvington, New York 10533, USA*
[11]*Dapnia, CEA Saclay, F-91191, Gif-sur-Yvette, France*
[12]*Debrecen University, H-4010 Debrecen, Egyetem tér 1, Hungary*
[13]*ELTE, Eötvös Loránd University, H - 1117 Budapest, Pázmány P. s. 1/A, Hungary*
[14]*Florida State University, Tallahassee, Florida 32306, USA*
[15]*Georgia State University, Atlanta, Georgia 30303, USA*
[16]*Hiroshima University, Kagamiyama, Higashi-Hiroshima 739-8526, Japan*
[17]*IHEP Protvino, State Research Center of Russian Federation, Institute for High Energy Physics, Protvino, 142281, Russia*
[18]*University of Illinois at Urbana-Champaign, Urbana, Illinois 61801, USA*
[19]*Iowa State University, Ames, Iowa 50011, USA*
[20]*Joint Institute for Nuclear Research, 141980 Dubna, Moscow Region, Russia*
[21]*KEK, High Energy Accelerator Research Organization, Tsukuba, Ibaraki 305-0801, Japan*
[22]*KFKI Research Institute for Particle and Nuclear Physics of the Hungarian Academy of Sciences (MTA KFKI RMKI), H-1525 Budapest 114, P.O. Box 49, Budapest, Hungary*
[23]*Korea University, Seoul, 136-701, Korea*
[24]*Russian Research Center "Kurchatov Institute", Moscow, Russia*
[25]*Kyoto University, Kyoto 606-8502, Japan*
[26]*Laboratoire Leprince-Ringuet, Ecole Polytechnique, CNRS-IN2P3, Route de Saclay, F-91128, Palaiseau, France*
[27]*Lawrence Livermore National Laboratory, Livermore, California 94550, USA*
[28]*Los Alamos National Laboratory, Los Alamos, New Mexico 87545, USA*
[29]*LPC, Université Blaise Pascal, CNRS-IN2P3, Clermont-Fd, 63177 Aubiere Cedex, France*
[30]*Department of Physics, Lund University, Box 118, SE-221 00 Lund, Sweden*
[31]*Institut für Kernphysik, University of Muenster, D-48149 Muenster, Germany*
[32]*Myongji University, Yongin, Kyonggido 449-728, Korea*
[33]*Nagasaki Institute of Applied Science, Nagasaki-shi, Nagasaki 851-0193, Japan*
[34]*University of New Mexico, Albuquerque, New Mexico 87131, USA*
[35]*New Mexico State University, Las Cruces, New Mexico 88003, USA*
[36]*Oak Ridge National Laboratory, Oak Ridge, Tennessee 37831, USA*
[37]*IPN-Orsay, Universite Paris Sud, CNRS-IN2P3, BP1, F-91406, Orsay, France*
[38]*Peking University, Beijing, People's Republic of China*
[39]*PNPI, Petersburg Nuclear Physics Institute, Gatchina, Leningrad region, 188300, Russia*
[40]*RIKEN (The Institute of Physical and Chemical Research), Wako, Saitama 351-0198, JAPAN*
[41]*RIKEN BNL Research Center, Brookhaven National Laboratory, Upton, New York 11973-5000, USA*
[42]*Universidade de São Paulo, Instituto de Física, Caixa Postal 66318, São Paulo CEP05315-970, Brazil*
[43]*System Electronics Laboratory, Seoul National University, Seoul, South Korea*
[44]*Chemistry Department, Stony Brook University, SUNY, Stony Brook, New York 11794-3400, USA*
[45]*Department of Physics and Astronomy, Stony Brook University, SUNY, Stony Brook, New York 11794, USA*
[46]*SUBATECH (Ecole des Mines de Nantes, CNRS-IN2P3, Université de Nantes) BP 20722 - 44307, Nantes, France*
[47]*University of Tennessee, Knoxville, Tennessee 37996, USA*
[48]*Department of Physics, Tokyo Institute of Technology, Oh-okayama, Meguro, Tokyo 152-8551, Japan*
[49]*Institute of Physics, University of Tsukuba, Tsukuba, Ibaraki 305, Japan*
[50]*Vanderbilt University, Nashville, Tennessee 37235, USA*
[51]*Waseda University, Advanced Research Institute for Science and Engineering, 17 Kikui-cho, Shinjuku-ku, Tokyo 162-0044, Japan*
[52]*Weizmann Institute, Rehovot 76100, Israel*
[53]*Yonsei University, IPAP, Seoul 120-749, Korea*
(Received 12 May 2006; published 5 October 2006)

The properties of jets produced in $p + p$ collisions at $\sqrt{s} = 200$ GeV are measured using the method of two-particle correlations. The trigger particle is a leading particle from a large transverse momentum jet while the associated particle comes from either the same jet or the away-side jet. Analysis of the angular width of the near-side peak in the correlation function determines the jet-fragmentation transverse momentum j_T. The extracted value, $\sqrt{\langle j_T^2 \rangle} = 585 \pm 6(\text{stat}) \pm 15(\text{sys})$ MeV$/c$, is constant with respect to the trigger particle transverse momentum, and comparable to the previous lower $\sqrt{s}$ measurements. The

*Deceased.
†PHENIX Spokesperson: zajc@nevis.columbia.edu

width of the away-side peak is shown to be a convolution of j_T with the fragmentation variable, z, and the partonic transverse momentum, k_T. The $\langle z \rangle$ is determined through a combined analysis of the measured π^0 inclusive and associated spectra using jet-fragmentation functions measured in e^+e^- collisions. The final extracted values of k_T are then determined to also be independent of the trigger particle transverse momentum, over the range measured, with value of $\sqrt{\langle k_T^2 \rangle} = 2.68 \pm 0.07(\text{stat}) \pm 0.34(\text{sys})$ GeV/c.

DOI: 10.1103/PhysRevD.74.072002 PACS numbers: 13.85.−t, 25.75.Dw

I. INTRODUCTION

The goal of this paper is to explore the systematics of jet production and fragmentation in $p + p$ collisions at $\sqrt{s} =$ 200 GeV by the method of two-particle azimuthal correlations. Knowledge of the jet-fragmentation process is useful not only as a reference measurement for a similar analysis in Au + Au collisions, but can be used as a stringent test of perturbative QCD (pQCD) calculations beyond leading order.

The two-particle azimuthal correlations method worked well at ISR energies ($\sqrt{s} = 63$ GeV) and below [1–3], where it is difficult to directly reconstruct jets, but has not been attempted at higher values of $\sqrt{s}$. This method is also suitable for jet-analysis in heavy-ion data where the large particle multiplicity severely interferes with direct jet reconstruction.

With the beginning of RHIC operation, heavy-ion physics entered a new regime, where pQCD phenomena can be fully explored. High-energy partons materializing into hadronic jets can be used as sensitive probes of the early stage of heavy-ion collisions. Measurements carried out during the first three years of RHIC operation at $\sqrt{s_{\text{NN}}} =$ 130 and 200 GeV exhibit many new and interesting features. The high-p_T particle yield was found to be strongly suppressed in Au + Au central collisions [4–6]. Furthermore, the nonsuppression of the high-p_T particle yield in d + Au induced collisions [7–10] confirmed that the suppression can be fully attributed to the final state interaction of high-energy partons with an extremely opaque nuclear medium formed in Au + Au collisions at RHIC.

Other striking features found in RHIC data are the large asymmetry of particle azimuthal distributions which is attributed to sizable elliptic flow [11,12] and the observation of the apparent disappearance of the back-to-back jet correlation in central Au + Au collisions [13].

Many of the above mentioned observations can be explained by a large opacity of the medium produced in central Au + Au collisions which causes the scattered partons to lose energy via coherent (Landau-Pomeranchuk-Migdal [14]) gluon bremsstrahlung [15–18]. It is expected that the medium effect will cause the apparent modification of fundamental properties of hard-scattering like broadening of intrinsic parton transverse momentum k_T [19,20] and modification of jet fragmentation [21]. Thus the measurement of jet fragmentation properties and intrinsic parton transverse momentum k_T for $p + p$ collisions presented here provides a baseline for comparison to the results in heavy-ion collisions, helping to disentangle the complex processes of propagation and possible fragmentation of partons within the excited nuclear medium.

This paper is organized as follows: Sec. II discusses the method of two-particle correlations and the relations between jet properties and the angular correlation between parton fragments. The details of the PHENIX experiment relevant to this analysis are outlined in Section III. Section IV deals with the analysis of the correlation functions extracted from the $p + p$ data and an evaluation of the $\langle j_T \rangle$ and $\langle k_T \rangle$ quantities. The combined analysis of the inclusive and associated p_T-distributions is discussed in Sec. V and the sensitivity of the associated p_T-distributions to the fragmentation function is discussed in Sec. VI. Section VII presents the resulting values of the partonic transverse momenta k_T corrected for the mean momentum fraction $\langle z_t \rangle$. Section VIII summarizes the results from this paper.

II. JET ANGULAR CORRELATIONS

Jets are produced in the hard scattering of two partons [22–25]. The overall $p + p$ hard-scattering cross section in ''leading logarithm'' pQCD is the sum over parton reactions $a + b \rightarrow c + d$ (e.g. $g + q \rightarrow g + q$) at parton-parton center-of-mass (c.m.) energy $\sqrt{\hat{s}}$,

$$\frac{d^3\sigma}{dx_1 dx_2 d\cos\theta^*} = \frac{1}{s}\sum_{ab} f_a(x_1) f_b(x_2) \frac{\pi \alpha_s^2(Q^2)}{2x_1 x_2} \Sigma^{ab}(\cos\theta^*), \tag{1}$$

where $f_a(x_1)$, $f_b(x_2)$, are parton distribution functions, the differential probabilities for partons a and b to carry momentum fractions x_1 and x_2 of their respective protons (e.g. $u(x_2)$), and where θ^* is the scattering angle in the parton-parton c.m. system. The parton-parton c.m. energy squared is $\hat{s} = x_1 x_2 s$, where $\sqrt{s}$ is the c.m. energy of the $p + p$ collision. The parton-parton c.m. system moves with rapidity $y = (1/2)\ln(x_1/x_2)$ in the $p + p$ c.m. system.

Equation (1) gives the p_T spectrum of outgoing parton c (emitted at θ^*), which then fragments into hadrons, e.g. a π^0. The fragmentation function $D_c^{\pi^0}(z, \mu^2)$ is the probability for a π^0 to carry a fraction $z = p^{\pi^0}/p^c$ of the momentum of outgoing parton c. Equation (1) must be summed over all subprocesses leading to a π^0 in the final state. The parameter μ^2 is an unphysical ''factorization'' scale intro-

duced to account for collinear singularities in the structure and fragmentation functions [26,27], which will be ignored for the purposes of this paper.

In this formulation, $f_a(x_1)$, $f_b(x_2)$, and $D_c^{\pi^0}(z)$ represent the ''long-distance phenomena'' to be determined by experiment; while the characteristic subprocess angular distributions, $\Sigma^{ab}(\cos\theta^*)$, and the coupling constant, $\alpha_s(Q^2) = \frac{12\pi}{25\ln(Q^2/\Lambda^2)}$, are fundamental predictions of QCD [28–30] for the short-distance, large-Q^2, phenomena. The momentum scale $Q^2 \sim p_T^2$ for the scattering subprocess, while $Q^2 \sim \hat{s}$ for a Compton or annihilation subprocess, but the exact meaning of Q^2 tends to be treated as a parameter rather than a dynamical quantity.

Figure 1 shows a schematic view of a hard-scattering event. The transverse momentum of the outgoing scattered parton is

$$p_T = p_T^* = \frac{\sqrt{\hat{s}}}{2}\sin\theta^*. \tag{2}$$

The two scattered partons propagate nearly back-to-back in azimuth from the collision point and fragment into the jetlike spray of final state particles [see Fig. 1(a) where only one fragment of each parton is shown).

It was originally thought that parton collisions were collinear with the $p + p$ collision axis so that the two emerging partons would have the same magnitude of transverse momenta pointing opposite in azimuth.

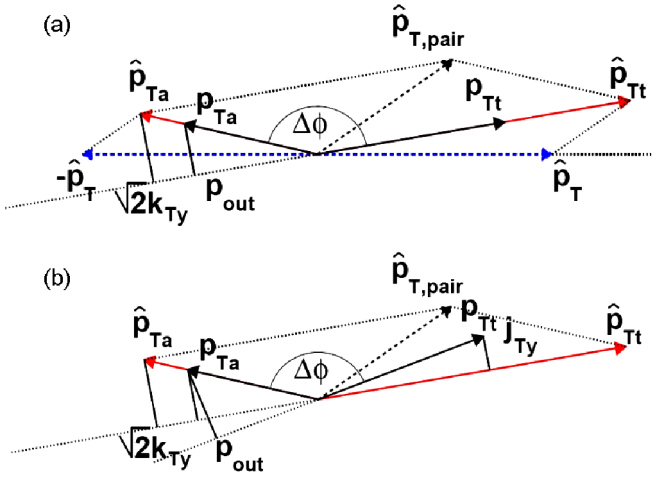

FIG. 1 (color online). (a) Schematic view of a hard-scattering event in the plane perpendicular to the beam. Two scattered partons with transverse momenta $\hat{p}_T$ in the partons' center-of-mass frame are seen in the laboratory frame to have a momenta $\hat{p}_{Tt}$ and $\hat{p}_{Ta}$. The net pair transverse momentum $\hat{p}_{T,pair}$ pair corresponds to the sum of the $\vec{k}_T$-vectors of the two colliding partons. The trigger and associated jet fragments producing high-p_T particles are labeled as p_{Tt} and p_{Ta}. The projection of $\vec{k}_T$ perpendicular to $\hat{p}_{Tt}$ is labeled as k_{Ty}. The transverse momentum component of the away-side particle $\vec{p}_{Ta}$ perpendicular to trigger particle $\vec{p}_{Tt}$ is labeled as p_{out}. (b) The same schematics as in (a), but the jet-fragmentation transverse momentum component j_{Ty} of the trigger jet is also shown.

However, it was found [3] that each of the partons carries initial transverse momentum $\vec{k}_T$, originally described as ''intrinsic'' [31]. This results in a momentum imbalance (the partons' p_T are not equal) and an acoplanarity (the transverse momentum of one jet does not lie in the plane determined by the transverse momentum of the second jet and the beam axes). The jets are noncollinear having a net transverse momentum $\langle p_T^2\rangle_{pair} = 2\cdot\langle k_T^2\rangle$.

It is important to emphasize that the $\langle k_T\rangle$ denotes the effective magnitude of the apparent transverse momentum of each colliding parton. The net transverse momentum of the outgoing parton-pair is $\sqrt{2}\cdot\langle k_T\rangle$. The naive expectation for the pure intrinsic parton transverse momentum based on nucleon constituent quark mass is about $\approx$ 300 MeV/c [31,32]. However, the measurement of net transverse momenta of diphotons, dileptons, or dijets over a wide range of center-of-mass energies gives $\langle k_T\rangle$ as large as 5 GeV/c [33]. It is common to think of the net transverse momentum of a dilepton or dijet pair as composed of 3 components:

$$\frac{\langle p_T^2\rangle_{pair}}{2} = \langle k_T^2\rangle = \langle k_T^2\rangle_{intrinsic} + \langle k_T^2\rangle_{soft} + \langle k_T^2\rangle_{NLO}, \tag{3}$$

where the intrinsic part refers to the possible ''fermi motion'' of the confined quarks or gluons inside a proton, the NLO part refers to the power law tail at large values of $p_{T_{pair}}$ due to the radiation of an initial state or final state hard gluon, which is divergent as the momentum of the radiated gluon goes to zero, and the soft part refers to the actual Gaussian-like distribution observed as $p_{T_{pair}} \to 0$, which is explained by resummation [34].

In the discussion below we will assume that the two components of the vector $\vec{k}_T$, k_{Tx} and k_{Ty} are Gaussian distributed with equal standard deviations $\sigma_{1parton,1D}$, in which case $k_T^2 = k_{Tx}^2 + k_{Ty}^2$ is distributed according to a 2-dimensional (2D) Gaussian [33]. For the net transverse momentum of the jet pair, $\langle p_T^2\rangle_{pair} = \sigma^2_{2partons,2d} = 2\sigma^2_{1parton,2d}$. Note that the principal difference between the 1 and 2 dimensional Gaussians is that $\langle k_{Tx}\rangle = \langle k_{Ty}\rangle = 0$, while $\langle k_T\rangle \neq 0$ since $\vec{k}_T$ is a 2D radius vector.

The two components of k_T result in different experimentally measurable effects. k_{Ty} leads to the acoplanarity of the dijet pair while k_{Tx} makes the momenta of the jets unequal which results in the smearing of the steeply falling p_T spectrum. This causes the measured inclusive jet or single particle cross section to be larger than the pQCD value given by Eq. (1). This was observed in the original discovery of high p_T particle production at the CERN ISR in 1972 [35] and led to much confusion until the existence and effects of k_T were understood.

Before the advent of QCD, the invariant cross section for the hard-scattering of the electrically charged partons of deeply inelastic scattering was predicted for $p + p$ collisions to follow a general scaling form [22,36]:

$$E\frac{d^3\sigma}{d^3p} = \frac{1}{p_{\mathrm{T}}^n}F(x_T) = \frac{1}{\sqrt{s}^n}G(x_T), \tag{4}$$

where $x_T = 2p_{\mathrm{T}}/\sqrt{s}$. The cross section has two factors, a function $F(x_T)$ ($G(x_T)$) which "scales," i.e. depends only on the ratio of momenta, and a dimensioned factor, $1/p_{\mathrm{T}}^n$ ($1/\sqrt{s}^n$), where n equals 4 for QED, and for LO-QCD [Eq. (4)], analogous to the $1/q^4$ form of Rutherford scattering. The structure and fragmentation functions are all in the $F(x_T)$ ($G(x_T)$) term. The original high p_T measurements at CERN [35] and Fermilab [37], showed beautiful x_T scaling, but with a value of $n = 8$ instead of $n = 4$, for values of $3 \le p_{\mathrm{T}} \le 7$ GeV/c. Later measurements at larger p_{T} showed the correct scaling in agreement with pQCD and it was realized that the value $n = 8$ at lower values of p_{T} and $\sqrt{s}$ was produced by the $k_{T\mathrm{x}}$ smearing [23,24]. More recently, the deviation of π^0 and direct photon inclusive cross sections measurements from pQCD predictions has been used to derive the values of k_T required to bring the measured and smeared pQCD predictions into agreement [33].

A more direct method to determine k_{Ty} is to measure the acoplanarity of the dijet pair. Such measurements were originally performed at the CERN-ISR using two-particle correlations [1–3,31]. The same method will be used in the present work.

Hard-scattering in $p + p$ collisions at $\sqrt{s} = 200$ GeV is detected by triggering on a π^0 with transverse momentum $p_{\mathrm{T_t}} \ge 3$ GeV/c; and the properties of jets are measured using the method of two-particle correlations. The trigger π^0 is a leading particle from a large transverse momentum jet while the associated particle comes from either the same jet or the away-side jet. We will analyze an outgoing dijet pair, with trigger jet transverse momentum magnitude $\hat{p}_{\mathrm{Tt}}$ which fragments to a trigger particle with transverse momentum $\vec{p}_{\mathrm{Tt}}$, and an away-side jet transverse momentum magnitude of $\hat{p}_{\mathrm{Ta}}$ which fragments to a particle with transverse momentum $\vec{p}_{\mathrm{Ta}}$. The average transverse momentum component of the away-side particle $\vec{p}_{\mathrm{Ta}}$ perpendicular to trigger particle $\vec{p}_{\mathrm{Tt}}$ in the azimuthal plane is labeled as p_{out}. If the magnitude of the jet transverse fragmentation momentum j_{T} [Fig. 1(a)] is neglected, the magnitude of $\sqrt{2}k_{\mathrm{Ty}}$ can be related to p_{out}: $\sqrt{2}k_{\mathrm{Ty}} = p_{\mathrm{out}}\hat{p}_{\mathrm{Ta}}/p_{\mathrm{Ta}} \equiv p_{\mathrm{out}}/z_{\mathrm{a}}$. Thus the measurement of p_{out} and the knowledge of the fragmentation variable (z_{a}) determines the magnitude of the parton's transverse momentum k_{T}.

The smearing of the steeply falling parton $\hat{p}_{\mathrm{T}}$ spectrum by the k_{Tx} distribution tends to make the trigger jet transverse momentum $\hat{p}_{\mathrm{Tt}}$ larger than the away-jet transverse momentum $\hat{p}_{\mathrm{Ta}}$. The component of the net transverse momentum of the parton pair along the trigger direction is smeared by $\sqrt{2}k_{T\mathrm{x}}$ such that

$$\langle(\hat{p}_{\mathrm{Tt}} - \hat{p}_{\mathrm{Tax}})^2\rangle = 2\langle k_{\mathrm{Tx}}^2\rangle = \langle k_{\mathrm{T}}^2\rangle. \tag{5}$$

For a flat $\hat{p}_T$ spectrum, the smearing would average to zero so that there would be no net shift in the transverse momentum spectrum:

$$\langle\hat{p}_{\mathrm{Tt}} - \hat{p}_{\mathrm{T}}\rangle = \langle\hat{p}_{\mathrm{T}} - \hat{p}_{\mathrm{Tax}}\rangle = 0. \tag{6}$$

However, due to the steeply falling $\hat{p}_{\mathrm{T}}$ spectrum, the k_{Tx} smearing results in a net imbalance of the jet-pair towards the trigger direction. In the limit when k_{T} is collinear with the trigger jet and with the requirement of the Lorentz invariance of $\hat{s}$ ($\hat{p}_{\mathrm{T}}^2 = \hat{p}_{\mathrm{Tt}}\hat{p}_{\mathrm{Ta}}$) it is easy to see that

$$\langle\hat{p}_{\mathrm{Tt}} - \hat{p}_{\mathrm{T}}\rangle = \left\langle\frac{\hat{p}_{\mathrm{Tt}}}{\hat{p}_{\mathrm{T}}}(\hat{p}_{\mathrm{T}} - \hat{p}_{\mathrm{Ta}})\right\rangle \simeq \frac{1}{2}\langle\hat{p}_{\mathrm{Tt}} - \hat{p}_{\mathrm{Ta}}\rangle > 0. \tag{7}$$

We denote the imbalance of $\hat{p}_{\mathrm{Ta}}$ and $\hat{p}_{\mathrm{Tt}}$ by the quantity

$$\hat{x}_{\mathrm{h}} = \langle\hat{p}_{\mathrm{Ta}}\rangle/\langle\hat{p}_{\mathrm{Tt}}\rangle. \tag{8}$$

Jet fragments have a momentum $\vec{j}_{\mathrm{T}}$ perpendicular to the partonic transverse momentum [Fig. 1(b)]. This vector is again a two-dimensional vector with one component perpendicular to the jet transverse axis, $\vec{j}_{\mathrm{T}}$, in the transverse plane and the other component perpendicular to the jet transverse axis in the longitudinal plane (defined by the beam and jet axes). The component of $\vec{j}_{\mathrm{T}}$ projected onto the azimuthal plane is labeled as j_{Ty}. The magnitude of $\langle j_{\mathrm{Ty}}\rangle$, the mean value of j_{T} projected into the plane perpendicular to the jet thrust (see Appendix A), measured at lower energies [1] has been found to be p_{T} independent and $\approx$ 400 MeV/c, consistent with measurements in e^+e^- collisions [38,39].

This analysis uses two-particle azimuthal correlation functions to measure the average relative angles between a trigger π^0 and an associated charged hadron. The angular width of the near- and away-side peak in the correlation function is used to extract the value of $\langle j_{\mathrm{T}}^2\rangle$ and $\hat{x}_{\mathrm{h}}^{-1}\langle z_{\mathrm{t}}\rangle \times \sqrt{\langle k_{\mathrm{T}}^2\rangle}$. An analysis of the associated yields is used to confirm the fragmentation function which provides the $\langle z_{\mathrm{t}}\rangle$ and $\langle z_{\mathrm{a}}\rangle$ values used for $\langle k_{\mathrm{T}}^2\rangle$ extraction. The details on the PHENIX experiment relevant to this analysis follow.

III. EXPERIMENTAL DETAILS

The PHENIX experiment consists of four spectrometer arms—two around mid-rapidity (the central arms) and two at forward rapidity (the muon arms)—along with a set of global detectors. The layout of the PHENIX experiment during the 2003 RHIC run is shown in Fig. 2.

Each central arm covers the pseudorapidity range $|\eta| <$ 0.35 and 90 degrees in azimuthal angle ϕ. In each of the central arms, charged particles are tracked by a drift chamber (DC) positioned from 2.0 to 2.4 m radially outward from the beam axis and 2 or 3 layers of pixel pad chambers (PC1, PC2, PC3 located at 2.4 m, 4.2 m, 5 m in the radial direction, respectively). Particle identification is provided

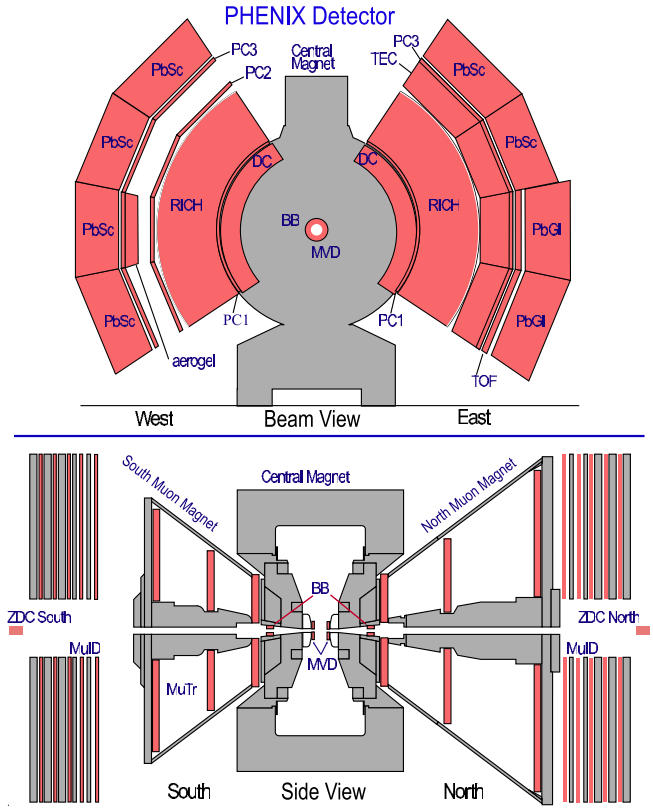

FIG. 2 (color online). The PHENIX experimental layout for the 2003 Au + Au run. The top panel shows the PHENIX central arm spectrometers viewed along the beam axis. The bottom panel shows a side view of the PHENIX muon arm spectrometers and the position of the global detectors (BBC and ZDC).

by ring imaging Čerenkov counters (RICH), a time of flight scintillator wall (TOF), and two types of electromagnetic calorimeters (EMCal), lead scintillator (PbSc) and lead glass (PbGl). The magnetic field for the central arm spectrometers is axially symmetric around the beam axis. Its component parallel to the beam axis has an approximately Gaussian dependence on the radial distance from the beam axis, dropping from 0.48 T at the center to 0.096 T (0.048 T) at the inner (outer) radius of the DC. A pair of zero-degree calorimeters (ZDC) and a pair of beam-beam counters (BBC) were used for global event characterization. Further details about the design and performance of PHENIX can be found in [40–42].

A $p + p$ data sample corresponding to an integrated luminosity 0.35 pb^{-1} at $\sqrt{s} = 200$ GeV has been used for the present analysis. It contains a minimum bias (MB) sample of 121 M events and a high-p_T triggered sample of 50 M events. The MB trigger is obtained from the charge multiplicity in the two BBCs situated at large pseudorapidity ($\eta \approx \pm(3.0\text{–}3.9)$). The BBCs were also used to determine the collision vertex, which is limited to a ± 30 cm range in this analysis. The high-p_T trigger requests an additional discrimination on sums of the analog signals from nonoverlapping, 2×2 groups of adjacent EMCal towers situated at mid-rapidity ($|\eta| < 0.35$) equivalent to an energy deposition of 750 MeV [43]. The analysis has been performed separately on the two data sets and no trigger selection bias was found within the quoted errors.

Neutral pions, which are used as trigger particles, are detected by the reconstruction of their $\gamma\gamma$ decay channel. Photons are detected in the EMCal, which has a timing resolution of ≈ 100 ps (PbSc) and ≈ 300 ps (PbGl) and energy resolution of $\sigma_E/E = 1.9\% \oplus 8.2\%/\sqrt{E(\text{GeV})}$ (PbSc) and $\sigma_E/E = 0.8\% \oplus 8.4\%/\sqrt{E(\text{GeV})}$ (PbGl). In order to improve the signal/background ratio we require the minimum hit energy >0.3 GeV, a shower profile cut as described in [41], and no accompanying hit in the RICH detector, which serves as a veto for conversion electrons. A sample of the invariant mass distribution of photon pairs detected in the EMCal is shown in Fig. 3.

Charged particles are reconstructed in each PHENIX central arm using a drift chamber, followed by two layers of multiwire proportional chambers with pad readout [40]. Particle momenta are measured with a resolution $\delta p/p = 0.7\% \oplus 1.1\% p\,(\text{GeV}/c)$. A confirmation hit is required in PC3. We also require that no signal in the RICH detector is associated with these tracks. These requirements eliminate charged particles which do not originate from the event vertex, such as beam albedo and weak decays, as well as conversion electrons.

High momentum charged pions (above the RICH Čerenkov threshold) are identified using the RICH and EMCal detectors. Candidate tracks must be associated

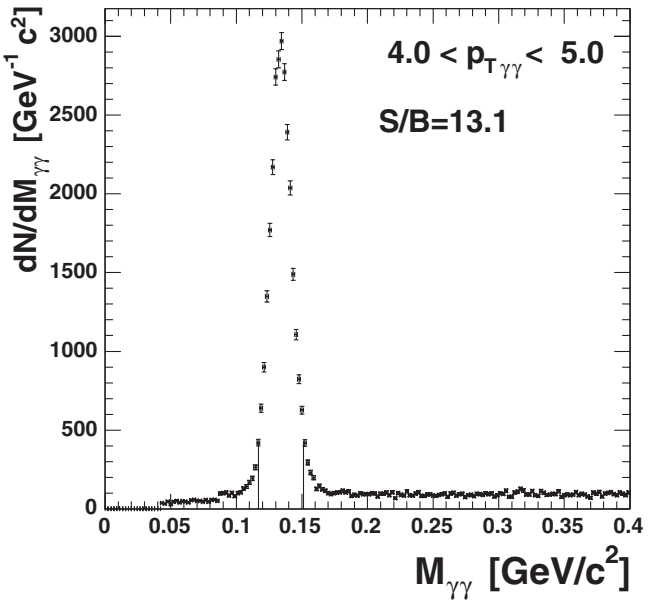

FIG. 3. The measured $\gamma\gamma$ invariant mass distribution for pair p_T in $4 < p_{T\gamma\gamma} < 5$ GeV/c. The peak is fitted with a Gaussian. The signal/background ratio within 2σ of the mean ranges from ≈ 6 at p_T of 3 GeV/c up to ≈ 15 at 8 GeV/c.

with a hit in the RICH [44], which corresponds to a minimum momentum of 18 MeV/c for electrons, 3.5 GeV/c for muons, and 4.9 GeV/c for charged pions. In a previous PHENIX publication [45], we have shown that charged particles with reconstructed p_T above 4.9 GeV/c, which have an associated hit in the RICH, are dominantly charged pions and background electrons from photon conversions albedo. The efficiency for detecting charged pions rises quickly past 4.9 GeV/c, reaching an efficiency of >90% at $p_T > 6$ GeV/c.

To reject the electron background in the charged pion candidates, the shower information at the EMCal is used. Since most of the background electrons are genuine low p_T particles that were misreconstructed as high p_T particles, simply requiring a large deposition of shower energy in the EMCal is effective in suppressing the electron background. In this analysis, a momentum- dependent energy cut on the EMCal is applied

$$\mathrm{E}\ \ (\mathrm{GeV}) > 0.3 + 0.15 p_T. \tag{9}$$

In addition to this energy cut, the shower shape information [41] is used to further separate the broad hadronic showers from the narrow electromagnetic showers and hence reduce the conversion backgrounds. The difference of the EM shower and hadronic shower is typically characterized by a χ^2 variable [41],

$$\chi^2 = \sum_i \frac{(\mathrm{E}_i^{\mathrm{meas}} - \mathrm{E}_i^{\mathrm{pred}})^2}{\sigma_i^2}, \tag{10}$$

where $\mathrm{E}_i^{\mathrm{meas}}$ is the energy measured at tower i and $\mathrm{E}_i^{\mathrm{pred}}$ is the predicted energy for an electromagnetic particle of total energy $\sum_i \mathrm{E}_i^{\mathrm{meas}}$.

In this analysis we use the probability calculated from this χ^2 value for an EM shower, ranging from 0 to 1 with a flat distribution expected for an EM shower, and a peak around 0 for an hadronic shower.

Figure 4 shows the probability distribution for pion and electron candidates, each normalized to one. The pion candidates were required to pass the energy cut and the electrons were selected using particle ID cuts similar to that used in [46]. The electron distribution is relatively flat, while the charged pion distribution peaks at 0. A cut of shower shape probability <0.2 selects pions above the energy cut with an efficiency of $\gtrsim 80\%$. Detailed knowledge of the pion efficiency is not necessary, since we present in this paper the per trigger pion conditional-yield distributions, for which this efficiency cancels out.

Since the energy and shower shape cuts are independent of each other, we can fix one cut and then vary the second to check the remaining background level from conversions. The energy cut in Eq. (9) is chosen such that the raw pion yield is found to be insensitive to the variation in the shower shape probability. Figure 5 shows the raw pion spectra for EMCal-RICH triggered events as a function of p_T, with the above cuts applied. The pion turn on from

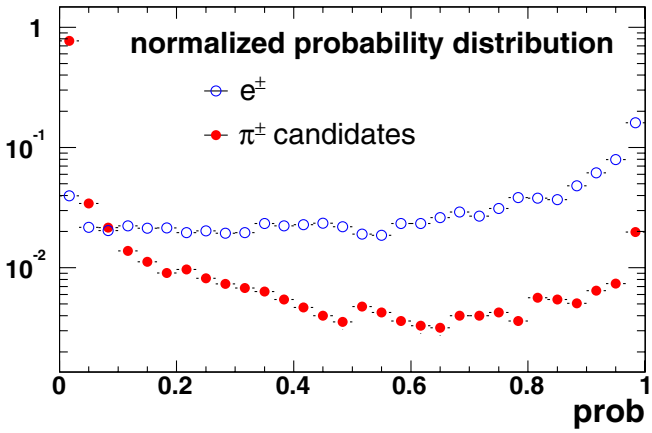

FIG. 4 (color online). The probability distribution for charged pion candidates and electrons derived from the EM shower shape using identified electrons and pions. The integrals have been normalized to one.

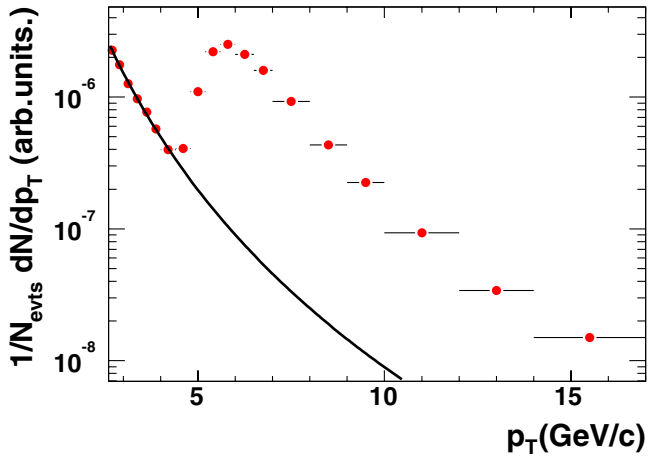

FIG. 5 (color online). The raw charged pion transverse momentum spectrum, with the final cuts applied. The level of the remaining background is estimated from an extrapolation from low-p_T and is shown as a black line.

4.9–7 GeV/c is clearly visible. Below p_T of 5 GeV/c, the remaining background comes mainly from the random association of charged particles with hits in the RICH detector. The background level is less than 5% from 5–16 GeV/c, which is the p_T range for the charged pion data presented in this paper.

IV. CORRELATION FUNCTION

The analysis uses two-particle azimuthal correlation functions between a neutral pion and an associated charged hadron to measure the distribution of the azimuthal angle difference $\Delta\phi = \phi_t - \phi_a$ (see Fig. 6). Whenever a π^0 was found in an event, the real, $dN_{\mathrm{uncorr}}/d\Delta\phi$, and mixed, $dN_{\mathrm{mix}}/d\Delta\phi$, distributions for given p_{Tt} (π^0) and p_{Ta} (charged hadron) were accumulated (upper panel of Fig. 6). Mixed events were obtained by randomly selecting

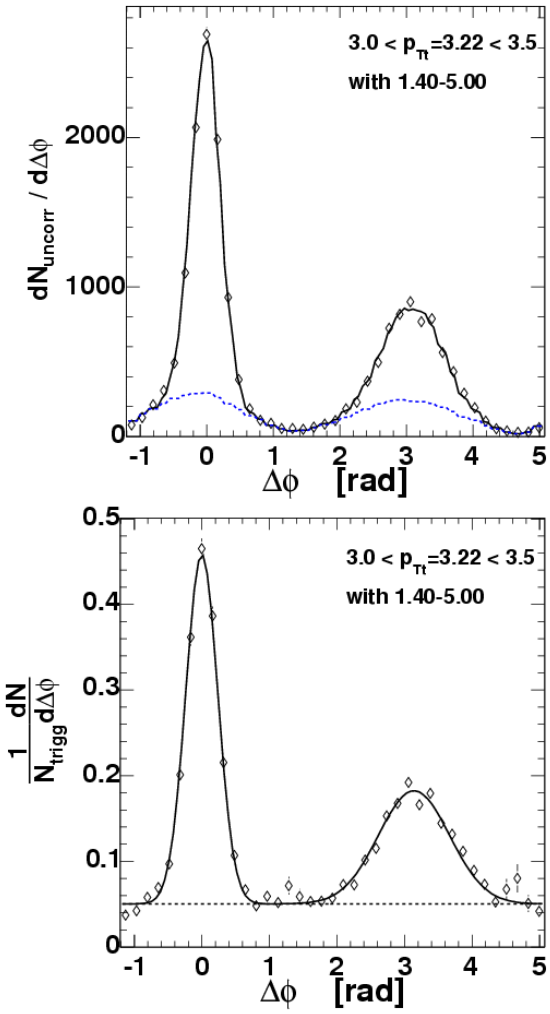

FIG. 6 (color online). An example of the correlation functions for $3 < p_{\mathrm{Tt}} < 3.5$ GeV/c and associated particles in $1.4 < p_{\mathrm{Ta}} < 5$ GeV/c. (upper) Unnormalized pair-yield distribution plotted with the fit function which is two Gaussians modulated by the pair detection efficiency derived from the mixed distribution (dashed line). (lower) Per π^0 trigger yield distribution corrected for the pair detection efficiency. Dashed line represents the constant term in the fit.

each member of a particle pair from different events having similar vertex position. Then the mixed event distribution was used to correct the correlation function for effects of the limited PHENIX azimuthal acceptance and for the detection efficiency, to the extent that it remains constant over the data sample.

We fit the raw $dN_{\mathrm{uncorr}}/d\Delta\phi$ distribution with the product

$$\frac{dN_{\mathrm{uncorr}}}{d\Delta\phi} = \frac{1}{\mathcal{N}} \frac{dN_{\mathrm{mix}}}{d\Delta\phi} \cdot (C_0 + C_1 \cdot f_{\mathrm{near}}(\Delta\phi) + C_2 \cdot f_{\mathrm{away}}(\Delta\phi)), \tag{11}$$

where the mixed event distribution is normalized to 2π ($\mathcal{N} = \sum dN^i_{\mathrm{mix}}/d\Delta\phi$ see dashed line on the upper panel of Fig. 6), C_{0-2} are constant factors to be determined from the fit, $f_{\mathrm{near}}(\Delta\phi)$ and $f_{\mathrm{away}}(\Delta\phi)$ are the near- and away-side peak fit functions, respectively. Traditionally, the Gaussian functions, around $\Delta\phi = 0$ and around $\Delta\phi = \pi$, are used for $f_{\mathrm{near}}(\Delta\phi)$ and $f_{\mathrm{away}}(\Delta\phi)$. This leaves a total of five free parameters to be determined - the areas and widths of the above two Gaussians: Y_{N}, σ_{N} for the near-angle component and Y_F, σ_{A} for the away-angle component and the constant term describing an uncorrelated distribution of particle pairs which are not associated with jets. However, the assumption of the Gaussian shape of the angular correlation induced by jet fragmentation is justified only in the high-p_{T} region where the relative angles are small. In order to access also a lower p_{T} region we used an alternative parameterization of $f_{\mathrm{near}}(\Delta\phi)$ and $f_{\mathrm{away}}(\Delta\phi)$ which will be discussed later in the text.

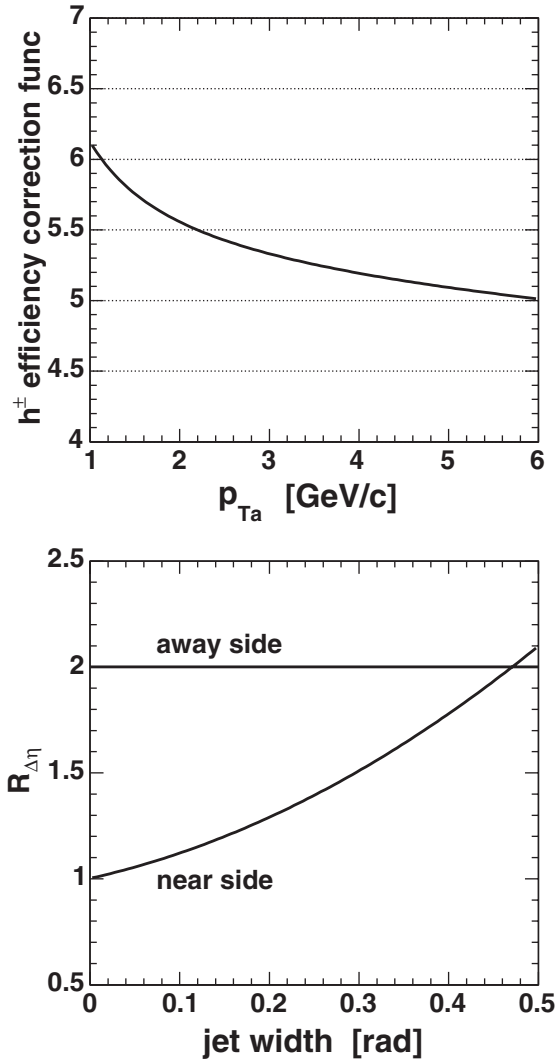

FIG. 7. (upper) Inclusive charged hadron efficiency correction function. (lower) η acceptance correction factor for loss of jet pairs outside the limited η-acceptance of the PHENIX experiment.

The normalized correlation function was constructed as a ratio of real and mixed distributions multiplied by η-acceptance correction factor $R_{\Delta\eta}$, divided by p_T-dependent efficiency correction $\epsilon(p_T)$ (see upper panel of Fig. 7) and divided by the number of π^0 triggers.

$$\frac{1}{N_{\rm trigg}}\frac{dN}{d\Delta\phi} = \frac{R_{\Delta\eta}}{N_{\rm trigg}\epsilon(p_T)}\frac{dN_{\rm uncorr}(\Delta\phi)/d\Delta\phi}{dN_{\rm mix}(\Delta\phi)/d\Delta\phi}\cdot\mathcal{N}. \tag{12}$$

The $R_{\Delta\eta}$ correction factor which accounts for limited η acceptance of the PHENIX experiment (see right panel of Fig. 7) for the near-side yield, with an assumption that the angular jet width is the same in $\Delta\eta$ and in $\Delta\phi$, can be written as

$$R_{\Delta\eta} = \frac{1}{\frac{1}{\sqrt{2\pi\sigma_N^2}}\int_{-0.7}^{0.7}\exp(-\frac{\Delta\eta}{2\sigma_N^2})acc(\Delta\eta)d\Delta\eta}, \tag{13}$$

where $acc(\Delta\eta)$ represent the PHENIX pair acceptance function in $|\Delta\eta|$. It can be obtained by convolving two flat distributions in $|\Delta\eta| < 0.35$, so $acc(\Delta\eta)$ has a simple triangular shape: $acc(\Delta\eta) = (0.7 - |\Delta\eta|)/0.7$. For the away-side yield the corresponding $R_{\Delta\eta}$ is

$$\mathrm{R}_{\Delta\eta} = \frac{2(0.7)}{\int_{-0.7}^{0.7}\mathrm{acc}(\Delta\eta)d\Delta\eta} = 2. \tag{14}$$

$R_{\Delta\eta}$ equals 2, because the pair efficiency has a triangular shape in $|\Delta\eta| < 0.7$, which results in 50% average efficiency when the real jet-pair distribution is flat in $|\Delta\eta| < 0.7$. Figure 8 and Table I show the normalized correlation functions for various $p_{\rm Tt}$ and $p_{\rm Ta}$.

For two particles with transverse momenta $p_{\rm Tt}$, $p_{\rm Ta}$ from the same jet, the width of the near-side correlation distribution can be related to the RMS value of the j_T vector component, $j_{\rm Ty}$, perpendicular to the parton momentum as

$$\sigma_N^2 = \langle\Delta\phi^2\rangle = \left\langle\left(\frac{j_{\rm Ty}}{p_{\rm Ta}}\right)^2 + \left(\frac{j_{\rm Ty}}{p_{\rm Tt}}\right)^2\right\rangle, \tag{15}$$

where we assume $\langle j_{\rm Ty}^2\rangle \ll p_{\rm Tt}^2$ and $p_{\rm Ta}^2$ and thus the arcsine function can be approximated by its argument and we

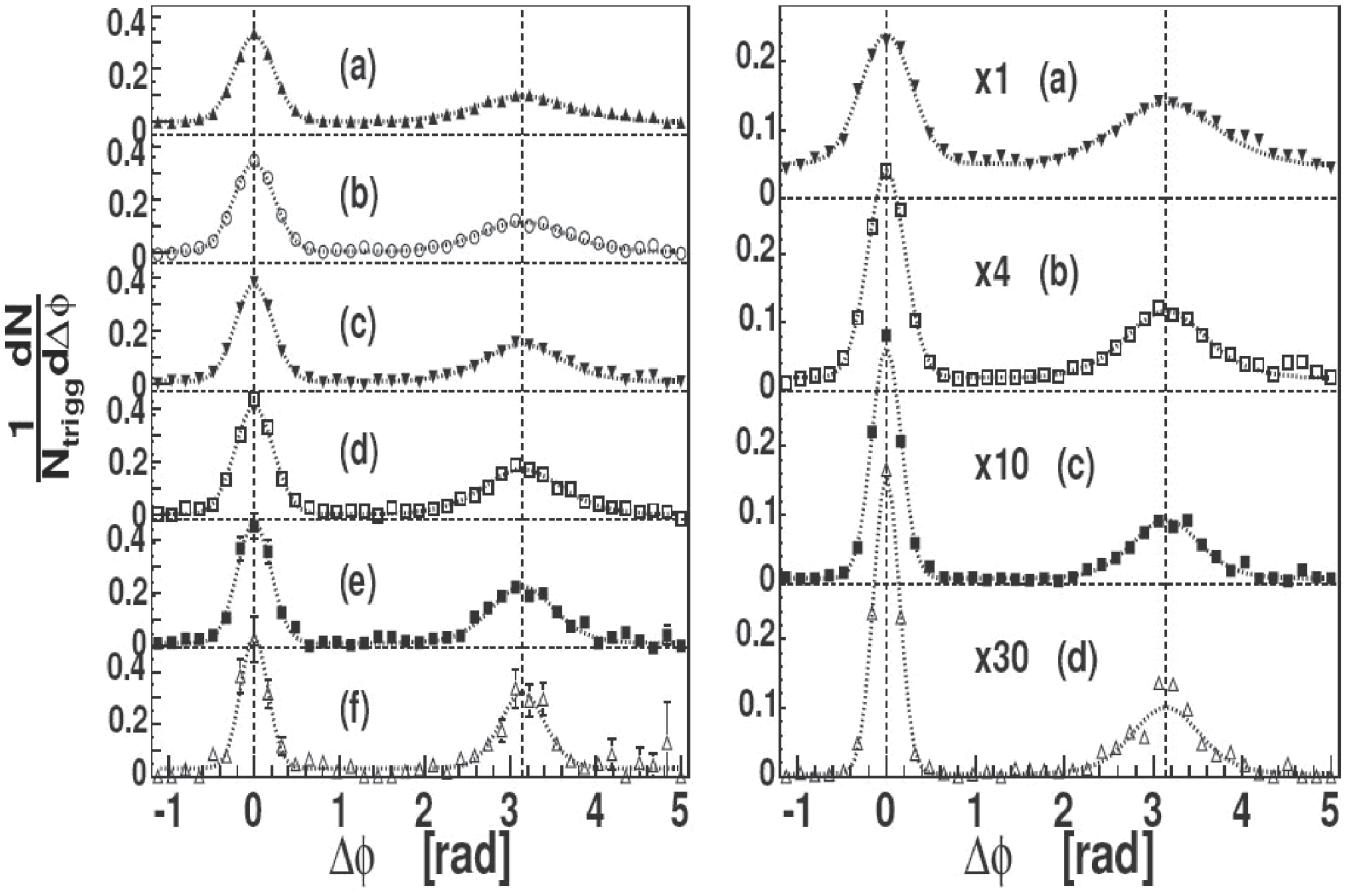

FIG. 8. (left) Measured yield of charged hadrons with away-side transverse momentum $1.4 < p_{\rm Ta} < 5.0$ GeV/c associated with a trigger π^0 of transverse momenta given in in Table I. (right) Measured yield of charged hadrons associated with a trigger π^0 of fixed transverse momentum $3.0 < p_{\rm Tt} < 10.0$ GeV/c and the away-side transverse momenta given in Table I. The dashed lines corresponds to the fit of two Gaussian functions representing the trigger (t) jet and away-side (a) jet correlation. The χ^2 (d.o.f.) σ_N and $\sqrt{\langle p_{\rm out}^2\rangle}$ values extracted from these fits are tabulated in Table I.

TABLE I. The χ^2 (d.o.f.) σ_N and $\sqrt{\langle p_{\rm out}^2\rangle}$ values extracted for the correlation function shown in Fig. 8. All units in rad and GeV/c. Only the statistical errors are shown.

	$1.4 < p_{\rm Ta} < 5.0$ GeV/c				$3.0 < p_{\rm Tt} < 10.0$ GeV/c		
$p_{\rm Tt}$	χ^2(d.o.f.=34)	$\sigma_{\rm N}$	$\sqrt{\langle p_{\rm out}^2\rangle}$	$p_{\rm Ta}$	χ^2(d.o.f.=34)	$\sigma_{\rm N}$	$\sqrt{\langle p_{\rm out}^2\rangle}$
(a) 2.5–3.0	69.4	$0.26 \pm 4 \times 10^{-3}$	1.17 ± 0.07	(a) 1.0–2.0	188.4	$0.29 \pm 4 \times 10^{-3}$	0.87 ± 0.03
(b) 3.0–3.5	79.6	$0.24 \pm 4 \times 10^{-3}$	1.19 ± 0.05	(b) 2.0–3.0	63.2	$0.21 \pm 3 \times 10^{-3}$	1.16 ± 0.04
(c) 3.5–4.5	61.2	$0.22 \pm 3 \times 10^{-3}$	1.04 ± 0.04	(c) 3.0–4.0	50.3	$0.16 \pm 4 \times 10^{-3}$	1.36 ± 0.06
(d) 4.5–5.5	52.7	$0.22 \pm 6 \times 10^{-3}$	1.08 ± 0.06	(d) 4.0–5.0	63.2	$0.14 \pm 4 \times 10^{-3}$	1.69 ± 0.13
(e) 5.5–6.5	38.4	$0.20 \pm 8 \times 10^{-3}$	0.90 ± 0.06				
(f) 6.5–8.0	31.6	$0.16 \pm 1 \times 10^{-2}$	0.64 ± 0.06				

can solve for [47]

$$\sqrt{\langle j_{\rm T}^2\rangle} = \sqrt{2\langle j_{\rm Ty}^2\rangle} \simeq \sqrt{2}\frac{p_{\rm Tt}p_{\rm Ta}}{\sqrt{p_{\rm Tt}^2 + p_{\rm Ta}^2}}\sigma_{\rm N}. \quad (16)$$

In order to extract $\langle|k_{\rm Ty}|\rangle$, or $\langle k_{\rm T}^2\rangle$, we start with the relation [1,31] between the magnitude of $p_{\rm out}$ (see Fig. 1),

$$p_{\rm out} = p_{\rm Ta}\sin\Delta\phi, \quad (17)$$

which is the transverse momentum component of the away-side particle $\vec{p}_{\rm Ta}$ perpendicular to trigger particle $\vec{p}_{\rm Tt}$ in the azimuthal plane (see Fig. 1), and $k_{\rm Ty}$:

$$\langle|p_{\rm out}|\rangle^2 = x_{\rm E}^2[2\langle|k_{\rm Ty}|\rangle^2 + \langle|j_{\rm Ty}|\rangle^2] + \langle|j_{\rm Ty}|\rangle^2, \quad (18)$$

where

$$x_{\rm E} = -\frac{\vec{p}_{\rm Tt}\cdot\vec{p}_{\rm Ta}}{p_{\rm Tt}^2} = -\frac{p_{\rm Ta}\cos\Delta\phi}{p_{\rm Tt}} \simeq \frac{z_{\rm a}\hat{p}_{\rm Ta}}{z_{\rm t}\hat{p}_{\rm Tt}} \quad (19)$$

represents the fragmentation variable of the away-side jet. [2,3] We note however, that [31] explicitly neglected $\langle z_{\rm t}\rangle = \langle p_{\rm Tt}/\hat{p}_{\rm Tt}\rangle$ in the formula at ISR energies, where $\langle z_{\rm t}\rangle \simeq 0.85$, while it is not negligible at $\sqrt{s} = 200$ GeV. Furthermore, as mentioned earlier, the average values of trigger and associated jet momenta are generally not the same. There is a systematic momentum imbalance due to $k_{\rm T}$-smearing of the steeply falling parton momentum distribution. The event sample with a condition of $p_{\rm Tt} > p_{\rm Ta}$ is dominated by configurations where the $k_{\rm T}$-vector is parallel to the trigger jet and antiparallel to the associated jet and $\langle\hat{p}_{\rm Tt} - \hat{p}_{\rm Ta}\rangle \neq 0$. Here we introduce the hadronic variable $x_{\rm h}$ in analogy to the partonic variable $\hat{x}_{\rm h}$

$$x_{\rm h} \equiv \frac{p_{\rm Ta}}{p_{\rm Tt}}, \qquad \hat{x}_{\rm h} = \hat{x}_{\rm h}(\langle k_{\rm T}^2\rangle, x_{\rm h}) \equiv \frac{\langle\hat{p}_{\rm Ta}\rangle}{\langle\hat{p}_{\rm Tt}\rangle}. \quad (20)$$

The detailed discussion on the magnitude of this imbalance is given later. In order to derive the relation between the magnitude of $p_{\rm out}$ and $k_{\rm T}$ let us first consider the simple case where we have neglected both trigger and associated $\langle j_{\rm T}\rangle$ [see panel (a) on Fig. 1]. In this case one can see that

$$\langle|p_{\rm out}|\rangle|_{j_{\rm Tt}=j_{\rm Ta}=0} \equiv \langle|p_{\rm out}|\rangle_{00} = \sqrt{2}\langle|k_{\rm Ty}|\rangle\frac{p_{\rm Ta}}{\langle\hat{p}_{\rm Ta}\rangle}$$
$$= \sqrt{2}\langle|k_{\rm Ty}|\rangle\langle z_{\rm t}\rangle\frac{x_{\rm h}}{\hat{x}_{\rm h}}.$$

Rewriting the formula for $p_{\rm out}$ in terms of RMS we get

$$\sqrt{\langle p_{\rm out}^2\rangle_{00}} = \langle z_{\rm t}\rangle\sqrt{\langle k_{\rm T}^2\rangle}\frac{x_{\rm h}}{\hat{x}_{\rm h}},$$

where we have taken $\langle k_{\rm T}^2\rangle = \langle 2k_{\rm Ty}^2\rangle$.

However, the jet fragments are produced with finite jet transverse momentum $j_{\rm T}$. The situation when the trigger particle is produced with $j_{\rm Tty} > 0$ GeV/c and the associated particle with $j_{\rm Tay} = 0$ GeV/c is shown in Fig. 1(b). The $p_{\rm out}$ vector picks up an additional component

$$\langle p_{\rm out}^2\rangle|_{j_{\rm Tt}>0, j_{\rm Ta}=0} = \left[\langle p_{\rm out}^2\rangle_{00} + \frac{\langle j_{\rm Tty}^2\rangle}{p_{\rm Tt}^2}(p_{\rm Ta}^2 - \langle p_{\rm out}^2\rangle_{00})\right]$$
$$\times \frac{p_{\rm Tt}^2 - \langle j_{\rm Tty}^2\rangle}{p_{\rm Tt}^2}.$$

With an assumption of $j_{\rm Tty} \ll p_{\rm Tt}$ we found that

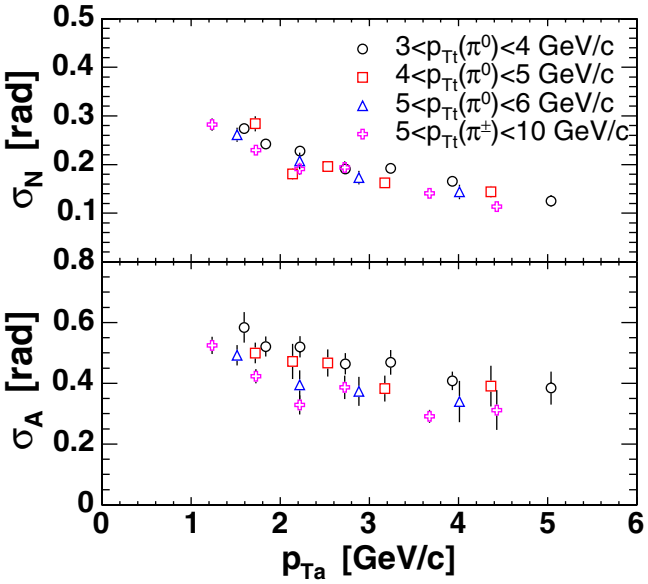

FIG. 9 (color online). (top) The width of the near-side peak $\sigma_{\rm N}$ with $p_{\rm Ta}$ for various values of $p_{\rm Tt}$ as indicated in legend. (bottom) The width of the far-side peak $\sigma_{\rm A}$ with $p_{\rm Ta}$ for the same $p_{\rm Tt}$ selection. The data values are given in Table II.

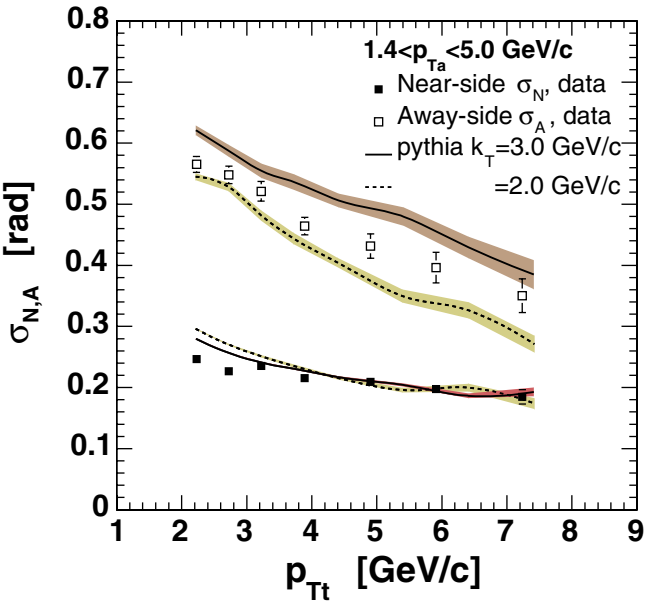

FIG. 10 (color online). The near-side (squares) and away-side (circles) width as a function or trigger-π^0 p_{Tt}. The associated charged particle momenta are in the $1.4 < p_{\mathrm{Ta}} < 5.0$ GeV/c region. The curves are from a PYTHIA calculation with the values of k_{T} indicated. The data values are given in Table III.

$$\langle p_{\mathrm{out}}^2\rangle|_{j_{\mathrm{Tt}}>0,j_{\mathrm{Ta}}=0} = x_{\mathrm{h}}^2\left[\langle z_{\mathrm{t}}\rangle^2\langle k_{\mathrm{T}}^2\rangle\frac{1}{\hat{x}_{\mathrm{h}}^2} + \langle j_{\mathrm{T_{ty}}}^2\rangle\right].$$

We include j_{Ta} in the same approximation, $j_{\mathrm{Tay}} \ll p_{\mathrm{Ta}}$, i.e. collinearity of j_{Ta} and p_{out} with result

$$\langle p_{\mathrm{out}}^2\rangle = x_{\mathrm{h}}^2\left[\langle z_{\mathrm{t}}\rangle^2\langle k_{\mathrm{T}}^2\rangle\frac{1}{\hat{x}_{\mathrm{h}}^2} + \langle j_{\mathrm{Tty}}^2\rangle\right] + \langle j_{\mathrm{Tay}}^2\rangle \qquad (21)$$

and we solve for $\langle z_{\mathrm{t}}\rangle\sqrt{\langle k_{\mathrm{T}}^2\rangle}/\hat{x}_h$

$$\frac{\langle z_{\mathrm{t}}\rangle\sqrt{\langle k_{\mathrm{T}}^2\rangle}}{\hat{x}_{\mathrm{h}}} = \frac{1}{x_{\mathrm{h}}}\sqrt{\langle p_{\mathrm{out}}^2\rangle - \langle j_{\mathrm{Tay}}^2\rangle - x_{\mathrm{h}}^2\langle j_{\mathrm{Tty}}^2\rangle}.$$

If we assume no difference between j_{Tt} and j_{Ta} then we have

TABLE III. The σ_{N} and σ_{A} values shown in Fig. 10. All units in rad and GeV/c. Only the statistical errors are shown.

p_{Tt}	σ_{N}	σ_{A}
2.23	0.247 ± 0.002	0.565 ± 0.013
2.72	0.227 ± 0.003	0.548 ± 0.014
3.22	0.235 ± 0.004	0.521 ± 0.016
3.89	0.215 ± 0.004	0.464 ± 0.014
4.90	0.210 ± 0.006	0.431 ± 0.020
5.91	0.197 ± 0.009	0.396 ± 0.025
7.23	0.185 ± 0.012	0.350 ± 0.028

$$\frac{\langle z_{\mathrm{t}}(k_{\mathrm{T}},x_{\mathrm{h}})\rangle\sqrt{\langle k_{\mathrm{T}}^2\rangle}}{\hat{x}_{\mathrm{h}}(k_{\mathrm{T}},x_{\mathrm{h}})} = \frac{1}{x_{\mathrm{h}}}\sqrt{\langle p_{\mathrm{out}}^2\rangle - \langle j_{\mathrm{Ty}}^2\rangle(1+x_{\mathrm{h}}^2)}. \qquad (22)$$

All quantities on the right-hand side of Eq. (22) can be directly extracted from the correlation function. The correlation functions are measured in the variable $\Delta\phi$ in bins of p_{Tt} and p_{Ta} (e.g. see Fig. 8), and the rms of the near and away peaks σ_{N} and σ_{A} are extracted. We tabulated σ_{N} and σ_{A} for many combinations of p_{Tt} and p_{Ta} (see Figs. 9 and 10 and Tables II and III).

Initially, we used the approximation $\sqrt{\langle p_{\mathrm{out}}^2\rangle} \sim p_{\mathrm{Ta}}\sin\sigma_{\mathrm{A}}$ in Eq. (22). However, we have noticed that this approximation and other approximations for $\sqrt{\langle p_{\mathrm{out}}^2\rangle}$ proposed e.g. in Ref. [48] (see Appendix B) are inadequate for $\sigma_{\mathrm{A}} > 0.4$ radians, so we do not use σ_{A} to calculate k_{T}.

We extract $\sqrt{\langle p_{\mathrm{out}}^2\rangle}$ directly for all values of p_{Tt} p_{Ta} (even for wide bins in p_{Ta} using the $\langle p_{\mathrm{Ta}}\rangle$ of the bin) by fitting the correlation function in the $\pi/2 < \Delta\phi < 3\pi/2$ region by

$$\frac{dN_{\mathrm{away}}}{d\Delta\phi}\Big|_{\pi/2}^{3\pi/2} = \frac{dN}{dp_{\mathrm{out}}}\frac{dp_{\mathrm{out}}}{d\Delta\phi} = \frac{-p_{\mathrm{Ta}}\cos\Delta\phi}{\sqrt{2\pi\langle p_{\mathrm{out}}^2\rangle}\,\mathrm{Erf}\left(\frac{\sqrt{2}p_{\mathrm{Ta}}}{\sqrt{\langle p_{\mathrm{out}}^2\rangle}}\right)}\exp\left(-\frac{p_{\mathrm{Ta}}^2\sin^2\Delta\phi}{2\langle p_{\mathrm{out}}^2\rangle}\right), \qquad (23)$$

where we assumed a Gaussian distribution in p_{out}. We still use a Gaussian function in $\Delta\phi$ in the near-angle peak to

TABLE II. Measured widths of the near- and away-angle $\pi^0 - h^{\pm}$ correlation peaks for various trigger particle momenta, as shown in Fig. 9. Only the statistical errors are shown.

$p_{\mathrm{Tt}} = 3.39$ GeV/c			$p_{\mathrm{Tt}} = 4.40$ GeV/c			$p_{\mathrm{Tt}} = 5.41$ GeV/c			$p_{\mathrm{Tt}} = 6.40$ GeV/c		
p_{Ta}	σ_{N} rad	σ_A rad	p_{Ta}	σ_{N} rad	σ_A rad	p_{Ta}	σ_{N} rad	σ_A rad	p_{Ta}	σ_{N} rad	σ_A rad
1.59	0.27 ± 0.01	0.58 ± 0.05	1.72	0.28 ± 0.02	0.50 ± 0.03	1.51	0.26 ± 0.01	0.49 ± 0.03	1.34	0.40 ± 0.03	0.68 ± 0.05
1.84	0.24 ± 0.01	0.52 ± 0.03	2.14	0.18 ± 0.01	0.47 ± 0.06	2.22	0.21 ± 0.02	0.39 ± 0.05	1.64	0.30 ± 0.02	0.58 ± 0.05
2.22	0.23 ± 0.01	0.52 ± 0.03	2.53	0.20 ± 0.01	0.47 ± 0.04	2.88	0.17 ± 0.01	0.37 ± 0.05	1.94	0.23 ± 0.02	0.52 ± 0.06
2.73	0.19 ± 0.01	0.46 ± 0.04	3.17	0.16 ± 0.01	0.38 ± 0.04	4.01	0.14 ± 0.02	0.34 ± 0.07	2.29	0.23 ± 0.02	0.40 ± 0.03
3.24	0.19 ± 0.01	0.47 ± 0.04	4.36	0.14 ± 0.01	0.39 ± 0.07				2.74	0.17 ± 0.01	0.41 ± 0.05
3.93	0.17 ± 0.01	0.41 ± 0.03							3.36	0.17 ± 0.02	0.36 ± 0.04
5.04	0.12 ± 0.01	0.38 ± 0.05									

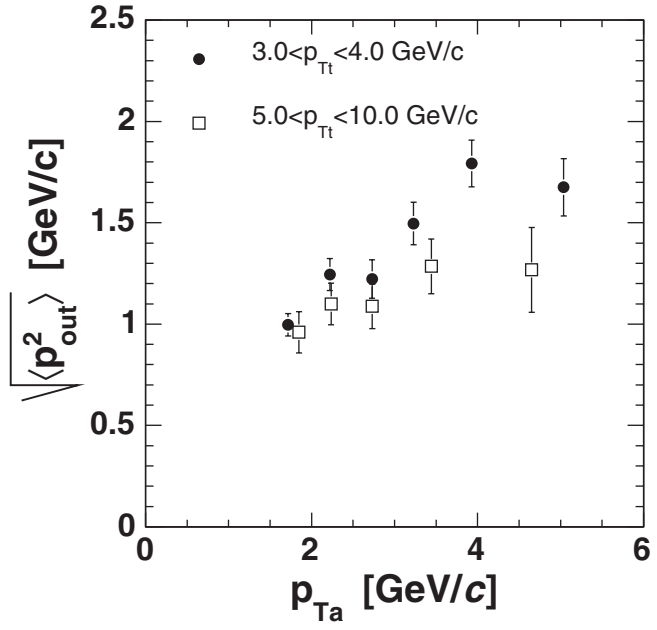

FIG. 11. Extracted values of $\sqrt{\langle p_{\rm out}^2\rangle}$ for $3.0 < p_{\rm Tt} < 4.0$ and $5.0 < p_{\rm Tt} < 10.0$ GeV/c for various values of $p_{\rm Ta}$ using the direct $p_{\rm out}$ extraction method based on fitting the away-side peak by Eq. (23).

extract $\sqrt{\langle j_{\rm T}^2\rangle}$. The $\sqrt{\langle p_{\rm out}^2\rangle}$ values extracted from the fit of the functional form (23) are shown in Figs. 11 and 12 and Table IV.

The per-trigger yields as a function of $p_{\rm Tt}$ for fixed associated $1.4 < p_{\rm Ta} < 5.0$ GeV/c bin are shown in Fig. 13 and Table V. There is a distinct behavior of the near-side yield which varies with trigger $p_{\rm Tt}$ much less than the away-side yield. For the away-side, this reflects the fact that the particle detected in the fixed associated bin are produced from the lower z region of the fragmentation function for events with higher trigger $p_{\rm Tt}$. For the near-side jet, this multiplicity increase is reduced due to the fact that with increasing $p_{\rm Tt}$ the near-side jet energy increases; however, at the same time the larger fraction of this energy is taken away by the more energetic trigger particle. Thus the relative change in z is smaller on the near side.

In order to extract $\langle z_{\rm t}\rangle$ and $\hat{x}_{\rm h}$ knowledge of the fragmentation function is needed; a detailed discussion is given in following sections.

TABLE IV. The $\sqrt{\langle p_{\rm out}^2\rangle}$ values shown in Fig. 11 and 12. All units in GeV/c. Only the statistical errors are shown.

$1.4 < p_{\rm Ta} < 5.0$		$3 < p_{\rm Tt} < 4$		$5 < p_{\rm Tt} < 10$	
$p_{\rm Tt}$	$\sqrt{\langle p_{\rm out}^2\rangle}$	$p_{\rm Ta}$	$\sqrt{\langle p_{\rm out}^2\rangle}$	$p_{\rm Ta}$	$\sqrt{\langle p_{\rm out}^2\rangle}$
2.23	1.315 ± 0.043	1.72	0.996 ± 0.056	1.85	0.960 ± 0.102
2.72	1.250 ± 0.046	2.22	1.244 ± 0.079	2.24	1.100 ± 0.103
3.22	1.182 ± 0.049	2.73	1.222 ± 0.095	2.73	1.088 ± 0.110
3.89	1.011 ± 0.038	3.23	1.496 ± 0.105	3.44	1.285 ± 0.136
4.90	0.953 ± 0.052	3.93	1.793 ± 0.115	4.65	1.268 ± 0.210
5.91	0.868 ± 0.064	5.04	1.675 ± 0.141		
7.24	0.798 ± 0.068				

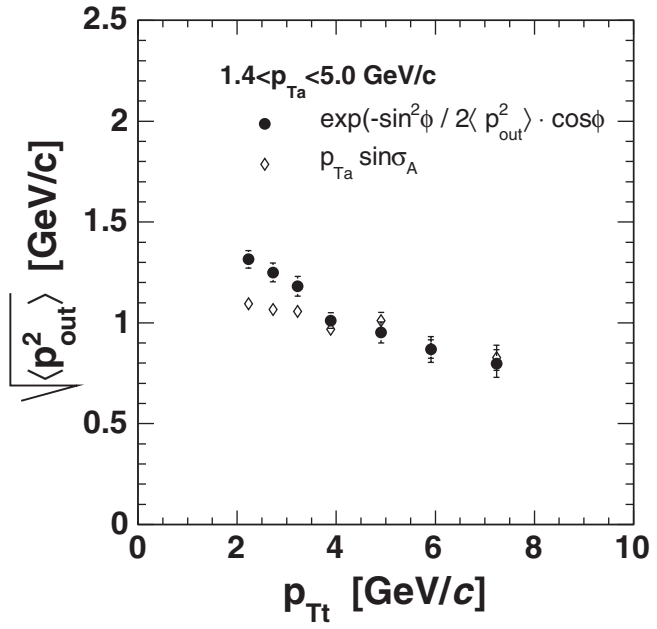

FIG. 12. (solid circles) Extracted values of $\sqrt{\langle p_{\rm out}^2\rangle}$ for $1.4 < p_{\rm Ta} < 5.0$ GeV/c for various values of $p_{\rm Tt}$ from Eq. (23). (open diamonds) Indirect $p_{\rm out} = p_{\rm Ta}\sin(\sigma_{\rm A})$ values.

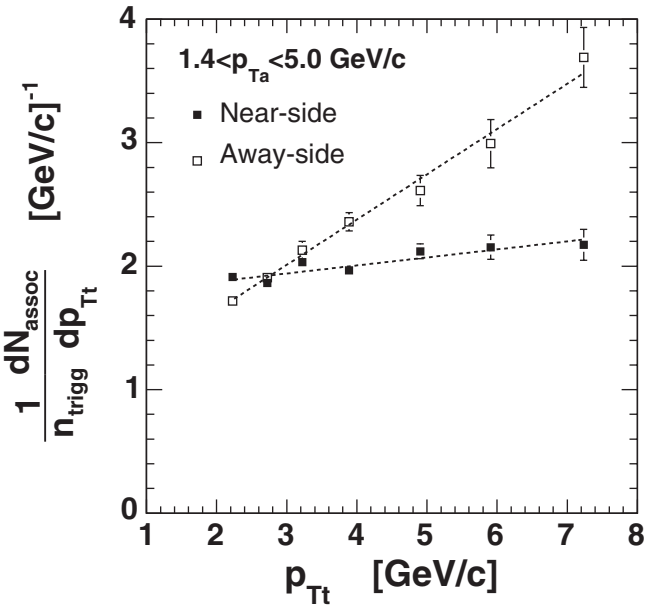

FIG. 13. Measured yield of charged hadrons associated with one trigger π^0 with transverse momenta indicated in Table I and associated charged hadron with $1.4 < p_{\rm T<} 5.0$ GeV/c. Dashed lines represent the linear fit. The data values are given in Table V.

TABLE V. The near and away-side conditional-yield per number of triggers for $1.4 < p_{\mathrm{Ta}} < 5.0$ GeV/c shown in Fig. 13. All units in rad and GeV/c. Only the statistical errors are shown.

p_{Tt}	Y_N	Y_A
2.23	1.911 ± 0.018	1.717 ± 0.044
2.72	1.863 ± 0.022	1.908 ± 0.055
3.22	2.032 ± 0.032	2.130 ± 0.071
3.89	1.966 ± 0.033	2.360 ± 0.074
4.90	2.120 ± 0.061	2.611 ± 0.123
5.91	2.153 ± 0.098	2.992 ± 0.196
7.24	2.174 ± 0.125	3.690 ± 0.242

A. $\sqrt{\langle j_{\mathrm{T}}^2\rangle}$ and $\hat{x}_{\mathrm{h}}^{-1}\langle z_{\mathrm{t}}\rangle\sqrt{\langle k_T^2\rangle}$ results

The measurement is performed in two different kinematical regimes; first the transverse momentum of the trigger particle, p_{Tt}, is fixed and the peak width is measured for different values of associated particle transverse momenta p_{Ta} (Fig. 9). (Note that in the region of overlap, the data are in excellent agreement with a previous measurement [9].) In the second case, particle pairs with a fixed associated bin $1.4 < p_{\mathrm{Ta}} < 5.0$ GeV/c and various p_{Tt} are selected (Fig. 10). It is evident that both near and away-side correlation peaks in all cases reveal a decreasing trend with p_{Ta} and p_{Tt}.

However, the asymptotic behavior of σ_{N} and σ_{A} is different. Whereas the magnitude of σ_{N}, according to Eq. (16), should vanish for large values of p_{Tt} and p_{Ta}, the σ_{A} according to Eq. (22) should be approximately constant around $\hat{x}_{\mathrm{h}}^{-1}\langle z_{\mathrm{t}}\rangle\sqrt{\langle k_{\mathrm{T}}^2\rangle}/p_{\mathrm{Tt}}$ for large values of p_{Ta}.

TABLE VI. The $\sqrt{\langle j_{\mathrm{T}}^2\rangle}$ values shown in Figs. 14 and 15. All units in rad and GeV/c. Only the statistical errors are shown.

$1.4 < p_{\mathrm{Ta}} < 5.0$		$3 < p_{\mathrm{Tt}} < 4$	
p_{Tt}	$\sqrt{\langle j_{\mathrm{T}}^2\rangle}$	p_{Ta}	$\sqrt{\langle j_{\mathrm{T}}^2\rangle}$
3.22	0.587 ± 0.009	1.72	0.562 ± 0.011
3.89	0.577 ± 0.009	2.22	0.597 ± 0.014
4.90	0.600 ± 0.017	2.73	0.572 ± 0.017
5.91	0.596 ± 0.026	3.23	0.590 ± 0.020
7.24	0.597 ± 0.038	3.93	0.603 ± 0.017
8.34	0.632 ± 0.085	5.04	0.506 ± 0.029
$4 < p_{\mathrm{Tt}} < 5$		$5 < p_{\mathrm{Tt}} < 6$	
p_{Ta}	$\sqrt{\langle j_{\mathrm{T}}^2\rangle}$	p_{Ta}	$\sqrt{\langle j_{\mathrm{T}}^2\rangle}$
1.72	0.643 ± 0.036	1.52	0.529 ± 0.030
2.14	0.492 ± 0.032	2.22	0.581 ± 0.049
2.53	0.608 ± 0.035	2.88	0.590 ± 0.047
3.17	0.590 ± 0.032	4.01	0.603 ± 0.063
4.36	0.631 ± 0.052		

The $\langle z_{\mathrm{t}}\rangle$ and $\hat{x}_{\mathrm{h}}$ quantities are implicitly p_{Ta} dependent, however, their ratio is roughly ~1 so that the asymptotic value of $\sigma_{\mathrm{A}}|_{p_{\mathrm{Ta}}\to\infty} \sim \langle k_{\mathrm{T}}^2\rangle/p_{\mathrm{Tt}}$.

Extracted values of $\langle j_{\mathrm{T}}^2\rangle$ as a function of p_{Ta} and p_{Tt} according to Eq. (16) are shown in Fig. 14 and 15 and Table VI. All $\langle j_{\mathrm{T}}^2\rangle$ values are constant in the explored region ($p_{\mathrm{Ta}} > 1.5$ GeV/c). It is expected that $\langle j_{\mathrm{T}}^2\rangle$ can not remain constant for arbitrarily small values of p_{Ta} because of the phase space limitation. In the region where

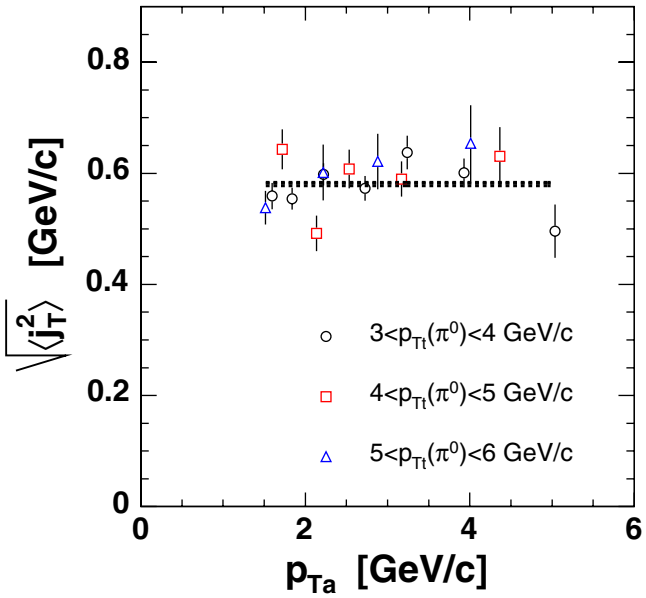

FIG. 14 (color online). $\sqrt{\langle j_{\mathrm{T}}^2\rangle}$ values calculated according Eq. (16). The dashed line represents a fit to a constant in the $1.5 < p_{\mathrm{Ta}} < 5$ GeV/c region. The data values are shown in Table VI.

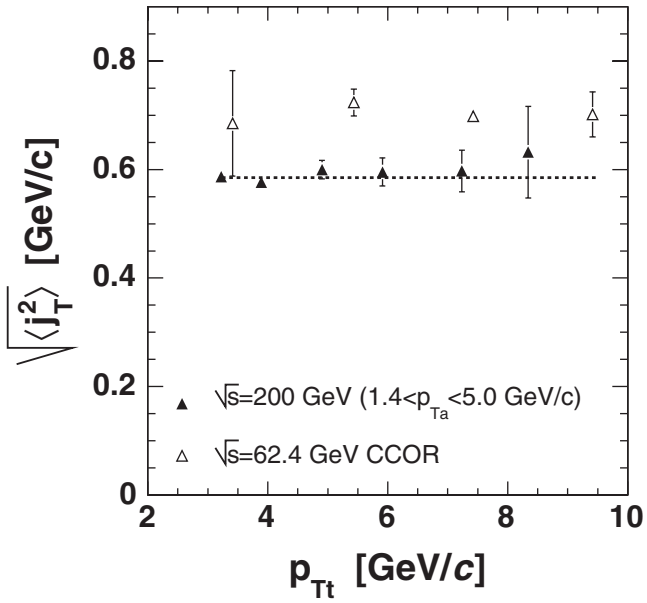

FIG. 15. Averaged values of $\sqrt{\langle j_{\mathrm{T}}^2\rangle}$ in ($1.5 < p_{\mathrm{Ta}} < 5$ GeV/c) as a function of the trigger transverse momentum p_{Tt} (solid triangles). The CCOR values measured at $\sqrt{s} = 62.4$ GeV shown by open triangles. The data values are shown in Table VI.

$p_{\mathrm{Ta}} \leq \sqrt{\langle j_T^2 \rangle}$, the magnitude of the j_{T}-vector is truncated, similar to the "seagull effect" [49]. Since the $\sqrt{\langle j_{\mathrm{T}}^2 \rangle}$ values are on the order of 600 MeV/c, we assume that the phase space limitation can be safely neglected for $p_{\mathrm{Ta}} > 1.5$ GeV/c and extract the value of $\sqrt{\langle j_{\mathrm{T}}^2 \rangle}$ averaged over p_{Ta} and p_{Tt}:

$$\sqrt{\langle j_{\mathrm{T}}^2 \rangle} = 585 \pm 6(\mathrm{stat}) \pm 15(\mathrm{sys})\ \mathrm{MeV/c}. \qquad (24)$$

The systematic error originates from the finite momentum resolution and Eq. (16) where we assume that the arcsine function can be approximated by its argument. For the angular width of the near-angle peak (see Fig. 9 and 10) it corresponds to an uncertainty of order of 3%.

The independence of $\langle j_T^2 \rangle$ on either p_{Tt} or $\sqrt{s}$ has been observed by the CCOR experiment in the range $\sqrt{s} =$ 31–62.4 GeV [1]. The $\langle j_{\mathrm{T}}^2 \rangle$ values at $\sqrt{s} = 62.4$ GeV (open triangles on Fig. 15) are systematically larger then values found in this analysis. The discrepancy should not be taken as significant, as CCOR used a slightly different technique than in this paper. CCOR extracted the $\langle j_{\mathrm{T}}^2 \rangle$ values from measurements of $\langle |p_{\mathrm{out}}| \rangle$ for different values of the x_E variable Eq. (19). According to Eq. (18) the $\langle |p_{\mathrm{out}}| \rangle^2$ magnitude should depend linearly on x_{E}^2; and the $\langle |j_{\mathrm{Ty}}| \rangle$ value was extracted from the intercept of the $\langle p_{\mathrm{out}}^2 \rangle(x_{\mathrm{E}})$ fit at $x_{\mathrm{E}} = 0$, rather than from a measurement of σ_{N}.

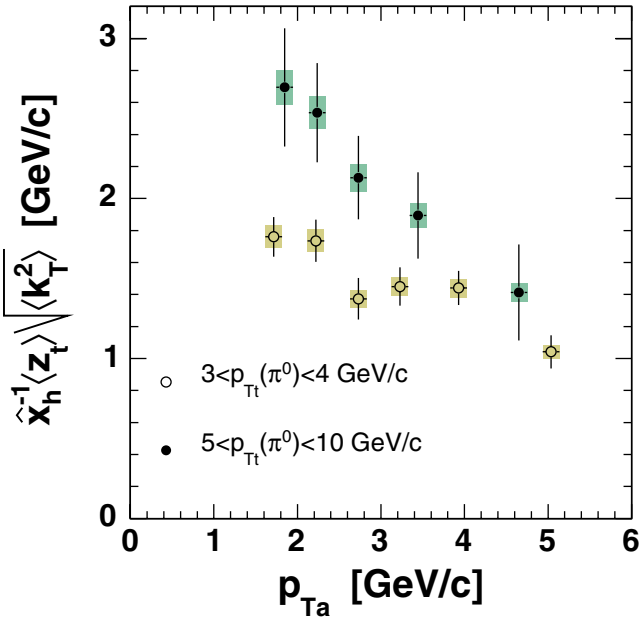

FIG. 16 (color online). $\hat{x}_{\mathrm{h}}^{-1}\langle z_{\mathrm{t}} \rangle \sqrt{\langle k_{\mathrm{T}}^2 \rangle}$ values calculated according to Eq. (22) for trigger π^0 in $3 < p_{\mathrm{Tt}} < 4$ GeV/c and $5 < p_{\mathrm{Tt}} < 6$ GeV/c as a function of p_{Ta}. The systematic uncertainties are indicated by the shaded boxes.

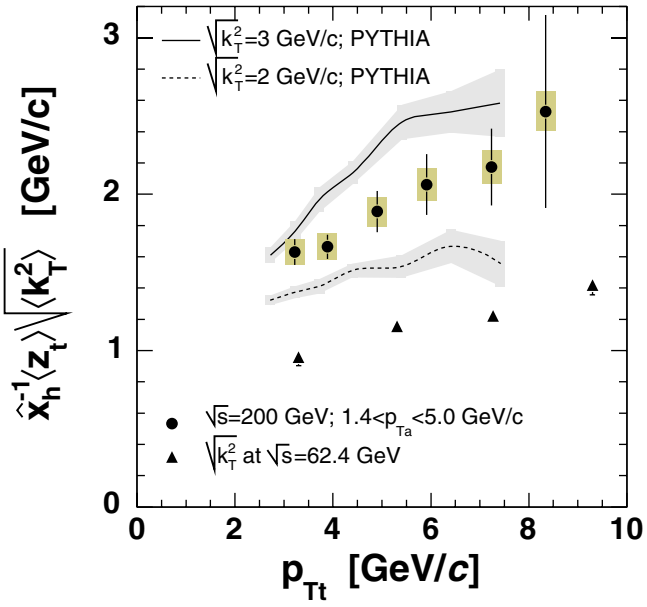

FIG. 17 (color online). The same calculation according Eq. (22) for fixed associated bin $1.4 < p_{\mathrm{Ta}} < 5.0$ GeV/c as a function of p_{Tt}. The systematic errors indicated by colored rectangles. The $\sqrt{\langle k_T^2 \rangle}$ results obtained by CCOR Collaboration at $\sqrt{s} = 62.4$ GeV [1] displayed by solid triangles.

Knowing the $\langle j_{\mathrm{T}}^2 \rangle$ and $\langle p_{\mathrm{out}}^2 \rangle$ values, we used Eq. (22) to determine $\hat{x}_{\mathrm{h}}^{-1}\langle z_t \rangle \sqrt{\langle k_{\mathrm{T}}^2 \rangle}$ (see Fig. 16 and Fig. 17). The systematic error was estimated with Monte Carlo simulations to be on the order of 5%. The main source of systematic error originates from the assumption [Eqs. (16) and (21)] of the relative smallness of $\langle j_{\mathrm{T}}^2 \rangle$, collinearity between p_{out} and j_{Tay} and from the limited momentum resolution discussed in Sec. III.

The p_{Ta} dependence of the extracted $\hat{x}_{\mathrm{h}}^{-1}\langle z_t \rangle \sqrt{\langle k_{\mathrm{T}}^2 \rangle}$ (Fig. 16) reveals a strikingly decreasing trend. It was originally expected that by fixing the value of p_{Tt}, the kinematics of the hard scattering (i.e. $\hat{p}_{\mathrm{Tt}} \simeq \hat{p}_{\mathrm{Ta}}$) would be fixed, independently of the value of p_{Ta}. Various values of p_{Ta} would then sample the $\hat{p}_{\mathrm{Ta}}$ fragmentation function, and the value of $\hat{x}_{\mathrm{h}}^{-1}\langle z_{\mathrm{t}} \rangle \langle k_{\mathrm{T}}^2 \rangle$ was expected to be constant. It is evident that this assumption is not quite correct.

A similar line of argument applies also for the rising trend when p_{Ta} is fixed and p_{Tt} varies (Fig. 17). It is interesting to note that the CCOR $\sqrt{\langle k_{\mathrm{T}}^2 \rangle}$ values measured at $\sqrt{s} = 62.4$ GeV (open triangles on Fig. 17) reveal a similar rising trend. However, the rising trend of $\hat{x}_{\mathrm{h}}^{-1}\langle z_{\mathrm{t}} \rangle \times \sqrt{\langle k_{\mathrm{T}}^2 \rangle}$ with p_{Tt} and falling with p_{Ta} suggests that the variation of $\sqrt{\langle k_{\mathrm{T}}^2 \rangle}$ with p_{Tt} seen by the CCOR Collaboration [1] may be indicative of the $\langle z_{\mathrm{t}} \rangle \hat{x}_{\mathrm{h}}^{-1}$ variation which was there neglected [50]. In order to understand

variation of $\langle z_t \rangle$ and $\hat{x}_h^{-1}$ we have to explore the process of dijet fragmentation.

V. FRAGMENTATION FUNCTIONS

We have shown in Eq. (22) that the width of the away-side correlation peak is related to the product of $\hat{x}_h^{-1}\langle z_t \rangle \times \sqrt{\langle k_T^2 \rangle}$. In order to evaluate $\langle z_t \rangle$, knowledge of the scattered parton $\hat{p}_T$ spectrum and fragmentation function is required.

Fragmentation functions from e^+e^- collisions, weighted by the appropriate hard-scattering constituent cross sections and Q^2 evolution could in principle be used. However, it was originally thought that the shape of the fragmentation function could be deduced from present measurements using the combined analysis of the inclusive trigger p_{Tt} and associated particle p_{Ta} distributions. Although this idea turned out to be incorrect, we will follow this line of reasoning for a while as it is instructive.

Generally, the invariant cross section for inclusive hadron production from jets can be parametrized in the following way. First, we assume that the number of parton fragments (consider only pions for simplicity) at a given p_T corresponds to the sum over all contributions from parton momenta, $\hat{p}_T$ from $p_T < \hat{p}_T < \sqrt{s}/2$. The joint probability of detecting a pion with $p_T = z\hat{p}_T$ originating from a parton with $\hat{p}_T$ can be written as

$$\frac{d^2\sigma_\pi}{\hat{p}_T d\hat{p}_T dz} = \frac{d\sigma_q}{\hat{p}_T d\hat{p}_T} \times D_\pi^q(z) = f_q(\hat{p}_T) \times D_\pi^q(z). \quad (25)$$

Here we use $f_q(\hat{p}_T)$ to represent the final state scattered-parton invariant spectrum $d\sigma_q/\hat{p}_T d\hat{p}_T$ and $D_\pi^q(z)$ to represent the fragmentation function. The first term in Eq. (25) can be viewed as a probability of finding a parton with transverse momentum $\hat{p}_T$ and the second term corresponds to the probability that the parton fragments into a particle of momentum $p_T = z\hat{p}_T$. With a simple change of variables from $\hat{p}_T$ to $p_T = z\hat{p}_T$, we obtain the joint probability of a pion with p_T which is a fragment with momentum fraction z from a parton with $\hat{p}_T = p_T/z$:

$$\frac{d^2\sigma_\pi}{p_T dp_T dz} = f_q\left(\frac{p_T}{z}\right) \cdot D_\pi^q(z)\frac{1}{z^2}. \quad (26)$$

The p_T and z dependences do not factorize. However, the p_T spectrum may be found by integrating over all values of $\hat{p}_T \geq p_T$ to $\hat{p}_T\,\mathrm{max} = \sqrt{s}/2$, which corresponds to values of z from $x_T = 2p_T/\sqrt{s}$ to 1.

$$\frac{1}{p_T}\frac{d\sigma_\pi}{dp_T} = \int_{x_T}^1 f_q\left(\frac{p_T}{z}\right) \cdot D_\pi^q(z)\frac{dz}{z^2}. \quad (27)$$

Alternatively, for any fixed value of p_T one can evaluate the $\langle z(p_T) \rangle$, integrated over the parton spectrum:

$$\langle z(p_T) \rangle = \frac{\int_{x_T}^1 z D_\pi^q(z) f_q(p_T/z)\frac{dz}{z^2}}{\int_{x_T}^1 D_\pi^q(z) f_q(p_T/z)\frac{dz}{z^2}}. \quad (28)$$

From the scaling properties of QCD and from the shape of the π^0 invariant cross section itself, which is a pure power law for $p_T \geq 3$ GeV/c [43], one can deduce that $f_q(\hat{p}_T)$ should have a power law shape, $f_q(\hat{p}_T) = A\hat{p}_T^{-n}$. In this case the hadron spectrum also has a power law shape because

$$\frac{1}{p_T}\frac{d\sigma_\pi}{dp_T} \approx \int_{x_T}^1 A D_\pi^q(z) \cdot \left(\frac{p_T}{z}\right)^{-n}\frac{dz}{z^2} \approx \frac{A}{p_T^n}\int_{x_T}^1 D_\pi^q(z) \cdot z^{n-2} dz \quad (29)$$

and the last integral depends only weakly on p_T due to the small value of x_T. For small parton $\hat{p}_T$ (below 3–4 GeV/c) the power law shape is no longer valid, but the region $p_T <$ 3 GeV/c is outside the scope of this paper. The $f_q(\hat{p}_T)$ should also diminish for very high $\hat{p}_T \rightarrow \sqrt{s}/2$ where the phase space available for hard parton production diminishes, again not relevant for the present purposes.

We used the power law parameterization for the final state scattered-parton invariant spectrum $f_q(\hat{p}_T) \propto \hat{p}_T^{-n}$ where n is a free parameter which can be determined from the fit of Eq. (27) to the measured π^0 cross section. There is, however, one more missing piece of information—the shape of the fragmentation function D_q^π. In an attempt to extract this information from the data, we have analyzed associated x_E-distributions, as shown in Table VII and Figs. 18–22.

A. "Scaling" variable x_E

It was expected [2] that the x_E variable, defined by Eq. (19), to first order, approximates the fragmentation function in the limit of high values of p_{Tt}, where there is sufficient collinearity between the trigger particle and the fragmenting parton. In this case where $j_T \ll p_{Tt}$ and $k_T \ll p_{Tt}$ one can assume that $p_{Tt} = \hat{p}_{Tt}/z_t$ and $x_E z_t = \hat{x}_h p_{Ta}\cos\Delta\phi/\hat{p}_{Ta} \simeq \hat{x}_h z_a$, and thus the slopes of $D(z_a)$ and x_E are related as

$$\langle z_a \rangle \approx \langle x_E \rangle \langle z_t \rangle \hat{x}_h^{-1}. \quad (30)$$

The x_E distributions of particles associated with trigger particles in the 3–8 GeV/c range of transverse momentum are plotted in Fig. 18. The dashed lines represent exponential fits. The slopes of these exponentials range from $-5.8 (3 < p_{Tt} < 4$ GeV/$c)$ to -7.8 (open symbols on Fig. 19). This is qualitatively and quantitatively different from the similar measurement done by CCOR Collaboration at $\sqrt{s} = 62.4$ GeV where the slopes of exponential fits to the x_E distributions were found to be ≈ -5.3 and independent of the trigger transverse momenta. That observation also supported the hypothesis of the x_E distribution being a good approximation of the fragmentation function. We also note that the x_E distributions are not quite exponential and at large values of x_E there is a tail similar to the power law tail of the single inclusive p_T distribution.

TABLE VII. Measured x_E distributions associated with various transverse momenta of the trigger π^0. Only the statistical errors are shown. See also Figs. 18–22.

$p_{Tt} = 3.39$ GeV/c		$p_{Tt} = 4.40$ GeV/c		$p_{Tt} = 5.41$ GeV/c		$p_{Tt} = 6.40$ GeV/c		$p_{Tt} = 7.39$ GeV/c	
x_E	dn/dx_E	x_E	dn/dx_E	x_E	dn/dx_E	x_E	dn/dx_E	x_E	dn/dx_E
0.32	$2.7 \pm 4.7 \times 10^{-2}$	0.23	$2.2 \pm 7.5 \times 10^{-2}$	0.22	$2.3 \pm 1.2 \times 10^{-1}$	0.18	$2.7 \pm 2.1 \times 10^{-1}$	0.17	$1.8 \pm 3.1 \times 10^{-1}$
0.37	$1.9 \pm 4.0 \times 10^{-2}$	0.27	$2.3 \pm 7.5 \times 10^{-2}$	0.27	$1.4 \pm 9.6 \times 10^{-2}$	0.22	$1.5 \pm 1.6 \times 10^{-1}$	0.24	$9.0 \times 10^{-1} \pm 1.5 \times 10^{-1}$
0.42	$1.4 \pm 3.3 \times 10^{-2}$	0.32	$1.6 \pm 6.2 \times 10^{-2}$	0.32	$9.4 \times 10^{-1} \pm 7.7 \times 10^{-2}$	0.27	$1.0 \pm 1.3 \times 10^{-1}$	0.33	$4.4 \times 10^{-1} \pm 1.0 \times 10^{-1}$
0.47	$9.6 \times 10^{-1} \pm 2.8 \times 10^{-2}$	0.37	$9.5 \times 10^{-1} \pm 4.8 \times 10^{-2}$	0.37	$5.7 \times 10^{-1} \pm 6.0 \times 10^{-2}$	0.35	$5.5 \times 10^{-1} \pm 6.6 \times 10^{-2}$	0.45	$2.8 \times 10^{-1} \pm 8.1 \times 10^{-2}$
0.52	$7.3 \times 10^{-1} \pm 2.4 \times 10^{-2}$	0.42	$7.2 \times 10^{-1} \pm 4.1 \times 10^{-2}$	0.43	$4.1 \times 10^{-1} \pm 5.0 \times 10^{-2}$	0.44	$2.7 \times 10^{-1} \pm 4.6 \times 10^{-2}$	0.55	$6.9 \times 10^{-2} \pm 4.0 \times 10^{-2}$
0.57	$5.2 \times 10^{-1} \pm 2.0 \times 10^{-2}$	0.47	$4.9 \times 10^{-1} \pm 3.4 \times 10^{-2}$	0.47	$2.8 \times 10^{-1} \pm 4.2 \times 10^{-2}$	0.54	$1.3 \times 10^{-1} \pm 3.1 \times 10^{-2}$	0.64	$4.5 \times 10^{-2} \pm 3.2 \times 10^{-2}$
0.62	$3.8 \times 10^{-1} \pm 1.7 \times 10^{-2}$	0.52	$2.7 \times 10^{-1} \pm 2.5 \times 10^{-2}$	0.52	$2.3 \times 10^{-1} \pm 3.8 \times 10^{-2}$	0.64	$8.1 \times 10^{-2} \pm 2.4 \times 10^{-2}$		
0.67	$3.0 \times 10^{-1} \pm 1.5 \times 10^{-2}$	0.57	$2.9 \times 10^{-1} \pm 2.6 \times 10^{-2}$	0.57	$1.9 \times 10^{-1} \pm 3.4 \times 10^{-2}$	0.81	$3.1 \times 10^{-2} \pm 8.6 \times 10^{-3}$		
0.75	$2.1 \times 10^{-1} \pm 9.0 \times 10^{-3}$	0.62	$1.9 \times 10^{-1} \pm 2.1 \times 10^{-2}$	0.63	$1.1 \times 10^{-1} \pm 2.5 \times 10^{-2}$				
0.85	$1.1 \times 10^{-1} \pm 6.5 \times 10^{-3}$	0.68	$1.6 \times 10^{-1} \pm 1.9 \times 10^{-2}$	0.67	$1.1 \times 10^{-1} \pm 2.5 \times 10^{-2}$				
0.95	$8.2 \times 10^{-2} \pm 5.5 \times 10^{-3}$	0.75	$1.1 \times 10^{-1} \pm 1.1 \times 10^{-2}$	0.76	$5.6 \times 10^{-2} \pm 1.3 \times 10^{-2}$				
1.04	$5.4 \times 10^{-2} \pm 4.5 \times 10^{-3}$	0.85	$6.5 \times 10^{-2} \pm 8.4 \times 10^{-3}$	0.85	$2.9 \times 10^{-2} \pm 9.2 \times 10^{-3}$				
1.15	$3.6 \times 10^{-2} \pm 3.6 \times 10^{-3}$	0.94	$5.2 \times 10^{-2} \pm 7.5 \times 10^{-3}$	0.97	$2.3 \times 10^{-2} \pm 8.1 \times 10^{-3}$				
1.25	$2.8 \times 10^{-2} \pm 3.2 \times 10^{-3}$	1.04	$2.3 \times 10^{-2} \pm 5.0 \times 10^{-3}$	1.07	$8.3 \times 10^{-3} \pm 4.8 \times 10^{-3}$				

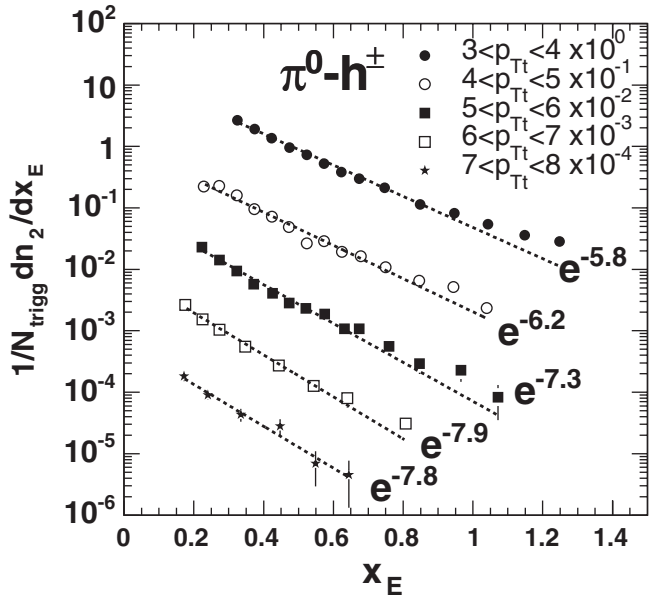

FIG. 18. The distribution of associated particles with x_E variable for various trigger particle p_{Tt} indicated in the legend. Exponential fits indicated by dashed lines.

The reason why the x_E distributions do not have the same slope for different p_{Tt} and why there is a ''power law'' tail at large x_E is the same as that which causes $\hat{x}_h^{-1}\langle z_t\rangle\sqrt{\langle k_T^2\rangle}$ to decrease with the associated particle transverse momentum. It turns out that by sampling different regions of p_{Ta} for fixed p_{Tt}, the average momentum of the parton fragmenting into a trigger particle, $\langle z_t\rangle$, also changes. This kind of trigger bias causes the hard-

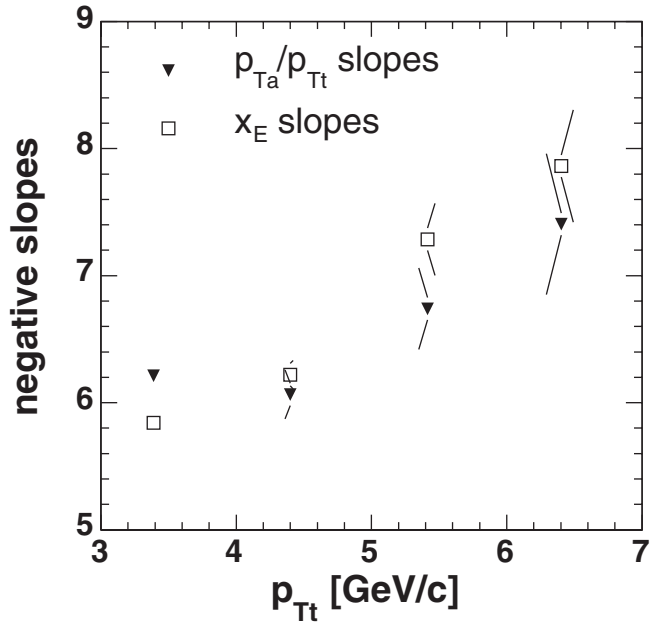

FIG. 19. The negative slope parameters extracted from the fit of a plain exponential function into a x_E (see Fig. 18) and p_{Ta}/p_{Tt} (see Fig. 20) distributions.

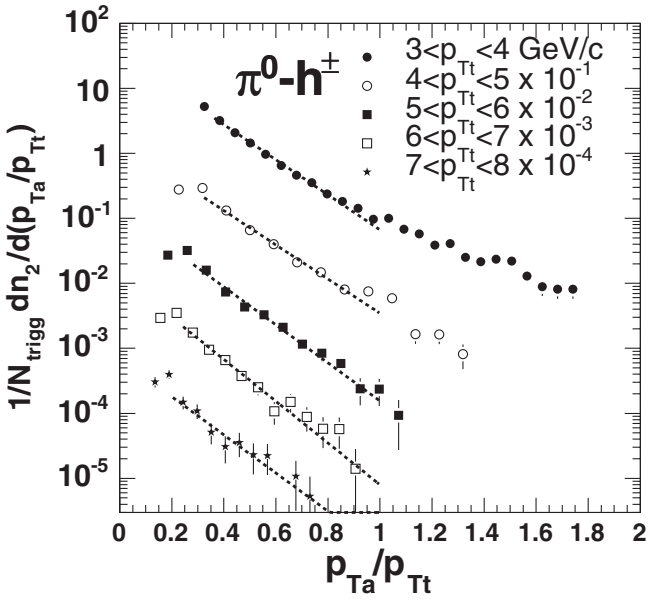

FIG. 20. The distribution of associated particles with p_{Ta}/p_{Tt} variable for various trigger particle p_{Tt} indicated in the legend. The distribution were fitted in the limited range $0.2 < p_{Ta}/p_{Tt} < 0.4$ by an exponential function (dashed lines).

scattering kinematics, the value of $\hat{p}_T$, to not be fixed for the case where p_{Tt} is fixed but p_{Ta} varies.

Taking this into account, one can not treat the associated x_E distribution as a rescaled fragmentation function, but rather as a folding of the two fragmentation processes of trigger and associated jets. The same line of arguments applies also for other two-particle variables, e.g. p_{Ta}/p_{Tt}, [51] used for an approximation of the fragmentation variable z (see Fig. 20). The negative slopes of an exponential fit in the $0.2 < p_{Ta}/p_{Tt} < 0.4$ range (solid symbols on Fig. 19) are, within the error bars, the same as for x_E.

In conclusion: the slope parameters extracted from associated x_E distributions reveal the rising trend with p_{Tt} which reflects the fact, that the different p_{Ta} samples not only different z_a but also different z_t.

The description of an associated distribution detected under the condition of the existence of a trigger particle requires an extension of the formulae discussed in Sec. V and is a subject of the next section.

VI. DIJET FRAGMENTATION

For the description of the detection of a single particle which is the result of jet fragmentation, recall Eq. (25)

$$\frac{d^2\sigma_\pi}{d\hat{p}_T dz_t} = \frac{d\sigma_q}{d\hat{p}_T} \times D_\pi^q(z_t) = \hat{p}_T f_q(\hat{p}_T) \times D_\pi^q(z_t) \equiv \Sigma_q(\hat{p}_T) \times D_\pi^q(z_t), \quad (31)$$

where we have now explicitly labeled the z of the trigger particle as z_t, and defined

$$\Sigma_q(\hat{p}_T) \equiv \hat{p}_T f_q(\hat{p}_T) = \frac{d\sigma_q}{d\hat{p}_T}. \quad (32)$$

When k_T smearing is introduced, configurations for which the high p_T parton pair is on the average moving towards the trigger particle are favored due to the steeply falling $\hat{p}_T$ spectrum, such that

$$\langle \hat{p}_{Tt} - \hat{p}_T \rangle \simeq \tfrac{1}{2}\langle \hat{p}_{Tt} - \hat{p}_{Ta} \rangle \equiv s(k_T)$$

with small variance σ_s^2, and we explicitly introduced $\hat{p}_{Tt}$ and $\hat{p}_{Ta}$ to represent the transverse momenta of the trigger and away partons. The single inclusive p_{Tt} spectrum is now given by

$$\frac{d^2\sigma_\pi}{d\hat{p}_{Tt}dz_t} = \Sigma'_q(\hat{p}_{Tt}) \times D_\pi^q(z_t) = \frac{z_t d^2\sigma_\pi}{dp_{T_t}dz_t}, \quad (33)$$

where the trigger parton $\hat{p}_{Tt}$ spectrum after k_T smearing is

$$\Sigma'_q(\hat{p}_{Tt}) \equiv \hat{p}_{Tt} f'_q(\hat{p}_{Tt}) = \frac{d\sigma_q}{d\hat{p}_{Tt}}. \quad (34)$$

Then, the conditional probability for finding the away-side parton with $\hat{p}_{Ta}$ and z_a, given $\hat{p}_{Tt}$ (and z_t), is

$$\left.\frac{dP(\hat{p}_{Ta}, z_a)}{d\hat{p}_{Ta}dz_a}\right|_{\hat{p}_{Tt}} = C(\hat{p}_{Ta}, \hat{p}_{Tt}, k_T) D_\pi^q(z_a),$$

where $C(\hat{p}_{Ta}, \hat{p}_{Tt}, k_T)$ represents the distribution of the transverse momentum of the away parton $\hat{p}_{Ta}$, given $\hat{p}_{Tt}$ and k_T, which can be written as

$$C(\hat{p}_{Ta}, \hat{p}_{Tt}, k_T) = \frac{1}{\sqrt{2\pi\sigma_s^2}} \times \exp\left(\frac{-[\hat{p}_{Ta} - (\hat{p}_{Tt} - 2s(k_T))]^2}{2\sigma_s^2}\right). \quad (35)$$

Then

$$\frac{d^4\sigma_\pi}{d\hat{p}_{Tt}dz_t d\hat{p}_{Ta}dz_a} = \frac{d^2\sigma_\pi}{d\hat{p}_{Tt}dz_t} \times \left.\frac{dP(\hat{p}_{Ta}, z_a)}{d\hat{p}_{Ta}dz_a}\right|_{\hat{p}_{Tt}}.$$

In general, $\sigma_s/s(k_T)$ is small (see Sec. VI B) so that $C(\hat{p}_{Ta}, \hat{p}_{Tt}, k_T)$ is well approximated by a δ function and we may take

$$\hat{p}_{Ta} = \hat{p}_{Tt} - 2s(k_T) = \hat{x}_h \hat{p}_{Tt},$$

so that

$$\frac{d^3\sigma_\pi}{d\hat{p}_{Tt}dz_t dz_a} = \Sigma'_q(\hat{p}_{Tt}) D_\pi^q(z_t) D_\pi^q(z_a),$$

where

$$z_a = \frac{p_{Ta}}{\hat{p}_{Ta}} = \frac{p_{Ta}}{\hat{x}_h \hat{p}_{Tt}} = \frac{z_t p_{Ta}}{\hat{x}_h p_{Tt}}.$$

Changing variables from $\hat{p}_{Tt}$, z_t to p_{Tt}, z_t as above, and similarly from z_a to p_{Ta}, we obtain

$$\frac{d^3\sigma_\pi}{dp_{Tt}dz_t dp_{Ta}} = \frac{1}{\hat{x}_h p_{Tt}} \Sigma'_q\left(\frac{p_{Tt}}{z_t}\right) D_\pi^q(z_t) D_\pi^q\left(\frac{z_t p_{Ta}}{\hat{x}_h p_{Tt}}\right), \quad (36)$$

where for integrating over z_t or finding $\langle z_t \rangle$ for fixed p_{Tt}, p_{Ta}, the minimum value of z_t is $z_t^{\min} = 2p_{Tt}/\sqrt{s} = x_{Tt}$ and the maximum value is

$$z_t^{\max} = \hat{x}_h \frac{p_{Tt}}{p_{Ta}} = \frac{\hat{x}_h}{x_h},$$

where $\hat{x}_h(p_{Tt}, p_{Ta})$ is also a function of k_T [Eq. (20)].

Thus, in order to evaluate $\hat{x}_h(p_{Tt}, p_{Ta})$ for use in Eq. (36), k_T must be known. We attack this problem by successive approximations. First we solve for k_T and $D_\pi^q(z)$ assuming $\hat{x}_h = 1$ as done at the ISR where the smearing correction was small. Then we solve for $\hat{x}_h(p_{Tt}, p_{Ta})$ with this value of k_T and iterate. On the first solution we solve only for $\Sigma'_q(\hat{p}_{Tt})$ while on the iteration we include the k_T smearing to solve for the unsmeared parton spectrum $\Sigma_{q(\hat{p}_T)} = \hat{p}_T f_q(\hat{p}_T)$ [Eq. (32)].

A. Sensitivity of the associated spectra to the fragmentation function

As discussed in Sec. V A, the associated x_E distribution was thought to approximate the fragmentation function of the away jet. Equation (36) can be transformed to the x_E distribution at fixed p_{Tt} with a change of variables from p_{Ta} to x_E followed by integration over z_t:

$$\frac{d^2\sigma}{dp_{Tt}dx_E} = \frac{dp_{Ta}}{dx_E} \times \frac{d^2\sigma}{dp_{Tt}dp_{Ta}} \simeq \frac{1}{\hat{x}_h} \int_{x_{Tt}}^{\hat{x}_h(p_{Tt}/p_{Ta})} D_\pi^q(z_t) D_\pi^q\left(\frac{z_t p_{Ta}}{\hat{x}_h p_{Tt}}\right) \Sigma'_q\left(\frac{p_{Tt}}{z_t}\right) dz_t. \quad (37)$$

We at first attempted to solve for the fragmentation function by simultaneous fits of the measured x_E distributions to Eq. (37) constrained by a fit of the inclusive invariant π^0 cross section to Eq. (27). There were difficulties with convergence.

The reason for the lack of convergence became apparent when we calculated x_E distributions according to Eq. (37) (Fig. 21) for two different fragmentation functions corresponding to quark and gluon jet fragmentation. A simple exponential parameterization was used and the slopes were obtained from the fit to the LEP data [52,53] (Fig. 22). For quark and gluon jets, we found $D_q(z) \approx \exp(-8.2 \cdot z)$ and $D_g(z) \approx \exp(-11.4 \cdot z)$ respectively. For the parton final state spectrum, we used $\Sigma'_q \propto \hat{p}_T^{-8}$. It is evident that the x_E distributions calculated for the quite different quark and gluon fragmentation functions do not differ significantly (the difference between solid and dashed lines on Fig. 21). Clearly, the x_E distributions are rather insensitive to the fragmentation functions of the away jet in contradiction to the previous conventional wisdom. The evidence of this explicit counter example led to attempts to perform the

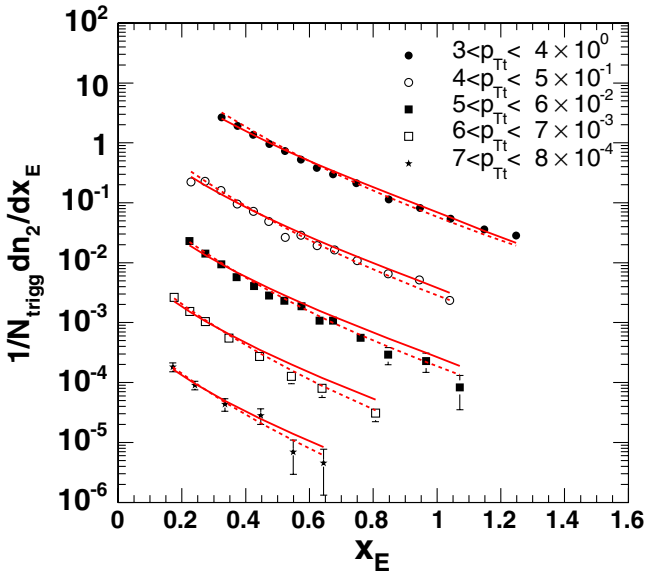

FIG. 21 (color online). The same x_E distributions as on Fig. 18 shown with calculations according to Eq. (37) for quark (solid lines) and for gluon (dashed lines) $D(z)$. An exponential approximation was used and the slopes for quark and gluon fragmentation function were obtained by fitting to LEP data [52,53] (see Fig. 22).

integrals of Eq. (33) and (36) analytically which straightforwardly confirmed the observation that the x_E distribution is not sensitive to the fragmentation function.

If the smeared trigger parton spectrum is taken as a power law,

$$\Sigma'_q\left(\frac{p_{\mathrm{Tt}}}{z_t}\right) = A\left(\frac{p_{\mathrm{Tt}}}{z_t}\right)^{-(n-1)}$$

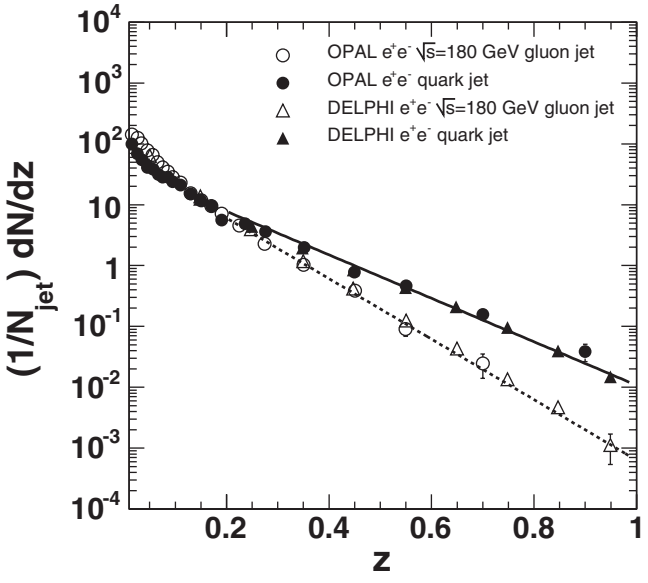

FIG. 22. Fragmentation function measured in e^+e^- collisions at $\sqrt{s} = 180$ GeV for gluon and quark jets. The solid and dashed lines represent the exponential fit in the $0.2 < z < 1$ region.

and the fragmentation function as an exponential, $D(z) = B\exp(-bz)$, then the integral of Eq. (36) over z_t becomes

$$\frac{d\sigma_\pi}{dp_{\mathrm{Tt}}dp_{\mathrm{Ta}}} = \frac{B^2}{\hat{x}_h}\frac{A}{p_{\mathrm{T_t}}^n}\int_{x_{\mathrm{T_t}}}^{\hat{x}_h(p_{\mathrm{Tt}}/p_{\mathrm{Ta}})} dz_t z_t^{n-1} \times \exp\left[-bz_t\left(1+\frac{p_{\mathrm{Ta}}}{\hat{x}_h p_{\mathrm{Tt}}}\right)\right], \quad (38)$$

which is an incomplete gamma function. Since $\hat{x}_h \sim 1$, we make the assumption that it is constant. Similarly, the integrals of Eqs. (29) and (33) are also incomplete gamma functions:

$$\frac{d\sigma_\pi}{dp_{\mathrm{Tt}}} = \frac{AB}{p_{\mathrm{T_t}}^{n-1}}\int_{x_{\mathrm{T_t}}}^1 dz_t z_t^{n-2}\exp[-bz_t]. \quad (39)$$

A reasonable approximation for the inclusive single, and two-particle cross sections is obtained by taking the lower limit to zero and the upper limit to infinity, leading to the replacement of the incomplete gamma functions by gamma functions, with the result that

$$\frac{d^2\sigma_\pi}{dp_{\mathrm{Tt}}dp_{\mathrm{Ta}}} \approx \frac{\Gamma(n)}{b^n}\frac{B^2}{\hat{x}_h}\frac{A}{p_{\mathrm{T_t}}^n}\frac{1}{(1+\frac{p_{\mathrm{Ta}}}{\hat{x}_h p_{\mathrm{Tt}}})^n}, \quad (40)$$

$$\frac{d\sigma_\pi}{dp_{\mathrm{Tt}}} \approx \frac{\Gamma(n-1)}{b^{n-1}}\frac{AB}{p_{\mathrm{T_t}}^{n-1}}, \quad (41)$$

where $\Gamma(n) = (n-1)\Gamma(n-1)$.

The conditional probability is just the ratio of the joint probability Eq. (40) to the inclusive probability Eq. (41), or

$$\left.\frac{dP_\pi}{dp_{\mathrm{Ta}}}\right|_{p_{\mathrm{Tt}}} \approx \frac{B(n-1)}{bp_{\mathrm{Tt}}}\frac{1}{\hat{x}_h}\frac{1}{(1+\frac{p_{\mathrm{Ta}}}{\hat{x}_h p_{\mathrm{Tt}}})^n}. \quad (42)$$

In the collinear limit, where $p_{\mathrm{Ta}} = x_E p_{\mathrm{Tt}}$:

$$\left.\frac{dP_\pi}{dx_E}\right|_{p_{\mathrm{Tt}}} \approx \frac{B(n-1)}{b}\frac{1}{\hat{x}_h}\frac{1}{(1+\frac{x_E}{\hat{x}_h})^n}. \quad (43)$$

The only dependence on the fragmentation function, in this approximation, is in the normalization constant B/b which equals $\langle m\rangle$, the multiplicity in the away-jet from the integral of the fragmentation function. The dominant term in Eq. (43) is the Hagedorn function $1/(1+x_E/\hat{x}_h)^n$, so that at fixed p_{Tt} the x_E distribution is predominantly a function only of x_E and thus does exhibit "x_E" scaling. Also, the Hagedorn function explains the "power law" tail at large x_E noted in Sec. VA. The reason that the x_E distribution is not very sensitive to the fragmentation function is that the integral over z_t for fixed p_{Tt} and p_{Ta} [Eq. (38)] is actually an integral over the jet transverse momentum $\hat{p}_{\mathrm{T_t}}$. However since both the trigger and away jets are always roughly equal and opposite in transverse momentum, integrating over $\hat{p}_{\mathrm{T_t}}$ simultaneously integrates over $\hat{p}_{\mathrm{T_a}}$, and thus also integrates over the away jet-fragmentation function. This can be seen directly by the

presence of z_t in both the same and away fragmentation functions in Eqs. (36) and (37), so that the integral over z_t integrates over both fragmentation functions simultaneously.

B. k_T smearing

In order to evaluate $\hat{x}_h(p_{Tt}, p_{Ta})$ and $\langle z_t \rangle$, k_T must be known. We attack this problem by successive approximations: first we solve for k_T assuming $\hat{x}_h = 1$ as done at the ISR, where the smearing correction was small. Then we iterate for finite k_T. The Gaussian approximation for the smearing function Eq. (35) does not work so well in the low $\hat{p}_T$ region. The product of the steeply falling parton distribution function and the fragmentation function is peaked at $z \approx 1$ preferring "small" parton momenta. We have developed more accurate description of the conditional yields taking into account the k_T smearing.

Let us consider the configuration depicted on Fig. 23. The two back-to-back partons in $\hat{s}$ frame undergo the Lorentz boost determined by net pair momentum

$$\vec{p}_{\,n} \equiv \vec{p}_{Tpair} \equiv \vec{\hat{p}}_{Tt} + \vec{\hat{p}}_{Ta} = \vec{k}_{Tt} + \vec{k}_{Ta}. \tag{44}$$

If we denote an angle between the unsmeared parton momentum and k_T-vector (or $\vec{p}_n$) as α (see Fig. 23) then we can write the conditional probability distribution of trigger parton momenta, $\hat{p}_{Tt}$, as

$$\left.\frac{d^3\sigma}{d\hat{p}_{Tt}d\alpha d\hat{p}_T}\right|_{p_{Tt},p_{Ta}} = \hat{p}_{Tt}\cdot\Sigma_q(\hat{p}_T)\cdot\hat{p}_n\cdot G(\hat{p}_n(\vec{r}_t)) \cdot D_\pi^q\!\left(\frac{p_{Tt}}{\hat{p}_{Tt}}\right)\frac{p_{Tt}}{\hat{p}_{Tt}^2}\cdot D_\pi^q\!\left(\frac{p_{Ta}}{\hat{p}_{Ta}(\vec{r}_t)}\right) \times \frac{p_{Ta}}{\hat{p}_{Ta}^2(\vec{r}_t)}, \tag{45}$$

where $G(\hat{p}_n) = \exp(-\hat{p}_n^2/2\langle k_T^2\rangle)$ describes the Gaussian probability distribution of the net pair momentum magnitude distribution, $\Sigma_q(\hat{p}_T)$ is the unsmeared parton momentum distribution, D_π^q is the fragmentation function and $\vec{r}_t = (\hat{p}_{Tt}, \phi, \hat{p}_T, k_T)$ is the phase space vector. The $\hat{p}_{Tt}$ is chosen to be an integration variable and $\hat{p}_{Ta}$ is fully determined by given values of $\hat{p}_{Tt}$, $\hat{p}_T$, angle ϕ and by the requirement of Lorentz invariance.

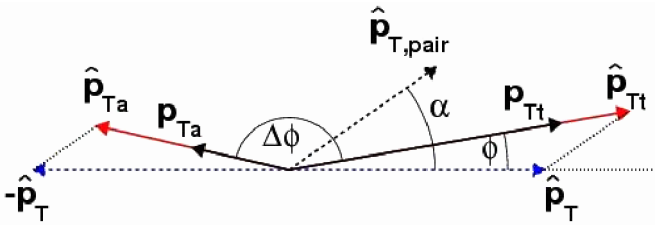

FIG. 23 (color online). Back-to-back partons in hard-scattering rest frame (back-to-back dashed arrows) with four-momenta $(\hat{p}_T, 0, 0, \hat{p}_T)$ and $(-\hat{p}_T, 0, 0, \hat{p}_T)$ in $(-,-,-,+)$ metrics moving along $\hat{p}_n$ ($\hat{p}_n = \hat{p}_{Tpair}$) for an event where detection of p_{Tt} and p_{Ta} is required (the j_T contribution is neglected). The $p_{Tt} > p_{Ta}$ condition implies that the events with $\hat{p}_n$ pointing more in the direction of p_{Tt} are selected.

In order to evaluate $\langle z_t(k_T)\rangle|_{p_{Tt},p_{Ta}}$ and $\hat{x}_h(k_T)|_{p_{Tt},p_{Ta}}$ we have to evaluate first the parton distribution for events where given p_{Tt} and p_{Ta} are detected. This conditional cross section can be expressed as a definite integral over the unobserved variables ϕ and $\hat{p}_T$ (see Fig. 23)

$$\begin{aligned}\left.\frac{d\sigma}{d\hat{p}_{Tt}}\right|_{p_{Tt},p_{Ta}} &= 2\int_0^{\sqrt{s}/2}\int_0^{\pi}\left.\frac{d^3\sigma}{d\hat{p}_{Tt}d\hat{p}_T d\phi}\right|_{p_{Tt},p_{Ta}} d\phi d\hat{p}_T \\ &= D_\pi^q\!\left(\frac{p_{Tt}}{\hat{p}_{Tt}}\right)\frac{2}{\hat{p}_{Tt}}\int_0^{\sqrt{s}/2}\Sigma_q(\hat{p}_T) \\ &\quad\times\int_0^{\pi}\hat{p}_n(\vec{r}_t)G(\hat{p}_n(\vec{r}_t)) \\ &\quad\cdot D_\pi^q\!\left(\frac{p_{Ta}}{\hat{p}_{Ta}(\vec{r}_t)}\right)\frac{1}{\hat{p}_{Ta}^2(\vec{r}_t)}\,d\phi d\hat{p}_T.\end{aligned} \tag{46}$$

The $d\sigma/d\hat{p}_{Ta}|_{p_{Tt},p_{Ta}}$ distribution can be derived from Eq. (46) just by rotation $\hat{p}_{Tt} \to \hat{p}_{Ta}$ and $\hat{p}_{Ta} \to \hat{p}_{Tt}$. The $\langle z_t(k_T)\rangle|_{p_{Tt},p_{Ta}}$ and $\hat{x}_h(k_T)|_{p_{Tt},p_{Ta}}$ quantities can then be evaluated as

$$\langle z_t(k_T)\rangle|_{p_{Tt},p_{Ta}} = \frac{\mathcal{Z}(1)}{\mathcal{Z}(0)}, \tag{47}$$

where

$$\begin{aligned}\mathcal{Z}(n) &= \int_{x_{Tt}}^1 z_t^{n-1}D_\pi^q(z_t)\int_0^{\sqrt{s}/2}\Sigma_q(\hat{p}_T) \\ &\quad\times\int_0^{\pi}\hat{p}_n G(\hat{p}_n(\vec{r}_{zt}))\cdot D_\pi^q\!\left(\frac{p_{Ta}}{\hat{p}_{Ta}(\vec{r}_{zt})}\right) \\ &\quad\times\frac{1}{\hat{p}_{Ta}^2(\vec{r}_{zt})}\,d\phi d\hat{p}_T dz_t\end{aligned}$$

and $\vec{r}_{zt} = (p_{Tt}/z_t, \phi, \hat{p}_T, k_T)$. The $\hat{x}_h(k_T)|_{p_{Tt},p_{Ta}}$ is evaluated as

$$\hat{x}_h(k_T)|_{p_{Tt},p_{Ta}} = \left.\frac{\langle\hat{p}_{Ta}\rangle}{\langle\hat{p}_{Tt}\rangle}\right|_{p_{Tt},p_{Ta}} = \frac{\mathcal{X}_a(1)}{\mathcal{X}_a(0)}\,\frac{\mathcal{X}_t(0)}{\mathcal{X}_t(1)}, \tag{48}$$

where

$$\begin{aligned}\mathcal{X}_t(n) &= \int_{p_{Tt}}^{\sqrt{s}/2}\hat{p}_{Tt}^{n-1}D_\pi^q\!\left(\frac{p_{Tt}}{\hat{p}_{Tt}}\right)\int_0^{\sqrt{s}/2}\Sigma_q(\hat{p}_T) \\ &\quad\times\int_0^{\pi}\hat{p}_n(\vec{r}_t)G(\hat{p}_n(\vec{r}_t))\cdot D_\pi^q\!\left(\frac{p_{Ta}}{\hat{p}_{Ta}(\vec{r}_t)}\right) \\ &\quad\times\frac{1}{\hat{p}_{Ta}^2(\vec{r}_t)}\,d\phi d\hat{p}_T\hat{p}_{Tt} \\ \mathcal{X}_a(n) &= \int_{p_{Ta}}^{\sqrt{s}/2}\hat{p}_{Ta}^{n-1}D_\pi^q\!\left(\frac{p_{Ta}}{\hat{p}_{Ta}}\right)\int_0^{\sqrt{s}/2}\Sigma_q(\hat{p}_T) \\ &\quad\times\int_0^{\pi}\hat{p}_n(\vec{r}_a)G(\hat{p}_n(\vec{r}_a))\cdot D_\pi^q\!\left(\frac{p_{Tt}}{\hat{p}_{Tt}(\vec{r}_a)}\right) \\ &\quad\times\frac{1}{\hat{p}_{Tt}^2(\vec{r}_a)}\,d\phi d\hat{p}_T\hat{p}_{Ta}.\end{aligned}$$

We have tested the above formulae on PYTHIA simulation. We have generated events with $\sqrt{\langle k_T^2 \rangle} = 3$ GeV/c and evaluated the partons' momenta unbalance variation with p_{Tt} for fixed $3 < p_{Ta} < 4$ GeV/c bin. The results from the PYTHIA simulation (solid points on Fig. 24) are compared to calculation based on Eq. (48) (solid line on Fig. 24). The magnitude of momentum unbalance saturates at $p_{Tt} \approx 10$ GeV/c around $\sqrt{\langle k_{Tx}^2 \rangle}$ and then starts to decrease. The maximum value depends on the k_T magnitude and on the asymmetry between p_{Tt} and p_{Ta}. Eventually, the unbalance should vanish at high p_{Tt} as a consequence of $\Sigma_q(\hat{p}_T)$ flattening.

The comparison of $\langle z_t \rangle$ and $\langle z_a \rangle$ found in PYTHIA and derived according to Eq. (47) is shown in Fig. 25. The overall agreement between the PYTHIA simulations and the calculation is excellent. The small deviations may be attributed to the fact that in the PYTHIA simulation, 1 GeV/c-wide bins were used for trigger and associated particle identification, whereas the calculation was performed for fixed values of p_{Tt} and p_{Ta}.

The last missing piece of information needed before solving Eq. (22) is the fragmentation function D_π^q and unsmeared $\Sigma_q(\hat{p}_T)$. The description of how this knowledge was extracted from the data is a subject of the next section.

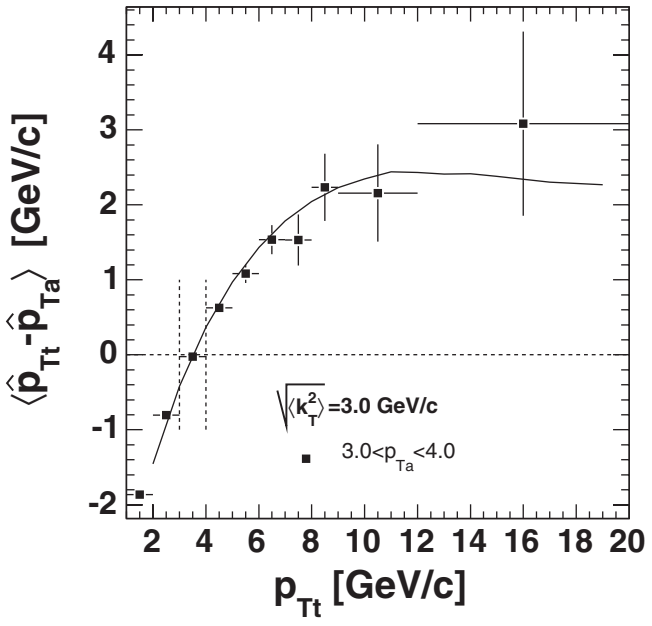

FIG. 24. PYTHIA simulated average momentum unbalance for the associated particles in $3.0 < p_{Ta} < 4.0$ GeV/c bin and calculated according Eq. (48). The two vertical dashed line indicates the range where p_{Tt} and p_{Ta} bins are equal and the parton momenta unbalance vanishes (fixed correlations).

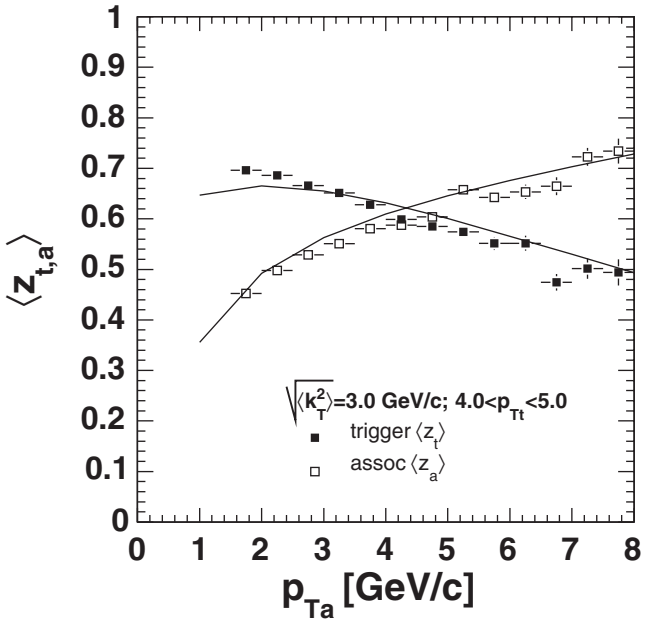

FIG. 25. Average z of a trigger and associated particle as a function of p_{Ta} from PYTHIA and according Eq. (47).

VII. CORRECTED $\langle k_T \rangle$ RESULTS

The $\hat{x}_h^{-1} \langle z_t \rangle \sqrt{\langle k_T^2 \rangle}$ extracted according to Eq. (22) for various p_{Tt} and p_{Ta} are shown in Fig. 16 and 17. In order to extract $\sqrt{\langle k_T^2 \rangle}$ values we have solved

$$x_h^{-1} \sqrt{\langle p_{out}^2 \rangle - \langle j_{Ty}^2 \rangle (x_h^2 + 1)} - \hat{x}_h^{-1} \langle z_t \rangle \sqrt{\langle k_T^2 \rangle} = 0 \quad (49)$$

for $\sqrt{\langle k_T^2 \rangle}$ where the $\langle z_t \rangle$ and $\hat{x}_h = \langle \hat{p}_{Ta} \rangle / \langle \hat{p}_{Tt} \rangle$ are evaluated according Eq. (47) and (48) respectively. These two quantities depend on $\sqrt{\langle k_T^2 \rangle}$ so we solved Eq. (49) iteratively by varying a $\sqrt{\langle k_T^2 \rangle}$ value and in every step the $\langle z_t \rangle$ and $\hat{x}_h$ were recalculated. To do so we need to know the unsmeared final state parton spectrum $\Sigma_q(\hat{p}_T)$ and the fragmentation function. For the latter we used the LEP data (see Fig. 22) where the fragmentation functions of gluon and quark jets were measured in e^+e^- collision at $\sqrt{s} = 180$ GeV. We have chosen

$$D_\pi^q \propto z^{-\alpha}(1 - z)^\beta (1 + z)^{-\gamma} \quad (50)$$

form used e.g. in [52] and extracted α, β, and γ parameters from the fit to distributions shown in Fig. 22 and Table VIII.

For a given set of parameters α, β, and γ the power of the unsmeared final state parton spectra $\Sigma_q(\hat{p}_T)$ was evaluated from the fit formula Eq. (27) to the single inclusive π^0 invariant cross section [43]. Here we used the simplified k_T smearing

$$f'_q(\hat{p}_{\mathrm{Tt}}) = \frac{1}{\hat{p}_{\mathrm{Tt}}}\Sigma'_q(\hat{p}_{\mathrm{Tt}}) = \frac{1}{\hat{p}_{\mathrm{T}}}\Sigma_q(\hat{p}_{\mathrm{T}}) \otimes \exp\frac{-(\hat{p}_{\mathrm{T}} - \hat{p}_{\mathrm{Tt}})^2}{\langle k_{\mathrm{Tx}}^2\rangle}$$

and for the fixed value of $\sqrt{\langle k_{\mathrm{T}}^2\rangle} = \sqrt{2}\sqrt{\langle k_{\mathrm{Tx}}^2\rangle} = 2.5$ GeV/c the power n of $\Sigma q(\hat{p}_{\mathrm{T}})$ distribution was determined.

The measurement of the fragmentation functions at LEP was done separately for quark and gluon jets and the slopes of these two $D(z)$ distributions are different. Quark jets produce a significantly harder spectrum than gluon jets (see Fig. 22). Since the relative abundance of quark and gluon jets at $\sqrt{s} = 200$ GeV is not known, for the final results we assumed that the numbers of quark and gluon jets are equal; the final $D(z)$ uses the averaged parameter values between quark and gluon and the difference was used as a measure of the systematic uncertainty.

Resulting $\sqrt{\langle k_{\mathrm{T}}^2\rangle}$ values for $3 < p_{\mathrm{Tt}} < 4$ GeV/c and $5 < p_{\mathrm{Tt}} < 10$ GeV/c as a function of p_{Ta} are shown in Fig. 26 and Table IX. The solid and dashed lines bracket the systematic error due to the unknown ratio of quark and gluon jets. These data points correspond to the uncorrected $\hat{x}_{\mathrm{h}}^{-1}\langle z_{\mathrm{t}}\rangle\sqrt{\langle k_{\mathrm{T}}^2\rangle}$ values shown in Fig. 16. The $\sqrt{\langle k_{\mathrm{T}}^2\rangle}$ values for varying p_{Tt} corresponding to the data of Fig. 17 are shown in Fig. 27 and Table X. The solid lines bracket the systematic error due to the unknown ratio of quark and gluon jets. It is evident that unfolded $\sqrt{\langle k_{\mathrm{T}}^2\rangle}$ values reveal, within the error bars, no dependence neither on p_{Ta} nor on p_{Tt}.

We compared the $\sqrt{\langle k_{\mathrm{T}}^2\rangle}$ data obtained in this analysis to $\sqrt{\langle k_{\mathrm{T}}^2\rangle}$ values found by the CCOR Collaboration at $\sqrt{s} = 62.4$ GeV [1] (empty triangles on Fig. 27). Although the trend with p_{Tt} seems to be similar the overall magnitude at $\sqrt{s} = 200$ GeV is significantly higher.

The $\langle z_{\mathrm{t}}\rangle$ and $\hat{x}_{\mathrm{h}}$ values from the iterative solution of Eq. (49) as a function of the π^0 trigger momenta p_{Tt} and associated momenta p_{Ta} are shown in Fig. 28 and 29 and Tables XI and XII. There is an opposite trend; whereas the $\langle z_{\mathrm{t}}\rangle$ rises with p_{Tt} it is falling with p_{Ta}. It is an interesting consequence of two effects: competition between steeply falling final state parton spectra and rising fragmentation function with parton momentum. Secondly, the detection of trigger particle biases the $\vec{k}_{\mathrm{T}}$ vector in the direction of the trigger jet as discussed in Sec. VI B.

TABLE VIII. Extracted values of $D(z)$ parameters according Eq. (50) from the fit to the LEP data (see Fig. 22) and power n of the unsmeared final state parton spectra $\Sigma_q(\hat{p}_{\mathrm{T}})$ extracted from the fit to the single inclusive π^0 invariant cross section [43] for corresponding fragmentation function and fixed value of $\sqrt{\langle k_{\mathrm{T}}^2\rangle} = 2.5$ GeV/c.

	Gluon	Quark	(gluon + quark)/2
α	0.16	0.49	0.32
β	0.88	0.57	0.72
γ	13.29	8.00	10.65
n	7.53	7.28	7.40

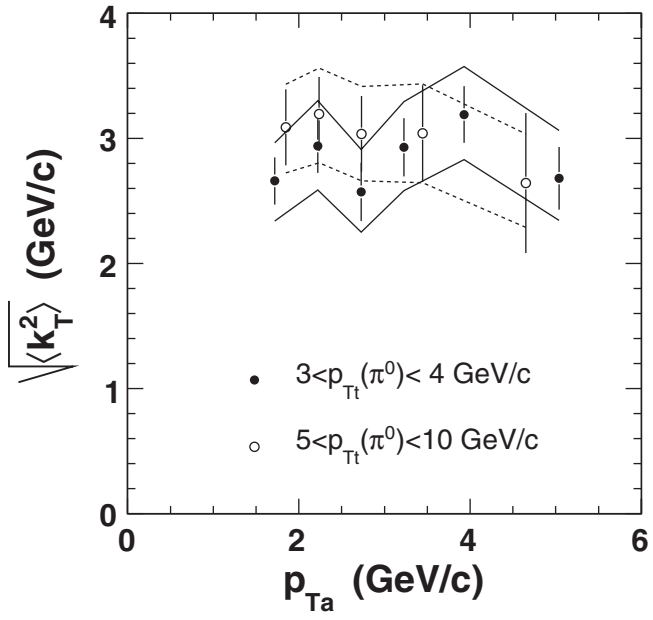

FIG. 26. $\sqrt{\langle k_{\mathrm{T}}^2\rangle}$ values corresponding to Fig. 16 as a solution to Eq. (49) for trigger π^0 in $3 < p_{\mathrm{Tt}} < 4$ GeV/c (solid symbols) and $5 < p_{\mathrm{Tt}} < 10$ GeV/c (open symbols) range. The solid and dashed lines bracket the systematic uncertainty due to the unknown ratio of quark and gluon jets, for the solid and open symbols, respectively.

The p_{Tt} averaged value of $\sqrt{\langle k_{\mathrm{T}}^2\rangle}$ (Fig. 27) is compared to the average parton-pair momentum, $\langle \hat{p}_{\mathrm{n}}\rangle = \langle p_{\mathrm{T}}\rangle$pair, presented in [33] (see Fig. 30). The value of $\langle p_{\mathrm{T}}\rangle$ pair is determined as a sum of the two partons' $\langle k_{\mathrm{T}}\rangle$. In the present

TABLE IX. The $\hat{x}_{\mathrm{h}}^{-1}\langle z_{\mathrm{t}}\rangle\sqrt{\langle k_{\mathrm{T}}^2\rangle}$ and $\sqrt{\langle k_{\mathrm{T}}^2\rangle}$ values as a function of p_{Ta} for two different trigger π^0 transverse momentum bins shown in Fig. 16 and Fig. 26. All units in rad and GeV/c.

$3 < p_{\mathrm{Tt}} < 4$ p_{Ta}	$\frac{\langle z_{\mathrm{t}}\rangle\sqrt{\langle k_{\mathrm{T}}^2\rangle}}{\hat{x}_{\mathrm{h}}}$	$\sqrt{\langle k_{\mathrm{T}}^2\rangle}$
1.7	1.76 ± 0.12	2.66 ± 0.19
2.2	1.74 ± 0.13	2.94 ± 0.22
2.7	1.37 ± 0.13	2.57 ± 0.23
3.2	1.45 ± 0.12	2.93 ± 0.23
3.9	1.44 ± 0.11	3.19 ± 0.23
5.0	1.04 ± 0.10	2.68 ± 0.25
$5 < p_{\mathrm{Tt}} < 10$ p_{Ta}	$\frac{\langle z_{\mathrm{t}}\rangle\sqrt{\langle k_{\mathrm{T}}^2\rangle}}{\hat{x}_{\mathrm{h}}}$	$\sqrt{\langle k_{\mathrm{T}}^2\rangle}$
1.9	2.69 ± 0.37	3.09 ± 0.30
2.2	2.54 ± 0.31	3.19 ± 0.30
2.7	2.13 ± 0.26	3.04 ± 0.30
3.4	1.89 ± 0.27	3.04 ± 0.38
4.7	1.41 ± 0.30	2.64 ± 0.56

TABLE X. Values of $\hat{x}_h^{-1}\langle z_t\rangle\sqrt{\langle k_T^2\rangle}$ and $\sqrt{\langle k_T^2\rangle}$ for various trigger particle p_{Tt} and associated momenta in the $1.4 < p_{Ta} < 5.0$ GeV/c region shown in Fig. 17 and 27.

p_{Tt} GeV/c	$\hat{x}_h^{-1}\langle z_t\rangle\sqrt{\langle k_T^2\rangle}$ GeV/c	$\sqrt{\langle k_T^2\rangle}$ GeV/c
3.22	1.63 ± 0.08	2.79 ± 0.13 ± 0.35
3.89	1.66 ± 0.08	2.57 ± 0.11 ± 0.33
4.90	1.89 ± 0.13	2.66 ± 0.17 ± 0.35
5.91	2.06 ± 0.19	2.74 ± 0.20 ± 0.34
7.24	2.17 ± 0.25	2.83 ± 0.25 ± 0.32
8.34	2.53 ± 0.62	3.11 ± 0.60 ± 0.33

analysis the $\sqrt{\langle k_T^2\rangle}$ is determined and thus the value of $\langle p_T\rangle$ *pair* is evaluated as $\langle p_T\rangle_{pair} = \sqrt{2}\times\langle k_T\rangle = \sqrt{\pi/2}\times\sqrt{\langle k_T^2\rangle}$.

The present value of $\langle p_T\rangle$ *pair*

$$\langle p_T\rangle_{pair} = 3.36 \pm 0.09(\text{stat}) \pm 0.43(\text{sys})\ \text{GeV/c}$$

appears to be in a good agreement with the lower energy dijet and dilepton measurements or the higher energy measurement in diphoton production [54]. A UA2 measurement of $\langle p_T\rangle$ of Z^0 production at $\sqrt{s} \sim 600$ GeV gives 8.6 ± 1.5 GeV/c [55,56].

VIII. SUMMARY

We have made the first measurement of jet j_T and k_T for $p + p$ collisions at $\sqrt{s} = 200$ GeV using the method of two-particle correlations. Analysis of the angular widths of the near-side peak in the correlation function has determined that the jet-fragmentation transverse momentum j_T is constant with trigger particle p_{Tt} and the extracted value $\sqrt{\langle j_T^2\rangle} = 585 \pm 6(\text{stat}) \pm 15(\text{sys})$ MeV/c is comparable with previous lower $\sqrt{s}$ measurements. The width of the

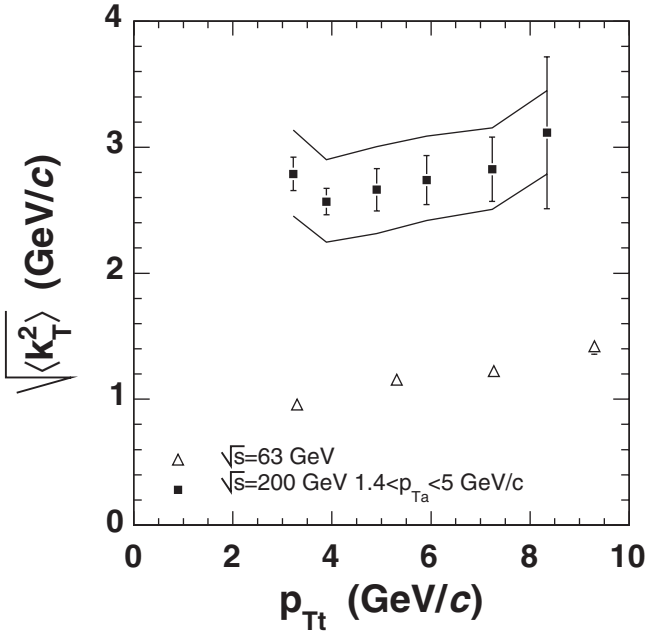

FIG. 27. $\sqrt{\langle k_T^2\rangle}$ values corresponding to Fig. 17 as a solution to Eq. (49) for associated particles in $1.4 < p_{Ta} < 5$ GeV/c region (solid symbols). The solid lines bracket the systematic error due to the unknown ratio of quark and gluon jets. The CCOR measurement at $\sqrt{s} = 62.4$ GeV [1] (empty triangles).

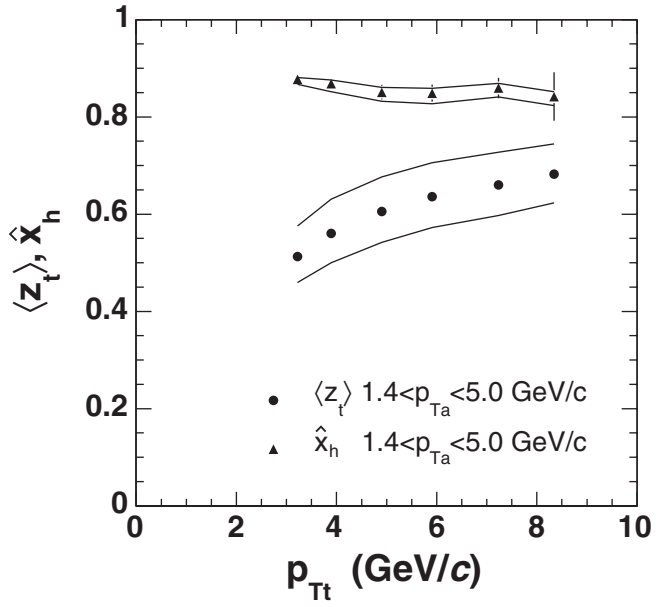

FIG. 28. $\langle z_t\rangle$ and $\hat{x}_h$ as a function of p_{Tt} for the $1.4 < p_{Ta} < 5.0$ GeV/c associated region. The data values are shown in Table XI.

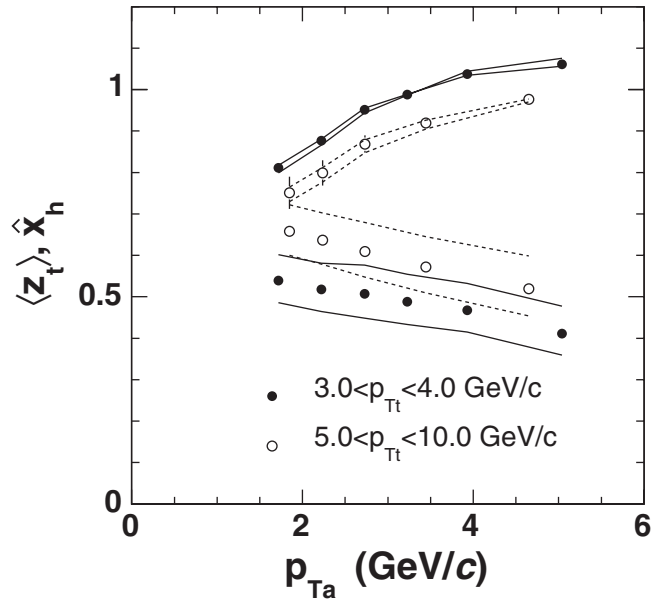

FIG. 29. The values of $\hat{x}_h$(upper two curves) and $\langle z_t\rangle$ (lower two curves) as a function of p_{Ta} are shown as solutions of Eq. (48) for $3 < p_{Tt} < 4$ GeV/c and $5 < p_{Tt} < 10$ GeV/c. Equation (20) defines $\langle z_t\rangle$ and $\hat{x}_h$. The data values are shown in Table XII.

TABLE XI. The $\langle z_t \rangle$ and $\hat{x}_h$ values with p_{Tt} shown in Fig. 28.

p_{Tt} (GeV/c)	$\langle z_t \rangle$	$\hat{x}_h$
3.22	$0.51 \pm 4 \times 10^{-3} \pm 0.06$	0.88 ± 0.01
3.89	$0.56 \pm 2 \times 10^{-3} \pm 0.07$	0.87 ± 0.01
4.90	$0.61 \pm 1 \times 10^{-3} \pm 0.07$	0.85 ± 0.01
5.91	$0.64 \pm 1 \times 10^{-4} \pm 0.07$	0.85 ± 0.02
7.24	$0.66 \pm 1 \times 10^{-3} \pm 0.07$	0.86 ± 0.02
8.34	$0.68 \pm 5 \times 10^{-3} \pm 0.06$	0.84 ± 0.05

TABLE XII. The $\langle z_t \rangle$ and $\hat{x}_h$ values with p_{Ta} for two trigger π^0 momenta bins as shown on Fig. 29.

$3 < p_{Tt} < 4$ GeV/c		
p_{Ta}	$\langle z_t \rangle$	$\hat{x}_h$
1.72	$0.54 \pm 8 \times 10^{-3} \pm 0.06$	0.81 ± 0.01
2.22	$0.52 \pm 6 \times 10^{-3} \pm 0.06$	0.88 ± 0.01
2.73	$0.51 \pm 1 \times 10^{-3} \pm 0.07$	0.95 ± 0.01
3.23	$0.49 \pm 1 \times 10^{-3} \pm 0.06$	0.99 ± 0.01
3.93	$0.47 \pm 5 \times 10^{-3} \pm 0.06$	1.04 ± 0.01
5.04	$0.41 \pm 6 \times 10^{-3} \pm 0.06$	1.06 ± 0.01
$5 < p_{Tt} < 10$ GeV/c		
p_{Ta}	$\langle z_t \rangle$	$\hat{x}_h$
1.85	$0.66 \pm 4 \times 10^{-3} \pm 0.06$	0.75 ± 0.04
2.24	$0.64 \pm 1 \times 10^{-3} \pm 0.06$	0.80 ± 0.03
2.73	$0.61 \pm 2 \times 10^{-3} \pm 0.07$	0.87 ± 0.02
3.44	$0.57 \pm 2 \times 10^{-3} \pm 0.07$	0.92 ± 0.02
4.65	$0.52 \pm 5 \times 10^{-3} \pm 0.08$	0.98 ± 0.01

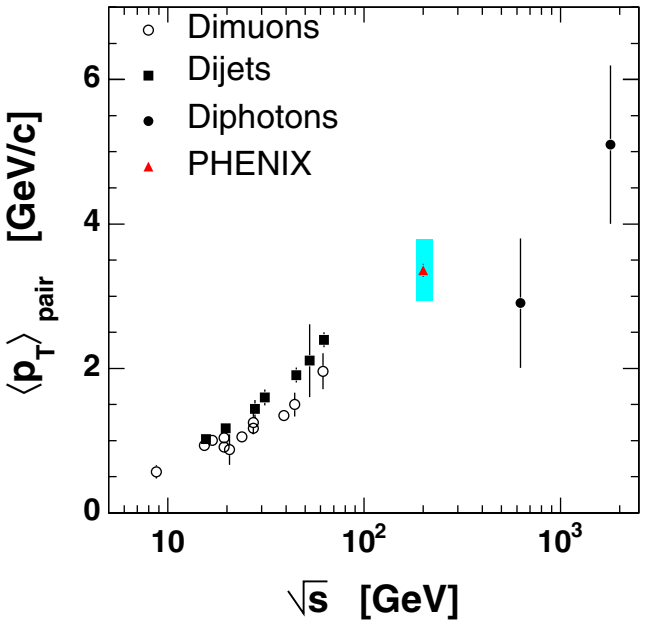

FIG. 30 (color online). Compilation of mean pair p_T measurements [33] and comparisons to the $\langle p_T \rangle$ pair measured in this analysis.

away-side peak is shown to be a measure of the convolution of j_T with the jet momentum fraction z and the partonic transverse momentum k_T. $\langle z_t \rangle$ is determined through a combined analysis of the measured π^0 inclusive and associated spectra using the jet-fragmentation functions from e^+e^- measurements. The average of $\langle z_t \rangle$ from the gluon and quark fragmentation functions is used and the difference is taken as the measure of the systematic error. The final extracted values of k_T are then determined to be also independent of the transverse momentum of the trigger π^0, in the range measured, with values of $\sqrt{\langle k_T^2 \rangle} = 2.68 \pm 0.07(\text{stat}) \pm 0.34(\text{sys})$ GeV/c.

ACKNOWLEDGMENTS

We thank the staff of the Collider-Accelerator and Physics Departments at Brookhaven National Laboratory and the staff of the other PHENIX participating institutions for their vital contributions. We acknowledge support from the Department of Energy, Office of Science, Office of Nuclear Physics, the National Science Foundation, Abilene Christian University Research Council, Research Foundation of SUNY, and Dean of the College of Arts and Sciences, Vanderbilt University (USA), Ministry of Education, Culture, Sports, Science, and Technology and the Japan Society for the Promotion of Science (Japan), Conselho Nacional de Desenvolvimento Científico e Tecnológico and Fundação de Amparo à Pesquisa do Estado de São Paulo (Brazil), Natural Science Foundation of China (People's Republic of China), Centre National de la Recherche Scientifique, Commissariat à l'Énergie Atomique, and Institut National de Physique Nucléaire et de Physique des Particules (France), Ministry of Industry, Science and Tekhnologies, Bundesministerium für Bildung und Forschung, Deutscher Akademischer Austausch Dienst, and Alexander von Humboldt Stiftung (Germany), Hungarian National Science Fund, OTKA (Hungary), Department of Atomic Energy (India), Israel Science Foundation (Israel), Korea Research Foundation, Center for High Energy Physics, and Korea Science and Engineering Foundation (Korea), Ministry of Education and Science, Russia Academy of Sciences, Federal Agency of Atomic Energy (Russia), V. R. and the Wallenberg Foundation (Sweden), the U.S. Civilian Research and Development Foundation for the Independent States of the Former Soviet Union, the US-Hungarian NSF-OTKA-MTA, and the US-Israel Binational Science Foundation.

APPENDIX A: FIRST AND SECOND MOMENTS OF NORMALLY DISTRIBUTED QUANTITIES

Let x be a 1D variable with normal (Gaussian) distribution and $r = \sqrt{x^2 + y^2}$ is a 2D variable with x and y of

normal distribution then the following relations can be easily derived.

$$\begin{array}{llll} \langle x\rangle & = & 0 & \langle r\rangle = \sqrt{\frac{\pi}{2}}\sigma_1 \\ \langle |x|\rangle & = & \sqrt{\frac{2}{\pi}}\sigma_1 & \langle |r|\rangle = \langle r\rangle \\ \langle x\rangle^2 & = & \sigma_1^2 & \langle r\rangle^2 = 2\sigma_1^2 \equiv \sigma_2^2 \end{array}$$

Both $\vec{j}_T$ and $\vec{k}_T$ are two-dimensional vectors. We assume Gaussian distributed x and y components and thus the mean value $\langle k_{Tx}\rangle$ and $\langle k_{Ty}\rangle$ is equal to zero. The nonzero moments of 2D Gaussian distribution are e.g. the root mean squares $\sqrt{\langle j_T^2\rangle}$, $\sqrt{\langle k_T^2\rangle}$ or the mean absolute values of the $\vec{j}_T$, $\vec{k}_T$ projections into the perpendicular plane to the jet axes $\langle |j_{Ty}|\rangle$ and $\langle |k_{Ty}|\rangle$. Note that there are a trivial correspondences

$$\sqrt{\langle k_T^2\rangle} = \frac{2}{\sqrt{\pi}}\langle k_T\rangle = \sqrt{\pi}\langle |k_{Ty}|\rangle. \quad (51)$$

APPENDIX B: THE CORRECT WAY TO ANALYZE THE AZIMUTHAL CORRELATION FUNCTION

Construction and fitting of the two-particle azimuthal correlation function is discussed in Sec. IV. Traditionally the correlation function is fitted by two Gaussian functions—one for intrajet correlation (near peak) and one for the interjet correlations (away-side peak). From the extracted variances of the Gaussian functions the j_T and p_{out} magnitudes are extracted.

There is, however, a fundamental problem with this approach. The p_{out}-vector defined in Eq. (17) is equal to $p_{Ta}\sin\Delta\phi$ event by event. However, we measure the width of the correlation peak and this corresponds to $\sqrt{\langle\Delta\phi^2\rangle} = \sigma_A$. The relation $\sqrt{\langle p_{out}^2\rangle} \approx p_{Ta}\sin\sigma_A$ is not a good approximation for $\sigma_A > 0.4$ rad (see Fig. 31). The assumption that the away-side correlation has a Gaussian shape is also good only for small values of σ_A (see Fig. 31).

One way of relating $\sqrt{\langle p_{out}^2\rangle}$ and σ_A was proposed e.g. by Peter Levai [48] and used in several other analyzes. Since $\sqrt{\langle p_{out}^2\rangle} = p_{Ta}\sqrt{\langle\sin^2\Delta\phi\rangle}$ one possibility how to relate p_{out} and σ_A is to expand

$$\langle\sin^2\Delta\phi\rangle = \left\langle \Delta\phi^2 - \frac{1}{3}\Delta\phi^4 + \frac{2}{45}\Delta\phi^6 \ldots \right\rangle$$
$$= \sigma_A^2 - \sigma_A^4 + \frac{2}{3}\sigma_A^6 \ldots,$$

where we assumed a Gaussian distribution of $\Delta\phi$. The comparison of $p_{Ta}\cdot(\sigma_A^2 - \sigma_A^4 + \frac{2}{3}\sigma_A^6\ldots)$ with the true p_{out} magnitude (simple monte carlo) for various σ_A values is shown in Fig. 31. It is obvious that there is only a little

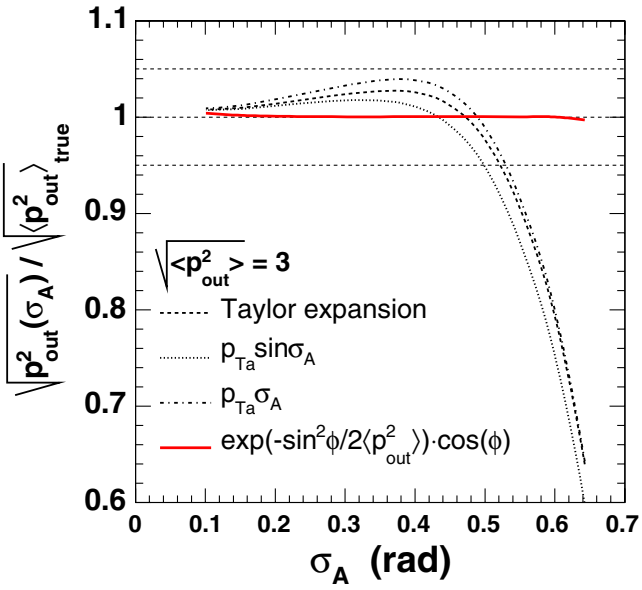

FIG. 31 (color online). The relative error on p_{out} determination from the azimuthal correlation function based on the Taylor expansion of $\langle\sin\Delta\phi^2\rangle$ (dashed line), with an assumption of $\sqrt{\langle p_{out}^2\rangle} = p_{Ta}\sin\sigma_A$ (dotted line) and $\sqrt{\langle p_{out}^2\rangle} = p_{Ta}\sigma_A$ (dotted-dashed line). The solid red line corresponds to $\sqrt{\langle p_{out}^2\rangle}$ from Eq. (23).

difference between $\sqrt{\langle p_{out}^2\rangle} = p_{Ta}\sin\sigma_A$, $\sqrt{\langle p_{out}^2\rangle} = p_{Ta}\sigma_A$ and the Taylor series. In the region where $\sigma_A > 0.4$ rad, all approximations seems to be equally bad.

However, p_{out}, the only quantity with a truly Gaussian distribution (if we neglect the radiative corrections responsible for non-Gaussian tails in the p_{out} distribution which are anyway not relevant for the k_T analysis) can be directly extracted from the correlation function. With the assumption of Gaussian distribution in p_{out}, we can write the away-side $\Delta\phi$-distribution (normalized to unity) as

$$\left.\frac{dN_{away}}{d\Delta\phi}\right|_{\pi/2}^{3\pi/2} = \frac{dN}{dp_{out}}\frac{dp_{out}}{d\Delta\phi} = \frac{-p_{Ta}\cos\Delta\phi}{\sqrt{2\pi\langle p_{out}^2\rangle}\,\mathrm{Erf}\left(\frac{\sqrt{2}p_{Ta}}{\sqrt{\langle p_{out}^2\rangle}}\right)} \times \exp\left(-\frac{p_{Ta}^2\sin^2\Delta\phi}{2\langle p_{out}^2\rangle}\right).$$

This is the correct way of extracting a dimensional quantity from the azimuthal correlation function in the case of narrow associated bin. Similar line of arguments can be drawn also in the case of near peak. However, given the narrowness of the near-angle peak, the simple Gaussian approximation is good enough.

[1] A. L. S. Angelis *et al.* (CERN-Columbia-Oxford-Rockefeller Collaboration), Phys. Lett. B **97**, 163 (1980).
[2] P. Darriulat *et al.*, Nucl. Phys. **B107**, 429 (1976).
[3] M. Della Negra *et al.* (CERN-College de France-Heidelberg-Karlsruhe Collaboration), Nucl. Phys. **B127**, 1 (1977).
[4] K. Adcox *et al.* (PHENIX Collaboration), Phys. Rev. Lett. **88**, 022301 (2001).
[5] C. Adler *et al.* (STAR Collaboration), Phys. Rev. Lett. **89**, 202301 (2002).
[6] S. S. Adler *et al.* (PHENIX Collaboration), Phys. Rev. Lett. **91**, 072301 (2003).
[7] B. B. Back *et al.* (PHOBOS Collaboration), Phys. Rev. Lett. **91**, 072302 (2003).
[8] S. S. Adler *et al.* (PHENIX Collaboration), Phys. Rev. Lett. **91**, 072303 (2003).
[9] J. Adams *et al.* (STAR Collaboration), Phys. Rev. Lett. **91**, 072304 (2003).
[10] I. Arsene *et al.* (BRAHMS Collaboration), Phys. Rev. Lett. **91**, 072305 (2003).
[11] S. S. Adler *et al.* (PHENIX Collaboration), Phys. Rev. Lett. **91**, 182301 (2003).
[12] C. Adler *et al.* (STAR Collaboration), Phys. Rev. Lett. **90**, 032301 (2003).
[13] C. Adler *et al.* (STAR Collaboration), Phys. Rev. Lett. **90**, 082302 (2003).
[14] A. B. Migdal, Phys. Rev. **103**, 1811 (1956).
[15] X.-N. Wang and M. Gyulassy, Phys. Rev. Lett. **68**, 1480 (1992).
[16] X.-N. Wang, Phys. Rev. C **58**, 2321 (1998).
[17] R. Baier, Y. L. Dokshitzer, S. Peigne, and D. Schiff, Phys. Lett. B **345**, 277 (1995).
[18] B. G. Zakharov, JETP Lett. **63**, 952 (1996).
[19] C. A. Salgado and U. A. Wiedemann, Phys. Rev. Lett. **93**, 042301 (2004).
[20] J.-w. Qiu and I. Vitev, Phys. Lett. B **570**, 161 (2003).
[21] X.-N. Wang, Nucl. Phys. **A702**, 238 (2002).
[22] S. M. Berman, J. D. Bjorken, and J. B. Kogut, Phys. Rev. D **4**, 3388 (1971).
[23] J. F. Owens and J. D. Kimel, Phys. Rev. D **18**, 3313 (1978).
[24] J. F. Owens, E. Reya, and M. Gluck, Phys. Rev. D **18**, 1501 (1978).
[25] R. P. Feynman, R. D. Field, and G. C. Fox, Phys. Rev. D **18**, 3320 (1978).
[26] J. F. Owens, Rev. Mod. Phys. **59**, 465 (1987).
[27] G. Bunce, N. Saito, J. Soffer, and W. Vogelsang, Annu. Rev. Nucl. Part. Sci. **50**, 525 (2000).
[28] R. Cutler and D. W. Sivers, Phys. Rev. D **17**, 196 (1978).
[29] R. Cutler and D. W. Sivers, Phys. Rev. D **16**, 679 (1977).
[30] B. L. Combridge, J. Kripfganz, and J. Ranft, Phys. Lett. B **70**, 234 (1977).
[31] R. P. Feynman, R. D. Field, and G. C. Fox, Nucl. Phys. **B128**, 1 (1977).
[32] Y. L. Dokshitzer, V. A. Khoze, A. H. Mueller, and S. I. Troian, *Basics of Perturbative QCD* (Editions Frontieres, Gif-sur-Yvette, France, 1991), p. 274.
[33] L. Apanasevich *et al.*, Phys. Rev. D **59**, 074007 (1999).
[34] A. Kulesza, G. Sterman, and W. Vogelsang, Nucl. Phys. **A721**, C591 (2003).
[35] F. W. Busser *et al.*, Phys. Lett. B **46**, 471 (1973).
[36] R. Blankenbecler, S. J. Brodsky, and J. F. Gunion, Phys. Lett. B **42**, 461 (1972).
[37] D. Antreasyan *et al.*, Phys. Rev. D **19**, 764 (1979).
[38] P. Darriulat, Annu. Rev. Nucl. Part. Sci. **30**, 159 (1980).
[39] K. Adachi *et al.* (TOPAZ Collaboration), Phys. Lett. B **451**, 256 (1999).
[40] K. Adcox *et al.* (PHENIX Collaboration), Nucl. Instrum. Methods Phys. Res., Sect. A **499**, 469 (2003).
[41] L. Aphecetche *et al.* (PHENIX Collaboration), Nucl. Instrum. Methods Phys. Res., Sect. A **499**, 521 (2003).
[42] K. Adcox *et al.* (PHENIX Collaboration), Nucl. Instrum. Methods Phys. Res., Sect. A **499**, 489 (2003).
[43] S. S. Adler *et al.* (PHENIX Collaboration), Phys. Rev. Lett. **91**, 241803 (2003).
[44] M. Aizawa *et al.* (PHENIX Collaboration), Nucl. Instrum. Methods Phys. Res., Sect. A **499**, 508 (2003).
[45] S. S. Adler *et al.* (PHENIX Collaboration), Phys. Rev. C **69**, 034910 (2004).
[46] S. S. Adler *et al.* (PHENIX Collaboration), Phys. Rev. Lett. **94**, 082301 (2005).
[47] For relations between $\sqrt{\langle X^2\rangle}$ and $\langle|X_y|\rangle$, where X is any 2D quantity, see Appendix A
[48] P. Levai, G. Fai, and G. Papp, Phys. Lett. B 634, 383 (2006).
[49] G. W. van Apeldoorn *et al.*, Nucl. Phys. **B91**, 1 (1975).
[50] Note, however that the method was different. CCOR determined j_T and k_T from the slope and intercept of Eq. (21) with respect to $p_{T\mathrm{a}}$ at each value of $p_{T\mathrm{t}}$, with the implicit assumption that $\langle z_t\rangle\hat{x}_h^{-1} = 1$.
[51] X.-N. Wang, Phys. Lett. B **595**, 165 (2004).
[52] P. Abreu *et al.* (DELPHI Collaboration), Eur. Phys. J. C **13**, 573 (2000).
[53] G. Alexander *et al.* (OPAL Collaboration), Z. Phys. C **69**, 543 (1996).
[54] F. Abe *et al.* (CDF Collaboration), Phys. Rev. Lett. **70**, 2232 (1993).
[55] R. Ansari *et al.* (UA2 Collaboration), Phys. Lett. B **194**, 158 (1987).
[56] R. Ansari *et al.* (UA2 Collaboration), Z. Phys. C **41**, 395 (1988).

Azimuthal Angle Correlations for Rapidity Separated Hadron Pairs in d + Au Collisions at $\sqrt{s_{NN}} = 200$ GeV

S. S. Adler,[5] S. Afanasiev,[20] C. Aidala,[10] N. N. Ajitanand,[44] Y. Akiba,[21,40] A. Al-Jamel,[35] J. Alexander,[44] K. Aoki,[25] L. Aphecetche,[46] R. Armendariz,[35] S. H. Aronson,[5] R. Averbeck,[45] T. C. Awes,[36] V. Babintsev,[17] A. Baldisseri,[11] K. N. Barish,[6] P. D. Barnes,[28] B. Bassalleck,[34] S. Bathe,[6,31] S. Batsouli,[10] V. Baublis,[39] F. Bauer,[6] A. Bazilevsky,[5,41] S. Belikov,[19,17] M. T. Bjorndal,[10] J. G. Boissevain,[28] H. Borel,[11] M. L. Brooks,[28] D. S. Brown,[35] N. Bruner,[34] D. Bucher,[31] H. Buesching,[5,31] V. Bumazhnov,[17] G. Bunce,[5,41] J. M. Burward-Hoy,[28,27] S. Butsyk,[45] X. Camard,[46] P. Chand,[4] W. C. Chang,[2] S. Chernichenko,[17] C. Y. Chi,[10] J. Chiba,[21] M. Chiu,[10] I. J. Choi,[53] R. K. Choudhury,[4] T. Chujo,[5] V. Cianciolo,[36] Y. Cobigo,[11] B. A. Cole,[10] M. P. Comets,[37] P. Constantin,[19] M. Csanád,[13] T. Csörgő,[22] J. P. Cussonneau,[46] D. d'Enterria,[10] K. Das,[14] G. David,[5] F. Deák,[13] H. Delagrange,[46] A. Denisov,[17] A. Deshpande,[41] E. J. Desmond,[5] A. Devismes,[45] O. Dietzsch,[42] J. L. Drachenberg,[1] O. Drapier,[26] A. Drees,[45] A. Durum,[17] D. Dutta,[4] V. Dzhordzhadze,[47] Y. V. Efremenko,[36] H. En'yo,[40,41] B. Espagnon,[37] S. Esumi,[49] D. E. Fields,[34,41] C. Finck,[46] F. Fleuret,[26] S. L. Fokin,[24] B. D. Fox,[41] Z. Fraenkel,[52] J. E. Frantz,[10] A. Franz,[5] A. D. Frawley,[14] Y. Fukao,[25,40,41] S.-Y. Fung,[6] S. Gadrat,[29] M. Germain,[46] A. Glenn,[47] M. Gonin,[26] J. Gosset,[11] Y. Goto,[40,41] R. Granier de Cassagnac,[26] N. Grau,[19] S. V. Greene,[50] M. Grosse Perdekamp,[18,41] H.-Å. Gustafsson,[30] T. Hachiya,[16] J. S. Haggerty,[5] H. Hamagaki,[8] A. G. Hansen,[28] E. P. Hartouni,[27] M. Harvey,[5] K. Hasuko,[40] R. Hayano,[8] X. He,[15] M. Heffner,[27] T. K. Hemmick,[45] J. M. Heuser,[40] P. Hidas,[22] H. Hiejima,[18] J. C. Hill,[19] R. Hobbs,[34] W. Holzmann,[44] K. Homma,[16] B. Hong,[23] A. Hoover,[35] T. Horaguchi,[40,41,48] T. Ichihara,[40,41] V. V. Ikonnikov,[24] K. Imai,[25,40] M. Inaba,[49] M. Inuzuka,[8] D. Isenhower,[1] L. Isenhower,[1] M. Ishihara,[40] M. Issah,[44] A. Isupov,[20] B. V. Jacak,[45] J. Jia,[45] O. Jinnouchi,[40,41] B. M. Johnson,[5] S. C. Johnson,[27] K. S. Joo,[32] D. Jouan,[37] F. Kajihara,[8] S. Kametani,[8,51] N. Kamihara,[40,48] M. Kaneta,[41] J. H. Kang,[53] K. Katou,[51] T. Kawabata,[8] A. V. Kazantsev,[24] S. Kelly,[9,10] B. Khachaturov,[52] A. Khanzadeev,[39] J. Kikuchi,[51] D. J. Kim,[53] E. Kim,[43] G.-B. Kim,[26] H. J. Kim,[53] E. Kinney,[9] A. Kiss,[13] E. Kistenev,[5] A. Kiyomichi,[40] C. Klein-Boesing,[31] H. Kobayashi,[41] L. Kochenda,[39] V. Kochetkov,[17] R. Kohara,[16] B. Komkov,[39] M. Konno,[49] D. Kotchetkov,[6] A. Kozlov,[52] P. J. Kroon,[5] C. H. Kuberg,[1,*] G. J. Kunde,[28] K. Kurita,[40] M. J. Kweon,[23] Y. Kwon,[53] G. S. Kyle,[35] R. Lacey,[44] J. G. Lajoie,[19] Y. Le Bornec,[37] A. Lebedev,[19,24] S. Leckey,[45] D. M. Lee,[28] M. J. Leitch,[28] M. A. L. Leite,[42] X. H. Li,[6] H. Lim,[43] A. Litvinenko,[20] M. X. Liu,[28] C. F. Maguire,[50] Y. I. Makdisi,[5] A. Malakhov,[20] V. I. Manko,[24] Y. Mao,[38,40] G. Martinez,[46] H. Masui,[49] F. Matathias,[45] T. Matsumoto,[8,51] M. C. McCain,[1] P. L. McGaughey,[28] Y. Miake,[49] T. E. Miller,[50] A. Milov,[45] S. Mioduszewski,[5] G. C. Mishra,[15] J. T. Mitchell,[5] A. K. Mohanty,[4] D. P. Morrison,[5] J. M. Moss,[28] D. Mukhopadhyay,[52] M. Muniruzzaman,[6] S. Nagamiya,[21] J. L. Nagle,[9,10] T. Nakamura,[16] J. Newby,[47] A. S. Nyanin,[24] J. Nystrand,[30] E. O'Brien,[5] C. A. Ogilvie,[19] H. Ohnishi,[40] I. D. Ojha,[3,50] H. Okada,[25,40] K. Okada,[40,41] A. Oskarsson,[30] I. Otterlund,[30] K. Oyama,[8] K. Ozawa,[8] D. Pal,[52] A. P. T. Palounek,[28] V. Pantuev,[45] V. Papavassiliou,[35] J. Park,[43] W. J. Park,[23] S. F. Pate,[35] H. Pei,[19] V. Penev,[20] J.-C. Peng,[18] H. Pereira,[11] V. Peresedov,[20] A. Pierson,[34] C. Pinkenburg,[5] R. P. Pisani,[5] M. L. Purschke,[5] A. K. Purwar,[45] J. M. Qualls,[1] J. Rak,[19] I. Ravinovich,[52] K. F. Read,[36,47] M. Reuter,[45] K. Reygers,[31] V. Riabov,[39] Y. Riabov,[39] G. Roche,[29] A. Romana,[26,*] M. Rosati,[19] S. S. E. Rosendahl,[30] P. Rosnet,[29] V. L. Rykov,[40] S. S. Ryu,[53] N. Saito,[25,40,41] T. Sakaguchi,[8,51] S. Sakai,[49] V. Samsonov,[39] L. Sanfratello,[34] R. Santo,[31] H. D. Sato,[25,40] S. Sato,[5,49] S. Sawada,[21] Y. Schutz,[46] V. Semenov,[17] R. Seto,[6] T. K. Shea,[5] I. Shein,[17] T.-A. Shibata,[40,48] K. Shigaki,[16] M. Shimomura,[49] A. Sickles,[45] C. L. Silva,[42] D. Silvermyr,[28] K. S. Sim,[23] A. Soldatov,[17] R. A. Soltz,[27] W. E. Sondheim,[28] S. P. Sorensen,[47] I. V. Sourikova,[5] F. Staley,[11] P. W. Stankus,[36] E. Stenlund,[30] M. Stepanov,[35] A. Ster,[22] S. P. Stoll,[5] T. Sugitate,[16] J. P. Sullivan,[28] S. Takagi,[49] E. M. Takagui,[42] A. Taketani,[40,41] K. H. Tanaka,[21] Y. Tanaka,[33] K. Tanida,[40] M. J. Tannenbaum,[5] A. Taranenko,[44] P. Tarján,[12] T. L. Thomas,[34] M. Togawa,[25,40] J. Tojo,[40] H. Torii,[25,41] R. S. Towell,[1] V.-N. Tram,[26] I. Tserruya,[52] Y. Tsuchimoto,[16] H. Tydesjö,[30] N. Tyurin,[17] T. J. Uam,[32] H. W. van Hecke,[28] J. Velkovska,[5] M. Velkovsky,[45] V. Veszprémi,[12] A. A. Vinogradov,[24] M. A. Volkov,[24] E. Vznuzdaev,[39] X. R. Wang,[15] Y. Watanabe,[40,41] S. N. White,[5] N. Willis,[37] F. K. Wohn,[19] C. L. Woody,[5] W. Xie,[6] A. Yanovich,[17] S. Yokkaichi,[40,41] G. R. Young,[36] I. E. Yushmanov,[24] W. A. Zajc,[10,†] C. Zhang,[10] S. Zhou,[7] J. Zimányi,[22] L. Zolin,[20] and X. Zong[19]

(PHENIX Collaboration)

[1]*Abilene Christian University, Abilene, Texas 79699, USA*
[2]*Institute of Physics, Academia Sinica, Taipei 11529, Taiwan*

 © 2006 The American Physical Society

[3]Department of Physics, Banaras Hindu University, Varanasi 221005, India
[4]Bhabha Atomic Research Centre, Bombay 400 085, India
[5]Brookhaven National Laboratory, Upton, New York 11973-5000, USA
[6]University of California-Riverside, Riverside, California 92521, USA
[7]China Institute of Atomic Energy (CIAE), Beijing, People's Republic of China
[8]Center for Nuclear Study, Graduate School of Science, University of Tokyo, 7-3-1 Hongo, Bunkyo, Tokyo 113-0033, Japan
[9]University of Colorado, Boulder, Colorado 80309, USA
[10]Columbia University, New York, New York 10027, and Nevis Laboratories, Irvington, New York 10533, USA
[11]Dapnia, CEA Saclay, F-91191, Gif-sur-Yvette, France
[12]Debrecen University, H-4010 Debrecen, Egyetem tér 1, Hungary
[13]ELTE, Eötvös Loránd University, H - 1117 Budapest, Pázmány P. s. 1/A, Hungary
[14]Florida State University, Tallahassee, Florida 32306, USA
[15]Georgia State University, Atlanta, Georgia 30303, USA
[16]Hiroshima University, Kagamiyama, Higashi-Hiroshima 739-8526, Japan
[17]IHEP Protvino, State Research Center of Russian Federation, Institute for High Energy Physics, Protvino, 142281, Russia
[18]University of Illinois at Urbana-Champaign, Urbana, Illinois 61801, USA
[19]Iowa State University, Ames, Iowa 50011, USA
[20]Joint Institute for Nuclear Research, 141980 Dubna, Moscow Region, Russia
[21]KEK, High Energy Accelerator Research Organization, Tsukuba, Ibaraki 305-0801, Japan
[22]KFKI Research Institute for Particle and Nuclear Physics of the Hungarian Academy of Sciences (MTA KFKI RMKI), H-1525 Budapest 114, POBox 49, Budapest, Hungary
[23]Korea University, Seoul, 136-701, Korea
[24]Russian Research Center "Kurchatov Institute", Moscow, Russia
[25]Kyoto University, Kyoto 606-8502, Japan
[26]Laboratoire Leprince-Ringuet, Ecole Polytechnique, CNRS-IN2P3, Route de Saclay, F-91128, Palaiseau, France
[27]Lawrence Livermore National Laboratory, Livermore, California 94550, USA
[28]Los Alamos National Laboratory, Los Alamos, New Mexico 87545, USA
[29]LPC, Université Blaise Pascal, CNRS-IN2P3, Clermont-Fd, 63177 Aubiere Cedex, France
[30]Department of Physics, Lund University, Box 118, SE-221 00 Lund, Sweden
[31]Institut für Kernphysik, University of Muenster, D-48149 Muenster, Germany
[32]Myongji University, Yongin, Kyonggido 449-728, Korea
[33]Nagasaki Institute of Applied Science, Nagasaki-shi, Nagasaki 851-0193, Japan
[34]University of New Mexico, Albuquerque, New Mexico 87131, USA
[35]New Mexico State University, Las Cruces, New Mexico 88003, U.S., USA
[36]Oak Ridge National Laboratory, Oak Ridge, Tennessee 37831, USA
[37]IPN-Orsay, Universite Paris Sud, CNRS-IN2P3, BP1, F-91406, Orsay, France
[38]Peking University, Beijing, People's Republic of China
[39]PNPI, Petersburg Nuclear Physics Institute, Gatchina, Leningrad region, 188300, Russia
[40]RIKEN (The Institute of Physical and Chemical Research), Wako, Saitama 351-0198, Japan
[41]RIKEN BNL Research Center, Brookhaven National Laboratory, Upton, New York 11973-5000, USA
[42]Universidade de São Paulo, Instituto de Física, Caixa Postal 66318, São Paulo CEP05315-970, Brazil
[43]System Electronics Laboratory, Seoul National University, Seoul, South Korea
[44]Chemistry Department, Stony Brook University, SUNY, Stony Brook, New York 11794-3400, USA
[45]Department of Physics and Astronomy, Stony Brook University, SUNY, Stony Brook, New York 11794, USA
[46]SUBATECH (Ecole des Mines de Nantes, CNRS-IN2P3, Université de Nantes), BP 20722 - 44307, Nantes, France
[47]University of Tennessee, Knoxville, Tennessee 37996, USA
[48]Department of Physics, Tokyo Institute of Technology, Oh-okayama, Meguro, Tokyo 152-8551, Japan
[49]Institute of Physics, University of Tsukuba, Tsukuba, Ibaraki 305, Japan
[50]Vanderbilt University, Nashville, Tennessee 37235, USA
[51]Advanced Research Institute for Science and Engineering, Waseda University, 17 Kikui-cho, Shinjuku-ku, Tokyo 162-0044, Japan
[52]Weizmann Institute, Rehovot 76100, Israel
[53]Yonsei University, IPAP, Seoul 120-749, Korea

(Received 17 March 2006; published 8 June 2006)

Deuteron-gold (d + Au) collisions at the Relativistic Heavy Ion Collider provide ideal platforms for testing QCD theories in dense nuclear matter at high energy. In particular, models suggesting strong saturation effects for partons carrying small nucleon momentum fraction (x) predict modifications to jet production at forward rapidity (deuteron-going direction) in d + Au collisions. We report on two-particle azimuthal angle correlations between charged hadrons at forward/backward (deuteron/gold going direction) rapidity and charged hadrons at midrapidity in d + Au and p + p collisions at $\sqrt{s_{NN}} = 200$ GeV. Jet structures observed in the correlations are quantified in terms of the conditional yield and angular

width of away-side partners. The kinematic region studied here samples partons in the gold nucleus with $x \sim 0.1$ to ~ 0.01. Within this range, we find no x dependence of the jet structure in d + Au collisions.

DOI: 10.1103/PhysRevLett.96.222301 PACS numbers: 25.75.Dw, 25.75.Gz

Observations in d + Au collisions at $\sqrt{s_{NN}} = 200$ GeV at the Relativistic Heavy Ion Collider (RHIC) reveal a significant suppression of hadron production at forward rapidity (deuteron-going direction) relative to $p + p$ collisions scaled up by the equivalent number of nucleon-nucleon collisions (N_{coll}) [1–3]. This suppression is observed for hadrons with momentum transverse to the beam direction in the range $p_T \approx 1.5$–4 GeV/c. In contrast, measurements at midrapidity [4–7] and backward rapidity [1–3] show a modest enhancement relative to N_{coll} scaling in the same p_T range. Particle production at forward rapidity is sensitive to partons in the gold nucleus which carry a small nucleon momentum fraction (small Bjorken x). The suppression has generated significant theoretical interest including different calculational frameworks for understanding the data [8–11].

One such framework, the color glass condensate (CGC), attempts to describe the data in terms of gluon saturation [8]. At small x the probability of emitting an extra gluon is large and the number of gluons grows in a limited transverse area. When the transverse density becomes large, partons start to overlap and gluon-gluon fusion processes start to dominate the parton evolution in the hadronic wave functions. Thus the gluon density saturates. Since the nonlinear growth of the gluon density depends on the transverse size of the system, gluon saturation effects are expected to set in at higher x for heavy nuclei than for free nucleons.

In the leading order pQCD framework, a quark or gluon jet with large transverse momentum produced in a hard-scattering process (high momentum transfer or large Q^2) must be momentum balanced by another quark or gluon jet in the opposite direction but with almost the same p_T. Thus the azimuthal angle correlation between particles from the pair of jets (referred to as dijets) is characterized by two peak structures separated by 180°. In CGC calculations, the momentum to balance a jet may come from a large multiplicity of gluons in the saturation regime, and thus no single partner jet may appear on the opposite side [12]. This effect is analogous to the nuclear Mössbauer effect, and is often referred to as the appearance of monojets. Alternative calculations, describing the suppression of single hadrons at forward rapidity in d + Au reactions in terms of leading twist pQCD effects, predict no such monojet feature [13].

We want to probe this high gluon density regime in d + Au collisions with relatively high p_T particles at forward rapidity. Such particles are likely to result from hard-scattering collisions involving small x partons in the gold nucleus. At small x the gluon density increases rapidly with Q^2 and saturation effects may be relevant for $x \approx 0.01$ at modest p_T. CGC calculations [12] predict significant suppression of the conditional yield and widening of away-side jet azimuthal correlations between rapidity-separated hadron pairs when one of those hadrons is at forward rapidity.

In this Letter we report on measurements of two-particle azimuthal angle correlations between unidentified charged hadrons in $p + p$ and d + Au collisions at $\sqrt{s_{NN}} =$ 200 GeV. In our analysis, the two particles are referred to as the *trigger* and *associated* particles. The trigger particle is at forward ($1.4 < \eta < 2.0$) or backward ($-2.0 < \eta < -1.4$) rapidity and the associated particle is at midrapidity, $|\eta| < 0.35$. The particles are separated by an average pseudorapidity gap $\langle \Delta\eta \rangle \sim 1.5$. The criteria for trigger particles, associated particles, and event selection are described elsewhere [3,14]. The two-particle azimuthal angle correlation technique has been used extensively by RHIC experiments and is described in detail elsewhere [14–18]. In this technique the azimuthal correlation function is formed from the angular difference, $\Delta\phi = \phi^{\text{assoc}} - \phi^{\text{trig}}$, between each trigger and associated particle pair. Two jet peaks are normally observed in such correlation functions: the near-side peak ($\Delta\phi \sim 0$) in which the two particles come from the same jet, and the away-side peak ($\Delta\phi \sim \pi$) in which they come from back-to-back jets. In addition to these peaks the correlation functions also have a $\Delta\phi$ independent combinatoric background contribution due to trigger-associated pairs from different jets or from non-jet processes.

We can construct separate correlation functions that are sensitive to partons in the gold nucleus with different x ranges. By choosing trigger particles with $1.0 < p_T < 5.0$ GeV/c at forward (backward) rapidity and associated particles with $0.5 < p_T < 2.5$ GeV/c at midrapidity, we sample partons in gold nuclei with $x \sim 0.01(0.1)$. We do not expect our data at $x \sim 0.1$ to be sensitive to saturation effects, but they may at $x \sim 0.01$ [19]. The comparison in d + Au reactions between these two cases, as well as with the $p + p$ case, may give insights into possible saturation effects on jet production and other mechanisms for forward rapidity single-particle suppression. It should be noted that the prediction of monojets in [12] assumes one particle at $\eta = 3.8$ and one at midrapidity, thus demonstrating sensitivity at smaller x ($\sim 10^{-4}$) than presented in this analysis.

Data for this analysis were collected by PHENIX [20] in 2003. For d + Au collisions, we divide the data into two centrality (impact parameter) classes based on the number of hits in the backward-rapidity PHENIX beam-beam counter (BBC, $-3.9 < \eta < -3.0$). Central (peripheral)

collisions comprise 0%–40% (40%–88%) of the minimum bias cross section. Using a Glauber model [3] and a simulation of the BBC, we determine $\langle N_{\rm coll}\rangle = 13.0 \pm 0.9(4.7 \pm 0.4)$ for central (peripheral) collisions.

Trigger particles are unidentified charged hadrons measured in the PHENIX muon spectrometers [20]. We only select particles from $1.4 < |\eta| < 2.0$ to obtain homogenous acceptance from $1 < p_T < 5$ GeV/c and to reduce beam correlated backgrounds. We identify hadrons, as opposed to muons, in the muon spectrometers by comparing their momentum and penetration depth [3]. It is notable that our trigger hadrons have a modified composition (pion/kaon/proton ratio) relative to that at the collision vertex due to species-dependent nuclear interaction cross sections. Detailed simulations show that kaons make up 65%–90% of positively charged trigger particles and pions make up 70%–90% of negatively charged trigger particles. The sizes of the quoted ranges of particle composition are due to uncertainties on the input particle compositions in simulation and due to variations, correlated with polar angle and therefore rapidity, in the length of absorber material that particles traverse. The baryon contribution to our trigger particle sample is negligible. We find the two-particle azimuthal angle correlations for positively and negatively charged trigger particles to be consistent and therefore combined the results. Associated particles are unidentified charged hadrons measured in the PHENIX central spectrometers [20] which cover $|\eta| < 0.35$ and in this analysis have $0.5 < p_T < 2.5$ GeV/c. Standard track selection criteria [14] are applied.

For comparison we have also included measurements where trigger particles and associated particles are both measured in the PHENIX central spectrometers at midrapidity. The d + Au points for this comparison are from [14] and the $p + p$ point is an extension in p_T of the analysis that was published in [16].

We define the azimuthal angle correlation function as $\mathrm{CF} = \frac{dN(\Delta\phi)/d(\Delta\phi)}{\mathrm{acc}(\Delta\phi)}$, where $dN(\Delta\phi)/d(\Delta\phi)$ is the measured two-particle distribution and $\mathrm{acc}(\Delta\phi)$ is the two-particle acceptance obtained by mixing trigger particles and associated particles from different events within the same centrality and collision vertex category. This correction is necessary because the PHENIX central arm detector is not azimuthally symmetric and the pair acceptance varies as a function of $\Delta\phi$.

Figure 1 shows the correlation functions for trigger particles with $p_T = 2$–5 GeV/c and associated particles with $p_T = 0.5$–1.0 GeV/c. A clear peak is seen near $\Delta\phi = \pi$ on all plots corresponding to the away-side jet. It is notable that there is no peak near $\Delta\phi = 0$, as expected, because the rapidity gap between the two particles is larger than the width of the near-side jet. Although the rapidity of away-side particles is not necessarily the same as the rapidity of the away-side jet, PYTHIA [21] studies show that the distribution of final state particles around the jet axis is symmetric in $\Delta\eta$ and $\Delta\phi$ and the jet cone width is less than 1 unit of rapidity, which is smaller than the rapidity gap.

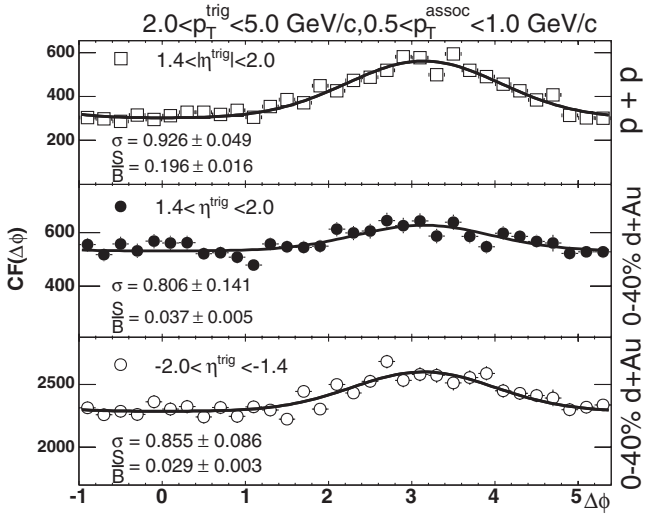

FIG. 1. Azimuthal angle correlation functions. Gaussian widths from the fits and the signal to background ratio integrated over $\pi - 1 < \Delta\phi < \pi + 1$ are shown. Note that the y axis is zero suppressed on the middle and bottom panels.

After constructing the correlation functions in various bins in $p_T^{\rm assoc}$, $p_T^{\rm trig}$, and $\eta^{\rm trig}$ we used two methods to determine the unnormalized number of trigger-associated particle pairs, $N_{\rm pair}$, above a constant background. In the first method, we define $N_{\rm pair} = \sum_{\Delta\phi=\pi-1}^{\pi+1} \mathrm{CF}(\Delta\phi) - \sum_{\Delta\phi=-1}^{+1} \mathrm{CF}(\Delta\phi)$, where the first term is the integral of the correlation function (CF) in the area of the correlation peak ($\pi - 1 < \Delta\phi < \pi + 1$) and the second term is the integral away from the peak ($-1 < \Delta\phi < 1$). In the second method we fit the correlation function with a Gaussian distribution centered at $\Delta\phi = \pi$ plus a constant background. The values of $N_{\rm pair}$ obtained by both methods are found to be consistent and the small differences are included in our systematic errors. The solid lines in Fig. 1 show the resulting fits. Gaussian width parameters (σ) and the integrated signal to background ratios ($\frac{S}{B}$) over the signal region ($\pi - 1 < \Delta\phi < \pi + 1$) are quoted.

The conditional yield (CY) (per trigger particle) is defined to be $\mathrm{CY} = \frac{N_{\rm pair}/\varepsilon_{\rm assoc}}{N_{\rm trig}}$, where $\varepsilon_{\rm assoc}$ ($\sim 0.15 \pm 0.015$) is the efficiency times acceptance for associated particles and $N_{\rm trig}$ is the number of trigger particles used to generate the correlation function. $\varepsilon_{\rm assoc}$ is obtained for each colliding system, centrality class, and p_T bin by a GEANT based simulation of the PHENIX detector [14].

It is interesting to plot the conditional yields as a function of $\eta^{\rm trig}$. Changing $\eta^{\rm trig}$ from -2.0 to 2.0 effectively changes the range of Bjorken x of sampled partons in gold nuclei from $0.1^{+0.06}_{-0.04}$ to $0.01^{+0.02}_{-0.007}$. Figure 2 shows the

results. The first observation is that there is no difference beyond statistical fluctuations in the conditional yields for $p + p$, $d + \mathrm{Au}$ peripheral, or $d + \mathrm{Au}$ central collisions at any trigger particle pseudorapidity.

We further quantify any nuclear modification in the conditional yield by defining a ratio $I_{d\mathrm{Au}} = \frac{\mathrm{CY}|_{d+\mathrm{Au}}}{\mathrm{CY}|_{p+p}}$. The technique of comparing conditional yields per trigger to investigate the source of single-particle nuclear modifications in the trigger particle region of phase space is well established at RHIC [14–16]. The fact that single-particle yields are strongly modified in the trigger particle p_T range makes $I_{d\mathrm{Au}}$ particularly interesting since it may shed light on the nature of the single-particle suppression. For our rapidity-separated pairs two different models [12,13], which posit different mechanisms to be responsible for the single-particle suppression, predict very different results for the evolution of the correlation function vs centrality and x.

Figure 3 shows the ratio $I_{d\mathrm{Au}}$ vs p_T^{assoc} for different p_T^{trig}, η^{trig} and $d + \mathrm{Au}$ centrality bins. Shaded bands on each data point show point-to-point independent systematic errors due to differences in N_{pair} obtained from the two methods described above. There is also a point-to-point correlated $\sim 2\%$ systematic uncertainty in the centrality dependence of $\varepsilon_{\mathrm{assoc}}$ determined by embedding Monte Carlo tracks into real events. The size of this uncertainty is comparable to the width of the $I_{d\mathrm{Au}} = 1$ line.

For trigger particles at both forward rapidity (sampling low-x partons in the gold nucleus) and backward rapidity (sampling high-x partons in the gold nucleus), the measured $I_{d\mathrm{Au}}$ is consistent with one. There may even be some evidence of slight enhancement for the case with trigger particles at forward rapidity in central $d + \mathrm{Au}$ collisions. We note that if monojets were a major contributor to the trigger particle sample in our x range, we would have expected a decrease in the conditional yield for $d + \mathrm{Au}$ central collisions with the trigger particle at forward rapidity.

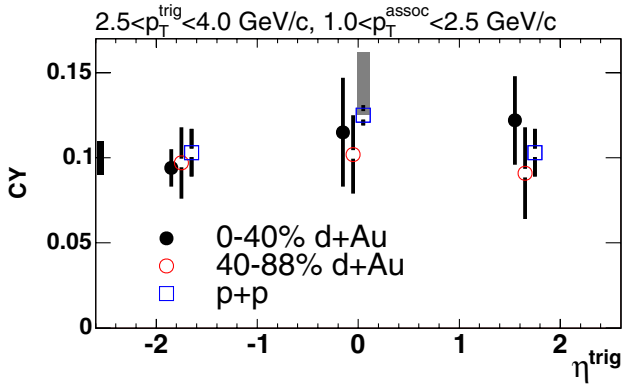

FIG. 2 (color online). Conditional yields are shown as a function of trigger particle pseudorapidity. Data points at midrapidity for $d + \mathrm{Au}$ collisions are from [14]. To increase visibility, we artificially shift data points belonging to the same η^{trig} bin. The errors on each point are statistical. The black bar around 0.1 on the y axis indicates a 10% common systematic error for all the data points due to uncertainties in $\varepsilon_{\mathrm{assoc}}$. There is an additional $+0.037$ systematic error on the midrapidity $p + p$ point from jet yield extraction, which is shown as the gray bar on that point (similar analysis as [16]).

Our measurement is inconsistent with any large nuclear suppression (i.e., monojets) of the jet structure in this kinematic range, but it is in agreement with leading twist pQCD calculations that predict suppression of single-particle yields at forward rapidity, with little modification of the conditional yield [13]. However, we note that in these modest p_T ranges, there may be contributions from both "hard" (large Q^2) processes and "soft" coherent (small Q^2) processes. In $d + \mathrm{Au}$ collisions soft particle production is shifted backwards in rapidity [22]. Thus, the fraction of hadrons at forward rapidity from hard processes may be increased in central $d + \mathrm{Au}$ reactions. This may offer an explanation for the modest enhancement seen in the conditional yield for this case and could also mask a small monojet signal.

We have also compared the Gaussian widths of the correlation peaks in $d + \mathrm{Au}$ collisions vs $p + p$ collisions. Ratios of the $d + \mathrm{Au}$ to $p + p$ widths are plotted in Fig. 4 vs p_T^{assoc}. There may be a hint of a slight p_T^{assoc} dependence in the ratio, but overall there is no significant difference in the width in $d + \mathrm{Au}$ collisions for different η^{trig}.

In conclusion, we measured two-particle azimuthal correlations with trigger particles at forward, backward, and midrapidity and correlated them with associated particles at midrapidity in $d + \mathrm{Au}$ and $p + p$ collisions. Associated particle conditional yields in central $d + \mathrm{Au}$ collisions are consistent with those in $p + p$ collisions and are consistent over the range $|\eta^{\mathrm{trig}}| < 2.0$. We have also compared the widths of the away-side jet peaks in $d + \mathrm{Au}$ and in $p + p$ collisions, and find no evidence for η^{trig}-dependent modification within our statistical errors. Overall the results

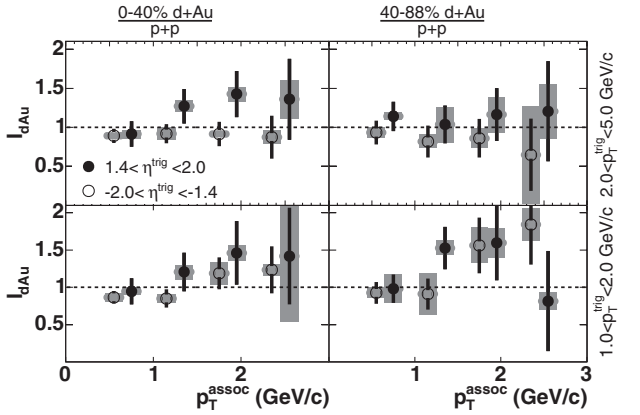

FIG. 3. $I_{d\mathrm{Au}}$ vs p_T^{assoc} for different centrality, p_T^{trig} and η^{trig} bins. To increase visibility, we artificially shift data points belonging to the same p_T^{assoc} bin.

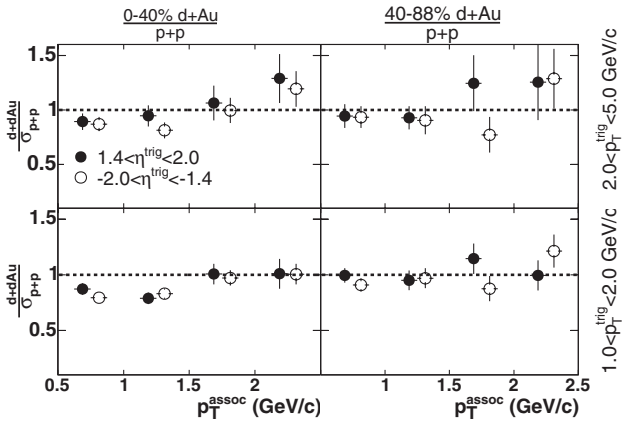

FIG. 4. The ratio of correlation peak widths between d + Au and $p + p$ collisions. Only statistical errors are shown. To increase visibility, we artificially shift the data points belonging to the same p_T^{assoc} bin.

presented here do not support models that predict strong modifications on jet production in the kinematic range covered by this analysis. However, we also note that the backwards rapidity shift of soft particle production may reduce the amplitude of such modifications.

We thank the staff of the Collider-Accelerator and Physics Departments at BNL for their vital contributions. We acknowledge support from the Department of Energy and NSF (U.S.A.), MEXT, and JSPS (Japan), CNPq and FAPESP (Brazil), NSFC (China), IN2P3/CNRS, CEA, and ARMINES (France), BMBF, DAAD, and AvH (Germany), OTKA (Hungary), DAE and DST (India), ISF (Israel), KRF and CHEP (Korea), RMIST, RAS, and RMAE (Russia), VR and KAW (Sweden), U.S. CRDF for the FSU, US-Hungarian NSF-OTKA-MTA, and US-Israel BSF.

*Deceased.
†PHENIX Spokesperson.
Electronic address: zajc@nevis.columbia.edu

[1] I. Arsene *et al.*, Phys. Rev. Lett. **93**, 242303 (2004).
[2] J. Adams *et al.*, Phys. Rev. C **70**, 064907 (2004).
[3] S. S. Adler *et al.*, Phys. Rev. Lett. **94**, 082302 (2005).
[4] S. S. Adler *et al.*, Phys. Rev. Lett. **91**, 072303 (2003).
[5] J. Adams *et al.*, Phys. Rev. Lett. **91**, 072304 (2003).
[6] B. B. Back *et al.*, Phys. Rev. Lett. **91**, 072302 (2003).
[7] I. Arsene *et al.*, Phys. Rev. Lett. **91**, 072305 (2003).
[8] L. McLerran and R. Venugopalan, Phys. Rev. D **49**, 2233 (1994); Phys. Rev. D **49**, 3352 (1994).
[9] R. Vogt, Phys. Rev. C **70**, 064902 (2004).
[10] J. Qiu and I. Vitev, hep-ph/0410218.
[11] R. C. Hwa, C. B. Yang, and R. J. Fries, Phys. Rev. C **71**, 024902 (2005).
[12] D. Kharzeev, E. Levin, and L. McLerran, Nucl. Phys. **A748**, 627 (2005).
[13] J. Qiu and I. Vitev, Phys. Lett. B **632**, 507 (2006).
[14] S. S. Adler *et al.*, nucl-ex/0510021.
[15] C. Adler *et al.*, Phys. Rev. Lett. **90**, 082302 (2003).
[16] S. S. Adler *et al.*, Phys. Rev. C **71**, 051902(R) (2005).
[17] J. Adams *et al.*, Phys. Rev. Lett. **95**, 152301 (2005).
[18] S. S. Adler *et al.*, nucl-ex/0507004.
[19] M. Arneodo, Phys. Rep. **240**, 301 (1994).
[20] K. Adcox *et al.*, Nucl. Instrum. Methods Phys. Res., Sect. A **499**, 469 (2003).
[21] T. Sjoestrand *et al.*, Comput. Phys. Commun. **135**, 238 (2001).
[22] B. B. Back *et al.*, Phys. Rev. C **72**, 031901 (2005).

Nuclear effects on hadron production in d + Au collisions at $\sqrt{s_{NN}}$ = 200 GeV revealed by comparison with p + p data

S. S. Adler,[5] S. Afanasiev,[20] C. Aidala,[10] N. N. Ajitanand,[44] Y. Akiba,[21,40] A. Al-Jamel,[35] J. Alexander,[44] K. Aoki,[25] L. Aphecetche,[46] R. Armendariz,[35] S. H. Aronson,[5] R. Averbeck,[45] T. C. Awes,[36] V. Babintsev,[17] A. Baldisseri,[11] K. N. Barish,[6] P. D. Barnes,[28] B. Bassalleck,[34] S. Bathe,[6,31] S. Batsouli,[10] V. Baublis,[39] F. Bauer,[6] A. Bazilevsky,[5,41] S. Belikov,[17,19] M. T. Bjorndal,[10] J. G. Boissevain,[28] H. Borel,[11] M. L. Brooks,[28] D. S. Brown,[35] N. Bruner,[34] D. Bucher,[31] H. Buesching,[5,31] V. Bumazhnov,[17] G. Bunce,[5,41] J. M. Burward-Hoy,[27,28] S. Butsyk,[45] X. Camard,[46] P. Chand,[4] W. C. Chang,[2] S. Chernichenko,[17] C. Y. Chi,[10] J. Chiba,[21] M. Chiu,[10] I. J. Choi,[53] R. K. Choudhury,[4] T. Chujo,[5] V. Cianciolo,[36] Y. Cobigo,[11] B. A. Cole,[10] M. P. Comets,[37] P. Constantin,[19] M. Csanád,[13] T. Csörgö,[22] J. P. Cussonneau,[46] D. d'Enterria,[10] K. Das,[14] G. David,[5] F. Deák,[13] H. Delagrange,[46] A. Denisov,[17] A. Deshpande,[41] E. J. Desmond,[5] A. Devismes,[45] O. Dietzsch,[42] J. L. Drachenberg,[1] O. Drapier,[26] A. Drees,[45] A. Durum,[17] D. Dutta,[4] V. Dzhordzhadze,[47] Y. V. Efremenko,[36] H. En'yo,[40,41] B. Espagnon,[37] S. Esumi,[49] D. E. Fields,[34,41] C. Finck,[46] F. Fleuret,[26] S. L. Fokin,[24] B. D. Fox,[41] Z. Fraenkel,[52] J. E. Frantz,[10] A. Franz,[5] A. D. Frawley,[14] Y. Fukao,[25,40,41] S.-Y. Fung,[6] S. Gadrat,[29] M. Germain,[46] A. Glenn,[47] M. Gonin,[26] J. Gosset,[11] Y. Goto,[40,41] R. Granier de Cassagnac,[26] N. Grau,[19] S. V. Greene,[50] M. Grosse Perdekamp,[18,41] H.-Å. Gustafsson,[30] T. Hachiya,[16] J. S. Haggerty,[5] H. Hamagaki,[8] A. G. Hansen,[28] E. P. Hartouni,[27] M. Harvey,[5] K. Hasuko,[40] R. Hayano,[8] X. He,[15] M. Heffner,[27] T. K. Hemmick,[45] J. M. Heuser,[40] P. Hidas,[22] H. Hiejima,[18] J. C. Hill,[19] R. Hobbs,[34] W. Holzmann,[44] K. Homma,[16] B. Hong,[23] A. Hoover,[35] T. Horaguchi,[40,41,48] T. Ichihara,[40,41] V. V. Ikonnikov,[24] K. Imai,[25,40] M. Inaba,[49] M. Inuzuka,[8] D. Isenhower,[1] L. Isenhower,[1] M. Ishihara,[40] M. Issah,[44] A. Isupov,[20] B. V. Jacak,[45] J. Jia,[45] O. Jinnouchi,[40,41] B. M. Johnson,[5] S. C. Johnson,[27] K. S. Joo,[32] D. Jouan,[37] F. Kajihara,[8] S. Kametani,[8,51] N. Kamihara,[40,48] M. Kaneta,[41] J. H. Kang,[53] K. Katou,[51] T. Kawabata,[8] A. V. Kazantsev,[24] S. Kelly,[9,10] B. Khachaturov,[52] A. Khanzadeev,[39] J. Kikuchi,[51] D. J. Kim,[53] E. Kim,[43] G.-B. Kim,[26] H. J. Kim,[53] E. Kinney,[9] A. Kiss,[13] E. Kistenev,[5] A. Kiyomichi,[40] C. Klein-Boesing,[31] H. Kobayashi,[41] L. Kochenda,[39] V. Kochetkov,[17] R. Kohara,[16] B. Komkov,[39] M. Konno,[49] D. Kotchetkov,[6] A. Kozlov,[52] P. J. Kroon,[5] C. H. Kuberg,[1,*] G. J. Kunde,[28] K. Kurita,[40] M. J. Kweon,[23] Y. Kwon,[53] G. S. Kyle,[35] R. Lacey,[44] J. G. Lajoie,[19] Y. Le Bornec,[37] A. Lebedev,[19,24] S. Leckey,[45] D. M. Lee,[28] M. J. Leitch,[28] M. A. L. Leite,[42] X. H. Li,[6] H. Lim,[43] A. Litvinenko,[20] M. X. Liu,[28] C. F. Maguire,[50] Y. I. Makdisi,[5] A. Malakhov,[20] V. I. Manko,[24] Y. Mao,[38,40] G. Martinez,[46] H. Masui,[49] F. Matathias,[45] T. Matsumoto,[8,51] M. C. McCain,[1] P. L. McGaughey,[28] Y. Miake,[49] T. E. Miller,[50] A. Milov,[45] S. Mioduszewski,[5] G. C. Mishra,[15] J. T. Mitchell,[5] A. K. Mohanty,[4] D. P. Morrison,[5] J. M. Moss,[28] D. Mukhopadhyay,[52] M. Muniruzzaman,[6] S. Nagamiya,[21] J. L. Nagle,[9,10] T. Nakamura,[16] J. Newby,[47] A. S. Nyanin,[24] J. Nystrand,[30] E. O'Brien,[5] C. A. Ogilvie,[19] H. Ohnishi,[40] I. D. Ojha,[3,50] H. Okada,[25,40] K. Okada,[40,41] A. Oskarsson,[30] I. Otterlund,[30] K. Oyama,[8] K. Ozawa,[8] D. Pal,[52] A. P. T. Palounek,[28] V. Pantuev,[45] V. Papavassiliou,[35] J. Park,[43] W. J. Park,[23] S. F. Pate,[35] H. Pei,[19] V. Penev,[20] J.-C. Peng,[18] H. Pereira,[11] V. Peresedov,[20] A. Pierson,[34] C. Pinkenburg,[5] R. P. Pisani,[5] M. L. Purschke,[5] A. K. Purwar,[45] J. M. Qualls,[1] J. Rak,[19] I. Ravinovich,[52] K. F. Read,[36,47] M. Reuter,[45] K. Reygers,[31] V. Riabov,[39] Y. Riabov,[39] G. Roche,[29] A. Romana,[26] M. Rosati,[19] S. S. E. Rosendahl,[30] P. Rosnet,[29] V. L. Rykov,[40] S. S. Ryu,[53] N. Saito,[25,40,41] T. Sakaguchi,[8,51] S. Sakai,[49] V. Samsonov,[39] L. Sanfratello,[34] R. Santo,[31] H. D. Sato,[25,40] S. Sato,[5,49] S. Sawada,[21] Y. Schutz,[46] V. Semenov,[17] R. Seto,[6] T. K. Shea,[5] I. Shein,[17] T.-A. Shibata,[40,48] K. Shigaki,[16] M. Shimomura,[49] A. Sickles,[45] C. L. Silva,[42] D. Silvermyr,[28] K. S. Sim,[23] A. Soldatov,[17] R. A. Soltz,[27] W. E. Sondheim,[28] S. P. Sorensen,[47] I. V. Sourikova,[5] F. Staley,[11] P. W. Stankus,[36] E. Stenlund,[30] M. Stepanov,[35] A. Ster,[22] S. P. Stoll,[5] T. Sugitate,[16] J. P. Sullivan,[28] S. Takagi,[49] E. M. Takagui,[42] A. Taketani,[40,41] K. H. Tanaka,[21] Y. Tanaka,[33] K. Tanida,[40] M. J. Tannenbaum,[5] A. Taranenko,[44] P. Tarján,[12] T. L. Thomas,[34] M. Togawa,[25,40] J. Tojo,[40] H. Torii,[25,41] R. S. Towell,[1] V-N. Tram,[26] I. Tserruya,[52] Y. Tsuchimoto,[16] H. Tydesjö,[30] N. Tyurin,[17] T. J. Uam,[32] H. W. van Hecke,[28] J. Velkovska,[5] M. Velkovsky,[45] V. Veszprémi,[12] A. A. Vinogradov,[24] M. A. Volkov,[24] E. Vznuzdaev,[39] X. R. Wang,[15] Y. Watanabe,[40,41] S. N. White,[5] N. Willis,[37] F. K. Wohn,[19] C. L. Woody,[5] W. Xie,[6] A. Yanovich,[17] S. Yokkaichi,[40,41] G. R. Young,[36] I. E. Yushmanov,[24] W. A. Zajc,[10,†] C. Zhang,[10] S. Zhou,[7] J. Zimányi,[22] L. Zolin,[20] and X. Zong[19]

(PHENIX Collaboration)

[1]*Abilene Christian University, Abilene, Texas 79699, USA*

[2]*Institute of Physics, Academia Sinica, Taipei 11529, Taiwan*

[3]*Department of Physics, Banaras Hindu University, Varanasi 221005, India*

[4]*Bhabha Atomic Research Centre, Bombay 400 085, India*

[5]*Brookhaven National Laboratory, Upton, New York 11973-5000, USA*

[6]*University of California-Riverside, Riverside, California 92521, USA*

[7]*China Institute of Atomic Energy (CIAE), Beijing, People's Republic of China*

[8]*Center for Nuclear Study, Graduate School of Science, University of Tokyo, 7-3-1 Hongo, Bunkyo, Tokyo 113-0033, Japan*

[9]*University of Colorado, Boulder, Colorado 80309, USA*

[10]*Columbia University, New York, New York 10027, and Nevis Laboratories, Irvington, New York 10533, USA*

[11]*Dapnia, CEA Saclay, F-91191, Gif-sur-Yvette, France*

[12]*Debrecen University, H-4010 Debrecen, Egyetem tér 1, Hungary*

[13]*ELTE, Eötvös Loránd University, H-1117 Budapest, Pázmány P. s. 1/A, Hungary*

 ©2006 The American Physical Society

[14]*Florida State University, Tallahassee, Florida 32306, USA*
[15]*Georgia State University, Atlanta, Georgia 30303, USA*
[16]*Hiroshima University, Kagamiyama, Higashi-Hiroshima 739-8526, Japan*
[17]*IHEP Protvino, State Research Center of Russian Federation, Institute for High Energy Physics, Protvino, RU-142281, Russia*
[18]*University of Illinois at Urbana-Champaign, Urbana, Illinois 61801, USA*
[19]*Iowa State University, Ames, Iowa 50011, USA*
[20]*Joint Institute for Nuclear Research, RU-141980 Dubna, Moscow Region, Russia*
[21]*KEK, High Energy Accelerator Research Organization, Tsukuba, Ibaraki 305-0801, Japan*
[22]*KFKI Research Institute for Particle and Nuclear Physics of the Hungarian Academy of Sciences (MTA KFKI RMKI), H-1525 Budapest 114, P.O. Box 49, Budapest, Hungary*
[23]*Korea University, Seoul, 136-701, Korea*
[24]*Russian Research Center "Kurchatov Institute," Moscow, Russia*
[25]*Kyoto University, Kyoto 606-8502, Japan*
[26]*Laboratoire Leprince-Ringuet, Ecole Polytechnique, CNRS-IN2P3, Route de Saclay, F-91128, Palaiseau, France*
[27]*Lawrence Livermore National Laboratory, Livermore, California 94550, USA*
[28]*Los Alamos National Laboratory, Los Alamos, New Mexico 87545, USA*
[29]*LPC, Université Blaise Pascal, CNRS-IN2P3, Clermont-Fd, F-63177 Aubiere Cedex, France*
[30]*Department of Physics, Lund University, Box 118, SE-22100 Lund, Sweden*
[31]*Institut für Kernphysik, University of Muenster, D-48149 Muenster, Germany*
[32]*Myongji University, Yongin, Kyonggido 449-728, Korea*
[33]*Nagasaki Institute of Applied Science, Nagasaki-shi, Nagasaki 851-0193, Japan*
[34]*University of New Mexico, Albuquerque, New Mexico 87131, USA*
[35]*New Mexico State University, Las Cruces, New Mexico 88003, USA*
[36]*Oak Ridge National Laboratory, Oak Ridge, Tennessee 37831, USA*
[37]*IPN-Orsay, Université Paris Sud, CNRS-IN2P3, BP1, F-91406, Orsay, France*
[38]*Peking University, Beijing, People's Republic of China*
[39]*PNPI, Petersburg Nuclear Physics Institute, Gatchina, Leningrad region, RU-188300, Russia*
[40]*RIKEN (Institute of Physical and Chemical Research), Wako, Saitama 351-0198, JAPAN*
[41]*RIKEN BNL Research Center, Brookhaven National Laboratory, Upton, New York 11973-5000, USA*
[42]*Universidade de São Paulo, Instituto de Física, Caixa Postal 66318, São Paulo CEP05315-970, Brazil*
[43]*System Electronics Laboratory, Seoul National University, Seoul, Korea*
[44]*Chemistry Department, Stony Brook University, SUNY, Stony Brook, New York 11794-3400, USA*
[45]*Department of Physics and Astronomy, Stony Brook University, SUNY, Stony Brook, New York 11794, USA*
[46]*SUBATECH (Ecole des Mines de Nantes, CNRS-IN2P3, Université de Nantes) BP 20722, F-44307, Nantes, France*
[47]*University of Tennessee, Knoxville, Tennessee 37996, USA*
[48]*Department of Physics, Tokyo Institute of Technology, Oh-okayama, Meguro, Tokyo 152-8551, Japan*
[49]*Institute of Physics, University of Tsukuba, Tsukuba, Ibaraki 305, Japan*
[50]*Vanderbilt University, Nashville, Tennessee 37235, USA*
[51]*Waseda University, Advanced Research Institute for Science and Engineering, 17 Kikui-cho, Shinjuku-ku, Tokyo 162-0044, Japan*
[52]*Weizmann Institute, Rehovot 76100, Israel*
[53]*Yonsei University, IPAP, Seoul 120-749, Korea*
(Received 8 March 2006; published 16 August 2006)

PHENIX has measured the centrality dependence of midrapidity pion, kaon, and proton transverse momentum distributions in $d + \mathrm{Au}$ and $p + p$ collisions at $\sqrt{s_{NN}} = 200$ GeV. The $p + p$ data provide a reference for nuclear effects in $d + \mathrm{Au}$ and previously measured $\mathrm{Au} + \mathrm{Au}$ collisions. Hadron production is enhanced in $d + \mathrm{Au}$, relative to independent nucleon-nucleon scattering, as was observed in lower energy collisions. The nuclear modification factor for (anti)protons is larger than that for pions. The difference increases with centrality but is not sufficient to account for the abundance of baryon production observed in central $\mathrm{Au} + \mathrm{Au}$ collisions at the BNL Relativistic Heavy Ion Collider (RHIC). The centrality dependence in $d + \mathrm{Au}$ shows that the nuclear modification factor increases gradually with the number of collisions encountered by each participant nucleon. We also present comparisons with lower energy data as well as with parton recombination and other theoretical models of nuclear effects on particle production.

DOI: 10.1103/PhysRevC.74.024904 PACS number(s): 25.75.Dw

I. INTRODUCTION

Since the early 1970s, it has been well established [1–3] that energetic particle production in proton-nucleus ($p + A$) collisions increases faster than the number of binary nucleon-nucleon collisions. This effect, called the "Cronin effect," is a manifestation of the fact that particle production and propagation is influenced by the nucleus. If the A dependence of the invariant cross section I of particle i in $p + A$ collisions is parametrized as

$$I_i(p_T, A) = I_i(p_T, 1)A^{\alpha_i(p_T)}, \quad (1)$$

then it has been observed that α_i is greater than unity above some transverse momentum value, typically 1–1.5 GeV/c, denoting significant enhancement of particle production in $p + A$ collisions. The enhancement depends on the momentum and the type of particle produced, with protons and antiprotons exhibiting a much larger enhancement than pions and kaons at $p_T > 2$–3 GeV/c. At $\sqrt{s_{NN}} = 27.4$ GeV, the enhancement peaks at around $p_T = 4.5$ GeV/c, with $\alpha_{K^+} \simeq \alpha_{\pi^+} = 1.109 \pm 0.007$, while, at the same momentum, the protons can be described by an α factor of $\alpha_p - \alpha_{\pi^+} = 0.231 \pm 0.013$ [2].

Although the observables in Eq. (1) have been clearly related to the nuclear medium, the cause of the Cronin enhancement and its species dependence are not yet completely understood, and further experimental study is warranted in its own right. Furthermore, in the search for the quark gluon plasma at the BNL Relativistic Heavy Ion Collider (RHIC), the Cronin effect is extremely important, as novel effects observed in central Au + Au collisions require good control of the initial state conditions. At RHIC energies, it was discovered that hadron production at high transverse momentum ($p_T \geqslant 2$ GeV/c) is suppressed in central Au + Au collisions [4] compared to nucleon-nucleon collisions. Such suppression may be interpreted as a consequence of the energy loss suffered by the hard-scattered partons as they propagate through the hot, dense medium. However, since the Cronin effect acts in the opposite direction, enhancing the hadron yields, it has to be taken into account when the parton energy loss is determined from the data.

Another unexpected discovery at RHIC energies is that the yields of p and $\bar{p}$ at intermediate p_T ($1.5 < p_T < 5$ GeV/c) in central Au + Au collisions [5–7] are comparable to the yield of pions, in striking contrast to the proton to pion (p/π) ratios of $\sim$0.1–0.3 measured in $p + p$ collisions [8]. Novel mechanisms of particle production in the environment of dense matter, such as recombination of boosted quarks [9] or contributions from baryon junctions [10], which can become dominant in the presence of pion suppression, were proposed to explain the data. Since it has been observed that at lower energies Cronin enhancement is stronger for protons than for pions [2], this effect has to be considered at RHIC energies before new physics is invoked.

The effects from the initial state are best studied by performing a control experiment in which no hot and dense matter is produced. Deuteron + gold collisions at $\sqrt{s_{NN}} = 200$ GeV serve this purpose. Since there is no hot and dense final state medium, the initial state conditions become accessible to the experiment. In addition to Cronin enhancement, known initial state effects also include nuclear shadowing and gluon saturation [11]. The Cronin enhancement is usually attributed to momentum broadening due to multiple initial state soft [12] or semihard [13–16] scattering. Such models typically do not predict the particle species dependence observed in the data. Recently, Hwa and collaborators provided an alternative explanation due to final state interactions. The particle species dependent enhancement is attributed to recombination of shower quarks with those from the medium, where no distinction is made if hot or cold nuclear matter is produced [17]. Identified hadron production measured as a function of centrality brings important experimental data relevant to the long-outstanding problem of the baryon Cronin effect. The dependence of the enhancement upon the thickness of the medium, or the number of collisions suffered by each participating nucleon, can help differentiate among the different scattering models, and the species dependence helps to separate initial from final state effects in $d + $Au.

The paper is arranged as follows. Section II describes the experiment, data analysis, and systematic uncertainties. Section III presents hadron spectra, yields, and the resulting nuclear modification factors. Discussion of the centrality, energy, and species dependence of the nuclear modification factors and implications for understanding of the Cronin effect are in Sec. IV. Section V presents conclusions.

II. EXPERIMENT AND DATA ANALYSIS

A. Data sets and trigger

Data presented here include collisions at $\sqrt{s_{NN}} = 200$ GeV of Au + Au taken in the 2002 run of RHIC and of $d + $Au and $p + p$ collisions collected in 2003. In the following, we discuss our analysis of the $p + p$ and $d + $Au data; details of the Au + Au analysis and the Au + Au results are found in [7]. Events with vertex position along the beam axis within $|z| < 30$ cm were triggered by the beam-beam counters (BBCs) located at $|\eta| = 3.0$–3.9 [18]. The minimum bias trigger accepts 88.5($\pm$4)% of all $d + $Au collisions that satisfy the vertex condition, and 51.6($\pm$9.8)% of $p + p$ collisions. A total of 42 and 25 million minimum bias events were analyzed for $d + $Au and $p + p$ collisions, respectively.

In $p + p$ collisions, PHENIX determines the differential invariant cross section via

$$E\frac{d^3\sigma}{dp^3} = \frac{\sigma_{\rm BBC}}{N_{\rm BBC}^{\rm total}}\frac{1}{2\pi}\frac{1}{p_T}C_{\rm eff}^{\rm geo}(p_T)\,C_{\rm bias}^{\rm BBC}\frac{d^2N}{dp_T dy}. \quad (2)$$

The BBC cross section $\sigma_{\rm BBC}$ was determined via the van der Meer scan technique [19]. In this $p + p$ data set, $\sigma_{\rm BBC} = 23.0 \pm 2.2(9.6\%)$ mb. $N_{\rm BBC}^{\rm total}$ is the total number of BBC triggers analyzed. The factor $C_{\rm eff}^{\rm geo}(p_T)$ denotes the efficiency and geometrical acceptance correction, calculated

*Deceased.
†PHENIX spokesperson, electronic address: zajc@nevis.columbia.edu

TABLE I. Mean number of binary collisions, participating nucleons from the Au nucleus, number of collisions per participating deuteron nucleon, and trigger bias corrections for the d + Au centrality bins.

	00%–20%	20%–40%	40%–60%	60%–88%
$\langle N_{\rm coll}\rangle$	15.4 ± 1.0	10.6 ± 0.7	7.0 ± 0.6	3.1 ± 0.3
$\langle N_{\rm part}\rangle$	15.6 ± 0.9	11.1 ± 0.6	7.7 ± 0.4	4.2 ± 0.3
$\langle \nu = N_{\rm coll}/N^{d}_{\rm part}\rangle$	7.5 ± 0.5	5.6 ± 0.4	4.0 ± 0.3	2.2 ± 0.2
Trigger bias correction	0.95 ± 0.3	0.99 ± 0.007	1.03 ± 0.009	1.04 ± 0.027

with a detailed GEANT Monte Carlo simulation [20] of the PHENIX detector. $C^{\rm geo}_{\rm eff}(p_T)$ normalizes the cross section in one unit of rapidity and full azimuthal coverage. The $C^{\rm BBC}_{\rm bias}$ factor corrects for the fact that the forward BBCs measure only a fraction of the inelastic $p + p$ cross section. This subset of events on which the BBC triggers contains only a fraction of the inclusive particle yield at midrapidity. For charged hadrons, this fraction was determined using triggers on the beam crossing clock; the fraction was found to be 0.80 ± 0.02, independent of p_T. The $C^{\rm BBC}_{\rm bias}$ term is, in our nomenclature, the inverse of this fraction.

In d + Au collisions, PHENIX measures the inelastic yield per BBC triggered event.[1] The collision centrality is selected in d + Au using the south (Au-going side) BBC (BBCS). We assume that the BBCS signal is proportional to the number of participating nucleons ($N^{\rm Au}_{\rm part}$) in the Au nucleus, and that the hits in the BBCS are uncorrelated to each other. We use a Glauber model [22] and simulation of the BBC to define four centrality classes in d + Au collisions, as discussed in detail in [23]. The deuteron nucleus is modeled after a wave function derived by Hulthèn [24]

$$\phi_{\rm d}(\mathbf{r}_{pn}) = \left(\frac{\alpha\beta(\alpha+\beta)}{2\pi(\alpha-\beta)^2}\right)^{\frac{1}{2}} \frac{(e^{-\alpha \mathbf{r}_{pn}} - e^{-\beta \mathbf{r}_{pn}})}{\mathbf{r}_{pn}}, \qquad (3)$$

where $\alpha = 0.228\,{\rm fm}^{-1}$; $\beta = 1.18\,{\rm fm}^{-1}$; and $\mathbf{r}_{pn}$ refers to the separation between the proton and the neutron. The Au nucleus is modeled using a Woods-Saxon density distribution

$$\rho(r) = \frac{\rho_0}{1 + \exp\left(\frac{r-c}{a}\right)}, \qquad (4)$$

where $a = 0.54$ fm and $c = 1.12\,A^{1/3} - 0.86\,A^{-1/3} = 6.40$ fm, a value which agrees well with the measured charge radius of $R = 6.38$ fm for gold.

Using the above parameters and taking into account the BBC efficiency, the mean number of binary collisions along with the mean number of participating nucleons from the Au nucleus that correspond to each centrality bin are shown in Table I. For the minimum bias d + Au collisions, $\langle N_{\rm coll}\rangle = 8.5 \pm 0.4$ and $\langle N_{\rm part}\rangle = 9.1 \pm 0.4$.

As for $p + p$ collisions, there is a BBC trigger bias, but it is much smaller in d + Au. In addition, a second bias occurs in d + Au centrality selected collisions. This second bias arises from the fact that events containing high-p_T hadrons from hard scatterings may have larger multiplicity, and consequently they produce a larger signal in the BBCS. Such events would be considered more central than events without a hard scattering. This effect gives an opposite bias from the first trigger bias effect in the most peripheral bin as events can be shifted out of this bin but not into it. We correct for both biases in d + Au collisions using simulations and a Glauber model. The combined corrections for these effects range from 0% to 5%, depending on the centrality category, and are shown in Table I. Systematic uncertainties on these corrections are less than 4%.

B. Tracking and particle identification

Charged particles are reconstructed using a drift chamber (DC) and two layers of multiwire proportional chambers with pad readout (PC1, PC3) [18]. Pattern recognition is based on a combinatorial Hough transform in the track bend plane, while the polar angle is determined by PC1 and the location of the collision vertex along the beam direction [25]. The track reconstruction efficiency is approximately 98%.

Particle momenta are measured with a resolution $\delta p/p = 0.7\% \oplus 1.1\%\, p$ (GeV/c). The momentum scale is known to 0.7%. Particle identification is based on particle mass calculated from the measured momentum and the velocity obtained from the time-of-flight and path length along the trajectory. The measurement uses the portion of the spectrometer containing the high-resolution time-of-flight (TOF) detector, which covers pseudorapidity $-0.35 \leqslant \eta \leqslant 0.35$ and $\Delta\phi = \pi/8$ in azimuthal angle. The timing uses the BBC for the global start and the stop signals from the TOF scintillators located at a radial distance of 5.06 m. Tracks are required to match a hit on the TOF within ± 3 standard deviations, σ, of the track projection to the TOF radial location. The particle yields are corrected for losses due to this matching cut.

Figure 1 illustrates the performance of the hadron identification system. The system resolution is $\sigma \approx 130$ ps for both d + Au and $p + p$; the start time resolution is limited by the low hit multiplicity in the BBC. The TOF resolution achieved allows for a clear separation of π/K and K/p up to $p_T = 2$ and $p_T = 3.6$ GeV/c, respectively. A 2σ cut in mass squared is used to separate the different hadron species, as shown in Fig. 2 for hadrons in the p_T range 1.2–1.6 GeV/c. A clear separation between pions and kaons is seen. The particle yields are corrected for losses due to the 2σ cut. A simple cut on mass would leave the pion spectrum above 2 GeV/c in p_T with an admixture of kaons. This is avoided by calculating a pion and kaon probability for each particle,

[1] To convert the reported inelastic yield to differential cross section, one must multiply by the BBC trigger cross section of $\sigma^{\rm tot}_{\rm MB}(d{\rm Au})\epsilon^{\rm BBC}_{\rm MB}(d{\rm Au}) = 1.99 \pm 0.10$ b [21].

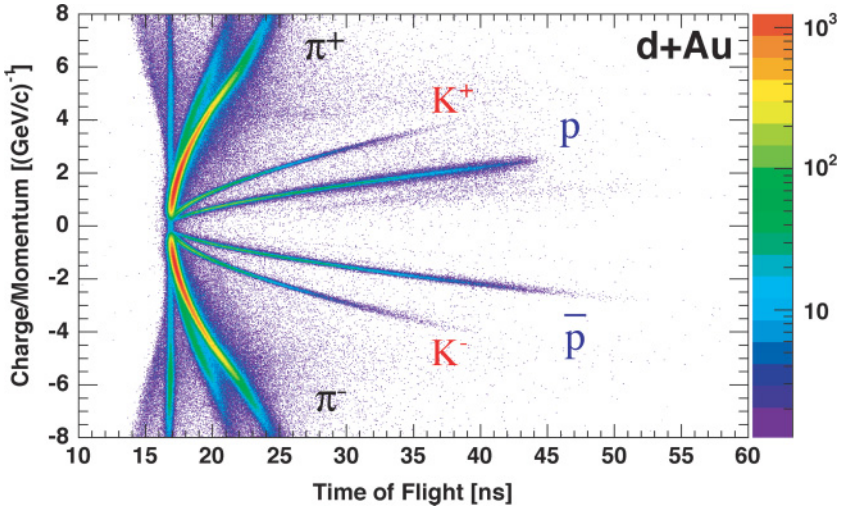

FIG. 1. (Color online) Time of flight vs charge/momentum for particles in minimum bias $d + \mathrm{Au}$ collisions. Bands corresponding to the different hadrons are labeled. Electron and muon bands are also visible, though not labeled.

utilizing the measured pion and kaon centroid and width in mass squared. For $2.0 \leqslant p_T \leqslant 2.7$ GeV/c, particles within the 2σ particle identification (PID) cut for pions that also fall inside the 2σ kaon band are vetoed from the pion spectrum. The resulting loss in efficiency is corrected by applying the same procedure in the Monte Carlo simulations. This procedure has been verified using 1σ PID cuts, which allows full pion-kaon separation to 2.7 GeV/c.

Corrections to the charged-particle spectrum for geometrical acceptance, decays in flight, reconstruction efficiency, energy loss in detector material, and momentum resolution are determined using a single-particle GEANT Monte Carlo simulation.

The proton and antiproton spectra are corrected for feed down from weak decays via a Monte Carlo simulation using as input experimental data on Λ production. The total number of protons produced in the collisions can be written as $p + 0.64(\Lambda + \Sigma^0 + \Xi^0 + \Xi^- + \Omega^-) + 0.52\Sigma^+$, where p denotes the primordial number of protons produced, the other symbols denote the primordial number of those particles produced in the collision, and 0.64 and 0.52 are the branching ratios for $\Lambda \to p\pi^-$ and $\Sigma^+ \to p\pi^0$, respectively. The hyperons listed together with Λ decay to Λ with approximately 100% branching ratio, and so yield protons with the $\Lambda \to p\pi$ branching ratio. We estimate the proton and antiproton spectra from weak decays and subtract them from the measured yields, using experimental data from UA5 [26] from nonsingle diffractive $\sqrt{s} = 200$ GeV $p + \bar{p}$ collisions, and preliminary Λ and $\overline{\Lambda}$ spectra from STAR in $p + p$ and $d + \mathrm{Au}$ collisions at the same energy [27–30]. The shape of the Σ^0, Ξ^0, and Ξ^- spectra are constructed from the Λ spectrum by m_T scaling (i.e., under the assumption that these hadrons are all produced with roughly the same spectrum in transverse mass [30]). The relative normalization of Λ, Σ^0, Ξ^0, and Ξ^- from UA5 [26] is used for both $p + p$ and $d + \mathrm{Au}$ collisions. This is justified by the similarity of the Cronin effect for different baryons. The contribution of Ω^- is negligible, and is not included in the correction. The Monte Carlo simulation decays these baryons and propagates the products through the PHENIX magnetic field and central arm detectors, accounting also for the change of momentum distributions between parent and daughter particles due to decay kinematics. The resulting proton and antiproton spectra are then subtracted from the measured inclusive spectra. The fractional contribution from

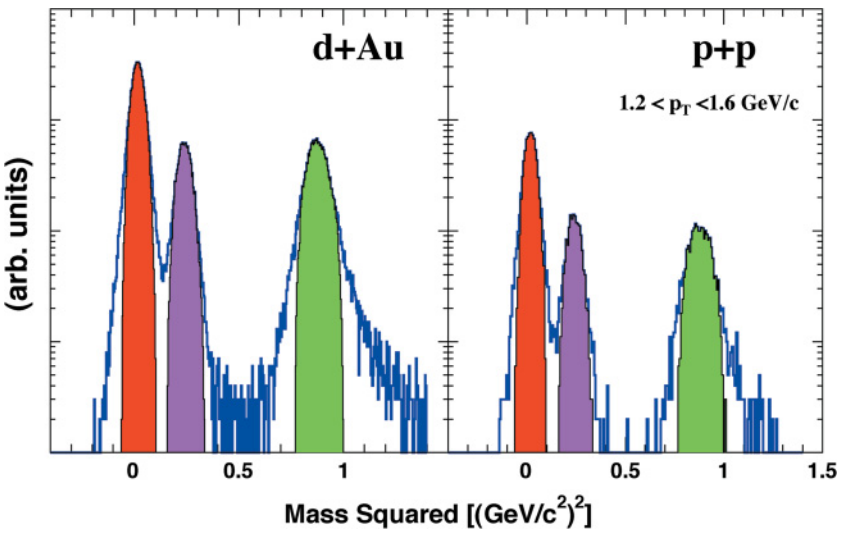

FIG. 2. (Color online) Mass squared distribution for positively charged tracks with $1.2 \leqslant p_T \leqslant 1.6$ GeV/c, using the high-resolution TOF measurement. Solid regions indicate the mass squared ranges for accepted pions, kaons, and protons, respectively, from left to right.

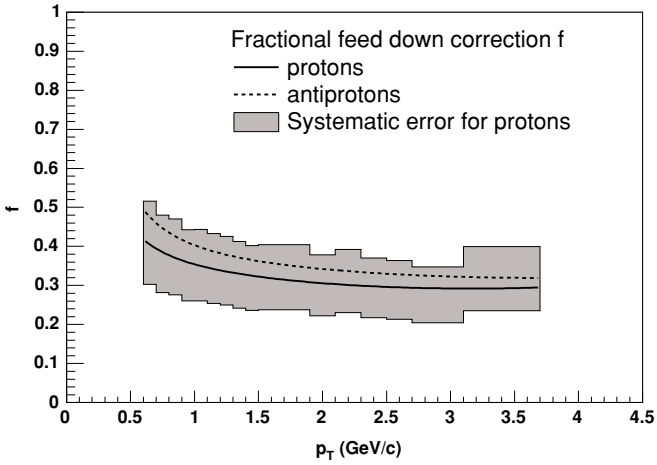

FIG. 3. Fractional contributions of protons f (solid line) and antiprotons (dashed line), as a function of p_T, from weak decays in all measured protons and antiprotons. Systematic error band (26%) for the protons is shown and discussed in the text. The same systematic error applies for the antiprotons.

feed-down protons from weak decays to the total measured proton spectrum, f, is approximately 30% at moderate and high p_T growing slowly for lower p_T and reaching 40% at $p_T = 0.6$ GeV/c. f is shown as a function of p_T in Fig. 3, along with the corresponding fractional contribution for the antiprotons.

C. Systematic uncertainties

Systematic uncertainties on the hadron spectra are estimated as in Ref. [7]. Various sets of p_T spectra and ratios of different particle types were made by varying the cut parameters such as the fiducial cut to check acceptance corrections, track association (i.e., matching) windows, and PID cuts, from those used in the analysis. For each of these spectra and ratios, the same changes in cuts were made in the Monte Carlo analysis. The uncertainties were evaluated by comparing fully corrected spectra and ratios from different cuts. The resulting uncertainties from each cut are given in Table II and added in quadrature to yield overall systematic uncertainties.

Additional systematic uncertainties on the hadron spectra arise from time variations in the TOF timing (slat-by-slat and run-by-run variations), the small remaining contamination by other species after matching and PID cuts, uncertainty in the corrections for track reconstruction efficiency, and uncertainty on particle energy loss in the detector material. These uncertainties, which do not depend measurably on the hadron momentum, are listed in Table II. The sizable uncertainty in the matching cut is due to the non-Gaussian tails on the z-coordinate matching distributions. The track matching in this direction is limited by a relatively poor vertex resolution determined by the BBC in $p + p$ and $d +$ Au collisions due to the small multiplicities. The quoted 3%–4% uncertainty in the reconstruction efficiency correction represents the maximum local discrepancy between efficiencies measured with strict and loose track quality cuts.

TABLE II. Systematic errors in percent on particle yields in $d +$ Au and $p + p$ collisions. These values are independent of p_T.

	$d +$ Au	$p + p$
Geometric acceptance correction	4	4
Track matching	9	8
Timing variations	5	5
Reconstruction efficiency correction	3	4
Energy loss correction	1	2
Trigger bias	–	4

Uncertainties due to particle identification cuts are momentum dependent. For protons and antiprotons, the identification uncertainty is 8% at low p_T and decreases to 3% at high p_T. Kaons at low momentum have 10% PID uncertainty, decreasing to 3% at high p_T. For pions, the uncertainty increases from 4% to 10% with increasing p_T. Kaon and proton uncertainties decrease with increasing p_T because energy loss and decay corrections become smaller. The pion uncertainties are dominated by the particle identification performance, which worsens with increasing p_T.

The systematic error on the feed-down proton spectrum is 26%, primarily due to uncertainty in the measured Λ spectra and particle composition. The resulting systematic error on the final prompt proton and antiproton spectra is of the order of 10% in both $p + p$ and $d +$ Au. The systematic error on the proton to pion ratio is 12%, including the uncertainty on $\overline{\Lambda}/\Lambda$.

Systematic uncertainties on the $d +$ Au nuclear modification factors mostly cancel as the $p + p$ and $d +$ Au data were collected immediately following one another, and detector performance was very similar. The overall systematic error in the nuclear modification factor is due to uncertainties in the reconstruction efficiencies, fiducial volumes, and small run-by-run variations. It is approximately 10%, independent of particle species and p_T. An additional $d +$ Au scale uncertainty is shown as boxes around 1.0 in the figures; this is the quadrature sum of uncertainties on the $p + p$ cross section of 9.6% and the number of binary collisions in the each centrality bin (presented in Table I).

The systematic error on the Au + Au nuclear modification factors is derived by propagating the systematic errors on $p + p$ and Au + Au data [7] to the final ratio. The average systematic error for pions is approximately 15%, while for protons and antiprotons it is on the order of 19%. The normalization uncertainty, as in $d +$ Au, is the quadrature sum of uncertainties on the $p + p$ cross section and the error on the number of binary collisions in the corresponding Au + Au centrality bin from Ref. [7]. We note that for the most central Au + Au bin (0%–5%), $N_{\rm coll} = 1065.4$ and the uncertainty is ± 105.3; in the most peripheral bin (60%–92%), $N_{\rm coll} = 14.5 \pm 4.0$.

III. RESULTS

A. Hadron spectra

The fully corrected p_T distributions of π, K, p, and $\bar{p}$ for the four $d +$ Au centrality bins and for $p + p$ collisions are

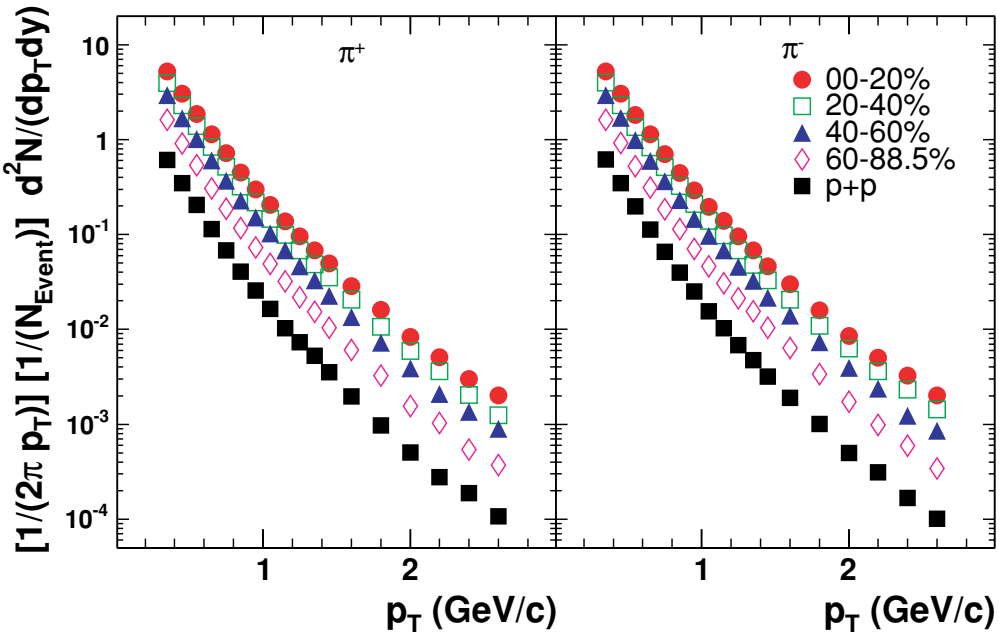

FIG. 4. (Color online) Invariant yields at midrapidity for positive and negative pions as a function of p_T for various centrality classes in $d + \text{Au}$ and $p + p$ collisions. The error bars show statistical uncertainties only and are typically smaller than the data points.

shown in Figs. 4, 5, and 6, respectively. Pions show a power law spectral shape, while kaons and protons are exponential.

To probe the hadron production mechanism, it is instructive to compare particle and antiparticle spectra. Figures 7, 8, and 9 show the ratios of antiparticle to particle production as a function of p_T in $p + p$, $d + \text{Au}$, and (for comparison) central $\text{Au} + \text{Au}$ collisions from [7] for π, K, and p, respectively. For all three hadron species, the ratios are flat with p_T in the PHENIX p_T range. The values agree within uncertainties with measurements by the STAR Collaboration [31]. The $d + \text{Au}$ yield ratios are in good agreement with $p + p$ collisions, and the ratios remain the same even in central $\text{Au} + \text{Au}$ collisions. The production ratio of antiparticle to particle is $0.99 \pm 0.01(\text{stat}) \pm 0.06(\text{syst})$ for pions and $0.92 \pm 0.01(\text{stat}) \pm 0.07(\text{syst})$ for kaons in both minimum bias $d + \text{Au}$ and $p + p$ collisions. The antiproton to proton ratio is measured to be $0.70 \pm 0.01(\text{stat}) \pm 0.08(\text{syst})$ in minimum bias $d + \text{Au}$ collisions and $0.71 \pm 0.01(\text{stat}) \pm 0.08(\text{syst})$ in $p + p$ collisions. All ratios are consistent within errors with values reported by PHOBOS [32] and BRAHMS [33].

B. Nuclear modification factors

The measurement of identified hadrons in both $d + \text{Au}$ and $p + p$ collisions allows study of the centrality dependence of the nuclear modification factor in $d + \text{Au}$. A standard way to quantify nuclear medium effects on high-p_T particle production in nucleus-nucleus collisions is provided by the

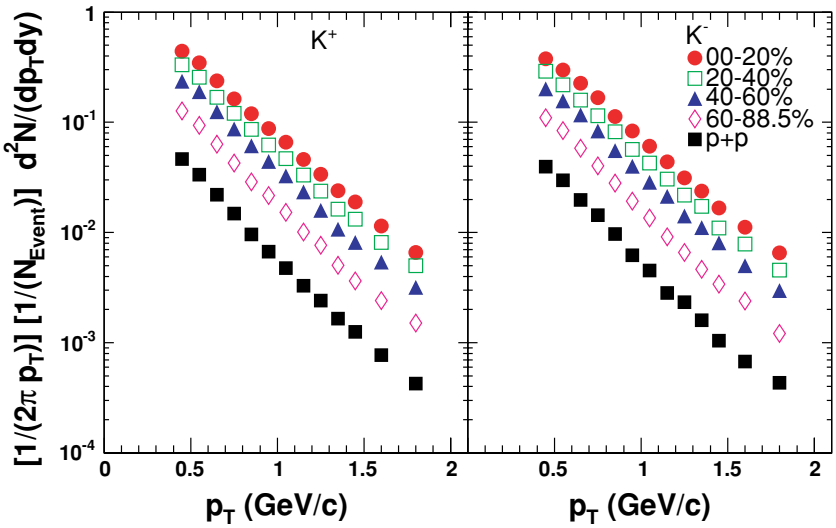

FIG. 5. (Color online) Same as Fig. 4, but for kaons.

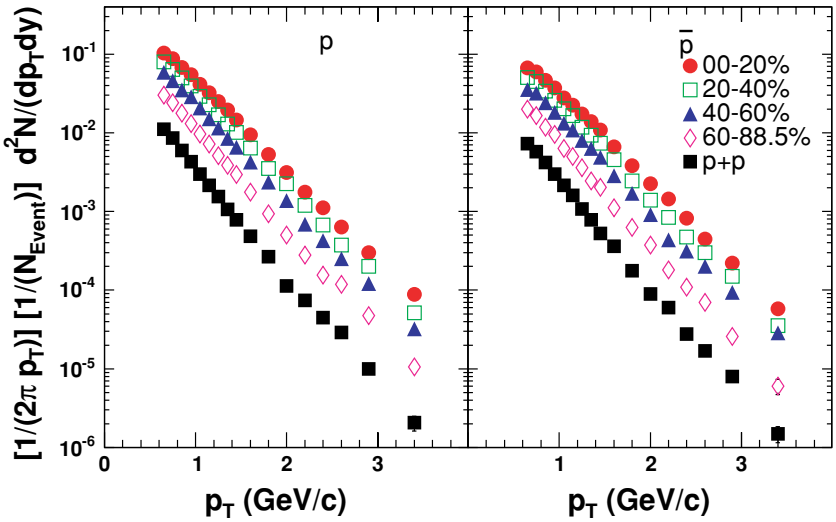

FIG. 6. (Color online) Same as Fig. 4, but for protons and antiprotons.

nuclear modification factor. This is the ratio of the $d + \mathrm{Au}$ invariant yields to the binary collision scaled $p + p$ invariant yields, that is,

$$R_{d\mathrm{Au}}(p_T) = \frac{\left(1/N_{d\mathrm{Au}}^{\mathrm{evt}}\right) d^2N_{d\mathrm{Au}}/dy\,dp_T}{T_{d\mathrm{Au}}\, d^2\sigma_{\mathrm{inel}}^{pp}/dy\,dp_T}, \qquad (5)$$

where $T_{d\mathrm{Au}} = \langle N_{\mathrm{coll}}\rangle/\sigma_{\mathrm{inel}}^{pp}$ describes the nuclear geometry, and $d^2\sigma_{\mathrm{inel}}^{pp}/dy dp_T$ for $p + p$ collisions is derived from the measured $p + p$ cross section. $\langle N_{\mathrm{coll}}\rangle$ is the average number of inelastic nucleon-nucleon collisions determined from simulation using the Glauber model as input, as described in Sec. II A. $N_{d\mathrm{Au}}^{\mathrm{evt}}$ is the number of $d + \mathrm{Au}$ events in the relevant centrality class.

Figure 10 shows $R_{d\mathrm{Au}}$ for pions, kaons, and protons for minimum bias $d + \mathrm{Au}$ collisions. We observe a nuclear enhancement in the production of hadrons with $p_T \gtrsim 1.5$–2 GeV/c in $d + \mathrm{Au}$ collisions, compared to that in $p + p$. As was already suggested when comparing the enhancement for inclusive charged hadrons with that of neutral pions [34], there is a species dependence in the Cronin effect. The Cronin effect for charged pions is small, as was observed for neutral pions. The nuclear enhancement for protons and antiprotons is considerably larger. The kaon measurement has a more limited kinematic range, but the $R_{d\mathrm{Au}}$ agrees with that of the pions at comparable p_T.

Figure 11 shows $R_{d\mathrm{Au}}$ for pions, kaons, and protons in the four $d + \mathrm{Au}$ centrality bins. Peripheral $d + \mathrm{Au}$ collisions ($\langle N_{\mathrm{coll}}\rangle = 3.1 \pm 0.3$) do not show any modification of high-momentum hadron production, compared to that in $p + p$ collisions. At $p_T \leqslant 1$ GeV/c, the nuclear modification factor falls below 1.0. This is to be expected as soft particle production scales with the number of participating nucleons, not with the number of binary nucleon-nucleon collisions. More central collisions show increasing nuclear enhancement in both high-p_T pion and proton production.

The bands in Fig. 11 show a calculation of the Cronin effect for pions by Accardi and Gyulassy, using a pQCD model of multiple semihard collisions and taking geometrical shadowing into account [13]. The agreement above 1 GeV/c, where the calculation should be reliable, is very good for all four centrality bins. This agreement illustrates that the multiple

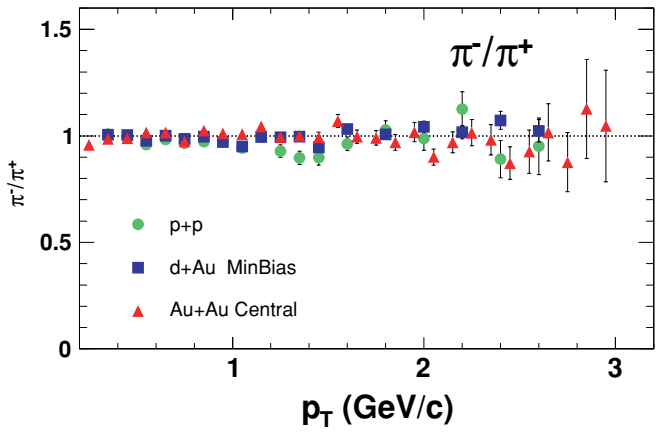

FIG. 7. (Color online) Ratio of midrapidity spectra for π^- to π^+ in $d + \mathrm{Au}$, $p + p$, and central $\mathrm{Au} + \mathrm{Au}$ collisions. Error bars show statistical uncertainties only.

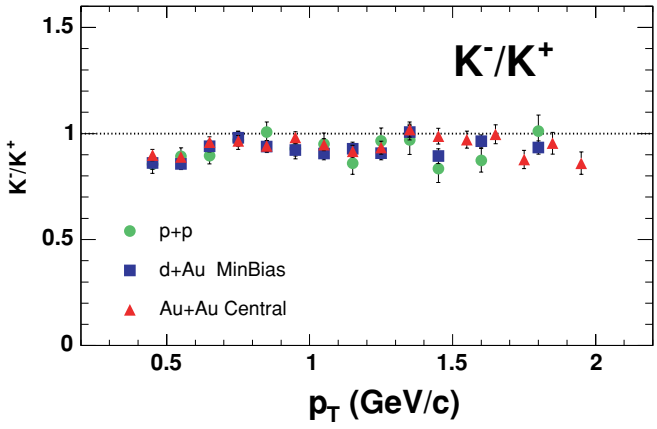

FIG. 8. (Color online) Same as Fig. 7, but for K^- to K^+.

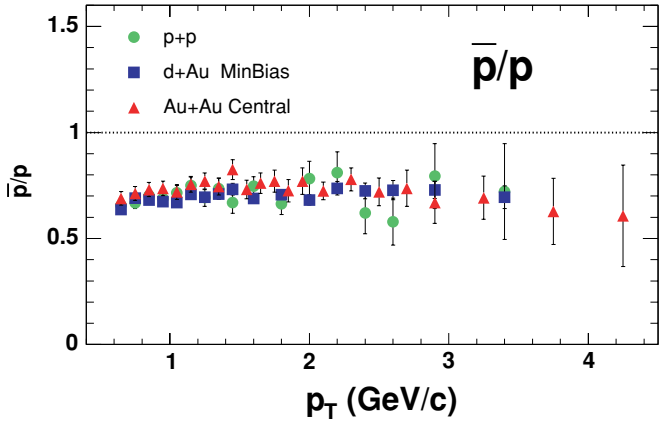

FIG. 9. (Color online) Same as Fig. 7, but antiprotons to protons.

partonic scattering and nuclear shadowing alone can explain the observed Cronin effect and leaves very little room for gluon saturation effects in the nuclear initial state at midrapidity at RHIC energies [13].

C. Centrality dependence

We further probe the effect of cold nuclear matter upon hadron production using the number of collisions suffered by each projectile nucleon for the four centrality bins. Figure 12 compares the centrality dependence of $R_{d\mathrm{Au}}$ for pions and protons in two momentum bins. The modification factors are plotted as a function of $\nu = N_{\mathrm{coll}}/N^{d}_{\mathrm{part}}$, the number of collisions per participating deuteron nucleon. The lower momentum bin, $0.6 \leqslant p_T \leqslant 1.0\ \mathrm{GeV}/c$, is chosen in the region

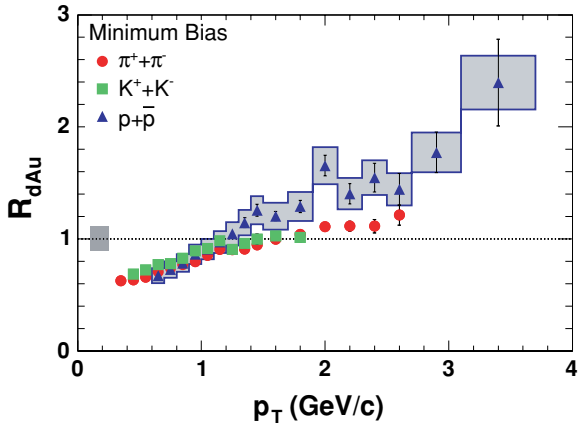

FIG. 10. (Color online) Nuclear modification factor $R_{d\mathrm{Au}}$ for pions, kaons, and protons in $d + \mathrm{Au}$ collisions for minimum bias events. The error bars represent the statistical errors. The box around 1.0 shows uncertainties in the $p + p$ absolute cross section and in the calculation of N_{coll}. For the proton and antiproton $R_{d\mathrm{Au}}$, the ~10% systematic uncertainty is also presented as boxes around the points. The systematic uncertainty on the pion and kaon $R_{d\mathrm{Au}}$ is similar but not shown in the picture for clarity.

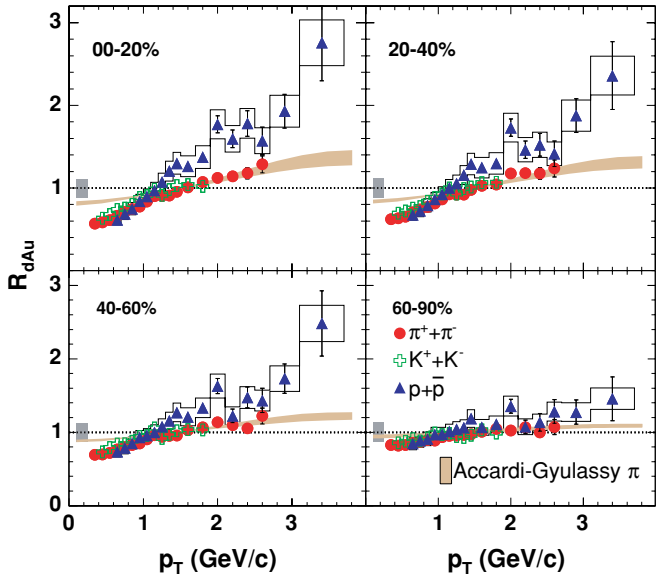

FIG. 11. (Color online) Nuclear modification factor $R_{d\mathrm{Au}}$ for pions, kaons, and protons in $d + \mathrm{Au}$ collisions in four centrality bins. The error bars represent the statistical errors. Boxes around 1.0 show uncertainties in the $p + p$ absolute cross section and in the calculation of N_{coll}. For the proton and antiproton $R_{d\mathrm{Au}}$, the ~10% systematic uncertainty is also presented as boxes around the points. The systematic uncertainty on the pion and kaon $R_{d\mathrm{Au}}$ is similar but not shown in the picture for clarity. Solid bands show the calculation of the nuclear modification factors for pions by Accardi and Gyulassy [13].

where $R_{d\mathrm{Au}}$ is less than 1.0, and hadron yields scale very nearly with the number of nucleons participating in the collision, rather than with the number of binary collisions. As expected,

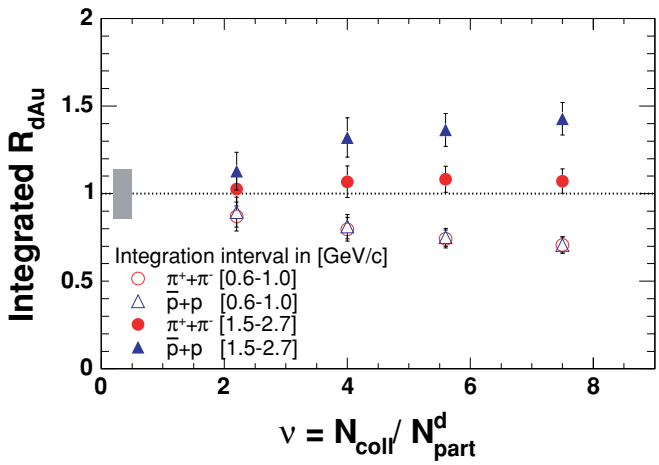

FIG. 12. (Color online) Integrated $R_{d\mathrm{Au}}$ for pions and protons in two momentum bins as a function of the number of collisions suffered by the deuteron participant ν. Error bars indicate the quadrature sum of statistical errors and uncertainties on the number of collisions bin by bin. The solid box on the left shows the magnitude of the centrality independent uncertainties.

$R_{d\mathrm{Au}}$ decreases with ν in this p_T range, with negligible difference between pions and protons. In the higher p_T bin, $R_{d\mathrm{Au}}$ increases with the number of collisions, with a notably larger rate of increase for baryons than for mesons. Though the $R_{d\mathrm{Au}}$ values for higher p_T hadrons appear to flatten with increasing centrality, the uncertainties are too large to allow a definitive conclusion about saturation with the number of collisions encountered by each participant nucleon [14].

D. Cronin effect for baryons

Figure 13 shows the ratio of the nuclear modification factors observed for protons and antiprotons to that for pions in the most central and most peripheral $d+\mathrm{Au}$ collisions. The enhancement for protons is stronger, by approximately 30–50% in the most central collisions; this was also reported by STAR [31,35]. The increasing difference between baryons and mesons for more central collisions indicates that the baryon production mechanism appears to depend upon the surrounding nuclear medium already found in $d+\mathrm{Au}$ collisions. We note, however, that the species dependence of the Cronin effect in $d+\mathrm{Au}$ collisions is much smaller than the factor of $\approx$3 enhancement of protons in central Au + Au collisions, as can be seen by comparing the nuclear modification factors for pions and protons in central Au + Au collisions shown below in Sec. IV A.

By converting the nuclear modification factors to beam per-nucleon cross section ratios and vice versa, it is possible to compare them to measurements of the Cronin effect at other energies. Figure 14 shows nuclear modification factors from this work compared to those derived from α factors measured at lower energies [2], in a manner similar to that used in [3] to calculate per-nucleon cross section ratios. To make the transition to nuclear modification factors from per-nucleon cross section ratios we assume that $\sigma_{d+\mathrm{Au}} = 2\sigma_{p+A}$ and that $\sigma_{p+d} = 2\,\sigma_{p+p}$ at the low energy of interest, which is a very reasonable approximation for all particle species [2].

The observed species dependence of the enhancement is similar to that measured in lower energy collisions [3]. The

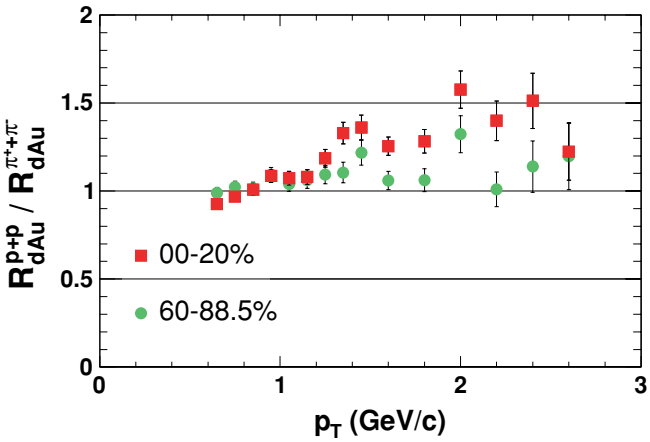

FIG. 13. (Color online) Ratio of the proton over the pion nuclear modification in $d+\mathrm{Au}$ collisions, for central and peripheral events. Error bars indicate statistical errors only.

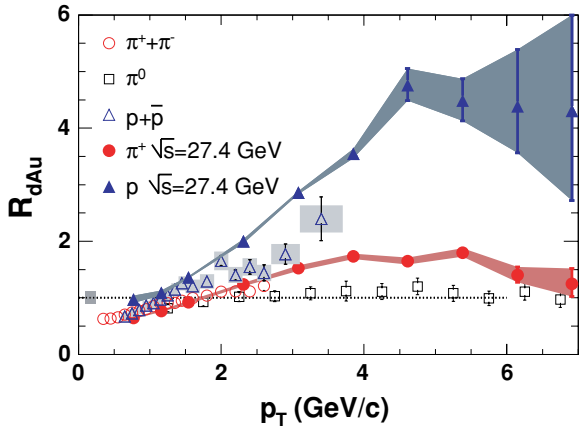

FIG. 14. (Color online) Nuclear modification factors for charged pions, neutral pions [34], and protons and antiprotons from minimum bias $d+\mathrm{Au}$ from this work (open symbols) compared to nuclear modification factors calculated from the per-beam nucleon cross sections reported for $\sqrt{s} = 27.4$ GeV $p+A$ collisions [2] (closed symbols and continuous bands).

magnitude of the enhancement for pions at $p_T > 3$ GeV/c is larger at $\sqrt{s} = 27.4$ GeV than at 200 GeV. Protons and antiprotons are also more enhanced at the lower beam energy: a factor of 3.5 at $p_T \approx 4$ GeV, as compared with a factor of 2 at $\sqrt{s} = 200$ GeV. This energy dependence of the Cronin effect for pions has been interpreted as evidence for a different production mechanism for high-p_T hadrons at RHIC energies compared to lower energies [36]. In this model, high-p_T hadrons are produced incoherently on different nucleons at low energy, while in higher energy collisions the production amplitudes can interfere because the process of gluon radiation is long compared to the binary collision time. Coherent radiation from different nucleons is subject to Landau-Pomeranchuk suppression. However, the difference between the baryon and meson Cronin effects is not predicted by this model.

IV. DISCUSSION

Traditional explanations of the Cronin effect all involve multiple scattering of incoming partons that lead to an enhancement at intermediate p_T [12]. Various theoretical models of multiple scattering predict somewhat different dependence upon the number of scattering centers. The observed centrality or ν dependence for pions is well reproduced by semihard initial state scattering [13] as shown in Fig. 11; see also [14–16]. The models include initial state multiple scattering as well as geometrical shadowing. However, none of these models would predict a species-dependent Cronin effect, as initial state parton scattering precedes fragmentation into the different hadronic species. The markedly larger Cronin effect for protons and antiprotons requires processes in addition to initial state multiple scattering in baryon production at moderate transverse momenta.

Recently, Hwa and Yang [17] demonstrated an alternative explanation of the Cronin effect, attributed to the recombination of shower quarks with those from the medium in

d + Au collisions. Such models do predict a larger Cronin effect for protons than for pions, which may be justified by the rather short formation times of $p_T = 2$–4 GeV/c protons. According to the uncertainty principle, the formation time in the rest frame of the hadron can be related to the hadron size R_h. In the laboratory frame, the formation time of a hadron with mass m_h and energy E_h is given by $\tau_f \approx R_h \frac{E_h}{m_h}$. For a $p_T = 2.5$ GeV/c pion, the formation time is 9–18 fm/c (for $R_h = 0.5$–1.0 fm), well outside the collision region. However, for $p_T = 2.5$ GeV/c protons, the corresponding formation time is only 2.7 fm/c, suggesting that the hadronization process may well begin in or near the nuclear medium.

A. Comparison to Au + Au collisions

The proton to pion ratio from minimum bias $p + p$ and minimum bias d + Au are compared to each other and to central and peripheral Au + Au collisions in Fig. 15. As noted above, protons and antiprotons are feed-down corrected in each system.

The p/π ratio in d + Au is very similar to that in peripheral Au + Au collisions and lies slightly above the $p + p$ ratio. The p/π ratio in central Au + Au collisions, however, is much larger. The difference between the ratio in d + Au and central Au + Au clearly indicates that baryon yield enhancement is not simply an effect of sampling a large nucleus in the initial state. The large enhancement requires the presence of a substantial volume of nuclear medium.

Figures 16–18 compare the nuclear modification factors for pions, kaons and (anti)protons in Au + Au and d + Au collisions. The $p + p$ data from this work allow, for the first time, the calculation of nuclear modification factors in Au + Au by PHENIX. The Au + Au data are taken from [7]. It should be noted that common fluctuations between $R_{d\mathrm{Au}}$ and R_{AuAu} in Figs. 17 and 18 arise because the $p + p$ denominators are common.

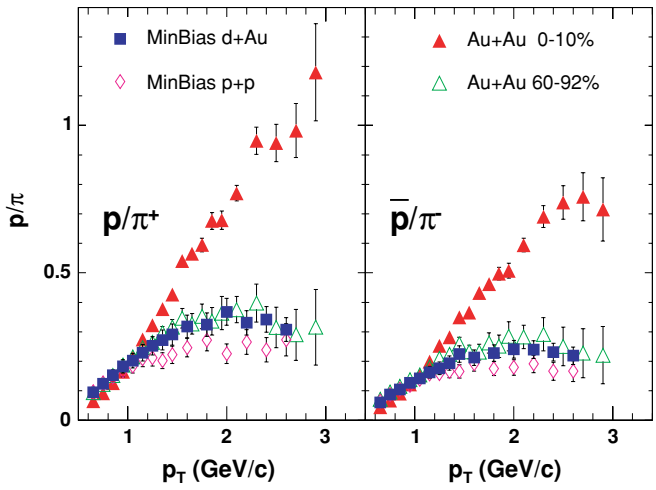

FIG. 15. (Color online) Ratio of feed-down-corrected protons to π^+ and antiprotons to π^- in minimum bias $p + p$ and d + Au compared to peripheral and central Au + Au collisions. Statistical error bars are shown.

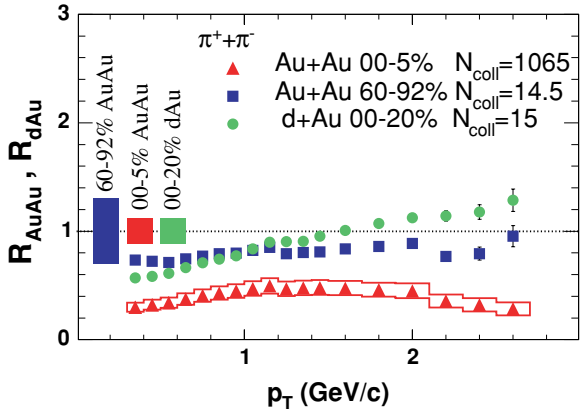

FIG. 16. (Color online) Nuclear modification factors for pions, comparing central and peripheral Au + Au collisions to central d + Au. Note that the number of binary nucleon-nucleon collisions in peripheral Au + Au and in central d + Au are very similar. Solid bars on the left indicate normalization uncertainties in the $p + p$ absolute cross section and in the calculation of N_{coll} for the three systems. Error bars indicate statistical errors only; for the most central Au + Au case, the systematic errors discussed in the text are shown as boxes around the points.

Central and peripheral Au + Au collisions are compared to central d + Au collisions, which have a similar number of binary collisions as the peripheral Au + Au sample. Pions show a much lower R_{AuAu} at high p_T in central than in peripheral Au + Au collisions, as expected from the large energy loss suffered by the partons in central collisions. The nuclear modification factor rises faster with p_T in d + Au than in peripheral Au + Au, despite the comparable number of binary collisions. As Au + Au involves a second Au nucleus, shadowing effects can be expected to be larger, reducing the observed Cronin effect.

The proton and antiproton nuclear modification factors show a quite different trend. The Cronin effect, larger than 1.0 at higher p_T values, is independent of centrality in Au + Au collisions. This feature was already observed as binary collision scaling of proton and antiproton production in the central/peripheral collision yield ratios [6]. The Cronin effect in d + Au is at least as large as that in peripheral

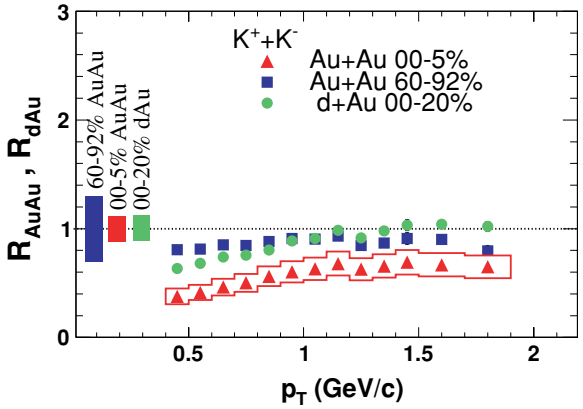

FIG. 17. (Color online) Same as Fig. 16, but for kaons.

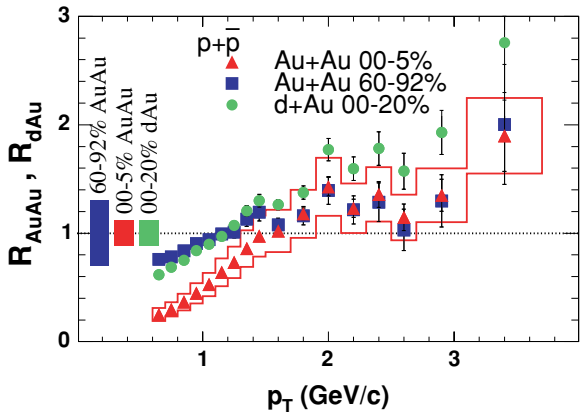

FIG. 18. (Color online) Same as Fig. 16, but for protons and antiprotons.

Au + Au. The difference indicates that baryon production must involve a complex interplay of processes in addition to initial state nucleon-nucleon collisions.

V. CONCLUSION

We have presented the centrality and species dependence of identified particle spectra in d + Au collisions, including the dependence of the nuclear modification factor upon the number of collisions per participant nucleon. We also presented the first measurement of R_{AuAu} for pions, kaons, protons, and antiprotons in Au + Au collisions.

The Cronin effect for charged pions is small, but nonzero. The proton to pion ratio in d + Au is similar to that in peripheral Au + Au, while the corresponding ratio in $p + p$ is somewhat lower. The nuclear modification factor in d + Au for protons shows a larger Cronin effect than that for pions, and the difference increases with collision centrality. This difference was seen, but never fully understood, in lower energy collisions; but it is not large enough to account for the abundance of protons in central Au + Au collisions. The difference between pions and protons does, however, indicate that the Cronin effect is not simply due to multiple scattering of the incoming partons. R_{AuAu} for protons and antiprotons confirms previous observations that the production of high-p_T baryons in Au + Au scales with the number of binary nucleon-nucleon collisions, but the baryon yield per collision in Au + Au exceeds that in $p + p$.

ACKNOWLEDGMENTS

We thank the staff of the Collider-Accelerator and Physics Departments at Brookhaven National Laboratory and the staff of the other PHENIX participating institutions for their vital contributions. We acknowledge support from the Department of Energy, Office of Science, Office of Nuclear Physics, the National Science Foundation, Abilene Christian University Research Council, Research Foundation of SUNY, and Dean of the College of Arts and Sciences, Vanderbilt University (U.S.A), Ministry of Education, Culture, Sports, Science, and Technology and the Japan Society for the Promotion of Science (Japan), Conselho Nacional de Desenvolvimento Científico e Tecnológico and Fundação de Amparo à Pesquisa do Estado de São Paulo (Brazil), Natural Science Foundation of China (People's Republic of China), Centre National de la Recherche Scientifique, Commissariat à l'Énergie Atomique, and Institut National de Physique Nucléaire et de Physique des Particules (France), Ministry of Industry, Science and Technologies, Bundesministerium für Bildung und Forschung, Deutscher Akademischer Austausch Dienst, and Alexander von Humboldt Stiftung (Germany), Hungarian National Science Fund, OTKA (Hungary), Department of Atomic Energy (India), Israel Science Foundation (Israel), Korea Research Foundation, Center for High Energy Physics, and Korea Science and Engineering Foundation (Korea), Ministry of Education and Science, Russian Academy of Sciences, Federal Agency of Atomic Energy (Russia), VR and the Wallenberg Foundation (Sweden), the U.S. Civilian Research and Development Foundation for the Independent States of the Former Soviet Union, the U.S.-Hungarian NSF-OTKA-MTA, and the U.S.-Israel Binational Science Foundation.

[1] J. W. Cronin *et al.*, Phys. Rev. D **11**, 3105 (1975).
[2] D. Antreasyan, J. W. Cronin, H. J. Frisch, M. J. Shochet, L. Kluberg, P. A. Piroue, and R. L. Sumner, Phys. Rev. D **19**, 764 (1979).
[3] P. B. Straub *et al.*, Phys. Rev. Lett. **68**, 452 (1992).
[4] K. Adcox *et al.* (PHENIX Collaboration), Phys. Rev. Lett. **88**, 022301 (2002).
[5] K. Adcox *et al.* (PHENIX Collaboration), Phys. Rev. Lett. **88**, 242301 (2002).
[6] S. S. Adler *et al.* (PHENIX Collaboration), Phys. Rev. Lett. **91**, 172301 (2003).
[7] S. S. Adler *et al.* (PHENIX Collaboration), Phys. Rev. C **69**, 034909 (2004).
[8] B. Alper *et al.*, Nucl. Phys. **B100**, 237 (1975).
[9] R. C. Hwa and C. B. Yang, Phys. Rev. C **67**, 034902 (2003); **70**, 037901 (2003); R. J. Fries, B. Muller, C. Nonaka, and S. A. Bass, Phys. Rev. Lett. **90**, 202303 (2003); Phys. Rev. C **68**, 044902 (2003); V. Greco, C. M. Ko, and P. Levai, Phys. Rev. Lett. **90**, 202302 (2003); Phys. Rev. C **68**, 034904 (2003).
[10] G. Rossi and G. Veneziano, Nucl. Phys. **B123**, 507 (1977); D. Kharzeev, Phys. Lett. **B378**, 238 (1996); S. E. Vance, M. Gyulassy, and X.-N. Wang, Phys. Lett. **B443**, 45 1998.
[11] D. Kharzeev, E. Levin, and L. McLerran, Phys. Lett. **B561**, 93 (2003).
[12] M. Lev and B. Petersson, Z. Phys. C **21**, 155 (1983).
[13] A. Accardi and M. Gyulassy, Phys. Lett. **B586**, 244 (2004).
[14] G. Papp, P. Levai, and G. Fai, Phys. Rev. C **61**, 021902(R) (1999).
[15] I. Vitev and M. Gyulassy, Phys. Rev. Lett. **89**, 252301 (2002).
[16] X. N. Wang, Phys. Rev. C **61**, 064910 (2000).
[17] R. C. Hwa and C. B. Yang, Phys. Rev. Lett. **93**, 082302 (2004).
[18] K. Adcox *et al.* (PHENIX Collaboration), Nucl. Instrum. Methods A **499**, 469 (2003). In addition to this overview, detailed

descriptions of individual subsystems are published in the same volume.
[19] K. A. Drees and Z. Xu, "Proceedings of the PAC2001 Conference" 3120, 2001 (unpublished). http://epaper.kek.jp/p03/PAPERS/TPPB032.PDF
[20] R. Brun, R. Hagelberg, N. Hansroul, and J. Lassalle, CERN-DD-78-2, 1978 (unpublished).
[21] S. S. Adler *et al*. (PHENIX Collaboration), Phys. Rev. Lett. **96**, 012304 (2006).
[22] R. J. Glauber and G. Matthiae, Nucl. Phys. **B21**, 135 (1970).
[23] S. S. Adler *et al*. (PHENIX Collaboration), Phys. Rev. Lett. **94**, 082302 (2005).
[24] L. Hulthèn and M. Sagawara, Handbuch der Physik (Springer-Verlag, Berlin, 1957), Vol. 39.
[25] K. Adcox *et al*. (PHENIX Collaboration), Nucl. Instrum. Methods A **482**, 491 (2002).
[26] R. E. Ansorge *et al*. (UA5 Collaboration), Nucl. Phys. **B328**, 36 (1989).
[27] J. Adams and M. Heinz (STAR Collaboration), nucl-ex/0403020 (2004).
[28] M. Heinz (STAR Collaboration), J. Phys. G **31**, S141 (2005).
[29] X. Z. Cai (STAR Collaboration), J. Phys. G **31**, S1015 (2005).
[30] R. Witt (STAR Collaboration), nucl-ex/0403021 (2004).
[31] J. Adams, *et al*. (STAR Collaboration), Phys. Lett. **B616**, 8 (2005).
[32] B. B. Back *et al*. (PHOBOS Collaboration), Phys. Rev. C **70**, 011901 (2004); **71**, 021901 (2005).
[33] I. G. Bearden *et al*. (BRAHMS Collaboration), Phys. Lett. **B607**, 42 (2005).
[34] S. S. Adler *et al*. (PHENIX Collaboration), Phys. Rev. Lett. **91**, 072303 (2003).
[35] J. Adams *et al*. (STAR Collaboration), Phys. Lett. **B616**, 8 (2005).
[36] B. Z. Kopeliovich, J. Nemchik, A. Schafer, and A. V. Tarasov, Phys. Rev. Lett. **88**, 232303 (2002).

PHYSICAL REVIEW D **73,** 091102(R) (2006)

Improved measurement of double helicity asymmetry in inclulsive midrapidity π^0 production for polarized $p + p$ collisions at $\sqrt{s} = 200$ GeV

S. S. Adler,[5] S. Afanasiev,[20] C. Aidala,[10] N. N. Ajitanand,[47] Y. Akiba,[22,41,42] A. Al-Jamel,[36] J. Alexander,[47] K. Aoki,[26,41] L. Aphecetche,[49] R. Armendariz,[36] S. H. Aronson,[5] R. Averbeck,[48] T. C. Awes,[37] B. Azmoun,[5] V. Babintsev,[17] A. Baldisseri,[11] K. N. Barish,[6] P. D. Barnes,[29] B. Bassalleck,[35] S. Bathe,[6,32] S. Batsouli,[10] V. Baublis,[40] F. Bauer,[6] A. Bazilevsky,[5,42] S. Belikov,[5,17,19] R. Bennett,[48] Y. Berdnikov,[44] M. T. Bjorndal,[10] J. G. Boissevain,[29] H. Borel,[11] K. Boyle,[48] M. L. Brooks,[29] D. S. Brown,[36] N. Bruner,[35] D. Bucher,[32] H. Buesching,[5,32] V. Bumazhnov,[17] G. Bunce,[5,42] J. M. Burward-Hoy,[28,29] S. Butsyk,[48] X. Camard,[49] S. Campbell,[48] J.-S. Chai,[21] P. Chand,[4] W. C. Chang,[2] S. Chernichenko,[17] C. Y. Chi,[10] J. Chiba,[22] M. Chiu,[10] I. J. Choi,[56] R. K. Choudhury,[4] T. Chujo,[5,53] V. Cianciolo,[37] C. R. Cleven,[15] Y. Cobigo,[11] B. A. Cole,[10] M. P. Comets,[38] P. Constantin,[19] M. Csanád,[13] T. Csörgő,[23] J. P. Cussonneau,[49] D. d'Enterria,[10] T. Dahms,[48] K. Das,[14] G. David,[5] F. Deák,[13] H. Delagrange,[49] A. Denisov,[17] A. Deshpande,[42,48] E. J. Desmond,[5] A. Devismes,[48] O. Dietzsch,[45] A. Dion,[48] J. L. Drachenberg,[1] O. Drapier,[27] A. Drees,[48] A. K. Dubey,[55] A. Durum,[17] D. Dutta,[4] V. Dzhordzhadze,[50] Y. V. Efremenko,[37] J. Egdemir,[48] A. Enokizono,[16] H. En'yo,[41,42] B. Espagnon,[38] S. Esumi,[52] D. E. Fields,[35,42] C. Finck,[49] F. Fleuret,[27] S. L. Fokin,[25] B. Forestier,[30] B. D. Fox,[42] Z. Fraenkel,[55] J. E. Frantz,[10] A. Franz,[5] A. D. Frawley,[14] Y. Fukao,[26,41,42] S.-Y. Fung,[6] S. Gadrat,[30] F. Gastineau,[49] M. Germain,[49] A. Glenn,[50] M. Gonin,[27] J. Gosset,[11] Y. Goto,[41,42] R. Granier de Cassagnac,[27] N. Grau,[19] S. V. Greene,[53] M. Grosse Perdekamp,[18,42] T. Gunji,[8] H.-Å. Gustafsson,[31] T. Hachiya,[16,41] A. Hadj Henni,[49] J. S. Haggerty,[5] M. N. Hagiwara,[1] H. Hamagaki,[8] A. G. Hansen,[29] H. Harada,[16] E. P. Hartouni,[28] K. Haruna,[16] M. Harvey,[5] E. Haslum,[31] K. Hasuko,[41] R. Hayano,[8] X. He,[15] M. Heffner,[28] T. K. Hemmick,[48] J. M. Heuser,[41] P. Hidas,[23] H. Hiejima,[18] J. C. Hill,[19] R. Hobbs,[35] M. Holmes,[53] W. Holzmann,[47] K. Homma,[16] B. Hong,[24] A. Hoover,[36] T. Horaguchi,[41,42,51] M. G. Hur,[21] T. Ichihara,[41,42] V. V. Ikonnikov,[25] K. Imai,[26,41] M. Inaba,[52] M. Inuzuka,[8] D. Isenhower,[1] L. Isenhower,[1] M. Ishihara,[41] T. Isobe,[8] M. Issah,[47] A. Isupov,[20] B. V. Jacak,[48] J. Jia,[10,48] J. Jin,[10] O. Jinnouchi,[41,42] B. M. Johnson,[5] S. C. Johnson,[28] K. S. Joo,[33] D. Jouan,[38] F. Kajihara,[8,41] S. Kametani,[8,54] N. Kamihara,[41,51] M. Kaneta,[42] J. H. Kang,[56] K. Katou,[54] T. Kawabata,[8] T. Kawagishi,[52] A. V. Kazantsev,[25] S. Kelly,[9,10] B. Khachaturov,[55] A. Khanzadeev,[40] J. Kikuchi,[54] D. J. Kim,[56] E. Kim,[46] G.-B. Kim,[27] H. J. Kim,[56] Y.-S. Kim,[21] E. Kinney,[9] A. Kiss,[13] E. Kistenev,[5] A. Kiyomichi,[41] C. Klein-Boesing,[32] H. Kobayashi,[42] L. Kochenda,[40] V. Kochetkov,[17] R. Kohara,[16] B. Komkov,[40] M. Konno,[52] D. Kotchetkov,[6] A. Kozlov,[55] P. J. Kroon,[5] C. H. Kuberg,[1,*] G. J. Kunde,[29] N. Kurihara,[8] K. Kurita,[41,43] M. J. Kweon,[24] Y. Kwon,[56] G. S. Kyle,[36] R. Lacey,[47] J. G. Lajoie,[19] Y. Le Bornec,[38] A. Lebedev,[19,25] S. Leckey,[48] D. M. Lee,[29] M. K. Lee,[56] M. J. Leitch,[29] M. A. L. Leite,[45] X. H. Li,[6] H. Lim,[46] A. Litvinenko,[20] M. X. Liu,[29] C. F. Maguire,[53] Y. I. Makdisi,[5] A. Malakhov,[20] M. D. Malik,[35] V. I. Manko,[25] Y. Mao,[39,41] G. Martinez,[49] H. Masui,[52] F. Matathias,[48] T. Matsumoto,[8,54] M. C. McCain,[1,18] P. L. McGaughey,[29] Y. Miake,[52] T. E. Miller,[53] A. Milov,[48] S. Mioduszewski,[5] G. C. Mishra,[15] J. T. Mitchell,[5] A. K. Mohanty,[4] D. P. Morrison,[5] J. M. Moss,[29] T. V. Moukhanova,[25] D. Mukhopadhyay,[53,55] M. Muniruzzaman,[6] J. Murata,[43,41] S. Nagamiya,[22] Y. Nagata,[52] J. L. Nagle,[9,10] M. Naglis,[55] T. Nakamura,[16] J. Newby,[28,50] M. Nguyen,[48] B. E. Norman,[29] A. S. Nyanin,[25] J. Nystrand,[31] E. O'Brien,[5] C. A. Ogilvie,[19] H. Ohnishi,[41] I. D. Ojha,[3,53] H. Okada,[26,41] K. Okada,[41,42] O. O. Omiwade,[1] A. Oskarsson,[31] I. Otterlund,[31] K. Oyama,[8] K. Ozawa,[8] D. Pal,[53,55] A. P. T. Palounek,[29] V. Pantuev,[48] V. Papavassiliou,[36] J. Park,[46] W. J. Park,[24] S. F. Pate,[36] H. Pei,[19] V. Penev,[20] J.-C. Peng,[18] H. Pereira,[11] V. Peresedov,[20] D. Yu. Peressounko,[25] A. Pierson,[35] C. Pinkenburg,[5] R. P. Pisani,[5] M. L. Purschke,[5] A. K. Purwar,[48] H. Qu,[15] J. M. Qualls,[1] J. Rak,[19] I. Ravinovich,[55] K. F. Read,[37,50] M. Reuter,[48] K. Reygers,[32] V. Riabov,[40] Y. Riabov,[40] G. Roche,[30] A. Romana,[27,*] M. Rosati,[19] S. S. E. Rosendahl,[31] P. Rosnet,[30] P. Rukoyatkin,[20] V. L. Rykov,[41] S. S. Ryu,[56] B. Sahlmueller,[32] N. Saito,[26,41,42] T. Sakaguchi,[8,54] S. Sakai,[52] V. Samsonov,[40] L. Sanfratello,[35] R. Santo,[32] H. D. Sato,[26,41] S. Sato,[5,22,52] S. Sawada,[22] Y. Schutz,[49] V. Semenov,[17] R. Seto,[6] D. Sharma,[55] T. K. Shea,[5] I. Shein,[17] T.-A. Shibata,[41,51] K. Shigaki,[16] M. Shimomura,[52] T. Shohjoh,[52] K. Shoji,[26,41] A. Sickles,[48] C. L. Silva,[45] D. Silvermyr,[29,37] K. S. Sim,[24] C. P. Singh,[3] V. Singh,[3] S. Skutnik,[19] W. C. Smith,[1] A. Soldatov,[17] R. A. Soltz,[28] W. E. Sondheim,[29] S. P. Sorensen,[50] I. V. Sourikova,[5] F. Staley,[11] P. W. Stankus,[37] E. Stenlund,[31] M. Stepanov,[36] A. Ster,[23] S. P. Stoll,[5] T. Sugitate,[16] C. Suire,[38] J. P. Sullivan,[29] J. Sziklai,[23] T. Tabaru,[42] S. Takagi,[52] E. M. Takagui,[45] A. Taketani,[41,42] K. H. Tanaka,[22] Y. Tanaka,[34] K. Tanida,[41,42] M. J. Tannenbaum,[5] A. Taranenko,[47] P. Tarján,[12] T. L. Thomas,[35] M. Togawa,[26,41] J. Tojo,[41] H. Torii,[26,41,42] R. S. Towell,[1] V-N. Tram,[27] I. Tserruya,[55] Y. Tsuchimoto,[16,41] S. K. Tuli,[3] H. Tydesjö,[31] N. Tyurin,[17] T. J. Uam,[33] H. Valle,[53] H. W. van Hecke,[29] J. Velkovska,[5,53] M. Velkovsky,[48] R. Vertesi,[12] V. Veszprémi,[12] A. A. Vinogradov,[25] M. A. Volkov,[25] E. Vznuzdaev,[40] M. Wagner,[26,41] X. R. Wang,[15,36] Y. Watanabe,[41,42] J. Wessels,[32] S. N. White,[5] N. Willis,[38] D. Winter,[10] F. K. Wohn,[19] C. L. Woody,[5]

 © 2006 The American Physical Society

M. Wysocki,[9] W. Xie,[6,42] A. Yanovich,[17] S. Yokkaichi,[41,42] G. R. Young,[37] I. Younus,[35] I. E. Yushmanov,[25] W. A. Zajc,[10,†] O. Zaudtke,[32] C. Zhang,[10] S. Zhou,[7] J. Zimányi,[23] L. Zolin,[20] and X. Zong[19]

(PHENIX Collaboration)

[1]*Abilene Christian University, Abilene, Texas 79699, U.S., USA*
[2]*Institute of Physics, Academia Sinica, Taipei 11529, Taiwan*
[3]*Department of Physics, Banaras Hindu University, Varanasi 221005, India*
[4]*Bhabha Atomic Research Centre, Bombay 400 085, India*
[5]*Brookhaven National Laboratory, Upton, New York 11973-5000, USA*
[6]*University of California - Riverside, Riverside, California 92521, USA*
[7]*China Institute of Atomic Energy (CIAE), Beijing, People's Republic of China*
[8]*Center for Nuclear Study, Graduate School of Science, University of Tokyo, 7-3-1 Hongo, Bunkyo, Tokyo 113-0033, Japan*
[9]*University of Colorado, Boulder, Colorado 80309, USA*
[10]*Columbia University, New York, New York 10027, USA and Nevis Laboratories, Irvington, New York 10533, USA*
[11]*Dapnia, CEA Saclay, F-91191, Gif-sur-Yvette, France*
[12]*Debrecen University, H-4010 Debrecen, Egyetem tér 1, Hungary*
[13]*ELTE, Eötvös Loránd University, H - 1117 Budapest, Pázmány P. s. 1/A, Hungary*
[14]*Florida State University, Tallahassee, Florida 32306, USA*
[15]*Georgia State University, Atlanta, Georgia 30303, USA*
[16]*Hiroshima University, Kagamiyama, Higashi-Hiroshima 739-8526, Japan*
[17]*IHEP Protvino, State Research Center of Russian Federation, Institute for High Energy Physics, Protvino, 142281, Russia*
[18]*University of Illinois at Urbana-Champaign, Urbana, Illinois 61801, USA*
[19]*Iowa State University, Ames, Iowa 50011, USA*
[20]*Joint Institute for Nuclear Research, 141980 Dubna, Moscow Region, Russia*
[21]*KAERI, Cyclotron Application Laboratory, Seoul, South Korea*
[22]*KEK, High Energy Accelerator Research Organization, Tsukuba, Ibaraki 305-0801, Japan*
[23]*KFKI Research Institute for Particle and Nuclear Physics of the Hungarian Academy of Sciences (MTA KFKI RMKI), H-1525 Budapest 114, POBox 49, Budapest, Hungary*
[24]*Korea University, Seoul, 136-701, Korea*
[25]*Russian Research Center "Kurchatov Institute", Moscow, Russia*
[26]*Kyoto University, Kyoto 606-8502, Japan*
[27]*Laboratoire Leprince-Ringuet, Ecole Polytechnique, CNRS-IN2P3, Route de Saclay, F-91128, Palaiseau, France*
[28]*Lawrence Livermore National Laboratory, Livermore, California 94550, USA*
[29]*Los Alamos National Laboratory, Los Alamos, New Mexico 87545, USA*
[30]*LPC, Université Blaise Pascal, CNRS-IN2P3, Clermont-Fd, 63177 Aubiere Cedex, France*
[31]*Department of Physics, Lund University, Box 118, SE-221 00 Lund, Sweden*
[32]*Institut für Kernphysik, University of Muenster, D-48149 Muenster, Germany*
[33]*Myongji University, Yongin, Kyonggido 449-728, Korea*
[34]*Nagasaki Institute of Applied Science, Nagasaki-shi, Nagasaki 851-0193, Japan*
[35]*University of New Mexico, Albuquerque, New Mexico 87131, USA*
[36]*New Mexico State University, Las Cruces, New Mexico 88003, USA*
[37]*Oak Ridge National Laboratory, Oak Ridge, Tennessee 37831, USA*
[38]*IPN-Orsay, Universite Paris Sud, CNRS-IN2P3, BP1, F-91406, Orsay, France*
[39]*Peking University, Beijing, People's Republic of China*
[40]*PNPI, Petersburg Nuclear Physics Institute, Gatchina, Leningrad region, 188300, Russia*
[41]*RIKEN, The Institute of Physical and Chemical Research, Wako, Saitama 351-0198, Japan*
[42]*RIKEN BNL Research Center, Brookhaven National Laboratory, Upton, New York 11973-5000, USA*
[43]*Physics Department, Rikkyo University, 3-34-1 Nishi-Ikebukuro, Toshima, Tokyo 171-8501, Japan*
[44]*Saint Petersburg State Polytechnic University, St. Petersburg, Russia*
[45]*Universidade de São Paulo, Instituto de Física, Caixa Postal 66318, São Paulo CEP05315-970, Brazil*
[46]*System Electronics Laboratory, Seoul National University, Seoul, South Korea*
[47]*Chemistry Department, Stony Brook University, Stony Brook, SUNY, New York 11794-3400, USA*
[48]*Department of Physics and Astronomy, Stony Brook University, SUNY, Stony Brook, New York 11794, USA*
[49]*SUBATECH (Ecole des Mines de Nantes, CNRS-IN2P3, Université de Nantes) BP 20722 - 44307, Nantes, France*
[50]*University of Tennessee, Knoxville, Tennessee 37996, USA*

*Deceased
†PHENIX Spokesperson: zajc@nevis.columbia.edu

[51]Department of Physics, Tokyo Institute of Technology, Oh-okayama, Meguro, Tokyo 152-8551, Japan
[52]Institute of Physics, University of Tsukuba, Tsukuba, Ibaraki 305, Japan
[53]Vanderbilt University, Nashville, Tennessee 37235, USA
[54]Waseda University, Advanced Research Institute for Science and Engineering, 17 Kikui-cho, Shinjuku-ku, Tokyo 162-0044, Japan
[55]Weizmann Institute, Rehovot 76100, Israel
[56]Yonsei University, IPAP, Seoul 120-749, Korea
(Received 1 February 2006; published 25 May 2006)

We present an improved measurement of the double helicity asymmetry for π^0 production in polarized proton-proton scattering at $\sqrt{s} = 200$ GeV employing the PHENIX detector at the Relativistic Heavy Ion Collider (RHIC). The improvements to our previous measurement come from two main factors: Inclusion of a new data set from the 2004 RHIC run with higher beam polarizations than the earlier run and a recalibration of the beam polarization measurements for the earlier run, which resulted in reduced uncertainties and increased beam polarizations. The results are compared to a Next to Leading Order (NLO) perturbative Quantum Chromodynamics (pQCD) calculation with a range of polarized gluon distributions.

DOI: 10.1103/PhysRevD.73.091102 PACS numbers: 13.85.Ni, 13.88.+e, 21.10.Hw, 25.40.Ep

From polarized lepton-nucleon deep inelastic scattering (DIS) experiments it is known that only ~25% of the proton spin can be attributed to the spins of the quarks and antiquarks [1]. The rest of the proton spin is assumed to be carried by the gluons and orbital angular momentum.

The double helicity asymmetry of inclusive π^0 production in polarized $p + p$ collisions, $A_{LL}^{\pi^0}$, is directly sensitive to the polarized gluon distribution function in the proton through gluon-gluon and gluon-quark subprocesses [2]. Results on $A_{LL}^{\pi^0}$ from polarized $p + p$ collisions at $\sqrt{s} =$ 200 GeV using the PHENIX detector at the Relativistic Heavy Ion Collider (RHIC) were published earlier [3]. The unpolarized cross section for π^0 production is described well by next-to-leading-order perturbative QCD (NLO pQCD) calculations within the theoretical scale uncertainty [4]. The double spin asymmetry can hence be reliably interpreted in terms of the polarized gluon and polarized quark distributions in the nucleon.

$A_{LL}^{\pi^0}$ is the difference between π^0 production cross sections for like helicity and unlike helicity proton collisions, divided by the sum. Experimentally, $A_{LL}^{\pi^0}$ is obtained from the difference in production rates for polarized collisions of like and unlike helicities, divided by the sum, and normalized by the product of the polarizations of each beam.

The published $A_{LL}^{\pi^0}$ data [3] were collected in the 2003 RHIC run (Run-3) when the average polarization of the beams in RHIC was 0.35 and 0.30 for the ''blue'' and ''yellow'' ring, respectively. Recalibration of the proton-carbon CNI polarimeter [5], based on a polarized atomic hydrogen gas jet at RHIC [6], changed the absolute scale of beam polarizations by 22%. In addition, this recalibration reduced the uncertainty in the polarization measurement for each beam from ~34% to ~18% (and for a product of two beam polarizations from 65% to 28%). An important, but less significant, change in Run-3 data as published occurred when we found a polarization pattern error in 10% of the data files of Run-3, and this was corrected.

In 2004, one week of RHIC operation was dedicated to the study and improvement of the beam polarization in RHIC. The PHENIX detector took data during this time. The results of this run (Run-4) are presented here combined with the data from the previous year.

The statistical uncertainty of a double spin asymmetry is inversely proportional to the square root of the figure of merit defined by $\mathcal{L}P_B^2P_Y^2$, where the P_B and P_Y are the beam polarization values of the blue and yellow RHIC beams, respectively, and $\mathcal{L}$ is the integrated luminosity collected by the experiment. Table I shows the average beam polarization values, the integrated luminosities and the figures of merit of the two runs. The Run-3 figure of merit in [3] was 1.2 nb^{-1}.

The stable spin direction in RHIC is vertical, and spin rotators are used to provide longitudinal polarization at PHENIX [7]. For the Run-3 and Run-4 data sets, the longitudinal fraction of the beam polarization was >0.98 and >0.99, respectively. Details of the Run-4 analysis method including the handling of detector efficiency, relative luminosity, determination of the longitudinal fraction of the beam polarization in the PHENIX interaction region, and the background subtraction are described in our Run-3 publication [3].

Table II and Fig. 1 show the results of the Run-3 reanalysis and the Run-4 analysis. Bunch-to-bunch and fill-to-fill systematic uncertainties for the asymmetry measurements are negligible. Also indicated for each data set are the total scale uncertainties due to the uncertainty in beam polarization, which consists of two terms: an 18% scale

TABLE I. Comparison of the data sets from 2003 (Run-3) and 2004 (Run-4) RHIC runs.

Run	$\langle P_B \rangle$	$\langle P_Y \rangle$	$\mathcal{L}$ (nb^{-1})	$\mathcal{L}\langle P_B P_Y \rangle^2$ (nb^{-1})
Run-3	0.35	0.30	220	2.6
Run-4	0.45	0.44	75	2.9

TABLE II. $A_{LL}^{\pi^0}$ for four p_T bins. The total point-to-point uncertainties are shown. Scale uncertainties of 28%, 24% and 18% for Run-3, Run-4 and combined runs are not included. For the combined results, uncorrelated systematic uncertainties for Run-3 and Run-4 have been included as point-to-point uncertainties, and are shown in parenthesis.

p_T ($\langle p_T \rangle$) (GeV/c)	Run-3 (10^{-2})	Run-4 (10^{-2})	Run-3+Run-4 (10^{-2})
1–2 (1.59)	-0.97 ± 0.85	-0.35 ± 0.72	$-0.60 \pm 0.56(0.10)$
2–3 (2.39)	-0.92 ± 0.90	0.56 ± 0.82	$-0.10 \pm 0.61(0.10)$
3–4 (3.37)	-0.90 ± 1.88	0.03 ± 1.79	$-0.41 \pm 1.30(0.09)$
4–5 (4.38)	-1.37 ± 4.19	7.90 ± 4.04	3.23 ± 2.98 (0.65)

uncertainty (9% for each beam), due to the proton-carbon CNI polarimeter calibration, common for each data set; and an uncorrelated uncertainty (21% in Run-3 and 16% in Run-4). The additional p_T-independent systematic uncertainty related to the relative luminosity measurement between colliding bunches with the same and opposite helicities was estimated to be below 1.5×10^{-3}.

Table II and Fig. 2 show the combined asymmetries for Run-3 and Run-4 data. The point-to-point uncertainties include the uncorrelated polarization uncertainties described above. Figure 2 also presents two NLO pQCD calculations using different assumptions for the polarized gluon distribution. One uses the best global fit to the inclusive DIS data (GRSV-std) and the other uses a polarized gluon distribution equal to the unpolarized distribution at the input scale of $Q^2 = 0.4$ GeV^2 (GRSV-max) [2,8].

Following the discussion in [3], we compared our results with theoretical curves, calculating confidence levels (C.L.) for all p_T points (> 1 GeV/c) and for the three highest p_T points (> 2 GeV/c). The data are consistent with GRSV-std with a C.L. = 61–63% (73–74%) for the range in polarization uncertainty of the measurement, considering all four points (the three highest p_T points). The results are less consistent with the large gluon polarization, with C.L. = 0.04–2% (0.3–5%) for GRSV-max [2,8]. These confidence levels do not include the theoretical uncertainty from the choice of scales or of the parton distribution functions or fragmentation function.

In summary, we present results for $A_{LL}^{\pi^0}$ that are improved over our previous publication [3]. Both the statistical and systematic uncertainties are reduced by more than a factor of 2. The new results probe the polarized gluon distribution in the proton with improved resolving power. We conclude that the observed asymmetry is small and not consistent with a maximal gluon polarization.

We thank the RHIC Polarimeter Group and the staff of the Collider-Accelerator and Physics Departments at BNL for their vital contributions. We acknowledge support from

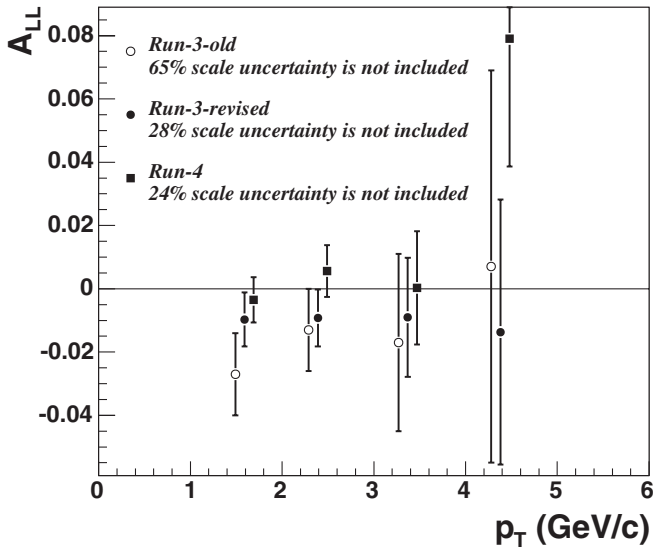

FIG. 1. Run-3 and Run-4 results on $A_{LL}^{\pi^0}$ versus mean p_T in each bin. Run-3-old results from [3] are also shown for comparison. For clarity, Run-3-old and Run-4 points are shifted by -0.1 GeV/c and $+0.1$ GeV/c, respectively.

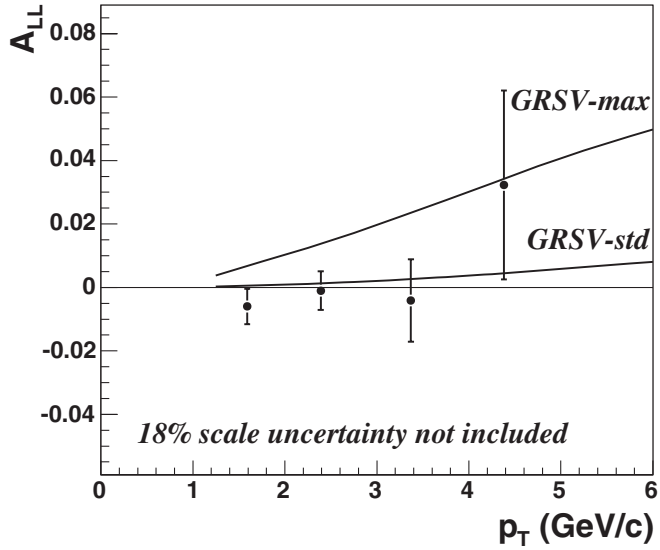

FIG. 2. Run-3+Run-4 combined results on $A_{LL}^{\pi^0}$ versus mean p_T in each bin. Two theoretical calculations based on NLO pQCD are also shown for comparison with the data (see text and [2,8] for details).

the Department of Energy and NSF (U.S.A.), MEXT and JSPS (Japan), CNPq and FAPESP (Brazil), NSFC (China), IN2P3/CNRS, and CEA (France), BMBF, DAAD, and AvH (Germany), OTKA (Hungary), DAE (India), ISF (Israel), KRF, CHEP, and KOSEF (Korea), MES, RAS, and FAAE (Russia), VR and KAW (Sweden), U.S. CRDF for the FSU, US-Hungarian NSF-OTKA-MTA, and US-Israel BSF.

[1] J. Ashman *et al.*, Phys. Lett. B **206**, 364 (1988); Nucl. Phys. **B328**, 1 (1989); E. Hughes and R. Voss, Annu. Rev. Nucl. Part. Sci. **49**, 303 (1999).
[2] B. Jäger, A. Schäfer, M. Stratmann, and W. Vogelsang, Phys. Rev. D **67**, 054005 (2003).
[3] S. S. Adler *et al.*, Phys. Rev. Lett. **93**, 202002 (2004).
[4] S. S. Adler *et al.*, Phys. Rev. Lett. **91**, 241803 (2003).
[5] O. Jinnouchi *et al.*, RHIC/CAD Accelerator Physics Note (2004), Vol. 171.
[6] T. Wise *et al.*, Proceedings of the Spin 2004 Symposium, p. 757, 507 (unpublished).
[7] W. W. MacKay *et al.*, Proceedings of the 2003 Particle Accelerator Conference, p. 1697 (unpublished).
[8] M. Glück, E. Reya, M. Stratmann, and W. Vogelsang, Phys. Rev. D **63**, 094005 (2001).

Common Suppression Pattern of η and π^0 Mesons at High Transverse Momentum in Au + Au Collisions at $\sqrt{s_{NN}} = 200$ GeV

S. S. Adler,[5] S. Afanasiev,[18] C. Aidala,[5] N. N. Ajitanand,[44] Y. Akiba,[21,39] J. Alexander,[44] R. Amirikas,[12] L. Aphecetche,[46] S. H. Aronson,[5] R. Averbeck,[45] T. C. Awes,[36] R. Azmoun,[45] V. Babintsev,[15] A. Baldisseri,[10] K. N. Barish,[6] P. D. Barnes,[28] B. Bassalleck,[34] S. Bathe,[31] S. Batsouli,[9] V. Baublis,[38] A. Bazilevsky,[40,15] S. Belikov,[17,15] Y. Berdnikov,[41] S. Bhagavatula,[17] J. G. Boissevain,[28] H. Borel,[10] S. Borenstein,[26] M. L. Brooks,[28] D. S. Brown,[35] N. Bruner,[34] D. Bucher,[31] H. Buesching,[31] V. Bumazhnov,[15] G. Bunce,[5,40] J. M. Burward-Hoy,[27,45] S. Butsyk,[45] X. Camard,[46] J.-S. Chai,[19] P. Chand,[4] W. C. Chang,[2] S. Chernichenko,[15] C. Y. Chi,[9] J. Chiba,[21] M. Chiu,[9] I. J. Choi,[53] J. Choi,[20] R. K. Choudhury,[4] T. Chujo,[5] V. Cianciolo,[36] Y. Cobigo,[10] B. A. Cole,[9] P. Constantin,[17] D. d'Enterria,[46] G. David,[5] H. Delagrange,[46] A. Denisov,[15] A. Deshpande,[40] E. J. Desmond,[5] A. Devismes,[45] O. Dietzsch,[42] O. Drapier,[26] A. Drees,[45] R. du Rietz,[30] A. Durum,[15] D. Dutta,[4] Y. V. Efremenko,[36] K. El Chenawi,[50] A. Enokizono,[14] H. En'yo,[39,40] S. Esumi,[49] L. Ewell,[5] D. E. Fields,[34,40] F. Fleuret,[26] S. L. Fokin,[24] B. D. Fox,[40] Z. Fraenkel,[52] J. E. Frantz,[9] A. Franz,[5] A. D. Frawley,[12] S.-Y. Fung,[6] S. Garpman,[30,*] T. K. Ghosh,[50] A. Glenn,[47] G. Gogiberidze,[47] M. Gonin,[26] J. Gosset,[10] Y. Goto,[40] R. Granier de Cassagnac,[26] N. Grau,[17] S. V. Greene,[50] M. Grosse Perdekamp,[40] W. Guryn,[5] H.-Å. Gustafsson,[30] T. Hachiya,[14] J. S. Haggerty,[5] H. Hamagaki,[8] A. G. Hansen,[28] E. P. Hartouni,[27] M. Harvey,[5] R. Hayano,[8] N. Hayashi,[39] X. He,[13] M. Heffner,[27] T. K. Hemmick,[45] J. M. Heuser,[45] M. Hibino,[51] H. Hiejima,[16] J. C. Hill,[17] W. Holzmann,[44] K. Homma,[14] B. Hong,[23] A. Hoover,[35] T. Ichihara,[39,40] V. V. Ikonnikov,[24] K. Imai,[25,39] D. Isenhower,[1] M. Ishihara,[39] M. Issah,[44] A. Isupov,[18] B. V. Jacak,[45] W. Y. Jang,[23] Y. Jeong,[20] J. Jia,[45] O. Jinnouchi,[39] B. M. Johnson,[5] S. C. Johnson,[27] K. S. Joo,[32] D. Jouan,[37] S. Kametani,[8,51] N. Kamihara,[48,39] J. H. Kang,[53] S. S. Kapoor,[4] K. Katou,[51] S. Kelly,[9] B. Khachaturov,[52] A. Khanzadeev,[38] J. Kikuchi,[51] D. H. Kim,[32] D. J. Kim,[53] D. W. Kim,[20] E. Kim,[43] G.-B. Kim,[26] H. J. Kim,[53] E. Kistenev,[5] A. Kiyomichi,[49] K. Kiyoyama,[33] C. Klein-Boesing,[31] H. Kobayashi,[39,40] L. Kochenda,[38] V. Kochetkov,[15] D. Koehler,[34] T. Kohama,[14] M. Kopytine,[45] D. Kotchetkov,[6] A. Kozlov,[52] P. J. Kroon,[5] C. H. Kuberg,[1,28,*] K. Kurita,[40] Y. Kuroki,[49] M. J. Kweon,[23] Y. Kwon,[53] G. S. Kyle,[35] R. Lacey,[44] V. Ladygin,[18] J. G. Lajoie,[17] A. Lebedev,[17,24] S. Leckey,[45] D. M. Lee,[28] S. Lee,[20] M. J. Leitch,[28] X. H. Li,[6] H. Lim,[43] A. Litvinenko,[18] M. X. Liu,[28] Y. Liu,[37] C. F. Maguire,[50] Y. I. Makdisi,[5] A. Malakhov,[18] V. I. Manko,[24] Y. Mao,[7,39] G. Martinez,[46] M. D. Marx,[45] H. Masui,[49] F. Matathias,[45] T. Matsumoto,[8,51] P. L. McGaughey,[28] E. Melnikov,[15] F. Messer,[45] Y. Miake,[49] J. Milan,[44] T. E. Miller,[50] A. Milov,[45,52] S. Mioduszewski,[5] R. E. Mischke,[28] G. C. Mishra,[13] J. T. Mitchell,[5] A. K. Mohanty,[4] D. P. Morrison,[5] J. M. Moss,[28] F. Mühlbacher,[45] D. Mukhopadhyay,[52] M. Muniruzzaman,[6] J. Murata,[39,40] S. Nagamiya,[21] J. L. Nagle,[9] T. Nakamura,[14] B. K. Nandi,[6] M. Nara,[49] J. Newby,[47] P. Nilsson,[30] A. S. Nyanin,[24] J. Nystrand,[30] E. O'Brien,[5] C. A. Ogilvie,[17] H. Ohnishi,[5,39] I. D. Ojha,[50,3] K. Okada,[39] M. Ono,[49] V. Onuchin,[15] A. Oskarsson,[30] I. Otterlund,[30] K. Oyama,[8] K. Ozawa,[8] D. Pal,[52] A. P. T. Palounek,[28] V. Pantuev,[45] V. Papavassiliou,[35] J. Park,[43] A. Parmar,[34] S. F. Pate,[35] T. Peitzmann,[31] J.-C. Peng,[28] V. Peresedov,[18] C. Pinkenburg,[5] R. P. Pisani,[5] F. Plasil,[36] M. L. Purschke,[5] A. K. Purwar,[45] J. Rak,[17] I. Ravinovich,[52] K. F. Read,[36,47] M. Reuter,[45] K. Reygers,[31] V. Riabov,[38,41] Y. Riabov,[38] G. Roche,[29] A. Romana,[26,*] M. Rosati,[17] P. Rosnet,[29] S. S. Ryu,[53] M. E. Sadler,[1] B. Sahlmueller,[31] N. Saito,[39,40] T. Sakaguchi,[8,51] M. Sakai,[33] S. Sakai,[49] V. Samsonov,[38] L. Sanfratello,[34] R. Santo,[31] H. D. Sato,[25,39] S. Sato,[5,49] S. Sawada,[21] Y. Schutz,[46] V. Semenov,[15] R. Seto,[6] M. R. Shaw,[1,28] T. K. Shea,[5] T.-A. Shibata,[48,39] K. Shigaki,[14,21] T. Shiina,[28] C. L. Silva,[42] D. Silvermyr,[28,30] K. S. Sim,[23] C. P. Singh,[3] V. Singh,[3] M. Sivertz,[5] A. Soldatov,[15] R. A. Soltz,[27] W. E. Sondheim,[28] S. P. Sorensen,[47] I. V. Sourikova,[5] F. Staley,[10] P. W. Stankus,[36] E. Stenlund,[30] M. Stepanov,[35] A. Ster,[22] S. P. Stoll,[5] T. Sugitate,[14] J. P. Sullivan,[28] E. M. Takagui,[42] A. Taketani,[39,40] M. Tamai,[51] K. H. Tanaka,[21] Y. Tanaka,[33] K. Tanida,[39] M. J. Tannenbaum,[5] P. Tarján,[11] J. D. Tepe,[1,28] T. L. Thomas,[34] J. Tojo,[25,39] H. Torii,[25,39] R. S. Towell,[1] I. Tserruya,[52] H. Tsuruoka,[49] S. K. Tuli,[3] H. Tydesjö,[30] N. Tyurin,[15] H. W. van Hecke,[28] J. Velkovska,[5,45] M. Velkovsky,[45] V. Veszprémi,[11] L. Villatte,[47] A. A. Vinogradov,[24] M. A. Volkov,[24] E. Vznuzdaev,[38] X. R. Wang,[13] Y. Watanabe,[39,40] S. N. White,[5] F. K. Wohn,[17] C. L. Woody,[5] W. Xie,[6] Y. Yang,[7] A. Yanovich,[15] S. Yokkaichi,[39,40] G. R. Young,[36] I. E. Yushmanov,[24] W. A. Zajc,[9,†] C. Zhang,[9] S. Zhou,[7] S. J. Zhou,[52] and L. Zolin[18]

(PHENIX Collaboration)

[1]*Abilene Christian University, Abilene, Texas 79699, USA*
[2]*Institute of Physics, Academia Sinica, Taipei 11529, Taiwan*
[3]*Department of Physics, Banaras Hindu University, Varanasi 221005, India*

 © 2006 The American Physical Society

[4]Bhabha Atomic Research Centre, Bombay 400 085, India
[5]Brookhaven National Laboratory, Upton, New York 11973-5000, USA
[6]University of California - Riverside, Riverside, California 92521, USA
[7]China Institute of Atomic Energy (CIAE), Beijing, People's Republic of China
[8]Center for Nuclear Study, Graduate School of Science, University of Tokyo, 7-3-1 Hongo, Bunkyo, Tokyo 113-0033, Japan
[9]Columbia University, New York, New York 10027, USA and Nevis Laboratories, Irvington, New York 10533, USA
[10]Dapnia, CEA Saclay, F-91191, Gif-sur-Yvette, France
[11]Debrecen University, H-4010 Debrecen, Egyetem tér 1, Hungary
[12]Florida State University, Tallahassee, Florida 32306, USA
[13]Georgia State University, Atlanta, Georgia 30303, USA
[14]Hiroshima University, Kagamiyama, Higashi-Hiroshima 739-8526, Japan
[15]IHEP Protvino, State Research Center of Russian Federation, Institute for High Energy Physics, Protvino, 142281, Russia
[16]University of Illinois at Urbana-Champaign, Urbana, Illinois 61801, USA
[17]Iowa State University, Ames, Iowa 50011, USA
[18]Joint Institute for Nuclear Research, 141980 Dubna, Moscow Region, Russia
[19]KAERI, Cyclotron Application Laboratory, Seoul, South Korea
[20]Kangnung National University, Kangnung 210-702, South Korea
[21]KEK, High Energy Accelerator Research Organization, Tsukuba, Ibaraki 305-0801, Japan
[22]KFKI Research Institute for Particle and Nuclear Physics of the Hungarian Academy of Sciences (MTA KFKI RMKI), H-1525 Budapest 114, PO Box 49, Budapest, Hungary
[23]Korea University, Seoul, 136-701, Korea
[24]Russian Research Center "Kurchatov Institute," Moscow, Russia
[25]Kyoto University, Kyoto 606-8502, Japan
[26]Laboratoire Leprince-Ringuet, Ecole Polytechnique, CNRS-IN2P3, Route de Saclay, F-91128, Palaiseau, France
[27]Lawrence Livermore National Laboratory, Livermore, California 94550, USA
[28]Los Alamos National Laboratory, Los Alamos, New Mexico 87545, USA
[29]LPC, Université Blaise Pascal, CNRS-IN2P3, Clermont-Fd, 63177 Aubiere Cedex, France
[30]Department of Physics, Lund University, Box 118, SE-221 00 Lund, Sweden
[31]Institut für Kernphysik, University of Muenster, D-48149 Muenster, Germany
[32]Myongji University, Yongin, Kyonggido 449-728, Korea
[33]Nagasaki Institute of Applied Science, Nagasaki-shi, Nagasaki 851-0193, Japan
[34]University of New Mexico, Albuquerque, New Mexico 87131, USA
[35]New Mexico State University, Las Cruces, New Mexico 88003, USA
[36]Oak Ridge National Laboratory, Oak Ridge, Tennessee 37831, USA
[37]IPN-Orsay, Universite Paris Sud, CNRS-IN2P3, BP1, F-91406, Orsay, France
[38]PNPI, Petersburg Nuclear Physics Institute, Gatchina, Leningrad Region, 188300, Russia
[39]RIKEN, The Institute of Physical and Chemical Research, Wako, Saitama 351-0198, Japan
[40]RIKEN BNL Research Center, Brookhaven National Laboratory, Upton, New York 11973-5000, USA
[41]Saint Petersburg State Polytechnic University, St. Petersburg, Russia
[42]Instituto de Física, Universidade de São Paulo, Caixa Postal 66318, São Paulo CEP05315-970, Brazil
[43]System Electronics Laboratory, Seoul National University, Seoul, South Korea
[44]Chemistry Department, Stony Brook University, SUNY, Stony Brook, New York 11794-3400, USA
[45]Department of Physics and Astronomy, Stony Brook University, SUNY, Stony Brook, New York 11794, USA
[46]SUBATECH (Ecole des Mines de Nantes, CNRS-IN2P3, Université de Nantes) BP 20722 - 44307, Nantes, France
[47]University of Tennessee, Knoxville, Tennessee 37996, USA
[48]Department of Physics, Tokyo Institute of Technology, Oh-okayama, Meguro, Tokyo, 152-8551, Japan
[49]Institute of Physics, University of Tsukuba, Tsukuba, Ibaraki 305, Japan
[50]Vanderbilt University, Nashville, Tennessee 37235, USA
[51]Waseda University, Advanced Research Institute for Science and Engineering, 17 Kikui-cho, Shinjuku-ku, Tokyo 162-0044, Japan
[52]Weizmann Institute, Rehovot 76100, Israel
[53]Yonsei University, IPAP, Seoul 120-749, Korea

(Received 26 January 2006; published 22 May 2006)

Inclusive transverse momentum spectra of η mesons have been measured within $p_T = 2$–10 GeV/c at midrapidity by the PHENIX experiment in Au + Au collisions at $\sqrt{s_{NN}} = 200$ GeV. In central Au + Au the η yields are significantly suppressed compared to peripheral Au + Au, d + Au, and $p + p$ yields scaled by the corresponding number of nucleon-nucleon collisions. The magnitude, centrality, and p_T dependence of the suppression is common, within errors, for η and π^0. The ratio of η to π^0 spectra at high p_T amounts to $0.40 < R_{\eta/\pi^0} < 0.48$ for the three systems, in agreement with the world average measured in hadronic and nuclear reactions and, at large scaled momentum, in e^+e^- collisions.

DOI: 10.1103/PhysRevLett.96.202301 PACS numbers: 25.75.Dw

The major motivation for the study of high energy nucleus-nucleus ($A + A$) collisions is the opportunity to probe strongly interacting matter at extremely high energy densities. Of particular interest are energy densities well above the expected transition from normal hadronic matter to a deconfined system of quarks and gluons. Lattice quantum chromodynamics (QCD) calculations [1] predict that this transition will occur at a temperature of $T \approx 170$ MeV $\approx 10^{12}$ K. The formation of a quark-gluon plasma (QGP) in $A + A$ reactions should manifest itself in a variety of experimental signatures [2].

At center-of-mass energies reached by the Relativistic Heavy Ion Collider (RHIC), arguably the most exciting experimental results so far are connected with the predicted "jet quenching" phenomenon [3–5] due to energy loss of hard-scattered partons as they traverse the dense medium formed in the reaction. Since (leading) hadrons with $p_T > 4$ GeV/c at RHIC carry a large fraction of the momentum of the parent quark or gluon [$\langle z \rangle = p_{\mathrm{hadron}}/p_{\mathrm{parton}} \approx 0.5$–$0.7$ [6,7]], parton energy loss results in a significantly suppressed production of high-p_T hadrons [4]. The inclusive spectra of high-p_T neutral pions [8,9] and charged hadrons [10,11] in Au + Au at $\sqrt{s_{NN}} = 200$ GeV are indeed suppressed by as much as a factor of 5 compared to the corresponding yields in $p + p$ [12] and $d +$ Au [13,14], scaled by the number of incoherent nucleon-nucleon (NN) collisions. The centrality [15], p_T [16–18] and center-of-mass energy [19] dependences of the observed quenching are consistent with theoretical calculations of QCD energy loss due to multiple gluon emission in a dense medium. Assuming a thermalized parton system, the magnitude of the suppression for central Au + Au at $\sqrt{s_{NN}} = 200$ GeV implies initial energy densities above 15 GeV/fm^3, $\sim$100 times larger than normal nuclear matter [20].

The equal amount of suppression for π^0 and $h^{\pm}$ observed above $p_T \approx 5$ GeV/c for the same Au + Au centrality seems to indicate that the mechanism of quenching is independent of the identity of the high-p_T light-quark hadron. This is expected if the suppression takes place at the parton level *prior* to its fragmentation into a given hadron. Indeed, in this case the high-p_T deficit depends only on the energy lost in the medium by the parent (u, d, s) quark or gluon and not on the nature of the final leading hadron which will be produced with the same *universal* probabilities (fragmentation functions) which govern hadron production in the vacuum in more elementary systems. The partons involved in high-p_T hadroproduction considered in this work have typical momenta $\gtrsim 5$ GeV/c, 10 times larger than the "bulk" average momenta $\langle p_T \rangle \approx 0.55$ GeV/c of the system [21]. Such energetic partons are then supposed to traverse (and lose energy in) the medium and hadronize in the *vacuum* a few tens of fm/c later [15]. The equal suppression of $h^{\pm}$ and π^0 does not by itself provide a conclusive argument for parton energy loss *before* fragmentation in the vacuum because above $p_T \approx 5$ GeV/c, unidentified charged hadron yields are dominated by $\pi^{\pm}$ [11]. Measurement of the yields of an additional light-quark species like the η meson at large enough p_T allows a confirmation of the independence of the quenching with respect to the nature of the produced hadron, and tests the consistency of the data with medium-induced *partonic* energy loss prior to vacuum hadronization. Besides its interest as a *signal* in its own right, the η meson constitutes, after the π^0, the second most important source of decay $e^{\pm}$ and γ. Reliable knowledge of their production cross sections is thus required in order to eliminate the *background* of secondary $e^{\pm}$ and γ in single electron [22], dielectron [23], and direct γ [24] measurements.

This Letter presents measurements of the η meson by the PHENIX experiment [25] in Au + Au collisions at $\sqrt{s_{NN}} = 200$ GeV during the second RHIC run (2001–2002) and compares them to η from $p + p$ and $d +$ Au [26] and to π^0 [8,9] and direct γ [24] from Au + Au, all measured in the same experiment at the same $\sqrt{s_{NN}}$. The η measurement reaches the second largest p_T for identified hadrons at RHIC, after the π^0. The analysis reported here uses beam-beam counters (BBC, $3.0 < |\eta| < 3.9$) plus the zero degree calorimeters (ZDC) for trigger and global event characterization. For each collision, the reaction centrality is obtained by cuts in the correlated distribution of the charge detected in the BBC and the energy measured in the ZDC [27]. A Glauber Monte Carlo model combined with a simulation of BBC and ZDC responses is used to determine the corresponding nuclear overlap function $\langle T_{AA} \rangle$ for each centrality [8]. The η mesons are reconstructed at midrapidity in the lead-scintillator (PbSc) electromagnetic calorimeter [28] via their $\gamma\gamma$ decay mode (BR = 39.43%). The PbSc consists of 15 552 individual lead-scintillator sandwich modules (5.54 cm $\times$ 5.54 cm $\times$ 37.5 cm, 18 X_0), grouped in six sectors located at a radial distance of 5.1 m from the beam line, covering a total solid angle of $\Delta\eta \approx 0.7$ and $\Delta\phi \approx 3\pi/4$ rad. The energy calibration of the PbSc modules is obtained from the beam-test values and confirmed with the measured position of the π^0 mass peak, the energy deposited by minimum ionizing particles traversing the calorimeter, as well as with the expected $E_{\mathrm{PbSc}}/p_{\mathrm{tracking}} \sim 1$ value for $e^{\pm}$ identified by the Ring-Imaging Čerenkov detector. The systematic error on the absolute energy scale is less than 1.5%, which translates into a maximum 8% uncertainty in the final η yields.

For this analysis a minimum bias (MB) trigger sample of 34×10^6 events, also used for the previously published π^0 analysis [8], is combined with a Level-2 trigger event sample for centralities 0%–60%, equivalent to an additional 30×10^6 minimum bias events. The Level-2 trigger sample is obtained with a software trigger on highly energetic particles (3.5 GeV threshold). The resulting trigger reaches a 50% (100%) efficiency for η above $p_T = 5(7)$ GeV/c. The normalization of the Level-2 data sample

relative to the MB data sample is accurate to 2%. Both sets of events are required to have a vertex position $|z| < 30$ cm along the beam axis. Photon candidates are identified in the PbSc by applying particle identification (PID) cuts based on the time-of-flight and shower profile [8,26]. The systematic uncertainty on the yields related to the applied PID cuts is ~8%. The η yields are determined by an invariant mass analysis of photon pairs with asymmetries $|E_{\gamma 1} - E_{\gamma 2}|/(E_{\gamma 1} + E_{\gamma 2}) < 0.5$. The combinatorial background is obtained by combining uncorrelated photon pairs from different events with similar centrality and vertex, and by normalizing the distribution in a region below ($m_{\rm inv} = 400$–450 MeV$/c^2$) and above ($m_{\rm inv} = 750$–1000 MeV$/c^2$) the η mass peak. The resulting distribution is fit to a Gaussian plus an exponential to account for the residual background not described by the mixed-event background (inset of Fig. 1). The open (solid) symbols depict the η signal after mixed (plus residual) background subtraction. To estimate the uncertainty in the subtraction procedure, different pair asymmetries and an alternative linear parametrization of the residual background are used. The signal-to-background ratio in peripheral (central) collisions is approximately 1.3 (1.5) for the highest p_T and 0.05 (0.002) for the lowest p_T.

The raw spectra are normalized to one unit of rapidity and full azimuth. This purely geometrical acceptance factor amounts to ~4 at large p_T. The spectra are further corrected for the detector response (energy resolution, dead areas), the reconstruction efficiency (analysis cuts), and occupancy effects (cluster overlaps). These corrections are quantified by embedding simulated single η from a full PHENIX GEANT [29] simulation into real events, and analyzing the merged events with the same analysis cuts used to obtain the real yields. The total η yield efficiency correction is ~3 and rises $\lesssim 20\%$ with centrality. The losses are dominated by fiducial and asymmetry cuts. The nominal energy resolution is adjusted in the simulation by adding a p_T-independent energy smearing of 3% for each PbSc tower. The shape, position, and width of the η peak measured for all p_T's and centralities are well reproduced by the embedded data.

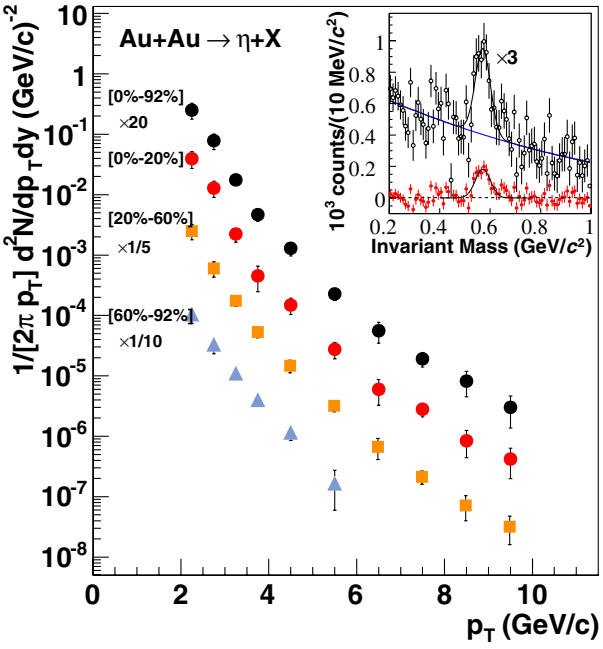

FIG. 1 (color online). Invariant η yields as a function of transverse momentum for 3 centralities and MB Au + Au at $\sqrt{s_{NN}} = 200$ GeV scaled by the factors indicated in the plot. Inset: invariant mass distribution of γ pairs with $p_T = 4$–5 GeV$/c$ measured in MB Au + Au, after mixed-event (black open circles) plus residual (red solid circles) background subtraction.

The main sources of systematic errors in the measurement are the uncertainties in the yield extraction (10%–30%), the yield correction (10%), and the energy scale (a maximum of 8%). The final combined systematic errors on the spectra are at the level of 10%–30% (point-to-point) and 10%–20% (p_T-correlated) depending on the p_T and centrality bin [26]. A correction in the yield to account for the true mean value of each p_T bin is applied to the steeply falling spectra. The fully corrected p_T distributions are shown in Fig. 1 for MB and 3 centrality bins (0%–20%, 20%–60%, and 60%–92%) scaled for clarity by the factors indicated. The error bars are the quadratic sum of statistical and systematic errors.

Medium effects in $A + A$ collisions are quantitatively determined using the *nuclear modification factor* given as the ratio of the measured $A + A$ invariant yield over the $p + p$ cross section scaled by the Glauber nuclear overlap function $\langle T_{AA} \rangle$ in the centrality bin under consideration:

$$R_{AA}(p_T) = \frac{d^2N_{AA}/dp_T dy}{\langle T_{AA} \rangle d^2\sigma_{pp}/dp_T dy}. \quad (1)$$

Deviations from $R_{AA}(p_T) = 1$ quantify the degree of departure of the hard $A + A$ yields from an incoherent superposition of NN collisions. Figure 2 compares the nuclear modification factor for η in central (0%–20%), semicentral (20%–60%), and peripheral (60%–92%) Au + Au reactions using the reference $d^2\sigma_{pp}/dp_T dy$ spectrum measured in $p + p$ collisions [26]. As observed for high-p_T π^0 [8,9], the η yields are consistent with the expectation of independent NN scatterings in peripheral reactions ($R_{AA} \approx 1$) but are increasingly reduced for smaller centralities. The p_T dependence of R_{AA} is flat above 4 GeV$/c$ as seen also for the π^0.

Figure 3 compares the $R_{AA}(p_T)$ measured in Au + Au at $\sqrt{s_{NN}} = 200$ GeV for η (0%–20% centrality), π^0 [8,9], and γ [24] (0%–10% centralities). Whereas direct γ are unsuppressed compared to the T_{AA}-scaled reference given here by a next-to-leading-order (NLO) calculation [24,30] that reproduces the PHENIX $p + p$ photon data well [31], π^0 and η are suppressed by a similar factor of ~5 compared to the corresponding $p + p$ cross sections [9,26]. Within the current uncertainties, light-quark mesons at

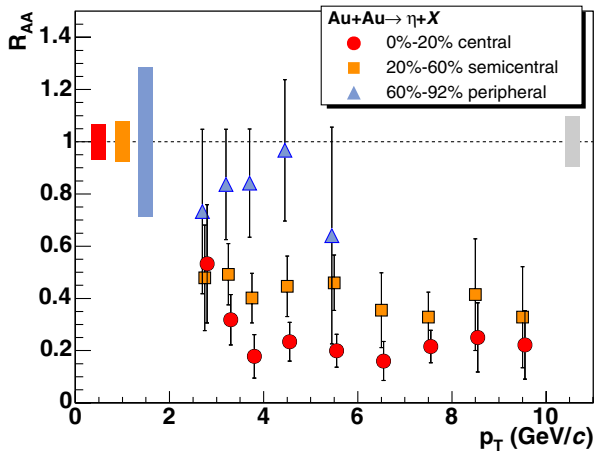

FIG. 2 (color online). Nuclear modification factors for η in Au + Au centralities: 0%–20%, 20%–60%, 60%–92%. The error bars show point-to-point uncertainties. The absolute normalization error bands at $R_{AA} = 1$ show the uncertainties in $\langle T_{AA} \rangle$ for decreasing centralities. The error box on the right indicates the 9.7% $p + p$ cross-section uncertainty [14].

RHIC show a flat suppression in the range $p_T = 4$–14 GeV/c, independent of their mass (note that the η is 4 times heavier than the π^0). The results are in agreement with expectations of in-medium non-Abelian energy loss of the parent parton prior to its fragmentation in the vacuum. The initial gluon densities needed to quench the high-p_T hadrons by such an amount are of the order of $dN^g/dy = 1100$ (solid curve in Fig. 3) [16].

An additional way to determine possible differences in the suppression pattern of π^0 and η is to study the centrality dependence of the η/π^0 ratio in Au + Au collisions and compare it with the ratio in more elementary systems (e^+e^-, $p + p$, d + Au). The η/π^0 ratio in hadron-hadron, hadron-nucleus, and nucleus-nucleus collisions is seen to increase rapidly with p_T and flatten out above $p_T \approx 2.5$ GeV/c at an asymptotically constant $R_{\eta/\pi^0} \approx 0.5$ for all systems [26]. Likewise, in e^+e^- at the Z pole ($\sqrt{s} = 91.2$ GeV) one also finds $R_{\eta/\pi^0} \approx 0.5$ for η and π^0 at large scaled momenta $x_p = p_{\text{hadron}}/p_{\text{beam}} \gtrsim 0.3$–$0.7$ [26] consistent with the range of fractional momenta $\langle z \rangle$ relevant for high-p_T production discussed here. It is interesting to test if this ratio is modified in any way by final- and/or initial-state medium effects in Au + Au collisions at RHIC.

Figure 4 shows $R_{\eta/\pi^0}(p_T)$ for three Au + Au centrality selections and for $p + p$ and d + Au collisions [26]. A fit to a constant for $p_T > 2$ GeV/c gives $R_{\eta/\pi^0}^{\text{AuAu0\%–20\%}} = 0.40 \pm 0.04$, $R_{\eta/\pi^0}^{d\text{AuMB}} = 0.47 \pm 0.03$, and $R_{\eta/\pi^0}^{pp} = 0.48 \pm 0.03$, where the quoted errors are the quadratic sum of statistical and systematic uncertainties. The Au + Au ratio is consistent within $\sim 1\sigma$ with both the essentially identical d + Au and $p + p$ ratios. The R_{η/π^0} ratio shows thus no apparent collision system, centrality, or p_T dependence. The dotted curve is the predicted PYTHIA [32] result for the $p + p$ ratio at $\sqrt{s} = 200$ GeV which is also coincident with the world data measured in the same momentum range in hadronic, nuclear, and e^+e^- collisions in a wide range of energies ($\sqrt{s} \approx 3$–1800 GeV) [26].

In summary, the transverse momentum spectra of η mesons have been measured at midrapidity in the range $p_T = 2$–10 GeV/c in Au + Au at $\sqrt{s_{NN}} = 200$ GeV. The invariant yields per nucleon-nucleon collision are increasingly depleted with centrality in comparison to $p + p$ results at the same center-of-mass energy. The maximum

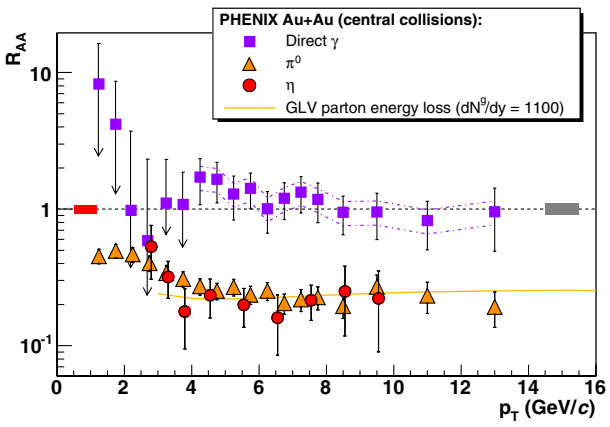

FIG. 3 (color online). $R_{AA}(p_T)$ measured in central Au + Au at $\sqrt{s_{NN}} = 200$ GeV for η, π^0 [8,9], and direct γ [24]. The error bars include all point-to-point errors. The error bands at $R_{AA} = 1$ have the same meaning as in Fig. 2. The baseline $p + p \rightarrow \gamma + X$ reference used is a NLO calculation [24,30], that reproduces our own data well [31], with theoretical uncertainties indicated by the dash-dotted lines around the points. The solid yellow curve is a parton energy loss prediction for a medium with density $dN^g/dy = 1100$ [16].

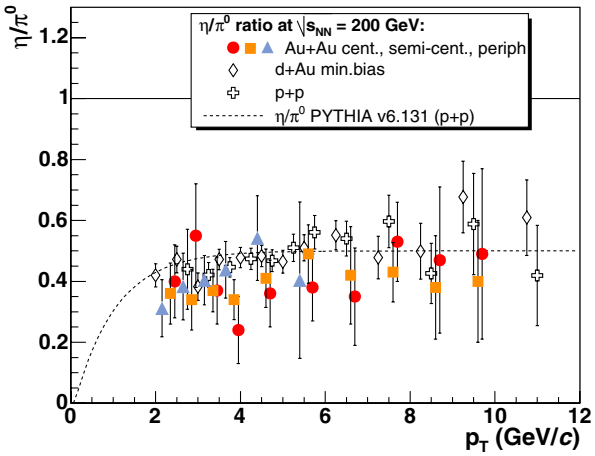

FIG. 4 (color online). η/π^0 ratio in Au + Au (centralities: 0%–20%, 20%–60%, 60%–92%) compared to the ratio in $p + p$ and d + Au [26] at $\sqrt{s_{NN}} = 200$ GeV. The error bars include all point-to-point errors that do not cancel in the ratio of yields. The dashed curve is the PYTHIA [32] prediction for $p + p$ at $\sqrt{s} = 200$ GeV consistent with the asymptotic $R_{\eta/\pi^0} \approx 0.5$ measured in hadronic and e^+e^- collisions in a wide range of c.m. energies [26].

suppression factor is ~5 in central Au + Au. The magnitude, p_T, and centrality dependences of the suppression are the same for η and π^0 suggesting that the production of light neutral mesons at large p_T in nuclear collisions at RHIC is affected by the medium in the same way. The measured η/π^0 ratio is flat with p_T and amounts to $R_{\eta/\pi^0} = 0.40 \pm 0.04$. This value is consistent with the world value at high p_T in hadronic and nuclear reactions and, at high x_p, in e^+e^- collisions. We conclude that all these observations are in agreement with a scenario where the parent parton first loses energy in the produced dense medium and then fragments into a leading meson in the vacuum according to the same probabilities that govern high-p_T hadroproduction in more elementary systems ($p + p$, e^+e^-).

We thank the staff of the Collider-Accelerator and Physics Departments at BNL for their vital contributions. We acknowledge support from the Department of Energy and NSF (USA), MEXT and JSPS (Japan), CNPq and FAPESP (Brazil), NSFC (China), CNRS-IN2P3 and CEA (France), BMBF, DAAD, and AvH (Germany), OTKA (Hungary), DAE and DST (India), ISF (Israel), KRF and CHEP (Korea), RMIST, RAS, and RMAE (Russia), VR and KAW (Sweden), US CRDF for the FSU, US-Hungarian NSF-OTKA-MTA, and US-Israel BSF.

*Deceased.
†PHENIX Spokesperson.
Email address: zajc@nevis.columbia.edu

[1] F. Karsch, Lect. Notes Phys. **583**, 209 (2002).
[2] J. W. Harris and B. Müller, Annu. Rev. Nucl. Part. Sci. **46**, 71 (1996).
[3] J. D. Bjorken, Fermilab Report No. FERMILAB-PUB-82-059-THY, 1982 (unpublished).
[4] M. Gyulassy and M. Plümer, Phys. Lett. B **243**, 432 (1990); X. N. Wang and M. Gyulassy, Phys. Rev. Lett. **68**, 1480 (1992).
[5] R. Baier, Y. L. Dokshitzer, A. H. Mueller, S. Peigné, and D. Schiff, Nucl. Phys. **B484**, 265 (1997); R. Baier, D. Schiff, and B. G. Zakharov, Annu. Rev. Nucl. Part. Sci. **50**, 37 (2000); U. Wiedemann, Nucl. Phys. **B588**, 303 (2000).
[6] S. S. Adler *et al.* (PHENIX Collaboration), hep-ex/0605039 (to be published).
[7] S. Kretzer, Acta Phys. Pol. B **36**, 179 (2005).
[8] S. S. Adler *et al.* (PHENIX Collaboration), Phys. Rev. Lett. **91**, 072301 (2003).
[9] S. S. Adler *et al.* (PHENIX Collaboration) (to be published).
[10] J. Adams *et al.* (STAR Collaboration), Phys. Rev. Lett. **91**, 172302 (2003).
[11] S. S. Adler *et al.* (PHENIX Collaboration), Phys. Rev. C **69**, 034910 (2004).
[12] S. S. Adler *et al.* (PHENIX Collaboration), Phys. Rev. Lett. **91**, 241803 (2003).
[13] S. S. Adler *et al.* (PHENIX Collaboration), Phys. Rev. Lett. **91**, 072303 (2003).
[14] S. S. Adler *et al.* (PHENIX Collaboration) (to be published).
[15] X. N. Wang, Phys. Lett. B **579**, 299 (2004).
[16] I. Vitev and M. Gyulassy, Phys. Rev. Lett. **89**, 252301 (2002); I. Vitev, J. Phys. G **30**, S791 (2004).
[17] K. J. Eskola, H. Honkanen, C. A. Salgado, and U. A. Wiedemann, Nucl. Phys. **A747**, 511 (2005).
[18] S. Jeon and G. D. Moore, Phys. Rev. C **71**, 034901 (2005).
[19] D. d'Enterria, Eur. Phys. J. C **43**, 295 (2005).
[20] K. Adcox *et al.* (PHENIX Collaboration), Nucl. Phys. **A757**, 184 (2005).
[21] S. S. Adler *et al.* (PHENIX Collaboration), Phys. Rev. C **69**, 034909 (2004).
[22] K. Adcox *et al.* (PHENIX Collaboration), Phys. Rev. Lett. **88**, 192303 (2002); S. S. Adler *et al.* (PHENIX Collaboration), Phys. Rev. C **72**, 024901 (2005); Phys. Rev. Lett. **96**, 032301 (2006).
[23] A. Toia (PHENIX Collaboration), *Proceedings of the QM'05*, nucl-ex/0510006.
[24] S. S. Adler *et al.* (PHENIX Collaboration), Phys. Rev. Lett. **94**, 232301 (2005).
[25] K. Adcox *et al.* (PHENIX Collaboration), Nucl. Instrum. Methods Phys. Res., Sect. A **499**, 469 (2003).
[26] S. S. Adler *et al.* (PHENIX Collaboration) (to be published).
[27] K. Adcox *et al.* (PHENIX Collaboration), Phys. Rev. Lett. **86**, 3500 (2001).
[28] L. Aphecetche *et al.* (PHENIX Collaboration), Nucl. Instrum. Methods Phys. Res., Sect. A **499**, 521 (2003).
[29] F. Carminati *et al.*, *GEANT 3.21: Detector Description and Simulation Tool*, CERN Program Library Long Writeup No. W5013, 1993 (unpublished).
[30] L. E. Gordon and W. Vogelsang, Phys. Rev. D **48**, 3136 (1993); Phys. Rev. D **50**, 1901 (1994).
[31] S. S. Adler *et al.* (PHENIX Collaboration), Phys. Rev. D **71**, 071102 (2005); K. Okada (PHENIX Collaboration), *Proceedings of SPIN04*, hep-ex/0501066.
[32] T. Sjöstrand, Comput. Phys. Commun. **82**, 74 (1994); computer code PYTHIA v6.131 with default parameters.

Available online at www.sciencedirect.com
ScienceDirect
ELSEVIER
Nuclear Physics A 774 (2006) 731–734
NUCLEAR PHYSICS A

Direct photons in 200 GeV $p+p$, d+Au, and Au+Au from PHENIX

S. Bathe[a*] for the PHENIX Collaboration[†]

[a]University of California at Riverside

Direct photons were measured with the PHENIX experiment in $p+p$, d+Au, and Au+Au at $\sqrt{s_{NN}} = 200$ GeV. To tackle the p_T region below 5 GeV/c, direct photons were measured through their internal conversion into e^+e^- in Au+Au collisions.

1. Introduction

Direct photons are a unique probe of the hot and dense matter created at RHIC: they allow access to the initial, thermalized state of the collision. Their measurement, however, is challenging. One has to cope with a large background from hadronic decays.

Direct photon measurements in $p+p$ constrain the hard-scattering contribution in Au+Au. A comparison to d+Au allows to quantify contributions from initial-state effects. In heavy ion collisions, thermal direct photons constrain the temperature of the collision system in its hottest phase while hard direct photons serve as a crucial baseline for the interpretation of the high-p_T hadron suppression observed earlier [1].

2. Direct Photon Analysis Via Low-Mass Electron Pairs

The conventional direct photon measurement with the EMCal has been described elsewhere [2,3]. In the following we will focus on the measurement through internal conversion of direct photons into e^+e^-. Compared to the conventional measurement, this technique improves both the signal-to-background ratio and the energy resolution at intermediate p_T where thermal production is expected to contribute substantially [4]. The measurement relies on a combination of excellent mass resolution at low invariant mass, m_{ee}, and a low conversion probability due to little material in the aperture. It has been carried out in heavy ion experiments for the first time [5,6].

The full 2004 data set of about 900 M minimum bias events was analyzed. Events and centrality were selected as described in [7]. Electrons in the central arms were identified by matching charged particle tracks to clusters in the EMCal and to rings in a ring imaging Čerenkov (RICH) detector.

To illustrate the underlying idea we consider the π^0 Dalitz decay where one decay photons is a virtual photon that further decays into an e^+-e^- pair. The invariant-mass distribution of the virtual photon is given by [8]

*Building 510 C, Brookhaven National Laboratory, Upton, NY11973-5000, USA
[†]For the full PHENIX Collaboration author list and acknowledgements, see Appendix "Collaboration" of this volume.

0375-9474/$ – see front matter © 2006 Elsevier B.V. All rights reserved.
doi:10.1016/j.nuclphysa.2006.06.125

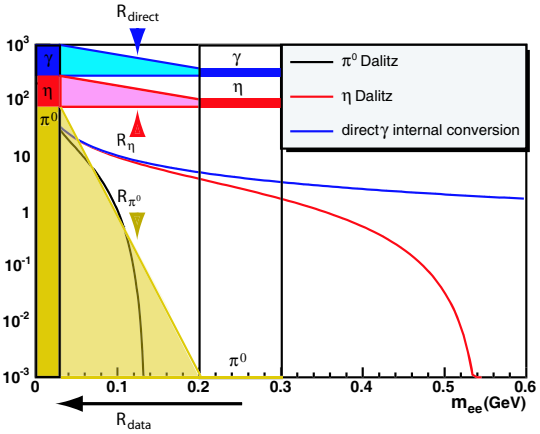

Figure 1. Invariant-mass distribution of virtual photons from the π^0 and η Dalitz decays as well as from direct photons according to Eq. 1. It is illustrated how the various contributions decrease to a fraction R when going to higher invariant mass with the π^0 contribution exhausting.

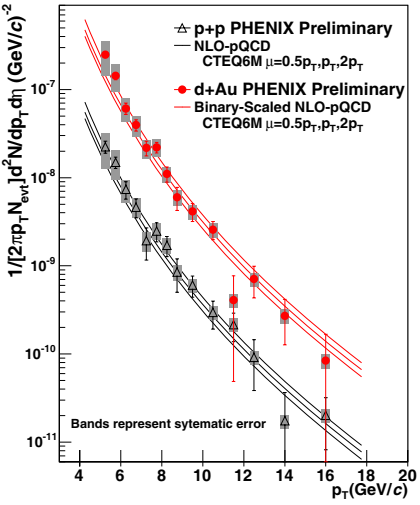

Figure 2. Preliminary direct photon invariant yield as a function of p_T for $p+p$ [3] and minimum-bias d+Au collisions at $\sqrt{s_{NN}} = 200$ GeV. The solid curves are pQCD predictions [9] for three different scales that represent the uncertainty on the calculation.

$$\frac{1}{N_\gamma}\frac{dN_{ee}}{dm_{ee}} = \frac{2\alpha}{3\pi}\sqrt{1-\frac{4m_e^2}{m_{ee}^2}}\left(1+\frac{2m_e^2}{m_{ee}^2}\right)\frac{1}{m_{ee}} \mid F(m_{ee}^2) \mid^2 \left(1-\frac{m_{ee}^2}{M^2}\right)^3 , \qquad (1)$$

and depicted in Fig. 1. In general, any source of real photons produces virtual photons with very low invariant mass. The rate and mass distribution of those virtual photons is given by the same formula[3]. For direct photons the phase space is not limited when $m_{ee} << p_T^{photon}$.

To obtain a clean invariant-mass distribution of e^+-e^- pairs, pairs originating from photon conversions in the beam pipe or detector material are rejected by an analysis cut. The combinatorial background is removed by the mixed-events technique. In this measurement decay photons can mostly be eliminated by measuring the yield of e^+-e^- pairs in an invariant-mass region where pairs from the π^0 Dalitz decay are largely suppressed due to their limited phase space. In order to convert the measured virtual photons into real photons, the obtained yield has to be related to the yield in an region where the phase space is unrestricted, so that $\gamma^\star_{direct}/\gamma^\star_{incl.} = \gamma_{direct}/\gamma_{incl.}$. The term $\gamma^\star_{direct}/\gamma^\star_{incl.}$ can be calculated from the ratio of total yields in the two intervals, $R_{\rm data} = N(90\text{-}300\ {\rm MeV})/N(0\text{-}30\ {\rm MeV})$,

[3]Since the virtual photons decay in the medium, this relation might be slightly modified. This would not affect the significance of the observed excess of direct photons, only its translation into an absolute yield of real direct photons.

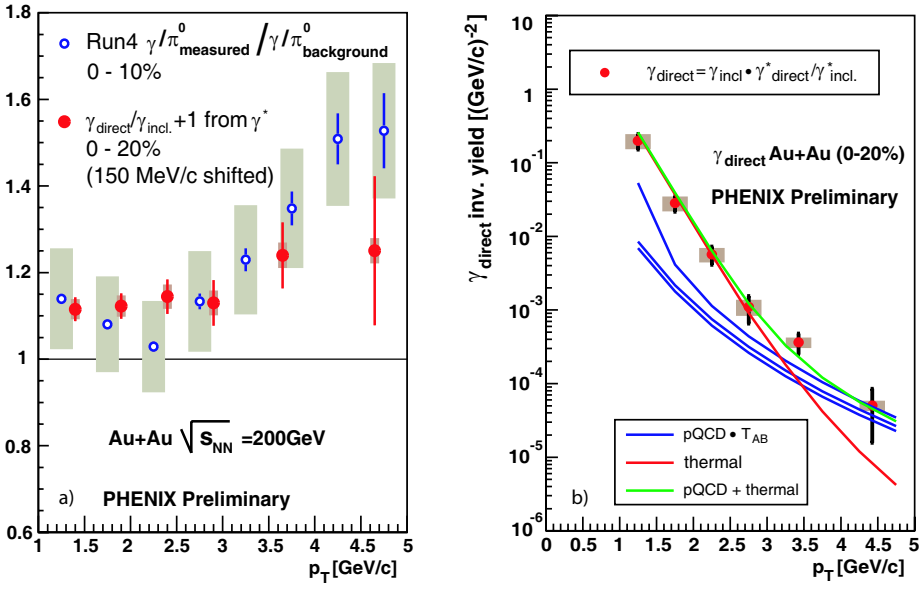

Figure 3. a) Direct photon excess for the conventional and the internal-conversion measurement in central Au+Au. b) Direct photon spectrum from the latter compared to pQCD [9], thermal-photon [11], and the sum of both calculations.

which is known from the measurement, and the ratios, $R_i, i = \{\gamma_{\rm direct}, \pi^0, \eta, {\rm other}\}$, for the various contributions, which can precisely be calculated from Eq. 1 (cf. Fig.1). Decay photons from a cocktail of hadrons are considered here. Finally, the yield of real inclusive photons known from the EMCal measurement [2] is needed to obtain the yield of real direct photons.

Since only the ratio of decay photon yields in the two invariant-mass intervals is needed, the uncertainty on the η-to-π^0 ratio of about 20 % [10] is the main source of uncertainty, translating into an uncertainty of 20 % on the measured direct photon yield. Other sources are the EMCal-measured inclusive photon yield (10 %) and the e^+-e^--pair acceptance (5 %). The total systematic uncertainty is 25 %.

3. Results

The preliminary direct photon spectra from the conventional measurement for $p + p$ [3] and minimum-bias d+Au at $\sqrt{s_{NN}} = 200$ GeV is shown in Fig. 2. For the whole p_T range of 5 to 16 GeV/c the observed yield is consistent with a next-to-leading-order perturbative-QCD (NLO pQCD) calculation [9] for both $p+p$ and d+Au. This supports the validity of the pQCD calculation as a reference for hard direct photon production in Au+Au. As shown by PHENIX in the 2002 run [2], at high p_T direct photon production is consistent with the pQCD expectation also in Au+Au. In the following we will focus on the region at intermediate p_T.

In a preliminary analysis with the conventional method, a small but stable subset of the 2004 data was selected to revisit the intermediate-p_T region, where no significant result had been previously obtained for $p_T \lesssim 3$ GeV/c. The new result is shown in Fig. 3 a) in terms of the double ratio $(\gamma/\pi^0|_{meas.})/(\gamma/\pi^0|_{bckgrd.})$. This ratio indicates a direct photon excess as an enhancement above 1. There is still no significant excess below 3 GeV/c. Further work is ongoing to increase the significance.

The preliminary result from the measurement of virtual photons is presented in the same figure in terms of $\gamma_{direct}/\gamma_{incl.} + 1$, which also indicates a direct photon excess as an enhancement above 1. (Note that the two quantities aren't exactly equivalent.). The result shows a significant direct photon excess of about 10 % for $1 < p_T < 5$ GeV/c and the 20 % most central Au+Au collisions. It is consistent with the EMCal measurement. In Fig. 3 b) the direct photon invariant yield from the virtual photon measurement is shown and compared to various theoretical calculations. With large significance, a direct photon spectrum was obtained for $1 < p_T < 5$ GeV/c. The spectrum lies significantly above a T_{AB}-scaled pQCD calculation [9] for $p_T \lesssim 3$ GeV/c. A 2+1 hydrodynamical model [11] for thermal-photon emission with an average initial temperature of $T_0^{ave} = 360$ MeV ($T_0^{max} = 570$ MeV) and a formation time of $\tau_0 = 0.15$ fm/c underpredicts the data for $p_T \gtrsim 3$ GeV/c. The data can be described when both sources are combined. The obtained temperature is only meaningful if the observed excess is of thermal origin. To confirm the result, an analysis of $p + p$ and d+Au using the same technique is needed. If the excess in Au+Au is mainly from thermal photons the reference data will show a much smaller effect.

4. Summary

Direct photons were measured with the PHENIX experiment in $p + p$, d+Au, and Au+Au at $\sqrt{s_{NN}} = 200$ GeV. At high p_T ($\gtrsim 5$ GeV/c), the measured yield in all systems is consistent with a NLO pQCD calculation. To tackle the p_T region below 5 GeV/c, direct photons were measured through their internal conversion into e^+e^- in Au+Au collisions. With this powerful technique a significant measurement for $1 < p_T < 5$GeV/c was achieved, lying significantly above the NLO pQCD expectation, but consistent with calculations when thermal photon emission is taken into account.

REFERENCES

1. Adler S S et al. *Phys. Rev. Lett.*, **91**:072301, 2003.
2. Adler S S et al. *Phys. Rev. Lett.*, **94**:232301, 2005.
3. Okada K, 2005. hep-ex/0501066.
4. Turbide S, Rapp R, and Gale C. *Phys. Rev.*, C**69**:014903, 2004.
5. Cobb J H, et al. *Phys. Lett.*, B**78**:519, 1978.
6. Albajar C, et al. *Phys. Lett.*, B**209**:397, 1988.
7. Adcox K, et al. *Phys. Rev.*, C**69**:024904, 2004.
8. Kroll N M, and Wada W. *Phys. Rev.*, **98**:1355–1359, 1955.
9. Gordon L E and Vogelsang W. *Phys. Rev.*, D**48**:3136–59, 1993.
10. Adler S S, et al. *Phys. Rev. Lett.*, **94**:082301, 2005.
11. d'Enterria D and Peressounko D, 2005. nucl-th/0503054.

Institute of Physics Publishing Journal of Physics: Conference Series **50** (2006) 328–331
doi:10.1088/1742-6596/50/1/041 5th International Conference on Physics and Astrophysics of Quark Gluon Plasma

Measurement of direct photons in $\sqrt{s_{NN}} = 200\,\mathbf{GeV}$ $p+p$ and Au+Au collisions with the PHENIX Experiment at RHIC

Stefan Bathe for the PHENIX Collaboration

University of California, Riverside, CA, USA

E-mail: bathe@bnl.gov

Abstract. The measurement of direct photons in $\sqrt{s_{NN}} = 200\,\mathrm{GeV}$ p+p and Au+Au collisions is presented. The signal is compared to NLO pQCD calculations, which, in case of Au+Au, are scaled with the number of underlying nucleon-nucleon collisions. The agreement of the calculation with the data in both cases confirms the scaling of hard processes with the number of nucleon-nucleon collisions and supports the explanation of the earlier-observed pion suppression as a final-state effect.

1. Introduction

Direct photons are a unique probe of the hot and dense matter created at RHIC: they allow access to the initial, thermalized state of the nuclear collision. Their measurement, however, is challenging. One has to cope with a large background from hadronic decays.

While several definitions of direct photons are used, we pragmatically attribute this term to all photons that are not decay photons. The main direct photon production processes are quark-antiquark annihilation and quark-gluon Compton scattering [1]. In addition, direct photons are produced through fragmentation of hard partons. These are also called bremsstrahlung photons.

Direct photon measurements in p+p collisions provide a superb test of pQCD. They probe the gluon distribution function. At RHIC they can also probe the spin gluon distribution function [2] in the polarized-proton program. In contrast to hadron measurements, their interpretation does not suffer much from uncertainties on the fragmentation function. Furthermore, they provide a constraint on the hard-scattering contribution to direct photon production in Au+Au collisions.

In heavy ion collisions, thermal direct photons allow, in principle, measurement of the temperature of the collision system in its hottest phase. Also, hard direct photons serve as a crucial baseline for the interpretation of the earlier observed high-p_T hadron suppression [3]. Interactions of hard partons with the medium provide an additional source of direct photons, either through annihilation and Compton scattering [4] or through medium-induced bremsstrahlung [5].

With its high-resolution, highly-segmented electromagnetic calorimeter PHENIX [6] has an excellent capability to measure photons. PHENIX has made precision measurements of neutral pions and η mesons up to transverse momenta of 15 GeV/c. With this crucial measurement of the direct photon background, PHENIX has extracted direct photons in $p+p$ and Au+Au collisions at $\sqrt{s_{NN}} = 200\,\mathrm{GeV}$.

© 2006 IOP Publishing Ltd

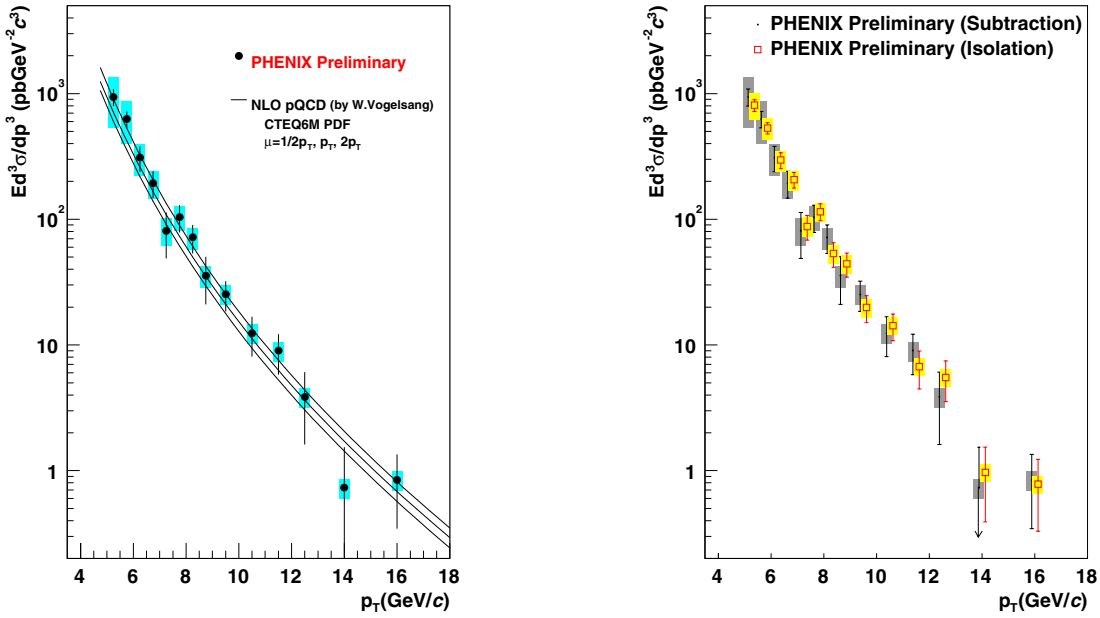

Figure 1. PHENIX preliminary direct photon invariant cross section [7] in $p+p$ collisions at $\sqrt{s}$ = 200 GeV . The left panel shows the result obtained with even-by-event subtraction of decay photons. The curves represent a NLO pQCD calculation for three different scales. The right panel compares this result to the result obtained by an isolation cut.

2. Direct Photon Analysis

The first step in the direct photon analysis in Au+Au is to get a clean inclusive photon sample. To achieve this, non-photon backgrounds, as from charged particles, have to be subtracted. The next step is to measure the p_T spectrum of π^0's and η's. From these spectra, the number of decay photons is determined in a Monte Carlo calculation, which also considers contributions from other hadronic decays. Finally, the decay photon spectrum is subtracted from the inclusive photon spectrum to obtain the direct photon spectrum. This method makes no attempt to identify direct photons on an event-by-event basis. Therefore it is called the subtraction method or statistical method. Further details can be found in [8].

In p+p collisions, where the multiplicity and the occupancy on the detector are small, it is possible to tag and subtract decay photons event by event. In addition, an isolation cut, *i. e.* a cut on the maximum energy allowed in a cone around a direct photon, allows further suppression of decay photons on an event-by-event basis. As an additional feature the isolation cut helps to identify fragmentation photons. Further details on the $p+p$ analysis can be found in [7].

For the measurement of direct photon production in $p+p$ collisions, an integrated luminosity of 266 nbarn^{-1} sampled in the 2003 RHIC $p+p$ run was analyzed. The Au+Au result is based on the 2002 run with an integrated luminosity of 24 μbarn^{-1}. Photons were detected by the electromagnetic calorimeter (EMCal), which is located in the two central arms of the PHENIX detector, each covering $2 * 90°$ in azimuth and a pseudorapidity (η) range of ± 0.35. For the $p+p$ measurement, only one arm was used. The energy calibration was checked by the position and width of the π^0 invariant-mass peak. The fraction of charged-particle contamination was determined with the central-arm tracking detectors which are located in front of the EMCal.

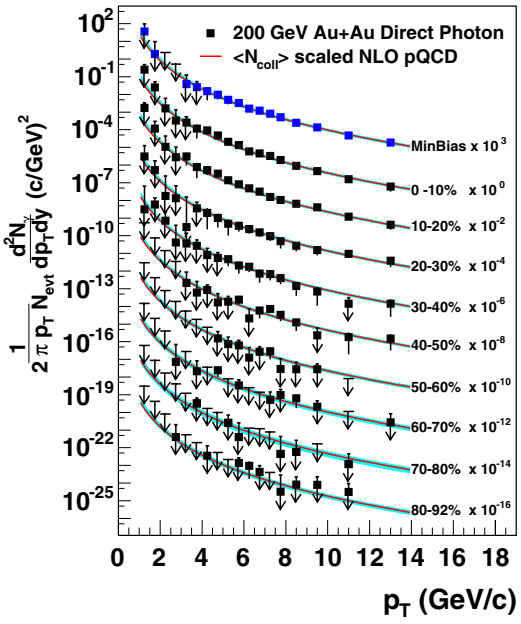

Figure 2. Direct photon invariant yields [8] as a function of p_T for 9 centrality selections and minimum bias Au+Au collisions at $\sqrt{s_{NN}}$ = 200 GeV. The error bars indicate the total error. Arrows indicate measurements consistent with zero yield with the tail of the arrow indicating the 90% confidence level upper limit. The solid curves are pQCD predictions.

3. Direct Photon Cross Section in $p+p$ Collisions

Figure 1 shows the PHENIX preliminary direct photon cross section measured in $\sqrt{s} = 200\,\mathrm{GeV}$ $p+p$ collisions as a function of p_T [7]. The left panel shows the result obtained with event-by-event tagging and subtraction of decay photons. The curves represent a NLO pQCD calculation for three different scales [9]. The calculation agrees well with the measurement. The right panel of Fig. 1 compares this result to the result obtained by an isolation cut. No significant reduction of the direct photon yield by the isolation cut is observed. This suggests that either the contribution from fragmentation photons is small or that the efficiency of the isolation cut to discount fragmentation photons is low. These preliminary results substantially increase the statistical significance and the p_T reach of the published result from the 2002 run [10].

4. Direct Photon Yield in Au+Au Collisions

The direct photon spectra measured in $\sqrt{s_{NN}} = 200\,\mathrm{GeV}$ Au+Au collisions [8] are shown in Fig. 2 for different centrality selections. They are compared to NLO pQCD calculations [9] scaled by the corresponding number of binary nucleon collisions. It can be seen that the pQCD calculations provide a good description of the measured direct photon spectra.

A common way to study possible medium effects in AA collisions is the *nuclear modification factor* R_{AA}, *i. e.* the ratio of the AA invariant yields to the NN-collision-scaled $p+p$ invariant yields [3]. The centrality dependence of R_{AA} for the integrated yield in $p_T > 6$ GeV/c for direct photons (closed circles) is now compared to that of π^0's (open circles) in Fig. 3. The direct photon $p+p$ yield is taken as the NLO pQCD calculation [9] as in the previous figure, while the π^0 $p+p$ yield is taken from the measured π^0 yield [11]. The R_{AA} trend confirms the observation from above in more detail: the direct photon production in Au+Au is consistent with the binary-scaled $p+p$ pQCD calculation. This is in sharp contrast [3] to the centrality dependence of the π^0 R_{AA}, indicating that the observed large suppression of high-p_T hadron production in central Au+Au collisions is dominantly a final-state effect due to parton energy loss in the dense produced medium, rather than an initial-state effect.

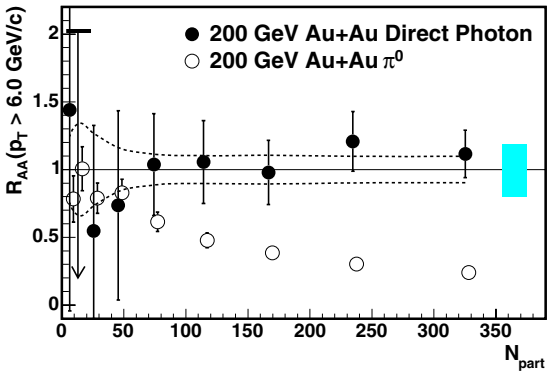

Figure 3. $R_{AA}(p_T > 6\text{GeV}/c)$ as a function of centrality (N_{part}) for direct photons (closed circles) and π^0's (open circles) [8]. The error bars indicate the total error excluding the error on $\langle N_{coll} \rangle$ shown by the dashed lines and the scale uncertainty of the NLO calculation shown by the shaded region at the right.

5. Summary

Direct photon production has been measured in $p + p$ and Au+Au collisions at $\sqrt{s_{NN}} = 200$ GeV. In $p + p$, NLO pQCD calculations agree well with the measurement. The equally good agreement between measurement and binary scaled pQCD calculations in Au+Au suggests that nuclear modifications at mid-rapidity are small. The result provides strong confirmation that the observed large suppression of high p_T hadron production in central Au+Au collisions is dominantly a final-state effect.

References

[1] Peitzmann T and Thoma M H. Direct photons from relativistic heavy-ion collisions. *Phys. Rept.*, **364**:175–246, 2002.

[2] Saito N et al. Spin physics with the PHENIX detector system. *Nucl. Phys.*, A**638**:575–578, 1998.

[3] Adler S S et al. Suppressed π^0 production at large transverse momentum in central Au + Au collisions at $\sqrt{s_{NN}} = 200$ GeV. *Phys. Rev. Lett.*, **91**:072301, 2003.

[4] Fries R J, Muller B and Srivastava D K. High energy photons from passage of jets through quark gluon plasma. *Phys. Rev. Lett.*, **90**:132301, 2003.

[5] Jeon S, Jalilian-Marian J and Sarcevic I. Prompt photon and inclusive π^0 production at RHIC and LHC. *Nucl. Phys.*, A**715**:795, 2003.

[6] Adcox K et al. PHENIX detector overview. *Nucl. Instrum. Meth.*, A**499**:469–479, 2003.

[7] Okada K. Measurement of prompt photons in $\sqrt{s} = 200$ GeV $p + p$ collisions, 2005. hep-ex/0501066. To appear in the proceedings of the 16th International Spin Physics Symposium (SPIN 2004), Trieste, Italy, October 10–16, 2004.

[8] Adler S S et al. Centrality dependence of direct photon production in $\sqrt{s_{NN}} = 200$ GeV Au + Au collisions. *Phys. Rev. Lett.*, **94**:232301, 2005.

[9] Gordon L E and Vogelsang W. Polarized and unpolarized prompt photon production beyond the leading order. *Phys. Rev.*, D**48**:3136–59, 1993.

[10] Adler S S et al. Mid-rapidity direct-photon production in p + p collisions at $\sqrt{s} = 200$ GeV. *Phys. Rev.*, D**71**:071102, 2005.

[11] Adler S S et al. Mid-rapidity neutral pion production in proton proton collisions at $\sqrt{s} = 200$ GeV. *Phys. Rev. Lett.*, **91**:241803, 2003.

Nuclear Modification of Electron Spectra and Implications for Heavy Quark Energy Loss in Au + Au Collisions at $\sqrt{s_{NN}} = 200$ GeV

S. S. Adler,[5] S. Afanasiev,[17] C. Aidala,[5] N. N. Ajitanand,[43] Y. Akiba,[20,38] J. Alexander,[43] R. Amirikas,[12] L. Aphecetche,[45] S. H. Aronson,[5] R. Averbeck,[44] T. C. Awes,[35] R. Azmoun,[44] V. Babintsev,[15] A. Baldisseri,[10] K. N. Barish,[6] P. D. Barnes,[27] B. Bassalleck,[33] S. Bathe,[30] S. Batsouli,[9] V. Baublis,[37] A. Bazilevsky,[39,15] S. Belikov,[16,15] Y. Berdnikov,[40] S. Bhagavatula,[16] J. G. Boissevain,[27] H. Borel,[10] S. Borenstein,[25] M. L. Brooks,[27] D. S. Brown,[34] N. Bruner,[33] D. Bucher,[30] H. Buesching,[30] V. Bumazhnov,[15] G. Bunce,[5,39] J. M. Burward-Hoy,[26,44] S. Butsyk,[44] X. Camard,[45] J.-S. Chai,[18] P. Chand,[4] W. C. Chang,[2] S. Chernichenko,[15] C. Y. Chi,[9] J. Chiba,[20] M. Chiu,[9] I. J. Choi,[52] J. Choi,[19] R. K. Choudhury,[4] T. Chujo,[5] V. Cianciolo,[35] Y. Cobigo,[10] B. A. Cole,[9] P. Constantin,[16] D. d'Enterria,[45] G. David,[5] H. Delagrange,[45] A. Denisov,[15] A. Deshpande,[39] E. J. Desmond,[5] A. Devismes,[44] O. Dietzsch,[41] O. Drapier,[25] A. Drees,[44] R. du Rietz,[29] A. Durum,[15] D. Dutta,[4] Y. V. Efremenko,[35] J. Egdemir,[44] K. El Chenawi,[49] A. Enokizono,[14] H. En'yo,[38,39] S. Esumi,[48] L. Ewell,[5] D. E. Fields,[33,39] F. Fleuret,[25] S. L. Fokin,[23] B. D. Fox,[39] Z. Fraenkel,[51] J. E. Frantz,[9] A. Franz,[5] A. D. Frawley,[12] S.-Y. Fung,[6] S. Garpman,[29,*] T. K. Ghosh,[49] A. Glenn,[46] G. Gogiberidze,[46] M. Gonin,[25] J. Gosset,[10] Y. Goto,[39] R. Granier de Cassagnac,[25] N. Grau,[16] S. V. Greene,[49] M. Grosse Perdekamp,[39] W. Guryn,[5] H.-Å. Gustafsson,[29] T. Hachiya,[14] J. S. Haggerty,[5] H. Hamagaki,[8] A. G. Hansen,[27] E. P. Hartouni,[26] M. Harvey,[5] R. Hayano,[8] N. Hayashi,[38] X. He,[13] M. Heffner,[26] T. K. Hemmick,[44] J. M. Heuser,[44] M. Hibino,[50] J. C. Hill,[16] W. Holzmann,[43] K. Homma,[14] B. Hong,[22] A. Hoover,[34] T. Ichihara,[38,39] V. V. Ikonnikov,[23] K. Imai,[24,38] D. Isenhower,[1] M. Ishihara,[38] M. Issah,[43] A. Isupov,[17] B. V. Jacak,[44] W. Y. Jang,[22] Y. Jeong,[19] J. Jia,[44] O. Jinnouchi,[38] B. M. Johnson,[5] S. C. Johnson,[26] K. S. Joo,[31] D. Jouan,[36] S. Kametani,[8,50] N. Kamihara,[47,38] J. H. Kang,[52] S. S. Kapoor,[4] K. Katou,[50] S. Kelly,[9] B. Khachaturov,[51] A. Khanzadeev,[37] J. Kikuchi,[50] D. H. Kim,[31] D. J. Kim,[52] D. W. Kim,[19] E. Kim,[42] G.-B. Kim,[25] H. J. Kim,[52] E. Kistenev,[5] A. Kiyomichi,[48] K. Kiyoyama,[32] C. Klein-Boesing,[30] H. Kobayashi,[38,39] L. Kochenda,[37] V. Kochetkov,[15] D. Koehler,[33] T. Kohama,[14] M. Kopytine,[44] D. Kotchetkov,[6] A. Kozlov,[51] P. J. Kroon,[5] C. H. Kuberg,[1,27,*] K. Kurita,[39] Y. Kuroki,[48] M. J. Kweon,[22] Y. Kwon,[52] G. S. Kyle,[34] R. Lacey,[43] V. Ladygin,[17] J. G. Lajoie,[16] A. Lebedev,[16,23] S. Leckey,[44] D. M. Lee,[27] S. Lee,[19] M. J. Leitch,[27] X. H. Li,[6] H. Lim,[42] A. Litvinenko,[17] M. X. Liu,[27] Y. Liu,[36] C. F. Maguire,[49] Y. I. Makdisi,[5] A. Malakhov,[17] V. I. Manko,[23] Y. Mao,[7,38] G. Martinez,[45] M. D. Marx,[44] H. Masui,[48] F. Matathias,[44] T. Matsumoto,[8,50] P. L. McGaughey,[27] E. Melnikov,[15] F. Messer,[44] Y. Miake,[48] J. Milan,[43] T. E. Miller,[49] A. Milov,[44,51] S. Mioduszewski,[5] R. E. Mischke,[27] G. C. Mishra,[13] J. T. Mitchell,[5] A. K. Mohanty,[4] D. P. Morrison,[5] J. M. Moss,[27] F. Mühlbacher,[44] D. Mukhopadhyay,[51] M. Muniruzzaman,[6] J. Murata,[38,39] S. Nagamiya,[20] J. L. Nagle,[9] T. Nakamura,[14] B. K. Nandi,[6] M. Nara,[48] J. Newby,[46] P. Nilsson,[29] A. S. Nyanin,[23] J. Nystrand,[29] E. O'Brien,[5] C. A. Ogilvie,[16] H. Ohnishi,[5,38] I. D. Ojha,[49,3] K. Okada,[38] M. Ono,[48] V. Onuchin,[15] A. Oskarsson,[29] I. Otterlund,[29] K. Oyama,[8] K. Ozawa,[8] D. Pal,[51] A. P. T. Palounek,[27] V. Pantuev,[44] V. Papavassiliou,[34] J. Park,[42] A. Parmar,[33] S. F. Pate,[34] T. Peitzmann,[30] J.-C. Peng,[27] V. Peresedov,[17] C. Pinkenburg,[5] R. P. Pisani,[5] F. Plasil,[35] M. L. Purschke,[5] A. K. Purwar,[44] J. Rak,[16] I. Ravinovich,[51] K. F. Read,[35,46] M. Reuter,[44] K. Reygers,[30] V. Riabov,[37,40] Y. Riabov,[37] G. Roche,[28] A. Romana,[25] M. Rosati,[16] P. Rosnet,[28] S. S. Ryu,[52] M. E. Sadler,[1] N. Saito,[38,39] T. Sakaguchi,[8,50] M. Sakai,[32] S. Sakai,[48] V. Samsonov,[37] L. Sanfratello,[33] R. Santo,[30] H. D. Sato,[24,38] S. Sato,[5,48] S. Sawada,[20] Y. Schutz,[45] V. Semenov,[15] R. Seto,[6] M. R. Shaw,[1,27] T. K. Shea,[5] T.-A. Shibata,[47,38] K. Shigaki,[14,20] T. Shiina,[27] C. L. Silva,[41] D. Silvermyr,[27,29] K. S. Sim,[22] C. P. Singh,[3] V. Singh,[3] M. Sivertz,[5] A. Soldatov,[15] R. A. Soltz,[26] W. E. Sondheim,[27] S. P. Sorensen,[46] I. V. Sourikova,[5] F. Staley,[10] P. W. Stankus,[35] E. Stenlund,[29] M. Stepanov,[34] A. Ster,[21] S. P. Stoll,[5] T. Sugitate,[14] J. P. Sullivan,[27] E. M. Takagui,[41] A. Taketani,[38,39] M. Tamai,[50] K. H. Tanaka,[20] Y. Tanaka,[32] K. Tanida,[38] M. J. Tannenbaum,[5] P. Tarján,[11] J. D. Tepe,[1,27] T. L. Thomas,[33] J. Tojo,[24,38] H. Torii,[24,38] R. S. Towell,[1] I. Tserruya,[51] H. Tsuruoka,[48] S. K. Tuli,[3] H. Tydesjö,[29] N. Tyurin,[15] H. W. van Hecke,[27] J. Velkovska,[5,44] M. Velkovsky,[44] V. Veszprémi,[11] L. Villatte,[46] A. A. Vinogradov,[23] M. A. Volkov,[23] E. Vznuzdaev,[37] X. R. Wang,[13] Y. Watanabe,[38,39] S. N. White,[5] F. K. Wohn,[16] C. L. Woody,[5] W. Xie,[6] Y. Yang,[7] A. Yanovich,[15] S. Yokkaichi,[38,39] G. R. Young,[35] I. E. Yushmanov,[23] W. A. Zajc,[9,†] C. Zhang,[9] S. Zhou,[7] S. J. Zhou,[51] and L. Zolin[17]

(PHENIX Collaboration)

[1]*Abilene Christian University, Abilene, Texas 79699, USA*
[2]*Institute of Physics, Academia Sinica, Taipei 11529, Taiwan*
[3]*Department of Physics, Banaras Hindu University, Varanasi 221005, India*

 © 2006 The American Physical Society

[4]Bhabha Atomic Research Centre, Bombay 400 085, India
[5]Brookhaven National Laboratory, Upton, New York 11973-5000, USA
[6]University of California—Riverside, Riverside, California 92521, USA
[7]China Institute of Atomic Energy (CIAE), Beijing, People's Republic of China
[8]Center for Nuclear Study, Graduate School of Science, University of Tokyo, 7-3-1 Hongo, Bunkyo, Tokyo 113-0033, Japan
[9]Columbia University, New York, New York 10027, USA,
and Nevis Laboratories, Irvington, New York 10533, USA
[10]Dapnia, CEA Saclay, F-91191 Gif-sur-Yvette, France
[11]Debrecen University, H-4010 Debrecen, Egyetem tér 1, Hungary
[12]Florida State University, Tallahassee, Florida 32306, USA
[13]Georgia State University, Atlanta, Georgia 30303, USA
[14]Hiroshima University, Kagamiyama, Higashi-Hiroshima 739-8526, Japan
[15]IHEP Protvino, State Research Center of Russian Federation, Institute for High Energy Physics, Protvino 142281, Russia
[16]Iowa State University, Ames, Iowa 50011, USA
[17]Joint Institute for Nuclear Research, 141980 Dubna, Moscow Region, Russia
[18]KAERI, Cyclotron Application Laboratory, Seoul, South Korea
[19]Kangnung National University, Kangnung 210-702, South Korea
[20]KEK, High Energy Accelerator Research Organization, Tsukuba, Ibaraki 305-0801, Japan
[21]KFKI Research Institute for Particle and Nuclear Physics of the Hungarian Academy of Sciences (MTA KFKI RMKI),
H-1525 Budapest 114, P.O. Box 49, Budapest, Hungary
[22]Korea University, Seoul 136-701, Korea
[23]Russian Research Center "Kurchatov Institute," Moscow, Russia
[24]Kyoto University, Kyoto 606-8502, Japan
[25]Laboratoire Leprince-Ringuet, Ecole Polytechnique, CNRS-IN2P3, Route de Saclay, F-91128 Palaiseau, France
[26]Lawrence Livermore National Laboratory, Livermore, California 94550, USA
[27]Los Alamos National Laboratory, Los Alamos, New Mexico 87545, USA
[28]LPC, Université Blaise Pascal, CNRS-IN2P3, Clermont-Fd, 63177 Aubiere Cedex, France
[29]Department of Physics, Lund University, Box 118, SE-221 00 Lund, Sweden
[30]Institut für Kernphysik, University of Muenster, D-48149 Muenster, Germany
[31]Myongji University, Yongin, Kyonggido 449-728, Korea
[32]Nagasaki Institute of Applied Science, Nagasaki-shi, Nagasaki 851-0193, Japan
[33]University of New Mexico, Albuquerque, New Mexico 87131, USA
[34]New Mexico State University, Las Cruces, New Mexico 88003, USA
[35]Oak Ridge National Laboratory, Oak Ridge, Tennessee 37831, USA
[36]IPN-Orsay, Universite Paris Sud, CNRS-IN2P3, BP1, F-91406 Orsay, France
[37]PNPI, Petersburg Nuclear Physics Institute, Gatchina, Leningrad Region 188300, Russia
[38]RIKEN, The Institute of Physical and Chemical Research, Wako, Saitama 351-0198, Japan
[39]RIKEN BNL Research Center, Brookhaven National Laboratory, Upton, New York 11973-5000, USA
[40]Saint Petersburg State Polytechnic University, St. Petersburg, Russia
[41]Instituto de Física, Universidade de São Paulo, Caixa Postal 66318, São Paulo CEP05315-970, Brazil
[42]System Electronics Laboratory, Seoul National University, Seoul, South Korea
[43]Chemistry Department, Stony Brook University, SUNY, Stony Brook, New York 11794-3400, USA
[44]Department of Physics and Astronomy, Stony Brook University, SUNY, Stony Brook, New York 11794, USA
[45]SUBATECH (Ecole des Mines de Nantes, CNRS-IN2P3, Université de Nantes), BP 20722-44307, Nantes, France
[46]University of Tennessee, Knoxville, Tennessee 37996, USA
[47]Department of Physics, Tokyo Institute of Technology, Oh-okayama, Meguro, Tokyo 152-8551, Japan
[48]Institute of Physics, University of Tsukuba, Tsukuba, Ibaraki 305, Japan
[49]Vanderbilt University, Nashville, Tennessee 37235, USA
[50]Advanced Research Institute for Science and Engineering, Waseda University, 17 Kikui-cho, Shinjuku-ku, Tokyo 162-0044, Japan
[51]Weizmann Institute, Rehovot 76100, Israel
[52]Yonsei University, IPAP, Seoul 120-749, Korea
(Received 17 October 2005; published 26 January 2006)

The PHENIX experiment has measured midrapidity ($|\eta| < 0.35$) transverse momentum spectra ($0.4 < p_T < 5.0$ GeV/c) of electrons as a function of centrality in Au + Au collisions at $\sqrt{s_{NN}} = 200$ GeV. Contributions from photon conversions and from light hadron decays, mainly Dalitz decays of π^0 and η mesons, were removed. The resulting nonphotonic electron spectra are primarily due to the semileptonic decays of hadrons carrying heavy quarks. Nuclear modification factors were determined by comparison to nonphotonic electrons in $p + p$ collisions. A significant suppression of electrons at high p_T is observed in central Au + Au collisions, indicating substantial energy loss of heavy quarks.

DOI: 10.1103/PhysRevLett.96.032301 PACS numbers: 25.75.Dw

It is well established that neutral pions and charged hadrons are strongly suppressed at high transverse momentum (p_T) in high energy Au + Au collisions [1–5]. The suppression, which is absent in d + Au collisions at midrapidity, implies that hard scattered partons traversing the medium created in Au + Au collisions experience considerable energy loss. Although high p_T suppression is expected for charm quarks as well, their interaction with the medium has been predicted to be smaller than for light quarks, i.e., they should lose a lower fraction of their energy, as their large mass decreases the phase space available for gluon radiation, which is known as the ''dead cone'' effect [6]. If the medium is indeed less opaque to charm quarks, they will also participate less in the collective expansion of the medium, leading to a smaller elliptic flow strength v_2 [7] for particles carrying charm quarks compared to those solely composed of light quarks. Such medium effects should be even less pronounced for bottom than for charm quarks.

The interaction of heavy quarks with the medium can be studied experimentally through systematic measurements of the p_T spectra of open heavy flavor, i.e., hadrons composed of a heavy and a light quark. While the full reconstruction of D meson decays at the Relativistic Heavy Ion Collider (RHIC) is reported for d + Au collisions [8], indirect measurements of open heavy flavor via semileptonic decays are available for $p + p$ and d + Au collisions at $\sqrt{s_{NN}} = 200$ GeV [8–10] as well as for Au + Au collisions at 130 and 200 GeV [11,12]. In $p + p$ collisions, the extracted electron p_T spectrum from heavy flavor decays is in reasonable agreement with perturbative quantum chromodynamics (pQCD) calculations in next-to-leading order. However, the data leave room for contributions from further production mechanisms in which the heavy quarks are not created in the initial hard parton scattering, e.g., via jet fragmentation [9]. In d + Au collisions, no indications for strong cold nuclear matter effects were found [8,10]. For Au + Au collisions of different centrality, the total electron yield from heavy flavor decays was observed to scale with the nuclear overlap integral $\langle T_{AA} \rangle$ as expected for pointlike pQCD processes [12]. However, these electrons show an azimuthal anisotropy with respect to the reaction plane [13], consistent with the notion of charm quark flow in Au + Au collisions. It has been pointed out that if the charm quarks flow along with the bulk of the medium, this is evidence for thermalization of charm. In this situation, the medium modifications of the charm spectrum should be substantial [14].

In this Letter, we report on the p_T spectra of nonphotonic electrons, $(e^+ + e^-)/2$, measured at midrapidity ($|\eta| < 0.35$) up to $p_T = 5$ GeV/c by the PHENIX experiment in Au + Au collisions at $\sqrt{s_{NN}} = 200$ GeV. The photonic electron background was removed by a *cocktail* subtraction, in contrast to the *converter* subtraction used in [12], where a subset of the current data sample was analyzed. The converter method is better suited for a determination of the total yield of heavy flavor electrons, while the cocktail subtraction used here provides a precision measurement of the spectral shape [15]. The nuclear modification is then determined by comparing the spectra to those in $p + p$ collisions [9].

The data used in this analysis were collected by the PHENIX detector [16] during the 2001 run of RHIC. A coincidence of the beam-beam counters (BBC) and the zero degree calorimeters (ZDC) provided the minimum bias trigger ($92.2^{+2.5}_{-3.0}\%$ of the Au + Au inelastic cross section). The centrality was determined by the correlation between the multiplicity measured by the BBC and the energy of spectator neutrons measured by the ZDC. After restricting the vertex range to $|z| < 20$ cm to eliminate background originating from the central magnet, a data sample of 25×10^6 minimum bias events was analyzed.

For the electron analysis, charged particle tracks were reconstructed with the drift chamber and the first layer of pad chambers of the PHENIX east-arm spectrometer ($|\eta| < 0.35$, $\Delta\phi = \pi/2$), as discussed in detail elsewhere [12]. Tracks were confirmed by matching hits in the electromagnetic calorimeter (EMC) within 2σ in position. Electron candidates had at least three associated hits in the ring imaging Čerenkov detector (RICH). After an additional cut on the correlation between the momentum p and the energy E deposited in the EMC [$-2\sigma < (E - p)/p < 3\sigma$], the only background remaining in the electron sample was due to accidental coincidences between RICH hits and hadron tracks. This background was estimated ($\approx$15% at low p_T in central collisions, decreasing towards high p_T and for peripheral events) and subtracted statistically by an event-mixing method.

The raw electron spectra were corrected as a function of p_T for geometrical acceptance and reconstruction efficiency [12]. The multiplicity dependent efficiency loss was estimated by embedding simulated electrons into real events. This loss increased from 5% to 26% from peripheral to central collisions without a significant p_T dependence in the range relevant here. The 1σ systematic uncertainty of all corrections is 11.8%, after correction for the effect of finite bin width in p_T. The fully corrected inclusive electron spectrum is shown in Fig. 1(a) for minimum bias collisions.

The spectra of electrons from heavy flavor decays were determined by subtracting cocktails of background contributions from other sources from the inclusive data. The most important background is the π^0 Dalitz decay which was calculated individually for each centrality class with a hadron decay generator using parametrizations of measured π^0 [2] and $\pi^\pm$ [17] spectra as input. The spectral shapes of other light hadrons h were obtained from the pion spectra, assuming a universal spectrum in $m_T = \sqrt{p_T^2 + m_h^2}$. Within this approach the ratios h/π^0 are constant at high p_T with the values [11]: $\eta/\pi^0 = 0.45 \pm 0.10$, $\rho/\pi^0 = 1.0 \pm 0.3$, $\omega/\pi^0 = 1.0 \pm 0.3$, $\eta'/\pi^0 = 0.25 \pm 0.08$, and $\phi/\pi^0 = 0.40 \pm 0.12$. Only the η contribution

is of any practical relevance, and the chosen parametrization is in good agreement with the measured η meson spectra [18]. Another major electron source is the conversion of photons, mainly from $\pi^0 \to \gamma\gamma$ decays, in material in the acceptance ($\approx 1\%\ X/X_0$). The spectra of electrons from conversions and Dalitz decays are very similar. In a GEANT simulation [19] of π^0 decays, the ratio of conversion electrons to Dalitz electrons was determined to be 1.25 ± 0.10, essentially p_T independent. Contributions from photon conversions from other sources were taken into account as well. Electrons from kaon decays (K_{e3}), determined in a GEANT simulation based on measured kaon spectra [17], and electrons from external as well as internal conversions of direct photons [20,21] were included.

All background sources are compared with the inclusive data in Fig. 1(a). Further background from $J/\psi \to e^+e^-$ decays and from Drell-Yan pairs [22] is negligible. A possible low mass dilepton enhancement through $\pi + \pi \to \rho \to e^+e^-$, as reported in Pb + Pb collisions at lower $\sqrt{s_{NN}}$ [23], would constitute another background source

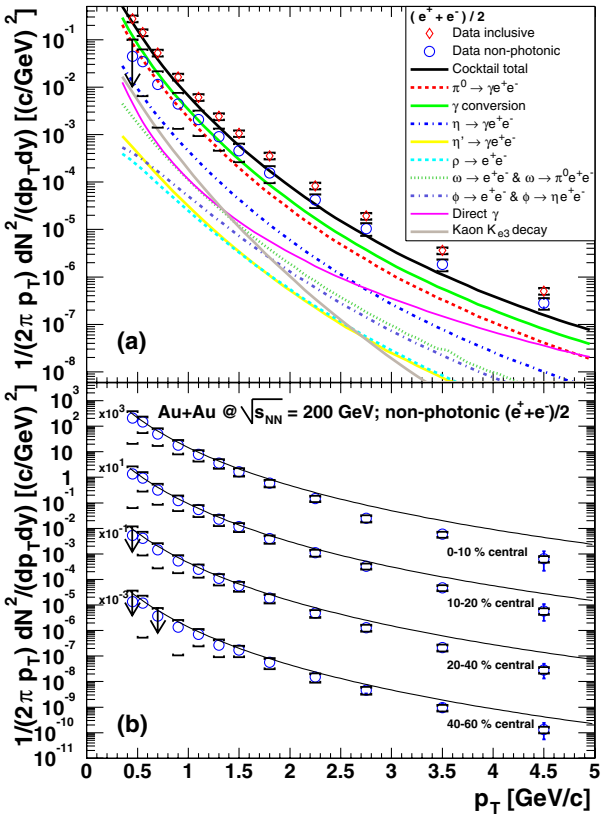

FIG. 1 (color online). (a) Inclusive and nonphotonic electron invariant yields in minimum bias Au + Au collisions at $\sqrt{s_{NN}} = 200$ GeV, compared with contributions from all background electron sources included in the cocktail. (b) Invariant yields of electrons from heavy flavor decays for different Au + Au centrality classes, scaled by powers of ten for clarity, together with the best fit to the $p + p$ reference scaled with the appropriate nuclear overlap integrals $\langle T_{AA} \rangle$. The error bars (brackets) correspond to statistical (systematic) uncertainties.

which is neglected here since the estimated ρ contribution in the absence of enhancement is small ($<1\%$ at all p_T). The total cocktail systematic uncertainty increases from 10% (at $p_T = 0.4$ GeV/c) to 15% (at $p_T = 5$ GeV/c), dominated by the systematic error of the pion input spectra ($\approx 8\%$–10%). Other systematic uncertainties, mainly the η/π^0 normalization and, at high p_T, the contribution from direct radiation, are much smaller. The background cocktail calculated here and the photonic electron background measured via the converter method [12] agree within 10%.

After subtracting the cocktail from the inclusive electron data, the invariant spectrum of electrons from heavy flavor decays is shown in Fig. 1(a) for minimum bias collisions. For $p_T > 2$ GeV/c the signal to background ratio is larger than 1. Figure 1(b) shows the electron spectra from heavy flavor decays in four centrality classes, 0%–10%, 10%–20%, 20%–40%, and 40%–60% central collisions. More peripheral collisions have insufficient electron statistics to reach $p_T = 5$ GeV/c.

PHENIX has also measured electrons from heavy flavor decays in $p + p$ collisions at $\sqrt{s} = 200$ GeV [9]. The curves shown in Fig. 1(b) depict the best fit of the corresponding spectrum from $p + p$ collisions, scaled by the nuclear overlap integral $\langle T_{AA} \rangle$ calculated within a Glauber model [2] for each Au + Au centrality class. At low p_T the Au + Au spectra are in reasonable agreement with the $p + p$ fit in all centrality bins, but a clear suppression of the spectra in Au + Au with respect to $p + p$ develops towards high p_T.

To quantify this effect we calculate for each individual bin in p_T the nuclear modification factor R_{AA} defined as

$$R_{AA} = \frac{dN_{\mathrm{Au+Au}}}{\langle T_{AA} \rangle d\sigma_{p+p}}, \tag{1}$$

where $dN_{\mathrm{Au+Au}}$ is the differential electron yield from heavy flavor decays in Au + Au collisions and $d\sigma_{p+p}$ is the corresponding differential cross section in $p + p$ collisions [9] in any given p_T bin.

Figure 2 shows R_{AA} as a function of p_T in the four Au + Au centrality classes. At low p_T, the electron R_{AA} is consistent with one within substantial uncertainties in all centrality classes, in agreement with the observation of binary collision scaling of the total charm yield in Au + Au collisions at RHIC [12]. Since the ratio of electrons from heavy flavor decays to background increases with increasing p_T, the systematic uncertainties of R_{AA} decrease towards high p_T. R_{AA} falls well below one for electron $p_T \geq 2$ GeV/c, providing clear evidence for heavy quark medium modifications. The observed high p_T suppression is most significant for central collisions. However, the limited statistics do not allow one to quantify the centrality dependence of heavy quark medium modifications. At the highest p_T, the electron R_{AA} becomes as small as that for π^0 [2], indicating substantial energy loss of heavy quarks in the medium. It is important to note that electrons at a given p_T originate from decays of higher p_T D or B

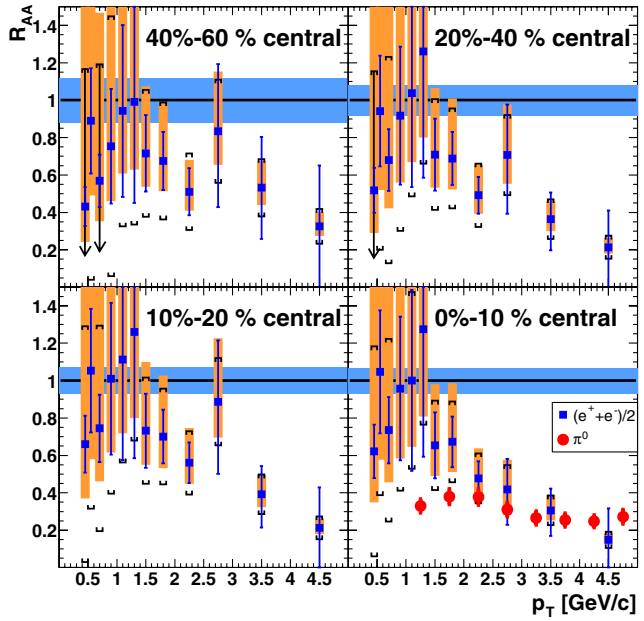

FIG. 2 (color online). Nuclear modification factor R_{AA} for electrons from heavy flavor decays as function of p_T in Au + Au collisions at $\sqrt{s_{NN}} = 200$ GeV for the different centrality classes. The error bars are statistical only. Error brackets (boxes) indicate the systematic errors related to the uncertainties in the Au + Au ($p + p$) measurements. The bands around one show the relative systematic uncertainties in T_{AA}. For the most central collisions the π^0 R_{AA} is shown for comparison [2]. For these data, a 13% p_T independent systematic uncertainty (not plotted) represents the uncertainty in $\langle T_{AA} \rangle$ and in the π^0 yield normalization.

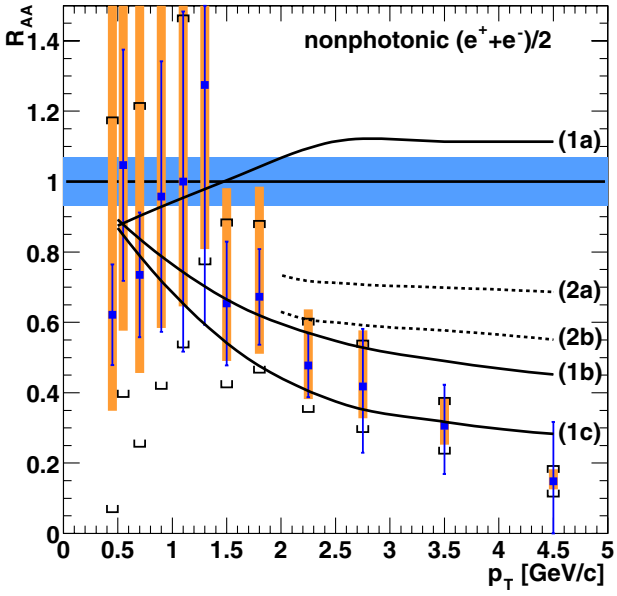

FIG. 3 (color online). Nuclear modification factor R_{AA} for electrons from heavy quark decays as function of p_T for the 10% most central Au + Au collisions at $\sqrt{s_{NN}} = 200$ GeV in comparison with predictions from models incorporating charm quark energy loss. Curves (1a)–(1c) and (2a)–(2b) are taken from [24,25], respectively, where contributions from B meson decays are included in (2a) and (2b) only. Experimental uncertainties are shown as described in Fig. 2.

mesons, making model independent comparisons of R_{AA} for light and heavy quarks impossible.

The observed R_{AA} is remarkable, as electrons with $p_T > 3.5$ GeV/c are expected to include significant contributions from B meson decays, and B mesons should suffer less than D mesons from medium modifications. Depending on their time scales, mechanisms by which heavy quarks are produced after the initial hard parton scattering, such as gluon splitting in jets, might lead to an attenuation at high p_T which then is due to a mixture of light parton and heavy quark energy loss in the medium created at RHIC.

Figure 3 confronts current model calculations [24,25] utilizing induced gluon radiation as the heavy quark energy loss mechanism with the data for the 10% most central collisions. The three curves (1a)–(1c) include electrons from charm decays only [24]. They correspond to different values of the time-averaged transport coefficient $\hat{q}$, which denotes the average squared transverse momentum transferred from a hard parton per unit path length while traversing the medium and, as such, is proportional to the density of scattering centers in the medium. Curve (1a) applies for the case without the presence of any medium causing heavy quark energy loss ($\hat{q} = 0$ GeV^2/fm). The $\hat{q}$ values of 4 and 14 GeV^2/fm, which correspond to curves (1b) and (1c), lead to light quark energy losses which bracket the observed high p_T suppression of neutral pions and charged hadrons. Predictions for charm energy loss from [24] for medium densities at the extreme high end of those allowed by the observed light quark energy loss are consistent with the electron data. Contributions from bottom decays, which are expected to be significant for $p_T > 3$ GeV/c, should lead to an increase of the predicted R_{AA} since b quarks are presumably less affected by energy loss than c quarks [6]. Curves (2a) and (2b) are taken from [25]. They include electrons from both D and B meson decays and correspond to initial gluon densities of $dN_g/dy = 1000$ and 3500 for curves (2a) and (2b), respectively, which again lead to light parton energy losses bracketing the observed high p_T pion suppression. However, at high p_T the predicted R_{AA} for electrons from heavy flavor decays is larger than observed. The present data pose a challenge to existing calculations of radiative energy loss in the medium produced at RHIC, and will help to distinguish between different energy loss scenarios.

In conclusion, we have measured electron spectra from heavy flavor decays in Au + Au collisions at $\sqrt{s_{NN}} = 200$ GeV. In central collisions, nuclear modification factors $R_{AA} \ll 1$ are observed at high p_T, providing clear evidence for strong medium effects. Current models involving energy loss via induced gluon radiation for heavy quarks traversing the medium created in heavy ion collisions at RHIC are challenged by the data even considering extremely high medium densities.

We thank the staff of the Collider-Accelerator and Physics Departments at BNL for their vital contributions. We acknowledge support from the Department of Energy and NSF (USA), MEXT and JSPS (Japan), CNPq and FAPESP (Brazil), NSFC (China), CNRS-IN2P3 and CEA (France), BMBF, DAAD, and AvH (Germany), OTKA (Hungary), DAE and DST (India), ISF (Israel), KRF and CHEP (Korea), RMIST, RAS, and RMAE (Russia), VR and KAW (Sweden), U.S. CRDF for the FSU, U.S.-Hungarian NSF-OTKA-MTA, and U.S.-Israel BSF.

*Deceased.
†PHENIX Spokesperson.
Electronic address: zajc@nevis.columbia.edu

[1] K. Adcox *et al.*, Phys. Rev. Lett. **88**, 022301 (2002).
[2] S. S. Adler *et al.*, Phys. Rev. Lett. **91**, 072301 (2003).
[3] I. Arsene *et al.*, Phys. Rev. Lett. **91**, 072305 (2003).
[4] B. B. Back *et al.*, Phys. Lett. B **578**, 297 (2004).
[5] J. Adams *et al.*, Phys. Rev. Lett. **91**, 172302 (2003).
[6] Y. L. Dokshitzer and D. E. Kharzeev, Phys. Lett. B **519**, 199 (2001).
[7] J.-Y. Ollitrault, Phys. Rev. D **46**, 229 (1992); S. Voloshin and Y. Zhang, Z. Phys. C **70**, 665 (1996).
[8] J. Adams *et al.*, Phys. Rev. Lett. **94**, 062301 (2005).
[9] S. S. Adler *et al.* (PHENIX Collaboration), Phys. Rev. Lett. **96**, LH10414 (2006).
[10] S. Kelly *et al.*, J. Phys. G **30**, S1189 (2004).
[11] K. Adcox *et al.*, Phys. Rev. Lett. **88**, 192303 (2002).
[12] S. S. Adler *et al.*, Phys. Rev. Lett. **94**, 082301 (2005).
[13] S. S. Adler *et al.*, Phys. Rev. C **72**, 024901 (2005).
[14] H. van Hees and R. Rapp, Phys. Rev. C **71**, 034907 (2005); G. D. Moore and D. Teaney, Phys. Rev. C **71**, 064904 (2005).
[15] R. Averbeck *et al.*, J. Phys. G **31**, S259 (2005).
[16] K. Adcox *et al.*, Nucl. Instrum. Methods Phys. Res., Sect. A **499**, 469 (2003).
[17] S. S. Adler *et al.*, Phys. Rev. C **69**, 034909 (2004).
[18] S. S. Adler *et al.* (to be published).
[19] GEANT 3.21, CERN program library.
[20] L. E. Gordon and W. Vogelsang, Phys. Rev. D **50**, 1901 (1994).
[21] S. S. Adler *et al.*, Phys. Rev. Lett. **94**, 232301 (2005).
[22] S. Gavin, P. L. McGaughey, P. V. Ruuskanen, and R. Vogt, Phys. Rev. C **54**, 2606 (1996).
[23] G. Agakichiev *et al.*, Phys. Lett. B **422**, 405 (1998).
[24] N. Armesto, A. Dainese, C. A. Salgado, and U. A. Wiedemann, Phys. Rev. D **71**, 054027 (2005).
[25] M. Djordjevic, M. Gyulassy, R. Vogt, and S. Wicks, Phys. Lett. B **632**, 81 (2006).

Jet structure from dihadron correlations in d + Au collisions at $\sqrt{s_{NN}} = 200$ GeV

S. S. Adler,[5] S. Afanasiev,[20] C. Aidala,[10] N. N. Ajitanand,[44] Y. Akiba,[21,40] A. Al-Jamel,[35] J. Alexander,[44] K. Aoki,[25] L. Aphecetche,[46] R. Armendariz,[35] S. H. Aronson,[5] R. Averbeck,[45] T. C. Awes,[36] V. Babintsev,[17] A. Baldisseri,[11] K. N. Barish,[6] P. D. Barnes,[28] B. Bassalleck,[34] S. Bathe,[6,31] S. Batsouli,[10] V. Baublis,[39] F. Bauer,[6] A. Bazilevsky,[5,41] S. Belikov,[17,19] M. T. Bjorndal,[10] J. G. Boissevain,[28] H. Borel,[11] M. L. Brooks,[28] D. S. Brown,[35] N. Bruner,[34] D. Bucher,[31] H. Buesching,[5,31] V. Bumazhnov,[17] G. Bunce,[5,41] J. M. Burward-Hoy,[27,28] S. Butsyk,[45] X. Camard,[46] P. Chand,[4] W. C. Chang,[2] S. Chernichenko,[17] C. Y. Chi,[10] J. Chiba,[21] M. Chiu,[10] I. J. Choi,[53] R. K. Choudhury,[4] T. Chujo,[5] V. Cianciolo,[36] Y. Cobigo,[11] B. A. Cole,[10] M. P. Comets,[37] P. Constantin,[19] M. Csanád,[13] T. Csörgö,[22] J. P. Cussonneau,[46] D. d'Enterria,[10] K. Das,[14] G. David,[5] F. Deák,[13] H. Delagrange,[46] A. Denisov,[17] A. Deshpande,[41] E. J. Desmond,[5] A. Devismes,[45] O. Dietzsch,[42] J. L. Drachenberg,[1] O. Drapier,[26] A. Drees,[45] A. Durum,[17] D. Dutta,[4] V. Dzhordzhadze,[47] Y. V. Efremenko,[36] H. En'yo,[40,41] B. Espagnon,[37] S. Esumi,[49] D. E. Fields,[34,41] C. Finck,[46] F. Fleuret,[26] S. L. Fokin,[24] B. D. Fox,[41] Z. Fraenkel,[52] J. E. Frantz,[10] A. Franz,[5,40] A. D. Frawley,[14] Y. Fukao,[25,40,41] S.-Y. Fung,[6] S. Gadrat,[29] M. Germain,[46] A. Glenn,[47] M. Gonin,[26] J. Gosset,[11] Y. Goto,[40,41] R. Granier de Cassagnac,[26] N. Grau,[19] S. V. Greene,[50] M. Grosse Perdekamp,[18,41] H.-Å. Gustafsson,[30] T. Hachiya,[16] J. S. Haggerty,[5] H. Hamagaki,[8] A. G. Hansen,[28] E. P. Hartouni,[27] M. Harvey,[5] K. Hasuko,[40] R. Hayano,[8] X. He,[15] M. Heffner,[27] T. K. Hemmick,[45] J. M. Heuser,[40] P. Hidas,[22] H. Hiejima,[18] J. C. Hill,[19] R. Hobbs,[34] W. Holzmann,[44] K. Homma,[16] B. Hong,[23] A. Hoover,[35] T. Horaguchi,[40,41,48] T. Ichihara,[40,41] V. V. Ikonnikov,[24] K. Imai,[25,40] M. Inaba,[49] M. Inuzuka,[8] D. Isenhower,[1] L. Isenhower,[1] M. Ishihara,[40] M. Issah,[44] A. Isupov,[20] B. V. Jacak,[45] J. Jia,[45] O. Jinnouchi,[40,41] B. M. Johnson,[5] S. C. Johnson,[27] K. S. Joo,[32] D. Jouan,[37] F. Kajihara,[8] S. Kametani,[8,51] N. Kamihara,[40,48] M. Kaneta,[41] J. H. Kang,[53] K. Katou,[51] T. Kawabata,[8] A. V. Kazantsev,[24] S. Kelly,[9,10] B. Khachaturov,[52] A. Khanzadeev,[39] J. Kikuchi,[51] D. J. Kim,[53] E. Kim,[43] G.-B. Kim,[26] H. J. Kim,[53] E. Kinney,[9] A. Kiss,[13] E. Kistenev,[5] A. Kiyomichi,[40] C. Klein-Boesing,[31] H. Kobayashi,[41] L. Kochenda,[39] V. Kochetkov,[17] R. Kohara,[16] B. Komkov,[39] M. Konno,[49] D. Kotchetkov,[6] A. Kozlov,[52] P. J. Kroon,[5] C. H. Kuberg,[1,*] G. J. Kunde,[28] K. Kurita,[40] M. J. Kweon,[23] Y. Kwon,[53] G. S. Kyle,[35] R. Lacey,[44] J. G. Lajoie,[19] Y. Le Bornec,[37] A. Lebedev,[19,24] S. Leckey,[45] D. M. Lee,[28] M. J. Leitch,[28] M. A. L. Leite,[42] X. H. Li,[6] H. Lim,[43] A. Litvinenko,[20] M. X. Liu,[28] C. F. Maguire,[50] Y. I. Makdisi,[5] A. Malakhov,[20] V. I. Manko,[24] Y. Mao,[38,40] G. Martinez,[46] H. Masui,[49] F. Matathias,[45] T. Matsumoto,[8,51] M. C. McCain,[1] P. L. McGaughey,[28] Y. Miake,[49] T. E. Miller,[50] A. Milov,[45] S. Mioduszewski,[5] G. C. Mishra,[15] J. T. Mitchell,[5] A. K. Mohanty,[4] D. P. Morrison,[5] J. M. Moss,[28] D. Mukhopadhyay,[52] M. Muniruzzaman,[6] S. Nagamiya,[21] J. L. Nagle,[9,10] T. Nakamura,[16] J. Newby,[47] A. S. Nyanin,[24] J. Nystrand,[30] E. O'Brien,[5] C. A. Ogilvie,[19] H. Ohnishi,[40] I. D. Ojha,[3,50] H. Okada,[25,40] K. Okada,[40,41] A. Oskarsson,[30] I. Otterlund,[30] K. Oyama,[8] K. Ozawa,[8] D. Pal,[52] A. P. T. Palounek,[28] V. Pantuev,[45] V. Papavassiliou,[35] J. Park,[43] W. J. Park,[23] S. F. Pate,[35] H. Pei,[19] V. Penev,[20] J.-C. Peng,[18] H. Pereira,[11] V. Peresedov,[20] A. Pierson,[34] C. Pinkenburg,[5] R. P. Pisani,[5] M. L. Purschke,[5] A. K. Purwar,[45] J. M. Qualls,[1] J. Rak,[19] I. Ravinovich,[52] K. F. Read,[36,47] M. Reuter,[45] K. Reygers,[31] V. Riabov,[39] Y. Riabov,[39] G. Roche,[29] A. Romana,[26,*] M. Rosati,[19] S. S. E. Rosendahl,[30] P. Rosnet,[29] V. L. Rykov,[40] S. S. Ryu,[53] N. Saito,[25,40,41] T. Sakaguchi,[8,51] S. Sakai,[49] V. Samsonov,[39] L. Sanfratello,[34] R. Santo,[31] H. D. Sato,[25,40] S. Sato,[5,49] S. Sawada,[21] Y. Schutz,[46] V. Semenov,[17] R. Seto,[6] T. K. Shea,[5] I. Shein,[17] T.-A. Shibata,[40,48] K. Shigaki,[16] M. Shimomura,[49] A. Sickles,[45] C. L. Silva,[42] D. Silvermyr,[28] K. S. Sim,[23] A. Soldatov,[17] R. A. Soltz,[27] W. E. Sondheim,[28] S. P. Sorensen,[47] I. V. Sourikova,[5] F. Staley,[11] P. W. Stankus,[36] E. Stenlund,[30] M. Stepanov,[35] A. Ster,[22] S. P. Stoll,[5] T. Sugitate,[16] J. P. Sullivan,[28] S. Takagi,[49] E. M. Takagui,[42] A. Taketani,[40,41] K. H. Tanaka,[21] Y. Tanaka,[33] K. Tanida,[40] M. J. Tannenbaum,[5] A. Taranenko,[44] P. Tarján,[12] T. L. Thomas,[34] M. Togawa,[25,40] J. Tojo,[40] H. Torii,[25,41] R. S. Towell,[1] V-N. Tram,[26] I. Tserruya,[52] Y. Tsuchimoto,[16] H. Tydesjö,[30] N. Tyurin,[17] T. J. Uam,[32] H. W. van Hecke,[28] J. Velkovska,[5] M. Velkovsky,[45] V. Veszprémi,[12] A. A. Vinogradov,[24] M. A. Volkov,[24] E. Vznuzdaev,[39] X. R. Wang,[15] Y. Watanabe,[40,41] S. N. White,[5] N. Willis,[37] F. K. Wohn,[19] C. L. Woody,[5] W. Xie,[6] A. Yanovich,[17] S. Yokkaichi,[40,41] G. R. Young,[36] I. E. Yushmanov,[24] W. A. Zajc,[10,†] C. Zhang,[10] S. Zhou,[7] J. Zimányi,[22] L. Zolin,[20] and X. Zong[19]

(PHENIX Collaboration)

[1]*Abilene Christian University, Abilene, Texas 79699, USA*

[2]*Institute of Physics, Academia Sinica, Taipei 11529, Taiwan*

[3]*Department of Physics, Banaras Hindu University, Varanasi 221005, India*

[4]*Bhabha Atomic Research Centre, Bombay 400 085, India*

[5]*Brookhaven National Laboratory, Upton, New York 11973-5000, USA*

[6]*University of California–Riverside, Riverside, California 92521, USA*

[7]*China Institute of Atomic Energy (CIAE), Beijing, People's Republic of China*

[8]*Center for Nuclear Study, Graduate School of Science, University of Tokyo, 7-3-1 Hongo, Bunkyo, Tokyo 113-0033, Japan*

[9]*University of Colorado, Boulder, Colorado 80309, USA*

[10]*Columbia University, New York, New York 10027 and Nevis Laboratories, Irvington, New York 10533, USA*

[11]*Dapnia, CEA Saclay, F-91191, Gif-sur-Yvette, France*

[12]*Debrecen University, H-4010 Debrecen, Egyetem tér 1, Hungary*

[13]*ELTE, Eötvös Loránd University, H-1117 Budapest, Pázmány P.s. 1/A, Hungary*

[14]*Florida State University, Tallahassee, Florida 32306, USA*

 ©2006 The American Physical Society

[15]*Georgia State University, Atlanta, Georgia 30303, USA*
[16]*Hiroshima University, Kagamiyama, Higashi-Hiroshima 739-8526, Japan*
[17]*IHEP Protvino, State Research Center of Russian Federation, Institute for High Energy Physics, Protvino, RU-142281, Russia*
[18]*University of Illinois at Urbana-Champaign, Urbana, Illinois 61801, USA*
[19]*Iowa State University, Ames, Iowa 50011, USA*
[20]*Joint Institute for Nuclear Research, RU-141980 Dubna, Moscow Region, Russia*
[21]*KEK, High Energy Accelerator Research Organization, Tsukuba, Ibaraki 305-0801, Japan*
[22]*KFKI Research Institute for Particle and Nuclear Physics of the Hungarian Academy of Sciences (MTA KFKI RMKI), H-1525 Budapest 114, P.O. Box 49, Budapest, Hungary*
[23]*Korea University, Seoul, 136-701, Korea*
[24]*Russian Research Center "Kurchatov Institute," Moscow, Russia*
[25]*Kyoto University, Kyoto 606-8502, Japan*
[26]*Laboratoire Leprince-Ringuet, Ecole Polytechnique, CNRS-IN2P3, Route de Saclay, F-91128, Palaiseau, France*
[27]*Lawrence Livermore National Laboratory, Livermore, California 94550, USA*
[28]*Los Alamos National Laboratory, Los Alamos, New Mexico 87545, USA*
[29]*LPC, Université Blaise Pascal, CNRS-IN2P3, Clermont-Fd, F-63177 Aubiere Cedex, France*
[30]*Department of Physics, Lund University, Box 118, SE-221 00 Lund, Sweden*
[31]*Institut für Kernphysik, University of Muenster, D-48149 Muenster, Germany*
[32]*Myongji University, Yongin, Kyonggido 449-728, Korea*
[33]*Nagasaki Institute of Applied Science, Nagasaki-shi, Nagasaki 851-0193, Japan*
[34]*University of New Mexico, Albuquerque, New Mexico 87131, USA*
[35]*New Mexico State University, Las Cruces, New Mexico 88003, USA*
[36]*Oak Ridge National Laboratory, Oak Ridge, Tennessee 37831, USA*
[37]*IPN-Orsay, Universite Paris Sud, CNRS-IN2P3, BP1, F-91406, Orsay, France*
[38]*Peking University, Beijing, People's Republic of China*
[39]*PNPI, Petersburg Nuclear Physics Institute, Gatchina, Leningrad region, RU-188300, Russia*
[40]*RIKEN (The Institute of Physical and Chemical Research), Wako, Saitama 351-0198, JAPAN*
[41]*RIKEN BNL Research Center, Brookhaven National Laboratory, Upton, New York 11973-5000, USA*
[42]*Universidade de São Paulo, Instituto de Física, Caixa Postal 66318, São Paulo CEP05315-970, Brazil*
[43]*System Electronics Laboratory, Seoul National University, Seoul, South Korea*
[44]*Chemistry Department, Stony Brook University, Stony Brook, SUNY, New York 11794-3400, USA*
[45]*Department of Physics and Astronomy, Stony Brook University, SUNY, Stony Brook, New York 11794, USA*
[46]*SUBATECH (Ecole des Mines de Nantes, CNRS-IN2P3, Université de Nantes) BP 20722-44307, Nantes, France*
[47]*University of Tennessee, Knoxville, Tennessee 37996, USA*
[48]*Department of Physics, Tokyo Institute of Technology, Oh-okayama, Meguro, Tokyo 152-8551, Japan*
[49]*Institute of Physics, University of Tsukuba, Tsukuba, Ibaraki 305, Japan*
[50]*Vanderbilt University, Nashville, Tennessee 37235, USA*
[51]*Waseda University, Advanced Research Institute for Science and Engineering, 17 Kikui-cho, Shinjuku-ku, Tokyo 162-0044, Japan*
[52]*Weizmann Institute, Rehovot 76100, Israel*
[53]*Yonsei University, IPAP, Seoul 120-749, Korea*
(Received 7 October 2005; published 10 May 2006)

Dihadron correlations at high transverse momentum p_T in $d+$Au collisions at $\sqrt{s_{NN}} = 200$ GeV at midrapidity are measured by the PHENIX experiment at the Relativistic Heavy Ion Collider. From these correlations, we extract several structural characteristics of jets: the root-mean-squared transverse momentum of fragmenting hadrons with respect to the jet $\sqrt{\langle j_T^2 \rangle}$, the mean sine-squared of the azimuthal angle between the jet axes $\langle \sin^2 \phi_{jj} \rangle$, and the number of particles produced within the dijet that are associated with a high-p_T particle (dN/dx_E distributions). We observe that the fragmentation characteristics of jets in $d+$Au collisions are very similar to those in $p+p$ collisions and that there is little dependence on the centrality of the $d+$Au collision. This is consistent with the nuclear medium having little influence on the fragmentation process. Furthermore, there is no statistically significant increase in the value of $\langle \sin^2 \phi_{jj} \rangle$ from $p+p$ to $d+$Au collisions. This constrains the effect of multiple scattering that partons undergo in the cold nuclear medium before and after a hard collision.

DOI: 10.1103/PhysRevC.73.054903 PACS number(s): 25.75.−q, 13.87.−a, 24.85.+p

I. INTRODUCTION

Jet production in high energy collisions is a useful tool to study the passage of scattered partons through a nuclear

*Deceased.
†PHENIX spokesperson: zajc@nevis.columbia.edu

medium. A dominant hard-scattering process is two partons scattering to produce two high-transverse momentum (high-p_T) partons which then fragment to produce a dijet. In a nuclear environment, the partons that participate in the collision can undergo multiple scattering within the nucleus, potentially changing the structure of the dijet. Such changes can provide information on the interaction of colored partons with the cold nuclear medium.

Some information on this interaction is already available at Relativistic Heavy Ion Collider (RHIC) energies via the Cronin enhancement of the p_T spectra [1]. In d + Au collisions at RHIC [2–4], the cross section for high-p_T particle production in d + Au collisions is enhanced compared to $p + p$ collisions, consistent with multiple scattering in the cold nuclear medium increasing the transverse momentum of the partons. In this paper, we report on a complementary observable to the Cronin effect: the broadening of dijet distributions. Such broadening is directly related to the additional transverse momentum delivered to the partons during multiple scattering, and hence it provides a complementary tool for comparing experiment against theory.

Interpreting both d + Au and Au + Au collisions requires solid knowledge of baseline $p + p$ collisions, especially those dijet events at midrapidity that contain two nearly back-to-back jets produced from a hard (large Q^2) parton-parton interaction. Experimentally, the jets were not exactly back to back, and the acoplanarity momentum vector $\vec{k}_T$ was measured in $p + p$ collisions at the Intersecting Storage Rings at CERN (ISR) to have a magnitude k_T on the order of 1 GeV/c [5]. This was much larger than the magnitude expected if k_T was due to an intrinsic parton transverse momentum governed by the hadron size, which would lead to $k_T \sim 300$ MeV/c. It was realized early [6] that additional gluon radiation either before or after the hard scattering will increase the value of k_T and the dijet acoplanarity.

In collisions involving nuclei at laboratory energies from 400 to 800 GeV/c, multiple scattering within the nucleus increases the parton transverse momentum. Fermilab experiments E557 [7], E609 [8], and E683 [9] all measured an increase in the dijet acoplanarity with atomic mass of the target. In E683, they measured an $A^{\frac{1}{3}}$ dependence of $\langle k_T^2 \rangle$ for both $\gamma + A$ and $\pi + A$ collisions. This dependence is expected since the number of scatterings should be proportional to the length traversed in the nucleus ($L \sim A^{\frac{1}{3}}$). For large A, the extracted $\langle k_T^2 \rangle$ values are about 50% above those for collisions with the hydrogen target, implying that the multiple-scattering effects are as important to the broadening of the dijets as are the initial state effects at that energy. In the case of $p + A$ reactions, the measured $\langle k_T^2 \rangle$ values increase more slowly than $A^{\frac{1}{3}}$ [8]. Since the $\langle k_T^2 \rangle$ values show a strong energy dependence [9], we need to establish the initial and multiple-scattering contributions to $\langle k_T^2 \rangle$ for $p + A$ reactions at RHIC energies. The $\langle k_T^2 \rangle$ values are also known to be dependent on the Q^2 of the parton-parton interaction, increasing with rising Q^2 [10,11].

No model is currently available that can reproduce all data on the Cronin effect and dijet broadening, although most include multiple scattering as the underlying mechanism. A recent review [12] considered two large classes of models: (1) soft or Glauber scattering where the multiple scattering is at either the hadronic or partonic level and (2) semihard multiple scattering where the multiple scattering is at the partonic level.

In both the soft and hard scattering models, the increase $\Delta\langle k_T^2 \rangle = \langle k_T^2 \rangle_{p+A} - \langle k_T^2 \rangle_{p+p}$ is proportional to the product of the scattering cross section and the nuclear thickness function,

$$\Delta\langle k_T^2 \rangle \propto \nu(b, \sqrt{s}) - 1 = \sigma_{\mathrm{MS}}(\sqrt{s}) T_A(b), \tag{1}$$

where $\nu(b, \sqrt{s})$ is the number of interactions, b is the impact parameter of the collision, σ_{MS} is the multiple-scattering cross section, and $T_A(b)$ is the nuclear thickness function. For the soft scattering models, σ_{MS} is defined to be $\sigma_{NN}(\sqrt{s})$, the nucleon-nucleon scattering cross section: while for the semihard models, σ_{MS} is $\sigma_{i|H}^{N}(\sqrt{s})$, the parton-nucleon semihard cross section. In the specific case of hard sphere nucleon scattering [13],

$$\nu(b, \sqrt{s}) = \sigma_{NN}(\sqrt{s}) \frac{3A}{2\pi R^2} \sqrt{1 - \frac{b^2}{R^2}}$$

where R is the nuclear radius, which gives an $A^{\frac{1}{3}}$ increase in $\Delta\langle k_T^2 \rangle$.

Both types of these models give the same trend in centrality and the same dependence on the target's atomic mass. The difference between them is in the strength of the increase with respect to $T_A(b)$ and how this changes with beam energy. We will compare the data in this paper to two specific implementations of the hard-scattering models from Qiu and Vitev [14] and Barnafoldi *et al.* [15].

An alternative view of the Cronin effect was recently proposed by Hwa and Yang [16]. These authors calculate the recombination of hard partons with soft partons released during the multiple collisions. Because this model reproduces the measured Cronin effect at RHIC without imparting successive transverse momentum kicks to the scattered partons, the authors suggest that there may be little to no increase in k_T from $p + p$ to d + Au collisions.

We also use jet-fragmentation observables to probe multiple scattering in cold nuclei, in particular, $\sqrt{\langle j_T^2 \rangle}$, the rms of the mean transverse momentum of hadrons with respect to the fragmenting parton, and the fragmentation function of the parton, $D(z, Q^2)$, where z is the fraction of the parton's momentum that a hadron carries. If the parton suffers semihard inelastic collisions within the nuclear environment, the parton will lose energy and its subsequent hadronization will produce fewer high-z fragments and more low-z fragments. We cannot directly measure fragmentation functions via dihadron correlations, but we can measure the distribution of hadrons produced in association with a high-p_T trigger particle. We plot these distributions as a function of x_E, where x_E is defined as

$$x_E = \frac{\vec{p}_{T,\mathrm{trig}} \cdot \vec{p}_{T,\mathrm{assoc}}}{|\vec{p}_{T,\mathrm{trig}}|^2}. \tag{2}$$

The motivation for the variable x_E can be most easily seen in the simple case where $\langle z \rangle = 1$ for the trigger particle and the two hadrons are emitted back to back. In this case, $p_{T,\mathrm{trig}}$ is the transverse momentum of the scattered parton

($q_{T,\mathrm{parton}}$), and for the far side, $x_E = z_{\mathrm{assoc}} = p_{T,\mathrm{assoc}}/q_{T,\mathrm{parton}}$. Relaxing the assumption on z_{trig}, there is still a simple relation between x_E and z for back-to-back jets at high p_T, where $x_E \simeq z_{\mathrm{assoc}}/z_{\mathrm{trig}}$. Hence the dN/dx_E distribution for hadrons emitted back to back from the trigger hadron can be related to the fragmentation function; for more details, see the end of Sec. II.

There is considerable information on x_E distributions from $p + p$ collisions. The CCHK Collaboration [5] demonstrated that the x_E distribution scaled, i.e., the distribution was approximately independent of $p_{T,\mathrm{trig}}$. Scaling at higher $p_{T,\mathrm{trig}}$ was also established by Fisk *et al.* [17] and the CCOR Collaboration [18,19], providing support for the idea that fragmentation of high-p_T partons is independent of the momentum of the parton.

This scaling is, however, approximate, and scaling violation was understood by Feynman *et al.* [6] to be caused by the radiation of semihard gluons. Scaling violation of the fragmentation function $D(z, Q^2)$ is now well established experimentally ([20] and references therein). For the Q^2 range considered in this paper ($10 < Q^2 < 1000\ \mathrm{GeV}/c^2$), the fragmentation functions used in next-to-leading order (NLO) calculations [21] drop by 25% for $z = 0.6$ over the range $10 < Q^2 < 100\ \mathrm{GeV}/c^2$. At higher Q^2, the fragmentation functions are less dependent on Q^2, e.g., the fragmentation drops by less than 20% at $z = 0.6$ over the much larger range of $100 < Q^2 < 1500\ \mathrm{GeV}/c^2$.

In this paper, we quantify the extent to which our measured x_E distributions in d + Au collision scale, and we compare the x_E distributions to those from $p + p$ collisions at RHIC. The goal is to establish whether inelastic scattering in the cold medium or the recombination mechanism changes the effective fragmentation function. The x_E distributions provide a stringent test of the recombination model from Hwa and Yang [22]. This model reproduces the Cronin effect in d + Au collisions through a shower thermal recombination mechanism and predicts an increase in jet-associated multiplicity [22,23], i.e., an increase in the near-angle dN/dx_E, in d + Au relative to $p + p$ collisions.

The measured x_E distributions in d + Au also serve as a critical baseline for Au + Au collisions, where the strong energy loss in the dense, hot medium is expected to dramatically change the shape of these distributions.

Our three goals for this paper are (1) to report the characteristics of jet structures in d + Au collisions at RHIC energies, (2) to establish the extent to which multiple scattering changes these structures as a function of centrality and by comparison with data from $p + p$ collisions, and (3) to establish the baseline for jet-structure measurements in heavy ion reactions. Any difference between jet properties in Au + Au and d + Au collisions should be attributable to the hot, dense nuclear matter created in the heavy ion collisions. The main results in this paper are presented in Sec. IV, which details the measured values of $\langle j_T^2 \rangle$ and $\langle \sin^2 \phi_{jj} \rangle$ and the p_T and x_E distributions from d + Au collisions at $\sqrt{s_{NN}} = 200$ GeV. These results are derived from the fitted widths and yields of two-particle azimuthal correlations, which are reported in Sec. IV. The experimental methods used to obtain these correlations are described in Sec. III, and the jet quantities we use throughout the paper are fully defined in Sec. II.

II. JET ANGULAR (AZIMUTHAL) CORRELATIONS

A. Two-particle correlation

The defining characteristic of a jet is the production of a large number of particles clustered in a cone in the direction of the fragmenting parton. Traditionally, energetic jets are identified directly using standard jet reconstruction algorithms [24,25]. In heavy ion collisions, the large amount of soft background makes direct jet reconstruction difficult. Even in $p + A$ or $p + p$ collisions, the range of energy accessible to direct jet reconstruction is probably limited to $p_T > 5{-}10\ \mathrm{GeV}/c$, below which the jet cone becomes too broad and contamination from the "underlying event" background is significant. Jet identification is even more complicated for detectors with limited acceptance, such as the PHENIX central arms, because of leakage of the jet cone outside the acceptance.

The two-particle azimuthal angle correlation technique provides an alternative way to access the properties of jets. It is based on the fact that the fragments are strongly correlated in azimuth ϕ and pseudorapidity η. Thus, the jet signal manifests itself as a narrow peak in $\Delta\phi$ and $\Delta\eta$ space. Jet properties can be extracted on a statistical basis by accumulating many events to build a $\Delta\phi$ distribution or a $\Delta\phi$ correlation function. Furthermore, we assume that the soft background is isotropic. Distributions in $\Delta\phi$ were initially used in the 1970s to search for jet signals in $p + p$ collisions at CERN's ISR facility [5,10,26]. More recently, $\Delta\phi$ distributions and correlation functions have been exploited for analysis of jet correlations at RHIC [27–31]. A detailed discussion of the two-particle correlation method can be found in [32]. These approaches overcome problems due to background and limited acceptance, and they extend the study of jet observables to lower p_T.

In the correlation method, two classes of particles are correlated with each other: trigger particles and associated particles. Although the distinction between these two classes is artificial, trigger particles are typically selected from a higher p_T range. In this work, we distinguish between two primary categories of correlations:

(i) Assorted-p_T correlation, where the p_T ranges for the trigger and associated particles do not overlap.
(ii) Fixed-p_T correlation, where the p_T ranges for the trigger and associated particles are identical.

In this paper, correlations are further categorized via a scheme which uses the identity of the trigger and associated particles. Denoting the trigger-particle p_T as $p_{T,\mathrm{trig}}$ and associated-particle p_T as $p_{T,\mathrm{assoc}}$, we present four different types of such correlations:

(i) $h^{\pm} - h^{\pm}$ fixed-p_T correlations. The p_T range of both the trigger and associated particle is $1 < p_T < 5\ \mathrm{GeV}/c$.

(ii) $h^{\pm} - h^{\pm}$ assorted-p_T correlations. There are three different selections:
   (a) $2.5 < p_{T,\mathrm{trig}} < 4\ \mathrm{GeV}/c$ with $0.5 < p_{T,\mathrm{assoc}} < 2.5\ \mathrm{GeV}/c$.
   (b) $4 < p_{T,\mathrm{trig}} < 6\ \mathrm{GeV}/c$ with $0.5 < p_{T,\mathrm{assoc}} < 4\ \mathrm{GeV}/c$.
   (c) $3 < p_{T,\mathrm{trig}} < 5\ \mathrm{GeV}/c$ with $0.5 < p_{T,\mathrm{assoc}} < 3\ \mathrm{GeV}/c$.

(iii) $\pi^0 - h^{\pm}$ assorted-p_T correlations. The trigger particle is a neutral pion and the associated particle is a charged hadron, where $5 < p_{T,\mathrm{trig}} < 10\ \mathrm{GeV}/c$ with $1 < p_{T,\mathrm{assoc}} < 5\ \mathrm{GeV}/c$.

(iv) $\pi^{\pm} - h^{\pm}$ assorted-p_T correlations. The trigger particle is a charged pion and the associated particle is a charged hadron, where $5 < p_{T,\mathrm{trig}} < 16\ \mathrm{GeV}/c$ with $1 < p_{T,\mathrm{assoc}} < 5\ \mathrm{GeV}/c$.

For each type of correlation, we study jet structure as a function of centrality and the momentum of the trigger and associated particles.

B. Extraction of j_T, $\sin^2\phi_{jj}$ from the correlation function

In this section, we discuss the framework for the two-particle correlation method. Figures 1 and 2 illustrate the relation between the two particles and their parent jet when the parents are the same jet or the dijet, respectively. The figures also show the relationship between j_T, $\sin^2(\phi_{jj})$, and the kinematic variables describing the trigger and associated particle. j_T is the component of the particle momentum perpendicular to the jet momentum. Its projection into the azimuthal plane is j_{T_y}. The quantity p_{out} (denoted with N or F for near or far side, respectively) is the component of the associated particle's p_T that is perpendicular to the trigger particle's p_T. The vector sum of $k_{T,1}$ and $k_{T,2}$ produces the dijet acoplanarity, and the azimuthal angle between the jet axes is ϕ_{jj}.

The rms value of j_{T_y} can be derived from the correlation functions. For the single jet fragmentation of Fig. 1, if we denote $\Delta\phi$, ϕ_{tj}, and ϕ_{aj} as the angles between trigger-associated, trigger-jet, and associated-jet, respectively, then the following relations are true:

$$\sin(\phi_{tj}) = \frac{j_{T_y,\mathrm{trig}}}{p_{T,\mathrm{trig}}} \equiv x_{j,\mathrm{trig}},$$
$$\sin(\phi_{aj}) = \frac{j_{T_y,\mathrm{assoc}}}{p_{T,\mathrm{assoc}}} \equiv x_{j,\mathrm{assoc}},$$

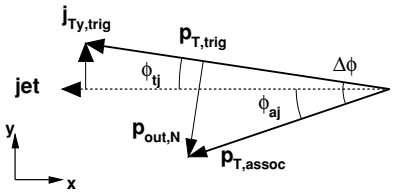

FIG. 1. Near-side or single jet fragmentation kinematics in the azimuthal plane perpendicular to the beam axis. Angles ϕ_{tj} and ϕ_{aj} are the angles (in the plane transverse to the beam axis) between the trigger-jet and associated-jet axes, respectively. Also shown are the p_T vectors for the trigger and associated particles, as well as p_{out} and j_{T_y} of the trigger particle.

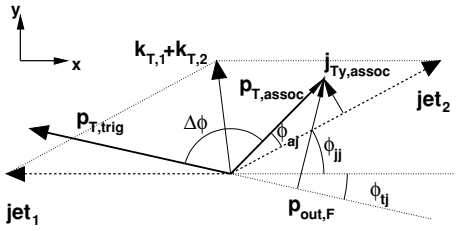

FIG. 2. Far-side jet fragmentation kinematics in the azimuthal plane perpendicular to the beam axis. Similar to Fig.1, the ϕ indices aj, jj, and tj denote the angles between the associated-jet, jet-jet, and trigger-jet axes.

$$\sin(\Delta\phi) = \frac{p_{\mathrm{out},N}}{p_{T,\mathrm{assoc}}},$$
$$\Delta\phi = \phi_{tj} + \phi_{aj}. \tag{3}$$

Assuming ϕ_{tj} and ϕ_{aj} are statistically independent, we have (cross terms average to 0) for the near side,

$$\langle \sin^2 \Delta\phi_N \rangle = \langle \sin^2 \phi_{tj} \rangle \cos^2 \phi_{aj} + \langle \sin^2 \phi_{aj} \rangle \cos^2 \phi_{tj}. \tag{4}$$

Substituting the sine and cosine terms from Eq. (3) into Eq. (4), we obtain the equation for the rms value of j_{T_y}

$$\sqrt{\left\langle j_{T_y}^2 \right\rangle} = \sqrt{\left\langle p_{\mathrm{out},N}^2 \right\rangle / \left(1 + \left\langle x_h^2 \right\rangle - 2\left\langle x_{j,\mathrm{trig}}^2 \right\rangle\right)}, \tag{5}$$

where $x_h = p_{T,\mathrm{assoc}}/p_{T,\mathrm{trig}}$.

In the Gaussian approximation for the near-side azimuthal distributions, a simple Taylor expansion connects p_{out} with the jet width σ such that

$$\left\langle p_{\mathrm{out}}^2 \right\rangle = \left\langle p_{T,\mathrm{assoc}}^2 \sin^2 \Delta\phi \right\rangle \approx \left\langle p_{T,\mathrm{assoc}}^2 \right\rangle \left[\sin\langle \Delta\phi^2 \rangle - \frac{\langle \Delta\phi^4 \rangle}{3} \right]$$
$$\approx \left\langle p_{T,\mathrm{assoc}}^2 \right\rangle [\sin\sigma^2 - \sigma^4]. \tag{6}$$

Since Eq. (5) contains the variable $x_{j,\mathrm{trig}}$ that depends on j_{T_y}, we should calculate $\sqrt{\langle j_{T_y}^2 \rangle}$ iteratively. In cases when trigger and associated particle p_T are much larger than the typical j_T value, the near-side jet width σ_N is small and $x_{j,\mathrm{trig}} \approx 0$. Hence Eq. (5) can be simplified as

$$\sqrt{\left\langle j_{T_y}^2 \right\rangle} \simeq \frac{\sigma_N \langle p_{T,\mathrm{assoc}} \rangle}{\sqrt{1 + \left\langle x_h^2 \right\rangle}} \simeq \sigma_N \frac{\langle p_{T,\mathrm{trig}} \rangle \langle p_{T,\mathrm{assoc}} \rangle}{\sqrt{\langle p_{T,\mathrm{trig}} \rangle^2 + \langle p_{T,\mathrm{assoc}} \rangle^2}}. \tag{7}$$

Since j_{T_y} is the projection of hadron p_T perpendicular to $p_{T,\mathrm{jet}}$, j_{T_y} is necessarily less than p_T. So, for any given p_T range, there is always an upper kinematic cutoff on the j_{T_y} distribution. This effect, known as the "seagull effect", leads to a reduction in the observed $\sqrt{\langle j_{T_y}^2 \rangle}$ from the expected value. It is important at low $p_{T,\mathrm{trig}}$ and becomes negligible once $p_{T,\mathrm{trig}} \gg \sqrt{\langle j_{T_y}^2 \rangle}$. The seagull effect can be parametrized and removed from the j_{T_y} values [33].

For the far-side correlation from Fig. 2 we have

$$\pi - \Delta\phi_F = \phi_{tj} + \phi_{aj} + \phi_{jj},$$
$$\sin(\Delta\phi_F) = \frac{p_{\mathrm{out},F}}{p_{T,\mathrm{assoc}}}, \tag{8}$$

where ϕ_{jj} is the azimuthal angle between the two jet axes. Expanding $\sin^2 \Delta\phi_F$ and dropping all cross terms (which average to 0), we get

$$\begin{aligned}\langle \sin^2 \Delta\phi_F \rangle = &\langle (\sin\phi_{tj} \cos\phi_{aj} \cos\phi_{jj})^2 \rangle \\ &+ \langle (\sin\phi_{aj} \cos\phi_{tj} \cos\phi_{jj})^2 \rangle \\ &+ \langle (\sin\phi_{jj} \cos\phi_{aj} \cos\phi_{tj})^2 \rangle \\ &+ \langle (\sin\phi_{tj} \sin\phi_{aj} \sin\phi_{jj})^2 \rangle. \end{aligned} \quad (9)$$

We substitute Eq. (4) to get

$$\begin{aligned}&\langle \sin^2 \Delta\phi_F \rangle \\ &= \langle \sin^2 \Delta\phi_N \rangle \langle \cos^2 \phi_{jj} \rangle + \langle \cos^2 \Delta\phi_N \rangle \langle \sin^2 \phi_{jj} \rangle \\ &= \langle \sin^2 \Delta\phi_N \rangle \langle 1 - \sin^2 \phi_{jj} \rangle + \langle 1 - \sin^2 \Delta\phi_N \rangle \langle \sin^2 \phi_{jj} \rangle \\ &= \langle \sin^2 \Delta\phi_N \rangle + \langle \sin^2 \phi_{jj} \rangle - 2 \langle \sin^2 \Delta\phi_N \rangle \langle \sin^2 \phi_{jj} \rangle. \end{aligned} \quad (10)$$

Collecting terms in ϕ_{jj} produces

$$\langle \sin^2 \phi_{jj} \rangle = \frac{\langle \sin^2 \Delta\phi_F \rangle - \langle \sin^2 \Delta\phi_N \rangle}{1 - 2\langle \sin^2 \Delta\phi_N \rangle}. \quad (11)$$

Note that since ϕ_{jj} is the azimuthal angle between the jet axes, $\sin^2(\phi_{jj})$ is one measure of the extent to which the jets are not back to back, and hence it is a quantity that is sensitive to any additional scattering in $d + \mathrm{Au}$ collisions. We express the right side in terms of the observables σ_N and σ_F, the rms widths of distribution that we measure by expanding the sine term

$$\langle \sin^2 \Delta\phi \rangle = \sigma^2 - \sigma^4 + 2/3\sigma^6, \quad (12)$$

which is good to 2% for rms widths at 0.5 rad and good to 0.6% for rms widths of 0.2 rad. Therefore,

$$\langle \sin^2 \phi_{jj} \rangle = \frac{\left(\sigma_F^2 - \sigma_F^4 + 2/3\sigma_F^6\right) - \left(\sigma_N^2 - \sigma_N^4 + 2/3\sigma_N^6\right)}{1 - 2\left(\sigma_N^2 - \sigma_N^4 + 2/3\sigma_N^6\right)}. \quad (13)$$

The right-hand side is now in terms of experimental observables which we will use to extract $\sin(\phi_{jj})$.

We have attempted to extract k_T from $\sin^2(\phi_{jj})$. This requires assumptions on the scattered quark distribution, the magnitude of the momentum asymmetry between the partons due to the k_T kick, as well as the detailed shape of the fragmentation function. The current paper is focused on the comparison between $p + p$ and $d + \mathrm{Au}$ collisions, which can be made with $\sin^2(\phi_{jj})$. Hence, we leave the extraction of k_T to future work.

In this paper, we report the rms values of j_T and $\sin(\phi_{jj})$, where $\sqrt{\langle j_T^2 \rangle} = \sqrt{2}\sqrt{\langle j_{T_y}^2 \rangle}$. In the literature, a j_T value is sometimes reported as the geometrical mean $\langle |j_{T_y}| \rangle$. The relation to the rms value is $\langle |j_{T_y}| \rangle = \sqrt{2/\pi}\sqrt{\langle j_{T_y}^2 \rangle}$.

C. Conditional yields

We also present in this paper the associated yield per trigger particle, referred to as the conditional yield (CY), as a function of p_T and x_E. CY is the number of particles produced in the same or opposite jet associated with a trigger particle,

$$\mathrm{CY}(p_T) = \frac{1}{N_{\mathrm{trig}}} \frac{dN_h}{dp_T}, \quad (14)$$

$$\mathrm{CY}(x_E) = \frac{1}{N_{\mathrm{trig}}} \frac{dN_h}{dx_E}, \quad (15)$$

and can be directly extracted from the measured Gaussian yields in the correlation functions.

To emphasize the importance of the CY, we note that it is related to the single- and two-particle cross sections:

$$\mathrm{CY} = \frac{d^2\sigma}{dp_a dp_b} \Big/ \frac{d\sigma}{dp_T}. \quad (16)$$

The interpretation for the two-particle cross section depends on whether one is studying the near- or far-side jet correlations. The conditional yield for particles from the near-side jet depends on the dihadron fragmentation function, while the conditional yield from the far side jet depends on two independent fragmentation functions: one parton fragments to produce a hadron with $p_{T,\mathrm{trig}}$, while the other scattered parton on the far side fragments to produce a hadron with $p_{T,\mathrm{assoc}}$. For the far side conditional yield at high p_T, $x_E \simeq z_{\mathrm{assoc}}/z_{\mathrm{trig}}$ [see Eq. (2)]. Hence, $d(x_E) \simeq d(z_{\mathrm{assoc}})/z_{\mathrm{trig}}$, and the slope of the far-side $\mathrm{CY}(x_E)$ is z_{trig} times the slope of the fragmentation function $D(z)$.

III. EXPERIMENT AND DATA ANALYSIS

A. Data collection

The data presented in this paper were collected by the PHENIX experiment at the RHIC facility during the $d + \mathrm{Au}$ and $p + p$ run of January–May 2003. During that time, integrated luminosities were recorded of 2.7 nb^{-1} for $d + \mathrm{Au}$ collisions and 0.35 pb^{-1} for $p + p$ collisions each at $\sqrt{s_{NN}} = 200$ GeV.

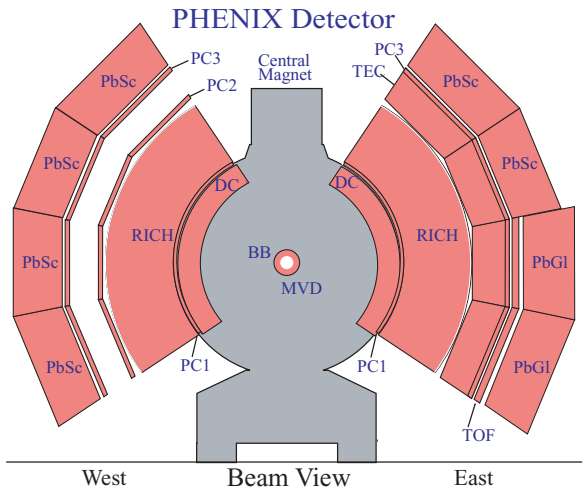

FIG. 3. (Color online) Two central spectrometer arms of the PHENIX experiment used to collect the charged hadron and charged and neutral pion tracks.

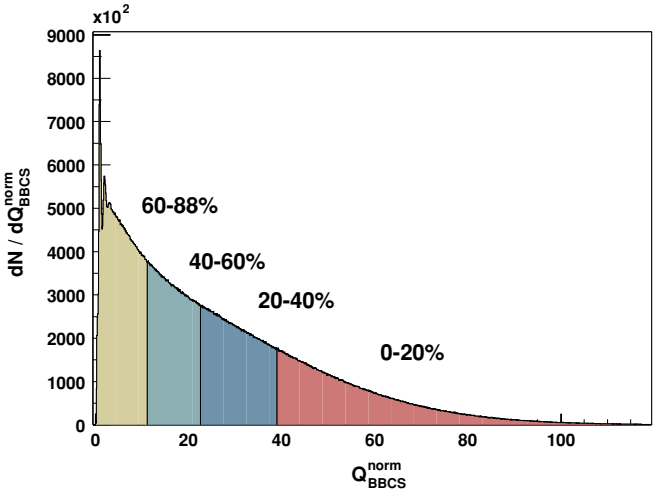

FIG. 4. (Color online) Total charge distribution on the Au-going side BBC for d + Au collisions and the centrality selection (see Table I).

The PHENIX detector consists of two central spectrometer arms, two forward muon arms, and several global detectors used for triggering, vertex detection, and centrality selection. This analysis utilizes the two central spectrometer arms that each cover a region of $|\eta| < 0.35$ units of pseudorapidity and 90° in azimuth. The spectrometer arms are not exactly back to back in azimuth; so while there is large acceptance for the detection of two particles separated by 180°, there is also finite acceptance for two particles separated by 90°. Figure 3 shows a beam cross-section view of the PHENIX central spectrometer arms. A complete overview of the whole PHENIX detector is found in Ref. [34]. In this section, we will only focus on those subsystems relevant to the analysis of the dihadron data.

1. Global event characteristics

For event characterization, the beam-beam counters (BBCs) [35] are utilized. The BBCs are sets of 64 Cherenkov counters placed symmetrically along the beam line, covering $3 < |\eta| < 3.9$ units of pseudorapidity and located 144 cm from the center of the interaction region. The BBCs determine the initial collision time t_0 and the event vertex from the time difference between particles reaching each BBC. For this analysis, we include only events with an offline cut of $|z_{\text{vertex}}| < 30$ cm.

The BBC facing the direction of the Au beam was used to determine the centrality. Figure 4 shows the BBC charge distribution and the centrality classes used in this analysis. The centrality is defined as

$$\%\text{Centrality} = 88.5\%(1 - \text{frac}(Q_{\text{BBC}})), \tag{17}$$

where $\text{frac}(Q_{\text{BBC}})$ is the fraction of the total BBC charge distribution integrated from zero to Q_{BBC}, and 88.5% is the efficiency of the minimum-bias trigger. This centrality can be related to the mean number of Au participants $\langle N_{\text{part}} \rangle$ and mean number of collisions $\langle N_{\text{coll}} \rangle$. To determine the centrality, we model the BBC charge distribution as a negative binomial distribution with a width and mean proportional to N_{part}. So, for a given centrality, several negative binomial distributions (defined by N_{part}) contribute to the overall distribution, and as such N_{part} is not uniquely defined. We calculate a weighted average of N_{part}, where the weight is given by the negative binomial distribution for a given N_{part} and the probability for having a collision with N_{part}. The latter probabilities were computed using a Glauber model, with a Hulthen wave function for the deuteron and an inelastic cross section of 42 mb. Finally, the $\langle N_{\text{coll}} \rangle$ was determined for a given $\langle N_{\text{part}} \rangle$ from the same Glauber model. The resulting centrality bins and $\langle N_{\text{coll}} \rangle$ used in this analysis are outlined in Table I.

TABLE I. Mean number of collisions for d + Au, N_{coll}, the percentage of the total inelastic cross section, and nuclear overlap function $T_A(b)$.

Percent σ_{inel}	$\langle N_{\text{coll}} \rangle$	$\langle T_A(b) \rangle (\text{mb}^{-1})$
0–20%	15.4 ± 1.0	0.367 ± 0.024
20–40%	10.6 ± 0.7	0.252 ± 0.017
40–88%	4.7 ± 0.3	0.112 ± 0.007

The dihadron events were recorded using several different level-1 triggers. The minimum-bias trigger required at least one hit in each of the BBCs and a collision vertex (computed online) that satisfies $|z_{\text{vertex}}| < 75$ cm. It was sensitive to 88.5% of the inelastic d + Au cross section. PHENIX also employed a series of level-1 triggers to select electrons, photons, and, with lower efficiency, high-p_T hadrons. These triggers utilized the ring imaging cherenkov (RICH) for electron identification, together with the electromagnetic calorimeter (EMC) [36], which consists of eight sectors, six of which are lead-scintillator (PbSc) sampling calorimeters and two are lead-glass (PbGl) Cherenkov counters. The EMC has excellent timing and energy resolution for electromagnetic showers. The triggers are called EMC/RICH triggers (ERTs) and were produced by summing signals from tiles, which were 4×5 photomultipliers (PMTs) in the RICH and either 2×2 or 4×4 PMTs in the EMC.

The electron trigger was defined by the coincidence between the minimum-bias trigger and the RICH and EMC 2×2 triggers where the threshold for the RICH tile was three photo-electrons and the EMC threshold varied between 400 and 800 MeV. Three different thresholds were available for the 4×4 photon triggers. These thresholds differed between the PbGl and PbSc and varied within and between the $p + p$ and d + Au runs. The lowest threshold setting (1.4–2.8 GeV) was most sensitive to hadron showers in the EMC. The threshold values and rejection factors (rejection = $N_{\text{minBiasEvents}}/N_{\text{triggerEvents}}$) for the ERT triggers, in coincidence with the minimum-bias trigger, are given in Table II. The $h^{\pm} - h^{\pm}$ correlations use only the minimum-bias-triggered data, while the $\pi^0 - h^{\pm}$ correlations use only the ERT photon triggers. The $\pi^{\pm} - h^{\pm}$ correlations use the minimum-bias, ERT photon, and ERT electron triggers. Above the energy threshold, the ERT electron trigger typically reached an efficiency of approximately 75%, and the ERT photon triggers reached efficiencies of 85–90%. A detailed knowledge of the ERT trigger efficiency is not necessary, since we present

TABLE II. EMC threshold and rejection factors for the electron and photon ERT triggers in coincidence with the minimum-bias trigger for $p + p$ and $d +$ Au. The photon triggers are defined by the energy sum of 4×4 PMTs in the EMC above threshold. The electron trigger requires the coincidence of the RICH trigger (threshold of three photoelectrons for both $p + p$ and $d +$ Au runs) and the energy sum of 2×2 PMTs in the EMC above threshold.

	$p + p$		$d +$ Au		$p + p$	$d +$ Au
	PbSc threshold (GeV)	PbGl threshold (GeV)	PbSc threshold (GeV)	PbGl threshold (GeV)	Rejection	Rejection
Gamma 1	2.1	2.1	2.8	3.5	400–1200	125–300
Gamma 2	2.8	2.8	2.8–3.5	3.5–4.2	1500–3100	450–900
Gamma 3	1.4	1.4	2.1	2.8	70–160	15–60
Electron	0.4–0.8	0.4–0.8	0.6–0.8	0.6–0.8	5–1200	30–170

the conditional yield distributions per trigger, for which this efficiency cancels out.

2. Tracking and particle identification

In this section, we discuss the tracking and identification of the particles used in the different correlation analyses. Three types of particles are included. Charged hadrons are used in all analyses, neutral pions are used as trigger particles for the $\pi^0 - h^\pm$ correlations, and charged pions are used as trigger particles for the $\pi^\pm - h^\pm$ correlations.

Charged hadron tracks are measured outside the PHENIX central magnetic field by the drift chamber (DC), located 2.0 m from the vertex, and two layers of multiwire proportional chamber (PC1 and PC3), located 2.5 and 5.0 m, respectively, from the vertex [37]. The DC determines the momentum and the azimuthal position of the track, while PC1 determines the polar angle [38]. The momentum resolution is determined to be $0.7\% \oplus 1.1\% p$ (GeV/c) [2]. Tracks are confirmed by requiring that an associated hit in PC3 lies within a 2.5σ (for $h^\pm - h^\pm$) or 3σ (for $\pi - h^\pm$) matching window in both the ϕ and z directions. This cut reduces the background from particles not originating in the direction of the vertex. The remaining background tracks are mainly decays and conversion particles [39]. The background level for single tracks is less than 5% below 3 GeV/c, increasing to about 30% at 5 GeV/c. However, the background is smaller for high-p_T triggered events (see Sec. III B). The charged particle tracking efficiency for the active region of the DC, PC1, and PC3 is better than 98%. Since we perform a pair analysis, the two-track resolution is important. For the DC, the two-track separation is better than 1.5 mm, while at PC1 it is 4 cm, and at PC3 it is 8 cm.

Neutral pions are detected by the statistical reconstruction of their $\gamma\gamma$ decay channel. These decay photons are detected by the EMC and identified by their time of flight (TOF) and shower shape. The electromagnetic shower shape is typically characterized by the χ^2 variable [36],

$$\chi^2 = \sum_i \frac{\left(E_i^{\text{meas}} - E_i^{\text{pred}}\right)^2}{\sigma_i^2}, \tag{18}$$

where E_i^{meas} is the energy measured at tower i and E_i^{pred} is the predicted energy for an electromagnetic particle of total energy $\sum_i E_i^{\text{meas}}$. This χ^2 value is useful for the discrimination of electromagnetic from hadron showers. The χ^2 and TOF cuts used give a very clean sample of photons with contamination of other particles at $\ll 1\%$.

Using pairs of photons that pass these EMC cuts, we create the invariant mass spectra for each photon pair p_T. A sample invariant mass distribution with a signal/background S/B of approximately 12 is given in Fig. 5. The background distribution can be reproduced by mixing clusters from different events and normalizing that distribution to the real event distribution outside the π^0 mass region. The peak position and width of the invariant mass distribution were parametrized as a function of pair p_T, in order to select π^0 candidates from a region of invariant mass within 2σ of the peak position. The S/B for a π^0 with $p_T > 5$ GeV is 10−20, increasing as a function of p_T. There is a slight dependence on centrality with the $\pi^0 S/B$ decreasing with increasing centrality.

PHENIX identifies high momentum charged pions with the RICH and EMC detectors. Charged particles with velocities above the Cherenkov threshold of $\gamma_{\text{th}} = 35$ (CO_2 radiator) emit Cherenkov photons, which are detected by photomultiplier tubes (PMTs) in the RICH [40]. This threshold corresponds to 18 MeV/c for electrons, 3.5 GeV/c for muons, and 4.9 GeV/c for charged pions. In a previous PHENIX publication [39], we showed that charged particles with reconstructed p_T above

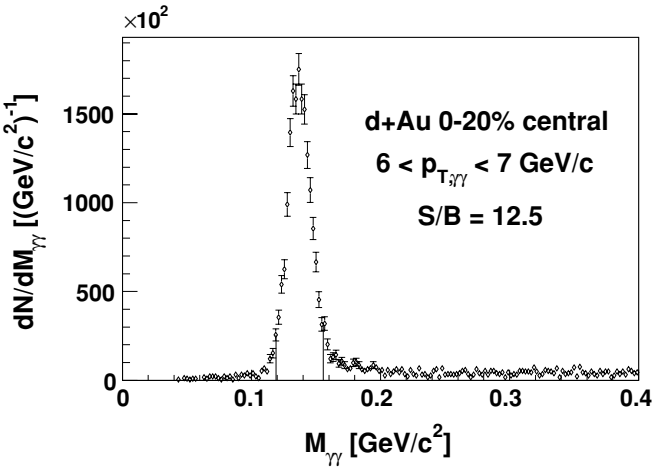

FIG. 5. Measured $\gamma\gamma$ invariant mass distribution for $6 < p_T < 7$ GeV/c in central $d +$ Au collisions. The peak is fitted with a Gaussian to extract the centroid mass and σ. The S/B within 2σ of the centroid ranges from ∼6 at 3 GeV/c up to 20 at ∼8 GeV/c.

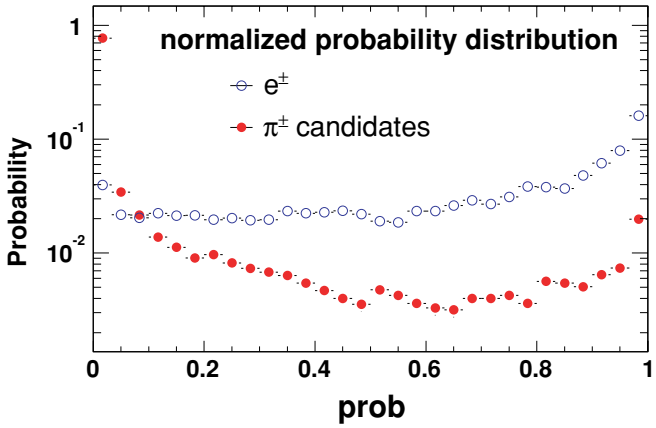

FIG. 6. (Color online) Probability distribution for charged pion candidates and electrons. Histogram integral has been normalized to unity.

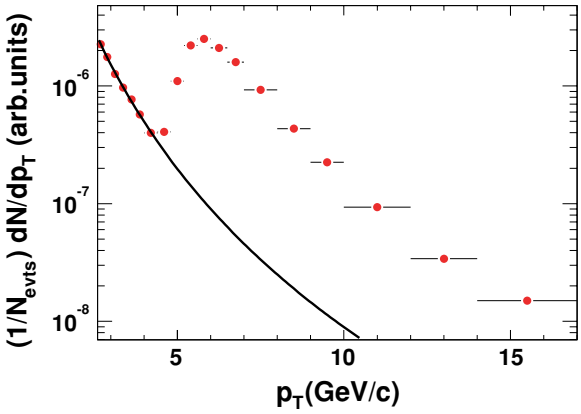

FIG. 7. (Color online) Raw charged pion transverse momentum spectrum, with the final cuts applied. Remaining background level is estimated from an extrapolation from low p_T and is shown as a black line.

4.9 GeV/c, which have an associated hit in the RICH, are dominantly charged pions and background electrons from photon conversions. The efficiency for detecting charged pions rises quickly past 4.9 GeV/c, reaching an efficiency of >90% at $p_T > 6$ GeV/c.

To reject the conversion backgrounds in the pion candidates, the shower information at the EMC is used. Since most of the background electrons are genuine low-p_T particles that were misreconstructed as high-p_T particles, simply requiring a large deposit of shower energy in the EMC is very effective in suppressing the electron background. In this analysis, a momentum-dependent energy cut applied at EMC is

$$E > 0.3 + 0.15\, p_T. \tag{19}$$

In addition to this energy cut, the shower shape information [36] is used to further separate the broad hadronic showers from the narrow electromagnetic (EM) showers and hence reduce the conversion backgrounds. In this analysis, we use the probability (prob) calculated from the χ^2 value [Eq. (18)] for an EM shower. The probability values range from 0 to 1, with a flat distribution expected for an EM shower and a peak around 0 for a hadronic shower. Figure 6 shows the probability distribution for the pion candidates and electrons, normalized by the integral, where the pion candidates were required to pass the energy cut and the electrons were selected using particle ID cuts similar to that used in Ref. [41]. Indeed, the electron distribution is relatively flat, while the charged pions peak at 0. A cut of prob <0.2 selects pions above the energy cut with an efficiency of $\gtrsim$80%. Detailed knowledge of the pion efficiency is not necessary, since we present in this paper the per-trigger pion conditional yield distributions, for which this efficiency cancels out.

Since the energy and prob cuts are independent of each other, we can fix one cut and then vary the second to check the remaining background level for conversions. The energy cut in Eq. (19) is chosen such that the raw pion yield is found to be insensitive to the variation in prob. Figure 7 shows the raw pion spectra for ERT-triggered events as a function of p_T, with the above cuts applied. The pion turnon from 4.9 to 7 GeV/c is clearly visible. Below a p_T of 5 GeV/c, the remaining background comes mainly from the random association of charged particles with hits in the RICH detector. The background level is less than 5% from 5 to 16 GeV/c, which is the p_T range for the charged pion data presented in this paper.

B. Data analysis

In this section, we outline the method used to obtain correlation functions and distributions. From these, we extract the jet shapes and yields outlined in Sec. II. For the extraction of the jet yield from the azimuthal distributions, we discuss how we obtain the absolute normalization of the distribution; while for the jet shape properties, j_{T_y} and $\langle \sin^2\phi_{jj} \rangle$, the absolute normalization is not necessary.

1. Correlation functions

Azimuthal correlation functions are generally defined as

$$C(\Delta\phi) \propto \frac{N_{\rm cor}(\Delta\phi)}{N_{\rm mix}(\Delta\phi)}. \tag{20}$$

Similarly, one can also define the correlation function in pseudorapidity as

$$C(\Delta\eta) \propto \frac{N_{\rm cor}(\Delta\eta)}{N_{\rm mix}(\Delta\eta)}. \tag{21}$$

The same-event pair distribution, $N_{\rm cor}(\Delta\phi)$ or $N_{\rm cor}(\Delta\eta)$, is constructed for trigger-associated particle pairs. The mixed-event pair distribution, $N_{\rm mix}(\Delta\phi)$ or $N_{\rm mix}(\Delta\eta)$, is determined by combining trigger particles with associated particles from randomly selected events.

This definition of the correlation function relies on the fact that detector acceptance and efficiency cancel out. It is therefore important that the pair efficiencies of the average mixed-event background and the average foreground distributions are the same. For this reason, we generate mixed-event distributions only for events with similar centralities and event vertices. More precisely, mixed events were required to match within ±10% centrality, and the event vertices were required to

be within ±3 cm. For $h^{\pm} - h^{\pm}$ correlations, the real and mixed events are minimum-bias data. For $\pi^0 - h^{\pm}$ correlations, the real and mixed events are ERT-triggered data. For $\pi^{\pm} - h^{\pm}$ correlations, the real events are ERT-triggered and minimum-bias data, while the mixed events mix ERT-triggered events with minimum-bias events.

For $h^{\pm} - h^{\pm}$ and $\pi^{\pm} - h^{\pm}$ correlations, due to finite two-track resolution for charged particles at the DC and PC, the reconstruction efficiency for same-event charged track pair drops at small $\Delta\phi$ and $\Delta\eta$. To minimize the difference in the pair efficiency between $N_{\rm cor}(\Delta\phi)$ and $N_{\rm mix}(\Delta\phi)$, the pairs are required to have a minimal separation of about two times the resolution at the various tracking detectors. This corresponds to about 0.28, 8, and 15 cm at the DC, PC1, and PC3, respectively. However, these pair cuts are not required for $\pi^0 - h^{\pm}$ correlations, because different detector subsystems are used for reconstructing trigger-π^0 and the associated charged tracks as outlined earlier.

Given the similarity of the analysis techniques between $\Delta\phi$ and $\Delta\eta$ correlations, in this paper we focus on the $\Delta\phi$ correlation. The $\Delta\phi$ correlation functions are obtained with two different normalizations. For $h^{\pm} - h^{\pm}$ assorted correlations, the correlation function is area normalized

$$C_{\rm norm}(\Delta\phi) = \frac{N_{\rm cor}(\Delta\phi)}{N_{\rm mix}(\Delta\phi)} \times \frac{\int d\Delta\phi (N_{\rm mix}(\Delta\phi))}{\int d\Delta\phi (N_{\rm cor}(\Delta\phi))}. \quad (22)$$

The details concerning this normalization are discussed in Sec. IV A. The second normalization is used in both the $\pi^0 - h^{\pm}$ and $\pi^{\pm} - h^{\pm}$ correlations. It was shown in Ref. [32] that the CY can be derived from the measured correlation function with an appropriate normalization,

$$\frac{1}{N^0_{\rm trig}} \frac{dN_0}{d\Delta\phi} = \frac{R_{\Delta\eta}}{N_{\rm trig}\epsilon} \frac{\frac{dN_{\rm cor}}{d\Delta\phi}(\Delta\phi)}{\frac{2\pi N_{\rm mix}(\Delta\phi)}{\int d\Delta\phi N_{\rm mix}(\Delta\phi)}}, \quad (23)$$

where $N^0_{\rm trig}$ and $N_{\rm trig}$ are the true and detected number of triggers, respectively, and ϵ is the average single-particle efficiency for the associated particles in 2π in azimuth and ± 0.35 in pseudorapidity. $R_{\Delta\eta}$ corrects for the loss of jet pairs outside a given $\Delta\eta$ acceptance, determined by PHENIX's finite acceptance in η. This second normalization is defined so that the integral of the resulting correlation function should be $N_0/N^0_{\rm trig}$, the total number of pairs per trigger particle in a given azimuthal and η range.

For the normalization in Eq. (23), two separate efficiencies must be determined, the $\Delta\eta$ correction and the single-particle efficiency. The near-side correlation has a well-behaved peak around $\Delta\eta = 0$. As we show in Sec. IV A, the near-side jet width in $\Delta\phi$ and $\Delta\eta$ are consistent with each other within errors. So we correct the near-side yield to the full-jet yield assuming the shape of the jet is Gaussian and the widths are equal in $\Delta\phi$ and $\Delta\eta$. This correction, according to Ref. [32], is

$$R_{\Delta\eta} = \frac{1}{\int_{-0.7}^{0.7} d\Delta\eta \frac{1}{\sqrt{2\pi}\sigma} \exp\left[-\frac{\Delta\eta^2}{2\sigma^2}\right] {\rm acc}(\Delta\eta)}, \quad (24)$$

where $\mathrm{acc}(\Delta\eta)$ represents the PHENIX pair acceptance function in $|\Delta\eta|$. It can be obtained by convoluting two flat distributions in $|\eta| < 0.35$, so $\mathrm{acc}(\Delta\eta)$ has a simple triangular shape: $\mathrm{acc}(\Delta\eta) = (0.7 - |\Delta\eta|)/0.7$. The PHENIX single-particle acceptance is flat in η to within 5%.

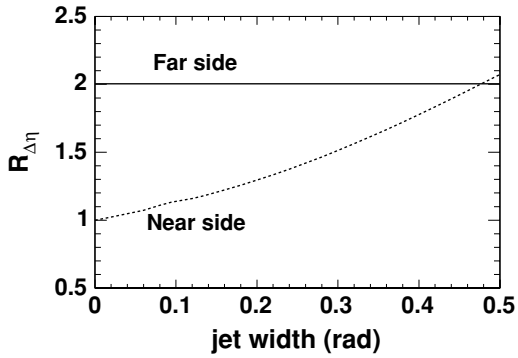

FIG. 8. Correction factor $R_{\Delta\eta}$ plotted as function of jet width for near and far sides.

In the far side, the jet signal is much broader than the PHENIX acceptance due to the broad range of momentum fraction x of the partons that participate in the hard scattering. In fact, we studied the far-side jet shape for the $\pi^{\pm} - h^{\pm}$ correlation (Fig. 17b) and found the true jet correlation strength to be almost constant in the PHENIX pair acceptance $|\Delta\eta| < 0.7$. Based on that, we assume that the far-side jet strength is constant and correct the far-side yield to the corresponding accessible pair range of $|\Delta\eta| < 0.7$,

$$R^{\rm far}_{\Delta\eta} = \frac{2 \times 0.7}{\int_{-0.7}^{0.7} d\Delta\eta \left[\frac{0.7 - |\Delta\eta|}{0.7}\right]} = 2. \quad (25)$$

$R^{\rm far}_{\Delta\eta}$ equals 2 because the pair efficiency has a triangular shape in $|\Delta\eta| < 0.7$, which results in 50% average efficiency when the real jet pair distribution is flat in $|\Delta\eta| < 0.7$. Figure 8 shows the correction factor $R_{\Delta\eta}$ as a function of jet width. The typical range of the near-side jet width in all analyses (see Sec. IV A) is below 0.5 rad. The maximum correction is about a factor of 2 for the near-side jet.

The single-particle efficiency for associated particles ϵ includes detector acceptance and reconstruction efficiency. It is evaluated in a way similar to previously published Au + Au [39] and d + Au [2] analyses. However, the jet-associated charged hadron spectrum in d + Au is much flatter than the inclusive charged hadron spectra [48],[1] so the corrections due to momentum scale and momentum resolution are much smaller than those for inclusive charged hadrons. For the same reason, the background contamination at high p_T, mainly coming from decay and photon conversions which are falsely reconstructed as high-p_T tracks [2,39], is also reduced. We studied both effects using a full GEANT simulation of PYTHIA events through PHENIX detectors. The jet-associated yields were extracted in the same manner as for the real data analysis. By comparing it with the input jet-associated yield spectra, we can quantitatively study the effect of momentum smearing and high-p_T background contamination. The corrections due to

[1]For example, in Fig. 21, the jet associated yields decrease by a factor of 100 from 0.5 to 5 GeV/c. However, the typical single inclusive hadron spectra decrease by a factor of 100 000 [2].

momentum scale and resolution are found to be less than 5% with 3% systematic errors. For high-p_T triggered events, the background contamination to the associated charged hadrons is found to be 5% independent of p_T from 1−5 GeV/c.

2. Extracting jet properties

The normalized correlation functions and conditional yield distributions are both fitted with a sum of two Gaussians to extract the jet widths and the conditional yield of hadrons in the near side ($\Delta\phi \sim 0$) and far side ($\Delta\phi \sim \pi$). The fit for the normalized correlation functions is described in Sec. IV A. For the conditional yield, we fit with the function

$$\frac{1}{N^0_{\rm trig}}\frac{dN_0}{d\Delta\phi} = B + \frac{{\rm Yield}_N}{\sqrt{2\pi}\sigma_N}\exp\left[\frac{-\Delta\phi^2}{2\sigma_N^2}\right] + \frac{{\rm Yield}_F}{\sqrt{2\pi}\sigma_F}\exp\left[\frac{-(\Delta\phi-\pi)^2}{2\sigma_F^2}\right], \quad (26)$$

where B reflects the combinatoric background level in the real distribution relative to the mixed distribution, and the other two terms represent the near-side jet and far-side jet signal, respectively. The resulting widths, σ_N and σ_F, are then used to calculate the jet shapes via Eqs. (7) and (13). For each choice of trigger and associated particle p_T range, Yield$_N$ and Yield$_F$ directly reflect the jet-associated yield $dN/dp_{T,\rm assoc}$ at the near and far side, respectively.

Two methods were used to calculate the dN/dx_E distribution. The first method was used for $\pi^0 - h^\pm$ correlations. Since these correlations are binned in p_T there is a distribution of x_E for each trigger-associated p_T bin. This distribution is approximately Gaussian. The fitted peak value is used as the bin center of the dN/dx_E distributions and the fitted Gaussian width is used as the horizontal error bar. To estimate the bin width in x_E, we used the definition Eq. (2) which can be written as (ignoring the sign) $x_E = p_{T,\rm assoc}\cos(\Delta\phi)/p_{T,\rm trig}$. We estimate $\cos(\Delta\phi) \approx 1$ and write the bin width as

$$\Delta x_E = \frac{p^{\rm max}_{T,\rm assoc} - p^{\rm min}_{T,\rm assoc}}{\langle p_{T,\rm trig}\rangle}, \quad (27)$$

where we have an associated p_T bin from $[p^{\rm min}_{T,\rm assoc}, p^{\rm max}_{T,\rm assoc}]$ and a trigger p_T bin with a mean $\langle p_{T,\rm trig}\rangle$.

The second method is adopted by $\pi^\pm - h^\pm$ analysis. It is statistically based and can be used to calculate the distribution for any pair variable $p_{T,\rm trig}$, $p_{T,\rm assoc}$, $\Delta\phi$, $\Delta\eta$, x_E, $p_{\rm out}$ etc. In the following we show two examples: the $dN/d\Delta\phi$ and dN/dx_E distributions. For each pair we calculate the $\Delta\phi$ and x_E value, then from Eq. (23) we calculate the same correction factor that was used for the $dN/d\Delta\phi$ distribution.

$$w(\Delta\phi) = \frac{R_{\Delta\eta}}{N_{\rm trig}\epsilon}\frac{1}{\frac{2\pi N_{\rm mix}(\Delta\phi)}{\int d\Delta\phi N_{\rm mix}(\Delta\phi)}}. \quad (28)$$

If this weight is used to fill the $\Delta\phi$ histogram for the real and mixed distribution, we obtain the CY for the true real pairs, and for the mixed pair the sum is,

$$\begin{aligned}{\rm background}(\Delta\phi) &= \sum_{\rm mix}\delta(\Delta\phi)w(\Delta\phi)\\ &= N_{\rm mix}(\Delta\phi)w(\Delta\phi)\\ &= \frac{N_{\rm trig}\epsilon}{R_{\Delta\eta}}\frac{\int d\Delta\phi N_{\rm mix}(\Delta\phi)}{2\pi}\end{aligned} \quad (29)$$

we have used the fact that $N_{\rm mix}(\Delta\phi) = \sum_{\rm mix}\delta(\Delta\phi)$.

Thus the jet signal can be extracted from Eq. (26) as

$$\begin{aligned}\frac{1}{N^0_{\rm trig}}\frac{dN^{\rm jet}_0}{d\Delta\phi} &= \sum_{\rm real}\delta(\Delta\phi)w(\Delta\phi) - B\\ &= \sum_{\rm real}\delta(\Delta\phi)w(\Delta\phi) - C\sum_{\rm mix}\delta(\Delta\phi)w(\Delta\phi),\end{aligned} \quad (30)$$

where

$$C = \frac{BR_{\Delta\eta}}{N_{\rm trig}\epsilon}\frac{2\pi}{\int d\Delta\phi N_{\rm mix}(\Delta\phi)}. \quad (31)$$

When this weight is used to fill the x_E histogram for both real and mixed distributions, we obtain the dN/dx_E by subtracting the mixed x_E distribution from the real x_E distribution,

$$\frac{1}{N^0_{\rm trig}}\frac{dN^{\rm jet}_0}{dx_E} = \sum_{\rm real}\delta(x_E)w(\Delta\phi) - C\sum_{\rm mix}\delta(x_E)w(\Delta\phi). \quad (32)$$

Equation (31) is rather trivial, because the weighting procedure is equivalent to Eq. (23), for which we know the shape of the distribution (Eq. (26)). But the advantage of the weighting procedure is that it allows for the determination of the absolute background pair distribution in any pair variables.

Similarly, the statistical method is used to extract the $p_{T,\rm assoc}$ and $p_{\rm out}$ spectra as

$$\frac{1}{N^0_{\rm trig}}\frac{dN^{\rm jet}_0}{dp_{T,\rm assoc}} = \sum_{\rm real}\delta(p_{T,\rm assoc})w(\Delta\phi) - C\sum_{\rm mix}\delta(p_{T,\rm assoc})w(\Delta\phi) \quad (33)$$

$$\frac{1}{N^0_{\rm trig}}\frac{dN^{\rm jet}_0}{dp_{\rm out}} = \sum_{\rm real}\delta(p_{\rm out})w(\Delta\phi) - C\sum_{\rm mix}\delta(p_{\rm out})w(\Delta\phi). \quad (34)$$

By construction, the integral of the jet yield should be conserved independent of the pair variable used, i.e.:

$$\begin{aligned}\int d\Delta\phi\frac{dN_0}{d\Delta\phi} &= \int dx_E\frac{dN^{\rm jet}_0}{dx_E}\\ \int dp_{T,\rm assoc}\frac{dN^{\rm jet}_0}{dp_{T,\rm assoc}} &= \int dp_{\rm out}\frac{dN^{\rm jet}_0}{dp_{\rm out}}.\end{aligned} \quad (35)$$

C. Systematic uncertainties

The correlation analyses presented here consist of several steps ranging from the generation of correlation functions to the extraction of the final physics variables [j_T, $\sin(\phi_{jj})$, per-trigger yields, etc.] from these correlation functions. Systematic error estimations for each of these steps have been evaluated and combined to determine the overall error quoted for each measurement. All errors quoted are maximum extent.

Systematic errors associated with the generation of correlation functions can result from shape distortions in either the foreground or background distributions. These distortions can arise if the requisite quality cuts (see Sec. III A) are not stable. In order to minimize such errors, the track pair and quality cuts were assigned such that the correlation functions were essentially insensitive to reasonable cut variations. Systematic errors associated with such cut variations are estimated to be less than 4%. A further source of systematic error is related to the efficiency of the background rejection when requiring a confirmation hit in the outer pad chamber. The yields have been corrected for remaining background. The systematic error on the background estimate is ≈3% for tracks with a transverse momentum (p_T) < 4 GeV/c and ≈7% for particles with 4 < p_T < 6 GeV/c. For the calculation of the conditional yields, the systematic error is dominated by the uncertainties associated with the determination of the efficiency corrected single-particle yields. These systematic errors have been estimated to be ≈10% as obtained from Ref. [2]. This error on the efficiency has two parts: the normalization error includes the error on PC3 matching and active area; the momentum smearing error includes contributions from momentum resolution and momentum scale.

A separate error is estimated for $\pi^0 - h^{\pm}$ correlations due to the background contamination of the π^0 within the mass bin. To estimate the width and yield contribution of the background $\gamma\gamma$ pairs, we created correlations of $\gamma\gamma$ outside the π^0 mass with hadrons. From these, we extrapolated the background contribution at the π^0 mass. These systematic errors are p_T dependent. For the near and far angle width, the variation is 1−3%, the near yield variation is 1%, the far yield variation is 1−5% and increases with increasing p_T.

The event-mixing technique has been used to correct for the limited detector acceptance and inefficiency. In addition, the CY has been corrected for limited $\Delta\eta$ coverage. To cross-check these procedures, we ran a detailed simulation using the PYTHIA event generator [42] coupled to a single-particle acceptance filter that randomly accepts charged particles according to the detector efficiency. In the following, we shall use $\pi^{\pm} - h^{\pm}$ as an example for this cross-check. Figure 9 shows a typical PHENIX two-dimensional single-particle acceptance used in this analysis.

We generated 1 million PYTHIA events, each required to have at least one >6 GeV/c charged pion. To speed up the event generation, a Q^2 cut of 100 GeV^2 on the underlying parton-parton scattering was required. These events were filtered through the single-particle acceptance filter. As an approximation, we ignore the p_T dependence of acceptance. The same event and mixed pair $\Delta\phi$ distributions were then

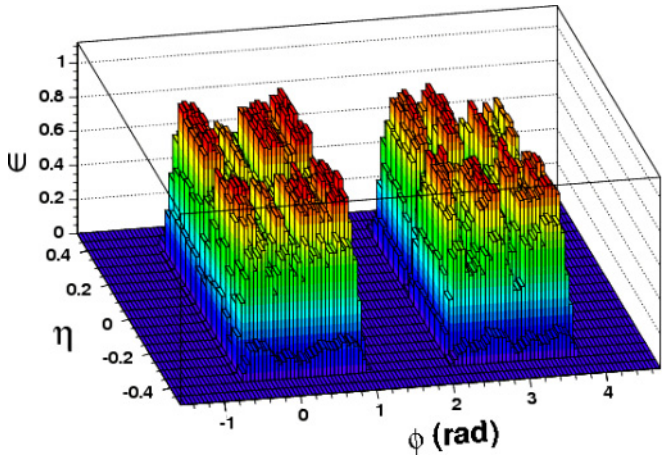

FIG. 9. (Color online) Typical PHENIX single-particle acceptance for charged hadrons.

built by combining the accepted $\pi^{\pm}$ and charged hadrons. The jet width and raw yield were extracted by fitting the $\frac{dN_{\rm fg}}{d\Delta\phi} / \frac{dN_{\rm mix}}{d\Delta\phi}$ with a constant plus double Gaussian function. The raw yields were then corrected via Eq. (24) to full jet yield for the near side and the yield in $|\Delta\eta| < 0.7$ for the far side. We also extracted the true CY and jet width without the acceptance requirement. The comparison of the CY and jet width with and without the acceptance requirement are shown in Fig. 10. The trigger particles are $\pi^{\pm}$ with 6 < $p_{T,\rm trig}$ < 10 GeV/c, the associated particles are $h^{\pm}$. In the near side, the corrected yield (top left panel) and width (bottom left panel) are compared with those extracted without the acceptance filter. In the far side, the yield corrected back to $|\Delta\eta| < 0.7$ and the width are compared with those extracted without the acceptance filter. The data requiring the acceptance filter are always indicated

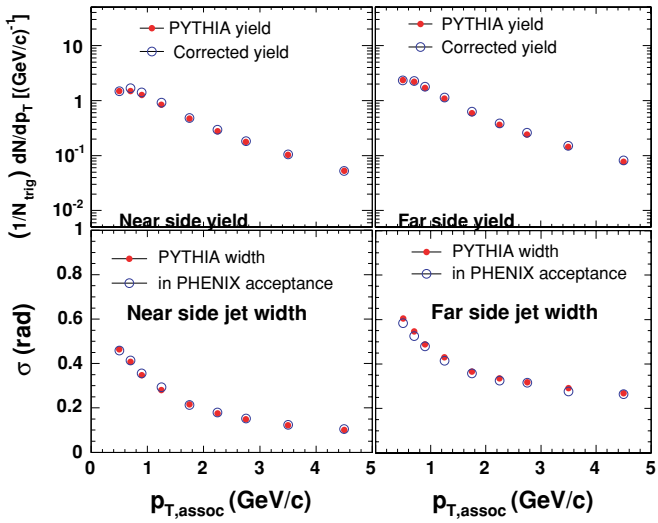

FIG. 10. (Color online) Comparison of near-side yield, near-side width, far-side yield, and far-side width as functions of p_T of charged hadrons. These are obtained for $\pi^{\pm} - h^{\pm}$ correlation from PYTHIA, with a trigger pion of 6−10 GeV/c. Filled circles represent quantities calculated with PHENIX acceptance filter.

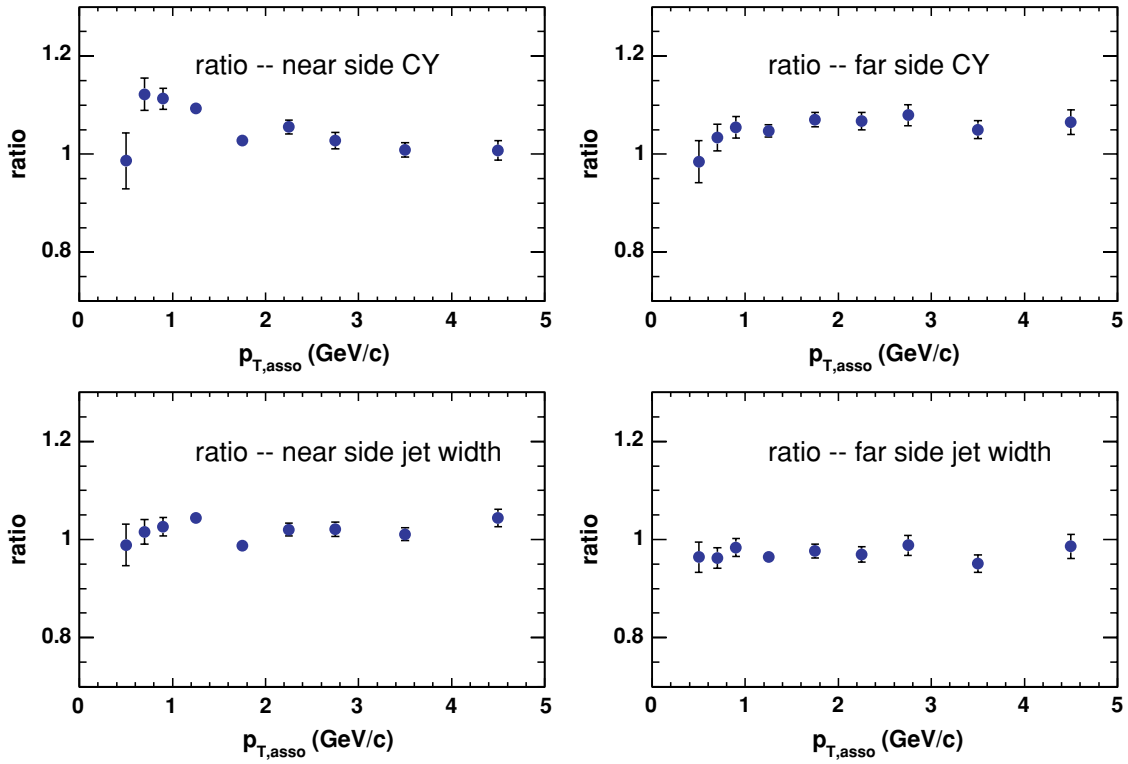

FIG. 11. (Color online) Ratio of the jet width or corrected yield obtained from the event-mixing method to those without the acceptance filter.

by the filled circles, while the expected yield or width are indicated with open circles.

The agreement between the two data sets can be better seen by plotting the ratios, which are shown in Fig. 11. The yields agree within 10% and the widths agree within 5%. Since $\sqrt{\langle j_T^2 \rangle}$, $\langle \sin^2(\phi_{jj}) \rangle$ are derived from the jet widths, the agreement in width naturally leads to the agreement in the $\sqrt{\langle j_T^2 \rangle}$ and $\langle \sin^2(\phi_{jj}) \rangle$. One notices that there are some systematic differences in the comparison of the yield at low $p_{T,\text{assoc}}$. This might indicate that the Gaussian assumption is not good enough when the jet width is wide and the extrapolation for $|\Delta\eta| > 0.7$ becomes sizable. (At $p_{T,\text{assoc}} = 0.5$ GeV/c, the jet width $\sigma_N = 0.5$ rad and the extrapolation is about 20%.)

The approximations in the formulas used to extract j_{T_y} and $\sin^2(\phi_{jj})$ are used to estimate the systematic error on these quantities. We estimate the systematic uncertainty in the formulation at the level of 5% for $\sqrt{\langle j_T^2 \rangle}$ and 3–4% for $\sqrt{\langle \sin^2(\phi_{jj}) \rangle}$.

Table III summarizes the systematic errors for the extracted widths $\sqrt{\langle j_T^2 \rangle}$ and $\sqrt{\langle \sin^2(\phi_{jj}) \rangle}$, while Tables IV, V, and VI summarize the list of systematic errors on the CY for the hadron-hadron, neutral pion-hadron, and charged pion-hadron correlations, respectively. Table VII outlines the systematic errors on the p_{out} extraction from pion-hadron correlations.

IV. RESULTS

We present the minimum-bias and centrality-dependent results on extracted jet widths and yields in Sec. IV A,

TABLE III. Summary of the systematic errors on the widths and j_T, $\langle \sin^2(\phi_{jj}) \rangle$.

Error source	
Tracking cuts, pair cuts	<4%
Assumptions used in formula	<5%
S/B correction (π^0 only)	1−3%

TABLE IV. Summary of the systematic errors on the conditional yields for $h^{\pm} - h^{\pm}$ analysis.

Error source	<4 GeV/c	4−6 GeV/c
Quality cuts	<4%	<4%
Background correction	3%	30%
Error on single particle yields	10%	10%

TABLE V. Summary of the systematic errors on the conditional yields for $\pi^0 - h^{\pm}$ analysis.

Single particle	Pair cuts		3%	
ϵ_{single}	Normalization		6.5%	
	p smearing (reso+scale)		3%	
	Near-side yield		1%	
S/B	$p_{T,\text{assoc}}$ (GeV/c)	<2	2−3	>3
	Far-side yield	5%	2%	1%

TABLE VI. Summary of the systematic errors on the conditional yields for $\pi^{\pm} - h^{\pm}$ analysis.

Single particle	Normalization			6.5%		
	p smearing (reso+scale)			3%		
ϵ_{single}	Trigger pion background			5%		
	Centrality dependent part			5%		
	$p_{T,\text{assoc}}$ (GeV/c)	<1	1−2	2−3	3−4	4−5
Yield extraction	Pair cuts	1%	1%	2%	3%	4%
	Near-side yield	20%	10%	6%	6%	6%
	Far-side yield			6%		
	Error on the fit	10−20%	6%	4%	4%	4%

TABLE VII. Summary of the systematic errors on the p_{out} distribution for $\pi^{\pm} - h^{\pm}$ analysis.

p_{out} (GeV/c)	<0.5	0.5−1	1−2	2−2.5
Yield extraction (near)	8%	15%	20%	20%
Yield extraction (far)	8%	15%	20%	30%
Other errors	10.6%	10.6%	10.6%	10.6%

which are used in Sec. IV B to calculate quantities describing the jet structures: the values of $\sqrt{\langle j_T^2 \rangle}$, $\langle \sin^2(\phi_{jj}) \rangle$, and jet fragmentation conditional yields dN/dp_T and dN/dx_E. The minimum-bias $d + \text{Au}$ results are compared with results from $p + p$ in Sec. IV C to establish the extent of effects due to medium modification in $d + \text{Au}$ with as much statistical precision as possible. The $d + \text{Au}$ centrality dependence of the derived quantities is presented in Sec. IV D. This provides a larger lever arm in nuclear thickness function, at the cost of dividing the available minimum-bias data into different centrality bins.

A. Correlation functions, widths, and yields

The baseline data from which jet structures are extracted are the correlation functions and conditional pair distributions that were defined in Sec. II. Figure 12 shows representative correlation functions between two charged hadrons, while Figs. 13 and 14 show representative conditional yield distributions triggered on neutral pions (π^0) and charged pions, respectively. All three correlation sets (Figs. 12–14) show relatively narrow peaks centered at $\Delta\phi = 0$ and π radians. The widths of these structures decrease with larger p_T, which is consistent with narrowing of the jet cone for increasing p_T. The fractional area under the jet peak relative to the flat underlying background also increases significantly as a function of associated-particle p_T, indicating increasing (di)jet

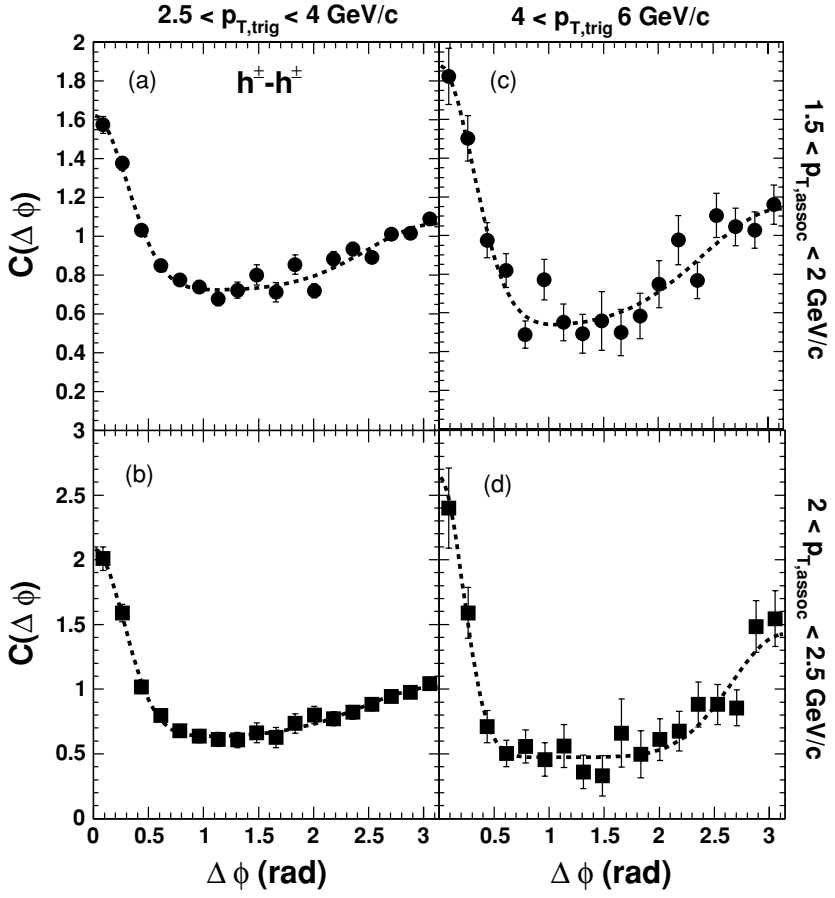

FIG. 12. Assorted $h^{\pm} - h^{\pm}$ correlation functions from $d + \text{Au}$ collisions for centrality 0–80% and several p_T cuts. Trigger p_T range is $2.5 < p_{T,\text{trig}} < 4.0$ GeV/c in (a) and (b) and $4.0 < p_{T,\text{trig}} < 6.0$ in (c) and (d). Associated hadron is in the range $1.5 < p_T < 2.0$ GeV/c or $2.0 < p_T < 2.5$ GeV/c. Correlations are for the centrality class 0−80%. Dashed line represents a fit to the correlation function using Eq. (37).

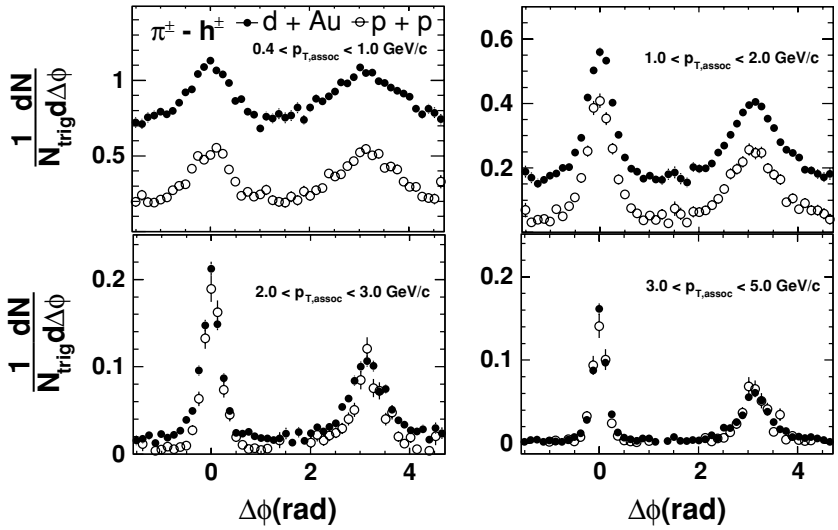

FIG. 13. Fully corrected assorted charged pion-hadron conditional pair distributions for $d+$Au collisions for centrality 0−88% and $p+p$ collisions. Trigger $\pi^{\pm}$ are within $5 < p_{T,\mathrm{trig}} < 10$ GeV/c and are correlated with hadrons with four $p_{T,\mathrm{assoc}}$ ranges as given in each plot.

contributions to the correlation function. In particular, Fig. 13 shows that for events where there is a high-p_T trigger, a large fraction of the low-p_T (as low as 0.4−1 GeV/c) particles are coming from the dijet fragmentation, and the jet contribution dominates at $p_T > 2$ GeV/c. Events tagged with a high-p_T jet are much harder than a typical minimum-bias event.

We characterize the jet correlations shown in Figs. 12–14 by assuming that there are only two contributions to the correlation function—(di)jet correlations and an isotropic underlying event. This scenario can then be expressed as

$$C(\Delta\phi) = A_o(1 + J(\Delta\phi)), \tag{36}$$

where A_o denotes the isotropic background and $J(\Delta\phi)$ is the jet function. Approximating the jet function as the sum of two Gaussians, we fit the correlations with

$$C(\Delta\phi) = A_o\left[1 + \frac{\lambda_N}{\sqrt{2\pi}\sigma_N}\exp\left(\frac{-\Delta\phi^2}{2\sigma_N^2}\right) + \frac{\lambda_F}{\sqrt{2\pi}\sigma_F} \times \exp\left(\frac{-(\Delta\phi-\pi)^2}{2\sigma_F^2}\right)\right]. \tag{37}$$

Here, $\lambda_{N,F}$ are the normalized Gaussian areas and $\sigma_{N,F}$ are the Gaussian widths for the near- and far-side jets, respectively. For the pair distribution functions, we fit with the same shaped function, but with a different normalization [Eq. (26)] as outlined in Sec. III B.

Figure 15 shows the associated-p_T dependence of the extracted widths for both the near- and far-side peaks[2] from the charged-hadron correlation functions with the trigger range for the charged hadron being 3−5 GeV/c. The data are tabulated in Table VIII.

In Fig. 16, we present the same quantities from the high-p_T identified pion correlations, where there is excellent agreement between the π^0 and charged-pion data sets. For both types of identified pions, the trigger p_T range is 5−10 GeV/c; these data are tabulated in Tables IX and X.

The far-side widths shown in Figs. 15 and 16 are larger than the near-side widths, as expected, since the far-side structure is a convolution of two jet fragmentations as well as any k_T of

[2]The results here are not sensitive to the slightly different range in centrality used.

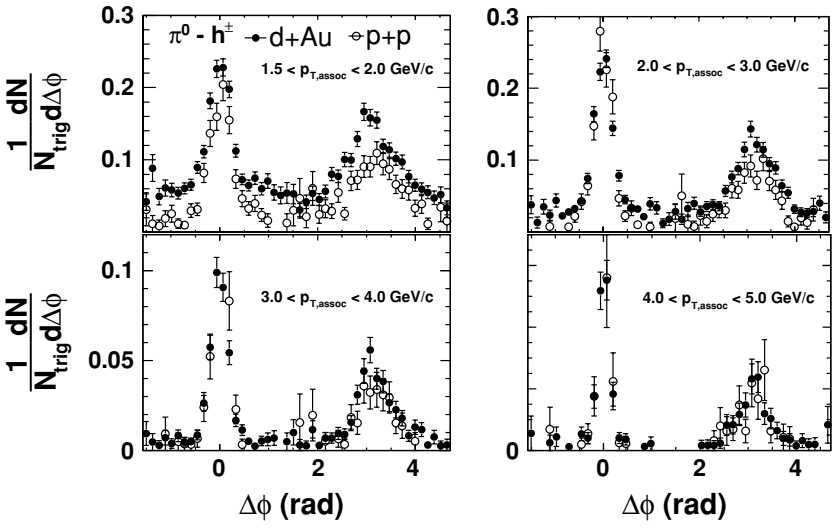

FIG. 14. Fully corrected assorted π^0-hadron conditional pair distributions for $d+$Au collisions for centrality 0−88% and $p+p$ collisions. Trigger π^0 are within $5 < p_{T,\mathrm{trig}} < 10$ GeV/c and are correlated with hadrons with four $p_{T,\mathrm{assoc}}$ ranges as given in each plot.

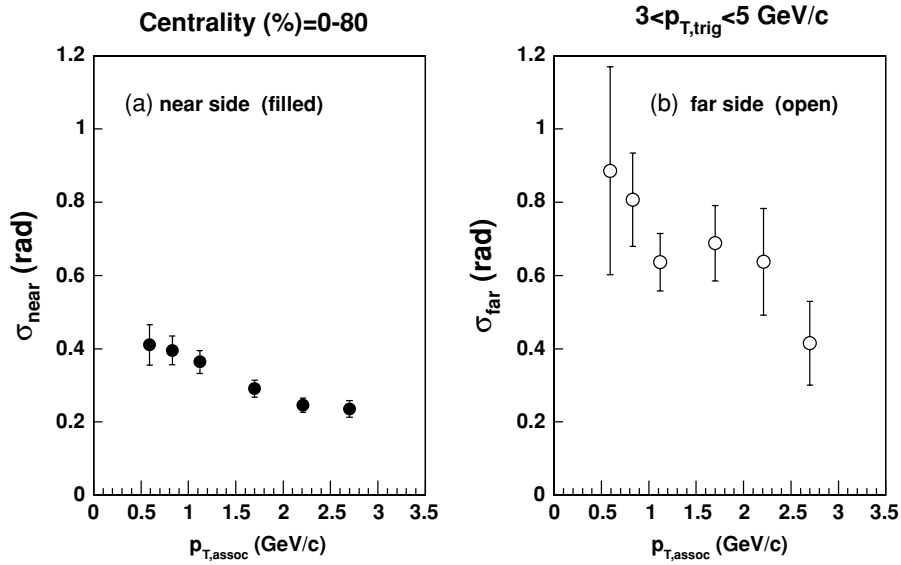

FIG. 15. Near- and far-side widths as a function of $p_{T,\mathrm{assoc}}$ for charged hadron azimuthal correlations from minimum-bias d + Au collisions (see text). Bars are statistical errors.

the scattered partons. The widths of the correlation functions also steadily decrease as a function of $p_{T,\mathrm{assoc}}$ as expected from (di)jet fragmentation. For completeness, we also tabulate the near- and far-side widths extracted as a function of $p_{T,\mathrm{trig}}$ for identified pions. These data are tabulated in Tables XI and XII.

Although the PHENIX single-particle acceptance is limited to $|\eta| < 0.35$, it can sample jet pairs in twice as large of a window in $\Delta\eta$ ($|\Delta\eta| < 0.7$) with varying pair efficiency. Similar to azimuthal correlation, the pair efficiency in $\Delta\eta$ can be estimated via mixed events and can subsequently be divided out [Eq. (21)]. Assuming that the underlying event is flat[3] in $|\Delta\eta| < 0.7$, we fix the background level to be equal to that in azimuthal correlation function Eq. (36) and subsequently extract the jet distribution as a function of $\Delta\eta$. In Fig. 17(a), we compare the near-side jet shape in $\Delta\phi$ and $\Delta\eta$ in the angular range of $|\Delta\phi, \Delta\eta| < 0.7$ for the $\pi^{\pm} - h^{\pm}$ correlation with $1.0 < p_{T,\mathrm{assoc}} < 2.0$ GeV/c. There is no significant difference

TABLE VIII. Near- and far-side widths as a function of $p_{T,\mathrm{assoc}}$ for charged hadron triggers (3−5 GeV/c) and associated charged hadrons from d + Au collisions.

$\langle p_{T,\mathrm{assoc}} \rangle$ (GeV/c)	σ_{near} (rad)	σ_{far} (rad)
0.59	0.411 ± 0.055	0.89 ± 0.28
0.83	0.395 ± 0.039	0.807 ± 0.128
1.12	0.364 ± 0.032	0.636 ± 0.079
1.7	0.291 ± 0.023	0.688 ± 0.103
2.2	0.246 ± 0.019	0.637 ± 0.146
2.7	0.236 ± 0.023	0.415 ± 0.114

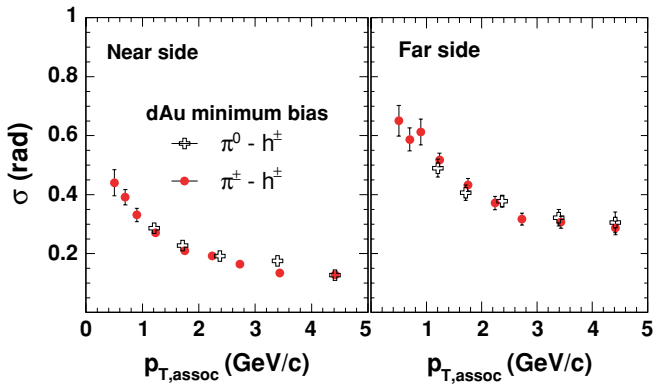

FIG. 16. (Color online) Near- and far-side widths as a function of $p_{T,\mathrm{assoc}}$ from pion-hadron azimuthal correlations for charged pion (closed symbols) and neutral pion (open symbols) triggers from the $p_{T,\mathrm{trig}}$ range of 5−10 GeV/c in minimum-bias d + Au collisions (see text). Bars are statistical errors.

[3] η dependence of the single-particle yield is very weak in $0 < |\eta| < 1$ [43]. Thus, the underlying pair distribution in $|\Delta\eta| < 0.7$ is almost flat.

TABLE IX. Near- and far-side widths as a function of $p_{T,\mathrm{assoc}}$ for charged pion triggers (5−10 GeV/c) and associated charged hadrons from minimum-bias d + Au collisions.

$\langle p_{T,\mathrm{assoc}} \rangle$ (GeV/c)	σ_{near} (rad)	σ_{far} (rad)
0.50	0.440 ± 0.044	0.651 ± 0.052
0.70	0.391 ± 0.026	0.587 ± 0.039
0.90	0.331 ± 0.023	0.613 ± 0.044
1.23	0.271 ± 0.010	0.517 ± 0.024
1.75	0.210 ± 0.008	0.433 ± 0.022
2.24	0.193 ± 0.009	0.372 ± 0.023
2.73	0.165 ± 0.007	0.317 ± 0.020
3.44	0.135 ± 0.006	0.307 ± 0.020
4.42	0.128 ± 0.008	0.287 ± 0.023

TABLE X. Same as Table IX, but for neutral pion triggers.

$\langle p_{T,\mathrm{assoc}} \rangle$ (GeV/c)	σ_{near} (rad)	σ_{far} (rad)
1.21	0.284 ± 0.011	0.494 ± 0.022
1.71	0.227 ± 0.007	0.410 ± 0.019
2.37	0.193 ± 0.005	0.380 ± 0.015
3.39	0.177 ± 0.006	0.322 ± 0.020
4.41	0.130 ± 0.007	0.315 ± 0.026

TABLE XI. Near- and far-side widths as a function of $p_{T,\mathrm{trig}}$ for charged pion triggers and associated charged hadrons (2–4.5 Gev/c) from minimum-bias d + Au collisions.

$\langle p_{T,\mathrm{trig}}\rangle$ (GeV/c)	σ_{near} (rad)	σ_{far} (rad)
5.44	0.176 ± 0.008	0.393 ± 0.030
6.31	0.165 ± 0.007	0.342 ± 0.020
7.27	0.162 ± 0.007	0.322 ± 0.022
8.60	0.157 ± 0.008	0.301 ± 0.019
10.6	0.149 ± 0.020	0.231 ± 0.039
13.2	0.177 ± 0.019	0.329 ± 0.042

in jet shape between $\Delta\eta$ and $\Delta\phi$, and the widths are consistent in both directions. Figure 17(b) shows the far-side jet shape in $\Delta\eta$; the associated pair distribution is flat within $\pm 10\%$.

Figure 18(a) shows the comparison of the near-side jet widths in $\Delta\phi$ and $\Delta\eta$ from d + Au. There is overall very good agreement between the two data sets. However, the width in $\Delta\eta$ is systematically lower than that in $\Delta\phi$ at small $p_{T,\mathrm{assoc}}$. This is because the underlying background is not completely flat in $\Delta\eta$, but varies by up to 10% in $|\Delta\eta| < 0.7$. Thus the procedure of dividing by the mixed-event distribution [Eq. (21)] introduces some distortion of the jet shape at large $\Delta\eta$ and consequently leads to a slightly different value for the jet width. In fact, for $p + p$ collisions, Fig. 18(b) indicates a similar discrepancy between $\Delta\phi$ and $\Delta\eta$ at small $p_{T,\mathrm{assoc}}$ for $p + p$ collisions. Thus this deviation is not likely due to the cold medium effect in d + Au.

We extract not only the widths of the jet structures but also the conditional yields of how many hadrons are in the near- and far-side structures for each high-p_T trigger. The conditional yield defined in Eq. (14) can be obtained from either a correlation function or conditional pair distribution, both of which produce identical results. For the conditional pair distributions, the conditional yield is directly extracted from the fit parameters [Eq. (26)]; for correlation functions, several normalization factors need to be applied to obtain the per-trigger yield [44, 45], as described below.

For correlation functions, it is convenient to define the fraction of jet-correlated particle pairs per event, $n_{\mathrm{jet\,pair}}/n_{\mathrm{total\,pair}}$. Following the basic ansatz outlined in Eq. (36), the fraction of jet-correlated particle pairs is obtained by summing the jet function over all bins in $\Delta\phi$ and dividing by the total sum of the correlation function such that

$$\frac{n_{\mathrm{jet\,pair}}}{n_{\mathrm{total\,pair}}} = \frac{\sum A_o J(\Delta\phi)}{\sum C(\Delta\phi)}. \tag{38}$$

Such pair fractions are shown as a function of $p_{T,\mathrm{assoc}}$ for a trigger hadron of $3.0 < p_T < 5.0$ GeV/c and a centrality selection of 0−80% in Fig. 19. The results, shown for both

TABLE XII. Same as Table XI, but for neutral pion triggers.

$\langle p_{T,\mathrm{trig}}\rangle$ (GeV/c)	σ_{near} (rad)	σ_{far} (rad)
5.39	0.207 ± 0.007	0.409 ± 0.025
6.40	0.151 ± 0.008	0.304 ± 0.034
7.66	0.144 ± 0.012	0.295 ± 0.035

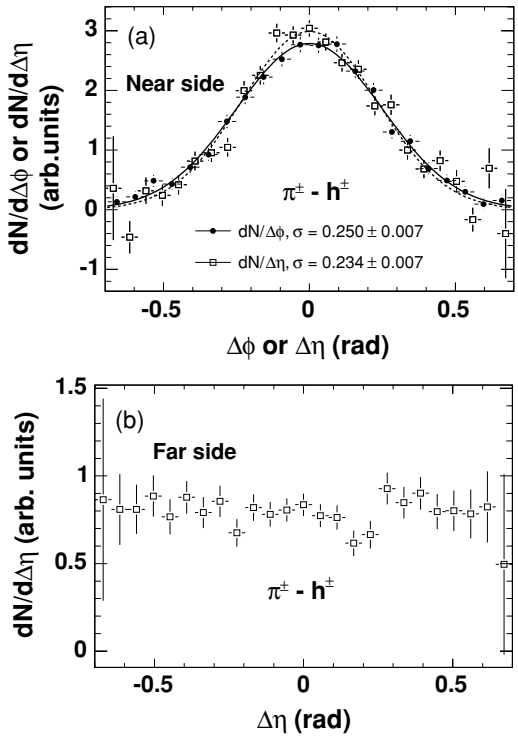

FIG. 17. Jet shapes in $\Delta\phi$ and $\Delta\eta$ from $\pi^{\pm} - h^{\pm}$ correlation with $5 < p_{T,\mathrm{trig}} < 10$ GeV/c and $1.0 < p_{T,\mathrm{assoc}} < 2.0$ GeV/c from minimum-bias d + Au collisions. (a) Near-side jet shape in $\Delta\phi$ and $\Delta\eta$. (b) Far-side jet shape in $\Delta\eta$.

the near- and far-side jets, indicate an increase in the average fraction of jet-correlated particle pairs with p_T as might be expected if jet fragmentation becomes the dominant particle production mechanism as p_T is increased.

The pair fraction is multiplied by the ratio $n_{\mathrm{pairs}}/n_{\mathrm{trig}}n_{\mathrm{assoc}}$ to obtain

$$\frac{n_{\mathrm{jet\,pair}}}{n_{\mathrm{trig}}n_{\mathrm{assoc}}} = \frac{n_{\mathrm{jet\,pair}}}{n_{\mathrm{total\,pair}}} \times \frac{n_{\mathrm{pairs}}}{n_{\mathrm{trig}}n_{\mathrm{assoc}}}, \tag{39}$$

where n_{pairs} denotes the average number of detected particle pairs per event, and n_{trig} and n_{assoc} are the detected

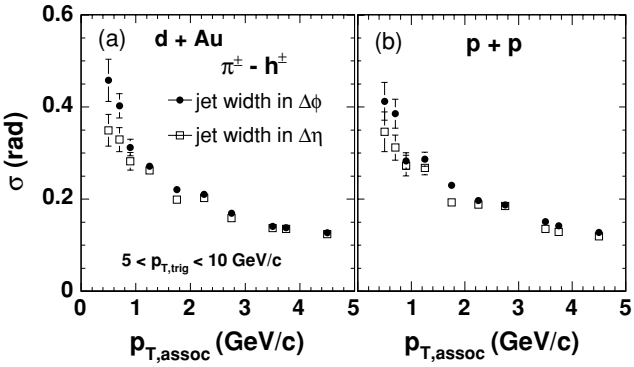

FIG. 18. Comparison of jet widths as function of $p_{T,\mathrm{assoc}}$ in $\Delta\phi$ and $\Delta\eta$ from $\pi^{\pm} - h^{\pm}$ correlation with $5 < p_{T,\mathrm{trig}} < 10$ GeV/c. (a) Results for d + Au. (b) Results for $p + p$. Bars are statistical errors.

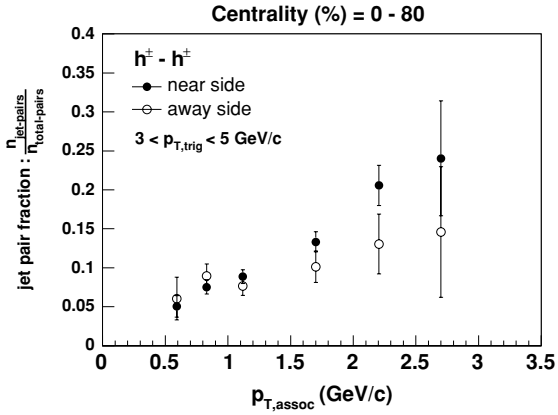

FIG. 19. Average jet pair fraction per event as a function of $p_{T,\mathrm{assoc}}$. Results are shown for the trigger hadron selection $3.0 < p_T < 5.0$ GeV/c from $d+$Au collisions and a centrality of 0−80%. Bars are statistical errors.

single-particle yields per event for trigger and associated particles, respectively. This gives the average number of jet-correlated pairs per event over the combinatoric background $n_{\mathrm{jet\,pair}}/n_{\mathrm{trig}}n_{\mathrm{assoc}}$. The conditional per-trigger yield, $n_{\mathrm{jet\,pair}}/n_{\mathrm{trig}}$, is obtained via multiplication by the efficiency corrected single-particle yield $n_{\mathrm{assoc}}^{\mathrm{eff\text{-}corr.}}$ for the selected associated p_T bin of interest;

$$\frac{n_{\mathrm{jet\,pair}}}{n_{\mathrm{trig}}} = \frac{n_{\mathrm{jet\,pair}}}{n_{\mathrm{trig}}n_{\mathrm{assoc}}} \times n_{\mathrm{assoc}}^{\mathrm{eff\text{-}corr.}}. \tag{40}$$

The per-trigger yields for hadron triggers [found using Eq. (40)] are corrected for the azimuthal acceptance and tracking efficiency but are reported within the PHENIX η acceptance for the central arms, i.e., no $R(\Delta\eta)$ correction is applied to the hadron-triggered conditional yields.

Figure 20 plots the near- and far-side invariant conditional yields extracted via Eq. (40) for different trigger p_T selections as indicated. An approximate exponential decrease with p_T is observed, i.e., there are more low-p_T particles associated with each high-p_T trigger hadron. The data are tabulated in Tables XIII and XIV.

In Fig. 21, the conditional yields for identified pion triggers are plotted as a function of $p_{T,\mathrm{assoc}}$ for both near- and far-side correlations. For this high-p_T data, the conditional yields are extracted from the fits to the data in Figs. 13 and 14 using Eq. (26), then corrected for pair efficiency in $\Delta\eta$ using Eqs. (24) and (25). The conditional yields are tabulated in Tables XV and XVI.

TABLE XIII. Near- and far-side conditional yields as a function of $p_{T,\mathrm{assoc}}$ for charged hadron triggers (2.5−4 GeV/c) and associated charged hadrons from $d+$Au collisions.

$\langle p_{T,\mathrm{assoc}}\rangle$ (GeV/c)	dN/dp_T^{near}	dN/dp_T^{far}
0.592	0.327 ± 0.092	0.383 ± 0.182
0.831	0.307 ± 0.045	0.339 ± 0.079
1.190	0.174 ± 0.018	0.158 ± 0.024
1.702	0.081 ± 0.009	0.066 ± 0.014
2.205	0.042 ± 0.006	0.028 ± 0.009

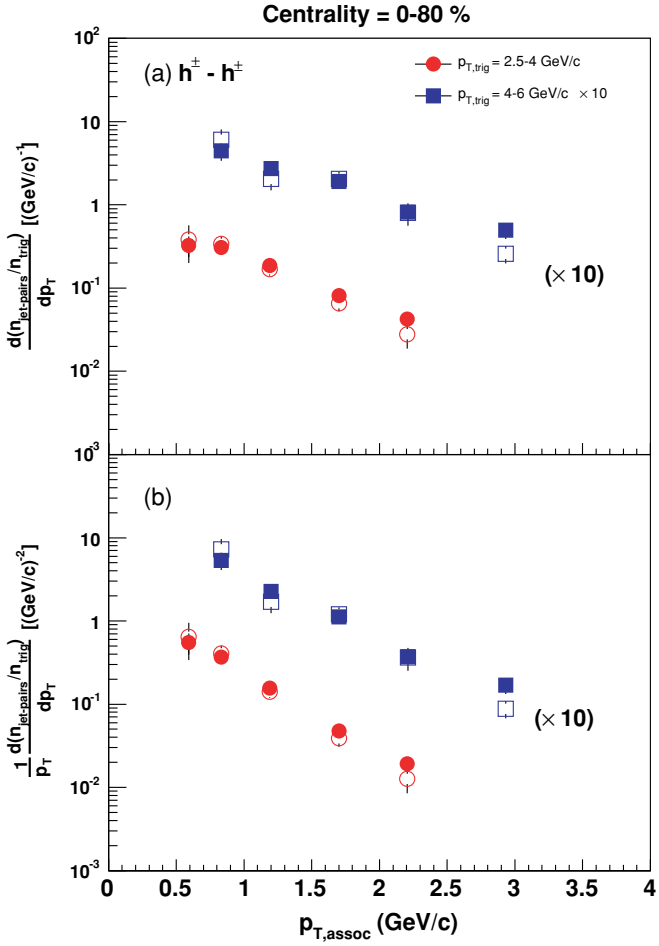

FIG. 20. (Color online) Per-trigger yield (a) and invariant conditional yield (b) as a function of $p_{T,\mathrm{assoc}}$ for the trigger hadron ranges shown. Closed points are the near-side yields; open points are the far-side yields. Centrality range is 0−80% in $d+$Au collisions. Yields are corrected for efficiency and reported in the PHENIX η acceptance. Bars are statistical errors.

The agreement between the two pion-triggered data sets is good, which indicates that the jet fragmentation function is independent of whether a neutral pion or a charged pion trigger is used. The difference in the magnitudes of the far- and near-side yields reflects the fact that the far-side correlation measure a hadron triggered effective fragmentation while the near-side correlation measures dihadron fragmentation.

The conditional yields presented in Figs. 20 and 21 can be considered as the basic information, whereas the near and far

TABLE XIV. Same as Table XIII, but for charged hadron triggers (4−6 GeV/c).

$\langle p_{T,\mathrm{assoc}}\rangle$ (GeV/c)	dN/dp_T^{near}	dN/dp_T^{far}
0.831	4.437 ± 1.040	6.031 ± 2.010
1.200	2.725 ± 0.506	2.051 ± 0.562
1.700	1.907 ± 0.278	2.046 ± 0.447
2.210	0.819 ± 0.152	0.804 ± 0.244
2.931	0.497 ± 0.107	0.258 ± 0.061

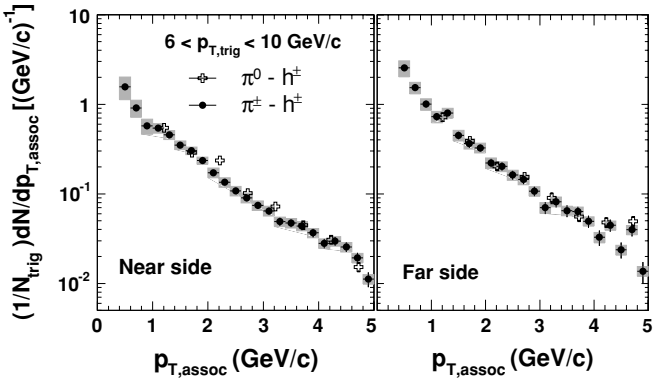

FIG. 21. Conditional yield as function of $p_{T,\mathrm{assoc}}$ for near- and far-side correlations from minimum-bias $d+$ Au collisions. Bars are statistical errors. Shaded boxes represent the total systematic error on each point.

dN/dx_E distributions in Sec. IV B have a closer relationship to parton fragmentation functions, as described in Sec. II.

Since multiple scattering should increase with centrality, we examine whether these jet characteristics exhibit any centrality dependence. Figure 22 reports on widths and conditional yields in the PHENIX η acceptance for dihadron correlations with a trigger hadron in the range $2.5 < p_{T,\mathrm{trig}} < 4$ GeV/c. The data are tabulated in Tables XVII and XVIII. Centrality-dependent widths for the $\pi^0 - h^{\pm}$ correlations are shown in Fig. 23 for a mean $\pi^0 p_T$ of approximately 5.4 GeV/c. The data for the widths are tabulated in Table XIX, while the yields can be found in Table XX.

Neither the widths nor the per-trigger yields change significantly with centrality, indicating that the influence of multiple scattering on jet properties is small in this region. This work is extended in Sec. IV D, where we present the centrality dependence of various jet-structure observables.

TABLE XV. Near- and far-side conditional yields as a function of $p_{T,\mathrm{assoc}}$ for charged pion triggers (5−10 GeV/c) and associated charged hadrons from minimum-bias $d+$ Au collisions.

$\langle p_{T,\mathrm{assoc}}\rangle$ (GeV/c)	dN/dp_T^{near}	dN/dp_T^{far}
0.5	1.57 ± 0.083	2.54 ± 0.15
0.7	0.911 ± 0.049	1.53 ± 0.13
0.9	0.574 ± 0.031	1.00 ± 0.087
1.1	0.542 ± 0.032	0.727 ± 0.068
1.3	0.456 ± 0.026	0.801 ± 0.058
1.5	0.351 ± 0.022	0.451 ± 0.044
1.7	0.303 ± 0.018	0.365 ± 0.038
1.9	0.235 ± 0.015	0.327 ± 0.031
2.1	0.172 ± 0.012	0.222 ± 0.025
2.3	0.135 ± 0.010	0.203 ± 0.022
2.5	0.108 ± 0.008	0.162 ± 0.018
2.7	0.0905 ± 0.0075	0.145 ± 0.017
2.9	0.0742 ± 0.0064	0.107 ± 0.013
3.1	0.0645 ± 0.0059	0.070 ± 0.011
3.3	0.0490 ± 0.0052	0.0819 ± 0.0113
3.5	0.0473 ± 0.0047	0.0647 ± 0.0097
3.7	0.0439 ± 0.0045	0.0636 ± 0.0084
3.9	0.0367 ± 0.0040	0.0495 ± 0.0075
4.1	0.0281 ± 0.0034	0.0327 ± 0.0064
4.3	0.0297 ± 0.0034	0.0446 ± 0.0068
4.5	0.0256 ± 0.0031	0.0238 ± 0.0048
4.7	0.0192 ± 0.0027	0.0397 ± 0.0061
4.9	0.0112 ± 0.0021	0.0137 ± 0.0036

TABLE XVI. Same as Table XV, but for neutral pion triggers.

$\langle p_{T,\mathrm{assoc}}\rangle$ (GeV/c)	dN/dp_T^{near}	dN/dp_T^{far}
1.21	0.545 ± 0.035	0.718 ± 0.076
1.71	0.289 ± 0.014	0.389 ± 0.030
2.21	0.236 ± 0.009	0.203 ± 0.018
2.72	0.102 ± 0.006	0.155 ± 0.012
3.22	0.0724 ± 0.0049	0.090 ± 0.012
3.73	0.0448 ± 0.0039	0.0560 ± 0.0071
4.23	0.0308 ± 0.0029	0.0481 ± 0.0058
4.72	0.0152 ± 0.0017	0.0495 ± 0.0060

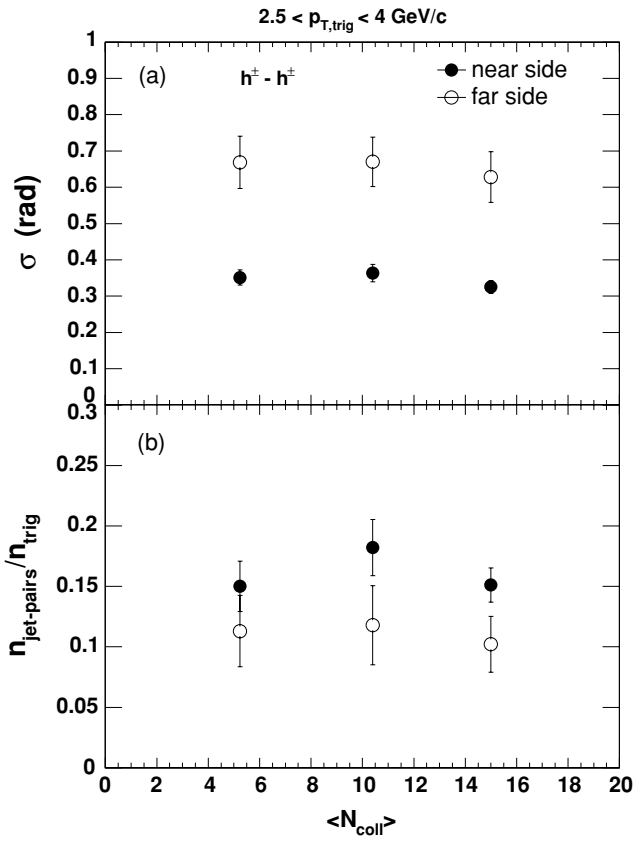

FIG. 22. Near- and far-side widths and conditional yields in the PHENIX pseudorapidity acceptance for several centrality selections from $d+$ Au collisions. Results are shown for the trigger hadron selection $2.5 < p_T < 4.0$ GeV/c and the associated p_T range of $1 < p_T < 2.5$ GeV/c. Bars are statistical errors.

TABLE XVII. Near- and far-side widths as a function of N_{coll} for charged hadron triggers (2.5−4 GeV/c) and associated charged hadrons (1–2.5 GeV/c) from d + Au collisions.

Centrality	σ_{near}(rad)	σ_{far}(rad)
0−20%	0.351 ± 0.021	0.669 ± 0.072
20−40%	0.364 ± 0.024	0.670 ± 0.068
40−80%	0.325 ± 0.018	0.628 ± 0.070

B. Jet properties in minimum-bias d + Au collisions

From the angular widths and yields discussed in the previous section, we calculate the following quantities that characterize the jet structures: transverse momentum of hadrons with respect to the jet (j_T), the dijet acoplanarity $\langle \sin^2(\phi_{jj}) \rangle$, and the dN/dx_E distributions. These quantities are first presented for minimum-bias d + Au collisions, which have the highest statistical precision, and are then compared with results from $p + p$ in Sec. IV C.

Figure 24 shows the compilation of $\sqrt{\langle j_T^2 \rangle}$ values extracted from $\pi^0 - h$ and $\pi^\pm - h$ correlations, and assorted-p_T and fixed-p_T correlation results for $h - h$ at low p_T. The $\sqrt{\langle j_T^2 \rangle}$ values were calculated using Eq. (7). The systematic errors are mainly due to the uncertainties of Eq. (7) and the fitting procedure, which are about 5% (independent of p_T) and are approximately the same for all four analyses. The $\sqrt{\langle j_T^2 \rangle}$ values for $\pi^\pm - h$ and $\pi^0 - h$ indicate a steady increase at p_T below 2 GeV/c followed by a saturation around 560−640 MeV/c at $p_T > 2$ GeV/c. The initial increase is due to the seagull effect [46,47]. The approximately constant behavior of $\sqrt{\langle j_T^2 \rangle}$ above 2 GeV/c is consistent with the scaling behavior of the fragmentation functions. The $\sqrt{\langle j_T^2 \rangle}$ results from the $h - h$ correlation analyses have a similar increase and saturation behavior. They seem to reach a slightly higher plateau value at a lower p_T (around 1.5 GeV/c).

A combined fit based on $\sqrt{\langle j_T^2 \rangle}$ data points at $p_T > 2$ GeV/c gives a plateau value of $\sqrt{\langle j_T^2 \rangle} = 0.64 \pm 0.02(\text{stat}) \pm 0.04(\text{sys})$ GeV/c for minimum-bias d + Au collisions.

TABLE XVIII. Same as Table XVII, but for near- and far-side conditional yields.

Centrality	dN/dp_T^{near}	dN/dp_T^{far}
0–20%	0.150 ± 0.021	0.113 ± 0.030
20–40%	0.182 ± 0.023	0.118 ± 0.033
40–80%	0.151 ± 0.014	0.102 ± 0.023

TABLE XIX. Near- and far-side widths as a function of centrality for neutral pion triggers (5−10 GeV/c) and associated charged hadrons (2–3 GeV/c) from d + Au collisions.

Centrality	σ_{near}(rad)	σ_{far}(rad)
0–20%	0.199 ± 0.009	0.387 ± 0.024
20–40%	0.195 ± 0.009	0.401 ± 0.031
40–88%	0.190 ± 0.008	0.376 ± 0.024

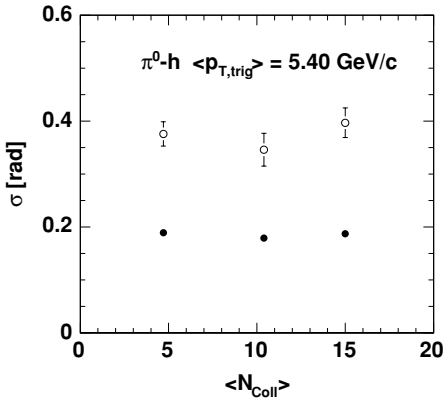

FIG. 23. Near- and far-side widths for several centrality selections from d + Au collisions. Results are shown for $\pi^0 - h$ correlations with the trigger π^0 $5 < p_T < 10$ GeV/c and the associated p_T range of $2 < p_T < 3$ GeV/c. Bars are statistical errors.

A key quantity that provides information on multiple scattering in the cold nuclear medium is $\langle \sin^2(\phi_{jj}) \rangle$, where ϕ_{jj} is the azimuthal angle between the jet axes. As described in Sec. II, we calculate $\langle \sin^2 \phi_{jj} \rangle$ from the experimental values of the near- and far-side widths [Eq. (13)]. Figure 25 shows $\langle \sin^2 \phi_{jj} \rangle$ as function of $p_{T,assoc}$ for high-p_T pion triggers. We observe that the rms of the sine of the angle between the jet axes, $\langle \sin^2 \phi_{jj} \rangle$, decreases as higher-$p_T$ associated particles are selected. There is good agreement between the two data sets. Figure 26 plots $\langle \sin^2 \phi_{jj} \rangle$ as a function of $p_{T,trig}$, where a similar decrease with p_T is observed.

In the next section we will calculate the quadrature difference $\langle \sin^2 \phi_{jj} \rangle$ between d + Au and $p + p$ collisions and use that to quantify the affect of additional final-state scattering in d + Au collisions.

In Sec. II we defined the near and far-side p_{out}. With this observable, it is possible to move beyond calculating means or rms values, and hence the p_{out} distribution potentially carries more information about the dijet acoplanarity. The measured p_{out} distributions for $\pi^\pm - h^\pm$ are shown in Fig. 27 for the near and far sides. The far-side p_{out} has a broader distribution than the near-side p_{out}, reflecting the fact that k_T is larger than j_T. The p_{out} distributions have a power law tail, possibly due to strong radiative processes driving large values of p_{out}.

In Sec. IV A we reported the yields of associated hadrons per trigger particle, or the conditional yield. A more comprehensive way of quantifying the fragmentation function is to plot the conditional yields as a function of x_E. This is shown in Fig. 28 for $\pi^\pm - h$ and $\pi^0 - h$.

TABLE XX. Same as Table XIX, but for near- and far-side conditional yields.

Centrality	dN/dp_T^{near}	dN/dp_T^{far}
0–20%	0.0816 ± 0.0037	0.116 ± 0.008
20–40%	0.0947 ± 0.0045	0.141 ± 0.011
40–88%	0.0967 ± 0.0043	0.144 ± 0.009

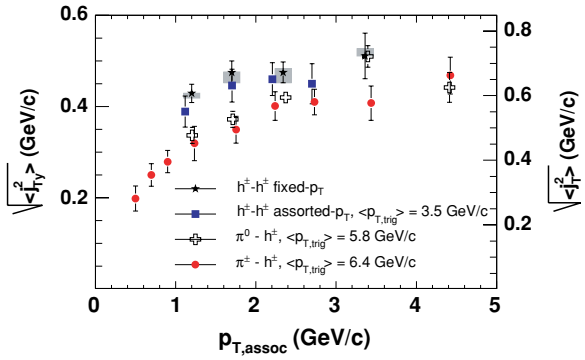

FIG. 24. (Color online) Extracted $\sqrt{\langle j_T^2 \rangle}$ for minimum-bias d + Au collisions from all four dihadron correlations. Trigger p_T ranges are 3–5, 5–10, and 5–10 GeV/c, respectively, for $h^{\pm} - h^{\pm}$, $\pi^0 - h^{\pm}$, and $\pi^{\pm} - h^{\pm}$ assorted-p_T correlations. Statistical and systematic errors are combined for the assorted-p_T correlations; the fixed-p_T correlation shows the systematic error separately as shaded boxes.

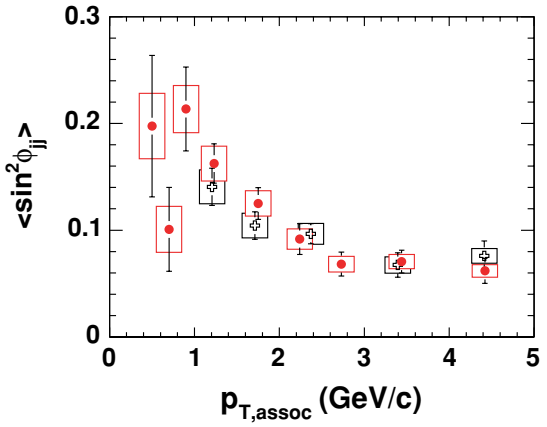

FIG. 25. (Color online) $\langle \sin^2 \phi_{jj} \rangle$ for minimum-bias d + Au collisions as function of associated particle p_T for $\pi^{\pm} - h^{\pm}$ (filled circles) and $\pi^0 - h^{\pm}$ (open crosses) correlations where the trigger particles have a p_T between 5 and 10 GeV/c. Data points are plotted at the mean $p_{T,\mathrm{assoc}}$. Bars are statistical errors. Boxes represent the total systematic error on each point.

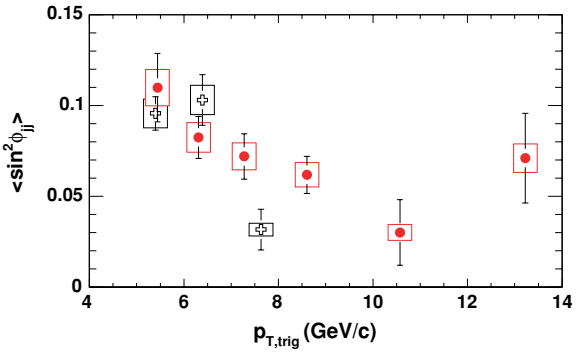

FIG. 26. (Color online) Same as Fig. 25, but as function of trigger particle p_T.

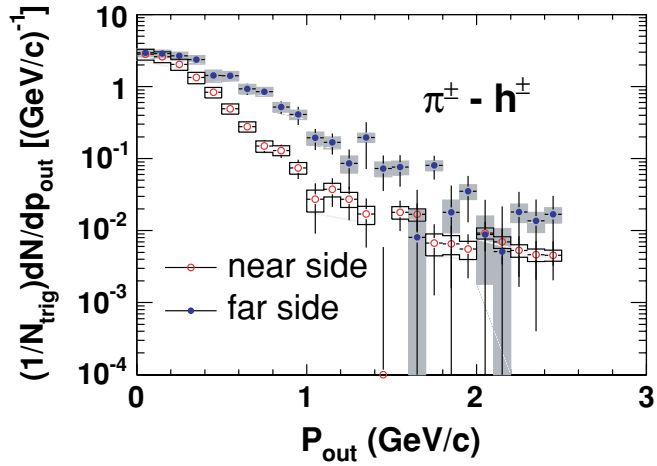

FIG. 27. (Color online) Near- and far-side p_{out} distributions for minimum-bias d + Au collisions obtained from $\pi^{\pm} - h^{\pm}$ correlation. The trigger is $5 < p_{T,\mathrm{trig}} < 10$ GeV/c, the associated particle is $0.5 < p_{T,\mathrm{assoc}} < 5.0$ GeV/c. Bars are statistical errors. Boxes represent the total systematic error on each point.

Previously, in ISR experiments, the slope of the x_E distribution had been determined to be around 5.3 [26]. In Fig. 29, the conditional yields as a function of x_E are plotted for the trigger p_T range of 5–6 GeV/c. In order to compare data with the previous ISR results, we determine the exponential inverse slope for $0.3 < x_E < 0.7$ and obtain the inverse slope parameter of 6.0 ± 0.3 in the near side and 7.1 ± 0.5 in the far side. The near-side x_E inverse slope is smaller than that for the far side, reflecting the difference between dihadron fragmentation and single hadron fragmentation. By requiring a trigger particle on the near side, one reduces the jet energy available for fragmenting to the second hadrons, and consequently a smaller inverse slope occurs for the near side. Note, however, that the x_E distributions do not have pure exponential shape, and the fitted inverse slope is sensitive to the fitting ranges.

It is well known that fragmentation functions $D(z)$ approximately scale in e^+e^- or $p + p$ collisions, i.e., they are

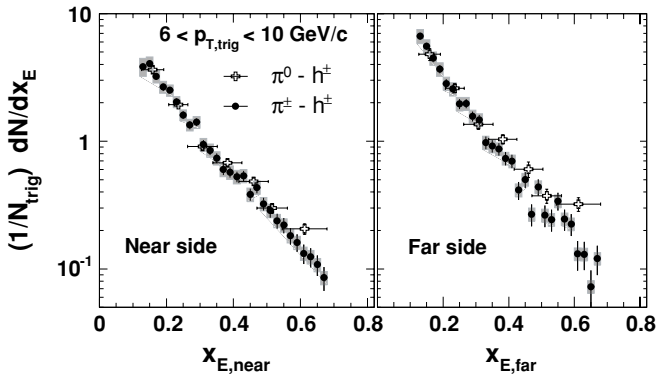

FIG. 28. Conditional yield as a function of x_E for near- and far sides for $\pi^{\pm} - h^{\pm}$ and $\pi^0 - h^{\pm}$ from minimum-bias d + Au collisions. Bars are statistical errors. Boxes represent the total systematic error on each point.

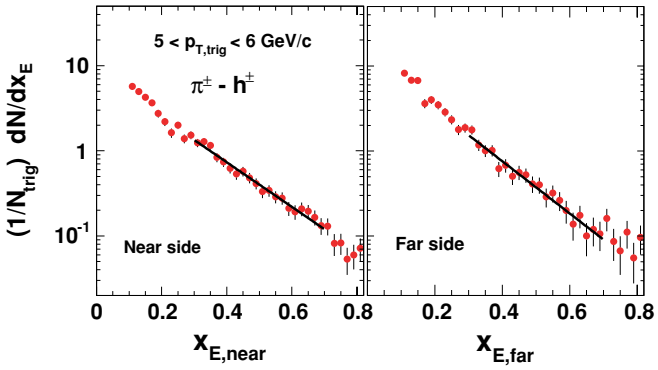

FIG. 29. (Color online) Conditional yield as a function of x_E for near- and far-side correlations for $\pi^{\pm} - h^{\pm}$ correlations from minimum-bias d + Au collisions. Trigger pions are $5 < p_{T,\mathrm{trig}} < 6$ GeV/c, and the black lines are fits to an exponential function for $0.3 < x_E < 0.7$. Bars are statistical errors.

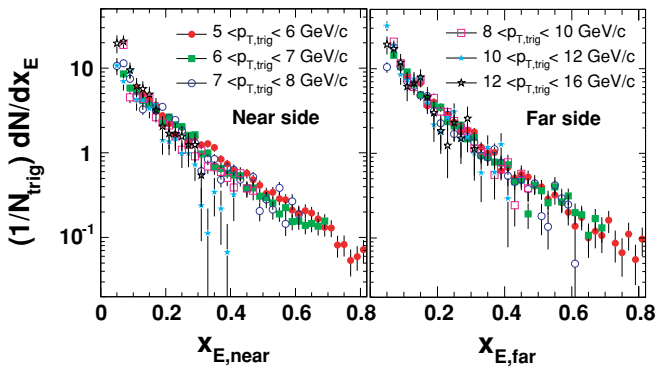

FIG. 30. (Color online) Conditional yield as a function of x_E for near- and far-side correlations for $\pi^{\pm} - h^{\pm}$ correlations for several different trigger p_T's for minimum-bias d + Au collisions. Bars are statistical errors.

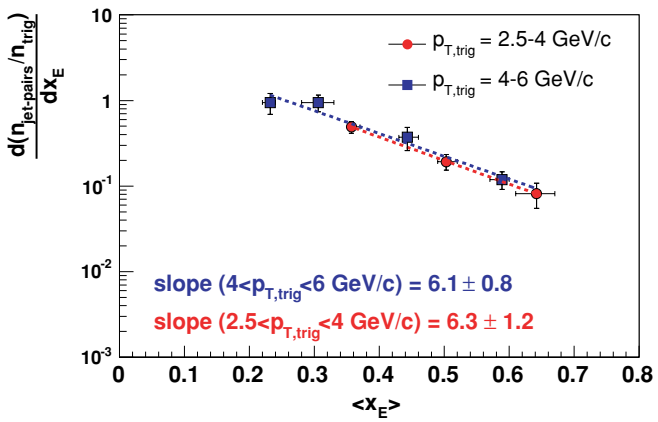

FIG. 31. (Color online) Conditional yield as a a function of $\langle x_E \rangle$ for the far-side $h - h$ correlations for two trigger p_T ranges. Dashed lines are exponential fits to the data. Bars are statistical errors.

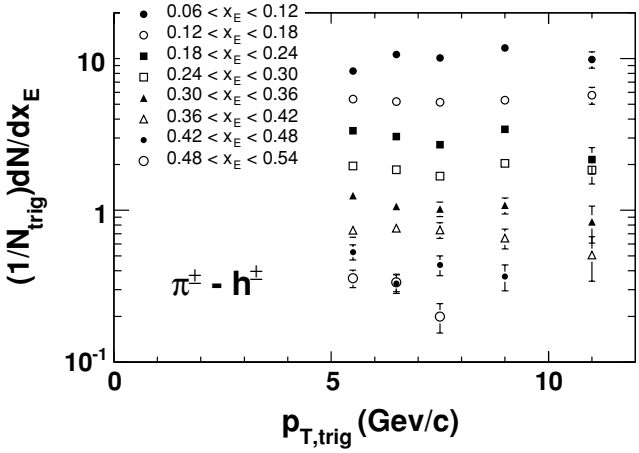

FIG. 32. Far-side conditional yield as a function of $p_{T,\mathrm{trig}}$ for different ranges of x_E for $\pi^{\pm} - h^{\pm}$ correlation for minimum-bias d + Au collisions. Bars are statistical errors.

independent of jet energy. To check whether this is still true in d + Au collisions, we plot in Fig. 30 the conditional yield as a function of x_E for different ranges of trigger p_T from $\pi^{\pm} - h^{\pm}$ correlations. All curves fall on top of each other, indicating a universal behavior of the jet fragmentation function.

At lower p_T, we have x_E distributions from the $h - h$ correlations. In Fig. 31, far-side conditional yields as obtained from charged hadron correlation functions are plotted versus $\langle x_E \rangle$. Here, $\langle x_E \rangle$ has been calculated from the $\langle p_{T,\mathrm{trig}} \rangle$, $\langle p_{T,\mathrm{assoc}} \rangle$ and extracted angular widths. Results are shown for two trigger p_T ranges, $2.5 < p_{T,\mathrm{trig}} < 4$ GeV/c and $4 < p_{T,\mathrm{trig}} < 6$ GeV/c, respectively. The slopes extracted are 6.3 ± 1.2 for the lower trigger p_T range and 6.1 ± 0.8 for the higher trigger p_T window. Within the statistics of the charged hadron data set, we do not observe a strong sensitivity of the slope of the x_E distributions to the trigger p_T.

A direct way of quantifying the scale dependence of the x_E distribution is to plot the far-side conditional yields versus $p_{T,\mathrm{trig}}$ for a fixed range of x_E. This is shown in Fig. 32, where the conditional yields are found to be independent of $p_{T,\mathrm{trig}}$, i.e., there is no significant deviation from scaling. We will quantify any scaling violation in these data when we compare these x_E distributions from d + Au to distributions from $p + p$ collisions in Sec. IV C.

C. Comparison between d + Au and $p + p$

As discussed in Sec. I, multiple scattering in the cold nuclear medium may broaden the far-side correlation and possibly modify the fragmentation properties. In the previous section, we presented the measured jet structures from minimum-bias d + Au collisions. In this section, we compare that data to results from $p + p$ collisions. The goal is to establish the extent to which the nuclear medium modifies the properties of jets.

Figure 33 compares the extracted $\sqrt{\langle j_T^2 \rangle}$ values as functions of $p_{T,\mathrm{assoc}}$ from d + Au and $p + p$ collisions. The $\sqrt{\langle j_T^2 \rangle}$ values show no change from $p + p$ to d + Au collisions.

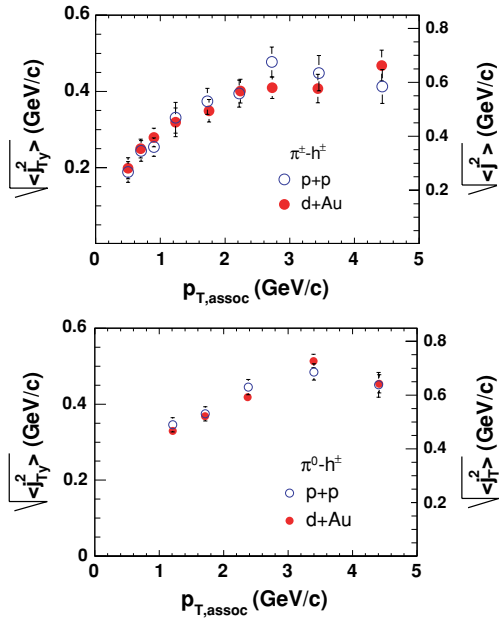

FIG. 33. (Color online) Comparison of $\sqrt{\langle j_T^2 \rangle}$ values between $d+$ Au and $p+p$ for $\pi^{\pm}-h^{\pm}$ and $\pi^0-h^{\pm}$ correlations. Trigger pion range is 5–10 GeV/c. Bars are statistical errors. Systematic errors are given in Table III.

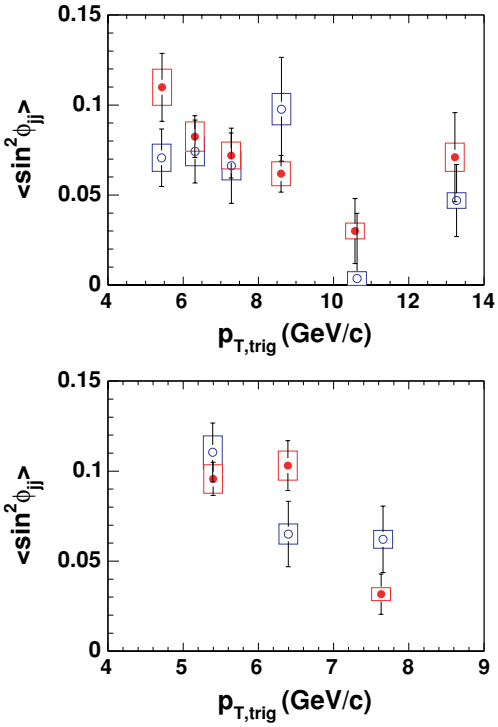

FIG. 34. (Color online) Comparison of $\langle \sin^2(\phi_{jj}) \rangle$ values between $d+$ Au (filled circles) and $p+p$ (open circles) for $\pi^{\pm}-h^{\pm}$ correlations (top panel) and $\pi^0-h^{\pm}$ correlations (lower panel). Associated hadron range is $2 < p_{T,\mathrm{assoc}} < 4.5$ GeV/c for the charged pion triggers and $2.5 < p_{T,\mathrm{assoc}} < 5$ GeV/c for the neutral pions. Bars are statistical errors. Boxes represent the total systematic error on each point.

Similarly, the $\langle \sin^2(\phi_{jj}) \rangle$ values shown in Fig. 34 for $d+$ Au are comparable to those from $p+p$ within errors, although the values from $d+$ Au collisions are systematically higher for $\pi^{\pm}-h^{\pm}$. Since there is no strong difference between the $d+$Au and $p+p$ results, there is little indication for increased multiple scattering in the $d+$ Au final state.

Any additional radiation can be quantified by calculating the point-by-point quadrature difference in $\langle \sin^2 \phi_{jj} \rangle$ between $d+$ Au and $p+p$ collisions. As shown in Fig. 35, this difference is consistent with zero. The average value for π^0-h is $\Delta\langle \sin^2 \phi_{jj} \rangle = -0.005 \pm 0.012(\mathrm{stat}) \pm 0.003(\mathrm{sys})$; for $\pi^{\pm}-h$, $\Delta\langle \sin^2 \phi_{jj} \rangle = 0.011 \pm 0.011(\mathrm{stat}) \pm 0.010(\mathrm{sys})$. Combining the two data sets, we find $\Delta\langle \sin^2 \phi_{jj} \rangle = +0.004 \pm 0.008(\mathrm{stat}) \pm 0.009(\mathrm{sys})$.

Figure 36 shows the comparison of the p_{out} distribution between central $d+$Au and $p+p$ from $\pi^{\pm}-h^{\pm}$ correlations; no apparent differences are observed in either the near or far side. This is consistent with the observation that both $\sqrt{\langle j_T^2 \rangle}$ and $\langle \sin^2 \phi_{jj} \rangle$ are similar between $d+$ Au and $p+p$.

A second set of comparisons between $d+$ Au and $p+p$ collisions is the number of hadrons in the near- and far-angle jet structures associated with a high-p_T trigger. Figure 37 shows the comparison of the conditional yield as function of x_E and no apparent difference between $d+$ Au and $p+p$ collisions is observed for either the near or far side.

In the previous section, we examined the level of scaling violations in the far-side dN/dx_E distribution for $d+$ Au collisions by plotting different x_E ranges as a function of $p_{T,\mathrm{trig}}$ (Fig. 32). The comparable plot for $p+p$ collisions is shown in Fig. 38. For both $d+$ Au and $p+p$ collisions, the amount of scaling violations, i.e., the dependence of dN/dx_E on $p_{T,\mathrm{trig}}$, can be quantified by fitting the data in each x_E range with a straight line as a function of $p_{T,\mathrm{trig}}$, that is,

$$\frac{dN}{dx_E} = \frac{dN}{dx_{E\,0}}(1+\beta p_T). \tag{41}$$

The fitted slopes β represent the fractional change in dN/dx_E per GeV/c and are shown in Fig. 39. For the $d+$ Au data,

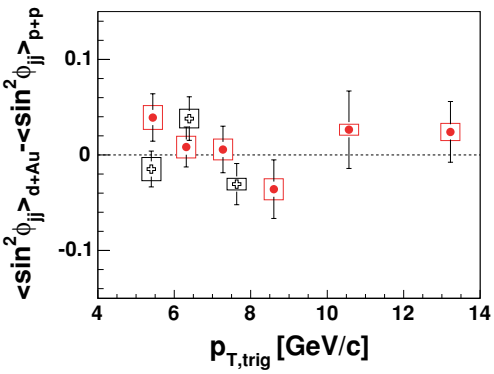

FIG. 35. (Color online) Quadrature difference between minimum-bias $d+$ Au and $p+p$ $\langle \sin^2 \phi_{jj} \rangle$ values. Closed circles are $\pi^{\pm}-h$ values and the open circles are π^0-h values. Bars are statistical errors. Boxes represent the total systematic error on each point.

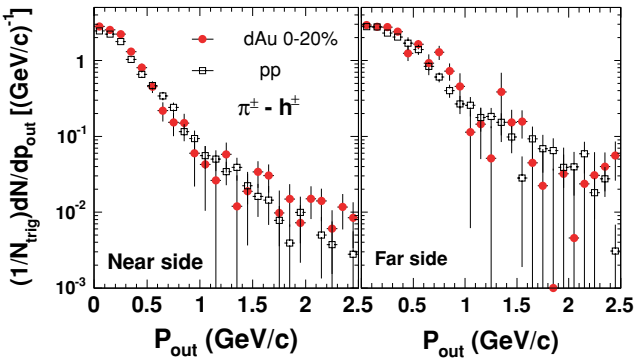

FIG. 36. (Color online) Comparison of the $p_{\rm out}$ distribution at the near and far sides between central $d+$Au collisions and $p+p$ collisions. Results are obtained for $\pi^{\pm}-h^{\pm}$ correlations with the associated hadron range $0.5 < p_{T,\rm assoc} < 5$ GeV/c and trigger pion range of $5 < p_{T,\rm trig} < 10$ GeV/c. Bars are statistical errors.

β is consistent with zero, i.e., there is no significant scaling violation across the whole x_E range, while there may be a slight scaling violation at high x_E for the $p+p$ data. On a point-by-point basis, there is no systematic difference between the $d+$Au and $p+p$ data.

Taken as a whole, all the results presented in this section indicate that the presence of the cold nuclear medium causes no significant change in jet fragmentation between $d+$Au and $p+p$ collisions. In addition, no strong evidence supports an increase in $\langle\sin^2(\phi_{jj})\rangle$ due to multiple scattering in the Au nucleus. Using the minimum-bias $d+$Au data has the advantage of the highest statistical precision. In the next section, we examine whether there is any change in jet structures as a function of collision centrality in $d+$Au, i.e., we split the statistics into a few centrality classes to increase the lever arm of the nuclear thickness function.

D. Centrality dependence

As discussed in Sec. I, $\langle\sin^2(\phi_{jj})\rangle$ is expected to increase as $d+$Au collisions become more central because of increased multiple scattering. Models of multiple scattering [12] predict that the increase in $\langle k_T^2\rangle$ is proportional to $T_A(b)$, the nuclear

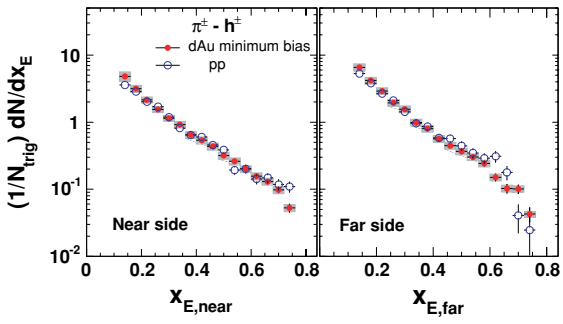

FIG. 37. (Color online) Comparison of the x_E distribution from $\pi^{\pm}-h^{\pm}$ correlations at the near and far sides between minimum-bias $d+$Au collisions and $p+p$ collisions. Triggers are $\pi^{\pm}$ from 5−10 GeV/c. Bars are statistical errors. Boxes represent the total systematic error on each point.

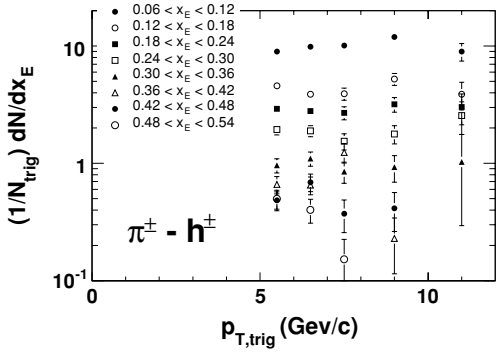

FIG. 38. Far-side conditional yield as function of $p_{T,\rm trig}$ for different ranges of x_E from $p+p$ collisions; triggers are $\pi^{\pm}$ from 5−10 GeV/c. Bars are statistical errors.

thickness function. We are not aware of predictions of how $\langle\sin^2(\phi_{jj})\rangle$ will change with centrality, but note that any increase in $\langle k_T^2\rangle$ will also increase $\langle\sin^2(\phi_{jj})\rangle$.

To probe this physics, we measured angular correlations in three centrality bins for $d+$Au collisions (0–20%, 20–40%, and 40–88%) to extract angular widths of the jet structures and hence $\sqrt{\langle j_T^2\rangle}$ and $\langle\sin^2(\phi_{jj})\rangle$. Figure 40 shows the independent data sets of $\langle\sin^2(\phi_{jj})\rangle$ including results from $p+p$ collisions and the three centrality classes from $d+$Au collisions.

All the $\langle\sin^2(\phi_{jj})\rangle$ data in Fig. 40 have been simultaneously fit with the following linear equation in $T_A(b)$:

$$\langle\sin^2(\phi_{jj})\rangle = \langle\sin^2(\phi_{jj})\rangle_0(1 + a_{\rm frac}T_A(b)). \qquad (42)$$

The slope parameter $a_{\rm frac}$ is assumed to be common to all data sets, while the pre-factors $\langle\sin^2(\phi_{jj})\rangle_0$ depend on the p_T of the trigger and associated particles. The extracted slope $a_{\rm frac} = -0.01 \pm 0.40$ mb with χ-squared per degree of freedom, $\chi^2/\nu = 27/22$. This slope is consistent with zero; i.e., we do not observe any significant increase in $\langle\sin^2(\phi_{jj})\rangle$ with centrality.

This can be compared to predictions from Hwa and Yang [16], who assume no increase in k_T with centrality to reproduce the Cronin effect data at RHIC, and Qiu and Vitev [14], who calculate

$$\langle k_T^2\rangle_{\rm dijet} = 2\langle k_T^2\rangle_{\rm vac} + \frac{0.72}{T_{A\,\rm minbias}}T_A(b). \qquad (43)$$

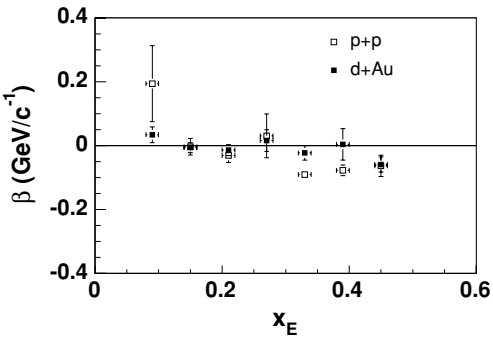

FIG. 39. Fitted fractional change in dN/dx_E per unit $p_{T,\rm trig}$ [β in Eq. (41)] of the far-side conditional yield for different ranges of x_E. Bars are statistical errors.

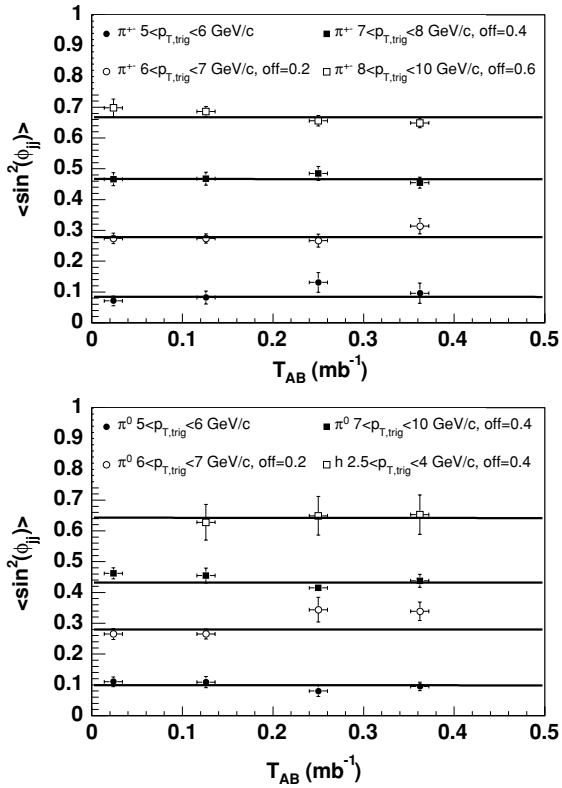

FIG. 40. Measured values of $\langle \sin^2(\phi_{jj})\rangle$ as a function of the nuclear thickness function $T_A(b)$. Left-most points are from $p+p$ collisions; other points are from the three centrality classes in $d+$Au collisions. Data sets are offset as indicated for clarity. Top plot shows data for $\pi^{\pm}$; bottom plot, for π^0 and hadron triggered data. Lines are a simultaneous fit to all the data with Eq. (42) to extract a common fractional increase in $\langle \sin^2(\phi_{jj})\rangle$ with $T_A(b)$. Bars are statistical errors.

To gain some insight into the magnitude of Qiu and Vitev's predicted effect compared to our experimental results, we recast Eq. (43) into the same form as Eq. (42).

$$\langle k_T^2\rangle_{\rm dijet} = 2\langle k_T^2\rangle_{\rm vac}\left(1+\frac{0.72}{2\langle k_T^2\rangle_{\rm vac} T_{A\,\rm minbias}}T_A(b)\right). \quad (44)$$

Hence, their prediction for the fractional increase in $\langle k_T^2\rangle$ with $T_A(b)$ is from 0.51 to 0.72 depending on the range $0.25 < \langle k_T^2\rangle_{\rm vac} < 0.35$ (GeV/c)^2 suggested by Qiu and Vitev [14].[4] Though the predicted fractional increase is of a different quantity, it should provide an estimate of the magnitude of the fractional increase in $\langle \sin^2(\phi_{jj})\rangle$. The prediction is slightly larger than one standard deviation (statistical) from our experimental result, $a_{\rm frac} = -0.01 \pm 0.40$ mb. If the measured value for $\langle k_T^2\rangle_{\rm vac}$ at RHIC turns out to be larger than assumed by Qiu and Vitev [14], then the predicted fractional increase in Eq. (44) will be smaller.

Barnafoldi *et al.* [15] have also predicted the increase in k_T due to multiple scattering in $d+$Au collisions at RHIC. They calculated that $\langle k_T^2\rangle$ increases by $C = 0.35$(GeV/c)^2 per collision up to the first four collisions, then it saturates. Their prediction is

$$\langle k_T^2\rangle = \langle k_T^2\rangle_0\left(1+\frac{0.35}{\langle k_T^2\rangle_0}(40\times T_A)\right), \qquad T_A < 0.1,$$
$$\langle k_T^2\rangle = \langle k_T^2\rangle_0\left(1+\frac{0.35}{\langle k_T^2\rangle_0}(40\times 0.1)\right), \qquad T_A > 0.1. \quad (45)$$

Barnafoldi *et al.* do not provide values for $\langle k_T^2\rangle_0$; however, if we use the range $0.25 < \langle k_T^2\rangle_0 < 0.35$ (GeV/c)^2 suggested by Qiu and Vitev [14] then the fractional increase with T_A is 40 to 56 for $T_A < 0.1$ followed by no further increase. This rapid increase is not observable in our data set because the model saturates already in the most peripheral $d+$Au bin, where $\langle T_A\rangle = 0.11$ mb^{-1}.

As discussed in Sec. I, inelastic scattering of the hard parton in the cold medium may also increase the conditional yields (CY) of hadrons that are associated with a high-p_T trigger. Figure 41 shows the centrality dependence of the extracted CY, together with CY from $p+p$ collisions. The difference can be better illustrated by taking the ratio ($d+$Au/$p+p$) of the per-trigger yield as shown in Fig. 42. There is a possible increase in near-side particle yield for $p_T < 1$ GeV/c in the $d+$Au collisions. In other momentum ranges, there is no consistent difference between yields in $d+$Au and $p+p$ collisions. The recombination model of Ref. [22] predicted a factor of 2 increase in CY peripheral to central $d+$Au collisions which is much larger than observed in the data. A later recombination calculation by the same authors [23] using

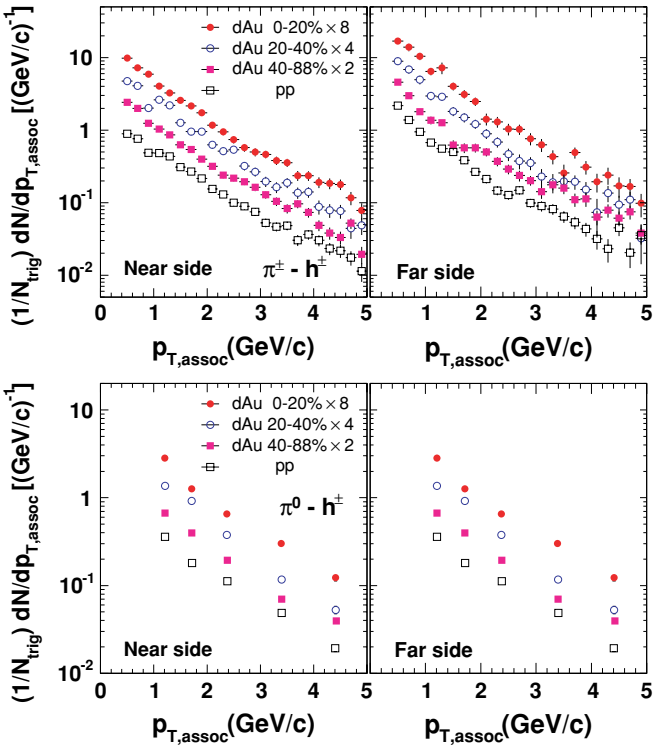

FIG. 41. (Color online) Centrality dependence of near and far CY(p_T) for $\pi^{\pm}-h^{\pm}$ and $\pi^0-h^{\pm}$ correlations. Bars are statistical errors.

[4]For 0−88% $d+$Au collisions, $T_{A\,\rm minbias} = 0.20$ mb^{-1}.

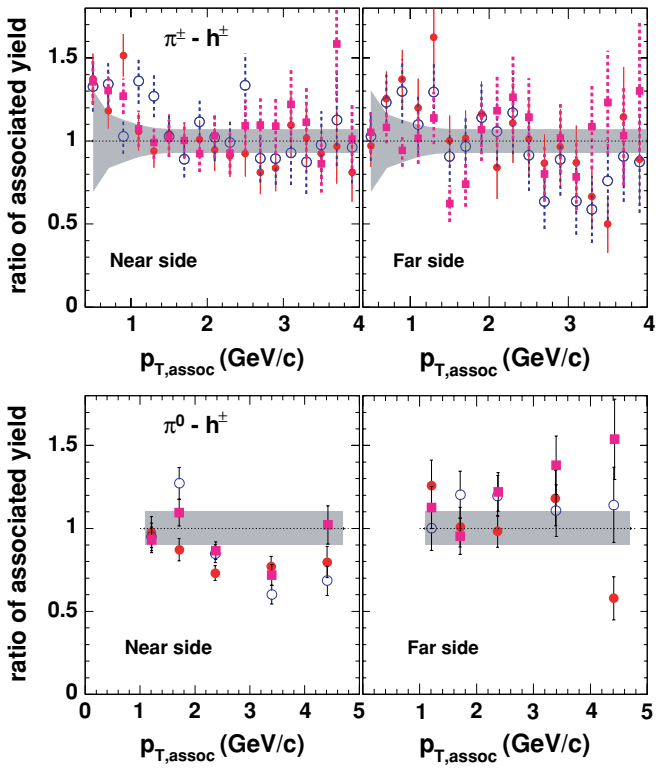

FIG. 42. (Color online) Centrality dependence related to the ratio of near and far CY(p_T) for d + Au to $p + p$ from the $\pi^{\pm} - h^{\pm}$ and $\pi^0 - h^{\pm}$ correlations. Shaded bands are the systematic errors due to normalization of the yields. Symbols are the same as in Fig. 41.

the same definition as the experiment [Eq. (16)] postdicted only a 30% increase in CY for associated particles at $p_T = 2$ GeV/c, which is comparable to or perhaps slightly larger than observed in the data.

V. CONCLUSIONS

We have measured several properties of jet fragmentation and dijet correlations using two-particle correlations with three different particle combinations: $h^{\pm} - h^{\pm}$, $\pi^0 - h^{\pm}$, and $\pi^{\pm} - h^{\pm}$. From the correlation functions, we have extracted the widths of the near- and far-angle correlations as a function of the momentum of the two hadrons, $p_{T,\mathrm{trig}}$ and $p_{T,\mathrm{assoc}}$. These widths decrease as a function of both the trigger and associated particle's momenta. From the near-angle widths, we calculate $\sqrt{\langle j_T^2 \rangle}$, the rms of the transverse momentum of fragmented hadrons with respect to the hard parton. The value of $\sqrt{\langle j_T^2 \rangle}$ saturates at $0.64 \pm 0.02(\mathrm{stat}) \pm 0.04(\mathrm{sys})$ GeV/c for $p_{T,\mathrm{assoc}} > 2$ GeV/c and is consistent with being independent of $p_{T,\mathrm{trig}}$ and trigger species. The $\sqrt{\langle j_T^2 \rangle}$ is similar for d + Au and $p + p$ collisions, which is consistent with the fragmentation process not being affected by the presence of the cold nuclear medium.

We have also compared the measured x_E distributions in d + Au collisions to the baseline distributions from $p + p$ collisions. The x_E distributions extracted from the far-angle correlations provide information on the fragmentation of a back-to-back parton triggered on a high-p_T hadron in the opposite hemisphere. The measured dN_{far}/dx_E distributions in d + Au are approximately independent of $p_{T,\mathrm{trig}}$; i.e., they scale. We have quantified the level of scaling violation by extracting the slope $\beta = d(dN/dx_E)/dp_{T,\mathrm{trig}}$ for different ranges of x_E. The slopes are consistent with zero for d + Au collisions; i.e., there is no significant scaling violation. Point by point, the scaling-violation slopes for $p + p$ collisions are not significantly different than the d + Au data. This suggests that if there is any additional gluon radiation in d + Au reactions due to multiple scattering, then it has little observable influence on the fragmentation of the hard parton.

We observe no centrality dependence of the conditional yield in d + Au, and these yields are very similar to those from $p + p$ collisions. The recombination model of Ref. [23] postdicted a 30% increase in conditional yield between d + Au and $p + p$, which is perhaps slightly larger than observed in the data.

We have extracted the dijet acoplanarity $\langle \sin^2(\phi_{jj}) \rangle$ from the widths of the back-to-back correlations in d + Au and $p + p$ collisions. In collisions involving nuclei, multiple interactions within the nucleus would tend to increase the parton transverse momentum which would be observable as a larger dijet acoplanarity; i.e., the back-to-back distribution of jets should broaden. However, in d + Au collisions, the extracted values of $\langle \sin^2(\phi_{jj}) \rangle$ are very similar to those observed in $p + p$ collisions. Indeed, the quadrature difference Δ between $\langle \sin^2(\phi_{jj}) \rangle$ in d + Au and $p + p$ is consistent with zero, $\Delta \langle \sin^2(\phi_{jj}) \rangle = +0.004 \pm 0.008(\mathrm{stat}) \pm 0.000(\mathrm{sys})$. The extracted $\langle \sin^2(\phi_{jj}) \rangle$ is also measured to be independent of the nuclear thickness function $T_A(b)$, which is in contrast to the strong A dependence of k_T observed at lower beam energies [7–9].

We have compared the centrality dependence of the extracted $\langle \sin^2(\phi_{jj}) \rangle$ with the multiple-scattering model of Qiu and Vitev [14]. This model reproduces the measured Cronin effect of single-particle spectra at RHIC [2–4] and predicts a finite increase of k_T with nuclear thickness function. When converted to a fractional increase, the prediction is at a level that is within the experimental uncertainty of the current data. Hence, our present data on $\langle \sin^2(\phi_{jj}) \rangle$ are not inconsistent with the level of multiple scattering deduced from the single-particle Cronin effect.

Taken together, we observe no change in fragmentation and no indication of the effects of multiple scattering; i.e., the jet structures are very similar in d + Au and $p + p$ collisions at RHIC energies. Our measurements also provide a critical baseline for jet measurements in Au + Au collisions at RHIC.

ACKNOWLEDGMENTS

We thank the staff of the Collider-Accelerator and Physics Departments at Brookhaven National Laboratory and the staff of the other PHENIX participating institutions for their vital contributions. We acknowledge support from the Department of Energy, Office of Science, Nuclear Physics Division, the National Science Foundation, Abilene Christian University Research Council, Research Foundation of SUNY, and Dean of the College of Arts and Sciences, Vanderbilt University

(U.S.A); Ministry of Education, Culture, Sports, Science, and Technology and the Japan Society for the Promotion of Science (Japan); Conselho Nacional de Desenvolvimento Científico e Tecnológico and Fundação de Amparo à Pesquisa do Estado de São Paulo (Brazil); Natural Science Foundation of China (People's Republic of China); Centre National de la Recherche Scientifique, Commissariat à l'Énergie Atomique, Institut National de Physique Nucléaire et de Physique des Particules, and Association pour la Recherche et le Développement des Méthodes et Processus Industriels (France); Ministry of Industry, Science and Tekhnologies, Bundesministerium für Bildung und Forschung, Deutscher Akademischer Austausch Dienst, and Alexander von Humboldt Stiftung (Germany); Hungarian National Science Fund, OTKA (Hungary); Department of Atomic Energy and Department of Science and Technology (India); Israel Science Foundation (Israel); Korea Research Foundation and Center for High Energy Physics (Korea); Russian Ministry of Industry, Science and Tekhnologies, Russian Academy of Science, Russian Ministry of Atomic Energy (Russia); VR and the Wallenberg Foundation (Sweden); the U.S. Civilian Research and Development Foundation for the Independent States of the Former Soviet Union; the US-Hungarian NSF-OTKA-MTA; and the US-Israel Binational Science Foundation.

[1] J. W. Cronin *et al*., Phys. Rev. D **11**, 3105 (1975).
[2] S. S. Adler *et al*. (PHENIX Collaboration), Phys. Rev. Lett. **91**, 072303 (2003).
[3] J. Adams *et al*. (STAR Collaboration), Phys. Rev. Lett. **91**, 072304 (2003).
[4] B. B. Back *et al*. (PHOBOS Collaboration), Phys. Rev. Lett. **91**, 072302 (2003).
[5] M. Della Negra *et al*. (CERN-College de France-Heidelberg-Karlsruhe Collaboration), Nucl. Phys. **B127**, 1 (1977).
[6] R. P. Feynman, R. D. Field, and G. C. Fox, Phys. Rev. D **18**, 3320 (1978).
[7] C. Stewart *et al*. (Fermilab E557 Collaboration), Phys. Rev. D **42**, 1385 (1990).
[8] M. D. Corcoran *et al*. (Fermilab E609 Collaboration), Phys. Lett. **B259**, 209 (1991).
[9] D. Naples *et al*., Phys. Rev. Lett. **72**, 2341 (1994).
[10] A. Angelis *et al*., Phys. Lett. **B97**, 163 (1980).
[11] M. R. Adams *et al*., Phys. Rev. Lett. **72**, 466 (1994).
[12] A. Accardi (2002), hep-ph/0212148.
[13] X. N. Wang, Phys. Rev. C **61**, 064910 (2000).
[14] J.-W. Qiu and I. Vitev, Phys. Lett. **B632**, 507 (2006).
[15] G. G. Barnafoldi, G. Papp, P. Levai, and G. Fai, J. Phys. G **30**, S1125 (2004).
[16] R. C. Hwa and C. B. Yang, Phys. Rev. Lett. **93**, 082302 (2004).
[17] R. J. Fisk *et al*., Phys. Rev. Lett. **40**, 984 (1978).
[18] M. Jacob, rapporteur's talk given at EPS Int. Conf, Geneva, Switzerland, Jun 27–Jul 4, 1979.
[19] A. L. S. Angelis *et al*. (CERN-Columbia-Oxford-Rockefeller Collaboration), Phys. Scripta **19**, 116 (1979).
[20] G. Abbiendi *et al*. (OPAL Collaboration), Eur. Phys. J. C **37**, 25 (2004).
[21] B. A. Kniehl, G. Kramer, and B. Potter, Nucl. Phys. **B582**, 514 (2000).
[22] R. C. Hwa and C. B. Yang, Phys. Rev. C **70**, 054902 (2004).
[23] R. C. Hwa and Z. Tan, Phys. Rev. C **72**, 057902 (2005).
[24] J. Huth *et al*., in *Proceedings of Research Directions for the Decade: Snowmass 1990*, edited by E. Berger (World Scientific, Singapore, 1992), p. 134.
[25] S. Catani, Y. L. Dokshitzer, M. H. Seymour, and B. R. Webber, Nucl. Phys. **B406**, 187 (1993).
[26] A. Angelis *et al*., Nucl. Phys. **B209**, 284 (1982).
[27] C. Adler *et al*. (STAR Collaboration), Phys. Rev. Lett. **90**, 032301 (2003).
[28] C. Adler *et al*. (STAR Collaboration), Phys. Rev. Lett. **90**, 082302 (2003).
[29] J. Rak, J. Phys. G **30**, S1309 (2004).
[30] S. S. Adler *et al*. (PHENIX Collaboration), Phys. Rev. C **71**, 051902 (2005).
[31] N. N. Ajitanand (PHENIX Collaboration), Nucl. Phys. **A715**, 765 (2003).
[32] J. Jia, J. Phys. G **31**, S521 (2005).
[33] P. Constantin, Ph.D. thesis, Iowa State University, 2004.
[34] K. Adcox *et al*. (PHENIX Collaboration), Nucl. Instrum. Methods A **499**, 469 (2003).
[35] M. Allen *et al*. (PHENIX Collaboration), Nucl. Instrum. Methods A **499**, 549 (2003).
[36] L. Aphecetche *et al*. (PHENIX Collaboration), Nucl. Instrum. Methods A **499**, 521 (2003).
[37] K. Adcox *et al*. (PHENIX Collaboration), Nucl. Instrum. Methods A **499**, 489 (2003).
[38] J. T. Mitchell *et al*. (PHENIX Collaboration), Nucl. Instrum. Methods A **482**, 491 (2002).
[39] S. S. Adler *et al*. (PHENIX Collaboration), Phys. Rev. C **69**, 034910 (2004).
[40] M. Aizawa *et al*. (PHENIX Collaboration), Nucl. Instrum. Methods A **499**, 508 (2003).
[41] S. S. Adler *et al*. (PHENIX Collaboration), Phys. Rev. Lett. **94**, 082301 (2005).
[42] T. Sjöstrand, L. Lönnblad, and S. Mrenna (2001), hep-ph/0108264.
[43] J. Adams *et al*. (STAR Collaboration), Phys. Rev. C **70**, 064907 (2004).
[44] P. Stankus, PHENIX Technical Note 412 (to be published).
[45] N. N. Ajitanand, J. Alexander, P. Chung, W. Holzmann, M. Issah, R. Lacey, A. Shevel, and Ataranenkopd Anielewicz, Phys. Rev. C **72**, 011902(R) (2005).
[46] G. van Apeldoorn, R. Blokzijl, D. Holthuizen, B. Jongejans, J. Kluyver, J. Warmerdam-de Leeuw, W. Metzger, H. Tiecke, and J. Timmermans, Nucl. Phys. **B91**, 1 (1975).
[47] N. M. Agababyan *et al*. (EHS-NA22 Collaboration), Phys. Lett. **B320**, 411 (1994).

Measurement of Identified π^0 and Inclusive Photon Second-Harmonic Parameter v_2 and Implications for Direct Photon Production in $\sqrt{s_{NN}} = 200$ GeV Au + Au

S. S. Adler,[5] S. Afanasiev,[17] C. Aidala,[5] N. N. Ajitanand,[43] Y. Akiba,[20,38] J. Alexander,[43] R. Amirikas,[12] L. Aphecetche,[45] S. H. Aronson,[5] R. Averbeck,[44] T. C. Awes,[35] R. Azmoun,[44] V. Babintsev,[15] A. Baldisseri,[10] K. N. Barish,[6] P. D. Barnes,[27] B. Bassalleck,[33] S. Bathe,[30] S. Batsouli,[9] V. Baublis,[37] A. Bazilevsky,[39,15] S. Belikov,[16,15] Y. Berdnikov,[40] S. Bhagavatula,[16] J. G. Boissevain,[27] H. Borel,[10] S. Borenstein,[25] M. L. Brooks,[27] D. S. Brown,[34] N. Bruner,[33] D. Bucher,[30] H. Buesching,[30] V. Bumazhnov,[15] G. Bunce,[5,39] J. M. Burward-Hoy,[26,44] S. Butsyk,[44] X. Camard,[45] J.-S. Chai,[18] P. Chand,[4] W. C. Chang,[2] S. Chernichenko,[15] C. Y. Chi,[9] J. Chiba,[20] M. Chiu,[9] I. J. Choi,[52] J. Choi,[19] R. K. Choudhury,[4] T. Chujo,[5] V. Cianciolo,[35] Y. Cobigo,[10] B. A. Cole,[9] P. Constantin,[16] D. d'Enterria,[45] G. David,[5] H. Delagrange,[45] A. Denisov,[15] A. Deshpande,[39] E. J. Desmond,[5] A. Devismes,[44] O. Dietzsch,[41] O. Drapier,[25] A. Drees,[44] R. du Rietz,[29] A. Durum,[15] D. Dutta,[4] Y. V. Efremenko,[35] K. El Chenawi,[49] A. Enokizono,[14] H. En'yo,[38,39] S. Esumi,[48] L. Ewell,[5] D. E. Fields,[33,39] F. Fleuret,[25] S. L. Fokin,[23] B. D. Fox,[39] Z. Fraenkel,[51] J. E. Frantz,[9] A. Franz,[5] A. D. Frawley,[12] S.-Y. Fung,[6] S. Garpman,[29,*] T. K. Ghosh,[49] A. Glenn,[46] G. Gogiberidze,[46] M. Gonin,[25] J. Gosset,[10] Y. Goto,[39] R. Granier de Cassagnac,[25] N. Grau,[16] S. V. Greene,[49] M. Grosse Perdekamp,[39] W. Guryn,[5] H.-Å. Gustafsson,[29] T. Hachiya,[14] J. S. Haggerty,[5] H. Hamagaki,[8] A. G. Hansen,[27] E. P. Hartouni,[26] M. Harvey,[5] R. Hayano,[8] N. Hayashi,[38] X. He,[13] M. Heffner,[26] T. K. Hemmick,[44] J. M. Heuser,[44] M. Hibino,[50] J. C. Hill,[16] W. Holzmann,[43] K. Homma,[14] B. Hong,[22] A. Hoover,[34] T. Ichihara,[38,39] V. V. Ikonnikov,[23] K. Imai,[24,38] D. Isenhower,[1] M. Ishihara,[38] M. Issah,[43] A. Isupov,[17] B. V. Jacak,[44] W. Y. Jang,[22] Y. Jeong,[19] J. Jia,[44] O. Jinnouchi,[38] B. M. Johnson,[5] S. C. Johnson,[26] K. S. Joo,[31] D. Jouan,[36] S. Kametani,[8,50] N. Kamihara,[47,38] M. Kaneta,[39] J. H. Kang,[52] S. S. Kapoor,[4] K. Katou,[50] S. Kelly,[9] B. Khachaturov,[51] A. Khanzadeev,[37] J. Kikuchi,[50] D. H. Kim,[31] D. J. Kim,[52] D. W. Kim,[19] E. Kim,[42] G.-B. Kim,[25] H. J. Kim,[52] E. Kistenev,[5] A. Kiyomichi,[48] K. Kiyoyama,[32] C. Klein-Boesing,[30] H. Kobayashi,[38,39] L. Kochenda,[37] V. Kochetkov,[15] D. Koehler,[33] T. Kohama,[14] M. Kopytine,[44] D. Kotchetkov,[6] A. Kozlov,[51] P. J. Kroon,[5] C. H. Kuberg,[1,27] K. Kurita,[39] Y. Kuroki,[48] M. J. Kweon,[22] Y. Kwon,[52] G. S. Kyle,[34] R. Lacey,[43] V. Ladygin,[17] J. G. Lajoie,[16] A. Lebedev,[16,23] S. Leckey,[44] D. M. Lee,[27] S. Lee,[19] M. J. Leitch,[27] X. H. Li,[6] H. Lim,[42] A. Litvinenko,[17] M. X. Liu,[27] Y. Liu,[36] C. F. Maguire,[49] Y. I. Makdisi,[5] A. Malakhov,[17] V. I. Manko,[23] Y. Mao,[7,38] G. Martinez,[45] M. D. Marx,[44] H. Masui,[48] F. Matathias,[44] T. Matsumoto,[8,50] P. L. McGaughey,[27] E. Melnikov,[15] F. Messer,[44] Y. Miake,[48] J. Milan,[43] T. E. Miller,[49] A. Milov,[44,51] S. Mioduszewski,[5] R. E. Mischke,[27] G. C. Mishra,[13] J. T. Mitchell,[5] A. K. Mohanty,[4] D. P. Morrison,[5] J. M. Moss,[27] F. Mühlbacher,[44] D. Mukhopadhyay,[51] M. Muniruzzaman,[6] J. Murata,[38,39] S. Nagamiya,[20] J. L. Nagle,[9] T. Nakamura,[14] B. K. Nandi,[6] M. Nara,[48] J. Newby,[46] P. Nilsson,[29] A. S. Nyanin,[23] J. Nystrand,[29] E. O'Brien,[5] C. A. Ogilvie,[16] H. Ohnishi,[5,38] I. D. Ojha,[49,3] K. Okada,[38] M. Ono,[48] V. Onuchin,[15] A. Oskarsson,[29] I. Otterlund,[29] K. Oyama,[8] K. Ozawa,[8] D. Pal,[51] A. P. T. Palounek,[27] V. Pantuev,[44] V. Papavassiliou,[34] J. Park,[42] A. Parmar,[33] S. F. Pate,[34] T. Peitzmann,[30] J.-C. Peng,[27] V. Peresedov,[17] C. Pinkenburg,[5] R. P. Pisani,[5] F. Plasil,[35] M. L. Purschke,[5] A. K. Purwar,[44] J. Rak,[16] I. Ravinovich,[51] K. F. Read,[35,46] M. Reuter,[44] K. Reygers,[30] V. Riabov,[37,40] Y. Riabov,[37] G. Roche,[28] A. Romana,[25] M. Rosati,[16] P. Rosnet,[28] S. S. Ryu,[52] M. E. Sadler,[1] N. Saito,[38,39] T. Sakaguchi,[8,50] M. Sakai,[32] S. Sakai,[48] V. Samsonov,[37] L. Sanfratello,[33] R. Santo,[30] H. D. Sato,[24,38] S. Sato,[5,48] S. Sawada,[20] Y. Schutz,[45] V. Semenov,[15] R. Seto,[6] M. R. Shaw,[1,27] T. K. Shea,[5] T.-A. Shibata,[47,38] K. Shigaki,[14,20] T. Shiina,[27] C. L. Silva,[41] D. Silvermyr,[27,29] K. S. Sim,[22] C. P. Singh,[3] V. Singh,[3] M. Sivertz,[5] A. Soldatov,[15] R. A. Soltz,[26] W. E. Sondheim,[27] S. P. Sorensen,[46] I. V. Sourikova,[5] F. Staley,[10] P. W. Stankus,[35] E. Stenlund,[29] M. Stepanov,[34] A. Ster,[21] S. P. Stoll,[5] T. Sugitate,[14] J. P. Sullivan,[27] E. M. Takagui,[41] A. Taketani,[38,39] M. Tamai,[50] K. H. Tanaka,[20] Y. Tanaka,[32] K. Tanida,[38] M. J. Tannenbaum,[5] P. Tarján,[11] J. D. Tepe,[1,27] T. L. Thomas,[33] J. Tojo,[24,38] H. Torii,[24,38] R. S. Towell,[1] I. Tserruya,[51] H. Tsuruoka,[48] S. K. Tuli,[3] H. Tydesjö,[29] N. Tyurin,[15] H. W. van Hecke,[27] J. Velkovska,[5,44] M. Velkovsky,[44] V. Veszprémi,[11] L. Villatte,[46] A. A. Vinogradov,[23] M. A. Volkov,[23] E. Vznuzdaev,[37] X. R. Wang,[13] Y. Watanabe,[38,39] S. N. White,[5] F. K. Wohn,[16] C. L. Woody,[5] W. Xie,[6] Y. Yang,[7] A. Yanovich,[15] S. Yokkaichi,[38,39] G. R. Young,[35] I. E. Yushmanov,[23] W. A. Zajc,[9,†] C. Zhang,[9] S. Zhou,[7] S. J. Zhou,[51] and L. Zolin[17]

(PHENIX Collaboration)

[1]*Abilene Christian University, Abilene, Texas 79699, USA*
[2]*Institute of Physics, Academia Sinica, Taipei 11529, Taiwan*
[3]*Department of Physics, Banaras Hindu University, Varanasi 221005, India*

 © 2006 The American Physical Society

[4]Bhabha Atomic Research Centre, Bombay 400 085, India
[5]Brookhaven National Laboratory, Upton, New York 11973-5000, USA
[6]University of California - Riverside, Riverside, California 92521, USA
[7]China Institute of Atomic Energy (CIAE), Beijing, People's Republic of China
[8]Center for Nuclear Study, Graduate School of Science, University of Tokyo, 7-3-1 Hongo, Bunkyo, Tokyo 113-0033, Japan
[9]Columbia University, New York, New York 10027, USA
and Nevis Laboratories, Irvington, New York 10533, USA
[10]Dapnia, CEA Saclay, F-91191, Gif-sur-Yvette, France
[11]Debrecen University, H-4010 Debrecen, Egyetem tér 1, Hungary
[12]Florida State University, Tallahassee, Florida 32306, USA
[13]Georgia State University, Atlanta, Georgia 30303, USA
[14]Hiroshima University, Kagamiyama, Higashi-Hiroshima 739-8526, Japan
[15]IHEP Protvino, State Research Center of Russian Federation, Institute for High Energy Physics, Protvino, 142281, Russia
[16]Iowa State University, Ames, Iowa 50011, USA
[17]Joint Institute for Nuclear Research, 141980 Dubna, Moscow Region, Russia
[18]KAERI, Cyclotron Application Laboratory, Seoul, South Korea
[19]Kangnung National University, Kangnung 210-702, South Korea
[20]KEK, High Energy Accelerator Research Organization, Tsukuba, Ibaraki 305-0801, Japan
[21]KFKI Research Institute for Particle and Nuclear Physics of the Hungarian Academy of Sciences (MTA KFKI RMKI), H-1525 Budapest 114, POBox 49, Budapest, Hungary
[22]Korea University, Seoul, 136-701, Korea
[23]Russian Research Center "Kurchatov Institute", Moscow, Russia
[24]Kyoto University, Kyoto 606-8502, Japan
[25]Laboratoire Leprince-Ringuet, Ecole Polytechnique, CNRS-IN2P3, Route de Saclay, F-91128, Palaiseau, France
[26]Lawrence Livermore National Laboratory, Livermore, California 94550, USA
[27]Los Alamos National Laboratory, Los Alamos, New Mexico 87545, USA
[28]LPC, Université Blaise Pascal, CNRS-IN2P3, Clermont-Fd, 63177 Aubiere Cedex, France
[29]Department of Physics, Lund University, Box 118, SE-221 00 Lund, Sweden
[30]Institut für Kernphysik, University of Muenster, D-48149 Muenster, Germany
[31]Myongji University, Yongin, Kyonggido 449-728, Korea
[32]Nagasaki Institute of Applied Science, Nagasaki-shi, Nagasaki 851-0193, Japan
[33]University of New Mexico, Albuquerque, New Mexico 87131, USA
[34]New Mexico State University, Las Cruces, New Mexico 88003, USA
[35]Oak Ridge National Laboratory, Oak Ridge, Tennessee 37831, USA
[36]IPN-Orsay, Universite Paris Sud, CNRS-IN2P3, Boîte Postale 1, F-91406, Orsay, France
[37]PNPI, Petersburg Nuclear Physics Institute, Gatchina, Leningrad region, 188300, Russia
[38]RIKEN, The Institute of Physical and Chemical Research, Wako, Saitama 351-0198, Japan
[39]RIKEN BNL Research Center, Brookhaven National Laboratory, Upton, New York 11973-5000, USA
[40]Saint Petersburg State Polytechnic University, St. Petersburg, Russia
[41]Universidade de São Paulo, Instituto de Física, Caixa Postal 66318, São Paulo CEP05315-970, Brazil
[42]System Electronics Laboratory, Seoul National University, Seoul, South Korea
[43]Chemistry Department, Stony Brook University, SUNY, Stony Brook, New York 11794-3400, USA
[44]Department of Physics and Astronomy, Stony Brook University, SUNY, Stony Brook, New York 11794, USA
[45]SUBATECH, Ecole des Mines de Nantes, CNRS-IN2P3, Université de Nantes Boîte Postale 20722 - 44307, Nantes, France
[46]University of Tennessee, Knoxville, Tennessee 37996, USA
[47]Department of Physics, Tokyo Institute of Technology, Tokyo, 152-8551, Japan
[48]Institute of Physics, University of Tsukuba, Tsukuba, Ibaraki 305, Japan
[49]Vanderbilt University, Nashville, Tennessee 37235, USA
[50]Waseda University, Advanced Research Institute for Science and Engineering, 17 Kikui-cho, Shinjuku-ku, Tokyo 162-0044, Japan
[51]Weizmann Institute, Rehovot 76100, Israel
[52]Yonsei University, IPAP, Seoul 120-749, Korea
(Received 16 August 2005; published 26 January 2006)

The azimuthal distribution of identified π^0 and inclusive photons has been measured in $\sqrt{s_{NN}} = 200$ GeV Au + Au collisions with the PHENIX experiment at the Relativistic Heavy-Ion Collider (RHIC). The second-harmonic parameter (v_2) was measured to describe the observed anisotropy of the azimuthal distribution. The measured inclusive photon v_2 is consistent with the value expected for the photons from hadron decay and is also consistent with the lack of direct photon signal over the measured p_T range 1–6 GeV/c. An attempt is made to extract v_2 of direct photons.

DOI: 10.1103/PhysRevLett.96.032302 PACS numbers: 25.75.Dw

Among the most exciting features of the experimental data from the Relativistic Heavy-Ion Collider (RHIC) are the suppression of high p_T hadron yields [1–5], the baryon excess at intermediate p_T [6–9], and the quark number scaling of the identified hadron v_2 [10,11]. Theoretically, the observed high p_T suppression has been attributed to energy loss of the hard-scattered partons [12,13]. Experimentally, the absence of the suppression in d + Au collisions has shown that it is a final-state effect due to the hot and dense matter created in central Au + Au collisions [14–17]. The quark number scaling of the measured elliptic flow parameter v_2 and the nuclear modification factor $R_{\rm cp}$ of baryons versus mesons may suggest the existence of a thermalized partonic phase before hadronization [18,19].

The second-harmonic coefficient parameter v_2 of the azimuthal distribution of the particles produced in heavy-ion collisions is defined by

$$\frac{dN}{d\phi} \propto 1 + 2v_2 \cos[2(\phi - \Phi_{\rm RP})], \tag{1}$$

where ϕ is the azimuthal direction of the particle and $\Phi_{\rm RP}$ is the direction of the nuclear impact parameter (reaction plane) in a given collision. The v_2 in high-energy heavy-ion collisions is considered to be sensitive to the initial geometric overlap of the colliding nuclei as well as the later expansion driven by the initial pressure. Theoretically, the dominant source of v_2 at low p_T is the expansion of the dense matter in the direction of the short axis of the overlap zone, and at high p_T is the parton energy loss given by the shape of the geometrical overlap. The quark coalescence (recombination) might be responsible for the v_2 in the intermediate p_T region. However, the experimental definition of v_2 includes any second-harmonic correlation with respect to the event plane, which is given by the beam direction and the impact parameter direction. Detailed v_2 measurements of identified particles at higher p_T than 2 GeV/c, where hydrodynamics alone does not describe the measurements, would enable us to understand the different mechanisms that generate v_2 and to investigate the transition region from low to high p_T. Especially, the v_2 of identified π^0 will give a baseline measurement of inclusive photon v_2 to extract the direct photon v_2.

The direct photons produced in hard scattering are penetrating probes of the produced dense matter in heavy-ion collisions. Recently, we observed that the centrality dependence of the direct photon yield in $\sqrt{s_{NN}} = 200$ GeV Au + Au collisions is consistent with binary collision scaling [20]. The lack of suppression of direct photons is further evidence in favor of the final-state effect in hadron suppression. In addition to the initially produced hard photons that should inherently follow binary scaling, there may be other counteracting effects resulting in apparent binary scaling. For example, some fraction of the photons may originate from partons having experienced energy loss, causing an analogous suppression of these photons [21] similar to hadrons. On the other hand, the parton energy loss may enhance the photon yield via bremsstrahlung while passing through the hot and dense matter [22]. The thermal emission of photons radiated from the hot and dense matter is also expected to increase direct photon yield for central Au + Au collisions [23].

The v_2 measurement of the direct photons could help to confirm that the observed binary scaling of the direct photon excess is attributable to the direct photon production being dominated by the initial hard scattering. The v_2 measurement of the direct photons would give additional and complementary information to help disentangle the various scenarios of direct photon production, as well as to provide more information on the dynamics and properties of the produced hot and dense matter. The v_2 of photons from the initial Compton-like hard scattering is expected to be zero if they do not interact with the hot and dense matter produced during the collision. However, when the v_2 of high p_T hadrons is given purely by the parton energy loss, the photons from the parton fragmentation outside of the reaction zone should have v_2 similar to the hadrons at high p_T. Such photon fraction is expected to be about 50% of total direct photon yield at 3.5 GeV/c in p_T [21,22]. On the other hand, one would expect that the photons originating from bremsstrahlung due to the passage of partons through the hot and dense matter should have the opposite (negative) sign in v_2 compared with hadrons, because the parton energy loss is larger in the long axis of the overlapping region (out-of-plane). Finally, the photons from the thermal radiation should reflect the dynamical evolution of the produced hot and dense matter. There are recent theoretical predictions for different mechanisms [24].

In this Letter we present measurements of the v_2 of π^0 and inclusive γ, as a function of transverse momentum and collision centrality, and we discuss the implications for the yield and v_2 of direct photons. The data are for 200 GeV Au + Au collisions from the PHENIX experiment [25] recorded during Run 2 at RHIC. The event trigger and centrality definition are given by the beam-beam counters (BBCs) and the zero degree calorimeters (ZDCs). The number of charged particles measured with the BBCs and the neutral spectators measured with the ZDCs are correlated with the number of participating nucleons, thus together providing a measure of the centrality. The event plane, which is a measure of reaction plane, is determined using the two BBCs at $|\eta| = 3.1 \sim 3.9$, where each counter consists of 64 photomultiplier tubes (PMTs) with quartz Cherenkov radiators in front, surrounding the beam pipe. The elliptic axis of the event plane $\Phi_{\rm measured}$ is calculated by the angle weighted with the PMT amplitude using the second-harmonic moment as described in Refs. [10,26]. The measured event anisotropy is corrected for a finite resolution of the measured event plane. The

estimated event plane resolution $\sigma_{\mathrm{RP}} = \langle \cos[2(\Phi_{\mathrm{measured}} - \Phi_{\mathrm{RP}})] \rangle$ is 0.3 on average, with a maximum of ~0.4 in the midcentral collisions. The corrected v_2 is calculated via the formula $v_2 = \langle \cos[2(\phi - \Phi_{\mathrm{measured}})] \rangle / \sigma_{\mathrm{RP}}$. The phase space used for the determination of the event plane for this analysis is 3–4 units away from the midrapidity, while the inclusive photon and the identified π^0 are measured at $|\eta| < 0.35$.

The photon identification and the π^0 reconstruction are performed in the same way as presented elsewhere [4]. The photon candidate clusters for both inclusive photon and π^0 measurement are first selected by their times of flight and the corresponding shower profiles in the electromagnetic calorimeter (EMCal). Neutral pions are reconstructed via $\pi^0 \rightarrow \gamma\gamma$ decay channel with an invariant mass analysis of γ pairs. An additional energy asymmetry cut, $|E_{\gamma 1} - E_{\gamma 2}|/(E_{\gamma 1} + E_{\gamma 2}) < 0.8$ is applied to the pairs of photon candidates in the π^0 reconstruction. The combinatorial background is estimated and subtracted by mixing pairs from different events with similar centrality, z-vertex position, and event plane orientation. The background is normalized in a region outside the π^0 mass peak for each bin in relative angle with respect to the measured event plane direction. A typical signal over background ratio is about 1 to 1 at $p_T = 3$ GeV/c in midcentral collisions (20–40% centrality). The v_2 of π^0 is calculated from the azimuthal distribution after the combinatorial background is subtracted for each centrality and p_T bin. For the inclusive photon analysis, the charged particle contamination in the sample of the photon candidate cluster is identified by associating the photon candidates with charged particle hits in the pad chamber (PC3) directly in front of the EMCal. The fraction of photon candidates removed by this charge veto cut is about 15–25% depending on centrality. The effect of hadron contamination on the measured v_2 of inclusive photons is estimated by varying the size of the charged particle association window in the PC3, and no significant effect is seen. Neutron and antineutron contamination and off-vertex photons in the identified photon sample are studied with full detector Monte Carlo simulation. The correction for these effects is applied to the data; it is 2% relative to the measured v_2 at 2 GeV/c and negligible at 4 GeV/c. The systematic error includes the effects from the π^0 and photon identification cuts and from the event plane determination: 5% for π^0 and 5% for photon identification and 5–10% for event plane determination given by the error on the correction factor from the finite event plane resolution. The analysis includes both a minimum-bias sample (30×10^6 events) and a Level 2 trigger sample (equivalent to 55×10^6 events), where the Level 2 algorithm is described in Ref. [20].

Figure 1 shows the measured v_2 of π^0 and inclusive photons as a function of p_T for different centrality selections. Data are compared with previous measurements of charged pions [10]. The p_T and centrality dependences of

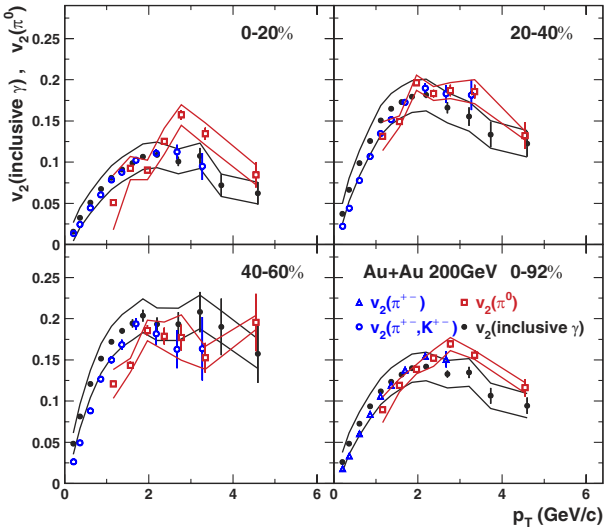

FIG. 1 (color online). The measured v_2 of inclusive photon ($v_2^{\mathrm{inclusive}\gamma}$, solid circles) and v_2 of π^0 ($v_2^{\pi^0}$, open squares) for 4 centrality selections. The statistical (vertical error bars) and systematic errors (lines) are plotted separately. The highest p_T point corresponds to 4–6 GeV/c. Charged pion data are from previous measurements [10].

both the π^0 and the inclusive photon v_2 is consistent with that of other mesons [10]. The v_2 values are significantly above zero up to the highest p_T points. The nonzero v_2 of π^0 up to the highest p_T cannot be explained by flow effects alone, but may be attributed to jet quenching and/or quark coalescence (recombination).

Figure 2 compares for different centralities the v_2 of inclusive photons with the expected photon v_2 from hadronic decays. The expected photon v_2 from hadronic decays (v_2^{bg}) is calculated by Monte Carlo simulation with the measured v_2 of π^0 and other hadronic sources of photon. The relative yield of other sources (mainly η) is about 20% of the total hadronic decay photons, which corresponds to about 4% relative contribution in v_2 at 1 GeV/c and negligible at 3 GeV/c. In the simulation, we assume that the v_2 of η is similar to the kaon (the closest in mass particle) v_2 measured in [10,11].

The v_2 of the inclusive photons $v_2^{\mathrm{inclusive}\gamma}$ can be expressed as

$$v_2^{\mathrm{inclusive}\gamma} = \frac{v_2^{\mathrm{direct}\gamma} N_{\mathrm{direct}\gamma} + v_2^{\mathrm{bg}} N_{\mathrm{bg}}}{N_{\mathrm{direct}\gamma} + N_{\mathrm{bg}}}, \qquad (2)$$

where $v_2^{\mathrm{direct}\gamma}$ is the direct photon v_2, $N_{\mathrm{direct}\gamma}$ is the direct photon yield, and N_{bg} is the background photon yield. Using the direct photon excess ratio $R = (N_{\mathrm{direct}\gamma} + N_{\mathrm{bg}})/N_{\mathrm{bg}}$, previously measured in Ref. [20], one can express the direct photon v_2 as

$$v_2^{\mathrm{direct}\gamma} = \frac{R v_2^{\mathrm{inclusive}\gamma} - v_2^{\mathrm{bg}}}{R - 1}. \qquad (3)$$

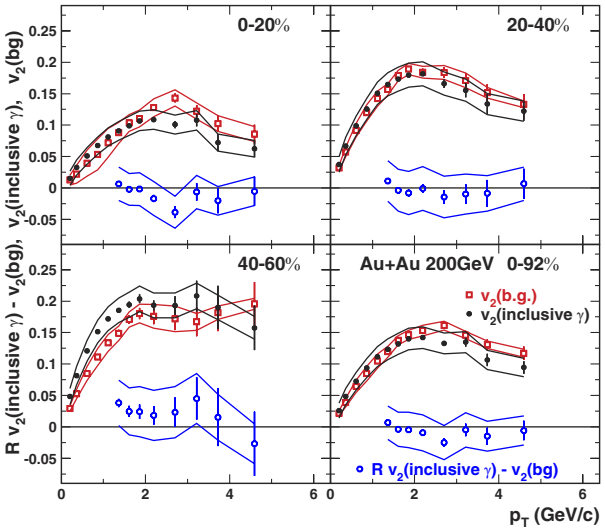

FIG. 2 (color online). The measured v_2 of inclusive photons ($v_2^{\text{inclusive}\gamma}$, solid circles) and expected photon v_2 from hadronic decay (v_2^{bg}, open squares). A subtracted v_2 quantity $Rv_2^{\text{inclusive}\gamma} - v_2^{\text{bg}}$ is plotted at the bottom of each panel (open circles), where $R = (N_{\text{direct}\gamma} + N_{\text{bg}})/N_{\text{bg}}$. The quantity corresponds to a product of the direct photon v_2 and a positive factor $R - 1$, ($v_2^{\text{direct}\gamma}(R - 1)$).

The bottom data points in each panel of Fig. 2 show the difference: $Rv_2^{\text{inclusive}\gamma} - v_2^{\text{bg}}$ (the numerator in the above equation), which corresponds to a product of the direct photon v_2 times a positive factor $R - 1$, $v_2^{\text{direct}\gamma}(R - 1)$. Alternatively, it would be possible to calculate $v_2^{\text{direct}\gamma}$ using the measured ratio R [20]. However, we have chosen this subtracted quantity in order to show the direct photon v_2 and its sign, because $R - 1$ is measured to be small, especially at low p_T, and is sometimes negative experimentally. The comparison between $v_2^{\text{inclusive}\gamma}$ and v_2^{bg} in each panel indicates that the measured inclusive photon v_2 is consistent with the expected photon v_2 from hadronic decay over the measured p_T range. The subtracted points are close to zero, which is also expected because of the lack of the direct photon signal in the measured p_T range, where R is close to unity [20]. The subtraction is especially meaningful where the measured R value goes above 1.0 at about 4–6 GeV/c and higher p_T in central Au + Au collisions [20]; a region where one could extract the direct photon v_2. The measurement indicates that v_2 of the direct photon is small at least in the highest p_T (4–6 GeV/c) range in central Au + Au collisions. However, some hidden important trends (slightly negative or positive v_2 of direct photon) as a function of p_T and centrality could be extracted, once the errors on those two v_2's and on the measured R are small enough. This is because the plotted subtracted quantity needs to be magnified by $1/(R - 1)$ in order to get the direct photon v_2. The extracted direct photon v_2 at 4–6 GeV/c is -1.5% with $\pm 6.4\%$ statistical and $\pm 6.4\%$ systematic errors for 0–20% central events and $-2.4\% \pm 6.7\%$(sta.) $\pm$ 9.8%(sys.) for 0–92% (minimum-bias) events.

Figure 3 shows the ratio of $v_2^{\text{bg}}/v_2^{\text{inclusive}\gamma}$ and a comparison to the measured ratio R of the yields from [20]. If the direct photon v_2 is assumed to be zero, the ratio R should be equal to $v_2^{\text{bg}}/v_2^{\text{inclusive}\gamma}$ according to the Eq. (3). If the measured direct photon excess comes from the initial hard scattering, that would correspond to zero $v_2^{\text{direct}\gamma}$, then the measured v_2 ratio $v_2^{\text{bg}}/v_2^{\text{inclusive}\gamma}$ gives a consistent check of the direct photon excess ratio R measurement, especially where R is significantly above 1.0. The measured v_2 ratio as a function of p_T and centrality is consistent with the conventional relative yield measurement of the direct photon excess ratio R, but has somewhat larger errors.

In conclusion, the v_2 of identified π^0 and inclusive photons as a function of p_T and centrality are measured with the PHENIX central arm spectrometer at $|\eta| < 0.35$ with respect to the event plane defined at $|\eta| = 3.1 \sim 3.9$ in 200 GeV Au + Au collisions at RHIC. The v_2 of identified π^0 shows a similar trend as a function of p_T and centrality compared with other mesons and has values significantly above zero up to the highest p_T point. The measured v_2 of the inclusive photons is consistent with the v_2 of photons from hadronic decays, which is furthermore consistent with the absence of direct photon signal over the measured p_T range. However, the measurement indicates a small direct photon v_2 for the highest p_T (4–6 GeV/c) range in central Au + Au collisions. The ratio of the estimated photon v_2 from the hadronic decay over the measured inclusive photon v_2 is also consistent with the

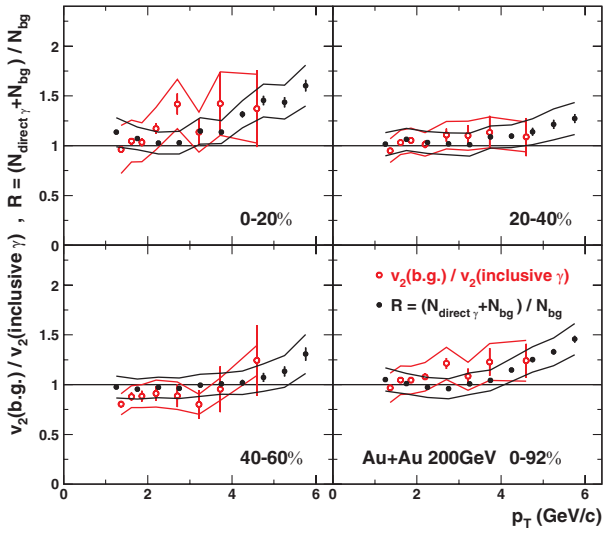

FIG. 3 (color online). The ratio of the hadronic decay photon v_2 over inclusive photon v_2 ($v_2^{\text{bg}}/v_2^{\text{inclusive}\gamma}$, open circles) compared with the direct photon excess ratio $R = (N_{\text{direct}\gamma} + N_{\text{bg}})/N_{\text{bg}}$, (solid circles).

direct photon excess ratio measured via conventional yields ratio. This should also imply that the v_2 of direct photons is zero where the measured direct photon excess ratio R is significantly above 1.0. The present statistics and systematic accuracy of the data from the second year of RHIC running do not allow us to explicitly state the magnitude of direct photon v_2. However, the indication of small v_2 for direct photons would favor the naive scenario of direct photon production from initial hard scattering and its small interaction with produced matter in high-energy Au + Au collisions.

We thank the staff of the Collider-Accelerator and Physics Departments at BNL for their vital contributions. We acknowledge support from the Department of Energy and NSF (U.S.A.), MEXT and JSPS (Japan), CNPq and FAPESP (Brazil), NSFC (China), CNRS-IN2P3 and CEA (France), BMBF, DAAD, and AvH (Germany), OTKA (Hungary), DAE and DST (India), ISF (Israel), KRF and CHEP (Korea), RMIST, RAS, and RMAE (Russia), VR and KAW (Sweden), U.S. CRDF for the FSU, US-Hungarian NSF-OTKA-MTA, and US-Israel BSF.

*Deceased.
†Email address: zajc@nevis.columbia.edu

[1] K. Adcox *et al.*, Phys. Rev. Lett. **88**, 022301 (2002).
[2] C. Adler *et al.*, Phys. Rev. Lett. **89**, 202301 (2002).
[3] K. Adcox *et al.*, Phys. Lett. B **561**, 82 (2003).
[4] S. S. Adler *et al.*, Phys. Rev. Lett. **91**, 072301 (2003).
[5] S. S. Adler *et al.*, Phys. Rev. C **69**, 034910 (2004).
[6] S. S. Adler *et al.*, Phys. Rev. Lett. **91**, 172301 (2003).
[7] S. S. Adler *et al.*, Phys. Rev. C **69**, 034909 (2004).
[8] K. Adcox *et al.*, Phys. Rev. C **69**, 024904 (2004).
[9] S. S. Adler *et al.*, Phys. Rev. C **72**, 014903 (2005).
[10] S. S. Adler *et al.*, Phys. Rev. Lett. **91**, 182301 (2003).
[11] J. Adams *et al.*, Phys. Rev. Lett. **92**, 052302 (2004).
[12] X.-N. Wang, Phys. Lett. B **579**, 299 (2004).
[13] M. Gyulassy, P. Levai, and I. Vitev, Phys. Lett. B **538**, 282 (2002).
[14] S. S. Adler *et al.*, Phys. Rev. Lett. **91**, 072303 (2003).
[15] J. Adams *et al.*, Phys. Rev. Lett. **91**, 072304 (2003).
[16] B. B. Back *et al.*, Phys. Rev. Lett. **91**, 072302 (2003).
[17] I. Arsene *et al.*, Phys. Rev. Lett. **91**, 072305 (2003).
[18] R. J. Fries, B. Müller, C. Nonaka, and S. A. Bass, Phys. Rev. C **68**, 044902 (2003).
[19] V. Greco, C. M. Ko, and P. Levai, Phys. Rev. C **68**, 034904 (2003).
[20] S. S. Adler *et al.*, Phys. Rev. Lett. **94**, 232301 (2005).
[21] B. G. Zakharov, JETP Lett. **80**, 1 (2004).
[22] R. J. Fries, B. Müller, and D. K. Srivastava, Phys. Rev. Lett. **90**, 132301 (2003).
[23] E. L. Feinberg, Nuovo Cimento **34**, 391 (1976); E. V. Shuryak, Phys. Lett. **78B**, 150 (1978); S. Turbide, R. Rapp, and C. Gale, Phys. Rev. C **69**, 014903 (2004).
[24] S. Turbide, C. Gale, R. J. Fries, hep-ph/0508201.
[25] K. Adcox *et al.*, Nucl. Instrum. Methods Phys. Res., Sect. A **499**, 469 (2003).
[26] A. M. Poskanzer and S. A. Voloshin, Phys. Rev. C **58**, 1671 (1998).

Single Electrons from Heavy-Flavor Decays in $p + p$ Collisions at $\sqrt{s} = 200$ GeV

S. S. Adler,[5] S. Afanasiev,[17] C. Aidala,[5] N. N. Ajitanand,[43] Y. Akiba,[20,38] J. Alexander,[43] R. Amirikas,[12] L. Aphecetche,[45] S. H. Aronson,[5] R. Averbeck,[44] T. C. Awes,[35] R. Azmoun,[44] V. Babintsev,[15] A. Baldisseri,[10] K. N. Barish,[6] P. D. Barnes,[27] B. Bassalleck,[33] S. Bathe,[30] S. Batsouli,[9] V. Baublis,[37] A. Bazilevsky,[39,15] S. Belikov,[16,15] Y. Berdnikov,[40] S. Bhagavatula,[16] J. G. Boissevain,[27] H. Borel,[10] S. Borenstein,[25] M. L. Brooks,[27] D. S. Brown,[34] N. Bruner,[33] D. Bucher,[30] H. Buesching,[30] V. Bumazhnov,[15] G. Bunce,[5,39] J. M. Burward-Hoy,[26,44] S. Butsyk,[44] X. Camard,[45] J.-S. Chai,[18] P. Chand,[4] W. C. Chang,[2] S. Chernichenko,[15] C. Y. Chi,[9] J. Chiba,[20] M. Chiu,[9] I. J. Choi,[52] J. Choi,[19] R. K. Choudhury,[4] T. Chujo,[5] V. Cianciolo,[35] Y. Cobigo,[10] B. A. Cole,[9] P. Constantin,[16] D. d'Enterria,[45] G. David,[5] H. Delagrange,[45] A. Denisov,[15] A. Deshpande,[39] E. J. Desmond,[5] A. Devismes,[44] O. Dietzsch,[41] O. Drapier,[25] A. Drees,[44] R. du Rietz,[29] A. Durum,[15] D. Dutta,[4] Y. V. Efremenko,[35] K. El Chenawi,[49] A. Enokizono,[14] H. En'yo,[38,39] S. Esumi,[48] L. Ewell,[5] D. E. Fields,[33,39] F. Fleuret,[25] S. L. Fokin,[23] B. D. Fox,[39] Z. Fraenkel,[51] J. E. Frantz,[9] A. Franz,[5] A. D. Frawley,[12] S.-Y. Fung,[6] S. Garpman,[29,*] T. K. Ghosh,[49] A. Glenn,[46] G. Gogiberidze,[46] M. Gonin,[25] J. Gosset,[10] Y. Goto,[39] R. Granier de Cassagnac,[25] N. Grau,[16] S. V. Greene,[49] M. Grosse Perdekamp,[39] W. Guryn,[5] H.-Å. Gustafsson,[29] T. Hachiya,[14] J. S. Haggerty,[5] H. Hamagaki,[8] A. G. Hansen,[27] E. P. Hartouni,[26] M. Harvey,[5] R. Hayano,[8] N. Hayashi,[38] X. He,[13] M. Heffner,[26] T. K. Hemmick,[44] J. M. Heuser,[44] M. Hibino,[50] J. C. Hill,[16] W. Holzmann,[43] K. Homma,[14] B. Hong,[22] A. Hoover,[34] T. Ichihara,[38,39] V. V. Ikonnikov,[23] K. Imai,[24,38] D. Isenhower,[1] M. Ishihara,[38] M. Issah,[43] A. Isupov,[17] B. V. Jacak,[44] W. Y. Jang,[22] Y. Jeong,[19] J. Jia,[44] O. Jinnouchi,[38] B. M. Johnson,[5] S. C. Johnson,[26] K. S. Joo,[31] D. Jouan,[36] S. Kametani,[8,50] N. Kamihara,[47,38] J. H. Kang,[52] S. S. Kapoor,[4] K. Katou,[50] S. Kelly,[9] B. Khachaturov,[51] A. Khanzadeev,[37] J. Kikuchi,[50] D. H. Kim,[31] D. J. Kim,[52] D. W. Kim,[19] E. Kim,[42] G.-B. Kim,[25] H. J. Kim,[52] E. Kistenev,[5] A. Kiyomichi,[48] K. Kiyoyama,[32] C. Klein-Boesing,[30] H. Kobayashi,[38,39] L. Kochenda,[37] V. Kochetkov,[15] D. Koehler,[33] T. Kohama,[14] M. Kopytine,[44] D. Kotchetkov,[6] A. Kozlov,[51] P. J. Kroon,[5] C. H. Kuberg,[1,27] K. Kurita,[39] Y. Kuroki,[48] M. J. Kweon,[22] Y. Kwon,[52] G. S. Kyle,[34] R. Lacey,[43] V. Ladygin,[17] J. G. Lajoie,[16] A. Lebedev,[16,23] S. Leckey,[44] D. M. Lee,[27] S. Lee,[19] M. J. Leitch,[27] X. H. Li,[6] H. Lim,[42] A. Litvinenko,[17] M. X. Liu,[27] Y. Liu,[36] C. F. Maguire,[49] Y. I. Makdisi,[5] A. Malakhov,[17] V. I. Manko,[23] Y. Mao,[7,38] G. Martinez,[45] M. D. Marx,[44] H. Masui,[48] F. Matathias,[44] T. Matsumoto,[8,50] P. L. McGaughey,[27] E. Melnikov,[15] F. Messer,[44] Y. Miake,[48] J. Milan,[43] T. E. Miller,[49] A. Milov,[44,51] S. Mioduszewski,[5] R. E. Mischke,[27] G. C. Mishra,[13] J. T. Mitchell,[5] A. K. Mohanty,[4] D. P. Morrison,[5] J. M. Moss,[27] F. Mühlbacher,[44] D. Mukhopadhyay,[51] M. Muniruzzaman,[6] J. Murata,[38,39] S. Nagamiya,[20] J. L. Nagle,[9] T. Nakamura,[14] B. K. Nandi,[6] M. Nara,[48] J. Newby,[46] P. Nilsson,[29] A. S. Nyanin,[23] J. Nystrand,[29] E. O'Brien,[5] C. A. Ogilvie,[16] H. Ohnishi,[5,38] I. D. Ojha,[49,3] K. Okada,[38] M. Ono,[48] V. Onuchin,[15] A. Oskarsson,[29] I. Otterlund,[29] K. Oyama,[8] K. Ozawa,[8] D. Pal,[51] A. P. T. Palounek,[27] V. Pantuev,[44] V. Papavassiliou,[34] J. Park,[42] A. Parmar,[33] S. F. Pate,[34] T. Peitzmann,[30] J.-C. Peng,[27] V. Peresedov,[17] C. Pinkenburg,[5] R. P. Pisani,[5] F. Plasil,[35] M. L. Purschke,[5] A. K. Purwar,[44] J. Rak,[16] I. Ravinovich,[51] K. F. Read,[35,46] M. Reuter,[44] K. Reygers,[30] V. Riabov,[37,40] Y. Riabov,[37] G. Roche,[28] A. Romana,[25] M. Rosati,[16] P. Rosnet,[28] S. S. Ryu,[52] M. E. Sadler,[1] N. Saito,[38,39] T. Sakaguchi,[8,50] M. Sakai,[32] S. Sakai,[48] V. Samsonov,[37] L. Sanfratello,[33] R. Santo,[30] H. D. Sato,[24,38] S. Sato,[5,48] S. Sawada,[20] Y. Schutz,[45] V. Semenov,[15] R. Seto,[6] M. R. Shaw,[1,27] T. K. Shea,[5] T.-A. Shibata,[47,38] K. Shigaki,[14,20] T. Shiina,[27] C. L. Silva,[41] D. Silvermyr,[27,29] K. S. Sim,[22] C. P. Singh,[3] V. Singh,[3] M. Sivertz,[5] A. Soldatov,[15] R. A. Soltz,[26] W. E. Sondheim,[27] S. P. Sorensen,[46] I. V. Sourikova,[5] F. Staley,[10] P. W. Stankus,[35] E. Stenlund,[29] M. Stepanov,[34] A. Ster,[21] S. P. Stoll,[5] T. Sugitate,[14] J. P. Sullivan,[27] E. M. Takagui,[41] A. Taketani,[38,39] M. Tamai,[50] K. H. Tanaka,[20] Y. Tanaka,[32] K. Tanida,[38] M. J. Tannenbaum,[5] P. Tarján,[11] J. D. Tepe,[1,27] T. L. Thomas,[33] J. Tojo,[24,38] H. Torii,[24,38] R. S. Towell,[1] I. Tserruya,[51] H. Tsuruoka,[48] S. K. Tuli,[3] H. Tydesjö,[29] N. Tyurin,[15] H. W. van Hecke,[27] J. Velkovska,[5,44] M. Velkovsky,[44] V. Veszprémi,[11] L. Villatte,[46] A. A. Vinogradov,[23] M. A. Volkov,[23] E. Vznuzdaev,[37] X. R. Wang,[13] Y. Watanabe,[38,39] S. N. White,[5] F. K. Wohn,[16] C. L. Woody,[5] W. Xie,[6] Y. Yang,[7] A. Yanovich,[15] S. Yokkaichi,[38,39] G. R. Young,[35] I. E. Yushmanov,[23] W. A. Zajc,[9,†] C. Zhang,[9] S. Zhou,[7] S. J. Zhou,[51] and L. Zolin[17]

(PHENIX Collaboration)

[1]*Abilene Christian University, Abilene, Texas 79699, USA*
[2]*Institute of Physics, Academia Sinica, Taipei 11529, Taiwan*
[3]*Department of Physics, Banaras Hindu University, Varanasi 221005, India*
[4]*Bhabha Atomic Research Centre, Bombay 400 085, India*

 © 2006 The American Physical Society

[5]Brookhaven National Laboratory, Upton, New York 11973-5000, USA
[6]University of California - Riverside, Riverside, California 92521, USA
[7]China Institute of Atomic Energy (CIAE), Beijing, People's Republic of China
[8]Center for Nuclear Study, Graduate School of Science, University of Tokyo, 7-3-1 Hongo, Bunkyo, Tokyo 113-0033, Japan
[9]Columbia University, New York, New York 10027, USA
and Nevis Laboratories, Irvington, New York 10533, USA
[10]Dapnia, CEA Saclay, F-91191, Gif-sur-Yvette, France
[11]Debrecen University, H-4010 Debrecen, Egyetem tér 1, Hungary
[12]Florida State University, Tallahassee, Florida 32306, USA
[13]Georgia State University, Atlanta, Georgia 30303, USA
[14]Hiroshima University, Kagamiyama, Higashi-Hiroshima 739-8526, Japan
[15]IHEP Protvino, Institute for High Energy Physics, State Research Center of Russian Federation, Protvino, 142281, Russia
[16]Iowa State University, Ames, Iowa 50011, USA
[17]Joint Institute for Nuclear Research, 141980 Dubna, Moscow Region, Russia
[18]KAERI, Cyclotron Application Laboratory, Seoul, South Korea
[19]Kangnung National University, Kangnung 210-702, South Korea
[20]KEK, High Energy Accelerator Research Organization, Tsukuba, Ibaraki 305-0801, Japan
[21]KFKI Research Institute for Particle and Nuclear Physics of the Hungarian Academy of Sciences (MTA KFKI RMKI), H-1525
Budapest 114, Post Office Box 49, Budapest, Hungary
[22]Korea University, Seoul, 136-701, Korea
[23]Russian Research Center "Kurchatov Institute", Moscow, Russia
[24]Kyoto University, Kyoto 606-8502, Japan
[25]Laboratoire Leprince-Ringuet, Ecole Polytechnique, CNRS-IN2P3, Route de Saclay, F-91128, Palaiseau, France
[26]Lawrence Livermore National Laboratory, Livermore, California 94550, USA
[27]Los Alamos National Laboratory, Los Alamos, New Mexico 87545, USA
[28]LPC, Université Blaise Pascal, CNRS-IN2P3, Clermont-Fd, 63177 Aubiere Cedex, France
[29]Department of Physics, Lund University, Box 118, SE-221 00 Lund, Sweden
[30]Institut für Kernphysik, University of Muenster, D-48149 Muenster, Germany
[31]Myongji University, Yongin, Kyonggido 449-728, Korea
[32]Nagasaki Institute of Applied Science, Nagasaki-shi, Nagasaki 851-0193, Japan
[33]University of New Mexico, Albuquerque, New Mexico 87131, USA
[34]New Mexico State University, Las Cruces, New Mexico 88003, USA
[35]Oak Ridge National Laboratory, Oak Ridge, Tennessee 37831, USA
[36]IPN-Orsay, Universite Paris Sud, CNRS-IN2P3, Boîte Postale 1, F-91406, Orsay, France
[37]PNPI, Petersburg Nuclear Physics Institute, Gatchina, Leningrad region, 188300, Russia
[38]The Institute of Physical and Chemical Research, RIKEN, Wako, Saitama 351-0198, Japan
[39]RIKEN BNL Research Center, Brookhaven National Laboratory, Upton, New York 11973-5000, USA
[40]Saint Petersburg State Polytechnic University, St. Petersburg, Russia
[41]Instituto de Física, Universidade de São Paulo, Caixa Postal 66318, São Paulo CEP05315-970, Brazil
[42]System Electronics Laboratory, Seoul National University, Seoul, South Korea
[43]Chemistry Department, Stony Brook University, SUNY, Stony Brook, New York 11794-3400, USA
[44]Department of Physics and Astronomy, Stony Brook University, SUNY, Stony Brook, New York 11794, USA
[45]SUBATECH (Ecole des Mines de Nantes, CNRS-IN2P3, Université de Nantes) Boîte Postale 20722 - 44307, Nantes, France
[46]University of Tennessee, Knoxville, Tennessee 37996, USA
[47]Department of Physics, Tokyo Institute of Technology, Tokyo, 152-8551, Japan
[48]Institute of Physics, University of Tsukuba, Tsukuba, Ibaraki 305, Japan
[49]Vanderbilt University, Nashville, Tennessee 37235, USA
[50]Waseda University, Advanced Research Institute for Science and Engineering, 17 Kikui-cho, Shinjuku-ku, Tokyo 162-0044, Japan
[51]Weizmann Institute, Rehovot 76100, Israel
[52]Yonsei University, IPAP, Seoul 120-749, Korea
(Received 15 August 2005; published 26 January 2006)

The invariant differential cross section for inclusive electron production in $p + p$ collisions at $\sqrt{s} = 200$ GeV has been measured by the PHENIX experiment at the BNL Relativistic Heavy Ion Collider over the transverse momentum range $0.4 \leq p_T \leq 5.0$ GeV/c in the central rapidity region ($|\eta| \leq 0.35$). The contribution to the inclusive electron spectrum from semileptonic decays of hadrons carrying heavy flavor, i.e., charm quarks or, at high p_T, bottom quarks, is determined via three independent methods. The resulting electron spectrum from heavy-flavor decays is compared to recent leading and next-to-leading order perturbative QCD calculations. The total cross section of charm quark-antiquark pair production is determined to be $\sigma_{c\bar{c}} = 0.92 \pm 0.15(\text{stat}) \pm 0.54(\text{syst})$ mb.

DOI: 10.1103/PhysRevLett.96.032001 PACS numbers: 13.85.Qk, 13.20.Fc, 13.20.He, 25.75.Dw

The production of hadrons carrying heavy quarks, i.e., charm or bottom, serves as a crucial proving ground for quantum chromodynamics (QCD), the theory of the strong interaction. Because of the large quark masses, charm and bottom production can be treated by perturbative QCD (pQCD) even at small momenta without being significantly affected by additional soft processes [1]. This is in distinct contrast to the production of particles composed solely of light quarks, which can be evaluated perturbatively only for sufficiently large momenta. Consequently, pQCD calculations of heavy quark production are expected to be reliable over the full momentum range experimentally accessible at collider energies.

For bottom production, next-to-leading order (NLO) calculations are in reasonable agreement with data [2]. Charm measurements at $\sqrt{s} = 1.96$ TeV exist for high transverse momentum (p_T) only [3], where the cross section is higher than NLO predictions by $\geq 50\%$. However, these discrepancies are within the substantial experimental and theoretical uncertainties [3]. At the Relativistic Heavy Ion Collider (RHIC), charm yields have been measured for $p + p$ and $d + \mathrm{Au}$ collisions at $\sqrt{s_{\mathrm{NN}}} = 200$ GeV [4,5] as well as for Au + Au collisions at 130 and 200 GeV [6,7]. Further measurements are crucial for a better understanding of heavy-flavor production at RHIC. In particular, the relevance of higher order processes and other production mechanisms like jet fragmentation is unclear.

We report on the central rapidity production ($|\eta| \leq 0.35$) of inclusive electrons, $(e^+ + e^-)/2$, in $p + p$ collisions at $\sqrt{s} = 200$ GeV measured by the PHENIX experiment [8] at RHIC. Contributions from semileptonic heavy-flavor decays are extracted in the electron p_T range $0.4 \leq p_T \leq 5.0$ GeV/c. The resulting invariant differential cross section is an important benchmark for pQCD calculations of heavy quark production. Furthermore, it provides a crucial baseline for measurements in nuclear collisions at RHIC. Since hadronic heavy-flavor production is expected to be dominated by initial parton scattering, systematic studies in $p + p$ and $d + \mathrm{Au}$ collisions should be sensitive to the nucleon parton distribution functions as well as to their nuclear modifications such as shadowing [9]. In Au + Au collisions, heavy quarks constitute a unique and, with the data presented here, calibrated probe for the hot and dense medium created in the collisions. Possible medium modification of heavy-flavor probes include energy loss [10,11], azimuthal asymmetry [12], and quarkonia suppression [13] or enhancement [14,15].

The data used here were recorded by PHENIX during RHIC Run 2. Beam-beam counters (BBCs), positioned at pseudorapidities $3.1 < |\eta| < 3.9$, measured the collision vertex and provided the minimum bias (MB) interaction trigger defined by at least one hit on each side of the vertex. Events containing high p_T electrons were selected by an additional level 1 trigger in coincidence with the MB trigger. This level 1 trigger required a minimum energy deposit of 0.75 GeV in a 2×2 tile of towers in the electromagnetic calorimeter (EMC) [16]. After a vertex cut of $|z_{\mathrm{vtx}}| < 20$ cm, an equivalent of 465×10^6 MB events sampled by the EMC trigger was analyzed in addition to the 15×10^6 events recorded with the MB trigger itself.

The PHENIX east arm spectrometer ($|\eta| < 0.35$, $\Delta\phi = \pi/2$) includes a drift chamber and a pad chamber layer for charged particle tracking. Tracks were confirmed by hits in the EMC matching in position with the track projection within 3σ. Electron candidates required at least two associated hits in the ring imaging Čerenkov detector (RICH) in the projected ring area. Random coincidences of hadron tracks and hits in the RICH occurred with a probability of $(3.0 \pm 1.5) \times 10^{-4}$. For electrons the energy E deposited in the EMC must be consistent with the momentum p. Requiring $|(E - p)/p| < 3\sigma$, a total charged hadron rejection factor of about 10^4 (10^5) was achieved for $p_T = 0.4\,(\geq 2.0)$ GeV/c. Remaining background ($<1\%$) was measured via event mixing and subtracted statistically.

The differential cross section for electron production was calculated as

$$E\frac{d^3\sigma}{dp^3} = \frac{1}{\epsilon_{\mathrm{bias}} \int \mathcal{L}dt} \frac{N_e}{2\pi p_T \Delta y \Delta p_T} \frac{1}{A\epsilon_{\mathrm{rec}}}, \qquad (1)$$

where $\int \mathcal{L}dt$ is the integrated luminosity measured with the MB trigger or sampled with the EMC trigger, respectively; ϵ_{bias} is the probability for an electron event to fulfill the MB trigger condition; N_e is the measured electron yield; and $A\epsilon_{\mathrm{rec}}$ is the product of geometrical acceptance and reconstruction efficiency. For the EMC triggered sample, ϵ_{rec} includes the trigger efficiency ϵ_{lvl1}.

$\int \mathcal{L}dt$ is calculated as $N_{\mathrm{MB}}/\sigma_{\mathrm{BBC}}$, where N_{MB} is the number of MB triggers or, for the EMC triggered sample, the number of EMC triggers divided by the measured fraction of MB events which simultaneously fulfill the EMC trigger criterion. With the MB trigger cross section $\sigma_{\mathrm{BBC}} = 21.8 \pm 2.1$ mb [16], the analyzed data samples correspond to integrated luminosities of 0.7 nb^{-1} (MB trigger) and 21 nb^{-1} (EMC trigger), respectively. The p_T independent trigger bias $\epsilon_{\mathrm{bias}} = 0.75 \pm 0.02$ was measured for events containing a π^0 with $p_T > 1.5$ GeV/c [16] and confirmed for charged hadrons with $p_T > 0.2$ GeV/c [17], indicating a universal bias both for hard and soft processes. $A\epsilon_{\mathrm{rec}}$ was calculated as a function of p_T ($< 10\%$ variation over the full p_T range) in a GEANT [18] simulation of electrons with flat distributions in rapidity ($|y| < 0.6$), azimuth ($0 < \phi < 2\pi$), and event vertex ($|z| < 30$ cm) as input. The simulated detector response was carefully tuned to match the real detector. Rigorous fiducial cuts were applied to eliminate active area mismatches between data and simulation as well as run-by-run variations. The trigger efficiency ϵ_{lvl1}, evaluated for single electrons in the fiducial area, rises from zero at low p_T to $95 \pm 5\%$ for $p_T > 2$ GeV/c. Finally, we appropriately corrected for the effect of finite bin width in p_T.

The corrected electron spectra from the MB and EMC triggered samples cover p_T ranges of $0.4 < p_T < 2.0$ GeV/c and $0.6 < p_T < 5.0$ GeV/c, respectively. They are consistent with each other within the statistical uncertainties in the p_T region of overlap. The weighted average of both measurements is shown in Fig. 1(a).

The systematic uncertainty of the inclusive electron spectrum is about 12%, almost p_T independent, calculated as the sum in quadrature of contributions from the acceptance calculation (7%), electron identification cuts (5.2%), run-by-run variations (4%), tracking efficiency (3%), momentum scale (1–5%), and other smaller uncertainties (more details on the uncertainty estimations can be found in Ref. [19]). The value of 12% does not include the 9.6% uncertainty of the absolute normalization.

The invariant cross section of electrons from heavy-flavor decays was determined by subtracting a *cocktail* of contributions from other sources from the inclusive data. The most important background is the π^0 Dalitz decay which was calculated with a hadron decay generator using a parameterization of measured π^0 [16] and $\pi^{\pm}$ [20] spectra as input. The spectral shapes of other light hadrons h were obtained from the pion spectra by m_T scaling.

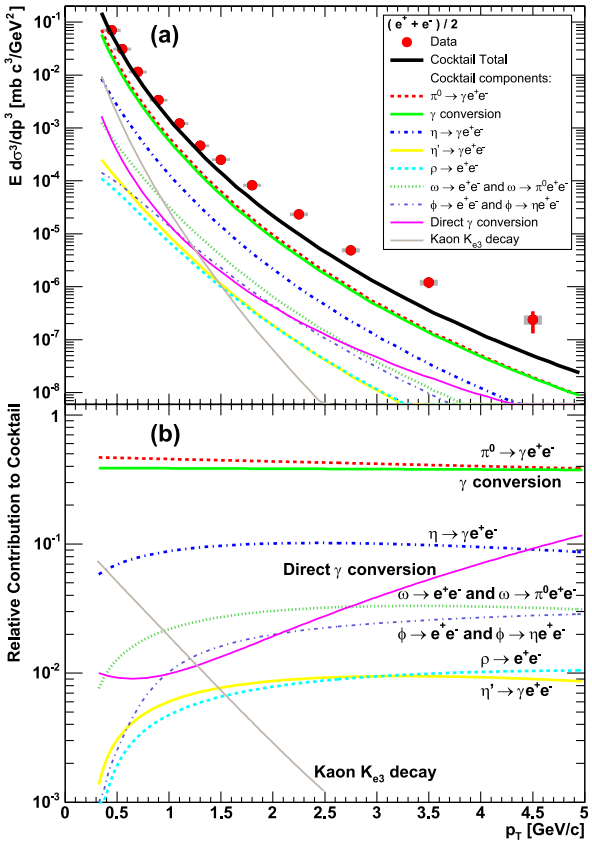

FIG. 1 (color online). (a) Inclusive electron invariant differential cross section, measured in $p + p$ collisions at $\sqrt{s} =$ 200 GeV, compared with all contributions from electron sources included in the background *cocktail*. Error bars (boxes) correspond to statistical (systematic) uncertainties. (b) Relative contributions of all electron sources to the background *cocktail*.

Within this approach the ratios h/π^0 are constant at high p_T and for the relative normalization we used: $\eta/\pi^0 = 0.45 \pm 0.10$ [21], $\rho/\pi^0 = 1.0 \pm 0.3$, $\omega/\pi^0 = 1.0 \pm 0.3$, $\eta'/\pi^0 = 0.25 \pm 0.08$, and $\phi/\pi^0 = 0.40 \pm 0.12$. Only the η contribution is of any practical relevance. Another major electron source is the conversion of photons, mainly from $\pi^0 \to \gamma\gamma$ decays, in material within the acceptance. The spectra of electrons from conversions and Dalitz decays are very similar. In a GEANT simulation of π^0 decays, the ratio of electrons from conversions to electrons from Dalitz decays was determined to be 0.73 ± 0.07, essentially p_T independent. Contributions from photon conversions from other sources were taken into account as well. In addition, electrons from kaon decays (K_{e3}), determined in a GEANT simulation based on measured kaon spectra [20], and electrons from external as well as internal conversions of direct photons [22,23] were considered in the cocktail. All background sources are compared with the inclusive data in Fig. 1(a) with the relative contributions shown in Fig. 1(b). The total systematic uncertainty of the cocktail is about 12%, essentially p_T independent. This uncertainty is dominated by the systematic error of the pion parameterization ($\approx$10%). Other systematic uncertainties, mainly the η/π^0 normalization and, at high p_T, the contribution from direct radiation, are much smaller.

Given the small amount of material within the acceptance (Be beam pipe: 0.29% X_0; air: 0.28% X_0) the ratio R_{NP} of nonphotonic electrons from heavy-flavor decays to background from photonic sources is large ($R_{\mathrm{NP}} > 1$ for $p_T > 1.5$ GeV/c) as shown in Fig. 2. Two complementary analysis methods confirm the *cocktail* result:

The *converter* technique [7] compares electron spectra measured with an additional photon converter $X_C = 1.67\% X_0$ introduced into the acceptance to measurements without converter. The converter increases the contribution from conversions and Dalitz decays by a fixed factor, which was determined precisely via GEANT simulations. Thus, the electron spectra from photonic and nonphotonic sources can be deduced (Fig. 2). The drawbacks of the *converter* method are the limitation in statistics of the converter run period and the fact that the photonic contribution is small at high p_T.

The *$e\gamma$ coincidence* technique evaluates the correlation of electrons and photons via their invariant mass. Electrons from π^0 Dalitz decays or the conversion of one of the photons from $\pi^0 \to \gamma\gamma$ decays are correlated with a photon, in contrast to electrons from semileptonic heavy-flavor decays. Comparing the measured $e\gamma$ coincidence rate with the simulated rate for single π^0 events allows R_{NP} to be deduced as shown in Fig. 2, once corrections for contributions from other photonic sources are applied.

After subtracting the background cocktail from the inclusive electron spectrum the invariant differential cross section of electrons from heavy-flavor decays is shown in Fig. 3 compared with two theoretical predictions. A leading order (LO) PYTHIA calculation, tuned to existing charm and bottom hadroproduction measurements [24,25], is in

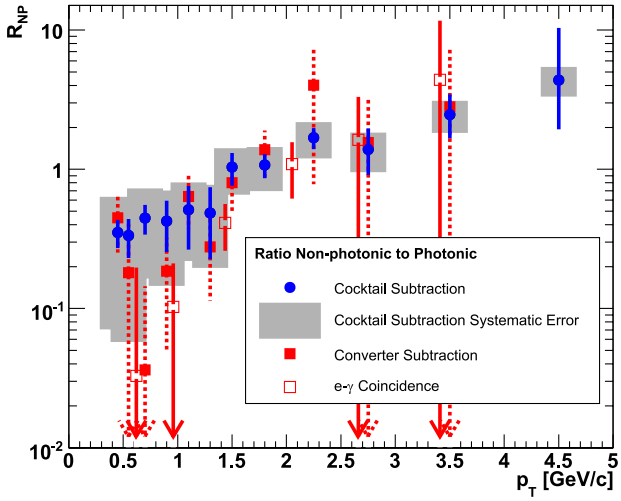

FIG. 2 (color online). Ratio of electrons from heavy-flavor decays (nonphotonic) and other sources (photonic), R_{NP}, for three independent analysis methods. Error bars (boxes) are statistical (*cocktail* systematic) uncertainties.

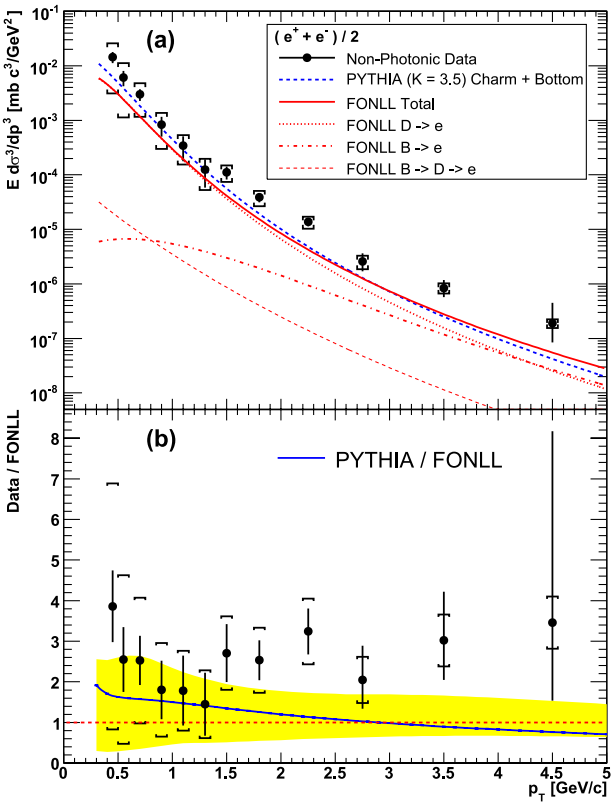

FIG. 3 (color online). (a) Invariant differential cross section of electrons from heavy-flavor decays compared with PYTHIA LO (with $K = 3.5$) and FONLL pQCD calculations. Error bars (brackets) show statistical (systematic) uncertainties. For the FONLL calculation contributions from charm, bottom and bottom cascade decays are shown separately. (b) Ratio of data and FONLL calculations with experimental statistical (error bars) and systematic (brackets) uncertainties as well as the theoretical uncertainty (shaded band). The solid line corresponds to the ratio of PYTHIA and FONLL.

reasonable agreement with the data for $p_T < 1.5$ GeV/c, but underestimates the cross section at higher p_T. It is important to note that this calculation includes a scale factor $K = 3.5$ to accommodate neglected NLO contributions. A *Fixed-Order plus Next-to-Leading-Log* (FONLL) pQCD calculation [26] still leaves room for further contributions beyond the included NLO processes. The predicted contribution from bottom decays is irrelevant for the electron cross section at $p_T < 3$ GeV/c and becomes significant only for $p_T > 4$ GeV/c.

The charm production cross section was derived from the integrated electron cross section for $p_T > p_{T,\mathrm{low}} = 0.6(0.8)$ GeV/c ($d\sigma_e^{p_{T,\mathrm{low}}}/dy = 4.78(2.15) \pm 0.78(0.46) \times$ (stat) $\pm$ 1.74(0.68)(syst) $\times 10^{-3}$ mb). Since in the low p_T region, which dominates the total cross section, PYTHIA describes the measured spectrum reasonably well, the total charm cross section was determined by extrapolating the properly scaled PYTHIA spectrum to $p_T = 0$ GeV/c. First the PYTHIA spectra for electrons from charm and bottom decays were fitted to the data for $p_T > 0.6$ GeV/c, with only the normalizations as free parameters. The resulting central rapidity charm production cross section was determined to be $d\sigma_{c\bar{c}}/dy = 0.20 \pm 0.03(\mathrm{stat}) \pm 0.11(\mathrm{syst})$ mb, where the systematic error is dominated by the uncertainty of the electron spectrum itself ($\approx$56%), evaluated by refitting PYTHIA to the data at the minimum and maximum of the 1σ systematic error band. Additional uncertainties from the relative ratios of different charmed hadron species and their branching ratios into electrons ($\approx$9%) and the variation of the PYTHIA spectral shape ($\approx$11%) [7] were added in quadrature. The rapidity integrated cross section was determined to be $\sigma_{c\bar{c}} = 0.92 \pm 0.15(\mathrm{stat}) \pm 0.54(\mathrm{syst})$ mb, where various parton distribution functions [GRV98LO and MRST(cg) [27] in addition to the default CTEQ5L [25]] were used for the extrapolation, with an associated extra systematic error of $\approx$6% [7] added in quadrature.

Within errors the integrated charm cross section is compatible with data from Au + Au collisions [7] (minimum bias value: $0.622 \pm 0.057 \pm 0.160$ mb per NN collision) and from d + Au collisions [4] ($1.3 \pm 0.2 \pm 0.4$ mb) at the same $\sqrt{s_{\mathrm{NN}}} = 200$ GeV. The FONLL cross section is smaller ($\sigma_{c\bar{c}}^{\mathrm{FONLL}} = 0.256^{+0.400}_{-0.146}$ mb) but it is still compatible with the data. Our measurement does not allow a bottom cross section to be deduced, which is predicted by FONLL to be $\sigma_{b\bar{b}}^{\mathrm{FONLL}} = 1.87^{+0.99}_{-0.67}$ μb.

In conclusion, we have measured single electrons from heavy-flavor decays in $p + p$ collisions at $\sqrt{s} = 200$ GeV. These data provide a crucial benchmark for pQCD heavy quark calculations. We observe that above $p_T \approx 2$ GeV/c the electron spectrum is significantly harder than predicted by a LO PYTHIA charm and bottom calculation. Contributions to the charm production cross section in excess of the considered FONLL calculation, e.g., from jet fragmentation, cannot be excluded. Similar excess at high p_T was ob-

served by Fermilab experiments (CDF and D0) at $\sqrt{s} = 1.96$ TeV [3]. The new data reported here provide an important baseline for the study of possible medium modification of heavy quark production at RHIC.

We thank the staff of the Collider-Accelerator and Physics Departments at BNL for their vital contributions. We acknowledge support from the Department of Energy and NSF (U.S.A.), MEXT and JSPS (Japan), CNPq and FAPESP (Brazil), NSFC (China), CNRS-IN2P3 and CEA (France), BMBF, DAAD, and AvH (Germany), OTKA (Hungary), DAE and DST (India), ISF (Israel), KRF and CHEP (Korea), RMIST, RAS, and RMAE (Russia), VR and KAW (Sweden), U.S. CRDF for the FSU, US-Hungarian NSF-OTKA-MTA, and US-Israel BSF.

*Deceased.
†Corresponding author.
Email address: zajc@nevis.columbia.edu

[1] M. L. Mangano *et al.*, Nucl. Phys. **B405**, 507 (1993).
[2] M. Cacciari, hep-ph/0407187; M. L. Mangano, hep-ph/0411020.
[3] D. Acosta *et al.*, Phys. Rev. Lett. **91**, 241804 (2003).
[4] J. Adams *et al.*, Phys. Rev. Lett. **94**, 062301 (2005).
[5] S. Kelly *et al.*, J. Phys. G **30**, S1189 (2004).
[6] K. Adcox *et al.*, Phys. Rev. Lett. **88**, 192303 (2002).
[7] S. S. Adler *et al.*, Phys. Rev. Lett. **94**, 082301 (2005).
[8] K. Adcox *et al.*, Nucl. Instrum. Methods Phys. Res., Sect. A **499**, 469 (2003).
[9] Z. Lin and M. Gyulassy, Phys. Rev. Lett. **77**, 1222 (1996).
[10] Y. L. Dokshitzer and D. E. Kharzeev, Phys. Lett. B **519**, 199 (2001).
[11] N. Armesto, A. Dainese, C. A. Salgado, and U. A. Wiedemann, Phys. Rev. D **71**, 054027 (2005).
[12] Z. W. Lin and D. Molnar, Phys. Rev. C **68**, 044901 (2003); V. Greco, C. M. Ko, and R. Rapp, Phys. Lett. B **595**, 202 (2004).
[13] T. Matsui and H. Satz, Phys. Lett. B **178**, 416 (1986).
[14] P. Braun-Munzinger and J. Stachel, Phys. Lett. B **490**, 196 (2000).
[15] R. L. Thews, M. Schroedter, and J. Rafelski, Phys. Rev. C **63**, 054905 (2001).
[16] S. S. Adler *et al.*, Phys. Rev. Lett. **91**, 241803 (2003).
[17] S. S. Adler *et al.*, Phys. Rev. Lett. **95**, 202001 (2005).
[18] GEANT 3.21, CERN program library.
[19] S. A. Butsyk, hep-ex/0511048.
[20] F. Matathias *et al.*, J. Phys. G **30**, S1113 (2004).
[21] S. S. Adler *et al.* (to be published).
[22] L. E. Gordon and W. Vogelsang, Phys. Rev. D **50**, 1901 (1994).
[23] S. S. Adler *et al.*, Phys. Rev. D **71**, 071102(R) (2005).
[24] We used PYTHIA 6.205 with a modified set of parameters [6] and CTEQ5L parton distribution functions [25].
[25] H. H. Lai *et al.*, Eur. Phys. J. C **12**, 375 (2000).
[26] M. Cacciari, P. Nason, and R. Vogt, Phys. Rev. Lett. **95**, 122001 (2005).
[27] M. Glück, E. Reya, and A. Vogt, Eur. Phys. J. C **5**, 461 (1998); A. D. Martin, R. G Roberts, W. J. Stirling, and R. S. Thorne, Eur. Phys. J. C **4**, 463 (1998).

J/ψ Production and Nuclear Effects for d + Au and p + p Collisions at $\sqrt{s_{NN}} = 200$ GeV

S. S. Adler,[5] S. Afanasiev,[20] C. Aidala,[10] N. N. Ajitanand,[44] Y. Akiba,[21,40] A. Al-Jamel,[35] J. Alexander,[44] K. Aoki,[25] L. Aphecetche,[46] R. Armendariz,[35] S. H. Aronson,[5] E. T. Atomssa,[26] R. Averbeck,[45] T. C. Awes,[36] V. Babintsev,[17] A. Baldisseri,[11] K. N. Barish,[6] P. D. Barnes,[28] B. Bassalleck,[34] S. Bathe,[6,31] S. Batsouli,[10] V. Baublis,[39] F. Bauer,[6] A. Bazilevsky,[5,41] S. Belikov,[19,17] M. T. Bjorndal,[10] J. G. Boissevain,[28] H. Borel,[11] M. L. Brooks,[28] D. S. Brown,[35] N. Bruner,[34] D. Bucher,[31] H. Buesching,[5,31] V. Bumazhnov,[17] G. Bunce,[5,41] J. M. Burward-Hoy,[28,27] S. Butsyk,[45] X. Camard,[46] P. Chand,[4] W. C. Chang,[2] S. Chernichenko,[17] C. Y. Chi,[10] J. Chiba,[21] M. Chiu,[10] I. J. Choi,[53] R. K. Choudhury,[4] T. Chujo,[5] V. Cianciolo,[36] Y. Cobigo,[11] B. A. Cole,[10] M. P. Comets,[37] P. Constantin,[19] M. Csanád,[13] T. Csörgő,[22] J. P. Cussonneau,[46] D. d'Enterria,[10] K. Das,[14] G. David,[5] F. Deák,[13] H. Delagrange,[46] A. Denisov,[17] A. Deshpande,[41] E. J. Desmond,[5] A. Devismes,[45] O. Dietzsch,[42] J. L. Drachenberg,[1] O. Drapier,[26] A. Drees,[45] A. Durum,[17] D. Dutta,[4] V. Dzhordzhadze,[47] Y. V. Efremenko,[36] H. En'yo,[40,41] B. Espagnon,[37] S. Esumi,[49] D. E. Fields,[34,41] C. Finck,[46] F. Fleuret,[26] S. L. Fokin,[24] B. D. Fox,[41] Z. Fraenkel,[52] J. E. Frantz,[10] A. Franz,[5] A. D. Frawley,[14] Y. Fukao,[25,40,41] S.-Y. Fung,[6] S. Gadrat,[29] M. Germain,[46] A. Glenn,[47] M. Gonin,[26] J. Gosset,[11] Y. Goto,[40,41] R. Granier de Cassagnac,[26] N. Grau,[19] S. V. Greene,[50] M. Grosse Perdekamp,[18,41] H.-Å. Gustafsson,[30] T. Hachiya,[16] J. S. Haggerty,[5] H. Hamagaki,[8] A. G. Hansen,[28] E. P. Hartouni,[27] M. Harvey,[5] K. Hasuko,[40] R. Hayano,[8] X. He,[15] M. Heffner,[27] T. K. Hemmick,[45] J. M. Heuser,[40] P. Hidas,[22] H. Hiejima,[18] J. C. Hill,[19] R. Hobbs,[34] W. Holzmann,[44] K. Homma,[16] B. Hong,[23] A. Hoover,[35] T. Horaguchi,[40,41,48] T. Ichihara,[40,41] V. V. Ikonnikov,[24] K. Imai,[25,40] M. Inaba,[49] M. Inuzuka,[8] D. Isenhower,[1] L. Isenhower,[1] M. Ishihara,[40] M. Issah,[44] A. Isupov,[20] B. V. Jacak,[45] J. Jia,[45] O. Jinnouchi,[40,41] B. M. Johnson,[5] S. C. Johnson,[27] K. S. Joo,[32] D. Jouan,[37] F. Kajihara,[8] S. Kametani,[8,51] N. Kamihara,[40,48] M. Kaneta,[41] J. H. Kang,[53] K. Katou,[51] T. Kawabata,[8] A. V. Kazantsev,[24] S. Kelly,[9,10] B. Khachaturov,[52] A. Khanzadeev,[39] J. Kikuchi,[51] D. J. Kim,[53] E. Kim,[43] G.-B. Kim,[26] H. J. Kim,[53] E. Kinney,[9] A. Kiss,[13] E. Kistenev,[5] A. Kiyomichi,[40] C. Klein-Boesing,[31] H. Kobayashi,[41] L. Kochenda,[39] V. Kochetkov,[17] R. Kohara,[16] B. Komkov,[39] M. Konno,[49] D. Kotchetkov,[6] A. Kozlov,[52] P. J. Kroon,[5] C. H. Kuberg,[1,*] G. J. Kunde,[28] K. Kurita,[40] M. J. Kweon,[23] Y. Kwon,[53] G. S. Kyle,[35] R. Lacey,[44] J. G. Lajoie,[19] Y. Le Bornec,[37] A. Lebedev,[19,24] S. Leckey,[45] D. M. Lee,[28] M. J. Leitch,[28] M. A. L. Leite,[42] X. H. Li,[6] H. Lim,[43] A. Litvinenko,[20] M. X. Liu,[28] C. F. Maguire,[50] Y. I. Makdisi,[5] A. Malakhov,[20] V. I. Manko,[24] Y. Mao,[38,40] G. Martinez,[46] H. Masui,[49] F. Matathias,[45] T. Matsumoto,[8,51] M. C. McCain,[1] P. L. McGaughey,[28] Y. Miake,[49] T. E. Miller,[50] A. Milov,[45] S. Mioduszewski,[5] G. C. Mishra,[15] J. T. Mitchell,[5] A. K. Mohanty,[4] D. P. Morrison,[5] J. M. Moss,[28] D. Mukhopadhyay,[52] M. Muniruzzaman,[6] S. Nagamiya,[21] J. L. Nagle,[9,10] T. Nakamura,[16] J. Newby,[47] A. S. Nyanin,[24] J. Nystrand,[30] E. O'Brien,[5] C. A. Ogilvie,[19] H. Ohnishi,[40] I. D. Ojha,[3,50] H. Okada,[25,40] K. Okada,[40,41] A. Oskarsson,[30] I. Otterlund,[30] K. Oyama,[8] K. Ozawa,[8] D. Pal,[52] A. P. T. Palounek,[28] V. Pantuev,[45] V. Papavassiliou,[35] J. Park,[43] W. J. Park,[23] S. F. Pate,[35] H. Pei,[19] V. Penev,[20] J.-C. Peng,[18] H. Pereira,[11] V. Peresedov,[20] A. Pierson,[34] C. Pinkenburg,[5] R. P. Pisani,[5] M. L. Purschke,[5] A. K. Purwar,[45] J. M. Qualls,[1] J. Rak,[19] I. Ravinovich,[52] K. F. Read,[36,47] M. Reuter,[45] K. Reygers,[31] V. Riabov,[39] Y. Riabov,[39] G. Roche,[29] A. Romana,[26,*] M. Rosati,[19] S. S. E. Rosendahl,[30] P. Rosnet,[29] V. L. Rykov,[40] S. S. Ryu,[53] N. Saito,[25,40,41] T. Sakaguchi,[8,51] S. Sakai,[49] V. Samsonov,[39] L. Sanfratello,[34] R. Santo,[31] H. D. Sato,[25,40] S. Sato,[5,49] S. Sawada,[21] Y. Schutz,[46] V. Semenov,[17] R. Seto,[6] T. K. Shea,[5] I. Shein,[17] T.-A. Shibata,[40,48] K. Shigaki,[16] M. Shimomura,[49] A. Sickles,[45] C. L. Silva,[42] D. Silvermyr,[28] K. S. Sim,[23] A. Soldatov,[17] R. A. Soltz,[27] W. E. Sondheim,[28] S. P. Sorensen,[47] I. V. Sourikova,[5] F. Staley,[11] P. W. Stankus,[36] E. Stenlund,[30] M. Stepanov,[35] A. Ster,[22] S. P. Stoll,[5] T. Sugitate,[16] J. P. Sullivan,[28] S. Takagi,[49] E. M. Takagui,[42] A. Taketani,[40,41] K. H. Tanaka,[21] Y. Tanaka,[33] K. Tanida,[40] M. J. Tannenbaum,[5] A. Taranenko,[44] P. Tarján,[12] T. L. Thomas,[34] M. Togawa,[25,40] J. Tojo,[40] H. Torii,[25,41] R. S. Towell,[1] V-N. Tram,[26] I. Tserruya,[52] Y. Tsuchimoto,[16] H. Tydesjö,[30] N. Tyurin,[17] T. J. Uam,[32] H. W. van Hecke,[28] J. Velkovska,[5] M. Velkovsky,[45] V. Veszprémi,[12] A. A. Vinogradov,[24] M. A. Volkov,[24] E. Vznuzdaev,[39] X. R. Wang,[15] Y. Watanabe,[40,41] S. N. White,[5] N. Willis,[37] F. K. Wohn,[19] C. L. Woody,[5] W. Xie,[6] A. Yanovich,[17] S. Yokkaichi,[40,41] G. R. Young,[36] I. E. Yushmanov,[24] W. A. Zajc,[10,†] C. Zhang,[10] S. Zhou,[7] J. Zimányi,[22] L. Zolin,[20] and X. Zong[19]

(PHENIX Collaboration)

[1]*Abilene Christian University, Abilene, Texas 79699, USA*
[2]*Institute of Physics, Academia Sinica, Taipei 11529, Taiwan*
[3]*Department of Physics, Banaras Hindu University, Varanasi 221005, India*

 © 2006 The American Physical Society

[4]Bhabha Atomic Research Centre, Bombay 400 085, India
[5]Brookhaven National Laboratory, Upton, New York 11973-5000, USA
[6]University of California - Riverside, Riverside, California 92521, USA
[7]China Institute of Atomic Energy (CIAE), Beijing, People's Republic of China
[8]Center for Nuclear Study, Graduate School of Science, University of Tokyo, 7-3-1 Hongo, Bunkyo, Tokyo 113-0033, Japan
[9]University of Colorado, Boulder, Colorado 80309, USA
[10]Columbia University, New York, New York 10027, USA
and Nevis Laboratories, Irvington, New York 10533, USA
[11]Dapnia, CEA Saclay, F-91191, Gif-sur-Yvette, France
[12]Debrecen University, H-4010 Debrecen, Egyetem tér 1, Hungary
[13]ELTE, Eötvös Loránd University, H - 1117 Budapest, Pázmány P. s. 1/A, Hungary
[14]Florida State University, Tallahassee, Florida 32306, USA
[15]Georgia State University, Atlanta, Georgia 30303, USA
[16]Hiroshima University, Kagamiyama, Higashi-Hiroshima 739-8526, Japan
[17]IHEP Protvino, State Research Center of Russian Federation, Institute for High Energy Physics, Protvino, 142281, Russia
[18]University of Illinois at Urbana-Champaign, Urbana, Illinois 61801, USA
[19]Iowa State University, Ames, Iowa 50011, USA
[20]Joint Institute for Nuclear Research, 141980 Dubna, Moscow Region, Russia
[21]KEK, High Energy Accelerator Research Organization, Tsukuba, Ibaraki 305-0801, Japan
[22]KFKI Research Institute for Particle and Nuclear Physics of the Hungarian Academy of Sciences (MTA KFKI RMKI),
H-1525 Budapest 114, P.O. Box 49, Budapest, Hungary
[23]Korea University, Seoul, 136-701, Korea
[24]Russian Research Center "Kurchatov Institute", Moscow, Russia
[25]Kyoto University, Kyoto 606-8502, Japan
[26]Laboratoire Leprince-Ringuet, Ecole Polytechnique, CNRS-IN2P3, Route de Saclay, F-91128, Palaiseau, France
[27]Lawrence Livermore National Laboratory, Livermore, California 94550, USA
[28]Los Alamos National Laboratory, Los Alamos, New Mexico 87545, USA
[29]LPC, Université Blaise Pascal, CNRS-IN2P3, Clermont-Fd, 63177 Aubiere Cedex, France
[30]Department of Physics, Lund University, Box 118, SE-221 00 Lund, Sweden
[31]Institut für Kernphysik, University of Muenster, D-48149 Muenster, Germany
[32]Myongji University, Yongin, Kyonggido 449-728, Korea
[33]Nagasaki Institute of Applied Science, Nagasaki-shi, Nagasaki 851-0193, Japan
[34]University of New Mexico, Albuquerque, New Mexico 87131, USA
[35]New Mexico State University, Las Cruces, New Mexico 88003, USA
[36]Oak Ridge National Laboratory, Oak Ridge, Tennessee 37831, USA
[37]IPN-Orsay, Universite Paris Sud, CNRS-IN2P3, BP1, F-91406, Orsay, France
[38]Peking University, Beijing, People's Republic of China
[39]PNPI, Petersburg Nuclear Physics Institute, Gatchina, Leningrad Region, 188300, Russia
[40]RIKEN (The Institute of Physical and Chemical Research), Wako, Saitama 351-0198, Japan
[41]RIKEN BNL Research Center, Brookhaven National Laboratory, Upton, New York 11973-5000, USA
[42]Universidade de São Paulo, Instituto de Física, Caixa Postal 66318, São Paulo CEP05315-970, Brazil
[43]System Electronics Laboratory, Seoul National University, Seoul, South Korea
[44]Chemistry Department, Stony Brook University, Stony Brook, SUNY, New York 11794-3400, USA
[45]Department of Physics and Astronomy, Stony Brook University, SUNY, Stony Brook, New York 11794, USA
[46]SUBATECH (Ecole des Mines de Nantes, CNRS-IN2P3, Université de Nantes) BP 20722 - 44307, Nantes, France
[47]University of Tennessee, Knoxville, Tennessee 37996, USA
[48]Department of Physics, Tokyo Institute of Technology, Oh-okayama, Meguro, Tokyo 152-8551, Japan
[49]Institute of Physics, University of Tsukuba, Tsukuba, Ibaraki 305, Japan
[50]Vanderbilt University, Nashville, Tennessee 37235, USA
[51]Waseda University, Advanced Research Institute for Science and Engineering, 17 Kikui-cho, Shinjuku-ku, Tokyo 162-0044, Japan
[52]Weizmann Institute, Rehovot 76100, Israel
[53]Yonsei University, IPAP, Seoul 120-749, Korea
(Received 28 July 2005; published 10 January 2006)

J/ψ production in d + Au and $p + p$ collisions at $\sqrt{s_{NN}} = 200$ GeV has been measured by the PHENIX experiment at rapidities $-2.2 < y < +2.4$. The cross sections and nuclear dependence of J/ψ production versus rapidity, transverse momentum, and centrality are obtained and compared to lower energy $p + A$ results and to theoretical models. The observed nuclear dependence in d + Au collisions is found to be modest, suggesting that the absorption in the final state is weak and the shadowing of the gluon distributions is small and consistent with Dokshitzer-Gribov-Lipatov-Altarelli-Parisi-based parametrizations that fit deep-inelastic scattering and Drell-Yan data at lower energies.

DOI: 10.1103/PhysRevLett.96.012304 PACS numbers: 25.75.Dw

J/ψ production in hadron collisions, since it proceeds predominantly through diagrams involving gluons (e.g., gluon fusion) [1], is a sensitive probe of the gluon structure function in the nucleon and its modification in nuclei. It is also a leading signal for the creation of hot-dense matter in heavy-ion collisions [2]. Shadowing of partons (quarks or gluons) in nuclei is a depletion of their population at small momentum fraction of the nucleon, x, compared to that in a free nucleon, with a corresponding enhancement at moderate x (antishadowing). In $\sqrt{s_{NN}} = 200$ GeV deuteron-gold ($d + \mathrm{Au}$) collisions at the Relativistic Heavy-Ion Collider (RHIC), for positive (deuteron direction) rapidities, gluons are probed that lie well into the shadowing region with momentum fractions in Au, $x_2 \sim 3 \times 10^{-3}$. Models of gluon shadowing predict suppressions of J/ψ production in nuclei that differ by as much as a factor of 3 [3–5]. Recent theoretical developments, e.g., the color glass condensate model [6], suggest that at very low x nonlinear gluon saturation effects become important and cause substantial modifications of the gluon densities.

The connection of the observed J/ψ suppression to the modified gluon distribution in nuclei can be clouded by the absorption of the final-state $c\bar{c}$ [7] which depends on the poorly known production mechanism [1] and by the energy loss of the intial-state gluon—although the latter is thought to be small at RHIC energies [5]. This connection is also distorted by the fact that approximately a third of the J/ψ's come from decays of higher-mass resonances [8].

Here we present measurements made by the PHENIX experiment at RHIC for the production of J/ψ's in $\sqrt{s_{NN}} = 200$ GeV $d + \mathrm{Au}$ and proton-proton ($p + p$) collisions. These data provide the first measurement of the nuclear dependence of J/ψ production at this energy, a much higher energy than previous $p + A$ measurements from fixed-target experiments at $\sqrt{s_{NN}} \lesssim 40$ GeV [9–13]. Although our measurements are for $d + A$, the nuclear effects on the J/ψ in deuterium were found to be small at lower energies [14]. Besides the shadowing region at small x, these data also probe larger gluon momentum fractions (at negative rapidity) nearer the rest frame of the residual nucleus. Finally, these measurements also serve as a baseline for the upcoming results from the high-luminosity Au + Au and Cu + Cu runs and must be understood in order to look for effects beyond what is expected from cold nuclear matter.

The measurements described here are similar to earlier ones with PHENIX [15] for $p + p$ [16] and Au + Au [17] collisions, but with a second muon spectrometer added and higher luminosity. The two muon spectrometers are especially valuable for asymmetric collisions such as $d + \mathrm{Au}$ where simultaneous measurements at positive ($1.2 < y < 2.4$) and negative ($-2.2 < y < -1.2$) rapidities, along with central ($|y| \leq 0.35$) rapidity from e^+e^-, are then available. Electrons in the central arms are identified by matching charged particle tracks to clusters in an electromagnetic calorimeter (EMC) and to rings in a ring imaging Čerenkov (RICH) detector. Muons are identified by their detection in Iarocci tubes after their penetration through 8 to 11 interaction lengths of copper and steel absorber.

The data used in this analysis were recorded in 2003 using a trigger that required hits in each of the two beam-beam counters located at negative and positive rapidity ($3 < |\eta| < 3.9$). In addition, for the di-muons at least two tracks in the muon identifier of appropriate absorber depth were required, while for the di-electrons a one-track trigger with a signal above threshold in the EMC with a matching hit in the RICH was required. After quality and vertex cuts, the samples for the three arms correspond to integrated luminosities from 180 to 250 nb^{-1} ($p + p$) and 1.4 to 1.7 nb^{-1} ($d + \mathrm{Au}$).

For the di-muons the J/ψ yield is obtained after subtraction of the combinatoric background using like-sign muon pairs ($2\sqrt{N_{++}N_{--}}$) and by fitting the resulting mass peak with a Gaussian plus an exponential to represent the small remaining continuum background underneath the peak. A variety of continuum shapes were checked for each fit in order to establish the uncertainty due to the low-statistics background. For the di-electrons the combinatoric background was subtracted using the sum of like-sign pairs and the J/ψ yield was taken as all remaining events in the mass range 2.6 to 3.6 GeV/c^2. A total ($p + p$ plus $d + \mathrm{Au}$) of about 2100 and 500 J/ψ's were obtained in the $\mu\mu$ and ee channels, respectively.

The differential cross sections are calculated as

$$B_{ll}\frac{d\sigma_{J/\psi}}{dy} = \frac{N_{J/\psi}}{A\epsilon_{\mathrm{rec}}\epsilon_{\mathrm{trig}}\epsilon^{\mathrm{BBC}}_{J/\psi}(N_{\mathrm{evt}}/(\sigma^{\mathrm{tot}}_{\mathrm{MB}}\cdot\epsilon^{BBC}_{\mathrm{MB}}))}\frac{1}{\Delta y} \quad (1)$$

and the nuclear modification factor, R_{dA}, is

$$R_{dA} = \frac{d\sigma^{d\mathrm{Au}}_{J/\psi}/dy}{(2\times 197)\times d\sigma^{pp}_{J/\psi}/dy}. \quad (2)$$

In the above expressions B_{ll} is the J/ψ branching ratio to di-leptons, $N_{J/\psi}$ is the measured J/ψ yield, A is the geometrical acceptance, ϵ_{rec} is the di-lepton reconstruction efficiency, ϵ_{trig} is the trigger efficiency, N_{evt} is the number of minimum-bias triggers sampled, $\sigma^{\mathrm{tot}}_{\mathrm{MB}}$ is the total minimum-bias (MB) cross section, Δy is the rapidity bin width, and $\epsilon^{\mathrm{BBC}}_{\mathrm{MB}}$ and $\epsilon^{\mathrm{BBC}}_{J/\psi}$ are the beam-beam trigger efficiencies for minimum-bias and J/ψ events, respectively. The factor of 2×197 causes R_{dA} to be one if the $d + A$ cross section is just additive from $p + p$, i.e., if there are no nuclear modifications.

For $p + p$ we use the cross section for our beam-beam trigger, $\sigma^{\mathrm{tot}}_{\mathrm{MB}}(pp)\epsilon^{\mathrm{BBC}}_{\mathrm{MB}}(pp) = 23.0 \pm 2.2$ mb, and the efficiency for events with a J/ψ, $\epsilon^{\mathrm{BBC}}_{J/\psi}(pp) = 0.79 \pm 0.02$.

For d + Au collisions we use a beam-beam trigger cross section of $\sigma_{\rm MB}^{\rm tot}(d{\rm Au})\epsilon_{\rm MB}^{\rm BBC}(d{\rm Au}) = 1.99 \pm 0.10$ b from our measurement [18] using photodissociation of the deuteron as a reference [19], which is consistent with our calculated Glauber result of 1.92 ± 0.18 b. For the J/ψ we use $\epsilon_{J/\psi}^{\rm BBC}(d{\rm Au}) = 0.94 \pm 0.02$ [20].

For d + Au collisions, the centrality of the collision can be characterized by measuring the charge deposited in the beam-beam counter in the Au beam direction [20]. An approximate number of nucleon + nucleon collisions $\langle N_{\rm coll}\rangle$ can be obtained through a Glauber calculation that relates this $\langle N_{\rm coll}\rangle$ to the observed charge. In this case $R_{dA}(N_{\rm coll})$ is calculated as

$$R_{dA}(\langle N_{\rm coll}\rangle) = \frac{N_{\rm inv}^{d{\rm Au}}(\langle N_{\rm coll}\rangle)}{\langle N_{\rm coll}\rangle \times N_{\rm inv}^{pp}}, \quad (3)$$

where the invariant yield $N_{\rm inv}$ is

$$N_{\rm inv}(\langle N_{\rm coll}\rangle) = \frac{N_{J/\psi} C_{\rm bias}(\langle N_{\rm coll}\rangle)}{A\epsilon_{\rm rec}\epsilon_{\rm trig}[N_{\rm evt}(\Delta w/w)]} \quad (4)$$

with $\langle N_{\rm coll}\rangle$ being the average number of binary collisions for a particular d + Au centrality bin and $N_{\rm evt}(\Delta w/w)$ the number of d + Au minimum-bias triggers sampled that lie in this fraction, Δw, of the total minimum-bias centrality range, w. This prescription is equivalent to that of Eq. (1) and (2) for minimum bias. For p + p collisions $\Delta w/w$ is one. $C_{\rm bias} = \epsilon_{\rm MB}^{\rm BBC}/\epsilon_{J/\psi}^{\rm BBC}$ is a correction for the smaller trigger efficiency in minimum-bias events compared to those with a J/ψ. For d + Au, $C_{\rm bias}$ depends on $\langle N_{\rm coll}\rangle$ and takes into account the effect of the underlying event multiplicity on both the trigger efficiency and the centrality measurement [20]. Its variation with centrality is up to 7% from unity.

For the electron analysis, $A\epsilon_{\rm rec}$ and $\epsilon_{\rm trig}$ were determined using a GEANT [21] simulation of the central arms and a trigger response software emulation [16]. $\epsilon_{\rm rec}$ was confirmed by studying pairs identified as photon conversions in the data. The systematic uncertainty of 10.4% is dominated by run-to-run efficiencies (5%), yield extraction (5%), and the occupancy dependence of the efficiency (4.4%).

For the muon arms, $A\epsilon_{\rm rec}\epsilon_{\rm trig}$ was determined within each rapidity and p_T bin, using a GEANT simulation with J/ψ events generated by PYTHIA [22]. The dominant systematic uncertainties in our result are $+6/-9\%$ from the muon identifier efficiency and up to 10% (for the most central negative rapidity d + Au data) from the combinatoric background.

Figure 1(a) shows the measured p + p differential cross section times branching ratio versus rapidity with a di-electron point at midrapidity and two di-muon points at negative and positive rapidities. A fit to a shape generated with PYTHIA is performed and, using a di-lepton branching ratio of 5.9% [23], gives a total cross section $\sigma_{pp}^{J/\psi} = 2.61 \pm 0.20({\rm fit}) \pm 0.26({\rm abs})$ μb. Variations in the parton distribution functions and models used to determine the shape are negligible compared to the fit errors. This result is smaller by about two sigma than our previous lower statistics result [16].

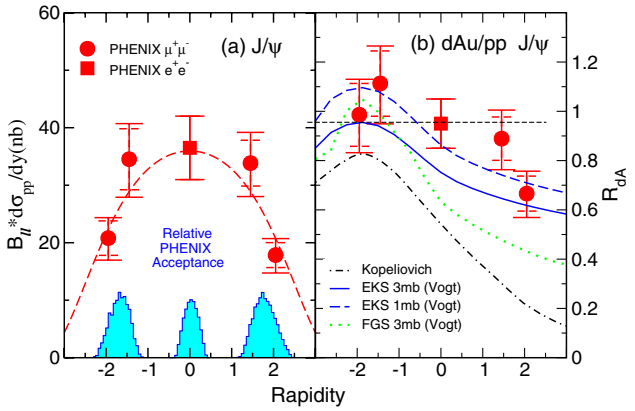

FIG. 1 (color online). (a) The 200 GeV J/ψ p + p differential cross section times di-lepton branching ratio versus rapidity (10% overall normalization uncertainty is not included). (b) The minimum-bias R_{dA} vs rapidity (12% overall normalization uncertainty not included). For both panels the dashed error bars represent systematic uncertainties relevant for comparing the two rapidity bins in each muon arm, while the solid error bars represent the overall uncertainties relevant for comparing points at negative, central, or positive rapidity. The curve in (a) represents a fit as described in the text while the curves in (b) are theoretical calculations [5,24,25] as described in the text.

Figure 1(b) shows the nuclear modification factor R_{dA} [Eq. (2)] versus rapidity, where a value of one would correspond to no nuclear modification. While this ratio is consistent with unity at negative rapidity, it is significantly lower at the most positive rapidity where gluons are expected to be shadowed in a heavy nucleus. Theoretical predictions [5,24,25] that include the effects of absorption and shadowing are shown for comparison in Fig. 1(b). The data favor a relatively modest shadowing in agreement with the parametrization of Eskola-Kolhinen-Salgado (EKS) [3] based on a leading-twist Dokshitzer-Gribov-Lipatov-Altarelli-Parisi-evolved parametrization of nuclear deep-inelastic scattering and Drell-Yan data at lower energies, rather than the stronger gluon shadowing of Kopeliovich [5] or Frankfurt-Guzey-Strikman (FGS) [4] based on models involving coherence for a $q\bar{q}$ dipole in the nucleus. The $c\bar{c}$ absorption cross section is not well determined by our data, but is probably nearer to 1 mb and is certainly smaller than the 4.1 ± 0.4 mb found at lower energy [26].

Lower energy $p + A$ measurements showed that J/ψ suppression did not follow a universal behavior versus x_2 [27], the momentum fraction in the heavy nucleus, as would be expected if the suppression was dominated by shadowing [10]. As shown in Fig. 2(a), our data confirm this x_2 scaling violation with the addition of a smaller x_2

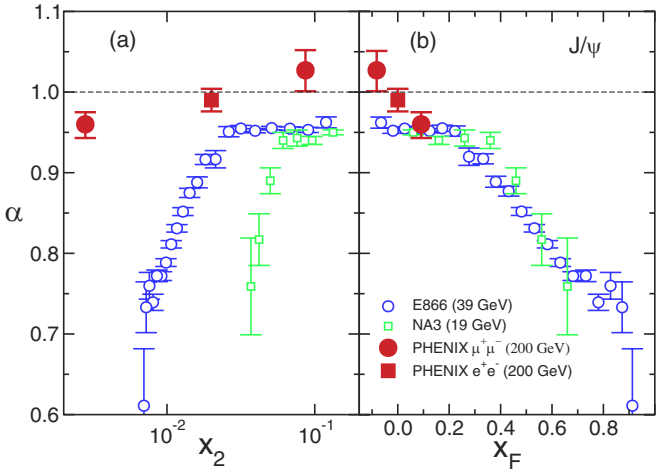

FIG. 2 (color online). α vs (a) x_2 and (b) x_F with present 200 GeV J/ψ results compared to lower energy results [10,13]. An additional overall uncertainty of 0.02 in our α values is not shown.

point, but with our small range in x_F have little to add to the approximate x_F scaling observed in these lower energy measurements [Fig. 2(b)]. Here α is defined by $\sigma_{dA} = \sigma_{pp} \times (2A)^{\alpha}$ and $x_F = x_1 - x_2$, where x_1 is the momentum fraction of the gluon in the deuteron. This x_F scaling may be caused by energy loss of the gluon in the initial state [7], or by an energy conservation effect ("Sudakov suppression") [28] which causes a universal suppression that increases with x_F for production of J/ψ's and other hadrons. It is also similar to that observed for more positive rapidity hadron production in the d + Au "limiting fragmentation" region [29].

Invariant cross sections versus transverse momentum, $(d^2\sigma/dydp_T)/(2\pi p_T)$, have been fit to the form $A \times (1 + (p_T/B)^2)^{-6}$ [30]. Average p_T^2 values resulting from these fits are 4.28 ± 0.31, 3.03 ± 0.40, and 3.63 ± 0.25 GeV$/c^2$ for d + Au collisions at negative, zero, and positive x_F, respectively; compared with 2.51 ± 0.21 and 4.31 ± 0.85 GeV$/c^2$ for negative/positive and zero x_F $p + p$ collisions, respectively. The observed p_T broadening is shown in Fig. 3(a). For negative x_F it is consistent with that of the lower energy ($\sqrt{s_{NN}} = 39$ GeV) measurements from E866/NuSea [10], but may be flatter at positive x_F. At zero x_F no p_T broadening is seen within errors.

R_{dA} [Eq. (3)] is shown in Fig. 3(b) for four centrality classes and for minimum-bias collisions. This classification into centrality bins for these results can only be approximate, as indicated by the overlapping histograms of $N_{\rm coll}$. At positive rapidity (small x_2, or the shadowing region), a weak drop for more central collisions is observed, while no significant centrality dependence is seen

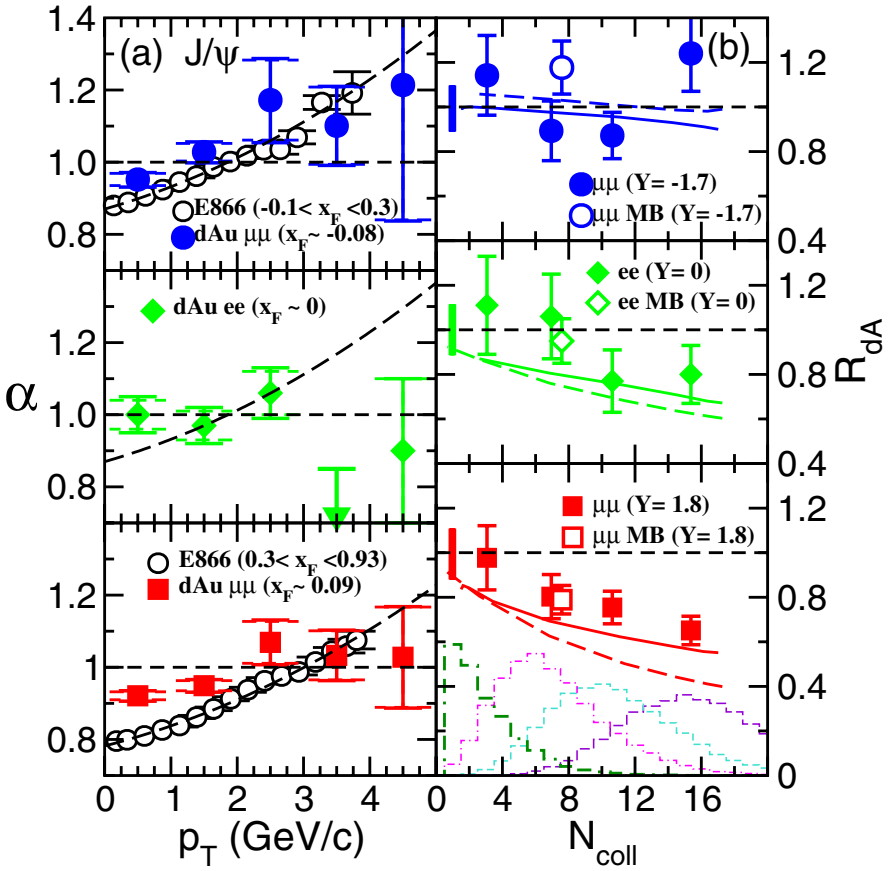

FIG. 3 (color online). (a) α vs p_T compared to lower energy measurements, shown for three different x_F ranges. The error bars have the same meaning as in Fig. 1. An additional 0.02 overall uncertainty is not shown. The dashed curves are simple fits [10] to the lower energy results. (b) Nuclear modification factor vs centrality as given by the number of nucleon + nucleon collisions shown for three different rapidity ranges, compared to theoretical calculations [24,25] including final-state absorption and EKS (solid) or FGS (dashed) shadowing. The bars at the low end of each plot represent the systematic errors between different rapidity ranges. An additional 12% global error bar is not shown. The histograms at the bottom of the lower panel indicate the distribution of the number of collisions for each of the four centrality bins.

for negative rapidity or for central rapidity. The theoretical curves on Fig. 3(b) correspond to different amounts of density dependent shadowing and antishadowing [24,25] and also include absorption. They are consistent with our data except at positive rapidity where the EKS shadowing curve is closest to our results, although slightly lower perhaps due to the amount of absorption that is included.

In summary, during the RHIC 2003 run, the PHENIX experiment measured nuclear effects on J/ψ production for $d + \mathrm{Au}$ collisions at $\sqrt{s_{NN}} = 200$ GeV. Increasing suppression for larger rapidity (smaller x_2) and for more central collisions (higher nuclear densities sampled) both are consistent with models containing a small amount of impact-parameter dependent shadowing and with weak absorption. Theoretical calculations which include EKS shadowing seem most consistent with the data. However, comparisons with other measurements at lower energies show that shadowing cannot be the dominant effect, at least not for the lower energy measurements. We also see some transverse momentum broadening which is consistent with that seen at lower energy. Higher luminosity $d + \mathrm{Au}$ running in the future yielding higher numbers of J/ψ's will be necessary to quantify these nuclear effects and to more clearly distinguish between various theoretical models of shadowing, absorption, and other cold nuclear matter effects.

We thank the staff of the Collider-Accelerator and Physics Departments at BNL for their vital contributions. We acknowledge support from the Department of Energy and NSF (USA), MEXT and JSPS (Japan), CNPq and FAPESP (Brazil), NSFC (China), IN2P3/CNRS, CEA, and ARMINES (France), BMBF, DAAD, and AvH (Germany), OTKA (Hungary), DAE and DST (India), ISF (Israel), KRF and CHEP (Korea), RMIST, RAS, and RMAE (Russia), VR and KAW (Sweden), US CRDF for the FSU, US-Hungarian NSF-OTKA-MTA, and US-Israel BSF.

*Deceased.
†PHENIX Spokesperson.
Email address: zajc@nevis.columbia.edu

[1] M. Bedjidian *et al.* hep-ph/0311048.
[2] T. Matsui and H. Satz, Phys. Lett. **178B**, 416 (1986).
[3] K. J. Eskola, V. J. Kolhinen, and C. A. Salgado, Eur. Phys. J. C **9**, 61 (1999).
[4] L. Frankfurt, V. Guzey, and M. Strikman, Phys. Rev. D **71**, 054001 (2005).
[5] B. Kopeliovich, A. Tarasov, and J. Hüfner, Nucl. Phys. **A696**, 669 (2001).
[6] L. McLerran and R. Venugopalan, Phys. Rev. D **49**, 2233 (1994).
[7] R. Vogt, Phys. Rev. C **61**, 035203 (2000).
[8] L. Antoniazzi *et al.*, Phys. Rev. Lett. **70**, 383 (1993).
[9] D. M. Alde *et al.*, Phys. Rev. Lett. **66**, 133 (1991).
[10] M. J. Leitch *et al.*, Phys. Rev. Lett. **84**, 3256 (2000).
[11] B. Alessandro *et al.*, Phys. Lett. B **553**, 167 (2003).
[12] J. Spengler, J. Phys. G **30**, S871 (2004).
[13] J. Badier *et al.*, Z. Phys. C **20**, 101 (1983).
[14] M. J. Leitch, Eur. Phys. J. A **S19**, 129 (2004).
[15] S. S. Adler *et al.*, Nucl. Instrum. Methods Phys. Res., Sect. A **499**, 469 (2003).
[16] S. S. Adler *et al.*, Phys. Rev. Lett. **92**, 051802 (2004).
[17] S. S. Adler *et al.*, Phys. Rev. C **69**, 014901 (2004).
[18] S. N. White, *Proceedings of the XIIIth International Workshop DIS'05, Madison, WI, 2005*, edited by W. H. Smith [AIP Conf. Proc. 792, No. 1, 527 (2005)].
[19] S. R. Klein and R. Vogt, Phys. Rev. C **67**, 047901 (2003).
[20] S. S. Adler *et al.*, Phys. Rev. Lett. **94**, 082302 (2005).
[21] F. Carminati *et al.*, "*GEANT: Detector Description and Simulation Tool*," CERN Program Library Long Writeup No. W5013, 1993 (unpublished).
[22] T. Sjostrand *et al.*, Comput. Phys. Commun. **135**, 238 (2001).
[23] S. Eidelman *et al.*, Phys. Lett. B **592**, 1 (2004).
[24] S. R. Klein and R. Vogt, Phys. Rev. Lett. **91**, 142301 (2003).
[25] R. Vogt, Phys. Rev. C **71**, 054902 (2005).
[26] G. Borges *et al.* hep-ex/0505065.
[27] $x_2 = 0.5(-x_F + \sqrt{x_F^2 + 4M_{J/\psi}^2/s_{NN}})$.
[28] B. Z. Kopeliovich *et al.*, Phys. Rev. C **72**, 054606 (2005).
[29] B. B. Back *et al.*, Phys. Rev. Lett. **93**, 082301 (2004).
[30] J. K. Yoh *et al.*, Phys. Rev. Lett. **41**, 684 (1978).

Measurement of Transverse Single-Spin Asymmetries for Midrapidity Production of Neutral Pions and Charged Hadrons in Polarized $p + p$ Collisions at $\sqrt{s} = 200$ GeV

S. S. Adler,[5] S. Afanasiev,[17] C. Aidala,[5] N. N. Ajitanand,[43] Y. Akiba,[20,38] J. Alexander,[43] R. Amirikas,[12] L. Aphecetche,[45] S. H. Aronson,[5] R. Averbeck,[44] T. C. Awes,[35] R. Azmoun,[44] V. Babintsev,[15] A. Baldisseri,[10] K. N. Barish,[6] P. D. Barnes,[27] B. Bassalleck,[33] S. Bathe,[30] S. Batsouli,[9] V. Baublis,[37] F. Bauer,[6] A. Bazilevsky,[39,15] S. Belikov,[16,15] Y. Berdnikov,[40] S. Bhagavatula,[16] J. G. Boissevain,[27] H. Borel,[10] S. Borenstein,[25] M. L. Brooks,[27] D. S. Brown,[34] N. Bruner,[33] D. Bucher,[30] H. Buesching,[30] V. Bumazhnov,[15] G. Bunce,[5,39] J. M. Burward-Hoy,[26,44] S. Butsyk,[44] X. Camard,[45] J.-S. Chai,[18] P. Chand,[4] W. C. Chang,[2] S. Chernichenko,[15] C. Y. Chi,[9] J. Chiba,[20] M. Chiu,[9] I. J. Choi,[52] J. Choi,[19] R. K. Choudhury,[4] T. Chujo,[5] V. Cianciolo,[35] Y. Cobigo,[10] B. A. Cole,[9] P. Constantin,[16] D. d'Enterria,[45] G. David,[5] H. Delagrange,[45] A. Denisov,[15] A. Deshpande,[39] E. J. Desmond,[5] A. Devismes,[44] O. Dietzsch,[41] O. Drapier,[25] A. Drees,[44] K. A. Drees,[5] R. du Rietz,[29] A. Durum,[15] D. Dutta,[4] Y. V. Efremenko,[35] K. El Chenawi,[49] A. Enokizono,[14] H. En'yo,[38,39] S. Esumi,[48] L. Ewell,[5] D. E. Fields,[33,39] F. Fleuret,[25] S. L. Fokin,[23] B. D. Fox,[39] Z. Fraenkel,[51] J. E. Frantz,[9] A. Franz,[5] A. D. Frawley,[12] S.-Y. Fung,[6] S. Garpman,[29,*] T. K. Ghosh,[49] A. Glenn,[46] G. Gogiberidze,[46] M. Gonin,[25] J. Gosset,[10] Y. Goto,[39] R. Granier de Cassagnac,[25] N. Grau,[16] S. V. Greene,[49] M. Grosse Perdekamp,[39] W. Guryn,[5] H.-Å. Gustafsson,[29] T. Hachiya,[14] J. S. Haggerty,[5] H. Hamagaki,[8] A. G. Hansen,[27] E. P. Hartouni,[26] M. Harvey,[5] R. Hayano,[8] N. Hayashi,[38] X. He,[13] M. Heffner,[26] T. K. Hemmick,[44] J. M. Heuser,[44] M. Hibino,[50] J. C. Hill,[16] W. Holzmann,[43] K. Homma,[14] B. Hong,[22] A. Hoover,[34] T. Ichihara,[38,39] V. V. Ikonnikov,[23] K. Imai,[24,38] D. Isenhower,[1] M. Ishihara,[38] M. Issah,[43] A. Isupov,[17] B. V. Jacak,[44] W. Y. Jang,[22] Y. Jeong,[19] J. Jia,[44] O. Jinnouchi,[38] B. M. Johnson,[5] S. C. Johnson,[26] K. S. Joo,[31] D. Jouan,[36] S. Kametani,[8,50] N. Kamihara,[47,38] J. H. Kang,[52] S. S. Kapoor,[4] K. Katou,[50] S. Kelly,[9] B. Khachaturov,[51] A. Khanzadeev,[37] J. Kikuchi,[50] D. H. Kim,[31] D. J. Kim,[52] D. W. Kim,[19] E. Kim,[42] G.-B. Kim,[25] H. J. Kim,[52] E. Kistenev,[5] A. Kiyomichi,[48] K. Kiyoyama,[32] C. Klein-Boesing,[30] H. Kobayashi,[38,39] L. Kochenda,[37] V. Kochetkov,[15] D. Koehler,[33] T. Kohama,[14] M. Kopytine,[44] D. Kotchetkov,[6] A. Kozlov,[51] P. J. Kroon,[5] C. H. Kuberg,[1,27,*] K. Kurita,[39] Y. Kuroki,[48] M. J. Kweon,[22] Y. Kwon,[52] G. S. Kyle,[34] R. Lacey,[43] V. Ladygin,[17] J. G. Lajoie,[16] A. Lebedev,[16,23] S. Leckey,[44] D. M. Lee,[27] S. Lee,[19] M. J. Leitch,[27] X. H. Li,[6] H. Lim,[42] A. Litvinenko,[17] M. X. Liu,[27] Y. Liu,[36] C. F. Maguire,[49] Y. I. Makdisi,[5] A. Malakhov,[17] V. I. Manko,[23] Y. Mao,[7,38] G. Martinez,[45] M. D. Marx,[44] H. Masui,[48] F. Matathias,[44] T. Matsumoto,[8,50] P. L. McGaughey,[27] E. Melnikov,[15] F. Messer,[44] Y. Miake,[48] J. Milan,[43] T. E. Miller,[49] A. Milov,[44,51] S. Mioduszewski,[5] R. E. Mischke,[27] G. C. Mishra,[13] J. T. Mitchell,[5] A. K. Mohanty,[4] D. P. Morrison,[5] J. M. Moss,[27] F. Mühlbacher,[44] D. Mukhopadhyay,[51] M. Muniruzzaman,[6] J. Murata,[38,39] S. Nagamiya,[20] J. L. Nagle,[9] T. Nakamura,[14] B. K. Nandi,[6] M. Nara,[48] J. Newby,[46] P. Nilsson,[29] A. S. Nyanin,[23] J. Nystrand,[29] E. O'Brien,[5] C. A. Ogilvie,[16] H. Ohnishi,[5,38] I. D. Ojha,[49,3] K. Okada,[38] M. Ono,[48] V. Onuchin,[15] A. Oskarsson,[29] I. Otterlund,[29] K. Oyama,[8] K. Ozawa,[8] D. Pal,[51] A. P. T. Palounek,[27] V. Pantuev,[44] V. Papavassiliou,[34] J. Park,[42] A. Parmar,[33] S. F. Pate,[34] T. Peitzmann,[30] J.-C. Peng,[27] V. Peresedov,[17] C. Pinkenburg,[5] R. P. Pisani,[5] F. Plasil,[35] M. L. Purschke,[5] A. K. Purwar,[44] J. Rak,[16] I. Ravinovich,[51] K. F. Read,[35,46] M. Reuter,[44] K. Reygers,[30] V. Riabov,[37,40] Y. Riabov,[37] G. Roche,[28] A. Romana,[25] M. Rosati,[16] P. Rosnet,[28] S. S. Ryu,[52] M. E. Sadler,[1] N. Saito,[38,39] T. Sakaguchi,[8,50] M. Sakai,[32] S. Sakai,[48] V. Samsonov,[37] L. Sanfratello,[33] R. Santo,[30] H. D. Sato,[24,38] S. Sato,[5,48] S. Sawada,[20] Y. Schutz,[45] V. Semenov,[15] R. Seto,[6] M. R. Shaw,[1,27] T. K. Shea,[5] T.-A. Shibata,[47,38] K. Shigaki,[14,20] T. Shiina,[27] C. L. Silva,[41] D. Silvermyr,[27,29] K. S. Sim,[22] C. P. Singh,[3] V. Singh,[3] M. Sivertz,[5] A. Soldatov,[15] R. A. Soltz,[26] W. E. Sondheim,[27] S. P. Sorensen,[46] I. V. Sourikova,[5] F. Staley,[10] P. W. Stankus,[35] E. Stenlund,[29] M. Stepanov,[34] A. Ster,[21] S. P. Stoll,[5] T. Sugitate,[14] J. P. Sullivan,[27] E. M. Takagui,[41] A. Taketani,[38,39] M. Tamai,[50] K. H. Tanaka,[20] Y. Tanaka,[32] K. Tanida,[38] M. J. Tannenbaum,[5] P. Tarján,[11] J. D. Tepe,[1,27] T. L. Thomas,[33] J. Tojo,[24,38] H. Torii,[24,38] R. S. Towell,[1] I. Tserruya,[51] H. Tsuruoka,[48] S. K. Tuli,[3] H. Tydesjö,[29] N. Tyurin,[15] H. W. van Hecke,[27] J. Velkovska,[5,44] M. Velkovsky,[44] V. Veszprémi,[11] L. Villatte,[46] A. A. Vinogradov,[23] M. A. Volkov,[23] E. Vznuzdaev,[37] X. R. Wang,[13] Y. Watanabe,[38,39] S. N. White,[5] F. K. Wohn,[16] C. L. Woody,[5] W. Xie,[6] Y. Yang,[7] A. Yanovich,[15] S. Yokkaichi,[38,39] G. R. Young,[35] I. E. Yushmanov,[23] W. A. Zajc,[9,†] C. Zhang,[9] S. Zhou,[7] S. J. Zhou,[51] and L. Zolin[17]

(PHENIX Collaboration)

[1]*Abilene Christian University, Abilene, Texas 79699, USA*
[2]*Institute of Physics, Academia Sinica, Taipei 11529, Taiwan*
[3]*Department of Physics, Banaras Hindu University, Varanasi 221005, India*

 © 2005 The American Physical Society

[4]Bhabha Atomic Research Centre, Bombay 400 085, India
[5]Brookhaven National Laboratory, Upton, New York 11973-5000, USA
[6]University of California—Riverside, Riverside, California 92521, USA
[7]China Institute of Atomic Energy (CIAE), Beijing, People's Republic of China
[8]Center for Nuclear Study, Graduate School of Science, University of Tokyo, 7-3-1 Hongo, Bunkyo, Tokyo 113-0033, Japan
[9]Columbia University, New York, New York 10027, USA,
and Nevis Laboratories, Irvington, New York 10533, USA
[10]Dapnia, CEA Saclay, F-91191 Gif-sur-Yvette, France
[11]Debrecen University, H-4010 Debrecen, Egyetem tér 1, Hungary
[12]Florida State University, Tallahassee, Florida 32306, USA
[13]Georgia State University, Atlanta, Georgia 30303, USA
[14]Hiroshima University, Kagamiyama, Higashi-Hiroshima 739-8526, Japan
[15]IHEP Protvino, State Research Center of Russian Federation, Institute for High Energy Physics, Protvino 142281, Russia
[16]Iowa State University, Ames, Iowa 50011, USA
[17]Joint Institute for Nuclear Research, 141980 Dubna, Moscow Region, Russia
[18]KAERI, Cyclotron Application Laboratory, Seoul, South Korea
[19]Kangnung National University, Kangnung 210-702, South Korea
[20]KEK, High Energy Accelerator Research Organization, Tsukuba, Ibaraki 305-0801, Japan
[21]KFKI Research Institute for Particle and Nuclear Physics of the Hungarian Academy of Sciences (MTA KFKI RMKI),
H-1525 Budapest 114, P.O. Box 49, Budapest, Hungary
[22]Korea University, Seoul 136-701, Korea
[23]Russian Research Center "Kurchatov Institute," Moscow, Russia
[24]Kyoto University, Kyoto 606-8502, Japan
[25]Laboratoire Leprince-Ringuet, Ecole Polytechnique, CNRS-IN2P3, Route de Saclay, F-91128 Palaiseau, France
[26]Lawrence Livermore National Laboratory, Livermore, California 94550, USA
[27]Los Alamos National Laboratory, Los Alamos, New Mexico 87545, USA
[28]LPC, Université Blaise Pascal, CNRS-IN2P3, Clermont-Fd, 63177 Aubiere Cedex, France
[29]Department of Physics, Lund University, Box 118, SE-221 00 Lund, Sweden
[30]Institut für Kernphysik, University of Muenster, D-48149 Muenster, Germany
[31]Myongji University, Yongin, Kyonggido 449-728, Korea
[32]Nagasaki Institute of Applied Science, Nagasaki-shi, Nagasaki 851-0193, Japan
[33]University of New Mexico, Albuquerque, New Mexico 87131, USA
[34]New Mexico State University, Las Cruces, New Mexico 88003, USA
[35]Oak Ridge National Laboratory, Oak Ridge, Tennessee 37831, USA
[36]IPN-Orsay, Universite Paris Sud, CNRS-IN2P3, BP 1, F-91406 Orsay, France
[37]PNPI, Petersburg Nuclear Physics Institute, Gatchina, Russia
[38]RIKEN, The Institute of Physical and Chemical Research, Wako, Saitama 351-0198, Japan
[39]RIKEN BNL Research Center, Brookhaven National Laboratory, Upton, New York 11973-5000, USA
[40]Saint Petersburg State Polytechnic University, St. Petersburg, Russia
[41]Universidade de São Paulo, Instituto de Física, Caixa Postal 66318, São Paulo CEP05315-970, Brazil
[42]System Electronics Laboratory, Seoul National University, Seoul, South Korea
[43]Chemistry Department, Stony Brook University, SUNY, Stony Brook, New York 11794-3400, USA
[44]Department of Physics and Astronomy, Stony Brook University, SUNY, Stony Brook, New York 11794, USA
[45]SUBATECH (Ecole des Mines de Nantes, CNRS-IN2P3, Université de Nantes) BP 20722-44307, Nantes, France
[46]University of Tennessee, Knoxville, Tennessee 37996, USA
[47]Department of Physics, Tokyo Institute of Technology, Tokyo 152-8551, Japan
[48]Institute of Physics, University of Tsukuba, Tsukuba, Ibaraki 305, Japan
[49]Vanderbilt University, Nashville, Tennessee 37235, USA
[50]Advanced Research Institute for Science and Engineering, Waseda University,
17 Kikui-cho, Shinjuku-ku, Tokyo 162-0044, Japan
[51]Weizmann Institute, Rehovot 76100, Israel
[52]Yonsei University, IPAP, Seoul 120-749, Korea
(Received 17 July 2005; published 11 November 2005)

Transverse single-spin asymmetries to probe the transverse-spin structure of the proton have been measured for neutral pions and nonidentified charged hadrons from polarized proton-proton collisions at midrapidity and $\sqrt{s} = 200$ GeV. The data cover a transverse momentum (p_T) range 1.0–5.0 GeV/c for neutral pions and 0.5–5.0 GeV/c for charged hadrons, at a Feynman-x value of approximately zero. The asymmetries seen in this previously unexplored kinematic region are consistent with zero within errors of a few percent. In addition, the inclusive charged hadron cross section at midrapidity from $0.5 < p_T < 7.0$ GeV/c is presented and compared to next-to-leading order perturbative QCD (pQCD) calculations.

Successful description of the unpolarized cross section above ~ 2 GeV/c suggests that pQCD is applicable in the interpretation of the asymmetry results in the relevant kinematic range.

DOI: 10.1103/PhysRevLett.95.202001 PACS numbers: 14.20.Dh, 13.85.Ni, 13.88.+e, 25.40.Ep

The spin structure of the proton persists as an intricate problem in quantum chromodynamics (QCD). In particular, its transverse-spin structure remains poorly understood. The measurement of transverse single-spin asymmetries (SSAs) in proton-proton collisions and lepton-nucleon deep-inelastic scattering (DIS) probes the quark and gluon structure of transversely polarized nucleons. Interest in these measurements is heightened by the large transverse SSAs observed in spin-dependent proton-proton scattering experiments spanning a wide range of energies. At $\sqrt{s} = 5$–10 GeV, asymmetries approaching 30% were seen in forward inclusive pion production [1,2]. At midrapidity, asymmetries were also observed in inclusive π^0 and π^+ but not π^- production [3–5]. At higher center-of-mass energies of 20 and 200 GeV, π^+, π^-, and π^0 asymmetries were found to persist at large Feynman-x (x_F) [6–8] while the asymmetry in π^0 production at midrapidity was found to be consistent with zero at $\sqrt{s} = 20$ GeV [9]. Nonzero transverse asymmetries have also been observed in semi-inclusive DIS experiments [10–12].

Three different mechanisms have been studied as the possible origin of transverse SSAs in hadron collisions at high energies: (1) Transversity distributions, the quark spin distributions in a transversely polarized proton, can give rise to SSAs in combination with spin-dependent fragmentation functions (FFs), e.g., the Collins function [13]. Spin-dependent FFs serve as analyzers for the transverse spin of the struck quark. (2) Quark and gluon distributions that are asymmetric in the transverse intrinsic parton momentum, k_T, first suggested by Sivers [14], can lead to SSAs. (3) Alternatively, interference between quark and gluon fields in the initial or final state can also generate SSAs [15,16]. Sivers parton distributions can exist for both quarks and gluons, and a possible connection to orbital angular momentum of partons in the nucleon has been suggested [14,17].

It is expected that SSAs measured at the Relativistic Heavy Ion Collider (RHIC) result from a combination of these three effects (see [8], and references therein). Model calculations leading to predictions for the Sivers and transversity distributions have been performed to describe existing data at forward rapidities. Precision measurements of SSAs in different regions of x_F and transverse momentum (p_T) and their QCD analysis may serve to quantify contributions from the competing mechanisms. In this Letter, we present first measurements of transverse single-spin asymmetries at midrapidity and collider energies.

These data were collected during the 2001–2002 polarized proton run at RHIC, in which approximately 0.15 pb^{-1} of integrated luminosity were collected using the PHENIX detector. Two beams of 55 bunches of polarized protons, with approximately 5×10^{10} protons per bunch, were injected into RHIC and accelerated to 100 GeV each.

Measurements of the unpolarized production of charged hadrons and of the spin-dependent production of neutral pions and charged hadrons were made in the central arms of the PHENIX detector. These cover a pseudorapidity range $|\eta| < 0.35$ and two azimuthal angle intervals of 90°, offset 33.75° from vertical [18].

A minimum-bias (MB) collision trigger and the vertex position in the beam direction are provided by two beam-beam counters (BBCs) [19]. The BBCs, which cover 2π in azimuth and $3.0 < |\eta| < 3.9$, are sensitive to charged particles and select approximately half of the total inelastic proton-proton cross section. A ± 30 cm event vertex cut was applied for all analyses, corresponding to the central arm acceptance. The approximate vertex resolution was 2 cm in the beam direction.

Charged-particle tracks from MB events were reconstructed using a drift chamber and pad chambers [20] as well as the collision vertex, which is the assumed point of origin because the tracking chambers are placed outside the magnetic field. Thus charged particles that do not originate at the vertex have incorrectly reconstructed momentum, leading to low-momentum, long-lived particle decays (e.g., $K^{\pm}$, K^0_L) and conversion electrons as the two main sources of background.

For the charged hadron cross section, approximately 17×10^6 MB events were analyzed. The luminosity was measured as $N_{\mathrm{BBC}}/\sigma_{\mathrm{BBC}}$ with $\sigma_{\mathrm{BBC}} = 21.8$ mb [21], accounting for the fraction of the yield for which the MB condition was satisfied. Backgrounds were estimated and subtracted statistically following the method of [22]: Conversion electrons were estimated using the different response of the ring-imaging Čerenkov detector (RICH) [23] to electrons and charged pions, and decay particles were estimated using the track bend in the residual magnetic field in the tracking detectors. Weak decays of short-lived particles, mainly K^0_S, Λ, and $\bar{\Lambda}$, remain, especially when they decay close to the vertex. Based on a Monte Carlo simulation, the reported cross section was reduced by 7% over the entire p_T range to correct for these decays.

The unpolarized cross section for inclusive charged hadron production at midrapidity is presented in Fig. 1 and Table I. The dominant systematic uncertainty for $p_T > 5$ GeV/c is from the background subtraction, while for $p_T < 5$ GeV/c it is due to the weak-decay correction.

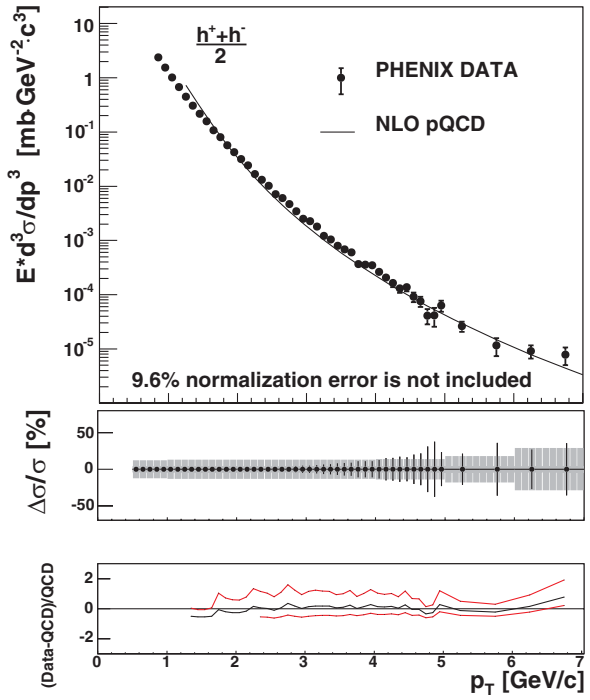

FIG. 1 (color online). Top panel: Invariant cross section vs p_T for the production of charged hadrons at midrapidity, averaged over sign. A 9.6% normalization uncertainty is not shown. The curve represents a NLO pQCD calculation at a renormalization scale of p_T [26]. Middle panel: The relative statistical (points) and point-to-point systematic (band) errors. Bottom panel: The relative difference between the data and the theory with scales of $p_T/2$ (lower curve), p_T, and $2p_T$ (upper curve).

There is a 9.6% normalization uncertainty due to the luminosity measurement. In Fig. 1 the cross section is compared to a next-to-leading-order (NLO) perturbative QCD (pQCD) calculation using the CTEQ6M [24] parton distribution functions and Kniel-Kramer-Pötter FFs [25] and found to be consistent above $p_T \sim 2$ GeV/c. The unpolarized cross sections for midrapidity and forward production of neutral pions have also been measured in 200 GeV proton-proton collisions at RHIC [8,21] and have been found to agree well with NLO pQCD calculations [26–28]. This agreement between all of these unpolarized measurements and theory indicates that NLO pQCD is applicable in interpreting polarized data at $\sqrt{s} =$ 200 GeV and provides a solid theoretical foundation for the study of the spin structure of the proton at RHIC.

The stable spin direction of the protons through acceleration and storage is vertical, and there is an approximately equal number of bunches filled with the spin of the protons up as there is down. With both beams polarized, single-spin analyses were performed by taking into account the spin states of one beam, averaging over those of the other. The beam polarization at 100 GeV was obtained using the same analyzing power (A_N^{pC}) in proton-carbon elastic scattering in the Coulomb-nuclear interference region measured at 22 GeV (see [29], and references therein), near RHIC injection energy. The average beam polarization was $15 \pm 5\%$.

TABLE I. Selected invariant cross section values for $(h^+ + h^-)/2$ corresponding to Fig. 1. A 9.6% normalization uncertainty is not included.

p_T (GeV/c)	Invariant cross section (mb/GeV^2)	Statistical error (%)	Systematic error (%)
0.55	1.06×10^{1}	0.2	8
1.05	1.02×10^{0}	0.4	8.5
1.55	1.58×10^{-1}	0.9	8.5
2.05	3.16×10^{-2}	1.7	9
2.55	7.14×10^{-3}	3.2	9
3.05	2.28×10^{-3}	5.1	9
3.55	6.86×10^{-4}	8.5	9
4.05	2.63×10^{-4}	12.8	9.5
4.55	9.12×10^{-5}	20.2	9.5
5.25	2.61×10^{-5}	21.2	16
5.75	1.16×10^{-5}	36.3	16
6.25	9.12×10^{-6}	27.2	28
6.75	7.82×10^{-6}	35.7	28

The left-right transverse single-spin asymmetry, A_N, can be extracted using

$$A_N = \frac{1}{P_{\mathrm{b}}}\left(\frac{\sigma^{\uparrow} - \sigma^{\downarrow}}{\sigma^{\uparrow} + \sigma^{\downarrow}}\right) = \frac{1}{P_{\mathrm{b}}}\frac{1}{\langle|\cos\phi|\rangle}\left(\frac{N^{\uparrow} - \mathcal{R}N^{\downarrow}}{N^{\uparrow} + \mathcal{R}N^{\downarrow}}\right), \quad (1)$$

where P_{b} is the beam polarization, $\sigma^{\uparrow}$ ($\sigma^{\downarrow}$) the production cross section when the protons in the bunch are polarized up (down), $N^{\uparrow}$ ($N^{\downarrow}$) the experimental yield from up- (down-) polarized bunches, and $\mathcal{R} = \mathcal{L}^{\uparrow}/\mathcal{L}^{\downarrow}$ the relative integrated luminosity of bunches of opposite polarization sign. The azimuthal term accounts for the coverage of the central arms. The above formula as written applies to yields observed to the left of the polarized beam. An overall minus sign is required for yields observed to the right of the polarized beam. Alternatively, we derive the asymmetry using

$$A_N = \frac{1}{P_{\mathrm{b}}}\frac{1}{\langle|\cos\phi|\rangle}\left(\frac{\sqrt{N_L^{\uparrow}N_R^{\downarrow}} - \sqrt{N_L^{\downarrow}N_R^{\uparrow}}}{\sqrt{N_L^{\uparrow}N_R^{\downarrow}} + \sqrt{N_L^{\downarrow}N_R^{\uparrow}}}\right), \quad (2)$$

which calculates a single value for the asymmetry taking into account yields from both the left (N_L) and right (N_R) sides of the polarized beam and provides a consistency check on the relative luminosity [30].

The BBCs were used to determine the relative luminosity [$\mathcal{R}$ in Eq. (1)] between bunches of opposite polarization sign fill-by-fill. A typical $\mathcal{R}$ for the data sample analyzed here was approximately 1.09, measured to better than 10^{-3}. In the asymmetry analysis of charged hadrons, which utilized ~13 M minimum-bias events, it was required that

TABLE II. Neutral pion transverse single-spin asymmetry values and statistical uncertainties for all photon pairs falling within the π^0 mass peak, for the background (bg), and for the π^0 background corrected. The third column (r) indicates the background contribution under the π^0 peak. An A_N scale uncertainty of $\pm 35\%$ is not included.

p_T (GeV/c)	$\langle p_T \rangle$ (GeV/c)	r (%)	A_N^{peak} (%)	A_N^{bg} (%)	$A_N^{\pi^0}$ (%)
1–2	1.45	34	-0.6 ± 0.8	-0.7 ± 0.9	-0.5 ± 1.2
2–3	2.34	12	-1.4 ± 1.7	-3.1 ± 3.4	-1.2 ± 2.0
3–4	3.36	6	-1.3 ± 4.2	3.6 ± 12.2	-1.6 ± 4.7
4–5	4.38	5	7.0 ± 10.1	42 ± 39	5.2 ± 10.9

there be no hits in the RICH in order to eliminate electrons from photon conversions which mimic high-p_T charged tracks. The momentum threshold for production of Čerenkov radiation by pions was 4.7 GeV/c, allowing the RICH veto to preserve nearly all charged pions. The electron contamination in the final data sample was less than 1%. The decay background from long-lived particles was less than 5%.

Neutral pions were reconstructed via their decay to two photons using finely segmented ($\Delta\phi \times \Delta\eta \approx 0.01 \times 0.01$) electromagnetic calorimeters (EMCal) [31]. Photon clusters were selected by their shower shape and a charged track veto. Approximately 18 M events recorded by an EMCal–based high-energy photon trigger in coincidence with the BBC collision trigger were analyzed [21]. The trigger efficiency for neutral pions varied from ~24% in the 1–2 GeV/c bin to ~78% in the 4–5 GeV/c bin. Only triggered events were used in this analysis. The π^0 peak widths varied from 13.2 MeV/c^2 in the 1–2 GeV/c bin to 10.6 MeV/c^2 in the 4–5 GeV/c bin. The contribution from combinatorial background ranged from 34% to 5% across these bins; in order to avoid errors associated with peak extraction it was not subtracted.

The asymmetry for neutral pions and charged hadrons was determined for each fill using Eq. (1), then averaged over all fills. The contribution to the π^0 asymmetry by the background under the peak was estimated by calculating the asymmetry of 50 MeV/c^2 regions on both sides of the signal, from 60–110 MeV/c^2 and 170–220 MeV/c^2 (see Table II). The asymmetry of the signal region and its uncertainty were then corrected using

$$A_N^{\pi^0} = \frac{A_N^{\text{peak}} - r A_N^{\text{bg}}}{1 - r}, \qquad \sigma_{A_N^{\pi^0}} = \frac{\sqrt{\sigma^2_{A_N^{\text{peak}}} + r^2 \sigma^2_{A_N^{\text{bg}}}}}{1 - r}, \quad (3)$$

where r is the fraction of background under the peak.

As the dominant systematic uncertainty is expected to be from the determination of the relative luminosity, systematic errors were evaluated by direct comparison of the asymmetry values calculated using Eqs. (1) and (2). Any potential effect should be the same for both the charged hadron and neutral pion analyses. No p_T dependence was expected or observed; therefore, we take the weighted average of the systematic uncertainties calculated for each bin, 0.002, as the overall, uniform systematic uncertainty.

The asymmetries are plotted vs p_T in Fig. 2 and shown in Tables II and III. The asymmetries are consistent with zero over the entire transverse momentum range.

In this Letter we have presented the first measurement of transverse-spin asymmetries A_N at midrapidity and high p_T at collider energies and the cross section for inclusive charged hadrons at midrapidity. NLO pQCD calculations have been found to reproduce experimental results for $p_T \gtrsim 2$ GeV/c not only for the cross section presented here but also for inclusive neutral pion production, indicating that pQCD can be used to interpret the high-p_T asymmetries. The transverse SSAs observed for midrapidity production of both neutral pions and charged hadrons are consistent with zero within statistical errors of a few percent, measured over $0.5 < p_T < 5$ GeV/c. The result is consistent with the midrapidity results for neutral pions at $\sqrt{s} = 20$ GeV [9]. The present measurement is complementary to that of [8]. The large asymmetries observed in neutral pion production at forward rapidity at $\sqrt{s} = 200$ GeV [8] are expected to originate from partonic processes involving valence quarks ($x > 0.1$), whereas the

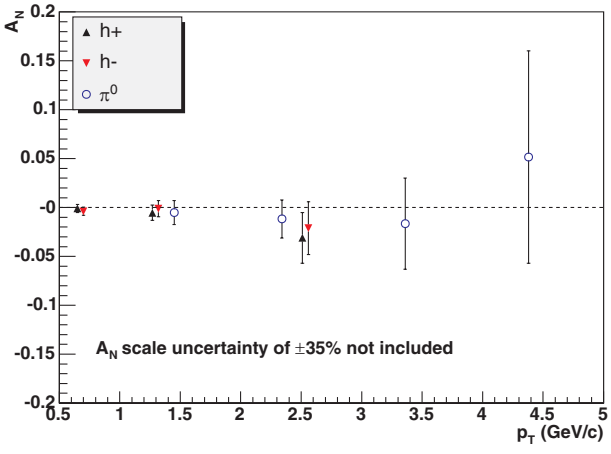

FIG. 2 (color online). Midrapidity neutral pion and charged hadron transverse single-spin asymmetry A_N vs transverse momentum. Points for positive hadrons have been shifted down by 50 MeV/c to improve readability. The error bars indicate statistical uncertainties.

TABLE III. Charged hadron transverse single-spin asymmetry values and statistical uncertainties. An A_N scale uncertainty of $\pm 35\%$ is not included.

p_T (GeV/c)	$\langle p_T \rangle$ (GeV/c)	$A_N^{h^-}$ (%)	$A_N^{h^+}$ (%)
0.5–1	0.70	-0.38 ± 0.42	-0.09 ± 0.41
1–2	1.32	-0.12 ± 0.82	-0.54 ± 0.78
2–5	2.56	-2.1 ± 2.7	-3.1 ± 2.6

particle production at midrapidity presented here is dominated by gluon-gluon and quark-gluon processes ($x < 0.1$). Our results are consistent with the pQCD expectation that quark-gluon correlations are suppressed at high p_T and midrapidity [15,32]. A QCD analysis of the presented A_N may lead to constraints on gluon-Sivers contributions to observed transverse-spin phenomena. The present transverse single-spin asymmetries represent an early measurement in a rigorous program to study transverse proton spin structure at hard scales using a pQCD framework at RHIC.

We thank the staff of the Collider-Accelerator Department, Magnet Division, and Physics Department at BNL and the RHIC polarimetry group for their vital contributions. We thank W. Vogelsang for calculations as well as numerous useful discussions. We acknowledge support from the Department of Energy and NSF (USA), MEXT and JSPS (Japan), CNPq and FAPESP (Brazil), NSFC (China), CNRS-IN2P3 and CEA (France), BMBF, DAAD, and AvH (Germany), OTKA (Hungary), DAE and DST (India), ISF (Israel), KRF and CHEP (Korea), RMIST, RAS, and RMAE (Russia), VR and KAW (Sweden), U.S. CRDF for the FSU, U.S.-Hungarian NSF-OTKA-MTA, and U.S.-Israel BSF.

*Deceased.
†PHENIX Spokesperson.
Electronic address: zajc@nevis.columbia.edu

[1] W. H. Dragoset *et al.*, Phys. Rev. D **18**, 3939 (1978).
[2] C. E. Allgower *et al.*, Phys. Rev. D **65**, 092008 (2002).
[3] J. Antille *et al.*, Phys. Lett. B **94**, 523 (1980).
[4] S. Saroff *et al.*, Phys. Rev. Lett. **64**, 995 (1990).
[5] V. D. Apokin *et al.*, Phys. Lett. B **243**, 461 (1990).
[6] D. L. Adams *et al.*, Phys. Lett. B **261**, 201 (1991).
[7] D. L. Adams *et al.*, Phys. Lett. B **264**, 462 (1991).
[8] J. Adams *et al.*, Phys. Rev. Lett. **92**, 171801 (2004).
[9] D. L. Adams *et al.*, Phys. Rev. D **53**, 4747 (1996).
[10] A. Airapetian *et al.*, Phys. Rev. Lett. **84**, 4047 (2000).
[11] A. Airapetian *et al.*, Phys. Lett. B **535**, 85 (2002).
[12] A. Airapetian *et al.*, Phys. Rev. Lett. **94**, 012002 (2005).
[13] J. C. Collins, Nucl. Phys. **B396**, 161 (1993).
[14] D. Sivers, Phys. Rev. D **41**, 83 (1990).
[15] J. Qiu and G. Sterman, Phys. Rev. D **59**, 014004 (1999).
[16] Y. Kanazawa and Y. Koike, Phys. Lett. B **478**, 121 (2000).
[17] M. Burkardt and D. S. Hwang, Phys. Rev. D **69**, 074032 (2004).
[18] K. Adcox *et al.*, Nucl. Instrum. Methods Phys. Res., Sect. A **499**, 469 (2003).
[19] M. Allen *et al.*, Nucl. Instrum. Methods Phys. Res., Sect. A **499**, 549 (2003).
[20] K. Adcox *et al.*, Nucl. Instrum. Methods Phys. Res., Sect. A **499**, 489 (2003).
[21] S. S. Adler *et al.*, Phys. Rev. Lett. **91**, 241803 (2003).
[22] S. S. Adler *et al.*, Phys. Rev. C **69**, 034910 (2004).
[23] M. Aizawa *et al.*, Nucl. Instrum. Methods Phys. Res., Sect. A **499**, 508 (2003).
[24] J. Pumplin *et al.*, J. High Energy Phys. 07 (2002) 012.
[25] B. A. Kniehl, G. Kramer, and B. Pötter, Nucl. Phys. **B597**, 337 (2001).
[26] B. Jäger, A. Schäfer, M. Stratmann, and W. Vogelsang, Phys. Rev. D **67**, 054005 (2003).
[27] F. Aversa, P. Chiappetta, M. Greco, and J. P. Guillet, Nucl. Phys. **B327**, 105 (1989).
[28] D. de Florian, Phys. Rev. D **67**, 054004 (2003).
[29] O. Jinnouchi *et al.*, AIP Conf. Proc. **675**, 817 (2003).
[30] H. Spinka, Argonne National Laboratory Report No. ANL-HEP-TR-99-113, 1999.
[31] L. Aphecetche *et al.*, Nucl. Instrum. Methods Phys. Res., Sect. A **499**, 521 (2003).
[32] G. L. Kane, J. Pumplin, and W. Repko, Phys. Rev. Lett. **41**, 1689 (1978).

Dense-Medium Modifications to Jet-Induced Hadron Pair Distributions in Au + Au Collisions at $\sqrt{s_{NN}} = 200$ GeV

S. S. Adler,[5] S. Afanasiev,[17] C. Aidala,[5] N. N. Ajitanand,[43] Y. Akiba,[20,38] J. Alexander,[43] R. Amirikas,[12] L. Aphecetche,[45] S. H. Aronson,[5] R. Averbeck,[44] T. C. Awes,[35] R. Azmoun,[44] V. Babintsev,[15] A. Baldisseri,[10] K. N. Barish,[6] P. D. Barnes,[27] B. Bassalleck,[33] S. Bathe,[30] S. Batsouli,[9] V. Baublis,[37] A. Bazilevsky,[39,15] S. Belikov,[16,15] Y. Berdnikov,[40] S. Bhagavatula,[16] J. G. Boissevain,[27] H. Borel,[10] S. Borenstein,[25] M. L. Brooks,[27] D. S. Brown,[34] N. Bruner,[33] D. Bucher,[30] H. Buesching,[30] V. Bumazhnov,[15] G. Bunce,[5,39] J. M. Burward-Hoy,[26,44] S. Butsyk,[44] X. Camard,[45] J.-S. Chai,[18] P. Chand,[4] W. C. Chang,[2] S. Chernichenko,[15] C. Y. Chi,[9] J. Chiba,[20] M. Chiu,[9] I. J. Choi,[52] J. Choi,[19] R. K. Choudhury,[4] T. Chujo,[5] V. Cianciolo,[35] Y. Cobigo,[10] B. A. Cole,[9] P. Constantin,[16] D. d'Enterria,[45] G. David,[5] H. Delagrange,[45] A. Denisov,[15] A. Deshpande,[39] E. J. Desmond,[5] A. Devismes,[44] O. Dietzsch,[41] O. Drapier,[25] A. Drees,[44] R. du Rietz,[29] A. Durum,[15] D. Dutta,[4] Y. V. Efremenko,[35] K. El Chenawi,[49] A. Enokizono,[14] H. En'yo,[38,39] S. Esumi,[48] L. Ewell,[5] D. E. Fields,[33,39] F. Fleuret,[25] S. L. Fokin,[23] B. D. Fox,[39] Z. Fraenkel,[51] J. E. Frantz,[9] A. Franz,[5] A. D. Frawley,[12] S.-Y. Fung,[6] S. Garpman,[29,*] T. K. Ghosh,[49] A. Glenn,[46] G. Gogiberidze,[46] M. Gonin,[25] J. Gosset,[10] Y. Goto,[39] R. Granier de Cassagnac,[25] N. Grau,[16] S. V. Greene,[49] M. Grosse Perdekamp,[39] W. Guryn,[5] H.-Å. Gustafsson,[29] T. Hachiya,[14] J. S. Haggerty,[5] H. Hamagaki,[8] A. G. Hansen,[27] E. P. Hartouni,[26] M. Harvey,[5] R. Hayano,[8] N. Hayashi,[38] X. He,[13] M. Heffner,[26] T. K. Hemmick,[44] J. M. Heuser,[44] M. Hibino,[50] J. C. Hill,[16] W. Holzmann,[43] K. Homma,[14] B. Hong,[22] A. Hoover,[34] T. Ichihara,[38,39] V. V. Ikonnikov,[23] K. Imai,[24,38] D. Isenhower,[1] M. Ishihara,[38] M. Issah,[43] A. Isupov,[17] B. V. Jacak,[44] W. Y. Jang,[22] Y. Jeong,[19] J. Jia,[44] O. Jinnouchi,[38] B. M. Johnson,[5] S. C. Johnson,[26] K. S. Joo,[31] D. Jouan,[36] S. Kametani,[8,50] N. Kamihara,[47,38] J. H. Kang,[52] S. S. Kapoor,[4] K. Katou,[50] S. Kelly,[9] B. Khachaturov,[51] A. Khanzadeev,[37] J. Kikuchi,[50] D. H. Kim,[31] D. J. Kim,[52] D. W. Kim,[19] E. Kim,[42] G.-B. Kim,[25] H. J. Kim,[52] E. Kistenev,[5] A. Kiyomichi,[48] K. Kiyoyama,[32] C. Klein-Boesing,[30] H. Kobayashi,[38,39] L. Kochenda,[37] V. Kochetkov,[15] D. Koehler,[33] T. Kohama,[14] M. Kopytine,[44] D. Kotchetkov,[6] A. Kozlov,[51] P. J. Kroon,[5] C. H. Kuberg,[1,27,*] K. Kurita,[39] Y. Kuroki,[48] M. J. Kweon,[22] Y. Kwon,[52] G. S. Kyle,[34] R. Lacey,[43] V. Ladygin,[17] J. G. Lajoie,[16] A. Lebedev,[16,23] S. Leckey,[44] D. M. Lee,[27] S. Lee,[19] M. J. Leitch,[27] X. H. Li,[6] H. Lim,[42] A. Litvinenko,[17] M. X. Liu,[27] Y. Liu,[36] C. F. Maguire,[49] Y. I. Makdisi,[5] A. Malakhov,[17] V. I. Manko,[23] Y. Mao,[7,38] G. Martinez,[45] M. D. Marx,[44] H. Masui,[48] F. Matathias,[44] T. Matsumoto,[8,50] P. L. McGaughey,[27] E. Melnikov,[15] F. Messer,[44] Y. Miake,[48] J. Milan,[43] T. E. Miller,[49] A. Milov,[44,51] S. Mioduszewski,[5] R. E. Mischke,[27] G. C. Mishra,[13] J. T. Mitchell,[5] A. K. Mohanty,[4] D. P. Morrison,[5] J. M. Moss,[27] F. Mühlbacher,[44] D. Mukhopadhyay,[51] M. Muniruzzaman,[6] J. Murata,[38,39] S. Nagamiya,[20] J. L. Nagle,[9] T. Nakamura,[14] B. K. Nandi,[6] M. Nara,[48] J. Newby,[46] P. Nilsson,[29] A. S. Nyanin,[23] J. Nystrand,[29] E. O'Brien,[5] C. A. Ogilvie,[16] H. Ohnishi,[5,38] I. D. Ojha,[49,3] K. Okada,[38] M. Ono,[48] V. Onuchin,[15] A. Oskarsson,[29] I. Otterlund,[29] K. Oyama,[8] K. Ozawa,[8] D. Pal,[51] A. P. T. Palounek,[27] V. Pantuev,[44] V. Papavassiliou,[34] J. Park,[42] A. Parmar,[33] S. F. Pate,[34] T. Peitzmann,[30] J.-C. Peng,[27] V. Peresedov,[17] C. Pinkenburg,[5] R. P. Pisani,[5] F. Plasil,[35] M. L. Purschke,[5] A. K. Purwar,[44] J. Rak,[16] I. Ravinovich,[51] K. F. Read,[35,46] M. Reuter,[44] K. Reygers,[30] V. Riabov,[37,40] Y. Riabov,[37] G. Roche,[28] A. Romana,[25,*] M. Rosati,[16] P. Rosnet,[28] S. S. Ryu,[52] M. E. Sadler,[1] N. Saito,[38,39] T. Sakaguchi,[8,50] M. Sakai,[32] S. Sakai,[48] V. Samsonov,[37] L. Sanfratello,[33] R. Santo,[30] H. D. Sato,[24,38] S. Sato,[5,48] S. Sawada,[20] Y. Schutz,[45] V. Semenov,[15] R. Seto,[6] M. R. Shaw,[1,27] T. K. Shea,[5] T.-A. Shibata,[47,38] K. Shigaki,[14,20] T. Shiina,[27] C. L. Silva,[41] D. Silvermyr,[27,29] K. S. Sim,[22] C. P. Singh,[3] V. Singh,[3] M. Sivertz,[5] A. Soldatov,[15] R. A. Soltz,[26] W. E. Sondheim,[27] S. P. Sorensen,[46] I. V. Sourikova,[5] F. Staley,[10] P. W. Stankus,[35] E. Stenlund,[29] M. Stepanov,[34] A. Ster,[21] S. P. Stoll,[5] T. Sugitate,[14] J. P. Sullivan,[27] E. M. Takagui,[41] A. Taketani,[38,39] M. Tamai,[50] K. H. Tanaka,[20] Y. Tanaka,[32] K. Tanida,[38] M. J. Tannenbaum,[5] P. Tarján,[11] J. D. Tepe,[1,27] T. L. Thomas,[33] J. Tojo,[24,38] H. Torii,[24,38] R. S. Towell,[1] I. Tserruya,[51] H. Tsuruoka,[48] S. K. Tuli,[3] H. Tydesjö,[29] N. Tyurin,[15] H. W. van Hecke,[27] J. Velkovska,[5,44] M. Velkovsky,[44] V. Veszprémi,[11] L. Villatte,[46] A. A. Vinogradov,[23] M. A. Volkov,[23] E. Vznuzdaev,[37] X. R. Wang,[13] Y. Watanabe,[38,39] S. N. White,[5] F. K. Wohn,[16] C. L. Woody,[5] W. Xie,[6] Y. Yang,[7] A. Yanovich,[15] S. Yokkaichi,[38,39] G. R. Young,[35] I. E. Yushmanov,[23] W. A. Zajc,[9,†] C. Zhang,[9] S. Zhou,[7] S. J. Zhou,[51] and L. Zolin[17]

(PHENIX Collaboration)

[1]*Abilene Christian University, Abilene, Texas 79699, USA*
[2]*Institute of Physics, Academia Sinica, Taipei 11529, Taiwan*
[3]*Department of Physics, Banaras Hindu University, Varanasi 221005, India*

 © 2006 The American Physical Society

[4]*Bhabha Atomic Research Centre, Bombay 400 085, India*
[5]*Brookhaven National Laboratory, Upton, New York 11973-5000, USA*
[6]*University of California—Riverside, Riverside, California 92521, USA*
[7]*China Institute of Atomic Energy (CIAE), Beijing, People's Republic of China*
[8]*Center for Nuclear Study, Graduate School of Science, University of Tokyo, 7-3-1 Hongo, Bunkyo, Tokyo 113-0033, Japan*
[9]*Columbia University, New York, New York 10027, USA,*
and Nevis Laboratories, Irvington, New York 10533, USA
[10]*Dapnia, CEA Saclay, F-91191 Gif-sur-Yvette, France*
[11]*Debrecen University, H-4010 Debrecen, Egyetem tér 1, Hungary*
[12]*Florida State University, Tallahassee, Florida 32306, USA*
[13]*Georgia State University, Atlanta, Georgia 30303, USA*
[14]*Hiroshima University, Kagamiyama, Higashi-Hiroshima 739-8526, Japan*
[15]*IHEP Protvino, State Research Center of Russian Federation, Institute for High Energy Physics, Protvino 142281, Russia*
[16]*Iowa State University, Ames, Iowa 50011, USA*
[17]*Joint Institute for Nuclear Research, 141980 Dubna, Moscow Region, Russia*
[18]*KAERI, Cyclotron Application Laboratory, Seoul, South Korea*
[19]*Kangnung National University, Kangnung 210-702, South Korea*
[20]*KEK, High Energy Accelerator Research Organization, Tsukuba, Ibaraki 305-0801, Japan*
[21]*KFKI Research Institute for Particle and Nuclear Physics of the Hungarian Academy of Sciences (MTA KFKI RMKI),*
H-1525 Budapest 114, P.O. Box 49, Budapest, Hungary
[22]*Korea University, Seoul 136-701, Korea*
[23]*Russian Research Center "Kurchatov Institute," Moscow, Russia*
[24]*Kyoto University, Kyoto 606-8502, Japan*
[25]*Laboratoire Leprince-Ringuet, Ecole Polytechnique, CNRS-IN2P3, Route de Saclay, F-91128 Palaiseau, France*
[26]*Lawrence Livermore National Laboratory, Livermore, California 94550, USA*
[27]*Los Alamos National Laboratory, Los Alamos, New Mexico 87545, USA*
[28]*LPC, Université Blaise Pascal, CNRS-IN2P3, Clermont-Fd, 63177 Aubiere Cedex, France*
[29]*Department of Physics, Lund University, Box 118, SE-221 00 Lund, Sweden*
[30]*Institut für Kernphysik, University of Muenster, D-48149 Muenster, Germany*
[31]*Myongji University, Yongin, Kyonggido 449-728, Korea*
[32]*Nagasaki Institute of Applied Science, Nagasaki-shi, Nagasaki 851-0193, Japan*
[33]*University of New Mexico, Albuquerque, New Mexico 87131, USA*
[34]*New Mexico State University, Las Cruces, New Mexico 88003, USA*
[35]*Oak Ridge National Laboratory, Oak Ridge, Tennessee 37831, USA*
[36]*IPN-Orsay, Universite Paris Sud, CNRS-IN2P3, BP1, F-91406 Orsay, France*
[37]*PNPI, Petersburg Nuclear Physics Institute, Gatchina, Russia*
[38]*RIKEN, The Institute of Physical and Chemical Research, Wako, Saitama 351-0198, Japan*
[39]*RIKEN BNL Research Center, Brookhaven National Laboratory, Upton, New York 11973-5000, USA*
[40]*Saint Petersburg State Polytechnic University, St. Petersburg, Russia*
[41]*Instituto de Física, Universidade de São Paulo, Caixa Postal 66318, São Paulo CEP05315-970, Brazil*
[42]*System Electronics Laboratory, Seoul National University, Seoul, South Korea*
[43]*Chemistry Department, Stony Brook University, SUNY, Stony Brook, New York 11794-3400, USA*
[44]*Department of Physics and Astronomy, Stony Brook University, SUNY, Stony Brook, New York 11794, USA*
[45]*SUBATECH (Ecole des Mines de Nantes, CNRS-IN2P3, Université de Nantes), BP 20722-44307, Nantes, France*
[46]*University of Tennessee, Knoxville, Tennessee 37996, USA*
[47]*Department of Physics, Tokyo Institute of Technology, Tokyo 152-8551, Japan*
[48]*Institute of Physics, University of Tsukuba, Tsukuba, Ibaraki 305, Japan*
[49]*Vanderbilt University, Nashville, Tennessee 37235, USA*
[50]*Advanced Research Institute for Science and Engineering, Waseda University,*
17 Kikui-cho, Shinjuku-ku, Tokyo 162-0044, Japan
[51]*Weizmann Institute, Rehovot 76100, Israel*
[52]*Yonsei University, IPAP, Seoul 120-749, Korea*
(Received 1 July 2005; published 2 August 2006)

Azimuthal correlations of jet-induced high-p_T charged hadron pairs are studied at midrapidity in Au + Au collisions at $\sqrt{s_{NN}} = 200$ GeV. The distribution of jet-associated partner hadrons ($1.0 < p_T < 2.5$ GeV/c) per trigger hadron ($2.5 < p_T < 4.0$ GeV/c) is found to vary with collision centrality, in both shape and yield, indicating a significant effect of the nuclear collision medium on the jet fragmentation process.

DOI: 10.1103/PhysRevLett.97.052301 PACS numbers: 25.75.Dw

Energetic collisions between heavy ions at the Relativistic Heavy Ion Collider (RHIC) have been shown to produce matter with extremely high energy density [1]. This matter has been observed to strongly suppress the yield of hadrons with large transverse momenta in central Au + Au collisions, compared to yields in $p + p$ collisions scaled by the number of binary nucleon-nucleon collisions [2–5]. Such a suppression was predicted to result from energy loss of hard-scattered partons (light quarks and gluons) traversing the dense matter prior to forming the observed hadrons [6,7]. If the parton encounters a sufficient amount of dense matter, the energy loss could strongly modify its fragmentation into jets of hadrons.

Strong suppression of the awayside jet has been observed at RHIC [8]. However, it is unclear at present how the lost energy is transported by the dense medium, and how the parton-medium interaction affects the fragmentation process. Recently, there have been predictions that the coupling of jets to a strongly interacting medium may modify the angular distribution and number of jet fragments [9–16]. Quarks from hard scattering processes may recombine with thermal quarks from the dense medium [9,10]. Comoving radiated gluons may produce a ''wake'' in the medium, further increasing the number of quarks available for building hadrons in the jet fragmentation process [11,13]. It has even been proposed that the energy deposited in the medium creates a shock wave around the propagating parton, thereby creating a ''conical flow'' akin to a sonic boom in a fluid [14–16]. To investigate the transport of lost parton energy, the PHENIX experiment at RHIC measures azimuthally correlated hadrons arising from jet fragmentation as a function of centrality in Au + Au collisions. Such studies, in effect, use hard-scattered partons as short-wavelength probes of the produced medium.

The analysis presented in this Letter uses data from $\sqrt{s_{NN}} = 200$ GeV Au + Au collisions in the PHENIX 2002 data set. Charged particles are reconstructed in the central arms of PHENIX using drift chambers, each with azimuthal coverage of $\pi/2$, and two layers of multiwire proportional chambers with pad readout (PC1, PC3) [17]. Pattern recognition is based on a combinatorial Hough transform in the track bend plane, with the polar angle determined by PC1 and the collision vertex along the beam direction [18]. Particle momenta are measured with a resolution $\delta p/p = 0.7\% \oplus 1.0\% p$ (GeV/c). To reject most background from albedo, conversions, and decays, a confirmation hit is required within a 2σ matching window in PC3 [2]. The Au + Au event centrality is determined using the PHENIX beam-beam counters (BBC) and zero-degree calorimeters [19].

The traditional identification of jets through hadronic calorimetry and cluster algorithms is problematic in Au + Au collisions at RHIC, since low-energy jets (<10–20 GeV) are overwhelmed by other produced particles in the underlying event and high-energy jets are relatively rare at $\sqrt{s_{NN}} = 200$ GeV. Instead, we study hard-scattered single partons and parton pairs through angular correlations of high-p_T hadron pairs. We examine the distribution of pairs over relative azimuthal angle $dN^{AB}/d(\Delta\phi)$, where A and B denote charged particles in the PHENIX pseudorapidity acceptance ($|\eta| < 0.35$) and in p_T bins $2.5\ \text{GeV}/c < p_T^A < 4.0\ \text{GeV}/c$ (''trigger'') and $1.0\ \text{GeV}/c < p_T^B < 2.5\ \text{GeV}/c$ (''partner''). Pairs from fragments of the same jet are expected to appear near $\Delta\phi \sim 0$, while $\Delta\phi \sim \pi$ indicates one hadron each from the outgoing hard-scattered parton pair (hereafter ''dijet'').

The PHENIX acceptance at central rapidity is nonuniform in azimuth. We correct for the shape of the acceptance in $\Delta\phi$ through the standard approach of constructing a correlation function, area normalized, utilizing pairs from mixed events:

$$C(\Delta\phi) \equiv \frac{Y^{AB}_{\text{same}}(\Delta\phi)}{Y^{AB}_{\text{mixed}}(\Delta\phi)} \frac{\int Y^{AB}_{\text{mixed}}(\Delta\phi)d(\Delta\phi)}{\int Y^{AB}_{\text{same}}(\Delta\phi)d(\Delta\phi)} \propto \frac{dN^{AB}}{d(\Delta\phi)}, \quad (1)$$

where $Y^{AB}_{\text{same}}(\Delta\phi)$ and $Y^{AB}_{\text{mixed}}(\Delta\phi)$ are, respectively, the uncorrected yields of pairs in the same event and in mixed events, each of which are chosen uniformly within each data sample.

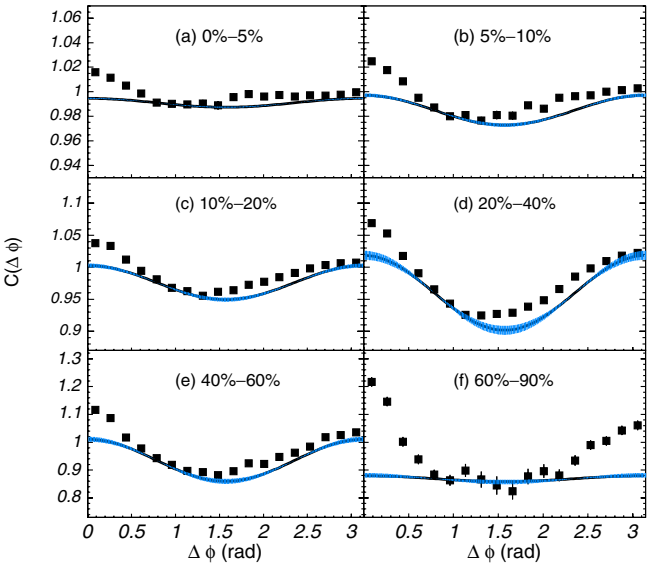

FIG. 1 (color online). Correlation functions, $C(\Delta\phi)$, for pairs of charged hadrons with $2.5\ \text{GeV}/c < p_T^A < 4.0\ \text{GeV}/c$ and $1.0\ \text{GeV}/c < p_T^B < 2.5\ \text{GeV}/c$ in different bins of collision centrality from the most central (a) 0%–5% to the most peripheral (f) 60%–90%. The solid bands indicate the estimate of the background pair component (see text) within one unit of its systematic error.

The correlation functions are shown in Fig. 1, folded into the range $0 < \Delta\phi < \pi$. For the most peripheral collisions [cf. Fig. 1(f)], the correlation function shows two well-defined peaks centered at $\Delta\phi = 0$ and $\Delta\phi = \pi$, which we can attribute to (di)jet pairs. For more central collisions, there is a similar peak at $\Delta\phi = 0$, a broader peak at $\Delta\phi = \pi$, and the apparent minima appear at $\Delta\phi < \pi/2$. These features reflect a mixture of (di)jet pairs and underlying events with particle flow along the reaction plane [20].

In order to extract and examine the jet-induced pairs, we analyze the pair distribution in the context of a *two-source model*, assuming that each hadron can be attributed to either (i) a jet fragmentation source or (ii) the underlying event. Additionally, we assume that the ϕ distributions for A or B inclusive single particles, summed over both sources, have a shape proportional to $\{1 + 2\langle v_2^{A\text{ or }B}\rangle \times \cos[2(\phi - \Phi_{\mathrm{RP}})]\}$ relative to azimuthal angle Φ_{RP} of the reaction plane of each event. All pairs which are not from the same jet or dijet fragmentation are termed *background pairs*, and are taken to have no angular correlation beyond having their distributions respect the same reaction plane. In principle, contributions from resonance decays and global transverse momentum conservation can also affect the distribution of background pairs, but we estimate these effects to be negligible for these p_T ranges and the PHENIX η acceptance. The distribution of background pairs over $\Delta\phi$ is then proportional to $[1 + 2\langle v_2^A v_2^B\rangle \times \cos(2\Delta\phi)]$ [20].

Given a normalization, $C(\Delta\phi)$ can then be decomposed into two pieces, one proportional to the distribution of background pairs and another $J(\Delta\phi)$ proportional to that of the (di)jet pairs:

$$C(\Delta\phi) = b_0[1 + 2\langle v_2^A v_2^B\rangle \cos(2\Delta\phi)] + J(\Delta\phi). \quad (2)$$

We approximate $\langle v_2^A v_2^B\rangle = \langle v_2^A\rangle\langle v_2^B\rangle$, and we measure $\langle v_2^A\rangle$ and $\langle v_2^B\rangle$ for each centrality and particle p_T bin through a standard reaction-plane analysis using the PHENIX BBC to reconstruct the reaction plane event by event. The large rapidity gap, $\Delta\eta > 2.75$, between the central arm acceptance and the BBC acceptance substantially reduces nonflow contributions to the measured v_2 values, particularly those arising from (di)jets. The results are shown in Table I; they are consistent with prior PHENIX v_2 measurements [21], where available.

The average level of the background b_0 can, in principle, be fixed by making an assumption about the shape of the (di)jet-pair distribution. However, since we wish to measure the shape of the (di)jet azimuthal correlations, we use a technique that requires no such *a priori* assumptions. The simplest assumption allowing b_0 to be fixed is that $dN^{AB}_{(\mathrm{di})\mathrm{jet}}/d(\Delta\phi)$ is zero for at least one value of $\Delta\phi$ (i.e., $\Delta\phi_{\mathrm{min}}$). We refer to this as the ZYAM ("zero yield at minimum") assumption for the (di)jet-pair distribution. The ZYAM condition is met by varying b_0 until the background component matches a functional fit to the correlation function at one point $\Delta\phi_{\mathrm{min}}$, as illustrated by the solid bands in Fig. 1. The systematic error on b_0 associated with this procedure (see Fig. 2) was estimated by using a variety of functional forms that matched the data.

TABLE I. Anisotropy values for bins A ($2.5 < p_T < 4.0$ GeV/c) and B ($1.0 < p_T < 2.5$ GeV/c), shown with statistical errors, and values of ϕ_{min} (see text). The relative systematic errors on the anisotropies are estimated to be $\pm 6\%$ for the five most central samples and $\pm 40\%$ for the most peripheral sample. The systematic errors on the v_2's are dominated by the uncertainty in the correction for reaction plane resolution [21], and we assume them to be completely correlated between the two p_T bins in each centrality sample.

Centrality (%)	$\langle v_2^B\rangle$	$\langle v_2^A\rangle$	ϕ_{min} (rad)
0–5	0.035 ± 0.001	0.052 ± 0.007	0.94
5–10	0.062 ± 0.001	0.100 ± 0.005	0.96
10–20	0.095 ± 0.0005	0.144 ± 0.003	0.98
20–40	0.146 ± 0.0004	0.208 ± 0.003	0.91
40–60	0.171 ± 0.001	0.236 ± 0.006	0.86
60–90	0.066 ± 0.001	0.091 ± 0.004	1.06

A nonzero yield of (di)jet pairs at $\Delta\phi_{\mathrm{min}}$ would invalidate the ZYAM assumption and result in an overestimate of the value of b_0. To verify that we are not making a significant error in the normalization of the background, we have independently estimated the b_0 values using the AB pair combinatorial rate, corrected for a slight bias

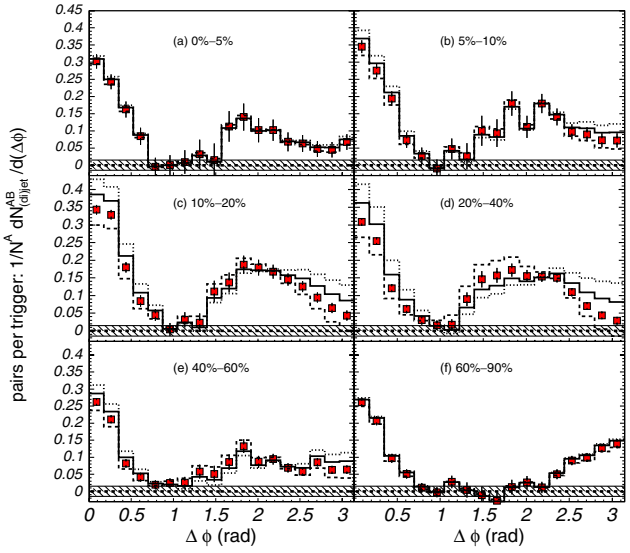

FIG. 2 (color online). Jet-pair distributions $dN^{AB}_{(\mathrm{di})\mathrm{jet}}/d(\Delta\phi)$ for different centralities, normalized per trigger particle. The shaded bands indicate the systematic error associated with the determination of $\Delta\phi_{\mathrm{min}}$. The dashed (solid) curves are the distributions that would result from increasing (decreasing) $\langle v_2^A v_2^B\rangle$ by one unit of the systematic error; the dotted curve would result from decreasing by two units.

introduced by mixing events of different multiplicity within the same centrality class [22]. These independent estimates are consistent with the ZYAM-determined values for b_0, confirming that we are not significantly overestimating the background levels.

Once $\langle v_2^A v_2^B \rangle$ and b_0 are fixed, we can extract $J(\Delta\phi)$ and the fully corrected (di)jet pairs distribution $dN^{AB}_{(\mathrm{di})\mathrm{jet}}/d(\Delta\phi)$. We construct the conditional yield distribution of jet-associated partners per trigger:

$$\frac{1}{N^A}\frac{dN^{AB}_{(\mathrm{di})\mathrm{jet}}}{d(\Delta\phi)} = \frac{J(\Delta\phi)}{\int C(\Delta\phi')d(\Delta\phi')}\frac{N^{AB}}{N^A}. \quad (3)$$

Here, N^A is the number of triggers and N^{AB} is the total number of AB pairs in the event sample. Assuming that the pair efficiency is the product of the single particle efficiencies, the trigger (A) efficiency cancels in Eq. (3). Thus, the ratio is corrected for acceptance and reconstruction efficiency [5] of the lower-p_T B particles; the systematic error on this correction leads to a 10% uncertainty on the associated yields.

The conditional yields of (di)jet-induced partners per trigger are shown in Fig. 2. For the most peripheral event sample the (di)jet-associated yield distribution has an appearance we might expect from a normal (di)jet fragmentation process [23]: a well-defined nearside peak around $\Delta\phi = 0$ and a somewhat wider awayside peak around $\Delta\phi = \pi$. For more central event samples the shape of the nearside peak is essentially unchanged while the associated yield in the nearside peak increases, indicating some change in the fragmentation process.

The much more dramatic change, however, is in the awayside peak, which is considerably broader in all the event samples more central than 60%. In midcentral and central collisions there is a local minimum at $\Delta\phi = \pi$. The existence of these local minima *per se* is not significant once we take the systematic errors on $\langle v_2^A v_2^B \rangle$ into account (see below), but it is clear that the awayside peaks in all the more central samples have a very different shape than in the most peripheral sample.

Given the dramatic results for the awayside peaks seen in Fig. 2, it is important to establish that they are not simply artifacts created by our method for background pair subtraction. If we relax the ZYAM assumption and lower b_0 slightly, the effect on any (di)jet-pair distribution would essentially be to raise it by a constant, which would not change the presence of the local minima at $\Delta\phi = \pi$, but would increase the per trigger yields. ZYAM derived yields are lower limit yields [20].

Changes to our estimate for $\langle v_2^A v_2^B \rangle$ can alter the shape of the (di)jet distribution for some centrality samples, but the result of awayside broadening with centrality remains robust. The curves in Fig. 2 show the distributions that would result if the $\langle v_2^A v_2^B \rangle$ products were arbitrarily lowered by one and two units of their systematic error. With a two-unit shift the shape in the midcentral would no longer show significant local minima at $\Delta\phi = \pi$. However, the widths of the awayside peaks are clearly still much greater than in the peripheral sample and the distributions in the two most central samples are hardly changed at all in shape. Even lower values of $\langle v_2^A v_2^B \rangle$ could be contemplated, but they would still not change the qualitative result of awayside broadening. And, such low $\langle v_2^A v_2^B \rangle$ values would also require a severe breakdown of the assumption $\langle v_2^A v_2^B \rangle = \langle v_2^A \rangle \langle v_2^B \rangle$, indicating that these background pairs have a large, hitherto-unknown source of azimuthal anticorrelation.

Convoluting the jet fragments' angles with respect to their parent partons and the acoplanarity between the two partons [23] would yield a Gaussian-like shape in $\Delta\phi$, possibly broadened through jet quenching [13,24]. The observed shapes in the awayside peaks cannot result from such a convolution.

We define the part of the $\Delta\phi$ distribution in $|\Delta\phi| < \Delta\phi_{\mathrm{min}}$ as the "nearside" peak and $|\Delta\phi| > \Delta\phi_{\mathrm{min}}$ as the "awayside" peak. Each peak is characterized by its yield of associated partners per trigger and by its rms width. We measure these for the full peak in the distribution over all values of $\Delta\phi$; the folded distributions over $0 < \Delta\phi < \pi$ shown here contain only half of each full peak's shape. These yields and widths are plotted in Fig. 3 for the different Au + Au centrality samples, along with the same quantities for 0%–20% central d + Au collisions at $\sqrt{s_{NN}} = 200$ GeV [23]. The yields and widths for the near- and awayside peaks in peripheral Au + Au collisions are consistent with those in d + Au collisions. The yields of both the near- and awayside peaks increase from peripheral to midcentral collisions, and then decrease for the most central collisions. The nearside width is unchanged with centrality, while the awayside width in-

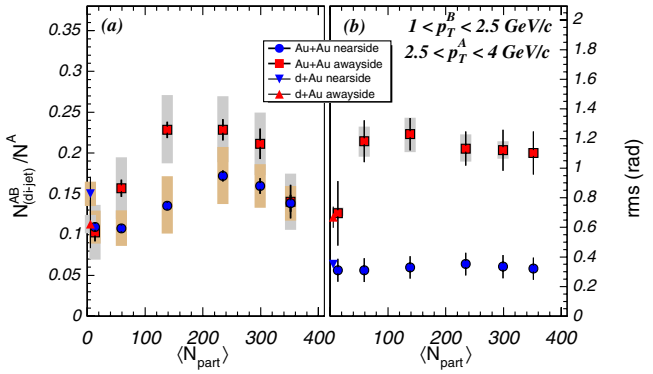

FIG. 3 (color online). (a) Associated yields for near- and awayside peaks in the jet-pair distribution, and (b) widths (rms) of the peaks in the full 0–2π distributions; plotted versus the mean number of participating nucleons for each event sample. Triangles show results from 0%–20% central d + Au collisions at the same $\sqrt{s_{NN}}$ [23]. Bars show statistical errors, shaded bands systematic.

creases substantially from the 60%–90% sample to the 40%–60% sample, and then remains constant with centrality.

In summary, we have presented correlations of high momentum charged hadron pairs as a function of collision centrality in Au + Au collisions. Utilizing a novel technique, we extract the jet-induced hadron pair distributions and show that the dense medium formed in Au + Au collisions at RHIC modifies jet fragmentation. In central and midcentral collisions the awayside angular distribution is significantly broadened relative to peripheral and d + Au collisions, and appears to be non-Gaussian. The shapes of the awayside $\Delta\phi$ distributions for non-peripheral collisions are apparently not consistent with Gaussian broadening of the peripheral Au + Au awayside. However, the broadening and possible changes in shape of the awayside jet are suggestive of recent theoretical predictions of dense-medium effects on fragment distributions [14–16,25]. The broadened shapes of the awayside distributions also imply that integration of the awayside peak in a narrow angular range around $\Delta\phi = \pi$ yields fewer associated partners in central collisions than in peripheral or d + Au collisions, as seen elsewhere [8,22]; but integrating over the entire broadened peak recovers the jet partners in the range $1.0\ \mathrm{GeV}/c < p_T^B < 2.5\ \mathrm{GeV}/c$ used here. Even though two-particle correlations do not allow for full reconstruction of the jet fragmentation function, these data provide an entirely new way to probe the hot, dense medium formed in heavy ion collisions.

We thank the staff of the Collider-Accelerator and Physics Departments at BNL for their vital contributions. We acknowledge support from the Department of Energy and NSF (USA), MEXT and JSPS (Japan), CNPq and FAPESP (Brazil), NSFC (China), CNRS-IN2P3 and CEA (France), BMBF, DAAD, and AvH (Germany), OTKA (Hungary), DAE and DST (India), ISF (Israel), KRF and CHEP (Korea), RMIST, RAS, and RMAE (Russia), VR and KAW (Sweden), U.S. CRDF for the FSU, U.S.-Hungarian NSF-OTKA-MTA, and U.S.-Israel BSF.

*Deceased.
†PHENIX spokesperson.
Electronic address: zajc@nevis.columbia.edu

[1] K. Adcox *et al.*, Nucl. Phys. **A757**, 184 (2005).
[2] K. Adcox *et al.*, Phys. Rev. Lett. **88**, 022301 (2001).
[3] S. S. Adler *et al.*, Phys. Rev. Lett. **91**, 072301 (2003).
[4] J. Adams *et al.*, Phys. Rev. Lett. **91**, 172302 (2003).
[5] S. S. Adler *et al.*, Phys. Rev. C **69**, 034910 (2004).
[6] J. D. Bjorken, Fermilab Report No. FERMILAB-PUB-82-059-THY, 1982.
[7] X. N. Wang and M. Gyulassy, Phys. Rev. Lett. **68**, 1480 (1992); X. N. Wang, Phys. Rev. C **58**, 2321 (1998).
[8] C. Adler *et al.*, Phys. Rev. Lett. **90**, 032301 (2003); **90**, 082302 (2003).
[9] V. Greco *et al.*, Phys. Rev. Lett. **90**, 202302 (2003); Phys. Rev. C **68**, 034904 (2003).
[10] R. C. Hwa and C. B. Yang, Phys. Rev. C **70**, 024905 (2004); J. Phys. G **30**, S1117 (2004).
[11] R. Fries *et al.*, Phys. Rev. Lett. **94**, 122301 (2005).
[12] A. Majumder, E. Wang, and X. N. Wang, nucl-th/0412061.
[13] N. Armesto, C. Salgado, and U. A. Wiedemann, Phys. Rev. Lett. **93**, 242301 (2004).
[14] J. Casalderrey-Solana, E. V. Shuryak, and D. Teaney, J. Phys.: Conf. Ser. **27**, 22 (2005).
[15] H. Stöcker, Nucl. Phys. **A750**, 121 (2005).
[16] J. Ruppert and B. Muller, Phys. Lett. B **618**, 123 (2005).
[17] K. Adcox *et al.*, Nucl. Instrum. Methods Phys. Res., Sect. A **499**, 469 (2003).
[18] J. Mitchell *et al.*, Nucl. Instrum. Methods Phys. Res., Sect. A **482**, 491 (2002).
[19] K. Adcox *et al.*, Phys. Rev. C **69**, 024904 (2004).
[20] N. N. Ajitanand *et al.*, Phys. Rev. C **72**, 011902 (2005).
[21] S. S. Adler *et al.*, Phys. Rev. Lett. **91**, 182301 (2003).
[22] S. S. Adler *et al.*, Phys. Rev. C **71**, 051902 (2005).
[23] S. S. Adler *et al.*, Phys. Rev. C **73**, 054903 (2006).
[24] J.-W. Qiu and I. Vitev, hep-ph/0410218.
[25] N. Armesto *et al.*, Phys. Rev. C **72**, 064910 (2005).

Centrality Dependence of Direct Photon Production in $\sqrt{S_{NN}} = 200$ GeV Au + Au Collisions

S. S. Adler,[5] S. Afanasiev,[17] C. Aidala,[5] N. N. Ajitanand,[43] Y. Akiba,[20,38] J. Alexander,[43] R. Amirikas,[12] L. Aphecetche,[45] S. H. Aronson,[5] R. Averbeck,[44] T. C. Awes,[35] R. Azmoun,[44] V. Babintsev,[15] A. Baldisseri,[10] K. N. Barish,[6] P. D. Barnes,[27] B. Bassalleck,[33] S. Bathe,[30] S. Batsouli,[9] V. Baublis,[37] A. Bazilevsky,[39,15] S. Belikov,[16,15] Y. Berdnikov,[40] S. Bhagavatula,[16] J. G. Boissevain,[27] H. Borel,[10] S. Borenstein,[25] M. L. Brooks,[27] D. S. Brown,[34] N. Bruner,[33] D. Bucher,[30] H. Buesching,[30] V. Bumazhnov,[15] G. Bunce,[5,39] J. M. Burward-Hoy,[26,44] S. Butsyk,[44] X. Camard,[45] J.-S. Chai,[18] P. Chand,[4] W. C. Chang,[2] S. Chernichenko,[15] C. Y. Chi,[9] J. Chiba,[20] M. Chiu,[9] I. J. Choi,[52] J. Choi,[19] R. K. Choudhury,[4] T. Chujo,[5] V. Cianciolo,[35] Y. Cobigo,[10] B. A. Cole,[9] P. Constantin,[16] D. d'Enterria,[45] G. David,[5] H. Delagrange,[45] A. Denisov,[15] A. Deshpande,[39] E. J. Desmond,[5] A. Devismes,[44] O. Dietzsch,[41] O. Drapier,[25] A. Drees,[44] R. du Rietz,[29] A. Durum,[15] D. Dutta,[4] Y. V. Efremenko,[35] K. El Chenawi,[49] A. Enokizono,[14] H. En'yo,[38,39] S. Esumi,[48] L. Ewell,[5] D. E. Fields,[33,39] F. Fleuret,[25] S. L. Fokin,[23] B. D. Fox,[39] Z. Fraenkel,[51] J. E. Frantz,[9] A. Franz,[5] A. D. Frawley,[12] S.-Y. Fung,[6] S. Garpman,[29,*] T. K. Ghosh,[49] A. Glenn,[46] G. Gogiberidze,[46] M. Gonin,[25] J. Gosset,[10] Y. Goto,[39] R. Granier de Cassagnac,[25] N. Grau,[16] S. V. Greene,[49] M. Grosse Perdekamp,[39] W. Guryn,[5] H.-Å. Gustafsson,[29] T. Hachiya,[14] J. S. Haggerty,[5] H. Hamagaki,[8] A. G. Hansen,[27] E. P. Hartouni,[26] M. Harvey,[5] R. Hayano,[8] N. Hayashi,[38] X. He,[13] M. Heffner,[26] T. K. Hemmick,[44] J. M. Heuser,[44] M. Hibino,[50] J. C. Hill,[16] W. Holzmann,[43] K. Homma,[14] B. Hong,[22] A. Hoover,[34] T. Ichihara,[38,39] V. V. Ikonnikov,[23] K. Imai,[24,38] D. Isenhower,[1] M. Ishihara,[38] M. Issah,[43] A. Isupov,[17] B. V. Jacak,[44] W. Y. Jang,[22] Y. Jeong,[19] J. Jia,[44] O. Jinnouchi,[38] B. M. Johnson,[5] S. C. Johnson,[26] K. S. Joo,[31] D. Jouan,[36] S. Kametani,[8,50] N. Kamihara,[47,38] J. H. Kang,[52] S. S. Kapoor,[4] K. Katou,[50] S. Kelly,[9] B. Khachaturov,[51] A. Khanzadeev,[37] J. Kikuchi,[50] D. H. Kim,[31] D. J. Kim,[52] D. W. Kim,[19] E. Kim,[42] G.-B. Kim,[25] H. J. Kim,[52] E. Kistenev,[5] A. Kiyomichi,[48] K. Kiyoyama,[32] C. Klein-Boesing,[30] H. Kobayashi,[38,39] L. Kochenda,[37] V. Kochetkov,[15] D. Koehler,[33] T. Kohama,[14] M. Kopytine,[44] D. Kotchetkov,[6] A. Kozlov,[51] P. J. Kroon,[5] C. H. Kuberg,[1,27] K. Kurita,[39] Y. Kuroki,[48] M. J. Kweon,[22] Y. Kwon,[52] G. S. Kyle,[34] R. Lacey,[43] V. Ladygin,[17] J. G. Lajoie,[16] A. Lebedev,[16,23] S. Leckey,[44] D. M. Lee,[27] S. Lee,[19] M. J. Leitch,[27] X. H. Li,[6] H. Lim,[42] A. Litvinenko,[17] M. X. Liu,[27] Y. Liu,[36] C. F. Maguire,[49] Y. I. Makdisi,[5] A. Malakhov,[17] V. I. Manko,[23] Y. Mao,[7,38] G. Martinez,[45] M. D. Marx,[44] H. Masui,[48] F. Matathias,[44] T. Matsumoto,[8,50] P. L. McGaughey,[27] E. Melnikov,[15] F. Messer,[44] Y. Miake,[48] J. Milan,[43] T. E. Miller,[49] A. Milov,[44,51] S. Mioduszewski,[5] R. E. Mischke,[27] G. C. Mishra,[13] J. T. Mitchell,[5] A. K. Mohanty,[4] D. P. Morrison,[5] J. M. Moss,[27] F. Mühlbacher,[44] D. Mukhopadhyay,[51] M. Muniruzzaman,[6] J. Murata,[38,39] S. Nagamiya,[20] J. L. Nagle,[9] T. Nakamura,[14] B. K. Nandi,[6] M. Nara,[48] J. Newby,[46] P. Nilsson,[29] A. S. Nyanin,[23] J. Nystrand,[29] E. O'Brien,[5] C. A. Ogilvie,[16] H. Ohnishi,[5,38] I. D. Ojha,[49,3] K. Okada,[38] M. Ono,[48] V. Onuchin,[15] A. Oskarsson,[29] I. Otterlund,[29] K. Oyama,[8] K. Ozawa,[8] D. Pal,[51] A. P. T. Palounek,[27] V. Pantuev,[44] V. Papavassiliou,[34] J. Park,[42] A. Parmar,[33] S. F. Pate,[34] T. Peitzmann,[30] J.-C. Peng,[27] V. Peresedov,[17] C. Pinkenburg,[5] R. P. Pisani,[5] F. Plasil,[35] M. L. Purschke,[5] A. K. Purwar,[44] J. Rak,[16] I. Ravinovich,[51] K. F. Read,[35,46] M. Reuter,[44] K. Reygers,[30] V. Riabov,[37,40] Y. Riabov,[37] G. Roche,[28] A. Romana,[25] M. Rosati,[16] P. Rosnet,[28] S. S. Ryu,[52] M. E. Sadler,[1] N. Saito,[38,39] T. Sakaguchi,[8,50] M. Sakai,[32] S. Sakai,[48] V. Samsonov,[37] L. Sanfratello,[33] R. Santo,[30] H. D. Sato,[24,38] S. Sato,[5,48] S. Sawada,[20] Y. Schutz,[45] V. Semenov,[15] R. Seto,[6] M. R. Shaw,[1,27] T. K. Shea,[5] T.-A. Shibata,[47,38] K. Shigaki,[14,20] T. Shiina,[27] C. L. Silva,[41] D. Silvermyr,[27,29] K. S. Sim,[22] C. P. Singh,[3] V. Singh,[3] M. Sivertz,[5] A. Soldatov,[15] R. A. Soltz,[26] W. E. Sondheim,[27] S. P. Sorensen,[46] I. V. Sourikova,[5] F. Staley,[10] P. W. Stankus,[35] E. Stenlund,[29] M. Stepanov,[34] A. Ster,[21] S. P. Stoll,[5] T. Sugitate,[14] J. P. Sullivan,[27] E. M. Takagui,[41] A. Taketani,[38,39] M. Tamai,[50] K. H. Tanaka,[20] Y. Tanaka,[32] K. Tanida,[38] M. J. Tannenbaum,[5] P. Tarján,[11] J. D. Tepe,[1,27] T. L. Thomas,[33] J. Tojo,[24,38] H. Torii,[24,38] R. S. Towell,[1] I. Tserruya,[51] H. Tsuruoka,[48] S. K. Tuli,[3] H. Tydesjö,[29] N. Tyurin,[15] H. W. van Hecke,[27] J. Velkovska,[5,44] M. Velkovsky,[44] V. Veszprémi,[11] L. Villatte,[46] A. A. Vinogradov,[23] M. A. Volkov,[23] E. Vznuzdaev,[37] X. R. Wang,[13] Y. Watanabe,[38,39] S. N. White,[5] F. K. Wohn,[16] C. L. Woody,[5] W. Xie,[6] Y. Yang,[7] A. Yanovich,[15] S. Yokkaichi,[38,39] G. R. Young,[35] I. E. Yushmanov,[23] W. A. Zajc,[9,†] C. Zhang,[9] S. Zhou,[7] S. J. Zhou,[51] and L. Zolin[17]

(PHENIX Collaboration)

[1]*Abilene Christian University, Abilene, Texas 79699, USA*
[2]*Institute of Physics, Academia Sinica, Taipei 11529, Taiwan*
[3]*Department of Physics, Banaras Hindu University, Varanasi 221005, India*
[4]*Bhabha Atomic Research Centre, Bombay 400 085, India*

 © 2005 The American Physical Society

[5]Brookhaven National Laboratory, Upton, New York 11973-5000, USA
[6]University of California–Riverside, Riverside, California 92521, USA
[7]China Institute of Atomic Energy (CIAE), Beijing, People's Republic of China
[8]Center for Nuclear Study, Graduate School of Science, University of Tokyo, 7-3-1 Hongo, Bunkyo, Tokyo 113-0033, Japan
[9]Columbia University, New York, New York 10027, USA and Nevis Laboratories, Irvington, New York 10533, USA
[10]Dapnia, CEA Saclay, F-91191, Gif-sur-Yvette, France
[11]Debrecen University, H-4010 Debrecen, Egyetem tér 1, Hungary
[12]Florida State University, Tallahassee, Florida 32306, USA
[13]Georgia State University, Atlanta, Georgia 30303, USA
[14]Hiroshima University, Kagamiyama, Higashi-Hiroshima 739-8526, Japan
[15]Institute for High Energy Physics (IHEP), Protvino, Russia
[16]Iowa State University, Ames, Iowa 50011, USA
[17]Joint Institute for Nuclear Research, 141980 Dubna, Moscow Region, Russia
[18]KAERI, Cyclotron Application Laboratory, Seoul, South Korea
[19]Kangnung National University, Kangnung 210-702, South Korea
[20]KEK, High Energy Accelerator Research Organization, Tsukuba-shi, Ibaraki-ken 305-0801, Japan
[21]KFKI Research Institute for Particle and Nuclear Physics (RMKI), H-1525 Budapest 114, P.O. Box 49, Hungary
[22]Korea University, Seoul, 136-701, Korea
[23]Russian Research Center "Kurchatov Institute," Moscow, Russia
[24]Kyoto University, Kyoto 606-8502, Japan
[25]Laboratoire Leprince-Ringuet, Ecole Polytechnique, CNRS-IN2P3, Route de Saclay, F-91128, Palaiseau, France
[26]Lawrence Livermore National Laboratory, Livermore, California 94550, USA
[27]Los Alamos National Laboratory, Los Alamos, New Mexico 87545, USA
[28]LPC, Université Blaise Pascal, CNRS-IN2P3, Clermont-Fd, 63177 Aubiere Cedex, France
[29]Department of Physics, Lund University, Box 118, SE-221 00 Lund, Sweden
[30]Institut für Kernphysik, University of Muenster, D-48149 Muenster, Germany
[31]Myongji University, Yongin, Kyonggido 449-728, Korea
[32]Nagasaki Institute of Applied Science, Nagasaki-shi, Nagasaki 851-0193, Japan
[33]University of New Mexico, Albuquerque, New Mexico 87131, USA
[34]New Mexico State University, Las Cruces, New Mexico 88003, USA
[35]Oak Ridge National Laboratory, Oak Ridge, Tennessee 37831, USA
[36]IPN-Orsay, Universite Paris Sud, CNRS-IN2P3, BP1, F-91406, Orsay, France
[37]PNPI, Petersburg Nuclear Physics Institute, Gatchina, Russia
[38]RIKEN (The Institute of Physical and Chemical Research), Wako, Saitama 351-0198, Japan
[39]RIKEN BNL Research Center, Brookhaven National Laboratory, Upton, New York 11973-5000, USA
[40]St. Petersburg State Technical University, St. Petersburg, Russia
[41]Universidade de São Paulo, Instituto de Física, Caixa Postal 66318, São Paulo CEP05315-970, Brazil
[42]System Electronics Laboratory, Seoul National University, Seoul, South Korea
[43]Chemistry Department, Stony Brook University, SUNY, Stony Brook, New York 11794-3400, USA
[44]Department of Physics and Astronomy, Stony Brook University, SUNY, Stony Brook, New York 11794, USA
[45]SUBATECH (Ecole des Mines de Nantes, CNRS-IN2P3, Université de Nantes) BP 20722-44307, Nantes, France
[46]University of Tennessee, Knoxville, Tennessee 37996, USA
[47]Department of Physics, Tokyo Institute of Technology, Tokyo, 152-8551, Japan
[48]Institute of Physics, University of Tsukuba, Tsukuba, Ibaraki 305, Japan
[49]Vanderbilt University, Nashville, Tennessee 37235, USA
[50]Waseda University, Advanced Research Institute for Science and Engineering, 17 Kikui-cho, Shinjuku-ku, Tokyo 162-0044, Japan
[51]Weizmann Institute, Rehovot 76100, Israel
[52]Yonsei University, IPAP, Seoul 120-749, Korea

(Received 7 March 2005; published 16 June 2005)

The first measurement of direct photons in Au + Au collisions at $\sqrt{s_{NN}} = 200$ GeV is presented. The direct photon signal is extracted as a function of the Au + Au collision centrality and compared to next-to-leading order perturbative quantum chromodynamics calculations. The direct photon yield is shown to scale with the number of nucleon-nucleon collisions for all centralities.

DOI: 10.1103/PhysRevLett.94.232301 PACS numbers: 25.75.Dw

One of the most exciting observations from experiments at the Relativistic Heavy Ion Collider (RHIC) is the strong suppression of the yield of hadrons at large transverse momenta ($p_T > 2$ GeV/c) in central Au + Au collisions, as compared to measured yields in $p + p$ collisions scaled by the number of binary nucleon-nucleon collisions [1–4].

Such quenching was predicted to result from the energy loss of hard-scattered partons propagating through the high density matter created in heavy ion collisions [5]. It was later proposed that the observed hadron suppression could be an initial-state effect due to saturation of the initial parton distributions in large nuclei [6]. The high-p_T hadron suppression was not observed in d + Au collisions [7,8]. This indicates that the suppression in Au + Au collisions is due to the extended dense matter in the final state that is absent in d + Au collisions.

Measurement of direct photon production allows more definitive discrimination between initial- and final-state suppression due to the fact that photons, once produced, are essentially unaffected by the surrounding matter. Hence photons produced directly in initial parton scatterings are not quenched unless the initial parton distributions are suppressed in the nucleus. In fact, there may be additional direct photon yield in AA collisions [9] due to various processes such as momentum broadening of the incoming partons, additional fragmentation contributions [10,11], or additional scatterings in the thermalizing dense matter of the final state.

This Letter reports on direct photon production in Au + Au collisions at $\sqrt{s_{NN}} = 200$ GeV with data taken by the PHENIX experiment [12] during the second RHIC run (2001–2002). This analysis used the beam-beam counters (BBC, $3.0 < |\eta| < 3.9$) and the zero degree calorimeter (ZDC) for trigger and event characterization, the electromagnetic calorimeter (EMCal) in the two central arms ($|\eta| \leq 0.35$) to measure the inclusive γ, π^0, and η yields, and the tracking system of the central arms to estimate the charged particle contamination. The EMCal consists of two subsystems: six sectors of lead-scintillator sandwich calorimeter (PbSc) and two sectors of lead-glass Čerenkov calorimeter (PbGl). Located at a radial distance of about 5 m, each sector covers an azimuthal interval of $\Delta\phi \approx 22.5°$. The fine segmentation of the EMCal ($\Delta\phi \times \Delta\eta \sim 0.01 \times 0.01$) ensures that the two photons from a decayed π^0 are well resolved up to transverse momenta of 15–20 GeV/c.

The event centrality was selected by cuts on the correlated distribution of charged particles detected in the BBCs versus energy measured in the ZDC detectors. A Glauber model Monte Carlo combined with a simulation of the BBC and ZDC responses gave an estimate of the associated number of binary collisions ($N_{\rm coll}$) and participating nucleons ($N_{\rm part}$) for each centrality bin (values tabulated in Ref. [3]).

For this analysis a minimum bias trigger sample of 30×10^6 events, also used for the previously published π^0 analysis [3], was combined with a level-2 trigger event sample equivalent to additional 55×10^6 minimum bias events. The level-2 trigger sample was obtained by the use of an EMCal software trigger on highly energetic showers equivalent to the level-1 hardware trigger used in Ref. [13]. The threshold energy of the trigger was set at 3.5 GeV with a resulting trigger efficiency plateau at 100% for single photons above $p_T \approx 5$ GeV/c (6.5 GeV/c) for the PbSc (PbGl). The normalization of the level-2 data sample relative to the minimum bias data sample is accurate to 2%. In the following, the minimum bias result refers to the combined level-2 and minimum bias trigger samples without selection on centrality.

The direct photon yield is extracted on a statistical basis, without isolation cuts, by a comparison of the inclusive photon spectra to the expected background from hadronic decays [14,15] (mainly $\pi^0 \rightarrow 2\gamma$). Photonlike clusters are identified in the EMCal by applying appropriate particle identification (PID) cuts based on time of flight and the shower profile. The consistency of the final results obtained independently with the PbSc and PbGl, and with different PID cuts, including no PID cut, is used to check the systematic error estimates. The π^0 and η yields are determined as described in [3,16] by an invariant mass analysis of photon pairs, with the combinatorial background established by combining uncorrelated photon pairs from different events.

The raw inclusive photon-candidate spectra must be corrected for charged and neutral hadron contaminations not removed by the PID cuts, as well as for photon conversions. Charged contaminants are identified by associating photon candidates in the EMCal with charged hits in the pad chamber (PC3) positioned directly in front of the EMCal. The charged contaminant spectra are subtracted from the photon-candidate spectra. The charged hadron contamination depends strongly on the PID cut and increases significantly for $p_T < 3$ GeV/c with a contribution of 4% above 3 GeV/c for the tightest PID cut. The contamination of neutral hadrons (mainly antineutrons) is determined with a full GEANT simulation of the detector response to neutrons and antineutrons with input spectra based on the proton and antiproton yields measured by PHENIX [4]. The neutral hadron contamination is found to be negligible above $p_T = 5$ GeV/c ($< 1\%$). The neutral photon-candidate spectra are corrected for conversions removed by the charged contaminant subtraction with a p_T-independent factor (5.9%–7.3% for different sectors based on simulation).

The raw spectra are normalized to one unit of rapidity and full azimuth (the purely geometrical acceptance correction is $\sim 1/0.35$). The spectra are further corrected for (i) the detector response (energy resolution, dead areas), (ii) the reconstruction efficiency (PID cuts), and (iii) occupancy effects (cluster overlaps). These corrections are quantified by embedding simulated single γ's, π^0's, or η's from a full PHENIX GEANT simulation into real events and by analyzing the merged events with the same analysis cuts used to obtain the real yields. The overall π^0 yield correction was ~ 2.5 with a centrality dependence of $\lesssim 25\%$. The losses were dominated by fiducial and asym-

metry cuts. The nominal energy resolution was adjusted in the simulation by smearing the energies with a constant term of ~5% for PbSc and ~7% for PbGl to reproduce the measured width of the π^0 peak observed at each p_T. The shape, position, and width of the π^0 peak measured for all centralities were confirmed to be well reproduced by the embedded data.

The energy calibration of the EMCal was corroborated by the position of the π^0 invariant mass peak, by the energy deposit from minimum ionizing charged particles traversing the EMCal (PbSc), and by the correlation between the measured momentum of electron and positron tracks identified by the ring-imaging Čerenkov detector and the associated energy deposit in the EMCal. From these studies it is determined that the accuracy of the energy measurement was better than 1.5%.

The main sources of systematic errors in the PbSc and PbGl measurements are the uncertainties in (i) the yield extraction, (ii) the yield correction, and (iii) the energy scale. The relative contributions of these effects to the total error differ for the PbSc and PbGl (Table I). The weighted average of the two independent measurements reduces the total error. The final systematic errors on the spectra are at the level of ~15%–20% (Table I). A correction for the true mean value of the p_T bin is applied to the steeply falling spectra.

TABLE I. Summary of the dominant sources of systematic errors on the π^0 and inclusive γ yields extracted independently with the PbGl and PbSc electromagnetic calorimeters. The error estimates are quoted at two p_T values in central events for the PbGl and PbSc. For the combined π^0 and inclusive γ spectra and γ/π^0 ratios, the approximate statistical and systematical errors are quoted for the most peripheral and most central reactions.

	PbGl (Central)		PbSc (Central)	
π^0 error source	3 GeV/c	8.5 GeV/c	3 GeV/c	8.5 GeV/c
Yield extraction	8.7%	7.0%	9.8%	7.2%
Yield correction	12.1%	12.0%	10.3%	12.5%
Energy scale	13.8%	14.1%	10.5%	11.4%
Total systematic	20.3%	19.8%	17.7%	18.4%
Statistical	10.6%	32.5%	2.1%	10.5%
Inclusive γ error				
Non-γ correction	2.4%	2.4%	3.2%	3.2%
Yield correction	10.2%	12.0%	9.1%	12.5%
Energy scale	15.7%	13.7%	12.4%	10.8%
Total systematic	18.9%	18.4%	15.7%	16.8%
Statistical	1.2%	14.1%	0.6%	4.1%
γ/π^0 syst.	13.6%	12.6%	14.0%	13.4%
γ/π^0 stat.	10.7%	35.4%	2.2%	11.3%
Total errors PbGl and PbSc combined				
	Peripheral		Central	
Error	3 GeV/c	8.5 GeV/c	3 GeV/c	8.5 GeV/c
π^0 syst.	13.2%	17.0%	13.9%	16.1%
π^0 stat.	3.0%	35.3%	1.8%	9.6%
γ syst.	11.4%	15.6%	11.5%	15.9%
γ stat.	3.0%	28.8%	0.6%	3.8%
γ/π^0 syst.	9.9%	13.1%	9.7%	11.2%
γ/π^0 stat.	4.2%	45.6%	1.9%	10.3%
γ/π^0 bkg calc.	4%		4%	

The completely corrected and combined PbSc and PbGl inclusive photon yields are compared to the expected yields of background photons from hadronic decays in Fig. 1 for minimum bias Au + Au collisions (0%–92% of the geometric cross section) and for five centrality bins. The decay photon calculations are based on the measured π^0 and η spectra [16] assuming m_T scaling for all other radiative decays (η', K^0_s, ω). The comparison is made as the ratio of measured (inclusive) γ/π^0 and calculated background γ/π^0 since this has the advantage that many uncertainties, such as the energy scale, cancel to a varying extent in the ratio. Since the π^0 spectra of the background calculations are taken to be the same as the measured spectra, we have

$$R_\gamma = \frac{(\gamma/\pi^0)_{\text{Measured}}}{(\gamma/\pi^0)_{\text{Background}}} \approx \frac{\gamma_{\text{Measured}}}{\gamma_{\text{Background}}}, \qquad (1)$$

and any significant deviation of the double ratio above unity indicates a direct photon excess. In Fig. 1 an excess

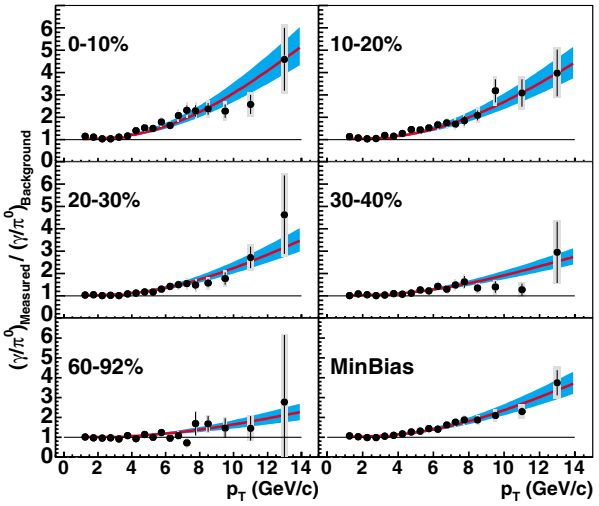

FIG. 1 (color online). Double ratio of measured $(\gamma/\pi^0)_{\text{Measured}}$ invariant yield ratio to the background decay $(\gamma/\pi^0)_{\text{Background}}$ ratio as a function of p_T for minimum bias and for five centralities of Au + Au collisions at $\sqrt{s_{NN}} = 200$ GeV (0%–10% is the most central). Statistical and total errors are indicated separately on each data point by the vertical bar and shaded region, respectively. The solid curves are the ratio of pQCD predictions described in the text to the background photon invariant yield based on the measured π^0 yield for each centrality class. The shaded regions around the curves indicate the variation of the pQCD calculation for scale changes from $p_T/2$ to $2p_T$, plus the $\langle N_{\text{coll}} \rangle$ uncertainty.

is observed at high p_T with a magnitude that increases with increasing centrality of the collision.

The measured results are compared to NLO perturbative QCD (pQCD) predictions [17], scaled by the number of binary nucleon collisions for each centrality selection. The same calculations are in agreement with the PHENIX direct photon measurement [15] for $p + p$ collisions at the same $\sqrt{s}$, and similar NLO pQCD calculations provide a good description of the measured π^0 production in $p + p$ collisions [13]. The calculations were performed [15,17] with normalization and factorization scales set equal to p_T, and using the CTEQ6 [18] set of parton distribution functions and the GRV set of fragmentation functions [19]. The direct photon spectra extracted as $\gamma_{\text{Direct}} = (1 - R_\gamma^{-1}) \cdot \gamma_{\text{Measured}}$ are shown in Fig. 2 for all nine centrality selections as well as minimum bias, and compared to the same NLO calculations. The binary collision scaled predictions are seen to provide a good description of the measured direct photon spectra (Fig. 2). The increasing ratio with centrality seen in Fig. 1 is therefore attributed to the decreasing decay background due to π^0 suppression [3].

Medium effects in AA collisions are often presented using the *nuclear modification factor* given as the ratio of the measured AA invariant yields to the NN-collision-scaled $p + p$ invariant yields:

$$R_{AA}(p_T) = \frac{(1/N_{AA}^{\text{evt}}) d^2N_{AA}/dp_T dy}{\langle N_{\text{coll}}\rangle/\sigma_{pp}^{\text{inel}} \times d^2\sigma_{pp}/dp_T dy}, \qquad (2)$$

where the $\langle N_{\text{coll}}\rangle/\sigma_{pp}^{\text{inel}}$ is the average nuclear thickness function, $\langle T_{AA}\rangle$, in the centrality bin under consideration (Ref. [3]). $R_{AA}(p_T)$ measures the deviation of AA data from an incoherent superposition of NN collisions.

The centrality dependence of the high p_T γ production represented as a function of the number of participating nucleons, N_{part}, is shown by the closed circles in Fig. 3. The production in Au + Au collisions relative to $p + p$ is characterized by the $R_{AA}(p_T > 6\ \text{GeV}/c)$ ratio of Eq. (2) as the ratio of Au + Au over the $\langle N_{\text{coll}}\rangle$ scaled $p + p$ yields each integrated above 6 GeV/c. The direct photon $p + p$ yields are taken as the NLO pQCD predictions described above. As noted above, the high p_T direct γ production is well described by the $p + p$ direct γ yield prediction scaled by $\langle N_{\text{coll}}\rangle$ for all centralities. This is in sharp contrast [3] to the centrality dependence of the π^0 $R_{AA}(p_T > 6\ \text{GeV}/c)$ shown by open circles in Fig. 3 where the measured π^0 yield [13] is used as the $p + p$ reference in Eq. (2).

The observed close agreement between the measured yields and NLO calculations is in contrast to observations for central Pb + Pb collisions at $\sqrt{s_{NN}} = 17.3$ GeV [14] where the measured photon yield exceeds the scaled NN photon yield by about a factor of 2. The present result constrains modifications of the initial parton distributions, or of the fragmentation contributions [10,11] (in these

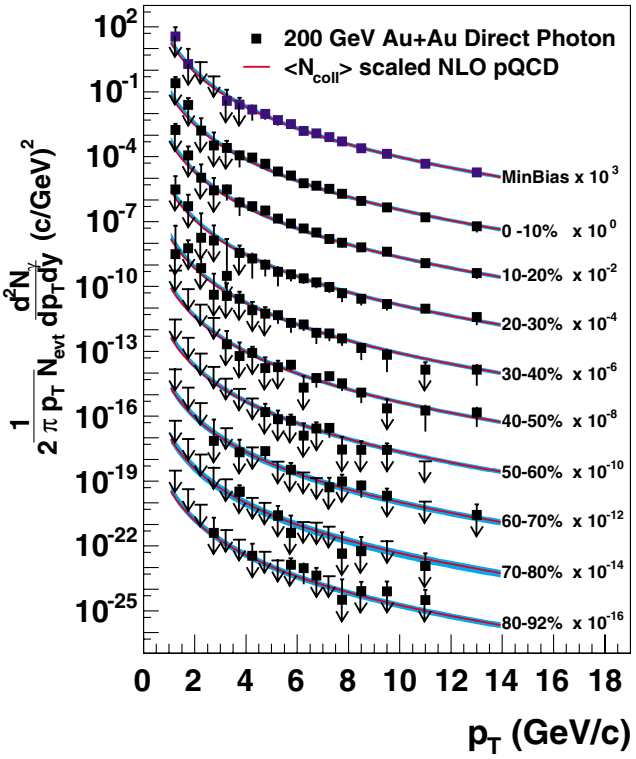

FIG. 2 (color online). Direct γ invariant yields as a function of transverse momentum for 9 centrality selections and minimum bias Au + Au collisions at $\sqrt{s_{NN}} = 200$ GeV. The vertical error bar on each point indicates the total error. Arrows indicate measurements consistent with zero yield with the tail of the arrow indicating the 90% confidence level upper limit. The solid curves are pQCD predictions described in the text.

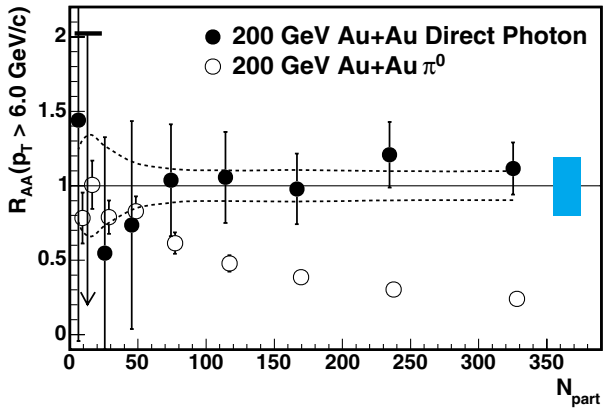

FIG. 3 (color online). Ratio of Au + Au yield to $p + p$ yield normalized by the number of binary nucleon collisions as a function of centrality given by N_{part} for direct γ (closed circles) and π^0 (open circles) yields integrated above 6 GeV/c. The $p + p$ direct photon yield is taken as the NLO pQCD prediction described in the text. The error bars indicate the total error excluding the error on $\langle N_{\text{coll}}\rangle$ shown by the dashed lines and the scale uncertainty of the NLO calculation shown by the shaded region at the right.

NLO calculations the contribution is significant: ~50% at 3.5 GeV/c and ~35% at 10 GeV/c), or additional photon yield from thermal radiation to levels comparable to the present measurement uncertainty.

In summary, the transverse momentum spectra of direct photons have been measured at midrapidity up to $p_T \approx 13$ GeV/c for nine centrality bins of Au + Au collisions at $\sqrt{s_{NN}} = 200$ GeV. The significance of the direct photon signal increases with collision centrality due to the increasingly suppressed π^0 production and associated decrease in the photon background from hadron decays. The direct photon spectral shapes and invariant yields are consistent with NLO pQCD predictions for $p + p$ reactions scaled by the average number of inelastic NN collisions for each centrality class. The close agreement between measurement and the binary scaled pQCD predictions of the direct photon yield suggests that nuclear modifications of the quark and gluon distribution functions in the relevant region of momentum fraction x are minor. The result provides strong confirmation that the observed large suppression of high p_T hadron production in central Au + Au collisions is dominantly a final-state effect due to parton energy loss in the dense produced medium, rather than an initial-state effect.

We thank the staff of the Collider-Accelerator and Physics Departments at BNL for their vital contributions. We acknowledge support from the Department of Energy and NSF (U.S.A.), MEXT and JSPS (Japan), CNPq and FAPESP (Brazil), NSFC (China), CNRS-IN2P3 and CEA (France), BMBF, DAAD, and AvH (Germany), OTKA (Hungary), DAE and DST (India), ISF (Israel), KRF and CHEP (Korea), RMIST, RAS, and RMAE (Russia), VR and KAW (Sweden), U.S. CRDF for the FSU, U.S.-Hungarian NSF-OTKA-MTA, and U.S.-Israel BSF.

*Deceased.
†PHENIX Spokesperson.
Electronic address: zajc@nevis.columbia.edu

[1] K. Adcox *et al.*, Phys. Rev. Lett. **88**, 022301 (2002).
[2] C. Adler *et al.*, Phys. Rev. Lett. **89**, 202301 (2002).
[3] S. S. Adler *et al.*, Phys. Rev. Lett. **91**, 072301 (2003).
[4] S. S. Adler *et al.*, Phys. Rev. C **69**, 034909 (2004).
[5] M. Gyulassy and M. Plumer, Phys. Lett. B **243**, 432 (1990).
[6] D. Kharzeev, E. Levin, and L. McLerran, Phys. Lett. B **561**, 93 (2003).
[7] S. S. Adler *et al.*, Phys. Rev. Lett. **91**, 072303 (2003).
[8] J. Adams *et al.*, Phys. Rev. Lett. **91**, 072304 (2003).
[9] T. Peitzmann and M. H. Thoma, Phys. Rep. **364**, 175 (2002).
[10] R. J. Fries, B. Muller, and D. K. Srivastava, Phys. Rev. Lett. **90**, 132301 (2003).
[11] B. G. Zakharov, JETP Lett. **80**, 1 (2004).
[12] K. Adcox *et al.*, Nucl. Instrum. Methods Phys. Res., Sect. A **499**, 469 (2003).
[13] S. S. Adler *et al.*, Phys. Rev. Lett. **91**, 241803 (2003).
[14] M. M. Aggarwal *et al.*, Phys. Rev. Lett. **85**, 3595 (2000).
[15] S. S. Adler *et al.*, Phys. Rev. D **71**, 071102 (2005).
[16] S. S. Adler *et al.* (to be published). An η/π^0 ratio of $R_{\eta/\pi^0}(p_T \to \infty) = 0.45 \pm 0.05$ has been used.
[17] L. E. Gordon and W. Vogelsang, Phys. Rev. D **48**, 3136 (1993).
[18] J. Pumplin *et al.*, J. High Energy Phys. 07 (2002) 012.
[19] M. Gluck, E. Reya, and A. Vogt, Phys. Rev. D **48**, 116 (1993).

Measurement of single electron event anisotropy in Au+Au collisions at $\sqrt{s_{NN}} = 200$ GeV

S. S. Adler,[5] S. Afanasiev,[17] C. Aidala,[5] N. N. Ajitanand,[43] Y. Akiba,[20,38] J. Alexander,[43] R. Amirikas,[12] L. Aphecetche,[45] S. H. Aronson,[5] R. Averbeck,[44] T. C. Awes,[35] R. Azmoun,[44] V. Babintsev,[15] A. Baldisseri,[10] K. N. Barish,[6] P. D. Barnes,[27] B. Bassalleck,[33] S. Bathe,[30] S. Batsouli,[9] V. Baublis,[37] A. Bazilevsky,[39,15] S. Belikov,[16,15] Y. Berdnikov,[40] S. Bhagavatula,[16] J. G. Boissevain,[27] H. Borel,[10] S. Borenstein,[25] M. L. Brooks,[27] D. S. Brown,[34] N. Bruner,[33] D. Bucher,[30] H. Buesching,[30] V. Bumazhnov,[15] G. Bunce,[5,39] J. M. Burward-Hoy,[26,44] S. Butsyk,[44] X. Camard,[45] J.-S. Chai,[18] P. Chand,[4] W. C. Chang,[2] S. Chernichenko,[15] C. Y. Chi,[9] J. Chiba,[20] M. Chiu,[9] I. J. Choi,[52] J. Choi,[19] R. K. Choudhury,[4] T. Chujo,[5] V. Cianciolo,[35] Y. Cobigo,[10] B. A. Cole,[9] P. Constantin,[16] D. d'Enterria,[45] G. David,[5] H. Delagrange,[45] A. Denisov,[15] A. Deshpande,[39] E. J. Desmond,[5] A. Devismes,[44] O. Dietzsch,[41] O. Drapier,[25] A. Drees,[44] K. A. Drees,[5] R. du Rietz,[29] A. Durum,[15] D. Dutta,[4] Y. V. Efremenko,[35] K. El Chenawi,[49] A. Enokizono,[14] H. En'yo,[38,39] S. Esumi,[48] L. Ewell,[5] D. E. Fields,[33,39] F. Fleuret,[25] S. L. Fokin,[23] B. D. Fox,[39] Z. Fraenkel,[51] J. E. Frantz,[9] A. Franz,[5] A. D. Frawley,[12] S.-Y. Fung,[6] S. Garpman,[29,*] T. K. Ghosh,[49] A. Glenn,[46] G. Gogiberidze,[46] M. Gonin,[25] J. Gosset,[10] Y. Goto,[39] R. Granier de Cassagnac,[25] N. Grau,[16] S. V. Greene,[49] M. Grosse Perdekamp,[39] W. Guryn,[5] H.-Å. Gustafsson,[29] T. Hachiya,[14] J. S. Haggerty,[5] H. Hamagaki,[8] A. G. Hansen,[27] E. P. Hartouni,[26] M. Harvey,[5] R. Hayano,[8] N. Hayashi,[38] X. He,[13] M. Heffner,[26] T. K. Hemmick,[44] J. M. Heuser,[44] M. Hibino,[50] J. C. Hill,[16] W. Holzmann,[43] K. Homma,[14] B. Hong,[22] A. Hoover,[34] T. Ichihara,[38,39] V. V. Ikonnikov,[23] K. Imai,[24,38] D. Isenhower,[1] M. Ishihara,[38] M. Issah,[43] A. Isupov,[17] B. V. Jacak,[44] W. Y. Jang,[22] Y. Jeong,[19] J. Jia,[44] O. Jinnouchi,[38] B. M. Johnson,[5] S. C. Johnson,[26] K. S. Joo,[31] D. Jouan,[36] S. Kametani,[8,50] N. Kamihara,[47,38] J. H. Kang,[52] S. S. Kapoor,[4] K. Katou,[50] S. Kelly,[9] B. Khachaturov,[51] A. Khanzadeev,[37] J. Kikuchi,[50] D. H. Kim,[31] D. J. Kim,[52] D. W. Kim,[19] E. Kim,[42] G.-B. Kim,[25] H. J. Kim,[52] E. Kistenev,[5] A. Kiyomichi,[48] K. Kiyoyama,[32] C. Klein-Boesing,[30] H. Kobayashi,[38,39] L. Kochenda,[37] V. Kochetkov,[15] D. Koehler,[33] T. Kohama,[14] M. Kopytine,[44] D. Kotchetkov,[6] A. Kozlov,[51] P. J. Kroon,[5] C. H. Kuberg,[1,27] K. Kurita,[39] Y. Kuroki,[48] M. J. Kweon,[22] Y. Kwon,[52] G. S. Kyle,[34] R. Lacey,[43] V. Ladygin,[17] J. G. Lajoie,[16] A. Lebedev,[16,23] S. Leckey,[44] D. M. Lee,[27] S. Lee,[19] M. J. Leitch,[27] X. H. Li,[6] H. Lim,[42] A. Litvinenko,[17] M. X. Liu,[27] Y. Liu,[36] C. F. Maguire,[49] Y. I. Makdisi,[5] A. Malakhov,[17] V. I. Manko,[23] Y. Mao,[7,38] G. Martinez,[45] M. D. Marx,[44] H. Masui,[48] F. Matathias,[44] T. Matsumoto,[8,50] P. L. McGaughey,[27] E. Melnikov,[15] F. Messer,[44] Y. Miake,[48] J. Milan,[43] T. E. Miller,[49] A. Milov,[44,51] S. Mioduszewski,[5] R. E. Mischke,[27] G. C. Mishra,[13] J. T. Mitchell,[5] A. K. Mohanty,[4] D. P. Morrison,[5] J. M. Moss,[27] F. Mühlbacher,[44] D. Mukhopadhyay,[51] M. Muniruzzaman,[6] J. Murata,[38,39] S. Nagamiya,[20] J. L. Nagle,[9] T. Nakamura,[14] B. K. Nandi,[6] M. Nara,[48] J. Newby,[46] P. Nilsson,[29] A. S. Nyanin,[23] J. Nystrand,[29] E. O'Brien,[5] C. A. Ogilvie,[16] H. Ohnishi,[5,38] I. D. Ojha,[49,3] K. Okada,[38] M. Ono,[48] V. Onuchin,[15] A. Oskarsson,[29] I. Otterlund,[29] K. Oyama,[8] K. Ozawa,[8] D. Pal,[51] A. P. T. Palounek,[27] V. Pantuev,[44] V. Papavassiliou,[34] J. Park,[42] A. Parmar,[33] S. F. Pate,[34] T. Peitzmann,[30] J.-C. Peng,[27] V. Peresedov,[17] C. Pinkenburg,[5] R. P. Pisani,[5] F. Plasil,[35] M. L. Purschke,[5] A. K. Purwar,[44] J. Rak,[16] I. Ravinovich,[51] K. F. Read,[35,46] M. Reuter,[44] K. Reygers,[30] V. Riabov,[37,40] Y. Riabov,[37] G. Roche,[28] A. Romana,[25] M. Rosati,[16] P. Rosnet,[28] S. S. Ryu,[52] M. E. Sadler,[1] N. Saito,[38,39] T. Sakaguchi,[8,50] M. Sakai,[32] S. Sakai,[48] V. Samsonov,[37] L. Sanfratello,[33] R. Santo,[30] H. D. Sato,[24,38] S. Sato,[5,48] S. Sawada,[20] Y. Schutz,[45] V. Semenov,[15] R. Seto,[6] M. R. Shaw,[1,27] T. K. Shea,[5] T.-A. Shibata,[47,38] K. Shigaki,[14,20] T. Shiina,[27] C. L. Silva,[41] D. Silvermyr,[27,29] K. S. Sim,[22] C. P. Singh,[3] V. Singh,[3] M. Sivertz,[5] A. Soldatov,[15] R. A. Soltz,[26] W. E. Sondheim,[27] S. P. Sorensen,[46] I. V. Sourikova,[5] F. Staley,[10] P. W. Stankus,[35] E. Stenlund,[29] M. Stepanov,[34] A. Ster,[21] S. P. Stoll,[5] T. Sugitate,[14] J. P. Sullivan,[27] E. M. Takagui,[41] A. Taketani,[38,39] M. Tamai,[50] K. H. Tanaka,[20] Y. Tanaka,[32] K. Tanida,[38] M. J. Tannenbaum,[5] P. Tarján,[11] J. D. Tepe,[1,27] T. L. Thomas,[33] J. Tojo,[24,38] H. Torii,[24,38] R. S. Towell,[1] I. Tserruya,[51] H. Tsuruoka,[48] S. K. Tuli,[3] H. Tydesjö,[29] N. Tyurin,[15] H. W. van Hecke,[27] J. Velkovska,[5,44] M. Velkovsky,[44] V. Veszprémi,[11] L. Villatte,[46] A. A. Vinogradov,[23] M. A. Volkov,[23] E. Vznuzdaev,[37] X. R. Wang,[13] Y. Watanabe,[38,39] S. N. White,[5] F. K. Wohn,[16] C. L. Woody,[5] W. Xie,[6] Y. Yang,[7] A. Yanovich,[15] S. Yokkaichi,[38,39] G. R. Young,[35] I. E. Yushmanov,[23] W. A. Zajc,[9,†] C. Zhang,[9] S. Zhou,[7] S. J. Zhou,[51] and L. Zolin[17]

(PHENIX Collaboration)

[1]*Abilene Christian University, Abilene, Texas 79699, USA*

[2]*Institute of Physics, Academia Sinica, Taipei 11529, Taiwan*

[3]*Department of Physics, Banaras Hindu University, Varanasi 221005, India*

[4]*Bhabha Atomic Research Centre, Bombay 400 085, India*

[5]*Brookhaven National Laboratory, Upton, New York 11973-5000, USA*

[6]*University of California, Riverside, California 92521, USA*

[7]*China Institute of Atomic Energy (CIAE), Beijing, People's Republic of China*

[8]*Center for Nuclear Study, Graduate School of Science, University of Tokyo, 7-3-1 Hongo, Bunkyo, Tokyo 113-0033, Japan*

[9]*Columbia University, New York, New York 10027 and Nevis Laboratories, Irvington, New York 10533, USA*

[10]*Dapnia, CEA Saclay, F-91191, Gif-sur-Yvette, France*

[11]*Debrecen University, Egyetem tér 1, H-4010 Debrecen, Hungary*

[12]*Florida State University, Tallahassee, Florida 32306, USA*

[13]*Georgia State University, Atlanta, Georgia 30303, USA*

[14]*Hiroshima University, Kagamiyama, Higashi-Hiroshima 739-8526, Japan*

[15]*Institute for High Energy Physics (IHEP), Protvino, Russia*

 ©2005 The American Physical Society

[16]*Iowa State University, Ames, Iowa 50011, USA*
[17]*Joint Institute for Nuclear Research, 141980 Dubna, Moscow Region, Russia*
[18]*KAERI, Cyclotron Application Laboratory, Seoul, South Korea*
[19]*Kangnung National University, Kangnung 210-702, South Korea*
[20]*KEK, High Energy Accelerator Research Organization, Tsukuba-shi, Ibaraki-ken 305-0801, Japan*
[21]*KFKI Research Institute for Particle and Nuclear Physics of the Hungarian Academy of Sciences (MTA KFKI RMKI), Post Office Box 49, H-1525 Budapest 114, Hungary*
[22]*Korea University, Seoul, 136-701, Korea*
[23]*Russian Research Center "Kurchatov Institute," Moscow, Russia*
[24]*Kyoto University, Kyoto 606-8502, Japan*
[25]*Laboratoire Leprince-Ringuet, Ecole Polytechnique, CNRS-IN2P3, Route de Saclay, F-91128, Palaiseau, France*
[26]*Lawrence Livermore National Laboratory, Livermore, California 94550, USA*
[27]*Los Alamos National Laboratory, Los Alamos, New Mexico 87545, USA*
[28]*LPC, Université Blaise Pascal, CNRS-IN2P3, Clermont-Fd, F-63177 Aubiere Cedex, France*
[29]*Department of Physics, Lund University, Box 118, SE-221 00 Lund, Sweden*
[30]*Institut für Kernphysik, University of Muenster, D-48149 Muenster, Germany*
[31]*Myongji University, Yongin, Kyonggido 449-728, South Korea*
[32]*Nagasaki Institute of Applied Science, Nagasaki-shi, Nagasaki 851-0193, Japan*
[33]*University of New Mexico, Albuquerque, New Mexico 87131, USA*
[34]*New Mexico State University, Las Cruces, New Mexico 88003, USA*
[35]*Oak Ridge National Laboratory, Oak Ridge, Tennessee 37831, USA*
[36]*IPN-Orsay, Universite Paris Sud, CNRS-IN2P3, BP1, F-91406, Orsay, France*
[37]*PNPI, Petersburg Nuclear Physics Institute, Gatchina, Leningrad Region, 188300, Russia*
[38]*RIKEN (The Institute of Physical and Chemical Research), Wako, Saitama 351-0198, Japan*
[39]*RIKEN BNL Research Center, Brookhaven National Laboratory, Upton, New York 11973-5000, USA*
[40]*St. Petersburg State Technical University, St. Petersburg, Russia*
[41]*Universidade de São Paulo, Instituto de Física, Caixa Postal 66318, São Paulo CEP05315-970, Brazil*
[42]*System Electronics Laboratory, Seoul National University, Seoul, South Korea*
[43]*Chemistry Department, Stony Brook University, SUNY, Stony Brook, New York 11794-3400, USA*
[44]*Department of Physics and Astronomy, Stony Brook University, SUNY, Stony Brook, New York 11794, USA*
[45]*SUBATECH (Ecole des Mines de Nantes, CNRS-IN2P3, Université de Nantes) Bôite Postale 20722, F-44307 Nantes, France*
[46]*University of Tennessee, Knoxville, Tennessee 37996, USA*
[47]*Department of Physics, Tokyo Institute of Technology, Oh-okayama, Meguro, Tokyo 152-8551, Japan*
[48]*Institute of Physics, University of Tsukuba, Tsukuba, Ibaraki 305, Japan*
[49]*Vanderbilt University, Nashville, Tennessee 37235, USA*
[50]*Waseda University, Advanced Research Institute for Science and Engineering, 17 Kikui-cho, Shinjuku-ku, Tokyo 162-0044, Japan*
[51]*Weizmann Institute, Rehovot 76100, Israel*
[52]*Yonsei University, IPAP, Seoul 120-749, Korea*
(Received 4 February 2005; published 10 August 2005)

The transverse momentum dependence of the azimuthal anisotropy parameter v_2, the second harmonic of the azimuthal distribution, for electrons at midrapidity ($|\eta| < 0.35$) has been measured with the PHENIX detector in Au+Au collisions at $\sqrt{s_{NN}} = 200$ GeV. The measurement was made with respect to the reaction plane defined at high rapidities ($|\eta| = 3.1$–3.9). From the result we have measured the v_2 of electrons from heavy flavor decay after subtraction of the v_2 of electrons from other sources such as photon conversions and Dalitz decay from light neutral mesons. We observe a nonzero single electron v_2 with a 90% confidence level in the intermediate-p_T region. The precision of the present data set does not permit us to conclude definitively that heavy quarks exhibit thermalization with the transverse flow of the bulk matter.

DOI: 10.1103/PhysRevC.72.024901 PACS number(s): 25.75.Dw

I. INTRODUCTION

The azimuthal anisotropy of particle emission is a powerful tool to study the early stage of ultrarelativistic nuclear collisions. The spatial anisotropy in the initial stage of noncentral nucleus-nucleus collisions is transferred into momentum anisotropy in the final state. The azimuthal anisotropy is defined by

$$\frac{dN}{d\phi} = N_0 \left\{ 1 + \sum_n 2v_n \cos[n(\phi - \Psi_{\mathrm{R.P.}})] \right\}, \qquad (1)$$

*Deceased.
†PHENIX spokesperson: zajc@nevis.columbia.edu

where N_0 is a normalization constant, ϕ is the azimuthal angle of particles, and $\Psi_{\mathrm{R.P.}}$ is the direction of the nuclear impact parameter ("reaction plane") in a given collision. The harmonic coefficients, v_n, indicate the strength of the nth anisotropy. The azimuthal anisotropy parameter v_2 (the second harmonic coefficient of the Fourier expansion of the azimuthal distribution) may be especially sensitive to the early pressure [1]. The transverse momentum (p_T) dependence of v_2 has been measured for identified particles at Brookhaven National Laboratory's Relativistic Heavy Ion Collider (RHIC) [2–5]. Previous measurements are limited to hadrons made of light quarks. These results show a clear mass dependence of v_2, which is well reproduced by a hydrodynamical calculation [6] in the low-p_T region ($p_T < 2$ GeV/c). The agreement is considered as evidence that the collective motion develops in the very early stages of the reaction. It is also observed that v_2 as a function of p_T scales via the coalescence prescription; that is, v_2/n as a function of p_T/n is universal, where n is the number of valence quarks plus valence antiquarks. This scaling behavior is consistent with the prediction of the quark coalescence model, which assumes a finite v_2 of quarks [7]. This suggests that the v_2 already develops in the partonic phase for hadrons made of light quarks. In addition, if the v_2 of heavy quarks is nonzero, it would support partonic level thermalization and very high density at the early stage of the collisions.

Electrons are a useful tool to study the production of heavy quarks such as charm quarks. In the PHENIX experiment at RHIC, transverse momentum spectra of single electrons have been measured in Au+Au collisions at $\sqrt{s_{NN}} = 130$ GeV [8] and 200 GeV [9]. The results are consistent with that expected from semileptonic charm decays in addition to decays of light mesons and photon conversions [8]. However, electrons originating from semileptonic decays of D mesons have a significant angular deviation from the original D meson direction. The effect on v_2 has been shown in [10] and [11]. The results suggest that the effect is not significant for the decay electron v_2, and the electron v_2 reflects the v_2 of the D meson. Therefore the single-electron v_2 measurement is a useful method for studying open charm v_2 [12,13].

Currently the single-electron spectra from PHENIX are consistent with two opposing scenarios: (1) initial perturbative QCD charm production without final-state interactions and (2) complete thermal equilibrium for charmed hadrons [14]. Therefore the measurement of the azimuthal anisotropy of electrons from semileptonic charm decays could give us important new information regarding the charm dynamics in high-energy heavy-ion collisions. The measurement is also important for the quark coalescence model, because of the large difference between the charm quark and light quark masses, and for the prediction of v_2 for the J/ψ and the D meson, those contain charm quarks.

In this paper, we present the first measurement of the single-electron v_2, which is expected to reflect the heavy flavor azimuthal anisotropy, below 4 GeV/c with respect to the reaction plane in Au+Au collisions at $\sqrt{s_{NN}} = 200$ GeV. The single-electron v_2 was measured by subtracting from the inclusive electron v_2 the v_2 of electrons from other sources such as photon conversions and Dalitz decays from light neutral mesons.

II. DATA ANALYSIS

About 16 million minimum bias events in RHIC-Run2 (2001) for $\sqrt{s_{NN}} = 200$ GeV are used in this analysis after a vertex cut is applied ($|z_{\mathrm{vertex}}| < 20$ cm). In this section we present a brief overview of the PHENIX detectors [15] used in this analysis and then present details of event selection, electron identification, and reaction-plane determination.

A. Overview of PHENIX detector

PHENIX consists of four spectrometer arms (central arms and muon arms) and a set of global detectors. The central arms are located east and west of the interaction region at midrapidity. The muon arms are located to the north and south at forward rapidity. Figure 1 shows the configuration of the central arms in Run2.

The global detectors consist of the beam-beam-counters (BBCs) and the zero-degree calorimeters (ZDCs). These detectors provide the time of the Au+Au collision, the collision vertex, the event trigger, and the collision centrality. In this analysis the BBCs are also used to determine the reaction plane. The BBCs are installed on the north and south sides of the collision point along the beam axis. Each BBC is placed 144 cm from the center of the interaction region and surrounds the beam pipe. This corresponds to a pseudorapidity range from 3.1 to 3.9 over the full azimuth. Each BBC is composed of 64 elements and a single BBC element consists of a 1-in-diameter mesh dynode photomultiplier tube mounted on a 3-cm-long quartz radiator. The ZDC is a hadron calorimeter and measures the energy of spectator neutrons. The ZDCs are located 18 m downstream and upstream along the beam axis, and each ZDC covers 2 mrad of forward angular cone, corresponding to $\eta > 6.0$.

The central arms are designed to track particles emitted from collisions, identify charged particles, and reconstruct invariant masses. The central arms each cover the pseudorapidity range $|\eta| < 0.35$ and 90° in azimuthal angle. The central arms consist of several subsystems. In this analysis drift chambers (DCs), pad chambers (PCs), ring imaging Cherenkov counters (RICHs), and electromagnetic calorimeters (EMCals) are used. The DCs are located between 2.0 and 2.4 m from the beam axis on each central arm and measure charged particle trajectories in the r-ϕ plane. The central arms have three layers of PCs, which are multiwire proportional chambers. The PCs are located at 2.4 m (PC1), 4.2 m (PC2), and 5.0 m (PC3) from the beam axis. PC1 and PC3 are installed in each central arm, but PC2 is installed only in the west arm. The PC measures three-dimensional space points along the straight-line particle trajectories. A RICH, the primary detector for electron identification, is installed in each central arm. The RICH consists of a gas vessel, a thin reflector, and a photon detector consisting of an array of photomultiplier tubes (PMTs). During Run2 CO_2 was used as the Cherenkov radiator so only pions with $p > 4.7$ GeV/c emit Cherenkov light in the

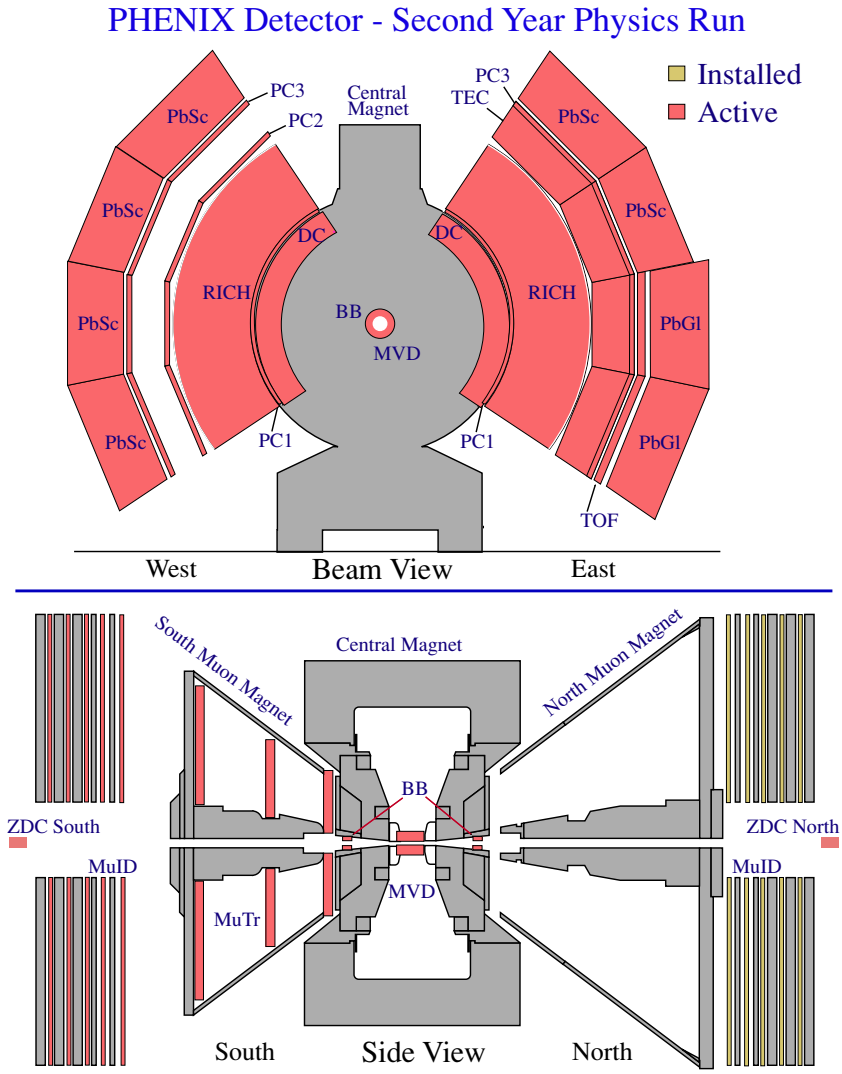

FIG. 1. (Color online) PHENIX experiment configuration in Run2. (Top) Cross section perpendicular to the beam pipe. (Bottom) East side view of the cross section along the beam pipe.

RICH. The EMCal is used to measure the spatial position and energy of electrons and photons. It covers the full central arm acceptance of $70^\circ < \theta < 110^\circ$ with each of the two walls subtending 90° in azimuth. One wall comprises four sectors of Pb-scintillator sampling calorimeter; the other has two sectors of Pb scintillator and two of Pb-glass Cherenkov calorimeter. The central magnet (CM) provides a magnetic field around the interaction vertex that is parallel to the beam. The CM allows momentum analysis of charged particles in the polar angle range $70^\circ < \theta < 110^\circ$ and provides a field integral of about 0.8 T m [16].

B. Event selection

Event selection was done with the BBC and the ZDC in this analysis. The minimum-bias trigger requires a coincidence between north and south BBC signals. The trigger included $92.2^{+2.5}_{-3.0}\%$ of the 6.9-b Au+Au inelastic cross section [17]. The event centrality is determined by combining information on spectator neutrons measured by the ZDC and the charge sum information measured by the BBC. The collision vertex point along the beam line is determined by the timing difference of the two BBCs. We required $|z_{\text{vertex}}| < 20$ cm for this analysis.

C. Charged particle selection and electron identification

Charged particle tracks are reconstructed by the DC and the first pad chamber plane (PC1) installed in each central arm together with the collision vertex determined by the BBC [18]. For a reconstructed track to be selected, the track projection to the EMCal and the position of the associated hit in the EMCal must match within two standard deviations. The electron candidates are required to have at least three associated hits in the RICH that pass a ring-shape cut and are also required to pass a timing cut. To reduce background from hadrons and photon conversions far from the vertex, energy is measured in the EMCal, and momentum matching (E/p) is required. Electrons deposit all of their energy in the EMCal; therefore the E/p is approximately 1.0. In this analysis we require $-2\sigma < (E-p)/p < 3\sigma$ to reduce background. Figure 2 shows the $(E-p)/p/\sigma$ distribution. Here the σ means a standard deviation of $(E-p)/p$. A background of less than 10% remains, caused by accidental association of

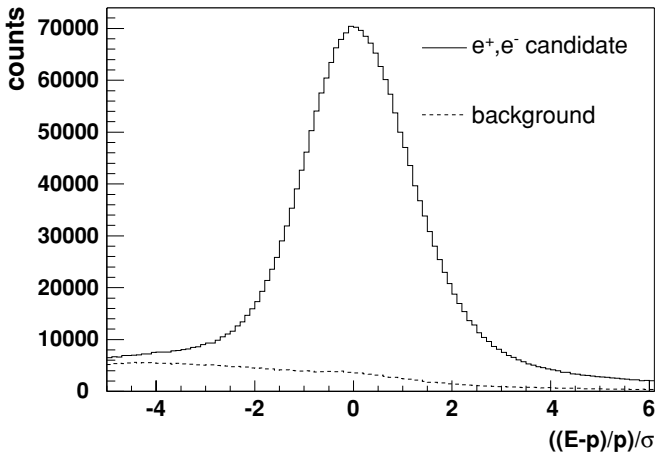

FIG. 2. $(E-p)/p/\sigma$ distribution. We require $-2\sigma < (E-p)/p < 3\sigma$ to reduce background from hadrons and photon conversions far from the vertex.

tracks with RICH hits. The background level is estimated by an event-mixing method and is subtracted when we calculate the electron v_2.

D. Reaction-plane determination

In this analysis the values of v_2 are calculated by the reaction-plane method, which measures the azimuthal angle of the particle emission with respect to the reaction plane [19]. The azimuthal angle of the reaction plane for the nth harmonic is determined by [19]

$$\psi_n^{\text{meas}} = \left[\tan^{-1}\frac{\sum_i w_i \sin(n\phi_i)}{\sum_i w_i \cos(n\phi_i)}\right] \Big/ n, \tag{2}$$

where ϕ_i is the azimuthal angle of each particle used in the reaction-plane determination and w_i is the corresponding weight. The azimuthal angle distribution of the particle emission measured with respect to the reaction plane can be written as Eq. (1). Because of finite reaction-plane resolution, coefficients in the Fourier expansion of the azimuthal distribution with respect to the "measured" reaction plane (v_n^{meas}) are smaller than coefficients measured with respect to the "real" reaction plane (v_n). The resolution correction necessary for v_n^{meas} is given by

$$v_n = v_n^{\text{meas}}/\sigma_{v_n}, \tag{3}$$

where v_n is the real coefficient and σ_{v_n} is the reaction-plane resolution for the nth harmonic. The reaction-plane resolution is defined as $\langle \cos n(\psi_n^{\text{meas}} - \psi_n^{\text{real}})\rangle$ [19]. The value of v_n^{meas} is obtained by fitting the azimuthal distribution (relative to the reaction plane) with

$$\frac{dN}{d\phi} = N_0\left[1 + 2v_n^{\text{meas}}\cos(n\phi)\right], \tag{4}$$

where N_0 and v_n^{meas} are fitting parameters. We can also calculate v_n^{meas} directly by

$$v_n^{\text{meas}} = \langle \cos(n\phi)\rangle. \tag{5}$$

In this analysis the v_2 is estimated by using the reaction plane found from the second harmonic ($n = 2$), since better accuracy of v_n is obtained by using the same harmonic's reaction plane [19]. The reaction planes are determined by using both BBCs. In the PHENIX experiment the reaction plane is also determined by using the central arm detectors. One of the key issues of the reaction-plane determination involves nonflow effects such as jets, resonance decays, and Hanbury-Brown and Twiss (HBT). Since each BBC is roughly three units of pseudorapidity away from the central arms, it is expected that the nonflow effects are smaller there than in the central arm detectors [2].

Using the BBC information the reaction plane is measured by

$$\psi = \left[\tan^{-1}\frac{\sum_{i=1}^{64} q_i \sin(2\phi_i)}{\sum_{i=1}^{64} q_i \cos(2\phi_i)}\right] \Big/ 2, \tag{6}$$

where ϕ_i is the azimuthal angle of each PMT and q_i is the charge information of each PMT. Owing to the random distribution of the impact-parameter direction in collisions, the reaction plane should have an isotropic azimuthal distribution. Because of the possible azimuthal asymmetries in the BBC response, however, the measured reaction-plane distribution is anisotropic. In this paper, we use the following two-step method to correct the reaction plane. First, the distribution of $\sum_{i=1}^{64} q_i \sin(2\phi_i)$ and $\sum_{i=1}^{64} q_i \cos(2\phi_i)$ are recentered by subtracting $\langle\sum_{i=1}^{64} q_i \sin(2\phi_i)\rangle$ and $\langle\sum_{i=1}^{64} q_i \cos(2\phi_i)\rangle$ over all events [19]:

$$\psi = \left[\tan^{-1}\frac{\sum_{i=1}^{64} q_i \sin(2\phi_i) - \left\langle\sum_{i=1}^{64} q_i \sin(2\phi_i)\right\rangle}{\sum_{i=1}^{64} q_i \cos(2\phi_i) - \left\langle\sum_{i=1}^{64} q_i \cos(2\phi_i)\right\rangle}\right] \Big/ 2. \tag{7}$$

This method does not remove higher harmonic components of the determined reaction plane, so we apply an additional correction method [20]. In this method flattening the reaction plane is accomplished by using a shift

$$n\psi^{\text{flat}} = n\psi_{\text{obs}} + \Delta\psi, \tag{8}$$

where $\Delta\psi$ is the correction factor for the reaction plane. $\Delta\psi$ is determined by

$$\Delta\psi = \sum_n A_n \cos(2n\psi_{\text{obs}}) + B_n \sin(2n\psi_{\text{obs}}), \tag{9}$$

where A_n and B_n are defined by requiring the nth Fourier moment of the new reaction plane (ψ^{flat}) to vanish. Hence

$$A_n = -\frac{2}{n}\langle \sin(2n\psi_{\text{obs}})\rangle, \tag{10}$$

$$B_n = \frac{2}{n}\langle \cos(2n\psi_{\text{obs}})\rangle. \tag{11}$$

Since the reaction plane depends on collision centrality and the z vertex, the reaction planes are divided into 40 samples (20 centrality bins and 2 vertex bins), and these corrections are determined independently for each sample. To measure the v_2 in this analysis, use is made of a combined reaction-plane, which is defined by weighted averaging of the

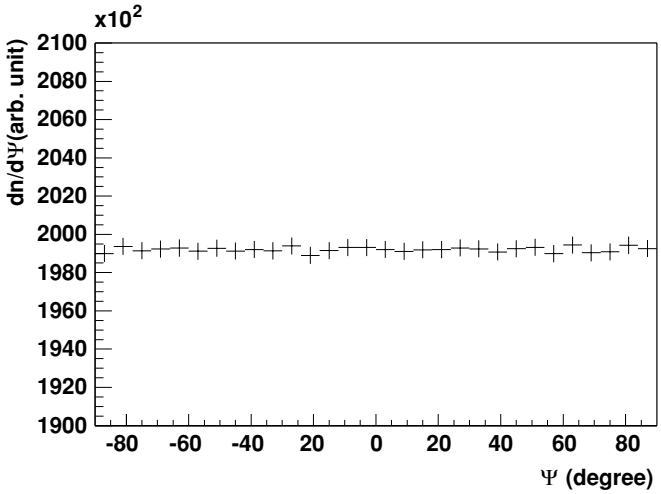

FIG. 3. The azimuthal angle distribution of the combined reaction plane after applying the flattening corrections. (Note that the vertical scale is zero suppressed.) After applying the corrections, the reaction plane has an isotropic azimuthal distribution.

reaction-plane angles obtained by the south-side BBC and the north-side BBC. Figure 3 shows the azimuthal angle distribution of the combined reaction plane after applying the flattening corrections. After applying the corrections, the reaction plane has an isotropic azimuthal distribution. The resolution of the combined reaction plane is estimated by using Eq. 11 in [19]. Figure 4 shows the centrality dependence of the resolution (σ_{v_2}).

III. RESULTS AND DISCUSSION

In this section we present a method to calculate the single-electron v_2 from inclusive electrons and show its transverse momentum dependence.

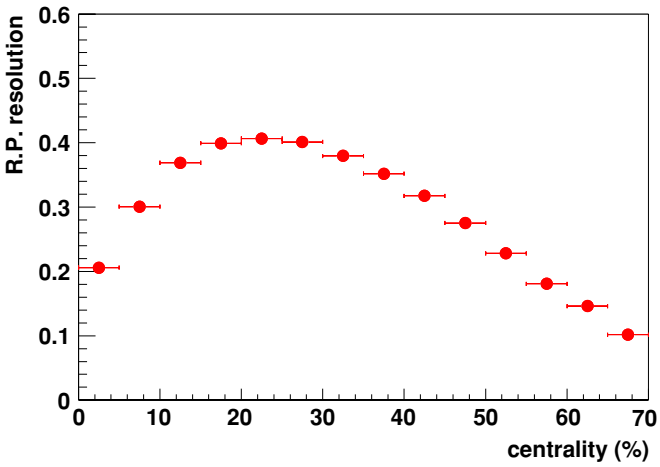

FIG. 4. (Color online) Centrality dependence of the combined reaction plane (R.P.) resolution determined by the BBC. The resolution is estimated by using Eq. 11 in [19].

A. Inclusive electron v_2

The azimuthal distributions of electrons relative to the reaction plane are shown in the middle panel of Fig. 5. The distributions are overlaid by shifting them on the vertical axis such that the spacing between each is equal. Each symbol represents the measured p_T region indicated in the left panel, which shows the raw yields of each distribution with large symbols. As described in Sec. II C, less than 10% background remains from accidental RICH associations. The azimuthal distributions of the background are shown in the right panel, and the yields are shown as small symbols in the left panel. The electron v_2 are measured after subtraction of this background ($dN^{e_{\rm back}}/d\phi$) from electrons that are identified by the RICH ($dN^{e_{\rm cand}}/d\phi$):

$$\frac{dN^e}{d\phi} = \frac{dN^{e_{\rm cand}}}{d\phi} - \frac{dN^{e_{\rm back}}}{d\phi}. \tag{12}$$

The transverse momentum dependence of the electron v_2 for minimum-bias events (centrality 0–92%) after subtracting background is shown in Fig. 6. The statistical errors are shown as vertical lines in the figure. The 1σ systematic uncertainties are shown as vertical bands. The systematic uncertainties include the systematic uncertainty of the reaction-plane determination and electron identification. The systematic uncertainty of the reaction-plane determination is about 5%. The uncertainty was estimated by measuring v_2 with a reaction plane determined by the north-side BBC, the south-side BBC, and a combination of the north and south sides. The systematic uncertainty from electron identification was estimated by measuring electron v_2 with several different sets of electron identification cuts. A comparison with v_2 for a charged pion [2] is also shown in Fig. 6. At low p_T ($p_T < 1.0$ GeV/c), the electron v_2 is larger than the v_2 of the pion. In this region electrons come mainly from π^0 decays, directly from the Dalitz decays, or indirectly from photon conversions. Because the decay angle of the π^0 decay is small, the electron has about the same azimuthal angle as the parent π^0, wheres the electron p_T is smaller than the π^0 p_T. Therefore the electron v_2 at a given p_T corresponds to the larger v_2 of the π^0 at higher p_T. The v_2 of charged pions is consistent with that of neutral pions [12]; therefore the inclusive electron v_2 is higher than the pion v_2. The v_2 at high p_T is thought to reflect parton energy loss in the initial stage of the collisions [21]. As described in Sec. III B, the primary source of electrons at high p_T is semileptonic decays of mesons containing heavy quarks. If these heavy quarks experience energy loss, the trend of the electron v_2 at high p_T might be the same as for pions. However, the electron v_2 at high p_T might be smaller than the pion v_2 if the heavy quarks do not lose energy. Owing to the large systematic and statistical uncertainty of the current measurement, the electron v_2 is consistent with the pion v_2.

B. Heavy-flavor electron v_2

The inclusive electron sample has two components: (1) a nonphotonic component, consisting of primarily semi-leptonic decays of mesons containing heavy (charm and bottom) quarks, and (2) a photonic component, consisting of Dalitz

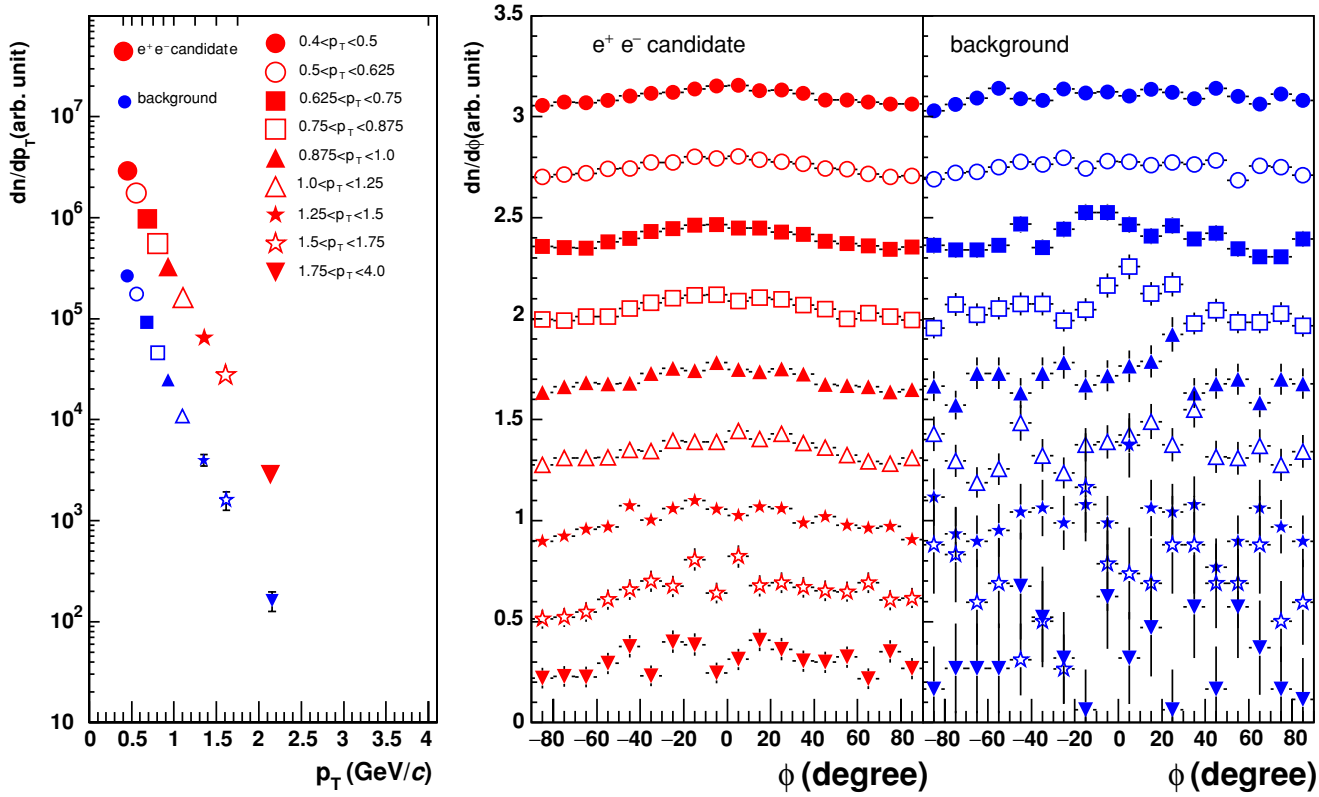

FIG. 5. (Color online) Azimuthal distributions relative to the reaction plane of electrons (middle panel) and the background (right panel) in each momentum bin. The distributions are overlaid by shifting them on the vertical axis such that the spacing between each is equal. The raw yields of each distribution are shown in the left panel.

decays of light neutral mesons (π_0, η, η', ω, and ϕ) and photon conversions in the detector material [9]. The azimuthal distribution of electrons ($dN^e/d\phi$) is the sum of the azimuthal distributions of photonic electrons ($dN^\gamma/d\phi$) and nonphotonic electrons ($dN^{\text{non}-\gamma}/d\phi$):

$$\frac{dN_e}{d\phi} = \frac{dN_e^\gamma}{d\phi} + \frac{dN_e^{\text{non}-\gamma}}{d\phi}. \tag{13}$$

The second harmonic of the Fourier expansion of each azimuthal distribution is defined according to

$$\begin{aligned} &N_e\left[1 + 2v_{2_e}\cos(2\phi)\right] \\ &= N_e^\gamma\left[1 + 2v_{2_e}^\gamma\cos(2\phi)\right] + N_e^{\text{non}-\gamma}\left[1 + 2v_{2_e}^{\text{non}-\gamma}\cos(2\phi)\right] \\ &= \left(N_e^\gamma + N_e^{\text{non}-\gamma}\right)\left[1 + 2\frac{N_e^\gamma v_{2_e}^\gamma + N_e^{\text{non}-\gamma}v_{2_e}^{\text{non}-\gamma}}{N_e^\gamma + N_e^{\text{non}-\gamma}}\cos(2\phi)\right], \end{aligned} \tag{14}$$

where v_{2_e} is the v_2 of inclusive electron, $v_{2_e}^\gamma$ is the v_2 of the photonic electrons, and $v_{2_e}^{\text{non}-\gamma}$ is the v_2 of the nonphotonic electrons. From Eq. (14), the inclusive electron v_2 is given by

$$\begin{aligned} v_{2_e} &= \frac{N_e^\gamma v_{2_e}^\gamma + N_e^{\text{non}-\gamma}v_{2_e}^{\text{non}-\gamma}}{N_e^\gamma + N_e^{\text{non}-\gamma}} \\ &= \frac{N_e^\gamma v_{2_e}^\gamma + \left(N_e - N_e^\gamma\right)v_{2_e}^{\text{non}-\gamma}}{N_e} \\ &= r v_{2_e}^\gamma + (1-r)v_{2_e}^{\text{non}-\gamma}, \end{aligned} \tag{15}$$

where r is defined as $r = 1/(1 + R_{\text{NP}})$, and R_{NP} is the ratio of the number of nonphotonic electrons to photonic electrons

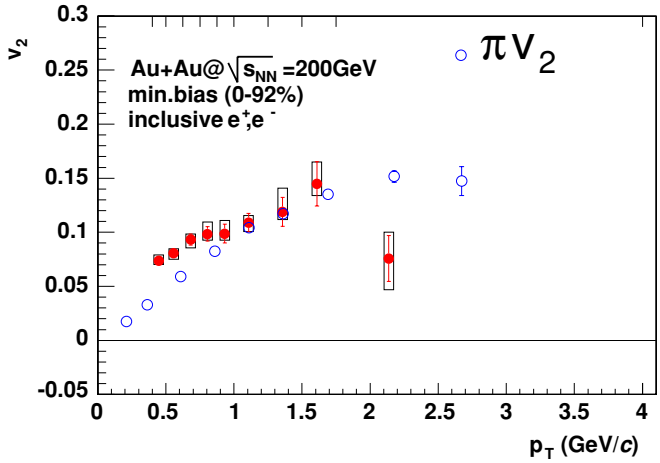

FIG. 6. (Color online) Transverse momentum dependence of the electron v_2 for minimum-bias events (centrality 0–92%). The data points for the electrons represent the inclusive single electrons (e^+ and e^-). The upper horizontal scale shows the bin size in p_T. The statistical errors are shown as vertical lines in the figure. The systematic uncertainty from the determination of the reaction plane and electron identification are shown as boxes. A comparison with the pionπ v_2 is also shown.

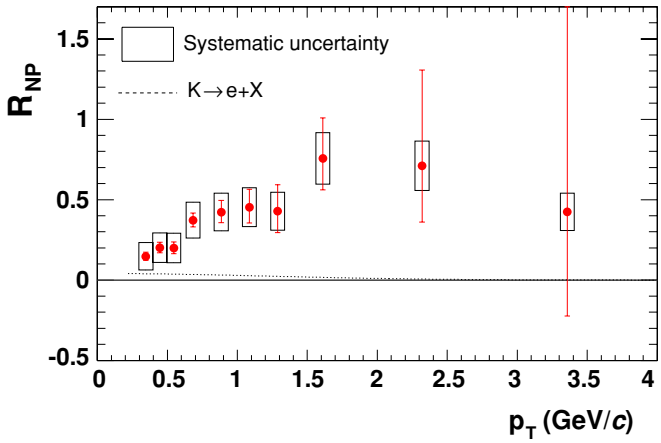

FIG. 7. (Color online) Ratio of nonphotonic to photonic $e^{\pm}$ yields ($R_{\rm NP}$, points) and contribution from kaon decays (dashed line) [9].

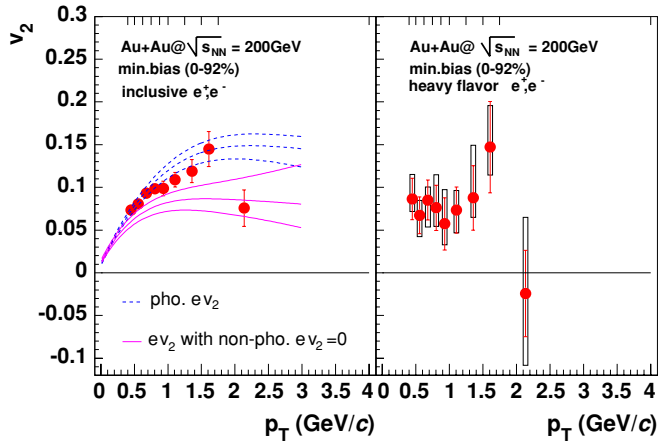

FIG. 8. (Color online) (Left) A comparison of the inclusive electron v_2 with the photonic electron v_2 (dashed line). The solid line is $r v_{2_e^\gamma}$, the photonic electron v_2 scaled by the ratio of the number of inclusive to photonic electrons. The electron v_2 is the same as $r v_{2_e^\gamma}$ if the nonphotonic electron v_2 is zero; that is, the v_2 of the parent particle, such as a D meson, is zero. (Right) Transverse momentum dependence of the heavy quark electron v_2 for minimum-bias events. The vertical line is the statistical error, which is propagated from the statistical errors of the electron v_2 for minimum-bias events. The systematic uncertainty from the electron v_2, the photonic electron v_2, and the ratio $R_{\rm NP}$ is shown as a band.

($N_e^{\rm non-\gamma}/N_e^{\gamma}$). We experimentally determined the ratio from analysis of special runs in which an additional an photon converter was installed. The details of the method are described in [9], and the measured ratio is shown in Fig. 7. The increase in the number of nonphotonic electrons is consistent with that expected from semileptonic charm decays [9]. From Eq. (15) $v_{2_e}^{\rm non-\gamma}$ can be expressed as

$$v_{2_e}^{\rm non-\gamma} = \frac{v_{2_e} - r v_{2_e}^{\gamma}}{1 - r}. \tag{16}$$

The dominant sources of photonic electrons are photon conversions and Dalitz decays from π^0 [8]. In addition, we also took into account electrons from η decays when calculating photonic electron v_2. We assumed that the contributions from η decays is 17% by taking into account $\eta/\pi_0 = 0.45$ [9]. The other sources are ignored when calculating the photonic electron v_2 because of their small contribution. The decay electron v_2 from decay electrons of π^0 and η were calculated by Monte Carlo simulation. The transverse momentum dependence of the $\pi^0 v_2$ was obtained from the measured $\pi^0 v_2$ [12] ($p_T > 1.0$ GeV/c) and the measured charged pion v_2 ($p_T < 1.0$ GeV/c). Both measurements were used since the $\pi^0 v_2$ has been measured only above 1.0 GeV/c, and both v_2 measurements are consistent at intermediate p_T ($1.0 < p_T < 3.0$). The measured π^0 spectra [22] were used to give the input transverse momentum spectrum. We assumed that the transverse momentum dependence of the η v_2 is the same as for the kaon v_2 because their mass difference is small. The transverse momentum spectrum of η was approximated by assuming m_T scaling of π^0 spectra. The photonic electron v_2 calculated from the results is shown as the dashed line in the left panel of Fig. 8. The middle dashed line is the mean value of the photonic electron v_2 and the upper and lower dashed lines show the 1σ systematic uncertainty. The systematic uncertainty of the photonic electron v_2 was estimated from the statistical error and the systematic error of the measured parent v_2. If the nonphotonic electron v_2 is zero, that means the v_2 of the parent particle, such as a D meson, is zero. Additionally, the inclusive electron v_2 is the same as that of the scaled photonic electron ($r v_{2_e^\gamma}$) from Eq. (15). The scaled photonic electron v_2 is shown as the solid line in the left panel in Fig. 8. At intermediate p_T ($1.0 < p_T < 1.5$) the electron v_2 is higher than $r v_{2_e^\gamma}$. This might suggest that the nonphotonic electron has nonzero v_2 at intermediate p_T. The details of this discussion are presented in the next section.

Background from kaon decays ($K \to \pi\ e\ \nu$) remains in the nonphotonic yield. The contribution of kaon decays to the nonphotonic yield, shown in Fig. 7 as a dashed line, is 18% at $p_T = 0.4$ GeV/c and decreases rapidly to less than 6% for $p_T = 1$ GeV/c [9]. The transverse momentum dependence of the kaon v_2 has been measured up to 3.0 GeV/c and that of the K_S^0 v_2 has been measured up to 6.0 GeV/c [5]. The kaon and K_S^0 v_2 are consistent up to 3.0 GeV/c, and the quark coalescence model predicts that these two meson v_2 values are the same. Therefore, kaon and K_S^0 v_2 were combined as input for the kaon v_2. The transverse momentum spectrum of kaons was obtained from measured kaon spectra up to 2.0 GeV/c. In the high-p_T region we used scaled π^0 spectra and assumed that the shapes of the kaon spectra were the same as for the π^0 spectra, which are matched with measured kaon spectra around 2.0 GeV/c.

The nonphotonic electrons mainly come from semileptonic decays of heavy flavor (charm and beauty). Therefore the non-photonic electron v_2 that was obtained by subtracting photonic electron and kaon decays from inclusive electrons should be heavy-flavor electron [9] v_2, which reflects the azimuthal anisotropy of heavy quarks. The result of the heavy-flavor electron v_2 for minimum-bias events is shown in the right panel of Fig. 8. The vertical lines are the statistical errors that are propagated from the statistical errors of the inclusive

TABLE I. The relative systematic uncertainty of heavy-quark electron v_2.

p_T Range	Systematic Error Bound	Inclusive ev_2 (%)	Photonic ev_2 (%)	R_{NP} (%)	R.P. (%)	Total (%)
$0.4 < p_T < 1.0$	lower	<32	<26	<21	4.5	<42
	upper	<63	<21	<21	4.5	<70
$1.0 < p_T < 1.75$	lower	<25	<21	<14	4.5	<36
	upper	<67	<17	<15	4.5	<70
$1.75 < p_T < 4.0$	lower	280	78	190	4.5	340
	upper	220	64	280	4.5	360
Type		A	A	A	B	

electron v_2 shown in Fig. 6. The 1σ systematic uncertainties of heavy-flavor electron v_2 are shown as bands. The systematic uncertainty includes the systematic uncertainty of the reaction plane, the measured inclusive electron v_2 (without the reaction plane), the photonic electron v_2 (without the reaction plane), and R_{NP}. The systematic uncertainty of R_{NP} is the quadratic sum of the statistical and systematic errors because R_{NP} is measured with a different data set. There are two categories of uncertainty: Type A is a point-to-point error uncorrected between p_T bins, and type B is a common displacement of all points by the same factor independent of p_T. The total systematic uncertainty is calculated by propagating the errors on the individual quantities that enter into Eq. (16). Table I shows the relative systematic uncertainty of heavy-quark electron v_2.

From the result we calculated the confidence level for a nonzero v_2. We assumed that the data of measured heavy-flavor electron v_2 follow a Gaussian distribution; the σ was obtained by calculating the quadratic sum of the statistical and systematic errors of the heavy-flavor electron v_2 assuming these errors to be independent. In the intermediate-p_T region ($1.0\ \text{GeV}/c < p_T < 1.75\ \text{GeV}/c$), the confidence level for a nonzero value for the measured heavy-flavor electron v_2 is 90%.

There are various scenarios to consider that lead to different elliptic flow values for D mesons [14]. One is that the charm quarks do not interact at all in the medium after being produced and eventually fragment in vacuum into D mesons. This scenario leads to zero elliptic flow ($v_2 = 0$). It is also possible that charm quarks do not flow with the medium but do suffer energy loss in the medium and then eventually fragment in vacuum into D mesons. This scenario may yield a nonzero v_2. Alternatively, the charm quarks may flow in the medium and then hadronize via coalescence or recombination with other partons from the medium, which could produce significant nonzero values for v_2. Finally, even if the charm quarks do not flow with the medium, but do hadronize via recombination, they may pick up some v_2 from the light quarks in the medium.

By assuming the quark coalescence model, the decay electron v_2 from D mesons has been predicted [10]. In the model D mesons are formed from charm quark coalescence with thermal light quarks at hadronization. For charm quark momentum spectra, two extreme scenarios are considered. The first scenario assumes no reinteractions after the production of charm-anticharm quark pairs in initial-state hard processes (calculated from PYTHIA). The second scenario assumes complete thermalization with the transverse flow of the bulk matter. Figure 9 shows a comparison of the heavy-flavor electron v_2 with decay electrons from D mesons in the "no reinteraction" scenario as a solid line; the dashed line reflects the "thermalization" scenario. Because of large systematic and statistical uncertainty of the current measurement, neither scenario is excluded by this single-electron v_2 measurement.

IV. SUMMARY

In summary, we have measured the elliptic flow, v_2, of single electrons from heavy-flavor decay. This single-electron v_2 is produced by subtracting the v_2 of electron sources such as photon conversion from the v_2 of inclusive electrons measured with the PHENIX detector in Au+Au collisions at $\sqrt{s_{NN}} = 200$ GeV with respect to the reaction plane defined at high rapidities ($|\eta| = 3$–4). The measured heavy-flavor electron v_2 is nonzero with a 90% confidence level. Two model calculations from [10] assume extremely different scenarios: either no reinteraction of the initially produced charm quarks or complete thermalization with the bulk matter. Both of these calculations are consistent within errors with the measured heavy-flavor electron v_2.

High-luminosity Au+Au collisions at $\sqrt{s_{NN}} = 200$ GeV have been recorded by the PHENIX experiment during Run4

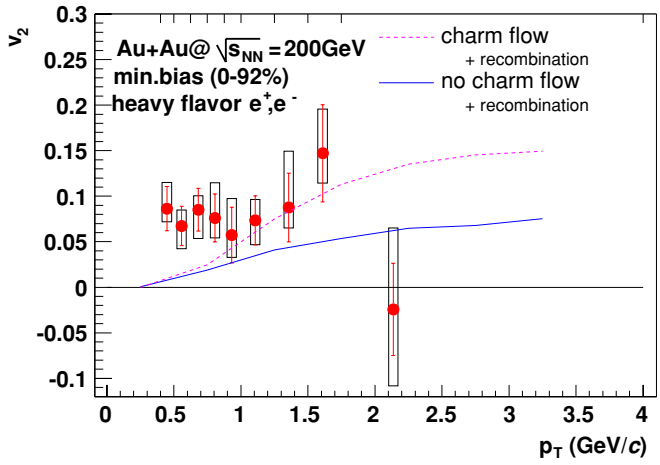

FIG. 9. (Color online) Comparison of the heavy-flavor electron v_2 with two different charm flow scenarios from [10]. The solid line corresponds to no rescattering of the initially produced charm quarks (without flow); the dashed line reflects the effect of complete thermalization (with flow).

(2003–2004). The much higher statistical precision of these data should allow an unambiguous result on the important issue of charm flow.

ACKNOWLEDGMENTS

We thank the staff of the Collider-Accelerator and Physics Departments at Brookhaven National Laboratory and the staff of the other PHENIX participating institutions for their vital contributions. We acknowledge support from the Department of Energy, Office of Science, Nuclear Physics Division, the National Science Foundation, Abilene Christian University Research Council, Research Foundation of SUNY, and Dean of the College of Arts and Sciences, Vanderbilt University (USA); Ministry of Education, Culture, Sports, Science, and Technology and the Japan Society for the Promotion of Science (Japan); Conselho Nacional de Desenvolvimento Científico e Tecnológico and Fundac oa de Amparo à Pesquisa do Estado de São Paulo (Brazil); Natural Science Foundation of China (People's Republic of China); Centre National de la Recherche Scientifique, Commissariat à l'Éenergie Atomique, Institut National de Physique Nucléaire et de Physique des Particules, and Institut National de Physique Nucléaire et de Physique des Particules (France); Bundesministerium für Bildung und Forschung, Deutscher Akademischer Austausch Dienst, and Alexander von Humboldt Stiftung (Germany); Hungarian National Science Fund, OTKA (Hungary); Department of Atomic Energy and Department of Science and Technology (India); Israel Science Foundation (Israel); Korea Research Foundation and Center for High Energy Physics (Korea), Russian Ministry of Industry, Science and Tekhnologies, Russian Academy of Science, and Russian Ministry of Atomic Energy (Russia), Vetenskapsrådet/Swedish Research Council (VR) and the Wallenberg Foundation (Sweden), the U.S. Civilian Research and Development Foundation for the Independent States of the Former Soviet Union; the US-Hungarian NSF-OTKA-MTA; the US-Israel Binational Science Foundation; and the 5th European Union TMR Marie-Curie Programme.

[1] H. Sorge, Phys. Rev. Lett. **82**, 2048 (1999).
[2] S. S. Adler *et al*. (PHENIX Collaboration), Phys. Rev. Lett. **91**, 182301 (2003).
[3] J. Adams *et al*. (STAR Collaboration), Phys. Rev. Lett. **87**, 182301 (2001).
[4] J. Adams *et al*. (STAR Collaboration), Phys. Rev. Lett. **89**, 132301 (2002).
[5] J. Adams *et al*. (STAR Collaboration), Phys. Rev. Lett. **92**, 052302 (2004).
[6] P. Houvinen, P. E. Kolb, U. W. Heinz, P. V. Ruuskanen, and S. A. Voloshin, Phys. Lett. **B503**, 58 (2001).
[7] D. Molnar and S. A. Voloshin, Phys. Rev. Lett. **91**, 092301 (2003).
[8] K. Adcox *et al*., Phys. Rev. Lett. **88**, 192303 (2002).
[9] S. S. Adler *et al*. (PHENIX Collaboration), Phys. Rev. Lett. **94**, 082301 (2005).
[10] V. Greco, C. M. Ko, and R. Rapp, Phys. Lett. **B595**, 202 (2004).
[11] X. Dong, S. Esumi, P. Sorensen, N. Xu, and Z. Xu, Phys. Lett. **B597**, 328 (2004).
[12] M. Kaneta *et al*., *Proceedings of the 17th International Conference Ultra Relativistic Nucleus-Nucleus Collisions (Quark Matter 2004)*; J. Phys. G **30**, S1217 (2004); nucl-ex/0404014.
[13] F. Laue, Proceedings of Hot Quarks 2004: Workshop for Young Scientists on the Physics of Ultrarelativistic Nucleus-Nucleus Collisions (HQ'04); J. Phys. G **31**, S27 (2005); nucl-ex/0411007.
[14] S. Batsouli *et al*., Phys. Lett. **B577**, 26 (2003).
[15] K. Adcox *et al*., Nucl. Instrum. Methods Phys. Res. A **499**, 469 (2003).
[16] S. H. Aronson *et al*. (PHENIX Collaboration), Nucl. Instrum. Methods Phys. Res. A **499**, 480 (2003).
[17] S. S Adler *et al*. (PHENIX Collaboration), Phys. Rev. Lett. **91**, 072301 (2003).
[18] J. T. Mitchell *et al*. (PHENIX Collaboration), Nucl. Instrum. Methods Phys. Res. A **482**, 491 (2002).
[19] A. M. Poskanzer and S. A. Voloshin, Phys. Rev. C **58**, 1671 (1998).
[20] J. Barrette *et al*. (E877 Collaboration), Phys. Rev. C **56**, 3254 (1998).
[21] M. Gyulassy, I. Vitev, and X.-N. Wang, Phys. Rev. Lett. **86**, 2537 (2001).
[22] S. S. Adler *et al*., Phys. Rev. Lett. **89**, 202301 (2002).

PHYSICAL REVIEW D **71,** 071102(R) (2005)

Midrapidity direct-photon production in $p+p$ collisions at $\sqrt{s}=200$ GeV

S. S. Adler,[5] S. Afanasiev,[17] C. Aidala,[5] N. N. Ajitanand,[43] Y. Akiba,[20,38] J. Alexander,[43] R. Amirikas,[12] L. Aphecetche,[45] S. H. Aronson,[5] R. Averbeck,[44] T. C. Awes,[35] R. Azmoun,[44] V. Babintsev,[15] A. Baldisseri,[10] K. N. Barish,[6] P. D. Barnes,[27] B. Bassalleck,[33] S. Bathe,[30] S. Batsouli,[9] V. Baublis,[37] A. Bazilevsky,[39,15] S. Belikov,[16,15] Y. Berdnikov,[40] S. Bhagavatula,[16] J. G. Boissevain,[27] H. Borel,[10] S. Borenstein,[25] M. L. Brooks,[27] D. S. Brown,[34] N. Bruner,[33] D. Bucher,[30] H. Buesching,[30] V. Bumazhnov,[15] G. Bunce,[5,39] J. M. Burward-Hoy,[26,44] S. Butsyk,[44] X. Camard,[45] J.-S. Chai,[18] P. Chand,[4] W. C. Chang,[2] S. Chernichenko,[15] C. Y. Chi,[9] J. Chiba,[20] M. Chiu,[9] I. J. Choi,[52] J. Choi,[19] R. K. Choudhury,[4] T. Chujo,[5] V. Cianciolo,[35] Y. Cobigo,[10] B. A. Cole,[9] P. Constantin,[16] D. d'Enterria,[45] G. David,[5] H. Delagrange,[45] A. Denisov,[15] A. Deshpande,[39] E. J. Desmond,[5] A. Devismes,[44] O. Dietzsch,[41] O. Drapier,[25] A. Drees,[44] K. A. Drees,[5] R. du Rietz,[29] A. Durum,[15] D. Dutta,[4] Y. V. Efremenko,[35] K. El Chenawi,[49] A. Enokizono,[14] H. En'yo,[38,39] S. Esumi,[48] L. Ewell,[5] D. E. Fields,[33,39] F. Fleuret,[25] S. L. Fokin,[23] B. D. Fox,[39] Z. Fraenkel,[51] J. E. Frantz,[9] A. Franz,[5] A. D. Frawley,[12] S.-Y. Fung,[6] S. Garpman,[29,*] T. K. Ghosh,[49] A. Glenn,[46] G. Gogiberidze,[46] M. Gonin,[25] J. Gosset,[10] Y. Goto,[39] R. Granier de Cassagnac,[25] N. Grau,[16] S. V. Greene,[49] M. Grosse Perdekamp,[39] W. Guryn,[5] H.-Å. Gustafsson,[29] T. Hachiya,[14] J. S. Haggerty,[5] H. Hamagaki,[8] A. G. Hansen,[27] E. P. Hartouni,[26] M. Harvey,[5] R. Hayano,[8] N. Hayashi,[38] X. He,[13] M. Heffner,[26] T. K. Hemmick,[44] J. M. Heuser,[44] M. Hibino,[50] J. C. Hill,[16] W. Holzmann,[43] K. Homma,[14] B. Hong,[22] A. Hoover,[34] T. Ichihara,[38,39] V. V. Ikonnikov,[23] K. Imai,[24,38] D. Isenhower,[1] M. Ishihara,[38] M. Issah,[43] A. Isupov,[17] B. V. Jacak,[44] W. Y. Jang,[22] Y. Jeong,[19] J. Jia,[44] O. Jinnouchi,[38] B. M. Johnson,[5] S. C. Johnson,[26] K. S. Joo,[31] D. Jouan,[36] S. Kametani,[8,50] N. Kamihara,[47,38] J. H. Kang,[52] S. S. Kapoor,[4] K. Katou,[50] S. Kelly,[9] B. Khachaturov,[51] A. Khanzadeev,[37] J. Kikuchi,[50] D. H. Kim,[31] D. J. Kim,[52] D. W. Kim,[19] E. Kim,[42] G.-B. Kim,[25] H. J. Kim,[52] E. Kistenev,[5] A. Kiyomichi,[48] K. Kiyoyama,[32] C. Klein-Boesing,[30] H. Kobayashi,[38,39] L. Kochenda,[37] V. Kochetkov,[15] D. Koehler,[33] T. Kohama,[14] M. Kopytine,[44] D. Kotchetkov,[6] A. Kozlov,[51] P. J. Kroon,[5] C. H. Kuberg,[1,27] K. Kurita,[39] Y. Kuroki,[48] M. J. Kweon,[22] Y. Kwon,[52] G. S. Kyle,[34] R. Lacey,[43] V. Ladygin,[17] J. G. Lajoie,[16] A. Lebedev,[16,23] S. Leckey,[44] D. M. Lee,[27] S. Lee,[19] M. J. Leitch,[27] X. H. Li,[6] H. Lim,[42] A. Litvinenko,[17] M. X. Liu,[27] Y. Liu,[36] C. F. Maguire,[49] Y. I. Makdisi,[5] A. Malakhov,[17] V. I. Manko,[23] Y. Mao,[7,38] G. Martinez,[45] M. D. Marx,[44] H. Masui,[48] F. Matathias,[44] T. Matsumoto,[8,50] P. L. McGaughey,[27] E. Melnikov,[15] F. Messer,[44] Y. Miake,[48] J. Milan,[43] T. E. Miller,[49] A. Milov,[44,51] S. Mioduszewski,[5] R. E. Mischke,[27] G. C. Mishra,[13] J. T. Mitchell,[5] A. K. Mohanty,[4] D. P. Morrison,[5] J. M. Moss,[27] F. Mühlbacher,[44] D. Mukhopadhyay,[51] M. Muniruzzaman,[6] J. Murata,[38,39] S. Nagamiya,[20] J. L. Nagle,[9] T. Nakamura,[14] B. K. Nandi,[6] M. Nara,[48] J. Newby,[46] P. Nilsson,[29] A. S. Nyanin,[23] J. Nystrand,[29] E. O'Brien,[5] C. A. Ogilvie,[16] H. Ohnishi,[5,38] I. D. Ojha,[49,3] K. Okada,[38] M. Ono,[48] V. Onuchin,[15] A. Oskarsson,[29] I. Otterlund,[29] K. Oyama,[8] K. Ozawa,[8] D. Pal,[51] A. P. T. Palounek,[27] V. Pantuev,[44] V. Papavassiliou,[34] J. Park,[42] A. Parmar,[33] S. F. Pate,[34] T. Peitzmann,[30] J.-C. Peng,[27] V. Peresedov,[17] C. Pinkenburg,[5] R. P. Pisani,[5] F. Plasil,[35] M. L. Purschke,[5] A. K. Purwar,[44] J. Rak,[16] I. Ravinovich,[51] K. F. Read,[35,46] M. Reuter,[44] K. Reygers,[30] V. Riabov,[37,40] Y. Riabov,[37] G. Roche,[28] A. Romana,[25] M. Rosati,[16] P. Rosnet,[28] S. S. Ryu,[52] M. E. Sadler,[1] N. Saito,[38,39] T. Sakaguchi,[8,50] M. Sakai,[32] S. Sakai,[48] V. Samsonov,[37] L. Sanfratello,[33] R. Santo,[30] H. D. Sato,[24,38] S. Sato,[5,48] S. Sawada,[20] Y. Schutz,[45] V. Semenov,[15] R. Seto,[6] M. R. Shaw,[1,27] T. K. Shea,[5] T.-A. Shibata,[47,38] K. Shigaki,[14,20] T. Shiina,[27] C. L. Silva,[41] D. Silvermyr,[27,29] K. S. Sim,[22] C. P. Singh,[3] V. Singh,[3] M. Sivertz,[5] A. Soldatov,[15] R. A. Soltz,[26] W. E. Sondheim,[27] S. P. Sorensen,[46] I. V. Sourikova,[5] F. Staley,[10] P. W. Stankus,[35] E. Stenlund,[29] M. Stepanov,[34] A. Ster,[21] S. P. Stoll,[5] T. Sugitate,[14] J. P. Sullivan,[27] E. M. Takagui,[41] A. Taketani,[38,39] M. Tamai,[50] K. H. Tanaka,[20] Y. Tanaka,[32] K. Tanida,[38] M. J. Tannenbaum,[5] P. Tarján,[11] J. D. Tepe,[1,27] T. L. Thomas,[33] J. Tojo,[24,38] H. Torii,[24,38] R. S. Towell,[1] I. Tserruya,[51] H. Tsuruoka,[48] S. K. Tuli,[3] H. Tydesjö,[29] N. Tyurin,[15] H. W. van Hecke,[27] J. Velkovska,[5,44] M. Velkovsky,[44] V. Veszprémi,[11] L. Villatte,[46] A. A. Vinogradov,[23] M. A. Volkov,[23] E. Vznuzdaev,[37] X. R. Wang,[13] Y. Watanabe,[38,39] S. N. White,[5] F. K. Wohn,[16] C. L. Woody,[5] W. Xie,[6] Y. Yang,[7] A. Yanovich,[15] S. Yokkaichi,[38,39] G. R. Young,[35] I. E. Yushmanov,[23] W. A. Zajc,[9,†] C. Zhang,[9] S. Zhou,[7] S. J. Zhou,[51] and L. Zolin[17]

(PHENIX Collaboration)

[1]*Abilene Christian University, Abilene, Texas 79699, USA*
[2]*Institute of Physics, Academia Sinica, Taipei 11529, Taiwan*
[3]*Department of Physics, Banaras Hindu University, Varanasi 221005, India*
[4]*Bhabha Atomic Research Centre, Bombay 400 085, India*
[5]*Brookhaven National Laboratory, Upton, New York 11973-5000, USA*

 © 2005 The American Physical Society

[6]*University of California–Riverside, Riverside, California 92521, USA*
[7]*China Institute of Atomic Energy (CIAE), Beijing, People's Republic of China*
[8]*Center for Nuclear Study, Graduate School of Science, University of Tokyo, 7-3-1 Hongo, Bunkyo, Tokyo 113-0033, Japan*
[9]*Columbia University, New York, New York 10027, USA, and Nevis Laboratories, Irvington, New York 10533, USA*
[10]*Dapnia, CEA Saclay, F-91191, Gif-sur-Yvette, France*
[11]*Debrecen University, H-4010 Debrecen, Egyetem tér 1, Hungary*
[12]*Florida State University, Tallahassee, Florida 32306, USA*
[13]*Georgia State University, Atlanta, Georgia 30303, USA*
[14]*Hiroshima University, Kagamiyama, Higashi-Hiroshima 739-8526, Japan*
[15]*Institute for High Energy Physics (IHEP), Protvino, Russia*
[16]*Iowa State University, Ames, Iowa 50011, USA*
[17]*Joint Institute for Nuclear Research, 141980 Dubna, Moscow Region, Russia*
[18]*KAERI, Cyclotron Application Laboratory, Seoul, Korea*
[19]*Kangnung National University, Kangnung 210-702, Korea*
[20]*KEK, High Energy Accelerator Research Organization, Tsukuba-shi, Ibaraki-ken 305-0801, Japan*
[21]*KFKI Research Institute for Particle and Nuclear Physics (RMKI), H-1525 Budapest 114, P.O. Box 49, Hungary*
[22]*Korea University, Seoul, 136-701, Korea*
[23]*Russian Research Center "Kurchatov Institute," Moscow, Russia*
[24]*Kyoto University, Kyoto 606-8502, Japan*
[25]*Laboratoire Leprince-Ringuet, Ecole Polytechnique, CNRS-IN2P3, Route de Saclay, F-91128, Palaiseau, France*
[26]*Lawrence Livermore National Laboratory, Livermore, California 94550, USA*
[27]*Los Alamos National Laboratory, Los Alamos, New Mexico 87545, USA*
[28]*LPC, Université Blaise Pascal, CNRS-IN2P3, Clermont-Fd, 63177 Aubiere Cedex, France*
[29]*Department of Physics, Lund University, Box 118, SE-221 00 Lund, Sweden*
[30]*Institut für Kernphysik, University of Muenster, D-48149 Muenster, Germany*
[31]*Myongji University, Yongin, Kyonggido 449-728, Korea*
[32]*Nagasaki Institute of Applied Science, Nagasaki-shi, Nagasaki 851-0193, Japan*
[33]*University of New Mexico, Albuquerque, New Mexico 87131, USA*
[34]*New Mexico State University, Las Cruces, New Mexico 88003, USA*
[35]*Oak Ridge National Laboratory, Oak Ridge, Tennessee 37831, USA*
[36]*IPN-Orsay, Universite Paris Sud, CNRS-IN2P3, BP1, F-91406, Orsay, France*
[37]*PNPI, Petersburg Nuclear Physics Institute, Gatchina, Russia*
[38]*RIKEN (The Institute of Physical and Chemical Research), Wako, Saitama 351-0198, Japan*
[39]*RIKEN BNL Research Center, Brookhaven National Laboratory, Upton, New York 11973-5000, USA*
[40]*St. Petersburg State Technical University, St. Petersburg, Russia*
[41]*Instituto de Física, Universidade de São Paulo, Caixa Postal 66318, São Paulo CEP05315-970, Brazil*
[42]*System Electronics Laboratory, Seoul National University, Seoul, Korea*
[43]*Chemistry Department, Stony Brook University, SUNY, Stony Brook, New York 11794-3400, USA*
[44]*Department of Physics and Astronomy, Stony Brook University, SUNY, Stony Brook, New York 11794, USA*
[45]*SUBATECH (Ecole des Mines de Nantes, CNRS-IN2P3, Université de Nantes), BP 20722-44307, Nantes, France*
[46]*University of Tennessee, Knoxville, Tennessee 37996, USA*
[47]*Department of Physics, Tokyo Institute of Technology, Tokyo, 152-8551, Japan*
[48]*Institute of Physics, University of Tsukuba, Tsukuba, Ibaraki 305, Japan*
[49]*Vanderbilt University, Nashville, Tennessee 37235, USA*
[50]*Waseda University, Advanced Research Institute for Science and Engineering, 17 Kikui-cho, Shinjuku-ku, Tokyo 162-0044, Japan*
[51]*Weizmann Institute, Rehovot 76100, Israel*
[52]*Yonsei University, IPAP, Seoul 120-749, Korea*

(Received 2 February 2005; published 8 April 2005)

A measurement of direct photons in $p + p$ collisions at $\sqrt{s} = 200$ GeV is presented. A photon excess above background from $\pi^0 \to \gamma + \gamma$, $\eta \to \gamma + \gamma$ and other decays is observed in the transverse momentum range $5.5 < p_T < 7$ GeV/c. The result is compared to a next-to-leading-order perturbative QCD calculation. Within errors, good agreement is found between the QCD calculation and the measured result.

DOI: 10.1103/PhysRevD.71.071102 PACS numbers: 13.85.Qk, 25.75.Dw

*Deceased.
†PHENIX spokesperson. Electronic address: zajc@nevis.columbia.edu

Measurements of particle production at large transverse momenta (p_T) in hadronic interactions provide the possibility to test perturbative quantum chromodynamics (pQCD). Neutral-pion production in $p + p$ collisions at $\sqrt{s} = 200$ GeV in the range $2 < p_T < 13$ GeV/c measured by the PHENIX experiment at the Relativistic Heavy Ion Collider (RHIC) can be well described by next-to-leading-order (NLO) pQCD [1]. This comparison, however, relies on the choice of the parton-to-pion fragmentation function. Measurement of direct-photon production provides a more direct test of pQCD. Quark-antiquark annihilation ($q\bar{q} \rightarrow \gamma g$) and quark-gluon Compton scattering ($qg \rightarrow q\gamma$) contribute to direct-photon production at leading order [2]. Because of the latter process, which dominates the production, the measurement of direct photons can be used to obtain information on the parton distribution function of the gluon inside the proton.

Previous direct-photon measurements in $p + p$ collisions were made up to energies of $\sqrt{s} = 63$ GeV (see e.g. [3–5]). For $p + \bar{p}$ collisions direct-photon data are available at considerably higher energies, $\sqrt{s} = 546$, 630 GeV [6–8] up to $\sqrt{s} = 1800$ GeV [9,10]. At these energies NLO pQCD calculations describe the direct-photon data within about 20%, although systematic differences in the spectral shapes were observed [11]. At energies below $\sqrt{s} = 63$ GeV the agreement between NLO pQCD and data is generally worse. With phenomenological approaches based on soft-gluon radiation of the incoming parton, which leads to an additional transverse momentum k_T, a better description of the data can be obtained [12]. The RHIC at the Brookhaven National Laboratory provides $p + p$ collisions at energies between the existing data sets, allowing better constraints on the processes affecting incoming partons. A further incentive to study direct-photon production in $p + p$ at $\sqrt{s} =$ 200 GeV comes from the measurement of direct photons in collisions of gold nuclei at the same center-of-mass energy per nucleon-nucleon pair [13,14]. In central Au + Au collisions high-p_T neutral-pion production is suppressed [15] which is due to energy loss of the scattered quarks and gluons in the hot and dense fireball created in these collisions (jet quenching) [16]. As direct photons are not subject to the strong interaction they should not be suppressed in the jet-quenching model. In this context, the $p + p$ direct-photon results serve as a baseline against which possible nuclear effects can be identified.

The data presented in this report were collected during the 2001–2002 run period (Run 2) of RHIC. The neutral-pion cross sections obtained from this data set were published in [1]. The unpolarized neutral-pion spectrum and the unpolarized direct-photon spectrum presented here were obtained by averaging over proton bunches with varying vertical polarization delivered by RHIC.

Direct photons and background photons from decays $\pi^0 \rightarrow \gamma + \gamma$ and $\eta \rightarrow \gamma + \gamma$ were measured with the electromagnetic calorimeter (EMCal) of the PHENIX experiment [17]. The background from charged particles was subtracted with the aid of a layer of multiwire proportional chambers with pad readout (PC3) which was located directly in front of the EMCal. The minimum-bias trigger was provided by two beam-beam counters (BBC) which were also used to determine the collision vertex. In addition to the minimum-bias trigger conditions, a high-p_T photon trigger was used, derived from the analog energy signal measured with the EMCal.

The two BBC's were located symmetrically around the nominal interaction point at ± 1.44 m along the beam line. The BBC's subtended the pseudorapidity range $\pm(3.1–3.9)$ with full azimuthal coverage. The collision vertex was determined by measuring the difference of particle arrival times in the two BBC's. This analysis was restricted to events with a vertex in the range ± 30 cm. The BBC's were calibrated as a luminosity detector with absolute luminosity measurements based on the van der Meer scan technique [18]. With these scans the cross section for firing the BBC minimum-bias trigger was determined to be 21.8 ± 2.1 mb [1]. Thus, roughly 50% of the inelastic $p + p$ events satisfy the minimum-bias trigger condition if an inelastic $p + p$ cross section of 42 mb at $\sqrt{s} = 200$ GeV is assumed. This trigger efficiency is determined by the geometrical acceptance of the BBC's.

The PHENIX EMCal comprises two arms each with 4 sectors [19]. The EMCal consists of two different subdetectors, a lead-scintillator calorimeter (PbSc, 6 sectors) and a lead-glass calorimeter (PbGl, 2 sectors). Each sector covers a pseudorapidity range of $|\eta| < 0.35$ and an azimuthal range of $\Delta\phi \approx 22.5°$. Each PbSc (PbGl) sector is highly segmented and consists of 72×36 (96×48) individual detector modules, called towers, with a lateral size of 5.5×5.5 cm^2 (4×4 cm^2). With a radial distance of the sectors to the beam line of roughly 5 m this corresponds to a segmentation of $\Delta\phi \times \Delta\eta \approx 0.01 \times 0.01$ such that the two decay photons of a π^0 are well separated up to neutral-pion momenta of $p_T \approx 20$ GeV/c. The different detection mechanisms of the two subdetectors (measurement of scintillation light in PbSc and detection of Cherenkov photons in PbGl) result in a different response to hadrons. Thus, the PbSc and PbGl provide photon measurements with different systematic uncertainties. The energy calibration of the detector was obtained from the position of the π^0 invariant-mass peaks. A $\sim$4% ($\sim$ 5%) shift of the π^0 peak position due to energy smearing in conjunction with the influence of the steeply falling π^0 p_T spectrum was taken into account in the PbSc (PbGl) calibration. The calibration was corroborated by correlating the EMCal energy with the momentum of electrons measured with the PHENIX tracking detectors and, in case of the PbSc, by measuring the energy deposited by minimum-ionizing particles. From these studies the systematic uncertainty of the energy measurement was estimated to be less than 1.5%. In

a direct-photon analysis it is essential to exclude bad detector modules ("hot towers") which might give rise to spurious direct-photon signals. A detailed quality assessment was carried out to identify such towers.

The EMCal high-p_T trigger (called 2×2) was based on the analog energy signal measured in 2×2 groups of adjacent EMCal towers (called trigger tiles). The average threshold of the trigger corresponded to an energy signal of 0.75 GeV. The probability as a function of the photon p_T to fire the trigger was determined by Monte Carlo simulations which included the variation of the trigger tile thresholds, the EMCal detector response, and the geometry of the active trigger tiles. This trigger efficiency was confirmed with minimum-bias data. The photon trigger efficiencies for PbSc and PbGl reached a plateau above $p_T = 1.5$–2 GeV/c at the limit of about 0.78 expected from the number of active towers and 2×2 trigger tiles. The high-p_T-trigger photon sample was used above $p_T = 3$ GeV/c in the final spectrum.

Another EMCal trigger which did not require a coincidence with the minimum-bias trigger was used to account for the bias on the particle measurement due to the minimum-bias event selection. To this end the fraction of π^0's measured with this EMCal trigger for events which in addition satisfied the minimum-bias trigger condition was determined to be $f = 0.75 \pm 0.02$. The unbiased photon and neutral pions cross sections were then determined by dividing the total number of measured photons and neutral pions by this number.

The minimum-bias data sample in this analysis consisted of 16.7×10^6 events, corresponding to an integrated luminosity of 0.77 nb^{-1}. About 1 in 47 minimum-bias events also satisfied the 2×2 high-p_T trigger condition. The 18.7×10^6 analyzed 2×2 events thus corresponded to an integrated luminosity of 40.3 nb^{-1}.

The first step in the direct-photon analysis was to define a sample of direct-photon-candidate hits. An EMCal hit was rejected as a direct-photon candidate if it formed an invariant mass in the π^0 or η range with other hits in the same or adjacent sectors. The invariant-mass window was $110 < m_{\gamma\gamma} < 170$ MeV/c^2 for the π^0 and $500 < m_{\gamma\gamma} < 620$ MeV/c^2 for the η, corresponding roughly to a $\pm 2\sigma$ window around the observed π^0 and η peaks. To keep the rate of accidental rejections of genuine direct photons low it was required that the partner hits had a transverse momentum of $p_T > 0.4$ GeV/c. This cut effectively corresponded to a p_T-dependent upper limit on the energy asymmetry $\alpha = |E_{\gamma 1} - E_{\gamma 2}|/(E_{\gamma 1} + E_{\gamma 2})$ in the rejection procedure. In spite of this requirement, a small fraction of genuine direct photons is rejected. This was studied by inserting artificially generated direct-photon hits into real events. In order to keep the hit multiplicity constant, a randomly selected real hit was removed from an event in this procedure. It was found that the loss of genuine direct photons was less than 2% for $p_T > 3$ GeV/c. The final direct-photon spectrum was corrected for this effect. In order to increase the chances of finding the partner photon for a π^0 or η decay photon, direct-photon candidates were required to lie within a restricted fiducial area which was defined by a minimum distance of 16 (20) towers to the edge of the detector for the PbSc (PbGl). For example, for π^0's with $p_T = 4$ GeV/c and the requirement that one decay photon has a $p_T > 0.4$ GeV/c the average distance of the decay photons in tower units is ~ 8 (~ 11) for PbSc (PbGl). With the chosen fiducial area basically all decay photons from neutral pions with $p_T \gtrsim 4$ GeV/c could be tagged, if all towers were active. Monte Carlo studies showed that the rejection of direct-photon candidates based on the π^0 and η tagging lead to a reduction of background photons from hadron decays in the fiducial area of about a factor of 2 for $p_T > 5$ GeV/c. Some direct-photon analyses only measure isolated direct photons for which the total transverse energy or the number of charged tracks in a cone centered around the direct photon is required to lie below a threshold. No such cut was used in this analysis.

In order to reduce the background from hadronic hits in the EMCal, cuts were applied on the lateral shower shape and on the time of flight of the hits. The remaining contamination of charged particles was subtracted on a statistical basis by employing the PC3 as a charged-particle veto detector. The intrinsic efficiency of the PC3 for detecting a charged particle was higher than 99% and the active PC3 area in the EMCal acceptance was roughly 90%. PC3 hits were projected onto the EMCal surface using a straight line given by the PC3 hit and the event vertex. An EMCal hit within a certain veto radius was counted as a charged hit. The chosen veto radius decreased with increasing p_T and for $p_T > 0.8$ GeV/c a constant value of 15 cm was used. The fraction of charged hits was corrected for random associations with the help of a mixed-event technique. The charged-particle background in the direct-photon-candidate sample was $\sim 15\%$ around $p_T = 5$ GeV/c for both PbSc and PbGl. A large fraction of these background hits, however, comes from photon conversion in the field-free region between the vertex and PC3. The photon loss due to conversion was calculated based on the material budget up to PC3. The photon conversion probability was 4.1% for the 2 PbSc sectors in the East Arm of the central spectrometer, 5.3% for the 4 sectors in the West Arm, and 7.4% for the PbGl. These conversion losses were taken into account in the final photon cross section. The correction for the contamination of the raw spectrum of neutral EMCal hits with neutrons and antineutrons was determined with a detailed GEANT simulation [20]. In the case of the PbGl calorimeter the simulation was based on the creation of Cherenkov photons in order to achieve a realistic description of the detector response. The background from neutral particles was found to decrease with p_T and was already less than 1% for $p_T > 2$ GeV/c for both PbSc and PbGl.

The geometric acceptance and the efficiency of the photon detection were calculated with a Monte Carlo

simulation. The efficiency takes the distortion of the direct-photon-candidate spectrum due to energy smearing into account. Moreover, it corrects the small ($\lesssim 5\%$) loss of photons due to the shower shape and time-of-flight cuts. The final direct-photon spectrum was corrected for the difference between the average direct-photon cross section within a finite p_T bin and the value of the cross section at the bin center.

With the described corrections the unbiased differential cross section $\gamma_{\text{direct}}^{\text{cand}} \equiv E\mathrm{d}^3\sigma/\mathrm{d}^3p$ for the direct-photon candidates calculated from the minimum-bias data sample reads

$$E\frac{\mathrm{d}^3\sigma}{\mathrm{d}^3p} = \frac{1}{\hat{\mathcal{L}}} \cdot \frac{1}{2\pi p_T} \cdot \frac{C_{\text{reco}} \cdot C_{\text{conv}} \cdot C_{\text{loss}}}{f} \cdot \frac{N_{\text{direct}\gamma}^{\text{cand}}}{\Delta p_T \cdot \Delta y} \quad (1)$$

where $N_{\text{direct}\gamma}^{\text{cand}}$ is the total number of direct-photon candidates in a p_T bin Δp_T and rapidity bin Δy; C_{reco} is the acceptance and efficiency correction for photons; C_{conv} is the correction for photon conversions; C_{loss} is the correction for the loss of genuine direct photons in the π^0 and η tagging; $f = 0.75 \pm 0.02$ is the fraction of the unbiased direct-photon yield which is measured under the minimum-bias trigger condition; and $\hat{\mathcal{L}}$ is the integrated luminosity for the analyzed data sample. The high-p_T triggered sample required an additional correction for the efficiency of this trigger for photon detection.

The p_T spectrum of the direct-photon candidates contains direct photons as well as remaining background photons from hadron decays. These background photons mostly come from π^0 and η decays for which one decay photon misses the detector. At a representative bin of $p_T = 6.75$ GeV/c about 93% of the background photons originate from π^0 and η decays, the remaining background photons come from decays of other hadrons like ω and η'. The background was calculated with the same Monte Carlo code that was used for the acceptance and efficiency calculation. The Monte Carlo code took a parametrization of the measured π^0 spectrum as input. The π^0 and η tagging was done with the same reconstruction cuts as in the analysis of real events. The spectra of η mesons and other hadrons with photon decay branches were assumed to have the same shape as the π^0 spectrum as a function of $m_T = \sqrt{p_T^2 + m_0^2}$ (m_T scaling [21,22]). The η/π^0 invariant cross section ratio as a function of m_T was taken as 0.48 ± 0.1 which was confirmed by the measured η spectrum.

The dominant systematic uncertainty of the neutral-pion spectrum and the direct-photon-candidate spectrum came from the uncertainty of the energy scale and the uncertainty of the yield correction. At $p_T = 6.75$ GeV/c, the 1.5% uncertainty of the energy scale resulted in a 9% uncertainty in the photon yield. The yield correction included the correction for energy and position smearing of the detector, for photon losses due to particle-identification cuts, for photon conversions, and for the detector acceptance. For the neutral pions an additional 5% uncertainty came from the extraction of the π^0-peak content. In the case of the photon measurement the uncertainty due to the subtraction of charged and neutral backgrounds was taken into account. In the ratio $\gamma_{\text{direct}}^{\text{cand}}/\pi^0$ of the direct-photon-candidate spectrum and the neutral-pion spectrum systematic uncertainties partially cancel. Monte Carlo studies showed that the uncertainty of this ratio at $p_T = 6.75$ GeV/c due to a possible nonlinearity of the energy scale was $\sim 2\%$.

For the determination of the direct-photon spectrum the expected background photons from hadronic decays need to be subtracted from the spectrum of direct-photon candidates. To this end the ratio $R_\gamma = (\gamma_{\text{direct}}^{\text{cand}}/\pi^0)/(\gamma_{\text{bckg}}/\pi^0)$ of the measured direct-photon candidates to the calculated background was determined. The direct-photon spectrum was then calculated as

$$\gamma_{\text{direct}} = (1 - R_\gamma^{-1}) \cdot \gamma_{\text{direct}}^{\text{cand}}. \quad (2)$$

The relative systematic uncertainty of the direct-photon cross section was calculated as the quadratic sum of the relative uncertainties of the two factors in Eq. (2). The factor $1 - R_\gamma^{-1}$ contains the (statistical and systematic) significance of the direct-photon signal. When multiplying with $\gamma_{\text{direct}}^{\text{cand}}$, only the systematic uncertainties that cancelled in the ratio R_γ are added (e.g. the energy scale error). The overall normalization uncertainty from the luminosity determination was 9.6%. The estimated systematic uncertainties for the measured neutral-pion spectrum and the measured direct-photon-candidate spectrum are shown in Table I for a representative bin ($p_T = 6.75$ GeV/c) of the spectrum. The systematic uncertainty of the direct-photon measurement was corroborated by comparing results obtained for the different photon-identification criteria. Moreover, the individual PbGl and PbSc results were found to agree within systematic errors.

TABLE I. Systematic uncertainties of the neutral-pion spectrum, the direct-photon-candidate spectrum, and the measured and simulated γ/π^0 ratios at $p_T = 6.75$ GeV/c.

π^0 error source	PbGl	PbSc
Yield extraction	5%	5%
Yield correction	8%	6%
Energy scale	9%	8%
Total	13%	12%
$\gamma_{\text{direct}}^{\text{cand}}$ error source	PbGl	PbSc
Non-γ background correction	4%	4%
Yield correction	6%	5%
Energy scale	9%	9%
Total	12%	11%
Total error	PbGl + PbSc combined	
$\gamma_{\text{direct}}^{\text{cand}}/\pi^0$	9%	
$\gamma_{\text{bckg}}/\pi^0$	4%	

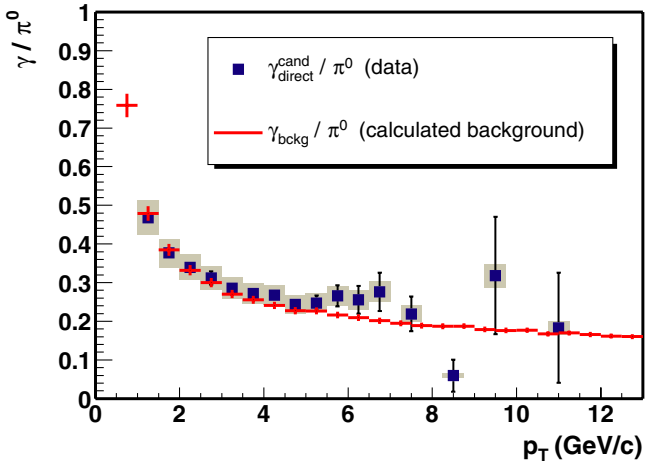

FIG. 1 (color online). Ratio of direct-photon candidates to the π^0 spectrum. The histogram represents the expected background signal from the Monte Carlo calculation. The error bars represent the statistical error and the boxes the systematic error.

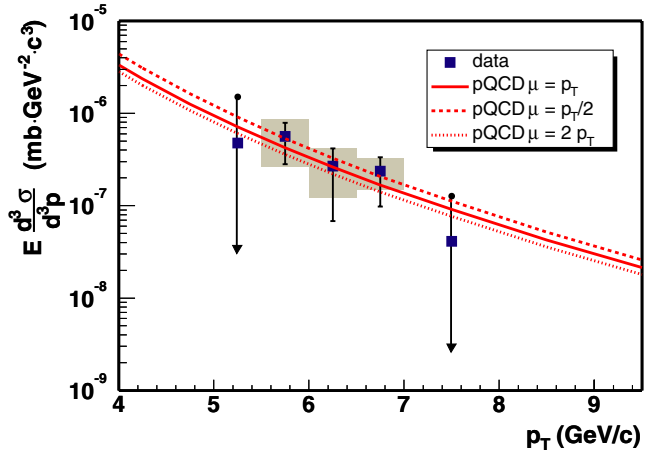

FIG. 2 (color online). Measured cross section and NLO pQCD calculations for direct-photon production in $p + p$ collisions at $\sqrt{s} = 200$ GeV. The normalization error of 9.6% is not shown. The two data points plotted with an arrow indicate the beginning of the low- and high-p_T ranges where the direct-photon signal is consistent with zero. The upper edges of the arrows indicate an upper limit (90% confidence level) for the direct-photon cross section calculated from the statistical and systematic uncertainty.

To make the best use of the available Run-2 statistics the photon and π^0 spectra from PbSc and PbGl were combined for the final result. The ratio of the acceptance- and efficiency-corrected direct-photon candidate p_T spectrum to the measured π^0 spectrum is depicted in Fig. 1. In addition, the Monte Carlo calculation for the ratio of the expected background photons to the π^0 spectrum is shown. At high p_T the statistical significance of the direct-photon-candidate spectrum is weak. However, around $p_T \approx$ 6–7 GeV/c there is clear evidence of a photon signal above the background.

The extracted invariant direct-photon spectrum is shown in Fig. 2 and the numerical values are given in Table II. The experimental result was compared to NLO pQCD calculations [23–28] which used the CTEQ6 parton distribution functions [29] and the Glück-Reya-Vogt parton-to-photon fragmentation function [30]. There are in general two mechanisms for the production of direct photons: the direct contribution from elementary scattering processes of quarks and gluons, described in the introduction, and the contribution from photons which are produced in the fragmentation of quark or gluon jets. The latter is a long-distance process which is not perturbatively calculable. It is described by a parton-to-photon fragmentation function which is determined experimentally. Since no isolation cut was used in the data analysis the pQCD calculation in Fig. 2 includes contributions from the direct production mechanism and the fragmentation mechanism. The separation of short-distance and long-distance processes in the pQCD calculation introduces unphysical renormalization, factorization, and fragmentation scales. Identical values for all three scales were used in the pQCD calculation. In Fig. 2, results are shown for three choices of the scales ($\mu = p_T$, $\mu = p_T/2$, and $\mu = 2p_T$). The theoretical and experimental results agree within the large uncertainties of the data points.

TABLE II. Invariant differential cross section for direct-photon production in $p + p$ collisions at $\sqrt{s} = 200$ GeV. Asymmetric uncertainties ($\sigma_{\rm low}$, $\sigma_{\rm high}$) are given for the cross section. The absolute normalization error of 9.6% is not included.

		Stat. error		Sys. error	
p_T (GeV/c)	$E\mathrm{d}^3\sigma/\mathrm{d}^3p$ (mb GeV$^{-2}c^3$)	$\sigma_{\rm low}$	$\sigma_{\rm high}$	$\sigma_{\rm low}$	$\sigma_{\rm high}$
5.75	5.61×10^{-7}	50%	42%	53%	54%
6.25	2.68×10^{-7}	75%	56%	55%	56%
6.75	2.37×10^{-7}	59%	42%	37%	38%

Prior to the Run-2 $p + p$ beam time PHENIX took data from Au + Au collisions at $\sqrt{s_{\rm NN}} = 200$ GeV. A clear direct-photon signal was observed in midcentral and central Au + Au reactions [13]. The strong suppression of π^0's and η's in Au + Au significantly reduced the number of background photons and eased the extraction of the direct-photon signal. The $p + p$ NLO pQCD was used as a baseline reference for the interpretation of the Au + Au result. In contrast to neutral pions no sign of a suppression of direct photons in Au + Au collisions was found. The direct-photon measurement presented in this paper supports the use of the NLO pQCD calculation as a reference for the results measured in Au + Au.

In summary, a small but significant direct-photon signal has been observed at midrapidity in $p + p$ collisions at $\sqrt{s} = 200$ GeV. The measured direct-photon cross section is in agreement with pQCD calculation, albeit within large errors.

We thank the staff of the Collider-Accelerator and Physics Departments at BNL for their vital contributions. We thank Werner Vogelsang for providing the NLO pQCD direct-photon calculations. We acknowledge support from the Department of Energy and NSF (U.S.A.), MEXT and JSPS (Japan), CNPq and FAPESP (Brazil), NSFC (China), CNRS-IN2P3 and CEA (France), BMBF, DAAD, and AvH (Germany), OTKA (Hungary), DAE and DST (India), ISF (Israel), KRF and CHEP (Korea), RMIST, RAS, and RMAE (Russia), VR and KAW (Sweden), U.S. CRDF for the FSU, US-Hungarian NSF-OTKA-MTA, and US-Israel BSF.

[1] PHENIX Collaboration, S. S. Adler *et al.*, Phys. Rev. Lett. **91**, 241803 (2003).
[2] H. Fritzsch and P. Minkowski, Phys. Lett. **69B**, 316 (1977).
[3] E. Anassontzis *et al.*, Z. Phys. C **13**, 277 (1982).
[4] Fermilab E706 Collaboration, L. Apanasevich *et al.*, Phys. Rev. D **70**, 092009 (2004).
[5] UA6 Collaboration, G. Ballocchi *et al.*, Phys. Lett. B **436**, 222 (1998).
[6] UA1 Collaboration, C. Albajar *et al.*, Phys. Lett. B **209**, 385 (1988).
[7] UA2 Collaboration, R. Ansari *et al.*, Z. Phys. C **41**, 395 (1988).
[8] UA2 Collaboration, J. Alitti *et al.*, Phys. Lett. B **263**, 544 (1991).
[9] CDF Collaboration, F. Abe *et al.*, Phys. Rev. Lett. **73**, 2662 (1994).
[10] D0 Collaboration, B. Abbott *et al.*, Phys. Rev. Lett. **84**, 2786 (2000).
[11] CDF Collaboration, D. Acosta *et al.*, Phys. Rev. D **65**, 112003 (2002).
[12] L. Apanasevich *et al.*, Phys. Rev. D **59**, 074007 (1999).
[13] PHENIX Collaboration, J. Frantz *et al.*, J. Phys. G **30**, S1003 (2004).
[14] PHENIX Collaboration, S. S. Adler *et al.* (unpublished).
[15] PHENIX Collaboration, S. S. Adler *et al.*, Phys. Rev. Lett. **91**, 072301 (2003).
[16] M. Gyulassy, I. Vitev, X.-N. Wang, and B.-W. Zhang, in *Quark Gluon Plasma 3*, edited by R. C. Hwa and X. N. Wang (World Scientific, Singapore, 2004).
[17] PHENIX Collaboration, K. Adcox *et al.*, Nucl. Instrum. Methods Phys. Res., Sect. A **499**, 469 (2003).
[18] S. van der Meer, CERN Internal Report No. ISR-PO/68-31, 1968.
[19] PHENIX Collaboration, L. Aphecetche *et al.*, Nucl. Instrum. Methods Phys. Res., Sect. A **499**, 521 (2003).
[20] GEANT 3.21, CERN program library.
[21] British-Scandinavian Collaboration, B. Alper *et al.*, Nucl. Phys. **B87**, 19 (1975).
[22] UA5 Collaboration, K. Alpgard *et al.*, Phys. Lett. **107B**, 310 (1981).
[23] L. E. Gordon and W. Vogelsang, Phys. Rev. D **48**, 3136 (1993).
[24] L. E. Gordon and W. Vogelsang, Phys. Rev. D **50**, 1901 (1994).
[25] P. Aurenche, A. Douiri, R. Baier, M. Fontannaz, and D. Schiff, Phys. Lett. **140B**, 87 (1984).
[26] P. Aurenche, R. Baier, M. Fontannaz, and D. Schiff, Nucl. Phys. **B297**, 661 (1988).
[27] H. Baer, J. Ohnemus, and J. F. Owens, Phys. Lett. B **234**, 127 (1990).
[28] H. Baer, J. Ohnemus, and J. F. Owens, Phys. Rev. D **42**, 61 (1990).
[29] J. Pumplin *et al.*, J. High Energy Phys. 07 (2002) 012.
[30] M. Gluck, E. Reya, and A. Vogt, Phys. Rev. D **48**, 116 (1993); **51**, 1427(E) (1995).

Nuclear Modification Factors for Hadrons at Forward and Backward Rapidities in Deuteron-Gold Collisions at $\sqrt{s_{NN}} = 200$ GeV

S. S. Adler,[5] S. Afanasiev,[20] C. Aidala,[10] N. N. Ajitanand,[44] Y. Akiba,[21,40] A. Al-Jamel,[35] J. Alexander,[44] K. Aoki,[25] L. Aphecetche,[46] R. Armendariz,[35] S. H. Aronson,[5] R. Averbeck,[45] T. C. Awes,[36] V. Babintsev,[17] A. Baldisseri,[11] K. N. Barish,[6] P. D. Barnes,[28] B. Bassalleck,[34] S. Bathe,[6,31] S. Batsouli,[10] V. Baublis,[39] F. Bauer,[6] A. Bazilevsky,[5,41] S. Belikov,[19,17] M. T. Bjorndal,[10] J. G. Boissevain,[28] H. Borel,[11] M. L. Brooks,[28] D. S. Brown,[35] N. Bruner,[34] D. Bucher,[31] H. Buesching,[5,31] V. Bumazhnov,[17] G. Bunce,[5,41] J. M. Burward-Hoy,[28,27] S. Butsyk,[45] X. Camard,[46] P. Chand,[4] W. C. Chang,[2] S. Chernichenko,[17] C. Y. Chi,[10] J. Chiba,[21] M. Chiu,[10] I. J. Choi,[53] R. K. Choudhury,[4] T. Chujo,[5] V. Cianciolo,[36] Y. Cobigo,[11] B. A. Cole,[10] M. P. Comets,[37] P. Constantin,[19] M. Csanád,[13] T. Csörgő,[22] J. P. Cussonneau,[46] D. d'Enterria,[10] K. Das,[14] G. David,[5] F. Deák,[13] H. Delagrange,[46] A. Denisov,[17] A. Deshpande,[41] E. J. Desmond,[5] A. Devismes,[45] O. Dietzsch,[42] J. L. Drachenberg,[1] O. Drapier,[26] A. Drees,[45] A. Durum,[17] D. Dutta,[4] V. Dzhordzhadze,[47] Y. V. Efremenko,[36] H. En'yo,[40,41] B. Espagnon,[37] S. Esumi,[49] D. E. Fields,[34,41] C. Finck,[46] F. Fleuret,[26] S. L. Fokin,[24] B. D. Fox,[41] Z. Fraenkel,[52] J. E. Frantz,[10] A. Franz,[5] A. D. Frawley,[14] Y. Fukao,[25,40,41] S.-Y. Fung,[6] S. Gadrat,[29] M. Germain,[46] A. Glenn,[47] M. Gonin,[26] J. Gosset,[11] Y. Goto,[40,41] R. Granier de Cassagnac,[26] N. Grau,[19] S. V. Greene,[50] M. Grosse Perdekamp,[18,41] H.-Å. Gustafsson,[30] T. Hachiya,[16] J. S. Haggerty,[5] H. Hamagaki,[8] A. G. Hansen,[28] E. P. Hartouni,[27] M. Harvey,[5] K. Hasuko,[40] R. Hayano,[8] X. He,[15] M. Heffner,[27] T. K. Hemmick,[45] J. M. Heuser,[40] P. Hidas,[22] H. Hiejima,[18] J. C. Hill,[19] R. Hobbs,[34] W. Holzmann,[44] K. Homma,[16] B. Hong,[23] A. Hoover,[35] T. Horaguchi,[40,41,48] T. Ichihara,[40,41] V. V. Ikonnikov,[24] K. Imai,[25,40] M. Inaba,[49] M. Inuzuka,[8] D. Isenhower,[1] L. Isenhower,[1] M. Ishihara,[40] M. Issah,[44] A. Isupov,[20] B. V. Jacak,[45] J. Jia,[45] O. Jinnouchi,[40,41] B. M. Johnson,[5] S. C. Johnson,[27] K. S. Joo,[32] D. Jouan,[37] F. Kajihara,[8] S. Kametani,[8,51] N. Kamihara,[40,48] M. Kaneta,[41] J. H. Kang,[53] K. Katou,[51] T. Kawabata,[8] A. Kazantsev,[24] S. Kelly,[9,10] B. Khachaturov,[52] A. Khanzadeev,[39] J. Kikuchi,[51] D. J. Kim,[53] E. Kim,[43] G.-B. Kim,[26] H. J. Kim,[53] E. Kinney,[9] A. Kiss,[13] E. Kistenev,[5] A. Kiyomichi,[40] C. Klein-Boesing,[31] H. Kobayashi,[41] L. Kochenda,[39] V. Kochetkov,[17] R. Kohara,[16] B. Komkov,[39] M. Konno,[49] D. Kotchetkov,[6] A. Kozlov,[52] P. J. Kroon,[5] C. H. Kuberg,[1] G. J. Kunde,[28] K. Kurita,[40] M. J. Kweon,[23] Y. Kwon,[53] G. S. Kyle,[35] R. Lacey,[44] J. G. Lajoie,[19] Y. Le Bornec,[37] A. Lebedev,[19,24] S. Leckey,[45] D. M. Lee,[28] M. J. Leitch,[28] M. A. L. Leite,[42] X. H. Li,[6] H. Lim,[43] A. Litvinenko,[20] M. X. Liu,[28] C. F. Maguire,[50] Y. I. Makdisi,[5] A. Malakhov,[20] V. I. Manko,[24] Y. Mao,[38,40] G. Martinez,[46] H. Masui,[49] F. Matathias,[45] T. Matsumoto,[8,51] M. C. McCain,[1] P. L. McGaughey,[28] Y. Miake,[49] T. E. Miller,[50] A. Milov,[45] S. Mioduszewski,[5] G. C. Mishra,[15] J. T. Mitchell,[5] A. K. Mohanty,[4] D. P. Morrison,[5] J. M. Moss,[28] D. Mukhopadhyay,[52] M. Muniruzzaman,[6] S. Nagamiya,[21] J. L. Nagle,[9,10] T. Nakamura,[16] J. Newby,[47] A. S. Nyanin,[24] J. Nystrand,[30] E. O'Brien,[5] C. A. Ogilvie,[19] H. Ohnishi,[40] I. D. Ojha,[3,50] H. Okada,[25,40] K. Okada,[40,41] A. Oskarsson,[30] I. Otterlund,[30] K. Oyama,[8] K. Ozawa,[8] D. Pal,[52] A. P. T. Palounek,[28] V. Pantuev,[45] V. Papavassiliou,[35] J. Park,[43] W. J. Park,[23] S. F. Pate,[35] H. Pei,[19] V. Penev,[20] J.-C. Peng,[18] H. Pereira,[11] V. Peresedov,[20] A. Pierson,[34] C. Pinkenburg,[5] R. P. Pisani,[5] M. L. Purschke,[5] A. K. Purwar,[45] J. M. Qualls,[1] J. Rak,[19] I. Ravinovich,[52] K. F. Read,[36,47] M. Reuter,[45] K. Reygers,[31] V. Riabov,[39] Y. Riabov,[39] G. Roche,[29] A. Romana,[26] M. Rosati,[19] S. S. E. Rosendahl,[30] P. Rosnet,[29] V. L. Rykov,[40] S. S. Ryu,[53] N. Saito,[25,40,41] T. Sakaguchi,[8,51] S. Sakai,[49] V. Samsonov,[39] L. Sanfratello,[34] R. Santo,[31] H. D. Sato,[25,40] S. Sato,[5,49] S. Sawada,[21] Y. Schutz,[46] V. Semenov,[17] R. Seto,[6] T. K. Shea,[5] I. Shein,[17] T.-A. Shibata,[40,48] K. Shigaki,[16] M. Shimomura,[49] A. Sickles,[45] C. L. Silva,[42] D. Silvermyr,[28] K. S. Sim,[23] A. Soldatov,[17] R. A. Soltz,[27] W. E. Sondheim,[28] S. P. Sorensen,[47] I. V. Sourikova,[5] F. Staley,[11] P. W. Stankus,[36] E. Stenlund,[30] M. Stepanov,[35] A. Ster,[22] S. P. Stoll,[5] T. Sugitate,[16] J. P. Sullivan,[28] S. Takagi,[49] E. M. Takagui,[42] A. Taketani,[40,41] K. H. Tanaka,[21] Y. Tanaka,[33] K. Tanida,[40] M. J. Tannenbaum,[5] A. Taranenko,[44] P. Tarján,[12] T. L. Thomas,[34] M. Togawa,[25,40] J. Tojo,[40] H. Torii,[25,41] R. S. Towell,[1] V-N. Tram,[26] I. Tserruya,[52] Y. Tsuchimoto,[16] H. Tydesjö,[30] N. Tyurin,[17] T. J. Uam,[32] H. W. van Hecke,[28] J. Velkovska,[5] M. Velkovsky,[45] V. Veszprémi,[12] A. A. Vinogradov,[24] M. A. Volkov,[24] E. Vznuzdaev,[39] X. R. Wang,[15] Y. Watanabe,[40,41] S. N. White,[5] N. Willis,[37] F. K. Wohn,[19] C. L. Woody,[5] W. Xie,[6] A. Yanovich,[17] S. Yokkaichi,[40,41] G. R. Young,[36] I. E. Yushmanov,[24] W. A. Zajc,[10,*] C. Zhang,[10] S. Zhou,[7] J. Zimányi,[22] L. Zolin,[20] and X. Zong[19]

(PHENIX Collaboration)

[1]*Abilene Christian University, Abilene, Texas 79699, USA*
[2]*Institute of Physics, Academia Sinica, Taipei 11529, Taiwan*
[3]*Department of Physics, Banaras Hindu University, Varanasi 221005, India*

 © 2005 The American Physical Society

[4]Bhabha Atomic Research Centre, Bombay 400 085, India
[5]Brookhaven National Laboratory, Upton, New York 11973-5000, USA
[6]University of California–Riverside, Riverside, California 92521, USA
[7]China Institute of Atomic Energy (CIAE), Beijing, People's Republic of China
[8]Center for Nuclear Study, Graduate School of Science, University of Tokyo, 7-3-1 Hongo, Bunkyo, Tokyo 113-0033, Japan
[9]University of Colorado, Boulder, Colorado 80309, USA
[10]Columbia University, New York, New York 10027, USA and Nevis Laboratories, Irvington, New York 10533, USA
[11]Dapnia, CEA Saclay, F-91191, Gif-sur-Yvette, France
[12]Debrecen University, H-4010 Debrecen, Egyetem tér 1, Hungary
[13]ELTE, Eötvös Loránd University, H-1117 Budapest, Pázmány P. s. 1/A, Hungary
[14]Florida State University, Tallahassee, Florida 32306, USA
[15]Georgia State University, Atlanta, Georgia 30303, USA
[16]Hiroshima University, Kagamiyama, Higashi-Hiroshima 739-8526, Japan
[17]Institute for High Energy Physics (IHEP), Protvino, Russia
[18]University of Illinois at Urbana-Champaign, Urbana, Illinois 61801, USA
[19]Iowa State University, Ames, Iowa 50011, USA
[20]Joint Institute for Nuclear Research, 141980 Dubna, Moscow Region, Russia
[21]KEK, High Energy Accelerator Research Organization, Tsukuba-shi, Ibaraki-ken 305-0801, Japan
[22]KFKI Research Institute for Particle and Nuclear Physics (RMKI), H-1525 Budapest 114, PO Box 49, Hungary
[23]Korea University, Seoul, 136-701, Korea
[24]Russian Research Center "Kurchatov Institute," Moscow, Russia
[25]Kyoto University, Kyoto 606, Japan
[26]Laboratoire Leprince-Ringuet, Ecole Polytechnique, CNRS-IN2P3, Route de Saclay, F-91128, Palaiseau, France
[27]Lawrence Livermore National Laboratory, Livermore, California 94550, USA
[28]Los Alamos National Laboratory, Los Alamos, New Mexico 87545, USA
[29]LPC, Université Blaise Pascal, CNRS-IN2P3, Clermont-Fd, 63177 Aubiere Cedex, France
[30]Department of Physics, Lund University, Box 118, SE-221 00 Lund, Sweden
[31]Institut für Kernphysik, University of Muenster, D-48149 Muenster, Germany
[32]Myongji University, Yongin, Kyonggido 449-728, Korea
[33]Nagasaki Institute of Applied Science, Nagasaki-shi, Nagasaki 851-0193, Japan
[34]University of New Mexico, Albuquerque, New Mexico 87131, USA
[35]New Mexico State University, Las Cruces, New Mexico 88003, USA
[36]Oak Ridge National Laboratory, Oak Ridge, Tennessee 37831, USA
[37]IPN-Orsay, Universite Paris Sud, CNRS-IN2P3, BP1, F-91406, Orsay, France
[38]Peking University, Beijing, People's Republic of China
[39]PNPI, Petersburg Nuclear Physics Institute, Gatchina, Russia
[40]RIKEN (The Institute of Physical and Chemical Research), Wako, Saitama 351-0198, Japan
[41]RIKEN BNL Research Center, Brookhaven National Laboratory, Upton, New York 11973-5000, USA
[42]Universidade de São Paulo, Instituto de Física, Caixa Postal 66318, São Paulo CEP05315-970, Brazil
[43]System Electronics Laboratory, Seoul National University, Seoul, South Korea
[44]Chemistry Department, Stony Brook University, SUNY, Stony Brook, New York 11794-3400, USA
[45]Department of Physics and Astronomy, Stony Brook University, SUNY, Stony Brook, New York 11794, USA
[46]SUBATECH (Ecole des Mines de Nantes, CNRS-IN2P3, Université de Nantes), BP 20722-44307, Nantes, France
[47]University of Tennessee, Knoxville, Tennessee 37996, USA
[48]Department of Physics, Tokyo Institute of Technology, Tokyo, 152-8551, Japan
[49]Institute of Physics, University of Tsukuba, Tsukuba, Ibaraki 305, Japan
[50]Vanderbilt University, Nashville, Tennessee 37235, USA
[51]Waseda University, Advanced Research Institute for Science and Engineering, 17 Kikui-cho, Shinjuku-ku, Tokyo 162-0044, Japan
[52]Weizmann Institute, Rehovot 76100, Israel
[53]Yonsei University, IPAP, Seoul 120-749, Korea

(Received 29 November 2004; published 3 March 2005)

We report on charged hadron production in deuteron-gold reactions at $\sqrt{s_{NN}} = 200$ GeV. Our measurements in the deuteron direction cover $1.4 < \eta < 2.2$, referred to as forward rapidity, and in the gold direction $-2.0 < \eta < -1.4$, referred to as backward rapidity, and a transverse momentum range $p_T = 0.5$–4.0 GeV/c. We compare the relative yields for different deuteron-gold collision centrality classes. We observe a suppression relative to binary collision scaling at forward rapidity, sensitive to low momentum fraction (x) partons in the gold nucleus, and an enhancement at backward rapidity, sensitive to high momentum fraction partons in the gold nucleus.

DOI: 10.1103/PhysRevLett.94.082302 PACS numbers: 25.75.Dw

Deep inelastic scattering of leptons on the proton revealed the proton's substructure of pointlike parton constituents [1]. This substructure, usually described quantitatively as parton distribution functions, evolves as one probes the proton at shorter wavelength or equivalently higher momentum transfer, Q^2. Using the measured quark and antiquark distribution functions and the DGLAP [2] and BFKL [3] evolution equations, a strong increase in the gluon density is expected at high Q^2 and small x (fraction of the proton momentum carried by the parton). Such an increase is, indeed, observed at HERA [4], suggesting that at sufficiently small x, gluons should overlap in space and time. This overlap should result in gluon fusion, and thus reduce the gluon density at low x and enhance it at larger x. This gluon fusion limits the achievable gluon density, leading to gluon saturation. This saturation is sometimes described as the formation of a color glass condensate [5]. Gluon saturation is expected to be a larger effect in nuclei where the partons from different nucleons overlap as well. Suppression of low x partons in nuclei relative to nucleons has been experimentally observed and is referred to as nuclear shadowing [6]. However, this shadowing is often described in terms of modification of the leading-twist parton densities in nuclei [7].

In 2003 the Relativistic Heavy Ion Collider (RHIC) collided deuteron and gold nuclei at $\sqrt{s_{NN}} = 200$ GeV. At this energy, most hadrons with $p_T > 2.0$ GeV/c arise from parton-parton interactions and can be used as a probe of nuclear partonic structure. Hadrons with $p_T > 2.0$ GeV/c at forward rapidity $1.4 < \eta < 2.2$ are sensitive to low x partons in the gold nucleus $0.001 < x < 0.03$. Hadrons at backward rapidity $-2.0 < \eta < -1.4$ are sensitive to high x partons in the gold nucleus $0.04 < x < 0.5$. It has been predicted that gluon saturation at small x will suppress hadronic yields at forward rapidity [8] with the transverse momentum scale for the onset of the gluon saturation set by $Q_s^2[\mathrm{GeV}^2] = 0.13 N_{\mathrm{coll}} e^{\lambda y}$ [9] for d + Au collisions at RHIC. Here $\lambda \sim 0.3$ is determined from HERA data [10] and N_{coll} is the number of nucleon-nucleon inelastic collisions. Thus, for central collisions and within our forward rapidity coverage Q_s^2 is expected to be of order 2–4 GeV^2 and may have observable consequences. Novel hadron production mechanisms, such as quark recombination [11], can also impact the distribution of particles in the forward rapidity region.

Results on charged hadron yields at forward rapidity from the BRAHMS experiment have shown a suppression of the yield of hadrons in central, compared to peripheral, d + Au collisions [12]. At midrapidity, PHENIX has reported a modest enhancement of the yield of hadrons with $p_T > 1.5$ GeV/c [13]. This enhancement, generally referred to as the "Cronin effect" is often ascribed to initial state scattering of the parton traversing the nucleus prior to the high Q^2 scattering [14]. At backward rapidities (large x), antishadowing and other effects of the surrounding nuclear medium (e.g., the EMC effect) [15] may compete, making predictions challenging.

It is important to note that in the transverse momentum range of this measurement, $0.5 < p_T < 4.0$ GeV/c, hadron production is also sensitive to soft physics phenomena which are determined by coherent hadron-hadron interactions. In $p + A$ reactions at lower energies soft hadron production shifts from forward to backward rapidity, with a larger shift for larger nuclear targets. Thus, at low p_T one may observe an increase (decrease) in hadron yields at backward (forward) rapidity which is not necessarily a reflection of changes at the partonic structure level.

In this Letter, we present results from the PHENIX experiment [16] on the ratio of hadron yields at forward and backward pseudorapidity for different centrality classes of d + Au collisions. PHENIX has two spectrometers designed for measuring muon production over the pseudorapidity range $-2.2 < \eta < -1.2$ (backward spectrometer) and $1.2 < \eta < 2.4$ (forward spectrometer) [16]. The spectrometers start with a thick hadron absorber composed of 19 cm of brass and 60 cm of low-carbon steel between the collision point and active detectors along the beam axis, primarily to reduce hadronic background for muon measurements [17]. After this material, the Muon Tracker (MuTr) detector, consisting of three stations of cathode strip chambers, tracks charged particles in a magnetic field. The momentum resolution is 5% (for typical momenta in this analysis) and the absolute scale is known to better than 1%. Following the muon magnet backplate [30 (20) cm of steel in the forward (backward) spectrometer] there is a Muon Identifier (MuID) detector. The MuID consists of five layers of planar drift tubes interleaved with layers of steel for further hadron absorption (10 cm thick in the first two layers and 20 cm thick for the remaining layers). The layers are numbered 0–4, with 4 being the most downstream. The MuID is used to separate muons from hadrons and provide triggering capabilities.

Although these spectrometers were designed to detect muons, they can also be used to measure charged hadrons via two independent methods. The first method is via the identification of hadrons which penetrate part way through the MuID, referred to as "punch-through hadrons." The second method is via muons from light mesons π, K which decay before interacting in the absorber material. By measuring these decay muons, we can reconstruct the yield of their parent light mesons. In both of these methods the absolute yield of hadrons is difficult to determine due to uncertainties in the punch-through and decay probabilities. However, this small probability is independent of d + Au collision centrality, and thus not knowing the absolute yields does not affect the precision of measured ratios of hadron yields between the different classes of events.

The punch-through hadron identification is achieved by studying particles that stop somewhere within the MuID before the last layer. For muons penetrating up to layers 2

and 3 we expect the average momenta measured in the MuTr of $p = 1.0$ and $1.2\ \mathrm{GeV}/c$, respectively, corresponding to the average ionization energy loss in traversing the spectrometer material. The reconstructed momentum distributions for particles stopping in layers 2 and 3 of the MuID are shown in Fig. 1. In addition to the expected muon peaks, there is a broad distribution extending to higher momentum which is the result of punch-through hadrons. These hadrons also suffer ionization energy loss up to the relevant layer, then suffer an inelastic collision in the MuID steel, and do not penetrate further. We thus select a clean sample of hadrons by demanding that a track stop in MuID layer 2 or 3 and have momentum more than 3σ away from the muon peaks. Muon contamination in our sample is estimated from simulations to be less than 5%.

Another source of background for the punch-through hadrons is secondary particles produced from hadronic showering in the absorber. This background is reduced by requiring that the track point back to the primary collision vertex, as determined from the beam-beam counter (BBC). The background from secondary particles varies as a function of p_T and is typically ~1%–5% of the signal based on simulations. We also apply acceptance cuts $-2.0 < \eta < -1.4$ and $1.4 < \eta < 2.2$ in order to reduce the background at small angles.

Some hadrons will decay into muons before the absorber, and the decay muons are then measured by the muon spectrometers. Muons can result from many sources including decays of π, K, D mesons, and J/ψ. These particles have a finite decay probability P_{decay} before they reach the absorber

$$P_{\mathrm{decay}}(p, L) = 1 - e^{-Lm/\tau p}, \tag{1}$$

where $L \sim 41$ cm is the distance from the collision vertex to the absorber; p, m, and τ are the momentum, mass, and proper lifetime of the parent particle.

Thus, collisions that occur far from the absorber are more likely to produce muons from light meson decays than those that occur close to the absorber. Charm hadrons, however, due to their very short proper decay lengths, $e^{-Lm/\tau p} \ll 1$, will have minimal collision vertex dependence. The right panel of Fig. 1 shows the collision vertex distribution from events in which muons are detected at forward rapidity, corrected for the minimum bias collision vertex distribution. The large vertex dependence indicates a significant fraction of the muons are from pion and kaon decay. Using this distribution, we can separate the muons from pion and kaon decay from other contributions. The acceptance and efficiency vary by less than 5% over the z vertex range, which establishes an upper bound on the systematic error attributable to the subtraction of these nonsignal contributions. It should be noted that the measured muon p_T is approximately 15% lower on average than the parent hadron p_T, which is not corrected for in this analysis.

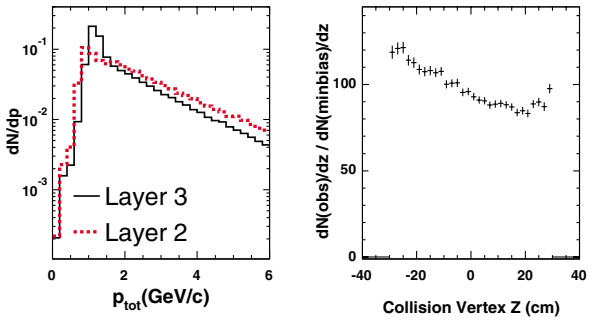

FIG. 1 (color online). Left: The total momentum p_{tot} measured in the MuTr without energy loss correction of all charged tracks penetrating to MuID layers 2 (gray) and 3 (black). Right: Collision vertex distribution for events with muons at forward rapidity, corrected for the minimum bias collision vertex distribution.

The data set for this analysis was collected under two different trigger conditions. We recorded 67×10^6 minimum bias triggers which required at least one hit in both the PHENIX forward $3.0 < \eta < 3.9$ and backward $-3.9 < \eta < -3.0$ BBC and a reconstructed vertex position within $|z| < 30$ cm along the beam axis. The minimum bias trigger accepts $88\% \pm 4\%$ of all inelastic d + Au collisions [13]. The second data set, sampling 5.3×10^9 minimum bias events, was collected with the MuID trigger which requires at least one track penetrating the first four layers of the MuID.

We divide these events into four centrality classes based on the number of particle hits in the backward BBC counter covering $-3.9 < \eta < -3.0$. Using a Glauber model [13] and simulation of the BBC, we determine the average number of binary collisions in each centrality class. The classes are categorized as follows: 60%–88% ($\langle N_{\mathrm{coll}} \rangle = 3.1 \pm 0.3$), 40%–60% ($\langle N_{\mathrm{coll}} \rangle = 7.0 \pm 0.6$), 20%–40% ($\langle N_{\mathrm{coll}} \rangle = 10.6 \pm 0.7$), and 0%–20% ($\langle N_{\mathrm{coll}} \rangle = 15.4 \pm 1.0$).

There is a correlation between having a particular physics process (for example, the production of a high p_T hadron) and the BBC response. The BBC coverage in pseudorapidity is well separated from the muon spectrometers so the correlation is not predominantly due to jet fragmentation, but rather an underlying event correlation. We have studied this effect in detail using proton-proton and d + Au data, as well as in simulations, and have accounted for this correlation bias. The bias correction factors we apply range from 0%–7% depending on the centrality category and the physics process. The systematic errors on these corrections are less than 4%.

The *nuclear modification factor* R_{cp} is defined as the ratio of the particle yield in central collisions to the particle yield in peripheral collisions, each normalized by the average number of nucleon-nucleon binary collisions ($\langle N_{\mathrm{coll}} \rangle$):

$$R_{cp} = \frac{\langle (\frac{dN}{d\eta dp_T})^{\mathrm{central}} \rangle / \langle N_{\mathrm{coll}}^{\mathrm{central}} \rangle}{\langle (\frac{dN}{d\eta dp_T})^{\mathrm{peripheral}} \rangle / \langle N_{\mathrm{coll}}^{\mathrm{peripheral}} \rangle}. \tag{2}$$

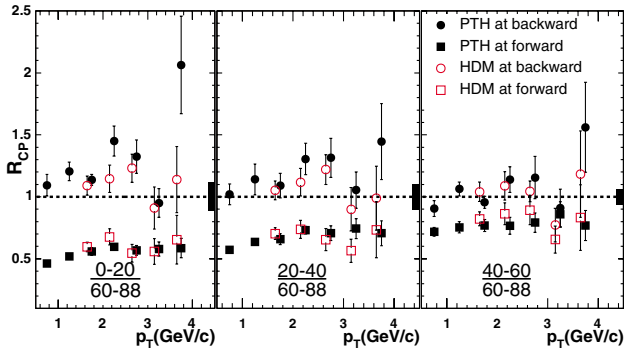

FIG. 2 (color online). R_{cp} as a function of p_T at forward rapidity (squares) and backward rapidity (circles) for different centrality classes.

The hadron R_{cp}, using the most peripheral centrality class (60%–88%) for normalization, is shown in Fig. 2 as a function of p_T at forward and backward rapidities. The results from the punch-through hadron and hadron decay muon techniques are both shown and are in quite good agreement. We also show the results integrated over $1.5 < p_T < 4.0$ GeV/c as a function of pseudorapidity in Fig. 3.

There are two types of systematic uncertainties in our analysis. Common systematic errors which move all data points up and down together include the error on $\frac{N_{\rm coll}^{\rm central}}{N_{\rm coll}^{\rm peripheral}}$ (10.8% for the most central bin), the centrality bias correction factors (4%), and the centrality-dependent tracking efficiency (4%) determined by embedding Monte Carlo particles in real data. Common systematic errors are shown as a black bar. Point-to-point systematic errors result from sensitivities to analysis cuts and are 5%–10%. They are added in quadrature with the statistical errors and shown as error bars.

It is notable that our two measurement methods have different sensitivity to different hadrons. The particle composition ($\pi/K/p$ ratio) of the observed sample is modified relative to the particle composition at the collision vertex due to species-dependent nuclear interaction cross sections affecting the punch-through hadrons and due to species-dependent decay lifetimes affecting the hadron decay muons. Both effects enhance the kaon contribution to our R_{cp} measurements. The uncertainty on our charged hadron R_{cp} values introduced by this effect is estimated to be less than 4% by calculating the difference between the kaon R_{cp} and inclusive charged particle R_{cp} determined by PHENIX at midrapidity [18].

We observe that R_{cp} shows a suppression at forward rapidity that is largest for the most central events. The opposite trend is observed at backward rapidity where R_{cp} shows an enhancement that is also largest for the most central events. We observe a weak p_T dependence with slightly smaller R_{cp} values at lower p_T. We observe a clear pseudorapidity dependence at forward rapidity with R_{cp} dropping further at larger η values. Within our current uncertainties we are unable to discern any pseudorapidity dependence at backward rapidity.

In Fig. 4 we compare results from the BRAHMS experiment [12] with our results at forward rapidity. The PHENIX data and the BRAHMS data are in agreement within systematic uncertainties.

The suppression of hadron yields relative to binary collision scaling at forward rapidity is expected from initial state nuclear effects. However, detailed comparisons with various theoretical approaches is necessary in order to discriminate between different models. In particular, the lack of a strong p_T dependence at both forward and backward rapidities must be understood as the physics processes transition from "soft" to "hard" physics scales.

To summarize, we observe a suppression in hadron yields relative to binary collision scaling at forward rapidities and an enhancement at backward rapidity for central relative to peripheral d + Au reactions at $\sqrt{s_{NN}} =$ 200 GeV. The forward rapidity suppression is in qualitative agreement with the expectation of shadowing and saturation effects in the small x region in the gold nucleus.

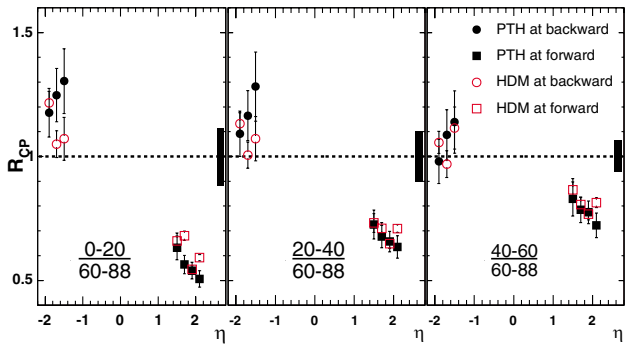

FIG. 3 (color online). R_{cp} as a function of η for $1.5 < p_T < 4.0$ GeV/c for different centrality classes.

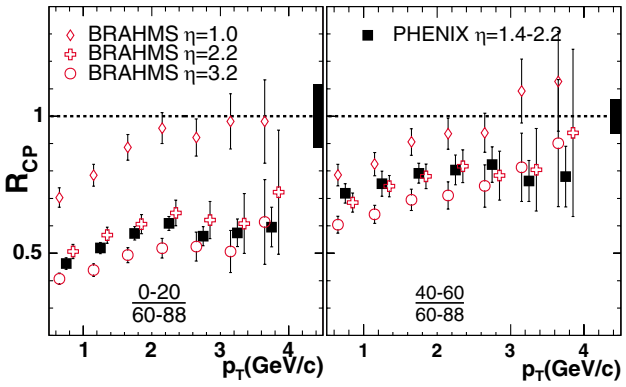

FIG. 4 (color online). PHENIX R_{cp} as a function of p_T at forward rapidities shown as the average of the two methods. Note that the BRAHMS results are for negative hadrons at $\eta =$ 2.2 and 3.2, and their centrality ranges (0%–20%/60%–80% and 30%–50%/60%–80%) are somewhat different from ours.

However, other physics effects must also be considered in understanding the full p_T and η dependence. The source of the backward rapidity enhancement, and the possible contribution of antishadowing of large x partons, has yet to be understood.

We thank the staff of the Collider-Accelerator and Physics Departments at BNL for their vital contributions. We acknowledge support from the Department of Energy and NSF (U.S.A.), MEXT and JSPS (Japan), CNPq and FAPESP (Brazil), NSFC (China), IN2P3/CNRS, CEA, and ARMINES (France), BMBF, DAAD, and AvH (Germany), OTKA (Hungary), DAE and DST (India), ISF (Israel), KRF and CHEP (Korea), RMIST, RAS, and RMAE (Russia), VR and KAW (Sweden), U.S. CRDF for the FSU, U.S.-Hungarian NSF-OTKA-MTA, and U.S.-Israel BSF.

*PHENIX Spokesperson.
Electronic address: zajc@nevis.columbia.edu

[1] J. D. Bjorken and E. A. Paschos, Phys. Rev. **185**, 1975 (1969).
[2] G. Altarelli and G. Parisi, Nucl. Phys. **B126**, 298 (1977); Y. L. Dokshitzer, Sov. Phys. JETP **46**, 641 (1977); V. N. Gribov and L. N. Lipatov, Sov. J. Nucl. Phys. **15**, 438 (1972).
[3] I. I. Balitsky and L. N. Lipatov, Sov. J. Nucl. Phys. **28**, 822 (1978); E. A. Kuraev, L. N. Lipatov, and V. S. Fadin, Sov. Phys. JETP **45**, 199 (1977); **44**, 443 (1976).
[4] H. Abramowicz and A. C. Caldwell, Rev. Mod. Phys. **71**, 1275 (1999).
[5] L. McLerran and R. Venugopalan, Phys. Rev. D **49**, 2233 (1994); **49**, 3352 (1994).
[6] J. Ashman *et al.*, Phys. Lett. B **202**, 603 (1988).
[7] V. Guzey, M. Strikman, and W. Vogelsang, hep-ph/0407201.
[8] A. Dumitru and J. Jalilian-Marian, Phys. Lett. B **547**, 15 (2002); F. Gelis and J. Jalilian-Marian, Phys. Rev. D **66**, 014021 (2002).
[9] D. Kharzeev, Y. V. Kovchegov, and K. Tuchin, Phys. Lett. B **599**, 23 (2004).
[10] K. Golec-Biernat and M. Wusthoff, Phys. Rev. D **59**, 014017 (1999); **60**, 114023 (1999).
[11] R. Hwa, C. B. Yang, and R. J. Fries, nucl-th/0410111.
[12] I. Arsene *et al.*, Phys. Rev. Lett. **93**, 242303 (2004).
[13] S. S. Adler *et al.*, Phys. Rev. Lett. **91**, 072303 (2003).
[14] D. Antreasyan *et al.*, Phys. Rev. D **19**, 764 (1979).
[15] M. Arneodo, Phys. Rep. **240**, 301 (1994).
[16] K. Adcox *et al.*, Nucl. Instrum. Methods Phys. Res., Sect. A **499**, 469 (2003), and references therein.
[17] S. H. Aronson *et al.*, Nucl. Instrum. Methods Phys. Res., Sect. A **499**, 480 (2003).
[18] F. Matathias *et al.*, J. Phys. G **30**, S1113 (2004).

Saturation of Azimuthal Anisotropy in Au + Au Collisions at $\sqrt{s_{NN}} = 62$–200 GeV

S. S. Adler,[5] S. Afanasiev,[20] C. Aidala,[5,10] N. N. Ajitanand,[48] Y. Akiba,[23,42,43] A. Al-Jamel,[37] J. Alexander,[48] R. Amirikas,[14] K. Aoki,[27,42] L. Aphecetche,[50] R. Armendariz,[37] S. H. Aronson,[5] R. Averbeck,[49] T. C. Awes,[38] B. Azmoun,[5] R. Azmoun,[49] V. Babintsev,[17] A. Baldisseri,[11] K. N. Barish,[6] P. D. Barnes,[30] B. Bassalleck,[36] S. Bathe,[6,33] S. Batsouli,[10] V. Baublis,[41] F. Bauer,[6] A. Bazilevsky,[5,17,43] S. Belikov,[5,17,19] R. Bennett,[49] Y. Berdnikov,[45] S. Bhagavatula,[19] M. T. Bjorndal,[10] J. G. Boissevain,[30] H. Borel,[11] S. Borenstein,[28] K. Boyle,[49] M. L. Brooks,[30] D. S. Brown,[37] N. Bruner,[36] D. Bucher,[33] H. Buesching,[5,33] V. Bumazhnov,[17] G. Bunce,[5,43] J. M. Burward-Hoy,[29,30,49] S. Butsyk,[49] X. Camard,[50] S. Campbell,[49] J.-S. Chai,[21] P. Chand,[4] W. C. Chang,[2] S. Chernichenko,[17] C. Y. Chi,[10] J. Chiba,[23] M. Chiu,[10] I. J. Choi,[57] J. Choi,[22] R. K. Choudhury,[4] T. Chujo,[5,54] V. Cianciolo,[38] C. R. Cleven,[15] Y. Cobigo,[11] B. A. Cole,[10] M. P. Comets,[39] P. Constantin,[19] M. Csanád,[13] T. Csörgő,[24] D. d'Enterria,[10,50] T. Dahms,[49] K. Das,[14] G. David,[5] H. Delagrange,[50] A. Denisov,[17] A. Deshpande,[43,49] E. J. Desmond,[5] A. Devismes,[49] O. Dietzsch,[46] A. Dion,[49] J. L. Drachenberg,[1] O. Drapier,[28] A. Drees,[49] K. A. Drees,[5] A. K. Dubey,[56] R. du Rietz,[32] A. Durum,[17] D. Dutta,[4] V. Dzhordzhadze,[51] Y. V. Efremenko,[38] J. Egdemir,[49] K. El Chenawi,[54] A. Enokizono,[16] H. En'yo,[42,43] B. Espagnon,[39] S. Esumi,[53] L. Ewell,[5] D. E. Fields,[36,43] F. Fleuret,[28] S. L. Fokin,[26] B. Forestier,[31] B. D. Fox,[43] Z. Fraenkel,[56] J. E. Frantz,[10] A. Franz,[5] A. D. Frawley,[14] Y. Fukao,[27,42] S.-Y. Fung,[6] S. Gadrat,[31] S. Garpman,[32,*] F. Gastineau,[50] M. Germain,[50] T. K. Ghosh,[54] A. Glenn,[51] G. Gogiberidze,[51] M. Gonin,[28] J. Gosset,[11] Y. Goto,[42,43] R. Granier de Cassagnac,[28] N. Grau,[19] S. V. Greene,[54] M. Grosse Perdekamp,[18,43] T. Gunji,[8] W. Guryn,[5] H.-Å. Gustafsson,[32] T. Hachiya,[16,42] A. Hadj Henni,[50] J. S. Haggerty,[5] M. N. Hagiwara,[1] H. Hamagaki,[8] A. G. Hansen,[30] H. Harada,[16] E. P. Hartouni,[29] K. Haruna,[16] M. Harvey,[5] E. Haslum,[32] K. Hasuko,[42] R. Hayano,[8] N. Hayashi,[42] X. He,[15] M. Heffner,[29] T. K. Hemmick,[49] J. M. Heuser,[42,49] M. Hibino,[55] H. Hiejima,[18] J. C. Hill,[19] R. Hobbs,[36] M. Holmes,[54] W. Holzmann,[48] K. Homma,[16] B. Hong,[25] A. Hoover,[37] T. Horaguchi,[42,52] H. M. Hur,[21] T. Ichihara,[42,43] V. V. Ikonnikov,[26] K. Imai,[27,42] M. Inaba,[53] D. Isenhower,[1] L. Isenhower,[1] M. Ishihara,[42] T. Isobe,[8] M. Issah,[48] A. Isupov,[20] B. V. Jacak,[49] W. Y. Jang,[25] Y. Jeong,[22] J. Jia,[10,49] J. Jin,[10] O. Jinnouchi,[42,43] B. M. Johnson,[5] S. C. Johnson,[29] K. S. Joo,[34] D. Jouan,[39] F. Kajihara,[8,42] S. Kametani,[8,55] N. Kamihara,[42,52] M. Kaneta,[43] J. H. Kang,[57] S. S. Kapoor,[4] K. Katou,[55] T. Kawagishi,[53] A. V. Kazantsev,[26] S. Kelly,[9,10] B. Khachaturov,[56] A. Khanzadeev,[41] J. Kikuchi,[55] D. H. Kim,[34] D. J. Kim,[57] D. W. Kim,[22] E. Kim,[47] G.-B. Kim,[28] H. J. Kim,[57] Y.-S. Kim,[21] E. Kinney,[9] W. W. Kinnison,[30] A. Kiss,[13] E. Kistenev,[5] A. Kiyomichi,[42,53] K. Kiyoyama,[35] C. Klein-Boesing,[33] H. Kobayashi,[42,43] L. Kochenda,[41] V. Kochetkov,[17] D. Koehler,[36] T. Kohama,[16] B. Komkov,[41] M. Konno,[53] M. Kopytine,[49] D. Kotchetkov,[6] A. Kozlov,[56] P. J. Kroon,[5] C. H. Kuberg,[1,30] G. J. Kunde,[30] N. Kurihara,[8] K. Kurita,[42,43,44] Y. Kuroki,[53] M. J. Kweon,[25] Y. Kwon,[57] G. S. Kyle,[37] R. Lacey,[48] V. Ladygin,[20] J. G. Lajoie,[19] Y. Le Bornec,[39] A. Lebedev,[19,26] S. Leckey,[49] D. M. Lee,[30] M. K. Lee,[57] S. Lee,[22] M. J. Leitch,[30] M. A. L. Leite,[46] X. H. Li,[6] H. Lim,[47] A. Litvinenko,[20] M. X. Liu,[30] Y. Liu,[39] C. F. Maguire,[54] Y. I. Makdisi,[5] A. Malakhov,[20] M. D. Malik,[36] V. I. Manko,[26] Y. Mao,[7,42] G. Martinez,[50] M. D. Marx,[49] H. Masui,[53] F. Matathias,[49] T. Matsumoto,[8,55] M. C. McCain,[18] P. L. McGaughey,[30] E. Melnikov,[17] F. Messer,[49] Y. Miake,[53] J. Milan,[48] T. E. Miller,[54] A. Milov,[49,56] S. Mioduszewski,[5] R. E. Mischke,[30] G. C. Mishra,[15] J. T. Mitchell,[5] A. K. Mohanty,[4] D. P. Morrison,[5] J. M. Moss,[30] T. V. Moukhanova,[26] F. Mühlbacher,[49] D. Mukhopadhyay,[54,56] M. Muniruzzaman,[6] J. Murata,[42,43,44] S. Nagamiya,[23] Y. Nagata,[53] J. L. Nagle,[9,10] M. Naglis,[56] T. Nakamura,[16] B. K. Nandi,[6] M. Nara,[53] J. Newby,[29,51] M. Nguyen,[49] P. Nilsson,[32] B. Norman,[30] A. S. Nyanin,[26] J. Nystrand,[32] E. O'Brien,[5] C. A. Ogilvie,[19] H. Ohnishi,[5,42] I. D. Ojha,[3,54] H. Okada,[27,42] K. Okada,[42,43] O. O. Omiwade,[1] M. Ono,[53] V. Onuchin,[17] A. Oskarsson,[32] I. Otterlund,[32] K. Oyama,[8] K. Ozawa,[8] D. Pal,[54,56] A. P. T. Palounek,[30] V. Pantuev,[49] V. Papavassiliou,[37] J. Park,[47] W. J. Park,[25] A. Parmar,[36] S. F. Pate,[37] H. Pei,[19] T. Peitzmann,[33] J.-C. Peng,[18,30] H. Pereira,[11] V. Peresedov,[20] D. Yu. Peressounko,[26] C. Pinkenburg,[5] R. P. Pisani,[5] F. Plasil,[38] M. L. Purschke,[5] A. K. Purwar,[49] H. Qu,[15] J. Rak,[19] I. Ravinovich,[56] K. F. Read,[38,51] M. Reuter,[49] K. Reygers,[33] V. Riabov,[41,45] Y. Riabov,[41] G. Roche,[31] A. Romana,[28] M. Rosati,[19] S. S. E. Rosendahl,[32] P. Rosnet,[31] P. Rukoyatkin,[20] V. L. Rykov,[42] S. S. Ryu,[57] M. E. Sadler,[1] B. Sahlmueller,[33] N. Saito,[27,42,43] T. Sakaguchi,[8,55] M. Sakai,[35] S. Sakai,[53] V. Samsonov,[41] L. Sanfratello,[36] R. Santo,[33] H. D. Sato,[27,42] S. Sato,[5,23,53] S. Sawada,[23] Y. Schutz,[50] V. Semenov,[17] R. Seto,[6] D. Sharma,[56] M. R. Shaw,[1,30] T. K. Shea,[5] I. Shein,[17] T.-A. Shibata,[42,52] K. Shigaki,[16,23] T. Shiina,[30] M. Shimomura,[53] T. Shohjoh,[53] K. Shoji,[27,42] A. Sickles,[49] C. L. Silva,[46] D. Silvermyr,[30,32,38] K. S. Sim,[25] J. Simon-Gillo,[30] C. P. Singh,[3] V. Singh,[3] M. Sivertz,[5] S. Skutnik,[19] W. C. Smith,[1] A. Soldatov,[17] R. A. Soltz,[29] W. E. Sondheim,[30] S. P. Sorensen,[51] I. V. Sourikova,[5] F. Staley,[11] P. W. Stankus,[38] E. Stenlund,[32] M. Stepanov,[37] A. Ster,[24] S. P. Stoll,[5] T. Sugitate,[16] C. Suire,[39] J. P. Sullivan,[30] J. Sziklai,[24] T. Tabaru,[43] S. Takagi,[53] E. M. Takagui,[46]

 © 2005 The American Physical Society

A. Taketani,[42,43] M. Tamai,[55] K. H. Tanaka,[23] Y. Tanaka,[35] K. Tanida,[42,43] M. J. Tannenbaum,[5] A. Taranenko,[48] P. Tarján,[12] J. D. Tepe,[1,30] T. L. Thomas,[36] M. Togawa,[27,42] J. Tojo,[27,42] H. Torii,[27,42] R. S. Towell,[1] V.-N. Tram,[28] I. Tserruya,[56] Y. Tsuchimoto,[16,42] H. Tsuruoka,[53] S. K. Tuli,[3] H. Tydesjö,[32] N. Tyurin,[17] H. Valle,[54] H. W. van Hecke,[30] J. Velkovska,[5,49,54] M. Velkovsky,[49] R. Vertesi,[12] V. Veszprémi,[12] L. Villatte,[51] A. A. Vinogradov,[26] M. A. Volkov,[26] E. Vznuzdaev,[41] M. Wagner,[27] X. R. Wang,[15,37] Y. Watanabe,[42,43] J. Wessels,[33] S. N. White,[5] N. Willis,[39] D. Winter,[10] F. K. Wohn,[19] C. L. Woody,[5] M. Wysocki,[9] W. Xie,[6,43] Y. Yang,[7] A. Yanovich,[17] S. Yokkaichi,[42,43] G. R. Young,[38] I. Younus,[36] I. E. Yushmanov,[26] W. A. Zajc,[10,†] O. Zaudkte,[33] C. Zhang,[10] S. Zhou,[7] S. J. Zhou,[56] J. Zimányi,[24] and L. Zolin[20]

(PHENIX Collaboration)

[1]*Abilene Christian University, Abilene, Texas 79699, USA*
[2]*Institute of Physics, Academia Sinica, Taipei 11529, Taiwan*
[3]*Department of Physics, Banaras Hindu University, Varanasi 221005, India*
[4]*Bhabha Atomic Research Centre, Bombay 400 085, India*
[5]*Brookhaven National Laboratory, Upton, New York 11973-5000, USA*
[6]*University of California - Riverside, Riverside, California 92521, USA*
[7]*China Institute of Atomic Energy (CIAE), Beijing, People's Republic of China*
[8]*Center for Nuclear Study, Graduate School of Science, University of Tokyo, 7-3-1 Hongo, Bunkyo, Tokyo 113-0033, Japan*
[9]*University of Colorado, Boulder, Colorado 80309, USA*
[10]*Columbia University, New York, New York 10027, USA*
and Nevis Laboratories, Irvington, New York 10533, USA
[11]*Dapnia, CEA Saclay, F-91191, Gif-sur-Yvette, France*
[12]*Debrecen University, H-4010 Debrecen, Egyetem tér 1, Hungary*
[13]*ELTE, Eötvös Loránd University, H - 1117 Budapest, Pázmány P. s. 1/A, Hungary*
[14]*Florida State University, Tallahassee, Florida 32306, USA*
[15]*Georgia State University, Atlanta, Georgia 30303, USA*
[16]*Hiroshima University, Kagamiyama, Higashi-Hiroshima 739-8526, Japan*
[17]*Institute for High Energy Physics (IHEP), Protvino, Russia*
[18]*University of Illinois at Urbana-Champaign, Urbana, Illinois 61801, USA*
[19]*Iowa State University, Ames, Iowa 50011, USA*
[20]*Joint Institute for Nuclear Research, 141980 Dubna, Moscow Region, Russia*
[21]*KAERI, Cyclotron Application Laboratory, Seoul, South Korea*
[22]*Kangnung National University, Kangnung 210-702, Korea*
[23]*KEK, High Energy Accelerator Research Organization, Tsukuba-shi, Ibaraki-ken 305-0801, Japan*
[24]*KFKI Research Institute for Particle and Nuclear Physics (RMKI), H-1525 Budapest 114, P.O. Box 49, Hungary*
[25]*Korea University, Seoul, 136-701, Korea*
[26]*Russian Research Center "Kurchatov Institute", Moscow, Russia*
[27]*Kyoto University, Kyoto 606-8502, Japan*
[28]*Laboratoire Leprince-Ringuet, Ecole Polytechnique, CNRS-IN2P3, Route de Saclay, F-91128, Palaiseau, France*
[29]*Lawrence Livermore National Laboratory, Livermore, California 94550, USA*
[30]*Los Alamos National Laboratory, Los Alamos, New Mexico 87545, USA*
[31]*LPC, Université Blaise Pascal, CNRS-IN2P3, Clermont-Fd, 63177 Aubiere Cedex, France*
[32]*Department of Physics, Lund University, Box 118, SE-221 00 Lund, Sweden*
[33]*Institut für Kernphysik, University of Muenster, D-48149 Muenster, Germany*
[34]*Myongji University, Yongin, Kyonggido 449-728, Korea*
[35]*Nagasaki Institute of Applied Science, Nagasaki-shi, Nagasaki 851-0193, Japan*
[36]*University of New Mexico, Albuquerque, New Mexico 87131, USA*
[37]*New Mexico State University, Las Cruces, New Mexico 88003, USA*
[38]*Oak Ridge National Laboratory, Oak Ridge, Tennessee 37831, USA*
[39]*IPN-Orsay, Universite Paris Sud, CNRS-IN2P3, BP1, F-91406, Orsay, France*
[40]*Peking University, Beijing, People's Republic of China*
[41]*PNPI, Petersburg Nuclear Physics Institute, Gatchina, Russia*
[42]*RIKEN (The Institute of Physical and Chemical Research), Wako, Saitama 351-0198, Japan*
[43]*RIKEN BNL Research Center, Brookhaven National Laboratory, Upton, New York 11973-5000, USA*
[44]*Physics Department, Rikkyo University, 3-34-1 Nishi-Ikebukuro, Toshima, Tokyo 171-8501, Japan*
[45]*St. Petersburg State Technical University, St. Petersburg, Russia*
[46]*Instituto de Física, Universidade de São Paulo, Caixa Postal 66318, São Paulo CEP05315-970, Brazil*
[47]*System Electronics Laboratory, Seoul National University, Seoul, Korea*

[48]Chemistry Department, Stony Brook University, Stony Brook, SUNY, New York 11794-3400, USA
[49]Department of Physics and Astronomy, Stony Brook University, SUNY, Stony Brook, New York 11794, USA
[50]SUBATECH (Ecole des Mines de Nantes, CNRS-IN2P3, Université de Nantes) BP 20722 - 44307, Nantes, France
[51]University of Tennessee, Knoxville, Tennessee 37996, USA
[52]Department of Physics, Tokyo Institute of Technology, Tokyo, 152-8551, Japan
[53]Institute of Physics, University of Tsukuba, Tsukuba, Ibaraki 305, Japan
[54]Vanderbilt University, Nashville, Tennessee 37235, USA
[55]Waseda University, Advanced Research Institute for Science and Engineering, 17 Kikui-cho, Shinjuku-ku, Tokyo 162-0044, Japan
[56]Weizmann Institute, Rehovot 76100, Israel
[57]Yonsei University, IPAP, Seoul 120-749, Korea
(Received 19 November 2004; published 17 June 2005)

New measurements are presented for charged hadron azimuthal correlations at midrapidity in Au + Au collisions at $\sqrt{s_{NN}} = 62.4$ and 200 GeV. They are compared to earlier measurements obtained at $\sqrt{s_{NN}} =$ 130 GeV and in Pb + Pb collisions at $\sqrt{s_{NN}} = 17.2$ GeV. Sizeable anisotropies are observed with centrality and transverse momentum (p_T) dependence characteristic of elliptic flow (v_2). For a broad range of centralities, the observed magnitudes and trends of the differential anisotropy, $v_2(p_T)$, change very little over the collision energy range $\sqrt{s_{NN}} = 62$–200 GeV, indicating saturation of the excitation function for v_2 at these energies. Such a saturation may be indicative of the dominance of a very soft equation of state for $\sqrt{s_{NN}} \sim 60$–200 GeV.

DOI: 10.1103/PhysRevLett.94.232302 PACS numbers: 25.75.Ld

Extremely high energy-density nuclear matter is produced in energetic Au + Au collisions at the relativistic heavy ion collider (RHIC) [1,2]. The dynamical evolution of this matter is predicted to reflect the presence and evolution of the quark gluon plasma (QGP)—a new phase of nuclear matter [3–5]. Azimuthal correlation measurements are important in several ways. They serve as a ''barometric sensor'' for pressure gradients developed in the collision and hence yield insight into crucial issues of thermalization and the equation of state (EOS) [6–8]. They provide important constraints for the density of the medium and the effective energy loss of partons which traverse it [9]. They can provide valuable information on the gluon saturation scale in the nucleus [10].

Recent measurements at RHIC ($\sqrt{s_{NN}} = 130$ and 200 GeV) indicate a mixture of (di-)jet and harmonic contributions to azimuthal correlations in Au + Au collisions [11–14]. The asymmetric (di-)jet contributions are found to be relatively small but can be separated; they show an increase with p_T and indicate strong suppression of away-side jet yields [13]. Significant modifications to the away-side jet topology have also been reported [15]. These observations, which are particularly striking for very central collisions, have been interpreted as evidence for parton energy loss and jet quenching in the produced medium [3]. The harmonic contributions show significant strength at midrapidity with characteristic dependencies on p_T and centrality [11,16–18]. They are typically characterized by the second order Fourier coefficient, $v_2 = \langle e^{i2(\phi_1 - \Phi_{\mathrm{RP}})} \rangle$, where ϕ_1 represents the azimuthal emission angle of a charged hadron and ϕ_{RP} is the azimuth of the reaction plane. The brackets denote statistical averaging over particles and events. At low p_T ($p_T \lesssim 2.0$ GeV/c) the magnitude and trends of v_2 are under-predicted by hadronic cascade models supplemented with string dynamics [19], but are well reproduced by models which incorporate hydrodynamic flow [5,7]. This has been interpreted as evidence for the production of a thermalized state of partonic matter [3–5]. At higher p_T the predictions of quark coalescence [20] are consistent with the data [18,21], and quantitative agreement has been achieved with transport model calculations which incorporate large opacities [22].

At Super Proton Synchrotron (SPS) energies ($\sqrt{s_{NN}} \sim$ 17 GeV) azimuthal correlation measurements also indicate a mixture of (di-)jet and harmonic contributions [23,24]. However, the observed anisotropy of the harmonic contribution is approximately 50% of the value observed at full RHIC energy ($\sqrt{s_{NN}} = 200$ GeV). Therefore, an important outstanding issue is the detailed behavior of v_2 over the range which spans SPS-RHIC energies. In recent work, the PHOBOS Collaboration has investigated the patterns for p_T-integrated v_2 over a broad range of pseudorapidities [25]. We present more revealing differential measurements for Au + Au collisions at $\sqrt{s_{NN}} = 62.4$–200 GeV and the first excitation function for differential v_2 which spans beam energies from the Alternating Gradient Synchrotron (AGS) to RHIC ($\sqrt{s_{NN}} \sim$ 3–200 GeV).

The colliding Au beams ($\sqrt{s_{NN}} = 62.4$, 130, and 200 GeV) used in the measurements presented here have been provided by RHIC in three separate experimental running periods (years 2004, 2000, and 2001, respectively). Charged tracks were detected in the two central arms ($|\eta| \leq 0.35$) of PHENIX [26]. Track reconstruction was accomplished at each collision energy via pattern recognition using a drift chamber (DC) followed by two layers of multiwire proportional chambers with pad readout (PC1 and PC3) located at radii of 2, 2.5, and 5 m, respectively [26]. For each analysis, the collision vertex z

along the beam direction was constrained to be within $|z| < 30$ cm. A confirmation hit within a 2σ matching window was required in PC3 to eliminate most albedo, conversions, and decays. Particle momenta were measured with resolutions $\delta p/p = 0.7\% \oplus 0.91\% p$, $\delta p/p = 0.6\% \oplus 3.6\% p$, and $\delta p/p = 0.7\% \oplus 1.0\% p(\mathrm{GeV}/c)$ at $\sqrt{s_{NN}} = 62.4$, 130, and 200 GeV, respectively.

Event centralities were obtained at $\sqrt{s_{NN}} = 62.4$ GeV via a series of cuts on the analog response of the PHENIX beam counters (BBC). For $\sqrt{s_{NN}} = 130$ and 200 GeV, cuts in the space of BBC versus zero-degree calorimeter analog response were employed; they reflect percentile cuts on the total interaction cross section at each beam energy [27]. Estimates for the number of participant nucleons N_{part} were also made for each of these cuts following the Glauber-based model detailed in Ref. [27]. Systematic uncertainties associated with these determinations are estimated to be less than $\sim 10\%$ for central and midcentral collisions.

The differential v_2 measurements reported in this Letter have been obtained via three separate methods of analysis:

First, we used the reaction plane technique which correlates the azimuthal angles of charged tracks detected in the central arms with the azimuth of an estimated event plane Φ_2, determined via hits in the north and south BBC's located at $|\eta| \sim 3$–3.9 [18]. This method was used for the analysis of data taken at both $\sqrt{s_{NN}} = 62.4$ and 200 GeV. Corrections [18,28] were applied to account for possible azimuthal distortions in the distribution of the estimated reaction planes. Values of v_2 were calculated via the expression

$$v_2 = \frac{\langle \cos(2(\phi - \Phi_2)) \rangle}{\langle \cos(2(\Phi_2 - \Phi_{RP})) \rangle}, \quad (1)$$

where the denominator represents a resolution factor which corrects for the difference between the estimated and the true azimuth of the reaction plane Φ_{RP} [18,28]. The estimated resolution of the combined reaction plane from both BBC's [18] has an average of 0.33(0.16) over centrality with a maximum of about 0.42(0.19) for $\sqrt{s_{NN}} =$ 200(62.4) GeV. Thus, the estimated correction factor, which is the inverse of the resolution for the combined reaction plane, ranges from 2.4(5.4) to 5.0(13).

Second, we performed a cumulant analysis on data collected at $\sqrt{s_{NN}} = 200$ and 62.4 GeV to obtain the anisotropy directly [29]

$$\langle e^{2i(\phi_1 - \phi_2)} \rangle = \langle e^{2i\phi_1} \rangle \langle e^{-i2\phi_2} \rangle + \langle\langle e^{2i(\phi_1 - \phi_2)} \rangle\rangle, \quad (2)$$

where the double brackets denote an average over pairs of particles emitted in an event followed by further averaging over events. For a detector having full azimuthal acceptance, the averages $\langle e^{2i\phi_1} \rangle$ and $\langle e^{-2i\phi_2} \rangle$ vanish due to symmetry considerations to give the second order cumulant estimate $v_2\{2\}$ [29] of v_2

$$\langle\langle e^{2i(\phi_1 - \phi_2)} \rangle\rangle = v_2\{2\}^2. \quad (3)$$

Since PHENIX does not have full azimuthal acceptance, $\langle e^{2i\phi_1} \rangle$ and $\langle e^{-2i\phi_2} \rangle$ do not vanish and this leads to an initial underestimate of the extracted anisotropy. To correct for this underestimate, separate correction factors ($\sim 30\%$) were evaluated and applied for each centrality and p_T cut, at each collision energy, following the procedures detailed in Ref. [29].

Third, we extracted the anisotropy at $\sqrt{s_{NN}} = 62.4$, 130, and 200 GeV via assorted two-particle correlation functions [11,18]: $C(\Delta\phi) = N_{\mathrm{cor}}(\Delta\phi)/N_{\mathrm{mix}}(\Delta\phi)$, where $N_{\mathrm{cor}}(\Delta\phi)$ is the observed $\Delta\phi$ distribution for charged particle pairs selected from the same event, and $N_{\mathrm{mix}}(\Delta\phi)$ is the $\Delta\phi$ distribution for particle pairs selected from mixed events. Mixed events were obtained by randomly selecting each member of a particle pair from different events with the same multiplicity and vertex cuts.

To extract the anisotropy of these correlations, two correlation functions were generated for each p_T and centrality selection [11,18]. For the first, charged hadron pairs were formed by selecting both particles from a reference range $p_{T,\mathrm{ref}}$, which excluded the p_T range of interest (i.e., a reference correlation). For the second, assorted hadron pairs were formed by selecting one member from the p_T range of interest and the other from $p_{T,\mathrm{ref}}$. The elliptic flow v_2 was obtained via the ratio $A_{2,a}/\sqrt{A_{2,\mathrm{ref}}} = v_2$, where $A_{2,a}$ and $A_{2,\mathrm{ref}}$ are the anisotropies extracted from the assorted and reference correlation functions (respectively) with the fit function:

$$C(\Delta\phi) = a_1[1 + 2A_2 \cos(2\Delta\phi) + \lambda e^{[-0.5(\Delta\phi/\sigma)^2]}], \quad (4)$$

where the Gaussian and harmonic terms are used to characterize the asymmetry (at small $\Delta\phi$) and the anisotropy of the correlation function, respectively [11,13].

Figure 1 shows representative $\Delta\phi$ correlation functions obtained for charged hadrons detected in the PHENIX central arms ($-0.35 < \eta < 0.35$) at $\sqrt{s_{NN}} = 62.4$ GeV. Correlation functions for midcentral events (centrality = 20%–40%) are shown for hadrons with $0.5 < p_T < 0.7$ GeV/c and $1.0 < p_T < 1.5$ GeV/c in Fig. 1(a) and Fig. 1(c), respectively. The same p_T cuts have been made for the correlation functions shown in Figs. 1(b) and 1(d) but for more peripheral collisions (centrality = 40%–60%). For both sets of correlation functions $0.65 < p_{T,\mathrm{ref}} < 2.5$ GeV/c. Figures 1(a)–1(d) show a clear anisotropic pattern with relatively small asymmetries (0°/180° ratios). Such asymmetries have been attributed to small jet contributions to the correlation functions [11,13], and are expected to decrease with decreasing $\sqrt{s_{NN}}$. The curves in Fig. 1 indicate a fit to the correlation function with Eq. (4); they show an increase of the anisotropy with increasing impact parameter and p_T. These trends are similar to those of prior AGS, SPS, and RHIC measurements [16,23,24,30] and are consistent with the expected patterns for in-plane elliptic flow [5,7].

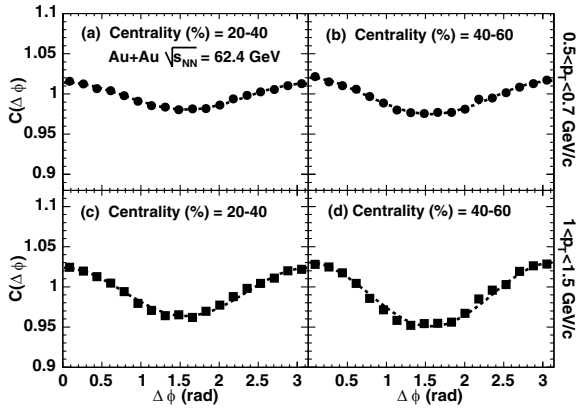

FIG. 1. Assorted-p_T correlation functions ($0.65 < p_{T,\mathrm{ref}} < 2.5$ GeV/c) for charged hadrons of $0.5 < p_T < 0.7$ GeV/c (top panels) and $1.0 < p_T < 1.5$ GeV/c (bottom panels) obtained in Au + Au collisions at $\sqrt{s_{NN}} = 62.4$ GeV. The left and right panels show correlation functions for centrality cuts of 20%–40% and 40%–60%, respectively. The lines represent fits to the correlation functions (see text).

Figure 2 compares the differential anisotropy $v_2(p_T)$, obtained at $\sqrt{s_{NN}} = 62.4$ GeV for all three methods of extraction. The error bars shown indicate statistical errors. Systematic errors are estimated to be ~10%, 5%, and 5% for extractions via the reaction plane, cumulant, and correlation function methods of analysis, respectively. The results, which are shown for two separate centrality cuts (0%–20% and 20%–40%) in each case, indicate an initial increase of v_2 with p_T followed by the previously observed plateau for $p_T \gtrsim 2.5$ GeV/c [11,17]. The close agreement of $v_2(p_T)$ values obtained from the cumulant and correlation function methods of analysis serve to confirm the reliability of these methods of extraction. On the other hand, the agreement between results from these latter methods and that obtained from the reaction plane method is quite striking, given the large rapidity gap (~3 units) between the particles used for reaction plane determination and the midrapidity particles correlated with this plane. It is expected that the latter correlations are less influenced by nonflow contributions, especially for $p_T < 2.0$ GeV/c. Consequently, we attribute this agreement to the absence of strong nonflow contributions to the hadron correlations (for $p_T < 2.0$ GeV/c) at midrapidity. A similarly good agreement between the different methods of analysis was obtained for all centralities presented in this work.

Figure 3 compares the centrality and p_T dependence (respectively) of the anisotropy obtained at several collision energies. The circles, stars, and squares in Fig. 3(a) show $v_2(N_{\mathrm{part}})$ for $\langle p_T \rangle$ selections of 0.4, 0.75, and 1.35 GeV/c obtained via the cumulant and correlation function methods of analysis. The same results obtained via the reaction plane method are consistent with prior results [18]. The open and filled symbols show measurements performed at $\sqrt{s_{NN}} = 62.4$ and 130 (200) GeV as indicated; they show rather striking agreement between the magnitudes of the v_2 values obtained at all three collision energies. Further evidence that this agreement persists down to $\sqrt{s_{NN}} = 62.4$ GeV is given in Fig. 3(b). The open and filled circles compare the differential anisotropy $v_2(p_T)$, obtained at $\sqrt{s_{NN}} = 62.4$ and 200 GeV for the 13%–26% most central collisions ($\langle N_{\mathrm{part}} \rangle = 200$). The comparison indicates that $v_2(p_T)$ saturates above 2 GeV/c independent of beam energy. Such a saturation is compatible with surface emission from a relatively opaque source [22]. More importantly, very little change in v_2 is observed as the collision energy is raised from $\sqrt{s_{NN}} = 62.4$ to 200 GeV. The latter contrasts with the much lower v_2 values measured in Pb + Pb collisions (filled squares) by the CERES Collaboration at $\sqrt{s_{NN}} = 17.2$ GeV for the same centrality cut (13%–26%) [23].

Figure 4 summarizes the $\sqrt{s_{NN}}$ dependence of v_2 for charged hadrons produced in Au + Au collisions for two separate p_T selections (0.65 and 1.75 GeV/c) and

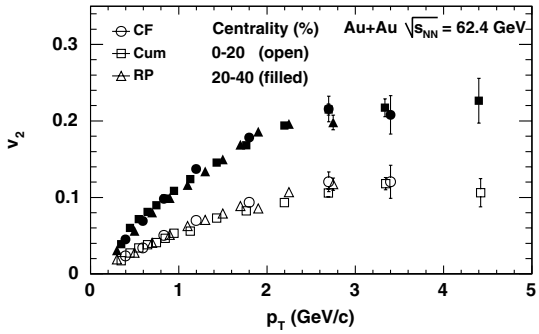

FIG. 2. Differential anisotropy $v_2(p_T)$ for charged hadrons in Au + Au collisions at $\sqrt{s_{NN}} = 62.4$ GeV with centrality cuts of 0%–20% (open symbols) and 20%–40% (filled symbols), obtained via the methods of correlation functions (CF), cumulants (Cum), and reaction plane (RP).

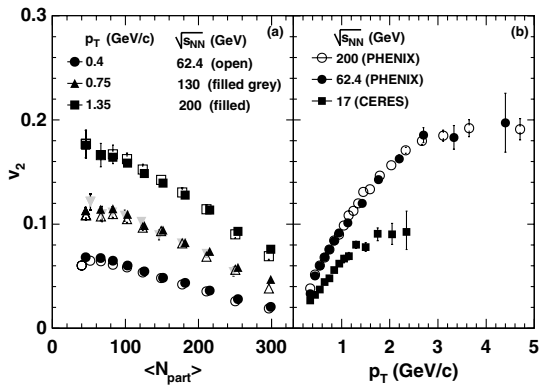

FIG. 3. Differential anisotropy $v_2(N_{\mathrm{part}})$ (left) and $v_2(p_T)$ (right) for several energies as indicated. $v_2(p_T)$ is shown for the centrality selection 13%–26% ($\langle N_{\mathrm{part}} \rangle = 200$) which facilitates a comparison with CERES data (filled squares) from Ref. [23].

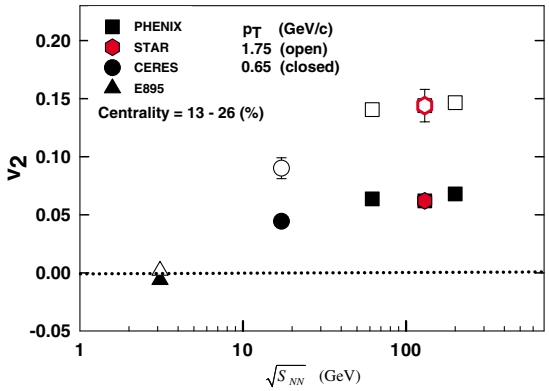

FIG. 4 (color online). Differential v_2 vs $\sqrt{s_{NN}}$ for charged hadrons in nucleus-nucleus collisions. Results are shown for the centrality cut of 13%–26% and p_T selections of 1.75 GeV/c (open symbols) and 0.65 GeV/c (closed symbols). The STAR, CERES, and E895 data are taken from Refs. [17,23,30–32], respectively.

centrality = 13%–26%. These data are taken from the current measurements and earlier measurements at the SPS [23] and the AGS [30–32]. The AGS [E895] measurements [30–32] are for protons but the transition energy is not very different for pions and protons. The STAR results were obtained for a slightly different centrality selection (10%–30%) [17] having essentially the same mean centrality. For both p_T cuts, the magnitude of v_2 shows a significant increase with collision energy (~50% increase from SPS to RHIC) up to the energy $\sqrt{s_{NN}} = 62.4$ GeV. Thereafter, it appears to saturate for larger beam energies. We note that this saturation is not in conflict with the recent observation of an increase of the p_T-integrated v_2 with $\sqrt{s_{NN}}$ [25]. The latter increase is expected if the $\langle p_T \rangle$ increases with $\sqrt{s_{NN}}$.

To summarize, we have measured differential azimuthal anisotropies for charged hadrons in Au + Au collisions spanning the energy range $\sqrt{s_{NN}} = 62.4$–200 GeV. Detailed comparisons of these differential measurements indicate no significant collision energy dependence of the anisotropy over this range. By contrast, comparisons to differential measurements obtained at AGS and SPS energies indicate that v_2 increases with collision energy up to $\sqrt{s_{NN}} = 62.4$ GeV. The energy density is estimated to increase by approximately 30% over the range $\sqrt{s_{NN}} = 62.4$–200 GeV. In a hydrodynamic scenario v_2 is driven by a pressure gradient which is related to the energy density via the equation of state [5,7]. Thus, the apparent saturation of v_2 above $\sqrt{s_{NN}} = 62.4$ GeV may be indicative of the role of a rather soft equation of state. Such a softening could result from the production of a mixed phase [31] for the range $\sqrt{s_{NN}} = 62.4$–200 GeV. Additional combined measurements of v_2, particle spectra, and the space-time extent of emission sources are required to further constrain the EOS.

We thank the staff of the Collider-Accelerator and Physics Departments at BNL for their vital contributions. We acknowledge support from the Department of Energy and NSF (USA), MEXT and JSPS (Japan), CNPq and FAPESP (Brazil), NSFC (China), IN2P3/CNRS, and CEA (France), BMBF, DAAD, and AvH (Germany), OTKA (Hungary), DAE and DST (India), ISF (Israel), KRF, CHEP, and KOSEF (Korea), RMIST, RAS, and RMAE (Russia), VR and KAW (Sweden), US CRDF for the FSU, US-Hungarian NSF-OTKA-MTA, and US-Israel BSF.

*Deceased.
†PHENIX Spokesperson.
Email: zajc@nevis.columbia.edu

[1] See, for example, the *Proceedings of the Quark Matter Conference, Oakland, CA, 2004* [J. Phys. G 30, S633–S1430 (2004).
[2] J. L. Nagle, nucl-ex/0405012.
[3] M. Gyulassy *et al.*, Nucl. Phys. **A750**, 30 (2005).
[4] B. Muller, nucl-th/0404015.
[5] E. V. Shuryak, Nucl. Phys. **A750**, 64 (2005).
[6] J.-Y. Ollitrault, Phys. Rev. D **46**, 229 (1992).
[7] P. F. Kolb *et al.*, Nucl. Phys. **A696**, 197 (2001).
[8] T. Hirano *et al.*, Nucl. Phys. **A743**, 305 (2004).
[9] M. Gyulassy, I. Vitev, and X. N. Wang, Phys. Rev. Lett. **86**, 2537 (2001).
[10] Y. Kovchegov *et al.*, Nucl. Phys. **A708**, 413 (2002).
[11] N. N. Ajitanand *et al.*, Nucl. Phys. **A715**, 765 (2003).
[12] M. Chiu *et al.*, Nucl. Phys. **A715**, 761 (2003).
[13] C. Adler *et al.*, Phys. Rev. Lett. **90**, 082302 (2003).
[14] S. S. Adler *et al.*, nucl-ex/0408007.
[15] J. Rak, J. Phys. G **30**, S1309 (2004).
[16] K. Adcox *et al.*, Phys. Rev. Lett. **89**, 212301 (2002).
[17] C. Adler *et al.*, Phys. Rev. C **66**, 034904 (2002).
[18] S. S. Adler *et al.*, Phys. Rev. Lett. **91**, 182301 (2003).
[19] M. Bleicher *et al.*, Phys. Lett. B **526**, 309 (2002).
[20] R. J. Fries, B. Muller, C. Nonaka, and S. A. Bass, Phys. Rev. C **68**, 044902 (2003).
[21] J. Adams *et al.*, Phys. Rev. Lett. **92**, 052302 (2004).
[22] D. Molnar, nucl-th/0503051.
[23] G. Agakichiev *et al.*, Phys. Rev. Lett. **92**, 032301 (2004).
[24] C. Alt *et al.*, Phys. Rev. C **68**, 034903 (2003).
[25] B. Back *et al.*, Phys. Rev. Lett. **94**, 122303 (2005).
[26] K. Adcox *et al.*, Nucl. Instrum. Methods Phys. Res., Sect. A **499**, 469 (2003).
[27] K. Adcox *et al.*, Phys. Rev. C **69**, 024904 (2004).
[28] A. M. Poskanzer and S. A. Voloshin, Phys. Rev. C **58**, 1671 (1998).
[29] N. Borghini, P. M. Dinh, and J. Y. Ollitrault, Phys. Rev. C **64**, 054901 (2001).
[30] P. Chung *et al.*, Phys. Rev. C **66**, 021901 (2002).
[31] P. Danielewicz *et al.*, Science **298**, 1592 (2002).
[32] C. Pinkenburg *et al.*, Phys. Rev. Lett. **83**, 1295 (1999).

Available online at www.sciencedirect.com
SCIENCE DIRECT
ELSEVIER
Nuclear Physics A 762 (2005) 129–146
NUCLEAR PHYSICS A

Centrality and transverse momentum dependence of collective flow in 158 *A* GeV Pb + Pb collisions measured via inclusive photons

WA98 Collaboration

M.M. Aggarwal [a], Z. Ahammed [k], A.L.S. Angelis [b,✠], V. Antonenko [c], V. Arefiev [d], V. Astakhov [d], V. Avdeitchikov [d], T.C. Awes [e,*], P.V.K.S. Baba [f], S.K. Badyal [f], S. Bathe [g], B. Batiounia [d], T. Bernier [h], V.S. Bhatia [a], C. Blume [g], D. Bucher [g], H. Büsching [g], L. Carlén [j], S. Chattopadhyay [k], M.P. Decowski [l], H. Delagrange [h], P. Donni [b], M.R. Dutta Majumdar [k], A.K. Dubey [s], K. El Chenawi [j], K. Enosawa [m], S. Fokin [c], V. Frolov [d], M.S. Ganti [k], S. Garpman [j,✠], O. Gavrishchuk [d], F.J.M. Geurts [n], T.K. Ghosh [o], R. Glasow [g], B. Guskov [d], H.Å. Gustafsson [j], H.H. Gutbrod [p], I. Hrivnacova [q], M. Ippolitov [c], H. Kalechofsky [b], R. Kamermans [n], K. Karadjev [c], K. Karpio [r], B.W. Kolb [p], I. Kosarev [d], I. Koutcheryaev [c], A. Kugler [q], P. Kulinich [l], M. Kurata [m], A. Lebedev [c], H. Löhner [o], L. Luquin [h], D.P. Mahapatra [s], V. Manko [c], M. Martin [b], G. Martínez [h], A. Maximov [d], Y. Miake [m], G.C. Mishra [s], B. Mohanty [s], M.-J. Mora [h], D. Morrison [t], T. Mukhanova [c], D.S. Mukhopadhyay [k], H. Naef [b], B.K. Nandi [s], S.K. Nayak [f], T.K. Nayak [k], A. Nianine [c], V. Nikitine [d], S. Nikolaev [c], P. Nilsson [j], S. Nishimura [m], P. Nomokonov [d], J. Nystrand [j], A. Oskarsson [j], I. Otterlund [j], T. Peitzmann [n], D. Peressounko [c], V. Petracek [q], S.C. Phatak [s], W. Pinganaud [h], F. Plasil [e], M.L. Purschke [p], J. Rak [q], R. Raniwala [i], S. Raniwala [i], N.K. Rao [f], F. Retiere [h], K. Reygers [g], G. Roland [l], L. Rosselet [b], I. Roufanov [d], C. Roy [h], J.M. Rubio [b], S.S. Sambyal [f], R. Santo [g], S. Sato [m], H. Schlagheck [g], H.-R. Schmidt [p], Y. Schutz [h], G. Shabratova [d], T.H. Shah [f], I. Sibiriak [c], T. Siemiarczuk [r], D. Silvermyr [j], B.C. Sinha [k], N. Slavine [d], K. Söderström [j], G. Sood [a],

0375-9474/$ – see front matter © 2005 Elsevier B.V. All rights reserved.
doi:10.1016/j.nuclphysa.2005.08.004

S.P. Sørensen [t], P. Stankus [e], G. Stefanek [r], P. Steinberg [l], E. Stenlund [j], M. Sumbera [q], T. Svensson [j], A. Tsvetkov [c], L. Tykarski [r], E.C.V.D. Pijll [n], N.V. Eijndhoven [n], G.J.V. Nieuwenhuizen [l], A. Vinogradov [c], Y.P. Viyogi [k], A. Vodopianov [d], S. Vörös [b], B. Wysłouch [l], G.R. Young [e]

[a] *University of Panjab, Chandigarh 160014, India*
[b] *University of Geneva, CH-1211 Geneva 4, Switzerland*
[c] *RRC "Kurchatov Institute", RU-123182 Moscow, Russia*
[d] *Joint Institute for Nuclear Research, RU-141980 Dubna, Russia*
[e] *Oak Ridge National Laboratory, Oak Ridge, TN 37831-6372, USA*
[f] *University of Jammu, Jammu 180001, India*
[g] *University of Münster, D-48149 Münster, Germany*
[h] *SUBATECH, Ecole des Mines, Nantes, France*
[i] *University of Rajasthan, Jaipur 3020inst4, Rajasthan, India*
[j] *Lund University, SE-221 00 Lund, Sweden*
[k] *Variable Energy Cyclotron Centre, Calcutta 700 064, India*
[l] *MIT Cambridge, MA 02139, USA*
[m] *University of Tsukuba, Ibaraki 305, Japan*
[n] *Universiteit Utrecht/NIKHEF, NL-3508 TA Utrecht, The Netherlands*
[o] *KVI, University of Groningen, NL-9747 AA Groningen, The Netherlands*
[p] *Gesellschaft für Schwerionenforschung (GSI), D-64220 Darmstadt, Germany*
[q] *Nuclear Physics Institute, CZ-250 68 Rez, Czech Republic*
[r] *Institute for Nuclear Studies, 00-681 Warsaw, Poland*
[s] *Institute of Physics, 751-005 Bhubaneswar, India*
[t] *University of Tennessee, Knoxville, TN 37966, USA*

Received 2 November 2004; received in revised form 8 July 2005; accepted 1 August 2005

Available online 26 August 2005

Abstract

Directed and elliptic flow of inclusive photons near mid-rapidity in 158 A GeV Pb + Pb collisions has been studied. The data have been obtained with the photon spectrometer LEDA of the WA98 experiment at the CERN SPS. The flow strength has been measured for various centralities as a function of p_T and rapidity over $0.18 < p_T < 1.5$ GeV/c and $2.3 < y < 2.9$. The angular anisotropy has been studied relative to an event plane obtained in the target fragmentation region that shows the elliptic flow to be in-plane. The elliptic flow has also been studied using two-particle correlations and shown to give similar results. A small directed flow component is observed. Both the directed and elliptic flow strengths increase with p_T. The photon flow results are used to estimate the corresponding neutral pion flow.
© 2005 Elsevier B.V. All rights reserved.

Keywords: NUCLEAR REACTIONS ^{208}Pb(^{208}Pb, X), $E = 158$ GeV/nucleon; measured inclusive photons direct and elliptic flow vs. centrality, rapidity and transverse momentum; deduced neutral pion flow features.

* Corresponding author.
E-mail address: awes@bnl.gov (T.C. Awes).
✠ Deceased.

1. Introduction

Heavy ion collisions at relativistic energies provide a means to study the properties of nuclear matter at high temperature and density. In such collisions it is expected that a high density interaction zone is formed. If this system thermalizes, the thermal pressure will generate collective transverse expansion [1]. Such collective flow, and especially its anisotropy, will reflect the time evolution of the pressure gradients of the system and can provide information on the equation of state (EOS) in the initial phase [2,3] and during the expansion [4], and in particular about the possible formation of the quark–gluon plasma (QGP) [5,6].

QGP formation requires high energy density and local thermalisation of the system. While transverse energy measurements indicate the attainment of high energy densities [7], the degree of thermalization has not been unambiguously determined. Measurements of collective flow may be one of the strongest hints related to the degree of thermalisation. One may consider two extreme cases: the low density limit, where the mean free path is comparable or larger than the system size for which cascade models may be appropriate, and the hydrodynamic limit, where the mean free path of the particles is much less than the system size. The detailed study of collective flow as a function of beam energy, system size, transverse momentum, rapidity, and particle species may allow to separate these two scenarios and to recognize the hadronic or partonic (QGP) nature of the reaction [8].

The anisotropic flow of charged fragments has been measured in nuclear collisions at various beam energies: at 0.1–1.0 A GeV [9–11], at 10 A GeV [12], at 158 A GeV [13–17] and also at $\sqrt{s_{NN}} = 130$ and 200 GeV [18–20]. The first p_T-integrated photon flow measurement was performed by the WA93 experiment [15] for 200 A GeV S + Au collisions, where photons were measured with the Photon Multiplicity Detector (PMD). In the present work we report first results of photon collective flow measurements in 158 A GeV Pb + Pb collisions using photons identified and momentum analyzed in the lead glass calorimeter LEDA of the WA98 experiment. Preliminary results have been presented in [21,22].

2. Experimental setup

The data presented here were obtained in the WA98 experiment [23] for 158 A GeV Pb + Pb collisions at the CERN SPS. The WA98 setup consisted of large acceptance hadron and photon spectrometers, calorimeters for forward and transverse energy measurements, and detectors for photon and charged particle multiplicity measurements.

The centrality of the event was determined by the total transverse energy, E_T, measured with the mid-rapidity calorimeter (MIRAC) [24], which covered the pseudo-rapidity range of $3.5 < \eta < 5.5$. It was placed at 24.7 meters downstream from the target and consisted of 30 stacks, each divided vertically into 6 towers, of size 20×20 cm^2 each. The MIRAC measured both the transverse electromagnetic E_T^{em} and hadronic E_T^{had} energies. Events with large E_T correspond to the most central collisions with small impact parameter. The minimum bias trigger required a beam trigger with a MIRAC transverse energy greater than a low threshold. During datataking, central collision events were accumulated preferentially without prescale by use of a high transverse energy trigger (15% of event sample with largest E_T) [25].

The Plastic Ball spectrometer, used for the reaction plane (RP) determination, had full azimuthal coverage in the pseudorapidity range of $-1.7 < \eta < 0.5$ (i.e., in the target fragmentation region with polar angles $70^\circ < \theta < 160^\circ$). It consisted of 655 detector modules and allowed to identify pions, protons, deutrons, tritons, ^{3}He, and ^{4}He with kinetic energies of 50 to 250 MeV by

the ΔE–E method. Each module comprised a slow 4 mm thick CaF_2 ΔE scintillator followed by a fast plastic scintillator, both read out by a common photomultiplier [26].

Photons, of which $\sim 85\%$ originate from π^0 decay [25], were detected in the electromagnetic calorimeter LEDA, a highly segmented photon detector located 22.1 m downstream the target and covering the photon rapidity region $2.3 < y < 2.9$, i.e., backwards of mid-rapidity ($y = 2.9$). LEDA consisted of 10 080 TF1 lead-glass modules, read out by FEU-84 photomultipliers. The photomultiplier high voltage was generated on-base with custom developed [27] Cockcroft–Walton voltage-multiplier type bases which were individually controlled by a VME processor. The photomultiplier signals were digitized with a custom-built ADC system [28]. The dimensions of each module were $4 \times 4 \times 40$ cm^3 (14.3 radiation lengths depth and 1.1 Moliere radius width). Each group of 24 modules had its own calibration and gain monitoring system based on a set of 3 LEDs mounted inside a sealed reflecting cover dome. Each module viewed the reflected LED light through an aperture on the front surface, while the LED light was simultaneously monitored by a PIN-photodiode [29].

LEDA was calibrated with 10 GeV electrons in the X1 beam at the CERN SPS in the years 1993–1994. Electron beams with energies from 3 to 20 GeV were used to measure the energy and position resolution, and the energy non-linearity. The measured energy resolution was $\sigma/E = (5.5 \pm 0.6)\%/\sqrt{E} + (0.8 \pm 0.2)\%$ and the measured position resolution was $\sigma/E = (8.35 \pm 0.25)\text{mm}/\sqrt{E} + (0.15 \pm 0.07)$ mm. A more detailed description of the WA98 setup is given in [16,23,25].

3. The methods

Two complementary methods have been used in this analysis of anisotropic flow: the study of single-particle angular distributions with respect to an estimated reaction plane (*reaction plane method*) and the study of two-particle correlations (*correlation method*). Both methods assume that the underlying azimuthal distribution of particles with respect to the reaction plane (RP), which is the plane that contains the impact parameter and beam direction vectors, can be described by a Fourier decomposition

$$\frac{1}{N}\frac{dN}{d(\phi - \Psi_{\mathrm{RP}})} = 1 + 2v_1\cos(\phi - \Psi_{\mathrm{RP}}) + 2v_2\cos\bigl(2(\phi - \Psi_{\mathrm{RP}})\bigr), \tag{1}$$

where ϕ is the azimuthal angle of the emitted particle, and Ψ_{RP} is the azimuthal angle of the RP. The anisotropic flow is characterized by the values of the Fourier coefficients v_1, for directed flow, and v_2, for elliptic flow.

3.1. The reaction plane method

The conventional reaction plane method [30,31] uses the distribution of particles in their azimuthal angle relative to the estimated reaction plane. Because the true reaction plane is not known in the experiment, one has to establish an *event plane* (EP) from the measured particles as an estimate for the reaction plane.

Particles measured in the target fragmentation region show significant directed flow—proton, deuterons, and heavier fragments are emitted in the reaction plane in one direction, while pions are emitted in the opposite direction, as has been measured with the Plastic Ball detector [32].

This information has been used to calculate an event plane angle from the particles measured in the Plastic Ball

$$\Phi_{\mathrm{EP}} = \tan^{-1}\left(\frac{\sum_{i=1}^{N} E_T^i \sin\phi_i}{\sum_{i=1}^{N} E_T^i \cos\phi_i}\right), \tag{2}$$

where the sum runs over all fragments and identified positive pions. E_T^i and ϕ_i are the transverse kinetic energy and azimuthal angle in the laboratory frame of the ith particle, respectively. For pions, ϕ was replaced by $\phi + \pi$ to account for the opposite sign pion directed flow [32].

The azimuthal distribution of photons detected by the LEDA calorimeter has been studied relative to this event plane angle. The distributions are studied as a function of $\Delta\Phi = \phi_\gamma - \Phi_{\mathrm{EP}}$ and are fitted with:

$$\frac{1}{N}\frac{dN}{d\Delta\Phi} = 1 + 2v_1^{\mathrm{obs}}\cos(\Delta\Phi) + 2v_2^{\mathrm{obs}}\cos(2\Delta\Phi). \tag{3}$$

The measured EP does not coincide exactly with the true RP because of the finite number of detected particles and resulting fluctuations. Because of this finite reaction plane resolution, the coefficients obtained from the fits have to be corrected by dividing them by the event plane resolution correction factors (RCF_n):

$$v_n = \frac{v_n^{\mathrm{obs}}}{RCF_n}. \tag{4}$$

The resolution correction functions RCF_n are given by [31]

$$\begin{aligned} RCF_n &= \left\langle \cos\big(n(\Phi_{\mathrm{EP}} - \Psi_{\mathrm{RP}})\big)\right\rangle \\ &= \frac{\sqrt{\pi}}{2\sqrt{2}}\chi_m \exp\left(\frac{-\chi_m^2}{4}\right)\left[I_{\frac{k-1}{2}}\left(\frac{\chi_m^2}{4}\right) + I_{\frac{k+1}{2}}\left(\frac{\chi_m^2}{4}\right)\right], \end{aligned} \tag{5}$$

where Ψ_{RP} is the true RP angle, χ_m is the resolution parameter, which is proportional to the square root of the multiplicity, m is the order of the Fourier component used for calculation of the event plane and $k = n/m$.

Since Ψ_{RP} is unknown, the RCF's must be determined from the measured EP themselves. This can be done by a subevent analysis in which each event, in this case consisting of hits in the Plastic Ball detector, is randomly divided into two subevents (A and B) and for each subevent the EP angle Φ_{EP} (Φ_A or Φ_B) is calculated. The quantity $\langle\cos(n(\Phi_A - \Phi_B))\rangle$ is determined directly from the subevent correlation function. It is then equated to the lefthand side of equation 5 to obtain the parameter χ_m^{sub} for the subevent multiplicity, which is then used to calculate $\chi_m = \sqrt{2}\chi_m^{\mathrm{sub}}$ for the full event, and finally to obtain RCF_n. In this analysis we have used $m = 1$ ($k = 1$) for RCF_1 and for RCF_2 ($k = 2$).

3.2. The correlation method

Alternatively, the flow values have been obtained from the azimuthal correlations of photon pairs as described in [2,31,33–35]. The correlation function is calculated as

$$C_{\gamma\gamma}(\Delta\phi) \equiv \frac{d^2N/d\phi_1\, d\phi_2}{dN/d\phi_1 \cdot dN/d\phi_2}, \tag{6}$$

where $\Delta\phi = \phi_1 - \phi_2$. The $C_{\gamma\gamma}$ are calculated as the ratio of the true two-photon distribution to the pair distribution from mixed events. This is necessary to correct for distortions from the

limited acceptance of the photon detector. In the event-mixing procedure we have taken care to mix only events with similar global properties and to use identical cuts, especially regarding the two-cluster separation within the detector. The two-photon correlation functions have then been fitted with

$$C_{\gamma\gamma}(\Delta\phi) = 1 + 2v_1^2\cos(\Delta\phi) + 2v_2^2\cos\big(2(\Delta\phi)\big). \tag{7}$$

From these fits, no significant v_1 component was observed. Since very little directed flow is expected near mid-rapidity, we have set $v_1 \equiv 0$ in this analysis.

If collective flow is dominant, this method should be equivalent to the previous one since (a) the correlation between every particle and the RP induces a correlation amongst the particles, and (b) correlating two subevents amounts to summing two-particle correlations [36]. The correlation method has the advantage that no EP determination, and therefore no resolution correction, is needed. However, non-flow correlations, such as back-to-back correlations due to momentum conservation [22], should be taken into account.

4. Analysis

The data presented here were taken in 1995 and 1996 with the 158 A GeV Pb ion beams of the CERN SPS. Pb targets of 495 and 239 mg/cm^2 thickness were used. About 10^7 events were analyzed. The events were divided into 8 centrality classes defined by intervals in the total E_T measured by MIRAC, as summarized in Table 1. The centralities are expressed as fractions of the minimum bias cross sections as a function of the total E_T, measured by MIRAC. In addition, a multiplicity of greater than 3 fragments measured in the Plastic Ball was demanded to allow for a reasonable determination of the EP. This has a significant effect for the peripheral bins and causes a slight bias towards higher multiplicity within the bin.

In addition to the 8 classes of centrality shown in Table 1, studies were performed with combined centrality classes: $3 + 4$ (24–65%), $5 + 6$ (13–24%) and $7 + 8$ (0–13%). The table also shows the number of participants N_{part} as calculated in a Glauber type calculation discussed in [37].

To further suppress the hadron contamination in the photon sample, only those showers in the calorimeter have been used which satisfy the following cuts:

- The measured energy was greater than 0.75 GeV. This cut suppressed minimum ionizing particles.
- The lateral dispersion of the shower was less than a maximum value. This suppressed showering hadrons.

These cuts kept the hadron contamination in the photon sample to less than $\approx 7\%$ [25,39].

The observed raw Φ_{EP}-distributions showed a variation due to detector biases, such as dead channels and inefficiency, of less than 5%. This non-uniformity has to be removed before extracting the flow strength from the measured correlation functions. This has been done by two methods:

- The real distribution was divided by the equivalent distribution for mixed events, where ϕ_γ and Φ_{EP} are taken from different events.
- In accumulating the distributions, the entries were weighted with the inverse of the Φ_{EP} distribution.

Table 1
Centrality classes used in this analysis. The percentage of the measured minimum bias cross section included in each class is given. Also given is the corresponding average number of participants for each class with an estimate of the systematic error. Cuts on E_T are for 1995 data set, 1996 data set cuts are shown in [38]

	E_T class	E_T (GeV)	N_{part}
1	83–100%	0–28.35	10 ± 2
2	65–83%	28.35–79.05	28 ± 2
3	47–65%	79.05–161.55	63 ± 2
4	24–47%	161.55–281.05	133 ± 3
5	19–24%	281.05–318.05	205 ± 2
6	13–19%	318.05–361.55	247 ± 2
7	6.5–13%	361.55–410.95	291 ± 2
8	0–6.5%	> 410.95	351 ± 1

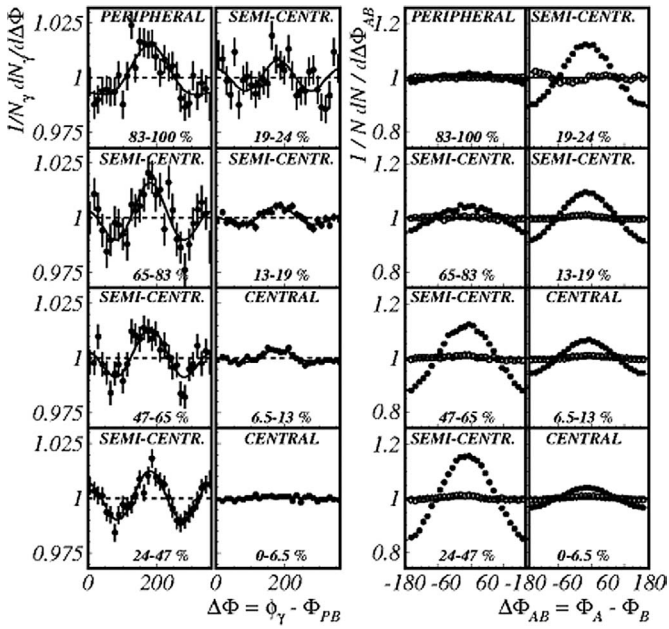

Fig. 1. Left: the measured photon azimuthal correlation functions for different centralities. The solid lines show fits to Eq. (3). Right: subevent correlation functions of particles measured in the Plastic Ball for different centralities. The filled circles show the measured correlation functions. The open circles show the results for mixed subevents.

Both methods gave consistent results within errors, we have used the second method for the final result.

Fig. 1 (left) shows examples of the measured photon azimuthal correlation functions for different centralities. A clear modulation is seen, especially in the semi-central classes, which can be described well with fits to Eq. (3).

The resolution correction factors RCF's for each centrality were determined as described above from the subevent correlation functions as shown in Fig. 1 (right). In this case the Plastic Ball acceptance correction was done by using mixed subevents, i.e., subevents from different events. The deviation of the mixed subevents from unity, i.e., the order of magnitude of this correction, was less than 2% (as shown in Fig. 1 (right)).

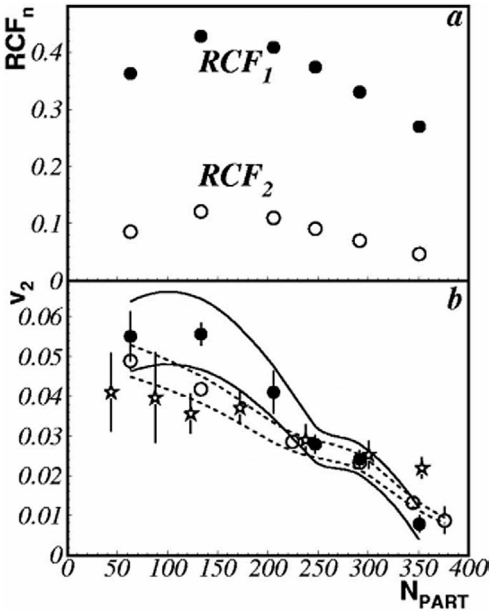

Fig. 2. (a) The resolution correction factors obtained from subevent correlation functions of particles measured in the target fragmentation region as a function of the number of participants. The filled circles show the values for directed flow, the open circles for elliptic flow. (b) The elliptic flow v_2 of photons extracted by the reaction plane method (solid circles, $p_T \geqslant 0.18$ GeV/c) and by the correlation method (open circles, $p_{T1} \geqslant 0.18$ GeV/c, $p_{T2} \geqslant 0.18$ GeV/c), integrated over $p_T > 0.18$ GeV/c and $y = 2.3$–2.9 as a function of the number of participants. The solid and dashed lines indicate the systematic error regions of the two measurements. The inclusive photon v_2 results from Ref. [42] integrated over all p_T and with $y = 3.25$–3.75 are shown by stars with error bars which include both statistical and systematical errors.

Fig. 2(a) shows the values of the resolution correction factors RCF's determined in this way as a function of the number of participants. A stronger subevent correlation implies a better determination of the RP, and the corresponding values of the RCF's are larger [40]. It is seen, that the subevent correlation is strongest for semi-central events, whereas for peripheral and central events the quality of the EP—determination is worse. The RCF's shown in Fig. 2(a) have been obtained for the 1996 beam time. The RCF's have been calculated and applied independently for the 1995 beam time, with values found to be smaller by ~ 20–40%.

Possible non-flow correlations in the RCF determination have been estimated and corrections have been applied. Among such non-flow effects relevant for azimuthal correlations are the correlations due to momentum conservation, long- and short-range two- and many-particle correlations (due to quantum statistics, resonances, jet or mini-jet production, etc.). The contribution of non-flow correlations scales as $1/N$, where N is the multiplicity of particles used to determine the event plane. The "momentum conservation" contribution increases with the fraction of particles detected, and the relative contribution of Bose–Einstein correlations would be independent of N. The effect of non-flow correlations in the reaction plane method is expected to be small as the event plane is determined from particle which have a large pseudorapidity separation $\Delta\eta > 1.8$ from the photons. The non-flow contributions to the event plane determination have been investigated by studying the dependence of the RCF's on the Plastic Ball multiplicity. The conventional subevent analysis was performed excluding various fractions of the Plastic Ball particles to investigate the deviation of the flow pa-

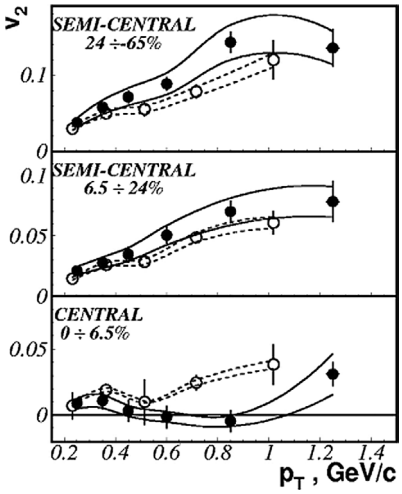

Fig. 3. The elliptic flow v_2 of photons extracted by the reaction plane method (solid circles, $p_T \geqslant 0.18$ GeV/c) and by the correlation method (open circles, $p_{T1} \geqslant 0.18$ GeV/c, $p_{T2} \geqslant 0.18$ GeV/c), integrated over $y = 2.3$–2.9 for three centrality selections.

rameter χ_m from $\chi_m \approx \sqrt{N}$ (see Eq. (5)). A multiplicity-dependent bias was observed and used to extrapolate an $M = \infty$ RCF value. These corrections varied from 2–4% with a systematic error of $< 4\%$. The determination of the RCF's for the two most peripheral centrality bins has been deemed unreliable due to the fact that the non-target background corrections are significant [25] and the average multiplicity in the Plastic Ball is too low (less than 5 hits). Therefore final v_n results for the two most peripheral centralities are not presented.

The v_2 elliptic flow values for photons have also been obtained from the two-photon correlation functions for various centrality classes, although not all of these precisely match those used for the reaction plane method analysis [41]. The v_2 elliptic flow values for photons obtained by the two methods are compared in Figs. 2(b) and 3. The two photon correlation functions have been fitted with Eq. (7) to extract v_2 with $v_1 \equiv 0$. Fig. 2(b) shows the centrality dependence of v_2 integrated over $p_T > 0.18$ GeV/c. The solid circles are the values obtained from the reaction plane method and the open circles are those from the correlation method. The inclusive photon v_2 results measured with the WA98 Photon Multiplicity Detector (PMD) preshower detector are also shown [42] in Fig. 2(b). The PMD provides a p_T integrated result in the rapidity region $y = 3.25$–3.75. For centralities corresponding to $N_{\text{part}} > 50$ there is good agreement between the different results. Fig. 3 shows the elliptic flow as a function of p_T for central and two semi-central classes for the reaction plane and two-particle correlation methods. There is reasonably good agreement between the methods.

One should note that the reaction plane and correlation methods suffer from systematic effects. The determination of the reaction plane has a large uncertainty due to fluctuations and backgrounds for low multiplicities. The correlation method is more susceptible to non-flow components [22] which would influence the extraction of the flow. Furthermore, the directed flow has been neglected in the correlation analysis which may also lead to systematic errors in the v_2 determination. The results from the reaction plane method are used in the discussions that follow.

As a consistency check we have performed the reaction plane analysis independently on the data from the two different beam periods, where the quality of the RP determination was found to be different. The resulting flow values are in good agreement.

5. Systematic error

The systematic errors of the obtained coefficients include:

- Uncertainties in the event plane determination in the Plastic Ball due to non-uniformity of acceptance and efficiency or imperfect particle identification, estimated as $< 2\%$.
- Uncertainties due to non-flow effects in the determination of the RCFs from the Plastic Ball event plane, estimated as $< 4\%$.
- Uncertainties in the photon angular distributions due to charge particle contamination of photons in LEDA. This contamination is less than $\approx 7\%$ [25]. The uncertainties are related to a difference in the observed flow between charged pions and pion decay photons and were estimated as $< 3.5\%$.

Other sources of the systematic errors have been investigated by comparing the results obtained under different conditions. The following checks have been performed:

(1) Different weights (E_T vs. p_T) have been used for the determination of the event plane.
(2) Different acceptance regions of the Plastic Ball detector ($70^\circ < \theta < 160^\circ$ or $60^\circ < \theta < 160^\circ$) have been used.
(3) Different identification cuts for the Plastic Ball fragments were used.
(4) The event plane was determined with and without including pions in the Plastic Ball.
(5) Results of the two different beam periods were analyzed separately.

All of these systematic checks lead to a total systematic error estimate of $\pm 16\%$ ($\pm 50\%$ for the most central bin) for the measured values of both flow coefficients. Unless explicitly stated otherwise, the systematic errors are not included in the figures.

6. Results

Fig. 4(a), (b) shows the final values of the directed flow v_1 and the elliptic flow v_2 coefficients as a function of the number of participants. The data were integrated over $p_T > 0.18\,\mathrm{GeV}/c$ and over rapidity $y = 2.3$–2.9.

Both types of flow decrease in strength with the number of participants. The sign of all values is positive with the sign convention that positive v_1 corresponds to the directed flow direction of the protons in the projectile fragmentation direction and positive v_2 corresponds to the in-plane direction. Thus, the directed flow of photons below mid-rapidity is in the same direction as the directed flow of pions, opposite to the protons, in the target fragmentation region, and the elliptic flow is oriented in the reaction plane.

The transverse momentum dependence of the photon flow integrated over $y = 2.3$–2.9 is shown in Fig. 4(c), (d) for different centrality classes. Both flow coefficients show an increase with p_T which is compatible with a blast-wave fit (see below [19,43]).

To be able to compare the flow of photons to other experimental results we have attempted to establish the relation between the observed photon flow and the underlying flow of the parent

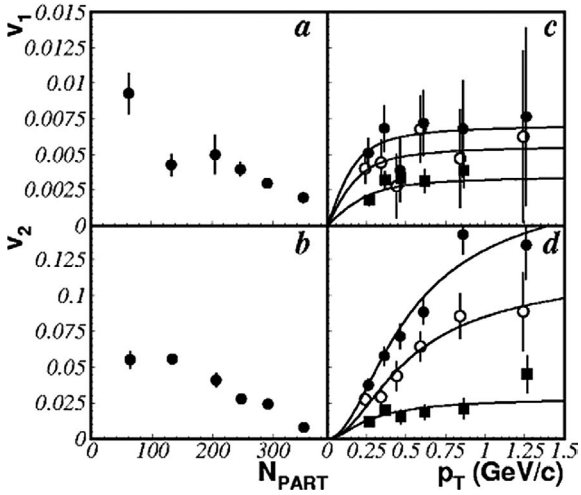

Fig. 4. Directed flow (v_1) (a) and elliptic flow (v_2) (b) of inclusive photons integrated over $p_T > 0.18$ GeV/c and $y = 2.3$–2.9 as a function of the number of participants. Directed flow (v_1) (c) and elliptic flow (v_2) (d) of inclusive photons integrated over $y = 2.3$–2.9 as a function of p_T for various centralities. Solid circles show results for semi-central events (24–65%), open circles show results for semi-central events (13–24%), solid squares show results for central events (0–13%). Solid lines are fitted results to a blast-wave model functional form (Eqs. (9) and (10)).

neutral pions. This has been investigated in Monte Carlo simulations. In the simulations, π^0's and η were generated according to the p_T spectra measured by WA98 [25]. The π^0 and η azimuthal distributions were modulated with directed and elliptic flow components. The values of the π^0 v_1 and v_2 and their p_T-dependence have been constrained by the photon measurement. The p_T-dependence of the azimuthal asymmetry has been parameterized following a simple hydrodynamically motivated blast-wave model, described in [19,44], and generalized in [43] to also describe v_1:

$$v_n(p_T) = \frac{\int_0^{2\pi} d\phi_b \cos(n\phi_b) I_n(\alpha) K_1(\beta)[1 + 2s_n \cos(n\phi_b)]}{\int_0^{2\pi} d\phi_b I_0(\alpha) K_1(\beta)[1 + 2s_n \cos(n\phi_b)]}, \tag{8}$$

where the harmonic n can be either 1 or 2, I_0, I_n, and K_1 are the modified Bessel functions, $\phi_b = \phi - \Psi_{\mathrm{RP}}$, $\alpha(\phi_b) = (p_T/T_f)\sinh[\rho(\phi_b)]$, $\beta(\phi_b) = (m_T/T_f)\cosh[\rho(\phi_b)]$, s_n is the surface emission parameter, and T_f is the freeze-out temperature. The azimuthal flow rapidity is given as $\rho(\phi_b) = \rho_0 + \rho_a \cos(n\phi_b)$ with ρ_0 is the mean transverse expansion rapidity ($v_0 = \tanh[\rho_0]$) and ρ_a is the amplitude of its azimuthal variation, respectively. Further details are given in [43].

Without regard to the physical interpretation of the parameters of this model it can be used to provide a convenient parameterization of the p_T dependence of the flow. For this purpose Eq. (8) can be further simplified by setting $\rho_a = 0$. The integrals can be solved to reduce the expression to two parameters, a_n and b_n. The expressions for the p_T dependence of the directed and elliptic flow are then

$$v_1(p_T) = a_1 \frac{I_1(b_1 p_T)}{I_0(b_1 p_T)}, \tag{9}$$

$$v_2(p_T) = a_2 \left(1 - 2\frac{I_1(b_2 p_T)}{b_2 p_T I_0(b_2 p_T)}\right). \tag{10}$$

Table 2
The blast-wave parameters a_n and b_n of Eqs. (9) and (10) for various centralities obtained by fits to the WA98 inclusive photon data (left) and the corresponding parameters extracted for neutral pions (right) from simulations that reproduce the inclusive photon results

Centrality	Fit to γ				Extracted for π^0			
	a_1	b_1	a_2	b_2	a_1	b_1	a_2	b_2
3	0.0072	3.06	0.22	5.2	0.0072	3.06	0.28	3.09
4	0.006	3.06	0.17	5.1	0.0078	3.06	0.217	2.98
5	0.005	3.06	0.12	5.0	0.005	3.256	0.158	2.87
6	0.0045	3.06	0.095	4.9	0.0044	3.06	0.118	2.93
7	0.004	3.06	0.06	4.8	0.0042	3.06	0.068	3.1
8	0.003	3.06	0.03	4.7	0.0026	3.06	0.028	3.8

The measured photon $v_n(p_T)$ are described well by these expressions as shown by the solid lines of Fig. 4(c), (d). The extracted a_n and b_n were constrained to have a smooth centrality dependence and are tabulated in Table 2.

In order to extract the π^0 $v_n(p_T)$ from the measured photon $v_n(p_T)$, the simulated π^0 p_T distributions have been parameterized as

$$\frac{1}{N_{\text{Event}}}\frac{d^2N}{dy\,dp_T} = \frac{1}{N_{\text{Event}}}E\frac{d^3N}{dp^3}p_T = C' p_T \left(\frac{p_0'}{p_0' + p_T}\right)^{n'} \tag{11}$$

with parameters C', p_0', n' taken from the measured π^0 results [25]. The η photon decay contributions were also included with the η yield assumed to proportional to the π^0 yield at the same transverse mass (m_T-scaling) [25]. Jetset 7.4 was used to generate the π^0- and η-decay photons which were then filtered in the simulations with the detector acceptance and efficiency.

In the simulations, the π^0's were generated with an azimuthal asymmetry with p_T dependent v_n parameterized by Eqs. (9) and (10). The η v_n were taken to be the same as those of the π^0's, $v_n^\eta(p_T) = v_n^\pi(p_T)$. As an initial ansatz, the measured photon $v_n(p_T) = g(p_T)$ for each centrality was used for the $v_n(p_T) = f(p_T)$ of the simulated pions. The output $v_n(p_T) = g'(p_T)$ of the simulated decay photons was compared to the measured photon dependence and used to adjust the π^0 $v_n(p_T)$ for the next iteration. The procedure was iterated until the simulated (g') and measured (g) photon results were in agreement, which typically required two to three iterations. The a_n and b_n coefficients obtained from the fit to the photon results and the coefficients extracted for the π^0's by the iteration procedure are summarized in Table 2. The ratio of the flow coefficients extracted for the simulated decay photons to the input pion flow coefficients provided the correction factors $k_n(p_T) = v_n^\gamma(p_T)/v_n^\pi(p_T)$ used to extract the π^0 $v_n^\pi(p_T)$ from the measured photon $v_n^\gamma(p_T)$. To extract p_T integrated correction factors k_n over the region of measurement $p_T > 0.18$ GeV/c, or k_n^0 extrapolated to zero transverse momentum, $p_T > 0$ GeV/c, the fitted $v_n(p_T)$ results were weighted by the measured inclusive photon or π^0 spectra extrapolated to $p_T = 0$ GeV/c and integrated over p_T. The systematic errors on the k_n were determined from the uncertainties Δ of the fit parameters: $a_n \pm \Delta a_n$, $b_n \pm \Delta b_n$, $p_0' \pm \Delta p_0'$ and $n' \pm \Delta n'$. The analysis was repeated assuming instead a linear or a square-root dependence of v_n on p_T and the variation of the results was found to be about 10% and 2% for k_1 and k_2, respectively, and has been included in the systematic errors on k_n. The systematic error on k_n from the η contribution in the simulations is estimated to be less than 5%.

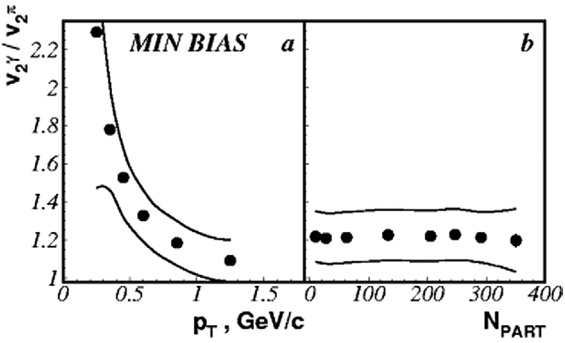

Fig. 5. The ratio of photon elliptic flow to parent pion elliptic flow coefficients. (a) $k_2 = v_2^\gamma / v_2^\pi$ for min. bias, (b) $k_2 = v_2^\gamma / v_2^\pi$ for different centrality bins.

Fig. 5(a), (b) shows k_2, the ratio of the v_2 coefficients of photons and pions, obtained from the simulations. The k_1 ratio is found to be independent of centrality and p_T with a value of $\langle k_1 \rangle = 1.183 \pm 0.03$ with a systematic error ranging from 14% to 22% from peripheral to central collisions. Since v_1^π is small, $k_1 \approx 1$.

The k_2 are seen in Fig. 5(a) to be strongly dependent on p_T, rising at low p_T where the v_2 are small. However, the p_T-integrated k_2 ratios are found to be independent of centrality with $\langle k_2 \rangle = 1.215 \pm 0.002$ and a systematic error which varies from 11% to 14% from peripheral to central collisions. The observation that the k_n ratios are greater than unity can be understood as a simple effect of the π^0 decay and the fact that the v_n increase with p_T. Comparing photons and π^0's at a given p_T, the decay photons will have been produced from π^0's with larger p_T and hence larger v_n, giving $k_n > 1$ (see Fig. 5(a) and (b)).

The π^0 v_2 extracted from the measured WA98 photon v_2 as a function of centrality are compared to the results from NA49 for charged pions [43] in Fig. 6. For this comparison the WA98 results for photons with $p_T > 0.18\,\mathrm{GeV}/c$ were extrapolated to the expectation for the pions without p_T threshold ($p_T > 0\,\mathrm{GeV}/c$) as for NA49 results, with the correction factor $k_1^0 = 1.43 \pm 0.036$ and $k_2^0 = 1.59 \pm 0.003$. The estimated systematic errors on the WA98 points including the errors of the measured photon v_n values and the additional error of the k_n^0 correction are less than $\pm 20\%$ ($\pm 55\%$ for the most central bin), except for the lowest p_T points where the upper systematic errors increase (Fig. 8). The systematic errors on the NA49 data points vary from 13% for the most peripheral to 80% for the most central bin. The two measurements are seen to be in agreement.

The rapidity dependence of the pion flow coefficients is shown in Fig. 7 for two centrality selections. The WA98 photon v_n with $p_T > 0.18\,\mathrm{GeV}/c$ were extrapolated to the expectation for π^0's without p_T threshold using the correction factors k_n^0 described above. The NA49 results for pions with $p_T > 0\,\mathrm{GeV}/c$ with appropriate corrections ([43]) are also shown and the two measurements are seen to be in agreement. Similar agreement between the NA49 and WA98 results is seen in the transverse momentum dependence of the v_2 shown in Fig. 8.

Fig. 9 shows the WA98 π^0 v_2 coefficient deduced from the measured photon v_2 (corrected by k_2^0) together with a compilation of results [43] from other experiments. Results are shown from E877 [8,12], CERES [45], NA49 [43], PHOBOS [46], PHENIX [47], and STAR [48]. The WA98 result follows the general trend of the smooth increase of the elliptic flow with increasing

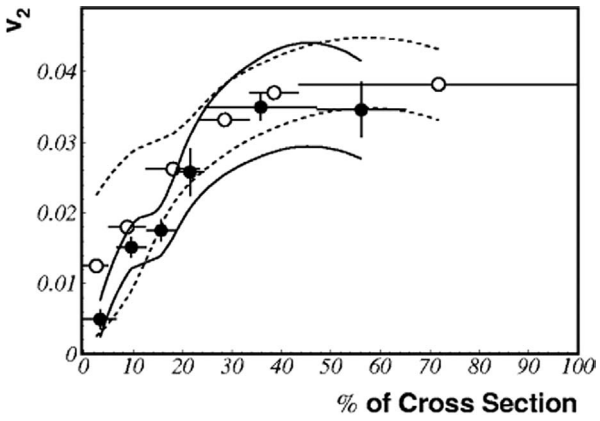

Fig. 6. The centrality dependence of pion elliptic flow v_2 extracted from the measured photon flow from WA98 (solid circles, $-0.6 < y_{\mathrm{CM}} < 0$), compared to pion flow results of NA49 (open circles, $0 < y_{\mathrm{CM}} < 2.1$, [43]).

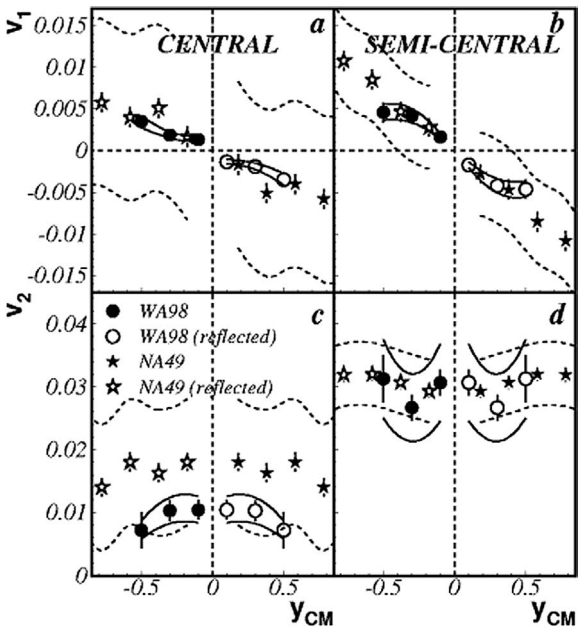

Fig. 7. The rapidity dependence of pion flow extracted from the measured photon flow from WA98 (circles) compared to pion flow results of NA49 (stars, [43]). The results are shown for central on the left panel (WA98: 0–13%, NA49: 0–12.5%) and semi-central on the right panel (WA98: 13–47%, NA49: 12.5–33.5%) selections for the directed flow (a), (b) and elliptic flow (c), (d). Systematic error bands are shown on (c) for NA49 (dashed curves) and for WA98 (solid curves). Open points are reflected at mid-rapidity.

beam energy. It should be kept in mind that the p_T and rapidity coverages as well as centrality selections differ somewhat for the various experiments.

Since the strength of the elliptic flow should be proportional to the initial eccentricity of the collision zone, it is useful to normalize the measured v_2 to the eccentricity of the reaction geom-

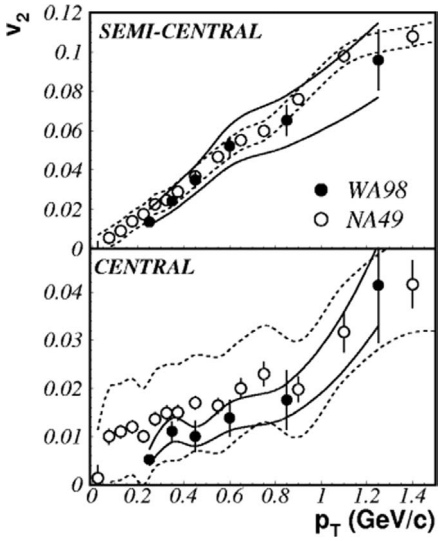

Fig. 8. The transverse momentum dependence of the π^0 elliptic flow extracted from the measured photon flow from WA98 (solid circles) compared to π^+ elliptic flow results of NA49 (open circles, [43]). The results are shown for semi-central selections (top: WA98: 13–47%, $-0.6 < y_{\mathrm{CM}} < 0$, NA49: 12.5–33.5%, $0 < y_{\mathrm{CM}} < 0.8$) and for central selections (bottom: WA98: 0–13%, $-0.6 < y_{\mathrm{CM}} < 0$, NA49: 0–12.5%, $0 < y_{\mathrm{CM}} < 0.8$). Systematic error bands are shown for NA49 (dashed curves) and for WA98 (solid curves).

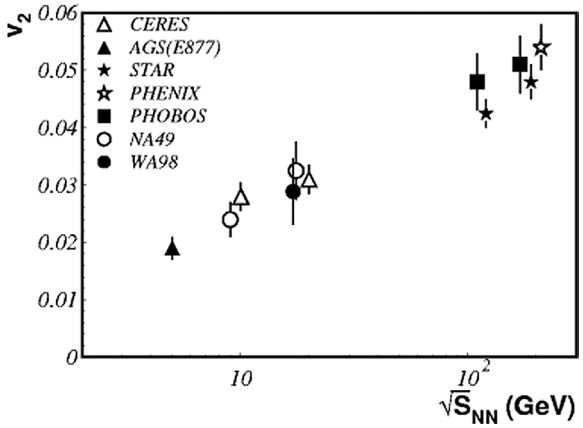

Fig. 9. Comparison of the WA98 p_T-integrated elliptic flow results at $\sqrt{s_{NN}} = 17$ GeV (13–47%, $-0.6 < y_{\mathrm{CM}} < 0$) with results from other experiments for different collision energies. The WA98 result is the π^0 elliptic flow extracted from the measured photon elliptic flow, as described in the text. The total statistical and systematic error is shown on the WA98 point.

etry when investigating the systematics of the elliptical flow [49]. The initial spatial eccentricity was calculated within a Glauber model calculation [37] as

$$\epsilon = \frac{\langle y^2 \rangle - \langle x^2 \rangle}{\langle y^2 \rangle + \langle x^2 \rangle},$$

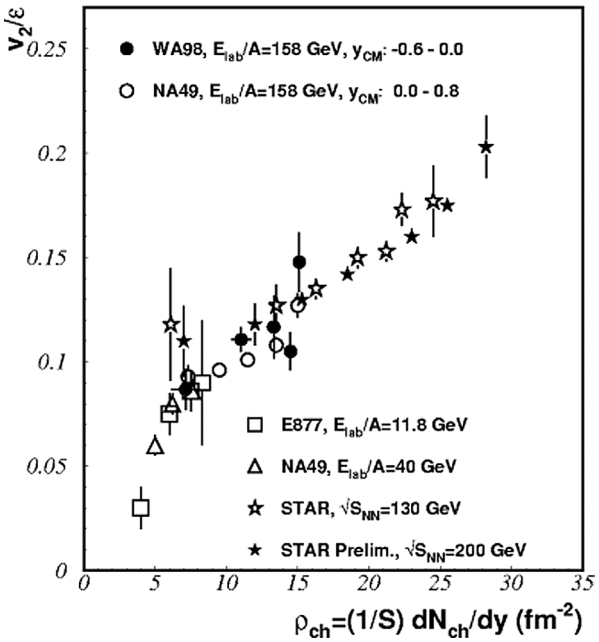

Fig. 10. The scaled elliptic flow v_2/ϵ as a function of particle density. Results are shown for the WA98 p_T-integrated v_2 values at $\sqrt{s_{NN}} = 17$ GeV ($-0.6 < y_{\mathrm{CM}} < 0$). The WA98 results are compared to results from the E877, NA49, and STAR experiments. The WA98 result is the π^0 elliptic flow extracted from the measured photon elliptic flow, as described in the text.

where x and y are the participant nucleon coordinates in the plane perpendicular to the beam and x denotes the in-plane direction.

It is of interest to plot the quantity v_2/ϵ versus the particle density as estimated by the dN/dy of charged particles divided by the area of the overlap region S [8,43]. Neglecting the weak incident energy and centrality dependence of the average p_T, the scaled particle density is proportional to the initial energy density in the Bjorken estimate [52]. Fig. 10 shows the WA98 result for v_2/ϵ for neutral pions together with results for charged pions from NA49 [43] and results for charged particles from STAR [50,51] and E877 [8]. The RHIC data have been corrected for their p_T cutoff, the errors are statistical. For the WA98 points the dN/dy are taken from WA98 measurements [37].

The WA98 results confirm the previous observation [8,43] of a universal dependence of v_2/ϵ on the particle density. It should be noted that results at different incident energies but similar average particle density correspond to dramatically different collision geometries. Generally, a central collision at low energy will have a particle density similar to a more peripheral collision at higher energy. Thus, the universal dependence demonstrates that the scaled v_2 depends only on the initial energy density, or initial pressure, rather than being dependent on the particle density times pathlength, which would be the expectation if only partial thermalization was attained. The observed increase of the scaled elliptic flow with increasing particle density is qualitatively similar to that seen in a recent hydrodynamical model study [53] in which the v_2 value for fixed impact parameter increases smoothly with increasing dN_{ch}/dy corresponding to the increase in pressure. That systematic study of hadron spectra and flow results indicated that existing data are best reproduced by hydrodynamic model calculations with an equation of state which include a

transition to a quark gluon plasma phase at a critical temperature of $T_c = 165$ MeV with a latent heat of 800 MeV [53].

7. Summary

Directed and elliptic flow of photons have been measured in 158 A GeV Pb + Pb collisions using the LEDA electromagnetic calorimeter and the Plastic Ball detector of the WA98 experiment. The conventional reaction plane method for directed and elliptic flow and the pair-correlation method for elliptic flow have been used in the analysis. The elliptic flow values obtained by the two methods are consistent.

The centrality and p_T dependences of the photon directed and elliptic flow coefficients were presented. In-plane elliptic flow is observed. Both flow values increase for more peripheral collisions and with increasing p_T.

For comparison with charged pion measurements, the neutral pion flow coefficients have been extracted from the measured photon flow coefficients using Monte Carlo simulations. The Monte Carlo simulations demonstrate that the average photon flow coefficients are $\approx$ 7–21% greater than the parent π^0 flow coefficients. The extracted neutral pion flow results are compatible with the NA49 charged pion flow and with the general trend of the elliptic flow behaviour as a function of beam energy. The universal dependence of the elliptic flow, scaled by the eccentricity of the initial nuclear overlap, on particle density is confirmed.

References

[1] M. Hofmann, et al., Nucl. Phys. A 566 (1994) 15c.
[2] J.-Y. Ollitrault, Phys. Rev. D 46 (1992) 229;
J.-Y. Ollitrault, Phys. Rev. D 48 (1993) 1132;
J.-Y. Ollitrault, Nucl. Phys. A 638 (1998) 195c.
[3] H. Sorge, Phys. Rev. Lett. 78 (1997) 2309.
[4] H. Stocker, W. Greiner, Phys. Rep. 137 (1986) 277.
[5] C.M. Hung, E.V. Shuryak, Phys. Rev. Lett. 75 (1995) 4003.
[6] D.H. Rischke, Nucl. Phys. A 610 (1996) 88c.
[7] NA49 Collaboration, T. Alber, et al., Phys. Rev. Lett. 75 (1995) 3814;
WA98 Collaboration, M.M. Aggarwal, et al., Eur. Phys. J. C 18 (2001) 0651;
PHENIX Collaboration, K. Adcox, et al., Phys. Rev. Lett. 87 (2001) 052301.
[8] S. Voloshin, A. Poskanzer, Phys. Lett. B 474 (2000) 27.
[9] Plastic Ball Collaboration, H.A. Gustafsson, et al., Phys. Rev. Lett. 52 (1984) 1590;
H.H. Gutbrod, et al., Phys. Lett. B 216 (1989) 267;
H.H. Gutbrod, et al., Rep. Prog. Phys. 52 (1989) 1267;
H.A. Gustafsson, et al., Phys. Rev. C 42 (1990) 640.
[10] KAOS Collaboration, D. Brill, et al., Phys. Rev. Lett. 71 (1993) 336;
D. Brill, et al., Z. Phys. A 355 (1996) 61;
D. Brill, et al., Z. Phys. A 357 (1996) 207;
Y. Shin, Phys. Rev. Lett. 81 (1998) 1576.
[11] FOPI Collaboration, G. Poggi, et al., Nucl. Phys. A 586 (1995) 755;
J.L. Ritman, et al., Z. Phys. A 352 (1995) 355;
N. Bastid, et al., Nucl. Phys. A 622 (1997) 573.
[12] E877 Collaboration, J. Barette, et al., Phys. Rev. Lett. 70 (1993) 2996;
J. Barette, et al., Phys. Rev. Lett. 73 (1994) 2532;
J. Barette, et al., Phys. Rev. C 55 (1997) 1420;
J. Barette, et al., Phys. Rev. C 56 (1997) 3254;
S.A. Voloshin, et al., Nucl. Phys. A 638 (1998) 455c.

[13] NA49 Collaboration, T. Wienold, et al., Nucl. Phys. A 610 (1996) 76c;
H. Appelshauser, et al., Phys. Rev. Lett. 80 (1998) 4136;
A.M. Poskanzer, et al., Nucl. Phys. A 638 (1998) 463c;
A.M. Poskanzer, et al., Nucl. Phys. A 661 (1999) 341c;
A. Wetzler, et al., Nucl. Phys. A 715 (2003) 583c.
[14] WA80 Collaboration, T.C. Awes, et al., Phys. Lett. B 381 (1996) 29.
[15] WA93 Collaboration, M.M. Aggarwal, et al., Phys. Lett. B 403 (1997) 390.
[16] WA98 Collaboration, M. Kurata, et al., Prog. Theor. Phys. Suppl. 129 (1997) 179;
B. Wyslouch, et al., Nucl. Phys. A 638 (1998) 147c;
S. Nishimura, et al., Nucl. Phys. A 638 (1998) 459c;
S. Nishimura, et al., Nucl. Phys. A 661 (1999) 464c;
M.M. Aggarwal, et al., nucl-ex/9807004;
M.M. Aggarwal, et al., Phys. Lett. B 469 (1999) 30;
S. Nishimura, et al., Nucl. Phys. A 663-664 (2000) 729c.
[17] CERES Collaboration, G. Agakichiev, et al., Phys. Rev. Lett. 92 (2004) 032301.
[18] PHENIX Collaboration, K. Adcox, et al., Phys. Rev. Lett. 89 (2002) 212301;
S. Esumi, et al., nucl-ex/0210012.
[19] STAR Collaboration, K.H. Ackermann, et al., Phys. Rev. Lett. 86 (2001) 402;
C. Adler, et al., Phys. Rev. Lett. 87 (2001) 182301.
[20] PHOBOS Collaboration, B. Back, et al., Phys. Rev. Lett. 94 (2005) 122303.
[21] WA98 Collaboration, S. Nikolaev, et al., Nucl. Phys. A 715 (2003) 579c.
[22] WA98 Collaboration, S. Bathe, et al., Nucl. Phys. A 715 (2003) 729c.
[23] WA98 Collaboration, Proposal for a large acceptance hadron and photon spectrometer, preprint CERN/SPSLC 91-17, SPSLC/P260, 1991.
[24] T.C. Awes, et al., Nucl. Instrum. Methods Phys. Res. Sect. A 279 (1989) 479.
[25] WA98 Collaboration, M.M. Aggarwal, et al., nucl-ex/0006007.
[26] A. Baden, et al., Nucl. Instrum. Methods Phys. Res. Sect. A 203 (1982) 189.
[27] S. Neumaier, et al., Nucl. Instrum. Methods Phys. Res. Sect. A 360 (1995) 593.
[28] A.L. Wintenberg, et al., in: Proceedings of Electronics for Future Colliders Conference, LeCroy Corp, May 1994.
[29] T. Peitzmann, et al., Nucl. Instrum. Methods Phys. Res. Sect. A 376 (1996) 368.
[30] S. Voloshin, Y. Zhang, Z. Phys. C 70 (1996) 665.
[31] A. Poskanzer, S. Voloshin, Phys. Rev. C 58 (1998) 1671.
[32] WA98 Collaboration, H. Schlagheck, et al., Nucl. Phys. A 661 (1999) 337c.
[33] S. Wang, et al., Phys. Rev. C 44 (1991) 1091.
[34] R. Lacey, et al., Phys. Rev. Lett. 70 (1993) 1224.
[35] PHENIX Collaboration, R. Lacey, Nucl. Phys. A 698 (2002) 559.
[36] N. Borghini, et al., Phys. Rev. C 64 (2001) 054901.
[37] WA98 Collaboration, M.M. Aggarwal, et al., Eur. Phys. J. C 18 (2001) 651–663.
[38] WA98 Collaboration, M.M. Aggarwal, et al., Eur. Phys. J. C 23 (2002) 225–236.
[39] F. Berger, et al., Nucl. Instrum. Methods Phys. Res. Sect. A 321 (1992) 152.
[40] P. Danielewicz, G. Odyniec, Phys. Lett. B 157 (1985) 146.
[41] H. Büsching, PhD thesis, Universitat Münster, 2002.
[42] WA98 Collaboration, M.M. Aggarwal, et al., Eur. Phys. J. C 41 (2005) 287–296.
[43] NA49 Collaboration, C. Alt, et al., Phys. Rev. C 68 (2003) 034903.
[44] P. Huovinen, et al., Phys. Lett. B 503 (2001) 58.
[45] CERES Collaboration, K. Filimonov, et al., nucl-ex/0109017.
[46] PHOBOS Collaboration, S. Manly, et al., Nucl. Phys. A 715 (2003) 611c.
[47] PHENIX Collaboration, S. Esumi, et al., Nucl. Phys. A 715 (2003) 599c.
[48] STAR Collaboration, L. Ray, et al., Nucl. Phys. A 715 (2003) 45c.
[49] H. Sorge, Phys. Rev. Lett. 82 (1999) 2048.
[50] STAR Collaboration, L. Ray, in: Quark Matter'02, Nucl. Phys. A 715 (2003) 45c.
[51] STAR Collaboration, C. Adler, et al., Phys. Rev. C 66 (2002) 034904.
[52] J.D. Bjorken, Phys. Rev. D 27 (1983) 140.
[53] D. Teaney, J. Lauret, E.V. Shuryak, et al., nucl-th/0110037.

Production of ϕ mesons at midrapidity in $\sqrt{s_{NN}} = 200$ GeV Au+Au collisions at relativistic energies

S. S. Adler,[5] S. Afanasiev,[17] C. Aidala,[5] N. N. Ajitanand,[43] Y. Akiba,[20,38] J. Alexander,[43] R. Amirikas,[12] L. Aphecetche,[45] S. H. Aronson,[5] R. Averbeck,[44] T. C. Awes,[35] R. Azmoun,[44] V. Babintsev,[15] A. Baldisseri,[10] K. N. Barish,[6] P. D. Barnes,[27] B. Bassalleck,[33] S. Bathe,[30] S. Batsouli,[9] V. Baublis,[37] A. Bazilevsky,[39,15] S. Belikov,[16,15] Y. Berdnikov,[40] S. Bhagavatula,[16] J. G. Boissevain,[27] H. Borel,[10] S. Borenstein,[25] M. L. Brooks,[27] D. S. Brown,[34] N. Bruner,[33] D. Bucher,[30] H. Buesching,[30] V. Bumazhnov,[15] G. Bunce,[5,39] J. M. Burward-Hoy,[26,44] S. Butsyk,[44] X. Camard,[45] J.-S. Chai,[18] P. Chand,[4] W. C. Chang,[2] S. Chernichenko,[15] C. Y. Chi,[9] J. Chiba,[20] M. Chiu,[9] I. J. Choi,[52] J. Choi,[19] R. K. Choudhury,[4] T. Chujo,[5] V. Cianciolo,[35] Y. Cobigo,[10] B. A. Cole,[9] P. Constantin,[16] D. G. d'Enterria,[45] G. David,[5] H. Delagrange,[45] A. Denisov,[15] A. Deshpande,[39] E. J. Desmond,[5] A. Devismes,[44] O. Dietzsch,[41] O. Drapier,[25] A. Drees,[44] R. du Rietz,[29] A. Durum,[15] D. Dutta,[4] Y. V. Efremenko,[35] K. El Chenawi,[49] A. Enokizono,[14] H. En'yo,[38,39] S. Esumi,[48] L. Ewell,[5] D. E. Fields,[33,39] F. Fleuret,[25] S. L. Fokin,[23] B. D. Fox,[39] Z. Fraenkel,[51] J. E. Frantz,[9] A. Franz,[5] A. D. Frawley,[12] S.-Y. Fung,[6] S. Garpman,[29,*] T. K. Ghosh,[49] A. Glenn,[46] G. Gogiberidze,[46] M. Gonin,[25] J. Gosset,[10] Y. Goto,[39] R. Granier de Cassagnac,[25] N. Grau,[16] S. V. Greene,[49] M. Grosse Perdekamp,[39] W. Guryn,[5] H.-Å. Gustafsson,[29] T. Hachiya,[14] J. S. Haggerty,[5] H. Hamagaki,[8] A. G. Hansen,[27] E. P. Hartouni,[26] M. Harvey,[5] R. Hayano,[8] N. Hayashi,[38] X. He,[13] M. Heffner,[26] T. K. Hemmick,[44] J. M. Heuser,[44] M. Hibino,[50] J. C. Hill,[16] W. Holzmann,[43] K. Homma,[14] B. Hong,[22] A. Hoover,[34] T. Ichihara,[38,39] V. V. Ikonnikov,[23] K. Imai,[24,38] D. Isenhower,[1] M. Ishihara,[38] M. Issah,[43] A. Isupov,[17] B. V. Jacak,[44] W. Y. Jang,[22] Y. Jeong,[19] J. Jia,[44] O. Jinnouchi,[38] B. M. Johnson,[5] S. C. Johnson,[26] K. S. Joo,[31] D. Jouan,[36] S. Kametani,[8,50] N. Kamihara,[47,38] J. H. Kang,[52] S. S. Kapoor,[4] K. Katou,[50] S. Kelly,[9] B. Khachaturov,[51] A. Khanzadeev,[37] J. Kikuchi,[50] D. H. Kim,[31] D. J. Kim,[52] D. W. Kim,[19] E. Kim,[42] G.-B. Kim,[25] H. J. Kim,[52] E. Kistenev,[5] A. Kiyomichi,[48] K. Kiyoyama,[32] C. Klein-Boesing,[30] H. Kobayashi,[38,39] L. Kochenda,[37] V. Kochetkov,[15] D. Koehler,[33] T. Kohama,[14] M. Kopytine,[44] D. Kotchetkov,[6] A. Kozlov,[51] P. J. Kroon,[5] C. H. Kuberg,[1,27] K. Kurita,[39] Y. Kuroki,[48] M. J. Kweon,[22] Y. Kwon,[52] G. S. Kyle,[34] R. Lacey,[43] V. Ladygin,[17] J. G. Lajoie,[16] A. Lebedev,[16,23] S. Leckey,[44] D. M. Lee,[27] S. Lee,[19] M. J. Leitch,[27] X. H. Li,[6] H. Lim,[42] A. Litvinenko,[17] M. X. Liu,[27] Y. Liu,[36] C. F. Maguire,[49] Y. I. Makdisi,[5] A. Malakhov,[17] V. I. Manko,[23] Y. Mao,[7,38] G. Martinez,[45] M. D. Marx,[44] H. Masui,[48] F. Matathias,[44] T. Matsumoto,[8,50] P. L. McGaughey,[27] E. Melnikov,[15] F. Messer,[44] Y. Miake,[48] J. Milan,[43] T. E. Miller,[49] A. Milov,[44,51] S. Mioduszewski,[5] R. E. Mischke,[27] G. C. Mishra,[13] J. T. Mitchell,[5] A. K. Mohanty,[4] D. P. Morrison,[5] J. M. Moss,[27] F. Mühlbacher,[44] D. Mukhopadhyay,[51] M. Muniruzzaman,[6] J. Murata,[38,39] S. Nagamiya,[20] J. L. Nagle,[9] T. Nakamura,[14] B. K. Nandi,[6] M. Nara,[48] J. Newby,[46] P. Nilsson,[29] A. S. Nyanin,[23] J. Nystrand,[29] E. O'Brien,[5] C. A. Ogilvie,[16] H. Ohnishi,[5,38] I. D. Ojha,[49,3] K. Okada,[38] M. Ono,[48] V. Onuchin,[15] A. Oskarsson,[29] I. Otterlund,[29] K. Oyama,[8] K. Ozawa,[8] D. Pal,[51] A. P. T. Palounek,[27] V. S. Pantuev,[44] V. Papavassiliou,[34] J. Park,[42] A. Parmar,[33] S. F. Pate,[34] T. Peitzmann,[30] J.-C. Peng,[27] V. Peresedov,[17] C. Pinkenburg,[5] R. P. Pisani,[5] F. Plasil,[35] M. L. Purschke,[5] A. K. Purwar,[44] J. Rak,[16] I. Ravinovich,[51] K. F. Read,[35,46] M. Reuter,[44] K. Reygers,[30] V. Riabov,[37,40] Y. Riabov,[37] G. Roche,[28] A. Romana,[25] M. Rosati,[16] P. Rosnet,[28] S. S. Ryu,[52] M. E. Sadler,[1] N. Saito,[38,39] T. Sakaguchi,[8,50] M. Sakai,[32] S. Sakai,[48] V. Samsonov,[37] L. Sanfratello,[33] R. Santo,[30] H. D. Sato,[24,38] S. Sato,[5,48] S. Sawada,[20] Y. Schutz,[45] V. Semenov,[15] R. Seto,[6] M. R. Shaw,[1,27] T. K. Shea,[5] T.-A. Shibata,[47,38] K. Shigaki,[14,20] T. Shiina,[27] C. L. Silva,[41] D. Silvermyr,[27,29] K. S. Sim,[22] C. P. Singh,[3] V. Singh,[3] M. Sivertz,[5] A. Soldatov,[15] R. A. Soltz,[26] W. E. Sondheim,[27] S. P. Sorensen,[46] I. V. Sourikova,[5] F. Staley,[10] P. W. Stankus,[35] E. Stenlund,[29] M. Stepanov,[34] A. Ster,[21] S. P. Stoll,[5] T. Sugitate,[14] J. P. Sullivan,[27] E. M. Takagui,[41] A. Taketani,[38,39] M. Tamai,[50] K. H. Tanaka,[20] Y. Tanaka,[32] K. Tanida,[38] M. J. Tannenbaum,[5] P. Tarján,[11] J. D. Tepe,[1,27] T. L. Thomas,[33] J. Tojo,[24,38] H. Torii,[24,38] R. S. Towell,[1] I. Tserruya,[51] H. Tsuruoka,[48] S. K. Tuli,[3] H. Tydesjö,[29] N. Tyurin,[15] H. W. van Hecke,[27] J. Velkovska,[5,44] M. Velkovsky,[44] V. Veszprémi,[11] L. Villatte,[46] A. A. Vinogradov,[23] M. A. Volkov,[23] E. Vznuzdaev,[37] X. R. Wang,[13] Y. Watanabe,[38,39] S. N. White,[5] F. K. Wohn,[16] C. L. Woody,[5] W. Xie,[6] Y. Yang,[7] A. Yanovich,[15] S. Yokkaichi,[38,39] G. R. Young,[35] I. E. Yushmanov,[23] W. A. Zajc,[9,†] C. Zhang,[9] S. Zhou,[7] S. J. Zhou,[51] and L. Zolin[17]

(PHENIX Collaboration)

[1]*Abilene Christian University, Abilene, Texas 79699, USA*

[2]*Institute of Physics, Academia Sinica, Taipei 11529, Taiwan*

[3]*Department of Physics, Banaras Hindu University, Varanasi 221005, India*

[4]*Bhabha Atomic Research Centre, Bombay 400 085, India*

[5]*Brookhaven National Laboratory, Upton, New York 11973-5000, USA*

[6]*University of California, Riverside, California 92521, USA*

[7]*China Institute of Atomic Energy (CIAE), Beijing, People's Republic of China*

[8]*Center for Nuclear Study, Graduate School of Science, University of Tokyo, 7-3-1 Hongo, Bunkyo, Tokyo 113-0033, Japan*

[9]*Columbia University, New York, New York 10027 and Nevis Laboratories, Irvington, New York 10533, USA*

*Deceased.

†PHENIX Spokesperson: zajc@nevis.columbia.edu

 ©2005 The American Physical Society

[10]*Dapnia, CEA Saclay, F-91191 Gif-sur-Yvette, France*
[11]*Debrecen University, Egyetem tér 1, H-4010 Debrecen, Hungary*
[12]*Florida State University, Tallahassee, Florida 32306, USA*
[13]*Georgia State University, Atlanta, Georgia 30303, USA*
[14]*Hiroshima University, Kagamiyama, Higashi-Hiroshima 739-8526, Japan*
[15]*Institute for High Energy Physics (IHEP), Protvino, Russia*
[16]*Iowa State University, Ames, Iowa 50011, USA*
[17]*Joint Institute for Nuclear Research, 141980 Dubna, Moscow Region, Russia*
[18]*KAERI, Cyclotron Application Laboratory, Seoul, South Korea*
[19]*Kangnung National University, Kangnung 210-702, South Korea*
[20]*KEK, High Energy Accelerator Research Organization, Tsukuba-shi, Ibaraki-ken 305-0801, Japan*
[21]*KFKI Research Institute for Particle and Nuclear Physics (RMKI), Post Office Box 49, H-1525 Budapest 114, Hungary*
[22]*Korea University, Seoul, 136-701, Korea*
[23]*Russian Research Center "Kurchatov Institute," Moscow, Russia*
[24]*Kyoto University, Kyoto 606-8502, Japan*
[25]*Laboratoire Leprince-Ringuet, Ecole Polytechnique, CNRS-IN2P3, Route de Saclay, F-91128 Palaiseau, France*
[26]*Lawrence Livermore National Laboratory, Livermore, California 94550, USA*
[27]*Los Alamos National Laboratory, Los Alamos, New Mexico 87545, USA*
[28]*LPC, Université Blaise Pascal, CNRS-IN2P3, Clermont-Fd, F-63177 Aubiere Cedex, France*
[29]*Department of Physics, Lund University, Box 118, SE-221 00 Lund, Sweden*
[30]*Institut für Kernphysik, University of Muenster, D-48149 Muenster, Germany*
[31]*Myongji University, Yongin, Kyonggido 449-728, Korea*
[32]*Nagasaki Institute of Applied Science, Nagasaki-shi, Nagasaki 851-0193, Japan*
[33]*University of New Mexico, Albuquerque, New Mexico 87131, USA*
[34]*New Mexico State University, Las Cruces, New Mexico 88003, USA*
[35]*Oak Ridge National Laboratory, Oak Ridge, Tennessee 37831, USA*
[36]*IPN-Orsay, Universite Paris Sud, CNRS-IN2P3, BP1, F-91406 Orsay, France*
[37]*PNPI, Petersburg Nuclear Physics Institute, Gatchina, Russia*
[38]*RIKEN (The Institute of Physical and Chemical Research), Wako, Saitama 351-0198, Japan*
[39]*RIKEN BNL Research Center, Brookhaven National Laboratory, Upton, New York 11973-5000, USA*
[40]*St. Petersburg State Technical University, St. Petersburg, Russia*
[41]*Universidade de São Paulo, Instituto de Física, Caixa Postal 66318, São Paulo CEP05315-970, Brazil*
[42]*System Electronics Laboratory, Seoul National University, Seoul, South Korea*
[43]*Chemistry Department, Stony Brook University, SUNY, Stony Brook, New York 11794-3400, USA*
[44]*Department of Physics and Astronomy, Stony Brook University, SUNY, Stony Brook, New York 11794, USA*
[45]*SUBATECH (Ecole des Mines de Nantes, CNRS-IN2P3, Université de Nantes) Bôite Postale 20722, F-44307 Nantes, France*
[46]*University of Tennessee, Knoxville, Tennessee 37996, USA*
[47]*Department of Physics, Tokyo Institute of Technology, Tokyo 152-8551, Japan*
[48]*Institute of Physics, University of Tsukuba, Tsukuba, Ibaraki 305, Japan*
[49]*Vanderbilt University, Nashville, Tennessee 37235, USA*
[50]*Waseda University, Advanced Research Institute for Science and Engineering, 17 Kikui-cho, Shinjuku-ku, Tokyo 162-0044, Japan*
[51]*Weizmann Institute, Rehovot 76100, Israel*
[52]*Yonsei University, IPAP, Seoul 120-749, Korea*
(Received 8 October 2004; published 14 July 2005)

We present the results of ϕ meson production in the K^+K^- decay channel from Au+Au collisions at $\sqrt{s_{NN}} = 200$ GeV as measured at midrapidity by the PHENIX detector at Brookhaven National Laboratory's Relativistic Heavy Ion Collider. Precision resonance centroid and width values are extracted as a function of collision centrality. No significant variation from the Particle Data Group accepted values is observed, contrary to some model predictions. The ϕ transverse mass spectra are fitted with a linear exponential function for which the derived inverse slope parameter is seen to be constant as a function of centrality. However, when these data are fitted by a hydrodynamic model the result is that the centrality-dependent freeze-out temperature and the expansion velocity values are consistent with the values previously derived from fitting identified charged hadron data. As a function of transverse momentum the collisions scaled peripheral-to-central yield ratio R_{CP} for the ϕ is comparable to that of pions rather than that of protons. This result lends support to theoretical models that distinguish between baryons and mesons instead of particle mass for explaining the anomalous (anti) proton yield.

DOI: 10.1103/PhysRevC.72.014903 PACS number(s): 25.75.Dw

I. INTRODUCTION

Relativistic heavy-ion experiments have a goal of producing matter at extreme temperatures and energy densities such that conditions are favorable for the transition to a deconfined state of quarks and gluons, the quark gluon plasma (QGP). Theoretical calculations predict that the temperatures and energy densities that can be reached at the Brookhaven National Laboratory's Relativistic Heavy Ion Collider (RHIC) will exceed those needed for the formation of the QGP [1–3].

The production and decay of the ϕ meson have long been recognized as an important probe for the state of matter produced in relativistic heavy-ion (RHI) collisions [4–21]. In pp collisions the creation of the ϕ is suppressed according to the Okubo-Zweig-Iizuka rule [22]. Hence, if there is an enhancement of the ϕ yield in RHI collisions relative to pp collisions, this could be evidence of nonconventional production mechanisms such as strange quark coalescence via the formation and subsequent hadronization of the QGP. The fact that the ϕ yield is undistorted by feed-down from higher mass resonances makes it an attractive probe in this respect.

The decay modes of the ϕ, specifically the dilepton channels (e^+e^- or $\mu^+\mu^-$) and the K^+K^- channel, will probe the final state differently should the decay take place in the presence of the QGP-mixed or the completely hadronized phase. The dileptons will have insignificant interactions with the medium, whereas the kaons can scatter until freeze-out. The lifetime of the ϕ in vacuum is large ($\approx$45 fm/c) compared to say a 10-fm-sized interaction region. However, several theoretical calculations [13,21,23] predict that the ϕ mass and width could be significantly modified in either the hot or the cold nuclear medium. These medium-induced effects could be manifested through measured shifts in the mass centroid of the resonance or changes in the resonance width. Also predicted are changes in the relative branching ratio between kaon and lepton pairs, with respect to the Particle Data Group (PDG) [24].

The production mechanism of strangeness in heavy-ion collisions can be investigated through the measurement of the particle yields. In this paper, we study system size dependence by analyzing centrality-selected data. A comparison between different systems can be made by normalizing to the number of participant pairs. The expectation is that for production dominated by soft processes, the yields scale as the number of participants. We compare the centrality dependence of strange and nonstrange particle yields to reveal a possible flavor dependence.

An additional important question is whether the ϕ mesons participate in radial flow together with the other hadrons, or if they freeze-out earlier, as might be true if the small vacuum cross sections of the ϕ with hadrons persist in the fireball. Previous measurements have yielded contradictory results [25, 26]. One of the important advantages of RHIC experiments is the capability to examine the momentum spectrum as a function of centrality for a variety of hadrons, which should yield important additional information on the radial flow issue. A spectral shape analysis including a simultaneous treatment of the ϕ and the more abundant hadrons (π, K, p) will be presented here.

At high p_T, hadrons are primarily produced from the fragmentation of hard-scattered partons. One of the most exciting results from RHIC was the discovery of hadron suppression in central Au+Au collisions [27,28]; this suppression is absent in d + Au collisions [29]. Surprisingly, it was also discovered that proton and antiproton production at intermediate p_T (1.5–4.5 GeV/c) scales with the number of binary nucleon-nucleon collisions ($N_{\rm coll}$) as would be expected for hard scattering in the absence of any nuclear modification [30]. In fact, the intermediate p_T antiproton to pion ratios were found to exceed by a factor of 3 the values expected from parton fragmentation [30,31]. These experimental results lead to the conclusion that protons and pions have different production mechanisms at intermediate p_T [30]. One possible explanation invokes parton recombination from the QGP [32–35]. A measurement of the nuclear modification factor for the ϕ meson, which has a mass comparable to the proton but carries only two quarks, is crucial for understanding the hadron production at intermediate p_T. In this work we have measured the nuclear modification factor through the ratio $R_{\rm CP}$ of central to peripheral yields scaled by their respective $N_{\rm coll}$ value.

To put our results into perspective, we begin by describing the currently available ϕ data obtained in RHI collisions. The production of ϕ mesons has been studied systematically at ever increasing $\sqrt{s}$ from the AGS to RHIC. The E802 collaboration made the first observation of the ϕ in fixed-target central collisions of 14.6A GeV Si+Au ($\sqrt{s_{NN}} = 5.39$ GeV) via the K^+K^- channel [36]. They obtained a ratio $N_\phi/N_{K^-} = 11.6\%$, roughly consistent with the ratio obtained in pp data over a wide range of $\sqrt{s}$ [37]. The analysis of the E802 rapidity distributions indicated that the ϕ production scaled with the product of the K^+ and K^- separate yields and that either there was significant rescattering of the ϕ after production or the production itself came after rescattering of the colliding participants.

Also at the AGS the E917 experiment has reported another ϕ measurement with 11.7A GeV Au+Au ($\sqrt{s_{NN}} = 4.87$ GeV) in the rapidity range $1.2 < y < 1.6$ in five centrality bins [38]. The observed yield of the ϕ increased toward more central collisions with a distinctly greater than linear dependence on the number of participants. The yield increase of the ϕ in central collisions was stronger than that of the π since the N_ϕ/N_π ratio increased in central collisions. However, the N_ϕ/N_{K^+} and N_ϕ/N_{K^-} ratios were constant as a function of centrality.

At the SPS the NA49 experiment has measured ϕ production in pp, p+Pb, and Pb+Pb collisions with $E_{\rm beam} =$ 158A GeV ($\sqrt{s_{NN}} = 17.5$ GeV) in the rapidity range $3.0 < y < 3.8$ [39]. Relative to the pp yields, these data showed that the ratio of the ϕ yield to the π yield in central Pb+Pb collisions was enhanced by a factor of 3.0 ± 0.7. Another SPS collaboration, NA38/NA50, has measured the ϕ in the $\mu^+\mu^-$ channel [40,41], for which the extracted effective temperature and dN/dy differ from those obtained in the K^+K^- channel in the same systems. The yield difference between the two SPS experiments has been calculated to be factors of 2–4 [42], with the NA38/NA50 result being higher.

The first measurement of the ϕ meson at RHIC was reported by the STAR Collaboration [43], in the collisions of Au+Au

at $\sqrt{s_{NN}} = 130$ GeV at three centralities, 0–11%, 11–26%, and 26–85%, in the rapidity range $-0.5 < y < +0.5$. The extracted temperature T and the ratio $N_\phi/N_{\text{hadrons}}$ did not vary with centrality.

One may summarize the current state of knowledge on ϕ production in heavy-ion collisions by stating that the topic remains highly unexplored territory. The heavy-ion measurements do indicate that the observed ϕ yield is not a simple linear superposition of nucleon-nucleon collisions. Rather, the data imply the influence of some collective effects. Whether those effects are induced by cold and/or hot nuclear matter is not known since there does not yet exist definitive evidence. Moreover, thus far there has not been precise enough heavy-ion data that can address the question of the change in the ϕ mass or its width in the cold nuclear or the hot QGP medium. And except for one experiment measuring the dimuon channel, there is a scarcity of useful quantitative information in heavy-ion collisions concerning the ϕ decay into dileptons.

In this paper we report on a measurement of the ϕ yield at midrapidity in collisions of Au+Au beams from RHIC at $\sqrt{s_{NN}} = 200$ GeV as measured in the K^+K^- channel by the PHENIX detector. The paper is organized as follows. In Sec. II we give a short review of the PHENIX detector configuration. In Sec. III we describe the data analysis procedure. Section IV presents and discusses the results. The first precision measurements of ϕ mass and width values obtained in RHI collisions as a function of centrality are given in Sec. IV A. Absolute yields as a function of p_T for three centrality bins are shown in Sec. IV B. The centrality dependence of yields and ratios are studied in Sec. IV D. In Sec. IV D the spectra shapes are interpreted in the framework of a hydrodynamical model and the freeze-out conditions are extracted. Finally, the nuclear modification factor R_{CP} for the ϕ is obtained and compared to those of pions and protons in Sec. IV E.

II. PHENIX DETECTOR

The PHENIX detector consists of two spectrometer arms at near zero rapidity, two forward rapidity muon spectrometers, and three global event characterization detectors. The central arm spectrometers, shown schematically in Fig. 1, are located east and west of the beam line with $\pi/2$ radian azimuthal coverage each. These spectrometers are designed to detect photons, electrons, and charged hadrons. The ϕ data for this paper were obtained with the central arm detector subsystems, which provide high-resolution particle identification and momentum reconstruction. A complete description of the PHENIX apparatus has been published elsewhere [44–49]. We present a brief review of the relevant detector subsystems in the following sections.

A. Global detectors

The global detectors furnish the start time signals, collision vertex measurements, and interaction centrality. The centrality for events in the Au+Au collisions is determined [50] by combining the data from two subsystems: the zero degree calorimeters (ZDC) [48] and the beam-beam counters (BBC)

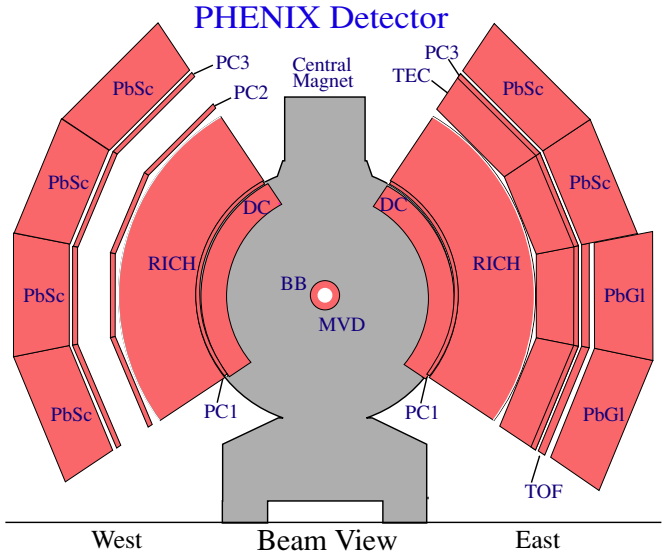

FIG. 1. (Color online) Beam's-eye view of the PHENIX central arm detector subsystems.

[47]. The ZDC are hadronic calorimeters located 18 m downstream and upstream of the interaction point along the beam line. These calorimeters detect the energy carried by spectator neutrons. The BBC are Čerenkov telescopes placed ± 1.44 m from the center of the beam collision region in the pseudorapidity region $3.0 < |\eta| < 3.9$. The correlation between the ZDC energy sum and the charge sum recorded in the BBC determines the centrality of the collision event. The BBC data also determine the longitudinal collision coordinate (z_{vertex}) and the start time for the time-of-flight measurements.

B. Central arm detectors

The central arm spectrometers [49] in PHENIX provide charged particle tracking and particle identification. This analysis was done with the east arm spectrometer. The $\phi \to K^+K^-$ decay kinematics are such that that the PHENIX detector has negligible acceptance for the very low p_T ϕ particles, which would decay into east-west kaon pairs. The data included information from the drift chamber (DC), the pad chambers (PC1 and PC3), the high-resolution time-of-flight (TOF) wall, and the electromagnetic calorimeter (EMCal) lead-scintillator detectors (PbSc), as depicted in Fig. 1.

Pattern recognition and tracking of the charged particles are accomplished using the DC information by a combinatorial Hough transform method [51]. The DC subsystem is located at an average radial distance of 2.2 m from the beam line. It is a projective tracking detector providing high-precision measurements in the azimuthal XY plane, which are combined with the XYZ single spatial point measurement from the PC1 located at 2.45 m. These data, together with the BBC z_{vertex} information, are sufficient to determine the track's initial momentum vector, whose magnitude is obtained with a resolution $\delta p/p \simeq 0.7\% \oplus 1.0\% \times p$ (GeV/c). The first term in this expression is due to the multiple scattering before the DC and the second term is the angular resolution of the DC.

Based on identified mass measurements obtained with the TOF subsystem, the absolute momentum scale is known to $\pm 0.7\%$.

Tracks obtained from the DC/PC1 detectors are projected to the PC3, TOF, and PbSc detectors where associations can be made. The high-resolution TOF subsystem provides one set of mass measurements while the PbSc detectors provide a geometrically independent set of mass measurements. The TOF wall is positioned 5.06 m from the beam line and consists of 960 scintillator slats oriented along the azimuthal direction. It is designed to cover $|\eta| < 0.35$ and $\Delta\phi = \pi/4$ in azimuthal angle.

The PbSc detector, covering half of the east arm and entire west arm, can also be used for hadron timing measurements. The present analysis uses the PbSc modules in the east arm, which are located at 5.1 m in radial distance from the beam line and cover a $\Delta\phi = \pi/4$ azimuthal range. This detector is constructed as separate towers of dimension $5.25 \times 5.25 \times 37\ \mathrm{cm}^3$, in an alternating lead-scintillator sandwich-type structure ("shish-kebob"), approximately 18 radiation lengths in depth. As illustrated in Fig. 1 the TOF and the PbSc sectors are completely nonoverlapping.

III. DATA ANALYSIS

In this section, we describe the event and track selection, particle identification, the details of K^+K^- pair reconstruction, and the corrections for geometrical acceptance, particle decay in flight, multiple scattering, and detector occupancy factors, all of which couple into deriving the ϕ meson spectra.

A. Event selection

The events selected for this analysis were based on the PHENIX minimum-bias trigger provided by the BBC and ZDC. As noted previously, the centrality of each Au+Au collision event was determined by correlating the BBC charge sum and the ZDC total energy [50]. The PHENIX minimum-bias data sample included $92.2^{+2.5}_{-3.0}\%$ of the 6.9-b Au+Au total inelastic cross section [29]. This analysis used 20 million minimum-bias events with a vertex position within $|z_{\mathrm{vertex}}| < 30$ cm.

To study the centrality-dependent physics, we divided these events into different centrality bins. For the ϕ meson lineshape analysis, we used five centrality bins: 0–10%, 10–20%, 20–40%, 40–60%, and 60–92%. The transverse mass (m_T) spectra were reconstructed for three centrality bins: 0–10%, 10–40%, and 40–92%. These bin divisions were chosen to have approximately equal statistical significance for their respective data points. The centrality of collisions is additionally characterized by the average number of participants ($\langle N_{\mathrm{part}} \rangle$) and the average number of binary nucleon–nucleon collisions ($\langle N_{\mathrm{coll}} \rangle$). These two global quantities, shown in Table I as a function of centrality, are derived from a Glauber model calculation [29].

B. Track selection

Only tracks with valid information from the DC and the PC1 were used for the analysis. These tracks were then confirmed by matching the projected and associated hit information at the TOF wall for the TOF analysis, or at the PC3 and the EMCal for the PbSc analysis. The differences between the actual azimuthal and longitudinal hit coordinates compared to the projected hit coordinates were determined. These tracking coordinate residuals were converted to standard deviation residuals by a momentum-dependent function that computed the expected residual coordinate value. On this basis, a 3σ track-matching cut was used to accept track associations. Lastly, for the TOF wall, an energy-loss cut is applied on the analog signal height from the scintillator slat. This cut has been described in a previous publication [50].

TABLE I. Average number of participants and collisions in Au+Au reaction at RHIC for different centralities determined from a Glauber model [29]. The error associated with each number is the systematic error.

Centrality (%)	$\langle N_{\mathrm{part}} \rangle$	$\langle N_{\mathrm{coll}} \rangle$
0–10	325.2 ± 3.3	955.4 ± 93.6
10–20	234.6 ± 4.7	602.6 ± 59.3
20–40	140.4 ± 4.9	296.8 ± 31.1
10–40	171.8 ± 4.8	398.7 ± 40.5
40–60	59.9 ± 3.5	90.6 ± 11.8
60–92	14.5 ± 2.5	14.5 ± 4.0
40–92	32.0 ± 2.9	45.2 ± 7.3
Minimum Bias	109.1 ± 4.1	257.8 ± 25.4

C. Particle identification

As mentioned earlier, the PHENIX central arm spectrometer utilizes the high-resolution TOF wall and PbSc modules for hadron mass identification. The kaons in the TOF wall were identified via reconstructed momentum combined with a TOF measurement. The timing resolution of this subsystem is $\sigma \simeq 115$ ps. A momentum range of 0.3–2.0 GeV/c was selected to compute the mass distributions [52]. Figure 2 shows the mass-squared distribution of all tracks passing through the TOF module for six different momentum bins. The kaons were identified by applying a 2σ mass-squared cut, which is shown by the shaded region in each plot.

The particle identification with the electromagnetic calorimeter modules is sensitive to the fact that the electromagnetic and hadronic interactions produce quite different patterns of energy sharing between calorimeter towers [53]. As a consequence, the hadron timing properties of the PbSc depend on the energy deposited on the central tower of the cluster, particle momentum, particle type, charge, angle of incidence of the track, etc. The PbSc hadronic timing response was corrected for these effects and we obtained an overall timing resolution of $\sigma \simeq 450$ ps, which is sufficient to enable a clear π/K separation within $0.3 < p(\mathrm{GeV/c}) < 1.0$ using a 2σ mass-squared selection criterion. In Fig. 3 the mass-squared distributions are plotted for four different momentum slices for all tracks passing through PC3 and PbSc. The identified kaons are also shown in the figure by the 2σ width shaded histograms superimposed on the M^2 distributions for all tracks in different momentum bins.

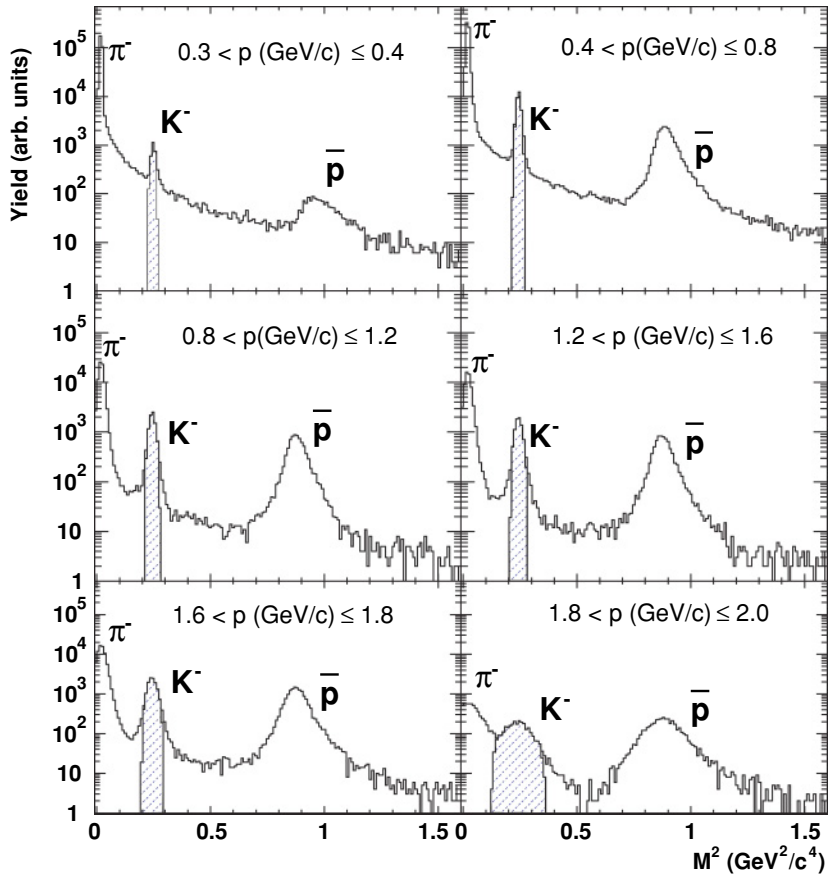

FIG. 2. (Color online) Mass-squared distribution of all accepted tracks passing through the TOF for six selected momentum bins. The identified kaons within 2σ mass-squared boundaries at the different momentum bins are shown by the shaded region on each plot.

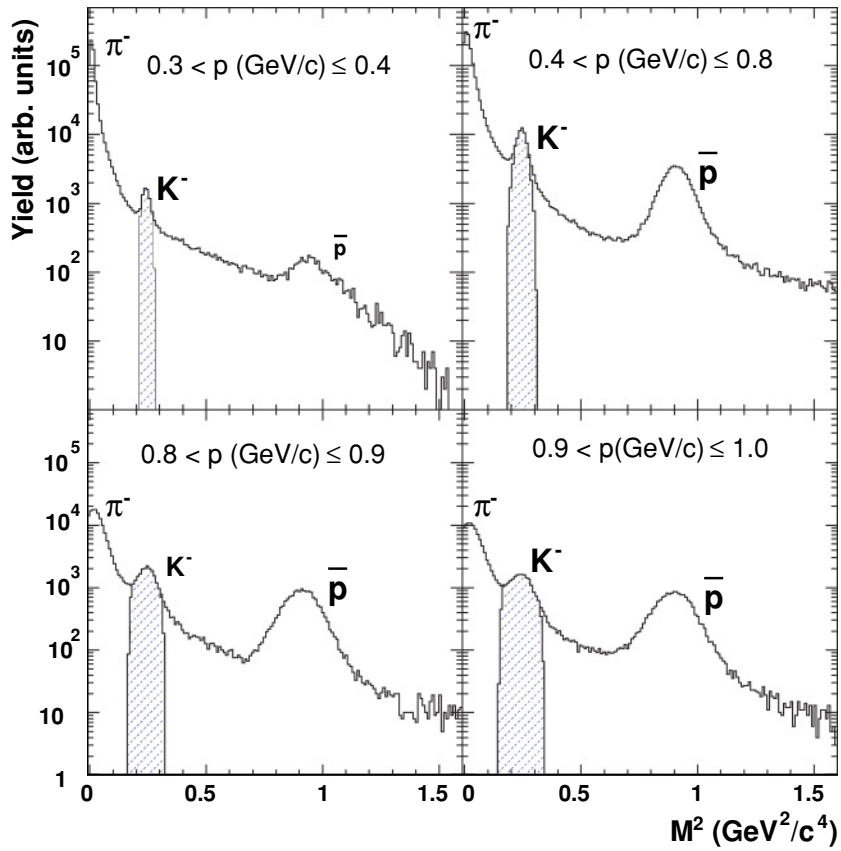

FIG. 3. (Color online) Mass-squared distribution of all selected tracks passing through the PbSc for four momentum bins. The identified kaons within 2σ mass-squared boundaries at the different momentum bins are shown by the shaded region on each plot.

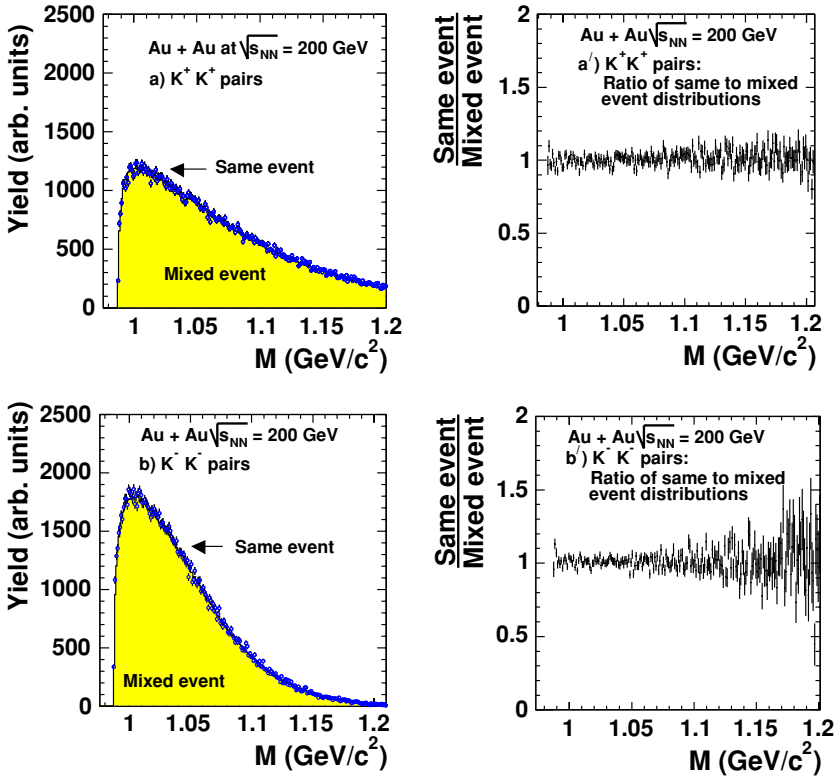

FIG. 4. (Color online) K^+K^+ [(a) and (a′)] and K^-K^- [(b) and (b′)] invariant mass spectra and ratio of real to mixed event spectra, respectively, for the TOF-PbSc combination.

D. K^+K^- invariant mass spectra and ϕ signal extraction

All identified K^+ and K^- tracks in a given event were combined to form the invariant pair mass distributions. Three different pair combinations were used:

(a) both K^+ and K^- identified by the TOF detector (TOF-TOF combination),
(b) K^+ identified with TOF and K^- identified with the PbSc detector (TOF-PbSc combination), and
(c) both K^+ and K^- identified with the PbSc detector (PbSc-PbSc combination).

We did not use the K^+ from PbSc and K^- from TOF in the (b) combination. This is because the PHENIX central arm geometry, in the presence of a 0.8 T m magnetic field, does not have any acceptance for such pairs below an invariant mass of 1.06 GeV/c^2 in the TOF-PbSc combination.

A large combinatorial background is inherent to the K^+K^- pair invariant mass distribution. The combinatorial background was estimated by an event-mixing method in which all K^+ tracks from one event were combined with K^- tracks of ten other events within the same centrality and vertex class. The mixed-event technique reproduces the shape of the unlike-sign combinatorial background. Finally, the size of the combinatorial background is obtained by normalizing the mixed-event invariant mass spectra to $2\sqrt{N_{++}N_{--}}$, where N_{++} and N_{--} represent the measured yields in K^+K^+ and K^-K^- mass distributions, respectively. This normalization is derived analytically starting from the assumption that the number of $K^\pm$ tracks per event-follows a Poisson distribution. A complete derivation of this is given in Appendix A.

The ability of this event-mixing method to reproduce correctly the shape of the combinatorial background distribution was confirmed by constructing, in a similar way, the mixed-event like-sign spectrum and comparing it to the same-event like-sign pair distribution. The assumption is that the like-sign pair distributions are purely combinatoric. For the three detector combinations, TOF-TOF, TOF-PbSc, and PbSc-PbSc, the ratio of the measured and combinatorial like-sign invariant mass distributions were found to be consistent with 1.0 as a function of the pair mass within statistical errors for all centrality bins. As an example, in Fig. 4 we plot the measured and combinatorial "$+\,+$" and "$-\,-$" invariant mass distributions and their ratios for the TOF-PbSc combination as a function of the invariant mass of K^+K^+ and K^-K^- pairs for minimum-bias events. As can be seen from the figures, these ratios are equal to the expected value of 1.0 within the statistical fluctuations.

The systematic uncertainty associated with this normalization procedure was estimated to vary between 0.5% and 2% for the different centralities in the different detector combinations. When we added all data together to derive the ϕ spectrum, the range of the systematic uncertainty is reduced to 0.7–1.0%.

Finally, the ϕ meson signal was obtained by subtracting the combinatorial background from the measured unlike-sign invariant mass spectrum. An example of the K^+K^- invariant mass spectrum for the TOF-PbSc combination is shown in Fig. 5, where we plotted the measured and scaled mixed-event invariant mass distributions for minimum-bias events. The lower panel of the figure shows the subtracted mass spectrum. The corrected yield of the ϕ mesons from the experimental data is then determined by integrating the subtracted invariant

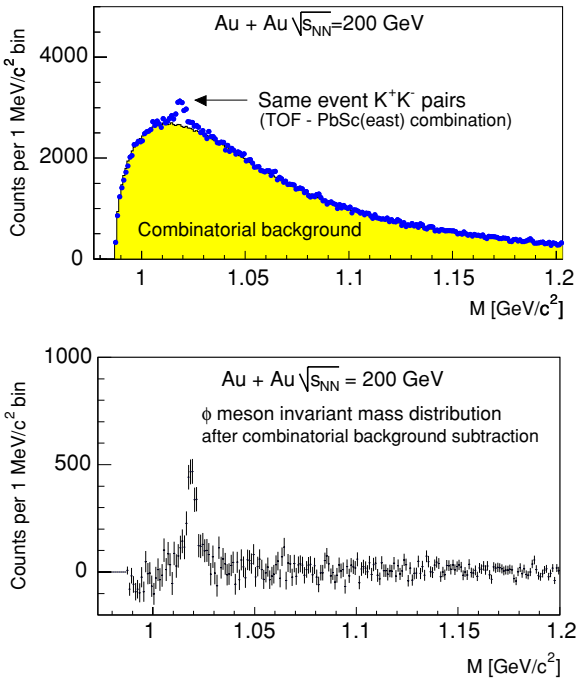

FIG. 5. (Color online) K^+K^- invariant mass spectra for the measured and mixed events (top) in the TOF-PbSc combination, and the subtracted mass spectrum showing the ϕ meson peak clearly above the background (bottom).

mass spectrum within a mass window of $\pm 5\,\mathrm{MeV}/c^2$ about the measured ϕ mass centroid. This narrow mass window was used as it provided a better signal-to-background ratio compared with a wider window. Since we will show that there is no significant centrality dependence of the intrinsic width, then the extracted yields as a function of centrality are not being biased by the use of a constant integration window. The systematic effect of the mass integration window itself on the corrected yield was studied by varying the stated integration limit and was found to contribute 2.6–3.2%, depending on centrality, to the total systematic uncertainty in the integrated yield.

E. Acceptance, decay, and multiple-scattering corrections

The ϕ meson yields were corrected for the geometrical acceptance of the detectors, in-flight kaon decay, multiple-scattering effects, and nuclear interactions with materials in the detector using the PISA software package, which is a GEANT-based [54] Monte Carlo detector simulation of the PHENIX detector. The simulation was carried out by generating 34 million single ϕ mesons in a ± 0.6 rapidity interval with an exponential transverse momentum distribution

$$dN/dp_T = p_T \exp[-m_T/(t_{\mathrm{fo}} + \beta^2 M_\phi)] \qquad (1)$$

with $t_{\mathrm{fo}} = 157$ MeV and $\beta = 0.4$, that is, an effective slope of $T = 320$ MeV in the range $0 < p_T < 10$ GeV/c. The generated ϕ mesons were then propagated through the simulation package. In this simulation, the BBC, DC, PC, TOF, and PbSc detector responses were tuned to match the real data by including their dead areas and by matching their track

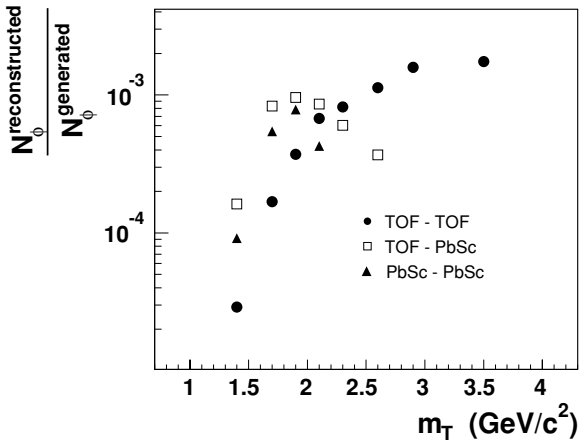

FIG. 6. Detector acceptance efficiency vs transverse mass of the simulated K^+K^- pairs for the TOF-TOF, TOF-PbSc, and PbSc-PbSc combinations. The statistical errors are smaller than the size of the data symbols.

associations and mass-squared resolutions. That is, the track association and mass-squared cut boundaries in the Monte Carlo analysis were parametrized to match the real data. The K^+K^- pair acceptance efficiency as a function of transverse mass was calculated as

$$\epsilon(m_T) = \frac{N_\phi^{\mathrm{reconstructed}}(m_T)}{N_\phi^{\mathrm{generated}}(m_T)}. \qquad (2)$$

The calculated acceptance efficiencies for the TOF-TOF, TOF-PbSc, and PbSc-PbSc combinations are shown in Fig. 6 as a function of m_T. The points in the figure are located at the center of the bins. In the actual m_T spectra, the proper bin centroids were used. The figure shows that the TOF detector (closed circles) has low acceptance for the low-momentum kaon pairs owing to their large opening angles. However, the TOF covers the largest m_T range for the ϕ particles. As a result, the TOF efficiency function increases toward higher transverse mass. In contrast, the TOF-PbSc (open squares) and PbSc-PbSc (closed triangles) combinations offer better low-pair-momentum acceptance than the TOF. However, the high-momentum kaon identification limit in the PbSc leads to the efficiency function decreasing at the highest transverse mass values.

To check the sensitivity of the acceptance correction factors to the input inverse slope of the ϕ mesons, the acceptance corrections are calculated for two input inverse slope parameters, $T = 320$ and 440 MeV. Both are found to be almost consistent within $\sim$1% uncertainty as a function of the momentum of the generated ϕ mesons. This is added as a systematic uncertainty to the acceptance correction factor.

In general, the PHENIX east arm ($|\eta| < 0.35$) particle identification detectors, in the presence of the central arm magnetic field, accepts 0.5% of the $\phi \to K^+K^-$ pairs generated within $|y| < 0.5$ and $1.2 < m_T^\phi(\mathrm{GeV}/c^2) < 4.0$. The factors that influence this geometrical acceptance are the geometry of TOF and PbSc at the PHENIX east arm, in-flight kaon decay, multiple-scattering effects, nuclear interactions of the kaons with detector materials, and the central arm magnetic

field. Out of those, about 17% of the kaon pairs are finally reconstructed after single-track reconstruction, track selection criteria, particle identification cuts, and finally the ϕ meson reconstruction within ± 5 MeV mass window with respect to its centroid.

The systematic error associated with the acceptance correction factor originates from

(i) tuning of detector alignments and mass-squared parameters in the Monte Carlo with reference to the real data ($\sim$3%),
(ii) systematics in the fiducial geometries in the data and the Monte Carlo ($\sim$12%), and
(iii) variation of the input inverse slope of the event generator ($\sim$1%).

F. Detector-occupancy correction

The high-multiplicity environment in the heavy-ion collisions produces multiple hits in a detector cell such as in the slats of the TOF or in the towers of the PbSc. These occupancy effects reduce the track reconstruction efficiency in central collisions compared to that in peripheral collisions, and these occupancy-dependent effects need to accounted for in calculating the invariant yields. The multiplicity-dependent efficiency ($\epsilon_{\text{occupancy}}$) factors were calculated by embedding simulated K^+K^- pairs into real data events. This study was done for different centrality bins from 0 to 92% in steps of 10%. We calculated the multiplicity-dependent efficiencies for TOF-TOF, TOF-PbSc, and PbSc-PbSc pairs separately. The systematic uncertainty associated with the embedding procedure was estimated for the three centrality bins used in the yield determinations, namely, 0–10%, 10–40%, and 40–92%. The systematic errors, calculated by estimating the occupancy-efficiency corrections for different track-confirming criteria, were found to vary from 7% to 10% for the three centrality bins used here, independent of the pair momenta. Figure 7 shows the $\epsilon_{\text{occupancy}}$ factors as a function of collision centrality

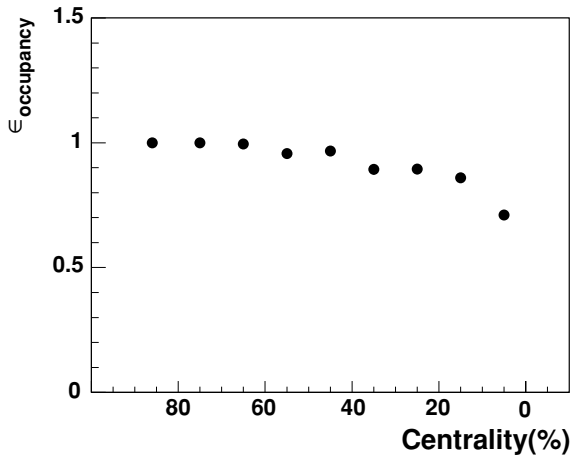

FIG. 7. Multiplicity-(occupancy-)dependent efficiency correction for detecting the ϕ meson in the PHENIX detector as a function of the collision centrality. The most central collisions are to the right; the most peripheral collisions are to the left. The statistical errors are less than the size of the data points.

for the K^+K^- pairs both identified in the TOF detector. The occupancy-dependent efficiency factors were found to be independent of the transverse momenta of the pairs.

IV. RESULTS AND DISCUSSION

In this section, we present and discuss the results of our measurements, which consist of (1) the ϕ line-shape analysis, (2) the transverse mass spectra analysis, (3) the integrated yields and ratios analysis, (4) hydrodynamical fits to $\pi^{\pm}$, $K^{\pm}$, p, $\overline{p}$, and ϕ transverse momentum spectra, and (5) the centrality dependence of the yields and nuclear modification factor R_{CP} as compared to that of pions and (anti)protons.

A. Line-shape analysis

The invariant mass spectra of the ϕ mesons are obtained by subtracting the combinatorial backgrounds from the same event K^+K^- mass spectra. The details of the combinatorial background analysis were described in Sec. III D. For the best statistical precision, we combine data from TOF and PbSc detectors to analyze the ϕ mass centroids and widths at the five different centrality bins. This is done by simply adding the measured and combinatorial invariant mass spectra from the three independent subsystem combinations mentioned in Sec. III D and then subtracting the total combinatorial background from the total measured mass spectra.

Figure 8 shows the minimum-bias $\phi \rightarrow K^+K^-$ invariant mass spectrum for the PHENIX data. The subtracted ϕ mass

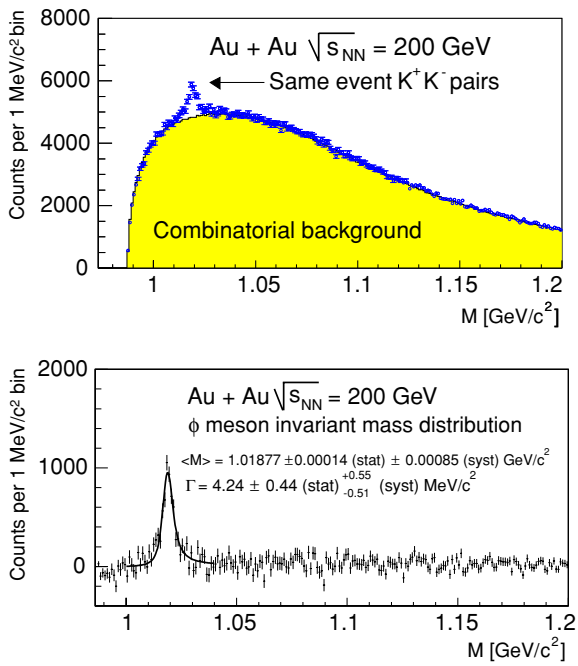

FIG. 8. (Color online) Minimum-bias $\phi \rightarrow K^+K^-$ invariant mass spectrum using the kaons identified in the PHENIX detector. The top panel shows the same event (circles) and combinatorial background K^+K^- mass distributions. The bottom panel shows the subtracted mass spectrum fitted with a relativistic Breit-Wigner function convolved with a Gaussian resolution function.

TABLE II. ϕ meson mass centroid and width for the minimum-bias Au+Au collisions at $\sqrt{s_{NN}} = 200$ GeV. The corresponding PDG values are $M_\phi = 1.019456$ GeV/c^2, $\Gamma_\phi = 4.26$ MeV/c^2.

Parameter	Value (MeV/c^2)
Centroid	1.01877 ± 0.00014 (stat) ± 0.00085 (syst)
Width	4.24 ± 0.45 (stat) $\pm \frac{0.55}{0.51}$ (syst)

spectrum (lower panel), containing approximately 5100 ϕ mesons in the fit region, is fitted with a relativistic Breit-Wigner (RBW) mass distribution function [38] convolved with a Gaussian experimental mass resolution function. Using Monte Carlo studies based on the experimentally measured single-kaon momentum resolution, the experimental ϕ mass resolution is calculated to be 1.0 MeV/c^2. This pair mass resolution value is found to be almost constant across the kinematic region of acceptance.

The errors on the data points in Fig. 8 reflect the statistical errors only. The systematic errors associated with the mass centroid and width measurements originate from the magnetic field uncertainties in the kaon momentum determination and the combinatorial background normalization procedure. The minimum-bias line-shape parameters (centroid and width) derived in our analysis are listed in Table II. The fitted minimum-bias ϕ mass centroid and width are consistent at the one standard deviation (1σ) level with the PDG values [55], taking into account both systematic and statistical errors. The centroids and widths from the mass spectra of the three independent subsystem combinations are also found to be consistent with PDG values within errors.

We investigated the centrality dependence of the ϕ meson line shapes. For each centrality bin, we again fitted the ϕ mass spectrum with the RBW function convolved with a Gaussian experimental ϕ mass resolution. The results are presented in Fig. 9. The left panel of the figure shows the centrality dependence of the fitted centroids. The upper and lower 1σ systematic error limits are indicated. The dotted line shows the PDG mass centroid. The solid line indicates the result obtained with a one-parameter constant fit through the measured data points. These results lead to two immediate conclusions. First, to within less than 1 MeV/c^2 there is no observed centrality dependence of the ϕ meson mass centroid, and second, the fitted centroids at all centralities are consistent with the PDG value within the statistical and systematic uncertainties of our measurements.

The ϕ mass widths, as shown in the right panel of the figure, are studied as a function of the centrality. The error bar on each point shows the statistical error; the bands on the points indicate the systematic errors. The dotted line shows the PDG ϕ mass width. The solid line shows the results of the constant-fit assumption to the data points. Again, within the statistical and systematic error limits shown, there is no convincing evidence of a variation of the ϕ width as a function of centrality.

The topic of medium effects on meson masses has been actively investigated in the recent literature [7–10,20,23,56–58]. The predictions are that for both cold and hot nuclear matter there could be a decrease of the ϕ mass value by a few MeV/c^2 or even tens of MeV/c^2. Even more dramatically the width could increase by several multiples above the PDG value of 4.26 MeV/c^2. A sample of such predictions is given in Table III. However, one of the models [20] considers the $\phi \to K^+K^-$ channel largely insensitive to medium effects since the kaons are "unlikely to escape without reacting further, thus destroying any useful information possessed about the ϕ." In this sense the $\phi \to K^+K^-$ is inherently biased in that only ϕ decays that are unaffected by the medium changes, for example those produced peripherally, can be detected.

It is sometimes thought that because the vacuum $c\tau$ of the ϕ is ≈ 45 fm/c there will be only limited sensitivity to medium effects in any case. However, if the resonance width were to actually increase by several times, as indicated in Table III, then the $c\tau$ would then approach or be even substantially less than 10 fm/c, which is a size compatible with the expected collision volume. The dramatic width changes predicted in either cold or hot nuclear matter might be visible, at least in the dilepton channel if not also the K^+K^- channel, as a function of centrality.

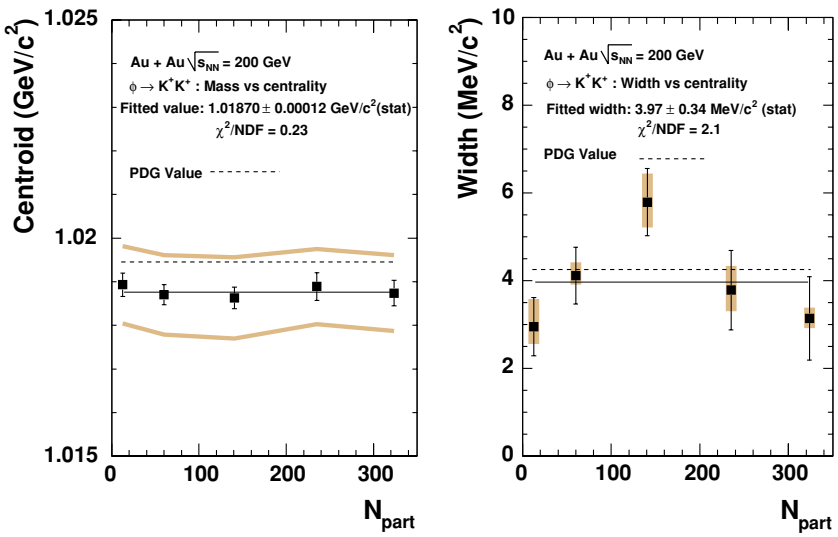

FIG. 9. (Color online) Centrality dependence of the ϕ mass centroid (left panel) and ϕ intrinsic width (right panel), where the $N_{\rm part}$ to Centrality correspondence is given in Table I. For the mass centroid plot, the 1σ systematic error limits on the data points are shown by the two continuous bands. The dotted line shows the PDG centroid value (1.019456 GeV/c^2). The solid line indicates the centroid value obtained from a one-parameter-fit assumption. For the width plot the systematic errors on the RBW widths are indicated as bands on each data point. Similarly, the dotted line shows the PDG width value (4.26 MeV/c^2), and the solid line shows a one-parameter-fit result for the measured data points.

TABLE III. Theoretical predictions for changes in the ϕ resonance.

Authors	Models	Environment	Predictions
Caberara and Vicente Vacas [23]	Chiral SU(3)	Cold hadronic	$M_\phi \rightarrow 1.011$ Gev $\Gamma_\phi \rightarrow 30\,\mathrm{MeV}/c^2$
Pal, Ko, and Lin [13]	AMPT Chiral Lagrangian	Hot hadronic	$M_\phi \rightarrow 0.95\,\mathrm{GeV}/c^2$ at twice normal nuclear density (ρ_0) $\Gamma_\phi \rightarrow 45$ MeV/c^2 at $2\rho_0$ Suppression of $\phi \rightarrow K^+K^-$ relative to $\phi \rightarrow e^+e^-$
Oset and Ramos [21]	Kaon mass renormalization	Cold hadronic	M_ϕ unchanged $\Gamma_\phi \rightarrow 22$ MeV/c^2
Smith and Haglin [20]	One-Boson exchange	Hot hadronic	M_ϕ unchanged $\Gamma_\phi \rightarrow 14$–$24$ MeV/c^2
Blaizot and Mendez Galain [12]	Nambu-Jona-Lasino	Hot hadronic	$M_\phi \rightarrow 2M_K$ at $T \approx T_{\mathrm{critical}}$ Γ_ϕ *reduced* by a factor of 6 $\phi \rightarrow K^+K^-$ disappears
Bi and Rafelski [14]	Bag model Chiral invariance	Hot hadronic	$M_\phi \rightarrow 1.029\,\mathrm{GeV}/c^2$ at $T \approx T_{\mathrm{critical}}$ $\Gamma_\phi \rightarrow 10$ MeV/c^2

The present mass centroid and width data, which are integrated over the available m_T range, rule out any major changes with respect to the PDG values. Specifically, the one-parameter fit result of 3.97 ± 0.34 MeV/c^2 obtained here excludes at the 99% confidence level a width value of 4.75 MeV/c^2 or greater. Possibly at the lowest m_T values, where the ϕ would remain longer in the collision volume, or with the availability of more finely binned centralities, there could be visible evidence of in-medium effects. However, the current data sample is insufficient to explore these possibilities.

It seems clear from the current set of theoretical models that an observed change in the ϕ width would not be itself indicative of a QGP formation. One would first have to constrain the cold nuclear medium effects on the ϕ as could be obtained in d+Au collisions, or by comparing peripheral Au+Au collision data results with central collision data. It is also important to measure the ϕ mass in the dilepton e^+e^- channel. That channel should be more sensitive to the ϕ that are produced deeper or earlier in the collision volume.

B. Spectral-shapes analysis

At low m_T, the spectral shapes carry information about the kinetic freeze–out conditions. Since the centrality dependence reveals the effect of the system size on the fireball evolution it becomes desirable to study the centrality dependence of the spectral shapes. Transverse mass spectra were obtained in three centrality bins corresponding to 0–10%, 10–40%, and 40–92% of the total geometrical cross section. We count the same event K^+K^- pairs within a defined mass window (± 5 MeV/c^2 with respect to the ϕ mass centroid) and estimate the number of combinatorial background pairs within that window. In each centrality bin, the data are divided into different m_T bins. The invariant mass spectrum for the same events and the background distributions are obtained for each of these m_T bins. Finally, the background is subtracted from the same-event invariant mass spectrum within the aforementioned ± 5 MeV/c^2 ϕ mass window to determine the number of reconstructed ϕ mesons within that m_T bin. The reconstruction of the ϕ in the Monte Carlo simulation takes into account the effect of the ϕ mass window size.

The ϕ mesons are reconstructed using kaons identified in the TOF and the PbSc detectors. Three detector combinations (TOF-TOF, TOF-PbSc, and PbSc-PbSc) are used to obtain three independent transverse mass spectra. Figure 10 shows the minimum-bias m_T spectra for these three combinations. The combined result, which is the weighted sum of the three combinations, is also included. For better visibility of the data points, TOF-TOF, TOF-PbSc, and PbSc-PbSc spectra are

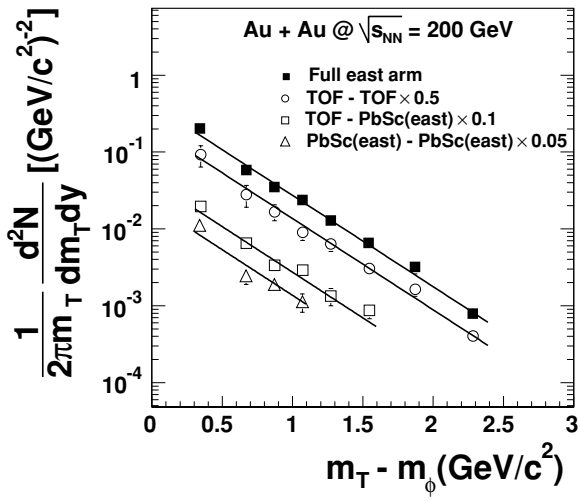

FIG. 10. Minimum-bias m_T spectra of the measured ϕ mesons for three different PHENIX subsystem combinations, with scale factors as indicated. The combined spectrum is fitted with an exponential function in m_T, Eq. (3). The lines drawn through the individual spectra (TOF-TOF, TOF-PbSc, and PbSc-PbSc) represent the same fit parameters as in the minimum-bias case. Statistical error bars are shown.

TABLE IV. Minimum-bias dN/dy and T for different subsystem combinations. The statistical and systematic errors are shown after the first and second $\pm$ signs, respectively.

Subsystem Combination	TOF-TOF	TOF-PbSc	PbSc-PbSc	Full Data Set
dN/dy	$1.16 \pm 0.17 \pm 0.19$	$1.37 \pm 0.15 \pm 0.22$	$1.47 \pm 0.26 \pm 0.27$	$1.34 \pm 0.09 \pm 0.21$
T (MeV)	$380 \pm 18 \pm 22$	$385 \pm 34 \pm 28$	$311 \pm 47 \pm 65$	$366 \pm 11 \pm 18$

scaled by a factor of 0.5, 0.1, and 0.05, respectively. The m_T spectrum obtained from the PHENIX detector is fitted with the exponential function

$$\frac{1}{2\pi m_T}\frac{d^2N}{dm_T dy} = \frac{dN/dy}{2\pi T(T+M_\phi)} e^{-(m_T - M_\phi)/T}, \qquad (3)$$

where dN/dy and the inverse slope T are returned as two fitting parameters. The lines drawn through the TOF-TOF, TOF-PbSc, and PbSc-PbSc spectra represent the same fit but are scaled with the same scaling factors as the data points. Comparison of the individual spectra to the fit obtained from the combined spectrum demonstrates the consistency among the different measurements, which have different systematic uncertainties. The TOF-TOF, TOF-PbSc, and PbSc-PbSc spectra are also independently fitted using Eq. (3). The resulting dN/dy and T are tabulated in Table IV. Both statistical and systematic errors are quoted. The systematic errors on dN/dy originate from the systematic uncertainties associated with extraction of the yields in each m_T bin (see Appendix C) and the uncertainties from the fitting procedure. The latter is sensitive to the extrapolation of the m_T spectra to $m_T = m_\phi$. A detailed account of systematic errors on dN/dy and T in the full dataset from all sources is shown in Appendix C. We also fitted the TOF-TOF and TOF-PbSc data over the smaller m_T range of the PbSc-PbSc data and obtained consistent sets of dN/dy and T values from that check.

Figure 10 and Table IV indicate that the three different analyses with different systematic uncertainties give consistent results. This allowed us to combine the results and make use of the maximum available statistics in each m_T bin. This combined spectrum was used to obtain the physics results discussed in the next sections.

Figure 11 shows m_T spectra of the ϕ mesons in 0–10%, 10–40%, 40–92%, and minimum-bias centrality classes. The data points representing the invariant yield as a function of transverse momentum are given in Appendix B. Each spectrum is fitted with an m_T-exponential function, Eq. (3). The ϕ yield per unit of rapidity (dN/dy) and inverse slope (T) obtained from the fits are shown in Table V and are summarized in Figs. 12 and 13 [59].

C. Yields and ratios

Hadron yields and ratios carry information about the chemical properties of the system. The yields of strange particles have been of particular interest as they help in understanding the strangeness enhancement in heavy-ion collisions and the equilibration of strangeness. It is important to study these phenomena as a function of system size. Centrality-selected data can be particularly useful in this respect. Here we present the yield of the ϕ mesons at midrapidity as a function of centrality and compare this yield to the yields of other hadrons and the results from lower energy heavy-ion collisions. The dN/dy of ϕ (shown in Fig. 12) is found to increase steadily with centrality. In the right panel, the yield is normalized to the number of participant pairs to take into account the size of the system. Within the error bars this normalized rapidity density is approximately independent of centrality with a possible slight increase from peripheral to the midperipheral collisions. The trend is quite different from lower energy results measured at the AGS. In [38], the yield of ϕ was reported to be increasing greater than linearly with the number of participants.

We now consider the ratio of strange to nonstrange particles to understand the extent and mechanism of the strangeness enhancement in heavy-ion collisions. The ratios K^+/π^+ and K^-/π^- are shown in Figs. 14 (a) and (b). Both ratios show an increase of $\approx$60% from peripheral to central collisions. Most of this increase is for $N_{\rm part} < 100$. Only a mild increase or saturation is observed from midcentral to the top centrality bin [50]. Figures 14 (c) and (d) show the centrality dependence of the ϕ/π and ϕ/K ratios. The limited statistics prevent us from extending the ϕ measurements into larger number of centrality bins spanning the more peripheral events. The ϕ/K ratio, in this limited number of centrality bins, is approximately flat as a function of centrality. The possibility of structure in the

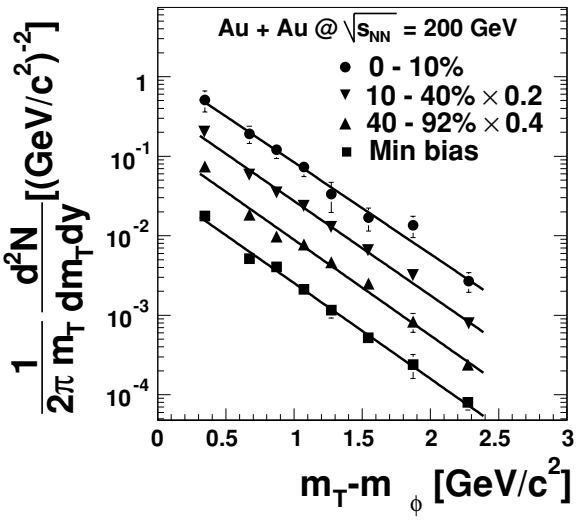

FIG. 11. m_T spectra of ϕ mesons for 0–10%, 10–40%, 40–92%, and minimum-bias (0–92%) centrality classes, with scale factors as indicated. Each spectrum is fitted with an exponential function in m_T, Eq. (3), with the fit parameters listed in Table V. Statistical error bars are shown.

TABLE V. dN/dy and T for different centrality bins.

Centrality (%)	dN/dy	T (MeV)
0–10	3.94 ± 0.60 (stat) ± 0.62 (syst)	376 ± 24 (stat) ± 20 (syst)
10–40	2.22 ± 0.18 (stat) ± 0.35 (syst)	360 ± 13 (stat) ± 23 (syst)
40–92	0.32 ± 0.03 (stat) ± 0.05 (syst)	359 ± 15 (stat) ± 16 (syst)
Minimum Bias	1.34 ± 0.09 (stat) ± 0.21 (syst)	366 ± 11 (stat) ± 18 (syst)

ϕ/π ratio is difficult to infer from our data within the error bars. One might expect to see some centrality dependence in the ϕ/π ratio because there is obviously a centrality dependence to the K/π ratio. However, we do not have enough centrality bins, nor enough signal in each bin, from which to conclusively identify a centrality dependence in ϕ/π. The flat behavior of the ϕ/K ratio indicates that there is no pronounced difference in the production of open (kaon) and hidden (ϕ) strangeness in heavy ion collisions at RHIC energies. Production in the hadronic stage via kaon coalescence $K^+K^- \rightarrow \phi$ seems to be excluded by these data, as it would result in an increase in ϕ/K^- as a function of N_{part}, which is not observed.

The collision energy dependence of the ϕ yield is shown in Fig. 15, where we plot the dN/dy per participant pair as a function of the number of participants for different colliding energies. The figure indicates two aspects of ϕ meson production at various energies. First, as we go from AGS to SPS to RHIC, the ϕ meson yield per participant increases by an order of magnitude overall. Secondly, at the AGS energy, we find a steady increase of ϕ production per participant pair from peripheral to central collisions. It is worth mentioning that the NA50 experiment [25] at CERN SPS reported an increase in fiducial ϕ yield (in the $\mu^+\mu^-$ decay channel) per participant from peripheral to central collisions although the yield per participant showed saturation within the error for the top centrality bins. The yield of ϕ mesons at RHIC, on the contrary, is found to be almost independent of centrality.

To investigate further the mechanism of ϕ enhancement with increase in collision energy, we study the two ratios ϕ/π and ϕ/K^- as a function of collision energy as illustrated in Fig. 16. The ϕ/π ratio is found to increase with the collision energy from AGS to RHIC. The ϕ/K^- ratio, in contrast, remains almost constant within the error bar with increasing collision energy.

D. Hydrodynamical model fits to the spectral-shape data

From the ϕ spectral data shown in the preceding sections, we can conclude that the transverse mass distributions are well described by an exponential distribution and are quite similar for all the centralities. There is little, if any, centrality dependence of the inverse slope parameter in the measured centrality bins, as shown in Fig. 13. The exponential behavior is expected for particle production from a thermal source.

If the system develops collective motion, particles experience a velocity boost resulting in an additional transverse kinetic energy component. This motivates the use of the transverse kinetic energy (i.e., transverse mass minus the particle rest mass) for studying flow effects. Traditionally, the CERN experiments [60,61] have used simple exponential fits to the transverse kinetic energy distributions and often quote just one number, the inverse slope T, to characterize the spectra. These fits are usually done in the range $(m_T - m_0) < 1$ GeV/c^2 to minimize the contribution from hard processes.

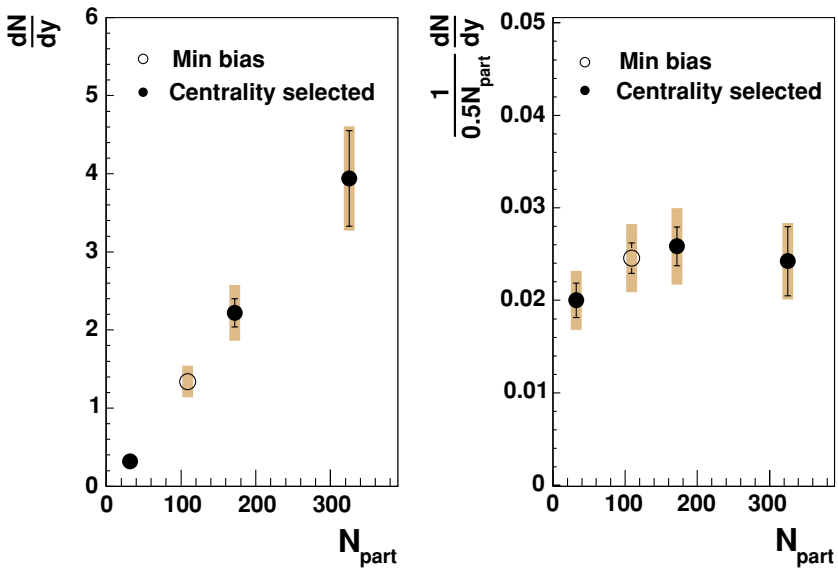

FIG. 12. (Color online) Centrality dependence of ϕ yield at midrapidity. The value of dN/dy increases steadily with the number of participants N_{part} (left) whereas the dN/dy per participant pairs increases slightly from peripheral to midcentral events and saturates after that (right). The error bars indicate the statistical errors. The shaded boxes on each data point are the systematic errors.

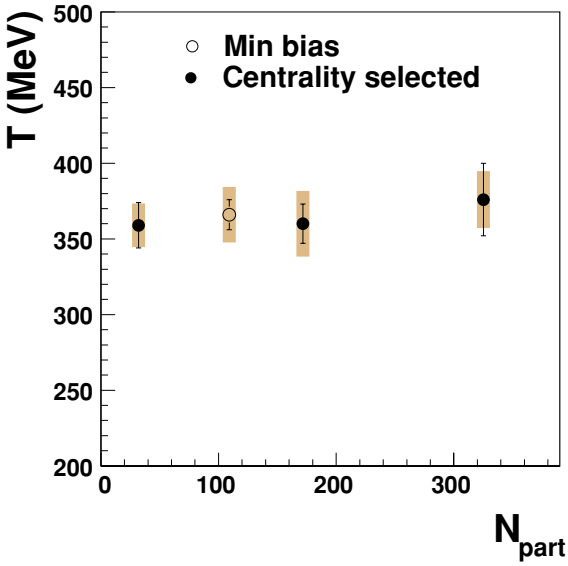

FIG. 13. (Color online) Centrality dependence of the inverse slope T.

The results of such fits, obtained from previously published PHENIX $\pi^{\pm}$, $K^{\pm}$, p, and $\overline{p}$ data [50] are shown in Fig. 17. The slope parameters show a clear mass dependence, as expected from radial flow. The mass dependence increases from peripheral to central collisions, indicating stronger collectivity in the more central events. The ϕ meson has mass similar to that of the proton. Hence we expect that if the ϕ participates in the collective flow then its inverse slope will be affected by this motion. For protons, the slope parameter changes significantly from peripheral to central collisions. As just noted, the ϕ inverse slopes show no such centrality dependence. An important difference between the results obtained for p, $\overline{p}$, and ϕ is that those for the proton and antiproton have been fitted within a limited low-m_T range [$(m_T - m_0) < 1$ GeV/c^2] as motivated by the previous discussion. In the case of the ϕ the full measured range has been used for the fit because of the limited data at low m_T. As shown in Fig. 11, the three data points below 1 GeV/c^2 are consistent with the fit over the entire m_T range.

The detailed study of the higher statistics (anti)proton spectra [50] indicated that (anti)proton spectra cannot be described by a single exponential in $m_T - m_0$, if the full measured range is considered. Although easy to visualize, the one-parameter inverse-slope analysis proves to be too simplistic as a way to infer the kinetic properties of the system. In particular, the degree to which the ϕ mesons participate in the collective expansion will be shown (see Fig. 22) to be obscured in this simple approach.

A more sophisticated approach to this problem is to compare the particle spectra to a functional form that describes a boosted thermal source, based on relativistic hydrodynamics [62]. This is a two-parameter model, termed the "blast-wave" model, in which the surface radial flow velocity (β_T) and the freeze-out temperature ($T_{\rm fo}$) are extracted from the invariant

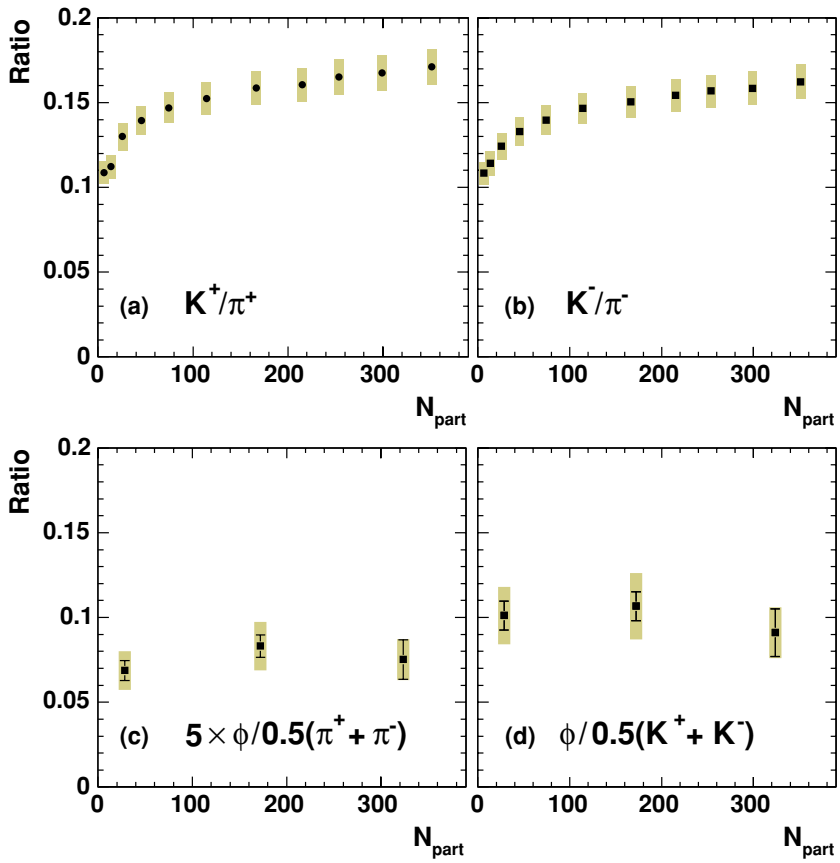

FIG. 14. (Color online) Centrality dependence of particle ratios for (a) K^+/π^+, (b) K^-/π^-, (c) $\phi/[0.5(\pi^+ + \pi^-)]$ (scaled by a factor of 5), and (d) $\phi/[0.5(K^+ + K^-)]$ in Au+Au collisions at $\sqrt{s_{NN}} = 200$ GeV. The data points have been placed in the center of each centrality bin. An increase in ϕ production, similar to kaons, would shift the lowest bin slightly to the right by about 20% to an $N_{\rm part}$ of about 40, in (c).

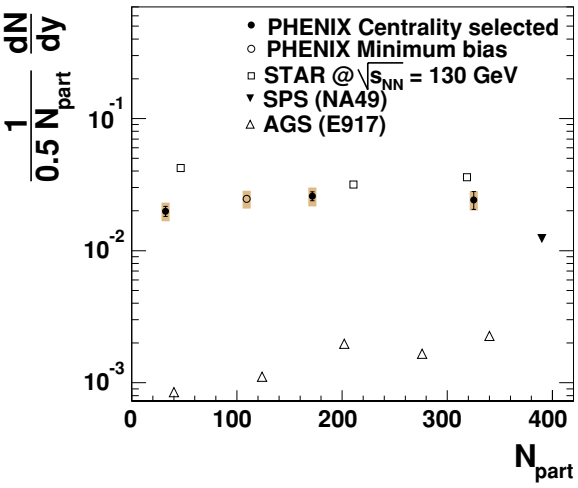

FIG. 15. (Color online) Centrality dependence of ϕ yields at different collision energies. STAR data are from [43], NA49 data are from [39], and E917 are from [38].

cross-section data according to the equation

$$\frac{dN}{m_T\, dm_T} \propto \int_0^R f(r)\, r\, dr m_T I_0\left(\frac{p_T \sinh\rho}{T_{\rm fo}}\right) K_1\left(\frac{m_T \cosh\rho}{T_{\rm fo}}\right), \tag{4}$$

where I_0 and K_1 represent modified Bessel functions with ρ being the transverse boost, which depends on the radial position according to

$$\rho = \tanh^{-1}(\beta_T) r/R. \tag{5}$$

Here the parameter R is the maximum radius of the expanding source at freeze-out. The function $f(r)$ represents the density, which is taken to be uniform in this calculation. A detailed comparison between our implementation of the blast-wave model and the results of full hydrodynamics calculations has been reported previously in [63] and the results were found to be consistent.

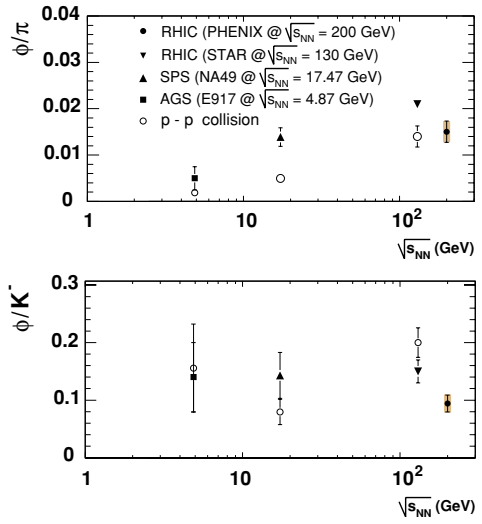

FIG. 16. (Color online) ϕ/π (top) and ϕ/K^- (bottom) ratios as a function of collision energy. The data symbols have the same meanings in both the top and the bottom parts of the figure.

To study the parameter correlations, we make a grid of ($T_{\rm fo}$, β_T) pairs and then for each pair we perform a chi-squared minimization for each particle type. We use a linear velocity profile and constant particle density distribution. The first fit attempt is performed simultaneously for the six particle species $\pi^{\pm}$, $K^{\pm}$, p, and $\overline{p}$ in the range $(m_T - m_0) < 1.0$ GeV/c^2.

The experimental data for p and $\overline{p}$ have been corrected for Λ and $\overline{\Lambda}$ decays. However, the invariant yields of $\pi^{\pm}$ and $K^{\pm}$ include feed-down from the decay of resonances and weak decays. To take this into account we add the decay of mesonic (ρ, η, ω, K^*, . . .) and baryonic (Δ, Λ, Σ, . . .) resonances as follows:

(1) Generate resonances with the transverse momentum distribution determined by each combination of $T_{\rm fo}$ and β_T.
(2) Simulate the decays using a Monte Carlo approach and obtain $\pi^{\pm}$ and $K^{\pm}$ distributions.
(3) Merge all particles, where the particle abundance is calculated with chemical parameters [64]$T_{\rm ch} = 177$ MeV, $\mu_B = 29$ MeV.

The two-parameter $T_{\rm fo}$ versus β_T fit results obtained in this analysis for the most central bin are shown in Fig. 18. Shown in the lower panel of the figure are the χ^2 contour levels obtained from fitting each particle spectrum separately. We observe that the parameters $T_{\rm fo}$ and β_T are anticorrelated; the different particles have different preferred parameter space and different sensitivity to the parameters. For example, the contours for the heavier particles are more sensitive to the flow velocity than to the kinetic freeze-out temperature. The minimum valleys in the contours for the six particle species do overlap at a single common point at the 2σ level. To find the values of the parameters at this overlap point, a simultaneous fit for the six single-particle spectra ($\pi^{\pm}$, $K^{\pm}$, p, and $\overline{p}$) was done; the result converges to a best fit value of $T_{\rm fo} = 108.9^{+2.6}_{-2.4}$ MeV and $\beta_T = 0.771^{+0.003}_{-0.004}$. Using these parameters, we obtain the transverse momentum shapes shown in Fig. 19, where we also include the prediction for the ϕ spectrum shape, which was not part of the original fit. The shape of the ϕ spectrum is reproduced well.

For the two other centrality bins in this study, 10–40% and 40–92%, we show the best-fit hydrodynamical results in Figs. 20 and 21, respectively. Again we see that the ϕ transverse momentum shapes are reproduced by the same flow parameters that fit the identified hadron data at the same centrality bins.

For a second hydrodynamical fit attempt, we include the ϕ transverse momentum 0–10% centrality data along with the previously identified hadron data as part of the χ^2 minimization search. The flow parameters derived with the ϕ data included are numerically consistent with the flow parameters derived previously without the ϕ data being included.

The two-dimensional grid-search best-fit values for the blast-wave parametrization as a function of centrality are tabulated in Table VI. The radial average expansion velocity $\langle\beta_T\rangle$ is also given in this table. For the range of centralities studied here, the expansion velocity parameter is seen to decrease moderately for more peripheral collisions whereas

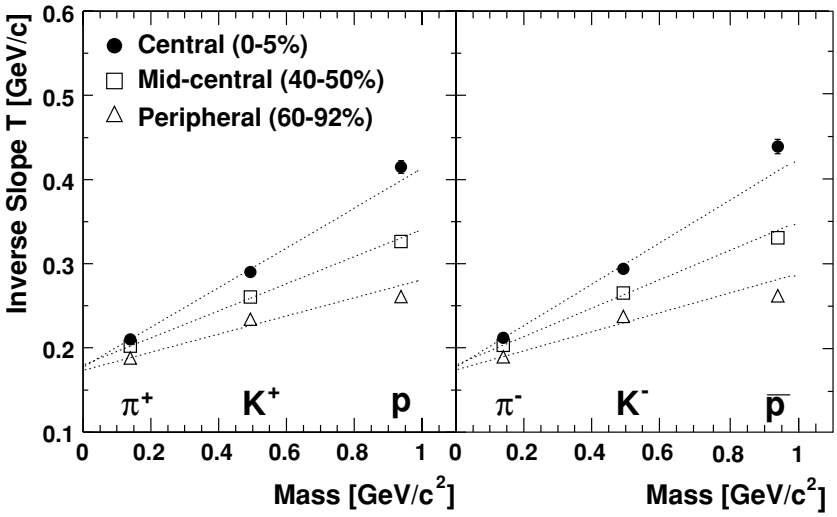

FIG. 17. Mass and centrality dependence of inverse slope parameters T in m_T spectra for positive (left) and negative (right) particles in Au+Au collisions at $\sqrt{s_{NN}} = 200$ GeV. The fit ranges are 0.2–1.0 GeV/c^2 for pions and 0.1–1.0 GeV/c^2 for kaons, protons, and antiprotons in $m_T - m_0$. Figure taken from Ref. [50].

the kinetic freeze-out temperature increases more significantly, by approximately 40%. If one takes these parameters literally, then the more peripheral collisions are subject to decreased radial flow while correspondingly the particles are decoupling kinetically from each other at temperatures closer to the chemical freeze-out temperature. This is a physically reasonable scenario given fewer participants in the initial expansion phase.

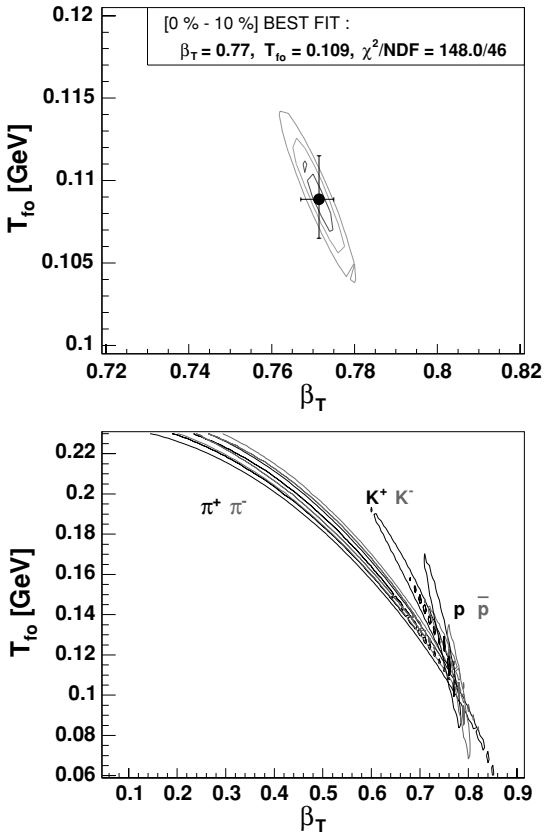

FIG. 18. (Color online) Contour plots for the hydrodynamical fit to the 200-GeV single-particle transverse momentum spectra for the $\pi^{\pm}$, $K^{\pm}$, p, and $\overline{p}$ in the 0–10% centrality bin. The contour lines are in 1σ steps. The upper plot is from a simultaneous fit with the best value shown as the dot. The lower plot is from independent fits for the six-particle spectra.

It should be pointed out that our present ϕ transverse momentum range does not extend below 0.8 GeV/c. The spectral shapes at low m_T, especially for the heavier particles, are mostly sensitive to the expansion velocity. In the range of our ϕ measurement, it is more appropriate to consider the asymptotic behavior of the spectral shapes, which for $m_T \gg m_0$ is given by [62]

$$T_{\text{eff}} = T_{\text{fo}}\sqrt{(1+\beta_T)/(1-\beta_T)}, \tag{6}$$

where T_{eff} is the slope parameter obtained using an m_T exponential fit, as in Eq. (3). It is interesting to note that the measured asymptotic slopes do not seem to depend on centrality, although both T_{fo} and β_T show a clear centrality dependence. This either is due to a cancellation effect in Eq. (6), since the parameters are anticorrelated, or indicates that the hydrodynamics description is no longer valid at these large transverse momenta. We conclude that although the ϕ data themselves cannot constrain the kinematic freeze-out conditions, they are consistent with the hydrodynamical results obtained from the simultaneous fit to the $\pi^{\pm}$, $K^{\pm}$, p, and $\overline{p}$ spectra.

TABLE VI. Blast-wave-model parameters [62] as a function of centrality from fitting $\pi^{\pm}$, $K^{\pm}$, p, and $\overline{p}$ spectra. The fit parameters quoted here are the results from fitting the six identified hadrons spectra simultaneously, without including the ϕ.

Centrality (%)	T_{fo} [MeV]	β_T	$\langle\beta_T\rangle$	χ^2/NDF
0–10	$108.9^{+2.6}_{-2.4}$	$0.771^{+0.003}_{-0.004}$	$0.572^{+0.003}_{-0.003}$	148.0/46
10–40	$119.0^{+1.5}_{-1.5}$	$0.748^{+0.003}_{-0.003}$	$0.550^{+0.002}_{-0.002}$	212.1/46
40–92	150^{+2}_{-2}	$0.630^{+0.005}_{-0.005}$	$0.447^{+0.004}_{-0.004}$	150.9/46

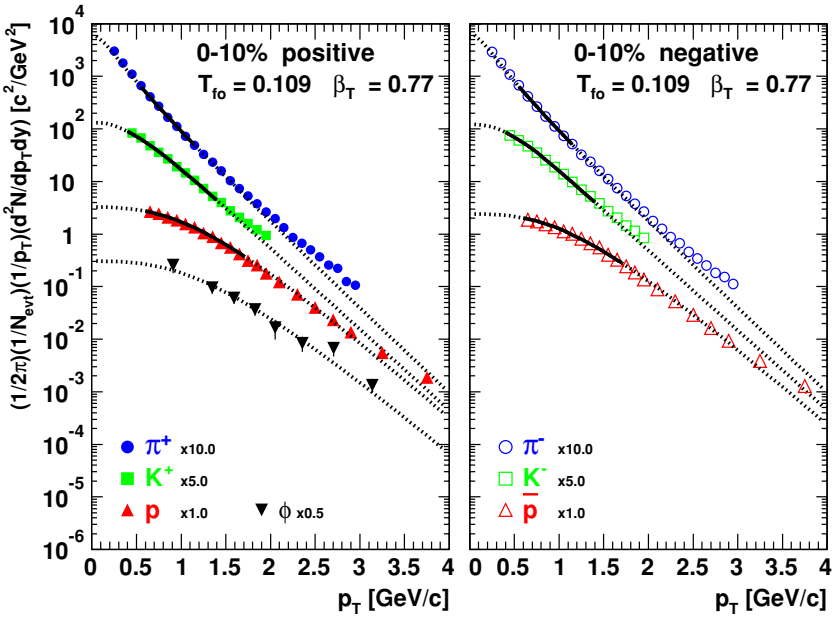

FIG. 19. (Color online) Transverse momentum data and best-fit hydrodynamical results for the 0–10% centrality bin for the 200-GeV $\pi^{\pm}$, $K^{\pm}$, p, and $\overline{p}$, along with the prediction for the ϕ transverse momentum spectrum. The transverse momentum ranges for the fit are indicated by the solid lines; the dashed lines indicate the extrapolated predictions for each particle species.

E. Nuclear modification factor R_{CP} for ϕ mesons

One of the most important result demonstrated so far in the study of relativistic heavy ions at RHIC is the observed suppression of high-p_T pions in central collisions as compared to either pp collisions or peripheral Au+Au collisions [65]. A second, quite surprising observation is the unusually large (anti)proton-to-pion ratio at high p_T. In particular, PHENIX has observed [30] that in central Au+Au collisions the p/π and $\overline{p}/\pi$ ratios are enhanced by a factor of 3 at intermediate p_T ($1.5 < p_T < 4.5$ GeV/c) as compared to the ratios in pp collisions and the ratios obtained in quark and gluon jets measured in e^+e^- collisions [66]. It was also observed that proton and antiproton production scales with $N_{\rm coll}$ in this p_T region, in sharp contrast to the strong suppression of pion production [30]. In pp collisions high-p_T particles are the result of the fragmentation of partons. Because of the power-law nature of the hard-scattering spectrum, most of the particles at high p_T are expected to be leading hadrons. The fragmentation functions, at least in vacuum, are expected to be universal and independent of the colliding system under consideration. However, at intermediate p_T (1.5–4.5 GeV/c) the PHENIX results from central Au+Au collisions are inconsistent with the known fragmentation functions.

There are several conjectures that may explain the unexpected PHENIX result:

(1) hydrodynamic flow generated from the hadronic stage [67],

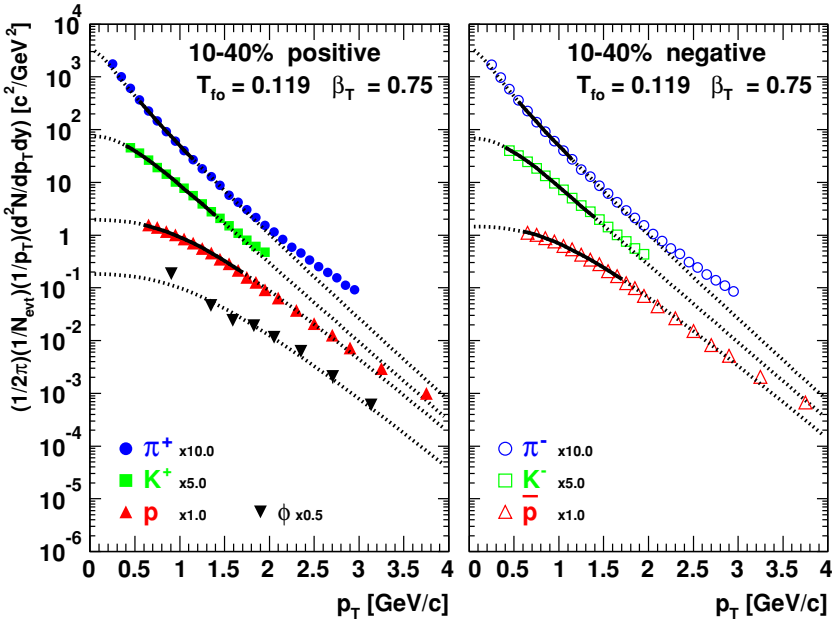

FIG. 20. (Color online) Transverse momentum data and best-fit hydrodynamical results for the 10–40% centrality bin for the 200-GeV $\pi^{\pm}$, $K^{\pm}$, and p, $\overline{p}$, along with the prediction for the ϕ transverse momentum spectrum.

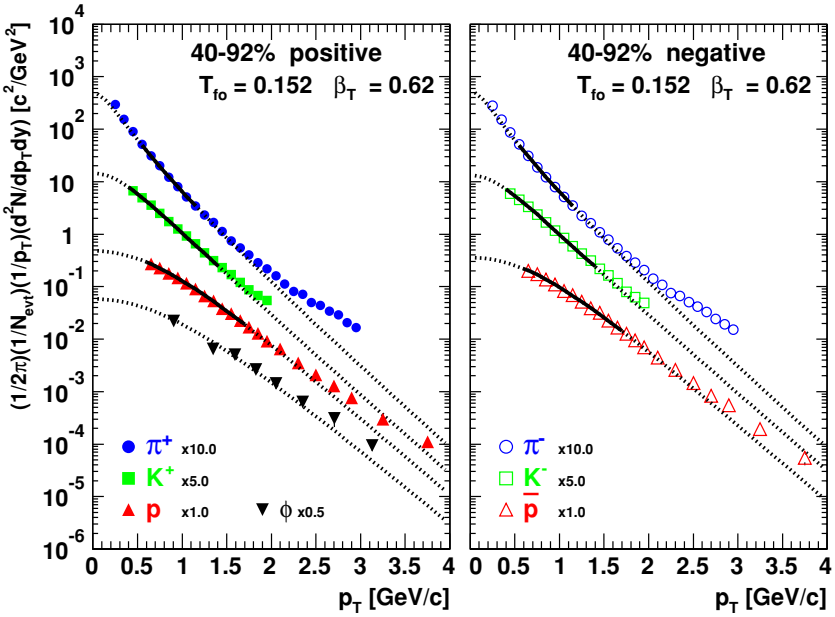

FIG. 21. (Color online) Transverse momentum data and best-fit hydrodynamical results for the 40–92% centrality bin for the 200-GeV $\pi^{\pm}$, $K^{\pm}$, and p, $\overline{p}$, along with the prediction for the ϕ transverse momentum spectrum.

(2) hydrodynamic flow generated at a partonic stage together with particle production from the recombination [32–34],
(3) baryon junctions as a mechanism for an usually large buildup of baryons and antibaryons at midrapidity [68], or
(4) in-medium modified fragmentation functions [69].

The first three possibilities invoke soft processes to populate a region of p_T that is dominated by hard scattering in pp collisions. The soft production at intermediate p_T is enhanced for protons and antiprotons, whereas pions remain dominated by hard scattering. In conjecture 4, the production for both pions and p, $\overline{p}$ is by hard scattering, but the fragmentation functions are modified in the medium, thus resulting in enhanced p/π and $\overline{p}/\pi$ ratios.

The second of these conjectures is particularly important since this hypothesis presupposes a partonic state with collective behavior. A critical factor that may differentiate among these scenarios is whether the large abundance of protons is due to its mass or to the number of constituent quarks [32–35]. Hydrodynamic flow generated at the hadronic stage imparts a single velocity to the moving matter; hence similar mass particles should exhibit the same momentum increase from this effect. In contrast, hypotheses 2 and 3 depend on whether the particles are baryons or mesons.

The ϕ meson which has a mass similar to that of a proton yet, like the pion, has two constituent quarks, should distinguish between conjecture 1 and 2 or 3. We examine the scaling properties of the intermediate-p_T yields of the ϕ and compare those to the yields of $(p + \overline{p})/2$. Figure 22 shows the transverse momentum spectra measured in three different centralities, each scaled down by the number of binary nucleon-nucleon collisions. The (anti)proton spectra show two pronounced features. Below $p_T < 1.5$ GeV/c, the spectral shapes are strongly influenced by the radial flow and thus the more central data have a harder slope. Above $p_T = 1.5$ GeV/c, the effect of radial flow is negligible. The spectra converge to the same line. Moreover, they scale with $N_{\rm coll}$ for all centrality classes, as expected for hardscattering unaffected by the nuclear medium. The ϕ spectra have a quite different behavior. There is no visible curvature at lower p_T. This could be because the ϕ spectra have only two (rather wide) bins below $p_T = 1.5$ GeV/c—the region where the curvature in the proton spectra is most pronounced. A curved functional form can be fit to the spectra with acceptable χ^2, as already discussed in Sec. IV D. At higher p_T the ϕ spectra run parallel to the (anti)proton spectra, but they do not obey $N_{\rm coll}$ scaling. To examine this feature on a linear scale, we plot the ratio between the central and peripheral data, that is, the ratio $R_{\rm CP}$

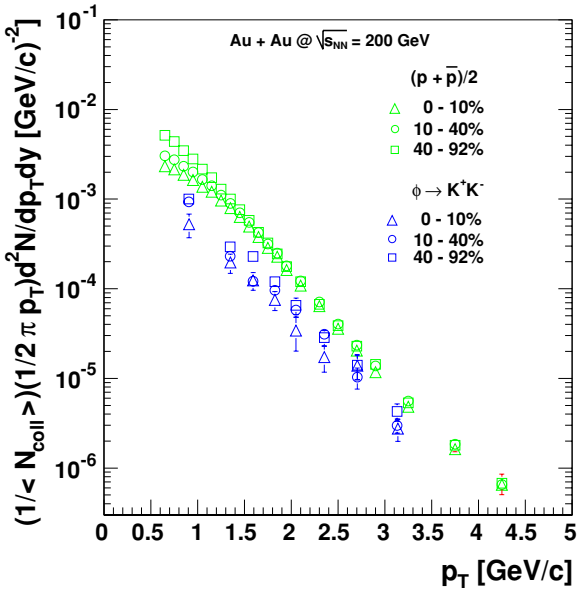

FIG. 22. (Color online) p_T spectra of protons and ϕ mesons at different centralities scaled down by their respective number of $N_{\rm coll}$.

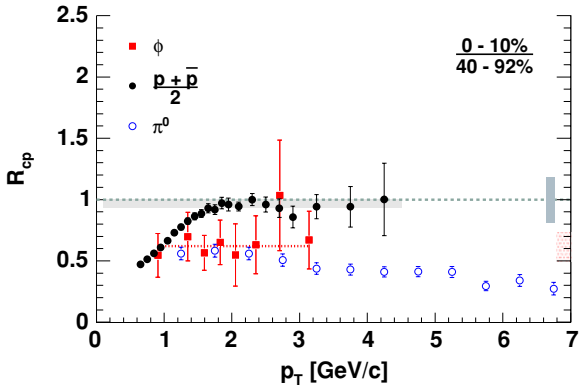

FIG. 23. (Color online) $N_{\rm coll}$ scaled central to peripheral ratio $R_{\rm CP}$ for $(p+\overline{p})/2$, π^0, and ϕ. The proton and pion results are published [30]. The vertical dotted bar on the right represents the error on $N_{\rm coll}^{0-10\%}/N_{\rm coll}^{40-92\%}$. The shaded solid bar around $R_{\rm CP}=1$ represents 12% systematic error, which can move the proton and/or ϕ points with respect to one another. The dotted horizontal line at $R_{\rm CP}=0.62$ is a straight-line fit to the ϕ data.

(Fig. 23). The systematic error arising from the determination of $N_{\rm coll}$ is about 19%. It is common for all three particle species shown in the figure, because the nuclear modification factors were obtained from the same centrality classes. The dotted horizontal line at $R_{\rm CP}=0.62$ is a straight-line fit to the ϕ data. To facilitate the comparison between the proton results and the ϕ including systematic errors, the $N_{\rm coll}$ error is plotted in two places: with a solid bar around $R_{\rm CP}=1$ and with a dotted bar around $R_{\rm CP}=0.62$. Since these errors are correlated, if the curves in the figure were to change owing to a change in the value of $N_{\rm coll}$, they will move together up or down within the extent of the error bars shown. We would like to emphasize the *comparison* between the $R_{\rm CP}$ values for the protons and the ϕ. In this comparison, the systematic errors in determining $N_{\rm coll}$ cancel. The important systematic errors to consider are those that can move the ϕ points with respect to the proton points. When determining a ratio of spectra measured at different centralities, most systematic errors cancel. After removing the $N_{\rm coll}$ error, the sources of error that remain for the ϕ come from the multiplicity-dependent corrections and the effect of the mass window as described previously. For the protons and pions [29,30], the error that remains that is independent of the error determined for the ϕ comes from the multiplicity-dependent corrections. The relative error between the ϕ and the proton measurements is evaluated at 7% and is represented by the extended solid bar just below $R_{\rm CP}=1$. Clearly, the ϕ's behavior is more like that of the pions and not like that of the protons. Thus we conclude that the ϕ meson exhibits a suppression effect at intermediate p_T similar to that of the pions. Although we cannot conclude whether ϕ production at this intermediate p_T is dominated by soft or hard processes, this observation provides support for models that depend on the number of constituent quarks in the particle as opposed to models that depend on just the mass of the particle to explain the anomalous proton yields. Other RHIC data on this subject are reviewed in Ref. [70].

V. CONCLUSIONS

A systematic measurement has been made of ϕ production at midrapidity in Au+Au collisions with $\sqrt{s_{NN}}=200$ GeV at RHIC. The general features of the data include the yield, which rises from 0.318 ± 0.028 (stat) $\pm$ 0.051 (syst) in peripheral collisions to 3.94 ± 0.60 (stat) $\pm$ 0.62 (syst) in central collisions. There is seen to be little centrality dependence to the inverse slope, which is about 360 MeV. The centroid mass and resonance width are extracted with high enough precision to rule out any large (MeV/c^2 scale) deviations from the accepted PDG values. At p_T below 1.5 GeV/c, a blast-wave analysis of the most central pion, kaon, and proton spectra with a freeze-out temperature $T_{\rm fo}$ of 109 MeV and a transverse velocity β_T of 0.77 describes the most central ϕ data as well. A similar conclusion, with monotonically changing results for $T_{\rm fo}$ and β_T, holds for the less central events. At higher transverse momenta, all particles lie above the blast-wave fits, which suggests that the dominant particle production mechanism is no longer soft physics but is giving way to the expected jet fragmentation. A study of the ratio $R_{\rm CP}$ of the ϕ provides a critical new piece of information in understanding the anomalous proton-to-pion ratio seen in central heavy ion collisions at RHIC, since the ϕ is a meson with a mass similar to that of a proton. The $R_{\rm CP}$ value for the ϕ above a transverse momentum of 1.5 GeV/c is about 0.6, similar to that of the pions but inconsistent with the proton value of 1. This indicates that the ϕ meson is being suppressed in this p_T range for the more central collisions. The lower p_T blast-wave fits imply hydrodynamic behavior at the hadronic stage, whereas the inconsistency with simple hydrodynamics at higher p_T is something one would expect in the jet fragmentation region. This transition is an important factor to consider as one begins to understand the mechanism of particle production in central collisions at RHIC.

ACKNOWLEDGMENTS

We thank the staff of the Collider-Accelerator and Physics Departments at Brookhaven National Laboratory and the staff of the other PHENIX participating institutions for their vital contributions. We acknowledge support from the Department of Energy, Office of Science, Nuclear Physics Division, the National Science Foundation, Abilene Christian University Research Council, Research Foundation of SUNY, and the Dean of the College of Arts and Sciences at Vanderbilt University (U.S.A); Ministry of Education, Culture, Sports, Science, and Technology and the Japan Society for the Promotion of Science (Japan); Conselho Nacional de Desenvolvimento Científico e Tecnológico and Fundação de Amparo à Pesquisa do Estado de São Paulo (Brazil); Natural Science Foundation of China (People's Republic of China); Centre National de la Recherche Scientifique, Commissariat à l'Énergie Atomique, Institut National de Physique Nucléaire et de Physique des Particules, and Institut National de Physique Nucléaire et de Physique des Particules (France); Bundesministerium für Bildung und Forschung, Deutscher Akademischer Austausch Dienst, and Alexander von Humboldt Stiftung (Germany); Hungarian

National Science Fund, OTKA (Hungary); Department of Atomic Energy and Department of Science and Technology (India); Israel Science Foundation (Israel); Korea Research Foundation and Center for High Energy Physics (Korea); Russian Ministry of Industry, Science and Tekhnologies, Russian Academy of Science, and Russian Ministry of Atomic Energy (Russia); VR and the Wallenberg Foundation (Sweden); the U.S. Civilian Research and Development Foundation for the Independent States of the Former Soviet Union; the US-Hungarian NSF-OTKA-MTA; the US-Israel Binational Science Foundation, and the 5th European Union TMR Marie-Curie Programme.

APPENDIX A: COMBINATORIAL BACKGROUND

Assume there are N tracks per event of which n are positive and $N-n$ are negative, the probability of the partition being $P(n)$ such that $\sum_{n=0}^{N} P(n) = 1$.

All the following expressions refer to the average number of pairs per event

1. General relation between the number of like and unlike pairs

The total number of pairs is

$$N_{\text{pairs}} = \frac{N(N-1)}{2}. \tag{A1}$$

The number of $+-$ pairs is

$$n_{+-} = \sum_{n=0}^{N} n(N-n)P(n) = N\langle n\rangle - \langle n^2\rangle. \tag{A2}$$

The number of $++$ pairs is

$$n_{++} = \sum_{n=0}^{N} \frac{n(n-1)}{2} P(n) = \frac{\langle n^2\rangle - \langle n\rangle}{2}. \tag{A3}$$

The number of $--$ pairs is

$$n_{--} = \sum_{n=0}^{N} \frac{(N-n)(N-n-1)}{2} P(n) \tag{A4}$$

$$= \frac{N(N-1)}{2} - \left(N - \frac{1}{2}\right)\langle n\rangle + \langle n^2\rangle. \tag{A5}$$

We therefore get

$$n_{++} + n_{--} = \frac{N(N-1)}{2} - (N\langle n\rangle - \langle n^2\rangle). \tag{A6}$$

The last expression is trivial: The number of like-sign pairs is equal to the total number pairs minus the number of unlike-sign pairs.

The ratio R of unlike to like pairs is therefore

$$R = \frac{n_{+-}}{n_{++} + n_{--}} = \frac{N\langle n\rangle - \langle n^2\rangle}{N(N-1)/2 - (N\langle n\rangle - \langle n^2\rangle)}. \tag{A7}$$

This is a general result, free of any assumption, and should always be fulfilled, in pure combinatorial background as well as in a mixture of signal plus combinatorial background.

2. Combinatorial background

Consider a pure combinatorial background sample. By its essence there are *no correlations* between tracks in such a sample; that is, within an event the probability p to have a positive (or a negative) track is constant and independent of the number of tracks. Therefore the probability $P(n)$ of having n positive tracks out of the total of N tracks is given by a binomial distribution

$$P(n) = \frac{N!}{n!(N-n)!} p^n (1-p)^{N-n}, \tag{A8}$$

$$\langle n\rangle = pN, \tag{A9}$$

$$\langle n^2\rangle = \sigma^2 + \langle n\rangle^2 = Np(1-p) + p^2N^2. \tag{A10}$$

Replacing these values in expression (6) gives

$$R = \frac{(p-p^2)}{(1/2 - p + p^2)}. \tag{A11}$$

If there is charge symmetry (i.e., $p = 0.5$) one gets $R = 1$ and consequently the combinatorial background is given by

$$n_{+-}^{\text{CB}} = n_{++} + n_{--}. \tag{A12}$$

This is an exact relation. It holds with quite good accuracy even if there is some charge asymmetry. For example, for an asymmetry of 10% (i.e., $p = 0.525$), $R = 0.995$.

3. The formula $N_{+-}^{\text{CB}} = 2\sqrt{N_{++}N_{--}}$

The combinatorial background is rigorously given by this formula provided that the number N of tracks per event has a Poisson distribution:

$$\mathcal{P}(N) = \frac{\langle N\rangle^N e^{-N}}{N!}. \tag{A13}$$

Again we assume that the N tracks are divided into n positive and $N-n$ negative tracks, the partition is given by the binomial distribution (A7), and all expressions to follow refer to average number of pairs per event.

The number of $++$ pairs is

$$N_{++} = \sum_{N=2}^{\infty} \mathcal{P}(N) \sum_{n=0}^{N} P(n) \frac{n(n-1)}{2}. \tag{A14}$$

Using relations (A7) and (A11) and some algebra leads to

$$N_{++} = \tfrac{1}{2} p^2 \langle N\rangle^2. \tag{A15}$$

Similarly, the number of $--$ pairs is given by

$$N_{--} = \sum_{N=2}^{\infty} \mathcal{P}(N) \sum_{n=0}^{N} P(n) \frac{(N-n)(N-n-1)}{2} \tag{A16}$$

$$= \frac{1}{2}(1-p)^2 \langle N\rangle^2. \tag{A17}$$

TABLE VII. m_T spectra of ϕ mesons in different centrality bins. The systematic errors on invariant yields are from combinatorial background normalization, ϕ counting mass window, acceptance correction efficiencies from Monte Carlo and occupancy-dependent corrections.

Centrality (%)	m_T (GeV/c^2)	m_T Bin Size (GeV/c^2)	$\frac{1}{2\pi m_T}\frac{d^2N}{dm_T dy}$ [(GeV^2/c^4)$^{-2}$]	Stat. Error [(GeV^2/c^4)$^{-2}$]	Syst. Error [(GeV^2/c^4)$^{-2}$]
0–10	1.365	0.4	0.51114	0.15120	0.0778747
	1.691	0.2	0.19114	0.04656	0.029121
	1.891	0.2	0.12065	0.02702	0.018382
	2.091	0.2	0.07313	0.01758	0.011142
	2.291	0.2	0.03335	0.01372	0.005081
	2.565	0.4	0.01683	0.00541	0.002564
	2.891	0.2	0.01353	0.00406	0.002061
	3.300	1.0	0.00268	0.00074	0.000408
10–40	1.364	0.4	0.37232	0.04145	0.05667
	1.691	0.2	0.09224	0.01255	0.01404
	1.891	0.2	0.04872	0.00719	0.00742
	2.091	0.2	0.03867	0.00483	0.00589
	2.291	0.2	0.02320	0.00389	0.00353
	2.564	0.4	0.01246	0.00160	0.00189
	2.891	0.2	0.00415	0.00110	0.00063
	3.294	1.0	0.00120	0.00021	0.00018
40–92	1.364	0.4	0.04432	0.00622	0.00645
	1.691	0.2	0.01295	0.00185	0.00189
	1.891	0.2	0.01009	0.00110	0.00147
	2.091	0.2	0.00531	0.00074	0.00077
	2.291	0.2	0.00287	0.00060	0.00042
	2.563	0.4	0.00126	0.00024	0.00018
	2.891	0.2	0.00062	0.00019	0.00009
	3.293	1.0	0.00019	0.00004	0.00003

The number of combinatorial background $+-$ pairs is

$$N_{+-}^{\mathrm{CB}} = \sum_{N=2}^{\infty} \mathcal{P}(N) \sum_{n=0}^{N} P(n) n(N-n) \quad \text{(A18)}$$

$$= p(1-p)\langle N^2 \rangle. \quad \text{(A19)}$$

Inspecting (A15), (A16), and (A17) shows that

$$N_{+-}^{\mathrm{CB}} = 2\sqrt{N_{++}N_{--}}. \quad \text{(A20)}$$

APPENDIX B: DATA TABLES OF CENTRALITY-SELECTED ϕ SPECTRA

The invariant yields, $(\frac{1}{2\pi m_T})(\frac{d^2N}{dm_T dy})$, of the ϕ mesons in different centrality bins are shown in Table VII.

APPENDIX C: SYSTEMATIC ERRORS ON dN/dy, T, AND m_T- SPECTRA

The sources of the systematic errors on yield (dN/dy), T, and m_T- spectra measurements come from the following sources:

(a) Systematic error on the combinatorial background normalization δ_{norm}: This originates from the systematics of the event mixing. Since both same-event and mixed-event like-sign distributions represent pure combinatorials, we estimated unlike-sign combinatorial background by normalizing the mixed-event unlike-sign distributions to $2\sqrt{N_{++}^{\text{Same event}} N_{--}^{\text{Same event}}}$ and $2\sqrt{N_{++}^{\text{Mixed event}} N_{--}^{\text{Mixed event}}}$, and the difference in the extracted ϕ signal from the real data between these two normalizations are attributed to the systematic uncertainty.

TABLE VIII. Systematic error in dN/dy.

Centrality (%)	δ_{norm} (%)	δ_{mass} (%)	δ_{extrap} (%)	δ_{MC} (%)	δ_{occu} (%)	$\delta_{\mathrm{sys}}^{\mathrm{tot}}$ (%)
Minimum Bias	0.7	2.6	4.0	12.4	7.8	15
0–10	0.8	4.2	5.2	12.4	10	17
10–40	1.1	2.3	5.9	12.4	8.5	16
40–92	0.7	3.1	6.0	12.4	7	16

TABLE IX. Systematic error in T.

Centrality (%)	δ_{mass} (%)	δ_{fit} (%)	$\delta_{\mathrm{sys}}^{\mathrm{tot}}$ (%)
Minimum Bias	0.6	4.9	5
0–10	1.1	5.2	5
10–40	1.1	6.2	6
40–92	1.1	4.2	4

We use the same normalization factor for all m_T bins. So, these systematics are applicable to the measured dN/dy only and the absolute normalization of the m_T spectra, but they do not affect their shape and the inverse slope, T.

(b) Systematics of the ϕ mass window, δ_{mass}: We count the number of reconstructed ϕ mesons by integrating the ϕ meson invariant mass spectra within a ± 5 MeV mass window with respect to the measured centroids in both data and Monte Carlo. The systematic associated with this mass window is estimated by measuring the extent of the changes in dN/dy and T after constructing ϕ meson m_T spectra within five different mass windows (± 3, ± 5, ± 8, ± 10, and ± 15 MeV) with respect to the measured ϕ centroids.

(c) Uncertainties in extrapolation of ϕ meson m_T spectra to $m_T = m_\phi$, δ_{extrap}: This is studied by

(i) fitting the m_T distributions with two different fitting functions (exponential and Boltzmann functions) and

(ii) fitting the transverse mass spectra within different m_T ranges. These are applied to both dN/dy and T.

(d) Acceptance correction systematics, δ_{MC}: The systematics associated with acceptance correction factors derived from Monte Carlo analysis are investigated by considering two sources:

(i) tuning of detector alignments in Monte Carlo with reference to the real data ($\sim 3\%$) and

(ii) systematics in the fiducial geometries in data and Monte Carlo ($\sim 12\%$).

The systematic error from this source is independent of the momenta of reconstructed ϕ mesons. So, this is attributed to dN/dy and the absolute normalization of the m_T spectra.

(e) Systematic error in the occupancy-dependent efficiency corrections, δ_{occu}: The systematic error associated with this efficiency is estimated by calculating the occupancy-dependent correction with different track confirmation criteria and is independent of the pair momenta. This systematic effect was shown to be momentum independent and hence affects these normalization of spectra and dN/dy, but not the extracted slope parameters.

These systematic errors are quoted in Tables VIII and IX for dN/dy and T, respectively.

[1] E. Laermann and O. Philipsen, Ann. Rev. Nucl. Part. Sci. **53**, 163 (2003).
[2] J. D. Bjorken, Phys. Rev. D **27**, 140 (1983).
[3] K. Adcox *et al.* (PHENIX Collaboration), Phys. Rev. Lett. **87**, 052301 (2001).
[4] J. Rafelski and B. Müller, Phys. Rev. Lett. **48**, 1066 (1982).
[5] A. Shor, Phys. Rev. Lett. **54**, 1122 (1985).
[6] P. Koch, B. Müller, and J. Rafelski, Phys. Rep. **142**, 167 (1986).
[7] C. P. Singh, Phys. Rev. Lett. **56**, 1750 (1986).
[8] C. P. Singh, Phys. Lett. **B188**, 369 (1987).
[9] C. P. Singh, Phys. Rep. **236**, 147 (1993).
[10] C. P. Singh, *et al.*, Phys. Lett. **B393**, 188 (1997).
[11] S. A. Bass *et al.*, Nucl. Phys. **A661**, 205 (1999).
[12] J.-P. Blaizot and R. Mendez Galain, Phys. Lett. **B271**, 32 (1991).
[13] S. Pal, C. M. Ko, and Z. Lin, Nucl. Phys. **A707**, 525 (2002).
[14] P. Bi and J. Rafelski, Phys. Lett. **B262**, 485 (1991).
[15] M. Asakawa and C. M. Ko, Nucl. Phys. **A572**, 732 (1994).
[16] C. Song, Phys. Lett. **B388**, 141 (1996).
[17] M. Asakawa and C. M. Ko, Phys. Lett. **B322**, 33 (1994).
[18] C. M. Ko and D. Seibert, Phys. Rev. C **49**, 2198 (1994).
[19] K. Haglin, Nucl. Phys. **A584**, 719 (1995).
[20] W. Smith and K. L. Haglin, Phys. Rev. C **57**, 1449 (1998).
[21] E. Oset and A. Ramos, Nucl. Phys. **A679**, 616 (2001).
[22] S. Okubo, Phys. Lett. **B5**, 165 (1963).
[23] D. Cabrera and M. J. Vicente Vacas, Phys. Rev. C **67**, 045203 (2003).
[24] S. Eidelman *et al.*, Phys. Lett. **B592**, 11 (2004).
[25] B. Alessandro *et al.*, Phys. Lett. **B555**, 147 (2003).
[26] V. Friese *et al.*, Nucl. Phys. **A698**, 487 (2002).
[27] K. Adcox *et al.* (PHENIX Collaboration), Phys. Rev. Lett. **88**, 022301 (2002).
[28] K. Adcox *et al.* (PHENIX Collaboration), Phys. Lett. **B561**, 82 (2003).
[29] S. S. Adler *et al.* (PHENIX Collaboration), Phys. Rev. Lett. **91**, 072303 (2003).
[30] S. S. Adler *et al.* (PHENIX Collaboration), Phys. Rev. Lett. **91**, 172301 (2003).
[31] K. Adcox *et al.* (PHENIX Collaboration), Phys. Rev. Lett. **88**, 242301 (2002).
[32] R. J. Fries, B. Müller, C. Nonaka, and S. A. Bass, Phys. Rev. C **68**, 044902 (2003); Phys. Rev. Lett. **90**, 202303 (2003).
[33] R. C. Hwa and C. B. Yang, Phys. Rev. C **70**, 024905 (2004).
[34] V. Greco, C. M. Ko, and P. Lévai, Phys. Rev. C **68**, 034904 (2003).
[35] V. Greco, C. M. Ko, and P. Lévai, Phys. Rev. Lett. **90**, 202302 (2003).
[36] Y. Akiba *et al.*, Phys. Rev. Lett. **76**, 2021 (1996).
[37] H. Fesefeldt *et al.*, Nucl. Phys. **B147**, 317 (1979); D. Drijard *et al.*, Z. Phys. C. **9**, 293 (1981), and references therein.
[38] B. B. Back *et al.* (E917 Collaboration), Phys. Rev. C **69**, 054901 (2004).
[39] S. V. Afanasiev *et al.* (NA49 Collaboration), Phys. Lett. **B491**, 59 (2000).
[40] M. C. Abreu *et al.* (NA38 Collaboration), Phys. Lett. **B368**, 239 (1996).
[41] M. C. Abreu *et al.* (NA50 Collaboration), Phys. Lett. **B555**, 147 (2003); **B561**, 294(E) (2003).
[42] D. Rohrich *et al.*, J. Phys. G **27**, 355 (2001).
[43] C. Adler *et al.* (STAR Collaboration), Phys. Rev. C **65**, 041901(R) (2002).
[44] K. Adcox *et al.* (PHENIX Collaboration), Nucl. Instrum. Methods A **499**, 469 (2003).
[45] M. Aizawa *et al.* (PHENIX Collaboration), Nucl. Instrum. Methods A **499**, 508 (2003).
[46] L. Aphecetche *et al.* (PHENIX Collaboration), Nucl. Instrum. Methods A **499**, 521 (2003).

[47] M. Allen *et al.* (PHENIX Collaboration), Nucl. Instrum. Methods A **499**, 549 (2003).
[48] C. Adler, A. Denisov, E. Garcia, M. Murray, H. Stroebele, and S. White, Nucl. Instrum. Methods A **470**, 488 (2001).
[49] K. Adcox *et al.* (PHENIX Collaboration), Nucl. Instrum. Methods A **499**, 489 (2003).
[50] S. S. Adler *et al.* (PHENIX Collaboration), Phys. Rev. C **69**, 034909 (2004).
[51] J. T. Mitchell *et al.*, Nucl. Instrum. Methods A **482**, 491 (2002).
[52] The mass squared for each track is defined as $M^2 = p^2(t^2c^2/L^2 - 1)$, where p is the momentum, t is the time of flight, c is the speed of light, and L is the length of the path traversed by the track from vertex to the detector.
[53] L. Aphecetche *et al.*, Nucl. Instrum. Methods A **499**, 521 (2003).
[54] GEANT 3.21, CERN program library.
[55] The PDG value for the ϕ mass centroid is $1019.456 \pm 0.020\,\mathrm{MeV}/c^2$, and for the ϕ width the value is $4.26 \pm 0.05\,\mathrm{MeV}/c^2$ [24].
[56] F. Klingl, T. Waas, and W. Weise, Phys. Lett. **B431**, 254 (1998).
[57] R. Rapp and J. Wambach, Adv. Nucl. Phys. **25**, 1 (2000), edited by A. Perlmutter, J. W. Negele, and E. W. Vogt (Kluwer Academic Publishers).
[58] L. Alvarez-Ruso and V. Koch, Phys. Rev. C **65**, 054901 (2002).
[59] The STAR experiment at RHIC has recently reported its analysis of the $\phi \to K^+K^-$ data for Au+Au at $\sqrt{s_{NN}} = 200$ GeV [71]. The analyses for PHENIX and STAR have one common centrality bin, 0–10%, for which the extracted dN/dy are not in agreement. The STAR value is $6.65 \pm 0.35\,(\mathrm{stat}) \pm 0.73\,(\mathrm{sys})$, compared with the PHENIX value $3.94 \pm 0.60\,(\mathrm{stat}) \pm 0.62\,(\mathrm{sys})$. The discrepancy persists even if one eliminates the four lowest m_T data points from the STAR data set to fit over the same m_T range for both the STAR and the PHENIX data. There is not a discrepancy between the quoted inverse slope parameters.
[60] I. G. Bearden *et al.* (NA44 Collaboration), Phys. Rev. Lett. **78**, 2080 (1997); H. Boggild *et al.*, Phys. Rev. C **59**, 328 (1999); I. G. Bearden *et al.*, Phys. Lett. **B388**, 431 (1996); I. G. Bearden *et al.*, Phys. Rev. C. **57**, 837 (1998).
[61] E. Andersen *et al.* (WA97 Collaboration), J. Phys. G **25**, 171 (1999).
[62] E. Schnedermann, J. Sollfrank, and U. Heinz, Phys. Rev. C **48**, 2462 (1993).
[63] K. Adcox *et al.* (PHENIX Collaboration), Phys. Rev. C **69**, 024904 (2004).
[64] P. Braun-Munzinger, D. Magestro, K. Redlich, and J. Stachel, Phys. Lett. **B518**, 41 (2001).
[65] S. Adler *et al.* (PHENIX Collaboration), Phys. Rev. C **69**, 034910 (2004).
[66] P. Abreu *et al.* (DELPHI Collaboration), Eur. Phys. J. C **17**, 207 (2000).
[67] T. Hirano and Y. Nara, Nucl. Phys. **A743**, 305 (2004); T. Hirano and K. Tsuda, Phys. Rev. C **66**, 054905 (2002); D. Teaney, J. Lauret, and E. V. Shuryak, Phys. Rev. Lett. **86**, 4783 (2001); P. Kolb *et al.*, Nucl. Phys. **A696**, 197 (2001); P. Huovinen *et al.*, Phys. Lett. **B503**, 58 (2001).
[68] G. C. Rossi and G. Veneziano, Nucl. Phys. **B123**, 507 (1977); D. Kharzeev, Phys. Lett. **B378**, 238 (1996); S. E. Vance, M. Gyulassy, and X.-N. Wang, *ibid.* **B443**, 45 (1998); I. Vitev and M. Gyulassy, Phys. Rev. C **65**, 041902(R) (2002).
[69] X-.N. Wang, Nucl. Phys. **A702**, 238 (2002).
[70] J. Velkovska, J. Phys. G **30**, S835 (2004).
[71] J. Adams *et al.* (STAR Collaboration), Phys. Lett. **B612**, 181 (2005).

Available online at www.sciencedirect.com
SCIENCE DIRECT®
ELSEVIER
Nuclear Physics A 757 (2005) 184–283
NUCLEAR PHYSICS A

Formation of dense partonic matter in relativistic nucleus–nucleus collisions at RHIC: Experimental evaluation by the PHENIX Collaboration

PHENIX Collaboration

K. Adcox [bd], S.S. Adler [e], S. Afanasiev [t], C. Aidala [e,j], N.N. Ajitanand [aw], Y. Akiba [w,aq,ar], A. Al-Jamel [al], J. Alexander [aw], R. Amirikas [n], K. Aoki [aa,aq], L. Aphecetche [ay], Y. Arai [w], R. Armendariz [al], S.H. Aronson [e], R. Averbeck [ax], T.C. Awes [am], R. Azmoun [e,ax], V. Babintsev [q], A. Baldisseri [k], K.N. Barish [f], P.D. Barnes [ad], J. Barrette [ag], B. Bassalleck [ak], S. Bathe [f,ah], S. Batsouli [j], V. Baublis [ap], F. Bauer [f], A. Bazilevsky [e,q,ar], S. Belikov [e,q,s], F.G. Bellaiche [am], S.T. Belyaev [z], M.J. Bennett [ad], Y. Berdnikov [at], S. Bhagavatula [s], M.T. Bjorndal [j], J.G. Boissevain [ad], H. Borel [k], S. Borenstein [ab], S. Botelho [au], M.L. Brooks [ad], D.S. Brown [al], N. Bruner [ak], D. Bucher [ah], H. Buesching [e,ah], V. Bumazhnov [q], G. Bunce [e,ar], J.M. Burward-Hoy [ac,ad,ax], S. Butsyk [ap,ax], X. Camard [ay], T.A. Carey [ad], J.-S. Chai [u], P. Chand [d], J. Chang [f], W.C. Chang [b], L.L. Chavez [ak], S. Chernichenko [q], C.Y. Chi [j], J. Chiba [w], M. Chiu [j], I.J. Choi [bg], J. Choi [v], R.K. Choudhury [d], T. Christ [ax], T. Chujo [e,bc,bd], M.S. Chung [y,ad], P. Chung [aw], V. Cianciolo [am], C.R. Cleven [o], Y. Cobigo [k], B.A. Cole [j], M.P. Comets [an], P. Constantin [s], M. Csanád [m], T. Csörgő [x], J.P. Cussonneau [ay], D. d'Enterria [j], T. Dahms [ax], K. Das [n], G. David [e], F. Deák [m], H. Delagrange [ay], A. Denisov [q], A. Deshpande [ar,ax], E.J. Desmond [e], A. Devismes [ax], O. Dietzsch [au], B.V. Dinesh [d],

0375-9474/$ – see front matter © 2005 Elsevier B.V. All rights reserved.
doi:10.1016/j.nuclphysa.2005.03.086

J.L. Drachenberg [a], O. Drapier [ab], A. Drees [ax], A.K. Dubey [bf], R. du Rietz [af], A. Durum [q], D. Dutta [d], V. Dzhordzhadze [az], K. Ebisu [aj], Y.V. Efremenko [am], J. Egdemir [ax], K. El Chenawi [bd], A. Enokizono [p], H. En'yo [aa,aq,ar], B. Espagnon [an], S. Esumi [bc], L. Ewell [e], T. Ferdousi [f], D.E. Fields [ak,ar], C. Finck [ay], F. Fleuret [ab], S.L. Fokin [z], B. Forestier [ae], B.D. Fox [ar], Z. Fraenkel [bf], J.E. Frantz [j], A. Franz [e], A.D. Frawley [n], Y. Fukao [aa,aq,ar], S.-Y. Fung [f], S. Gadrat [ae], S. Garpman [af,✠], F. Gastineau [ay], M. Germain [ay], T.K. Ghosh [bd], A. Glenn [az], A.L. Godoi [au], G. Gogiberidze [az], M. Gonin [ab], J. Gosset [k], Y. Goto [aq,ar], R. Granier de Cassagnac [ab], N. Grau [s], S.V. Greene [bd], M. Grosse Perdekamp [r,ar], T. Gunji [h], S.K. Gupta [d], W. Guryn [e], H.-Å. Gustafsson [af], T. Hachiya [p,aq], A. Hadjhenni [ay], J.S. Haggerty [e], M.N. Hagiwara [a], H. Hamagaki [h], A.G. Hansen [ad], H. Hara [aj], H. Harada [p], E.P. Hartouni [ac], K. Haruna [p], M. Harvey [e], E. Haslum [af], K. Hasuko [aq], R. Hayano [h,bb], N. Hayashi [aq], X. He [o], M. Heffner [ac], T.K. Hemmick [ax], J.M. Heuser [aq,ax], M. Hibino [be], P. Hidas [x], H. Hiejima [r], J.C. Hill [s], D.S. Ho [bg], R. Hobbs [ak], M. Holmes [bd], W. Holzmann [aw], K. Homma [p], B. Hong [y], A. Hoover [al], T. Horaguchi [aq,ar,ba], H.M. Hur [u], T. Ichihara [aq,ar], V.V. Ikonnikov [z], K. Imai [aa,aq], M. Inaba [bc], M. Inuzuka [h], M.S. Ippolitov [z], D. Isenhower [a], L. Isenhower [a], M. Ishihara [aq,ar], T. Isobe [h], M. Issah [aw], A. Isupov [t], B.V. Jacak [ar,ax], W.Y. Jang [y], Y. Jeong [v], J. Jia [j,ax], J. Jin [j], O. Jinnouchi [aq,ar], B.M. Johnson [e], S.C. Johnson [ac,ax], K.S. Joo [ai], D. Jouan [an], F. Kajihara [h,aq], S. Kametani [h,be], N. Kamihara [aq,ba], M. Kaneta [ar], J.H. Kang [bg], M. Kann [ap], S.S. Kapoor [d], K. Katou [be], T. Kawabata [h], T. Kawagishi [bc], A.V. Kazantsev [z], S. Kelly [i,j], B. Khachaturov [bf], A. Khanzadeev [ap], J. Kikuchi [be], D.H. Kim [ai], D.J. Kim [bg], D.W. Kim [v], E. Kim [av], G.-B. Kim [ab], H.J. Kim [bg], S.Y. Kim [bg], Y.-S. Kim [u], Y.G. Kim [bg], E. Kinney [i], W.W. Kinnison [ad], A. Kiss [m], E. Kistenev [e], A. Kiyomichi [aq,bc], K. Kiyoyama [aj], C. Klein-Boesing [ah], S. Klinksiek [ak], H. Kobayashi [aq,ar], L. Kochenda [ap], V. Kochetkov [q], D. Koehler [ak], T. Kohama [p], R. Kohara [p], B. Komkov [ap], M. Konno [bc], M. Kopytine [ax], D. Kotchetkov [f], A. Kozlov [bf], P.J. Kroon [e], C.H. Kuberg [a,ad], G.J. Kunde [ad], N. Kurihara [h], K. Kurita [aq,ar,as], Y. Kuroki [bc], M.J. Kweon [y], Y. Kwon [bg], G.S. Kyle [al], R. Lacey [aw],

V. Ladygin [t], J.G. Lajoie [s], J. Lauret [aw], Y. Le Bornec [an], A. Lebedev [s,z], S. Leckey [ax], D.M. Lee [ad], M.K. Lee [bg], S. Lee [v], M.J. Leitch [ad], M.A.L. Leite [au], X.H. Li [f], Z. Li [g,aq], D.J. Lim [bg], H. Lim [av], A. Litvinenko [t], M.X. Liu [ad], X. Liu [g], Y. Liu [an], Z. Liu [g], C.F. Maguire [bd], J. Mahon [e], Y.I. Makdisi [e], A. Malakhov [t], M.D. Malik [ak], V.I. Manko [z], Y. Mao [g,ao,aq], S.K. Mark [ag], S. Markacs [j], G. Martinez [ay], M.D. Marx [ax], A. Masaike [aa], H. Masui [bc], F. Matathias [ax], T. Matsumoto [h,be], M.C. McCain [a,r], P.L. McGaughey [ad], E. Melnikov [q], M. Merschmeyer [ah], F. Messer [ax], M. Messer [e], Y. Miake [bc], J. Milan [aw], T.E. Miller [bd], A. Milov [ax,bf], S. Mioduszewski [e,az], R.E. Mischke [ad], G.C. Mishra [o], J.T. Mitchell [e], A.K. Mohanty [d], D.P. Morrison [e], J.M. Moss [ad], T.V. Moukhanova [z], F. Mühlbacher [ax], D. Mukhopadhyay [bd,bf], M. Muniruzzaman [f], J. Murata [aq,ar,as], S. Nagamiya [w], Y. Nagasaka [aj], Y. Nagata [bc], J.L. Nagle [i,j], M. Naglis [bf], Y. Nakada [aa], T. Nakamura [p], B.K. Nandi [f], M. Nara [bc], J. Newby [ac,az], M. Nguyen [ax], L. Nikkinen [ag], P. Nilsson [af], S. Nishimura [h], B. Norman [ad], A.S. Nyanin [z], J. Nystrand [af], E. O'Brien [e], C.A. Ogilvie [s], H. Ohnishi [e,p,aq], I.D. Ojha [c,bd], H. Okada [aa,aq], K. Okada [aq,ar], O.O. Omiwade [a], M. Ono [bc], V. Onuchin [q], A. Oskarsson [af], L. Österman [af], I. Otterlund [af], K. Oyama [h,bb], K. Ozawa [h], L. Paffrath [e,✠], D. Pal [bd,bf], A.P.T. Palounek [ad], V. Pantuev [ax], V. Papavassiliou [al], J. Park [av], W.J. Park [y], A. Parmar [ak], S.F. Pate [al], H. Pei [s], T. Peitzmann [ah], V. Penev [t], J.-C. Peng [r,ad], H. Pereira [k], V. Peresedov [t], D.Yu. Peressounko [z], A.N. Petridis [s], A. Pierson [ak], C. Pinkenburg [e,aw], R.P. Pisani [e], P. Pitukhin [q], F. Plasil [am], M. Pollack [ax,az], K. Pope [az], M.L. Purschke [e], A.K. Purwar [ax], H. Qu [o], J.M. Qualls [a], J. Rak [s], I. Ravinovich [bf], K.F. Read [am,az], M. Reuter [ax], K. Reygers [ah], V. Riabov [ap,at], Y. Riabov [ap], G. Roche [ae], A. Romana [ab], M. Rosati [s], A.A. Rose [bd], S.S.E. Rosendahl [af], P. Rosnet [ae], P. Rukoyatkin [t], V.L. Rykov [aq], S.S. Ryu [bg], M.E. Sadler [a], B. Sahlmueller [ah], N. Saito [aa,aq,ar], A. Sakaguchi [p], T. Sakaguchi [h,be], M. Sakai [aj], S. Sakai [bc], H. Sako [bc], T. Sakuma [aq,ba], V. Samsonov [ap], L. Sanfratello [ak], T.C. Sangster [ac], R. Santo [ah], H.D. Sato [aa,aq], S. Sato [e,w,bc], S. Sawada [w], B.R. Schlei [ad], Y. Schutz [ay], V. Semenov [q], R. Seto [f], D. Sharma [bf], M.R. Shaw [a,ad], T.K. Shea [e], I. Shein [q],

T.-A. Shibata [aq,ba], K. Shigaki [p,w], T. Shiina [ad], M. Shimomura [bc], Y.H. Shin [bg], T. Shohjoh [bc], K. Shoji [aa,aq], I.G. Sibiriak [z], A. Sickles [ax], C.L. Silva [au], D. Silvermyr [ad,af,am], K.S. Sim [y], J. Simon-Gillo [ad], C.P. Singh [c], V. Singh [c], M. Sivertz [e], S. Skutnik [s], W.C. Smith [a], A. Soldatov [q], R.A. Soltz [ac], W.E. Sondheim [ad], S.P. Sorensen [am,az], I.V. Sourikova [e], F. Staley [k], P.W. Stankus [am], N. Starinsky [ag], P. Steinberg [j], E. Stenlund [af], M. Stepanov [al], A. Ster [x], S.P. Stoll [e], M. Sugioka [aq,ba], T. Sugitate [p], C. Suire [an], J.P. Sullivan [ad], Y. Sumi [p], Z. Sun [g], M. Suzuki [bc], J. Sziklai [x], T. Tabaru [ar], S. Takagi [bc], E.M. Takagui [au], A. Taketani [aq,ar], M. Tamai [be], K.H. Tanaka [w], Y. Tanaka [aj], K. Tanida [aq,ar], E. Taniguchi [aq,ba], M.J. Tannenbaum [e], A. Taranenko [aw], P. Tarján [l], J.D. Tepe [a,ad], J. Thomas [ax], J.H. Thomas [ac], T.L. Thomas [ak], W. Tian [g,az], M. Togawa [aa,aq], J. Tojo [aa,aq], H. Torii [aa,aq,ar], R.S. Towell [a,ad], V.-N. Tram [ab], I. Tserruya [bf], Y. Tsuchimoto [p,aq], H. Tsuruoka [bc], A.A. Tsvetkov [z], S.K. Tuli [c], H. Tydesjö [af], N. Tyurin [q], T.J. Uam [ai], T. Ushiroda [aj], H. Valle [bd], H.W. van Hecke [ad], C. Velissaris [al], J. Velkovska [e,ax,bd], M. Velkovsky [ax], R. Vertesi [l], V. Veszprémi [l], L. Villatte [az], A.A. Vinogradov [z], M.A. Volkov [z], A. Vorobyov [ap], E. Vznuzdaev [ap], M. Wagner [aa], H. Wang [f], X.R. Wang [o,al], Y. Watanabe [aq,ar], J. Wessels [ah], S.N. White [e], N. Willis [an], D. Winter [j], C. Witzig [e], F.K. Wohn [s], C.L. Woody [e], M. Wysocki [i], W. Xie [f,ar,bf], K. Yagi [bc], Y. Yang [g], A. Yanovich [q], S. Yokkaichi [aq,ar], G.R. Young [am], I. Younus [ak], I.E. Yushmanov [z], W.A. Zajc [j,*], O. Zaudke [ah], C. Zhang [j], Z. Zhang [ax], S. Zhou [g], S.J. Zhou [bf], J. Zimányi [x], L. Zolin [t], X. Zong [s]

[a] *Abilene Christian University, Abilene, TX 79699, USA*
[b] *Institute of Physics, Academia Sinica, Taipei 11529, Taiwan*
[c] *Department of Physics, Banaras Hindu University, Varanasi 221005, India*
[d] *Bhabha Atomic Research Centre, Bombay 400 085, India*
[e] *Brookhaven National Laboratory, Upton, NY 11973-5000, USA*
[f] *University of California - Riverside, Riverside, CA 92521, USA*
[g] *China Institute of Atomic Energy (CIAE), Beijing, People's Republic of China*
[h] *Center for Nuclear Study, Graduate School of Science, University of Tokyo, 7-3-1 Hongo, Bunkyo, Tokyo 113-0033, Japan*
[i] *University of Colorado, Boulder, CO 80309, USA*
[j] *Columbia University, New York, NY 10027 and Nevis Laboratories, Irvington, NY 10533, USA*
[k] *Dapnia, CEA Saclay, F-91191, Gif-sur-Yvette, France*
[l] *Debrecen University, Egyetem tér 1, H-4010 Debrecen, Hungary*
[m] *ELTE, Eötvös Loránd University, Pázmány P.s. 1/A, H-1117 Budapest, Hungary*

[n] *Florida State University, Tallahassee, FL 32306, USA*
[o] *Georgia State University, Atlanta, GA 30303, USA*
[p] *Hiroshima University, Kagamiyama, Higashi-Hiroshima 739-8526, Japan*
[q] *Institute for High Energy Physics (IHEP), Protvino, Russia*
[r] *University of Illinois at Urbana-Champaign, Urbana, IL 61801, USA*
[s] *Iowa State University, Ames, IA 50011, USA*
[t] *Joint Institute for Nuclear Research, 141980 Dubna, Moscow Region, Russia*
[u] *KAERI, Cyclotron Application Laboratory, Seoul, South Korea*
[v] *Kangnung National University, Kangnung 210-702, South Korea*
[w] *KEK, High Energy Accelerator Research Organization, Tsukuba-shi, Ibaraki-ken 305-0801, Japan*
[x] *KFKI Research Institute for Particle and Nuclear Physics (RMKI), PO Box 49, H-1525 Budapest 114, Hungary*
[y] *Korea University, Seoul 136-701, South Korea*
[z] *Russian Research Center "Kurchatov Institute", Moscow, Russia*
[aa] *Kyoto University, Kyoto 606, Japan*
[ab] *Laboratoire Leprince-Ringuet, Ecole Polytechnique, CNRS-IN2P3, Route de Saclay, F-91128, Palaiseau, France*
[ac] *Lawrence Livermore National Laboratory, Livermore, CA 94550, USA*
[ad] *Los Alamos National Laboratory, Los Alamos, NM 87545, USA*
[ae] *LPC, Université Blaise Pascal, CNRS-IN2P3, Clermont-Fd, 63177 Aubiere cedex, France*
[af] *Department of Physics, Lund University, Box 118, SE-221 00 Lund, Sweden*
[ag] *McGill University, Montreal, PQ H3A 2T8, Canada*
[ah] *Institut für Kernphysik, University of Muenster, D-48149 Muenster, Germany*
[ai] *Myongji University, Yongin, Kyonggido 449-728, South Korea*
[aj] *Nagasaki Institute of Applied Science, Nagasaki-shi, Nagasaki 851-0193, Japan*
[ak] *University of New Mexico, Albuquerque, NM 87131, USA*
[al] *New Mexico State University, Las Cruces, NM 88003, USA*
[am] *Oak Ridge National Laboratory, Oak Ridge, TN 37831, USA*
[an] *IPN-Orsay, Universite Paris Sud, CNRS-IN2P3, BP1, F-91406, Orsay, France*
[ao] *Peking University, Beijing, People's Republic of China*
[ap] *PNPI, Petersburg Nuclear Physics Institute, Gatchina, Russia*
[aq] *RIKEN (Institute of Physical and Chemical Research), Wako, Saitama 351-0198, Japan*
[ar] *RIKEN BNL Research Center, Brookhaven National Laboratory, Upton, NY 11973-5000, USA*
[as] *Physics Department, Rikkyo University, 3-34-1 Nishi-Ikebukuro, Toshima, Tokyo 171-8501, Japan*
[at] *St. Petersburg State Technical University, St. Petersburg, Russia*
[au] *Universidade de São Paulo, Instituto de Física, Caixa Postal 66318, São Paulo CEP05315-970, Brazil*
[av] *System Electronics Laboratory, Seoul National University, Seoul, South Korea*
[aw] *Chemistry Department, Stony Brook University, SUNY, Stony Brook, NY 11794-3400, USA*
[ax] *Department of Physics and Astronomy, Stony Brook University, SUNY, Stony Brook, NY 11794, USA*
[ay] *SUBATECH (Ecole des Mines de Nantes, CNRS-IN2P3, Université de Nantes), BP 20722-44307, Nantes, France*
[az] *University of Tennessee, Knoxville, TN 37996, USA*
[ba] *Department of Physics, Tokyo Institute of Technology, Tokyo, 152-8551, Japan*
[bb] *University of Tokyo, Tokyo, Japan*
[bc] *Institute of Physics, University of Tsukuba, Tsukuba, Ibaraki 305, Japan*
[bd] *Vanderbilt University, Nashville, TN 37235, USA*
[be] *Waseda University, Advanced Research Institute for Science and Engineering, 17 Kikui-cho, Shinjuku-ku, Tokyo 162-0044, Japan*
[bf] *Weizmann Institute, Rehovot 76100, Israel*
[bg] *Yonsei University, IPAP, Seoul 120-749, South Korea*

Received 15 October 2004; received in revised form 29 March 2005; accepted 1 June 2005

Available online 17 May 2005

Abstract

Extensive experimental data from high-energy nucleus-nucleus collisions were recorded using the PHENIX detector at the Relativistic Heavy Ion Collider (RHIC). The comprehensive set of measurements from the first three years of RHIC operation includes charged particle multiplicities, transverse energy, yield ratios and spectra of identified hadrons in a wide range of transverse momenta (p_T), elliptic flow, two-particle correlations, nonstatistical fluctuations, and suppression of particle production at high p_T. The results are examined with an emphasis on implications for the formation of a new state of dense matter. We find that the state of matter created at RHIC cannot be described in terms of ordinary color neutral hadrons.
© 2005 Elsevier B.V. All rights reserved.

1. Introduction

1.1. Historical introduction

A recurring theme in the history of physics is the desire to study matter under extreme conditions. The latter half of the twentieth century saw this quest extended from "ordinary" atomic systems to those composed of nuclear matter. Even prior to the identification of quantum chromodynamics (QCD) as the underlying theory of the strong interaction, there was considerable interest in the fate of nuclear matter when subjected to density and temperature extremes [1–3]. Particularly intriguing was the suggestion that new phases of nuclear matter could be associated with a corresponding change in the structure of the vacuum [4]. These considerations gained additional impetus with the realizations that (a) QCD was the correct theory of the strong interaction, (b) the phenomena of quark confinement was a consequence of the nonperturbative structure of the vacuum and (c) this vacuum structure is modified at high temperatures and/or densities, suggesting that quarks and gluons under such conditions would be deconfined. Taken together, these facts suggest that QCD is a fundamental theory of nature containing a phase transition *that is accessible to experimental investigation*.

It is quite remarkable that this understanding was achieved very early in the development of QCD. Collins and Perry noted in 1975 [5] that the reduction of the coupling constant at small distances indicated that the dense nuclear matter at the center of neutron stars would consist of deconfined quarks and gluons.[1] Their treatment focused on the high-density, low-temperature regime of QCD, but they did note that similar arguments might apply to the high temperatures present in the early universe. An extensive review by Shuryak in 1980 [7] is the first to have examined the high-temperature phase in detail,

* Corresponding author.
E-mail address: zajc@nevis.columbia.edu (W.A. Zajc).
✠ Deceased.

[1] In fact, prior to the development of QCD the quark hypothesis raised serious issues concerning the stability of neutron stars [6].

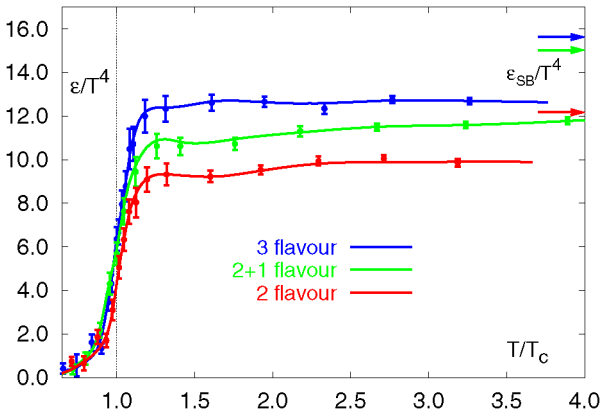

Fig. 1. Lattice QCD results [11] for the energy density/T^4 as a function of the temperature scaled by the critical temperature T_C. Note the arrows on the right side indicating the values for the Stefan–Boltzmann limit.

and is also notable for proposing the phrase "quark–gluon plasma" (QGP) to describe the deconfined state:

> When the *energy* density ε exceeds some typical hadronic value (~ 1 GeV/fm^3), matter no longer consists of separate hadrons (protons, neutrons, etc.), but as their fundamental constituents, quarks and gluons. Because of the apparent analogy with similar phenomena in atomic physics we may call this phase of matter the QCD (or quark–gluon) plasma.

Developing a quantitative understanding of the deconfining phase transition in hadronic matter and of QGP properties has proven to be a challenging task. While simple dimensional arguments suffice to identify both the critical energy density $\varepsilon_C \sim 1$ GeV/fm^3 and the associated critical temperature $T_C \sim 170$ MeV, these values also imply that the transition occurs in a regime where the coupling constant is of order unity, thereby making perturbative descriptions highly suspect.

Progress in understanding QCD in the extremely nonperturbative domain near the critical temperature has relied on an essential contribution by Creutz [8], who showed that numerical implementations of Wilson's lattice formulation [9] could be used to study phase transition phenomena. This work, together with the continued exponential increases in computing power, stimulated the development of lattice QCD, which in turn has led to detailed investigations of the thermodynamic properties of quarks and gluons [10].

Lattice QCD predicts a phase transformation to a quark–gluon plasma at a temperature of approximately $T \approx 170$ MeV $\approx 10^{12}$ K, as shown in Fig. 1 [11]. This transition temperature corresponds to an energy density $\varepsilon \approx 1$ GeV/fm^3, nearly an order of magnitude larger than that of normal nuclear matter. As noted above, this value is plausible based on dimensional grounds, since such densities correspond to the total overlap of several (light) hadrons within a typical hadron volume of 1–3 fm^3. No plausible mechanism exists under

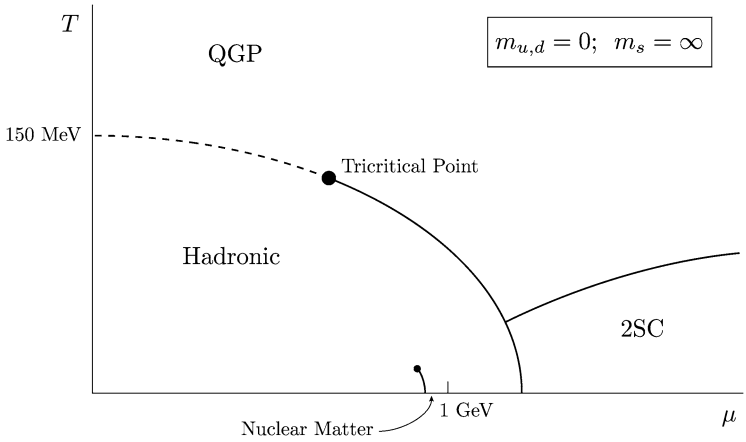

Fig. 2. Theoretical phase diagram of nuclear matter for two massless quarks as a function of temperature T and baryon chemical potential μ [12].

which hadrons could retain their *in vacuo* properties under these conditions. Lattice calculations also indicate that this significant change in the behavior of the system occurs over a small range in temperature (~ 20 MeV), and suggest that the change of phase includes the restoration of approximate chiral symmetry resulting from greatly reduced or vanishing quark constituent masses.

In the limit of massless noninteracting particles, each bosonic degree of freedom contributes $\frac{\pi^2}{30}T^4$ to the energy density; each fermionic degree of freedom contributes $\frac{7}{8}$ this value. The corresponding "Stefan–Boltzmann" limits of the energy density $\varepsilon_{\mathrm{SB}}$ for the case of 2(3) active flavor quark–gluon plasma is then

$$\varepsilon_{\mathrm{SB}} = \begin{cases} \left\{2_f \cdot 2_s \cdot 2_q \cdot 3_c \frac{7}{8} + 2_s \cdot 8_c\right\} \frac{\pi^2}{30} T^4 = 37 \frac{\pi^2}{30} T^4, & (1) \\ \left\{3_f \cdot 2_s \cdot 2_q \cdot 3_c \frac{7}{8} + 2_s \cdot 8_c\right\} \frac{\pi^2}{30} T^4 = 47.5 \frac{\pi^2}{30} T^4 & (2) \end{cases}$$

after summing over the appropriate flavor, spin, quark/antiquark and color factors for quarks and spin times color factors for gluons. The large numerical coefficients (37 and 47.5) stand in stark contrast to the value of ~ 3 expected for a hadron gas with temperature $T < T_C$, in which case the degrees of freedom are dominated by the three pion species π^-, π^0, π^+.

The exact order of this phase transition is not known. In a pure gauge theory containing only gluons the transition appears to be first order. However, inclusion of two light quarks (up and down) or three light quarks (adding the strange quark) can change the transition from first order to second order to a smooth crossover. These results are obtained at zero net baryon density; dramatic changes in the nature of the transition and in the medium itself are expected when the net baryon density becomes significant. A schematic version of the phase diagram for an idealized form of nuclear matter with vanishing light quark (up and down) masses and infinite strange quark mass is presented in Fig. 2 [12]. For sufficiently large values of the baryon chemical potential μ this system exhibits a first order phase transition between hadronic matter and QGP, along with a tricritical point below which

the transition becomes second order. However, nonzero values of the light quark masses dramatically alter this simple picture: the second order phase transition denoted by the dashed line in Fig. 2 becomes a smooth crossover, and the tricritical point correspondingly becomes a critical point designating the end of the first order transition found at higher values of μ. For example, recent calculations [13,14] indicate that the transition is a crossover for values of $\mu \lesssim 400$ MeV. Given that both theoretical arguments and experimental data suggest that nucleus–nucleus collisions at RHIC (at least near mid-rapidity) are characterized by low net baryon density, we will restrict our attention to this regime, while noting that the predicted smooth nature of the transition in this region increases the experimental challenges of unambiguously establishing that such a transition has occurred. We also note that while Fig. 2 shows that the region of low temperature and high baryon density is expected to show a transition to a color superconducting phase of matter, this regime is not accessible to RHIC collisions and will not be discussed further.

While the lattice results plotted in Fig. 1 show that the energy density reaches a significant fraction (~ 0.8) of the Stefan–Boltzmann values in the deconfined phase, the deviation from $\varepsilon_{\mathrm{SB}}$, and the reason for the persistence of that deviation to the highest studied values of T/T_C, are of great interest. For instance, Greiner has noted [15] that "in order to allow for simple calculations the QGP is usually described as a free gas consisting of quarks and gluons. This is theoretically not well founded at $T \approx T_C$". In fact, analysis of the gluon propagator in a thermal system [16,17] has demonstrated that effective masses of order $g(T)T$ are generated, suggesting that the relevant degrees of freedom are in fact massive near T_C. $m_g \approx T_C$ could be generated by gluons. Especially interesting is recent work which indicates that both heavy [18–20] and light [21] flavor states may remain bound above T_C, calling into question the naive interpretation of $\varepsilon(T)$ as an indicator of the explicit appearance of quark and gluon degrees of freedom. This is supported by explicit calculations of the spectrum of bound states above T_C [22] which predict a rich structure of states that belies a description as a weakly interacting parton gas.

To emphasize this point, consider the standard measure of the degree of coupling in a classical plasma, obtained by comparing the relative magnitudes of the average kinetic and potential energies:

$$\Gamma \equiv \frac{\langle V(r)\rangle}{\langle E_{\mathrm{kin}}\rangle}. \tag{3}$$

In the case of the QCD plasma the mean inter-particle spacing should scale as some numerical coefficient times $1/T$. Naively, this gives a mean potential energy $\langle V(r)\rangle \sim \alpha_s(T)\langle 1/r\rangle \sim \alpha_s(T)T$, leading to

$$\Gamma \sim \frac{\alpha_s(T)T}{3T} \sim \alpha_s(T). \tag{4}$$

Any reasonable estimate for the numerical coefficients leads to $\Gamma > 1$, which is the condition for a "strongly-coupled" plasma. In reality, the screening present at such densities (or equivalently, the generation of effective gluon masses) modifies the mean potential energy to $\langle V(r)\rangle \sim g(T)T$, which only increases the estimated value of Γ [23].[2] Considerations

[2] We wish to acknowledge B. Müller for this observation.

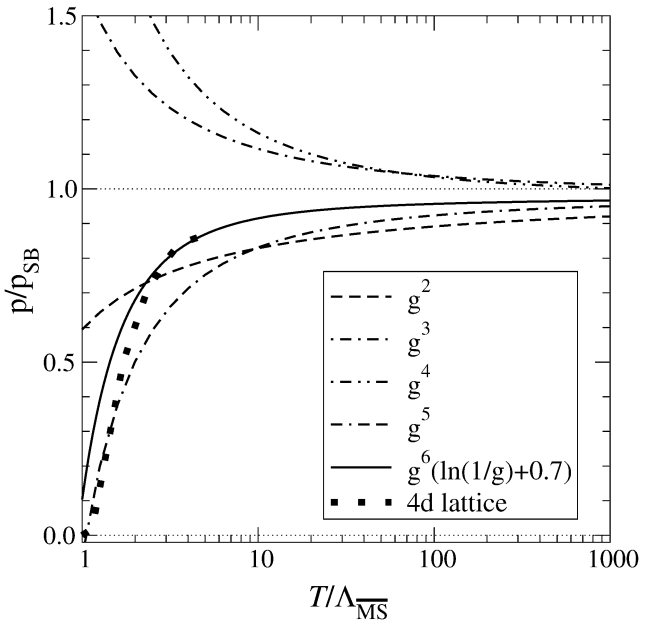

Fig. 3. Perturbative QCD results for the pressure as a function of temperature at various orders normalized to the Stefan–Boltzmann value p_{SB} [29].

such as these have led some authors [24,25] to denote quark–gluon plasma in this regime as "sQGP" for "strongly interacting QGP".

It is worth noting that this state of affairs has been anticipated by many authors. Whether the argument was based on the divergence of perturbative expansions [26], on phenomenological descriptions of confinement [27], on the development of effective gluon masses from plasmon modes [28] or on general principles [15], it is clear that the QGP near T_C should not be regarded as an ideal gas of quarks and gluons.

How high a temperature is needed not just to form a quark–gluon plasma, but to approach this "weakly" interacting plasma? A calculation of the pressure of hot matter within perturbative QCD [29] is shown in Fig. 3. The pressure result oscillates significantly as one considers contributions of different orders. These oscillations are an indication that the expansion is not yielding reliable results. However at temperatures approaching 1000 times of T_C ($\approx \Lambda_{\overline{\mathrm{MS}}}$), they appear to be converging toward the Stefan–Boltzmann limit (asymptotically free partons). It is interesting that in considering the highest-order term, the results are still nonconvergent though one seems to approach the lattice calculated pressure. Unlike the case of single parton–parton scattering at zero temperature, the infrared problems of finite-temperature field theory prevent further analytic progress even for very small values of the coupling constant [29–31].

The goal of relativistic heavy ion physics is the experimental study of the nature of QCD matter under conditions of extreme temperature. A great emphasis has been placed on "the discovery of the quark–gluon plasma", where the terminology "quark–gluon plasma" is used as a generic descriptor for a system in which the degrees of freedom are no

longer the color neutral hadron states observed as isolated particles and resonances. This definition is limited since high-energy proton–proton reactions cannot be described purely in terms of color-neutral hadrons, but rather require analysis of the underlying partonic interactions. The hoped-for essential difference in heavy ion collisions is the dominance of the partonic-level description for essentially all momentum scales and over nuclear size distances. Beyond this simple criterion, in order to characterize the produced system as a state of matter it is necessary to establish that these nonhadronic degrees of freedom form a statistical ensemble, so that concepts such as temperature, chemical potential and flow velocity apply and the system can be characterized by an experimentally determined equation of state. Additionally, experiments eventually should be able to determine the physical characteristics of the transition, for example the critical temperature, the order of the phase transition, and the speed of sound along with the nature of the underlying quasi-particles. While at (currently unobtainable) very high temperatures $T \gg T_C$ the quark–gluon plasma may act as a weakly interacting gas of quarks and gluons, in the transition region near T_C the fundamental degrees of freedom may be considerably more complex. It is therefore appropriate to argue that the quark–gluon plasma must be defined in terms of its unique properties *at a given temperature*. To date the definition is provided by lattice QCD calculations. Ultimately we would expect to validate this by characterizing the quark–gluon plasma in terms of its experimentally observed properties. However, the real discoveries will be of the fascinating properties of high temperature nuclear matter, and not the naming of that matter.

1.2. Experimental program

The theoretical discussion of the nature of hadronic matter at extreme densities has been greatly stimulated by the realization that such conditions could be studied via relativistic heavy ion collisions [32]. Early investigations at the Berkeley Bevalac (c. 1975–1985), the BNL AGS (c. 1987–1995) and the CERN SPS (c. 1987–present) have reached their culmination with the commissioning of BNL's Relativistic Heavy Ion Collider (RHIC), a dedicated facility for the study of nuclear collisions at ultra-relativistic energies [33].

The primary goal of RHIC is the experimental study of the QCD phase transition. The 2002 Long-Range Plan for Nuclear Science [34] clearly enunciates this objective:

> ...the completion of RHIC at Brookhaven has ushered in a new era. Studies are now possible of the most basic interactions predicted by QCD in bulk nuclear matter at temperatures and densities great enough to excite the expected phase transition to a quark–gluon plasma. As the RHIC program matures, experiments will provide a unique window into the hot QCD vacuum, with opportunities for fundamental advances in the understanding of quark confinement, chiral symmetry breaking, and, very possibly, new and unexpected phenomena in the realm of nuclear matter at the highest densities.

The RHIC accelerator and its four experiments were commissioned and brought online in the summer of 2000. The initial operation of both RHIC and the experiments has been remarkably successful. In these first three years the accelerator has collided, and the experiments have acquired data on, Au + Au collisions at five energies, an essential $p + p$

baseline data set, and a critical $d + \mathrm{Au}$ comparison. The analyses of these various systems have resulted in a correspondingly rich abundance of results, with over 90 publications in the refereed literature.

It is therefore appropriate to reflect on the physics accomplishments to date, with a particular emphasis on their implications for the discovery of a new state of matter. At the same time, it is essential to identify those features of the data (if any) that are at odds with canonical descriptions of the produced matter, to specify those crucial measurements which remain to be made, and to outline a program for continued exploration and characterization of strongly interacting matter at RHIC. The PHENIX Collaboration [35] has performed such an assessment; this document represents a summary of its findings.

The PHENIX Conceptual Design Report [36], submitted to BNL/RHIC management on January 29th, 1993, outlined a comprehensive physics program focused on the search for and characterization of new states of nuclear matter. The measurement of electromagnetic probes and high-transverse-momentum phenomena formed a major thrust of the proposed program. It was also realized that the measurement of global variables and soft identified hadron spectra in the same apparatus was essential to the goal of understanding the evolution of the produced matter over all relevant timescales. These diverse criteria required combining an unprecedented number of subsystems together with a high-bandwidth trigger and data-acquisition system into an integrated detector design. Particular attention was given to minimizing the conflicting design criteria of the central arm spectrometers, with their requirement for minimal mass in the aperture, and those of the muon spectrometers which require maximal absorption of the incident hadron flux. The data acquisition and trigger system was designed to accommodate the great variety of interaction rates and event sizes provided by RHIC. Every effort was made to provide for future upgrades, both in the geometry of the experiment and in the architecture and design parameters of the read-out system.

The published PHENIX results of $\mathrm{Au} + \mathrm{Au}$ collision at a center-of-mass energy per nucleon pair, $\sqrt{s_{NN}}$, of 130 GeV [37–48] and at $\sqrt{s_{NN}} = 200$ GeV [49–59], $p + p$ collisions at $\sqrt{s} = 200$ GeV [60–63], and $d + \mathrm{Au}$ at $\sqrt{s_{NN}} = 200$ GeV [64,65] clearly demonstrate that PHENIX's goal to make high-quality measurements in both hadronic and leptonic channels for collisions ranging from $p + p$ to $\mathrm{Au} + \mathrm{Au}$ has been realized. A summary of these results illustrates this point.

- First measurement of the dependence of the charged particle pseudo-rapidity density [37] and the transverse energy [38] on the number of participants in $\mathrm{Au} + \mathrm{Au}$ collisions at $\sqrt{s_{NN}} = 130$ GeV; systematic study of the centrality and $\sqrt{s_{NN}}$ dependence of $dE_T/d\eta$ and $dN_{\mathrm{ch}}/d\eta$ [59].
- Discovery of suppressed production for π^0's and charged particles at high p_T in $\mathrm{Au} + \mathrm{Au}$ collisions at $\sqrt{s_{NN}} = 130$ GeV [39] and a systematic study of the scaling properties of the suppression [47]; extension of these results to much higher transverse momenta in $\mathrm{Au} + \mathrm{Au}$ collisions at $\sqrt{s_{NN}} = 200$ GeV [49,53].
- Co-discovery (together with BRAHMS [66], PHOBOS [67] and STAR [68]) of absence of high-p_T suppression in $d + \mathrm{Au}$ collisions at $\sqrt{s_{NN}} = 200$ GeV [64].
- Discovery of the anomalously large proton and antiproton yields at intermediate transverse momentum in $\mathrm{Au} + \mathrm{Au}$ collisions at $\sqrt{s_{NN}} = 130$ GeV through the system-

atic study of $\pi^{\pm}$, $K^{\pm}$, p and $\bar{p}$ spectra [40]; study of the scaling properties of the proton and antiproton yields in Au + Au collisions at $\sqrt{s_{NN}} = 200$ GeV [52];

- Measurement of Λ's and $\bar{\Lambda}$'s in Au + Au collisions at $\sqrt{s_{NN}} = 130$ GeV [43]; measurement of ϕ's at $\sqrt{s_{NN}} = 200$ GeV [69]; measurement of deuteron and antideuteron spectra at $\sqrt{s_{NN}} = 200$ GeV [58].
- Measurement of Hanbury–Brown–Twiss (HBT) correlations in $\pi^+\pi^+$ and $\pi^-\pi^-$ pairs in Au + Au collisions at $\sqrt{s_{NN}} = 130$ GeV [41] and 200 GeV [56], establishing that the "HBT puzzle" of $R_{\text{out}} \approx R_{\text{side}}$ extends to high pair momentum.
- First measurement of single electron spectra in Au + Au collisions at $\sqrt{s_{NN}} = 130$ GeV, suggesting that charm production scales with the number of binary collisions [42]; measurement of centrality dependence of charm production in Au + Au collisions at $\sqrt{s_{NN}} = 200$ GeV [57].
- Sensitive measures of charge fluctuations [44] and fluctuations in mean p_T and transverse energy per particle [45,55] in Au + Au collisions at $\sqrt{s_{NN}} = 130$ GeV and 200 GeV.
- Measurements of elliptic flow for charged particles from Au + Au collisions at $\sqrt{s_{NN}} = 130$ GeV [46] and 62 GeV to 200 GeV [70] and identified charged hadrons from Au + Au collisions at $\sqrt{s_{NN}} = 200$ GeV [50].
- Extensive study of hydrodynamic flow, particle yields, ratios and spectra from Au + Au collisions at $\sqrt{s_{NN}} = 130$ GeV [48] and 200 GeV [54].
- First observation of J/ψ production in Au + Au collisions at $\sqrt{s_{NN}} = 200$ GeV [51].
- Measurement of the nuclear modification factor for hadrons at forward and backward rapidities in d + Au collisions at $\sqrt{s_{NN}} = 200$ GeV [65].
- First measurement of the jet structure of baryon excess in Au + Au collisions at $\sqrt{s_{NN}} = 200$ GeV [71].
- First measurement of elliptic flow of single electrons from charm decay in Au + Au collisions at $\sqrt{s_{NN}} = 200$ GeV [72].
- First measurement of direct photons in Au + Au collisions at $\sqrt{s_{NN}} = 200$ GeV [73].
- Measurement of crucial baseline data on π^0 spectra [60], direct photon production [63], and J/ψ production [61] in $p + p$ collisions at $\sqrt{s} = 200$ GeV.
- First measurement of the double longitudinal spin asymmetry A_{LL} in π^0 production for polarized $p + p$ collisions at $\sqrt{s} = 200$ GeV [62].

These publications encompass physics from the barn to the picobarn level; their very breadth precludes a detailed presentation here. These data, together with a rich program of future RHIC measurements, will allow us to address many of the features that would characterize a quark–gluon plasma:

- temperature;
- parton number density;
- energy density;
- opacity;
- collective behavior;
- thermalization leading to the quark–gluon phase;
- deconfinement;
- number and nature of degrees of freedom;

- recombination of quarks and gluons to form final-state hadrons;
- chiral symmetry restoration;
- time evolution of system parameters;
- equation of state;
- color and thermal transport properties;
- critical behavior.

As emphasized above, the present PHENIX data set from RHIC runs in year 2000 to 2003 already provides an extensive set of measurements on global variables: (transverse energy and multiplicity, elliptic flow); correlations and fluctuations: (fluctuations in charge and $\langle p_T \rangle$, HBT measurements), hadron spectra: (low-p_T single-hadron spectra and radial flow, particle ratios, resonances, anomalous p/π ratio at intermediate p_T); high-p_T physics: (high-p_T singles spectra, suppression phenomena in $A + A$, nonsuppression in $d + A$, high-p_T two-particle correlations, nuclear suppression/enhancement in forward/backward directions), heavy flavor production: (charm, J/ψ), and electromagnetic probes: (direct photons). However, an important conclusion of this report is that systematic studies of these observables (vs. collision species and energy) are needed to extract unambiguous information on most of these features.

1.3. Organization of this document

As a result, this paper concentrates on those aspects of the present data that address the broad features of energy density, thermalization, deconfinement and critical behavior. The focus in most cases will be on the data of the PHENIX experiment, but the data of the other RHIC experiments will be cited to support and to extend the discussion.[3] The experimental tools that allow the systematic study of all phenomena as a function of the inferred impact parameter are presented in the context of hard-scattering phenomena. These methods and the associated data are then used to discuss the experimental evidence for the formation of a state of high-density matter. The measured abundances, spectra and flow patterns are used to analyze the degree of thermalization and collectivity in the produced matter. These results are then examined for evidence establishing the role of deconfined quarks and gluons in the produced system, along with the implications for its description as a quark–gluon plasma. A concluding section summarizes the findings and identifies key future measurements required to further refine our observations.

2. Energy density and E_T, N_{ch}

A prerequisite for creating a quark–gluon plasma is producing a system with sufficiently large energy density. From both elementary estimates [22] and from extensive numerical studies in lattice QCD [10,11], the required density is known to be on the order of

[3] An underappreciated aspect of the RHIC program is the excellent agreement between the various experiments in almost all measured channels.

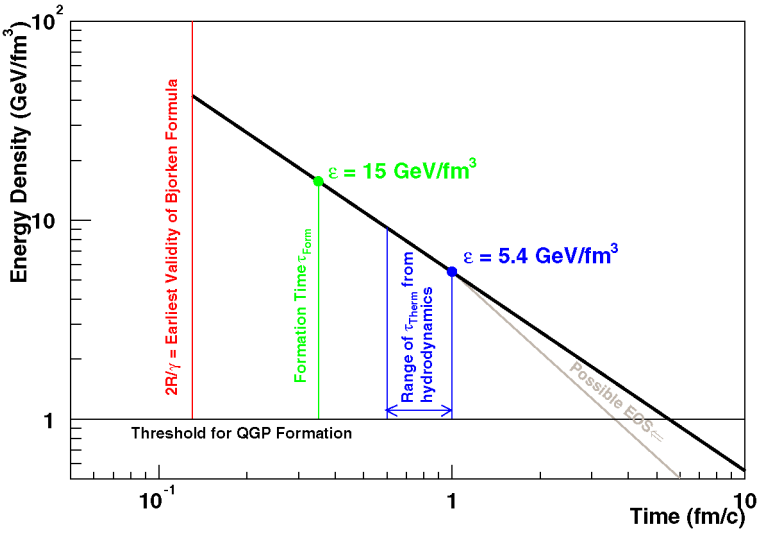

Fig. 4. Schematic drawing of the time and energy density scales derived through the Bjorken picture.

1 GeV/fm^3. Establishing that this energy density is created in RHIC collisions is a basic ingredient in establishing the creation of a QGP at RHIC.

In this section we explore what can be deduced about the energy densities achieved in RHIC $A + A$ collisions from measurements of the global transverse energy and multiplicity. In later sections these estimates will be compared to densities inferred from hydrodynamics-based models (Section 3) and from jet quenching evidence (Section 6).

Specifically, we will address three different energy density estimates, and introduce two distinct time scales: (i) The peak *general energy density* that is achieved when the incoming nuclei overlap; (ii) The peak *formed energy density* involving created particles at proper time τ_{Form}; and (iii) The peak *thermalized energy density* present at proper time τ_{Therm} when local thermal equilibrium is first achieved (assuming that this occurs). The values and time scales for formed and thermalized energy densities are indicated schematically in Fig. 4; detailed explanations follow in Sections 2.3 and 2.4.

In this section we will also review data on overall particle multiplicities, and through them distinguish between different models of the initial particle production.

2.1. General energy density

The simplest definition of "energy density" is the total mass-energy within some region of space divided by the volume of that region, as seen at some instant of time in some Lorentz frame. However, this definition is not satisfactory since we can "trivially" raise any simple energy density by viewing the system in a different frame. For example, a static system with constant energy density ρ_0 in its rest frame—say, a gold nucleus—will appear to have energy density $\gamma^2\rho_0$ when viewed in a frame boosted by Lorentz γ. Accordingly, we can only calculate a *meaningful* energy density $\langle\varepsilon\rangle$ as mass-energy/volume for some region *in the case* when the total momentum in the region is zero.

Now let us imagine a symmetric RHIC $A + A$ collision at a moment when the two original nuclei are overlapping in space, as seen in the laboratory/center-of-mass frame. The total momentum in any overlap region is zero by symmetry, so we can calculate a meaningful—if short-lived—energy density for such a region. If each nucleus has energy density ρ_0 in its rest frame then the total energy density in the overlap region is just $\langle\varepsilon\rangle = 2\rho_0\gamma^2$. If we take a nominal $\rho_0 = 0.14$ GeV/fm^3 for a nucleus at rest and $\gamma = 106$ for a full-energy RHIC collision, then the result for the peak general energy density is $\langle\varepsilon\rangle = 3150$ GeV/fm^3. This is a spectacularly, almost absurdly high number on the scale of ~ 1 GeV/fm^3 associated with the familiar transition described by lattice QCD.

This energy density is of course artificial, in that it would be temporarily present even in the case of no interactions between the two nuclei. It is instructive to consider the (again artificial) case where the nucleons in the two nuclei have only elastic interactions. Then the time during which a high energy density is present over *any* volume cannot last longer than $t = 2R/\gamma$, where R is the rest-frame radius of the nucleus. With $R = 7$ fm for Au this time is only 0.13 fm/c at RHIC, and after this time all energy densities will fall precipitously back to ρ_0 if no secondary particles are created. The scale of this interval is so short that a scattering cannot even be said to have occurred within that volume unless its momentum transfer scale Q exceeds at least 1.5 GeV/c, or more. Accordingly, we will turn our attention instead to energy densities involving only produced particles as the potential source for a QCD transition.

2.2. *Formed energy density*

In any frame (not just the center-of-mass frame) where the two incoming nuclei have very high energies the region when/where the nuclei overlap will be very thin in the longitudinal direction and very short in duration. In this limit, then, it is fair to describe all secondary produced particles as having been radiated out from a very thin "disk", and that they are all created at essentially the same time. These realizations lead directly to the picture described by Bjorken [74], whose original diagram is reproduced in Fig. 5 and whose derivation we retrace briefly here.

Once the beam "pancakes" recede after their initial overlap, the region between them is occupied by secondaries at intermediate rapidities. We can calculate the local energy density of these created particles if we make one further assumption: that the secondaries can be considered "formed" at some proper time τ_{Form} after they are radiated out from the thin source disk.

Our region of interest, in any frame, will be a slab perpendicular to the beam direction, with longitudinal thickness dz, with one face on the "source" plane in this frame, and transverse extent with area A covering the nuclear overlap region.[4] At time $t = \tau_{\text{Form}}$ this volume will contain all the (now-formed) particles with longitudinal velocities $0 \leqslant \beta_\parallel \leqslant dz/\tau_{\text{Form}}$ (since we assume that the particles cannot scatter before they are formed!). We can then write this number of particles as $dN = (dz/\tau_{\text{Form}})\frac{dN}{d\beta_\parallel}$, or equivalently $dN =$

[4] The region described here corresponds to half the shaded region shown in Fig. 5. Since $\beta_\parallel \simeq 0$ for particles near the source location, this is an appropriate region over which we can calculate a meaningful energy density.

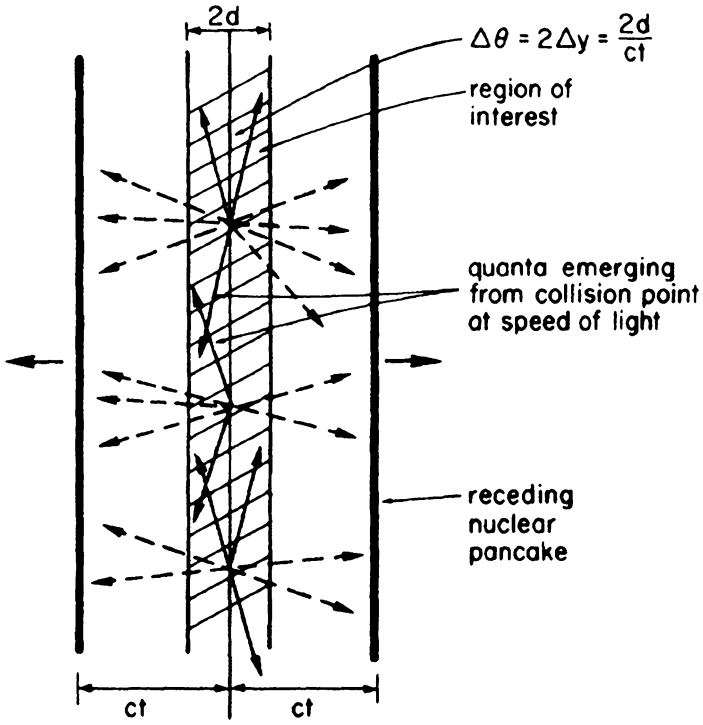

Fig. 5. Figure from Bjorken [74] illustrating the geometry of initially produced particles at a time t after the overlap of the incoming nuclei in some frame. The picture is valid in any frame in which the incoming nuclei have very high energies and so are highly Lorentz contracted.

$(dz/\tau_{\rm Form})\frac{dN}{dy}$, where y is longitudinal rapidity, since $dy = d\beta_\parallel$ at $y = \beta_\parallel = 0$. If these particles have an average total energy $\langle m_T\rangle$ in this frame ($E = m_T$ for particles with no longitudinal velocity), then the total energy divided by the total volume of the slab at $t = \tau_{\rm Form}$ is just

$$\left\langle \varepsilon(\tau_{\rm Form})\right\rangle = \frac{dN\langle m_T\rangle}{dz\,A} = \frac{dN(\tau_{\rm Form})}{dy}\frac{\langle m_T\rangle}{\tau_{\rm Form}A} = \frac{1}{\tau_{\rm Form}A}\frac{dE_T(\tau_{\rm Form})}{dy}, \tag{5}$$

where we have equated $\frac{dE_T}{dy} = \langle m_T\rangle\frac{dN}{dy}$ and emphasized that Eq. (5) is true for the transverse energy density present at time $t = \tau_{\rm Form}$.

Eq. (5) here is essentially identical[5] to Eq. (4) of Bjorken's result [74], and so is usually referred to as the *Bjorken energy density* $\varepsilon_{\rm Bj}$. It should be valid as a measure of peak energy density in created particles, on very general grounds and in all frames, as long as two conditions are satisfied: (1) A finite formation time $\tau_{\rm Form}$ can meaningfully be defined for the created secondaries; and (2) The thickness/"crossing time" of the source disk is small compared to $\tau_{\rm Form}$, that is, $\tau_{\rm Form} \gg 2R/\gamma$. In particular, the validity of Eq. (5) is completely independent of the shape of the $dE_T(\tau_{\rm Form})/dy$ distribution to the extent that

[5] A (well-known) factor of 2 error appears in the original.

$\beta_\parallel$ is infinitesimally small in a comoving frame; a plateau in dE_T/dy is *not* required. For present practical purposes, we will consider condition (2) above to be satisfied as long as $\tau_{\rm Form} > 2R/\gamma$ is true, corresponding to $\tau_{\rm Form} > 0.13$ fm/c for full-energy Au + Au collisions at RHIC.

Bjorken's original motivation was to estimate, in advance of data, the energy densities that would be reached in high-energy $A + A$ collisions using knowledge of $p(\bar{p}) + p$ collisions to estimate $\langle m_T \rangle$ and dN/dy, and choosing $\tau_{\rm Form} \sim 1$ fm/c without any particular justification other than as an order-of-magnitude estimate. With $A + A$ collision data in hand, attempts have been made to use Eq. (5) to estimate the energy densities that are actually achieved in the collisions. Historically, $\varepsilon_{\rm Bj}$ has been calculated using the final-state dE_T/dy and simply inserting a nominal value of 1 fm/c for $\tau_{\rm Form}$. In addition, fixed target experiments have been using $dE_T/d\eta$ as an estimate for dE_T/dy, which is a good approximation for these experiments; at RHIC a correction is made for the Jacobian $dy/d\eta$ which is important for a collider geometry. These "nominal Bjorken energy density" estimates, which we term $\varepsilon_{\rm Bj}^{\rm Nominal}$, range for central event samples from about 1.5 GeV/fm^3 in Au + Au collisions at AGS energies [75] ($\sqrt{s_{NN}} = 5$ GeV), to about 2.9 GeV/fm^3 in Pb + Pb collisions at SPS energies [38,76] ($\sqrt{s_{NN}} = 17$ GeV; and see also [59]) to about 5.4 GeV/fm^3 in Au + Au collisions at full RHIC energy [59] ($\sqrt{s_{NN}} = 200$ GeV).

It has often been noted that all of these values are similar to, or higher than, the 1 GeV/fm^3 scale required for the QCD transition. However, we cannot take these $\varepsilon_{\rm Bj}^{\rm Nominal}$ estimates seriously as produced energy densities without some justification for the value of 1 fm/c taken for $\tau_{\rm Form}$. An indication of potential problems with this choice arises immediately when considering AGS Au+Au and SPS Pb+Pb collisions, where the center-of-mass "crossing times" $2R/\gamma$ are 5.3 fm/c and 1.6 fm/c respectively, which implies that this choice for $\tau_{\rm Form} = 1$ fm/c actually violates the validity condition $\tau_{\rm Form} > 2R/\gamma$ we set for the use of Eq. (5). So we will deprecate the use of $\varepsilon_{\rm Bj}^{\rm Nominal}$ as an quantitative estimate of actual produced energy density, and instead treat it only as a compact way of comparing $dE_T/d\eta$ measurements across different systems, centralities and beam energies.

2.3. *Realistic $\tau_{\rm Form}$ and $\varepsilon_{\rm Bj}$ estimates*

Can we justify a better estimate for $\tau_{\rm Form}$? We might say, on general quantum mechanical grounds, that in a frame where its motion is entirely transverse a particle of energy m_T can be considered to have "formed" after a time $t = \hbar/m_T$ since its creation in that frame. To estimate the average transverse mass, we can use the final-state $dE_T/d\eta$ to estimate $dE_T(\tau_{\rm Form})/dy$ and, correspondingly, use the final-state $dN/d\eta$ as an estimate for $dN(\tau_{\rm Form})/dy$ to obtain

$$\langle m_T \rangle = \frac{dE_T(\tau_{\rm Form})/dy}{dN(\tau_{\rm Form})/dy} \simeq \frac{dE_T/d\eta}{dN/d\eta} \quad \text{(Final state)}. \tag{6}$$

PHENIX has measured the ratio of final-state transverse-energy density to charged-particle density, each per unit pseudorapidity, and the results are shown in Fig. 6. For a wide range of centralities the ratio is remarkably constant at about 0.85 GeV for full-energy central

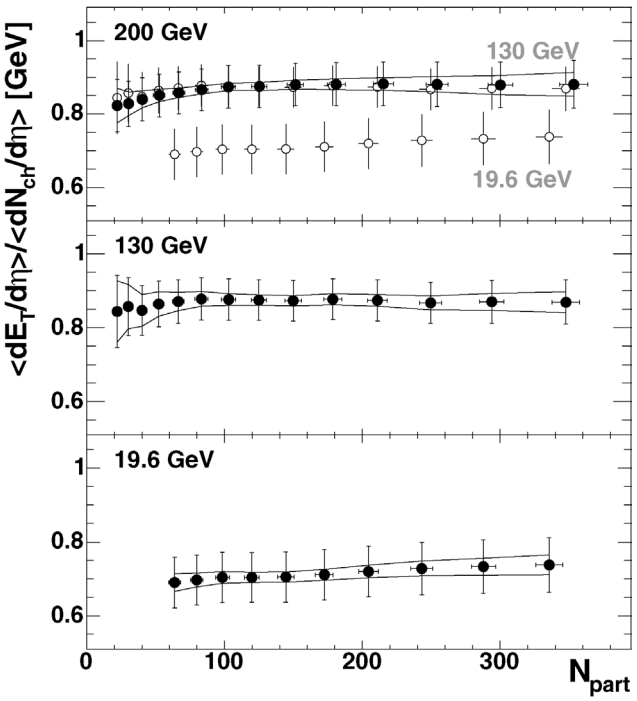

Fig. 6. The ratio of transverse energy density in pseudorapidity to charged particle density in pseudorapidity, at mid-rapidity; shown as a function of centrality, represented by the number of nucleons participating in the collision, N_{part}, for three different RHIC beam energies [59].

Au + Au collisions and shows very little change with beam energy, decreasing to only 0.7 GeV when $\sqrt{s_{NN}}$ is decreased by an order of magnitude down to 19.6 GeV.

If we approximate $dN^{Ch}/d\eta = (2/3)\,dN/d\eta$ in the final state then Eq. (6) would imply $\langle m_T \rangle \simeq 0.57$ GeV and corresponding $\tau_{\text{Form}} \simeq 0.35$ fm/c, a value shorter than the "nominal" 1 fm/c but still long enough to satisfy our validity condition $\tau_{\text{Form}} > 2R/\gamma$ at RHIC. Inserting this value into Eq. (5), along with the highest $dE_T/d\eta = 600$ GeV for 0–5% central events as measured by PHENIX [59], yields a value of $\langle \varepsilon \rangle = 15$ GeV/fm^3 for the energy density in initially produced, mid-rapidity particles in a central RHIC Au + Au collision, that is, roughly 100 times the mass-energy density of cold nuclear matter.

It is important to note that this large value of the energy density as obtained from Eq. (5) represents a conservative *lower* limit on the actual $\langle \varepsilon(\tau_{\text{Form}}) \rangle$ achieved in RHIC collisions. This follows from two observations: (1) The final-state measured $dE_T/d\eta$ is a solid lower limit on the $dE_T(\tau_{\text{Form}})/dy$ present at formation time; and (2) The final-state ratio $(dE_T/d\eta)/(dN/d\eta)$ is a good lower limit on $\langle m_T \rangle$ at formation time, and so yields a good *upper* limit on τ_{Form}. We justify these statements as follows.

Several mechanisms are known that will decrease dE_T/dy as the collision system evolves after the initial particle formation, while no mechanism is known that can cause it to increase (for $y = 0$, at least). Therefore, its final-state value should be a solid lower limit on its value at any earlier time. A partial list of the mechanisms through which dE_T/dy

will decrease after $t = \tau_{\rm Form}$ includes: (i) The initially formed secondaries in any local transverse "slab" will, in a comoving frame, have all their energy in transverse motion and none in longitudinal motion; if they start to collide and thermalize, at least some of their E_T will be converted to longitudinal modes in the local frame; (ii) Should rough local thermal equilibrium be obtained while the system's expansion is still primarily longitudinal, then each local fluid element will lose internal energy through pdV work and so its E_T will decrease; (iii) If there are pressure gradients during a longitudinal hydrodynamic expansion then some fluid elements may be accelerated to higher or lower rapidities; these effects are complicated to predict, but we can state generally that they will always tend to *decrease* dE_T/dy where it has its maximum, namely at $y = 0$. Given that we have strong evidence that thermalization and hydrodynamical evolution do occur in RHIC collisions (Section 3), it is likely that all these effects are present to some degree, and so we should suspect that final-state $dE_T/d\eta$ is substantially lower than $dE_T(\tau_{\rm Form})/dy$ at mid-rapidity.

Turning to our estimate of $\tau_{\rm Form}$, the assumption that $\tau_{\rm Form} = \hbar/\langle m_T \rangle$ cannot be taken as exact, even if the produced particles' m_T's are all identical, since "formed" is not an exact concept. However, if we accept the basic validity of this uncertainty principle argument, then we can see that the approximation in Eq. (6) provides a lower limit on $\langle m_T \rangle$. First, the numerator $dE_T/d\eta$ is a lower limit on $dE_T(\tau_{\rm Form})/dy$, as above. Second, the argument is often made on grounds of entropy conservation that the local number density of particles can never decrease [77], which would make the final-state denominator in Eq. (6) an upper limit on its early-time value.

With these limits in mind, then, it is not unreasonable for us to claim that the peak energy density of created particles reached in central Au + Au collision at RHIC is at least 15 GeV/fm^3, and in all likelihood is significantly higher.

2.4. Thermalized energy density

We have arrived at a reasonably solid, lower-limit estimate for the energy density in produced particles in a RHIC Au + Au collision, and it is more than enough to drive a QCD transition. But the situation at $t = \tau_{\rm Form}$ pictured in Fig. 5 looks nothing like local thermal equilibrium. It is an important question, then, to ask: if and when the system evolves to a state of local thermal equilibrium, is the energy density still sufficient to drive the transition to a QGP?

To answer this we begin by looking at the state of the system at $t = \tau_{\rm Form}$ and immediately afterward. At the time they are formed the particles have sorted themselves out automatically, with all the particles on a "sheet" at a longitudinal position z having the same longitudinal velocity $\beta_\parallel = z/t$; and so in the rest frame of a sheet all the sheet's particles have only transverse motion. If the particles continue free-streaming and never reinteract then the energy density will continue to fall as $\varepsilon \sim 1/t$ and the Bjorken formula in Eq. (5) will be valid, with t in place of $\tau_{\rm Form}$, as long as the expansion is primarily longitudinal.[6]

[6] For long times $t > R$ transverse expansion will become significant and the energy density will decrease as $\varepsilon \sim 1/t^3$.

For thermalization to occur the particles will have to start interacting and/or radiating. Once this happens the particles which were originally together on one "sheet" will start to spread in longitudinal velocity, though on short time scales we would expect their group average longitudinal velocity to remain the same. If the thermalization process is fast enough, then, we would expect that at time $t = \tau_{\rm Therm}$ these groups will have formed locally equilibrated fluid elements, with a velocity profile following $\beta_{\parallel}^{\rm Fluid} = z/t$. The energy density at this time will be reduced from the energy density at formation time $\varepsilon(\tau_{\rm Form})$ by a factor $\tau_{\rm Form}/\tau_{\rm Therm}$; i.e., the $\varepsilon_{\rm Bj}$ of Eq. (5) but with $\tau_{\rm Therm}$ in place of $\tau_{\rm Form}$. This evolution is illustrated in Fig. 4.

Once local equilibration is achieved we would then expect the system to evolve hydrodynamically, and the behavior of $\varepsilon(t)$ will depend on the details of the local equations of state (EOS). Without knowing those details, though, we can say that in the limit of low pressure, $p/\varepsilon \sim 0$, the energy density will continue to evolve (during longitudinal expansion) as $\varepsilon \sim 1/t$, while in the limit of high pressure, $p/\varepsilon \sim 1/3$, the energy density will decrease somewhat more quickly, $\varepsilon \sim 1/t^{4/3}$, within a fluid element. This range of possible behaviors for $t > \tau_{\rm Therm}$ is indicated schematically in Fig. 4.

A direct theoretical determination of $\tau_{\rm Therm}$ would require a detailed description of both the parton–parton interactions and the resulting evolution of the system density. However, other lines of reasoning may provide information on $\tau_{\rm Therm}$. For example, it has been argued [78] that the strong elliptic flow in RHIC collisions can be taken as evidence for fast thermalization (see Section 3.3). In a hydrodynamic picture the source of elliptic flow is the spatial anisotropy of the energy density in the transverse plane at the time hydrodynamics becomes valid. If local equilibration and the onset of hydrodynamics is delayed because interactions between the initially produced particles are weak at first, then the spatial anisotropy which could give rise to elliptic flow will be reduced (see Fig. 14). This, in effect, limits how high $\tau_{\rm Therm}$ can be if hydrodynamics is the mechanism for generating elliptic flow.

We can see from Table 1 in Section 3.5 that hydrodynamical models typically require quite short thermalization times, in the range of 0.6–1.0 fm/c, in order to reproduce the magnitude of elliptic flow which is observed at RHIC. If we take this range as typical of what hydrodynamics would imply for $\tau_{\rm Therm}$, then we can calculate the corresponding "typical" implied energy densities at thermalization time as in range of 5.4 to 9.0 GeV/fm^3. These densities are well above that required to drive the QCD transition, so the combination of our transverse energy measurements and the fast thermalization times from hydrodynamics can be taken, to some degree, as evidence that conditions to create the equilibrated upper phase of QCD matter are achieved at RHIC.

2.5. What are the initial quanta?

With our extensive use of the picture in Fig. 5 it is only natural to ask, "What are these initially produced particles?" that Bjorken referred to, nonspecifically, as "quanta". What models do we have for initial production, and what can we say about them using our data on E_T and multiplicity?

The simplest assumption is that the initially produced particles in a RHIC collision are scattered partons at mid- to low-p_T, traditionally known as "mini-jets". For a long period in

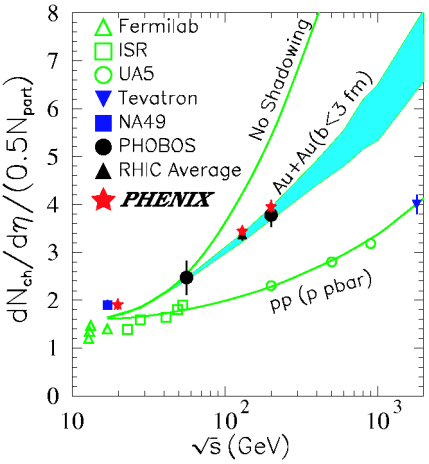

Fig. 7. Figure from Li and Wang [79] showing trends in final-state charged multiplicity per participant pair vs. (nucleon–nucleon) beam energy. (PHENIX data points [59] have been added.) The curves are the result of their two-component "hard/soft" model, which reproduces well the multiplicities from elementary $p(\bar{p}) + p$ collisions at RHIC energies. The same model extended to nuclear collisions with no regulating mechanism on hard processes (the "no shadowing" line) over-predicts the multiplicities in central RHIC collisions, while the data can be matched if substantial nuclear shadowing of gluons is invoked (shaded band).

advance of RHIC data, it was widely expected that mini-jets would be the dominant channel for E_T and particle production, and this led to two further, general expectations. First, that multiplicity and E_T per interacting nucleon would go up sharply at collider energies, as compared to fixed-target energies, since jet and mini-jet cross sections are increasing quickly with $\sqrt{s_{NN}}$ (see Fig. 7). And, secondly, that E_T and multiplicity per participating nucleon would increase steeply in more central events, since the rate of hard pQCD scatterings goes up faster with centrality than does the number of interacting nucleons.

It was therefore quite surprising when the first RHIC data [37,38,80] showed lower multiplicities than had been predicted from mini-jet models, and only a modest increase in E_T and multiplicity per participant as functions of centrality. Compared to the sharp rise, shown in Fig. 7, predicted by straightforward factorized pQCD, it was clear that some mechanism must be acting at RHIC energies to restrict, or regulate, particle production [79,81].

pQCD-based models have parameters regulating the momentum scales; these include a lower-momentum cutoff, and the factorization and fragmentation scales. Fig. 8 shows that the pQCD-based HIJING model, circa 2002, was able to reproduce 130 GeV and 200 GeV $dN_{\mathrm{ch}}/d\eta$ reasonably well. However, in that model jet production via hard scattering is an important mechanism for particle production, and the combination of the $\sqrt{s}$ dependence of hard-scattering cross sections with the growth of the nuclear overlap with centrality causes the model to predict an increase in the ratio between the two data sets with centrality. The observed ratio is, instead, quite constant. Thus the authors found it necessary to introduce a centrality-dependent shadowing to regulate the jet growth [79].

An alternative to models which use collinearly factorized pQCD is found in the "color glass condensate" picture, in which the gluon population of low-x, low-p_T states in the

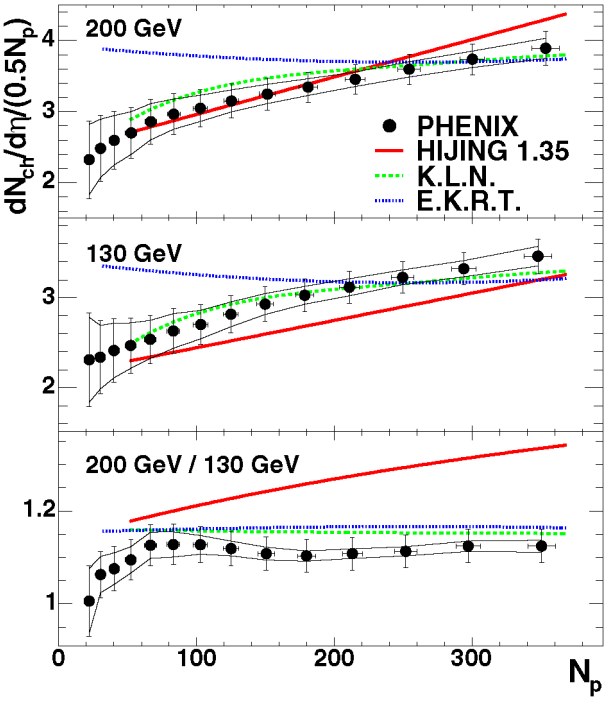

Fig. 8. Multiplicity per participant nucleon pair, as a function of centrality, for $\sqrt{s_{NN}} = 130$ GeV and 200 GeV Au + Au collisions as measured in PHENIX [59]; compared to theoretical predictions available in 2002. "HIJING" is a pQCD-based model [82], while "KLN" features gluon saturation in the initial state [83,84]; "EKRT" assumes saturation in the final state [85,86].

initial nuclear wave function is limited by transverse overlap and fusion of these low-p_T gluons. The phase-space density saturates because of the competition between extra gluon radiation from higher-x gluons and nonlinear fusion of the gluons at high density. Au + Au collisions are then collisions of two sheets of colored glass, with the produced quarks and gluons materializing at a time given by the inverse of the saturation momentum, $\tau = 1/Q_s$. Saturation of gluons with momenta below Q_s provides a regulating mechanism that limits the rise in gluon—and later, hadron—multiplicity with centrality and beam energy. Models featuring this initial-state gluon saturation agree well with essentially all RHIC data on the multiplicity density, which is dominated by low-momentum particles [83,84]. This is seen, for instance, in Fig. 8.

In this picture, the total gluon multiplicity is proportional to $1/\alpha_s \cdot Q_s^2$, which limits the number of low-momentum charged particles produced. Q_s evolves slowly with collision centrality and beam energy. For central Au + Au collisions, it has been estimated that the typical m_T scale of the gluons "liberated" from the colored glass is about 1 GeV per particle [77], which is above the lower limit of 0.53 GeV per particle that we set above using the PHENIX data. Though there are fewer predictions of E_T than total charged-particle production from gluon-saturation models, the existing models are broadly consistent with

data at RHIC. Consequently, gluon saturation is considered to be a promising candidate for describing the initial state of RHIC collisions.

2.6. Conclusions

Using reasoning similar to that of Bjorken [74], combined with some simple formation-time arguments, we can draw the following conclusions from the PHENIX data on transverse energy production and overall particle multiplicity.

- The peak energy density in created secondary particles is at least 15 GeV/fm^3, and this is most likely an underestimate. This is well in excess of the ~ 1 GeV/fm^3 required, according to lattice QCD predictions, to drive a QCD transition to QGP.
- We note that hydrodynamical calculations which reproduce the magnitude of elliptic flow observed at RHIC require local thermalization to occur very quickly, typically by 1 fm/c or earlier (see Section 3.5). If the system does reach local equilibrium on this time scale then the energy density of the first thermalized state would be in excess of 5 GeV/fm^3, well above the amount required to create the QGP.
- Pre-RHIC expectations that E_T and charged particle production would be dominated by factorized pQCD processes were contradicted by data, which showed only very modest increases with centrality and beam energy. A new class of models featuring initial-state gluon saturation compares well with RHIC multiplicity and E_T data, and are also consistent with our Bjorken-style arguments for estimating energy densities at early times.

3. Thermalization

A key question is whether the matter formed at RHIC is thermalized, and if so when in the collision was equilibration achieved. If thermalization is established early then evidence for strong transverse expansion can be potentially related to the equation of state of the dense matter produced at RHIC. To explore these issues we review several experimental observables from integral quantities (numbers of particles produced and in what ratios), to differential distributions (measured p_T and azimuthal distributions), to two-particle (HBT) correlations.

3.1. Chemical equilibrium

For many years it has been known that the abundances of different hadron species in $e^+ + e^-$ and $p + \bar{p}$ reactions can be reproduced by statistical models [87,88]. This success is often attributed to hadronization statistically filling the available phase space. At RHIC there is also the possibility that the strong scattering deduced from the measurements of elliptic flow (Section 3.3) may prove sufficient to establish chemical equilibrium.

The production of strange particles provides a means to check whether chemical equilibrium is achieved. For $e^+ + e^-$ and $p + \bar{p}$ reactions strange particle production is suppressed due to the small size of the system. This canonical suppression is largely removed for central heavy-ion collisions. If the measured strangeness yields are still lower than full

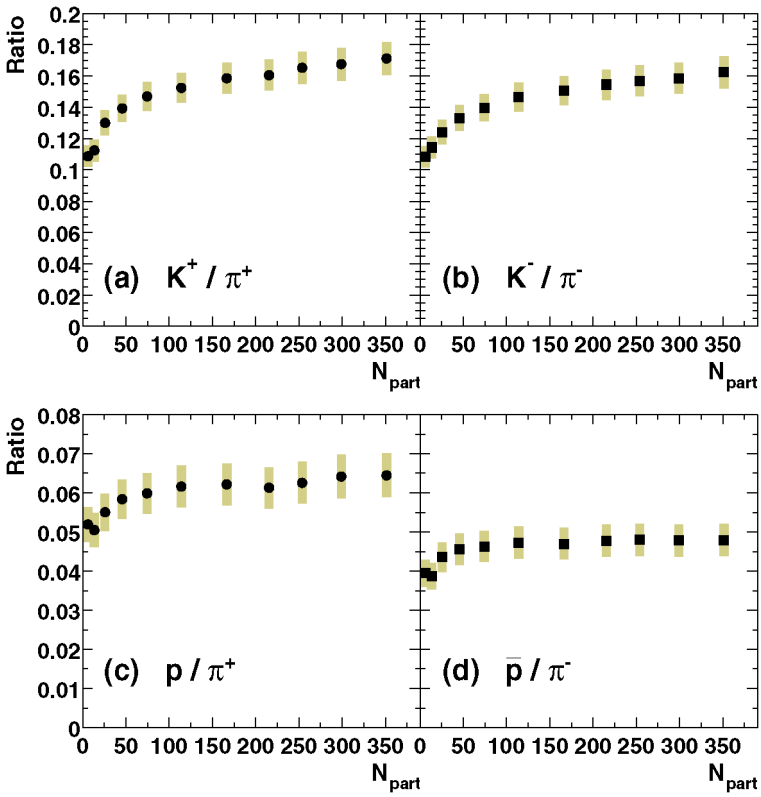

Fig. 9. Centrality dependence of particle ratios for (a) K^+/π^+, (b) K^-/π^-, (c) p/π^+, and (d) $\bar{p}/\pi^-$ in Au+Au collisions at $\sqrt{s_{NN}} = 200$ GeV [54].

equilibrium predictions, then the partial equilibrium can be quantified by a multiplicative factor of γ_s for each strange quark in a hadron, where $\gamma_s = 1$ for complete equilibration and $\gamma_s < 1$ for partial equilibration.

Fig. 9 shows the centrality dependence of K/π and p/π ratios in Au + Au collisions at $\sqrt{s_{NN}} = 200$ GeV [54]. Both K^+/π^+ and K^-/π^- increase rapidly for peripheral collisions, and then saturate or rise slowly from mid-central to the most central collisions. The ratios p/π^+ and $\bar{p}/\pi^-$ also increase from peripheral collisions but appear flatter than the K/π ratios. Canonical statistical models [89] predict an increase in these ratios with centrality, as the larger system-size effectively places less of a constraint on conserved quantities. In addition the chemical parameters, $T_{\rm chem}$ and μ_B, can also vary with centrality [90,91].

Focusing on the ratios from central collisions at $\sqrt{s_{NN}} = 200$ GeV, the data are compared to the thermal model data analysis of Kaneta and Xu [90] in Fig. 10. The extracted thermal parameters from this fit are $T_{\rm chem} = 157 \pm 3$ MeV, $\mu_B = 23 \pm 3$ MeV, and $\gamma_s = 1.03 \pm 0.04$. A large γ_s is also found by STAR [92] who extract $\gamma_s = 0.96 \pm 0.06$, while Cleymans et al., [91] extract γ_s that increases from $\gamma_s \simeq 0.85$ in peripheral collisions

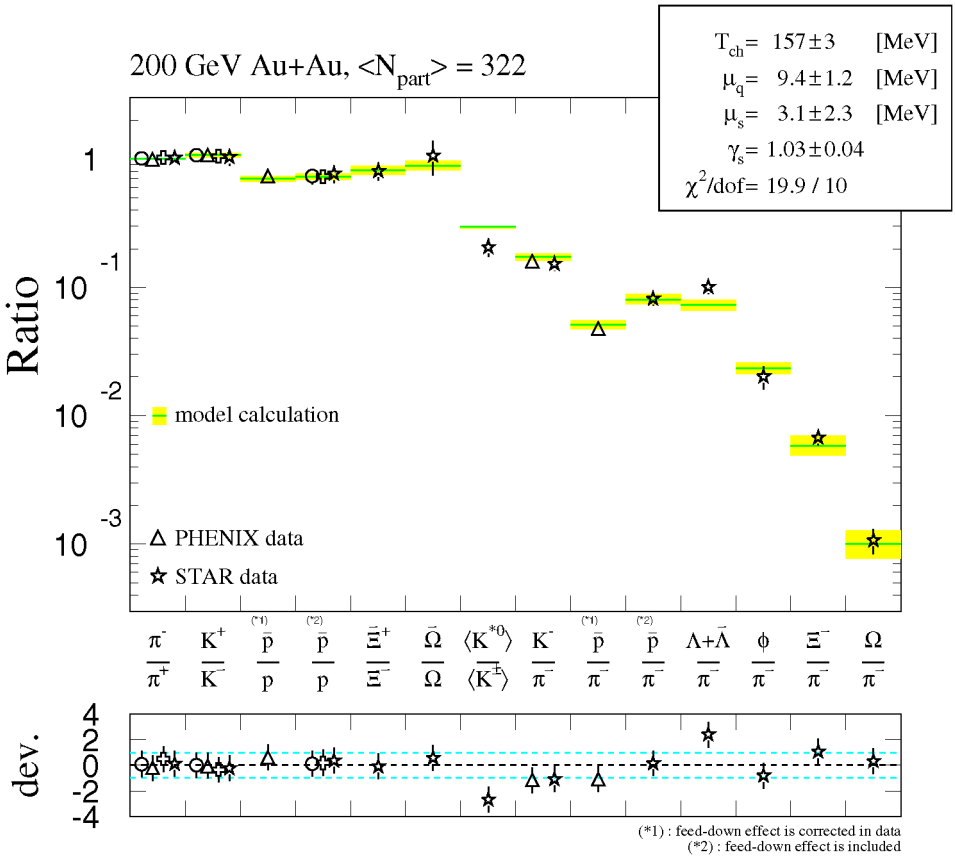

Fig. 10. Comparison of PHENIX (triangles), STAR (stars), BRAHMS (circles), and PHOBOS (crosses) particle ratios from central Au + Au collisions at $\sqrt{s_{NN}} = 200$ GeV at mid-rapidity. The thermal model descriptions from Kaneta and Xu [90] are also shown as lines. See Kaneta and Xu [90] for the experimental references.

to $\gamma_s \simeq 0.95$ for central collisions at RHIC. Similar fits to the central RHIC data are obtained by Braun-Munzinger et al., [93] who assume complete chemical equilibration, i.e., $\gamma_s = 1$.

We note that there are differences in the temperature parameter extracted by the different authors. Kaneta and Xu [90] extract $T_{\text{chem}} = 157 \pm 3$ MeV which is lower than that extracted by both Braun-Munzinger et al., [89] of $T_{\text{chem}} = 177 \pm 7$ MeV and Cleymans et al. [91] of $T_{\text{chem}} = 165 \pm 7$ MeV. However, both Braun-Munzinger et al. [89] and Magestro [94] discuss the sensitivity of the extracted temperature to corrections from feed-down from decays. Cleymans et al., [91] estimate that over 70% of π^+ in the thermal model fits come from the decay of resonances.

At lower beam energies there is controversy over whether strangeness is in full chemical equilibrium. Becattini et al. [95] use data that is integrated over the full rapidity and find that strangeness is in partial equilibrium, i.e., at the AGS $\gamma_s = 0.65 \pm 0.07$ and at the SPS $\gamma_s = 0.84 \pm 0.03$. Braun-Munzinger et al. [89] instead use ratios measured at mid-

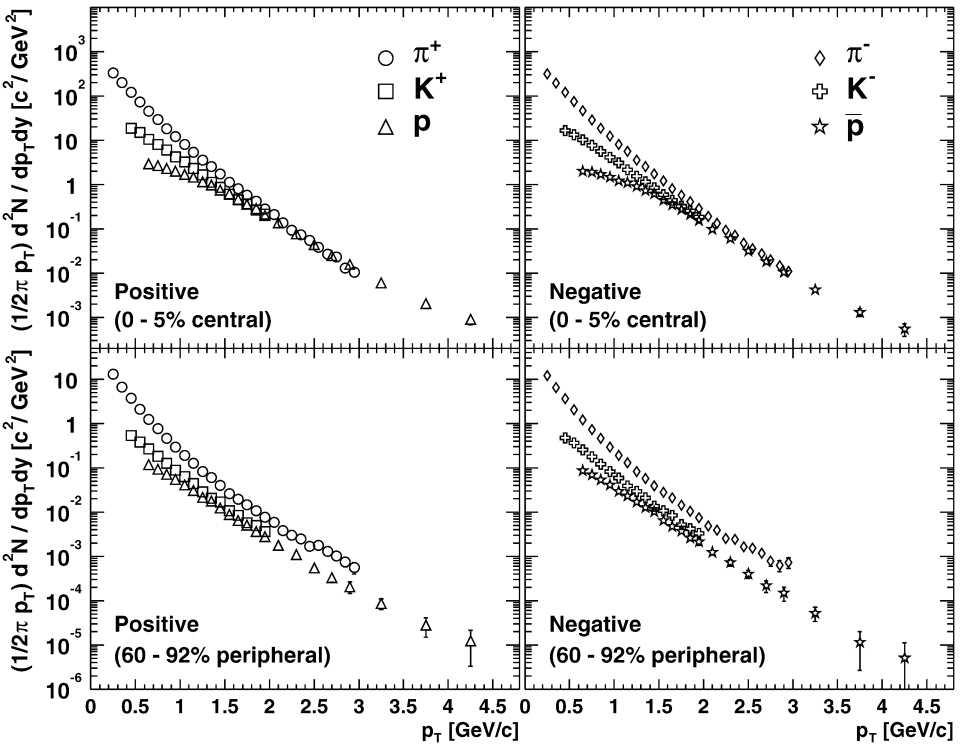

Fig. 11. Transverse momentum distributions for pions, kaons, protons, and antiprotons in Au + Au collisions at $\sqrt{s_{NN}} = 200$ GeV [54].

rapidity which typically have larger strange/nonstrange values, and, hence, they obtain acceptable fits with $\gamma_s = 1$ at both AGS and SPS energies. At RHIC energies thermal model comparisons all use mid-rapidity data; a choice that is motivated in part by the separation between fragmentation regions and central particle production.

In contrast to the controversies at lower beam energies, the observation that strangeness is equilibrated is common to all thermal calculations that reproduce RHIC data. This is consistent with chemical equilibrium being obtained before hadronization, though does not prove that this is the case. An alternative explanation is that scattering in the hadronic phase could increase γ_s to 1, though small interaction cross sections imply that it may be difficult to equilibrate the multi-strange baryons before the hadrons freezeout.

3.2. Spectra

Hadron spectra reflect conditions late in the reaction, as well as the integrated effects of expansion from the beginning of the collision. Fig. 11 shows the p_T distributions for pions, kaons, protons, and antiprotons in both central (top panel) and peripheral collisions (bottom panel) [54]. The pion spectra have a concave shape at low p_T where many of the pions may come from the decay of resonances: Δ, ρ, etc. The kaon spectra are approximately

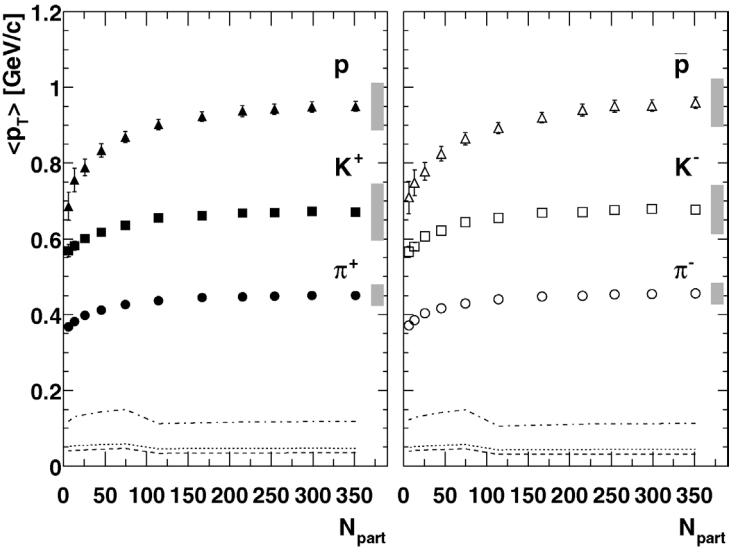

Fig. 12. Mean transverse momentum as a function of N_{part} for pions, kaons, protons and antiprotons in Au + Au collisions at $\sqrt{s_{NN}} = 200$ GeV [54]. The systematic errors from extrapolation, which are scaled by a factor of two for clarity, are shown in the bottom for protons and antiprotons (dashed-dotted lines), kaons (dotted lines), and pions (dashed lines). The shaded bars to the right represent the systematic error.

exponential over the full measured p_T range, whereas the proton spectra flatten at low p_T for the most central collisions. A striking feature is that the proton and antiproton spectra in central collisions become comparable in yield to the pion spectra above 2 GeV/c. This is more fully discussed in Section 7.

One way to characterize the change in spectra as a function of centrality is to calculate $\langle p_T \rangle$ for each spectrum [54] as shown in Fig. 12. The $\langle p_T \rangle$ increases for all particles as a function of centrality with the largest change occurring in peripheral collisions ($N_{\text{part}} < 100$). Across the different particles the increase is largest for protons and antiprotons. This is consistent with a collective expansion velocity that increases with centrality to produce the largest increase in $\langle p_T \rangle$ for the heaviest particles.

The pion, kaon, and proton spectra can all be fit using an ansatz of a thermal, expanding source [48,96] to extract the collective transverse expansion velocity $\langle \beta_T \rangle$ as well as the temperature at freezeout, T_{fo}. Fig. 13 shows $\langle \beta_T \rangle \sim 0.45$ at AGS energies [97,98], which increases to $\langle \beta_T \rangle \sim 0.5$ at the SPS [99–101] and RHIC [48,102]. All the above fits use similar model assumptions of a linear velocity profile and a Woods–Saxon density profile. That the spectra at these beam energies can be reproduced by a thermal source is necessary, but not sufficient, evidence for thermal equilibrium at each of these energies. However, it is difficult to draw strong conclusions from the increase in $\langle \beta_T \rangle$ as a function of beam energy since the parameters $\langle \beta_T \rangle$ and T_{fo} are strongly anticorrelated and their values depend on fit ranges and treatment of decays.

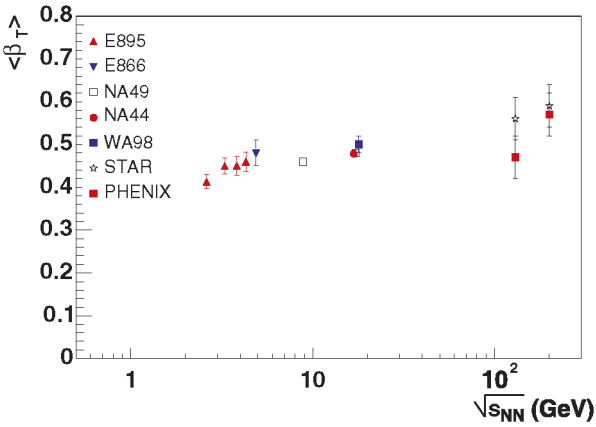

Fig. 13. Beam-energy dependence of the extracted mean transverse expansion velocity as a function of beam energy from simultaneous fits to spectra of different mass [48,97–102].

3.3. *Elliptic flow*

At the beginning of a heavy ion collision, the spatial distribution of the colliding matter resembles an ellipsoid due to the incomplete overlap of the two colliding nuclei. Any strong scattering in this early stage converts the spatial anisotropy to a momentum anisotropy which is observable as an elliptic flow of the emitted hadrons. Elliptic flow is a self-limiting phenomenon, which is readily understood in the thermodynamic limit. If strong scattering is sufficient to establish local thermal equilibrium, then the pressure gradient is largest in the shortest direction of the ellipsoid. This gradient produces higher momenta in that direction, quickly reducing the spatial asymmetry.

The absence of any strong scattering in the early stage of the collision would reduce the amount of elliptic flow that could be created. If the initially produced particles are allowed to initially free stream and reach local equilibrium only after some time delay, then the spatial anisotropy at the start of hydrodynamic evolution will be reduced; the longer the delay, the greater the reduction. Following the prescription of Kolb et al. [78], we plot in Fig. 14 the eccentricity after a time delay Δt compared to its value at formation time, as a function of Au + Au collision centrality. The eccentricity (ε) of the reaction zone is

$$\varepsilon = \frac{\langle y^2 \rangle - \langle x^2 \rangle}{\langle y^2 \rangle + \langle x^2 \rangle}. \tag{7}$$

The eccentricity can be analytically calculated once the density profile of the nuclei is chosen (typically a Woods–Saxon shape). It can also be calculated using Monte Carlo techniques, where the positions of those nucleons that participate in the reaction are used to calculate the averages in Eq. (7). From Fig. 14 we can see that for time delays of 2 fm/c or greater the magnitude of the eccentricity is significantly reduced, and its shape vs. centrality is also altered.

If locally equilibrated hydrodynamics is taken as the mechanism for generating elliptic flow, then the observation of *any* substantial amount of elliptic flow can be taken as

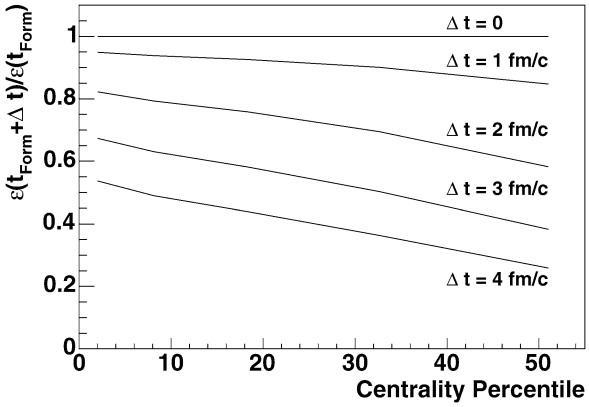

Fig. 14. The ratio of the eccentricity after a time delay Δt compared to its value at formation time, as a function of Au + Au collision centrality. The calculations follow the prescription of [78] where the produced particles are allowed to free-stream at first and reach local equilibrium only after some time delay.

evidence that local thermal equilibrium is achieved on a time scale before the spatial anisotropy would be completely erased. The order of this time-scale would be $t \sim R/c$, where R is the nuclear radius. However, the hydrodynamical calculations we will examine here (see Section 3.5 and Table 1) all require quite short thermalization times, from 0.6–1.0 fm/c, in order to reproduce the magnitude of elliptic flow observed at RHIC.

The azimuthal anisotropy of the spectra can be characterized in terms of Fourier coefficients, which at RHIC are dominated by the elliptic flow, the second Fourier coefficient, $v_2(p_T)$, where

$$\frac{d^2N}{d\phi\, dp_T} = N_0\big(1 + 2v_2(p_T)\cos(2\phi)\big). \tag{8}$$

Both the first Fourier coefficient, v_1, and higher order coefficients have been neglected in the above expression.

The most direct evidence that v_2 is related to spatial asymmetries present early in the reaction is that v_2 at low p_T approximately scales with the initial eccentricity (ε) of the reaction zone. The measured values of v_2 normalized by ε are shown in Fig. 15 vs. centrality for two different p_T ranges [46]. At low momentum v_2/ε is independent of centrality to within 20%. This scaling is increasingly broken at higher p_T.

The measured values of the integrated v_2 at RHIC are larger than those at lower energies, but this is in part due to the fact that $v_2(p_T)$ increases with p_T and $\langle p_T \rangle$ increases as a function of beam energy. To remove this effect we will concentrate on the differential flow, i.e., the shape of $v_2(p_T)$.

To make a uniform comparison between different colliding nuclei (Pb + Pb at SPS and Au + Au at RHIC) as well as different impact parameter selections from the different experiments, we normalize v_2 by the eccentricity, ε, as shown in Fig. 16. The values of ε have been calculated via a Glauber Monte Carlo using Woods–Saxon density distributions for the Au and Pb nuclei. The averages in Eq. (7) are over the participating nucleons, hence ε is calculated at the start of the collision. The pion data in Fig. 16 show that $v_2(p_T)/\varepsilon$

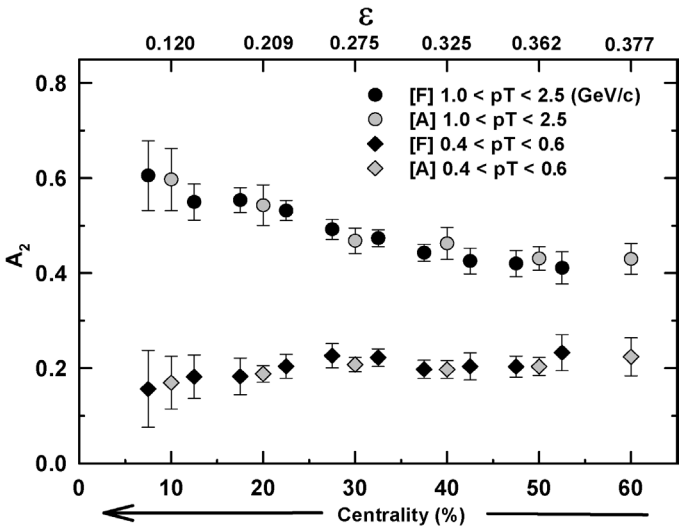

Fig. 15. $A_2 = v_2/\varepsilon$ vs. centrality for Au + Au collisions at $\sqrt{s_{NN}} = 130$ GeV [46]. The data points come from two different types of two-particle correlations: "fixed" p_T correlations when both particles are at the same p_T (points are labeled as "F"), and "assorted" p_T correlations when the two particles have different p_T (points are labeled as "A"). In this case the labeled p_T range is for the higher-momentum particle of the pair.

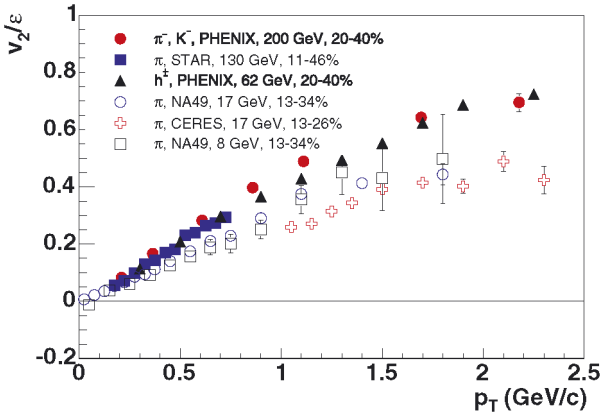

Fig. 16. $v_2(p_T)/\varepsilon$ vs. p_T for mid-central collisions at RHIC (filled symbols) and SPS (open symbols). Dividing by eccentricity removes to first order the effect of different centrality selections across the experiments [50,70, 103–105].

increases approximately linearly with p_T for low p_T. The rate of increase of v_2/ε as a function of p_T is larger at RHIC [50,103] than at SPS [104,105] as can most easily be seen by calculating the slope of v_2/ε below $p_T = 1$ GeV/c (Fig. 17). The slope $(dv_2/dp_T)/\varepsilon$ increases from SPS to RHIC by approximately 50%. Hydrodynamical calculations [106] shown in Fig. 17 reproduce the data both at RHIC and at CERN SPS within one standard deviation. More extensive comparisons with hydro calculations will be discussed in Sec-

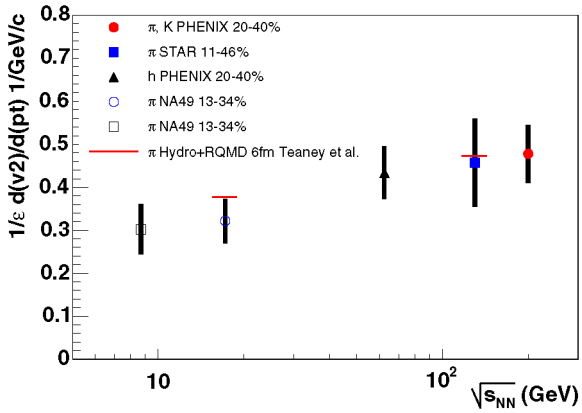

Fig. 17. The slope of the scaled elliptic flow, $(dv_2/dp_T)/\varepsilon$, for mid-central collisions at RHIC (filled symbols) and the SPS (open symbols). The slope is calculated from the data in Fig. 16 for the data $p_T < 1$ GeV/c. The solid error bars represent the total systematic error including the systematic error on v_2 and ε [50,70,103,104].

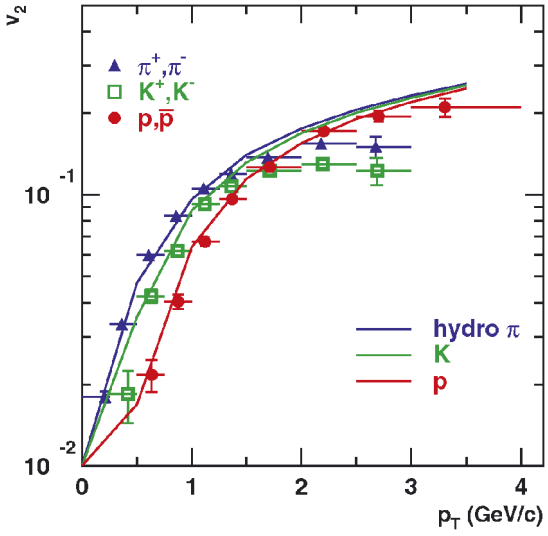

Fig. 18. $v_2(p_T)$ for pions, kaons and protons produced in minimum-bias collisions at RHIC [50] compared to hydro calculations from Huovinen et al. [107].

tion 3.5, while the behavior of v_2 at higher p_T, which follows a scaling with respect to the number of quarks, is discussed in Section 7.

Further insight into the expansion dynamics can be obtained from the mass dependence of $v_2(p_T)$ shown in Fig. 18 for pions, kaons and protons [50] along with a comparison with an early hydrodynamic model calculation [107]. The $v_2(p_T)$ for pions is larger than for kaons and protons at low p_T, and this mass ordering has been explained as resulting from radial expansion [107] that produces a larger distortion of the elliptic flow

induced velocity profile for larger hadron masses. However, as will be discussed in Section 3.5, this calculation fails to reproduce the proton spectra, and attempts to remedy this failure lead to calculations that no longer reproduce the measured v_2 for pions and protons.

3.4. HBT

Bose–Einstein correlations between identical particles provide a measure of the space–time extent of the source at the end of the reaction. Because the extracted source parameters as measured by the HBT technique are driven by space–time correlations, HBT results are sensitive to expansion dynamics integrated throughout the collision. HBT measurements were originally motivated by theoretical predictions of a large source size and/or a long duration of particle emission [108–110]—which would result from the presence of a long-lived mixture of phases in the matter as it undergoes a first-order phase transition from a quark–gluon plasma back to the hadronic phase.

In HBT analyses, multidimensional Gaussian fits are made to the normalized relative momentum distributions yielding fit parameters, R_{long}, R_{side}, R_{out} [111], also referred to as HBT radii, where

$$C_2 = 1 + \lambda \exp\bigl(-R_{\text{side}}^2 q_{\text{side}}^2 - R_{\text{out}}^2 q_{\text{out}}^2 - R_{\text{long}}^2 q_{\text{long}}^2\bigr). \tag{9}$$

The coordinate system is chosen so that the longitudinal direction is parallel to the beam axis, the out direction is in the direction of the pair's total transverse momentum, and the side direction is in the transverse plane perpendicular to the out axis. For dynamic (i.e., expanding) sources, the HBT radii depend on the mean transverse momentum of the particle pairs, $k_T = |\mathbf{p}_{1\text{T}} + \mathbf{p}_{2\text{T}}|/2$, and correspond to lengths of homogeneity: regions of the source which emit particles of similar momentum [112]. Measuring the k_T dependence of HBT radii provides essential constraints on dynamical models [113]. In particular, the ratio $R_{\text{out}}/R_{\text{side}}$ is predicted to be larger than unity for sources which emit particles over a long time.

The measured k_T dependence of all radii [56] and the ratio $R_{\text{out}}/R_{\text{side}}$ are shown in Fig. 19, along with STAR results [114]. The data from PHENIX and STAR are in excellent agreement. Both sets of data have been corrected for Coulomb repulsion between the detected particles.

The measured radii all decrease with increasing k_T as expected for a rapidly expanding source. The ratio $R_{\text{out}}/R_{\text{side}}$ was measured to be 1 within errors, with a slight systematic decrease for increasing k_T. As is discussed in the next section, these data have excluded the validity of a large majority of hydrodynamical models developed to describe Au + Au collisions at RHIC, indicating that in their present form these models do not describe well the space–time evolution of the Au + Au collisions.

3.5. Hydrodynamic model comparisons

Many of the experimental features in the spectra and elliptic flow are consistent with equilibrium being established early in the collision with large pressure gradients that drive

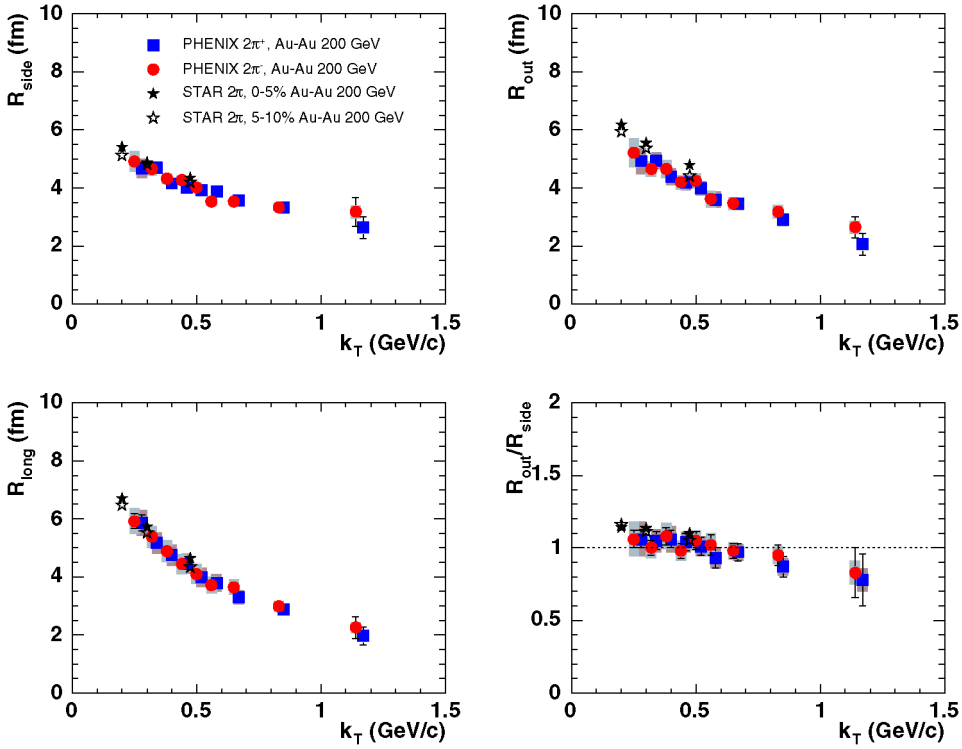

Fig. 19. The k_T dependence of the Bertsch–Pratt parameters for $\pi^+\pi^+$ (blue square) and $\pi^-\pi^-$ (red circle) for 0–30% centrality with statistical error bars and systematic error bands. Results from PHENIX [56] and STAR [114] are overlaid. (For interpretation of the references to colour in this figure legend, the reader is referred to the web version of this article.)

a strong expansion. Moving from a statement of "consistency" to a statement that equilibrium has been "established" is difficult. Some progress can be made by comparing the data to hydrodynamic models that assume full equilibrium early in the collision.

A variety of hydrodynamic models have been published. Our approach is to confront these models with the following broad set of data; $v_2(p_T)$, spectra, and HBT. In this paper we will not compare the data with hydro-inspired parameterized fits, e.g., blast-wave [115] or Buda–Lund [116] models, but will restrict ourselves to dynamical hydro models.

In Figs. 20 and 21, hydro calculations that include a phase transition from the QGP phase to a hadronic phase are shown with solid lines, while hydro calculations that do not include a pure QGP phase at any stage in the dynamics are drawn with dashed lines. The four calculations that include a QGP phase all assume an ideal gas EOS for the QGP phase, a resonance gas for the hadronic phase and connect the two using a first-order phase transition and a Maxwell construction. These calculations use latent heats that range from 0.8 GeV/fm^3 (Teaney et al. [106]) to 1.15 GeV/fm^3 (Huovinen et al. [107] and Kolb et al. [117]), to 1.7 GeV/fm^3 (Hirano et al. [118,119]). For comparison the bag model of the nucleon with external bag pressure $B = (230\ \text{MeV})^4$ and a $T_{\text{crit}} = 164$ MeV produces

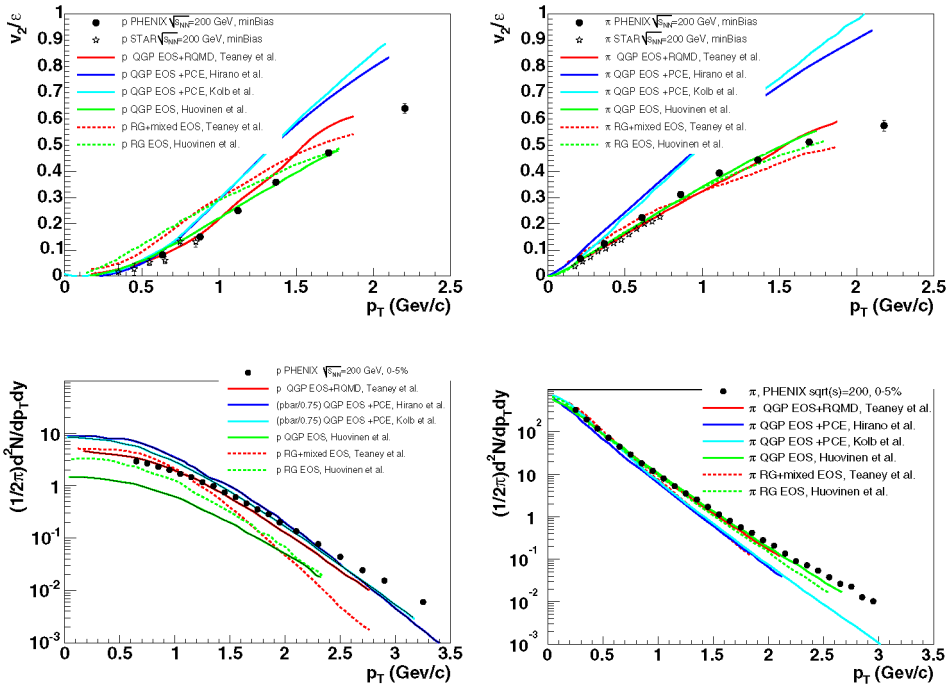

Fig. 20. Top two panels: on the left, proton $\frac{1}{\varepsilon}v_2(p_T)$ vs. p_T for minimum-bias collisions at RHIC [50,103] are compared with hydro calculations [106,107,118,120], and on the right is the same comparison for pions. Bottom two panels: on the left, proton spectra for 0–5% collisions at RHIC [54] are compared with the same hydro calculations and on the right is the same comparison for pions.

a latent heat of 1.15 GeV/fm^3 [120]. The calculations that do not include a QGP phase (dashed lines) either include a hadron phase and a phase mixture by forcing the latent heat of the transition to infinity [106], or use an hadronic resonance gas equation of state, i.e., no mixed or QGP phases [107].

The calculations also differ in how they solve the hydro equations and how they treat the final hadronic phase. The work of Hirano, Tsuda, and Nara cited here are the only calculations in this paper that solve the hydro equations in 3D [118,119]. For the final hadronic stage Teaney [106] uses a hybrid model that couples the hadronic phase to RQMD to allow hadrons to freezeout according to their cross section, i.e., for chemical equilibrium to be broken in the hadronic phase. Hirano [118] and Kolb [120] both allow for partial chemical equilibrium by chemically freezing out earlier than the kinetic freezeout. This has been done in order to reproduce the large proton yield measured at RHIC (see later in this section). In contrast, Huovinen [107] maintains full chemical equilibrium throughout the hadronic phase.

Fig. 20 compares these calculations to the measured minimun-bias proton and pion $v_2(p_T)/\varepsilon$. Minimum-bias results were chosen in order to have the broadest set of data and model calculations for comparison. The four calculations that include a phase transition from the QGP phase to a hadronic phase (solid lines) reproduce the low-p_T proton data

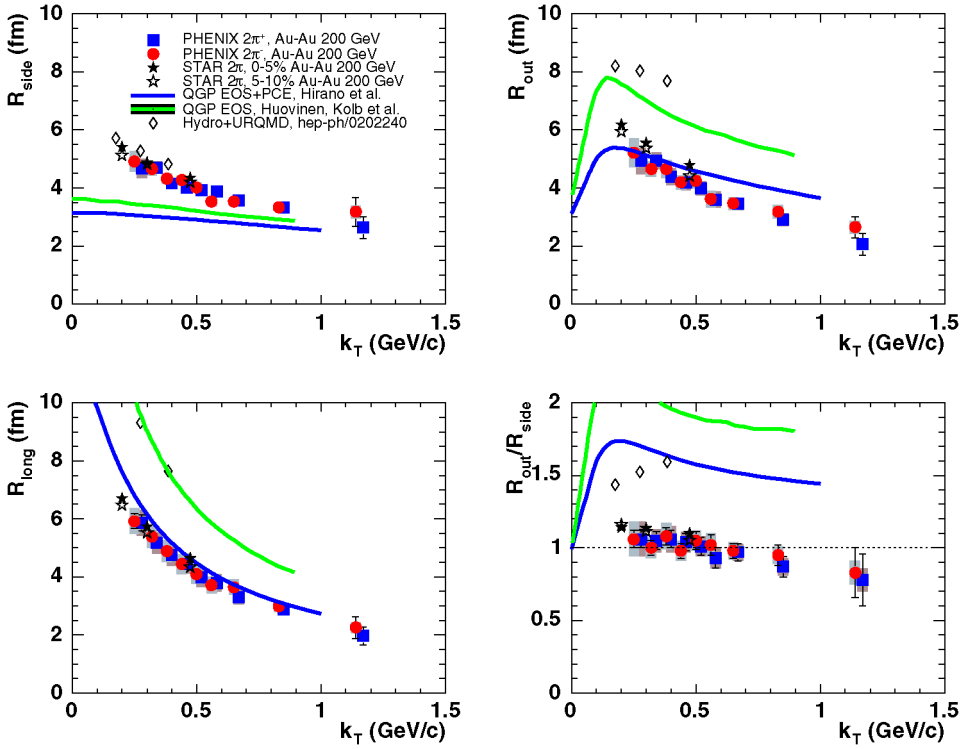

Fig. 21. The k_T dependence of the Bertsch–Pratt parameters for $\pi^+\pi^+$ (blue square) and $\pi^-\pi^-$ (red circle) for 0–30% centrality with statistical error bars and systematic error bands. Results from PHENIX [56], STAR [114] and hydrodynamics models (Hirano [118], Kolb/Huovinen [123] and Soff [130], diamonds) are overlaid. (For interpretation of the references to colour in this figure legend, the reader ir referred to the web version of this article.)

better than the two hydro calculations that do not have a QGP phase at any stage in the dynamics (dashed lines). The presence of the first-order QGP phase transition softens the EOS which reduces the elliptic flow. At higher p_T there is considerable variation between the models. Part of this is due to how the final hadronic stage is modeled. For example, Kolb's (solid light-blue line)[7] and Hirano's (solid dark-blue line) calculations allow for partial chemical equilibrium in the final stage compared to Huovinen (solid green line) which chemically freezes out late in the collision. The difference is observable above $p_T \sim 1\ \mathrm{GeV}/c$.

The same hydro models are compared to the pion $v_2(p_T)/\varepsilon$ measurements from STAR and PHENIX in Fig. 20. The Kolb (solid light-blue line) and Hirano (solid dark-blue line) calculations fail completely by predicting too strong a v_2. These two models have very similar partial chemical equilibrium assumptions in the late hadronic stage. It is worth noting that the Kolb calculation is the same as the Huovinen (solid green line) calculation with the exception of the final hadronic stage.

[7] For interpretation of the references to colour in Fig. 20, the reader is referred to the web version of this article.

All the above models have assumed ideal hydrodynamics, i.e., with no viscosity and zero mean free path. Nonzero viscosity in the QGP reduces v_2 [121,122] and since the early hydro calculations from Teaney and Huovinen reproduced the magnitude of the pion v_2 data, it is often stated that viscosity of the matter at RHIC must be small [24]. However recent calculations from Hirano (3D) (solid dark-blue line) and Kolb (solid light-blue line) overpredict the measured v_2. As these results do not include dissipative effects, such as those resulting from hadronic interactions in the final state, their failure indicates that further work will be necessary before a quantitative determination of the viscosity in the QGP phase is possible. Progress will require both theoretical development and experimental measures that are less sensitive to how the azimuthal asymmetry of the energy–momentum tensor is distributed between different particles in the final stage of the reaction, e.g., the elliptic flow of the total transverse energy.

The same hydro models are now compared to the measured spectra from central collisions. The bottom right panel of Fig. 20 shows that all the hydro models reproduce the pion spectra below $p_T \sim 1$ GeV/c; at higher p_T the particles are less likely to be equilibrated and hydro models are not expected to work well. In the bottom left panel the calculated proton spectra from Huovinen [107] (solid green line) are lower than the data, due to the calculation maintaining chemical equilibrium throughout the hadronic phase. The lower temperature chemical freezeout suppresses the final calculated yield of heavier particles such as protons. Of the two calculations from Teaney [106] the calculation that includes the QGP phase (solid red line) reproduces the proton spectra, presumably because of the increased transverse flow from the stronger early pressure gradients. Hirano's and Kolb's (solid dark and light-blue lines) calculations break chemical equilibrium during the hadronic phase and overpredict the proton spectra at low p_T.

One difficulty is that the spectra comparison with hydrodynamic models is for central collisions while the v_2 comparison is for minimum-bias collisions. It is difficult to use central collisions for the v_2 comparison since the collisions are nearly symmetric and hence v_2 is small. In addition, hydrodyamic calculations that reproduce v_2 values over a broad range of centrality (from 0–45% in Ref. [103]) tend to overpredict the data for more peripheral collisions by approximately 25%, presumably because of a breakdown in the hydrodynamic assumptions. Hence when comparing to minimum-bias data sets, an overprediction of v_2 from the hydro models of less than 20% should be acceptable.

These comparisons between data and hydro models are summarized in Table 1 and in the following conclusions.

- $v_2(p_T, PID)$ is sensitive to all stages of the reaction. Elliptic flow is produced by strong scattering in the initial phase, while the detailed shape of $v_2(p_T)$ and how the momentum asymmetry is distributed to different particles is affected by the transition from a QGP to hadronic phase and scattering in the final hadronic stage.
- The hydro models that reproduce the low-p_T proton v_2 are those that include both a QGP and hadronic phase.
- The hadronic phase critically affects the final values of $v_2(p_T, PID)$. Models (Hirano, Kolb) that include partial chemical equilibrium to reproduce the baryon yield, completely fail on the pion v_2.

Table 1
Summary of various hydro model assumptions and a comparison between measurements and hydro calculations. Two initial energies are tabulated, either the maximum energy density at the center of the collision or the energy density averaged over the transverse profile

	QGP + mixed + RG				mixed + RG	RG
	Teaney	Hirano	Kolb	Huovinen	Teaney	Huovinen
Reference	[106]	[118]	[117,123]	[107]	[106]	[107]
latent heat ($\mathrm{GeV/fm^3}$)	0.8	1.7	1.15	1.15	0.8	
init. $\varepsilon_{\max}$ ($\mathrm{GeV/fm^3}$)	16.7		23	23	16.7	23
init. $\langle\varepsilon\rangle$ ($\mathrm{GeV/fm^3}$)	11.0	13.5			11.0	
τ_0 fm/c	1.0	0.6	0.6	0.6	1.0	0.6
hadronic stage	RQMD	partial chemical equil.	partial chemical equil.	full equil.	RQMD	full equil.
proton v2	yes	< 0.7 GeV/c	< 0.7 GeV/c	yes	no	no
pion v2	yes	no	no	yes	yes	yes
proton spectra	yes	overpredict	overpredict	no	no	no
pion spectra	yes	< 1 GeV/c	< 1 GeV/c	yes	< 0.7 GeV/c	yes
HBT	Not available	No	No	No	Not available	Not available

- The only model that survives this comparison with measured v_2 and spectra is Teaney's (solid red line) which includes a strong expansion in a QGP phase, a phase transition to a mixed phase, and then a hadronic cascade in the final hadronic state. There are open questions in this hybrid model, e.g., the sensitivity of the results to the matching conditions between hydro and RQMD. All other models fail in at least one v_2 or spectra comparison, partially due to differences in modeling the final hadronic state.
- Until the model uncertainty in the final state is reduced, it is not yet possible to use the measured splitting between proton and pion $v_2(p_T)$ to extract quantitative information on the EOS during the reaction, including the possible softening of the EOS due to the presence of a mixed phase.

A comparison with the HBT data and some of the hydro models is shown in Fig. 21. It is unfortunate that not all hydro models have been compared to HBT data, e.g., the hydro + RQMD model from Teaney [106] has not been confronted with this observable. The hydro calculation from Kolb, Heinz and Huovinen [123] (solid green line) includes a first-order phase transition which leads to a long lifetime for the system. The source parameter R_{long} is considered most sensitive to the duration of the whole collision, i.e., from initial overlap to final particle emission, and the Kolb/Huovinen hydro calculation [123] (solid green line) overpredicts the measured R_{long} data. Changing to partial chemical equilibrium in the hadronic stage [118], indicated with the dark blue line, reduces the lifetime of the collision which improves the agreement with R_{long}. However the ratio $R_{\mathrm{out}}/R_{\mathrm{side}}$, which is sensitive to the duration over which particles are emitted, is still overpredicted.

There have been many attempts to understand what may be causing the disagreement with data (known collectively as the HBT puzzle).

• Sinyukov et al. [124] and Grassi et al. [125] have suggested that the sharp Cooper–Frye freezeout condition [126] should be replaced by an emission function that decouples hadrons depending on their hadronic cross section.

• However when this has been effectively implemented by using a hadronic cascade (URQMD) for the final hadronic stage, the predicted ratio $R_{\rm out}/R_{\rm side}$ increases and diverges further from the data [127]. Modeling the final stage with a hadronic cascade effectively includes dissipative effects which should increase the duration of emission and produce a larger ratio $R_{\rm out}/R_{\rm side}$.

• One method to reduce the lifetime of the reaction is to change the QGP EOS. Using a crossover instead of a first-order transition reduces the ratio $R_{\rm out}/R_{\rm side}$ by about 50% to $R_{\rm out}/R_{\rm side} \sim 1.5$ [128] which is still larger than the data. Because the calculation was restricted to $\eta = 0$ Zschiesche et al. were unable to compare with the measured values of $R_{\rm long}$.

In summary, model comparisons seem to be closer to the HBT data when the lifetime of the collision is made smaller than the long time resulting from a first-order phase transition. The small values of $R_{\rm out}/R_{\rm side}$ may indicate that there is little to no mixed phase present in the reactions. One possible direction for future comparisons with data is to include a more realistic EOS into the hydro models, e.g., to take the EOS from lattice QCD calculations [129]. Such a calculation needs to be compared with all the available data, including spectra and v_2, as well as HBT.

3.6. Conclusions

In summary we can make the following conclusions.

• The measured yields and spectra of hadrons are consistent with thermal emission from a strongly expanding source.

• Strangeness is fully saturated at RHIC, consistent with full chemical equilibrium.

• The scaling of v_2 with eccentricity shows that collective behavior is established early in the collision.

• Elliptic flow is stronger at RHIC than at the SPS, since the measured slope of $v_2(p_T)$ for pions is 50% larger at RHIC.

• The measured proton $v_2(p_T)$ is less than that for pions at low p_T; the small magnitude of the proton v_2 at low p_T is reproduced by hydro models that include both a QGP and hadronic phase.

• However several of the hydro models that reproduce the proton $v_2(p_T)$ fail for the pion $v_2(p_T)$.

• The HBT source parameters, especially the small value of $R_{\rm long}$ and the ratio $R_{\rm out}/R_{\rm side}$, suggest that the mixed phase is too long-lived in the current hydro calculations.

Hence we currently do not have a consistent picture of the space–time dynamics of reactions at RHIC as revealed by spectra, v_2, and HBT. The lack of a consistent picture of the dynamics means that it is not yet possible to extract quantitative properties of the QGP or mixed phase using the observables v_2, spectra, or HBT.

4. Fluctuations

4.1. Net-charge fluctuations

In the study of the fluctuations of multiplicity as a means to understand the dynamics of charged particle production, one important realization was to use small regions of phase space, where energy–momentum conservation constraints would not be significant [131–133]. Such studies led to the important observation that the distribution of multiplicity, even in small intervals near mid-rapidity, was negative binomial rather than Poisson, which indicated large multiplicity correlations even in small $\delta\eta$ intervals [134]. No such studies are yet available at RHIC.

Based on predictions that event-by-event fluctuations of the net charge in local phase space regions would show a large decrease as a signature of the QGP [135–137], net-charge fluctuations were measured in PHENIX [44]. The idea is that in a QGP composed of fractionally charged quarks, the larger number of fractionally charged particles compared to unit-charged hadrons would result in smaller relative net-charge fluctuations in a QGP than for a pure gas of hadrons and that this original fluctuation would survive the transition back to ordinary hadrons.

It is important to realize that the study of net-charge fluctuations represents the study of fluctuations in a quantity that is conserved over all phase space. Consider $N = N_+ + N_-$ charged particles produced in the full phase space. By charge conservation $N_+ = N_- = N/2$, and the net charge $Q \equiv N_+ - N_-$ is identically zero so that there are no net-charge fluctuations—the variance $V(Q) = 0$, where

$$V(Q) \equiv \left\langle Q^2 \right\rangle - \langle Q \rangle^2. \tag{10}$$

In a smaller region of phase space, where p is the fraction of N observed in a stochastic scenario, the mean and variance of the number of positive n_+ and negative n_- particles are equal, but the variance of Q is no longer identically zero:

$$\langle n_+ \rangle = \langle n_- \rangle = pN/2, \tag{11}$$

$$V(n_+) = V(n_-) = p(1-p)N/2, \tag{12}$$

from which it follows that

$$V(Q) = (1-p)n_{\mathrm{ch}}, \tag{13}$$

where $n_{\mathrm{ch}} = pN$ is the expected number of charged particles on the interval. Thus the normalized variance in Q (normalized to Poisson statistics) is defined as

$$v(Q) = \frac{V(Q)}{n_{\mathrm{ch}}} = (1-p). \tag{14}$$

In the limit $n_{\mathrm{ch}} \gg 0$, the variance of the charge ratio $R = n_+/n_-$ approaches $V(R) = 4(1-p)/n_{\mathrm{ch}}$. However, it is well known in mathematical statistics that moments of the inverse of a stochastic variable, e.g., $1/n_-$, diverge if there is any finite probability, no matter how small, for $n_- = 0$. Thus, the charge ratio is not a stable measure of fluctuations.

The previous arguments are based on fixed N. The results where N varies according to a specified distribution are also interesting. If n_- is Poisson distributed, with mean value

$\mu = N/2$ over the whole phase space, then in the region of phase space with probability p the distribution is also Poisson, with mean $\langle n_- \rangle|_p = \mu_p = pN/2$. If, on the other hand n_- is negative binomial distributed, with mean value $\mu = N/2$ and NBD parameter $\sigma^2/\mu^2 - 1/\mu = 1/k$ for the whole phase space, then in the region of phase space with probability p, the distribution is negative binomial with mean $\langle n_- \rangle|_p = \mu_p = pN/2$ and the same value of $1/k$.

Actually, the binomial division preserves $\sigma_p^2/\mu_p^2 - 1/\mu_p = 1/k$, for any distribution [138]. This appears to indicate that smaller intervals, which tend to have larger values of σ_p^2/μ_p^2 would be less sensitive to the global $1/k$, the long-range correlation. This would be true except for the fact that there are short-range correlations which are better seen on small intervals of phase space. Another important thing to note regarding a binomial split of a negative binomial distribution is that the two subintervals are not statistically independent. The conditional probability distribution on the interval $(1 - p)$ depends upon the outcome on the interval p [139]. It is unfortunate that these elegant arguments cannot be applied to the net-charge fluctuations since $\langle Q \rangle = 0$.

The PHENIX measurement [44] of the normalized variance $v(Q)$ of net-charge fluctuations is shown in Fig. 22 in the interval $-0.35 \leqslant \delta\eta \leqslant +0.35$ as a function of the azimuthal angular interval of reconstructed tracks, either at the detector, $\Delta\phi_d$, or at the vertex, $\Delta\phi_r$, chosen symmetrically around the detector acceptance. For smaller $\Delta\phi_r$ the data agree with the purely stochastic $(1 - p)$ dependence shown as the solid line, but deviate from the stochastic prediction at larger values due to correlations from resonance decay, such as $\rho^0 \to \pi^+ + \pi^-$ as nicely explained by RQMD [140].

Absent new theoretical insight, it is difficult to understand how quark-level net-charge fluctuations in a QGP can be related to net-charge fluctuations of hadrons, where, by definition, strong correlations exist, e.g., in the formation of a meson from a q–$\bar{q}$ pair. Also, the study of the fluctuations of net charge, which is conserved, may not be as useful to detect interesting fluctuations as the study of fluctuations of the total charged multiplicity, which is much less constrained by conservation laws. This has yet to be tried at RHIC.

4.2. Event-by-event average-p_T fluctuations

Fluctuations in the event-by-event average p_T, denoted M_{p_T}, have been measured and provide a severely small limit on possible fluctuations from a sharp phase transition. For events with n detected charged particles with magnitudes of transverse momenta, p_{T_i}, the event-by-event average p_T, denoted M_{p_T} is defined as

$$M_{p_T} = \overline{p_T} = \frac{1}{n} \sum_{i=1}^{n} p_{T_i}. \tag{15}$$

Mixed events are used to define the baseline for random fluctuations of M_{p_T} in PHENIX [45,55]. This has the advantage of effectively removing any residual detector-dependent effects. The event-by-event average distributions are very sensitive to the number of tracks in the event (denoted n or N_{tracks}), so the mixed event sample is produced with the *identical* N_{tracks} distribution as the data. Additionally, no two tracks from the same data event are placed in the same mixed event in order to remove any intra-event correlations in p_T. Finally, $\langle M_{p_T} \rangle$ must exactly match the semi-inclusive $\langle p_T \rangle$.

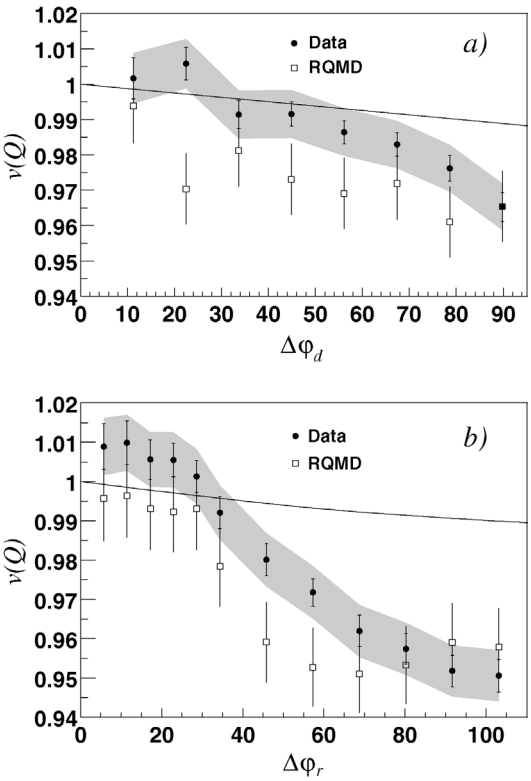

Fig. 22. $v(Q)$ for the 10% most central events in data and RQMD, as a function of the azimuthal interval in degrees of reconstructed tracks, either (a) at the detector, $\Delta\phi_d$, or (b) at the vertex, $\Delta\phi_r$, chosen symmetrically around the detector acceptance. For data, the error band shows the total statistical error, whereas the error bars indicate the uncorrelated part. The solid line shows the expected reduction in $v(Q)$ in the stochastic scenario when global charge conservation is taken into account [44]. Note that the data points are correlated since the data in one bin is a subset of the data in the next bin.

For the case of statistical independent emission, where the fluctuations are purely random, an analytical formula for the distribution in M_{p_T} can be obtained assuming negative binomial distributed event-by-event multiplicity, with gamma distributed semi-inclusive p_T spectra [141]. The formula depends on the four semi-inclusive parameters $\langle n\rangle$, $1/k$, b and p which are derived from the means and standard deviations of the semi-inclusive p_T and multiplicity distributions, $\langle n\rangle$, σ_n, $\langle p_T\rangle$, σ_{p_T}:

$$f(y) = \sum_{n=n_{\min}}^{n_{\max}} f_{\mathrm{NBD}}\big(n, 1/k, \langle n\rangle\big)\, f_{\Gamma}(y, np, nb), \tag{16}$$

where $y = M_{p_T}$. For fixed n, and purely random fluctuations, the mean and standard deviation of M_{p_T} follow the expected behavior, $\langle M_{p_T}\rangle = \langle p_T\rangle$, $\sigma_{M_{p_T}} = \sigma_{p_T}/\sqrt{n}$. In PHENIX, Eq. (16) is used to confirm the randomness of mixed events which are used to define the baseline for random fluctuations of M_{p_T} [45,55].

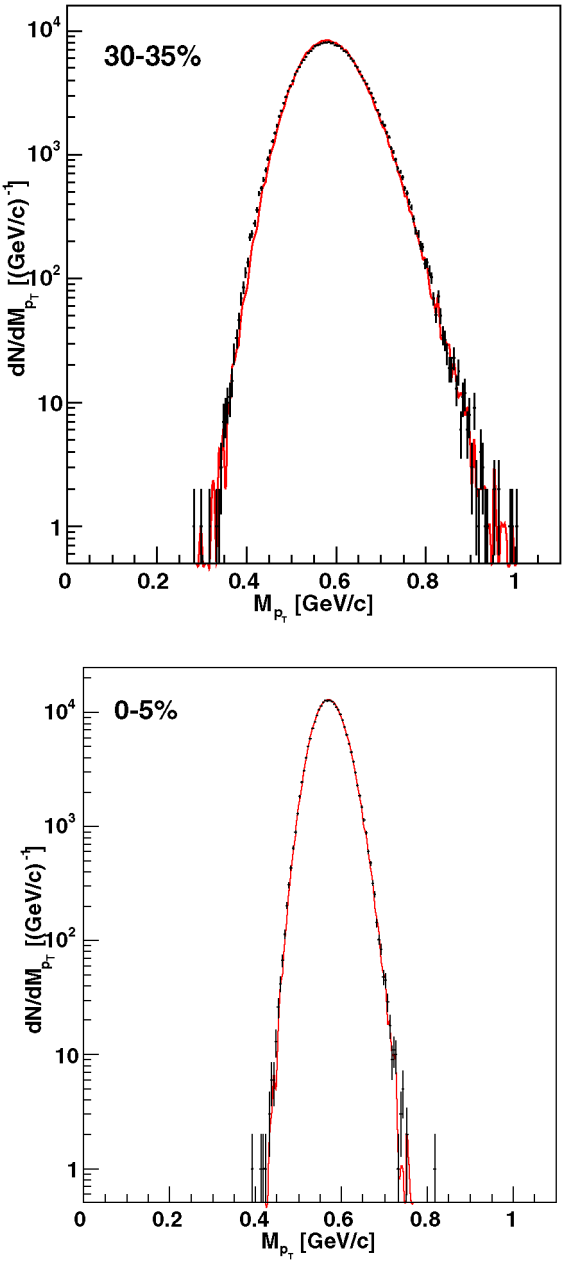

Fig. 23. M_{pT} for 30–35% and 0–5% centrality classes: data (points) mixed events (histogram) [55].

The measured M_{p_T} distributions for the data in two centrality classes for $\sqrt{s_{NN}} =$ 200 GeV Au + Au collisions in PHENIX [55] are shown in Fig. 23 (data points) compared to the mixed-event distributions (histograms). The non-Gaussian, gamma-distribution

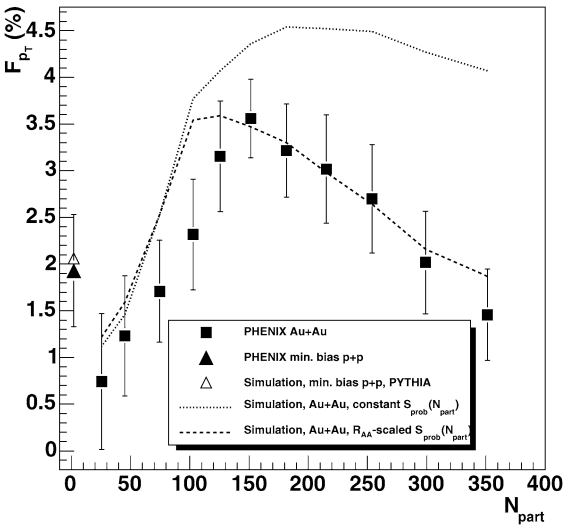

Fig. 24. F_{p_T} vs. centrality, represented as the average number of participants (N_{part}) in a centrality class, compared to jet simulation [55].

shape of the M_{p_T} distributions is evident. The difference between the data and the mixed-event random baseline distributions is not visible to the naked eye. The nonrandom fluctuation is quantified by the fractional difference of ω_{p_T}, the normalized standard deviation of M_{p_T}, for the data and the mixed-event (random) samples:

$$\omega_{p_T} = \frac{\sigma_{M_{p_T}}}{\langle M_{p_T} \rangle}, \tag{17}$$

$$F_{p_T} = \frac{\omega_{p_T,\text{data}} - \omega_{p_T,\text{mixed}}}{\omega_{p_T,\text{mixed}}}. \tag{18}$$

The results are shown as a function of centrality, represented by N_{part} in Fig. 24.

The dependence of F_{p_T} on N_{part} is striking. To further understand this dependence and the source of these nonrandom fluctuations, F_{p_T} was measured over a varying p_T range, $0.2\ \text{GeV}/c \leqslant p_T \leqslant p_T^{\text{max}}$ (Fig. 25), where $p_T^{\text{max}} = 2.0\ \text{GeV}/c$ for the N_{part} dependence.

The increase of F_{p_T} with p_T^{max} suggests elliptic flow or jet origin. This was investigated using a Monte Carlo simulation of correlations due to elliptic flow and jets in the PHENIX acceptance. The flow was significant only in the lowest centrality bin and negligible ($F_{p_T} < 0.1\%$) at higher centralities. Jets were simulated by embedding (at a uniform rate per generated particle, $S_{\text{prob}}(N_{\text{part}})$) $p + p$ hard-scattering events from the PYTHIA event generator into simulated Au + Au events assembled at random according to the measured N_{tracks} and semi-inclusive p_T distributions. This changed $\langle p_T \rangle$ and σ_{p_T} by less than 0.1%. $S_{\text{prob}}(N_{\text{part}})$ was either constant for all centrality classes, or scaled by the measured hard-scattering suppression factor $R_{AA}(N_{\text{part}})$ for $p_T > 4.5\ \text{GeV}/c$ [49]. A value $F_{p_T} = 2.06\%$ for $p + p$ collisions was extracted from pure PYTHIA events in the PHENIX acceptance in agreement with the $p + p$ measurement (Fig. 24). The value of $S_{\text{prob}}(N_{\text{part}})$ was chosen so that the simulation with $S_{\text{prob}}(N_{\text{part}}) \times R_{AA}(N_{\text{part}})$ agreed with

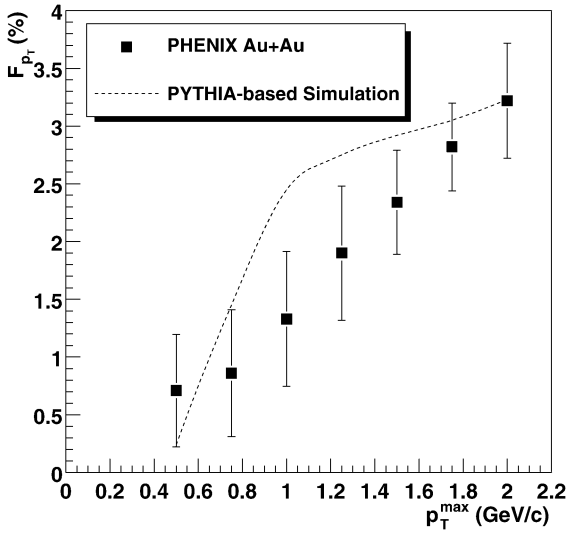

Fig. 25. F_{pT} vs. $p_T^{\max}$ compared to R_{AA}-scaled jet simulation for the 20–25% centrality class ($N_{\text{part}} = 181.6$) [55].

the data at $N_{\text{part}} = 182$. The centrality and $p_T^{\max}$ dependences of the measured F_{pT} match the simulation very well, but only when the R_{AA} scaling is included.

A less experiment-dependent method to compare nonrandom fluctuations is to assume that the entire F_{pT} is due to temperature fluctuations of the initial state, with RMS variation $\sigma_T/\langle T\rangle$ [45,142]. Then,

$$\omega^2_{p_T,\text{data}} - \omega^2_{p_T,\text{mixed}} = \left(1 - \frac{1}{\langle n\rangle}\right)\frac{\sigma_T^2}{\langle T\rangle^2} = 2F_{p_T}\omega^2_{p_T,\text{mixed}}, \tag{19}$$

This yields $\sigma_T/\langle T\rangle = 1.8\%$ for central collisions in PHENIX with similarly small values for the other Relativistic Heavy Ion experiments [143], 1.7% in STAR, 1.3% in CERES, and 0.6% in NA49. These results put severely small limits on the critical fluctuations that were expected for a sharp phase transition, both at SPS energies and at RHIC, but are consistent with the expectation from lattice QCD that the transition is a smooth crossover [12].

Other proposed explanations of the centrality and $p_T^{\max}$ dependences of F_{pT} include: overlapping color strings which form clusters so that the number of sources and $\langle p_T\rangle$ per source is modified as a function of centrality [144]; and near equilibrium p_T correlations induced by spatial inhomogeneity [145].

4.3. Conclusions

Critical behavior near the phase boundary can produce nonrandom fluctuations in observables such as the net-charge distribution and the average transverse momentum distribution. Our search for net-charge fluctuations has ruled out the most naive model of charge fluctuations in a QGP, but it is unclear whether the charge fluctuation signature can survive

hadronization. Our measurement of the event-by-event average p_T distribution shows a nonrandom fluctuation that is consistent with the effect expected from high-p_T jets. This puts a severe constraint on the critical fluctuations that were expected for a sharp phase transition but is consistent with the expectation from lattice QCD that the transition is a smooth crossover [12].

5. Binary scaling

5.1. Hard scattering and pQCD

One way to get a partonic probe into the midst of an $A + A$ collision is to use the high-p_T partons produced by hard scattering. For $p + p$ collisions in the RHIC energy range, hard scattering is considered to be the dominant process of particle production with $p_T \geqslant 2$ GeV/c at mid-rapidity. Typically, particles with $p_T \geqslant 2$ GeV/c are produced from states with two roughly back-to-back jets which are the result of scattering of constituents of the nucleons (partons) as described by pQCD [146].

The overall $p + p$ hard-scattering cross section in "leading logarithm" pQCD is the sum over parton reactions $a + b \to c + d$ (e.g., $g + q \to g + q$) at parton–parton center-of-mass (c.m.) energy $\sqrt{\hat{s}}$:

$$\frac{d^3\sigma}{dx_1\,dx_2\,d\cos\theta^*} = \frac{1}{s}\sum_{ab} f_a(x_1)\,f_b(x_2)\,\frac{\pi\alpha_s^2(Q^2)}{2x_1x_2}\,\Sigma^{ab}\big(\cos\theta^*\big), \tag{20}$$

where $f_a(x_1)$, $f_b(x_2)$, are parton distribution functions, the differential probabilities for partons a and b to carry momentum fractions x_1 and x_2 of their respective protons (e.g., $u(x_2)$), and where θ^* is the scattering angle in the parton–parton c.m. system. The parton–parton c.m. energy squared is $\hat{s} = x_1x_2s$, where $\sqrt{s}$ is the c.m. energy of the $p+p$ collision. The parton–parton c.m. system moves with rapidity $y = 1/2\ln(x_1/x_2)$ in the $p + p$ c.m. system.

Eq. (20) gives the p_T spectrum of outgoing parton c, which then fragments into hadrons, e.g., π^0. The fragmentation function $D_c^{\pi^0}(z,\mu^2)$ is the probability for a π^0 to carry a fraction $z = p^{\pi^0}/p^c$ of the momentum of outgoing parton c. Eq. (20) must be summed over all subprocesses leading to a π^0 in the final state. The parameter μ^2 is an unphysical "factorization" scale introduced to account for collinear singularities in the structure and fragmentation functions [146,147].

In this formulation, $f_a(x_1,\mu^2)$, $f_b(x_2,\mu^2)$ and $D_c^C(z,\mu^2)$ represent the "long-distance phenomena" to be determined by experiment; while the characteristic subprocess angular distributions, $\Sigma^{ab}(\cos\theta^*)$, and the coupling constant, $\alpha_s(Q^2) = \frac{12\pi}{25}\ln(Q^2/\Lambda^2)$, are fundamental predictions of QCD [148–150] for the short-distance, large-Q^2, phenomena. The momentum scale $Q^2 \sim p_T^2$ for the scattering subprocess, while $Q^2 \sim \hat{s}$ for a Compton or annihilation subprocess, but the exact meaning of Q^2 tends to be treated as a parameter rather than a dynamical quantity. The transverse momentum of a scattered constituent is

$$p_T = p_T^* = \frac{\sqrt{\hat{s}}}{2}\sin\theta^*. \tag{21}$$

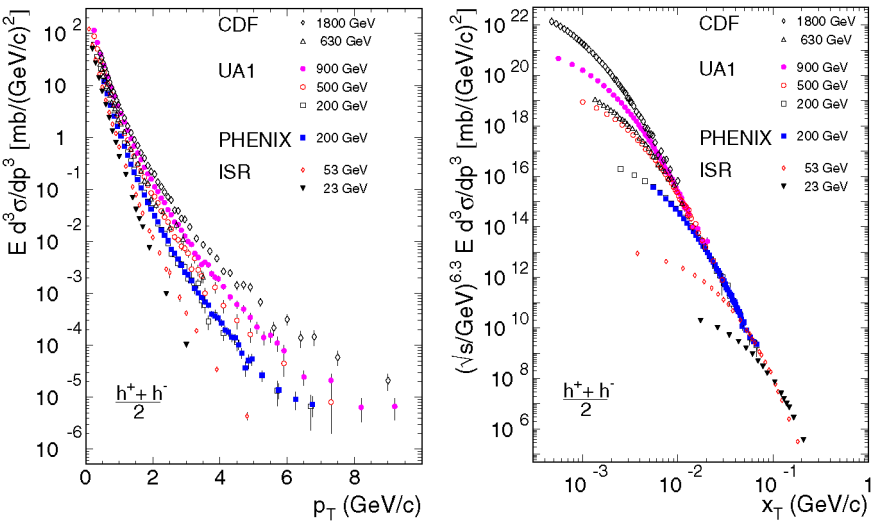

Fig. 26. Left: $E\,d^3\sigma(p_T)/d^3p$ at mid-rapidity as a function of $\sqrt{s}$ in $p+p$ collisions. Right: $(\sqrt{s}/\mathrm{GeV})^{6.3} \times E\,d^3\sigma/d^3p$ vs. $x_T = 2p_T/\sqrt{s}$ [53] (and references therein).

Eq. (20) leads to a general "x_T-scaling" form for the invariant cross section of high-p_T particle production:

$$E\frac{d^3\sigma}{d^3p} = \frac{1}{p_T^n}F(x_T) = \frac{1}{\sqrt{s}^n}G(x_T), \tag{22}$$

where $x_T = 2p_T/\sqrt{s}$. The cross section has two factors, a function $F(x_T)$ ($G(x_T)$) which "scales", i.e., depends only on the ratio of momenta, and a dimensioned factor, $1/p_T^n$ ($1/\sqrt{s}^n$), where n equals 4 in lowest-order (LO) calculations, analogous to the $1/q^4$ form of Rutherford Scattering in QED. The structure and fragmentation functions are all in the $F(x_T)$ ($G(x_T)$) term. Due to higher-order effects such as the running of the coupling constant, $\alpha_s(Q^2)$, the evolution of the structure and fragmentation functions, and the initial-state transverse momentum k_T, n is not a constant but is a function of x_T, $\sqrt{s}$. Measured values of $n(x_T, \sqrt{s})$ in $p+p$ collisions are between 5 and 8.

5.2. *Mid-rapidity p_T spectra from $p+p$ collisions*

The scaling and power-law behavior of hard scattering are evident from the $\sqrt{s}$ dependence of the p_T dependence of the $p+p$ invariant cross sections. This is shown for nonidentified charged hadrons, $(h^+ + h^-)/2$, in Fig. 26 (left). At low $p_T \leqslant 1$ GeV/c the cross sections exhibit a "thermal" $\exp(-6p_T)$ dependence, which is largely independent of $\sqrt{s}$, while at high p_T there is a power-law tail, due to hard scattering, which depends strongly on $\sqrt{s}$. The characteristic variation with $\sqrt{s}$ at high p_T is produced by the funda-

mental power-law and scaling dependence of Eqs. (20), (22). This is best illustrated by a plot of

$$\sqrt{s}^{n(x_T,\sqrt{s})} \times E\frac{d^3\sigma}{d^3p} = G(x_T), \tag{23}$$

as a function of x_T, with $n(x_T, \sqrt{s}) = 6.3$, which is valid for the x_T range of the present RHIC measurements (Fig. 26 (right)). The data show an asymptotic power law with increasing x_T. Data at a given $\sqrt{s}$ fall below the asymptote at successively lower values of x_T with increasing $\sqrt{s}$, corresponding to the transition region from hard to soft physics in the p_T region of about 2 GeV/c.

The PHENIX measurement of the invariant cross section for π^0 production in $p + p$ collisions at $\sqrt{s} = 200$ GeV [60] agrees with NLO pQCD predictions over the range $2.0 \leqslant p_T \leqslant 15$ GeV/c (Fig. 27).

5.3. Scaling hard scattering from $p + p$ to $p + A$ and $A + B$ collisions

Since hard scattering is point-like, with distance scale $1/p_T \leqslant 0.1$ fm, and the hard-scattering cross section factorizes as shown in Eq. (20), the cross section in $p + A$ or $A + B$ collisions, compared to $p + p$, is proportional to the relative number of possible point-like encounters. The number of encounters of point-like constituents of nucleons is then proportional to A (AB), for $p + A$ ($A + B$) minimum-bias collisions. For $A + B$ collisions at impact parameter b, it is proportional to $T_{AB}(b)$, the nuclear thickness function, which is the integral of the product of nuclear thickness over the geometrical overlap region of the two nuclei. In detail, the semi-inclusive invariant yield of, e.g., high-p_T π^0's for $A + B$ inelastic collisions, with centrality f, is related to the $p + p$ cross section by

$$\left.\frac{1}{N_{AB}^{\text{evt}}}\frac{d^2N_{AB}^{\pi^0}}{dp_T dy}\right|_f = \langle T_{AB}\rangle_f \times \frac{d^2\sigma_{pp}^{\pi^0}}{dp_T dy}. \tag{24}$$

Note that

$$\langle T_{AB}\rangle_f = \frac{\int_f T_{AB}(b)\,d^2b}{\int_f (1 - e^{-\sigma_{NN}T_{AB}(b)})\,d^2b} = \frac{\langle N_{\text{coll}}\rangle_f}{\sigma_{NN}}, \tag{25}$$

where $\langle N_{\text{coll}}\rangle_f$ is the average number of binary nucleon–nucleon inelastic collisions, with cross section σ_{NN}, in the centrality class f. This leads to the description of the scaling for point-like processes as binary-collision (or N_{coll}) scaling.

Nuclear medium effects, either in the initial or final state, can modify the expected scaling. These modifications can be quantitatively studied by measurement of the *nuclear modification factor* R_{AB}, which is defined as

$$R_{AB} = \frac{dN_{AB}^P}{\langle T_{AB}\rangle_f \times d\sigma_{NN}^P} = \frac{dN_{AB}^P}{\langle N_{\text{coll}}\rangle_f \times dN_{NN}^P}, \tag{26}$$

where dN_{AB}^P is the differential yield of a point-like process P in a $A + B$ collision and $d\sigma_{NN}^P$ is the cross section of P in $N + N$ collision. If there are no initial- or final-state effects that modify the yield of P in $A + B$ collisions, the process P scales with $\langle T_{AB}\rangle_f$

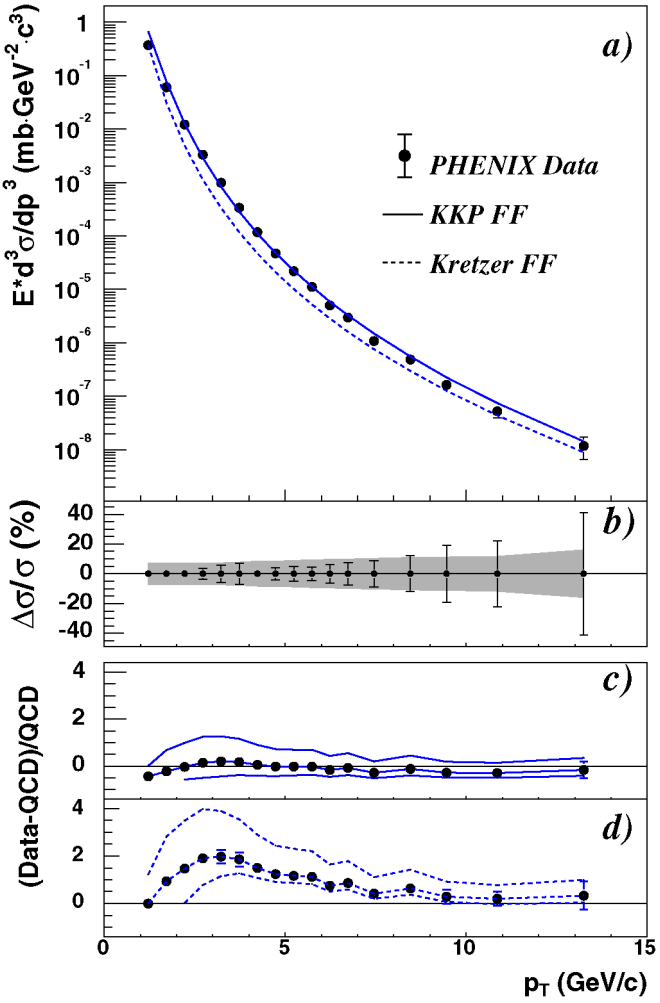

Fig. 27. PHENIX π^0 invariant cross section at mid-rapidity from $p+p$ collisions at $\sqrt{s} = 200$ GeV, together with NLO pQCD predictions from Vogelsang [151,152]. (a) The invariant differential cross section for inclusive π° production (points) and the results from NLO pQCD calculations with equal renormalization and factorization scales of p_T using the "Kniehl–Kramer–Pötter" (solid line) and "Kretzer" (dashed line) sets of fragmentation functions. (b) The relative statistical (points) and point-to-point systematic (band) errors. (c), (d) The relative difference between the data and the theory using KKP (c) and Kretzer (d) fragmentation functions with scales of $p_T/2$ (lower curve), p_T, and $2p_T$ (upper curve). In all figures, the normalization error of 9.6% is not shown [60].

and $R_{AB} = 1$. Sometimes, the central to peripheral ratio, R_{CP}, is used as an alternative to R_{AB}. The central to peripheral ratio is defined as

$$R_{CP} = \frac{dN^{\text{Central}}/\langle N_{\text{coll}}^{\text{Central}}\rangle}{dN^{\text{Peripheral}}/\langle N_{\text{coll}}^{\text{Peripheral}}\rangle}, \tag{27}$$

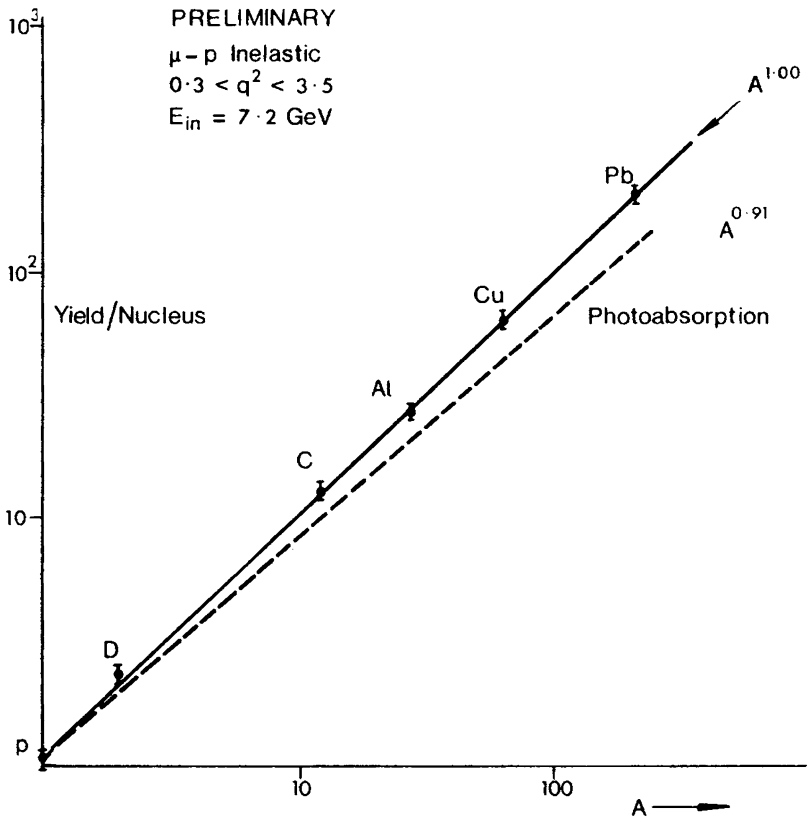

Fig. 28. μ–A cross section vs. A [156].

where dN^{Central} and $dN^{\text{Peripheral}}$ are the differential yield per event of the studied process in a central and peripheral collision, respectively. If the yield of the process scales with the number of binary collisions, $R_{CP} = 1$.

5.4. Binary scaling in $l + A$, $p + A$, and low-energy $A + A$

In deeply inelastic lepton scattering, where hard scattering was discovered [153–155], the cross section for $\mu + A$ collisions is indeed proportional to $A^{1.00}$ (Fig. 28). This indicates that the structure function of a nucleus of mass A is simply A times the structure function of a nucleon (with only minor deviations, $\leqslant 10\%$ for $0.02 \leqslant x \leqslant 0.50$ [157]), which means that the nucleus acts like an incoherent superposition of nucleons for hard scattering of leptons.

The situation is rather different in $p + A$ collisions: the cross section at a given p_T also scales as a power law, $A^{\alpha(p_T)}$ (Fig. 29), but the power $\alpha(p_T)$ is greater than 1. This is called the "Cronin effect" [158]. The enhancement (relative to $A^{1.00}$) is thought to be due to the multiple scattering of the incident partons while passing through the nucleus A before the collision [159,160], which smears the axis of the hard scattering relative to the axis of the

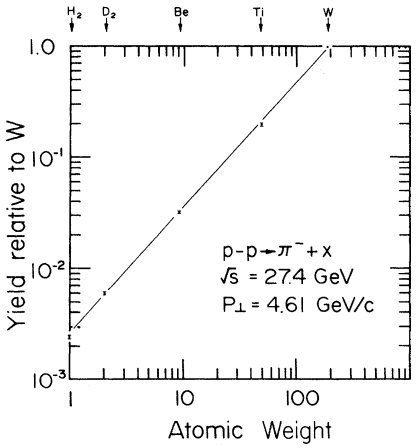

Fig. 29. Cronin effect in $p + A$, for π^- with $p_T = 4.61$ GeV/c. $\alpha(p_T) = 1.148 \pm 0.010$ [158].

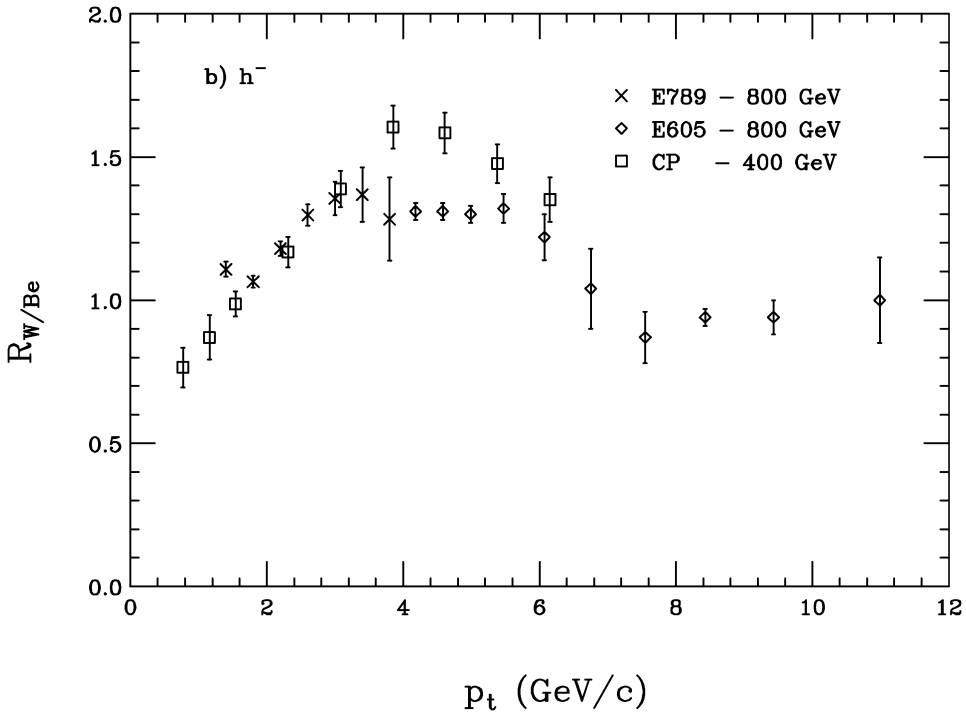

Fig. 30. Cronin effect at fixed target energies expressed as $R_{\mathrm{W/Be}}$, the ratio of the point-like scaled cross sections in $p + \mathrm{W}$ and $p + \mathrm{Be}$ collisions vs. p_T [161].

incident beam, leading to the characteristic "Cronin effect" shape for $R_A(p_T)$ (Fig. 30). At low $p_T < 1$ GeV/c, the cross-section is no longer point-like, so the scattering is shadowed ($\propto A^{2/3}$), thus $R_A < 1$. At larger $p_T > 2$ GeV/c, as the hard-scattering, power-law p_T

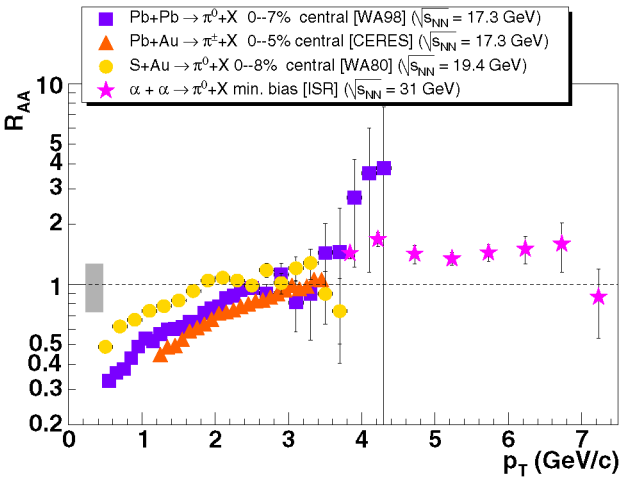

Fig. 31. Nuclear modification factors for π^0 production at the CERN-ISR in minimum-bias $\alpha + \alpha$ reactions at $\sqrt{s_{NN}} = 31$ GeV [162] and for pion production at the CERN-SPS in central Pb + Pb [163], Pb + Au [164], and S + Au [165] reactions at $\sqrt{s_{NN}} \approx 20$ GeV. The R_{AA} from SPS are obtained using the $p + p$ parametrization proposed in Ref. [166]. The shaded band around $R_{AA} = 1$ represents the overall fractional uncertainty of the SPS data (including in quadrature the 25% uncertainty of the $p + p$ reference and the 10% error of the Glauber calculation of N_{coll}). There is an additional overall uncertainty of ±15% for the CERES data not shown in the plot [164].

spectrum begins to dominate, the multiple scattering smears the spectrum to larger p_T leading to an enhancement relative to binary-scaling which dissipates with increasing p_T as the influence of the multiple scattering diminishes.

Previous measurements of high-p_T particle production in $A + A$ collisions at $\sqrt{s_{NN}} \leqslant 31$ GeV (Fig. 31) and in $p + A$ (or $d + A$) collisions (Fig. 30) including measurements at RHIC [64] at mid-rapidity (Fig. 32) all show binary scaling or a Cronin effect.

This establishes that the initial condition for hard scattering at RHIC at mid-rapidity is an incoherent superposition of nucleon structure functions, including gluons, where multiple scattering before the hard collision smears the p_T spectrum of scattered particles to be somewhat above the simple point-like binary (N_{coll}) scaling.

An alternative view of the initial state of a nucleus at RHIC is provided by the color glass condensate (CGC), in which the gluon population at low x is not an incoherent superposition of nucleon structure functions but is limited with increasing A by nonlinear gluon–gluon fusion resulting from the overlap of gluons from several nucleons in the plane of the nucleus transverse to the collision axis [168]. A Cronin effect in $d + A$ collisions, as shown in Fig. 32, can be reproduced in the CGC with a suitable choice of initial state parameters, which must also reproduce quantitatively the observed binary scaling of the direct photon production and total charm production in Au + Au collisions to be shown below (Figs. 33, 34). However, at this writing, no detailed quantitative description of the CGC initial state which satisfies these three conditions has been published.

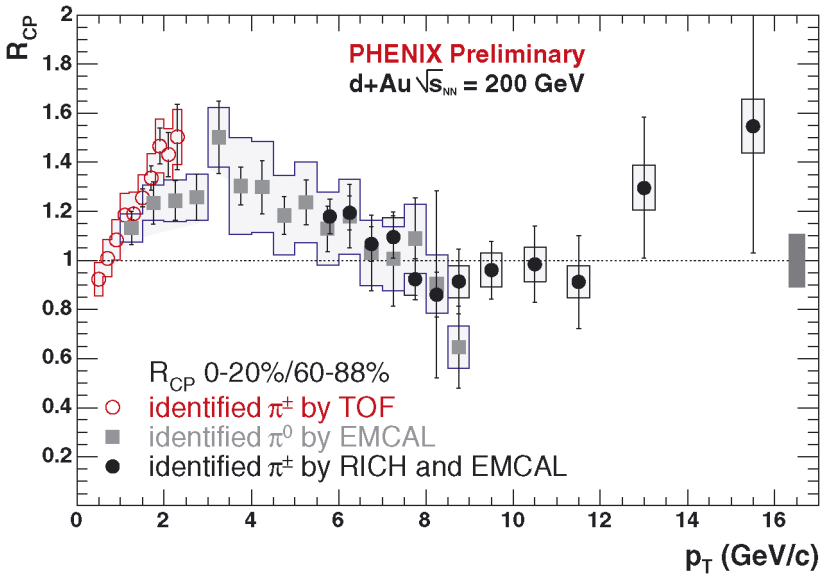

Fig. 32. Cronin effect in R_{CP}, the ratio of point-like scaled central to peripheral collisions for pions in $d + \mathrm{Au}$ at $\sqrt{s_{NN}} = 200$ GeV [167]. Data points for low p_T are $\pi^{\pm}$ identified by Time of Flight (TOF). Data at medium p_T are for π^0 identified by reconstruction in the Electromagnetic Calorimeter (EMCAL). Highest p_T data are for $\pi^{\pm}$ identified by a count in the Ring Imaging Cerenkov Counter (RICH) and a deposited energy/momentum and shower shape in the EMCAL inconsistent with those of a photon or electron. The shaded band on the right represents the overall fractional systematic uncertainty due to N_{coll}.

5.5. *Binary scaling in Au + Au collisions at RHIC—direct photons and charm yield*

The production of hard photons in Au + Au collisions at RHIC via the constituent reactions (e.g., $g + q \to \gamma + q$) is a very important test of QCD and the initial state, because the photons only interact electromagnetically, hence hardly at all, with any final-state medium produced. The direct-photon cross section and centrality dependence should then reflect only the properties of the initial state, notably the product of the gluon and quark structure functions of the Au nuclei.

The first measurement of direct photon production in Au + Au collisions at RHIC has been reported by the PHENIX Collaboration (Fig. 33) [73]. The data exhibit pure point-like (N_{coll}) scaling as a function of centrality relative to a pQCD calculation for $p + p$ collisions. The statistical and systematic errors still leave some room for a small Cronin effect and/or some thermal photon production. The observation of direct photon production establishes the importance of gluon degrees of freedom at RHIC.

PHENIX measured the single-electron yield from nonphotonic sources in Au + Au collision at 130 GeV [42] and 200 GeV [57]. Since semi-leptonic decay of charm is the dominant source of the nonphotonic electrons at low p_T ($p_T \leqslant 3\ \mathrm{GeV}/c$), the total yield of charm can be determined from the integrated yield of nonphotonic electrons in the low-p_T region. Fig. 34 shows the yield of nonphotonic electrons ($0.8 < p_T < 4.0\ \mathrm{GeV}/c$) per NN collision in Au + Au reactions at $\sqrt{s_{NN}} = 200$ GeV as a function of N_{coll} [57]. The N_{coll}

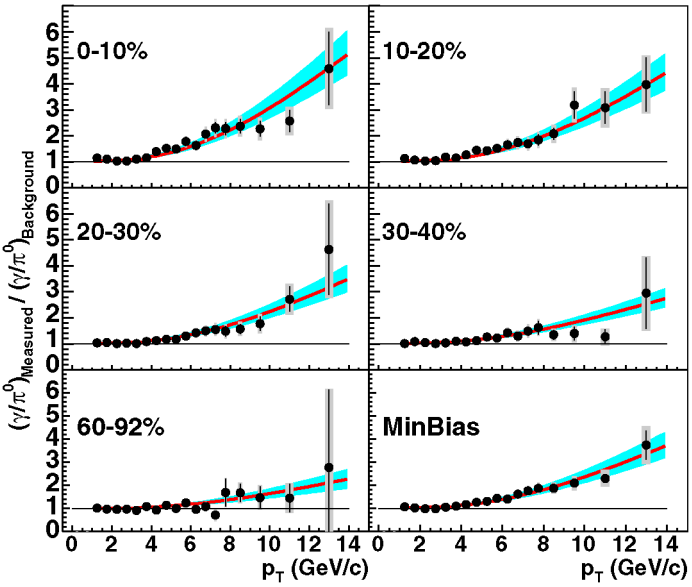

Fig. 33. PHENIX direct photon measurements relative to the background for minimum bias and for five centralities of Au + Au collisions at $\sqrt{s_{NN}} = 200$ GeV (0–10% is the most central). Statistical and total errors are indicated separately on each data point by the vertical bar and shaded region, respectively. The curves represent a pQCD calculation of direct photons in $p + p$ collisions from Vogelsang [169–172] scaled to Au + Au assuming pure point-like ($N_{\rm coll}$) scaling, with no suppression. The shaded region around the curves indicate the variation of the pQCD calculation for scale changes from $p_T/2$ to $2p_T$, plus the $\langle N_{\rm coll}\rangle$ uncertainty [73].

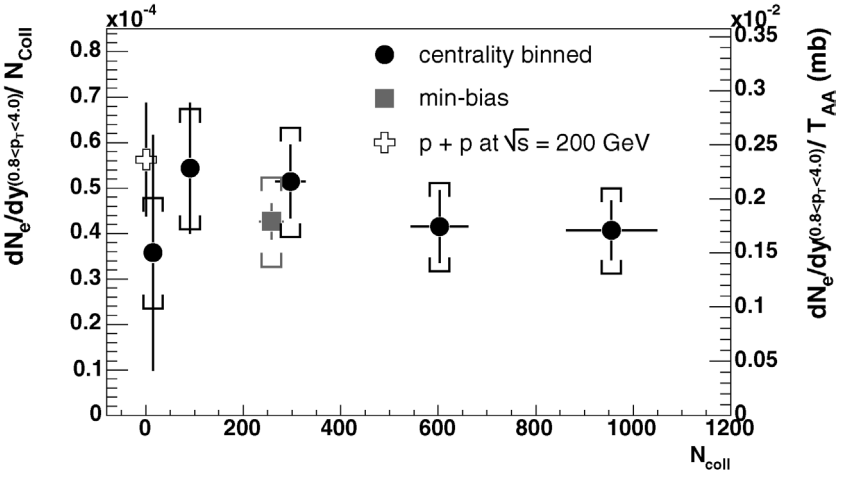

Fig. 34. Nonphotonic electron yield ($0.8 < p_T < 4.0$ GeV/c), dominated by semi-leptonic charm decays, measured in Au + Au collisions at $\sqrt{s_{NN}} = 200$ GeV scaled by $N_{\rm coll}$ as a function of $N_{\rm coll}$. The right-hand scale shows the corresponding electron cross section per NN collision in the above p_T range. The yield in $p + p$ collision at 200 GeV is also shown [57].

dependence of the yield is fit to $N_{\rm coll}^{\alpha}$, where $\alpha = 1$ is the expectation for binary scaling. We find $\alpha = 0.938 \pm 0.075(\text{stat.}) \pm 0.018(\text{sys.})$, showing that the total yield of charm-decay electrons is consistent with binary scaling. It should be noted that medium effects, such as energy loss of charm in the dense hot medium, can only influence the momentum distribution of charm, and have little effect on the total yield of charm. Initial-state effects, such as shadowing, and other effects, such as thermal production of charm, are believed to be very small for charm production at RHIC energy. Therefore, the observation of binary scaling of the total charm yield in Au + Au collisions at RHIC may also be considered as an experimental verification of the binary scaling of a point-like pQCD process.

5.6. Conclusions

In this section evidence has been presented to show that the initial condition for hard-scattering at RHIC at mid-rapidity is an incoherent superposition of nucleon structure functions, including gluons, where multiple scattering before the hard collision can smear the p_T spectrum of scattered particles to be somewhat above the simple point-like binary ($N_{\rm coll}$) scaling. This was demonstrated using the reactions: pion production in d + Au collisions, where there is no final-state medium, and direct photon production in Au + Au collisions, where the outgoing photons interact electromagnetically, hence hardly at all, with any final-state medium produced. The total charm yield in Au + Au, a reaction dominated by the subprocess $g + g \to c + \bar{c}$, and which is not sensitive to final-state medium effects for the total yield of $c + \bar{c}$ pairs, also exhibits binary scaling. The latter two measurements provide experimental evidence for the binary scaling of point-like pQCD processes in Au + Au collisions.

The color glass condensate (CGC) provides an alternative view of the initial state of a nucleus at RHIC in which coherence of gluons due to nonlinear gluon–gluon fusion can produce a Cronin-like effect, depending on the initial conditions and the kinematic range covered. However, at the present writing, there is no CGC description of the initial state nuclear structure function which reproduces the observed Cronin effect for pions in d + Au collisions and the observed binary scaling for both direct photon production and the total charm yield in Au + Au collisions.

6. Number density and high p_T suppression

To study the initial properties of the matter created in heavy ion collisions we need a probe that is already present at the earliest times and that is directly sensitive to the properties of the medium. Partons resulting from hard scatterings during the initial crossing of the two nuclei in $A + A$ collisions provide such a probe. Energetic partons propagating through a dense medium are predicted to lose energy [173–181] thus producing a suppression in the yield of high-p_T hadrons produced from the fragmentation of these partons. Initial measurements from RHIC Run 1 [39,47,182] and Run 2 [49,53,183,184] demonstrated such a suppression, and the results of d + Au measurements [64,66–68] showed that the suppression was not due to initial-state effects. Further measurements have in-

dicated a modification of dijet angular correlations [68] that has also been attributed to in-medium parton energy loss [185,186].

While the energy loss of hard-scattered partons was originally proposed as a signature of the quark–gluon plasma and deconfinement, it has been argued recently that the energy loss is sensitive only to the density of unscreened color charges and not directly to deconfinement [177–181,187,188]. Ideally, a measurement of initial parton densities together with constraints on initial energy density might allow an estimate of the temperature of the medium. As will be seen below, the current high-p_T measurements and theoretical tools for interpreting the experimental data are not yet sufficient to take such a step. Instead, the energy loss results are currently being used to provide estimates of the initial energy density. The remainder of this section summarizes PHENIX experimental data related to high-p_T suppression, discusses the current state of theoretical understanding of the energy loss process and concludes with a statement of estimates for initial parton number and energy densities that currently can be made.

6.1. Single particle spectra, R_{AA}

As described in Section 5, in the absence of modifications due to initial-state or final-state effects, the rate for the production of particles through hard-scattering processes in nucleus–nucleus collisions is expected to be given by the equivalent $p+p$ hard-scattering cross section multiplied by T_{AB}. Fig. 35 shows PHENIX π^0 spectra, $d^2N/dp_T\,dy$, measured in $\sqrt{s_{NN}}$ GeV [49] peripheral (80–92%) and central (0–10%) Au + Au collisions compared to measured [60] $p+p$ cross sections multiplied by the peripheral and central T_{AB} values estimated using the procedure described in Section 5. The error bands on the $p+p$ data points reflect both the systematic errors on the $p+p$ cross sections and the uncertainties in the T_{AB} values. As the figure clearly demonstrates, the central Au + Au π^0 yields are strongly suppressed relative to the "expected" yields over the entire measured p_T range. In contrast, the peripheral yields compared to the T_{AB}-scaled $p+p$ cross sections show little or no suppression. The results incontrovertibly demonstrate that there is a strong and centrality-dependent suppression of the production of high-p_T pions relative to pQCD-motivated expectations. This is quite different from measurements of R_{AA} in Pb + Pb collisions at $\sqrt{s_{NN}} = 17.3$ GeV where in semi-peripheral Pb + Pb collisions there is a nuclear enhancement increasing with p_T similar to the well-known Cronin effect, while in central collisions the Cronin enhancement appears to be weaker than expected (see Fig. 31).

To better demonstrate quantitatively the suppression in central collisions indicated in Fig. 35, we show in Fig. 36 $R_{AA}(p_T)$ for mid-rapidity π^0's in central and peripheral 200 GeV Au + Au collisions. We also show the values obtained from minimum-bias 200 GeV d + Au collisions [64] which provide a stringent test of the possible contribution of initial-state nuclear effects to the observed suppression in Au + Au collisions. The error bands on the data indicate combined statistical and point-to-point systematic errors and the bars shown next to the different data sets indicate common systematic errors due to uncertainties in the $p+p$ cross section normalization and T_{AB}.

Fig. 36 shows that the central Au + Au π^0 suppression changes only slightly over the measured p_T range and reaches an approximately p_T-independent factor of 5 ($R_{AA} \approx 0.2$)

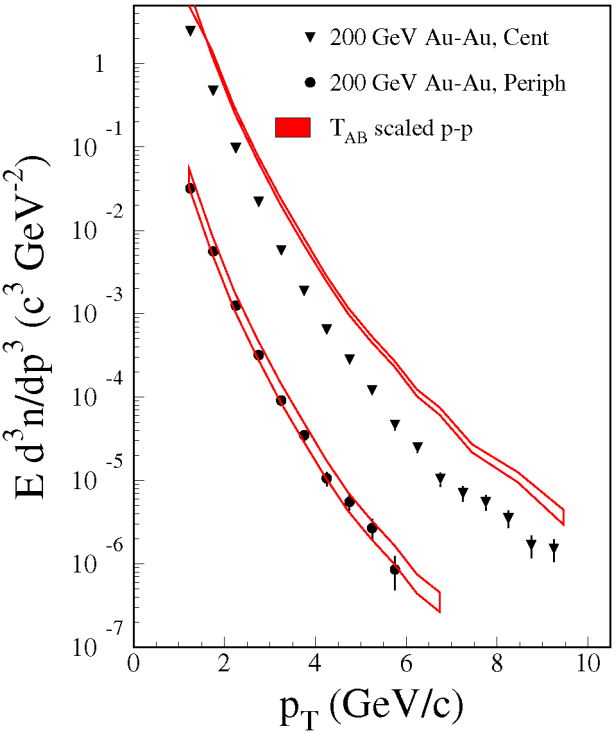

Fig. 35. π^0 p_T spectra in 200 GeV Au + Au collisions [49] compared to a T_{AB} scaling of the 200 GeV $p+p$ π^0 differential cross section [60]. The central data were obtained with a 0–10% centrality cut while the peripheral data were obtained with an 80–92% cut.

for $p_T > 4$–5 GeV/c. The peripheral Au + Au R_{AA} values are consistent with one after taking into account systematic errors but we cannot rule out a slight suppression suggested by the peripheral R_{AA} values. In all of the data sets R_{AA} decreases with decreasing p_T for $p_T < 2$ GeV/c. This decrease, known since the original measurements of the A dependence of particle production in $p+A$ collisions is due to contributions of soft hadronic processes at low p_T that are expected to increase more slowly than proportional to T_{AB}. The $d+$Au R_{dA} values are also consistent with one within systematic uncertainties, but in contrast to the Au + Au results, the data suggest a slight enhancement. The $d+$Au R_{dA} values above 2 GeV/c exceed one for nearly the entire experimentally covered p_T range. As shown previously in Fig. 32, only for $p_T \gtrsim 6$ GeV/c does the $d+$Au pion yield return to the T_{AB}-scaling expectation. Such a small enhancement is consistent with expectations based on prior measurements of the Cronin effect [189,190], and it is also quantitatively consistent with calculations incorporating the initial-state multiple scattering that is thought to produce the Cronin effect [191–197]. Therefore the Cronin effect at RHIC is small and cannot mask a strong suppression of high p_T particle production due to initial-state parton saturation as suggested by Ref. [198].

To better demonstrate the systematic behavior of the high-p_T suppression we show in Fig. 37 π^0 [49] and unidentified charged particle R_{AA} values [53] as a function of p_T for

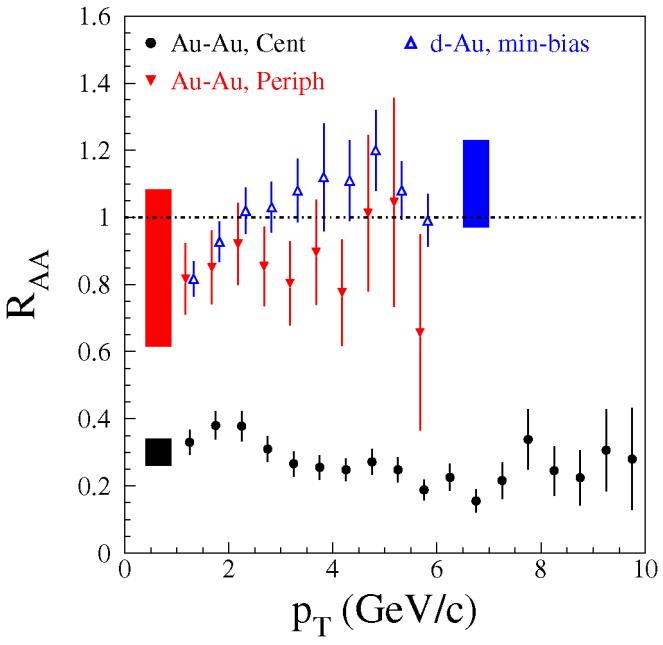

Fig. 36. π^0 $R_{AA}(p_T)$ for central (0–10%) and peripheral (80–92%) Au + Au collisions [49] and minimum-bias d + Au collisions [64]. The shaded boxes on the left show the systematic errors for the Au + Au R_{AA} values resulting from overall normalization of spectra and uncertainties in T_{AB}. The shaded box on the right shows the same systematic error for the d + Au points.

various centrality bins. While for moderate p_T values ($2 < p_T < 5$ GeV/c) total charged particle production is suppressed less than pion production, the charged particle and π^0 R_{AA} values become equal, within errors, at high p_T. This evolution in the charged particle suppression is related to contributions from the (anti)protons that will be discussed further below. Despite the differences resulting from the protons, the charged particles and π^0's exhibit very similar trends in the suppression vs. p_T and vs. centrality. The suppression increases smoothly with centrality though the change in R_{AA} values at high p_T is most rapid in the middle of the centrality range. Fig. 37 also shows that the suppression is approximately constant as a function of p_T for $p_T > 4.5$ GeV/c in all centrality bins. We take advantage of this feature of the data to better illustrate the centrality dependence of the suppression by integrating both the Au + Au spectra and the reference $p + p$ cross sections over $p_T > 4.5$ GeV/c and using these integrated quantities to determine an average suppression factor, R_{AA} for $p_T > 4.5$ GeV/c. We plot the charged particle and π^0 R_{AA} values vs. N_{part} in Fig. 38 (top). This figure suggests that the suppression evolves smoothly with N_{part}, showing no abrupt onset of suppression. The charged particles and π^0's exhibit similar evolution of suppression with N_{part}. In the most central collisions we obtain R_{AA} values of 0.24 ± 0.04 (total) and 0.23 ± 0.05 (total) for charged particles and π^0's, respectively. In peripheral collisions, R_{AA} approaches one, but the systematic errors on the most peripheral T_{AB} values are sufficiently large that we cannot rule out $\sim 20\%$ deviations of the peripheral Au + Au hard-scattering yields from the T_{AB}-scaled $p + p$ cross sections.

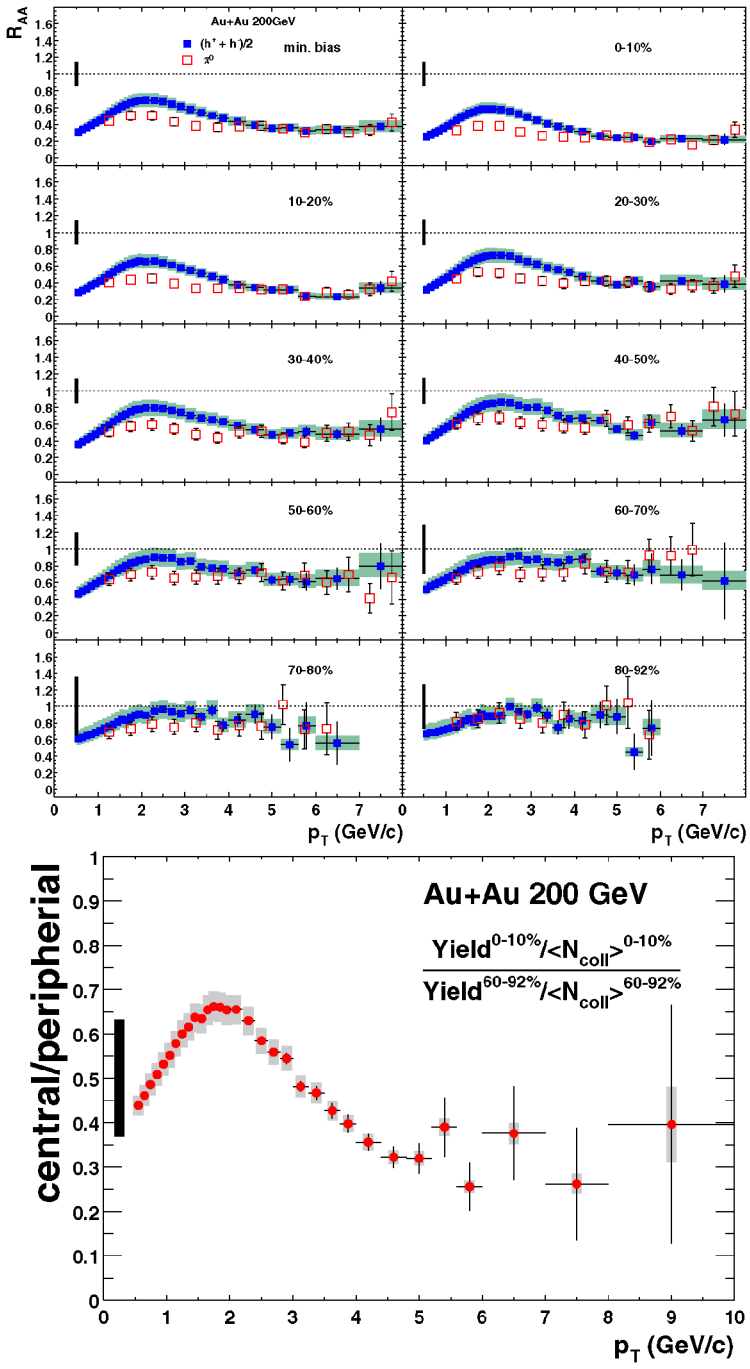

Fig. 37. Centrality and p_T dependence of nuclear modification factors in 200 GeV Au + Au collisions [53]. Top panel: π^0 and charged particle $R_{AA}(p_T)$ for ten centrality bins. Bottom panel: charged particle R_{CP} vs. p_T.

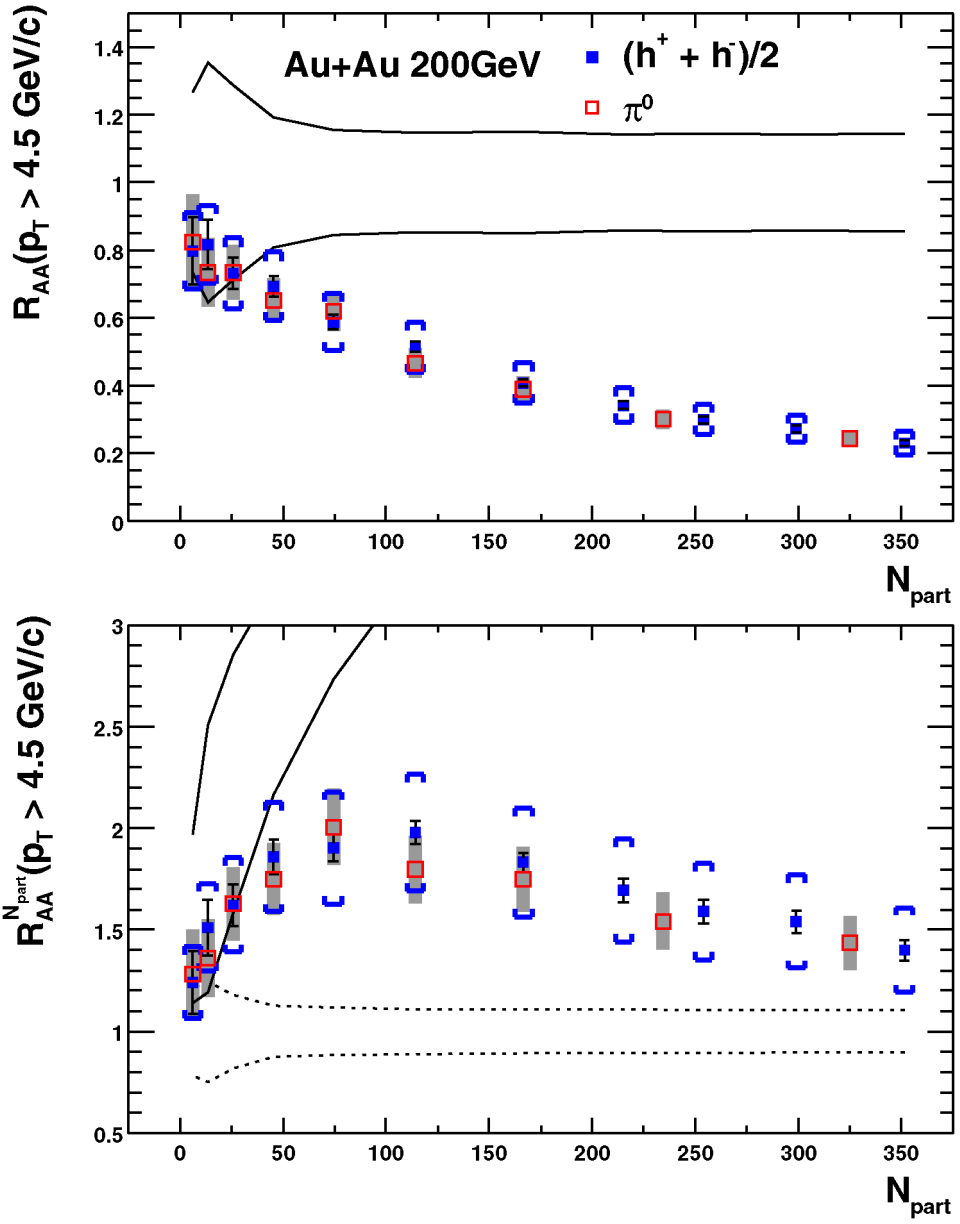

Fig. 38. Top panel: R_{AA} vs. N_{part} obtained from p_T-integrated ($p_T > 4.5$ GeV/c) Au + Au π^0 and charged-hadron spectra. The band indicates the systematic error bands on a hypothetical T_{AB} scaling of the $p + p$ p_T-integrated cross section. Bottom panel: π^0 and charged hadron yield per participant vs. N_{part} divided by the same quantity in $p + p$ collisions ($R_{AA} N_{\text{part}}$). The solid band shows the same band as in the top panel expressed in terms of yield per participant pair while the dashed band indicates the systematic error bands around a hypothetical N_{part} scaling. Both plots are from [53].

An alternative method for evaluating the evolution of the high-p_T suppression with centrality is provided in Fig. 38 (bottom) which presents the charged and π^0 yields per participant integrated over $p_T > 4.5$ GeV/c as a function of $N_{\rm part}$ [53] divided by the same quantity in $p+p$ collisions. Also shown in the figure are curves demonstrating the $N_{\rm part}$ dependence that would result if the π^0 and charged particle yields exactly T_{AB} scaled and what an $N_{\rm part}$ scaling from $p+p$ collisions would imply. As Fig. 38 demonstrates, the high-p_T yields of both charged hadrons and π^0's *per participant* increase proportional to T_{AB} for small $N_{\rm part}$ but level off and then decrease with increasing $N_{\rm part}$ in more central collisions. The PHENIX measurements do not naturally support an approximate $N_{\rm part}$ scaling of high-p_T particle production suggested in an analysis of PHOBOS data [184]. The PHENIX $R_{AA}^{N_{\rm part}}$ values decrease from mid-peripheral ($N_{\rm part} \approx 75$) to central collisions by an amount larger than the systematic errors in the measurement. For more peripheral collisions, $R_{AA}^{N_{\rm part}}$ increases with $N_{\rm part}$ consistent with the modest suppression of high-p_T production shown for peripheral collisions in the top panel of Fig. 38. The initial rise and subsequent decrease of $R_{AA}^{N_{\rm part}}$ with increasing $N_{\rm part}$ suggests that the high-p_T hadron yield in Au + Au collisions has no simple dependence on $N_{\rm part}$. The observation that the high-p_T yields initially increase proportional to T_{AB} demonstrates that in the most peripheral Au + Au collisions the hard-scattering yields are consistent with point-like scaling. However, the deviation from T_{AB} scaling sets in rapidly, becoming significant by $N_{\rm part} = 50$. By $N_{\rm part} = 100$ the high-p_T suppression is so strong that high-p_T yields grow even more slowly than proportional to $N_{\rm part}$.

6.2. x_T scaling in Au + Au collisions at RHIC

If the production of high-p_T particles in Au + Au collisions is the result of hard scattering according to pQCD, then x_T scaling should work just as well in Au + Au collisions as in $p+p$ collisions and should yield the same value of the exponent $n(x_T, \sqrt{s})$. The only assumption required is that the structure and fragmentation functions in Au + Au collisions should scale, in which case Eq. (23) still applies, albeit with a $G(x_T)$ appropriate for Au + Au. In Fig. 39, $n(x_T, \sqrt{s_{NN}})$ in Au + Au is derived from Eq. (23), for peripheral and central collisions, by taking the ratio of $E\,d^3\sigma/dp^3$ at a given x_T for $\sqrt{s_{NN}} = 130$ and 200 GeV, in each case. The π^0's exhibit x_T scaling, with the same value of $n = 6.3$ as in $p+p$ collisions, for both Au + Au peripheral and central collisions, while the nonidentified charged hadrons x_T-scale with $n = 6.3$ for peripheral collisions only. Notably, the $h^{\pm}$ in Au + Au central collisions exhibit a significantly larger value of n, indicating different physics, which will be discussed below. The x_T scaling establishes that high-p_T π^0 production in peripheral and central Au + Au collisions and $h^{\pm}$ production in peripheral Au + Au collisions follow pQCD as in $p+p$ collisions, with parton distributions and fragmentation functions that scale with x_T, at least within the experimental sensitivity of the data.

6.3. Two-hadron azimuthal-angle correlations

We argued in Section 5 that the production of hadrons at high-p_T results predominantly from hard scattering followed by fragmentation of the outgoing parton(s). While

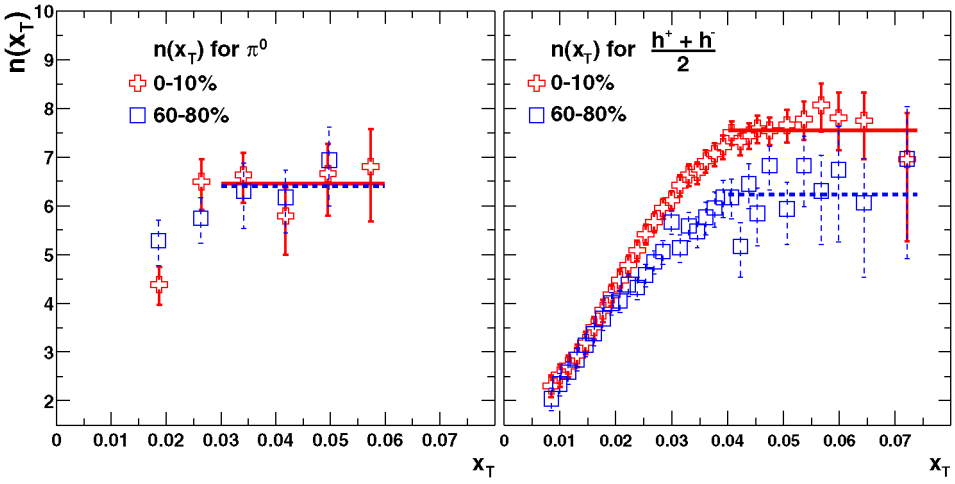

Fig. 39. Power-law exponent $n(x_T)$ for π^0 and h spectra in central and peripheral Au + Au collisions at $\sqrt{s_{NN}} = 130$ and 200 GeV [53].

this result is well established in $p(\bar{p}) + p$ collisions, it might not be true in Au + Au collisions when the yield of high-p_T particles is modified so dramatically compared to expectations. Since a hard-scattered parton fragments into multiple particles within a restricted angular region (i.e., a jet) a reasonable way to check the assumption that high-p_T hadron production in Au + Au collisions is due to hard scattering is to directly observe the angular correlations between hadrons in the jets. None of the experiments at RHIC are currently capable of reconstructing jets in the presence of the large soft background of a Au + Au collision. However, both STAR [199,200] and PHENIX [201,202] have directly observed the presence of jets by studying two-hadron azimuthal-angle correlations. Fig. 40 shows preliminary distributions [201] of the relative azimuthal angle ($\Delta\phi$) between pairs of charged particles detected within the PHENIX acceptance in d + Au collisions and peripheral (60–90%) and central (0–10%) Au + Au collisions after the subtraction of combinatoric background. The pairs of particles are chosen such that one particle lies within a "trigger" p_T range ($2.5 < p_{T\,\mathrm{trig}} < 4$ GeV/c) while the other "associated" particle falls within a lower p_T window $1.0 < p_T < 2.5$ GeV/c. The distributions show the differential yield per $\Delta\phi$ of associated particles per detected trigger particle within the given p_T ranges and within the η acceptance of the PHENIX central arms ($-0.35 < \eta < 0.35$).

The peaks observed at $\Delta\phi = 0$ (near side) reflect the correlation between hadrons produced within the same jet while the broader peaks observed at $\Delta\phi = \pi$ (away side) reflect the correlations between hadrons produced in one jet and hadrons produced in the "balance" jet. In the Au + Au cases, a $\cos 2\Delta\phi$ modulation underlies the jet angular correlations due to the elliptic flow of particles in the combinatoric background and possibly also in part due to azimuthal anisotropies in the jets themselves (see below). Nonetheless, the $\cos 2\Delta\phi$ contribution has little effect on the narrow same-jet (near-side) peak in the $\Delta\phi$ distribution.

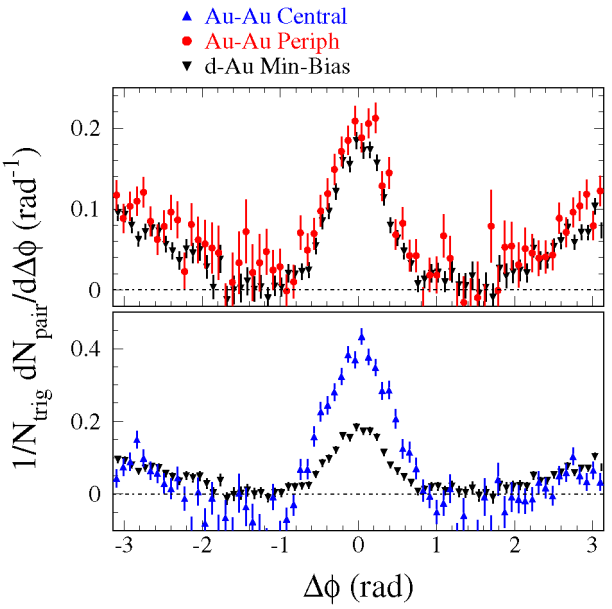

Fig. 40. Differential yields per $\Delta\phi$ and per trigger particle of pairs of charged hadrons in $d+\mathrm{Au}$, peripheral $\mathrm{Au}+\mathrm{Au}$ and central $\mathrm{Au}+\mathrm{Au}$ collisions at $\sqrt{s_{NN}} = 200$ GeV [201]. The pairs were selected with the higher-momentum "trigger" particle in the range $2.5 < p_T < 4.0$ GeV/c and the lower-momentum "associated" particle in the range $1.0 < p_T < 2.5$ GeV/c. A constant background has been subtracted for all three distributions.

We observe that the angular widths of the same-jet correlations are the same within errors in all three data sets in spite of the factor of two larger yield of associated hadrons in central $\mathrm{Au}+\mathrm{Au}$ collisions compared to $d+\mathrm{Au}$ and peripheral $\mathrm{Au}+\mathrm{Au}$ collisions. This result is demonstrated more quantitatively in Fig. 41 which shows the centrality dependence of the Gaussian widths of the same-jet peaks in the $\mathrm{Au}+\mathrm{Au}$ $\Delta\phi$ compared to the jet widths extracted from $d+\mathrm{Au}$ collisions [201]. We see that the $\mathrm{Au}+\mathrm{Au}$ two-hadron correlation functions show peaks with the same jet width as $d+\mathrm{Au}$ collisions. Since this width is a unique characteristic of the parton fragmentation process, we conclude that high-p_T hadrons in $\mathrm{Au}+\mathrm{Au}$ collisions result from hard scattering followed by jet fragmentation regardless of any medium modifications of the fragmentation multiplicity.

6.4. High-p_T suppression and energy loss

The suppression of the production of high-p_T hadrons in heavy ion collisions at RHIC had been predicted long before RHIC started running [173–179,203]. It is now generally accepted that partons propagating in colored matter lose energy predominantly through medium-induced emission of gluon radiation [204,205]. An energetic parton scatters off color charges in the high-parton-density medium and radiates gluon bremsstrahlung. The reduction in the parton energy translates to a reduction in the average momentum of the fragmentation hadrons, which, in turn, produces a suppression in the yield of high-p_T

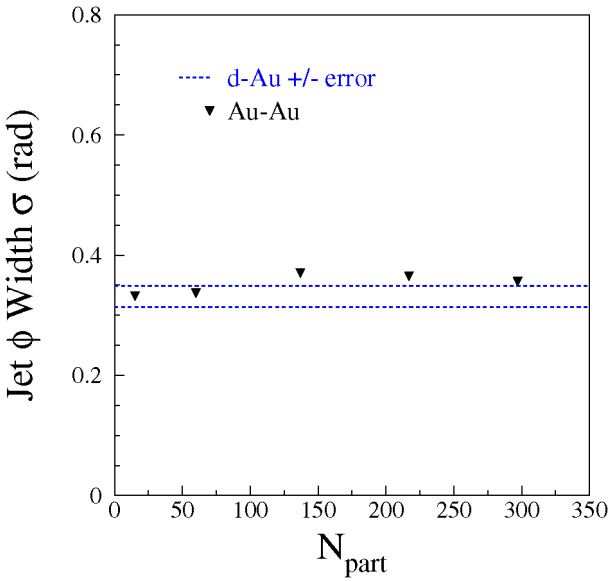

Fig. 41. The azimuthal angle width of jets in 200 GeV Au + Au collisions extracted as the σ's of Gaussian fits to the 0° peak in the two-charged-hadron azimuthal-angle ($\Delta\phi$) correlation functions [201]. The correlation functions were formed from pairs with trigger hadron in the p_T range $2.5 < p_T < 4.0$ GeV/c and the associated hadron in the range $1.0 < p_T < 2.5$ GeV/c. The dashed lines show the $\pm 1\sigma$ range of the jet widths in d + Au collisions using the same momentum bins. In the Au + Au data, the effect of the elliptic flow has been subtracted in the extraction of the jet width.

hadrons relative to the corresponding yield in $p + p$ collisions. The power-law spectrum for $p_T \geqslant 3$ GeV/c implies that a modest reduction in fragmenting parton energy can produce a significant decrease in the yield of hadrons at a given p_T. Thus, the suppression of the yield of high-p_T hadrons is generally believed to provide a direct experimental probe of the density of color charges in the medium through which the parton passes [188,194, 206]. However, before proceeding to an interpretation of our results, we briefly discuss the theoretical understanding of the radiative energy loss mechanism and limitations in that understanding.

The dominant role of radiative gluon emission was identified early on [175], but it took several years and much effort before rigorous calculations of the energy loss taking into account Landau–Pomeranchuk–Migdal suppression [176] and the time evolution of the medium were available. Initial estimates of the radiative energy loss suggested an approximately constant $\Delta E/\Delta x$ [174,176], but later calculations [177,180,181,207] showed that the quantum interference can produce a loss of energy that grows faster than linearly with the propagation path length, L, of the parton in the medium. However, this ideal growth of $\Delta E/\Delta x$ with increasing path length is never realized in heavy ion collisions due to the rapid decrease of the energy density and the corresponding color charge density with time [179,185,188,194]. Generally, all energy loss calculations predict that the fractional energy loss of a propagating parton decreases with increasing parton energy. However, the precise evolution with parton energy depends on the assumptions in the energy loss models and on

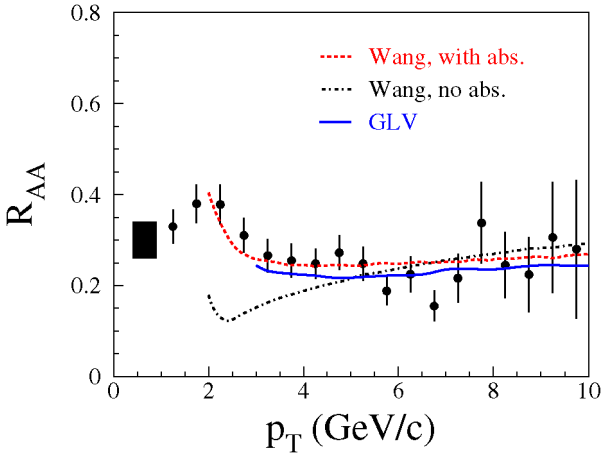

Fig. 42. Comparisons of energy loss calculations [185,212] used to extract estimates for the initial parton number or energy density (see text for details) to the central 200 GeV Au + Au π^0 $R_{AA}(p_T)$ measured by PHENIX. The Wang curves compare results with and without energy absorption from the medium.

the treatment of details like kinematic limits and nonleading terms in the radiation spectrum [204,205]. There are many different calculations of medium-induced energy loss currently available based on a variety of assumptions about the thickness of the medium, the energy of the radiating parton, and the coherence in the radiation process itself (see [204,205,208] for recent reviews). The p_T dependence of the PHENIX π^0 R_{AA} values has ruled out the possibility of a constant (energy independent) $\Delta E/\Delta x$ [203] and the original BDMS energy loss formulation (which the authors argued should not be applied at RHIC energies). In fact, the only detailed energy loss model that *predicted* the flat p_T dependence of R_{AA} over the p_T range covered by RHIC data was the GLV prescription [181,194,209–211]. In the GLV formulation, the fractional energy loss for large jet energies varies approximately as $\log(E)/E$ but the authors observe that below 20 GeV the full numerical calculation of the energy loss produces a nearly constant $\Delta E/E$ [205]. However, the same authors argue that the flat $R_{AA}(p_T)$ observed at high p_T at 200 GeV also requires an accidental cancellation of several different contributions including the separate p_T dependences of the quark and gluon jet contributions, the p_T dependence of the Cronin enhancement, and shadowing/EMC effect. A comparison of the GLV results for the p_T dependence of the π^0 suppression to the PHENIX data is shown in Fig. 42.

One of the most critical issues in the energy loss calculation is the treatment of the time evolution of the energy density of the matter through which the radiating parton is propagating. Even if transverse expansion of the created matter is ignored, the longitudinal expansion produces a rapid reduction in the energy density as a function of time. Most energy loss calculations assume that the color charge density decreases as a function of proper time as $\rho(\tau) = \rho_0\tau_0/\tau$ in which case the measured R_{AA} can be used to infer the product $\rho_0\tau_0$. Here τ_0 represents the formation time of the partons from which the medium is composed and ρ_0 the initial number density of those partons. Since the gluons have the largest cross section for scattering with other partons, the initial color-charge density is

interpreted as the gluon density. Making the usual assumption that the produced partons are spread over a longitudinal spatial width $\delta z = \tau_0 \delta y$, the GLV authors relate the product $\rho_0 \tau_0$ to the initial dn_g/dy and e obtain $dn_g/dy = 1000 \pm 200$ from the PHENIX π^0 R_{AA} values [194]. The sensitivity of the GLV calculations to the details of the description of the transverse parton density and the transverse expansion of the matter has been tested by using the results of hydrodynamic calculations of the energy density as a function of position and time [213]. The average energy loss for partons in central Au + Au collisions evaluated under dramatically different assumptions was shown to be remarkably insensitive to details of the description of the parton density. The GLV results are also potentially sensitive to a "screening mass" that determines both the transverse momentum distributions of the virtual gluons absorbed from the medium in the bremsstrahlung process and an energy cutoff for the radiated gluons. This mass is related to the local energy density using lattice QCD calculations of the plasma screening mass [194]. However, it was shown by the authors that a factor of two change in the screening mass produces only a 15% change in the dn_g/dy needed to describe the data.

An alternative analysis of parton energy loss [214] starts from explicit calculation of higher-twist matrix elements for $e + A$ collisions that account for coherent rescattering of the struck quark in the nucleus. The contributions of these higher-twist terms can be incorporated into modified jet fragmentation functions, producing an effective energy loss. This calculation can reproduce [188] the HERMES measurements of modified jet fragmentation in nuclear deep-inelastic scattering [215]. By relating the modified fragmentation functions from the higher-twist calculation to energy-loss results obtained from the leading term in an opacity expansion calculation (e.g., GLV) of medium-induced energy loss the parameters describing the rescattering in the nucleus in $e + A$ collisions can be related to the parameters describing the medium in an explicit energy-loss calculation. By relating the two sets of parameters, the parton density in the hot medium can be related to the parton density in a cold nucleus [188]. Results of this analysis are shown in Fig. 42 for parameters that give an initial energy loss per unit length of 13.8 ± 3.9 GeV/fm when the HIJING [79] parameterization of shadowing is used [185] (Note: this result is a factor of two larger that in [188] which was based on analysis of the 130 GeV results). However, an alternative (EKS) [216] shadowing description results in an initial energy loss of 16.1 ± 3.9 GeV/fm [185] in the same calculation indicating at least a 25% systematic error in the energy loss estimates due to uncertainties in the description of nuclear shadowing. Nonetheless, these initial-energy-loss values are much larger than the time-averaged energy loss extracted from the calculation, 0.85 ± 0.24 GeV/fm for HIJING shadowing [185], due to the assumed $1/\tau$ decrease in the color-charged density. In fact, the average energy loss per unit path length in central Au + Au collisions [188] is comparable to the value for cold nuclear matter extracted from HERMES data [188]. However, the initial energy loss is estimated by Wang to be a factor of ~ 30 larger than that in a cold nucleus [185] implying that the initial Au + Au parton density is larger by a factor > 30 than in cold nuclear matter [217].

As shown in Fig. 42 the Wang higher-twist calculation predicts a suppression that varies strongly with p_T over the range where the experimental $R_{AA}(p_T)$ values are flat. However, Wang and Wang have argued that absorption of energy from the medium needs to be accounted for in calculating the energy loss of moderate-p_T partons [187]. They provide a formula which incorporates both parton energy loss and "feedback" from the medium that

can reproduce the shape of the observed high-p_T suppression as shown by the lower curve in Fig. 42. This formula, then, provides the energy loss estimate given above. This explanation for the observed p_T independence of R_{AA}, a crucial feature of the experimental data, is disquieting, however, because it contradicts the explanation provided by the GLV model which provides a consistent estimate of the initial energy density. The feedback of energy from the medium is *not* included in the GLV calculations and if this contribution is significant, then the agreement of the GLV predictions with the π^0 $R_{AA}(p_T)$ over the entire p_T range would have to be considered "accidental". Also, the variation of the suppression in the Wang higher-twist calculation with p_T reflects the $\Delta E \propto \log E$ variation of parton energy loss naturally obtained from approximations to the full opacity expansion [205]. As noted above, the GLV approach finds that incorporating nonleading terms in the opacity expansion produces $\Delta E \propto E$. Thus, while the absorption of energy from the medium in the Wang et al. approach may only be significant below $p_T = 5$ GeV/c, the differences between the variation of energy loss with parton energy in the two approaches will not be confined to low p_T.

One source of uncertainty in the interpretation of the high-p_T suppression is the role of possible inelastic scattering of hadrons after fragmentation. It was originally argued that final-state inelastic scattering of hadrons could produce all of the observed suppression [218]. The persistence of the jet signal with the correct width in Au + Au collisions would be difficult to reconcile with this hypothesis. Indeed, more recent analyses [219] discount the possibility that hadronic re-interaction could account for the observed high-p_T suppression and indicate that only $\sim 1/3$ of fragmentation hadrons undergo final-state inelastic scattering [219]. Wang has also argued [220] that the complete pattern of high-p_T phenomena observed in the RHIC data cannot be explained by hadronic rescattering. However, this leaves open the question of whether hadronic re-interactions after jet fragmentation can be partially responsible for the observed high-p_T suppression. There are a number of other open issues with the quantitative interpretation of the observed high-p_T suppression. The calculations all assume that the jets radiate by scattering off static color charges while the typical initial gluon p_T is often assumed to be ~ 1 GeV. Also the radiated gluons are assumed to be massless though a plasmon cutoff equal to the screening mass is applied. The systematic errors introduced by these and other assumptions made in the current energy loss calculations have not yet been evaluated though the gluon screening mass is being included in analyses of heavy-quark energy loss.

6.5. *Empirical energy loss estimate*

The observation that the suppression of high-p_T particle production is approximately independent of p_T above 4 GeV/c and that the $p + p$ p_T spectra are well described by a pure power-law function in the same p_T range allows a simple empirical estimate of the energy loss of hard-scattered partons in the medium. The π^0 invariant cross section measured by PHENIX in $p + p$ collisions [60] is found to be well described by a power law

$$E\frac{d^3n}{dp^3} = \frac{1}{2\pi}\frac{d^2n}{p_T\,dp_T\,dy} = \frac{A}{p_T^n} \tag{28}$$

for $p_T > 3.0$ GeV/c with an exponent $n = 8.1 \pm 0.1$. If we assume that none of the hard-scattered partons escape from the medium without losing energy, then the approximately p_T-independent suppression above 4.5 GeV/c can be interpreted as resulting from an average fractional shift in the momentum of the final-state hadrons due to energy loss of the parent parton. The suppressed spectrum can be evaluated from the unsuppressed $(p + p)$ spectrum by noting that hadrons produced in Au + Au collisions at a particular p_T value, would have been produced at a larger p_T value $p'_T = p_T + S(p_T)$ in $p + p$ collisions. If the energy loss is proportional to p_T then we can write $S(p_T) = S_0 p_T$ so $p'_T = (1 + S_0) p_T$ Then, the number of particles observed after suppression in a given Δp_T interval is given by

$$\frac{dn}{dp_T} = \frac{dn}{dp'_T}\frac{dp'_T}{dp_T} = \frac{A}{(1+S_0)^{(n-2)}\, p_T^{(n-1)}}. \tag{29}$$

We note that the factor $\frac{dp'_T}{dp_T}$ accounts for the larger relative density of particles per measured p_T interval due to the effective compression of the p_T scale caused by the induced energy loss; this factor is necessary for the total number of particles to be conserved. The nuclear modification factor then can be expressed in terms of S_0,

$$R_{AA}(p_T) = \frac{1}{(1+S_0)^{(n-2)}}. \tag{30}$$

Using this very simple picture, we can estimate the fraction of energy lost by hard-scattered partons in the medium from our measured R_{AA} values. First we obtain S_0 from Eq. (30)

$$S_0 = \frac{1}{R_{AA}^{1/(n-2)}} - 1. \tag{31}$$

Then we observe that the hadrons that would have been produced in $p + p$ collisions at a momentum $(1 + S_0) p_T$ were actually produced at p_T, implying a fractional energy loss

$$S_{\rm loss} = 1 - 1/(1 + S_0) = 1 - R_{AA}^{1/(n-2)}. \tag{32}$$

Fig. 43 shows the centrality dependence of $S_{\rm loss}$ obtained from the p_T-averaged R_{AA} values shown in Fig. 38. For the most central Au + Au collisions at 200 GeV we obtain $S_{\rm loss} = 0.2$, which naively implies that an average 20% reduction in the energy of partons in the medium will produce the suppression observed in the π^0 spectra above 4.5 GeV/c. The extracted $S_{\rm loss}$ values are well described by an $N_{\rm part}^{2/3}$ dependence using the most central bin to fix the proportionality constant. This result agrees with the GLV prediction for the centrality dependence of the medium-induced energy loss.

It has been shown previously [221,222] that fluctuations in the radiation process can distort an estimate of parton energy loss using the procedure described above. Because of the steeply falling p_T spectrum, the partons that lose less energy dominate the yield at a given p_T so our determination of $S_{\rm loss}$ will significantly underestimate the true energy loss. However, it has also been observed that this distortion can largely be compensated by a single multiplicative factor of value ~ 1.5–2.0 [221]. While we cannot use the empirically extracted energy loss to estimate an initial gluon density, we can evaluate the consistency of our results with estimates of $\langle dE/dx \rangle$ in the medium. If we take into account the factor

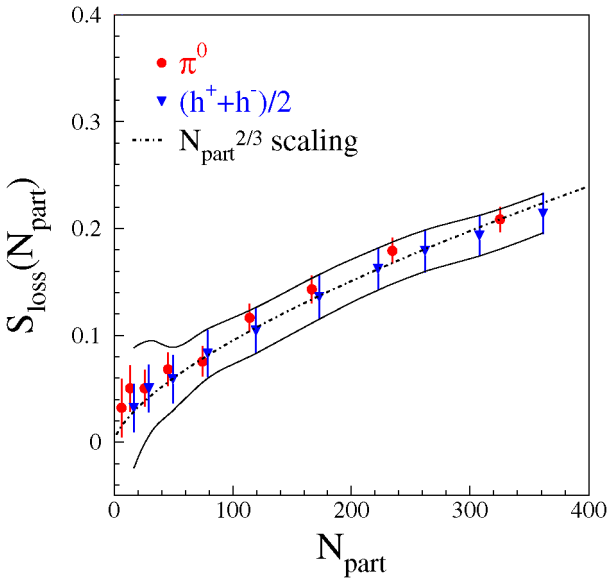

Fig. 43. Calculated energy loss shift factor, S_{loss} vs. N_{part} for π^0 and charged hadron production in 200 GeV Au + Au collisions. The band around the values indicates systematic errors resulting from uncertainties in T_{AB} and the normalization of the $p + p$ spectrum. The dot-dashed curve shows an $N_{\text{part}}^{2/3}$ scaling of S_{loss} using the most central bin to fix the proportionality constant.

of 1.5–2.0 renormalization of S_{loss}, we estimate that 10 GeV partons lose $\sim$ 3–4 GeV of energy. If the typical path length of these partons is on the order of the nuclear radius then we can infer a $\Delta E/\Delta x \sim 0.5$ GeV/fm which is in good agreement with the estimate from Wang [188]. We can also use the above empirical energy loss approach to evaluate possible systematic errors in the estimate of the initial gluon density. For example, if one third of the observed suppression were a result of final-state hadronic interactions in the medium, then the suppression due to energy loss would be a factor of 1.5 smaller than that implied by the measured R_{AA} values, assuming that every fragmentation hadron that interacts effectively "disappears" by being shifted to much lower momentum. As a result, S_0 in central Au + Au collisions would be reduced from 0.25 to 0.17, implying 30% reduction in the estimated energy loss. If this energy loss is indeed proportional to the initial gluon density then the uncertainty in the effect of the final-state hadronic interactions would introduce a 30% systematic error in dn_g/dy.

6.6. Conclusions

The observed suppression of high-p_T particle production at RHIC is a unique phenomenon that has not been previously observed in any hadronic or heavy ion collisions at any energy. The suppression provides direct evidence that Au + Au collisions at RHIC have produced matter at extreme densities, greater than ten times the energy density of normal nuclear matter and the highest energy densities ever achieved in the laboratory. Medium-induced energy loss, predominantly via gluon bremsstrahlung emission, is the

only currently known physical mechanism that can fully explain the magnitude and p_T dependence of the observed high-p_T suppression. This conclusion is based on evidence provided above that we summarize here:

- Observation of the x_T scaling of the high-p_T hadron spectra and measurements of two-hadron azimuthal-angle correlations at high p_T confirm the dominant role of hard scattering and subsequent jet fragmentation in the production of high-p_T hadrons.
- $d+\mathrm{Au}$ measurements demonstrate that any initial-state modification of nuclear-parton distributions has little effect on the production of hadrons with $p_T > 2$ GeV/c at mid-rapidity.
- This conclusion is further strengthened by preliminary PHENIX measurements showing that the yield of direct photons with $p_T > 5$ GeV/c is consistent with a T_{AB} scaling of a pQCD-calculated $p+p$ direct-photon spectrum.
- Analyses described above indicate that final-state hadronic interactions can only account for a small fraction of the observed high-p_T suppression.

Interpreted in the context of in-medium energy loss, the high-p_T suppression data rule out the simplest energy loss prescription—a jet energy independent $\Delta E/\Delta x$. The approximately flat $R_{AA}(p_T)$ was predicted by the GLV energy loss model from which the most explicit estimates of the initial gluon-number density, $dn_g/dy = 1000 \pm 200$ and a corresponding initial energy density $\varepsilon_0 \approx 15$ GeV/fm^3 [194], have been obtained. An alternative estimate from the analysis of Wang et al. [188] yields a path-length-averaged energy loss of 0.5 GeV/fm. Assuming a $1/\tau$ time evolution of the energy density a much larger initial energy loss of 13–16 GeV/fm is obtained. That estimate combined with the estimated 0.5 GeV/fm energy loss of partons in cold nuclear matter yields an initial $\mathrm{Au}+\mathrm{Au}$ gluon density > 30 times larger than that in nuclei [217]. From this result, Wang concludes that the initial energy density is a factor of ~ 100 times larger than that of a nucleus which would correspond to 16 GeV/fm^3 [217]. While this conclusion is consistent with the independent estimate from GLV, we note that the two models provide completely different explanations for the nearly p_T-independent R_{AA}—the most unique feature of the single-particle high-p_T suppression—and the differences between the approaches may not be confined to low p_T. An empirical analysis of the parton energy loss suggests that the Wang estimate of > 0.5 GeV/fm for the average parton $\Delta E/\Delta x$ is consistent with the measured R_{AA} values in central $\mathrm{Au}+\mathrm{Au}$ collisions. However, some outstanding issues with current energy loss calculations and the interpretation of high-p_T suppression were noted above. Most notably, rescattering of hadrons after parton fragmentation could affect the observed high-p_T suppression even if such rescattering cannot explain the pattern of jet quenching observations. Using results from [219] and our empirical energy loss analysis, we estimated that hadronic interactions *could* modify extracted values for initial parton densities by only 30%. However, we cannot evaluate the potential systematic error in extracted parton densities due to other untested assumptions of the energy loss calculations. Therefore, to be conservative we interpret the extracted initial gluon number and energy densities as order-of-magnitude estimates. Even then, the 15 GeV/fm^3 estimated by Gyulassy and Vitev from the central 200 GeV $\mathrm{Au}+\mathrm{Au}$ π^0 $R_{AA}(p_T)$ measurements indicates that the

matter produced in central Au + Au collision has an energy density greater than 10 times normal nuclear matter density.

7. Hadron production

Descriptions of heavy ion collisions have provided an understanding of early energy densities of production rates and medium effects of hard partons, and of collective flow of matter. However, hadronization—the process by which partons are converted into hadrons—is not well understood. The process of hadronization is particularly important since it includes both the dressing of the quarks from their bare masses, i.e., the breaking of approximate chiral symmetry, and the confinement of quarks into colorless hadrons. One could conclude that a quark–gluon plasma had been formed if one had conclusive evidence of hadronization occurring from a thermal distribution of quarks and gluons.

Hadronization processes have been studied over many years in proton–proton and electron–positron reactions. Hadron formation, by its very nature a nonperturbative process, has often been parameterized from data (e.g., fragmentation functions $D(z)$) or phenomenologically described (e.g., string models) [223]. From QCD one expects that hadron production at high transverse momentum is dominated by hard scattering of partons followed by fragmentation into "jets" or "mini-jets" of hadrons. Following the assumptions of collinear factorization, the fragmentation functions should be universal. This universality has proved a powerful tool in comparing e^+e^- annihilation to hadron-hadron reactions. One feature of jet fragmentation is that baryons and antibaryons are always suppressed relative to mesons at a given p_T [224,225]. Phenomenologically this can be thought of as a large penalty for creating a diquark–antidiquark pair for baryon formation vs. a quark–antiquark pair for meson formation.

In hadron–hadron reactions, hard scattering followed by fragmentation is considered to be the dominant process of hadron production for particles with $p_T \geqslant 2$ GeV/c at mid-rapidity. At low transverse momentum, where particles have $p_T < 2$ GeV/c, particle interactions are often referred to as "soft". In small momentum transfer reactions the effective wavelength of interactions is longer than the spacing of individual partons in a nucleon or nucleus. Thus coherence effects are expected to result in large violations of factorization and universality of fragmentation functions. Hadron formation mechanisms in this "soft" regime are poorly understood. We are particularly interested in the study of hadron formation in the region of $p_T \approx 2$–5 GeV/c, where production is expected to make the transition from "soft" to "hard" mechanisms.

7.1. Baryons and antibaryons

One of the most striking and unexpected observations in heavy ion reactions at RHIC is the large enhancement of baryons and antibaryons relative to pions at intermediate $p_T \approx 2$–5 GeV/c. As shown in Fig. 44, the (anti)proton to pion ratio is enhanced by almost a factor

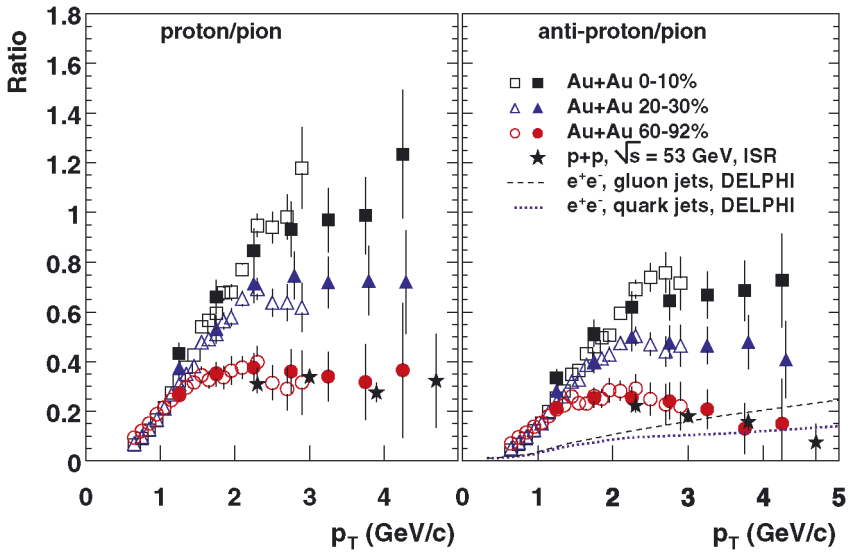

Fig. 44. p/π (left) and $\bar{p}/\pi$ (right) ratios for central (0–10%), mid-central (20–30%) and peripheral (60–92%) Au + Au collisions at $\sqrt{s_{NN}} = 200$ GeV [52]. Open (filled) points are for $\pi^{+/-}$ (π^0), respectively. Data from $\sqrt{s} = 53$ GeV $p + p$ collisions [224] are shown with stars. The dashed and dotted lines are $(\bar{p} + p)/(\pi^+ + \pi^-)$ ratio in gluon and in quark jets [225].

of three when one compares peripheral reactions to the most central gold-gold reactions [52].[8] This of course is in sharp contrast to the suppression of pions in this region.

We can study this (anti)baryon excess at much higher p_T by comparing our inclusive charged spectra (primarily pions, kaons and protons) with our neutral pion measurements [52]. Shown in Fig. 45 is the charged hadron to π^0 ratio as a function of transverse momentum in ten centrality bins. We observe a significant increase of the $(h^+ + h^-)/\pi^0$ ratio above 1.6 in the p_T range 1–5 GeV/c that increases as a function of collision centrality. The ratio of $h/\pi = 1.6$ is the value measured in $p + p$ reactions [224], and is thought to arise from jet fragmentation. In Au + Au central reactions, above $p_T \approx 5$ GeV/c, h/π returns to the $p + p$ measured baseline. This implies that the (anti)baryon excess occurs only in the limited p_T window $\approx$ 2–5 GeV/c, and then returns to the universal fragmentation function expectation.

As discussed in Section 6, pions in this p_T range are suppressed by almost a factor of five relative to binary collision scaling for central Au + Au reactions. Thus, one possible interpretation of the large (anti)proton to pion ratio is that somehow the baryons are not suppressed in a manner similar to the pions. Fig. 46 shows that in fact (anti)proton production appears to follow binary collision scaling over the transverse momentum range $p_T = 2$–5 GeV/c [52]. However, the h/π^0 ratios shown in Fig. 45 imply that above $p_T > 5$ GeV/c, the (anti)protons must be as suppressed as the pions.

[8] All PHENIX (anti)proton spectra shown in this section are corrected for feed down from weak decays.

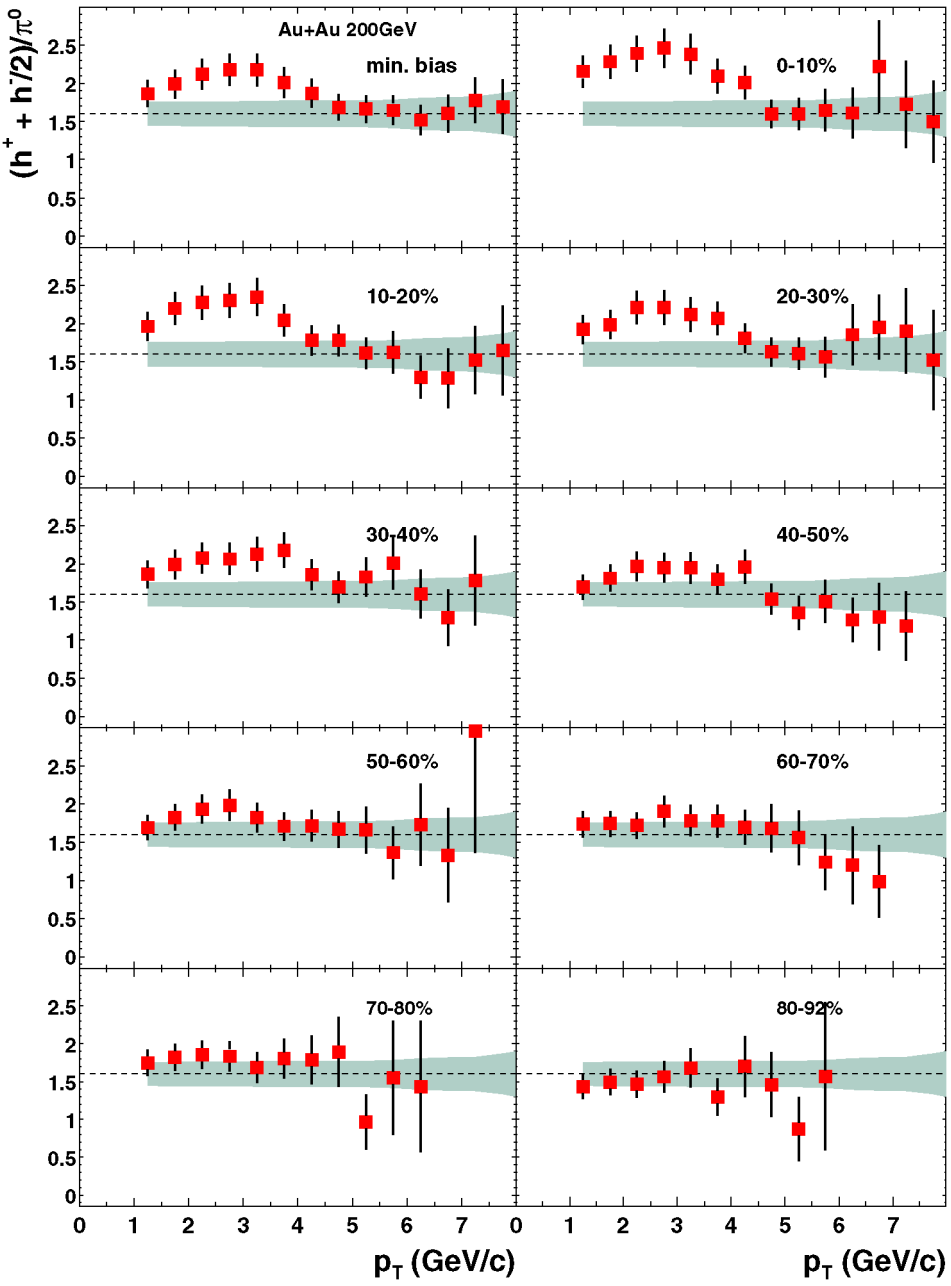

Fig. 45. Charged hadron to π^0 ratio for different centrality classes for Au + Au collisions at $\sqrt{s_{NN}} = 200$ GeV [53]. Error bars represent the quadratic sum of statistical and point to point systematic errors. The shaded band shows the normalization error common to all centrality classes. The line at 1.6 is the h/π ratio measured in $p + p$ collisions at $\sqrt{s} = 53$ GeV [224] and in $e^+ + e^-$ collisions [225].

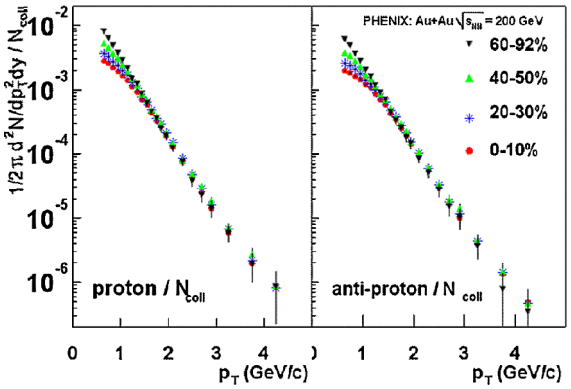

Fig. 46. p and $\bar{p}$ invariant yields scaled by $N_{\rm coll}$ in Au + Au collision at $\sqrt{s_{NN}} = 200$ GeV [52]. Error bars are statistical. Systematic errors on $N_{\rm coll}$ range from $\approx 10\%$ for central to $\approx 28\%$ for 60–92% centrality. Multiplicity dependent normalization errors are $\approx 3\%$.

Characteristics of the intermediate p_T (anti)protons are:

- A large enhancement of the p/π and $\bar{p}/\pi$ ratios in central Au + Au collisions.
- A ratio in peripheral collisions which is in agreement with that from $p + p$ collisions.
- A smooth increase from peripheral to central Au + Au collisions.
- A similar effect for protons and antiprotons.
- Approximate scaling of (anti)proton production at $p_T \approx 2$–4 GeV/c with the number of binary nucleon–nucleon collisions.
- Suppression relative to binary collision scaling similar for (anti)protons and pions for $p_T > 5$ GeV/c.

Large proton to pion ratios have also been observed in heavy ion collisions at lower energies. Fig. 47 shows p_T distributions of protons, antiprotons, and pions in central Pb + Pb collisions at the SPS and in central Au + Au collisions at the AGS. The p/π ratio in central Pb + Pb collisions at the SPS is greater than unity for $p_T \geqslant 1.3$ GeV/c. At the AGS, the proton spectrum crosses pion spectra at $p_T \sim 0.5$ GeV/c, and the p/π ratio is about 20 at $p_T = 1.6$ GeV/c. The p/π ratios in the low-energy heavy-ion collisions are also enhanced compared with $p + p$ collisions at the same energy.

Most of the protons in these lower-energy heavy-ion collisions are not produced in the collision. Rather they are protons from the beam or target nucleus (Pb or Au) that are transported to large p_T at mid-rapidity. As discussed in Section 3, a strong radial flow with velocity $\beta_T \sim 0.5$ is produced in heavy ion collisions at AGS and SPS energies. The large p/π ratio can be interpreted as a result of this radial flow. Since the proton is heavier, a fixed velocity boost results is a larger momentum boost than for pions, and thus enhances p/π ratio at higher p_T. In contrast, at RHIC energies, most of protons are produced particles [40]. The anomalously large antibaryon-to-meson ratio $\bar{p}/\pi \sim 1$ at high $p_T \geqslant 2$ GeV/c is a unique result from RHIC. Such a large $\bar{p}/\pi$ ratio has not been observed in any other collision system. Fig. 47 shows that $\bar{p}/\pi$ is less than ~ 0.1 at the SPS, and it is less than $1/100$ at the AGS. It should also be noted that the measurements from the

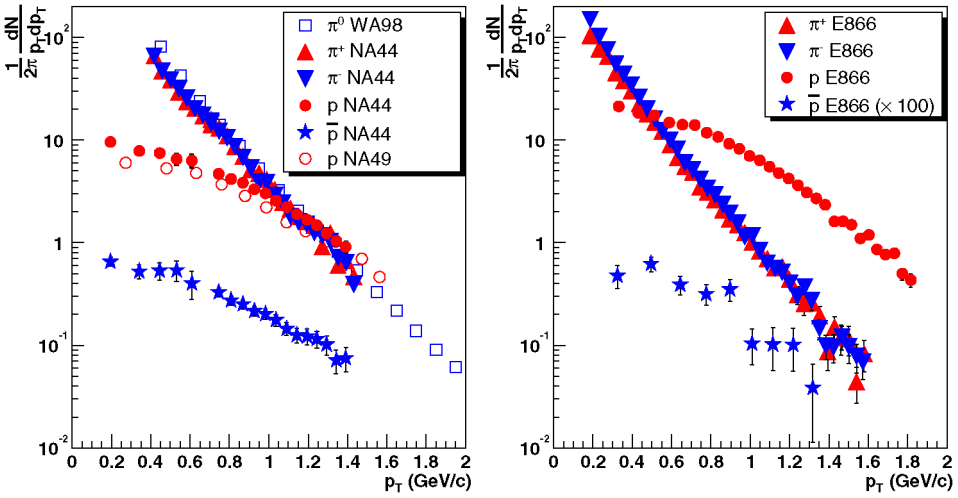

Fig. 47. Invariant yields of p, $\bar{p}$, and π as function of p_T in central Pb + Pb collisions at the SPS ($\sqrt{s_{NN}} = 17$ GeV) (left panel) and in central Au + Au collisions at the AGS ($\sqrt{s_{NN}} = 5$ GeV) (right panel). The $\bar{p}$ spectrum from the AGS is scaled up by a factor 100. All data are at mid-rapidity ($y - y_{\rm cm} \approx 0$) and are from W98 [163], NA44 [226], NA49 [227], and E866 [228,229].

AGS/SPS are limited to lower p_T ($p_T < 2$ GeV/c), where soft physics is still dominant, while at RHIC we observe a large $p(\bar{p})/\pi$ ratio in $p_T \approx 2$–5 GeV/c where hard processes are expected to be the dominant mechanism of particle production.

7.2. The ϕ meson

We have extended our identified hadron studies to include the ϕ vector meson as measured in the K^+K^- decay channel. The ϕ is a meson, and is in that sense similar to the pion with a valence quark and antiquark, yet its mass is comparable to that of the proton.

Fig. 48 shows R_{CP}, the ratio of production in central to peripheral Au + Au collisions scaled by binary collisions, for protons, pions and ϕ mesons detected via its KK decay channel [69] in Au + Au collisions at $\sqrt{s_{NN}} = 200$ GeV. A large suppression of pions at $p_T > 2$ GeV/c is observed (as detailed in Section 6), and a lack of suppression for the protons and antiprotons as expected from Fig. 46. The ϕ follows the suppression pattern of the pions within errors, indicating that the surprising behavior of the protons is not followed by the ϕ. Fig. 49 shows a comparison between the p_T spectral shape for protons and the ϕ in central and peripheral Au + Au reactions. The two spectra agree with each other within errors for the most central events. Thus, although the yields are evolving differently with collision centrality, giving rise to the deviation from unity of R_{CP}, the p_T distributions appear quite similar.

7.3. Jet correlations

A crucial test of the origin for the enhanced (anti)proton to pion ratio is to see if baryons in this intermediate p_T regime exhibit correlations characteristic of the structure

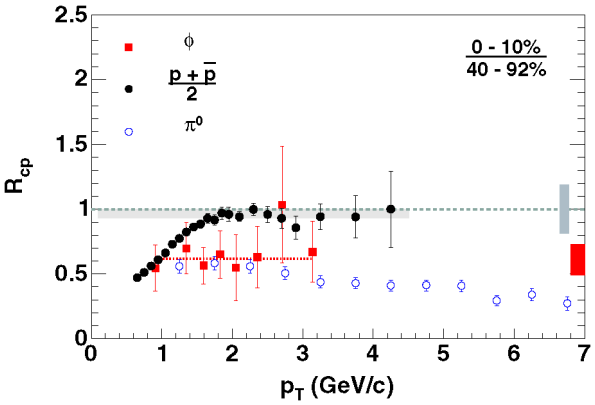

Fig. 48. The R_{CP} of the ϕ as measured in the KK channel, compared to the protons and pions for Au + Au collisions at $\sqrt{s_{NN}} = 200$ GeV [69].

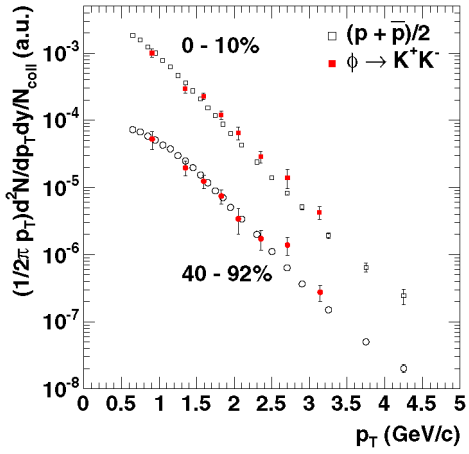

Fig. 49. $(p + \bar{p})$ and ϕ invariant yield as a function of transverse momentum for central 0–10% and peripheral 40–92% Au + Au reactions at $\sqrt{s_{NN}} = 200$ GeV. The two distributions for each centrality class are given an arbitrary relative normalization to allow for comparison of the p_T dependent shapes. Data are from [69].

of jets from hard-scattered partons. Particles which exhibit these correlations are termed "jet-like". Fig. 50 shows the associated partner particle yield within the relative angular range $0.0 < \phi < 0.94$ radians on the same side as trigger baryons and mesons [71]. Correlated pairs are then formed between the trigger particle and other particles within the above mentioned angular range. Mixed events are used to determine the combinatorial (i.e., non-jet-like) background distribution, which is subtracted after accounting for modulation according to the measured v_2.

The partner yield increases for both trigger baryons and mesons by almost a factor of two from deuteron–gold to peripheral and mid-central Au + Au reactions. We then observe a decrease in the jet-like correlations for baryons relative to mesons for the most

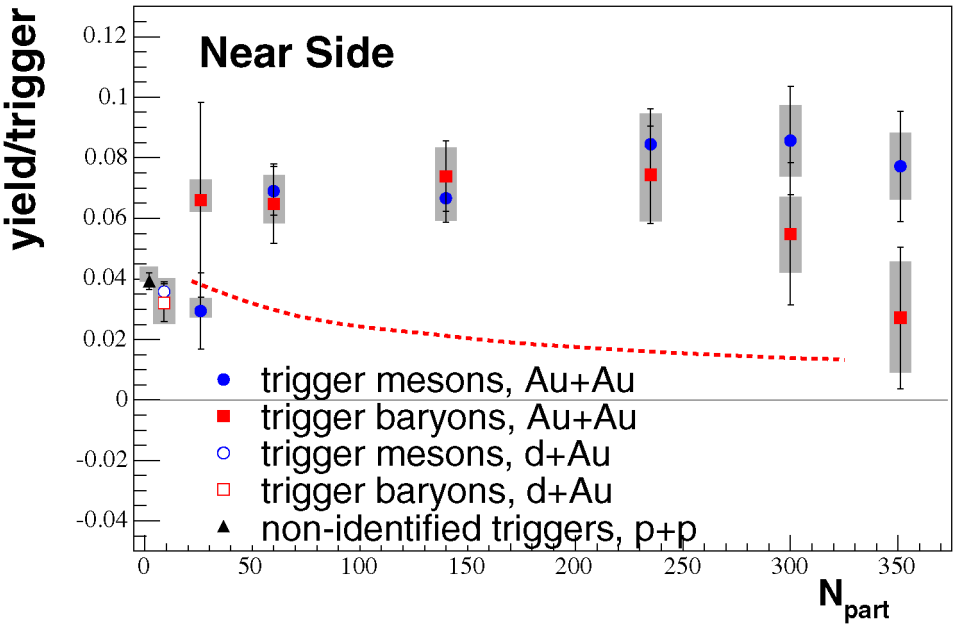

Fig. 50. Centrality dependence of associated charged hadron yield ($1.7 < p_T < 2.5$ GeV/c) above combinatorial background for trigger baryons and trigger mesons in the p_T range 2.5–4.0 GeV/c in a 54° cone around the trigger particle in Au + Au collisions at $\sqrt{s_{NN}} = 200$ GeV [71]. The error bars are statistical errors and the gray boxes are systematic errors. The dashed line represents an upper limit of the centrality dependence of the near-side partner yield from thermal recombination (see text).

central collisions. We note that this observation is of limited significance within our current statistical and systematic errors. Over a broad range of centrality 10–60% the partner yield is the same for protons and pions within errors. This is notable since the (anti)proton to pion ratio has already increased by a factor of two for mid-central Au + Au relative to proton–proton reactions, with the implication that the increase in the p/π ratio is inclusive of the particles with jet-like correlations.

The dashed line in Fig. 50 shows the expected centrality dependence of partners per baryon if all the "extra" baryons which increase the p/π over that in $p + p$ collisions were to arise solely from soft processes. Baryons from thermal quark recombination should have no jet-like partner hadrons and would dilute the per-trigger conditional yield. Because this simple estimate does not allow for meson production by recombination, which must also occur along with baryon production, it represents an upper limit to the centrality dependence of jet partner yield from thermal recombination. The data clearly disagree with both the centrality dependence and also the absolute yields of this estimation, indicating that the baryon excess has the same jet-like origin as the mesons, except perhaps in the highest centrality bin.

The characteristics of the jet-like particles are compared to inclusive hadrons in Fig. 51, which shows the centrality dependence of the p_T distributions of jet-like partners and inclusive hadrons. One can see that, within the available statistics, the slopes of the associated

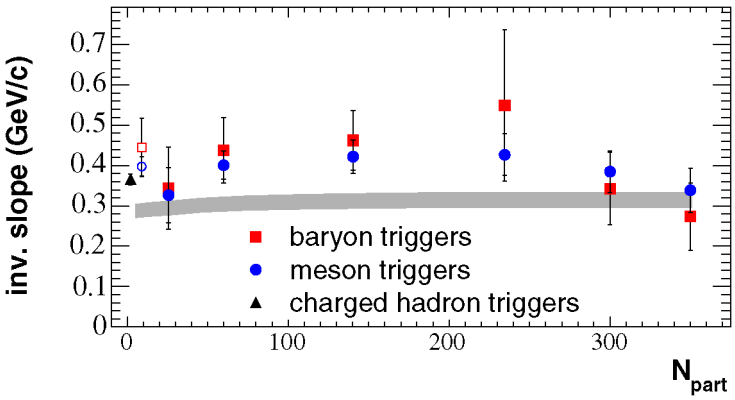

Fig. 51. The inverse slopes for the momentum distributions of the associated particles shown in Fig. 50. The gray band is the inverse slope of the momentum distribution of the inclusive hadrons from Au + Au collisions at $\sqrt{s_{NN}} = 200$ GeV [71].

particle spectra in $p + p$, $d +$ Au, peripheral and mid-central Au + Au collisions are very similar for both trigger mesons and trigger baryons. The partner spectra are harder than the inclusive hadron spectra, as expected from jet fragmentation. In the most central collisions, the number of particles associated with trigger baryons is very small, resulting in large statistical error bars. However, the inverse slopes of the jet-like partners and inclusive hadron distributions agree better in central collisions than in peripheral collisions.

We can then make the following general observations.

- Trigger (anti)protons and mesons have comparable near-side associated-particle yields over a broad range in centrality, indicating a significant jet-like component for both.
- There is an indication that the proton partner yield tends to diminish for the most central collisions, unlike for leading mesons.
- Within the limited statistics available for the measurement, the inverse slopes of the associated particles are similar for both mesons and baryons. These are harder than for the inclusive spectra.
- Trigger particles in Au + Au collisions appear to have *more* associated particles than in $d +$ Au collisions. This is true for all centralities aside from the most peripheral, and except for leading baryons in central collisions.

7.4. Soft physics

As previously noted, hard scattering followed by fragmentation is considered to be the dominant process of hadron production with $p_T \geqslant 2$ GeV/c in hadron–hadron reactions at mid-rapidity. However, as detailed Section 3, there is strong evidence for explosive collective motion of particles in the medium. If the mean free path for particles in the medium is small, then all particles must move with a common local velocity as described by hydrodynamics. Therefore, heavier particles receive a larger momentum boost than lighter

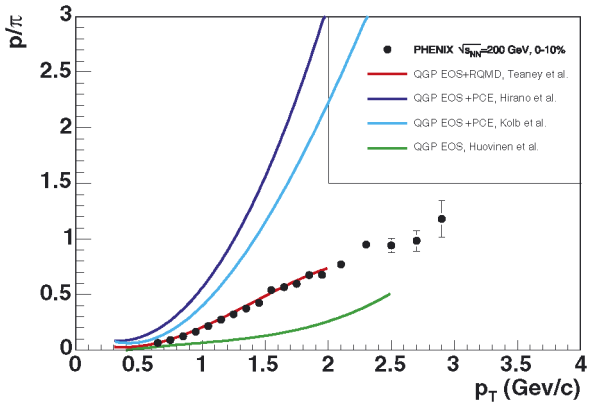

Fig. 52. p/π ratios for central (0–10%) Au + Au collisions at $\sqrt{s_{NN}} = 200$ GeV [52] compared to hydrodynamic models [106,107,117–119].

particles. This effective shifting of particles to higher p_T results in a "shoulder-arm" shape for the (anti)proton p_T spectra, visible in Fig. 49.

7.4.1. Hydrodynamics

Is it possible that this soft hadron production extends to higher p_T for baryons than mesons? Hydrodynamic boosting of "soft" physics for heavier particles into the $p_T > 2$ GeV/c offers a natural explanation for the enhanced p/π and $\bar{p}/\pi$ ratios [106].

As seen in Section 3, some hydrodynamical models can describe both the proton and the pion spectra. Consequently, the p/π ratio is also reproduced (Fig. 52). It is clear that the description of the p/π ratio is not unique and different calculations yield quite different results. Above some p_T, hydrodynamics should fail to describe the data and fragmentation should dominate. Pure hydrodynamics predicts that this ratio would continue to increase essentially up to $p_T \to \infty$. However, these particles cannot have a zero mean free path in the medium. Any finite mean free path and a finite volume will limit the number of p_T "kicks" a particle can receive. For this reason many of the hydrodynamic calculations are not extended into the p_T region 2–5 GeV/c in which we are interested.

Hydrodynamic calculations do not specify the quanta that flow; rather they assume an equation of state. When applied at RHIC, most calculations start with a quark–gluon-plasma equation of state and transition to a resonance gas. The mapping of the fluid onto hadrons is somewhat ad hoc, and often uses the Cooper–Frye freezeout [126], giving the typical hierarchies of momenta one sees where heavier particles receive a larger boost.

As mentioned previously, this generic feature of a transverse velocity boost yielding an increase in the baryon to meson ratio relative to proton–proton reactions is not unique to RHIC as shown in Fig. 47. However, a major difference between lower-energy results and those at $\sqrt{s_{NN}} = 200$ GeV is that at these highest energies there is a significant hard-process contribution. If the source of the excess baryons is the transport of soft baryons to the intermediate p_T range, then it is purely coincidental that the baryons scale with binary collisions. More importantly, we should expect a significant decrease in the jet-like partner yield for baryons relative to mesons. Although there may be a hint of this for the

most central reactions, one expects this decrease to follow the centrality dependence of the increase in p/π ratio. Thus, this effect should already reduce the partner yield by a factor of two in mid-central Au + Au reactions. This is ruled out by the data.

7.4.2. Recombination models

The quark recombination or coalescence model is a different physics framework in which baryons receive a larger p_T boost than mesons. These models were frequently invoked in the 1970s [230,231] in an attempt to describe the rapidity distribution of various hadronic species in *hadron–hadron* reactions. More recently, these models have been applied to describe the forward charm hadron production in *hadron–nucleus* reactions at Fermilab [232]. In this case they calculate a significant probability for D meson formation from a hard-scattering-created charm quark with a light valence quark in the projectile. The quark coalescence mechanisms have some similarities to light nuclei coalescence. However, wave functions are relatively well determined for light nuclei, whereas the hadron wave functions are neither easily described by partons nor directly calculable from QCD.

Recently, quark recombination has been successfully applied to describe a number of features of heavy ion collisions [233,234] (Duke model). In this picture, quarks in a densely populated phase space combine to form the final-state hadrons. This model uses the simplifying assumption that the mass is small relative to the momentum giving a prediction largely independent of the final hadron wave function.[9] The coalescing parton distribution was assumed to be exponential, i.e., thermal, and recombination applied for hadrons where $m^2/p_T^2 \ll 1$. At very high p_T particles are assumed to arise from fragmentation of hard partons with a standard power law distribution; the relative normalization of the thermal source with respect to this process is an important external parameter to the model. A crucial component of recombination models is the assumption that the partons which recombine carry a mass which is essentially equal to the mass of the dressed constituent quarks.[10] If all observables of intermediate p_T hadrons can be explained by recombination of only thermal quarks, this would essentially prove the existence of a quark–gluon plasma in the early stage of the collisions.

Three essential features are predicted by recombination models. First, baryons at moderate p_T are greatly enhanced relative to mesons as their transverse momentum is the sum of 3 quarks rather than 2. Recombination dominates over parton fragmentation in this region, because, for an exponential spectrum recombination is a more efficient means of producing particles at a particular p_T. This enhancement should return to its fragmentation values at higher p_T. In the intermediate range, all mesons should behave in a similar manner regardless of mass, as should all baryons. Secondly, recombination predicts that the collective flow of the final-state hadrons should follow the collective flow of their constituent quarks. Finally, recombination causes thermal features to extend to higher transverse momentum, $p_T \gg T_C$ than one might naively expect since the underlying thermal spectrum of the con-

[9] The recombination model prediction of these models is independent of the final hadron wave function with an accuracy of about 20% for protons and 10% for pions.

[10] The actual source of this mass is under discussion. It may be that the chiral phase transition is slightly above the deconfinement transition. In this case, the mass would be from the dressing of the quarks. Another possibility is that the mass is a thermal mass which happens to be similar to the constituent quark mass.

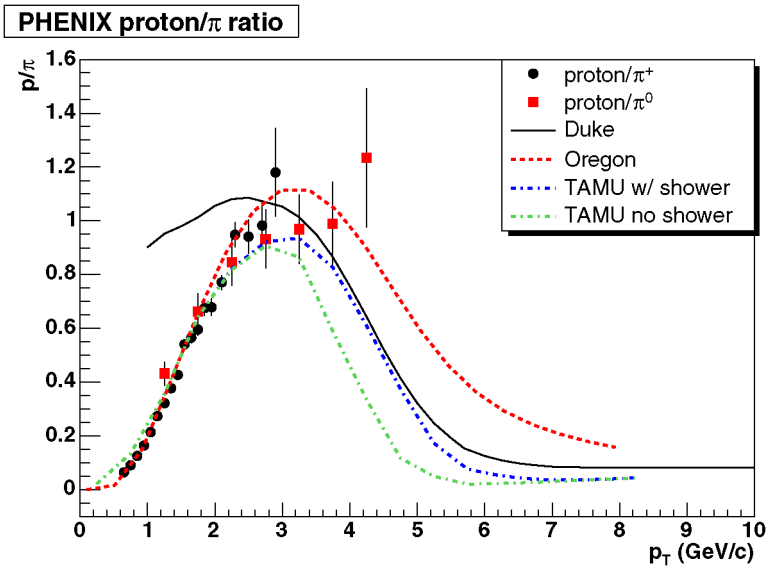

Fig. 53. The proton to pion ratio measured by PHENIX for Au + Au collisions at $\sqrt{s_{NN}} = 200$ GeV [52]. Several comparisons to recombination models as mentioned in the text are shown.

stituents gets a multiplication factor of essentially 3 for baryons and 2 for mesons. A last general feature which is true for the simplest of the models, but may not necessarily be true for more complex models, is that at intermediate p_T, recombination is the dominant mechanism for the production of hadrons—particularly of baryons.

Other recombination calculations have relaxed the assumptions previously described, at the cost of much more dependence on the particular form of the hadronic wave function used. One such calculation [235,236] (Oregon model) uses a description of hadronization which assumes that all hadrons—including those from fragmentation—arise from recombination. Hard partons are allowed to fragment into a shower of partons, which can in turn recombine—both with other partons in the shower and partons in the thermal background. Another model [237] (TAMU model) uses a Monte Carlo method to model the production of hadrons allowing recombination of hard partons with thermal partons, and includes particle decays, such as $\rho \to 2\pi$ which produces low-p_T pions.

Fig. 53 shows several recombination model calculations compared to the p/π ratio from PHENIX. The general features at $p_T > 3$ GeV/c are reasonably reproduced—that is the protons show a strong enhancement at moderate p_T which disappears at $p_T > 5$ GeV/c consistent with the measured h/π ratio shown in Fig. 45. The more complicated models do a better job, as one might expect in the $p_T < 3$ GeV/c region, where the assumptions made by the Duke model begin to break down. Since the recombination model's essential ingredient is the number of constituent quarks in a hadron, the similarity of R_{CP} for the ϕ and pions is nicely explained.

Fig. 54 shows the fraction of hadrons arising from recombination of only thermal quarks, as a function of p_T. For p_T between 2.5 and 4 GeV/c the fraction of protons from recombination is greater than 90% for all impact parameters, and is essentially 100%

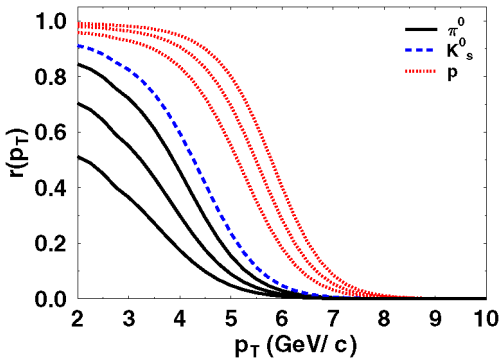

Fig. 54. The ratio $r(P_T) = R/(R+F)$ of recombined hadrons to the sum of recombination (R) and fragmentation (F) for pions (solid), K^0s (dashed) and p (dotted lines) [234] in Au + Au collisions at $\sqrt{s_{NN}} = 200$ GeV. For protons and pions different impact parameters $b = 0$, 7.5 and 12 fm (from top to bottom) are shown. K^0s is for $b = 0$ fm only.

for the most central collisions. For pions the value is between 40 and 80%, depending on the centrality. This is contradicted by the data in Fig. 50 which clearly shows jet-like correlations for both pions and protons in mid-central collisions. It should be noted that the yield of particles associated with baryons in very central collisions appears to decrease, indicating a possible condition where the simple picture of recombination of purely thermal quarks may apply.

One can examine the general prediction for the elliptic flow of identified particles by rescaling both the v_2 and the transverse momentum by the number of constituent quarks as shown in Fig. 55. This scaling was first suggested by Voloshin [238]. Above p_T/n of 1 GeV/c (corresponding to 3 GeV/c in the proton transverse momentum) all particles essentially plateau at a value of about 0.35 presumably reflecting the elliptic flow of the underlying partons. Interestingly, even at lower values of the transverse momentum, all particles also fall on the same curve aside from pions.

It is clear from the jet correlations observed that the majority of moderate p_T baryons in peripheral and mid-central collisions cannot arise from a purely thermal source, as that would dilute the per-trigger partner yield. The jet structure and collision scaling indicate that at least some of the baryon excess is jet-like in origin. The relatively short formation time for baryons of such momenta suggests that allowing recombination of fragmentation partons with those from the medium may solve the problem and better reproduce the data. Both the Oregon and TAMU models have mechanisms to do this. However, such modification of the jet fragmentation function must also modify the elliptic flow, and could break the quark scaling needed to reproduce the observed v_2 trends. Hence, the jet structure of hadrons at 2–5 GeV/c p_T presents a challenge to models of the hadron formation.

Fig. 56 shows a comparison of the elliptic flow calculated by the TAMU model [241] with PHENIX data from Au + Au collisions at $\sqrt{s_{NN}} = 200$ GeV. The model includes the recombination of hard and soft partons, as well as the decay of resonances such as the ρ. In this model, at least, the agreement of v_2 with the data is preserved—in addition a simple explanation is given for the excess of pion v_2 at low p_T. A similar conclusion in shown

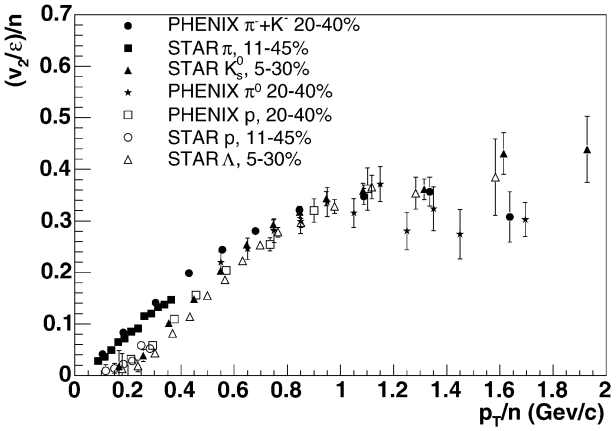

Fig. 55. v_2 as a function of transverse momentum for a variety of particles for Au + Au collisions where both v_2 and p_T have been scaled by the number of constituent quarks in the particle. The meson data are shown with filled symbols; $\pi^- + K^-$ from PHENIX at $\sqrt{s_{NN}} = 200$ GeV [50] (filled circles), charged π from STAR at $\sqrt{s_{NN}} = 130$ GeV [103] (filled squares), K_s^0 from STAR at $\sqrt{s_{NN}} = 200$ GeV [239] (filled triangles), and π^0 from PHENIX at $\sqrt{s_{NN}} = 200$ GeV [240] (filled stars). While the baryons are shown with open symbols; p from PHENIX at $\sqrt{s_{NN}} = 200$ GeV [50] (open squares), p from STAR at $\sqrt{s_{NN}} = 130$ GeV [103] (open circles), and Λ from STAR at $\sqrt{s_{NN}} = 200$ GeV [239] (open triangles).

in [242]. This would seemingly attribute all the elliptic flow to the partonic phase leaving no room for additional flow to be produced in the later, hadronic stage—which may be in contradiction to hydrodynamic interpretations of the hadronic state as demanded by a variety of signatures such as the p_T spectra of the protons and pions (see Section 3). It is clear that a more comprehensive comparison of observables should be undertaken to check the validity of these models. Higher-statistics jet studies with different identified particles by PHENIX in Run-4 will help clarify the situation.

7.5. Hadron formation time

In the discussion of the suppression of pions for $p_T > 2$ GeV/c, we treat the pions as resulting from the fragmentation of hard-scattered quarks and gluons. The explanation of this suppression in terms of partonic energy loss assumes that the hadronic wave function only becomes coherent outside the medium. Protons have a different hadronic structure and larger mass, and so may have a different, shorter time scale for coherence.

Following [220], we can estimate the formation time for the different mass hadrons at moderate p_T in two different ways. According to the uncertainty principle, the formation time in the rest frame of the hadron can be related to the hadron size, R_h. In the laboratory frame, the hadron formation time is then given by

$$\tau_f \approx R_h \frac{E_h}{m_h}, \tag{33}$$

where R_h is taken to be 0.5–1 fm. For a 10 GeV/c pion, this gives a formation time of 35–70 fm/c. For the $p_T = 2.5$ GeV/c pions considered in this section, the formation time

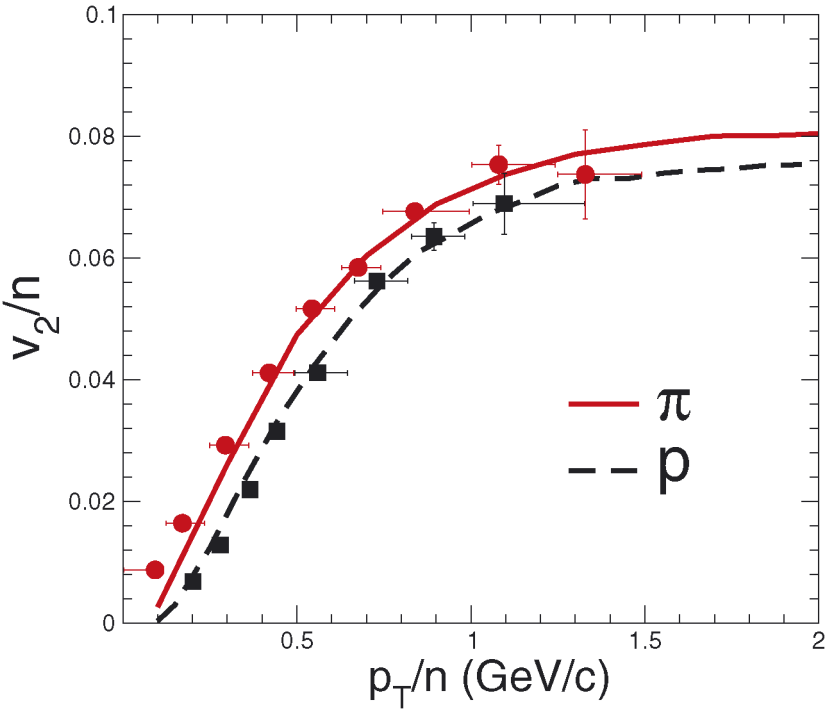

Fig. 56. v_2/n in the TAMU model, where n is the number of constituent quarks in a particle for protons and pions [241]. Scaled pion (dashed line) and proton (dotted line) results from the TAMU model are shown in addition to charged pion and proton measurements from the PHENIX experiment from minimum bias Au + Au reactions at $\sqrt{s_{NN}} = 200$ GeV [50]. This model allows for the recombination of hard partons and soft partons, as well as the decay of resonances such as the two pion decay of the ρ meson. One sees that, at least in this calculation, the addition of processes which mix hard and soft partons do not destroy the agreement for the model with v_2/n which is presumably a soft process.

is 9–18 fm/c, well outside the collision region. However for $p_T = 2.5$ GeV/c protons, the corresponding formation time is only 2.7 fm/c in the vacuum, suggesting the possibility that the hadronization process may begin inside the medium. However the formation of such heavy particles would presumably be delayed in a deconfined medium until the entire system began to hadronize.

If quarks and antiquarks from gluon splitting are assumed to combine into dipole color singlets leading to the final hadrons, the formation time may be estimated from the gluon emission time. Then the formation time for a hadron carrying a fraction z of the parton energy is given by

$$\tau_f \approx \frac{2E_h(1-z)}{k_T^2 + m_h^2}. \tag{34}$$

If z is 0.6–0.8 and $k_T \approx \Lambda_{\mathrm{QCD}}$, proton formation times in the range of 1–4 fm result [220]. Such values again imply formation of the proton within the medium. Thus, it is possible that differing (and perhaps complicated) interactions with the medium may produce differ-

ent scalings of proton and pion production and result in modified fragmentation functions in Au + Au collisions. However, most expectations are that this should lead to greater suppression rather than less. In fact, modified fragmentation functions measured in electron deep-inelastic scattering on nuclei by the HERMES experiment are often interpreted in terms of additional suppression for hadrons forming in the nuclear material.

7.6. Hard-scattering physics

If the dominant source of (anti)protons at intermediate p_T is not soft physics, is the explanation a medium-modified hard-process source? The near-side partner yields indicate that a significant fraction of the baryons have jet-like partners. However, in the parton energy loss scenario as described in Section 6, hard-scattered partons lose energy in medium prior to hadronization. Thus one would expect the same suppression for baryons and mesons. Furthermore, we know that the (anti)protons are as suppressed above $p_T = 5$ GeV/c in a manner similar to pions. Hence for this explanation to be correct, there must exist a mechanism by which only partons leading to baryons between 2 and 5 GeV/c in p_T escape suppression.

Another key piece of information is that the elliptic flow v_2 for protons is large for p_T in the range 2–4 GeV/c. At low p_T this collective motion is attributed to different pressure gradients along and perpendicular to the impact parameter direction in semi-central collisions. At higher p_T it has been hypothesized that one could observe a v_2 due to smaller partonic energy loss for partons traveling along the impact parameter direction (shorter path in the medium) as opposed to larger partonic energy loss in the perpendicular direction (larger path in the medium). However, the data suggest that the pions have a large energy loss (a factor of five suppression in central Au + Au reactions), while the protons do not. In this case one might expect that if the source of proton v_2 were energy loss, then proton v_2 would be significantly less than the v_2 for the pions. In fact, the opposite is experimentally observed: for $p_T > 2$ GeV/c, the proton v_2 is always larger than the pion v_2.

The contradictions the data create for both the “soft”- and “hard”-physics explanations may indicate that the correct physics involves an interplay between the two.

7.7. Conclusions

The anomalous enhancement of (anti)protons relative to pions at intermediate $p_T = 2$–5 GeV remains a puzzle. At lower transverse momentum particle production is a long-wavelength “soft” process and the transport of these hadrons and their precursor partons is reasonably described by hydrodynamics. As observed at lower energies, soft particles emitted from an expanding system receive a collective velocity boost to higher p_T resulting in an enhanced p/π and $\bar{p}/\pi$ ratio relative to proton–proton reactions at the same energy. We observe a similar phenomena at RHIC, for which the (anti)proton spectra and v_2 are roughly described in some hydrodynamic models up to approximately 2 GeV/c. Another class of calculations, referred to as recombination models, also boosts soft physics to higher p_T by coalescence of “dressed” partons. In the hydrodynamic models the quanta which are flowing are initially partons and then hadrons. The recombination models de-

scribe comoving valence partons which coalesce into hadrons, and do not reinteract. These two points of view may not be entirely contradictory, since both include a flowing partonic phase. In fact, it may be that the recombination models provide a mechanism by which hydrodynamics works to a much higher p_T than one might expect. The simplifying assumption of hadrons which do not interact is most probably an oversimplification and further refinement of the models will include this, though it may be that the hadronic phase will not modify the spectra as much as the hydrodynamic models might predict.

In both models, the (anti)proton enhancement as a function of centrality can be tuned to reproduce the apparent binary collision scaling observed in the data. An important distinction between the two is that in one case this enhancement is mass dependent and in the other it comes from the combination of quark momenta and thus distinguishes between baryons and mesons.[11] R_{CP} for the ϕ is similar to other mesons despite the fact that they are more massive than protons. This scaling with quark content, as opposed to mass, favors recombination models.

Further investigations into these intermediate p_T baryons reveals a near-angle correlation between particles, in a fashion characteristic of jet fragmentation. The near-angle associated particle yield increases by almost a factor of two in going from proton–proton and deuteron–gold reactions to gold–gold peripheral collisions. In addition, the partner yield is similar for trigger pions and protons, except in the most central gold–gold reactions. This appears to indicate a hard process source for a significant fraction of these baryons in contrast to the previous mentioned physics scenarios. Quantifying the precise contribution is an important goal for future measurements.

The large (anti)baryon to pion excess relative to expectations from parton fragmentation functions at intermediate $p_T = 2$–5 GeV/c remains one of the most striking unpredicted experimental observations at RHIC. The data clearly indicate a new mechanism other than universal parton fragmentation as the dominant source of baryons and antibaryons at intermediate p_T in heavy ion collisions. The boosting of soft physics, that dominates hadron production at low p_T, to higher transverse momentum has been explored with the context of hydrodynamic and recombination models. However, investigations into these intermediate p_T baryons reveals a near-angle correlation between particles, in a fashion characteristic of jet fragmentation. If instead these baryons have a partonic hard scattering followed by fragmentation source, this fragmentation process must be significantly modified. It is striking that these baryons have a large v_2 (typically 20%) indicative of strong collective motion and also a large "jet-like" near-side partner yield. At present, no theoretical framework provides a complete understanding of hadron formation in the intermediate p_T region.

8. Future measurements

The previous sections have documented the breadth and depth of the PHENIX data from the first three years of RHIC operations, along with the physics implications of those

[11] A caveat to this fact is that in the recombination models, it is the constituent-quark mass that is important, thereby giving a slightly larger mass to the strange quark.

results. Here we describe those measurements required to further define and characterize the state of matter formed at RHIC. In particular, we note that the study of penetrating probes, which are the most sensitive tools in this endeavor, is just beginning. The PHENIX experiment was specifically designed to address these probes with capabilities that are unique within the RHIC program and unprecedented in the field of relativistic heavy ion physics.

One can distinguish two broad classes of penetrating probes.

(1) Hard probes created at the very early stage of the collision which propagate through, and could be modified by, the medium. These are the QCD hard-scattering probes and the main observables are high-p_T particles coming from the fragmentation of jets, hidden charm (J/ψ production), open charm and eventually also bottom quark and Υ production.
(2) Electromagnetic probes (either real or virtual photons) which are created by the medium. Due to their large mean free path these probes can leave the medium without final-state interaction thus carrying direct information about the medium's conditions and properties. The main observables here are low-mass e^+e^- pairs and the thermal radiation of the medium.

By their very nature, penetrating probes are also rare probes and consequently depend on the development of large values of the integrated luminosity. In the present data set the reach for high-p_T particles in PHENIX extends to roughly 10 GeV/c, and lower-cross-section measurements such as charmonium are severely limited. The dramatic improvement of the machine performance in the year 2004 run provides confidence that both this data set and those from future RHIC runs will dramatically extend our reach in the rare probes sector.

As part of a decadal planning of the RHIC operation, PHENIX has prepared a comprehensive document that outlines in great detail its scientific goals and priorities for the next 10 years together with the associated detector upgrade program needed to achieve them. The decadal plan [243] is centered around the systematic study of the penetrating probes listed above. The program is broad and can accommodate additions or modifications provided that a compelling physics case can be made. Measurements are mainly planned in Au + Au collisions at the full RHIC energy but they will be supplemented by other measurements varying the energy and/or the species and by the necessary reference measurements of $p + p$ and $p + A$ collisions. A short summary is given below.

8.1. High-p_T suppression and jet physics

The most exciting results to date at RHIC are the discovery of high-p_T suppression of mesons, interpreted in terms of energy loss of quarks in a high-density medium, and the nonsuppression of baryons or equivalently, the anomalously high p/π ratio which still awaits a clear explanation. These two topics were extensively discussed in Sections 6 and 7, respectively.

The data collected so far are superb. However, they suffer from limited reach in transverse momentum, limited particle identification capabilities and limited statistics in par-

ticular for detailed studies of jet correlations. PHENIX has a program for further studies of the high-p_T-suppression phenomena and jet physics which aims at overcoming these limitations.

It will be necessary to trace the suppression pattern to much higher p_T to determine whether (and if so, when) the suppression disappears and normal perturbative QCD behavior sets in. High-luminosity runs will be needed, with at least a factor of 50 more statistics. PHENIX is particularly able to perform these measurements with its excellent capability of triggering on high-momentum π^0's.

PHENIX has performed several particle correlation analyses and has demonstrated that the experiment's aperture at mid-rapidity is sufficient to conduct these studies. Currently, these analyses are limited by the available statistics. Again, increasing the data sample by a factor of 50–100 will allow a variety of correlation studies using trigger particles with much-higher-momentum than studied to date. A particularly interesting case is the study of high-momentum γ-jet correlations, which have vastly reduced trigger bias, since the trigger photons propagate through the medium with a very long mean free path.

To further elucidate the baryon puzzle, additional data is required with better separation between baryons and mesons. An upgrade consisting of an aerogel Cerenkov counter and a high-resolution TOF detector is expected to be completed in time for the year 2006. A portion of this aerogel counter was already installed prior of the year 2004 run and performed according to expectations. Once completed, this high-p_T detector will allow identification of π, K/p to beyond 8 GeV/c in p_T.

8.2. J/ψ production

Suppression of heavy quarkonia is one of the earliest and most striking proposed signatures of deconfinement. The suppression mechanism follows directly from the Debye screening expected in the medium, which reduces the range of the potential between charm quark and antiquark pairs [244]. The NA38 and NA50 experiments have carried out a systematic study of J/ψ and ψ' at the CERN-SPS in $p+p$, $p+A$, light ion, and Pb + Pb collisions providing some of the most intriguing results of the relativistic heavy ion program for more than ten years. The NA50 experiment observed an anomalous suppression of J/ψ in central Pb + Pb collisions at $\sqrt{s_{NN}} = 17.2$ GeV [245]. The suppression, which is of the order of 25% with respect to the normal suppression in nuclear matter, has been interpreted by the NA50 authors as evidence for deconfinement of quarks and gluons. Although this interpretation is not universally shared [246,247], the results of NA38 and NA50 demonstrate the utility and great interest in understanding the fate of charmonium in dense nuclear matter.

The theoretical expectations at RHIC energies are not at all clear. They range from total suppression in the traditional Debye screening scenario to enhancement in coalescence models [248–250] and in statistical hadronization models [251,252], of c and $\bar{c}$ quarks. Although some versions of the coalescence model seem disfavored from our very limited data set [51], a more conclusive statement on these models has to await the much larger data set of the year 2004 run.

PHENIX has unprecedented capabilities for the study of the J/ψ in Au + Au collisions. The J/ψ can be measured via its $\mu^+\mu^-$ decay channel at forward and backward

rapidities in the muon spectrometers and via its e^+e^- decay channel at mid-rapidity in the central arm spectrometers. From the recorded luminosity of the year 2004 run, we expect several thousand and ~ 500 J/ψ in the muon and central arms, respectively. This data set will allow us a first look at the J/ψ production pattern at RHIC. However, it could well be marginal for a complete characterization as a function of centrality and p_T, so that it is likely that further higher-luminosity runs will be required. Also the $p + p$ and $d +$ Au baseline measurements performed in the year 2001–2003 runs have large statistical uncertainties, and higher-statistics versions for these colliding species will be needed. A high-luminosity $p + p$ run is planned in the year 2005 and high-luminosity $d + A$ or $p + A$ are still to be scheduled in the next years.

8.3. Charm production

Charm quarks are expected to be produced in the initial hard collisions between the incoming partons. The dominant mechanism is gluon fusion and thus the production cross section is sensitive to the gluon density in the initial state. The $c\bar{c}$ production cross section is sizable at RHIC energies with a few $c\bar{c}$ pairs and therefore several open charm mesons per unit of rapidity in central Au + Au collisions. As a result, charm observables become readily accessible at RHIC and offer additional and extraordinarily valuable diagnostic tools. For example, it is vitally important to perform measurements of charm flow and to determine the energy loss of charm quarks in the medium. Such measurements will determine if the bulk dynamics observed for light quarks extend to charm quarks, which could in fact have very different behavior due to their much larger mass. Again the potential of PHENIX in this domain is unique with its capability of measuring open charm in a broad rapidity range, in the central and muon arms, via both the electron and muon decay channels. An additional unique feature is the possibility to measure correlated semileptonic charm decays by detecting e–μ coincidences from correlated $D\bar{D}$ decays. Such a measurement is particularly interesting for the study of charm-quark energy loss which may differ significantly from that observed for lighter quarks [253–255]. A first study of e–μ coincidences should be feasible with the year 2004 data.

To date PHENIX has measured charm production cross section in an indirect way through high-p_T single electrons [42,57] assuming that all electrons (after measuring and subtracting the contributions from light hadrons and photon conversions) originate from the semileptonic decays of charm quarks. Although the charm cross section has large uncertainties, the centrality dependence of the charm rapidity density demonstrates that charm production follows binary scaling as shown in Fig. 34. Improvements and additional information are expected from the much higher statistic of the year 2004 data.

A qualitatively new advance for PHENIX in the charm and also the beauty sector will be provided by the implementation of the silicon vertex detector. An upgrade project is underway to install in the next five years a silicon vertex tracker, including a central arm barrel and two end caps in front of the two muon spectrometers. The vertex tracker will allow us to resolve displaced vertices and therefore to directly identify open charm mesons via hadronic, e.g., $D \to K\pi$, as well as semi-leptonic decays. The heavy-quark physics topics accessible with the vertex tracker include production cross section and energy loss

of open charm and open beauty, and spectroscopy of charmonium and bottomonium states, each of which should provide incisive new details on the properties of the created medium.

8.4. Low-mass dileptons

Low-mass dileptons are considered the most sensitive probe of chiral symmetry restoration primarily through ρ meson decays. Due to its very short lifetime ($\tau = 1.3$ fm/c) compared to that of the typical fireball of ~ 10 fm/c, most of the ρ mesons decay inside the medium providing an unique tool to observe in-medium modifications of its properties (mass and/or width) which could be linked to chiral symmetry restoration. The situation is somewhat different but still interesting for the ω and ϕ mesons. Because of their much longer lifetimes ($\tau = 23$ fm/c and 46 fm/c for the ω and ϕ, respectively) they predominantly decay outside the medium, after regaining their vacuum properties, with only a small fraction decaying inside the medium. Since the measurement integrates over the history of the collision, this may result in a small modification of the line shape of these two mesons which PHENIX might be able to observe with its excellent mass resolution. PHENIX also has the unprecedented capability of simultaneously measuring within the same apparatus the ϕ meson decay through e^+e^- and K^+K^- channels. The comparison of the branching ratios to these two channels provides a very sensitive tool for in-medium modifications of the ϕ and K mesons.

The CERES experiment at CERN has confirmed the unique physics potential of low-mass dileptons [256–258]. An enhancement of electron pairs was observed in the mass region $m = 0.2$–0.6 GeV/c^2 in Pb + Au collisions at $\sqrt{s_{NN}} = 17.2$ GeV with respect to $p + p$ collisions. The results have triggered a wealth of theoretical activity and can be explained by models which invoke in-medium modification of the ρ meson (dropping of its mass and/or broadening of its width) [259]. The precision of the CERES data has been so far insufficient to distinguish between the different models. Results with higher statistics and better mass resolution are expected from the NA60 experiment that is studying the production of low-mass dimuons in In + In collisions [260]. Theoretical calculations [261] show that the enhancement should persist at RHIC energies and that PHENIX with its excellent mass resolution has an unique opportunity to do precise spectroscopy of the light vector mesons and to shed more light on the origin of the enhancement of the low-mass-pair continuum.

The measurement of low-mass electron pairs is however a very challenging one. The main difficulty stems from the huge combinatorial background created by the pairing of e^+ and e^- tracks from unrecognized π^0 Dalitz decays and γ conversions. PHENIX is developing a novel Cerenkov detector that, in combination with the recently installed coil which makes the magnetic field zero close to the beam axis, will effectively reduce this combinatorial background by almost two orders of magnitude [262]. The detector, operated in pure CF_4, consists of a 50-cm-long radiator directly coupled, in a windowless configuration, to a triple GEM detector which has a CsI photocathode evaporated on the top face of the first GEM foil and pad read out at the bottom of the GEM stack [263]. The R&D phase to demonstrate the validity of the concept is nearing completion. The detector construction phase is starting now with installation foreseen in time for the year 2006–2007. With this detector PHENIX will have the unprecedented ability to perform high-quality measure-

ments over the whole dilepton mass range from the π^0 Dalitz decay up to the charmonium states.

8.5. Thermal radiation

A prominent topic of interest in the field of relativistic heavy-ion collisions is the identification of the thermal radiation emitted by the system and in particular the thermal radiation emitted by the quark–gluon plasma via $q\bar{q}$ annihilation. Such radiation is a direct fingerprint of the matter formed and is regarded as a very strong signal of deconfinement. Its spectral shape should provide a direct measurement of the plasma temperature.

In principle the thermal radiation can be studied through real photons or dileptons, since real and virtual photons carry basically the same physics message. In practice the measurements are extremely challenging. The thermal radiation is expected to be a small signal compared to the large background from competing processes, hadron decays for real photons and Dalitz decays and γ conversions for dileptons, the former being larger by orders of magnitude compared to the latter. But in both cases, a very precise knowledge of all these sources is an absolutely necessary prerequisite. After subtracting these sources, one still needs to disentangle other contributions which might be comparable or even stronger, mainly the contributions of initial hard-parton scattering to direct photons and of semileptonic decays of charm mesons to dileptons.

Theoretical calculations have singled out the dilepton mass range $m = 1$–3 GeV$/c^2$ as the most appropriate window where the QGP radiation could dominate over other contributions [264,265]. Measurements in this intermediate mass range carried out at the CERN SPS by HELIOS and NA50 have revealed an excess of dileptons, but this excess could be explained by hadronic contributions [266].

There is no conclusive evidence for QGP thermal photons from the CERN experiments (for a recent review see [267]). From the theoretical point of view it is clear that in the low-p_T region ($p_T < 2$ GeV$/c$) the real photon spectrum is dominated by hadronic sources and the thermal radiation from the hadron gas. It is only in the high-p_T region where one might have a chance to observe the thermal radiation from the QGP.

PHENIX has measured direct real photons at $p_T > 4$ GeV$/c$ from the initial hard scatterings [73]. The errors are relatively large leaving room for a comparable contribution of thermal photons. The high statistics of the year 2004 run will provide the first real opportunity to search for the QGP thermal radiation in PHENIX both in the dilepton and real photon channels. However, the search for this elusive signal might take some time as it will probably require equally-high-statistics runs of reference data in $p + p$ and $p + A$ collisions for a precise mapping of all the other contributions (hadronic + pQCD for real photons and hadronic + charm for dileptons).

9. Summary and conclusions

The PHENIX data set from the first three years of RHIC operation provides an extensive set of measurements, from global variables to hadron spectra to high-p_T physics to heavy-flavor production. From this rich menu we have reviewed those aspects of the present data

that address the broad features of the matter created in Au + Au collisions at RHIC, namely, energy and number density, thermalization, critical behavior, hadronization, and possible deconfinement.

We first investigated whether the transverse energy and multiplicity measurements of PHENIX demonstrate that a state of high-energy-density matter is formed in Au + Au collision at RHIC. We estimated from our $dE_T/d\eta$ measurement that the peak energy density in the form of created secondary particles is at least 15 GeV/fm^3. If we use a thermalization time of 1 fm/c provided by the hydrodynamic models from the elliptic flow, then the value of the energy density of the first thermalized state would be in excess of 5 GeV/fm^3. These values are well in excess of the ~ 1 GeV/fm^3 obtained in lattice QCD as the energy density needed to form a deconfined phase. Naïve expectations prior to RHIC turn-on that $dE_T/d\eta$ and $dN_{\rm ch}/d\eta$ could be factorized into a "soft" and a pQCD jet component are not supported by the data. Results from a new class of models featuring initial-state gluon saturation compare well with RHIC multiplicity and E_T data.

We then examined our data and various theoretical models to investigate the degree to which the matter formed at RHIC appears to be thermalized. The measured yields and spectra of hadrons are consistent with thermal emission from a strongly expanding source, and the observed strangeness production is consistent with predictions based on complete chemical equilibrium. The scaling of the strength of the elliptic flow v_2 with eccentricity shows that a high degree of collectivity is built up at a very early stage of the collision. The hydro models which include both hadronic and QGP phases reproduce the qualitative features of the measured $v_2(p_T)$ of pions, kaons, and protons. These hydro models require early thermalization ($\tau_{\rm therm} \leqslant 1$ fm/c) and high initial energy density $\varepsilon \geqslant 10$ GeV/fm^3. These points of agreement between the data and the hydrodynamic and thermal models can be interpreted as strong evidence for formation of high-density matter that thermalizes very rapidly.

However several of the hydro models fail to reproduce the $v_2(p_T)$ of pions, protons, and spectra of pions and protons simultaneously. Given this disagreement it is not yet possible to make an unequivocal statement regarding the presence of a QGP phase based on comparisons to hydrodynamic calculations. The experimentally measured HBT source parameters, especially the small value of $R_{\rm long}$ and the ratio $R_{\rm out}/R_{\rm side} \approx 1$, are not reproduced by the hydrodynamic calculations. Hence we currently do not have a consistent picture of the space–time dynamics of reactions at RHIC as revealed by spectra, v_2 and HBT. These inconsistencies prevent us from drawing firm conclusions on properties of the matter such as the equation of state and the presence of a mixed phase.

Critical behavior near the phase boundary can produce nonstatistical fluctuations in observables such as the net-charge distribution and the average transverse momentum. Our search for charge fluctuations has ruled out the most naïve model of charge fluctuations in a QGP, but it is unclear if the charge fluctuation signature can survive hadronization. Our measurement of $\langle p_T \rangle$ fluctuations is consistent with the effect expected of high-p_T jets, and it gives a severe constraint on the fluctuations that were expected for a sharp phase transition.

Many of these observables—for instance, large $dE/d\eta$ and $dN_{\rm ch}/d\eta$, strangeness enhancement, strong radial flow, and elliptic flow—have been observed in heavy ion collisions at lower energies. We have found smooth changes in these observables as a function

of $\sqrt{s_{NN}}$ from AGS energies to SPS energies to RHIC energy. The $dE_T/d\eta$ increases by about 100% and the strength of the elliptic flow increase by about 50% from SPS to RHIC. The strangeness suppression factor γ_s and the radial expansion velocity $\langle\beta_T\rangle$ vary smoothly from AGS to RHIC energies. No sudden change with collision energy has been observed.

The strong suppression of high-p_T particle production at RHIC is a unique phenomenon that has not been previously observed. Measurements of two-hadron azimuthal-angle correlations at high p_T and the x_T scaling in Au + Au collisions confirm the dominant role of hard scattering and subsequent jet fragmentation in the production of high-p_T hadrons. Measurements in deuteron–gold collisions demonstrate that any initial-state modification of nuclear parton distributions causes little or no suppression of hadron production for $p_T > 2$ GeV/c at mid-rapidity. This conclusion is further strengthened by the observed binary scaling of direct photon and open charm yields in Au + Au. Combined together, these observations provide direct evidence that Au + Au collisions at RHIC have produced matter at extreme densities.

Medium-induced energy loss, predominantly via gluon bremsstrahlung emission, is the only currently known physical mechanism that can fully explain the magnitude of the observed high-p_T suppression. The approximately flat suppression factor $R_{AA}(p_T)$ observed in the data, which was predicted by the GLV energy loss model, rules out the simplest energy loss models which predicted a constant energy loss per unit length. However, the model by Wang et al. obtains the same flat $R_{AA}(p_T)$ from apparently different physics. From the GLV model, the initial gluon number density, $dn_g/dy \approx 1000$ and initial energy density, $\varepsilon_0 \approx 15$ GeV/fm^3, have been obtained. These values are consistent with the energy density obtained from our $dE_T/d\eta$ measurement as well as ones from the hydro models.

The large (anti)baryon to pion excess relative to expectations from parton fragmentation functions at intermediate p_T (2–5 GeV/c) is both an unpredicted and one of the most striking experimental observation at RHIC. The data demonstrate that a mechanism other than universal parton fragmentation is the dominant source of (anti)baryons in the intermediate p_T range in heavy ion collisions. Explanations based on the boosting of soft physics to higher transverse momentum have been examined within the context of hydrodynamics and recombination models. While hydrodynamic models can readily explain the baryon to meson ratio as a consequence of strong radial flow, these models have difficulties reproducing the difference in v_2 between protons and mesons above 2 GeV/c. In contrast, recombination models provide a natural explanation for the large baryon to meson ratio as well as the apparent quark-number scaling of the elliptic flow. However, the near-angle correlation between particles is characteristic of jet fragmentation. It is truly remarkable that these baryons have a large v_2 of $\approx 20\%$ typically indicative of strong collective motion and also a large jet-like near-side partner yield. At present, no model provides a complete understanding of hadron formation in the intermediate p_T regime.

The initial operation of RHIC has produced the impressive quantity of significant results described above. These striking findings call for additional efforts to define, clarify and characterize the state of matter formed at RHIC. Further study of the collisions using hard probes such as high-p_T particles, open charm, and J/ψ, and electromagnetic probes such as direct photons, thermal photons, thermal dileptons, and low-mass lepton pairs are

particularly important. The utilization of these penetrating probes is just beginning, and we expect these crucial measurements based on the very-high-statistics data of the year 2004 run will provide essential results towards understanding of the dense matter created at RHIC.

Advances in the theoretical understanding of relativistic heavy ion collisions is vital for the quantitative study of the dense matter formed at RHIC. While there is rapid and significant progress in this area, a coherent and consistent picture of heavy ion collisions at RHIC, from the initial formation of the dense matter to the thermalization of the system to the hadronization to the freezeout, remains elusive. With such a consistent model, it will become possible to draw definitive conclusions on the nature of the matter and to quantitatively determine its properties. The comprehensive data sets ranging from global variables to penetrating probes provided by PHENIX at present and in the future will prove essential in constructing and constraining a consistent model of heavy ion collisions to determine the precise nature of the matter created at RHIC.

In conclusion, there is compelling experimental evidence that heavy-ion collisions at RHIC produce a state of matter characterized by very high energy densities, density of unscreened color charges ten times that of a nucleon, large cross sections for the interaction between strongly interacting particles, strong collective flow, and early thermalization. Measurements indicate that this matter modifies jet fragmentation and has opacity that is too large to be explained by any known hadronic processes. This state of matter is not describable in terms of ordinary color-neutral hadrons, because there is no known self-consistent theory of matter composed of ordinary hadrons at the measured densities. The most economical description is in terms of the underlying quark and gluon degrees of freedom. Models taking this approach have scored impressive successes in explaining many, but not all, of the striking features measured to date. There is not yet irrefutable evidence that this state of matter is characterized by quark deconfinement or chiral symmetry restoration, which would be a direct indication of quark–gluon plasma formation. The anticipated program of additional incisive experimental measurements combined with continued refinement of the theoretical description is needed to achieve a complete understanding of the state of matter created at RHIC.

Acknowledgements

We thank the staff of the Collider-Accelerator and Physics Departments at Brookhaven National Laboratory and the staff of the other PHENIX participating institutions for their vital contributions. We acknowledge support from the Department of Energy, Office of Science, Nuclear Physics Division, the National Science Foundation, Abilene Christian University Research Council, Research Foundation of SUNY, and Dean of the College of Arts and Sciences, Vanderbilt University (USA); Ministry of Education, Culture, Sports, Science, and Technology and the Japan Society for the Promotion of Science (Japan); Conselho Nacional de Desenvolvimento Científico e Tecnológico and Fundaçao de Amparo à Pesquisa do Estado de Sao Paulo (Brazil); Natural Science Foundation of China (People's Republic of China); Centre National de la Recherche Scientifique, Commissariat à l'Énergie Atomique, Institut National de Physique Nucléaire et de Physique des Particules, and

Association pour la Recherche et le Développement des Méthodes et Processus Industriels (France); Ministry of Industry, Science and Tekhnologies, Bundesministerium für Bildung und Forschung, Deutscher Akademischer Austausch Dienst, and Alexander von Humboldt Stiftung (Germany); Hungarian National Science Fund, OTKA (Hungary); Department of Atomic Energy and Department of Science and Technology (India); Israel Science Foundation (Israel); Korea Research Foundation and Center for High Energy Physics (Korea); Russian Ministry of Industry, Science and Tekhnologies, Russian Academy of Science, Russian Ministry of Atomic Energy (Russia); VR and the Wallenberg Foundation (Sweden); the US Civilian Research and Development Foundation for the Independent States of the Former Soviet Union; the US–Hungarian NSF-OTKA-MTA; and the US–Israel Binational Science Foundation.

References

[1] G.F. Chapline, M.H. Johnson, E. Teller, M.S. Weiss, Phys. Rev. D 8 (1973) 4302.
[2] T.D. Lee, G.C. Wick, Phys. Rev. D 9 (1974) 2291.
[3] T.D. Lee, Rev. Mod. Phys. 47 (1975) 267.
[4] T.D. Lee, cU-TP-170, Trans. N.Y. Acad. Sci. Ser. 2 40 (1979) 0111.
[5] J.C. Collins, M.J. Perry, Phys. Rev. Lett. 34 (1975) 1353.
[6] N. Itoh, Prog. Theor. Phys. 44 (1970) 291.
[7] E.V. Shuryak, Phys. Rep. 61 (1980) 71.
[8] M. Creutz, Phys. Rev. D 15 (1977) 1128.
[9] K.G. Wilson, Phys. Rev. D 10 (1974) 2445.
[10] E. Laermann, O. Philipsen, Annu. Rev. Nucl. Part. Sci. 53 (2003) 163.
[11] F. Karsch, in: Lecture Notes in Physics, vol. 583, 2002, p. 209.
[12] K. Rajagopal, Acta Phys. Pol. B 31 (2000) 3021.
[13] Z. Fodor, S.D. Katz, JHEP 0404 (2004) 050.
[14] S. Ejiri, et al., Prog. Theor. Phys. Suppl. 153 (2004) 118.
[15] W. Greiner, S. Schramm, E. Stein, Quantum Chromodynamics, second ed., Springer-Verlag, Berlin, 2002.
[16] V.V. Klimov, Sov. Phys. JETP 55 (1982) 199.
[17] H.A. Weldon, Phys. Rev. D 26 (1982) 1394.
[18] S. Datta, F. Karsch, P. Petreczky, I. Wetzorke, Nucl. Phys. B (Proc. Suppl.) 119 (2003) 487.
[19] M. Asakawa, T. Hatsuda, Phys. Rev. Lett. 92 (2004) 012001.
[20] S. Datta, F. Karsch, P. Petreczky, I. Wetzorke, Phys. Rev. D 69 (2004) 094507.
[21] F. Karsch, et al., Nucl. Phys. A 715 (2003) 701.
[22] E.V. Shuryak, I. Zahed, Phys. Rev. D 70 (2004) 054507.
[23] B. Müller, private communication, 2004.
[24] E. Shuryak, Prog. Part. Nucl. Phys. 53 (2004) 273.
[25] M. Gyulassy, L. McLerran, Nucl. Phys. A 750 (2005) 30.
[26] G. Baym, in: M. Jacob, H. Satz (Eds.), Proceedings of the Bielefeld Workshop on Quark Matter Formation and Heavy Ion Collisions, 1982.
[27] M. Plümer, S. Raha, R. Weiner, Nucl. Phys. A 418 (1984) 549c.
[28] B. Müller, nucl-th/9211010.
[29] K. Kajantie, M. Laine, K. Rummukainen, Y. Schröder, Phys. Rev. D 67 (2003) 105008.
[30] A.D. Linde, Phys. Lett. B 96 (1980) 289.
[31] D.J. Gross, R.D. Pisarski, L.G. Yaffe, Rev. Mod. Phys. 53 (1981) 43.
[32] Bear-Mountain, nearly the entire history of the various experimental efforts is documented in the proceedings of the various "Quark Matter" conferences, which began in 1981. A seminal document in the history of the field is the report of the "Bear Mountain" conference: Report of the Workshop on BeV/Nucleon Collisions of Heavy Ions—How and Why, Bear Mountain, New York, 29 November–1 December 1974, BNL-AUI, 1975.

[33] G. Baym, Nucl. Phys. A 698 (2002) xxiii.
[34] NSAC, 2002 NSAC Long-Range Plan: Opportunities in Nuclear Science, A Long-Range Plan for the Next Decade, April 2002, available from http://www.sc.doe.gov/henp/np/nsac/nsac.html, 2002.
[35] PHENIX Collaboration, PHENIX ≡ Pioneering High Energy Nuclear Interaction eXperiment. Full details are available from http://www.phenix.bnl.gov/, 2004.
[36] PHENIX, PHENIX Conceptual Design Report 1993 (PX20, BNL48922, internal report) 1993.
[37] K. Adcox, et al., Phys. Rev. Lett. 86 (2001) 3500.
[38] K. Adcox, et al., Phys. Rev. Lett. 87 (2001) 052301.
[39] K. Adcox, et al., Phys. Rev. Lett. 88 (2002) 022301.
[40] K. Adcox, et al., Phys. Rev. Lett. 88 (2002) 242301.
[41] K. Adcox, et al., Phys. Rev. Lett. 88 (2002) 192302.
[42] K. Adcox, et al., Phys. Rev. Lett. 88 (2002) 192303.
[43] K. Adcox, et al., Phys. Rev. Lett. 89 (2002) 092302.
[44] K. Adcox, et al., Phys. Rev. Lett. 89 (2002) 082301.
[45] K. Adcox, et al., Phys. Rev. C 66 (2002) 024901.
[46] K. Adcox, et al., Phys. Rev. Lett. 89 (2002) 212301.
[47] K. Adcox, et al., Phys. Lett. B 561 (2003) 82.
[48] K. Adcox, et al., Phys. Rev. C 69 (2004) 024904.
[49] S.S. Adler, et al., Phys. Rev. Lett. 91 (2003) 072301.
[50] S.S. Adler, et al., Phys. Rev. Lett. 91 (2003) 182301.
[51] S.S. Adler, et al., Phys. Rev. C 69 (2004) 014901.
[52] S.S. Adler, et al., Phys. Rev. Lett. 91 (2003) 172301.
[53] S.S. Adler, et al., Phys. Rev. C 69 (2004) 034910.
[54] S.S. Adler, et al., Phys. Rev. C 69 (2004) 034909.
[55] S.S. Adler, et al., Phys. Rev. Lett. 93 (2004) 092301.
[56] S.S. Adler, et al., Phys. Rev. Lett. 93 (2004) 152302.
[57] S.S. Adler, et al., Phys. Rev. Lett. 94 (2004) 082301.
[58] S.S. Adler, et al., Phys. Rev. Lett. 94 (2005) 122302.
[59] S.S. Adler, et al., Phys. Rev. C 71 (2005) 034908;
S.S. Adler, et al., Phys. Rev. C 71 (2005) 049901, Erratum.
[60] S.S. Adler, et al., Phys. Rev. Lett. 91 (2003) 241803.
[61] S.S. Adler, et al., Phys. Rev. Lett. 92 (2004) 051802.
[62] S.S. Adler, et al., Phys. Rev. Lett. 93 (2004) 202002.
[63] S.S. Adler, et al., Phys. Rev. D 71 (2005) 071102.
[64] S.S. Adler, et al., Phys. Rev. Lett. 91 (2003) 072303.
[65] S.S. Adler, et al., Phys. Rev. Lett. 94 (2004) 082302.
[66] I. Arsene, et al., Phys. Rev. Lett. 91 (2003) 072305.
[67] B.B. Back, et al., Phys. Rev. Lett. 91 (2003) 072302.
[68] J. Adams, et al., Phys. Rev. Lett. 91 (2003) 072304.
[69] S.S. Adler, et al., nucl-ex/0410012.
[70] S.S. Adler, et al., nucl-ex/0411040.
[71] S.S. Adler, et al., nucl-ex/0408007.
[72] S.S. Adler, et al., nucl-ex/0502009.
[73] S.S. Adler, et al., nucl-ex/0503003.
[74] J.D. Bjorken, Phys. Rev. D 27 (1983) 140.
[75] L. Ahle, et al., Phys. Lett. B 332 (1994) 258.
[76] T. Alber, et al., Phys. Rev. Lett. 75 (1995) 3814.
[77] A. Krasnitz, Y. Nara, R. Venugopalan, Nucl. Phys. A 717 (2003) 268.
[78] P.F. Kolb, J. Sollfrank, U.W. Heinz, Phys. Rev. C 62 (2000) 054909.
[79] S.-Y. Li, X.-N. Wang, Phys. Lett. B 527 (2002) 85.
[80] B.B. Back, et al., Phys. Rev. Lett. 85 (2000) 3100.
[81] X.-N. Wang, M. Gyulassy, Phys. Rev. Lett. 86 (2001) 3496.
[82] V. Topor Pop, et al., Phys. Rev. C 68 (2003) 054902.
[83] D. Kharzeev, M. Nardi, Phys. Lett. B 507 (2001) 121.

[84] D. Kharzeev, E. Levin, Phys. Lett. B 523 (2001) 79.
[85] K.J. Eskola, K. Kajantie, P.V. Ruuskanen, K. Tuominen, Nucl. Phys. B 570 (2000) 379.
[86] K.J. Eskola, P.V. Ruuskanen, S.S. Rasanen, K. Tuominen, Nucl. Phys. A 696 (2001) 715.
[87] F. Becattini, Z. Phys. C 69 (1996) 485.
[88] F. Becattini, U.W. Heinz, Z. Phys. C 76 (1997) 269 (e).
[89] P. Braun-Munzinger, K. Redlich, J. Stachel, nucl-th/0304013.
[90] M. Kaneta, N. Xu, nucl-th/0405068.
[91] J. Cleymans, B. Kampfer, M. Kaneta, N. Wheaton, S. Xu, Phys. Rev. C 71 (2005) 054901.
[92] J. Adams, et al., Phys. Rev. Lett. 92 (2004) 182301.
[93] P. Braun-Munzinger, D. Magestro, K. Redlich, J. Stachel, Phys. Lett. B 518 (2001) 41.
[94] D. Magestro, J. Phys. G 28 (2002) 1745.
[95] F. Becattini, M. Gazdzicki, A. Keranen, J. Manninen, R. Stock, Phys. Rev. C 69 (2004) 024905.
[96] E. Schnedermann, J. Sollfrank, U.W. Heinz, Phys. Rev. C 48 (1993) 2462.
[97] G. Rai, Nucl. Phys. A 681 (2001) 181.
[98] H. Dobler, J. Sollfrank, U.W. Heinz, Phys. Lett. B 457 (1999) 353.
[99] C. Alt, et al., J. Phys. G 30 (2004) S119.
[100] T. Peitzmann, Eur. Phys. J. C 26 (2003) 539.
[101] M.M. Aggarwal, et al., Phys. Rev. C 67 (2003) 014906.
[102] J. Adams, et al., Phys. Rev. Lett. 92 (2004) 112301.
[103] C. Adler, et al., Phys. Rev. Lett. 87 (2001) 182301.
[104] C. Alt, et al., Phys. Rev. C 68 (2003) 034903.
[105] G. Agakichiev, et al., Phys. Rev. Lett. 92 (2004) 032301.
[106] D. Teaney, J. Lauret, E.V. Shuryak, nucl-th/0110037.
[107] P. Huovinen, P.F. Kolb, U.W. Heinz, P.V. Ruuskanen, S.A. Voloshin, Phys. Lett. B 503 (2001) 58.
[108] D.H. Rischke, M. Gyulassy, Nucl. Phys. A 597 (1996) 701.
[109] G.F. Bertsch, Nucl. Phys. A 498 (1989) 173c.
[110] S. Pratt, Phys. Rev. D 33 (1986) 1314.
[111] S. Pratt, Phys. Rev. Lett. 53 (1984) 1219.
[112] A.N. Makhlin, Y.M. Sinyukov, Z. Phys. C 39 (1988) 69.
[113] S. Pratt, T. Csoergoe, J. Zimanyi, Phys. Rev. C 42 (1990) 2646.
[114] J. Adams, et al., Phys. Rev. Lett. 93 (2004) 012301.
[115] F. Retiere, J. Phys. G 30 (2004) S827.
[116] M. Csanad, T. Csorgo, B. Lorstad, A. Ster, J. Phys. G 30 (2004) S1079.
[117] P.F. Kolb, R. Rapp, Phys. Rev. C 67 (2003) 044903.
[118] T. Hirano, K. Tsuda, Phys. Rev. C 66 (2002) 054905.
[119] T. Hirano, Y. Nara, Nucl. Phys. A 743 (2004) 305.
[120] P.F. Kolb, U. Heinz, nucl-th/0305084.
[121] D. Molnar, P. Huovinen, Phys. Rev. Lett. 94 (2005) 012302.
[122] D.A. Teaney, J. Phys. G 30 (2004) S1247.
[123] U.W. Heinz, P.F. Kolb, hep-ph/0204061.
[124] Y.M. Sinyukov, S.V. Akkelin, Y. Hama, Phys. Rev. Lett. 89 (2002) 052301.
[125] F. Grassi, Y. Hama, S.S. Padula, J. Socolowski, Octavio, Phys. Rev. C 62 (2000) 044904.
[126] F. Cooper, G. Frye, Phys. Rev. D 10 (1974) 186.
[127] S. Soff, S.A. Bass, A. Dumitru, Phys. Rev. Lett. 86 (2001) 3981.
[128] D. Zschiesche, S. Schramm, H. Stocker, W. Greiner, Phys. Rev. C 65 (2002) 064902.
[129] F. Karsch, E. Laermann, hep-lat/0305025.
[130] S. Soff, hep-ph/0202240.
[131] G.N. Fowler, R.M. Weiner, Phys. Lett. B 70 (1977) 201.
[132] G.N. Fowler, E.M. Friedlander, R.M. Weiner, Phys. Lett. B 104 (1981) 239.
[133] L. Van Hove, Physica A 147 (1987) 19.
[134] G.J. Alner, et al., Phys. Lett. B 160 (1985) 193.
[135] S. Jeon, V. Koch, Phys. Rev. Lett. 85 (2000) 2076.
[136] M. Asakawa, U.W. Heinz, B. Muller, Phys. Rev. Lett. 85 (2000) 2072.
[137] H. Heiselberg, A.D. Jackson, Phys. Rev. C 63 (2001) 064904.

[138] R. Albrecht, et al., Z. Phys. C 45 (1989) 31.
[139] P. Carruthers, C.C. Shih, Phys. Lett. B 165 (1985) 209.
[140] H. Sorge, Phys. Rev. C 52 (1995) 3291.
[141] M.J. Tannenbaum, Phys. Lett. B 498 (2001) 29.
[142] R. Korus, S. Mrowczynski, M. Rybczynski, Z. Wlodarczyk, Phys. Rev. C 64 (2001) 054908.
[143] J.T. Mitchell, J. Phys. G 30 (2004) S819.
[144] E.G. Ferreiro, F. del Moral, C. Pajares, Phys. Rev. C 69 (2004) 034901.
[145] S. Gavin, Phys. Rev. Lett. 92 (2004) 162301.
[146] J.F. Owens, Rev. Mod. Phys. 59 (1987) 465.
[147] G. Bunce, N. Saito, J. Soffer, W. Vogelsang, Annu. Rev. Nucl. Part. Sci. 50 (2000) 525.
[148] R. Cutler, D.W. Sivers, Phys. Rev. D 17 (1978) 196.
[149] R. Cutler, D.W. Sivers, Phys. Rev. D 16 (1977) 679.
[150] B.L. Combridge, J. Kripfganz, J. Ranft, Phys. Lett. B 70 (1977) 234.
[151] F. Aversa, P. Chiappetta, M. Greco, J.P. Guillet, Nucl. Phys. B 327 (1989) 105.
[152] B. Jager, A. Schafer, M. Stratmann, W. Vogelsang, Phys. Rev. D 67 (2003) 054005.
[153] E.D. Bloom, et al., Phys. Rev. Lett. 23 (1969) 930.
[154] M. Breidenbach, et al., Phys. Rev. Lett. 23 (1969) 935.
[155] J.D. Bjorken, Phys. Rev. 179 (1969) 1547.
[156] M. May, et al., Phys. Rev. Lett. 35 (1975) 407.
[157] M. Arneodo, et al., Nucl. Phys. B 481 (1996) 3.
[158] D. Antreasyan, et al., Phys. Rev. D 19 (1979) 764.
[159] A. Krzywicki, J. Engels, B. Petersson, U. Sukhatme, Phys. Lett. B 85 (1979) 407.
[160] M. Lev, B. Petersson, Z. Phys. C 21 (1983) 155.
[161] C.N. Brown, et al., Phys. Rev. C 54 (1996) 3195.
[162] A.L.S. Angelis, et al., Phys. Lett. B 185 (1987) 213.
[163] M.M. Aggarwal, et al., Eur. Phys. J. C 23 (2002) 225.
[164] J. Slivova, PhD thesis, Charles University, Prague, 2003, from the CERES experiment.
[165] R. Albrecht, et al., Eur. Phys. J. C 5 (1998) 255.
[166] D. d'Enterria, Phys. Lett. B 596 (2004) 32.
[167] H. Busching, J. Phys. G 31 (2005) S473.
[168] D. Kharzeev, Y.V. Kovchegov, K. Tuchin, Phys. Rev. D 68 (2003) 094013.
[169] H. Baer, J. Ohnemus, J.F. Owens, Phys. Rev. D 42 (1990) 61.
[170] P. Aurenche, A. Douiri, R. Baier, M. Fontannaz, D. Schiff, Phys. Lett. B 140 (1984) 87.
[171] P. Aurenche, R. Baier, M. Fontannaz, D. Schiff, Nucl. Phys. B 297 (1988) 661.
[172] L.E. Gordon, W. Vogelsang, Phys. Rev. D 48 (1993) 3136.
[173] J.D. Bjorken, FERMILAB-PUB-82-059-THY (1982).
[174] M. Gyulassy, M. Plumer, Phys. Lett. B 243 (1990) 432.
[175] X.-N. Wang, M. Gyulassy, Phys. Rev. Lett. 68 (1992) 1480.
[176] X.-N. Wang, M. Gyulassy, M. Plumer, Phys. Rev. D 51 (1995) 3436.
[177] R. Baier, Y.L. Dokshitzer, S. Peigne, D. Schiff, Phys. Lett. B 345 (1995) 277.
[178] R. Baier, Y.L. Dokshitzer, A.H. Mueller, S. Peigne, D. Schiff, Nucl. Phys. B 483 (1997) 291.
[179] R. Baier, Y.L. Dokshitzer, A.H. Mueller, D. Schiff, Phys. Rev. C 58 (1998) 1706.
[180] M. Gyulassy, P. Levai, I. Vitev, Phys. Rev. Lett. 85 (2000) 5535.
[181] M. Gyulassy, P. Levai, I. Vitev, Nucl. Phys. B 594 (2001) 371.
[182] C. Adler, et al., Phys. Rev. Lett. 89 (2002) 202301.
[183] J. Adams, et al., Phys. Rev. Lett. 91 (2003) 172302.
[184] B.B. Back, et al., Phys. Lett. B 578 (2004) 297.
[185] X.-N. Wang, Phys. Lett. B 595 (2004) 165.
[186] J.-W. Qiu, I. Vitev, Phys. Lett. B 570 (2003) 161.
[187] E. Wang, X.-N. Wang, Phys. Rev. Lett. 87 (2001) 142301.
[188] E. Wang, X.-N. Wang, Phys. Rev. Lett. 89 (2002) 162301.
[189] J.W. Cronin, et al., Phys. Rev. D 11 (1975) 3105.
[190] D. Antreasyan, et al., Phys. Rev. Lett. 39 (1977) 513.
[191] M. Gyulassy, P. Levai, Phys. Lett. B 442 (1998) 1.

[192] X.-N. Wang, Phys. Rev. C 61 (2000) 064910.
[193] G. Papp, P. Levai, G.I. Fai, Phys. Rev. C 61 (2000) 021902.
[194] I. Vitev, M. Gyulassy, Phys. Rev. Lett. 89 (2002) 252301.
[195] I. Vitev, Phys. Lett. B 562 (2003) 36.
[196] X.-N. Wang, Phys. Lett. B 565 (2003) 116.
[197] P. Levai, G. Papp, G.G. Barnafoldi, G.I. Fai, nucl-th/0306019.
[198] D. Kharzeev, E. Levin, L. McLerran, Phys. Lett. B 561 (2003) 93.
[199] C. Adler, et al., Phys. Rev. Lett. 90 (2003) 032301.
[200] C. Adler, et al., Phys. Rev. Lett. 90 (2003) 082302.
[201] J. Rak, J. Phys. G 30 (2004) S1309.
[202] M. Chiu, Nucl. Phys. A 715 (2003) 761.
[203] S.A. Bass, et al., Nucl. Phys. A 661 (1999) 205.
[204] A. Kovner, U.A. Wiedemann, hep-ph/0304151.
[205] M. Gyulassy, I. Vitev, X.-N. Wang, B.-W. Zhang, nucl-th/0302077.
[206] M. Gyulassy, M. Plumer, M. Thoma, X.N. Wang, Nucl. Phys. A 538 (1992) 37c.
[207] B.G. Zakharov, JETP Lett. 65 (1997) 615.
[208] R. Baier, D. Schiff, B.G. Zakharov, Annu. Rev. Nucl. Part. Sci. 50 (2000) 37.
[209] M. Gyulassy, P. Levai, I. Vitev, Nucl. Phys. B 571 (2000) 197.
[210] P. Levai, et al., Nucl. Phys. A 698 (2002) 631.
[211] I. Vitev, M. Gyulassy, P. Levai, hep-ph/0109198.
[212] I. Vitev, J. Phys. G 30 (2004) S791.
[213] M. Gyulassy, I. Vitev, X.-N. Wang, P. Huovinen, Phys. Lett. B 526 (2002) 301.
[214] X.-f. Guo, X.-N. Wang, Phys. Rev. Lett. 85 (2000) 3591.
[215] A. Airapetian, et al., Eur. Phys. J. C 20 (2001) 479.
[216] K.J. Eskola, V.J. Kolhinen, C.A. Salgado, Eur. Phys. J. C 9 (1999) 61.
[217] X.-N. Wang, Nucl. Phys. A 750 (2005) 98.
[218] K. Gallmeister, C. Greiner, Z. Xu, Phys. Rev. C 67 (2003) 044905.
[219] W. Cassing, K. Gallmeister, C. Greiner, Nucl. Phys. A 735 (2004) 277.
[220] X.-N. Wang, Phys. Lett. B 579 (2004) 299.
[221] M. Gyulassy, P. Levai, I. Vitev, Phys. Lett. B 538 (2002) 282.
[222] R. Baier, Y.L. Dokshitzer, A.H. Mueller, D. Schiff, JHEP 0109 (2001) 033.
[223] B.R. Webber, Int. J. Mod. Phys. A 15S1 (2000) 577.
[224] B. Alper, et al., Nucl. Phys. B 100 (1975) 237.
[225] P. Abreu, et al., Eur. Phys. J. C 17 (2000) 207.
[226] I.G. Bearden, et al., Phys. Rev. C 66 (2002) 044907.
[227] T. Anticic, et al., Phys. Rev. C 69 (2004) 024902.
[228] L. Ahle, et al., Phys. Rev. C 55 (1997) 2604.
[229] L. Ahle, et al., Nucl. Phys. A 638 (1998) 427.
[230] K.P. Das, R.C. Hwa, Phys. Lett. B 68 (1977) 459.
[231] R.G. Roberts, R.C. Hwa, S. Matsuda, J. Phys. G 5 (1979) 1043.
[232] E. Braaten, Y. Jia, T. Mehen, Phys. Rev. Lett. 89 (2002) 122002.
[233] R.J. Fries, B. Muller, C. Nonaka, S.A. Bass, Phys. Rev. Lett. 90 (2003) 202303.
[234] R.J. Fries, B. Muller, C. Nonaka, S.A. Bass, Phys. Rev. C 68 (2003) 044902.
[235] R.C. Hwa, C.B. Yang, Phys. Rev. C 70 (2004) 024905.
[236] R.C. Hwa, C.B. Yang, Phys. Rev. C 67 (2003) 034902.
[237] V. Greco, C.M. Ko, P. Levai, Phys. Rev. Lett. 90 (2003) 202302.
[238] S.A. Voloshin, Nucl. Phys. A 715 (2003) 379c.
[239] J. Adams, et al., Phys. Rev. Lett. 92 (2004) 052302.
[240] M. Kaneta, J. Phys. G 30 (2004) S1217.
[241] V. Greco, C.M. Ko, Phys. Rev. C 70 (2004) 024901.
[242] X. Dong, S. Esumi, P. Sorensen, N. Xu, Z. Xu, Phys. Lett. B 597 (2004) 328.
[243] PHENIX Collaboration, BNL 72162-2004, internal report, 2003.
[244] T. Matsui, H. Satz, Phys. Lett. B 178 (1986) 416.
[245] M.C. Abreu, et al., Phys. Lett. B 477 (2000) 28.

[246] A. Capella, E.G. Ferreiro, A.B. Kaidalov, Phys. Rev. Lett. 85 (2000) 2080.
[247] A. Capella, A.B. Kaidalov, D. Sousa, Phys. Rev. C 65 (2002) 054908.
[248] R.L. Thews, M. Schroedter, J. Rafelski, Phys. Rev. C 63 (2001) 054905.
[249] R.L. Thews, J. Phys. G 30 (2004) S369.
[250] A.P. Kostyuk, M.I. Gorenstein, H. Stocker, W. Greiner, Phys. Rev. C 68 (2003) 041902.
[251] P. Braun-Munzinger, J. Stachel, Phys. Lett. B 490 (2000) 196.
[252] A. Andronic, P. Braun-Munzinger, K. Redlich, J. Stachel, Phys. Lett. B 571 (2003) 36.
[253] M.G. Mustafa, D. Pal, D.K. Srivastava, M. Thoma, Phys. Lett. B 428 (1998) 234.
[254] Z.-W. Lin, R. Vogt, X.-N. Wang, Phys. Rev. C 57 (1998) 899.
[255] Y.L. Dokshitzer, D.E. Kharzeev, Phys. Lett. B 519 (2001) 199.
[256] G. Agakishiev, et al., Phys. Rev. Lett. 75 (1995) 1272.
[257] G. Agakishiev, et al., Phys. Lett. B 422 (1998) 405.
[258] D. Adamova, et al., Phys. Rev. Lett. 91 (2003) 042301.
[259] R. Rapp, J. Wambach, Adv. Nucl. Phys. 25 (2000) 1.
[260] R. Arnaldi, et al., nucl-ex/0501028.
[261] R. Rapp, nucl-th/0204003.
[262] Z. Fraenkel, B. Khachaturov, A. Kozlov, A. Milov, D. Mukhopadhyay, D. Pal, I. Ravinovich, I. Tserruya, S. Zhou, PHENIX Technical Note 391, internal report, 2001.
[263] A. Kozlov, et al., Nucl. Instrum. Methods A 523 (2004) 345.
[264] R. Rapp, Phys. Rev. C 63 (2001) 054907.
[265] P.V. Ruuskanen, Nucl. Phys. A 544 (1992) 169.
[266] G.-Q. Li, C. Gale, Phys. Rev. Lett. 81 (1998) 1572.
[267] S. Turbide, R. Rapp, C. Gale, Phys. Rev. C 69 (2004) 014903.

Centrality Dependence of Charm Production from a Measurement of Single Electrons in Au + Au Collisions at $\sqrt{s_{NN}} = 200$ GeV

S. S. Adler,[5] S. Afanasiev,[17] C. Aidala,[5] N. N. Ajitanand,[43] Y. Akiba,[20,38] J. Alexander,[43] R. Amirikas,[12] L. Aphecetche,[45] S. H. Aronson,[5] R. Averbeck,[44] T. C. Awes,[35] R. Azmoun,[44] V. Babintsev,[15] A. Baldisseri,[10] K. N. Barish,[6] P. D. Barnes,[27] B. Bassalleck,[33] S. Bathe,[30] S. Batsouli,[9] V. Baublis,[37] A. Bazilevsky,[39,15] S. Belikov,[16,15] Y. Berdnikov,[40] S. Bhagavatula,[16] J. G. Boissevain,[27] H. Borel,[10] S. Borenstein,[25] M. L. Brooks,[27] D. S. Brown,[34] N. Bruner,[33] D. Bucher,[30] H. Buesching,[30] V. Bumazhnov,[15] G. Bunce,[5,39] J. M. Burward-Hoy,[26,44] S. Butsyk,[44] X. Camard,[45] J.-S. Chai,[18] P. Chand,[4] W. C. Chang,[2] S. Chernichenko,[15] C. Y. Chi,[9] J. Chiba,[20] M. Chiu,[9] I. J. Choi,[52] J. Choi,[19] R. K. Choudhury,[4] T. Chujo,[5] V. Cianciolo,[35] Y. Cobigo,[10] B. A. Cole,[9] P. Constantin,[16] D. G. d'Enterria,[45] G. David,[5] H. Delagrange,[45] A. Denisov,[15] A. Deshpande,[39] E. J. Desmond,[5] A. Devismes,[44] O. Dietzsch,[41] O. Drapier,[25] A. Drees,[44] R. du Rietz,[29] A. Durum,[15] D. Dutta,[4] Y. V. Efremenko,[35] K. El Chenawi,[49] A. Enokizono,[14] H. En'yo,[38,39] S. Esumi,[48] L. Ewell,[5] D. E. Fields,[33,39] F. Fleuret,[25] S. L. Fokin,[23] B. D. Fox,[39] Z. Fraenkel,[51] J. E. Frantz,[9] A. Franz,[5] A. D. Frawley,[12] S.-Y. Fung,[6] S. Garpman,[29,*] T. K. Ghosh,[49] A. Glenn,[46] G. Gogiberidze,[46] M. Gonin,[25] J. Gosset,[10] Y. Goto,[39] R. Granier de Cassagnac,[25] N. Grau,[16] S. V. Greene,[49] M. Grosse Perdekamp,[39] W. Guryn,[5] H.-Å. Gustafsson,[29] T. Hachiya,[14] J. S. Haggerty,[5] H. Hamagaki,[8] A. G. Hansen,[27] E. P. Hartouni,[26] M. Harvey,[5] R. Hayano,[8] N. Hayashi,[38] X. He,[13] M. Heffner,[26] T. K. Hemmick,[44] J. M. Heuser,[44] M. Hibino,[50] J. C. Hill,[16] W. Holzmann,[43] K. Homma,[14] B. Hong,[22] A. Hoover,[34] T. Ichihara,[38,39] V. V. Ikonnikov,[23] K. Imai,[24,38] D. Isenhower,[1] M. Ishihara,[38] M. Issah,[43] A. Isupov,[17] B. V. Jacak,[44] W. Y. Jang,[22] Y. Jeong,[19] J. Jia,[44] O. Jinnouchi,[38] B. M. Johnson,[5] S. C. Johnson,[26] K. S. Joo,[31] D. Jouan,[36] S. Kametani,[8,50] N. Kamihara,[47,38] J. H. Kang,[52] S. S. Kapoor,[4] K. Katou,[50] S. Kelly,[9] B. Khachaturov,[51] A. Khanzadeev,[37] J. Kikuchi,[50] D. H. Kim,[31] D. J. Kim,[52] D. W. Kim,[19] E. Kim,[42] G.-B. Kim,[25] H. J. Kim,[52] E. Kistenev,[5] A. Kiyomichi,[48] K. Kiyoyama,[32] C. Klein-Boesing,[30] H. Kobayashi,[38,39] L. Kochenda,[37] V. Kochetkov,[15] D. Koehler,[33] T. Kohama,[14] M. Kopytine,[44] D. Kotchetkov,[6] A. Kozlov,[51] P. J. Kroon,[5] C. H. Kuberg,[1,27] K. Kurita,[39] Y. Kuroki,[48] M. J. Kweon,[22] Y. Kwon,[52] G. S. Kyle,[34] R. Lacey,[43] V. Ladygin,[17] J. G. Lajoie,[16] A. Lebedev,[16,23] S. Leckey,[44] D. M. Lee,[27] S. Lee,[19] M. J. Leitch,[27] X. H. Li,[6] H. Lim,[42] A. Litvinenko,[17] M. X. Liu,[27] Y. Liu,[36] C. F. Maguire,[49] Y. I. Makdisi,[5] A. Malakhov,[17] V. I. Manko,[23] Y. Mao,[7,38] G. Martinez,[45] M. D. Marx,[44] H. Masui,[48] F. Matathias,[44] T. Matsumoto,[8,50] P. L. McGaughey,[27] E. Melnikov,[15] F. Messer,[44] Y. Miake,[48] J. Milan,[43] T. E. Miller,[49] A. Milov,[44,51] S. Mioduszewski,[5] R. E. Mischke,[27] G. C. Mishra,[13] J. T. Mitchell,[5] A. K. Mohanty,[4] D. P. Morrison,[5] J. M. Moss,[27] F. Mühlbacher,[44] D. Mukhopadhyay,[51] M. Muniruzzaman,[6] J. Murata,[38,39] S. Nagamiya,[20] J. L. Nagle,[9] T. Nakamura,[14] B. K. Nandi,[6] M. Nara,[48] J. Newby,[46] P. Nilsson,[29] A. S. Nyanin,[23] J. Nystrand,[29] E. O'Brien,[5] C. A. Ogilvie,[16] H. Ohnishi,[5,38] I. D. Ojha,[49,3] K. Okada,[38] M. Ono,[48] V. Onuchin,[15] A. Oskarsson,[29] I. Otterlund,[29] K. Oyama,[8] K. Ozawa,[8] D. Pal,[51] A. P. T. Palounek,[27] V. S. Pantuev,[44] V. Papavassiliou,[34] J. Park,[42] A. Parmar,[33] S. F. Pate,[34] T. Peitzmann,[30] J.-C. Peng,[27] V. Peresedov,[17] C. Pinkenburg,[5] R. P. Pisani,[5] F. Plasil,[35] M. L. Purschke,[5] A. K. Purwar,[44] J. Rak,[16] I. Ravinovich,[51] K. F. Read,[35,46] M. Reuter,[44] K. Reygers,[30] V. Riabov,[37,40] Y. Riabov,[37] G. Roche,[28] A. Romana,[25] M. Rosati,[16] P. Rosnet,[28] S. S. Ryu,[52] M. E. Sadler,[1] N. Saito,[38,39] T. Sakaguchi,[8,50] M. Sakai,[32] S. Sakai,[48] V. Samsonov,[37] L. Sanfratello,[33] R. Santo,[30] H. D. Sato,[24,38] S. Sato,[5,48] S. Sawada,[20] Y. Schutz,[45] V. Semenov,[15] R. Seto,[6] M. R. Shaw,[1,27] T. K. Shea,[5] T.-A. Shibata,[47,38] K. Shigaki,[14,20] T. Shiina,[27] C. L. Silva,[41] D. Silvermyr,[27,29] K. S. Sim,[22] C. P. Singh,[3] V. Singh,[3] M. Sivertz,[5] A. Soldatov,[15] R. A. Soltz,[26] W. E. Sondheim,[27] S. P. Sorensen,[46] I. V. Sourikova,[5] F. Staley,[10] P. W. Stankus,[35] E. Stenlund,[29] M. Stepanov,[34] A. Ster,[21] S. P. Stoll,[5] T. Sugitate,[14] J. P. Sullivan,[27] E. M. Takagui,[41] A. Taketani,[38,39] M. Tamai,[50] K. H. Tanaka,[20] Y. Tanaka,[32] K. Tanida,[38] M. J. Tannenbaum,[5] P. Tarján,[11] J. D. Tepe,[1,27] T. L. Thomas,[33] J. Tojo,[24,38] H. Torii,[24,38] R. S. Towell,[1] I. Tserruya,[51] H. Tsuruoka,[48] S. K. Tuli,[3] H. Tydesjö,[29] N. Tyurin,[15] H. W. van Hecke,[27] J. Velkovska,[5,44] M. Velkovsky,[44] V. Veszprémi,[11] L. Villatte,[46] A. A. Vinogradov,[23] M. A. Volkov,[23] E. Vznuzdaev,[37] X. R. Wang,[13] Y. Watanabe,[38,39] S. N. White,[5] F. K. Wohn,[16] C. L. Woody,[5] W. Xie,[6] Y. Yang,[7] A. Yanovich,[15] S. Yokkaichi,[38,39] G. R. Young,[35] I. E. Yushmanov,[23] W. A. Zajc,[9,†] C. Zhang,[9] S. Zhou,[7] S. J. Zhou,[51] and L. Zolin[17]

(PHENIX Collaboration)

[1]*Abilene Christian University, Abilene, Texas 79699, USA*
[2]*Institute of Physics, Academia Sinica, Taipei 11529, Taiwan*
[3]*Department of Physics, Banaras Hindu University, Varanasi 221005, India*

 © 2005 The American Physical Society

[4]Bhabha Atomic Research Centre, Bombay 400 085, India
[5]Brookhaven National Laboratory, Upton, New York 11973-5000, USA
[6]University of California at Riverside, Riverside, California 92521, USA
[7]China Institute of Atomic Energy (CIAE), Beijing, People's Republic of China
[8]Center for Nuclear Study, Graduate School of Science, University of Tokyo, 7-3-1 Hongo, Bunkyo, Tokyo 113-0033, Japan
[9]Columbia University, New York, New York 10027, USA
and Nevis Laboratories, Irvington, New York 10533, USA
[10]Dapnia, CEA Saclay, F-91191, Gif-sur-Yvette, France
[11]Debrecen University, H-4010 Debrecen, Egyetem tér 1, Hungary
[12]Florida State University, Tallahassee, Florida 32306, USA
[13]Georgia State University, Atlanta, Georgia 30303, USA
[14]Hiroshima University, Kagamiyama, Higashi-Hiroshima 739-8526, Japan
[15]Institute for High Energy Physics (IHEP), Protvino, Russia
[16]Iowa State University, Ames, Iowa 50011, USA
[17]Joint Institute for Nuclear Research, 141980 Dubna, Moscow Region, Russia
[18]KAERI, Cyclotron Application Laboratory, Seoul, Korea
[19]Kangnung National University, Kangnung 210-702, Korea
[20]KEK, High Energy Accelerator Research Organization, Tsukuba-shi, Ibaraki-ken 305-0801, Japan
[21]KFKI Research Institute for Particle and Nuclear Physics (RMKI), H-1525 Budapest 114, P.O. Box 49, Hungary
[22]Korea University, Seoul, 136-701, Korea
[23]Russian Research Center "Kurchatov Institute," Moscow, Russia
[24]Kyoto University, Kyoto 606, Japan
[25]Laboratoire Leprince-Ringuet, Ecole Polytechnique, CNRS-IN2P3, Route de Saclay, F-91128, Palaiseau, France
[26]Lawrence Livermore National Laboratory, Livermore, California 94550, USA
[27]Los Alamos National Laboratory, Los Alamos, New Mexico 87545, USA
[28]LPC, Université Blaise Pascal, CNRS-IN2P3, Clermont-Fd, 63177 Aubiere CEDEX, France
[29]Department of Physics, Lund University, Box 118, SE-221 00 Lund, Sweden
[30]Institut für Kernphysik, University of Muenster, D-48149 Muenster, Germany
[31]Myongji University, Yongin, Kyonggido 449-728, Korea
[32]Nagasaki Institute of Applied Science, Nagasaki-shi, Nagasaki 851-0193, Japan
[33]University of New Mexico, Albuquerque, New Mexico 87131, USA
[34]New Mexico State University, Las Cruces, New Mexico 88003, USA
[35]Oak Ridge National Laboratory, Oak Ridge, Tennessee 37831, USA
[36]IPN-Orsay, Universite Paris Sud, CNRS-IN2P3, BP 1, F-91406, Orsay, France
[37]PNPI, Petersburg Nuclear Physics Institute, Gatchina, Russia
[38]RIKEN (The Institute of Physical and Chemical Research), Wako, Saitama 351-0198, Japan
[39]RIKEN BNL Research Center, Brookhaven National Laboratory, Upton, New York 11973-5000, USA
[40]St. Petersburg State Technical University, St. Petersburg, Russia
[41]Universidade de São Paulo, Instituto de Física, Caixa Postal 66318, São Paulo CEP05315-970, Brazil
[42]System Electronics Laboratory, Seoul National University, Seoul, Korea
[43]Chemistry Department, Stony Brook University, SUNY, Stony Brook, New York 11794-3400, USA
[44]Department of Physics and Astronomy, Stony Brook University, SUNY, Stony Brook, New York 11794, USA
[45]SUBATECH (Ecole des Mines de Nantes, CNRS-IN2P3, Université de Nantes) BP 20722-44307, Nantes, France
[46]University of Tennessee, Knoxville, Tennessee 37996, USA
[47]Department of Physics, Tokyo Institute of Technology, Tokyo 152-8551, Japan
[48]Institute of Physics, University of Tsukuba, Tsukuba, Ibaraki 305, Japan
[49]Vanderbilt University, Nashville, Tennessee 37235, USA
[50]Waseda University, Advanced Research Institute for Science and Engineering, 17 Kikui-cho, Shinjuku-ku, Tokyo 162-0044, Japan
[51]Weizmann Institute, Rehovot 76100, Israel
[52]Yonsei University, IPAP, Seoul 120-749, Korea

(Received 28 September 2004; published 2 March 2005)

The PHENIX experiment has measured midrapidity transverse momentum spectra ($0.4 < p_T < 4.0$ GeV/c) of single electrons as a function of centrality in Au + Au collisions at $\sqrt{s_{NN}} = 200$ GeV. Contributions from photon conversions and Dalitz decays of light neutral mesons are measured by introducing a thin (1.7% X_0) converter into the PHENIX acceptance and are statistically removed. The subtracted nonphotonic electron spectra are primarily due to the semileptonic decays of hadrons containing heavy quarks, mainly charm at lower p_T. For all centralities, the charm production cross section is found to scale with the nuclear overlap function, T_{AA}. For minimum-bias collisions the charm cross section per binary collision is $N_{c\bar{c}}/T_{AA} = 622 \pm 57(\text{stat}) \pm 160(\text{syst})$ μb.

DOI: 10.1103/PhysRevLett.94.082301 PACS numbers: 25.75.Dw

In central Au + Au collisions at $\sqrt{s_{NN}} = 200$ GeV neutral pions and charged hadrons are strongly suppressed at high transverse momentum (p_T) [1–3]. In contrast, a modest high-p_T enhancement is observed in d + Au collisions at the same energy [4,5]. Taken together, these observations indicate that the suppression in Au + Au collisions is caused by final-state effects (e.g., parton energy loss in a dense medium produced in the reaction).

Heavy quarks (charm and bottom) are complementary probes of the hot and dense matter produced in high energy heavy ion collisions. Because of their large masses, charm and bottom cross sections are calculable via perturbative quantum chromodynamics (pQCD) and their yield is sensitive to the initial gluon density [6]. It has been predicted that heavy quarks suffer less energy loss than light quarks while traversing partonic matter due to the ''dead cone'' effect [7–9]. This can be studied through systematic measurements of the p_T spectra of open heavy flavor. In addition, the open-charm yield is an important baseline for understanding J/ψ production which has been predicted to be either suppressed [10] or enhanced [11] in deconfined partonic matter.

The PHENIX experiment observed that inclusive single electrons in central and minimum-bias Au + Au collisions at $\sqrt{s_{NN}} = 130$ GeV were produced in excess of purely ''photonic'' contributions (primarily due to π^0 Dalitz decays and conversion of π^0 photons in the detector material) [12]. This excess is consistent with the expected charm production, assuming that it scales with the number of binary nucleon-nucleon collisions ($N_{\rm coll}$) or, equivalently, with the nuclear overlap function, T_{AA}. In this Letter, we present results on the single electron measurement in $\sqrt{s_{NN}} = 200$ GeV Au + Au collisions. Our measurement is in a p_T range sensitive only to charm production. The new data have higher statistics and smaller systematic errors than the 130 GeV data, allowing us to measure charm production as a function of collision centrality.

The data used in this analysis were collected by the PHENIX detector [13] during the 2001 run period of the Relativistic Heavy Ion Collider. A coincidence of the beam-beam counters (BBC), a pair of detector arrays covering 2π in azimuth and $\eta = \pm(3.0$–$3.9)$, and the zero degree calorimeters (ZDC) provides the minimum-bias trigger ($92.2^{+2.5}_{-3.0}\%$ of the 6.8 ± 0.5 barn Au + Au inelastic cross section). The centrality is determined by the correlation between the multiplicity measured by the BBC and the energy of spectator neutrons measured by the ZDC. The BBC also measures the collision vertex, z, with resolution $\sigma = 0.7$ cm. We require $|z| < 20$ cm to eliminate electrons originating from the central magnet.

Charged particles are measured by the PHENIX east-arm spectrometer ($|\eta| < 0.35$, $\Delta\phi = \pi/2$) with resolution $\sigma_p/p \simeq 0.7\% \oplus 1.0\% p({\rm GeV}/c)$. Tracks are reconstructed with the drift chamber and the first layer of pad chambers and confirmed by requiring an electromagnetic calorimeter (EMCal) matching hit within 2σ in position. Electron candidates are required to have at least three associated hits in the ring imaging Čerenkov detector (RICH) that pass a ring shape cut, and are required to pass a timing cut in either the EMCal or the time-of-flight detector. After these cuts, a clear electron signal is observed as a narrow peak at $E/p = 1$. By requiring $-2\sigma < (E - p)/p < 3\sigma$, background from hadrons, which deposit only a fraction of their energy in the EMCal, and nonvertex electrons, which have misreconstructed momenta, is further reduced. Remaining background in the electron sample, due to accidental coincidences between RICH hits and hadron tracks, is estimated ($\approx 10\%$) and subtracted by an event-mixing method.

Inclusive electrons contain two components: (i) ''nonphotonic''—primarily semileptonic decays of mesons containing heavy quarks, and (ii) photonic—Dalitz decays of light neutral mesons (π^0, η, η', ρ, ω, and ϕ) and photon conversions in the detector material. To separate these two components, a photon converter (a thin brass tube of 1.7% radiation length surrounding the beam pipe at $r = 29$ cm) was installed.

We analyzed 2.2 M (2.5 M) events with the converter in (out). The corresponding raw electron p_T spectra for minimum-bias collisions are shown in Fig. 1(a). The photon converter multiplies the photonic contribution to the electron yield by a factor R_γ:

$$N_e^{\text{Conv-out}} = N_e^{\gamma} + N_e^{\text{non-}\gamma}, \tag{1}$$

$$N_e^{\text{Conv-in}} = R_\gamma N_e^{\gamma} + (1 - \epsilon) N_e^{\text{non-}\gamma}. \tag{2}$$

Here $N_e^{\text{Conv-in}}$ ($N_e^{\text{Conv-out}}$) is the measured electron yield with (without) the converter; N_e^{γ} ($N_e^{\text{non-}\gamma}$) is the electron yield due to the photonic (nonphotonic) component; and $\epsilon(\approx 2.1\%)$ represents a small loss of electrons due to the converter. We next define R_{CN} as the ratio of the raw electron yield with and without the converter. Dividing Eq. (2) by Eq. (1) and defining $R_{NP} \equiv N_e^{\text{non-}\gamma}/N_e^{\gamma}$, one has

$$R_{CN} \equiv \frac{N_e^{\text{Conv-in}}}{N_e^{\text{Conv-out}}} = \frac{R_\gamma + (1 - \epsilon) R_{NP}}{1 + R_{NP}}. \tag{3}$$

If there were no contribution from the nonphotonic component ($R_{NP} = 0$), then $R_{CN} = R_\gamma$.

The photonic electron yield per photon is approximately given by $Y \propto \delta + \frac{7}{9} t$, where δ is the Dalitz branching ratio per γ relative to 2γ (for π^0, η, and η') or 1γ (for ρ, ω, and ϕ) decay, and t is the thickness of the conversion material in radiation length (X_0). The factor $\frac{7}{9}$ is the approximate probability for a γ to convert in one X_0. Plugging in $\delta^{\pi^0} = 0.6\%$, $t \approx 1.1\%$ ($t \approx 2.8\%$) for converter out (in) we find $R_\gamma^{\pi^0} = Y^{\text{Conv-in}}/Y^{\text{Conv-out}} \approx 1.9$. There is some p_T depen-

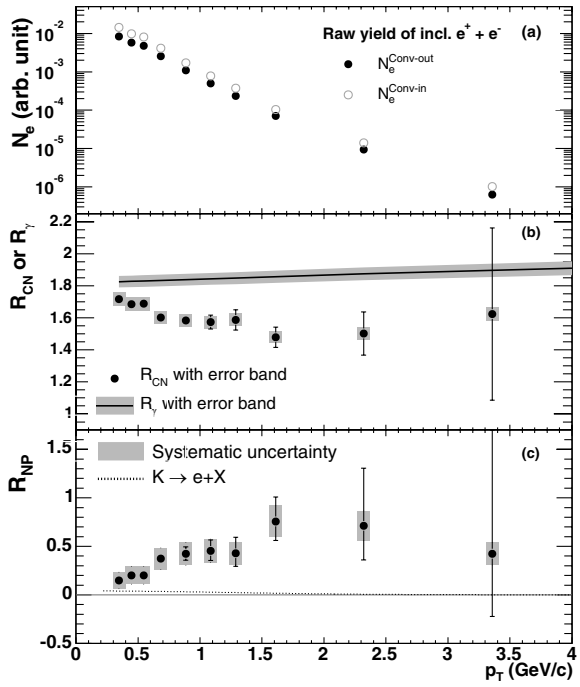

FIG. 1. Shown vs p_T (a) raw $e^{\pm}$ spectra measured with the converter in (open circles) and out (closed circles). (b) Ratio of the converter in/out $e^{\pm}$ yields (R_{CN}, points) and ratio of photonic $e^{\pm}$ yield with/without the converter (R_γ, line and shaded band). (c) Ratio of nonphotonic to photonic $e^{\pm}$ yields (R_{NP}, points) and contribution from kaon decays (dashed line).

dence in the complete formula for Y and the value of δ is species dependent ($\delta^\eta \approx 0.8\%$), so we perform a full GEANT [14] simulation with and without the converter to calculate R_γ. We determine R_γ for π^0 and η separately. We use the π^0 spectrum measured by PHENIX [1] as the input for the π^0 simulation and assume m_T scaling ($p_T \rightarrow \sqrt{p_T^2 + M_\eta^2 - M_\pi^2}$, normalized at high p_T to $\eta/\pi^0 = 0.45 \pm 0.1$) to obtain the input for the η simulation. Contributions from other mesons which undergo Dalitz decay (η', ρ, ω, ϕ) are small (6% at $p_T = 3$ GeV/c, and smaller at lower p_T). Since they have $\delta \approx \delta^\eta$, we assign them $R_\gamma = R_\gamma^\eta$. When calculating the combined R_γ, we use the particle ratios at high p_T ($\eta'/\pi^0 = 0.25 \pm 0.13$, $\rho/\pi^0 = \omega/\pi^0 = 1 \pm 0.5$, $\phi/\pi^0 = 0.4 \pm 0.2$). The ϕ/π^0 ratio used here is consistent with our π^0 and ϕ measurement [15]. The uncertainties in the particle ratios are included in the systematic uncertainties of R_γ. For this method it is essential that the amount of material is accurately modeled in the simulation. We compared the yield of identified photon conversion pairs in the data and in the simulation and conclude that the simulation reproduces R_γ within $\pm 2.0\%$. This uncertainty is included in the overall systematic uncertainty.

Figure 1(b) shows that R_{CN} gradually decreases with increasing p_T, while R_γ slightly increases with p_T. The difference between R_{CN} and R_γ indicates the existence of nonphotonic electrons. Figure 1(c) shows R_{NP} obtained from R_γ and R_{CN} using Eq. (3). R_{NP} increases with p_T and is more than 30% for $p_T > 0.6$ GeV/c. The small amount of conversion material in the PHENIX detector allows a sensitive measurement of R_{CN}.

Background from kaon decays ($K \rightarrow \pi e \nu$) and dielectron decays of ρ, ω, and ϕ remain in the nonphotonic electron yield. The background from kaon decays is estimated with a GEANT simulation using the kaon p_T spectrum measured by PHENIX [16] as input. The contribution of kaon decays to the nonphotonic yield, shown in Fig. 1(c), is 18% at $p_T = 0.4$ GeV/c and decreases rapidly to less than 6% for $p_T > 1$ GeV/c. To calculate background from the e^+e^- decays of ρ, ω, and ϕ, we first generate spectra by applying m_T scaling to the PHENIX π^0 spectrum, as described above. The contribution of these decays to the nonphotonic electrons is $<3\%$ for all p_T. Background from $J/\psi \rightarrow e^+e^-$ decays and from Drell-Yan pairs is negligible. Possible enhancement of low mass dileptons through $\pi + \pi \rightarrow \rho \rightarrow e^+e^-$, as reported in Pb + Pb collisions at the Super Proton Synchrotron [17], would contribute to the nonphotonic electrons. However, this is neglected since the estimated ρ contribution in the absence of enhancement is only $\approx 0.6\%$ over all p_T.

After these backgrounds are subtracted the only other significant source of nonphotonic electrons is the semileptonic decay of heavy flavor, overwhelmingly charm. We denote the remaining electrons as charm electrons. The raw spectrum of charm electrons is corrected for geometrical acceptance ($\epsilon_{\rm geo}$), track reconstruction efficiency ($\epsilon_{\rm rec}$), and electron identification efficiency ($\epsilon_{e\rm ID}$) determined by GEANT simulation. The efficiency $\epsilon_{\rm geo} \times \epsilon_{\rm rec}$ is about 11% of dN_e/dy, and $\epsilon_{e\rm ID}$ is about 65% as confirmed with electrons identified through photon conversion. Correction of multiplicity dependent efficiency losses, estimated by embedding simulated electron tracks into real events, is p_T independent and increases from 5% to 26% from peripheral to central collisions. The 1σ systematic uncertainty of these corrections is 11.8%. Fully corrected charm electron spectra are shown in Fig. 2 for minimum-bias collisions and for five centrality bins. We determined photonic electron spectra and found them to be in good agreement with the background calculated from the measured π^0 spectra using the method described in [12].

We also measured the charm electron spectrum in $p + p$ collisions at $\sqrt{s_{NN}} = 200$ GeV [18]. The lines in Fig. 2 show the best fit curve of this spectrum, scaled by T_{AA} for each Au + Au centrality bin. Here, T_{AA} is the nuclear overlap function calculated by a Glauber model [1] (Table I). The Au + Au data points are in reasonable agreement with the $p + p$ fit in all centrality bins.

To quantify the centrality dependence of charm production, we calculated the integrated yield dN_e/dy ($0.8 < p_T < 4.0$ GeV/c) and fit it to $AN_{\rm coll}^\alpha$, where A is constant. In the absence of medium effects $\alpha = 1$ is the expectation

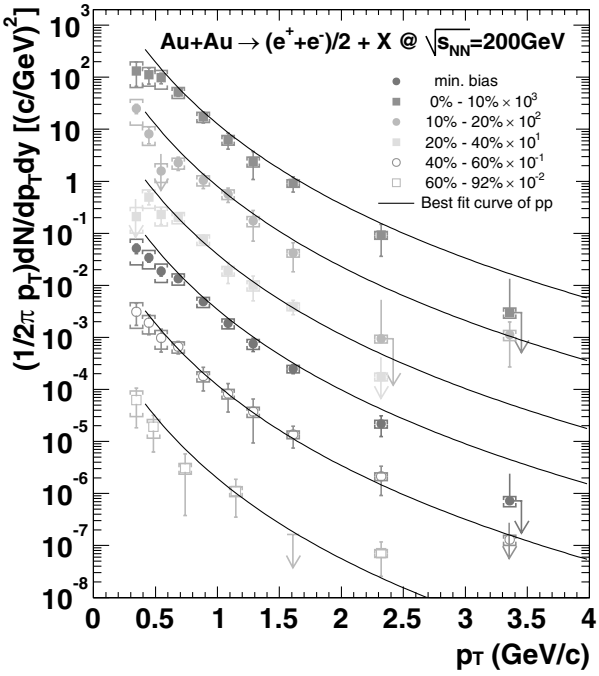

FIG. 2. Fully corrected charm electron p_T spectra for different Au + Au centralities scaled by successive factors of 10 for clarity. Error bars (brackets) correspond to statistical (systematic) uncertainties. Curves are described in the text.

in the absence of medium effects. In this comparison, most of the systematic effects will cancel. Figure 3 shows $dN_e/dy(0.8 < p_T < 4.0)/N_{\rm coll}$ vs $N_{\rm coll}$ for minimum bias and five centrality bins in Au + Au collisions and $p + p$ collisions. We find $\alpha = 0.938 \pm 0.075(\text{stat}) \pm 0.018(\text{syst})$. If $p + p$ data are included, $\alpha = 0.958 \pm 0.035(\text{stat})$. This shows that the total yield of charm electrons for all centralities is consistent with $N_{\rm coll}$ scaling.

For each centrality bin we scale the charm electron spectrum ($p_T > 0.8$ GeV/c) by T_{AA} and fit it with a PYTHIA calculation of the electron spectrum resulting from leading order charm and bottom production. We used PYTHIA 6.205 with a modified set of parameters (described in [12]) and CTEQ5L parton distribution functions [19]. Based on experimental input [20,21] we modified the PYTHIA default charm ratios, using instead $D^+/D^0 = 0.45 \pm 0.1$, $D_s/D^0 = 0.25 \pm 0.1$, and $\Lambda_c/D^0 = 0.1 \pm 0.05$.

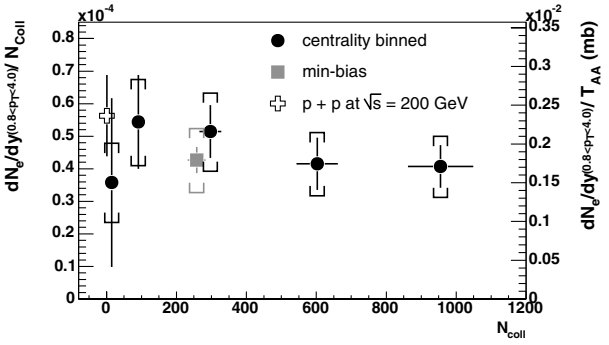

FIG. 3. Charm electron yield ($0.8 < p_T < 4.0$ GeV/c) measured in Au + Au collisions at 200 GeV scaled by $N_{\rm coll}$ as a function of $N_{\rm coll}$ (left-hand scale). Normalizing instead by the nuclear overlap function we obtain charm electron cross section per $N + N$ collision (right-hand scale).

This gives a $c \to e$ total branching ratio of $9.5 \pm 0.4\%$. Charmed hadron ratios from the statistical model [22] gives a similar branching ratio (9.3%). The scaled charm and bottom cross sections are treated as fit parameters, although our data are restricted to p_T values which are sensitive only to charm production. We evaluated the systematic error due to background subtraction ($\approx 21\%$) by refitting to the electron spectrum at the minimum and maximum of its 1σ systematic error band. The change of the p_T range for fitting the charm electron spectrum gives 3% systematic error for minimum-bias collisions. The systematic error due to the PYTHIA spectral shape ($\approx 11\%$) is dominated by the uncertainty in $\langle k_T \rangle = 1.5 \pm 0.5\,\text{GeV}/c$. Different parton distribution functions yield a systematic error of 6.2% for the rapidity-integrated cross section. These systematic errors are added in quadrature to give the overall systematic error on the charm cross section. For minimum-bias collisions we obtain $\frac{1}{T_{AA}} \frac{dN_{c\bar{c}}}{dy}|_{y=0} = 143 \pm 13(\text{stat}) \pm 36(\text{syst})\,\mu\text{b}$ and $N_{c\bar{c}}/T_{AA} = 622 \pm 57(\text{stat}) \pm 160(\text{syst})\,\mu\text{b}$. Results for all centrality bins are shown in Table I. The STAR collaboration reports a somewhat larger charm cross section ($\sigma_{c\bar{c}}^{NN} = 1.3 \pm 0.2 \pm 0.4 mb$) in $p + p$ and d + Au collision at $\sqrt{s_{NN}} = 200$ GeV [23]. Next-to leading order pQCD calculations of the charm production cross section have large associated uncertainties, with typical values between 300 and 450 μb [24].

TABLE I. Centrality bin, number of NN collisions, nuclear overlap function, charm cross section per NN collision, and total charm multiplicity per NN collision, in $\sqrt{s_{NN}} = 200$ GeV Au + Au reactions.

Centrality (%)	N_{coll}	T_{AA} (mb^{-1})	$\frac{1}{T_{AA}} \frac{dN_{c\bar{c}}}{dy}|_{y=0}$ (μb)	$N_{c\bar{c}}/T_{AA}$ (μb)
Minimum bias	258 ± 25	6.14 ± 0.45	143 ± 13 ± 36	622 ± 57 ± 160
0–10	955 ± 94	22.8 ± 1.6	137 ± 21 ± 35	597 ± 93 ± 156
10–20	603 ± 59	14.4 ± 1.0	137 ± 26 ± 35	596 ± 115 ± 158
20–40	297 ± 31	7.07 ± 0.58	168 ± 27 ± 45	731 ± 117 ± 199
40–60	91 ± 12	2.16 ± 0.26	193 ± 47 ± 52	841 ± 205 ± 232
60–92	14.5 ± 4.0	0.35 ± 0.10	116 ± 87 ± 43	504 ± 378 ± 190

We note that final-state effects influence only the momentum distribution of charm; they have little or no effect on the total open-charm yield. Therefore, our results indicate $N_{\rm coll}$ scaling of the initial charm production, as expected for pointlike pQCD processes. pQCD calculations without charm quark energy loss and hydrodynamic calculations assuming complete thermalization of charm quarks predict very similar charm electron spectra for $p_T < 2$ GeV/c [25]. Differentiating between these opposite physical pictures is possible only for $p_T > 2.5$ GeV/c, where statistics of the current analysis are limited.

In conclusion, we have measured single electrons from charm decays in Au + Au collisions at $\sqrt{s_{NN}} = 200$ GeV. We observe that the centrality dependence of charm quark production is consistent with $N_{\rm coll}$ scaling, as expected for hard processes. The much larger Au + Au data set collected by PHENIX in the 2003-04 run will allow us more detailed exploration of medium effects on charm production, both through deviations of the charm electron spectrum from $N_{\rm coll}$ scaling, and also through a measurement of charm quark flow.

We thank the staff of the Collider-Accelerator and Physics Departments at BNL for their vital contributions. We acknowledge support from the Department of Energy and NSF (USA), MEXT and JSPS (Japan), CNPq and FAPESP (Brazil), NSFC (China), CNRS-IN2P3 and CEA (France), BMBF, DAAD, and AvH (Germany), OTKA (Hungary), DAE and DST (India), ISF (Israel), KRF and CHEP (Korea), RMIST, RAS, and RMAE (Russia), VR and KAW (Sweden), U.S. CRDF for the FSU, U.S.-Hungarian NSF-OTKA-MTA, and U.S.-Israel BSF.

*Deceased.
†PHENIX Spokesperson.
Electronic address: zajc@nevis.columbia.edu

[1] S. S. Adler *et al.*, Phys. Rev. Lett. **91**, 072301 (2003).
[2] J. Adams *et al.*, Phys. Rev. Lett. **91**, 172302 (2003).
[3] S. S. Adler *et al.*, Phys. Rev. C **69**, 034910 (2004).
[4] S. S. Adler *et al.*, Phys. Rev. Lett. **91**, 072303 (2003).
[5] J. Adams *et al.*, Phys. Rev. Lett. **91**, 072304 (2003).
[6] J. A. Appel, Annu. Rev. Nucl. Part. Sci. **42**, 367 (1992).
[7] Y. L. Dokshitzer and D. E. Kharzeev, Phys. Lett. B **519**, 199 (2001).
[8] M. Djordjevic and M. Gyulassy, Phys. Lett. B **560**, 37 (2003).
[9] B. W. Zhang, E. Wang, and X.-N. Wang, Phys. Rev. Lett. **93**, 072301 (2004).
[10] T. Matsui and H. Satz, Phys. Lett. B **178**, 416 (1986).
[11] R. L. Thews, M. Schroedter, and J. Rafelski, Phys. Rev. C **63**, 054905 (2001).
[12] K. Adcox *et al.*, Phys. Rev. Lett. **88**, 192303 (2002).
[13] K. Adcox *et al.*, Nucl. Instrum. Methods Phys. Res., Sect. A **499**, 469 (2003).
[14] GEANT 3.2.1, CERN program library.
[15] R. Seto *et al.*, J. Phys. G **30**, S1017 (2004).
[16] S. S. Adler *et al.*, Phys. Rev. C **69**, 034909 (2004).
[17] G. Agakichiev *et al.*, Phys. Lett. B **422**, 405 (1998).
[18] S. Kelly *et al.*, J. Phys. G **30**, S1189 (2004).
[19] H. L. Lai *et al.*, Eur. Phys. J. C **12**, 375 (2000).
[20] D. Acosta *et al.*, Phys. Rev. Lett. **91**, 241804 (2003).
[21] K. Hagiwara *et al.*, Phys. Rev. D **66**, 010001 (2002).
[22] A. Andronic *et al.*, Phys. Lett. B **571**, 36 (2003).
[23] J. Adams *et al.*, nucl-ex/0407006.
[24] R. Vogt, hep-ph/0203151.
[25] S. Batsouli *et al.*, Phys. Lett. B **557**, 26 (2003).

Systematic studies of the centrality and $\sqrt{s_{NN}}$ dependence of the $dE_T/d\eta$ and $dN_{ch}/d\eta$ in heavy ion collisions at midrapidity

S. S. Adler,[5] S. Afanasiev,[17] C. Aidala,[5] N. N. Ajitanand,[43] Y. Akiba,[20,38] J. Alexander,[43] R. Amirikas,[12] L. Aphecetche,[45] S. H. Aronson,[5] R. Averbeck,[44] T. C. Awes,[35] R. Azmoun,[44] V. Babintsev,[15] A. Baldisseri,[10] K. N. Barish,[6] P. D. Barnes,[27] B. Bassalleck,[33] S. Bathe,[30] S. Batsouli,[9] V. Baublis,[37] A. Bazilevsky,[39,15] S. Belikov,[16,15] Y. Berdnikov,[40] S. Bhagavatula,[16] J. G. Boissevain,[27] H. Borel,[10] S. Borenstein,[25] M. L. Brooks,[27] D. S. Brown,[34] N. Bruner,[33] D. Bucher,[30] H. Buesching,[30] V. Bumazhnov,[15] G. Bunce,[5,39] J. M. Burward-Hoy,[26,44] S. Butsyk,[44] X. Camard,[45] J.-S. Chai,[18] P. Chand,[4] W. C. Chang,[2] S. Chernichenko,[15] C. Y. Chi,[9] J. Chiba,[20] M. Chiu,[9] I. J. Choi,[52] J. Choi,[19] R. K. Choudhury,[4] T. Chujo,[5] V. Cianciolo,[35] Y. Cobigo,[10] B. A. Cole,[9] P. Constantin,[16] D. G. d'Enterria,[45] G. David,[5] H. Delagrange,[45] A. Denisov,[15] A. Deshpande,[39] E. J. Desmond,[5] O. Dietzsch,[41] O. Drapier,[25] A. Drees,[44] R. du Rietz,[29] A. Durum,[15] D. Dutta,[4] Y. V. Efremenko,[35] K. El Chenawi,[49] A. Enokizono,[14] H. En'yo,[38,39] S. Esumi,[48] L. Ewell,[5] D. E. Fields,[33,39] F. Fleuret,[25] S. L. Fokin,[23] B. D. Fox,[39] Z. Fraenkel,[51] J. E. Frantz,[9] A. Franz,[5] A. D. Frawley,[12] S.-Y. Fung,[6] S. Garpman,[29,*] T. K. Ghosh,[49] A. Glenn,[46] G. Gogiberidze,[46] M. Gonin,[25] J. Gosset,[10] Y. Goto,[39] R. Granier de Cassagnac,[25] N. Grau,[16] S. V. Greene,[49] M. Grosse Perdekamp,[39] W. Guryn,[5] H.-Å. Gustafsson,[29] T. Hachiya,[14] J. S. Haggerty,[5] H. Hamagaki,[8] A. G. Hansen,[27] E. P. Hartouni,[26] M. Harvey,[5] R. Hayano,[8] X. He,[13] M. Heffner,[26] T. K. Hemmick,[44] J. M. Heuser,[44] M. Hibino,[50] J. C. Hill,[16] W. Holzmann,[43] K. Homma,[14] B. Hong,[22] A. Hoover,[34] T. Ichihara,[38,39] V. V. Ikonnikov,[23] K. Imai,[24,38] D. Isenhower,[1] M. Ishihara,[38] M. Issah,[43] A. Isupov,[17] B. V. Jacak,[44] W. Y. Jang,[22] Y. Jeong,[19] J. Jia,[44] O. Jinnouchi,[38] B. M. Johnson,[5] S. C. Johnson,[26] K. S. Joo,[31] D. Jouan,[36] S. Kametani,[8,50] N. Kamihara,[47,38] J. H. Kang,[52] S. S. Kapoor,[4] K. Katou,[50] S. Kelly,[9] B. Khachaturov,[51] A. Khanzadeev,[37] J. Kikuchi,[50] D. H. Kim,[31] D. J. Kim,[52] D. W. Kim,[19] E. Kim,[42] G.-B. Kim,[25] H. J. Kim,[52] E. Kistenev,[5] A. Kiyomichi,[48] K. Kiyoyama,[32] C. Klein-Boesing,[30] H. Kobayashi,[38,39] L. Kochenda,[37] V. Kochetkov,[15] D. Koehler,[33] T. Kohama,[14] M. Kopytine,[44] D. Kotchetkov,[6] A. Kozlov,[51] P. J. Kroon,[5] C. H. Kuberg,[1,27] K. Kurita,[39] Y. Kuroki,[48] M. J. Kweon,[22] Y. Kwon,[52] G. S. Kyle,[34] R. Lacey,[43] V. Ladygin,[17] J. G. Lajoie,[16] A. Lebedev,[16,23] S. Leckey,[44] D. M. Lee,[27] S. Lee,[19] M. J. Leitch,[27] X. H. Li,[6] H. Lim,[42] A. Litvinenko,[17] M. X. Liu,[27] Y. Liu,[36] C. F. Maguire,[49] Y. I. Makdisi,[5] A. Malakhov,[17] V. I. Manko,[23] Y. Mao,[7,38] G. Martinez,[45] M. D. Marx,[44] H. Masui,[48] F. Matathias,[44] T. Matsumoto,[8,50] P. L. McGaughey,[27] E. Melnikov,[15] M. Mendenhall,[49] F. Messer,[44] Y. Miake,[48] J. Milan,[43] T. E. Miller,[49] A. Milov,[44,51] S. Mioduszewski,[5] R. E. Mischke,[27] G. C. Mishra,[13] J. T. Mitchell,[5] A. K. Mohanty,[4] D. P. Morrison,[5] J. M. Moss,[27] F. Mühlbacher,[44] D. Mukhopadhyay,[51] M. Muniruzzaman,[6] J. Murata,[38,39] S. Nagamiya,[20] J. L. Nagle,[9] T. Nakamura,[14] B. K. Nandi,[6] M. Nara,[48] J. Newby,[46] P. Nilsson,[29] A. S. Nyanin,[23] J. Nystrand,[29] E. O'Brien,[5] C. A. Ogilvie,[16] H. Ohnishi,[5,38] I. D. Ojha,[49,3] K. Okada,[38] M. Ono,[48] V. Onuchin,[15] A. Oskarsson,[29] I. Otterlund,[29] K. Oyama,[8] K. Ozawa,[8] D. Pal,[51] A. P. T. Palounek,[27] V. S. Pantuev,[44] V. Papavassiliou,[34] J. Park,[42] A. Parmar,[33] S. F. Pate,[34] T. Peitzmann,[30] J.-C. Peng,[27] V. Peresedov,[17] C. Pinkenburg,[5] R. P. Pisani,[5] F. Plasil,[35] M. L. Purschke,[5] A. K. Purwar,[44] J. Rak,[16] I. Ravinovich,[51] K. F. Read,[35,46] M. Reuter,[44] K. Reygers,[30] V. Riabov,[37,40] Y. Riabov,[37] G. Roche,[28] A. Romana,[25] M. Rosati,[16] P. Rosnet,[28] S. S. Ryu,[52] M. E. Sadler,[1] N. Saito,[38,39] T. Sakaguchi,[8,50] M. Sakai,[32] S. Sakai,[48] V. Samsonov,[37] L. Sanfratello,[33] R. Santo,[30] H. D. Sato,[24,38] S. Sato,[5,48] S. Sawada,[20] Y. Schutz,[45] V. Semenov,[15] R. Seto,[6] M. R. Shaw,[1,27] T. K. Shea,[5] T.-A. Shibata,[47,38] K. Shigaki,[14,20] T. Shiina,[27] C. L. Silva,[41] D. Silvermyr,[27,29] K. S. Sim,[22] C. P. Singh,[3] V. Singh,[3] M. Sivertz,[5] A. Soldatov,[15] R. A. Soltz,[26] W. E. Sondheim,[27] S. P. Sorensen,[46] I. V. Sourikova,[5] F. Staley,[10] P. W. Stankus,[35] E. Stenlund,[29] M. Stepanov,[34] A. Ster,[21] S. P. Stoll,[5] T. Sugitate,[14] J. P. Sullivan,[27] E. M. Takagui,[41] A. Taketani,[38,39] M. Tamai,[50] K. H. Tanaka,[20] Y. Tanaka,[32] K. Tanida,[38] M. J. Tannenbaum,[5] P. Tarján,[11] J. D. Tepe,[1,27] T. L. Thomas,[33] J. Tojo,[24,38] H. Torii,[24,38] R. S. Towell,[1] I. Tserruya,[51] H. Tsuruoka,[48] S. K. Tuli,[3] H. Tydesjö,[29] N. Tyurin,[15] H. W. van Hecke,[27] J. Velkovska,[5,44] M. Velkovsky,[44] L. Villatte,[46] A. A. Vinogradov,[23] M. A. Volkov,[23] E. Vznuzdaev,[37] X. R. Wang,[13] Y. Watanabe,[38,39] S. N. White,[5] F. K. Wohn,[16] C. L. Woody,[5] W. Xie,[6] Y. Yang,[7] A. Yanovich,[15] S. Yokkaichi,[38,39] G. R. Young,[35] I. E. Yushmanov,[23] W. A. Zajc,[9,†] C. Zhang,[9] S. Zhou,[7] S. J. Zhou,[51] and L. Zolin[17]

(PHENIX Collaboration)

[1]*Abilene Christian University, Abilene, Texas 79699, USA*

[2]*Institute of Physics, Academia Sinica, Taipei 11529, Taiwan*

[3]*Department of Physics, Banaras Hindu University, Varanasi 221005, India*

[4]*Bhabha Atomic Research Centre, Bombay 400 085, India*

[5]*Brookhaven National Laboratory, Upton, New York 11973-5000, USA*

[6]*University of California–Riverside, Riverside, California 92521, USA*

[7]*China Institute of Atomic Energy (CIAE), Beijing, People's Republic of China*

[8]*Center for Nuclear Study, Graduate School of Science, University of Tokyo, 7-3-1 Hongo, Bunkyo, Tokyo 113-0033, Japan*

[9]*Columbia University, New York, New York 10027 and Nevis Laboratories, Irvington, New York 10533, USA*

[10]*Dapnia, Commissariat à l'Energie Atomique Saclay, F-91191 Gif-sur-Yvette, France*

[11]*Debrecen University, H-4010 Debrecen, Egyetem tér 1, Hungary*

[12]*Florida State University, Tallahassee, Florida 32306, USA*

[13]*Georgia State University, Atlanta, Georgia 30303, USA*

[14]*Hiroshima University, Kagamiyama, Higashi-Hiroshima 739-8526, Japan*

 ©2005 The American Physical Society

[15]*Institute for High Energy Physics (IHEP), Protvino, Russia*
[16]*Iowa State University, Ames, Iowa 50011, USA*
[17]*Joint Institute for Nuclear Research, 141980 Dubna, Moscow Region, Russia*
[18]*KAERI, Cyclotron Application Laboratory, Seoul, Korea*
[19]*Kangnung National University, Kangnung 210-702, Korea*
[20]*KEK, High Energy Accelerator Research Organization, Tsukuba-shi, Ibaraki-ken 305-0801, Japan*
[21]*Central Energy Research Establishment, Research Institute for Particle and Nuclear Physics (RMKI), P.O. Box 49, H-1525 Budapest 114, Hungary*
[22]*Korea University, Seoul 136-701, Korea*
[23]*Russian Research Center "Kurchatov Institute," Moscow, Russia*
[24]*Kyoto University, Kyoto 606, Japan*
[25]*Laboratoire Leprince-Ringuet, Ecole Polytechnique, Centre National de la Recherche Scientifique IN2P3, Route de Saclay, F-91128 Palaiseau, France*
[26]*Lawrence Livermore National Laboratory, Livermore, California 94550, USA*
[27]*Los Alamos National Laboratory, Los Alamos, New Mexico 87545, USA*
[28]*LPC, Université Blaise Pascal, Centre National de la Recherche Scientifique-IN2P3, Clermont-Fd, F-63177 Aubiere Cedex, France*
[29]*Department of Physics, Lund University, Box 118, SE-221 00 Lund, Sweden*
[30]*Institut für Kernphysik, University of Muenster, D-48149 Muenster, Germany*
[31]*Myongji University, Yongin, Kyonggido 449-728, Korea*
[32]*Nagasaki Institute of Applied Science, Nagasaki-shi, Nagasaki 851-0193, Japan*
[33]*University of New Mexico, Albuquerque, New Mexico 87131, USA*
[34]*New Mexico State University, Las Cruces, New Mexico 88003, USA*
[35]*Oak Ridge National Laboratory, Oak Ridge, Tennessee 37831, USA*
[36]*IPN-Orsay, Universite Paris Sud, Centre National de la Recherche Scientifique-IN2P3, BP1, F-91406 Orsay, France*
[37]*Petersburg Nuclear Physics Institute (PNPI), Gatchina, Russia*
[38]*Institute of Physical and Chemical Research (RIKEN), Wako, Saitama 351-0198, Japan*
[39]*RIKEN BNL Research Center, Brookhaven National Laboratory, Upton, New York 11973-5000, USA*
[40]*St. Petersburg State Technical University, St. Petersburg, Russia*
[41]*Universidade de São Paulo, Instituto de Física, Caixa Postal 66318, São Paulo CEP05315-970, Brazil*
[42]*System Electronics Laboratory, Seoul National University, Seoul, Korea*
[43]*Chemistry Department, SUNY at Stony Brook, Stony Brook, New York 11794-3400, USA*
[44]*Department of Physics and Astronomy, SUNY at Stony Brook, Stony Brook, New York 11794, USA*
[45]*SUBATECH, Ecole des Mines de Nantes, Centre National de la Recherche Scientifique-IN2P3, Université de Nantes, BP 20722-44307, Nantes, France*
[46]*University of Tennessee, Knoxville, Tennessee 37996, USA*
[47]*Department of Physics, Tokyo Institute of Technology, Tokyo 152-8551, Japan*
[48]*Institute of Physics, University of Tsukuba, Tsukuba, Ibaraki 305, Japan*
[49]*Vanderbilt University, Nashville, Tennessee 37235, USA*
[50]*Waseda University, Advanced Research Institute for Science and Engineering, 17 Kikui-cho, Shinjuku-ku, Tokyo 162-0044, Japan*
[51]*Weizmann Institute, Rehovot 76100, Israel*
[52]*Yonsei University, IPAP, Seoul 120-749, Korea*

(Received 20 September 2004; published 25 March 2005; corrected 6 April 2005)

The PHENIX experiment at the relativistic heavy ion collider (RHIC) has measured transverse energy and charged particle multiplicity at midrapidity in Au + Au collisions at center-of-mass energies $\sqrt{s_{NN}} = 19.6$, 130, and 200 GeV as a function of centrality. The presented results are compared to measurements from other RHIC experiments and experiments at lower energies. The $\sqrt{s_{NN}}$ dependence of $dE_T/d\eta$ and $dN_{\rm ch}/d\eta$ per pair of participants is consistent with logarithmic scaling for the most central events. The centrality dependence of $dE_T/d\eta$ and $dN_{\rm ch}/d\eta$ is similar at all measured incident energies. At RHIC energies, the ratio of transverse energy per charged particle was found to be independent of centrality and growing slowly with $\sqrt{s_{NN}}$. A survey of comparisons between the data and available theoretical models is also presented.

DOI: 10.1103/PhysRevC.71.034908 PACS number(s): 25.75.Dw

*Deceased.
†PHENIX Spokesperson: zajc@nevis.columbia.edu.

I. INTRODUCTION

The PHENIX experiment at the relativistic heavy ion collider (RHIC) at Brookhaven National Laboratory was designed to measure the properties of matter at extremely high temperatures and densities. Under such conditions, the possibility exists of producing states of matter that have not been observed and studied in the laboratory. Perhaps the best known of these is the quark-gluon plasma (QGP), a matter in which the quarks are not confined within individual baryons but exist as some form of plasma of individual quarks and gluons. It should be emphasized that the exact properties of this matter are not known and that the characterization of the deconfined state, if such a state is produced, will form an essential part of the RHIC program.

One fundamental element of the study of ultrarelativistic collisions is the characterization of the interaction in terms of variables such as the energy produced transverse to the beam direction or the number of charged particles. These variables are closely related to the collision geometry and are important in understanding global properties of the system during the collision.

This paper describes the PHENIX experiment's systematic study of $dE_T/d\eta$ and $dN_{\rm ch}/d\eta$ at midrapidity at center-of-mass energies $\sqrt{s_{NN}} = 19.6$, 130, and 200 GeV. The centrality dependence of $dE_T/d\eta$ and $dN_{\rm ch}/d\eta$ is characterized by the number of participants, determined with a Glauber model, and is studied as a function of the incident energy. $dE_T/d\eta$ and $dN_{\rm ch}/d\eta$ results for all four RHIC experiments are included in this study. The data taken at 19.6 GeV are particularly interesting because they can be compared with data taken at lower energies by the CERN super proton synchroton (SPS) program. Comparisons are also made with results of previous experiments conducted at the Brookhaven alternating-gradient synchroton (AGS) and the CERN SPS for c.m. energies of 4.8, 8.7, and 17.2 GeV. Finally, an extensive set of collision models describing the E_T and $N_{\rm ch}$ distributions are compared with existing data. Appendix A describes the recalculation of non-PHENIX data to make comparison possible. Appendix B contains the PHENIX measurement data.

II. PHENIX DETECTOR

PHENIX is one of four experiments located at RHIC [1]. The PHENIX detector consists of two central spectrometer arms, designated east and west for their location relative to the interaction region, and two muon spectrometers, similarly called north and south. Each central spectrometer arm covers a rapidity range of $|\eta| < 0.35$ and subtends 90° in azimuth. The muon spectrometers both have full azimuthal coverage with a rapidity range of $-2.2 < \eta < -1.2$ (south) and $1.2 < \eta < 2.4$ (north). Additional global detectors are used as input to the trigger and for global event characterization such as vertex, time of event, and centrality determination. A detailed description of the PHENIX detector can be found in [2]. The PHENIX detector subsystems relevant to the physics analysis presented in this paper are listed below.

Charged particle multiplicity was measured with two multiwire proportional chamber (MWPC) layers of the pad chambers (PCs) [3] called PC1 and PC3. These are located in both central arms at the radii of 2.5 and 5.0 m from the beam axis. The PCs cover the full central arm acceptance and have an efficiency greater than 99.5% for minimum ionizing particles. The position resolution of PC1 was measured to be 1.7 by 3 mm; it was twice that for PC3. PC1 and PC3 can distinguish between two particle tracks if they strike the detector with a separation greater than 4 and 8 cm, respectively.

For the transverse energy measurements, a PbSc sampling calorimeter (EMCal) [4] from the PHENIX central spectrometers was used. The front face of EMCal is located 5.1 m from the beam axis. Scintillation light produced in the PbSc EMCal towers is read out through wavelength shifting fibers that penetrate the module. The depth of the PbSc calorimeter is 18 radiation lengths (X_0) which corresponds to 0.85 nuclear interaction lengths. The PbSc calorimeter has an energy resolution of $8.1\%/\sqrt{E\,(\mathrm{GeV})} \oplus 2.1\%$ for test beam electrons, with a measured response proportional to the incident electron energy that is within $\pm 2\%$ over the range $0.3 \leqslant E_e \leqslant 40.0$ GeV [4].

Two identical beam-beam counters (BBCs) [5] each consisting of 64 individual Cherenkov counters with 3-cm quartz glass radiators cover the full azimuthal angle in the pseudorapidity range $3.0 < |\eta| < 3.9$. These detectors provide a minimum biased (MB) event trigger and timing and are also used for event vertex determination. The vertex position resolution for central Au + Au events was 6 mm along the beam axis.

The zero degree calorimeters (ZDCs) [6] are hadronic calorimeters located on both sides of the PHENIX detector. They cover a rapidity region of $|\eta| > 6$ and measure the energy of the spectator neutrons with approximately 20% energy resolution. The BBC and ZDC were used for the centrality determination.

III. DATA ANALYSIS

The analysis procedures for the $dE_T/d\eta$ and $dN_{\rm ch}/d\eta$ measured at $\sqrt{s_{NN}} = 130$ GeV are described in [7] and [8], respectively. In this paper the analysis was improved in the following ways:

- Inflow and outflow corrections were done based on the identified particle data, as opposed to HIJING.
- Corrected trigger efficiency was $92.2^{+2.5}_{-3.0}\%$ instead of $92.0 \pm 2 \pm 1\%$.
- Definition of E_T was modified as discussed below.

The results presented here for $\sqrt{s_{NN}} = 130$ GeV are consistent with results previously published.

The same data samples with zero magnetic field were used for both E_T and $N_{\rm ch}$ measurements at each beam energy. The analyzed numbers of events are approximately 40×10^3, 160×10^3, and 270×10^3 for $\sqrt{s_{NN}} = 19.6$, 130, and 200 GeV, respectively.

The main steps of the analysis procedure are discussed below in connection with the systematic errors associated with them. Some additional details can be found in [9–12].

A. E_T analysis

The transverse energy E_T is defined as

$$E_T = \sum_i E_i \sin\theta_i, \quad (1)$$

where θ_i is the polar angle. The sum is taken over all particles emitted into a fixed solid angle in an event. By convention, E_i is taken to be $E_i^{\rm tot} - m_N$ for baryons, $E_i^{\rm tot} + m_N$ for antibaryons, and $E_i^{\rm tot}$ for all other particles, where $E_i^{\rm tot}$ is the total energy of the particle and m_N is the nucleon mass.[1]

The E_T measurement presented in this paper was performed using the PHENIX PbSc EMCal. The EMCal absolute energy scale was set using the π^0 mass peak reconstructed from pairs of EMCal clusters. The value was checked against a measurement of the minimum ionizing peak for charged particles penetrating along the tower axis and the energy/momentum (E/p) peak of identified electrons and positrons. The uncertainty in the absolute energy scale is 3% in the $\sqrt{s_{NN}} =$ 19.6-GeV data and 1.5% in the 130- and 200-GeV data.

The EMCal acts as a thin but effective hadronic calorimeter at midrapidity at a collider [7]. The mean hadron momenta in the EMCal acceptance are approximately 0.4, 0.55, and 0.9 GeV/c for pion, kaons, and (anti)protons, respectively [13]. Most hadrons stop in the EMCal, depositing all their kinetic energy (at p_T less than 0.35 GeV/c for pions, 0.64 for kaons, and 0.94 for protons).

The average EMCal response to the different particle species was obtained with a GEANT-based [14] Monte Carlo (MC) simulation of the PHENIX detector using the HIJING [15] event generator. The HIJING particle composition and p_T spectra were tuned to the identified charged particle spectra and yields in Au + Au collisions measured by PHENIX [13,16] at $\sqrt{s_{NN}} = 200$ and 130 GeV. The NA49 results [17–19] were used for EMCal response studies for 19.6-GeV data. The "deposited" $E_{T_{\rm EMC}}$ was about 75% of the total E_T "striking" the EMCal. This value varied in the $\pm 1.5\%$ range for different centralities and beam energies.

The uncertainty in the EMCal response to hadrons gave a 3% error to the total E_T. This uncertainty was estimated using a comparison between the simulated energy deposited by hadrons with different momenta and from the test beam data [4]. An additional error of 1.3% at $\sqrt{s_{NN}} = 19.6$ and 200 GeV and 1% at 130 GeV comes from the systematic uncertainties in the particle composition and momentum distribution.

E_T was computed for each event [Eq. (1)] using clusters with energy greater than 30 MeV composed of adjacent towers with deposited energy of more than 10 MeV.[2] The energy losses at the EMCal edges and those due to energy thresholds, 6% each, were estimated with the absolute uncertainty 1.5%.

The first main issue for the E_T measurement is the correction for losses for particles originating within the aperture but whose decay products miss the EMCal ($\sim$10%). The second issue is the inflow contribution ($\sim$24%), which is principally of two types: (1) albedo from the magnet poles and (2) particles originating outside the aperture of the calorimeter but whose decay products hit the calorimeter. The inflow component was checked by comparing the MC simulation and the measurements for events with a vertex just at and inside a pole face of the axial central-spectrometer magnet, for which the calorimeter aperture was partly shadowed. The estimated contribution of the inflow uncertainty to the E_T uncertainty is 3% [7].

Since E_T measurements are based on the sum of all cluster energies in the EMCal, random noise even in a small portion of the total number of EMCal towers ($\sim$15,000 in PbSc) may affect the total energy in the EMCal, particularly in peripheral collisions. This effect was estimated by measuring the total energy in the EMCal in very peripheral events with the collision vertex inside the magnet poles. In this case, the EMCal is fully shadowed and no energy deposit from beam collisions is expected. The estimated contribution was consistent with zero. The uncertainty from this effect contributes 3.5% systematic error to the E_T measurement in the most peripheral bin of 45–50% at $\sqrt{s_{NN}} = 19.6$ GeV, 10% to the most peripheral bin of 65–70% at 130 GeV, and 6% to the bin of 65–70% at 200 GeV. The contribution to the systematic error for central events is negligible.

B. $N_{\rm ch}$ analysis

In the absence of a magnetic field, the particle tracks are straight lines. The number of tracks in the event was determined by combining all hits in PC3 with all hits in PC1. The resulting straight lines were projected onto a plane containing the beam line and perpendicular to the symmetry axis of the PCs. All tracks intersecting the plane at a radius less than 25 cm from the event vertex were accepted. $95\pm1\%$ of all real tracks in the event pointed back within this radius. The complete set of tracks thus formed contained both real tracks and tracks from a combinatorial background. The latter were determined using a mixed event technique in which each sector in PC1 was exchanged with its neighbor and the resulting combinatorial background measured. The average combinatorial background from the mixed event analysis was subtracted from the data obtained from the real events. Several corrections were subsequently applied.

A correction of 15.3% accounted for nonsensitive mechanical gaps between the PC sectors, inactive electronic readout cards, and dead pads in the PC1 and PC3 detectors. The data were also corrected for the PC efficiency for an isolated hit, measured to be 99.5% using cosmic rays [3]. The combined systematic error from these corrections was estimated to be 2.5% for a single east arm and 2.3% for both east and west arms.

Track losses from the finite double hit resolution of the PCs depend on the event multiplicity. Losses can occur in both the direct counting of tracks and in the combinatorial background subtraction. These two effects were studied in great detail using

[1]The definition of E_i in our earlier publication [7] is different for the antibaryon contribution: $E_i^{\rm tot}$ was used instead of $E_i^{\rm tot} + m_N$. The current definition increases the value of E_T by about 4%, independent of centrality.

[2]In [7] thresholds of 20 and 3 MeV were applied for the cluster and for the tower, respectively. Energy losses due to thresholds were properly accounted for in both analyses.

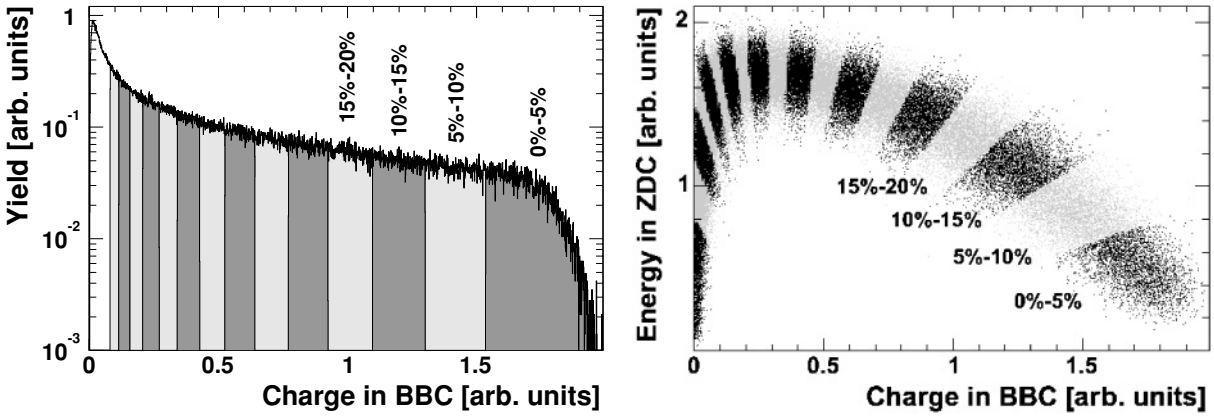

FIG. 1. Different centrality classes based on the BBC (left) and ZDC vs. BBC (right) distributions.

Monte Carlo techniques. To account for the track losses in the real event sample, a correction of 15%, 13%, and 6% for the 5% most central events was applied at $\sqrt{s_{NN}} = 200$, 130, and 19.6 GeV, respectively.

Track losses due to the finite double hit resolution reduce the combinatorial background in the real events more than in the mixed events. The number of tracks in the mixed events must be decreased by 3.6% to account for this. The uncertainty in the correction related to the finite double hit resolution of the PCs was estimated to be 3.5% of the number of reconstructed tracks in the most central events at $\sqrt{s_{NN}} = 200$ GeV. This number was deduced from the simulation and cross-checked with an artificial 50% increase of the double hit resolution of PC1 and PC3.

An additional correction is related to the decay of charged particles and feed-down from the decay of neutral particles. This correction is discussed in [8], where it was determined using the HIJING event generator. In this paper the measured composition of the produced particles at different centralities is used at $\sqrt{s_{NN}} = 200$ and 130 GeV [13,16]. The correction related to particle decay varies about $\pm 1\%$ over the full range of measured centralities. In midcentral events it is $-1 \pm 2.9\%$ and $+1 \pm 2.5\%$ at 200 and 130 GeV, respectively. At the lowest RHIC energy the correction is based on NA49 [17–19] measurements at close energy 17.2 GeV and is about $11 \pm 5.7\%$ independent of centrality. The difference between 19.6 and 130 GeV arises from the decrease of the particle momenta and the width of the η distribution at lower energy which affects the number of tracks from the decay of particles coming from adjacent rapidities. The uncertainty is also larger because the correction was based on non-PHENIX data. More details on the analysis can be found in [8,11,12].

C. Determination of trigger efficiency and N_p

The distribution of the number of participants (N_p) in Au + Au collisions was determined using a Monte Carlo simulation based on the Glauber model. The inelastic cross section of $p + p$ collisions used in the Glauber model was taken to be 31, 41, and 42 mb at $\sqrt{s_{NN}} = 19.6$, 130, and 200 GeV, respectively [20], and was varied within ± 3 mb in order to get the systematic errors. The nuclear density profile $\rho(r)$ was taken as the Woods-Saxon parametrization,

$$\rho(r) = 1/(1 + e^{(r-r_n)/d}), \tag{2}$$

where r_n is the nucleus radius and d is a diffuseness parameter. Based on the measurements of electron scattering from Au nuclei [21], r_n was set to (6.38 ± 0.27) fm and d to (0.54 ± 0.01) fm.

The BBC detectors are located in a region where the number of produced particles is proportional to N_p at $\sqrt{s_{NN}} =$ 130 and 200 GeV [22]. By comparing measured BBC spectra to simulations, the MB trigger efficiency was estimated to be $92.2^{+2.5}_{-3.0}\%$ at both 200 and 130 GeV, with less than 1% uncertainty in the difference between these two energies.

One can also use the BBC (or ZDC vs. BBC) response to define centrality for a given event as a percentage of the total geometrical cross section. The BBC amplitude distribution and ZDC vs. BBC signals divided into centrality classes are shown in Fig. 1.

By matching the detector response simulation to the data, N_p can be assigned to each centrality class. The results for N_p vary by less than 0.5% depending on the shape of the cut in the ZDC/BBC space and whether the BBC alone was used as a centrality measure. The larger error in N_p comes from model uncertainties and can be parametrized as $\Delta N_p/N_p = 0.02 + 3.0/N_p$.

At $\sqrt{s_{NN}} = 19.6$ GeV, the BBC acceptance partially covers the Au nuclei fragmentation region where the relation between the particle production and N_p is not well known for peripheral events. This makes the MB trigger efficiency model dependent. To avoid this problem, an approach based on the Glauber model and the negative binomial distribution (NBD) was applied to the data from the PHENIX central arm. For the centrality associations, the BBC signal can still be used after applying the following correction.

The NBD, written as

$$P(n, \mu, k) = \Gamma(n + k)/(\Gamma(k)n!) \cdot (\mu/k)^n/(1 + \mu/k)^{n+k}, \tag{3}$$

represents the number of independent trials n that are required to get a number of predetermined successes if the average number of successes per trial is μ. The parameter k is related

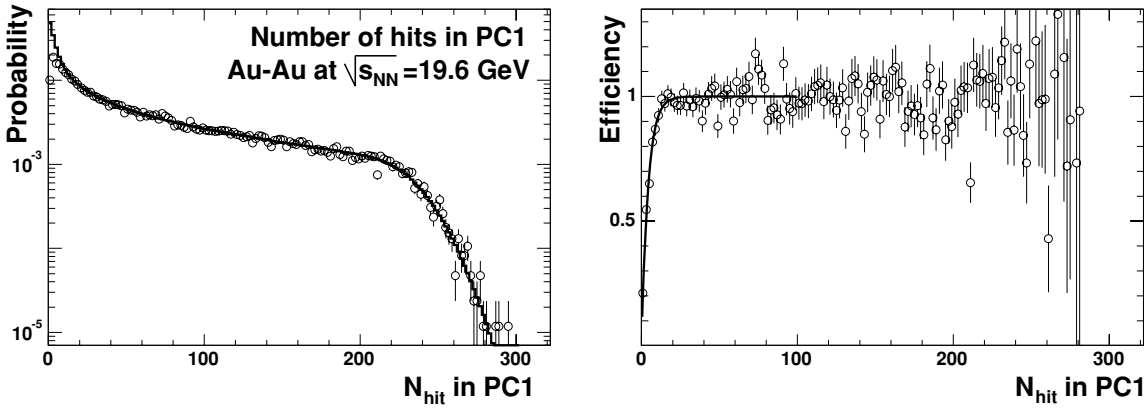

FIG. 2. Left panel: Glauber/NBD fit (line) to the distribution of the number of hits in the PC1 detector at $\sqrt{s_{NN}} = 19.6$ GeV (circles). Right panel: MB trigger efficiency as a function of the number of hits. The parametrization is to guide the eye.

to the variance of the distribution by the equation $(\sigma/\mu)^2 = 1/k + 1/\mu$. By associating n with the number of particles produced in the event such that $n = f(N_p)$, the NBD describes the distribution of hits in a detector [23,24] produced by a given number of N_p. In the simplest case when $n \propto N_p$, $\langle N_{\rm hit}\rangle = \mu\langle N_p\rangle$. Using probability weights for N_p from the Glauber model, one can construct a distribution of the number of hits in a detector. The coefficients μ and k can be obtained by fitting the constructed distribution to the experimentally measured distribution.

The number of hits in the PC1 detector shown in the left panel of Fig. 2 was used to determine the trigger efficiency. $N_{\rm hit} \propto dN_{\rm ch}/d\eta$ can be parametrized as scaling with the number of participants N_p^{α}, where α is between 1.0 and 1.1 as measured by WA98 at the CERN SPS [25]. The Glauber/NBD fit to the distribution of the number of hits in PC1 is shown as the solid line. The fitting range is constrained above some number of hits, where the trigger efficiency is equal to 1. The efficiency as a function of the number of hits in the detector can be found by taking the ratio of measured and reconstructed distributions. This is shown in the right panel of Fig. 2. Intergated over all $N_{\rm hits}$ the MB trigger efficiency was found to be $81.5 \pm 3\%$ at $\sqrt{s_{NN}} = 19.6$ GeV. The 1% uncertainty due to variation of α from 1.0 to 1.1 was included in the systematic error. An uncertainty in the difference between 19.6 and 200 GeV was 1.5%.

A fraction of events missing in the trigger at all energies belongs to the peripheral centrality classes outside the centrality range discussed in this paper.

As a cross-check, the same procedure was applied to the BBC response at 200 GeV. It was found that the MB trigger efficiency in Au + Au and d + Au collisions agrees with the procedure based on a full simulation within one standard deviation of the systematic error. In Au + Au the N_p in the centrality bins determined using the Glauber/NBD method agree better than 0.5% with the values used in this paper. In d + Au for a single nucleon-nucleon collision the MB trigger efficiency was found to be 57%, consistent with the $52 \pm 7\%$ measured for PHENIX $p + p$ trigger efficiency at the same energy using a different method [26]. Finally, the fraction of expected p + Au collisions in the d + Au sample agrees with the fraction of events in which the corresponding ZDC detects the spectator neutron from the deuteron within better than 1.5%.

As stated above, the BBC detector at $\sqrt{s_{NN}} = 19.6$ GeV covers a part of the Au nuclei fragmentation region, and its response is not linear with N_p [22]. Also, the number of hits in BBC has a strong vertex dependence mainly because the BBC samples different parts of the $dN_{\rm ch}/d\eta$ distribution at different vertices; see Fig. 3. The asymmetry of north and south BBC amplitudes in the same event was studied to correct for these two effects. Around vertex $z = 0$ the asymmetry between the number of hits in north BBC $N(z)$ and south BBC $S(z)$ is $(N(z) - S(z))/(S(z) + N(z)) \propto (d^2N_{\rm ch}/d\eta^2)/(dN_{\rm ch}/d\eta)$ reflects the slope of the η distribution at BBC rapidity. To use the BBC signal for the N_p determination, the observed signals were scaled such that the asymmetry between north and south was the same as in the most central events where the influence of the fragmentation region was negligible. The data were also corrected for vertex dependence. The results of the correction are shown in Fig. 3.

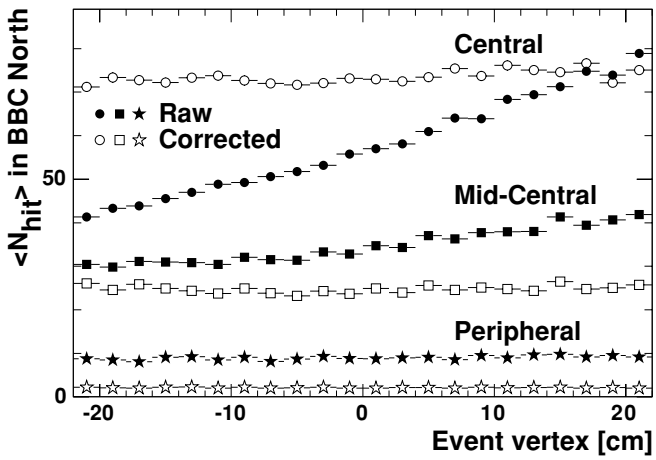

FIG. 3. Average number of hits in BBC north vs. event vertex at different centralities before correction (solid symbols) and after correction (open symbols).

TABLE I. Summary of systematic errors given in percent. When a range is given, the first number corresponds to the most central bin and the second to the most peripheral bin presented in Appendix B, Tables XIII–XV.

	$dE_T/d\eta$			$dN_{\rm ch}/d\eta$		
$\sqrt{s_{NN}}$ (GeV)	19.6	130	200	19.6	130	200
Energy resp.	4.7	3.8	3.9			
Bkg./noise	0.5–3.5	0.4–10	0.2–6	1.0	1.0	1.0
Acceptance	2.0	2.0	2.0	2.3	2.5	2.3
In- & outflow	3.0	3.0	3.0	5.7	2.5	2.9
Occupancy				1.6–0.3	3.1–0.1	3.5–0.1
Centrality	2.0	0.5	0.5		Same	
N_p	2.9–6.7	2.8–15	2.8–15		Same	
Trigger	0.4–8.8	0.3–16	0.3–16		Same	

The corrected BBC response was used for the centrality determination. Based on both data and Monte Carlo simulation, a systematic error of 2% was added to the determination of the centrality classes using the BBC correction procedure.

D. Systematic error summary

Table I summarizes the systematic errors discussed in this section. The "Energy resp." error for the E_T measurements combines the uncertainties in absolute energy scale, hadronic response, and energy losses on the EMCal edges and from energy thresholds. The resulting error for each centrality bin is a quadratic sum of the errors listed in the table.

IV. RESULTS

A. PHENIX results

The distribution of the raw transverse energy $E_{T_{\rm EMC}}$ into the fiducial aperture of two EMCal sectors is shown in the left three panels of Fig. 4 for the three RHIC energies. The lower scale represents the fully corrected E_T normalized to one unit of pseudorapidity and full azimuthal acceptance. The lower axis in the plot is not labeled beyond 200 GeV to avoid confusion between the true shape of the $dE_T/d\eta$ distribution and E_T as measured using the limited acceptance of two EMCal sectors.

For the measurements at $\sqrt{s_{NN}} = 19.6$ and 200 GeV, five EMCal sectors (with azimuthal coverage $\Delta\phi = 112^\circ$) were used, while only two sectors ($\Delta\phi = 45^\circ$) were available during

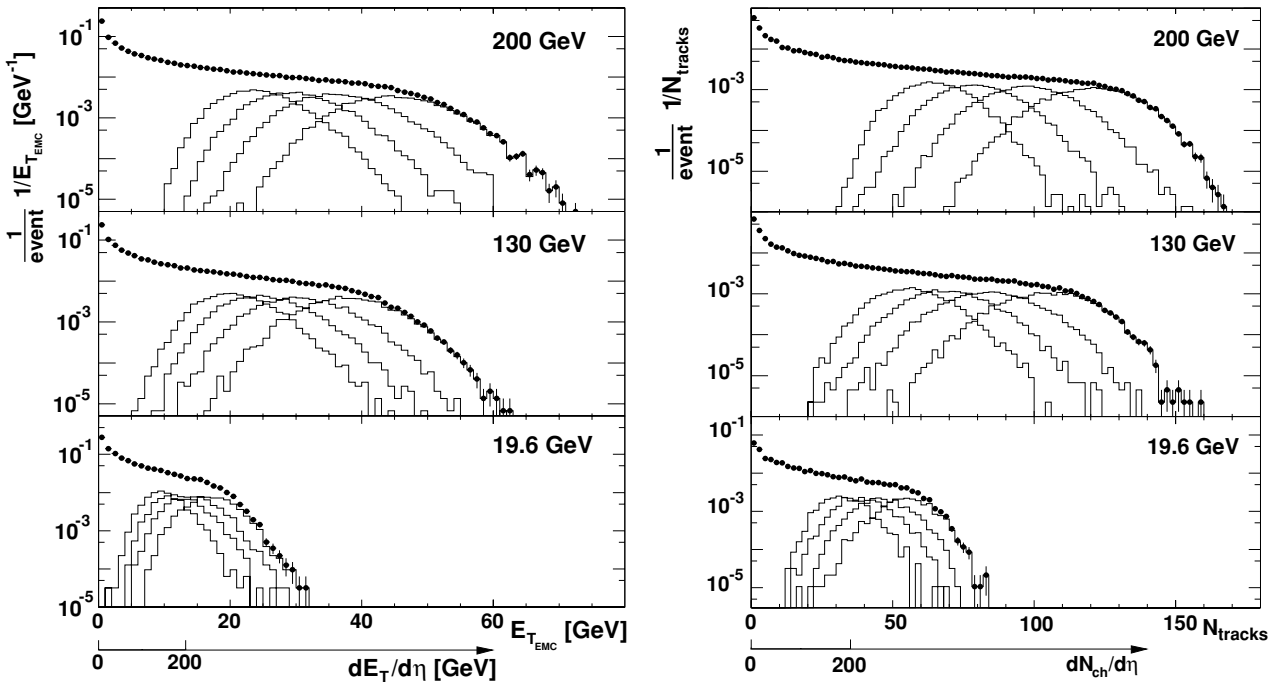

FIG. 4. The distribution of the raw E_T in two EMCal sectors (left) and the number of tracks in the east arm of the PHENIX detector (right) per MB trigger, measured at three energies. The lower axis corresponds to midrapidity values of $dE_T/d\eta$ and $dN_{\rm ch}/d\eta$, respectively. Distributions of the four 5% most central bins are also shown in each plot.

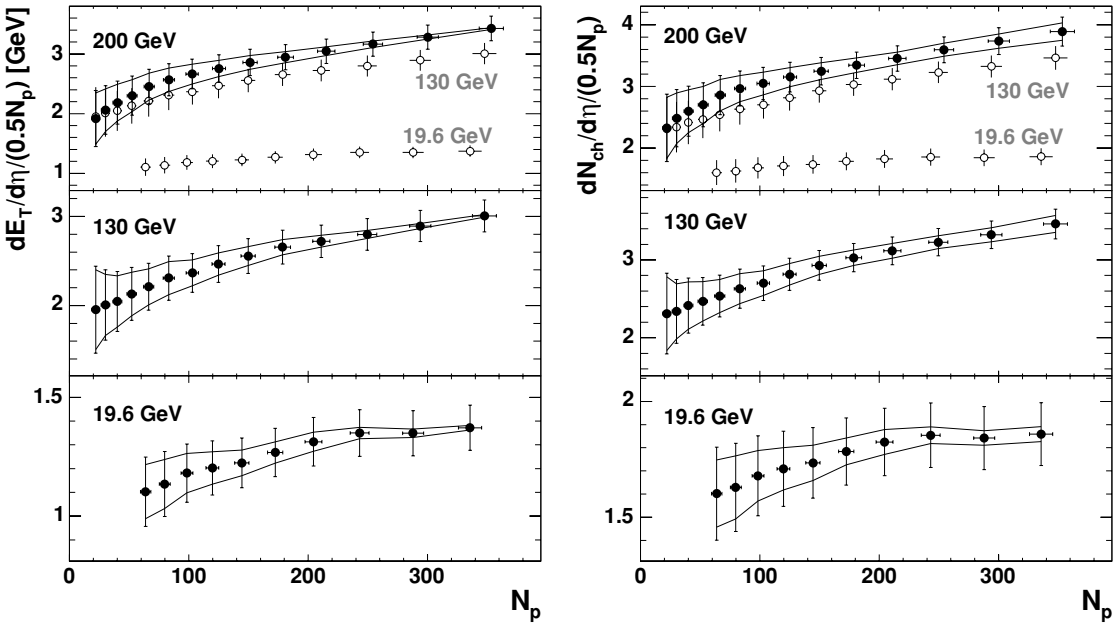

FIG. 5. $dE_T/d\eta$ (left) and $dN_{\rm ch}/d\eta$ (right) divided by the number of participant pairs at three RHIC energies. Errors shown with vertical bars are full systematic errors. Lines show the part of the systematic error that allows bending or inclination of the points. Horizontal errors denote the uncertainty in determination of N_p.

the PHENIX run at 130 GeV. Results obtained with different number of sectors at the same energy were consistent within 1.5%.

The right three panels in Fig. 4 show the number of tracks reconstructed in the east arm of the PHENIX detector after background subtraction and all corrections. The lower axis corresponds to measured distributions normalized to one unit of pseudorapidity and full azimuthal acceptance. For a similar reason as for the E_T measurement, the lower axis is not labeled above 200 GeV in $dN_{\rm ch}/d\eta$.

For the $N_{\rm ch}$ measurements at $\sqrt{s_{NN}} = 130\,\text{GeV}$, only the east arm was used; for the other two energies the measurements were made using both PHENIX central arms. The results obtained with two arms at 200 and 19.6 GeV are consistent with each other within 1.5%.

The distributions shown in Fig. 4 have a characteristic shape with a sharp peak that corresponds to the most peripheral events. Missing events caused by the finite MB trigger efficiency in peripheral events would make this peak even sharper than measured. The plateau in all distributions corresponds to midcentral events, and the falloff to the most central Au + Au events. The shape of the curves in Fig. 4 in the falloff region is a product of the intrinsic fluctuations of the measured quantities and the limited acceptance of the detector.

The distributions for the four most central bins (0–5% to 15–20%) are also shown in each panel. The centroids of these distributions were used to calculate the centrality dependence of $dE_T/d\eta$ and $dN_{\rm ch}/d\eta$.[3] The statistical uncertainties of all mean values (less than or about 1%) determined by the width of the distributions are small because of the large size of the event samples.

The magnitude of $dE_T/d\eta$ and $dN_{\rm ch}/d\eta$ at midrapidity divided by the number of participant pairs as a function of N_p is shown in Fig. 5 and tabulated in Appendix B, Tables XIII–XV. The right three panels show the same ratio for $dN_{\rm ch}/d\eta$ at the three RHIC energies.

The horizontal errors correspond to the uncertainty in N_p, determined within the framework of the Monte Carlo–Glauber model. The vertical bars show the full systematic errors of the measurements[4] added quadratically to the errors of N_p. The lines denote the corridor in which the points can be inclined or bent. The statistical errors are smaller than the size of the markers. The upper panel also shows the results of the two lower panels with open markers for comparison.

An important result from Fig. 5 is an evident consistency in the behavior of the centrality curves of E_T shown on the left and $N_{\rm ch}$ shown on the right for all measured energies. Both values demonstrate an increase from peripheral (65–70% bin) to the most central events by 50–70% at RHIC energies 130 and 200 GeV. For the lowest RHIC energy (19.6 GeV) this increase is at the level of systematic uncertainties of the measurement. One can note that results from PHOBOS [27] show that the total charged particle multiplicity is proportional to N_p, while the multiplicity at midrapidity over N_p increases with N_p, indicating that the pseudorapidity distribution gets more narrow for central events.

The ratios of the $dE_T/d\eta$ and $dN_{\rm ch}/d\eta$ per participant pair measured at different RHIC energies are shown in

[3]All plotted and quoted numbers correspond to average values in each centrality bin or ratios of those averages.

[4]Here and everywhere errors correspond to one standard deviation.

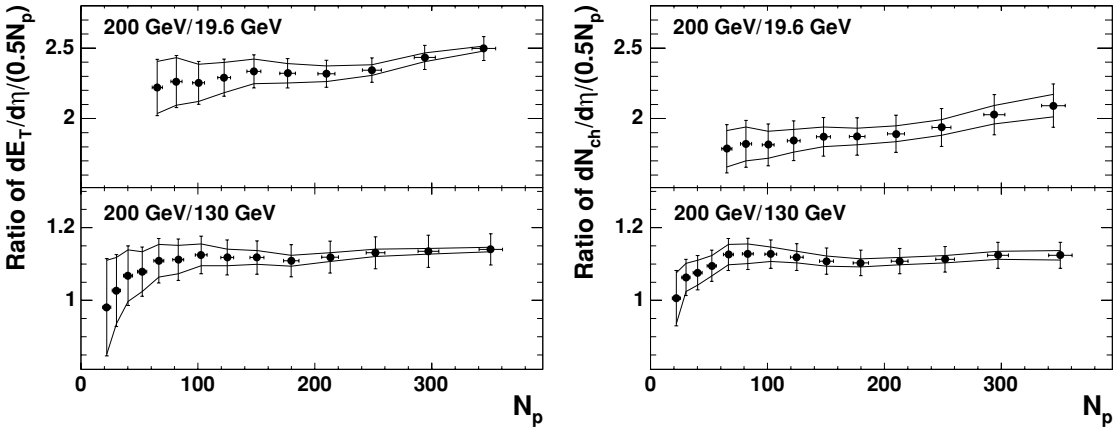

FIG. 6. Same as Fig. 5, but for ratios of $dE_T/d\eta$ (left) and $dN_{\rm ch}/d\eta$ (right) measured at different RHIC energies.

Fig. 6 and tabulated in Table XVI. In these ratios some common systematic errors cancel.

The increase in the E_T production between 19.6 and 200 GeV (with an average factor of 2.3) is larger than for $N_{\rm ch}$ (with average factor of 1.9). This is consistent with an increase in the particle production per participant common to both E_T and $N_{\rm ch}$ and a $\sim$20% increase in $\langle m_T \rangle$ of produced particles contributing to the E_T parameter only. See Appendix A 1 and [16,17].

The ratio of 200/19.6 GeV shows some increase from peripheral to central events; however, the increase is marginally at the level of the systematic errors of the measurement.

The ratio of 200/130 GeV is flat above $N_p \sim 80$ and is equal to 1.140 ± 0.043 for E_T and 1.126 ± 0.036 for $N_{\rm ch}$ in the most central bin. A rather sharp increase between $N_p = 22$ and 83 in the ratios of both quantities is still at the level of systematic uncertainties.

The ratio of the transverse energy and charged particle multiplicity at midrapidity as a function of centrality is shown in Fig. 7 for the three energies. The upper plot also shows the results displayed in the lower panels for comparison.

The ratio $E_T/N_{\rm ch}$,[5] sometimes called the "global barometric observable," triggered considerable discussion [28,29]. It is related to the $\langle m_T \rangle$ of the produced particles and is observed to be almost independent of centrality and incident energy of the collisions within the systematic errors of the previous measurements. The present paper forges a direct link between the highest SPS and lowest RHIC energies, making a more quantitative study of $E_T/N_{\rm ch}$ possible.

The results presented in Fig. 7 and tabulated in Tables XIII–XV show that the centrality dependence of $E_T/N_{\rm ch}$ is weak and lies within the systematic errors plotted with lines. There is a clear increase in $E_T/N_{\rm ch}$ between $\sqrt{s_{NN}} = 19.6$ and 200 GeV. The $\sqrt{s_{NN}}$ dependence of the results is discussed below.

B. Bjorken energy density

The Bjorken energy density [30] can be calculated using

$$\epsilon_{Bj} = \frac{1}{A_\perp \tau} \frac{dE_T}{dy}, \tag{4}$$

where τ is the formation time and $A_\perp$ is the nuclei transverse overlap area.

The transverse overlap area of two colliding nuclei was estimated using a Monte Carlo–Glauber model $A_\perp \sim \sigma_x \sigma_y$, where σ_x and σ_y are the widths of x and y position distributions of the participating nucleons in the transverse plane. The normalization to πR^2, where R is the sum of r_n and d parameters in a Woods-Saxon parametrization [Eq. (2)], was done for the most central collisions at the impact parameter $b = 0$. For the transformation from $dE_T/d\eta|_{\eta=0}$ to $dE_T/dy|_{y=0}$, a scale factor of 1.25 ± 0.05 was used; see Appendix A 1.

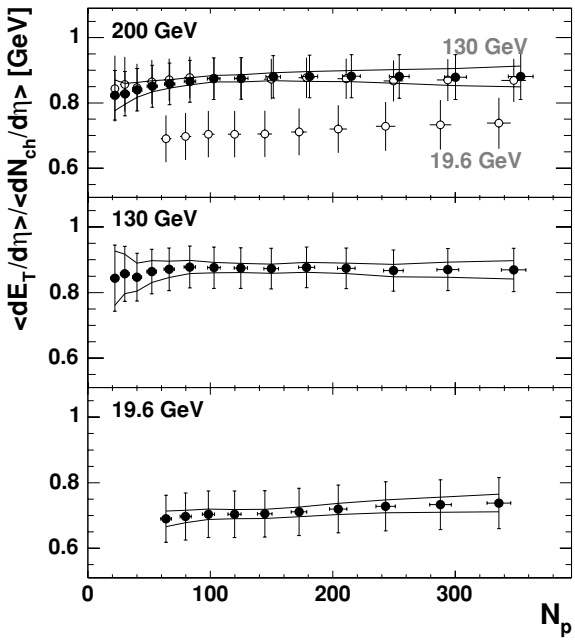

FIG. 7. Same as Fig. 5, but for $E_T/N_{\rm ch}$ vs. N_p at different RHIC energies.

[5] $E_T/N_{\rm ch}$ is used as a shortcut for $\langle dE_T/d\eta \rangle / \langle dN_{\rm ch}/d\eta \rangle$ at $\eta = 0$ in the c.m. system.

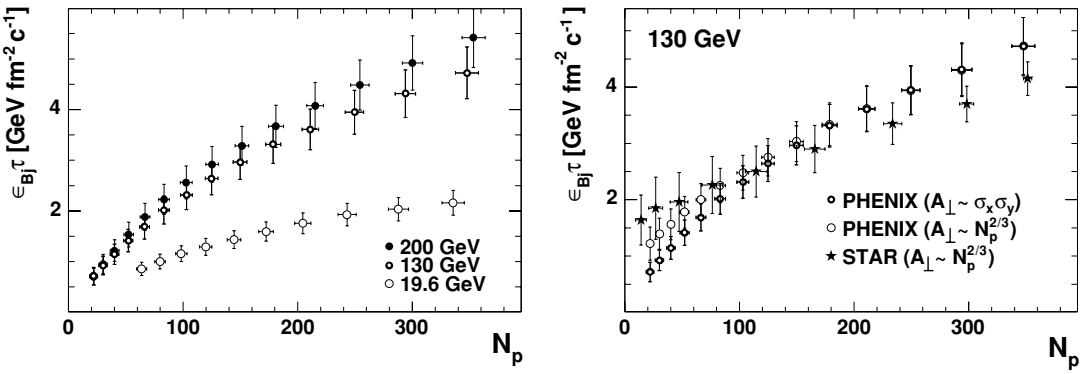

FIG. 8. $\epsilon_{Bj} \cdot \tau$ deduced from the PHENIX data at three RHIC energies (left) and using different estimates of the nuclear transverse overlap at $\sqrt{s_{NN}} = 130$ GeV (right).

The Bjorken energy density for three RHIC energies is plotted in the left panel of Fig. 8 and tabulated in Tables XIII–XV. For the 5% most central collisions, $\epsilon_{Bj} \cdot \tau$ was $2.2 \pm 0.2, 4.7 \pm 0.5$, and 5.4 ± 0.6 GeV fm$^{-2}c^{-1}$ for $\sqrt{s_{NN}} =$ 19.6, 130, and 200 GeV, respectively. These values increase by 2, 4, and 5%, respectively, for the maximal $N_p = 394$, as obtained from extrapolation of PHENIX data points. There is a factor of 2.6 increase between the SPS-like energy (19.6 GeV) and the top RHIC energy (200 GeV). The comparison of the only published $\epsilon_{Bj} = 3.2$ GeV/fm^3 at SPS for head-on collisions [31] and top RHIC energies, assuming the same $\tau = 1$ fm/c, reveals an increase in energy density by a factor of only 1.8, which may come from an overestimation in the SPS measurement, as shown latter in the left panel of Fig. 13 and discussed in Appendix A 3.

Another approach is used by STAR in [32] for the estimate of the transverse overlap area of the two nuclei $A_\perp \sim N_p^{2/3}$ in Eq. (4). This approach accounts for only the common area of colliding nucleons, not nuclei. The results are different only in the peripheral bins as shown in the right panel of Fig. 8. For a comparison, the same panel shows the result obtained by STAR which agrees with PHENIX results within systematic errors, though displaying a smaller increase of the energy density with N_p.

C. Comparison to other measurements

Comparison to the results of other experiments is complicated by several factors. AGS and SPS data were taken in the laboratory (Lab.) system while the RHIC data are in the center-of-mass system (c.m.s.). Since η and E_T are not boost-invariant quantities, the data should be converted into the same coordinate system. Some experiments provide a complete set of identified particle spectra from which information about E_T and $N_{\rm ch}$ can be deduced. For other experiments, additional assumptions are necessary for their published values. Appendix A describes how such recalculation was done in each particular case.

The PHENIX results for $N_{\rm ch}$ are compared to the data available from the other RHIC experiments. This comparison is shown in the left panels of Fig. 9.

There is good agreement between the results of BRAHMS [33,34], PHENIX, PHOBOS [35–37], and STAR [38,39] using N_p based on a Monte Carlo–Glauber model. This agreement is very impressive because all four experiments use different apparatuses and techniques to measure the charged particle production. The systematic errors of all results are uncorrelated, except for those related to the same Glauber model, which are small. That makes it possible to calculate the RHIC average and reduce the systematic uncertainty. The averaged results from all four RHIC experiments are plotted in the right panel of Fig. 9 and tabulated in Table XVII. See Appendix A 2 for the procedure.

Figure 10 compares E_T results from the PHENIX and STAR [40] experiments. The results are consistent for all centralities within systematic errors, though the STAR $dE_T/d\eta$ per participant pair has a smaller slope vs. N_p above $\sim$70 participants, and $E_T/N_{\rm ch}$ shown in the lower panel is consistent for all N_p.

The RHIC run at $\sqrt{s_{NN}} = 19.6$ GeV allows a connection between RHIC and SPS data to be made. The highest SPS energy per projectile nucleon of 158 A GeV corresponds to $\sqrt{s_{NN}} = 17.2$ GeV in the c.m.s., making a direct comparison of RHIC and SPS results possible. This comparison is shown in Fig. 11. See Appendixes A 3–A 6 for the details of the data compilation.

Several comments should be made about this comparison. For both measured parameters the PHENIX results and the SPS results agree. The WA98 results (see Appendix A 4) are systematically higher than the results of other experiments, especially for $dE_T/d\eta$. However, the WA98 data have an additional systematic error common to all points shown for the last bin. For $N_{\rm ch}$ the relative spread of the SPS results is larger than for the RHIC results shown in Fig. 9, though overall the $\sqrt{s_{NN}} = 17.2$ GeV SPS measurements are consistent with the PHENIX result at 19.6 GeV.

Different SPS and AGS experiments made measurements at lower energies. The combined data of AGS, SPS, and RHIC provide a complete picture of the centrality behavior of E_T and $N_{\rm ch}$ as a function of the nucleon-nucleon energy. The centrality dependence of $dN_{\rm ch}/d\eta$ at midrapidity measured at $\sqrt{s_{NN}} =$ 4.8, 8.7, and 17.2 GeV by different experiments is shown in Fig. 12. See Table XVII for the summary of these results and Appendixes A 5–A 7 for the details of the data compilation.

At the highest SPS energy the averaging procedure is the same as for RHIC energies, and weighted experimental errors are

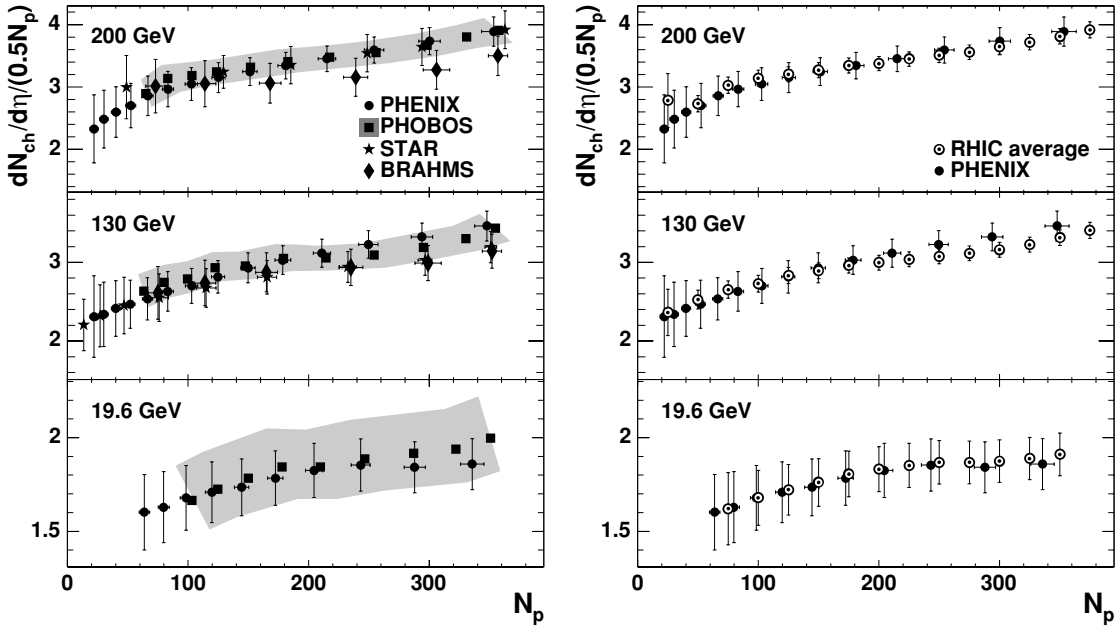

FIG. 9. Left panel: $dN_{\rm ch}/d\eta$ per pair of N_p measured by the four RHIC experiments at different energies. The shaded area is the PHOBOS systematic error. Right panel: RHIC average values (including PHENIX) compared to the PHENIX results.

scaled with the reduced χ^2-like factor S (described in Appendix A 2) reaching the value of 1.5 at some points. For the intermediate SPS energy $\sqrt{s_{NN}} = 8.7$ GeV, two experiments, NA45 [41] and NA50 [42], reported the centrality dependence of $dN_{\rm ch}/d\eta$ at midrapidity. The discrepancy in the measurements is close to three times the quadratic sum of their systematic error. However, the shapes of the two curves are almost the same. NA49 has published results (see Appendix A 3) that give one point in $dN_{\rm ch}/d\eta$ at $N_p = 352$. This point favors the NA45 result.[6]

[6]The NA57 results at both SPS energies are published without systematic errors in [43] They are currently not considered.

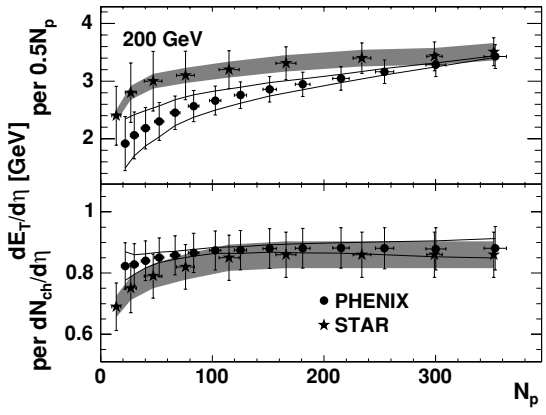

FIG. 10. $dE_T/d\eta$ divided by the number of N_p pairs (top) and $E_T/N_{\rm ch}$ (bottom) measured by the PHENIX and STAR [40] experiments at $\sqrt{s_{NN}} = 200$ GeV. PHENIX systematic errors are explained in the text. The shaded area is the STAR systematic scaling error.

The average centrality curve is produced taking into account the shape of the centrality curves reported by NA45 and NA50 and the single NA49 point. See Appendix A 8 for the averaging procedure at $\sqrt{s_{NN}} = 8.7$ GeV. The errors are scaled with the factor S, which reaches a value of 2.5 at some points. The AGS results are presented with a curve produced from the combined results of the E802/E917 experiments (see Appendix A 7). The averaging procedure in this case is a simple rebinning of the data.

The average SPS centrality dependence at $\sqrt{s_{NN}} = 17.2$ GeV shown in the upper panel in Fig. 12 and the average curve of the two RHIC experiments at 19.6 GeV shown in the lower panel in Fig. 9 are very similar. Less than a 5% increase is expected to result from the difference in the incident energy between the highest SPS and the lowest RHIC energies (see Sec. IV D below). The average values presented in Figs. 9 and 12 are summarized in Table XVII.

D. Dependence on the incident nucleon energy

The data compilation made in the previous section allows for a detailed study of the charged particle production in heavy ion reactions at different incident energies of colliding nuclei. Although the data on transverse energy production are not abundant, a similar comparison can be made [9,10].

1. Central collisions

Figure 13 shows the energy dependence of the $dE_T/d\eta$ and $dN_{\rm ch}/d\eta$ production per pair of participants in the most central collisions measured by different experiments. See Appendixes A 5–A 9 for the details of the data compilation.

The results shown in Fig. 13 are consistent with logarithmic scaling as described in [9,11,12]. Use of the logarithmic

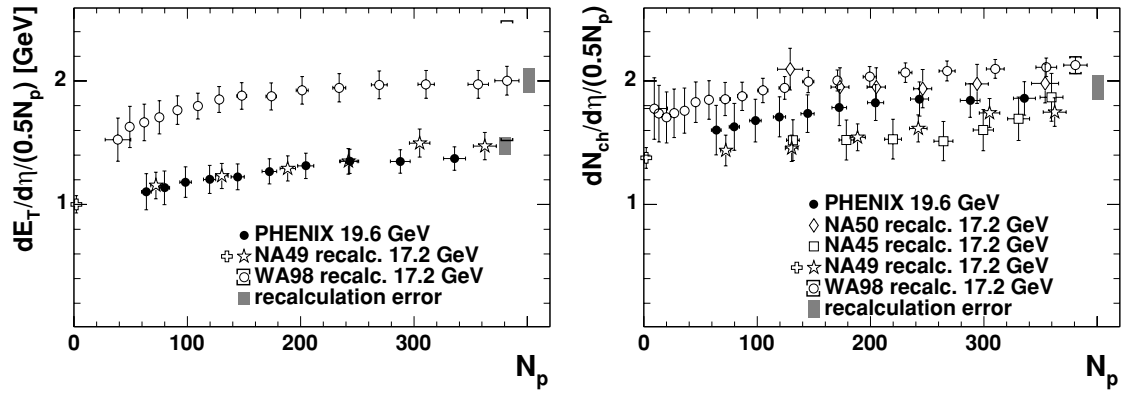

FIG. 11. $dE_T/d\eta$ (left) and $dN_{\rm ch}/d\eta$ (right) divided by the number of N_p pairs measured by PHENIX at $\sqrt{s_{NN}} = 19.6$ GeV (solid markers) and recalculated from the results of the SPS experiments at the highest energy $\sqrt{s_{NN}} = 17.2$ GeV (open markers). The $p + p$ result of NA49 is marked with an open cross.

function is phenomenological and is suggested by the trend of the data in the range of available measurements. The agreement of the fits with the data in both panels is very good, especially in the right panel where the averaged values are used for $N_p = 350$. The single point of NA49 [31] is excluded from the E_T fit (see Appendix A 3). The results of the fit $dX/d\eta = (0.5N_p \cdot A)\ln(\sqrt{s_{NN}}/\sqrt{s^0_{NN}})$ are

for E_T, $\sqrt{s^0_{NN}} = 2.35 \pm 0.2$ GeV and $A = 0.73 \pm 0.03$ GeV,
for $N_{\rm ch}$, $\sqrt{s^0_{NN}} = 1.48 \pm 0.02$ GeV and $A = 0.74 \pm 0.01$.

The parameter $\sqrt{s^0_{NN}} = 2.35$ GeV obtained from the E_T fit is slightly above although within 3σ from the minimum possible value of $\sqrt{s_{NN}} = 2 \times$ amu $= 1.86$ GeV. The measurement closest to it at $\sqrt{s_{NN}} = 2.05$ GeV done by the FOPI experiment

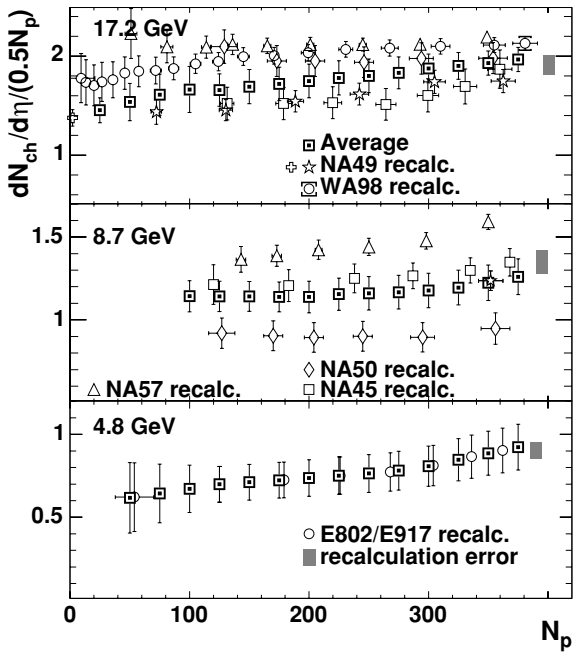

FIG. 12. $dN_{\rm ch}/d\eta$ divided by the number of N_p pairs measured by AGS and SPS experiments and the average taken at different energies recalculated in the c.m.s.

allows one to estimate the amount of $dE_T/d\eta$ produced to be 5.0 GeV in the most central collisions corresponding to $N_p = 359$. Appendix A 9 gives details of the estimate. This does not disagree with the extrapolation of the fit but does indicate that the logarithmic parametrization requires higher order terms to describe how the E_T production starts at very low $\sqrt{s_{NN}}$.

The right panel of Fig. 13 shows the logarithmic fit to the $N_{\rm ch}$ data. It agrees well with all $dN_{\rm ch}/d\eta$ results plotted for $N_p = 350$. Unlike that for E_T, the fit parameter $\sqrt{s^0_{NN}}$ for $N_{\rm ch}$ is 1.48 ± 0.02 GeV which is lower than the minimum allowed $\sqrt{s_{NN}}$. This suggests that above $2 \times$ amu the $N_{\rm ch}$ production as a function of $\sqrt{s_{NN}}$ should undergo threshold-like behavior, unlike the E_T production which must approach zero smoothly because of energy conservation.

The FOPI measurements at $\sqrt{s_{NN}} = 1.94$ and 2.05 GeV agree with the extrapolation of the fit at energy very close to $2 \times$ amu. It is an interesting result that colliding nuclei with kinetic energies of 0.037 and 0.095 GeV per nucleon in the c.m.s. follow the same particle production trend as seen at AGS, SPS, and RHIC energies.

A fit to the charged particle multiplicity shows a factor of 2.2 increase in $dN_{\rm ch}/d\eta$ per participant in the most central events from the highest energy at the AGS ($\sqrt{s_{NN}} = 4.8$ GeV) to the highest energy at the SPS (17.2 GeV) and a factor of 2.0 from the highest SPS energy to the highest RHIC energy (200 GeV). Assuming the same behavior extends to the Large Hadron Collider (LHC) highest energy (5500 GeV) one would expect $dN_{\rm ch}/d\eta = (6.1 \pm 0.13) \cdot (0.5N_p)$ and the increase in particle production from the highest RHIC energy to be $\sim$60% for the most central events. With the greater energy, the rapidity width should increase by $\sim$60%, i.e., the total charged particle multiplicity at LHC would increase by a factor of $\sim$2.6 from the top RHIC energy.

The ratio of $E_T/N_{\rm ch}$ for the most central bin as a function of $\sqrt{s_{NN}}$ is shown in Fig. 14. Note that the line shown in the figure is not the fit to the data points. Rather, it is calculated from the fits shown in Fig. 13. The calculation agrees well with the data. There are two regions in the plot which can be clearly separated. The region from the lowest allowed $\sqrt{s_{NN}}$ to SPS energy is characterized by a steep increase of

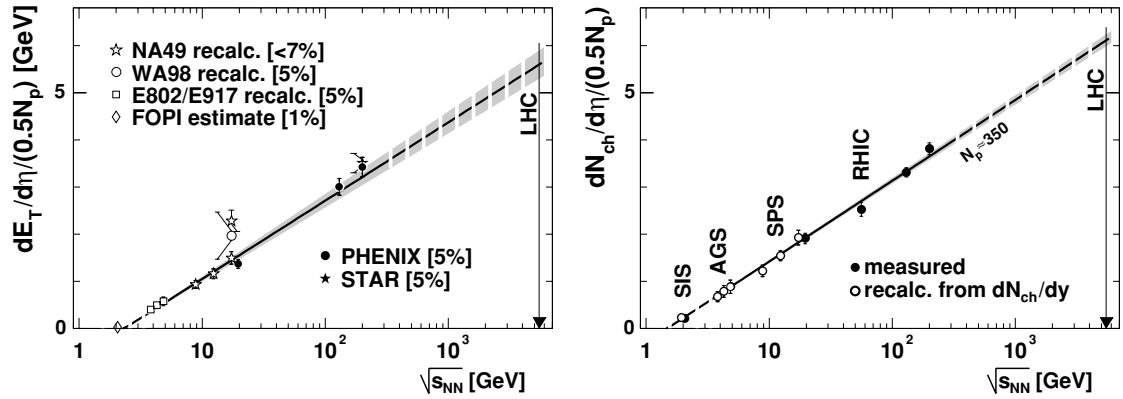

FIG. 13. Left panel: $dE_T/d\eta$ divided by the number of N_p pairs measured in the most central bin (value given in brackets) as a function of incident nucleon energy. The line is a logarithmic fit. The band corresponds to a 1σ statistical deviation of the fit parameters. Right panel: the same for $dN_{\rm ch}/d\eta$. The values of $N_{\rm ch}$ are the average values corresponding to $N_p = 350$. The single point at $\sqrt{s_{NN}} = 56\,{\rm GeV}$ is explained in Appendix A 10.

the $E_T/N_{\rm ch}$ ratio with $\sqrt{s_{NN}}$. In this region the increase in the incident energy causes an increase in the $\langle m_T \rangle$ of the produced particles. The second region starts from the SPS energies and continues above. In this region, the $E_T/N_{\rm ch}$ ratio is very weakly dependent on $\sqrt{s_{NN}}$. The incident energy is converted into particle production at midrapidity rather than into increasing the particle $\langle m_T \rangle$.

The shape of the $E_T/N_{\rm ch}$ curve in the first region is governed by the difference in the $\sqrt{s^0_{NN}}$ parameter between E_T and $N_{\rm ch}$. In the second region it is dominated by the ratio of the A parameters in the fits. This ratio is close to 1 GeV. Extrapolating to LHC energies one gets a $E_T/N_{\rm ch}$ value of (0.92 ± 0.06) GeV.

2. *Centrality shape*

Another interesting question is how the shapes of the centrality curves of E_T and $N_{\rm ch}$ change with $\sqrt{s_{NN}}$.

One approach previously used in a number of papers is to describe the shape of the centrality dependence as a sum of "soft" and "hard" contributions such that the soft component is proportional to N_p and the hard component to the the number of binary collisions N_c, that is, $A \times N_p + B \times N_c$. A disadvantage of this approach is that the contributions called soft and hard do not necessarily correspond to the physical processes associated with these notations. Another approach is to assume that the production of E_T or $N_{\rm ch}$ is proportional to N_p^α, although the parameter α has no physical meaning.

The results of B/A and α obtained from the fits to the data at different $\sqrt{s_{NN}}$ are summarized in Table II. Although the numbers tend to increase with beam energy, the values presented in Table II are consistent with each other within the systematic errors.

The availability of higher quality data would make it possible to derive a more conclusive statement about the shape of the curves plotted in Figs. 9 and 12. With the present set of data usually limited to N_p above 50, a large part of the

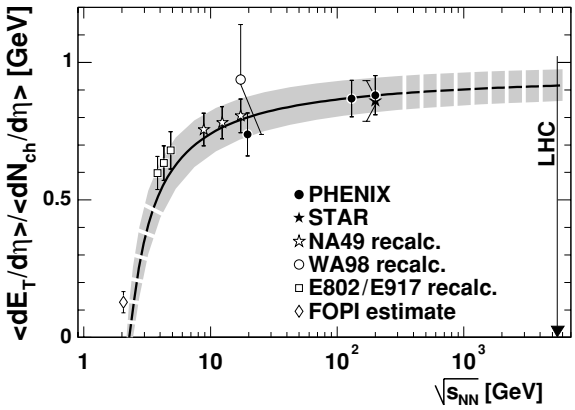

FIG. 14. Ratio of E_T over $N_{\rm ch}$ for the most central events as a function of $\sqrt{s_{NN}}$ recalculated into c.m.s. The line is the ratio of two fits shown in Fig. 13. The band corresponds to one standard deviation of the combined error.

TABLE II. B/A ratio and parameter α from the fit to the data. Errors are calculated assuming a change in the slope of the centrality curves within the limits of the bending errors for PHENIX and full errors for the averaged data (Table XVII).

$\sqrt{s_{NN}}$ (GeV)	$dE_T/d\eta$ PHENIX	$dN_{\rm ch}/d\eta$ PHENIX B/A	$dN_{\rm ch}/d\eta$ Average
200	$0.49^{+.69}_{-.22}$	$0.41^{+.57}_{-.21}$	$0.28^{+.18}_{-.15}$
130	$0.41^{+.52}_{-.23}$	$0.41^{+.45}_{-.23}$	$0.26^{+.18}_{-.11}$
19.6	$0.37^{+.48}_{-.22}$	$0.21^{+.30}_{-.15}$	$0.23^{+.73}_{-.23}$
17.2			$0.31^{+.46}_{-.24}$
8.7			$0.12^{+.64}_{-.20}$
	Parameter α		
200	1.20 ± 0.07	1.18 ± 0.08	1.16 ± 0.06
130	1.14 ± 0.08	1.17 ± 0.08	1.14 ± 0.05
19.6	1.13 ± 0.07	1.09 ± 0.06	1.10 ± 0.11
17.2			1.11 ± 0.08
8.7			1.06 ± 0.13
4.8			1.20 ± 0.24

centrality curve is missing or smeared by systematic errors. To avoid this, one can compare Au + Au collisions to $p + p$ ($N_p = 2$) at the same energy.

Figure 15 shows $dN_{\rm ch}/d\eta/(0.5N_p)$ divided by the parametrization plotted in the right panel of Fig. 13. The top panel shows the most central events with $N_p = 350$. All points are consistent with 1, demonstrating an agreement of the fit to the data. The points are connected with a line for visibility. The middle panel shows results for midcentral events, with $N_p = 100$ connected with a solid line. The dotted line is the same line as in the top panel for $N_p = 350$. The points for $N_p = 100$ are lower than for $N_p = 350$ by a factor of 0.8–0.9, over the plotted range of incident energies. The lower panel shows $p + p$ data corresponding to $N_p = 2$ measured by several experiments. The dotted lines are the same as appear in the upper two panels for $N_p = 350$ and 100, and the $p + p$ parametrizations are taken from [44,45]. In the range of RHIC energies these points are lower by a factor of 0.65–0.75 than the most central events.

These results indicate that the centrality curves normalized to the most central collisions have a similar shape for all RHIC energies within the errors of available measurements.

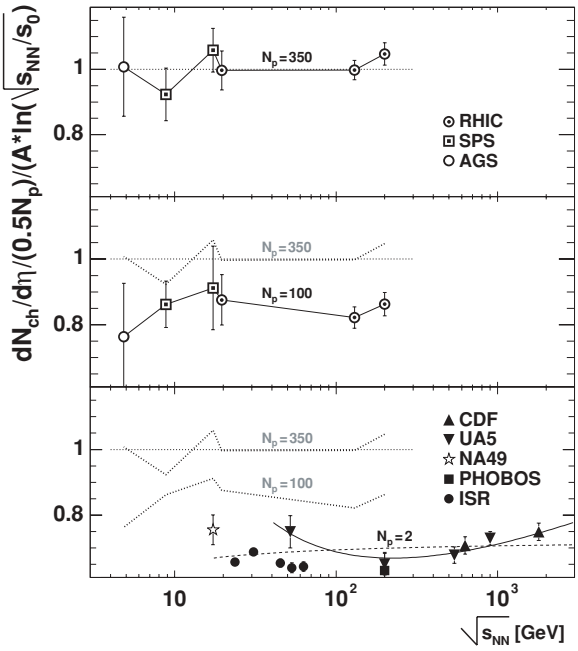

FIG. 15. The three panels show $dN_{\rm ch}/d\eta/(0.5N_p)$ divided by the logarithmic parametrization from Fig. 13. The panels correspond to $N_p = 350$, 100, and 2 ($p + p$) from top to bottom. Au + Au points are connected with lines also shown in lower panels for comparison. The Au + Au data are tabulated in Table XVII. $p + p$ data and parametrizations $dN/d\eta = 2.5 - 0.25\ln(s_{NN}) + 0.023\ln(s_{NN})^2$ (solid line) and $dN/d\eta = 0.27\ln(s_{NN}) - 0.32$ (dashed line) are taken from [44,45].

E. Comparison to models

A variety of models attempting to describe the behavior of E_T and $N_{\rm ch}$ as a function of centrality at different $\sqrt{s_{NN}}$ are available. An updated set of model results were collected from several theoretical groups to make a comparison as comprehensive as possible. Figures 16–18 show the comparison

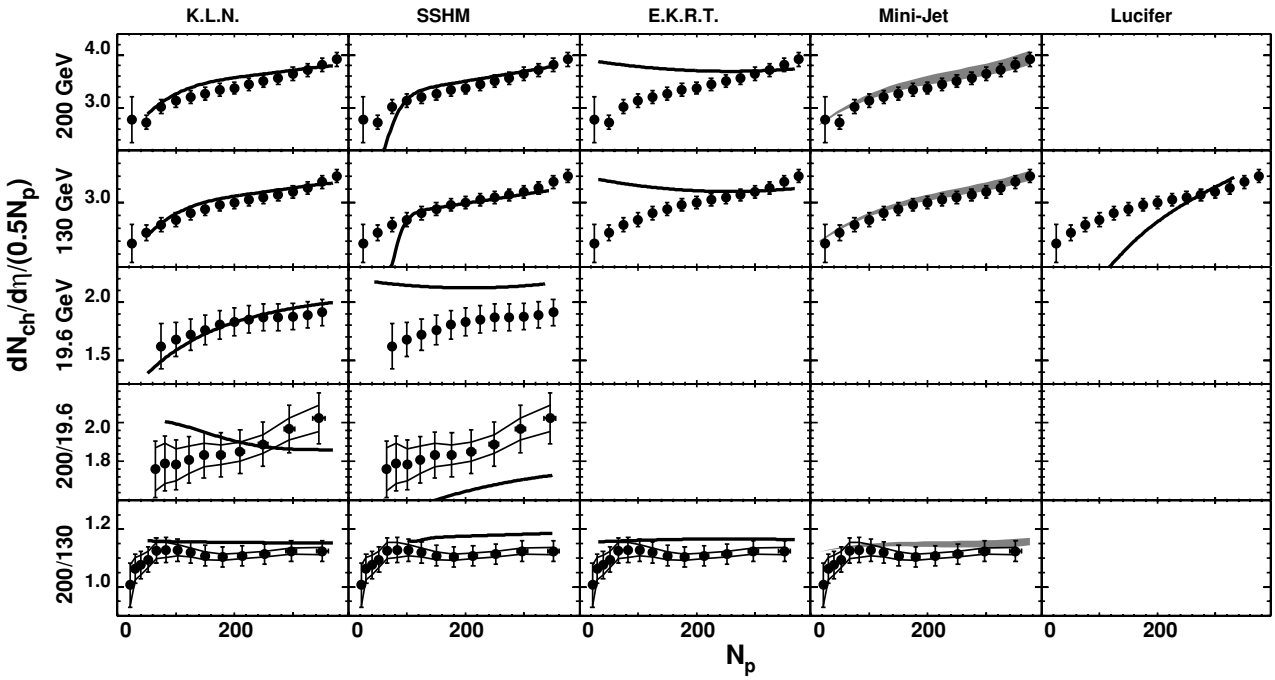

FIG. 16. $dN_{\rm ch}/d\eta$ per pair of participants compared to theoretical models. KLN [49], SSHM [52], EKRT [48], Minijet [50] and LUCIFER [56]. The band shows the range of prediction for the Minijet model.

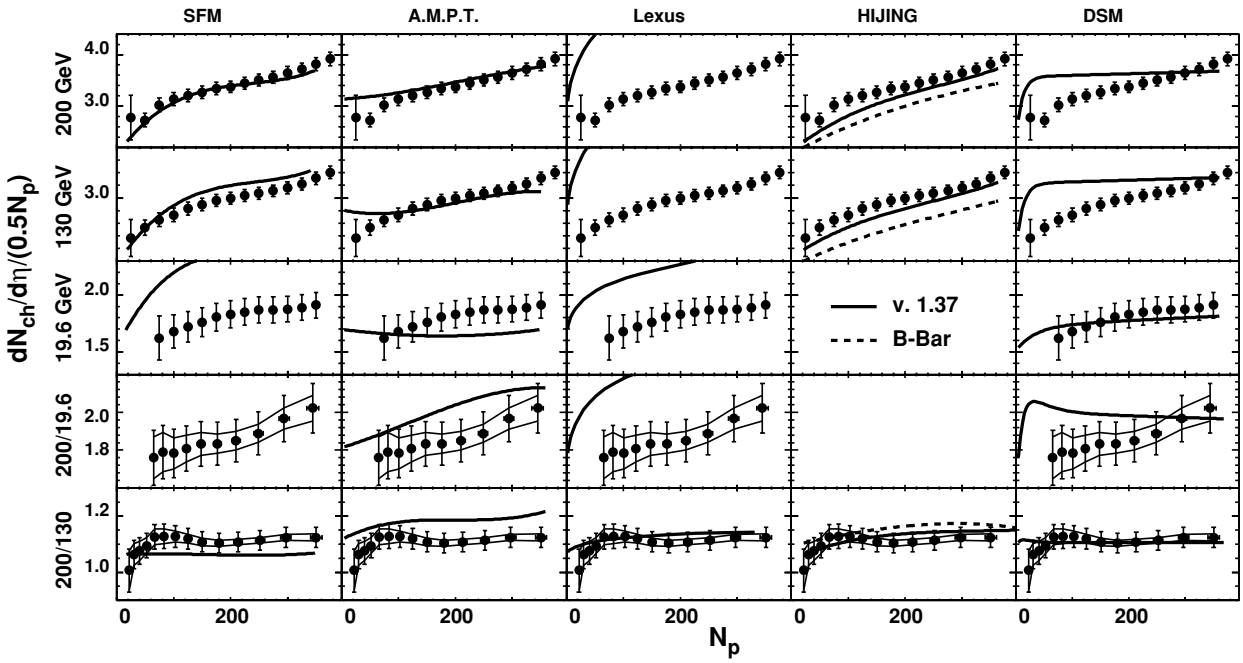

FIG. 17. Theoretical models compared to $dN_{\rm ch}/d\eta$ per pair of participants: SFM [55], AMPT [51], LEXUS [57], HIJING [15,46], and DSM [53].

between the existing theoretical models[7] and the data for 19.6, 130, and 200 GeV. Brief descriptions of the models and their main characteristics are given next.

One of the more commonly used Monte Carlo event generators is HIJING [15,46]. This model, like several others, uses pQCD for initial minijet production and the Lund string model [47] for jet fragmentation and hadronization. HIJING also includes jet quenching and nuclear shadowing. This type of model typically has two components, a soft part proportional to N_p and a hard part proportional to N_e, which partly motivated the discussion in Sec. IV D 2. There are also the so-called saturation models, which also rely on pQCD and predict that at some fixed scale the gluon and quark phase-space density saturates, thus limiting the number of produced quarks and gluons. An example of this type of model is EKRT [48], which is referred to as a final state saturation model. In this paper, comparisons are also made to another parton saturation type model, KLN [49], which is an initial state saturation model, and to models related to HIJING, namely, Minijet [50] and AMPT [51]. AMPT is a multiphase transport model and extends HIJING by including explicit interactions between initial minijet partons and final state hadronic interactions. Minijet follows the same two-component model as HIJING but also incorporates an energy-dependent cutoff scale, similar to the saturation models.

The other models are listed briefly below. SSHM and SFM do not have a designated short identifier, so they were named somewhat arbitrarily here, based on the physics the models incorporate. SSHM (saturation for semi-hard minijet) [52] is also a two-component model: it is pQCD-based for semihard partonic interactions, while for the soft particle production it uses the wounded nucleon model. DSM [53], the dual string model, is basically the dual parton model [54], with the inclusion of strings. SFM (string fusion model) [55] is a string model that includes hard collisions, collectivity in the initial state (string fusion), and rescattering of the produced secondaries. Finally, there are the hadronic models, LUCIFER [56], a cascade model with input fixed from lower energy data, and LEXUS [57], a linear extrapolation of ultrarelativistic nucleon-nucleon scattering data to nucleus-nucleus collisions.

The available model results range from predicting (or postdicting) $dN_{\rm ch}/d\eta$ at one energy to predicting both $dN_{\rm ch}/d\eta$ and $dE_T/d\eta$ at 19.6, 130 and 200 GeV. The models have varying success in reproducing the data.

In Fig. 16, KLN is among the most successful at describing the $dN_{\rm ch}/d\eta$ centrality dependence for all three energies. However, at $\sqrt{s_{NN}} = 19.6$ GeV, the theoretical curve is steeper than the data. This results in a reversed centrality dependence relative to the data for the 200 to 19.6 GeV ratio. SSHM describes the 130 and 200 GeV data well, for centralities above $N_p \sim 100$, which is the approximate limit of applicability for this and other saturation models. For the less central events, the model values are lower than the data. At 19.6 GeV, the model values are significantly higher than the data. The saturation model EKRT describes the central points at both energies but overshoots the more peripheral data points and thus does not reproduce the general centrality dependence of the data. For the nonsaturation models included in this figure, Minijet reproduces both the overall scale and the centrality and energy dependence of the data rather well, while the cascade model

[7]Models are presented as the best fit by the polynomial of the lowest degree which is closer than 1% to any theoretical point provided by the authors of the models. The polynomial is plotted in the range where points are provided.

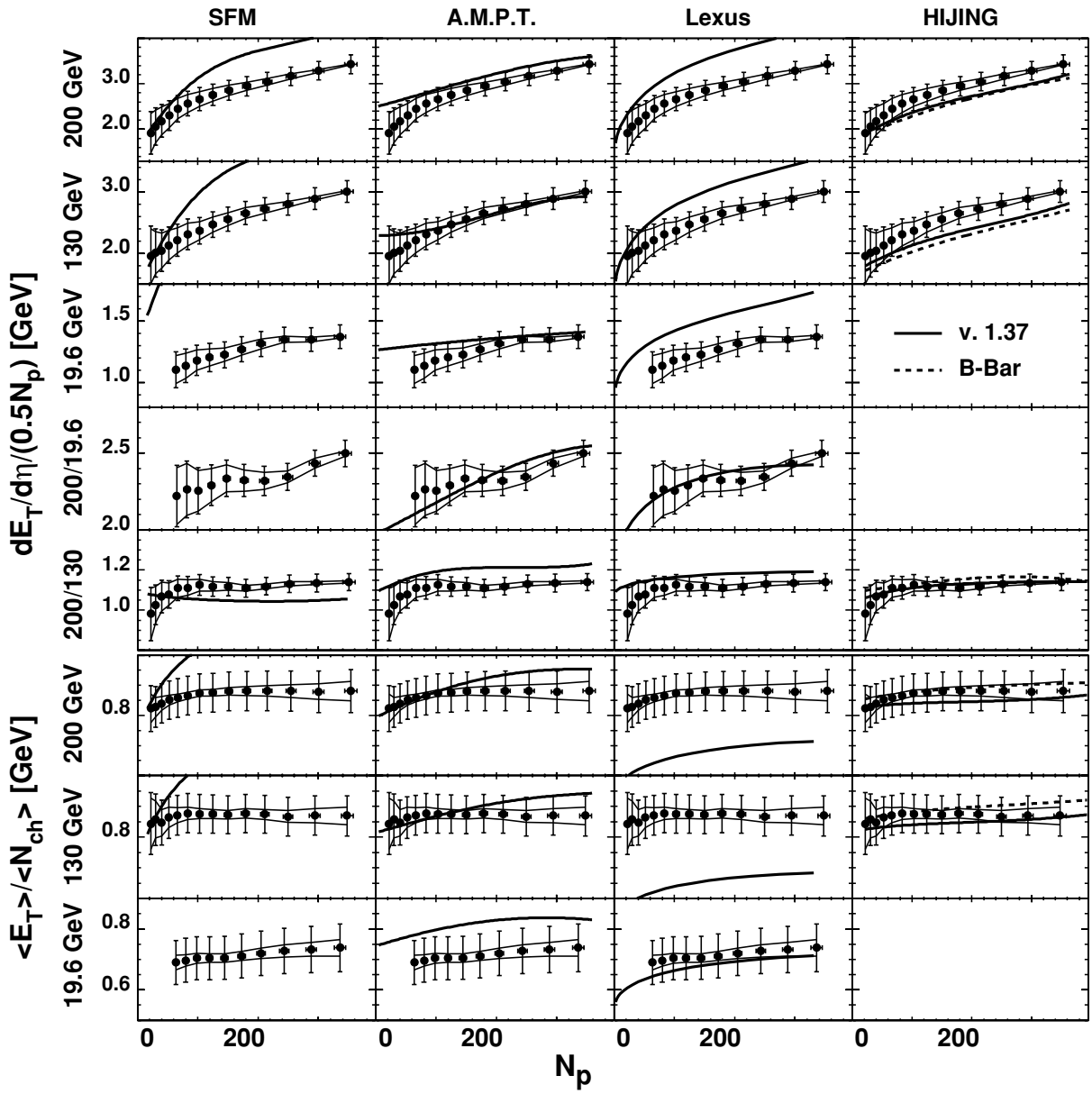

FIG. 18. Theoretical models compared to $dE_T/d\eta$ per pair of participants (upper panels) and per produced charged particle (lower panels): SFM [55], AMPT [51], LEXUS [57], and HIJING [15,46].

LUCIFER describes the central points at 130 GeV well but undershoots the less central values at this energy.

Most of the models included in Fig. 17 provided values for all three energies: 19.6, 130, and 200 GeV. SFM is in reasonable agreement with the 130 and 200 GeV data, but gives much larger values than the data at 19.6 GeV. AMPT is in overall good agreement with the data for the two higher energies, except for the increasing trend in $dN_{\rm ch}/d\eta$ at the most peripheral events, which is not seen in the experimental data. At the lower energy, the $N_{\rm ch}$ centrality behavior is underestimated. LEXUS rather severely overshoots the data for all energies, indicating that nucleus-nucleus effects are not accounted for. The HIJING models (version 1.37 and a new version with implemented baryon junctions, HIJING B-$\bar{\rm B}$) only provide points at 130 and 200 GeV and are in reasonable agreement with the data at those energies, but generally give somewhat lower values. The curves shown include quenching and shadowing implemented in HIJING. DSM describes 19.6 GeV reasonably well for all centralities and the more central bins for 130 and 200 GeV, but it overpredicts the values for semicentral and peripheral events.

Figure 18 shows the results for the models that provide data for both $dN_{\rm ch}/d\eta$ and $dE_T/d\eta$. For $dE_T/d\eta$, LEXUS and SFM consistently overshoot the data for all energies. In the ratio $E_T/N_{\rm ch}$, LEXUS gives values that are too low except at the lowest energy, 19.6 GeV. That might indicate that the hadronization mechanism allows too little energy per particle. The SFM gives values that are too large, except for the most peripheral bin, which suggests that the particles are assigned transverse masses that are too large. The HIJING versions and

the related AMPT model are in reasonable agreement with the data for both $dE_T/d\eta$ and $E_T/N_{\rm ch}$.[8]

Also shown in Fig. 18 are the ratios of results at 200 to 19.6 GeV, and 200 to 130 GeV, for $dE_T/d\eta$. These results, especially the comparison of the 200 to 19.6 GeV data, are intended to make a more precise check of the $\sqrt{s_{NN}}$ dependence of the models. SFM fails to describe the 19.6 GeV data and thus cannot describe the energy dependence probed by these ratios, unlike LEXUS which, however, does not agree well with the individual data curves for 19.6, 130, and 200 GeV. AMPT and the HIJING versions reproduce the values of the ratios well, as expected since they are in reasonable agreement with the individual curves. AMPT and HIJING are also successful in describing the $E_T/N_{\rm ch}$ ratio, as illustrated in the lower panels of Fig. 18.

To summarize, most models reproduce at least some of the data fairly well, but most fail in describing all the data. Since the model results typically are given without systematic errors, it is not entirely straightforward to quantify the level of agreement or disagreement with the data. Qualitatively, the models that are most successful in describing both $dE_T/d\eta$ and $dN_{\rm ch}/d\eta$ in terms of the overall trends, regarding both centrality dependence and energy dependence, are AMPT and the HIJING versions. KLN and Minijet unfortunately do not give information on $dE_T/d\eta$ but are successful in describing the $dN_{\rm ch}/d\eta$ results. The $dN_{\rm ch}/d\eta$ results thus can either be described by the initial state saturation scenario (KLN) or by the minijet models that need an energy-dependent minijet cutoff scale as described in [46,50] to reproduce the data.

V. SUMMARY

This paper presents a systematic study of the energy and centrality dependence of the charged particle multiplicity and transverse energy at midrapidity at $\sqrt{s_{NN}} = 19.6$, 130, and 200 GeV.

The yields, divided by the number of participant nucleons, show a consistent centrality dependence (increase from peripheral to central) between $dE_T/d\eta$ and $dN_{\rm ch}/d\eta$ for all energies. Furthermore, the increase in the ratio $E_T/N_{\rm ch}$ from 19.6 to 200 GeV is consistent with a 20% increase in $\langle m_T \rangle$ with increasing $\sqrt{s_{NN}}$. The ratio $E_T/N_{\rm ch}$ shows only a weak centrality dependence at RHIC energies.

For the $\sqrt{s_{NN}}$ dependence, comparisons were made not only among RHIC results but also with data from lower energy fixed-target experiments at SPS, AGS, and Schwer-Ionen-Synchrotron (SIS). A phenomenological fit, scaling logarithmically with $\sqrt{s_{NN}}$, describes well both $dE_T/d\eta$ and $dN_{\rm ch}/d\eta$ for the most central collisions for all energies.

Using the fit results, one can delineate two regions with different particle production mechanisms. The region below SPS energy is characterized by a steep increase in $E_T/N_{\rm ch} \sim \langle m_T \rangle$ with $\sqrt{s_{NN}}$, whereas for the energies above SPS, $E_T/N_{\rm ch}$ is weakly dependent on $\sqrt{s_{NN}}$.

Within the systematic errors of the measurements, the shape of the centrality curves of $dN_{\rm ch}/d\eta/(0.5N_p)$ vs. N_p were found to be the same in the range of RHIC energies and to scale with $\ln(\sqrt{s_{NN}})$. The same must be true for E_T because $E_T/N_{\rm ch}$ has a very weak centrality dependence.

Based on the $dE_T/d\eta$ measurements, the Bjorken energy density estimates were performed and $\epsilon_{Bj} \cdot \tau$ was determined to be 5.4 ± 0.6 GeV fm$^{-2}\,c^{-1}$ at $\sqrt{s_{NN}} = 200$ GeV for the most central bin. This is in excess of what is believed to be sufficient for a phase transition to the new state of matter. The energy density increases by about a factor of 2.6 from the top SPS energy to the top RHIC energy.

Finally, a comparison between the RHIC $dN_{\rm ch}/d\eta$ and $dE_T/d\eta$ data and a collection of models was performed. A few models, notably HIJING and AMPT, reproduce both $dE_T/d\eta$ and $dN_{\rm ch}/d\eta$ rather well for several energies.

ACKNOWLEDGMENTS

We thank the staff of the Collider-Accelerator and Physics Departments at Brookhaven National Laboratory and the staff of the other PHENIX participating institutions for their vital contributions. We are grateful for information provided by the model authors. In particular, we thank A. Accardi, S. Barshay, S. Jeon, S. Kahana, D. Kharzeev, Z. Lin, N. Armesto Perez, R. Ugoccioni, V. T. Pop, and X. N. Wang for helpful correspondence. We acknowledge support from the U.S. Department of Energy, Office of Science, Nuclear Physics Division; the National Science Foundation, Abilene Christian University Research Council, Research Foundation of SUNY, and Dean of the College of Arts and Sciences, Vanderbilt University (USA); Ministry of Education, Culture, Sports, Science, and Technology and the Japan Society for the Promotion of Science (Japan); Conselho Nacional de Desenvolvimento Científico e Tecnológico and Fundação de Amparo à Pesquisa do Estado de São Paulo (Brazil); Natural Science Foundation of China (People's Republic of China); Centre National de la Recherche Scientifique, Commissariat à l'Énergie Atomique, and Institut National de Physique Nucléaire et de Physique des Particules (France); Bundesministerium für Bildung und Forschung, Deutscher Akademischer Austausch Dienst, and Alexander von Humboldt Stiftung (Germany); Hungarian National Science Fund, OTKA (Hungary); Department of Atomic Energy and Department of Science and Technology (India); Israel Science Foundation (Israel); Korea Research Foundation and Center for High Energy Physics (Korea); Russian Ministry of Industry, Science and Tekhnologies, Russian Academy of Science, Russian Ministry of Atomic Energy (Russia); VR and the Wallenberg Foundation (Sweden); the U.S. Civilian Research and Development Foundation for the Independent States of the Former Soviet Union; the US-Hungarian NSF-OTKA-MTA; the US-Israel Binational Science Foundation; and the 5th European Union TMR Marie-Curie Programme.

APPENDIX A: RECALCULATION OF THE NON-PHENIX EXPERIMENTAL DATA

Comparisons of $dE_T/d\eta$ and $dN_{\rm ch}/d\eta$ between different experiments can be made only if the results are presented

[8]Note that the HIJING versions available at the time the data were collected and used for predictions were in worse agreement with the data [10]. This was before energy loss and minijet separation/cutoff scale parameters were updated.

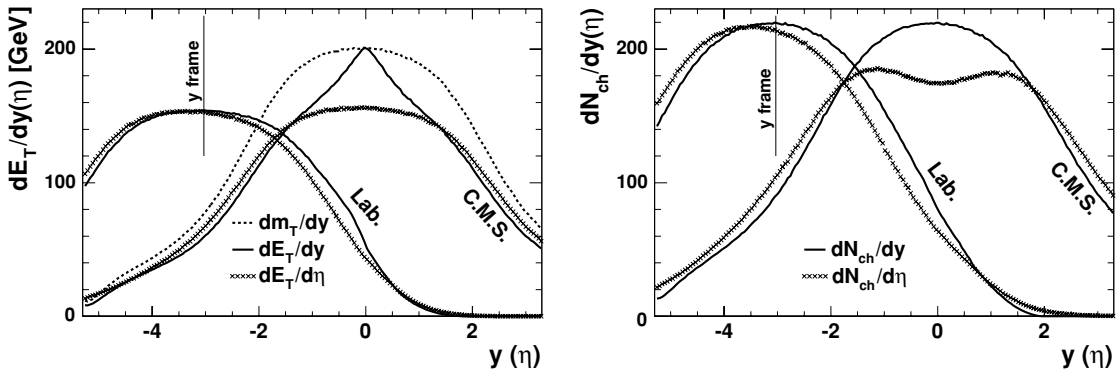

FIG. 19. Simulated E_T (left) and $N_{\rm ch}$ (right) distributions in rapidity and pseudorapidity units in c.m.s. and Lab. systems.

in the same coordinate system since these values are not boost invariants. In some cases a full set of identified particles measured by one experiment can be recalculated into E_T and $N_{\rm ch}$. Each case that involves handling non-PHENIX published data is separately explained in this Appendix.

1. General

Figure 19 shows simulated rapidity distributions for E_T and $N_{\rm ch}$ in the c.m.s. and Lab. frames. Plots presented here are for illustrative purposes only. The invariant distributions which do not change their shape under transition from Lab. to c.m.s. are dm_T/dy and $dN_{\rm ch}/dy$, while all others do.

In the c.m.s. system, the transition from η to y at midrapidity requires a scaling factor between 1.2 and 1.3. An accurate determination of this coefficient from the published data of other experiments is not always possible; therefore for the SPS and AGS energies a coefficient of 1.25 was used. Because of the definition of E_T used in this paper, $dE_T/dy \approx dm_T/dy$, around midrapidity, where m_T is a quadratic sum of the particle mass and transverse momentum: $m_T = \sqrt{m^2 + p_T^2}$.

In the Lab. system $dN_{\rm ch}/dy \approx dN_{\rm ch}/d\eta$ and $dE_T/dy \approx dE_T/d\eta$ at maximum rapidity. A 1.04 conversion factor was assigned to the transition from η to y in the Lab. system.

An error of 5% was assigned to any converted value. This error also absorbs uncertainties on various assumptions used in the calculations. For example, the contribution of neutral particles to the total E_T is assumed to be

$$E_T^{\pi^0} = \left(E_T^{\pi^+} + E_T^{\pi^-}\right)/2,$$
$$E_T^{K^0} = E_T^{K^+} + E_T^{K^-},$$
$$E_T^{n} + E_T^{\bar{n}} = E_T^{p} + E_T^{\bar{p}}. \qquad \text{(A1)}$$

2. Averaging procedure

Average values were calculated for $N_p = 25, 50, \ldots, 375$. The centrality bin corresponding to a given N_p can be different in different experiments. $dN_{\rm ch}/d\eta$ per participant and the associated error were deduced by a weighted average interpolation from the two nearest values of each experiment. The closest value was required to be within a proximity of 25 participants from the N_p value. The error bars are multiplied by the S factor, where $S = \sqrt{\chi^2/\text{n.d.f.}}$ if $\chi^2/\text{n.d.f.} > 1$ or $S = 1$ otherwise. See the Particle Data Group reference [20] for details.

3. NA49

Table III lists the identified particle yields in the most central events at midrapidity at $\sqrt{s_{NN}} = 17.2$ GeV, as shown in Fig. 6 in Ref. [17]. The total yields per participant and number of participants in Table IV are taken from Fig. 10 in Ref. [17]. Using shapes of the dN/dy distributions shown in Fig. 7 of Ref. [17] for different centrality bins, the quantities tabulated in Tables III and IV can be converted into $dE_T/d\eta$ and $dN_{\rm ch}/d\eta$ per participant pair at midrapidity. Systematic errors on particle yields are given in Table 1 in the same reference. The systematic errors for this value are not mentioned in the paper, therefore they were taken from [19]. The results used in this paper are also given in Table IV.

For the same and lower $\sqrt{s_{NN}}$, the identified particle yields and $\langle m_T \rangle$ were reconstructed using formula (1) and Fig. 1 in Ref. [18] and Table II and formulas (1) and (2) in Ref. [19]. The data obtained from the tables and the fits are summarized in Table V. Using dN/dy and $\langle m_T \rangle$, the values of $dE_T/d\eta$ and $dN_{\rm ch}/d\eta$, were recalculated in the c.m.s. frame. The accuracy of the procedure was verified by the consistency of results presented in Tables V and VI.

The single E_T point in Fig. 13 is taken from [31] as 405 GeV and scaled up by 10%, then divided by pairs of $N_p = 390$ as explained in the text. This point does not agree with the value of E_T deduced from [17–19].

4. WA98

The centrality dependencies of E_T, $N_{\rm ch}$, and $E_T/N_{\rm ch}$ were read from the plots in Figs. 7 and 14 in Ref. [25] and converted to the c.m.s. frame. Results are summarized in Table VII.

TABLE III. Results on identified particle yields in the most central events published by NA49 at midrapidity at $\sqrt{s_{NN}} = 17.2$ GeV taken from Fig. 6 in Ref. [17].

Particle	π^+	π^-	K^+	K^-	p	$\bar{p}$
dN/dy	167	165	32	15	33	5
Error	10	10	4	5	1.5	0.5

TABLE IV. Total yields of identified particles per participant and mean momentum at midrapidity in different centrality bins published by NA49 (P) at $\sqrt{s_{NN}} = 17.2$ GeV, from Figs. 8 and 10 in Ref. [17]. Recalculated values (R) are plotted in Figs. 11 and 12.

P	N_p	362	305	242	189	130	72	2
P	Error	10	15	15	15	10	5	
P	$\langle dN^{\pi}/dy/N_p \rangle$	1.65	1.64	1.55	1.48	1.40	1.42	1.42
P	Error	0.08	0.08	0.08	0.08	0.08	0.08	0.08
P	$\langle p_T^{\pi^+} \rangle$ (GeV/c)	0.29	0.31	0.30	0.30	0.30	0.29	0.28
P	$\langle p_T^{\pi^-} \rangle$ (GeV/c)	0.27	0.31	0.29	0.30	0.30	0.30	0.28
P	$dN^{K^+}/dy/N_p$	0.27	0.27	0.22	0.19	0.16	0.14	0.10
P	Error	0.02	0.02	0.02	0.02	0.02	0.02	0.02
P	$\langle p_T^{K^+} \rangle$ (GeV/c)	0.57	0.54	0.50	0.49	0.53	0.55	0.45
P	$dN^{K^-}/dy/N_p$	0.15	0.15	0.12	0.10	0.09	0.07	0.06
P	Error	0.01	0.01	0.01	0.01	0.01	0.01	0.01
P	$\langle p_T^{K^-} \rangle$ (GeV/c)	0.57	0.55	0.53	0.51	0.55	0.51	0.42
P	$\langle p_T^{p} \rangle$ (GeV/c)	0.77	0.74	0.75	0.73	0.70	0.65	0.54
P	$dN^{\bar{p}}/dy/N_p$	0.03	0.03	0.03	0.03	0.03	0.02	0.02
P	Error	0.005	0.005	0.005	0.005	0.005	0.005	0.005
P	$\langle p_T^{\bar{p}} \rangle$ (GeV/c)	0.87	0.84	0.80	0.75	0.78	0.70	0.48
R	$dE_T/d\eta/(0.5N_p)$ (GeV)	1.47	1.50	1.35	1.29	1.23	1.15	1.00
R	Error (GeV)	0.11	0.11	0.10	0.10	0.10	0.11	0.07
R	$dN_{\rm ch}/d\eta/(0.5N_p)$	1.75	1.74	1.62	1.54	1.46	1.44	1.38
R	Error	0.12	0.12	0.11	0.11	0.11	0.12	0.08

TABLE V. Temperatures of the identified particles published by NA49 at different $\sqrt{s_{NN}}$, as extracted from [18,19]. The yields are results of the fits of the parametrizations given in these publications.

	$\sqrt{s_{NN}} = 17.2$ GeV								
	π^+	π^-	K^+	K^-	p	$\bar{p}$	Λ	$\bar{\Lambda}$	d
T (GeV)	0.180	0.180	0.232	0.226	0.127	0.122	0.127	0.122	0.127
Error (GeV)	0.01	0.010	0.007	0.011	0.004	0.002	0.004	0.002	0.004
dN/dy	170.0	175.0	29.6	16.8	23.0	1.4	16.0	3.5	0.32
Error	9.0	9.0	1.5	0.8	7.4	0.23	6.1	0.67	0.23
	$\sqrt{s_{NN}} = 12.4$ GeV								
	π^+	π^-	K^+	K^-	p	$\bar{p}$	Λ	$\bar{\Lambda}$	d
T (GeV)	0.179	0.179	0.230	0.217	0.133	0.120	0.133	0.120	0.133
Error (GeV)	0.01	0.010	0.008	0.007	0.003	0.001	0.003	0.001	0.003
dN/dy	132.0	140.0	24.6	11.7	29.0	0.7	17.5	0.8	0.85
Error	7.0	7.0	1.2	0.6	6.2	0.06	4.4	0.08	0.28
	$\sqrt{s_{NN}} = 8.7$ GeV								
	π^+	π^-	K^+	K^-	p	$\bar{p}$	Λ	$\bar{\Lambda}$	d
T (GeV)	0.169	0.169	0.232	0.226	0.130	0.137	0.130	0.137	0.130
Error (GeV)	0.01	0.01	0.007	0.007	0.002	0.004	0.002	0.004	0.002
dN/dy	96.6	106.0	20.1	7.6	40.0	0.28	17.2	0.28	1.25
Error	6.0	6.0	1.0	0.4	5.8	0.08	2.9	0.08	0.37

TABLE VI. Recalculated NA49 results, as plotted in Figs. 13 and 14.

$\sqrt{s_{NN}}$ (GeV)	17.2	12.4	8.7
N_p	363 ± 10	352 ± 10	352 ± 10
$dE_T/d\eta/(0.5N_p)$ (GeV)	1.50 ± 0.11	1.16 ± 0.09	0.94 ± 0.07
$dN_{\rm ch}/d\eta/(0.5N_p)$	1.86 ± 0.08	1.54 ± 0.07	1.24 ± 0.06
$E_T/N_{\rm ch}$ (GeV)	0.81 ± 0.06	0.78 ± 0.06	0.76 ± 0.06

TABLE VII. Published (P) WA98 results at $\sqrt{s_{NN}} = 17.2$ GeV taken from Figs. 7 and 14 in Ref. [25], and recalculated (R) results plotted in Figs. 11–14. Additional systematic errors are shown in the plots.

P	N_p				382	357	311	269	234	201	174	148	128	109	91	75	62	49	39
P	Error				11	9	7	7	6	5	5	4	4	4	4	3	3	2	11
P	$dE_T/d\eta/(0.5N_p)$ (GeV)				2.09	2.06	2.06	2.05	2.03	2.00	1.95	1.96	1.93	1.87	1.84	1.78	1.73	1.70	1.59
P	Error (GeV)				0.12	0.12	0.12	0.12	0.12	0.12	0.11	0.11	0.11	0.11	0.12	0.14	0.15	0.17	0.18
R	$dE_T/d\eta/(0.5N_p)$ (GeV)				2.00	1.97	1.97	1.97	1.95	1.92	1.88	1.88	1.85	1.80	1.76	1.71	1.67	1.63	1.53
R	Error (GeV)				0.12	0.11	0.11	0.11	0.12	0.11	0.11	0.11	0.11	0.11	0.12	0.13	0.15	0.17	0.18
P	N_p	381	355	310	268	231	199	171	145	124	105	87	72	58	46	36	27	20	13	9
P	Error	10	9	8	7	6	6	6	5	5	5	4	5	4	3	3	3	2	2	12
P	$dN_{ch}/d\eta/(0.5N_p)$	2.66	2.64	2.62	2.60	2.58	2.54	2.50	2.49	2.43	2.40	2.34	2.32	2.31	2.29	2.20	2.17	2.13	2.17	2.22
P	Error	0.09	0.09	0.10	0.10	0.10	0.10	0.11	0.11	0.11	0.12	0.14	0.17	0.19	0.21	0.23	0.25	0.26	0.29	0.31
R	$dN_{ch}/d\eta/(0.5N_p)$	2.13	2.11	2.10	2.08	2.07	2.03	2.00	2.00	1.94	1.92	1.88	1.85	1.85	1.83	1.76	1.74	1.71	1.74	1.78
R	Error	0.07	0.08	0.08	0.08	0.08	0.08	0.09	0.09	0.09	0.10	0.12	0.14	0.16	0.16	0.18	0.20	0.21	0.23	0.25
P	N_p				383	359	315	276	242	211	185	160	140	123	106	91	78	66	56	49
P	Error				10	9	8	7	6	5	4	4	3	4	6	6	6	5	5	11
P	E_T/N_{ch} (GeV)				0.78	0.78	0.79	0.80	0.80	0.81	0.79	0.79	0.81	0.81	0.81	0.80	0.79	0.78	0.77	0.77
P	Error (GeV)				0.06	0.06	0.06	0.06	0.06	0.06	0.06	0.06	0.06	0.06	0.06	0.06	0.06	0.06	0.06	0.06
R	E_T/N_{ch} (GeV)				0.94	0.94	0.95	0.96	0.96	0.97	0.95	0.95	1.00	0.98	0.97	0.96	0.94	0.94	0.93	0.93
R	Error (GeV)				0.07	0.07	0.07	0.07	0.07	0.07	0.07	0.07	0.07	0.07	0.07	0.07	0.07	0.07	0.07	0.07

5. NA45

The NA45/CERES collaboration did not publish results for $dN_{ch}/d\eta$ as a function of centrality at $\sqrt{s_{NN}} = 17.2$ GeV. The data were taken from Fig. 6.5 in Ref. [58], and a 10% error was assigned based on the analysis procedure. The number of participants was taken from the corresponding cross-section bin reported by the NA50 results [42]. At the lower energy, the results were originally published in [59] and then N_p was subsequently corrected (see [41], for example). The results presented in Fig. 4 of Ref. [41] for charged hadrons h^- and $(h^+ - h^-)$ were added together to get $dh/d\eta$ and then converted to $dN_{ch}/d\eta$ in the c.m.s. frame. The published and recalculated results are summarized in Table VIII.

6. NA50

Results on N_p are taken from Tables 1 and 2 in Ref. [42] and on multiplicity from Figs. 2 and 4 tabulated in captions in Ref. [42]. The systematic errors are mentioned in the text. There is some discrepancy in the results of NA50 and NA45 as shown in Fig. 12. In this respect the comparison made in Table 3 of Ref. [42] is unclear. The results were converted to the c.m.s. frame. Recalculated values are given in Table IX.

7. E802/E917

The centrality dependence of π^+, K^+ yields and $\langle m_T \rangle$ were recalculated from Tables V and VI in Ref. [60]. Number of participants are taken from Table II in the same publication. The results are presented in Table X.

TABLE VIII. Published (P) NA45 results at $\sqrt{s_{NN}} = 17.2$ GeV taken from Fig. 6.5 in Ref. [58] and at $\sqrt{s_{NN}} = 8.7$ GeV from Fig. 4 in Ref. [41], and recalculated (R) results plotted in Figs. 11 and 12.

				$\sqrt{s_{NN}} = 17.2$ GeV				
P	Bin	0–2.3	2.3–5	5–8	8–12	12–18	18–23	23–35
P	$dN_{ch}/d\eta$	420	350	300	250	210	170	125
R	N_p	360	331	300	264	220	179	132
R	Error	10.	10	9	8	7	7	6
R	$dN_{ch}/d\eta/(0.5N_p)$	1.87	1.69	1.60	1.51	1.53	1.52	1.52
R	Error	0.19	0.18	0.17	0.16	0.16	0.16	0.17
				$\sqrt{s_{NN}} = 8.7$ GeV				
P	N_p	368	335	287	238	183	120	
P	h^-	129	113	94	78	58	38	
P	Error	15	14	12	11	9	9	
P	$h^+ - h^-$	52	46	39	30	22	15	
P	Error	12	8	8	7	6	6	
R	$dN_{ch}/d\eta/(0.5N_p)$	1.35	1.30	1.27	1.25	1.21	1.21	
R	Error	0.08	0.08	0.08	0.09	0.10	0.12	

TABLE IX. Recalculated NA50 results plotted in Figs. 11 and 12.

			$\sqrt{s_{NN}} = 17.2$ GeV			
N_p	354	294	246	205	173	129
Error	12	10	8	8	8	11
$dN_{\rm ch}/d\eta/(0.5N_p)$	1.98	1.98	1.94	1.95	1.95	2.10
Error	0.16	0.16	0.16	0.16	0.16	0.17
			$\sqrt{s_{NN}} = 8.7$ GeV			
N_p	356	295	245	204	170	127
Error	12	10	8	8	8	11
$dN_{\rm ch}/d\eta/(0.5N_p)$	0.95	0.90	0.90	0.89	0.90	0.92
Error	0.10	0.09	0.09	0.09	0.09	0.09

K^-/K^+ ratio was assigned a value of 0.17 for all centralities based on Tables II and III in Ref. [61]. This is consistent with results reported in Fig. 6 in Ref. [62] and Fig. 11 in [63]. The proton production reported in Table IV in Ref. [60] was compared to measurements reported in Fig. 2 in [64] and Fig. 10 in [63] for different centrality bins. The results are consistent. $\bar{p}/p$ ratio was assigned a value of 0.0003 based on Fig. 11 in Ref. [63]. A 25% enhancement in π^-/π^+ ratio for low m_T reported in [65] for the most central bin is not clearly seen in Fig. 11 in [63] for all centralities. Such an enhancement would contribute an additional 8–9% to the total particle and transverse energy production. This is less than the systematic error on the result and the recalculation error, and thus this effect is not considered. The resulting values shown in Table X were recalculated to midrapidity in the c.m.s. frame.

For the lower $\sqrt{s_{NN}}$ the information about particle yields and $\langle m_T \rangle$ was extracted for π^+ and K^+ from Tables II and I in Ref. [66], respectively; for K^- from Table I in [67]; and for p from Fig. 2 in [64]. The same assumptions as above were made to recalculate values plotted in Figs. 13 and 14. The numbers are given in Table XI.

8. Averaging procedure at $\sqrt{s_{NN}} = 8.7$ GeV

The averaging procedure is slightly different for this curve. First the average results of NA45 and NA50 are produced.

TABLE X. Centrality dependence of the identified particles measured by E802/E866/E917 collaborations. Number of participant pairs is published (P) in Table II in Ref. [60]. π^+ and K^+ values are obtained by extrapolation (E) from E802 measurement very close to midrapidity. Data were taken from Tables V and VI in Ref. [60]. Proton data are a compilation of the results taken from Table IV in [60] and Fig. 2 in [64]. Recalculated values (R) are plotted in Figs. 11 and 12.

P	N_p pairs	181	168	152	134	113	89.5	62.5	26.9
E	dN^{π^+}/dy	64.5	56.8	47.6	39.6	33.3	25.8	17.8	6.89
E	Error	3.13	2.55	2.75	1.75	1.68	1.37	0.89	0.28
E	$\langle m_T^{\pi^+} \rangle$ (GeV)	0.398	0.392	0.387	0.385	0.375	0.365	0.362	0.361
E	Error	0.013	0.013	0.014	0.012	0.041	0.011	0.010	0.011
E	dN^{K^+}/dy	10.6	9.28	8.12	6.17	4.91	3.73	2.22	0.74
E	Error	0.45	0.37	0.32	0.27	0.21	0.16	0.11	0.04
E	$\langle m_T^{K^+} \rangle$ (GeV)	0.809	0.787	0.774	0.785	0.770	0.740	0.743	0.685
E	Error	0.034	0.032	0.028	0.028	0.030	0.027	0.025	0.021
E	dN^p/dy	62.8	57.0	49.4	43.0	33.7	25.2	16.5	6.2
E	Error	1.7	1.5	1.4	1	1	1	1	1
E	$\langle m_T^p \rangle$ (GeV)	1.25	1.26	1.24	1.23	1.21	1.19	1.17	1.14
R	$dE_T/d\eta/(0.5N_p)$	0.608	0.580	0.527	0.492	0.460	0.426	0.396	0.335
R	Error (GeV)	0.146	0.138	0.125	0.116	0.111	0.103	0.098	0.131
R	$dN_{\rm ch}/d\eta/(0.5N_p)$	0.903	0.865	0.812	0.773	0.751	0.725	0.699	0.621
R	Error	0.135	0.130	0.122	0.116	0.112	0.108	0.108	0.207
R	$E_T/N_{\rm ch}$ (GeV)	0.673	0.670	0.649	0.636	0.612	0.588	0.567	0.540
R	Error (GeV)	0.127	0.123	0.120	0.117	0.115	0.111	0.111	0.112

TABLE XI. Recalculated values from E802/E917 experiments plotted in Figs. 13 and 14.

$\sqrt{s_{NN}}$ (GeV)	4.84	4.27	3.81
$dE_T/d\eta/(0.5N_p)$ (GeV)	0.579 ± 0.087	0.498 ± 0.075	0.405 ± 0.061
$dN_{\rm ch}/d\eta/(0.5N_p)$	0.851 ± 0.128	0.787 ± 0.118	0.678 ± 0.102
$E_T/N_{\rm ch}$ (GeV)	0.680 ± 0.068	0.634 ± 0.063	0.598 ± 0.060

TABLE XII. Particle yields measured by FOPI experiment at midrapidity extracted from Fig. 21 in Ref. [68].

Z	1	2	3	4	5–6
$dM/d(\cos\theta)$	43	12	2	0.5	0.25
Error	4.3	1.2	0.2	0.05	0.025

Then at $N_p = 350$, this result is combined with the NA49 measurement using the weighted error method. A scaling coefficient before and after NA49 averaging is calculated. The NA45/NA50 combined result is scaled by this factor for all values of N_p.

9. FOPI

The FOPI results for $N_{\rm ch}$ were calculated for 400 A MeV based on the data plotted in Fig. 21 of Ref. [68]. The points were read at the angle corresponding to the midrapidity angle ($\theta = 55^\circ$) and then converted to $dN_{\rm ch}/d\eta$ resulting in 39 ± 4 at $\sqrt{s_{NN}} = 2.053$ GeV.

The corresponding number of participants for a 42-mb event sample is 359 based on Fig. 8 in Ref. [69]. Data for 150 A MeV were compiled based on the comparison between Figs. 13 and 14 in [68] and the used definition of rapidity y, resulting in $dN_{\rm ch}/d\eta = 40 \pm 5$ at $\sqrt{s_{NN}} = 1.937$ GeV.

The estimate of the E_T production at 400 A MeV is made based on a comparison of the total yields of the particles with $Z = 1$ in [68] and yields of protons and deuterons published in [70]. That allowed us to determine the number of all pions at midrapidity to be 20.6 and the number of all hadrons with $Z = 1$ to be 15.2. Assuming that the particle temperatures are equal to $T = 40$ MeV (exact numbers are published in [69,70]), one can estimate that the contribution to E_T from pions is $m_\pi + 3/2T$ and from baryons is $3/2T$, according to the definition of E_T used in this paper. The resulting number of 5.0 GeV is a lower limit estimate because the contribution of heavier particles is not considered. A conservative error of 30% is assigned to this number.

10. PHOBOS measurement at $\sqrt{s_{NN}} = 56$ GeV

The PHOBOS experiment published $dN_{\rm ch}/d\eta = 408 \pm 12(\text{stat}) \pm 30(\text{syst})$ at $\sqrt{s_{NN}} = 56$ GeV measured for $N_p = 330 \pm 4(\text{stat})^{+10}_{-15}(\text{syst})$ in [35]. In the same paper, $dN_{\rm ch}/d\eta$ per participant between 130 and 56 GeV was measured to increase by $1.31 \pm 0.04(\text{stat}) \pm 0.05(\text{syst})$. That allows the use of the averaged value at $\sqrt{s_{NN}} = 130$ GeV consistent with the PHOBOS result published in [36] to recalculate $dN_{\rm ch}/d\eta$ at $\sqrt{s_{NN}} = 56$ GeV with smaller systematic error. This value is plotted in Fig. 13.

APPENDIX B: OUTPUT TABLES

TABLE XIII. Results of the measurements by PHENIX at $\sqrt{s_{NN}} = 200$ GeV. Errors have the same dimension as the preceding value. Results are plotted in Figs. 5, 7, and 8.

Bin (%)	0–5	5–10	10–15	15–20	20–25	25–30	30–35	35–40	40–45	45–50	50–55	55–60	60–65	65–70
N_p	353	300	254	215	181	151	125	103	83.3	66.7	52.5	40.2	30.2	22.0
Syst. error	10.0	9.0	8.1	7.3	6.6	6.0	5.5	5.1	4.7	4.3	4.1	3.8	3.6	3.4
$A_\perp$(fm^2)	140	125.0	112	100	90.8	82.2	73.9	66.8	60.0	54.3	49.3	45.1	40.9	37.5
Syst. error	11.0	10.0	9.1	8.2	7.4	6.8	6.2	5.7	5.2	4.8	4.6	4.5	4.5	4.9
$dE_T/d\eta$ (GeV)	606	493	402	328	266	216	173	137	107	81.8	60.4	43.9	31.1	21.1
Stat. error	0.6	0.6	0.5	0.5	0.4	0.4	0.3	0.3	0.2	0.2	0.2	0.1	0.1	0.1
Bending syst. error	2.4	5.1	7.0	7.6	8.2	8.5	8.2	8.1	7.6	6.9	6.4	5.5	4.6	3.9
Full syst. error	32.0	27.0	22.0	19.0	16.0	14.0	12.0	11.0	9.5	8.1	7.2	5.9	4.9	4.0
$\varepsilon_{Bj}\tau$ (GeV fm^{-2} c^{-1})	5.4	4.9	4.5	4.1	3.7	3.3	2.9	2.6	2.2	1.9	1.5	1.2	1.0	0.7
Full syst. error	0.6	0.5	0.5	0.5	0.4	0.4	0.4	0.3	0.3	0.3	0.2	0.2	0.2	0.2
$dE_T/d\eta/(0.5N_p)$ (GeV)	3.43	3.28	3.16	3.05	2.94	2.86	2.76	2.66	2.57	2.45	2.30	2.18	2.06	1.92
Bending syst. error	0.01	0.03	0.05	0.07	0.09	0.12	0.14	0.17	0.19	0.22	0.27	0.31	0.36	0.43
Full syst. error	0.21	0.20	0.20	0.20	0.21	0.22	0.23	0.25	0.27	0.29	0.33	0.36	0.41	0.47
$dN_{\rm ch}/d\eta$	687	560	457	372	302	246	197	156	124	95.3	70.9	52.2	37.5	25.6
Stat. error	0.7	0.6	0.5	0.5	0.4	0.4	0.3	0.3	0.2	0.2	0.2	0.1	0.1	0.1
Bending syst. error	25.0	17.0	14.0	11.0	10.0	9.9	9.4	9.0	8.2	7.8	7.1	6.1	5.2	4.4
Full syst. error	37.0	28.0	22.0	18.0	16.0	14.0	12.0	11.0	9.6	8.6	7.6	6.5	5.4	4.5
$dN_{\rm ch}/d\eta/(0.5N_p)$	3.89	3.73	3.59	3.45	3.34	3.25	3.15	3.05	2.96	2.86	2.70	2.60	2.48	2.33
Bending syst. error	0.14	0.12	0.11	0.10	0.12	0.14	0.16	0.19	0.21	0.25	0.30	0.35	0.41	0.49
Full syst. error	0.23	0.22	0.21	0.21	0.21	0.22	0.24	0.26	0.28	0.32	0.36	0.41	0.46	0.55
$E_T/N_{\rm ch}$ (GeV)	0.881	0.879	0.881	0.882	0.881	0.880	0.875	0.874	0.866	0.858	0.851	0.840	0.828	0.823
Bending syst. error	0.032	0.026	0.021	0.017	0.015	0.012	0.011	0.010	0.011	0.013	0.017	0.023	0.032	0.047
Full syst. error	0.071	0.069	0.067	0.066	0.065	0.065	0.064	0.064	0.064	0.064	0.064	0.065	0.068	0.076

TABLE XIV. Results of the measurements by PHENIX at $\sqrt{s_{NN}} = 130\,\text{GeV}$. Errors have the same dimension as the preceding value. Results are plotted in Figs. 5, 7, and 8.

Bin (%)	0–5	5–10	10–15	15–20	20–25	25–30	30–35	35–40	40–45	45–50	50–55	55–60	60–65	65–70
N_p	348	294	250	211	179	150	125	103	83.2	66.3	52.1	40.1	30.1	21.9
Syst. error	10.0	8.9	8.0	7.2	6.6	6.0	5.5	5.1	4.7	4.3	4.0	3.8	3.6	3.4
$A_\perp(\text{fm}^2)$	138	123	110	99.5	89.4	80.6	72.8	65.8	59.5	54.3	49.0	44.8	40.9	37.4
Syst. error	11.0	9.9	8.9	8.1	7.3	6.6	6.1	5.6	5.2	4.8	4.6	4.5	4.6	4.8
$dE_T/d\eta$ (GeV)	523	425	349	287	237	191	154	122	96.0	73.3	55.5	41.0	30.2	21.4
Stat. error	0.9	0.9	0.8	0.7	0.6	0.6	0.5	0.4	0.4	0.3	0.3	0.2	0.2	0.2
Bending syst. error	2.6	4.2	5.6	7.0	7.5	7.6	7.5	7.0	7.3	6.2	5.8	5.1	4.4	4.1
Full syst. error	27.0	22.0	19.0	16.0	14.0	12.0	11.0	9.4	8.8	7.3	6.5	5.5	4.7	4.2
$\varepsilon_{Bj}\tau$ (GeV fm^{-2} c^{-1})	4.7	4.3	3.9	3.6	3.3	3.0	2.6	2.3	2.0	1.7	1.4	1.1	0.9	0.7
Full syst. error	0.5	0.5	0.4	0.4	0.4	0.3	0.3	0.3	0.3	0.2	0.2	0.2	0.2	0.2
$dE_T/d\eta/(0.5N_p)$ (GeV)	3.01	2.89	2.80	2.72	2.65	2.56	2.47	2.37	2.31	2.21	2.13	2.05	2.01	1.95
Bending syst. error	0.01	0.03	0.05	0.07	0.09	0.10	0.12	0.14	0.19	0.20	0.24	0.29	0.34	0.45
Full syst. error	0.18	0.18	0.18	0.18	0.19	0.20	0.21	0.22	0.25	0.26	0.30	0.34	0.39	0.49
$dN_{\text{ch}}/d\eta$	602	488	403	329	270	219	176	139	109	84.1	64.3	48.4	35.2	25.3
Stat. error	1.4	1.2	1.1	0.9	0.8	0.7	0.6	0.5	0.4	0.3	0.3	0.3	0.2	0.2
Bending syst. error	19.0	13.0	10.0	9.9	8.6	8.4	8.3	7.7	7.5	6.4	5.9	5.2	4.3	4.1
Full syst. error	28.0	22.0	17.0	15.0	13.0	11.0	10.0	9.1	8.4	7.0	6.3	5.4	4.5	4.1
$dN_{\text{ch}}/d\eta/(0.5N_p)$	3.46	3.32	3.23	3.12	3.03	2.93	2.82	2.70	2.63	2.54	2.47	2.41	2.34	2.31
Bending syst. error	0.11	0.09	0.08	0.09	0.10	0.12	0.14	0.16	0.19	0.21	0.25	0.30	0.35	0.47
Full syst. error	0.19	0.18	0.17	0.18	0.18	0.19	0.21	0.22	0.25	0.27	0.31	0.35	0.41	0.52
E_T/N_{ch} (GeV)	0.869	0.870	0.867	0.874	0.877	0.873	0.875	0.876	0.878	0.871	0.864	0.847	0.857	0.844
Bending syst. error	0.028	0.023	0.019	0.016	0.015	0.014	0.014	0.016	0.020	0.025	0.033	0.043	0.060	0.083
Full syst. error	0.066	0.064	0.063	0.062	0.062	0.062	0.062	0.063	0.064	0.065	0.068	0.073	0.084	0.101

TABLE XV. Results of the measurements by PHENIX at $\sqrt{s_{NN}} = 19.6\,\text{GeV}$. Errors have the same dimension as the preceding value. Results are plotted in Figs. 5, 7, and 8.

Bin (%)	0–5	5–10	10–15	15–20	20–25	25–30	30–35	35–40	40–45	45–50
N_p	336	288	243	204	172	144	120	98.4	79.8	63.8
Syst. error	9.7	8.8	7.9	7.1	6.4	5.9	5.4	5.0	4.6	4.3
$A_\perp(\text{fm}^2)$	133.0	119	106	95.6	85.8	77.2	69.7	62.7	56.7	51.3
Syst. error	11.0	9.6	8.6	7.8	7.0	6.4	5.8	5.3	4.9	4.6
$dE_T/d\eta$ (GeV)	230	194	164	134	109	88.4	72.0	58.1	45.3	35.2
Stat. error	0.8	0.8	0.8	0.7	0.5	0.5	0.4	0.4	0.3	0.3
Bending syst. error	1.7	2.6	2.9	4.0	3.8	3.8	3.9	3.9	3.9	3.4
Full syst. error	14.	12.	11.	9.3	7.8	6.7	6.0	5.3	4.8	4.0
$\varepsilon_{Bj}\tau$ (GeV fm^{-2} c^{-1})	2.2	2.0	1.9	1.8	1.6	1.4	1.3	1.2	1.0	0.9
Full syst. error	0.2	0.2	0.2	0.2	0.2	0.2	0.2	0.2	0.1	0.1
$dE_T/d\eta/(0.5N_p)$ (GeV)	1.37	1.35	1.35	1.31	1.27	1.22	1.20	1.18	1.13	1.10
Bending syst. error	0.01	0.02	0.02	0.04	0.05	0.05	0.07	0.08	0.10	0.11
Full syst. error	0.09	0.09	0.10	0.10	0.10	0.10	0.11	0.12	0.14	0.15
$dN_{\text{ch}}/d\eta$	312	265	226	187	154	125	102	82.6	65.0	51.1
Stat. error	0.9	0.9	0.9	0.8	0.7	0.6	0.5	0.4	0.4	0.3
Bending syst. error	5.3	4.5	4.4	5.4	4.9	5.3	5.2	5.1	5.1	4.2
Full syst. error	21.0	18.0	15.0	13.0	11.0	9.7	8.5	7.4	6.6	5.4
$dN_{\text{ch}}/d\eta/(0.5N_p)$	1.86	1.84	1.85	1.83	1.78	1.74	1.71	1.68	1.63	1.60
Bending syst. error	0.03	0.03	0.04	0.05	0.06	0.08	0.09	0.11	0.14	0.14
Full syst. error	0.14	0.14	0.14	0.14	0.14	0.15	0.16	0.17	0.19	0.20

TABLE XV. (*Continued*.)

Bin (%)	0–5	5–10	10–15	15–20	20–25	25–30	30–35	35–40	40–45	45–50
$E_T/N_{\rm ch}$ (GeV)	0.738	0.733	0.728	0.720	0.711	0.705	0.704	0.704	0.697	0.690
Bending syst. error	0.027	0.023	0.020	0.017	0.015	0.014	0.014	0.016	0.019	0.024
Full syst. error	0.078	0.076	0.075	0.073	0.072	0.071	0.071	0.071	0.072	0.072

TABLE XVI. Ratios of measured quantities at 200/130 and 200/19.6 GeV. The number of N_p is the average between two energies. The data are plotted in Fig. 6.

Bin (%)	0–5	5–10	10–15	15–20	20–25	25–30	30–35	35–40	40–45	45–50	50–55	55–60	60–65	65–70
							200/130 GeV							
N_p	350	297	252	213	180	150	125	103	83.2	66.5	52.3	40.2	30.2	22.0
Syst. error	10.0	9.0	8.1	7.3	6.6	6.0	5.5	5.1	4.7	4.3	4.1	3.8	3.6	3.4
$dE_T/d\eta/(0.5N_p)$	1.14	1.13	1.13	1.12	1.11	1.12	1.12	1.12	1.11	1.11	1.08	1.07	1.03	0.98
Bending syst. error	0.01	0.01	0.01	0.01	0.01	0.02	0.02	0.03	0.04	0.05	0.05	0.07	0.09	0.13
Full syst. error	0.04	0.04	0.04	0.04	0.04	0.05	0.05	0.05	0.06	0.06	0.07	0.08	0.10	0.13
$dN_{\rm ch}/d\eta/(0.5N_p)$	1.12	1.12	1.11	1.11	1.10	1.11	1.12	1.13	1.13	1.13	1.10	1.08	1.06	1.01
Bending syst. error	0.01	0.01	0.01	0.01	0.01	0.01	0.02	0.02	0.03	0.03	0.03	0.03	0.04	0.07
Full syst. error	0.04	0.04	0.04	0.04	0.04	0.04	0.04	0.04	0.04	0.04	0.04	0.05	0.05	0.08
							200/19.6 GeV							
N_p	344	294	249	210	177	148	122	101	81.6	65.2				
Syst. error	10.0	9.0	8.1	7.3	6.6	6.0	5.5	5.1	4.7	4.3				
$dE_T/d\eta/(0.5N_p)$	2.50	2.43	2.34	2.32	2.32	2.34	2.29	2.25	2.26	2.22				
Bending syst. error	0.02	0.03	0.04	0.06	0.07	0.09	0.11	0.13	0.17	0.19				
Full syst. error	0.09	0.09	0.09	0.10	0.10	0.12	0.13	0.15	0.19	0.20				
$dN_{\rm ch}/d\eta/(0.5N_p)$	2.09	2.03	1.94	1.89	1.87	1.87	1.84	1.81	1.82	1.79				
Bending syst. error	0.08	0.06	0.06	0.06	0.06	0.07	0.08	0.10	0.12	0.13				
Full syst. error	0.15	0.14	0.13	0.13	0.13	0.14	0.14	0.15	0.17	0.17				

TABLE XVII. Average values of $dN_{\rm ch}/d\eta\,/(0.5N_p)$ at different $\sqrt{S_{NN}}$. An additional 5% error should be added to rows 17.2–4.8 GeV for the uncertainty related to recalculation to the center-of-mass system. The results are presented in Figs. 9 and 12.

N_p	375	350	325	300	275	250	225	200	175	150	125	100	75	50	25
$\sqrt{S_{NN}}$															
200 GeV	3.92	3.81	3.72	3.65	3.56	3.51	3.45	3.38	3.34	3.27	3.20	3.14	3.03	2.73	2.78
Error	0.13	0.13	0.12	0.12	0.12	0.12	0.12	0.11	0.12	0.12	0.12	0.13	0.13	0.13	0.43
130 GeV	3.41	3.31	3.22	3.16	3.11	3.07	3.04	3.00	2.96	2.89	2.83	2.73	2.65	2.53	2.36
Error	0.10	0.10	0.10	0.10	0.09	0.09	0.10	0.09	0.10	0.10	0.10	0.11	0.11	0.12	0.30
19.6 GeV		1.91	1.89	1.88	1.87	1.87	1.85	1.83	1.81	1.76	1.72	1.68	1.62		
Error		0.11	0.11	0.11	0.11	0.12	0.12	0.12	0.12	0.13	0.14	0.15	0.19		
17.2 GeV	1.97	1.93	1.90	1.88	1.83	1.80	1.78	1.75	1.72	1.69	1.66	1.66	1.61	1.54	1.45
Error	0.12	0.12	0.14	0.15	0.16	0.17	0.17	0.17	0.17	0.17	0.16	0.23	0.21	0.19	0.13
8.7 GeV	1.26	1.22	1.20	1.18	1.17	1.16	1.16	1.14	1.14	1.14	1.14	1.14			
Error	0.11	0.11	0.11	0.10	0.10	0.10	0.10	0.10	0.09	0.09	0.09	0.09			
4.8 GeV	0.92	0.89	0.85	0.81	0.78	0.76	0.75	0.74	0.72	0.71	0.70	0.67	0.64	0.63	
Error	0.14	0.13	0.13	0.12	0.12	0.11	0.11	0.11	0.11	0.11	0.11	0.14	0.18	0.21	

[1] H. Hahn *et al*., Nucl. Instrum. Methods A **499**, 245 (2003).
[2] PHENIX Collaboration, K. Adcox *et al*., Nucl. Instrum. Methods A **499**, 469 (2003).
[3] K. Adcox *et al*., Nucl. Instrum. Methods A **497**, 263 (2003).
[4] L. Aphechetche *et al*., Nucl. Instrum. Methods A **499**, 521 (2003).
[5] M. Allen *et al*., Nucl. Instrum. Methods A **499**, 549 (2003).
[6] S. Adler *et al*., Nucl. Instrum. Methods A **470**, 488 (2001).
[7] PHENIX Collaboration, K. Adcox *et al*., Phys. Rev. Lett. **87**, 052301 (2001).
[8] PHENIX Collaboration, K. Adcox *et al*., Phys. Rev. Lett. **86**, 3500 (2001).
[9] A. Milov for the PHENIX Collaboration, Nucl. Phys. **A698**, 171 (2002).
[10] A. Bazilevsky for the PHENIX Collaboration, Nucl. Phys. **A715**, 486 (2003).
[11] D. Silvermyr, Ph.D. thesis, Lund University, 2001.
[12] A. Milov, Ph.D. Thesis, Weizmann Institute of Science, 2002.
[13] PHENIX Collaboration, K. Adcox *et al*., Phys. Rev. Lett. **88**, 242301 (2002).
[14] GEANT 3.2.1, CERN program library.
[15] X. N. Wang and M. Gyulassy, Phys. Rev. D **44**, 3501 (1991).
[16] PHENIX Collaboration, S. S. Adler *et al*., Phys. Rev. C **69**, 034909 (2004).
[17] J. Bächler for the NA49 Collaboration, Nucl. Phys. **A661**, 45 (1999).
[18] M. van Leeuwen for the NA49 Collaboration, Nucl. Phys. **A715**, 161 (2003).
[19] NA49 Collaboration, S. V. Afanasiev *et al*., Phys. Rev. C **66**, 054902 (2002).
[20] K. Hagiwara *et al*., http://pdg.lbl.gov; Phys. Rev. D **66**, 010001 (2002).
[21] B. Hahn, D. G. Ravenhall, and R. Hofstadter, Phys. Rev. **101**, 1131 (1956); C. W. De Jager *et al*., At. Data Nucl. Data Tables **24**, 479 (1974).
[22] PHOBOS Collaboration, B. B. Back *et al*., Phys. Rev. Lett. **91**, 052303 (2003).
[23] E-802 Collaboration, T. Abbott *et al*., Phys. Rev. C **63**, 064602 (2001).
[24] PHENIX Collaboration, K. Adcox *et al*., Phys. Rev. C **66**, 024901 (2002).
[25] WA98 Collaboration, M. M. Aggarval *et al*., Eur. Phys. J. C **18**, 651 (2001).
[26] PHENIX Collaboration, S. S. Adler *et al*., Phys. Rev. Lett. **91**, 241803 (2003).
[27] PHOBOS Collaboration, B. B. Back *et al*., nucl-ex/0301017.
[28] M. Gyulassy, Lec. Note Phys. **583**, 37 (2002).
[29] A. Krasnitz, Y. Nara, and R. Venugopalan, hep-ph/0305112; Nucl. Phys. **A727**, 427 (2003).
[30] J. D. Bjorken, Phys. Rev. D **27**, 140 (1983).
[31] NA49 Collaboration, T. Alber *et al*., Phys. Rev. Lett. **75**, 3814 (1995).
[32] STAR Collaboration, J. Adams *et al*., nucl-ex/0311017.
[33] BRAHMS Collaboration, I. G. Bearden *et al*., Phys. Lett. **B523**, 227 (2001).
[34] BRAHMS Collaboration, I. G. Bearden *et al*., Phys. Rev. Lett. **88**, 202301 (2002).
[35] PHOBOS Collaboration, B. B. Back *et al*., Phys. Rev. Lett. **85**, 3100 (2000).
[36] PHOBOS Collaboration, B. B. Back *et al*., Phys. Rev. C **65**, 061901 (2002).
[37] M. D. Baker *et al*. for the PHOBOS Collaboration, Nucl. Phys. **A715**, 65c (2003).
[38] T. S. Ullrich for the STAR Collaboration, Heavy Ion Phys. **21**, 143 (2004).
[39] T. S. Ullrich for the STAR Collaboration, Nucl. Phys. **A715**, 399 (2003).
[40] STAR Collaboration, J. Adams *et al*., Phys. Rev. C **70**, 054907 (2004).
[41] CERES Collaboration, D. Miśkowiec, in *Proceedings of the 30th International Workshop on Gross Properties of Nuclei and Nuclear Excitations: Ultrarelativistic heavy-ion collisions, Hirschegg, Austria, January 13–19, 2002*, edited by M. Buballa, W. Nörenberg, B.-J. Schaefer, J. Wambach [Technical University of Darmstadt and Gesellschaft fürSchwerionenforschung (GSI), Darmstadt, 2002], p. 238–247, http://theory.gsi.de/hirschegg/2002/Proceedings/
[42] NA50 Collaboration, M. C. Abreu *et al*., Phys. Lett. **B530**, 43 (2002).
[43] NA57 Collaboration, F. Antinori *et al*., hep-ex/0406004.
[44] UA5 Collaboration, G. J. Alner *et al*., Z. Phys. C **33**, 1 (1986).
[45] W. Thome *et al*., Nucl. Phys. **B129**, 365 (1977).
[46] V. Topor Pop, M. Gyulassy, J. Barrette, C. Gale, X. N. Wang, N. Xu, and K. Filimonov, Phys. Rev. C **68**, 054902 (2003).
[47] B. Andersson *et al*., Nucl. Phys. **B281**, 289 (2003).
[48] K. J. Eskola *et al*., Nucl. Phys. **B570**, 379 (2000); Phys. Lett. **B497**, 39 (2001).
[49] D. Kharzeev and M. Nardi, Phys. Lett. **B507**, 121 (2001); D. Kharzeev and E. Levin, *ibid*. **B523**, 79 (2001).
[50] S. Lee and X. N. Wang, Phys. Lett. **B527**, 85 (2002).
[51] Z. W. Lin, S. Pal, C. M. Ko, B. A. Li, and B. Zhang, Phys. Rev. C **64**, 011902(R) (2001).
[52] A. Accardi, Phys. Rev. C **64**, 064905 (2001).
[53] R. Ugoccioni, Phys. Lett. **B491**, 253 (2000).
[54] A. Capella *et al*., Phys. Rep. **236**, 225 (1994).
[55] N. Armesto Perez *et al*., Phys. Lett. **B527**, 92 (2002); Eur. Phys. J. C **22**, 149 (2001).
[56] D. E. Kahana and S. H. Kahana, nucl-th/0208063.
[57] S. Jeon and J. Kapusta, Phys. Rev. C **63**, 011901(R) (2001).
[58] F. Ceretto, Ph.D. thesis, University of Heidelberg, 1998.
[59] H. Appelshäuser for the CERES Collaboration, Nucl. Phys. **A698**, 253 (2002).
[60] E802 Collaboration, L. Ahle *et al*., Phys. Rev. C **59**, 2173 (1999).
[61] E802 Collaboration, L. Ahle *et al*., Phys. Rev. C **58**, 3523 (1998).
[62] C. A. Ogilvie for the E866 and E917 Collaborations, Nucl. Phys. **A638**, 57c (1998).
[63] Y. Akiba for the E802 Collaboration, Nucl. Phys. **A610**, 139 (1996).
[64] E917 Collaboration, B. B. Back *et al*., Phys. Rev. Lett. **86**, 1970 (2001).
[65] E802 Collaboration, L. Ahle *et al*., Phys. Rev. C **57**, 466(R) (1998).
[66] E802 Collaboration, L. Ahle *et al*., Phys. Lett. **B476**, 1 (2000).
[67] E802 Collaboration, L. Ahle *et al*., Phys. Lett. **B490**, 53 (2000).
[68] FOPI Collaboration, W. Reisdorf *et al*., Nucl. Phys. **A612**, 493 (1997).
[69] FOPI Collaboration, D. Pelte *et al*., Z. Phys. A **357**, 215 (1997).
[70] FOPI Collaboration, B. Hong *et al*., Phys. Rev. C **66**, 034901 (2002).

Publisher's Note: Systematic studies of the centrality and $\sqrt{s_{NN}}$ dependence of the $dE_T/d\eta$ and $dN_{\rm ch}/d\eta$ in heavy ion collisions at midrapidity [Phys. Rev. C 71, 034908 (2005)]

S. S. Adler, S. Afanasiev, C. Aidala, N. N. Ajitanand, Y. Akiba, J. Alexander, R. Amirikas, L. Aphecetche, S. H. Aronson, R. Averbeck, T. C. Awes, R. Azmoun, V. Babintsev, A. Baldisseri, K. N. Barish, P. D. Barnes, B. Bassalleck, S. Bathe, S. Batsouli, V. Baublis, A. Bazilevsky, S. Belikov, Y. Berdnikov, S. Bhagavatula, J. G. Boissevain, H. Borel, S. Borenstein, M. L. Brooks, D. S. Brown, N. Bruner, D. Bucher, H. Buesching, V. Bumazhnov, G. Bunce, J. M. Burward-Hoy, S. Butsyk, X. Camard, J.-S. Chai, P. Chand, W. C. Chang, S. Chernichenko, C. Y. Chi, J. Chiba, M. Chiu, I. J. Choi, J. Choi, R. K. Choudhury, T. Chujo, V. Cianciolo, Y. Cobigo, B. A. Cole, P. Constantin, D. G. d'Enterria, G. David, H. Delagrange, A. Denisov, A. Deshpande, E. J. Desmond, O. Dietzsch, O. Drapier, A. Drees, R. du Rietz, A. Durum, D. Dutta, Y. V. Efremenko, K. El Chenawi, A. Enokizono, H. En'yo, S. Esumi, L. Ewell, D. E. Fields, F. Fleuret, S. L. Fokin, B. D. Fox, Z. Fraenkel, J. E. Frantz, A. Franz, A. D. Frawley, S.-Y. Fung, S. Garpman, T. K. Ghosh, A. Glenn, G. Gogiberidze, M. Gonin, J. Gosset, Y. Goto, R. Granier de Cassagnac, N. Grau, S. V. Greene, M. Grosse Perdekamp, W. Guryn, H. Å. Gustafsson, T. Hachiya, J. S. Haggerty, H. Hamagaki, A. G. Hansen, E. P. Hartouni, M. Harvey, R. Hayano, X. He, M. Heffner, T. K. Hemmick, J. M. Heuser, M. Hibino, J. C. Hill, W. Holzmann, K. Homma, B. Hong, A. Hoover, T. Ichihara, V. V. Ikonnikov, K. Imai, D. Isenhower, M. Ishihara, M. Issah, A. Isupov, B. V. Jacak, W. Y. Jang, Y. Jeong, J. Jia, O. Jinnouchi, B. M. Johnson, S. C. Johnson, K. S. Joo, D. Jouan, S. Kametani, N. Kamihara, J. H. Kang, S. S. Kapoor, K. Katou, S. Kelly, B. Khachaturov, A. Khanzadeev, J. Kikuchi, D. H. Kim, D. J. Kim, D. W. Kim, E. Kim, G.-B. Kim, H. J. Kim, E. Kistenev, A. Kiyomichi, K. Kiyoyama, C. Klein-Boesing, H. Kobayashi, L. Kochenda, V. Kochetkov, D. Koehler, T. Kohama, M. Kopytine, D. Kotchetkov, A. Kozlov, P. J. Kroon, C. H. Kuberg, K. Kurita, Y. Kuroki, M. J. Kweon, Y. Kwon, G. S. Kyle, R. Lacey, V. Ladygin, J. G. Lajoie, A. Lebedev, S. Leckey, D. M. Lee, S. Lee, M. J. Leitch, X. H. Li, H. Lim, A. Litvinenko, M. X. Liu, Y. Liu, C. F. Maguire, Y. I. Makdisi, A. Malakhov, V. I. Manko, Y. Mao, G. Martinez, M. D. Marx, H. Masui, F. Matathias, T. Matsumoto, P. L. McGaughey, E. Melnikov, M. Mendenhall, F. Messer, Y. Miake, J. Milan, T. E. Miller, A. Milov, S. Mioduszewski, R. E. Mischke, G. C. Mishra, J. T. Mitchell, A. K. Mohanty, D. P. Morrison, J. M. Moss, F. Mühlbacher, D. Mukhopadhyay, M. Muniruzzaman, J. Murata, S. Nagamiya, J. L. Nagle, T. Nakamura, B. K. Nandi, M. Nara, J. Newby, P. Nilsson, A. S. Nyanin, J. Nystrand, E. O'Brien, C. A. Ogilvie, H. Ohnishi, I. D. Ojha, K. Okada, M. Ono, V. Onuchin, A. Oskarsson, I. Otterlund, K. Oyama, K. Ozawa, D. Pal, A. P. T. Palounek, V. S. Pantuev, V. Papavassiliou, J. Park, A. Parmar, S. F. Pate, T. Peitzmann, J.-C. Peng, V. Peresedov, C. Pinkenburg, R. P. Pisani, F. Plasil, M. L. Purschke, A. K. Purwar, J. Rak, I. Ravinovich, K. F. Read, M. Reuter, K. Reygers, V. Riabov, Y. Riabov, G. Roche, A. Romana, M. Rosati, P. Rosnet, S. S. Ryu, M. E. Sadler, N. Saito, T. Sakaguchi, M. Sakai, S. Sakai, V. Samsonov, L. Sanfratello, R. Santo, H. D. Sato, S. Sato, S. Sawada, Y. Schutz, V. Semenov, R. Seto, M. R. Shaw, T. K. Shea, T.-A. Shibata, K. Shigaki, T. Shiina, C. L. Silva, D. Silvermyr, K. S. Sim, C. P. Singh, V. Singh, M. Sivertz, A. Soldatov, R. A. Soltz, W. E. Sondheim, S. P. Sorensen, I. V. Sourikova, F. Staley, P. W. Stankus, E. Stenlund, M. Stepanov, A. Ster, S. P. Stoll, T. Sugitate, J. P. Sullivan, E. M. Takagui, A. Taketani, M. Tamai, K. H. Tanaka, Y. Tanaka, K. Tanida, M. J. Tannenbaum, P. Tarján, J. D. Tepe, T. L. Thomas, J. Tojo, H. Torii, R. S. Towell, I. Tserruya, H. Tsuruoka, S. K. Tuli, H. Tydesjö, N. Tyurin, H. W. van Hecke, J. Velkovska, M. Velkovsky, L. Villatte, A. A. Vinogradov, M. A. Volkov, E. Vznuzdaev, X. R. Wang, Y. Watanabe, S. N. White, F. K. Wohn, C. L. Woody, W. Xie, Y. Yang, A. Yanovich, S. Yokkaichi, G. R. Young, I. E. Yushmanov, W. A. Zajc, C. Zhang, S. Zhou, S. J. Zhou, and L. Zolin

(Received 5 April 2005; published 22 April 2005)

DOI: 10.1103/PhysRevC.71.049901 PACS number(s): 25.75.Dw, 99.10.Fg

This paper was published online on 25 March 2005 with an error in Fig. 4. The left and right panels of Fig. 4 were identical. The correct right panel has been inserted as of 6 April 2005. The figure is correct in the printed version of the journal.

 ©2005 The American Physical Society

PHYSICAL REVIEW C **71**, 051902(R) (2005)

Jet structure of baryon excess in Au+Au collisions at $\sqrt{s_{NN}} = 200$ GeV

S. S. Adler,[5] S. Afanasiev,[20] C. Aidala,[5,10] N. N. Ajitanand,[47] Y. Akiba,[23,42] A. Al-Jamel,[37] J. Alexander,[47] R. Amirikas,[14] K. Aoki,[27] L. Aphecetche,[49] R. Armendariz,[37] S. H. Aronson,[5] R. Averbeck,[48] T. C. Awes,[38] R. Azmoun,[48] V. Babintsev,[17] A. Baldisseri,[11] K. N. Barish,[6] P. D. Barnes,[30] B. Bassalleck,[36] S. Bathe,[6,33] S. Batsouli,[10] V. Baublis,[41] F. Bauer,[6] A. Bazilevsky,[5,17,43] S. Belikov,[19,17] Y. Berdnikov,[44] S. Bhagavatula,[19] M. T. Bjorndal,[10] J. G. Boissevain,[30] H. Borel,[11] S. Borenstein,[28] M. L. Brooks,[30] D. S. Brown,[37] N. Bruner,[36] D. Bucher,[33] H. Buesching,[5,33] V. Bumazhnov,[17] G. Bunce,[5,43] J. M. Burward-Hoy,[29,30,48] S. Butsyk,[48] X. Camard,[49] J.-S. Chai,[21] P. Chand,[4] W. C. Chang,[2] S. Chernichenko,[17] C. Y. Chi,[10] J. Chiba,[23] M. Chiu,[10] I. J. Choi,[56] J. Choi,[22] R. K. Choudhury,[4] T. Chujo,[5] V. Cianciolo,[38] Y. Cobigo,[11] B. A. Cole,[10] M. P. Comets,[39] P. Constantin,[19] M. Csanád,[13] T. Csörgő,[24] J. P. Cussonneau,[49] D. d'Enterria,[10,49] K. Das,[14] G. David,[5] F. Deák,[13] H. Delagrange,[49] A. Denisov,[17] A. Deshpande,[43] E. J. Desmond,[5] A. Devismes,[48] O. Dietzsch,[45] J. L. Drachenberg,[1] O. Drapier,[28] A. Drees,[48] K. A. Drees,[5] R. du Rietz,[32] A. Durum,[17] D. Dutta,[4] V. Dzhordzhadze,[50] Y. V. Efremenko,[38] K. El Chenawi,[53] A. Enokizono,[16] H. En'yo,[42,43] B. Espagnon,[39] S. Esumi,[52] L. Ewell,[5] D. E. Fields,[36,43] C. Finck,[49] F. Fleuret,[28] S. L. Fokin,[26] B. D. Fox,[43] Z. Fraenkel,[55] J. E. Frantz,[10] A. Franz,[5] A. D. Frawley,[14] Y. Fukao,[27,42,43] S.-Y. Fung,[6] S. Gadrat,[31] S. Garpman,[32,*] M. Germain,[49] T. K. Ghosh,[53] A. Glenn,[50] G. Gogiberidze,[50] M. Gonin,[28] J. Gosset,[11] Y. Goto,[42,43] R. Granier de Cassagnac,[28] N. Grau,[19] S. V. Greene,[53] M. Grosse Perdekamp,[18,43] W. Guryn,[5] H.-Å. Gustafsson,[32] T. Hachiya,[16] J. S. Haggerty,[5] H. Hamagaki,[8] A. G. Hansen,[30] E. P. Hartouni,[29] M. Harvey,[5] K. Hasuko,[42] R. Hayano,[8] N. Hayashi,[42] X. He,[15] M. Heffner,[29] T. K. Hemmick,[48] J. M. Heuser,[42,48] M. Hibino,[54] P. Hidas,[24] H. Hiejima,[18] J. C. Hill,[19] R. Hobbs,[36] W. Holzmann,[47] K. Homma,[16] B. Hong,[25] A. Hoover,[37] T. Horaguchi,[42,43,51] T. Ichihara,[42,43] V. V. Ikonnikov,[26] K. Imai,[27,42] M. Inaba,[52] M. Inuzuka,[8] D. Isenhower,[1] L. Isenhower,[1] M. Ishihara,[42] M. Issah,[47] A. Isupov,[20] B. V. Jacak,[48] W. Y. Jang,[25] Y. Jeong,[22] J. Jia,[48] O. Jinnouchi,[42,43] B. M. Johnson,[5] S. C. Johnson,[29] K. S. Joo,[34] D. Jouan,[39] F. Kajihara,[8] S. Kametani,[8,54] N. Kamihara,[42,51] M. Kaneta,[43] J. H. Kang,[56] S. S. Kapoor,[4] K. Katou,[54] T. Kawabata,[8] A. Kazantsev,[26] S. Kelly,[9,10] B. Khachaturov,[55] A. Khanzadeev,[41] J. Kikuchi,[54] D. H. Kim,[34] D. J. Kim,[56] D. W. Kim,[22] E. Kim,[46] G.-B. Kim,[28] H. J. Kim,[56] E. Kinney,[9] W. W. Kinnison,[30] A. Kiss,[13] E. Kistenev,[5] A. Kiyomichi,[42,52] K. Kiyoyama,[35] C. Klein-Boesing,[33] H. Kobayashi,[42,43] L. Kochenda,[41] V. Kochetkov,[17] D. Koehler,[36] T. Kohama,[16] R. Kohara,[16] B. Komkov,[41] M. Konno,[52] M. Kopytine,[48] D. Kotchetkov,[6] A. Kozlov,[55] P. J. Kroon,[5] C. H. Kuberg,[1,30] G. J. Kunde,[30] K. Kurita,[42,43] Y. Kuroki,[52] M. J. Kweon,[25] Y. Kwon,[56] G. S. Kyle,[37] R. Lacey,[47] V. Ladygin,[20] J. G. Lajoie,[19] Y. Le Bornec,[39] A. Lebedev,[19,26] S. Leckey,[48] D. M. Lee,[30] S. Lee,[22] M. J. Leitch,[30] M. A. L. Leite,[45] X. H. Li,[6] H. Lim,[46] A. Litvinenko,[20] M. X. Liu,[30] Y. Liu,[39] C. F. Maguire,[53] Y. I. Makdisi,[5] A. Malakhov,[20] V. I. Manko,[26] Y. Mao,[7,40,42] G. Martinez,[49] M. D. Marx,[48] H. Masui,[52] F. Matathias,[48] T. Matsumoto,[8,54] M. C. McCain,[1] P. L. McGaughey,[30] E. Melnikov,[17] F. Messer,[48] Y. Miake,[52] J. Milan,[47] T. E. Miller,[53] A. Milov,[48,55] S. Mioduszewski,[5] R. E. Mischke,[30] G. C. Mishra,[15] J. T. Mitchell,[5] A. K. Mohanty,[4] D. P. Morrison,[5] J. M. Moss,[30] F. Mühlbacher,[48] D. Mukhopadhyay,[55] M. Muniruzzaman,[6] J. Murata,[42,43] S. Nagamiya,[23] J. L. Nagle,[9,10] T. Nakamura,[16] B. K. Nandi,[6] M. Nara,[52] J. Newby,[50] P. Nilsson,[32] A. S. Nyanin,[26] J. Nystrand,[32] E. O'Brien,[5] C. A. Ogilvie,[19] H. Ohnishi,[5,42] I. D. Ojha,[3,53] H. Okada,[27,42] K. Okada,[42,43] M. Ono,[52] V. Onuchin,[17] A. Oskarsson,[32] I. Otterlund,[32] K. Oyama,[8] K. Ozawa,[8] D. Pal,[55] A. P. T. Palounek,[30] V. Pantuev,[48] V. S. Pantuev,[48] V. Papavassiliou,[37] J. Park,[46] W. J. Park,[25] A. Parmar,[36] S. F. Pate,[37] H. Pei,[19] T. Peitzmann,[33] V. Penev,[20] J.-C. Peng,[18,30] H. Pereira,[11] V. Peresedov,[20] A. Pierson,[36] C. Pinkenburg,[5] R. P. Pisani,[5] F. Plasil,[38] M. L. Purschke,[5] A. K. Purwar,[48] J. Qualls,[1] J. Rak,[19] I. Ravinovich,[55] K. F. Read,[38,50] M. Reuter,[48] K. Reygers,[33] V. Riabov,[41,44] Y. Riabov,[41] G. Roche,[31] A. Romana,[28] M. Rosati,[19] S. Rosendahl,[32] P. Rosnet,[31] V. L. Rykov,[42] S. S. Ryu,[56] M. E. Sadler,[1] N. Saito,[27,42,43] T. Sakaguchi,[8,54] M. Sakai,[35] S. Sakai,[52] V. Samsonov,[41] L. Sanfratello,[36] R. Santo,[33] H. D. Sato,[27,42] S. Sato,[5,52] S. Sawada,[23] Y. Schutz,[49] V. Semenov,[17] R. Seto,[6] M. R. Shaw,[1,30] T. K. Shea,[5] I. Shein,[17] T.-A. Shibata,[42,51] K. Shigaki,[16,23] T. Shiina,[30] M. Shimomura,[52] A. Sickles,[48] C. L. Silva,[45] D. Silvermyr,[30,32] K. S. Sim,[25] J. Simon-Gillo,[30] C. P. Singh,[3] V. Singh,[3] M. Sivertz,[5] A. Soldatov,[17] R. A. Soltz,[29] W. E. Sondheim,[30] S. Sorensen,[50] S. P. Sorensen,[50] I. V. Sourikova,[5] F. Staley,[11] P. W. Stankus,[38] E. Stenlund,[32] M. Stepanov,[37] A. Ster,[24] S. P. Stoll,[5] T. Sugitate,[16] J. P. Sullivan,[30] S. Takagi,[52] E. M. Takagui,[45] A. Taketani,[42,43] M. Tamai,[54] K. H. Tanaka,[23] Y. Tanaka,[35] K. Tanida,[42] M. J. Tannenbaum,[5] A. Taranenko,[47] P. Tarján,[12] J. D. Tepe,[1,30] T. L. Thomas,[36] M. Togawa,[27,42] J. Tojo,[27,42] H. Torii,[27,42,43] R. S. Towell,[1] V.-N. Tram,[28] I. Tserruya,[55] Y. Tsuchimoto,[16] H. Tsuruoka,[52] S. K. Tuli,[3] H. Tydesjö,[32] N. Tyurin,[17] T. J. Uam,[34] H. W. van Hecke,[30] J. Velkovska,[5,48] M. Velkovsky,[48] V. Veszprémi,[12] L. Villatte,[50] A. A. Vinogradov,[26] M. A. Volkov,[26] E. Vznuzdaev,[41] X. R. Wang,[15] Y. Watanabe,[42,43] S. N. White,[5] N. Willis,[39] F. K. Wohn,[19] C. L. Woody,[5] W. Xie,[6] Y. Yang,[7] A. Yanovich,[17] S. Yokkaichi,[42,43] G. R. Young,[38] I. E. Yushmanov,[26] W. A. Zajc,[10,†] C. Zhang,[10] S. Zhou,[7] S. J. Zhou,[55] J. Zimányi,[24] L. Zolin,[20] and X. Zong[19]

(PHENIX Collaboration)

[1]*Abilene Christian University, Abilene, Texas 79699, USA*

[2]*Institute of Physics, Academia Sinica, Taipei 11529, Taiwan*

[3]*Department of Physics, Banaras Hindu University, Varanasi 221005, India*

[4]*Bhabha Atomic Research Centre, Bombay 400 085, India*

[*]Deceased.

[†]PHENIX Spokesperson: zajc@nevis.columbia.edu

 ©2005 The American Physical Society

[5]*Brookhaven National Laboratory, Upton, New York 11973-5000, USA*
[6]*University of California - Riverside, Riverside, California 92521, USA*
[7]*China Institute of Atomic Energy (CIAE), Beijing, People's Republic of China*
[8]*Center for Nuclear Study, Graduate School of Science, University of Tokyo, 7-3-1 Hongo, Bunkyo, Tokyo 113-0033, Japan*
[9]*University of Colorado, Boulder, Colorado 80309, USA*
[10]*Columbia University, New York, New York 10027 and Nevis Laboratories, Irvington, New York 10533, USA*
[11]*Dapnia, CEA Saclay, F-91191, Gif-sur-Yvette, France*
[12]*Debrecen University, H-4010 Debrecen, Egyetem tér 1, Hungary*
[13]*ELTE, Eötvös Loránd University, H-1117 Budapest, Pázmány P. s. 1/A, Hungary*
[14]*Florida State University, Tallahassee, Florida 32306, USA*
[15]*Georgia State University, Atlanta, Georgia 30303, USA*
[16]*Hiroshima University, Kagamiyama, Higashi-Hiroshima 739-8526, Japan*
[17]*Institute for High Energy Physics (IHEP), Protvino, Russia*
[18]*University of Illinois at Urbana-Champaign, Urbana, Illinois 61801, USA*
[19]*Iowa State University, Ames, Iowa 50011, USA*
[20]*Joint Institute for Nuclear Research, RU-141980 Dubna, Moscow Region, Russia*
[21]*KAERI, Cyclotron Application Laboratory, Seoul, Korea*
[22]*Kangnung National University, Kangnung 210-702, Korea*
[23]*KEK, High Energy Accelerator Research Organization, Tsukuba-shi, Ibaraki-ken 305-0801, Japan*
[24]*KFKI Research Institute for Particle and Nuclear Physics (RMKI), H-1525 Budapest 114, P.O. Box 49, Hungary*
[25]*Korea University, Seoul, 136-701, Korea*
[26]*Russian Research Center "Kurchatov Institute," Moscow, Russia*
[27]*Kyoto University, Kyoto 606, Japan*
[28]*Laboratoire Leprince-Ringuet, Ecole Polytechnique, CNRS-IN2P3, Route de Saclay, F-91128, Palaiseau, France*
[29]*Lawrence Livermore National Laboratory, Livermore, California 94550, USA*
[30]*Los Alamos National Laboratory, Los Alamos, New Mexico 87545, USA*
[31]*LPC, Université Blaise Pascal, CNRS-IN2P3, Clermont-Fd, F-63177 Aubiere Cedex, France*
[32]*Department of Physics, Lund University, Box 118, SE-221 00 Lund, Sweden*
[33]*Institut für Kernphysik, University of Muenster, D-48149 Muenster, Germany*
[34]*Myongji University, Yongin, Kyonggido 449-728, Korea*
[35]*Nagasaki Institute of Applied Science, Nagasaki-shi, Nagasaki 851-0193, Japan*
[36]*University of New Mexico, Albuquerque, New Mexico 87131, USA*
[37]*New Mexico State University, Las Cruces, New Mexico 88003, USA*
[38]*Oak Ridge National Laboratory, Oak Ridge, Tennessee 37831, USA*
[39]*IPN-Orsay, Universite Paris Sud, CNRS-IN2P3, BP1, F-91406, Orsay, France*
[40]*Peking University, Beijing, People's Republic of China*
[41]*PNPI, Petersburg Nuclear Physics Institute, Gatchina, Russia*
[42]*RIKEN (The Institute of Physical and Chemical Research), Wako, Saitama 351-0198, Japan*
[43]*RIKEN BNL Research Center, Brookhaven National Laboratory, Upton, New York 11973-5000, USA*
[44]*St. Petersburg State Technical University, St. Petersburg, Russia*
[45]*Universidade de São Paulo, Instituto de Física, Caixa Postal 66318, São Paulo CEP05315-970, Brazil*
[46]*System Electronics Laboratory, Seoul National University, Seoul, Korea*
[47]*Chemistry Department, Stony Brook University, Stony Brook, SUNY, New York 11794-3400, USA*
[48]*Department of Physics and Astronomy, Stony Brook University, SUNY, Stony Brook, New York 11794, USA*
[49]*SUBATECH (Ecole des Mines de Nantes, CNRS-IN2P3, Université de Nantes) BP 20722 - 44307, Nantes, France*
[50]*University of Tennessee, Knoxville, Tennessee 37996, USA*
[51]*Department of Physics, Tokyo Institute of Technology, Tokyo, 152-8551, Japan*
[52]*Institute of Physics, University of Tsukuba, Tsukuba, Ibaraki 305, Japan*
[53]*Vanderbilt University, Nashville, Tennessee 37235, USA*
[54]*Waseda University, Advanced Research Institute for Science and Engineering, 17 Kikui-cho, Shinjuku-ku, Tokyo 162-0044, Japan*
[55]*Weizmann Institute, Rehovot 76100, Israel*
[56]*Yonsei University, IPAP, Seoul 120-749, Korea*
(Received 7 August 2004; published 27 May 2005)

Two particle correlations between identified meson and baryon trigger particles with $2.5 < p_T < 4.0$ GeV/c and lower p_T charged hadrons have been measured at midrapidity by the PHENIX experiment at RHIC in p+p, d+Au, and Au+Au collisions at $\sqrt{s_{NN}} = 200$ GeV. In noncentral Au+Au collisions, the probability of finding a hadron near in azimuthal angle to the trigger particles is almost identical for mesons and baryons and significantly higher than in p+p collisions. The *associated* yields for trigger baryons decrease in the most central collisions, consistent with some baryon production by thermal recombination in addition to hard scattering.

DOI: 10.1103/PhysRevC.71.051902 PACS number(s): 25.75.Dw

A remarkable feature of relativistic heavy ion collisions is greatly enhanced production of baryons and antibaryons relative to mesons. This enhancement over elementary $p+p$ collisions occurs at transverse momenta (p_T) of 2–5 GeV/c [1–3]. In this range, particle production shifts from soft processes (nonperturbative, low momentum transfer scattering) to hard (high momentum transfer parton-parton scattering). Hard scattering is followed by fragmentation of the scattered partons to jets of hadrons. Baryon and antibaryon production is suppressed in fragmentation in vacuum. Phenomenologically, this can be thought of as a large penalty for creating a diquark/antidiquark pair for baryons vs. a quark/antiquark pair for meson formation.

Since there is no sharp separation of scales between hard and soft processes, it is natural to ask which causes the baryon excess in Au+Au collisions. Hadron formation by coalescence of quarks from the expanding thermal fireball can explain single particle yields [4–7] but causes no jetlike correlations. The yield of baryons in this momentum range scales approximately with the number of binary nucleon-nucleon collisions [2], which is typical of hard processes. However, if hard scattering is at the root of the baryon excess, additional mechanisms absent in elementary $p+p$ collisions are required, such as alteration of the jet fragmentation function in the dense medium formed in Au+Au collisions, or recombination of hard scattered quarks with accidental comoving quarks from the medium. Models include hard parton fragmentation but recombination of thermal quarks only [5], thermal quark recombination with jet fragments [6,8], and recombination of quarks from hard scattering with a modified fireball distribution [7]. Hadron production via recombination between jet fragments and thermal quarks [6–8] could preserve jetlike correlations among the final hadrons, presuming that each hadron contains at least one quark arising from a fragmenting hard scattered parton.

To determine the role of jets in production of intermediate p_T protons, the PHENIX experiment at RHIC has measured energetic hadronic partners near the baryons. These are the additional fragmentation products from the same jet as the baryon. We present first results on two particle correlations where the *trigger* particle is an identified meson (π, K) or baryon (p, $\bar{p}$) at $2.5 < p_T < 4.0$ GeV/c. *Associated* particles, i.e., lower p_T charged hadrons near the trigger particle in azimuthal angle are counted. A Monte Carlo study shows that for these trigger particle momenta, resonance decays do not contribute associated particles at $p_T > 1.2$ GeV/c; at lower p_T, there is a small contribution, but it is less than the statistical uncertainty. The centrality and collision system dependence of the associated particle yield per trigger is measured. Trigger particles from recombination of boosted thermal quarks only should not have correlated partners beyond effects of elliptic flow, as a thermal source is by definition uncorrelated. However, trigger particles from hard scattered partons should have jetlike partners with a probability depending upon the medium effect on fragmentation. We use $p+p$ collisions without trigger identification to provide a comparison baseline.

Collisions at $\sqrt{s_{NN}} = 200$ GeV of Au+Au (24 million events), d+Au (42 million events), and $p+p$ (23 million events) are analyzed. Charged particles are reconstructed in the central arms of PHENIX using drift chambers, each with azimuthal coverage of $\pi/2$, and two layers of multiwire proportional chambers with pad readout (PC1, PC3) [9]. Pattern recognition is based on a combinatorial Hough transform in the track bend plane, with the polar angle determined by PC1 and the collision vertex along the beam direction [1]. Particle momenta are measured with a resolution $\delta p/p = 0.7\% \oplus 1.0(1.1)\% p(\mathrm{GeV}/c)$ in Au+Au (d+Au, $p+p$). The portion of the east arm spectrometer containing the high resolution time-of-flight (TOF) detector, which covers pseudorapidity $|\eta| < 0.35$ and $\phi = \pi/4$ in azimuthal angle, is used for trigger particle identification. Beam counters (BBC) [9] provide the global start; stop signals are from TOF scintillators at a radial distance of 5.06 m. The timing resolution is $\sigma = 120$ ps, which allows a 4σ separation of mesons/baryons up to $p_T \approx 4$ GeV/c. The Au+Au centrality determination is described in Ref. [10].

Distributions of azimuthal angular difference $\Delta\phi$ are constructed for trigger-partner pairs. The combinatorial background is determined by constructing mixed events in two steps: the number of trigger and partner particles per event is determined by sampling the measured particle multiplicity distributions in the relevant momentum and centrality ranges. The measured trigger and partner particle momentum distributions are then sampled to yield three-momenta of particles in each mixed event. To correct for the limited acceptance of PHENIX, the real event $\Delta\phi$ distributions are divided by $\Delta\phi$ distributions from mixed events, with the integral fixed to correspond to perfect acceptance as a function of $\Delta\phi$. The shape of this distribution corrects for the $\Delta\phi$ dependence of the PHENIX azimuthal acceptance, but has no true correlations. The $\Delta\phi$ distributions are shown in Fig. 1; mixed events are indicated by solid lines. The partner yield is corrected for the reconstruction efficiency, detector aperture, and (for Au+Au only) detector occupancy [11]. No extrapolation is made to $|\eta| > 0.35$. No correction for the PHENIX $\Delta\eta$ acceptance is needed in Figs. 1 and 2, as the same acceptance is used for both trigger type and the different collision systems. Since d+Au and Au+Au collisions contain uncorrelated combinatorial background from other particles in the underlying event, the mixed event partner yield per trigger, after the same efficiency correction, is subtracted. The absolute normalization of the background is obtained independently by a convolution of the trigger and partner single particle rates.

In real events, collisions from the more central edge of the bin contribute more pairs than those from the less central edge. Mixed events are constructed by randomly sampling single particle multiplicity distributions within a 5% centrality bin. As the particle multiplicity is not flat with centrality, mixed events underweight the upper edge of the bin compared to real events. The mixed event background is corrected for this effect. The spread of trigger and partner number within a bin is determined from the measured centrality dependence of particle multiplicity in the relevant momentum region and particle species [10–13]. The correction modifies the background level by $\approx$0.2% in the most central and $\approx$25% in the most peripheral Au+Au collisions.

Elliptic flow causes an angular correlation in Au+Au unrelated to jet fragmentation, and is a background to this

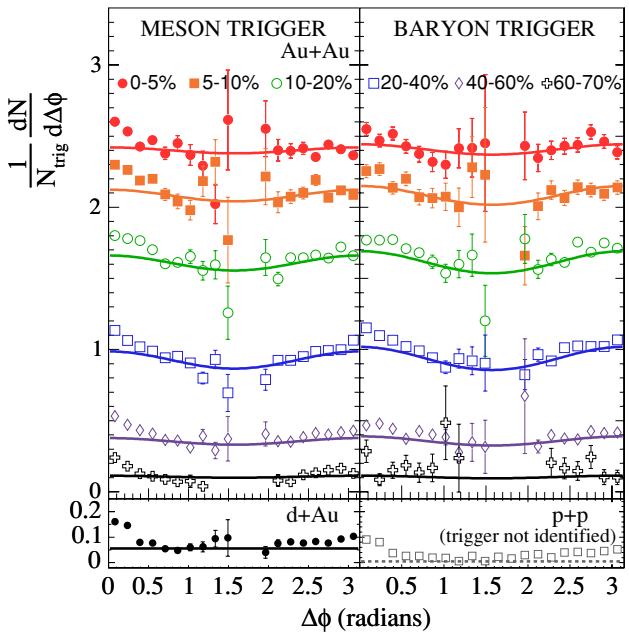

FIG. 1. (Color online) Top panels show $\Delta\phi$ distributions for meson (left) and baryon (right) triggers with $2.5 < p_T < 4.0$ GeV/c and associated charged hadrons with $1.7 < p_T < 2.5$ GeV/c in Au+Au collisions. Bottom panels show the same quantity for meson triggers in d+Au collisions (left) and unidentified triggers in p+p collisions (right). Lines indicate the calculated combinatorial background in the event modulated by the measured elliptic flow (Au+Au only).

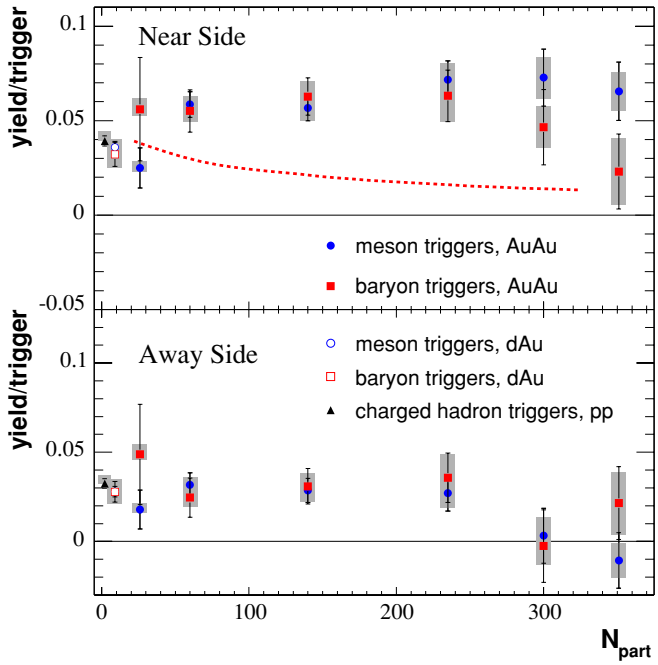

FIG. 2. (Color online) Yield per trigger for associated charged hadrons between $1.7 < p_T < 2.5$ GeV/c for the near- (top) and away- (bottom) side jets. The error bars are statistical errors, and the gray boxes are centrality-dependent systematic errors There is an additional 12% error on the overall normalization, which moves all points together. The dashed line (top) represents an upper limit of the centrality dependence of the near-side partner yield from thermal recombination (see text).

measurement. The elliptic flow correlation is removed by modulating the azimuthally uniform combinatorial background by $1 + 2v_2^{\text{assoc}} v_2^{\text{trig}} \cos(\Delta\phi)$, where v_2^{assoc} and v_2^{trig} are the v_2 values measured for the partner and trigger p_T ranges, respectively [14]. The reaction plane is measured by the BBC at $3 < |\eta| < 4$ in order to minimize the influence of jets in the v_2 values. Because the centrality binning in this analysis is finer than in [14], the p_T integrated centrality dependence is used to interpolate v_2 for collisions more central than 20%. The modulation of the mixed event $\Delta\phi$ distributions is visible in Fig. 1.

Systematic uncertainties in Au+Au and d+Au partner yields arise from uncertainties in the corrections for centrality bin width, systematic and statistical errors on v_2 [14] (Au+Au only), uncertainty in the background subtraction due to the event mixing technique, and uncertainty in the detector occupancy correction. Cross-contamination of mesons and protons is less than 5%. The error on the occupancy correction reaches a maximum of 5% in the most central Au+Au collisions. For most Au+Au bins, the dominant systematic uncertainty on the partner yields is the uncertainty in v_2. This produces a systematic error of approximately 0.01 partners per trigger baryon in semicentral and central collisions; for trigger mesons, the corresponding error is 60% of this. The event mixing uncertainty is nearly comparable. In peripheral Au+Au collisions, the dominant systematic error is from uncertainty on centrality bias corrections and v_2. In d+Au collisions, there is no v_2, and the partner yield uncertainty is driven by the correction for centrality bias. In p+p collisions, the systematic error is taken to be the same size as the combinatorial background, which is subtracted. The total systematic errors are shown in Fig. 2.

The background shown in Fig. 1 is subtracted from the data points, which in most cases lie systematically above the line. The number of associated partners per trigger is integrated to determine the conditional yield of partners. The near- (far-) side yield is the integral over $0 < \Delta\phi < 0.94$ radians ($2.2 < \Delta\phi < \pi$ radians). This range maximizes the partner acceptance while omitting the region around $\Delta\phi = \pi/2$, where the TOF coverage creates an acceptance hole. Nonbackground associated partners are observed in the angular range characteristic of jet fragmentation in p+p, which was measured by PHENIX to be $\approx$0.25 radians in a similar p_T range [15].

Figure 2 shows the conditional yield per trigger of partner particles in p+p, d+Au, and Au+Au collisions, as a function of the number of participant nucleons. Small relative angle yields, from the same jet as the trigger hadron, are in the top panel. The partners increase for both trigger baryons and mesons by almost a factor of two from d+Au to peripheral and midcentral Au+Au. There is an indication that jetlike correlations for baryons relative to mesons decrease in the most central collisions, as expected for production of a fraction of the baryons by recombination of thermal quarks. It is notable, however, that the baryon excess

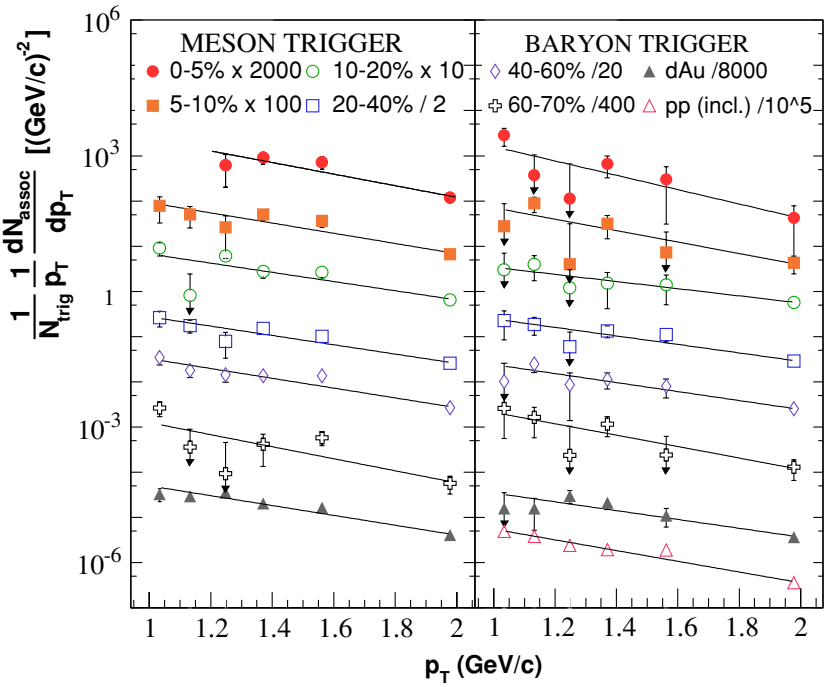

FIG. 3. (Color online) p_T spectra of the near-side associated charged hadrons corrected to the full jet yield for meson (left) and baryon (right) triggers at $2.5 < p_T < 4.0$ GeV/c and $|\eta| < 0.35$. Errors are statistical only. The curves are exponential fits.

observed via p/π ratios [1–3] is already large in midcentral collisions. In d+Au collisions, the near-side yields per trigger are the same for meson and baryon triggers, and they agree with results from p+p collisions generated with PYTHIA [16].

The dashed line in Fig. 2 shows the expected centrality dependence of partners per baryon if all the "extra" baryons [10], that increase p/π over that in p+p collisions, were to arise solely from soft processes; such baryons dilute the per-trigger conditional yield. Because this simple estimate omits meson production by recombination, which must also occur along with baryon production, it represents an upper limit to the centrality dependence of the jet partner yield from thermal recombination. The data clearly disagree with both the centrality dependence and the absolute yields of this estimate, indicating that hard processes must also contribute to the baryon excess. The bottom panel of Fig. 2 shows the conditional yield of partners on the away side. The partner yield in $2.2 < \Delta\phi < \pi$ radians drops equally for both trigger baryons and mesons from p+p and d+Au to central Au+Au, in agreement with the observed disappearance [17] and/or broadening [15] of the away-side jet. It further supports the conclusion that the baryons originate from the same jetlike mechanism as mesons.

Figure 3 shows the p_T spectra of associated particles [18] on the near side with trigger mesons and baryons. The measured transverse momentum of jet hadrons with respect to the initial parton direction $\langle j_T \rangle$ is constant as a function of collision energy and p_T [15,19]. Thus, the angular size of jets increases as the partner p_T decreases. We use the PHENIX measurement of $\langle |j_{Ty}| \rangle = 0.359 \pm 0.011$ GeV/c [15] to correct the near-side conditional yield measured in $\Delta\phi < 0.94$ radians, and the PHENIX η acceptance to the full jet yield, assuming that jets are symmetric gaussians in both ϕ and η. The conditional yields in Fig. 2 do not have this additional correction as they are measured in a single p_T bin. The partner spectra in Fig. 3 are fitted with exponentials, and the inverse slopes are given in Fig. 4. The systematic uncertainty on the associated

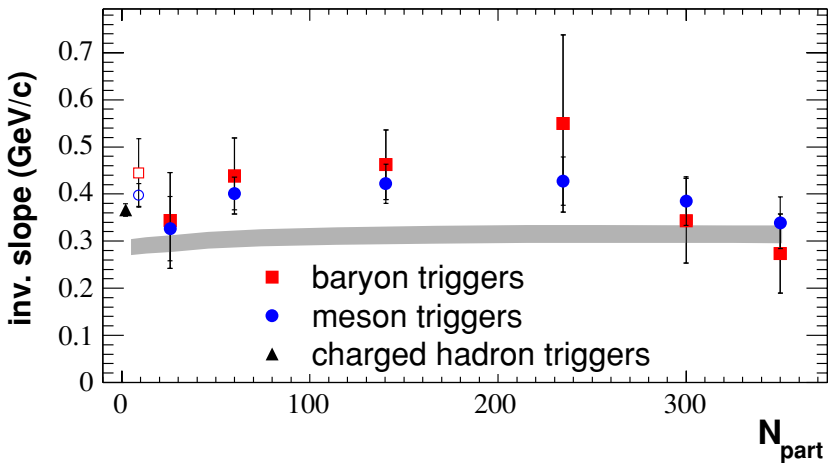

FIG. 4. (Color online) Inverse slopes from the fits in Fig. 3. Solid (open) squares and circles are Au+Au (d+Au), collisions and the triangle is p+p collisons. The solid band indicates the slopes of inclusive particle spectra in Au+Au collisions [11]. Errors are statistical only.

particle slope in central collisions is approximately 20%, based on a conservative estimate of 50% uncertainty on the correction to the full jet yield. We note that this is comparable to the statistical error for leading mesons and smaller than the statistical error for leading baryons. Within the available statistics, the inverse slopes of the associated particles are similar for trigger mesons and baryons in $p+p$, $d+$Au, peripheral, and midcentral Au+Au. The spectra are harder than inclusive hadron spectra, as expected from jet fragmentation. In the most central Au+Au collisions, the partner and inclusive hadron spectra are in better agreement.

We have presented the first study of the jet structure of baryons $(p, \overline{p})$ and mesons (π, K) in the momentum region where baryon production is greatly enhanced in central Au+Au collisions at RHIC. Three observations indicate that mesons and baryons arise from hard processes in all but the most central Au+Au collisions. First, baryons and mesons both have jetlike partner particles. Second, within the limited statistics available, the inverse slopes of the associated particles are similar for both baryons and mesons; these are larger than for inclusive hadrons. Finally, on the away side, the jet partner yield into a 0.94 radian opening angle has the same centrality dependence for trigger baryons and mesons, consistent with attenuation in central collisions. The increase in jetlike partners between $p+p$ and Au+Au is strong evidence for medium modification of the fragmentation process. Recombination of thermal quarks with jet fragments [6,8] and a "wake effect" from comoving radiated gluons [7] are two examples of how the medium might modify jet fragmentation. The decrease with centrality of partner yields for trigger baryons suggests a growing contribution of baryons from thermal recombination.

We thank the staff of the Collider-Accelerator and Physics Departments at Brookhaven National Laboratory, and the staff of the other PHENIX participating institutions, for their vital contributions. We acknowledge support from the Department of Energy; the Office of Science, Nuclear Physics Division, the National Science Foundation; Abilene Christian University Research Council; the Research Foundation of SUNY; the Dean of the College of Arts and Sciences, Vanderbilt University; the Ministry of Education, Culture, Sports, Science, and Technology, and the Japan Society for the Promotion of Science (Japan); Conselho Nacional de Desenvolvimento Científico e Tecnológico and Fundação de Amparo à Pesquisa do Estado de São Paulo (Brazil); the Natural Science Foundation of China (People's Republic of China); Centre National de la Recherche Scientifique, Commissariat à l'Énergie Atomique, Institut National de Physique Nucléaire et de Physique des Particules, and Institut National de Physique Nucléaire et de Physique des Particules (France); Bundesministerium für Bildung und Forschung, Deutscher Akademischer Austausch Dienst, and Alexander von Humboldt Stiftung (Germany); the Hungarian National Science Fund, OTKA (Hungary); the Department of Atomic Energy and Department of Science and Technology (India); the Israel Science Foundation (Israel); the Korea Research Foundation and Center for High Energy Physics (Korea); the Russian Ministry of Industry, Science and Technologies, Russian Academy of Science, Russian Ministry of Atomic Energy (Russia); VR and the Wallenberg Foundation (Sweden); the U.S. Civilian Research and Development Foundation for the Independent States of the Former Soviet Union; the US-Hungarian NSF-OTKA-MTA; the US-Israel Binational Science Foundation; and the 5th European Union TMR Marie-Curie Program.

[1] K. Adcox *et al.* (PHENIX Collaboration), Phys. Rev. Lett. **88**, 022301 (2002).
[2] S. S. Adler *et al.* (PHENIX Collaboration), Phys. Rev. Lett. **91**, 172301 (2003).
[3] J. Adams *et al.* (STAR Collaboration), Phys. Rev. Lett. **92**, 052302 (2004).
[4] R. C. Hwa and C. B. Yang, Phys. Rev. C **67**, 034902 (2003).
[5] R. J. Fries, B. Muller, C. Nonaka, and S. A. Bass, Phys. Rev. Lett. **90**, 202303 (2003); Phys. Rev. C **68**, 044902 (2003).
[6] V. Greco, C. M. Ko, and P. Levai, Phys. Rev. Lett. **90**, 202302 (2003); Phys. Rev. C **68**, 034904 (2003).
[7] R. J. Fries, S. A. Bass, and B. Muller, Phys. Rev. Lett. **94**, 122301 (2005).
[8] R. C. Hwa and C. B. Yang, Phys. Rev. C **70**, 024905 (2004); J. Phys. G **30**, S1117 (2004).
[9] K. Adcox *et al.* (PHENIX Collaboration), Nucl. Instrum. Methods **A499**, 469 (2003).
[10] S. S. Adler *et al.* (PHENIX Collaboration), Phys. Rev. C **69**, 034909 (2004).
[11] S. S. Adler *et al.* (PHENIX Collaboration), Phys. Rev. C **69**, 034910 (2004).
[12] C. Klein-Bösing (PHENIX Collaboration), J. Phys. G **30**, S975 (2004).
[13] F. Matathias (PHENIX Collaboration), J. Phys. G **30**, S1113 (2004).
[14] S. S. Adler *et al.* (PHENIX Collaboration), Phys. Rev. Lett. **91**, 182301 (2003).
[15] J. Rak (PHENIX Collaboration), J. Phys. G **30**, S1309 (2004).
[16] T. Sjöstrand *et al.*, Comput. Phys. Commun. **135**, 238 (2001).
[17] C. Adler *et al.* (STAR Collaboration), Phys. Rev. Lett. **90**, 082302 (2003).
[18] F. Wang (STAR Collaboration), J. Phys. G **30**, S1299 (2004).
[19] A. L. S. Angelis *et al.* (CCOR Collaboration), Phys. Lett. **B97**, 163 (1980).

Eur. Phys. J. C 41, 287–296 (2005)
Digital Object Identifier (DOI) 10.1140/epjc/s2005-02249-2

THE EUROPEAN PHYSICAL JOURNAL C

Azimuthal anisotropy of photon and charged particle emission in ^{208}Pb + ^{208}Pb collisions at 158 $\cdot A$ GeV/c

The WA98 Collaboration

M.M. Aggarwal[4], Z. Ahammed[2], A.L.S. Angelis[7,†], V. Antonenko[13], V. Arefiev[6], V. Astakhov[6], V. Avdeitchikov[6], T.C. Awes[16], P.V.K.S. Baba[10], S.K. Badyal[10], S. Bathe[14], B. Batiounia[6], T. Bernier[15], V.S. Bhatia[4], C. Blume[14], D. Bucher[14], H. Büsching[14], L. Carlén[12], S. Chattopadhyay[2], M.P. Decowski[3], H. Delagrange[15], P. Donni[7], M.R. Dutta Majumdar[2], A.K. Dubey[1], K. El Chenawi[12], K. Enosawa[18], S. Fokin[13], V. Frolov[6], M.S. Ganti[2], S. Garpman[12,†], O. Gavrishchuk[6], F.J.M. Geurts[19], T.K. Ghosh[8], R. Glasow[14], R. Gupta[10], B. Guskov[6], H.Å. Gustafsson[12], H.H. Gutbrod[5], I. Hrivnacova[17], M. Ippolitov[13], H. Kalechofsky[7], R. Kamermans[19], K. Karadjev[13], K. Karpio[20], B.W. Kolb[5], I. Kosarev[6], I. Koutcheryaev[13], A. Kugler[17], P. Kulinich[3], M. Kurata[18], A. Lebedev[13], H. Löhner[8], L. Luquin[15], D.P. Mahapatra[1], V. Manko[13], M. Martin[7], G. Martínez[15], A. Maximov[6], Y. Miake[18], G.C. Mishra[1], B. Mohanty[2], M.-J. Mora[15], D. Morrison[11], T. Moukhanova[13], D.S. Mukhopadhyay[2], H. Naef[7], B.K. Nandi[2], S.K. Nayak[10], T.K. Nayak[2], A. Nianine[13], V. Nikitine[6], S. Nikolaev[13], P. Nilsson[12], S. Nishimura[18], P. Nomokonov[6], J. Nystrand[12], A. Oskarsson[12], I. Otterlund[12], T. Peitzmann[19], D. Peressounko[13], V. Petracek[17], S.C. Phatak[1], W. Pinganaud[15], F. Plasil[16], M.L. Purschke[5], J. Rak[17], R. Raniwala[9,a], S. Raniwala[9], N.K. Rao[10], F. Retiere[15], K. Reygers[14], G. Roland[3], L. Rosselet[7], I. Roufanov[6], C. Roy[15], J.M. Rubio[7], S.S. Sambyal[10], R. Santo[14], S. Sato[18], H. Schlagheck[14], H.-R. Schmidt[5], Y. Schutz[15], G. Shabratova[6], T.H. Shah[10], A. Sharma[10], I. Sibiriak[13], T. Siemiarczuk[20], D. Silvermyr[12], B.C. Sinha[2], N. Slavine[6], K. Söderström[12], G. Sood[4], S.P. Sørensen[11], P. Stankus[16], G. Stefanek[20], P. Steinberg[3], E. Stenlund[12], M. Sumbera[17], T. Svensson[12], A. Tsvetkov[13], L. Tykarski[20], E.C. v.d. Pijll[19], N. v. Eijndhoven[19], G.J. v. Nieuwenhuizen[3], A. Vinogradov[13], Y.P. Viyogi[2], A. Vodopianov[6], S. Vörös[7], B. Wysłouch[3], G.R. Young[16]

[1] Institute of Physics, 751-005 Bhubaneswar, India
[2] Variable Energy Cyclotron Centre, Calcutta 700 064, India
[3] MIT Cambridge, MA 02139, USA
[4] University of Panjab, Chandigarh 160014, India
[5] Gesellschaft für Schwerionenforschung (GSI), 64220 Darmstadt, Germany
[6] Joint Institute for Nuclear Research, 141980 Dubna, Russia
[7] University of Geneva, 1211 Geneva 4, Switzerland
[8] KVI, University of Groningen, 9747 AA Groningen, The Netherlands
[9] University of Rajasthan, Jaipur 302004, Rajasthan, India
[10] University of Jammu, Jammu 180001, India
[11] University of Tennessee, Knoxville, Tennessee 37966, USA
[12] Lund University, 221 00 Lund, Sweden
[13] RRC "Kurchatov Institute", 123182 Moscow, Russia
[14] University of Münster, 48149 Münster, Germany
[15] SUBATECH, Ecole des Mines, Nantes, France
[16] Oak Ridge National Laboratory, Oak Ridge, Tennessee 37831-6372, USA
[17] Nuclear Physics Institute, 250 68 Rez, Czech Republic
[18] University of Tsukuba, Ibaraki 305, Japan
[19] Universiteit Utrecht/NIKHEF, 3508 TA Utrecht, The Netherlands
[20] Institute for Nuclear Studies, 00-681 Warsaw, Poland
[†] Deceased

Received: 22 May 2004 / Revised version: 14 April 2005 /
Published online: 4 May 2005 – © Springer-Verlag / Società Italiana di Fisica 2005

Abstract. The azimuthal distributions of photons and charged particles with respect to the event plane are investigated as a function of centrality in ^{208}Pb + ^{208}Pb collisions at 158 $\cdot A$ GeV/c in the WA98 experiment at the CERN SPS. The anisotropy of the azimuthal distributions is characterized using a Fourier analysis. For both the photon and charged particle distributions the first two Fourier coefficients are observed to decrease with increasing centrality. The observed anisotropies of the photon distributions compare well with the expectations from the charged particle measurements for all centralities.

PACS. 25.75.Dw

1 Introduction

Non-isotropic emission of particles with respect to the reaction plane, as first observed at the Bevalac [1], provides evidence for collective flow in high energy heavy ion collisions. Flow, or anisotropic particle emission, has been observed for a large variety of interacting systems from incident energies of a few A GeV/c at the Bevalac (SIS) and AGS to much greater energies at the SPS and RHIC [2–13].

Anisotropic flow manifests itself as asymmetries in the azimuthal distribution of particles and can be reproduced in theoretical models with different underlying assumptions. One scenario is incorporated in transport models where the particles have a mean free path comparable to the system size [14–16]. The models can describe the observed flow up to AGS energies. The other scenario applies when the mean free path is much smaller than the system size which allows the description of the equilibrated system in terms of macroscopic quantities [17,18]. Hydrodynamic models are able to describe the qualitative features of the observed flow [19] for p_T below about 3 GeV/c.

The initial asymmetry in the overlap zone of the colliding nuclei translates into unequal pressure gradients in different directions that leads to an elliptic final state momentum distribution of the particles [17], causing an elliptic pattern of flow. The elliptic flow is therefore expected to be sensitive to the system evolution at the time of maximum compression [20] and is shown to be sensitive to the equation of state of the compressed nuclear matter. The variation of asymmetry with centrality enables to relate the observed flow to the geometry of the overlap region [21,16]. One would then expect a scaling of the data from AGS to SPS and RHIC provided the physics of elliptic flow remains the same [22]. In the case that there is a phase transition from hadronic matter to a quark gluon plasma, it is expected that the reflection of this transition in the equation of state of the dense nuclear matter would result in changes in the pressure gradients which would then be reflected in changes in the particle flow pattern.

The first evidence of azimuthal anisotropy at SPS energies was observed in the distribution of photons from S+Au collisions at 200 $\cdot A$ GeV measured in the preshower photon multiplicity detector of the WA93 experiment at CERN [8]. Since almost 90% of photons produced in ultra-relativistic nuclear collisions originate from the decay of π^0's, the anisotropy of the observed photon distributions should reflect the anisotropy of the π^0 production followed by the effects of decay of the π^0's. Methods have been proposed to estimate the anisotropy of the neutral pion emission by measuring the anisotropy of photons [23]. The decay introduces non-flow correlations between the photon pairs due to four-momentum conservation and may dilute the correlations between the π^0's and the event plane. Determination of the effect of decay enables the deduction of the anisotropy of the neutral pions. The photon anisotropy measurement thus complements the study of the anisotropy of charged particle distributions.

In the present work we report results from the WA98 experiment on the centrality dependence of the anisotropy coefficients extracted from measurement of the azimuthal distributions with respect to the event plane of photons and charged particles in the same pseudorapidity interval. Preliminary results on the anisotropy of photon emission in Pb+Pb collisions have been reported earlier [24,25]. The paper is organized in the following manner: Sect. 2 describes the experimental setup and data selection. The analysis technique is discussed in Sect. 3. The results on the centrality dependence of the azimuthal anisotropy of charged particles and photons are discussed in Sect. 4 and Sect. 5 summarises our investigations.

2 WA98 experiment and data selection

The WA98 experiment at CERN [26] placed emphasis on simultaneous detection of hadrons and photons. The experimental setup consisted of large acceptance hadron and photon spectrometers, detectors for photon and charged particle multiplicity measurements, and calorimeters for transverse and forward energy measurements. The experiment recorded data with 158$\cdot A$ GeV Pb beams from the CERN SPS in 1994, 1995, and 1996. The results presented here are from a portion of the Pb run in 1996 during which the magnet (GOLIATH) was turned off. The analysis presented here used data recorded with the photon multiplicity detector (PMD) and the silicon pad multiplicity detector (SPMD). The data from the mid-rapidity calorimeter (MIRAC) was used to characterize events on the basis of centrality of the collision.

The circular Silicon Pad Multiplicity Detector (SPMD), used for measurement of the charged particle multiplicity, was located 32.8 cm from the target. It had full azimuthal coverage in the region $2.35 \leq \eta \leq 3.75$ (beam rapidity $y_{\rm beam} = 5.81$). The detector had four overlapping quadrants, each fabricated from a single 300 μm thick silicon wafer. The active area of each quadrant was divided into 1012 pads forming 46 azimuthal wedges and 22 radial bins with pad size increasing with radius to provide a uniform pseudo-rapidity coverage. The intrinsic efficiency of the detector was better than 99%. During the datataking, 95% of the pads worked properly. The SPMD was nearly transparent to high energy photons since only about 0.2% are expected to interact in the silicon. Multiple hits of charged particles on a single pad were treated as a single hit for the present analysis, and are counted as $N_{\rm hits}$. The detector is sensitive to all charged particles. The energy cutoff appears as a low noise threshold. Details of the characteristics of the SPMD can be found in [27,28].

The photon multiplicity was measured using the preshower photon multiplicity detector (PMD) located at a distance of 21.5 meters from the target. The detector consisted of 3 radiation length (X_0) thick lead converter plates placed in front of an array of square scintillator pads of four different sizes that varied from 15 mm×15 mm to 25 mm×25 mm, placed in 28 box modules. Each box module had a matrix of 38×50 pads which were read

[a] e-mail: rashmi@mail.cern.ch

Table 1. Centrality selections used in the present analysis based on the measured total transverse energy. The corresponding fraction of the minimum bias cross section, number of participants, and the average photon and charged particle multiplicities measured in the pseudo-rapidity interval $3.25 \leq \eta \leq 3.75$ are given for each centrality selection

E_T(GeV)	% σ_{MB}	$N_{\rm part}$	$\langle N_{\rm photon}\rangle$	$\langle N_{\rm hits}\rangle$
40.0–89.9	50–80	43.7	41.1	34.3
89.9–124.3	40–50	87.5	65.6	56.9
124.3–170.2	30–40	123.0	88.0	78.1
170.2–225.5	20–30	172.2	116.9	105.5
225.5–298.6	10–20	237.7	163.1	150.5
298.6–347.6	5–10	300.4	190.1	177.1
>347.6	0–5	353.4	222.9	210.3

out using one image intensifier + CCD camera. Details of the design and characteristics of the PMD may be found in [29,30].

The clusters of hit pads with a signal above a hadron rejection threshold were identified as photon-like. The present analysis has been performed with the photon-like clusters, which are referred to as photons for brevity. Detailed simulations showed that the photon counting efficiencies for the central to peripheral cases varied from 68% to 73%. The purity of the photon sample in the two cases varied from 65% to 54%. Most of the contaminants of the photon sample are charged particles which deposit enough energy to fall above the hadron rejection threshold. The hadron rejection threshold is taken as three times the energy deposited by a minimum ionizing particle. For photons this leads to a low p_T threshold of 30 MeV/c.

The transverse energy was measured with the MIRAC calorimeter [31] located at 24.7 meters downstream from the target. The MIRAC was used to measure the total transverse energy by measurement of both the transverse electromagnetic ($E_{\rm T}^{\rm em}$) and hadronic ($E_{\rm T}^{\rm had}$) energies in the pseudorapidity interval $3.5 \leq \eta \leq 5.5$. The measured total transverse energy, $E_{\rm T}$, provides a measure of the centrality of the reaction. Events with large $E_{\rm T}$ correspond to very central reactions with small impact parameter, and vice versa.

The minimum bias $E_{\rm T}$ distribution has been divided into different fractions of the minimum bias cross section corresponding to different centrality bins [30]. The most central selection corresponds to that 5% of the minimum bias cross section σ_{MB} with largest measured $E_{\rm T}$. A total of about 0.25 Million events have been analysed. The minimum number of events in any centrality selection is 15K and the maximum is 70K. Table 1 shows the percentage cross section and the corresponding number of participants for each centrality bin. The results presented here use only the data for the pseudorapidity region of common coverage of the PMD and SPMD ($3.25 \leq \eta \leq 3.75$) where both detectors have full azimuthal coverage. The average measured photon and charged particle multiplicities for this region of acceptance are also quoted for each centrality in Table 1.

3 Analysis

The anisotropy of the azimuthal distribution of particle emission with respect to the reaction plane (or event plane) is characterized by the coefficients of the Fourier expansion of the azimuthal distribution [32]. The first and the second coefficients are measures of the directed and elliptic flow when the expansion is made about the reaction plane, the plane defined by the beam direction and the impact parameter. This may be written as

$$\frac{2\pi dN}{d(\phi-\psi_R)} = 1 + 2v_1\cos(\phi-\psi_R) + 2v_2\cos 2(\phi-\psi_R) \quad (1)$$

where ϕ is the azimuthal angle of the measured particle and ψ_R denotes the azimuthal orientation of the reaction plane. The reaction plane can be most accurately determined in an experiment that measures the (transverse) momenta of the target or projectile fragments. Both v_1 and v_2 can take positive or negative values. By convention, positive (negative) values of v_1 in (1) denote flow (anti-flow) in the direction of the deflected projectile fragment, and positive (negative) values of v_2 indicate in-plane (out-of-plane) flow.

Though the most accurate determination of the reaction plane requires the measurement of target (or projectile) fragments, most experiments *assume* that the measurement of any particle type, in any kinematic window enables a determination of the reaction plane. We wish to distinguish between the plane determined by projectile or target fragments and the plane determined by any other particle type, and throughout this article refer to the latter as the *event plane*. Obtaining the values of coefficients after projecting azimuthal angles on the event plane determined from the same set (after removing auto correlations) maximises the values of anisotropy coefficients, and may include non-flow correlations. The values obtained are necessarily positive, and have been shown as such in the present work. The coefficients determined by projecting on an event plane from any other set of particles are expected to be smaller, and can also have negative values. The difference in the values determined using different sets of event planes have been included in systematic error by various experiments [10,11,13].

3.1 Method

In the present analysis, the azimuthal distributions of particles for any particle species in any pseudorapidity window is expanded as a Fourier series where the coefficients of expansion determine the shape of the event. Retaining terms up to second order coefficient in the expansion, the shape can be characterized by an ellipse for small values of

the coefficients. The direction of the centroid and the major axis of the ellipse are determined from the azimuthal distributions of the particles. These directions, along with the beam direction, define the first order and the second order event plane respectively, and are obtained as [32]

$$\psi'_m = \frac{1}{m}\left(\tan^{-1}\frac{\Sigma w_i \sin m\phi_i}{\Sigma w_i \cos m\phi_i}\right) \quad (2)$$

where $m = 1$ or 2 for the first and the second order, respectively. The ϕ_i are the azimuthal angles of the emitted particles with respect to a fixed laboratory direction and the w_i are the weight factors. For the azimuthal distribution of the particle yield, as in (1), the weight factors are set equal to one. In reality, due to finite particle multiplicities ψ'_1 and ψ'_2 fluctuate about the *actual* event planes that represent the direction of the centroid and the direction of the major axis of the elliptic shape. To the extent that initial state nuclear densities are spherically symmetric and the density fluctuations are negligible, the initial nucleon density in the overlap region is symmetric about the impact parameter or reaction plane and so it is expected that the two event plane angles are either the same or perpendicular to the reaction plane.

The anisotropy, or Fourier coefficients of order n, can be determined from the azimuthal distribution of the particles with respect to the event plane angle of order m, provided n is an integral multiple of m, by fitting to the following equation [32]

$$\frac{dN}{d(\phi - \psi'_m)} \propto 1 + \textstyle\sum_{n=1}^{\infty} 2v'_{nm}\cos nm(\phi - \psi'_m) \quad (3)$$

v'_{nm} is a measure of the offset of the centroid of the distribution when $n \cdot m = 1$ and is a measure of the difference between the major and the minor axes of the ellipse when $n \cdot m = 2$. The actual coefficients are obtained from the observed coefficients v'_{nm} as described later.

Since the event planes do not depend on the geometrical setup of the experiment, the distribution of the event plane angles determined for a large number of events is expected to be uniformly distributed in laboratory angle. Any non-uniformity in the acceptance of the detectors over the full azimuth will be reflected in a non-uniform distribution of event plane angles. Any non-uniformity that is identifiable within a large subset of events can be corrected for by appropriate correction methods. The method employed in the present work is summarized in the following.

3.2 Detector acceptance correction

The corrected event plane angle is obtained by shifting the observed event plane angles ψ'_m by $\Delta\psi'_m$ [32] where the latter is written as

$$\Delta\psi'_m = \sum_{n=1}^{N}\frac{2}{nm}(-\langle\sin(nm\ \psi'_m)\rangle\cos(nm\ \psi'_m) + \langle\cos(nm\ \psi'_m)\rangle\sin(nm\ \psi'_m)) \quad (4)$$

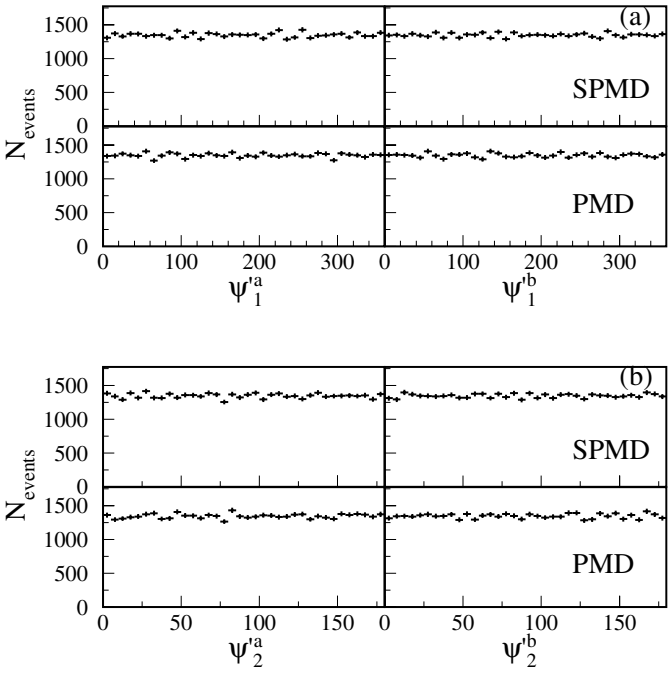

Fig. 1. Acceptance corrected distributions of **a** the first order event plane angle, ψ'_1, of the two subevents for the charged particles hits in the SPMD and the photons in the PMD in the region $3.25 \leq \eta \leq 3.75$ for the centrality class defined by 225.5 $\leq E_T \leq$ 298.6. **b** The same for second order event plane angle, ψ'_2

where $N = 4/m$ is sufficient to flatten the raw ψ distribution. The angular brackets denote an average over all events and are obtained from the raw distribution of the m^{th} order event plane distribution.

The distribution of the first and the second order event plane angles, corrected for acceptance, is shown in Fig. 1 for the charged particle hits in the SPMD and the photon hits in the PMD.

3.3 Event plane resolution correction

The average deviation of the estimated event plane from the true event plane due to multiplicity fluctuations can be determined experimentally and is termed as the resolution correction factor (RCF). Experimentally, RCF is obtained using the subevent method described in [32]. The particles in each event are sorted in ascending order of pseudorapidity. Each event is divided into two equal multiplicity subevents separated by a pseudorapidity interval. The two subevents are separated by one pad for the SPMD and by $\Delta\eta = 0.05$ for the PMD. The actual location of the pad in SPMD and the $\Delta\eta$ interval in PMD is allowed to vary in the region 3.25 to 3.75 to ensure equal multiplicity for the two subevents. The event plane angle ψ'_m is determined for each subevent.[1]

[1] The distribution of the corrected event plane angles for these subevents is observed to be flat, for both orders, for photons and for charged particles.

This enables determination of a parameter χ_m directly from the experimental data using the fraction of events where the correlation of the planes of the subevents is greater than $\pi/2$ [32,33]:

$$\frac{N_{\rm events}(m|\psi'^a_m - \psi'^b_m| > \pi/2)}{N_{\rm total}} = \frac{{\rm e}^{-\frac{\chi^2_m}{4}}}{2} \quad (5)$$

where $N_{\rm total}$ denotes the total number of events, ψ'^a_m, ψ'^b_m are the observed event plane angles of the two subevents (labeled a and b) and the numerator on the left denotes the number of events having the angle between subevents greater than $\pi/2m$. The parameter χ_m so obtained is then used to determine ${\rm RCF}_{nm} = \langle\cos(nm(\psi'_m - \psi^{true}_m))\rangle$, where ψ^{true}_m is the true direction of the event plane, and the average is over all events. The RCF can be determined from χ_m by the following relation from reference [32].

$$\langle\cos(nm(\psi'_m - \psi^{true}_m))\rangle = \frac{\sqrt{\pi}}{2\sqrt{2}}\chi_m \exp(-\chi^2_m/4) \cdot \left[I_{\frac{n-1}{2}}(\chi^2_m/4) + I_{\frac{n+1}{2}}(\chi^2_m/4)\right] \quad (6)$$

where $\rm I_\nu$ are the modified Bessel functions of order ν.

The errors on the RCF values have been obtained by considering that the error on $N_{\rm events}$ is statistical. The new values of χ_m are then calculated for values of $N_{\rm events} \pm \sqrt{N_{\rm events}}$ and used in (6) to calculate new values of RCF. The change in the RCF values gives the statistical error on the RCF determination. In general, the errors determined in this way are asymmetric. Symmetric errors have been quoted using the larger of the two asymmetric errors.

3.4 Anisotropy coefficients

The anisotropy coefficients are obtained by filling up particle azimuthal distributions of one subevent with respect to the event plane of the other subevent where the subevent division is described in the previous section. The anisotropy coefficients have been determined by three methods which differ in detail and provide a consistency check. In this analysis the Fourier coefficients prior to event plane resolution correction v'_{nm} are extracted for the case with event plane order equal to the order of the extracted Fourier coefficient, i.e. $v'_{nm} = v'_{nn}$ which we will denote by v'_n.

In the first method we determine $v'^a_n = \langle\cos n(\phi^a - \psi'^b_n)\rangle$ and $v'^b_n = \langle\cos n(\phi^b - \psi'^a_n)\rangle$ where ϕ^a represent the azimuthal angles of particles in subevent a and ψ'^b_n is the event plane angle determined using particles in subevent b. The averages are computed over all particles over all events. In the absence of non-flow correlations, v_n can be determined using

$$v_n = \sqrt{\frac{v'^a_n \cdot v'^b_n}{\langle\cos n(\psi'^a_n - \psi'^b_n)\rangle}} \quad (7)$$

This determines the magnitude of the coefficients and is necessarily positive.

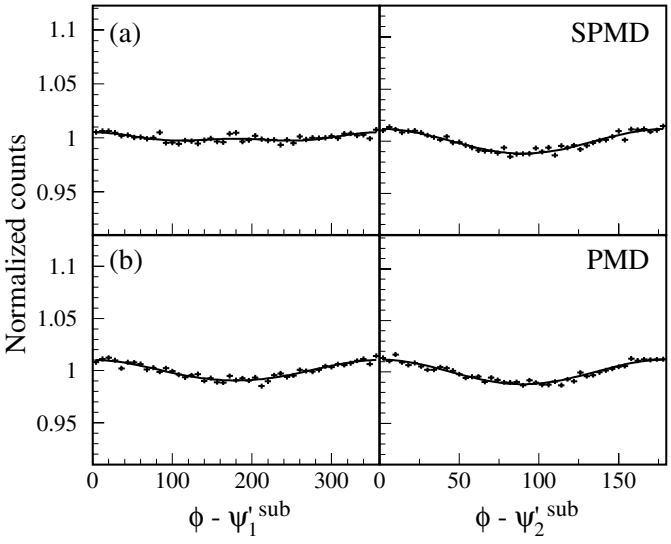

Fig. 2. Distributions of azimuthal angles with respect to the first and second order event plane for the centrality class defined by $225.5 \leq {\rm E}_T \leq 298.6$. **a** for charged particle hits in the SPMD and **b** for photons in the PMD, both in the pseudorapidity region $3.25 \leq \eta \leq 3.75$

The distributions with respect to the event plane are shown in Fig. 2 for both photon and charged particles, for both orders for the centrality selection corresponding to 10–20% of the cross section. In the second method the distributions have been fitted to (3) to determine v'_{11}. The corresponding distributions with respect to the second order event plane are shown in Fig. 2 and have been fitted to (3) to determine v'_{22}. For both orders, the fits have been made keeping terms up to values of $n \cdot m = 2$ in the summation in (3).

The v'_{nm} are the values determined with respect to the estimated event plane and must be corrected for the event plane resolution [32] to obtain the actual anisotropy values

$$v_{nm} = \frac{\sqrt{2} \cdot v'_{nm}}{RCF_{nm}} \quad (8)$$

The factor $\sqrt{2}$ arises because the particle distributions have been obtained with respect to the event plane of a subevent with half of the total event multiplicity. The subevent resolution, $\sqrt{\langle\cos(nm(\psi^a_n - \psi^b_n))\rangle}$, is averaged over all events and is in good agreement with ${\rm RCF}_{nm}/\sqrt{2}$.

In the third method, the values v_{nn} have been obtained directly by the subevent method from χ_m of (5) and the fluctuation in the average multiplicity M of the full events in that centrality bin.

$$v_{nn} = \frac{\chi_n}{\sqrt{2M}} \quad (9)$$

The different methods yield consistent results for both the first order and the second order anisotropy coefficients and the difference in the values is included in the systematic error. The equivalence of the first two methods arises due to the equivalence of the geometric mean (method

1) and the arithmetic mean (method 2) of the resolution uncorrected values v'_n of the two subevents and due to the $1/\sqrt{M}$ dependence of the fluctuation in event plane determination. The latter contributes to the equivalence of the third method with the first two. The three methods may yield different values in the presence of non-flow correlations where the differences will be governed by the nature and strength of these correlations. The most probable values are determined using method 1 above. The following sections discuss the systematic effects that distort the measured anisotropies and the centrality dependence of the anisotropies for charged particles and for photons.

4 Anisotropy in charged particles

The measured anisotropy is expected to be less than the actual anisotropy due to the finite granularity of the detector. The measured values of anisotropy may also be affected by the imprecision in the vertex position due to the finite spread of the beam. These effects are particularly relevant for the charged particle distribution measurement due to the relatively coarse segmentation and close proximity to the target of the SPMD detector. The effects are estimated using simulations.

4.1 Granularity

The finite granularity of the SPMD detector causes a dilution of the anisotropy of the azimuthal distribution primarily due to efficiency losses from multiple hits. The quantitative effect of the finite granularity on the measured anisotropy has been estimated and is briefly discussed in the following. This has been corroborated by simulations and is described in greater detail in [34].

Defining the mean occupancy as the ratio of the number of particles incident on the detector to the number of active cells

$$\mu = \frac{N_{\rm part}}{N_{\rm cell}} \tag{10}$$

one can show that

$$\mu = \ln\left(1 + \frac{N_{\rm occ}}{N_{\rm unocc}}\right) \tag{11}$$

where $N_{\rm occ}$ and $N_{\rm unocc}$ are the number of occupied and unoccupied cells [35]. One can further show that

$$\frac{N_{\rm hit}}{N_{\rm part}} = \frac{1 - {\rm e}^{-\mu}}{\mu} \tag{12}$$

where $N_{\rm hit}$ is the number of ocupied cells.

Since the intrinsic occupancy of cells increases with the increase in the number of incident particles, the occupancy will have the same azimuthal dependence as the incident particles. Substituting this for the occupancy in (12) gives us the azimuthal dependence of the hits. Expressing the resulting equation as a Fourier series and collecting coefficients of $\cos n\phi$ enables a determination of the ratio $v_n^{\rm hits}/v_n$, which to first order can be approximated by

$$\frac{v_n^{\rm hits}}{v_n} = -\frac{1-x}{x} \cdot \ln(1-x) \tag{13}$$

where $x = \frac{N_{\rm hit}}{N_{\rm cell}}$ $(= \frac{N_{\rm occ}}{N_{\rm cell}})$.

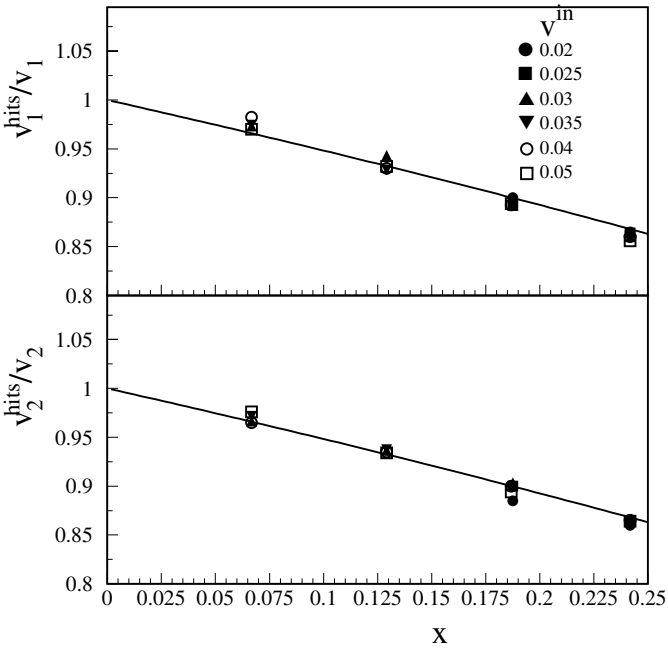

Fig. 3. The ratio $v_n^{\rm hits}/v_n$ for different number of occupied cells. x is the number of occupied cells scaled with the total number of cells. Different symbols correspond to different initial values of v_n. The solid line represents (13)

The anisotropy in the distribution of charged particles can be obtained using the measured value of anisotropy in the distribution of hits.

The azimuthal distributions of the charged particles were generated with different initial anisotropies with multiplicities corresponding to the measured results. The charged particle hits were sorted into the SPMD bins (2° ϕ-bin) assuming a 94% detection efficiency but taking into account hit losses due to multiple hits in a single SPMD pad. The resulting azimuthal distributions were then analyzed to determine the anisotropy coefficients using the method detailed in Sec 3.4 above. Figure 3 shows the results of the simulation for both orders, where the ratio of the estimated anisotropy from the hit distribution to the initial anisotropy is shown for varying hit multiplicities, far beyond the range of measured values in the SPMD. This is done for different values of initial anisotropy. The correction factor as given by (13) is shown as a solid line in the figure. One observes that the simulation results corroborate the results obtained above. The simulation results show that the extracted anisotropy is systematically lower than the initial anisotropy. Part of this loss occurs directly due to efficiency losses from multiple hits, and contributes both to the anisotropy and the event plane resolution.

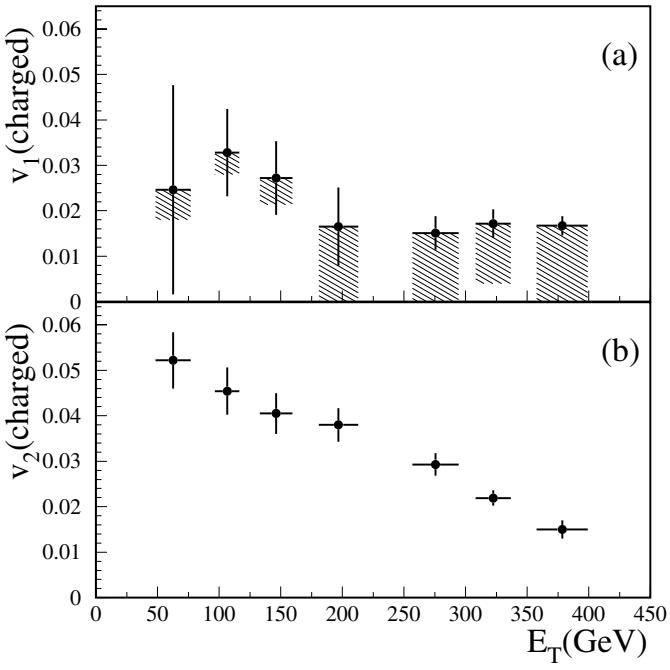

Fig. 4. Anisotropy coefficients of the azimuthal distributions of charged particles in the pseudorapidity region $3.25 \leq \eta \leq 3.75$ for different centralities characterised by the measured transverse energy. **a** First order, v_1, where the shaded region indicates the extent of the total systematic error due to uncertainty in the vertex position. **b** Second order, v_2

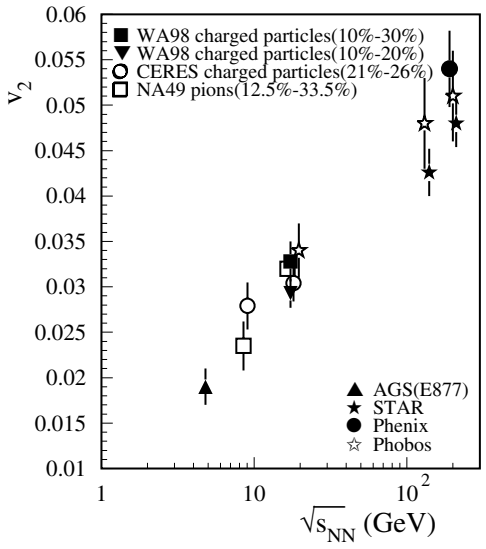

Fig. 5. Second order coefficient for different centre of mass energies. The results of the present work are for charged particles and are shown for two different centrality classes. The ordinates of CERES, NA49, STAR and PHENIX results have been shifted slightly for clarity. The error bars on WA98 points indicate the statistical and systematical errors added in quadrature. E877, STAR, PHENIX and PHOBOS v_2 values are for charged particles. The centrality cuts for all experiments are comparable

4.2 Shift in vertex and beam spread

The finite beam size caused an imprecision in the assumed vertex by up to one mm in the WA98 experiment. A small shift in the vertex position does not affect the azimuthal distribution in the fine granularity PMD, situated at 21.5 meters from the vertex. However, it can produce an apparent anisotropy in the hit distribution in the SPMD situated at 0.328 meters from the target.

The effect of vertex shifts due to the beam spread was also investigated by simulation. The vertex position was generated according to a two dimensional Gaussian with width σ. Particles were simulated to originate from this vertex position with a realistic η and p_T distribution and an azimuthally symmetric ϕ distribution. The particles were projected onto the SPMD plane, and their hit positions recorded according to the granularity and nominal location of the SPMD detector. The recorded positions corresponded to values of η and ϕ which differed from the generated values due to the shifted position of the vertex. The simulated distributions were then analyzed in the same manner as the experimental data. This was repeated for different values of σ and the values of v_n were obtained for each sample generated. The maximum possible shift has been deduced by assuming an azimuthally symmetric distribution for the most central class, and assigning the granularity corrected observed value for first order anisotropy to the shift in vertex. This corresponded to a maximum width of the Gaussian distribution due to beam spread of 0.3 mm.

A shift in the vertex position due to beam spread, or time variation during the 2.5 s SPS spill, produces an azimuthal distribution which has a shifted centroid. If the shift occurs on an event-by-event basis it cannot be corrected for by the acceptance correction methods discussed above, since they can only correct for average effects. To investigate the possibility of systematic shifts correlated with time during the SPS spill, the SPMD charged particle azimuthal distributions were analyzed for different times during the spill. No significant variations with time during the spill were observed.

The second order anisotropy is obtained from the fit to the elliptical shape of the measured hit distribution. A vertex shift does not affect the elliptical shape, as verified by simulations.

4.3 Results

The finite granularity requires a correction which is obtained using the measured values of v_n from the hit distributions and using (13). The corrected results are shown for both orders of anisotropy in Fig. 4. The error bars shown are statistical. The results for the first order anisotropy include contributions from a possible vertex shift. The upper and the lower limit of the boxes shown in Fig 4a show the asymmetric systematic error and correspond to no uncertainty and a maximum uncertainty in the position of the vertex, as discussed above.

Figure 5 shows v_2 as a function of centre of mass energy from various experiments (results mostly taken from com-

pilation of [36]). These have been measured in different experiments in different kinematic ranges using methods that vary in detail. The general behaviour shows a continuous increase in v_2 as a function of centre of mass energy. The results of the present work are shown for two different centrality ranges corresponding to 10–20% of cross section and 10-30% of cross section. For comparison to the present results, values of v_2 from PHOBOS, NA49 and CERES experiments [35–37] at nearly the same centre of mass energy are included. The various measurements are seen to agree well within errors.

5 Anisotropy in photons

The photons incident on the PMD predominantly result from the two photon decay of the neutral pion, and if both photons are detected in the PMD an additional apparent anisotropy will result from the kinematic correlation between the photons. The limited efficiency and purity of the detected photon sample in the PMD affect the measured photon anisotropy values. The quantitative effect is estimated using simulations and is described in the following.

5.1 Decay effect

The decay of neutral pions into two photons introduces correlations that can cause apparent anisotropies in the photon distributions which are greater than the actual anisotropy of the pions. On the other hand, the process of decay smears the photon momenta relative to the initial pion momenta and can thereby dilute the initial correlation present in the neutral pions. The relative importance of these two competing effects has been shown to scale with the experimentally measured quantity χ_m and enables a determination of the neutral pion anisotropy from the measured photon anisotropy [23]. However, the limited efficiency and the contamination of charged particles in the sample preclude a determination of the π^0 anisotropy from the measured γ anisotropy in the present work. Using the anisotropy values of the charged particles folded with the π^0 decay and experimental response allows one to determine the expected values of anisotropy of the photons in the PMD, as discussed below.

5.2 Efficiency and contamination

The PMD records particle hits which include incident photons and a contamination of charged particle hits. These charged particles could be primary, or secondary rescattered particles. As noted above, the photon counting efficiency (e) of the sample varies from 68% to 73% for central and peripheral events and the corresponding purity (p) of the sample varies from 65% to 54%.

The effect of decay, identification efficiency, and contamination on the observed photon anisotropy has been estimated using simulations. The simulations assume that the photon sample contains a contribution from charged particle contamination which directly reflects the measured charged particle anisotropy in addition to a contribution from photons from π^0 decays with a π^0 anisotropy which is also equal to the measured charged particle anisotropy. These simulations use the anisotropy values of the charged particles, π^0 decay kinematics, the PMD acceptance, and the purity of the PMD photon sample to generate simulated data. The simulated sample is analyzed to obtain an estimate of the expected photon anisotropy corresponding to the observed charged particle anisotropy.

The neutral pions were generated using the experimental pseudorapidity distribution of the charged pions [38] with an exponential p_T distribution ($dN/dp_T = p_T \cdot \exp(-6p_T)$). The π^0 multiplicity values were chosen as half of those measured for charged particles with the SPMD for the same centrality selection. The second order anisotropy values of π^0 were chosen to be linearly increasing with p_T before saturating at $p_T \sim 1.5$ GeV/c. For each centrality, the p_T dependence was chosen to reproduce the p_T integrated mean values of v_n of charged particles shown in Fig. 4. The linear dependence and the value of p_T at saturation were both varied to estimate the systematic errors. Neutral pions were generated and decayed and the decay photons were accepted if within the PMD acceptance. Using the measured photon multiplicity for a given centrality class, $p \cdot N_{photons}$ photons were randomly selected from those falling onto the PMD, where p was assigned a value of 0.65 to 0.54 corresponding to the centrality selection being simulated. A background contribution of $(1-p) \cdot N_{photons}$ charged particles was added to the simulated event. This simulated data was then analyzed using the methods detailed in Sect. 3.4.

The systematic errors in the simulated results have been estimated for both orders of anisotropy for each centrality. The contribution to the systematic error on the simulated results are shown for one particular centrality selection (20%–30% of minimum bias cross section) in Table 2.

The relation between the neutral pion anisotropy and photon anisotropy is not linear [23]. v_n^{PMD} has been estimated for a range of pion anisotropy values corresponding to the error measured in this experiment. An increase

Table 2. Contribution to systematic error from various sources for the simulated values of both orders of anisotropy of the $N_{photons}$ distributions for the centrality selection corresponding to 20–30% of minimum bias cross section

Source	First order	Second order
Charged particle anisotropy	+0.005	+0.002
	−0.004	−0.003
Purity of photon sample	±0.002	±0.001
Anisotropy of contaminants	−0.004	−0.007
η and p_T distribution of π^0	± 0.001	± 0.001
Neutral pion multiplicity	± 0.002	± 0.001

(decrease) in the charged particle anisotropy increases (decreases) the anisotropy in the simulated results of $v_n^{\rm PMD}$ for all centralities. The percentage change in $v_n^{\rm PMD}$ corresponding to a 10% change in the purity of photon sample is small and is about the same for all centralities. If 50% of the contaminants are assumed to be isotropic, then the resulting anisotropy decreases for all centralities, and contributes maximumally to the total systematic error. The uncertainty in the neutral pion multiplicity also has a small effect, which is almost independent of centrality.

The systematic error on the measured values of $v_n^{\rm PMD}$ have been obtained by

- increasing and decreasing the region of acceptance for the analysis
- varying the size of the interval $\Delta\eta$ between the two subevents in the range 0.03 to 0.07.
- randomly removing up to 20% of the photons in the PMD.
- obtaining the $v_n^{\rm PMD}$ values by the correlation between the subevents as described in Sect. 3.4 above.

Repeating the analysis by rejecting clusters closer than twice the size of the scintillator pads did not change the $v_n^{\rm PMD}$ values.

5.3 Results

The measured values of $v_n^{\rm PMD}$ are shown in Fig. 6. The errors on $v_n^{\rm PMD}$ are obtained by adding the systematic and the statistical error in quadrature and are also shown. The open triangles show the expected values of $v_n^{\rm PMD}$ from the simulations described above. The statistical and systematic errors are added in quadrature and are shown by the shaded regions. The photon anisotropy coefficients extracted from the simulated PMD data are consistent within errors with the measured PMD result. This demonstrates that the photon anisotropy results measured with the PMD are consistent with the charged particle results presented in Sect. 4. Note, however, that the results shown in Fig. 6 include π^0 decay and charged particle contamination effects, and should not be compared directly with other results. In particular, the use of the PMD photons themselves to determine the event plane gives a strong π^0 decay effect. This is shown by the open circles in Fig. 6 which show the simulation values of $v_n^{\rm PMD}$ for the assumption of isotropic π^0 emission, $v_n(\pi) = 0$. It is seen that the first order photon anisotropy results are dominated by the π^0 decay effect while the second order photon anisotropy results also have a significant decay contribution, which cannot simply be subtracted from the measured $v_2^{\rm PMD}$. Since the relationship between v_γ and v_{π^0} depends in a non-trivial way on the π^0 (p_T dependent) multiplicity and anisotropy [23,39] it is non-trivial to extract the π^0 anisotropy from the photon anisotropy measured with respect to the event plane determined using photons. It should be noted that the WA98 photon v_n results measured with the LEDA photon detector covering the photon rapidity region $2.3 \leq y \leq 2.9$ [39] were obtained with respect to an event plane determined in the target fragmentation region. The $v_n^{\rm PMD}$ measured using the PMD photons and

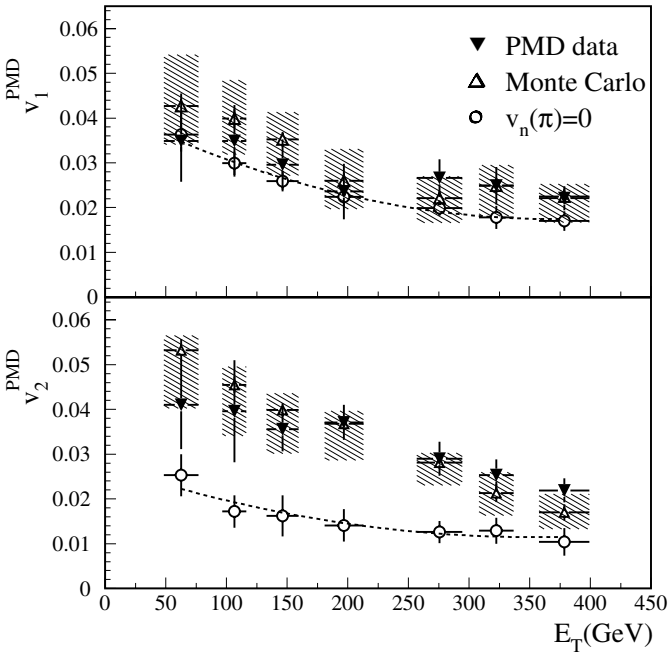

Fig. 6. a First order, $v_1^{\rm PMD}$, and **b** second order, $v_2^{\rm PMD}$, photon anisotropy coefficients in the pseudorapidity region $3.25 \leq \eta \leq 3.75$ for different centralities are shown by filled triangles. Statistical and systematical errors are added in quadrature and shown as bars on the filled triangles. Open triangles are the most probable values of $v_n^{\rm PMD}$ as expected from the simulation. The shaded regions indicate the simulation uncertainties as described in Sect. 5.4. The open circles show the calculated values of $v_n^{\rm PMD}(v_n(\pi) = 0)$ assuming an isotropic distribution of pions with the dashed curve indicating a smooth polynomial fit to the open points. Note, however, that $v_n^{\rm PMD}(v_n(\pi) = 0)$ can not be directly subtracted from the $v_n^{\rm PMD}(v_n(\pi) > 0)$ to obtain the anisotropy flow coefficents v_n, as explained in the text

v_n measured using the LEDA photons will therefore have different sensitivity to the π^0 decay effect. The PMD results include effect of decay correlations, and therefore the current measurement, $v_n^{\rm PMD}$, provides upper limits on the anisotropic flow coefficients v_n.

6 Summary

The azimuthal angle distributions with respect to the event plane have been measured for charged particles and photons with full azimuthal coverage in the pseudorapidity region of $3.25 \leq \eta \leq 3.75$ for ^{208}Pb + ^{208}Pb collisions at 158 $\cdot A$ GeV/c. A total of 0.25 million events, classified in seven centrality selections, have been used in the analysis. The Fourier coefficients of the azimuthal distributions have been extracted in several ways, all giving consistent results for the first order v_1 (directed) and v_2 second order (elliptic) anisotropies for photons and charged particles. The results show the expected trend of decreasing anisotropy with increasing centrality for both v_1 and v_2 for charged particles and photons. Our results agree with the

results reported by other experiments for near similar conditions. [35–37,39]. The observed anisotropies of the photon distributions compare well with those obtained from simulations that include the charged particle contamination and the correlations arising due to the decay of the neutral pions assumed to have the same anisotropies as measured for charged particles.

Acknowledgements. We wish to express our gratitude to the CERN accelerator division for the excellent performance of the SPS accelerator complex. We acknowledge with appreciation the effort of all engineers, technicians, and support staff who have participated in the construction of this experiment.

This work was supported jointly by the German BMBF and DFG, the U.S. DOE, the Swedish NFR and FRN, the Dutch Stichting FOM, the Polish KBN under Contract No. 621/E-78/SPUB-M/CERN/P-03/DZ211/, the Grant Agency of the Czech Republic under contract No. 202/95/0217, the Department of Atomic Energy, the Department of Science and Technology, the Council of Scientific and Industrial Research and the University Grants Commission of the Government of India, the Indo-FRG Exchange Program, the PPE division of CERN, the Swiss National Fund, the INTAS under Contract INTAS-97-0158, ORISE, Grant-in-Aid for Scientific Research (Specially Promoted Research & International Scientific Research) of the Ministry of Education, Science and Culture, the University of Tsukuba Special Research Projects, and the JSPS Research Fellowships for Young Scientists. ORNL is managed by UT-Battelle, LLC, for the U.S. Department of Energy under contract DE-AC05-00OR22725. The MIT group has been supported by the US Dept. of Energy under the cooperative agreement DE-FC02-94ER40818.

References

1. H.A. Gustafsson et al., Phys. Rev. Lett. **52**, 1590 (1984); H.H. Gutbrod et al., Phys. Lett. B **216**, 267 (1989); H.H. Gutbrod et al., Rep. Prog. Phys. **52**, 1267 (1989); H.H. Gutbrod et al., Phys. Rev. C **42**, 640 (1990)
2. W. Reisdorf, H.G. Ritter, Ann. Rev. Nucl. Part. Sci **47**, 663 (1997)
3. EOS Collaboration, J. Chance et al., Phys. Rev. Lett. **78**, 2535 (1997); M.A.Lisa et. al., nucl-ex/9610007
4. FOPI Collaboration, G. Poggi et al., Nucl. Phys. A **586**, 755 (1995); J.L. Ritman et al., Z. Phyc. **352**, 355 (1995); N. Bastid et al., Nucl. Phys. A **622**, 573 (1997)
5. KaoS Collaboration, D. Bril et al., Phys. Rev. Lett. **71**, 336 (1993); D. Brill et al., Z. Phys. A **355**, 61 (1996); Y. Shin et al., Phys. Rev. Lett. **81**, 1576 (1998)
6. E877 Collaboration, J.Barette et al., Phys. Rev. Lett. **73**, 2532 (1994); Phys. Rev. Lett. **70**, 2996 (1993); Phys. Rev. C **55**, 1420 (1997); Phys. Rev. C **56**, 3254 (1997)
7. E802 Collaboration, L. Ahle et.al., Phys. Rev. C **57**, 1416 (1998)
8. WA93 Collaboration, M.M. Aggarwal et.al., Phys. Lett. B **403**, 390 (1997)
9. WA98 Collaboration, M.M. Aggarwal et.al., Phys. Lett. B **469**, 30 (1999)
10. NA49 Collaboration, T. Wienold et al., Nucl. Phys. A **610**, 76c (1996); H. Appelshäuser et al., Phys. Rev. Lett. **80**, 4136 (1998)
11. STAR Collaboration, K.H. Ackermann et al., Phys. Rev. Lett **86**, 402 (2001); C. Adler et al., Phys. Rev. Lett. **87**, 182301 (2001)
12. PHENIX Collaboration, K. Adcox et al., Phys. Rev. Lett.**89**, 212301 (2002); S. Esumi et al., Nucl. Phys. A **715**, 599c (2003)
13. PHOBOS Collaboration, B.B. Back et al., Phys. Rev. Lett. **89**, 222301 (2002)
14. P. Danielewicz et al., Phys. Rev. Lett. **81**, 2438 (1998); Nucl. Phys. A **661**, 82c (1999)
15. G.Q. Li, C.M. Ko, B. Li, Phys. Rev. Lett. **74**, 235 (1995); H. Sorge, Phys. Rev. C **52**, 3291 (1995)
16. H. Heiselberg, Anne-Marie Levy, Phys. Rev. C **59**, 2716 (1999)
17. J.-Y. Ollitrault, Phys. Rev. D**46**, 229 (1992)
18. P.F. Kolb et al., Nucl. Phys. A **696**, 197 (2001)
19. P.F. Kolb, J. Sollfrank, U.W. Heinz, Phys. Rev. C **62**, 054909 (2000)
20. H. Sorge, Phys. Rev. Lett. **78**, 2309 (1997)
21. H. Sorge, Phys. Rev. Lett. **82**, 2048 (1999)
22. S.A. Voloshin, A.M. Poskanzer, Phys. Lett. B **474**, 27 (2000)
23. R. Raniwala, S. Raniwala, Y.P. Viyogi, Phys. Lett. B **489**, 9 (2000)
24. Gobinda Mishra, Ph.D thesis, Utkal University, 1999
25. Sudhir Raniwala, Pramana-Journal of Physics **60**, 739 (2003)
26. Proposal for a Large Acceptance Hadron and Photon Spectrometer, Preprint CERN/SPSLC 91-17, SPSLC/P260
27. WA98 Collaboration, M.M. Aggarwal et al., Phys. Lett. B **420**, 169 (1998)
28. W.T. Lin et al., Nucl. Instrum. Meth. A **389**, 415 (1997)
29. M.M. Aggarwal et al., Nucl. Instrum. Methods Phys. Res. A **424**, 395 (1999)
30. WA98 Collaboration, M.M. Aggarwal et al., Phys. Lett. B **458**, 422 (1999)
31. T. C. Awes et al., Nucl. Instrum. Methods Phys. Res. Sect. A **279**, 497 (1989)
32. A.M. Poskanzer, S. Voloshin, Phys. Rev. C **58**, 1671 (1998)
33. J.-Y. Ollitrault, e-print nucl-ex/9711003
34. R. Raniwala, S. Raniwala, Y.P. Viyogi, e-print nucl-ex/0502023
35. PHOBOS Collaboration, B.B. Back et al., nucl-ex/0406021
36. NA49 Collaboration, C. Alt et al., Phys. Rev. C **68**, 034903 (2003)
37. CERES/NA45 Collaboration, J. Slivova et al., Nucl. Phys. A **715**, 615c (2003)
38. WA98 Collaboration, M.M. Aggarwal et al., Eur. Phys. J. C **18**, 651 (2001)
39. WA98 Collaboration, M.M. Aggarwal et al., nucl-ex/0410045

Deuteron and Antideuteron Production in Au+Au Collisions at $\sqrt{s_{NN}}=200$ GeV

S. S. Adler,[5] S. Afanasiev,[17] C. Aidala,[5] N. N. Ajitanand,[43] Y. Akiba,[20,38] J. Alexander,[43] R. Amirikas,[12] L. Aphecetche,[45] S. H. Aronson,[5] R. Averbeck,[44] T. C. Awes,[35] R. Azmoun,[44] V. Babintsev,[15] A. Baldisseri,[10] K. N. Barish,[6] P. D. Barnes,[27] B. Bassalleck,[33] S. Bathe,[30] S. Batsouli,[9] V. Baublis,[37] A. Bazilevsky,[39,15] S. Belikov,[16,15] Y. Berdnikov,[40] S. Bhagavatula,[16] J. G. Boissevain,[27] H. Borel,[10] S. Borenstein,[25] M. L. Brooks,[27] D. S. Brown,[34] N. Bruner,[33] D. Bucher,[30] H. Buesching,[30] V. Bumazhnov,[15] G. Bunce,[5,39] J. M. Burward-Hoy,[26,44] S. Butsyk,[44] X. Camard,[45] J.-S. Chai,[18] P. Chand,[4] W. C. Chang,[2] S. Chernichenko,[15] C. Y. Chi,[9] J. Chiba,[20] M. Chiu,[9] I. J. Choi,[52] J. Choi,[19] R. K. Choudhury,[4] T. Chujo,[5] V. Cianciolo,[35] Y. Cobigo,[10] B. A. Cole,[9] P. Constantin,[16] D. d'Enterria,[45] G. David,[5] H. Delagrange,[45] A. Denisov,[15] A. Deshpande,[39] E. J. Desmond,[5] A. Devismes,[44] O. Dietzsch,[41] O. Drapier,[25] A. Drees,[44] R. du Rietz,[29] A. Durum,[15] D. Dutta,[4] Y. V. Efremenko,[35] K. El Chenawi,[49] A. Enokizono,[14] H. En'yo,[38,39] S. Esumi,[48] L. Ewell,[5] D. E. Fields,[33,39] F. Fleuret,[25] S. L. Fokin,[23] B. D. Fox,[39] Z. Fraenkel,[51] J. E. Frantz,[9] A. Franz,[5] A. D. Frawley,[12] S.-Y. Fung,[6] S. Garpman,[29,*] T. K. Ghosh,[49] A. Glenn,[46] G. Gogiberidze,[46] M. Gonin,[25] J. Gosset,[10] Y. Goto,[39] R. Granier de Cassagnac,[25] N. Grau,[16] S. V. Greene,[49] M. Grosse Perdekamp,[39] W. Guryn,[5] H.-Å. Gustafsson,[29] T. Hachiya,[14] J. S. Haggerty,[5] H. Hamagaki,[8] A. G. Hansen,[27] E. P. Hartouni,[26] M. Harvey,[5] R. Hayano,[8] N. Hayashi,[38] X. He,[13] M. Heffner,[26] T. K. Hemmick,[44] J. M. Heuser,[44] M. Hibino,[50] J. C. Hill,[16] W. Holzmann,[43] K. Homma,[14] B. Hong,[22] A. Hoover,[34] T. Ichihara,[38,39] V. V. Ikonnikov,[23] K. Imai,[24,38] D. Isenhower,[1] M. Ishihara,[38] M. Issah,[43] A. Isupov,[17] B. V. Jacak,[44] W. Y. Jang,[22] Y. Jeong,[19] J. Jia,[44] O. Jinnouchi,[38] B. M. Johnson,[5] S. C. Johnson,[26] K. S. Joo,[31] D. Jouan,[36] S. Kametani,[8,50] N. Kamihara,[47,38] J. H. Kang,[52] S. S. Kapoor,[4] K. Katou,[50] S. Kelly,[9] B. Khachaturov,[51] A. Khanzadeev,[37] J. Kikuchi,[50] D. H. Kim,[31] D. J. Kim,[52] D. W. Kim,[19] E. Kim,[42] G.-B. Kim,[25] H. J. Kim,[52] E. Kistenev,[5] A. Kiyomichi,[48] K. Kiyoyama,[32] C. Klein-Boesing,[30] H. Kobayashi,[38,39] L. Kochenda,[37] V. Kochetkov,[15] D. Koehler,[33] T. Kohama,[14] M. Kopytine,[44] D. Kotchetkov,[6] A. Kozlov,[51] P. J. Kroon,[5] C. H. Kuberg,[1,27] K. Kurita,[39] Y. Kuroki,[48] M. J. Kweon,[22] Y. Kwon,[52] G. S. Kyle,[34] R. Lacey,[43] V. Ladygin,[17] J. G. Lajoie,[16] A. Lebedev,[16,23] S. Leckey,[44] D. M. Lee,[27] S. Lee,[19] M. J. Leitch,[27] X. H. Li,[6] H. Lim,[42] A. Litvinenko,[17] M. X. Liu,[27] Y. Liu,[36] C. F. Maguire,[49] Y. I. Makdisi,[5] A. Malakhov,[17] V. I. Manko,[23] Y. Mao,[7,38] G. Martinez,[45] M. D. Marx,[44] H. Masui,[48] F. Matathias,[44] T. Matsumoto,[8,50] P. L. McGaughey,[27] E. Melnikov,[15] F. Messer,[44] Y. Miake,[48] J. Milan,[43] T. E. Miller,[49] A. Milov,[44,51] S. Mioduszewski,[5] R. E. Mischke,[27] G. C. Mishra,[13] J. T. Mitchell,[5] A. K. Mohanty,[4] D. P. Morrison,[5] J. M. Moss,[27] F. Mühlbacher,[44] D. Mukhopadhyay,[51] M. Muniruzzaman,[6] J. Murata,[38,39] S. Nagamiya,[20] J. L. Nagle,[9] T. Nakamura,[14] B. K. Nandi,[6] M. Nara,[48] J. Newby,[46] P. Nilsson,[29] A. S. Nyanin,[23] J. Nystrand,[29] E. O'Brien,[5] C. A. Ogilvie,[16] H. Ohnishi,[5,38] I. D. Ojha,[49,3] K. Okada,[38] M. Ono,[48] V. Onuchin,[15] A. Oskarsson,[29] I. Otterlund,[29] K. Oyama,[8] K. Ozawa,[8] D. Pal,[51] A. P. T. Palounek,[27] V. Pantuev,[44] V. Papavassiliou,[34] J. Park,[42] A. Parmar,[33] S. F. Pate,[34] T. Peitzmann,[30] J.-C. Peng,[27] V. Peresedov,[17] C. Pinkenburg,[5] R. P. Pisani,[5] F. Plasil,[35] M. L. Purschke,[5] A. K. Purwar,[44] J. Rak,[16] I. Ravinovich,[51] K. F. Read,[35,46] M. Reuter,[44] K. Reygers,[30] V. Riabov,[37,40] Y. Riabov,[37] G. Roche,[28] A. Romana,[25] M. Rosati,[16] P. Rosnet,[28] S. S. Ryu,[52] M. E. Sadler,[1] N. Saito,[38,39] T. Sakaguchi,[8,50] M. Sakai,[32] S. Sakai,[48] V. Samsonov,[37] L. Sanfratello,[33] R. Santo,[30] H. D. Sato,[24,38] S. Sato,[5,48] S. Sawada,[20] Y. Schutz,[45] V. Semenov,[15] R. Seto,[6] M. R. Shaw,[1,27] T. K. Shea,[5] T.-A. Shibata,[47,38] K. Shigaki,[14,20] T. Shiina,[27] C. L. Silva,[41] D. Silvermyr,[27,29] K. S. Sim,[22] C. P. Singh,[3] V. Singh,[3] M. Sivertz,[5] A. Soldatov,[15] R. A. Soltz,[26] W. E. Sondheim,[27] S. P. Sorensen,[46] I. V. Sourikova,[5] F. Staley,[10] P. W. Stankus,[35] E. Stenlund,[29] M. Stepanov,[34] A. Ster,[21] S. P. Stoll,[5] T. Sugitate,[14] J. P. Sullivan,[27] E. M. Takagui,[41] A. Taketani,[38,39] M. Tamai,[50] K. H. Tanaka,[20] Y. Tanaka,[32] K. Tanida,[38] M. J. Tannenbaum,[5] P. Tarján,[11] J. D. Tepe,[1,27] T. L. Thomas,[33] J. Tojo,[24,38] H. Torii,[24,38] R. S. Towell,[1] I. Tserruya,[51] H. Tsuruoka,[48] S. K. Tuli,[3] H. Tydesjö,[29] N. Tyurin,[15] H. W. van Hecke,[27] J. Velkovska,[5,44] M. Velkovsky,[44] V. Veszprémi,[11] L. Villatte,[46] A. A. Vinogradov,[23] M. A. Volkov,[23] E. Vznuzdaev,[37] X. R. Wang,[13] Y. Watanabe,[38,39] S. N. White,[5] F. K. Wohn,[16] C. L. Woody,[5] W. Xie,[6] Y. Yang,[7] A. Yanovich,[15] S. Yokkaichi,[38,39] G. R. Young,[35] I. E. Yushmanov,[23] W. A. Zajc,[9,†] C. Zhang,[9] S. Zhou,[7] S. J. Zhou,[51] and L. Zolin[17]

(PHENIX Collaboration)

[1]*Abilene Christian University, Abilene, Texas 79699, USA*
[2]*Institute of Physics, Academia Sinica, Taipei 11529, Taiwan*
[3]*Department of Physics, Banaras Hindu University, Varanasi 221005, India*
[4]*Bhabha Atomic Research Centre, Bombay 400085, India*

 © 2005 The American Physical Society

[5]Brookhaven National Laboratory, Upton, New York 11973-5000, USA
[6]University of California at Riverside, Riverside, California 92521, USA
[7]China Institute of Atomic Energy (CIAE), Beijing, People's Republic of China
[8]Center for Nuclear Study, Graduate School of Science, University of Tokyo, 7-3-1 Hongo, Bunkyo, Tokyo 113-0033, Japan
[9]Columbia University, New York, New York 10027, USA, and Nevis Laboratories, Irvington, New York 10533, USA
[10]Dapnia, CEA Saclay, F-91191, Gif-sur-Yvette, France
[11]Debrecen University, H-4010 Debrecen, Egyetem tér 1, Hungary
[12]Florida State University, Tallahassee, Florida 32306, USA
[13]Georgia State University, Atlanta, Georgia 30303, USA
[14]Hiroshima University, Kagamiyama, Higashi-Hiroshima 739-8526, Japan
[15]Institute for High Energy Physics (IHEP), Protvino, Russia
[16]Iowa State University, Ames, Iowa 50011, USA
[17]Joint Institute for Nuclear Research, 141980 Dubna, Moscow Region, Russia
[18]KAERI, Cyclotron Application Laboratory, Seoul, Korea
[19]Kangnung National University, Kangnung 210-702, Korea
[20]KEK, High Energy Accelerator Research Organization, Tsukuba-shi, Ibaraki-ken 305-0801, Japan
[21]KFKI Research Institute for Particle and Nuclear Physics (RMKI), H-1525 Budapest 114, P.O. Box 49, Hungary
[22]Korea University, Seoul 136-701, Korea
[23]Russian Research Center, "Kurchatov Institute," Moscow, Russia
[24]Kyoto University, Kyoto 606-8502, Japan
[25]Laboratoire Leprince-Ringuet, Ecole Polytechnique, CNRS-IN2P3, Route de Saclay, F-91128, Palaiseau, France
[26]Lawrence Livermore National Laboratory, Livermore, California 94550, USA
[27]Los Alamos National Laboratory, Los Alamos, New Mexico 87545, USA
[28]LPC, Université Blaise Pascal, CNRS-IN2P3, Clermont-Fd, 63177 Aubiere CEDEX, France
[29]Department of Physics, Lund University, Box 118, SE-221 00 Lund, Sweden
[30]Institut für Kernphysik, University of Muenster, D-48149 Muenster, Germany
[31]Myongji University, Yongin, Kyonggido 449-728, Korea
[32]Nagasaki Institute of Applied Science, Nagasaki-shi, Nagasaki 851-0193, Japan
[33]University of New Mexico, Albuquerque, New Mexico 87131, USA
[34]New Mexico State University, Las Cruces, New Mexico 88003, USA
[35]Oak Ridge National Laboratory, Oak Ridge, Tennessee 37831, USA
[36]IPN-Orsay, Universite Paris Sud, CNRS-IN2P3, BP 1, F-91406, Orsay, France
[37]PNPI, Petersburg Nuclear Physics Institute, Gatchina, Russia
[38]RIKEN (The Institute of Physical and Chemical Research), Wako, Saitama 351-0198, Japan
[39]RIKEN BNL Research Center, Brookhaven National Laboratory, Upton, New York 11973-5000, USA
[40]St. Petersburg State Technical University, St. Petersburg, Russia
[41]Universidade de São Paulo, Instituto de Física, Caixa Postal 66318, São Paulo CEP05315-970, Brazil
[42]System Electronics Laboratory, Seoul National University, Seoul, Korea
[43]Chemistry Department, Stony Brook University, SUNY, Stony Brook, New York 11794-3400, USA
[44]Department of Physics and Astronomy, Stony Brook University, SUNY, Stony Brook, New York 11794, USA
[45]SUBATECH (Ecole des Mines de Nantes, CNRS-IN2P3, Université de Nantes), BP 20722-44307, Nantes, France
[46]University of Tennessee, Knoxville, Tennessee 37996, USA
[47]Department of Physics, Tokyo Institute of Technology, Tokyo 152-8551, Japan
[48]Institute of Physics, University of Tsukuba, Tsukuba, Ibaraki 305, Japan
[49]Vanderbilt University, Nashville, Tennessee 37235, USA
[50]Waseda University, Advanced Research Institute for Science and Engineering, 17 Kikui-cho, Shinjuku-ku, Tokyo 162-0044, Japan
[51]Weizmann Institute, Rehovot 76100, Israel
[52]Yonsei University, IPAP, Seoul 120-749, Korea
(Received 1 June 2004; published 1 April 2005)

The production of deuterons and antideuterons in the transverse momentum range $1.1 < p_T < 4.3$ GeV/c at midrapidity in Au + Au collisions at $\sqrt{s_{NN}} = 200$ GeV has been studied by the PHENIX experiment at RHIC. A coalescence analysis, comparing the deuteron and antideuteron spectra with that of proton and antiproton, has been performed. The coalescence probability is equal for both deuterons and antideuterons and it increases as a function of p_T, which is consistent with an expanding collision zone. Comparing (anti)proton yields, $\overline{p}/p = 0.73 \pm 0.01$, with (anti)deuteron yields, $\overline{d}/d = 0.47 \pm 0.03$, we estimate that $\bar{n}/n = 0.64 \pm 0.04$. The nucleon phase space density is estimated from the coalescence measurement.

DOI: 10.1103/PhysRevLett.94.122302 PACS numbers: 25.75.Dw

Ultrarelativistic heavy-ion collisions are used to study the behavior of nuclear matter at extreme conditions of temperature and density, similar to those that existed in the universe a few microseconds after the Big Bang. Previous measurements indicate that high particle multiplicities [1] and large $\bar{p}/p$ ratios prevail at the Relativistic Heavy-Ion Collider (RHIC), which is expected for a nearly net baryon-free region [2]. As the hot, dense system of particles cools, it expands and the mean-free path increases until the particles cease interacting (''freeze-out''). At this point, light nuclei such as deuterons and antideuterons (d and $\bar{d}$) can be formed, with a probability proportional to the product of the phase space densities of its constituent nucleons [3,4]. Thus, the invariant yield of deuterons, compared to the protons [5,6] from which they coalesce, provides information about the size of the emitting system and its space-time evolution.

PHENIX [7] at RHIC is a versatile detector designed to study the production of leptons, photons, and hadrons over a wide momentum range. In this Letter, results on d and $\bar{d}$ production in Au + Au interactions at $\sqrt{s_{NN}} = 200$ GeV are presented. For the sake of brevity, in the rest of this Letter, our statements will generally apply to both particles and antiparticles.

The east central tracking spectrometer in the PHENIX detector [5,7,8] is used in this analysis. The information from the PHENIX beam-beam counters (BBCs) and zero-degree calorimeters (ZDCs) is used for triggering and event selection. The BBCs are Čerenkov counters surrounding the beam pipe in the pseudorapidity interval $3.0 < |\eta| < 3.9$, and provide the start timing signal. The ZDCs are hadronic calorimeters 18 m downstream of the interaction region and detect spectator neutrons in a narrow forward cone. Particle identification in the central rapidity region is achieved by measuring momentum (by drift chamber) and time of flight (by time-of-flight detector). The drift chamber (DC) and two layers of pad chambers are used for tracking and momentum reconstruction [8]. The time-of-flight (TOF) detector spans the pseudorapidity range $|\eta| < 0.35$ and $\Delta\phi = \pi/4$ azimuthally. The TOF consists of plastic scintillators, with a combined time resolution of ≈115 ps. The TOF thus provides identification of d and $\bar{d}$ in the transverse momentum (p_T) range $1.1 < p_T < 4.3$ GeV/c. For $p_T < 1.1$ GeV/c, the signal-to-background ratio suffers due to multiple scattering and energy loss effects.

The data set for this analysis includes 21.6×10^6 minimum bias events. The minimum bias cross section corresponds to $92.2^{+2.5}_{-3}\%$ of the total inelastic Au + Au cross section (6.9 b) [9]. Using the momentum determined by the DC, which has a resolution of $\delta p/p \approx 0.7\% \oplus 1\% p$ GeV/c, and the time of flight from the event vertex provided by the TOF, the mass of the particle is determined. The d and $\bar{d}$ yields are obtained by fitting the mass squared distributions to the sum of a Gaussian signal and an exponential background. Examples of mass squared distributions with fits for antideuterons in minimum bias collisions are shown in Fig. 1.

The raw yields are corrected for effects of detector acceptance, reconstruction efficiency, and detector occupancy. Corrections are determined by reconstructing single deuterons simulated using GEANT [10] and a detector response model of PHENIX, using the method described in [6]. The track reconstruction efficiency decreases in high multiplicity events because of high detector occupancy. This effect can be slightly larger for slower, heavier particles, due to detector dead times between successive hits. Occupancy effects on reconstruction efficiency (≈83.5% for 0%–20% most central events) are evaluated by embedding simulated single particle Monte Carlo (MC) events in real events. Since the hadronic interactions of nuclei are not treated by GEANT, a correction needs to be applied to account for the hadronic absorption of d and $\bar{d}$ (including annihilation). The d- and the $\bar{d}$-nucleus cross sections are calculated from parametrizations of the nucleon and antinucleon cross sections:

$$\sigma_{d/\bar{d},A} = \left[\sqrt{\sigma_{N/\bar{N},A}} + \Delta_d\right]^2. \quad (1)$$

The limited data available on deuteron induced interactions [11] indicate that the term Δ_d is independent of the nuclear mass number A and that $\Delta_d = 3.51 \pm 0.25$ mb$^{1/2}$. The hadronic absorption varies only slightly over the applicable p_T range and is ≈ 10% for d and ≈ 15% for $\bar{d}$. The background contribution from deuterons knocked out due to the interaction of the produced particles with the beam pipe is estimated using simulations and is found to be negligible in the momentum range of our measurement.

Figure 2 shows the corrected d and $\bar{d}$ invariant yields as a function of transverse mass [m_T in the range $1.1 < p_T < 4.3$ GeV/c, for minimum bias events, and two centrality bins: 0%–20% (most central) and 20%–92% (noncen-

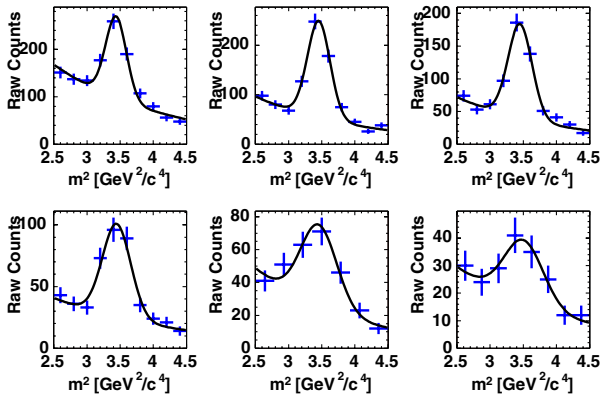

FIG. 1 (color online). Histograms of the mass squared for identified antideuterons in the transverse momentum range $1.1 < p_T < 3.5$ GeV/c (in 400 MeV/c increments), with Gaussian fits including an exponential background.

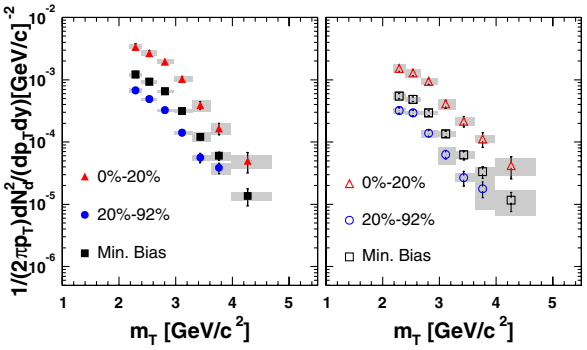

FIG. 2 (color online). Corrected spectra for deuterons (left panel) and antideuterons (right panel) for different centralities are plotted vs m_T. Error bars indicate statistical errors and gray bands the systematic errors. Values are plotted at the "true" mean value of m_T of each bin, the extent of which is indicated by the width of the gray bars along the x axis.

tral)]. The 20%–92% centrality bin is dominated by mid-central events, due to larger track multiplicities relative to peripheral events.

Systematic uncertainties have several sources: errors in particle identification, DC-TOF hit match efficiency, the uncertainty in momentum scale, d and $\bar{d}$ hadronic interaction correction, and uncertainty in occupancy corrections. All the systematic uncertainties are added in quadrature, depicted by the gray bars in Fig. 2.

The p_T spectra Ed^3N/d^3p are fitted in the range $1.1 < p_T < 3.5$ GeV/c to an exponential distribution in $m_T = \sqrt{p_T^2 + m^2}$. The inverse slopes ($T_{\rm eff}$) of the spectra are tabulated in Table I. The deuteron inverse slopes of $T_{\rm eff} =$ 500–520 MeV are considerably higher than the $T_{\rm eff} =$ 300–350 MeV observed for protons [5,6]. The invariant yields and the average transverse momenta ($\langle p_T \rangle$) are obtained by summing the data over p_T and using a Boltzmann distribution, $\frac{d^2N}{2\pi m_T dm_T dy} \propto m_T e^{-m_T/T_{\rm eff}}$, to extrapolate to low m_T regions where we have no data. The extrapolated yields constitute $\approx 42\%$ of our total yields. The rapidity distributions, dN/dy, and the mean transverse momenta, $\langle p_T \rangle$, are compiled in Table I for three different centrality bins. Systematic uncertainties in dN/dy and $\langle p_T \rangle$ are estimated by using an exponential in p_T and a "truncated" Boltzmann distribution (assumed flat for $p_T < 1.1$ GeV/c) for alternative extrapolations.

TABLE I. The inverse slope parameter $T_{\rm eff}$ obtained from a m_T exponential fit to the spectra along with multiplicity dN/dy and mean transverse momentum $\langle p_T \rangle$ obtained from a Boltzmann distribution for different centralities.

$T_{\rm eff}$ [MeV]	Deuterons	Antideuterons
Minimum bias	519 ± 27	512 ± 32
0%–20%	536 ± 32	562 ± 51
20%–92%	475 ± 29	456 ± 35
dN/dy		
Minimum bias	$0.0250 \pm ^{0.0006(\rm stat)}_{0.005(\rm syst)}$	$0.0117 \pm ^{0.0003(\rm stat)}_{0.002(\rm syst)}$
0%–20%	$0.0727 \pm ^{0.0022(\rm stat)}_{0.0141(\rm syst)}$	$0.0336 \pm ^{0.0013(\rm stat)}_{0.0057(\rm syst)}$
20%–92%	$0.0133 \pm ^{0.0004(\rm stat)}_{0.0029(\rm syst)}$	$0.0066 \pm ^{0.0002(\rm stat)}_{0.0015(\rm syst)}$
$\langle p_T \rangle$ [GeV/c]		
Minimum bias	$1.54 \pm ^{0.04(\rm stat)}_{0.13(\rm syst)}$	$1.52 \pm ^{0.05(\rm stat)}_{0.12(\rm syst)}$
0%–20%	$1.58 \pm ^{0.05(\rm stat)}_{0.13(\rm syst)}$	$1.62 \pm ^{0.07(\rm stat)}_{0.1(\rm syst)}$
20%–92%	$1.45 \pm ^{0.05(\rm stat)}_{0.15(\rm syst)}$	$1.41 \pm ^{0.06(\rm stat)}_{0.15(\rm syst)}$

With a binding energy of 2.24 MeV, the deuteron is a very loosely bound state. Thus, the observed deuterons can be formed only at a later stage in the collision. The proton and neutron must be close in space and tightly correlated in velocity to coalesce. As a result, d and $\bar{d}$ yields are a sensitive measure of correlations in phase space at freeze-out and can provide information about the space-time evolution of the system. If deuterons are formed by coalescence of protons and neutrons, the invariant deuteron yield can be related [12] to the primordial nucleon yields by

$$E_d \frac{d^3N_d}{d^3p_d}\Big|_{p_d=2p_p} = B_2 \left(E_p \frac{d^3N_p}{d^3p_p} \right)^2, \qquad (2)$$

where B_2 is the coalescence parameter, with the subscript implying that two nucleons are involved in the coalescence. The above equation includes an implicit assumption that the ratio of neutrons to protons is unity. The proton and antiproton spectra [6] are corrected for feed-down from Λ and $\bar{\Lambda}$ decays by using a MC simulation tuned to reproduce the particle ratios: (Λ/p and $\bar{\Lambda}/\bar{p}$) measured by PHENIX at 130 GeV [13].

Figure 3 displays the coalescence parameter B_2 as a function of p_T for different centralities. Thermodynamic models [4] predict that B_2 scales with the inverse of the effective volume $V_{\rm eff}$ ($B_2 \propto 1/V_{\rm eff}$). The lower B_2 in more central collisions may thus reflect the increase in the participant volume with centrality. We also observe that B_2 increases with p_T. This is consistent with an expanding

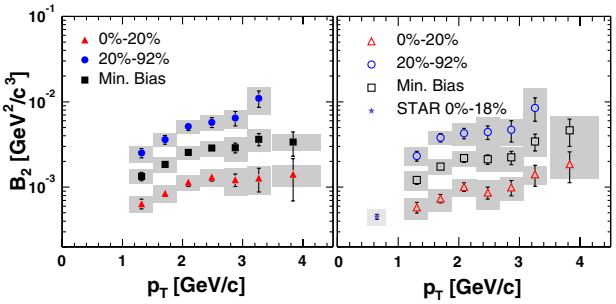

FIG. 3 (color online). Coalescence parameter B_2 vs p_T for deuterons (left panel) and antideuterons (right panel). Gray bands indicate the systematic errors. Values are plotted at the true mean value of p_T of each bin, the extent of which is indicated by the width of the gray bars along the x axis.

source because position-momentum correlations lead to a higher coalescence probability at larger p_T. The p_T dependence of B_2 can provide information about the density profile of the source as well as the expansion velocity distribution. It has been shown [14,15] that a Gaussian source density combined with a linear flow velocity profile leads to a constant B_2 with p_T. This is not supported by our data, which show a rise in B_2 with p_T. An increase of B_2 with p_T can be achieved if the Gaussian source density is replaced with a flat distribution [14,15]. The increase is a consequence of the flat density distribution giving greater weight to the outer parts of the system where the flow is strongest when a linear velocity profile is used.

Figure 4 compares B_2 for most central collisions to results at lower $\sqrt{s}$ [16–21]. Note that B_2 is nearly independent of $\sqrt{s}$, indicating that the source volume does not change appreciably with center-of-mass energy (with the caveat that B_2 varies as a function of p_T, centrality, and rapidity). This observation is consistent with what has been observed in Bose-Einstein correlation Hanbury Brown-Twiss analysis at RHIC [22] for identified particles. The coalescence parameter B_2 for d and $\bar{d}$ is equal within errors, indicating that nucleons and antinucleons have the same temperature, flow, and freeze-out density distributions.

The $\bar{d}/d$ ratio is independent of centrality and p_T within errors. The average value of $\bar{d}/d$ is 0.47 ± 0.03, consistent with the square of the ratio $\bar{p}/p = 0.73 \pm 0.01$ [6] within statistical and systematic uncertainties. This is expected if deuterons are formed by coalescence of comoving nucleons and $\bar{p}/p = \bar{n}/n$. The ratio $\bar{n}/n$ can, however, be estimated from the data based on the thermal chemical model. Assuming thermal and chemical equilibrium, the chemical fugacities are determined from the particle/antiparticle ratios [14]:

$$\frac{E_A(d^3N_A/d^3p_A)}{E_{\bar{A}}(d^3N_{\bar{A}}/d^3p_{\bar{A}})} = \exp\left(\frac{2\mu_A}{T}\right) = \lambda_A^2. \quad (3)$$

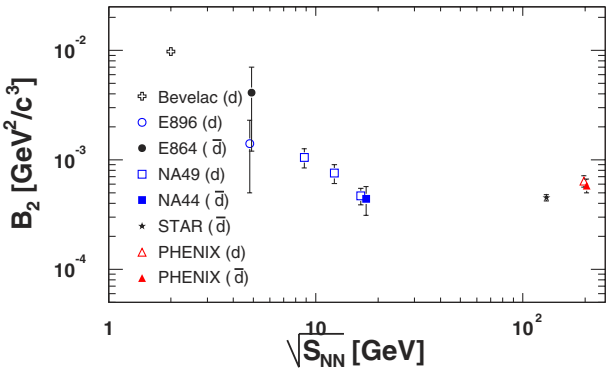

FIG. 4 (color online). Comparison of the coalescence parameter for deuterons and antideuterons ($p_T = 1.3$ GeV/c) with other experiments at different values of $\sqrt{s}$.

Using the ratio $p/\bar{p}$, the extracted proton fugacity is $\lambda_p = \exp(\mu_p/T) = 1.17 \pm 0.01$. Similarly, using the $d/\bar{d}$ ratio, the extracted deuteron fugacity is $\lambda_d = \exp[(\mu_p + \mu_n)/T] = 1.46 \pm 0.05$. From this, the neutron fugacity can be estimated to be $\lambda_n = \exp(\mu_n/T) = 1.25 \pm 0.04$, which results in $\bar{n}/n = 0.64 \pm 0.04$. The extracted $\bar{p}/p$ and $\bar{n}/n$ ratios are in agreement with what one would expect from the initial neutron excess in the Au nucleus if the same number of (anti)neutrons and (anti)protons are produced in the collision. Thermal models predict [23] $\bar{d}/d = 0.52$ and $\bar{n}/n = 0.73$ for $T = 177$ MeV and $\mu_B = 29$ MeV.

Finally, the coalescence requirement allows us to estimate the nucleon phase space distribution, i.e., the average number of nucleons per cell $(d^3pd^3x)/h$ in phase space. We define the phase space distribution averaged over the source volume as

$$\langle f(p)\rangle = \frac{1}{2S+1}\frac{(2\pi\hbar)^3}{V}\frac{d^3N}{dp^3}, \quad (4)$$

where $2S + 1$ is the spin degeneracy factor. From the coalescence equation [15], $f_A(\vec{r}, \vec{p}) = [f(\vec{r}, \vec{p}/A)]^A$, we can thus calculate $\langle f\rangle$ as a function of p_T from the measured invariant yields, if we assume that the protons, neutrons, and deuterons are emitted from the same volume. The results are shown in Fig. 5. The phase space density is well below 1 in the range of our measurement, and much lower than what has been found for pions produced in Au + Au collisions previously [24].

To summarize, the transverse momentum spectra of d and $\bar{d}$ in the range $1.1 < p_T < 4.3$ GeV/c have been measured at midrapidty in Au + Au collisions at $\sqrt{s_{NN}} = 200$ GeV, and are found to be less steeply falling than proton (and antiproton) spectra. The extracted coalescence parameter B_2 increases with p_T, which is indicative of an expanding source. The results rule out a Gaussian source density distribution combined with a linear flow velocity profile and seem to favor a flat density distribution. The B_2 measured in nucleus-nucleus collisions is independent of $\sqrt{s_{NN}}$ above 12 GeV, consistent with the energy depen-

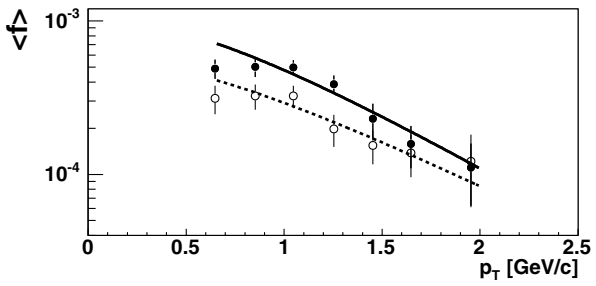

FIG. 5. Average nucleon phase space density as a function of p_T for central collisions. Solid circles correspond to nucleons and open circles correspond to antinucleons. The curves are fits to a Boltzmann function, $C\exp(-m_T/T)$, with $T = 568 \pm 96$ MeV (nucleons) and $T = 670 \pm 182$ MeV (antinucleons).

dence of the source radii extracted from Bose-Einstein correlation measurements. B_2 is equal within errors for both deuterons and antideuterons. From the measurements, it is estimated that $\bar{n}/n = 0.64 \pm 0.04$.

We thank the staff of the Collider-Accelerator and Physics Departments at BNL for their vital contributions. We acknowledge support from the Department of Energy and NSF (USA), MEXT and JSPS (Japan), CNPq and FAPESP (Brazil), NSFC (China), CNRS-IN2P3 and CEA (France), BMBF, DAAD, and AvH (Germany), OTKA (Hungary), DAE and DST (India), ISF (Israel), KRF and CHEP (Korea), RMIST, RAS, and RMAE, (Russia), VR and KAW (Sweden), U.S. CRDF for the FSU, U.S.-Hungarian NSF-OTKA-MTA, and U.S.-Israel BSF.

*Deceased.
†PHENIX Spokesperson.
Electronic address: zajc@nevis.columbia.edu

[1] K. Adcox *et al.*, Phys. Rev. Lett. **86**, 3500 (2001); B. B. Back *et al.*, Phys. Rev. Lett. **88**, 022302 (2002).
[2] K. Adcox *et al.*, Phys. Rev. Lett. **88**, 242301 (2002); B. B. Back *et al.*, Phys. Rev. C **67**, 021901 (2003); C. Adler *et al.*, Phys. Rev. Lett. **86**, 4778 (2001).
[3] L. P. Csernai and J. I. Kapusta, Phys. Rep. **131**, 223 (1986).
[4] A. Z. Mekjian, Phys. Rev. C **17**, 1051 (1978).
[5] K. Adcox *et al.*, Phys. Rev. C **69**, 024904 (2004).
[6] S. S. Adler *et al.*, Phys. Rev. C **69**, 034909 (2004).
[7] K. Adcox *et al.*, Nucl. Instrum. Methods Phys. Res., Sect. A **499**, 469 (2003), and references therein.
[8] J. T. Mitchell *et al.*, Nucl. Instrum. Methods Phys. Res., Sect. A **482**, 491 (2002).
[9] S. S. Adler *et al.*, Phys. Rev. Lett. **91**, 072301 (2003).
[10] GEANT 3.21, CERN program library.
[11] J. Jaros *et al.*, Phys. Rev. C **18**, 2273 (1978); E. O. Abdurakhmanov *et al.*, Z. Phys. C **5**, 1 (1980).
[12] S. T. Butler and C. A. Pearson, Phys. Rev. **129**, 836 (1963).
[13] K. Adcox *et al.*, Phys. Rev. Lett. **89**, 092302 (2002).
[14] R. Scheibl and U. Heinz, Phys. Rev. C **59**, 1585 (1999).
[15] A. Polleri, J. P. Bondorf, and I. N. Mishustin, Phys. Lett. B **419**, 19 (1998).
[16] S. Wang *et al.*, Phys. Rev. Lett. **74**, 2646 (1995).
[17] S. Albergo *et al.*, Phys. Rev. C **65**, 034907 (2002).
[18] T. A. Armstrong *et al.*, Phys. Rev. Lett. **85**, 2685 (2000).
[19] T. Anticic *et al.*, Phys. Rev. C **69**, 024902 (2004).
[20] I. G. Bearden *et al.*, Phys. Rev. Lett. **85**, 2681 (2000).
[21] C. Adler *et al.*, Phys. Rev. Lett. **87**, 262301 (2001).
[22] K. Adcox *et al.*, Phys. Rev. Lett. **88**, 192302 (2002); C. Adler *et al.*, Phys. Rev. Lett. **87**, 082301 (2001).
[23] P. Braun-Munzinger, D. Magestro, K. Redlich, and J. Stachel, Phys. Lett. B **518**, 41 (2001); J. Stachel (private communication).
[24] F. Laue *et al.*, Nucl. Phys. **A698**, 177c (2002).

Double Helicity Asymmetry in Inclusive Midrapidity π^0 Production for Polarized $p + p$ Collisions at $\sqrt{s} = 200$ GeV

S. S. Adler,[5] S. Afanasiev,[20] C. Aidala,[10] N. N. Ajitanand,[44] Y. Akiba,[21,40] A. Al-Jamel,[35] J. Alexander,[44] K. Aoki,[25] L. Aphecetche,[46] R. Armendariz,[35] S. H. Aronson,[5] R. Averbeck,[45] T. C. Awes,[36] V. Babintsev,[17] A. Baldisseri,[11] K. N. Barish,[6] P. D. Barnes,[28] B. Bassalleck,[34] S. Bathe,[6,31] S. Batsouli,[10] V. Baublis,[39] F. Bauer,[6] A. Bazilevsky,[5,41] S. Belikov,[19,17] M. T. Bjorndal,[10] J. G. Boissevain,[28] H. Borel,[11] M. L. Brooks,[28] D. S. Brown,[35] N. Bruner,[34] D. Bucher,[31] H. Buesching,[5,31] V. Bumazhnov,[17] G. Bunce,[5,41] J. M. Burward-Hoy,[28,27] S. Butsyk,[45] X. Camard,[46] P. Chand,[4] W. C. Chang,[2] S. Chernichenko,[17] C. Y. Chi,[10] J. Chiba,[21] M. Chiu,[10] I. J. Choi,[53] R. K. Choudhury,[4] T. Chujo,[5] V. Cianciolo,[36] Y. Cobigo,[11] B. A. Cole,[10] M. P. Comets,[37] P. Constantin,[19] M. Csanád,[13] T. Csörgő,[22] J. P. Cussonneau,[46] D. d'Enterria,[10] K. Das,[14] G. David,[5] F. Deák,[13] H. Delagrange,[46] A. Denisov,[17] A. Deshpande,[41] E. J. Desmond,[5] A. Devismes,[45] O. Dietzsch,[42] J. L. Drachenberg,[1] O. Drapier,[26] A. Drees,[45] A. Durum,[17] D. Dutta,[4] V. Dzhordzhadze,[47] Y. V. Efremenko,[36] H. En'yo,[40,41] B. Espagnon,[37] S. Esumi,[49] D. E. Fields,[34,41] C. Finck,[46] F. Fleuret,[26] S. L. Fokin,[24] B. D. Fox,[41] Z. Fraenkel,[52] J. E. Frantz,[10] A. Franz,[5] A. D. Frawley,[14] Y. Fukao,[25,40,41] S.-Y. Fung,[6] S. Gadrat,[29] M. Germain,[46] A. Glenn,[47] M. Gonin,[26] J. Gosset,[11] Y. Goto,[40,41] R. Granier de Cassagnac,[26] N. Grau,[19] S. V. Greene,[50] M. Grosse Perdekamp,[18,41] H.-Å. Gustafsson,[30] T. Hachiya,[16] J. S. Haggerty,[5] H. Hamagaki,[8] A. G. Hansen,[28] E. P. Hartouni,[27] M. Harvey,[5] K. Hasuko,[40] R. Hayano,[8] X. He,[15] M. Heffner,[27] T. K. Hemmick,[45] J. M. Heuser,[40] P. Hidas,[22] H. Hiejima,[18] J. C. Hill,[19] R. Hobbs,[34] W. Holzmann,[44] K. Homma,[16] B. Hong,[23] A. Hoover,[35] T. Horaguchi,[40,41,48] T. Ichihara,[40,41] V. V. Ikonnikov,[24] K. Imai,[25,40] M. Inaba,[49] M. Inuzuka,[8] D. Isenhower,[1] L. Isenhower,[1] M. Ishihara,[40] M. Issah,[44] A. Isupov,[20] B. V. Jacak,[45] J. Jia,[45] O. Jinnouchi,[40,41] B. M. Johnson,[5] S. C. Johnson,[27] K. S. Joo,[32] D. Jouan,[37] F. Kajihara,[8] S. Kametani,[8,51] N. Kamihara,[40,48] M. Kaneta,[41] J. H. Kang,[53] K. Katou,[51] T. Kawabata,[8] A. Kazantsev,[24] S. Kelly,[9,10] B. Khachaturov,[52] A. Khanzadeev,[39] J. Kikuchi,[51] D. J. Kim,[53] E. Kim,[43] G.-B. Kim,[26] H. J. Kim,[53] E. Kinney,[9] A. Kiss,[13] E. Kistenev,[5] A. Kiyomichi,[40] C. Klein-Boesing,[31] H. Kobayashi,[41] V. Kochetkov,[17] R. Kohara,[16] B. Komkov,[39] M. Konno,[49] D. Kotchetkov,[6] A. Kozlov,[52] P. J. Kroon,[5] C. H. Kuberg,[1] G. J. Kunde,[28] K. Kurita,[40] M. J. Kweon,[23] Y. Kwon,[53] G. S. Kyle,[35] R. Lacey,[44] J. G. Lajoie,[19] Y. Le Bornec,[37] A. Lebedev,[19,24] S. Leckey,[45] D. M. Lee,[28] M. J. Leitch,[28] M. A. L. Leite,[42] X. Li,[7] X. H. Li,[6] H. Lim,[43] A. Litvinenko,[20] M. X. Liu,[28] C. F. Maguire,[50] Y. I. Makdisi,[5] A. Malakhov,[20] V. I. Manko,[24] Y. Mao,[38,40] G. Martinez,[46] H. Masui,[49] F. Matathias,[45] T. Matsumoto,[8,51] M. C. McCain,[1] P. L. McGaughey,[28] Y. Miake,[49] T. E. Miller,[50] A. Milov,[45] S. Mioduszewski,[5] G. C. Mishra,[15] J. T. Mitchell,[5] A. K. Mohanty,[4] D. P. Morrison,[5] J. M. Moss,[28] D. Mukhopadhyay,[52] M. Muniruzzaman,[6] S. Nagamiya,[21] J. L. Nagle,[9,10] T. Nakamura,[16] J. Newby,[47] A. S. Nyanin,[24] J. Nystrand,[30] E. O'Brien,[5] C. A. Ogilvie,[19] H. Ohnishi,[40] I. D. Ojha,[3,50] H. Okada,[25,40] K. Okada,[40,41] A. Oskarsson,[30] I. Otterlund,[30] K. Oyama,[8] K. Ozawa,[8] D. Pal,[52] A. P. T. Palounek,[28] V. Pantuev,[45] V. Papavassiliou,[35] J. Park,[43] W. J. Park,[23] S. F. Pate,[35] H. Pei,[19] V. Penev,[20] J.-C. Peng,[18] H. Pereira,[11] V. Peresedov,[20] A. Pierson,[34] C. Pinkenburg,[5] R. P. Pisani,[5] M. L. Purschke,[5] A. K. Purwar,[45] J. Qualls,[1] J. Rak,[19] I. Ravinovich,[52] K. F. Read,[36,47] M. Reuter,[45] K. Reygers,[31] V. Riabov,[39] Y. Riabov,[39] G. Roche,[29] A. Romana,[26] M. Rosati,[19] S. Rosendahl,[30] P. Rosnet,[29] V. L. Rykov,[40] S. S. Ryu,[53] N. Saito,[25,40,41] T. Sakaguchi,[8,51] S. Sakai,[49] V. Samsonov,[39] L. Sanfratello,[34] R. Santo,[31] H. D. Sato,[25,40] S. Sato,[5,49] S. Sawada,[21] Y. Schutz,[46] V. Semenov,[17] R. Seto,[6] T. K. Shea,[5] I. Shein,[17] T.-A. Shibata,[40,48] K. Shigaki,[16] M. Shimomura,[49] A. Sickles,[45] C. L. Silva,[42] D. Silvermyr,[28] K. S. Sim,[23] A. Soldatov,[17] R. A. Soltz,[27] W. E. Sondheim,[28] S. Sorensen,[47] I. V. Sourikova,[5] F. Staley,[11] P. W. Stankus,[36] E. Stenlund,[30] M. Stepanov,[35] A. Ster,[22] S. P. Stoll,[5] T. Sugitate,[16] J. P. Sullivan,[28] S. Takagi,[49] E. M. Takagui,[42] A. Taketani,[40,41] K. H. Tanaka,[21] Y. Tanaka,[33] K. Tanida,[40] M. J. Tannenbaum,[5] A. Taranenko,[44] P. Tarján,[12] T. L. Thomas,[34] M. Togawa,[25,40] J. Tojo,[40] H. Torii,[25,41] R. S. Towell,[1] V-N. Tram,[26] I. Tserruya,[52] Y. Tsuchimoto,[16] H. Tydesjö,[30] N. Tyurin,[17] T. J. Uam,[32] H. W. van Hecke,[28] J. Velkovska,[5] M. Velkovsky,[45] V. Veszprémi,[12] A. A. Vinogradov,[24] M. A. Volkov,[24] E. Vznuzdaev,[39] X. R. Wang,[15] Y. Watanabe,[40,41] S. N. White,[5] N. Willis,[37] F. K. Wohn,[19] C. L. Woody,[5] W. Xie,[6] A. Yanovich,[17] S. Yokkaichi,[40,41] G. R. Young,[36] I. E. Yushmanov,[24] W. A. Zajc,[10,*] O. Zaudtke,[31] C. Zhang,[10] S. Zhou,[7] J. Zimányi,[22] L. Zolin,[20] and X. Zong[19]

(PHENIX Collaboration)

[1]*Abilene Christian University, Abilene, Texas 79699, USA*
[2]*Institute of Physics, Academia Sinica, Taipei 11529, Taiwan*
[3]*Department of Physics, Banaras Hindu University, Varanasi 221005, India*

 0031-9007/04/93(20)/202002(6)$22.50 © 2004 The American Physical Society

[4]*Bhabha Atomic Research Centre, Bombay 400 085, India*
[5]*Brookhaven National Laboratory, Upton, New York 11973-5000, USA*
[6]*University of California–Riverside, Riverside, California 92521, USA*
[7]*China Institute of Atomic Energy (CIAE), Beijing, People's Republic of China*
[8]*Center for Nuclear Study, Graduate School of Science, University of Tokyo, 7-3-1 Hongo, Bunkyo, Tokyo 113-0033, Japan*
[9]*University of Colorado, Boulder, Colorado 80309, USA*
[10]*Columbia University, New York, New York 10027, USA,*
and Nevis Laboratories, Irvington, New York 10533, USA
[11]*Dapnia, CEA Saclay, F-91191, Gif-sur-Yvette, France*
[12]*Debrecen University, H-4010 Debrecen, Egyetem tér 1, Hungary*
[13]*ELTE, Eötvös Loránd University, H-1117 Budapest, Pázmány P. s. 1/A, Hungary*
[14]*Florida State University, Tallahassee, Florida 32306, USA*
[15]*Georgia State University, Atlanta, Georgia 30303, USA*
[16]*Hiroshima University, Kagamiyama, Higashi-Hiroshima 739-8526, Japan*
[17]*Institute for High Energy Physics (IHEP), Protvino, Russia*
[18]*University of Illinois at Urbana-Champaign, Urbana, Illinois 61801, USA*
[19]*Iowa State University, Ames, Iowa 50011, USA*
[20]*Joint Institute for Nuclear Research, 141980 Dubna, Moscow Region, Russia*
[21]*KEK, High Energy Accelerator Research Organization, Tsukuba-shi, Ibaraki-ken 305-0801, Japan*
[22]*KFKI Research Institute for Particle and Nuclear Physics (RMKI), H-1525 Budapest 114, POBox 49, Hungary*
[23]*Korea University, Seoul, 136-701, Korea*
[24]*Russian Research Center "Kurchatov Institute," Moscow, Russia*
[25]*Kyoto University, Kyoto 606-8394, Japan*
[26]*Laboratoire Leprince-Ringuet, Ecole Polytechnique, CNRS-IN2P3, Route de Saclay, F-91128, Palaiseau, France*
[27]*Lawrence Livermore National Laboratory, Livermore, California 94550, USA*
[28]*Los Alamos National Laboratory, Los Alamos, New Mexico 87545, USA*
[29]*LPC, Université Blaise Pascal, CNRS-IN2P3, Clermont-Fd, 63177 Aubiere Cedex, France*
[30]*Department of Physics, Lund University, Box 118, SE-221 00 Lund, Sweden*
[31]*Institut fuer Kernphysik, University of Muenster, D-48149 Muenster, Germany*
[32]*Myongji University, Yongin, Kyonggido 449-728, Korea*
[33]*Nagasaki Institute of Applied Science, Nagasaki-shi, Nagasaki 851-0193, Japan*
[34]*University of New Mexico, Albuquerque, New Mexico 87131, USA*
[35]*New Mexico State University, Las Cruces, New Mexico 88003, USA*
[36]*Oak Ridge National Laboratory, Oak Ridge, Tennessee 37831, USA*
[37]*IPN-Orsay, Universite Paris Sud, CNRS-IN2P3, BP1, F-91406, Orsay, France*
[38]*Peking University, Beijing, People's Republic of China*
[39]*PNPI, Petersburg Nuclear Physics Institute, Gatchina, Russia*
[40]*RIKEN (The Institute of Physical and Chemical Research), Wako, Saitama 351-0198, Japan*
[41]*RIKEN BNL Research Center, Brookhaven National Laboratory, Upton, New York 11973-5000, USA*
[42]*Universidade de São Paulo, Instituto de Física, Caixa Postal 66318, São Paulo CEP05315-970, Brazil*
[43]*System Electronics Laboratory, Seoul National University, Seoul, South Korea*
[44]*Chemistry Department, Stony Brook University, SUNY, Stony Brook, New York 11794-3400, USA*
[45]*Department of Physics and Astronomy, Stony Brook University, SUNY, Stony Brook, New York 11794, USA*
[46]*SUBATECH (Ecole des Mines de Nantes, CNRS-IN2P3, Université de Nantes), BP 20722-44307, Nantes, France*
[47]*University of Tennessee, Knoxville, Tennessee 37996, USA*
[48]*Department of Physics, Tokyo Institute of Technology, Tokyo, 152-8551, Japan*
[49]*Institute of Physics, University of Tsukuba, Tsukuba, Ibaraki 305, Japan*
[50]*Vanderbilt University, Nashville, Tennessee 37235, USA*
[51]*Waseda University, Advanced Research Institute for Science and Engineering, 17 Kikui-cho, Shinjuku-ku, Tokyo 162-0044, Japan*
[52]*Weizmann Institute, Rehovot 76100, Israel*
[53]*Yonsei University, IPAP, Seoul 120-749, Korea*
(Received 21 April 2004; published 11 November 2004)

We present a measurement of the double longitudinal spin asymmetry in inclusive π^0 production in polarized proton-proton collisions at $\sqrt{s} = 200$ GeV. The data were taken at the Relativistic Heavy Ion Collider with average beam polarizations of 0.27. The measurements are the first in a program to study the longitudinal spin structure of the proton, using strongly interacting probes, at collider energies. The asymmetry is presented for transverse momenta 1–5 GeV/c at midrapidity, where next-to-leading-order perturbative quantum chromodynamic (NLO pQCD) calculations well describe the unpolarized cross section. The observed asymmetry is small and is compared to a NLO pQCD calculation with a range of polarized gluon distributions.

DOI: 10.1103/PhysRevLett.93.202002 PACS numbers: 13.85.Ni, 13.88.+e, 21.10.Hw, 25.40.Fq

From polarized lepton-nucleon deep inelastic scattering (DIS) experiments over the past 20 years it is known that only ~25% of the proton spin can be attributed to the spins of the quarks and antiquarks [1]. The rest of the proton spin must hence be carried by the gluons and orbital angular momentum. DIS experiments have constrained the possible gluon polarization in the proton through the measurement of scaling violation in inclusive polarized scattering [2], and through semi-inclusive measurements of two hadrons to utilize the photon-gluon fusion process [3]. A fixed target experiment at Fermilab first presented a measurement with strongly interacting probes [4]. The reach of these measurements was limited, due to the low energy available for fixed target experiments. Presently, the gluon contribution to the proton spin is largely unknown.

The polarized proton collisions at the Relativistic Heavy Ion Collider (RHIC) provide a new laboratory to study the proton spin structure with strongly interacting probes. The PHENIX experiment has reported the unpolarized cross section for π^0 production at midrapidity for $p_T = 1$–14 GeV/c, which is described well by next-to-leading-order perturbative QCD (NLO pQCD) calculations over 8 orders of magnitude [5]. In this Letter we report the first results on the double spin asymmetry A_{LL} for inclusive π^0 production at midrapidity in longitudinally polarized proton-proton collisions corresponding to $0.22\ \mathrm{pb}^{-1}$ integrated luminosity with the PHENIX detector.

In perturbative QCD A_{LL} is directly sensitive to the polarized gluon distribution function in the proton through gluon-gluon and gluon-quark subprocesses [6,7].

The double spin asymmetry in π^0 production is given by

$$A_{LL}^{\pi^0} = \frac{\sigma_{++} - \sigma_{+-}}{\sigma_{++} + \sigma_{+-}}, \tag{1}$$

where σ_{++} (σ_{+-}) is the cross section of the reaction when two colliding particles have the same (opposite) helicity. Here we neglect the parity violating difference in cross section between $(++) \leftrightarrow (--)$ and $(+-) \leftrightarrow (-+)$ beam helicity configurations. Since the cross section can be obtained by dividing the experimental yield (N) by the integrated luminosity (L), A_{LL} is expressed as

$$A_{LL} = \frac{1}{|\langle P_B P_Y \rangle|} \frac{N_{++} - R N_{+-}}{N_{++} + R N_{+-}}; \qquad R = \frac{L_{++}}{L_{+-}}, \tag{2}$$

where $P_{Y(B)}$ are the polarizations of the RHIC "yellow" ("blue") beams, and R is the ratio of luminosities of protons colliding with like to unlike helicities.

For the 2002–2003 RHIC run, 55 bunches of polarized protons, typically 5×10^{10} protons per bunch, were loaded into each of the yellow and blue accelerator/storage rings of RHIC and accelerated to 100 GeV. The bunch lengths and separations were ~1 and 213 ns, respectively. The beam polarization sign for each bunch was prepared independently at the source, with the successive bunches in one ring alternating in polarization sign, and with successive pairs of bunches in the other ring alternating in sign. The locations of the bunches were identified relative to a RHIC timing clock. In this way, the experiments collected data from collisions with all four combinations of blue-yellow ring beam polarization signs simultaneously.

The stable direction of the proton spin in RHIC is vertical, but the region around the PHENIX experiment includes sets of magnets (spin rotators) to rotate the spin to the longitudinal direction at the collision point, and then back to vertical after the interaction point, in order to provide collisions with longitudinal polarization, and to maintain the required vertical polarization around RHIC. The RHIC polarimeters measure the transverse beam polarization away from the interaction points, independent of the operation of the spin rotators.

The transverse beam polarization was measured in RHIC independently in each beam using proton-carbon elastic scattering in the Coulomb nuclear interference region [8]. The analyzing power A_N^{pC} was measured for 22 GeV beam energy, $A_N^{pC}(22)$, to ±30% [9]. The energy dependence of the analyzing power over the RHIC energies is expected to be small, <10% [10]. For the results reported here, we have used the same analyzing power at 100 GeV as at 22 GeV, and 10% is added in quadrature to the relative uncertainty for $A_N^{pC}(22)$ to give a ±32% uncertainty for $A_N^{pC}(100)$. With these assumptions, the average polarization in the analyzed data set in this paper was $\sqrt{\langle P_B P_Y \rangle} = 0.27 \pm 1\%(\mathrm{stat}) \pm 10\%(\mathrm{syst}) \pm 32\%(A_N^{pC}\ \mathrm{syst})$.

Local polarimeters, sensitive to the transverse polarization at collision, were used to set up the spin rotators, and to monitor the beam polarization direction at the PHENIX experiment. The local polarimeters utilized a transverse single-spin asymmetry in neutron production in p-p collisions at $\sqrt{s} = 200$ GeV [11]. For vertically polarized beam a left-right asymmetry is observed for neutrons produced at very forward angles, with no asymmetry for production at very backward angles. A fully longitudinally polarized beam produces no asymmetry.

Neutrons with $E_n > 20$ GeV and production angle $0.3 < \theta_n < 2.5$ mrad were observed by two hadronic calorimeters located ±18 m from the interaction point [zero degree calorimeter (ZDC) [12]]. Scintillator hodoscopes at 1.7 interaction length provided the neutron position at the ZDC, and thus the neutron production angle and azimuthal angle $\phi = \arctan(x/y)$ with $\hat{y}$ vertically upward. The $\hat{x}$ axis forms a right-handed coordinate system with the $\hat{z}$ axis defined by the beam direction for forward

production. The single-spin asymmetry ϵ was calculated versus azimuth, from the four rates $N_{\uparrow,\phi}$, $N_{\uparrow,\phi+\pi}$, $N_{\downarrow,\phi}$, $N_{\downarrow,\phi+\pi}$, using the geometric mean [13]. This method largely cancels differences in luminosity between $\uparrow$ and $\downarrow$ polarization collisions and between detector acceptance differences at ϕ and $\phi + \pi$. Figure 1 shows the observed asymmetry, for the spin rotators off and on, for the blue and yellow beams. With the spin rotators off, a left-right asymmetry is observed from the vertically polarized beam. With the spin rotators on, the measured transverse polarization, averaged over the run, was $\langle P_{Bx}\rangle = 0.033 \pm 0.019$, $\langle P_{By}\rangle = 0.008 \pm 0.020$, $\langle P_{Yx}\rangle = -0.020 \pm 0.013$, and $\langle P_{Yy}\rangle = 0.054 \pm 0.017$, out of $\langle P\rangle = 0.27$. The double spin transverse polarization was $\langle P_{Bx}P_{Yx}\rangle = (0.4 \pm 1.1) \times 10^{-3}$ and $\langle P_{By}P_{Yy}\rangle = (-0.2 \pm 0.8) \times 10^{-3}$, compared to $\langle P_B P_Y\rangle = 0.07$. Therefore, with the spin rotators on, the transverse asymmetry is greatly reduced, indicating a high degree of longitudinal polarization: the longitudinal fraction of the beam polarization was 0.99 and 0.98 for the blue and yellow beams, respectively.

A separate run with the spin rotators set to give radial polarization confirmed the direction of the polarization for each beam.

Collisions in PHENIX are defined by the coincidence of signals in two beam-beam counters (BBC) [14] located ± 1.44 m from the nominal interaction point and subtending a pseudorapidity range $\pm(3.0$–$3.9)$ with full azimuthal coverage. The BBCs select about half of the inelastic proton-proton collisions [5]. The vertex was reconstructed from the time difference of the hits in the two BBCs. The collision vertex was required to be within 30 cm of the nominal interaction point. Events satisfying this condition constitute the minimum bias (MB) trigger, which was used for relative luminosity measurements.

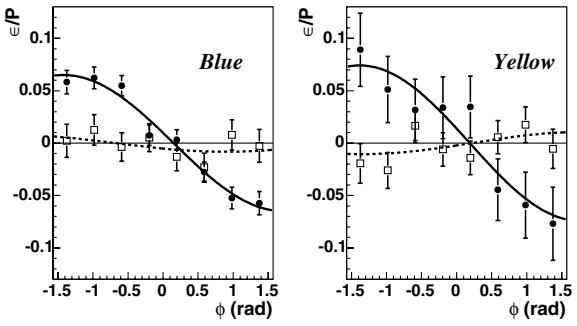

FIG. 1. The raw asymmetry normalized by the beam polarization ϵ/P as a function of azimuthal angle ϕ, for forward neutron production. The solid points and curve correspond to the spin rotators off (transverse polarization) and the open points and dashed curve correspond to the spin rotators on (longitudinal polarization). Curves are sine function fits to the data, representing possible transverse polarization. The data are for special runs used to set up the spin rotators, where the blue (yellow) polarization was 0.24 and 0.33 (0.08 and 0.28), for spin rotators off and on, correspondingly.

A coincidence of the two ZDCs was used to estimate the possible bias in the relative luminosity measurement from the BBCs. This was done by comparing the accumulated number of triggers in the ZDCs and BBCs for each bunch and each fill. The accuracy of relative luminosity measurements δR [Eq. (2)] was estimated to be 2.5×10^{-4}, which for the average beam polarization of 0.27 translated to $\delta A_{LL} = 1.8 \times 10^{-3}$, and, on the same uncertainty level, confirmed no A_{LL} asymmetry of BBC triggers relative to ZDC. The ratio R averaged over the data sample used in the analysis was within 0.5% of unity.

Neutral pions were reconstructed from the $\pi^0 \to \gamma\gamma$ decays using finely granulated ($\Delta\phi \times \Delta\eta \sim 0.01 \times 0.01$) electromagnetic calorimeters (EMCal) [15], which consisted of two subsystems: a lead scintillator (PbSc) and a lead glass (PbGl) calorimeter covering three quarters and one quarter of the EMCal acceptance, respectively. Located at a radial distance of $\sim$5 m from the beam line, the EMCal covered the pseudorapidity range of $|\eta| < 0.35$ and two azimuthal angle intervals of $\Delta\phi \approx 90°$ separated by $\phi \approx 70°$ (nearly back-to-back).

High p_T π^0's were collected using coincidences between a MB trigger and an EMCal-based high p_T photon trigger [5]. The trigger efficiency for π^0's varied from 8% in the 1–2 GeV/c p_T bin to 90% in the 4–5 GeV/c p_T bin.

The π^0 reconstruction and photon identification cuts were optimized to minimize the background contribution under the π^0 peak in the invariant mass distribution while keeping the π^0 efficiency high. For photon identification we used the shower shape and the time of flight measured by the EMCal, and charge veto cuts. The charge veto was set for those EMCal clusters associated with hit(s) in the pad chamber [16], which was located $\sim$20 cm in front of the EMCal surface. In order to avoid the effects of electronic noise and to suppress the very low energy background, only clusters with energy greater than 0.1 GeV in PbSc and 0.2 GeV in PbGl were used in the analysis.

The π^0 yield was extracted by integrating the two photon invariant mass spectrum over a ± 25 MeV/c^2 region around the π^0 mass (signal region). The EMCal resolution was such that the widths of the π^0 mass peaks varied from 12 MeV/c^2 in the 1–2 GeV/c p_T bin to 9.5 MeV/c^2 in the 4–5 GeV/c p_T bin, in both PbSc and PbGl. In the p_T range of 1 to 5 GeV/c, 4×10^6 π^0 candidates were collected. The background contribution (combinatorial + hadronic) under the π^0 peak r varied from 27% in the 1–2 GeV/c bin to 8% in the 4–5 GeV/c bin. The π^0 reconstruction efficiency due to photon identification cuts varied from 84% in the lowest p_T bin to 93% in the highest p_T bin.

The asymmetry of the background in the signal region A_{LL}^{BG} was evaluated using the asymmetry calculated from the data in $\gamma\gamma$ mass regions 50 MeV/c^2 wide on either side of the π^0 peak, centered at masses 75 and

195 MeV/c^2. The measured π^0 asymmetry $A_{LL}^{\rm raw}$ was corrected for the contribution of background using

$$A_{LL}^{\pi^0} = \frac{A_{LL}^{\rm raw} - rA_{LL}^{BG}}{1-r}, \qquad \sigma_{A_{LL}^{\pi^0}} = \frac{\sqrt{\sigma^2_{A_{LL}^{\rm raw}} + r^2\sigma^2_{A_{LL}^{BG}}}}{1-r}. \quad (3)$$

The spin asymmetry for each beam fill [17] $A_{LL}^{\rm fill}$ was calculated using Eq. (2). For the $A_{LL}^{\rm fill}$ error evaluation, we considered only the N_{++} and N_{+-} statistical errors. The resulting A_{LL} was obtained after fitting a constant to all $A_{LL}^{\rm fill}$'s. The fit $\chi^2_{\rm fit}$ and a "bunch shuffling" technique were used to evaluate the uncertainties assigned to A_{LL}. In each bunch shuffling we randomly assigned the helicity sign to every bunch crossing, keeping the balance between the number of bunches with correctly and inversely assigned helicities, so that the average polarization for each shuffled sample was nearly zero, and recalculated A_{LL}. The widths of the distributions of A_{LL} values obtained in all bunch shuffles were consistent with errors assigned to A_{LL} indicating that all noncorrelated bunch-to-bunch and fill-to-fill systematic errors were much smaller than the π^0 yield statistical errors.

A number of systematic checks, including variation of photon identification criteria and mass window range for π^0's and background, were performed to look for possible systematic effects on the measured A_{LL} values. None were found.

The double spin asymmetries between $(++)$ and $(--)$ and between $(+-)$ and $(-+)$ helicity configurations, as well as the single-spin asymmetries for each polarized beam ($A_L = -\frac{\sigma_+ - \sigma_-}{\sigma_+ + \sigma_-}$) were evaluated. These measure parity violating asymmetries, if any. All of these asymmetries were consistent with zero.

The results are presented in Table I and Fig. 2. Systematic uncertainties for the asymmetry measurements are negligible. A total scale uncertainty of $\pm 65\%$, from the correlated polarization analyzing power uncertainty δA_N^{pC} for the two beams and the uncorrelated measurement uncertainties, is not shown.

Two theoretical curves based on NLO pQCD are shown in Fig. 2, representing different assumptions for the gluon polarization, one using the best global fit to inclusive DIS data (GRSV-std), and another one using a gluon polarized distribution equal to the unpolarized distribution at the input scale of $Q^2 = 0.6$ GeV^2 (GRSV-max) [6,18]. The gluon polarization contributes to A_{LL} through gluon-gluon and gluon-quark subprocesses, with the gluon-gluon contribution significantly larger at midrapidity and for the estimated gluon momentum fraction for these results $x \approx 0.03$–0.1 [19]. Thus, the asymmetry A_{LL} is approximately proportional to the square of the gluon polarization and a negative value of A_{LL} is not expected [20]. The results are consistent with zero or small gluon polarization, with a confidence level (C.L.) of 16%–20% for GRSV-std, for the range in polarization uncertainty of the measurement. The results are less consistent with a large gluon polarization, with C.L. = 0.02%–5% for GRSV-max.

We emphasize the following points: (1) The lowest p_T point reported here can have a significant contribution from soft physics, since the agreement of the NLO pQCD calculation with the measured cross section [5] can only be checked to within the uncertainties of the calculation, estimated to be a factor two at this p_T [6,20]. If the soft physics is represented by an exponential falloff in p_T (e^{-6p_T} is typically used [21]), the soft physics contribution to the higher p_T data is small ($< 10\%$ to the 2–3 GeV/c p_T bin if we assume equal soft/hard contributions to the lowest bin). If we consider only the highest three p_T bins, the C.L. = 58%–67% for GRSV-std, and C.L. = 0.4%–29% for GRSV-max. (2) These confidence levels do not include a theoretical uncertainty, from either scales or from choices of parton distribution functions and fragmentation function. The comparisons are made for NLO pQCD, rather than extracting a leading-order estimate of the gluon polarization. (3) The range of theory curves in Fig. 2 reflects the uncertainty on gluon polarization from inclusive DIS measurements [18,22–24].

In summary, we have presented a new technique for determining the polarized gluon distribution using polarized protons acting as strongly interacting probes, at

TABLE I. Double and single-spin asymmetries for four p_T bins with mean $p_T(\pi^0)$ 1.59, 2.39, 3.37, and 4.38 GeV/c.

p_T (GeV/c)	$A_{LL}^{\rm raw}$ (10^{-2})	A_{LL}^{BG} (10^{-2})	$A_{LL}^{\pi^0}$ (10^{-2})	$A_L^{\pi^0}$ (10^{-2})
1–2	-1.5 ± 0.9	1.6 ± 1.4	-2.7 ± 1.3	-0.2 ± 0.3
2–3	-1.5 ± 1.1	-3.0 ± 2.4	-1.3 ± 1.3	-0.1 ± 0.3
3–4	-1.8 ± 2.5	-2.4 ± 6.8	-1.7 ± 2.8	-0.3 ± 0.6
4–5	2.6 ± 5.7	24 ± 17	0.7 ± 6.2	-1.0 ± 1.2

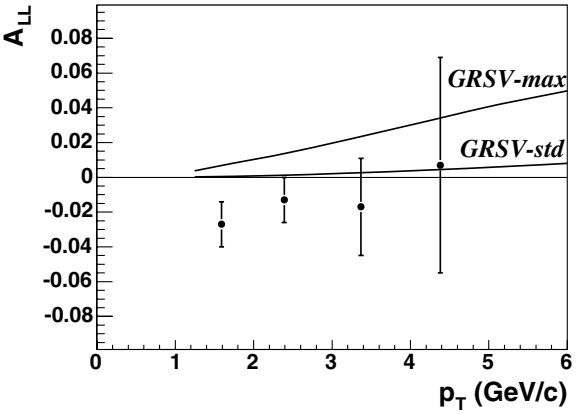

FIG. 2. $A_{LL}^{\pi^0}$ versus mean p_T of π^0's in each bin. A scale uncertainty of $\pm 65\%$ is not included. Two theoretical calculations based on NLO pQCD are also shown for comparison with the data (see text for details).

collider energies. The reported results of the double spin helicity asymmetries for π^0 production begin to probe the proton spin structure in the perturbative QCD regime with a sensitivity comparable to the polarized inclusive deep inelastic scattering data. The observed asymmetry is small and consistent with a small gluon polarization.

We thank the staff of the Collider-Accelerator Department, Magnet Division, and Physics Department at BNL and the RHIC polarimetry group for their vital contributions. We thank W. Vogelsang for informative discussions. We acknowledge support from the Department of Energy and NSF (U.S.A.), MEXT and JSPS (Japan), CNPq and FAPESP (Brazil), NSFC (China), IN2P3/CNRS, CEA, and ARMINES (France), BMBF, DAAD, and AvH (Germany), OTKA (Hungary), DAE and DST (India), ISF (Israel), KRF and CHEP (Korea), RAS, RMAE, and RMS (Russia), VR and KAW (Sweden), U.S. CRDF for the FSU, U.S.-Hungarian NSF-OTKA-MTA, and U.S.-Israel BSF.

*PHENIX Spokesperson.
Electronic address: zajc@nevis.columbia.edu

[1] J. Ashman *et al.*, Phys. Lett. B **206**, 364 (1988); Nucl. Phys. **B328**, 1 (1989); E. Hughes and R. Voss, Annu. Rev. Nucl. Part. Sci. **49**, 303 (1999).
[2] B. Adeva *et al.*, Phys. Rev. D **58**, 112002 (1998); P. L. Anthony *et al.*, Phys. Lett. B **493**, 19 (2000).
[3] A. Airapetian *et al.*, Phys. Rev. Lett. **84**, 2584 (2000); B. Adeva *et al.*, Phys. Rev. D **70**, 012002 (2004).
[4] D. L. Adams *et al.*, Phys. Lett. B **261**, 197 (1991).
[5] S. S. Adler *et al.*, Phys. Rev. Lett. **91**, 241803 (2003).
[6] B. Jäger, A. Schafer, M. Stratmann, and W. Vogelsang, Phys. Rev. D **67**, 054005 (2003).
[7] B. Jäger *et al.*, in the Proceedings of the 8th Workshop on High Energy Physics Phenomenology (WHEPP 8), Bombay, India, 2004 (to be published); hep-ph/0405069.
[8] O. Jinnouchi *et al.*, RHIC/CAD Accelerator Physics Note 171, 2004.
[9] J. Tojo *et al.*, Phys. Rev. Lett. **89**, 052302 (2002).
[10] T. L. Trueman, hep-ph/0203013.
[11] A. Bazilevsky *et al.*, in *SPIN 2002: 15th International Spin Physics Symposium and Workshop on Polarized Electron Sources and Polarimeters*, AIP Conf. Proc. 675 (AIP, New York, 2003), pp. 584–588.
[12] C. Adler *et al.*, Nucl. Instrum. Methods Phys. Res., Sect. A **470**, 488 (2001).
[13] G. G. Ohlsen and P. W. Keaton, Jr., Nucl. Instrum. Methods **109**, 41 (1973).
[14] M. Allen *et al.*, Nucl. Instrum. Methods Phys. Res., Sect. A **499**, 549 (2003).
[15] L. Aphecetche *et al.*, Nucl. Instrum. Methods Phys. Res., Sect. A **499**, 521 (2003).
[16] K. Adcox *et al.*, Nucl. Instrum. Methods Phys. Res., Sect. A **499**, 489 (2003).
[17] Each fill is characterized by a constant polarization of the beams.
[18] M. Glück, E. Reya, M. Stratmann, and W. Vogelsang, Phys. Rev. D **63**, 094005 (2001).
[19] B. Jäger, M. Stratmann, and W. Vogelsang, Phys. Rev. D **70**, 034010 (2004).
[20] B. Jäger, M. Stratmann, S. Kretzer, and W. Vogelsang, Phys. Rev. Lett. **92**, 121803 (2004).
[21] S. M. Berman, J. D. Bjorken, and J. B. Kogut, Phys. Rev. D **4**, 3388 (1971).
[22] J. Blümlein and H. Böttcher, Nucl. Phys. **B636**, 225 (2002).
[23] M. Hirai, S. Kumano, and N. Saito, Phys. Rev. D **69**, 054021 (2004).
[24] M. Hirai and K. Sudoh, hep-ph/0403102; RIKEN Report No. RIKEN-AF-NP-456.

Bose-Einstein Correlations of Charged Pion Pairs in Au + Au Collisions at $\sqrt{s_{NN}} = 200$ GeV

S. S. Adler,[5] S. Afanasiev,[17] C. Aidala,[5] N. N. Ajitanand,[43] Y. Akiba,[20,38] J. Alexander,[43] R. Amirikas,[12] L. Aphecetche,[45] S. H. Aronson,[5] R. Averbeck,[44] T. C. Awes,[35] R. Azmoun,[44] V. Babintsev,[15] A. Baldisseri,[10] K. N. Barish,[6] P. D. Barnes,[27] B. Bassalleck,[33] S. Bathe,[30] S. Batsouli,[9] V. Baublis,[37] A. Bazilevsky,[39,15] S. Belikov,[16,15] Y. Berdnikov,[40] S. Bhagavatula,[16] J. G. Boissevain,[27] H. Borel,[10] S. Borenstein,[25] M. L. Brooks,[27] D. S. Brown,[34] N. Bruner,[33] D. Bucher,[30] H. Buesching,[30] V. Bumazhnov,[15] G. Bunce,[5,39] J. M. Burward-Hoy,[26,44] S. Butsyk,[44] X. Camard,[45] J.-S. Chai,[18] P. Chand,[4] W. C. Chang,[2] S. Chernichenko,[15] C. Y. Chi,[9] J. Chiba,[20] M. Chiu,[9] I. J. Choi,[52] J. Choi,[19] R. K. Choudhury,[4] T. Chujo,[5] V. Cianciolo,[35] Y. Cobigo,[10] B. A. Cole,[9] P. Constantin,[16] D. G. d'Enterria,[45] G. David,[5] H. Delagrange,[45] A. Denisov,[15] A. Deshpande,[39] E. J. Desmond,[5] O. Dietzsch,[41] O. Drapier,[25] A. Drees,[44] R. du Rietz,[29] A. Durum,[15] D. Dutta,[4] Y. V. Efremenko,[35] K. El Chenawi,[49] A. Enokizono,[14] H. En'yo,[38,39] S. Esumi,[48] L. Ewell,[5] D. E. Fields,[33,39] F. Fleuret,[25] S. L. Fokin,[23] B. D. Fox,[39] Z. Fraenkel,[51] J. E. Frantz,[9] A. Franz,[5] A. D. Frawley,[12] S.-Y. Fung,[6] S. Garpman,[29,*] T. K. Ghosh,[49] A. Glenn,[46] G. Gogiberidze,[46] M. Gonin,[25] J. Gosset,[10] Y. Goto,[39] R. Granier de Cassagnac,[25] N. Grau,[16] S. V. Greene,[49] M. Grosse Perdekamp,[39] W. Guryn,[5] H.-Å. Gustafsson,[29] T. Hachiya,[14] J. S. Haggerty,[5] H. Hamagaki,[8] A. G. Hansen,[27] E. P. Hartouni,[26] M. Harvey,[5] R. Hayano,[8] X. He,[13] M. Heffner,[26] T. K. Hemmick,[44] J. M. Heuser,[44] M. Hibino,[50] J. C. Hill,[16] W. Holzmann,[43] K. Homma,[14] B. Hong,[22] A. Hoover,[34] T. Ichihara,[38,39] V. V. Ikonnikov,[23] K. Imai,[24,38] D. Isenhower,[1] M. Ishihara,[38] M. Issah,[43] A. Isupov,[17] B. V. Jacak,[44] W. Y. Jang,[22] Y. Jeong,[19] J. Jia,[44] O. Jinnouchi,[38] B. M. Johnson,[5] S. C. Johnson,[26] K. S. Joo,[31] D. Jouan,[36] S. Kametani,[8,50] N. Kamihara,[47,38] J. H. Kang,[52] S. S. Kapoor,[4] K. Katou,[50] S. Kelly,[9] B. Khachaturov,[51] A. Khanzadeev,[37] J. Kikuchi,[50] D. H. Kim,[31] D. J. Kim,[52] D. W. Kim,[19] E. Kim,[42] G.-B. Kim,[25] H. J. Kim,[52] E. Kistenev,[5] A. Kiyomichi,[48] K. Kiyoyama,[32] C. Klein-Boesing,[30] H. Kobayashi,[38,39] L. Kochenda,[37] V. Kochetkov,[15] D. Koehler,[33] T. Kohama,[14] M. Kopytine,[44] D. Kotchetkov,[6] A. Kozlov,[51] P. J. Kroon,[5] C. H. Kuberg,[1,27] K. Kurita,[39] Y. Kuroki,[48] M. J. Kweon,[22] Y. Kwon,[52] G. S. Kyle,[34] R. Lacey,[43] V. Ladygin,[17] J. G. Lajoie,[16] A. Lebedev,[16,23] S. Leckey,[44] D. M. Lee,[27] S. Lee,[19] M. J. Leitch,[27] X. H. Li,[6] H. Lim,[42] A. Litvinenko,[17] M. X. Liu,[27] Y. Liu,[36] C. F. Maguire,[49] Y. I. Makdisi,[5] A. Malakhov,[17] V. I. Manko,[23] Y. Mao,[7,38] G. Martinez,[45] M. D. Marx,[44] H. Masui,[48] F. Matathias,[44] T. Matsumoto,[8,50] P. L. McGaughey,[27] E. Melnikov,[15] F. Messer,[44] Y. Miake,[48] J. Milan,[43] T. E. Miller,[49] A. Milov,[44,51] S. Mioduszewski,[5] R. E. Mischke,[27] G. C. Mishra,[13] J. T. Mitchell,[5] A. K. Mohanty,[4] D. P. Morrison,[5] J. M. Moss,[27] F. Mühlbacher,[44] D. Mukhopadhyay,[51] M. Muniruzzaman,[6] J. Murata,[38,39] S. Nagamiya,[20] J. L. Nagle,[9] T. Nakamura,[14] B. K. Nandi,[6] M. Nara,[48] J. Newby,[46] P. Nilsson,[29] A. S. Nyanin,[23] J. Nystrand,[29] E. O'Brien,[5] C. A. Ogilvie,[16] H. Ohnishi,[5,38] I. D. Ojha,[49,3] K. Okada,[38] M. Ono,[48] V. Onuchin,[15] A. Oskarsson,[29] I. Otterlund,[29] K. Oyama,[8] K. Ozawa,[8] D. Pal,[51] A. P. T. Palounek,[27] V. S. Pantuev,[44] V. Papavassiliou,[34] J. Park,[42] A. Parmar,[33] S. F. Pate,[34] T. Peitzmann,[30] J.-C. Peng,[27] V. Peresedov,[17] C. Pinkenburg,[5] R. P. Pisani,[5] F. Plasil,[35] M. L. Purschke,[5] A. K. Purwar,[44] J. Rak,[16] I. Ravinovich,[51] K. F. Read,[35,46] M. Reuter,[44] K. Reygers,[30] V. Riabov,[37,40] Y. Riabov,[37] G. Roche,[28] A. Romana,[25] M. Rosati,[16] P. Rosnet,[28] S. S. Ryu,[52] M. E. Sadler,[1] N. Saito,[38,39] T. Sakaguchi,[8,50] M. Sakai,[32] S. Sakai,[48] V. Samsonov,[37] L. Sanfratello,[33] R. Santo,[30] H. D. Sato,[24,38] S. Sato,[5,48] S. Sawada,[20] Y. Schutz,[45] V. Semenov,[15] R. Seto,[6] M. R. Shaw,[1,27] T. K. Shea,[5] T.-A. Shibata,[47,38] K. Shigaki,[14,20] T. Shiina,[27] C. L. Silva,[41] D. Silvermyr,[27,29] K. S. Sim,[22] C. P. Singh,[3] V. Singh,[3] M. Sivertz,[5] A. Soldatov,[15] R. A. Soltz,[26] W. E. Sondheim,[27] S. P. Sorensen,[46] I. V. Sourikova,[5] F. Staley,[10] P. W. Stankus,[35] E. Stenlund,[29] M. Stepanov,[34] A. Ster,[21] S. P. Stoll,[5] T. Sugitate,[14] J. P. Sullivan,[27] E. M. Takagui,[41] A. Taketani,[38,39] M. Tamai,[50] K. H. Tanaka,[20] Y. Tanaka,[32] K. Tanida,[38] M. J. Tannenbaum,[5] P. Tarján,[11] J. D. Tepe,[1,27] T. L. Thomas,[33] J. Tojo,[24,38] H. Torii,[24,38] R. S. Towell,[1] I. Tserruya,[51] H. Tsuruoka,[48] S. K. Tuli,[3] H. Tydesjö,[29] N. Tyurin,[15] H. W. van Hecke,[27] J. Velkovska,[5,44] M. Velkovsky,[44] L. Villatte,[46] A. A. Vinogradov,[23] M. A. Volkov,[23] E. Vznuzdaev,[37] X. R. Wang,[13] Y. Watanabe,[38,39] S. N. White,[5] F. K. Wohn,[16] C. L. Woody,[5] W. Xie,[6] Y. Yang,[7] A. Yanovich,[15] S. Yokkaichi,[38,39] G. R. Young,[35] I. E. Yushmanov,[23] W. A. Zajc,[9,†] C. Zhang,[9] S. Zhou,[7] S. J. Zhou,[51] and L. Zolin[17]

(PHENIX Collaboration)

[1]*Abilene Christian University, Abilene, Texas 79699, USA*
[2]*Institute of Physics, Academia Sinica, Taipei 11529, Taiwan*
[3]*Department of Physics, Banaras Hindu University, Varanasi 221005, India*
[4]*Bhabha Atomic Research Centre, Bombay 400 085, India*

 0031-9007/04/93(15)/152302(6)$22.50 © 2004 The American Physical Society

[5]Brookhaven National Laboratory, Upton, New York 11973-5000, USA
[6]University of California–Riverside, Riverside, California 92521, USA
[7]China Institute of Atomic Energy (CIAE), Beijing, People's Republic of China
[8]Center for Nuclear Study, Graduate School of Science, University of Tokyo, 7-3-1 Hongo, Bunkyo, Tokyo 113-0033, Japan
[9]Columbia University, New York, New York 10027 and Nevis Laboratories, Irvington, New York 10533, USA
[10]Dapnia, CEA Saclay, F-91191, Gif-sur-Yvette, France
[11]Debrecen University, H-4010 Debrecen, Egyetem tér 1, Hungary
[12]Florida State University, Tallahassee, Florida 32306, USA
[13]Georgia State University, Atlanta, Georgia 30303, USA
[14]Hiroshima University, Kagamiyama, Higashi-Hiroshima 739-8526, Japan
[15]Institute for High Energy Physics (IHEP), Protvino, Russia
[16]Iowa State University, Ames, Iowa 50011, USA
[17]Joint Institute for Nuclear Research, 141980 Dubna, Moscow Region, Russia
[18]KAERI, Cyclotron Application Laboratory, Seoul, South Korea
[19]Kangnung National University, Kangnung 210-702, South Korea
[20]KEK, High Energy Accelerator Research Organization, Tsukuba-shi, Ibaraki-ken 305-0801, Japan
[21]KFKI Research Institute for Particle and Nuclear Physics (RMKI), H-1525 Budapest 114, POBox 49, Hungary
[22]Korea University, Seoul, 136-701, Korea
[23]Russian Research Center "Kurchatov Institute," Moscow, Russia
[24]Kyoto University, Kyoto 606, Japan
[25]Laboratoire Leprince-Ringuet, Ecole Polytechnique, CNRS-IN2P3, Route de Saclay, F-91128, Palaiseau, France
[26]Lawrence Livermore National Laboratory, Livermore, California 94550, USA
[27]Los Alamos National Laboratory, Los Alamos, New Mexico 87545, USA
[28]LPC, Université Blaise Pascal, CNRS-IN2P3, Clermont-Fd, 63177 Aubiere Cedex, France
[29]Department of Physics, Lund University, Box 118, SE-221 00 Lund, Sweden
[30]Institut für Kernphysik, University of Muenster, D-48149 Muenster, Germany
[31]Myongji University, Yongin, Kyonggido 449-728, Korea
[32]Nagasaki Institute of Applied Science, Nagasaki-shi, Nagasaki 851-0193, Japan
[33]University of New Mexico, Albuquerque, New Mexico, USA
[34]New Mexico State University, Las Cruces, New Mexico 88003, USA
[35]Oak Ridge National Laboratory, Oak Ridge, Tennessee 37831, USA
[36]IPN-Orsay, Universite Paris Sud, CNRS-IN2P3, BP1, F-91406, Orsay, France
[37]PNPI, Petersburg Nuclear Physics Institute, Gatchina, Russia
[38]RIKEN (The Institute of Physical and Chemical Research), Wako, Saitama 351-0198, Japan
[39]RIKEN BNL Research Center, Brookhaven National Laboratory, Upton, New York 11973-5000, USA
[40]St. Petersburg State Technical University, St. Petersburg, Russia
[41]Universidade de São Paulo, Instituto de Física, Caixa Postal 66318, São Paulo CEP05315-970, Brazil
[42]System Electronics Laboratory, Seoul National University, Seoul, South Korea
[43]Chemistry Department, Stony Brook University, SUNY, Stony Brook, New York 11794-3400, USA
[44]Department of Physics and Astronomy, Stony Brook University, SUNY, Stony Brook, New York 11794, USA
[45]SUBATECH (Ecole des Mines de Nantes, CNRS-IN2P3, Université de Nantes), BP 20722, 44307, Nantes, France
[46]University of Tennessee, Knoxville, Tennessee 37996, USA
[47]Department of Physics, Tokyo Institute of Technology, Tokyo, 152-8551, Japan
[48]Institute of Physics, University of Tsukuba, Tsukuba, Ibaraki 305, Japan
[49]Vanderbilt University, Nashville, Tennessee 37235, USA
[50]Waseda University, Advanced Research Institute for Science and Engineering, 17 Kikui-cho, Shinjuku-ku, Tokyo 162-0044, Japan
[51]Weizmann Institute, Rehovot 76100, Israel
[52]Yonsei University, IPAP, Seoul 120-749, Korea

(Received 5 January 2004; published 8 October 2004)

Bose-Einstein correlations of identically charged pion pairs were measured by the PHENIX experiment at midrapidity in Au + Au collisions at $\sqrt{s_{NN}} = 200$ GeV. The Bertsch-Pratt radius parameters were determined as a function of the transverse momentum of the pair and as a function of the centrality of the collision. Using the standard core-halo partial Coulomb fits, and a new parametrization which constrains the Coulomb fraction as determined from the unlike-sign pion correlation, the ratio $R_{\mathrm{out}}/R_{\mathrm{side}}$ is within 0.8–1.1 for $0.25 < \langle k_{\mathrm{T}} \rangle < 1.2$ GeV/c. The centrality dependence of all radii is well described by a linear scaling in $N_{\mathrm{part}}^{1/3}$, and $R_{\mathrm{out}}/R_{\mathrm{side}}$ for $\langle k_{\mathrm{T}} \rangle \sim 0.45$ GeV/c is approximately constant at unity as a function of centrality.

DOI: 10.1103/PhysRevLett.93.152302 PACS numbers: 25.75.Gz, 25.75.Dw

Following its application in the study of proton-antiproton annihilations [1], the study of Bose-Einstein correlations has been used extensively to measure source distributions in relativistic heavy ion collisions [2,3]. These measurements were originally motivated by theoretical predictions of a large source size and/or a long duration of particle emission [4–6] which would result from a softening of the equation of state in a first-order phase transition to a quark-gluon plasma (QGP). The technique of Bose-Einstein correlations is based upon quantum statistical interference, but final state interactions such as Coulomb repulsion modify the relative momentum distributions for pairs of identical particles emanating from the collision region. Both effects are included in multidimensional Gaussian fits to the normalized relative momentum distributions yielding fit parameters which are the rms widths in each dimension, R_{long}, R_{side}, R_{out} [7,8], also referred to as HBT radii to honor the radio astronomers Hanbury Brown and Twiss who pioneered a similar technique to determine the angular diameters of stars [9]. For dynamic (i.e., expanding) sources, the HBT radii depend on the mean transverse momentum of the particle pairs, $k_{\mathrm{T}} = (\mathbf{p}_{1\mathrm{T}} + \mathbf{p}_{2\mathrm{T}})/2$, and correspond to lengths of homogeneity, regions of the source which emit particles of similar momentum [10]. Measuring the k_{T} dependence of the HBT radii provides essential constraints on dynamical models that include the space-time evolution of the source [11,12].

Most hydrodynamical models for the space-time evolution of a rehadronizing QGP predicted that the measurement of the $R_{\mathrm{out}}/R_{\mathrm{side}}$ ratio at moderate values of k_{T} provides a sensitive measure of the expected long duration of particle emission, a signal of a slowly burning first-order phase transition from QGP to hadrons at the Relativistic Heavy Ion Collider (RHIC) [4]. Predictions that the $R_{\mathrm{out}}/R_{\mathrm{side}}$ ratio should reach ~ 1.5 at k_{T} of ~ 0.5 GeV/c were not borne out by initial measurements of Bose-Einstein correlations of pions from Au + Au collisions at $\sqrt{s_{NN}} = 130$ GeV [13,14]. Disagreement between theory and data is known as the "RHIC HBT puzzle" [15].

We present here data on Bose-Einstein correlations of charged pion pairs measured by the PHENIX experiment at RHIC for Au + Au collisions at $\sqrt{s_{NN}} = 200$ GeV. In this analysis, we adopt a recent fitting technique that provides for a self-consistent treatment of the Coulomb final state interaction for a source that is made up of a smaller core and a more extended halo of long-lived resonances. We introduce a new parametrization in which the strength of the Coulomb interaction is constrained by the measured unlike-sign pion correlation.

The PHENIX detector provides particle identification (PID) capabilities for hadrons, leptons, and photons over a wide momentum range. The setup of the PHENIX detector has been described in detail elsewhere [16]. In this analysis, we use the west arm of the central spectrometer, which covers the pseudorapidity region $|\eta| < 0.35$ and $\Delta\phi = \pi/2$ in an azimuthal angle over a region of $0.2 < k_{\mathrm{T}} < 2.0$ GeV/c. The drift chamber (DC), at a radial distance between 2.0 and 2.4 m, provides trajectory information in the azimuthal direction. A pad chamber (PC1) at 2.5 m provides z-coordinate information. Combining the DC and PC1 information, a track model provides a three-dimensional trajectory and momentum vector for charged particles. The momentum resolution is $\delta p/p \simeq 0.7\% \oplus 1.0\% \times p$ (GeV/c), where the first term is due to the multiple scattering before the DC, and the second term results from the angular resolution of the DC. For this analysis, the electromagnetic calorimeter (EMCal) provides the time of arrival of particles at its front face located 5.1 m from the beam axis. The timing resolution is approximately 400 psec for hadrons. This analysis is based on a sample of 34×10^6 minimum-bias events taken with an integrated magnetic field of 0.78 T m and triggered by the coincidence of the beam-beam counters (BBCs) and zero-degree calorimeters (ZDCs)—corresponding to $92\% \pm 2\%$ of the total inelastic cross section of 6.8 b. Event centrality is determined using a correlation measurement between neutral energy deposited in the ZDCs and fast particles recorded in the BBCs [17]. A Monte Carlo Glauber model [18,19] is used with a simulation of the BBC and ZDC responses to determine the number of nucleons participating in the collisions (N_{part}) for the minimum-bias events. About 23×10^6 events are selected with a requirement that the collision vertex position measured by the BBC is within ± 30 cm from the center of the spectrometer. Each track is required to have an associated hit on the EMCal within 2σ of the track's projection to the EMCal, where σ refers to the resolution of the projection. Charged particles are identified by the time-of-flight technique using timing information between the BBC and the EMCal, combined with momentum and path length calculated by the track model. Charged particles in the PID zone within 1.5σ of the ideal squared-mass peak of pions but 1.5σ away from the kaon bands are identified as pions. After the track quality and PID cuts, $\sim 45 \times 10^6$ positive pions and $\sim 51 \times 10^6$ negative pions are selected in a momentum range from 0.2 to 2.0 GeV/c.

The pion correlation function is experimentally defined as $C_2(\mathbf{q}) = A(\mathbf{q})/B(\mathbf{q})$, where $A(\mathbf{q})$ is the measured two-pion (actual pair) distribution of pair momentum difference $\mathbf{q}$, and $B(\mathbf{q})$ is the background pair (mixed pair) distribution generated using mixed events from the same data sample. Event mixing is done selecting events that have similar multiplicities and event vertices. We remove ghost tracks and inefficiencies by removing pairs of tracks in three regions at the drift chambers: $\Delta Z_{\mathrm{DC}} < 1$ cm and $\Delta\phi_{\mathrm{DC}} < 60$ mr, $\Delta Z_{\mathrm{DC}} < 5$ cm and

$\Delta\phi_{\rm DC} < 30$ mr, and $\Delta\phi_{\rm DC} < 5$ mr. We also remove hits affected by EMCal cluster sharing by eliminating tracks with hits separated by less than 8 cm at the EMCal. The event-mixed background pairs are subjected to the same cuts. After pair cuts, $\sim 110 \times 10^6$ positive and 140×10^6 negative pion pairs remain, approximately 40 times the data sample acquired by PHENIX at $\sqrt{s_{NN}} = 130$ GeV [13]. Remaining inefficiencies in the DC and EMCal are small, and for these we apply a correction from a GEANT-based [20] Monte Carlo simulation of the detector. The multiplicity dependence is estimated by embedding simulated pion pairs into real events. The systematic errors from pair cuts and corrections are estimated to be $\sim 4\%$ for $R_{\rm side}$ and $R_{\rm long}$, and $\sim 8\%$ for $R_{\rm out}$. Systematic errors for the Coulomb correction (discussed below) are $\sim 2\%$, and we assign an additional systematic error of 1% to each radius for the so-called residual HBT effect [21] in the event-mixed background. All systematic errors are determined as a function of $k_{\rm T}$ and centrality.

To compare directly to previous analyses, we fit the correlations using a standard *full* Coulomb correction, in which the Coulomb correction is determined iteratively by calculating the Coulomb wave function [6] for a 3D Gaussian parametrization of the source using the radius fit parameters from the previous iteration. We fit the Bose-Einstein correlation with the *full* Coulomb correction to the 1D $q_{\rm inv}$ parametrization, $C_2^{\rm FC}(q_{\rm inv}) = 1 + \lambda_{\rm inv} \times \exp(-R_{\rm inv}^2 q_{\rm inv}^2)$, and the 3D Bertsch-Pratt parametrization is given by

$$C_2^{\rm FC} = 1 + \lambda \exp(-R_{\rm side}^2 q_{\rm side}^2 - R_{\rm out}^2 q_{\rm out}^2 - R_{\rm long}^2 q_{\rm long}^2). \quad (1)$$

The relative momentum $\mathbf{q}$ is decomposed into $q_{\rm side}$, $q_{\rm out}$, and $q_{\rm long}$, where the longitudinal component ($q_{\rm long}$) is parallel to the beam axis, the out component ($q_{\rm out}$) is parallel to the mean transverse momentum of the pair, $\mathbf{k}_{\rm T}$, and the side component ($q_{\rm side}$) is perpendicular to both $q_{\rm long}$ and $q_{\rm out}$ [7,8]. Analysis is performed in the longitudinal center-of-mass system (LCMS), where the mean longitudinal momentum of the pair vanishes. In this frame, the duration of particle emission couples exclusively to $q_{\rm out}$. Cross terms may appear in Eq. (1), but they vanish in our measurement of central collisions at midrapidity for symmetry reasons [22].

In the core-halo model of the source many relatively long-lived particles (e.g., η, η') decay into pions too far from the core to be experimentally resolved by Bose-Einstein interference [23]. These pions also have Coulomb interactions that are negligible. To account for this effect, and to assess the systematic errors that arise from making a clean distinction between the core and halo components of the source, we perform two fits to the correlation function using Eqs. (2) and (3):

$$C_2^{\rm raw} = C_{\rm core} + C_{\rm halo} = [\lambda(1 + G)F] + [1 - \lambda], \quad (2)$$

$$C_2^{\rm raw} = [\lambda(1 + G)F] + [(\lambda_{+-} - \lambda)F] + [1 - \lambda_{+-}], \quad (3)$$

where G corresponds to the Gaussian term in Eq. (1). In Eq. (2) [24–26], the fit is applied to the correlation function without Coulomb correction ($C_2^{\rm raw}$), and the Coulomb correction term F is included in the fit function itself. In Eq. (3) we introduce a new parameter, λ_{+-}, to decouple the Coulomb and Bose-Einstein fractions. This form extends the formalism to allow for intermediate range decay pions, such as from the ω, which may contribute to the Coulomb strength without being resolved in the measured Bose-Einstein correlation [27]. λ_{+-} is determined by fitting Coulomb correlation functions calculated with several Coulomb strengths, assuming the 1D HBT radius obtained from the like-sign pion data, to the unlike-sign correlation function in the range $0.2 < k_{\rm T} < 2.0$ GeV/c, as shown in Fig. 1(a). The test yields a value of Coulomb strength $\lambda_{+-} = 0.50 \pm 0.04$, where χ^2 of the fit becomes minimum (χ^2/d.o.f. $= 32.9/11$).

Figures 1(b)–1(d) show fits to the $\pi^-\pi^-$ correlation functions for the full [Eq. (1)] and partial [Eq. (2)] Coulomb corrections. Figure 2 shows the fit parameters most affected by the strength of the Coulomb correction, and the physically interesting ratio $R_{\rm out}/R_{\rm side}$ for the full Coulomb correction and two types of partial Coulomb corrections. The partial Coulomb correction leads to a reduction in λ at low $k_{\rm T}$ and increases in $R_{\rm out}$ and $R_{\rm out}/R_{\rm side}$, which are most prominent at intermediate $k_{\rm T}$. In all subsequent results, Eq. (2) is used exclusively, and

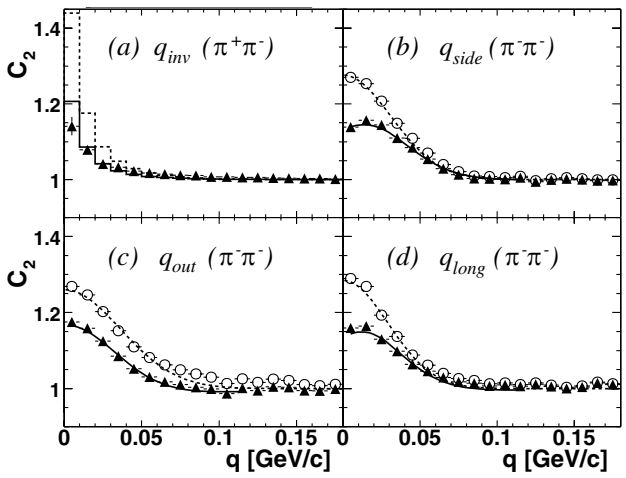

FIG. 1. (a) The one-dimensional correlation function of unlike-sign pions for $0.2 < k_{\rm T} < 2.0$ GeV/c. The two overlaid histograms show calculations for the *full* (dashed) and the 50% partial (solid) Coulomb corrections. (b)–(d) The three-dimensional $\pi^-\pi^-$ correlation function slices for $0.2 < k_{\rm T} < 2.0$ GeV/c and 0%–30% centrality averaged over the lowest 40 MeV/c in the orthogonal directions. The full Coulomb corrected data (open circles) are fit to Eq. (1) (dashed lines), and the data without Coulomb correction (filled triangles) are fit to Eq. (2) (solid lines).

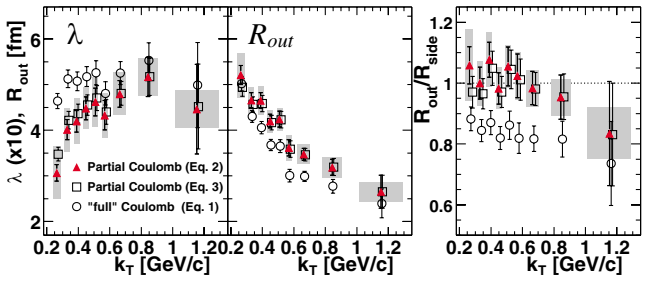

FIG. 2 (color online). The k_T dependence of λ, R_{out}, and R_{out}/R_{side} for $\pi^-\pi^-$ for 0%–30% centrality. Filled triangles show the results from fits to a core-halo structure by Eq. (2), with statistical error bars and systematic error bands. Open circles and squares show the results from the *full* and partial Coulomb corrections by Eqs. (1) and (3), respectively, with statistical error bars.

differences arising from the use of Eq. (3) are incorporated into the total systematic errors.

Figure 3 shows the k_T dependence of all radii and the ratio R_{out}/R_{side}, along with the recently published STAR results [28], and the radii from hydrodynamical model calculations of Hirano [29] and Soff [30]. The results of PHENIX and STAR are in excellent agreement, and reveal in great detail the characteristic ~50% overprediction of these models in R_{out}/R_{side}. The k_T dependence of these radii is reproduced by parametrizations of hydrodynamic freeze-out hypersurfaces [31–33] that are fit to previously published data.

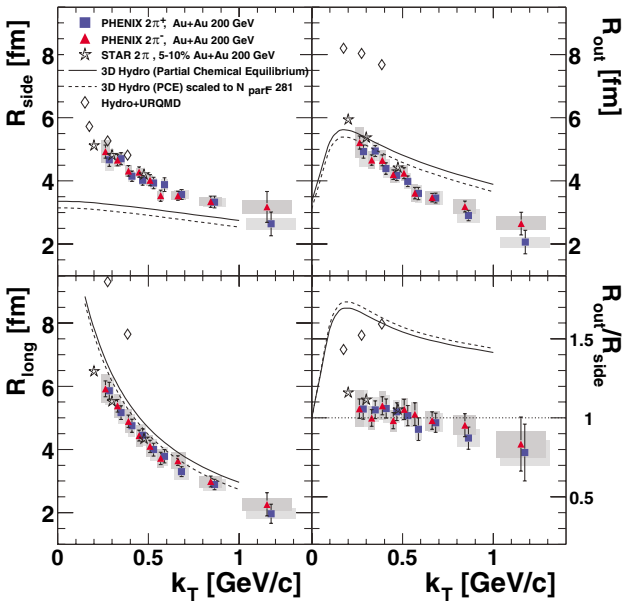

FIG. 3 (color online). The k_T dependence of the Bertsch-Pratt parameters for $\pi^+\pi^+$ (blue square) and $\pi^-\pi^-$ (red triangle) for 0%–30% centrality, from fits to a core-halo structure by Eq. (2), with statistical error bars and systematic error bands. Results from STAR [28] and hydrodynamics models (Hirano [29], solid and dashed lines, and Soff [30], diamonds) are overlaid.

Figure 4 shows that the centrality dependency is well described by a linear function of $N_{part}^{1/3}$. The slope parameters for R_{side} and R_{out} are similar to those measured at 11.6 and 14.6A GeV/c [34], while R_{long} is significantly larger. Therefore the approximate independence of R_{side} and R_{out}, and the increase in R_{long} with $\sqrt{s_{NN}}$ documented in Fig. 2 of [13], can be extended to peripheral collisions as well.

In conclusion, we have presented the Bertsch-Pratt HBT radii in the LCMS for identified charged pions measured by PHENIX in Au + Au collisions at $\sqrt{s_{NN}} = 200$ GeV. The k_T dependence of the HBT radii was measured for $\langle N_{part}\rangle = 281$, and the centrality dependence was measured for $\langle k_T\rangle \sim 0.45$ GeV/c. We performed two different partial Coulomb analyses: one based upon a self-consistent treatment of the Coulomb correction, and the other based upon direct comparison to the unlike-sign correlations. The methods give different results for λ, R_{out}, and R_{out}/R_{side} from those of the full Coulomb correction. Using the partial Coulomb correction of Eq. (2), we observe that the value of R_{out}/R_{side}, as a function of k_T, decreases from ~1.1 to ~0.8 over the range of $k_T = 0.2$–1.2 GeV/c for $\langle N_{part}\rangle = 281$. This ratio remains approximately constant at unity when plotted as a function of the number of participants for $\langle k_T\rangle \sim 0.45$ GeV/c. These measurements are consistent with recent results from STAR for the same system, but they

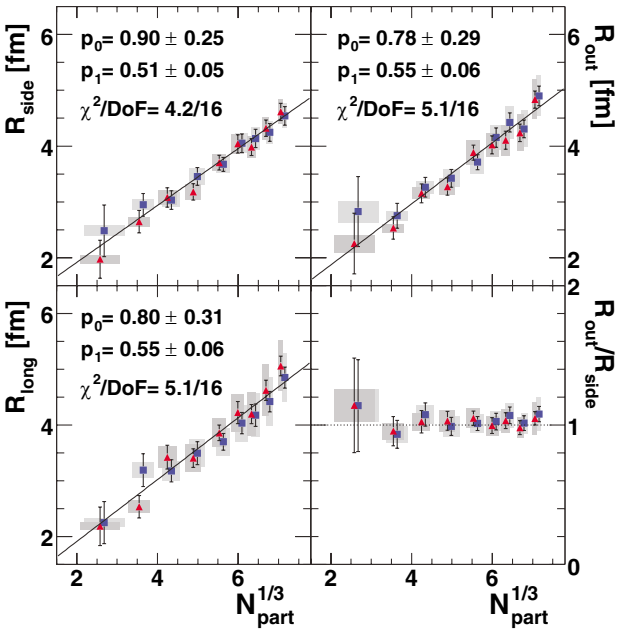

FIG. 4 (color online). Bertsch-Pratt radius parameters versus the cube root of the number of participants ($N_{part}^{1/3}$) for $\pi^+\pi^+$ (blue square) and $\pi^-\pi^-$ (red triangle) for the fits to a core-halo structure by Eq. (2) with statistical error bars and systematic error bands, in the $0.2 < k_T < 2.0$ GeV/c range, with $\langle k_T\rangle \sim 0.45$ GeV/c. The solid line shows fits to $p_0 + p_1 * N_{part}^{1/3}$ for both signs.

are inconsistent with recent hydrodynamical calculations assuming the first-order phase transition from QGP to hadrons. These detailed measurements of the transverse momentum dependence of the HBT radii, in particular, that of $R_{\mathrm{out}}/R_{\mathrm{side}}$, provide extremely strong constraints for models of particle production at RHIC.

We thank the staff of the Collider-Accelerator and Physics Departments at BNL for their vital contributions. We acknowledge support from the Department of Energy and NSF (USA), MEXT and JSPS (Japan), CNPq and FAPESP (Brazil), NSFC (China), CNRS-IN2P3 and CEA (France), BMBF, DAAD, and AvH (Germany), OTKA (Hungary), DAE and DST (India), ISF (Israel), KRF and CHEP (Korea), RMIST, RAS, and RMAE (Russia), VR and KAW (Sweden), U.S. CRDF for the FSU, U.S.-Hungarian NSF-OTKA-MTA, and U.S.-Israel BSF.

*Deceased.
†PHENIX Spokesperson.
Electronic address: zajc@nevis.columbia.edu

[1] G. Goldhaber *et al.*, Phys. Rev. **120**, 300 (1960).
[2] U. A. Wiedemann and U. Heinz, Phys. Rep. **319**, 145 (1999).
[3] T. Csörgő, Heavy Ion Phys. **15**, 1 (2002).
[4] D. H. Rischke and M. Gyulassy, Nucl. Phys. **A597**, 701 (1996).
[5] G. F. Bertsch, Nucl. Phys. **A498**, 173 (1989).
[6] S. Pratt, Phys. Rev. D **33**, 72 (1986).
[7] S. Pratt, Phys. Rev. Lett. **53**, 1219 (1984).
[8] G. Bertsch and G. E. Brown, Phys. Rev. C **40**, 1830 (1989).
[9] R. Hanbury Brown and R. Twiss, Philos. Mag. **45**, 663 (1954).
[10] A. Makhlin and Yu. M. Sinyukov, Z. Phys. C **39**, 69 (1988).
[11] S. Pratt, T. Csörgő, and J. Zimányi, Phys. Rev. C **42**, 2646 (1990).
[12] D. E. Fields *et al.*, Phys. Rev. C **52**, 986 (1995).
[13] K. Adcox *et al.*, Phys. Rev. Lett. **88**, 192302 (2002).
[14] C. Adler *et al.*, Phys. Rev. Lett. **87**, 082301 (2001).
[15] M. Gyulassy, Lect. Notes Phys. **583**, 37 (2002).
[16] K. Adcox *et al.*, Nucl. Instrum. Methods Phys. Res., Sect. A **499**, 469 (2003).
[17] K. Adcox *et al.*, Phys. Rev. Lett. **86**, 3500 (2001).
[18] R. Glauber and G. Matthiae, Nucl. Phys. **B21**, 135 (1970).
[19] Woods-Saxon Au nuclear radius $R = 6.38 \pm 0.06$ fm, diffusivity $a = 0.535 \pm 0.027$ fm [B. Hahn, D. G. Ravenhall, and R. Hofstadter, Phys. Rev. **101**, 1131 (1956)], and nucleon-nucleon cross section $\sigma_{NN}^{\mathrm{inel}} = 42 \pm 3$ mb.
[20] GEANT 3.2.1, CERN program library.
[21] W. A. Zajc *et al.*, Phys. Rev. C **29**, 2173 (1984).
[22] S. Chapman, P. Scotto, and U.W. Heinz, Phys. Rev. Lett. **74**, 4400 (1995); Heavy Ion Phys. **1**, 1 (1995).
[23] P. Avery *et al.*, Phys. Rev. D **32**, 2294 (1985).
[24] M. G. Bowler, Phys. Lett. B **270**, 69 (1991).
[25] Y. M. Sinyukov, R. Lednicky, S.V. Akkelin, J. Pluta, and B. Erazmus, Phys. Lett. B **432**, 248 (1998).
[26] D. Adamova *et al.*, Nucl. Phys. **A714**, 124 (2003).
[27] U. A. Wiedemann and U. Heinz, Phys. Rev. C **56**, 3265 (1997).
[28] J. Adams *et al.*, Phys. Rev. Lett. **93**, 012301 (2004).
[29] T. Hirano and K. Tsuda, Phys. Rev. C **66**, 054905 (2002).
[30] S. Soff, hep-ph/0202240.
[31] F. Retiere and M. A. Lisa, nucl-th/0312024.
[32] M. Csanád, T. Csörgő, B. Lörstad, and A. Ster, J. Phys. G **30**, S1079 (2004).
[33] W. Broniowski, A. Baran, and W. Florkowski, AIP Conf. Proc. **660**, 185 (2003).
[34] L. Ahle *et al.*, Phys. Rev. C **66**, 054906 (2002).

Interferometry of Direct Photons in Central ^{208}Pb + ^{208}Pb Collisions at 158A GeV

M. M. Aggarwal,[1] Z. Ahammed,[2] A. L. S. Angelis,[3,*] V. Antonenko,[4] V. Arefiev,[5] V. Astakhov,[5] V. Avdeitchikov,[5] T. C. Awes,[6] P. V. K. S. Baba,[7] S. K. Badyal,[7] S. Bathe,[8] B. Batiounia,[5] T. Bernier,[9] K. B. Bhalla,[10] V. S. Bhatia,[1] C. Blume,[8] D. Bucher,[8] H. Büsching,[8] L. Carlén,[11] S. Chattopadhyay,[2] M. P. Decowski,[12] H. Delagrange,[9] P. Donni,[3] M. R. Dutta Majumdar,[2] K. El Chenawi,[11] A. K. Dubey,[13] K. Enosawa,[14] S. Fokin,[4] V. Frolov,[5] M. S. Ganti,[2] S. Garpman,[11,*] O. Gavrishchuk,[5] F. J. M. Geurts,[15] T. K. Ghosh,[16] R. Glasow,[8] B. Guskov,[5] H. Å. Gustafsson,[11] H. H. Gutbrod,[17] I. Hrivnacova,[18] M. Ippolitov,[4] H. Kalechofsky,[3] K. Karadjev,[4] K. Karpio,[19] B. W. Kolb,[17] I. Kosarev,[5] I. Koutcheryaev,[4] A. Kugler,[18] P. Kulinich,[12] M. Kurata,[14] A. Lebedev,[4] H. Löhner,[16] L. Luquin,[9] D. P. Mahapatra,[13] V. Manko,[4] M. Martin,[3] G. Martínez,[9] A. Maximov,[5] Y. Miake,[14] G. C. Mishra,[13] B. Mohanty,[13] M.-J. Mora,[9] D. Morrison,[20] T. Moukhanova,[4] D. S. Mukhopadhyay,[2] H. Naef,[3] B. K. Nandi,[13] S. K. Nayak,[7] T. K. Nayak,[2] A. Nianine,[4] V. Nikitine,[5] S. Nikolaev,[4] P. Nilsson,[11] S. Nishimura,[14] P. Nomokonov,[5] J. Nystrand,[11] A. Oskarsson,[11] I. Otterlund,[11] T. Peitzmann,[15] D. Peressounko,[4] V. Petracek,[18] S. C. Phatak,[13] W. Pinganaud,[9] F. Plasil,[6] M. L. Purschke,[17] J. Rak,[18] R. Raniwala,[10] S. Raniwala,[10] N. K. Rao,[7] F. Retiere,[9] K. Reygers,[8] G. Roland,[12] L. Rosselet,[3] I. Roufanov,[5] C. Roy,[9] J. M. Rubio,[3] S. S. Sambyal,[7] R. Santo,[8] S. Sato,[14] H. Schlagheck,[8] H.-R. Schmidt,[17] Y. Schutz,[9] G. Shabratova,[5] T. H. Shah,[7] I. Sibiriak,[4] T. Siemiarczuk,[19] D. Silvermyr,[11] B. C. Sinha,[2] N. Slavine,[5] K. Söderström,[11] G. Sood,[1] S. P. Sørensen,[20] P. Stankus,[6] G. Stefanek,[19] P. Steinberg,[12] E. Stenlund,[11] M. Sumbera,[18] T. Svensson,[11] A. Tsvetkov,[4] L. Tykarski,[19] E. C. v.d. Pijll,[15] N. v. Eijndhoven,[15] G. J. v. Nieuwenhuizen,[12] A. Vinogradov,[4] Y. P. Viyogi,[2] A. Vodopianov,[5] S. Vörös,[3] B. Wysłouch,[12] and G. R. Young[6]

(WA98 Collaboration)

[1]*University of Panjab, Chandigarh 160014, India*
[2]*Variable Energy Cyclotron Centre, Calcutta 700064, India*
[3]*University of Geneva, CH-1211, Geneva 4, Switzerland*
[4]*RRC "Kurchatov Institute", RU-123182, Moscow*
[5]*Joint Institute for Nuclear Research, RU-141980 Dubna, Russia*
[6]*Oak Ridge National Laboratory, Oak Ridge, Tennessee 37831-6372, USA*
[7]*University of Jammu, Jammu 180001, India*
[8]*University of Münster, D-48149 Münster, Germany*
[9]*SUBATECH, Ecole des Mines, Nantes, France*
[10]*University of Rajasthan, Jaipur 302004, Rajasthan, India*
[11]*University of Lund, SE-221 00 Lund, Sweden*
[12]*MIT, Cambridge, Massachusetts 02139, USA*
[13]*Institute of Physics, Bhubaneswar 751005, India*
[14]*University of Tsukuba, Ibaraki 305, Japan*
[15]*Universiteit Utrecht/NIKHEF, NL-3508 TA Utrecht, The Netherlands*
[16]*KVI, University of Groningen, NL-9747 AA Groningen, The Netherlands*
[17]*Gesellschaft für Schwerionenforschung (GSI), D-64220 Darmstadt, Germany*
[18]*Nuclear Physics Institute, CZ-250 68 Rez, Czech Republic*
[19]*Institute for Nuclear Studies, 00-681 Warsaw, Poland*
[20]*University of Tennessee, Knoxville, Tennessee 37966, USA*
(Received 22 October 2003; published 6 July 2004)

Two-particle correlations of direct photons were measured in central ^{208}Pb + ^{208}Pb collisions at 158A GeV. The invariant interferometric radii were extracted for $100 < K_T < 300$ MeV/c and compared to radii extracted from charged pion correlations. The yield of soft direct photons, $K_T < 300$ MeV/c, was extracted from the correlation strength and compared to theoretical calculations.

DOI: 10.1103/PhysRevLett.93.022301 PACS numbers: 25.75.Gz

Hanbury Brown–Twiss (HBT) interferometry provides a powerful tool to explore the space-time dimensions of the emitting source created in elementary particle or heavy ion collisions. Historically, such measurements have concentrated on pion pair correlations, but have also been applied to kaons, protons, and even heavy fragments [1]. Hadron correlations reflect the space-time extent of the emitting source at the time of freeze-out.

The importance of direct photon Bose-Einstein interferometry for investigation of the history of heavy ion

 © 2004 The American Physical Society

collisions, especially of the very early phase, has been extensively discussed in the literature [2–6]. It has been shown that photon-photon correlations can provide information about the space-time distribution of the hot matter prior to freeze-out. Moreover, the correlations of direct photons of different transverse momenta will reflect different stages of the collision. Unfortunately, photon interferometry is faced with considerable difficulties compared to hadron interferometry primarily due to the small yield of photons emitted directly from the hot zone in comparison to the huge background of photons produced by the electromagnetic decay of the final hadrons (π^0's). For this reason, there has been only one experimental measurement of photon-photon correlations in heavy ion collisions obtained at low incident energy and low photon momenta ($K_T \leq 20$ MeV/c) [7]. In this Letter, we present first measurements of direct photon correlations in central ultrarelativistic heavy-ion collisions.

A detailed description of the layout of the CERN experiment WA98 can be found in [8]. Here we briefly discuss those subsystems used in the present analysis. The WA98 photon spectrometer, comprising the LEad-glass photon Detector Array (LEDA), was located at a distance of 21.5 m downstream from the ^{208}Pb target. It provided partial azimuthal coverage over the rapidity interval $2.35 < y < 2.95$. Further downstream, the total transverse energy was measured in the MIRAC calorimeter. The total transverse energy measured in MIRAC was used for offline centrality selection. The analysis was performed on data collected in 1995 and 1996 for the 10% most central and 20% most peripheral fractions of the ^{208}Pb + ^{208}Pb minimum bias cross section with total data samples of 5.8×10^6 and 3.9×10^6 events, respectively. No significant signal was observed in the peripheral data sample, consistent with the absence of any significant direct photon signal reported in [8].

In order to reject most of the hadron background, all showers reconstructed in the LEDA spectrometer were required to have a deposited energy of greater than 750 MeV, well above the minimum ionizing peak energy of 550 MeV. Hadron showers could be further rejected by the requirement that the shower have a narrow width, consistent with an electromagnetic shower in LEDA [8]. In addition, during the 1996 run period, the LEDA charged particle veto was operational and provided a shower sample of $> 98\%$ photon purity.

The two-photon correlation function was calculated for each bin of the photon average transverse momentum, $K_T = |\vec{p}_{T_1} + \vec{p}_{T_2}|/2$ as the ratio of the distribution of photon pair invariant relative momenta, $Q_{\rm inv}$, where both photons were taken from the same event, to the same distribution but with the photons of the pair taken from different events. Sample correlation functions are shown in Fig. 1. The ratio was normalized to have an equal number of pairs in the numerator and denominator.

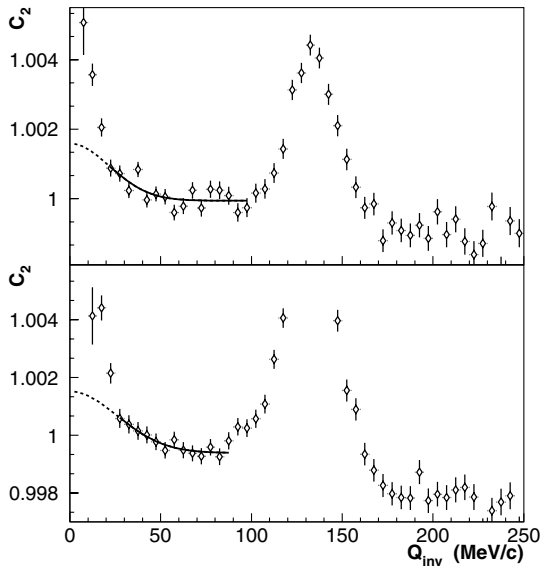

FIG. 1. The two-photon correlation function for narrow showers with $L_{\rm min} > 20$ cm (diamonds) and average photon momenta $100 < K_T < 200$ MeV/c (top) and $200 < K_T < 300$ MeV/c (bottom) fitted with Eq. (1). The solid line shows the fit result in the fit region used (excluding the π^0 peak at $Q_{\rm inv} \approx m_{\pi^0}$) and the dotted line shows the extrapolation into the low $Q_{\rm inv}$ region where backgrounds are large.

The correlation function has been fit with a Gaussian parameterization with normalization A, correlation strength $\lambda_{\rm inv}$, and radius parameter $R_{\rm inv}$:

$$C_2(Q_{\rm inv}) = A[1 + \lambda_{\rm inv} \exp(-R_{\rm inv}^2 Q_{\rm inv}^2)]. \qquad (1)$$

There are a large number of effects which may give rise to small $Q_{\rm inv}$ correlations and mimic a direct photon Bose-Einstein correlation. These include (i) single hadron or photon showers that are split into nearby clusters, (ii) photon conversions, (iii) HBT correlations of charged pions or other hadrons misidentified as photons, (iv) residual photon correlations from π^0 HBT correlations, (v) radiative decays of heavier resonances, and (vi) collective flow.

Apparatus or analysis effects which may result in the splitting of a single shower into multiple clusters, or the merging of nearby showers into a single cluster, may be investigated by studying the dependence of the correlation function on the relative distance L between the showers on the LEDA detector surface. These effects are expected to contribute strongly at small L and so can be suppressed effectively by a distance cut. Such a minimum cut on L introduces a lower cutoff in $Q_{\rm inv}$ [9].

The dependence of the correlation strength parameter $\lambda_{\rm inv}$ on the minimum distance cut $L_{\rm min}$ and the minimum invariant momentum $Q_{\rm min}$ used to define the fit region is shown in Fig. 2 for two K_T regions for narrow showers. The different symbols correspond to minimum distance cuts of $L_{\rm min} = 20$, 25, 30, and 35 cm (note that a single

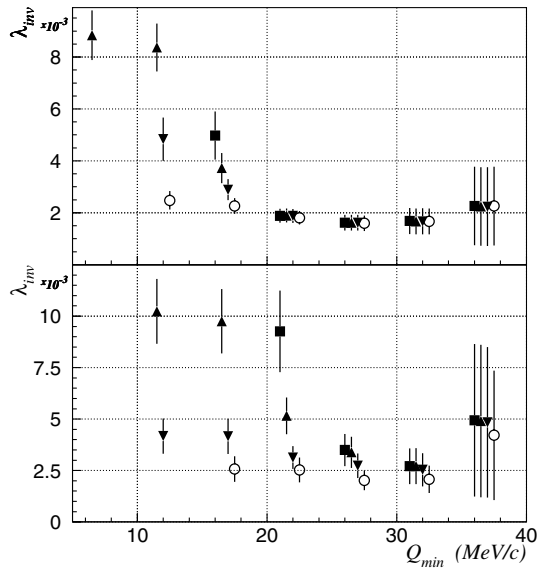

FIG. 2. Comparison of $\lambda_{\rm inv}$ parameter fit results for different fit regions for $100 < K_T < 200$ MeV/c (top) and $200 < K_T < 300$ MeV/c (bottom), calculated for narrow showers with different cuts on the minimum shower separation distance: $L_{\rm min} = 20$ cm, ■; 25 cm, ▲; 30 cm, ▼; 35 cm, ○ (same $Q_{\rm min}$ for each).

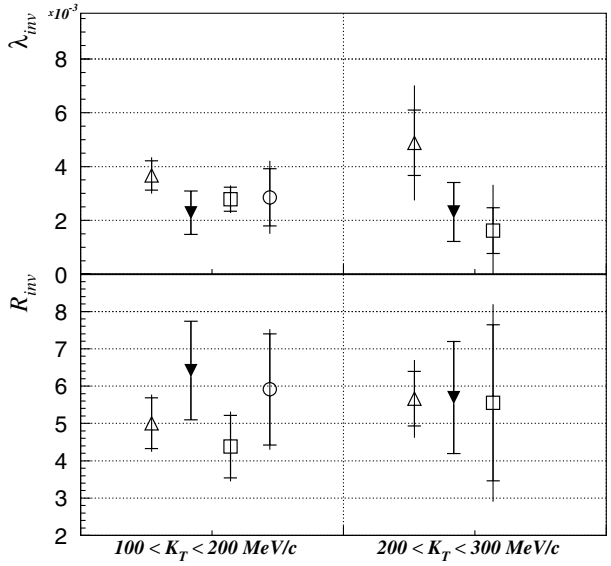

FIG. 3. Comparison of parameters of correlation functions with different particle identification criteria: △, all clusters; ▼, narrow electromagnetic; □, all neutral; ○, narrow neutral electromagnetic (no significant result for high K_T).

LEDA module is 4 cm in width). The results demonstrate that the extracted fit parameters vary strongly with $L_{\rm min}$ when the low $Q_{\rm inv}$ region is included in the fit, a result attributed to apparatus effects and conversion background, but that stable results are obtained with a sufficiently large minimum separation distance cut, or by restricting the $Q_{\rm inv}$ fit region. When no charged veto or narrow shape cuts are applied to the showers, stable results are also obtained, but with larger minimum distance cut (or $Q_{\rm min}$) required, consistent with the larger expected backgrounds.

As mentioned above, the observed correlations could be caused by residual correlations of charged pions, neutrons, antineutrons, or conversion electrons misidentified as photons. To investigate possible contributions from nonphoton contamination, the correlation functions were constructed with four different identification criteria applied to the showers reconstructed in LEDA. These criteria have somewhat different photon efficiencies, which should not affect the photon correlation, but more importantly have very different levels of nonphoton contamination which should only affect $\lambda_{\rm inv}$ if the contamination forms uncorrelated background. The charged hadron contamination decreases from 37% and 22% to 16% and 4%, respectively, for the two K_T bins, after applying the narrow electromagnetic shower shape condition [8] and is negligible after application of the charged veto condition. The correlation parameters extracted from these four types of correlation functions, corrected for contamination, are shown in Fig. 3. The consistency of the parameters extracted with the different identification criteria indicates that the nonphoton contribution to the observed correlation is not significant.

The estimated systematic errors on the correlation fit parameters are summarized in Table I. Besides the uncertainties associated with the apparatus and fit range discussed with respect to Fig. 2, and nonphoton contamination (Fig. 3), the dependence on the fit function has been investigated. In addition to the Gaussian form of Eq. (1), an exponential form and a student's t distribution form have also been used to fit the correlation functions. The student's t distribution provides a good fit to the correlation for parameter $n \geq 2$. The variation of the fit results with n and comparison with the Gaussian fit results has been used to estimate the fit function error. Reasonable fit functions leading to significantly smaller values of $\lambda_{\rm inv}$ could not be found. An exponential form gives larger

TABLE I. Summary of relative systematic errors on the photon-photon correlation parameters (in %).

	$100 < K_T < 200$		$200 < K_T < 300$	
Source	$\lambda_{\rm inv}$	$R_{\rm inv}$	$\lambda_{\rm inv}$	$R_{\rm inv}$
Apparatus	7	5	16	6
Contamination	17	14	42	14
Fit function	5	5	18	6
Fit range	8	5	26	10
$Q_{\rm inv}$ slope (flow + BE)	2	3	12	8
Total systematic error (%)	21	17	56	21
$N_\gamma^{\rm total}$ total error (%)	12	...	4	...

$\lambda_{\rm inv}$ values but also exhibits a strong dependence of the fit parameters on fit range.

Finally, correlations might exist in the background decay photons, e.g., correlations due to collective flow, Bose-Einstein correlations of π^0's, or from decays of heavier resonances. Monte Carlo simulations have been performed to estimate each of these effects. For these simulations, the transverse momentum and rapidity distributions of the π^0's were taken from measurements [8]. The effect of flow was investigated by introducing an elliptic flow pattern with a magnitude equal to that measured for charged pions [10]. Similarly, the effect of π^0 Bose-Einstein correlations was introduced with the same parameters as measured for charged pions [11]. Finally, residual correlations due to decays of heavier resonances were estimated by including all resonances having high yield and large branching ratios for electromagnetic decay: K^0_S, K^0_L, η, and ω. The heavy resonances were included based on experimental spectra where available and thermodynamic extrapolations otherwise. In all simulations, the acceptance, identification cuts, and energy and position resolution of LEDA were applied. The simulations showed that elliptic flow results in the appearance of a small slope in the correlation function and that Bose-Einstein correlations of π^0's lead to a characteristic steplike structure in the photon-pair correlation function at the π^0 mass, with a small slope in the $Q_{\rm inv} < 100$ MeV/c region, also shown by analytical calculations [5]. The height of the step in simulations agrees with that seen in the correlation functions of Fig. 1. The contribution of residual correlations due to decays of heavier resonances results in a deviation from unity which is smaller than 10^{-4}. The combination of these effects in simulation results in a predicted slope in the photon-pair correlation of 5×10^{-6} (MeV/c)$^{-1}$ in the region of fit. The data sample with the highest statistics has been fit with an additional parameter for the slope, and the extracted value of $(5 \pm 3) \times 10^{-6}$ (MeV/c)$^{-1}$ was found to be consistent with the simulation result. However, limited statistics did not allow to extract a slope value for all data samples. Therefore, the final values of the correlation strength and radii have been corrected for the presence of an overall slope using the simulation result (typically a 10% decrease of $\lambda_{\rm inv}$ and 10% increase of $R_{\rm inv}$).

Averaging over the different particle identification criteria, we obtain the following correlation parameters:

$$\lambda^{\rm I}_{\rm inv} = 0.0028 \pm 0.0004({\rm stat}) \pm 0.0006({\rm syst}), \qquad R^{\rm I}_{\rm inv} = 5.9 \pm 0.8({\rm stat}) \pm 0.9({\rm syst})\ {\rm fm},$$

$$\lambda^{\rm II}_{\rm inv} = 0.0029 \pm 0.0007({\rm stat}) \pm 0.0016({\rm syst}), \qquad R^{\rm II}_{\rm inv} = 6.1 \pm 0.8({\rm stat}) \pm 1.2({\rm syst})\ {\rm fm},$$

for regions (I) $100 < K_T < 200$ MeV/c and (II) $200 < K_T < 300$ MeV/c, respectively.

The correlation function can be written as an integral over directions of the relative momenta in the pair c.m. frame. For massless particles it can be expressed as

$$C_2(Q_{\rm inv}, K_T) = 1 + \frac{\lambda}{4\pi} \int d\Omega \exp\{-(Q^2_{\rm inv} + 4K^2_T)R^2_O \cos^2\theta - Q^2_{\rm inv}(R^2_S \sin^2\theta \sin^2\phi + R^2_L \sin^2\theta \cos^2\phi)\},$$

where λ is the correlation strength ($\lambda = 1/2$ for a fully chaotic photon source), R_O, R_S, and R_L are the "out" "side," and "long" radius components of the source, measured in the local comover system. For large K_T ($\gg Q_{\rm inv}$), the photon $R_{\rm inv}$ is an average of R_S and R_L, and almost independent of R_O. However, the measured invariant correlation strength is dependent on R_O as $\lambda_{\rm inv} = \lambda \times \sqrt{\pi}\,{\rm Erf}(2K_T R_O)/4K_T R_O$. Therefore the direct photon invariant radii may be compared to measurements of the side and long components of interferometric radii of π^- for the same centrality selection and similar K_T region [12]: $R_S = 5.55 \pm 0.24$, 5.13 ± 0.32, and 4.81 ± 0.29 fm, $R_L = 5.95 \pm 0.27$, 5.45 ± 0.37, and 5.15 ± 0.34 at $K_T = 125$, 175, and 285 MeV/c, respectively. The similarity of the interferometric radii of direct photons and pions suggests that the direct photons of this K_T region are emitted in the late stage of the collision.

Under the assumption of a fully chaotic photon source, the direct photon yield $N^{\rm direct}_\gamma$ is related to the correlation strength λ and the total inclusive photon yield $N^{\rm total}_\gamma$ as [5]

$$N^{\rm direct}_\gamma / N^{\rm total}_\gamma = \sqrt{2\lambda} = \sqrt{8\lambda_{\rm inv} K_T R_O / \sqrt{\pi}\,{\rm Erf}(2K_T R_O)}.$$

Although the photon R_O has not been measured, a *lower* limit on the yield of direct photons is given by the assumption $R_O = 0$. A *most probable* yield is obtained by assuming a value of $R_O = 6$ fm [12]. The low p_T direct photon yields have been extracted for these two cases and are presented in Fig. 4 (assuming $p_T = \langle K_T \rangle$). The previously published direct photon yield at high transverse momenta obtained with the subtraction method [8] is also shown. The measured direct photon results are compared with recent fireball model predictions [13]. The calculated contributions to the total yield from the quark gluon plasma and hadronic stages of the collision are shown. It is seen that the contribution from the hadron gas phase dominates the direct photon yield at small p_T, with predicted yields below the measured direct photon yield.

In summary, two-photon correlation functions have been measured for the first time in central

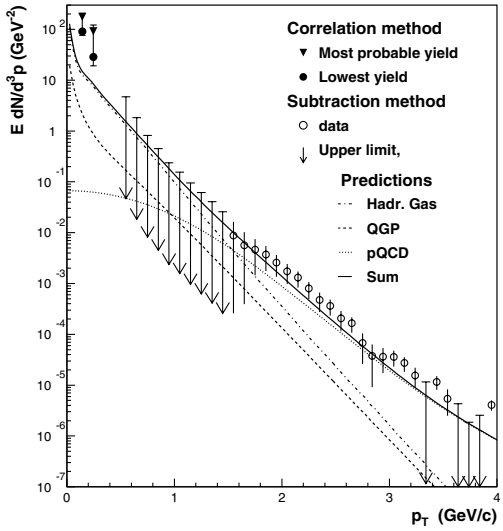

FIG. 4. Yield of direct photons extracted from the strength of the two-photon correlation ($R_O = 0$ fm, closed circles; $R_O = 6$ fm, closed triangles) and by the statistical subtraction method (open circles, or arrows indicating upper limits) [8]. Total statistical plus systematical errors are shown. The calculations are described in the text.

^{208}Pb + ^{208}Pb collisions at 158A GeV. The observed correlations are attributed to Bose-Einstein correlations of directly radiated photons. An invariant photon source radius of about 6 fm is extracted at low momenta, comparable to correlation radii extracted for pions of similar momenta. The correlation strength parameter was used to determine the yield of direct photons at $p_T < 300$ MeV/c. The measured yield exceeds theoretical expectations which attribute the dominant contribution in this p_T region to the hadronic phase.

We wish to acknowledge useful discussions with R. Rapp, C. Gale, and D. Srivastava. This work was supported jointly by Russian NS-1885.2003.2, the German BMBF and DFG, the U.S. DOE, the Swedish NFR and FRN, the Dutch Stichting FOM, the Polish KBN under Contract No. 621/E-78/SPUB-M/CERN/P-03/DZ211/, the Grant Agency of the Czech Republic under Contract No. 202/95/0217, the Department of Atomic Energy, the Department of Science and Technology, the Council of Scientific and Industrial Research and the University Grants Commission of the Government of India, the Indo-FRG Exchange Program, the PPE division of CERN, the Swiss National Fund, the INTAS under Contract No. INTAS-97-0158, ORISE, Grant-in-Aid for Scientific Research (Specially Promoted Research & International Scientific Research) of the Ministry of Education, Science and Culture, the University of Tsukuba Special Research Projects, and the JSPS. ORNL is managed by UT-Battelle, LLC, for the U.S. Department of Energy under Contract No. DE-AC05-00OR22725. The MIT group has been supported by the U.S. Department of Energy under the cooperative agreement DE-FC02-94ER40818.

*Deceased.

[1] See, e.g., W. Bauer, C. K. Gelbke, and S. Pratt, Annu. Rev. Nucl. Part. Sci. **42**, 77 (1992); U. Heinz and B. Jacak, Annu. Rev. Nucl. Part. Sci. **49**, 529 (1999).
[2] D. K. Srivastava and J. I. Kapusta, Phys. Lett. B **307**, 1 (1993);Phys. Rev. C **48**, 1335 (1993); Phys. Rev. C **50**, 505 (1994).
[3] A. Timmermann, M. Plumer, L. Razumov, and R. M. Weiner, Phys. Rev. C **50**, 3060 (1994).
[4] U. Ornik *et al.*, hep-ph/9509367.
[5] D. Peressounko, Phys. Rev. C **67**, 014905 (2003).
[6] J. Alam, B. Mohanty, P. Roy, S. Sarkar, and B. Sinha, Phys. Rev. C **67**, 054902 (2003).
[7] M. Marques *et al.*, Phys. Rep. **284**, 91(1997); Phys. Rev. Lett. **73**, 34 (1994); Phys. Lett. B **349**, 30 (1995).
[8] M. M. Aggarwal *et al.*, Phys. Rev. Lett. **85**, 3595 (2000); M. M. Aggarwal *et al.*, nucl-ex/0006007.
[9] Since $Q_{\rm inv}$ is proportional to K_T, the distance cut implies that the low $Q_{\rm inv}$ Bose-Einstein enhancement of the correlation is observable here only at low K_T.
[10] H. Appelshauser *et al.*, Phys. Rev. Lett. **80**, 4136 (1998).
[11] K. Kadija *et al.*, Nucl. Phys. **A610**, 248c (1996).
[12] M. M. Aggarwal *et al.*, Phys. Rev. C **67**, 014906 (2003).
[13] S. Turbide, R. Rapp, and C. Gale, Phys. Rev. C **69**, 014903 (2004).

Measurement of Nonrandom Event-by-Event Fluctuations of Average Transverse Momentum in $\sqrt{s_{NN}} = 200$ GeV Au + Au and $p + p$ Collisions

S. S. Adler,[5] S. Afanasiev,[17] C. Aidala,[5] N. N. Ajitanand,[43] Y. Akiba,[20,38] J. Alexander,[43] R. Amirikas,[12] L. Aphecetche,[45] S. H. Aronson,[5] R. Averbeck,[44] T. C. Awes,[35] R. Azmoun,[44] V. Babintsev,[15] A. Baldisseri,[10] K. N. Barish,[6] P. D. Barnes,[27] B. Bassalleck,[33] S. Bathe,[30] S. Batsouli,[9] V. Baublis,[37] A. Bazilevsky,[39,15] S. Belikov,[16,15] Y. Berdnikov,[40] S. Bhagavatula,[16] J. G. Boissevain,[27] H. Borel,[10] S. Borenstein,[25] M. L. Brooks,[27] D. S. Brown,[34] N. Bruner,[33] D. Bucher,[30] H. Buesching,[30] V. Bumazhnov,[15] G. Bunce,[5,39] J. M. Burward-Hoy,[26,44] S. Butsyk,[44] X. Camard,[45] J.-S. Chai,[18] P. Chand,[4] W. C. Chang,[2] S. Chernichenko,[15] C. Y. Chi,[9] J. Chiba,[20] M. Chiu,[9] I. J. Choi,[52] J. Choi,[19] R. K. Choudhury,[4] T. Chujo,[5] V. Cianciolo,[35] Y. Cobigo,[10] B. A. Cole,[9] P. Constantin,[16] D. G. d'Enterria,[45] G. David,[5] H. Delagrange,[45] A. Denisov,[15] A. Deshpande,[39] E. J. Desmond,[5] O. Dietzsch,[41] O. Drapier,[25] A. Drees,[44] R. du Rietz,[29] A. Durum,[15] D. Dutta,[4] Y. V. Efremenko,[35] K. El Chenawi,[49] A. Enokizono,[14] H. En'yo,[38,39] S. Esumi,[48] L. Ewell,[5] D. E. Fields,[33,39] F. Fleuret,[25] S. L. Fokin,[23] B. D. Fox,[39] Z. Fraenkel,[51] J. E. Frantz,[9] A. Franz,[5] A. D. Frawley,[12] S.-Y. Fung,[6] S. Garpman,[29,*] T. K. Ghosh,[49] A. Glenn,[46] G. Gogiberidze,[46] M. Gonin,[25] J. Gosset,[10] Y. Goto,[39] R. Granier de Cassagnac,[25] N. Grau,[16] S. V. Greene,[49] M. Grosse Perdekamp,[39] W. Guryn,[5] H.-Å. Gustafsson,[29] T. Hachiya,[14] J. S. Haggerty,[5] H. Hamagaki,[8] A. G. Hansen,[27] E. P. Hartouni,[26] M. Harvey,[5] R. Hayano,[8] X. He,[13] M. Heffner,[26] T. K. Hemmick,[44] J. M. Heuser,[44] M. Hibino,[50] J. C. Hill,[16] W. Holzmann,[43] K. Homma,[14] B. Hong,[22] A. Hoover,[34] T. Ichihara,[38,39] V. V. Ikonnikov,[23] K. Imai,[24,38] D. Isenhower,[1] M. Ishihara,[38] M. Issah,[43] A. Isupov,[17] B. V. Jacak,[44] W. Y. Jang,[22] Y. Jeong,[19] J. Jia,[44] O. Jinnouchi,[38] B. M. Johnson,[5] S. C. Johnson,[26] K. S. Joo,[31] D. Jouan,[36] S. Kametani,[8,50] N. Kamihara,[47,38] J. H. Kang,[52] S. S. Kapoor,[4] K. Katou,[50] S. Kelly,[9] B. Khachaturov,[51] A. Khanzadeev,[37] J. Kikuchi,[50] D. H. Kim,[31] D. J. Kim,[52] D. W. Kim,[19] E. Kim,[42] G.-B. Kim,[25] H. J. Kim,[52] E. Kistenev,[5] A. Kiyomichi,[48] K. Kiyoyama,[32] C. Klein-Boesing,[30] H. Kobayashi,[38,39] L. Kochenda,[37] V. Kochetkov,[15] D. Koehler,[33] T. Kohama,[14] M. Kopytine,[44] D. Kotchetkov,[6] A. Kozlov,[51] P. J. Kroon,[5] C. H. Kuberg,[1,27] K. Kurita,[39] Y. Kuroki,[48] M. J. Kweon,[22] Y. Kwon,[52] G. S. Kyle,[34] R. Lacey,[43] V. Ladygin,[17] J. G. Lajoie,[16] A. Lebedev,[16,23] S. Leckey,[44] D. M. Lee,[27] S. Lee,[19] M. J. Leitch,[27] X. H. Li,[6] H. Lim,[42] A. Litvinenko,[17] M. X. Liu,[27] Y. Liu,[36] C. F. Maguire,[49] Y. I. Makdisi,[5] A. Malakhov,[17] V. I. Manko,[23] Y. Mao,[7,38] G. Martinez,[45] M. D. Marx,[44] H. Masui,[48] F. Matathias,[44] T. Matsumoto,[8,50] P. L. McGaughey,[27] E. Melnikov,[15] F. Messer,[44] Y. Miake,[48] J. Milan,[43] T. E. Miller,[49] A. Milov,[44,51] S. Mioduszewski,[5] R. E. Mischke,[27] G. C. Mishra,[13] J. T. Mitchell,[5] A. K. Mohanty,[4] D. P. Morrison,[5] J. M. Moss,[27] F. Mühlbacher,[44] D. Mukhopadhyay,[51] M. Muniruzzaman,[6] J. Murata,[38,39] S. Nagamiya,[20] J. L. Nagle,[9] T. Nakamura,[14] B. K. Nandi,[6] M. Nara,[48] J. Newby,[46] P. Nilsson,[29] A. S. Nyanin,[23] J. Nystrand,[29] E. O'Brien,[5] C. A. Ogilvie,[16] H. Ohnishi,[5,38] I. D. Ojha,[49,3] K. Okada,[38] M. Ono,[48] V. Onuchin,[15] A. Oskarsson,[29] I. Otterlund,[29] K. Oyama,[8] K. Ozawa,[8] D. Pal,[51] A. P. T. Palounek,[27] V. S. Pantuev,[44] V. Papavassiliou,[34] J. Park,[42] A. Parmar,[33] S. F. Pate,[34] T. Peitzmann,[30] J.-C. Peng,[27] V. Peresedov,[17] C. Pinkenburg,[5] R. P. Pisani,[5] F. Plasil,[35] M. L. Purschke,[5] A. K. Purwar,[44] J. Rak,[16] I. Ravinovich,[51] K. F. Read,[35,46] M. Reuter,[44] K. Reygers,[30] V. Riabov,[37,40] Y. Riabov,[37] G. Roche,[28] A. Romana,[25] M. Rosati,[16] P. Rosnet,[28] S. S. Ryu,[52] M. E. Sadler,[1] N. Saito,[38,39] T. Sakaguchi,[8,50] M. Sakai,[32] S. Sakai,[48] V. Samsonov,[37] L. Sanfratello,[33] R. Santo,[30] H. D. Sato,[24,38] S. Sato,[5,48] S. Sawada,[20] Y. Schutz,[45] V. Semenov,[15] R. Seto,[6] M. R. Shaw,[1,27] T. K. Shea,[5] T.-A. Shibata,[47,38] K. Shigaki,[14,20] T. Shiina,[27] C. L. Silva,[41] D. Silvermyr,[27,29] K. S. Sim,[22] C. P. Singh,[3] V. Singh,[3] M. Sivertz,[5] A. Soldatov,[15] R. A. Soltz,[26] W. E. Sondheim,[27] S. P. Sorensen,[46] I. V. Sourikova,[5] F. Staley,[10] P. W. Stankus,[35] E. Stenlund,[29] M. Stepanov,[34] A. Ster,[21] S. P. Stoll,[5] T. Sugitate,[14] J. P. Sullivan,[27] E. M. Takagui,[41] A. Taketani,[38,39] M. Tamai,[50] K. H. Tanaka,[20] Y. Tanaka,[32] K. Tanida,[38] M. J. Tannenbaum,[5] P. Tarján,[11] J. D. Tepe,[1,27] T. L. Thomas,[33] J. Tojo,[24,38] H. Torii,[24,38] R. S. Towell,[1] I. Tserruya,[51] H. Tsuruoka,[48] S. K. Tuli,[3] H. Tydesjö,[29] N. Tyurin,[15] H. W. van Hecke,[27] J. Velkovska,[5,44] M. Velkovsky,[44] L. Villatte,[46] A. A. Vinogradov,[23] M. A. Volkov,[23] E. Vznuzdaev,[37] X. R. Wang,[13] Y. Watanabe,[38,39] S. N. White,[5] F. K. Wohn,[16] C. L. Woody,[5] W. Xie,[6] Y. Yang,[7] A. Yanovich,[15] S. Yokkaichi,[38,39] G. R. Young,[35] I. E. Yushmanov,[23] W. A. Zajc,[9,†] C. Zhang,[9] S. Zhou,[7] S. J. Zhou,[51] and L. Zolin[17]

(PHENIX Collaboration)

[1]*Abilene Christian University, Abilene, Texas 79699, USA*
[2]*Institute of Physics, Academia Sinica, Taipei 11529, Taiwan*
[3]*Department of Physics, Banaras Hindu University, Varanasi 221005, India*

 0031-9007/04/93(9)/092301(6)$22.50 © 2004 The American Physical Society

[4]*Bhabha Atomic Research Centre, Bombay 400 085, India*
[5]*Brookhaven National Laboratory, Upton, New York 11973-5000, USA*
[6]*University of California - Riverside, Riverside, California 92521, USA*
[7]*China Institute of Atomic Energy (CIAE), Beijing, People's Republic of China*
[8]*Center for Nuclear Study, Graduate School of Science, University of Tokyo, 7-3-1 Hongo, Bunkyo, Tokyo 113-0033, Japan*
[9]*Columbia University, New York, New York 10027*
and Nevis Laboratories, Irvington, New York 10533, USA
[10]*Dapnia, CEA Saclay, F-91191, Gif-sur-Yvette, France*
[11]*Debrecen University, H-4010 Debrecen, Egyetem tér 1, Hungary*
[12]*Florida State University, Tallahassee, Florida 32306, USA*
[13]*Georgia State University, Atlanta, Georgia 30303, USA*
[14]*Hiroshima University, Kagamiyama, Higashi-Hiroshima 739-8526, Japan*
[15]*Institute for High Energy Physics (IHEP), Protvino, Russia*
[16]*Iowa State University, Ames, Iowa 50011, USA*
[17]*Joint Institute for Nuclear Research, 141980 Dubna, Moscow Region, Russia*
[18]*KAERI, Cyclotron Application Laboratory, Seoul, South Korea*
[19]*Kangnung National University, Kangnung 210-702, South Korea*
[20]*KEK, High Energy Accelerator Research Organization, Tsukuba-shi, Ibaraki-ken 305-0801, Japan*
[21]*KFKI Research Institute for Particle and Nuclear Physics (RMKI), H-1525 Budapest 114, POBox 49, Hungary*
[22]*Korea University, Seoul, 136-701, Korea*
[23]*Russian Research Center "Kurchatov Institute," Moscow, Russia*
[24]*Kyoto University, Kyoto 606, Japan*
[25]*Laboratoire Leprince-Ringuet, Ecole Polytechnique, CNRS-IN2P3, Route de Saclay, F-91128, Palaiseau, France*
[26]*Lawrence Livermore National Laboratory, Livermore, California 94550, USA*
[27]*Los Alamos National Laboratory, Los Alamos, New Mexico 87545, USA*
[28]*LPC, Université Blaise Pascal, CNRS-IN2P3, Clermont-Fd, 63177 Aubiere Cedex, France*
[29]*Department of Physics, Lund University, Box 118, SE-221 00 Lund, Sweden*
[30]*Institut für Kernphysik, University of Muenster, D-48149 Muenster, Germany*
[31]*Myongji University, Yongin, Kyonggido 449-728, Korea*
[32]*Nagasaki Institute of Applied Science, Nagasaki-shi, Nagasaki 851-0193, Japan*
[33]*University of New Mexico, Albuquerque, New Mexico, USA*
[34]*New Mexico State University, Las Cruces, New Mexico 88003, USA*
[35]*Oak Ridge National Laboratory, Oak Ridge, Tennessee 37831, USA*
[36]*IPN-Orsay, Universite Paris Sud, CNRS-IN2P3, BP1, F-91406, Orsay, France*
[37]*PNPI, Petersburg Nuclear Physics Institute, Gatchina, Russia*
[38]*RIKEN (The Institute of Physical and Chemical Research), Wako, Saitama 351-0198, Japan*
[39]*RIKEN BNL Research Center, Brookhaven National Laboratory, Upton, New York 11973-5000, USA*
[40]*St. Petersburg State Technical University, St. Petersburg, Russia*
[41]*Universidade de São Paulo, Instituto de Física, Caixa Postal 66318, São Paulo CEP05315-970, Brazil*
[42]*System Electronics Laboratory, Seoul National University, Seoul, South Korea*
[43]*Chemistry Department, Stony Brook University, SUNY, Stony Brook, New York 11794-3400, USA*
[44]*Department of Physics and Astronomy, Stony Brook University, SUNY, Stony Brook, New York 11794, USA*
[45]*SUBATECH (Ecole des Mines de Nantes, CNRS-IN2P3, Université de Nantes) BP 20722 - 44307, Nantes, France*
[46]*University of Tennessee, Knoxville, Tennessee 37996, USA*
[47]*Department of Physics, Tokyo Institute of Technology, Tokyo, 152-8551, Japan*
[48]*Institute of Physics, University of Tsukuba, Tsukuba, Ibaraki 305, Japan*
[49]*Vanderbilt University, Nashville, Tennessee 37235, USA*
[50]*Waseda University, Advanced Research Institute for Science and Engineering, 17 Kikui-cho, Shinjuku-ku, Tokyo 162-0044, Japan*
[51]*Weizmann Institute, Rehovot 76100, Israel*
[52]*Yonsei University, IPAP, Seoul 120-749, Korea*
(Received 6 October 2003; published 24 August 2004)

Event-by-event fluctuations of the average transverse momentum of produced particles near mid-rapidity have been measured by the PHENIX Collaboration in $\sqrt{s_{NN}} = 200$ GeV Au + Au, and $p + p$ collisions at the Relativistic Heavy Ion Collider. The fluctuations are observed to be in excess of the expectation for statistically independent particle emission for all centralities. The excess fluctuations exhibit a dependence on both the centrality of the collision and on the p_T range over which the average is calculated. Both the centrality and p_T dependence can be well reproduced by a simulation of random particle production with the addition of contributions from hard-scattering processes.

DOI: 10.1103/PhysRevLett.93.092301 PACS numbers: 25.75.Dw

The measurement of fluctuations in the event-by-event average transverse momentum of produced particles in relativistic heavy ion collisions has been proposed as a probe of phase instabilities near the QCD phase transition [1–3], which could result in classes of events with different properties, such as the effective temperature of the collision. Fluctuation measurements could also provide information about the onset of thermalization in the system [4]. The resulting phenomena can be observed by measuring deviations of the event-by-event average p_T, referred to here as M_{p_T}, of produced charged particles from the expectation for statistically independent particle emission [5,6] after subtracting contributions from fluctuations arising from physical processes such as elliptic flow and jet production.

Several M_{p_T} fluctuation measurements have been reported in heavy ion collisions [7–10], including a study by PHENIX [9] in $\sqrt{s_{NN}} = 130$ GeV Au + Au collisions, which set limits on the magnitude of nonrandom fluctuations in M_{p_T}. Recently, STAR has reported fluctuations in excess of the random expectation, within the PHENIX limits, at the same collision energy [10]. For the first results from $\sqrt{s_{NN}} = 200$ GeV Au + Au and $p + p$ collisions reported here, upgrades of the PHENIX central arm spectrometers [11] have expanded the azimuthal acceptance from 58.5° to 180.0° within the pseudorapidity range of $|\eta| < 0.35$. Pad chamber and calorimeter detectors have also been utilized for improved background rejection. As a result, the sensitivity of the PHENIX spectrometer to the observation of fluctuations in M_{p_T} due to event-by-event fluctuations in the effective temperature [9,12] has improved by greater than a factor of 2.

Minimum bias events triggered by a coincidence between the zero degree calorimeters (ZDC) and the beam-beam counters (BBC), with a requirement that the collision vertex, which is measured with an rms resolution of less than 6 mm in central collisions and 8 mm in the most peripheral collisions, be within 5 cm of the nominal origin, are used in this analysis. Event centrality for Au + Au collisions, which is defined using correlations in the BBC and ZDC analog response [13], is divided into several classes, each containing an average of 244 000 analyzed events. These classes are associated to the estimated average number of participants in the collision, $\langle N_{\text{part}} \rangle$, which is derived using a Glauber model Monte Carlo calculation with the BBC and ZDC detector response taken into account [14].

Charged particle momenta are reconstructed in the PHENIX central arm spectrometers with a drift chamber and a radially adjacent pixel pad chamber. Nonvertex track background rejection is provided by pixel pad chambers and calorimeters located further outward radially from the collision vertex [15]. The momentum resolution is $(\delta p/p) \simeq 0.7\% \oplus 1.0\% \times p$ (GeV/c).

M_{p_T} is calculated for each event, which contains a number of reconstructed tracks within a specified p_T range, N_{tracks}. The p_T range is always given a lower bound of 200 MeV/c and a varying upper bound, $p_T^{\max}$, from 500 MeV to 2.0 GeV/c. There is a minimum N_{tracks} cut of three in both Au + Au events (removing 0%, 4.6%, and 29% of events in the 0%–50%, 50%–60%, and 60%–70% centrality ranges, respectively, when $p_T^{\max} = 2.0$ GeV/c) and $p + p$ events (removing 59% of the events).

There are several measures by which the magnitude of nonrandom fluctuations can be quantified, namely ϕ_{p_T} [16,17], ν_{dynamic} [18], and F_{p_T} [9]. The calculation of F_{p_T} is based upon the magnitude of the fluctuation, ω_{p_T}, defined as

$$\omega_{p_T} = \frac{(\langle M_{p_T}^2 \rangle - \langle M_{p_T} \rangle^2)^{1/2}}{\langle M_{p_T} \rangle} = \frac{\sigma_{M_{p_T}}}{\langle M_{p_T} \rangle}. \quad (1)$$

F_{p_T} is defined as the fractional deviation of ω_{p_T} from a baseline estimate defined using mixed events,

$$F_{p_T} = \frac{[\omega_{(p_T,\text{data})} - \omega_{(p_T,\text{mixed})}]}{\omega_{(p_T,\text{mixed})}}. \quad (2)$$

Mixed event M_{p_T} distributions are validated by comparisons to a calculation of M_{p_T} assuming statistically independent particle emission using parameters extracted from the inclusive p_T distributions of the data [19]. For the 0%–5% centrality class, which suffers the most from tracking inefficiency, the effects of two-track resolution, and background contributions, the mixed event M_{p_T} distribution yields a value of $F_{p_T} = 0.04\%$ with respect to the calculation. The results of this comparison are included in the estimates of the systematic errors. Further details on the mixed event procedure and a discussion of contributions to the value of F_{p_T} from detector efficiency and resolution effects can be found in the description of the data analysis of $\sqrt{s_{NN}} = 130$ GeV Au + Au collisions [9].

Comparisons of the data and mixed event M_{p_T} distributions for the 0%–5% and 30%–35% centrality classes are shown in Fig. 1. Any excess fluctuations are small and are difficult to distinguish by eye in a direct overlay of the M_{p_T} distributions. Therefore, the comparison is also shown as residuals of the difference between the data and mixed event distributions in units of standard deviations of the individual data points. The double-peaked shape in the residual distributions is an artifact of the fact that the mixed event distributions, which always have a smaller standard deviation in M_{p_T} than the data, are normalized to minimize the total χ^2 of the residual distribution.

Figure 2 shows the magnitude of F_{p_T}, expressed in percent, as a function of centrality for Au + Au collisions with $p_T^{\max} = 2.0$ GeV/c. The error bars are dominated by time-dependent systematic effects during the data taking period due to detector variations, which are minimized using strict time-dependent cuts on the mean and standard deviations of the inclusive p_T and N_{tracks}

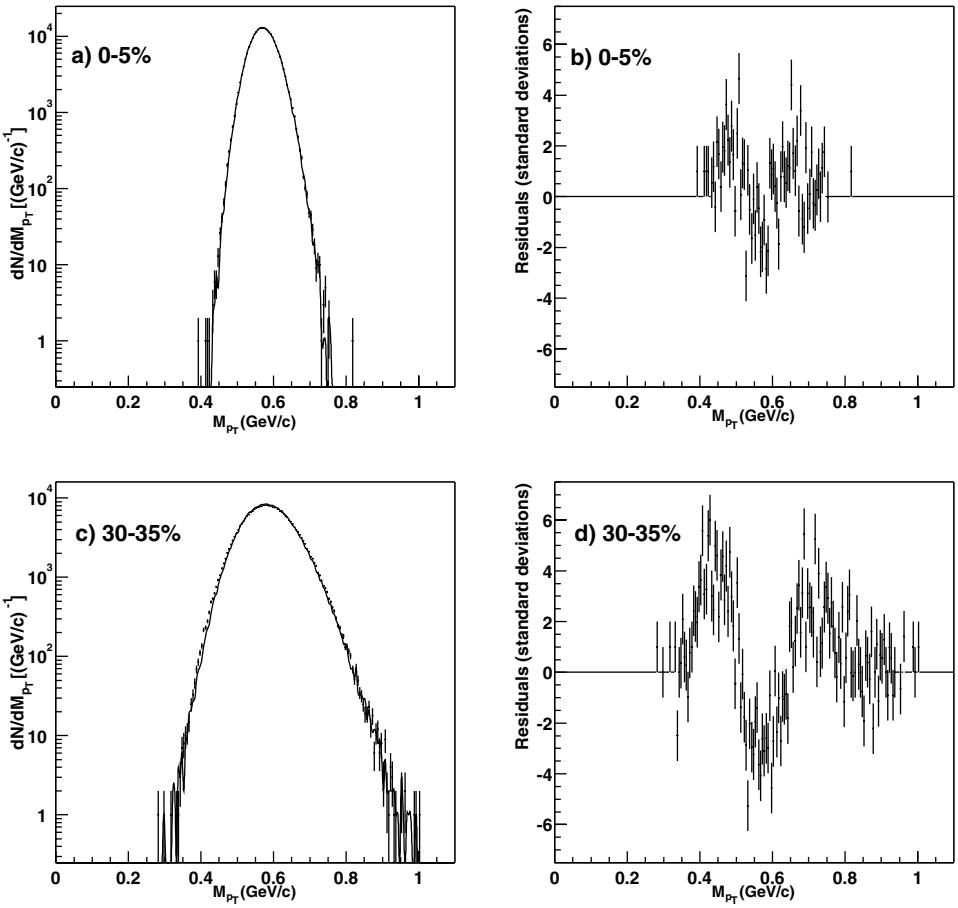

FIG. 1. Comparisons between the data and mixed event M_{p_T} distributions for the representative 0%–5% and 30%–35% centrality classes. Plots (a) and (c) show direct comparisons of the data (points) and normalized mixed event (solid line) M_{p_T} distributions. Plots (b) and (d) show the residuals between the data and mixed events in units of standard deviations of the data points from the mixed event points.

distributions. Statistical errors are below $F_{p_T} = 0.05\%$ for all centralities. The systematic errors are determined by dividing the entire dataset into ten separate subsets for each centrality class and extracting the standard deviation of the F_{p_T} values calculated for each subset. From Fig. 2, a significant nonrandom fluctuation is seen that appears to peak in midcentral collisions. However, the magnitude of the observed fluctuations are within previously published limits [9]. In addition, the value of F_{p_T} for the most peripheral Au + Au collisions is consistent with, albeit slightly below, the value measured by the same PHENIX apparatus in minimum bias $\sqrt{s_{NN}} = 200$ GeV $p + p$ collisions. If the magnitude of F_{p_T} is entirely due to fluctuations in the effective temperature of the system [12], this measurement corresponds to a fluctuation of $\sigma_T/\langle T\rangle = 1.8\%$ at 0%–5% centrality and 3.7% at 20%–25% centrality.

To further understand the source of the nonrandom fluctuations, F_{p_T} is measured over a varying p_T range for which M_{p_T} is calculated, $0.2\ \mathrm{GeV}/c < p_T < p_T^{\max}$. Figure 3 shows F_{p_T} plotted as a function of $p_T^{\max}$ for the 20%–25% centrality class. A trend of increasing F_{p_T} for increasing $p_T^{\max}$ is observed for this and all other centrality classes. The majority of the contribution to F_{p_T} appears to be due to correlations of particles with $p_T > 1.0$ GeV/c, where F_{p_T} increases disproportionately to the small increase (only 14%) of N_{tracks} in this region.

The behavior of F_{p_T} as a function of centrality and p_T is similar to trends seen in measurements of elliptic flow [20]. The contribution of elliptic flow to the magnitude of F_{p_T} is investigated using a Monte Carlo simulation whereby events are generated with a Gaussian distribution of N_{tracks} particles determined by a fit to the data and a random reaction plane azimuthal angle, Φ, between 0 and 2π. Independent particles within an event are generated following the inclusive p_T distribution with azimuthal angles, ϕ, distributed according to collective elliptic flow described by the function $[dN/d(\phi - \Phi)] = 1 + 2v_2\cos[2(\phi - \Phi)]$. The values of the v_2 parameter are linearly parametrized as a function of p_T and centrality using PHENIX measurements of inclusive charged hadrons [20]. Only generated particles that lie within the PHENIX azimuthal acceptance are included in the calculation of M_{p_T}. This simulation estimates that the

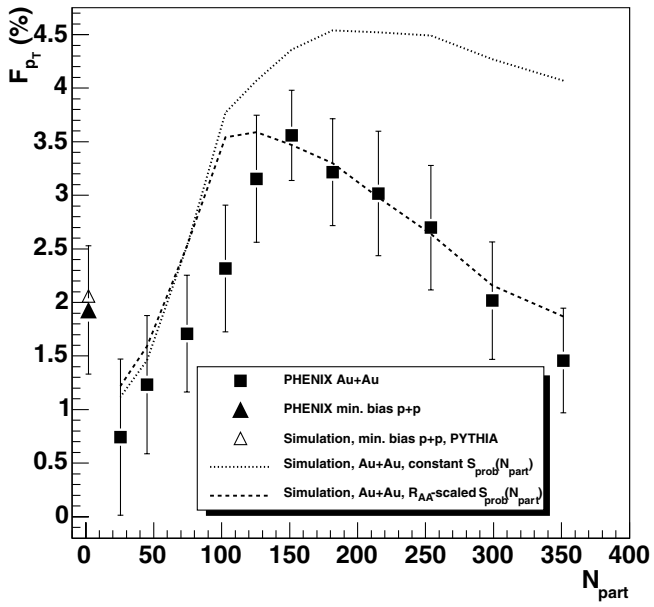

FIG. 2. F_{p_T} (in percent, $0.2\ \mathrm{GeV}/c < p_T < 2.0\ \mathrm{GeV}/c$) as a function of centrality, which is expressed in terms of the number of participants in the collision, N_{part}. The solid squares represent the Au + Au data. The solid triangle represents the minimum bias $p + p$ data point. The open triangle is the result from an analysis of PYTHIA minimum bias $p + p$ events within the PHENIX acceptance. The error bars include statistical and systematic errors and are dominated by the latter. The curves are the results of a Monte Carlo simulation with hard processes modeled using PYTHIA with a constant (dotted curve) and R_{AA}-scaled (dashed curve) hard-scattering probability factor, and include the estimated contribution due to elliptic flow.

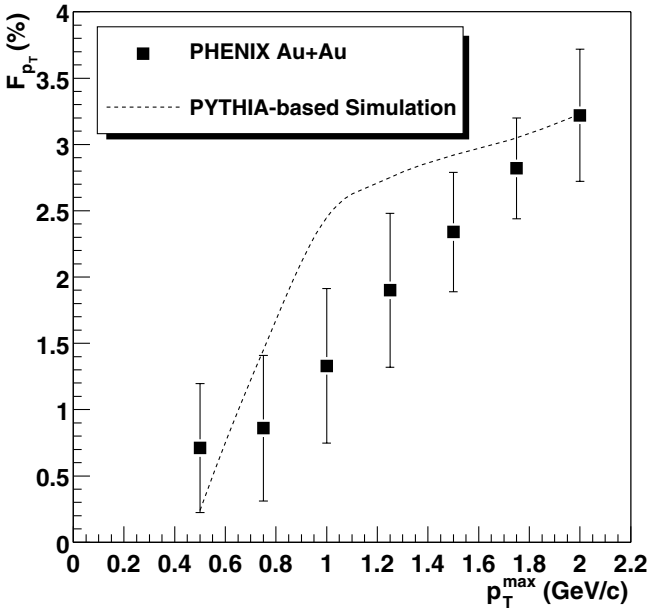

FIG. 3. F_{p_T} (in percent) of nonrandom fluctuations as a function of the p_T range over which M_{p_T} is calculated, $0.2\ \mathrm{GeV}/c < p_T < p_T^{\mathrm{max}}$, for the 20%–25% centrality class ($N_{\mathrm{part}} = 181.6$). The curve is the result of a Monte Carlo simulation with hard-scattering processes modeled using PYTHIA with $S_{\mathrm{prob}}(N_{\mathrm{part}}) = 0.075$ and $R_{AA} = 0.41$ [23]. The error bars include statistical and systematic errors and are dominated by the latter. The contribution of elliptic flow is estimated to be negligible at this centrality.

contribution of elliptic flow to F_{p_T} is largely canceled out by the symmetry of the PHENIX acceptance, and is negligible for central collisions. The estimated elliptic flow contribution to the value of F_{p_T} is less than 0.1% for $N_{\mathrm{part}} > 150$, increasing to about 0.6% for $N_{\mathrm{part}} < 100$. Note that F_{p_T} measured for minimum bias $p + p$ collisions, where collective flow is not expected to contribute, is nonzero ($1.9 \pm 0.6\%$), implying that a nonflow contribution may also be present in peripheral Au+Au collisions.

Figure 3 illustrates that a large contribution to the observed nonrandom fluctuations is due to the correlation of high p_T particles, such as might be expected from correlations due to jet production [21]. In order to estimate the contribution due to jets, a Monte Carlo simulation is again applied. Events are generated with a Gaussian distribution of N_{tracks} particles as independent particles that follow an m_T exponential fit to the inclusive data p_T distribution. Hard processes are defined to occur at a uniform rate per generated particle, $S_{\mathrm{prob}}(N_{\mathrm{part}})$, for each centrality class. This is the only parameter that is allowed to vary in the simulation. As Au + Au events are being generated, single $\sqrt{s_{NN}} = 200$ GeV $p + p$ hard-scattering events generated by the PYTHIA event generator [22] and filtered by the PHENIX acceptance are embedded into the event. The addition of the PYTHIA events affects the mean and standard deviation of the inclusive p_T spectra by less than 0.1%. The value of F_{p_T} has been extracted from 100 000 PYTHIA events for minimum bias $p + p$ collisions, yielding $F_{p_T} = 2.06\%$ within the PHENIX acceptance, which is consistent with the measured value of $F_{p_T} = 1.9 \pm 0.6\%$.

Two scenarios are considered for studies of the centrality dependence of jet contributions to the value of F_{p_T}: (i) with $S_{\mathrm{prob}}(N_{\mathrm{part}})$ set at a constant rate for all centrality classes, and (ii) with $S_{\mathrm{prob}}(N_{\mathrm{part}})$ scaled for each centrality class by the PHENIX measurement of the suppression of high p_T charged particles, which is characterized by the nuclear modification factor, R_{AA}, integrated over $p_T > 4.5\ \mathrm{GeV}/c$ [23]. The p_T value at which R_{AA} is extracted has little effect on the simulation results, which change by less than 0.2% for 0%–5% centrality if the R_{AA} measurement at $p_T = 2.0\ \mathrm{GeV}/c$ is used instead. The latter scenario is intended to model the effect of the suppression of jets due to energy loss in the nuclear medium [24] on the fluctuation signal. The initial value of $S_{\mathrm{prob}}(N_{\mathrm{part}})$ for both scenarios is normalized so that the F_{p_T} result from the R_{AA}-scaled simulation matches that of the data for the 20%–25% centrality class. The results of the simulation

as a function of $p_T^{\max}$, with $S_{\text{prob}}(N_{\text{part}})$ scaled by R_{AA}, are represented by the dashed curve in Fig. 3 for the 20%–25% centrality class, The trend of increasing F_{p_T} with increasing $p_T^{\max}$ observed in the data is reproduced by the simulation reasonably well.

The results of the two hard-scattering simulation scenarios are shown in Fig. 2 as a function of centrality. The model curves include the small contribution estimated from the elliptic flow simulation. The dotted curve is the result with $S_{\text{prob}}(N_{\text{part}})$ fixed for all centralities. The dashed curve is the result with $S_{\text{prob}}(N_{\text{part}})$ scaled by R_{AA} as a function of centrality. Within this simulation, the decrease of F_{p_T} for the more peripheral events is explained as a decrease in the signal strength relative to number fluctuations from the small and decreasing value of N_{tracks}. If $S_{\text{prob}}(N_{\text{part}})$ remains constant, the value of F_{p_T} decreases only slightly when going from midcentral to central collisions, in contradiction with the large decrease seen in the data over this centrality range. When $S_{\text{prob}}(N_{\text{part}})$ is scaled by R_{AA} as a function of centrality, the trend in the simulation of decreasing F_{p_T} with increasing centrality is more consistent with the data.

To summarize, the PHENIX experiment has observed a positive nonrandom fluctuation signal in event-by-event average transverse momentum, measured as a function of centrality and p_T in $\sqrt{s_{NN}} = 200$ GeV Au + Au and $p + p$ collisions. The increase of F_{p_T} with increasing p_T implies that the majority of the fluctuations are due to correlated high p_T particles. A Monte Carlo simulation that includes elliptic flow and a PYTHIA-based hard-scattering description can consistently describe contributions to the signal as a function of centrality and p_T with a simple implementation of jet suppression.

We thank the staff of the Collider-Accelerator and Physics Departments at BNL for their vital contributions. We acknowledge support from the Department of Energy and NSF (USA), MEXT and JSPS (Japan), CNPq and FAPESP (Brazil), NSFC (China), CNRS-IN2P3 and CEA (France), BMBF, DAAD, and AvH (Germany), OTKA (Hungary), DAE and DST (India), ISF (Israel), KRF and CHEP (Korea), RMIST, RAS, and RMAE (Russia), VR and KAW (Sweden), U.S. CRDF for the FSU, U.S.-Hungarian NSF-OTKA-MTA, and U.S.-Israel BSF.

*Deceased.
†PHENIX Spokesperson.
Email address: zajc@nevis.columbia.edu

[1] H. Heiselberg, Phys. Rep. **351**, 161 (2001).
[2] M. Stephanov *et al.*, Phys. Rev. Lett. **81**, 4816 (1998).
[3] M. Stephanov *et al.*, Phys. Rev. D **60**, 114028 (1999).
[4] S. Gavin, Phys. Rev. Lett. **92**, 162301 (2004).
[5] L. Stodolsky, Phys. Rev. Lett. **75**, 1044 (1995).
[6] E. Shuryak, Phys. Lett. B **423**, 9 (1998).
[7] NA49 Collaboration, H. Appelshäuser *et al.*, Phys. Lett. B **459**, 679 (1999).
[8] CERES Collaboration, D. Adamová *et al.*, Nucl. Phys. **A727** 97 (2003).
[9] PHENIX Collaboration, K. Adcox *et al.*, Phys. Rev. C **66**, 024901 (2002).
[10] STAR Collaboration, nucl-ex/0308033 (to be published).
[11] PHENIX Collaboration, K. Adcox *et al.*, Nucl. Instrum. Methods Phys. Res., Sect. A **499**, 235 (2003).
[12] R. Korus and S. Mrówczyński, Phys. Rev. C **64**, 054908 (2001).
[13] PHENIX Collaboration, K. Adcox *et al.*, Phys. Rev. Lett. **86**, 3500 (2001).
[14] PHENIX Collaboration, S. S. Adler *et al.*, Phys. Rev. C **69**, 034909 (2004).
[15] J. T. Mitchell *et al.*, Nucl. Instrum. Methods Phys. Res., Sect. A **482**, 491 (2002).
[16] M. Gaździcki and S. Mrówczyński, Z. Phys. C **54**, 127 (1992).
[17] S. Mrówczyński, Phys. Lett. B **439**, 6 (1998).
[18] C. Pruneau *et al.*, Phys. Rev. C **66**, 044904 (2002).
[19] M. J. Tannenbaum, Phys. Lett. B **498**, 29 (2001).
[20] PHENIX Collaboration, S. S. Adler *et al.*, Phys. Rev. Lett. **91**, 182301 (2003); PHENIX Collaboration, K. Adcox *et al.*, Phys. Rev. Lett. **89**, 212301 (2002); STAR Collaboration, C. Adler *et al.* Phys. Rev. C **66**, 034904 (2002).
[21] Q. Liu and T. Trainor, Phys. Lett. B **567**, 184 (2003).
[22] T. Sjöstrand, Comput. Phys. Commun. **82**, 74 (1994). Version 5.720 with MSEL = 1 for embedded hard-scattering events and MSEL = 2 for min. bias $p + p$ events, CKIN(3) = 0.0, MSTP(32) = 4, and MSTP(33) = 1.
[23] PHENIX Collaboration, S. S. Adler *et al.*, Phys. Rev. C **69**, 034910 (2004).
[24] X. N. Wang, Phys. Rev. C **58**, 2321 (1998).

Available online at www.sciencedirect.com
SCIENCE DIRECT®
Nuclear Instruments and Methods in Physics Research A 499 (2003) 521–536
NUCLEAR INSTRUMENTS & METHODS IN PHYSICS RESEARCH Section A
www.elsevier.com/locate/nima

PHENIX calorimeter

L. Aphecetche[a], T.C. Awes[b], J. Banning[b], S. Bathe[c], A. Bazilevsky[d], S. Belikov[e,f], S.T. Belyaev[g], C. Blume[c], M. Bobrek[b], D. Bucher[c], V. Bumazhnov[f], H. Büsching[c], S. Chernichenkov[f], V. Cianciolo[b], M. Cutshaw[b], D.G. D'Enterria[a], S. Daniels[b], G. David[h,*], H. Delagrange[a], A. Denisov[a], A. Durum[a], Y.V. Efremenko[b], M.S. Emery[b], S.L. Fokin[g], S. Frank[b], Y. Goto[d], M. Grosse Perdekamp[d], N. Heine[c], D.E. Hurst[b], V.V. Ikonnikov[g], M.S. Ippolitov[g], G. Jackson[b], J.P. Jones[b], K.V. Karadjev[g], E. Kistenev[h], C. Klein-Bösing[c], V. Kochetkov[f], Iou.A. Koutcheryaev[g], V.A. Lebedev[g], V.I. Manko[g], G. Martinez[a], Y. Melnikov[f], T. Moore[b], M. Musrock[b], S.A. Nikolaev[e], A.S. Nyanin[e], V. Onuchin[f], T. Peitzmann[c], P. Pitukhin[f], F. Plasil[b], K.F. Read[b], K. Reygers[c], R. Santo[c], Y. Schutz[a], V. Semenov[f], V. Shelikhov[f], Iou.G. Sibiriak[g], M. Simpson[b], D.C. Smith[b], M. Smith[b], A. Soldatov[f], P.W. Stankus[b], J. Stewering[c], S.P. Stoll[h], H. Torii[i], A.A. Tsvetkov[g], N. Tyurin[f], A. Usachev[f], A.A. Vasiliev[g], W. Verhoeven[c], A.A. Vinogradov[g], M.A. Volkov[g], J.W. Walker[b], S.N. White[h], A.L. Wintenberg[b], C.L. Woody[h], G.R. Young[b], I.E. Yushmanov[g]

[a] *SUBATECH (Ecole des Mines de Nantes, IN2P3/CRNS, Université de Nantes), BP 20722-44307, Nantes-cedex 3, France*
[b] *Oak Ridge National Laboratory, Oak Ridge, TN 37831, USA*
[c] *University of Münster, D-411980 Münster, Germany*
[d] *BNL Research Center, Brookhaven National Laboratory, Upton, NY 11973-5000, USA*
[e] *Iowa State University, Ames, IA 50011, USA*
[f] *Institute for High Energy Physics (IHEP), Protvino, Russia*
[g] *Russian Research Center "Kurchatov Institute", RU-123182 Moscow, Russia*
[h] *Brookhaven National Laboratory, Upton, NY 11973-5000, USA*
[i] *Kyoto University, Kyoto 606, Japan*

The PHENIX Collaboration

Abstract

The PHENIX Electromagnetic Calorimeter (EMCal) is used to measure the spatial position and energy of electrons and photons produced in heavy ion collisions. It covers the full central spectrometer acceptance of $70^\circ \leqslant \theta \leqslant 110^\circ$ with two walls, each subtending 90° in azimuth. One wall comprises four sectors of a Pb-scintillator sampling calorimeter and the other has two sectors of Pb-scintillator and two of a Pb-glass Cherenkov calorimeter. Both detectors have very

*Corresponding author. Tel.: +1-631-344-3016; fax: +1-631-344-3253.
E-mail address: david@bnl.gov (G. David).

0168-9002/03/$ - see front matter © 2002 Elsevier Science B.V. All rights reserved.
PII: S0168-9002(02)01954-X

good energy, spatial and timing resolution, while the Pb-scintillator excels in timing and the Pb-glass in energy measurements. Also, having two detectors with different systematics increases the confidence level of the physics results. Design and operational parameters of the Pb-scintillator, Pb-glass and special readout electronics for EMCal are presented and running experience during the first year of data taking with PHENIX is discussed. Some examples of data taken during the first run are shown.
© 2002 Elsevier Science B.V. All rights reserved.

PACS: 01.52.+r; 29.30.−h; 29.40.Mc; 29.40.Ka; 29.40.Vj

Keywords: RHIC; PHENIX; Calorimeter; Pb-glass; Scintillator; Electronics

1. Introduction

The PHENIX detector [1] at the Relativistic Heavy Ion Collider is designed to measure the properties of nuclear matter at the highest temperatures and energy densities yet produced in terrestrial experiments and to search for new phenomena such as the quark-gluon plasma. The primary role of the Electromagnetic Calorimeter (EMCal) in PHENIX is to provide a measurement of the energies and spatial positions of photons and electrons produced in heavy ion collisions. It also plays a major role in particle identification and is an important part of the PHENIX trigger system. The EMCal system can trigger on rare events with high transverse momentum (p_T) photons and electrons. Its signals are incorporated in Level-1 triggers for high multiplicity or large total transverse energy (E_T) events. In addition the EMCal provides a good measurement of the *hadronic* energy produced at mid-rapidity and thus of the E_T produced in the reaction.

The EMCal system consists of a total of 24,768 individual detector modules divided between the Pb-Scintillator calorimeter, which provides six sectors of azimuthal coverage and the Pb-glass calorimeter comprised of two sectors. Both sub-detectors are read out with photomultipliers and have good energy resolution and intrinsic timing characteristics but their design is quite different and they will be described separately. A description of special EMCal front-end electronics is also given. The position of the EMCal relative to the rest of the PHENIX detector is illustrated in Fig. 2 in the article entitled "PHENIX Detector Overview" in this volume [1] and a view in a cut through the collision vertex is shown in Fig. 1 in the article entitled "PHENIX Central Arm Tracking Detectors" also in this volume [2].

The properties of the Pb-scintillator and Pb-glass calorimeters are very different and they have different strengths and weaknesses. The Pb-scintillator is a sampling calorimeter while the Pb-glass is a Cherenkov detector. For the two detectors the granularity, energy resolution, linearity, response to hadrons, timing properties and shower shape at normal and non-normal impact on the face of the tower differ significantly. For example, the Pb-glass has the best granularity and energy resolution but the Pb-scintillator has the best linearity and timing and the response to hadrons is better understood. Due to this the data analysis, particle identification cuts and the resulting systematic errors are also different and will be discussed in separate sections. Nevertheless choosing two different technologies was a deliberate decision by PHENIX which has the advantage of producing independent cross-checks of results within the same experiment.

2. Lead-scintillator calorimeter

The Pb-scintillator electromagnetic calorimeter is a shashlik type sampling calorimeter made of alternating tiles of Pb and scintillator consisting of 15,552 individual towers and covering an area of approximately 48 m^2. The basic building block is a module consisting of four (optically isolated) towers which are read out individually. The modules were manufactured in Russia and subjected to quality control procedures designed to

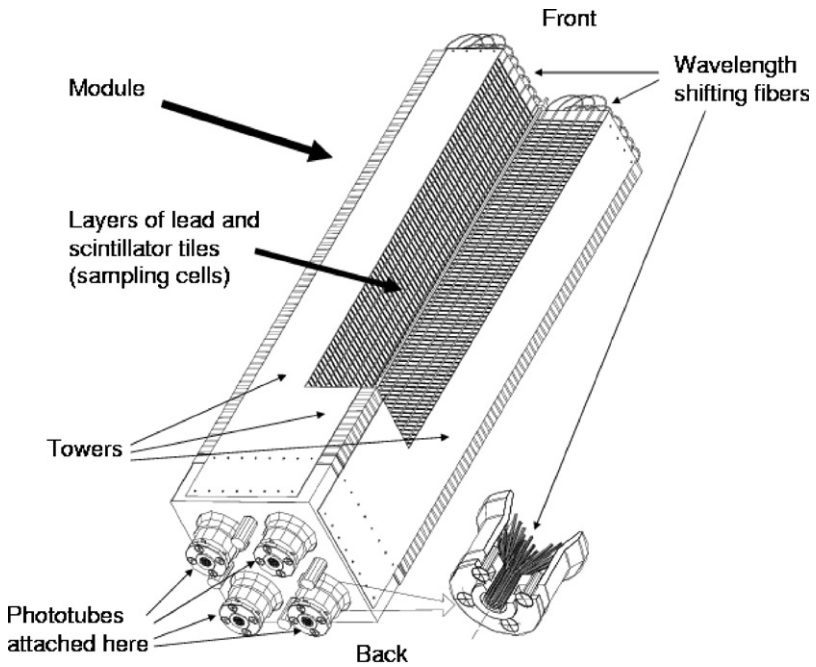

Fig. 1. Interior view of a Pb-scintillator calorimeter module showing a stack of scintillator and lead plates, wavelength shifting fiber readout and leaky fiber inserted in the central hole.

achieve consistent large light yield in all towers ($\sim 12,500$ photons/GeV). The PbSc calorimeter has a nominal energy resolution of $8.1\%/\sqrt{E(\mathrm{GeV})} \oplus 2.1\%$ and an intrinsic timing resolution better than 200 ps for electromagnetic showers [3]. A high precision calibration and monitoring system has been developed to achieve an absolute energy calibration better than 5% for day one operation at RHIC, and to maintain an overall long term gain stability of the order of 1%. Details of the two calorimeter types are given in Sections 2 and 3 below and the front-end electronics for both are discussed in Section 4.

2.1. Pb-scintillator calorimeter design

2.1.1. Opto-mechanical design

Each Pb-scintillator tower contains 66 sampling cells consisting of alternating tiles of Pb and scintillator. The edges of the tiles are plated with Al. These cells are optically connected by 36 longitudinally penetrating wavelength shifting fibers for light collection. Light is read out by 30 mm FEU115M phototubes at the back of the towers. Four towers are mechanically grouped together into a single structural entity called a module as shown in Fig. 1. Thirty six modules are attached to a backbone and held together by welded stainless-steel skins on the outside to form a rigid structure called a supermodule. Eighteen supermodules make a "sector", a $2 \times 4\ \mathrm{m}^2$ plane with its own rigid steel frame. Details of the design and methods of construction of the Pb-scintillator modules have been given in an earlier publication [4]. All major Pb-scintillator design parameters are listed in Table 1. The scintillating plastic contains an organic scintillator p-bis[2-(5-phenyloxazolyl)]-benzene (POPOP) and a fluorescent additive p-terphenyl (PT).

2.1.2. Monitoring system design

The calibration and monitoring system is based on a UV laser which supplies light to the calorimeter through a series of optical splitters and fibers. The block diagram of the monitoring system is shown schematically in Fig. 2 [5].

Table 1
Individual Pb-scintillator calorimeter tower parameters

Parameter	Value
Lateral segmentation	5.535×5.535 cm^2
Active sampling cells	66
Scintillator	Polystyrene (1.5% PT/0.01% POPOP), 0.4 cm
Absorber	Pb, 0.15 cm
Cell thickness	0.56 cm (0.277 $X_\circ$)
Active depth	37.5 cm
Radiation length	18
Nuclear interaction Length	0.85
WLS fiber	BCF-99-29a, 0.1 cm
WLS fibers per tower	36
PMT type	FEU115M, MELS, Russia, 3.0 cm
Photocathode	Sb–K–Na–Cs
Luminous sensitivity	$\geqslant$80 μa/lm
Rise time (20–80%)	$\leqslant$5 ns

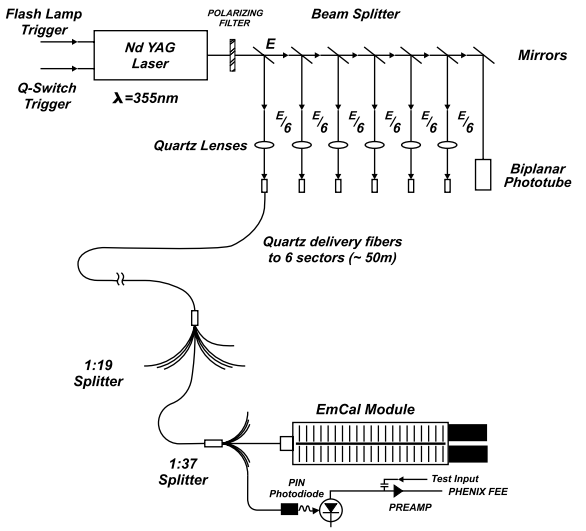

Fig. 2. Laser light distribution and monitoring system.

Light from a high power YAG laser is initially split into six equal intensity beams using a set of partially reflecting mirrors. The beam from each mirror passes through a quartz lens and is focused to a point just in front of a quartz fiber which is used to transport the light over a distance of approximately 50 m to one sector of the calorimeter. Optical splitters are used to distribute the light to each of the individual calorimeter modules. At the very last stage the light is injected into a 38 cm long, 2 mm diameter plastic fiber that penetrates the center of the module (there is a small gap in the optical isolation of the towers). This "leaky fiber" is grated such that light exits along its length simulating the depth profile of a 1 GeV electromagnetic shower in the four surrounding towers. The overall efficiency to produce one photoelectron in each of the 15,592 towers from the primary photons of the laser is of the order of 4×10^{-12}. Given that the calorimeter has an intrinsic light output of $\sim$1500 photoelectrons per GeV, this leads to an energy requirement of $\sim$0.2 mJ per pulse from the YAG laser to deliver 1 GeV of equivalent energy into each tower.

2.2. Energy calibration and gain monitoring

The initial calibration coefficients were established as follows. The calorimeter response to cosmic ray muons penetrating the supermodule in a direction nearly orthogonal to the tower axis was recorded along with the response to laser pulses. The absolute energy scale for muons was in turn established by test-beam measurements using electrons of known energy [4]. During the same test-beam exposure the response to relativistic (1 GeV/c)$\pi^{\pm}$ charged particles which traverse the calorimeter was characterized by the minimum ionizing peak (MIP).

A lego plot of the energies deposited by a laterally penetrating muon in neighboring towers of a supermodule is shown in the bottom left plot of Fig. 3. The top left plot in the same figure shows the energy spectrum in one tower exposed to laterally penetrating muons. The MIP peak corresponds to 38 MeV in this case (270 MeV for longitudinally traversing particles) and has a nearly gaussian shape with $\sigma(E)/E \sim 30\%$. On average the EMCal towers produce 12,500 photons per GeV of deposited electromagnetic energy. The distribution of the light yield (normalized to an average value) for $\sim$8000 towers is also shown in the same figure. Both the precalibration and original light yield measurements were performed with a "standard set" of phototubes,

whose quantum efficiencies and gains differ from the actual tubes used in the final assembly. The laser monitoring system was used to transfer the initial calibration into the RHIC operational environment. After renormalization, the dispersion in the actual response of each tower with respect to the original muon calibration was only 2.3%. This residual dispersion is due mainly to the non-uniformities in the quantum efficiencies of the phototubes over the active photocathode area. The implemented scheme for calorimeter precalibration and further monitoring ensured a very low uncertainty in the absolute energy scale for day one operation at RHIC, well below the design goal of 5%.

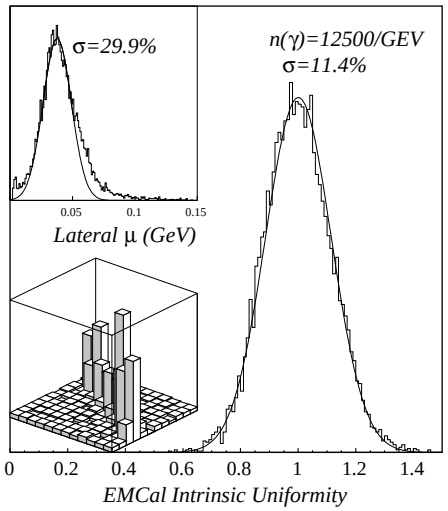

Fig. 3. Light yield uniformity in the Pb-scintillator calorimeter. The energy distribution in the towers exposed to laterally penetrating cosmic muons is shown in the top left inset and a lego plot of energies deposited in the towers by laterally penetrating cosmic muons is shown at the bottom left.

2.3. Energy and position measurements with the test beam

The Pb-scintillator calorimeter went through a rather extensive sequence of preconstruction tests in the particle beams from U70 (IHEP, Protvino), from the AGS (BNL) and finally from the SPS (CERN). The correlation plot between the incident beam energy and the energy measured in the calorimeter is presented in Fig. 4. Data are normalized to 1 GeV. The finite light attenuation length (100 cm) in the WS fibers is a major contributor to the response non-uniformities at the low end of the energy scale, although this effect

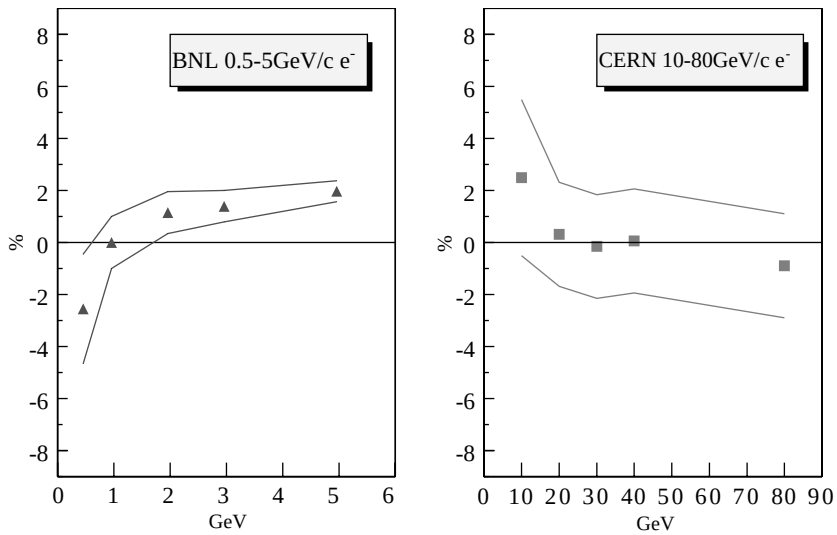

Fig. 4. Pb-scintillator EMCal energy linearity measured in beam tests at BNL (left) and CERN (right). The residual (calorimeter measured energy less the beam energy, divided by the beam energy) is for the 5×5 tower energy sum. The solid lines show total systematic uncertainties in the analysis.

is mitigated by the fact that each fiber is looped back (see Fig. 1), and the light collected always has a short and a long path to the phototube. Other contributors at low energies are coarse sampling [6] and energy leakage at the front face [7]. At high momenta the "positive" effect of the light attenuation in the fibers is overcompensated by the "negative" effect of energy leakage from the back of the calorimeter. The resulting nonlinearity is about a factor of 2 lower than what one would expect from the effect of light attenuation alone.

The calorimeter energy resolution (corrected for the noise contribution) is shown in Fig. 5. The resolution is given by

$$8.1\%\sqrt{E(\mathrm{GeV})}\oplus 2.1\%. \quad (1)$$

The 8.1% value for the stochastic term is close to the expected resolution from sampling as predicted by GEANT.

The main contributors to the constant term are intrinsic non-uniformities, in particular tower boundaries, hot spots at fiber positions and shower depth fluctuations. (The latter are responsible for the variations in the amount of the light seen and in the energy leaking from the calorimeter via the front and back surfaces.)

In order to study the lateral response non-uniformity, different areas of the calorimeter were exposed to 1 GeV/c electrons whose impact point was measured to better than 3 mm. The response variation was $\pm 2.5\%$. The 8% loss in the calorimeter response from particles hitting the corner of the towers is the main factor in the relatively large constant term in the expression for the energy resolution.

The depth of the Pb-scintillator electromagnetic calorimeter measured in units of nuclear interaction length at normal incidence is 0.85 L_{abs}. Lineshapes for protons and pions are shown in Fig. 6 along with electrons of the same momentum for comparison.

Both simulated (GEANT) and experimental data (taken at different impact angles) show that the measured shower shape (the projection onto the front face of the calorimeter) becomes skewed for non-normal angles of incidence. The data also show a gradual spread of the shower core mainly related to the longitudinal shower fluctuations contributing to the observed width, which in turn depends on impact angle θ as

$$b(\theta) = b_0 \oplus a(E) \times \sin^2(\theta) \quad (2)$$

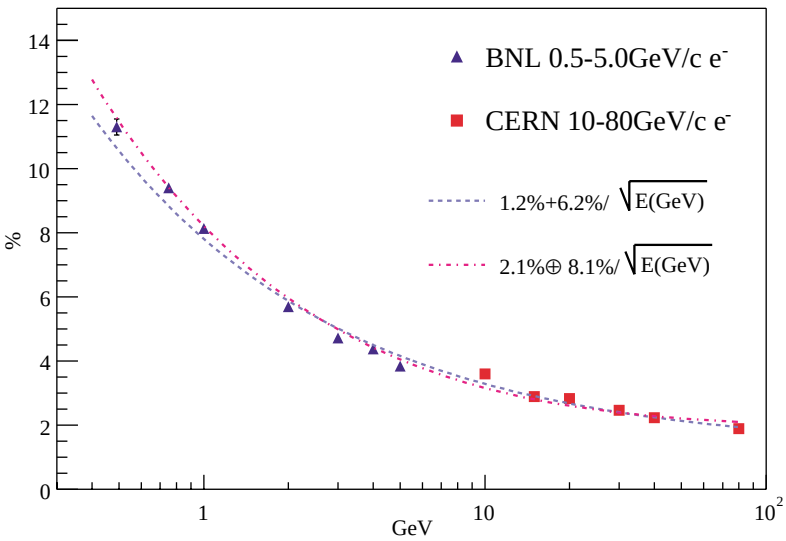

Fig. 5. Pb-scintillator EMCal energy resolution obtained by beam tests at CERN and BNL. The dashed line shows a fit to the linear formula $\sigma(E)/E = 1.2\% + 6.2\%/\sqrt{(E(\mathrm{GeV}))}$. The dashed-dotted line shows the fit to the quadratic formula $\sigma(E)/E = 2.1\% \oplus 8.1\%/\sqrt{(E(\mathrm{GeV}))}$.

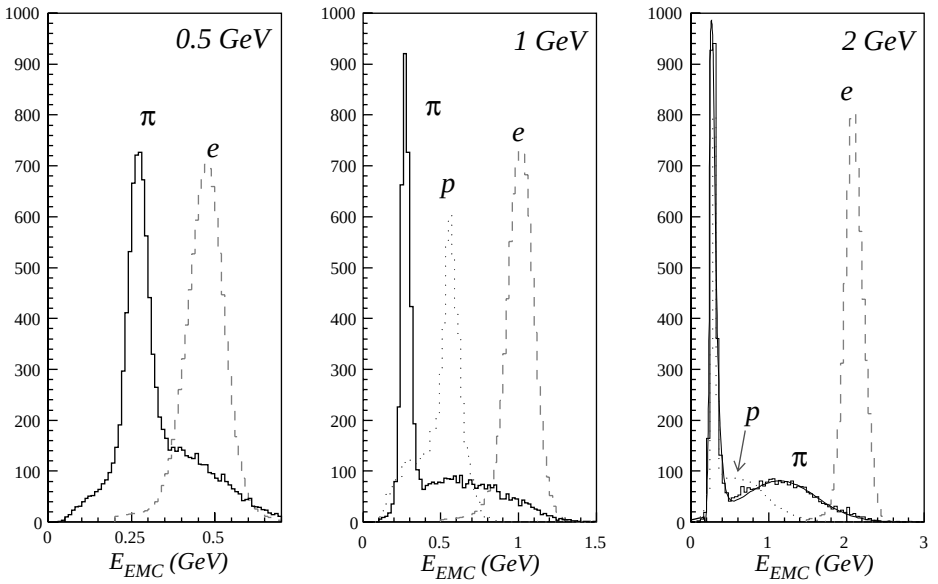

Fig. 6. The energy spectra measured in the PHENIX EMCal when exposed to electrons, pions and protons of 0.5, 1 and 2 GeV/c.

where $b_0 = 7.3$ mm is the average width of 1 GeV electromagnetic showers for $\theta = 0$ (orthogonal impact). At larger angles the contribution from longitudinal fluctuations becomes dominant and the position resolution degrades. All available data on position resolution can be well described by the simple formula

$$\sigma_x(E,\theta) = \sigma_0(E) \oplus \Delta \times \sin(\theta) \tag{3}$$

where

$$\sigma_0(E) = 1.55 \oplus \frac{5.7}{\sqrt{E}}(\text{mm}), \quad E(\text{GeV}) \tag{4}$$

is the position resolution for normal incidence and $\Delta \sim L_{\text{rad}}$.

2.4. Particle identification with the Pb-scintillator calorimeter

2.4.1. Effect of shower-shape measurements on photon identification and hadron rejection

Since electromagnetic and hadronic particles produce quite different patterns of energy sharing between calorimeter towers, second moments of the measured showers are often used to differentiate between them. However, in an earlier paper [8] we introduced a model which uses an analytical parametrization of the energy sharing and its fluctuations based upon measurements of identified electrons. The parameterization is used to compute $\chi^2 = \sum_i (E_i^{\text{pred}} - E_i^{\text{meas}})^2/\sigma_i^2$ where E_i^{meas} is the energy measured in tower i and E_i^{pred} is the predicted energy (using the parametrization and the actual measured impact point) for an electromagnetic particle of total energy $\sum_i E_i^{\text{meas}}$. This χ^2 value characterizes how "electromagnetic" a particular shower is and can be used to discriminate against hadrons. The important new feature of this model is that the fluctuations are also parameterized. Therefore, the resulting χ^2 distribution is close to the theoretical one and it is nearly independent of the energy or the impact angle of the electron. The χ^2 distributions for 2 GeV/c electrons and pions (with energy deposit above minimum ionization) are shown in Fig. 7. The arrow marks the χ^2 cut corresponding to 90% electron efficiency.

2.4.2. Time-of-flight measurements with the calorimeter

Timing information from the calorimeter is used both for particle identification and in the pattern

recognition to find overlapping showers. In particular, timing is the only tool to reject neutral baryons, and interacting antineutrons are a major contributor to clusters with energy ~ 2 GeV. Also, large inconsistencies between the measured times in different towers of the same cluster often indicate the overlap of two particles with very different time-of-flight.

Slew corrected arrival times measured by exposing the calorimeter to electrons, pions and protons at 1 GeV/c momenta are shown in Fig. 8 (top). The distribution for electrons has a perfectly Gaussian shape with only a few events in the tails. Both the pion and proton distributions show the presence of tails and are slightly asymmetric. The timing resolution curves (stochastic term) plotted in Fig. 8 combine the points measured by exposing the calorimeter to the particles in the 0.3–1.0 GeV/c momentum range.

For energy deposits in the calorimeter $\geqslant 0.5$ GeV the calorimeter timing resolution is nearly constant at ~ 120 ps for electrons and protons and ~ 270 ps for pions where shower fluctuations are the major contributor to the measured resolution. In general the data can be well fitted by the function:

$$\sigma_t = \sigma_{t0} + \sigma_{t1}/(E - E_{\text{threshold}}) \quad (5)$$

which includes a pole type divergence close to the threshold. Here σ_{t0} is an intrinsic timing resolution limit, presumably due to fluctuations in the localization of the shower, and σ_{t1} includes contributions due to photon statistics as well as pulse shape fluctuations.

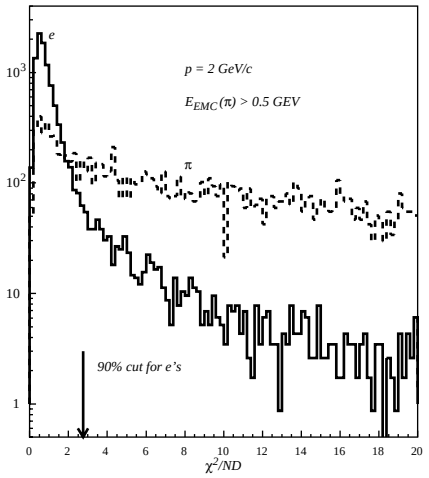

Fig. 7. χ^2 distribution for showers induced by 2 GeV/c electrons and pions in the Pb-scintillator calorimeter.

2.5. Pb-scintillator performance during first year running

Photons are identified using time-of-flight and showershape (χ^2) cuts. The inset in Fig. 9 shows the $\gamma\gamma$ invariant mass distribution for minimum bias data of the same reaction.

2.6. Summary for the Pb-scintillator calorimeter

We have designed and successfully constructed a 15,552 channel electromagnetic calorimeter covering a total area of 48 m^2 using an approach optimized for industrial mass production. We relied heavily on industrial style quality control procedures to insure conformity to physics specifications. The calorimeter has a light yield of $\sim 12{,}500$ photons/GeV of electromagnetic energy. The calorimeter has energy and position resolutions $\sim 8\%$ and ~ 7 mm, respectively, for 1 GeV photons and electrons at normal incidence and gives a π^0 mass with resolution of ~ 15 MeV. It has an excellent timing resolution of ~ 100 ps for electromagnetic and ~ 270 ps for hadronic showers which is nearly independent of the energy well above a threshold of about 10 MeV.

3. Lead-glass calorimeter

The Pb-glass calorimeter array comprises 9216 elements of a system previously used in CERN experiment WA98 [9]. It has a nominal energy resolution of $6\%/\sqrt{E(\text{GeV})}$ and an intrinsic timing resolution of better than 300 ps for electromagnetic showers above the minimum ionizing peak energy.

3.1. Pb-glass calorimeter design

3.1.1. Mechanical design

The Pb-glass calorimeter occupies the two lower sectors of the East Central arm of PHENIX. The

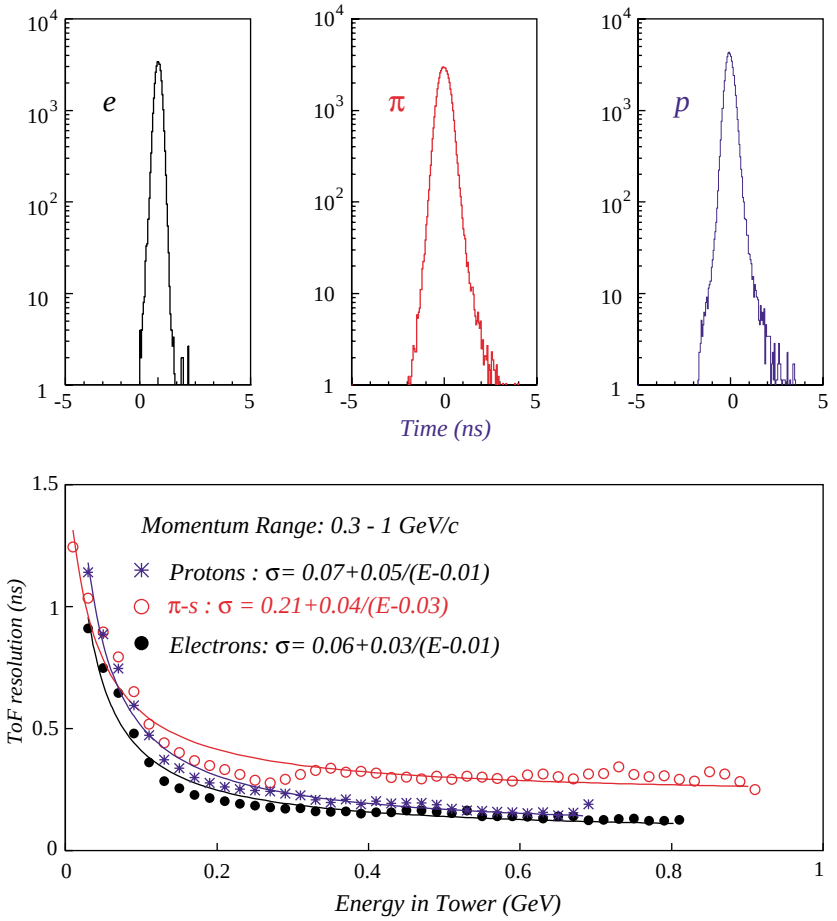

Fig. 8. Pb-scintillator timing resolution for different particles. Top: lineshape for 1 GeV/c electrons, pions and protons. Bottom: resolution in the momentum range 0.3–1.0 GeV/c.

PHENIX Time-of-flight system [10] is located on the Pb-glass sectors. Each Pb-glass sector comprises 192 supermodules (SM) in an array of 16 Pb-glass SM wide by 12 SM high as shown in Fig. 10. Each Pb-glass SM comprises 24 Pb-glass modules in a array of 6 Pb-glass modules wide by 4 modules high. Each Pb-glass module is 40 mm × 40 mm × 400 mm in size. The Pb-glass modules within a SM are individually wrapped with aluminized mylar and shrink tube and 24 modules are glued together with carbon fiber and epoxy resin to form a self-supporting SM with a shared calibration system (see Fig. 10). Steel sheets 0.5 mm in thickness were used to house the phototubes and bases. The sheets were incorporated during the gluing process. An aluminized plastic foil on the front of the SM contains a hole for each Pb-glass module which allows entry for the LED light used for gain monitoring. A polystyrene reflective dome encloses the LED system on the front surface of the SM.

Each Pb-glass module is read out with an FEU-84 photomultiplier. The high voltage for each photomultiplier is generated in a Cockcroft–Walton type photomultiplier base [11]. The high voltage for each module is individually controlled and read out with a custom VME based control system (HIVOC). Each HIVOC VME control

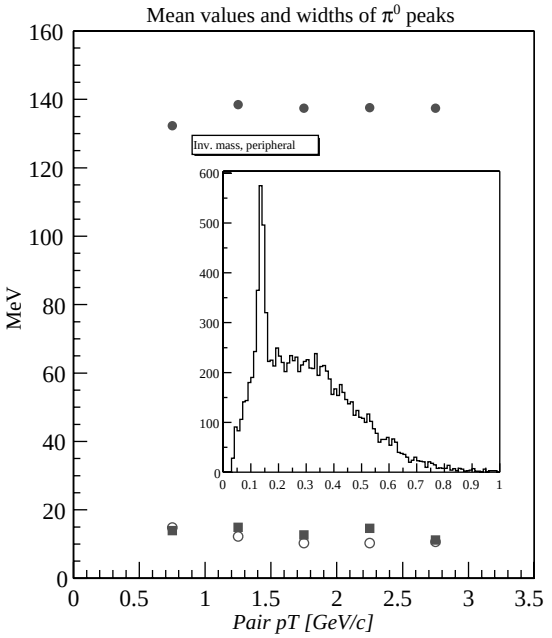

Fig. 9. Position and width of π^0 invariant mass peaks as a function of transverse momentum for peripheral Au–Au collisions at 130 GeV. The insert shows the $\gamma\gamma$ invariant mass distribution for minimum bias data of the same reaction. Closed squares show measured widths and open circles show simulated widths.

module can control up to 2048 photomultipliers. Six PbGl SMs, 2 SM wide by 3 SM high, (144 individual Pb-glass modules) are read out with a single Front End Electronics (FEE) motherboard. The physical parameters of the Pb-glass detector system are summarized in Table 2.

3.1.2. Calibration and monitoring system

Each Pb-glass supermodule (SM) has its own gain monitoring system based on a set of 3 LEDs which are viewed by all 24 Pb-glass modules within a SM [12]. Three LEDs with different characteristics are employed. They are a fixed amplitude avalanche yellow LED with pulse shape most like real showers together with a yellow and a blue LED which have amplitudes which may be varied. The absolute light yields of the LEDs of each SM are monitored by a photodiode which, together with preamp, is permanently attached to the SM. The photodiode-normalized avalanche yellow LED signal observed in each Pb-glass module was calibrated in GeV-equivalents using 10 GeV electrons in the CERN X1 beamline in Fall 1993 and Spring 1994. The GeV equivalent of the avalanche yellow LEDs in individual modules ranged from 5 to 10 GeV. The Pb-glass calibration has been maintained to within approximately 10% for PHENIX using the LED/photodiode system.

3.2. Test beam performance

The response of the Pb-glass electromagnetic calorimeter was studied extensively in test beams at the AGS(BNL) and SPS(CERN) to investigate the performance of the device with respect to energy, position and timing measurements and their variation with energy, position and angle of incidence.

3.2.1. Energy and position measurements

The measured energy resolution of e^+ showers versus the incident energy is shown in Fig. 11 for various angles of incidence on the calorimeter surface. The energy resolution results of Fig. 11 are shown with the fit parameterization

$$\frac{\sigma(E)}{E} = \frac{[5.9 \pm 0.1]\%}{\sqrt{E/\mathrm{GeV}}} \oplus [0.8 \pm 0.1]\%. \quad (6)$$

The measured position resolution can be fit with the parameterization

$$\sigma_x(E) = \frac{[8.4 \pm 0.3]\mathrm{mm}}{\sqrt{E/\mathrm{GeV}}} \oplus [0.2 \pm 0.1]\ \mathrm{mm}. \quad (7)$$

3.2.2. Particle identification

The EMCal is designed to identify and measure the total energy of electrons and photons. The identification is assisted by the fact that hadrons typically do not shower or they deposit only a small fraction of their total energy in the calorimeter, since it is only about one interaction length in thickness (see Table 2). The hadron response of the PbGl calorimeter is further reduced by the fact that it observes only Cherenkov light. The Cherenkov threshold momenta (energies) for muons, pions and protons are 81, 106 and 715 MeV/c (27, 36 and 241 MeV), respectively. When the hadron momenta fall below

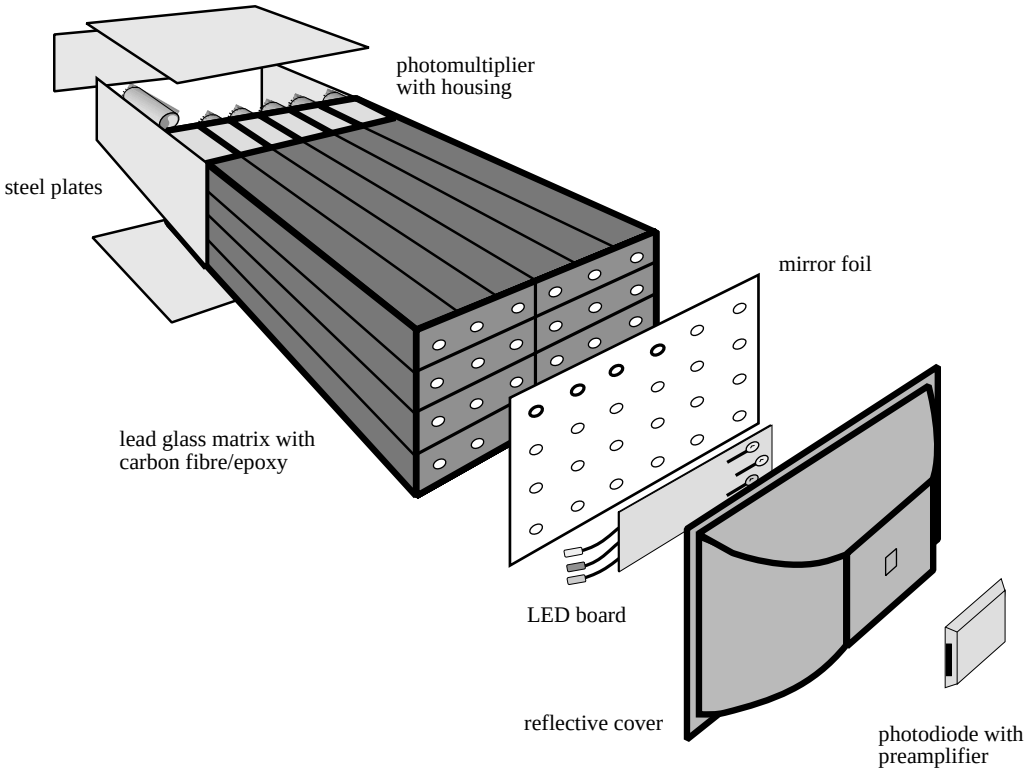

Fig. 10. Exploded view of a lead-glass detector supermodule.

these thresholds they will no longer produce Cherenkov light and their signal will be reduced. This is illustrated in Fig. 12 for 1 GeV/c protons and pions in comparison to electrons. The pions show a peak at around 460 MeV on a broad tail below the peak while the protons peak at around 80 MeV. At 4 GeV/c both protons and pions show a peak at about 540 MeV. At 500 MeV/c no significant signal is observed for protons and the pions show only a broad plateau from 0 to 500 MeV. At 150 MeV/c muons and pions deposit 55 and 25 MeV of apparent energy, respectively, when the electron signal is normalized to 150 MeV.

When the momentum of the charged hadron is measured in the PHENIX tracking system, the mismatch between the measured momentum and the deposited energy in the EMCal can be used to differentiate between hadrons and electrons. This is illustrated in the lower panel of Fig. 12. Using the fact that a 1 GeV/c track has been identified by the tracking system, the figure illustrates the fraction of electron tracks which would be accepted, as well as the fraction of pion tracks rejected, as a function of the required corresponding energy deposit in the Pb-glass. The pion rejection factors which can be obtained for various electron acceptance fractions as a function of the incident energy are shown in Fig. 13. An additional factor of about 2 can be obtained based on differences in the shower shape for hadrons which deposit the same energy as electromagnetic energy above about 1 GeV of energy deposit.

3.2.3. *Time-of-flight measurements*

The EMCal provides time-of-flight information to assist with hadron identification in the tracking system and to reject neutron and anti-neutron showers. The measured time-of-flight resolution as a function of the energy deposited in a single Pb-glass module is shown in Fig. 14 for electrons of various incident energies and pions of 1 GeV/c.

Table 2
Lead-glass physical parameters

Quantity	Value
Geometry:	384 Super Modules
Number of SM per sector	192 (16 wide by 12 high)
Number of modules per SM	24 (6 wide by 4 high)
Total number of modules	9216
Module gront surface	4 cm × 4 cm
Module length	40 cm ($14.4X_0$)
Mylar foil thickness	12 μm
Shrink tube thickness	150 μm
Super module front surface	24.6 ± 0.02 cm × 16.4 ± 0.02 cm
Pb-glass: Type	TF1
Pb-oxide content	51%
Density	3.85 g/cm^2
Weight per module	2.46 kg
Index of refraction	1.648
Total internal reflection angle	36°
Radiation length	2.8 cm
Moliere radius	3.68 cm
Interaction length	38.0 cm
Critical energy	16 MeV

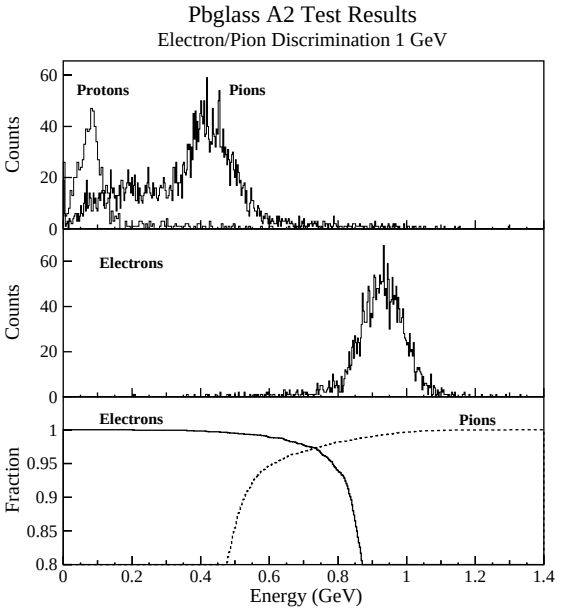

Fig. 12. Measured energy signal for protons, π^+ and e^+ of 1 GeV/c incident momentum. The lower panel shows the fraction of e^+ accepted or π^+ rejected for a varying threshold on the measured energy.

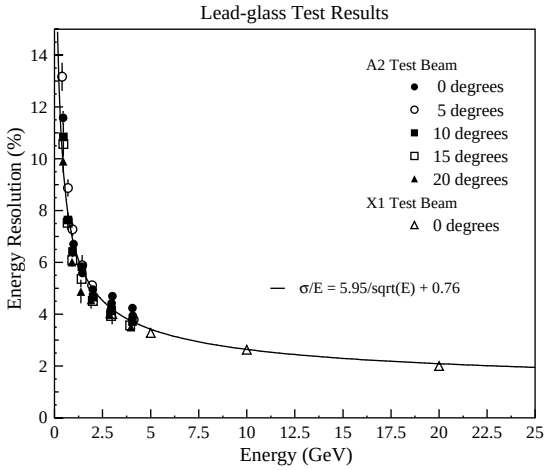

Fig. 11. PbGl energy resolution versus incident energy.

The timing resolution can be parameterized in the form

$$\sigma_t(E_{\mathrm{Dep.}}) = \frac{3.75\ \mathrm{ns}}{\sqrt{500 E_{\mathrm{Dep.}}/\mathrm{GeV}}} \oplus 0.075\ \mathrm{ns}. \qquad (8)$$

The intrinsic timing resolution is seen to be similar for electromagnetic showers and decreasing with the increasing energy deposit according to the light produced (about 500 photoelectrons per GeV). The resolution falls below 200 ps in the upper range of momenta of interest to PHENIX. However, the use of the timing information from the PbGl is complicated by the fact that the arrival time of hadrons or hadron showers which pass through the PbGl (those which deposit more than about 500 MeV) have apparent arrival times which are about 800 ps faster than an electron of the same momentum. This is due to light from the faster transit time of the hadron to the rear of the lead-glass module compared to that of the Cherenkov light from the electromagnetic shower produced near the front of the module.

3.3. Pb-glass calorimeter performance in PHENIX

One full sector of the Pb-glass calorimeter was fully instrumented for the first PHENIX run

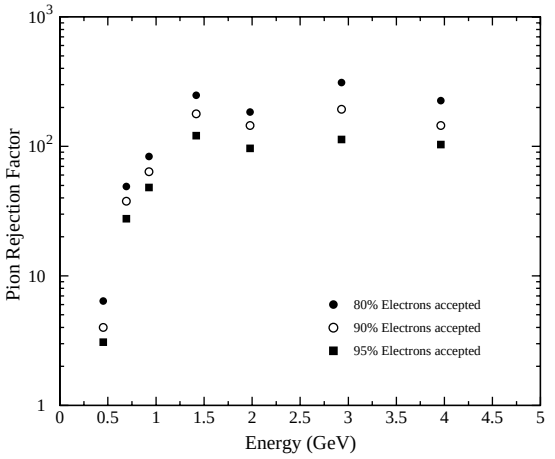

Fig. 13. Pion rejection factor versus incident energy.

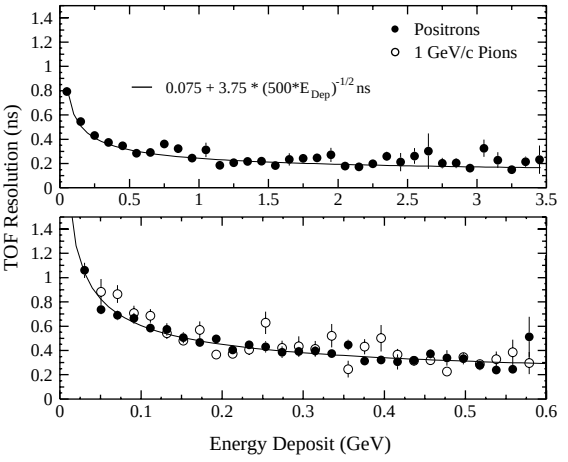

Fig. 14. Pb-glass timing resolution versus energy deposit in a single module for positrons of incident momenta 0.5, 0.75, 1.0, 1.5, 2,3 and 4.0 GeV/c and for 1.0 GeV/c pions.

period at RHIC with Au beams. An example of the performance is shown in Fig. 15 where the π^0 peak is observed in the two photon invariant mass distribution. The result is shown for peripheral Au–Au collisions at $\sqrt{s} = 130$ GeV per nucleon for photon pair transverse momentum in the range of 1.5–2.0 GeV/c.

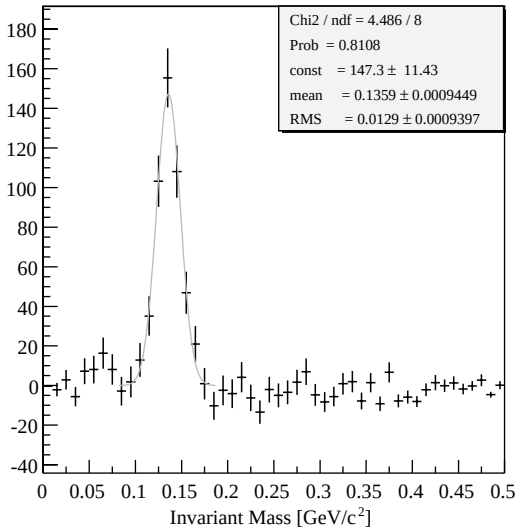

Fig. 15. The two photon invariant mass distribution after subtraction of the combinatorial pair background. The result is shown for peripheral Au–Au collisions at $\sqrt{s} = 130$ GeV per nucleon for photon pair transverse momentum in the range of 1.5–2.0 GeV/c.

4. Calorimeter front-end electronics

The readout electronics for the EMCal system conform to the general PHENIX Front-End Electronics (FEE) scheme [13] which includes periodic sampling synchronous with the RHIC RF clock and pipelined, deadtime-less conversion and readout. This section describes those features unique to the EMCal readout electronics and the way in which they satisfy the needs of the physics measurements made with the EMCal detector. Analog processing, digital processing and triggering are discussed below in Sections 4.1–4.3, respectively.

4.1. Analog processing

On every event, for either physics or calibration data, each EMCal PMT emits a negative current pulse and each of these is processed by a chain as shown in Fig. 16. The salient features of the chain are discussed below.

There is no preamp or shaping stage other than passive integration. The 93 Ω resistor terminates

the signal line from the PMT so the voltage profile at point A in Fig. 16 simply follows the current profile from the PMT which is a pulse with a $\leqslant 5$ ns rise time. The charge is collected onto the 500 pF capacitor so the voltage profile at point B in Fig. 16 follows the integral of the current. The current pulse is a step function with a ~ 100 ns rise time. The large resistor sets the quiescent voltage at this stage to +4 V to allow for negative-going pulses.

The fast voltage pulse discussed above is the "timing signal" that is used to measure the arrival time of the EM shower in the detector. During the pulse integration process a voltage step function is generated whose height is proportional to the total charge collected and thus the energy.collected during the time window of the event. All of the remaining analog processing stages up to ADC conversion are carried out within an ASIC [14] chip, as illustrated in Fig. 16. This chip was custom designed for the EMCal system. Each of these ASIC chips services four PMT channels and also contains the circuitry for the fast trigger function which is described below.

In the arrival time measurement the voltage pulse is discriminated, either in a leading-edge mode or a constant-fraction mode. The choice of mode, as well as the threshold voltages, are remotely selected in situ via ARCNet [13] which is the system used for monitoring and slow control of the PHENIX FEMs. The discriminator firing starts a voltage ramp generator. The ramp is stopped on the next edge of the RHIC clock providing a *common-stop mode* TAC for each channel. After stopping the ramp voltage is held for two clock cycles where it settles and is then sampled and converted in the AMU/ADC stage (see Section 4.2). The final reported ADC value then varies linearly with the pulse arrival time. The relationship between time and the resulting ADC output voltage can be adjusted by programming the ramp slope and offset voltage remotely via ARCNet.

The energy signal is first put through a Variable Gain Amplifier (VGA). Each PMT channel has its own VGA and each of whose gains can be set remotely in the range $\times 4$–$\times 12$ with 5-bit resolution. This allows the readout electronics to compensate, to within a few percent over its range, for gain variations among PMTs which share the same high voltage supply. Uniform response for the energy signal is useful in the performance of the trigger circuit (see Section 4.3) and in general for maximizing the use of the ADC dynamic range for all channels.

The dynamic range of physics signals from the EMCal is quite large and the detector is expected to resolve energy deposits from 20 MeV up to 15–30 GeV with a noise contribution from the electronics of no more than 0.1% for large signals and 5 MeV for small signals. This range is impossible to cover with a single 12-bit ADC

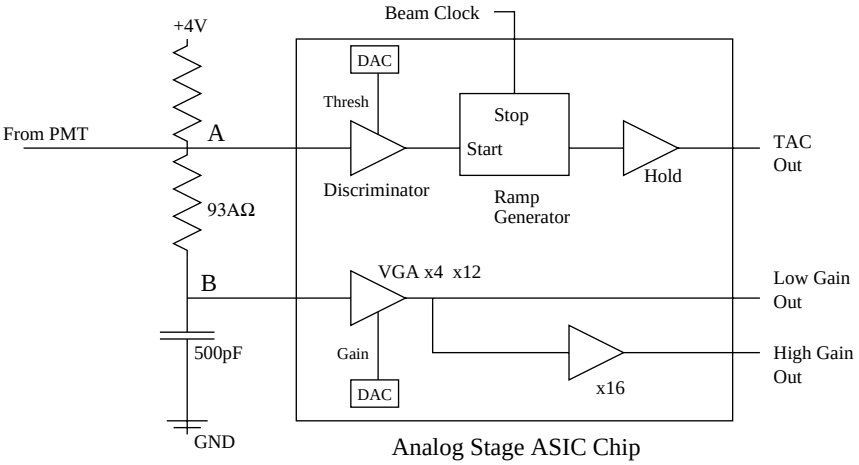

Fig. 16. Block diagram of the energy and timing measurement circuits.

conversion. Thus the energy signal is converted twice with two different levels of amplification. The "low gain" signal is converted straight from the VGA and the "high gain" signal is converted separately after a second stage of $\times 16$ amplification. The results of both conversions are available when the digital output packet is assembled as discussed in Section 4.2.

4.2. Conversion and digital processing

The voltage waveforms from the high- and low-gain energy stages and the TAC for each channel are sampled once per RHIC clock tick and stored in a series of Analog Memory Units (AMUs) as in several other PHENIX FEE systems [13]. Each waveform is sampled into a ring buffer of 64 AMUs, effectively preserving it for 64 RHIC clock ticks or about 7 μs, which easily covers the PHENIX LVL-1 (Level-1) trigger [13] latency of 40 RHIC clock ticks.

Upon receiving a LVL-1 Accept instruction the FEM identifies the energy and TAC AMU cells corresponding to the event. These AMU cells are then taken out of the ring buffer and converted in the ADC. The AMU rings and the ADC units are contained within another ASIC chip which was custom-designed for PHENIX and is used in several PHENIX readout systems. These ADC outputs are controlled, collected and reformatted by several Xilinx FPGAs, which are programmable remotely in situ. The formatted data "packet" for each event is then sent to a PHENIX Data Collection Module (DCM) [13] via GLINK across a PHENIX standard optical fiber.

4.3. EMCal fast trigger function

At design luminosities, the rate of basic interactions in both A–A and p–p running in RHIC is too high for PHENIX to digitize and record all events. Since it is an explicit goal of PHENIX to use the full available luminosity to measure rare processes such as the production of heavy flavors and very high-energy secondaries, an ability to trigger on such processes is necessary. The EMCal FEE provides a fast-trigger function intended to signal the presence of a high-energy shower in the EMCal detector. Electromagnetic showers with a large energy deposit (generally taken as above several GeV) are natural indicators of several kinds of interesting rare events, including high-energy photons and neutral mesons as well as high-energy electrons from heavy-flavor decays.

A traditional approach for a high-energy cluster trigger in a laterally segmented calorimeter is to make a fast analog sum of a group of towers and discriminate that sum against a threshold. In the simplest scheme each tower contributes to only one sum leaving the summed trigger groups disjointed. This arrangement has the drawback that the effective threshold is position dependent since showers which spread across more than one group need to have a much higher energy than those contained within one group.

The PHENIX EMCal fast trigger avoids this problem by summing over non-disjoint overlapping groups of towers. The design is illustrated in Fig. 17. Groups of 2×2 towers are served by one ASIC chip described above. Within each ASIC the four analog PMT signals are summed creating an array of disjoint 2×2 sums. To negate the influence of "hot" PMTs, each channel in each ASIC can be masked out of the sum individually by remote ARCNET control. Each ASIC relays copies of its signal generated by summing the current to three immediate neighbors. These are relayed between FEMs at supermodule boundaries making the trigger circuitry effectively seamless.

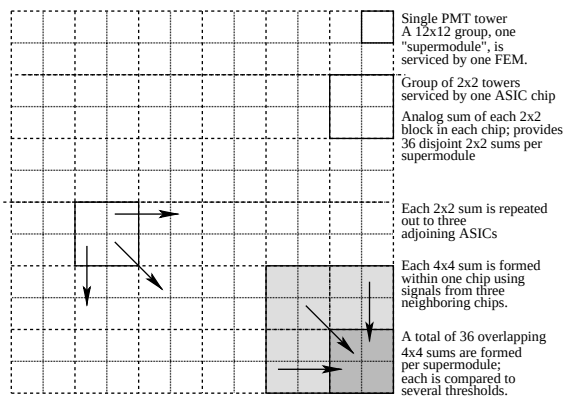

Fig. 17. Schematic of the EMCal fast trigger summing operation.

Each ASIC also receives three signals from its neighbors and combines them with its own to form a 4×4 sum. The entire circuitry then produces 36 overlapping 4×4 sums in each FEM. Within each ASIC the 4×4 sum signal is compared to three separate thresholds, each remotely programmable, to provide extra flexibility for different physics processes.

Acknowledgements

This work was supported by the Department of Energy (USA).

References

[1] J.C. Hill, et al., PHENIX Detector Overview, Nucl. Instr. and Meth. A (2003), this issue.
[2] T.K. Hemmick, et al., PHENIX Central Arm Tracking Detectors, Nucl. Instr. and Meth. A (2003), this issue.
[3] E. Kistenev, et al., Proceedings of the 5th International Conference on Calorimetry in High Energy Physics, World Scientific, Singapore, 1994, p. 211.
[4] G. David, et al., IEEE Trans. Nucl. Sci. NS-45 (1998) 692.
[5] G. David, et al., IEEE Trans. Nucl. Sci. NS-45 (1998) 705.
[6] J. Stumer, private communication.
[7] R. Wigmans, private communication.
[8] G. David, et al., IEEE Trans. Nucl. Sci. NS-47 (2000) 1982.
[9] WA98 Collaboration, CERN Report No. SPSLC 91-17 (1991).
[10] A.D. Frawley, et al., PHENIX Central Arm Particle I.D. Detectors, Nucl. Instr. and Meth. A (2003), this issue.
[11] S. Neumaier, et al., Nucl. Instr. and Meth. A 360 (1995) 593.
[12] T. Peitzmann, et al., Nucl. Instr. and Meth. A 376 (1996) 368.
[13] J.C. Hill, et al., PHENIX On-Line Systems, Nucl. Instr. and Meth. A (2003), this issue.
[14] M.S. Emery, et al., IEEE Trans. Nucl. Sci. NS-44 (1997) 374.

Available online at www.sciencedirect.com
SCIENCE DIRECT®
Nuclear Instruments and Methods in Physics Research A 499 (2003) 469–479
NUCLEAR INSTRUMENTS & METHODS IN PHYSICS RESEARCH Section A
www.elsevier.com/locate/nima

PHENIX detector overview

K. Adcox[a], S.S. Adler[b], M. Aizama[c], N.N. Ajitanand[d], Y. Akiba[e], H. Akikawa[f], J. Alexander[d], A. Al-Jamel[g], M. Allen[h], G. Alley[i], R. Amirikas[j], L. Aphecetche[k], Y. Arai[e], J.B. Archuleta[l], J.R. Archuleta[l], R. Armendariz[g], V. Armijo[l], S.H. Aronson[b], D. Autrey[m], R. Averbeck[n], T.C. Awes[i], B. Azmoun[n], A. Baldisseri[o], J. Banning[i], K.N. Barish[p], A.B. Barker[q], P.D. Barnes[l], J. Barrette[r], F. Barta[b], B. Bassalleck[s], S. Bathe[t], S. Batsouli[u], V.V. Baublis[v], A. Bazilevsky[w,x], R. Begay[n], J. Behrendt[s], S. Belikov[y,z], R. Belkin[b], F.G. Bellaiche[i], S.T. Belyaev[aa], M.J. Bennett[l], Y. Berdnikov[ab], S. Bhaganatula[z], J.C. Biggs[b], A.W. Bland[q], C. Blume[t], M. Bobrek[i], J.G. Boissevain[l], S. Boose[b], H. Borel[o], D. Borland[a], E. Bosze[p], S. Botelho[ac], J. Bowers[m], C. Britton[i], L. Britton[i], M.L. Brooks[l], A.W. Brown[q], D.S. Brown[g], N. Bruner[s], W.L. Bryan[i], D. Bucher[t], H. Buesching[t], V. Bumazhnov[w], G. Bunce[b,x], J. Burward-Hoy[n], S.A. Butsyk[n,v], M.M. Cafferty[l], T.A. Carey[l], J.S. Chai[ad], P. Chand[ae], J. Chang[p], W.C. Chang[af], R.B. Chappell[j], L.L. Chavez[s], S. Chernichenko[w], C.Y. Chi[u], J. Chiba[e], M. Chiu[u], S. Chollet[ag], R.K. Choudhury[ae], T. Christ[n], T. Chujo[b,c], M.S. Chung[ah,l], P. Chung[d], V. Cianciolo[i], D.J. Clark[l], Y. Cobigo[o], B.A. Cole[u], P. Constantin[z], R. Conway[l], K.C. Cook[z], D.W. Crook[j], H. Cunitz[u], R. Cunningham[l], M. Cutshaw[i], D.G. D'Enterria[k], C.M. Dabrowski[b], G. Danby[b], S. Daniels[i], A. Danmura[c], G. David[b], A. Debraine[ag], H. Delagrange[k], J. DeMoss[s], A. Denisov[w], A. Deshpande[x], E.J. Desmond[b], O. Dietzsch[ac], B.V. Dinesh[ae], J.L. Drachenberg[q], O. Drapier[ag], A. Drees[n], R. du Rietz[ai], A. Durum[w], D. Dutta[ae], K. Ebisu[aj], M.A. Echave[l], Y.V. Efremenko[i], K. El Chenawi[a], M.S. Emery[i], D. Engo[b], A. Enokizono[ak], K. Enosawa[c], H. En'yo[al,f], N. Ericson[i], S. Esumi[c], V.A. Evseev[v], L. Ewell[b], O. Fackler[m], J. Fellenstein[a], T. Ferdousi[p], J. Ferrierra[n], D.E. Fields[s], F. Fleuret[ag], S.L. Fokin[aa], B. Fox[x], Z. Fraenkel[am], S. Frank[i], A. Franz[b], J.E. Frantz[u], A.D. Frawley[j], J. Fried[b], J.P. Freidberg[an], E. Fujisawa[ao], H. Funahashi[f], S.-Y. Fung[p], S. Gadrat[ap], J. Gannon[b], S. Garpman[ai], F. Gastaldi[ag], T.F. Gee[i], R. Gentry[i], T.K. Ghosh[a], P. Giannotti[b], A. Glenn[h], A.L. Godoi[ac], M. Gonin[ag], G. Gogiberidze[h], J. Gosset[o], Y. Goto[x], R. Granier de Cassagnac[ag],

*Corresponding author. Tel.: +1-515-294-6580; fax: +1-515-294-6027.
E-mail address: jhill@iastate.edu (J.C. Hill).

0168-9002/03/$ - see front matter © 2002 Elsevier Science B.V. All rights reserved.
PII: S0168-9002(02)01950-2

S.V. Greene[a], V. Griffin[j], M. Grosse Perdekamp[x], S.K. Gupta[ae], W. Guryn[b], H.-Å. Gustafsson[ai], T. Hachiya[ak], J.S. Haggerty[b], S. Hahn[l], J. Halliwell[i], H. Hamagaki[aq], R.H. Hance[q], A.G. Hansen[l], H. Hara[aj], J. Harder[b], G.W. Hart[l], E.P. Hartouni[m], A. Harvey[m], L. Hawkins[b], R.S. Hayano[ar], H. Hayashi[c], N. Hayashi[al], X. He[as], N. Heine[t], F. Heistermann[b], S. Held[h], T.K. Hemmick[n], J.M. Heuser[n], M. Hibino[at], J.S. Hicks[i], R. Higuchi[c], J.C. Hill[z,*], T. Hirano[c], D.S. Ho[au], R. Hoade[b], W. Holzmann[d], K. Homma[ak], B. Hong[ah], A. Hoover[g], T. Honaguchi[x,ao], C.T. Hunter[q], D.E. Hurst[i], R. Hutter[n], T. Ichihara[al,x], V.V. Ikonnikov[aa], K. Imai[f,al], M. Inaba[c], M.S. Ippolitov[aa], L. Davis Isenhower[q], L. Donald Isenhower[q], M. Ishihara[al,x], M. Issah[d], V.I. Ivanov[v], B.V. Jacak[n,x], G. Jackson[i], J. Jackson[b], D. Jaffe[i], U. Jagadish[i], W.Y. Jang[ah], R. Jayakumar[an], J. Jia[n], B.M. Johnson[b], J. Johnson[i], S.C. Johnson[m,n], J.P. Jones[i], K. Jones[b], K.S. Joo[av], D. Jouan[aw], S. Kahn[b], F. Kajihara[aq], S. Kametani[at], N. Kamihara[x,ao], Y. Kamyshkov[i,h], A. Kandasamy[b], J.H. Kang[au], M.R. Kann[v], S.S. Kapoor[ae], J. Kapustinsky[l], K.V. Karadjev[aa], V. Kashikhin[y], S. Kato[c], K. Katou[at], H.-J. Kehayias[b], M.A. Kelley[b], S. Kelly[u], M. Kennedy[j], B. Khachaturov[am], A.V. Khanzadeev[v], A. Khomutnikov[ab], J. Kikuchi[at], D.J. Kim[au], D.-W. Kim[ax], G.-B. Kim[ag], H.J. Kim[au], S.Y. Kim[au], Y.G. Kim[au], W.W. Kinnison[l], E. Kistenev[b], A. Kiyomichi[c], C. Klein-Boesing[t], S. Klinksiek[s], L. Kluberg[ag], H. Kobayashi[x], V. Kochetkov[w], D. Koehler[s], T. Kohama[ak], B.G. Komkov[v], M.L. Kopytine[n], K. Koseki[c], L. Kotchenda[v,ay], D. Kotchetkov[p], Iou.A. Koutcheryaev[aa], A. Kozlov[am], V.S. Kozlov[v], P.A. Kravtsov[v], P.J. Kroon[b], C.H. Kuberg[q], L.G. Kudin[v], M. Kurata-Nishimura[c], V.V. Kuriatkov[v], K. Kurita[al,x], Y. Kuroki[c], M.J. Kweon[ah], Y. Kwon[au], G.S. Kyle[g], J.J. LaBounty[b], R. Lacey[d], J.G. Lajoie[z], J. Lauret[d], A. Lebedev[z], V.A. Lebedev[aa], V.D. Lebedev[v], D.M. Lee[l], S. Lee[ax], M.J. Leitch[l], M. Lenz[b], W. Lenz[b], X.H. Li[p], Z. Li[az,al], B. Libby[z], M. Libkind[m], W. Liccardi[b], D.J. Lim[au], S. Lin[b], M.X. Liu[l], X. Liu[az], Y. Liu[aw], Z. Liu[az], E. Lockner[s], N. Longbotham[q], J.D. Lopez[l], R. Machnowski[b], C.F. Maguire[a], J. Mahon[b], Y.I. Makdisi[b], V.I. Manko[aa], Y. Mao[az,al], S. Marino[b], S.K. Mark[r], S. Markacs[u], D.G. Markushin[v], G. Martinez[k], X.B. Martinez[l], M.D. Marx[n], A. Masaike[f], F. Matathias[n], T. Matsumoto[aq,at], P.L. McGaughey[l], M.C. McCain[q], J. Mead[b], E. Melnikov[w], Y. Melnikov[w], W.Z. Meng[b], M. Merschmeyer[t], F. Messer[n], M. Messer[b], Y. Miake[c], N.M. Miftakhov[v], S. Migluolio[an], J. Milan[d], T.E. Miller[a], A. Milov[am], K. Minuzzo[m], S. Mioduszewski[b,h], R.E. Mischke[l], G.C. Mishra[as], J.T. Mitchell[b], Y. Miyamoto[c], A.K. Mohanty[ae], B.C. Montoya[l], A. Moore[i], T. Moore[i], D.P. Morrison[b], G.G. Moscone[i], J.M. Moss[l], F. Mühlbacher[n], M. Muniruzzaman[p], J. Murata[al], M.M. Murray[l], M. Musrock[i], S. Nagamiya[e], Y. Nagasaka[aj], J.L. Nagle[y], Y. Nakada[f], T. Nakamura[ak],

B.K. Nandi[p], J. Negrin[b], J. Newby[h], L. Nikkinen[r], S.A. Nikolaev[aa], P. Nilsson[ai], S. Nishimura[aq], A.S. Nyanin[aa], J. Nystrand[ai], E. O'Brien[b], P. O'Conner[b], F. Obenshain[i], C.A. Ogilvie[z], H. Ohnishi[b,ak], I.D. Ojha[ba,a], M. Ono[c], V. Onuchin[w], A. Oskarsson[ai], L. Österman[ai], I. Otterlund[ai], K. Oyama[aq,ar], L. Paffrath[b], A.P.T. Palounek[l], C.E. Pancake[n], V.S. Pantuev[n], V. Papavassiliou[g], S.F. Pate[g], T. Peitzmann[t], R. Petersen[m], A.N. Petridis[z], C.H. Pinkenburg[b,d], R.P. Pisani[b], P. Pitukhin[w], T. Plagge[z], F. Plasil[i], M. Pollack[n,h], K. Pope[h], R. Prigl[b], M.L. Purschke[b], A.K. Purwar[n], J.M. Qualls[q], S. Rankowitz[b], G. Rao[i], R. Rao[i], M. Rau[b], I. Ravinovich[am], R. Raynis[b], K.F. Read[i,h], K. Reygers[t], G. Riabov[v], V.G. Riabov[v,ab], Yu.G. Riabov[v], S.H. Robinson[l], G. Roche[ap], A. Romana[ag], M. Rosati[z], E.V. Roschin[v], A.A. Rose[a], P. Rosnet[ap], R. Roth[l], R. Ruggiero[b], S.S. Ryu[au], N. Saito[al,x], A. Sakaguchi[ak], T. Sakaguchi[aq,at], S. Sakai[c], H. Sako[c], T. Sakuma[al,ao], S. Salomone[n], V.M. Samsonov[v], W.F. Sandhoff Jr.[b], L. Sanfratello[s], T.C. Sangster[m], R. Santo[t], H.D. Sato[f,al], S. Sato[c], R. Savino[b], S. Sawada[e], B.R. Schlei[l], R. Schleuter[bb], Y. Schutz[k], M. Sekimoto[e], V. Semenov[w], R. Seto[p], Y. Severgin[y], A. Shajii[an], V. Shangin[y], M.R. Shaw[q], T.K. Shea[b], I. Shein[w], V. Shelikhov[w], T.-A. Shibata[al,ao], K. Shigaki[e], T. Shiina[l], T. Shimada[c], Y.H. Shin[au], I.G. Sibiriak[aa], D. Silvermyr[ai], K.S. Sim[ah], J. Simon-Gillo[l], M. Simpson[i], C.P. Singh[ba], V. Singh[ba], W. Sippach[u], M. Sivertz[b], H.D. Skank[z], S. Skutnik[z], G.A. Sleege[z], D.C. Smith[i], G.D. Smith[l], M. Smith[i], A. Soldatov[w], G.P. Solodov[v], R.A. Soltz[m], W.E. Sondheim[l], S. Sorensen[i,h], I. Sourikova[b], F. Staley[o], P.W. Stankus[i], N. Starinsky[r], S. Steffens[h], E.M. Stein[b], P. Steinberg[u], E. Stenlund[ai], M. Stepanov[g], A. Ster[bc], J. Stewering[t], W. Stokes[b], S.P. Stoll[b], M. Sugioka[al,ao], T. Sugitate[ak], J.P. Sullivan[l], Y. Sumi[ak], Z. Sun[az], M. Suzuki-Nara[c], E.M. Takagui[ac], A. Taketani[al], M. Tamai[at], K.H. Tanaka[e], Y. Tanaka[aj], E. Taniguchi[al,ao], M.J. Tannenbaum[b], V.I. Tarakanov[v], O.P. Tarasenkova[v], J.D. Tepe[q], R. Thern[b], J.H. Thomas[m], J.L. Thomas[n], T.L. Thomas[s], W.D. Thomas[z], G.W. Thornton[l], W. Tian[az,h], R. Todd[i], J. Tojo[f,al], F. Toldo[b], H. Torii[f,al], R.S. Towell[q,l], J. Tradeski[b], V.A. Trofimov[v], I. Tserruya[am], H. Tsuruoka[c], A.A. Tsvetkov[aa], S.K. Tuli[ba], G. Turner[i], H. Tydesjö[ai], N. Tyurin[w], S. Urasawa[c], A. Usachev[w], T. Ushiroda[aj], H.W. van Hecke[l], M. Van Lith[b], A.A. Vasiliev[aa], V. Vasiliev[y], M. Vassent[ap], C. Velissaris[g], J. Velkovska[n], M. Velkovsky[n], W. Verhoeven[t], L. Villatte[h], A.A. Vinogradov[aa], V.I. Vishnevskii[v], M.A. Volkov[aa], W. Von Achen[b], A.A. Vorobyov[v], E.A. Vznuzdaev[v], M. Vznuzdaev[v], J.W. Walker[i], Y. Wan[az], H.Q. Wang[p], S. Wang[j], Y. Watanabe[al,x], L.C. Watkins[i], T. Weimer[z], S.N. White[b], B.R. Whitus[i], C. Williams[i], P.S. Willis[q], A.L. Wintenberg[i], C. Witzig[b], F.K. Wohn[z], K. Wolniewicz[b], B.G. Wong-Swanson[l], L. Wood[z], C.L. Woody[b], L.W. Wright[j], J. Wu[n], W. Xie[p,am],

N. Xu[h], K. Yagi[c], R. Yamamoto[m], Y. Yang[b,az], S. Yokkaichi[al], Y. Yokota[c], S. Yoneyama[ao], G.R. Young[i], I.E. Yushmanov[aa], W.A. Zajc[u], C. Zhang[u], L. Zhang[u], Z. Zhang[n], S. Zhou[az]

[a] *Vanderbilt University, Nashville, TN 37235, USA*
[b] *Brookhaven National Laboratory, Upton, NY 11973-5000, USA*
[c] *Institute of Physics, University of Tsukuba, Tsukuba, Ibaraki 305, Japan*
[d] *Chemistry Department, State University of New York—Stony Brook, Stony Brook, NY 11794, USA*
[e] *KEK, High Energy Accelerator Research Organization, Tsukuba-shi, Ibaraki-ken 305-0801, Japan*
[f] *Kyoto University, Kyoto 606, Japan*
[g] *New Mexico State University, Las Cruces, NM 88003, USA*
[h] *University of Tennessee, Knoxville, TN 37996, USA*
[i] *Oak Ridge National Laboratory, Oak Ridge, TN 37831, USA*
[j] *Florida State University, Tallahassee, FL 32306, USA*
[k] *SUBATECH (Ecole des Mines de Nantes, IN2P3/CNRS, Universite de Nantes) BP 20722-44307, Nantes Cedex 3, France*
[l] *Los Alamos National Laboratory, Los Alamos, NM 87545, USA*
[m] *Lawrence Livermore National Laboratory, Livermore, CA 94550, USA*
[n] *Department of Physics and Astronomy, State University of New York - Stony Brook, Stony Brook, NY 11794, USA*
[o] *DSM/Dapnia/SPhN, CEA/Saclay, 91191 Gif-sur-Yvette Cedex, France*
[p] *University of California—Riverside, Riverside, CA 92521, USA*
[q] *Abilene Christian University, Abilene, TX 79699, USA*
[r] *McGill University, Montreal, Que., Canada H3A 2T8*
[s] *University of New Mexico, Albuquerque, NM 87131, USA*
[t] *Institut für Kernphysik, University of Münster, D-48149 Münster, Germany*
[u] *Columbia University, New York, NY 10027 and Nevis Laboratories, Irvington, NY 10533, USA*
[v] *PNPI, Petersburg Nuclear Physics Institute, Gatchina, Russia*
[w] *Institute for High Energy Physics (IHEP), Protvino, Russia*
[x] *RIKEN BNL Research Center, Brookhaven National Laboratory, Upton, NY 11973-5000, USA*
[y] *Efremov Institute for Electrophysical Research, St. Petersburg, Russia*
[z] *Iowa State University, Ames, IA 50011, USA*
[aa] *Russian Research Center ''Kurchatov Institute'', Moscow, Russia*
[ab] *St. Petersburg State Technical University, St. Petersburg, Russia*
[ac] *Universidade de São Paulo, Instituto de Física, Caixa Postal 66318, São Paulo CEP05315-970, Brazil*
[ad] *C.A.L., Korea Cancer Hospital, Seoul 139-706, South Korea*
[ae] *Bhabha Atomic Research Centre, Bombay 400 085, India*
[af] *Institute of Physics, Academia Sinica, Taipei 11529, Taiwan*
[ag] *L.L.R., Ecole Polytechnique, 91128 Palaiseau, France*
[ah] *Korea University, Seoul 136-701, South Korea*
[ai] *Department of Physics, Lund University, Box 118, SE-221 00 Lund, Sweden*
[aj] *Nagasaki Institute of Applied Science, Nagasaki-shi, Nagasaki 851-0193, Japan*
[ak] *Hiroshima University, Kagamiyama, Higashi-Hiroshima 739-8526, Japan*
[al] *RIKEN (The Institute of Physical and Chemical Research), Wako, Saitama 351-0198, Japan*
[am] *Weizmann Institute, Rehovot 76100, Israel*
[an] *Plasma Science and Fusion, Center Massachusetts Institute of Technology, Cambridge, MA 02139, USA*
[ao] *Department of Physics, Tokyo Institute of Technology, Tokyo, 152-8551, Japan*
[ap] *L.P.C., Universite Blaise Pascal, 63177 Aubiere Cedex, France*
[aq] *Center for Nuclear Study, Graduate School of Science, University of Tokyo, 7-3-1 Hongo, Bunkyo, Tokyo 113-0033, Japan*
[ar] *University of Tokyo, Tokyo, Japan*
[as] *Georgia State University, Atlanta, GA 30303, USA*
[at] *Waseda University, Advanced Research Institute for Science and Engineering, 17 Kikui-cho, Shinjuku-ku, Tokyo 162-0044, Japan*
[au] *Yonsei University, IPAP, Seoul 120-749, South Korea*
[av] *Myongji University, Yongin, Kyonggido 449-728, South Korea*
[aw] *I.P.N., BP 1, 91406 Orsay, France*
[ax] *Kangnung National University, Kangnung 210-702, South Korea*
[ay] *State Interphysica, Protvino, Russia*
[az] *China Institute of Atomic Energy (CIAE), Beijing, People's Republic of China*

[ba] Department of Physics, Banaras Hindu University, Varanasi 221005, India
[bb] Lawrence Berkeley National Laboratory, Berkeley, CA 94720, USA
[bc] KFKI Research Institute for Particle and Nuclear Physics (RMKI), Budapest, Hungary

The PHENIX Collaboration

Abstract

The PHENIX detector is designed to perform a broad study of A–A, p–A, and p–p collisions to investigate nuclear matter under extreme conditions. A wide variety of probes, sensitive to all timescales, are used to study systematic variations with species and energy as well as to measure the spin structure of the nucleon. Designing for the needs of the heavy-ion and polarized-proton programs has produced a detector with unparalleled capabilities. PHENIX measures electron and muon pairs, photons, and hadrons with excellent energy and momentum resolution. The detector consists of a large number of subsystems that are discussed in other papers in this volume. The overall design parameters of the detector are presented.
© 2002 Elsevier Science B.V. All rights reserved.

PACS: 25.75.−q; 29.30.−h; 29.40.−n

Keywords: RHIC; PHENIX; Heavy ions; Spectrometer

1. Introduction

The Relativistic Heavy Ion Collider (RHIC) at Brookhaven National Laboratory accelerates nuclear beams from protons to gold. For the heaviest beams an energy of 100 GeV/nucleon is reached. Four detectors, BRAHMS, PHENIX, PHOBOS and STAR, are operating to study collisions ranging from p–p to Au–Au. The Pioneering High Energy Nuclear Interaction eXperiment (PHENIX) is carried out by a collaboration of about 500 physicists and engineers from 54 participating institutions in 13 countries [1]. Fig. 1 shows a subset of the Collaboration standing in front of parts of the PHENIX detector.

The PHENIX experiment probes several fundamental features of the strong interaction. A prime goal for experiments with heavy ion beams is to produce a deconfined state of nuclear matter called the Quark Gluon Plasma (QGP) and study it's properties. This is thought to be the state of the universe a μs after its birth in the "big bang". Measuring leptons and photons probes the QGP phase directly, while studying the copiously produced hadrons gives information on the later hadronization of the QGP. RHIC also provides the opportunity to study collisions of polarized protons. The aim is to measure the spin structure of the nucleon [2].

In order to carry out this broad physics agenda the PHENIX detector utilizes a variety of detector technologies. It uses global detectors to characterize the collisions, a pair of central spectrometers at mid-rapidity to measure electrons, hadrons, and photons, and a pair of forward spectrometers to measure muons. Each spectrometer has a large geometric acceptance of about one steradian and excellent energy and momentum resolution and particle identification.

2. Physics goals of PHENIX

Quantum Chromodynamics (QCD) predicts that heavy nuclei colliding at ultrarelativistic energies will undergo a phase transition from hadronic matter to a deconfined state of quarks and gluons moving freely over a volume approximately 10 fm^3, namely the QGP.

This process can be thought of as proceeding through a series of steps from the initial collision through QGP formation (deconfinement) and

Fig. 1. Members of the PHENIX collaboration in front of the PHENIX detector.

possible chiral symmetry restoration. The QGP would thermalize followed by expansion and cooling leading to hadronization. PHENIX is able to probe each phase of the above process by virtue of its ability to study the rare processes involving photons, electrons and muons as well as the predominant hadronic production. The experiment has a high rate capability and fine granularity combined with excellent momentum, energy and mass resolution.

Direct photons and lepton pairs which emerge from the collision with a minimum of final state interaction are sensitive to the full time evolution from the initial state through thermalization. The capability to measure direct photons over a wide range of p_T is unique to PHENIX and is important for relating their momentum to the temperature of the emitting source.

Jets from the hard scattering of constituent quarks and gluons are produced in the initial state and are sensitive to the properties of the medium during the evolution so that a significant modification of the structure of the jet is expected if a QGP is formed. PHENIX studies the deconfined state and Debye screening by observing the yields of the J/Ψ and Ψ' relative to that of the Υ. Chiral symmetry restoration is predicted to result in the reduction of quark masses and possible changes in the lifetime and width of the ϕ and possibly the ρ and ω. All of the above vector mesons are studied by observation of their decays into lepton pairs.

After hadronization the expansion of the fireball is studied by measurement of Hanbury–Brown–Twiss correlations and the coalescence probabilities of various nuclei and anti-nuclei give insights into the space-time evolution of the collision. Precision time-of-flight (ToF) allows measurement of the identified charged hadron spectrum over a wide p_T range. Many of the above signals can also be produced from interactions between particles in hot hadronic matter. It is thus necessary to understand the purely hadronic effects. For this reason PHENIX studies the above signals using p–p and p–A collisions to gain a better understanding of effects distorting signals from the QGP.

A second major goal of the PHENIX experiment is to measure the spin structure of the nucleon. RHIC accelerates beams of polarized protons up to 250 GeV with polarizations up to 50%. Work of the EMC [3] collaboration and others indicated that the fraction of the proton spin carried by the quarks was only about half of the expected value. PHENIX studies the gluon polarization by measuring high p_T prompt photon production using the highly segmented EM Calorimeter to minimize interference from photons from π^0 decays. The anti-quark polarization is measured by observing the parity violating asymmetry for W production. The W particles are identified by the detection of muons or electrons with $p_T \geqslant 20$ GeV/c using the PHENIX north and south muon arms or the central spectrometer, respectively.

3. PHENIX detector subsystems

The PHENIX detector comprises four instrumented spectrometers or arms and three global detectors [4]. The detector consists of a number of subsystems. The rapidity and ϕ coverages and other features of these subsystems is given in Table 1 and a perspective drawing of the PHENIX detector with the major subsystems labeled is shown in Fig. 2. Also an overview of the subsystems is given below. The east and west central arms are centered at zero rapidity and instrumented to detect electrons, photons and charged hadrons. The north and south forward arms have full azimuthal coverage and are instrumented to detect muons. Each of the four arms has a geometric acceptance of approximately one steradian. The global detectors measure the start time, vertex and multiplicity of the interactions. A photograph of the PHENIX detector from above is shown in Fig. 3.

3.1. Global detectors

In order to characterize the nature of an event following a heavy ion collision, three global detectors are employed. They consist of Zero-Degree Calorimeters (ZDC), Beam-Beam Counters (BBC) and the Multiplicity-Vertex Detector (MVD). A pair of ZDCs [5] detect neutrons from grazing collisions and form a trigger for the most peripheral collisions. The ZDC is used by all four RHIC detectors and is discussed elsewhere in this volume [6]. A pair of BBCs [7] provide a measure of the ToF of forward particles to determine the time of a collision, provide a trigger for the more central collisions and provide a measure of the collision position along the beam axis. The MVD [7] provides a more precise determination of event position and multiplicity and measures fluctuations of the charged particle distributions. It is composed of concentric barrels of silicon-strip detectors and endcaps made of silicon pads. Recently a Normalization Trigger Counter (NTC) [7] has been added between the MVD endcaps and the central magnet pole tips. The NTC extends the coverage of the BBC for p–p and p–A running.

3.2. Central spectrometers

The magnetic field for the central spectrometer is supplied by the central magnet [8] that provides an axial field parallel to the beam and around the interaction vertex. The central arms consist of tracking systems for charged particles and electromagnetic calorimetry. The calorimeter [9] is the outermost subsystem on the central arms and provides measurements of both photons and energetic electrons. A lead-scintillator (PbSc) calorimeter is used for good timing and a lead–glass (PbGl) calorimeter gives good energy resolution.

The tracking system uses three sets of Pad Chambers (PC) [10] to provide precise three-dimensional space points needed for pattern recognization. The precise projective tracking of the drift chambers (DC) [10] is the basis of the excellent momentum resolution. A Time Expansion Chamber (TEC) [10] in the east arm provides additional tracking and particle identification. The ToF and Ring-Imaging Cherenkov (RICH) detectors also provide particle identification [11]. The 85 ps timing resolution of the ToF allows separation of kaons from pions up to 2.5 GeV/c and proton identification out to 5 Gev/c. For p–p

Table 1
Summary of the PHENIX detector subsystems

Element	$\Delta\eta$	$\Delta\phi$	Purpose and special features
Magnet			
Central (CM)	± 0.35	360°	Up to 1.15 T m
Muon (MMS)	-1.1–-2.2	360°	0.72 T m for $\eta = 2$
Muon (MMN)	1.1–2.4	360°	0.72 T m for $\eta = 2$
Silicon (MVD)	± 2.6	360°	$d^2N/d\eta\, d\phi$, precise vertex, Reaction plane determination
Beam–beam (BBC)	$\pm(3.1$–$3.9)$	360°	Start timing, fast vertex
NTC	$\pm(1$–$2)$	320°	Extend coverage of BBC for p–p and p–A
ZDC	± 2 mrad	360°	Minimum bias trigger
Drift chambers (DC)	± 0.35	$90^\circ \times 2$	Good momentum and mass resolution $\Delta m/m = 1.0\,\%$ at $m = 1$ GeV
Pad chambers (PC)	± 0.35	$90^\circ \times 2$	Pattern recognition, tracking for nonbend direction
TEC	± 0.35	90°	Pattern recognition, dE/dx Good momentum resolution for $p_T > 4$ GeV/c
RICH	± 0.35	$90^\circ \times 2$	Electron identification
ToF	± 0.35	45°	Good hadron identification, $\sigma < 100$ ps
T0	± 0.35	45°	Improve ToF timing for p–p and p–A
PbSc EMCal	± 0.35	$90^\circ + 45^\circ$	For both calorimeters, photon and electron detection and energy measurement
PbGl EMCal	± 0.35	45°	Good $e^\pm/\pi^\pm$ separation at $p > 1$ GeV/c by EM shower and $p < 0.35$ GeV/c by ToF $K^\pm/\pi^\pm$ separation up to 1 GeV/c by ToF
μ *tracker*			
(μTS)	-1.15 to -2.25	360°	Tracking for muons
(μTN)	1.15 to 2.44	360°	Muon tracker north installed for year-3
μ *identifier*			
(μIDS)	-1.15 to -2.25	360°	Steel absorbers and Iarocci tubes for
(μIDN)	1.15 to 2.44	360°	muon/hadron separation

running the ToF timing resolution would be poorer than for heavy ions due to a reduced number of particles in the BBC. The ToF timing is improved by the use of a T0 counter [11] outside the barrel of the MVD. This is needed for p–p and p–A experiments. The RICH provides separation of electrons from the large number of copiously produced pions. Using information from the RICH, the TEC and the electromagnetic calorimeter it is possible to reject pion contamination of identified electrons to one part in 10^4 over a wide range of momentum.

3.3. Muon spectrometers

The two forward muon spectrometers [12] give PHENIX acceptance for J/Ψ decaying into dimuons at rapidities of $-2.25 \leqslant y \leqslant -1.15$ for the south arm and $1.15 \leqslant y \leqslant 2.44$ for the north arm. Each spectrometer is based on a muon tracker inside a radial magnetic field [8] followed by a muon identifier, both with full azimuthal acceptance. The muon trackers consist of three stations of multi-plane drift chambers that provide precision tracking. The muon identifiers consist of

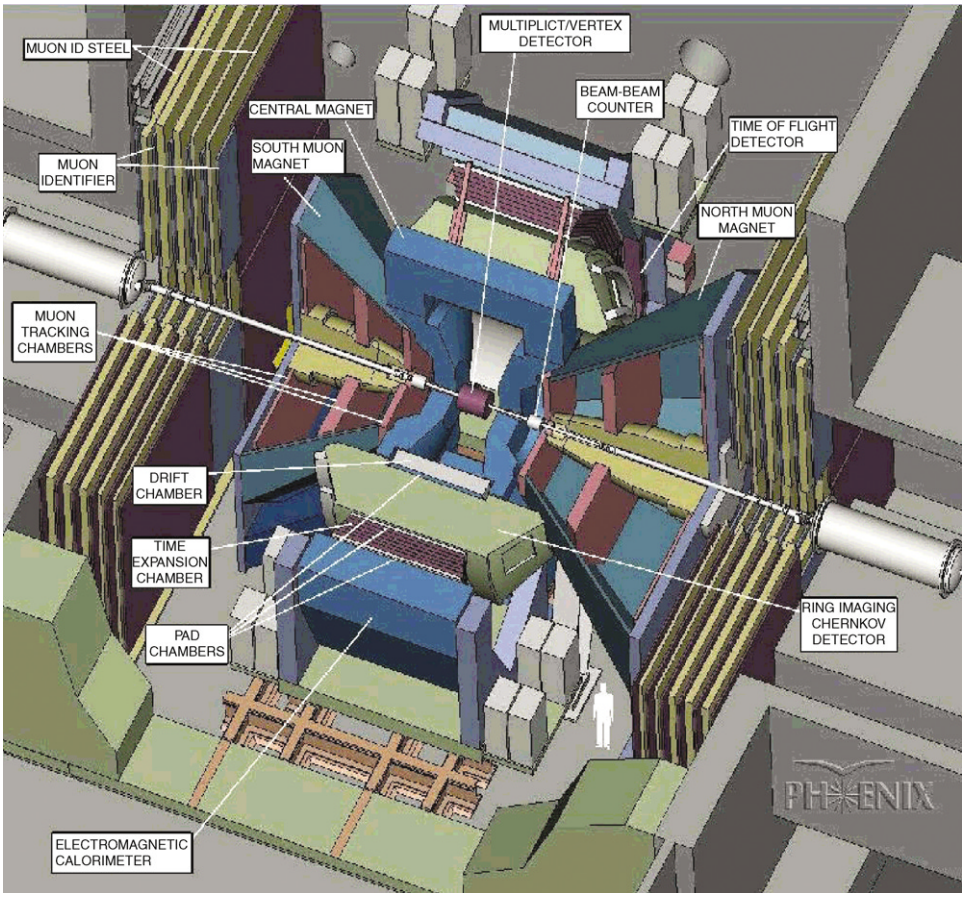

Fig. 2. A cutaway drawing of the PHENIX detector. Labeled arrows point to the major detector subsystems.

alternating layers of steel absorbers and low resolution tracking layers of streamer tubes of the Iarocci type. With this combination the pion contamination of identified muons is typically 3×10^{-3}. The complete north arm will be installed prior to the year-3 PHENIX run.

3.4. Electronics and computing

PHENIX selects and archives events of potential physics interest at the maximum rate consistent with the available RHIC luminosity. The channel count for the PHENIX detector is large and details for the various subdetectors is given in Table 2. Note that for some subsystems two ADCs are required per channel to get the needed dynamic range. In order to obtain a high data-collection efficiency a high degree of coordination between the electronics and computing efforts is required. Custom Front-End Electronics (FEE) were designed for the PHENIX subsystems. Signals from the FEEs [13] are transported by optical fibers to the level-1 trigger [13] that processes signals from a number of subsystems and then either accepts or rejects the event. The trigger operates in a synchronous pipelined mode with a latency of 40 beam crossings, and thus generates a decision for each crossing. The timing of the above operations is coordinated by a master timing system [13] that distributes the RHIC clocks to granule timing modules that communicate with the FEEs.

In order to study the rare event physics for which PHENIX was designed, it is necessary to have a higher level of event rejection than possible

with the level-1 trigger alone. Therefore a level-2 software trigger [13] that makes its selection after a complete event is assembled was developed.

Table 2
Channel counts, digitizer channels and LVL-1 trigger bits/sums for PHENIX

Subsystem symbol	Detector channels	ADC channels	TDC channels	LVL-1 inputs
BB	128	128	256	128 bits
MVD	20,736	20,736		
NTC	8	8	16	8 bits
DC	12,800		12,800	
PC	172,800		172,800	
TEC	20,480	20,480		
RICH	5120	5120	5120	256 bits
ToF	1920	1920	1920	1920 bits
T0	22	22	44	22 bits
EMCal	24,768	49,536	24,768	688 bits
μTR	43,968	43,968		
μID	6340		6340	6340 bits

Once the level-1 trigger accepts an event, the data from the various subsystems is routed via fiber-optic cable to the data collection modules [13]

Table 3
Performance of the PHENIX detector

Physics	Year-2 version
Electrons	$\pi/e < 10^{-4}$ at $p \leqslant 4.7$ GeV/c RICH for <4.7 GeV/c TEC (dE/dx) for <2 GeV/c EMCal for >0.5 GeV/c
Photons	$p_T \geqslant 1$ GeV/c for 0.5 sr with PbGl $p_T \geqslant 1$ GeV/c for 1.5 sr with PbSc Single γs resolved from merging $\pi^0 \to \gamma + \gamma$ out to $p_T \geqslant 25$ GeV/c
Hadrons	$\leqslant 2.3$ GeV/c π for 0.38 sr $\leqslant 1.6$ GeV/c K for 0.38 sr $\leqslant 5.0$ GeV/c p for 0.38 sr ToF with $\sigma < 100$ ps
Muons	$\pi/\mu < 3 \times 10^{-3}$ at $p \geqslant 2.3$ GeV/c with 5 layers of μID.
Global	$d^2N/d\eta\, d\phi$ for $\lvert\eta\rvert < 2.6$

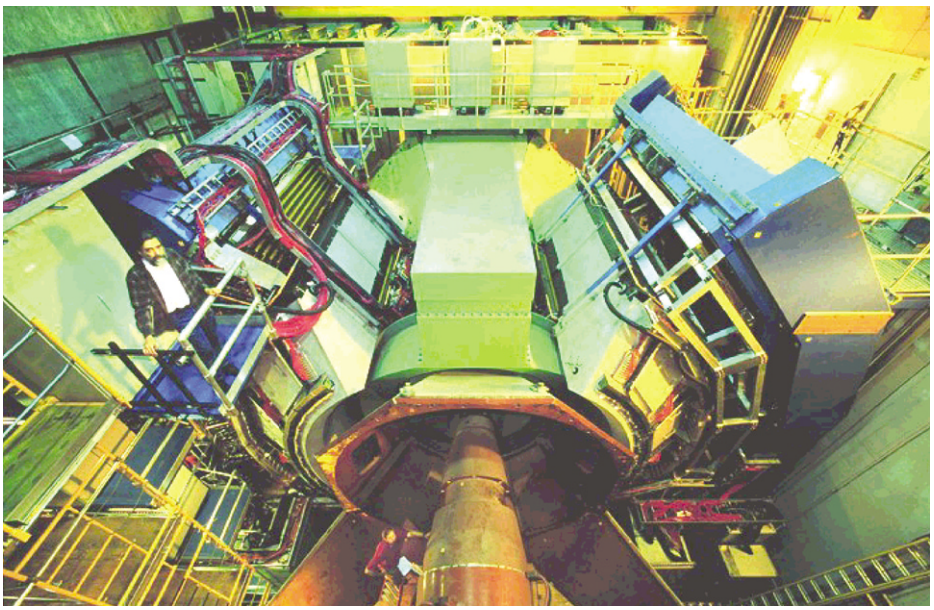

Fig. 3. Photograph of the PHENIX detector viewed from north to south. The central arms are visible on the right (west) and east (left) sides. In the back the south muon magnet and the muon identifier detectors are visible.

that interact with the subsystems by means of daughter cards that format and zero-suppress the data. Data packets are generated by digital signal processors and sent to event builders [13] that assemble the events in their final form. The control and monitoring of the electronics and triggering is handled by the On-Line Computing System (ONCS) [14]. ONCS configures and initializes the on-line system, monitors and controls the data flow and interlocks the data acquisition process with the slow controls systems. After the data is collected the off-line system [14] provides event reconstruction, data analysis and information management. It provides the tools to convert raw data into physics results.

4. Conclusion

The performance of the PHENIX detector is summarized in Table 3. It is designed to carry out the broadest possible study of collisions from Au–Au to p–p. The goal is to examine nuclear matter under a variety of extreme conditions using a variety of probes sensitive to all time scales. In addition, studies of various signals are carried out as a function of both energy and nuclear species in order to separate QGP signals from those of hadronic origin. Another goal is to measure the spin structure of the nucleon by determining the contributions from anti-quarks and gluons. The above goals have resulted in the production of a detector with unparalled capabilities. In the summer of 2000 a number of Au–Au collisions were observed between Au ions with energies of 65 GeV/nucleon using the central spectrometer. In the first PHENIX physics publication [15] results from the measurement of the charged-particle multiplicity are presented. Subsequently results from the first measurement of energy transverse to the beam direction [16], on mass dependence of two-pion correlations [17], on measurement of single electrons with implications for charm production [18] and on the centrality dependence of pion, kaon, proton and antiproton production [19] have been published and studies of results from Au–Au collisions with 100 Gev/nucleon beams are underway.

Acknowledgements

We thank the staff of the RHIC project, Collider-Accelerator, and Physics Departments at BNL and the staff of PHENIX participating institutions for their vital contributions. We acknowledge support from the Department of Energy and NSF (USA), Monbu-sho and STA (Japan), RAS, RMAE, and RMS (Russia), BMBF and DAAD (Germany), FRN, NFR, and the Wallenberg Foundation (Sweden), MIST and NSERC (Canada), CNPq and FAPESP (Brazil), IN2P3/CNRS and DAPNIA/CEA (France), DAE (India), KRF and KOSEF (Korea) and the US–Israel Binational Science Foundation.

References

[1] Y. Akiba, et al., Nucl. Phys. A 638 (1998) 565c.
[2] N. Saito, et al., Nucl. Phys. A 638 (1998) 575c.
[3] J. Ashman, et al. (EM Collaboration), Phys. Lett. B 202 (1988) 603;
J.J. Aubert, et al. (EM Collaboration), Phys. Lett. B 123 (1983) 275.
[4] PHENIX Conceptual Design Report, BNL, 1993, unpublished.
[5] C. Adler, et al., Nucl. Instr. and Meth. A 470 (2001) 488.
[6] ZDC article, Nucl. Instr. and Meth. A (2003), this issue.
[7] M. Allen, et al., PHENIX inner detectors, Nucl. Instr. and Meth. A (2003), this issue.
[8] S.M. Aronson, et al., PHENIX magnet system, Nucl. Instr. and Meth. A (2003), this issue.
[9] L. Aphecetche, et al., PHENIX calorimeter, Nucl. Instr. and Meth. A (2003), this issue.
[10] K. Adcox, et al., PHENIX central arm tracking detectors, Nucl. Instr. and Meth. A (2003), this issue.
[11] M. Aizawa, et al., PHENIX central arm particle ID detectors, Nucl. Instr. and Meth. A (2003), this issue.
[12] H. Akikawa, et al., PHENIX muon arms, Nucl. Instr. and Meth. A (2003), this issue.
[13] S.S. Adler, et al., PHENIX on-line systems, Nucl. Instr. and Meth. A (2003), this issue.
[14] S.S. Adler, et al., PHENIX on-line and off-line computing, Nucl. Instr. and Meth. A (2003), this issue.
[15] K. Adcox, et al., Phys. Rev. Lett. 86 (2001) 3500.
[16] K. Adcox, et al., Phys. Rev. Lett. 87 (2001) 052301.
[17] K. Adcox, et al., Phys. Rev. Lett. 88 (2002) 192 302.
[18] K. Adcox, et al., Phys. Rev. Lett. 88 (2002) 192 303.
[19] K. Adcox, et al., Phys. Rev. Lett. 88 (2002) 242 301.

High-p_T charged hadron suppression in Au+Au collisions at $\sqrt{s_{NN}}$=200 GeV

S. S. Adler,[5] S. Afanasiev,[17] C. Aidala,[5] N. N. Ajitanand,[43] Y. Akiba,[20,38] J. Alexander,[43] R. Amirikas,[12] L. Aphecetche,[45] S. H. Aronson,[5] R. Averbeck,[44] T. C. Awes,[35] R. Azmoun,[44] V. Babintsev,[15] A. Baldisseri,[10] K. N. Barish,[6] P. D. Barnes,[27] B. Bassalleck,[33] S. Bathe,[30] S. Batsouli,[9] V. Baublis,[37] A. Bazilevsky,[39,15] S. Belikov,[16,15] Y. Berdnikov,[40] S. Bhagavatula,[16] J. G. Boissevain,[27] H. Borel,[10] S. Borenstein,[25] M. L. Brooks,[27] D. S. Brown,[34] N. Bruner,[33] D. Bucher,[30] H. Buesching,[30] V. Bumazhnov,[15] G. Bunce,[5,39] J. M. Burward-Hoy,[26,44] S. Butsyk,[44] X. Camard,[45] J.-S. Chai,[18] P. Chand,[4] W. C. Chang,[2] S. Chernichenko,[15] C. Y. Chi,[9] J. Chiba,[20] M. Chiu,[9] I. J. Choi,[52] J. Choi,[19] R. K. Choudhury,[4] T. Chujo,[5] V. Cianciolo,[35] Y. Cobigo,[10] B. A. Cole,[9] P. Constantin,[16] D. G. d'Enterria,[45] G. David,[5] H. Delagrange,[45] A. Denisov,[15] A. Deshpande,[39] E. J. Desmond,[5] O. Dietzsch,[41] O. Drapier,[25] A. Drees,[44] R. du Rietz,[29] A. Durum,[15] D. Dutta,[4] Y. V. Efremenko,[35] K. El Chenawi,[49] A. Enokizono,[14] H. En'yo,[38,39] S. Esumi,[48] L. Ewell,[5] D. E. Fields,[33,39] F. Fleuret,[25] S. L. Fokin,[30] B. D. Fox,[39] Z. Fraenkel,[51] J. E. Frantz,[9] A. Franz,[5] A. D. Frawley,[12] S.-Y. Fung,[6] S. Garpman,[29,*] T. K. Ghosh,[49] A. Glenn,[46] G. Gogiberidze,[46] M. Gonin,[25] J. Gosset,[10] Y. Goto,[39] R. Granier de Cassagnac,[25] N. Grau,[16] S. V. Greene,[49] M. Grosse Perdekamp,[39] W. Guryn,[5] H.-Å. Gustafsson,[29] T. Hachiya,[14] J. S. Haggerty,[5] H. Hamagaki,[8] A. G. Hansen,[27] E. P. Hartouni,[26] M. Harvey,[5] R. Hayano,[8] X. He,[13] M. Heffner,[26] T. K. Hemmick,[44] J. M. Heuser,[44] M. Hibino,[50] J. C. Hill,[16] W. Holzmann,[43] K. Homma,[14] B. Hong,[22] A. Hoover,[34] T. Ichihara,[38,39] V. V. Ikonnikov,[23] K. Imai,[24,38] D. Isenhower,[1] M. Ishihara,[38] M. Issah,[43] A. Isupov,[17] B. V. Jacak,[44] W. Y. Jang,[22] Y. Jeong,[19] J. Jia,[44] O. Jinnouchi,[38] B. M. Johnson,[5] S. C. Johnson,[26] K. S. Joo,[31] D. Jouan,[36] S. Kametani,[8,50] N. Kamihara,[47,38] J. H. Kang,[52] S. S. Kapoor,[4] K. Katou,[50] S. Kelly,[9] B. Khachaturov,[51] A. Khanzadeev,[37] J. Kikuchi,[50] D. H. Kim,[31] D. J. Kim,[52] D. W. Kim,[19] E. Kim,[42] G.-B. Kim,[25] H. J. Kim,[52] E. Kistenev,[5] A. Kiyomichi,[48] K. Kiyoyama,[32] C. Klein-Boesing,[30] H. Kobayashi,[38,39] L. Kochenda,[37] V. Kochetkov,[15] D. Koehler,[33] T. Kohama,[14] M. Kopytine,[44] D. Kotchetkov,[6] A. Kozlov,[51] P. J. Kroon,[5] C. H. Kuberg,[1,27] K. Kurita,[39] Y. Kuroki,[48] M. J. Kweon,[22] Y. Kwon,[52] G. S. Kyle,[34] R. Lacey,[43] V. Ladygin,[17] J. G. Lajoie,[16] A. Lebedev,[16,23] S. Leckey,[44] D. M. Lee,[27] S. Lee,[19] M. J. Leitch,[27] X. H. Li,[6] H. Lim,[42] A. Litvinenko,[17] M. X. Liu,[27] Y. Liu,[36] C. F. Maguire,[49] Y. I. Makdisi,[5] A. Malakhov,[17] V. I. Manko,[23] Y. Mao,[7,38] G. Martinez,[45] M. D. Marx,[44] H. Masui,[48] F. Matathias,[44] T. Matsumoto,[8,50] P. L. McGaughey,[27] E. Melnikov,[15] F. Messer,[44] Y. Miake,[48] J. Milan,[43] T. E. Miller,[49] A. Milov,[44,51] S. Mioduszewski,[5] R. E. Mischke,[27] G. C. Mishra,[13] J. T. Mitchell,[5] A. K. Mohanty,[4] D. P. Morrison,[5] J. M. Moss,[27] F. Mühlbacher,[44] D. Mukhopadhyay,[51] M. Muniruzzaman,[6] J. Murata,[38,39] S. Nagamiya,[20] J. L. Nagle,[9] T. Nakamura,[14] B. K. Nandi,[6] M. Nara,[48] J. Newby,[46] P. Nilsson,[29] A. S. Nyanin,[23] J. Nystrand,[29] E. O'Brien,[5] C. A. Ogilvie,[16] H. Ohnishi,[5,38] I. D. Ojha,[49,3] K. Okada,[38] M. Ono,[48] V. Onuchin,[15] A. Oskarsson,[29] I. Otterlund,[29] K. Oyama,[8] K. Ozawa,[8] D. Pal,[51] A. P. T. Palounek,[27] V. S. Pantuev,[44] V. Papavassiliou,[34] J. Park,[42] A. Parmar,[33] S. F. Pate,[34] T. Peitzmann,[30] J.-C. Peng,[27] V. Peresedov,[17] C. Pinkenburg,[5] R. P. Pisani,[5] F. Plasil,[35] M. L. Purschke,[5] A. K. Purwar,[44] J. Rak,[16] I. Ravinovich,[51] K. F. Read,[35,46] M. Reuter,[44] K. Reygers,[30] V. Riabov,[37,40] Y. Riabov,[37] G. Roche,[28] A. Romana,[25] M. Rosati,[16] P. Rosnet,[28] S. S. Ryu,[52] M. E. Sadler,[1] N. Saito,[38,39] T. Sakaguchi,[8,50] M. Sakai,[32] S. Sakai,[48] V. Samsonov,[37] L. Sanfratello,[33] R. Santo,[30] H. D. Sato,[24,38] S. Sato,[5,48] S. Sawada,[20] Y. Schutz,[45] V. Semenov,[15] R. Seto,[6] M. R. Shaw,[1,27] T. K. Shea,[5] T.-A. Shibata,[47,38] K. Shigaki,[14,20] T. Shiina,[27] C. L. Silva,[41] D. Silvermyr,[27,29] K. S. Sim,[22] C. P. Singh,[3] V. Singh,[3] M. Sivertz,[5] A. Soldatov,[15] R. A. Soltz,[26] W. E. Sondheim,[27] S. P. Sorensen,[46] I. V. Sourikova,[5] F. Staley,[10] P. W. Stankus,[35] E. Stenlund,[29] M. Stepanov,[34] A. Ster,[21] S. P. Stoll,[5] T. Sugitate,[14] J. P. Sullivan,[27] E. M. Takagui,[41] A. Taketani,[38,39] M. Tamai,[50] K. H. Tanaka,[20] Y. Tanaka,[32] K. Tanida,[38] M. J. Tannenbaum,[5] P. Tarján,[11] J. D. Tepe,[1,27] T. L. Thomas,[33] J. Tojo,[24,38] H. Torii,[24,38] R. S. Towell,[1] I. Tserruya,[51] H. Tsuruoka,[48] S. K. Tuli,[3] H. Tydesjö,[29] N. Tyurin,[15] H. W. van Hecke,[27] J. Velkovska,[5,44] M. Velkovsky,[44] L. Villatte,[46] A. A. Vinogradov,[23] M. A. Volkov,[23] E. Vznuzdaev,[37] X. R. Wang,[13] Y. Watanabe,[38,39] S. N. White,[5] F. K. Wohn,[16] C. L. Woody,[5] W. Xie,[6] Y. Yang,[7] A. Yanovich,[15] S. Yokkaichi,[38,39] G. R. Young,[35] I. E. Yushmanov,[23] W. A. Zajc,[9,†] C. Zhang,[9] S. Zhou,[7,51] and L. Zolin[17]

(PHENIX Collaboration)

[1]*Abilene Christian University, Abilene, Texas 79699, USA*
[2]*Institute of Physics, Academia Sinica, Taipei 11529, Taiwan*
[3]*Department of Physics, Banaras Hindu University, Varanasi 221005, India*
[4]*Bhabha Atomic Research Centre, Bombay 400 085, India*
[5]*Brookhaven National Laboratory, Upton, New York 11973-5000, USA*
[6]*University of California, Riverside, Riverside, California 92521, USA*
[7]*China Institute of Atomic Energy (CIAE), Beijing, People's Republic of China*
[8]*Center for Nuclear Study, Graduate School of Science, University of Tokyo, 7-3-1 Hongo, Bunkyo, Tokyo 113-0033, Japan*
[9]*Columbia University, New York, New York 10027 and Nevis Laboratories, Irvington, New York 10533, USA*
[10]*Dapnia, CEA Saclay, F-91191 Gif-sur-Yvette, France*
[11]*Debrecen University, H-4010 Debrecen, Egyetem tér 1, Hungary*
[12]*Florida State University, Tallahassee, Florida 32306, USA*
[13]*Georgia State University, Atlanta, Georgia 30303, USA*
[14]*Hiroshima University, Kagamiyama, Higashi-Hiroshima 739-8526, Japan*
[15]*Institute for High Energy Physics (IHEP), Protvino, Russia*

 ©2004 The American Physical Society

[16]*Iowa State University, Ames, Iowa 50011, USA*
[17]*Joint Institute for Nuclear Research, 141980 Dubna, Moscow Region, Russia*
[18]*KAERI, Cyclotron Application Laboratory, Seoul, South Korea*
[19]*Kangnung National University, Kangnung 210-702, South Korea*
[20]*KEK, High Energy Accelerator Research Organization, Tsukuba-shi, Ibaraki-ken 305-0801, Japan*
[21]*KFKI Research Institute for Particle and Nuclear Physics (RMKI), P. O. Box 49, H-1525 Budapest 114, Hungary*
[22]*Korea University, Seoul 136-701, Korea*
[23]*Russian Research Center "Kurchatov Institute," Moscow, Russia*
[24]*Kyoto University, Kyoto 606, Japan*
[25]*Laboratoire Leprince-Ringuet, Ecole Polytechnique, CNRS-IN2P3, Route de Saclay, F-91128 Palaiseau, France*
[26]*Lawrence Livermore National Laboratory, Livermore, California 94550, USA*
[27]*Los Alamos National Laboratory, Los Alamos, New Mexico 87545, USA*
[28]*LPC, Université Blaise Pascal, CNRS-IN2P3, Clermont-Fd, 63177 Aubiere Cedex, France*
[29]*Department of Physics, Lund University, Box 118, SE-221 00 Lund, Sweden*
[30]*Institut fuer Kernphysik, University of Muenster, D-48149 Muenster, Germany*
[31]*Myongji University, Yongin, Kyonggido 449-728, Korea*
[32]*Nagasaki Institute of Applied Science, Nagasaki-shi, Nagasaki 851-0193, Japan*
[33]*University of New Mexico, Albuquerque, New Mexico 87131, USA*
[34]*New Mexico State University, Las Cruces, New Mexico 88003, USA*
[35]*Oak Ridge National Laboratory, Oak Ridge, Tennessee 37831, USA*
[36]*IPN-Orsay, Universite Paris Sud, CNRS-IN2P3, Boîte Postale 1, F-91406 Orsay, France*
[37]*PNPI, Petersburg Nuclear Physics Institute, Gatchina, Russia*
[38]*RIKEN (The Institute of Physical and Chemical Research), Wako, Saitama 351-0198, Japan*
[39]*RIKEN BNL Research Center, Brookhaven National Laboratory, Upton, New York 11973-5000, USA*
[40]*St. Petersburg State Technical University, St. Petersburg, Russia*
[41]*Universidade de São Paulo, Instituto de Física, Caixa Postal 66318, São Paulo CEP05315-970, Brazil*
[42]*System Electronics Laboratory, Seoul National University, Seoul, South Korea*
[43]*Chemistry Department, Stony Brook University, SUNY, Stony Brook, New York 11794-3400, USA*
[44]*Department of Physics and Astronomy, Stony Brook University, SUNY, Stony Brook, New York 11794, USA*
[45]*SUBATECH (Ecole des Mines de Nantes, CNRS-IN2P3, Université de Nantes) Boîte Postale 20722-44307, Nantes, France*
[46]*University of Tennessee, Knoxville, Tennessee 37996, USA*
[47]*Department of Physics, Tokyo Institute of Technology, Tokyo 152-8551, Japan*
[48]*Institute of Physics, University of Tsukuba, Tsukuba, Ibaraki 305, Japan*
[49]*Vanderbilt University, Nashville, Tennessee 37235, USA*
[50]*Waseda University, Advanced Research Institute for Science and Engineering, 17 Kikui-cho, Shinjuku-ku, Tokyo 162-0044, Japan*
[51]*Weizmann Institute, Rehovot 76100, Israel*
[52]*Yonsei University, IPAP, Seoul 120-749, Korea*
(Received 8 August 2003; published 30 March 2004)

The PHENIX experiment at the Relativistic Heavy Ion Collider has measured charged hadron yields at midrapidity over a wide range of transverse momenta ($0.5<p_T<10$ GeV/c) in Au+Au collisions at $\sqrt{s_{NN}}=200$ GeV. The data are compared to π^0 measurements from the same experiment. For both charged hadrons and neutral pions, the yields per nucleon-nucleon collision are significantly suppressed in central compared to peripheral and nucleon-nucleon collisions. The suppression sets in gradually and increases with increasing centrality of the collisions. Above 4–5 GeV/c in p_T, a constant and almost identical suppression of charged hadrons and π^0's is observed. The p_T spectra are compared to published spectra from Au+Au at $\sqrt{s_{NN}}=130$ in terms of x_T scaling. Central and peripheral π^0 as well as peripheral charged spectra exhibit the same x_T scaling as observed in $p+p$ data.

DOI: 10.1103/PhysRevC.69.034910 PACS number(s): 25.75.Dw

*Deceased.
†Email address: zajc@nevis.columbia.edu

I. INTRODUCTION

Lattice quantum chromodynamic (QCD) calculations predict a new state of matter of deconfined quarks and gluons at an energy density exceeding ~ 1 GeV/ fm^3 [1]. It has long been suggested that such a "quark gluon plasma" may be produced in collisions between ultrarelativistic heavy nuclei [2]. Indeed, measurements of transverse energy produced in high-energy Pb+Pb and Au+Au collisions suggest that energy densities above 3 GeV/fm^3 at the CERN SPS [3] and 5 GeV/fm^3 at the Relativistic Heavy Ion Collider (RHIC) [4,5] have been reached. However, this conclusion relies on model assumptions [6–9] to relate the properties of the hadronic final state to the initial state dynamics.

The spectra of high transverse momentum (p_T) hadrons resulting from the fragmentation of hard-scattered partons potentially provide a direct probe of the properties of the initial state. Theoretical calculations show that the outgoing high-p_T partons radiate substantially more energy when propagating through dense matter than when propagating in the vacuum, resulting in a softening of the hadron p_T spectrum [10], with the energy loss of the partons depending on the gluon density of the matter [11,12]. Formation time considerations suggest that hard scattered partons are "produced" at the earliest stage of the collision, thus directly probe the dense matter from the time of their creation. Therefore, a detailed analysis of high-p_T hadron production may reveal information on the properties of the dense medium created early in the collisions [12–14].

At the energies reached at RHIC, high-p_T hadrons are copiously produced. In nucleon-nucleon collisions, it has been well established that hadrons with $p_T \geqslant 2$ GeV/c result primarily from the fragmentation of hard-scattered partons, and that the p_T spectra of these hadrons can be calculated using perturbative QCD (pQCD) [15,16]. Initial measurements of hadron p_T spectra in Au+Au collisions at $\sqrt{s_{NN}}$ =130 GeV led to the discovery of a substantial suppression of hadron yields per nucleon-nucleon collision relative to pp data [17–19]. Data from $\sqrt{s_{NN}}$=200 GeV confirm these results [20–23]. The suppression is observed in central but not in peripheral collisions. These observations are consistent with pQCD-inspired modeling of parton energy loss in dense matter [24,25]. However, alternative interpretations that do not assume the formation of a deconfined phase have been proposed based on the modifications of the parton distribution functions in the initial state [26] or final-state hadronic interactions [27].

In addition to hadron suppression, an unexpectedly large fraction of baryons has been observed in central Au+Au collisions for p_T up to 4–5 GeV/c [28–30], which complicates the interpretation of the high-p_T results. The observed baryon to meson ratio from PHENIX [29] is inconsistent with jet fragmentation in $p+p$ [31] and e^+e^- collisions [32]. While the origin of this effect is unclear, it could point towards bulk particle production ("soft physics") contributing to the p_T spectra out to 4–5 GeV/c. It has been suggested that coalescence of thermalized quarks combining with energy loss of hard-scattered partons can account for the unusual particle composition, which shifts the region dominated by hard scattering to higher p_T [33].

Systematic measurements of the p_T, centrality, particle species, and $\sqrt{s_{NN}}$ dependence of the suppression can constrain competing descriptions of high-p_T hadron production. In this paper, we present new data on inclusive charged hadron production for $0.5 < p_T < 10$ GeV/c, measured over a broad range of centrality in Au+Au collisions at $\sqrt{s_{NN}}$ =200 GeV by the PHENIX Collaboration at RHIC. These data are compared to data on neutral pion production [21] and to data from Au+Au collisions at $\sqrt{s_{NN}}$=130 GeV [17,19], all measured within the same experiment.

The remainder of the paper is organized as follows. Section II gives a detailed account of the charged particle analysis. Centrality and p_T dependence of the charged hadron p_T spectra are discussed in Sec. III A. Section III B studies the charged hadron suppression and compares the results to π^0 data. In Sec. III C, we discuss the $\sqrt{s_{NN}}$ dependence of both charged hadron and neutral pion production and test possible x_T scaling. A summary is given in Sec. IV.

II. DATA ANALYSIS

A. PHENIX detector

The PHENIX experiment consists of four spectrometer arms—two around midrapidity (the central arms) and two at forward rapidity (the muon arms)—and a set of global detectors. The central arm and south muon arm detectors were completed in 2001 and took data during Au+Au operation of RHIC the same year (RUN-2). The layout of the PHENIX experiment during RUN-2 is shown in Fig. 1. Each central arm covers $|\eta| < 0.35°$ in pseudorapidity and 90° in azimuthal angle ϕ. In each of the central arms, charged particles are tracked by a drift chamber (DC) positioned from 2.0 to 2.4 m radially outward from the beam axis and two or three layers of pixel pad chambers [PC1, (PC2), PC3 located at 2.4 m, (4.2 m), 5 m in radial direction, respectively]. Particle identification is provided by ring imaging Cerenkov counters (RICH), a time of flight scintillator wall (TOF), and two types of electromagnetic calorimeters (lead scintillator and lead glass). The magnetic field for the central spectrometer is axially symmetric around the beam axis. Its component parallel to the beam axis has an approximately Gaussian dependence on the radial distance from the beam axis, dropping from 0.48 T at the center to 0.096 T (0.048 T) at the inner (outer) radius of the DC. A pair of zero-degree calorimeters (ZDC) and a pair of beam-beam counters (BBC) were used for global event characterization. Further details about the design and performance of PHENIX can be found in Ref. [34].

B. Event selection

During RUN-2, PHENIX sampled an integrated luminosity of 24 μb^{-1} for Au+Au collisions at $\sqrt{s_{NN}}$=200 GeV. Minimum bias events were selected by a coincidence between the ZDCs and the BBCs. This selection corresponds to $92.2^{+2.5}_{-3.0}$% of the 6.9 b Au+Au inelastic cross section. The event centrality is determined by correlating the charge detected in the BBCs with the energy measured in the ZDCs. Two sets of centrality definitions are used in this analysis: a

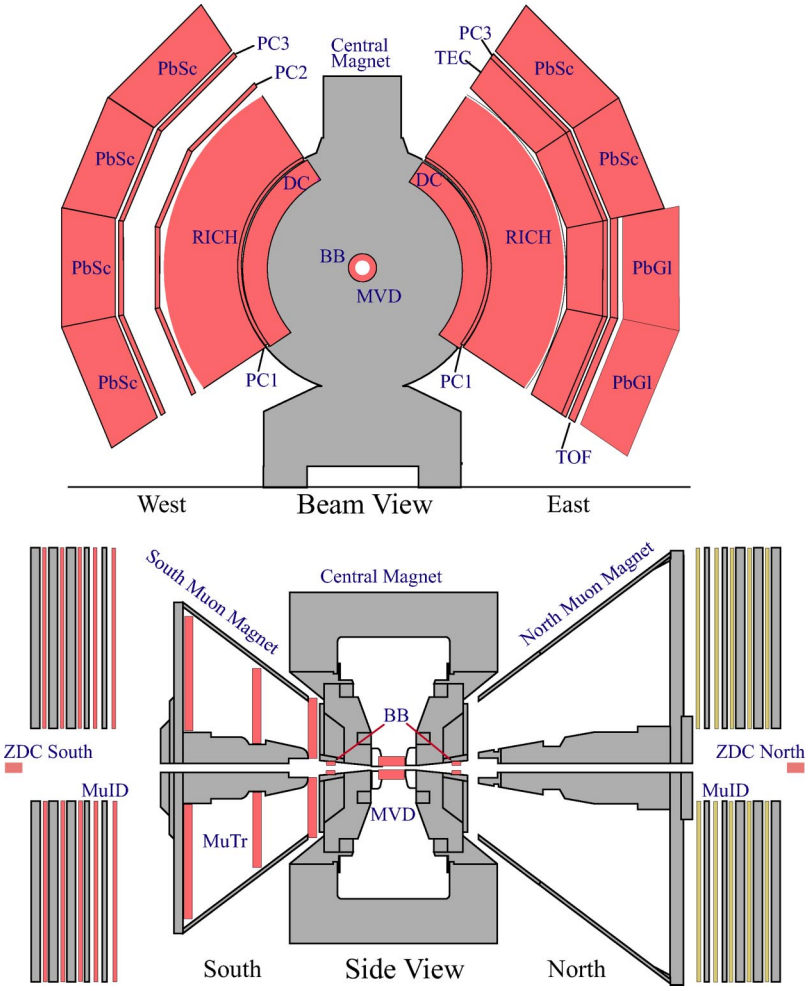

FIG. 1. (Color online) PHENIX experimental layout for the Au+Au run in 2001. The top panel shows the PHENIX central arm spectrometers viewed along the beam axis. The bottom panel shows a side view of the PHENIX muon arm spectrometers.

"Fine" set of centralities, which corresponds to 0–5%, …, 15–20%, 20–30%, …, 80–92%, and a "Coarse" set of centralities, which corresponds to 0–10%, 10–20%, 20–30%, …, 80–92%. A Glauber model Monte Carlo simulation [35–38] that includes the responses of BBC and ZDC gives an estimate of the average number of binary collisions $\langle N_{coll}\rangle$, participating nucleons $\langle N_{part}\rangle$, and nuclear overlap function $\langle T_{\mathrm{AuAu}}\rangle$ for each centrality class. The calculated values of $\langle N_{coll}\rangle$, $\langle N_{part}\rangle$, and $\langle T_{\mathrm{AuAu}}\rangle$ for each centrality class are listed in Table I.

In addition to the event selection, the BBCs also allow us to reconstruct the collision vertex in the beam direction (z) with a resolution of 0.5 cm. An offline z-vertex cut, $|z_{vtx}|<30$ cm, was applied to the minimum bias events. After this selection, a total of 27×10^6 minimum bias Au+Au events were analyzed to obtain the charged hadron spectra presented in this paper.

C. Charged particle tracking and momentum measurement

Charged hadron tracks are measured using information from the DC, PC1, PC2, and PC3 detectors of the west central arm and the BBC. The projections of the charged particle trajectories into a plane perpendicular to the beam axis are detected typically in 12 wire planes in the DC. The wire planes are spaced at 0.6 cm intervals along the radial direction from the beam axis. Each wire provides a projective measurement, with better than 150 μm spacial resolution in the azimuthal (ϕ) direction. Eight additional wire planes in the DC provide stereoscopic projections, which together with the space point measured at the PC1 and the vertex position measured by the BBC determine the polar angle of the track. Trajectories are confirmed by requiring matching hits at both PC2 and PC3 to reduce the secondary background.

Tracks are then projected back to the collision vertex through the magnetic field to determine the momentum $\vec{p}$. The transverse momentum p_T is related to the deflection angle α measured at the DC with respect to an infinite momentum trajectory. For tracks emitted perpendicular to the beam axis, this relation can be approximated by

$$\alpha \simeq \frac{K}{p_T}, \tag{1}$$

where $K=87$ mrad GeV/c is the effective field integral.

The momentum scale is verified by comparing the known proton mass to the value measured for charged particles identified as protons from their time of flight. The flight time is measured in the TOF detector, which cover $\pi/4$ of the

TABLE I. Centrality classes, average number of $N+N$ collisions, average number of participant nucleons, and average nuclear overlap function obtained from a Glauber Monte Carlo simulation of the BBC and ZDC responses for Au+Au at $\sqrt{s_{NN}}=200$ GeV. Each centrality class is expressed as a percentage of $\sigma_{\mathrm{AuAu}}=6.9$ b. Two sets of centrality definitions are used in this analysis: a "Fine" set of centralities, which corresponds to 0–5%, …, 15–20%, 20–30%,…, 80–92%, and a "Coarse" set of centralities, which corresponds to 0–10%, 10–20%, 20–30%, …, 80–92%.

Centrality (%)	$\langle N_{coll}\rangle$	$\langle N_{part}\rangle$	$\langle T_{\mathrm{AuAu}}\rangle$ (mb^{-1})
0–5	1065±105.5	351.4±2.9	25.37±1.77
5–10	854.4±82.1	299±3.8	20.13±1.36
10–15	672.4±66.8	253.9±4.3	16.01±1.15
15–20	532.7±52.1	215.3±5.3	12.68±0.86
0–10	955.4±93.6	325.2±3.3	22.75±1.56
10–20	602.6±59.3	234.6±4.7	14.35±1.00
20–30	373.8±39.6	166.6±5.4	8.90±0.72
30–40	219.8±22.6	114.2±4.4	5.23±0.44
40–50	120.3±13.7	74.4±3.8	2.86±0.28
50–60	61.0±9.9	45.5±3.3	1.45±0.23
60–70	28.5±7.6	25.7±3.8	0.68±0.18
70–80	12.4±4.2	13.4±3.0	0.30±0.10
80–92	4.9±1.2	6.3±1.2	0.12±0.03
60–92	14.5±4	14.5±2.5	0.35±0.10
Minimum bias	257.8±25.4	109.1±4.1	6.14±0.45

azimuthal acceptance in the east arm. The absolute value of the momentum scale is known to be correct to better than 0.7%.

The momentum resolution is directly related to the α resolution,

$$\delta p/p = \delta\alpha/\alpha = \frac{1}{K}\sqrt{\left(\frac{\sigma_{ms}}{\beta}\right)^2 + (\sigma_\alpha p)^2}, \tag{2}$$

where $\delta\alpha$ is the measured angular spread, which can be decomposed into the contribution from multiple scattering σ_{ms} and the contribution from the intrinsic pointing resolution σ_α of the DC. At high p_T, σ_α is the dominating contribution, i.e., $\delta_\alpha \simeq \sigma_\alpha$. We measure $\sigma_\alpha \approx 0.84\pm0.05$ mrad/(GeV/c) using zero field data, where we select high-momentum tracks by requiring energetic hadronic showers in the electromagnetic calorimeters. The width of the proton mass as function of p_T independently confirms the momentum resolution. In summary, the momentum resolution is determined to be $\delta p/p \simeq 0.7\% \oplus 1.0\% p$ (GeV/c). Further details on track reconstruction and momentum determination can be found in Ref. [39].

D. Background rejection and subtraction

Approximately 95% of the tracks reconstructed by the DC originate from the event vertex. The remainder have to be investigated as potential background to the charged particle measurement. The main background sources include secondary particles from decays and e^+e^- pairs from the conversion of photons in materials between the vertex and the DC. Depending on how close the conversion or decay point is to the DC, or depending on the Q value of the decay, these tracks may have a small deflection angle α at the DC. Thus, according to Eq. (1), they are incorrectly assigned a large momentum. In this analysis, the p_T range over which charged particle production is accessible in PHENIX is limited by this background. We exploit the track match to PC2 and PC3 to reject as much of the background as possible, then employ a statistical method to measure and subtract the irreducible background.

For primary tracks, the distance in both the $r-\phi$ and the z direction between the track projection point and the measured PC hit position is approximately Gaussian with a mean of 0 and a width given by

$$\sigma_{match} = \sqrt{\sigma_{det}^{match2} + \left(\frac{\sigma_{ms}^{match}}{p\beta}\right)^2}, \tag{3}$$

where σ_{det}^{match} is the finite detector resolution [which includes DC pointing (or α) resolution and the PC2, PC3 spacial resolution], and σ_{ms}^{match} is the multiple scattering contribution.

Despite being incorrectly reconstructed with large p_T, the majority of the background particles have low momenta. While traveling from the DC to the PC2 and PC3, they multiple scatter and receive an additional deflection from the fringe field. This causes a correlated deflection between the measured positions at PC2, PC3, and the projections calculated from tracks measured by the DC and PC1. The displacements in $r-\phi$ and z directions are represented by D_ϕ and D_z. Since the residual bend depends on the z component of the fringe field, which decreases rapidly at large $|\eta|$, a fiducial cut of $|\eta|<0.18$ was applied to ensure that the residual bend due to the fringe field is almost independent of z.

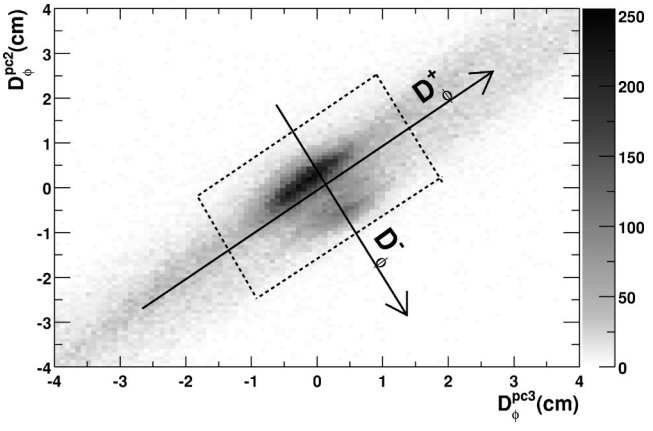

FIG. 2. D_ϕ^{pc2} (the difference between projection and hit location in r-ϕ direction at PC2) vs D_ϕ^{pc3} in centimeters for tracks with reconstructed $p_T>4$ GeV/c. PC2, PC3 matching differences are correlated, with signal tracks peaked around 0 and background tracks extend along the D_ϕ^+ direction. The double-peak structure along D_ϕ^- is related to the finite granularity of PC2 and PC3 pads. The positive directions of D_ϕ^+ and D_ϕ^- are indicated by the arrow. A $\pm 2\sigma$ cut on these variables is illustrated by the box region inside the dashed lines.

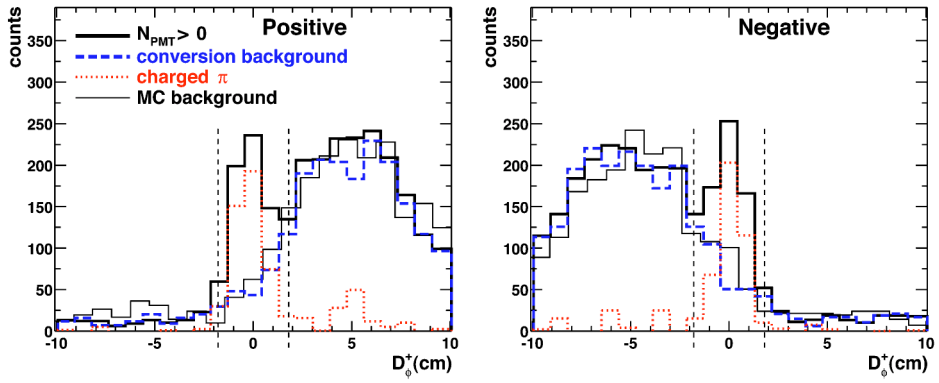

FIG. 3. (Color online) Background contamination due to electrons, illustrated by the track match in D^+_ϕ for tracks with associated RICH PMTs and $6<p_T<7$ GeV/c. The matching distributions are shown for minimum bias events and separately for positive (left) and negative (right) charged tracks. The first three distributions represent the raw counts for all tracks with RICH association (thick solid line), estimated conversion backgrounds (dashed line), and charged pions (dot-dashed line) that were obtained by subtracting the dashed line from the solid line. The thin solid line represents the matching distribution of background electrons from Monte Carlo simulation, arbitrarily scaled to match the data. The $\pm 2\sigma$ matching windows are illustrated by the vertical dashed line. Since e^+ and e^- are deflected in opposite directions by the fringe field, they are shifted to positive and negative directions, respectively.

We focus on the displacement in $r-\phi$, D_ϕ, which are large for low momentum tracks due to the residual bend. The D_ϕ's at PC2 and PC3 are correlated with each other, as shown in Fig. 2. Most of the tracks lie in a narrow window around the diagonal line. The width of this window is given by the PC2 and PC3 detector resolutions, which are of the order of a few millimeters. Multiple scattering and residual bend broaden the matching distribution along the diagonal line. To optimize background rejection, we define two orthogonal projections,

$$D^+_\phi = \frac{1}{\sqrt{2}}(D^{pc2}_\phi + D^{pc3}_\phi),$$

$$D^-_\phi = \frac{1}{\sqrt{2}}(D^{pc2}_\phi - D^{pc3}_\phi). \quad (4)$$

D^+_ϕ is the variable along the correlated direction, D^-_ϕ is the direction normal to D^+_ϕ. A $\pm 2\sigma$ cut on these variables is applied in the data analysis. In the remaining discussion, unless stated otherwise, only tracks satisfying these cuts are included.

After matching cuts, the background level is less than 6% for $p_T<4$ GeV/c, but increases rapidly at higher p_T. For $4<p_T<10$ GeV/c, the most significant remaining background sources are e^+e^- from conversion of photons close to the DC and particles from weak decays of long lived particles, mainly of $K^\pm$ and K^0_L. These backgrounds are estimated and subtracted separately from the D^+_ϕ distribution for all tracks, as will be discussed in the rest of this section.

To separate the two background sources, we take advantage of the RICH to tag electrons. Charged particles with velocities above the Cherenkov threshold $\gamma_{th}=35$ (CO_2 radiator) will emit Cherenkov photons, which are detected by photon multiplier tubes (PMTs) in the RICH [40]. We characterize the Cherenkov photon yield for a charged particle by N_{PMT}, the number of PMTs with signals above threshold associated with the track. For reconstructed electrons ($p_T>150$ MeV/c), the average number of associated PMTs is $\langle N_{PMT}\rangle \approx 4.5$. The probability to find at least one PMT above threshold is more than 99%. For pions, the Cherenkov threshold is 4.8 GeV/c, and the number of associated PMTs reaches its asymptotic value only well above 10 GeV/c; $\langle N_{PMT}\rangle$ increases from 1.4 at 6 GeV/c to 2.8 at 8 GeV/c and 3.6 at 10 GeV/c.

Tracks (N_R) with at least one associated RICH PMT contain both conversion electrons and real pions. Their matching distributions in D^+_ϕ are presented in Fig. 3 for a sample range of $6<p_T<7$ GeV/c. Also shown is the matching distribution for conversion electrons from Monte Carlo simulation. The contributions from pions and electrons are clearly distinguishable. For pions with $p_T<10$ GeV/c, $\langle N_{PMT}\rangle$ has not reached its asymptotic value. A requirement of $N_{PMT}\geqslant 5$ rejects most of the pions while preserving a well-defined fraction (R_e) of the electrons. To measure R_e from the data, we select tracks with an apparent $p_T>10$ GeV/c. [1] The fraction of tracks with $N_{PMT}\geqslant 5$ is measured to be $R_e=0.458\pm 0.05$. Both Monte Carlo and data show a small variation of R_e with p_T and centrality. This variation is included in the error on R_e. The total electron background is calculated using tracks with $N_{PMT}\geqslant 5(N_e)$ as, N_e/R_e. The number of real pions in the RICH-associated sample for each p_T bin is then calculated as

$$S_R = N_R - \frac{N_e}{R_e}. \quad (5)$$

With this method, a small fraction of genuine pions, which satisfy $N_{PMT}\geqslant 5$, is subtracted. This fraction is negligible

[1] In this p_T range, the background yield decreases slowly with p_T, while the true π yield decreases rapidly as p_T increases. By comparing the measured π^0 spectrum from PHENIX [21] with the charged hadron spectrum before background subtraction at $p_T>10$ GeV/c, the integrated signal yield is estimated to be less than 3% and thus may be neglected.

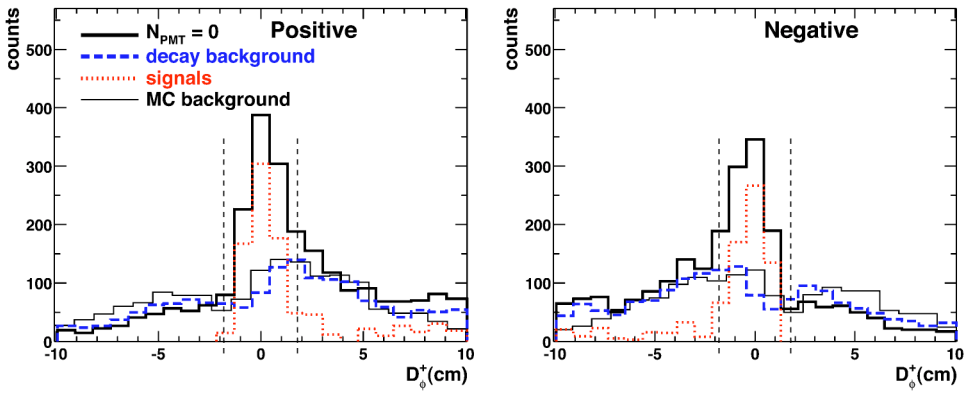

FIG. 4. (Color online) Background contamination due to decays, illustrated by the track match in D_ϕ^+ for tracks without an associated RICH PMT and with $6<p_T<7$ GeV/c, shown for minimum bias events and separately for positive (left) and negative (right) charged tracks. The first three distributions represent the raw counts for all tracks without RICH association (thick solid line), estimated decay backgrounds (dashed line), and signal tracks (dot-dashed line) that were calculated as the difference of the two. The thin solid line represents the matching distribution of decay background from Monte Carlo simulation, arbitrarily scaled to match the data. The two $\pm 2\sigma$ matching windows are illustrated by the vertical dashed line. Outside the signal window, the shape of the dashed line matches the solid line rather well, the difference of 10% level is taken into account in the error estimation of R_{decay}.

below 7 GeV/c, but increases rapidly towards higher p_T. This loss is corrected using the PHENIX Monte Carlo simulation. In this case, a 100% error on the correction is assigned.

The sample of tracks (N_{NR}) with no associated RICH PMT contains a mixture of π, K, p, contaminated by the decay background. Their matching distributions in D_ϕ^+ are shown in Fig. 4 for $6<p_T<7$ GeV/c, together with the matching distribution for decay particles from MC simulation. A Monte Carlo study shows that the apparent momentum of these tracks is nearly uncorrelated with true momentum and therefore the distribution of this background in D_ϕ^+ is nearly independent of the apparent momentum. We select a nearly pure background sample using tracks with reconstructed $p_T>10$ GeV/c and measure the ratio of the number of tracks passing a $|D_\phi^+|<2\sigma$ cut to tracks in the interval $3\sigma<|D_\phi^+|<9\sigma$:

$$R_{decay}=\frac{N_{NR}(p_T>10\ \text{GeV/}c, |D_\phi^+|<2\sigma)}{N_{NR}(p_T>10\ \text{GeV/}c, 3\sigma<|D_\phi^+|<9\sigma)} = 0.424\pm 0.05. \quad (6)$$

The error quoted takes into account the small variation of R_{decay} with p_T and centrality. Since the average yield of real hadrons in this interval is small, we estimate the decay contribution as a function of p_T to be $N_{NR}(3\sigma<|D_\phi^+|<9\sigma)\times R_{decay}$. Finally, the signal is calculated as

$$S_{NR}=N_{NR}(|D_\phi^+|<2\sigma)-N_{NR}(3\sigma<|D_\phi^+|<9\sigma)\times R_{decay}. \quad (7)$$

Figure 5 gives the total signal, obtained as S_R+S_{NR}, with the decay and conversion background subtracted. On the right hand side, the signal-to-background ratio is shown. The background increases with increasing p_T. At 4 GeV/c the signal-to-background ratio is about 10, and decreases to 1 at 7.5 GeV/c and to ~0.3 at 10 GeV/c.

Weak decays of short lived particles, mainly K_s^0, Λ, and $\overline{\Lambda}$ within the magnetic field provide an additional source of background. A significant fraction of this background is subtracted using the R_{decay} method described above. However, secondary particles from decays close to the event vertex are not subtracted since they are nearly indistinguishable from primary particles. This "feed-down" contaminates the track sample without the associated RICH PMTs, S_{NR} (about 40% of all charged particles at high p_T), and needs to be subtracted from the data.

To estimate the feed-down contribution we generate Au+Au events with HIJING [41], reconstruct them through the PHENIX Monte Carlo simulation, and count the secondaries which survive all analysis cuts. The secondaries from Λ and $\overline{\Lambda}$ decays are counted relative to the reconstructed $(p+\overline{p})$, and correspondingly, those from K_s^0 relative to $(K^++K^-)/2$. We tune the $(\Lambda+\overline{\Lambda})/(p+\overline{p})$, $K_s^0/[0.5(K^++K^-)]$ ratios by weighting the particle distributions generated according to HIJING such that they reproduce the nearly p_T independent experimentally observed ratios from Au+Au collisions at $\sqrt{s_{NN}}=130$ GeV [42,43].

The final feed-down contribution depends on the choice of the Λ and K_s^0 p_T spectra and of their yields in the high-p_T range where they are not measured. Both yields and spectral shapes are varied within limits imposed by the spectrum for tracks that do not fire the RICH. The average feed-down contribution depends on p_T and varies between 6% to 13% relative to the total charged hadron yield; it is subtracted from the charged spectra. The systematic uncertainties are estimated from the spread of the feed-down contributions obtained with different assumptions. The uncertainties are approximately 60% of the subtraction, and depend on p_T and centrality.

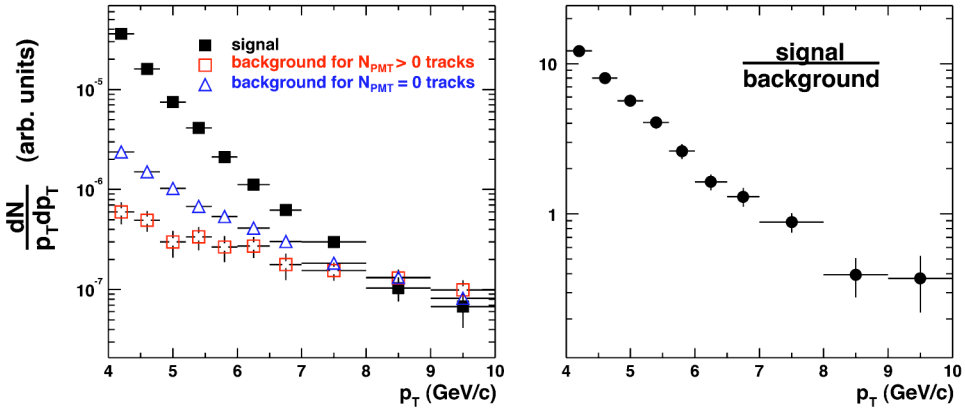

FIG. 5. (Color online) Amount of background estimated as a function of p_T for minimum bias collision. The left part shows the background subtracted charged hadron spectra (filled square), the background from γ conversions (open square), and decays (open triangle). The right part shows the signal to background ratio. Only statistical errors are shown.

Table II summarizes the systematic errors on the background subtraction.[2] All errors are correlated with p_T and are presented as relative errors to the charged hadron yield. The uncertainty on the pion oversubtraction correction ($\delta_{\pi loss}$) was rescaled by the fraction of signal tracks with RICH association, i.e., $S_R/(S_R+S_{NR})$. Errors on the scaling factors R_e and R_{decay} were individually folded with the signal-to-background ratios in the two samples. The resulting uncertainties on the charged yields were then added in quadrature ($\delta_{R_e \oplus R_{decay}}$). The uncertainty of the K_s^0, Λ, and $\bar{\Lambda}$ feed-down subtraction is denoted by $\delta_{feeddown}$.

E. Corrections and systematic uncertainties

After background subtraction, we have determined a single, p_T-dependent correction function to correct the hadron spectra for acceptance, decay in flight, reconstruction efficiency, and momentum resolution. This function is determined using a GEANT [44] Monte Carlo simulation [45] of the PHENIX detector in which simulated single tracks are reconstructed using the same analysis chain applied to the real data. Because of decays and multiple scattering, the correction function depends on the particle species. This is reflected in Fig. 6, where the correction functions averaged between π^+ and π^-, K^+ and K^-, p^+ and p^- are shown separately. At $p_T<3$ GeV/c, the kaon correction function is significantly larger than those for pions and protons. For $p_T>3$ GeV/c, this difference is less than 15%. To take into account this species dependence, we determine the correction function separately for pions, kaons, protons, and their antiparticles. The final correction function is then obtained by combining the correction functions for the different particle species weighted by the measured p_T-dependent particle composition from Ref. [46]. Above 2 GeV/c, where kaon data are not available, we assume the K/π ratio is constant within ±10% from the value observed at 2 GeV/c. This assumption leads to a 2.5% systematic error in the correction function. The resulting correction function is plotted in the upper left panel of Fig. 7. The sharp rise below 2 GeV/c is due to loss in acceptance and decays in flight. Above 2 GeV/c, the correction decreases only slowly with p_T. For $p_T>4$ GeV/c, the correction varies by less than ±5%.

The data are also corrected for efficiency losses due to detector occupancy. Though this is negligible for peripheral collisions, these losses are important in central collisions, and are evaluated by embedding simulated tracks into real events. The average track reconstruction efficiency in the active detector area is larger than 98% for peripheral collisions, but decreases to (70±3.5)% for central collisions. As shown in the lower part of Fig. 7, the efficiency loss is independent of p_T within a ±3% systematic uncertainty from 1.5 to 10 GeV/c. Based on this observation, the full correction can be factorized into centrality-dependent (i.e., detector occupancy dependent) correction function $c(N_{part})$, and p_T-dependent correction function $c(p_T)$. The centrality-dependent correction function is shown on the upper right panel of Fig. 7. Most of the efficiency loss is due to hit overlaps, which can shift the hit positions in the DC or PC's outside of the matching windows. The $\pm 2\sigma$ matching windows are larger at low p_T to account for multiple scattering [see Eq. (3)], thus the tracks are less vulnerable to the effect of hit merging. This effect has been taken into account by applying a slightly smaller, p_T-dependent, occupancy correction at $p_T<1.5$ GeV/c.

Figure 7 also shows systematic errors on the correction functions. These errors include not only the errors on the correction itself, but also the uncertainty due to the background subtraction procedure.

Finally, the inclusive charged hadron yield is obtained by multiplying the p_T-dependent correction function $c(p_T)$ and centrality-dependent correction function $c(N_{part})$ with the background subtracted spectra and dividing by the number of events for every centrality class as

$$\frac{1}{N_{evts}}\frac{dN}{2\pi p_T dp_T d\eta} = \frac{1}{N_{evts}} \times c(p_T) \times c(N_{part}) \times \left(\frac{dN}{p_T dp_T d\eta}\right)^{bgr\text{-}subtracted}. \quad (8)$$

The systematic errors on the spectra, which are common to all centrality classes, are listed in Table III. Sources of systematic uncertainties are the matching cuts (δ_{match}), normalization (δ_{norm}), particle composition (δ_{mix}), momentum

[2]We should emphasize that, in the remaining discussion unless stated otherwise, all systematic errors listed in tables have been adjusted to 1σ errors.

TABLE II. Systematic errors on background subtraction. All errors are given in percent and are quoted as 1σ errors. These errors are correlated with p_T.

p_T (GeV/c)	$\delta_{\pi loss}$ (%)	$\delta_{R_e \oplus R_{decay}}$ (%)	$\delta_{feeddown}$ (%)	Total (%)
<5	0.3	0.3	5	5
5–6	0.6	1.8	5	5.3
6–7	1.4	4.1	8.5	9.5
7–8	4.6	7.1	7.8	11.5
8–9	9.9	17.6	6	21.1
9–10	19.4	23.5	6	31.1

resolution (δ_{reso}), momentum scale (δ_{scale}), and background subtraction (δ_{bgr}) from Table II. The normalization error is independent of p_T. All other errors vary with p_T but are highly correlated bin-to-bin, which means that points in neighboring p_T bins can move in the same direction by similar factors.

The centrality-dependent systematic errors are quantified in terms of the central-to-peripheral ratio R_{cp}, as given in Table IV. Besides the uncertainty on the occupancy correction ($\delta_{occupancy}$) illustrated in Fig. 7, the background subtraction procedure has a centrality-dependent uncertainty. As discussed in Sec. II D, the errors on R_e and R_{decay} reflect the p_T and centrality dependencies. The centrality-dependent part contributes about half of the error on both R_e and R_{decay}, and hence does not cancel in R_{cp}. Since the errors on R_e and R_{decay} are independent, the uncertainty on R_{cp} is approximately equal to $\delta_{R_e \oplus R_{decay}}$ from Table II. Finally, $\delta_{feeddown}$ is the centrality-dependent error from feed-down subtraction.

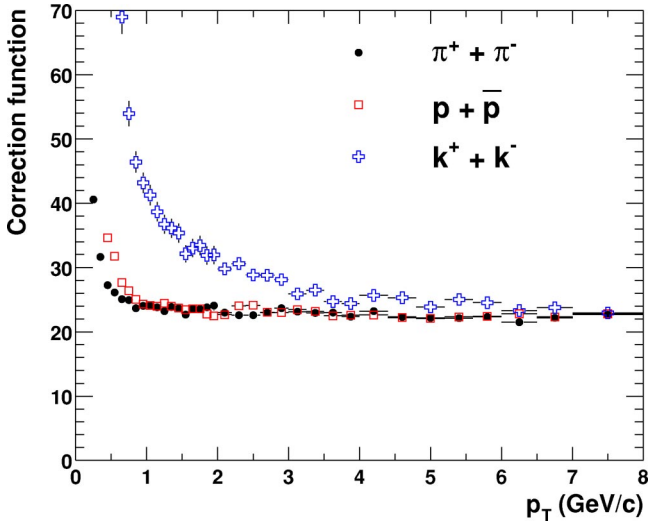

FIG. 6. (Color online) Averaged correction functions for π^+ and π^-, p and $\bar{p}$, and K^+ and K^-.

III. RESULTS

A. Inclusive charged hadron p_T spectra

Figure 8 shows the inclusive charged hadron p_T spectra for various centrality classes. All spectra exhibit power-law tails at high p_T. But for peripheral collisions, the power-law shape is more concave than for central collisions. More details of the centrality dependence of the spectral shape can be seen from Fig. 9, which shows for each centrality class the ratio of the spectra to the minimum-bias spectrum. In these ratios, most systematic errors cancel or affect the overall scale only. The characteristic centrality dependence of the shape already observed in $\sqrt{s_{NN}}$=130 GeV Au+Au collisions

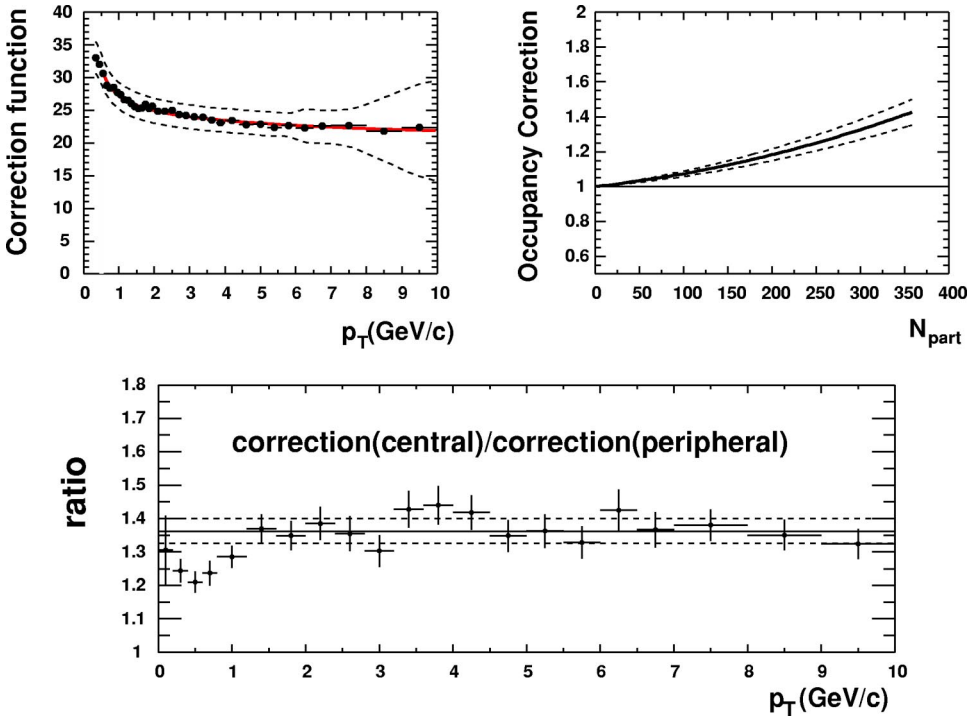

FIG. 7. (Color online) Functions used to correct the charged particle p_T spectra. The upper left panel shows the p_T-dependent correction $c(p_T)$. The upper right panel shows the centrality dependent correction $c(N_{part})$. Systematic uncertainties are indicated by the dashed lines. The two corrections factorize at $p_T > 1.5$ GeV/c, so that for given centrality the full correction function is given by $c(p_T) \times c(N_{part})$. The accuracy of this factorization is demonstrated in the lower panel. The ratio of the full correction for central collisions (5% most central) to the correction for single particle events varies by less than 3% above 1.5 GeV/c (the error bar is the statistical error from the Monte Carlo calculation).

TABLE III. Systematic errors on the p_T spectra. All errors are given in percent and are quoted as 1σ errors. They are either normalization errors or are p_T correlated errors.

p_T (GeV/c)	δ_{match} (%)	δ_{norm} (%)	δ_{mix} (%)	δ_{reso} (%)	δ_{scale} (%)	δ_{bgr} (%)	Total (%)
<1	3.5	3.2	2.4	0.6	0.6	5	7.3
1–5	3	3.2	2.4	0.6	3	5	7.6
5–6	3	3.2	1.8	0.6	3.6	5.3	7.9
6–7	3	3.2	1.8	0.6	3.3	9.5	11.1
7–8	3	3.2	1.8	0.6	3.1	11.5	12.8
8–9	3	3.2	1.8	0.9	3.1	21.1	21.9
9–10	3	3.2	1.8	5.3	3.1	31.1	32.1

[18,19] is more apparent at $\sqrt{s_{NN}}=200$ GeV. In peripheral collisions, the ratio decreases up to $p_T\sim 2$ GeV/c and then rises up to about 4 GeV/c. The trends are reversed in the most central collisions. In the range above 4–5 GeV/c, all ratios appear to be constant as a function of p_T, which would imply that they have a similar centrality independent shape.

Based on the different trends observed in Fig. 9, we can distinguish three p_T regions: 0.5–2, 2–4.5, and >4.5 GeV/c. The different centrality dependence of the spectral shape in these regions can be quantified by a truncated average p_T:

$$\langle p_T^{trunc}\rangle \equiv \frac{\int_{p_T^{min}}^{8\ \mathrm{GeV}/c} p_T\, dN/dp_T}{\int_{p_T^{min}}^{8\ \mathrm{GeV}/c} dN/dp_T} - p_T^{min}, \tag{9}$$

which is insensitive to the normalization of the spectra. The upper bound of 8 GeV/c in the integral is given by the limited p_T reach for peripheral centrality classes as shown in Fig. 8. In Fig. 10, the values of $\langle p_T^{trunc}\rangle$ for the three p_T^{min} values are plotted as a function of centrality, represented by the average number of participating nucleons (N_{part}) for each centrality class.

For $p_T^{min}=0.5$ GeV/c, where particle production is expected to be governed by soft physics, $\langle p_T^{trunc}\rangle$ increases with N_{part}. This trend is also seen for the average p_T of identified charged hadrons, and reflects the increased radial flow of soft particles in more central collisions [46]. For $p_T^{min}=2$ GeV/c, the trend is significantly different. For peripheral collisions, $\langle p_T^{trunc}\rangle$ is substantially larger than the value obtained with $p_T^{min}=0.5$ GeV/c due to the presence of the power-law tail. With increasing N_{part}, $\langle p_T^{trunc}\rangle$ for $p_T^{min}=2$ GeV/c decreases and the values obtained with $p_T^{min}=0.5$ and 2 GeV/c approach each other, which indicates an almost exponential spectrum in central collisions between 0.5 and 2 GeV/c. For the highest p_T range ($p_T^{min}=4.5$ GeV/c), $\langle p_T^{trunc}\rangle$ is approximately constant. This implies that the shape of the spectrum is nearly independent of centrality, as would be expected if this region is dominated by hard scattering.

However, the yields at high p_T do not scale with the number of nucleon-nucleon collisions; they are suppressed comparing to the binary collision scaling expected for hard scattering processes. This can be clearly seen from Fig. 11, which shows R_{cp}, the ratio of yields for central and peripheral collisions normalized to the average number of nucleon-nucleon collisions in each event sample. The ratio is below unity for all p_T. The three p_T regions show different trends as outlined in the discussion of Fig. 10.

(i) In the "soft" region with $p_T<2$ GeV/c, the ratio increases as a function of p_T.

(ii) In the "hard" region with $p_T>4.5$ GeV/c, the suppression appears to be constant at $\sim$0.3, which again indicates that the spectra have a similar shape, but with the yield in central collisions being suppressed by a constant factor from 4.5 to 10 GeV/c.

(iii) In the transition region from 2 to $\sim$4.5 GeV/c, the ratio decreases as a function of p_T.

TABLE IV. Systematic errors on the central-to-peripheral ratio. All errors are given in percent and are quoted as 1σ errors. Most of the systematic errors listed in Table III cancel in the central-to-peripheral ratio. Only those errors that are uncorrelated with centrality are shown here.

p_T (GeV/c)	$\delta_{occupancy}$ (%)	$\delta_{feeddown}$ (%)	$\delta_{R_e\oplus R_{decay}}$ (%)	Total (%)
<6	5	5	1.8	7.3
6–7	5	5	4.1	8.2
7–8	5	5	7.1	10
8–9	5	5	17.6	19
9–10	5	5	23.5	24.6

B. Suppression of high-p_T hadrons in Au+Au at $\sqrt{s_{NN}}=200$ GeV

At finite Q^2, nuclear modifications of the parton distribution [26,47] and initial [48] and final state [10] interactions of the scattering partons can modify the high-p_T hadron production rates in hard scattering processes. Medium modifications of hadron spectra are often quantified by the "nuclear modification factor" R_{AA}, which we calculate for each centrality class as the ratio of the yield per nucleon-nucleon collision in Au+Au to the yield in nucleon-nucleon collisions:

$$R_{AA}(p_T,\eta) = \left(\frac{1}{N_{evt}}\frac{d^2N^{A+A}}{dp_T d\eta}\right) \Bigg/ \left(\frac{\langle N_{coll}\rangle}{\sigma_{inel}^{N+N}}\frac{d^2\sigma^{N+N}}{dp_T d\eta}\right), \tag{10}$$

$\langle N_{coll}\rangle/\sigma_{inel}^{N+N}$ is the average Glauber nuclear overlap function, $\langle T_{\mathrm{AuAu}}\rangle$, for each centrality class. In order to calculate R_{AA},

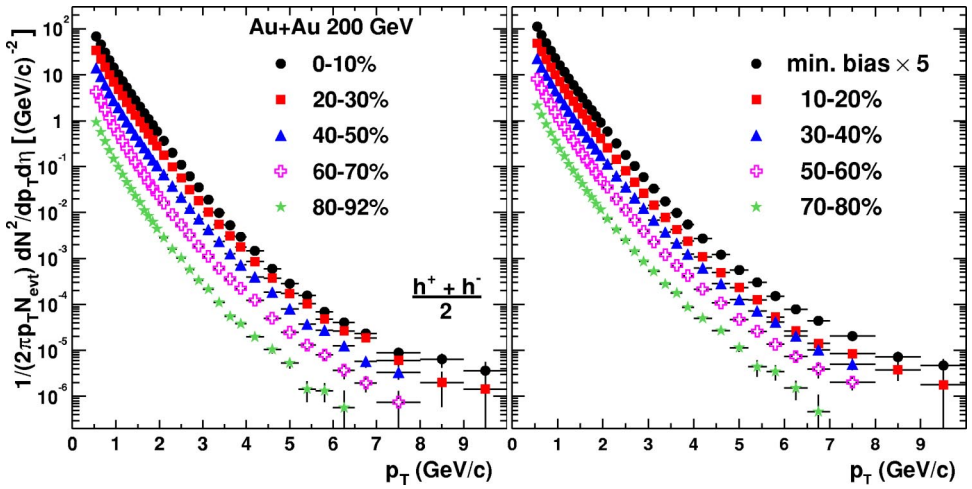

FIG. 8. (Color online) p_T spectra of charged hadrons for minimum bias collisions along with spectra for nine centrality classes derived from the pseudorapidity region $|\eta|<0.18$. The minimum bias spectrum has been multiplied by 5 for visibility. Only statistical errors are shown in the spectra. Most of the p_T-dependent systematic errors are independent of centrality and are tabulated in Table III.

we need a reference spectrum for nucleon-nucleon collisions. Due to the lack of charged hadron data with sufficient reach in p_T from our own experiment, we construct the $N+N$ reference for charged hadrons from the π^0 spectra in $p+p$ collisions at $\sqrt{s}=200$ GeV/c measured by PHENIX [16], and the charged hadron to pion ratio observed in other experiments, as described below.

The PHENIX π^0 spectra from $p+p$ collisions are measured out to 14 GeV/c. These data can be parametrized by a power-law function,

$$\frac{1}{2\pi p_T}\frac{d^2\sigma^{\pi^0}_{N+N}}{dp_T d\eta} = A\left(\frac{p_0}{p_0+p_T}\right)^n, \tag{11}$$

with $A=386$ mb/(GeV/c)^2, $p_0=1.219$ GeV/c, and $n=9.99$ [16].

In $p+p$ experiments at the ISR, the h/π ratio was measured to be 1.6 ± 0.16, independent of p_T from 1.5 to 5 GeV/c, and independent of $\sqrt{s}$ from 23 to 63 GeV [31]. Below 1.5 GeV/c, h/π decreases towards lower p_T. The ISR data are consistent with data on π, K, P production from FNAL E735 experiment [49] at $\sqrt{s}=1.8$ TeV. The h/π ratio computed from these data increases with p_T and reaches a value of 1.6 at the end of the measured p_T range, ~1.5 GeV/c. At high momentum, a h/π ratio of ~1.6 is also observed for quark and gluon jet fragmentation in e^+e^- collisions at LEP by the DELPHI Collaboration [32]. Finally, charged hadron data measured by PHENIX in $p+p$ collisions and data measured by UA1 [50] in $\bar{p}+p$ collisions, both at $\sqrt{s}=200$ GeV/c, give consistent h/π ratios when compared to the PHENIX $p+p$ π^0 data.

Based on these findings, we assume that h/π is constant above 1.5 GeV/c in $p+p$ collisions at RHIC and that we can scale up the π^0 cross section [Eq. (11)] by this factor to obtain a reference for charged hadron production. To be consistent with the data described above, we correct this reference below 1.5 GeV/c using an empirical function,

$$r(p_T) = \begin{cases} R_{h/\pi} - a(p_{max}-p_T)^2 & \text{for } p_T \leqslant p_{max} \\ R_{h/\pi} & \text{for } p_T > p_{max}, \end{cases} \tag{12}$$

where $R_{h/\pi}=1.6$, $p_{max}=1.6$ GeV/c, and $a=0.28$ (GeV/c)$^{-2}$. The charged hadron reference used in this analysis is then given by the product of the power-law function from Eq. (11) and the empirical correction from Eq. (12) as

$$\frac{1}{2\pi p_T}\frac{d^2\sigma^{h^++h^-}_{N+N}}{dp_T d\eta} = A\left(\frac{p_0}{p_0+p_T}\right)^n \times r(p_T). \tag{13}$$

The systematic errors on the charged hadron $N+N$ reference are summarized in Table V. The main sources of uncer-

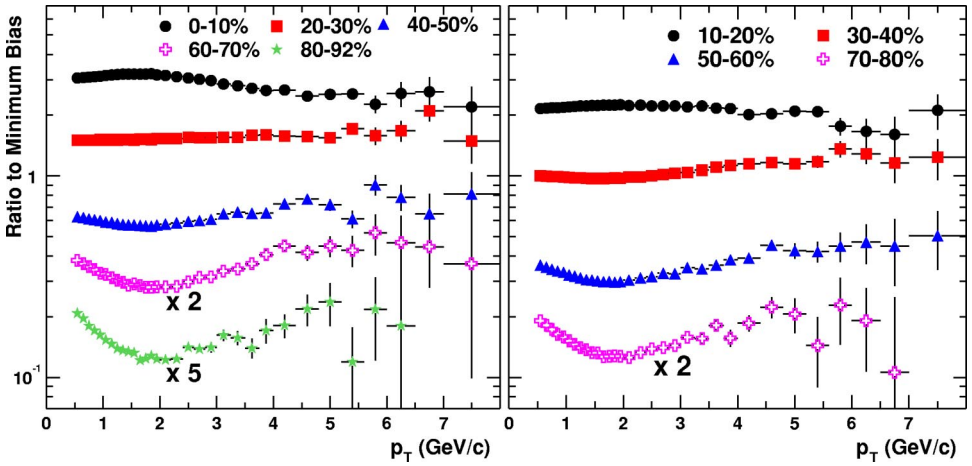

FIG. 9. (Color online) Ratios of centrality selected p_T spectra to the minimum bias spectrum. Ratios for peripheral classes are scaled up for clarity. For the p_T range shown, most of the systematic errors cancel in the ratio. The remaining systematic errors that can change the shape are less than 10% (see Table IV) and are correlated bin-to-bin in p_T.

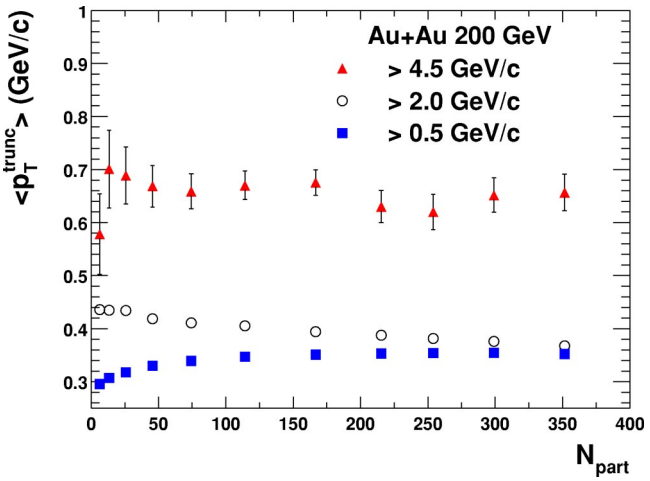

FIG. 10. (Color online) Centrality dependence of $\langle p_T^{trunc} \rangle$, the average p_T of charged particles above a p_T threshold as defined in Eq. (9). Shown are $\langle p_T^{trunc} \rangle$ values for three p_T^{min} cuts, with p_T^{min} =0.5, 2, and 4.5 GeV/c, respectively. The errors shown are statistical only. The systematical errors for all data points are less than 3%.

TABLE V. Systematic errors on the charged hadron $N+N$ reference spectrum. All errors are given in percent and are quoted as 1σ errors. Positive and negative errors are given separately where appropriate. Most of the errors are correlated with p_T.

p_T(GeV/c)	$\delta^{\pi^0}_{norm}$ (%)	$\delta^{\pi^0}_{fit}$ (%)	$\delta_{R_{h/\pi}}$ (%)	Total (%)
0.75	±10.4	−3.9+9.1	−15.1+5.9	−18.7+15.0
1.00	±10.4	−4.1+8.9	−14.4+5.9	−18.3+14.9
1.50	±10.4	−4.6+8.3	−11.6+5.9	−16.3+14.6
2.00	±10.4	−5.1+7.7	−7.9+5.9	−14.0+14.2
2.50	±10.4	−5.5+7.2	−5.9+5.9	−13.1+13.9
3.00	±10.4	−5.9+6.7	−5.9+5.9	−13.3+13.7
3.50	±10.4	−6.4+6.4	−5.9+5.9	−13.5+13.5
4.50	±10.4	−7.5+6.5	−5.9+5.9	−14.1+13.6
5.50	±10.4	−8.9+7.9	−5.9+5.9	−14.9+14.3
6.50	±10.4	−10.7+10.5	−5.9+5.9	−16.0+15.9
7.50	±10.4	−12.9+14.3	−5.9+5.9	−17.6+18.7
8.50	±10.4	−15.8+19.4	−5.9+5.9	−19.8+22.8
9.50	±10.4	−19.3+25.9	−5.9+5.9	−22.7+28.5

tainties include: (i) the systematic errors on the absolute normalization of the PHENIX π^0 data ($\delta^{\pi^0}_{norm}$), which are independent of p_T; (ii) uncertainties due to the power-law fit to the π^0 data ($\delta^{\pi^0}_{fit}$); and (iii) uncertainties on $R_{h/\pi}$ ($\delta_{h/\pi}$), which are estimated from the spread of $R_{h/\pi}$ obtained from different data sets used to constrain h/π^0.

Figure 12 shows the nuclear modification factor $R_{AA}(p_T)$ for charged hadrons from minimum bias and nine centrality classes. The systematic errors on R_{AA} are described in the figure captions. At low p_T, the charged hadron R_{AA} increase monotonically up to 2 GeV/c for all centrality classes. At $p_T>2$ GeV/c, R_{AA} remains constant and close to unity for the most peripheral centrality class. However, in central collisions, it decreases at higher p_T, down to an approximately constant value of 0.2–0.3 for $p_T>4$–5 GeV/c. This is consistent with Fig. 11, where the central to peripheral ratio also saturates above 4–5 GeV/c. This approximately p_T independent suppression pattern has been interpreted as a result of the detailed interplay between the Cronin effect, nuclear shadowing, and partonic energy loss [51].

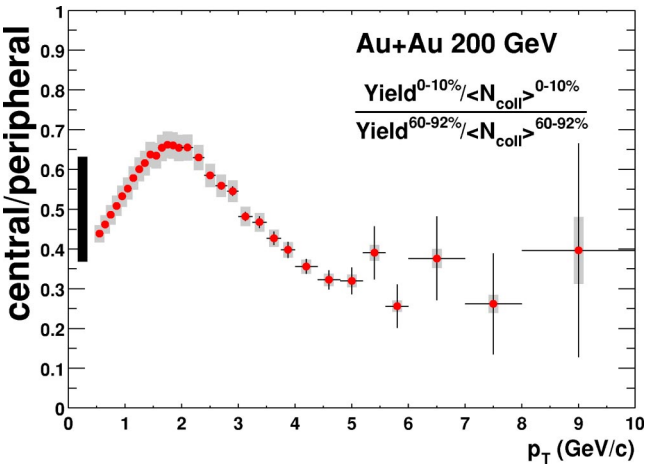

FIG. 11. (Color online) Ratio of charged hadron yields per nucleon-nucleon collision between central (0–10%) and peripheral (60–92%) Au+Au collisions. The solid error bars on each data point are statistical. The error bar on the left hand side of the figure is the overall scale error relative to 0.5, which is the quadrature sum of (i) the uncertainty of $\langle N_{coll} \rangle$ (see Table I) and (ii) the uncertainty on the occupancy correction ($\delta_{occupancy}$). The shaded error band on each data point is the p_T-dependent systematic error from $\delta_{R_e \oplus R_{decay}}$ and centrality dependent feed down correction ($\delta_{feeddown}$) as given in Table IV.

Also shown in Fig. 12 are R_{AA} for neutral pions from Ref. [21]. The neutral pion R_{AA} values also seem to reach maximum around 2 GeV/c, but the changes are smaller than those for charged hadrons. Except for the most peripheral bin, the neutral pion R_{AA} are always below the charged R_{AA} in the range of $2<p_T<4.5$ GeV/c. However, at $p_T>4.5$ GeV/c, R_{AA} for both neutral pions and hadrons saturate at roughly the same level, indicating a similar suppression for neutral pions and charged hadrons at high p_T.

The fact that the neutral pion R_{AA} values are smaller than inclusive charged hadron R_{AA} at intermediate $p_T(2<p_T<4.5$ GeV/$c)$ has already been observed at $\sqrt{s_{NN}}$ =130 GeV [17]. This difference can be explained by the large p/π ratio observed in the same p_T range in central Au+Au collisions [28,29]. This large relative proton and antiproton yield indicates a deviation from the standard picture of hadron production at $p_T>2$ GeV/c, which assumes that the hadrons are created by the fragmentation of energetic partons. Such a deviation has led to models of quark coalescence [33] or baryon junctions [52] as the possible mechanisms to enhance the proton production rate at medium p_T. Both models predict that baryon enhancement is limited to $p_T<5$ GeV/c, beyond which jet fragmentation should eventually become the dominant production mechanism for all particle species. In that case, one would expect a similar

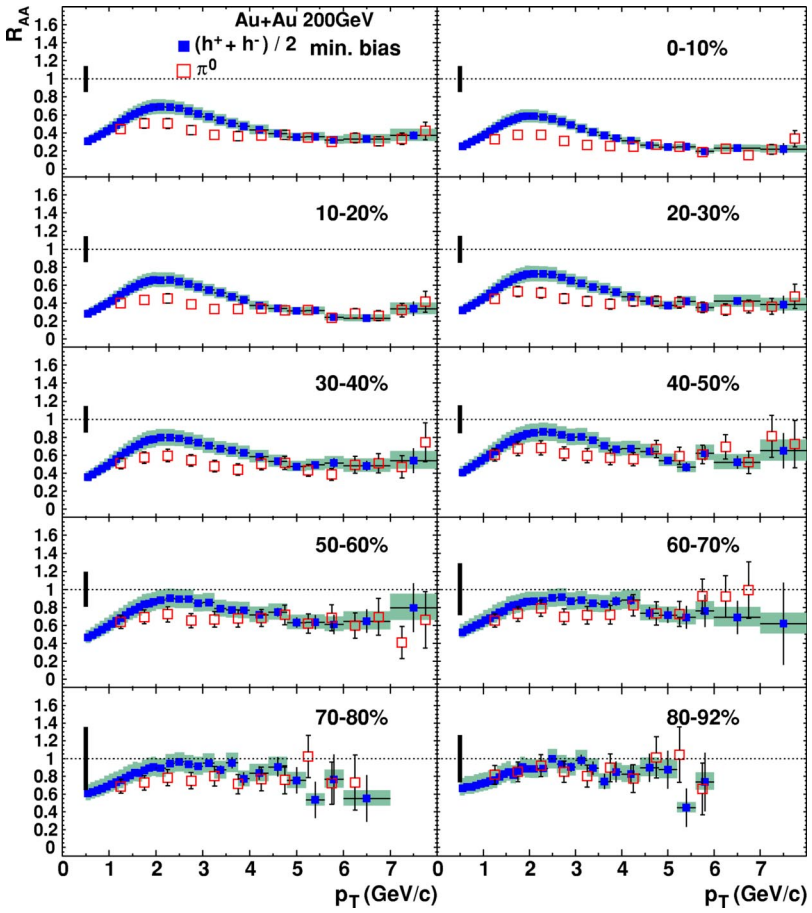

FIG. 12. (Color online) R_{AA} for $(h^+ + h^-)/2$ and π^0 as a function of p_T for minimum bias and nine centrality classes according to the "Fine" type of centrality classes defined in Table I. The error bars on the π^0 data points include statistical and systematical errors on the Au+Au data and the $N+N$ reference. The error bars on $(h^+ + h^-)/2$ data points are statistical errors only. The common normalization errors ($\delta^{\pi^0}_{norm}$ from Table V) on the references for charged hadrons and π^0's are added in quadrature with the uncertainly on $\langle N_{coll}\rangle$ and are indicated by the black bar on the left side of each panel. This error ranges from 15% to 36% from central to peripheral collisions and can shift all points in the charged and neutral pion R_{AA} up and down together. The shaded band on charged R_{AA} includes the remaining systematic errors on the charged $N+N$ reference summed in quadrature with the systematic errors from the Au+Au spectra. This error amounts to $-12.5\% + 18\%$ at low p_T and changes to $\pm 12.5\%$ at $p_T = 4.5$ GeV/c and $\pm 18.5\%$ at $p_T = 8$ GeV/c.

suppression factor for charged hadron and π^0, in agreement with the data at $p_T > 4.5$ GeV/c. Recently, the difference of R_{AA} between charged hadrons and pions was also argued as the consequence of centrality and particle species dependent $\langle k_T\rangle$ broadening effect [53].

If hard-scattering dominates charged hadron production at $p_T > 4.5$ GeV/c, the particle composition should be determined by the jet fragmentation function, similar to nucleon-nucleon collisions. Figure 13 shows h/π^0 for all centrality classes. The systematic errors are explained in the figure captions. In the most peripheral collisions, the h/π^0 ratio is consistent with the $p+p$ values down to $p_T \approx 2$ GeV/c . In central collisions, the h/π^0 ratio is enhanced by as much as 50% above the $p+p$ value in the region $1 < p_T < 4.5$ GeV/c. This enhancement gradually decreases towards more peripheral collisions and reflects the difference of R_{AA} between the charged hadrons and π^0's, which is due to large baryon contribution. The enhancement also strongly depends on p_T. It reaches a maximum between 2.5 and 3.5 GeV/c, then decreases. At $p_T > 4.5$ GeV/c, the h/π^0 ratios for all centralities reach an approximately constant value of 1.6, which is consistent with the h/π value observed in $p+p$ [31] collisions and in jet fragmentation in e^+e^- [32] collisions. The similarity of the spectral shape and of the particle composition between Au+Au and $p+p$ collisions suggest that fragmentation of hard-scattered partons is the dominant mechanism of particle production in Au+Au collisions above p_T of 4–5 GeV/c, regardless of the fact that the yields do not scale with N_{coll}.

Since R_{AA} values for charged hadrons and π^0's are approximately constant at $p_T > 4.5$ GeV/c, we can quantify the centrality dependence of the R_{AA} value by calculating it from yields integrated above 4.5 GeV/c. The upper panel of Fig. 14 shows R_{AA} for $p_T > 4.5$ GeV/c as a function of N_{part}. The R_{AA} values for charged hadrons and π^0 agree for all centrality classes within errors. In peripheral collisions with $N_{part} < 50$, R_{AA} is consistent with binary collision scaling. With increasing N_{part}, R_{AA} decreases monotonically, reaching a value of 0.23 ± 0.03 (0–5% most central) for charged hadrons and 0.24 ± 0.02 (0–10% most central) for π^0's. There is an additional 14% error common to charged hadrons and π^0's, which originates from the uncertainty on the $N+N$ reference and N_{coll}.

To address suggestions that the yield of high-p_T hadrons in Au+Au collisions may be proportional to N_{part} instead of N_{coll} [26,54], we have investigated a different ratio,

$$R_{AA}^{N_{part}} = 2\langle N_{coll}\rangle / \langle N_{part}\rangle \times R_{AA}. \tag{14}$$

$R_{AA}^{N_{part}}$ for $p_T > 4.5$ GeV/c is shown in the lower panel of Fig. 14, together with solid (or dashed) bands representing the allowed range if the data follow binary collision (or participant) scaling. As discussed above, for peripheral collisions, $R_{AA}^{N_{part}}$ follows more closely the binary collision scaling. Above 50 participants, $R_{AA}^{N_{part}}$ varies by only ±20%.

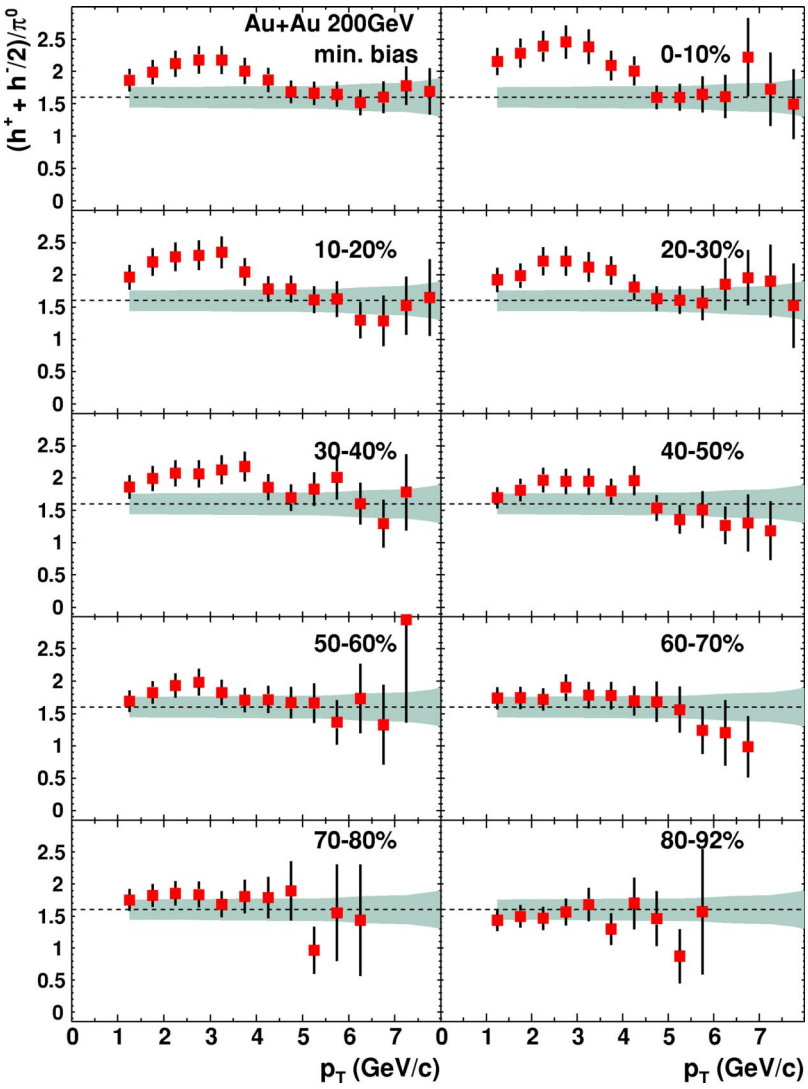

FIG. 13. (Color online) Charged hadron to π^0 ratios for minimum bias events and nine centrality classes according to the "Fine" type of centrality classes defined in Table I. The error bars represent the quadratic sum of statistical and point-by-point systematic errors from $(h^+ + h^-)/2$ and π^0. The shaded band shows the percent normalization error [dominantly from $(h^+ + h^-)/2$ data] common to all centrality classes. The dashed line at 1.6 is the h/π ratio measured in $p+p$ [31] and e^+e^- [32] collisions.

However, it peaks at $\langle N_{part} \rangle = 100$ and decreases monotonically towards more central collisions.[3]

The decrease of $R_{AA}^{N_{part}}$ could be a natural consequence of energy loss of hard scattered partons in the medium [54]. If the energy loss is large, hard scattered partons may only escape near the surface of the reaction volume. In a cylindrical collision geometry, for which the number of collisions from the surface is proportional to N_{part}, binary collision scaling is reduced to an approximate participant scaling. Detailed calculations show that in this case, $R_{AA}^{N_{part}}$ slightly decreases with N_{part} depending in details on how the energy loss is modeled [54]. This interpretation is also consistent with our previous conclusion that, above 4.5 GeV/c, hadron production is dominated by hard scattering although the yield does not scale with the number of binary collisions. Gluon saturation scenarios [26] also suggest approximate participant scaling, with a 30% increase in R_{AA} over the p_T range 4.5–9 GeV/c in central collisions. This increase cannot be excluded by the data.

C. Energy dependence and x_T scaling

The inclusive charged hadron and $\pi^0 p_T$ spectra and h/π^0 ratios suggest that fragmentation of hard scattered partons is the dominant production mechanism of high-p_T hadrons not only in $p+p$ but also in Au+Au collisions. For $p+p$ collisions this fact was demonstrated on general principles well before the advent of QCD by the method of "x_T scaling." This method does not depend on whether the initial projectiles are protons or Au ions, so it should be directly applicable to Au+Au collisions. Since our data show a suppression of high-p_T particles in central Au+Au collisions with respect to pointlike scaling from $p+p$ and peripheral Au+Au collisions, it is important to investigate whether the production dynamics of high-p_T particles in central (and peripheral) Au+Au collisions are the same or different from those in $p+p$ collisions. We first review the x_T-scaling method in $p+p$ collisions and then apply it to the present Au+Au data.

[3]In the p_T range from 3–4 GeV/c, $R_{AA}^{N_{part}}$ for charged hadrons is approximately constant, which is consistent with earlier measurements at $\sqrt{s_{NN}} = 130$ GeV [19] and $\sqrt{s_{NN}} = 200$ GeV [20]. To interpret this constancy as participant scaling is misleading, since pion and proton yields change differently with centrality in this p_T region, and $R_{AA}^{N_{part}}$ accidentally appears constant for inclusive charged hadron. The data above 4.5 GeV/c shown in Fig. 14 are free of this effect.

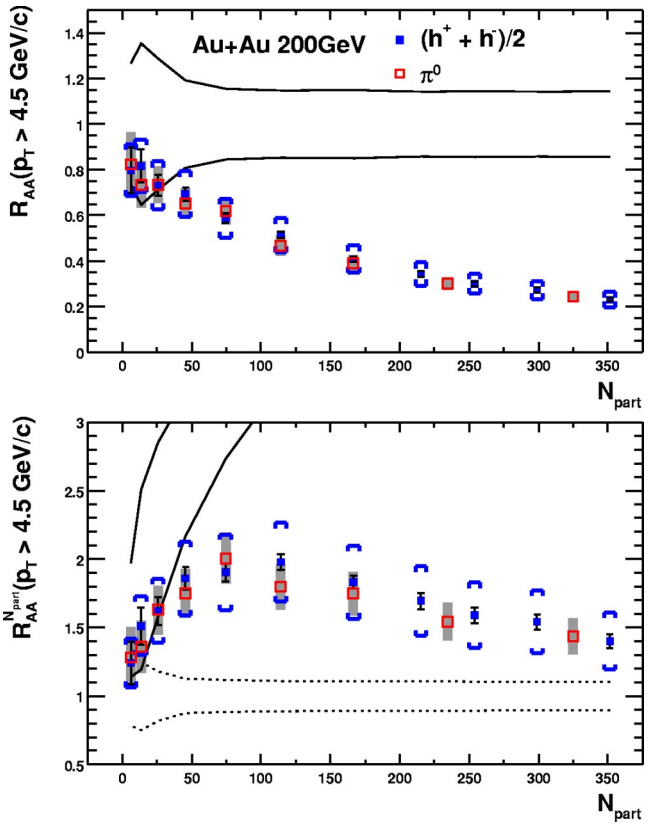

FIG. 14. (Color online) Au+Au yield integrated for $p_T > 4.5$ GeV/c over the $N+N$ yield, normalized using either N_{coll} (R_{AA} in the top panel) or N_{part} ($R_{AA}^{N_{part}}$ in the bottom panel), plotted as a function of $\langle N_{part}\rangle$. The bands represent the expectation of binary collisions (solid) and participant pair (dashed) scaling. The width of the bands gives the systematic errors on $N_{coll}(N_{part})$ added in quadrature with the common normalization errors on the $N+N$ references for charged hadrons and neutral pions. For charged hadrons, the statistical errors are given by the bars. The systematic errors, which are not common with the errors for neutral pions and which are correlated in p_T, are shown as brackets. The shaded bars around each neutral pion point represent the systematic and statistical errors; these errors are not correlated with the errors shown for the charged hadron data.

The idea of hard scattering in $N+N$ collisions dates from the first indication of pointlike structure inside the proton, in 1968, found in deep inelastic electron-proton scattering [55], i.e., scattering with large values of four-momentum transfer squared Q^2 and energy loss ν. The discovery that the deep inelastic scattering (DIS) structure function

$$F_2(Q^2,\nu) = F_2\left(\frac{Q^2}{\nu}\right) \tag{15}$$

"scales," or in other words, depends on the ratio

$$x = \frac{Q^2}{2M\nu} \tag{16}$$

independent of Q^2 as suggested by Bjorken [56], led to the concept of a proton being composed of pointlike "partons." Since the partons of DIS are charged, and hence must scatter electromagnetically from each other in $p+p$ collisions, a general formula for the cross section of the single-particle inclusive reaction

$$p + p \rightarrow C + X \tag{17}$$

was derived [57] using the principle of factorization of the reaction into parton distribution functions for the protons, fragmentation functions to particle C for the scattered partons, and a short-distance parton-parton hard scattering cross section.

The invariant cross section for the single-particle inclusive reaction [Eq. (17)], where particle C has transverse momentum p_T near midrapidity, was given by the general scaling form [58]

$$E\frac{d^3\sigma}{dp^3} = \frac{1}{p_T^n}F\left(\frac{2p_T}{\sqrt{s}}\right) \quad \text{where} \quad x_T = 2p_T/\sqrt{s}. \tag{18}$$

The cross section has two factors: a function F which depends only on the ratio of momenta, and a dimensioned factor p_T^{-n}, where n depends on the quantum exchanged in the hard-scattering. For QED or vector gluon exchange [57], $n=4$. For the case of quark-meson scattering by the exchange of a quark [58], $n=8$. The discovery of high-p_T pions in $p+p$ scattering at the CERN-ISR, in 1972 [59–61], at a rate much larger than predicted by electromagnetic scattering, but with the scaling form of Eq. (18), proved that the partons of DIS strongly interact with each other.

Inclusion of QCD [62] into the scaling form [Eq. (18)] led to the x_T-scaling law,

$$E\frac{d^3\sigma}{dp^3} = \frac{1}{\sqrt{s}^{n(x_T,\sqrt{s})}}\,G(x_T), \tag{19}$$

where the "x_T-scaling power" $n(x_T,\sqrt{s})$ should equal 4 in lowest order (LO) calculations, analogous to the $1/q^4$ form of Rutherford scattering in QED. The structure and fragmentation functions, which scale as the ratios of momenta are all in the $G(x_T)$ term. Due to higher order effects such as the running of the coupling constant, $\alpha_s(Q^2)$, the evolution of the structure and fragmentation functions, and the initial state k_T, measured values of $n(x_T,\sqrt{s})$ in $p+p$ collisions are in the range from 5 to 8.

The compilation of single particle inclusive transverse momentum spectra at midrapidity from $p+p$ and $p+\bar{p}$ collisions at center-of-mass (c.m.) energy $\sqrt{s}$ from 23 to 1800 GeV [31,50,63,64] is shown in Fig. 15(a) for $(h^+ + h^-)/2$, and in Fig. 16(a) for π^0 [16,65–68]. The spectra exhibit a characteristic shape: an exponential part at low $p_T \leqslant 1$ GeV/c which depends very little on $\sqrt{s}$ (soft physics), and a power-law tail for $p_T \geqslant 2$ GeV/c which depends very strongly on $\sqrt{s}$ (hard physics). The high-p_T part of the spectra shows a characteristic scaling behavior indicative of fragmentation of jets produced by hard scattering of the quark and gluon constituents of the proton as described by QCD [69–71].

The x_T scaling of the single particle inclusive data is nicely illustrated by a plot of

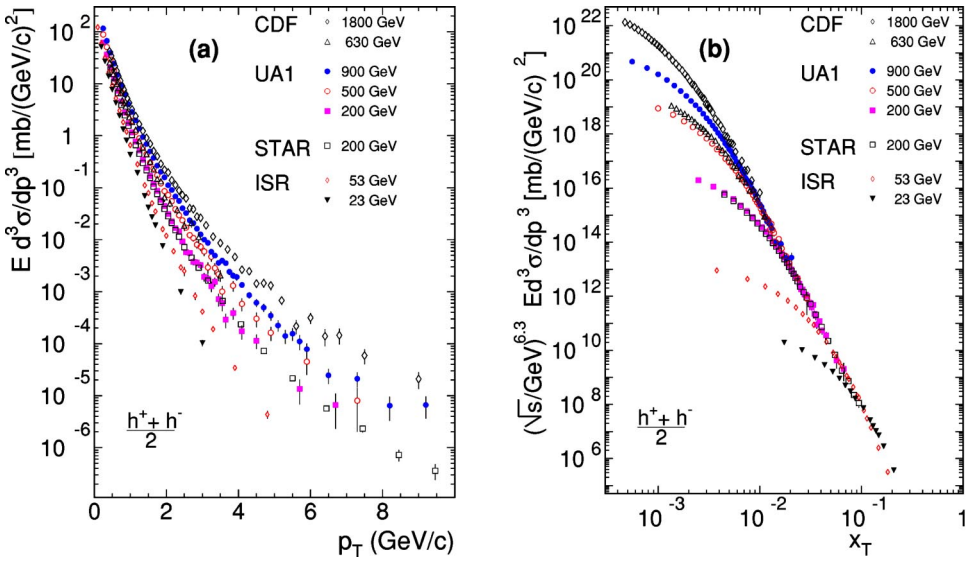

FIG. 15. (Color online) (a) Transverse momentum dependence of the invariant cross section at seven center-of-mass energies from different experiments [31,50,63,64]. (b) The same data multiplied by $\sqrt{s}^{6.3}$, plotted as a function of $x_T = 2p_T/\sqrt{s}$.

$$\sqrt{s}^{n(x_T,\sqrt{s})} \times E\frac{d^3\sigma}{dp^3} = G(x_T), \tag{20}$$

as a function of x_T, with $n(x_T,\sqrt{s})=6.3$. The $(h^+ + h^-)/2$ data [Fig. 15(b)] show an asymptotic power law with increasing x_T. Data at a given $\sqrt{s}$ fall below the asymptote at successively lower values of x_T with increasing $\sqrt{s}$, corresponding to the transition region from hard to soft physics in the p_T range of 1–2 GeV/c. The π^0 data [Fig. 16(b)] show a similar x_T scaling but without the deviation at low x_T, since all available data are for p_T larger than 1–2 GeV/c. For larger $x_T \geqslant 0.3$, a value of $n=5.1$ [66,72] improves the scaling for the three lower c.m. energies, $\sqrt{s}=38.7$, 52.7, and 62.4 GeV. It will be a challenge at RHIC to obtain data in this x_T range to see whether the value of $n\sim 5$ is the asymptotic limit for inclusive single particle production or whether n reaches the (LO) QCD value of 4. x_T scaling has also been studied in jet production at $\sqrt{s}=630$ and 1800 GeV [73], where $n=4.45$ is observed in the jet x_T range 0.15–0.3.

In Au+Au collisions, x_T scaling should work just as well as in $p+p$ collisions and should yield the same value of $n(x_T,\sqrt{s})$ if the high-p_T particles are the result of hard scattering according to QCD. This is because the structure and fragmentation functions in Au+Au collisions should scale, so that Eq. (19) applies, albeit with a different $G(x_T)$. Thus, if the suppression of high-p_T particles with respect to pointlike scaling from $p+p$ collisions is due to shadowing of the structure functions [47] or gluon saturation [26], which are basi-

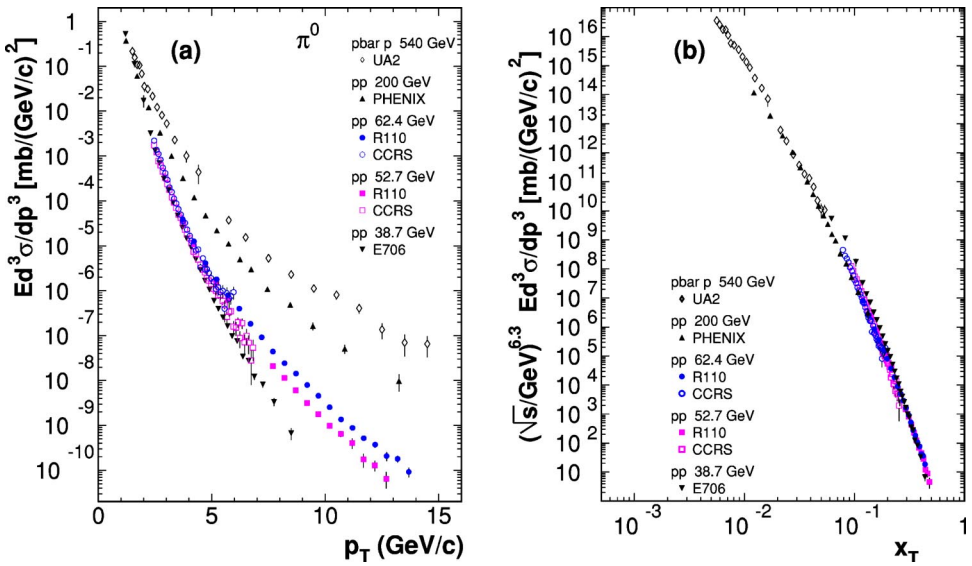

FIG. 16. (Color online) (a) Transverse momentum dependence of the invariant cross section for π^0 at five center-of-mass energies from different experiments [16,65–68]. (b) The same data multiplied by $\sqrt{s}^{6.3}$, plotted vs $x_T = 2p_T/\sqrt{s}$.

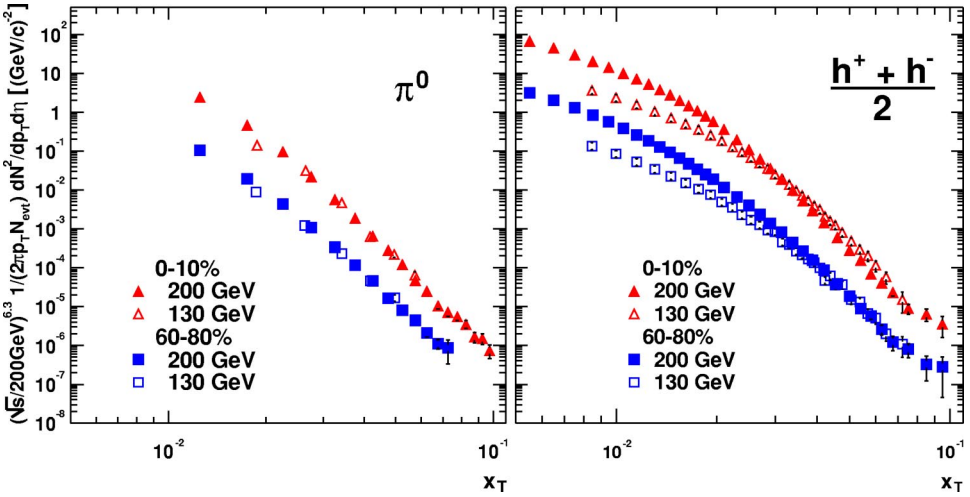

FIG. 17. (Color online) x_T scaled spectra for central collisions and peripheral collisions at $\sqrt{s_{NN}}=130$ and 200 GeV. The left figure shows the π^0 x_T spectra, and the right figure shows the $(h^++h^-)/2$ x_T spectra. The central (0–10%) x_T spectra are represented by triangular symbols, and the peripheral (60–80%) x_T spectra are represented by square symbols. The open symbols represent x_T spectra from $\sqrt{s_{NN}}=130$ GeV scaled by a factor of $(130/200)^{6.3}$. The solid symbols represent x_T spectra from $\sqrt{s_{NN}}=200$ GeV The error bars are statistical only.

cally scaling effects,[4] rather than due to a final state interaction with the dense medium, which may not scale, the cross sections [Eq. (19)] at a given x_T (and centrality) should all exhibit the same suppression. The initial state shadowing may cause $G(x_T)$ to change with centrality, but $n(x_T,\sqrt{s})$ should remain constant. In the case of the interaction with the dense medium, x_T scaling may or may not hold, depending on the details of the energy loss, for instance, whether or not the energy loss of the hard-scattered parton scales with its energy. It is also conceivable that the high-p_T particles observed in Au+Au collisions at RHIC have nothing to do with QCD hard scattering [27,33,52]. In this case, striking differences from Eq. (19) and the systematics observed in $p+p$ collisions should be expected.

To test x_T scaling in Au+Au collisions, we plot the quantities defined by Eq. (20) in Fig. 17 for charged hadron and π^0 data from $\sqrt{s_{NN}}=130$ GeV and 200 GeV for central (0–10%) and peripheral (60–80%) collisions. For the power n, we use the same value $n(x_T,\sqrt{s})=6.3$ that was used for the $p+p$ data shown in Fig. 15(b) and Fig. 16(b). The data are consistent with x_T scaling over the range $0.03\leqslant x_T\leqslant 0.06$ for π^0 and $0.04\leqslant x_T\leqslant 0.075$ for $(h^++h^-)/2$.

According to Eq. (19), the ratio of inclusive cross sections at fixed x_T equals $(200/130)^n$. Thus, the power $n(x_T,\sqrt{s})$ is related directly to the logarithm of the ratio of invariant hadron yield at fixed x_T as

$$n(x_T)=\frac{\log\left[\text{yield}(x_T,130\text{ GeV})/\text{yield}(x_T,200\text{ GeV})\right]}{\log(200/130)}. \tag{21}$$

The power n's for both neutral pions and charged hadrons for central and peripheral collisions are shown in Fig. 18.

While the π^0 data in central and peripheral collisions and charged hadron data in peripheral collisions seem to favor a similar power n, the charged hadron data from central collisions require a larger value of n.

For a more quantitative analysis, the Au+Au data for a given centrality and hadron selection are fitted simultaneously for $\sqrt{s_{NN}}=130$ and 200 GeV to the form

$$\left(\frac{A}{\sqrt{s}}\right)^n (x_T)^{-m}, \tag{22}$$

where we have approximated Eq. (19) by using a constant power $n(x_T,\sqrt{s})$ and a power law, x_T^{-m}, for $G(x_T)$ over a limited range in x_T. The fit results and errors are quoted in Table VI. The corresponding ratios of yields are presented by lines in Figure 18, where the fit ranges ($0.03\leqslant x_T\leqslant 0.06$ for π^0s and $0.04\leqslant x_T\leqslant 0.074$ for charged hadrons) are indicated by the length of the line.

For peripheral collisions the fitted values for the power are $n=6.33\pm0.54$ and $n=6.12\pm0.49$, for π^0 and charged hadrons respectively, which are in quantitative agreement with the expectation from $p+p$ collisions. Approximate x_T scaling in peripheral Au+Au collisions with the same power as observed in $p+p$ collisions indicates that hard scattering is the dominating production mechanism for high-p_T particles. In central collisions, neutral pions also exhibit x_T scaling with a similar power, $n=6.41\pm0.55$. Thus, it seems that high-p_T π^0 production is consistent with hard scattering, with scaling structure and fragmentation functions, for all centralities.

For charged hadrons, the power found for central collisions is $n=7.53\pm0.44$. Most of the systematic errors are common and cancel between central and peripheral collisions, thus the difference of the two powers found for charged hadrons, $\Delta n=n_{cent}-n_{periph}=1.41\pm0.43$ compared with that for neutral pion $\Delta n=0.09\pm0.47$, is significant.

This difference is consistent with the large proton and antiproton enhancement in central Au+Au collisions for in-

[4]There is a slight nonscaling effect of the structure functions [47] since for fixed x_T, Q^2 changes by a factor of 2.4 between the two $\sqrt{s_{NN}}$.

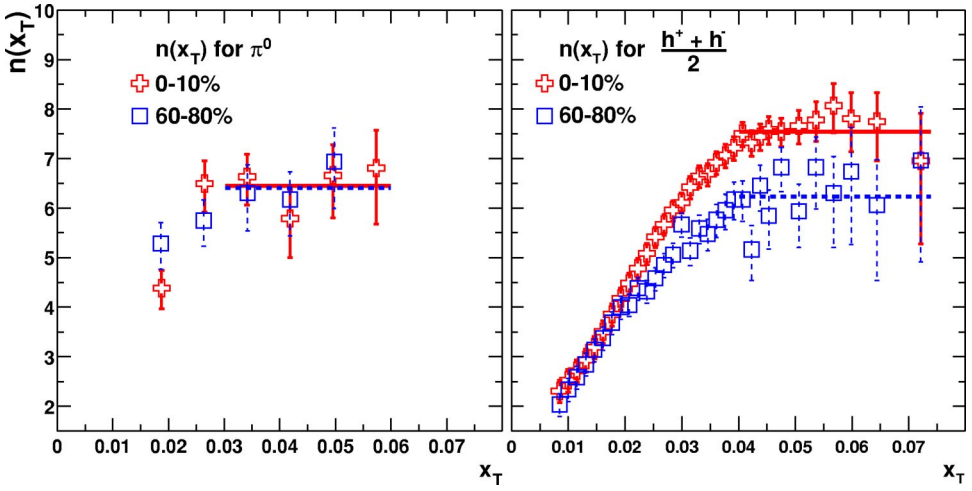

FIG. 18. (Color online) The x_T scaling power n [according to Eq. (21)] plotted as a function of x_T calculated for π^0 (left) and $(h^+ + h^-)/2$ (right) in central (0–10%) and peripheral (60–80%) collisions. The solid (and dashed) lines indicate a constant fit along with the fitting ranges to the central (and peripheral) $n(x_T)$ functions. The error bars at each data point include statistical and point-to-point systematic errors from $\sqrt{s_{NN}}$=130 and 200 GeV. The scale errors on x_T spectra are 20.7%(15.9%) for π^0 x_T spectra ratio in central (peripheral) collisions, and 18.6%(15.7%) for $(h^+ + h^-)/2$ x_T spectra ratio in central (peripheral) collisions. These type of errors propagate into the systematic errors on x_T scaling power n listed in Table VI.

termediate p_T seen at $\sqrt{s_{NN}}$=130 and 200 GeV, which appears to violate x_T scaling. The x_T range $0.04 \leqslant x_T \leqslant 0.074$ corresponds to $4 < p_T < 7.4$ GeV/c at $\sqrt{s_{NN}}$=200 GeV, but it corresponds to $2.6 < p_T < 4.8$ GeV/c at $\sqrt{s_{NN}}$=130 GeV. If protons are enhanced at $2 < p_T < 4.5$ GeV/c in central collisions at both $\sqrt{s_{NN}}$=130 GeV and 200 GeV, then n_{cent} will be larger than n_{periph} in the measured x_T range. Since $\sqrt{s_{NN}}$ =200 GeV data indicate that the proton enhancement is limited to the medium p_T range, based on the equality of R_{AA} for charged hadrons and π^0 at $p_T > 4.5$ GeV/c (Fig. 12), this difference should go away at larger x_T.

IV. SUMMARY

We have presented a systematic study of the p_T and centrality dependence of charged hadron production at $|\eta| < 0.18$ at $\sqrt{s_{NN}}$=200 GeV. The yields per nucleon-nucleon collision in central collisions are significantly suppressed compared to peripheral and nucleon-nucleon collisions. The suppression is approximately independent of p_T above 4.5 GeV/c for all centrality classes, suggesting a similar spectral shape between Au+Au and $p+p$ collisions. At $p_T > 4.5$, charged hadron suppression is the same as for neutral pions; the ratio h/π^0 is ~1.6 for all centralities, similar to the h/π value measured in $p+p$ and e^+e^- collisions. The similar spectral shape and particle composition at high p_T are consistent with jet fragmentation as the dominating mechanism of particle production in Au+Au collisions for $p_T > 4$–5 GeV/c. For both charged hadrons and neutral pions, the suppression sets in gradually from peripheral to central collisions, consistent with the expectation of partonic

TABLE VI. Results of the simultaneous fit to $\sqrt{s_{NN}}$=130 and 200 GeV data using Eq. (22). The fit ranges are $0.03 \leqslant x_T \leqslant 0.06$ for π^0 and $0.04 \leqslant x_T \leqslant 0.074$ for charged hadron. Only statistical and point-to-point systematic errors on the data points are included in the fit, which gives the statistical error on n. The normalization errors and other p_T correlated systematic errors are not included in the fit but are directly translated into a systematic error on n.

Fitting results for π^0 over $0.03 < x_T < 0.06$		
Parameters	0–10% centrality bin	60–80% centrality bin
A	0.973±0.232	0.843±0.3
m	8.48±0.17	7.78±0.22
n	6.41±0.25(stat) ±0.49(sys)	6.33±0.39(stat) ±0.37(sys)
Fitting results for $h^+ + h^-$ over $0.04 < x_T < 0.074$		
A	2.30±0.44	0.62±0.27
m	8.74±0.28	8.40±0.43
n	7.53±0.18(stat) ±0.40(sys)	6.12±0.33(stat) ±0.36(sys)

energy loss and surface emission of high-p_T hadrons. The x_T-scaled hadron yields are compared between $\sqrt{s_{NN}}$ = 130 GeV and $\sqrt{s_{NN}}$ = 200 GeV Au+Au collisions. We find that the x_T scaling power n calculated for neutral pions in central and peripheral collisions and charged hadron in peripheral collisions is 6.3 ± 0.6, similar to $p+p$ collisions. This again points towards similar production dynamics, i.e., hard scattering processes as described by QCD. However, n is 7.5 ± 0.5 for charged hadrons in central collisions, indicating a strong nonscaling modification of particle composition of charged hadron spectra from that of $p+p$ at intermediate p_T, 2–4.5 GeV/c. This is consistent with the large h/π^0 ratios observed over the same p_T range in central collisions.

ACKNOWLEDGMENTS

We thank the staff of the Collider-Accelerator and Physics Departments at Brookhaven National Laboratory and the staff of the other PHENIX participating institutions for their vital contributions. We acknowledge support from the Department of Energy, Office of Science, Nuclear Physics Division, the National Science Foundation, Abilene Christian University Research Council, Research Foundation of SUNY, and Dean of the College of Arts and Sciences, Vanderbilt University (USA), Ministry of Education, Culture, Sports, Science, and Technology and the Japan Society for the Promotion of Science (Japan), Conselho Nacional de Desenvolvimento Científico e Tecnológico and Fundação de Amparo à Pesquisa do Estado de São Paulo (Brazil), Natural Science Foundation of China (People's Republic of China), Centre National de la Recherche Scientifique, Commissariat à l'Énergie Atomique, Institut National de Physique Nucléaire et de Physique des Particules and Institut National de Physique Nucléaire et de Physique des Particules, (France), Bundesministerium fuer Bildung und Forschung, Deutscher Akademischer Austausch Dienst, and Alexander von Humboldt Stiftung (Germany), Hungarian National Science Fund, OTKA (Hungary), Department of Atomic Energy and Department of Science and Technology (India), Israel Science Foundation (Israel), Korea Research Foundation and Center for High Energy Physics (Korea), Russian Ministry of Industry, Science and Tekhnologies, Russian Academy of Science, Russian Ministry of Atomic Energy (Russia), VR and the Wallenberg Foundation (Sweden), the U.S. Civilian Research and Development Foundation for the Independent States of the Former Soviet Union, the US-Hungarian NSF-OTKA-MTA, the US-Israel Binational Science Foundation, and the 5th European Union TMR Marie-Curie Programme.

[1] F. Karsch, Lect. Notes Phys. **583**, 209 (2002).
[2] L. Mclerran, Lect. Notes Phys. **221**, 1 (1985); M. Gyulassy, Z. Phys. C **38**, 1 (1988).
[3] T. Alber *et al.*, NA49 Collaboration, Phys. Rev. Lett. **75**, 3814 (1995).
[4] K. Adcox *et al.*, PHENIX Collaboration, Phys. Rev. Lett. **87**, 052301 (2001).
[5] A. Bazilevsky *et al.*, PHENIX Collaboration, Nucl. Phys. **A715**, 486 (2003).
[6] J. D. Bjorken, Phys. Rev. D **27**, 140 (1983).
[7] D. Teaney *et al.*, Phys. Rev. Lett. **86**, 4783 (2001).
[8] U. Heinz and P. Kolb, Nucl. Phys. **A702**, 269 (2002).
[9] W. Broniowski and W. Florkowski, Phys. Rev. Lett. **87**, 272302 (2001); W. Florkowski and W. Broniowski, Phys. Rev. C **65**, 064905 (2002).
[10] M. Gyulassy and M. Plümer, Phys. Lett. B **243**, 432 (1990); X. N. Wang and M. Gyulassy, Phys. Rev. Lett. **68**, 1480 (1992); R. Baier *et al.*, Phys. Lett. B **345**, 277 (1995).
[11] R. Baier, D. Schiff, and B. G. Zakharov, Annu. Rev. Nucl. Part. Sci. **50**, 37 (2000).
[12] R. Baier, Y. L. Dokshitzer, A. H. Mueller, and D. Schiff, J. High Energy Phys. **9**, 33 (2001).
[13] X. N. Wang, Phys. Rev. C **63**, 054902 (2001).
[14] X. N. Wang, Nucl. Phys. **A715**, 775 (2003).
[15] J. F. Owens *et al.*, Phys. Rev. D **18**, 1501 (1978).
[16] S. S. Adler *et al.*, PHENIX Collaboration, Phys. Rev. Lett. **91**, 241803 (2003) and reference therein.
[17] K. Adcox *et al.*, PHENIX Collaboration, Phys. Rev. Lett. **88**, 022301 (2002).
[18] C. Adler *et al.*, STAR Collaboration, Phys. Rev. Lett. **89**, 202301 (2002).
[19] K. Adcox *et al.*, PHENIX Collaboration, Phys. Lett. B **561**, 82 (2003).
[20] B. B. Back *et al.*, PHOBOS Collaboration, nucl-ex/0302015.
[21] S. S Adler *et al.*, PHENIX Collaboration, Phys. Rev. Lett. **91**, 072301 (2003).
[22] J. Adams *et al.*, STAR Collaboration, Phys. Rev. Lett. **91**, 172302 (2003).
[23] I Arsene, *et al.*, BRAHMS Collaboration, Phys. Rev. Lett. **91**, 072305 (2003).
[24] M. Gyulassy, I. Vitev, and X. N. Wang, Phys. Rev. Lett. **86**, 2537 (2001).
[25] G. G. Barnafoldi, P. Levai, G. Papp, G. Fai, and Y. Zhang, nucl-th/0212111.
[26] D. Kharzeev, E. Levin, and L. McLerran, Phys. Lett. B **561**, 93 (2003), and references therein.
[27] K. Gallmeister, C. Greiner, and Z. Xu, nucl-th/0202051; K. Gallmeister, C. Greiner, and Z. Xu, Phys. Rev. C **67**, 044905 (2003).
[28] K. Adcox *et al.*, PHENIX Collaboration, Phys. Rev. Lett. **88**, 242301 (2002).
[29] S. S Adler *et al.*, PHENIX Collaboration, Phys. Rev. Lett. **91**, 172301 (2003).
[30] J. Adams *et al.*, STAR Collaboration, nucl-ex/0306007.
[31] B. Alper *et al.*, Nucl. Phys. **B100**, 237 (1975).
[32] P. Abreu *et al.*, Eur. Phys. J. C **17**, 207 (2000); O. Klapp, Doctoral thesis, University Wuppertal, 1999.
[33] R. C. Hwa and C. B. Yang, Phys. Rev. C **67**, 034902 (2003); R. J. Fries, B. Muller, C. Nonaka, and S. A. Bass, Phys. Rev. Lett. **90**, 202303 (2003); V. Greco, C. M. Ko, and P. Levai, *ibid.* **90**, 202302 (2003); Phys. Rev. C **68**, 034904 (2003); R. J. Fries, B Müller, C. Nonaka, and S. A. Bass, *ibid.* **68**,

044902 (2003).
[34] K. Adcox *et al.*, Nucl. Instrum. Methods Phys. Res. A **499**, 469 (2003).
[35] R. J. Glauber and G. Matthiae, Nucl. Phys. **B21**, 135 (1970).
[36] Woods-Saxon Au nuclear radius $R=6.38^{+0.27}_{-0.13}$ fm, diffusivity $a=0.53\pm0.01$ fm [B. Hahn, D. G. Ravenhall, and R. Hofstadter, Phys. Rev. **101**, 1131 (1956)], and nucleon-nucleon cross section $\sigma_{NN}^{inel}=42\pm3$ mb.
[37] K. Adcox *et al.*, PHENIX Collaboration, Phys. Rev. Lett. **86**, 3500 (2001).
[38] K. Adcox *et al.*, PHENIX Collaboration, nucl-ex/0307010.
[39] K. Adcox *et al.*, Nucl. Instrum. Methods Phys. Res. A **499**, 489 (2003); J. T. Mitchell *et al.*, *ibid.* **482**, 491 (2002).
[40] M. Aizawa *et al.*, Nucl. Instrum. Methods Phys. Res. A **499**, 508 (2003).
[41] X. N. Wang and M. Gyulassy, Phys. Rev. D **44**, 3501 (1991).
[42] K. Adcox *et al.*, PHENIX Collaboration, Phys. Rev. Lett. **89**, 092302 (2002).
[43] C. Adler *et al.*, STAR Collaboration, nucl-ex/0206008.
[44] GEANT 3.2.1, CERN program library.
[45] S. S. Adler *et al.*, Nucl. Instrum. Methods Phys. Res. A **409**, 593 (2003).
[46] S. S. Adler *et al.*, PHENIX Collaboration, nucl-ex/0307022.
[47] K. J. Eskola, V. J. Kolhinen, and P. V. Ruuskanen, Nucl. Phys. **B535**, 351 (1998); K. J. Eskola, V. J. Kolhinen, and C. A. Salgado, Eur. Phys. J. C **9**, 61 (1999).
[48] D. Antreasyan *et al.*, Phys. Rev. D **19**, 764 (1979).
[49] T. Alexopoulos *et al.*, Phys. Rev. D **48**, 984 (1993).
[50] C. Albajar *et al.*, Nucl. Phys. **B335**, 261 (1990).
[51] I. Vitev and M. Gyulassy, Phys. Rev. Lett. **89**, 252301 (2002).
[52] I. Vitev and M. Gyulassy, Phys. Rev. C **65**, 041902(R) (2002).
[53] X. F. Zhang and G. Fai, hep-ph/0306227.
[54] B. Müller, Phys. Rev. C **67**, 061901 (2003).
[55] M. Breidenbach *et al.*, Phys. Rev. Lett. **23**, 935 (1969); see also W. K. H. Panofsky, in *Proceedings of the Fourteenth International Conference On High Energy Physics, Vienna, Austria, 1968* (CERN Scientific Information Service, Geneva, Switzerland, 1968), p. 23.
[56] J. D. Bjorken, Phys. Rev. **179**, 1547 (1969).
[57] S. M. Berman, J. D. Bjorken, and J. B. Kogut, Phys. Rev. D **4**, 3388 (1971).
[58] R. Blankenbecler, S. J. Brodsky, and J. F. Gunion, Phys. Lett. **42B**, 461 (1972).
[59] F. W. Büsser *et al.*, Phys. Lett. **46B**, 471 (1973); see also *Proceedings of the 16th International Conference of HEP*, edited by J. D. Jackson and A. Roberts (NAL, Batavia, IL, 1972), Vol. 3, p. 317.
[60] M. Banner *et al.*, Phys. Lett. **44B**, 537 (1973).
[61] B. Alper *et al.*, Phys. Lett. **44B**, 521 (1973).
[62] R. F. Cahalan, K. A. Geer, J. Kogut, and L. Susskind Phys. Rev. D **11**, 1199 (1975).
[63] F. Abe *et al.*, Phys. Rev. Lett. **61**, 1819 (1988).
[64] J. Adams *et al.*, STAR Collaboration, Phys. Rev. Lett. **91**, 072304 (2003).
[65] F. W. Büsser *et al.*, Nucl. Phys. **B106**, 1 (1976).
[66] A. L.S. Angelis *et al.*, Phys. Lett. **79B**, 505 (1978); see also, A. G. Clark *et al.*, *ibid.* **74B**, 267 (1978).
[67] M. Banner *et al.*, Phys. Lett. **115B**, 59 (1982); Z. Phys. C **27**, 329 (1985).
[68] L. Apanasevich *et al.*, Phys. Rev. D **68**, 052001 (2003).
[69] P. Darriulat, Annu. Rev. Nucl. Part. Sci. **30**, 159 (1980).
[70] L. DiLella, Annu. Rev. Nucl. Part. Sci. **35**, 107 (1985).
[71] J. F. Owens, Phys. Rev. D **11**, 1199 (1975); Rev. Mod. Phys. **59**, 465 (1987).
[72] C. Kourkoumelis *et al.*, Phys. Lett. **84B**, 271 (1979).
[73] J. Huston, in *Proceedings of the 29th International Conference of HRP (ICHEP 98), Vancouver, Canada, 1998*, edited by A. Astbury and J. Robinson (World Scientific, Singapore, 1999).

Identified charged particle spectra and yields in Au+Au collisions at $\sqrt{s_{NN}}$=200 GeV

S. S. Adler,[5] S. Afanasiev,[17] C. Aidala,[5] N. N. Ajitanand,[43] Y. Akiba,[20,38] J. Alexander,[43] R. Amirikas,[12] L. Aphecetche,[45] S. H. Aronson,[5] R. Averbeck,[44] T. C. Awes,[35] R. Azmoun,[44] V. Babintsev,[15] A. Baldisseri,[10] K. N. Barish,[6] P. D. Barnes,[27] B. Bassalleck,[33] S. Bathe,[30] S. Batsouli,[9] V. Baublis,[37] A. Bazilevsky,[39,15] S. Belikov,[16,15] Y. Berdnikov,[40] S. Bhagavatula,[16] J. G. Boissevain,[27] H. Borel,[10] S. Borenstein,[25] M. L. Brooks,[27] D. S. Brown,[34] N. Bruner,[33] D. Bucher,[30] H. Buesching,[30] V. Bumazhnov,[15] G. Bunce,[5,39] J. M. Burward-Hoy,[26,44] S. Butsyk,[44] X. Camard,[45] J.-S. Chai,[18] P. Chand,[4] W. C. Chang,[2] S. Chernichenko,[15] C. Y. Chi,[9] J. Chiba,[20] M. Chiu,[9] I. J. Choi,[52] J. Choi,[19] R. K. Choudhury,[4] T. Chujo,[5] V. Cianciolo,[35] Y. Cobigo,[10] B. A. Cole,[9] P. Constantin,[16] D. G. d'Enterria,[45] G. David,[5] H. Delagrange,[45] A. Denisov,[15] A. Deshpande,[39] E. J. Desmond,[5] O. Dietzsch,[41] O. Drapier,[25] A. Drees,[44] R. du Rietz,[29] A. Durum,[15] D. Dutta,[4] Y. V. Efremenko,[35] K. El Chenawi,[49] A. Enokizono,[14] H. En'yo,[38,39] S. Esumi,[48] L. Ewell,[5] D. E. Fields,[33,39] F. Fleuret,[25] S. L. Fokin,[23] B. D. Fox,[39] Z. Fraenkel,[51] J. E. Frantz,[9] A. Franz,[5] A. D. Frawley,[12] S.-Y. Fung,[6] S. Garpman,[29,*] T. K. Ghosh,[49] A. Glenn,[46] G. Gogiberidze,[46] M. Gonin,[25] J. Gosset,[10] Y. Goto,[39] R. Granier de Cassagnac,[25] N. Grau,[16] S. V. Greene,[49] M. Grosse Perdekamp,[39] W. Guryn,[5] H.-Å. Gustafsson,[29] T. Hachiya,[14] J. S. Haggerty,[5] H. Hamagaki,[8] A. G. Hansen,[27] E. P. Hartouni,[26] M. Harvey,[5] R. Hayano,[8] X. He,[13] M. Heffner,[26] T. K. Hemmick,[44] J. M. Heuser,[44] M. Hibino,[50] J. C. Hill,[16] W. Holzmann,[43] K. Homma,[14] B. Hong,[22] A. Hoover,[34] T. Ichihara,[38,39] V. V. Ikonnikov,[23] K. Imai,[24,38] D. Isenhower,[1] M. Ishihara,[38] M. Issah,[43] A. Isupov,[17] B. V. Jacak,[44] W. Y. Jang,[22] Y. Jeong,[19] J. Jia,[44] O. Jinnouchi,[38] B. M. Johnson,[5] S. C. Johnson,[26] K. S. Joo,[31] D. Jouan,[36] S. Kametani,[8,50] N. Kamihara,[47,38] J. H. Kang,[52] S. S. Kapoor,[4] K. Katou,[50] S. Kelly,[9] B. Khachaturov,[51] A. Khanzadeev,[37] J. Kikuchi,[50] D. H. Kim,[31] D. J. Kim,[52] D. W. Kim,[19] E. Kim,[42] G.-B. Kim,[25] H. J. Kim,[52] E. Kistenev,[5] A. Kiyomichi,[48] K. Kiyoyama,[32] C. Klein-Boesing,[30] H. Kobayashi,[38,39] L. Kochenda,[37] V. Kochetkov,[15] D. Koehler,[33] T. Kohama,[14] M. Kopytine,[44] D. Kotchetkov,[6] A. Kozlov,[51] P. J. Kroon,[5] C. H. Kuberg,[1,27] K. Kurita,[39] Y. Kuroki,[48] M. J. Kweon,[22] Y. Kwon,[52] G. S. Kyle,[34] R. Lacey,[43] V. Ladygin,[17] J. G. Lajoie,[16] A. Lebedev,[16,23] S. Leckey,[44] D. M. Lee,[27] S. Lee,[19] M. J. Leitch,[27] X. H. Li,[6] H. Lim,[42] A. Litvinenko,[17] M. X. Liu,[27] Y. Liu,[36] C. F. Maguire,[49] Y. I. Makdisi,[5] A. Malakhov,[17] V. I. Manko,[23] Y. Mao,[7,38] G. Martinez,[45] M. D. Marx,[44] H. Masui,[48] F. Matathias,[44] T. Matsumoto,[8,50] P. L. McGaughey,[27] E. Melnikov,[15] F. Messer,[44] Y. Miake,[48] J. Milan,[43] T. E. Miller,[49] A. Milov,[44,51] S. Mioduszewski,[5] R. E. Mischke,[27] G. C. Mishra,[13] J. T. Mitchell,[5] A. K. Mohanty,[4] D. P. Morrison,[5] J. M. Moss,[27] F. Mühlbacher,[44] D. Mukhopadhyay,[51] M. Muniruzzaman,[6] J. Murata,[38,39] S. Nagamiya,[20] J. L. Nagle,[9] T. Nakamura,[14] B. K. Nandi,[6] M. Nara,[48] J. Newby,[46] P. Nilsson,[29] A. S. Nyanin,[23] J. Nystrand,[29] E. O'Brien,[5] C. A. Ogilvie,[16] H. Ohnishi,[5,38] I. D. Ojha,[49,3] K. Okada,[38] M. Ono,[48] V. Onuchin,[15] A. Oskarsson,[29] I. Otterlund,[29] K. Oyama,[8] K. Ozawa,[8] D. Pal,[51] A. P.T. Palounek,[27] V. S. Pantuev,[44] V. Papavassiliou,[34] J. Park,[42] A. Parmar,[33] S. F. Pate,[34] T. Peitzmann,[30] J.-C. Peng,[27] V. Peresedov,[17] C. Pinkenburg,[5] R. P. Pisani,[5] F. Plasil,[35] M. L. Purschke,[5] A. K. Purwar,[44] J. Rak,[16] I. Ravinovich,[51] K. F. Read,[35,46] M. Reuter,[44] K. Reygers,[30] V. Riabov,[37,40] Y. Riabov,[37] G. Roche,[28] A. Romana,[25] M. Rosati,[16] P. Rosnet,[28] S. S. Ryu,[52] M. E. Sadler,[1] N. Saito,[38,39] T. Sakaguchi,[8,50] M. Sakai,[32] S. Sakai,[48] V. Samsonov,[37] L. Sanfratello,[33] R. Santo,[30] H. D. Sato,[24,38] S. Sato,[5,48] S. Sawada,[20] Y. Schutz,[45] V. Semenov,[15] R. Seto,[6] M. R. Shaw,[1,27] T. K. Shea,[5] T.-A. Shibata,[47,38] K. Shigaki,[14,20] T. Shiina,[27] C. L. Silva,[41] D. Silvermyr,[27,29] K. S. Sim,[22] C. P. Singh,[3] V. Singh,[3] M. Sivertz,[5] A. Soldatov,[15] R. A. Soltz,[26] W. E. Sondheim,[27] S. P. Sorensen,[46] I. V. Sourikova,[5] F. Staley,[10] P. W. Stankus,[35] E. Stenlund,[29] M. Stepanov,[34] A. Ster,[21] S. P. Stoll,[5] T. Sugitate,[14] J. P. Sullivan,[27] E. M. Takagui,[41] A. Taketani,[38,39] M. Tamai,[50] K. H. Tanaka,[20] Y. Tanaka,[32] K. Tanida,[38] M. J. Tannenbaum,[5] P. Tarján,[11] J. D. Tepe,[1,27] T. L. Thomas,[33] J. Tojo,[24,38] H. Torii,[24,38] R. S. Towell,[1] I. Tserruya,[51] H. Tsuruoka,[48] S. K. Tuli,[3] H. Tydesjö,[29] N. Tyurin,[15] H. W. van Hecke,[27] J. Velkovska,[5,44] M. Velkovsky,[44] L. Villatte,[46] A. A. Vinogradov,[23] M. A. Volkov,[23] E. Vznuzdaev,[37] X. R. Wang,[13] Y. Watanabe,[38,39] S. N. White,[5] F. K. Wohn,[16] C. L. Woody,[5] W. Xie,[6] Y. Yang,[7] A. Yanovich,[15] S. Yokkaichi,[38,39] G. R. Young,[35] I. E. Yushmanov,[23] W. A. Zajc,[9,†] C. Zhang,[9] S. Zhou,[7] S. J. Zhou,[51] and L. Zolin[17]

(PHENIX Collaboration)

[1]*Abilene Christian University, Abilene, Texas 79699, USA*

[2]*Institute of Physics, Academia Sinica, Taipei 11529, Taiwan*

[3]*Department of Physics, Banaras Hindu University, Varanasi 221005, India*

[4]*Bhabha Atomic Research Centre, Bombay 400 085, India*

[5]*Brookhaven National Laboratory, Upton, New York 11973-5000, USA*

[6]*University of California—Riverside, Riverside, California 92521, USA*

[7]*China Institute of Atomic Energy (CIAE), Beijing, People's Republic of China*

[8]*Center for Nuclear Study, Graduate School of Science, University of Tokyo, 7-3-1 Hongo, Bunkyo, Tokyo 113-0033, Japan*

[9]*Columbia University, New York, New York 10027, USA and Nevis Laboratories, Irvington, New York 10533, USA*

[10]*Dapnia, CEA Saclay, F-91191 Gif-sur-Yvette, France*

[11]*Debrecen University, H-4010 Debrecen, Egyetem tér 1, Hungary*

[12]*Florida State University, Tallahassee, Florida 32306, USA*

[13]*Georgia State University, Atlanta, Georgia 30303, USA*

[14]*Hiroshima University, Kagamiyama, Higashi-Hiroshima 739-8526, Japan*

[15]*Institute for High Energy Physics (IHEP), Protvino, Russia*

 ©2004 The American Physical Society

[16]*Iowa State University, Ames, Iowa 50011, USA*
[17]*Joint Institute for Nuclear Research, 141980 Dubna, Moscow Region, Russia*
[18]*KAERI, Cyclotron Application Laboratory, Seoul, South Korea*
[19]*Kangnung National University, Kangnung 210-702, South Korea*
[20]*KEK, High Energy Accelerator Research Organization, Tsukuba-shi, Ibaraki-ken 305-0801, Japan*
[21]*KFKI Research Institute for Particle and Nuclear Physics (RMKI), H-1525 Budapest 114, P. O. Box 49, Hungary*
[22]*Korea University, Seoul 136-701, Korea*
[23]*Russian Research Center "Kurchatov Institute," Moscow, Russia*
[24]*Kyoto University, Kyoto 606, Japan*
[25]*Laboratoire Leprince-Ringuet, Ecole Polytechnique, CNRS-IN2P3, Route de Saclay, F-91128 Palaiseau, France*
[26]*Lawrence Livermore National Laboratory, Livermore, California 94550, USA*
[27]*Los Alamos National Laboratory, Los Alamos, New Mexico 87545, USA*
[28]*LPC, Université Blaise Pascal, CNRS-IN2P3, Clermont-Fd, 63177 Aubiere Cedex, France*
[29]*Department of Physics, Lund University, Box 118, SE-221 00 Lund, Sweden*
[30]*Institut fuer Kernphysik, University of Muenster, D-48149 Muenster, Germany*
[31]*Myongji University, Yongin, Kyonggido 449-728, Korea*
[32]*Nagasaki Institute of Applied Science, Nagasaki-shi, Nagasaki 851-0193, Japan*
[33]*University of New Mexico, Albuquerque, New Mexico 87131, USA*
[34]*New Mexico State University, Las Cruces, New Mexico 88003, USA*
[35]*Oak Ridge National Laboratory, Oak Ridge, Tennessee 37831, USA*
[36]*IPN-Orsay, Universite Paris Sud, CNRS-IN2P3, BP1, F-91406 Orsay, France*
[37]*PNPI, Petersburg Nuclear Physics Institute, Gatchina, Russia*
[38]*RIKEN (The Institute of Physical and Chemical Research), Wako, Saitama 351-0198, Japan*
[39]*RIKEN BNL Research Center, Brookhaven National Laboratory, Upton, New York 11973-5000, USA*
[40]*St. Petersburg State Technical University, St. Petersburg, Russia*
[41]*Universidade de São Paulo, Instituto de Física, Caixa Postal 66318, São Paulo CEP05315-970, Brazil*
[42]*System Electronics Laboratory, Seoul National University, Seoul, South Korea*
[43]*Chemistry Department, Stony Brook University, SUNY, Stony Brook, New York 11794-3400, USA*
[44]*Department of Physics and Astronomy, Stony Brook University, SUNY, Stony Brook, New York 11794, USA*
[45]*SUBATECH (Ecole des Mines de Nantes, CNRS-IN2P3, Université de Nantes), BP 20722, 44307 Nantes, France*
[46]*University of Tennessee, Knoxville, Tennessee 37996, USA*
[47]*Department of Physics, Tokyo Institute of Technology, Tokyo 152-8551, Japan*
[48]*Institute of Physics, University of Tsukuba, Tsukuba, Ibaraki 305, Japan*
[49]*Vanderbilt University, Nashville, Tennessee 37235, USA*
[50]*Waseda University, Advanced Research Institute for Science and Engineering, 17 Kikui-cho, Shinjuku-ku, Tokyo 162-0044, Japan*
[51]*Weizmann Institute, Rehovot 76100, Israel*
[52]*Yonsei University, IPAP, Seoul 120-749, Korea*
(Received 28 July 2003; published 29 March 2004)

The centrality dependence of transverse momentum distributions and yields for $\pi^{\pm}, K^{\pm}, p$, and $\bar{p}$ in Au + Au collisions at $\sqrt{s_{NN}} = 200$ GeV at midrapidity are measured by the PHENIX experiment at the Relativistic Heavy Ion Collider. We observe a clear particle mass dependence of the shapes of transverse momentum spectra in central collisions below ~ 2 GeV/c in p_T. Both mean transverse momenta and particle yields per participant pair increase from peripheral to midcentral and saturate at the most central collisions for all particle species. We also measure particle ratios of π^-/π^+, K^-/K^+, $\bar{p}/p$, K/π, p/π, and $\bar{p}/\pi$ as a function of p_T and collision centrality. The ratios of equal mass particle yields are independent of p_T and centrality within the experimental uncertainties. In central collisions at intermediate transverse momenta $\sim 1.5-4.5$ GeV/c, proton and antiproton yields constitute a significant fraction of the charged hadron production and show a scaling behavior different from that of pions.

DOI: 10.1103/PhysRevC.69.034909 PACS number(s): 25.75.Dw

*Deceased.
†PHENIX spokesperson.
Email address: zajc@nevis.columbia.edu

I. INTRODUCTION

The motivation for ultrarelativistic heavy-ion experiments at the Relativistic Heavy Ion Collider (RHIC) at Brookhaven National Laboratory is the study of nuclear matter at extremely high temperature and energy density with the hope of creating and detecting deconfined matter consisting of quarks and gluons—the quark gluon plasma (QGP). Lattice QCD calculations [1] predict that the transition to a deconfined state occurs at a critical temperature $T_c \approx 170$ MeV and an energy density $\epsilon \approx 2$ GeV/fm^3. Based on the Bjorken estimation [2] and the measurement of transverse energy (E_T) in Au+Au collisions at $\sqrt{s_{NN}}=130$ GeV [3] and 200 GeV, the spatial energy density in central Au+Au collisions at RHIC is believed to be high enough to create such deconfined matter in a laboratory [3].

The hot and dense matter produced in relativistic heavy-ion collisions may evolve through the following scenario: preequilibrium, thermal (or chemical) equilibrium of partons, possible formation of QGP or a QGP-hadron gas mixed state, a gas of hot interacting hadrons, and finally, a freeze-out state when the produced hadrons no longer strongly interact with each other. Since produced hadrons carry information about the collision dynamics and the entire space-time evolution of the system from the initial to the final stage of collisions, a precise measure of the transverse momentum (p_T) distributions and yields of identified hadrons as a function of collision geometry is essential for the understanding of the dynamics and properties of the created matter.

In the low p_T region (<2 GeV/c), hydrodynamic models [4,5] that include radial flow successfully describe the measured p_T distributions in Au+Au collisions at $\sqrt{s_{NN}}=130$ GeV [6–8]. The p_T spectra of identified charged hadrons below $p_T \approx 2$ GeV/c in central collisions have been well reproduced by two simple parameters: transverse flow velocity β_T and freeze-out temperature T_{fo} [8] under the assumption of thermalization with longitudinal and transverse flow [4]. The particle production in this p_T region is considered to be dominated by secondary interactions among produced hadrons and participating nucleons in the reaction zone. Another model which successfully describes the particle abundances at low p_T is the statistical thermal model [9]. Particle ratios have been shown to be well reproduced by two parameters: a baryon chemical potential μ_B and a chemical freeze-out temperature T_{ch}. It is found that there is an overall good agreement between measured particle ratios at $\sqrt{s_{NN}}=130$ GeV Au+Au and the thermal model calculations [10,11].

On the other hand, at high p_T ($\geqslant 4$ GeV/c) the dominant particle production mechanism is the hard scattering described by perturbative quantum chromodynamics (pQCD), which produces particles from the fragmentation of energetic partons. One of the most interesting observations at RHIC is that the yield of high p_T neutral pions and nonidentified charged hadrons in central Au+Au collisions at RHIC are below the expectation of the scaling with the number of nucleon-nucleon binary collisions, N_{coll} [12–14]. This effect could be a consequence of the energy loss suffered by partons moving through deconfined matter [15,16]. It has also been observed that the yield of neutral pions is more strongly suppressed than that for nonidentified charged hadrons [12] in central Au+Au collisions at RHIC. Another interesting feature is that the proton and antiproton yields in central events are comparable to that of pions at $p_T \approx 2$ GeV/c [6], differing from the expectation of pQCD. These observations suggest that a detailed study of particle composition at intermediate $p_T (\approx 2-4$ GeV/$c)$ is very important to understand hadron production and collision dynamics at RHIC.

The PHENIX experiment [17] has a unique hadron identification capability in a broad momentum range. Pions and kaons are identified up to 3 GeV/c and 2 GeV/c in p_T, respectively, and protons and antiprotons can be identified up to 4.5 GeV/c by using a high resolution time-of-flight detector [18]. Neutral pions are reconstructed via $\pi^0 \rightarrow \gamma\gamma$ up to $p_T \approx 10$ GeV/c through an invariant mass analysis of γ pairs detected in an electromagnetic calorimeter [19] with wide azimuthal coverage. During the measurements of Au+Au collisions at $\sqrt{s_{NN}}=200$ GeV in year 2001 at RHIC, the PHENIX experiment accumulated enough events to address the above issues at intermediate p_T as well as the particle production at low p_T with precise centrality dependences. In this paper, we present the centrality dependence of p_T spectra, $\langle p_T \rangle$, yields, and ratios for $\pi^{\pm}$, $K^{\pm}$, p, and $\overline{p}$, in Au+Au collisions at $\sqrt{s_{NN}}=200$ GeV at midrapidity measured by the PHENIX experiment. We also present results on the scaling behavior of charged hadrons compared with results of π^0 measurements [14], which have been published separately.

The paper is organized as follows. Section II describes the PHENIX detector used in this analysis. In Sec. III the analysis details including event selection, track selection, particle identification, and corrections applied to the data are described. The systematic errors on the measurements are also discussed in this section. For the experimental results, centrality dependence of p_T spectra for identified charged particles is presented in Sec. IV A, and transverse mass spectra are given in Sec. IV B. Particle yields and mean transverse momenta as a function of centrality are presented in Sec. IV C. In Sec. IV D the systematic study of particle ratios as a function p_T and centrality is presented. Section IV E studies the scaling behavior of identified charged hadrons. A summary is given in Sec. V.

II. PHENIX DETECTOR

The PHENIX experiment is composed of two central arms, two forward muon arms, and three global detectors. The east and west central arms are placed at zero rapidity and designed to detect electrons, photons, and charged hadrons. The north and south forward muon arms have full azimuthal coverage and are designed to detect muons. The global detectors measure the start time, vertex, and multiplicity of the interactions. The following sections describe the parts of the detector that are used in the present analysis. A detailed description of the complete detector can be found elsewhere [17–22].

A. Global detectors

In order to characterize the centrality of Au+Au collisions, zero-degree calorimeters (ZDCs) [21] and beam-beam

counters (BBCs) [20] are employed. The zero-degree calorimeters are small hadronic calorimeters which measure the energy carried by spectator neutrons. They are placed 18 m upstream and downstream of the interaction point along the beam line. Each ZDC consists of three modules. Each module has a depth of two hadronic interaction lengths and is read out by a single photomultiplier tube (PMT). Both time and amplitude are digitized for each PMT along with the analog sum of the three PMT signals for each ZDC.

Two sets of beam-beam counters are placed 1.44 m from the nominal interaction point along the beam line (one on each side). Each counter consists of 64 Čerenkov telescopes, arranged radially around the beam line. The BBC measures the number of charged particles in the pseudorapidity region $3.0<|\eta|<3.9$. The correlation between BBC charge sum and ZDC total energy is used for centrality determination. The BBC also provides a collision vertex position and start time information for time-of-flight measurement.

B. Central arm detectors

Charged particles are tracked using the central arm spectrometers [22]. The spectrometer on the east side of the PHENIX detector (east arm) contains the following subsystems used in this analysis: drift chamber (DC), pad chamber (PC), and time-of-flight (TOF).

The drift chambers are the closest tracking detectors to the beam line—at a radial distance of 2.2 m. They measure charged particle trajectories in the azimuthal direction to determine the transverse momentum of each particle. By combining the polar angle information from the first layer of the PC with the transverse momentum, the total momentum p is determined. The momentum resolution is $\delta p/p \simeq 0.7\% \oplus 1.0\% \times p(\mathrm{GeV}/c)$, where the first term is due to the multiple scattering before the DC and the second term is the angular resolution of the DC. The momentum scale is known to 0.7%, from the reconstructed proton mass using the TOF.

The pad chambers are multiwire proportional chambers that form three separate layers of the central tracking system. The first pad chamber layer (PC1) is located at the radial outer edge of each drift chamber at a distance of 2.49 m, while the third layer (PC3) is 4.98 m from the interaction point. The second layer (PC2) is located at a radial distance of 4.19 m in the west arm only. PC1 and the DC, along with the vertex position measured by the BBC, are used in the global track reconstruction to determine the polar angle of each charged track.

The time-of-flight detector serves as the primary particle identification device for charged hadrons by measuring the stop time. The start time is given by the BBC. The TOF wall is located at a radial distance of 5.06 m from the interaction point in the east central arm. This contains 960 scintillator slats oriented along the azimuthal direction. It is designed to cover $|\eta|<0.35$ and $\Delta\phi=45°$ in azimuthal angle. The intrinsic timing resolution is $\sigma \simeq 115$ ps, which allows for a 3σ π/K separation up to $p_T \simeq 2.5$ GeV/c, and 3σ K/p separation up to $p_T \simeq 4$ GeV/c.

III. DATA ANALYSIS

In this section, we describe the event and track selection, charged particle identification and various corrections, including geometrical acceptance, particle decay, multiple scattering and absorption effects, detector occupancy corrections, and weak decay contributions from Λ and $\bar{\Lambda}$ to proton and antiproton spectra. The estimations of systematic uncertainties on the measurements are addressed at the end of this section.

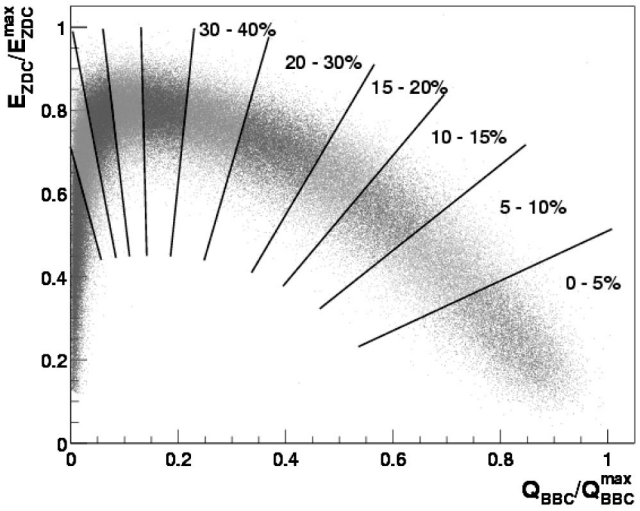

FIG. 1. BBC vs ZDC analog response. The lines represent the centrality cut boundaries.

A. Event selection

For the present analysis, we use the PHENIX minimum bias trigger events, which are determined by a coincidence between north and south BBC signals. We also require a collision vertex within ±30 cm from the center of the spectrometer. The collision vertex resolution determined by the BBC is about 6 mm in Au+Au collisions in minimum bias events [20]. The PHENIX minimum bias trigger events include $92.2^{+2.5}_{-3.0}$% of the 6.9 b Au+Au total inelastic cross section [14]. Figure 1 shows the correlation between the BBC charge sum and ZDC total energy for Au+Au at $\sqrt{s_{NN}}$ =200 GeV. The lines on the plot indicate the centrality definition in the analysis. For the centrality determination, these events are subdivided into 11 bins using the BBC and ZDC correlation: 0–5%, 5–10%, 10–15%, 15–20%, 20–30%, …, 70–80%, and 80–92%. Due to the statistical limitations in the peripheral events, we also use the 60–92% centrality bin as the most peripheral bin. After event selection, we analyze 2.02×10^7 minimum bias events, which represents ~140 times more events than used in our published Au+Au data at 130 GeV [6,8]. Based on a Glauber model calculation [8,14] we use two global quantities to characterize the event centrality: the average number of participants $\langle N_{part}\rangle$ and the average number of collisions $\langle N_{coll}\rangle$ associated with each centrality bin (Table I).

B. Track selection

Charged particle tracks are reconstructed by the DC based on a combinatorial Hough transform [25]—which gives the angle of the track in the main bend plane. The main bend

TABLE I. The average nuclear overlap function ($\langle T_{\mathrm{AuAu}}\rangle$), the number of nucleon-nucleon binary collisions ($\langle N_{coll}\rangle$), and the number of participant nucleons ($\langle N_{part}\rangle$) obtained from a Glauber Monte Carlo [8,14] correlated with the BBC and ZDC response for Au+Au at $\sqrt{s_{NN}}=200$ GeV as a function of centrality. Centrality is expressed as percentiles of $\sigma_{\mathrm{AuAu}}=6.9$ b with 0% representing the most central collisions. The last line refers to minimum bias collisions.

Centrality	$\langle T_{\mathrm{AuAu}}\rangle$ (mb^{-1})	$\langle N_{coll}\rangle$	$\langle N_{part}\rangle$
0–5%	25.37±1.77	1065.4±105.3	351.4±2.9
0–10%	22.75±1.56	955.4±93.6	325.2±3.3
5–10%	20.13±1.36	845.4±82.1	299.0±3.8
10–15%	16.01±1.15	672.4±66.8	253.9±4.3
10–20%	14.35±1.00	602.6±59.3	234.6±4.7
15–20%	12.68±0.86	532.7±52.1	215.3±5.3
20–30%	8.90±0.72	373.8±39.6	166.6±5.4
30–40%	5.23±0.44	219.8±22.6	114.2±4.4
40–50%	2.86±0.28	120.3±13.7	74.4±3.8
50–60%	1.45±0.23	61.0±9.9	45.5±3.3
60–70%	0.68±0.18	28.5±7.6	25.7±3.8
60–80%	0.49±0.14	20.4±5.9	19.5±3.3
60–92%	0.35±0.10	14.5±4.0	14.5±2.5
70–80%	0.30±0.10	12.4±4.2	13.4±3.0
70–92%	0.20±0.06	8.3±2.4	9.5±1.9
80–92%	0.12±0.03	4.9±1.2	6.3±1.2
min. bias	6.14±0.45	257.8±25.4	109.1±4.1

plane is perpendicular to the beam axis (azimuthal direction). PC1 is used to measure the position of the hit in the longitudinal direction (along the beam axis). When combined with the location of the collision vertex along the beam axis (from the BBC), the PC1 hit gives the polar angle of the track. Only tracks with valid information from both the DC and PC1 are used in the analysis. In order to associate a track with a hit on the TOF, the track is projected to its expected hit location on the TOF. Tracks are required to have a hit on the TOF within $\pm 2\sigma$ of the expected hit location in both the azimuthal and beam directions. Finally, a cut on the energy loss in the TOF scintillator is applied to each track. This β-dependent energy loss cut is based on a parametrization of the Bethe-Bloch formula, i.e., $dE/dx \approx \beta^{-5/3}$, where $\beta = L/(ct_{\mathrm{TOF}})$, L is the path length of the track trajectory from the collision vertex to the hit position of the TOF wall, t_{TOF} is the time of flight, and c is the speed of light. The flight path length is calculated from a fit to the reconstructed track trajectory. The background due to random association of DC/PC1 tracks with TOF hits is reduced to a negligible level when the mass cut used for particle identification is applied (described in the following) section.

C. Particle identification

The charged particle identification (PID) is performed by using the combination of three measurements: time of flight from the BBC and TOF, momentum from the DC, and flight path length from the collision vertex point to the hit position on the TOF wall. The square of the mass is derived from the following formula:

$$m^2 = \frac{p^2}{c^2}\left[\left(\frac{t_{\mathrm{TOF}}}{L/c}\right)^2 - 1\right], \tag{1}$$

where p is the momentum, t_{TOF} is the time of flight, L is a flight path length, and c is the speed of light. The charged particle identification is performed using cuts in m^2 and momentum space.

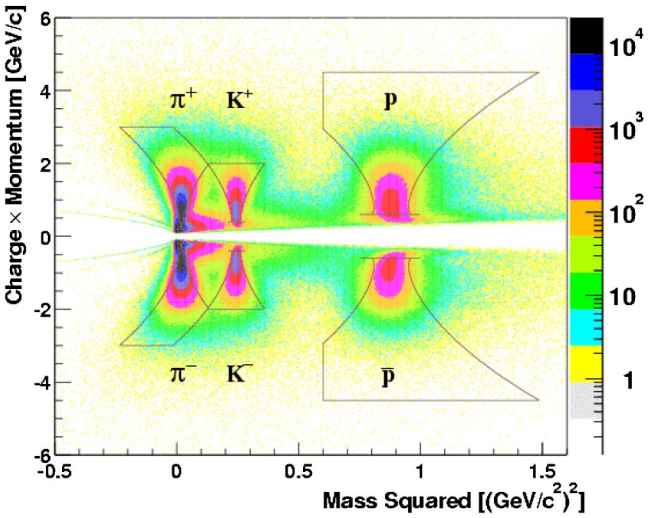

FIG. 2. (Color online) Mass-squared vs momentum multiplied by charge distribution in Au+Au collisions at $\sqrt{s_{NN}}=200$ GeV. The lines indicate the PID cut boundaries for pions, kaons, and protons (antiprotons) from left to right, respectively.

In Fig. 2, a plot of m^2 versus momentum multiplied by charge is shown together with applied PID cuts as solid curves. We use 2σ standard deviation PID cuts in m^2 and momentum space for each particle species. The PID cut is based on a parametrization of the measured m^2 width as a function of momentum,

$$\sigma_{m^2}^2 = \frac{\sigma_\alpha^2}{K_1^2}(4m^4p^2) + \frac{\sigma_{ms}^2}{K_1^2}\left[4m^4\left(1+\frac{m^2}{p^2}\right)\right] + \frac{\sigma_t^2 c^2}{L^2}[4p^2(m^2+p^2)], \tag{2}$$

where σ_α is the angular resolution, σ_{ms} is the multiple scattering term, σ_t is the overall time-of-flight resolution, m is the centroid of m^2 distribution for each particle species, and K_1 is a magnetic field integral constant term of 87.0 mrad GeV. The parameters for PID are $\sigma_\alpha = 0.835$ mrad, $\sigma_{ms}=0.86$ mrad GeV, and $\sigma_t=120$ ps. Through improvements in alignment and calibrations, the momentum resolution is improved over the 130 GeV data [8]. The centrality dependence of the width and the mean position of the m^2 distribution has also been checked. There is no clear difference seen between central and peripheral collisions. For pion identification above 2 GeV/c, we apply an asymmetric PID cut to reduce kaon contami-

nation of the pions. As shown by the lines in Fig. 2, the overlap region which is within the 2σ cuts for both pions and kaons is excluded. For kaons, the upper momentum cutoff is 2 GeV/c since the pion contamination level for kaons is ≈10% at that momentum. The upper momentum cutoff on the pions is p_T=3 GeV/c—where the kaon contamination reaches ≈10%. The contamination of protons by kaons reaches about 5% at 4 GeV/c. Electron (positron) and decay muon background at very low p_T (<0.3 GeV/c) are well separated from the pion mass-squared peak. The contamination background on each particle species is not subtracted in the analysis. For protons, the upper momentum cutoff is set at 4.5 GeV/c due to statistical limitations and background at high p_T. An additional cut on m^2 for protons and antiprotons, $m^2 > 0.6$ (GeV/c^2)^2, is introduced to reduce background. The lower momentum cutoffs are 0.2 GeV/c for pions, 0.4 GeV/c for kaons, and 0.6 GeV/c for p and $\bar{p}$. This cutoff value for p and $\bar{p}$ is larger than those for pions and kaons due to the large energy loss effect.

D. Acceptance, decay, and multiple scattering corrections

In order to correct for (1) the geometrical acceptance, (2) in-flight decay for pions and kaons, (3) the effect of multiple scattering, and (4) nuclear interactions with materials in the detector (including antiproton absorption), we use PISA (PHENIX Integrated Simulation Application), a GEANT [26] based Monte Carlo (MC) simulation program of the PHENIX detector. The single-particle tracks are passed from GEANT through the PHENIX event reconstruction software [25]. In this simulation, the BBC, TOF, and DC detector responses are tuned to match the real data. For example, dead areas of DC and TOF are included, and momentum and time-of-flight resolution are tuned. The track association to TOF in both azimuth (ϕ) and along the beam axis (z) as a function of momentum and the PID cut boundaries are parametrized to match the real data. A fiducial cut is applied to choose identical active areas on the TOF in both the simulation and data. We generate 1×10^7 single-particle events for each particle species ($\pi^{\pm}$, $K^{\pm}$, p, and $\bar{p}$) with low p_T enhanced (<2 GeV/c)+flat p_T distributions for high p_T (2–4 GeV/c for pions and kaons, 2–8 GeV/c for p and $\bar{p}$). [1] The efficiencies are determined in each p_T bin by dividing the reconstructed output by the generated input as expressed as follows:

$$\epsilon_{\rm acc}(j,p_T) = \frac{\text{No. of reconstructed MC tracks}}{\text{No. of generated MC tracks}}, \qquad (3)$$

where j is the particle species. The resulting correction factors ($1/\epsilon_{\rm acc}$) are applied to the data in each p_T bin and for each individual particle species.

[1]Due to the good momentum resolution at the high p_T region, the momentum smearing effect for a steeply falling spectrum is <1% at p_T=5 GeV/c. The flat p_T distribution up to 5 GeV/c can be used to obtain the correction factors.

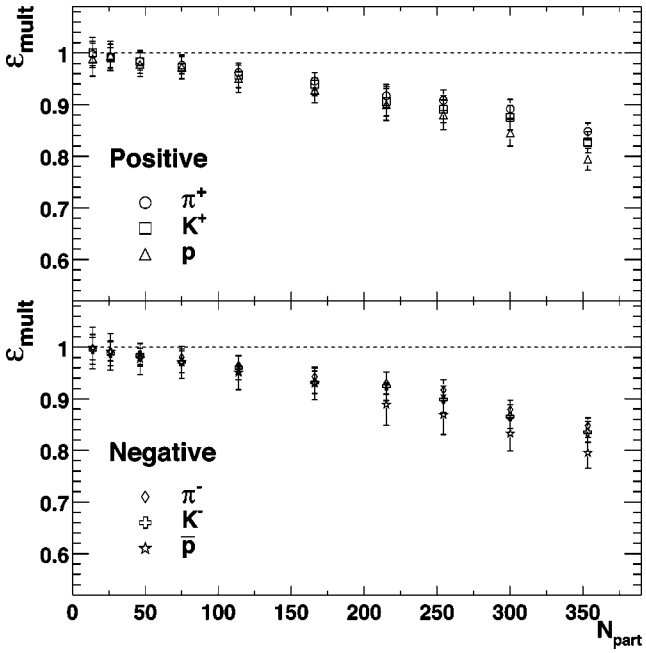

FIG. 3. Track reconstruction efficiency ($\epsilon_{\rm mult}$) as a function of centrality. The error bars on the plot represent the systematic errors.

E. Detector occupancy correction

Due to the high multiplicity environment in heavy ion collisions, which causes high occupancy and multiple hits on a detector cell such as scintillator slats of the TOF, it is expected that the track reconstruction efficiency in central events is lower than that in peripheral events. The typical occupancy at TOF is less than 10% in the most central Au+Au collisions. To correct for this effect, we merge single particle simulated events with real events and calculate the track reconstruction efficiency for each simulated track as follows:

$$\epsilon_{\rm mult}(i,j) = \frac{\text{No. of reconstructed embedded tracks}}{\text{No. of embedded tracks}}, \qquad (4)$$

where i is the centrality bins and j is the particle species. This study has been performed for each particle species and each centrality bin. The track reconstruction efficiencies are factorized (into independent terms depending on centrality and p_T) for $p_T > 0.4$ GeV/c, since there is no p_T dependence in the efficiencies above that p_T. Figure 3 shows the dependence of track reconstruction efficiency for $\pi^{\pm}$, $K^{\pm}$, p, and $\bar{p}$ as a function of centrality expressed as N_{part}. The efficiency in the most central 0–5% events is about 80% for protons ($\bar{p}$), 83% for kaons, and 85% for pions. Slower particles are more likely lost due to high occupancy in the TOF because the system responds to the earliest hit. For the most peripheral 80–92% events, the efficiency for detector occupancy effect is ≈99% for all particle species. The factors are applied to the spectra for each particle species and centrality bin. Systematic uncertainties on detector occupancy corrections ($1/\epsilon_{\rm mult}$) are less than 3%.

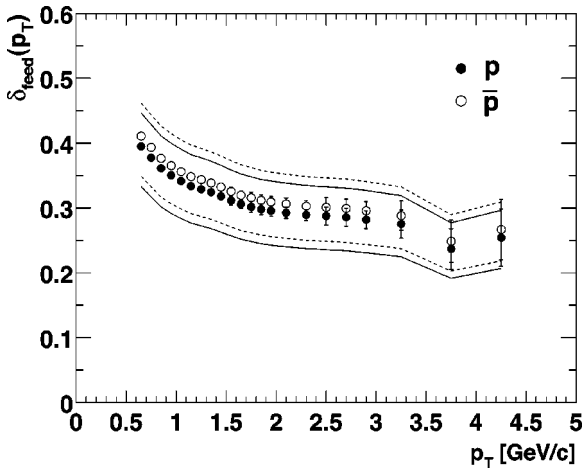

FIG. 4. The fractional contribution of protons ($\bar{p}$) from Λ ($\bar{\Lambda}$) decays in all measured protons ($\bar{p}$), $\delta_{\text{feed}}(p_T)$, as a function of p_T. The solid (dashed) lines represent the systematic errors for protons ($\bar{p}$). The error bars are statistical errors.

F. Weak decay correction

Protons and antiprotons from weak decays (e.g., from Λ and $\bar{\Lambda}$) can be reconstructed as tracks in the PHENIX spectrometer. The proton and antiproton spectra are corrected to remove the feed-down contribution from weak decays using a HIJING [27] simulation. HIJING output has been tuned to reproduce the measured particle ratios of Λ/p and $\bar{\Lambda}/\bar{p}$ along with their p_T dependencies in $\sqrt{s_{NN}}=130$ GeV Au+Au collisions [28] which include contribution from Ξ and Σ^0. Corrections for feed-down from $\Sigma^{\pm}$ are not applied, as these yields were not measured. About 2×10^6 central HIJING events (impact parameter $b=0-3$ fm) covering the TOF acceptance have been generated and processed through the PHENIX reconstruction software. To calculate the feed-down corrections, the $\bar{p}/p$ and $\bar{\Lambda}/\Lambda$ yield ratios were assumed to be independent of p_T and centrality. The systematic error due to the feed-down correction is estimated at 6% by varying the Λ/p and $\bar{\Lambda}/\bar{p}$ ratios within the systematic errors of the $\sqrt{s_{NN}}=130$ GeV Au+Au measurement [28] (±24%) and assuming m_T scaling at high p_T. This uncertainty could be larger if the Λ/p and $\bar{\Lambda}/\bar{p}$ ratios change significantly with p_T and beam energy. The fractional contribution to the p ($\bar{p}$) yield from Λ ($\bar{\Lambda}$), $\delta_{\text{feed}}(p_T)$, is shown in Fig. 4. The solid (dashed) lines represent the systematic errors for protons ($\bar{p}$). The obtained factor is about 40% below 1 GeV/c and 30% at 4 GeV/c. We multiply the proton and antiproton spectra by the factor C_{feed} for all centrality bins as a function of p_T:

$$C_{\text{feed}}(j,p_T) = 1 - \delta_{\text{feed}}(j,p_T), \tag{5}$$

where $j=p,\bar{p}$.

G. Invariant yield

Applying the data cuts and corrections discussed above, the final invariant yield for each particle species and centrality bin are derived using the following equation:

$$\frac{1}{2\pi p_T}\frac{d^2N}{dp_T dy} = \frac{1}{2\pi p_T}\frac{1}{N_{evt}(i)}C_{ij}(p_T)\frac{N_j(i,p_T)}{\Delta p_T \Delta y}, \tag{6}$$

where y is rapidity, $N_{evt}(i)$ is the number of events in each centrality bin i, $C_{ij}(p_T)$ is the total correction factor, and $N_j(i,p_T)$ is the number of counts in each centrality bin i, particle species j, and p_T. The total correction factor is composed of

$$C_{ij}(p_T) = \frac{1}{\epsilon_{\text{acc}}(j,p_T)}\frac{1}{\epsilon_{\text{mult}}(i,j)}C_{\text{feed}}(j,p_T). \tag{7}$$

H. Systematic uncertainties

To estimate systematic uncertainties on the p_T distribution and particle ratios, various sets of p_T spectra and particle ratios were made by changing the cut parameters including the fiducial cut, PID cut, and track association windows slightly from what was used in the analysis. For each of these spectra and ratios using modified cuts, the same changes in the cuts were made in the Monte Carlo analysis. The absolutely normalized spectra with different cut conditions are divided by the spectra with the baseline cut conditions, resulting in uncertainties associated with each cut condition as a function of p_T. The various uncertainties are added in quadrature. Three different centrality bins (minimum bias, central 0–5%, and peripheral 60–92%) are used to study the centrality dependence of systematic errors. The same procedure has been applied for the following particle ratios: π^-/π^+, K^-/K^+, $\bar{p}/p$, K/π, p/π^+, and $\bar{p}/\pi^-$.

TABLE II. Systematic errors on the p_T spectra for central events. All errors are given in percent.

	π^+	π^-	K^+	K^-	p		$\bar{p}$	
p_T range (GeV/c)	0.2–3.0	0.2–3.0	0.4–2.0	0.4–2.0	0.6–3.0	3.0–4.5	0.6–3.0	3.0–4.5
Cuts	6.2	6.2	11.2	9.5	6.6	11.6	6.6	11.6
Momentum scale	3	3	3	3	3	3	3	3
Occupancy correction	2	2	3	3	3	3	3	3
Feed-down correction					6.0	6.0	6.0	6.0
Total	7.2	7.2	12.0	10.4	9.9	13.7	9.9	9.9

TABLE III. Systematic errors on central-to-peripheral ratio (R_{CP}). All errors are given in percent.

Source	$(\pi^+ + \pi^-)/2$	$(K^+ + K^-)/2$	$(p+\bar{p})/2$
Occupancy correction (central)	2	3	3
Occupancy correction (peripheral)	2	3	3
$\langle T_{\mathrm{AuAu}} \rangle$ (0–10%)	6.9	6.9	6.9
$\langle T_{\mathrm{AuAu}} \rangle$ (60–92%)	28.6	28.6	28.6
Total	29.5	29.7	29.7

Table II shows the systematic errors of the p_T spectra for central collisions. The systematic uncertainty on the absolute value of momentum (momentum scale) is estimated as 3% in the measured p_T range by comparing the known proton mass to the value measured as protons in real data. It is found that the total systematic error on the p_T spectra is 8–14% in both central and peripheral collisions. For the particle ratios, the typical systematic error is about 6% for all particle species. The dominant source of uncertainties on the central-to-peripheral ratio scaled by N_{coll} (R_{CP}) are the systematic errors on the nuclear overlap function, T_{AuAu} (see Table III). The systematic errors on dN/dy and $\langle p_T \rangle$ are discussed in Sec. IV C together with the procedure for the determination of these quantities.

IV. RESULTS

In this section, the p_T and transverse mass spectra and yields of identified charged hadrons as a function of centrality are shown. Also a systematic study of particle ratios in Au+Au collisions at $\sqrt{s_{NN}}=200$ GeV at midrapidity is presented.

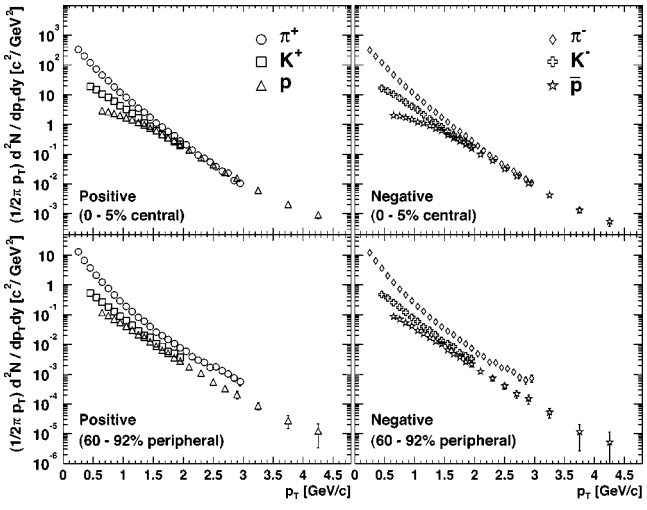

FIG. 5. Transverse momentum distributions for pions, kaons, protons, and antiprotons in Au+Au collisions at $\sqrt{s_{NN}}=200$ GeV. The top two figures show p_T spectra for the most central 0–5% collisions. The bottom two are for the most peripheral 60–92% collisions. The error bars are statistical only. The Λ ($\bar{\Lambda}$) feed-down corrections for protons (antiprotons) have been applied.

A. Transverse momentum distributions

Figure 5 shows the p_T distributions for pions, kaons, protons, and antiprotons. The top two plots are for the most central 0–5% collisions, and the bottom two are for the most peripheral 60–92% collisions. The spectra for positive particles are presented on the left, and those for negative particles on the right. For $p_T < 1.5$ GeV/c in central events, the data show a clear mass dependence in the shapes of the spectra. The p and $\bar{p}$ spectra have a shoulder-arm shape, the pion spectra have a concave shape, and the kaons fall exponentially. On the other hand, in the peripheral events, the mass dependences of the p_T spectra are less pronounced and the p_T spectra are more nearly parallel to each other. Another notable observation is that at p_T above $\approx$2.0 GeV/c in central events, the p and $\bar{p}$ yields become comparable to the pion yields, which is also observed in 130 GeV Au+Au collisions [6]. This observation shows that a significant fraction of the total particle yield at $p_T \approx 2.0$–4.5 GeV/c in Au+Au central collisions consists of p and $\bar{p}$.

These high statistics Au+Au data at $\sqrt{s_{NN}}=200$ GeV allow us to perform a detailed study of the centrality dependence of the p_T spectra. In this analysis, we use the 11 centrality bins described in Sec. III A as well as the combined peripheral bin (60–92%) for each particle species. Figure 6 shows the centrality dependence of the p_T spectrum for π^+ (left) and π^- (right). For clarity, the data points are scaled

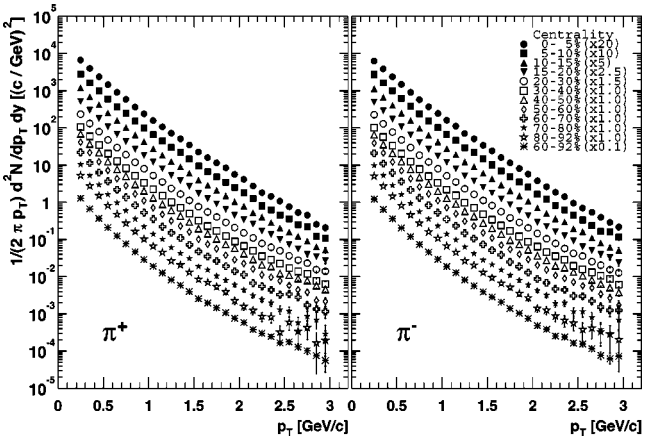

FIG. 6. Centrality dependence of the p_T distribution for π^+ (left) and π^- (right) in Au+Au collisions at $\sqrt{s_{NN}}=200$ GeV. The different symbols correspond to different centrality bins. The error bars are statistical only. For clarity, the data points are scaled vertically as quoted in the figure.

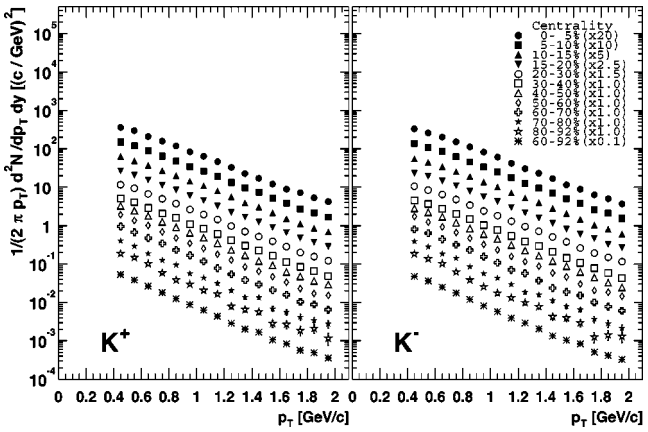

FIG. 7. Centrality dependence of the p_T distribution for K^+ (left) and K^- (right) in Au+Au collisions at $\sqrt{s_{NN}}$=200 GeV. The different symbols correspond to different centrality bins. The error bars are statistical only. For clarity, the data points are scaled vertically as quoted in the figure.

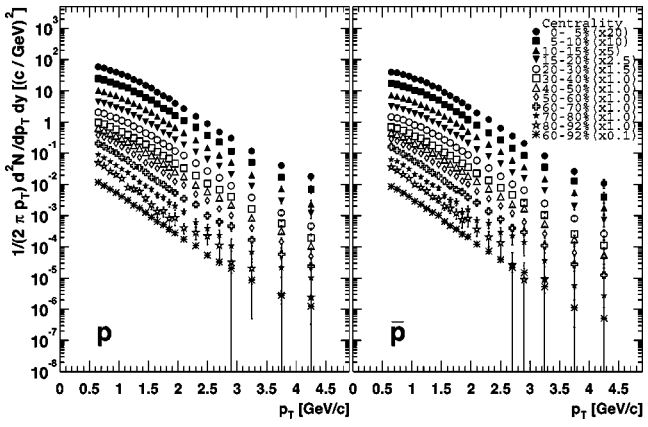

FIG. 8. Centrality dependence of the p_T distribution for protons (left) and antiprotons (right) in Au+Au collisions at $\sqrt{s_{NN}}$ =200 GeV. The different symbols correspond to different centrality bins. The error bars are statistical only. Feed-down corrections for Λ ($\bar{\Lambda}$) decaying into proton ($\bar{p}$) have been applied. For clarity, the data points are scaled vertically as quoted in the figure.

vertically as quoted in the figures. The error bars are statistical only. The pion spectra show an approximately power-law shape for all centrality bins. The spectra become steeper (fall faster with increasing p_T) for more peripheral collisions.

Figure 7 shows similar plots for kaons. The data can be well approximated by an exponential function in p_T for all centralities. Finally, the centrality dependence of the p_T spectra for protons (left) and antiprotons (right) is shown in Fig. 8. As in Fig. 5, both p and $\bar{p}$ spectra show a strong centrality dependence below 1.5 GeV/c, i.e., they develop a shoulder at low p_T and the spectra flatten (fall more slowly with increasing p_T) with increasing collision centrality.

Up to p_T=1.5–2 GeV/c, it has been found that hydrodynamic models can reproduce the data well for $\pi^{\pm}$, $K^{\pm}$, p, and $\bar{p}$ spectra at 130 GeV [8], and also the preliminary data at 200 GeV in Au+Au collisions (e.g., Refs. [5,29]). These models assume thermal equilibrium and that the created particles are affected by a common transverse flow velocity β_T and freeze-out (stop interacting) at a temperature T_{fo} with a fixed initial condition governed by the equation of state (EOS) of matter. There are several types of hydrodynamic calculations, e.g., (1) a conventional hydrodynamic fit to the experimental data with two free parameters, β_T and T_{fo} [30], (2) a combination of hydrodynamics and a hadronic cascade model [5], (3) transverse and longitudinal flow with simultaneous chemical and thermal freeze-outs within the statistical thermal model [31], (4) requiring the early thermalization with a QGP type EOS [32]. Despite the differences between the hydrodynamic models, all models are in qualitative agreement with the identified single-particle spectra in central collisions at low p_T as seen in Ref. [8]. However, they fail to reproduce the peripheral spectra above $p_T \simeq 1$ GeV/c and their applicability in the high p_T region (>2 GeV/c) is limited. Comparison with the detailed centrality dependence of hadron spectra presented here would shed light on further understanding of the EOS, chemical properties in the model, and the freeze-out conditions at RHIC.

B. Transverse mass distributions

In order to quantify the observed particle mass dependence of the p_T spectra shape and their centrality dependence, the transverse mass spectra for identified charged hadrons are presented here. From former studies at lower beam energies, it is known that the invariant differential cross sections in $p+p$, $p+A$, and $A+A$ collisions generally show a shape of an exponential in m_T-m_0, where m_0 is particle mass, and $m_T=\sqrt{p_T^2+m_0^2}$ is transverse mass. For an m_T spectrum with an exponential shape, one can parametrize it as follows:

$$\frac{d^2N}{2\pi m_T dm_T dy} = \frac{1}{2\pi T(T+m_0)} A \exp\left(-\frac{m_T-m_0}{T}\right), \quad (8)$$

where T is referred to as the inverse slope parameter, and A is a normalization parameter which contains information on dN/dy. In Fig. 9, m_T distributions for $\pi^{\pm}$, $K^{\pm}$, p, and $\bar{p}$ for central 0–5% (top panels), midcentral 40–50% (middle panels), and peripheral 60–92% (bottom panels) collisions are shown. The spectra for positive particles are on the left and for negative particles are on the right. The solid lines overlaid on each spectra are the fit results using Eq. (8). The error bars are statistical only. As seen in Fig. 9, all the m_T spectra display an exponential shape in the low m_T region. However, at higher m_T, the spectra become less steep, which corresponds to a power-law behavior in p_T. Thus, the inverse slope parameter in Eq. (8) depends on the fitting range. In this analysis, the fits cover the range 0.2–1.0 GeV/c^2 for pions and 0.1–1.0 GeV/c^2 for kaons, protons, and antiprotons in m_T-m_0. The low m_T region ($m_T-m_0<0.2$ GeV/c^2) for pions is excluded from the fit to eliminate the contributions from resonance decays. The inverse slope parameters for each particle species in the three centrality bins are summarized in Fig. 10 and in Table IV. The inverse slope parameters increase with increasing particle mass in all centrality bins. This

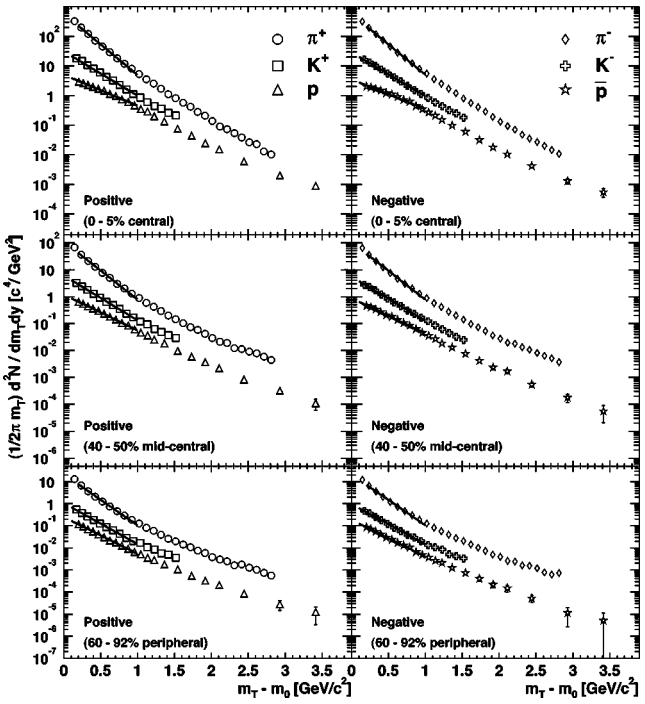

FIG. 9. Transverse mass distributions for $\pi^{\pm}$, $K^{\pm}$, protons, and antiprotons for central 0–5% (top panels), midcentral 40–50% (middle panels), and peripheral 60–92% (bottom panels) in Au+Au collisions at $\sqrt{s_{NN}}=200$ GeV. The lines on each spectra are the fitted results using m_T exponential function. The fit ranges are 0.2–1.0 GeV/c^2 for pions and 0.1–1.0 GeV/c^2 for kaons, protons, and antiprotons in m_T-m_0. The error bars are statistical errors only.

increase for central collisions is more rapid for heavier particles.

Such a behavior was derived, under certain conditions, by Schnedermann *et al.* [33] for central collisions and by Csörgő *et al.* [34] for noncentral heavy-ion collisions:

$$T = T_0 + m\langle u_t\rangle^2. \tag{9}$$

Here T_0 is a freeze-out temperature and $\langle u_t\rangle$ is a measure of the strength of the (average radial) transverse flow. The dotted lines in Fig. 10 represent a linear fit of the results from each centrality bin as a function of mass using Eq. (9). The fit parameters for positive and negative particles are shown in Table IV. It indicates, that the linear extrapolation of the slope parameter $T(m)$ to zero mass has the same intercept parameters T_0 in all the centrality classes, indicating that the freeze-out temperature is approximately independent of the centrality. On the other hand, $\langle u_t\rangle$, the strength of the average transverse flow is increasing with increasing centrality, supporting the hydrodynamic picture.

Motivated by the idea of a color glass condensate, the authors of Ref. [35] argued that the m_T spectra (not m_T-m_0) of identified hadrons at RHIC energy follow a generalized scaling law for all centrality classes when the proton (kaon) spectrum is multiplied by a factor of 0.5 (2.0). The 200 GeV Au+Au pion and kaon spectra seem to follow this m_T scaling, but proton and antiproton spectra are below it by a factor of $\sim$2 for all centralities. Since p and $\bar{p}$ spectra presented here are corrected for weak decays from Λ and $\bar{\Lambda}$, the model also needs to study the feed-down effect to conclude that a universal m_T scaling law is seen at RHIC.

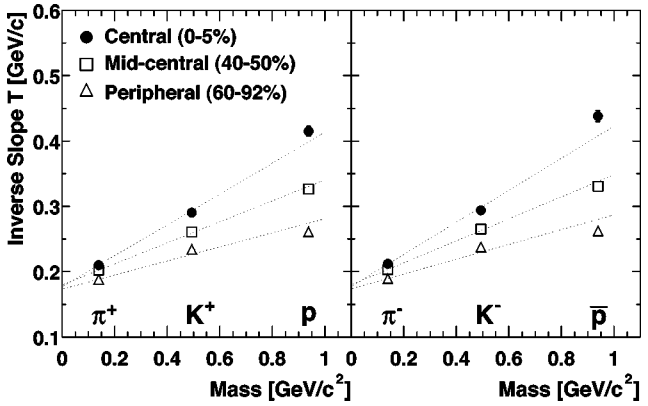

FIG. 10. Mass and centrality dependence of inverse slope parameters T in m_T spectra for positive (left) and negative (right) particles in Au+Au collisions at $\sqrt{s_{NN}}=200$ GeV. The fit ranges are 0.2–1.0 GeV/c^2 for pions and 0.1–1.0 GeV/c^2 for kaons, protons, and antiprotons in m_T-m_0. The dotted lines represent a linear fit of the results from each centrality bin as a function of mass using Eq. (9).

C. Mean transverse momentum and particle yields versus N_{part}

By integrating a measured p_T spectrum over p_T, one can determine the mean transverse momentum $\langle p_T\rangle$ and particle yield per unit rapidity, dN/dy, for each particle species. The procedure to determine the mean p_T and dN/dy is described below.

TABLE IV. (Top) Inverse slope parameters for π, K, p, and $\bar{p}$ for the 0–5%, 40–50%, and 60–92% centrality bins, in units of MeV/c^2. The errors are statistical only. (Bottom) The extracted fit parameters of the freeze-out temperature T_0 in units of MeV/c^2 and the measure of the strength of the average radial transverse flow ($\langle u_t\rangle$) using Eq. (9). The fit results shown here are for positive and negative particles, as denoted in the superscripts, and for three different centrality bins.

Particle	0–5%	40–50%	60–92%
π^+	210.2±0.8	201.9±0.8	187.8±0.7
π^-	211.9±0.7	203.0±0.7	189.2±0.7
K^+	290.2±2.2	260.6±2.4	233.9±2.6
K^-	293.8±2.2	265.1±2.3	237.4±2.6
p	414.8±7.5	326.3±5.9	260.7±5.4
$\bar{p}$	437.9±8.5	330.5±6.4	262.1±5.9
Fit parameter	0–5%	40–50%	60–92%
$T_0^{(+)}$	177.0±1.2	179.5±1.2	173.1±1.2
$T_0^{(-)}$	177.3±1.2	179.6±1.2	173.7±1.1
$\langle u_t\rangle^{(+)}$	0.48±0.07	0.40±0.07	0.32±0.07
$\langle u_t\rangle^{(-)}$	0.49±0.07	0.41±0.07	0.33±0.07

TABLE V. Systematic errors on dN/dy for central 0–5% (top) and peripheral 60–92% (bottom) collisions. All errors are given in percent.

Source	π^+	π^-	K^+	K^-	p	$\bar{p}$
			Central 0–5%			
Cuts + occupancy	6.5	6.5	11.6	10.0	7.2	7.2
Extrapolation	5.4	4.8	5.7	5.6	9.6	9.2
Contamination background	<1	<1	<1	<1	<1	<1
Feed-down					8.0	8.0
Total	8.4	8.0	12.9	11.4	14.4	14.4
			Peripheral 60–92%			
Cuts + occupancy	6.5	6.5	8.3	7.2	8.3	8.3
Extrapolation	8.4	8.0	7.4	7.5	13.6	13.6
Contamination background	<1	<1	<1	<1	<1	<1
Feed-down					8.0	8.0
Total	10.6	10.3	11.1	10.3	17.8	17.8

(1) Determine dN/dy and $\langle p_T \rangle$ by integrating over the measured p_T range from the data.

(2) Fit several appropriate functional forms (detailed below) to the p_T spectra. Note that all of the fits are reasonable approximations to the data. Integrate from zero to the first data point and from the last data point to infinity.

(3) Sum the data yield and the two functional yield pieces together to get dN/dy and $\langle p_T \rangle$ in each functional form.

(4) Take the average between the upper and lower bounds from the different functional forms to obtain the final dN/dy and $\langle p_T \rangle$. The statistical uncertainties are determined from the data. The systematic errors from the extrapolation of yield are defined as half of the difference between the upper and lower bounds.

(5) Determine the final systematic errors on dN/dy and $\langle p_T \rangle$ for each centrality bin by taking the quadrature sum of the extrapolation errors, errors associated with cuts, detector occupancy corrections (for dN/dy), and feed-down corrections (for p and $\bar{p}$).

For the extrapolation of dN/dy and $\langle p_T \rangle$, the following functional forms are used for different particle species: a power-law function and a p_T exponential for pions, a p_T exponential and an m_T exponential for kaons, and a Boltzmann function, p_T exponential, and m_T exponential for protons and antiprotons. The effects of contamination background at high-p_T region for both dN/dy and $\langle p_T \rangle$ are estimated as less than 1% for all particle species. The overall systematic uncertainties on both dN/dy and $\langle p_T \rangle$ are about 10–15%. See Table V for the systematic errors of dN/dy and Table VI for those of $\langle p_T \rangle$.

In Fig. 11, the centrality dependence of $\langle p_T \rangle$ for $\pi^{\pm}$, $K^{\pm}$, p, and $\bar{p}$ is shown. The error bars in the figure represent the

TABLE VI. Systematic errors on $\langle p_T \rangle$ for central 0–5 % (top) and peripheral 60–92% (bottom) collisions. All errors are given in percent.

Source	π^+	π^-	K^+	K^-	p	$\bar{p}$
			Central 0–5%			
Cuts	6.2	6.2	11.2	9.5	6.6	6.6
Extrapolation	3.9	3.5	3.5	3.3	6.2	5.9
Contamination background	<1	<1	<1	<1	<1	<1
Feed-down					1.0	1.0
Total	7.3	7.1	13.5	10.0	9.1	8.9
			Peripheral 60–92%			
Cuts	6.2	6.2	7.7	6.6	7.7	7.7
Extrapolation	5.4	5.3	4.6	4.4	8.6	8.6
Contamination background	<1	<1	<1	<1	<1	<1
Feed-down					1.0	1.0
Total	8.2	8.1	8.9	7.9	11.5	11.5

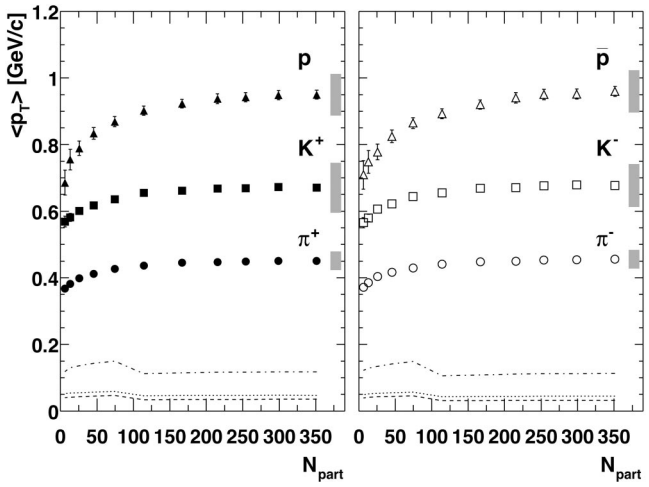

FIG. 11. Mean transverse momentum as a function of N_{part} for pions, kaons, protons, and antiprotons in Au+Au collisions at $\sqrt{s_{NN}}=200$ GeV. The left (right) panel shows the $\langle p_T \rangle$ for positive (negative) particles. The error bars are statistical errors. The systematic errors from cut conditions are shown as shaded boxes on the right for each particle species. The systematic errors from extrapolations, which are scaled by a factor of 2 for clarity, are shown in the bottom for protons and antiprotons (dashed-dot lines), kaons (dotted lines), and pions (dashed lines).

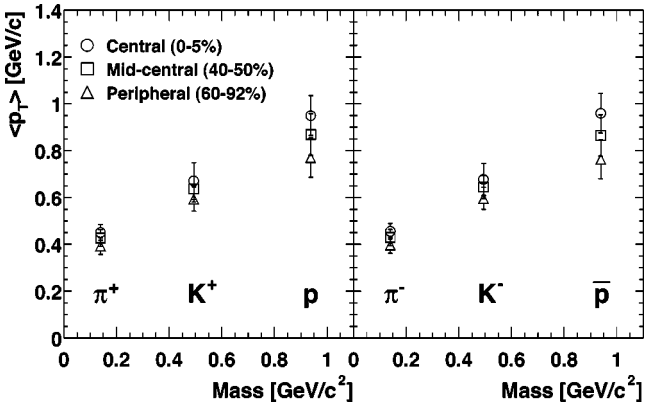

FIG. 12. Mean transverse momentum versus particle mass for central 0–5%, midcentral 40–50%, and peripheral 60–92% in Au+Au collisions at $\sqrt{s_{NN}}=200$ GeV. The left (right) panel shows the $\langle p_T \rangle$ for positive (negative) particles. The error bars represent the total systematic errors. The statistical errors are negligible.

statistical errors. The systematic errors from cut conditions are shown as shaded boxes on the right for each particle species. The systematic errors from extrapolations, which are scaled by a factor of 2 for clarity, are shown in the bottom for each particle species. The data are also summarized in Table VII. It is found that $\langle p_T \rangle$ for all particle species increases from the most peripheral to midcentral collisions, and appears to saturate from the midcentral to central collisions (although the $\langle p_T \rangle$ values for p and $\bar{p}$ may continue to rise). It should be noted that while the total systematic errors on $\langle p_T \rangle$ listed in Table VI is large, the trend shown in the figure is significant. One of the main sources of the uncertainty is the yield extrapolation in unmeasured p_T range (e.g., $p_T < 0.6$ GeV/c for protons and antiprotons). These systematic errors are correlated, and therefore move the curve up and down simultaneously. In Fig. 12, the particle mass and centrality dependence of $\langle p_T \rangle$ are shown. The data presented here are the $\langle p_T \rangle$ for the 0–5%, 40–50% and 60–92% centrality bins. Figure 12 is similar to Fig. 10, which shows the inverse slope parameters, in that the $\langle p_T \rangle$ increases with particle mass and with centrality. This is qualitatively consistent with the hydrodynamic expansion picture [29,33,34].

Figure 13 shows the centrality dependence of dN/dy per participant pair (0.5 N_{part}). The data are summarized in Table VIII. The error bars on each point represent the quadratic sum of the statistical errors and systematic errors from cut conditions. The statistical errors are negligible. The lines represent the effect of the systematic error on N_{part} which affects all curves in the same way. The data indicate that dN/dy per participant pair increases for all particle species with N_{part} up to $\approx$100, and saturates from the midcentral to the most central collisions. From dN/dy for protons and antiprotons, we obtain the net proton number at midrapidity for the most central 0–5% collisions, $dN/dy|_p - dN/dy|_{\bar{p}} = 18.47-13.52$

TABLE VII. Centrality dependence of $\langle p_T \rangle$ for $\pi^{\pm}$, $K^{\pm}$, p, and $\bar{p}$ in MeV/c. The errors are systematic only. The statistical errors are negligible.

N_{part}	π^+	π^-	K^+	K^-	p	$\bar{p}$
351.4	451±33	455±32	670±78	677±68	949±85	959±84
299.0	450±33	454±33	672±78	679±68	948±84	951±83
253.9	448±33	453±33	668±78	676±68	942±84	950±83
215.3	447±34	449±33	667±78	670±67	937±84	940±83
166.6	444±35	447±34	661±77	668±67	923±85	920±83
114.2	436±35	440±35	655±77	654±66	901±83	892±82
74.4	426±35	429±35	636±54	644±48	868±88	864±88
45.5	412±35	416±34	617±53	621±47	833±86	824±86
25.7	398±34	403±33	600±52	606±46	788±84	777±83
13.4	381±32	385±32	581±51	579±46	755±82	747±80
6.3	367±30	371±30	568±51	565±45	685±78	708±81

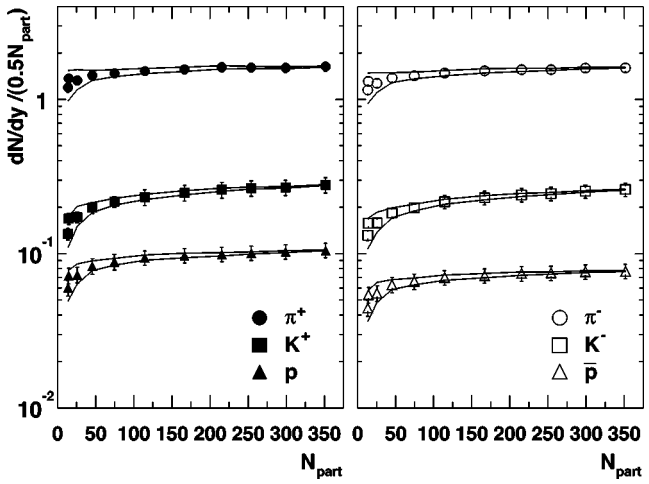

FIG. 13. Particle yield per unit rapidity (dN/dy) per participant pair ($0.5N_{part}$) as a function of N_{part} for pions, kaons, protons, and antiprotons in Au+Au collisions at $\sqrt{s_{NN}}=200$ GeV. The left (right) panel shows the dN/dy for positive (negative) particles. The error bars represent the quadratic sum of statistical errors and systematic errors from cut conditions. The lines represent the effect of the systematic error on N_{part} which affects all curves in the same way.

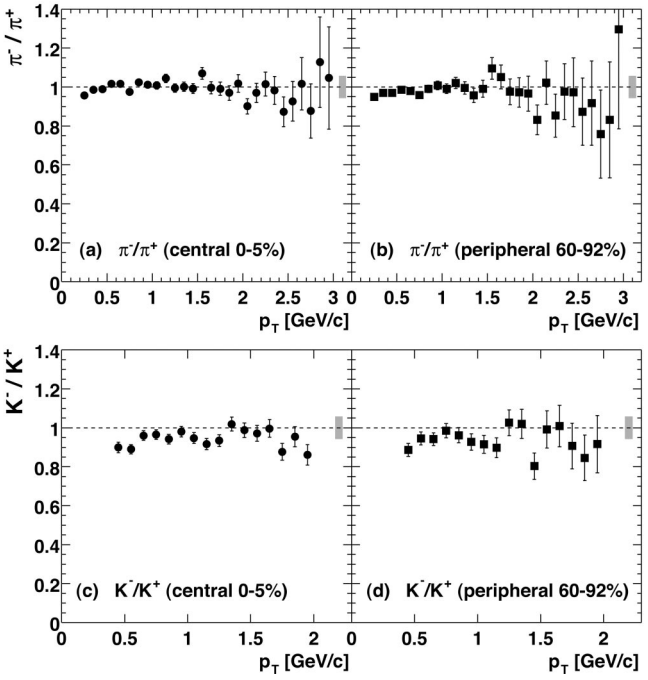

FIG. 14. Particle ratios of (a) π^-/π^+ for central 0–5%, (b) π^-/π^+ for peripheral 60–92%, (c) K^-/K^+ for central 0–5%, and (d) K^-/K^+ for peripheral 60–92% in Au+Au collisions at $\sqrt{s_{NN}}=200$ GeV. The error bars indicate the statistical errors and shaded boxes around unity on each panel indicate the systematic errors.

$=4.95\pm2.74$, which is consistent with the preliminary result at 200 GeV Au+Au (midrapidity) reported by the BRAHMS Collaboration [36].

D. Particle ratios

The ratios of π^-/π^+, K^-/K^+, $p/\bar{p}$, K/π, p/π, and $\bar{p}/\pi$ measured as a function of p_T and centrality at $\sqrt{s_{NN}}=200$ GeV in Au+Au collisions are presented here.

1. Particle Ratios versus p_T

Figure 14 shows the particle ratios of (a) π^-/π^+ for central 0–5%, (b) π^-/π^+ for peripheral 60–92%, (c) K^-/K^+ for central 0–5%, and (d) K^-/K^+ for peripheral 60–92%. Similar plots for the $\bar{p}/p$ ratios are shown in Fig. 15. The error bars represent statistical errors and the shaded boxes on each panel represent the systematic errors. For each of these particle species and centralities, the particle ratios are constant within the experimental errors over the measured p_T range. Similar centrality and p_T dependences are observed in 130 GeV Au+Au data [8,37–42] and previously published 200 GeV Au+Au data [43,44].

To investigate the p_T dependence of the $\bar{p}/p$ ratio in detail, it is shown in Fig. 16 for minimum bias events with two theoretical calculations: a pQCD calculation (dashed line) and a baryon junction model with jet-quenching [46] (solid line). The baryon junction calculation agrees well with the measured $\bar{p}/p$ ratio over the measured p_T range within the experimental uncertainties, while the pQCD calculation does not explain the constant $\bar{p}/p$ ratio over the wide p_T range.

TABLE VIII. Centrality dependence of dN/dy for $\pi^{\pm}$, $K^{\pm}$, p, and $\bar{p}$. The errors are systematic only. The statistical errors are negligible.

N_{part}	π^+	π^-	K^+	K^-	p	$\bar{p}$
351.4	286.4±24.2	281.8±22.8	48.9±6.3	45.7±5.2	18.4±2.6	13.5±1.8
299.0	239.6±20.5	238.9±19.8	40.1±5.1	37.8±4.3	15.3±2.1	11.4±1.5
253.9	204.6±18.0	198.2±16.7	33.7±4.3	31.1±3.5	12.8±1.8	9.5±1.3
215.3	173.8±15.6	167.4±14.4	27.9±3.6	25.8±2.9	10.6±1.5	7.9±1.1
166.6	130.3±12.4	127.3±11.6	20.6±2.6	19.1±2.2	8.1±1.1	5.9±0.8
114.2	87.0±8.6	84.4±8.0	13.2±1.7	12.3±1.4	5.3±0.7	3.9±0.5
74.4	54.9±5.6	52.9±5.2	8.0±0.8	7.4±0.6	3.2±0.5	2.4±0.3
45.5	32.4±3.4	31.3±3.1	4.5±0.4	4.1±0.4	1.8±0.3	1.4±0.2
25.7	17.0±1.8	16.3±1.6	2.2±0.2	2.0±0.1	0.93±0.15	0.71±0.12
13.4	7.9±0.8	7.7±0.7	0.89±0.09	0.88±0.09	0.40±0.07	0.29±0.05
6.3	4.0±0.4	3.9±0.3	0.44±0.04	0.42±0.04	0.21±0.04	0.15±0.02

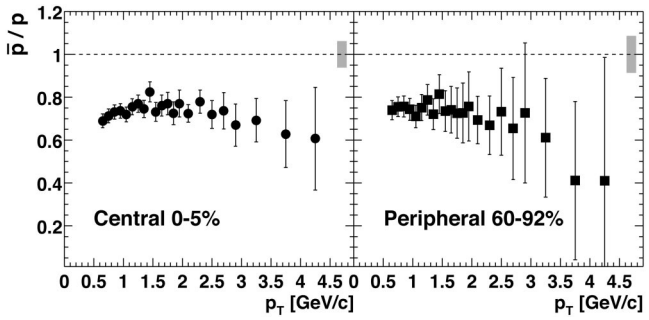

FIG. 15. Ratio of $\overline{p}/p$ as a function of p_T for central 0–5% (left) and peripheral 60–92% (right) in Au+Au collisions at $\sqrt{s_{NN}}$ =200 GeV. The error bars indicate the statistical errors and shaded boxes around unity on each panel indicate the systematic errors.

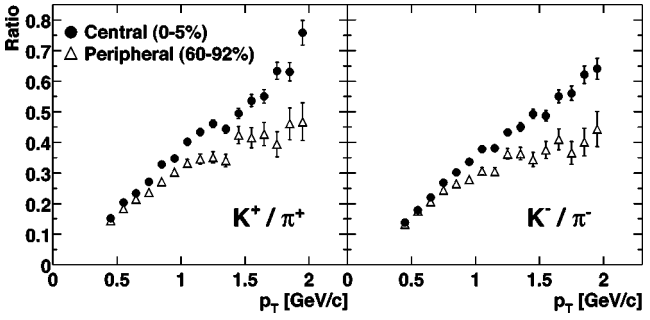

FIG. 17. K/π ratios as a function of p_T for central 0–5% and peripheral 60–92% in Au+Au collisions at $\sqrt{s_{NN}}$=200 GeV. The left is for K^+/π^+ and the right is for K^-/π^-. The error bars indicate the statistical errors.

The statistical thermal model (discussed in more detail later in this section) predicted [10] a baryon chemical potential of μ_B=29 MeV and a freeze-out temperature of T_{ch} =177 MeV for central Au+Au collisions at 200 GeV. From these, the expected $\overline{p}/p$ ratio is $e^{-2\mu_B/T_{ch}}$=0.72, which agrees with our data (0.73). The parton recombination model [45] also reproduces the $\overline{p}/p$ ratio and its flat p_T dependence. The $\overline{p}/p$ ratio in this model is 0.72 since the statistical thermal model is used.

In Fig. 17, the p_T dependence of the K/π ratio is shown for the most central 0–5% and the most peripheral 60–92% centrality bins. The K^+/π^+ (K^-/π^-) ratios are shown on the left (right). Both ratios increase with p_T and the increase is faster in central collisions than in peripheral ones.

In Fig. 18, the p/π and $\overline{p}/\pi$ ratios are shown as a function of p_T for the 0–10%, 20–30% and 60–92% centrality bins. In this figure, the results of p/π^0 and $\overline{p}/\pi^0$ [14] are presented above 1.5 GeV/c and overlaid on the results of p/π^+ and $\overline{p}/\pi^-$, respectively. The absolutely normalized p_T spectra of

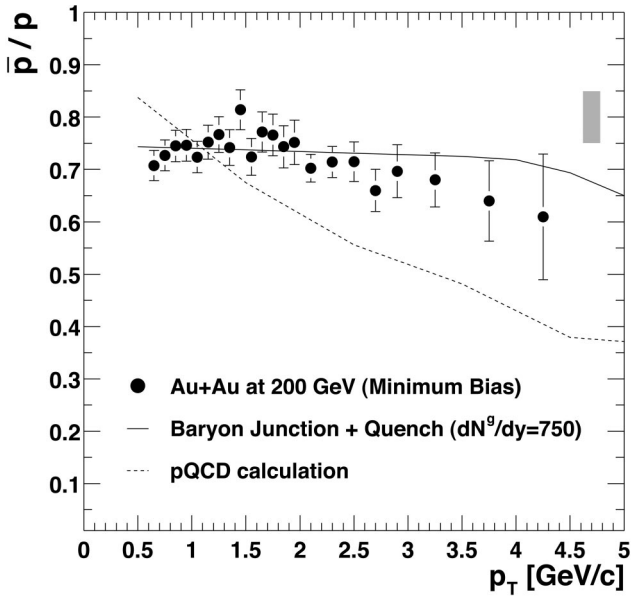

FIG. 16. $\overline{p}/p$ ratios as a function of p_T for minimum bias events in Au+Au at $\sqrt{s_{NN}}$=200 GeV. The error bars indicate the statistical errors and shaded box on the right indicates the systematic errors. Two theoretical calculations are shown: baryon junction model (solid line) and pQCD calculation (dashed line) taken from Ref. [46].

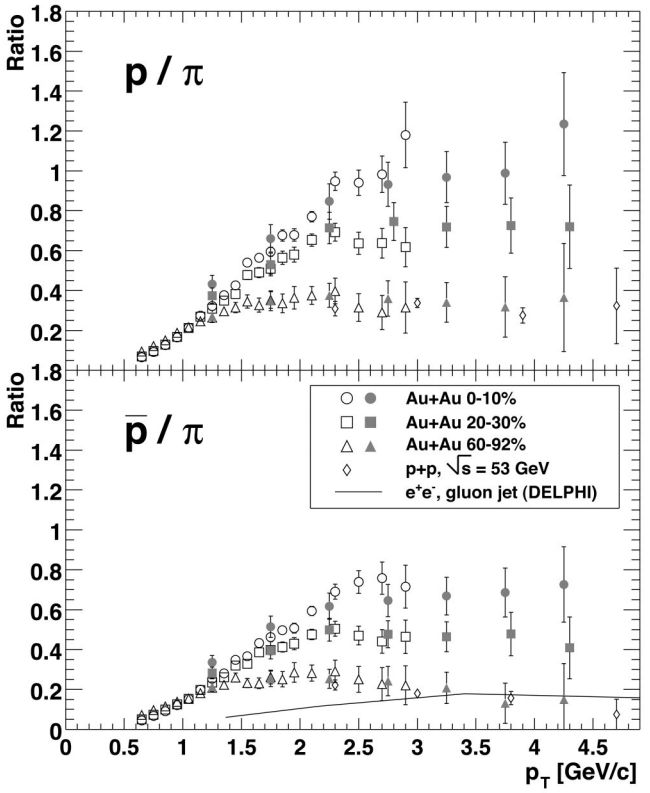

FIG. 18. Proton/pion (top) and antiproton/pion (bottom) ratios for central 0–10%, midcentral 20–30%, and peripheral 60–92% in Au+Au collisions at $\sqrt{s_{NN}}$=200 GeV. Open (filled) points are for charged (neutral) pions. The data at $\sqrt{s}$=53 GeV $p+p$ collisions [47] are also shown. The solid line is the $(\overline{p}+p)/(\pi^+ + \pi^-)$ ratio measured in gluon jets [48].

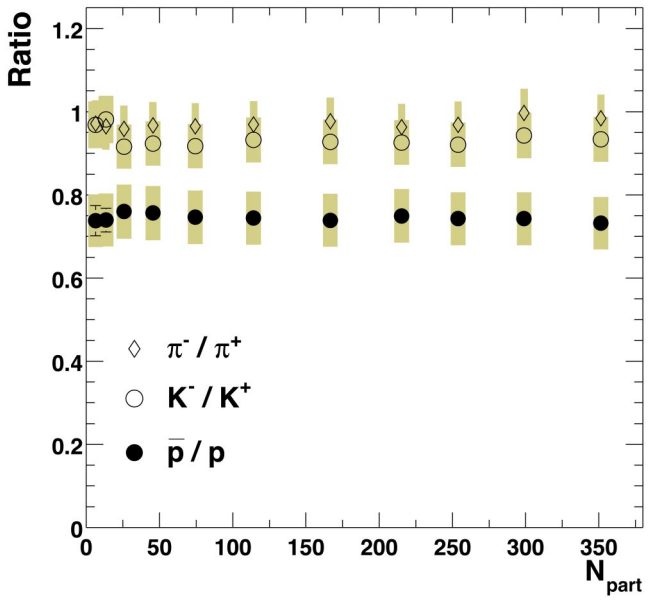

FIG. 19. (Color online) Centrality dependence of particle ratios for π^-/π^+, K^-/K^+, and $\bar{p}/p$ in Au+Au collisions at $\sqrt{s_{NN}}$ =200 GeV. The error bars indicate the statistical errors. The shaded boxes on each data point are the systematic errors.

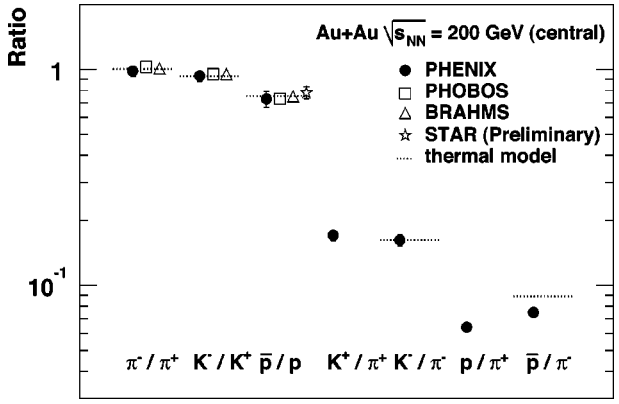

FIG. 20. Comparison of PHENIX particle ratios with those of PHOBOS [44], BRAHMS [43], and STAR (preliminary) [51] results in Au+Au central collisions at $\sqrt{s_{NN}}$=200 GeV at midrapidity. The thermal model prediction [10] for 200 GeV Au+Au central collisions are also shown as dotted lines. The error bars on data indicate the systematic errors.

charged and neutral pions agree within 5–15%. The error bars on the PHENIX data points in the figure show the quadratic sum of the statistical errors and the point-to-point systematic errors. There is an additional normalization uncertainty of 8% for p/π^+, $\bar{p}/\pi^-$ and 12% for p/π^0, $\bar{p}/\pi^0$ [the quadratic sum of the systematic errors on p (or $\bar{p}$) normalization and p_T independent systematic errors from π^0 [23]], which may shift the data up or down for all three centrality bins together, but does not affect their shape. The ratios increase rapidly at low p_T, but saturate at different values of p_T which increase from peripheral to central collisions. In central collisions, the yields of both protons and antiprotons are comparable to that of pions for $p_T>2$ GeV/c. For comparison, the corresponding ratios for $p_T>2$ GeV/c observed in $p+p$ collisions at lower energies [47], and in gluon jets produced in e^++e^- collisions [48], are also shown. Within the uncertainties those ratios are compatible with the peripheral Au+Au results. In hard-scattering processes described by pQCD, the p/π and $\bar{p}/\pi$ ratios at high p_T are determined by the fragmentation of energetic partons, independent of the initial colliding system, which is seen as agreement between $p+p$ and e^++e^- collisions. Thus, the clear increase in the p/π ($\bar{p}/\pi$) ratios at high p_T from $p+p$ and peripheral to the midcentral and to the central Au+Au collisions requires ingredients other than pQCD.

The first observation of the enhancement of protons and antiprotons compared to pions in the intermediate p_T region was in the 130 GeV Au+Au data [6]. The data inspired several new theoretical interpretations and models. Hydrodynamics calculations [32] predict that the $\bar{p}/\pi$ ratio at high p_T exceeds unity for central collisions. The expected $\bar{p}/\pi$ ratio in the thermal model at fixed and sufficiently large p_T is determined by $2e^{-\mu_B/T_{ch}}\approx 1.7$ using T_{ch}=1.77 MeV and μ_B =29 MeV [10] for 200 GeV Au+Au central collisions. Due to the strong radial flow effect at RHIC at relativistic transverse momenta ($p_T \gg m$), all hadron spectra have a similar shape. The hydrodynamic model thus explains the excess of $\bar{p}/\pi$ in central collisions at intermediate p_T. However, the hydrodynamic model [49] predicts no or very little dependence on the centrality, which clearly disagrees with the present data. This model predicts, within 10%, the same p_T dependence of p/π ($\bar{p}/\pi$) for all centrality bins.

Recently, two new models have been proposed to explain the experimental results on the p_T dependence of p/π and $\bar{p}/\pi$ ratios. One model is the parton recombination and fragmentation model [45] and the other model is the baryon junction model [50]. Both models explain qualitatively the observed feature of p/π enhancement in central collisions, and their centrality dependencies. Furthermore, both theoretical models predict that this baryon enhancement is limited to $p_T<5-6$ GeV/c. This will be discussed in Sec. IV E in detail.

2. Particle ratio versus N_{part}

Figure 19 shows the centrality dependence of particle ratios for π^-/π^+, K^-/K^+, and $\bar{p}/p$. The ratios presented here are derived from the integrated yields over p_T (i.e., dN/dy). The shaded boxes on each data point indicate the systematic errors. Within uncertainties, the ratios are all independent of N_{part} over the measured range. Figure 20 shows a comparison of the PHENIX particle ratios with those from PHOBOS [44], BRAHMS [43], and STAR (preliminary) [51] in Au+Au central collisions at $\sqrt{s_{NN}}$=200 GeV at midrapidity. The PHENIX antiparticle-to-particle ratios are consistent with other experimental results within the systematic uncertainties.

Figure 21 shows the centrality dependence of K/π and p/π ratios. Both K^+/π^+ and K^-/π^- ratios increase rapidly

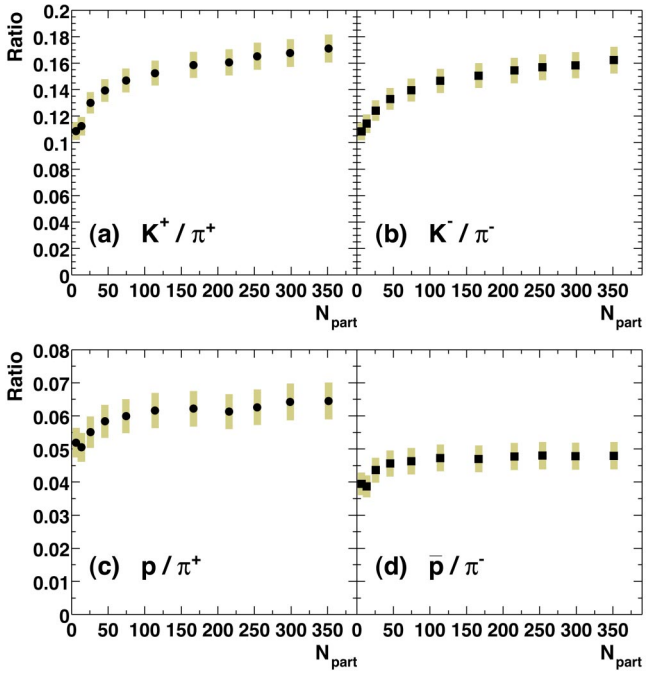

FIG. 21. (Color online) Centrality dependence of particle ratios for (a) K^+/π^+, (b) K^-/π^-, (c) p/π^+, and (d) $\bar{p}/\pi^-$ in Au+Au collisions at $\sqrt{s_{NN}}=200$ GeV. The error bars indicate the statistical errors. The shaded boxes on each data point are the systematic errors.

for peripheral collisions ($N_{part}<100$), and then saturate or rise slowly from the midcentral to the most central collisions. The p/π^+ and $\bar{p}/\pi^-$ ratios increase for peripheral collisions ($N_{part}<50$) and saturate from midcentral to central collisions—similar to the centrality dependence of K/π ratio (but possibly flatter).

Within the framework of the statistical thermal model [9] in a grand canonical ensemble with baryon number, strangeness, and charge conservation [10], particle ratios measured at $\sqrt{s_{NN}}=130$ GeV at midrapidity have been analyzed with the extracted chemical freeze-out temperature $T_{ch}=174\pm7$ MeV and baryon chemical potential $\mu_B=46\pm5$ MeV. A set of chemical parameters at $\sqrt{s_{NN}}=200$ GeV in Au+Au were also predicted by using a phenomenological parametrization of the energy dependence of μ_B. The predictions were $\mu_B=29\pm8$ MeV and $T_{ch}=177\pm7$ MeV at $\sqrt{s_{NN}}=200$ GeV. The comparison between the PHENIX data at 200 GeV for 0–5% central and the thermal model prediction is shown in Table IX and Fig. 20. There is a good agreement between data and the model. The thermal model calculation was performed by assuming a 50% reconstruction efficiency of all weakly decaying baryons in Ref. [10]. However, our results have been corrected to remove these contributions. Therefore, Table IX includes $\bar{p}/p$ and $\bar{p}/\pi^-$ ratios with and without Λ ($\bar{\Lambda}$) feed-down corrections to the proton and antiproton spectra. The ratios without the Λ ($\bar{\Lambda}$) feed-down correction are labeled "inclusive." The small μ_B is qualitatively consistent with our measurement of the number of net protons (≈5) in central Au+Au collisions at $\sqrt{s_{NN}}=200$ GeV at midrapidity.

TABLE IX. Comparison between the data for the 0–5% central collisions and the thermal model prediction at $\sqrt{s_{NN}}=200$ GeV with $T_{ch}=177$ MeV and $\mu_B=29$ MeV [10].

Particles	Ratio ± stat. ± sys.	Thermal model
π^-/π^+	0.984±0.004±0.057	1.004
K^-/K^+	0.933±0.007±0.054	0.932
$\bar{p}/p$	0.731±0.011±0.062	
$\bar{p}/p$ (Inclusive)	0.747±0.007±0.046	0.752
K^+/π^+	0.171±0.001±0.010	
K^-/π^-	0.162±0.001±0.010	0.147
p/π^+	0.064±0.001±0.003	
p/π^+ (Inclusive)	0.099±0.001±0.006	
$\bar{p}/\pi^-$	0.047±0.001±0.002	
$\bar{p}/\pi^-$ (Inclusive)	0.075±0.001±0.004	0.089

E. Binary collision scaling of p_T spectra

One of the most striking features in Au+Au collisions at RHIC is that π^0 and nonidentified hadron yields at $p_T>2$ GeV/c in central collisions are suppressed with respect to the number of nucleon-nucleon binary collisions (N_{coll}) scaled by $p+p$ and peripheral Au+Au results [12–14]. Moreover, the suppression of π^0 is stronger than that for nonidentified charged hadrons [12], and the yields of protons and antiprotons in central collisions are comparable to that of pions around $p_T=2$ GeV/c [6]. The enhancement of the p/π ($\bar{p}/\pi$) ratio in central collisions at intermediate p_T (2.0–4.5 GeV/c), which was presented in the preceding section, is consistent with the above observations. These results show the significant contributions of proton and antiproton yields to the total particle composition at this intermediate p_T region. We present here the N_{coll} scaling behavior for charged pions, kaons, and protons (antiprotons) in order to quantify the particle composition at intermediate p_T.

Figure 22 shows the p_T spectra scaled by the averaged number of binary collisions, $\langle N_{coll}\rangle$, for $(\pi^++\pi^-)/2$, $(K^++K^-)/2$, and $(p+\bar{p})/2$ in three centrality bins: central 0–10%, midcentral 40–50%, and peripheral 60–92%. For $(p+\bar{p})/2$ in the range of $p_T=1.5$–4.5 GeV/c, it is clearly seen that the spectra are on top of each other. This indicates that proton and antiproton production at high p_T scales with the number of binary collisions. On the other hand, at p_T below 1.5 GeV/c, different shapes for different centrality bins are observed, which indicates a strong contribution from radial flow. The scaling behavior of the kaons seems to be similar to protons, but this is not conclusive due to our PID limitations. For pions, the N_{coll} scaled yield in central events is suppressed compared to that for peripheral events at $p_T>2$ GeV/c, which is consistent with the results in the π^0 spectra [12,14].

Figure 23 shows the central (0–10%) to peripheral (60–92%) ratio for N_{coll} scaled p_T spectra ($R_{\rm CP}$: the nuclear modification factor) of $(\bar{p}+p)/2$, kaons, charged pions, and π^0. In this paper we define $R_{\rm CP}$ as

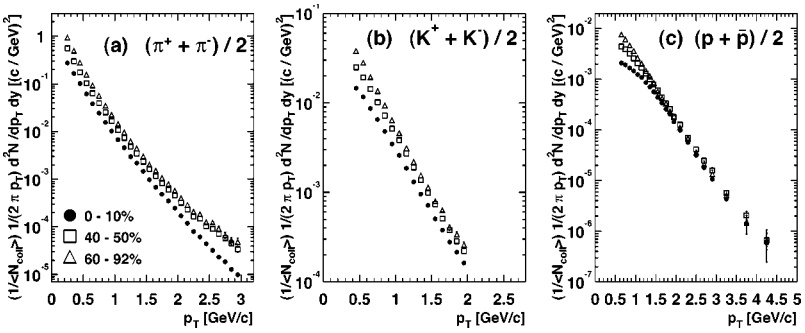

FIG. 22. p_T spectra scaled by the averaged number of binary collisions for averaged charged (a) pions, (b) kaons, and (c) $(p+\bar{p})/2$ in three different centrality bins: central 0–10%, midcentral 40–50%, and peripheral 60–92% in Au+Au collisions at $\sqrt{s_{NN}}=200$ GeV. The error bars are statistical only. Note the different horizontal and vertical scales on the three plots.

$$R_{\mathrm{CP}} = \frac{\mathrm{Yield}^{0-10\%}/\langle {N_{coll}}^{0-10\%}\rangle}{\mathrm{Yield}^{60-92\%}/\langle {N_{coll}}^{60-92\%}\rangle}. \tag{10}$$

The peripheral 60–92 % Au+Au spectrum is used as an approximation of the yields in $p+p$ collisions, based on the experimental fact that the peripheral spectra scale with N_{coll} by using the yields in $p+p$ collisions measured by PHENIX [14,24]. Thus the meaning of the R_{CP} is expected to be the same as R_{AA} used in our previous publications [12–14]. The lines in Fig. 23 indicate the expectations of N_{part} (dotted) and N_{coll} (dashed) scaling. The shaded bars at the end of each line represent the systematic error associated with the determination of these quantities for central and peripheral events. The error bars on charged particles are statistical errors only, and those for π^0 are the quadratic sum of the statistical errors and the point-to-point systematic errors. The data show that $(\bar{p}+p)/2$ reaches unity for $p_T \gtrsim 1.5$ GeV/c, consistent with N_{coll} scaling. The data for kaons also show the N_{coll} scaling behavior around 1.5–2.0 GeV/c, but the behavior is weaker than for protons. As with neutral pions [14], charged pions are also suppressed at 2–3 GeV/c with respect to peripheral Au+Au collisions.

Motivated by the observation that the $(\bar{p}+p)/2$ spectra scale with N_{coll} above $p_T=1.5$ GeV/c, the ratio of the integrated yield between central and peripheral events (scaled by the corresponding N_{coll}) above $p_T=1.5$ GeV/c are shown in Fig. 24 as a function of N_{part}. The p_T ranges for the integration are 1.5–4.5 GeV/c for $(\bar{p}+p)/2$, 1.5–2.0 GeV/c for kaons, and 1.5–3.0 GeV/c for charged pions. The data points are normalized to the most peripheral data point. The shaded boxes in the figure indicate the systematic errors, which include the normalization errors on the p_T spectra, the errors on the detector occupancy corrections, and the uncertainties of the $\langle T_{\mathrm{AuAu}}\rangle$ determination for the numerator only. Only at the most peripheral data point, the uncertainty on the denominator $\langle T_{\mathrm{AuAu}}^{60-92\%}\rangle$ is also added. The figure shows that $(\bar{p}+p)/2$ scales with N_{coll} for all centrality bins, while the data for charged pions show a decrease with N_{part}. The kaon data points are between the charged pions and the $(\bar{p}+p)/2$ spectra.

The standard picture of hadron production at high momentum is the fragmentation of energetic partons. While the observed suppression of the π^0 yield at high p_T in central collisions may be attributed to the energy loss of partons during their propagation through the hot and dense matter

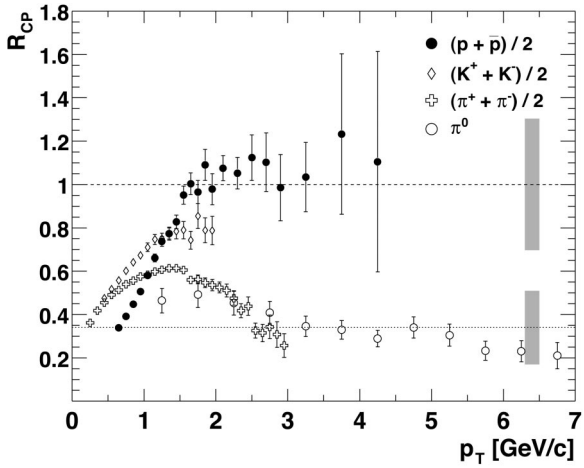

FIG. 23. Central (0–10%) to peripheral (60–92%) ratios of binary-collision-scaled p_T spectra, R_{CP}, as a function of p_T for $(\bar{p}+p)/2$, charged kaons, charged pions, and π^0 [14] in Au+Au collisions at $\sqrt{s_{NN}}=200$ GeV. The lines indicate the expectations of N_{part} (dotted) and N_{coll} (dashed) scaling, the shaded bars represent the systematic errors on these quantities.

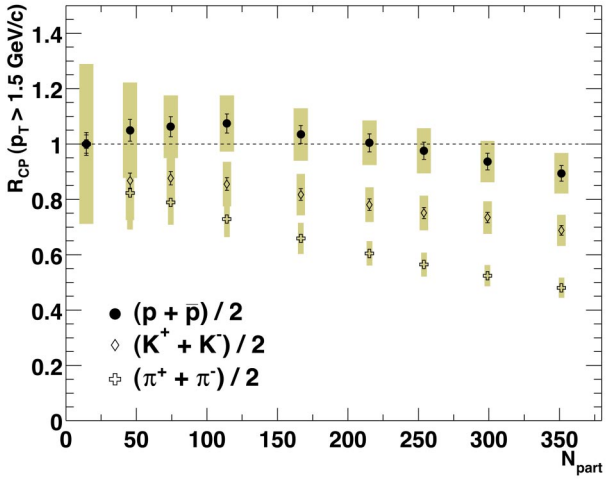

FIG. 24. (Color online) Centrality dependence of integrated R_{CP} above 1.5 GeV/c normalized to the most peripheral 60–92% value. The data show R_{CP} for $(\bar{p}+p)/2$, charged kaons, and charged pions in Au+Au collisions at $\sqrt{s_{NN}}=200$ GeV. The error bars are statistical only. The shaded boxes represent the systematic errors (see text for details).

created in the collisions, i.e., jet quenching [15,16], it is a theoretical challenge to explain the absence of suppression for baryons up to 4.5 GeV/c for all centralities along with the enhancement of the p/π ratio at $p_T=2-4$ GeV/c for central collisions.

It has been recently proposed that such observations can be explained by the dominance of parton recombination at intermediate p_T, rather than by fragmentation [45]. The competition between recombination and fragmentation of partons may explain the observed features. The model predicts that the effect is limited to $p_T<5$ GeV/c, beyond which fragmentation becomes the dominant production mechanism for all particle species.

Another possible explanation is the baryon junction model [50]. It invokes a topological gluon configuration with jet quenching. With pion production above 2 GeV/c suppressed by jet quenching, gluon junctions produce copious baryons at intermediate p_T, thus leading to the enhancement of baryons in this p_T region. The model reproduces the baryon-to-meson ratio and its centrality dependence qualitatively [52].

Both theoretical models predict that baryon enhancement is limited to $p_T<5-6$ GeV/c, which is unfortunately beyond our current PID capability. However, it is possible to test the two predictions indirectly by using the nonidentified charged hadrons to neutral pion ratio (h/π^0) as a measure of the baryon content at high p_T, as published in Ref. [23]. The results support the limited behavior of baryon enhancement up to 5 GeV/c in p_T. Similar trends are observed in Λ, K^0_S, and $K^{\pm}$ measurements by the STAR Collaboration [53].

On the other hand, it is also possible that nuclear effects, such as the "Cronin effect" [54,55], attributed to initial state multiple scattering (p_T broadening) [56], contribute to the observed species dependence. At center-of-mass energies up to $\sqrt{s}=38.8$ GeV, a nuclear enhancement beyond N_{coll} scaling has been observed for π, K, p, and their antiparticles in $p+A$ collisions. The effect is stronger for protons and antiprotons than for pions, which leads to an enhancement of the p/π and $\bar{p}/\pi$ ratios compared to $p+p$ collisions. In proton-tungsten reactions, the increase is a factor of ~ 2 in the range $3<p_T<6$ GeV. For pions, theoretical calculations at RHIC energies [57] predict a reduced strength of the Cronin effect compared to lower energies, although no prediction exists for protons. New data from d+Au collisions at $\sqrt{s_{NN}}=200$ GeV will help to clarify this issue.

V. SUMMARY AND CONCLUSION

In summary, we present the centrality dependence of identified charged hadron spectra and yields for $\pi^{\pm}$, $K^{\pm}$, p and $\bar{p}$ in Au+Au collisions at $\sqrt{s_{NN}}=200$ GeV at midrapidity. In central events, the low p_T region ($\leqslant 2.0$ GeV/c) of the p_T spectra show a clear particle mass dependence in their shapes, namely, p and $\bar{p}$ spectra have a shoulder-arm shape while the pion spectra have a concave shape. The spectra can be well fit with an exponential function in m_T at the region below 1.0 GeV/c^2 in m_T-m_0. The resulting inverse slope parameters show clear particle mass and centrality dependences that increase with particle mass and centrality. These observations are consistent with the hydrodynamic radial flow picture. Moreover, at around $p_T=2.0$ GeV/c in central events, the p and $\bar{p}$ yields are comparable to the pion yields. Here, baryons comprise a significant fraction of the hadron yield in this intermediate p_T range. The $\langle p_T\rangle$ and dN/dy per participant pair increase from peripheral to midcentral collisions and saturate for the most central collisions for all particle species. The net proton number in Au+Au central collisions at $\sqrt{s_{NN}}=200$ GeV is ~ 5 at midrapidity.

The particle ratios of π^-/π^+, K^-/K^+, $p/\bar{p}$, K/π, p/π, and $\bar{p}/\pi$ as a function of p_T and centrality have been measured. Particle ratios in central Au+Au collisions are well reproduced by the statistical thermal model with a baryon chemical potential of $\mu_B=29$ MeV and a chemical freeze-out temperature of $T_{ch}=177$ MeV. Regardless of the particle species and centrality, it is found that ratios for equal mass particles are constant as a function of p_T, within the systematic uncertainties in the measured p_T range. On the other hand, both K/π and p/π ($\bar{p}/\pi$) ratios increase as a function of p_T. This increase with p_T is stronger for central than for peripheral events. The p/π and $\bar{p}/\pi$ ratios in central events both increase with p_T up to 3 GeV/c and approach unity at $p_T\approx 2$ GeV/c. However, in peripheral collisions these ratios saturate at the value of 0.3–0.4 around $p_T=1.5$ GeV/c. The observed centrality dependence of p/π and $\bar{p}/\pi$ ratios in intermediate p_T region is not explained by the hydrodynamic model alone, but both the parton recombination model and the baryon junction model qualitatively agree with data.

The scaling behavior of identified charged hadrons is compared with results for neutral pions. In the N_{coll} scaled p_T spectra for $(p+\bar{p})/2$, the spectra scale with N_{coll} from $p_T=1.5$ to 4.5 GeV/c. The central-to-peripheral ratio R_{CP} approaches unity for $(\bar{p}+p)/2$ from $p_T=1.5$ up to 4.5 GeV/c. Meanwhile, charged and neutral pions are suppressed. The ratio of integrated R_{CP} from $p_T=1.5$ to 4.5 GeV/c exhibits an N_{coll} scaling behavior for all centrality bins in the $(\bar{p}+p)/2$ data, which is in contrast to the stronger pion suppression that increases with centrality.

ACKNOWLEDGMENTS

We thank the staff of the Collider-Accelerator and Physics Departments at Brookhaven National Laboratory and the staff of the other PHENIX participating institutions for their vital contributions. We acknowledge support from the Department of Energy, Office of Science, Nuclear Physics Division, the National Science Foundation, Abilene Christian University Research Council, Research Foundation of SUNY, and Dean of the College of Arts and Sciences, Vanderbilt University (USA), Ministry of Education, Culture, Sports, Science, and Technology and the Japan Society for the Promotion of Science (Japan), Conselho Nacional de Desenvolvimento Científico e Tecnológico and Fundação de Amparo à Pesquisa do Estado de São Paulo (Brazil), Natural Science Foundation of China (People's Republic of China), Centre National de la Recherche Scientifique, Commissariat à l'Énergie Atomique, Institut National de Physique Nucléaire et de Physique des Particules, and Institut National de Physique Nucléaire et de Physique des Particules (France),

Bundesministerium fuer Bildung und Forschung, Deutscher Akademischer Austausch Dienst, and Alexander von Humboldt Stiftung (Germany), Hungarian National Science Fund, OTKA (Hungary), Department of Atomic Energy and Department of Science and Technology (India), Israel Science Foundation (Israel), Korea Research Foundation and Center for High Energy Physics (Korea), Russian Ministry of Industry, Science and Tekhnologies, Russian Academy of Science, Russian Ministry of Atomic Energy (Russia), VR and the Wallenberg Foundation (Sweden), the U.S. Civilian Research and Development Foundation for the Independent States of the Former Soviet Union, the US-Hungarian NSF-OTKA-MTA, the US-Israel Binational Science Foundation, and the Fifth European Union TMR Marie-Curie Programme.

APPENDIX: TABLE OF INVARIANT YIELDS

The invariant yields for $\pi^{\pm}$, $K^{\pm}$, p, and $\bar{p}$ in Au+Au collisions at $\sqrt{s_{NN}}=200$ GeV at midrapidity are tabulated in Tables X–XXIX. The data presented here are for the minimum bias events and each centrality bin (0–5%, 5–10%, 10–15%, 15–20%, 20–30%,…, 70–80%, 80–92%, and 60–92%). Errors are statistical only.

TABLE X. Invariant yields for π^{+} at midrapidity in the minimum bias, 0–5%, 5–10%, and 10–15% centrality bins, normalized to unit rapidity. Errors are statistical only.

p_T (GeV/c)	Minimum bias	0–5%	5–10%	10–15%
0.25	$1.07\times10^{2}\pm8.8\times10^{-1}$	$3.29\times10^{2}\pm2.7\times10^{0}$	$2.76\times10^{2}\pm2.3\times10^{0}$	$2.39\times10^{2}\pm2.0\times10^{0}$
0.35	$6.06\times10^{1}\pm5.0\times10^{-1}$	$1.97\times10^{2}\pm1.6\times10^{0}$	$1.64\times10^{2}\pm1.4\times10^{0}$	$1.39\times10^{2}\pm1.2\times10^{0}$
0.45	$3.63\times10^{1}\pm3.1\times10^{-1}$	$1.20\times10^{2}\pm1.1\times10^{0}$	$9.93\times10^{1}\pm8.7\times10^{-1}$	$8.41\times10^{1}\pm7.4\times10^{-1}$
0.55	$2.18\times10^{1}\pm2.0\times10^{-1}$	$7.26\times10^{1}\pm6.7\times10^{-1}$	$6.02\times10^{1}\pm5.6\times10^{-1}$	$5.08\times10^{1}\pm4.7\times10^{-1}$
0.65	$1.34\times10^{1}\pm1.3\times10^{-1}$	$4.49\times10^{1}\pm4.5\times10^{-1}$	$3.74\times10^{1}\pm3.8\times10^{-1}$	$3.16\times10^{1}\pm3.2\times10^{-1}$
0.75	$8.71\times10^{0}\pm9.5\times10^{-2}$	$2.93\times10^{1}\pm3.3\times10^{-1}$	$2.43\times10^{1}\pm2.7\times10^{-1}$	$2.05\times10^{1}\pm2.3\times10^{-1}$
0.85	$5.41\times10^{0}\pm6.3\times10^{-2}$	$1.82\times10^{1}\pm2.2\times10^{-1}$	$1.53\times10^{1}\pm1.8\times10^{-1}$	$1.29\times10^{1}\pm1.6\times10^{-1}$
0.95	$3.59\times10^{0}\pm4.5\times10^{-2}$	$1.21\times10^{1}\pm1.6\times10^{-1}$	$1.01\times10^{1}\pm1.3\times10^{-1}$	$8.56\times10^{0}\pm1.1\times10^{-1}$
1.05	$2.35\times10^{0}\pm3.1\times10^{-2}$	$7.96\times10^{0}\pm1.1\times10^{-1}$	$6.56\times10^{0}\pm9.3\times10^{-2}$	$5.56\times10^{0}\pm8.0\times10^{-2}$
1.15	$1.58\times10^{0}\pm2.2\times10^{-2}$	$5.32\times10^{0}\pm8.0\times10^{-2}$	$4.47\times10^{0}\pm6.8\times10^{-2}$	$3.72\times10^{0}\pm5.7\times10^{-2}$
1.25	$1.05\times10^{0}\pm1.5\times10^{-2}$	$3.55\times10^{0}\pm5.7\times10^{-2}$	$2.99\times10^{0}\pm4.9\times10^{-2}$	$2.51\times10^{0}\pm4.2\times10^{-2}$
1.35	$7.59\times10^{-1}\pm1.2\times10^{-2}$	$2.55\times10^{0}\pm4.5\times10^{-2}$	$2.15\times10^{0}\pm3.9\times10^{-2}$	$1.81\times10^{0}\pm3.3\times10^{-2}$
1.45	$5.16\times10^{-1}\pm8.3\times10^{-3}$	$1.72\times10^{0}\pm3.3\times10^{-2}$	$1.45\times10^{0}\pm2.8\times10^{-2}$	$1.23\times10^{0}\pm2.5\times10^{-2}$
1.55	$3.37\times10^{-1}\pm5.6\times10^{-3}$	$1.13\times10^{0}\pm2.3\times10^{-2}$	$9.36\times10^{-1}\pm2.0\times10^{-2}$	$7.93\times10^{-1}\pm1.7\times10^{-2}$
1.65	$2.44\times10^{-1}\pm4.2\times10^{-3}$	$8.05\times10^{-1}\pm1.8\times10^{-2}$	$6.68\times10^{-1}\pm1.6\times10^{-2}$	$5.78\times10^{-1}\pm1.4\times10^{-2}$
1.75	$1.77\times10^{-1}\pm3.3\times10^{-3}$	$5.70\times10^{-1}\pm1.4\times10^{-2}$	$4.84\times10^{-1}\pm1.3\times10^{-2}$	$4.19\times10^{-1}\pm1.1\times10^{-2}$
1.85	$1.27\times10^{-1}\pm2.4\times10^{-3}$	$4.18\times10^{-1}\pm1.2\times10^{-2}$	$3.42\times10^{-1}\pm1.0\times10^{-2}$	$2.99\times10^{-1}\pm9.1\times10^{-3}$
1.95	$9.01\times10^{-2}\pm1.9\times10^{-3}$	$2.80\times10^{-1}\pm9.0\times10^{-3}$	$2.50\times10^{-1}\pm8.3\times10^{-3}$	$2.07\times10^{-1}\pm7.3\times10^{-3}$
2.05	$6.68\times10^{-2}\pm1.2\times10^{-3}$	$2.09\times10^{-1}\pm6.1\times10^{-3}$	$1.82\times10^{-1}\pm5.6\times10^{-3}$	$1.56\times10^{-1}\pm5.0\times10^{-3}$
2.15	$4.71\times10^{-2}\pm8.9\times10^{-4}$	$1.36\times10^{-1}\pm4.8\times10^{-3}$	$1.27\times10^{-1}\pm4.6\times10^{-3}$	$1.05\times10^{-1}\pm4.1\times10^{-3}$
2.25	$3.27\times10^{-2}\pm6.8\times10^{-4}$	$9.10\times10^{-2}\pm3.8\times10^{-3}$	$8.06\times10^{-2}\pm3.5\times10^{-3}$	$8.05\times10^{-2}\pm3.5\times10^{-3}$
2.35	$2.60\times10^{-2}\pm6.2\times10^{-4}$	$7.20\times10^{-2}\pm3.6\times10^{-3}$	$6.28\times10^{-2}\pm3.3\times10^{-3}$	$5.78\times10^{-2}\pm3.1\times10^{-3}$
2.45	$1.94\times10^{-2}\pm5.3\times10^{-4}$	$5.40\times10^{-2}\pm3.2\times10^{-3}$	$4.57\times10^{-2}\pm2.9\times10^{-3}$	$4.06\times10^{-2}\pm2.7\times10^{-3}$
2.55	$1.49\times10^{-2}\pm4.7\times10^{-4}$	$3.78\times10^{-2}\pm2.8\times10^{-3}$	$3.59\times10^{-2}\pm2.7\times10^{-3}$	$3.18\times10^{-2}\pm2.5\times10^{-3}$
2.65	$1.13\times10^{-2}\pm4.2\times10^{-4}$	$2.65\times10^{-2}\pm2.5\times10^{-3}$	$2.50\times10^{-2}\pm2.4\times10^{-3}$	$2.44\times10^{-2}\pm2.3\times10^{-3}$
2.75	$9.30\times10^{-3}\pm4.0\times10^{-4}$	$2.27\times10^{-2}\pm2.5\times10^{-3}$	$2.19\times10^{-2}\pm2.4\times10^{-3}$	$1.83\times10^{-2}\pm2.1\times10^{-3}$
2.85	$6.20\times10^{-3}\pm3.2\times10^{-4}$	$1.28\times10^{-2}\pm1.9\times10^{-3}$	$1.21\times10^{-2}\pm1.8\times10^{-3}$	$1.30\times10^{-2}\pm1.8\times10^{-3}$
2.95	$5.17\times10^{-3}\pm3.1\times10^{-4}$	$1.03\times10^{-2}\pm1.8\times10^{-3}$	$1.08\times10^{-2}\pm1.8\times10^{-3}$	$1.04\times10^{-2}\pm1.8\times10^{-3}$

TABLE XI. Invariant yields for π^+ at midrapidity in 15–20%, 20–30%, 30–40%, and 40–50% centrality bins, normalized to unit rapidity. Errors are statistical only.

p_T (GeV/c)	15–20%	20–30%	30–40%	40–50%
0.25	$2.04\times10^{2}\pm1.7\times10^{0}$	$1.57\times10^{2}\pm1.3\times10^{0}$	$1.07\times10^{2}\pm8.9\times10^{-1}$	$6.84\times10^{1}\pm5.7\times10^{-1}$
0.35	$1.18\times10^{2}\pm9.9\times10^{-1}$	$8.82\times10^{1}\pm7.4\times10^{-1}$	$5.86\times10^{1}\pm4.9\times10^{-1}$	$3.67\times10^{1}\pm3.1\times10^{-1}$
0.45	$7.09\times10^{1}\pm6.2\times10^{-1}$	$5.27\times10^{1}\pm4.6\times10^{-1}$	$3.46\times10^{1}\pm3.0\times10^{-1}$	$2.15\times10^{1}\pm1.9\times10^{-1}$
0.55	$4.28\times10^{1}\pm4.0\times10^{-1}$	$3.17\times10^{1}\pm2.9\times10^{-1}$	$2.06\times10^{1}\pm1.9\times10^{-1}$	$1.26\times10^{1}\pm1.2\times10^{-1}$
0.65	$2.65\times10^{1}\pm2.7\times10^{-1}$	$1.95\times10^{1}\pm2.0\times10^{-1}$	$1.26\times10^{1}\pm1.3\times10^{-1}$	$7.66\times10^{0}\pm8.0\times10^{-2}$
0.75	$1.73\times10^{1}\pm2.0\times10^{-1}$	$1.27\times10^{1}\pm1.4\times10^{-1}$	$8.29\times10^{0}\pm9.4\times10^{-2}$	$4.99\times10^{0}\pm5.8\times10^{-2}$
0.85	$1.07\times10^{1}\pm1.3\times10^{-1}$	$7.94\times10^{0}\pm9.5\times10^{-2}$	$5.10\times10^{0}\pm6.3\times10^{-2}$	$3.04\times10^{0}\pm3.9\times10^{-2}$
0.95	$7.12\times10^{0}\pm9.6\times10^{-2}$	$5.31\times10^{0}\pm7.0\times10^{-2}$	$3.38\times10^{0}\pm4.6\times10^{-2}$	$2.02\times10^{0}\pm2.9\times10^{-2}$
1.05	$4.77\times10^{0}\pm6.9\times10^{-2}$	$3.49\times10^{0}\pm4.9\times10^{-2}$	$2.22\times10^{0}\pm3.2\times10^{-2}$	$1.30\times10^{0}\pm2.0\times10^{-2}$
1.15	$3.16\times10^{0}\pm5.0\times10^{-2}$	$2.34\times10^{0}\pm3.5\times10^{-2}$	$1.50\times10^{0}\pm2.4\times10^{-2}$	$8.78\times10^{-1}\pm1.5\times10^{-2}$
1.25	$2.10\times10^{0}\pm3.6\times10^{-2}$	$1.56\times10^{0}\pm2.5\times10^{-2}$	$9.99\times10^{-1}\pm1.7\times10^{-2}$	$5.98\times10^{-1}\pm1.1\times10^{-2}$
1.35	$1.52\times10^{0}\pm2.9\times10^{-2}$	$1.12\times10^{0}\pm2.0\times10^{-2}$	$7.17\times10^{-1}\pm1.4\times10^{-2}$	$4.26\times10^{-1}\pm9.0\times10^{-3}$
1.45	$1.05\times10^{0}\pm2.2\times10^{-2}$	$7.57\times10^{-1}\pm1.5\times10^{-2}$	$4.98\times10^{-1}\pm1.0\times10^{-2}$	$2.91\times10^{-1}\pm6.9\times10^{-3}$
1.55	$6.78\times10^{-1}\pm1.5\times10^{-2}$	$5.07\times10^{-1}\pm1.0\times10^{-2}$	$3.24\times10^{-1}\pm7.4\times10^{-3}$	$1.97\times10^{-1}\pm5.2\times10^{-3}$
1.65	$4.93\times10^{-1}\pm1.2\times10^{-2}$	$3.67\times10^{-1}\pm8.3\times10^{-3}$	$2.31\times10^{-1}\pm5.9\times10^{-3}$	$1.42\times10^{-1}\pm4.2\times10^{-3}$
1.75	$3.60\times10^{-1}\pm1.0\times10^{-2}$	$2.67\times10^{-1}\pm6.7\times10^{-3}$	$1.69\times10^{-1}\pm4.9\times10^{-3}$	$1.03\times10^{-1}\pm3.5\times10^{-3}$
1.85	$2.56\times10^{-1}\pm8.2\times10^{-3}$	$1.92\times10^{-1}\pm5.3\times10^{-3}$	$1.22\times10^{-1}\pm3.9\times10^{-3}$	$7.29\times10^{-2}\pm2.8\times10^{-3}$
1.95	$1.78\times10^{-1}\pm6.6\times10^{-3}$	$1.38\times10^{-1}\pm4.3\times10^{-3}$	$8.80\times10^{-2}\pm3.3\times10^{-3}$	$5.80\times10^{-2}\pm2.5\times10^{-3}$
2.05	$1.35\times10^{-1}\pm4.6\times10^{-3}$	$1.00\times10^{-1}\pm2.9\times10^{-3}$	$6.67\times10^{-2}\pm2.3\times10^{-3}$	$4.13\times10^{-2}\pm1.7\times10^{-3}$
2.15	$1.02\times10^{-1}\pm4.0\times10^{-3}$	$7.41\times10^{-2}\pm2.4\times10^{-3}$	$4.90\times10^{-2}\pm1.9\times10^{-3}$	$2.92\times10^{-2}\pm1.4\times10^{-3}$
2.25	$6.65\times10^{-2}\pm3.1\times10^{-3}$	$5.16\times10^{-2}\pm2.0\times10^{-3}$	$3.58\times10^{-2}\pm1.6\times10^{-3}$	$2.09\times10^{-2}\pm1.2\times10^{-3}$
2.35	$5.43\times10^{-2}\pm3.0\times10^{-3}$	$4.12\times10^{-2}\pm1.9\times10^{-3}$	$2.84\times10^{-2}\pm1.5\times10^{-3}$	$1.87\times10^{-2}\pm1.2\times10^{-3}$
2.45	$3.97\times10^{-2}\pm2.6\times10^{-3}$	$3.28\times10^{-2}\pm1.7\times10^{-3}$	$2.27\times10^{-2}\pm1.4\times10^{-3}$	$1.21\times10^{-2}\pm9.8\times10^{-4}$
2.55	$2.88\times10^{-2}\pm2.4\times10^{-3}$	$2.41\times10^{-2}\pm1.5\times10^{-3}$	$1.70\times10^{-2}\pm1.3\times10^{-3}$	$1.11\times10^{-2}\pm1.0\times10^{-3}$
2.65	$2.21\times10^{-2}\pm2.2\times10^{-3}$	$1.85\times10^{-2}\pm1.4\times10^{-3}$	$1.40\times10^{-2}\pm1.2\times10^{-3}$	$8.92\times10^{-3}\pm9.5\times10^{-4}$
2.75	$1.58\times10^{-2}\pm2.0\times10^{-3}$	$1.55\times10^{-2}\pm1.4\times10^{-3}$	$1.20\times10^{-2}\pm1.2\times10^{-3}$	$7.80\times10^{-3}\pm9.5\times10^{-4}$
2.85	$1.37\times10^{-2}\pm1.9\times10^{-3}$	$1.03\times10^{-2}\pm1.1\times10^{-3}$	$7.69\times10^{-3}\pm9.7\times10^{-4}$	$5.80\times10^{-3}\pm8.3\times10^{-4}$
2.95	$1.08\times10^{-2}\pm1.8\times10^{-3}$	$9.32\times10^{-3}\pm1.2\times10^{-3}$	$6.39\times10^{-3}\pm9.6\times10^{-4}$	$4.49\times10^{-3}\pm7.9\times10^{-4}$

TABLE XII. Invariant yields for π^+ at midrapidity in 50–60%, 60–70%, 70–80%, and 80–92% centrality bins, normalized to unit rapidity. Errors are statistical only.

p_T(GeV/c)	50–60%	60–70%	70–80%	80–92%
0.25	$4.10\times10^{1}\pm3.4\times10^{-1}$	$2.19\times10^{1}\pm1.9\times10^{-1}$	$1.03\times10^{1}\pm9.2\times10^{-2}$	$5.20\times10^{0}\pm5.0\times10^{-2}$
0.35	$2.17\times10^{1}\pm1.9\times10^{-1}$	$1.13\times10^{1}\pm1.0\times10^{-1}$	$5.27\times10^{0}\pm5.0\times10^{-2}$	$2.75\times10^{0}\pm2.8\times10^{-2}$
0.45	$1.24\times10^{1}\pm1.1\times10^{-1}$	$6.37\times10^{0}\pm6.0\times10^{-2}$	$2.95\times10^{0}\pm3.1\times10^{-2}$	$1.49\times10^{0}\pm1.8\times10^{-2}$
0.55	$7.20\times10^{0}\pm7.0\times10^{-2}$	$3.65\times10^{0}\pm3.8\times10^{-2}$	$1.62\times10^{0}\pm1.9\times10^{-2}$	$8.20\times10^{-1}\pm1.1\times10^{-2}$
0.65	$4.33\times10^{0}\pm4.7\times10^{-2}$	$2.18\times10^{0}\pm2.6\times10^{-2}$	$9.63\times10^{-1}\pm1.3\times10^{-2}$	$4.72\times10^{-1}\pm8.1\times10^{-3}$
0.75	$2.78\times10^{0}\pm3.4\times10^{-2}$	$1.36\times10^{0}\pm1.9\times10^{-2}$	$5.91\times10^{-1}\pm9.9\times10^{-3}$	$2.69\times10^{-1}\pm5.9\times10^{-3}$
0.85	$1.67\times10^{0}\pm2.3\times10^{-2}$	$8.36\times10^{-1}\pm1.3\times10^{-2}$	$3.53\times10^{-1}\pm7.1\times10^{-3}$	$1.63\times10^{-1}\pm4.4\times10^{-3}$
0.95	$1.11\times10^{0}\pm1.7\times10^{-2}$	$5.29\times10^{-1}\pm9.6\times10^{-3}$	$2.22\times10^{-1}\pm5.4\times10^{-3}$	$1.02\times10^{-1}\pm3.4\times10^{-3}$
1.05	$7.11\times10^{-1}\pm1.2\times10^{-2}$	$3.51\times10^{-1}\pm7.3\times10^{-3}$	$1.41\times10^{-1}\pm4.1\times10^{-3}$	$6.51\times10^{-2}\pm2.6\times10^{-3}$
1.15	$4.71\times10^{-1}\pm9.2\times10^{-3}$	$2.21\times10^{-1}\pm5.4\times10^{-3}$	$1.01\times10^{-1}\pm3.4\times10^{-3}$	$4.48\times10^{-2}\pm2.2\times10^{-3}$
1.25	$3.14\times10^{-1}\pm6.9\times10^{-3}$	$1.51\times10^{-1}\pm4.3\times10^{-3}$	$6.06\times10^{-2}\pm2.5\times10^{-3}$	$2.63\times10^{-2}\pm1.6\times10^{-3}$
1.35	$2.31\times10^{-1}\pm5.8\times10^{-3}$	$1.10\times10^{-1}\pm3.6\times10^{-3}$	$4.25\times10^{-2}\pm2.1\times10^{-3}$	$2.07\times10^{-2}\pm1.5\times10^{-3}$
1.45	$1.59\times10^{-1}\pm4.6\times10^{-3}$	$7.17\times10^{-2}\pm2.8\times10^{-3}$	$3.04\times10^{-2}\pm1.8\times10^{-3}$	$1.30\times10^{-2}\pm1.1\times10^{-3}$
1.55	$1.02\times10^{-1}\pm3.4\times10^{-3}$	$4.72\times10^{-2}\pm2.2\times10^{-3}$	$1.89\times10^{-2}\pm1.3\times10^{-3}$	$8.48\times10^{-3}\pm8.8\times10^{-4}$
1.65	$7.47\times10^{-2}\pm2.8\times10^{-3}$	$3.50\times10^{-2}\pm1.8\times10^{-3}$	$1.52\times10^{-2}\pm1.2\times10^{-3}$	$7.00\times10^{-3}\pm8.1\times10^{-4}$
1.75	$5.60\times10^{-2}\pm2.4\times10^{-3}$	$2.63\times10^{-2}\pm1.6\times10^{-3}$	$1.03\times10^{-2}\pm1.0\times10^{-3}$	$5.37\times10^{-3}\pm7.1\times10^{-4}$
1.85	$3.80\times10^{-2}\pm2.0\times10^{-3}$	$1.92\times10^{-2}\pm1.3\times10^{-3}$	$8.04\times10^{-3}\pm8.7\times10^{-4}$	$3.87\times10^{-3}\pm6.0\times10^{-4}$
1.95	$2.86\times10^{-2}\pm1.7\times10^{-3}$	$1.41\times10^{-2}\pm1.2\times10^{-3}$	$6.06\times10^{-3}\pm7.6\times10^{-4}$	$2.26\times10^{-3}\pm4.6\times10^{-4}$
2.05	$2.26\times10^{-2}\pm1.2\times10^{-3}$	$1.12\times10^{-2}\pm8.4\times10^{-4}$	$4.34\times10^{-3}\pm5.3\times10^{-4}$	$1.56\times10^{-3}\pm3.1\times10^{-4}$
2.15	$1.60\times10^{-2}\pm1.0\times10^{-3}$	$6.73\times10^{-3}\pm6.6\times10^{-4}$	$3.09\times10^{-3}\pm4.5\times10^{-4}$	$1.23\times10^{-3}\pm2.8\times10^{-4}$
2.25	$1.13\times10^{-2}\pm8.6\times10^{-4}$	$5.46\times10^{-3}\pm5.9\times10^{-4}$	$2.43\times10^{-3}\pm4.0\times10^{-4}$	$8.48\times10^{-4}\pm2.3\times10^{-4}$
2.35	$9.73\times10^{-3}\pm8.5\times10^{-4}$	$4.42\times10^{-3}\pm5.7\times10^{-4}$	$1.98\times10^{-3}\pm3.9\times10^{-4}$	$8.16\times10^{-4}\pm2.5\times10^{-4}$
2.45	$7.73\times10^{-3}\pm7.8\times10^{-4}$	$3.27\times10^{-3}\pm5.0\times10^{-4}$	$1.30\times10^{-3}\pm3.2\times10^{-4}$	$3.19\times10^{-4}\pm1.6\times10^{-4}$
2.55	$5.77\times10^{-3}\pm7.2\times10^{-4}$	$3.38\times10^{-3}\pm5.5\times10^{-4}$	$1.17\times10^{-3}\pm3.3\times10^{-4}$	$5.92\times10^{-4}\pm2.3\times10^{-4}$
2.65	$4.48\times10^{-3}\pm6.7\times10^{-4}$	$2.82\times10^{-3}\pm5.2\times10^{-4}$	$5.70\times10^{-4}\pm2.4\times10^{-4}$	$3.37\times10^{-4}\pm1.8\times10^{-4}$
2.75	$3.84\times10^{-3}\pm6.7\times10^{-4}$	$1.72\times10^{-3}\pm4.4\times10^{-4}$	$8.51\times10^{-4}\pm3.2\times10^{-4}$	$4.22\times10^{-4}\pm2.2\times10^{-4}$
2.85	$2.30\times10^{-3}\pm5.2\times10^{-4}$	$1.35\times10^{-3}\pm4.0\times10^{-4}$	$6.79\times10^{-4}\pm2.9\times10^{-4}$	$1.65\times10^{-4}\pm1.4\times10^{-4}$
2.95	$2.16\times10^{-3}\pm5.5\times10^{-4}$	$1.16\times10^{-3}\pm4.0\times10^{-4}$	$2.88\times10^{-4}\pm2.0\times10^{-4}$	$1.90\times10^{-4}\pm1.6\times10^{-4}$

TABLE XIII. Invariant yields for π^- at midrapidity in the minimum bias, 0–5%, 5–10%, and 10–15% centrality bins, normalized to unit rapidity. Errors are statistical only.

p_T (GeV/c)	Minimum bias	0–5%	5–10%	10–15%
0.25	$1.02\times10^{2}\pm7.9\times10^{-1}$	$3.15\times10^{2}\pm2.4\times10^{0}$	$2.71\times10^{2}\pm2.1\times10^{0}$	$2.27\times10^{2}\pm1.8\times10^{0}$
0.35	$5.92\times10^{1}\pm4.6\times10^{-1}$	$1.94\times10^{2}\pm1.5\times10^{0}$	$1.64\times10^{2}\pm1.3\times10^{0}$	$1.35\times10^{2}\pm1.1\times10^{0}$
0.45	$3.56\times10^{1}\pm2.9\times10^{-1}$	$1.19\times10^{2}\pm9.8\times10^{-1}$	$9.93\times10^{1}\pm8.2\times10^{-1}$	$8.18\times10^{1}\pm6.8\times10^{-1}$
0.55	$2.18\times10^{1}\pm1.9\times10^{-1}$	$7.37\times10^{1}\pm6.5\times10^{-1}$	$6.17\times10^{1}\pm5.4\times10^{-1}$	$5.04\times10^{1}\pm4.5\times10^{-1}$
0.65	$1.34\times10^{1}\pm1.2\times10^{-1}$	$4.57\times10^{1}\pm4.3\times10^{-1}$	$3.82\times10^{1}\pm3.6\times10^{-1}$	$3.15\times10^{1}\pm3.0\times10^{-1}$
0.75	$8.36\times10^{0}\pm8.2\times10^{-2}$	$2.86\times10^{1}\pm2.9\times10^{-1}$	$2.40\times10^{1}\pm2.4\times10^{-1}$	$1.96\times10^{1}\pm2.0\times10^{-1}$
0.85	$5.44\times10^{0}\pm5.7\times10^{-2}$	$1.86\times10^{1}\pm2.0\times10^{-1}$	$1.56\times10^{1}\pm1.7\times10^{-1}$	$1.28\times10^{1}\pm1.4\times10^{-1}$
0.95	$3.58\times10^{0}\pm4.1\times10^{-2}$	$1.22\times10^{1}\pm1.4\times10^{-1}$	$1.02\times10^{1}\pm1.2\times10^{-1}$	$8.47\times10^{0}\pm1.0\times10^{-1}$
1.05	$2.35\times10^{0}\pm2.8\times10^{-2}$	$8.02\times10^{0}\pm1.0\times10^{-1}$	$6.75\times10^{0}\pm8.7\times10^{-2}$	$5.57\times10^{0}\pm7.2\times10^{-2}$
1.15	$1.62\times10^{0}\pm2.1\times10^{-2}$	$5.55\times10^{0}\pm7.7\times10^{-2}$	$4.64\times10^{0}\pm6.5\times10^{-2}$	$3.83\times10^{0}\pm5.5\times10^{-2}$
1.25	$1.04\times10^{0}\pm1.4\times10^{-2}$	$3.53\times10^{0}\pm5.2\times10^{-2}$	$2.94\times10^{0}\pm4.4\times10^{-2}$	$2.46\times10^{0}\pm3.8\times10^{-2}$
1.35	$7.54\times10^{-1}\pm1.1\times10^{-2}$	$2.55\times10^{0}\pm4.1\times10^{-2}$	$2.19\times10^{0}\pm3.6\times10^{-2}$	$1.80\times10^{0}\pm3.0\times10^{-2}$
1.45	$5.07\times10^{-1}\pm7.6\times10^{-3}$	$1.71\times10^{0}\pm3.0\times10^{-2}$	$1.48\times10^{0}\pm2.7\times10^{-2}$	$1.22\times10^{0}\pm2.2\times10^{-2}$
1.55	$3.61\times10^{-1}\pm5.7\times10^{-3}$	$1.20\times10^{0}\pm2.3\times10^{-2}$	$1.02\times10^{0}\pm2.0\times10^{-2}$	$8.63\times10^{-1}\pm1.8\times10^{-2}$
1.65	$2.46\times10^{-1}\pm4.0\times10^{-3}$	$8.02\times10^{-1}\pm1.7\times10^{-2}$	$6.94\times10^{-1}\pm1.5\times10^{-2}$	$5.86\times10^{-1}\pm1.3\times10^{-2}$
1.75	$1.73\times10^{-1}\pm3.0\times10^{-3}$	$5.65\times10^{-1}\pm1.3\times10^{-2}$	$4.91\times10^{-1}\pm1.2\times10^{-2}$	$4.10\times10^{-1}\pm1.0\times10^{-2}$
1.85	$1.25\times10^{-1}\pm2.3\times10^{-3}$	$4.05\times10^{-1}\pm1.1\times10^{-2}$	$3.48\times10^{-1}\pm9.6\times10^{-3}$	$3.00\times10^{-1}\pm8.5\times10^{-3}$
1.95	$8.97\times10^{-2}\pm1.8\times10^{-3}$	$2.85\times10^{-1}\pm8.8\times10^{-3}$	$2.53\times10^{-1}\pm8.1\times10^{-3}$	$2.12\times10^{-1}\pm7.1\times10^{-3}$
2.05	$6.10\times10^{-2}\pm1.1\times10^{-3}$	$1.89\times10^{-1}\pm5.8\times10^{-3}$	$1.64\times10^{-1}\pm5.4\times10^{-3}$	$1.42\times10^{-1}\pm4.8\times10^{-3}$
2.15	$4.43\times10^{-2}\pm8.7\times10^{-4}$	$1.32\times10^{-1}\pm4.8\times10^{-3}$	$1.20\times10^{-1}\pm4.5\times10^{-3}$	$1.01\times10^{-1}\pm4.0\times10^{-3}$
2.25	$3.20\times10^{-2}\pm7.0\times10^{-4}$	$9.24\times10^{-2}\pm4.0\times10^{-3}$	$8.31\times10^{-2}\pm3.8\times10^{-3}$	$7.21\times10^{-2}\pm3.4\times10^{-3}$
2.35	$2.52\times10^{-2}\pm6.3\times10^{-4}$	$7.07\times10^{-2}\pm3.7\times10^{-3}$	$6.29\times10^{-2}\pm3.5\times10^{-3}$	$5.95\times10^{-2}\pm3.3\times10^{-3}$
2.45	$1.79\times10^{-2}\pm5.1\times10^{-4}$	$4.71\times10^{-2}\pm3.0\times10^{-3}$	$4.47\times10^{-2}\pm2.9\times10^{-3}$	$3.97\times10^{-2}\pm2.7\times10^{-3}$
2.55	$1.41\times10^{-2}\pm4.8\times10^{-4}$	$3.50\times10^{-2}\pm2.8\times10^{-3}$	$3.33\times10^{-2}\pm2.7\times10^{-3}$	$3.28\times10^{-2}\pm2.7\times10^{-3}$
2.65	$1.06\times10^{-2}\pm4.1\times10^{-4}$	$2.69\times10^{-2}\pm2.5\times10^{-3}$	$2.36\times10^{-2}\pm2.3\times10^{-3}$	$2.22\times10^{-2}\pm2.2\times10^{-3}$
2.75	$8.05\times10^{-3}\pm3.7\times10^{-4}$	$1.99\times10^{-2}\pm2.3\times10^{-3}$	$1.67\times10^{-2}\pm2.1\times10^{-3}$	$1.61\times10^{-2}\pm2.0\times10^{-3}$
2.85	$6.45\times10^{-3}\pm3.5\times10^{-4}$	$1.45\times10^{-2}\pm2.1\times10^{-3}$	$1.63\times10^{-2}\pm2.2\times10^{-3}$	$1.21\times10^{-2}\pm1.9\times10^{-3}$
2.95	$4.95\times10^{-3}\pm3.2\times10^{-4}$	$1.08\times10^{-2}\pm1.9\times10^{-3}$	$1.16\times10^{-2}\pm2.0\times10^{-3}$	$1.03\times10^{-2}\pm1.8\times10^{-3}$

TABLE XIV. Invariant yields for π^- at midrapidity in 15–20%, 20–30%, 30–40%, and 40–50% centrality bins, normalized to unit rapidity. Errors are statistical only.

p_T (GeV/c)	15–20%	20–30%	30–40%	40–50%
0.25	$1.95\times10^{2}\pm1.5\times10^{0}$	$1.51\times10^{2}\pm1.2\times10^{0}$	$1.02\times10^{2}\pm7.9\times10^{-1}$	$6.53\times10^{1}\pm5.1\times10^{-1}$
0.35	$1.13\times10^{2}\pm9.0\times10^{-1}$	$8.62\times10^{1}\pm6.8\times10^{-1}$	$5.68\times10^{1}\pm4.5\times10^{-1}$	$3.56\times10^{1}\pm2.8\times10^{-1}$
0.45	$6.86\times10^{1}\pm5.7\times10^{-1}$	$5.18\times10^{1}\pm4.3\times10^{-1}$	$3.36\times10^{1}\pm2.8\times10^{-1}$	$2.08\times10^{1}\pm1.7\times10^{-1}$
0.55	$4.22\times10^{1}\pm3.7\times10^{-1}$	$3.17\times10^{1}\pm2.8\times10^{-1}$	$2.04\times10^{1}\pm1.8\times10^{-1}$	$1.24\times10^{1}\pm1.1\times10^{-1}$
0.65	$2.61\times10^{1}\pm2.5\times10^{-1}$	$1.95\times10^{1}\pm1.8\times10^{-1}$	$1.26\times10^{1}\pm1.2\times10^{-1}$	$7.57\times10^{0}\pm7.4\times10^{-2}$
0.75	$1.63\times10^{1}\pm1.7\times10^{-1}$	$1.22\times10^{1}\pm1.2\times10^{-1}$	$7.81\times10^{0}\pm8.0\times10^{-2}$	$4.67\times10^{0}\pm4.9\times10^{-2}$
0.85	$1.06\times10^{1}\pm1.2\times10^{-1}$	$7.96\times10^{0}\pm8.7\times10^{-2}$	$5.06\times10^{0}\pm5.7\times10^{-2}$	$3.04\times10^{0}\pm3.5\times10^{-2}$
0.95	$7.01\times10^{0}\pm8.6\times10^{-2}$	$5.31\times10^{0}\pm6.3\times10^{-2}$	$3.37\times10^{0}\pm4.1\times10^{-2}$	$1.99\times10^{0}\pm2.6\times10^{-2}$
1.05	$4.68\times10^{0}\pm6.2\times10^{-2}$	$3.45\times10^{0}\pm4.4\times10^{-2}$	$2.18\times10^{0}\pm2.9\times10^{-2}$	$1.30\times10^{0}\pm1.8\times10^{-2}$
1.15	$3.19\times10^{0}\pm4.6\times10^{-2}$	$2.36\times10^{0}\pm3.3\times10^{-2}$	$1.52\times10^{0}\pm2.2\times10^{-2}$	$8.96\times10^{-1}\pm1.4\times10^{-2}$
1.25	$2.05\times10^{0}\pm3.2\times10^{-2}$	$1.55\times10^{0}\pm2.3\times10^{-2}$	$9.75\times10^{-1}\pm1.5\times10^{-2}$	$5.68\times10^{-1}\pm9.8\times10^{-3}$
1.35	$1.49\times10^{0}\pm2.6\times10^{-2}$	$1.10\times10^{0}\pm1.8\times10^{-2}$	$7.11\times10^{-1}\pm1.2\times10^{-2}$	$4.18\times10^{-1}\pm8.2\times10^{-3}$
1.45	$9.90\times10^{-1}\pm1.9\times10^{-2}$	$7.55\times10^{-1}\pm1.3\times10^{-2}$	$4.76\times10^{-1}\pm9.2\times10^{-3}$	$2.75\times10^{-1}\pm6.1\times10^{-3}$
1.55	$7.11\times10^{-1}\pm1.5\times10^{-2}$	$5.41\times10^{-1}\pm1.1\times10^{-2}$	$3.42\times10^{-1}\pm7.4\times10^{-3}$	$2.01\times10^{-1}\pm5.0\times10^{-3}$
1.65	$4.85\times10^{-1}\pm1.2\times10^{-2}$	$3.71\times10^{-1}\pm7.9\times10^{-3}$	$2.37\times10^{-1}\pm5.7\times10^{-3}$	$1.40\times10^{-1}\pm3.9\times10^{-3}$
1.75	$3.43\times10^{-1}\pm9.2\times10^{-3}$	$2.56\times10^{-1}\pm6.1\times10^{-3}$	$1.68\times10^{-1}\pm4.5\times10^{-3}$	$9.60\times10^{-2}\pm3.1\times10^{-3}$
1.85	$2.38\times10^{-1}\pm7.3\times10^{-3}$	$1.93\times10^{-1}\pm5.0\times10^{-3}$	$1.20\times10^{-1}\pm3.7\times10^{-3}$	$7.36\times10^{-2}\pm2.7\times10^{-3}$
1.95	$1.74\times10^{-1}\pm6.2\times10^{-3}$	$1.36\times10^{-1}\pm4.1\times10^{-3}$	$8.73\times10^{-2}\pm3.1\times10^{-3}$	$5.34\times10^{-2}\pm2.3\times10^{-3}$
2.05	$1.16\times10^{-1}\pm4.2\times10^{-3}$	$9.65\times10^{-2}\pm2.9\times10^{-3}$	$6.46\times10^{-2}\pm2.2\times10^{-3}$	$3.64\times10^{-2}\pm1.6\times10^{-3}$
2.15	$8.98\times10^{-2}\pm3.7\times10^{-3}$	$6.97\times10^{-2}\pm2.4\times10^{-3}$	$4.55\times10^{-2}\pm1.9\times10^{-3}$	$2.72\times10^{-2}\pm1.4\times10^{-3}$
2.25	$6.55\times10^{-2}\pm3.2\times10^{-3}$	$5.15\times10^{-2}\pm2.1\times10^{-3}$	$3.60\times10^{-2}\pm1.7\times10^{-3}$	$1.95\times10^{-2}\pm1.2\times10^{-3}$
2.35	$5.02\times10^{-2}\pm2.9\times10^{-3}$	$3.83\times10^{-2}\pm1.9\times10^{-3}$	$2.83\times10^{-2}\pm1.6\times10^{-3}$	$1.76\times10^{-2}\pm1.2\times10^{-3}$
2.45	$3.62\times10^{-2}\pm2.5\times10^{-3}$	$2.84\times10^{-2}\pm1.6\times10^{-3}$	$1.94\times10^{-2}\pm1.3\times10^{-3}$	$1.33\times10^{-2}\pm1.0\times10^{-3}$
2.55	$2.55\times10^{-2}\pm2.3\times10^{-3}$	$2.37\times10^{-2}\pm1.6\times10^{-3}$	$1.57\times10^{-2}\pm1.3\times10^{-3}$	$1.06\times10^{-2}\pm1.0\times10^{-3}$
2.65	$2.01\times10^{-2}\pm2.1\times10^{-3}$	$1.68\times10^{-2}\pm1.4\times10^{-3}$	$1.30\times10^{-2}\pm1.2\times10^{-3}$	$8.20\times10^{-3}\pm9.1\times10^{-4}$
2.75	$1.57\times10^{-2}\pm1.9\times10^{-3}$	$1.35\times10^{-2}\pm1.3\times10^{-3}$	$1.06\times10^{-2}\pm1.1\times10^{-3}$	$6.35\times10^{-3}\pm8.5\times10^{-4}$
2.85	$1.30\times10^{-2}\pm1.9\times10^{-3}$	$1.03\times10^{-2}\pm1.2\times10^{-3}$	$8.61\times10^{-3}\pm1.1\times10^{-3}$	$5.10\times10^{-3}\pm8.3\times10^{-4}$
2.95	$9.44\times10^{-3}\pm1.7\times10^{-3}$	$8.45\times10^{-3}\pm1.2\times10^{-3}$	$6.16\times10^{-3}\pm9.8\times10^{-4}$	$3.72\times10^{-3}\pm7.5\times10^{-4}$

TABLE XV. Invariant yields for π^- at midrapidity in 50–60%, 60–70%, 70–80%, and 80–92% centrality bins, normalized to unit rapidity. Errors are statistical only.

p_T (GeV/c)	50–60%	60–70%	70–80%	80–92%
0.25	$3.92\times10^{1}\pm3.1\times10^{-1}$	$2.07\times10^{1}\pm1.7\times10^{-1}$	$9.77\times10^{0}\pm8.2\times10^{-2}$	$5.03\times10^{0}\pm4.5\times10^{-2}$
0.35	$2.10\times10^{1}\pm1.7\times10^{-1}$	$1.09\times10^{1}\pm9.0\times10^{-2}$	$5.19\times10^{0}\pm4.6\times10^{-2}$	$2.67\times10^{0}\pm2.6\times10^{-2}$
0.45	$1.21\times10^{1}\pm1.0\times10^{-1}$	$6.21\times10^{0}\pm5.5\times10^{-2}$	$2.84\times10^{0}\pm2.8\times10^{-2}$	$1.45\times10^{0}\pm1.6\times10^{-2}$
0.55	$7.13\times10^{0}\pm6.6\times10^{-2}$	$3.59\times10^{0}\pm3.5\times10^{-2}$	$1.62\times10^{0}\pm1.8\times10^{-2}$	$8.13\times10^{-1}\pm1.1\times10^{-2}$
0.65	$4.30\times10^{0}\pm4.4\times10^{-2}$	$2.16\times10^{0}\pm2.4\times10^{-2}$	$9.32\times10^{-1}\pm1.2\times10^{-2}$	$4.54\times10^{-1}\pm7.3\times10^{-3}$
0.75	$2.61\times10^{0}\pm2.9\times10^{-2}$	$1.30\times10^{0}\pm1.6\times10^{-2}$	$5.61\times10^{-1}\pm8.6\times10^{-3}$	$2.70\times10^{-1}\pm5.3\times10^{-3}$
0.85	$1.68\times10^{0}\pm2.1\times10^{-2}$	$8.30\times10^{-1}\pm1.2\times10^{-2}$	$3.52\times10^{-1}\pm6.4\times10^{-3}$	$1.59\times10^{-1}\pm3.9\times10^{-3}$
0.95	$1.10\times10^{0}\pm1.5\times10^{-2}$	$5.26\times10^{-1}\pm8.7\times10^{-3}$	$2.27\times10^{-1}\pm5.0\times10^{-3}$	$1.07\times10^{-1}\pm3.2\times10^{-3}$
1.05	$7.13\times10^{-1}\pm1.1\times10^{-2}$	$3.45\times10^{-1}\pm6.6\times10^{-3}$	$1.41\times10^{-1}\pm3.8\times10^{-3}$	$6.63\times10^{-2}\pm2.4\times10^{-3}$
1.15	$4.88\times10^{-1}\pm8.8\times10^{-3}$	$2.32\times10^{-1}\pm5.2\times10^{-3}$	$9.75\times10^{-2}\pm3.1\times10^{-3}$	$4.46\times10^{-2}\pm2.0\times10^{-3}$
1.25	$3.12\times10^{-1}\pm6.3\times10^{-3}$	$1.47\times10^{-1}\pm3.8\times10^{-3}$	$6.31\times10^{-2}\pm2.4\times10^{-3}$	$2.65\times10^{-2}\pm1.5\times10^{-3}$
1.35	$2.29\times10^{-1}\pm5.3\times10^{-3}$	$1.05\times10^{-1}\pm3.2\times10^{-3}$	$4.17\times10^{-2}\pm1.9\times10^{-3}$	$2.02\times10^{-2}\pm1.3\times10^{-3}$
1.45	$1.51\times10^{-1}\pm4.1\times10^{-3}$	$7.32\times10^{-2}\pm2.6\times10^{-3}$	$2.81\times10^{-2}\pm1.6\times10^{-3}$	$1.28\times10^{-2}\pm1.0\times10^{-3}$
1.55	$1.10\times10^{-1}\pm3.4\times10^{-3}$	$5.15\times10^{-2}\pm2.2\times10^{-3}$	$2.11\times10^{-2}\pm1.4\times10^{-3}$	$9.27\times10^{-3}\pm8.8\times10^{-4}$
1.65	$7.11\times10^{-2}\pm2.6\times10^{-3}$	$3.83\times10^{-2}\pm1.8\times10^{-3}$	$1.53\times10^{-2}\pm1.1\times10^{-3}$	$6.56\times10^{-3}\pm7.3\times10^{-4}$
1.75	$5.38\times10^{-2}\pm2.2\times10^{-3}$	$2.51\times10^{-2}\pm1.4\times10^{-3}$	$1.08\times10^{-2}\pm9.5\times10^{-4}$	$5.14\times10^{-3}\pm6.5\times10^{-4}$
1.85	$4.00\times10^{-2}\pm1.9\times10^{-3}$	$1.87\times10^{-2}\pm1.2\times10^{-3}$	$8.06\times10^{-3}\pm8.2\times10^{-4}$	$3.51\times10^{-3}\pm5.3\times10^{-4}$
1.95	$2.88\times10^{-2}\pm1.6\times10^{-3}$	$1.30\times10^{-2}\pm1.1\times10^{-3}$	$6.03\times10^{-3}\pm7.3\times10^{-4}$	$2.70\times10^{-3}\pm4.8\times10^{-4}$
2.05	$2.04\times10^{-2}\pm1.2\times10^{-3}$	$8.63\times10^{-3}\pm7.4\times10^{-4}$	$4.23\times10^{-3}\pm5.3\times10^{-4}$	$1.40\times10^{-3}\pm3.0\times10^{-4}$
2.15	$1.53\times10^{-2}\pm1.0\times10^{-3}$	$6.88\times10^{-3}\pm6.7\times10^{-4}$	$3.17\times10^{-3}\pm4.6\times10^{-4}$	$1.25\times10^{-3}\pm2.9\times10^{-4}$
2.25	$1.08\times10^{-2}\pm8.8\times10^{-4}$	$4.71\times10^{-3}\pm5.7\times10^{-4}$	$1.89\times10^{-3}\pm3.7\times10^{-4}$	$8.66\times10^{-4}\pm2.5\times10^{-4}$
2.35	$8.95\times10^{-3}\pm8.4\times10^{-4}$	$4.42\times10^{-3}\pm5.8\times10^{-4}$	$1.96\times10^{-3}\pm4.0\times10^{-4}$	$6.65\times10^{-4}\pm2.3\times10^{-4}$
2.45	$7.17\times10^{-3}\pm7.6\times10^{-4}$	$3.04\times10^{-3}\pm4.9\times10^{-4}$	$1.17\times10^{-3}\pm3.1\times10^{-4}$	$5.61\times10^{-4}\pm2.1\times10^{-4}$
2.55	$5.72\times10^{-3}\pm7.5\times10^{-4}$	$2.96\times10^{-3}\pm5.3\times10^{-4}$	$1.16\times10^{-3}\pm3.4\times10^{-4}$	$3.79\times10^{-4}\pm1.9\times10^{-4}$
2.65	$4.94\times10^{-3}\pm7.1\times10^{-4}$	$2.21\times10^{-3}\pm4.7\times10^{-4}$	$8.05\times10^{-4}\pm2.9\times10^{-4}$	$4.14\times10^{-4}\pm2.0\times10^{-4}$
2.75	$3.43\times10^{-3}\pm6.3\times10^{-4}$	$1.54\times10^{-3}\pm4.2\times10^{-4}$	$3.78\times10^{-4}\pm2.1\times10^{-4}$	$3.34\times10^{-4}\pm2.0\times10^{-4}$
2.85	$2.67\times10^{-3}\pm6.0\times10^{-4}$	$1.24\times10^{-3}\pm4.1\times10^{-4}$	$2.87\times10^{-4}\pm2.0\times10^{-4}$	$2.85\times10^{-4}\pm2.0\times10^{-4}$
2.95	$1.73\times10^{-3}\pm5.1\times10^{-4}$	$1.25\times10^{-3}\pm4.3\times10^{-4}$	$6.75\times10^{-4}\pm3.2\times10^{-4}$	$2.04\times10^{-4}\pm1.8\times10^{-4}$

TABLE XVI. Invariant yields for K^+ at midrapidity in the minimum bias, 0–5%, 5–10%, and 10–15% centrality bins, normalized to unit rapidity. Errors are statistical only.

p_T (GeV/c)	Minimum bias	0–5%	5–10%	10–15%
0.45	$5.46\times10^{0}\pm1.1\times10^{-1}$	$1.83\times10^{1}\pm3.9\times10^{-1}$	$1.50\times10^{1}\pm3.3\times10^{-1}$	$1.29\times10^{1}\pm2.8\times10^{-1}$
0.55	$4.28\times10^{0}\pm7.8\times10^{-2}$	$1.48\times10^{1}\pm2.9\times10^{-1}$	$1.20\times10^{1}\pm2.4\times10^{-1}$	$9.88\times10^{0}\pm2.0\times10^{-1}$
0.65	$3.11\times10^{0}\pm5.4\times10^{-2}$	$1.05\times10^{1}\pm2.0\times10^{-1}$	$8.75\times10^{0}\pm1.7\times10^{-1}$	$7.38\times10^{0}\pm1.4\times10^{-1}$
0.75	$2.27\times10^{0}\pm3.9\times10^{-2}$	$7.97\times10^{0}\pm1.5\times10^{-1}$	$6.48\times10^{0}\pm1.2\times10^{-1}$	$5.39\times10^{0}\pm1.0\times10^{-1}$
0.85	$1.69\times10^{0}\pm3.0\times10^{-2}$	$5.96\times10^{0}\pm1.2\times10^{-1}$	$4.81\times10^{0}\pm9.5\times10^{-2}$	$4.02\times10^{0}\pm8.1\times10^{-2}$
0.95	$1.20\times10^{0}\pm2.2\times10^{-2}$	$4.19\times10^{0}\pm8.5\times10^{-2}$	$3.47\times10^{0}\pm7.2\times10^{-2}$	$2.91\times10^{0}\pm6.1\times10^{-2}$
1.05	$9.06\times10^{-1}\pm1.7\times10^{-2}$	$3.20\times10^{0}\pm6.8\times10^{-2}$	$2.61\times10^{0}\pm5.7\times10^{-2}$	$2.21\times10^{0}\pm5.0\times10^{-2}$
1.15	$6.57\times10^{-1}\pm1.3\times10^{-2}$	$2.31\times10^{0}\pm5.2\times10^{-2}$	$1.91\times10^{0}\pm4.4\times10^{-2}$	$1.63\times10^{0}\pm3.9\times10^{-2}$
1.25	$4.55\times10^{-1}\pm8.9\times10^{-3}$	$1.64\times10^{0}\pm3.9\times10^{-2}$	$1.32\times10^{0}\pm3.3\times10^{-2}$	$1.14\times10^{0}\pm2.9\times10^{-2}$
1.35	$3.24\times10^{-1}\pm6.5\times10^{-3}$	$1.13\times10^{0}\pm2.9\times10^{-2}$	$9.63\times10^{-1}\pm2.5\times10^{-2}$	$7.88\times10^{-1}\pm2.2\times10^{-2}$
1.45	$2.43\times10^{-1}\pm5.1\times10^{-3}$	$8.52\times10^{-1}\pm2.4\times10^{-2}$	$7.33\times10^{-1}\pm2.1\times10^{-2}$	$6.05\times10^{-1}\pm1.8\times10^{-2}$
1.55	$1.76\times10^{-1}\pm3.8\times10^{-3}$	$6.03\times10^{-1}\pm1.8\times10^{-2}$	$5.16\times10^{-1}\pm1.6\times10^{-2}$	$4.33\times10^{-1}\pm1.4\times10^{-2}$
1.65	$1.27\times10^{-1}\pm2.9\times10^{-3}$	$4.43\times10^{-1}\pm1.5\times10^{-2}$	$3.84\times10^{-1}\pm1.3\times10^{-2}$	$3.04\times10^{-1}\pm1.1\times10^{-2}$
1.75	$9.47\times10^{-2}\pm2.3\times10^{-3}$	$3.61\times10^{-1}\pm1.3\times10^{-2}$	$2.76\times10^{-1}\pm1.1\times10^{-2}$	$2.28\times10^{-1}\pm9.3\times10^{-3}$
1.85	$7.24\times10^{-2}\pm1.8\times10^{-3}$	$2.64\times10^{-1}\pm1.0\times10^{-2}$	$2.17\times10^{-1}\pm9.0\times10^{-3}$	$1.72\times10^{-1}\pm7.7\times10^{-3}$
1.95	$5.67\times10^{-2}\pm1.5\times10^{-3}$	$2.12\times10^{-1}\pm9.1\times10^{-3}$	$1.67\times10^{-1}\pm7.8\times10^{-3}$	$1.37\times10^{-1}\pm6.9\times10^{-3}$

TABLE XVII. Invariant yields for K^+ at midrapidity in 15–20%, 20–30%, 30–40%, and 40–50% centrality bins, normalized to unit rapidity. Errors are statistical only.

p_T (GeV/c)	15–20%	20–30%	30–40%	40–50%
0.45	$1.04\times10^{1}\pm2.3\times10^{-1}$	$7.81\times10^{0}\pm1.7\times10^{-1}$	$5.11\times10^{0}\pm1.1\times10^{-1}$	$3.28\times10^{0}\pm7.8\times10^{-2}$
0.55	$8.30\times10^{0}\pm1.7\times10^{-1}$	$6.22\times10^{0}\pm1.2\times10^{-1}$	$4.06\times10^{0}\pm8.3\times10^{-2}$	$2.43\times10^{0}\pm5.3\times10^{-2}$
0.65	$6.20\times10^{0}\pm1.2\times10^{-1}$	$4.51\times10^{0}\pm8.5\times10^{-2}$	$2.89\times10^{0}\pm5.7\times10^{-2}$	$1.78\times10^{0}\pm3.8\times10^{-2}$
0.75	$4.46\times10^{0}\pm8.8\times10^{-2}$	$3.31\times10^{0}\pm6.2\times10^{-2}$	$2.07\times10^{0}\pm4.1\times10^{-2}$	$1.26\times10^{0}\pm2.7\times10^{-2}$
0.85	$3.36\times10^{0}\pm7.0\times10^{-2}$	$2.50\times10^{0}\pm4.9\times10^{-2}$	$1.60\times10^{0}\pm3.3\times10^{-2}$	$9.00\times10^{-1}\pm2.1\times10^{-2}$
0.95	$2.40\times10^{0}\pm5.2\times10^{-2}$	$1.74\times10^{0}\pm3.6\times10^{-2}$	$1.08\times10^{0}\pm2.4\times10^{-2}$	$6.46\times10^{-1}\pm1.6\times10^{-2}$
1.05	$1.81\times10^{0}\pm4.2\times10^{-2}$	$1.31\times10^{0}\pm2.8\times10^{-2}$	$8.42\times10^{-1}\pm2.0\times10^{-2}$	$4.82\times10^{-1}\pm1.3\times10^{-2}$
1.15	$1.29\times10^{0}\pm3.2\times10^{-2}$	$9.60\times10^{-1}\pm2.2\times10^{-2}$	$6.01\times10^{-1}\pm1.5\times10^{-2}$	$3.48\times10^{-1}\pm1.0\times10^{-2}$
1.25	$8.82\times10^{-1}\pm2.4\times10^{-2}$	$6.54\times10^{-1}\pm1.6\times10^{-2}$	$4.22\times10^{-1}\pm1.1\times10^{-2}$	$2.34\times10^{-1}\pm7.5\times10^{-3}$
1.35	$6.60\times10^{-1}\pm1.9\times10^{-2}$	$4.68\times10^{-1}\pm1.2\times10^{-2}$	$2.99\times10^{-1}\pm8.7\times10^{-3}$	$1.70\times10^{-1}\pm5.9\times10^{-3}$
1.45	$4.91\times10^{-1}\pm1.5\times10^{-2}$	$3.50\times10^{-1}\pm9.9\times10^{-3}$	$2.22\times10^{-1}\pm7.2\times10^{-3}$	$1.20\times10^{-1}\pm4.8\times10^{-3}$
1.55	$3.55\times10^{-1}\pm1.2\times10^{-2}$	$2.59\times10^{-1}\pm7.9\times10^{-3}$	$1.63\times10^{-1}\pm5.8\times10^{-3}$	$9.25\times10^{-2}\pm4.0\times10^{-3}$
1.65	$2.62\times10^{-1}\pm1.0\times10^{-2}$	$1.88\times10^{-1}\pm6.3\times10^{-3}$	$1.14\times10^{-1}\pm4.6\times10^{-3}$	$6.22\times10^{-2}\pm3.1\times10^{-3}$
1.75	$1.92\times10^{-1}\pm8.3\times10^{-3}$	$1.34\times10^{-1}\pm5.1\times10^{-3}$	$8.52\times10^{-2}\pm3.8\times10^{-3}$	$4.81\times10^{-2}\pm2.7\times10^{-3}$
1.85	$1.48\times10^{-1}\pm7.0\times10^{-3}$	$1.04\times10^{-1}\pm4.2\times10^{-3}$	$6.58\times10^{-2}\pm3.2\times10^{-3}$	$3.66\times10^{-2}\pm2.3\times10^{-3}$
1.95	$1.14\times10^{-1}\pm6.1\times10^{-3}$	$8.21\times10^{-2}\pm3.7\times10^{-3}$	$4.87\times10^{-2}\pm2.7\times10^{-3}$	$2.91\times10^{-2}\pm2.0\times10^{-3}$

TABLE XVIII. Invariant yields for K^+ at midrapidity in 50–60%, 60–70%, 70–80%, and 80–92% centrality bins, normalized to unit rapidity. Errors are statistical only.

p_T (GeV/c)	50–60%	60–70%	70–80%	80–92%
0.45	$1.93\times10^{0}\pm5.0\times10^{-2}$	$9.56\times10^{-1}\pm2.9\times10^{-2}$	$4.06\times10^{-1}\pm1.7\times10^{-2}$	$1.88\times10^{-1}\pm1.1\times10^{-2}$
0.55	$1.36\times10^{0}\pm3.3\times10^{-2}$	$6.72\times10^{-1}\pm2.0\times10^{-2}$	$2.89\times10^{-1}\pm1.2\times10^{-2}$	$1.48\times10^{-1}\pm7.8\times10^{-3}$
0.65	$1.01\times10^{0}\pm2.4\times10^{-2}$	$4.81\times10^{-1}\pm1.4\times10^{-2}$	$1.88\times10^{-1}\pm8.0\times10^{-3}$	$1.02\times10^{-1}\pm5.6\times10^{-3}$
0.75	$6.82\times10^{-1}\pm1.7\times10^{-2}$	$3.40\times10^{-1}\pm1.1\times10^{-2}$	$1.24\times10^{-1}\pm5.8\times10^{-3}$	$5.88\times10^{-2}\pm3.9\times10^{-3}$
0.85	$4.77\times10^{-1}\pm1.3\times10^{-2}$	$2.33\times10^{-1}\pm8.1\times10^{-3}$	$9.39\times10^{-2}\pm4.8\times10^{-3}$	$3.87\times10^{-2}\pm3.0\times10^{-3}$
0.95	$3.51\times10^{-1}\pm1.0\times10^{-2}$	$1.69\times10^{-1}\pm6.4\times10^{-3}$	$5.66\times10^{-2}\pm3.5\times10^{-3}$	$2.99\times10^{-2}\pm2.5\times10^{-3}$
1.05	$2.54\times10^{-1}\pm8.2\times10^{-3}$	$1.19\times10^{-1}\pm5.1\times10^{-3}$	$4.40\times10^{-2}\pm3.0\times10^{-3}$	$2.07\times10^{-2}\pm2.0\times10^{-3}$
1.15	$1.80\times10^{-1}\pm6.4\times10^{-3}$	$7.84\times10^{-2}\pm3.9\times10^{-3}$	$3.12\times10^{-2}\pm2.4\times10^{-3}$	$1.64\times10^{-2}\pm1.7\times10^{-3}$
1.25	$1.28\times10^{-1}\pm5.1\times10^{-3}$	$5.43\times10^{-2}\pm3.1\times10^{-3}$	$2.07\times10^{-2}\pm1.9\times10^{-3}$	$7.94\times10^{-3}\pm1.1\times10^{-3}$
1.35	$8.53\times10^{-2}\pm3.9\times10^{-3}$	$3.85\times10^{-2}\pm2.5\times10^{-3}$	$1.38\times10^{-2}\pm1.5\times10^{-3}$	$6.53\times10^{-3}\pm9.9\times10^{-4}$
1.45	$6.40\times10^{-2}\pm3.3\times10^{-3}$	$2.94\times10^{-2}\pm2.1\times10^{-3}$	$1.34\times10^{-2}\pm1.4\times10^{-3}$	$5.70\times10^{-3}\pm9.2\times10^{-4}$
1.55	$4.73\times10^{-2}\pm2.7\times10^{-3}$	$2.10\times10^{-2}\pm1.8\times10^{-3}$	$6.85\times10^{-3}\pm1.0\times10^{-3}$	$2.84\times10^{-3}\pm6.4\times10^{-4}$
1.65	$3.39\times10^{-2}\pm2.2\times10^{-3}$	$1.60\times10^{-2}\pm1.5\times10^{-3}$	$5.62\times10^{-3}\pm8.9\times10^{-4}$	$2.67\times10^{-3}\pm6.1\times10^{-4}$
1.75	$2.31\times10^{-2}\pm1.8\times10^{-3}$	$1.04\times10^{-2}\pm1.2\times10^{-3}$	$4.19\times10^{-3}\pm7.6\times10^{-4}$	$1.85\times10^{-3}\pm5.0\times10^{-4}$
1.85	$1.72\times10^{-2}\pm1.5\times10^{-3}$	$8.75\times10^{-3}\pm1.1\times10^{-3}$	$3.39\times10^{-3}\pm6.7\times10^{-4}$	$2.09\times10^{-3}\pm5.2\times10^{-4}$
1.95	$1.53\times10^{-2}\pm1.4\times10^{-3}$	$6.49\times10^{-3}\pm9.2\times10^{-4}$	$2.75\times10^{-3}\pm6.1\times10^{-4}$	$1.16\times10^{-3}\pm3.9\times10^{-4}$

TABLE XIX. Invariant yields for K^- at midrapidity in the minimum bias, 0–5%, 5–10%, and 10–15% centrality bins, normalized to unit rapidity. Errors are statistical only.

p_T (GeV/c)	Minimum bias	0–5%	5–10%	10–15%
0.45	$4.87\times10^{0}\pm9.3\times10^{-2}$	$1.64\times10^{1}\pm3.4\times10^{-1}$	$1.36\times10^{1}\pm2.8\times10^{-1}$	$1.12\times10^{1}\pm2.4\times10^{-1}$
0.55	$3.88\times10^{0}\pm6.7\times10^{-2}$	$1.31\times10^{1}\pm2.4\times10^{-1}$	$1.09\times10^{1}\pm2.0\times10^{-1}$	$8.91\times10^{0}\pm1.7\times10^{-1}$
0.65	$2.96\times10^{0}\pm4.9\times10^{-2}$	$1.01\times10^{1}\pm1.8\times10^{-1}$	$8.57\times10^{0}\pm1.5\times10^{-1}$	$6.94\times10^{0}\pm1.3\times10^{-1}$
0.75	$2.20\times10^{0}\pm3.6\times10^{-2}$	$7.69\times10^{0}\pm1.4\times10^{-1}$	$6.27\times10^{0}\pm1.1\times10^{-1}$	$5.14\times10^{0}\pm9.5\times10^{-2}$
0.85	$1.59\times10^{0}\pm2.6\times10^{-2}$	$5.61\times10^{0}\pm1.0\times10^{-1}$	$4.55\times10^{0}\pm8.4\times10^{-2}$	$3.82\times10^{0}\pm7.2\times10^{-2}$
0.95	$1.14\times10^{0}\pm1.9\times10^{-2}$	$4.11\times10^{0}\pm7.7\times10^{-2}$	$3.36\times10^{0}\pm6.5\times10^{-2}$	$2.76\times10^{0}\pm5.4\times10^{-2}$
1.05	$8.50\times10^{-1}\pm1.5\times10^{-2}$	$3.03\times10^{0}\pm6.0\times10^{-2}$	$2.53\times10^{0}\pm5.2\times10^{-2}$	$2.05\times10^{0}\pm4.3\times10^{-2}$
1.15	$5.96\times10^{-1}\pm1.0\times10^{-2}$	$2.11\times10^{0}\pm4.4\times10^{-2}$	$1.79\times10^{0}\pm3.8\times10^{-2}$	$1.44\times10^{0}\pm3.2\times10^{-2}$
1.25	$4.29\times10^{-1}\pm7.8\times10^{-3}$	$1.53\times10^{0}\pm3.4\times10^{-2}$	$1.25\times10^{0}\pm2.9\times10^{-2}$	$1.05\times10^{0}\pm2.5\times10^{-2}$
1.35	$3.23\times10^{-1}\pm6.2\times10^{-3}$	$1.15\times10^{0}\pm2.8\times10^{-2}$	$9.45\times10^{-1}\pm2.4\times10^{-2}$	$8.03\times10^{-1}\pm2.1\times10^{-2}$
1.45	$2.32\times10^{-1}\pm4.6\times10^{-3}$	$8.42\times10^{-1}\pm2.2\times10^{-2}$	$6.97\times10^{-1}\pm1.9\times10^{-2}$	$5.62\times10^{-1}\pm1.6\times10^{-2}$
1.55	$1.67\times10^{-1}\pm3.4\times10^{-3}$	$5.86\times10^{-1}\pm1.7\times10^{-2}$	$4.97\times10^{-1}\pm1.5\times10^{-2}$	$4.16\times10^{-1}\pm1.3\times10^{-2}$
1.65	$1.21\times10^{-1}\pm2.6\times10^{-3}$	$4.42\times10^{-1}\pm1.4\times10^{-2}$	$3.82\times10^{-1}\pm1.2\times10^{-2}$	$2.93\times10^{-1}\pm1.0\times10^{-2}$
1.75	$8.78\times10^{-2}\pm2.0\times10^{-3}$	$3.17\times10^{-1}\pm1.1\times10^{-2}$	$2.64\times10^{-1}\pm9.6\times10^{-3}$	$2.11\times10^{-1}\pm8.2\times10^{-3}$
1.85	$6.76\times10^{-2}\pm1.6\times10^{-3}$	$2.52\times10^{-1}\pm9.4\times10^{-3}$	$2.10\times10^{-1}\pm8.4\times10^{-3}$	$1.61\times10^{-1}\pm7.0\times10^{-3}$
1.95	$5.10\times10^{-2}\pm1.3\times10^{-3}$	$1.83\times10^{-1}\pm7.9\times10^{-3}$	$1.53\times10^{-1}\pm7.1\times10^{-3}$	$1.22\times10^{-1}\pm6.1\times10^{-3}$

TABLE XX. Invariant yields for K^- at midrapidity in 15–20%, 20–30%, 30–40%, and 40–50% centrality bins, normalized to unit rapidity. Errors are statistical only.

p_T (GeV/c)	15–20%	20–30%	30–40%	40–50%
0.45	$9.24\times10^{0}\pm2.0\times10^{-1}$	$7.05\times10^{0}\pm1.5\times10^{-1}$	$4.60\times10^{0}\pm9.9\times10^{-2}$	$2.79\times10^{0}\pm6.4\times10^{-2}$
0.55	$7.61\times10^{0}\pm1.5\times10^{-1}$	$5.62\times10^{0}\pm1.0\times10^{-1}$	$3.68\times10^{0}\pm7.1\times10^{-2}$	$2.25\times10^{0}\pm4.7\times10^{-2}$
0.65	$5.78\times10^{0}\pm1.1\times10^{-1}$	$4.29\times10^{0}\pm7.7\times10^{-2}$	$2.74\times10^{0}\pm5.1\times10^{-2}$	$1.69\times10^{0}\pm3.4\times10^{-2}$
0.75	$4.33\times10^{0}\pm8.1\times10^{-2}$	$3.22\times10^{0}\pm5.8\times10^{-2}$	$2.04\times10^{0}\pm3.8\times10^{-2}$	$1.19\times10^{0}\pm2.5\times10^{-2}$
0.85	$3.13\times10^{0}\pm6.0\times10^{-2}$	$2.29\times10^{0}\pm4.2\times10^{-2}$	$1.49\times10^{0}\pm2.9\times10^{-2}$	$8.47\times10^{-1}\pm1.8\times10^{-2}$
0.95	$2.23\times10^{0}\pm4.5\times10^{-2}$	$1.61\times10^{0}\pm3.1\times10^{-2}$	$1.04\times10^{0}\pm2.1\times10^{-2}$	$6.04\times10^{-1}\pm1.4\times10^{-2}$
1.05	$1.70\times10^{0}\pm3.7\times10^{-2}$	$1.21\times10^{0}\pm2.5\times10^{-2}$	$7.74\times10^{-1}\pm1.7\times10^{-2}$	$4.49\times10^{-1}\pm1.1\times10^{-2}$
1.15	$1.17\times10^{0}\pm2.7\times10^{-2}$	$8.78\times10^{-1}\pm1.9\times10^{-2}$	$5.39\times10^{-1}\pm1.3\times10^{-2}$	$3.11\times10^{-1}\pm8.4\times10^{-3}$
1.25	$8.58\times10^{-1}\pm2.1\times10^{-2}$	$6.29\times10^{-1}\pm1.4\times10^{-2}$	$3.87\times10^{-1}\pm9.9\times10^{-3}$	$2.25\times10^{-1}\pm6.8\times10^{-3}$
1.35	$6.26\times10^{-1}\pm1.7\times10^{-2}$	$4.76\times10^{-1}\pm1.2\times10^{-2}$	$2.97\times10^{-1}\pm8.3\times10^{-3}$	$1.64\times10^{-1}\pm5.5\times10^{-3}$
1.45	$4.56\times10^{-1}\pm1.4\times10^{-2}$	$3.41\times10^{-1}\pm9.2\times10^{-3}$	$2.09\times10^{-1}\pm6.5\times10^{-3}$	$1.21\times10^{-1}\pm4.5\times10^{-3}$
1.55	$3.25\times10^{-1}\pm1.1\times10^{-2}$	$2.50\times10^{-1}\pm7.3\times10^{-3}$	$1.43\times10^{-1}\pm5.0\times10^{-3}$	$8.71\times10^{-2}\pm3.7\times10^{-3}$
1.65	$2.36\times10^{-1}\pm8.9\times10^{-3}$	$1.72\times10^{-1}\pm5.7\times10^{-3}$	$1.07\times10^{-1}\pm4.2\times10^{-3}$	$6.17\times10^{-2}\pm3.0\times10^{-3}$
1.75	$1.83\times10^{-1}\pm7.4\times10^{-3}$	$1.29\times10^{-1}\pm4.6\times10^{-3}$	$7.79\times10^{-2}\pm3.4\times10^{-3}$	$4.42\times10^{-2}\pm2.4\times10^{-3}$
1.85	$1.29\times10^{-1}\pm6.0\times10^{-3}$	$1.01\times10^{-1}\pm4.0\times10^{-3}$	$5.84\times10^{-2}\pm2.8\times10^{-3}$	$3.24\times10^{-2}\pm2.0\times10^{-3}$
1.95	$1.05\times10^{-1}\pm5.5\times10^{-3}$	$7.67\times10^{-2}\pm3.4\times10^{-3}$	$4.31\times10^{-2}\pm2.4\times10^{-3}$	$2.46\times10^{-2}\pm1.8\times10^{-3}$

TABLE XXI. Invariant yields for K^- at midrapidity in 50–60%, 60–70%, 70–80%, and 80–92% centrality bins, normalized to unit rapidity. Errors are statistical only.

p_T (GeV/c)	50–60%	60–70%	70–80%	80–92%
0.45	$1.73\times10^{0}\pm4.3\times10^{-2}$	$8.11\times10^{-1}\pm2.5\times10^{-2}$	$3.89\times10^{-1}\pm1.6\times10^{-2}$	$1.82\times10^{-1}\pm9.9\times10^{-3}$
0.55	$1.25\times10^{0}\pm2.9\times10^{-2}$	$6.37\times10^{-1}\pm1.8\times10^{-2}$	$2.80\times10^{-1}\pm1.1\times10^{-2}$	$1.37\times10^{-1}\pm7.1\times10^{-3}$
0.65	$9.30\times10^{-1}\pm2.1\times10^{-2}$	$4.43\times10^{-1}\pm1.3\times10^{-2}$	$1.83\times10^{-1}\pm7.5\times10^{-3}$	$1.02\times10^{-1}\pm5.4\times10^{-3}$
0.75	$6.59\times10^{-1}\pm1.6\times10^{-2}$	$3.16\times10^{-1}\pm9.5\times10^{-3}$	$1.40\times10^{-1}\pm5.9\times10^{-3}$	$6.21\times10^{-2}\pm3.8\times10^{-3}$
0.85	$4.65\times10^{-1}\pm1.2\times10^{-2}$	$2.31\times10^{-1}\pm7.4\times10^{-3}$	$8.42\times10^{-2}\pm4.2\times10^{-3}$	$3.81\times10^{-2}\pm2.7\times10^{-3}$
0.95	$3.22\times10^{-1}\pm9.0\times10^{-3}$	$1.56\times10^{-1}\pm5.7\times10^{-3}$	$5.67\times10^{-2}\pm3.2\times10^{-3}$	$2.57\times10^{-2}\pm2.1\times10^{-3}$
1.05	$2.32\times10^{-1}\pm7.2\times10^{-3}$	$1.09\times10^{-1}\pm4.5\times10^{-3}$	$4.26\times10^{-2}\pm2.7\times10^{-3}$	$1.73\times10^{-2}\pm1.7\times10^{-3}$
1.15	$1.60\times10^{-1}\pm5.5\times10^{-3}$	$7.06\times10^{-2}\pm3.4\times10^{-3}$	$2.98\times10^{-2}\pm2.1\times10^{-3}$	$1.32\times10^{-2}\pm1.4\times10^{-3}$
1.25	$1.15\times10^{-1}\pm4.4\times10^{-3}$	$5.72\times10^{-2}\pm2.9\times10^{-3}$	$1.84\times10^{-2}\pm1.6\times10^{-3}$	$9.79\times10^{-3}\pm1.2\times10^{-3}$
1.35	$8.85\times10^{-2}\pm3.8\times10^{-3}$	$3.67\times10^{-2}\pm2.3\times10^{-3}$	$1.59\times10^{-2}\pm1.5\times10^{-3}$	$7.78\times10^{-3}\pm1.0\times10^{-3}$
1.45	$5.83\times10^{-2}\pm3.0\times10^{-3}$	$2.38\times10^{-2}\pm1.8\times10^{-3}$	$1.12\times10^{-2}\pm1.2\times10^{-3}$	$4.22\times10^{-3}\pm7.5\times10^{-4}$
1.55	$4.60\times10^{-2}\pm2.5\times10^{-3}$	$1.89\times10^{-2}\pm1.6\times10^{-3}$	$7.86\times10^{-3}\pm1.0\times10^{-3}$	$3.92\times10^{-3}\pm7.1\times10^{-4}$
1.65	$3.05\times10^{-2}\pm2.0\times10^{-3}$	$1.53\times10^{-2}\pm1.4\times10^{-3}$	$6.44\times10^{-3}\pm9.0\times10^{-4}$	$2.92\times10^{-3}\pm6.0\times10^{-4}$
1.75	$2.07\times10^{-2}\pm1.6\times10^{-3}$	$1.00\times10^{-2}\pm1.1\times10^{-3}$	$3.65\times10^{-3}\pm6.6\times10^{-4}$	$1.27\times10^{-3}\pm3.9\times10^{-4}$
1.85	$1.84\times10^{-2}\pm1.5\times10^{-3}$	$7.82\times10^{-3}\pm9.5\times10^{-4}$	$2.81\times10^{-3}\pm5.8\times10^{-4}$	$1.44\times10^{-3}\pm4.1\times10^{-4}$
1.95	$1.46\times10^{-2}\pm1.3\times10^{-3}$	$6.14\times10^{-3}\pm8.6\times10^{-4}$	$2.12\times10^{-3}\pm5.1\times10^{-4}$	$1.30\times10^{-3}\pm4.0\times10^{-4}$

TABLE XXII. Invariant yields for protons at midrapidity in the minimum bias, 0–5%, 5–10%, and 10–15% centrality bins, normalized to unit rapidity. Errors are statistical only.

p_T (GeV/c)	Minimum bias	0–5%	5–10%	10–15%
0.65	$9.51\times10^{-1}\pm2.7\times10^{-2}$	$2.90\times10^{0}\pm9.3\times10^{-2}$	$2.44\times10^{0}\pm8.0\times10^{-2}$	$2.09\times10^{0}\pm6.9\times10^{-2}$
0.75	$8.47\times10^{-1}\pm2.4\times10^{-2}$	$2.65\times10^{0}\pm8.5\times10^{-2}$	$2.24\times10^{0}\pm7.3\times10^{-2}$	$1.87\times10^{0}\pm6.2\times10^{-2}$
0.85	$7.08\times10^{-1}\pm2.0\times10^{-2}$	$2.28\times10^{0}\pm7.3\times10^{-2}$	$1.91\times10^{0}\pm6.3\times10^{-2}$	$1.60\times10^{0}\pm5.3\times10^{-2}$
0.95	$6.06\times10^{-1}\pm1.8\times10^{-2}$	$2.00\times10^{0}\pm6.6\times10^{-2}$	$1.66\times10^{0}\pm5.5\times10^{-2}$	$1.41\times10^{0}\pm4.8\times10^{-2}$
1.05	$5.05\times10^{-1}\pm1.5\times10^{-2}$	$1.68\times10^{0}\pm5.7\times10^{-2}$	$1.43\times10^{0}\pm4.9\times10^{-2}$	$1.16\times10^{0}\pm4.1\times10^{-2}$
1.15	$4.23\times10^{-1}\pm1.3\times10^{-2}$	$1.46\times10^{0}\pm5.1\times10^{-2}$	$1.22\times10^{0}\pm4.3\times10^{-2}$	$9.85\times10^{-1}\pm3.6\times10^{-2}$
1.25	$3.30\times10^{-1}\pm1.0\times10^{-2}$	$1.16\times10^{0}\pm4.2\times10^{-2}$	$9.51\times10^{-1}\pm3.5\times10^{-2}$	$7.92\times10^{-1}\pm3.0\times10^{-2}$
1.35	$2.71\times10^{-1}\pm8.8\times10^{-3}$	$9.72\times10^{-1}\pm3.7\times10^{-2}$	$7.96\times10^{-1}\pm3.1\times10^{-2}$	$6.55\times10^{-1}\pm2.6\times10^{-2}$
1.45	$2.04\times10^{-1}\pm6.7\times10^{-3}$	$7.42\times10^{-1}\pm2.9\times10^{-2}$	$6.09\times10^{-1}\pm2.5\times10^{-2}$	$5.07\times10^{-1}\pm2.1\times10^{-2}$
1.55	$1.68\times10^{-1}\pm5.8\times10^{-3}$	$6.05\times10^{-1}\pm2.5\times10^{-2}$	$5.08\times10^{-1}\pm2.2\times10^{-2}$	$4.21\times10^{-1}\pm1.9\times10^{-2}$
1.65	$1.25\times10^{-1}\pm4.4\times10^{-3}$	$4.55\times10^{-1}\pm2.0\times10^{-2}$	$3.77\times10^{-1}\pm1.7\times10^{-2}$	$3.02\times10^{-1}\pm1.4\times10^{-2}$
1.75	$9.38\times10^{-2}\pm3.4\times10^{-3}$	$3.51\times10^{-1}\pm1.6\times10^{-2}$	$2.76\times10^{-1}\pm1.4\times10^{-2}$	$2.29\times10^{-1}\pm1.2\times10^{-2}$
1.85	$7.50\times10^{-2}\pm2.8\times10^{-3}$	$2.85\times10^{-1}\pm1.4\times10^{-2}$	$2.28\times10^{-1}\pm1.2\times10^{-2}$	$1.79\times10^{-1}\pm1.0\times10^{-2}$
1.95	$5.37\times10^{-2}\pm2.1\times10^{-3}$	$1.99\times10^{-1}\pm1.1\times10^{-2}$	$1.61\times10^{-1}\pm9.3\times10^{-3}$	$1.36\times10^{-1}\pm8.2\times10^{-3}$
2.10	$3.71\times10^{-2}\pm9.4\times10^{-4}$	$1.35\times10^{-1}\pm5.0\times10^{-3}$	$1.12\times10^{-1}\pm4.4\times10^{-3}$	$9.18\times10^{-2}\pm3.8\times10^{-3}$
2.30	$2.15\times10^{-2}\pm5.9\times10^{-4}$	$7.69\times10^{-2}\pm3.5\times10^{-3}$	$6.73\times10^{-2}\pm3.2\times10^{-3}$	$5.39\times10^{-2}\pm2.7\times10^{-3}$
2.50	$1.21\times10^{-2}\pm4.2\times10^{-4}$	$4.39\times10^{-2}\pm2.5\times10^{-3}$	$3.67\times10^{-2}\pm2.2\times10^{-3}$	$3.05\times10^{-2}\pm2.0\times10^{-3}$
2.70	$7.26\times10^{-3}\pm2.8\times10^{-4}$	$2.44\times10^{-2}\pm1.8\times10^{-3}$	$2.27\times10^{-2}\pm1.7\times10^{-3}$	$1.78\times10^{-2}\pm1.5\times10^{-3}$
2.90	$4.17\times10^{-3}\pm1.9\times10^{-4}$	$1.54\times10^{-2}\pm1.4\times10^{-3}$	$1.16\times10^{-2}\pm1.2\times10^{-3}$	$1.04\times10^{-2}\pm1.1\times10^{-3}$
3.25	$1.70\times10^{-3}\pm8.3\times10^{-5}$	$5.98\times10^{-3}\pm5.5\times10^{-4}$	$5.17\times10^{-3}\pm5.0\times10^{-4}$	$4.04\times10^{-3}\pm4.3\times10^{-4}$
3.75	$5.79\times10^{-4}\pm4.4\times10^{-5}$	$2.05\times10^{-3}\pm3.1\times10^{-4}$	$1.68\times10^{-3}\pm2.8\times10^{-4}$	$1.45\times10^{-3}\pm2.5\times10^{-4}$
4.25	$2.21\times10^{-4}\pm2.7\times10^{-5}$	$8.96\times10^{-4}\pm2.2\times10^{-4}$	$7.04\times10^{-4}\pm1.9\times10^{-4}$	$4.70\times10^{-4}\pm1.5\times10^{-4}$

TABLE XXIII. Invariant yields for protons at midrapidity in 15–20%, 20–30%, 30–40%, and 40–50% centrality bins, normalized to unit rapidity. Errors are statistical only.

p_T (GeV/c)	15–20%	20–30%	30–40%	40–50%
0.65	$1.76\times10^{0}\pm6.0\times10^{-2}$	$1.37\times10^{0}\pm4.4\times10^{-2}$	$9.68\times10^{-1}\pm3.2\times10^{-2}$	$6.31\times10^{-1}\pm2.2\times10^{-2}$
0.75	$1.59\times10^{0}\pm5.4\times10^{-2}$	$1.24\times10^{0}\pm4.0\times10^{-2}$	$8.52\times10^{-1}\pm2.9\times10^{-2}$	$5.39\times10^{-1}\pm1.9\times10^{-2}$
0.85	$1.34\times10^{0}\pm4.6\times10^{-2}$	$1.02\times10^{0}\pm3.3\times10^{-2}$	$7.06\times10^{-1}\pm2.4\times10^{-2}$	$4.33\times10^{-1}\pm1.6\times10^{-2}$
0.95	$1.16\times10^{0}\pm4.1\times10^{-2}$	$8.90\times10^{-1}\pm2.9\times10^{-2}$	$5.79\times10^{-1}\pm2.0\times10^{-2}$	$3.60\times10^{-1}\pm1.4\times10^{-2}$
1.05	$9.75\times10^{-1}\pm3.5\times10^{-2}$	$7.41\times10^{-1}\pm2.5\times10^{-2}$	$4.83\times10^{-1}\pm1.7\times10^{-2}$	$2.96\times10^{-1}\pm1.2\times10^{-2}$
1.15	$8.38\times10^{-1}\pm3.1\times10^{-2}$	$6.27\times10^{-1}\pm2.2\times10^{-2}$	$3.93\times10^{-1}\pm1.5\times10^{-2}$	$2.33\times10^{-1}\pm9.7\times10^{-3}$
1.25	$6.47\times10^{-1}\pm2.5\times10^{-2}$	$4.83\times10^{-1}\pm1.8\times10^{-2}$	$3.09\times10^{-1}\pm1.2\times10^{-2}$	$1.77\times10^{-1}\pm7.9\times10^{-3}$
1.35	$5.35\times10^{-1}\pm2.2\times10^{-2}$	$3.93\times10^{-1}\pm1.5\times10^{-2}$	$2.46\times10^{-1}\pm1.0\times10^{-2}$	$1.40\times10^{-1}\pm6.7\times10^{-3}$
1.45	$4.04\times10^{-1}\pm1.8\times10^{-2}$	$2.90\times10^{-1}\pm1.2\times10^{-2}$	$1.89\times10^{-1}\pm8.3\times10^{-3}$	$1.05\times10^{-1}\pm5.4\times10^{-3}$
1.55	$3.33\times10^{-1}\pm1.6\times10^{-2}$	$2.42\times10^{-1}\pm1.0\times10^{-2}$	$1.49\times10^{-1}\pm7.1\times10^{-3}$	$8.39\times10^{-2}\pm4.7\times10^{-3}$
1.65	$2.60\times10^{-1}\pm1.3\times10^{-2}$	$1.80\times10^{-1}\pm8.1\times10^{-3}$	$1.10\times10^{-1}\pm5.6\times10^{-3}$	$6.02\times10^{-2}\pm3.7\times10^{-3}$
1.75	$1.86\times10^{-1}\pm1.0\times10^{-2}$	$1.36\times10^{-1}\pm6.6\times10^{-3}$	$8.52\times10^{-2}\pm4.7\times10^{-3}$	$4.64\times10^{-2}\pm3.1\times10^{-3}$
1.85	$1.51\times10^{-1}\pm8.9\times10^{-3}$	$1.08\times10^{-1}\pm5.7\times10^{-3}$	$6.68\times10^{-2}\pm4.0\times10^{-3}$	$3.64\times10^{-2}\pm2.7\times10^{-3}$
1.95	$1.06\times10^{-1}\pm6.9\times10^{-3}$	$7.98\times10^{-2}\pm4.5\times10^{-3}$	$4.72\times10^{-2}\pm3.2\times10^{-3}$	$2.53\times10^{-2}\pm2.1\times10^{-3}$
2.10	$7.41\times10^{-2}\pm3.3\times10^{-3}$	$5.63\times10^{-2}\pm2.1\times10^{-3}$	$3.32\times10^{-2}\pm1.5\times10^{-3}$	$1.82\times10^{-2}\pm1.0\times10^{-3}$
2.30	$4.46\times10^{-2}\pm2.4\times10^{-3}$	$3.19\times10^{-2}\pm1.5\times10^{-3}$	$1.96\times10^{-2}\pm1.1\times10^{-3}$	$9.61\times10^{-3}\pm7.2\times10^{-4}$
2.50	$2.52\times10^{-2}\pm1.7\times10^{-3}$	$1.79\times10^{-2}\pm1.1\times10^{-3}$	$1.07\times10^{-2}\pm7.8\times10^{-4}$	$5.83\times10^{-3}\pm5.5\times10^{-4}$
2.70	$1.55\times10^{-2}\pm1.3\times10^{-3}$	$1.08\times10^{-2}\pm8.0\times10^{-4}$	$6.78\times10^{-3}\pm6.1\times10^{-4}$	$3.73\times10^{-3}\pm4.4\times10^{-4}$
2.90	$8.35\times10^{-3}\pm9.5\times10^{-4}$	$6.05\times10^{-3}\pm5.8\times10^{-4}$	$4.10\times10^{-3}\pm4.7\times10^{-4}$	$2.20\times10^{-3}\pm3.3\times10^{-4}$
3.25	$3.51\times10^{-3}\pm3.9\times10^{-4}$	$2.54\times10^{-3}\pm2.4\times10^{-4}$	$1.64\times10^{-3}\pm1.9\times10^{-4}$	$8.36\times10^{-4}\pm1.3\times10^{-4}$
3.75	$1.18\times10^{-3}\pm2.2\times10^{-4}$	$8.20\times10^{-4}\pm1.3\times10^{-4}$	$5.66\times10^{-4}\pm1.1\times10^{-4}$	$3.25\times10^{-4}\pm7.8\times10^{-5}$
4.25	$4.64\times10^{-4}\pm1.4\times10^{-4}$	$3.07\times10^{-4}\pm8.3\times10^{-5}$	$1.93\times10^{-4}\pm6.4\times10^{-5}$	$1.07\times10^{-4}\pm4.7\times10^{-5}$

TABLE XXIV. Invariant yields for protons at midrapidity in 50–60%, 60–70%, 70–80%, and 80–92% centrality bins, normalized to unit rapidity. Errors are statistical only.

p_T (GeV/c)	50–60%	60–70%	70–80%	80–92%
0.65	$3.82\times10^{-1}\pm1.5\times10^{-2}$	$2.04\times10^{-1}\pm9.7\times10^{-3}$	$9.09\times10^{-2}\pm5.9\times10^{-3}$	$4.96\times10^{-2}\pm4.2\times10^{-3}$
0.75	$3.25\times10^{-1}\pm1.3\times10^{-2}$	$1.65\times10^{-1}\pm8.1\times10^{-3}$	$7.04\times10^{-2}\pm4.9\times10^{-3}$	$3.79\times10^{-2}\pm3.4\times10^{-3}$
0.85	$2.60\times10^{-1}\pm1.1\times10^{-2}$	$1.27\times10^{-1}\pm6.5\times10^{-3}$	$5.41\times10^{-2}\pm4.0\times10^{-3}$	$2.62\times10^{-2}\pm2.7\times10^{-3}$
0.95	$2.08\times10^{-1}\pm9.1\times10^{-3}$	$1.00\times10^{-1}\pm5.5\times10^{-3}$	$4.11\times10^{-2}\pm3.3\times10^{-3}$	$2.06\times10^{-2}\pm2.3\times10^{-3}$
1.05	$1.61\times10^{-1}\pm7.5\times10^{-3}$	$7.43\times10^{-2}\pm4.5\times10^{-3}$	$3.14\times10^{-2}\pm2.8\times10^{-3}$	$1.54\times10^{-2}\pm1.9\times10^{-3}$
1.15	$1.24\times10^{-1}\pm6.2\times10^{-3}$	$5.88\times10^{-2}\pm3.8\times10^{-3}$	$2.40\times10^{-2}\pm2.3\times10^{-3}$	$8.08\times10^{-3}\pm1.3\times10^{-3}$
1.25	$9.20\times10^{-2}\pm5.0\times10^{-3}$	$3.98\times10^{-2}\pm3.0\times10^{-3}$	$1.68\times10^{-2}\pm1.9\times10^{-3}$	$6.94\times10^{-3}\pm1.2\times10^{-3}$
1.35	$7.34\times10^{-2}\pm4.4\times10^{-3}$	$3.41\times10^{-2}\pm2.7\times10^{-3}$	$1.21\times10^{-2}\pm1.6\times10^{-3}$	$5.84\times10^{-3}\pm1.1\times10^{-3}$
1.45	$4.98\times10^{-2}\pm3.3\times10^{-3}$	$2.41\times10^{-2}\pm2.2\times10^{-3}$	$9.02\times10^{-3}\pm1.3\times10^{-3}$	$3.61\times10^{-3}\pm8.1\times10^{-4}$
1.55	$4.43\times10^{-2}\pm3.1\times10^{-3}$	$1.69\times10^{-2}\pm1.8\times10^{-3}$	$6.98\times10^{-3}\pm1.1\times10^{-3}$	$2.19\times10^{-3}\pm6.3\times10^{-4}$
1.65	$3.29\times10^{-2}\pm2.6\times10^{-3}$	$1.30\times10^{-2}\pm1.5\times10^{-3}$	$4.57\times10^{-3}\pm9.0\times10^{-4}$	$1.36\times10^{-3}\pm4.8\times10^{-4}$
1.75	$2.37\times10^{-2}\pm2.1\times10^{-3}$	$9.76\times10^{-3}\pm1.3\times10^{-3}$	$3.81\times10^{-3}\pm8.0\times10^{-4}$	$1.40\times10^{-3}\pm4.8\times10^{-4}$
1.85	$1.80\times10^{-2}\pm1.8\times10^{-3}$	$7.16\times10^{-3}\pm1.1\times10^{-3}$	$2.56\times10^{-3}\pm6.6\times10^{-4}$	$8.09\times10^{-4}\pm3.7\times10^{-4}$
1.95	$1.24\times10^{-2}\pm1.4\times10^{-3}$	$5.34\times10^{-3}\pm9.1\times10^{-4}$	$2.04\times10^{-3}\pm5.7\times10^{-4}$	$8.46\times10^{-4}\pm3.6\times10^{-4}$
2.10	$9.33\times10^{-3}\pm7.2\times10^{-4}$	$3.47\times10^{-3}\pm4.2\times10^{-4}$	$1.34\times10^{-3}\pm2.7\times10^{-4}$	$4.08\times10^{-4}\pm1.5\times10^{-4}$
2.30	$4.86\times10^{-3}\pm5.0\times10^{-4}$	$2.28\times10^{-3}\pm3.4\times10^{-4}$	$6.06\times10^{-4}\pm1.8\times10^{-4}$	$2.88\times10^{-4}\pm1.2\times10^{-4}$
2.50	$3.01\times10^{-3}\pm3.9\times10^{-4}$	$9.91\times10^{-4}\pm2.2\times10^{-4}$	$3.91\times10^{-4}\pm1.4\times10^{-4}$	$2.19\times10^{-4}\pm1.0\times10^{-4}$
2.70	$1.66\times10^{-3}\pm2.9\times10^{-4}$	$6.31\times10^{-4}\pm1.7\times10^{-4}$	$2.37\times10^{-4}\pm1.1\times10^{-4}$	$1.12\times10^{-4}\pm7.4\times10^{-5}$
2.90	$1.03\times10^{-3}\pm2.2\times10^{-4}$	$4.62\times10^{-4}\pm1.5\times10^{-4}$	$1.06\times10^{-4}\pm7.3\times10^{-5}$	$3.22\times10^{-5}\pm4.0\times10^{-5}$
3.25	$4.01\times10^{-4}\pm8.7\times10^{-5}$	$1.66\times10^{-4}\pm5.5\times10^{-5}$	$6.73\times10^{-5}\pm3.6\times10^{-5}$	$2.02\times10^{-5}\pm2.0\times10^{-5}$
3.75	$1.45\times10^{-4}\pm5.2\times10^{-5}$	$5.72\times10^{-5}\pm3.2\times10^{-5}$	$2.13\times10^{-5}\pm1.9\times10^{-5}$	$2.89\times10^{-6}\pm7.7\times10^{-6}$
4.25	$4.94\times10^{-5}\pm3.2\times10^{-5}$	$2.40\times10^{-5}\pm2.2\times10^{-5}$	$1.02\times10^{-5}\pm1.5\times10^{-5}$	$2.43\times10^{-6}\pm6.7\times10^{-6}$

TABLE XXV. Invariant yields for antiprotons at midrapidity in the minimum bias, 0–5%, 5–10%, and 10–15% centrality bins, normalized to unit rapidity. Errors are statistical only.

p_T (GeV/c)	Minimum bias	0–5%	5–10%	10–15%
0.65	$6.73\times10^{-1}\pm2.0\times10^{-2}$	$2.00\times10^{0}\pm6.8\times10^{-2}$	$1.73\times10^{0}\pm6.0\times10^{-2}$	$1.48\times10^{0}\pm5.2\times10^{-2}$
0.75	$6.16\times10^{-1}\pm1.8\times10^{-2}$	$1.89\times10^{0}\pm6.2\times10^{-2}$	$1.61\times10^{0}\pm5.4\times10^{-2}$	$1.34\times10^{0}\pm4.6\times10^{-2}$
0.85	$5.28\times10^{-1}\pm1.5\times10^{-2}$	$1.67\times10^{0}\pm5.4\times10^{-2}$	$1.42\times10^{0}\pm4.7\times10^{-2}$	$1.19\times10^{0}\pm4.1\times10^{-2}$
0.95	$4.52\times10^{-1}\pm1.3\times10^{-2}$	$1.47\times10^{0}\pm4.8\times10^{-2}$	$1.25\times10^{0}\pm4.2\times10^{-2}$	$1.05\times10^{0}\pm3.6\times10^{-2}$
1.05	$3.65\times10^{-1}\pm1.1\times10^{-2}$	$1.21\times10^{0}\pm4.1\times10^{-2}$	$1.04\times10^{0}\pm3.6\times10^{-2}$	$8.82\times10^{-1}\pm3.1\times10^{-2}$
1.15	$3.19\times10^{-1}\pm9.7\times10^{-3}$	$1.10\times10^{0}\pm3.9\times10^{-2}$	$9.28\times10^{-1}\pm3.4\times10^{-2}$	$7.39\times10^{-1}\pm2.8\times10^{-2}$
1.25	$2.53\times10^{-1}\pm7.9\times10^{-3}$	$8.90\times10^{-1}\pm3.3\times10^{-2}$	$7.47\times10^{-1}\pm2.8\times10^{-2}$	$6.15\times10^{-1}\pm2.4\times10^{-2}$
1.35	$2.01\times10^{-1}\pm6.5\times10^{-3}$	$7.24\times10^{-1}\pm2.8\times10^{-2}$	$6.08\times10^{-1}\pm2.4\times10^{-2}$	$4.88\times10^{-1}\pm2.0\times10^{-2}$
1.45	$1.66\times10^{-1}\pm5.6\times10^{-3}$	$6.12\times10^{-1}\pm2.5\times10^{-2}$	$5.01\times10^{-1}\pm2.1\times10^{-2}$	$4.09\times10^{-1}\pm1.8\times10^{-2}$
1.55	$1.22\times10^{-1}\pm4.1\times10^{-3}$	$4.43\times10^{-1}\pm1.9\times10^{-2}$	$3.69\times10^{-1}\pm1.6\times10^{-2}$	$3.04\times10^{-1}\pm1.4\times10^{-2}$
1.65	$9.61\times10^{-2}\pm3.4\times10^{-3}$	$3.46\times10^{-1}\pm1.6\times10^{-2}$	$3.00\times10^{-1}\pm1.4\times10^{-2}$	$2.43\times10^{-1}\pm1.2\times10^{-2}$
1.75	$7.19\times10^{-2}\pm2.7\times10^{-3}$	$2.70\times10^{-1}\pm1.3\times10^{-2}$	$2.17\times10^{-1}\pm1.1\times10^{-2}$	$1.84\times10^{-1}\pm9.9\times10^{-3}$
1.85	$5.57\times10^{-2}\pm2.1\times10^{-3}$	$2.07\times10^{-1}\pm1.1\times10^{-2}$	$1.68\times10^{-1}\pm9.5\times10^{-3}$	$1.45\times10^{-1}\pm8.4\times10^{-3}$
1.95	$4.04\times10^{-2}\pm1.7\times10^{-3}$	$1.53\times10^{-1}\pm9.2\times10^{-3}$	$1.19\times10^{-1}\pm7.7\times10^{-3}$	$1.02\times10^{-1}\pm6.9\times10^{-3}$
2.10	$2.61\times10^{-2}\pm7.3\times10^{-4}$	$9.75\times10^{-2}\pm4.2\times10^{-3}$	$7.95\times10^{-2}\pm3.7\times10^{-3}$	$6.64\times10^{-2}\pm3.2\times10^{-3}$
2.30	$1.54\times10^{-2}\pm4.8\times10^{-4}$	$5.99\times10^{-2}\pm3.1\times10^{-3}$	$4.59\times10^{-2}\pm2.7\times10^{-3}$	$3.87\times10^{-2}\pm2.4\times10^{-3}$
2.50	$8.66\times10^{-3}\pm3.4\times10^{-4}$	$3.16\times10^{-2}\pm2.2\times10^{-3}$	$2.69\times10^{-2}\pm2.0\times10^{-3}$	$2.29\times10^{-2}\pm1.8\times10^{-3}$
2.70	$4.79\times10^{-3}\pm2.2\times10^{-4}$	$1.79\times10^{-2}\pm1.6\times10^{-3}$	$1.46\times10^{-2}\pm1.4\times10^{-3}$	$1.19\times10^{-2}\pm1.2\times10^{-3}$
2.90	$2.91\times10^{-3}\pm1.6\times10^{-4}$	$1.04\times10^{-2}\pm1.2\times10^{-3}$	$8.43\times10^{-3}\pm1.1\times10^{-3}$	$7.25\times10^{-3}\pm9.6\times10^{-4}$
3.25	$1.16\times10^{-3}\pm6.7\times10^{-5}$	$4.14\times10^{-3}\pm4.7\times10^{-4}$	$3.55\times10^{-3}\pm4.3\times10^{-4}$	$3.02\times10^{-3}\pm3.8\times10^{-4}$
3.75	$3.71\times10^{-4}\pm3.5\times10^{-5}$	$1.29\times10^{-3}\pm2.5\times10^{-4}$	$1.30\times10^{-3}\pm2.5\times10^{-4}$	$1.09\times10^{-3}\pm2.2\times10^{-4}$
4.25	$1.35\times10^{-4}\pm2.1\times10^{-5}$	$5.44\times10^{-4}\pm1.7\times10^{-4}$	$3.98\times10^{-4}\pm1.4\times10^{-4}$	$3.57\times10^{-4}\pm1.3\times10^{-4}$

TABLE XXVI. Invariant yields for antiprotons at midrapidity in 15–20%, 20–30%, 30–40%, and 40–50% centrality bins, normalized to unit rapidity. Errors are statistical only.

p_T (GeV/c)	15–20%	20–30%	30–40%	40–50%
0.65	$1.25\times10^{0}\pm4.5\times10^{-2}$	$9.68\times10^{-1}\pm3.2\times10^{-2}$	$6.98\times10^{-1}\pm2.4\times10^{-2}$	$4.51\times10^{-1}\pm1.7\times10^{-2}$
0.75	$1.16\times10^{0}\pm4.1\times10^{-2}$	$8.94\times10^{-1}\pm2.9\times10^{-2}$	$6.35\times10^{-1}\pm2.2\times10^{-2}$	$4.06\times10^{-1}\pm1.5\times10^{-2}$
0.85	$1.02\times10^{0}\pm3.5\times10^{-2}$	$7.83\times10^{-1}\pm2.5\times10^{-2}$	$5.21\times10^{-1}\pm1.8\times10^{-2}$	$3.37\times10^{-1}\pm1.3\times10^{-2}$
0.95	$8.85\times10^{-1}\pm3.1\times10^{-2}$	$6.61\times10^{-1}\pm2.2\times10^{-2}$	$4.42\times10^{-1}\pm1.5\times10^{-2}$	$2.70\times10^{-1}\pm1.0\times10^{-2}$
1.05	$7.26\times10^{-1}\pm2.6\times10^{-2}$	$5.25\times10^{-1}\pm1.8\times10^{-2}$	$3.54\times10^{-1}\pm1.3\times10^{-2}$	$2.05\times10^{-1}\pm8.4\times10^{-3}$
1.15	$6.43\times10^{-1}\pm2.5\times10^{-2}$	$4.63\times10^{-1}\pm1.6\times10^{-2}$	$2.99\times10^{-1}\pm1.2\times10^{-2}$	$1.79\times10^{-1}\pm7.7\times10^{-3}$
1.25	$4.99\times10^{-1}\pm2.0\times10^{-2}$	$3.65\times10^{-1}\pm1.4\times10^{-2}$	$2.33\times10^{-1}\pm9.5\times10^{-3}$	$1.37\times10^{-1}\pm6.4\times10^{-3}$
1.35	$4.11\times10^{-1}\pm1.8\times10^{-2}$	$2.88\times10^{-1}\pm1.1\times10^{-2}$	$1.80\times10^{-1}\pm7.8\times10^{-3}$	$1.03\times10^{-1}\pm5.2\times10^{-3}$
1.45	$3.40\times10^{-1}\pm1.5\times10^{-2}$	$2.41\times10^{-1}\pm1.0\times10^{-2}$	$1.42\times10^{-1}\pm6.7\times10^{-3}$	$8.40\times10^{-2}\pm4.6\times10^{-3}$
1.55	$2.45\times10^{-1}\pm1.2\times10^{-2}$	$1.77\times10^{-1}\pm7.8\times10^{-3}$	$1.06\times10^{-1}\pm5.3\times10^{-3}$	$6.14\times10^{-2}\pm3.6\times10^{-3}$
1.65	$1.90\times10^{-1}\pm1.0\times10^{-2}$	$1.43\times10^{-1}\pm6.7\times10^{-3}$	$8.53\times10^{-2}\pm4.6\times10^{-3}$	$4.50\times10^{-2}\pm3.0\times10^{-3}$
1.75	$1.45\times10^{-1}\pm8.4\times10^{-3}$	$1.02\times10^{-1}\pm5.2\times10^{-3}$	$6.32\times10^{-2}\pm3.8\times10^{-3}$	$3.49\times10^{-2}\pm2.6\times10^{-3}$
1.85	$1.20\times10^{-1}\pm7.4\times10^{-3}$	$7.97\times10^{-2}\pm4.4\times10^{-3}$	$4.76\times10^{-2}\pm3.1\times10^{-3}$	$2.66\times10^{-2}\pm2.2\times10^{-3}$
1.95	$8.41\times10^{-2}\pm6.0\times10^{-3}$	$5.83\times10^{-2}\pm3.7\times10^{-3}$	$3.56\times10^{-2}\pm2.7\times10^{-3}$	$1.84\times10^{-2}\pm1.8\times10^{-3}$
2.10	$5.22\times10^{-2}\pm2.8\times10^{-3}$	$3.90\times10^{-2}\pm1.7\times10^{-3}$	$2.30\times10^{-2}\pm1.3\times10^{-3}$	$1.27\times10^{-2}\pm8.8\times10^{-4}$
2.30	$3.19\times10^{-2}\pm2.1\times10^{-3}$	$2.24\times10^{-2}\pm1.2\times10^{-3}$	$1.34\times10^{-2}\pm9.2\times10^{-4}$	$7.39\times10^{-3}\pm6.6\times10^{-4}$
2.50	$1.83\times10^{-2}\pm1.5\times10^{-3}$	$1.22\times10^{-2}\pm9.0\times10^{-4}$	$7.78\times10^{-3}\pm6.9\times10^{-4}$	$4.11\times10^{-3}\pm4.8\times10^{-4}$
2.70	$9.79\times10^{-3}\pm1.1\times10^{-3}$	$6.65\times10^{-3}\pm6.4\times10^{-4}$	$4.66\times10^{-3}\pm5.2\times10^{-4}$	$2.30\times10^{-3}\pm3.5\times10^{-4}$
2.90	$6.28\times10^{-3}\pm8.7\times10^{-4}$	$4.33\times10^{-3}\pm5.1\times10^{-4}$	$2.57\times10^{-3}\pm3.8\times10^{-4}$	$1.67\times10^{-3}\pm3.0\times10^{-4}$
3.25	$2.55\times10^{-3}\pm3.4\times10^{-4}$	$1.64\times10^{-3}\pm2.0\times10^{-4}$	$1.05\times10^{-3}\pm1.5\times10^{-4}$	$5.44\times10^{-4}\pm1.1\times10^{-4}$
3.75	$8.03\times10^{-4}\pm1.9\times10^{-4}$	$5.39\times10^{-4}\pm1.1\times10^{-4}$	$2.59\times10^{-4}\pm7.3\times10^{-5}$	$1.75\times10^{-4}\pm5.9\times10^{-5}$
4.25	$2.92\times10^{-4}\pm1.2\times10^{-4}$	$1.74\times10^{-4}\pm6.3\times10^{-5}$	$1.12\times10^{-4}\pm4.9\times10^{-5}$	$5.56\times10^{-5}\pm3.5\times10^{-5}$

TABLE XXVII. Invariant yields for antiprotons at midrapidity in 50–60%, 60–70%, 70–80%, and 80–92% centrality bins, normalized to unit rapidity. Errors are statistical only.

p_T (GeV/c)	50–60%	60–70%	70–80%	80–92%
0.65	$2.84\times10^{-1}\pm1.2\times10^{-2}$	$1.58\times10^{-1}\pm8.1\times10^{-3}$	$6.22\times10^{-2}\pm4.7\times10^{-3}$	$3.55\times10^{-2}\pm3.4\times10^{-3}$
0.75	$2.50\times10^{-1}\pm1.1\times10^{-2}$	$1.25\times10^{-1}\pm6.6\times10^{-3}$	$5.43\times10^{-2}\pm4.0\times10^{-3}$	$2.77\times10^{-2}\pm2.8\times10^{-3}$
0.85	$1.89\times10^{-1}\pm8.3\times10^{-3}$	$9.50\times10^{-2}\pm5.2\times10^{-3}$	$4.16\times10^{-2}\pm3.3\times10^{-3}$	$2.06\times10^{-2}\pm2.2\times10^{-3}$
0.95	$1.58\times10^{-1}\pm7.1\times10^{-3}$	$7.38\times10^{-2}\pm4.3\times10^{-3}$	$3.13\times10^{-2}\pm2.7\times10^{-3}$	$1.56\times10^{-2}\pm1.8\times10^{-3}$
1.05	$1.19\times10^{-1}\pm5.8\times10^{-3}$	$5.50\times10^{-2}\pm3.5\times10^{-3}$	$2.12\times10^{-2}\pm2.1\times10^{-3}$	$1.01\times10^{-2}\pm1.4\times10^{-3}$
1.15	$9.60\times10^{-2}\pm5.1\times10^{-3}$	$4.34\times10^{-2}\pm3.1\times10^{-3}$	$1.73\times10^{-2}\pm1.9\times10^{-3}$	$7.94\times10^{-3}\pm1.2\times10^{-3}$
1.25	$7.11\times10^{-2}\pm4.1\times10^{-3}$	$3.19\times10^{-2}\pm2.5\times10^{-3}$	$1.22\times10^{-2}\pm1.5\times10^{-3}$	$6.05\times10^{-3}\pm1.1\times10^{-3}$
1.35	$5.31\times10^{-2}\pm3.4\times10^{-3}$	$2.40\times10^{-2}\pm2.1\times10^{-3}$	$9.65\times10^{-3}\pm1.3\times10^{-3}$	$4.08\times10^{-3}\pm8.4\times10^{-4}$
1.45	$4.43\times10^{-2}\pm3.1\times10^{-3}$	$1.90\times10^{-2}\pm1.9\times10^{-3}$	$7.69\times10^{-3}\pm1.2\times10^{-3}$	$3.31\times10^{-3}\pm7.6\times10^{-4}$
1.55	$3.13\times10^{-2}\pm2.4\times10^{-3}$	$1.28\times10^{-2}\pm1.4\times10^{-3}$	$4.43\times10^{-3}\pm8.5\times10^{-4}$	$2.02\times10^{-3}\pm5.6\times10^{-4}$
1.65	$2.39\times10^{-2}\pm2.1\times10^{-3}$	$9.29\times10^{-3}\pm1.2\times10^{-3}$	$3.09\times10^{-3}\pm7.0\times10^{-4}$	$1.70\times10^{-3}\pm5.2\times10^{-4}$
1.75	$1.79\times10^{-2}\pm1.7\times10^{-3}$	$6.92\times10^{-3}\pm1.0\times10^{-3}$	$2.79\times10^{-3}\pm6.6\times10^{-4}$	$1.21\times10^{-3}\pm4.3\times10^{-4}$
1.85	$1.28\times10^{-2}\pm1.4\times10^{-3}$	$5.66\times10^{-3}\pm9.3\times10^{-4}$	$1.27\times10^{-3}\pm4.4\times10^{-4}$	$7.33\times10^{-4}\pm3.3\times10^{-4}$
1.95	$1.00\times10^{-2}\pm1.3\times10^{-3}$	$3.93\times10^{-3}\pm7.8\times10^{-4}$	$1.54\times10^{-3}\pm4.9\times10^{-4}$	$7.92\times10^{-4}\pm3.5\times10^{-4}$
2.10	$6.03\times10^{-3}\pm5.9\times10^{-4}$	$2.58\times10^{-3}\pm3.8\times10^{-4}$	$6.91\times10^{-4}\pm2.0\times10^{-4}$	$3.59\times10^{-4}\pm1.4\times10^{-4}$
2.30	$3.46\times10^{-3}\pm4.4\times10^{-4}$	$1.37\times10^{-3}\pm2.7\times10^{-4}$	$5.66\times10^{-4}\pm1.8\times10^{-4}$	$2.03\times10^{-4}\pm1.1\times10^{-4}$
2.50	$2.04\times10^{-3}\pm3.4\times10^{-4}$	$7.56\times10^{-4}\pm2.0\times10^{-4}$	$2.85\times10^{-4}\pm1.3\times10^{-4}$	$1.35\times10^{-4}\pm8.5\times10^{-5}$
2.70	$1.20\times10^{-3}\pm2.5\times10^{-4}$	$3.92\times10^{-4}\pm1.4\times10^{-4}$	$2.26\times10^{-4}\pm1.1\times10^{-4}$	$2.67\times10^{-5}\pm3.8\times10^{-5}$
2.90	$6.21\times10^{-4}\pm1.8\times10^{-4}$	$2.92\times10^{-4}\pm1.2\times10^{-4}$	$1.40\times10^{-4}\pm8.8\times10^{-5}$	$8.76\times10^{-6}\pm2.2\times10^{-5}$
3.25	$2.61\times10^{-4}\pm7.3\times10^{-5}$	$1.10\times10^{-4}\pm4.7\times10^{-5}$	$3.63\times10^{-5}\pm2.8\times10^{-5}$	$9.16\times10^{-6}\pm1.4\times10^{-5}$
3.75	$6.52\times10^{-5}\pm3.6\times10^{-5}$	$2.77\times10^{-5}\pm2.3\times10^{-5}$	$5.76\times10^{-6}\pm1.1\times10^{-5}$	
4.25	$4.82\times10^{-5}\pm3.2\times10^{-5}$	$1.23\times10^{-5}\pm1.6\times10^{-5}$	$2.71\times10^{-6}\pm8.1\times10^{-6}$	

TABLE XXVIII. Invariant yields for $\pi^{\pm}$ and $K^{\pm}$ at midrapidity in 60–92% centrality bins, normalized to unit rapidity. Errors are statistical only.

p_T (GeV/c)	π^+	π^-	K^+	K^-
0.25	$1.28\times10^{1}\pm1.1\times10^{-1}$	$1.21\times10^{1}\pm9.5\times10^{-2}$		
0.35	$6.61\times10^{0}\pm5.7\times10^{-2}$	$6.42\times10^{0}\pm5.2\times10^{-2}$		
0.45	$3.71\times10^{0}\pm3.4\times10^{-2}$	$3.59\times10^{0}\pm3.1\times10^{-2}$	$5.35\times10^{-1}\pm1.5\times10^{-2}$	$4.74\times10^{-1}\pm1.3\times10^{-2}$
0.55	$2.09\times10^{0}\pm2.1\times10^{-2}$	$2.06\times10^{0}\pm1.9\times10^{-2}$	$3.83\times10^{-1}\pm9.7\times10^{-3}$	$3.62\times10^{-1}\pm8.8\times10^{-3}$
0.65	$1.24\times10^{0}\pm1.4\times10^{-2}$	$1.21\times10^{0}\pm1.3\times10^{-2}$	$2.66\times10^{-1}\pm6.8\times10^{-3}$	$2.50\times10^{-1}\pm6.2\times10^{-3}$
0.75	$7.63\times10^{-1}\pm9.6\times10^{-3}$	$7.31\times10^{-1}\pm8.4\times10^{-3}$	$1.81\times10^{-1}\pm4.9\times10^{-3}$	$1.78\times10^{-1}\pm4.6\times10^{-3}$
0.85	$4.64\times10^{-1}\pm6.6\times10^{-3}$	$4.60\times10^{-1}\pm5.9\times10^{-3}$	$1.26\times10^{-1}\pm3.7\times10^{-3}$	$1.21\times10^{-1}\pm3.4\times10^{-3}$
0.95	$2.93\times10^{-1}\pm4.8\times10^{-3}$	$2.95\times10^{-1}\pm4.3\times10^{-3}$	$8.85\times10^{-2}\pm2.9\times10^{-3}$	$8.21\times10^{-2}\pm2.5\times10^{-3}$
1.05	$1.91\times10^{-1}\pm3.5\times10^{-3}$	$1.89\times10^{-1}\pm3.2\times10^{-3}$	$6.34\times10^{-2}\pm2.3\times10^{-3}$	$5.80\times10^{-2}\pm2.0\times10^{-3}$
1.15	$1.26\times10^{-1}\pm2.6\times10^{-3}$	$1.28\times10^{-1}\pm2.5\times10^{-3}$	$4.35\times10^{-2}\pm1.8\times10^{-3}$	$3.91\times10^{-2}\pm1.5\times10^{-3}$
1.25	$8.15\times10^{-2}\pm2.0\times10^{-3}$	$8.12\times10^{-2}\pm1.8\times10^{-3}$	$2.87\times10^{-2}\pm1.4\times10^{-3}$	$2.94\times10^{-2}\pm1.3\times10^{-3}$
1.35	$5.96\times10^{-2}\pm1.7\times10^{-3}$	$5.71\times10^{-2}\pm1.5\times10^{-3}$	$2.03\times10^{-2}\pm1.1\times10^{-3}$	$2.07\times10^{-2}\pm1.0\times10^{-3}$
1.45	$3.95\times10^{-2}\pm1.3\times10^{-3}$	$3.91\times10^{-2}\pm1.2\times10^{-3}$	$1.68\times10^{-2}\pm9.7\times10^{-4}$	$1.35\times10^{-2}\pm8.2\times10^{-4}$
1.55	$2.56\times10^{-2}\pm9.7\times10^{-4}$	$2.81\times10^{-2}\pm9.7\times10^{-4}$	$1.06\times10^{-2}\pm7.5\times10^{-4}$	$1.05\times10^{-2}\pm7.0\times10^{-4}$
1.65	$1.96\times10^{-2}\pm8.4\times10^{-4}$	$2.07\times10^{-2}\pm8.1\times10^{-4}$	$8.39\times10^{-3}\pm6.5\times10^{-4}$	$8.47\times10^{-3}\pm6.2\times10^{-4}$
1.75	$1.44\times10^{-2}\pm7.1\times10^{-4}$	$1.41\times10^{-2}\pm6.5\times10^{-4}$	$5.68\times10^{-3}\pm5.2\times10^{-4}$	$5.15\times10^{-3}\pm4.6\times10^{-4}$
1.85	$1.07\times10^{-2}\pm6.0\times10^{-4}$	$1.04\times10^{-2}\pm5.6\times10^{-4}$	$4.91\times10^{-3}\pm4.7\times10^{-4}$	$4.15\times10^{-3}\pm4.1\times10^{-4}$
1.95	$7.68\times10^{-3}\pm5.1\times10^{-4}$	$7.42\times10^{-3}\pm4.8\times10^{-4}$	$3.59\times10^{-3}\pm4.1\times10^{-4}$	$3.29\times10^{-3}\pm3.7\times10^{-4}$
2.05	$5.87\times10^{-3}\pm3.6\times10^{-4}$	$4.87\times10^{-3}\pm3.3\times10^{-4}$		
2.15	$3.78\times10^{-3}\pm2.9\times10^{-4}$	$3.87\times10^{-3}\pm3.0\times10^{-4}$		
2.25	$2.99\times10^{-3}\pm2.6\times10^{-4}$	$2.55\times10^{-3}\pm2.5\times10^{-4}$		
2.35	$2.47\times10^{-3}\pm2.5\times10^{-4}$	$2.41\times10^{-3}\pm2.6\times10^{-4}$		
2.45	$1.68\times10^{-3}\pm2.1\times10^{-4}$	$1.63\times10^{-3}\pm2.1\times10^{-4}$		
2.55	$1.77\times10^{-3}\pm2.3\times10^{-4}$	$1.54\times10^{-3}\pm2.3\times10^{-4}$		
2.65	$1.28\times10^{-3}\pm2.1\times10^{-4}$	$1.18\times10^{-3}\pm2.0\times10^{-4}$		
2.75	$1.02\times10^{-3}\pm2.0\times10^{-4}$	$7.74\times10^{-4}\pm1.7\times10^{-4}$		
2.85	$7.49\times10^{-4}\pm1.7\times10^{-4}$	$6.23\times10^{-4}\pm1.7\times10^{-4}$		
2.95	$5.61\times10^{-4}\pm1.6\times10^{-4}$	$7.27\times10^{-4}\pm1.9\times10^{-4}$		

TABLE XXIX. Invariant yields for protons and antiprotons at midrapidity in 60–92% centrality bin, normalized to unit rapidity. Errors are statistical only.

p_T (GeV/c)	p	$\bar{p}$
0.65	$1.17\times10^{-1}\pm4.8\times10^{-3}$	$8.63\times10^{-2}\pm3.8\times10^{-3}$
0.75	$9.26\times10^{-2}\pm3.9\times10^{-3}$	$7.00\times10^{-2}\pm3.1\times10^{-3}$
0.85	$7.01\times10^{-2}\pm3.1\times10^{-3}$	$5.31\times10^{-2}\pm2.5\times10^{-3}$
0.95	$5.48\times10^{-2}\pm2.6\times10^{-3}$	$4.07\times10^{-2}\pm2.0\times10^{-3}$
1.05	$4.10\times10^{-2}\pm2.1\times10^{-3}$	$2.92\times10^{-2}\pm1.6\times10^{-3}$
1.15	$3.09\times10^{-2}\pm1.7\times10^{-3}$	$2.32\times10^{-2}\pm1.4\times10^{-3}$
1.25	$2.16\times10^{-2}\pm1.3\times10^{-3}$	$1.70\times10^{-2}\pm1.1\times10^{-3}$
1.35	$1.77\times10^{-2}\pm1.2\times10^{-3}$	$1.27\times10^{-2}\pm9.4\times10^{-4}$
1.45	$1.25\times10^{-2}\pm9.4\times10^{-4}$	$1.02\times10^{-2}\pm8.3\times10^{-4}$
1.55	$8.85\times10^{-3}\pm7.8\times10^{-4}$	$6.51\times10^{-3}\pm6.2\times10^{-4}$
1.65	$6.42\times10^{-3}\pm6.3\times10^{-4}$	$4.76\times10^{-3}\pm5.2\times10^{-4}$
1.75	$5.08\times10^{-3}\pm5.5\times10^{-4}$	$3.69\times10^{-3}\pm4.5\times10^{-4}$
1.85	$3.58\times10^{-3}\pm4.6\times10^{-4}$	$2.60\times10^{-3}\pm3.7\times10^{-4}$
1.95	$2.79\times10^{-3}\pm3.9\times10^{-4}$	$2.11\times10^{-3}\pm3.4\times10^{-4}$
2.10	$1.77\times10^{-3}\pm1.8\times10^{-4}$	$1.23\times10^{-3}\pm1.5\times10^{-4}$
2.30	$1.08\times10^{-3}\pm1.4\times10^{-4}$	$7.22\times10^{-4}\pm1.2\times10^{-4}$
2.50	$5.42\times10^{-4}\pm9.5\times10^{-5}$	$3.97\times10^{-4}\pm8.5\times10^{-5}$
2.70	$3.32\times10^{-4}\pm7.4\times10^{-5}$	$2.17\times10^{-4}\pm6.2\times10^{-5}$
2.90	$2.04\times10^{-4}\pm5.8\times10^{-5}$	$1.49\times10^{-4}\pm5.2\times10^{-5}$
3.25	$8.58\times10^{-5}\pm2.3\times10^{-5}$	$5.24\times10^{-5}\pm1.9\times10^{-5}$
3.75	$2.76\times10^{-5}\pm1.3\times10^{-5}$	$1.14\times10^{-5}\pm8.7\times10^{-6}$
4.25	$1.24\times10^{-5}\pm9.1\times10^{-6}$	$5.08\times10^{-6}\pm6.1\times10^{-6}$

[1] See E. Laermann and O. Philipsen, hep-ph/0303042. (Invited article for Annual Review of Nuclear and Particle Sciences.)
[2] J. D. Bjorken, Phys. Rev. D **27**, 140 (1983).
[3] K. Adcox *et al.*, PHENIX Collaboration, Phys. Rev. Lett. **87**, 052301 (2001).
[4] W. Broniowski and W. Florkowski, Phys. Rev. Lett. **87**, 272302 (2001); Phys. Rev. C **65**, 064905 (2002).
[5] D. Teaney, J. Lauret, and E. V. Shuryak, nucl-th/0110037; Phys. Rev. Lett. **86**, 4783 (2001).
[6] K. Adcox *et al.*, PHENIX Collaboration, Phys. Rev. Lett. **88**, 242301 (2002).
[7] C. Adler *et al.*, STAR Collaboration, Phys. Rev. Lett. **87**, 262302 (2001).
[8] K. Adcox *et al.*, PHENIX Collaboration, Phys. Rev. C **69**, 024904 (2004).
[9] F. Becattini *et al.*, Phys. Rev. C **64**, 024901 (2001).
[10] P. Braun-Munzinger, D. Magestro, K. Redlich, and J. Stachel, Phys. Lett. B **518**, 41 (2001).
[11] W. Florkowski, W. Broniowski, and M. Michalec, Acta Phys. Pol. B **33**, 761 (2002).
[12] K. Adcox *et al.*, PHENIX Collaboration, Phys. Rev. Lett. **88**, 022301 (2002).
[13] K. Adcox *et al.*, PHENIX Collaboration, Phys. Lett. B **561**, 82 (2003).
[14] S. S. Adler *et al.*, PHENIX Collaboration, Phys. Rev. Lett. **91**, 072301 (2003).
[15] X. N. Wang and M. Gyulassy, Phys. Rev. Lett. **68**, 1480 (1992); X. N. Wang, Phys. Rev. C **58**, 2321 (1998).
[16] M. Gyulassy and M. Plümer, Phys. Lett. B **243**, 432 (1990); R. Baier and *et al.*, *ibid.* **345**, 277 (1995).
[17] K. Adcox *et al.*, PHENIX Collaboration, Nucl. Instrum. Methods Phys. Res. A **499**, 469 (2003).
[18] M. Aizawa *et al.*, PHENIX Collaboration, Nucl. Instrum. Methods Phys. Res. A **499**, 508 (2003).
[19] L. Aphecetche *et al.*, PHENIX Collaboration, Nucl. Instrum. Methods Phys. Res. A **499**, 521 (2003).
[20] M. Allen *et al.*, PHENIX Collaboration, Nucl. Instrum. Methods Phys. Res. A **499**, 549 (2003).
[21] C. Adler *et al.*, PHENIX Collaboration, Nucl. Instrum. Methods Phys. Res. A **470**, 488 (2001).
[22] K. Adcox *et al.*, PHENIX Collaboration, Nucl. Instrum. Methods Phys. Res. A **499**, 489 (2003).
[23] S. S. Adler *et al.*, PHENIX Collaboration, Phys. Rev. Lett. **91**, 172031 (2003).
[24] S. S. Adler *et al.*, PHENIX Collaboration, Phys. Rev. Lett. **91**, 241803 (2003).
[25] J. T. Mitchell *et al.*, Nucl. Instrum. Methods Phys. Res. A **482**, 491 (2002).
[26] Computer code GEANT 3.21 (CERN, Geneva, 1993).
[27] X. N. Wang and M. Gyulassy, Phys. Rev. D **44**, 3501 (1991).
[28] K. Adcox *et al.*, PHENIX Collaboration, Phys. Rev. Lett. **89**, 092302 (2002).
[29] P. F. Kolb and R. Rapp, Phys. Rev. C **67**, 044903 (2003).
[30] E. Schnedermann, J. Sollfrank, and U. Heinz, Phys. Rev. C **48**, 2462 (1993).
[31] P. Kolb *et al.*, Nucl. Phys. **A696**, 197 (2001); P. Huovinen *et al.*, Phys. Lett. B **503**, 58 (2001).
[32] U. Heinz and P. Kolb, Nucl. Phys. **A702**, 269 (2002).
[33] E. Schnedermann, J. Sollfrank, and U. Heinz, Phys. Rev. C **48**, 2462 (1994); T. Csörgő and B. Lörstad, *ibid.* **54**, 1390 (1996).
[34] T. Csörgő, S. V. Akkelin, Y. Hama, B. Lukács, and Y. M. Sinyukov, Phys. Rev. C **67**, 034904 (2003).
[35] J. Schaffner-Bielich, D. Kharzeev, L. McLerran, and R. Venugopalan, Nucl. Phys. **A705**, 494 (2002).
[36] P. Christiansen, BRAHMS Collaboration, Nucl. Phys. **A721**, 239 (2003).
[37] C. Adler *et al.*, STAR Collaboration, Phys. Rev. Lett. **86**, 4778 (2001).
[38] J. Adams *et al.*, STAR Collaboration, Phys. Rev. Lett. **90**, 119903 (2003).
[39] C. Adler *et al.*, STAR Collaboration, nucl-ex/0206008, Phys. Lett. B (to be published).
[40] J. Adams *et al.*, STAR Collaboration, Phys. Lett. B **567**, 167 (2003).
[41] I. G. Bearden *et al.*, BRAHMS Collaboration, Phys. Rev. Lett. **87**, 112305 (2001).
[42] B. B. Back *et al.*, PHOBOS Collaboration, Phys. Rev. Lett. **87**, 102301 (2001).
[43] I. G. Bearden *et al.*, BRAHMS Collaboration, Phys. Rev. Lett. **90**, 102301 (2003).
[44] B. B. Back *et al.*, PHOBOS Collaboration, Phys. Rev. C **67**, 021901(R) (2003).
[45] R. C. Hwa and C. B. Yang, Phys. Rev. C **67** 034902 (2003); R. J. Fries, B. Müller, C. Nonaka, and S. A. Bass, Phys. Rev. Lett. **90**, 202303 (2003); V. Greco, C. M. Ko, and P. Lévai, Phys. Rev. Lett. **90**, 202302 (2003).
[46] I. Vitev and M. Gyulassy, Nucl. Phys. **A715**, 779c (2003).
[47] B. Alper *et al.*, Nucl. Phys. **B100**, 237 (1975).
[48] P. Abreu *et al.*, DELPHI Collaboration, Eur. Phys. J. C **17**, 207 (2000).
[49] B. Kämpfer, J. Cleymans, K. Gallmeister, and S. M. Wheaton, Heavy Ion Phys. **18**, 1 (2003).
[50] G. C. Rossi and G. Veneziano, Nucl. Phys. **B123**, 507 (1977); D. Kharzeev, Phys. Lett. B **378**, 238 (1996); S. E. Vance, M. Gyulassy, and X.-N. Wang, *ibid.* **443**, 45 (1998).
[51] G. Van Buren, Nucl. Phys. **A715**, 129c (2003).
[52] I. Vitev and M. Gyulassy, Phys. Rev. C **65**, 041902 (2002); I. Vitev, M. Gyulassy, and P. Lévai, hep-ph/0109198 (EPS-HEP 2001 conference proceedings).
[53] J. Adams *et al.*, STAR Collaboration, Phys. Rev. Lett. **92**, 052302 (2004).
[54] J. Cronin *et al.*, Phys. Rev. D **11**, 3105 (1975).
[55] D. Antreasyan *et al.*, Phys. Rev. D **19**, 764 (1979).
[56] M. Lev and B. Petersson, Z. Phys. C **21**, 155 (1983).
[57] B. Z. Kopeliovich, J. Nemchik, A. Schafer, and A. V. Tarasov, Phys. Rev. Lett. **88**, 232303 (2002).

Single identified hadron spectra from $\sqrt{s_{NN}}$=130 GeV Au+Au collisions

K. Adcox,[40] S. S. Adler,[4] N. N. Ajitanand,[33] Y. Akiba,[14] J. Alexander,[33] L. Aphecetche,[35] Y. Arai,[14] S. H. Aronson,[4] R. Averbeck,[34] T. C. Awes,[27] K. N. Barish,[5] P. D. Barnes,[19] J. Barrette,[21] B. Bassalleck,[25] S. Bathe,[22] V. Baublis,[28] A. Bazilevsky,[12,30] S. Belikov,[12,13] F. G. Bellaiche,[27] S. T. Belyaev,[16] M. J. Bennett,[19] Y. Berdnikov,[31] S. Botelho,[32] M. L. Brooks,[19] D. S. Brown,[26] N. Bruner,[25] D. Bucher,[22] H. Buesching,[22] V. Bumazhnov,[12] G. Bunce,[4,30] J. M. Burward-Hoy,[34] S. Butsyk,[34,28] T. A. Carey,[19] P. Chand,[3] J. Chang,[5] W. C. Chang,[1] L. L. Chavez,[25] S. Chernichenko,[12] C. Y. Chi,[8] J. Chiba,[14] M. Chiu,[8] R. K. Choudhury,[3] T. Christ,[34] T. Chujo,[4,39] M. S. Chung,[15,19] P. Chung,[33] V. Cianciolo,[27] B. A. Cole,[8] D. G. d'Enterria,[35] G. David,[4] H. Delagrange,[35] A. Denisov,[12] A. Deshpande,[30] E. J. Desmond,[4] O. Dietzsch,[32] B. V. Dinesh,[3] A. Drees,[34] A. Durum,[12] D. Dutta,[3] K. Ebisu,[24] Y. V. Efremenko,[27] K. El Chenawi,[40] H. En'yo,[17,29] S. Esumi,[39] L. Ewell,[4] T. Ferdousi,[5] D. E. Fields,[25] S. L. Fokin,[16] Z. Fraenkel,[42] A. Franz,[4] A. D. Frawley,[9] S.-Y. Fung,[5] S. Garpman,[20,*] T. K. Ghosh,[40] A. Glenn,[36] A. L. Godoi,[32] Y. Goto,[30] S. V. Greene,[40] M. Grosse Perdekamp,[30] S. K. Gupta,[3] W. Guryn,[4] H.-Å. Gustafsson,[20] J. S. Haggerty,[4] H. Hamagaki,[7] A. G. Hansen,[19] H. Hara,[24] E. P. Hartouni,[18] R. Hayano,[38] N. Hayashi,[29] X. He,[10] T. K. Hemmick,[34] J. M. Heuser,[34] M. Hibino,[41] J. C. Hill,[13] D. S. Ho,[43] K. Homma,[11] B. Hong,[15] A. Hoover,[26] T. Ichihara,[29,30] K. Imai,[17,29] M. S. Ippolitov,[16] M. Ishihara,[29,30] B. V. Jacak,[34,30] W. Y. Jang,[15] J. Jia,[34] B. M. Johnson,[4] S. C. Johnson,[18,34] K. S. Joo,[23] S. Kametani,[41] J. H. Kang,[43] M. Kann,[28] S. S. Kapoor,[3] S. Kelly,[8] B. Khachaturov,[42] A. Khanzadeev,[28] J. Kikuchi,[41] D. J. Kim,[43] H. J. Kim,[43] S. Y. Kim,[43] Y. G. Kim,[43] W. W. Kinnison,[19] E. Kistenev,[4] A. Kiyomichi,[39] C. Klein-Boesing,[22] S. Klinksiek,[25] L. Kochenda,[28] V. Kochetkov,[12] D. Koehler,[25] T. Kohama,[11] D. Kotchetkov,[5] A. Kozlov,[42] P. J. Kroon,[4] K. Kurita,[29,30] M. J. Kweon,[15] Y. Kwon,[43] G. S. Kyle,[26] R. Lacey,[33] J. G. Lajoie,[13] J. Lauret,[33] A. Lebedev,[13] D. M. Lee,[19] M. J. Leitch,[19] X. H. Li,[5] Z. Li,[6,29] D. J. Lim,[43] M. X. Liu,[19] X. Liu,[6] Z. Liu,[6] C. F. Maguire,[40] J. Mahon,[4] Y. I. Makdisi,[4] V. I. Manko,[16] Y. Mao,[6,29] S. K. Mark,[21] S. Markacs,[8] G. Martinez,[35] M. D. Marx,[34] A. Masaike,[17] F. Matathias,[34] T. Matsumoto,[7,41] P. L. McGaughey,[19] E. Melnikov,[12] M. Merschmeyer,[22] F. Messer,[34] M. Messer,[4] Y. Miake,[39] T. E. Miller,[40] A. Milov,[42] S. Mioduszewski,[4,36] R. E. Mischke,[19] G. C. Mishra,[10] J. T. Mitchell,[4] A. K. Mohanty,[3] D. P. Morrison,[4] J. M. Moss,[19] F. Mühlbacher,[34] M. Muniruzzaman,[5] J. Murata,[29] S. Nagamiya,[14] Y. Nagasaka,[24] J. L. Nagle,[8] Y. Nakada,[17] B. K. Nandi,[5] J. Newby,[36] L. Nikkinen,[21] P. Nilsson,[20] S. Nishimura,[7] A. S. Nyanin,[16] J. Nystrand,[20] E. O'Brien,[4] C. A. Ogilvie,[13] H. Ohnishi,[4,11] I. D. Ojha,[2,40] M. Ono,[39] V. Onuchin,[12] A. Oskarsson,[20] L. Österman,[20] I. Otterlund,[20] K. Oyama,[7,38] L. Paffrath,[4,*] A. P. T. Palounek,[19] V. S. Pantuev,[34] V. Papavassiliou,[26] S. F. Pate,[26] T. Peitzmann,[22] A. N. Petridis,[13] C. Pinkenburg,[4,33] R. P. Pisani,[4] P. Pitukhin,[12] F. Plasil,[27] M. Pollack,[34,36] K. Pope,[36] M. L. Purschke,[4] I. Ravinovich,[42] K. F. Read,[27,36] K. Reygers,[22] V. Riabov,[28,31] Y. Riabov,[28] M. Rosati,[13] A. A. Rose,[40] S. S. Ryu,[43] N. Saito,[29,30] A. Sakaguchi,[11] T. Sakaguchi,[7,41] H. Sako,[39] T. Sakuma,[29,37] V. Samsonov,[28] T. C. Sangster,[18] R. Santo,[22] H. D. Sato,[17,29] S. Sato,[39] S. Sawada,[14] B. R. Schlei,[19] Y. Schutz,[35] V. Semenov,[12] R. Seto,[5] T. K. Shea,[4] I. Shein,[12] T.-A. Shibata,[29,37] K. Shigaki,[14] T. Shiina,[19] Y. H. Shin,[43] I. G. Sibiriak,[16] D. Silvermyr,[20] K. S. Sim,[15] J. Simon-Gillo,[19] C. P. Singh,[2] V. Singh,[2] M. Sivertz,[4] A. Soldatov,[12] R. A. Soltz,[18] S. Sorensen,[27,36] P. W. Stankus,[27] N. Starinsky,[21] P. Steinberg,[8] E. Stenlund,[20] A. Ster,[44] S. P. Stoll,[4] M. Sugioka,[29,37] T. Sugitate,[11] J. P. Sullivan,[19] Y. Sumi,[11] Z. Sun,[6] M. Suzuki,[39] E. M. Takagui,[32] A. Taketani,[29] M. Tamai,[41] K. H. Tanaka,[14] Y. Tanaka,[24] E. Taniguchi,[29,37] M. J. Tannenbaum,[4] J. Thomas,[34] J. H. Thomas,[18] T. L. Thomas,[25] W. Tian,[6,36] J. Tojo,[17,29] H. Torii,[17,29] R. S. Towell,[19] I. Tserruya,[42] H. Tsuruoka,[39] A. A. Tsvetkov,[16] S. K. Tuli,[2] H. Tydesjö,[20] N. Tyurin,[12] T. Ushiroda,[24] H. W. van Hecke,[19] C. Velissaris,[26] J. Velkovska,[34] M. Velkovsky,[34] A. A. Vinogradov,[16] M. A. Volkov,[16] A. Vorobyov,[28] E. Vznuzdaev,[28] H. Wang,[5] Y. Watanabe,[29,30] S. N. White,[4] C. Witzig,[4] F. K. Wohn,[13] C. L. Woody,[4] W. Xie,[5,42] K. Yagi,[39] S. Yokkaichi,[29] G. R. Young,[27] I. E. Yushmanov,[16] W. A. Zajc,[8,†] Z. Zhang,[34] and S. Zhou[6]

(PHENIX Collaboration)

[1]*Institute of Physics, Academia Sinica, Taipei 11529, Taiwan*

[2]*Department of Physics, Banaras Hindu University, Varanasi 221005, India*

[3]*Bhabha Atomic Research Centre, Bombay 400 085, India*

[4]*Brookhaven National Laboratory, Upton, New York 11973-5000, USA*

[5]*University of California, Riverside, California 92521, USA*

[6]*China Institute of Atomic Energy (CIAE), Beijing, People's Republic of China*

[7]*Center for Nuclear Study, Graduate School of Science, University of Tokyo, 7-3-1 Hongo, Bunkyo, Tokyo 113-0033, Japan*

[8]*Columbia University, New York, New York 10027, USA and*

Nevis Laboratories, Irvington, New York 10533, USA

[9]*Florida State University, Tallahassee, Florida 32306, USA*

[10]*McGill University, Montreal, Quebec, Canada H3A 2T8*

[11]*Hiroshima University, Kagamiyama, Higashi-Hiroshima 739-8526, Japan*

[12]*Institute for High Energy Physics (IHEP), Protvino, Russia*

[13]*Iowa State University, Ames, Iowa 50011, USA*

[14]*KEK, High Energy Accelerator Research Organization, Tsukuba-shi, Ibaraki-ken 305-0801, Japan*

[15]*Korea University, Seoul, 136-701, Korea*

[16]*Russian Research Center "Kurchatov Institute," Moscow, Russia*

 ©2004 The American Physical Society

[17]*Kyoto University, Kyoto 606, Japan*
[18]*Lawrence Livermore National Laboratory, Livermore, California 94550, USA*
[19]*Los Alamos National Laboratory, Los Alamos, New Mexico 87545, USA*
[20]*Department of Physics, Lund University, Box 118, SE-221 00 Lund, Sweden*
[21]*Georgia State University, Atlanta, Georgia 30303, USA*
[22]*Institut für Kernphysik, University of Muenster, D-48149 Muenster, Germany*
[23]*Myongji University, Yongin, Kyonggido 449-728, Korea*
[24]*Nagasaki Institute of Applied Science, Nagasaki-shi, Nagasaki 851-0193, Japan*
[25]*University of New Mexico, Albuquerque, New Mexico, 87131 USA*
[26]*New Mexico State University, Las Cruces, New Mexico 88003, USA*
[27]*Oak Ridge National Laboratory, Oak Ridge, Tennessee 37831, USA*
[28]*PNPI, Petersburg Nuclear Physics Institute, Gatchina, Russia*
[29]*RIKEN (The Institute of Physical and Chemical Research), Wako, Saitama 351-0198, Japan*
[30]*RIKEN BNL Research Center, Brookhaven National Laboratory, Upton, New York 11973-5000, USA*
[31]*St. Petersburg State Technical University, St. Petersburg, Russia*
[32]*Universidade de São Paulo, Instituto de Física, Caixa Postal 66318, São Paulo CEP05315-970, Brazil*
[33]*Chemistry Department, State University of New York, Stony Brook, New York 11794, USA*
[34]*Department of Physics and Astronomy, State University of New York, Stony Brook, New York 11794, USA*
[35]*SUBATECH (Ecole des Mines de Nantes, CNRS-IN2P3, Université de Nantes) Boîte Postal 20722 - 44307, Nantes, France*
[36]*University of Tennessee, Knoxville, Tennessee 37996, USA*
[37]*Department of Physics, Tokyo Institute of Technology, Tokyo, 152-8551, Japan*
[38]*University of Tokyo, Tokyo, Japan*
[39]*Institute of Physics, University of Tsukuba, Tsukuba, Ibaraki 305, Japan*
[40]*Vanderbilt University, Nashville, Tennessee 37235, USA*
[41]*Waseda University, Advanced Research Institute for Science and Engineering, 17 Kikui-cho, Shinjuku-ku, Tokyo 162-0044, Japan*
[42]*Weizmann Institute, Rehovot 76100, Israel*
[43]*Yonsei University, IPAP, Seoul 120-749, Korea*
[44]*KFKI Research Institute for Particle and Nuclear Physics (RMKI), Budapest, Hungary*
(Received 9 July 2003; published 17 February 2004)

Transverse momentum spectra and yields of hadrons are measured by the PHENIX collaboration in Au + Au collisions at $\sqrt{s_{NN}}$=130 GeV at the Relativistic Heavy Ion Collider. The time-of-flight resolution allows identification of pions to transverse momenta of 2 GeV/c and protons and antiprotons to 4 GeV/c. The yield of pions rises approximately linearly with the number of nucleons participating in the collision, while the number of kaons, protons, and antiprotons increases more rapidly. The shape of the momentum distribution changes between peripheral and central collisions. Simultaneous analysis of all the p_T spectra indicates radial collective expansion, consistent with predictions of hydrodynamic models. Hydrodynamic analysis of the spectra shows that the expansion velocity increases with collision centrality and collision energy. This expansion boosts the particle momenta, causing the yield from soft processes to exceed that for hard to large transverse momentum, perhaps as large as 3 GeV/c.

DOI: 10.1103/PhysRevC.69.024904 PACS number(s): 25.75.Dw

I. INTRODUCTION

Heavy ion reactions at ultrarelativistic energies provide information on strongly interacting matter under extreme conditions. Lattice QCD and phenomenological predictions indicate that at high enough energy density a deconfined state of quarks and gluons, the quark-gluon plasma, is formed. It is expected that conditions in ultrarelativistic heavy ion reactions may produce this new state of matter, the study of which is the major goal of the experiments at the Relativistic Heavy Ion Collider (RHIC).

The high energy density state thus created will cool down and expand, undergoing a phase transition to "ordinary" hadronic matter. While the tools of choice to study the earliest phase of the reactions, and thereby the new state, are probes that do not interact via the strong force, such as photons, electrons, or muons, the global properties and dynamics of later stages in the system are best studied via hadronic observables. Hadron momentum spectra in proton-proton reactions are often separated into two parts, a soft part at low transverse momentum p_T, where the shape is roughly exponential in transverse mass $m_T=\sqrt{p_T^2+m_0^2}$, and a high p_T region where the shape more closely resembles a power law. Soft production (low p_T) is attributed to fragmentation of a string [1,2] between components of the struck nucleons, while hard (high p_T) hadrons are expected to originate predominantly

*Deceased.
†Spokesperson. Email address: zajc@nevis.columbia.edu

from fragmentation of hard-scattered partons. The transition between these two regimes is not sharply defined, but is commonly believed to be near $p_T \approx 2$ GeV/c [3].

In proton-nucleus ($p+A$) scattering, these two regimes depend on the colliding system size in different ways. The soft production depends on the number of nucleons struck or participating in the collision ($N_{\rm part}$). The number of hard scatterings should increase proportionally to the number of binary nucleon-nucleon encounters ($N_{\rm coll}$) since these processes have a small elementary cross section and may be considered as incoherent. Hard scattering also produces color strings which fragment and produce some low-p_T particles, though these are much fewer in number than those from the much more frequent soft scatterings. In $p+A$ these $N_{\rm part}$ and $N_{\rm coll}$ are connected by a very simple relation, namely, $N_{\rm part} = N_{\rm coll} + 1$.

In nucleus-nucleus collisions, the number of participant nucleons does not scale simply with A, so it is more useful to study scaling with $N_{\rm coll}$ or $N_{\rm part}$. Collisions are sorted according to centrality, allowing control of the geometry and determination of $N_{\rm coll}$ or $N_{\rm part}$.

In heavy ion collisions, one expects secondary collisions of particles (rescattering) to take place, especially among particles with low and intermediate transverse momentum. Rescattering may occur among partons early in the collision, and also among hadrons later in the collision. Both kinds of rescattering can lead to collective behavior among the particles, and the presence of elliptic flow [4–9] indicates that partonic rescattering is important at RHIC. In the extreme, rescattering can lead to thermalization. Rescattering has observable consequences on the final hadron momentum spectra, causing them to be broadened as shown in this paper. This relates to some of the key questions regarding the evolution of the collision: Are the size and lifetime sufficient to attain local equilibrium? Are the momentum distributions thermal, and, if so, what are the chemical and kinetic freeze-out temperatures? Can expansion be described by hydrodynamic models? Momentum distributions of hadrons as a function of centrality provide a means to investigate these questions and permit extraction of thermodynamic quantities which govern the predicted phase transition.

This paper reports semi-inclusive momentum spectra and yields of π, K, and p from Au-Au collisions at $\sqrt{s_{NN}} = 130$ GeV. The data are measured and analyzed by the PHENIX Collaboration in the first year of the physics program at RHIC (Run-1).

The paper is organized as follows. In Sec. II the PHENIX detectors used in the analysis are described. The data reduction techniques using the time-of-flight and drift chamber detectors, along with the corrections applied to the spectra, are described in Sec. III. Functions that describe the shape of the spectra are used to extrapolate the unmeasured portion in order to determine the total average momentum and particle yield for each particle. The overall systematic uncertainties in the spectra are discussed. The resulting minimum bias and centrality-selected particle spectra are presented in Sec. IV. In Sec. V a description of the particle production within a hydrodynamic picture is investigated. For each centrality selection, a hydrodynamic parametrization of the m_T distribution is fit simultaneously to the spectra of different species.

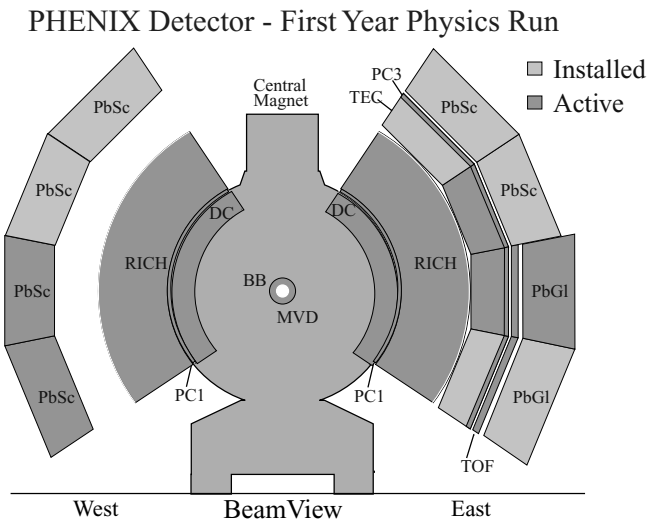

FIG. 1. A cross-sectional view of the PHENIX detector transverse to the beamline. Within the two central arm spectrometers the detectors that were instrumented and operational during the $\sqrt{s_{NN}} = 130$ GeV run are shown.

The data are compared to full hydrodynamic calculations. The transition region in p_T between hard (perturbative QCD) and soft (hydrodynamic behavior) physics is investigated by comparison of extrapolated soft spectra to the data. Finally, we study the dependence of the particle yields on the number of nucleons participating in the collision.

II. EXPERIMENT

The PHENIX [10,11] experiment at RHIC identifies hadrons over a large momentum range, by the addition of excellent time-of-flight capability to the detector suite optimized for photons, electrons, and muons. PHENIX has four spectrometer arms: two that are positioned about midrapidity (the central arms) and two at more forward rapidities (the muon arms). A cross-sectional view of the PHENIX detector, transverse to the beam line is shown in Fig. 1. Within the two central arm spectrometers, the detectors that were instrumented and operational during the $\sqrt{s_{NN}} = 130$ GeV run (Run-1) are shown. The detector systems in PHENIX are discussed in detail elsewhere [12]. The detector systems used for the measurements reported in this paper are described in detail in the following sections.

A. Central arm detectors

The central arm spectrometers use a central magnet that produces an approximately axially symmetric field that focuses charged particles into the detector acceptance. The two central arms are labeled as east and west arms. The east arm contains the following subsystems used in this analysis: drift chamber (DC), pad chamber (PC), and a time-of-flight (TOF) wall. The PHENIX hadron acceptance using the TOF system in the east arm is illustrated in Fig. 2 where the transverse momentum is plotted as a function of the particle rapidity (the phase space) within the central arm acceptance subtend-

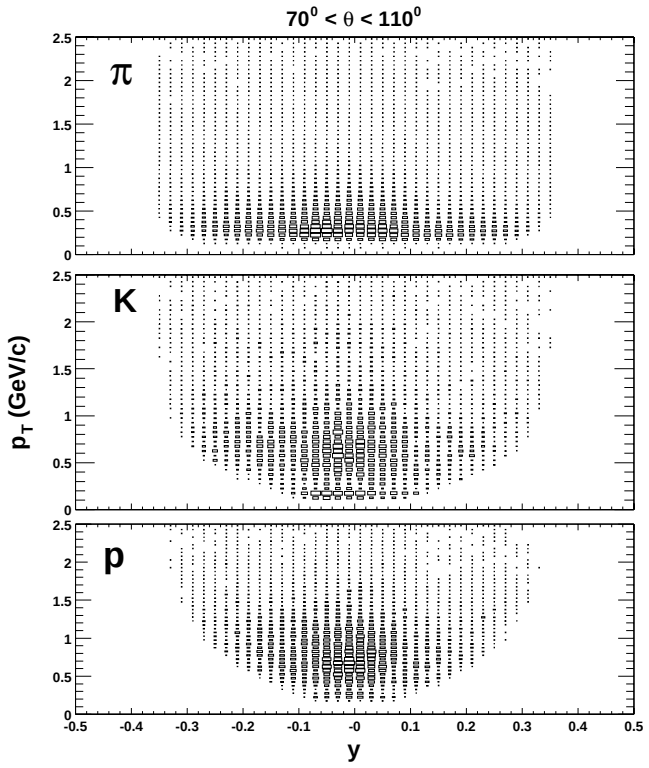

FIG. 2. The central arm spectrometer acceptance in rapidity and transverse momentum for pions (top), kaons (middle), and protons (bottom).

ing the polar angle θ from 70° to 110° for pions, kaons, and protons. The vertical lines are the equivalent pseudorapidity edges, corresponding to $|\eta|<0.35$. More details are discussed elsewhere [13].

1. Tracking chambers

The charged particle tracking chambers include three layers of pad chambers and two drift chambers. The chambers are designed to operate in a high particle multiplicity environment.

The drift chambers are the first tracking detectors that charged particles encounter as they travel from the collision vertex through the central arms. Each is 1.8 m in width in the beam direction, subtends 90° in azimuthal angle ϕ, centered at a radius $R_{\mathrm{DC}}=2.2$ m, and is filled with a 50-50 argon-ethane gas mixture. It consists of 40 planes of sense wires arranged in 80 drift cells placed cylindrically symmetric about the beam line. The wire planes are placed in an *X*-*U*-*V* configuration in the following order (moving outward radially): 12 *X* planes (*X*1)), four *U* planes (*U*1), four *V* planes (*V*1), 12 *X* planes (*X*2), four *U* planes (*U*2), and four *V* planes (*V*2). The *U* and *V* planes are tilted by a small ±5° stereo angle to allow for full three-dimensional track reconstruction. The field wire design is such that the electron drift to each sense wire is only from one side, thus removing most left-right ambiguities everywhere except within 2 mm of the sense wire. The wires are divided electrically in the middle at the beam-line center. The occupancy for a central RHIC Au+Au collision is about two hits per wire.

At the drift chamber location, the field of the central magnet is nearly zero, so the DC determines (nearly) straight-line track segments in the r-ϕ plane. Each track segment is intersected with a circle at R_{DC}, where it is characterized by two angles: the angular deflection in the main bend plane and the azimuthal position in ϕ. A combinatorial Hough transform technique is used to identify track segments by searching for location maxima in this angular space [14]. The DCs are calibrated with respect to the event collision time measurement (see Sec. II B). With this calibration, the single-wire resolution in the r-ϕ plane is 160 μm. The single-track wire efficiency is 99% and the two-track resolution is better than 1.5 mm.

The drift chambers are used to measure the momentum of charged particles and the direction vector for charged particles traversing the spectrometer. The angular deflection is inversely proportional to the component of momentum in the bend plane only. Both the bend angle and the measured track points are used in the momentum reconstruction and track model, which uses a look-up table of the measured central magnet field grid. For this dataset, the drift chamber momentum resolution is $\sigma_p/p=0.6\% \oplus 3.6\% p$, where the first term is multiple scattering up to the drift chambers and the second is the angular resolution of the detector.

In run-1, there were three pad chambers in PHENIX. Each pad chamber measures a three-dimensional space point of a charged track. The pad chambers are pixel-based detectors with effective readout sizes of 8.45 mm along the beam line by 8.40 mm in the plane transverse to the beam line. The first pad chamber layer (PC1) is fixed to the outer edge radially of each drift chamber at a radial distance of 2.49 m, while the third layer (PC3) is positioned at 4.98 m from the beam line. Both arms include PC1 chambers, while only the east arm is instrumented with PC3. The second layer (PC2) is located at an inner inscribed radius of 4.19 m in the west arm and was not installed for run-1.

The position resolution of PC1 is 1.6 mm along the beam axis and 2.3 mm in the plane transverse to the beam axis. The position resolutions of PC3 are 3.2 mm and 4.8 mm, respectively. The PC3 is used to reject background from albedo and nonvertex decay particles; however, only the PC1 is used for the results presented here. The PC1 is used in the global track reconstruction with the measured vertex position using the beam-line detectors (see Sec. II B) to determine the polar angle of each charged track. Both PC1 and the beam-line detectors provide z-coordinate information with a 1.89 mm resolution.

2. Time of flight

The TOF detector serves as the primary particle identification device for charged hadrons by the measurement of their arrival time at the TOF wall 5.1 m from the collision vertex. The TOF wall spans 30° in azimuth in the east arm. It consists of 10 panels of 96 scintillator slats each with an intrinsic timing resolution better than 100 ps. Each slat is oriented along the r-ϕ direction and provides timing as well as beam-axis position information for each particle hit recorded. The slats are viewed by two photomultiplier tubes (PMTs), attached to either end of the scintillator.

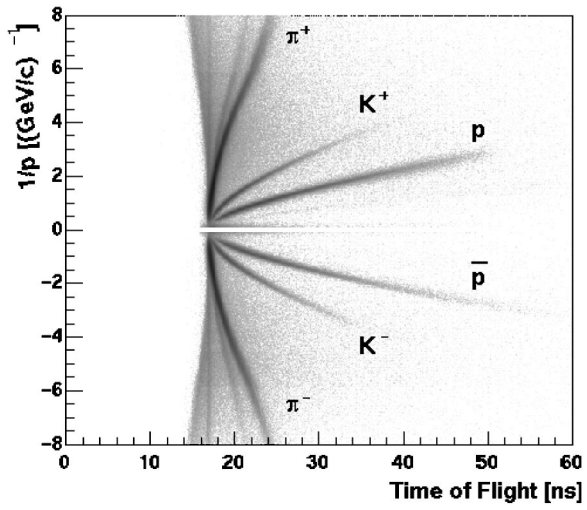

FIG. 3. Scaled time-of-flight vs reciprocal momentum in minimum-bias Au+Au collisions at $\sqrt{s_{NN}}=130$ GeV. The distribution demonstrates the particle identification capability using the TOF for the run-1 data taking period.

A $\pm 2\sigma$ π/K separation at momenta up to 2 GeV/c, and a $\pm 2\sigma$ $(\pi+K)$/proton separation up to 4 GeV/c can be achieved.

For each particle, the time, energy loss in the scintillator, and geometrical position are determined. The total time offset is calibrated slat by slat. A particle hit in the scintillator is defined by a measured pulse height which is also used to correct the time recorded at each end of the slat (slewing correction). After calibration, the average of the times at either end of the slat is the measured time for a particle. The azimuthal position is proportional to the time difference across the slat and the known velocity of light propagation in the scintillator (for Bicron BC404, this is 14 cm/ns). The slat position along the beam line determines the longitudinal coordinate position of the particle. The total time of flight is measured relative to the beam-beam counter (BBC) initial time (see Sec. II B), the measured time in the time-of-flight detector, and a global time offset from the RHIC clock. Positive pions in the momentum range $1.4<p_T<1.8$ GeV/c are used to determine the TOF resolution. The timing calibration in this analysis results in a resolution of $\sigma=115$ ps.[1]

Particle identification for charged hadrons is performed by combining the information from the tracking system with the timing information from the BBC and the TOF. Tracks at 1 GeV/c in momentum point to the TOF with a projected resolution σ_{proj} of 5 mrad in azimuthal angle and 2 cm along the beam axis. Tracks that point to the TOF with less than 2.0 σ_{proj} were selected. Figure 3 shows the resulting time of flight as a function of the reciprocal momentum in minimum-bias Au+Au collisions.

B. Beam-line detectors

The beam-line detectors determine the collision vertex position along the beam direction, and the trigger and timing information for each event. These detectors include the zero degree calorimeters (ZDCs), the BBCs, and the multiplicity vertex detector (MVD) and are positioned in PHENIX as shown in Fig. 4.

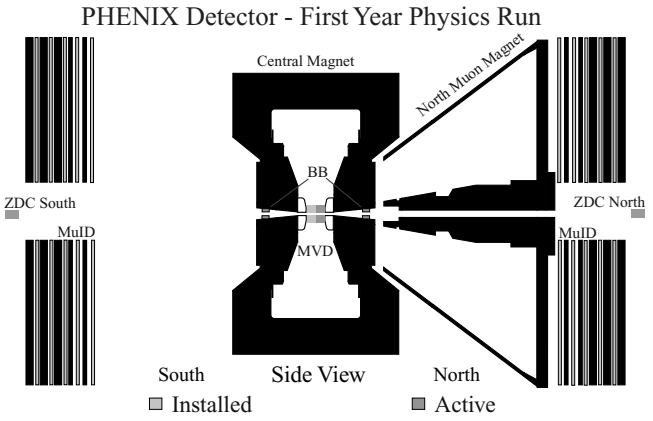

FIG. 4. A side view of the PHENIX detector parallel to the beam line. The beam line detectors determine the collision vertex position along the beam direction, and the trigger and timing information for each event.

The zero-degree calorimeters are small transverse area hadron calorimeters that are installed at each of the four RHIC experiments. They measure the fraction of the energy deposited by spectator neutrons from the collisions and serve as an event trigger for each RHIC experiment. The ZDCs measure the unbound neutrons in small forward cones ($\theta<2$ mrad) around each beam axis. Each ZDC is positioned 18 m upstream and downstream from the interaction point along the beam axis. A single ZDC consists of three modules each with a depth of two hadronic interaction lengths and read out by a single PMT. Both time and amplitude are digitized for each of the three PMTs as well as an analog sum of the PMTs for each ZDC [15].

There are two beam-beam counters each positioned 1.4 m from the interaction point, just behind the central magnet poles along the beam axis (see Fig. 4). The BBC consists of two identical sets of counters installed on both sides of the interaction point along the beam. Each counter consists of 64 Cherenkov telescopes, arranged radially about the collision axis and situated north and south of the MVD. The BBCs measure the fast secondary particles produced in each collision at forward angles, with $3.0\leqslant\eta\leqslant 3.9$, and full azimuthal coverage.

For both the ZDC and the BBC, the time and vertex position are determined using the measured time difference between the north and the south detector and the known distance between the two detectors. The start time T_0 and the vertex position along the beam axis (Z_{vertex}) are calculated as $T_0=(T_1+T_2)/2$ and $Z_{\text{vertex}}=(T_1-T_2)/2c$, where T_1 and T_2 are the average timing of particles in each counter and c is the speed of light. With an intrinsic timing resolution of 150 ps, the ZDC vertex is measured to within 3 cm. In run-1, the BBC timing resolution of 70 ps results in a vertex position resolution of 1.5 cm.

Event centrality is determined using a correlation measurement between neutral energy deposited in the ZDCs and

[1]Ultimately, 96 ps results after further calibration, as reported in Ref. [12].

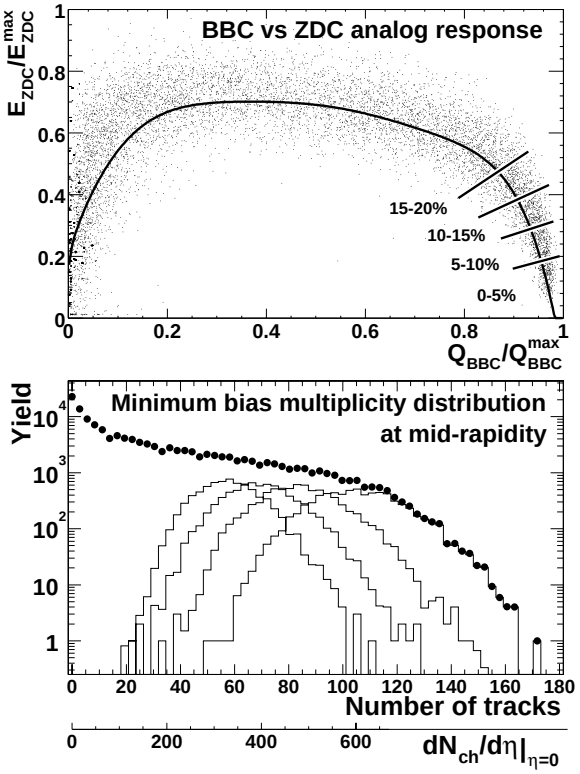

FIG. 5. The event centrality (upper plot) is determined using a correlation measurement of the fraction of neutron energy recorded in the ZDCs (vertical scale) and the fractional charge measured in the BBCs (horizontal scale). The equivalent track multiplicity in each centrality selection is shown in the lower plot.

fast particles recorded in the BBCs as shown in Fig. 5. The spectator nucleons are unaffected by the interaction and travel at their initial momentum from each respective ion. The number of neutrons measured by the ZDC is proportional to the number of spectators, while the BBC signal increases with the number of participants.

III. DATA REDUCTION AND ANALYSIS

A. Data reduction

The PHENIX Level-1 trigger selected events with hits coincident in both the ZDC and BBC detectors, and in time with the RHIC clock. A total of 5 million events were recorded at $\sqrt{s_{NN}}=130$ GeV in the ZDCs [11]. The collision position along the beam direction was required to be within ±30 cm of the center of PHENIX, using the collision vertex reconstructed by the BBC.

The trigger on both BBC and ZDC counters includes $92\pm4\%$ of the total inelastic cross section (6.8 ± 0.4 b). A Monte Carlo Glauber model [16] is used with a simulation of the BBC and ZDC responses to determine the number of nucleons participating in the collisions for the minimum-bias events. The Woods-Saxon parameters determined from electron scattering experiments are radius $R=6.38\pm0.06$ fm, diffusivity $d=0.54\pm0.01$ fm [17], and the nucleon-nucleon inelastic cross section, $\sigma^{inel}_{N+N}=40\pm3$ mb. An additional systematic uncertainty enters the radius parameter since the radial distribution of neutrons in large nuclei should be larger than for protons and is not well determined [18].

The centrality selections used in this paper are 0–5 %, 5–15 %, 15–30 %, 30–60 %, and 60–92 % of the total geometrical cross section, where 0–5 % corresponds to the most central collisions.

Only tracks that are reconstructed in all three dimensions are included in the spectra. These tracks are then matched within $2\sigma_{\rm proj}$ to the measured positions in the TOF detector. For each TOF hit, the time, position, and energy loss are measured in the TOF detector. The widths of residual distance distributions between projected tracks and TOF hit positions, $\sigma_{\rm proj}$, increase at lower momentum due to multiple scattering. Therefore, a momentum-dependent hit association criterion was defined.

Finally, a requirement on energy loss in the TOF is applied to each track to exclude false hits by requiring the energy deposit of at least minimum ionizing particle energy. A β-dependent energy loss cut whose form is a parametrization of the Bethe-Bloch formula [19] is used, where

$$dE/dx \approx \beta^{-5/3} \tag{1}$$

and $\beta=L/ct$, where L is the pathlength of the particle's trajectory from the BBC vertex to the TOF detector, t is the particle's time of flight, and c is the speed of light. The approximate Bethe-Bloch formula is scaled by a factor to fall below the data and thereby serve as a cut. The resulting equation is $\Delta E=A\beta^{-5/3}$, where A is a scaling factor equal to 1.6 MeV. The energy loss cut reduces low momentum background under the kaon and proton mass peaks. The fraction of tracks excluded after the energy loss cut is less than 5.5%.

The measured momentum p, pathlength L, and time of flight t in the spectrometer are used to calculate the particle mass, which is used for particle identification:

$$m^2 = \frac{p^2}{c^2}\left[\left(\frac{1}{\beta}\right)^2 - 1\right]. \tag{2}$$

The widths of the peaks in the mass-squared distribution depend on both momentum and time-of-flight resolutions. An analytic form for the width of m^2 as a function of momentum resolution σ_p and time-of-flight resolution is determined using Eq. (2). The error in the particle's pathlength L results in an effective time width that is included with the TOF resolution, σ_T,

$$\sigma^2_{m^2} = 4m^4\left(\frac{\sigma_p}{p}\right)^2 + 4p^4\left(\frac{\sigma_T}{\beta t}\right)^2. \tag{3}$$

The momentum resolution of the drift chambers is expressed in the following form:

$$\sigma^2_p = \left(C_1 p\frac{1}{\beta}\right)^2 + (C_2 p^2)^2, \tag{4}$$

$$C_1 = \frac{\delta\phi_{\rm ms}}{K_1}, \tag{5}$$

$$C_2 = \frac{\delta\phi_\alpha}{K_1}, \tag{6}$$

where C_1 and C_2 are the multiple scattering and angular resolution terms, respectively. The units of $\delta\phi_{\rm ms}$ are mrad GeV/c. The constant K_1 is the momentum kick on the particle from the magnetic field and is equal to 87.3 mrad GeV/c. The constant C_1 is the width in ϕ due to the multiple scattering (ms) of a charged particle with materials of the spectrometer up to the drift chambers. The C_2 term is the angular resolution of the bend angle α, which is the angular deflection in ϕ of the track segment relative to the radius to the collision vertex.

Equation (4) is used in Eq. (3) with $\beta = p/\sqrt{p^2+m^2}$, where m is the mass centroid of the particle's mass-squared distribution. The mass centroid is close to the rest mass of the particle; however due to residual misalignments and timing calibration, the centroid of the distribution is a fit parameter in order to avoid cutting into the distribution. The m^2 width for each particle is written as follows:

$$\sigma^2_{m^2} = C_1^2 4m^4\left(1+\frac{m^2}{p^2}\right) + C_2^2 4m^4p^2 + C_3^2[4p^2(m^2+p^2)], \tag{7}$$

where the coefficient C_3 is related to the combined TOF,

$$C_3 = \frac{\sigma_T c}{L}, \tag{8}$$

and pathlength contributions to the time width, σ_T in Eq. (8). From the measured drift chamber momentum resolution, $C_1 = 0.006$ and $C_2 = 0.036$ c/GeV. While the TOF resolution is 115 ± 15 ps, the pathlength uncertainty introduces a width of $\approx 20-40$ ps, so 145 ps is used for σ_T in C_3.

The pions, kaons, and protons are identified using the measured peak centroids of the m^2 distribution and selecting 2σ bands; shown as shaded regions in Fig. 6 for two different momentum slices. The 2σ bands for pions and kaons do not overlap up to $p_T = 2$ GeV/c. The protons are identified up to $p_T = 4$ GeV/c. By studying variations in the m^2 centroid and width before the particle identification cut is applied, the uncertainty in the particle identification is estimated to be 5% for all particles.

Kaons are depleted by decays in flight and geometrical acceptance. For the low momentum protons, energy loss and geometrical acceptance cause a drop in the raw yield for $p_T < 0.5$ GeV/c, as seen in Fig. 2.

The remaining background contribution was determined by reflecting the track about the midpoint of PHENIX along the beam line and repeating the association and particle identification cuts used in the TOF detector. This random background was evaluated separately for each particle type. The background contribution is $\approx 30\%$ for the kaon spectra at $0.2 < p_T < 0.4$ GeV/c and defines the low p_T limit in the spectra. The background is less than 5% in all other cases, and negligible above 0.8 GeV/c in the measured momentum range in this analysis. The background was not subtracted but is instead treated as a systematic uncertainty. This uncertainty is 2%, 5%, and 3% for pions, kaons, and protons, respectively, at $p_T < 0.6$ GeV/c and is negligible at higher momenta.

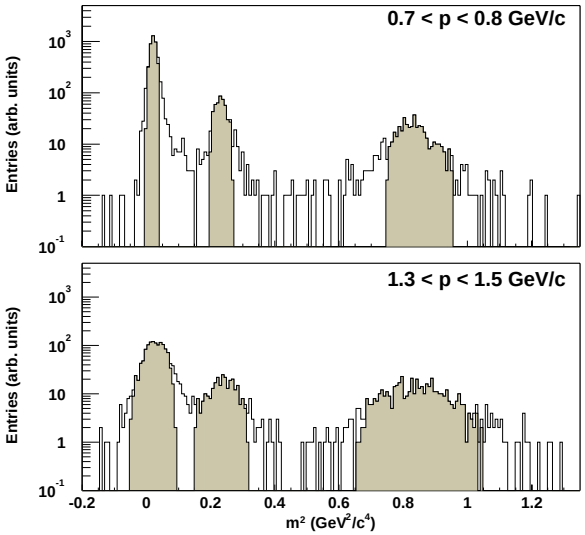

FIG. 6. (Color online) The mass-squared distributions of positive pions, kaons, and protons for two different momentum slices. The momentum slice $0.7 < p < 0.8$ GeV/c is the upper panel and $1.3 < p < 1.5$ GeV/c is the lower panel. The shaded regions correspond to the 2σ particle identification bands based on the calculated mass-squared width, the measured mass-squared centroids, and the known detector resolutions.

B. Analysis

The raw spectra include inefficiencies from detector acceptance, resolution, particle decays in flight and track reconstruction. The base-line efficiencies are determined by simulating and reconstructing single hadrons. Multiplicity dependent effects are then evaluated by embedding simulated single hadrons into real events and calculating the degradation of the reconstruction efficiency.

1. Corrections: Acceptance, decays in flight, and detector response

The corrections for the finite detector aperture, pion and kaon decays in flight, and the detector response are determined using single particles in the the GEANT [20] simulation of the detector. All details of each detector are modeled, including dead channels in the drift chambers, pad chambers, and time-of-flight detector. All physics processes are automatically taken into account, resulting in corrections for multiple scattering, antiproton annihilation, pion and kaon decays in flight, finite geometrical acceptance of the detector, and momentum resolution, which affects the spectral shape above 2.5 GeV/c.

The drift chamber simulated response is tuned to describe the response of the real drift chambers on the single-wire level. This is done using a simple geometrical model of the drift chamber and the straight-line trajectories of particles from the zero-field data. This simple model of the drift cell in the drift chamber is sufficient to describe the observed drift

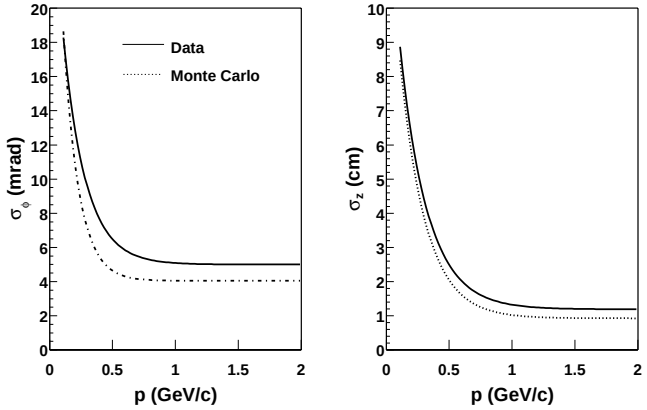

FIG. 7. Comparison of the momentum-dependent residuals of DC tracks matched to TOF hits in azimuthal angle ϕ (left) and z (right) between data (solid) and simulation (dashed).

distance distribution, the pulse width, the single-wire efficiency, and the detector resolution. The TOF response is simulated by smearing the true time of flight using a Gaussian distribution with a width as measured in the data.

Figure 7 shows the momentum dependence of the residual distance between projected tracks and TOF hits for the real (solid line) and simulated (dashed) events. These residuals are parametrized in the azimuthal angle ϕ and the beam-line direction z, separately for data and simulation. For each case, tracks that fall outside 2σ of the parametrized width are rejected, thus allowing use of the Monte Carlo to evaluate the correction for the 2σ match requirement for real tracks.

A fiducial cut is made in both the simulation and the data to ensure the same fiducial volume. The systematic uncertainty in the acceptance correction is $\approx 5\%$.

The simulated distributions are generated uniformly in p_T, ϕ, and y. For each hadron, sufficient Monte Carlo events are generated to obtain the correction factor for every measured p_T bin. The statistical errors from the correction factors were smaller than those in the data and both are added in quadrature.

The distribution of the number of particles generated in each p_T slice, dN/dp_T, is the "ideal" input distribution without detector and reconstruction effects. This distribution is normalized to 2π and 1 unit of rapidity. After detector response and track reconstruction, the output distribution is the number of particles found in each p_T slice. The final corrections are determined after an iterative weighting procedure. First, the flat input and output distributions are weighted by exponential functions for all particles using an inverse slope of 300 MeV. The ratio of input to output distributions is determined as a function of momentum. In each p_T slice, the corresponding ratio is applied to the data. The corrected data are next fitted with exponentials for kaons and protons [see Eq. (11)], and a power law for the pions [see Eq. (9)]. The original flat input and output distributions are weighted by these resulting functions. The procedure is repeated until the functions remain constant in their parameters. The weighted input and output distributions are divided to produce acceptance correction factors. The corrections are larger for kaons due to the decays in flight. The statistical error in determination of the correction factor is added in quadrature to the statistical error in the data.

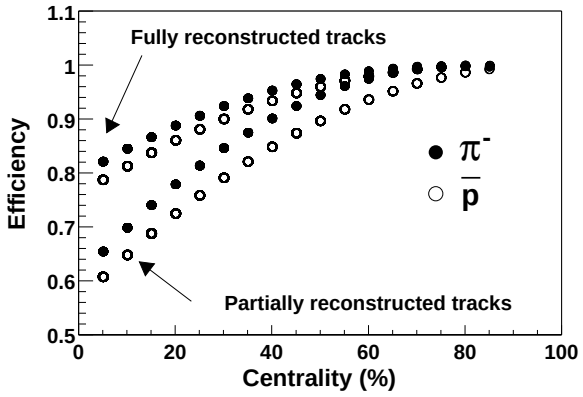

FIG. 8. The multiplicity dependent efficiency correction for pions (solid) and (anti)protons (open) for two types of tracks. The upper set of points correspond to fully reconstructed tracks in the drift chambers, while the lower set of points correspond to partially reconstructed tracks in the drift chambers.

2. High track-density efficiency correction

A final multiplicity dependent correction is determined using simulated single-particles embedded into real events. This correction depends on both the quality of the track reconstruction in a high multiplicity environment and the type of particle measured.

Depending on the centrality of the event, the correction factor is determined for each particle in the raw transverse momentum distribution and is applied as a weight. The final efficiency corrections are shown in Fig. 8, where the correction for pions is shown as solid circles and for (anti)protons as open circles. The horizontal axis ranges from the most central to the most peripheral events in increments of 5%. The systematic uncertainty in the multiplicity efficiency correction is 9%.

The difference between pions (solid) and (anti)protons (open) is due to the different TOF efficiencies for each particle (protons are slower than pions). In a small fraction of cases two particles may hit the same TOF slat at different times, and the slower particle is assigned an incorrect time. The particle will then fall outside the particle identification cuts. This effect depends on the type of particle.

For each particle, two curves are shown, representing the DC tracking inefficiency for two types of tracks: fully reconstructed and partially reconstructed tracks. Fully reconstructed tracks include $X1$ and $X2$ sections. In a high track-density environment, tracks may be partially reconstructed or hits may be incorrectly associated. There are two cases when this incorrect hit association occurs. In the first case, the direction vector in the azimuth prevents the track from pointing properly to the PC1 detector, and the correct hit cannot be associated. In the second case, the track is reconstructed properly, but there are two possible PC1 points. If no UV hits are found, then the wrong PC1 point can be associated with the track and the track's beam-line coordinate is misreconstructed. In both of these cases, the track fails the matching criteria in the TOF detector and is lost.

3. Determining the yield and mean p_T

The dN/dy and $\langle p_T \rangle$ are determined using the data in the measured region and an extrapolation to the unmeasured re-

TABLE I. The sources of systematic uncertainties in $\langle p_T \rangle$ and dN/dy.

	π(%)	K(%)	(anti)p(%)
Extrapolation	6	8	7.5
Background ($p_T < 0.6$ GeV/c)	2	5	3
$\langle p_T \rangle$ total	7	10	8
Corrections and cuts	11	11	11
dN/dy total	13	15	14

gion after integrating a functional form fit to the data. A function describing the spectral shape is fit to the data, with varying p_T ranges to control systematic uncertainties in the fit parameters. The fitted shape is extrapolated, integrated over the unmeasured range, and then combined with the measured data to get the full yield. Two different functions are used to estimate upper and lower bounds for each spectrum. The average between the upper and lower bounds is used for dN/dy and $\langle p_T \rangle$. The statistical error is determined from the data, and the systematic uncertainty is taken as half the difference between the upper and lower bounds.

For pions, a power law in p_T [Eq. (9)] and an exponential in $m_T (=\sqrt{p_T^2 + m_0^2})$ [Eq. (10)] are fit to the data. For kaons and (anti)protons, two exponentials—one in p_T [Eq. (11)] and the other in m_T—are used. The p_T exponential provides an upper limit for the extrapolated yield, which is most important for the (anti)protons. The power-law function has three parameters labeled A, p_0, and n in Eq. (9). The exponentials have two parameters, A and T.

$$\frac{d^2N}{2\pi p_T dp_T dy} = A\left(\frac{p_0}{p_0 + p_T}\right)^n, \tag{9}$$

$$\frac{d^2N}{2\pi m_T dm_T dy} = Ae^{-m_T/T}, \tag{10}$$

$$\frac{d^2N}{2\pi p_T dp_T dy} = Ae^{-p_T/T}. \tag{11}$$

C. Systematic uncertainties

In Table I, the sources of systematic uncertainties in both $\langle p_T \rangle$ and dN/dy are tabulated. The sources of uncertainty include the extrapolation in p_T, the background, and the Monte Carlo corrections, and cuts. The uncertainty in the Monte Carlo corrections is 11% and includes the multiplicity efficiency correction of 9%, the particle identification cut of 5%, and the fiducial cuts of 5%. The uncertainties in the correction functions are added in quadrature to the statistical error in the data. Background is only relevant for $p_T < 0.6$ GeV/c in the spectra.

The total systematic uncertainty in the $\langle p_T \rangle$ depends on the extrapolation and background uncertainties; the uncertainties are 7%, 10%, and 8% for pions, kaons, and protons, respectively. The overall uncertainty on dN/dy includes the uncertainties on $\langle p_T \rangle$ in addition to the uncertainties from the corrections and cuts; the uncertainties are 13%, 15%, and 14% for pions, kaons, and protons, respectively [21].

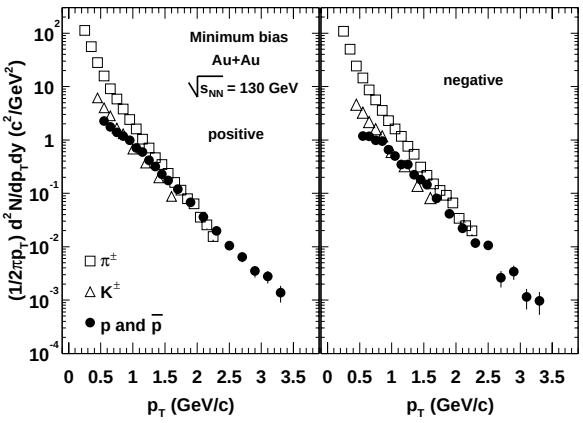

FIG. 9. The spectra of positive particles (left) and negative (right) in minimum-bias collisions from Au+Au collisions at $\sqrt{s_{NN}} = 130$ GeV. The errors include both statistical and systematic errors from the corrections.

The hadron yields and $\langle p_T \rangle$ values include an additional uncertainty arising from the fitting function used for extrapolation to the unmeasured region at low and high p_T. The magnitude of the extrapolation is $30 \pm 6\%$ of the spectrum for pions, $40 \pm 8\%$ for kaons, and $25 \pm 7.5\%$ for protons [21]. The systematic uncertainty quoted here is taken as half the difference between the results from the two different functional forms.

The momentum scale is known to better than 2%, and the momentum resolution affects the spectra shape, primarily for protons, above 2.5 GeV/c. The momentum resolution is corrected by the Monte Carlo. As other sources of uncertainty on the number of particles at any given momentum are much larger, momentum resolution effects are neglected in determining the overall systematic uncertainty from the data reduction.

IV. RESULTS

A. Transverse momentum distributions

The invariant yields as a function of p_T for identified hadrons are shown in Fig. 9, while Fig. 10 provides the centrality dependence of the spectra. The spectra are tabulated in Appendix B. The $\pi^{\pm}$, $K^{\pm}$, p, and $\bar{p}$ invariant yields for the most central, midcentral, and the most peripheral collisions, were reported previously [22]. Pion and (anti)proton invariant yields are comparable for $p_T > 1$ GeV in the most central collisions.

As can be seen already from Fig. 10 all the spectra seem to be exponential; however, upon closer inspection, small deviations from an exponential form are apparent for the more peripheral collisions. The spectrum in the most peripheral collisions is noticeably power-law-like when compared to the more exponential-like spectrum in central collisions. This is especially apparent for the pions. The effect can be seen more clearly in the ratio of the spectra for a given particle species in two different centrality classes. Such ratios

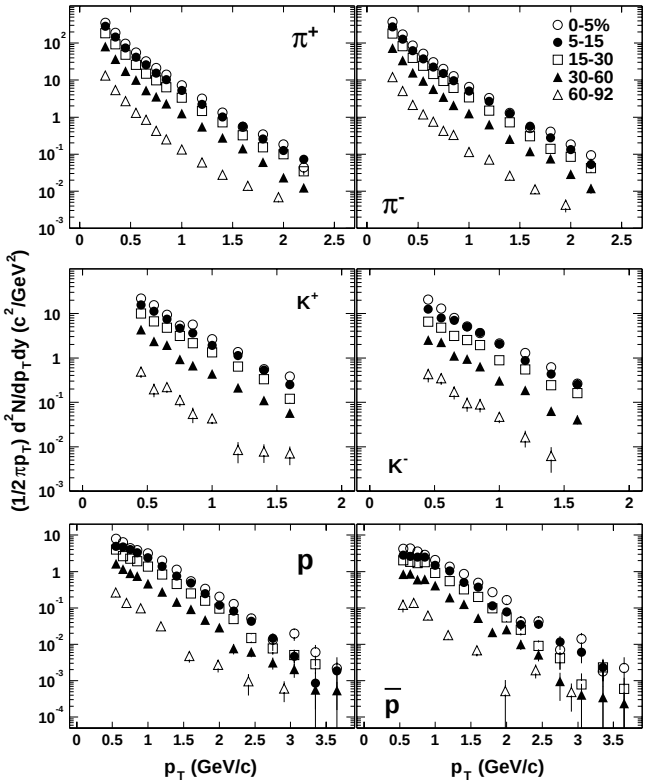

FIG. 10. The hadron spectra for five centralities from the most central 0–5 % to the most peripheral 60–92 % at $\sqrt{s_{NN}}=130$ GeV. Errors include both the statistical and point-by-point error in the corrections added in quadrature.

are shown in Fig. 11 for the 5% central and the most peripheral positive spectra (60–92 % centrality). The ratios for protons and antiprotons as well as for π^+ have a maximum at intermediate p_T and are lower at both low and high p_T. The kaon shape change is not very significant, given the current statistics.

The change in slope at low p_T in central collisions compared to peripheral is consistent with a more substantial hydrodynamic, pressure-driven transverse flow existing in central collisions, since the increased boost would tend to deplete particles at the lowest p_T (see Sec. IV C). This is observed at lower energies at the CERN SPS [23,24]. It is in contrast to results obtained at the ISR [25] for $p+p$ collisions at $\sqrt{s}=63$ GeV, where a shallow maximum or minimum exists at low p_T (in the range 0.3–0.6 GeV/c).

Feed-down contribution to p and $\bar{p}$ from inclusive Λ and $\bar{\Lambda}$

Inclusive Λ and $\bar{\Lambda}$ transverse momentum distributions have been measured in the west arm of the PHENIX spectrometer using the tracking detectors (DC, PC1) and a lead-scintillator electromagnetic calorimeter (EMCal) [26]. The invariant mass is reconstructed from the weak decays $\Lambda \rightarrow p+\pi^-$ and $\bar{\Lambda}\rightarrow \bar{p}+\pi^+$.

The tracks from the tracking detectors are required to fall within 3σ of EMCal measured space points. The EMCal timing resolution of the daughter particles is $\approx$700 ps. Using the DC momentum and the EMCal time of flight, the particle mass is calculated, and protons, antiprotons, and pions are

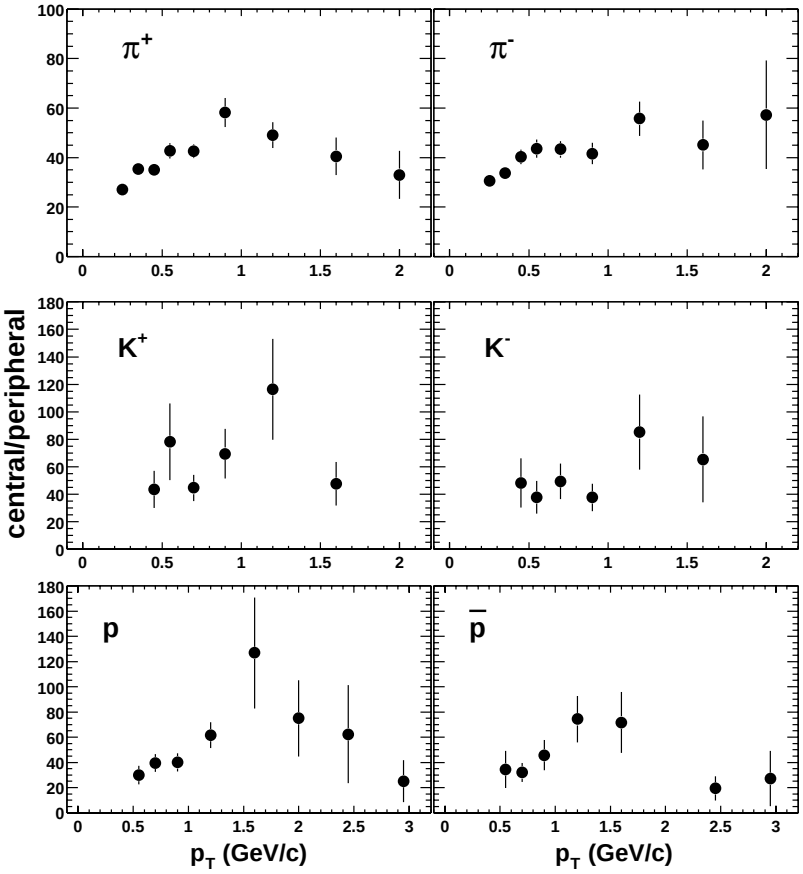

FIG. 11. The ratio of the most central to the most peripheral yields as a function of p_T for pions (top), kaons (middle), and (anti)protons (bottom).

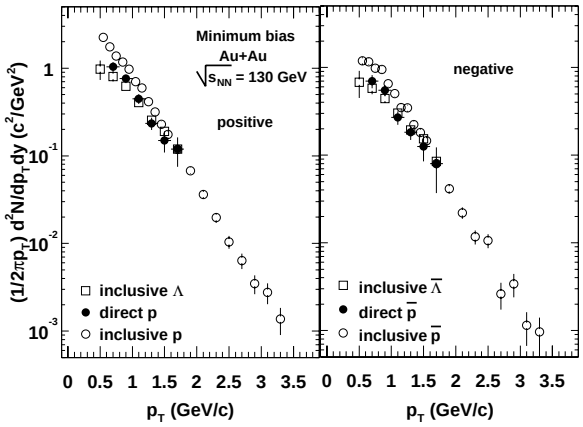

FIG. 12. For minimum-bias collisions, the inclusive Λ, inclusive p, and direct p transverse momentum distributions are plotted together in the left panel. The equivalent comparison for inclusive $\bar{\Lambda}$, $\bar{p}$, and direct $\bar{p}$ transverse momentum distributions is in the right panel.

identified using 2σ momentum-dependent mass-squared cuts. A clean particle separation is obtained using an upper momentum cut of 0.6 GeV/c and 1.4 GeV/c for pions and protons, respectively. The momentum is determined assuming the primary decay vertex is positioned at the event vertex and results in a momentum shift of 1–2% based on a Monte Carlo study.

Using all combinations of pions and protons, the invariant mass is determined. The mass distribution shows a Λ peak on top of a random combinatorial background, which is determined by combining protons and pions from different collisions with the same centrality. A signal-to-background ratio of 1/2 is obtained after applying a decay kinematic cut on the daughter particles. Fitting a Gaussian function to the mass distribution in the range $1.05 < m_{p\pi} < 1.20$ GeV/c^2, 12000 Λ and 9000 $\bar{\Lambda}$ are observed, with mass resolution $\delta m/m \approx 2\%$. The reconstructed Λ and $\bar{\Lambda}$ spectra are corrected for the acceptance, pion decay-in-flight, momentum resolution, and reconstruction efficiency [26]. The systematic uncertainty on the p_T spectra is 13% from the corrections and 3% from the combinatorial background subtraction. The feed-down contributions from heavier hyperons Σ^0 and Ω are not measured but are estimated to be $<5\%$.

Figure 12 shows the transverse momentum spectra of inclusive protons (left) and antiprotons (right) with the inclusive Λ and $\bar{\Lambda}$ transverse momentum distributions. The solid points are the (anti)proton spectra after the feed-down correction from Λ and $\bar{\Lambda}$ weak decays. From here forward, the data that are presented and discussed are not corrected for this feed-down effect; inclusive p and $\bar{p}$ yields are given. More details on the Λ and $\bar{\Lambda}$ measurement are included in Ref. [26].

TABLE III. The $\langle p_T \rangle$ in MeV/c for hadrons produced at midrapidity in each centrally class. The errors are statistical only. The systematic uncertainities are 7%, 10%, and 8% for pions, kaons, and (anti)protons, respectively.

	0–5 %	5–15 %	15–30 %	30–60 %	60–92 %
π^+	390±10	380±10	380±20	360±10	310±30
π^-	380±20	390±10	380±10	370±20	320±20
K^+	560±40	580±40	570±40	550±40	470±90
K^-	570±50	590±40	610±40	550±50	460±90
p	880±40	870±30	850±30	800±30	710±80
$\bar{p}$	900±50	890±40	840±40	820±40	800±100

B. Yield and $\langle p_T \rangle$

The yield dN/dy and the average transverse momentum $\langle p_T \rangle$ are determined for each particle as described in the preceding section and have been previously published in Ref. [22]. For each centrality, the rapidity density dN/dy and average transverse momentum $\langle p_T \rangle$ are tabulated in Tables II and III, respectively.

The $N_{\rm part}$ and $N_{\rm coll}$ in each centrality selection are determined using a Glauber-model calculation in Ref. [27]. The resulting values of $N_{\rm part}$ and $N_{\rm coll}$ are also tabulated in Table II. (See Appendix A for more detail.) The errors on $N_{\rm part}$ and $N_{\rm coll}$ include the uncertainties in the model parameters as

TABLE II. The dN/dy at midrapidity for hadrons produced at midrapidity in each centrality class. The errors are statistical only. The systematic errors are 13%, 15%, and 14% for pions, kaons, and (anti)protons, respectively. The $N_{\rm part}$ and $N_{\rm coll}$ in each centrality selection are from a Glauber-model calculation in Ref. [27], also shown with systematic errors based on a 92±4% coverage.

	0–5 %	5–15 %	15–30 %	30–60 %	60–92 %
$N_{\rm part}$	347.7±10	271.3±8.4	180.2±6.6	78.5±4.6	14.3±3.3
$N_{\rm coll}$	1008.8	712.2	405.5	131.5	14.2
π^+	276±3	216±2	141±1.5	57.0±0.6	9.6±0.2
π^-	270±3.5	200±2.2	129±1.4	53.3±0.6	8.6±0.2
K^+	46.7±1.5	35±1.3	22.2±0.8	8.3±0.3	0.97±0.11
K^-	40.5±2.3	30.4±1.4	15.5±0.7	6.2±0.3	0.98±0.1
p	28.7±0.9	21.6±0.6	13.2±0.4	5.0±0.2	0.73±0.06
$\bar{p}$	20.1±1.0	13.8±0.6	9.2±0.4	3.6±0.1	0.47±0.05

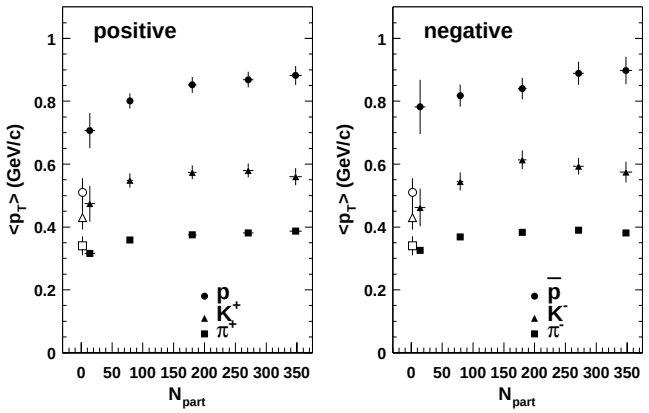

FIG. 13. The integrated mean p_T for pions, kaons, and (anti)protons produced in the five different classes of event centrality [22]. The error bars are statistical only. The systematic uncertainties are 7%, 10%, and 8% for pions, kaons, and (anti)protons, respectively. The open points are equivalent average transverse momenta from pp and $p\bar{p}$ data, interpolated to $\sqrt{s}=130$ GeV.

well as in the fraction of the total geometrical cross section $(92\% \pm 4\%)$ seen by the interaction trigger. The error due to model uncertainties is 2% [27]. An additional 3.5% error results from time dependencies in the centrality selection over the large data sample.

Pions dominate the charged particle multiplicity, but a large number of kaons and (anti)protons are produced. The inclusive yield of antiprotons is nearly comparable to that of protons. In the most central Au+Au collisions, the particle density at midrapidity (dN/dy) is ≈ 20 for antiprotons and 28 for protons, not corrected for feed-down from strange baryons.

The average transverse momenta increase with particle mass and with decreasing impact parameter. The mean transverse momentum increases with the number of participant nucleons by $20 \pm 5\%$ for pions and protons, as shown in Fig. 13. The $\langle p_T \rangle$ of particles produced in $p+p$ and $p\bar{p}$ collisions, extrapolated to RHIC energies, are consistent with the most peripheral pion and kaon data; however, the $\langle p_T \rangle$ of protons produced in Au+Au collisions is significantly higher. This dependence on the number of participant nucleons may be due to radial expansion. It should be noted that the feeding of protons and antiprotons from Λ decays affects $\langle p_T \rangle$. If the spectra are corrected for feed-down, $\langle p_T \rangle$ increases by approximately 15%.

C. Transverse mass distributions

Production of hadrons from a thermal source would make transverse mass the natural variable for analysis. Therefore we extract inverse slopes from the transverse mass distributions by separately fitting a thermal distribution to each particle species. The Boltzmann distribution is given in Eq. (12),

$$\frac{d^2N}{2\pi m_T dm_T dy} = A m_T e^{-m_T/T_{eff}}. \tag{12}$$

We use a simple exponential, however, with no powers of m_T in the prefactor, as shown in Eq. (10). This simplification is acceptable as the difference in the inverse slope is found to be less than 2%. The simple m_T exponential was also used in an equivalent analysis in Ref. [28]. The inverse slope T_{eff} can be compared to other experiments, provided the same momentum range of the spectrum is used for fitting.

If the system develops collective motion, particles experience a velocity boost from this motion, resulting in an additional transverse kinetic energy component. This motivates use of the transverse kinetic energy, i.e., transverse mass minus the particle rest mass, for plotting data. Figure 14 shows the transverse kinetic energy distributions (i.e., transverse mass minus the particle rest mass) for all positive particles (left) and negative particles (right). Pions are in the top panel, kaons in the middle panel, and (anti)protons in the bottom panel, with different symbols indicating different centrality bins. The solid lines are m_T exponential fits in the range $(m_T - m_0) < 1$ GeV for all particle species while the dashed lines are the extrapolated fits. The pion spectra follow an exponential for $0.38 < (m_T - m_0) < 1.0$ GeV while the kaons and protons appear exponential over the entire measured m_T range. The same is true for the negative particles in the right panel; however, the antiprotons have more curvature for $(m_T - m_0) < 0.5$ GeV. We extract T_{eff} by fitting exponentials of form (10) to the transverse mass spectra in the range $(m_T - m_0) < 1$ GeV.

This range is chosen common for all particle species and minimizes contributions from hard processes. Caution must be taken when comparing T_{eff} values as the local slope of the transverse mass spectra varies somewhat over m_T for pions and antiprotons even within this fit range. The resulting values of T_{eff} for all particles and centralities are tabulated in Table IV in units of MeV. The inverse slopes increase and then saturate for more central collisions for all particles except antiprotons. The fact that the inverse slope is different for mesons and baryons and for central and peripheral events is consistent with the mean p_T trends discussed above.

We compare to published inverse slopes of transverse mass distributions at midrapidity from m_T exponential fits in the region $(m_T - m_0) < 1.2$ GeV, listed in Table V. The comparison includes NA44 [28–31] and WA97 [32,33] at the SPS at $\sqrt{s_{NN}} = 17-29$ GeV; and, at $\sqrt{s_{NN}} = 23$ GeV at the ISR, Alper *et al.* [34] and Guettler *et al.* [35]. These data are chosen as they match the $m_T - m_0$ range used in fitting our data. For pions, the low-p_T region of $(m_T - m_0) < 0.3$ GeV, populated by decay of baryonic resonances, is systematically excluded from the fits. The effective temperatures are given in Table V with the references noted accordingly.

Radial flow imparts a radial velocity boost on top of the thermal distribution. Heavy particles are boosted to higher p_T, depleting the cross section at lower p_T and yielding a higher inverse slope. Therefore, the observed inverse slope dependence on both centrality and particle mass implies more radial expansion in more central collisions. At CERN SPS, the T_{eff} depends on both mass and system size (the number of participating nucleons in the collision), indicating collective expansion. The T_{eff} values at RHIC shown in Table IV are somewhat larger.

In p-p collisions at similar $\sqrt{s}$ at the ISR, hadron spectra were analyzed in transverse mass, m_T, rather than transverse

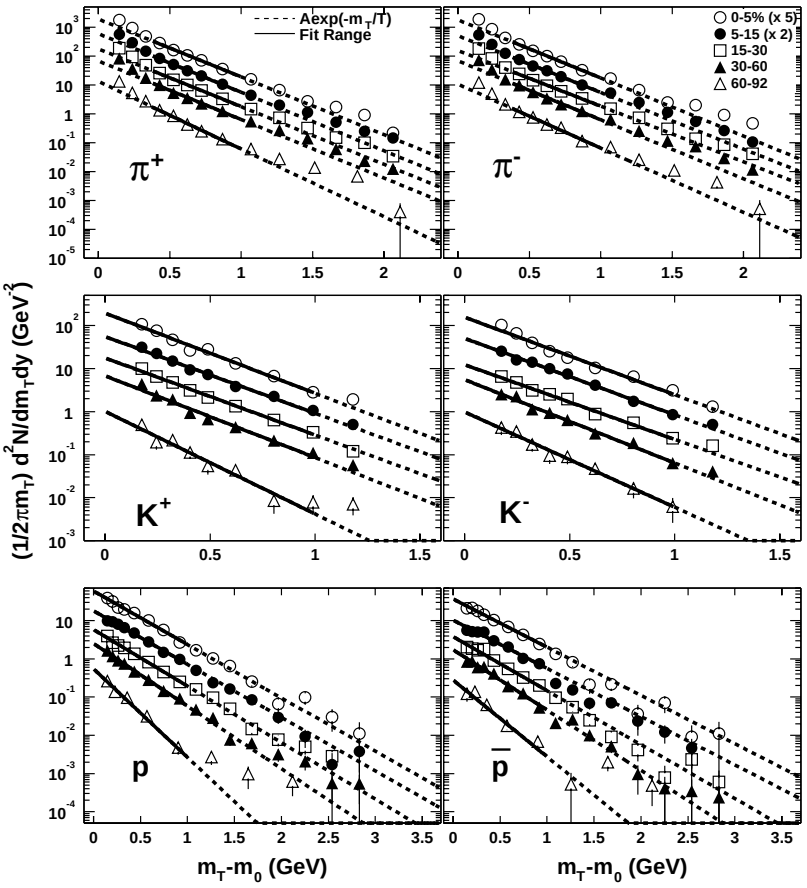

FIG. 14. Transverse mass distributions of pions (top), kaons (middle), and (anti)protons (bottom) in events with different centralities. Positive particle distributions are on the left and negative particle distributions are on the right. The solid lines are m_T exponential fits in the range $(m_T - m_0) < 1$ GeV for all particle species while the dashed lines are the extrapolated fits.

kinetic energy $m_T - m_0$ [36,37]. To facilitate a direct comparison, Fig. 15 shows the PHENIX hadron spectra, including π^0 from the 10% most central Au+Au collisions. The spectra approach one another, but do not fall upon a universal curve, and thereby fail the usual definition of scaling.

It has been suggested that at transverse mass significantly larger than the rest mass of the particle, thermal emission and radial flow may not be the only physics affecting the particle spectra. If heavy ion collisions can be described as collisions of two sheets of colored glass in which the gluon occupation number is sufficiently large to saturate, scaling of different hadron spectra with transverse mass is also predicted [38]. For Au+Au collisions at different impact parameters, the saturation scale differs, and some differences in the spectra may be expected. Nevertheless, the authors observe that the level of m_T scaling in our data is in qualitative agreement with expectations from gluon saturation [38]. Single-particle spectra alone, however, are not sufficient to disentangle saturation from flow effects.

It is often stated that m_T scaling holds in pp collisions at similar $\sqrt{s}$ to RHIC (see data, for example, in Refs. [36] and [37]). Scaling in m_T, i.e., spectra following a universal curve in m_T, might be expected if the hadrons are emitted from a source in thermal equilibrium. It is instructive to note that Ref. [36] states: "Although the curves for different particles do come together, there is no real evidence for any universal behavior in this variable." Thus, scaling at the ISR was never claimed by the original authors. In central Au+Au collisions, the slopes and yields of π, K, and p approach each other as well, but Figs. 15–17 also do not support a truly universal

TABLE IV. The resulting inverse slopes in MeV after fitting an m_T exponential to the spectra in the range $m_T - m_0 < 1$ GeV in each event centrality classes. The pion resonance is excluded in the fits. The equivalent p_T fit range for each particle is shown accordingly. The errors are statistical only.

	0–5 %	5–15 %	15–30 %	30–60 %	60–92 %
π^+ in $0.5 < p_T < 1.05$ GeV/c	216.8±5.7	214.3±4.6	217.4±4.7	214.4±5.2	176.9±9.5
π^- in $0.5 < p_T < 1.05$ GeV/c	215.8±6.5	221.2±5.6	225.3±5.8	212.8±5.7	215.8±16.8
K^+ in $0.45 < p_T < 1.35$ GeV/c	233.2±10.8	243.6±9.8	242.4±9.2	228.7±10.2	182.3±19.0
K^- in $0.45 < p_T < 1.35$ GeV/c	241.1±15.8	244.5±10.2	250.0±12.3	224.2±11.1	196.4±22.3
p in $0.55 < p_T < 1.85$ GeV/c	310.8±14.8	311.0±12.3	293.8±11.4	265.3±10.9	200.9±14.8
$\bar{p}$ in $0.55 < p_T < 1.85$ GeV/c	344.2±25.3	344.0±20.9	307.6±17.1	275.1±14.0	217.0±28.3

TABLE V. Inverse slope parameters (in MeV) of hadrons for $p+p$, $p+$nucleus, and central S+S, S+Pb, and Pb+Pb colliding at CERN energies. The errors are statistical and systematic, respectively.

Hadron	17 GeV/nucleon Pb+Pb	19.4 GeV/nucleon S+Pb	19.4 GeV/nucleon S+S	29 GeV/nucleon p+Pb	29 GeV/nucleon p+S	29 GeV/nucleon p+Be	23 GeV $p+p$
π^+	$156\pm6\pm23$[a]	$165\pm9\pm10$[b]	$148\pm4\pm22$[a]	$145\pm3\pm10$[b]	$139\pm3\pm10$[b]	$148\pm3\pm10$[b]	$139\pm13\pm21$[c]
K^+	$234\pm6\pm12$[a]	$181\pm8\pm10$[b]	$180\pm8\pm9$[a]	$172\pm9\pm10$[b]	$163\pm14\pm10$[b]	$154\pm8\pm10$[b]	$139\pm15\pm7$[c]
p	$289\pm7\pm14$[d]	$256\pm4\pm10$[e]	$208\pm8\pm10$[a]	$203\pm6\pm10$[e]	$175\pm30\pm10$[e]	$156\pm4\pm10$[e]	$148\pm20\pm7$[c]
Λ	$289\pm8\pm29$[f]			$203\pm9\pm20$[g]			
$\bar{\Lambda}$	$287\pm13\pm29$[f]			$180\pm15\pm18$[g]			

[a]Reference [28] (NA44 Collaboration).
[b]Reference [29] (NA44 Collaboration).
[c]References [34,35] (ISR).
[d]Reference [31] (NA44 Collaboration).
[e]Reference [30] (NA44 Collaboration).
[f]Reference [32] (WA97 Collaboration).
[g]Reference [33] (WA97 Collaboration).

behavior in m_T. Therefore the apparent puzzle of how the data could exhibit both m_T scaling and the mass-dependent p_T boost characteristic of radial flow is no puzzle at all, as any "m_T scaling" is only very approximate.

D. Summed charged particle multiplicity

As a consistency check we compare the measured rapidity densities as given in Sec. IV B to previously published pseudorapidity densities of charged particles. The measured dN/dy for each hadron species is converted to $dN/d\eta$, and the total $dN/d\eta$ is calculated by summation. Figure 18 shows $dN/d\eta$ per participant nucleon pair, compared to the measurement made by PHENIX using the pad chambers alone [27] as well as to PHOBOS and STAR yields in central collisions [40,41]. We note that the lines correspond to the fit of a linear parametrization of $N_{\rm part}$ and $N_{\rm coll}$ to the PHENIX measurement (open circles) with $a=0.88\pm0.28$ and $b=0.34\pm0.12$ as described in Ref. [42]. For the 5% central collisions, we measure 598 ± 30, and is comparable to the STAR result of 567 ± 38 [41], the PHOBOS result of 555 ± 37 [43], and the PHENIX pad chamber result of 622 ± 41 [27]. The agreement is excellent, allowing the results of this analysis to be used to decompose the particle-type dependence of the charge particle multiplicity increase with centrality.

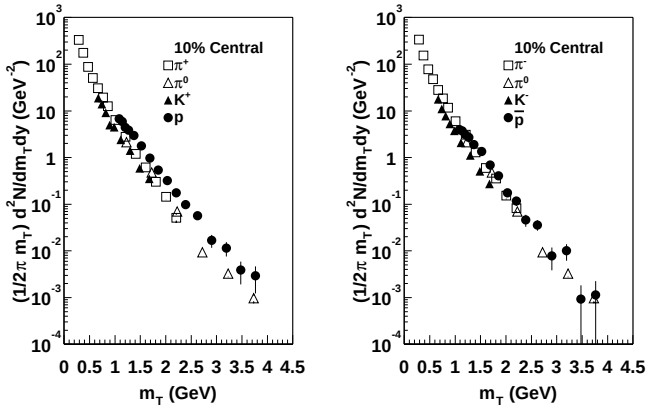

FIG. 15. The transverse mass distributions of inclusive identified hadrons produced in 10% central events, including the π^0 as measured in the electromagnetic calorimeter in PHENIX and published in Ref. [39].

V. COMPARISON WITH MODELS

A. Hydrodynamic-inspired fit

The charged particle pseudorapdity distributions are incompatible with a static thermal source, but the flat distribution observed in Ref. [43] reflects the strong longitudinal motion in the initial state. Consequently, the longitudinal momentum distribution is not an unambiguous sign of collective motion. Transverse momentum is, however, generated in the collision, so collective expansion may be more easily inferred from transverse momentum distributions.

Following the arguments of the preceding section, we analyze the particle m_T spectra. A parametrization of the m_T distribution of particles emitted from a hydrodynamic ex-

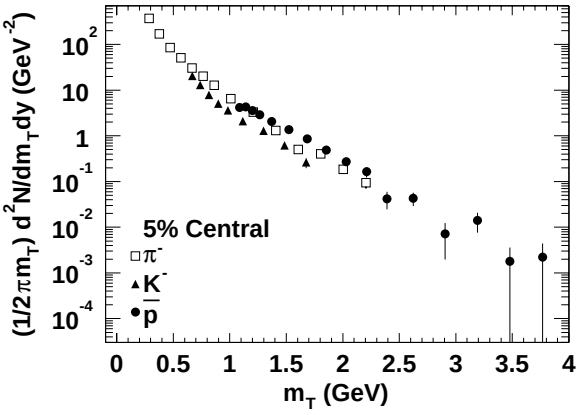

FIG. 16. The transverse mass distributions of the inclusive identified hadrons produced in the 5% central events.

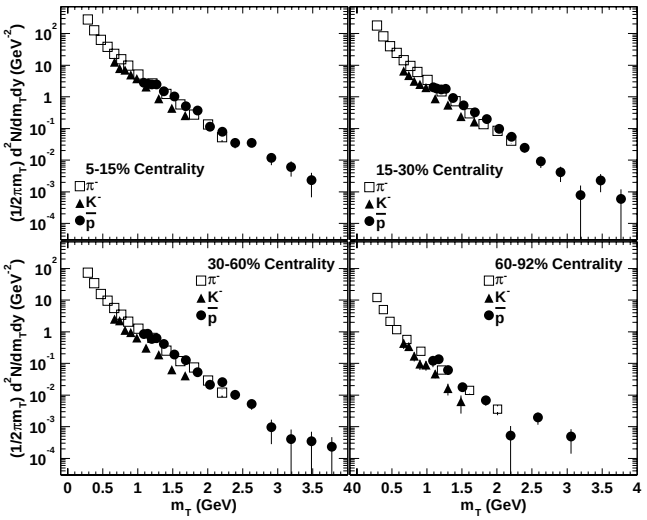

FIG. 17. The transverse mass distributions of the inclusive identified hadrons produced in events with different centralities.

panding hadron source is used. In order to determine the freeze-out temperature and collective flow without confusion from hard scattering processes, a limited p_T range is used in the fits. We include only particles with $(m_T-m_0)<1$ GeV in the fit. Pions with $(m_T-m_0)<0.38$ GeV are excluded to avoid resonance decays. All particles are assumed to decouple from the expanding hadron source [44] at the same freeze-out temperature $T_{\rm fo}$. This procedure allows us to extract $T_{\rm fo}$ and the magnitude of the collective boost in the transverse direction.

The inverse slope includes the local temperature of a section of the hadronic matter along with its collective velocity. The simple exponential fit of Eq. (10) treats each particle spectrum as a static thermal source, and a collective expansion velocity cannot be extracted reliably from a single-particle spectrum. However, the relative sensitivity to the

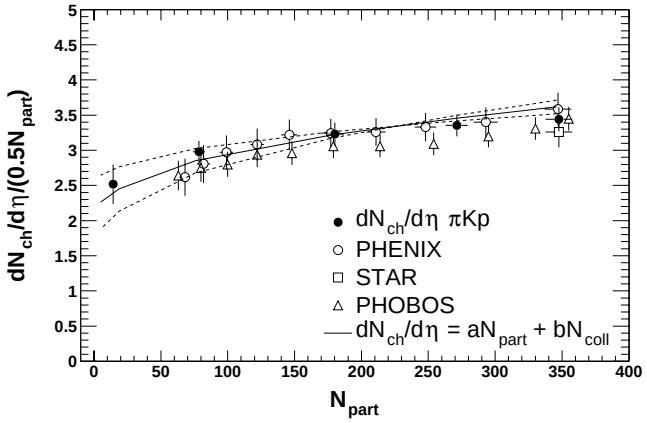

FIG. 18. Both the total charged multiplicity (open) in Refs. [40–42] and the total identified charged multiplicity (closed) scaled by the number of participant pairs are plotted together as a function of the number of participants. The lines correspond to the fit of a linear parametrization of $N_{\rm part}$ and $N_{\rm coll}$ to the PHENIX charged multiplicity measurement (open circles) with $a=0.88\pm0.28$ and $b=0.34\pm0.12$ as described in Ref. [42].

temperature and collective radial flow velocity differs for different particles. By using the information from all the particles, the expansion velocity can be inferred. We fit all particle species simultaneously with a functional form for a boosted thermal source based on relativistic hydrodynamics [44].

Use of this form assumes that (1) all particles decouple kinematically on a freeze-out hypersurface at the same freeze-out temperature $T_{\rm fo}$; (2) the particles collectively expand with a velocity profile increasing linearly with the radial position in the source (i.e., Hubble expansion where fluid elements do not pass through one another); and (3) the particle density distribution is independent of the radial position. Longitudinally boost-invariant expansion of the particle source is also assumed.

The transverse velocity profile is parametrized as:

$$\beta_T(\xi)=\beta_T^{\rm max}\xi^n, \tag{13}$$

where $\xi=r/R$, and R is the maximum radius of the expanding source at freeze-out $(0<\xi<1)$ [45]. The maximum surface velocity is given by $\beta_T^{\rm max}$, and for a linear velocity profile, $n=1$. The average of the transverse velocity is equal to

$$\langle\beta_T\rangle=\frac{\int\beta_T^{\rm max}\xi^n\xi d\xi}{\int\xi d\xi}=\frac{2}{2+n}\beta_T^{\rm max}. \tag{14}$$

Each fluid element is locally thermalized and receives a transverse boost ρ that depends on the radial position as

$$\rho=\tanh^{-1}(\beta_T(\xi)). \tag{15}$$

The m_T dependence of the invariant yield $dN/m_T dm_T$ is determined by integrating over the rapidity, azimuthal angle, and radial distribution of fluid elements in the source. This procedure, discussed in Appendix C, yields

$$\frac{d^2N}{m_T dm_T dy}=A\int_0^1 m_T f(\xi)K_1\left(\frac{m_T\cosh(\rho)}{T_{\rm fo}}\right)I_0\left(\frac{p_T\sinh(\rho)}{T_{\rm fo}}\right)\xi d\xi. \tag{16}$$

The parameters determined by fitting Eq. (16) to the data are the freeze-out temperature $T_{\rm fo}$, the normalization A, and the maximum surface velocity $\beta_T^{\rm max}$ using a flat particle density distribution [i.e., $f(\xi)=1$].

To study the parameter correlations, we make a grid of combinations of temperature and velocity, and perform a χ^2 minimization to extract the normalization A for each particle type. The fit is done simultaneously for all particles in the range $(m_T-m_0)<1$ GeV. In addition to this upper limit in the fit, the pion fit range includes a lower limit of $(m_T-m_0)>0.38$ GeV to avoid the resonance contribution to the low-p_T region (see Sec. V A 2).

The radial flow velocity and freeze-out temperature for all centralities are determined in the same way. The results are plotted together with the spectra in Fig. 19. The hydrody-

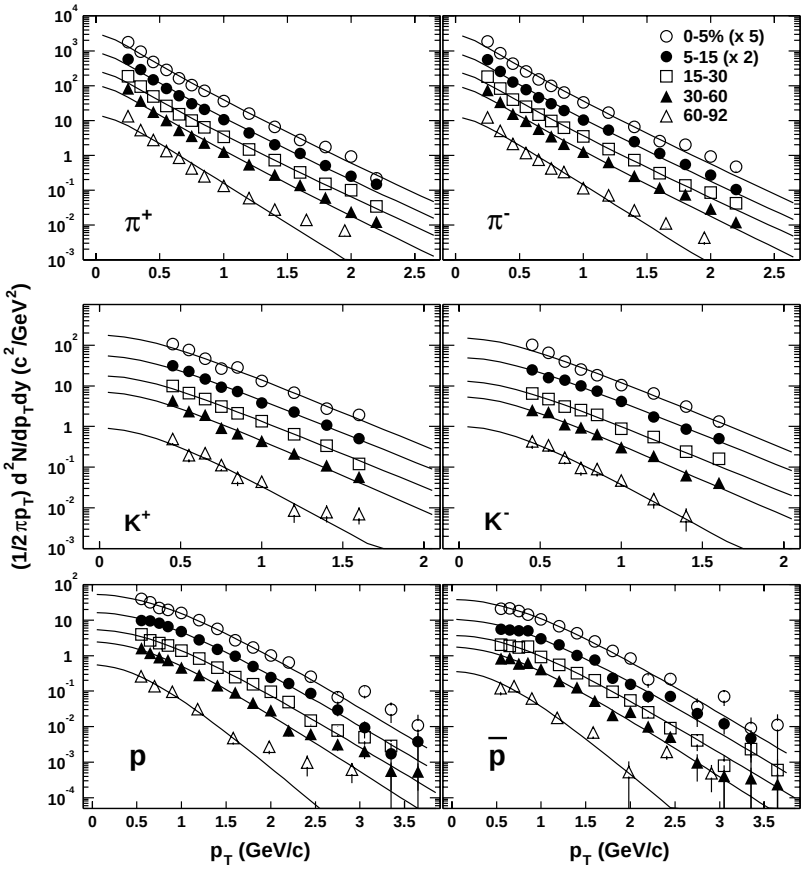

FIG. 19. The parametrization and the p_T hadron spectra for all five centrality selections.

namic form clearly describes the spectra better than the simple exponential in Fig. 14. The values for $T_{\rm fo}$ and $\beta_T^{\rm max}$ are tabulated in Table VI.

Figure 20 shows χ^2 contours for the temperature and velocity parameters for the 5% most central collisions. The n-sigma contours are labeled up to 8σ. The χ^2 contours indicate strong anticorrelation of the two parameters. If the freeze-out temperature decreases, the flow velocity increases. The minimum χ^2 is 34 and the total number of degrees of freedom (DOF) is 40. The parameters that correspond to this minimum are $T_{\rm fo}=121\pm4$ MeV and $\beta_T^{\rm max}=0.70\pm0.01$. The quoted errors are the 1σ contour widths of $\Delta\beta_T^{\rm max}$ and $\Delta T_{\rm fo}$. Within 3σ, the $T_{\rm fo}$ range is 106–141 MeV and the $\beta_T^{\rm max}$ range is 0.75–0.64.

TABLE VI. The minimum χ^2 and the parameters $T_{\rm fo}$ and $\beta_T^{\rm max}$ for each of the five centrality selections. The best fit parameters are determined by averaging all parameter pairs within the 1σ contour. The errors correspond to the standard deviation of the parameter pairs within the 1σ χ^2 contour. It is important to note that the fit range in Fig. 19 is the same as was used to fit m_T exponentials to the spectra in Fig. 14.

Centrality (%)	χ^2/DOF	$T_{\rm fo}$(MeV)	$\beta_T^{\rm max}$	$\langle\beta_T\rangle$
0–5	34.0/40	121 ± 4	0.70 ± 0.01	0.47 ± 0.01
5–15	34.7/40	125 ± 2	0.69 ± 0.01	0.46 ± 0.01
15–30	36.2/40	134 ± 2	0.65 ± 0.01	0.43 ± 0.01
30–60	68.9/40	140 ± 4	0.58 ± 0.01	0.39 ± 0.01
60–92	36.3/40	$161\pm^{19}_{12}$	$0.24\pm^{0.16}_{0.2}$	$0.16\pm^{0.16}_{0.2}$

As a linear velocity profile [$n=1$ in Eq. (13)] is assumed, the mean flow velocity in the transverse plane is $\langle\beta_T\rangle=2\beta_T^{\rm max}/3$. If a different particle density distribution [for instance, a Gaussian function for $f(\xi)$] were used, then the average should be determined after weighting accordingly [45].

A similar analysis for Pb+Pb collisions at 158A GeV, was reported by the NA49 Collaboration in Ref. [46]. Using the same hydrodynamic parametrization, simultaneous fits of several hadron species for the highest energy results in $T_{\rm fo}=127\pm1$ MeV and $\beta_T^{\rm max}=0.48\pm0.01$ with $\chi^2/NDF=120/43$ for positive particles and $T_{\rm fo}=114\pm2$ MeV and $\beta_T^{\rm max}=0.50\pm0.01$ with $\chi^2/NDF=91/41$ for negative particles (statistical errors only). Pions and deuterons are excluded from the fits to avoid dealing with resonance contributions to the pion yield and formation of deuterons by coalescence. The ϕ meson is included in the fit together with the negative particles. Previously, NA49 used a different parametrization to fit the charged hadron and deuteron spectra, as well as the m_T dependence of measured Hanbury Brown–Twiss source radii, resulting in overlapping χ^2 contours with $T_{\rm fo}=120\pm12$ MeV and $\beta_T^{\rm max}=0.55\pm0.12$ [47].

1. Velocity and particle density profile

In order to use $\beta_T^{\rm max}$ and $T_{\rm fo}$ from the fits described above, one needs to know their sensitivity to the assumed velocity and particle density profiles in the emitting source. The

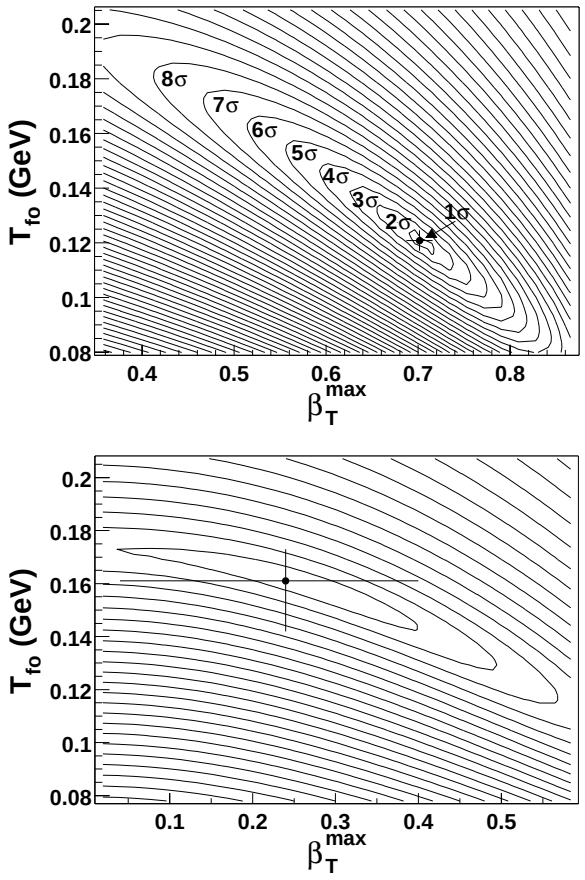

FIG. 20. The χ^2 contours in the parameter space $T_{\rm fo}$ and $\beta_T^{\rm max}$ that result after simultaneously fitting hadrons in the 0–5 % centrality (top) and 60–92 % (bottom). The *n*-sigma contours are labeled accordingly in the top panel. The fit results are tabulated in Table VI.

choice of a linear velocity profile within the source is motivated by the profile observed in a full hydrodynamic calculation [48], which shows a nearly perfect linear increase of $\beta(r)$ with r. Nevertheless, we also used a parabolic profile to check the sensitivity of the results to details of the velocity profile. For a parabolic velocity profile [$n=2$ in Eq. (13)], $\beta_T^{\rm max}$ increases by $\approx$13% and $T_{\rm fo}$ increases by $\approx$5%.

A Gaussian density profile used with a linear velocity profile increases $\beta_T^{\rm max}$ by $\approx$2%, with a negligible difference in the temperature $T_{\rm fo}$. As a test of the assumption that all the particles freeze out at a common temperature, the simultaneous fits were repeated without the kaons. The difference in $T_{\rm fo}$ is within the measured uncertainties.

2. Influence of resonance production

The functional forms given by Eqs. (10) and (17) do not include particles arising from resonance or weak decays. As resonance decays are known to result in pions at low transverse momenta [49–51], we place a p_T threshold of 500 MeV/c on pions included in the hydrodynamic fit. A similar approach was followed by NA44, E814, and other experiments at lower energies, which performed in-depth studies of resonance decays feeding hadron spectra. However, these were for systems with higher baryon density, so we performed a cross-check on possible systematic uncertainties arising from the pion threshold used in the fits. To estimate the effect of resonance decays were they not excluded from the fit, we calculate resonance contributions following Wiedemann [52].

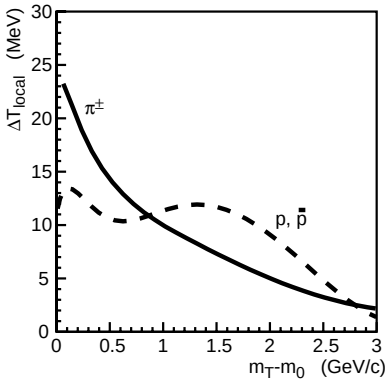

FIG. 21. The difference in the local slope for direct and inclusive pions (solid) and (anti)protons (dashed).

In order to reproduce the relative yields of different particle types, a chemical freeze-out temperature—different from the kinetic freeze-out temperature—and a baryonic chemical potential are introduced. Direct production and resonance contribution are calculated for pions and (anti)protons assuming a kinetic freeze-out temperature of 123 MeV, a transverse flow velocity of 0.612 (equivalent to $\langle\beta_T\rangle = 0.44$), a baryon chemical potential of 37 MeV, and a chemical freeze-out temperature (when particle production stops) of 172 MeV. These parameters are chosen as they provide a reasonable description of the (anti)proton and pion spectra and yields (10% most central) and are in good agreement with chemical freeze-out analyses [53]. Most spectra from resonance decays show a steeper falloff than the direct production, which should lead to a smaller apparent inverse slope, depending on what fraction of the low p_T part of the spectrum is included in the fits.

To measure the effect of resonance production on the spectral shape, the local slope is determined. For a given m_T bin number i, the local slope is defined as

$$T_{\rm local}(i) = -\frac{m_T(i+1) - m_T(i-1)}{\ln[N(i+1)] - \ln[N(i-1)]}, \qquad (17)$$

which is identical to the inverse slope independent of m_T for an exponential.

The difference in the local slope,

$$\Delta T_{\rm local} = T_{\rm local}^{\rm direct} - T_{\rm local}^{\rm incl}, \qquad (18)$$

is determined for direct and inclusive pions and (anti)protons. The differences are plotted as a function of $m_T - m_0$ in Fig. 21. The difference in the local slope for protons is below 13 MeV for the full transverse mass range; the nonmonotonic behavior for protons is caused by the relatively strong transverse flow. For pions, $\Delta T_{\rm local}$ decreases monotonically with m_T and is below 10 MeV above m_T

$=1$ GeV/c. A fit of an exponential to the pion spectra for $(m_T - m_0) > 0.38$ GeV (which corresponds to $p_T > 0.5$ GeV/c) yields a difference in the inverse slope of 16 MeV with and without resonances.

B. Comparison with hydrodynamic models

Hydrodynamic parametrizations as used in the preceding Section rely upon many simplifying assumptions. Another approach to the study of collective flow is to compare the data to hydrodynamic models. Such models assume rapid equilibration in the collision and describe the subsequent motion of the matter using the laws of hydrodynamics. Large pressure buildup is found, and we investigate this ansatz by checking the consistency of the data with calculations using a reasonable set of initial conditions. We compare to two separate models, the hydrodynamics model of Kolb and Heinz [54–56] and the "hydro to hadrons" (H2H) model of Teaney and Shuryak [57,58]. The H2H model consists of a hydrodynamics calculation, followed by a hadronic cascade after chemical freeze-out. The cascade step utilizes the relativistic quantum molecular dynamics (RQMD) model, developed for lower energy heavy ion collisions [59].

In both models, initial conditions are tuned to reproduce the shape of the transverse momentum spectra measured in the most central collisions, along with the charged particle yield. Each model also includes the formation and decay of resonances.

In the Kolb and Heinz model [54–56], the initial parameters are the entropy density, baryon number density, the equilibrium time, and the freeze-out temperature which controls the duration of the expansion. The chemical freeze-out temperature is the temperature at which particle production ceases. The initial entropy or energy density and maximum temperature are fixed to match the measured multiplicity for the most central collisions using a parametrization that is tuned to produce the measured $dN_{\rm ch}/d\eta$ dependence on both $N_{\rm part}$ and $N_{\rm coll}$. A kinetic freeze-out temperature of $T_{\rm fo} = 128$ MeV is used. Spectra from the Kolb-Heinz hydrodynamic model are shown in Fig. 22 for pions (upper) and for protons (lower) as dotted lines. The solid lines are the results from the fits described in the previous sections. Figure 22 thus allows two comparisons. The similarity of the dashed and solid lines shows that the hydrodynamic-inspired parametrization used to fit the data results in a p_T distribution similar to this hydrodynamic calculation. Comparing the dashed lines to the data points shows that the hydrodynamic model agrees quite well for most of the centrality ranges. It is important to note that the model parameters are uncertain at the level of 10%, and, more importantly, the application of hydrodynamics to peripheral collisions may be less reasonable than for central collisions, as hydrodynamic calculations assume strong rescattering and a sufficiently large system size (discussed in Ref. [56]).

In Refs. [57,60], the PHENIX $\bar{p}$ spectrum shape is well described by the H2H model with the LH8 equation of state. The cascade step in the H2H model removes the requirement that all particles freeze out at a common temperature. Thus the freeze-out temperature and its profile are predicted, rather

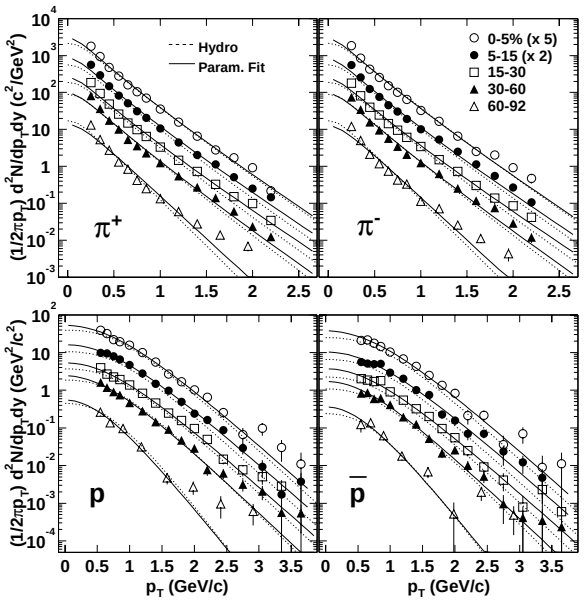

FIG. 22. The hydrodynamics calculation with initial parameters tuned to match the most central spectra in the p_T range 0.3–2.0 GeV/c.

than input parameters. Furthermore, following the hadronic interactions explicitly with RQMD removes the need to rescale the particle ratios at the end of the calculation, as they are fixed by the hadronic cross sections rather than at some particular freeze-out temperature. The LH8 equation of state includes a phase transition with a latent heat of 0.8 GeV. In Refs. [57,60], the Ω and the ϕ are shown to decouple from the expanding system at $T = 160$ MeV, and they receive a flow velocity boost of $0.45c$. Pions and kaons decouple at $T = 135$ MeV with flow velocity equal to 0.55c, while protons have $T = 120$ MeV and flow velocity greater than or equal to 0.6. These temperatures and flow velocities are consistent with the values extracted from the data for the most central events. However, the average initial energy density exceeds the experimental estimate using formation time $\tau_0 = 1$ fm/c.

Figure 23 shows radial flow from the fits of the preceding section as a function of the number of participants for $T_{\rm fo}$ (top) and $\langle \beta_T \rangle$ (bottom). There is a slight decrease of $T_{\rm fo}$, while $\langle \beta_T \rangle$ increases with $N_{\rm part}$, saturating at 0.45. The value of $\langle \beta_T \rangle$ from Kolb and Heinz [54–56] is also shown, and agrees with the data reasonably well. In the plot of $\langle \beta_T \rangle$, the dashed line indicates the results of fitting the parametrization to the data while keeping $T_{\rm fo}$ fixed at 128 MeV to agree with the value used by Kolb and Heinz. Radial flow values for central collisions remain unchanged, while those in peripheral collisions increase. Even with the extreme assumption that all collisions freeze out at the same temperature, regardless of centrality, the trend in the centrality dependence of the radial flow does not change. $\langle \beta_T \rangle$ would increase somewhat if a full feed-down correction for protons and antiprotons could be made. The low-p_T part of the spectrum would flatten slightly, as seen in Fig. 12. The resulting hydrodynamic-inspired fit to the data, shown as the solid line in Fig. 22, would be drawn nearer to the Kolb-Heinz hydrodynamic model indicated by the dashed lines in Fig. 22.

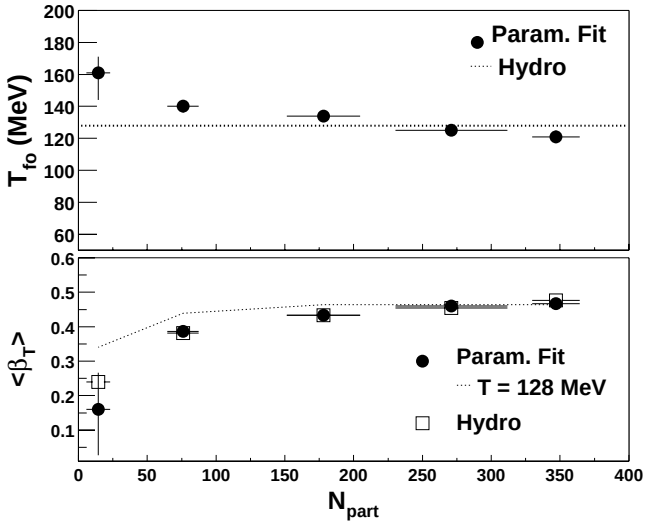

FIG. 23. The expansion parameters $T_{\rm fo}$ and $\beta_T^{\rm max}$ as a function of the number of participants. As a comparison, the results from a hydrodynamic model calculation are also shown (Refs. [54–56]). The dashed line corresponds to a fixed temperature of 128 MeV for all centralities in the parametrized fit to the data.

C. Hydrodynamic contributions at higher p_T

We use the parameters extracted from the fit to the charged hadron spectra in the low-p_T region to extrapolate the effect of the soft physics to higher p_T. This yields a prediction for the spectra of hadrons should a collective expanding thermal source be the only mechanism for particle production in heavy ion collisions. Comparing this prediction to the measured spectrum of charged particles or neutral pions should indicate the p_T range over which soft thermal processes dominate the cross section. Where the data deviate from the hydrodynamic extrapolation, other contributions, as, e.g., from hard processes or nonequilibrium production become visible. The approach described here differs from hydrodynamic fits to the entire hadron spectrum, as we fix the parameters from the low-p_T region alone, where soft physics should be dominant.

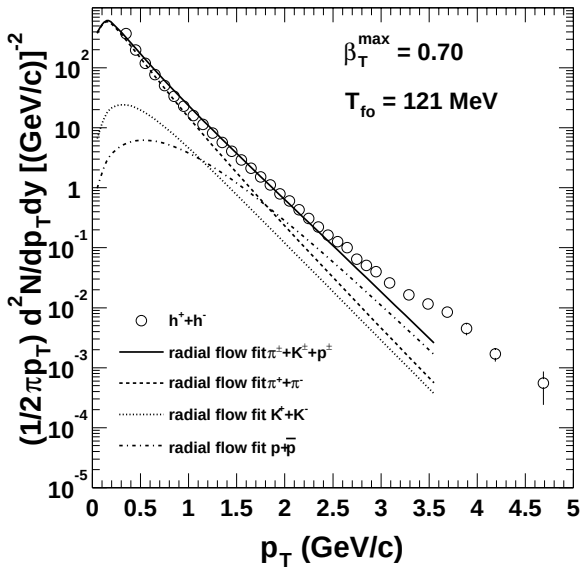

FIG. 24. The high-p_T hadron spectra in Ref. [39] compared to the fit results assuming radial flow from the π, K, p spectra in the 5% central events.

TABLE VII. Fit parameters for each particle species using Eqs. (19) and (20).

Particle	$\alpha_{\rm part}$	$\alpha_{\rm coll}$
π^+	1.06±0.01	0.79±0.01
π^-	1.08±0.01	0.80±0.01
K^+	1.18±0.02	0.88±0.02
K^-	1.20±0.03	0.89±0.02
p^+	1.16±0.02	0.86±0.02
p^-	1.14±0.03	0.84±0.02

The hadron spectrum is calculated using the fit parameters from the low-p_T region fits shown in the preceding section, and extrapolated to higher p_T. Figure 24 shows the calculated spectrum for each particle type, and the sum of the extrapolated spectra is compared to the measured charged hadrons $(h^+ + h^-)$ in the 5% most central collisions. As nonidentified charged hadrons are measured in η rather than in y, the extrapolated spectra are converted to units of η. This conversion is most important in the low-p_T region. No additional scale factor is applied—the extrapolation and data are compared absolutely. Below $\approx$2.5 GeV/c p_T, the agreement is very good, while at higher p_T the data begin to exceed the hydrodynamic extrapolation.

Other hydrodynamic calculations have been successful in describing the distributions over the full p_T range [61] with different parameter values. There are clear indications that particle production from a hydrodynamic source, if invoked to explain the spectra at low p_T, will have a non-negligible influence even at relatively large p_T. Furthermore, the range of p_T populated by hydrodynamically boosted hadrons is species dependent. This is clearly visible in Fig. 24, which shows that the extrapolated proton spectra have a flatter p_T distribution than the extrapolated pions and kaons. The yield of the "soft" protons reaches, and even exceeds, that of the extrapolated soft pions at 2.5 GeV/c p_T. Therefore the transition from soft to hard processes must also be species dependent, and the boost of the protons causes the region

TABLE VIII. Values of the parameters n_{pp} and x from fitting Eq. (21) to the observed dN/dy per $N_{\rm part}$.

	n_{pp}	x
π^+	1.41±0.11	0.028±0.020
π^-	1.10±0.11	0.085±0.030
K^+	0.130±0.021	0.232±0.076
K^-	0.089±0.020	0.326±0.132
p	0.089±0.013	0.181±0.062
$\bar{p}$	0.062±0.010	0.172±0.068

where hard processes dominate the inclusive charged particle spectrum to be at significantly higher transverse momenta in central Au+Au than in $p+p$ collisions. Our analysis suggests this occurs not lower than $p_T=3$ GeV/c.

D. Hadron yields as a function of centrality

The preceding discussion focused on the hadron spectra; now we turn to the centrality dependence of the pion, kaon, proton, and antiproton yields, which can shed further light on the importance of different mechanisms in particle production. It is instructive to see whether yields of the different hadrons scale with the number of participant nucleons, $N_{\rm part}$, the number of binary nucleon-nucleon collisions, $N_{\rm coll}$, or some combination of the two.

The total yields of the hadrons may be expected to be dominated by soft processes, and the wounded nucleon model of soft interactions suggests that the yields should scale as the number of participants, $N_{\rm part}$. If each participant loses a certain fraction of its incoming energy, as, e.g., in string models, where each pair of participants (or wounded nucleons) contributes a color flux tube, the total energy of the fireball formed at central rapidity would be proportional to the number $N_{\rm part}$ of participants. If, furthermore, the fireball is locally thermalized and particle production is determined at a single temperature, the multiplicity would scale with $N_{\rm part}$. On the other hand, at very high p_T, particle production may be dominated by hard processes and scale with $N_{\rm coll}$ [62,63].

In order to investigate the existence of scaling, the multiplicities are parametrized as

$$\frac{dN}{dy} = C(N_{\rm part})^{\alpha_{\rm part}} \tag{19}$$

and

$$\frac{dN}{dy} = C'(N_{\rm coll})^{\alpha_{\rm coll}}. \tag{20}$$

Fit results for these parametrizations are shown in Table VII. As can be seen, the exponents $\alpha_{\rm part}$ are >1 for all species, while $\alpha_{\rm coll}$ is consistently <1. The production of all particles increases more strongly than with $N_{\rm part}$, but not as strongly as with $N_{\rm coll}$. Small differences between the different particle species are apparent: The (anti)proton yield increases more strongly than the pion yield, and the kaon

TABLE IX. Invariant yields for $\pi^{\pm}$, $K^{\pm}$, and (anti)p measured in minimum-bias events at midrapidity and normalized to one rapidity unit. The errors are statistical only.

p_T(GeV/c)	$\pi^{\pm}$	$K^{\pm}$	$p(\overline{p})$
0.25	112±2		
	109±2		
0.35	56±1		
	49.9±0.9		
0.45	28.0±0.5	6.1±0.4	
	24.1±0.5	4.6±0.4	
0.55	15.7±0.3	4.0±0.3	2.3±0.1
	14.6±0.3	3.2±0.2	1.2±0.1
0.65	9.1±0.2	2.8±0.2	1.8±0.1
	8.7±0.2	2.1±0.2	1.17±0.09
0.75	5.8±0.1	1.7±0.1	1.38±0.08
	5.6±0.2	1.6±0.1	0.98±0.07
0.85	3.8±0.1	1.30±0.08	1.18±0.07
	3.6±0.1	1.17±0.09	0.95±0.07
0.95	2.40±0.08	0.87±0.06	0.98±0.06
	2.28±0.08	0.69±0.06	0.65±0.05
1.05	1.61±0.06	0.62±0.04	0.70±0.04
	1.61±0.06	0.53±0.05	0.50±0.04
1.15	103±0.04	0.43±0.03	0.60±0.04
	1.17±0.05	0.38±0.04	0.35±0.03
1.25	0.71±0.03	0.33±0.03	0.41±0.03
	0.76±0.04	0.27±0.03	0.34±0.03
1.35	0.46±0.02	0.20±0.02	0.32±0.02
	0.54±0.03	0.16±0.02	0.22±0.02
1.45	0.35±0.02	0.17±0.02	0.23±0.02
	0.31±0.02	0.13±0.02	0.18±0.02
1.55	0.24±0.02	0.10±0.01	0.17±0.02
	0.22±0.02	0.10±0.01	0.15±0.02
1.65	0.16±0.01	0.08±0.01	
	0.15±0.01	0.07±0.01	
1.70			0.119±0.008
			0.080±0.007
1.75	0.11±0.01		
	0.11±0.01		
1.85	0.079±0.008		
	0.092±0.009		
1.90			0.068±0.006
			0.041±0.005
1.95	0.063±0.007		
	0.066±0.008		
2.05	0.036±0.005		
	0.034±0.005		
2.10			0.036±0.004
			0.022±0.003
2.15	0.026±0.004		
	0.025±0.004		
2.25	0.015±0.003		

TABLE X. Pion inavariant yields in each event centrally and p_T bin measured at midrapidity, normalized to one rapidity unit. For each measured p_T bin, the postitive pion yield is the top row and the negative pion yield is the bottom row. Errors are statistical only.

p_T(GeV/c)	0–5 %	5–15 %	15–30 %	30–60 %	60–92 %
0.25	355±9	282±6	186±4	81±2	13.2±0.5
	371±10	275±7	180±4	74±2	12.1±0.5
0.35	188±5	146±3	93±2	36.6±0.8	5.3±0.2
	169±5	128±3	82±2	34.3±0.9	5.0±0.2
0.45	95±3	74±2	48±1	17.5±0.5	2.7±0.1
	86±3	63±2	40±1	15.7±0.5	2.1±0.1
0.55	56±2	41±1	26.0±0.7	10.1±0.3	1.32±0.09
	51±2	38±1	24.5±0.8	9.6±0.3	1.18±0.09
0.65	32±1	25.6±0.8	15.0±0.5	5.3±0.2	
	30±1	22.6±0.8	14.5±0.5	5.7±0.2	
0.70					0.62±0.04
					0.57±0.04
0.75	21.1±0.9	15.4±0.6	9.9±0.4	3.6±0.1	
	20±1	15.3±0.6	9.5±0.4	3.5±0.2	
0.85	14.0±0.7	10.3±0.4	6.4±0.3	2.3±0.1	
	12.8±0.8	9.6±0.5	6.1±0.3	2.1±0.1	
0.90					0.19±0.02
					0.24±0.02
1.00	7.1±0.3	5.3±0.2	3.4±0.1	1.25±0.05	
	6.5±0.3	5.0±0.2	3.4±0.1	1.25±0.05	
1.20	3.2±0.2	2.2±0.1	1.47±0.07	0.55±0.03	0.064±0.006
	3.3±0.2	2.6±0.1	1.51±0.08	0.63±0.04	0.061±0.007
1.40	1.3±0.1	1.01±0.07	0.72±0.04	0.27±0.02	
	1.3±0.1	1.25±0.09	0.72±0.05	0.26±0.02	
1.60	0.55±0.07	0.57±0.05	0.33±0.03	0.14±0.01	0.015±0.003
	0.51±0.07	0.57±0.05	0.30±0.03	0.12±0.01	0.014±0.003
1.80	0.35±0.05	0.25±0.03	0.15±0.02	0.060±0.008	
	0.40±0.06	0.27±0.03	0.14±0.02	0.075±0.009	
2.00	0.18±0.03	0.13±0.02	0.10±0.01	0.023±0.004	0.005±0.001
	0.18±0.04	0.13±0.02	0.09±0.01	0.029±0.005	0.004±0.001
2.20	0.043±0.02	0.07±0.01	0.034±0.007	0.012±0.003	
	0.09±0.03	0.05±0.01	0.042±0.009	0.012±0.003	

yield shows the strongest centrality dependence. Remarkably, the yield fraction scaling beyond linear with N_{part} is larger for kaons, protons, and antiprotons than for pions. Perhaps it is not surprising that the yields do not scale simply with N_{part}; the collective flow seen in the p_T spectra already shows that the nucleon-nucleon collisions cannot be independent.

It should be noted that scaling with multiplicity is not actually a good expectation for kaons. Kaon production at the CERN SPS can be well understood with a statistical hadronization model [64,65], if one takes into account the fact that strangeness must be produced in the collisions in $s\bar{s}$ pairs. Strangeness production is suppressed in pp collisions by phase space limitations for $s\bar{s}$ pair production. This suppression, well described by a canonical ensemble treatment, gradually fades away with increasing reaction volume, and grand canonical descriptions suffice for central Au+Au collisions [66]. Therefore, simple scaling with N_{part} should not be expected for kaons. This does not, of course, explain the rise of baryon and antibaryon production faster than linear with N_{part}.

We next check whether the simple model of hadron yields can be brought into agreement with the data by adding a component of the yields scaling as the number of binary collisions, N_{coll}. Such an admixture inspires simple two-component models [62,63]. The nonlinearity of dN/dy on the number of participants is illustrated by the ratio $(dN/dy)/N_{\mathrm{part}}$, shown in Fig. 25 as a function of centrality. The yields are seen to depend linearly on $N_{\mathrm{coll}}/N_{\mathrm{part}}$. As seen already from the exponents in Table VII, the increase with

TABLE XI. Kaon invariant yields in each event centrality and p_T bin, measured at midrapidity and normalized to one rapidity unit. The top row in each p_T bin is K^+, and the bottom row is K^-. Errors are statistical only.

p_T(GeV/c)	0–5 %	5–15 %	15–30 %	30–60 %	60–92 %
0.44					0.5±0.1
					0.4±0.1
0.45	21±3	16±2	10±1	4.3±0.5	
	21±3	13±2	7±1	2.5±0.4	
0.54					0.20±0.07
					0.3±0.1
0.55	15±2	11±1	6.6±0.7	2.4±0.3	
	13±2	8±1	4.8±0.6	2.3±0.3	
0.65	9±1	7.5±0.7	4.7±0.4	1.9±0.2	
	8±1	7.0±0.8	3.1±0.4	1.1±0.2	
0.69					0.18±0.03
					0.14±0.03
0.75	5.3±0.7	4.6±0.5	3.1±0.3	0.9±0.1	
	5.1±0.8	5.0±0.6	2.5±0.3	0.9±0.1	
0.85	5.7±0.7	3.6±0.4	2.1±0.2	0.67±0.08	
	3.6±0.6	3.7±0.4	2.0±0.2	0.64±0.09	
0.89					0.07±0.02
					0.09±0.02
0.95	3.0±0.4	2.3±0.2	1.5±0.2	0.51±0.07	
	2.4±0.4	2.3±0.3	1.0±0.2	0.35±0.06	
1.05	2.3±0.3	1.5±0.2	1.2±0.1	0.37±0.05	
	1.8±0.3	1.8±0.2	0.8±0.1	0.27±0.05	
1.15	1.6±0.3	1.3±0.2	0.62±0.09	0.29±0.04	
	1.4±0.3	0.9±0.2	0.7±0.1	0.23±0.04	
1.17					0.012±0.004
					0.015±0.005
1.25	1.1±0.2	1.0±0.1	0.66±0.09	0.15±0.03	
	1.2±0.2	0.8±0.1	0.41±0.08	0.15±0.03	
1.35	0.6±0.1	0.6±0.1	0.35±0.05	0.12±0.02	
	0.9±0.2	0.5±0.1	0.22±0.05	0.05±0.02	
1.45	0.5±0.1	0.45±0.08	0.32±0.05	0.10±0.02	
	0.4±0.1	0.36±0.08	0.26±0.05	0.07±0.02	
1.55	0.4±0.1	0.26±0.06	0.14±0.03	0.07±0.02	
	0.4±0.1	0.28±0.07	0.21±0.04	0.04±0.01	
1.57					0.008±0.002
					0.004±0.002
1.65	0.4±0.1	0.24±0.05	0.10±0.03	0.05±0.01	
	0.12±0.06	0.23±0.06	0.12±0.03	0.04±0.01	

centrality is strongest for kaons, intermediate for (anti)protons, and weakest for pions. This indicates that protons and antiprotons have a larger component scaling with N_{coll} than pions.

We fit the yields per participant with Eq. (21). As in Refs. [62,63] we parametrize the multiplicity using two free parameters: n_{pp}, the multiplicity in $p+p$ collisions, and x, the relative strength of the component scaling with N_{coll}.

$$R \equiv \frac{dN/dy}{N_{\mathrm{part}}} = (1-x)n_{pp}\frac{1}{2} + xn_{pp}\frac{N_{\mathrm{coll}}}{N_{\mathrm{part}}} = n_{pp}\left[\frac{1}{2} + x\left(\frac{N_{\mathrm{coll}}}{N_{\mathrm{part}}} - \frac{1}{2}\right)\right]. \quad (21)$$

The results of the fit are shown as solid lines in Fig. 25. The fit parameter values are given in Table VIII. All hadron spe-

TABLE XII. (Anti)proton invariant yields in each event centrality and p_T bin, measured at midrapidity and normalized to one rapidity unit. The top row in each p_T is the proton yield, and the bottom row the anitproton. The errors are statistical only.

p_T(GeV/c)	0–5 %	5–15 %	15–30 %	30–60 %	60–92 %
0.545					0.26±0.06
					0.12±0.05
0.55	8±1	4.9±0.5	4.0±0.4	1.6±0.2	
	4.2±0.8	2.8±0.5	2.0±0.3	0.8±0.1	
0.65	6.3±0.7	4.7±0.4	2.7±0.2	1.2±0.1	
	4.3±0.7	2.6±0.4	1.9±0.3	0.9±0.1	
0.695					0.14±0.02
					0.14±0.03
0.75	4.4±0.5	4.0±0.4	2.2±0.2	0.90±0.08	
	3.6±0.5	2.5±0.3	1.7±0.2	0.60±0.08	
0.85	3.9±0.4	3.3±0.3	1.9±0.2	0.75±0.07	
	2.9±0.5	2.5±0.3	1.8±0.2	0.62±0.08	
0.895					0.10±0.02
					0.06±0.01
1.00	3.1±0.2	2.4±0.2	1.37±0.09	0.46±0.03	
	2.1±0.2	1.5±0.1	0.91±0.08	0.41±0.04	
1.18					0.031±0.005
					0.018±0.004
1.20	2.0±0.2	1.4±0.1	0.82±0.06	0.28±0.02	
	1.4±0.2	1.0±0.1	0.54±0.05	0.19±0.02	
1.40	1.1±0.1	0.74±0.07	0.46±0.04	0.14±0.01	
	0.9±0.1	0.50±0.06	0.32±0.04	0.13±0.02	
1.58					0.005±0.002
					0.007±0.002
1.60	0.54±0.07	0.49±0.05	0.25±0.03	0.09±0.01	
	0.49±0.08	0.37±0.05	0.20±0.03	0.053±0.009	
1.80	0.34±0.05	0.25±0.03	0.16±0.02	0.047±0.007	
	0.27±0.06	0.11±0.02	0.10±0.02	0.021±0.005	
1.98					0.003±0.001
					0.0005±0.0005
2.00	0.20±0.04	0.12±0.02	0.10±0.01	0.029±0.005	
	0.16±0.04	0.08±0.02	0.05±0.01	0.026±0.006	
2.20	0.13±0.03	0.08±0.02	0.05±0.01	0.008±0.002	
	0.04±0.02	0.03±0.01	0.025±0.007	0.010±0.003	
2.41					0.0010±0.0006
					0.0020±0.0008
2.425	0.06±0.02	0.05±0.01	0.017±0.005	0.007±0.002	
	0.05±0.02	0.04±0.01	0.011±0.004	0.006±0.002	
2.675	0.014±0.008	0.019±0.006	0.010±0.003	0.004±0.001	
	0.005±0.005	0.018±0.007	0.002±0.002	0.0012±0.0008	
2.908					0.0006±0.0004
					0.0005±0.0003
2.925	0.017±0.007	0.006±0.003	0.006±0.002	0.003±0.001	
	0.020±0.009	0.009±0.004	0.003±0.002	0.0009±0.0006	
3.175	0.013±0.006	0.002±0.002	0.003±0.002	0.0012±0.0007	
	0.006±0.004	0.003±0.002	0.0010±0.001		
3.425	0.004±0.003	0.003±0.002	0.002±0.001	0.0007±0.0005	
	0.002±0.002	0.001±0.001	0.002±0.001	0.0003±0.0003	
3.675	0.003±0.003			0.0003±0.003	
	0.003±0.003		0.0008±0.0008		

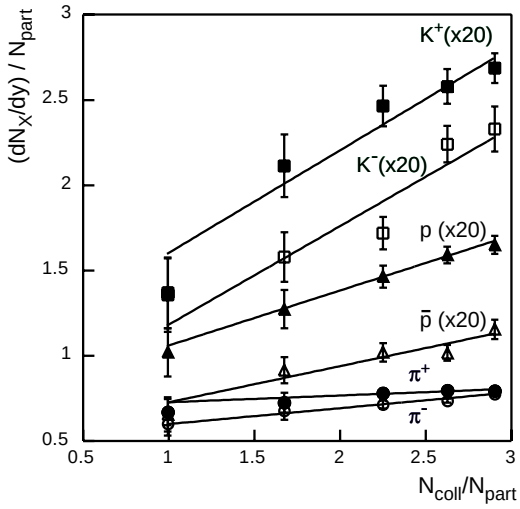

FIG. 25. dN/dy per participant of different particle species as a function of the number of collisions per participant. Kaon and (anti)proton multiplicities are scaled by a factor of 20.

cies are well fit. The importance of the component scaling as N_{coll} is the largest for kaons and smallest for pions.

We check the consistency of the fits in Fig. 25 with known hadron yields in $p+p$ collisions by extrapolating the fits down to two participants (and one binary nucleon-nucleon collision). Isospin differences between $p+p$ and Au+Au are ignored. The check is done by separately extrapolating the fitted fraction of yield which scales with N_{coll} and the fraction scaling with N_{part} down to one nucleon-nucleon collision and two participant nucleons, and summing the result. One obtains particle ratios of $K/\pi=(8.7\pm2.6)\%$ and $\overline{p}/\pi=(4.9\pm0.8)\%$. These values fall between those measured at lower $\sqrt{s}$ at the ISR [67] and those at higher $\sqrt{s}$ at the Tevatron [68], as expected since the RHIC energy lies in-between. Thus the Au+Au data are shown to scale down to $p+p$ reasonably.

One may expect that the particle ratios at very high p_T should be dominated by hard scattering, and therefore scale

TABLE IX. (*Continued.*)

p_T(GeV/c)	$\pi^{\pm}$	$K^{\pm}$	$p(\overline{p})$
	0.020 ± 0.004		
2.30			0.020 ± 0.003
			0.012 ± 0.002
2.50			0.010 ± 0.002
			0.011 ± 0.002
2.70			0.006 ± 0.001
			0.0026 ± 0.0009
2.90			0.0035 ± 0.0008
			0.003 ± 0.001
3.10			0.0028 ± 0.0007
			0.0011 ± 0.0005
3.30			0.0014 ± 0.0005
			0.0010 ± 0.0004

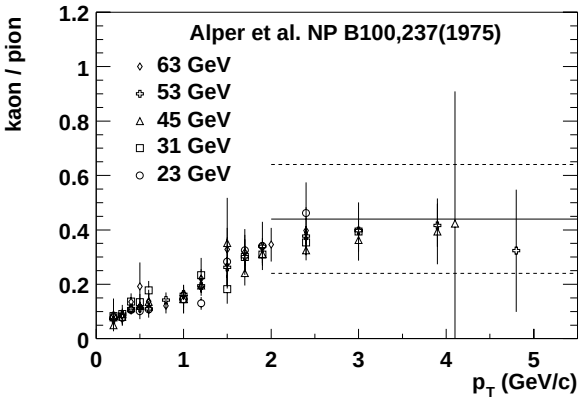

FIG. 26. Kaon to pion ratio as a function of p_T. The different points are measured in $p+p$ collisions (data from Ref. [69]). The solid line is the asymptotic value for high p_T in $p+p$ derived from the hard scattering component of the fits using Eq. (21) to the measured centrality dependence of dN/dy in Au-Au collisions at $\sqrt{s_{NN}}=130$ GeV. The dashed lines indicate the corresponding uncertainty.

with the number of binary collisions. Consequently, we look at ratios of the N_{coll} scaling components alone, extrapolated down to one binary collision. The values are compared to measurements of hadron ratios at the ISR [69] in Figs. 26 and 27. The ratios of the extrapolated Au+Au yield fractions scaling as N_{coll} are shown as solid lines for $p_T\geqslant2$ GeV/c. The agreement with the $p+p$ data at high p_T is quite good.

Finally, we directly compare p/π and $\overline{p}/\pi$ ratios in central Au+Au collisions with $p+p$, as a function of p_T. These ratios from the 10% most central data, using the charged particle measurement from this paper and neutral pions from Ref. [39], are shown in Fig. 28. The ratios show a steady increase up to 2.5 GeV/c in p_T. Even though the simple extrapolation of the N_{coll} scaling yield fraction agreed with $p+p$, the ratios of the full yield significantly exceed those in the ISR measurements [69]. According to Gyulassy and co-

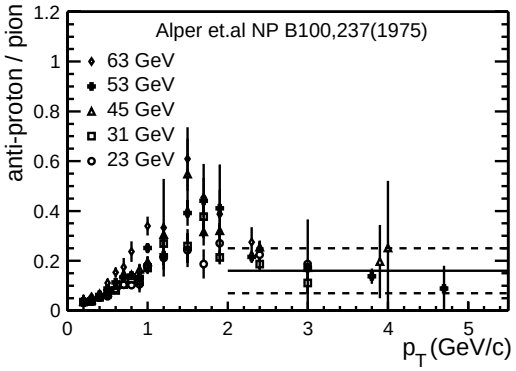

FIG. 27. Antiproton to π^- ratio as a function of p_T. The different points are measured in $p+p$ collisions (data from Ref. [69]). The solid line is the asymptotic value for high p_T in $p+p$ derived from the hard scattering component of the fits using Eq. (21) to the measured centrality dependence of dN/dy in Au-Au collisions at $\sqrt{s_{NN}}=130$ GeV. The dashed lines indicate the corresponding uncertainty.

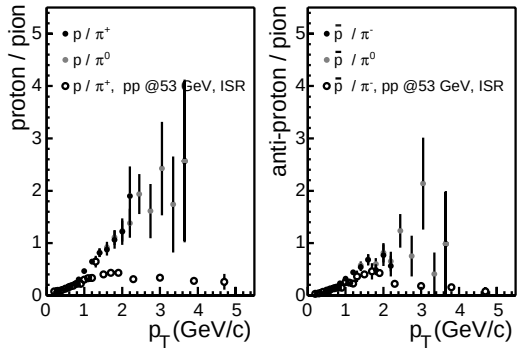

FIG. 28. (a) Proton to pion ratio as a function of p_T. (b) Antiproton to pion ratio as a function of p_T. The open circles represent measurements in $p+p$ collisions (data from Ref. [69]). The filled circles show the 10% most central Au+Au collisions. The neutral pion spectra are from the data published in Ref. [39].

workers [70] this result may give insight into baryon number transport and the interplay between soft and hard processes.

Of course, splitting the observed yields into portions that scale with $N_{\rm part}$ and $N_{\rm coll}$ is by no means a unique explanation of the data. The spectra and yields can also be well reproduced by thermal models, which break such simple scalings due to the multiple interactions suffered by the constituents.

Simple thermal models that ignore transverse and longitudinal flow [71] are able to describe the centrality dependence of the midrapidity $\pi^{\pm}$, $K^{\pm}$, p, and $\overline{p}$ yields by tuning the chemical freeze-out temperature $T_{\rm ch}$, the baryon chemical potential μ_B and by introducing a strangeness saturation factor γ_s. It was found that μ_B is independent of centrality, while both $\gamma_{\rm s}$ and $T_{\rm ch}$ increase from peripheral to central collisions. Within the same model, the centrality dependence of the particle yields at lower energy ($\sqrt{s_{NN}}=17$ GeV [72,73]) are described by constant $T_{\rm ch}$ and μ_B. The strong centrality dependence in kaon production at both energies is accounted for by the increase in the strangeness saturation factor γ_s. Although the integrated particle yields are very well described, such simple thermal models do not attempt a comparison to the single-particle spectra, which clearly indicate centrality dependent flow effects not included in the model.

Thermal models that include hydrodynamical parameters on a freeze-out hypersurface to account for longitudinal and transverse flow can reproduce the absolutely normalized particle spectra by introducing only two thermal parameters $T_{\rm ch}$ and μ_B [74,75]. In this approach, the thermal parameters are independent of centrality, while the geometric parameters are adjusted to reproduce the spectra. Good agreement with the data is obtained up to $p_T \approx 2-3$ GeV/c, however, an explicit comparison with the centrality dependence of the integrated midrapidity yields has not yet been made.

This section shows that the yields of all hadrons increase more rapidly than linearly with the number of participants, but the increase is weaker than scaling with the number of binary collisions. The excess beyond linear scaling with $N_{\rm part}$ is the strongest for kaons, intermediate for (anti)protons, and weakest for pions. The centrality dependence of the total yields can be well fit with a sum of these two kinds of scaling. At high p_T, the baryon and antibaryon yields greatly exceed expectations from $p+p$ collisions. Thermal models, which do not invoke strict scaling rules, can successfully reproduce the data as well, providing that they include the radial flow required by the p_T spectra.

VI. SUMMARY AND CONCLUSION

We have presented the spectra and yields of identified hadrons produced in $\sqrt{s_{NN}}=130$ GeV Au+Au collisions. The yields of pions increase approximately linearly with the number of participant nucleons, while the yield increase is faster than linear for kaons, protons, and antiprotons.

Hydrodynamic analyses of the particle spectra are performed: the spectra are fit with a hydrodynamic-inspired parametrization to extract freeze-out temperature and radial flow velocity of the particle source. The data are also compared to two full hydrodynamics calculations. The simultaneous fits of pion, kaon, proton, and antiproton spectra show that radial flow in central collisions at RHIC exceeds that at lower energies and increases with centrality of the collision. The hydrodynamic models are consistent with the measured spectral shapes, extracted freeze-out temperature $T_{\rm fo}$, and the flow velocity β_T in central collisions.

TABLE XIII. Minimum-bias invariant yields for all particles in equal p_T bins. For each p_T, the first line are the positive particle yields and the second are the negative particle yields. The units are c^2/Gev^2.

p_T(GeV/c)	$\pi^{\pm}$	$K^{\pm}$	(anti)p
0.25	112±2		
	109±2		
0.35	56±1		
	49.9±0.9		
0.45	28.0±0.5	6.1±0.4	
	24.1±0.5	4.6±0.4	
0.55	15.7±0.3	4.0±0.3	2.3±0.1
	14.6±0.3	3.2±0.2	0.38±0.02
0.70	7.3±0.1	2.18±0.09	1.55±0.06
	7.0±0.1	1.9±0.1	1.07±0.06
0.90	3.06±0.06	1.07±0.05	1.08±0.04
	2.89±0.07	0.91±0.05	0.79±0.04
1.20	0.91±0.02	0.38±0.02	0.49±0.02
	0.98±0.02	0.32±0.02	0.35±0.01
1.60	0.208±.007	0.104±0.006	0.157±0.007
	0.193±0.007	0.093±0.006	0.119±0.007
2.00	0.050±0.003		0.051±0.003
	0.053±0.003		0.031±0.003
2.45	0.0028±0.005		0.013±0.001
	0.0034±0.0006		0.009±0.001
2.95			0.0036±0.0006
			0.0022±0.0005
3.55			0.007±0.0002
			0.0006±0.0002

TABLE XIV. Pion invariant yields in each event centrality normalized to one rapidity unit at midrapidity. The first line corresponds to positive pions and the second to negative pions.

p_T(GeV/c)	0–5 %	5–15 %	15–30 %	30–60 %	60–92 %
0.25	355±9	282±6	186±4	81±2	13.2±0.5
	371±10	275±7	180±4	74±2	12.1±0.5
0.35	188±5	146±3	93±2	36.6±0.8	5.3±0.2
	169±5	128±3	82±2	34.3±0.9	5.0±0.2
0.45	95±3	74±2	48±1	17.5±0.5	2.7±0.1
	86±3	63±2	40±1	15.7±0.5	2.1±0.1
0.55	56±2	41±1	26.0±0.7	10.1±0.3	1.32±0.09
	51±2	38±1	24.5±0.8	9.6±0.3	1.18±0.09
0.70	26.3±0.8	20.2±0.5	12.3±0.3	4.4±0.1	0.62±0.04
	24.7±0.9	18.6±0.6	11.8±0.4	4.5±0.1	0.57±0.04
0.90	11.0±0.4	7.9±0.2	5.1±0.2	1.79±0.06	0.19±0.02
	10.0±0.5	7.9±0.3	5.0±0.2	1.76±0.07	0.24±0.02
1.20	3.1±0.1	2.37±0.09	1.50±0.05	0.58±0.02	0.064±0.006
	3.4±0.2	2.7±0.1	1.67±0.07	0.64±0.03	0.061±0.007
1.60	0.62±0.05	0.54±0.03	0.34±0.02	0.142±0.009	0.015±0.003
	0.63±0.06	0.58±0.04	0.32±0.02	0.129±0.009	0.014±0.003
2.00	0.17±0.02	0.14±0.01	0.083±0.009	0.027±0.003	0.005±0.001
	0.20±0.03	0.14±0.02	0.09±0.01	0.035±0.004	0.004±0.001
2.45	0.005±0.003	0.009±0.003	0.006±0.002	0.0017±0.0006	
	0.011±0.005	0.11±0.004	0.005±0.002	0.0025±0.0009	

Extrapolating the fits to estimate thermal particle production at higher p_T allows us to study the soft-hard physics boundary by comparing to measured spectra at high p_T. The yield of the soft protons reaches, and even exceeds, that of the extrapolated soft pions at 2 GeV/c p_T. The sum of the extrapolated soft spectra agrees with the measured inclusive data to $p_T \approx 2.5-3$ GeV/c. The transition from soft to hard processes must be species dependent, and the admixture of boosted nucleons implies that hard processes do not dominate the inclusive charged particle spectra until ≈ 3 GeV/c.

ACKNOWLEDGMENTS

We thank the staff of the RHIC Project, Collider-Accelerator, and Physics Departments at Brookhaven National Laboratory and the staff of the other PHENIX participating institutions for their vital contributions. We acknowledge support from the Department of Energy, Office of Science, Nuclear Physics Division, the National Science Foundation, and Dean of the College of Arts and Sciences, Vanderbilt University (U.S.), Ministry of Education, Culture,

TABLE XV. Kaon invariant yields in each event centrality normalized to one rapidity unit at midrapidity. The first line corresponds to positive kaons and the second to negative kaons.

p_T(GeV/c)	0–5 %	5–15 %	15–30 %	30–60 %	60–92 %
0.45	21±3	16±2	10±1	4.3±0.5	0.5±0.1
	21±3	13±2	7±1	2.5±0.4	0.4±0.1
0.55	15±2	11±1	6.6±0.7	2.4±0.3	0.20±0.07
	13±2	8±1	4.8±0.6	2.3±0.3	0.3±0.1
0.70	8.0±0.7	6.6±0.5	4.3±0.3	1.5±0.1	0.18±0.03
	7.0±0.8	6.5±0.6	3.1±0.3	1.1±0.1	0.14±0.03
0.90	4.5±0.4	3.1±0.2	1.9±0.1	0.62±0.06	0.06±0.02
	3.3±0.4	3.3±0.3	1.6±0.2	0.5±0.06	0.09±0.02
1.20	1.4±0.1	1.10±0.08	0.68±0.05	0.22±0.02	0.012±0.004
	1.3±0.1	0.97±0.08	0.50±0.05	0.17±0.02	0.015±0.005
1.60	0.36±0.05	0.29±0.03	0.17±0.02	0.062±0.007	0.008±0.002
	0.29±0.05	0.27±0.03	0.20±0.02	0.058±0.008	0.004±0.002

TABLE XVI. (Anti)proton invariant yields in each event centrality normalized to one rapidity unit at midrapidity. The first line corresponds to protons and the second to antiprotons.

p_T(GeV/c)	0–5 %	5–15 %	15–30 %	30–60 %	60–92 %
0.55	8±1	4.9±0.5	4.0±0.4	1.6±0.2	0.26±0.06
	4.2±0.8	2.8±0.5	2.0±0.3	0.8±0.1	0.12±0.05
0.70	5.4±0.4	4.5±0.3	2.5±0.2	1.06±0.07	0.14±0.02
	4.4±0.5	2.9±0.3	2.0±0.2	0.80±0.08	0.14±0.03
0.90	3.9±0.3	3.1±0.2	1.9±0.1	0.71±0.05	0.10±0.02
	2.8±0.3	2.1±0.2	1.4±0.1	0.58±0.05	0.06±0.01
1.20	1.9±0.1	1.37±0.08	0.78±0.04	0.26±0.02	0.031±0.005
	1.3±0.1	0.96±0.07	0.56±0.04	0.21±0.02	0.018±0.004
1.60	0.60±0.06	0.44±0.03	0.27±0.02	0.087±0.008	0.005±0.002
	0.49±0.06	0.34±0.03	0.19±0.02	0.062±0.007	0.007±0.002
2.00	0.20±0.03	0.15±0.02	0.09±0.01	0.025±0.003	0.003±0.001
	0.15±0.03	0.07±0.01	0.055±0.009	0.019±0.003	0.0005±0.0005
2.45	0.06±0.01	0.040±0.007	0.020±0.004	0.006±0.001	0.0010±0.0006
	0.04±0.01	0.028±0.006	0.011±0.003	0.005±0.001	0.0020±0.0008
2.95	0.015±0.005	0.007±0.002	0.005±0.002	0.0023±0.0007	0.0006±0.0004
	0.013±0.005	0.008±0.003	0.002±0.007	0.0003±0.0003	0.0005±0.0003
3.55	0.003±0.002	0.0012±0.007	0.0014±0.006	0.0005±0.0002	
	0.002±0.001	0.0011±0.007	0.0013±0.006	0.0002±0.0002	

Sports, Science, and Technology and the Japan Society for the Promotion of Science (Japan), Russian Academy of Science, Ministry of Atomic Energy of Russian Federation, Ministry of Industry, Science, and Technologies of Russian Federation (Russia), Bundesministerium für Bildung und Forschung, Deutscher Akademischer Auslandsdienst, and Alexander von Humboldt Stiftung (Germany), VR and the Wallenberg Foundation (Sweden), MIST and the Natural Sciences and Engineering Research Council (Canada), Conselho Nacional de Desenvolvimento Científico e Tecnológico and Fundação de Amparo à Pesquisa do Estado de São Paulo (Brazil), Natural Science Foundation of China (People's Republic of China), Centre National de la Recherche Scientifique, Commissariat à l'Énergie Atomique, Institut National de Physique Nucláire et de Physique des Particules, and Association pour la Recherche et le Développement des Méthodes et Processus Industriels (France), Department of Atomic Energy and Department of Science and Technology (India), Israel Science Foundation (Israel), Korea Research Foundation and Center for High Energy Physics (Korea), the U.S. Civilian Research and Development Foundation for the Independent States of the Former Soviet Union, and the U.S.-Israel Binational Science Foundation.

APPENDIX A: DETERMINING N_{part} AND N_{coll}

As only the fraction of the total cross section is measured in both ZDC and BBC detectors, a model-dependent calculation is used to map collision centrality to the number of participant nucleons, N_{part}, and the number of binary nucleon-nucleon collisions, N_{coll}. A discussion of this calculation at RHIC can be found elsewhere [62].

Using a Glauber model combined with a simulation of the BBC and ZDC responses, N_{part} and N_{coll} are determined in each centrality. The model provides the thickness of nuclear matter in the direct path of each oncoming nucleon, and uses the inelastic nucleon-nucleon cross section $\sigma_{N+N}^{\mathrm{inel}}$ to determine whether or not a nucleon-nucleon collision occurs. We assume the following.

(1) The nucleons travel in straight-line paths, parallel to the velocity of its respective nucleus.

(2) An inelastic collision occurs if the relative distance between two nucleons is less than $\sqrt{\sigma_{N+N}^{\mathrm{inel}}/\pi}$.

(3) Fluctuations are introduced by using the simulated detector response for both ZDC and BBC.

In this calculation, the Woods-Saxon nuclear density distribution $[\rho(r)]$ is used for each nucleus with two parameters, the nuclear radius $R=6.38^{+0.27}_{-0.13}$ fm and diffusivity $d=0.53\pm0.01$ fm [16]. The central density ρ_0 is determined by normalization to the correct number of nucleons. The inelastic nucleon-nucleon cross section is $\sigma_{N+N}^{\mathrm{inel}}=40\pm3$ mb,

$$\rho(r)=\frac{\rho_0}{1+e^{(r-r_n)/d}}. \tag{A1}$$

APPENDIX B: INVARIANT YIELDS

Tabulated here are the measured invariant yields of pions, kaons, and (anti)protons produced in Au+Au collisions at 130 GeV. Tables IX–XII show the invariant yields plotted in Figs. 9 and 10. Tables XIII–XVI show the invariant yields in equal p_T bins as used in Fig. 11.

APPENDIX C: FREEZE-OUT SURFACE ASSUMPTIONS

The freeze-out surface is $\sigma(r,\phi,\eta)$, where the radius r is between zero and R, the radius at freeze-out, the azimuthal

angle ϕ is between zero and 2π, and the longitudinal space-time rapidity variable η varies between $-\eta_{\max}$ and $\eta_{\max}$. In the Bjorken scenario, the freeze-out surface in space-time is hyperbolic, with contours of constant proper time $\tau = \sqrt{t^2 - z^2}$. Assuming instantaneous freeze-out in the radial direction and longitudinal boost invariance, the model dependence factors out of Eq. (17) and is included in the normalization constant A.

At 130 GeV, the PHOBOS experiment measures the total charged particle pseudorapidity distribution to be flat over 2 units of pseudorapidity [43]. The measured rapidity in PHOBOS is taken to be the same as the rapidity of the fireball, defined here as z. The rapidity variables in the integrand vanish for $|z| > 2$. Therefore, the integration over the fireball rapidity is generally taken to be from $-\infty$ to $+\infty$ using the modified K_1 Bessel function

$$K_1(m_T/T) = \int_0^\infty \cosh(z) e^{-m_T \cosh(z)/T} dz, \qquad \text{(C1)}$$

where the variable z is the fireball rapidity variable. The K_1 bessel function can also result by integration over the measured rapidity y with the assumption that the freeze-out is instantaneous in the radial direction. In this case, no assumption is made on the shape of the freeze-out hypersurface. This also assumes that the total rapidity distribution is measured in the detector. What results is the single differential $1/m_T\, dN/dm_T$ [76].

[1] B. Andersson *et al.*, Phys. Rep. **97**, 31 (1983).
[2] X. Artru, Phys. Rep. **97**, 147 (1983).
[3] J. Owens *et al.*, Phys. Rev. D **18**, 1501 (1978).
[4] K. Ackermann *et al.*, Phys. Rev. Lett. **86**, 402 (2001).
[5] C. Adler *et al.*, Phys. Rev. Lett. **87**, 182301 (2001).
[6] C. Adler *et al.*, Phys. Rev. C **66**, 034904 (2002).
[7] C. Adler *et al.*, Phys. Rev. Lett. **90**, 032301 (2003).
[8] K. Adcox *et al.*, Phys. Rev. Lett. **89**, 212301 (2002).
[9] B. Back *et al.*, Phys. Rev. Lett. **89**, 222301 (2002).
[10] D. Morrison *et al.*, Nucl. Phys. **A638**, 565c (1998).
[11] W. Zajc, Nucl. Phys. **A98**, 39 (2002).
[12] K. Adcox *et al.*, Nucl. Instrum. Methods Phys. Res. A **499**, 469 (2003).
[13] J. Mitchell *et al.*, Nucl. Instrum. Methods Phys. Res. A **482**, 491 (2002).
[14] D. Ben-Tzvi and M. Sandler, Pattern Recogn. Lett. **11**, 167 (1990).
[15] C. Adler *et al.*, Nucl. Instrum. Methods Phys. Res. A **470**, 488 (2001).
[16] R. Glauber and J. Natthiae, Nucl. Phys. **B21**, 135 (1970).
[17] B. Hahn, D. Ravenhall, and R. Hofstadter, Phys. Rev. **101**, 1131 (1956).
[18] S. J. Pollock *et al.*, Phys. Rev. C **46**, 2587 (1992).
[19] D. Groom, Eur. Phys. J. C **3**, 144 (1998).
[20] R. Brun, R. Hagelberg, N. Hansroul, and J. Lassalle, CERN-DD-78-2, 1978.
[21] J. M. Burward-Hoy, Ph.D. thesis, State University of New York at Stony Brook, 2001.
[22] K. Adcox *et al.*, Phys. Rev. Lett. **88**, 242301 (2002).
[23] R. Albrecht *et al.*, Eur. Phys. J. C **5**, 255 (1998).
[24] M. Aggarwal *et al.*, Eur. Phys. J. C **23**, 225 (2002).
[25] M. Faessler, Phys. Rep. **115**, 1 (1984).
[26] K. Adcox *et al.*, Phys. Rev. Lett. **89**, 092302 (2002).
[27] K. Adcox *et al.*, Phys. Rev. Lett. **86**, 3500 (2001).
[28] I. Bearden *et al.*, Phys. Rev. Lett. **78**, 2080 (1997).
[29] H. Boggild *et al.*, Phys. Rev. C **59**, 328 (1999).
[30] I. Bearden *et al.*, Phys. Rev. C **57**, 837 (1998).
[31] I. Bearden *et al.*, Phys. Lett. B **388**, 431 (1996).
[32] E. Andersen, J. Phys. G **25**, 171 (1999).
[33] F. Antinori *et al.*, Phys. Lett. B **433**, 209 (1998).
[34] B. Alper *et al.*, Nucl. Phys. **B100**, 237 (1975).
[35] K. Guettler *et al.*, Nucl. Phys. **B116**, 77 (1976).
[36] B. Alper *et al.*, Nucl. Phys. **B87**, 19 (1975).
[37] K. Guettler *et al.*, Nucl. Phys. **B116**, 77 (1976).
[38] J. Schaffner-Bielich, D. Kharzeev, L. McLerran, and R. Venugopalan, Nucl. Phys. **A705**, 494 (2002).
[39] K. Adcox *et al.*, Phys. Rev. Lett. **88**, 022301 (2002).
[40] B. Back *et al.*, PHOBOS Collaboration, Phys. Rev. C **65**, 061901(R) (2002).
[41] C. Adler *et al.*, STAR Collaboration, Phys. Rev. Lett. **87**, 112303 (2001).
[42] K. Adcox *et al.*, PHENIX Collaboration, Phys. Rev. Lett. **86**, 3500 (2001).
[43] B. Back *et al.*, Phys. Rev. Lett. **85**, 3100 (2000).
[44] E. Schnedermann, J. Sollfrank, and U. Heinz, Phys. Rev. C **48**, 2462 (1993).
[45] S. Esumi, S. Chapman, H. van Hecke, and N. Xu, Phys. Rev. C **55**, R2163 (1997).
[46] M. van Leeuwen for the NA49 Collaboration, Nucl. Phys. **A715**, 161 (2003).
[47] S. Afanasiev *et al.*, Eur. Phys. J. C **2**, 661 (1998).
[48] P. Kolb, Ph.D. thesis, University of Regensburg, 2001.
[49] J. Sollfrank, P. Koch, and U. Heinz, Phys. Lett. B **252**, 256 (1990).
[50] J. Barette *et al.*, Phys. Lett. B **351**, 93 (1995).
[51] H. Boggild *et al.*, Z. Phys. C **69**, 621 (1996).
[52] U. Wiedemann and U. Heinz, Phys. Rev. C **56**, 3265 (1997).
[53] P. Braun-Munzinger, D. Magestro, K. Redlich, and J. Stachel, Phys. Lett. B **518**, 41 (2001).
[54] P. F. Kolb (unpublished).
[55] P. F. Kolb, J. Sollfrank, and U. Heinz, Phys. Rev. C **62**, 054909 (2000).
[56] P. Kolb, P. Huovinen, U. Heinz, and H. Heiselberg, Phys. Lett. B **500**, 232 (2001).
[57] D. Teaney, Ph.D. thesis, State University of New York at Stony Brook, 2001.
[58] D. Teaney, J. Lauret, and E. Shuryak, Phys. Rev. Lett. **86**, 4783 (2001).
[59] H. Sorge, Phys. Rev. C **52**, 3291 (1995).
[60] D. Teaney, J. Lauret, and E. Shuryak, nucl-th/0110037.
[61] W. Broniowski and W. Florkowski, Phys. Rev. Lett. **87**, 272302 (2001).

[62] D. Kharzeev and M. Nardi, Phys. Lett. B **507**, 121 (2001).
[63] X.-N. Wang and M. Gyulassy, Phys. Rev. Lett. **86**, 3496 (2001).
[64] F. Becattini and U. Heinz, Z. Phys. C **76**, 269 (1997).
[65] F. Becattini, Eur. Phys. J. C **5**, 143 (1998).
[66] A. Tounsi and K. Redlich, J. Phys. G **28**, 1761 (2002).
[67] B. Alper *et al.*, Nucl. Phys. **B87**, 19 (1975).
[68] T. Alexopoulos *et al.*, Phys. Rev. D **48**, 984 (1993).
[69] B. Alper *et al.*, Nucl. Phys. **B100**, 237 (1975).
[70] I. Vitev and M. Gyulassy, Phys. Rev. C **65**, 041902 (2002).
[71] B. Kampfer, J. Cleymans, K. Gallmeister, and S. M. Wheaton, Heavy Ion Phys. **18**, 1 (2003).
[72] F. Sikler, Nucl. Phys. **A661**, 45c (1999).
[73] V. Freise, for the NA49 Collaboration, Proceedings of Strangeness in Quark Matter 2003, nucl-ex/0305017, J. Phys. G (to be published).
[74] W. Broniowski, A. Baran, and W. Florkowski, Acta Phys. Pol. B **33**, 4235 (2002).
[75] W. Broniowski and W. Florkowski, Acta Phys. Pol. B **33**, 1629 (2002).
[76] U. Heinz (private communication).

J/ψ Production from Proton-Proton Collisions at $\sqrt{s} = 200$ GeV

S. S. Adler,[5] S. Afanasiev,[17] C. Aidala,[5] N. N. Ajitanand,[43] Y. Akiba,[20,38] J. Alexander,[43] R. Amirikas,[12] L. Aphecetche,[45] S. H. Aronson,[5] R. Averbeck,[44] T. C. Awes,[35] R. Azmoun,[44] V. Babintsev,[15] A. Baldisseri,[10] K. N. Barish,[6] P. D. Barnes,[27] B. Bassalleck,[33] S. Bathe,[30] S. Batsouli,[9] V. Baublis,[37] A. Bazilevsky,[39,15] S. Belikov,[16,15] Y. Berdnikov,[40] S. Bhagavatula,[16] J. G. Boissevain,[27] H. Borel,[10] S. Borenstein,[25] M. L. Brooks,[27] D. S. Brown,[34] N. Bruner,[33] D. Bucher,[30] H. Buesching,[30] V. Bumazhnov,[15] G. Bunce,[5,39] J. M. Burward-Hoy,[26,44] S. Butsyk,[44] X. Camard,[45] J.-S. Chai,[18] P. Chand,[4] W. C. Chang,[2] S. Chernichenko,[15] C. Y. Chi,[9] J. Chiba,[20] M. Chiu,[9] I. J. Choi,[52] J. Choi,[19] R. K. Choudhury,[4] T. Chujo,[5] V. Cianciolo,[35] Y. Cobigo,[10] B. A. Cole,[9] P. Constantin,[16] D. G. d'Enterria,[45] G. David,[5] H. Delagrange,[45] A. Denisov,[15] A. Deshpande,[39] E. J. Desmond,[5] O. Dietzsch,[41] O. Drapier,[25] A. Drees,[44] K. A. Drees,[5] R. du Rietz,[29] A. Durum,[15] D. Dutta,[4] Y. V. Efremenko,[35] K. El Chenawi,[49] A. Enokizono,[14] H. En'yo,[38,39] S. Esumi,[48] L. Ewell,[5] D. E. Fields,[33,39] F. Fleuret,[25] S. L. Fokin,[23] B. D. Fox,[39] Z. Fraenkel,[51] J. E. Frantz,[9] A. Franz,[5] A. D. Frawley,[12] S.-Y. Fung,[6] S. Garpman,[29,*] T. K. Ghosh,[49] A. Glenn,[46] G. Gogiberidze,[46] M. Gonin,[25] J. Gosset,[10] Y. Goto,[39] R. Granier de Cassagnac,[25] N. Grau,[16] S. V. Greene,[49] M. Grosse Perdekamp,[39] W. Guryn,[5] H.-Å. Gustafsson,[29] T. Hachiya,[14] J. S. Haggerty,[5] H. Hamagaki,[8] A. G. Hansen,[27] E. P. Hartouni,[26] M. Harvey,[5] R. Hayano,[8] X. He,[13] M. Heffner,[26] T. K. Hemmick,[44] J. M. Heuser,[44] M. Hibino,[50] J. C. Hill,[16] W. Holzmann,[43] K. Homma,[14] B. Hong,[22] A. Hoover,[34] T. Ichihara,[38,39] V. V. Ikonnikov,[23] K. Imai,[24,38] D. Isenhower,[1] M. Ishihara,[38] M. Issah,[43] A. Isupov,[17] B. V. Jacak,[44] W. Y. Jang,[22] Y. Jeong,[19] J. Jia,[44] O. Jinnouchi,[38] B. M. Johnson,[5] S. C. Johnson,[26] K. S. Joo,[31] D. Jouan,[36] S. Kametani,[8,50] N. Kamihara,[47,38] J. H. Kang,[52] S. S. Kapoor,[4] K. Katou,[50] S. Kelly,[9] B. Khachaturov,[51] A. Khanzadeev,[37] J. Kikuchi,[50] D. H. Kim,[31] D. J. Kim,[52] D. W. Kim,[19] E. Kim,[42] G.-B. Kim,[25] H. J. Kim,[52] E. Kistenev,[5] A. Kiyomichi,[48] K. Kiyoyama,[32] C. Klein-Boesing,[30] H. Kobayashi,[38,39] L. Kochenda,[37] V. Kochetkov,[15] D. Koehler,[33] T. Kohama,[14] M. Kopytine,[44] D. Kotchetkov,[6] A. Kozlov,[51] P. J. Kroon,[5] C. H. Kuberg,[1,27] K. Kurita,[39] Y. Kuroki,[48] M. J. Kweon,[22] Y. Kwon,[52] G. S. Kyle,[34] R. Lacey,[43] V. Ladygin,[17] J. G. Lajoie,[16] A. Lebedev,[16,23] S. Leckey,[44] D. M. Lee,[27] S. Lee,[19] M. J. Leitch,[27] X. H. Li,[6] H. Lim,[42] A. Litvinenko,[17] M. X. Liu,[27] Y. Liu,[36] C. F. Maguire,[49] Y. I. Makdisi,[5] A. Malakhov,[17] V. I. Manko,[23] Y. Mao,[7,38] G. Martinez,[45] M. D. Marx,[44] H. Masui,[48] F. Matathias,[44] T. Matsumoto,[8,50] P. L. McGaughey,[27] E. Melnikov,[15] F. Messer,[44] Y. Miake,[48] J. Milan,[43] T. E. Miller,[49] A. Milov,[44,51] S. Mioduszewski,[5] R. E. Mischke,[27] G. C. Mishra,[13] J. T. Mitchell,[5] A. K. Mohanty,[4] D. P. Morrison,[5] J. M. Moss,[27] F. Mühlbacher,[44] D. Mukhopadhyay,[51] M. Muniruzzaman,[6] J. Murata,[38,39] S. Nagamiya,[20] J. L. Nagle,[9] T. Nakamura,[14] B. K. Nandi,[6] M. Nara,[48] J. Newby,[46] P. Nilsson,[29] A. S. Nyanin,[23] J. Nystrand,[29] E. O'Brien,[5] C. A. Ogilvie,[16] H. Ohnishi,[5,38] I. D. Ojha,[49,3] K. Okada,[38] M. Ono,[48] V. Onuchin,[15] A. Oskarsson,[29] I. Otterlund,[29] K. Oyama,[8] K. Ozawa,[8] D. Pal,[51] A. P. T. Palounek,[27] V. S. Pantuev,[44] V. Papavassiliou,[34] J. Park,[42] A. Parmar,[33] S. F. Pate,[34] T. Peitzmann,[30] J.-C. Peng,[27] V. Peresedov,[17] C. Pinkenburg,[5] R. P. Pisani,[5] F. Plasil,[35] M. L. Purschke,[5] A. K. Purwar,[44] J. Rak,[16] I. Ravinovich,[51] K. F. Read,[35,46] M. Reuter,[44] K. Reygers,[30] V. Riabov,[37,40] Y. Riabov,[37] G. Roche,[28] A. Romana,[25] M. Rosati,[16] P. Rosnet,[28] S. S. Ryu,[52] M. E. Sadler,[1] N. Saito,[38,39] T. Sakaguchi,[8,50] M. Sakai,[32] S. Sakai,[48] V. Samsonov,[37] L. Sanfratello,[33] R. Santo,[30] H. D. Sato,[24,38] S. Sato,[5,48] S. Sawada,[20] Y. Schutz,[45] V. Semenov,[15] R. Seto,[6] M. R. Shaw,[1,27] T. K. Shea,[5] T.-A. Shibata,[47,38] K. Shigaki,[14,20] T. Shiina,[27] C. L. Silva,[41] D. Silvermyr,[27,29] K. S. Sim,[22] C. P. Singh,[3] V. Singh,[3] M. Sivertz,[5] A. Soldatov,[15] R. A. Soltz,[26] W. E. Sondheim,[27] S. P. Sorensen,[46] I. V. Sourikova,[5] F. Staley,[10] P. W. Stankus,[35] E. Stenlund,[29] M. Stepanov,[34] A. Ster,[21] S. P. Stoll,[5] T. Sugitate,[14] J. P. Sullivan,[27] E. M. Takagui,[41] A. Taketani,[38,39] M. Tamai,[50] K. H. Tanaka,[20] Y. Tanaka,[32] K. Tanida,[38] M. J. Tannenbaum,[5] P. Tarján,[11] J. D. Tepe,[1,27] T. L. Thomas,[33] J. Tojo,[24,38] H. Torii,[24,38] R. S. Towell,[1] I. Tserruya,[51] H. Tsuruoka,[48] S. K. Tuli,[3] H. Tydesjö,[29] N. Tyurin,[15] H. W. van Hecke,[27] J. Velkovska,[5,44] M. Velkovsky,[44] L. Villatte,[46] A. A. Vinogradov,[23] M. A. Volkov,[23] E. Vznuzdaev,[37] X. R. Wang,[13] Y. Watanabe,[38,39] S. N. White,[5] F. K. Wohn,[16] C. L. Woody,[5] W. Xie,[6] Y. Yang,[7] A. Yanovich,[15] S. Yokkaichi,[38,39] G. R. Young,[35] I. E. Yushmanov,[23] W. A. Zajc,[9,†] C. Zhang,[9] S. Zhou,[7] S. J. Zhou,[51] and L. Zolin[17]

(PHENIX Collaboration)

[1]*Abilene Christian University, Abilene, Texas 79699, USA*
[2]*Institute of Physics, Academia Sinica, Taipei 11529, Taiwan*
[3]*Department of Physics, Banaras Hindu University, Varanasi 221005, India*
[4]*Bhabha Atomic Research Centre, Bombay 400 085, India*

 0031-9007/04/92(5)/051802(6)$22.50 © 2004 The American Physical Society

[5]*Brookhaven National Laboratory, Upton, New York 11973-5000, USA*
[6]*University of California–Riverside, Riverside, California 92521, USA*
[7]*China Institute of Atomic Energy (CIAE), Beijing, People's Republic of China*
[8]*Center for Nuclear Study, Graduate School of Science, University of Tokyo, 7-3-1 Hongo, Bunkyo, Tokyo 113-0033, Japan*
[9]*Columbia University, New York, New York 10027, USA, and Nevis Laboratories, Irvington, New York 10533, USA*
[10]*Dapnia, CEA Saclay, F-91191, Gif-sur-Yvette, France*
[11]*Debrecen University, H-4010 Debrecen, Egyetem tér 1, Hungary*
[12]*Florida State University, Tallahassee, Florida 32306, USA*
[13]*Georgia State University, Atlanta, Georgia 30303, USA*
[14]*Hiroshima University, Kagamiyama, Higashi-Hiroshima 739-8526, Japan*
[15]*Institute for High Energy Physics (IHEP), Protvino, Russia*
[16]*Iowa State University, Ames, Iowa 50011, USA*
[17]*Joint Institute for Nuclear Research, 141980 Dubna, Moscow Region, Russia*
[18]*KAERI, Cyclotron Application Laboratory, Seoul, South Korea*
[19]*Kangnung National University, Kangnung 210-702, South Korea*
[20]*KEK, High Energy Accelerator Research Organization, Tsukuba-shi, Ibaraki-ken 305-0801, Japan*
[21]*KFKI Research Institute for Particle and Nuclear Physics (RMKI), H-1525 Budapest 114, POBox 49, Hungary*
[22]*Korea University, Seoul, 136-701, Korea*
[23]*Russian Research Center "Kurchatov Institute," Moscow, Russia*
[24]*Kyoto University, Kyoto 606, Japan*
[25]*Laboratoire Leprince-Ringuet, Ecole Polytechnique, CNRS-IN2P3, Route de Saclay, F-91128, Palaiseau, France*
[26]*Lawrence Livermore National Laboratory, Livermore, California 94550, USA*
[27]*Los Alamos National Laboratory, Los Alamos, New Mexico 87545, USA*
[28]*LPC, Université Blaise Pascal, CNRS-IN2P3, Clermont-Fd, 63177 Aubiere Cedex, France*
[29]*Department of Physics, Lund University, Box 118, SE-221 00 Lund, Sweden*
[30]*Institut fuer Kernphysik, University of Muenster, D-48149 Muenster, Germany*
[31]*Myongji University, Yongin, Kyonggido 449-728, Korea*
[32]*Nagasaki Institute of Applied Science, Nagasaki-shi, Nagasaki 851-0193, Japan*
[33]*University of New Mexico, Albuquerque, New Mexico 87131, USA*
[34]*New Mexico State University, Las Cruces, New Mexico 88003, USA*
[35]*Oak Ridge National Laboratory, Oak Ridge, Tennessee 37831, USA*
[36]*IPN-Orsay, Universite Paris Sud, CNRS-IN2P3, BP1, F-91406, Orsay, France*
[37]*PNPI, Petersburg Nuclear Physics Institute, Gatchina, Russia*
[38]*RIKEN (The Institute of Physical and Chemical Research), Wako, Saitama 351-0198, Japan*
[39]*RIKEN BNL Research Center, Brookhaven National Laboratory, Upton, New York 11973-5000, USA*
[40]*St. Petersburg State Technical University, St. Petersburg, Russia*
[41]*Universidade de São Paulo, Instituto de Física, Caixa Postal 66318, São Paulo CEP05315-970, Brazil*
[42]*System Electronics Laboratory, Seoul National University, Seoul, South Korea*
[43]*Chemistry Department, Stony Brook University, SUNY, Stony Brook, New York 11794-3400, USA*
[44]*Department of Physics and Astronomy, Stony Brook University, SUNY, Stony Brook, New York 11794, USA*
[45]*SUBATECH (Ecole des Mines de Nantes, CNRS-IN2P3, Université de Nantes), BP 20722-44307, Nantes, France*
[46]*University of Tennessee, Knoxville, Tennessee 37996, USA*
[47]*Department of Physics, Tokyo Institute of Technology, Tokyo, 152-8551, Japan*
[48]*Institute of Physics, University of Tsukuba, Tsukuba, Ibaraki 305, Japan*
[49]*Vanderbilt University, Nashville, Tennessee 37235, USA*
[50]*Waseda University, Advanced Research Institute for Science and Engineering, 17 Kikui-cho, Shinjuku-ku, Tokyo 162-0044, Japan*
[51]*Weizmann Institute, Rehovot 76100, Israel*
[52]*Yonsei University, IPAP, Seoul 120-749, Korea*
(Received 8 July 2003; published 5 February 2004)

J/ψ production has been measured in proton-proton collisions at $\sqrt{s} = 200$ GeV over a wide rapidity and transverse momentum range by the PHENIX experiment at the Relativistic Heavy Ion Collider. Distributions of the rapidity and transverse momentum, along with measurements of the mean transverse momentum and total production cross section are presented and compared to available theoretical calculations. The total J/ψ cross section is $4.0 \pm 0.6(\text{stat}) \pm 0.6(\text{syst}) \pm 0.4(\text{abs})$ μb. The mean transverse momentum is $1.80 \pm 0.23(\text{stat}) \pm 0.16(\text{syst})$ GeV/c.

DOI: 10.1103/PhysRevLett.92.051802 PACS numbers: 13.85.Ni, 13.20.Fc, 14.40.Gx, 25.75.Dw

Understanding J/ψ production mechanisms requires data over a large range of collision energies and with broad coverage in rapidity and transverse momentum (p_T). Existing data at lower energies from fixed target hadron experiments yield total cross sections and mean p_T ($\langle p_T \rangle$) values in the energy range $\sqrt{s} = 7$–38.8 GeV [1]. Limited kinematic coverage in collider experiments [1–3] has so far meant that total cross sections and mean

p_T values could not be measured. The systematic study of J/ψ production at Relativistic Heavy Ion Collider (RHIC) energies with wide p_T and rapidity coverage should therefore provide crucial tests of J/ψ production models. In addition, the RHIC proton-proton results provide a baseline for studying cold and hot nuclear matter in proton-nucleus and nucleus-nucleus collisions using J/ψ yields as a probe.

Intense theoretical interest in the J/ψ production mechanism was stimulated when the color singlet model (CSM) was found [4] to dramatically underpredict the high p_T prompt J/ψ and $\psi(2S)$ cross sections measured with the collider detector at Fermilab (CDF) [3]. Attention turned toward models in which color octet $c\bar{c}$ states can also contribute to the J/ψ yield. The color octet model (COM), which is based on the nonrelativistic QCD (NRQCD) approach [5], has been successful in reproducing the high p_T CDF prompt J/ψ cross sections, as has the more phenomenological color evaporation model (CEM) [6].

In this Letter we report results of the first measurements of $pp \to J/\psi + X$ at RHIC, made at $\sqrt{s} = 200$ GeV by the PHENIX experiment. The data yield the first total cross sections for J/ψ production beyond fixed target energies, and the first measurement of $\langle p_T \rangle$ beyond $\sqrt{s} =$ 63 GeV. They will constrain models in the lower p_T region where gluon fusion is expected to dominate. At p_T beyond about 5 GeV/c, the direct J/ψ production cross section is expected to be dominated by fragmentation of high p_T gluons [7].

The PHENIX experiment [8] detects electrons in the pseudorapidity range $|\eta| \leq 0.35$ in two central spectrometer arms covering $\Delta\phi = 90°$, and forward rapidity muons in two muon arms covering $\Delta\phi = 360°$. Only one muon arm, covering $1.2 < \eta < 2.2$, was operational for this data set. Electrons are identified by matching charged particle tracks to energy deposits in the electromagnetic calorimeter (EMC) and to rings in the ring imaging Čerenkov detector (RICH), which has a threshold of 4.7 GeV/c for pions. Muons are identified by finding deeply penetrating roads in the muon identifier (MuID) and matching them to tracks in the muon tracker (MuTr).

The data were recorded during the $\sqrt{s} = 200$ GeV pp run covering the end of 2001 and the beginning of 2002. After quality assurance and vertex cuts (± 35 cm for ee and ± 38 cm for $\mu\mu$), 67 nb^{-1} were used for the $J/\psi \to \mu^+\mu^-$ analysis, and 82 nb^{-1} for $J/\psi \to e^+e^-$. The minimum bias interaction trigger required at least one hit on each side of the interaction vertex in the beam-beam counter (BBC), which covers $3.1 < |\eta| < 3.9$. Minimum bias trigger rates varied from 5 to 30 kHz. Events containing J/ψ decays were selected using level-1 triggers in coincidence with the minimum bias interaction trigger. The $J/\psi \to e^+e^-$ trigger required a minimum energy deposit of either 0.75 GeV in a 2×2 tile of EMC towers or 2.1 GeV in a 4×4 tile. The $J/\psi \to \mu^+\mu^-$ trigger required at least two deeply penetrating roads in separate azimuthal quadrants of the MuID [9].

J/ψ yields in the central arms were obtained by reconstructing electron-positron pairs. Electron candidates were charged particle tracks that were associated with a RICH ring (≥ 2 hit phototubes) and an EMC hit ($\pm 4\sigma$ position association cut), and which satisfied $0.5 < E/p < 1.5$, where E is the EMC cluster energy and p is the reconstructed track momentum. A 5 GeV/c upper limit on electron momentum prevented charged pions from firing the RICH.

J/ψ yields in the muon arm were obtained by reconstructing $\mu^+\mu^-$ pairs. Muon tracks were reconstructed by finding a track seed in the MuID and matching it to clusters of hits in each of the three MuTr stations. The momentum was determined by fitting, with a correction for energy loss, the MuID and MuTr hit positions and the BBC vertex position. Each track was required to pass 5σ cuts on the χ^2 from the track fit and on the radial distance of the fitted track from the measured z-vertex position.

Unlike-sign pairs and, for background estimation, like-sign pairs satisfying the above conditions were combined to form invariant mass spectra. Simulations show that the acceptance for like-sign and unlike-sign pairs is the same to within a few percent for invariant masses above 1 GeV/c^2 for electrons. In Fig. 1, unlike-sign and like-sign invariant mass spectra from the entire pp data set are shown together. For electrons, the net yield inside 2.8–3.4 GeV/c^2 is 46 ± 7.4, and for muons inside 2.71–3.67 GeV/c^2 it is 65 ± 9.5. For electrons, the peak width is 110 MeV/c^2 and the centroid agrees well with the Particle Data Group (PDG) value [10]. For muons, the width is 160 MeV/c^2. The muon peak centroid is higher than the PDG value by about 3%, consistent with the uncertainty in the muon magnetic field calibration. In both cases the width of the mass window was chosen to be 6 times the standard deviation expected from simulations.

The J/ψ cross sections were determined from the measured yields using

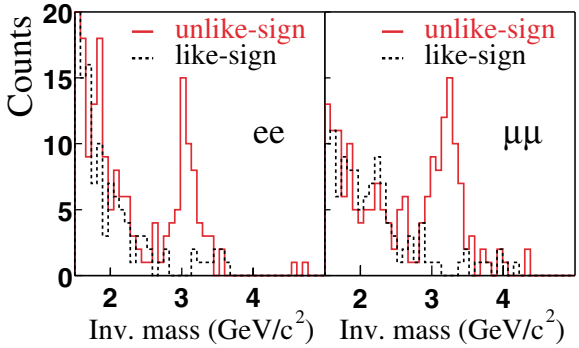

FIG. 1 (color online). The invariant mass spectra for dielectron and dimuon pairs. Unlike-sign pairs are shown as solid lines, and the sum of like-sign pairs as dashed lines.

$$B_{ll}\frac{d^2\sigma_{J/\psi}}{dydp_T} = \frac{N_{J/\psi}}{(\int \mathcal{L}dt)\Delta y \Delta p_T}\frac{1}{\epsilon_{\rm bias}\epsilon_{lvl1}}\frac{1}{A\epsilon_{\rm rec}},$$

where $N_{J/\psi}$ is the measured J/ψ yield, $\int \mathcal{L}dt$ is the integrated luminosity measured by the minimum bias trigger, B_{ll} is the branching fraction for the J/ψ to either e^+e^- or $\mu^+\mu^-$ pairs (PDG average value 5.9% [10]), $\epsilon_{\rm bias}$ is the minimum bias trigger efficiency for an event containing a J/ψ, ϵ_{lvl1} is the level-1 trigger efficiency for detecting a J/ψ, and $A\epsilon_{\rm rec}$ is the acceptance times reconstruction efficiency for a J/ψ.

The integrated luminosity can be written as $\int \mathcal{L}dt = N_{\rm MB}/\sigma_{\rm BBC}$, where $N_{\rm MB}$ is the number of minimum bias triggers and $\sigma_{\rm BBC}$ is the minimum bias trigger cross section. Using a van der Meer scan measurement, $\sigma_{\rm BBC}$ was determined to be 21.8 ± 2.1 mb [11]. We have estimated $\epsilon_{\rm bias}$ in two ways. First, the minimum bias trigger efficiency for J/ψ events from a simulation study using PYTHIA [12] [with the GRV94NLO parton distribution functions (PDFs)] was 0.74, with no p_T dependence. Good agreement is observed in the $dN_{ch}/d\eta$ distribution between PYTHIA simulations and measurements [13] for events involving high p_T π^0 production. Second, we measured [11] our minimum bias trigger efficiency for high p_T π^0 production using events recorded with a high p_T EMC trigger. The efficiency of $0.75 \pm 3\%$ is constant within uncertainties over the measured range of $1.5 < p_T < 9$ GeV/c. We chose to use our measured trigger efficiency from high p_T π^0 events when calculating the J/ψ cross section, assuming that the trigger efficiency is the same for both processes.

For the electron analysis, $A\epsilon_{\rm rec}$ was determined as a function of p_T using a full GEANT simulation of single J/ψ events with flat distributions in dN/dy ($|y| < 0.6$), p_T ($p_T < 6$ GeV/c), and collision vertex ($|z| < 35$ cm). The GEANT simulations were tuned to match real detector responses for single electrons. The reconstruction efficiency calculations used a typical dead channel map. An average correction for run-to-run variations in detector active area was determined from single electron yields. An estimate of the systematic uncertainty in $A\epsilon_{\rm rec}$ due to z vertex dependence of the acceptance, momentum resolution effects, the pair mass cut, and electron identification cuts is given in Table I, along with the uncertainty in the yield due to Drell-Yan and correlated charm decay contributions. The efficiency ϵ_{lvl1} of the level-1 J/ψ triggers in the central arms was determined as a function of p_T by using a software trigger-emulator to analyze simulated single J/ψ events. The results are shown in Table I. The trigger emulator was tuned by analyzing simulated single electrons and comparing with the real single electron trigger efficiency.

TABLE I. Table of quantities and their systematic error estimates (in parentheses). Ranges are given for p_T dependent quantities. For the $\mu^+\mu^-$ case the values of $A\epsilon_{\rm rec}$ and ϵ_{lvl1} are combined. The absolute cross section normalization uncertainty from $\epsilon_{\rm bias}$ and $\int \mathcal{L}dt$ is kept separate and is labeled (abs).

Quantity	e^+e^-	$\mu^+\mu^-$
Yield	($\pm$ 5%)	($\pm$5%)
$A\epsilon_{\rm rec}$	0.026–0.010($\pm$13%)	0.038–0.017($\pm$13%)
ϵ_{lvl1}	(2 × 2) 0.87–0.90($\pm$5%)	
	(4 × 4) 0.30–0.74($\pm$36%)	
$\epsilon_{\rm bias}$	0.75($\pm$3%)	0.75($\pm$3%)
$\int \mathcal{L}dt$	82 nb^{-1} ($\pm$9.6%)	67 nb^{-1} ($\pm$9.6%)
Total	$\pm$15%(syst) $\pm$ 10%(abs)	$\pm$14%(syst) $\pm$ 10%(abs)

For the muon arm, $A\epsilon_{\rm rec}\,\epsilon_{lvl1}$ was determined as an average within each rapidity and p_T bin, using a full GEANT simulation with J/ψ events generated by PYTHIA (with GRV94LO PDFs). The PYTHIA J/ψ rapidity and p_T distributions are very similar to those of the real data, so that bin averaging effects should be approximately accounted for by this procedure. The simulated events were reconstructed using the same reconstruction software and cuts as for the real data, assuming nominal detector efficiencies and typical realistic dead channel and dead high-voltage maps. Each event had to pass the simulated dimuon trigger. The systematic error includes discrepancies between Monte Carlo and real detector response, run to run variations in the detector state, and uncertainties in the PYTHIA distributions. The results, integrated over the rapidity range of the muon arm, are shown in Table I, along with an estimate of the systematic error on the yield due to the background subtraction technique. In both the electron and muon cases the J/ψ polarization was assumed to be zero, since existing J/ψ polarization measurements are consistent with zero at low p_T [14]. The effect of the unknown J/ψ polarization has not been included in the systematic error.

The p_T distributions for $J/\psi \to e^+e^-$ and $J/\psi \to \mu^+\mu^-$ are shown in Fig. 2, with predictions [15] from the COM. Predictions of the CSM, which greatly underpredicts the cross sections, are also shown. These

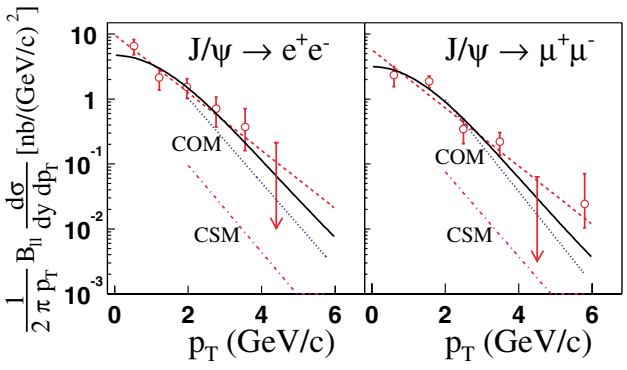

FIG. 2 (color online). The J/ψ p_T distributions for the dielectron and dimuon measurements, with statistical uncertainties. The solid line is a phenomenological fit of the form $(1/2\pi p_T)d\sigma/dp_T = A[1 + (p_T/B)^2]^{-6}$. The dashed line is an exponential fit. The CSM (dot-dashed) and COM (dotted) calculations are from [15].

predictions are limited to $p_T > 2$ GeV/c because parton intrinsic transverse momentum (k_T) broadening is not accounted for properly in the calculation. The COM calculations do not include fragmentation contributions, which become important at around 5 GeV/c [3]. Another calculation for the PHENIX muon arm using NRQCD is available in Ref. [16]. Calculations covering all p_T and including fragmentation contributions are needed. The solid lines are a phenomenological fit of a form that has been shown to fit J/ψ data well at fixed target energies [17]. The dashed line is an exponential fit. The phenomenological fits yield $\langle p_T \rangle$ values of $1.85 \pm 0.46(\text{stat}) \pm 0.16(\text{syst})$ GeV/c (central arm) and $1.78 \pm 0.27(\text{stat}) \pm 0.16(\text{syst})$ GeV/c (muon arm), with a combined value of $1.80 \pm 0.23(\text{stat}) \pm 0.16(\text{syst})$ GeV/c. The systematic uncertainties were estimated from the spread in $\langle p_T \rangle$ from a weighted mean of the binned data, the phenomenological fit, and the exponential fit. An additional 3% was assigned to the muon $\langle p_T \rangle$ due to the uncertainty in momentum scale.

The J/ψ rapidity distribution obtained by combining the dielectron and dimuon measurements is shown in Fig. 3, with the muon arm data divided into two rapidity bins. The COM curves are theoretical shape predictions [9] using the same models as are discussed in connection with Fig. 4(b), except that they are normalized to our data to make the shape comparison clearer. Since gluon fusion is the dominant process in all of the models, the rapidity shape depends mostly on the gluon distribution function and is not very sensitive to the production model. Most of the available PDFs are consistent with the data, and improved statistical precision will be needed to constrain them. A PYTHIA calculation that reproduces the shape of our data best is also shown in Fig. 3. Normalizing this to the data, the total cross section was determined to be $4.0 \pm 0.6(\text{stat}) \pm 0.6(\text{syst}) \pm 0.4(\text{abs})$ μb. The quoted systematic error was estimated by setting the measured cross sections all to their upper systematic error limits or all to their lower systematic error limits and noting how the cross section changed. The variation in the total cross section extracted if we use the same procedure with different PDF choices and models was estimated to be small (3%). We note that the minimum bias trigger efficiency for a single or double diffractive event producing a J/ψ will be different from the one we have assumed. However, the measured diffractive component of the J/ψ cross section at $\sqrt{s} = 1.8$ TeV and $p_T > 2$ GeV/c for both muons is only 1.45% [18], with little or no p_T dependence, suggesting that the diffractive component should be negligible in our case.

A comparison is made in Fig. 4(a) of the present $\langle p_T \rangle$ value with values from previous experiments [1]. There are no theoretical predictions that we can compare with the $\langle p_T \rangle$ measurements. The total J/ψ cross section determined in this analysis is shown in Fig. 4(b), along with cross sections determined by lower energy experiments [1] and predictions from the COM [9] using two different PDFs. The $\sqrt{s}$ dependence of the cross section is sensitive to the factorization scale Q, since the shape of the PDFs depends on Q. The values of Q (3.1 GeV for GRV98NLO and 2.3 GeV for MRST2001NLO) were chosen to give good agreement with the data. The total cross section normalization was obtained using color octet matrix elements from [19], but has large theoretical uncertainties associated with the charm quark mass and the renormalization scale. The renormalization scale was taken to be equal to the quark mass M_c, and their values (1.48 GeV for GRV98NLO and 1.55 GeV for MRST2001NLO) were chosen to give good agreement with the data. The CEM is also able to describe the total cross section data [6]. All measurements and models include feed-down from the χ_c and the ψ' to the J/ψ. We estimate [20] that B decay feed-down contributes less than 4% to the J/ψ total cross section at $\sqrt{s} = 200$ GeV.

In summary, we have presented the first $pp \to J/\psi + X$ measurements from RHIC, obtained at $\sqrt{s} = 200$ GeV. The rapidity distributions, p_T distributions,

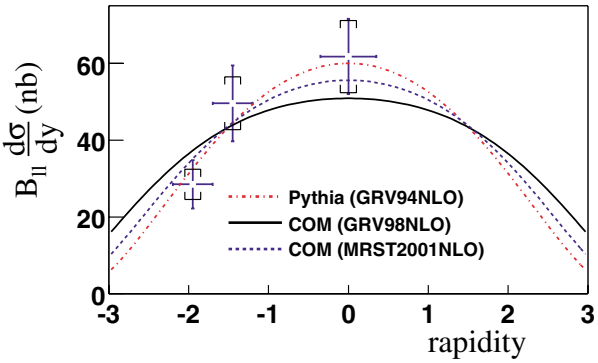

FIG. 3 (color online). The central rapidity point is from $J/\psi \to e^+e^-$, the others from $J/\psi \to \mu^+\mu^-$. The brackets represent systematic uncertainties. All curves have their overall normalization fitted to the data. The PYTHIA shape was used to determine the cross section. There is an overall 10% absolute normalization error not shown.

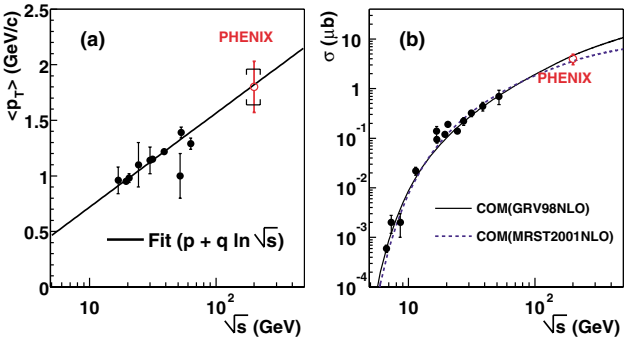

FIG. 4 (color online). (a) The present J/ψ mean p_T value compared with previous measurements at lower energy [1]. The linear fit parameters are $p = 0.53$, $q = 0.19$. (b) The present J/ψ total cross section compared with previous measurements at other values of $\sqrt{s}$ [1]. The curves are discussed in the text.

$\langle p_T \rangle$, and total cross sections have been presented and compared with available model calculations. The transverse momentum distributions above 2 GeV/c are reasonably well described by the COM. With the present statistical precision, our rapidity distribution shape is consistent with most of the available PDFs. COM calculations are able to reproduce the $\sqrt{s}$ dependence of the cross section using color octet matrix elements found in the literature, with a reasonable choice of QCD parameters.

RHIC is expected to have proton-proton runs with enhanced luminosity at $\sqrt{s} = 200$ and 500 GeV in the near future. The increased luminosity will improve the statistical precision and p_T reach of the PHENIX data, and will ultimately make it possible to measure the J/ψ polarization, which has been an important test for models [14].

We thank the staff of the Collider-Accelerator and Physics Departments at BNL for their vital contributions. We acknowledge support from the Department of Energy and NSF (U.S.A.), MEXT and JSPS (Japan), CNPq and FAPESP (Brazil), NSFC (China), CNRS-IN2P3 and CEA (France), BMBF, DAAD, and AvH (Germany), OTKA (Hungary), DAE and DST (India), ISF (Israel), KRF and CHEP (Korea), RMIST, RAS, and RMAE, (Russia), VR and KAW (Sweden), U.S. CRDF for the FSU, U.S.-Hungarian NSF-OTKA-MTA, and U.S.-Israel BSF.

*Deceased.
†PHENIX Spokesperson.
Email address: zajc@nevis.columbia.edu

[1] R. Vogt, Phys. Rep. **310**, 197 (1999); G. A. Schuler, hep-ph/9403387; A. Gribushin *et al.*, Phys. Rev. D **62**, 012001 (2000), and references therein.
[2] F. Abe *et al.*, Phys. Rev. Lett. **69**, 3704 (1992); F. Abe *et al.*, Phys. Rev. D **66**, 092001 (2002); S. Abachi *et al.*, Phys. Lett. B **370**, 239 (1996); B. Abbot *et al.*, Phys. Rev. Lett. **82**, 35 (1999).
[3] F. Abe *et al.*, Phys. Rev. Lett. **79**, 572 (1997).
[4] E. Braaten *et al.*, Annu. Rev. Nucl. Part. Sci. **46**, 197 (1996).
[5] G.T. Bodwin *et al.*, Phys. Rev. D **51**, 1125 (1995); **55**, 5853(E) (1997).
[6] J. F. Amundson *et al.*, Phys. Lett. B **390**, 323 (1997); (and private communication).
[7] E. Braaten *et al.*, Phys. Rev. Lett. **71**, 1673 (1993).
[8] K. Adcox *et al.*, Nucl. Instrum. Methods Phys. Res., Sect. A **499**, 469 (2003).
[9] H. D. Sato, Ph.D. thesis, Kyoto University, 2003; hep-ph/0305239.
[10] Particle Data Group, K. Hagiwara *et al.*, Phys. Rev. D **66**, 010001 (2002).
[11] S. S. Adler *et al.*, Phys. Rev. Lett. **91**, 241803 (2003).
[12] T. Sjöstrand, Comput. Phys. Commun. **135**, 238 (2001).
[13] R. Kephart *et al.*, Phys. Rev. D **14**, 2909 (1976).
[14] T. Affolder *et al.*, Phys. Rev. Lett. **85**, 2886 (2000); E. Braaten *et al.*, Phys. Rev. D **62**, 094005 (2000).
[15] G. C. Nayak, M. X. Liu, and F. Cooper, Phys. Rev. D **68**, 034003 (2003).
[16] M. Klasen *et al.*, Phys. Rev. D **68**, 034017 (2003).
[17] A. Gribushin *et al.*, Phys. Rev. D **62**, 012001 (2000), and references therein.
[18] T. Affolder *et al.*, Phys. Rev. Lett. **87**, 241802 (2001).
[19] M. Beneke and I. Z. Rothstein, Phys. Rev. D **54**, 2005 (1996).
[20] S. S. Adler *et al.*, Phys. Rev. C **69**, 014901 (2004).

Absence of Suppression in Particle Production at Large Transverse Momentum in $\sqrt{s_{NN}} = 200$ GeV d + Au Collisions

S. S. Adler,[4] S. Afanasiev,[19] C. Aidala,[9] N. N. Ajitanand,[43] Y. Akiba,[20,39] A. Al-Jamel,[34] J. Alexander,[43] K. Aoki,[24] L. Aphecetche,[45] R. Armendariz,[34] S. H. Aronson,[4] R. Averbeck,[44] T. C. Awes,[35] V. Babintsev,[16] A. Baldisseri,[10] K. N. Barish,[5] P. D. Barnes,[27] B. Bassalleck,[33] S. Bathe,[5,30] S. Batsouli,[9] V. Baublis,[38] F. Bauer,[5] A. Bazilevsky,[4,40] S. Belikov,[18,16] M. T. Bjorndal,[9] J. G. Boissevain,[27] H. Borel,[10] M. L. Brooks,[27] D. S. Brown,[34] N. Bruner,[33] D. Bucher,[30] H. Buesching,[4,30] V. Bumazhnov,[16] G. Bunce,[4,40] J. M. Burward-Hoy,[27,26] S. Butsyk,[44] X. Camard,[45] P. Chand,[3] W. C. Chang,[2] S. Chernichenko,[16] C. Y. Chi,[9] J. Chiba,[20] M. Chiu,[9] I. J. Choi,[52] R. K. Choudhury,[3] T. Chujo,[4] V. Cianciolo,[35] Y. Cobigo,[10] B. A. Cole,[9] M. P. Comets,[36] P. Constantin,[18] M. Csanád,[12] T. Csörgő,[21] J. P. Cussonneau,[45] D. d'Enterria,[9] K. Das,[13] G. David,[4] F. Deák,[12] H. Delagrange,[45] A. Denisov,[16] A. Deshpande,[40] E. J. Desmond,[4] A. Devismes,[44] O. Dietzsch,[41] J. L. Drachenberg,[1] O. Drapier,[25] A. Drees,[44] A. Durum,[16] D. Dutta,[3] V. Dzhordzhadze,[46] Y. V. Efremenko,[35] H. En'yo,[39,40] B. Espagnon,[36] S. Esumi,[48] D. E. Fields,[33,40] C. Finck,[45] F. Fleuret,[25] S. L. Fokin,[23] B. D. Fox,[40] Z. Fraenkel,[51] J. E. Frantz,[9] A. Franz,[4] A. D. Frawley,[13] Y. Fukao,[24,39,40] S.-Y. Fung,[5] S. Gadrat,[28] M. Germain,[45] A. Glenn,[46] M. Gonin,[25] J. Gosset,[10] Y. Goto,[39,40] R. Granier de Cassagnac,[25] N. Grau,[18] S. V. Greene,[49] M. Grosse Perdekamp,[17,40] H.-Å. Gustafsson,[29] T. Hachiya,[15] J. S. Haggerty,[4] H. Hamagaki,[7] A. G. Hansen,[27] E. P. Hartouni,[26] M. Harvey,[4] K. Hasuko,[39] R. Hayano,[7] X. He,[14] M. Heffner,[26] T. K. Hemmick,[44] J. M. Heuser,[39] P. Hidas,[21] H. Hiejima,[17] J. C. Hill,[18] R. Hobbs,[33] W. Holzmann,[43] K. Homma,[15] B. Hong,[22] A. Hoover,[34] T. Horaguchi,[39,40,47] T. Ichihara,[39,40] V. V. Ikonnikov,[23] K. Imai,[24,39] M. Inuzuka,[7] D. Isenhower,[1] L. Isenhower,[1] M. Issah,[43] A. Isupov,[19] B. V. Jacak,[44] J. Jia,[44] O. Jinnouchi,[39,40] B. M. Johnson,[4] S. C. Johnson,[26] K. S. Joo,[31] D. Jouan,[36] F. Kajihara,[7] S. Kametani,[7,50] N. Kamihara,[39,47] M. Kaneta,[40] J. H. Kang,[52] K. Katou,[50] T. Kawabata,[7] A. Kazantsev,[23] S. Kelly,[8,9] B. Khachaturov,[51] A. Khanzadeev,[38] J. Kikuchi,[50] D. J. Kim,[52] E. Kim,[42] G.-B. Kim,[25] H. J. Kim,[52] E. Kinney,[8] A. Kiss,[12] E. Kistenev,[4] A. Kiyomichi,[39] C. Klein-Boesing,[30] H. Kobayashi,[40] V. Kochetkov,[16] R. Kohara,[15] B. Komkov,[38] M. Konno,[48] D. Kotchetkov,[5] A. Kozlov,[51] P. J. Kroon,[4] C. H. Kuberg,[1] G. J. Kunde,[27] K. Kurita,[39] M. J. Kweon,[22] Y. Kwon,[52] G. S. Kyle,[34] R. Lacey,[43] J. G. Lajoie,[18] Y. Le Bornec,[36] A. Lebedev,[18,23] S. Leckey,[44] D. M. Lee,[27] M. J. Leitch,[27] M. A. L. Leite,[41] X. Li,[6] X. H. Li,[5] H. Lim,[42] A. Litvinenko,[19] M. X. Liu,[27] C. F. Maguire,[49] Y. I. Makdisi,[4] A. Malakhov,[19] V. I. Manko,[23] Y. Mao,[37,39] G. Martinez,[45] H. Masui,[48] F. Matathias,[44] T. Matsumoto,[7,50] M. C. McCain,[1] P. L. McGaughey,[27] Y. Miake,[48] T. E. Miller,[49] A. Milov,[44] S. Mioduszewski,[4] G. C. Mishra,[14] J. T. Mitchell,[4] A. K. Mohanty,[3] D. P. Morrison,[4] J. M. Moss,[27] D. Mukhopadhyay,[51] M. Muniruzzaman,[5] S. Nagamiya,[20] J. L. Nagle,[8,9] T. Nakamura,[15] J. Newby,[46] A. S. Nyanin,[23] J. Nystrand,[29] E. O'Brien,[4] C. A. Ogilvie,[18] H. Ohnishi,[39] I. D. Ojha,[49] H. Okada,[24,39] K. Okada,[39,40] A. Oskarsson,[29] I. Otterlund,[29] K. Oyama,[7] K. Ozawa,[7] D. Pal,[51] A. P. T. Palounek,[27] V. Pantuev,[44] V. Papavassiliou,[34] J. Park,[42] W. J. Park,[22] S. F. Pate,[34] H. Pei,[18] V. Penev,[19] J.-C. Peng,[17] H. Pereira,[10] V. Peresedov,[19] A. Pierson,[33] C. Pinkenburg,[4] R. P. Pisani,[4] M. L. Purschke,[4] A. K. Purwar,[44] J. Qualls,[1] J. Rak,[18] I. Ravinovich,[51] K. F. Read,[35,46] M. Reuter,[44] K. Reygers,[30] V. Riabov,[38] Y. Riabov,[38] G. Roche,[28] A. Romana,[25] M. Rosati,[18] S. Rosendahl,[29] P. Rosnet,[28] V. L. Rykov,[39] S. S. Ryu,[52] N. Saito,[24,39,40] T. Sakaguchi,[7,50] S. Sakai,[48] V. Samsonov,[38] L. Sanfratello,[33] R. Santo,[30] H. D. Sato,[24,39] S. Sato,[4,48] S. Sawada,[20] Y. Schutz,[45] V. Semenov,[16] R. Seto,[5] T. K. Shea,[4] I. Shein,[16] T.-A. Shibata,[39,47] K. Shigaki,[15] M. Shimomura,[48] A. Sickles,[44] C. L. Silva,[41] D. Silvermyr,[27] K. S. Sim,[22] A. Soldatov,[16] R. A. Soltz,[26] W. E. Sondheim,[27] S. Sorensen,[46] I. V. Sourikova,[4] F. Staley,[10] P. W. Stankus,[35] E. Stenlund,[29] M. Stepanov,[34] A. Ster,[21] S. P. Stoll,[4] T. Sugitate,[15] J. P. Sullivan,[27] S. Takagi,[48] E. M. Takagui,[41] A. Taketani,[39,40] K. H. Tanaka,[20] Y. Tanaka,[32] K. Tanida,[39] M. J. Tannenbaum,[4] A. Taranenko,[43] P. Tarján,[11] T. L. Thomas,[33] M. Togawa,[24,39] J. Tojo,[39] H. Torii,[24,40] R. S. Towell,[1] V-N. Tram,[25] I. Tserruya,[51] Y. Tsuchimoto,[15] H. Tydesjö,[29] N. Tyurin,[16] T. J. Uam,[31] H. W. van Hecke,[27] J. Velkovska,[4] M. Velkovsky,[44] V. Veszprémi,[11] A. A. Vinogradov,[23] M. A. Volkov,[23] E. Vznuzdaev,[38] X. R. Wang,[14] Y. Watanabe,[39,40] S. N. White,[4] N. Willis,[36] F. K. Wohn,[18] C. L. Woody,[4] W. Xie,[5] A. Yanovich,[16] S. Yokkaichi,[39,40] G. R. Young,[35] I. E. Yushmanov,[23] W. A. Zajc,[9,*] C. Zhang,[9] S. Zhou,[6] J. Zimányi,[21] L. Zolin,[19] and X. Zong[18]

(PHENIX Collaboration)

[1]*Abilene Christian University, Abilene, Texas 79699, USA*
[2]*Institute of Physics, Academia Sinica, Taipei 11529, Taiwan*
[3]*Bhabha Atomic Research Centre, Bombay 400 085, India*

 0031-9007/03/91(7)/072303(6)$20.00 © 2003 The American Physical Society

[4]*Brookhaven National Laboratory, Upton, New York 11973-5000, USA*
[5]*University of California–Riverside, Riverside, California 92521, USA*
[6]*China Institute of Atomic Energy (CIAE), Beijing, People's Republic of China*
[7]*Center for Nuclear Study, Graduate School of Science, University of Tokyo, 7-3-1 Hongo, Bunkyo, Tokyo 113-0033, Japan*
[8]*University of Colorado, Boulder, Colorado 80309, USA*
[9]*Columbia University, New York, New York 10027, USA, and Nevis Laboratories, Irvington, New York 10533, USA*
[10]*Dapnia, CEA Saclay, F-91191, Gif-sur-Yvette, France*
[11]*Debrecen University, H-4010 Debrecen, Egyetem tér 1, Hungary*
[12]*ELTE, Eötvös Loránd University, H-1117 Budapest, Pázmány P. s. 1/A, Hungary*
[13]*Florida State University, Tallahassee, Florida 32306, USA*
[14]*Georgia State University, Atlanta, Georgia 30303, USA*
[15]*Hiroshima University, Kagamiyama, Higashi-Hiroshima 739-8526, Japan*
[16]*Institute for High Energy Physics (IHEP), Protvino, Russia*
[17]*University of Illinois at Urbana-Champaign, Urbana, Illinois 61801, USA*
[18]*Iowa State University, Ames, Iowa 50011, USA*
[19]*Joint Institute for Nuclear Research, 141980 Dubna, Moscow Region, Russia*
[20]*KEK, High Energy Accelerator Research Organization, Tsukuba-shi, Ibaraki-ken 305-0801, Japan*
[21]*KFKI Research Institute for Particle and Nuclear Physics (RMKI), H-1525 Budapest 114, P.O. Box 49, Hungary*
[22]*Korea University, Seoul, 136-701, Korea*
[23]*Russian Research Center, "Kurchatov Institute," Moscow, Russia*
[24]*Kyoto University, Kyoto 606, Japan*
[25]*Laboratoire Leprince-Ringuet, Ecole Polytechnique, CNRS-IN2P3, Route de Saclay, F-91128, Palaiseau, France*
[26]*Lawrence Livermore National Laboratory, Livermore, California 94550, USA*
[27]*Los Alamos National Laboratory, Los Alamos, New Mexico 87545, USA*
[28]*LPC, Université Blaise Pascal, CNRS-IN2P3, Clermont-Fd, 63177 Aubiere Cedex, France*
[29]*Department of Physics, Lund University, Box 118, SE-221 00 Lund, Sweden*
[30]*Institut fuer Kernphysik, University of Muenster, D-48149 Muenster, Germany*
[31]*Myongji University, Yongin, Kyonggido 449-728, Korea*
[32]*Nagasaki Institute of Applied Science, Nagasaki-shi, Nagasaki 851-0193, Japan*
[33]*University of New Mexico, Albuquerque, New Mexico, USA*
[34]*New Mexico State University, Las Cruces, New Mexico 88003, USA*
[35]*Oak Ridge National Laboratory, Oak Ridge, Tennessee 37831, USA*
[36]*IPN-Orsay, Universite Paris Sud, CNRS-IN2P3, BP1, F-91406, Orsay, France*
[37]*Peking University, Beijing, People's Republic of China*
[38]*PNPI, Petersburg Nuclear Physics Institute, Gatchina, Russia*
[39]*RIKEN (The Institute of Physical and Chemical Research), Wako, Saitama 351-0198, Japan*
[40]*RIKEN BNL Research Center, Brookhaven National Laboratory, Upton, New York 11973-5000, USA*
[41]*Universidade de São Paulo, Instituto de Física, Caixa Postal 66318, São Paulo CEP05315-970, Brazil*
[42]*System Electronics Laboratory, Seoul National University, Seoul, South Korea*
[43]*Chemistry Department, Stony Brook University, SUNY, Stony Brook, New York 11794-3400, USA*
[44]*Department of Physics and Astronomy, Stony Brook University, SUNY, Stony Brook, New York 11794, USA*
[45]*SUBATECH (Ecole des Mines de Nantes, CNRS-IN2P3, Université de Nantes) BP 20722-44307, Nantes, France*
[46]*University of Tennessee, Knoxville, Tennessee 37996, USA*
[47]*Department of Physics, Tokyo Institute of Technology, Tokyo, 152-8551, Japan*
[48]*Institute of Physics, University of Tsukuba, Tsukuba, Ibaraki 305, Japan*
[49]*Vanderbilt University, Nashville, Tennessee 37235, USA*
[50]*Waseda University, Advanced Research Institute for Science and Engineering, 17 Kikui-cho, Shinjuku-ku, Tokyo 162-0044, Japan*
[51]*Weizmann Institute, Rehovot 76100, Israel*
[52]*Yonsei University, IPAP, Seoul 120-749, Korea*
(Received 18 June 2003; published 15 August 2003)

Transverse momentum spectra of charged hadrons with $p_T < 8$ GeV/c and neutral pions with $p_T < 10$ GeV/c have been measured at midrapidity by the PHENIX experiment at BNL RHIC in $d + \mathrm{Au}$ collisions at $\sqrt{s_{NN}} = 200$ GeV. The measured yields are compared to those in $p + p$ collisions at the same $\sqrt{s_{NN}}$ scaled up by the number of underlying nucleon-nucleon collisions in $d + \mathrm{Au}$. The yield ratio does not show the suppression observed in central Au + Au collisions at RHIC. Instead, there is a small enhancement in the yield of high momentum particles.

DOI: 10.1103/PhysRevLett.91.072303 PACS numbers: 25.75.Dw

High transverse momentum ($p_T > 2$ GeV/c) hadrons provide an excellent probe of the high energy density matter created in relativistic heavy ion collisions [1,2]. They arise from fragmentation of quarks and gluons (partons) scattered with large momentum transfer, Q^2, in the initial parton-parton interactions [3]. In the

absence of medium effects, these hard scattering yields in nucleus-nucleus collisions should scale with the average number of inelastic nucleon-nucleon collisions $N_{\rm coll}$ (binary scaling). One of the most intriguing observations from experiments at the BNL Relativistic Heavy Ion Collider (RHIC) is the large suppression of high p_T neutral pion and charged hadron yields in central Au + Au collisions with respect to $p + p$ results scaled by the number of binary nucleon-nucleon collisions [4–7].

Theoretical studies of parton propagation in high density matter suggest that partons lose a significant fraction of their energy through gluon bremsstrahlung [1,2], reducing the parton momentum and depleting the yield of high p_T hadrons [8–13]. This is a final-state effect in the spatially extended medium created in $A + A$ collisions. Initial-state effects include nuclear modifications to the parton momentum distributions (structure functions), and soft scatterings of the incoming parton prior to its hard scattering. These should be present in $p + A$, $d + A$, and $A + A$. Interpretations of Au + Au collisions based on initial-state parton saturation effects [14] or final-state hadronic interactions [15] also predict a considerable suppression of the hadron production at high p_T. It is therefore of paramount interest to determine experimentally the modification, if any, of high p_T hadron yields due to initial-state nuclear effects for a system in which a hot, dense medium is not produced in the final state. This Letter reports on charged hadron and π^0 production at midrapidity obtained by the PHENIX [16] experiment at RHIC in d + Au collisions at $\sqrt{s_{NN}} =$ 200 GeV. The results are compared to those in $p + p$ and Au + Au [7,17,18] at the same nucleon-nucleon center-of-mass energy. Similar d + Au measurements are also reported in [19,20].

The data were collected under two different trigger conditions. Minimum bias events with vertex position along the beam axis within $|z| < 30$ cm were triggered by the beam-beam counters (BBC) [16] which cover $|\eta| = 3.0$–3.9. The minimum bias trigger accepts $(88\% \pm 4\%)$ of all inelastic d + Au collisions that satisfy the vertex condition. A total of 1.2×10^7 and 1.7×10^7 events were analyzed for charged hadron and π^0 spectra, respectively. A second "photon triggered" sample, requiring showers above 2.5 GeV for lead-scintillator (PbSc) and 3.5 GeV for lead-glass (PbGl) electromagnetic calorimeters (EMCal) [16] in addition to the BBC requirement, is used to extend the π^0 measurements to higher p_T. This trigger sampled a total of 1.7×10^9 events.

Neutral pions were measured by the PHENIX EMCal via the $\pi^0 \to \gamma\gamma$ decay. The EMCal covers $|\eta| \leq 0.35$ in pseudorapidity and $\Delta\phi = \pi$ in azimuth. It consists of six PbSc and two PbGl sectors, each covering $\pi/8$ in azimuth. The data from PbSc and PbGl were analyzed separately. The energy calibration is obtained from beam tests, cosmic rays, minimum ionizing energy peaks of charged hadrons, and the energy/momentum ratio of electrons identified with the Ring Imaging Čerenkov Detector. The combined uncertainty on the energy scale and linearity is $\leq 1.5\%$, determined from the response to identified electrons, and confirmed by the positions and widths of the observed π^0 mass peaks.

Photonlike energy clusters in the calorimeter are selected via shower profile cuts. The invariant mass for all photon pairs with energy asymmetry $|E_1 - E_2|/(E_1 + E_2) < 0.7$ is calculated and binned in p_T. The π^0 yield in each p_T bin is determined by integrating the background subtracted two-photon invariant mass distribution [7]; the background is determined from mixed events. The peak-to-background ratio increases from ~ 0.3 at $p_T = 1.25$ GeV/c to more than 5 above 4.25 GeV/c. The raw π^0 spectra are corrected by Monte Carlo simulations for trigger efficiency and acceptance, and for π^0 reconstruction efficiency including dead areas, effects of energy resolution, photon identification cuts, and peak extraction window. Finally, the yields are corrected to the center of the p_T bin using the observed slope of the spectrum. Below $p_T =$ 5 GeV/c the yields are determined from the minimum bias data sample while above 5 GeV/c the photon triggered sample is used. The main sources of systematic errors are listed in Table I. The final systematic errors on the spectra are 10% to 16%, increasing with p_T.

Charged particles are reconstructed using a drift chamber (DC) followed by two layers of multiwire proportional chambers with pad readout (PC1, PC3) [16]. In this analysis tracks were reconstructed over a restricted pseudorapidity range $|\eta| < 0.18$. Pattern recognition in the DC is based on a combinatorial Hough transform in the track bend plane, while the polar angle is determined by PC1 and the location of the collision vertex along the beam direction [21]. The vertex was constrained to be within $|z| < 18$ cm for analysis of the charged tracks. The track reconstruction efficiency is approximately 98%, independent of p_T. Particle momenta are measured with

TABLE I. Systematic errors in percent on π^0 invariant yields for PbSc (PbGl), as a function of p_T (in GeV/c). There are three categories of uncertainty: Type A is a point-to-point error uncorrelated between p_T bins, type B is p_T correlated, where all points move in the same direction but not by the same factor, while in type C all points move by the same factor independent of p_T.

	Type	$p_T = 2$	$p_T = 6$	$p_T = 10$
Peak extraction	A	5.0(5.0)	5.0(5.0)	5.0(5.0)
Geom. accept.	B	3.0(3.0)	2.0(2.0)	2.0(2.0)
π^0 reconstr. eff.	B	4.0(4.0)	4.0(4.0)	4.5(4.5)
Energy scale	B	4.0(4.0)	9.0(9.0)	11.0(11.0)
Trigger eff.	B	···	5.0(10.0)	3.0(3.0)
Trigger norm.	C	···	5.0(5.0)	5.0(5.0)
Conversion corr.	C	2.8(2.8)	2.8(2.8)	2.8(2.8)
Total error		8.6(8.6)	14(16)	15(15)

a resolution $\delta p/p = 0.7\% \oplus 1.1\% p$ (GeV/c). The momentum scale is known to 0.7%, from the reconstructed proton mass using the time of flight. A confirmation hit is required in PC3, located at a radius of 5 m, within a 2.5σ matching window to eliminate most albedo, conversions, and decays. The remaining background above $p_T = 5$ GeV/c is subtracted statistically using identified conversions and weak decays (primarily kaons) [18].

Corrections to the charged particle spectrum for geometrical acceptance, decays in flight, reconstruction efficiency, and momentum resolution are determined using a single-particle GEANT Monte Carlo simulation. All analysis steps, including the outer detector matching cuts are applied consistently in simulation and data. As the DC and PC occupancies in d + Au are low, no multiplicity-dependent occupancy corrections are required. The yield was corrected to the center of the p_T bin. Table II lists the source and magnitude of each contribution to the systematic uncertainties on the charged particle spectra.

The fully corrected p_T distributions of π^0's and $(h^+ + h^-)/2$ are shown in Fig. 1. Each panel shows the reference spectrum from $p + p$ collisions along with the particle spectrum from d + Au. The reference for π^0 is the π^0 spectrum measured in $p + p$ by PHENIX [17], shown on the right panel. For charged hadrons, the reference is obtained by scaling up the π^0 spectrum by the p_T-dependent h/π ratio observed at the CERN Intersecting Storage Rings [22] at $\sqrt{s} = 23$ to 63 GeV and measured by PHENIX. The value of h/π is constant at 1.6 ± 0.16 above 1.5 GeV/c, and decreases at lower p_T to a value of $1.25^{+0.12}_{-0.25}$. Table III summarizes uncertainties on the reference spectra.

A standard way to quantify nuclear medium effects on high p_T production is by the *nuclear modification factor,* which we define for d + Au collisions as the ratio of invariant yield in d + Au to that of $p + p$, scaled by the number of binary collisions.

$$R_{dA}(p_T) = \frac{(1/N_{dA}^{\rm evt})\, d^2N_{dA}/d\eta dp_T}{\langle N_{\rm coll}\rangle/\sigma_{pp}^{\rm inel}\, d^2\sigma_{pp}/d\eta dp_T},$$

where $\langle N_{\rm coll}\rangle$ is the average number of inelastic nucleon-nucleon (NN) collisions per event in the minimum bias collisions, and $\langle N_{\rm coll}\rangle/\sigma_{pp}^{\rm inel}$ is the nuclear overlap function $\langle T_{dA}(b)\rangle$. Using a Glauber model [23] and simulation of the BBC, $\langle N_{\rm coll}\rangle$ is 8.5 ± 0.4 in minimum bias d + Au.

TABLE II. Systematic errors in percent on the $(h^+ + h^-)/2$ invariant yields. Error types are as in Table I.

	Type	$p_T < 4$	$p_T = 4$	$p_T = 6$	$p_T = 7$
PC3 match	C	2.4	2.4	2.4	2.4
Geometr. acc.	C	2.9	2.9	2.9	2.9
Monte Carlo corr.	C	3.7	3.7	3.7	3.7
Mom. resolution	B	···	<0.5	0.6	1.2
Mom. scale	B	<3.2	3.2	3.5	3.7
Backgd. subtrac.	B	<0.5	0.6	3.8	8.2
π oversubtrac.	B	···	···	1.8	4.7
Total error		6.2	6.2	7.6	11.5

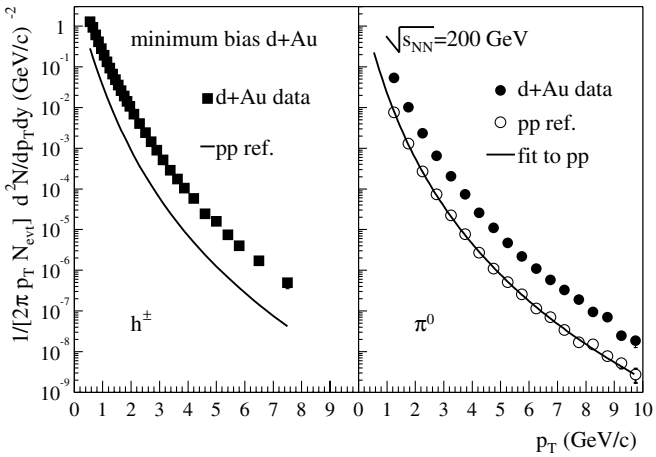

FIG. 1. Midrapidity p_T spectra for charged hadrons and π^0. Total uncertainties are shown. The π^0 below 5 GeV/c are from minimum bias triggered events, and above from photon triggered events. Lines show fits to reference spectra from $p + p$ collisions, and open points show the $p + p$ π^0 spectrum measured by PHENIX [17].

The ratio R_{dA} is plotted separately for π^0 measured in the PbGl and in the PbSc calorimeters in Fig. 2. The two analyses are consistent within errors. The data are compared to the corresponding nuclear modification factor R_{AA} obtained from central Au + Au collisions. The top panel of Fig. 3 shows R_{dA} for inclusive charged particles $(h^+ + h^-)/2$, again compared with R_{AA} observed in central Au + Au collisions, while the lower panel compares $(h^+ + h^-)/2$ with π^0. In both Figs. 2 and 3, the uncertainties are plotted as follows: error bars represent the quadrature sum of statistical errors and those systematic errors which vary point to point in p_T; systematic errors on the absolute yield and the systematic errors which are correlated point to point are shown as bands. All procedures for estimating the various systematic errors have been adjusted to provide estimates corresponding to 1σ error values.

The data clearly indicate that there is no suppression of high p_T particles in d + Au collisions. We do, however, observe an enhancement in inclusive charged particle production at $p_T > 2$ GeV/c. A similar enhancement

TABLE III. Systematic errors on the $p + p$ reference spectrum.

	Type	$p_T < 2$	$p_T = 4$	$p_T = 6$	$p_T = 10$
Normalization	C	10	10	10	10
Residual syst.	B	3	5	7	9
Charged (π^0) only[a]	B(A)	8(5)	7(5)	9(5)	20(5)

[a]Errors affect only the charged (neutral) analysis, and include h/π_0, and fits to reference (point by point pp) errors.

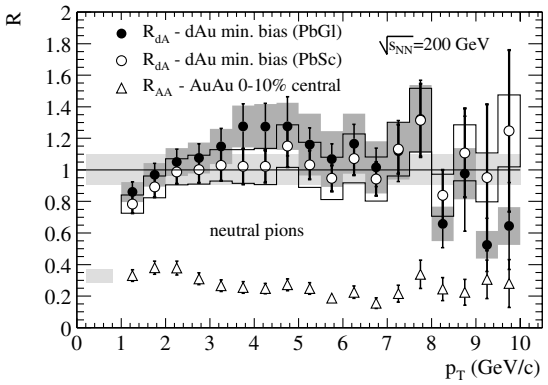

FIG. 2. Nuclear modification factor R_{dA} for π^0 in the PbGl and PbSc calorimeters in minimum bias d + Au. The bands around the data points show systematic errors which can vary with p_T, while the shaded band around unity indicates the normalization uncertainty. The nuclear modification factor R_{AA} in 10% most central Au + Au collisions is also shown.

was observed in $p + A$ fixed-target experiments [24] and is generally referred to as the "Cronin effect." To facilitate comparison of the Cronin effect in inclusive charged particles and π^0, the lower part of Fig. 3 shows all systematic uncertainties common to both analyses in the bar on the left. It should be noted that this uncertainty must be added in quadrature with the bands shown for each curve to obtain the 1σ allowed range of R_{dA} from the data. The π^0 data suggest a smaller enhancement for pions than for inclusive charged particles at $p_T = 2$–4 GeV/c. We note that the charged spectrum includes baryons and antibaryons, which may have a different nuclear enhancement than the mesons [24].

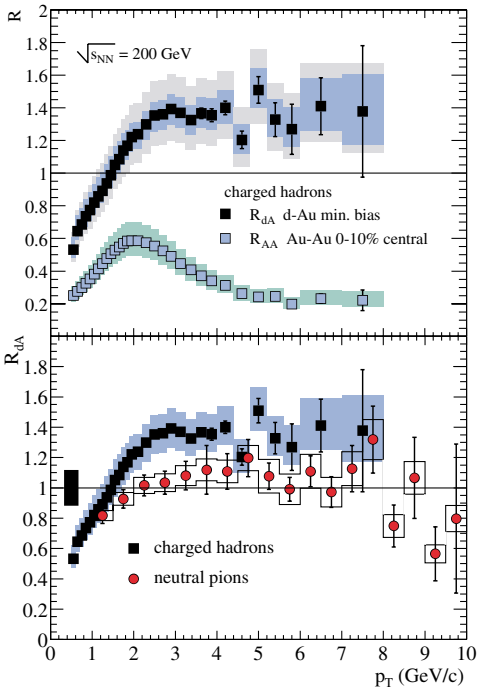

FIG. 3 (color online). Top: Nuclear modification factor R_{dA} for $(h^+ + h^-)/2$ in minimum bias d + Au compared to R_{AA} in the 10% most central Au + Au collisions. Inner bands show systematic errors which can vary with p_T, and outer bands include also the normalization uncertainty. Bottom: Comparison of R_{dA} for $(h^+ + h^-)/2$ and the average of the π^0 measurements in d + Au. The bar at the left indicates the systematic uncertainty in common for the charged and π^0 measurements.

The various models of the suppression observed in Au + Au predict a different dependence on $N_{\rm coll}$ in d + Au [14,25,26]. Therefore, a second data sample was selected by requiring observation of a neutron in the zero-degree calorimeter on the deuteron-going side of PHENIX. This, together with the requirement of particles entering both beam-beam counters, selects a class of events in which only the proton from the deuteron interacts with the Au nucleus. The mean number of binary collisions for this sample is calculated with the Glauber model to be 3.6 ± 0.3. Particle yields in this sample have a $<5\%$ uncertainty beyond that of the minimum bias sample, arising from trigger bias.

Figure 4 shows the ratios of R_{dA} in minimum bias d + Au to R_{pA} in the neutron tagged sample, for both $(h^+ + h^-)/2$ and π^0. Systematic uncertainties on the spectra cancel in the ratio; the band around unity shows the uncertainty on the ratio of the number of binary collisions in the two samples. Average values of $N_{\rm coll}$ are 3.6 per participating proton in the neutron tagged sample and 8.5 for 1.7 participating nucleons from the deuteron in minimum bias d + Au. Given the systematic uncertainties on $N_{\rm coll}$, we cannot exclude a small centrality dependence for $p_T > 1$ GeV/c. It should be noted that the figure also indicates that d + Au collisions provide a good measure of the physics of p + Au.

The observation of an enhancement of high-p_T hadron production in both the minimum bias d + Au and the neutron tagged sample of p + Au collisions indicates that the suppression in central Au + Au collisions is not an initial-state effect. Nor does it arise from modification of parton structure functions in nuclei. The data suggest,

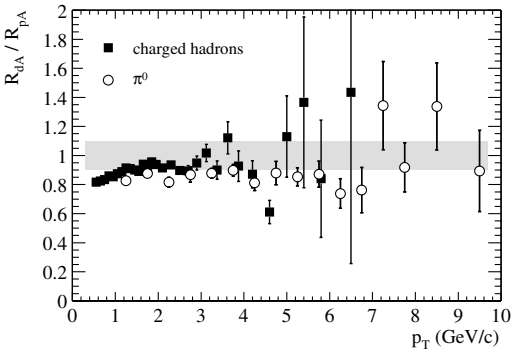

FIG. 4. Ratio of R_{dA} in minimum bias d + Au and R_{pA} from neutron tagged d + Au collisions for $(h^+ + h^-)/2$ and π^0. The band shows the uncertainty on the number of binary collisions; all other systematic errors cancel.

instead, that the suppression of high p_T hadrons in Au + Au is more likely a final-state effect of the produced dense medium.

We thank the staff of the Collider-Accelerator and Physics Departments at BNL for their vital contributions. We acknowledge support from the Department of Energy and NSF (U.S.A.), MEXT and JSPS (Japan), CNPq and FAPESP (Brazil), NSFC (China), IN2P3/CNRS and CEA (France), BMBF, DAAD, and AvH (Germany), OTKA (Hungary), DAE and DST (India), ISF (Israel), KRF and CHEP (Korea), RMIST, RAS, and RMAE (Russia), VR and KAW (Sweden), U.S. CRDF for the FSU, U.S.-Hungarian NSF-OTKA-MTA, and U.S.-Israel BSF.

*PHENIX spokesperson.
Email address: zajc@nevis.columbia.edu

[1] M. Gyulassy and M. Plümer, Phys. Lett. B **243**, 432 (1990); X. N. Wang and M. Gyulassy, Phys. Rev. Lett. **68**, 1480 (1992).
[2] R. Baier *et al.*, Phys. Lett. B **345**, 277 (1995).
[3] J. F. Owens *et al.*, Phys. Rev. D **18**, 1501 (1978).
[4] K. Adcox *et al.*, Phys. Rev. Lett. **88**, 022301 (2002).
[5] K. Adcox *et al.*, Phys. Lett. B **561**, 82 (2003).
[6] C. Adler *et al.*, Phys. Rev. Lett. **89**, 202301 (2002).
[7] S. S. Adler *et al.*, nucl-ex/0304022 (to be published).
[8] M. Gyulassy and X. N. Wang, Nucl. Phys. **B420**, 583 (1994); X. N. Wang, Phys. Rev. C **58**, 2321 (1998).
[9] I. Vitev and M. Gyulassy, Phys. Rev. Lett. **89**, 252301 (2002).
[10] S. Jeon, J. Jalilian-Marian, and I. Sarcevic, Phys. Lett. B **562**, 45 (2003).
[11] G. G. Barnaföldi *et al.*, nucl-th/0212111; V. Greco, C. M. Ko, and P. Lévai, Phys. Rev. Lett. **90**, 202302 (2003).
[12] X. N. Wang, Nucl. Phys. **A715**, 775 (2003).
[13] F. Arleo, J. High Energy Phys. 11 (2002) 044.
[14] D. Kharzeev, E. Levin, and L. McLerran, Phys. Lett. B **561**, 93 (2003).
[15] K. Gallmeister, C. Greiner, and Z. Xu, Phys. Rev. C **67**, 044905 (2003).
[16] K. Adcox *et al.*, Nucl. Instrum. Methods Phys. Res., Sect. A **499**, 469 (2003), and references therein.
[17] S. S. Adler *et al.*, hep-ex/0304038 (to be published).
[18] J. Jia *et al.*, Nucl. Phys. **A715**, 769c (2003).
[19] J. Adams *et al.*, Phys. Rev. Lett. **91**, 072304 (2003).
[20] B. B. Back *et al.*, Phys. Rev. Lett. **91**, 072302 (2003).
[21] J. T. Mitchell *et al.*, Nucl. Instrum. Methods Phys. Res., Sect. A **482**, 491 (2002).
[22] B. Alper *et al.*, Nucl. Phys. **B100**, 237 (1975).
[23] In the present work the Woods-Saxon nuclear density parameters radius $R = 6.38$ fm, diffusivity $a = 0.54$ fm, and N-N cross section $\sigma_{NN}^{\text{inel}} = 42$ mb were used. The deuteron is described by a Hulthén wave function [L. Hulthén and M. Sugawara, Handb. Phys. **39** 1 (1957)] with $\alpha = 0.228$ fm^{-1} and $\beta = 1.18$ fm^{-1}.
[24] D. Antreasyan *et al.*, Phys. Rev. D **19**, 764 (1979).
[25] I. Vitev, Phys. Lett. B **562**, 36 (2003).
[26] B. Kopeliovich, Phys. Rev. Lett. **88**, 232303 (2002).

Scaling Properties of Proton and Antiproton Production in $\sqrt{s_{NN}} = 200$ GeV Au + Au Collisions

S. S. Adler,[5] S. Afanasiev,[17] C. Aidala,[5] N. N. Ajitanand,[43] Y. Akiba,[20,38] J. Alexander,[43] R. Amirikas,[12] L. Aphecetche,[45] S. H. Aronson,[5] R. Averbeck,[44] T. C. Awes,[35] R. Azmoun,[44] V. Babintsev,[15] A. Baldisseri,[10] K. N. Barish,[6] P. D. Barnes,[27] B. Bassalleck,[33] S. Bathe,[30] S. Batsouli,[9] V. Baublis,[37] A. Bazilevsky,[39,15] S. Belikov,[16,15] Y. Berdnikov,[40] S. Bhagavatula,[16] J. G. Boissevain,[27] H. Borel,[10] S. Borenstein,[25] M. L. Brooks,[27] D. S. Brown,[34] N. Bruner,[33] D. Bucher,[30] H. Buesching,[30] V. Bumazhnov,[15] G. Bunce,[5,39] J. M. Burward-Hoy,[26,44] S. Butsyk,[44] X. Camard,[45] J.-S. Chai,[18] P. Chand,[4] W. C. Chang,[2] S. Chernichenko,[15] C. Y. Chi,[9] J. Chiba,[20] M. Chiu,[9] I. J. Choi,[52] J. Choi,[19] R. K. Choudhury,[4] T. Chujo,[5] V. Cianciolo,[35] Y. Cobigo,[10] B. A. Cole,[9] P. Constantin,[16] D. G. d'Enterria,[45] G. David,[5] H. Delagrange,[45] A. Denisov,[15] A. Deshpande,[39] E. J. Desmond,[5] O. Dietzsch,[41] O. Drapier,[25] A. Drees,[44] R. du Rietz,[29] A. Durum,[15] D. Dutta,[4] Y. V. Efremenko,[35] K. El Chenawi,[49] A. Enokizono,[14] H. En'yo,[38,39] S. Esumi,[48] L. Ewell,[5] D. E. Fields,[33,39] F. Fleuret,[25] S. L. Fokin,[23] B. D. Fox,[39] Z. Fraenkel,[51] J. E. Frantz,[9] A. Franz,[5] A. D. Frawley,[12] S.-Y. Fung,[6] S. Garpman,[29,*] T. K. Ghosh,[49] A. Glenn,[46] G. Gogiberidze,[46] M. Gonin,[25] J. Gosset,[10] Y. Goto,[39] R. Granier de Cassagnac,[25] N. Grau,[16] S. V. Greene,[49] G. Grosse Perdekamp,[39] W. Guryn,[5] H.-Å. Gustafsson,[29] T. Hachiya,[14] J. S. Haggerty,[5] H. Hamagaki,[8] A. G. Hansen,[27] E. P. Hartouni,[26] M. Harvey,[5] R. Hayano,[8] X. He,[13] M. Heffner,[26] T. K. Hemmick,[44] J. M. Heuser,[44] M. Hibino,[50] J. C. Hill,[16] W. Holzmann,[43] K. Homma,[14] B. Hong,[22] A. Hoover,[34] T. Ichihara,[38,39] V. V. Ikonnikov,[23] K. Imai,[24,38] L. D. Isenhower,[1] M. Ishihara,[38] M. Issah,[43] A. Isupov,[17] B. V. Jacak,[44] W. Y. Jang,[22] Y. Jeong,[19] J. Jia,[44] O. Jinnouchi,[38] B. M. Johnson,[5] S. C. Johnson,[26] K. S. Joo,[31] D. Jouan,[36] S. Kametani,[8,50] N. Kamihara,[47,38] J. H. Kang,[52] S. S. Kapoor,[4] K. Katou,[50] S. Kelly,[9] B. Khachaturov,[51] A. Khanzadeev,[47] J. Kikuchi,[50] D. H. Kim,[31] D. J. Kim,[52] D. W. Kim,[19] E. Kim,[42] G.-B. Kim,[25] H. J. Kim,[52] E. Kistenev,[5] A. Kiyomichi,[48] K. Kiyoyama,[32] C. Klein-Boesing,[30] H. Kobayashi,[38,39] L. Kochenda,[37] V. Kochetkov,[15] D. Koehler,[33] T. Kohama,[14] M. Kopytine,[44] D. Kotchetkov,[6] A. Kozlov,[51] P. J. Kroon,[5] C. H. Kuberg,[1,27] K. Kurita,[39] Y. Kuroki,[48] M. J. Kweon,[22] Y. Kwon,[52] G. S. Kyle,[34] R. Lacey,[43] V. Ladygin,[17] J. G. Lajoie,[16] A. Lebedev,[16,23] S. Leckey,[44] D. M. Lee,[27] S. Lee,[19] M. J. Leitch,[27] X. H. Li,[6] H. Lim,[42] A. Litvinenko,[17] M. X. Liu,[27] Y. Liu,[36] C. F. Maguire,[49] Y. I. Makdisi,[5] A. Malakhov,[17] V. I. Manko,[23] Y. Mao,[7,38] G. Martinez,[45] M. D. Marx,[44] H. Masui,[48] F. Matathias,[44] T. Matsumoto,[8,50] P. L. McGaughey,[27] E. Melnikov,[15] F. Messer,[44] Y. Miake,[48] J. Milan,[43] T. E. Miller,[49] A. Milov,[44,51] S. Mioduszewski,[5] R. E. Mischke,[27] G. C. Mishra,[13] J. T. Mitchell,[5] A. K. Mohanty,[4] D. P. Morrison,[5] J. M. Moss,[27] F. Mühlbacher,[44] D. Mukhopadhyay,[51] M. Muniruzzaman,[6] J. Murata,[38,39] S. Nagamiya,[20] J. L. Nagle,[9] T. Nakamura,[14] B. K. Nandi,[6] M. Nara,[48] J. Newby,[46] P. Nilsson,[29] A. S. Nyanin,[23] J. Nystrand,[29] E. O'Brien,[5] C. A. Ogilvie,[16] H. Ohnishi,[5,38] I. D. Ojha,[49,3] K. Okada,[38] M. Ono,[48] V. Onuchin,[15] A. Oskarsson,[29] I. Otterlund,[29] K. Oyama,[8] K. Ozawa,[8] D. Pal,[51] A. P. T. Palounek,[27] V. S. Pantuev,[44] V. Papavassiliou,[34] J. Park,[42] A. Parmar,[33] S. F. Pate,[34] T. Peitzmann,[30] J.-C. Peng,[27] V. Peresedov,[17] C. Pinkenburg,[5] R. P. Pisani,[5] F. Plasil,[35] M. L. Purschke,[5] A. Purwar,[44] J. Rak,[16] I. Ravinovich,[51] K. F. Read,[35,46] M. Reuter,[44] K. Reygers,[30] V. Riabov,[37,40] Y. Riabov,[37] G. Roche,[28] A. Romana,[25] M. Rosati,[16] P. Rosnet,[28] S. S. Ryu,[52] M. E. Sadler,[1] N. Saito,[38,39] T. Sakaguchi,[8,50] M. Sakai,[32] S. Sakai,[48] V. Samsonov,[37] L. Sanfratello,[33] R. Santo,[30] H. D. Sato,[24,38] S. Sato,[5,48] S. Sawada,[20] Y. Schutz,[45] V. Semenov,[15] R. Seto,[6] M. R. Shaw,[1,27] T. K. Shea,[5] T.-A. Shibata,[47,38] K. Shigaki,[14,20] T. Shiina,[27] C. L. Silva,[41] D. Silvermyr,[27,29] K. S. Sim,[22] C. P. Singh,[3] V. Singh,[3] M. Sivertz,[5] A. Soldatov,[15] R. A. Soltz,[26] W. E. Sondheim,[27] S. P. Sorensen,[46] I. V. Sourikova,[5] F. Staley,[10] P. W. Stankus,[35] E. Stenlund,[29] M. Stepanov,[34] A. Ster,[21] S. P. Stoll,[5] T. Sugitate,[14] J. P. Sullivan,[27] E. M. Takagui,[41] A. Taketani,[38,39] M. Tamai,[50] K. H. Tanaka,[20] Y. Tanaka,[32] K. Tanida,[38] M. J. Tannenbaum,[5] P. Tarján,[11] J. D. Tepe,[1,27] T. L. Thomas,[33] J. Tojo,[24,38] H. Torii,[24,38] R. S. Towell,[1] I. Tserruya,[51] H. Tsuruoka,[48] S. K. Tuli,[3] H. Tydesjö,[29] N. Tyurin,[15] H. W. van Hecke,[27] J. Velkovska,[5,44] M. Velkovsky,[44] L. Villatte,[46] A. A. Vinogradov,[23] M. A. Volkov,[23] E. Vznuzdaev,[37] X. R. Wang,[13] Y. Watanabe,[38,39] S. N. White,[5] F. K. Wohn,[16] C. L. Woody,[5] W. Xie,[6] Y. Yang,[7] A. Yanovich,[15] S. Yokkaichi,[38,39] G. R. Young,[35] I. E. Yushmanov,[23] W. A. Zajc,[9,†] C. Zhang,[9] S. Zhou,[7,51] and L. Zolin[17]

(PHENIX Collaboration)

[1]*Abilene Christian University, Abilene, Texas 79699, USA*
[2]*Institute of Physics, Academia Sinica, Taipei 11529, Taiwan*
[3]*Department of Physics, Banaras Hindu University, Varanasi 221005, India*

 0031-9007/03/91(17)/172301(6)$20.00 © 2003 The American Physical Society

[4]*Bhabha Atomic Research Centre, Bombay 40 085, India*
[5]*Brookhaven National Laboratory, Upton, New York 11973-5000, USA*
[6]*University of California–Riverside, Riverside, California 92521, USA*
[7]*China Institute of Atomic Energy (CIAE), Beijing, People's Republic of China*
[8]*Center for Nuclear Study, Graduate School of Science, University of Tokyo, 7-3-1 Hongo, Bunkyo, Tokyo 113-0033, Japan*
[9]*Columbia University, New York, New York 10027, USA and Nevis Laboratories, Irvington, New York 10533, USA*
[10]*Dapnia, CEA Saclay, F-91191, Gif-sur-Yvette, France*
[11]*Debrecen University, H-4010 Debrecen, Egyetem tér 1, Hungary*
[12]*Florida State University, Tallahassee, Florida 32306, USA*
[13]*Georgia State University, Atlanta, Georgia 30303, USA*
[14]*Hiroshima University, Kagamiyama, Higashi-Hiroshima 739-8526, Japan*
[15]*Institute for High Energy Physics (IHEP), Protvino, Russia*
[16]*Iowa State University, Ames, Iowa 50011, USA*
[17]*Joint Institute for Nuclear Research, 141980 Dubna, Moscow Region, Russia*
[18]*KAERI, Cyclotron Application Laboratory, Seoul, South Korea*
[19]*Kangnung National University, Kangnung 210-702, South Korea*
[20]*KEK, High Energy Accelerator Research Organization, Tsukuba-shi, Ibaraki-ken 305-0801, Japan*
[21]*KFKI Research Institute for Particle and Nuclear Physics (RMKI), H-1525 Budapest 114, PO Box 49, Hungary*
[22]*Korea University, Seoul, 136-701, Korea*
[23]*Russian Research Center "Kurchatov Institute," Moscow, Russia*
[24]*Kyoto University, Kyoto 606, Japan*
[25]*Laboratoire Leprince-Ringuet, Ecole Polytechnique, CNRS-IN2P3, Route de Saclay, F-91128, Palaiseau, France*
[26]*Lawrence Livermore National Laboratory, Livermore, California 94550, USA*
[27]*Los Alamos National Laboratory, Los Alamos, New Mexico 87545, USA*
[28]*LPC, Université Blaise Pascal, CNRS-IN2P3, Clermont-Fd, 63177 Aubiere Cedex, France*
[29]*Department of Physics, Lund University, Box 118, SE-221 00 Lund, Sweden*
[30]*Institut fuer Kernphysik, University of Muenster, D-48149 Muenster, Germany*
[31]*Myongji University, Yongin, Kyonggido 449-728, Korea*
[32]*Nagasaki Institute of Applied Science, Nagasaki-shi, Nagasaki 851-0193, Japan*
[33]*University of New Mexico, Albuquerque, New Mexico 87131, USA*
[34]*New Mexico State University, Las Cruces, New Mexico 88003, USA*
[35]*Oak Ridge National Laboratory, Oak Ridge, Tennessee 37831, USA*
[36]*IPN-Orsay, Universite Paris Sud, CNRS-IN2P3, BP1, F-91406, Orsay, France*
[37]*PNPI, Petersburg Nuclear Physics Institute, Gatchina, Russia*
[38]*RIKEN (The Institute of Physical and Chemical Research), Wako, Saitama 351-0198, Japan*
[39]*RIKEN BNL Research Center, Brookhaven National Laboratory, Upton, New York 11973-5000, USA*
[40]*St. Petersburg State Technical University, St. Petersburg, Russia*
[41]*Universidade de São Paulo, Instituto de Física, Caixa Postal 66318, São Paulo CEP05315-970, Brazil*
[42]*System Electronics Laboratory, Seoul National University, Seoul, South Korea*
[43]*Chemistry Department, Stony Brook University, SUNY, Stony Brook, New York 11794-3400, USA*
[44]*Department of Physics and Autonomy, Stony Brook University, SUNY, Stony Brook, New York 11794, USA*
[45]*SUBATECH (Ecole des Mines de Nantes, CNRS-IN2P3, Université de Nantes) BP 20722-44307, Nantes, France*
[46]*University of Tennessee, Knoxville, Tennessee 37996, USA*
[47]*Department of Physics, Tokyo Institute of Technology, Tokyo, 152-8551, Japan*
[48]*Institute of Physics, University of Tsukuba, Tsukuba, Ibaraki 305, Japan*
[49]*Vanderbilt University, Nashville, Tennessee 37235, USA*
[50]*Waseda University, Advanced Research Institute for Science and Engineering, 17 Kikui-cho, Shinjuku-ku, Tokyo 162-0044, Japan*
[51]*Weizmann Institute, Rehovot 76100, Israel*
[52]*Yonsei University, IPAP, Seoul 120-749, Korea*
(Received 30 May 2003; published 21 October 2003)

We report on the yield of protons and antiprotons, as a function of centrality and transverse momentum, in Au + Au collisions at $\sqrt{s_{NN}} = 200$ GeV measured at midrapidity by the PHENIX experiment at the BNL Relativistic Heavy Ion Collider. In central collisions at intermediate transverse momenta ($1.5 < p_T < 4.5$ GeV/c) a significant fraction of all produced particles are protons and antiprotons. They show a centrality-scaling behavior different from that of pions. The $\overline{p}/\pi$ and p/π ratios are enhanced compared to peripheral Au + Au, $p + p$, and e^+e^- collisions. This enhancement is limited to $p_T < 5$ GeV/c as deduced from the ratio of charged hadrons to π^0 measured in the range $1.5 < p_T < 9$ GeV/c.

DOI: 10.1103/PhysRevLett.91.172301 PACS numbers: 25.75.Dw

Heavy-ion collisions at the BNL Relativistic Heavy Ion Collider (RHIC) energies permit the study of nuclear matter at extreme energy densities. Hadrons originating from fragmentation of partons that have undergone large momentum transfer (hard) scatterings are sensitive probes of the hottest and densest stage of the collision. Data collected during the first RHIC run at $\sqrt{s_{NN}} = 130$ GeV led to the discovery of suppression of high transverse momentum ($p_T \geq 2$ GeV/c) hadron production in central Au + Au collisions [1–3] when compared to expectations from nucleon-nucleon collisions. This effect, quantified in terms of a nuclear modification factor $R_{\rm AA} = (\text{yield}_{\rm AA}/N_{\rm coll})/\text{yield}_{pp}$, where $N_{\rm coll}$ is the average number of binary nucleon-nucleon collisions, had been discussed as a possible consequence of the energy loss suffered by partons moving in a dense medium [4,5]. Unexpectedly, it was found that $R_{\rm AA}$ is more strongly suppressed for π^0 than for charged hadrons [1], and that the yields of p and $\overline{p}$ near 2 GeV/c in central events [6] are comparable to the yield of pions ($p/\pi \sim 1$). This is in contrast to the p/π ratios of ~0.1–0.3, measured in $p + p$ [7] and e^+e^- [8] collisions, and to perturbative quantum chromodynamics phenomenology [9]. These results suggest that an investigation of particle composition is important for understanding the medium effect on high-p_T phenomena at RHIC. During the 2001 Au + Au run at $\sqrt{s_{NN}} = 200$ GeV the PHENIX experiment collected data to study the scaling properties of p and $\overline{p}$ production as well as the p/π, $\overline{p}/\pi$, and charged hadron to pion (h/π) ratios as a function of centrality.

The PHENIX detector [10] combines high momentum resolution with diverse particle identification (PID), resulting in hadron identification over a broad momentum range. The present results combine the measurements of $\pi^{\pm}$, p, and $\overline{p}$ with those of neutral pions [11] and inclusive charged hadrons [12]. A "minimum bias" trigger based on signals from the beam-beam counters (BBC) and zero-degree calorimeter (ZDC) sampled $92.2^{+2.5}_{-3}\%$ of the inelastic Au + Au cross section of $\sigma^{\rm AuAu}_{\rm inel} = 6.9$ b [11]. The collision vertex is restricted to ± 30 cm of the nominal origin. Approximately 2×10^7 (3×10^7) minimum bias events are used in the charged (neutral) particle analysis. These samples are subdivided into seven centrality classes based on cuts in the combined ZDC and BBC response: 0–10%, 10–20%, 20–30%, 30–40%, 40–50%, 50–60%, and 60–92% of $\sigma^{\rm AuAu}_{\rm inel}$. The average number of participants ($N_{\rm part}$) and collisions ($N_{\rm coll}$) for each centrality class are derived from a Glauber model calculation [11].

Identified charged particles are measured over a subset of the PHENIX East-arm spectrometer covering pseudorapidity $|\eta| < 0.35$ and $\Delta\phi = \pi/8$ in azimuthal angle. PID is based on particle mass calculated from the measured momentum and velocity. The momentum resolution is $\delta p/p \simeq 0.7\% \oplus 1\% \times p(\text{GeV}/c)$ and is provided by a multilayer drift chamber followed by a multiwire proportional chamber with pad readout (PC1). The velocity is obtained by measuring the time of flight (TOF) and the path length along the trajectory. The timing system uses the BBC to provide a global start signal; hits on the TOF scintillator wall, located at a radial distance of 5.06 m, provide individual stop signals. The resolution is $\sigma \simeq 115$ ps, which allows a 4σ π/K and K/p separation up to $p_T \simeq 2$ GeV/c and $p_T \simeq 4$ GeV/c, respectively. A 2σ momentum dependent cut in mass squared is used up to $p_T = 2$ GeV/c and $p_T = 4$ GeV/c to select π and $(\overline{p})p$. Asymmetric cuts are applied at higher momenta to extend the π/K and K/p separation up to p_T of 3 and 4.5 GeV/c. The spectra are corrected for geometrical acceptance, decay in flight, and reconstruction efficiency using a GEANT-based Monte Carlo (MC) simulation and embedding simulated tracks into real events with different particle multiplicities.

The p and $\overline{p}$ yields are corrected for feed down from weak decays using a MC simulation and the measured Λ/p and $\overline{\Lambda}/\overline{p}$ ratios at $\sqrt{s_{NN}} = 130$ GeV [13] which include contributions from Ξ and Σ^0. Corrections for feed down from $\Sigma^{\pm}$ are not applied, but estimates based on HIJING MC give less than ~5% contribution. At $p_T = 0.65$ GeV/c, about 40% of the inclusive $(\overline{p})p$ come from weak decays. This fraction reduces to $\approx 25\%$ at 4 GeV/c. The systematic uncertainty of this correction is estimated at 6% by varying the Λ/p ($\overline{\Lambda}/\overline{p}$) ratios within the $\pm 24\%$ errors of the $\sqrt{s_{NN}} = 130$ GeV measurement and assuming m_T scaling at high p_T. The above uncertainty could be larger if the Λ/p ($\overline{\Lambda}/\overline{p}$) ratios change significantly with p_T and beam energy. The additional systematic error on the overall normalization is 8% for $p_T < 3$ GeV/c and 12% above 3 GeV/c. Added in quadrature, the total systematic errors are 11% and 14%; the larger value is for $p_T > 3$ GeV/c.

Inclusive charged hadrons are measured in the West-arm spectrometer covering $|\eta| < 0.35$ and $\Delta\phi = \pi/2$. Two pad chambers (PC2, PC3) located at 4.2 and 5 m, respectively, and a ring imaging Čerenkov counter [12] are used to reject and subtract high-p_T background. The systematic errors on the yields range from 11% for $p_T <$ 5 GeV/c to 45% at 9 GeV/c.

Neutral pions are reconstructed via the decay $\pi^0 \rightarrow \gamma\gamma$ through an invariant mass analysis of γ pairs detected in the electromagnetic calorimeter (EMCal), which covers $\Delta\eta = 0.7$ and $\Delta\phi = \pi$. The absolute energy scale is known to $\leq 1.5\%$. The systematic errors on the π^0 spectra range from 10% to 17%, from low to high p_T [11].

Figure 1 shows the p/π and $\overline{p}/\pi$ ratios as a function of p_T measured at midrapidity in central (0–10%), midcentral (20–30%), and peripheral (60–92%) Au + Au collisons. The open symbols represent the p/π^+ and $\overline{p}/\pi^-$ measurements, while the closed symbols represent the corresponding p/π^0 and $\overline{p}/\pi^0$ ratios. The error bars are the quadratic sum of statistical errors and point-to-point systematic errors. There is an additional normalization

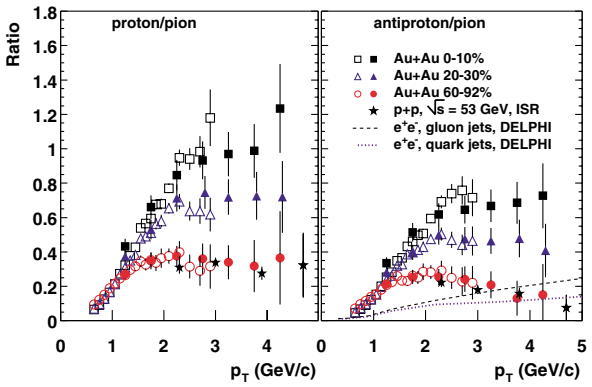

FIG. 1 (color online). p/π (left) and $\overline{p}/\pi$ ratios for central (0–10%), midcentral (20–30%), and peripheral (60–92%) Au + Au collisions at $\sqrt{s_{NN}} = 200$ GeV. Open (filled) points are for $\pi^{\pm}$ (π^0), respectively. Data from $\sqrt{s} = 53$ GeV $p + p$ collisions [7] are shown with stars. The dashed and dotted lines are $(\overline{p} + p)/(\pi^+ + \pi^-)$ ratios in gluon and in quark jets [8].

uncertainty of ~8% (for p/π^+, $\overline{p}/\pi^-$) and 12% (for p/π^0, $\overline{p}/\pi^0$), which may shift the curves up or down, but does not affect their shapes. In the region of overlap, the $\pi^{\pm}$ and π^0 measurements, with very different systematics, are consistent to within 5% to 15%. For all centralities the ratios rise steeply at low p_T and then, at a value of p_T which increases from peripheral to central collisions, level off. In central collisions the ratios are a factor of ~3 larger than in peripheral events. At $p_T > 2$ GeV/c the peripheral Au + Au data agree well with the ratios observed in $p + p$ collisions at lower energies [7] (shown with stars). The $(p + \overline{p})/(\pi^+ + \pi^-)$ ratios in gluon and quark jets produced in e^+e^- collisions [8] are shown with a dashed (dotted) line. Above 3 GeV/c the p/π, $\overline{p}/\pi$ ratios from peripheral collisions are also consistent with gluon and quark jet fragmentation, which should be independent of the collision system. Deviations from jet fragmentation below 3 GeV/c indicate the absence of soft hadron production in the e^+e^- data.

Hydrodynamic models have had success reproducing $(\overline{p})p$ [6,14] and π data [6] from $\sqrt{s_{NN}} = 130$ GeV Au + Au collisions [15,16] and preliminary 200 GeV data [17]. The calculations show good agreement with the central p, $\overline{p}$ and $\pi^{\pm}$ spectra up to $p_T \simeq 3$ and 2 GeV/c, respectively. In peripheral collisions the calculations deviate from the data above $p_T \simeq 1$ GeV/c. Within these models the large $\overline{p}/\pi$ ratio is a natural consequence of the strong radial flow [18]. All particle spectra converge to the same slope if p_T is sufficiently larger than the particle mass m_0. The $\overline{p}/\pi$ ratio is $R_{\overline{p}/\pi} \simeq 2\exp(-\mu_b/T_{\rm ch})$, governed only by the baryon chemical potential μ_b and the chemical freezeout temperature $T_{\rm ch}$. Using $T_{\rm ch} = 177$ MeV and $\mu_b = 29$ MeV [19], $R_{\overline{p}/\pi}$ reaches a limiting value of 1.7. Within 10%, the same limiting behavior is expected for all centralities, since the thermal parameters vary only weakly with centrality [20]. The data are not only below the asymptotic value but also show a more pronounced centrality dependence than can be accommodated by hydrodynamics models. This suggests that other mechanisms begin to play a role before the asymptotic value is reached. At intermediate p_T ($2 < p_T < 4$ GeV/c), hard scattering is one possible mechanism that competes with "soft" processes as described by hydrodynamics.

Figure 2 shows the p and $\overline{p}$ spectra for different centralities (0–10%, 20–30%, 40–50%, 60–92%) scaled by the corresponding value of $N_{\rm coll}$ [11]. Error bars are statistical only. Multiplicity dependent systematic errors are of the order of 3%. Errors on $N_{\rm coll}$ range from ~10% for central to ~28% for the peripheral event class. Below $p_T \simeq 1.5$ GeV/c the p and $\overline{p}$ yields scale slower than $N_{\rm coll}$ as expected for soft processes, and the effect of the radial flow on the shape of the spectra is clearly visible. The inverse slopes gradually increase from the most peripheral to the most central event class. Beyond $p_T \simeq 1.5$ GeV/c all spectra converge to the same slope and seem to obey $N_{\rm coll}$ scaling as expected for production due to hard processes in the absence of nuclear effects.

Figure 3 compares the $N_{\rm coll}$ scaled central to peripheral yield ratios,

$$R_{\rm CP} = \frac{\text{yield}^{0-10\%}/N_{\rm coll}^{0-10\%}}{\text{yield}^{60-92\%}/N_{\rm coll}^{60-92\%}}, \qquad (1)$$

for $(p + \overline{p})/2$ and π^0. In the p_T range from 1.5 to 4.5 GeV/c, p and $\overline{p}$ are not suppressed in contrast to π^0 which is reduced by a factor of 2–3. Moreover, this behavior holds for all centrality selections (Fig. 2), while the suppression in the π^0 yields increases from peripheral to central collisions [11]. The apparent scaling with $N_{\rm part}$ for $p_T \simeq 4$ GeV/c of inclusive charged hadrons [21], which has been interpreted in terms of saturation scenario [22], appears to be somewhat coincidental, since we

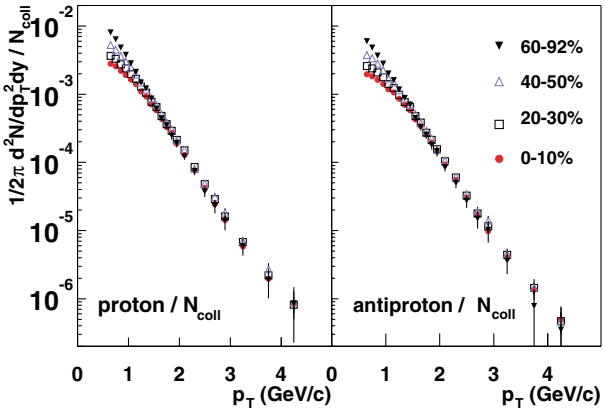

FIG. 2 (color online). p and $\overline{p}$ invariant yields scaled by $N_{\rm coll}$. Error bars are statistical. Systematic errors on $N_{\rm coll}$ range from ~10% for central to ~28% for 60–92% centrality. Multiplicity dependent normalization errors are ~3%.

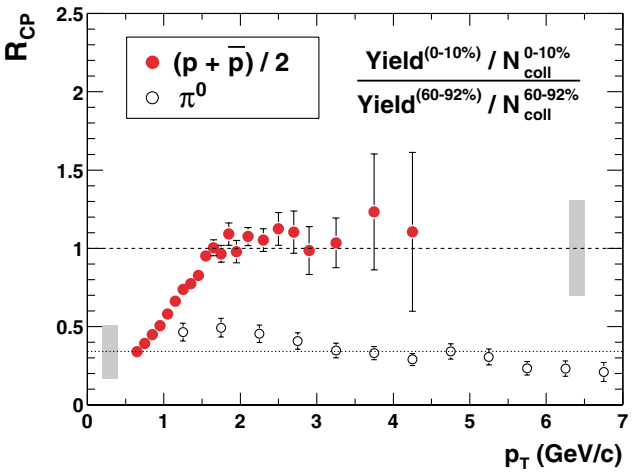

FIG. 3 (color online). Nuclear modification factor R_{CP} for $(p + \overline{p})/2$ (filled circles) and π^0. Dashed and dotted lines indicate N_{coll} and N_{part} scaling; the shaded bars show the systematic errors on these quantities.

observe a strong species dependence not expected in the model. However, the interpretation in terms of soft and hard processes is also not straightforward. If both π and p, $\overline{p}$ originate from the fragmentation of hard-scattered partons that lose energy in the medium, the nuclear modification factor R_{CP} should be independent of particle species contrary to our result. As discussed above, for a "hard" description to hold, the particle ratios $\overline{p}/\pi$ and p/π should reflect the fragmentation function, which favors pion production.

It is possible that nuclear effects such as the "Cronin effect" [23,24] contribute to the observed large $(\overline{p})p/\pi$ ratios. In $p + A$ collisions at energies up to $\sqrt{s} = 38.8$ GeV a nuclear enhancement beyond N_{coll} scaling has been observed for π, K, p and their antiparticles [25]. The effect is larger for $p(\overline{p})$ than for π which leads to an enhancement of the $(\overline{p})p/\pi$ ratio compared to $p + p$ collisions. For $p + W$ the increase is a factor of ~ 2 in the range $3 < p_T < 6$ GeV/c. Theoretical descriptions assume that the effect is due to initial state scattering or p_T broadening [26]. Recent results comparing charged hadrons to π^0 to $d + \mathrm{Au}$ at $\sqrt{s_{NN}} = 200$ GeV suggest that the Cronin effect in baryons is different from that in mesons [27]. Another possibility is that the variation in the p/π ratio with centrality reflects a medium-induced difference in the formation time of baryons and mesons—an effect which has been cited to explain DIS results [28].

Recently, the abundance of p relative to π in central collisions has been attributed to the recombination, rather than fragmentation, of quarks [29]. In this model, recombination for p and $\overline{p}$ is effective up to $p_T \simeq 5$ GeV above which fragmentation dominates for all particle species. Another explanation of the observed large baryon content invokes a topological gluon configuration: the baryon junction [30]. A centrality dependence, which is in qualitative agreement with our results, has been predicted [9]. In both theoretical models, the baryon/meson enhancement is limited to $p_T < 5$–6 GeV/c. The identification of charged particles beyond $p_T \approx 4.5$ GeV/c is not yet possible with the current PHENIX configuration; however, the baryon content at high p_T can be tracked indirectly using the h/π^0 ratio.

Figure 4 shows h/π^0 for central and peripheral Au + Au collisions. The error bars represent the quadratic sum of statistical and point-to-point systematic errors. In peripheral Au + Au collisions, R_{h/π^0} is consistent with the measurement in $p + p$. In central collisions in the region $1 < p_T < 4.5$ GeV/c, R_{h/π^0} is enhanced by as much as 50% above the $p + p$ value. As shown in Fig. 1, this enhancement is due to a large baryon contribution. Above $p_T \simeq 5$ GeV/c, the particle composition is consistent with that measured in $p + p$ collisions. This indicates that the centrality scaling of the p yields should become consistent with that of π at higher p_T ($\gtrsim 5$ GeV/c). Similar trends are observed in Λ and K^0_S measurements by the STAR Collaboration [31].

We have presented a systematic study of high-p_T particle composition in Au + Au collisions at $\sqrt{s_{NN}} = 200$ GeV as a function of centrality. A large p and $\overline{p}$ contribution which increases from peripheral to central collisions is observed in the range $1.5 < p_T < 4.5$ GeV/c. In this p_T range, the p and $\overline{p}$ yields scale with N_{coll}, as expected for hard scattering. This is in contrast to the

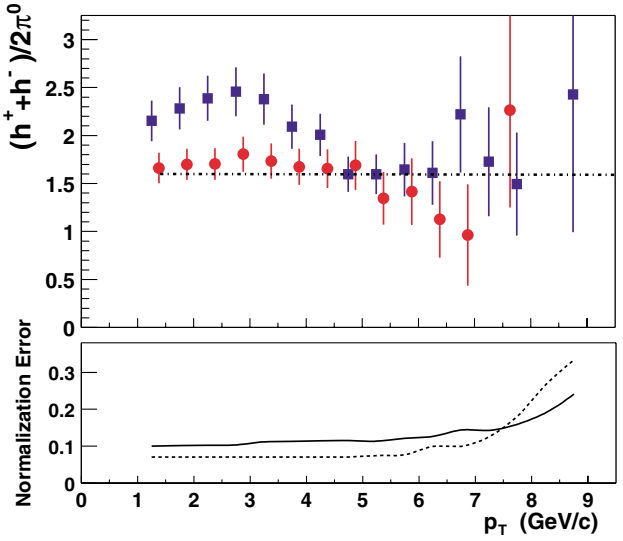

FIG. 4 (color online). Charged hadron to π^0 ratio in central (0–10% squares) and peripheral (60–92% circles) Au + Au collisions. The peripheral data points are offset by +130 MeV/c for clarity. The line at 1.6 is the h/π ratio measured in $p + p$ collisions [7]. The lower panel shows the fractional normalization error common to both centrality selections (solid line) and the relative error between the two (dashed line).

centrality-dependent suppression of π^0 production. The baryon enhancement with respect to π seems to be limited to transverse momenta $p_T \sim 5$ GeV/c, as deduced from the measurement of the ratio of inclusive charged hadrons to π^0. We conclude that π and $(\overline{p})p$ have different dominant production mechanisms for $p_T < 5$ GeV/c.

We thank the staff of the Collider-Accelerator and Physics Departments at BNL for their vital contributions. We acknowledge support from the Department of Energy and NSF (U.S.A.), MEXT and JSPS (Japan), CNPq and FAPESP (Brazil), NSFC (China), CNRS-IN2P3 and CEA (France), BMBF, DAAD, and AvH (Germany), OTKA (Hungary), DAE and DST (India), ISF (Israel), KRF and CHEP (Korea), RMIST, RAS, and RMAE, (Russia), VR and KAW (Sweden), U.S. CRDF for the FSU, US-Hungarian NSF-OTKA-MTA, and US-Israel BSF.

*Deceased.
†Corresponding author.
Email address: zajc@nevis.columbia.edu

[1] K. Adcox *et al.*, Phys. Rev. Lett. **88**, 022301 (2002).
[2] K. Adcox *et al.*, Phys. Lett. B **561**, 82 (2003).
[3] C. Adler *et al.*, Phys. Rev. Lett. **89**, 202301 (2002).
[4] X. N. Wang and M. Gyulassy, Phys. Rev. Lett. **68**, 1480 (1992); X. N. Wang, Phys. Rev. C **58**, 2321 (1998).
[5] M. Gyulassy and M. Plümer, Phys. Lett. B **243**, 432 (1990); R. Baier *et al.*, Phys. Lett. B **345**, 277 (1995).
[6] K. Adcox *et al.*, Phys. Rev. Lett. **88**, 242301 (2002).
[7] B. Alper *et al.*, Nucl. Phys. **B100**, 237 (1975).
[8] P. Abreu *et al.*, Eur. Phys. J. C **17**, 207 (2000).
[9] I. Vitev and M. Gyulassy, Phys. Rev. C **65**, 041902 (2002); I. Vitev, M. Gyulassy, and P. Levai, hep-ph/0109198.
[10] K. Adcox *et al.*, Nucl. Instrum. Methods Phys. Res., Sect. A **499**, 469 (2003), and references therein.
[11] S. S. Adler *et al.*, Phys. Rev. Lett. **91**, 072301 (2003).
[12] J. Jia, Nucl. Phys. **A715**, 769c (2003); S. S. Adler *et al.* (to be published).
[13] K. Adcox *et al.*, Phys. Rev. Lett. **89**, 092302 (2002).
[14] C. Adler *et al.*, Phys. Rev. Lett. **87**, 262302 (2001).
[15] D. Teaney *et al.*, Phys. Rev. Lett. **86**, 4783 (2001); P. Kolb *et al.*, Nucl. Phys. **A696**, 197 (2001); P. Huovinen *et al.*, Phys. Lett. B **503**, 58 (2001).
[16] W. Broniowski and W. Florkowski, Phys. Rev. C **65**, 064905 (2002); Phys. Rev. Lett. **87**, 272302 (2001).
[17] P. F. Kolb and R. Rapp, Phys. Rev. C **67**, 044903 (2003).
[18] U. Heinz and P. Kolb, Nucl. Phys. **A702**, 269 (2002).
[19] P. Braun-Munzinger, D. Magestro, K. Redlich, and J. Stachel, Phys. Lett. B **518**, 41 (2001).
[20] B. Kampfer, J. Cleymans, K. Gallmeister, and S. M. Wheaton, hep-ph/0204227.
[21] B. B. Back *et al.*, nucl-ex/0302015 (to be published).
[22] D. Kharzeev, E. Levin, and L. McLerran, Phys. Lett. B **561**, 93 (2003).
[23] J. Cronin *et al.*, Phys. Rev. D **11**, 3105 (1975).
[24] D. Antreasyan *et al.*, Phys. Rev. D **19**, 764 (1979).
[25] P. B. Straub *et al.*, Phys. Rev. D **45**, 3030 (1992).
[26] M. Lev and B. Petersson, Z. Phys. C **21**, 155 (1983).
[27] S. S. Adler *et al.*, Phys. Rev. Lett. **91**, 072303 (2003).
[28] A. Airapetian *et al.*, Eur. Phys. J. C **20**, 479 (2001).
[29] R. C. Hwa and C. B. Yang, Phys. Rev. C **67**, 034902 (2003); R. J. Fries, B. Muller, C. Nonaka, and S. A. Bass, nucl-th/0301087; V. Greco, C. M. Ko, and P. Levai, nucl-th/0301093.
[30] G. C. Rossi and G. Veneziano, Nucl. Phys. **B123**, 507 (1977); D. Kharzeev, Phys. Lett. B **378**, 238 (1996); S. E. Vance, M. Gyulassy, and X.-N. Wang, Phys. Lett. B **443**, 45 (1998).
[31] J. Adams *et al.*, nucl-ex/0306007 (to be published).

J/ψ production in Au-Au collisions at $\sqrt{s_{NN}}$ = 200 GeV

S. S. Adler,[5] S. Afanasiev,[17] C. Aidala,[5] N. N. Ajitanand,[43] Y. Akiba,[20,38] J. Alexander,[43] R. Amirikas,[12] L. Aphecetche,[45] S. H. Aronson,[5] R. Averbeck,[44] T. C. Awes,[35] R. Azmoun,[44] V. Babintsev,[15] A. Baldisseri,[10] K. N. Barish,[6] P. D. Barnes,[27] B. Bassalleck,[33] S. Bathe,[30] S. Batsouli,[9] V. Baublis,[37] A. Bazilevsky,[39,15] S. Belikov,[16,15] Y. Berdnikov,[40] S. Bhagavatula,[16] J. G. Boissevain,[27] H. Borel,[10] S. Borenstein,[25] M. L. Brooks,[27] D. S. Brown,[34] N. Bruner,[33] D. Bucher,[30] H. Buesching,[30] V. Bumazhnov,[15] G. Bunce,[5,39] J. M. Burward-Hoy,[26,44] S. Butsyk,[44] X. Camard,[45] J. -S. Chai,[18] P. Chand,[4] W. C. Chang,[2] S. Chernichenko,[15] C. Y. Chi,[9] J. Chiba,[20] M. Chiu,[9] I. J. Choi,[52] J. Choi,[19] R. K. Choudhury,[4] T. Chujo,[5] V. Cianciolo,[35] Y. Cobigo,[10] B. A. Cole,[9] P. Constantin,[16] D. G. d'Enterria,[45] G. David,[5] H. Delagrange,[45] A. Denisov,[15] A. Deshpande,[39] E. J. Desmond,[5] O. Dietzsch,[41] O. Drapier,[25] A. Drees,[44] R. du Rietz,[29] A. Durum,[15] D. Dutta,[4] Y. V. Efremenko,[35] K El Chenawi,[49] A. Enokizono,[14] H. En'yo,[38,39] S. Esumi,[48] L. Ewell,[5] D. E. Fields,[33,39] F. Fleuret,[25] S. L. Fokin,[23] B. D. Fox,[39] Z. Fraenkel,[51] J. E. Frantz,[9] A. Franz,[5] A. D. Frawley,[12] S. -Y. Fung,[6] S. Garpman,[29,*] T. K. Ghosh,[49] A. Glenn,[46] G. Gogiberidze,[46] M. Gonin,[25] J. Gosset,[10] Y. Goto,[39] R. Granier de Cassagnac,[25] N. Grau,[16] S. V. Greene,[49] M. Grosse Perdekamp,[39] W. Guryn,[5] H.-Å. Gustafsson,[29] T. Hachiya,[14] J. S. Haggerty,[5] H. Hamagaki,[8] A. G. Hansen,[27] E. P. Hartouni,[26] M. Harvey,[5] R. Hayano,[8] X. He,[13] M. Heffner,[26] T. K. Hemmick,[44] J. M. Heuser,[44] M. Hibino,[50] J. C. Hill,[16] W. Holzmann,[43] K. Homma,[14] B. Hong,[22] A. Hoover,[34] T. Ichihara,[38,39] V. V. Ikonnikov,[23] K. Imai,[24,38] L. D. Isenhower,[1] M. Ishihara,[38] M. Issah,[43] A. Isupov,[17] B. V. Jacak,[44] W. Y. Jang,[22] Y. Jeong,[19] J. Jia,[44] O. Jinnouchi,[38] B. M. Johnson,[5] S. C. Johnson,[26] K. S. Joo,[31] D. Jouan,[36] S. Kametani,[8,50] N. Kamihara,[47,38] J. H. Kang,[52] S. S. Kapoor,[4] K. Katou,[50] S. Kelly,[9] B. Khachaturov,[51] A. Khanzadeev,[37] J. Kikuchi,[50] D. H. Kim,[31] D. J. Kim,[52] D. W. Kim,[19] E. Kim,[42] G.-B. Kim,[25] H. J. Kim,[52] E. Kistenev,[15] A. Kiyomichi,[48] K. Kiyoyama,[32] C. Klein-Boesing,[30] H. Kobayashi,[38,39] L. Kochenda,[37] V. Kochetkov,[15] D. Koehler,[33] T. Kohama,[14] M. Kopytine,[44] D. Kotchetkov,[6] A. Kozlov,[51] P. J. Kroon,[5] C. H. Kuberg,[1,27] K. Kurita,[39] Y. Kuroki,[48] M. J. Kweon,[22] Y. Kwon,[52] G. S. Kyle,[34] R. Lacey,[43] V. Ladygin,[17] J. G. Lajoie,[16] A. Lebedev,[16,23] S. Leckey,[44] D. M. Lee,[27] S. Lee,[19] M. J. Leitch,[27] X. H. Li,[6] H. Lim,[42] A. Litvinenko,[17] M. X. Liu,[27] Y. Liu,[36] C. F. Maguire,[49] Y. I. Makdisi,[5] A. Malakhov,[17] V. I. Manko,[23] Y. Mao,[7,38] G. Martinez,[45] M. D. Marx,[44] H. Masui,[48] F. Matathias,[44] T. Matsumoto,[8,50] P. L. McGaughey,[27] E. Melnikov,[15] F. Messer,[44] Y. Miake,[48] J. Milan,[43] T. E. Miller,[49] A. Milov,[44,51] S. Mioduszewski,[5] R. E. Mischke,[27] G. C. Mishra,[13] J. T. Mitchell,[5] A. K. Mohanty,[4] D. P. Morrison,[5] J. M. Moss,[27] F. Mühlbacher,[44] D. Mukhopadhyay,[51] M. Muniruzzaman,[6] J. Murata,[38,39] S. Nagamiya,[20] J. L. Nagle,[9] T. Nakamura,[14] B. K. Nandi,[6] M. Nara,[48] J. Newby,[46] P. Nilsson,[29] A. S. Nyanin,[23] J. Nystrand,[29] E. O'Brien,[5] C. A. Ogilvie,[16] H. Ohnishi,[5,38] I. D. Ojha,[49,3] K. Okada,[38] M. Ono,[48] V. Onuchin,[15] A. Oskarsson,[29] I. Otterlund,[29] K. Oyama,[8] K. Ozawa,[8] D. Pal,[51] A. P. T. Palounek,[27] V. S. Pantuev,[44] V. Papavassiliou,[34] J. Park,[42] A. Parmar,[33] S. F. Pate,[34] T. Peitzmann,[30] J.-C. Peng,[27] V. Peresedov,[17] C. Pinkenburg,[5] R. P. Pisani,[5] F. Plasil,[35] M. L. Purschke,[5] A. Purwar,[44] J. Rak,[16] I. Ravinovich,[51] K. F. Read,[35,46] M. Reuter,[44] K. Reygers,[28] V. Riabov,[37,40] Y. Riabov,[37] G. Roche,[28] A. Romana,[25] M. Rosati,[16] P. Rosnet,[28] S. S. Ryu,[52] M. E. Sadler,[1] N. Saito,[38,39] T. Sakaguchi,[8,50] M. Sakai,[32] S. Sakai,[48] V. Samsonov,[37] L. Sanfratello,[33] R. Santo,[30] H. D. Sato,[24,38] S. Sato,[5,48] S. Sawada,[20] Y. Schutz,[45] V. Semenov,[15] R. Seto,[6] M. R. Shaw,[1,27] T. K. Shea,[5] T. -A. Shibata,[47,38] K. Shigaki,[14,20] T. Shiina,[27] C. L. Silva,[41] D. Silvermyr,[27,29] K. S. Sim,[22] C. P. Singh,[3] V. Singh,[3] M. Sivertz,[5] A. Soldatov,[15] R. A. Soltz,[26] W. E. Sondheim,[27] S. P. Sorensen,[46] I. V. Sourikova,[5] F. Staley,[10] P. W. Stankus,[35] E. Stenlund,[29] M. Stepanov,[34] A. Ster,[21] S. P. Stoll,[5] T. Sugitate,[14] J. P. Sullivan,[27] E. M. Takagui,[41] A. Taketani,[38,39] M. Tamai,[50] K. H. Tanaka,[20] Y. Tanaka,[32] K. Tanida,[38] M. J. Tannenbaum,[5] P. Tarján,[11] J. D. Tepe,[1,27] T. L. Thomas,[33] J. Tojo,[24,38] H. Torii,[24,38] R. S. Towell,[1] I. Tserruya,[51] H. Tsuruoka,[48] S. K. Tuli,[3] H. Tydesjö,[29] N. Tyurin,[15] H. W. van Hecke,[27] J. Velkovska,[5,44] M. Velkovsky,[44] L. Villatte,[46] A. A. Vinogradov,[23] M. A. Volkov,[23] E. Vznuzdaev,[37] X. R. Wang,[13] Y. Watanabe,[38,39] S. N. White,[5] F. K. Wohn,[16] C. L. Woody,[5] W. Xie,[6] Y. Yang,[7] A. Yanovich,[15] S. Yokkaichi,[38,39] G. R. Young,[35] I. E. Yushmanov,[23] W. A Zajc,[9,†] C. Zhang,[9] S. Zhou,[7] S. J. Zhou,[51] and L. Zolin[17]

(PHENIX Collaboration)

[1]*Abilene Christian University, Abilene, Texas 79699, USA*
[2]*Institute of Physics, Academia Sinica, Taipei 11529, Taiwan*
[3]*Department of Physics, Banaras Hindu University, Varanasi 221005, India*
[4]*Bhabha Atomic Research Centre, Bombay 400 085, India*
[5]*Brookhaven National Laboratory, Upton, New York 11973-5000, USA*
[6]*University of California-Riverside, Riverside, California 92521, USA*
[7]*China Institute of Atomic Energy (CIAE), Beijing, People's Republic of China*
[8]*Center for Nuclear Study, Graduate School of Science, University of Tokyo, 7-3-1 Hongo, Bunkyo, Tokyo 113-0033, Japan*
[9]*Columbia University, New York, New York 10027, USA and Nevis Laboratories, Irvington, New York 10533, USA*
[10]*Dapnia, CEA Saclay, Bâtiment 703, F-91191, Gif-sur-Yvette, France*
[11]*Debrecen University, H-4010 Debrecen, Egyetem tér 1, Hungary*
[12]*Florida State University, Tallahassee, Florida 32306, USA*
[13]*Georgia State University, Atlanta, Georgia 30303, USA*

 ©2004 The American Physical Society

[14]*Hiroshima University, Kagamiyama, Higashi-Hiroshima 739-8526, Japan*
[15]*Institute for High Energy Physics (IHEP), Protvino, Russia*
[16]*Iowa State University, Ames, Iowa 50011, USA*
[17]*Joint Institute for Nuclear Research, 141980 Dubna, Moscow Region, Russia*
[18]*KAERI, Cyclotron Application Laboratory, Seoul, South Korea*
[19]*Kangnung National University, Kangnung 210-702, South Korea*
[20]*KEK, High Energy Accelerator Research Organization, Tsukuba-shi, Ibaraki-ken 305-0801, Japan*
[21]*KFKI Research Institute for Particle and Nuclear Physics (RMKI), H-1525 Budapest 114, P.O. Box 49, Hungary*
[22]*Korea University, Seoul, 136-701, Korea*
[23]*Russian Research Center "Kurchatov Institute," Moscow, Russia*
[24]*Kyoto University, Kyoto 606, Japan*
[25]*Laboratoire Leprince-Ringuet, Ecole Polytechnique, CNRS-IN2P3, Route de Saclay, F-91128 Palaiseau, France*
[26]*Lawrence Livermore National Laboratory, Livermore, California 94550, USA*
[27]*Los Alamos National Laboratory, Los Alamos, New Mexico 87545, USA*
[28]*LPC, Université Blaise Pascal, CNRS-IN2P3, Clermont-Fd, 63177 Aubiere Cedex, France*
[29]*Department of Physics, Lund University, Box 118, SE-221 00 Lund, Sweden*
[30]*Institut fuer Kernphysik, University of Muenster, D-48149 Muenster, Germany*
[31]*Myongji University, Yongin, Kyonggido 449-728, Korea*
[32]*Nagasaki Institute of Applied Science, Nagasaki-shi, Nagasaki 851-0193, Japan*
[33]*University of New Mexico, Albuquerque, New Mexico 87131, USA*
[34]*New Mexico State University, Las Cruces, New Mexico 88003, USA*
[35]*Oak Ridge National Laboratory, Oak Ridge, Tennessee 37831, USA*
[36]*IPN-Orsay, Universite Paris Sud, CNRS-IN2P3, BP1, F-91406, Orsay, France*
[37]*PNPI, Petersburg Nuclear Physics Institute, Gatchina, Russia*
[38]*RIKEN (The Institute of Physical and Chemical Research), Wako, Saitama 351-0198, Japan*
[39]*RIKEN BNL Research Center, Brookhaven National Laboratory, Upton, New York 11973-5000, USA*
[40]*St. Petersburg State Technical University, St. Petersburg, Russia*
[41]*Universidade de São Paulo, Instituto de Física, Caixa Postal 66318, São Paulo CEP05315-970, Brazil*
[42]*System Electronics Laboratory, Seoul National University, Seoul, South Korea*
[43]*Chemistry Department, Stony Brook University, SUNY, Stony Brook, New York 11794-3400, USA*
[44]*Department of Physics and Astronomy, Stony Brook University, SUNY, Stony Brook, New York 11794, USA*
[45]*SUBATECH (Ecole des Mines de Nantes, CNRS-IN2P3, Université de Nantes) Boîte Postale 20722-44307, Nantes, France*
[46]*University of Tennessee, Knoxville, Tennessee 37996, USA*
[47]*Department of Physics, Tokyo Institute of Technology, Tokyo 152-8551, Japan*
[48]*Institute of Physics, University of Tsukuba, Tsukuba, Ibaraki 305, Japan*
[49]*Vanderbilt University, Nashville, Tennessee 37235, USA*
[50]*Waseda University, Advanced Research Institute for Science and Engineering, 17 Kikui-cho, Shinjuku-ku, Tokyo 162-0044, Japan*
[51]*Weizmann Institute, Rehovot 76100, Israel*
[52]*Yonsei University, IPAP, Seoul 120-749, Korea*
(Received 27 May 2003; published 26 January 2004)

First results on charm quarkonia production in heavy ion collisions at the Relativistic Heavy Ion Collider (RHIC) are presented. The yield of J/ψ's measured in the PHENIX experiment via electron-positron decay pairs at midrapidity for Au-Au reactions at $\sqrt{s_{NN}}=200$ GeV is analyzed as a function of collision centrality. For this analysis we have studied 49.3×10^6 minimum bias Au-Au reactions. We present the J/ψ invariant yield dN/dy for peripheral and midcentral reactions. For the most central collisions where we observe no signal above background, we quote 90% confidence level upper limits. We compare these results with our J/ψ measurement from proton-proton reactions at the same energy. We find that our measurements are not consistent with models that predict strong enhancement relative to binary collision scaling.

DOI: 10.1103/PhysRevC.69.014901 PACS number(s): 25.75.Dw

*Deceased.
†Spokesperson. Email address: zajc@nevis.columbia.edu

I. INTRODUCTION

Lattice quantum chromodynamics (QCD) calculations indicate that there is a transition of nuclear matter from confined to deconfined quarks and gluons at a temperature of order $T_c=170$ MeV. Characteristic of this deconfined state of matter is the dynamic screening of the long-range confining potential of QCD. Color screening is predicted to reduce the attraction between heavy quark-antiquark pairs, and thus leads to a decrease in the ratio of hidden charm and beauty (quarkonia) to open charm and beauty [1,2]. Thus, one expects a suppression of quarkonium states $[J/\psi, \psi', \chi_c, \Upsilon(1s, 2s, 3s)]$ depending on their binding energy and the temperature of the surrounding system.

In relativistic heavy ion collisions a state of a deconfined thermalized quark-gluon plasma may be created. Measurements in Pb-Pb reactions at $\sqrt{s_{NN}}=17.3$ GeV by the NA50 experiment [3] show a suppression of heavy quarkonia production relative to "normal" nuclear absorption, the dissociation of $c\bar{c}$ pairs by interactions with the nucleons into separate quarks that eventually hadronize into D mesons [4–7]. This suppression has been interpreted in the context of color screening in a quark-gluon plasma [6,8], additional absorption with comoving hadrons [9,10], and multiple scattering between the charm quarks and the surrounding medium [11,12].

At Relativistic Heavy Ion Collider (RHIC) energies, where of order 10 $c\bar{c}$ pairs are produced in central Au-Au reactions [13,14], some models predict an enhancement of heavy quarkonia due to $c\bar{c}$ coalescence in a quark-gluon plasma [15], detailed balance of $D+\bar{D}\leftrightarrow J/\psi+X$ [16], and/or statistical J/ψ production [17]. In addition, at RHIC energies initial state effects of shadowing and possible parton saturation may play a role in initial charm production [18]. Disentangling these competing effects will require a systematic study of yields of various quarkonium states in different colliding systems [proton-proton, proton (or deuteron)-ion, and ion-ion] and over a wide kinematic range in terms of transverse momentum and x_F.

We report here the first results on J/ψ production via electron-positron decay pairs at midrapidity from Au-Au collisions at $\sqrt{s_{NN}}=200$ GeV from data taken during Run 2 at RHIC in 2001. For peripheral and midcentral Au-Au collisions, we present the most probable yield values, while for central reactions, we observe no signal above background and thus quote 90% confidence level upper limits on J/ψ production.

II. PHENIX EXPERIMENT

The PHENIX experiment is specifically designed to make use of high-luminosity ion-ion, proton-ion, and proton-proton collisions at the Relativistic Heavy Ion Collider to sample rare physics probes including the J/ψ and other heavy quarkonium states. The PHENIX experiment includes two central rapidity spectrometer arms, each covering the pseudorapidity range $|\eta|<0.35$ and an interval of 90° in azimuthal angle ϕ. The spectrometers are composed from the inner radius outward of a multiplicity and vertex detector, drift chambers (DC), pixel pad chambers (PC), ring imaging cerenkov counters (RICH), time-of-flight scintillator wall, time expansion chambers (TEC), and two types of electromagnetic calorimeters (EMC). This combination of detectors allows for the clean identification of electrons over a broad range in transverse momentum. Further details of the detector design and performance are given in Ref. [19].

The Au-Au event centrality is estimated using the combined data from our beam-beam counters (BBCs) and zero degree calorimeters (ZDCs). While the ZDCs measure forward neutrons that result from fragmentation of the colliding nuclei, the BBCs are sensitive to charged particles produced in the collisions. Together, both detectors yield information on the impact parameter of the nuclear reaction [20]. These observables, combined with a Glauber model for the nuclear geometry, allow us to determine different collision geometry categories, referred to as centrality ranges [21].

For the analysis presented here, the electron (positron) momentum and charge sign are determined from tracking using the DC and the PC and then projecting back through the PHENIX axial magnetic field to the collision point determined by the BBC [22]. The momentum resolution achieved is $\delta p/p=0.7\% \oplus 1.0\% \times p$ (in GeV/c). Electrons are cleanly separated from the large background of charged pions and kaons by associating the tracks with at least three active photomultiplier tubes in the RICH [23]. In addition, we compare the track momentum (p) to the energy (E) measured in the electromagnetic calorimeter. The E/p ratio is used to further reduce the pion contamination in the electron sample. Pions typically deposit only a fraction of their energy in the calorimeter whereas electrons deposit all of their energy. These selections are augmented by requiring that the calorimeter shower position and time-of-flight information agree with the track projection. Thus, we obtain a clean sample of electron and positron candidates with less than 5% contamination.

III. DATA SELECTION AND TRIGGERS

The Au-Au data at $\sqrt{s_{NN}}=200$ GeV used in this analysis were recorded during Run 2 at RHIC in the fall of 2001. For our "minimum bias" Au-Au event selection, we use a level-1 trigger that requires a coincidence between our BBCs. We place an additional offline requirement of at least one forward neutron in each of our ZDCs to remove beam related backgrounds. Our "minimum bias" sample includes 92% of the 6.9 barn Au-Au inelastic cross section [21]. We further restrict our analysis to 90% of the inelastic cross section to remove a small remaining contribution from beam related background events.

We observed a Au-Au inelastic collision rate that increased during the running period from 100 to 1200 Hz. The level-2 triggers are implemented in a personal-computer-based farm with 30 processors in run 2, as part of the PHENIX Event Builder [19]. The level-2 J/ψ trigger algorithm identified electron candidates by starting with rings in the RICH and then searching for possible matching showers in the EMC. The EMC search window based on the RICH ring is obtained from a lookup table, generated using Monte Carlo simulations of single electrons. Possible matches were

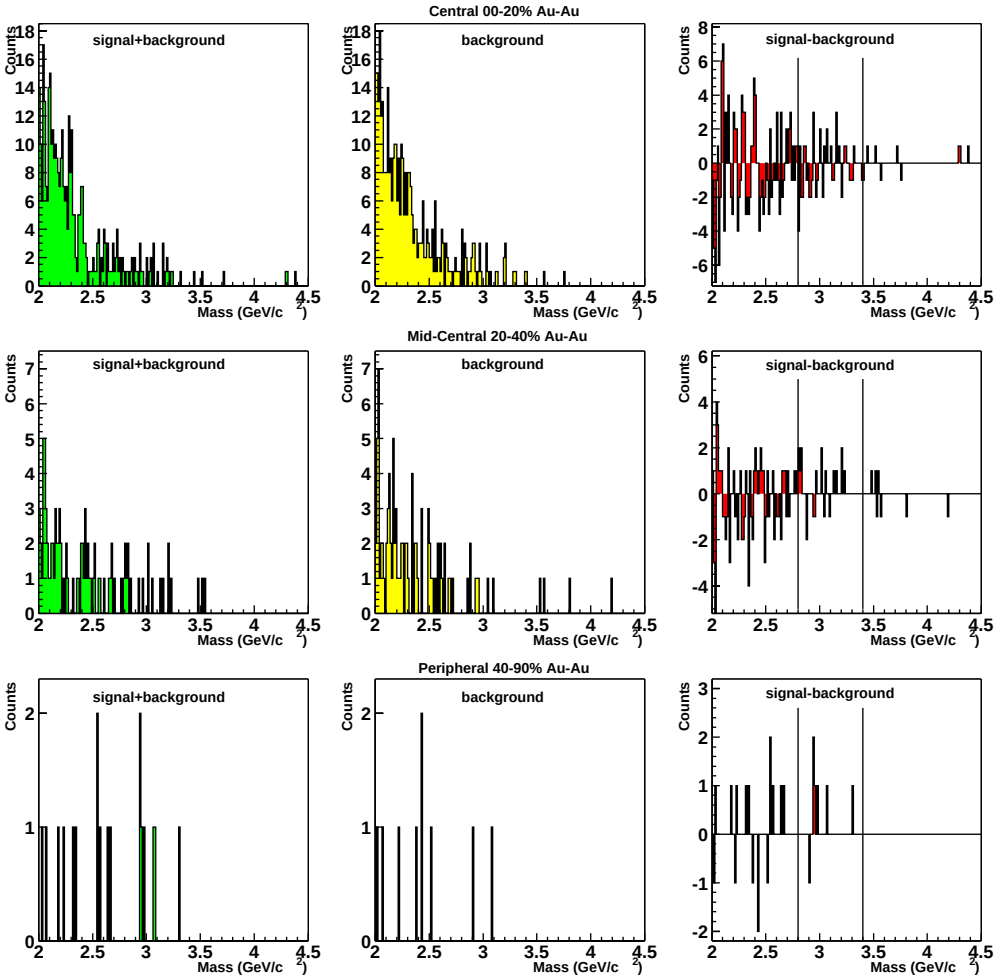

FIG. 1. (Color online) Dielectron invariant mass distribution in Au-Au reactions (top row, most central, 0–20 % central; middle row, midcentral, 20–40 % central; and bottom row, peripheral, 40–90 % central) for unlike sign pairs containing signal+background (left column), like sign pairs containing only background (center column), and the subtracted difference (right column).

assumed to be electron candidates, and the electron momentum was taken to be the EMC shower energy. The invariant mass was calculated for all electron candidate pairs within an event, regardless of the candidate's charge sign. If the invariant mass was higher than 2.2 GeV/c^2, the pair was accepted as a J/ψ candidate, and the entire event was archived. The level-2 trigger provided a rejection factor of order 30 relative to our "minimum bias" level-1 trigger sample.

An additional offline requirement was imposed that the collisions have a z vertex satisfying $|z|<30$ cm in order to eliminate collisions taking place near the PHENIX magnet. After this selection, we have analyzed 25.9×10^6 "minimum bias" Au-Au reactions as triggered by our BBC level-1 trigger. In addition, from the high-luminosity period of running, we also processed 23.4×10^6 "minimum bias" events with our J/ψ level-2 trigger.

IV. J/ψ SIGNAL COUNTING

For three exclusive centrality bins—0–20%, 20–40%, and 40–90% of the total Au-Au cross section, we show the dielectron invariant mass distributions for unlike sign pairs (e^+e^-), like sign pairs (e^+e^+ or e^-e^-), and the subtracted difference in Fig. 1. The number of J/ψ counts for each centrality range is determined from the number of signal counts above "background" within a fixed invariant mass window. The PHENIX acceptance and level-2 trigger efficiencies are the same within a few percent for unlike sign pairs and like sign pairs in the J/ψ mass region. Therefore, the sample of like sign pairs is a good representation with no additional scale factor of the "background" due to simple combinatorics.

In order to extract a J/ψ signal strength, we employ a counting method where we subtract from the number of unlike sign pairs the number of like sign pairs in the mass window $2.8<m<3.4$ GeV/c^2. We have chosen a wide invariant mass window to be consistent with the signal extraction method from our proton-proton analysis [24], and to limit our sensitivity to the exact mass width value. Although we expect from our Monte Carlo studies a mass width of order 60 MeV, we cannot quantitatively verify this even with our proton-proton data sample due to low statistics. We note, that in principle, there is more information to be utilized in the exact distribution of the candidates within the mass window. However, we have found that this does not add to the

TABLE I. Statistical results for J/ψ counts are shown for three exclusive centrality ranges. Shown are the number of unlike and like sign counts within the mass window ($2.8<m<3.4$ GeV/c^2). Also shown are the most likely signal value with the 68% statistics confidence interval (for the peripheral and midcentral cases), and the 90% confidence level upper limits.

Cent.	Unlike sign counts	Like sign counts	Most likely signal	90% C.L.
0–20 %	33	41	0	9.9
20–40 %	16	8	$8^{+4.8}_{-4.1}$	14.4
40–90 %	7	2	$5^{+3.1}_{-2.6}$	9.3

significance of the result, given the low counts and the lack of constraint on the J/ψ and background line shape.

Table I shows the number of unlike and like sign counts within the mass window. For given observed counts of N_l (like sign) and N_u (unlike sign), the likelihood $L(\nu_l, \nu_u)$ for the expectation values ν_l and ν_u is given as

$$L(\nu_l, \nu_u) = \frac{\nu_l^{N_l} e^{-\nu_l}}{N_l!} \times \frac{\nu_u^{N_u} e^{-\nu_u}}{N_u!}. \quad (1)$$

We then integrate $L(\nu_l, \nu_u)$ to give the likelihood $L(\nu_s)$ for the expectation value of the net signal counts $\nu_s = \nu_u - \nu_l$,

$$L(\nu_s) = \int_0^\infty \int_0^\infty L(\nu_l, \nu_u)\delta(\nu_s - \nu_u + \nu_l) d\nu_l d\nu_u \quad (2)$$

We show the likelihood distribution $L(\nu_s)$ for the midcentral (20–40 %) events in Fig. 2. Although $L(\nu_s)$ is normalized such that $\int_{-\infty}^{\infty} L(\nu_s) d\nu_s = 1$, it has a nonzero probability for negative expected net signal value ($\nu_s<0$). Since the unlike sign contains signal + background, and the like sign contains only *background*, the only physically allowed values for ν_s are greater than or equal to zero. Thus, we remove the probability range corresponding to $\nu_s<0$, and renormalize the remaining probability integral to one [25], as shown in Fig. 2. We then determine for each centrality the 90% confidence level upper limit, and the 68% confidence interval around the most likely value for the peripheral and midcentral ranges. These values are shown in Table I.

Since the net signal is negative for the 0–20 % central event class, we can only quote a 90% confidence level upper limit. Also, even for the 20–40 % and 40–90 % centrality classes, the signal observed is not significant at the two standard deviation level and thus we also show 90% confidence level upper limits for completeness. The limited statistical significance of the results is clear from the mass distributions shown in Fig. 1.

In the intermediate mass region below the J/ψ, $2.0<m<2.8$ GeV/c^2, the shapes and absolute yield of like sign and unlike sign dielectron mass distributions are well reproduced by an event mixing method within a few percent. This indicates that most of the dielectron pairs are from uncorrelated electron and positron candidates. They are originating from Dalitz decays, photon conversions, open charm/

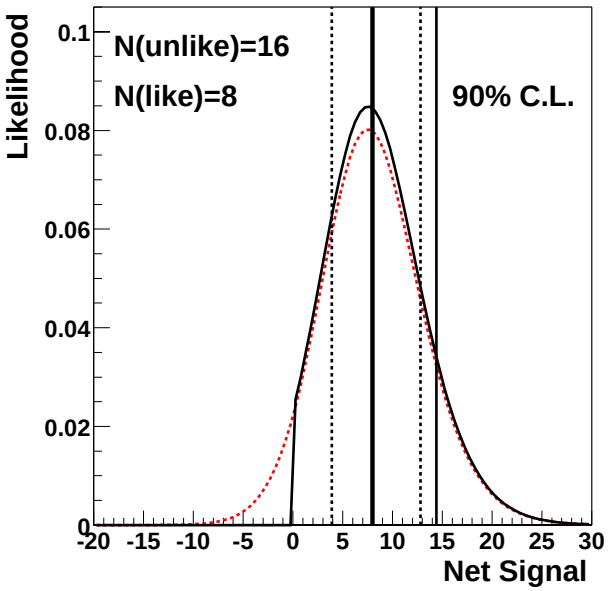

FIG. 2. (Color online) The Poisson statistical likelihood distribution as a function of the expected net signal. The distributions are for the midcentral case of $N_{unlike}=16$ and $N_{like}=8$. The dashed curve is the likelihood distribution, and the black is after eliminating the unphysical net signal less than zero and renormalizing. Vertical lines are shown to indicate the most likely value (8), the 68% confidence interval values, and the 90% confidence level upper limit.

beauty semileptonic decays, and a small contamination of misidentified hadrons. The unlike sign pairs should also have a component from semileptonic decays of charm and anticharm pairs, but its contribution is less than the statistical uncertainty of the data [26]. A complete analysis of the intermediate mass region will be presented elsewhere [27].

Our method of measurement does not separate contributions from decay feed-down from other states such as the χ_c and ψ', and thus our J/ψ counts include these feed-down sources. Our acceptance and efficiency is identical for the resulting J/ψ from these decays as for prompt J/ψ, and thus they enter our signal weighted simply by their relative production and branching fraction into $J/\psi+X$. Another contribution may result from B meson decays into J/ψ. However, if we assume a $b\bar{b}$ cross section in proton-proton reactions $\sigma_{b\bar{b}} \approx 2-5$ μb [28] and that beauty production scales with binary collisions, we would expect a contribution of order 1–4 % relative to primary J/ψ or J/ψ from χ_c. This percentage contribution calculation assumes that the primary J/ψ also scales with binary collisions. If primary J/ψ are substantially suppressed, the B meson decay contribution would constitute a larger fraction of our measured J/ψ, especially at higher p_T.

It should also be noted that some signal in the unlike sign pairs from correlated open charm $c\bar{c} \rightarrow D(\rightarrow e^+ + X) + D(\rightarrow e^- + X)$ will contribute in our mass window. Assuming binary scaling in charm production with a proton-proton cross section $\sigma_{c\bar{c}} \approx 650$ μb [14], this contribution in the J/ψ mass region is estimated to be about 0.1 events in the 0–20 %, 0.05 events in the 20–40 %, and 0.02 events in the 40–90 % centrality bins.

V. J/ψ YIELD CALCULATION

We quote our results as the branching fraction of $J/\psi \rightarrow e^+e^-$ ($B=5.93\pm0.10\times10^{-2}$ [25]) times the invariant yield at midrapidity $dN/dy|_{y=0}$. We calculate this quantity for three exclusive centrality ranges as detailed below,

$$B\left.\frac{dN}{dy}\right|_{y=0} = \frac{N_{J/\psi}}{N_{mb-evt} + (\epsilon_{lvl2-eff} N_{lvl2-evt})} \times \frac{1}{\Delta y} \frac{1}{\epsilon_{acc-eff} \times \epsilon_{cent}}. \tag{3}$$

The number of signal counts $N_{J/\psi}$ from both the "minimum bias" and level-2 triggered event samples are shown in Table I. The number of events from the "minimum bias" sample $N_{mb\text{-}evt}$ is 25.9×10^6 Au-Au events. The number of effective events sampled by the level-2 trigger is ($\epsilon_{lvl2\text{-}eff} \times N_{lvl2\text{-}evt}$), which is the level-2 trigger efficiency times the number of events processed by the level-2 trigger, 23.4×10^6 Au-Au events. This formulation appropriately weights the two data samples by the expected number of J/ψ.

The efficiency of the level-2 trigger $\epsilon_{lvl2\text{-}eff}$ was determined by running the trigger algorithm on simulated J/ψ and carrying out a full offline reconstruction of the resulting electron-positron decay pair. The efficiency was calculated via counting the fraction of successfully reconstructed J/ψ events that were also found by the trigger. In these trigger simulations, the channel-by-channel calibrations for the RICH and EMC were used to convert the simulated signals into realistic values representative of a specific period in the run, before passing them to the level-2 trigger.

The overall J/ψ trigger efficiency from the trigger simulations was $\epsilon_{lvl2\text{-}eff}=0.75\pm0.04$. The systematic error was determined by studying the dependence of the trigger efficiency on the collision vertex position, the assumed J/ψ transverse momentum and rapidity distribution, collision centrality, and the period of the run from which the channel-by-channel calibrations were taken. After evaluating all of the above dependencies, we assign a 5% systematic error to the J/ψ trigger efficiency.

The efficiency result from the trigger simulations was confirmed using real data in two ways. First, the minimum bias data sample in Au-Au collisions was analyzed to calculate the J/ψ trigger efficiency. This was done by taking the ratio of the events that have an electron pair with invariant mass between 2.8 and 3.4 GeV/c^2 that fired the J/ψ trigger to all of the events having electron pairs in that invariant mass range. The trigger efficiency estimate from this check is 0.67 ± 0.10 (stat). Second, the triggers were run on a sample of 26 events from the proton-proton dataset that passed all of the J/ψ cuts in the offline analysis and had invariant masses between 2.8 and 3.4 GeV/c^2. The level-2 J/ψ trigger accepted 19 of these events, yielding an estimate of $0.73\pm^{0.07}_{0.10}$ (stat), in very good agreement with the trigger simulation result. These results verify that the trigger performance is similar for real data and simulations.

The J/ψ acceptance and efficiency $\epsilon_{acc\text{-}eff}$ is determined with a GEANT based Monte Carlo simulation of the PHENIX experiment. The detector response has been tuned to reproduce the resolution and performance of the real detector. The efficiency includes not only the tracking efficiency, but also the probability for passing all of the electron identification selection cuts. The electron identification efficiency determined by the Monte Carlo simulation is verified by a clean electron sample from conversion photons. We also account for run by run efficiency changes by counting the relative number of reconstructed electrons and positrons per event in our data sample. We show the PHENIX acceptance and efficiency as a function of transverse momentum in Fig. 3.

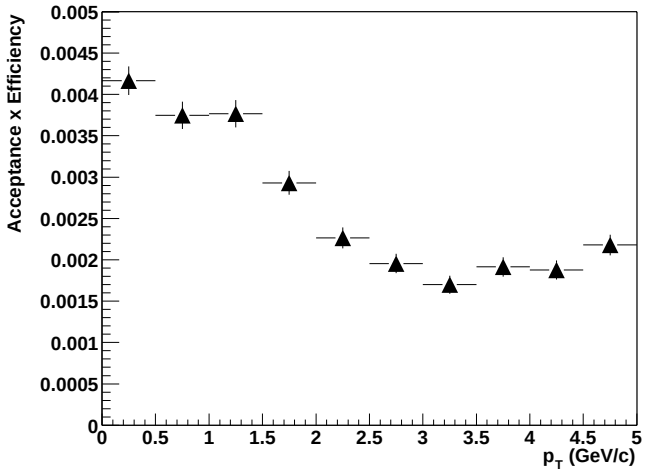

FIG. 3. The PHENIX J/ψ acceptance $\times$ efficiency as a function of the J/ψ transverse momentum is shown. Most of the acceptance is with one lepton into each of the two PHENIX central spectrometers. This contribution peaks at $p_T=0$ and decreases with increasing p_T. The rise in the acceptance at high p_T is from contributions where both electron and positron are accepted into one of the PHENIX central spectrometers.

Since we do not have the statistics to determine the transverse momentum distribution of the J/ψ, we must employ a model for the p_T dependence to determine an overall acceptance and efficiency. We use two different functional forms for the p_T distributions to test the model sensitivity of our acceptance. We use an exponential in p_T and an exponential in p_T^2 as motivated by fits to J/ψ data at lower energies [29]. The two models give similar acceptance values given a common $\langle p_T \rangle$ value input. The largest uncertainty comes from the value of $\langle p_T \rangle$ assumed. PHENIX has measured J/ψ production in proton-proton reactions at $\sqrt{s}=200$ GeV and finds a $\langle p_T \rangle = 1.80\pm0.23(\text{stat})\pm0.16(\text{syst})\text{GeV}/c$ [24]. We use this value to determine our acceptance and efficiency averaged over all p_T. The J/ψ $\langle p_T \rangle$ in Au-Au collisions may differ from that in proton-proton reactions. Therefore we vary the $\langle p_T \rangle$

TABLE II. The J/ψ acceptance $\times$ efficiency and the centrality dependent efficiency are shown for three exclusive Au-Au centrality event classes.

Centrality bin	$\epsilon_{acc\text{-}eff}$	ϵ_{cent}
0–20 %	$0.0027\pm^{0.0009}_{0.0005}$ (syst)	0.61 ± 0.06 (syst)
20–40 %	$0.0027\pm^{0.0009}_{0.0005}$ (syst)	0.78 ± 0.08 (syst)
40–90 %	$0.0027\pm^{0.0009}_{0.0005}$ (syst)	0.90 ± 0.09 (syst)

TABLE III. We show the statistically most likely J/ψ invariant yield ($B\ dN/dy|_{y=0}$) value and the 68% confidence interval for peripheral (40–90 %) and midcentral (20–40 %) collisions. We also show the 90% confidence level upper limit and the systematic error on this limit for all three different centrality ranges of Au-Au collisions.

	$B\ dN/dy\|_{y=0}(\times 10^{-4})$	
Centrality	Most likely value	90% C.L. upper limit
0–20 %	N.A.	$6.08+1.56$ (syst)
20–40 %	$4.00^{+2.34}_{-2.01}$ (stat)$^{+1.36}_{-1.60}$ (syst)	$7.19+2.43$ (syst)
40–90 %	$0.86^{+0.52}_{-0.44}$ (stat)$^{+0.29}_{-0.35}$ (syst)	$1.60+0.54$ (syst)

from 1.0 to 3.0 GeV/c to determine our model dependent systematic errors. We assume that the J/ψ rapidity distribution is flat over the range $-0.35<y<0.35$ where we measure. The final value for the J/ψ acceptance and efficiency is shown in Table II. This acceptance and efficiency has a 20% systematic error from uncertainties in matching the Monte Carlo to the detector response, a 10% systematic error from run-to-run variation corrections, and a $\pm^{32}_{24}$% systematic error from the uncertainty in the $\langle p_T\rangle$.

Our tracking and electron identification efficiencies exhibit a centrality dependence due to overlapping hits and energy contamination in the calorimeter. We determine this dependence by embedding Monte Carlo J/ψ into real data events of different centrality selections. The corresponding efficiency factor ϵ_{cent} varies from 56% for the 0–5 % most central events to 98% for the 85–90 % most peripheral events.

The final values for the embedding efficiency in our wide centrality bins are sensitive to the true centrality dependence of the J/ψ production. In order to estimate the systematic error due to this uncertainty we assume two different centrality dependence models: (1) binary collision scaling and (2) participant collision scaling. Within our centrality ranges, we find that these two models yield less than a 5% difference and we include this in our systematic error. We assign an additional 10% systematic error to account for uncertainties in the Monte Carlo embedding procedure. The centrality dependent efficiency values are shown in Table II.

In our $B\ dN/dy$ calculation, we have added the systematic errors from all of the contributing factors in quadrature and find +35% and −41% total systematic error on the invariant yield in each of the centrality ranges. The dominant systematic error results from the uncertainty in the $\langle p_T\rangle$ of the J/ψ distribution.

VI. RESULTS

The $B\ dN/dy|_{y=0}$ values for the three exclusive centrality selections are shown in Table III. We have calculated using a Glauber model [21] the number of expected participating nucleons N_{part} and the number of expected binary collisions N_{coll} for each centrality range. These results are shown in Table IV, in addition to the $B\ dN/dy|_{y=0}$ values divided by the expected number of binary collisions.

The PHENIX result for the J/ψ invariant yield in proton-proton induced reactions at $\sqrt{s}=200$ GeV at midrapidity [24] is

$$B dN/dy|_{y=0}(pp) = 1.46 \pm 0.23(\text{stat}) \pm 0.22(\text{syst}) \pm 0.15(\text{abs}) \times 10^{-6}. \quad (4)$$

The systematic error (abs) represents the uncertainty of the normalization of the total proton-proton invariant yield.

We show in Fig. 4 the results from the three Au-Au centrality bins and the proton-proton data normalized per binary collision as a function of the number of participating nucleons. Note that for proton-proton reactions, there are two participating nucleons and one binary collision.

VII. DISCUSSION

Despite the limited statistical significance and systematic uncertainty of these first J/ψ results, we can address some important physics questions raised by the numerous theoretical frameworks in which J/ψ rates are calculated.

We show in Fig. 5 binary scaling expectations as a gray band. We also show a calculation of the suppression expected from "normal" nuclear absorption using a $\sigma_{c\bar{c}-N}=4.4$ mb [30] and 7.1 mb [31,6]. A recent measurement in proton-nucleus collisions at lower energies [30] favors the smaller absorption cross section, thus underscoring the importance of measuring J/ψ in proton(deuteron)-nucleus collisions at RHIC energies. We also show the NA50 suppression pattern relative to binary scaling [3], normalized to

TABLE IV. We show the number of participating nucleons and the number of binary collisions for three different centrality ranges of Au-Au collisions, and the associated systematic errors. We show the statistically most likely value for the J/ψ invariant yield ($B\ dN/dy|_{y=0}$) divided by the expected number of binary collisions for peripheral (40–90 %) and midcentral (20–40 %) collisions. We also show the 90% confidence level upper limit and the systematic error on this limit for all three different centrality ranges of Au-Au collisions. The systematic error in the invariant yield per binary collision does not include the systematic error in the expected number of binary collisions. This error contribution is negligible for the central and midcentral categories and would increase the systematic error for the peripheral category by 6%.

			$B\ dN/dy\|_{y=0}$ per binary collision ($\times 10^{-6}$)	
Centrality	N_{part}	N_{coll}	Most likely value	90% C.L. upper limit
0–20 %	280 ± 4	779 ± 75	N.A.	$0.78+0.20$ (syst)
20–40 %	140 ± 5	296 ± 31	$1.35^{+0.79}_{-0.68}$ (stat)$^{+0.46}_{-0.54}$ (syst)	$2.43+0.82$ (syst)
40–90 %	34 ± 3	45 ± 7	$1.91^{+1.15}_{-0.97}$ (stat)$^{+0.65}_{-0.77}$ (syst)	$3.55+1.21$ (syst)

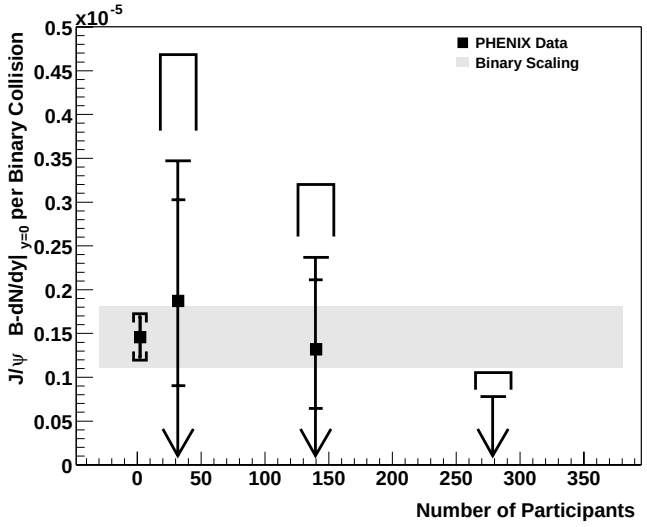

FIG. 4. The J/ψ invariant yield per binary collision is shown for proton-proton reactions and three exclusive centrality ranges of Au-Au reactions all at $\sqrt{s_{NN}}=200$ GeV. For the proton-proton reactions, we show the most likely value as a data point (square), the statistical error, and the estimated systematic errors as brackets. For the three Au-Au data points, we show as arrows the 90% confidence level upper limits. The bracket above the limit includes the estimated systematic error on these limits. In the case of the peripheral and midcentral ranges, we also show, as a square marker, the statistically most likely value and as two horizontal dashes the 68% confidence interval. The gray band indicates binary scaling and the width is the quadrature sum of the statistical and systematic error on our proton-proton data point. For the Au-Au points, the systematic error in the invariant yield per binary collision does not include the systematic error in the expected number of binary collisions. This error contribution is negligible for the central and midcentral categories and would increase the systematic error for the peripheral category by 6%.

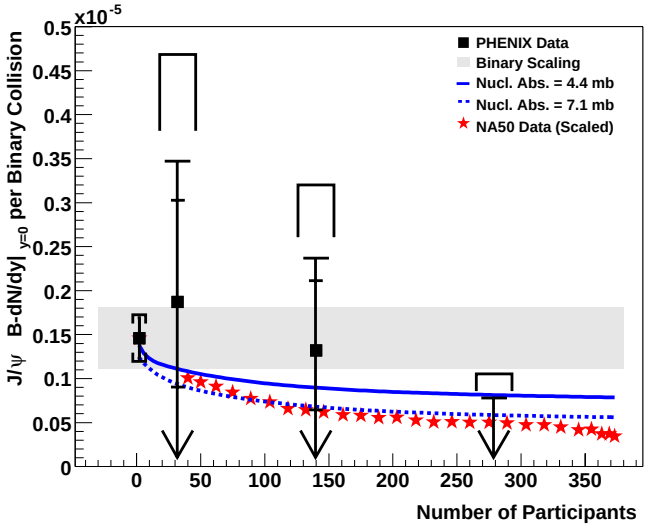

FIG. 5. (Color online) The J/ψ invariant yield per binary collision is shown from proton-proton reactions and three exclusive centrality ranges of Au-Au reactions all at $\sqrt{s_{NN}}=200$ GeV. The lines are the theoretical expectations from "normal" nuclear absorption with $\sigma_{c\bar{c}-N}=4.4$ mb (solid curve) and 7.1 mb (dashed curve) cross section. The stars are the J/ψ per binary collision measured by the NA50 experiment at lower collision energy. In order to compare the shapes of the distribution, we have normalized the NA50 data to match the central value for our proton-proton results.

match our proton-proton data point at 200 GeV. The data disfavor binary scaling, while they are consistent with "normal" nuclear absorption alone and also the NA50 suppression pattern measured at lower energies, within our large statistical errors.

One model calculation [16] including just the "normal" nuclear and plasma absorption components at RHIC energies is shown in Fig. 6. The higher temperature (T) and longer time duration of the system at RHIC lead to a predicted larger suppression of J/ψ relative to binary collision scaling. This specific model [16], and in general this class of models [32,8], cannot be ruled out at this time due to our null result (90% confidence level upper limit) for the most central collisions.

Many recent theoretical calculations also include the possibility for additional late stage re-creation or coalescence of J/ψ states. In Ref. [16], they include both breakup and creation reactions $D+D\leftrightarrow J/\psi+X$. At the lower fixed target CERN energies, this represents a very small contribution due to the small charm production cross section. However, at RHIC energies, where in central Au-Au collisions there are of order 10 $c\bar{c}$ pairs produced, the contribution is significant. The sum of the initial production, absorption, and re-creation as shown in Fig. 6 is also consistent with our experimental data.

A different calculation [15] assumes the formation of a quark-gluon plasma in which the mobility of heavy quarks in the deconfined region leads to increased $c\bar{c}$ coalescence. This leads to a very large enhancement of J/ψ production at RHIC energies for the most central reactions. The model considers the plasma temperature (T) and the rapidity width (Δy) of charm quark production as input parameters. Shown in Fig. 6 are the calculation results for $T=400$ MeV and $\Delta y=1.0, 2.0, 3.0, 4.0$. The narrower the rapidity window in which all charm quarks reside, the larger the probability for J/ψ formation. $\Delta y=1.0$ is consistent with the three dimensional spherically symmetric thermal distribution, and results in a charm yield at midrapidity that is inconsistent with the PHENIX preliminary charm yield as determined from single electron measurements [14]. $\Delta y=4.0$ is consistent with expectations from factorized QCD and PYTHIA with CTEQ5L structure functions [13]. All of these parameters within this model predict a J/ψ enhancement relative to binary collisions scaling, which is disfavored by our data.

Another framework for determining quarkonia yields is to assume a statistical distribution of charm quarks that may then form quarkonia. A calculation assuming thermal, but not chemical, equilibration [17] is shown in Figure 6, and is also consistent with our data.

Significantly larger datasets are required to address the various models that are still consistent with our first measurement. Key tests will be the p_T and x_F dependence of the J/ψ yields, and how these compare with other quarkonium states such as the ψ'.

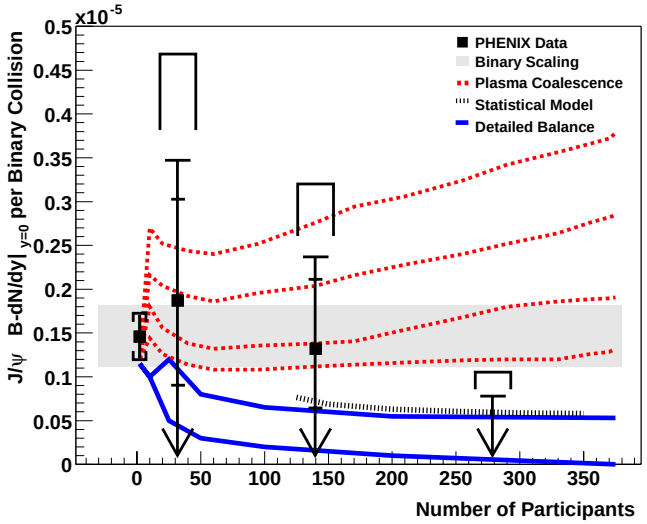

FIG. 6. (Color online) The J/ψ invariant yield per binary collision is shown from proton-proton reactions and three exclusive centrality ranges of Au-Au reactions all at $\sqrt{s_{NN}}=200$ GeV. The lowest curve is a calculation including "normal" nuclear absorption in addition to substantial absorption in a high-temperature quark-gluon plasma [16]. The curve above this is including backward reactions that recreate J/ψ. The statistical model [17] result is shown as a dotted curve for midcentral to central collisions just above that. The four highest dashed curves are from the plasma coalescence model [15] for a temperature parameter of $T=400$ MeV and charm rapidity widths of $\Delta y=1.0, 2.0, 3.0, 4.0$, from the highest to the lowest curve, respectively.

VIII. SUMMARY

PHENIX has shown first results on J/ψ production in Au-Au collisions at $\sqrt{s_{NN}}=200$ GeV at midrapidity as measured via electron-positron pairs. We find that models that predict J/ψ enhancement relative to binary collision scaling are disfavored, while we cannot discriminate between various scenarios leading to suppression relative to binary scaling.

This first measurement from PHENIX will be followed with high statistics measurements in both the electron channel at midrapidity and at forward and backward rapidities in the PHENIX muon spectrometers. Such measurements are expected in the next few years and will address the full range of heavy quarkonia production and evolution models.

ACKNOWLEDGMENTS

We thank the staff of the Collider-Accelerator and Physics Departments at Brookhaven National Laboratory and the staff of the other PHENIX participating institutions for their vital contributions. We acknowledge support from the Department of Energy, Office of Science, Nuclear Physics Division, the National Science Foundation, Abilene Christian University Research Council, Research Foundation of SUNY, and Dean of the College of Arts and Sciences, Vanderbilt University (USA), Ministry of Education, Culture, Sports, Science, and Technology and the Japan Society for the Promotion of Science (Japan), Conselho Nacional de Desenvolvimento Científico e Tecnológico and Fundação de Amparo à Pesquisa do Estado de São Paulo (Brazil), Natural Science Foundation of China (People's Republic of China), IN2P3/CNRS and Commissariat a l'Energie Atomique (France), Bundesministerium fuer Bildung und Forschung, Deutscher Akademischer Austausch Dienst, and Alexander von Humboldt Stiftung (Germany), Hungarian National Science Fund, OTKA (Hungary), Department of Atomic Energy and Department of Science and Technology (India), Israel Science Foundation (Israel), Korea Research Foundation and Center for High Energy Physics (Korea), Russian Academy of Science, Ministry of Atomic Energy of Russian Federation, Ministry of Industry, Science, and Technologies of Russian Federation (Russia), VR and the Wallenberg Foundation (Sweden), the U.S. Civilian Research and Development Foundation for the Independent States of the Former Soviet Union, the U.S.-Hungarian NSF-OTKA-MTA, the U.S.-Israel Binational Science Foundation, and the 5th European Union TMR Marie-Curie Programme.

[1] T. Matsui and H. Satz, Phys. Lett. B **178**, 416 (1986).
[2] F. Karsch, Lect. Notes Phys. **583**, 209 (2002).
[3] M. C. Abreu *et al.*, NA50 Collaboration, Phys. Lett. B **477**, 28 (2000); M. C. Abreu *et al.*, NA50 Collaboration, *ibid.* **521**, 195 (2001).
[4] M. Leitch *et al.*, E866-FNAL Collaboration, Phys. Rev. Lett. **84**, 3256 (2000).
[5] F. Arleo *et al.*, Phys. Rev. C **61**, 054906 (2000).
[6] D. Kharzeev *et al.*, Z. Phys. C **74**, 307 (1997).
[7] H. Fujii and T. Matsui, Phys. Lett. B **545**, 82 (2002).
[8] J. P. Blaizot, P. M. Dinh, and J. Y. Ollitrault, Phys. Rev. Lett. **85**, 4012 (2000).
[9] X.-M. Xu, C.-Y. Wong, and T. Barnes, Phys. Rev. C **67**, 014907 (2003); T. Barnes, E. S. Swanson, C.-Y. Wong, and X.-M. Xu, *ibid.* **68**, 014903 (2003).
[10] N. Armesto *et al.*, Nucl. Phys. **A698**, 583 (2002); A. Capella and D. Sousa, nucl-th/0303055.
[11] J. Qiu, J. P. Vary, and X. Zhang, Phys. Rev. Lett. **88**, 232301 (2002).
[12] A. K. Chaudhuri, nucl-th/0207082.
[13] K. Adcox *et al.*, Phys. Rev. Lett. **88**, 192303 (2002).
[14] R. Averbeck *et al.*, PHENIX Collaboration, Nucl. Phys. **A715**, 252c (2003).
[15] R. L. Thews, M. Schroedter, and J. Rafelski, Phys. Rev. C **63**, 054905 (2001); R. L. Thews (unpublished).
[16] L. Grandchamp and R. Rapp, Nucl. Phys. **A709**, 415 (2002); Phys. Lett. B **523**, 60 (2001).
[17] A. Andronic *et al.*, nucl-th/0303036.
[18] N. Hammon *et al.*, Phys. Rev. C **59**, 2744 (1999).
[19] K. Adcox, Nucl. Instrum. Methods Phys. Res. A **499**, 469

(2003).
[20] M. Chiu *et al.*, Phys. Rev. Lett. **89**, 012302 (2002).
[21] S. S. Adler *et al.*, Phys. Rev. Lett. **91**, 072301 (2003).
[22] J. T. Mitchell *et al.*, Nucl. Instrum. Methods Phys. Res. A **482**, 491 (2002).
[23] Y. Akiba *et al.*, Nucl. Instrum. Methods Phys. Res. A **433**, 143 (1999).
[24] S. S. Adler *et al.*, hep-ex/0307019.
[25] Particle Data Group, K. Hagiwara *et al.*, Phys. Rev. D **66**, 010001 (2002).
[26] J. L. Nagle *et al.*, PHENIX Collaboration, Nucl. Phys. **A715**, 695c (2003).
[27] PHENIX Collaboration (unpublished).
[28] C. H. Jaroschek, Masters thesis, State University of New York at Stony Brook, 2001.
[29] M. H. Schub *et al.*, Phys. Rev. D **52**, 1307 (1995).
[30] B. Alessandro *et al.*, NA50 Collaboration, Phys. Lett. B **553**, 167 (2003).
[31] J. L. Nagle and M. J. Bennett, Phys. Lett. B **465**, 21 (1999).
[32] S. Digal *et al.*, Phys. Lett. B **549**, 101 (2002).

Elliptic Flow of Identified Hadrons in Au + Au Collisions at $\sqrt{s_{NN}} = 200$ GeV

S. S. Adler,[5] S. Afanasiev,[17] C. Aidala,[5] N. N. Ajitanand,[43] Y. Akiba,[20,38] J. Alexander,[43] R. Amirikas,[12] L. Aphecetche,[45] S. H. Aronson,[5] R. Averbeck,[44] T. C. Awes,[35] R. Azmoun,[44] V. Babintsev,[15] A. Baldisseri,[10] K. N. Barish,[6] P. D. Barnes,[27] B. Bassalleck,[33] S. Bathe,[30] S. Batsouli,[9] V. Baublis,[37] A. Bazilevsky,[39,15] S. Belikov,[16,15] Y. Berdnikov,[40] S. Bhagavatula,[16] J. G. Boissevain,[27] H. Borel,[10] S. Borenstein,[25] M. L. Brooks,[27] D. S. Brown,[34] N. Bruner,[33] D. Bucher,[30] H. Buesching,[30] V. Bumazhnov,[15] G. Bunce,[5,39] J. M. Burward-Hoy,[26,44] S. Butsyk,[44] X. Camard,[45] J.-S. Chai,[18] P. Chand,[4] W. C. Chang,[2] S. Chernichenko,[15] C. Y. Chi,[9] J. Chiba,[20] M. Chiu,[9] I. J. Choi,[52] J. Choi,[19] R. K. Choudhury,[4] T. Chujo,[5] V. Cianciolo,[35] Y. Cobigo,[10] B. A. Cole,[9] P. Constantin,[16] D. G. d'Enterria,[45] G. David,[5] H. Delagrange,[45] A. Denisov,[15] A. Deshpande,[39] E. J. Desmond,[5] O. Dietzsch,[41] O. Drapier,[25] A. Drees,[44] R. du Rietz,[29] A. Durum,[15] D. Dutta,[4] Y. V. Efremenko,[35] K. El Chenawi,[49] A. Enokizono,[14] H. En'yo,[38,39] S. Esumi,[48] L. Ewell,[5] D. E. Fields,[33,39] F. Fleuret,[25] S. L. Fokin,[23] B. D. Fox,[39] Z. Fraenkel,[51] J. E. Frantz,[9] A. Franz,[5] A. D. Frawley,[12] S.-Y. Fung,[6] S. Garpman,[29,*] T. K. Ghosh,[49] A. Glenn,[46] G. Gogiberidze,[46] M. Gonin,[25] J. Gosset,[10] Y. Goto,[39] R. Granier de Cassagnac,[25] N. Grau,[16] S. V. Greene,[49] M. Grosse Perdekamp,[39] W. Guryn,[5] H.-Å. Gustafsson,[29] T. Hachiya,[14] J. S. Haggerty,[5] H. Hamagaki,[8] A. G. Hansen,[27] E. P. Hartouni,[26] M. Harvey,[5] R. Hayano,[8] X. He,[13] M. Heffner,[26] T. K. Hemmick,[44] J. M. Heuser,[44] M. Hibino,[50] J. C. Hill,[16] W. Holzmann,[43] K. Homma,[14] B. Hong,[22] A. Hoover,[34] T. Ichihara,[38,39] V. V. Ikonnikov,[23] K. Imai,[24,38] L. D. Isenhower,[1] M. Ishihara,[38] M. Issah,[43] A. Isupov,[17] B. V. Jacak,[44] W. Y. Jang,[22] Y. Jeong,[19] J. Jia,[44] O. Jinnouchi,[38] B. M. Johnson,[5] S. C. Johnson,[26] K. S. Joo,[31] D. Jouan,[36] S. Kametani,[8,50] N. Kamihara,[47,38] J. H. Kang,[52] S. S. Kapoor,[4] K. Katou,[50] S. Kelly,[9] B. Khachaturov,[51] A. Khanzadeev,[37] J. Kikuchi,[50] D. H. Kim,[31] D. J. Kim,[52] D. W. Kim,[19] E. Kim,[42] G.-B. Kim,[25] H. J. Kim,[52] E. Kistenev,[5] A. Kiyomichi,[48] K. Kiyoyama,[32] C. Klein-Boesing,[30] H. Kobayashi,[38,39] L. Kochenda,[37] V. Kochetkov,[15] D. Koehler,[33] T. Kohama,[14] M. Kopytine,[44] D. Kotchetkov,[6] A. Kozlov,[51] P. J. Kroon,[5] C. H. Kuberg,[1,27] K. Kurita,[39] Y. Kuroki,[48] M. J. Kweon,[22] Y. Kwon,[52] G. S. Kyle,[34] R. Lacey,[43] V. Ladygin,[17] J. G. Lajoie,[16] A. Lebedev,[16,23] S. Leckey,[44] D. M. Lee,[27] S. Lee,[19] M. J. Leitch,[27] X. H. Li,[6] H. Lim,[42] A. Litvinenko,[17] M. X. Liu,[27] Y. Liu,[36] C. F. Maguire,[49] Y. I. Makdisi,[5] A. Malakhov,[17] V. I. Manko,[23] Y. Mao,[7,38] G. Martinez,[45] M. D. Marx,[44] H. Masui,[48] F. Matathias,[44] T. Matsumoto,[8,50] P. L. McGaughey,[27] E. Melnikov,[15] F. Messer,[44] Y. Miake,[48] J. Milan,[43] T. E. Miller,[49] A. Milov,[44,51] S. Mioduszewski,[5] R. E. Mischke,[27] G. C. Mishra,[13] J. T. Mitchell,[5] A. K. Mohanty,[4] D. P. Morrison,[5] J. M. Moss,[27] F. Mühlbacher,[44] D. Mukhopadhyay,[51] M. Muniruzzaman,[6] J. Murata,[38,39] S. Nagamiya,[20] J. L. Nagle,[9] T. Nakamura,[14] B. K. Nandi,[6] M. Nara,[48] J. Newby,[46] P. Nilsson,[29] A. S. Nyanin,[23] J. Nystrand,[29] E. O'Brien,[5] C. A. Ogilvie,[16] H. Ohnishi,[5,38] I. D. Ojha,[49,3] K. Okada,[38] M. Ono,[48] V. Onuchin,[15] A. Oskarsson,[29] I. Otterlund,[29] K. Oyama,[8] K. Ozawa,[8] D. Pal,[51] A. P. T. Palounek,[27] V. S. Pantuev,[44] V. Papavassiliou,[34] J. Park,[42] A. Parmar,[33] S. F. Pate,[34] T. Peitzmann,[30] J.-C. Peng,[27] V. Peresedov,[17] C. Pinkenburg,[5] R. P. Pisani,[5] F. Plasil,[35] M. L. Purschke,[5] A. Purwar,[44] J. Rak,[16] I. Ravinovich,[51] K. F. Read,[35,46] M. Reuter,[44] K. Reygers,[30] V. Riabov,[37,40] Y. Riabov,[37] G. Roche,[28] A. Romana,[25] M. Rosati,[16] P. Rosnet,[28] S. S. Ryu,[52] M. E. Sadler,[1] N. Saito,[38,39] T. Sakaguchi,[8,50] M. Sakai,[32] S. Sakai,[48] V. Samsonov,[37] L. Sanfratello,[33] R. Santo,[30] H. D. Sato,[24,38] S. Sato,[5,48] S. Sawada,[20] Y. Schutz,[45] V. Semenov,[15] R. Seto,[6] M. R. Shaw,[1,27] T. K. Shea,[5] T.-A. Shibata,[47,38] K. Shigaki,[14,20] T. Shiina,[27] C. L. Silva,[41] D. Silvermyr,[27,29] K. S. Sim,[22] C. P. Singh,[3] V. Singh,[3] M. Sivertz,[5] A. Soldatov,[15] R. A. Soltz,[26] W. E. Sondheim,[27] S. P. Sorensen,[46] I. V. Sourikova,[5] F. Staley,[10] P. W. Stankus,[35] E. Stenlund,[29] M. Stepanov,[34] A. Ster,[21] S. P. Stoll,[5] T. Sugitate,[14] J. P. Sullivan,[27] E. M. Takagui,[41] A. Taketani,[38,39] M. Tamai,[50] K. H. Tanaka,[20] Y. Tanaka,[32] K. Tanida,[38] M. J. Tannenbaum,[5] P. Tarján,[11] J. D. Tepe,[1,27] T. L. Thomas,[33] J. Tojo,[24,38] H. Torii,[24,38] R. S. Towell,[1] I. Tserruya,[51] H. Tsuruoka,[48] S. K. Tuli,[3] H. Tydesjö,[29] N. Tyurin,[15] H. W. van Hecke,[27] J. Velkovska,[5,44] M. Velkovsky,[44] L. Villatte,[46] A. A. Vinogradov,[23] M. A. Volkov,[23] E. Vznuzdaev,[37] X. R. Wang,[13] Y. Watanabe,[38,39] S. N. White,[5] F. K. Wohn,[16] C. L. Woody,[5] W. Xie,[6] Y. Yang,[7] A. Yanovich,[15] S. Yokkaichi,[38,39] G. R. Young,[35] I. E. Yushmanov,[23] W. A. Zajc,[9,†] C. Zhang,[9] S. Zhou,[7,51] and L. Zolin[17]

(PHENIX Collaboration)

[1]*Abilene Christian University, Abilene, Texas 79699, USA*
[2]*Institute of Physics, Academia Sinica, Taipei 11529, Taiwan*
[3]*Department of Physics, Banaras Hindu University, Varanasi 221005, India*
[4]*Bhabha Atomic Research Centre, Bombay 400 085, India*

 0031-9007/03/91(18)/182301(6)$20.00 © 2003 The American Physical Society

[5]*Brookhaven National Laboratory, Upton, New York 11973-5000, USA*
[6]*University of California–Riverside, Riverside, California 92521, USA*
[7]*China Institute of Atomic Energy (CIAE), Beijing, People's Republic of China*
[8]*Center for Nuclear Study, Graduate School of Science, University of Tokyo, 7-3-1 Hongo, Bunkyo, Tokyo 113-0033, Japan*
[9]*Columbia University, New York, NY 10027*
and Nevis Laboratories, Irvington, New York 10533, USA
[10]*Dapnia, CEA Saclay, Bâtiment 703, F-91191, Gif-sur-Yvette, France*
[11]*Debrecen University, H-4010 Debrecen, Egyetem tér 1, Hungary*
[12]*Florida State University, Tallahassee, Florida 32306, USA*
[13]*Georgia State University, Atlanta, Georgia 30303, USA*
[14]*Hiroshima University, Kagamiyama, Higashi-Hiroshima 739-8526, Japan*
[15]*Institute for High Energy Physics (IHEP), Protvino, Russia*
[16]*Iowa State University, Ames, Iowa 50011, USA*
[17]*Joint Institute for Nuclear Research, 141980 Dubna, Moscow Region, Russia*
[18]*KAERI, Cyclotron Application Laboratory, Seoul, South Korea*
[19]*Kangnung National University, Kangnung 210-702, South Korea*
[20]*KEK, High Energy Accelerator Research Organization, Tsukuba-shi, Ibaraki-ken 305-0801, Japan*
[21]*KFKI Research Institute for Particle and Nuclear Physics (RMKI), H-1525 Budapest 114, POBox 49, Hungary*
[22]*Korea University, Seoul, 136-701, Korea*
[23]*Russian Research Center "Kurchatov Institute," Moscow, Russia*
[24]*Kyoto University, Kyoto 606, Japan*
[25]*Laboratoire Leprince-Ringuet, Ecole Polytechnique, CNRS-IN2P3, Route de Saclay, F-91128, Palaiseau, France*
[26]*Lawrence Livermore National Laboratory, Livermore, California 94550, USA*
[27]*Los Alamos National Laboratory, Los Alamos, New Mexico 87545, USA*
[28]*LPC, Université Blaise Pascal, CNRS-IN2P3, Clermont-Fd, 63177 Aubiere Cedex, France*
[29]*Department of Physics, Lund University, Box 118, SE-221 00 Lund, Sweden*
[30]*Institut für Kernphysik, University of Muenster, D-48149 Muenster, Germany*
[31]*Myongji University, Yongin, Kyonggido 449-728, Korea*
[32]*Nagasaki Institute of Applied Science, Nagasaki-shi, Nagasaki 851-0193, Japan*
[33]*University of New Mexico, Albuquerque, New Mexico 87131, USA*
[34]*New Mexico State University, Las Cruces, New Mexico 88003, USA*
[35]*Oak Ridge National Laboratory, Oak Ridge, Tennessee 37831, USA*
[36]*IPN-Orsay, Universite Paris Sud, CNRS-IN2P3, BP1, F-91406, Orsay, France*
[37]*PNPI, Petersburg Nuclear Physics Institute, Gatchina, Russia*
[38]*RIKEN (The Institute of Physical and Chemical Research), Wako, Saitama 351-0198, Japan*
[39]*RIKEN BNL Research Center, Brookhaven National Laboratory, Upton, New York 11973-5000, USA*
[40]*St. Petersburg State Technical University, St. Petersburg, Russia*
[41]*Universidade de São Paulo, Instituto de Física, Caixa Postal 66318, São Paulo CEP05315-970, Brazil*
[42]*System Electronics Laboratory, Seoul National University, Seoul, South Korea*
[43]*Chemistry Department, Stony Brook University, SUNY, Stony Brook, New York 11794-3400, USA*
[44]*Department of Physics and Astronomy, Stony Brook University, SUNY, Stony Brook, New York 11794, USA*
[45]*SUBATECH (Ecole des Mines de Nantes, CNRS-IN2P3, Université de Nantes) BP 20722 - 44307, Nantes, France*
[46]*University of Tennessee, Knoxville, Tennessee 37996, USA*
[47]*Department of Physics, Tokyo Institute of Technology, Tokyo, 152-8551, Japan*
[48]*Institute of Physics, University of Tsukuba, Tsukuba, Ibaraki 305, Japan*
[49]*Vanderbilt University, Nashville, Tennessee 37235, USA*
[50]*Waseda University, Advanced Research Institute for Science and Engineering, 17 Kikui-cho, Shinjuku-ku, Tokyo 162-0044, Japan*
[51]*Weizmann Institute, Rehovot 76100, Israel*
[52]*Yonsei University, IPAP, Seoul 120-749, Korea*
(Received 16 May 2003; published 30 October 2003)

The anisotropy parameter (v_2), the second harmonic of the azimuthal particle distribution, has been measured with the PHENIX detector in Au + Au collisions at $\sqrt{s_{NN}} = 200$ GeV for identified and inclusive charged particle production at central rapidities ($|\eta| < 0.35$) with respect to the reaction plane defined at high rapidities ($|\eta| = 3$–4). We observe that the v_2 of mesons falls below that of (anti)-baryons for $p_T > 2$ GeV/c, in marked contrast to the predictions of a hydrodynamical model. A quark-coalescence model is also investigated.

DOI: 10.1103/PhysRevLett.91.182301 PACS numbers: 25.75.Dw

Event anisotropy is expected to be sensitive to the early stage of ultrarelativistic nuclear collisions at the BNL Relativistic Heavy Ion Collider (RHIC). The possible formation of a quark-gluon plasma could affect how the initial anisotropy in coordinate space is transferred into momentum space in the final state. The anisotropy parameter

v_2 for a selection of produced particles is derived from the azimuthal distribution of those particles.

$$\frac{dN}{d\phi} \propto 1 + 2v_2 \cos 2(\phi - \Phi_{\mathrm{RP}}), \quad (1)$$

where ϕ is the azimuthal direction of the particle and Φ_{RP} is the direction of the nuclear impact parameter ("reaction plane") in a given collision. Measurements of the parameter v_2 in RHIC collisions have been performed [1–6] for charged particles and for identified particles. The current work reports results for charged particles versus transverse momentum (p_T) out to 5 GeV/c, and extends previous measurements for identified particles out to 3 GeV/c for π and K, and to 4 GeV/c for protons. (Previous measurements of the v_2 for π, K, and p extended to 1 GeV/c at $\sqrt{s_{NN}} = 130$ GeV[2].) Detailed measurements of the azimuthal anisotropy are important to eventually discriminate among different possible scenarios for its physical origin. Such scenarios include hydrodynamical flow of compressed hadronic matter, the production of multiple minijets, and an anisotropy developed during an early quark-matter phase of the collision. It has been observed that v_2 saturates at $p_T \sim 2$ GeV/c and above [4,5]. The cause of this saturation is not yet known; however, we note that at this momentum the particle composition is very different than at low momentum in that the proton yield is comparable to the pion yield [7]. This makes the measurement of v_2 for separately identified particles especially interesting.

The measurements described here were carried out in the PHENIX experiment at RHIC [8]. About 28×10^6 minimum-bias Au + Au collisions at $\sqrt{s_{NN}} = 200$ GeV from the 2001–2002 run period (Run-2) are used in the analysis. Charged particles are measured in the central arm spectrometers ($|\eta| < 0.35$) [9] where PHENIX has excellent particle identification capabilities[10]. The drift chamber and the first pad chamber plane (PC1) together with the collision vertex define the charged particle tracks. In order to reduce background, the reconstructed tracks are confirmed by requiring matching hits in the outer detectors, i.e., the third pad chamber plane (PC3) and the electromagnetic calorimeter or the time-of-flight detector (TOF). In this analysis, the TOF detector is used to identify charged particles up to 4 GeV/c in p_T. Particle time-of-flight is measured using the TOF with respect to the collision time defined by beam counters (BBC), and is used to calculate mass squared using the particle momentum and the flight path length [7]. The timing resolution of the system is $\simeq 120$ ps. A momentum dependent $\pm 2\sigma$ cut on mass squared allows particle identification in the following p_T ranges: $0.2 < p_T < 3$ GeV/c for pions, $0.3 < p_T < 3$ GeV/c for kaons, and $0.5 < p_T < 4$ GeV/c for protons. The contamination of misidentified particles is less than 10%. In addition to collision time, the BBC provide z-vertex position information. The two beam counters are located at $|z| = 1.5$ m from the collision point, covering $|\eta| = 3$–4. They consist of 64 photomultiplier tubes (PMT) equipped with quartz Cherenkov radiators in front surrounding the beam pipe. The large charged multiplicity (a few hundred) in $|\eta| = 3$–4 and the nonzero signal of event anisotropy in this η range enable us to estimate the azimuthal angle of the reaction plane in each event using the BBC with full azimuthal angle coverage.

Since the v_2 parameter is in effect a quadrupole moment, the anisotropy which gives rise to a nonzero v_2 is often referred to as an "elliptic flow." It is extracted by first determining the reaction plane angle Φ_{RP} for each event,

$$\tan 2\Phi_{\mathrm{RP}} = \frac{\Sigma n_{\mathrm{ch}} \sin 2\phi_{\mathrm{PMT}}}{\Sigma n_{\mathrm{ch}} \cos 2\phi_{\mathrm{PMT}}}, \quad (2)$$

where n_{ch} is the number of charged particles per PMT (determined from the pulse height in each PMT) and ϕ_{PMT} is the azimuthal angle of each PMT. Then, it is calculated by the Fourier moment $v_2 = \langle \cos 2(\phi - \Phi_{\mathrm{RP}}) \rangle$ over all particles, for all events in a given sample [11]. Corrections [11–14] are applied to account for finite resolution in the reaction plane determination, and for possible azimuthal asymmetries in the reaction plane detector response. The bottom-left panel in Fig. 1 shows the average cosine of the difference between the two reaction planes defined by the beam counters at $\eta = 3$–4 and at $\eta = -4$–-3 using the elliptic (second) moment definition. In order to improve the reaction plane resolution, a combined reaction plane is defined by averaging the reaction plane angles obtained from each BBC, using the elliptic moment in each. The estimated resolution of the combined reaction plane [11], $\langle \cos 2(\Phi_{\mathrm{meas}} - \Phi_{\mathrm{true}}) \rangle$, has an average of 0.3 over centrality with a maximum of about 0.4. The estimated correction factor, which is the inverse of the resolution

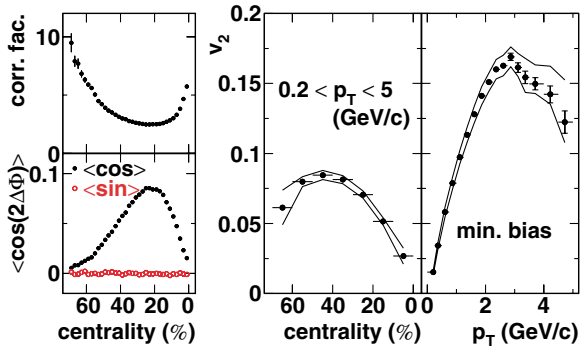

FIG. 1 (color online). Correlation of reaction planes between two beam counters for the second moment is shown as a function of centrality (bottom-left panel) and the correction factor for the combined reaction plane resolution of two beam counters is shown as a function of centrality (top-left panel). The value of v_2 for charged particles is shown as a function of centrality (middle panel) and as a function of p_T (right panel).

for the combined reaction plane, is shown in the top-left panel in Fig. 1.

The present technique is distinguished by defining the reaction plane angle using particles at high rapidity when measuring v_2 for particles at midrapidity. Other measurements of v_2 for midrapidity particles at RHIC have used reaction planes defined with midrapidity particles, or have employed a technique of measuring angular correlations between pairs of particles at midrapidity. While these different approaches generally seek to measure the same thing, they are not identical and a variety of physics effects can cause them to yield different results from the same collision sample [4,15,16]. Because of the large rapidity gap between the reaction plane and the midrapidity acceptance of about three units, it is expected that this analysis is less affected by nonflow contributions. However, we do not observe any substantial difference between the v_2 results shown here and published results for the v_2 of charged particles at RHIC in the p_T range where they are available.

The centrality of each collision is defined using the simultaneous measurement of the total number of particles measured in the BBC and the total energy measured in the zero degree calorimeter [17]. The middle panel in Fig. 1 shows the centrality dependence of v_2 for charged particles measured at midrapidity ($|\eta| < 0.35$) with respect to the reaction plane defined above. The centrality is measured in percentile from the most central collision. The v_2 parameter decreases for both peripheral and central collisions with a maximum at about 50% of the geometric cross section. Beyond 70%, the correction factor due to the reaction plane resolution is large, as shown in the leftmost panel in Fig. 1. This limits the centrality range used in this analysis.

The rightmost panel in Fig. 1 shows the transverse momentum dependence of v_2 for charged particles with respect to the reaction plane for minimum-bias events. The data above a p_T of 2 GeV/c clearly show a deviation from the monotonically increasing behavior seen at smaller p_T. The systematic errors are shown as line bands, which are estimated by several reaction plane methods using the two single beam counters or combined beam counters and by several different ways to correct nonuniform reaction plane distribution: "inverse weighting," "recentering of sine and cosine summation," "Fourier expansion," and combinations of those above [11,18]. Those systematic errors are estimated to be about 10%, depending on centrality, and are independent of p_T. Above 3 GeV/c, background tracks result in an additional systematic error of about 10%, depending on p_T, which is included in the upper error band [19].

In Fig. 2, the transverse momentum dependence of v_2 for identified particles is shown. The top-left panel shows negatively charged particles, while the top-right panel shows positively charged particles as described in the figure caption. The statistical errors and the systematic errors are plotted independently. From the lambda particle spectra measured in the PHENIX central arm, it is determined that approximately 35% of the protons originate from lambda decays ("lambda feed-down")[22]. The effect of the lambda feed-down on the measured v_2 of the proton is studied by varying the lambda v_2 with Monte Carlo simulation. Protons resulting from lambda feed-down increase the measured v_2 value. Using the value of the lambda v_2 measured at $\sqrt{s_{NN}} = 130$ GeV at RHIC [3], the effect on the proton v_2 would be less than 10%. Less than 5% of protons originate from decays of particles not involving the lambda. Based on further simulations of their decays to protons, we estimate that the total systematic error due to feed-down is at most 11% depending on p_T, which is included in the lower systematic error band in Fig. 2.

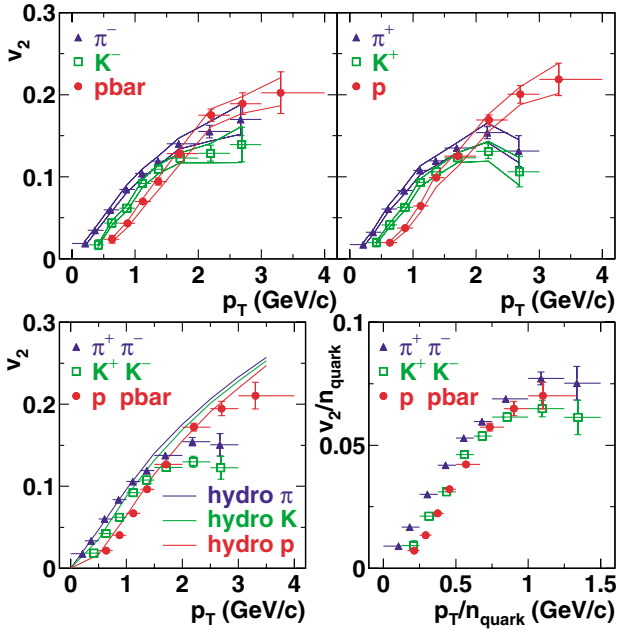

FIG. 2 (color online). Transverse momentum dependence of v_2 for identified particles, π^-, K^-, $\overline{p}$ (top-left panel) and π^+, K^+, p (top-right panel). The circles show p and $\overline{p}$, the squares show K^+ and K^-, and the triangles show π^+ and π^- for minimum-bias events. Statistical errors are represented by error bars and overall systematic error due to all sources by the solid lines in the top two panels. The combined positive particles and negative particles are shown in the bottom-left panel, and the lines there represent the result of a hydrodynamical calculation [20] including a first-order phase transition with a freeze-out temperature of 120 MeV for π, K, and p from upper to lower curves, respectively. The bottom-right panel shows the quark v_2 as a function of the quark p_T by scaling both axes with the number of quarks for each particle, as motivated by a quark-coalescence model [21].

The combined positive and negative particles are shown in the bottom-left panel. The lines in that panel represent a hydrodynamical calculation [20] including a first-order phase transition with a freeze-out temperature of 120 MeV. The data show that at lower p_T (<2 GeV/c), the lighter mass particles have a larger v_2 at a given p_T,

which is reproduced by the model calculations. We note, however, that the difference between the charged kaons and charged pions is larger than the model predicts.

A striking feature observed at higher p_T is that the v_2 of p and $\overline{p}$ are larger than for π and K at $p_T > 2$ GeV/c. This is in sharp contrast to the hydrodynamical picture, which would predict the same mass ordering for v_2 at all p_T. In our data the mesons begin to show a departure from the hydrodynamical prediction at p_T of about 1.5 GeV/c, while the (anti)baryons agree with the prediction up until 3 GeV/c but may be deviating at higher p_T. Such behavior is predicted by the quark-coalescence mechanism [21], as shown in the bottom-right panel where both v_2 and p_T have been scaled by the number of quarks. This could be an indication that the v_2 of measured hadrons is already established in a quark-matter phase, although it does not explain why the quark v_2 would saturate with p_T. There exist other scenarios that could be applicable at RHIC, but we have selected two simple models (hydrodynamical and quark coalescence) only to emphasize the experimental evidence of the crossing of v_2 for mesons and baryons.

As an additional illustration of the different behavior for mesons and baryons, the transverse momentum dependences of the v_2 parameter are shown in Fig. 3 for different particles and different centralities. Since the particle identification separation of K and p goes up to 4 GeV/c, the combined π and K can be compared with protons up to 4 GeV/c. The charged particle acceptance is larger than the TOF acceptance where the particle identification can be performed. Therefore, the statistical fluctuations for the charged particle v_2 are smaller than for the p, $\overline{p}$, and $\pi + K$. The trend exhibited in Fig. 2 for minimum-bias spectra, in which the v_2 for (anti)-baryons exceed those for mesons at $p_T > 2$ GeV/c, is shown here to occur for all centralities.

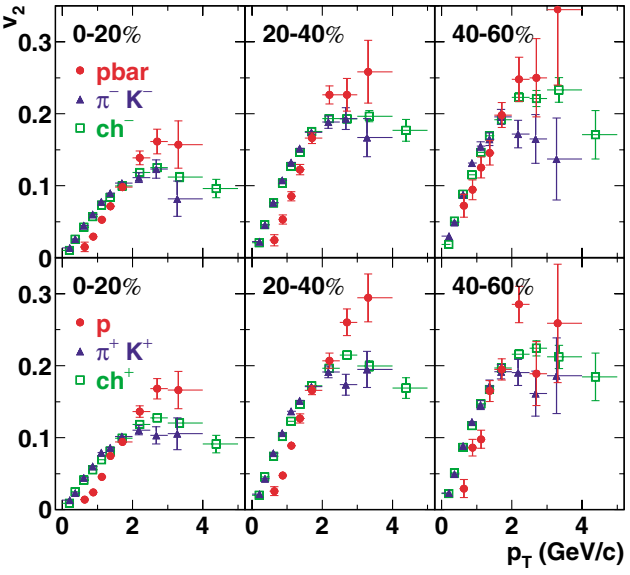

FIG. 3 (color online). Transverse momentum dependence of v_2 for combined π^- and K^- (top) or π^+ and K^+ (bottom) compared with $\overline{p}$ (top) and p (bottom). In addition, results for inclusive negative (top) and positive (bottom) charged particle distributions are plotted as open squares. From left to right, the different centrality selections are shown for 0%–20% (left), 20%–40% (middle), and 40%–60% (right).

In summary, the value of the v_2 parameter for identified and inclusive charged particle production at midrapidity has been measured with respect to the reaction plane defined in the forward and backward rapidity regions in $\sqrt{s_{NN}} = 200$ GeV Au + Au collisions, using the PHENIX experiment at RHIC. The value of v_2 for charged particles decreases for both peripheral and central collisions with a maximum at about the 50th percentile of the geometric cross section. We have observed that for charged particles v_2 increases with p_T up to about 2 GeV/c, then starts to saturate or decrease slightly. However, the detailed behavior is different for different particle species. The lighter particles have larger v_2 than the heavier particles for p_T below 2 GeV/c. This trend is partly reversed above 2 GeV/c where the proton and antiproton have larger v_2 than mesons, a pattern which persists over all centralities. A hydrodynamical calculation can reproduce the mass ordering and magnitude of v_2 for the different particles in the region up to 2 GeV/c, but fails to reproduce either in the p_T region above 2 GeV/c. As an alternative, we investigated the quark-coalescence scenario, in which the anisotropy of the final-state hadrons is largely inherited from the anisotropy of quarks in a preceding quark-matter phase. The quark-coalescence model makes a definite prediction for a simple scaling behavior between the v_2 for mesons and for (anti)baryons, and this scaling behavior is largely, though not perfectly, borne out in our data. Further measurements extending to higher p_T involving more identified species will be required to discriminate among alternative scenarios for the origin of elliptic flow at RHIC.

We thank the staff of the Collider-Accelerator and Physics Departments at BNL for their vital contributions. We acknowledge support from the Department of Energy and NSF (U.S.A.), MEXT and JSPS (Japan), CNPq and FAPESP (Brazil), NSFC (China), CNRS-IN2P3 and CEA (France), BMBF, DAAD, and AvH (Germany), OTKA (Hungary), DAE and DST (India), ISF (Israel), KRF and CHEP (Korea), RAS, RMAE, and RMS (Russia), VR and KAW (Sweden), U.S. CRDF for the FSU, US-Hungarian NSF-OTKA-MTA, and US-Israel BSF.

*Deceased.
†Spokesperson: zajc@nevis.columbia.edu

[1] K. H. Ackermann *et al.*, Phys. Rev. Lett. **86**, 402 (2001).
[2] C. Adler *et al.*, Phys. Rev. Lett. **87**, 182301 (2001).
[3] C. Adler *et al.*, Phys. Rev. Lett. **89**, 132301 (2002).
[4] C. Adler *et al.*, Phys. Rev. C **66**, 034904 (2002).

[5] C. Adler *et al.*, Phys. Rev. Lett. **90**, 032301 (2003).
[6] K. Adcox *et al.*, Phys. Rev. Lett. **89**, 212301 (2002).
[7] K. Adcox *et al.*, Phys. Rev. Lett. **88**, 242301 (2002).
[8] K. Adcox *et al.*, Nucl. Instrum. Methods Phys. Res., Sect. A **499**, 469 (2003).
[9] J. T. Mitchell *et al.*, Nucl. Instrum. Methods Phys. Res., Sect. A **482**, 491 (2002).
[10] H. Hamagaki *et al.*, Nucl. Phys. **A698**, 412 (2002).
[11] A. Poskanzer and S. Voloshin, Phys. Rev. C **58**, 1671 (1998).
[12] J. Barrette *et al.*, Phys. Rev. Lett. **73**, 2532 (1994).
[13] J. Barrette *et al.*, Phys. Rev. C **55**, 1420 (1997).
[14] J. Barrette *et al.*, Phys. Rev. C **56**, 3254 (1997).
[15] N. Borghini, P. M. Dinh, and J. Y. Ollitrault, Phys. Rev. C **63**, 054906 (2001).
[16] N. Borghini, P. M. Dinh, and J. Y. Ollitrault, Phys. Rev. C **64**, 054901 (2001).
[17] K. Adcox *et al.*, Phys. Rev. Lett. **86**, 3500 (2001).
[18] S. Esumi *et al.*, Nucl. Phys. **A715**, 599 (2003).
[19] K. Adcox *et al.*, Phys. Rev. Lett. **88**, 022301 (2002).
[20] P. Huovinen, P. F. Kolb, U. W. Heinz, P. V. Ruuskanen, and S. A. Voloshin, Phys. Lett. B **503**, 58 (2001).
[21] D. Molnar and S. Voloshin, nucl-th/0302014.
[22] K. Adcox *et al.*, Phys. Rev. Lett. **89**, 092302 (2002).

Suppressed π^0 Production at Large Transverse Momentum in Central Au + Au Collisions at $\sqrt{s_{NN}} = 200$ GeV

S. S. Adler,[5] S. Afanasiev,[17] C. Aidala,[5] N. N. Ajitanand,[43] Y. Akiba,[20,38] J. Alexander,[43] R. Amirikas,[12] L. Aphecetche,[45] S. H. Aronson,[5] R. Averbeck,[44] T. C. Awes,[35] R. Azmoun,[44] V. Babintsev,[15] A. Baldisseri,[10] K. N. Barish,[6] P. D. Barnes,[27] B. Bassalleck,[33] S. Bathe,[30] S. Batsouli,[9] V. Baublis,[37] A. Bazilevsky,[39,15] S. Belikov,[16,15] Y. Berdnikov,[40] S. Bhagavatula,[16] J. G. Boissevain,[27] H. Borel,[10] S. Borenstein,[25] M. L. Brooks,[27] D. S. Brown,[34] N. Bruner,[33] D. Bucher,[30] H. Buesching,[30] V. Bumazhnov,[15] G. Bunce,[5,39] J. M. Burward-Hoy,[26,44] S. Butsyk,[44] X. Camard,[45] J.-S. Chai,[18] P. Chand,[4] W. C. Chang,[2] S. Chernichenko,[15] C. Y. Chi,[9] J. Chiba,[20] M. Chiu,[9] I. J. Choi,[52] J. Choi,[19] R. K. Choudhury,[4] T. Chujo,[5] V. Cianciolo,[35] Y. Cobigo,[10] B. A. Cole,[9] P. Constantin,[16] D. G. d'Enterria,[45] G. David,[5] H. Delagrange,[45] A. Denisov,[15] A. Deshpande,[39] E. J. Desmond,[5] O. Dietzsch,[41] O. Drapier,[25] A. Drees,[44] K. A. Drees,[5] R. du Rietz,[29] A. Durum,[15] D. Dutta,[4] Y. V. Efremenko,[35] K. El Chenawi,[49] A. Enokizono,[14] H. En'yo,[38,39] S. Esumi,[48] L. Ewell,[5] D. E. Fields,[33,39] F. Fleuret,[25] S. L. Fokin,[23] B. D. Fox,[39] Z. Fraenkel,[51] J. E. Frantz,[9] A. Franz,[5] A. D. Frawley,[12] S.-Y. Fung,[6] S. Garpman,[29,*] T. K. Ghosh,[49] A. Glenn,[46] G. Gogiberidze,[46] M. Gonin,[25] J. Gosset,[10] Y. Goto,[39] R. Granier de Cassagnac,[25] N. Grau,[16] S. V. Greene,[49] M. Grosse Perdekamp,[39] W. Guryn,[5] H.-Å. Gustafsson,[29] T. Hachiya,[14] J. S. Haggerty,[5] H. Hamagaki,[8] A. G. Hansen,[27] E. P. Hartouni,[26] M. Harvey,[5] R. Hayano,[8] X. He,[13] M. Heffner,[26] T. K. Hemmick,[44] J. M. Heuser,[44] M. Hibino,[50] J. C. Hill,[16] W. Holzmann,[43] K. Homma,[14] B. Hong,[22] A. Hoover,[34] T. Ichihara,[38,39] V. V. Ikonnikov,[23] K. Imai,[24,38] L. Isenhower,[1] M. Ishihara,[38] M. Issah,[43] A. Isupov,[17] B. V. Jacak,[44] W. Y. Jang,[22] Y. Jeong,[19] J. Jia,[44] O. Jinnouchi,[38] B. M. Johnson,[5] S. C. Johnson,[26] K. S. Joo,[31] D. Jouan,[36] S. Kametani,[8,50] N. Kamihara,[47,38] J. H. Kang,[52] S. S. Kapoor,[4] K. Katou,[50] S. Kelly,[9] B. Khachaturov,[51] A. Khanzadeev,[37] J. Kikuchi,[50] D. H. Kim,[31] D. J. Kim,[52] D. W. Kim,[19] E. Kim,[42] G.-B. Kim,[25] H. J. Kim,[52] E. Kistenev,[5] A. Kiyomichi,[48] K. Kiyoyama,[32] C. Klein-Boesing,[30] H. Kobayashi,[38,39] L. Kochenda,[37] V. Kochetkov,[15] D. Koehler,[33] T. Kohama,[14] M. Kopytine,[44] D. Kotchetkov,[6] A. Kozlov,[51] P. J. Kroon,[5] C. H. Kuberg,[1,27] K. Kurita,[39] Y. Kuroki,[48] M. J. Kweon,[22] Y. Kwon,[52] G. S. Kyle,[34] R. Lacey,[43] V. Ladygin,[17] J. G. Lajoie,[16] A. Lebedev,[16,23] S. Leckey,[44] D. M. Lee,[27] S. Lee,[19] M. J. Leitch,[27] X. H. Li,[6] H. Lim,[42] A. Litvinenko,[17] M. X. Liu,[27] Y. Liu,[36] C. F. Maguire,[49] Y. I. Makdisi,[5] A. Malakhov,[17] V. I. Manko,[23] Y. Mao,[7,38] G. Martinez,[45] M. D. Marx,[44] H. Masui,[48] F. Matathias,[44] T. Matsumoto,[8,50] P. L. McGaughey,[27] E. Melnikov,[15] F. Messer,[44] Y. Miake,[48] J. Milan,[43] T. E. Miller,[49] A. Milov,[44,51] S. Mioduszewski,[5] R. E. Mischke,[27] G. C. Mishra,[13] J. T. Mitchell,[5] A. K. Mohanty,[4] D. P. Morrison,[5] J. M. Moss,[27] F. Mühlbacher,[44] D. Mukhopadhyay,[51] M. Muniruzzaman,[6] J. Murata,[38,39] S. Nagamiya,[20] J. L. Nagle,[9] T. Nakamura,[14] B. K. Nandi,[6] M. Nara,[48] J. Newby,[46] P. Nilsson,[29] A. S. Nyanin,[23] J. Nystrand,[29] E. O'Brien,[5] C. A. Ogilvie,[16] H. Ohnishi,[5,38] I. D. Ojha,[49,3] K. Okada,[38] M. Ono,[48] V. Onuchin,[15] A. Oskarsson,[29] I. Otterlund,[29] K. Oyama,[8] K. Ozawa,[8] D. Pal,[51] A. P. T. Palounek,[27] V. S. Pantuev,[44] V. Papavassiliou,[34] J. Park,[42] A. Parmar,[33] S. F. Pate,[34] T. Peitzmann,[30] J.-C. Peng,[27] V. Peresedov,[17] C. Pinkenburg,[5] R. P. Pisani,[5] F. Plasil,[35] M. L. Purschke,[5] A. K. Purwar,[44] J. Rak,[16] I. Ravinovich,[51] K. F. Read,[35,46] M. Reuter,[44] K. Reygers,[30] V. Riabov,[37,40] Y. Riabov,[37] G. Roche,[28] A. Romana,[25] M. Rosati,[16] P. Rosnet,[28] S. S. Ryu,[52] M. E. Sadler,[1] N. Saito,[38,39] T. Sakaguchi,[8,50] M. Sakai,[32] S. Sakai,[48] V. Samsonov,[37] L. Sanfratello,[33] R. Santo,[30] H. D. Sato,[24,38] S. Sato,[5,48] S. Sawada,[20] Y. Schutz,[45] V. Semenov,[15] R. Seto,[6] M. R. Shaw,[1,27] T. K. Shea,[5] T.-A. Shibata,[47,38] K. Shigaki,[14,20] T. Shiina,[27] C. L. Silva,[41] D. Silvermyr,[27,29] K. S. Sim,[22] C. P. Singh,[3] V. Singh,[3] M. Sivertz,[5] A. Soldatov,[15] R. A. Soltz,[26] W. E. Sondheim,[27] S. P. Sorensen,[46] I. V. Sourikova,[5] F. Staley,[10] P. W. Stankus,[35] E. Stenlund,[29] M. Stepanov,[34] A. Ster,[21] S. P. Stoll,[5] T. Sugitate,[14] J. P. Sullivan,[27] E. M. Takagui,[41] A. Taketani,[38,39] M. Tamai,[50] K. H. Tanaka,[20] Y. Tanaka,[32] K. Tanida,[38] M. J. Tannenbaum,[5] P. Tarján,[11] J. D. Tepe,[1,27] T. L. Thomas,[33] J. Tojo,[24,38] H. Torii,[24,38] R. S. Towell,[1] I. Tserruya,[51] H. Tsuruoka,[48] S. K. Tuli,[3] H. Tydesjö,[29] N. Tyurin,[15] H. W. van Hecke,[27] J. Velkovska,[5,44] M. Velkovsky,[44] L. Villatte,[46] A. A. Vinogradov,[23] M. A. Volkov,[23] E. Vznuzdaev,[37] X. R. Wang,[13] Y. Watanabe,[38,39] S. N. White,[5] F. K. Wohn,[16] C. L. Woody,[5] W. Xie,[6] Y. Yang,[7] A. Yanovich,[15] S. Yokkaichi,[38,39] G. R. Young,[35] I. E. Yushmanov,[23] W. A. Zajc,[9,†] C. Zhang,[9] S. Zhou,[7,51] and L. Zolin[17]

(PHENIX Collaboration)

[1]*Abilene Christian University, Abilene, Texas 79699, USA*
[2]*Institute of Physics, Academia Sinica, Taipei 11529, Taiwan*
[3]*Department of Physics, Banaras Hindu University, Varanasi 221005, India*

 0031-9007/03/91(7)/072301(6)$20.00 © 2003 The American Physical Society

[4]*Bhabha Atomic Research Centre, Bombay 400 085, India*
[5]*Brookhaven National Laboratory, Upton, New York 11973-5000, USA*
[6]*University of California–Riverside, Riverside, California 92521, USA*
[7]*China Institute of Atomic Energy (CIAE), Beijing, People's Republic of China*
[8]*Center for Nuclear Study, Graduate School of Science, University of Tokyo, 7-3-1 Hongo, Bunkyo, Tokyo 113-0033, Japan*
[9]*Columbia University, New York, New York 10027, USA, and Nevis Laboratories, Irvington, New York 10533, USA*
[10]*Dapnia, CEA Saclay, F-91191, Gif-sur-Yvette, France*
[11]*Debrecen University, H-4010 Debrecen, Egyetem tér 1, Hungary*
[12]*Florida State University, Tallahassee, Florida 32306, USA*
[13]*Georgia State University, Atlanta, Georgia 30303, USA*
[14]*Hiroshima University, Kagamiyama, Higashi-Hiroshima 739-8526, Japan*
[15]*Institute for High Energy Physics (IHEP), Protvino, Russia*
[16]*Iowa State University, Ames, Iowa 50011, USA*
[17]*Joint Institute for Nuclear Research, 141980 Dubna, Moscow Region, Russia*
[18]*KAERI, Cyclotron Application Laboratory, Seoul, South Korea*
[19]*Kangnung National University, Kangnung 210-702, South Korea*
[20]*KEK, High Energy Accelerator Research Organization, Tsukuba-shi, Ibaraki-ken 305-0801, Japan*
[21]*KFKI Research Institute for Particle and Nuclear Physics (RMKI), H-1525 Budapest 114, PO Box 49, Hungary*
[22]*Korea University, Seoul, 136-701, Korea*
[23]*Russian Research Center, "Kurchatov Institute," Moscow, Russia*
[24]*Kyoto University, Kyoto 606, Japan*
[25]*Laboratoire Leprince-Ringuet, Ecole Polytechnique, CNRS-IN2P3, Route de Saclay, F-91128, Palaiseau, France*
[26]*Lawrence Livermore National Laboratory, Livermore, California 94550, USA*
[27]*Los Alamos National Laboratory, Los Alamos, New Mexico 87545, USA*
[28]*LPC, Université Blaise Pascal, CNRS-IN2P3, Clermont-Fd, 63177 Aubiere Cedex, France*
[29]*Department of Physics, Lund University, Box 118, SE-221 00 Lund, Sweden*
[30]*Institut fuer Kernphysik, University of Muenster, D-48149 Muenster, Germany*
[31]*Myongji University, Yongin, Kyonggido 449-728, Korea*
[32]*Nagasaki Institute of Applied Science, Nagasaki-shi, Nagasaki 851-0193, Japan*
[33]*University of New Mexico, Albuquerque, New Mexico 87131, USA*
[34]*New Mexico State University, Las Cruces, New Mexico 88003, USA*
[35]*Oak Ridge National Laboratory, Oak Ridge, Tennessee 37831, USA*
[36]*IPN-Orsay, Universite Paris Sud, CNRS-IN2P3, BP1, F-91406, Orsay, France*
[37]*PNPI, Petersburg Nuclear Physics Institute, Gatchina, Russia*
[38]*RIKEN (The Institute of Physical and Chemical Research), Wako, Saitama 351-0198, Japan*
[39]*RIKEN BNL Research Center, Brookhaven National Laboratory, Upton, New York 11973-5000*
[40]*St. Petersburg State Technical University, St. Petersburg, Russia*
[41]*Universidade de São Paulo, Instituto de Física, Caixa Postal 66318, São Paulo CEP05315-970, Brazil*
[42]*System Electronics Laboratory, Seoul National University, Seoul, South Korea*
[43]*Chemistry Department, Stony Brook University, SUNY, Stony Brook, New York 11794-3400, USA*
[44]*Department of Physics and Astronomy, Stony Brook University, SUNY, Stony Brook, New York 11794, USA*
[45]*SUBATECH (Ecole des Mines de Nantes, CNRS-IN2P3, Université de Nantes) BP 20722-44307, Nantes, France*
[46]*University of Tennessee, Knoxville, Tennessee 37996, USA*
[47]*Department of Physics, Tokyo Institute of Technology, Tokyo, 152-8551, Japan*
[48]*Institute of Physics, University of Tsukuba, Tsukuba, Ibaraki 305, Japan*
[49]*Vanderbilt University, Nashville, Tennessee 37235, USA*
[50]*Waseda University, Advanced Research Institute for Science and Engineering, 17 Kikui-cho, Shinjuku-ku, Tokyo 162-0044, Japan*
[51]*Weizmann Institute, Rehovot 76100, Israel*
[52]*Yonsei University, IPAP, Seoul 120-749, Korea*
(Received 28 April 2003; published 13 August 2003)

Transverse momentum spectra of neutral pions in the range $1 < p_T < 10$ GeV/c have been measured at midrapidity by the PHENIX experiment at BNL RHIC in Au + Au collisions at $\sqrt{s_{NN}} = 200$ GeV. The π^0 multiplicity in central reactions is significantly below the yields measured at the same $\sqrt{s_{NN}}$ in peripheral Au + Au and $p + p$ reactions scaled by the number of nucleon-nucleon collisions. For the most central bin, the suppression factor is ~2.5 at $p_T = 2$ GeV/c and increases to ~4–5 at $p_T \approx 4$ GeV/c. At larger p_T, the suppression remains constant within errors. The deficit is already apparent in semiperipheral reactions and increases smoothly with centrality.

DOI: 10.1103/PhysRevLett.91.072301 PACS numbers: 25.75.Dw

High energy collisions of heavy ions provide the means to study quantum chromodynamics (QCD) at energy densities where lattice calculations [1] predict a transition from hadronic matter to a deconfined, chirally symmetric plasma of quarks and gluons (QGP). The large center-of-mass energies, $\sqrt{s_{NN}} \approx 200$ GeV, available in Au + Au collisions at the BNL Relativistic Heavy Ion Collider (RHIC), have resulted in a significant production of high transverse momentum hadrons ($p_T > 2$ GeV/c) for the first time in heavy-ion physics. High p_T particle production in hadronic collisions results from the fragmentation of quarks and gluons emerging from the initial high Q^2 parton-parton scatterings [2]. Thus, hard processes in nucleus-nucleus (AA) collisions provide direct information on the early partonic phases of the reaction. In the absence of nuclear medium effects, hard scattering yields in AA reactions are expected to scale like an incoherent superposition of nucleon-nucleon (NN) collisions because of the small probability of hard scattering processes per NN collision. In AA reactions, the number of NN collisions ($N_{\rm coll}$) at impact parameter b is simply proportional to the geometric nuclear overlap function, $T_{AA}(b)$, and can be calculated in an eikonal approach [3]. After scaling by the nuclear geometry, spectra of high p_T particles measured in AA reactions can be compared to the baseline $p + p$, $p + A$ data, as well as to perturbative [4–7] and classical-field [8] QCD predictions. Any departure from the expected $N_{\rm coll}$-scaled result provides information on the strongly interacting medium in central heavy-ion reactions.

One of the most significant observations from the first RHIC run (run 1) was the suppressed yield of moderately high p_T neutral pions ($p_T \approx 1.5$–4.0 GeV/c) in central Au + Au at $\sqrt{s_{NN}} = 130$ GeV with respect to the $N_{\rm coll}$-scaled $p + p$ and peripheral Au + Au data [9]. This result points to strong medium effects present in central Au + Au and has triggered extensive theoretical studies on its origin [4–8,10–13]. Most of these studies are based on the prediction [14,15] that a QGP would induce multiple gluon radiations from the scattered fast partons, effectively leading to a suppression of high p_T hadronic fragmentation products ("jet quenching"). Alternative interpretations have been proposed based on initial-state gluon saturation [8] or final-state hadronic interactions [13].

This Letter presents π^0 results obtained by the PHENIX experiment in Au + Au collisions at $\sqrt{s_{NN}} =$ 200 GeV and compares them to the $p + p \to \pi^0 X$ data measured in the same experiment at the same center-of-mass energy [16]. The analysis uses 30×10^6 minimum bias events, triggered by a coincidence between the zero degree calorimeters (ZDC) and the beam-beam counters (BBC), with vertex position $|z| < 30$ cm. In run 2, the electromagnetic calorimeter (EMCal) was fully instrumented providing a total solid angle coverage at midrapidity of approximately $\Delta\eta = 0.7$ and $\Delta\phi = \pi$ and the total collected π^0 statistics was a factor of $\sim$100 larger than in run 1 [9]. The combination of larger acceptance, high statistics, and the measurement of $p + p$ data in the same detector permits a precise study of the high p_T π^0 production mechanisms in AA collisions at RHIC.

Neutral pions are reconstructed via their $\pi^0 \to \gamma\gamma$ decay through an invariant mass analysis of γ pairs detected in the EMCal [17] which consists of six lead-scintillator (PbSc) and two lead-glass Čerenkov (PbGl) sectors. The large radial distance of the calorimeters to the interaction region (> 5 m) and their fine granularity ($\Delta\eta \times \Delta\phi \approx 0.01 \times 0.01$) keep the tower occupancy low, $<10\%$ even in the highest multiplicity Au + Au events. The energy calibration is obtained from beam tests and, in the case of PbSc, from cosmic rays data and the known minimum ionizing energy peak of charged hadrons traversing the calorimeter. It is then confirmed using the π^0 mass, as well as the agreement of the calorimeter energy with the measured momentum of identified electrons. The systematic error on the absolute energy scale is less than 1.5%. Photonlike clusters are identified in the EMCal by applying time-of-flight and shower profile cuts [17]. The selected clusters are binned in pair invariant mass $m_{\gamma\gamma}$ and p_T. An additional energy asymmetry cut, $|E_{\gamma 1} - E_{\gamma 2}|/(E_{\gamma 1} + E_{\gamma 2}) <$ 0.7(PbGl), 0.8(PbSc), is applied to the reconstructed pairs. The signal-to-background in peripheral (central) is approximately 20 (5) and 0.5 (0.01) for the highest and lowest p_T, respectively. The combinatorial background is estimated and subtracted by mixing clusters from different events with similar centrality and vertex, and normalizing the distribution in a region outside the π^0 mass peak. The π^0 yield in each p_T bin is determined by integrating the subtracted $m_{\gamma\gamma}$ distribution in a $\pm 3\sigma$ window determined by a p_T-dependent parametrization of Gaussian fits to the π^0 peaks.

The raw PbSc and PbGl π^0 spectra are normalized to one unit of rapidity and full azimuth (this acceptance correction quickly reaches the $\sim 1/0.35$ pure geometric factor at high p_T). The spectra are further corrected for (i) the detector response (energy resolution, dead areas), (ii) the reconstruction efficiency (analysis cuts), and (iii) the occupancy effects (cluster overlaps). These corrections are quantified by embedding simulated single π^0's from a full PHENIX GEANT [18] simulation into real events, and analyzing the merged events with the same analysis cuts used to obtain the real yields. Each correction is determined, for each centrality bin, as the ratio of the input to the reconstructed simulated p_T distributions. The overall yield correction amounts to $\sim$2.5 with a centrality dependence $\lesssim 25\%$. The losses are dominated by fiducial and asymmetry cuts.

The main sources of systematic errors in the PbSc and PbGl measurements are due to the uncertainties in (i) the yield extraction (background subtraction and $m_{\rm inv}$ integration), (ii) the yield correction (efficiency factors), and

TABLE I. Summary of the dominant sources of systematic errors on the PbSc and PbGl π^0 yields and total errors on the combined measurements. The error ranges are quoted for the lowest to highest p_T values.

Source		Syst. error PbSc	Syst. error PbGl	
Yield extraction		10%	6%–7%	
Yield correction		8%	8%	
Energy scale		3%–11%	7%–13%	
Total error (%)	Stat.	Syst.	Normalization Central	Peripheral
Comb. π^0 spectra	2–40	10–17	5	5
R_{AA}	2–45	11–22	14	30

(iii) the energy scale (absolute calibration of the calorimeter). The relative contributions of these effects to the total error differ for the PbSc and PbGl (Table I). The weighted average of the two independent measurements reduces the total error. The nominal energy resolution [17] is adjusted in the simulation to reproduce the true width of the π^0 peak observed at each p_T, smearing the energies with a constant term of 7% for PbSc and ~9% for PbGl. The shape, position, and width of the π^0 peak measured in all different centralities are then confirmed to be well reproduced by the embedded data. The final systematic errors on the spectra are at the level of ~10% at 1 GeV/c and ~17% at the highest p_T (Table I). A correction for the true mean value of the p_T bin is applied to the steeply falling spectra. No corrections have been applied to account for the contribution of feed-down π^0's (mainly coming from K^0_s and η decays) which are <5% based on HIJING [19] simulations.

The event centrality is determined by correlating the charge detected in the BBC with the energy measured in the ZDC detectors. A Glauber model Monte Carlo (MC) calculation combined with a simulation of the BBC and ZDC responses [20–22] gives an estimate of the associated averaged number of binary collisions ($\langle N_{\rm coll}\rangle$) and participating nucleons ($\langle N_{\rm part}\rangle$) in each centrality bin (Table II). Fully corrected and combined PbSc and PbGl π^0 p_T distributions are shown in Fig. 1 for minimum bias and for nine centrality bins scaled by factors of 10.

We quantify the medium effects on high p_T production in AA collisions with the *nuclear modification factor* given by the ratio of the measured AA invariant yields to the NN collision scaled $p + p$ invariant yields:

$$R_{AA}(p_T) = \frac{(1/N^{\rm evt}_{AA}) d^2N^{\pi^0}_{AA}/dp_T dy}{\langle N_{\rm coll}\rangle/\sigma^{\rm inel}_{pp} \times d^2\sigma^{\pi^0}_{pp}/dp_T dy}, \quad (1)$$

where the $\langle N_{\rm coll}\rangle/\sigma^{\rm inel}_{pp}$ is just the average Glauber nuclear overlap function, $\langle T_{\rm AuAu}\rangle$, in the centrality bin under consideration (Table II). $R_{AA}(p_T)$ measures the deviation of AA data from an incoherent superposition of NN collisions. For $p_T \lesssim 2$ GeV/c, R_{AA} is known to be below unity, since the bulk of particle production is due to soft processes which scale closer to the number of participant nucleons [20] than to $\langle N_{\rm coll}\rangle$.

TABLE II. Centrality bin, average nuclear overlap function, number of NN collisions, and number of participant nucleons from a Glauber MC [21,22] and the BBC and ZDC responses for Au + Au at $\sqrt{s_{NN}} = 200$ GeV. The centrality bin is expressed as percentiles of $\sigma_{\rm AuAu} = 6.9$ b.

Centrality	$\langle T_{\rm AuAu}\rangle$ (mb^{-1})	$\langle N_{\rm coll}\rangle$	$\langle N_{\rm part}\rangle$
0%–10%	22.75 ± 1.56	955.4 ± 93.6	325.2 ± 3.3
10%–20%	14.35 ± 1.00	602.6 ± 59.3	234.6 ± 4.7
20%–30%	8.90 ± 0.72	373.8 ± 39.6	166.6 ± 5.4
30%–40%	5.23 ± 0.44	219.8 ± 22.6	114.2 ± 4.4
40%–50%	2.86 ± 0.28	120.3 ± 13.7	74.4 ± 3.8
50%–60%	1.45 ± 0.23	61.0 ± 9.9	45.5 ± 3.3
60%–70%	0.68 ± 0.18	28.5 ± 7.6	25.7 ± 3.8
60%–80%	0.49 ± 0.14	20.4 ± 5.9	19.5 ± 3.3
60%–92%	0.35 ± 0.10	14.5 ± 4.0	14.5 ± 2.5
70%–80%	0.30 ± 0.10	12.4 ± 4.2	13.4 ± 3.0
70%–92%	0.20 ± 0.06	8.3 ± 2.4	9.5 ± 1.9
80%–92%	0.12 ± 0.03	4.9 ± 1.2	6.3 ± 1.2
Min. bias	6.14 ± 0.45	257.8 ± 25.4	109.1 ± 4.1

Figure 2 shows R_{AA} as a function of p_T for π^0 measured in 0%–10% central (closed circles) and 80%–92% peripheral (open circles) Au + Au. The PHENIX $p + p \rightarrow \pi^0$ data [16] is used as the reference in the denominator. The R_{AA} values for central collisions are noticeably below unity, as found at 130 GeV [9]. This is in contrast to the enhanced high p_T π^0 production ($R_{AA} > 1$) observed

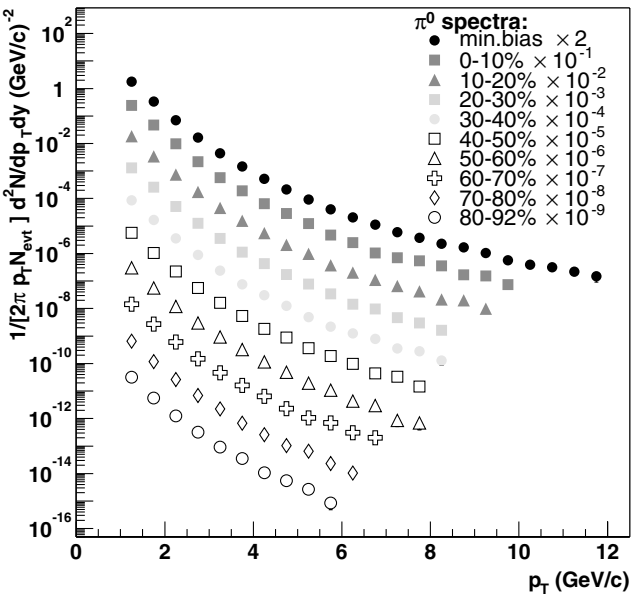

FIG. 1. Invariant π^0 yields at midrapidity as a function of p_T for minimum bias and nine centralities in Au + Au at $\sqrt{s_{NN}} = 200$ GeV [0%–10% (80%–92%) is most central (peripheral)].

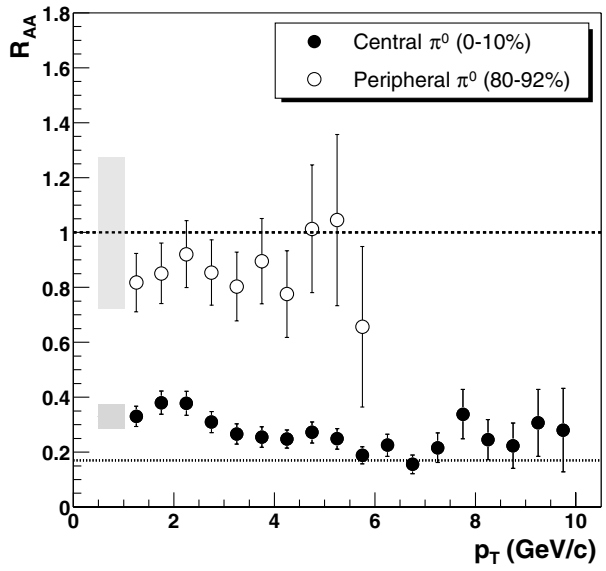

FIG. 2. Nuclear modification factor $R_{AA}(p_T)$ for π^0 in central (closed circles) and peripheral (open circles) Au + Au at $\sqrt{s_{NN}} = 200$ GeV. The error bars include all point-to-point experimental ($p + p$, Au + Au) errors. The shaded bands represent the fractional uncertainties in $\langle T_{\mathrm{AuAu}} \rangle$ and in the π^0 yields normalization added in quadrature, which can move all the points up or down together (in the central case the shaded band shown is the fractional error for the first point).

at CERN Super Proton Synchrotron energies [23], interpreted in terms of initial-state p_T broadening effects ("Cronin effect" [24]). Within errors, peripheral Au + Au collisions behave like a superposition of $p + p$ collisions with regard to high p_T π^0 production ($R_{AA} \approx 1$). In central collisions, the suppression is smallest at 2 GeV/c and increases to an approximately constant suppression factor of $1/R_{AA} \approx 4$–5 over the p_T range of 4–10 GeV/c, ~30% above the expectation from N_{part} scaling (dotted line in Fig. 2).

The magnitude and p_T dependence of R_{AA} (corresponding to parton fractional momenta $x \approx 2p_T/\sqrt{s} \sim 0.02$–$0.1$ at midrapidity) is inconsistent with the expectations of leading-twist "shadowing" effects on the nuclear parton distribution functions alone [25]. Different jet quenching calculations [4–7,10–12], based on medium-induced radiative energy loss, can reproduce the magnitude of the π^0 suppression assuming the formation of a hot and dense partonic system. The predicted p_T dependence of the quenching, however, varies in the different models. All models that include the Landau-Pomeranchuck-Migdal (LPM) interference effect [15,26] predict R_{AA} effectively $\propto \sqrt{p_T}$ [10]. Such a trend is not compatible with our data over the entire p_T range. Analyses which combine LPM jet quenching together with shadowing and initial-state p_T broadening generally reproduce the whole p_T dependence of the π^0 suppression [4], as do recent approaches that take into account detailed balance between parton emission and absorption [7]. However, based solely on the data presented here, we are not able to distinguish between partonic or hadronic [13] energy loss scenarios.

The centrality dependence of the high p_T π^0 suppression is shown in Fig. 3 as a function of $\langle N_{\mathrm{part}} \rangle$. The suppression is characterized as the ratio of Au + Au over $p + p$ yields integrated above 4 GeV/c and normalized using two different scalings. R_{AA} (circles) denotes the N_{coll} scaling as in Eq. (1), whereas R_{AA}^{part} (crosses) indicates N_{part} scaling expected in scenarios dominated either by gluon saturation [8] or by surface emission of the quenched jets [10]. Figure 3 indicates that the transition from the N_{coll} scaling behavior ($R_{AA} \sim 1$) apparent in the most peripheral region, to the strong suppression seen in central reactions ($R_{AA} \sim 0.25$) is smooth. In addition, although there is no exact participant scaling ($R_{AA}^{\mathrm{part}} > 1$ for all centralities), the π^0 production per participant pair above 4 GeV/c is approximately constant over a wide range of intermediate centralities, in qualitative agreement with a parton saturation model prediction [8].

In summary, transverse momentum spectra of neutral pions have been measured at midrapidity up to $p_T \approx 10$ GeV/c for nine centrality bins of Au + Au collisions at $\sqrt{s_{NN}} = 200$ GeV. The spectral shape and invariant yield for peripheral reactions are consistent with those of $p + p$ reactions scaled by the average number of inelastic NN collisions. Central yields, on the other hand, are significantly lower than peripheral Au + Au and $p + p$ scaled yields, as found at $\sqrt{s_{NN}} = 130$ GeV. The observed suppression increases slowly with p_T to as much as a factor of 4–5 in the 10% most central collisions,

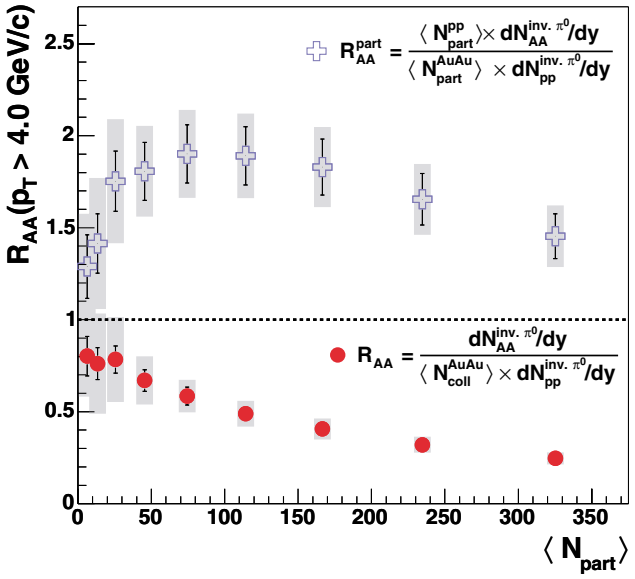

FIG. 3 (color online). Ratio of Au + Au over $p + p$ π^0 yields integrated above 4 GeV/c and normalized using $\langle N_{\mathrm{coll}} \rangle$ (circles) and $\langle N_{\mathrm{part}} \rangle$ (crosses), as a function of centrality given by $\langle N_{\mathrm{part}} \rangle$. The errors bands and bars are the same as for Fig. 2.

remaining constant within errors above ~ 4 GeV/c. The suppression is already apparent in semiperipheral reactions and increases smoothly with centrality. The magnitude of the deficit can be reproduced by parton energy loss calculations in an opaque medium, but its p_T and centrality dependence puts strong constraints on the details of energy loss and the properties of the medium. The role of initial-state effects, including shadowing, p_T broadening, and gluon saturation will be studied with data from the recent RHIC run using $d + \mathrm{Au}$, where final-state medium effects such as jet quenching are minimal.

We thank the staff of the Collider-Accelerator and Physics Departments at BNL for their vital contributions. We acknowledge support from the Department of Energy and NSF (U.S.A.), MEXT and JSPS (Japan), CNPq and FAPESP (Brazil), NSFC (China), CNRS-IN2P3 and CEA (France), BMBF, DAAD, and AvH (Germany), OTKA (Hungary), DAE and DST (India), ISF (Israel), KRF and CHEP (Korea), RMIST, RAS, and RMAE (Russia), VR and KAW (Sweden), U.S. CRDF for the FSU, U.S.-Hungarian NSF-OTKA-MTA, and U.S.-Israel BSF.

*Deceased.
†PHENIX Spokesperson.
Email address: zajc@nevis.columbia.edu

[1] See E. Laermann and O. Philipsen, hep-ph/0303042 [Annu. Rev. Nucl. Part. Sci. (to be published)], for a recent review.
[2] J. F. Owens *et al.*, Phys. Rev. D **18**, 1501 (1978).
[3] R. J. Glauber and G. Matthiae, Nucl. Phys. **B21**, 135 (1970).
[4] I. Vitev and M. Gyulassy, Phys. Rev. Lett. **89**, 252301 (2002).
[5] S. Jeon, J. Jalilian-Marian, and I. Sarcevic, Phys. Lett. B **562**, 45 (2003).
[6] G. G. Barnafoldi *et al.*, nucl-th/0212111.
[7] X. N. Wang, Nucl. Phys. **A715**, 775 (2003).
[8] D. Kharzeev, E. Levin, and L. McLerran, Phys. Lett. B **561**, 93 (2003).
[9] K. Adcox *et al.*, Phys. Rev. Lett. **88**, 022301 (2002).
[10] B. Müller, Phys. Rev. C **67**, 061901(R) (2003), and references therein.
[11] F. Arleo, J. High Energy Phys. 11 (2002) 044.
[12] C. A. Salgado and U. A. Wiedemann, Phys. Rev. D **68**, 014008 (2003).
[13] K. Gallmeister, C. Greiner, and Z. Xu, Phys. Rev. C **67**, 044905 (2003).
[14] M. Gyulassy and M. Plümer, Phys. Lett. B **243**, 432 (1990); X. N. Wang and M. Gyulassy, Phys. Rev. Lett. **68**, 1480 (1992).
[15] R. Baier, D. Schiff, and B. G. Zakharov, Annu. Rev. Nucl. Part. Sci. **50**, 37 (2000), and references therein.
[16] S. S. Adler *et al.*, hep-ex/0304038 (to be published).
[17] L. Aphecetche *et al.*, Nucl. Instrum. Methods Phys. Res., Sect. A **499**, 521 (2003).
[18] GEANT 3.21, CERN program library.
[19] X. N. Wang and M. Gyulassy, Phys. Rev. D **44**, 3501 (1991).
[20] K. Adcox *et al.*, Phys. Rev. Lett. **86**, 3500 (2001).
[21] The trigger is inefficient for very peripheral reactions and records $92.2^{+2.5}_{-3.0}\%$ of σ_{AuAu}.
[22] Woods-Saxon Au nuclear radius $R = 6.38 \pm 0.06$ fm, diffusivity $a = 0.535 \pm 0.027$ fm [B. Hahn, D. G. Ravenhall, and R. Hofstadter, Phys. Rev. **101**, 1131 (1956)], and nucleon-nucleon cross section $\sigma_{NN}^{\mathrm{inel}} = 42 \pm 3$ mb.
[23] M. M. Aggarwal *et al.*, Eur. Phys. J. C **23**, 225 (2002).
[24] D. Antreasyan *et al.*, Phys. Rev. D **19**, 764 (1979).
[25] K. J. Eskola, V. J. Kolhinen, and C. A. Salgado, Eur. Phys. J. C **9**, 61 (1999); S. R. Klein and R. Vogt, Phys. Rev. C **67**, 047901 (2003).
[26] M. Gyulassy, P. Levai, and I. Vitev, Phys. Rev. Lett. **85**, 5535 (2000); Nucl. Phys. **B594**, 371 (2001).

Midrapidity Neutral-Pion Production in Proton-Proton Collisions at $\sqrt{s} = 200$ GeV

S. S. Adler,[5] S. Afanasiev,[17] C. Aidala,[5] N. N. Ajitanand,[43] Y. Akiba,[20,38] J. Alexander,[43] R. Amirikas,[12] L. Aphecetche,[45] S. H. Aronson,[5] R. Averbeck,[44] T. C. Awes,[35] R. Azmoun,[44] V. Babintsev,[15] A. Baldisseri,[10] K. N. Barish,[6] P. D. Barnes,[27] B. Bassalleck,[33] S. Bathe,[30] S. Batsouli,[9] V. Baublis,[7] A. Bazilevsky,[39,15] S. Belikov,[16,15] Y. Berdnikov,[40] S. Bhagavatula,[16] J. G. Boissevain,[27] H. Borel,[10] S. Borenstein,[25] M. L. Brooks,[27] D. S. Brown,[34] N. Bruner,[33] D. Bucher,[30] H. Buesching,[30] V. Bumazhnov,[15] G. Bunce,[5,39] J. M. Burward-Hoy,[26,44] S. Butsyk,[44] X. Camard,[45] J.-S. Chai,[18] P. Chand,[4] W. C. Chang,[2] S. Chernichenko,[15] C. Y. Chi,[9] J. Chiba,[20] M. Chiu,[9] I. J. Choi,[52] J. Choi,[19] R. K. Choudhury,[4] T. Chujo,[5] V. Cianciolo,[35] Y. Cobigo,[10] B. A. Cole,[9] P. Constantin,[16] D. G. d'Enterria,[45] G. David,[5] H. Delagrange,[45] A. Denisov,[15] A. Deshpande,[39] E. J. Desmond,[5] O. Dietzsch,[41] O. Drapier,[25] A. Drees,[44] K. A. Drees,[5] R. du Rietz,[29] A. Durum,[15] D. Dutta,[4] Y. V. Efremenko,[35] K. El Chenawi,[49] A. Enokizono,[14] H. En'yo,[38,39] S. Esumi,[48] L. Ewell,[5] D. E. Fields,[33,39] F. Fleuret,[25] S. L. Fokin,[23] B. D. Fox,[39] Z. Fraenkel,[51] J. E. Frantz,[9] A. Franz,[5] A. D. Frawley,[12] S.-Y. Fung,[6] S. Garpman,[29,*] T. K. Ghosh,[49] A. Glenn,[46] G. Gogiberidze,[46] M. Gonin,[25] J. Gosset,[10] Y. Goto,[39] R. Granier de Cassagnac,[25] N. Grau,[16] S. V. Greene,[49] M. Grosse Perdekamp,[39] W. Guryn,[5] H.-Å. Gustafsson,[29] T. Hachiya,[14] J. S. Haggerty,[5] H. Hamagaki,[8] A. G. Hansen,[27] E. P. Hartouni,[26] M. Harvey,[5] R. Hayano,[8] X. He,[13] M. Heffner,[26] T. K. Hemmick,[44] J. M. Heuser,[44] M. Hibino,[50] J. C. Hill,[16] W. Holzmann,[43] K. Homma,[14] B. Hong,[22] A. Hoover,[34] T. Ichihara,[38,39] V. V. Ikonnikov,[23] K. Imai,[24,38] D. Isenhower,[1] M. Ishihara,[38] M. Issah,[43] A. Isupov,[17] B. V. Jacak,[44] W. Y. Jang,[22] Y. Jeong,[19] J. Jia,[44] O. Jinnouchi,[38] B. M. Johnson,[5] S. C. Johnson,[26] K. S. Joo,[31] D. Jouan,[36] S. Kametani,[8,50] N. Kamihara,[47,38] J. H. Kang,[52] S. S. Kapoor,[4] K. Katou,[50] S. Kelly,[9] B. Khachaturov,[51] A. Khanzadeev,[37] J. Kikuchi,[50] D. H. Kim,[31] D. J. Kim,[52] D. W. Kim,[19] E. Kim,[42] G.-B. Kim,[25] H. J. Kim,[52] E. Kistenev,[5] A. Kiyomichi,[48] K. Kiyoyama,[32] C. Klein-Boesing,[30] H. Kobayashi,[38,39] L. Kochenda,[37] V. Kochetkov,[15] D. Koehler,[33] T. Kohama,[14] M. Kopytine,[44] D. Kotchetkov,[6] A. Kozlov,[51] P. J. Kroon,[5] C. H. Kuberg,[1,27] K. Kurita,[39] Y. Kuroki,[48] M. J. Kweon,[22] Y. Kwon,[52] G. S. Kyle,[34] R. Lacey,[43] V. Ladygin,[17] J. G. Lajoie,[16] A. Lebedev,[16,23] S. Leckey,[44] D. M. Lee,[27] S. Lee,[19] M. J. Leitch,[27] X. H. Li,[6] H. Lim,[42] A. Litvinenko,[17] M. X. Liu,[27] Y. Liu,[36] C. F. Maguire,[49] Y. I. Makdisi,[5] A. Malakhov,[17] V. I. Manko,[23] Y. Mao,[7,38] G. Martinez,[45] M. D. Marx,[44] H. Masui,[48] F. Matathias,[44] T. Matsumoto,[8,50] P. L. McGaughey,[27] E. Melnikov,[15] F. Messer,[44] Y. Miake,[48] J. Milan,[43] T. E. Miller,[49] A. Milov,[44,51] S. Mioduszewski,[5] R. E. Mischke,[27] G. C. Mishra,[13] J. T. Mitchell,[5] A. K. Mohanty,[4] D. P. Morrison,[5] J. M. Moss,[27] F. Mühlbacher,[44] D. Mukhopadhyay,[51] M. Muniruzzaman,[6] J. Murata,[38,39] S. Nagamiya,[20] J. L. Nagle,[9] T. Nakamura,[14] B. K. Nandi,[6] M. Nara,[48] J. Newby,[46] P. Nilsson,[29] A. S. Nyanin,[23] J. Nystrand,[29] E. O'Brien,[5] C. A. Ogilvie,[16] H. Ohnishi,[5,38] I. D. Ojha,[49,3] K. Okada,[38] M. Ono,[48] V. Onuchin,[15] A. Oskarsson,[29] I. Otterlund,[29] K. Oyama,[8] K. Ozawa,[8] D. Pal,[51] A. P. T. Palounek,[27] V. S. Pantuev,[44] V. Papavassiliou,[34] J. Park,[42] A. Parmar,[33] S. F. Pate,[34] T. Peitzmann,[30] J.-C. Peng,[27] V. Peresedov,[17] C. Pinkenburg,[5] R. P. Pisani,[5] F. Plasil,[35] M. L. Purschke,[5] A. K. Purwar,[44] J. Rak,[16] I. Ravinovich,[51] K. F. Read,[35,46] M. Reuter,[44] K. Reygers,[30] V. Riabov,[37,40] Y. Riabov,[37] G. Roche,[28] A. Romana,[25] M. Rosati,[16] P. Rosnet,[28] S. S. Ryu,[52] M. E. Sadler,[1] N. Saito,[38,39] T. Sakaguchi,[8,50] M. Sakai,[32] S. Sakai,[48] V. Samsonov,[37] L. Sanfratello,[33] R. Santo,[30] H. D. Sato,[24,38] S. Sato,[5,48] S. Sawada,[20] Y. Schutz,[45] V. Semenov,[15] R. Seto,[6] M. R. Shaw,[1,27] T. K. Shea,[5] T.-A. Shibata,[47,38] K. Shigaki,[14,20] T. Shiina,[27] C. L. Silva,[41] D. Silvermyr,[27,29] K. S. Sim,[22] C. P. Singh,[3] V. Singh,[3] M. Sivertz,[5] A. Soldatov,[15] R. A. Soltz,[26] W. E. Sondheim,[27] S. P. Sorensen,[46] I. V. Sourikova,[5] F. Staley,[10] P. W. Stankus,[35] E. Stenlund,[29] M. Stepanov,[34] A. Ster,[21] S. P. Stoll,[5] T. Sugitate,[14] J. P. Sullivan,[27] E. M. Takagui,[41] A. Taketani,[38,39] M. Tamai,[50] K. H. Tanaka,[20] Y. Tanaka,[32] K. Tanida,[38] M. J. Tannenbaum,[5] P. Tarján,[11] J. D. Tepe,[1,27] T. L. Thomas,[33] J. Tojo,[24,38] H. Torii,[24,38] R. S. Towell,[1] I. Tserruya,[51] H. Tsuruoka,[48] S. K. Tuli,[3] H. Tydesjö,[29] N. Tyurin,[15] H. W. van Hecke,[27] J. Velkovska,[5,44] M. Velkovsky,[44] L. Villatte,[46] A. A. Vinogradov,[23] M. A. Volkov,[23] E. Vznuzdaev,[37] X. R. Wang,[13] Y. Watanabe,[38,39] S. N. White,[5] F. K. Wohn,[16] C. L. Woody,[5] W. Xie,[6] Y. Yang,[7] A. Yanovich,[15] S. Yokkaichi,[38,39] G. R. Young,[35] I. E. Yushmanov,[23] W. A. Zajc,[9,†] C. Zhang,[9] S. Zhou,[7,51] and L. Zolin[17]

(PHENIX Collaboration)

[1]*Abilene Christian University, Abilene, Texas 79699, USA*
[2]*Institute of Physics, Academia Sinica, Taipei 11529, Taiwan*
[3]*Department of Physics, Banaras Hindu University, Varanasi 221005, India*
[4]*Bhabha Atomic Research Centre, Bombay 400 085, India*

 0031-9007/03/91(24)/241803(6)$20.00 © 2003 The American Physical Society

[5]*Brookhaven National Laboratory, Upton, New York 11973-5000, USA*
[6]*University of California–Riverside, Riverside, California 92521, USA*
[7]*China Institute of Atomic Energy (CIAE), Beijing, Peopleś Republic of China*
[8]*Center for Nuclear Study, Graduate School of Science, University of Tokyo, 7-3-1 Hongo, Bunkyo, Tokyo 113-0033, Japan*
[9]*Columbia University, New York, New York 10027, USA*
and Nevis Laboratories, Irvington, New York 10533, USA
[10]*Dapnia, CEA Saclay, F-91191, Gif-sur-Yvette, France*
[11]*Debrecen University, H-4010 Debrecen, Egyetem tér 1, Hungary*
[12]*Florida State University, Tallahassee, Florida 32306, USA*
[13]*Georgia State University, Atlanta, Georgia 30303, USA*
[14]*Hiroshima University, Kagamiyama, Higashi-Hiroshima 739-8526, Japan*
[15]*Institute for High Energy Physics (IHEP), Protvino, Russia*
[16]*Iowa State University, Ames, Iowa 50011, USA*
[17]*Joint Institute for Nuclear Research, 141980 Dubna, Moscow Region, Russia*
[18]*KAERI, Cyclotron Application Laboratory, Seoul, South Korea*
[19]*Kangnung National University, Kangnung 210-702, South Korea*
[20]*KEK, High Energy Accelerator Research Organization, Tsukuba-shi, Ibaraki-ken 305-0801, Japan*
[21]*KFKI Research Institute for Particle and Nuclear Physics (RMKI), H-1525 Budapest 114, PO Box 49, Hungary*
[22]*Korea University, Seoul, 136-701, Korea*
[23]*Russian Research Center "Kurchatov Institute," Moscow, Russia*
[24]*Kyoto University, Kyoto 606, Japan*
[25]*Laboratoire Leprince-Ringuet, Ecole Polytechnique, CNRS-IN2P3, Route de Saclay, F-91128, Palaiseau, France*
[26]*Lawrence Livermore National Laboratory, Livermore, California 94550, USA*
[27]*Los Alamos National Laboratory, Los Alamos, New Mexico 87545, USA*
[28]*LPC, Université Blaise Pascal, CNRS-IN2P3, Clermont-Fd, 63177 Aubiere Cedex, France*
[29]*Department of Physics, Lund University, Box 118, SE-221 00 Lund, Sweden*
[30]*Institut für Kernphysik, University of Muenster, D-48149 Muenster, Germany*
[31]*Myongji University, Yongin, Kyonggido 449-728, Korea*
[32]*Nagasaki Institute of Applied Science, Nagasaki-shi, Nagasaki 851-0193, Japan*
[33]*University of New Mexico, Albuquerque, New Mexico 87131, USA*
[34]*New Mexico State University, Las Cruces, New Mexico 88003, USA*
[35]*Oak Ridge National Laboratory, Oak Ridge, Tennessee 37831, USA*
[36]*IPN-Orsay, Universite Paris Sud, CNRS-IN2P3, BP1, F-91406, Orsay, France*
[37]*PNPI, Petersburg Nuclear Physics Institute, Gatchina, Russia*
[38]*RIKEN (The Institute of Physical and Chemical Research), Wako, Saitama 351-0198, Japan*
[39]*RIKEN BNL Research Center, Brookhaven National Laboratory, Upton, New York 11973-5000, USA*
[40]*St. Petersburg State Technical University, St. Petersburg, Russia*
[41]*Universidade de São Paulo, Instituto de Física, Caixa Postal 66318, São Paulo CEP05315-970, Brazil*
[42]*System Electronics Laboratory, Seoul National University, Seoul, South Korea*
[43]*Chemistry Department, Stony Brook University, SUNY, Stony Brook, New York 11794-3400, USA*
[44]*Department of Physics and Astronomy, Stony Brook University, SUNY, Stony Brook, New York 11794, USA*
[45]*SUBATECH (Ecole des Mines de Nantes, CNRS-IN2P3, Université de Nantes) BP 20722 - 44307, Nantes, France*
[46]*University of Tennessee, Knoxville, Tennessee 37996, USA*
[47]*Department of Physics, Tokyo Institute of Technology, Tokyo, 152-8551, Japan*
[48]*Institute of Physics, University of Tsukuba, Tsukuba, Ibaraki 305, Japan*
[49]*Vanderbilt University, Nashville, Tennessee 37235, USA*
[50]*Waseda University, Advanced Research Institute for Science and Engineering, 17 Kikui-cho, Shinjuku-ku, Tokyo 162-0044, Japan*
[51]*Weizmann Institute, Rehovot 76100, Israel*
[52]*Yonsei University, IPAP, Seoul 120-749, Korea*
(Received 28 April 2003; published 11 December 2003)

The invariant differential cross section for inclusive neutral-pion production in $p + p$ collisions at $\sqrt{s} = 200$ GeV has been measured at midrapidity ($|\eta| < 0.35$) over the range $1 < p_T \lesssim 14$ GeV/c by the PHENIX experiment at the Relativistic Heavy Ion Collider. Predictions of next-to-leading order perturbative QCD calculations are consistent with these measurements. The precision of our result is sufficient to differentiate between prevailing gluon-to-pion fragmentation functions.

DOI: 10.1103/PhysRevLett.91.241803 PACS numbers: 13.85.Ni, 13.87.Fh, 25.75.Dw

Particle production at large transverse momenta, p_T, in hadronic reactions has provided an important testing ground for perturbative quantum chromodynamics (pQCD) [1]. Next-to-leading order (NLO) pQCD calculations describe Tevatron ($\sqrt{s} = 1.8$ TeV) measurements of inclusive jet production [2] within 10% and direct photon production [3], in which the elementary quark-gluon scattering produces a photon directly, within 50%.

For high-p_T pion production, the recent calculations have not been compared with the UA2 data [4] obtained at $\sqrt{s} = 540$ GeV. However, at lower center of mass energies ($\sqrt{s} \lesssim 63$ GeV), they underestimate the data by a factor of $\sim$2.5 [5]. Similar discrepancies were observed for direct photon measurements from fixed target experiments [6] and were attributed to effects of soft-gluon radiations beyond NLO [7], to effects of initial intrinsic transverse momentum, k_T [8], or to experimental problems in the difficult direct photon measurements [9,10]. The π^0 calculations, as compared to the jet or direct photon calculations, also require the probability for the scattered quark or gluon to fragment into a pion.

Information on fragmentation to pions [11–15] has principally come from global analyses of inclusive hadron production in e^+e^- annihilation. These analyses constrain the quark-to-pion fragmentation functions well but, via the scale dependence, the gluon-to-pion fragmentation function to a lesser extent. For example, the latter function at a scale of 100 GeV^2 can vary by a factor of 2 to 10 when the fraction of the initial gluon momentum carried by the pion is above 0.5. The more direct measurements of gluon fragmentation functions from b-tagged, three jet event data from the Large Electron-Positron Collider [16] have played a limited role in the global analyses because NLO corrections are unavailable for the quantitative treatment, including scale and scheme dependencies, of these data. As has been explored for measurements of inclusive hadron production in $p + \bar{p}$ collisions [17], results from inclusive pion production at high p_T can be included in the global NLO analyses and thus may provide meaningful constraints on the gluon-to-pion fragmentation. These results also provide a reference needed for quantifying the suppression of π^0 production observed in Au-Au collisions at the Relativistic Heavy Ion Collider (RHIC) [18] and, to the extent of agreement with the calculations, the foundations for the planned polarized gluon density measurement with polarized protons in the RHIC [19].

In this Letter, we report the first results on inclusive neutral-pion production in $p + p$ collisions at a center of mass energy ($\sqrt{s}$) of 200 GeV as extracted from the data collected during the 2001–2002 run period (Run-2) of RHIC. The bunched proton beams in the collider were vertically polarized with spin orientations alternating in successive bunches. By balancing the integrated luminosity in the different spin states, the effects from polarization were canceled at the 0.1% level.

In Run-2, the PHENIX experiment [20] operated two central arm spectrometers, one muon arm spectrometer, and other detectors for triggering and vertex determination. This work used the beam-beam counters (BBC) [21] for determining the collision vertex and constructing the minimum bias (MB) trigger, and the electromagnetic calorimeters (EMCal) [22] for detecting the neutral pions and deriving high-p_T triggers.

The unbiased differential cross section for π^0 production is calculated from the MB triggered data sample as

$$E\frac{d^3\sigma}{dp^3} = \frac{1}{\hat{\mathcal{L}}}\frac{1}{2\pi p_T^*}\frac{C_{\rm reco}C_{\rm conv}}{f_{\pi^0}}\frac{N_{\pi^0}}{\Delta p_T \Delta y}, \qquad (1)$$

where N_{π^0} is the number of π^0's observed in a Δp_T wide bin at p_T^* defined as the p_T for which the cross section equals its average over the bin; Δy is the rapidity range; $C_{\rm reco}$ is a correction for the acceptance, reconstruction efficiency, and p_T smearing; $C_{\rm conv}$ is a correction for the conversion of decay photons; f_{π^0} is the fraction of the inclusive π^0 yield for which the MB trigger condition was satisfied; and $\hat{\mathcal{L}}$ is the integrated luminosity for the analyzed data sample. The high-p_T triggered sample required an additional correction to account for the efficiency of this trigger for π^0 detection.

The MB trigger imposed the requirement that the collision vertex was within 75 cm of the center of the interaction region. This vertex was reconstructed from the difference in the arrival times of particles at the BBCs which were located along the beam line at ± 1.44 m from the nominal interaction point and subtended the pseudorapidity range $\pm(3.0$–$3.9)$ with full azimuthal coverage. In the analysis of the data, a more restrictive requirement of ± 30 cm was applied.

The EMCal consisted of two subsystems: a six sector, lead scintillator (PbSc) calorimeter and a two sector, lead glass (PbGl) calorimeter. Located at a radial distance of $\sim$5 m from the beam line, each of these sectors covered the pseudorapidity range of $|\eta| < 0.35$ and an azimuthal angle interval of $\Delta\phi \approx 22.5°$. Each of the towers in the calorimeter subtended $\Delta\phi \times \Delta\eta \sim 0.01 \times 0.01$, thus ensuring that the two photons from a decayed π^0 were clearly resolved up to a p_T of 12 GeV/c. Shower profile analysis can extend this p_T range beyond 20 GeV/c. The energy calibration was corroborated by the position of the π^0 invariant mass peak, the energy deposit from minimum ionizing charged particles traversing the EMCal (PbSc), and the correlation between the energy deposit in the EMCal and the measured momentum for electrons and positrons identified by the ring-imaging Čerenkov detector. These studies showed that the accuracy of the energy measurement was within 1.5%. At a p_T of $\sim$11 GeV/c, this uncertainty translates into a systematic error on the π^0 yield of $\sim$12%. The effective energy resolution for the data set was deduced from the widths of the π^0 mass peaks, which varied with p_T from 7% to 10% (PbSc) and from 12% to 13% (PbGl), and a comparison of the measured energy and momentum for identified electrons and positrons.

The number of recorded high-p_T π^0's was enhanced by a high-p_T trigger (denoted as 2×2) in which threshold discrimination was applied independently to sums of the analog signals from nonoverlapping, 2×2 groupings (called tiles) of adjacent EMCal towers. During this run, the thresholds corresponded to a deposited energy of 0.75 GeV. The efficiency of this trigger for π^0

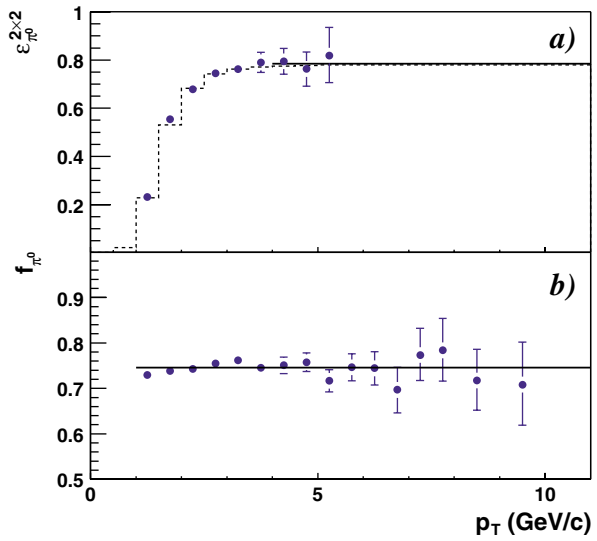

FIG. 1 (color online). (a) The efficiency of the 2×2 high-p_T trigger for π^0 as a function of the p_T of the π^0. The dashed and solid lines show the results of a Monte Carlo simulation based on the 2×2 trigger tile efficiencies and the limit derived from the fraction of active trigger tiles, respectively. (b) The fraction of the inclusive π^0 yield which satisfied the MB trigger condition. The solid line shows a fit of these data to a constant.

detection, $\varepsilon_{\pi^0}^{2\times2}(p_T)$, was obtained from the MB data. As shown in Fig. 1(a), this efficiency reached a plateau at a p_T of $\sim$3 GeV/c. This dependence was reproduced by Monte Carlo calculations which included the tile threshold curves, the EMCal detector response, and the geometry of the active trigger tiles. The plateau level, 0.78 ± 0.03 for both PbSc and PbGl, was consistent with the geometrical acceptance of the active trigger tiles.

Since only a fraction of inelastic $p + p$ collisions produce particles which enter both BBCs, the MB trigger condition biased the recorded data sample, so only a fraction, f_{π^0}, of the inclusive π^0 yield was detected. This fraction was determined from data collected by an additional, high-p_T trigger which had not been operated in coincidence with the MB trigger. This trigger was formed by threshold discrimination of the sums of the analog signals from overlapping 2×2 groupings of adjacent 2×2 trigger tiles. As shown in Fig. 1(b), the fraction of these high-p_T events with π^0's for which the MB condition was also satisfied was 0.75 ± 0.02, independent of p_T.

In each event, the two photon invariant mass was calculated for each pairing of clusters. Clusters were paired if the energy asymmetry, $|E_1 - E_2|/(E_1 + E_2)$, was less than 0.8 (PbSc) or 0.7 (PbGl). For the PbGl, the pairings were further restricted to those clusters which were identified as electromagnetic via the shower profile and time of flight. The π^0 yield was extracted by integrating the invariant mass spectrum over a region around the π^0 mass. The background contribution in each p_T bin was estimated and then subtracted by fitting the invariant mass distribution outside the peak region (PbSc) or using the mixed event technique (PbGl). For the PbSc and the PbGl, the background to signal ratio varied with increasing p_T from 1 to 0.1 and 1 to 0.03, respectively.

The raw yields were corrected for the p_T smearing arising from the EMCal energy resolution and the steeply falling spectrum, and for the losses due to disabled towers, incomplete azimuthal coverage, energy asymmetry cut, and photon identification cut (PbGl). The correction for these effects, C_{reco}, was calculated with Monte Carlo simulations which contained the configuration of the active EMCal towers. The energy and position of the decay photons were smeared with the measured test beam resolutions [22] augmented by a constant energy smearing of 5% (12%) for the PbSc (PbGl) to match the response of the EMCal.

The correction for the losses due to conversions of decay photons, C_{conv}, was determined to be 4% (PbSc) and 9% (PbGl) by using a GEANT3 [23] simulation of the PHENIX detector. The same simulation, using $p + p$ events from the PYTHIA generator [24], showed that the contribution of π^0's from secondary interactions was negligible and that the contribution from decays of other hadrons (e.g., K^0 and η mesons) was less than 6%. The π^0 spectrum was not corrected for these decays.

The integrated luminosity, $\hat{\mathcal{L}}$, was determined from the number of MB events using an absolute calibration of the trigger cross section obtained via the van der Meer scan technique [25]. In a scan, the transverse profile of the beam overlap is measured by sweeping one beam across the other in steps while monitoring the MB trigger rate. This information, the bunch intensities of the two beams ($\sim 10^{11}$/bunch), and the revolution frequency (78 kHz) are then used to compute the instantaneous luminosity. The trigger cross section is the ratio of the MB trigger rate when the beams were overlapping maximally to the instantaneous luminosity. Based on three scans, this cross section was 21.8 ± 0.9 (2.8) mb at the 68.5% (95%) confidence level with an absolute error of 0.7 mb. From the linear sum of the absolute error and half of the 95% confidence level, point-to-point systematic error, an error of 9.6% was assigned for the luminosity normalization.

During the run, the maximum and average instantaneous luminosities were 1.5×10^{30} and 0.5×10^{30} cm^{-2} s^{-1}, respectively. Contributions from multiple collisions per bunch crossing and beam-gas interactions were negligible. The MB trigger sample of 16×10^6 events corresponded to 0.7 nb^{-1}. As computed from the fraction of recorded MB events which also met the 2×2 high-p_T trigger condition ($\sim 1/47$), the 18×10^6 high-p_T triggered events corresponded to an effective luminosity of 39 nb^{-1}.

The invariant differential cross sections obtained from the MB and high-p_T samples were consistent within the statistical errors over the p_T region of overlap ($p_T \leq 5.5$ GeV/c). Moreover, the results determined

independently from the PbSc and the PbGl data samples were consistent within the total error as computed as the quadrature sum of the statistical and point-to-point systematic errors. The main sources of the latter were (i) the absolute energy scale, (ii) the extraction of the yield, (iii) the correction of the yield for reconstruction efficiency, and (iv) the correction of the yield for the geometric acceptance. The magnitude of these errors is tabulated for a low- and a high-p_T bin in Table I.

From the MB and the high-p_T trigger samples for p_T below and above 4 GeV/c, respectively, the cross section and the errors were obtained by averaging the PbSc and PbGl results using the total error for the weighting. Figures 2(a) and 2(b) show this combined result and its fractional statistical and systematic uncertainties ($\Delta\sigma/\sigma$). The data are well parametrized by a power-law form $A(1 + p_T/p_0)^{-n}$ with parameters of $A = 393\ \text{mb}\,\text{GeV}^{-2}\,c^3$, $p_0 = 1.212$ GeV/c, and $n = 9.97$.

In Fig. 2, our results are compared with NLO pQCD calculations [26–28]. In these calculations, the cross section is factorized into parton distribution functions (PDFs) for the protons, parton-to-pion fragmentation functions, and short-distance partonic hard-scattering cross sections which can be evaluated using perturbative QCD. Because of this factorization, the calculations depend on unphysical, factorization and renormalization scales which are of the order of the hard scale p_T. This dependence is reduced as higher order terms are included in the perturbation expansion and thus serves as a gauge for the uncertainty of calculations truncated at a given order.

The calculations in Fig. 2 were performed with equal renormalization and factorization scales of $p_T/2$, p_T, and $2p_T$, the CTEQ6M [29] set of PDFs, and two sets of fragmentation functions. In general, these calculations are consistent with the data, even at low p_T (<2 GeV/c) where the theory might be expected to be less applicable. The calculations vary slightly (~15%) with the choice of PDFs, whereas they change markedly with the choice of fragmentation functions. As shown in Figs. 2(c) and 2(d), the calculation with the "Kniehl-Kramer-Pötter" (KKP) set of fragmentation functions [12] agrees with our data better than the calculation with the "Kretzer" set [13] does. These two sets differ mainly in that the gluon-to-pion fragmentation function, D_g^π, is greater in the KKP set. This difference is exhibited primarily at low p_T because of the dominance of gluon-gluon and gluon-quark interactions for p_T below ~10 GeV/c [26]. Our data are the first from a hadron experiment from which an unambiguous conclusion may be drawn about D_g^π.

In summary, the invariant differential cross section for inclusive neutral-pion production in $p + p$ collisions at $\sqrt{s} = 200$ GeV was measured at midrapidity ($|\eta| < 0.35$) as a function of p_T up to ~14 GeV/c. These results were compared with two NLO pQCD calculations which differed in the choice of fragmentation functions. Over the full range of p_T, the calculations were consistent with the results within the uncertainty of the calculations as judged from the scale dependence, although the results favored a larger gluon-to-pion fragmentation function.

TABLE I. Summary of the sources of systematic errors on the π^0 yields and the total systematic error for p_T of 1.2 and 10.9 GeV/c. The normalization error of 9.6% is not listed.

	% Error (PbSc)		% Error (PbGl)	
p_T (in GeV/c)	1.2	10.9	1.2	10.9
Energy scale	3	11	6	12
Yield extraction	7	4	5	5
Yield correction	3	6	6	11
Acceptance stability	4.5	4.5	3	2
Total	9	14	10	17

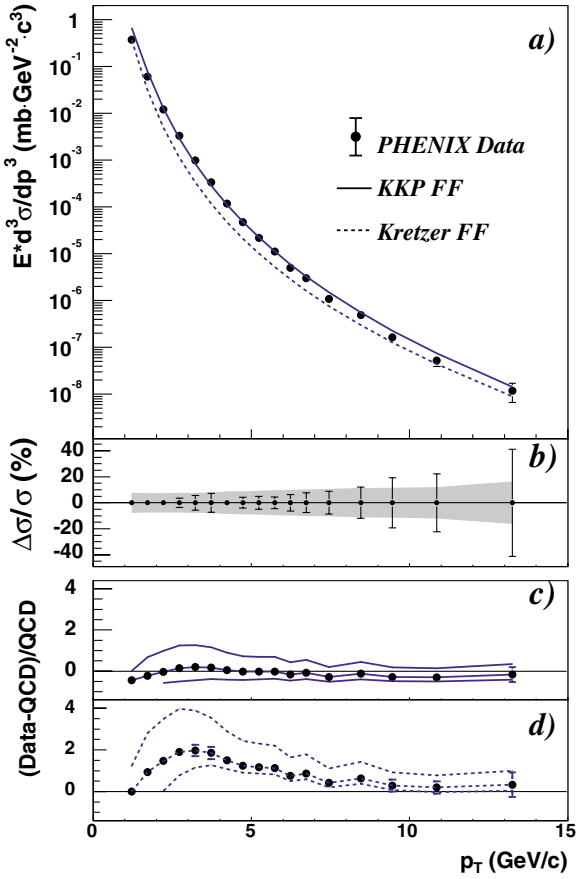

FIG. 2 (color online). (a) The invariant differential cross section for inclusive π^0 production (points) and the results from NLO pQCD calculations with equal renormalization and factorization scales of p_T using the "Kniehl-Kramer-Pötter" (solid line) and "Kretzer" (dashed line) sets of fragmentation functions. (b) The relative statistical (points) and point-to-point systematic (band) errors. (c),(d) The relative difference between the data and the theory using KKP (c) and Kretzer (d) fragmentation functions with scales of $p_T/2$ (lower curve), p_T, and $2p_T$ (upper curve). In all figures, the normalization error of 9.6% is not shown.

We thank the staff of the Collider-Accelerator and Physics Departments at BNL for their vital contributions. We thank Werner Vogelsang and Stefan Kretzer for their interest and input. We acknowledge support from the Department of Energy and NSF (U.S.A.), MEXT and JSPS (Japan), CNPq and FAPESP (Brazil), NSFC (China), CNRS-IN2P3 and CEA (France), BMBF, DAAD, and AvH (Germany), OTKA (Hungary), DAE and DST (India), ISF (Israel), KRF and CHEP (Korea), RAS, RMAE, and RMS (Russia), VR and KAW (Sweden), U.S. CRDF for the FSU, US-Hungarian NSF-OTKA-MTA, and US-Israel BSF.

*Deceased.
†PHENIX spokesperson.
Email address: zajc@nevis.columbia.edu

[1] J. F. Owens, Rev. Mod. Phys. **59**, 465 (1987).
[2] D. Stump *et al.*, J. High Energy Phys. 0310 (2003) 046.
[3] D. Acosta *et al.*, Phys. Rev. D **65**, 112003 (2002); V. M. Abazov *et al.*, Phys. Rev. Lett. **87**, 251805 (2001).
[4] M. Banner *et al.*, Z. Phys. C **27**, 329 (1985).
[5] P. Aurenche *et al.*, Eur. Phys. J. C **13**, 347 (2000).
[6] W. Vogelsang and M. R. Whalley, J. Phys. G **23**, Suppl. 7A, A1 (1997).
[7] E. Laenen *et al.*, Phys. Rev. D **63**, 114018 (2001).
[8] E706 Collaboration, L. Apanasevich *et al.*, Phys. Rev. D **68**, 052001 (2003).
[9] P. Aurenche *et al.*, Eur. Phys. J. C **9**, 107 (1999).
[10] L. Apanasevich *et al.*, Phys. Rev. D **63**, 014009 (2001).
[11] J. Binnewies *et al.*, Phys. Rev. D **52**, 4947 (1995).
[12] B. A. Kniehl *et al.*, Nucl. Phys. **B597**, 337 (2001).
[13] S. Kretzer, Phys. Rev. D **62**, 054001 (2000).
[14] S. Kretzer *et al.*, Eur. Phys. J. C **22**, 269 (2001).
[15] O. Biebel *et al.*, hep-ph/0109282.
[16] P. Abreu *et al.*, Eur. Phys. J. C **17**, 207 (2000); G. Abbiendi *et al.*, Eur. Phys. J. C **11**, 217 (1999); R. Barate *et al.*, Eur. Phys. J. C **17**, 1 (2000).
[17] L. Bourhis *et al.*, Eur. Phys. J. C **19**, 89 (2001).
[18] S. S. Adler *et al.*, Phys. Rev. Lett. **91**, 072301 (2003).
[19] G. Bunce *et al.*, Annu. Rev. Nucl. Part. Sci. **50**, 525 (2000).
[20] K. Adcox *et al.*, Nucl. Instrum. Methods Phys. Res., Sect. A **499**, 469 (2003).
[21] M. Allen *et al.*, Nucl. Instrum. Methods Phys. Res., Sect. A **499**, 549 (2003).
[22] L. Aphecetche *et al.*, Nucl. Instrum. Methods Phys. Res., Sect. A **499**, 521 (2003).
[23] GEANT 3.21, CERN program library.
[24] T. Sjöstrand, Comput. Phys. Commun. **82**, 74 (1994).
[25] K. A. Drees, Z. Xu, B. Fox, and H. Huang, in *Proceedings of the PAC2003 Conference, Portland, OR* (http://warrior.lbl.gov:7778/pac.html).
[26] F. Aversa *et al.*, Nucl. Phys. **B327**, 105 (1989); the authors wrote the computer code used for our calculations.
[27] B. Jäger *et al.*, Phys. Rev. D **67**, 054005 (2003).
[28] D. de Florian, Phys. Rev. D **67**, 054004 (2003).
[29] J. Pumplin *et al.*, J. High Energy Phys. 07 (2002) 012.

One-, two-, and three-particle distributions from 158*A* GeV/*c* central Pb+Pb collisions

M. M. Aggarwal,[1] A. L. S. Angelis,[4] V. Antonenko,[5] V. Arefiev,[6] V. Astakhov,[6] V. Avdeitchikov,[6] T. C. Awes,[7] P. V. K. S. Baba,[8] S. K. Badyal,[8] S. Bathe,[9] B. Batiounia,[6] T. Bernier,[10] K. B. Bhalla,[2] V. S. Bhatia,[1] C. Blume,[9] D. Bucher,[9] H. Büsching,[9] L. Carlén,[13] S. Chattopadhyay,[3] M. P. Decowski,[18] H. Delagrange,[10] P. Donni,[4] M. R. Dutta Majumdar,[3] K. El Chenawi,[13] K. Enosawa,[14] S. Fokin,[5] V. Frolov,[6] M. S. Ganti,[3] S. Garpman,[13] O. Gavrishchuk,[6] F. J. M. Geurts,[12] T. K. Ghosh,[16] R. Glasow,[9] B. Guskov,[6] H. Å. Gustafsson,[13] H. H. Gutbrod,[11] I. Hrivnacova,[15] M. Ippolitov,[5] H. Kalechofsky,[4] R. Kamermans,[12] K. Karadjev,[5] K. Karpio,[17] B. W. Kolb,[11] I. Kosarev,[6] I. Koutcheryaev,[5] A. Kugler,[15] P. Kulinich,[18] M. Kurata,[14] A. Lebedev,[5] H. Löhner,[16] D. P. Mahapatra,[19] V. Manko,[5] M. Martin,[4] G. Martínez,[10] A. Maximov,[6] Y. Miake,[14] G. C. Mishra,[19] B. Mohanty,[19] M.-J. Mora,[10] D. Morrison,[20] T. Mukhanova,[5] D. S. Mukhopadhyay,[3] H. Naef,[4] B. K. Nandi,[19] S. K. Nayak,[10] T. K. Nayak,[3] A. Nianine,[5] V. Nikitine,[6] S. Nikolaev,[5] P. Nilsson,[13] S. Nishimura,[14] P. Nomokonov,[6] J. Nystrand,[13] A. Oskarsson,[13] I. Otterlund,[13] T. Peitzmann,[9] D. Peressounko,[5] V. Petracek,[15] F. Plasil,[7] M. L. Purschke,[11] J. Rak,[15] R. Raniwala,[2] S. Raniwala,[2] N. K. Rao,[8] K. Reygers,[9] G. Roland,[18] L. Rosselet,[4] I. Roufanov,[6] J. M. Rubio,[4] S. S. Sambyal,[8] R. Santo,[9] S. Sato,[14] H. Schlagheck,[9] H.-R. Schmidt,[11] Y. Schutz,[10] G. Shabratova,[6] T. H. Shah,[8] I. Sibiriak,[5] T. Siemiarczuk,[17] D. Silvermyr,[13] B. C. Sinha,[3] N. Slavine,[6] K. Söderström,[13] G. Sood,[1] S. P. Sørensen,[20] P. Stankus,[7] G. Stefanek,[17] P. Steinberg,[18] E. Stenlund,[13] M. Sumbera,[15] T. Svensson,[13] A. Tsvetkov,[5] L. Tykarski,[17] E. C. v. d. Pijll,[12] N. v. Eijndhoven,[12] G. J. v. Nieuwenhuizen,[18] A. Vinogradov,[5] Y. P. Viyogi,[3] A. Vodopianov,[6] S. Vörös,[4] B. Wysłouch,[18] and G. R. Young[7]

(WA98 Collaboration)

[1]*University of Panjab, Chandigarh 160 014, India*
[2]*University of Rajasthan, Jaipur 302 004, Rajasthan, India*
[3]*Variable Energy Cyclotron Centre, Calcutta 700 064, India*
[4]*University of Geneva, CH-1211 Geneva 4, Switzerland*
[5]*RRC Kurchatov Institute, RU-123182 Moscow, Russia*
[6]*Joint Institute for Nuclear Research, RU-141980 Dubna, Russia*
[7]*Oak Ridge National Laboratory, Oak Ridge, Tennessee 37831-6372*
[8]*University of Jammu, Jammu 180 001, India*
[9]*University of Münster, D-48149 Münster, Germany*
[10]*SUBATECH, Ecole des Mines, Nantes, France*
[11]*Gesellschaft für Schwerionenforschung (GSI), D-64220 Darmstadt, Germany*
[12]*Universiteit Utrecht/NIKHEF, NL-3508 TA Utrecht, The Netherlands*
[13]*Lund University, SE-221 00 Lund, Sweden*
[14]*University of Tsukuba, Ibaraki 305, Japan*
[15]*Nuclear Physics Institute, CZ-250 68 Rez, Czech Republic*
[16]*KVI, University of Groningen, NL-9747 AA Groningen, The Netherlands*
[17]*Institute for Nuclear Studies, 00-681 Warsaw, Poland*
[18]*MIT, Cambridge, Massachusetts 02139*
[19]*Institute of Physics, 751-005 Bhubaneswar, India*
[20]*University of Tennessee, Knoxville, Tennessee 37966*

(Received 1 October 2002; published 31 January 2003)

Several hadronic observables have been studied in central 158*A* GeV Pb+Pb collisions using data measured by the WA98 experiment at CERN: single π^- and K^- production, as well as two- and three-pion interferometry. The Wiedemann-Heinz hydrodynamical model has been fitted to the pion spectrum, giving an estimate of the temperature and transverse flow velocity. Bose-Einstein correlations between two identified π^- have been analyzed as a function of k_T, using two different parametrizations. The results indicate that the source does not have a strictly boost invariant expansion or spend time in a long-lived intermediate phase. A comparison between data and a hydrodynamical based simulation shows very good agreement for the radii parameters as a function of k_T. The pion phase-space density at freeze-out has been measured, and agrees well with the Tomášik-Heinz model. A large pion chemical potential close to the condensation limit of m_π seems to be excluded. The three-pion Bose-Einstein interferometry shows a substantial contribution of the genuine three-pion correlation, but not quite as large as expected for a fully chaotic and symmetric source.

DOI: 10.1103/PhysRevC.67.014906 PACS number(s): 25.75.Gz

I. INTRODUCTION

The study of single-particle distributions of particles produced in heavy-ion collisions gives access to the degree of thermal and chemical equilibrium at freeze-out, and allows the determination of the parameters of hydrodynamical expansion models of the source. The spatiotemporal extension of the interaction region created in such collisions is not

 ©2003 The American Physical Society

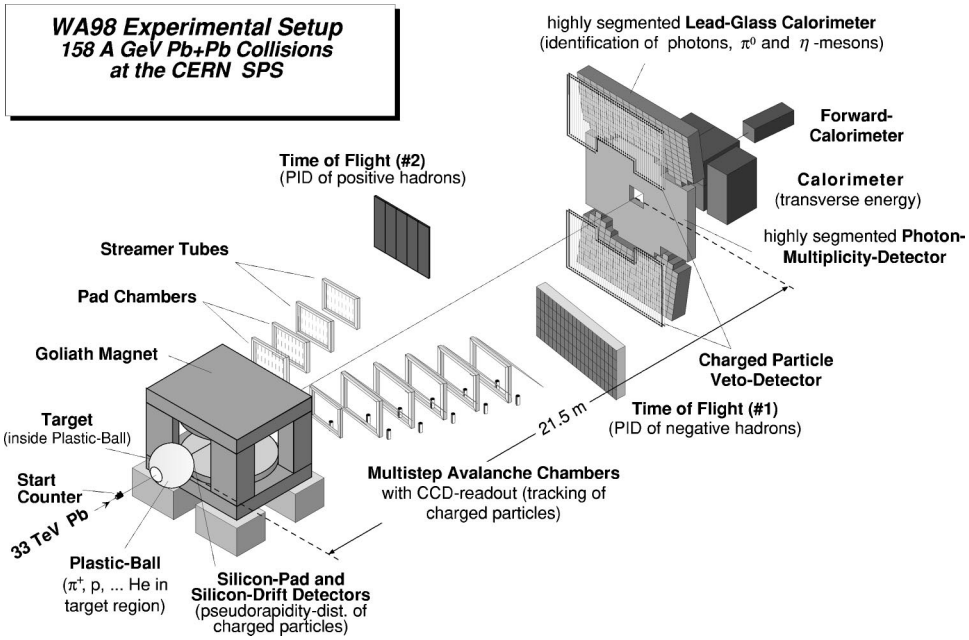

FIG. 1. The WA98 experimental setup.

directly observable, but the study of Bose-Einstein interferometry between identical particles provides information on the geometry and on the dynamical evolution of the particle emission sources. In particular, the correlations between produced pions give access to the size of the homogeneity region, to the duration of emission, and to various parameters characterizing the spatial extension of the fireball [1]. In addition, by combining information from the source size in momentum-space obtained by interferometry, and from the momentum-space density provided by the single-particle distributions, an average phase-space density at freeze-out can be calculated.

Compared to the two-particle correlation, the three-particle correlation can provide additional information on the chaoticity and asymmetry of the source emission [2–4]. In particular, the three-pion interference produced by a fully chaotic source is sensitive to the phase of the Fourier transform of the source emission function and, hence, to the asymmetry of the source.

In this paper, we present the analysis of single-particle production, and of two- and three-pion interferometry measured in the WA98 experiment for central 158*A* GeV ^{208}Pb+^{208}Pb collisions at the CERN SPS. In addition, estimates of hydrodynamical expansion model parameters, temperature and transverse flow velocity are extracted from these results.

II. EXPERIMENTAL SETUP AND DATA PROCESSING

The CERN SPS fixed target experiment WA98 [5] combined large acceptance photon detectors with a two arm charged particle tracking spectrometer. The experimental layout is shown in Fig. 1. The 158*A* GeV Pb beam interacted with a Pb target near the entrance of a large dipole magnet. The online trigger centrality selection used a forward calorimeter located at 0° and a midrapidity calorimeter measuring the total transverse energy in the pseudorapidity interval $3.2 \leqslant \eta \leqslant 5.4$. The results presented here have been obtained from an analysis of the complete data set. These data were taken with the most central triggers corresponding to about 10% of the minimum bias cross section of 6300 mb [6,7], with an average of 330 participating nucleons per collision. These quantities are estimated to have an overall systematic error of less than 10%. The charged particle spectrometer made use of a 1.6-Tm dipole magnet with a 2.4×1.6-m^2 air gap which deflected the charged particles in the horizontal plane into two tracking arms located downstream, one on each side of the beam axis. The results shown here are measurements of π^- and K^- observed in the negative particle tracking arm of the spectrometer. This tracking arm consisted of six multistep avalanche chambers with optical readout [8]. Inside the chambers, triethylamine photoemissive vapor produced UV photons along the path of charged particles, these photons being subsequently converted to visible light via wavelength shifter plates. On exit, the light was reflected by mirrors at 45° to CCD cameras equipped with two image intensifiers. The active area of the first chamber was 1.2×0.8 m^2 and that of the other five 1.6×1.2 m^2. Each CCD camera pixel viewed a region of about 3.1×3.1 mm^2 on the chambers. Downstream of the chambers, at a distance of 16.5 m from the target, a 4×1.9-m^2 time of flight wall allowed for particle identification with a time resolution of better than 120 ps. The resulting particle separation is shown in Fig. 2. The π^- rapidity acceptance ranged from $y=2.1$ to 3.1 with a rapidity average at 2.7, close to the midrapidity value of 2.9. The momentum resolution of the spectrometer was $\Delta p/p=0.005$ at $p=1.5$ GeV/c, resulting in an average precision of better than or equal to 10 MeV/c at vanishing p_T for all the Q variables used in the correlation analysis and defined in Secs. IV and VI: $\sigma(Q_{inv})=7$ MeV/c, $\sigma(Q_{TO})=10$ MeV/c, $\sigma(Q_{TS})=5$ MeV/c, $\sigma(Q_L)=3$ MeV/c, $\sigma(Q_T)=8$ MeV/c, $\sigma(Q_0)=5$ MeV/c, and $\sigma(Q_3)=7$ MeV/c. Severe track quality cuts were applied, resulting in a final sample of 7.9×10^6 π^-, providing 13.7×10^6 pairs

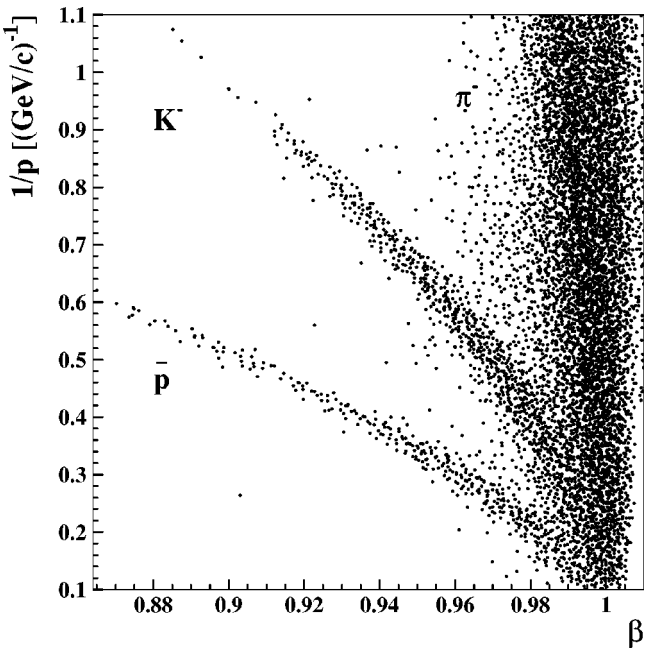

FIG. 2. Particle identification in the negative arm of the spectrometer.

and 13.1×10^6 triplets for the Bose-Einstein correlation analysis.

III. SINGLE-PARTICLE SPECTRA AND HYDRODYNAMICAL MODEL

The study of inclusive distributions of single particles produced in heavy-ion collisions can be interpreted in the context of models of the source using hydrodynamical expansion. Within the context of such models, which assume local thermal equilibration, parameters like the temperature and collective velocity at freeze-out can be determined. In the limit of a stationary fireball, the distribution takes the simple form [9]

$$E\frac{dN}{dp^3}\equiv\frac{dN}{m_T dm_T dy d\phi}\propto E\mathrm{e}^{-(E-\mu)/T}, \tag{1}$$

where p is the Cartesian particle momentum, $m_T \equiv\sqrt{p_T^2+m_0^2}$ is the transverse mass, p_T is the transverse momentum, m_0 is the rest mass, y is the rapidity, $E=m_T\cosh(y-y_{fireball})$, μ is the chemical potential, and T is the temperature.

In the limit where only a narrow rapidity interval close to $y_{fireball}$ is measured, the spectrum becomes

$$E\frac{dN}{dp^3}\sim m_T\mathrm{e}^{-m_T/T},$$

and, in the case of a rapidity-integrated spectrum,

$$\frac{dN}{m_T dm_T}\propto m_T K_1\left(\frac{m_T}{T}\right)\rightarrow\sim\sqrt{m_T}\mathrm{e}^{-m_T/T}$$

where K_1 is a modified Bessel function. The last approximation holds in the limit $m_T\gg T$. Plotted against m_T-m_0, all particles from a thermalized emitter should show the same universal exponential behavior. However, different additional features like transverse hydrodynamic expansion or particles originating from the decay of resonances will distort the shape of the spectrum. It was noted in Ref. [10] that for the popular fit with a simple exponential in m_T (without the m_T prefactor),

$$E\frac{dN}{dp^3}=C\mathrm{e}^{-m_T/T}, \tag{2}$$

an interpretation of the resulting slope parameter in terms of a temperature is not possible. However, since it is found to fit the measured spectrum better than the previous expressions, it is useful for obtaining an estimate of the inverse slope parameter T.

A. Data analysis

A detailed description of the analysis of the single particle spectra presented here can be found in Ref. [11]. The correction for detector acceptance and efficiency applied to the measured spectrum is based on a precise simulation of the detector, tuned in order to reproduce the measured detector response as accurately as possible using the VENUS [12] event generator as input. Multiple scattering, decays, and all other reactions within the detector material are taken into account. Efficiency maps depending on the hit position on each chamber, the particle momentum, and its identity are applied, together with position resolution and noise simulation. Simulated events are then reconstructed using the same code as for real data, ensuring that any software-induced systematics are also taken into account. The output is then matched to the VENUS input. This correction procedure ensures that the final result is little sensitive to remaining contamination, such as pions in a kaon sample. A detailed study of the systematic uncertainty has been performed and it is found to be small, especially as regards the slope of the spectrum ($\sim$3%). The absolute normalization, on the other hand, is more sensitive to detector instabilities which could not be perfectly simulated, and is found to have an estimated uncertainty of at most 20%.

Since the statistical uncertainty on the final m_T spectrum is negligible compared to the systematics, it is possible to apply very severe quality cuts on the reconstructed tracks and on the events used.

In contrast to the Bose-Einstein analysis, only a subset of all data is kept using only run periods where the detector operation remained particularly stable. The analysis is performed separately for identified π^- and K^-. The final data sample consists of 4.7×10^5 π^- tracks and 1.8×10^4 K^-

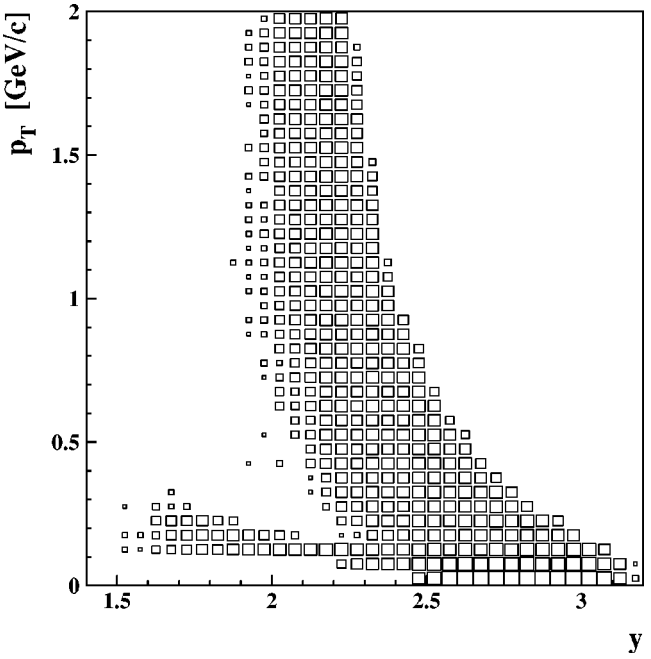

FIG. 3. Acceptance of tracking arm I in the (p_T, y) plane for pions.

drawn from 3.8×10^5 central events. Figures 3 and 4 show the detector acceptance for negative pions and kaons, respectively, obtained from the simulation. The π^-/π^+ ratio and the K^-/K^+ ratio of the number of detected pions and kaons have also been measured using two opposite magnetic field polarities. The results will be presented in a separate publication.

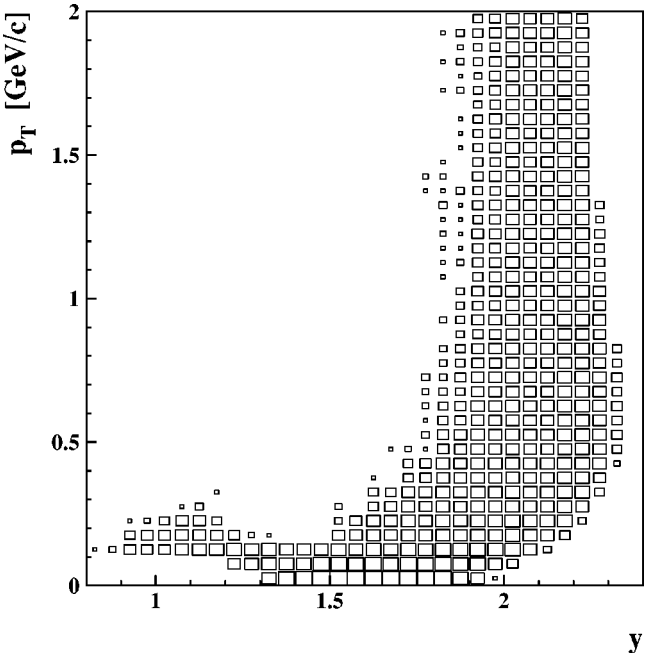

FIG. 4. Acceptance of tracking arm I in the (p_T, y) plane for kaons.

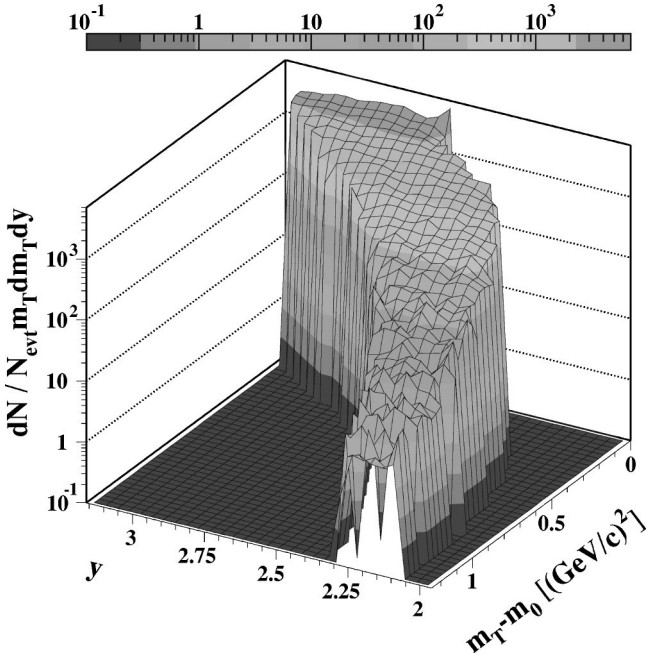

FIG. 5. Two-dimensional (fully corrected) single pion spectrum as a function of the two variables m_T and y.

B. Results

Figure 5 shows the final (fully corrected) single-particle spectrum for π^- plotted as a function of the two variables m_T and y. The form of the detector acceptance shown in Fig. 3 is clearly noticeable, except for the low p_T-low y lobe, which has been omitted here.

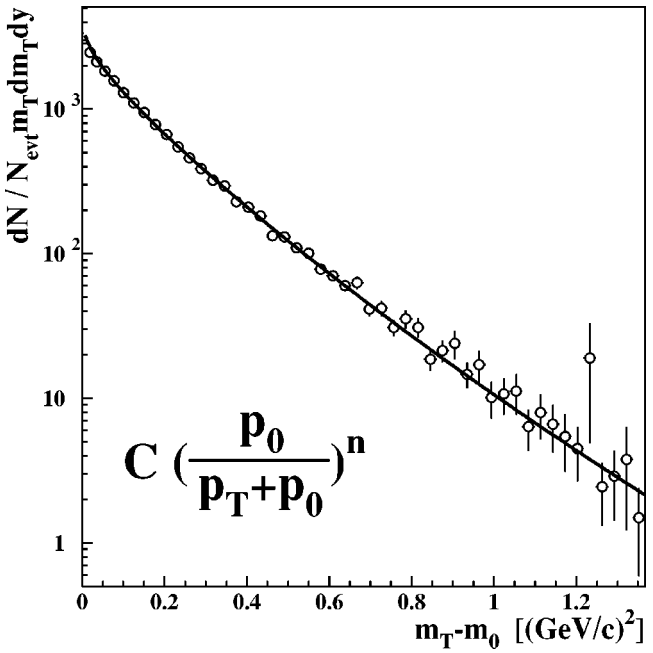

FIG. 6. One-dimensional (fully corrected) m_T spectrum for π^-. The errors are statistical. The power-law fit of Eq. (3) is superimposed on the data points. The fit interval is $m_T - m_0 = [0.05, 1.2]$ GeV/c^2.

Figure 6 shows the projection on the m_T axis (normalized to a unit rapidity interval using the VENUS profile) of the two-dimensional spectrum of Fig. 5. A fit to the exponential form of Eq. (2) over the interval $m_T - m_0 = [0.1,1.2]$ GeV/c^2 (not shown in Fig. 6) yields $C = 5220 \pm 80$ (stat.) $^{+1270}_{-200}$(syst.), and $T = 0.168 \pm 0.001$ (stat.) $^{+0.001}_{-0.005}$ (syst.) GeV, with a χ^2 per degree of freedom of 1.6. This result is in agreement with the NA49 result [13].

At high p_T, where perturbative QCD becomes applicable, the spectra are expected to attain a power-law behavior as observed in numerous high-energy pp measurements (see, for example, Ref. [14]). The heavy-ion data of this experiment seem to follow that trend even into the lower p_T range. Therefore, a parametrization originally inspired by QCD [15] and successfully applied already to *pp* data [14] and heavy-ion data [16] can be used to fit the spectrum,

$$E\frac{d^3\sigma}{dp^3} = C\left(\frac{p_0}{p_T + p_0}\right)^n, \tag{3}$$

with C, p_0, and n taken as free parameters. A link to the more familiar exponential slope parameter T is obtained from the derivative of this expression according to

$$T_{\text{power-law}} = -\frac{f(p_T)}{\dfrac{\partial f(p_T)}{\partial p_T}} = \frac{p_0}{n} + \frac{p_T}{n}.$$

Thus, p_0/n characterizes the slope of the transverse momentum spectrum in the limit $p_T \to 0$, while $1/n$ characterizes its gradient along p_T, i.e., the strength of the concave curvature. The extracted parameters are $C = 4150 \pm 70$, $p_0 = 4.80 \pm 1.04$ GeV/c and $n = 29.0 \pm 5.9$, which gives a slope parameter $T \equiv p_0/n = 0.166 \pm 0.005$ GeV. The χ^2 per degree of freedom is 1.0. The same fit performed on the π^0 spectrum, measured by the WA98 experiment [7,6,17,18], yields $C = 5120 \pm 140$, $p_0 = 5.08 \pm 0.18$ GeV/c, $n = 29.3 \pm 0.8$, and so $T = 0.173 \pm 0.002$ GeV. The acceptance for the π^0 measurement being different, it is interesting to note that fitting only the $p_T = [0.3,1.4]$ GeV/c common interval of both spectra yields $T = 0.169$ GeV for π^- and $T = 0.166$ GeV for π^0, showing that the result is stable with respect to the fit interval and that the spectra agree quite well.

It has also been shown that fluctuation of the parameter in an exponential distribution leads to a final distribution of the powerlike form [19]. This behavior can be interpreted in terms of a suitable application of the nonextensive statistics of Tsallis [20]. This interpretation is convenient to describe particle production at fluctuating T, as may occur near the phase transition. These fluctuations would exist in small parts of the hadronic system with respect to the whole system rather than between events. The average $\langle T \rangle$ around which the temperature fluctuates is given by $p_0/n = 0.166$ GeV, and the relative variance of $1/T$ is

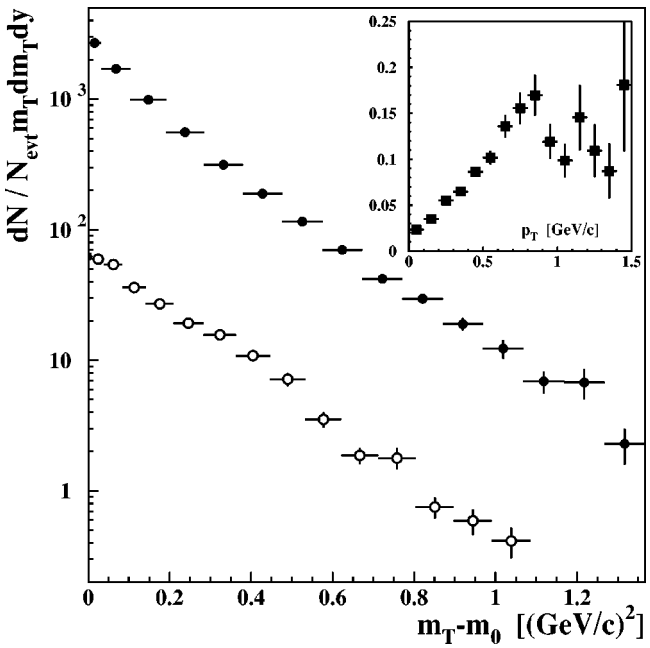

FIG. 7. π^- (black circles) and K^- (empty circles) single-particle spectra. The error bars are statistical only. Note that for the same transverse mass, p_T is different for pions and kaons. The inset shows the (bin by bin) ratio of the two p_T spectra.

$$\omega = \frac{\left\langle \left(\frac{1}{T}\right)^2 \right\rangle - \left\langle \frac{1}{T} \right\rangle^2}{\left\langle \frac{1}{T} \right\rangle^2} = \frac{1}{n} = 0.034,$$

both for π^- and π^0.

This corresponds to a nonextensivity parameter $q = 1 + \omega$ of 1.034. This result, interpreted in the spirit of Ref. [19], indicates a relative fluctuation $\Delta T/T$ of $18.4 \pm 1.9\%$ ($18.4 \pm 0.3\%$) for the π^- (π^0) measurement. However, this analysis neglects the contributions of resonance decays and flow velocity distributions. Both of these effects increase the curvature of the pion spectrum. Thus the value of $\Delta T/T = 18.4\%$ should be considered an upper limit on the temperature fluctuations.

The averaged negative pion yield per unit rapidity in the acceptance window is $1/N_{\text{evt}} dN/dy = 129 \pm 1$ (stat.) $^{+23}_{-5}$(syst.). Figure 7 shows the same plot as above for kaons. A fit to the exponential form 2 yields $C = 1000 \pm 120$ (stat.) $^{+260}_{-1}$ (syst.), and $T = 0.181 \pm 0.005$ (stat.) $^{+0.001}_{-0.009}$ (syst.) GeV. So the inverse slope T for kaons and pions are comparable. It should be noted that the rapidity acceptance is quite different for the two particle species, the π^- acceptance being much closer to midrapidity. An estimate of the effect induced by this difference in acceptance can be made using the term $\cosh(\Delta y)$ given below Eq. (1). The inverse slope for K^- would become of the order of 0.230 GeV. The K^-/π^- ratio at a common rapidity of 2.3 is 11.4 ± 0.4 (stat.) $^{+0.6}_{-2.7}$ (syst.)%, which is in agreement with the NA49 result [13].

C. Hydrodynamical source expansion model

The single pion spectrum has been fitted in the interval $0.05 < m_T - m_0 < 1.2$ GeV/c^2 with the Wiedemann-Heinz (W.-H.) model [21–26]. It relies on the following idea: the main characteristics of the particle phase-space distribution at freeze-out can be quantified by its widths in the spatial and temporal directions, a collective dynamical component (parametrized by a flow field) which determines the strength of the position-momentum correlations in the source, and a second, random dynamical component in momentum space (parametrized by a temperature). The model emission function contains seven parameters, but the shape of the single-particle transverse mass spectrum is fully determined by the temperature T and the transverse flow rapidity profile $\eta_T(r) = \eta_f(r/R)$ which is assumed to depend linearly on the transverse coordinate r, where η_f is the transverse flow rapidity strength, and R the Gaussian transverse spatial width. The mean transverse flow velocity $\langle \beta_T \rangle$ can be easily calculated as the mean value of $\tanh[\eta_T(r)]$ over the transverse source profile. The results will be given as a function of $\langle \beta_T \rangle$ rather than η_f, since its physical interpretation is more straightforward.

The three parameters that are allowed to vary freely during the fitting procedure are T, η_f, and an overall normalization factor. The result of the fit is $T = 0.084 \pm 0.003$ GeV and $\langle \beta_T \rangle = 0.50 \pm 0.02$, the χ^2/d.o.f. being 1.1. The resulting curve is not shown in Fig. 6 as it is hardly distinguishable from the power-law fit. The temperature and flow parameters are strongly correlated, so it is more interesting to consider a χ^2 contour plot of the fit to the measured single particle spectrum as a function of those two parameters. Figure 8 shows the result assuming a Gaussian transverse spatial profile, and Fig. 9 assuming a box profile of the same rms width as the Gaussian one. Only direct pions are considered in the model. Furthermore, only statistical errors are taken into account during the fit. The curves displayed represent different confidence levels for the $(T, \langle \beta_T \rangle)$ values.

The dependence of the χ^2/d.o.f. on the shape of the source is very small, the best χ^2/d.o.f. being slightly larger for the box profile (1.5). While the best fit temperature appears to be independent of the shape of the source, the best fit flow velocity is considerably smaller ($\langle \beta_T \rangle = 0.29$) for the box profile. Inclusion of the resonance decay contribution in the model calculation would be expected to reduce the extracted flow velocity parameters and increase the temperature parameters. The precise effects do however depend on details of the models used.

IV. TWO-PION CORRELATIONS

Bose-Einstein interferometry is most commonly used to study pairs of identical particles. The correlation function C_2 is defined, up to a proportionality factor $\mathcal{N}$, as the ratio of a two-particle spectrum $\mathcal{P}_2$ over the product of two single-particle spectra $\mathcal{P}_1$,

$$C_2(\vec{p}_1, \vec{p}_2) = \mathcal{N} \frac{\mathcal{P}_2(\vec{p}_1, \vec{p}_2)}{\mathcal{P}_1(\vec{p}_1) \cdot \mathcal{P}_1(\vec{p}_2)},$$

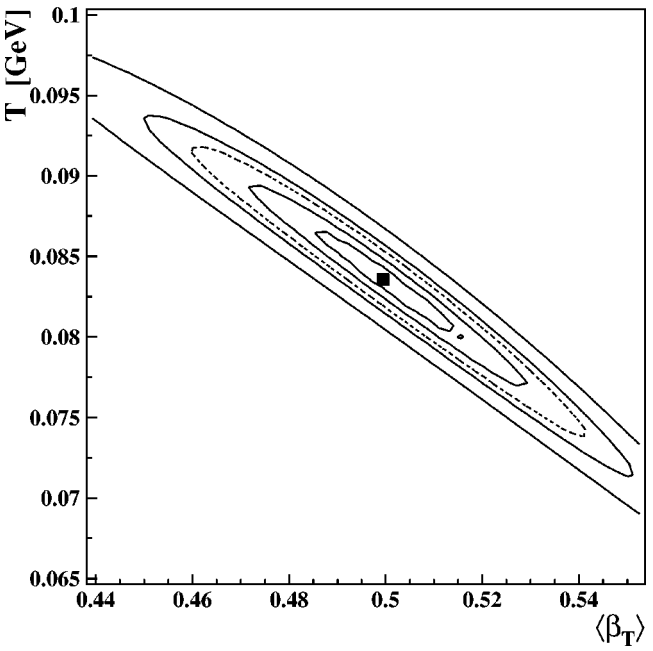

FIG. 8. χ^2 contour plot of the hydrodynamical model fit to the measured π^- single-particle spectrum of Fig. 6. A Gaussian profile is assumed for the transverse spatial profile of the source. The curves displayed represent successively (starting with the innermost one) contours at 50% C.L., 90% C.L., 99% C.L. (dashed line), and 99.9% C.L., and the last curve indicates a highly excluded region. The black square represents the best parameter values.

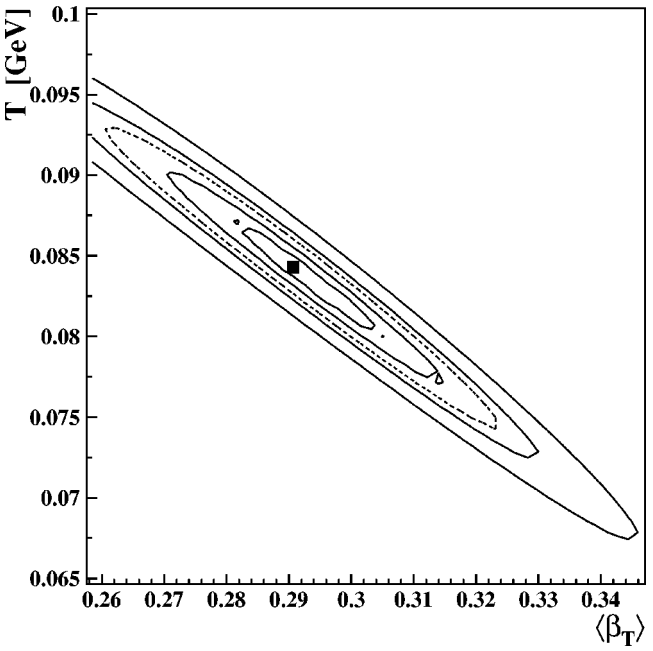

FIG. 9. Same plot as in Fig. 8, but assuming a box profile for the transverse spatial profile of the source.

with

$$\mathcal{P}_1(\vec{p}) = E\frac{dN}{dp^3}$$

and

$$\mathcal{P}_2(\vec{p}_1,\vec{p}_2) = E_1E_2\frac{dN}{dp_1^3 dp_2^3},$$

where E_i and $\vec{p}_i$ are the energy and momentum of particle i, respectively.

Experimentally, the product of one-particle distributions in the denominator is commonly obtained by a mixed event technique whereas the two-particle distribution in the numerator is constructed from all pair combinations of identical particles found in each event. C_2 is then normalized to unity far away from the interference region.

A fully chaotic source can be seen as a superposition of uncorrelated elementary sources, and one- and two-particle distributions may be expressed through the Wigner function of the source $S(x,k_{12})$ [1]. The correlation function is then written

$$C_2(\vec{p}_1,\vec{p}_2) = 1+\lambda\frac{\left|\int d^4x S(x,k_{12})\exp[iq_{12}x]\right|^2}{\left|\int d^4x S(x,k_{12})\right|^2}$$

with $q_{12}=p_1-p_2$ the four–momentum difference of the two particles, $k_{12}=(p_1+p_2)/2$, and $x=(x_1+x_2)/2$ the mean space-time coordinate of the pair emission point. The chaoticity parameter λ is inserted to take into account the possibility that the source may not be fully chaotic and also that any wrongly reconstructed tracks, or tracks originating from decays of long-lived resonances, will dilute the Bose-Einstein correlations in the data. A one-dimensional interferometry analysis is commonly made as a function of $Q_{inv} \equiv \sqrt{-q_{12}^2}$, whereas a multidimensional analysis uses a set of Q variables which are defined as various projections of q_{12}.

A. Data analysis and results

Two independent analyses were performed with the complete data set recorded in the negative tracking arm [11,27] totalling 13.7×10^6 pairs of identified π^-. These data were corrected for resolution and Coulomb effects in an iterative way [28]. The Gamow correction was not used as it overcorrects the data in the Q_{inv} range of 0.1–0.3 GeV/c. Because the finite resolution in the measurement of the Q variables leads to an underestimate of the radii and λ parameters, a correction has to be implemented in the fitting procedure. This is done by a convolution method, replacing the $C_2(\vec{Q})$ formula expressing the two-particle correlation function used to fit the data by

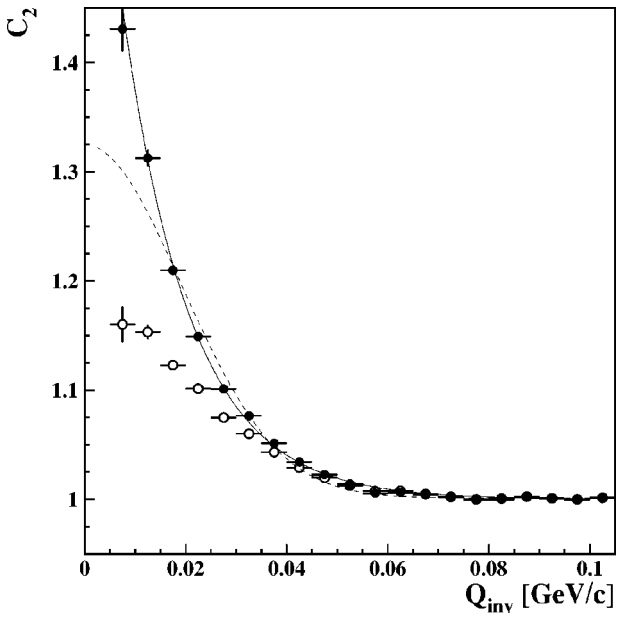

FIG. 10. The measured two-pion correlation function C_2 (full symbols), corrected for resolution and Coulomb effects, as a function of Q_{inv}. The full line is a fit to an exponential form, whereas the dashed curve is a fit to a Gaussian form. The empty symbols show the data before corrections.

$$C_2^{rc}(\vec{Q}) = \int\int\int r(\vec{Q},\vec{Q}')C_2(\vec{Q}')d\vec{Q}',$$

where $r(\vec{Q},\vec{Q}')$ is the resolution function which is chosen to be Gaussian:

$$r(\vec{Q},\vec{Q}') = 1/(2\pi)^{3/2}1/|V|^{1/2} \times\exp[-1/2(\vec{Q}-\vec{Q}')^T V^{-1}(\vec{Q}-\vec{Q}')].$$

The diagonal elements of the covariance matrix V are set equal to the square of the various Q resolutions, which are estimated by a full simulation of the experimental setup as a function of the $k_T=|\vec{p}_{T1}+\vec{p}_{T2}|/2$ of the pairs. The nondiagonal elements of V are neglected, as the resolution correction has a very small effect compared to the Coulomb correction. Figure 10 shows C_2, the measured $\pi^-\pi^-$ correlation function, plotted as a function of Q_{inv} before and after the resolution and Coulomb corrections. In the plot, the correction for resolution is obtained by multiplying each data point by $C_2^{rc}(Q_{inv})/C_2(Q_{inv})$. C_2 is clearly exponential [29]. The solid curve is a fit of the form $1+\lambda_e\exp[-2Q_{inv}R_{inv}]$ which gives $R_{inv}=7.33\pm0.08$ fm and $\lambda_e=0.788\pm0.009$ for $\langle k_T\rangle = 0.116$ GeV/c. This exponential behavior appears not to hold in the three-dimensional analysis, where projected slices are better represented by Gaussians.

The three-dimensional analysis of Bose-Einstein correlations has been done using two different parametrizations in the longitudinally comoving system (LCMS): the standard Pratt-Bertsch fit (PB) in the three-dimensional space of momentum differences Q_{TS} (perpendicular to the beam axis and

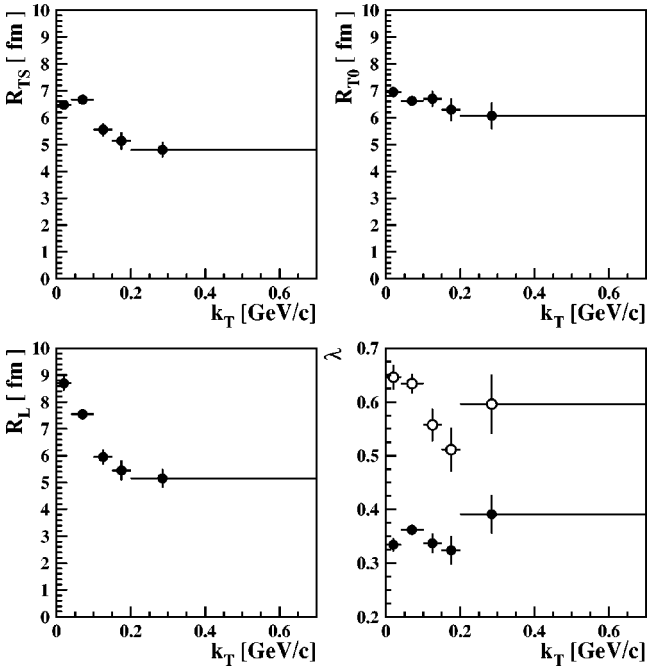

FIG. 11. The k_T dependence of the Pratt-Bertsch parameters. The points are plotted at the average k_T of the bin, and the horizontal bars indicate the bin width. The open symbols in the figure at bottom right show the λ parameter after correction for background from misidentified pions, as explained in Sec. V.

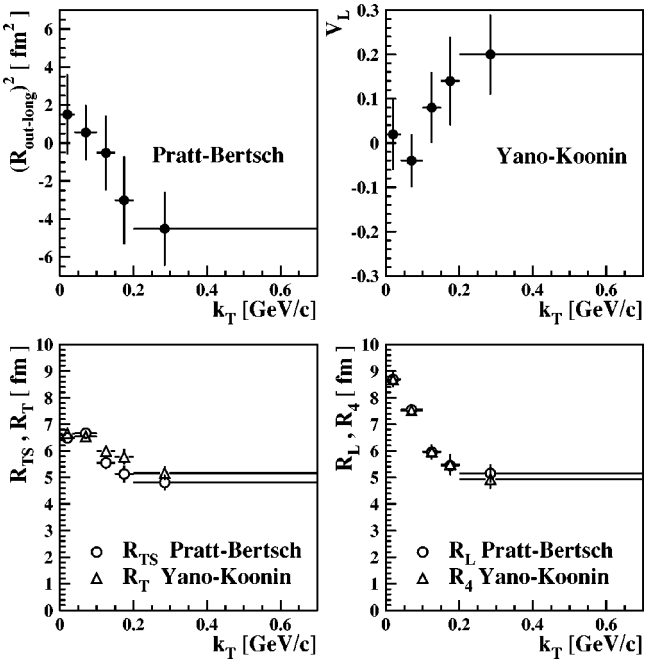

FIG. 12. Comparison between the PB and YKP fits in the LCMS. The cross term $R^2_{out\text{-}long}$ from the PB fit and v_L from the YKP fit both show a deviation from zero at large k_T when estimated in the LCMS. The R_{TS} and R_L parameters from the PB fit are in good agreement with, respectively, R_T and R_4 from the YKP fit.

to the transverse momentum of the pair), Q_{TO} (perpendicular to the beam axis and parallel to the transverse momentum of the pair), and Q_L (parallel to the beam axis) [30], including a cross term $R^2_{out\text{-}long}$ as predicted [31],

$$C_2 = 1 + \lambda \exp[-Q_{TS}^2 R_{TS}^2 - Q_{TO}^2 R_{TO}^2 - Q_L^2 R_L^2 - 2 Q_{TO} Q_L R^2_{out\text{-}long}],$$

and the Yano-Koonin-Podgoretskiĭ fit (YKP) [21] in the Q_0 (energy difference of the pair), Q_T, Q_L space,

$$C_2 = 1 + \lambda \exp[-Q_T^2 R_T^2 + (Q_0^2 - Q_L^2) R_4^2 - (Q \cdot U)^2 (R_0^2 + R_4^2)],$$

where $U = \gamma(1,0,0,v_L)$, $\gamma = 1/\sqrt{1 - v_L^2}$ with v_L in units of $c = 1$.

In the YKP parametrization the different radii are invariant under a longitudinal Lorentz boost, and the speed parameter v_L connects the local rest frame to the measurement frame (the LCMS in our case). The results as a function of the k_T of the pairs are shown in Figs. 11 and 12 and summarized in Table I. The λ parameters of the YKP fit (not shown in Table I) are found compatible with the λ parameters of the PB fit.

The systematic errors, not included in Figs. 11 and 12, and Table I, are estimated by varying the different analysis cuts, including the cuts used to identify the pion with the time of flight system. The systematic error on the Coulomb correction due to the error on the determination of the radius parameters is also taken into account. All these variations are added in quadrature. The total relative systematic errors on the radii $\Delta R/R$ amount to 0.8% for R_{inv}, 1.4% for R_{TS}, 3.5% for R_{TO}, 9.1% for R_L, 0.8% for R_T, and 9.7% for R_4. Systematic errors on $R^2_{out\text{-}long}$ and v_L are asymmetric and reach, respectively, $^{+2.2}_{-1.7}$ fm^2 and $^{+0.13}_{-0.08}$.

The R_{TS} and R_L parameters from the PB fit are in good agreement, respectively, with R_T and R_4 from the YKP fit. The cross term $R^2_{out\text{-}long}$ from the PB fit and v_L from the YKP fit deviate from zero.

In a source undergoing a boost invariant expansion the local rest frame coincides with the LCMS. Both the cross term and v_L expressed in the LCMS are then expected to vanish [21]. As this is not quite the case, it suggests that the source seen within the acceptance does not have a strictly boost invariant expansion. The strong decrease of the longitudinal radius R_L or R_4 with k_T compared to the transverse radii R_T, R_{TS}, and R_{TO} shows a longitudinal expansion which is larger than the transverse one. Finally, the R_0 parameter (not shown in the figures), which corresponds to the duration of emission of particles from the source, is compatible with zero for all k_T bins, excluding a long-lived intermediate phase. These results agree with the previously published WA98 results obtained using roughly half of the present data sample [29]. The WA98 analysis is compatible with the NA49 results obtained in a slightly different rapidity range ($\langle y \rangle = 3.2$) with unidentified negative particles [32]. The direct comparison with the NA44 results is not possible because NA44 and WA98 do not have the same rapidity range. The smaller R_{TO} measured by NA44 [33] can be explained by the larger rapidity range of its acceptance ($3.1 < y < 4.1$).

TABLE I. Three-dimensional analysis as a function of k_T for the PB and YKP fits. λ after correction for backgrounds from misidentified pions is also shown.

$\langle k_T \rangle$	0.02 GeV/c	0.07 GeV/c	0.125 GeV/c	0.175 GeV/c	0.285 GeV/c
R_{TS}	6.48±0.18 fm	6.67±0.15 fm	5.55±0.24 fm	5.13±0.32 fm	4.81±0.29 fm
R_{TO}	6.95±0.20 fm	6.62±0.16 fm	6.70±0.29 fm	6.29±0.43 fm	6.07±0.50 fm
R_L	8.69±0.26 fm	7.54±0.19 fm	5.95±0.27 fm	5.45±0.37 fm	5.15±0.34 fm
$R^2_{out\text{-}long}$	1.51±2.11 fm^2	0.55±1.45 fm^2	−0.52±1.96 fm^2	−3.01±2.31 fm^2	−4.51±1.94 fm^2
λ	0.334±0.012	0.362±0.010	0.337±0.018	0.324±0.026	0.391±0.036
λ_{cor}	0.646±0.023	0.634±0.018	0.557±0.030	0.511±0.041	0.596±0.055
R_T	6.66±0.14 fm	6.54±0.13 fm	5.99±0.19 fm	5.78±0.29 fm	5.17±0.26 fm
R_4	8.68±0.26 fm	7.52±0.19 fm	5.97±0.28 fm	5.49±0.39 fm	4.94±0.35 fm
v_L	0.02±0.08 fm	−0.04±0.06 fm	0.08±0.08 fm	0.14±0.10 fm	0.20±0.09 fm

B. Comparison with a hydrodynamical model based simulation

The W.-H. model can be used to generate correlation functions which can be compared to the data. For that purpose, all necessary integrations are performed numerically [25] to get the value of C_2 in the PB parameterization for given values of Q_{TS}, Q_{TO}, Q_L, k_T, and the rapidity $Y=(y_1+y_2)/2$ of a pair. To simulate properly the acceptance of the negative tracking arm, the mean values of k_T and Y for each (Q_{TS},Q_{TO},Q_L) bin are calculated using real data, and then for each bin the mean values $(\langle Q_{TS}\rangle,\langle Q_{TO}\rangle,\langle Q_L\rangle,\langle k_T\rangle,\langle Y\rangle)$ are used as input for the hydrodynamical calculation. This procedure is repeated for all five k_T intervals used in the data analysis. The correlation functions are generated neglecting contribution from resonances, using $T=85$ MeV, $\eta_f=0.5$ (values extracted from the single-particle spectra analysis), $R=8$ fm, $\tau_0=11$ fm/c, $\Delta\tau=2$ fm/c, and $\Delta\eta=1.3$ (see Ref. [25] for definitions of the parameters). Figure 13 shows the Bose-Einstein radii extracted from fitting the simulated correlation functions with the PB formula. The error bars used to perform these fits are taken to be the same as the ones calculated for the real data in each (Q_{TS},Q_{TO},Q_L) bin. The measured results are shown on the same plot, and the agreement is found to be good. The shift in the the cross term $R^2_{out\text{-}long}$ between data and simulation is compatible with the systematic uncertainty.

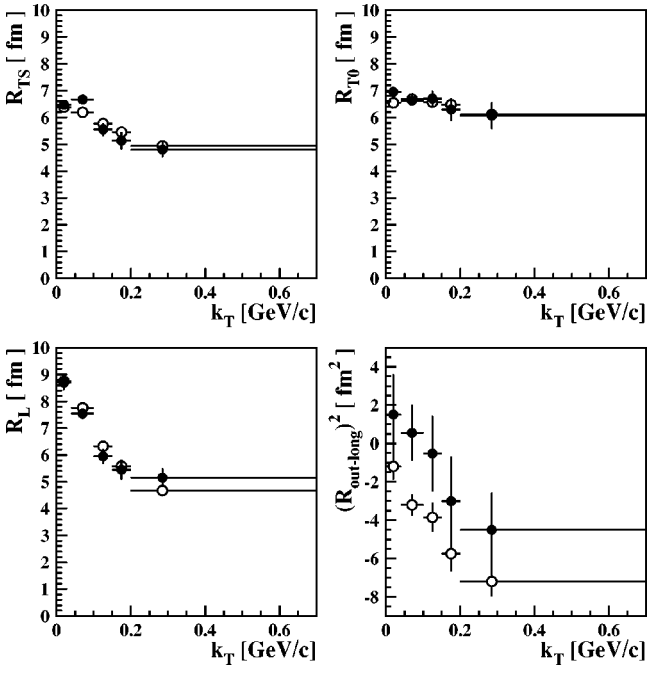

FIG. 13. Comparison between simulation and data as a function of k_T. The open symbols are the result of the fit of the PB formula to the correlation functions produced by the hydrodynamical model, whereas the full symbols are the result of the fit to the data.

V. AVERAGE PION PHASE-SPACE DENSITY AT FREEZE-OUT

As the m_T spectrum gives the momentum-space density at freeze-out and as the Bose-Einstein correlation radii provide information on the covariant volume for particles of momentum $\vec{p}$, it is possible, by combining these results, to extract the average phase-space density $\langle f\rangle(p_T,y)$ at freeze-out [34,35],

$$\langle f\rangle = \frac{\sqrt{\lambda}}{\left(\frac{E_\pi}{\pi^{3/2}}\right) R_{TS}\sqrt{R^2_{TO}R^2_L - R^4_{out\text{-}long}}} \frac{dn}{dy p_T dp_T d\phi}$$

with $E_\pi=\sqrt{m_\pi^2+p^2}=m_T\cosh y$. The radii and λ are functions of p_T and y. The factor λ, which comes from the two-pion correlation analysis, corrects for contributions of pions originating from long-lived resonances decaying close to the primary vertex. A difficulty of this method is to include only the contribution of the real pions in the determination of λ, excluding backgrounds from misidentified particles. This is achieved by applying to λ, separately for each k_T bin, a correction factor obtained from a full simulation of the experimental setup, taking into account geometrical acceptance, backgrounds and efficiency of the chamber-camera-time of flight system. The effects can be seen in Fig. 11, bottom right, where λ with and without correction is displayed.

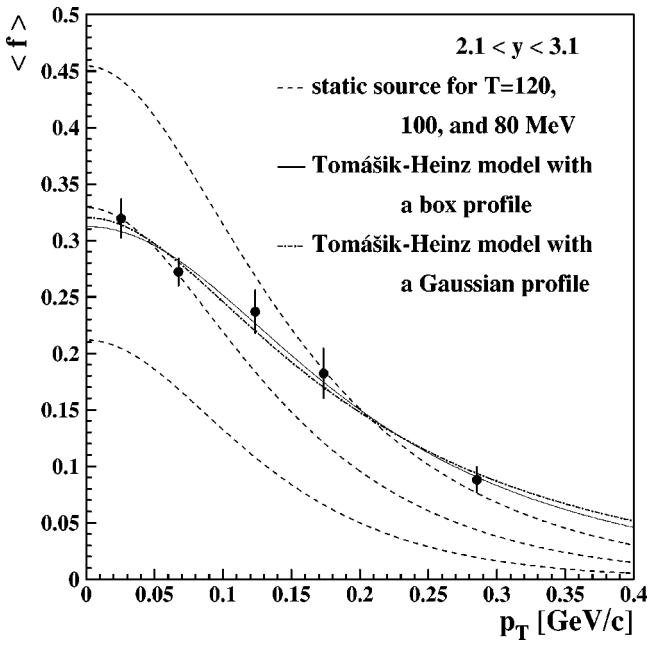

FIG. 14. Average pion phase-space density as a function of p_T compared to different models (see the text).

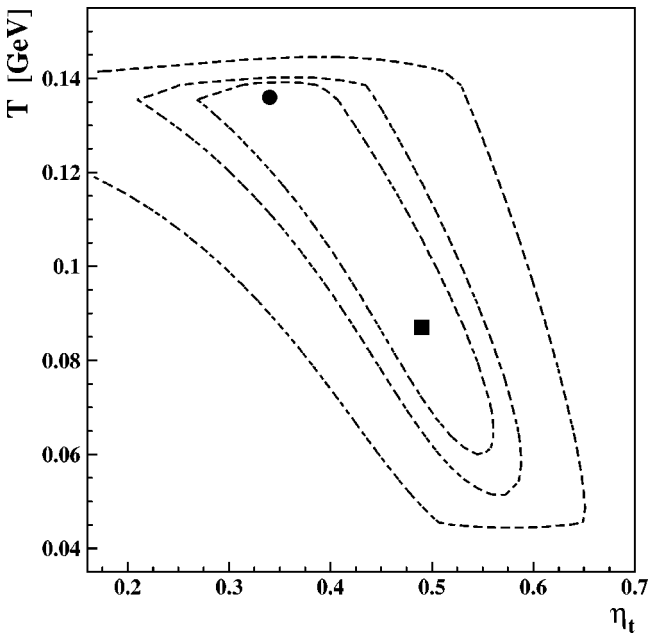

FIG. 15. χ^2 contour plot for the T.-H. model with a box profile. Starting from the center, the curves represent contours at 39%, 70%, and 99% confidence levels for T and η_t. The black square is the best fit ($\mu_0=57$ MeV). The full circle is the result with μ_0 excluded from the fit and set to zero.

Figure 14 and Table II show the results on the average phase-space density for π^- as a function of p_T. The error bars reflect the statistical errors only. The systematic uncertainties are dominated by the uncertainty of the correction on the λ parameter, which is estimated to be 20%, and by the systematic error on R_L, giving a total of 13.7% systematic error on $\langle f \rangle$. Within errors, all nuclear collision measurements at the SPS are found to be indistinguishable [36], and our result at mid-rapidity agrees well with these previous measurements. The dashed lines indicate Bose-Einstein density distributions $\langle f \rangle = [\exp(E_\pi/T)-1]^{-1}$ of static sources of pions ($E_\pi \approx m_T$) for three choices of the freeze-out temperature T: 80, 100, and 120 MeV, from the lower curve to the higher curve. The results are in rough agreement with the 100-MeV distribution at low p_T, but show a clear deviation from a Bose-Einstein distribution at high p_T. As pointed out in Ref. [37], this deviation is mainly due to the strong longitudinal expansion of the fireball which reduces the spatially averaged phase-space density and, to a lesser extent, due to the radial collective flow, which adds extra transverse momentum to the particles compared to particles emitted by a static source. Consequently, even in the absence of transverse flow, $\langle f \rangle$ will be reduced compared to a Bose-Einstein density distribution. This effect may necessitate a positive pion chemical potential in order to match the experimental observation. Such a positive potential can be related to the presence of pions from short-lived resonance decays. The Tomášik-Heinz (T.-H.) model [37] used to fit the data assumes a thermalized fireball with a longitudinally boost-invariant expansion and a transverse flow rapidity profile which depends linearly on the transverse coordinate. This model includes a pion chemical potential and has three free parameters, the freeze-out temperature T, the strength of the transverse flow rapidity profile η_t, and μ_0, the chemical potential value in the center of the fireball. In Fig. 14, the full line is a fit of the T.-H. model with a box transverse density profile, whereas the point-dashed line is a fit of the same model with a Gaussian transverse profile. Both fits agree well with the data with a χ^2/d.o.f. of 0.78 and 0.93 for, respectively, the box and Gaussian profiles, giving $T = 87^{+52}_{-27}$ MeV, $\eta_t = 0.49^{+0.07}_{-0.22}$, and $\mu_0 = 57^{+29}_{-125}$ MeV for the box profile. This η_t result corresponds to a mean transverse flow velocity $\langle \beta_T \rangle = 0.42^{+0.05}_{-0.18}$. Due to the lack of experimental points at large p_T, the T.-H. model with the Gaussian profile provides very loose estimates of these parameters, which are nevertheless compatible with those from the box profile. Figure 15 shows the χ^2 contour plot for the T.-H. model with the box profile for T and η_t. The curves represent (starting from the center) contours at 39%, 70% and 99% confidence level. The best fit is obtained for a pion chemical potential $\mu_0 = 57$ MeV (black square) but a solu-

TABLE II. Average π^- phase-space density $\langle f \rangle$ at freeze-out as a function of p_T.

$\langle p_T \rangle$	0.02 GeV/c	0.07 GeV/c	0.125 GeV/c	0.175 GeV/c	0.285 GeV/c
$\langle f \rangle$	0.319 ± 0.018	0.272 ± 0.012	0.237 ± 0.019	0.182 ± 0.022	0.088 ± 0.012

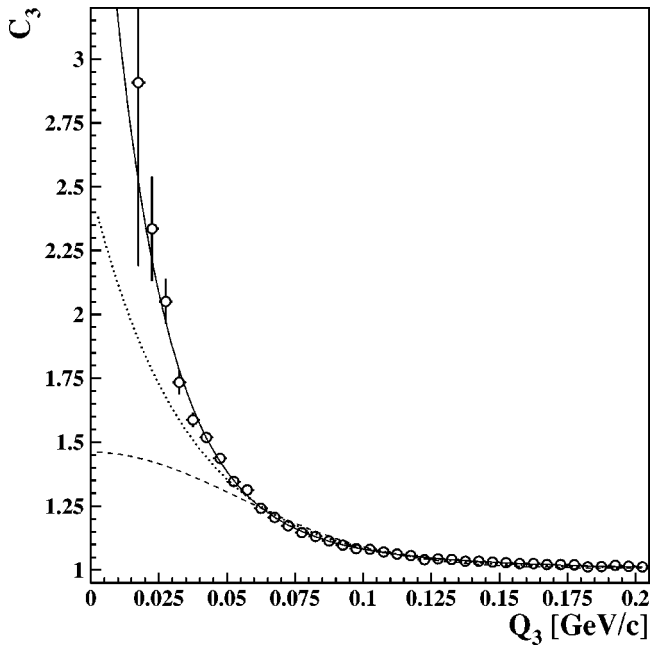

FIG. 16. The three-pion correlation function C_3 as a function of Q_3. The full line is a fit to a double exponential form (see the text). The dotted and dashed lines are fits, respectively, to a single exponential and a Gaussian form.

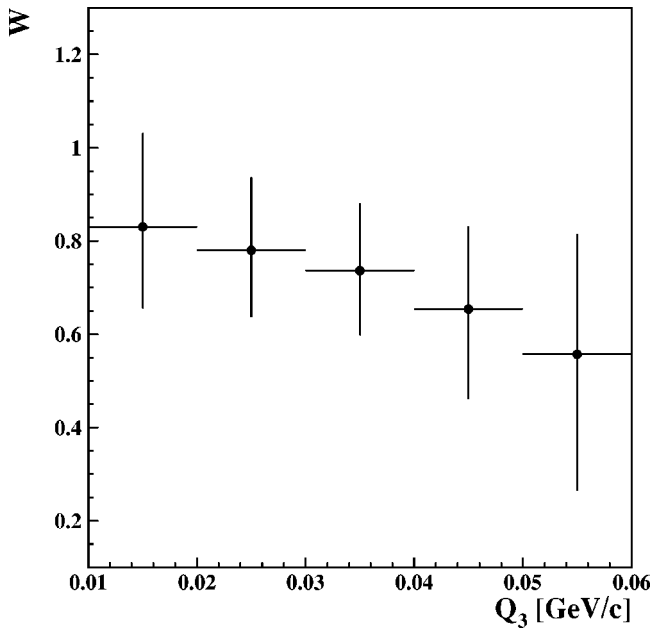

FIG. 17. The factor W as a function of Q_3. The error bars include statistical and systematic errors. The statistical errors alone are contained within the size of the symbols.

tion with $\mu_0=0$ MeV is also possible (full circle). On the other hand, a large pion chemical potential at freeze-out, close to the Bose condensation limit of $\mu_0=m_\pi$, as could be speculated given the rather low mass of the pion, seems to be excluded in view of the error bar on μ_0.

The results of the fit of the W.-H. model on the single π^- spectrum can be compared to the fit of the T.-H. model on the phase-space distribution. The agreement is good for T, and satisfactory for $\langle\beta_T\rangle$ when taking into account the systematic error. It should be noted that the constraint provided by the fit of the T.-H. model is weak compared to the one given by the W.-H. model because of the relatively small amount of experimental points in the phase-space distribution. Moreover the T.-H. model uses a pion chemical potential whereas the W.-H. model does not. Finally, as $\langle f\rangle$ is the pion occupation per six-dimensional position$\otimes$momentum cell, the obtained values do not provide striking evidence for the presence of an excess of pions or for the presence of large disoriented chiral condensates. This chiral condensate phenomena has been investigated by other means within WA98 [38,39].

VI. THREE-PION CORRELATIONS

In the hypothesis of a fully chaotic source of identical particles, the two-pion correlation function can be written $C_2=1+|F_{12}|^2$ where $|F_{12}|^2$ is the Fourier transform squared of the space-time source function. The three-pion correlation function is then $C_3=1+|F_{12}|^2+|F_{23}|^2+|F_{31}|^2+2\cdot\mathrm{Re}\{F_{12}\cdot F_{23}\cdot F_{31}\}$. The terms $|F_{ij}|^2$, which express the contribution of the three combinations of the two-pion correlations contained in the triplet (123), provide the largest contribution to C_3. The last term only represents the genuine three-body correlation. It can be written $2\cdot|F_{12}|\cdot|F_{23}|\cdot|F_{31}|\cdot W$, where F_{ij} is defined as $|F_{ij}|\exp[i\phi_{ij}]$ and $W\equiv\cos(\phi_{12}+\phi_{23}+\phi_{31})$. The simultaneous measurement of C_2 and C_3 provides information on W, the cosine of the sum of the three phases of the Fourier transforms. In contrast, the measurement of C_2 alone gives access only to the radii of the source and not to the phases. If the emission source is fully chaotic, W measures the asymmetry of the source. In the presence of not fully chaotic sources, which is likely to be the case, W, the strength of the true three-body correlation, is basically sensitive to the coherence. So, in the framework of the partially coherent model [40], W gives information on the de-

TABLE III. Weighted mean of the strength of the genuine three-pion correlations $\langle W\rangle$ as a function of Q_3.

Q_3 range	0.01–0.02 GeV/c	0.02–0.03 GeV/c	0.03–0.04 GeV/c	0.04–0.05 GeV/c	0.05–0.06 GeV/c
$\langle W\rangle$	$0.830^{+0.201}_{-0.175}$	$0.780^{+0.156}_{-0.143}$	$0.736^{+0.145}_{-0.138}$	$0.654^{+0.177}_{-0.193}$	$0.557^{+0.258}_{-0.293}$

gree of chaoticity of the emission source in a manner which is insensitive to backgrounds such as the contributions from resonances. The complete data set recorded with the negative tracking arm yielded a total of 13.1×10^6 triplets of π^-.

After correction for resolution and Coulomb effects,[1] a strong C_3 signal is observed (Fig. 16) as a function of $Q_3 \equiv \sqrt{Q_{12}^2+Q_{23}^2+Q_{31}^2}$ with $Q_{ij}\equiv\sqrt{-(p_i-p_j)^2}$, which can be fitted by a double exponential function

$$C_3 = 1+\lambda_1 \exp[-2Q_3R_1]+\lambda_2\exp[-2Q_3R_2],$$

with fitted parameters $R_1=5.08\pm0.26$ fm, $\lambda_1=3.12\pm0.27$, $R_2=1.66\pm0.08$ fm, $\lambda_2=0.341\pm0.046$, and χ^2/d.o.f. $=1.10$. Such a non-Gaussian behavior was in fact predicted by a final-state rescattering model [41]. After the measurement of C_2 and C_3, the data are analyzed again, and the experimental value of W is calculated using

$$W=\frac{\{C_3(Q_3)-1\}-\{C_2(Q_{12})-1\}-\{C_2(Q_{23})-1\}-\{C_2(Q_{31})-1\}}{2\cdot\sqrt{\{C_2(Q_{12})-1\}\{C_2(Q_{23})-1\}\{C_2(Q_{31})-1\}}}$$

individually for each triplet found, characterized by Q_3 and by the values Q_{12}, Q_{23}, and Q_{31} corresponding to the three pair combinations contained in the triplet.

As described earlier, the estimate of systematic errors is done by varying the different analysis cuts, both in the two- and three-pion correlation analysis. The effects on W of the statistical errors in the measurement of C_2 and C_3 are treated as systematic errors by changing C_2 (C_3) by $\pm\sigma_{C_2}$ ($\pm\sigma_{C_3}$). This last source of error dominates the other ones. All these variations are then added in quadrature.

Figure 17 and Table III show W as a function of Q_3 for $Q_3\leqslant 60$ MeV/c, beyond which the W significance is too low. The error bars include statistical and systematic errors. The statistical errors (not shown separately in Fig. 17) are by comparison negligible. In view of the errors, no significant Q_3 dependence is observed. The genuine three-pion correlation is found to be substantial with a weighted mean over the five bins $\langle W\rangle = 0.735\pm0.004(\text{stat.})\pm0.146(\text{syst.})$.[2]

This result is in agreement with the previously published WA98 result obtained using about half of the present data sample [42], where a more detailed description of the three-pion analysis method can also be found. More recently, the NA44 experiment [43] obtained with lower statistics a factor $\langle W\rangle$ which agrees with our results.

VII. CONCLUSIONS

We have studied m_T distributions for identified π^- and K^- produced in central Pb+Pb collisions at 158A GeV. The W.-H. hydrodynamical model has been fitted to the pion spectrum. The resulting fitted parameters favor a combination of a relatively low temperature $T\sim85$ MeV and an average transverse flow velocity $\langle\beta_T\rangle\sim0.50$. The shape of the π^- m_T distribution is in good agreement with the π^0 m_T distribution measured in the same experiment.

Bose-Einstein interferometry of π^- pairs gives fitted radii of typically 7 fm. This has to be compared to the equivalent rms radius of the initial Pb ion of 3.2 fm, indicating an expanded emission volume at freeze-out.

The analysis of two-pion correlations has been performed as a function of k_T using two different parametrizations in the LCMS. The results are consistent between the standard three-dimensional Pratt-Bertsch fit and the Yano-Koonin-Podgoretskiĭ fit.

A clear dependence of all radius parameters on k_T is observed, with a stronger dependence for the longitudinal radii, indicating a larger longitudinal than transverse expansion. Both the cross term $R^2_{out\text{-}long}$ from the PB fit and v_L from the YKP fit deviate from zero, which suggests that the source seen within the acceptance does not undergo a strictly boost invariant expansion. Moreover, the short duration of emission disfavors any long-lived intermediate phase.

A comparison of the data with a hydrodynamical simulation based on the Wiedemann-Heinz model, and taking into account acceptance and resolution effects has been made for the radii parameters as a function of k_T. The agreement is found to be very good.

The average pion phase-space density at freeze-out has been calculated from measured quantities as a function of p_T. The results indicate a clear deviation from a Bose-Einstein distribution at high p_T, but are very well fitted by the Tomášik-Heinz model. The pion chemical potential, which is included in the model, is found to be compatible with zero, while a large pion chemical potential close to the condensation limit of m_π, seems to be excluded.

Finally, we have studied the $\pi^-\pi^-\pi^-$ interference and found a substantial contribution of genuine three-pion correlations in central collisions. For $Q_3\leqslant60$ MeV/c a weighted mean of the strength of the genuine three-pion correlations $\langle W\rangle = 0.735\pm0.004(\text{stat.})\pm0.146(\text{syst.})$ was extracted. This

[1]The Coulomb correction applied to a particular triplet is the product of the Coulomb corrections used for the three pair combinations contained in that triplet.

[2]The weighted systematic error is obtained by calculating the weighted average over the five Q_3 bins separately for each kind of systematic error. These errors are then added in quadrature. On the other hand, adding quadratically the systematic errors of the five Q_3 bins, as done for weighted statistical errors, would give ±0.078 instead of ±0.146 for the systematic uncertainty.

is somewhat smaller than what is expected for a fully chaotic and symmetric source.

ACKNOWLEDGMENTS

We would like to thank the CERN-SPS accelerator crew for providing an excellent Pb beam. This work was supported jointly by the German BMBF and DFG, the U.S. DOE, the Swedish NFR, the Dutch Stichting FOM, the Swiss National Fund, the Humboldt Foundation, the Stiftung für deutsch-polnische Zusammenarbeit, the Department of Atomic Energy, the Department of Science and Technology and the University Grants Commission of the Government of India, the Indo-FRG Exchange Program, the PPE division of CERN, the INTAS under Contract No. INTAS-97-0158, the Polish KBN under Grant No. 2P03B16815, the Grant-in-Aid for Scientific Research (Specially Promoted Research & International Scientific Research) of the Ministry of Education, Science, Sports and Culture, JSPS Research financial support for Young Scientists, the University of Tsukuba Special Research Projects, and ORISE. ORNL is managed by UT-Battelle, LLC, for the U.S. Department of Energy under Contract No. DE-AC05-00OR22725.

[1] W. Zajc *et al.* Phys. Rev. C **29**, 2173 (1984), and references therein; U.A. Wiedemann and U. Heinz, Phys. Rep. **319**, 145 (1999), and references therein.
[2] I.V. Andreev, M. Plümer, and R.M. Weiner, Int. J. Mod. Phys. A **8**, 4577 (1993).
[3] B. Lörstad, Int. J. Mod. Phys. A **4**, 2861 (1989), and references therein.
[4] H. Heiselberg and A.P. Vischer, Phys. Rev. C **55**, 874 (1997).
[5] WA98 Collaboration, proposal for a large acceptance hadron and photon spectrometer, 1991, preprint CERN/SPSLC 91-17, SPSLC/P260.
[6] M.M. Aggarwal *et al.*, Eur. Phys. J. C **23**, 225 (2002).
[7] M.M. Aggarwal *et al.*, nucl-ex/0006007.
[8] J.M. Rubio *et al.*, Nucl. Instrum. Methods Phys. Res. A **367**, 358 (1995); A.L.S. Angelis *et al.*, Nucl. Phys. **A566**, 605c (1994); M. Iżycki *et al.*, Nucl. Instrum. Methods Phys. Res. A **310**, 98 (1991).
[9] E. Schnedermann *et al.*, Phys. Rev. C **48**, 2462 (1993).
[10] U. Heinz, in *Hot Hadronic Matter: Theory and Experiment*, Vol. 346 of NATO Advanced Study Institute, Series B: edited by H.H. Gutbrod, J. Letessier, and J. Rafelski (Plenum, New York, 1995), p. 413.
[11] S. Vörös, Ph.D. thesis, University of Geneva, 2001.
[12] K. Werner, Phys. Rep. **232**, 87 (1993).
[13] S.V. Afanasiev *et al.*, nucl-ex/0205002.
[14] G. Bocquet *et al.*, Phys. Lett. B **366**, 434 (1996).
[15] R. Hagedorn, Nuovo Cimento **6**, 1 (1983); also CERN-TH 3684, 1983.
[16] R. Albrecht *et al.*, Eur. Phys. J. C **5**, 255 (1998).
[17] M.M. Aggarwal *et al.*, Phys. Rev. Lett. **81**, 4087 (1998); **84**, 578(E) (2000).
[18] M.M. Aggarwal *et al.*, Phys. Rev. Lett. **83**, 926 (1999).
[19] G. Wilk and Z. Włodarczyk, Physica A **305**, 227 (2002), and references therein.
[20] C. Tsallis, J. Stat. Phys. **52**, 479 (1988).
[21] S. Chapman *et al.*, Phys. Rev. C **52**, 2694 (1995), and references therein.
[22] S. Chapman *et al.*, Heavy Ion Phys. **1**, 1 (1995).
[23] U. Heinz *et al.*, Phys. Lett. B **382**, 181 (1996).
[24] U.A. Wiedemann, P. Scotto, and U. Heinz, Phys. Rev. C **53**, 918 (1996).
[25] U.A. Wiedemann and U. Heinz, Phys. Rev. C **56**, 3265 (1997); these calculations were made with a FORTRAN program supplied by U.A. Wiedemann.
[26] U.A. Wiedemann and U. Heinz, Phys. Rep. **319**, 145 (1999).
[27] L. Rosselet *et al.*, Nucl. Phys. **A698**, 647c (2002).
[28] S. Pratt *et al.*, Phys. Rev. C **42**, 2646 (1990); these calculations were made with a FORTRAN program supplied by S. Pratt.
[29] M.M. Aggarwal *et al.*, Eur. Phys. J. C **16**, 445 (2000).
[30] S. Pratt, Phys. Rev. D **33**, 1314 (1986); G. Bertsch and G.E. Brown, Phys. Rev. C **40**, 1830 (1989).
[31] S. Chapman *et al.*, Phys. Rev. Lett. **74**, 4400 (1995).
[32] R. Ganz *et al.*, Nucl. Phys. **A661**, 448c (1999).
[33] I.G. Bearden *et al.*, Phys. Rev. C **58**, 1656 (1998).
[34] G.F. Bertsch, Phys. Rev. Lett. **72**, 2349 (1994); **77**, 789(E) (1996).
[35] J. Barrette *et al.*, Phys. Rev. Lett. **78**, 2916 (1997).
[36] D. Ferenc *et al.*, Phys. Lett. B **457**, 347 (1999).
[37] B. Tomášik and U. Heinz, Phys. Rev. C **65**, 031902(R) (2002).
[38] M.M. Aggarwal *et al.*, Phys. Lett. B **420**, 169 (1998).
[39] M.M. Aggarwal *et al.*, Phys. Rev. C **64**, 011901(R) (2001).
[40] U. Heinz and Q.H. Zhang, Phys. Rev. C **56**, 426 (1997).
[41] T.J. Humanic, Phys. Rev. C **60**, 014901 (1999).
[42] M.M. Aggarwal *et al.*, Phys. Rev. Lett. **85**, 2895 (2000).
[43] I.G. Bearden *et al.*, Phys. Lett. B **517**, 25 (2001).

ELSEVIER

Nuclear Physics A715 (2003) 729c–732c

NUCLEAR PHYSICS A

www.elsevier.com/locate/npe

High p_T π^0 Production and Angular Correlations in 158 AGeV p+A and Pb+Pb Collisions

S. Bathe[a] for the WA98-Collaboration

[a]University of Münster, 48149 Münster, Germany

Recent results of the WA98 experiment with p and Pb induced reactions at 158 AGeV are presented. Azimuthal γ-γ correlations at high p_T were studied in search for a signal of jet-like structures. A clear indication for back-to-back correlations can be seen in p+A with a strong dependence on the p_T of the photons and the size of the system. In Pb+Pb collisions in plane elliptic flow has been observed. Results on transverse mass spectra of neutral pions measured at central rapidity are presented for impact parameter selected Pb+Pb collisions. In going from peripheral to medium central collisions there is a nuclear enhancement increasing with transverse mass similar to the Cronin effect, while for very central collisions this enhancement appears to be weaker than expected.

1. Introduction

The CERN experiment WA98 [1,2] consisted of large acceptance photon and hadron spectrometers together with several other large acceptance devices which allow to measure various global variables on an event-by-event basis. The results presented here were obtained from an analysis of the data taken with p and Pb beams in 1995 and 1996 at 158 AGeV. The Pb-induced reactions have been subdivided into samples of different centrality using the transverse energy E_T measured in the MIRAC calorimeter. Photons are measured with the WA98 lead-glass photon detector, LEDA, which consisted of 10,080 individual modules with photomultiplier readout. The detector was located at a distance of 21.5 m from the target and covered the pseudorapidity interval $2.2 < \eta < 2.9$. Details about the photon measurement can be found in [2].

2. Azimuthal γ-γ-Correlations

We attempt to use azimuthal correlations of photons, which mainly originate from decays of neutral hadrons, π^0 or η, to gain information on the relative fraction of produced particles which still carry memory of the primary production process. Particles produced in a primary two-body collision of incoming nucleons must be correlated in transverse momentum due to local momentum conservation. Dominantly, especially if their individual transverse momenta are large, the particles will be anti-correlated in azimuthal angle. This is of course reminiscent of jet structure in the particle emission in high-energy physics. In fact, there is expected to be a smooth transition of this purely kinematical effect to mini-jet or jet production. At high enough transverse momenta, such an analysis

0375-9474/03/$ – see front matter © 2003 Elsevier Science B.V. All rights reserved.
doi:10.1016/S0375-9474(02)01475-6

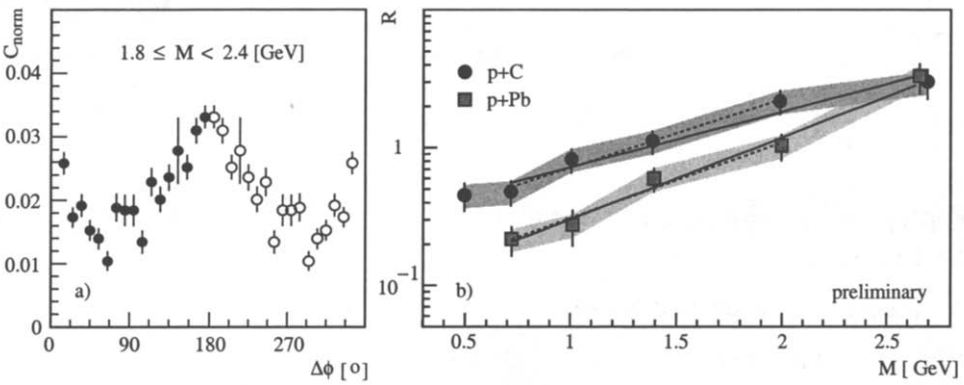

Figure 1. a) Exemplary $C(\Delta\phi)$ for p+C reactions. b) Ratio R of correlated to uncorrelated pairs at $\Delta\phi = 180°$ as function of the pseudo-mass M for p+C and p+Pb.

should allow to study minijet or jet production and eventually allow to investigate effects such as jet quenching. If the particles undergo secondary and further rescatterings, as in an equilibrated system, the memory of the correlation discussed above will be lost. Of course, anti-correlation of particle pairs will also be generated by collective effects like hydrodynamical elliptic flow. One therefore has to check how much the measured effects might be altered by flow phenomena. The γ-pairs are characterized by the difference of their azimuthal angle $\Delta\phi$ and the so-called pseudo-mass $M = p_{T1} + p_{T2}$. The correlation function $C(\Delta\phi)$ is introduced:

$$C(\Delta\phi) = \left.\frac{d^2N}{d\varphi_1 d\varphi_2}\right|_{p_{T1}+p_{T2}} \Big/ \left.\left(\frac{dN}{d\varphi_1}\frac{dN}{d\varphi_2}\right)\right|_{p_{T1}+p_{T2}}$$

The combinatorial background of uncorrelated pairs is obtained by event mixing taking into account different centrality and multiplicity classes. A clear correlation around $\Delta\phi = 180°$ can be seen for p+C (Fig 1a) and p+Pb reactions. It is assumed that the correlation originates from the direct production of π^0's in single binary collisions and that its strength therefore contains information about the ratio of directly produced to rescattered particles. The correlation function for the p+A data can be described by a Gaussian distribution, with the ratio R of correlated to uncorrelated pairs at $\Delta\phi = 180°$ increasing exponentially with the pseudo-mass M as shown in Figure 1b. Peripheral Pb+Pb data show a similar behaviour. Semi-peripheral and semi-central Pb+Pb data show a correlation function that is dominated by elliptic flow. The flow effects are evaluated by means of a Fourier expansion [3,4].

$$\frac{1}{N}\frac{dN}{d(\Delta\phi)} = 1 + 2v_1^2\cos\Delta\phi + 2v_2^2\cos 2\Delta\phi, \qquad (1)$$

The Fourier coefficient v_1 quantifies the directed flow, whereas v_2 quantifies the elliptic flow. The Fourier coefficients $v_n (n = 1, 2)$ can be extracted from the correlation function without determination of the reaction plane, and hence no event plane resolution correction has to be applied. Figure 2a shows v_2 for different cut-offs on the pseudo-mass as

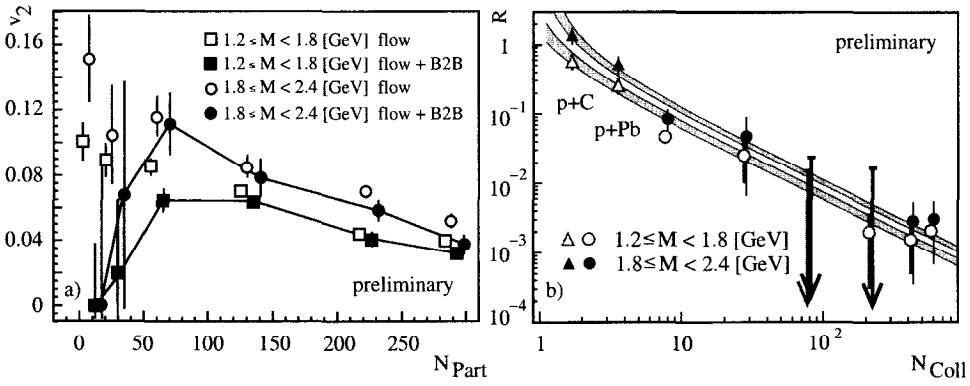

Figure 2. a) v_2 in Pb+Pb as function of the number of participants with and without consideration of back-to-back effects. b) Strength of back-to-back correlations in p+A and Pb+Pb reactions.

a function of different centralities in Pb+Pb with and without consideration of back-to-back effects. Especially in the more peripheral samples, elliptic flow does not describe the correlation completely. To compare the strength of an additional Gaussian-like correlation for different systems the ratio R of correlated to uncorrelated pairs at $\Delta\phi = 180°$ is shown in Figure 2b as a function of the number of binary collisions. A parametrisation of the p+A data points with $R(N_{Coll}) = 1/(aN_{Coll} - 1)$ is extrapolated to the Pb+Pb data, which represents scaling of the number of correlated pairs with N_{Coll}. No deviation from this scaling is observed.

3. Centrality Dependence of π^0-Production

Already from the experimentally determined shape of transverse mass spectra of hadrons it is evident that heavy ion reactions are not merely a superposition of nucleon-nucleon collisions [5]. In p+A collisions the flattening of the transverse mass spectra compared to p+p (Cronin effect [6]) has been attributed to initial state multiple scattering of partons [7]. In the analysis of central reactions of Pb+Pb at 158 AGeV, however, it is seen that both predictions of perturbative QCD [8] and hydrodynamical parameterizations [9] can describe the measured neutral pion spectra reasonably well. The understanding of the relative contributions of the various soft and hard processes in particle production is especially important in view of the recent interest in the energy loss of partons in dense matter [10,11], generally referred to as *jet quenching*, as a possible probe for the quark gluon plasma. Since one of the suggested experimental hints of jet quenching is the suppression of particle production at high transverse momenta, it is important to understand other possible nuclear modifications of particle production in detail.

More information in this respect may be gathered from the variation of the particle spectra for different reaction systems or different centralities [12]. Here we study the variations in absolute multiplicities. Especially at high transverse momentum one naïvely expects an increase of the multiplicity proportional to the number of collisions due to the

importance of hard scattering. In fact, it was already observed in p+A collisions at beam energies of 200 – 400 GeV [6] that the increase in cross section at high transverse momenta is even stronger than the increase in the target mass. The ratios of the measured pion multiplicity distributions for two different samples (labeled X and Y) normalized to the number of collisions

$$R_{XY}(m_T) \equiv \frac{\left(E\frac{d^3N}{dp^3}(m_T)/N_{coll}\right)_X}{\left(E\frac{d^3N}{dp^3}(m_T)/N_{coll}\right)_Y} \tag{2}$$

is introduced.

The ratio of peripheral Pb+Pb collisions to p+p increases strongly with increasing transverse mass – this is in line with the Cronin effect discussed above. A similar trend is observed when going from peripheral to medium-central data. In addition, the pion production is seen to increase roughly proportional to the number of collisions even at low transverse mass. Going from medium central to central the trend is reversed: the ratio decreases with increasing transverse mass and the pion multiplicities increase more weakly than the number of collisions. The ratio of very central to central collisions shows an indication of a similar effect although not very significant.

Neither results of HIJING[13] calculations nor a more refined pQCD calculation [14] can reproduce the experimental data. Here the ratios are all ≥ 1 and thus do not explain the centrality dependence observed.

REFERENCES

1. WA98 Collaboration, *Proposal for a large acceptance hadron and photon spectrometer*,1991, Preprint CERN/SPSLC 91-17, SPSLC/P260; WA98 Collaboration, M.M. Aggarwal et al., Nucl. Phys. **A 610**, 200c (1996).
2. WA98 Collaboration, M.M. Aggarwal et al, nucl-ex/0006007, submitted to Phys. Rev. C.
3. A. M. Poskanzer ans S. A. Voloshin, Phys. Rev. **C58**, 1671 (1998).
4. J. Y. Ollitrault, Phys. Rev. **D 46**, 229 (1992).
5. WA80 Collaboration, R. Albrecht et al., Eur. Phys. J. C **5**, 255–267 (1998).
6. D. Antreasyan, et al., Phys. Rev. D **19**, 764 (1979).
7. M. Lev and B. Petersson, Z. Phys. **C21** (1983) 155–161; A. Krzywicki et al., Phys. Lett. **B85** (1979) 407–416.
8. WA98 Collaboration, M. M. Aggarwal et al., Phys. Rev. Lett. **81** (1998) 4087; Phys. Rev. Lett. **84** (2000) 578 (erratum); X.-N. Wang, Phys. Rev. Lett. **81** (1998) 2655.
9. WA98 Collaboration, M. M. Aggarwal et al., Phys. Rev. Lett **83** (1999) 926.
10. X.-N. Wang and M. Gyulassy, Phys. Rev. Lett. **68** (1992) 1480; X.-N. Wang, Phys. Rev. C **58** (1998) 2321.
11. R. Baier, D. Schiff, and B. G. Zakharov Ann. Rev. Nucl. Part. Sci. **50** (2000) 37-69 and references therein.
12. M. M. Aggarwal et al., Eur.Phys.J. **C 23** (2002) 225-236.
13. X.-N. Wang and M. Gyulassy, Phys. Rev. **D 44**, 3501 (1991); Comp. Phys. Comm. **83**, 307 (1994).
14. E. Wang, and X.-N. Wang, preprint nucl-th/0104031.

Available online at www.sciencedirect.com
SCIENCE DIRECT®
PHYSICS LETTERS B
ELSEVIER
Physics Letters B 561 (2003) 82–92
www.elsevier.com/locate/npe

Centrality dependence of the high p_T charged hadron suppression in Au + Au collisions at $\sqrt{s_{\mathrm{NN}}} = 130$ GeV

PHENIX Collaboration

K. Adcox [an], S.S. Adler [c], N.N. Ajitanand [aa], Y. Akiba [n], J. Alexander [aa], L. Aphecetche [ah], Y. Arai [n], S.H. Aronson [c], R. Averbeck [ab], T.C. Awes [ac], K.N. Barish [e], P.D. Barnes [s], J. Barrette [u], B. Bassalleck [y], S. Bathe [v], V. Baublis [ad], A. Bazilevsky [l,af], S. Belikov [l,m], F.G. Bellaiche [ac], S.T. Belyaev [p], M.J. Bennett [s], Y. Berdnikov [ai], S. Botelho [ag], M.L. Brooks [s], D.S. Brown [z], N. Bruner [y], D. Bucher [v], H. Buesching [v], V. Bumazhnov [l], G. Bunce [c,af], J. Burward-Hoy [ab], S. Butsyk [ab,ad], T.A. Carey [s], P. Chand [b], J. Chang [e], W.C. Chang [a], L.L. Chavez [y], S. Chernichenko [l], C.Y. Chi [h], J. Chiba [n], M. Chiu [h], R.K. Choudhury [b], T. Christ [ab], T. Chujo [c,am], M.S. Chung [o,s], P. Chung [aa], V. Cianciolo [ac], B.A. Cole [h], D.G. D'Enterria [ah], G. David [c], H. Delagrange [ah], A. Denisov [l], A. Deshpande [af], E.J. Desmond [c], O. Dietzsch [ag], B.V. Dinesh [b], A. Drees [ab], A. Durum [l], D. Dutta [b], K. Ebisu [x], Y.V. Efremenko [ac], K. El Chenawi [an], H. En'yo [q,ae], S. Esumi [am], L. Ewell [c], T. Ferdousi [e], D.E. Fields [y], S.L. Fokin [p], Z. Fraenkel [ap], A. Franz [c], A.D. Frawley [i], S.-Y. Fung [e], S. Garpman [t], T.K. Ghosh [an], A. Glenn [aj], A.L. Godoi [ag], Y. Goto [af], S.V. Greene [an], M. Grosse Perdekamp [af], S.K. Gupta [b], W. Guryn [c], H.-Å. Gustafsson [t], J.S. Haggerty [c], H. Hamagaki [g], A.G. Hansen [s], H. Kara [x], E.P. Hartouni [r], R. Hayano [al], N. Hayashi [ae], X. He [j], T.K. Hemmick [ab], J.M. Heuser [ab], M. Hibino [ao], J.C. Hill [m], D.S. Ho [aq], K. Homma [k], B. Hong [o], A. Hoover [z], T. Ichihara [ae,af], K. Imai [q,ae], M.S. Ippolitov [p], M. Ishihara [ae,af], B.V. Jacak [ab,af], W.Y. Jang [o], J. Jia [ab], B.M. Johnson [c,*], S.C. Johnson [r,ab], K.S. Joo [w], S. Kametani [ao], J.H. Kang [aq], M. Kann [ad], S.S. Kapoor [b], S. Kelly [h], B. Khachaturov [ap], A. Khanzadeev [ad], J. Kikuchi [ao], D.J. Kim [aq], H.J. Kim [aq], S.Y. Kim [aq], Y.G. Kim [aq], W.W. Kinnison [s], E. Kistenev [c], A. Kiyomichi [am], C. Klein-Boesing [v], S. Klinksiek [y], L. Kochenda [ad], V. Kochetkov [l], D. Koehler [y], T. Kohama [k], D. Kotchetkov [e], A. Kozlov [ap], P.J. Kroon [c], K. Kurita [ae,af], M.J. Kweon [o], Y. Kwon [aq], G.S. Kyle [z], R. Lacey [aa], J.G. Lajoie [m], J. Lauret [aa], A. Lebedev [m,p], D.M. Lee [s], M.J. Leitch [s], X.H. Li [e], Z. Li [f,ae], D.J. Lim [aq], M.X. Liu [s], X. Liu [f], Z. Liu [f], C.F. Maguire [an], J. Mahon [c], Y.I. Makdisi [c], V.I. Manko [p], Y. Mao [f,ae], S.K. Mark [u], S. Markacs [h], G. Martinez [ah], M.D. Marx [ab], A. Masaike [q], F. Matathias [ab],

0370-2693/03/$ – see front matter © 2003 Published by Elsevier Science B.V.
doi:10.1016/S0370-2693(03)00423-4

T. Matsumoto [g,ao], P.L. McGaughey [s], E. Melnikov [l], M. Merschmeyer [v], F. Messer [ab], M. Messer [c], Y. Miake [am], T.E. Miller [an], A. Milov [ap], S. Mioduszewski [c,aj], R.E. Mischke [s], G.C. Mishra [j], J.T. Mitchell [c], A.K. Mohanty [b], D.P. Morrison [c], J.M. Moss [s], F. Mühlbacher [ab], M. Muniruzzaman [e], J. Murata [ae], S. Nagamiya [n], Y. Nagasaka [x], J.L. Nagle [h], Y. Nakada [q], B.K. Nandi [e], J. Newby [aj], L. Nikkinen [u], P. Nilsson [t], S. Nishimura [g], A.S. Nyanin [p], J. Nystrand [t], E. O'Brien [c], C.A. Ogilvie [m], H. Ohnishi [c,k], I.D. Ojha [d,an], M. Ono [am], V. Onuchin [l], A. Oskarsson [t], L. Österman [t], I. Otterlund [t], K. Oyama [g,al], L. Paffrath [c,1], A.P.T. Palounek [s], V.S. Pantuev [ab], V. Papavassiliou [z], S.F. Pate [z], T. Peitzmann [v], A.N. Petridis [m], C. Pinkenburg [c,aa], R.P. Pisani [c], P. Pitukhin [l], F. Plasil [ac], M. Pollack [ab,aj], K. Pope [aj], M.L. Purschke [c], I. Ravinovich [ap], K.F. Read [ac,aj], K. Reygers [v], V. Riabov [ad,ai], Y. Riabov [ad], M. Rosati [m], A.A. Rose [an], S.S. Ryu [aq], N. Saito [ae,af], A. Sakaguchi [k], T. Sakaguchi [g,ao], H. Sako [am], T. Sakuma [ae,ak], V. Samsonov [ad], T.C. Sangster [r], R. Santo [v], H.D. Sato [q,ae], S. Sato [am], S. Sawada [n], B.R. Schlei [s], Y. Schutz [ah], V. Semenov [l], R. Seto [e], T.K. Shea [c], I. Shein [l], T.-A. Shibata [ae,ak], K. Shigaki [n], T. Shiina [s], Y.H. Shin [aq], I.G. Sibiriak [p], D. Silvermyr [t], K.S. Sim [o], J. Simon-Gillo [s], C.P. Singh [d], V. Singh [d], M. Sivertz [c], A. Soldatov [l], R.A. Soltz [r], S. Sorensen [ac,aj], P.W. Stankus [ac], N. Starinsky [u], P. Steinberg [h], E. Stenlund [t], A. Ster [ar], S.P. Stoll [c], M. Sugioka [ae,ak], T. Sugitate [k], J.P. Sullivan [s], Y. Sumi [k], Z. Sun [f], M. Suzuki [am], E.M. Takagui [ag], A. Taketani [ae], M. Tamai [ao], K.H. Tanaka [n], Y. Tanaka [x], E. Taniguchi [ae,ak], M.J. Tannenbaum [c], J. Thomas [ab], J.H. Thomas [r], T.L. Thomas [y], W. Tian [f,aj], J. Tojo [q,ae], H. Torii [q,ae], R.S. Towell [s], I. Tserruya [ap], H. Tsuruoka [am], A.A. Tsvetkov [p], S.K. Tuli [d], H. Tydesjö [t], N. Tyurin [l], T. Ushiroda [x], H.W. van Hecke [s], C. Velissaris [z], J. Velkovska [ab], M. Velkovsky [ab], A.A. Vinogradov [p], A.M. Volkov [p], A. Vorobyov [ad], E. Vznuzdaev [ad], H. Wang [e], Y. Watanabe [ae,af], S.N. White [c], C. Witzig [c], F.K. Wohn [m], C.L. Woody [c], W. Xie [e,ap], K. Yagi [am], S. Yokkaichi [ae], G.R. Young [ac], I.E. Yushmanov [p], W.A. Zajc [h], Z. Zhang [ab], S. Zhou [f]

[a] *Institute of Physics, Academia Sinica, Taipei 11529, Taiwan*
[b] *Bhabha Atomic Research Centre, Bombay 400 085, India*
[c] *Brookhaven National Laboratory, Upton, NY 11973-5000, USA*
[d] *Department of Physics, Banaras Hindu University, Varanasi 221005, India*
[e] *University of California, Riverside, CA 92521, USA*
[f] *China Institute of Atomic Energy (CIAE), Beijing, People's Republic of China*
[g] *Center for Nuclear Study, Graduate School of Science, University of Tokyo, 7-3-1 Hongo, Bunkyo, Tokyo 113-0033, Japan*
[h] *Columbia University, New York, NY 10027 and Nevis Laboratories, Irvington, NY 10533, USA*
[i] *Florida State University, Tallahassee, FL 32306, USA*
[j] *Georgia State University, Atlanta, GA 30303, USA*
[k] *Hiroshima University, Kagamiyama, Higashi-Hiroshima 739-8526, Japan*
[l] *Institute for High Energy Physics (IHEP), Protvino, Russia*
[m] *Iowa State University, Ames, IA 50011, USA*
[n] *KEK, High Energy Accelerator Research Organization, Tsukuba-shi, Ibaraki-ken 305-0801, Japan*
[o] *Korea University, Seoul, 136-701, South Korea*
[p] *Russian Research Center "Kurchatov Institute", Moscow, Russia*
[q] *Kyoto University, Kyoto 606, Japan*

[r] Lawrence Livermore National Laboratory, Livermore, CA 94550, USA
[s] Los Alamos National Laboratory, Los Alamos, NM 87545, USA
[t] Department of Physics, Lund University, Box 118, SE-221 00 Lund, Sweden
[u] McGill University, Montreal, PQ H3A 2T8, Canada
[v] Institut fur Kernphysik, University of Münster, D-48149 Münster, Germany
[w] Myongji University, Yongin, Kyonggido 449-728, South Korea
[x] Nagasaki Institute of Applied Science, Nagasaki-shi, Nagasaki 851-0193, Japan
[y] University of New Mexico, Albuquerque, NM 87131, USA
[z] New Mexico State University, Las Cruces, NM 88003, USA
[aa] Chemistry Department, State University of New York, Stony Brook, NY 11794, USA
[ab] Department of Physics and Astronomy, State University of New York, Stony Brook, NY 11794, USA
[ac] Oak Ridge National Laboratory, Oak Ridge, TN 37831, USA
[ad] PNPI, Petersburg Nuclear Physics Institute, Gatchina, Russia
[ae] RIKEN (The Institute of Physical and Chemical Research), Wako, Saitama 351-0198, Japan
[af] RIKEN BNL Research Center, Brookhaven National Laboratory, Upton, NY 11973-5000, USA
[ag] Universidade de São Paulo, Institute de Física, Caixa Postal 66318, São Paulo CEP05315-970, Brazil
[ah] SUBATECH (Ecole des Mines de Nantes, 1N2P3/CNRS, Universite de Nantes) BP 20722 - 44307, Nantes cedex 3, France
[ai] St. Petersburg State Technical University, St. Petersburg, Russia
[aj] University of Tennessee, Knoxville, TN 37996, USA
[ak] Department of Physics, Tokyo Institute of Technology, Tokyo 152-8551, Japan
[al] University of Tokyo, Tokyo, Japan
[am] Institute of Physics, University of Tsukuba, Tsukuba, Ibaraki 305, Japan
[an] Vanderbilt University, Nashville, TN 37235, USA
[ao] Waseda University, Advanced Research Institute for Science and Engineering, 17 Kikui-cho, Shinjuku-ku, Tokyo 162-0044, Japan
[ap] Weizmann Institute, Rehovot 76100, Israel
[aq] Yonsei University, IPAP, Seoul 120-749, South Korea
[ar] KFKl Research Institute for Particle and Nuclear Physics (RMKI), Budapest, Hungary [2]

Received 17 July 2002; received in revised form 21 March 2003; accepted 21 March 2003

Editor: J.P. Schiffer

Abstract

PHENIX has measured the centrality dependence of charged hadron p_T spectra from Au+Au collisions at $\sqrt{s_{\mathrm{NN}}} = 130$ GeV. The truncated mean p_T decreases with centrality for $p_T > 2$ GeV/c, indicating an apparent reduction of the contribution from hard scattering to high p_T hadron production. For central collisions the yield at high p_T is shown to be suppressed compared to binary nucleon–nucleon collision scaling of p + p data. This suppression is monotonically increasing with centrality, but most of the change occurs below 30% centrality, i.e., for collisions with less than ~ 140 participating nucleons. The observed p_T and centrality dependence is consistent with the particle production predicted by models including hard scattering and subsequent energy loss of the scattered partons in the dense matter created in the collisions.
© 2003 Published by Elsevier Science B.V.

1. Introduction

Particle production at large transverse momentum (p_T) provides a new tool to study hot and dense nuclear matter created in high energy nuclear collisions. In nucleon–nucleon collisions, hadrons with $p_T \geqslant 2$ GeV/c are believed to originate mostly from the jet fragmentation of constituent partons, quarks and gluons, that were scattered with large momentum transfer Q^2 [1]. In nuclear collision these hard scattering processes between constituent partons occur early compared to the lifetime of the strongly interacting matter. Thus the hard scattered partons may traverse

* Corresponding author.
E-mail address: brant@bnl.gov (B.M. Johnson).
[1] Deceased.
[2] Not a participating institution.

the highest energy density matter produced. Theoretical studies of the propagation of partons in high density matter suggest that they lose a significant fraction of their energy through gluon bremsstrahlung [2] and that the energy lost reflects the density of color charges in the matter through which they pass [3]. The energy loss reduces the momenta of the partons, which results in a corresponding reduction of the momenta of the fragmentation products [4], observable as a reduced yield of high p_T hadrons.

The first measurements of hadron spectra at the Brookhaven National Laboratory Relativistic Heavy Ion Collider (RHIC) facility indicate a suppression of high-p_T hadron production in central Au + Au collisions relative to a binary collision scaling of p + p and $\bar{\text{p}}$ + p data [5,6]. No suppression is found for peripheral Au + Au collisions. So far no unique explanation of this apparent absence of the expected jet contribution to the p_T spectrum above 2 GeV/c has been identified.

Models of parton energy loss can reproduce the observed suppression in central Au + Au collisions [7–9]. Other final state effects such as rescattering of hadrons originally produced via the jet fragmentation have been proposed to explain the suppression [10]. It should be noted that models invoking thermal hadron production combined with collective transverse expansion of the reaction volume successfully describe the transverse momentum distributions of identified hadrons up to 3 GeV/c [11,12]. However, the mechanism of equilibration, which requires a reduction of the high p_T particle yield, is not specified in these models.

Alternatively, the initial state may be modified such that the number of hard scatterings is reduced. It is well known that nuclear modifications of the parton distributions exist [13]. These modifications cannot explain the suppression, since in the kinematic range of the measurements anti-shadowing enhances the parton distributions in nuclei [14–16]. However, models using a classical QCD picture of a highly relativistic nucleus [17,18] suggest that gluon distributions are saturated for momenta below a scale Q_s and thus reduced compared to expectations based on perturbative QCD [19]. As a consequence, a considerable suppression of hadron production might be expected even well above Q_s [20].

In this Letter we present the centrality dependence of the suppression of the high-p_T hadron yield to provide new experimental constraints on theoretical descriptions. These data are complementary to the previous study of the absolute yields [5] and have different systematic errors.

2. Experimental setup and data analysis

The results are obtained from 1.4×10^6 minimum bias Au + Au collisions at $\sqrt{s_{\text{NN}}} = 130$ GeV recorded by the PHENIX experiment during the Run-1 operation of RHIC (August–September 2000). Details on the PHENIX detector and its configuration in Run-1 operation can be found in [5,21].

In PHENIX semi-inclusive charged hadron spectra are measured over the range $0.5 < p_T < 5.0$ GeV/c in the east central arm spectrometer using data from a drift chamber (DC) and two segmented cathode pad chambers (PC1 and PC3), located outside of an axial magnetic field at a radial distance of 2.2, 2.5 and 5 m from the beam axis. The detectors cover an azimuthal acceptance of 90° and a pseudo-rapidity range of $|\eta| < 0.35$. In this analysis an additional fiducial cut $|\eta| < 0.18$ is applied to guarantee homogeneous track acceptance for collisions within $|z_{\text{vtx}}| < 30$ cm of the nominal interaction point. About $\sim 25\%$ of the azimuthal acceptance is covered by a time-of-flight system which allows proton identification out to 3.5 GeV/c, where the measurement is limited by statistics [22].

A pair of beam–beam counters provides the vertex position along the beam direction (z). Each charged track is reconstructed from the DC measurements of its projection into the bend plane of the magnetic field and two space points provided by PC1 and PC3. The unphysical background, resulting from false associations of drift chamber projections with pad chamber points, is estimated and subtracted by forming artificial events with the locations of pad chamber points inverted around the symmetry axis of the spectrometer. Physical background from decays in flight and photon conversions close to the DC, which only partially traverse the field and thus mimic high momentum tracks, are removed by requiring the track to point back to the event vertex within $|z_{\text{vtx}}| < 2.5$ cm. The remaining background level is negligible below 4 GeV/c and less than 40% at 5 GeV/c; this upper estimate is included in the systematic errors.

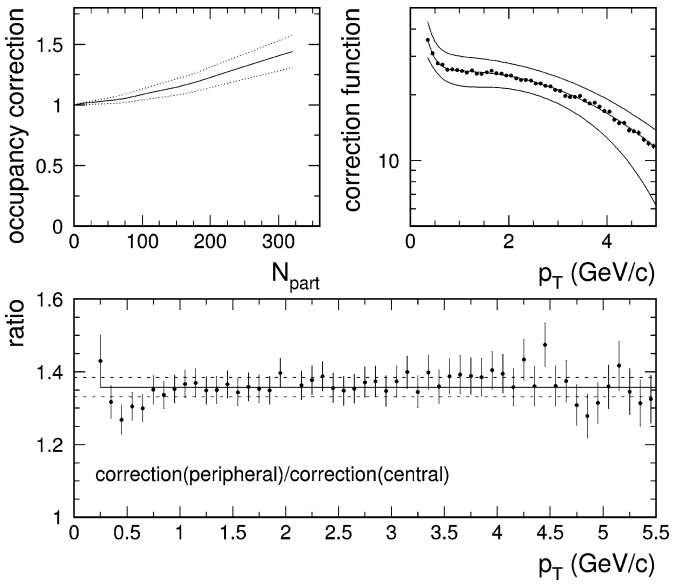

Fig. 1. Functions used to correct the charged particle p_T spectra. Upper left panel shows the centrality dependent correction $c(N_{\text{part}})$ and the right panel shows the p_T dependent correction $c(p_T)$. The systematic uncertainties are indicated by the dashed lines. The two corrections factorize, so that for any centrality the full correction function is given by $c(p_T) \times c(N_{\text{part}})$. The accuracy of this factorization is demonstrated in the lower panel. The ratio of the full correction for central collisions (top 5%) to the correction for single particle events varies by less than 2% above 1 GeV/c.

Corrections of the data are determined by tracing individual particles through a full GEANT simulation, simulating the detector response, then merging this response with that of all particles from a real event and passing the composite event through the PHENIX reconstruction software. The average track reconstruction efficiency in the active detector area is larger than 98% in peripheral collisions and decreases to $68 \pm 6\%$ for central collisions. The corresponding correction is shown on the upper left-hand side of Fig. 1. The full correction also depends on p_T. It is plotted for peripheral collision on the upper right-hand side of the figure. Between 0.8 and 2.5 GeV/c the correction factor varies slowly with p_T. Its value of ~ 25 corrects for geometrical acceptance ($\Delta\phi = \pi/4$; $\Delta\eta = 0.36$), dead areas of the detectors (45% DC, 5% PCs), and losses due to 2σ track matching cuts. At lower p_T the correction increases reflecting the gradual loss of acceptance. At higher p_T the observed particle yield is artificially increased because of the finite momentum resolution ($\delta p/p \simeq 0.6\% \oplus 3.6\% p$ (GeV/c)) and therefore the correction function decreases. Since this correction depends on the spectral shape of the true p_T distribution it was determined iteratively. At 5 GeV/c the correction is reduced by a factor of ~ 2. The systematic uncertainties are indicate by the dashed lines; they are also tabulated in Table 1. As shown in the lower part of Fig. 1 correction factorizes into functions of centrality (i.e., detector occupancy) and p_T within 2% systematic uncertainty in the range from 2 to 5 GeV/c.

Events are selected according to centrality following the procedure described in [5]. Six exclusive centrality bins are established using the energy measured in two zero-degree calorimeters and the number of charged-particles detected in the two beam–beam counters. A Monte Carlo simulation using measured nucleon density distributions calculated in the Glauber eikonal approximation was used to estimate the average number of binary nucleon–nucleon collisions (N_{coll}) and the corresponding average number of participating nucleons (N_{part}) for each bin. The results are quoted in Table 2.

3. Results

Fig. 2 presents charged hadron p_T spectra for the six centrality bins. For peripheral collisions the spectra

Table 1
Upper bounds of the systematic error on the p_T dependent single particle correction function

p_T (GeV/c)	δ_{track} (%)	δ_{decay} (%)	δ_{reso} (%)	δ_{bgr} (%)	Total
1	±13.5	+10	±0	0	−13.5+16.4
2	±13.5	+5	±1	0	−13.7+14.4
3	±13.5	+2.5	±4	−1.6	−14.2+14.2
4	±13.5	+1.25	±9	−11.5	−20 + 16
5	±13.5	+0.6	±15	−40	−45 + 16

Here δ_{track} includes the uncertainties of the acceptance, dead areas, track matching cuts and the track reconstruction efficiency. The δ_{decay} term accounts for the uncertainty of the decay correction. The effect of the momentum resolution contributes with δ_{reso} to the systematic error. Uncertainties due to potentially unsubtracted background are quantified by δ_{bgr}. The total systematic error given in the last column is calculated as quadrature sum of the individual contributions. It is calculated separately for positive and negative errors.

Table 2
Number of participants and binary collisions and their systematic errors for the individual centrality selections used in this analysis

Bin	Relative fraction (%)	N_{part}	N_{coll}	$N_{\text{coll}}^{\text{central}}/N_{\text{coll}}$	$2N_{\text{coll}}/N_{\text{part}}$
1	80–92	5.5±2.6	4.1±1.7	246 ± 98	1.5 ± 0.5
2	60–80	19.5±3.5	20 ± 6	50.4 ± 13	2.1 ± 0.5
3	30–60	79 ± 4.6	131 ± 23	7.68 ± 1.1	3.4 ± 0.6
4	15–30	180 ± 6.6	406 ± 46	2.49±0.13	4.5 ± 0.5
5	5–15	271 ± 9	712 ± 72	1.41±0.03	5.2 ± 0.6
6	0–5	348 ± 10	1009 ± 101	1	5.8 ± 0.6

Also given is the ratio of the number of binary collisions for the most central sample relative to the one for each sample. The last column quantifies the ratio of binary collisions to participant pairs.

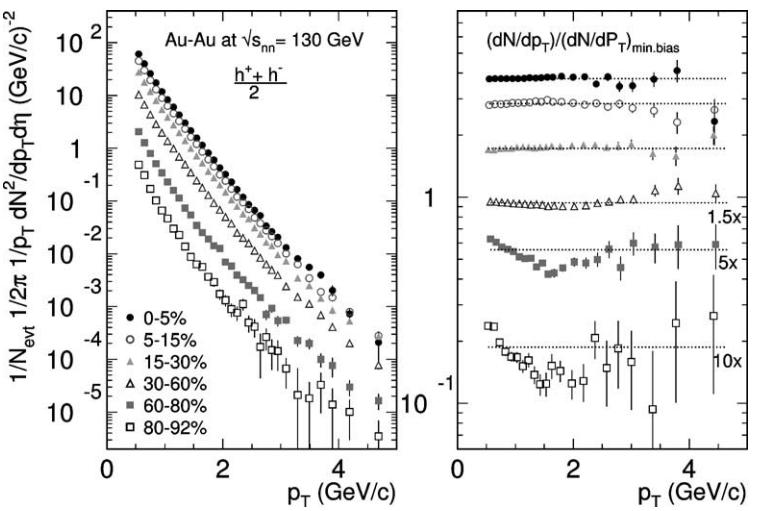

Fig. 2. The left panel shows p_T spectra of charged hadrons from six Au + Au centrality selections. Error bars indicate statistical errors only. The p_T dependent systematic errors are independent of centrality and not shown, they are given in Table 1. The centrality dependent errors are less than 10% and small compared to the symbol size. The right panel shows the ratio of each of the centrality selected p_T spectra to the minimum bias spectrum. Ratios for peripheral selections are scaled for clarity. Dotted lines indicate the average ratios for each centrality selection.

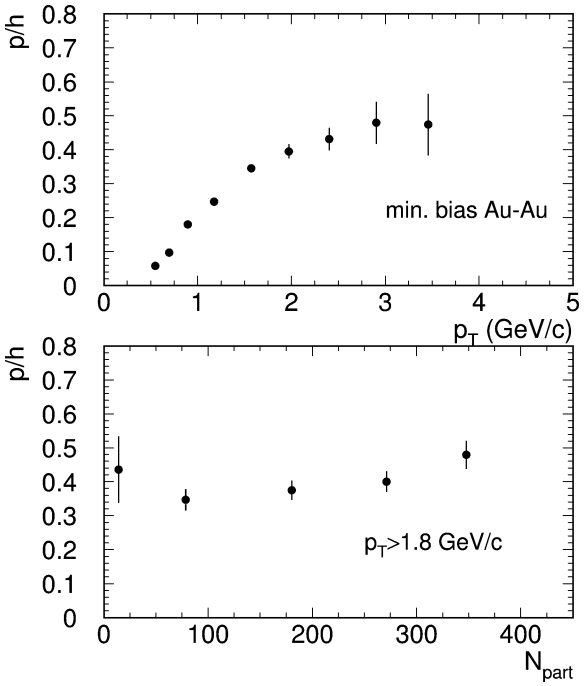

Fig. 3. The ratio p/h represents the proton plus anti-proton yield relative to the total charged hadron multiplicity. The top panel shows the p_T dependence of p/h for minimum bias events. In the bottom panel we show the centrality dependence of p/h for $p_T > 1.8$ GeV/c. Only statistical errors are shown.

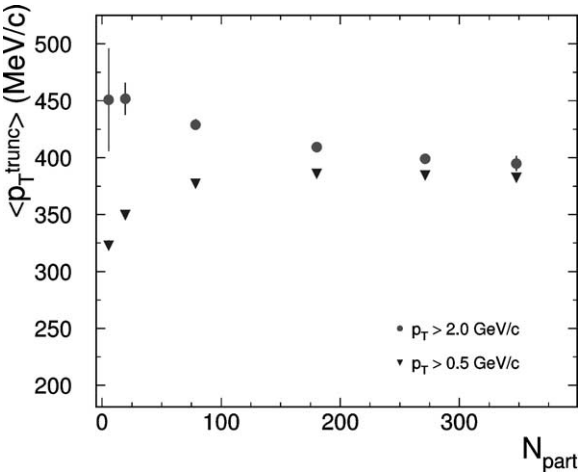

Fig. 4. Centrality dependence of $\langle p_T^{\text{trunc}} \rangle$, the average p_T of charged particles with p_T above a threshold p_T^{min} minus the threshold p_T^{min}. Shown are values for two p_T^{min} cuts, one at $p_T > 0.5$ GeV/c representing all data presented in Fig. 2 and the other one at $p_T > 2$ GeV/c. Only statistical errors are shown; see the text following Eq. (1) for a discussion of the systematic errors.

are more concave than those for central collisions. This shape difference is seen more clearly by taking the ratio of the spectrum for each centrality bin to the minimum-bias spectrum, as shown on the right-hand side of Fig. 2. In these ratios most systematic errors cancel or affect the overall scale only. The ratios for the central bins are almost independent of p_T since central collisions dominate the minimum bias yields. The peripheral bins show a decreasing ratio between 0.5 and 1.5 GeV/c thus in peripheral collisions the yield in this region decreases more rapidly with increasing p_T than in central collisions. For p_T above 1.5 GeV/c this trend is inverted.

Before analyzing the centrality dependence in more detail we demonstrate that the observed suppression of the yield at high p_T does not result from a reduced yield of protons and anti-protons [22]. To evaluate the effect of the (anti-)protons, we plot in the top panel of Fig. 3 the p_T dependence of p/h, the ratio of proton plus anti-proton yields to the total charged hadron yield for minimum bias collisions, which increases steadily. Above 1.5 GeV/c the ratio seem to saturate reaching a value of ~ 0.5 around 3 GeV/c. In the bottom panel of Fig. 3 we show p/h for p_T above 1.8 GeV/c as a function of centrality. Since there is clearly no significant decrease of the p/h ratio with either centrality or p_T, the observed hadron suppression is not due to a larger suppression of the (anti-)proton component than that of the mesons. On the contrary, within the range of the presented measurement the apparent slight increase in p/h with N_{part} could indicate a larger suppression of the meson component relative to all charged hadrons.

To evaluate the change of the hadron spectra more quantitatively we calculate the truncated average p_T:

$$\langle p_T^{\text{trunc}} \rangle \equiv \frac{\int_{p_T^{\text{min}}}^{\infty} p_T \, dN/dp_T}{\int_{p_T^{\text{min}}}^{\infty} dN/dp_T} - p_T^{\text{min}} \tag{1}$$

for $p_T^{\text{min}} = 0.5$ GeV/c and for $p_T^{\text{min}} = 2.0$ GeV/c for each centrality selection.[3] In Fig. 4 $\langle p_T^{\text{trunc}} \rangle$ is plotted as a function of N_{part}. The value of $\langle p_T^{\text{trunc}} \rangle$ is

[3] The value of $\langle p_T^{\text{trunc}} \rangle$ is closely related to the local inverse slope which is slightly smaller. The conversion to local slope depends on the spectral shape and also on p_T^{min}. For an exponential spectrum

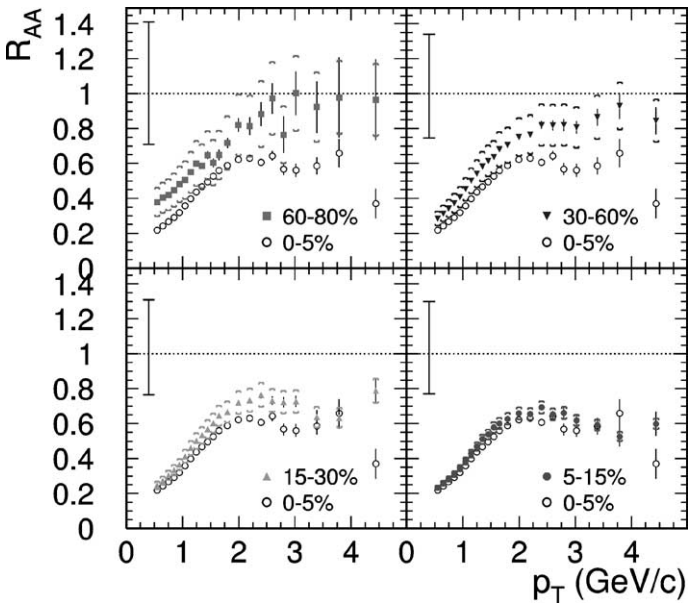

Fig. 5. Nuclear modification factor (R_{AA}) for the 60–80%, 30–60%, 15–30%, and 5–15% centrality selections compared to the one for the most central sample (0–5%). Due to insufficient statistics R_{AA} is not shown for the 80–92% sample. The solid error bars on each data point are statistical. The systematic error between the more peripheral and the central sample are given as brackets for the more peripheral data points. The error bar on the left-hand side of each panel indicates the overall systematic error on the R_{AA} scale.

insensitive to the normalization of the spectra. Systematic uncertainties of $\sim 20(50)$ MeV/c for $p_T^{\min} = 0.5(2.0)$ GeV/c result from an 1–2% uncertainty on the momentum scale and the p_T dependent uncertainties on the correction function. Since the centrality and p_T dependence of the correction factorize the error on $\langle p_T^{\text{trunc}} \rangle$ is independent of centrality to better than 2 MeV/c.

The $\langle p_T^{\text{trunc}} \rangle$ for $p_T^{\min} = 0.5$ GeV/c increases with N_{part} similar to the average p_T of identified charged hadrons [22]. For higher $p_T^{\min} = 2.0$ GeV/c the $\langle p_T^{\text{trunc}} \rangle$ drops by ~ 60 MeV/c with N_{part}, distinctly different from the expected increased role of hard particle production in the more central collisions. Absent any collective effects, the hard scattering contribution should increase relative to soft production by the factor $N_{\text{coll}}/N_{\text{part}}$ which grows from 1.5 to ~ 6 from peripheral to central collisions. Since the relative contribution of the hard component to the spectrum increases with p_T, this should lead to a rise of $\langle p_T^{\text{trunc}} \rangle$ for sufficiently large $p_T^{\min}$. The drop of $\langle p_T \rangle$ therefore indicates the suppression of the high p_T relative to the low p_T hadron yield independent of systematic errors associated with the absolute normalization of the spectra or any nucleon–nucleon reference distribution.

Changes of the hadron spectra at high p_T are often presented in terms of the nuclear modification factor R_{AA}. This measure relies on the absolute normalization and a reference and therefore has intrinsically larger systematic uncertainties, but it allows to quantify the suppression. We have calculated R_{AA} for each centrality bin as:

$$R_{AA}(p_T, \eta) = \left(\frac{1}{N_{\text{evt}}} \frac{d^2 N^{A+A}}{dp_T\, d\eta} \right) \times \left(\frac{\langle N_{\text{coll}} \rangle}{\sigma_{\text{inel}}^{\text{N+N}}} \frac{d^2 \sigma^{\text{N+N}}}{dp_T\, d\eta} \right)^{-1}. \quad (2)$$

For the N + N charged hadron cross section we use a power-law parameterization $1/\pi\ d^2\sigma/dp_T^2 = A/(1 + p_T/p_0)^n$, with $A = 330$ mb/(GeV/c)^2, $p_0 = 1.72$ GeV/c, and $n = 12.4$. The parameters were obtained by interpolating p + p and $\bar{\text{p}}$ + p data to $\sqrt{s} = 130$ GeV as described in [5]. In Fig. 5 the $R_{AA}(p_T)$

with an inverse slope of 350 MeV/c the conversion is approximately $-80(-60)$ MeV/c for $p_T^{\min} = 0.5(2.0)$ GeV/c.

values for all centrality bins excluding the most peripheral one are compared to the central (0–5%) bin. The systematic uncertainties in the normalization of the data, in $N_{\rm coll}$, and in the N + N reference (20%) result in overall systematic errors of about 41%, 34%, 31%, 31% and 30% for centrality bins 2–6, respectively. The errors are quoted for the range from 1 to 3.5 GeV/c; they increase somewhat towards higher p_T. Comparing R_{AA} for a given centrality bin to the most central bin, the systematic errors reduce to $\sim 6\%$ for bin 5 (5–15%) and nearly 27% for bin 2(60–80%). They are dominated the uncertainty in $N_{\rm coll}$ listed in Table 2.

For the 60–80% centrality bin, R_{AA} increases with p_T and reaches unity at high p_T. In comparison to the 60–80% bin, the R_{AA} values for the most central bin remain significantly below unity at a value of 0.55 for $p_T > 2$ GeV/c. At high p_T approximately constant R_{AA} values are detected in all centrality bins. The high p_T values decrease monotonically with centrality, clearly indicating that the magnitude of the suppression of high p_T hadrons increases with centrality. This is shown clearly in the upper part of Fig. 6, which presents R_{AA} obtained for the three p_T bins 1.6 to 2.6 GeV/c, 2.6 to 3.6 GeV/c, and above 3.6 GeV/c as a function of centrality. For central collisions we observe a suppression of about a factor of 2 ± 0.6 compared to binary collision scaling. Relative to peripheral collisions the suppression factor in central collisions increases with p_T from 1.25 ± 0.2 to 1.5 ± 0.2 to 1.8 ± 0.3 for the three p_T bins, respectively.

We note that for peripheral collisions the data do not indicate a significant increase of R_{AA} above unity, unlike data at lower energies [23]. However, such an increase, attributed to initial state scattering, the Cronin effect [24], may well be consistent with the peripheral data due to the large systematic uncertainty of the R_{AA} scale. While the relative difference between the peripheral and central spectra increases with p_T, the roughly constant nuclear modification factor at large p_T suggests an approximately p_T independent suppression of hard scattering contributions over the range $2 < p_T < 4.5$ GeV/c.

The physics that controls the production of high-p_T particles or the suppression of the hard scattering yields in the measured p_T range may not depend directly on $N_{\rm coll}$. Thus, we have calculated a different

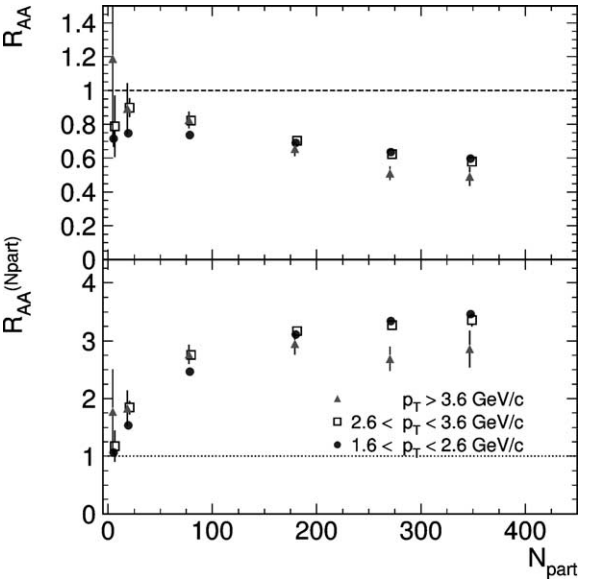

Fig. 6. The top panel gives the nuclear modification factor R_{AA} for three exclusive p_T regions as a function of the centrality of the collision. The lower panel shows essentially the same quantity but normalized to the number of participant pairs rather than to the number of binary collisions. The dotted line indicates the expectation for scaling with the number of binary collisions (top) or with the number of participants (bottom). Only statistical errors are shown. The systematic error on the scale and the centrality dependence are identical to the errors shown in Fig. 5. These errors are correlated, i.e., take their maximum or minimum value simultaneously for all centrality and p_T selections. In addition, there are also p_T dependent systematic errors, which are given in Table 1. The systematic errors do not alter the trends in the data.

ratio, $R_{AA}^{\rm part}$, defined similarly to R_{AA} but with $N_{\rm coll}$ replaced by the number of participant pairs, $N_{\rm part}/2$. If particle production increases proportional to the number of participants, $R_{AA}^{\rm part} = 1$.

The obtained $R_{AA}^{\rm part}$ values are shown in Fig. 6 (bottom) for the three p_T bins used above. The values of $R_{AA}^{\rm part}$ are larger than R_{AA} by a factor equal to $2N_{\rm coll}/N_{\rm part}$ the average number of nucleon–nucleon collisions suffered by each participant. For all p_T bins the yield per participant is consistent with unity for peripheral collisions as expected since peripheral collisions should closely resemble N + N collisions. For central collisions $R_{AA}^{\rm part}$ increases to approximately three. Most of this change occurs in the range of $N_{\rm part}$ from 40 to 140. For larger $N_{\rm part}$ the yield in the highest p_T bin is approximately constant while in both lower p_T bins it increases by 20 to 30%.

4. Concluding discussion

In this Letter we have presented the centrality dependence of charged hadron p_T spectra focusing on the behavior of the spectra at high p_T. A striking change of the spectral shape is observed when comparing spectra from different centrality selections. For peripheral collisions the spectrum exhibits a pronounced concave shape which is modified towards a more exponential spectrum as the centrality increases. The observed lack of variation with centrality in the proton to charged ratio at large transverse momenta indicates that the modification is not due to a change in the relative yields of protons.

We observe a decrease of $\langle p_T^{\text{trunc}} \rangle$ for $p_T > 2$ GeV/c with increasing centrality, which is distinctly different from the increase of $\langle p_T \rangle$ and demonstrates the suppression of the high p_T hadron yield independent of systematic errors associated with the absolute normalization of the spectra. The data are not consistent with binary collision scaling of hard scattering processes, which would results in an increase of $\langle p_T^{\text{trunc}} \rangle$. If the p_T spectra above 2 GeV/c are strongly affected by collective motion of matter before freeze-out, we would also expect an increase $\langle p_T^{\text{trunc}} \rangle$ since the corresponding flow velocities should increase in more central collisions [25]. Similarly, if gluon saturation is important for particle production in the p_T range above 2 GeV/c, $\langle p_T^{\text{trunc}} \rangle$ should increase with increasing N_{part} due to the predicted logarithmic increase of Q_s [26]. In contrast, the data are consistent with models assuming energy loss of hard scattered partons, which results in an increasing reduction of the hard scattering contribution to the hadron spectrum with increasing centrality of the collisions [7–9]. It remains to be seen whether this explanation is unique.

Comparing the measured differential yields in five centrality bins to an N_{coll} scaling of the N + N reference yields we see a suppression of the yields in central collisions at high p_T, consistent with the results in [5,6]. In the 0–30% centrality range (bins 1–3) the suppression is approximately independent of p_T for $2 < p_T < 5$ GeV/c at a value of $R_{AA} \sim 0.6$ and simultaneously nearly independent within 20% of centrality. The suppression sets in gradually with the largest change occurring over the 30–60% centrality range. This centrality bin covers a broad range of collision geometries. Whether the change is continuous or exhibits a threshold behavior, as predicted in [27], cannot be judged from the present data. The observed suppression is consistent with parton energy loss scenarios. In these models, the value of R_{AA} and its p_T dependence are very sensitive to the actual energy loss prescription. Due to the large systematic errors on the R_{AA} scale, the contribution from the protons and the limited p_T reach of the data presented here, we cannot distinguish between the different energy loss prescriptions on the basis of R_{AA}.

In summary, a detailed analysis of the centrality dependence of charged particle data from Au–Au collisions at $\sqrt{s_{\text{NN}}} = 130$ GeV measured by PHENIX reveals interesting features of the observed high p_T hadron suppression. The decrease of the average p_T with increasing centrality seems to favor models of particle production that consider energy loss effects, rather than saturation- or hydrodynamics-based approaches for this p_T range. The suppression sets in gradually with the largest changes occurring for peripheral collisions with less than about 140 participating nucleons. From there on it does not change substantially towards more central collisions.

Note added in proof

After submission of our manuscript, data from Au–Au collisions at $\sqrt{s_{\text{NN}}} = 200$ GeV were presented by the PHOBOS Collaboration [28,29], with an emphasis on the lack of variation in the scaled yields with N_{part} for $N_{\text{part}} > 65$. Keeping in mind that results from different energies are not directly comparable, we note that the broader range in N_{part} presented here shows that this effect does not apply over the entire range of centralities, and that when normalized with the appropriate p–p yields, is simply an aspect of the smooth variation of R_{AA}^{part} visible in Fig. 6.

Acknowledgements

We thank the staff of the Collider-Accelerator and Physics Departments at BNL for their vital contributions. We acknowledge support from the Department of Energy and NSF (USA), MEXT and JSPS (Japan), RAS, RMAE, and RMS (Russia), BMBF, DAAD, and AvH (Germany), VR and KAW (Sweden), MIST

and NSERC (Canada), CNPq and FAPESP (Brazil), IN2P3/CNRS (France), DAE and DST (India), KRF and CHEP (Korea), the US CRDF for the FSU, and the US-Israel BSF.

References

[1] H. Jöstlein, et al., Phys. Rev. D 20 (1979) 53.
[2] M. Gyulassy, M. Plümer, Phys. Lett. B 243 (1990) 432;
X.N. Wang, M. Gyulassy, Phys. Rev. Lett. 68 (1992) 1480.
[3] X.N. Wang, M. Gyulassy, M. Plümer, Phys. Rev. D 51 (1995) 3436;
R. Baier, et al., Phys. Lett. B 345 (1995) 277;
R. Baier, D. Schiff, B.C. Zakharov, Annu. Rev. Nucl. Part. Sci. 50 (2000) 37.
[4] M. Gyulassy, X.N. Wang, Nucl. Phys. B 420 (1994) 583;
X.N. Wang, Phys. Rev. C 58 (1998) 2321.
[5] PHENIX Collaboration, K. Adcox, et al., Phys. Rev. Lett. 88 (2002) 22301.
[6] STAR Collaboration, C. Adler, et al., Phys. Rev. Lett. 89 (2002) 202301.
[7] X.N. Wang, Phys. Rev. C 61 (2000) 64910.
[8] M. Gyulassy, P. Levai, I. Vitev, Phys. Rev. Lett. 85 (2000) 5535.
[9] P. Levai, et al., Nucl. Phys. A 698 (2002) 631.
[10] K. Gallmeister, C. Greiner, Z. Xu, nucl-th/0202051.
[11] P. Kolb, et al., Nucl. Phys. A 696 (2001) 197.
[12] D. Teaney, J. Lauret, E.V. Shuryak, nucl-th/0110037.
[13] J.J. Aubert, et al., Phys. Lett. B 123 (1983) 275.
[14] L.V. Gribov, E.M. Levin, M.G. Ryskin, Phys. Rep. 100 (1983).
[15] Z. Huang, H.J. Lu, I. Sarcevic, Nucl. Phys. A 637 (1998) 79.
[16] K.J. Eskola, V.J. Kolhinen, C.A. Salgado, Eur. Phys. J. C 9 (1999) 61.
[17] L.D. McLerran, R. Venugopalan, Phys. Rev. D 49 (1994) 2233.
[18] A. Kovner, L.D. McLerran, H. Weigert, Phys. Rev. D 52 (1995) 6231.
[19] A. Krasnitz, Y. Nara, R. Venugopalan, Phys. Rev. Lett. 87 (2001) 192302.
[20] D. Kharzeev, E. Levin, L.D. McLerran, hep-ph/0210332.
[21] PHENIX Collaboration, K. Adcox, et al., Phys. Rev. Lett. 86 (2001) 3500;
PHENIX Collaboration, K. Adcox, et al., Phys. Rev. Lett. 87 (2001) 052301.
[22] PHENIX Collaboration, K. Adcox, et al., Phys. Rev. Lett. 88 (2002) 242301.
[23] E. Wang, X.N. Wang, nucl-th/0104031, and references therein.
[24] D. Antreasyan, et al., Phys. Rev. D 19 (1979) 764.
[25] E. Shuryak, private communication.
[26] D. Kharzeev, E. Levin, nucl-th/0108006;
J. Schaffner-Bielich, et al., nucl-th/0108048.
[27] X.N. Wang, Phys. Rev. C 63 (2001) 54902.
[28] PHOBOS Collaboration, C. Roland, et al., hep-ex/0212006.
[29] PHOBOS Collaboration, B.B. Back, et al., nucl-ex/0302015, Phys. Lett. B, submitted for publication.

Centrality dependence of charged-neutral particle fluctuations in 158*A* GeV ^{208}Pb+^{208}Pb collisions

M. M. Aggarwal,[1] Z. Ahammed,[2] A. L. S. Angelis,[3] V. Antonenko,[4] V. Arefiev,[5] V. Astakhov,[5] V. Avdeitchikov,[5] T. C. Awes,[6] P. V. K. S. Baba,[7] S. K. Badyal,[7] S. Bathe,[8] B. Batiounia,[5] T. Bernier,[9] K. B. Bhalla,[10] V. S. Bhatia,[1] C. Blume,[8] D. Bucher,[8] H. Büsching,[8] L. Carlén,[11] S. Chattopadhyay,[2] M. P. Decowski,[12] H. Delagrange,[9] P. Donni,[3] M. R. Dutta Majumdar,[2] K. El Chenawi,[11] A. K. Dubey,[13] K. Enosawa,[14] S. Fokin,[4] V. Frolov,[5] M. S. Ganti,[2] S. Garpman,[11] O. Gavrishchuk,[5] F. J. M. Geurts,[15] T. K. Ghosh,[16] R. Glasow,[8] B. Guskov,[5] H. Å. Gustafsson,[11] H. H. Gutbrod,[17] I. Hrivnacova,[18] M. Ippolitov,[4] H. Kalechofsky,[3] K. Karadjev,[4] K. Karpio,[19] B. W. Kolb,[17] I. Kosarev,[5] I. Koutcheryaev,[4] A. Kugler,[18] P. Kulinich,[12] M. Kurata,[14] A. Lebedev,[4] H. Löhner,[16] L. Luquin,[9] D. P. Mahapatra,[13] V. Manko,[4] M. Martin,[3] G. Martínez,[9] A. Maximov,[5] Y. Miake,[14] G. C. Mishra,[13] B. Mohanty,[2,13,*] M.-J. Mora,[9] D. Morrison,[20] T. Mukhanova,[4] D. S. Mukhopadhyay,[2] H. Naef,[3] B. K. Nandi,[13] S. K. Nayak,[7] T. K. Nayak,[2] A. Nianine,[4] V. Nikitine,[5] S. Nikolaev,[4] P. Nilsson,[11] S. Nishimura,[14] P. Nomokonov,[5] J. Nystrand,[11] A. Oskarsson,[11] I. Otterlund,[11] T. Peitzmann,[16] D. Peressounko,[4] V. Petracek,[18] W. Pinganaud,[9] F. Plasil,[6] M. L. Purschke,[17] J. Rak,[18] R. Raniwala,[10] S. Raniwala,[10] N. K. Rao,[7] F. Retiere,[9] K. Reygers,[16] G. Roland,[12] L. Rosselet,[3] I. Roufanov,[5] C. Roy,[9] J. M. Rubio,[3] S. S. Sambyal,[7] R. Santo,[8] S. Sato,[14] H. Schlagheck,[8] H.-R. Schmidt,[17] Y. Schutz,[9] G. Shabratova,[5] T. H. Shah,[7] I. Sibiriak,[4] T. Siemiarczuk,[19] D. Silvermyr,[11] B. C. Sinha,[2] N. Slavine,[5] K. Söderström,[11] G. Sood,[1] S. P. Sørensen,[20] P. Stankus,[6] G. Stefanek,[19] P. Steinberg,[12] E. Stenlund,[11] M. Sumbera,[18] T. Svensson,[11] A. Tsvetkov,[4] L. Tykarski,[19] E. C. v. d. Pijll,[15] N. v. Eijndhoven,[15] G. J. v. Nieuwenhuizen,[12] A. Vinogradov,[4] Y. P. Viyogi,[2] A. Vodopianov,[5] S. Vörös,[3] B. Wysłouch,[12] and G. R. Young [6]

(WA98 Collaboration)

[1]*University of Panjab, Chandigarh 160014, India*
[2]*Variable Energy Cyclotron Centre, Calcutta 700064, India*
[3]*University of Geneva, CH-1211 Geneva 4, Switzerland*
[4]*RRC "Kurchatov Institute," RU-123182 Moscow, Russia*
[5]*Joint Institute for Nuclear Research, RU-141980 Dubna, Russia*
[6]*Oak Ridge National Laboratory, Oak Ridge, Tennessee 37831-6372*
[7]*University of Jammu, Jammu 180001, India*
[8]*University of Münster, D-48149 Münster, Germany*
[9]*SUBATECH, Ecole des Mines, Nantes, France*
[10]*University of Rajasthan, Jaipur 302004, Rajasthan, India*
[11]*University of Lund, SE-221 00 Lund, Sweden*
[12]*MIT, Cambridge, Massachusetts 02139*
[13]*Institute of Physics, Bhubaneswar 751005, India*
[14]*University of Tsukuba, Ibaraki 305, Japan*
[15]*Universiteit Utrecht/NIKHEF, NL-3508 TA Utrecht, The Netherlands*
[16]*KVI, University of Groningen, NL-9747 AA Groningen, The Netherlands*
[17]*Gesellschaft für Schwerionenforschung (GSI), D-64220 Darmstadt, Germany*
[18]*Nuclear Physics Institute, CZ-250 68 Rez, Czech Republic*
[19]*Institute for Nuclear Studies, 00-681 Warsaw, Poland*
[20]*University of Tennessee, Knoxville, Tennessee 37966*

(Received 25 June 2002; published 2 April 2003)

Results on the study of localized fluctuations in the multiplicity of charged particles and photons produced in 158*A* GeV/*c* Pb+Pb collisions are presented for varying centralities. The charged versus neutral particle multiplicity correlations in common phase space regions of varying azimuthal sizes are analyzed by two different methods. Various types of mixed events are constructed to probe fluctuations arising from different sources. The measured results are compared to those from simulations and from mixed events. The comparison indicates the presence of nonstatistical fluctuations in both the charged particle and photon multiplicities in limited azimuthal regions. However, no correlated charged-neutral fluctuations, a possible signature of formation of disoriented chiral condensates, are observed. An upper limit on the production of disoriented chiral condensates is set.

DOI: 10.1103/PhysRevC.67.044901 PACS number(s): 25.75.Gz, 13.40.−f, 24.90.+d

*Electronic address: bmohanty@veccal.ernet.in

 ©2003 The American Physical Society

I. INTRODUCTION

The large number of particles produced in relativistic heavy-ion collisions at the Super Proton Synchrotron (SPS) and the Relativistic Heavy-Ion Collider provide an opportunity to analyze and study, on an event-by-event basis, fluctuations in physical observables, such as particle multiplicities, transverse momenta, and their correlations. These studies provide information on the dynamics of multiparticle production and may help us to reveal the phase transition from hadronic matter to quark-gluon plasma [1,2]. The formation of hot and dense matter in high energy heavy-ion collisions also has the possibility to create matter in a chiral symmetry restored phase in the laboratory. After the initial stage of the collision, the system cools and expands, returning to the normal QCD vacuum in which the chiral symmetry is spontaneously broken. During this process, a metastable state may be formed in which the chiral condensate is disoriented from the true vacuum direction. This transient state would subsequently decay by emitting pions coherently within finite subvolumes or domains of the collision region. The possibility of formation of disoriented chiral condensate (DCC) has been discussed extensively in recent years [3–11]. The detection and study of the DCC state would provide valuable information about the chiral phase transition and the vacuum structure of strong interactions.

Theoretical studies [5–7] suggest that isospin fluctuations caused by the formation of a DCC would produce clusters of coherent pions in localized phase space domains. The formation of DCC domains would be associated with large event-by-event fluctuations in the ratio of neutral to charged pions. The probability distribution of the neutral pion fraction f in such a DCC domain has been shown [3] to follow the relation

$$P(f)=\frac{1}{2\sqrt{f}}, \quad \text{where} \quad f=N_{\pi^0}/N_{\pi}, \tag{1}$$

which is quite different from that of the normal pion production mechanism. For the normal pion production, where the production of π^0, π^+, and π^- are equally probable, the f distribution is binomial, peaking at 1/3.

In the experimental search for localized domains of DCC, a practical approach is to search for events with large and localized fluctuations (localized in pseudorapidity η and azimuthal angle ϕ) in the ratio of the number of photons to charged particles, which would directly reflect fluctuations in the neutral to charged pion ratio. Typical event structures would be similar to the Centauro and anti-Centauro events reported by the JACEE Collaboration [12]. Results from other cosmic ray experiments have not ruled out the possibility of the DCC formation mechanism [13]. The accelerator based studies carried out in p-$\bar{p}$ [14] and heavy-ion [15,16] reactions have investigated particle production over extended regions of phase space. These analyses were not sensitive to the presence of small domains of DCC localized in phase space. The first search for evidence of localized domains of DCC has been carried out at the SPS by the WA98 experiment in a detailed study of central Pb+Pb events [17]. The analysis showed the presence of localized nonstatistical fluctuations in the multiplicity of both photons and charged particles. However, the charged-neutral fluctuations were found not to be correlated event by event, as would be expected for a DCC production mechanism. An upper limit on the frequency of DCC formation in central Pb+Pb collisions was set. Recently, there have been theoretical suggestions to look for DCC formation in events for intermediate centralities [18]. In this paper we present first results on the centrality dependence of localized charged-neutral multiplicity fluctuations. It is based on an analysis of event-by-event fluctuation in the relative number of charged particles and photons detected within the common acceptance of the photon and charged particle multiplicity detectors of the WA98 experiment [19].

The paper is organized in the following manner: In the following section we describe the detectors used for the present analysis; the centrality selection criteria, the data reduction, and simulation. Section III deals with the analysis techniques where two analysis methods are presented, one based on the correlation of photons and charged particles, and the other based on a discrete wavelet transformation analysis. In Sec. IV, we present in detail the construction of mixed events used for this study. Section V discusses the ability of the mixed events to probe specific fluctuations. The final results and discussion are given in Sec. VI. A summary is presented in Sec. VII.

II. EXPERIMENTAL SETUP AND DATA REDUCTION

In the WA98 experiment at CERN [19], the main emphasis has been on high precision, simultaneous detection of both hadrons and photons. The experimental setup consisted of large acceptance hadron and photon spectrometers, detectors for charged particle and photon multiplicity measurements, and calorimeters for transverse and forward energy measurements. The present study makes use of the data from the photon multiplicity detector (PMD), the silicon pad multiplicity detector (SPMD), and the midrapidity calorimeter (MIRAC).

A. Centrality selection

The centrality of the interaction was determined from the total transverse energy (E_{T}) measured by the MIRAC [20]. The MIRAC measures both the transverse electromagnetic (E_{T}^{em}) and hadronic (E_{T}^{had}) energies in the interval $3.5 \leqslant \eta \leqslant 5.5$ with a resolution of $17.9\%/\sqrt{E}$ and $46.1\%/\sqrt{E}$, respectively, where E is expressed in GeV. The centrality, or impact parameter of the collision, has a strong correlation with the amount of E_{T} produced. Events with large E_{T} production correspond to the most central, small impact parameter, collisions [21].

The centralities are expressed as fractions of the minimum bias cross section as a function of the measured total E_{T}. For the present analysis we have used data selections in four centrality bins, the top 5% (henceforth referred to as centrality-1), 5–10 % (centrality-2), 15–30 % (centrality-3),

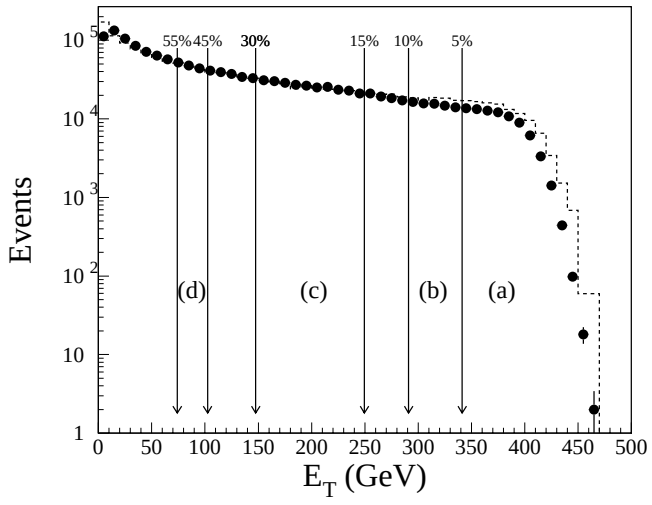

FIG. 1. The total E_{T} distribution (solid dots) measured in $3.5 \leqslant \eta \leqslant 5.5$ for Pb+Pb collision at 158*A* GeV/c. The total E_T distribution as obtained from VENUS is also shown as dashed histogram. The E_{T} values corresponding to the different centrality bins used in the analysis are shown. (a) Centrality-1 (0–5 %), (b) centrality-2 (5–10 %), (c) centrality-3 (15–30 %), and (d) centrality-4 (45–55 %) of the minimum bias cross section as determined by selection on the measured transverse energy distribution.

and 45–55 % (centrality-4) of the minimum bias cross section. The minimum bias distribution of the total E_{T} is shown in Fig. 1. The centrality bins used in this analysis are marked in the figure.

B. Photon multiplicity detector

The photon multiplicity is measured using the preshower PMD located at a distance of 21.5 m from the target. The PMD consists of three radiation length (X_0) thick lead converter plates in front of an array of square scintillator pads of four sizes, varying from 15×15 mm^2 to 25×25 mm^2, placed in 28 box modules. Each box module consists of a matrix of 38×50 scintillator pads read out using an image intensifier plus charged coupled device (CCD) camera system. The scintillation light is transmitted to the readout device via a short wavelength shifting fiber spliced to a long extramural absorber coated clear fiber. The total light amplification of the readout system is $\sim$40 000. Digitization of the CCD pixel charge is done by a set of custom built fast-bus modules employing an 8-bit, 20-MHz flash analog-to-digital converter (ADC) system. Details of the design and characteristics of the PMD may be found in Refs. [22,23]. The results presented here make use of the data from the central 22 box modules covering the pseudorapidity range of $2.9 \leqslant \eta \leqslant 4.2$. The clusters of hit pads, having total ADC content above a hadron rejection threshold are identified as photon-like, the multiplicity being denoted by $N_{\gamma\text{-like}}$. If the number of incident photons is denoted by N_γ^{inc} and the number of photons detected above the hadron rejection threshold as N_γ^{th}, then the photon counting efficiency ϵ_γ and purity of photon sample (f_p) are defined as $\epsilon_\gamma = N_\gamma^{th}/N_\gamma^{inc}$ and $f_p = N_\gamma^{th}/N_{\gamma\text{-like}}$, respectively. These are estimated from detector simulations [22,23]. The photon counting efficiencies for the central to peripheral cases varies from 68% to 73%. The purity of the photon sample in the two cases varies from 65% to 54% [22,23]. The acceptance in terms of transverse momentum p_T extends down to about 30 MeV/c, however, the PMD energy resolution is not sufficient for particle-by-particle p_T measurement.

C. Silicon pad multiplicity detector

The charged particle multiplicity N_{ch} is measured using the circular SPMD located 32.8 cm from the target and having full azimuthal coverage in the region $2.35 < \eta < 3.75$, corresponding to the central rapidity region at SPS energies (where $\eta_{CMS} = 2.92$). The detector consists of four overlapping quadrants, each fabricated from a single 300-μm-thick silicon wafer. The active area of each quadrant is divided into 1012 pads forming 46 azimuthal wedges and 22 radial bins, with the pad size increasing with increasing radius to provide equal sized pseudorapidity bins. The efficiency for detection of a charged particle in the active area has been determined in test beam measurements to be better than 99%. Conversely, the detector is transparent to high energy photons, since only about 0.2% are expected to interact in the silicon. During the data recording, 95% of the pads worked properly and are used in this analysis. Details of the characteristics of the SPMD can be found in Refs. [15,24]. The SPMD does not provide p_T measurement, but provides the multiplicity measurement integrated over transverse momentum p_T with a threshold which extends down to about 20 MeV/c.

D. Data reduction

The data presented here were taken in 1996 at the CERN SPS with the 158*A* GeV Pb ion beam on a Pb target of thickness 213 μm. The WA98 Goliath magnet was switched off during these runs. Events with beam pileup, downstream interactions, and pileup in the CCD camera system were rejected in the off-line analysis [15,23]. The data have been analyzed for the region of common η ($2.9 < \eta < 3.75$) and ϕ coverage of the SPMD charged particle and PMD photon multiplicity detectors. The $N_{\gamma\text{-like}}$ and the N_{ch} distributions for the four centrality bins are shown in Figs. 2 and 3. The number of events analyzed, the mean number of photons and charged particles, along with the root mean square deviations are shown in the figures. The PMD and SPMD detectors provide momentum integrated multiplicity measurements with very low thresholds. Since pions from DCC domains are expected to have small p_T values, below the pion mass, the momentum integration will dilute the DCC signal. On the other hand, the large coverage of the PMD and SPMD are important to overcome the limitations of small number fluctuations.

The various sources of systematic errors associated with the $N_{\gamma\text{-like}}$ and N_{ch} distributions have been investigated and described in detail previously [23,25]. These include the following.

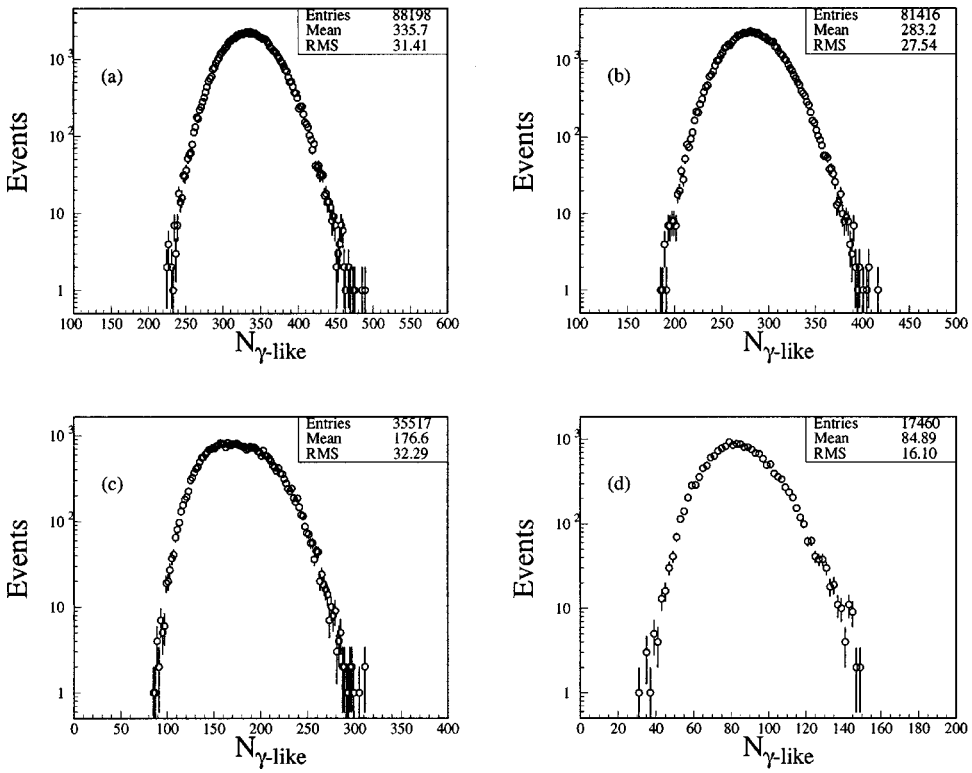

FIG. 2. The $N_{\gamma\text{-like}}$ multiplicity distributions for the four centrality selections for Pb+Pb collision at 158*A* GeV/*c*. (a) Centrality-1 (0–5 %), (b) centrality-2 (5–10 %), (c) centrality-3 (15–30 %), and (d) centrality-4 (45–55 %).

(a) The uncertainty in the energy calibration and the associated uncertainty in the energy threshold for hadron rejection in the PMD leads to an error in the efficiency for $N_{\gamma\text{-like}}$ clusters. The nominal hadron rejection threshold was set at three times the minimum ionizing particle (MIP) peak. The value of the threshold was reduced by 10% [23] in order to estimate the systematic error. The associated error in $N_{\gamma\text{-like}}$ is 2.5%.

(b) The error due to the effect of clustering of pad signals in the PMD is a major source of error in $N_{\gamma\text{-like}}$. This error is determined from GEANT [26] simulation by comparing the number of known photon tracks on the PMD with the total

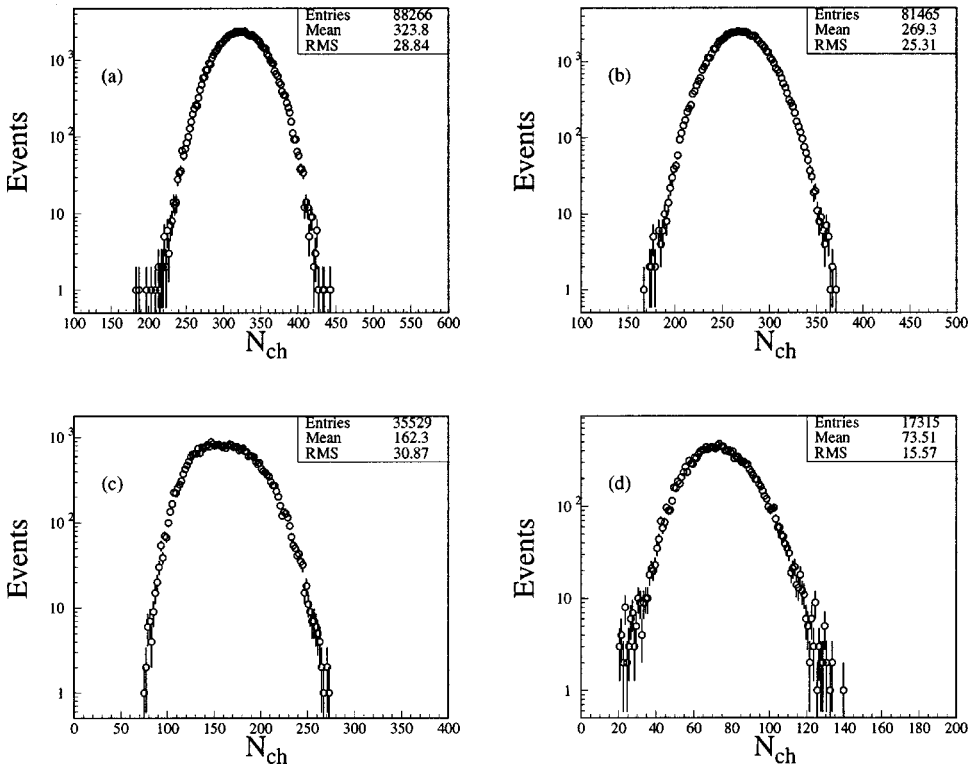

FIG. 3. The N_{ch} multiplicity distributions for the four centrality selections for Pb+Pb collision at 158*A* GeV/*c*. (a) Centrality-1 (0–5 %), (b) centrality-2 (5–10 %), (c) centrality-3 (15–30 %), and (d) centrality-4 (45–55 %).

number of reconstructed photonlike clusters. It is found that the number of clusters exceeds the number of tracks by 3% in the case of peripheral events and by 7% for high multiplicity central events.

(c) The error due to the variation in pad-to-pad gains of the scintillators in PMD was found to be less than 1%.

(d) The uncertainty in the $N_{\rm ch}$ determination with the SPMD has been estimated to be about 4% [15].

(e) The error due to the finite resolution in the measurement of the total transverse energy E_T in MIRAC [23] translates into an uncertainty in the centrality selection. The effect of this systematic error has been determined by performing the analysis with varying centrality cut within the MIRAC resolution.

The contribution of each of these various systematic errors to the final results is discussed in the following sections.

E. Simulated events

Simulated events were generated using the VENUS 4.12 event generator [27] with the default parameter values. The output was processed through a detector simulation package in the GEANT 3.21 [26] framework. This simulation includes the full WA98 experimental setup and includes experimental effects such as photon conversions, downstream interactions, hadron backgrounds in the PMD, etc., which might dilute or enhance the observed fluctuations. The effect of Landau fluctuations in the energy loss of charged particles in silicon was included in the SPMD simulation [15]. For the PMD simulation, the GEANT results in terms of energy deposition in pads were converted to the pad ADC values using the MeV-ADC calibration relation. After this the ADC distribution is convoluted with a Gaussian function of proper width taken from the readout resolution curve. If the energy deposition is less than three MIP, a Landau distribution is used for convolution. The details of the PMD simulations taking into account the detector and readout effects can be found in Ref. [22]. The centrality selection with the simulated data has been made in a manner identical to the data, determined from the simulated total transverse energy in MIRAC. The minimum bias total $E_{\rm T}$ distribution predicted by VENUS is shown by the dashed histogram in Fig. 1. The agreement with the data is seen to be quite reasonable. A total of 60 K VENUS events with simulated detector response were generated for the present study. These simulated events (henceforth referred to simply as VENUS events unless otherwise specified) were then processed with the same analysis codes as used for the analysis of the experimental data.

III. ANALYSIS TECHNIQUES

Two different analysis methods have been used in the present study. In the first analysis method, the magnitude of the $N_{\gamma\text{-like}}$ versus $N_{\rm ch}$ multiplicity fluctuations is obtained in decreasing phase space regions. The second method employed the discrete wavelet transformation technique to investigate the relative magnitude of the $N_{\gamma\text{-like}}$ versus $N_{\rm ch}$ fluctuations in adjacent phase space regions. The results from these methods of analysis applied to data, VENUS, and various sets of mixed events (to be discussed later) are compared to draw proper conclusions.

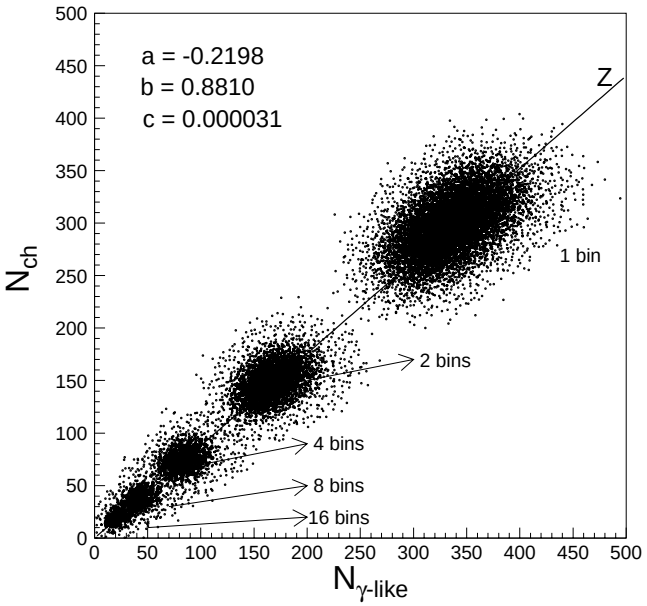

FIG. 4. The event-by-event correlation between $N_{\rm ch}$ and $N_{\gamma\text{-like}}$ for centrality bin 1. Overlaid on the plot is the common correlation axis (Z axis) obtained for the full distribution by fitting the $N_{\gamma\text{-like}}$ and $N_{\rm ch}$ correlations with a second-order polynomial. The values in the upper left are the coefficients of the polynomial of the form $N_{\rm ch}=a+bN_{\gamma\text{-like}}+cN^2_{\gamma\text{-like}}$. For the other three centrality classes, the plots are qualitatively similar.

A. N_γ versus $N_{\rm ch}$ correlations

In order to search for localized fluctuations in the photon and charged particle multiplicities, which may have non-statistical origin, the correlation between $N_{\gamma\text{-like}}$ and $N_{\rm ch}$ is investigated at various scales in ϕ.

The event-by-event correlation between $N_{\gamma\text{-like}}$ and $N_{\rm ch}$ has been studied in various ϕ intervals by dividing the entire ϕ space into 2, 4, 8, and 16 bins. The method of analysis is similar to that described in Refs. [15,17]. Figure 4 shows a scatter plot of the correlation between $N_{\gamma\text{-like}}$ and $N_{\rm ch}$ for the top centrality bin. The correlation plots for each ϕ interval size, including the case of the full interval with no segmentation, are shown. The distributions for the other three centrality bins are qualitatively similar. A common correlation axis Z has been obtained for the full distribution by fitting the $N_{\gamma\text{-like}}$ and $N_{\rm ch}$ correlation with a second-order polynomial. The correlation axis with fit parameters is shown in the figure. The distance of separation (D_Z) between a data point and the correlation axis has been calculated with the convention that D_Z is positive for points below the Z axis. The distribution of D_Z represents the relative fluctuations of $N_{\gamma\text{-like}}$ and $N_{\rm ch}$ from the correlation axis for any chosen ϕ bin size. In order to compare the fluctuations for different ϕ bins on a similar footing, a scaled variable $S_Z=D_Z/s(D_Z)$ is used, where $s(D_Z)$ represents the rms deviation of the D_Z distribution for VENUS events analyzed in the same manner. The D_Z distributions of data, mixed events, and the simu-

lated events for a given centrality and ϕ bin size are all scaled by the same $s(D_Z)$ corresponding to the VENUS events for the respective centrality and azimuthal bin size. The presence of events with localized fluctuations in $N_{\gamma\text{-like}}$ and N_{ch}, at a given ϕ bin, is expected to result in a broader distribution of S_Z compared to those for normal events. Comparing the rms deviations of the S_Z distributions of data, mixed events (to be discussed later), and VENUS events may allow us to infer the presence of nonstatistical localized fluctuations.

B. Multiresolution DWT analysis

A multiresolution analysis using discrete wavelet transform (DWT) [28] has been shown to be quite powerful in the search for localized domains of DCC [29–31]. The significance of the DWT technique lies in its power to analyze a spectrum at different resolutions, with the ability to identify fluctuations present at any scale. This method has been utilized very successfully in many fields including image processing, data compression, turbulence, human vision, radar, and earthquake prediction [28]. It should be noted that the DWT analysis provides information different from the moment analysis of the preceding section. It analyzes the event-by-event distribution in ϕ space to characterize the bin-to-bin fluctuations relative to the average behavior.

For the present DWT analysis, the full azimuthal region is divided into smaller bins in ϕ, the number of bins at a given scale j being 2^j. The input to the analysis is a spectrum of the sample function at the smallest bin in ϕ corresponding to the highest resolution scale j_{max}. In the present case the sample function is chosen to be the photon fraction, given by

$$f'(\phi)=N_{\gamma\text{-like}}(\phi)/[N_{\gamma\text{-like}}(\phi)+N_{\text{ch}}(\phi)]. \tag{2}$$

A multiresolution analysis has been carried out using the D-4 wavelet basis on the above sample function starting with $j_{max}=5$. It may be mentioned that there are several families of wavelet bases distinguished by the number of coefficients and the level of iteration; we have used the frequently employed D-4 wavelet basis [32]. The output of the DWT consists of a set of wavelet or father function coefficients (FFCs) at each scale, from $j=1,\ldots,(j_{max}-1)$. The coefficients obtained at a given scale j are derived from the distribution of the sample function at one higher scale, $j+1$. The FFCs quantify the bin-to-bin fluctuations in the sample function at that higher scale relative to the average behavior. The presence of localized nonstatistical fluctuations will increase the rms deviation of the distribution of FFCs and may result in non-Gaussian tails [29,31]. The DWT technique as used in this analysis has been demonstrated in our earlier publication [17]. Once again, comparing the rms deviations of the FFC distributions of data, mixed events, and VENUS events may allow us to infer the presence of localized fluctuations. The utility of the mixed events and the response of the analysis technique are demonstrated in Sec. V.

IV. CONSTRUCTION OF MIXED EVENTS

It is possible to search for nonstatistical fluctuations in the experimental data in a model independent way by comparison of the data with mixed events generated from the data itself. Furthermore, it is necessary to isolate the various contributions to the fluctuations and to understand all detector related effects in the data. This has been done by generating different types of mixed events which preserve the global multiplicity correlation between $N_{\gamma\text{-like}}$ and N_{ch}. Fluctuations in the ratio of N_γ to N_{ch} can arise due to fluctuations in N_γ only, fluctuations in N_{ch} only, or fluctuation in both N_γ and N_{ch}. Furthermore, the fluctuations in N_γ and N_{ch} may be correlated event by event, as nominally expected in the case of DCC formation. Each of these possibilities is investigated through the construction of four different kinds of mixed events. The method of construction of these mixed events and the type of fluctuations they probe are described next.

A. Maximally mixed events

The first set of mixed events, referred to as $M1$ events, are constructed to remove all correlations to the greatest extent possible to provide a base line for comparison to the real event data. They were generated by mixing hits in both the photon and charged particle detectors separately, but still satisfying the global $N_{\gamma\text{-like}}$-N_{ch} correlation of the real event in the full acceptance. This means that on an event-by-event basis, the total photon multiplicity and charged particle multiplicity of the mixed event were identical to those of the real event to which it corresponds. Thus, the scatter plot of the mixed events is identical to the real events for the single-bin case shown in Fig. 4. The idea is to constrain the mixed events to be identical to real events globally, and then compare them to the real data in localized regions of phase space to search for indications of nonstatistical localized fluctuations in the data.

The $M1$ type of mixed events was constructed from the pool of all photonlike and charged particle hits, in which the hit position (η and ϕ) and event information (event number and total multiplicity) were kept for both the photonlike and charged particle hits. For a given real event measured to have multiplicities $N_{\gamma\text{-like}}$ and N_{ch} in the full acceptance region, a mixed event was constructed by randomly selecting $N_{\gamma\text{-like}}$ photonlike hits from the pool of photonlike hits and N_{ch} charged particle hits from the pool of charged particle hits. This procedure was repeated for each real event. Care was taken such that no two hits from the same real event were used in the construction of a mixed event. Also, for the mixed events, hits within either the SPMD or PMD detector were not allowed to lie within the two-track resolution of that detector. In brief, the $M1$ mixed events randomly distribute the hits in each individual detector but keep the global correlation between the $N_{\gamma\text{-like}}$ and N_{ch} multiplicity. They provide a maximally randomized sample of PMD and SPMD hits. Comparisons of such mixed events to real events will be most sensitive to the presence of localized fluctuations. However, in themselves they would not isolate the source of fluctuations as being due to N_γ and/or N_{ch}, or correlations between N_γ and N_{ch}.

B. Minimally mixed events

A second type of mixed events, referred to as $M2$ mixed events, was constructed to investigate the presence of correlated event-by-event fluctuations between N_γ and $N_{\rm ch}$. These mixed events had a minimal amount of randomization since they were generated by mixing the photon hits taken unaltered from one event, with the charged particle hits taken unmodified from another event. As with the $M1$ mixed events, the global $N_{\gamma\text{-like}}$-$N_{\rm ch}$ multiplicity correlation was maintained to be exactly the same as the data. To construct such mixed events, for a given real event measured to have multiplicities $N_{\gamma\text{-like}}$ and $N_{\rm ch}$ in the full acceptance region, a mixed event was constructed by keeping the PMD $N_{\gamma\text{-like}}$ portion of the event intact, but combining it with the unaltered SPMD portion of a different randomly selected event, but constrained to have almost the same charged particle multiplicity $N_{\rm ch}$. This procedure was repeated for each real event. In brief, this type of mixed event keeps the event-by-event hit structure in each detector identical to that in real events. Thus, such mixed events keep the individual localized fluctuations present in N_γ or $N_{\rm ch}$, but remove the event-by-event localized correlated fluctuations between them. Comparison of such mixed events to real events may reveal the presence of correlated localized fluctuations between N_γ and $N_{\rm ch}$.

C. Partially mixed events

The intermediates between the $M1$ and $M2$ types of mixed events are third and fourth type of partially mixed events, referred to as $M3$-γ and $M1$-ch mixed events. These were constructed to provide information regarding the contribution to the localized fluctuations in the N_γ to $N_{\rm ch}$ ratio from the individual observables (N_γ and $N_{\rm ch}$). They were generated from real events by mixing hits in one of the detectors (following the procedure for construction of $M1$ mixed events) and keeping the hit structure of the event in the other detector intact. $M3$-γ mixed events correspond to the case where the hits within the photon detector are unaltered while the hits in the charged particle detector are mixed. Similarly, in $M3$-ch mixed events the hits in the charged particle detector were unaltered and the hits in the photon detector were mixed. In each type of mixed event, the global $N_{\gamma\text{-like}}$-$N_{\rm ch}$ correlation is maintained as in the real event. The two-track resolution in the detectors where the hits are mixed is kept identical to that in real events. The total number of mixed events is the same as the number of real events. Comparison of such mixed events to real events and the other types of mixed events will reveal the presence of localized fluctuations in N_γ or $N_{\rm ch}$ separately.

A summary of the different sources of fluctuations in the ratio of N_γ to $N_{\rm ch}$ probed by each of the types of mixed events is given in Table I.

TABLE I. Type of fluctuations preserved by various mixed events.

Fluctuation	Mixed Event			
	$M1$	$M2$	$M3$-ch	$M3$-γ
N_γ only	No	Yes	No	Yes
$N_{\rm ch}$ only	No	Yes	Yes	No
Correlated N_γ-$N_{\rm ch}$	No	No	No	No

V. DEMONSTRATION OF ANALYSIS METHOD

In this section we wish to demonstrate the analysis method and illustrate how the relationship of the measured result to that obtained with the various mixed events can be used to provide an essentially model-independent signature of DCC formation. To demonstrate the analysis method and the potential to observe DCC event formation, we have applied the DWT analysis to a simple DCC-like model. The analysis is applied to ''real'' DCC events from the model as well as the various types of mixed events described in the preceding section constructed from the model DCC events. Since event generators which include DCC formation do not exist, we have implemented a simple DCC model in which localized nonstatistical N_γ-N_{ch} fluctuations have been introduced by modification of the output of the VENUS event generator. To implement the fluctuations, the final state pions within a localized $\eta-\phi$ region from VENUS are interchanged pairwise ($\pi^+\pi^- \leftrightarrow \pi^0\pi^0$) according to the DCC probability distribution $P(f)=1/2\sqrt{f}$. The fluctuations were generated over a localized region of $\eta=3-4$ and a $\Delta\phi$ interval of 90°. The π^0's were then allowed to decay. The resulting events were then passed through the WA98 detector response simulation. The DCC events in the simple model used here give rise to an anticorrelation between N_γ and $N_{\rm ch}$. It also results in nonrand'om fluctuations in both N_γ and $N_{\rm ch}$ individually. Since the probability to produce events with localized charged-neutral fluctuations is unknown, ensembles of events, here referred to as ''nDCC events,'' were produced as a mixture of normal VENUS events and events with localized fluctuations. The fraction of events with localized DCC-like fluctuations in each nDCC sample was varied as a parameter to be studied.

By using VENUS events as the basis to introduce the DCC effect, it is ensured that the general features of the event, including the multiplicity, composition, and momenta of the produced particles, as well as correlations in the particle multiplicities due to impact parameter variation, are reasonably well described. Also the GEANT simulation of the detector response to these events ensures that other effects such as photon conversions and the response of the PMD to hadrons, which might affect the observed multiplicities and the observed correlations, are also taken into account. While the assumption of a 100% DCC contribution over an interval of fixed size in $\eta-\phi$ is certainly a gross simplification, it provides a well-defined reference to gauge the potential for DCC observation. Other assumptions, such as a varying fraction, which might also be momentum dependent (since DCCs are expected to be low-p_T phenomena), and different or varying sizes might be more realistic. However, without clear theoretical guidance, we have chosen this very simple model as a reasonable and well-defined reference.

The DWT analysis was carried out on an ensemble of nDCC events and their corresponding mixed event sets cre-

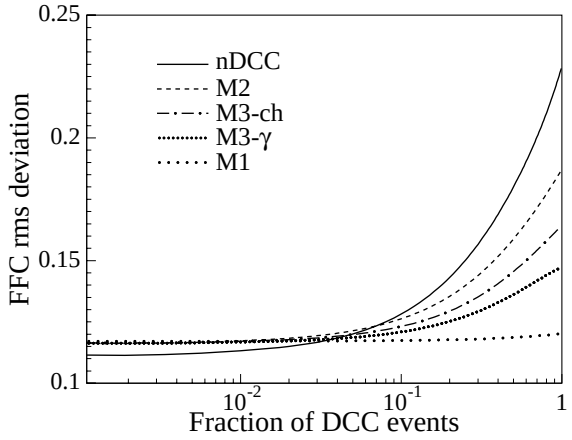

FIG. 5. The rms deviations of the FFC distributions for simulated VENUS events containing a variable fraction of localized DCC-like events with DCC extent $\Delta\phi_{DCC}=90°$, as a function of that fraction. Results are also shown for various mixed events constructed from those events.

ated from each set of nDCC events. By ensemble of nDCC events we mean sets of events having different percentages of events with localized fluctuations. The percentage varied from zero, that is, normal VENUS events with no localized fluctuations, to an event set where all events had localized charged-neutral fluctuations. For every nDCC event set, the four sets of mixed events ($M1$, $M2$, $M3$-γ, and $M3$-ch) were constructed from the nDCC events and analyzed. The rms deviations of the FFC distributions for each set of nDCC events and corresponding mixed event sets were obtained. The results for scale $j=1$ are plotted in Fig. 5 as a function of the percentage of localized DCC-type events in the nDCC event set.

It is seen that the rms deviations of the FFC distributions of the nDCC events increase as the percentage of events with localized fluctuations in N_γ-$N_{\rm ch}$ increases. This is the expected behavior and demonstrates the linear response of the DWT to the DCC events when the frequency of events with fluctuations increases. On the other hand, the rms deviations of the FFC distributions of the $M1$-type mixed events created from the nDCC events are found to be independent of the percentage of events having localized fluctuations. This is also the expected behavior and demonstrates that the $M1$ mixed events can be used as a base line from which to deduce the presence of fluctuations in a model-independent manner. However, the deviation of the real events from the $M1$ mixed events does not inform about the relative contributions of the individual N_γ and $N_{\rm ch}$ fluctuations. The rms deviations of the FFC distributions of the $M3$ mixed events are found to be intermediate to those obtained for nDCC events and $M1$ mixed events. They indicate the separate contributions of the N_γ or $N_{\rm ch}$ fluctuations alone to the ratio. The rms deviations of the $M2$ mixed events are higher than those of $M1$ and $M3$ mixed events. That is because the $M2$ mixed events keep the separate contributions of both the N_γ and $N_{\rm ch}$ fluctuations. However, the rms deviations of the $M2$ mixed events are consistently below those for the nDCC events. This is because the $M2$ events randomize the correlations between N_γ and $N_{\rm ch}$. The difference between the $M2$ mixed events and the nDCC events indicates the presence of the DCC-like correlated N_γ-$N_{\rm ch}$ fluctuations. The relative pattern of rms values for the real events and the various mixed events constructed from those real events seen in Fig. 5 provides a rather unambiguous model-independent signature for DCC-like fluctuations. Similar relative patterns of the rms deviations of the S_Z distributions for mixed events and simulated events were also observed for N_γ-$N_{\rm ch}$ correlation analysis. In particular, the observation of fluctuations in real events that are greater than the $M2$ mixed events would constitute what might be called ''smoking gun'' evidence for DCC formation. Conversely, the lack of a difference between real events and $M2$ mixed events would indicate the lack of DCC-like correlated charged-neutral fluctuations.

Figure 5 also demonstrates an effect which must be taken into account when comparing the measured result to the mixed events. For nDCC events with vanishing fraction of events with fluctuations, which is to say for normal VENUS events, it is seen that the rms deviations of the FFC distributions for all types of mixed events are higher than those for the nDCC events. In the VENUS simulations this is due to the presence of correlations between $N_{\rm ch}$ and $N_{\gamma\text{-like}}$. These are primarily due to residual impact parameter correlations (see Fig. 4) as well as due to the charged particle contamination in the $N_{\gamma\text{-like}}$ data sample whereby the charged particles register in both the PMD and SPMD (see Sec. II C) [33]. These correlations are removed by the event mixing procedure that results in a larger rms deviations for the mixed events. The real data are presumed to have similar residual correlations as observed in the VENUS simulations. In order to correct for the effects of these non-DCC correlations, all mixed event rms values constructed from real events have been rescaled by the percentage difference between the rms deviations of the VENUS distributions and those of the corresponding VENUS mixed events, as also discussed in Ref. [17].

For nDCC events with larger percentages of DCC-like events, the anticorrelation between $N_{\rm ch}$ and $N_{\gamma\text{-like}}$ overcomes the correlations between $N_{\rm ch}$ and $N_{\gamma\text{-like}}$, and hence the rms deviations of the FFC distributions of nDCC events become greater than those of the mixed events, despite the other correlation effects.

VI. RESULTS AND DISCUSSION

In the analysis of experimental data, the results from the measured data are compared with simulated and mixed events. Below we discuss the results obtained from such a comparison using two different analysis methods discussed earlier.

A. N_γ versus $N_{\rm ch}$ correlation results

The S_Z distributions calculated for different ϕ bin sizes are shown in Fig. 6 for data, $M1$, and VENUS events, for the four different centrality selections. The distributions for the other types of mixed events are not shown for clarity of presentation. The small differences in the S_Z distributions have been quantified in terms of the corresponding rms de-

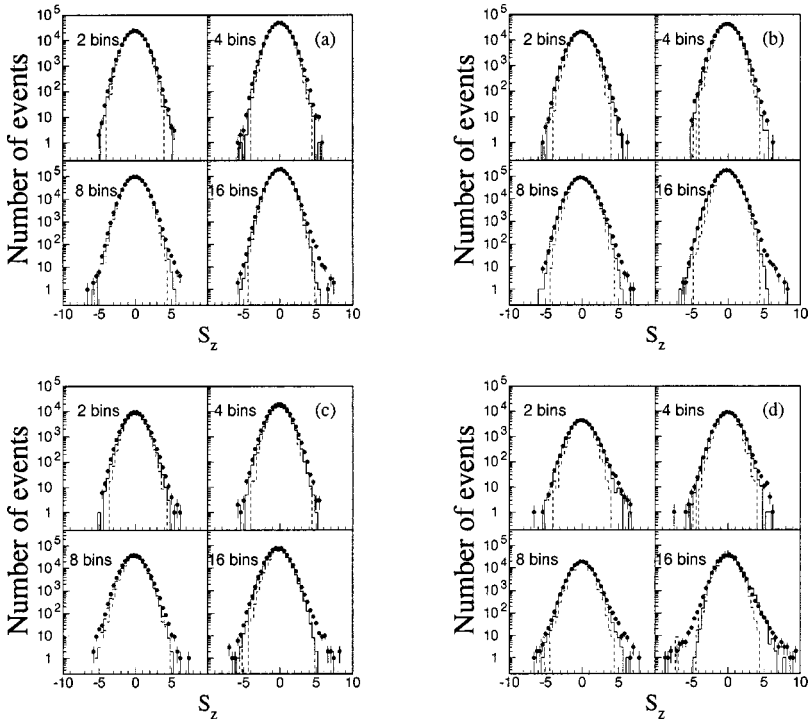

FIG. 6. The S_Z distributions for data (solid circles), mixed events (solid histogram), and simulated events (dashed histogram) for the four centrality bins. (a) Centrality-1 (0–5 %), (b) centrality-2 (5–10 %), (c) centrality-3 (15–30 %), and (d) centrality-4 (45–55 %).

viations; these rms distributions are shown in Fig. 7. The statistical errors on the values are small and are within the size of the symbols. The bars represent statistical and systematic errors added in quadrature. The various sources of systematic error have been discussed in an earlier section. An additional systematic error from the fit errors associated with the determination of the correlation axis Z is also included. In general, the width of the S_Z distribution increases from the most central to less central event selections, and decreases with decreasing bin size.

The rms deviations of the S_Z distribution for the VENUS simulated events are 1 (by definition) for all centrality and all bins in azimuth by definition of S_Z, and are significantly different from the measured results. This is primarily because the global particle multiplicity as predicted by VENUS and those measured in the experiment within the coverage of the detectors are not same.

As seen in Fig. 7, the widths of the S_Z distributions for mixed events closely follow those of the data. The mixed events have been constructed such that the global $N_{\gamma\text{-like}}$ versus $N_{\rm ch}$ multiplicity correlations are maintained. Therefore the rms deviations of the data and the mixed event reference are the same in the first ϕ bin of Fig. 7 by construction. Some correlations between $N_{\rm ch}$ and $N_{\gamma\text{-like}}$ are expected, mostly as a result of the charged particle contamination in the $N_{\gamma\text{-like}}$ data sample, but are removed by the event mixing

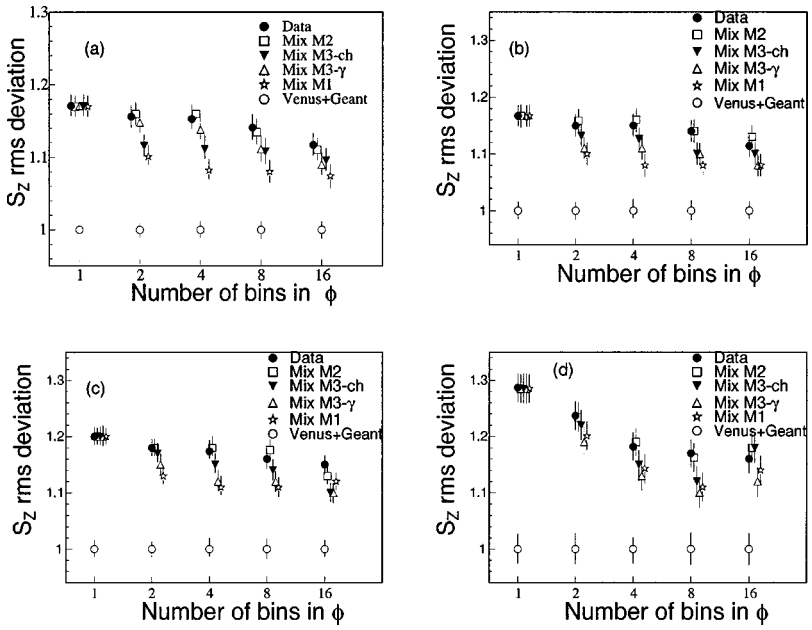

FIG. 7. The rms deviations of the S_Z distributions for data, various mixed events, and simulated events for the four centrality bins. (a) Centrality-1 (0–5 %), (b) centrality-2 (5–10 %), (c) centrality-3 (15–30 %), and (d) centrality-4 (45–55 %).

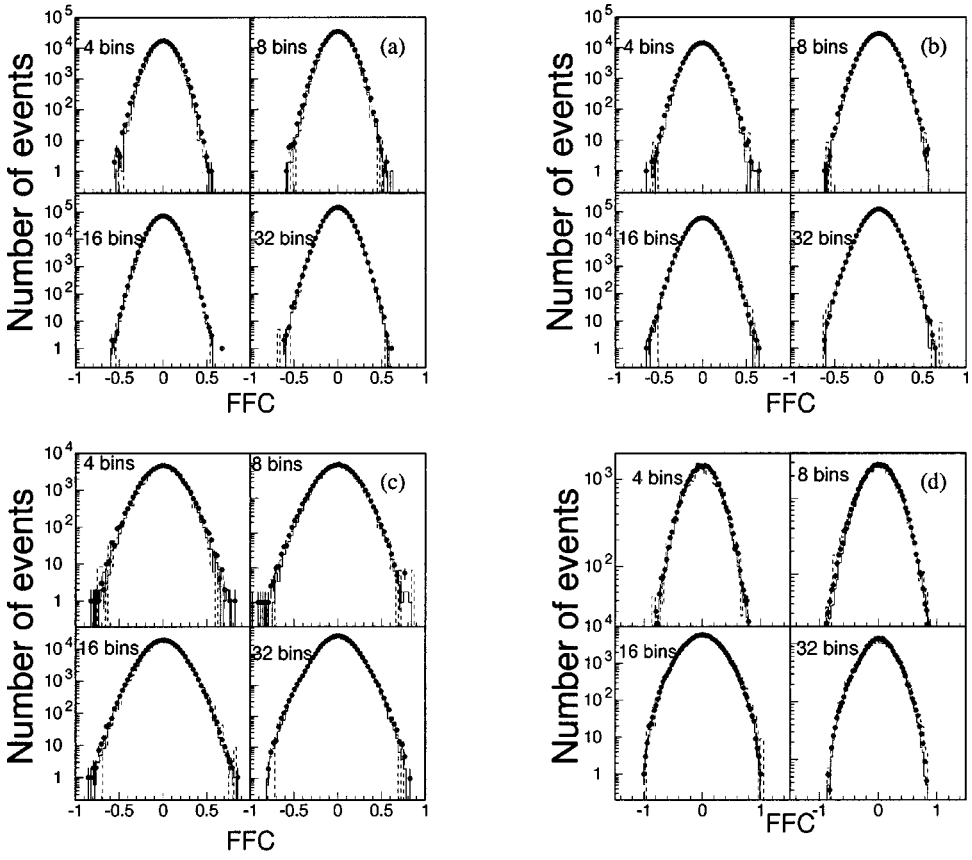

FIG. 8. The FFC distributions for data (solid circles), mixed events (solid histogram), and simulation (dashed histogram) for the four centrality bins. (a) Centrality-1 (0–5 %), (b) centrality-2 (5–10 %), (c) centrality-3 (15–30 %), and (d) centrality-4 (45–55 %).

procedure, and thereby result in a small difference between the real and mixed events, as seen in the analysis of the VENUS events discussed earlier. All of the mixed event S_Z distribution rms values (Fig. 7) have therefore been rescaled by the percentage difference between the rms deviations of the VENUS distributions and those of the corresponding VENUS mixed events for each centrality class (Ref. [17]).

The rms deviations of S_Z distributions of the $M2$ mixed events are found to agree with those of the experimental data within errors for all four centrality classes and for all azimuthal bin sizes. This indicates the absence of event-by-event localized correlated fluctuations in $N_{\gamma\text{-like}}$ and N_{ch}, as expected for DCC-like fluctuations. On the other hand, the rms deviations of the $M1$ mixed events are found to be sys-

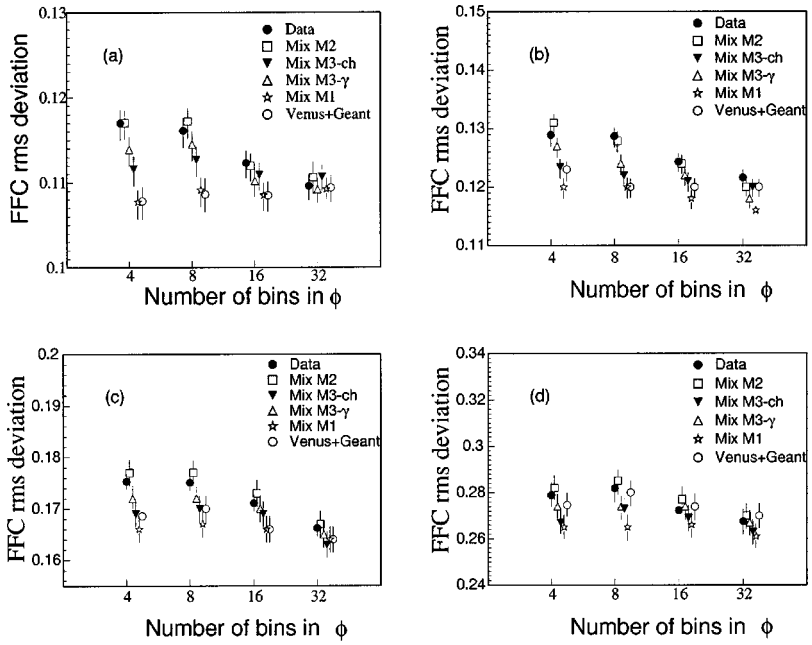

FIG. 9. The rms deviations of the FFC distributions for data, various mixed events, and simulation for the four centrality bins. (a) Centrality-1 (0–5 %), (b) centrality-2 (5–10 %), (c) centrality-3 (15–30 %), and (d) centrality-4 (45–55 %).

tematically lower than those of the data for 2, 4, and 8 bins in ϕ for centrality bins 1, 2, and 3. The results for both types of $M3$ mixed events are found to be intermediate between those of the data and the $M1$ mixed events. The results indicate the presence of localized fluctuations in the data in both the photon and charged particle multiplicities. For the case of the most peripheral centrality selection (centrality-4), the rms deviations of the S_Z distributions of data and the various mixed events are found to be in close agreement to each other within the quoted errors.

B. Multiresolution DWT analysis results

The FFC distributions at scales $j=1-4$, corresponding to 4–32 bins in azimuthal angle, are shown in Fig. 8 for data, $M1$, and VENUS events for the four centrality classes. The results for other types of mixed events are not shown for clarity of presentation. The widths of the FFC distributions are found to increase in going from the most central to most peripheral centrality class. The rms deviations of these FFC distributions are summarized in Fig. 9. Similar to the case for the S_Z distributions discussed above, the rms deviations of the mixed events have been rescaled by the percentage difference between the rms deviations of the VENUS FFC distributions and those of the VENUS mixed events for each centrality class. The statistical errors are small and are within the size of the symbols. The bars represent statistical and systematic errors added in quadrature.

The rms deviations of the FFC distributions for the data, VENUS, and mixed events are found to be close to each other (within quoted errors) for the case of 32 bins in ϕ for all of the four centrality classes. The rms deviations for the FFC distribution of $M2$ mixed events are found to closely follow those of the data for all centrality classes and all bins in ϕ, while the rms deviations for the $M3$ mixed events lie between those of the data and $M1$ mixed events. These results are consistent with those obtained from the analysis of the S_Z distributions. These observations indicate the absence of event-by-event localized correlated fluctuations (DCC-like) between $N_{\gamma\text{-like}}$ and N_{ch}. They also suggest the presence of localized fluctuations in both photons and charged particle multiplicities for intermediate bin sizes in azimuth. The rms values of the FFC distributions for VENUS events are close to those of the $M1$ mixed events for centrality classes 1, 2, and 3. However, they are slightly higher for the most peripheral centrality class (centrality-4).

C. Discussion

The results from the two independent methods of analysis are consistent and indicate the absence of event-by-event correlated DCC-like fluctuations in the photon and charged particle multiplicities. However, they do suggest the presence of uncorrelated fluctuations in both the photon and charged particle multiplicities for intermediate bin sizes in ϕ. The data have been compared to various kinds of mixed events and to simulated events which take into account many detector related effects. Still it is worthwhile to explore the extent of other possible experimental effects that might affect the observed rms deviations of the S_Z and FFC distributions. As discussed extensively in Refs. [15,22,23], care has been taken during the data taking and during the data processing to closely monitor the performance of the PMD and SPMD. The detector uniformity of the PMD was studied in detail by using the minimum ionizing particle (MIP) signal from the data for all pads of the 22 boxes. The fluctuations of the pad-to-pad relative gains were approximately 10%. The gain corrections were made for each pad. Corrections for gain variations during the data taking period were made periodically for both the PMD and SPMD. This reduces the possibility of abrupt gain or threshold changes during the run period. Events with obvious detector readout effects, such as missing or dead regions, were carefully removed from the data sample. It should be recalled that most detector effects are reflected in the mixed events.

The effect of local fluctuations in the performance of the PMD has been studied using simulated VENUS events. In one test, the gain of a group of pads corresponding to one or more PMD cameras was randomly varied. A 30% change of gain in one camera for all events resulted in an increase of 0.7% in the rms deviations. Changing the gains of three cameras by 30% for all events resulted in an increase of the rms deviations by 1.7%. Since the camera gains were closely monitored on-line and during the processing of the data, this is considered to be a highly unlikely scenario. Still, these changes are within the quoted errors of Figs. 7 and 9, which indicates that local gain and threshold variations would not account for the observed differences between the data and the $M1$ mixed events.

Several checks were performed to verify the quality of the data obtained with the SPMD. One of the differences between the previous analysis [15] and the present one is that while in the previous case the analysis was performed using the total charged particle multiplicity of the detector deduced from the magnitude of the measured SPMD signals, here we simply used the total number of hit SPMD pads. The reason for using hit pads is that the correction in going from deposited charge to hits for each event and small $\eta-\phi$ segments is nontrivial. Also, the effects of two-track resolution and possible shifts of the beam position on the target during the spill were studied in detail. However, all of these produced small effects that could not account for the differences observed between the data and $M1$ mixed events.

D. Strength of localized fluctuations

In order to quantify the strength of the $N_{\gamma\text{-like}}$ and N_{ch} fluctuations for various bins in ϕ and for different centrality classes, we define a quantity χ as

$$\chi=\frac{\sqrt{(s^2-s_1^2)}}{s_1}, \tag{3}$$

where s_1 and s correspond to the rms deviations of the FFC distributions of the $M1$ mixed events and real data, respectively. The results are shown in Fig. 10 as a function of the number of bins in ϕ for the four different centrality classes. Qualitatively similar results are obtained when χ is calculated using the rms deviations of the S_Z distributions. The

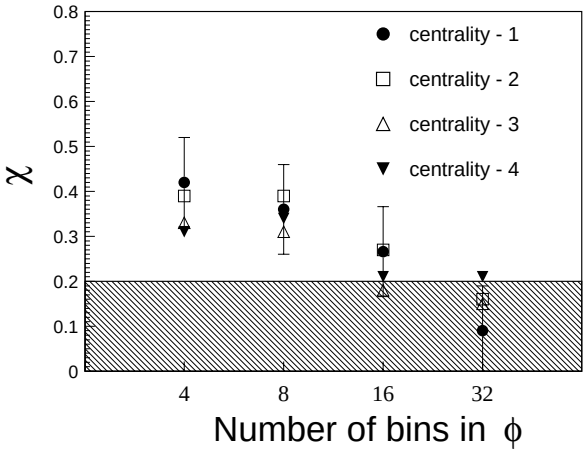

FIG. 10. The fluctuation strength parameter for the four centrality classes. Centrality-1 corresponds to the 5% most central, centrality-2 corresponds to 5–10 %, centrality-3 corresponds to 15–30 %, and centrality-4 corresponds to 45–55 % of the minimum bias cross section as determined by selection on the measured transverse energy distribution. The error bars are shown only on the centrality-1 selection for clarity of presentation. The errors are similar for the other centralities. The shaded portion represents the limit above which a signal is detectable (see text for details).

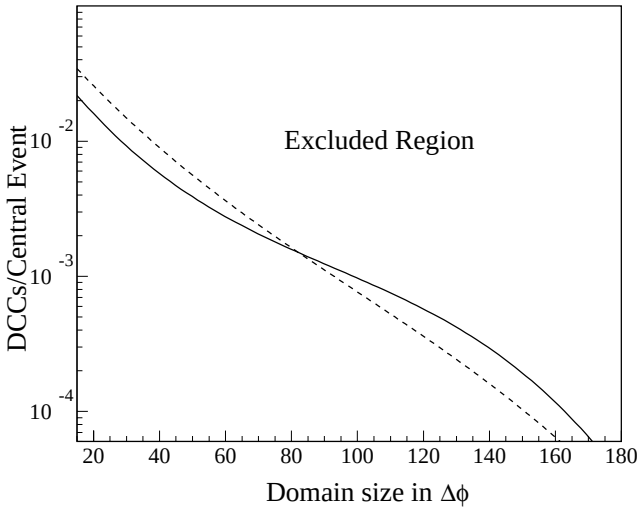

FIG. 11. The 90% confidence level upper limit on DCC production for central Pb+Pb collision at 158*A* GeV/*c*, as a function of the DCC domain size in azimuthal angle within the context of a simple DCC model and the measured photon and charged particle multiplicities in the interval $2.9<\eta<3.75$. The solid line corresponds to data from the top 5% and dashed line to top 5–10 % of the minimum bias cross section as determined by selection on the measured transverse energy distribution.

shaded portion indicates the region of χ where s is one σ greater than the rms deviation FFC distributions for $M1$ events, where σ is the total error on the $M1$ event rms deviation. It represents the limit above which a signal is detectable. Since χ is calculated from the rms deviations of the FFC distributions for data and $M1$ mixed events, it gives the combined strength of localized fluctuations in both the photon and charged particle multiplicities. We do not present χ values calculated using $M3$-type mixed events. However, it is clear from the rms deviation figures (Figs. 7 and 9) that both photons and charged particles contribute to the observed fluctuations. The result shows that the strength of the fluctuations decreases as the number of bins in ϕ increases, with a strength that decreases to below the detectable level (within the quoted errors) for 16 and 32 bins. There is an indication that the strength of the signal decreases with decreasing centrality for 4 and 8 bins in azimuthal angle, although the tendency is not very strong.

E. Upper limit on DCC production

It has been shown that the rms deviations of the S_Z and FFC distributions for data are very close to those of the $M2$ mixed events, within the quoted errors. If the DCC-like correlated fluctuations in $N_{\gamma\text{-like}}$ versus N_{ch} were large, the rms deviations (Figs. 7 and 9) of data would have been larger compared to those of the $M2$ mixed events. Since this is not the case, we may extract an upper limit on the production of DCCs at the 90% confidence level following the standard procedure as discussed in Ref. [34].

The errors are assumed to have Gaussian distribution, although they are asymmetric. The larger of the asymmetric errors is conservatively used for the limit calculation. The 90% C.L. upper limit contour has been calculated as $\chi + 1.28e_\chi$, where χ is calculated using Eq. (3). Here s_1 and s correspond to the rms deviations of the FFC (or S_Z) distributions for $M2$ mixed events and real data, respectively, and e_χ is the error in χ from the FFC (or S_Z) analysis. If the difference between the rms deviation of the FFC distributions for $M2$ mixed events and real data is negative, we take the value of χ to be zero. It may be mentioned that for the calculation of the upper limits we have assumed that the total difference in the rms values of data and $M2$ mixed events is due to DCC-like fluctuations only.

To relate the measured upper limit on the size of the fluctuations to a limit on DCC domain size and frequency of occurrence, we proceed as follows. Within the context of the simple simulated DCC model described earlier, we obtain the rms deviations of the FFC distributions with various domain sizes in azimuthal angle (15°,30°, . . . ,180°) and for each domain size also for different frequencies of occurrence of DCC (0–100 %). The $M2$ mixed events are then constructed for each of these sets of simulated events. For each set of DCC-type events of a given domain size and frequency of occurrence, the value of χ is calculated using Eq. (3), from the difference in rms deviations of the FFC distribution of the DCC event (s) and its corresponding $M2$ mixed event distribution ($s1$). The upper limit is set at that value of frequency of occurrence for a fixed DCC domain size at which the χ value from the DCC model matches with that of the $\chi+1.28e_\chi$ upper limit from the experimental data. This is used to set the upper limit contour in terms of domain size and frequency of occurrence of the DCC. The results for centrality classes 1 and 2 are shown in Fig. 11. It may be mentioned that the upper limit contour set by a similar analysis of the rms values of the S_Z distributions is very similar to

that from the FFC analysis. Also, from Fig. 10 it is seen that the total fluctuation is similar or weaker for centrality classes 3 and 4; hence the upper limit for these two classes would be similar or weaker than those shown in Fig. 11 for centrality classes 1 and 2.

VII. SUMMARY

A detailed event-by-event analysis of the $\eta-\phi$ phase space distributions of the multiplicity of charged particles and photons in Pb+Pb collisions at 158*A* GeV has been carried out using two different analysis methods for four different centrality classes. The results from the two analysis methods were found to be consistent with each other. The first analysis method studied the magnitude of the $N_{\gamma\text{-like}}$ versus N_{ch} multiplicity fluctuations in decreasing phase space regions. The second analysis employed the discrete wavelet transformation technique to investigate the relative magnitude of the $N_{\gamma\text{-like}}$ versus N_{ch} fluctuations in adjacent phase space regions. The results were compared to pure VENUS +GEANT simulation events and to various types of mixed events to search for and identify the source of nonstatistical fluctuations. Both analysis methods indicated fluctuations beyond those observed in simulated and fully mixed events for ϕ intervals of greater than 45° and which increased weakly in strength with increasing centrality. The additional fluctuations were found to be due to uncorrelated fluctuations in both $N_{\gamma\text{-like}}$ and N_{ch}. No significant correlated fluctuations in $N_{\gamma\text{-like}}$ versus N_{ch}, a likely signature of the formation of disoriented chiral condensates, were observed in all of the four centrality classes studied. Using the results from the data, mixed events, and within the limitations of a simple model of DCC formation, an upper limit on DCC production in 158 A GeV Pb+Pb collisions has been set.

ACKNOWLEDGMENTS

We wish to express our gratitude to the CERN accelerator division for the excellent performance of the SPS accelerator complex. We acknowledge with appreciation the effort of all engineers, technicians, and support staff who participated in the construction of this experiment. This work was supported jointly by the German BMBF and DFG, the U.S. Department of Energy, the Swedish NFR and FRN, the Dutch Stichting FOM, the Polish KBN under Contract No. 621/E-78/SPUB-M/CERN/P-03/DZ211, the Grant Agency of the Czech Republic under Contract No. 202/95/0217, the Department of Atomic Energy, the Department of Science and Technology, the Council of Scientific and Industrial Research, the University Grants Commission of the Government of India, the Indo-FRG Exchange Program, the PPE division of CERN, the Swiss National Fund, the INTAS under Contract No. INTAS-97-0158, the ORISE, a Grant-in-Aid for Scientific Research (specially promoted research and international scientific research) of the Ministry of Education, Science and Culture, the University of Tsukuba Special Research Projects, and the financial support of the JSPS. ORNL is managed by UT-Battelle, LLC, for the U.S. Department of Energy under Contract No. DE-AC05-00OR22725. The MIT group has been supported by the U.S. Department of Energy under the cooperative agreement under Grant No. DE-FC02-94ER40818.

[1] H. Heiselberg, Phys. Rep. **351**, 161 (2001).
[2] M. Stephanov, K. Rajagopal, and E. Shuryak, Phys. Rev. D **60**, 114028 (1999).
[3] A.A. Anselm and M.G. Ryskin, Phys. Lett. B **266**, 482 (1991).
[4] J.D. Bjorken, Int. J. Mod. Phys. A **7**, 4189 (1992).
[5] K. Rajagopal and F. Wilczek, Nucl. Phys. **B399**, 395 (1993); **B404**, 577 (1993).
[6] Zheng Huang and Xin-Nian Wang, Phys. Rev. D **49**, 4335 (1994).
[7] K. Rajagopal, hep-ph/9504310.
[8] Sean Gavin, Andreas Gocksch, and Robert D. Pisarski, Phys. Rev. Lett. **72**, 2143 (1994).
[9] M. Asakawa, Z. Huang, and X.-N. Wang, Phys. Rev. Lett. **74**, 3126 (1995).
[10] James V. Steele and Volker Koch, Phys. Rev. Lett. **81**, 4096 (1998).
[11] Sean Gavin and Joseph I. Kapusta, Phys. Rev. C **65**, 054910 (2002).
[12] *Proceedings of the Eighth International Symposium on Very High Energy Cosmic Ray Interactions*, edited by C.M.G. Lattes, Y. Fujimoto, and S. Hasegawa, Tokyo, 1994; C.M.G. Lattes, Y. Fujimoto, and S. Hasegawa, Phys. Rep. **65**, 151 (1980).
[13] C.R.A. Augusto *et al.*, Phys. Rev. D **59**, 054001 (1999).
[14] T.C. Brooks *et al.*, Minimax Collaboration, Phys. Rev. D **55**, 5667 (1997).
[15] M.M. Aggarwal *et al.*, WA98 Collaboration, Phys. Lett. B **420**, 169 (1998).
[16] H. Appelshauser *et al.*, NA49 Collaboration, Phys. Lett. B **459**, 679 (1999).
[17] M.M. Aggarwal *et al.*, WA98 Collaboration, Phys. Rev. C **64**, 011901(R) (2001).
[18] M. Asakawa, H. Minakata, and B. Muller, Nucl. Phys. **A638**, 443c (1998).
[19] H. H. Gutbrod *et al.*, CERN/SPSLC 91-17 (unpublished); SPSLC/P260 (unpublished).
[20] T.C. Awes *et al.*, Nucl. Instrum. Methods Phys. Res. A **279**, 479 (1989).
[21] M.M. Aggarwal *et al.*, WA98 Collaboration, Eur. Phys. J. C **18**, 651 (2001).
[22] M.M. Aggarwal *et al.*, Nucl. Instrum. Methods Phys. Res. A **424**, 395 (1999).
[23] M.M. Aggarwal *et al.*, WA98 Collaboration, Phys. Lett. B **458**, 422 (1999).
[24] W.T. Lin *et al.*, Nucl. Instrum. Methods Phys. Res. A **389**, 415 (1997).
[25] M.M. Aggarwal *et al.*, WA98 Collaboration, Phys. Rev. C **65**, 054912 (2002).

[26] R. Brun *et al.*, CERN/DD/EE/84-1 1984.
[27] K. Werner, Phys. Rep. **232**, 87 (1993).
[28] Amara Graps, IEEE Comput. Sci. Eng. **2**, 50 (1995).
[29] Zheng Huang, Ina Sarcevic, Robert Thews, and Xin-Nian Wang, Phys. Rev. D **54**, 750 (1996).
[30] B.K. Nandi, G.C. Mishra, B. Mohanty, D.P. Mahapatra, and T.K. Nayak, Phys. Lett. B **449**, 109 (1999).
[31] B.K. Nandi, T.K. Nayak, B. Mohanty, D.P. Mahapatra, and Y.P. Viyogi, Phys. Lett. B **461**, 142 (1999).
[32] *Numerical Recipes* (Cambridge University Press, Cambridge, England, 1998).
[33] B. Mohanty, Ph.D. thesis, Utkal University, 2002.
[34] G.J. Feldman and R.D. Cousins, Phys. Rev. D **57**, 3873 (1998).

Measurement of Λ and $\overline{\Lambda}$ Particles in Au + Au Collisions at $\sqrt{s_{NN}} = 130$ GeV

K. Adcox,[40] S. S. Adler,[3] N. N. Ajitanand,[27] Y. Akiba,[14] J. Alexander,[27] L. Aphecetche,[34] Y. Arai,[14] S. H. Aronson,[3] R. Averbeck,[28] T. C. Awes,[29] K. N. Barish,[5] P. D. Barnes,[19] J. Barrette,[21] B. Bassalleck,[25] S. Bathe,[22] V. Baublis,[30] A. Bazilevsky,[12,32] S. Belikov,[12,13] F. G. Bellaiche,[29] S. T. Belyaev,[16] M. J. Bennett,[19] Y. Berdnikov,[35] S. Botelho,[33] M. L. Brooks,[19] D. S. Brown,[26] N. Bruner,[25] D. Bucher,[22] H. Buesching,[22] V. Bumazhnov,[12] G. Bunce,[3,32] J. Burward-Hoy,[28] S. Butsyk,[28,30] T. A. Carey,[19] P. Chand,[2] J. Chang,[5] W. C. Chang,[1] L. L. Chavez,[25] S. Chernichenko,[12] C. Y. Chi,[8] J. Chiba,[14] M. Chiu,[8] R. K. Choudhury,[2] T. Christ,[28] T. Chujo,[3,39] M. S. Chung,[15,19] P. Chung,[27] V. Cianciolo,[29] B. A. Cole,[8] D. G. D'Enterria,[34] G. David,[3] H. Delagrange,[34] A. Denisov,[12] A. Deshpande,[32] E. J. Desmond,[3] O. Dietzsch,[33] B. V. Dinesh,[2] A. Drees,[28] A. Durum,[12] D. Dutta,[2] K. Ebisu,[24] Y. V. Efremenko,[29] K. El Chenawi,[40] H. En'yo,[17,31] S. Esumi,[39] L. Ewell,[3] T. Ferdousi,[5] D. E. Fields,[25] S. L. Fokin,[16] Z. Fraenkel,[42] A. Franz,[3] A. D. Frawley,[9] S. -Y. Fung,[5] S. Garpman,[20,*] T. K. Ghosh,[40] A. Glenn,[36] A. L. Godoi,[33] Y. Goto,[32] S. V. Greene,[40] M. Grosse Perdekamp,[32] S. K. Gupta,[2] W. Guryn,[3] H. -Å. Gustafsson,[20] J. S. Haggerty,[3] H. Hamagaki,[7] A. G. Hansen,[19] H. Hara,[24] E. P. Hartouni,[18] R. Hayano,[38] N. Hayashi,[31] X. He,[10] T. K. Hemmick,[28] J. M. Heuser,[28] M. Hibino,[41] J. C. Hill,[13] D. S. Ho,[43] K. Homma,[11] B. Hong,[15] A. Hoover,[26] T. Ichihara,[31,32] K. Imai,[17,31] M. S. Ippolitov,[16] M. Ishihara,[31,32] B. V. Jacak,[28,32] W. Y. Jang,[15] J. Jia,[28] B. M. Johnson,[3] S. C. Johnson,[18,28] K. S. Joo,[23] S. Kametani,[41] J. H. Kang,[43] M. Kann,[30] S. S. Kapoor,[2] S. Kelly,[8] B. Khachaturov,[42] A. Khanzadeev,[30] J. Kikuchi,[41] D. J. Kim,[43] H. J. Kim,[43] S. Y. Kim,[43] Y. G. Kim,[43] W. W. Kinnison,[19] E. Kistenev,[3] A. Kiyomichi,[39] C. Klein-Boesing,[22] S. Klinksiek,[25] L. Kochenda,[30] V. Kochetkov,[12] D. Koehler,[25] T. Kohama,[11] D. Kotchetkov,[5] A. Kozlov,[42] P. J. Kroon,[3] K. Kurita,[31,32] M. J. Kweon,[15] Y. Kwon,[43] G. S. Kyle,[26] R. Lacey,[27] J. G. Lajoie,[13] J. Lauret,[27] A. Lebedev,[13,16] D. M. Lee,[19] M. J. Leitch,[19] X. H. Li,[5] Z. Li,[6,31] D. J. Lim,[43] M. X. Liu,[19] X. Liu,[6] Z. Liu,[6] C. F. Maguire,[40] J. Mahon,[3] Y. I. Makdisi,[3] V. I. Manko,[16] Y. Mao,[6,31] S. K. Mark,[21] S. Markacs,[8] G. Martinez,[34] M. D. Marx,[28] A. Masaike,[17] F. Matathias,[28] T. Matsumoto,[7,41] P. L. McGaughey,[19] E. Melnikov,[12] M. Merschmeyer,[22] F. Messer,[28] M. Messer,[3] Y. Miake,[39] T. E. Miller,[40] A. Milov,[42] S. Mioduszewski,[3,36] R. E. Mischke,[19] G. C. Mishra,[10] J. T. Mitchell,[3] A. K. Mohanty,[2] D. P. Morrison,[3] J. M. Moss,[19] F. Mühlbacher,[28] D. Mukhopadhyay,[42] M. Muniruzzaman,[5] J. Murata,[31] S. Nagamiya,[14] Y. Nagasaka,[24] J. L. Nagle,[8] Y. Nakada,[17] B. K. Nandi,[5] J. Newby,[36] L. Nikkinen,[21] P. Nilsson,[20] S. Nishimura,[7] A. S. Nyanin,[16] J. Nystrand,[20] E. O'Brien,[3] C. A. Ogilvie,[13] H. Ohnishi,[3,11] I. D. Ojha,[4,40] M. Ono,[39] V. Onuchin,[12] A. Oskarsson,[20] L. Österman,[20] I. Otterlund,[20] K. Oyama,[7,38] L. Paffrath,[3,*] D. Pal,[42] A. P. T. Palounek,[19] V. S. Pantuev,[28] V. Papavassiliou,[26] S. F. Pate,[26] T. Peitzmann,[22] A. N. Petridis,[13] C. Pinkenburg,[3,27] R. P. Pisani,[3] P. Pitukhin,[12] F. Plasil,[29] M. Pollack,[28,36] K. Pope,[36] M. L. Purschke,[3] I. Ravinovich,[42] K. F. Read,[29,36] K. Reygers,[22] V. Riabov,[30,35] Y. Riabov,[30] M. Rosati,[13] A. A. Rose,[40] S. S. Ryu,[43] N. Saito,[31,32] A. Sakaguchi,[11] T. Sakaguchi,[7,41] H. Sako,[39] T. Sakuma,[31,37] V. Samsonov,[30] T. C. Sangster,[18] R. Santo,[22] H. D. Sato,[17,31] S. Sato,[39] S. Sawada,[14] B. R. Schlei,[19] Y. Schutz,[34] V. Semenov,[12] R. Seto,[5] T. K. Shea,[3] I. Shein,[12] T. -A. Shibata,[31,37] K. Shigaki,[14] T. Shiina,[19] Y. H. Shin,[43] I. G. Sibiriak,[16] D. Silvermyr,[20] K. S. Sim,[15] J. Simon-Gillo,[19] C. P. Singh,[4] V. Singh,[4] M. Sivertz,[3] A. Soldatov,[12] R. A. Soltz,[18] S. Sorensen,[29,36] P. W. Stankus,[29] N. Starinsky,[21] P. Steinberg,[8] E. Stenlund,[20] A. Ster,[44] S. P. Stoll,[3] M. Sugioka,[31,37] T. Sugitate,[11] J. P. Sullivan,[19] Y. Sumi,[11] Z. Sun,[6] M. Suzuki,[39] E. M. Takagui,[33] A. Taketani,[31] M. Tamai,[41] K. H. Tanaka,[14] Y. Tanaka,[24] E. Taniguchi,[31,37] M. J. Tannenbaum,[3] J. Thomas,[28] J. H. Thomas,[18] T. L. Thomas,[25] W. Tian,[6,36] J. Tojo,[17,31] H. Torii,[17,31] R. S. Towell,[19] I. Tserruya,[42] H. Tsuruoka,[39] A. A. Tsvetkov,[16] S. K. Tuli,[4] H. Tydesjö,[20] N. Tyurin,[12] T. Ushiroda,[24] H. W. van Hecke,[19] C. Velissaris,[26] J. Velkovska,[28] M. Velkovsky,[28] A. A. Vinogradov,[16] M. A. Volkov,[16] A. Vorobyov,[30] E. Vznuzdaev,[30] H. Wang,[5] Y. Watanabe,[31,32] S. N. White,[3] C. Witzig,[3] F. K. Wohn,[13] C. L. Woody,[3] W. Xie,[5,42] K. Yagi,[39] S. Yokkaichi,[31] G. R. Young,[29] I. E. Yushmanov,[16] W. A. Zajc,[8] Z. Zhang,[28] S. Zhou,[6] and S. Zhou[42]

(PHENIX Collaboration)

[1]*Institute of Physics, Academia Sinica, Taipei 11529, Taiwan*
[2]*Bhabha Atomic Research Centre, Bombay 400 085, India*
[3]*Brookhaven National Laboratory, Upton, New York 11973-5000*
[4]*Department of Physics, Banaras Hindu University, Varanasi 221005, India*
[5]*University of California–Riverside, Riverside, California 92521*
[6]*China Institute of Atomic Energy (CIAE), Beijing, People's Republic of China*
[7]*Center for Nuclear Study, Graduate School of Science, University of Tokyo, 7-3-1 Hongo, Bunkyo, Tokyo 113-0033, Japan*
[8]*Columbia University, New York, New York 10027 and Nevis Laboratories, Irvington, New York 10533*

 0031-9007/02/89(9)/092302(6)$20.00 © 2002 The American Physical Society

[9]*Florida State University, Tallahassee, Florida 32306*
[10]*Georgia State University, Atlanta, Georgia 30303*
[11]*Hiroshima University, Kagamiyama, Higashi-Hiroshima 739-8526, Japan*
[12]*Institute for High Energy Physics (IHEP), Protvino, Russia*
[13]*Iowa State University, Ames, Iowa 50011*
[14]*KEK, High Energy Accelerator Research Organization, Tsukuba-shi, Ibaraki-ken 305-0801, Japan*
[15]*Korea University, Seoul, 136-701, Korea*
[16]*Russian Research Center "Kurchatov Institute," Moscow, Russia*
[17]*Kyoto University, Kyoto 606, Japan*
[18]*Lawrence Livermore National Laboratory, Livermore, California 94550*
[19]*Los Alamos National Laboratory, Los Alamos, New Mexico 87545*
[20]*Department of Physics, Lund University, Box 118, SE-221 00 Lund, Sweden*
[21]*McGill University, Montreal, Quebec H3A 2T8, Canada*
[22]*Institut für Kernphysik, University of Münster, D-48149 Münster, Germany*
[23]*Myongji University, Yongin, Kyonggido 449-728, Korea*
[24]*Nagasaki Institute of Applied Science, Nagasaki-shi, Nagasaki 851-0193, Japan*
[25]*University of New Mexico, Albuquerque, New Mexico 87131*
[26]*New Mexico State University, Las Cruces, New Mexico 88003*
[27]*Chemistry Department, State University of New York–Stony Brook, Stony Brook, New York 11794*
[28]*Department of Physics and Astronomy, State University of New York–Stony Brook, Stony Brook, New York 11794*
[29]*Oak Ridge National Laboratory, Oak Ridge, Tennessee 37831*
[30]*PNPI, Petersburg Nuclear Physics Institute, Gatchina, Russia*
[31]*RIKEN (The Institute of Physical and Chemical Research), Wako, Saitama 351-0198, Japan*
[32]*RIKEN BNL Research Center, Brookhaven National Laboratory, Upton, New York 11973-5000*
[33]*Universidade de São Paulo, Instituto de Física, Caixa Postal 66318, São Paulo CEP05315-970, Brazil*
[34]*SUBATECH (Ecole des Mines de Nantes, IN2P3/CNRS, Universite de Nantes), BP 20722-44307, Nantes Cedex 3, France*
[35]*St. Petersburg State Technical University, St. Petersburg, Russia*
[36]*University of Tennessee, Knoxville, Tennessee 37996*
[37]*Department of Physics, Tokyo Institute of Technology, Tokyo, 152-8551, Japan*
[38]*University of Tokyo, Tokyo, Japan*
[39]*Institute of Physics, University of Tsukuba, Tsukuba, Ibaraki 305, Japan*
[40]*Vanderbilt University, Nashville, Tennessee 37235*
[41]*Waseda University, Advanced Research Institute for Science and Engineering, 17 Kikui-cho, Shinjuku-ku, Tokyo 162-0044, Japan*
[42]*Weizmann Institute, Rehovot 76100, Israel*
[43]*Yonsei University, IPAP, Seoul 120-749, Korea*
[44]*KFKI Research Institute for Particle and Nuclear Physics (RMKI), Budapest, Hungary*[†]
(Received 17 April 2002; published 12 August 2002)

We present results on the measurement of Λ and $\bar{\Lambda}$ production in Au + Au collisions at $\sqrt{s_{NN}} =$ 130 GeV with the PHENIX detector at the Relativistic Heavy Ion Collider. The transverse momentum spectra were measured for minimum bias and for the 5% most central events. The $\bar{\Lambda}/\Lambda$ ratios are constant as a function of p_T and the number of participants. The measured net Λ density is significantly larger than predicted by models based on hadronic strings (e.g., HIJING) but in approximate agreement with models which include the gluon-junction mechanism.

DOI: 10.1103/PhysRevLett.89.092302 PACS numbers: 25.75.Dw

In this Letter we report on the measurement by the PHENIX experiment at the Relativistic Heavy Ion Collider (RHIC) of the production of Λ and $\bar{\Lambda}$ particles and the ratio $\bar{\Lambda}/\Lambda$ as a function of transverse momentum p_T and centrality in Au + Au collisions at $\sqrt{s_{NN}} =$ 130 GeV. The production of strange baryons and of strange particles in general has been extensively studied in heavy ion collisions at the Alternating Gradient Synchrotron (AGS) and at the Super Proton Synchrotron (SPS) [1] to investigate the flavor composition of nuclear matter at high density and temperature. Furthermore, antibaryon-to-baryon ratios, or alternatively, a net baryon number such as $(\Lambda - \bar{\Lambda})$ at midrapidity provide insight into the baryon transport mechanism in these collisions [2–5]. The systematic study of baryon stopping (transport of baryon number in rapidity space) and hyperon production in proton-proton, proton-nucleus, and nucleus-nucleus collisions has been done over the past decade at the AGS [6,7] and CERN SPS [8–10]. The results have shown a high degree of baryon stopping and enhanced hyperon production in heavy nucleus-nucleus collisions. Clearly the measurement of these quantities at RHIC, at the highest energies so far available in the laboratory, is of great importance for our understanding of the sources of these processes.

The results reported here were obtained using the west arm of the PHENIX spectrometer [11] which covers an angular range of $\Delta\phi = \pi/4$ (during its first year of running) and a pseudorapidity range of $|\eta| < 0.35$. The detectors used were the drift chamber (DC), a set of multiwire proportional chambers with pixel-pad readout (PC1) [12], and a lead-scintillator electromagnetic calorimeter (EMCal) [13]. Signals from two sets of beam-beam counters (BBC) and two zero-degree calorimeters (ZDC) provided a trigger sensitive to $92\% \pm 4\%$ of the 6.8 b total Au + Au cross section [14]. The centrality selection was done using the correlation between the analog responses of the ZDC and BBC [14].

The present analysis is based on 1.3 M minimum-bias events with a vertex position of $|z| < 20$ cm. To reconstruct the Λ and $\bar{\Lambda}$ particles, their weak decays $\Lambda \rightarrow p\pi^-$ and $\bar{\Lambda} \rightarrow \bar{p}\pi^+$ are used. The tracks of the charged particles from the decay of Λ and $\bar{\Lambda}$ are reconstructed using DC and PC1, and their momentum is determined by the DC with a resolution of $\delta p/p \simeq 0.6\% \oplus 3.6\% p$ (GeV/c). Although these tracks do not point back to the primary vertex position (the mean distance of the Λ decay vertex to interaction vertex is $\sim$3.5 cm), their momentum is calculated assuming that they come from the interaction point, hence there is, in general, a shift in the momentum of the reconstructed Λ and $\bar{\Lambda}$ particles. A Monte Carlo (MC) study shows that the difference is of the order 1%–2% over the measured momentum range, within the measured momentum resolution, and thus neglected in the present study. The absolute momentum scale is known to better than 2% [15]. In order to reduce background the tracks are confirmed by requiring a matching hit in the EMCal within $\pm 3\sigma$. For the particle identification of the daughter charged particles the time-of-flight signal of the EMCal with a timing resolution of $\sim$700 ps is used. Using the momentum measured by the DC and the flight time, the particle mass is calculated and a 2σ momentum-dependent cut is applied to the mass-squared distribution to identify protons, antiprotons, and pions. An upper momentum cut of 0.6 and 1.4 GeV/c for pions and protons, respectively, provides clean particle separation. Then each proton is combined with each pion in the same event and the invariant mass is calculated. If Λ or $\bar{\Lambda}$ are produced, a peak appears in the mass distribution on top of a background from random combinations of particles and short lived resonances (Δ and N^*). In order to determine the number of Λ's and $\bar{\Lambda}$'s from such a distribution, an estimation of the background is essential. For this, the mass distribution with combinations of protons and pions from different events with the same centrality class (event mixing) is used. In order to reduce the background, the decay proton energy is required to be within $E_p^{\min} < E_p < E_p^{\max}$, where $E_p^{\min}$ and $E_p^{\max}$ are calculated from the two-body decay kinematics in the Λ center-of-mass system. A similar cut is used for the pions. This cut is particularly effective in reducing the contributions from short-lived resonances and gives an improvement of the signal-to-background ratio by a factor of 2 without affecting the Λ line shape and results in the final value of $S/B = 1/2$ for both Λ and $\bar{\Lambda}$. We obtain $\sim$12000 Λ and $\sim$9000 $\bar{\Lambda}$ particles in the mass range $1.05 < m_{p\pi} < 1.20$ GeV/c^2 with mass resolution $\delta m/m \simeq 2\%$ obtained from a Gaussian fit. The Λ ($\bar{\Lambda}$) peaks vary by less than the mass resolution over the measured p_T range.

Figure 1 shows the invariant mass spectra for the $\Lambda \rightarrow p\pi^-$ and $\bar{\Lambda} \rightarrow \bar{p}\pi^+$. The results represent the primary Λ and $\bar{\Lambda}$ and contributions from the feed-down from heavier hyperons (mainly Σ^0 and Ξ). The reconstructed number of Λ and $\bar{\Lambda}$ particles is corrected for acceptance, pion decay-in-flight, momentum resolution, and reconstruction efficiency. For this, single-particle MC events were generated over the full azimuth ϕ ($0 < \phi < 2\pi$) and one unit of rapidity y ($-0.5 < y < 0.5$). The simulated particles were passed through the entire PHENIX GEANT [16] simulation. The correction function is defined as the ratio of the input (generated) transverse momentum distribution to the p_T distribution of the particles reconstructed in the spectrometer. However, this correction does not take into account the decreasing track reconstruction efficiency due to the high multiplicity environment in more central events. A well-established method to obtain this efficiency drop is the embedding procedure [15]. We use single-particle MC tracks embedded into real events and analyze the merged events with the same analysis code as used for the reconstruction of the data set. The track reconstruction efficiency decreases from 90% for minimum bias to 70%

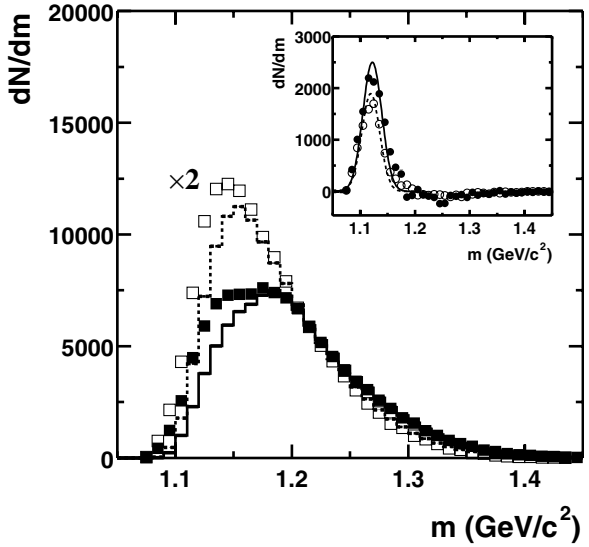

FIG. 1. Invariant mass spectra of $p\pi^-$ (solid squares) and $\bar{p}\pi^+$ (open squares) pairs. The histograms show the background for $p\pi^-$ (solid line) and $\bar{p}\pi^+$ (dashed line). For clarity the $\bar{p}\pi^+$ data are scaled up by a factor of 2. The inset shows the background-subtracted spectra of Λ (solid circles) and $\bar{\Lambda}$ (open circles). The lines are Gaussian fits to the Λ (solid line) and $\bar{\Lambda}$ (dashed line) mass spectra.

for central events, independently of the track p_T. The Σ^0 and Ξ hyperons decay to Λ with a branching ratio of essentially 100%. We have verified, using HIJING, that the kinematic properties (p_T and y distributions) of primary Λ and those produced by Σ^0 and Ξ decay are the same (within a few percent). We conclude that the correction function determined for primary Λ is valid for all Λ. Since there are no reliable data available for the yields of those hyperons at RHIC energies, we cannot quantitatively state the contributions from those heavier hyperons to our Λ production. Therefore, our data include the primordial Λ and $\bar{\Lambda}$, as well as the feed-down from the heavier hyperons.

Using the correction function determined from single-particle MC and multiplicity-dependent track reconstruction efficiency derived from the embedding procedure, we correct the transverse momentum distributions of Λ and $\bar{\Lambda}$. The invariant yields as a function of the transverse momentum p_T for Λ and $\bar{\Lambda}$ are shown in Fig. 2 for minimum-bias events (circles). Over the measured transverse momentum range ($0.4 < p_T < 1.8$ GeV/c), both the Λ and $\bar{\Lambda}$ spectra can be described by a distribution of the form $dN/dp_T^2 \propto p_T e^{-p_T/T}$ as shown in Fig. 2 by the solid line. The total yield dN/dy is obtained by integrating the functional fit from zero to infinity. The fraction of the extrapolated yield is 29%. In the same Fig. 2 we show the invariant yield for the 5% most central events (squares). In Table I the total yields dN/dy together with the average transverse momentum $\langle p_T \rangle$ and the slope parameters T are listed for both minimum bias and for the 5% most central events.

There are several sources which contribute to the systematic uncertainties of the total yield dN/dy and average transverse momentum $\langle p_T \rangle$ determination. One of the sources, the uncertainty in the correction function determination, is found to be 13%. By changing the fitting function used for the yield extrapolation to a pure exponential, we derive a systematic error of $\pm 9\%$. There is also an additional contribution to the systematic error which originates from the combinatorial background subtraction which is 3%. Combining the above uncertainties in quadrature gives a total systematic error in the yield of 16% (see Table I).

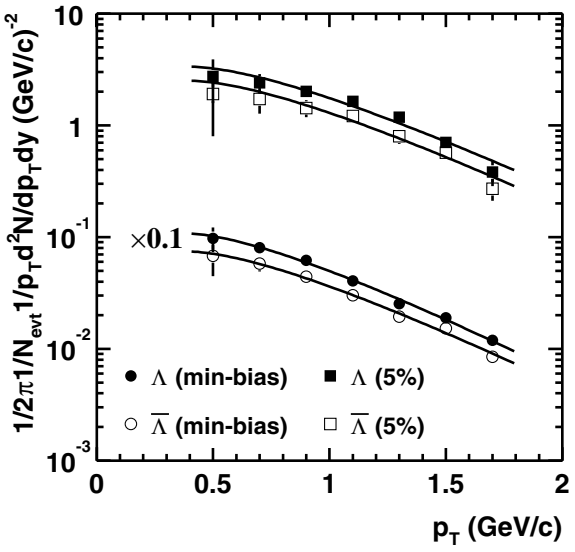

FIG. 2. Transverse momentum spectra of Λ and $\bar{\Lambda}$ for minimum bias and for the 5% most central events. For clarity of presentation the data points for minimum bias are scaled down by a factor of 10.

The $\bar{\Lambda}/\Lambda$ yield ratio determined in the mass window defined above versus p_T is shown in Fig. 3 (top panel). The ratio is constant over the whole p_T range $0.4 < p_T < 1.8$ GeV/c. There is also no significant variation of the $\bar{\Lambda}/\Lambda$ ratio as a function of the number of participants (bottom panel) which is calculated using a Glauber model together with a simulation of the ZDC and BBC responses [14]. The average $\bar{\Lambda}/\Lambda$ ratio is $0.75 \pm 0.09(\text{stat}) \pm 0.17(\text{syst})$. Both the p_T dependence and the integral $\bar{\Lambda}/\Lambda$ ratio are consistent with statistical thermal model calculations [17] at RHIC energies.

The present measurement of the total yield of Λ and $\bar{\Lambda}$ enables us to take the previously reported inclusive p and $\bar{p}$ spectra [18] and construct a feed-down correction for Λ decays. As the Σ yield has not been measured, we do

TABLE I. Inclusive Λ and feed-down corrected proton yields, average transverse momentum (in GeV/c), and slope parameters (in MeV/c) for minimum bias (MB) and for the 5% most central events. The errors listed are statistical. The systematic errors are 17% for the protons and 16% for the Λ.

		Λ	$\bar{\Lambda}$	p	$\bar{p}$
dN/dy	(MB)	4.8 ± 0.3	3.5 ± 0.3	5.4 ± 0.2	3.7 ± 0.2
	(5%)	17.3 ± 1.8	12.7 ± 1.8	19.3 ± 0.6	13.7 ± 0.7
$\langle p_T \rangle$	(MB)	1.06 ± 0.08	1.10 ± 0.12	0.88 ± 0.04	0.91 ± 0.06
	(5%)	1.15 ± 0.15	1.14 ± 0.21	0.95 ± 0.07	1.04 ± 0.12
T	(MB)	355 ± 11	366 ± 13	292 ± 21	304 ± 23
	(5%)	384 ± 16	380 ± 19	319 ± 31	327 ± 34

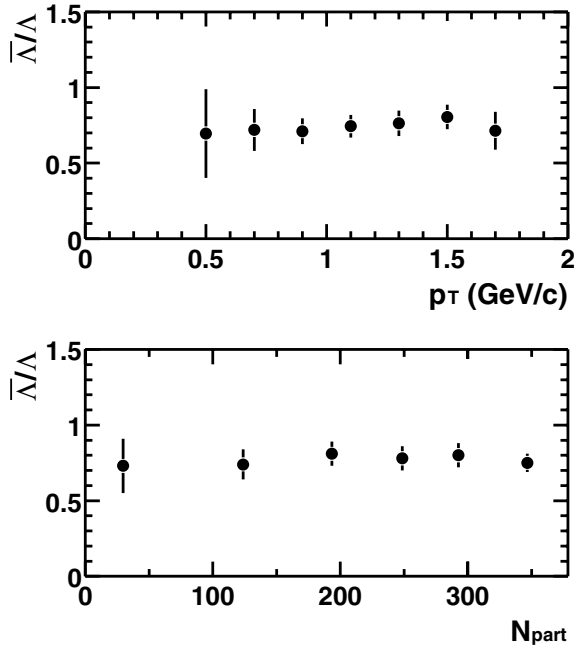

FIG. 3. The ratio $\bar{\Lambda}/\Lambda$ as a function of p_T (top) and as a function of the number of participants (bottom).

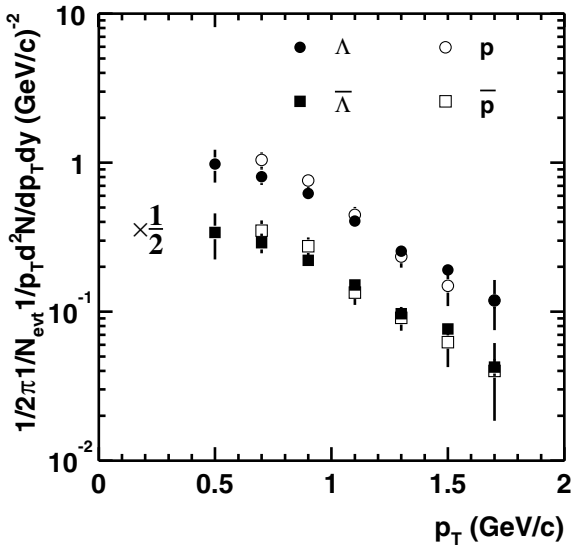

FIG. 4. Spectra of inclusive Λ ($\bar{\Lambda}$) and feed-down corrected protons (antiprotons) for minimum-bias events. The data points for antiprotons and $\bar{\Lambda}$ are scaled down by a factor of 2.

not include feed-down from $\Sigma^{\pm}$ decays, but this is expected to be $<5\%$, based on HIJING calculations. The feed-down corrections were done bin by bin on the proton (antiproton) p_T spectrum by the following method:

$$\frac{dN^p}{dydp_T}(i) = \frac{dN^m}{dydp_T}(i) - \sum_{j=1}^{N_{\text{bins}}} \frac{dN^{\Lambda}}{dydp_T}(j) \times BR \times w(j,i), \tag{1}$$

where $dN^p/dydp_T$ is the total yield of the primary protons, $dN^m/dydp_T$ is the total yield of the measured protons, $dN^{\Lambda}/dydp_T$ is the total yield of the measured Λ, BR is the branching ratio of the Λ decay $\Lambda \rightarrow p\pi^-$, i is the p_T bin number, N_{bins} is the number of bins, and $w(j,i)$ is the fraction of protons from Λ decay from bin number j which fall into the proton bin number i. These fractions were extracted from MC. The feed-down corrected proton and antiproton p_T spectra are shown in Fig. 4. We calculated the total yield, dN/dy, for protons and antiprotons by fitting them to the same distribution as used for the Λ and integrating from zero to infinity. The results for the total yields dN/dy, the average transverse momentum $\langle p_T \rangle$, and the slope parameters T for minimum bias and for the 5% most central events are also listed in Table I. The measured Λ/p and $\bar{\Lambda}/\bar{p}$ ratios after feed-down corrections are found to be $0.89 \pm 0.07(\text{stat}) \pm 0.21(\text{syst})$ and $0.95 \pm 0.09(\text{stat}) \pm 0.22(\text{syst})$.

The net baryon numbers are indicative of the baryon transport mechanism in relativistic heavy ion (RHI) collisions. In Table II we compare our results for minimum bias and for the 5% most central events with the predictions of the HIJING [19] model which assumes that the primary mechanism for baryon transport in RHI is due to quark-diquark hadronic strings. Vance *et al.* [4] implemented a nonperturbative gluon-junction mechanism in a new version of HIJING (called HIJING/B) to explain the enhanced baryon stopping at CERN SPS energies. The predictions of this model are also shown in Table II. For a valid comparison with the experimental data, the HIJING and HIJING/B results for Λ and $\bar{\Lambda}$ also include the feed-down from the heavier hyperons and the results for protons and antiprotons the feed-down from $\Sigma^{\pm}$. Table II shows a clear difference (by a factor of $\sim$4) between HIJING and HIJING/B for the net Λ number, with the HIJING/B predictions in much better agreement, in particular, for the minimum-bias data, where the experimental errors are relatively small. Moreover, HIJING/B rapidity densities for both Λ and $\bar{\Lambda}$ are closer to the experimental values though still below them. The difference between the two models for the net proton number is less obvious and, although the data seem

TABLE II. Total measured and predicted baryon yields for minimum bias (MB) and for the 5% most central events. The errors listed are statistical. The proton yields are corrected for feed-down. The systematic errors are 24% for the protons and 23% for the Λ.

Net baryon number	PHENIX	HIJING	HIJING/B
$(\Lambda - \bar{\Lambda})$ (MB)	1.3 ± 0.4	0.2	0.8
$(p - \bar{p})$ (MB)	1.7 ± 0.3	1.1	1.7
$(\Lambda - \bar{\Lambda})$ (5%)	4.6 ± 2.5	0.8	3.2
$(p - \bar{p})$ (5%)	5.6 ± 0.9	4.7	7.1

to favor HIJING/B, the present accuracy does not allow for a clear preference between the two models.

In conclusion, we have measured the transverse momentum spectra of Λ and $\bar{\Lambda}$ particles in the p_T range $0.4 < p_T < 1.8$ GeV/c in minimum bias and the 5% most central Au + Au collisions at $\sqrt{s_{NN}} = 130$ GeV at RHIC with the PHENIX experiment. The absolute yields of dN/dy, at midrapidity, of Λ hyperons are determined by extrapolating to all values of p_T. The average $\bar{\Lambda}/\Lambda$ ratio is found to be $0.75 \pm 0.09 \pm 0.17$. The ratio is constant over the whole p_T range and there is also no significant variation of the $\bar{\Lambda}/\Lambda$ ratio as a function of the number of participants. Using the measured Λ and $\bar{\Lambda}$ yields, the p and $\bar{p}$ yields corrected for feed-down from Λ decays are determined. The Λ/p and $\bar{\Lambda}/\bar{p}$ ratios after feed-down corrections are found to be $0.89 \pm 0.07 \pm 0.21$ and $0.95 \pm 0.09 \pm 0.22$. The measured net Λ number is substantially larger than predicted by HIJING as already seen at CERN SPS and which may indicate enhanced baryon stopping at RHI energies. The newly available high statistics data at $\sqrt{s_{NN}} = 200$ GeV will allow us to further study baryon transport and strangeness production in RHI collisions.

We thank the staff of the Collider-Accelerator and Physics Departments at BNL for their vital contributions. We acknowledge support from the Department of Energy and NSF (U.S.), MEXT and JSPS (Japan), RAS, RMAE, and RMS (Russia), BMBF, DAAD, and AvH (Germany), VR and KAW (Sweden), MIST and NSERC (Canada), CNPq and FAPESP (Brazil), IN2P3/CNRS (France), DAE and DST (India), KRF and CHEP (Korea), the U.S. CRDF for the FSU, and the US–Israel BSF.

*Deceased.
†Not a participating institution.

[1] *5th International Conference on Strangeness in Quark Matter 2000* [J. Phys. G **27**, 255 (2001)], and references therein.
[2] B. Z. Kopeliovich and B. G. Zakharov, Z. Phys. C **43**, 241 (1989).
[3] D. Kharzeev, Phys. Lett. B **378**, 238 (1996).
[4] S. E. Vance *et al.*, Phys. Lett. B **443**, 45 (1998).
[5] M. Gyulassy and I. Vitev, nucl-th/0104066.
[6] S. Ahmad *et al.*, Phys. Lett. B **382**, 35 (1996).
[7] K. Filimonov *et al.*, Nucl. Phys. **A661**, 198c (1999).
[8] T. Alber *et al.*, Eur. J. Phys. C **2**, 643 (1998).
[9] K. Wolf *et al.*, Phys. Rev. C **57**, 837 (1998).
[10] H. Appelshäuser *et al.*, Phys. Rev. Lett. **82**, 2471 (1999).
[11] PHENIX Collaboration, D. P. Morrison *et al.*, Nucl. Phys. **A638**, 565c (1998).
[12] P. Nilsson *et al.*, Nucl. Phys. **A661**, 665c (1999).
[13] PHENIX Collaboration, S. White *et al.*, Nucl. Phys. **A698**, 420c (2002).
[14] K. Adcox *et al.*, Phys. Rev. Lett. **86**, 3500 (2001).
[15] K. Adcox *et al.*, Phys. Rev. Lett. **88**, 022301 (2002).
[16] GEANT 3.21, CERN program library.
[17] P. Braun-Munzinger *et al.*, Phys. Lett. B **518**, 41 (2001).
[18] K. Adcox *et al.*, Phys. Rev. Lett. **88**, 242301 (2002).
[19] X. N. Wang and M. Gyulassy, Phys. Rev. D **44**, 3501 (1991).

Flow Measurements via Two-Particle Azimuthal Correlations in Au + Au Collisions at $\sqrt{s_{NN}} = 130$ GeV

K. Adcox,[40] S. S. Adler,[3] N. N. Ajitanand,[27] Y. Akiba,[14] J. Alexander,[27] L. Aphecetche,[34] Y. Arai,[14] S. H. Aronson,[3] R. Averbeck,[28] T. C. Awes,[29] K. N. Barish,[5] P. D. Barnes,[19] J. Barrette,[21] B. Bassalleck,[25] S. Bathe,[22] V. Baublis,[30] A. Bazilevsky,[12,32] S. Belikov,[12,13] F. G. Bellaiche,[29] S. T. Belyaev,[16] M. J. Bennett,[19] Y. Berdnikov,[35] S. Botelho,[33] M. L. Brooks,[19] D. S. Brown,[26] N. Bruner,[25] D. Bucher,[22] H. Buesching,[22] V. Bumazhnov,[12] G. Bunce,[3,32] J. Burward-Hoy,[28] S. Butsyk,[28,30] T. A. Carey,[19] P. Chand,[2] J. Chang,[5] W. C. Chang,[1] L. L. Chavez,[25] S. Chernichenko,[12] C. Y. Chi,[8] J. Chiba,[14] M. Chiu,[8] R. K. Choudhury,[2] T. Christ,[28] T. Chujo,[3,39] M. S. Chung,[15,19] P. Chung,[27] V. Cianciolo,[29] B. A. Cole,[8] D. G. D'Enterria,[34] G. David,[3] H. Delagrange,[34] A. Denisov,[12] A. Deshpande,[32] E. J. Desmond,[3] O. Dietzsch,[33] B. V. Dinesh,[2] A. Drees,[28] A. Durum,[12] D. Dutta,[2] K. Ebisu,[24] Y. V. Efremenko,[29] K. El Chenawi,[40] H. En'yo,[17,31] S. Esumi,[39] L. Ewell,[3] T. Ferdousi,[5] D. E. Fields,[25] S. L. Fokin,[16] Z. Fraenkel,[42] A. Franz,[3] A. D. Frawley,[9] S.-Y. Fung,[5] S. Garpman,[20,*] T. K. Ghosh,[40] A. Glenn,[36] A. L. Godoi,[33] Y. Goto,[32] S. V. Greene,[40] M. Grosse Perdekamp,[32] S. K. Gupta,[2] W. Guryn,[3] H.-Å. Gustafsson,[20] J. S. Haggerty,[3] H. Hamagaki,[7] A. G. Hansen,[19] H. Hara,[24] E. P. Hartouni,[18] R. Hayano,[38] N. Hayashi,[31] X. He,[10] T. K. Hemmick,[28] J. M. Heuser,[28] M. Hibino,[41] J. C. Hill,[13] D. S. Ho,[43] K. Homma,[11] B. Hong,[15] A. Hoover,[26] T. Ichihara,[31,32] K. Imai,[17,31] M. S. Ippolitov,[16] M. Ishihara,[31,32] B. V. Jacak,[28,32] W. Y. Jang,[15] J. Jia,[28] B. M. Johnson,[3] S. C. Johnson,[18,28] K. S. Joo,[23] S. Kametani,[41] J. H. Kang,[43] M. Kann,[30] S. S. Kapoor,[2] S. Kelly,[8] B. Khachaturov,[42] A. Khanzadeev,[30] J. Kikuchi,[41] D. J. Kim,[43] H. J. Kim,[43] S. Y. Kim,[43] Y. G. Kim,[43] W. W. Kinnison,[19] E. Kistenev,[3] A. Kiyomichi,[39] C. Klein-Boesing,[22] S. Klinksiek,[25] L. Kochenda,[30] V. Kochetkov,[12] D. Koehler,[25] T. Kohama,[11] D. Kotchetkov,[5] A. Kozlov,[42] P. J. Kroon,[3] K. Kurita,[31,32] M. J. Kweon,[15] Y. Kwon,[43] G. S. Kyle,[26] R. Lacey,[27] J. G. Lajoie,[13] J. Lauret,[27] A. Lebedev,[13,16] D. M. Lee,[19] M. J. Leitch,[19] X. H. Li,[5] Z. Li,[6,31] D. J. Lim,[43] M. X. Liu,[19] X. Liu,[6] Z. Liu,[6] C. F. Maguire,[40] J. Mahon,[3] Y. I. Makdisi,[3] V. I. Manko,[16] Y. Mao,[6,31] S. K. Mark,[21] S. Markacs,[8] G. Martinez,[34] M. D. Marx,[28] A. Masaike,[17] F. Matathias,[28] T. Matsumoto,[7,41] P. L. McGaughey,[19] E. Melnikov,[12] M. Merschmeyer,[22] F. Messer,[28] M. Messer,[3] Y. Miake,[39] T. E. Miller,[40] A. Milov,[42] S. Mioduszewski,[3,36] R. E. Mischke,[19] G. C. Mishra,[10] J. T. Mitchell,[3] A. K. Mohanty,[2] D. P. Morrison,[3] J. M. Moss,[19] F. Mühlbacher,[28] M. Muniruzzaman,[5] J. Murata,[31] S. Nagamiya,[14] Y. Nagasaka,[24] J. L. Nagle,[8] Y. Nakada,[17] B. K. Nandi,[5] J. Newby,[36] L. Nikkinen,[21] P. Nilsson,[20] S. Nishimura,[7] A. S. Nyanin,[16] J. Nystrand,[20] E. O'Brien,[3] C. A. Ogilvie,[13] H. Ohnishi,[3,11] I. D. Ojha,[4,40] M. Ono,[39] V. Onuchin,[12] A. Oskarsson,[20] L. Österman,[20] I. Otterlund,[20] K. Oyama,[7,38] L. Paffrath,[3,*] A. P. T. Palounek,[19] V. S. Pantuev,[28] V. Papavassiliou,[26] S. F. Pate,[26] T. Peitzmann,[22] A. N. Petridis,[13] C. Pinkenburg,[3,27] R. P. Pisani,[3] P. Pitukhin,[12] F. Plasil,[29] M. Pollack,[28,36] K. Pope,[36] M. L. Purschke,[3] I. Ravinovich,[42] K. F. Read,[29,36] K. Reygers,[22] V. Riabov,[30,35] Y. Riabov,[30] M. Rosati,[13] A. A. Rose,[40] S. S. Ryu,[43] N. Saito,[31,32] A. Sakaguchi,[11] T. Sakaguchi,[7,41] H. Sako,[39] T. Sakuma,[31,37] V. Samsonov,[30] T. C. Sangster,[18] R. Santo,[22] H. D. Sato,[17,31] S. Sato,[39] S. Sawada,[14] B. R. Schlei,[19] Y. Schutz,[34] V. Semenov,[12] R. Seto,[5] T. K. Shea,[3] I. Shein,[12] T.-A. Shibata,[31,37] K. Shigaki,[14] T. Shiina,[19] Y. H. Shin,[43] I. G. Sibiriak,[16] D. Silvermyr,[20] K. S. Sim,[15] J. Simon-Gillo,[19] C. P. Singh,[4] V. Singh,[4] M. Sivertz,[3] A. Soldatov,[12] R. A. Soltz,[18] S. Sorensen,[29,36] P. W. Stankus,[29] N. Starinsky,[21] P. Steinberg,[8] E. Stenlund,[20] A. Ster,[44] S. P. Stoll,[3] M. Sugioka,[31,37] T. Sugitate,[11] J. P. Sullivan,[19] Y. Sumi,[11] Z. Sun,[6] M. Suzuki,[39] E. M. Takagui,[33] A. Taketani,[31] M. Tamai,[41] K. H. Tanaka,[14] Y. Tanaka,[24] E. Taniguchi,[31,37] M. J. Tannenbaum,[3] J. Thomas,[28] J. H. Thomas,[18] T. L. Thomas,[25] W. Tian,[6,36] J. Tojo,[17,31] H. Torii,[17,31] R. S. Towell,[19] I. Tserruya,[42] H. Tsuruoka,[39] A. A. Tsvetkov,[16] S. K. Tuli,[4] H. Tydesjö,[20] N. Tyurin,[12] T. Ushiroda,[24] H. W. van Hecke,[19] C. Velissaris,[26] J. Velkovska,[28] M. Velkovsky,[28] A. A. Vinogradov,[16] M. A. Volkov,[16] A. Vorobyov,[30] E. Vznuzdaev,[30] H. Wang,[5] Y. Watanabe,[31,32] S. N. White,[3] C. Witzig,[3] F. K. Wohn,[13] C. L. Woody,[3] W. Xie,[5,42] K. Yagi,[39] S. Yokkaichi,[31] G. R. Young,[29] I. E. Yushmanov,[16] W. A. Zajc,[8] Z. Zhang,[28] and S. Zhou[6]

(PHENIX Collaboration)

[1]*Institute of Physics, Academia Sinica, Taipei 11529, Taiwan*
[2]*Bhabha Atomic Research Centre, Bombay 400 085, India*
[3]*Brookhaven National Laboratory, Upton, New York 11973-5000*
[4]*Department of Physics, Banaras Hindu University, Varanasi 221005, India*
[5]*University of California–Riverside, Riverside, California 92521*
[6]*China Institute of Atomic Energy (CIAE), Beijing, People's Republic of China*
[7]*Center for Nuclear Study, Graduate School of Science, University of Tokyo, 7-3-1 Hongo, Bunkyo, Tokyo 113-0033, Japan*

 0031-9007/02/89(21)/212301(6)$20.00 © 2002 The American Physical Society

[8]*Columbia University, New York, New York 10027 and Nevis Laboratories, Irvington, New York 10533*
[9]*Florida State University, Tallahassee, Florida 32306*
[10]*Georgia State University, Atlanta, Georgia 30303*
[11]*Hiroshima University, Kagamiyama, Higashi-Hiroshima 739-8526, Japan*
[12]*Institute for High Energy Physics (IHEP), Protvino, Russia*
[13]*Iowa State University, Ames, Iowa 50011*
[14]*KEK, High Energy Accelerator Research Organization, Tsukuba-shi, Ibaraki-ken 305-0801, Japan*
[15]*Korea University, Seoul, 136-701, Korea*
[16]*Russian Research Center "Kurchatov Institute," Moscow, Russia*
[17]*Kyoto University, Kyoto 606, Japan*
[18]*Lawrence Livermore National Laboratory, Livermore, California 94550*
[19]*Los Alamos National Laboratory, Los Alamos, New Mexico 87545*
[20]*Department of Physics, Lund University, Box 118, SE-221 00 Lund, Sweden*
[21]*McGill University, Montreal, Quebec, Canada H3A 2T8*
[22]*Institut für Kernphysik, University of Münster, D-48149 Münster, Germany*
[23]*Myongji University, Yongin, Kyonggido 449-728, Korea*
[24]*Nagasaki Institute of Applied Science, Nagasaki-shi, Nagasaki 851-0193, Japan*
[25]*University of New Mexico, Albuquerque, New Mexico 87131*
[26]*New Mexico State University, Las Cruces, New Mexico 88003*
[27]*Chemistry Department, State University of New York–Stony Brook, Stony Brook, New York 11794*
[28]*Department of Physics and Astronomy, State University of New York–Stony Brook, Stony Brook, New York 11794*
[29]*Oak Ridge National Laboratory, Oak Ridge, Tennessee 37831*
[30]*PNPI, Petersburg Nuclear Physics Institute, Gatchina, Russia*
[31]*RIKEN (The Institute of Physical and Chemical Research), Wako, Saitama 351-0198, Japan*
[32]*RIKEN BNL Research Center, Brookhaven National Laboratory, Upton, New York 11973-5000*
[33]*Instituto de Física, Universidade de São Paulo, Caixa Postal 66318, São Paulo CEP05315-970, Brazil*
[34]*SUBATECH (Ecole des Mines de Nantes, IN2P3/CNRS, Universite de Nantes), BP 20722-44307, Nantes-Cedex 3, France*
[35]*St. Petersburg State Technical University, St. Petersburg, Russia*
[36]*University of Tennessee, Knoxville, Tennessee 37996*
[37]*Department of Physics, Tokyo Institute of Technology, Tokyo, 152-8551, Japan*
[38]*University of Tokyo, Tokyo, Japan*
[39]*Institute of Physics, University of Tsukuba, Tsukuba, Ibaraki 305, Japan*
[40]*Vanderbilt University, Nashville, Tennessee 37235*
[41]*Advanced Research Institute for Science and Engineering, Waseda University, 17 Kikui-cho, Shinjuku-ku, Tokyo 162-0044, Japan*
[42]*Weizmann Institute, Rehovot 76100, Israel*
[43]*IPAP, Yonsei University, Seoul 120-749, Korea*
[44]*KFKI Research Institute for Particle and Nuclear Physics (RMKI), Budapest, Hungary*[†]

(Received 11 April 2002; published 30 October 2002)

Two-particle azimuthal correlation functions are presented for charged hadrons produced in Au + Au collisions at the Relativistic Heavy Ion Collider ($\sqrt{s_{NN}} = 130$ GeV). The measurements permit determination of elliptic flow without event-by-event estimation of the reaction plane. The extracted elliptic flow values (v_2) show significant sensitivity to both the collision centrality and the transverse momenta of emitted hadrons, suggesting rapid thermalization and relatively strong velocity fields. When scaled by the eccentricity of the collision zone ε, the scaled elliptic flow shows little or no dependence on centrality for charged hadrons with relatively low p_T. A breakdown of this ε scaling is observed for charged hadrons with $p_T > 1.0$ GeV/c.

DOI: 10.1103/PhysRevLett.89.212301 PACS numbers: 25.75.Ld

The primary goal of current relativistic heavy ion research is the creation and study of nuclear matter at high energy densities [1–7]. Open questions include the detailed properties of such excited matter, as well as the existence of a transition to the quark-gluon plasma (QGP) phase. Such a phase of deconfined quarks and gluons has been predicted to survive for $\approx$ 3–10 fm/c in Au + Au collisions at the Relativistic Heavy Ion Collider (RHIC) [8], and several experimental probes have been proposed for its possible detection and study [1]. Elliptic flow constitutes an important observable [9–16] because it is thought to be driven by pressure built up early in the collision and, therefore, can reflect conditions existing in the first few fm/c. Elliptic flow leads to an anisotropy in the azimuthal distribution of emitted particles. A Fourier decomposition of this distribution [17,18],

$$\frac{dN}{d(\phi - \Phi_R)} \propto \left(1 + \sum_{n=1}^{\infty} 2v_n \cos[n(\phi - \Phi_R)]\right), \qquad (1)$$

provides a characterization of the elliptic flow via the second Fourier coefficient v_2. Here, ϕ is the azimuthal angle of an emitted particle and Φ_R is the azimuth of the reaction plane, defined by the beam direction and the impact-parameter vector [19]. The apparent reaction plane is determined from the azimuthal correlations between emitted particles, and its dispersion correction from the azimuthal correlations between two "subevents" [19–21]. An alternative technique for elliptic flow analysis is the Fourier decomposition of the pairwise distribution in the azimuthal angle difference ($\Delta\phi = \phi_1 - \phi_2$) between pairs of emitted particles [22–24]:

$$\frac{dN}{d\Delta\phi} \propto \left(1 + \sum_{n=1}^{\infty} 2v_n^2 \cos(n\Delta\phi)\right). \quad (2)$$

In this case the magnitude of the elliptic flow is characterized by the square of the second Fourier coefficient in Eq. (1), i.e., v_2^2. These methods of analysis can be taken as equivalent since (i) the correlation between every particle and the reaction plane induces correlations among the particles, and (ii) correlating two subevents amounts to summing two-particle correlations [18]. The results in this Letter have several advantages over elliptic flow measurements obtained via the reaction plane method at the same beam energy by the STAR [5] and PHOBOS [6] Collaborations. First, two-particle correlations circumvent the need for full azimuthal detector acceptance. Second, it allows the determination of elliptic flow without event-by-event estimation of the reaction plane and the associated corrections for its dispersion. Third, the correlation method can provide insights on nonflow correlations and minimize many important systematic uncertainties (detector acceptance, efficiency, etc.) important to the accuracy of elliptic flow measurements [22,23,25] .

Elliptic flow is predicted and found to be negative for beam energies $\lesssim 4A$ GeV and positive for higher beam energies in Au + Au collisions [9,13–16]. Recent theoretical investigations have made predictions for the centrality dependence of the scaled elliptic flow $A_2 \equiv v_2/\varepsilon$ [26,27], where ε is the eccentricity or initial spatial anisotropy of the "participant" nucleons in the collision zone. The eccentricity ε shows an essentially linear variation with impact parameter b, for $0.2b_{\max} \lesssim b \lesssim 0.8b_{\max}$ [9] in Au + Au collisions ($b_{\max} \approx 14$ fm). For central collisions ($b \lesssim 5$–6 fm), it is predicted that higher energy densities are produced and rapid kinetic equilibration in the QGP phase leads to a characteristic rise in A_2 [26,27]. In addition, elliptic flow for high p_T particles has been proposed as an observable sensitive to the energy loss of scattered partons in a QGP phase [28].

The colliding Au beams ($\sqrt{s_{NN}} = 130$ GeV) used in these measurements have been provided by the Relativistic Heavy Ion Collider at Brookhaven National Laboratory (BNL). Charged reaction products were detected in the east and west central arms of the PHENIX detector [2,29]. Each of these arms subtends 90° in azimuth ϕ, and ± 0.35 units of pseudorapidity η. The axially symmetric magnetic field of PHENIX (0.5 T) allowed for the tracking of particles with $p_T \geq 200$ MeV/c in the fiducial volume of both arms. The drift chamber (DC) and a layer of pad chambers (PC1) located at radii of 2 m and 2.5 m, respectively, in each arm, served as the primary tracking detector for these measurements. A second layer of pad chambers (PC3), positioned at 5 m in the east arm, was employed to confirm the trajectory of charged particles which traversed both the DC and PC1. The zero degree calorimeters (ZDC) were used in conjunction with the beam-beam counters (BBC) to provide the position of the vertex along the beam direction as well as a trigger for a wide range of centrality selections.

The present data analysis uses two-particle azimuthal correlation functions to measure the distribution of the azimuthal angle difference ($\Delta\phi = \phi_1 - \phi_2$) between pairs of charged hadrons. Following an approach commonly exploited in interferometry studies, a two-particle azimuthal correlation function can be defined as follows [22–24]:

$$C(\Delta\phi) = \frac{N_{\text{cor}}(\Delta\phi)}{N_{\text{uncor}}(\Delta\phi)}, \quad (3)$$

where $N_{\text{cor}}(\Delta\phi)$ is the observed $\Delta\phi$ distribution for charged particle pairs selected from the same event, and $N_{\text{uncor}}(\Delta\phi)$ is the $\Delta\phi$ distribution for particle pairs selected from mixed events. Events were selected with a collision vertex position, $-20 < z < 20$ cm, along the beam axis. Mixed events were obtained by randomly selecting each member of a particle pair from different events having similar multiplicity and vertex position. In order to suppress an overefficiency in finding two tracks at close angles, hadron pairs within 1 cm of each other in the DC were removed from both the $N_{\text{cor}}(\Delta\phi)$ and $N_{\text{uncor}}(\Delta\phi)$ distributions. Event centralities were obtained via a series of cuts in the space of BBC versus ZDC analog response [2]; they reflect percentile selections of the total interaction cross section of 6.8 b [2]. Estimates for the impact parameter and the eccentricity, $\varepsilon \equiv (\langle y^2\rangle - \langle x^2\rangle)/(\langle y^2\rangle + \langle x^2\rangle)$, were also made for each of these selections following the model detailed in Ref. [2]. Here, $\langle \ldots \rangle$ represents the spatial average (weighted by the density) of participant nucleons over the transverse plane of the collision zone [11]. Systematic uncertainties associated with the determination of ε are estimated to be $\sim$7%. This estimate includes the variation of all of the inputs to the Glauber model within reasonable limits.

Correlation functions were obtained via two separate methods. In the first, charged hadron pairs were formed by selecting each particle from a common p_T range (fixed-p_T method). In the second hadron pairs were formed by selecting one member from a fixed p_T range

and the other from outside this range (assorted-p_T method). Within statistical errors, both methods of analysis yield similar results for the p_T range presented below, as would be expected for a system dominated by collective motion.

An important prerequisite for reliable flow extraction from PHENIX data is to establish whether or not the $\sim 180^o$ azimuthal coverage of the detector results in significant distortions to the correlation function. To this end, detailed simulations of the detector response, acceptance, and efficiency, have been performed for simulated data incorporating specific amounts of flow (parametrized by v_2). The results from these simulations indicated no significant distortion to the correlation functions due to the PHENIX acceptance. On the other hand, small distortions to the correlation function (for $\Delta\phi \lesssim 25^o$) as well as an incomplete recovery of v_2 could be attributed to background contributions from particle decay and interactions in detector material.

These background contributions principally affect the extraction of v_2 from the correlation function in two ways. The distortion to the correlation function at small relative angle introduces a small systematic distortion when fit with a Fourier function [cf. Eq. (2)]. A good representation of the data was obtained with the fit function $C(\Delta\phi) = \lambda \exp[-0.5(\Delta\phi/\sigma)^2] + a_1[1 + 2v_2^2 \cos(2\Delta\phi)]$, where the Gaussian term is used to characterize the background distortion at small angles. In addition, there is an isotropic background of false tracks which are predominantly misidentified as high p_T particles. These contributions can be efficiently suppressed in the east central arm of PHENIX, by requiring a relatively stringent association between tracks found in the DC and their associated hits in PC3. Using such a procedure, the fraction of background tracks has been evaluated as a function of p_T and used to correct v_2. Corrections range from $\sim 10\%$ at low p_T to $\sim 25\%$ at 2 GeV/c with a systematic uncertainty of 5%. The current analysis is restricted to the range $0.3 < p_t \leq 2.5$ GeV/c to maintain this relatively small systematic uncertainty.

Figures 1(a)–1(d) show representative $\Delta\phi$ correlation functions obtained for charged hadrons detected in the pseudorapidity range $-0.35 < \eta < 0.35$. Correlation functions for relatively central events (centrality = 20%–25%, $b \sim 7.0$ fm) are shown for hadrons with $0.3 < p_T < 2.5$ GeV/c and $0.5 < p_T < 2.5$ GeV/c in Figs. 1(a) and 1(c), respectively. The same p_T selections have been made for the correlation functions shown in Figs. 1(b) and 1(d) but for more peripheral collisions (centrality = 40%–45%, $b \sim 9.6$ fm) as indicated. Figures 1(a)–1(d) show a clear anisotropic pattern which is essentially symmetric about $\Delta\phi = 90^o$. There is also a visible increase of this anisotropy with increasing impact parameter and p_T. These trends are all consistent with those expected for in-plane elliptic flow [10,11,13,20].

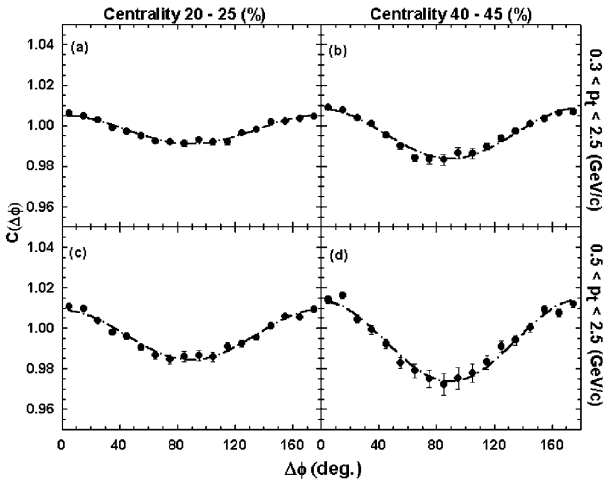

FIG. 1. Azimuthal correlation functions for charged hadrons as a function of centrality and p_T selection. The solid curves represent Fourier fits following Eq. (2). Error bars are statistical only.

The magnitude of elliptic flow and the mechanism for its development can be shown to be related to (a) the geometry of the collision zone, (b) the initial baryon and energy density developed in this zone, and (c) the detailed nature of the equation of state for the created nuclear matter [9–13,26]. Since differential flow measurements can serve to provide important insights for disentangling these separate aspects [10–13,26], we show the results of such measurements in Figs. 2 and 3. Figure 2 shows v_2 as a function of centrality for several p_T selections: $0.40 < p_T < 0.60$ GeV/c (diamonds), $0.60 < p_T < 1.00$ GeV/c (squares), and $1.0 < p_T < 2.5$ GeV/c (circles), respectively. Figure 3 compares the differential flow $v_2(p_T)$ for several centralities as indicated.

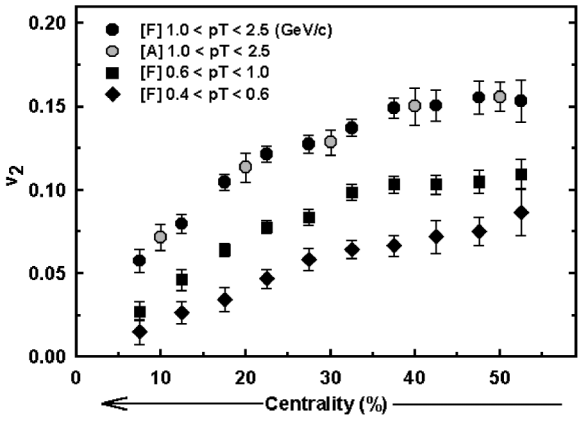

FIG. 2. v_2 vs centrality for several p_T selections. [F] and [A] indicate results obtained with the fixed-p_T and assorted-p_T methods, respectively. Systematic errors are estimated to be $\sim 5\%$; they are dominated by the normalization of the correction function for real tracks. For the centrality range 0%–5% the data points are statistically uncertain and the points are omitted.

Figures 2 and 3 both show relatively large differential flow values which increase with increasing impact parameter and the p_T of emitted hadrons. The separate effects of spatial asymmetry and the response of the collision zone, possibly due to the generated pressure are also evident in Fig. 2. That is, v_2 not only increases with increasing impact parameter for a fixed p_T, but also increases with increasing p_T for a fixed centrality selection. Trivially, the magnitude of flow should go to zero for very small and very large impact parameters. Similarly, its magnitude can be expected to be zero for $p_T = 0$. It is interesting that Fig. 3 indicates an essentially linear rise of v_2 with p_T for each of the centrality selections presented. Such a trend cannot be accounted for via simple geometric considerations alone [30]. However, it is compatible with model calculations which assume a strong transverse velocity field [30]. This suggests the presence of strong dynamically driven transverse flow at RHIC. The magnitude and trends for v_2 shown in Figs. 2 and 3 are consistent with other elliptic flow measurements at RHIC [5,6].

Figure 4 aims to disentangle the geometric and dynamical (p_T) contributions to the elliptic flow over a broad range of centralities or energy densities. To do this, we plot A_2 as a function of centrality to obtain the dynamical contributions [26,27]. This evaluation is performed for two p_T selections ($0.40 < p_T < 0.60$ and $1.0 < p_T < 2.5$ GeV/c) which give rise to relatively low and high p_T values, respectively. The underlying idea is that this ratio should remove the geometric dependence of v_2, while the p_T selections may provide greater sensitivity to different time scales and energy densities associated with the expanding system.

Figure 4 shows an increase in the magnitude of A_2 with increasing p_T. This increase can be attributed to the dynamical response of the created system, resulting from the generated pressure gradients. For hadrons of $0.4 < p_T < 0.6$ the observed centrality dependence of A_2 is compatible with ε scaling. However, a breakdown of this scaling is observed for hadrons with $1.0 < p_T < 2.5$. Such a trend may point to a change in the particle production mechanism or the possibility that pressures larger than those predicted by current hydrodynamic calculations [10,11] are being produced in the most central collisions at RHIC. It is also interesting to note that the species' composition of the charged particle spectra changes dramatically between the two p_T ranges used in Fig. 4 [31].

To summarize, we have measured two-particle azimuthal correlation functions for charged hadrons produced in Au + Au collisions at RHIC ($\sqrt{s_{NN}} = 130$ GeV). The integral, differential, and scaled elliptic flow values extracted from these measurements indicate strong sensitivity to the collision centrality and the transverse momenta of emitted hadrons. The centrality dependence of v_2 suggests that the high-energy-density nuclear matter created at RHIC efficiently translates the initial spatial asymmetry into a similar asymmetry in momentum space. The p_T dependence is consistent with the development of strong transverse velocity fields in the collision zone. The centrality dependence of A_2 for hadrons in the range $0.4 < p_T < 0.6$ is compatible with ε scaling. However, a breakdown of this scaling is observed for hadrons with $1.0 < p_T < 2.5$. Such a trend could result from a number of effects, the most intriguing of which is a possible change in the equation of state [26,27]. Additional experimental signatures and model calculations will undoubtedly be necessary to test the detailed implications of these results. Nevertheless, the results presented here clearly show that two-particle azimuthal

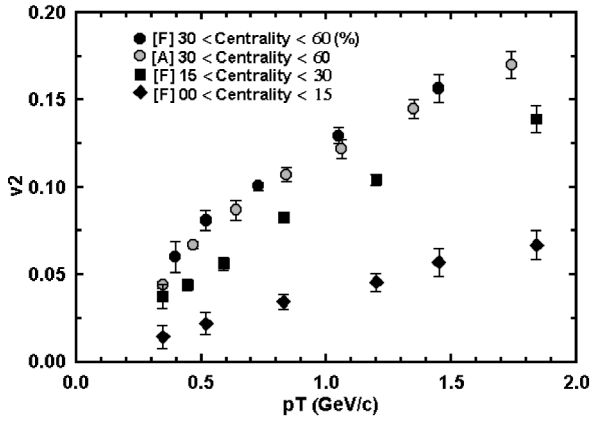

FIG. 3. v_2 vs p_T for several centrality selections. [F] and [A] follow the notation in Fig. 2. Systematic errors are estimated to be ~5%.

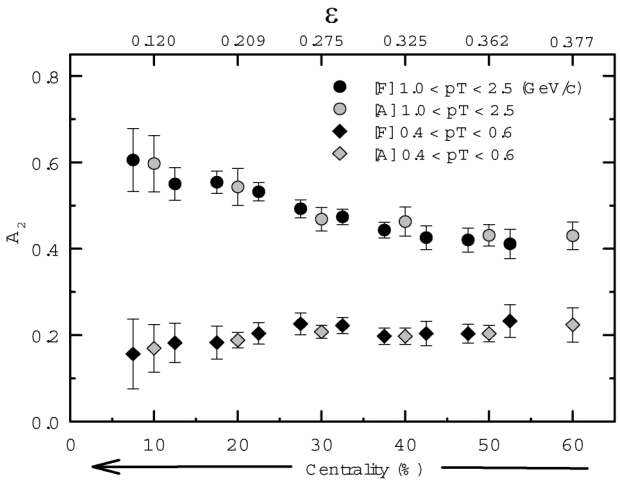

FIG. 4. The centrality dependence of A_2 for two different p_T selections. [F] and [A] follow the notation in Fig. 2. Estimates of the eccentricity ε for several centralities are indicated on the upper abscissa. Systematic errors are estimated to be ~10%, dominated by the normalization of the correction function and the model determination of ε.

correlation measurements provide an important probe for the high-energy-density nuclear matter created at RHIC.

We thank the staff of the Collider-Accelerator and Physics Departments at BNL for their vital contributions. We acknowledge support from the Department of Energy and NSF (U.S.A.), MEXT and JSPS (Japan), RAS, RMAE, and RMS (Russia), BMBF, DAAD, and AvH (Germany), VR and KAW (Sweden), MIST and NSERC (Canada), CNPq and FAPESP (Brazil), IN2P3/CNRS (France), DAE and DST (India), KRF and CHEP (Korea), the U.S. CRDF for the FSU, and the U.S.–Israel BSF.

*Deceased.
†Not a participating institution.

[1] S. Bass *et al.*, Nucl. Phys. **A661**, 205 (1999).
[2] K. Adcox *et al.*, Phys. Rev. Lett. **86**, 3500 (2001).
[3] K. Adcox *et al.*, Phys. Rev. Lett. **87**, 052301 (2001).
[4] PHENIX Collaboration, W. A. Zajc *et al.*, Nucl. Phys. **A698**, 39c (2002).
[5] K. H. Ackermann *et al.*, Phys. Rev. Lett. **86**, 402 (2001).
[6] PHOBOS Collaboration, I. Park *et al.*, Nucl. Phys. **A698**, 564c (2002).
[7] B. B. Back *et al.*, Phys. Rev. Lett. **85**, 3100 (2000).
[8] B. Zhang, M. Gyulassy, and C. M. Ko, Phys. Lett. B **455**, 45 (1999).
[9] J.-Y. Ollitrault, Phys. Rev. D **46**, 229 (1992).
[10] D. Teaney, J. Lauret, and E. V. Shuryak, Phys. Rev. Lett. **86**, 4783 (2001).
[11] P. F. Kolb *et al.*, Nucl. Phys. **A696**, 197c (2002).
[12] E. E. Zabrodin *et al.*, Phys. Lett. B **508**, 184 (2001).
[13] P. Danielewicz *et al.*, Phys. Rev. Lett. **81**, 2438 (1998).
[14] J. Barrette *et al.*, Phys. Rev. C **55**, 1420 (1997).
[15] H. Appelshäuser *et al.*, Phys. Rev. Lett. **80**, 4136 (1998).
[16] C. Pinkenburg *et al.*, Phys. Rev. Lett. **83**, 1295 (1999).
[17] H. H. Gutbrod *et al.*, Phys. Rev. C **42**, 640 (1990).
[18] N. Borghini, P. M. Dinh, and J.-Y. Ollitrault, Phys. Rev. C **64**, 054901 (2001).
[19] P. Danielewicz and G. Odyniec, Phys. Lett. **157B**, 146 (1985).
[20] J.-Y. Ollitrault, Nucl. Phys. **A638**, 195c (1998).
[21] A. M. Poskanzer *et al.*, Phys. Rev. C **58**, 1671 (1998).
[22] S. Wang *et al.*, Phys. Rev. C **44**, 1091 (1991).
[23] R. Lacey *et al.*, Phys. Rev. Lett. **70**, 1224 (1993).
[24] PHENIX Collaboration, R. Lacey *et al.*, Nucl. Phys. **A698**, 559c (2002).
[25] STAR Collaboration, K. H. Ackermann *et al.*, nucl-th/0207037; nucl-ex/0206001.
[26] H. Sorge, Phys. Rev. Lett. **82**, 2048 (1999).
[27] H. Heiselberg and A. M. Levy, Phys. Rev. C **59**, 2716 (1999).
[28] M. Gyulassy, I. Vitev, and X. N. Wang, Phys. Rev. Lett. **86**, 2537 (2000).
[29] PHENIX Collaboration, D. P. Morrison *et al.*, Nucl. Phys. **A638**, 565c (1998); N. Saito *et al.*, *ibid.* **A638**, 575c (1998).
[30] P. Huovinen, P. F. Kolb, and U. Heinz, Nucl. Phys. **A698**, 475c (2002).
[31] K. Adcox *et al.*, Phys. Rev. Lett. **88**, 242301 (2002).

Event-by-event fluctuations in mean p_T and mean e_T in $\sqrt{s_{NN}}$=130 GeV Au+Au collisions

K. Adcox,[40] S. S. Adler,[3] N. N. Ajitanand,[27] Y. Akiba,[14] J. Alexander,[27] L. Aphecetche,[34] Y. Arai,[14] S. H. Aronson,[3] R. Averbeck,[28] T. C. Awes,[29] K. N. Barish,[5] P. D. Barnes,[19] J. Barrette,[21] B. Bassalleck,[25] S. Bathe,[22] V. Baublis,[30] A. Bazilevsky,[12,32] S. Belikov,[12,13] F. G. Bellaiche,[29] S. T. Belyaev,[16] M. J. Bennett,[19] Y. Berdnikov,[35] S. Botelho,[33] M. L. Brooks,[19] D. S. Brown,[26] N. Bruner,[25] D. Bucher,[22] H. Buesching,[22] V. Bumazhnov,[12] G. Bunce,[3,32] J. Burward-Hoy,[28] S. Butsyk,[28,30] T. A. Carey,[19] P. Chand,[2] J. Chang,[5] W. C. Chang,[1] L. L. Chavez,[25] S. Chernichenko,[12] C. Y. Chi,[8] J. Chiba,[14] M. Chiu,[8] R. K. Choudhury,[2] T. Christ,[28] T. Chujo,[3,39] M. S. Chung,[15,19] P. Chung,[27] V. Cianciolo,[29] B. A. Cole,[8] D. G. D'Enterria,[34] G. David,[3] H. Delagrange,[34] A. Denisov,[12] A. Deshpande,[32] E. J. Desmond,[3] O. Dietzsch,[33] B. V. Dinesh,[2] A. Drees,[28] A. Durum,[12] D. Dutta,[2] K. Ebisu,[24] Y. V. Efremenko,[29] K. El Chenawi,[40] H. En'yo,[17,31] S. Esumi,[39] L. Ewell,[3] T. Ferdousi,[5] D. E. Fields,[25] S. L. Fokin,[16] Z. Fraenkel,[42] A. Franz,[3] A. D. Frawley,[9] S.-Y. Fung,[5] S. Garpman,[20,*] T. K. Ghosh,[40] A. Glenn,[36] A. L. Godoi,[33] Y. Goto,[32] S. V. Greene,[40] M. Grosse Perdekamp,[32] S. K. Gupta,[2] W. Guryn,[3] H.-Å. Gustafsson,[20] J. S. Haggerty,[3] H. Hamagaki,[7] A. G. Hansen,[19] H. Hara,[24] E. P. Hartouni,[18] R. Hayano,[38] N. Hayashi,[31] X. He,[10] T. K. Hemmick,[28] J. M. Heuser,[28] M. Hibino,[41] J. C. Hill,[13] D. S. Ho,[43] K. Homma,[11] B. Hong,[15] A. Hoover,[26] T. Ichihara,[31,32] K. Imai,[17,31] M. S. Ippolitov,[16] M. Ishihara,[31,32] B. V. Jacak,[28,32] W. Y. Jang,[15] J. Jia,[28] B. M. Johnson,[3] S. C. Johnson,[18,28] K. S. Joo,[23] S. Kametani,[41] J. H. Kang,[43] M. Kann,[30] S. S. Kapoor,[2] S. Kelly,[8] B. Khachaturov,[42] A. Khanzadeev,[30] J. Kikuchi,[41] D. J. Kim,[43] H. J. Kim,[43] S. Y. Kim,[43] Y. G. Kim,[43] W. W. Kinnison,[19] E. Kistenev,[3] A. Kiyomichi,[39] C. Klein-Boesing,[22] S. Klinksiek,[25] L. Kochenda,[30] V. Kochetkov,[12] D. Koehler,[25] T. Kohama,[11] D. Kotchetkov,[5] A. Kozlov,[42] P. J. Kroon,[3] K. Kurita,[31,32] M. J. Kweon,[15] Y. Kwon,[43] G. S. Kyle,[26] R. Lacey,[27] J. G. Lajoie,[13] J. Lauret,[27] A. Lebedev,[13,16] D. M. Lee,[19] M. J. Leitch,[19] X. H. Li,[5] Z. Li,[6,31] D. J. Lim,[43] M. X. Liu,[19] X. Liu,[6] Z. Liu,[6] C. F. Maguire,[40] J. Mahon,[3] Y. I. Makdisi,[3] V. I. Manko,[16] Y. Mao,[6,31] S. K. Mark,[21] S. Markacs,[8] G. Martinez,[34] M. D. Marx,[28] A. Masaike,[17] F. Matathias,[28] T. Matsumoto,[7,41] P. L. McGaughey,[19] E. Melnikov,[12] M. Merschmeyer,[22] F. Messer,[28] M. Messer,[3] Y. Miake,[39] T. E. Miller,[40] A. Milov,[42] S. Mioduszewski,[3,36] R. E. Mischke,[19] G. C. Mishra,[10] J. T. Mitchell,[3] A. K. Mohanty,[2] D. P. Morrison,[3] J. M. Moss,[19] F. Mühlbacher,[28] M. Muniruzzaman,[5] J. Murata,[31] S. Nagamiya,[14] Y. Nagasaka,[24] J. L. Nagle,[8] Y. Nakada,[17] B. K. Nandi,[5] J. Newby,[36] L. Nikkinen,[21] P. Nilsson,[20] S. Nishimura,[7] A. S. Nyanin,[16] J. Nystrand,[20] E. O'Brien,[3] C. A. Ogilvie,[13] H. Ohnishi,[3,11] I. D. Ojha,[4,40] M. Ono,[39] V. Onuchin,[12] A. Oskarsson,[20] L. Österman,[20] I. Otterlund,[20] K. Oyama,[7,38] L. Paffrath,[3,*] A. P. T. Palounek,[19] V. S. Pantuev,[28] V. Papavassiliou,[26] S. F. Pate,[26] T. Peitzmann,[22] A. N. Petridis,[13] C. Pinkenburg,[3,27] R. P. Pisani,[3] P. Pitukhin,[12] F. Plasil,[29] M. Pollack,[28,36] K. Pope,[36] M. L. Purschke,[3] I. Ravinovich,[42] K. F. Read,[29,36] K. Reygers,[22] V. Riabov,[30,35] Y. Riabov,[30] M. Rosati,[13] A. A. Rose,[40] S. S. Ryu,[43] N. Saito,[31,32] A. Sakaguchi,[11] T. Sakaguchi,[7,41] H. Sako,[39] T. Sakuma,[31,37] V. Samsonov,[30] T. C. Sangster,[18] R. Santo,[22] H. D. Sato,[17,31] S. Sato,[39] S. Sawada,[14] B. R. Schlei,[19] Y. Schutz,[34] V. Semenov,[12] R. Seto,[5] T. K. Shea,[3] I. Shein,[12] T.-A. Shibata,[31,37] K. Shigaki,[14] T. Shiina,[19] Y. H. Shin,[43] I. G. Sibiriak,[16] D. Silvermyr,[20] K. S. Sim,[15] J. Simon-Gillo,[19] C. P. Singh,[4] V. Singh,[4] M. Sivertz,[3] A. Soldatov,[12] R. A. Soltz,[18] S. Sorensen,[29,36] P. W. Stankus,[29] N. Starinsky,[21] P. Steinberg,[8] E. Stenlund,[20] A. Ster,[44,†] S. P. Stoll,[3] M. Sugioka,[31,37] T. Sugitate,[11] J. P. Sullivan,[19] Y. Sumi,[11] Z. Sun,[6] M. Suzuki,[39] E. M. Takagui,[33] A. Taketani,[31] M. Tamai,[41] K. H. Tanaka,[14] Y. Tanaka,[24] E. Taniguchi,[31,37] M. J. Tannenbaum,[3] J. Thomas,[28] J. H. Thomas,[18] T. L. Thomas,[25] W. Tian,[6,36] J. Tojo,[17,31] H. Torii,[17,31] R. S. Towell,[19] I. Tserruya,[42] H. Tsuruoka,[39] A. A. Tsvetkov,[16] S. K. Tuli,[4] H. Tydesjö,[20] N. Tyurin,[12] T. Ushiroda,[24] H. W. van Hecke,[19] C. Velissaris,[26] J. Velkovska,[28] M. Velkovsky,[28] A. A. Vinogradov,[16] M. A. Volkov,[16] A. Vorobyov,[30] E. Vznuzdaev,[30] H. Wang,[5] Y. Watanabe,[31,32] S. N. White,[3] C. Witzig,[3] F. K. Wohn,[13] C. L. Woody,[3] W. Xie,[5,42] K. Yagi,[39] S. Yokkaichi,[31] G. R. Young,[29] I. E. Yushmanov,[16] W. A. Zajc,[8] Z. Zhang,[28] and S. Zhou[6]

(PHENIX Collaboration)

[1]*Institute of Physics, Academia Sinica, Taipei 11529, Taiwan*
[2]*Bhabha Atomic Research Centre, Bombay 400 085, India*
[3]*Brookhaven National Laboratory, Upton, New York, 11973-5000*
[4]*Department of Physics, Banaras Hindu University, Varanasi 221005, India*
[5]*University of California–Riverside, Riverside, California 92521*
[6]*China Institute of Atomic Energy (CIAE), Beijing, People's Republic of China*
[7]*Center for Nuclear Study, Graduate School of Science, University of Tokyo, 7-3-1 Hongo, Bunkyo, Tokyo 113-0033, Japan*
[8]*Columbia University, New York, New York 10027*
and Nevis Laboratories, Irvington, New York 10533
[9]*Florida State University, Tallahassee, Florida 32306*
[10]*Georgia State University, Atlanta, Georgia 30303*
[11]*Hiroshima University, Kagamiyama, Higashi-Hiroshima 739-8526, Japan*
[12]*Institute for High Energy Physics (IHEP), Protvino, Russia*
[13]*Iowa State University, Ames, Iowa 50011*
[14]*KEK, High Energy Accelerator Research Organization, Tsukuba-shi, Ibaraki-ken 305-0801, Japan*

 ©0 The American Physical Society

[15]*Korea University, Seoul, 136-701, Korea*
[16]*Russian Research Center "Kurchatov Institute," Moscow, Russia*
[17]*Kyoto University, Kyoto 606, Japan*
[18]*Lawrence Livermore National Laboratory, Livermore, California 94550*
[19]*Los Alamos National Laboratory, Los Alamos, New Mexico 87545*
[20]*Department of Physics, Lund University, Box 118, SE-221 00 Lund, Sweden*
[21]*McGill University, Montreal, Quebec, Canada H3A 2T8*
[22]*Institut für Kernphysik, University of Münster, D-48149 Münster, Germany*
[23]*Myongji University, Yongin, Kyonggido 449-728, Korea*
[24]*Nagasaki Institute of Applied Science, Nagasaki-shi, Nagasaki 851-0193, Japan*
[25]*University of New Mexico, Albuquerque, New Mexico 87131*
[26]*New Mexico State University, Las Cruces, New Mexico 88003*
[27]*Chemistry Department, State University of New York–Stony Brook, Stony Brook, New York 11794*
[28]*Department of Physics and Astronomy, State University of New York–Stony Brook, Stony Brook, New York 11794*
[29]*Oak Ridge National Laboratory, Oak Ridge, Tennessee 37831*
[30]*PNPI, Petersburg Nuclear Physics Institute, Gatchina, Russia*
[31]*RIKEN (The Institute of Physical and Chemical Research), Wako, Saitama 351-0198, Japan*
[32]*RIKEN BNL Research Center, Brookhaven National Laboratory, Upton, New York 11973-5000*
[33]*Universidade de São Paulo, Instituto de Física, Caixa Postal 66318, São Paulo CEP05315-970, Brazil*
[34]*SUBATECH (Ecole des Mines de Nantes, IN2P3/CNRS, Universite de Nantes) Boîte Postale 20722-44307, Nantes-cedex 3, France*
[35]*St. Petersburg State Technical University, St. Petersburg, Russia*
[36]*University of Tennessee, Knoxville, Tennessee 37996*
[37]*Department of Physics, Tokyo Institute of Technology, Tokyo, 152-8551, Japan*
[38]*University of Tokyo, Tokyo, Japan*
[39]*Institute of Physics, University of Tsukuba, Tsukuba, Ibaraki 305, Japan*
[40]*Vanderbilt University, Nashville, Tennesse 37235*
[41]*Waseda University, Advanced Research Institute for Science and Engineering, 17 Kikui-cho, Shinjuku-ku, Tokyo 162-0044, Japan*
[42]*Weizmann Institute, Rehovot 76100, Israel*
[43]*Yonsei University, IPAP, Seoul 120-749, Korea*
[44]*KFKI Research Institute for Particle and Nuclear Physics (RMKI), Budapest, Hungary*
(Received 22 March 2002; published 2 August 2002)

Distributions of event-by-event fluctuations of the mean transverse momentum and mean transverse energy near mid-rapidity have been measured in Au+Au collisions at $\sqrt{s_{NN}}=130$ GeV at the Relativistic Heavy-Ion Collider. By comparing the distributions to what is expected for statistically independent particle emission, the magnitude of nonstatistical fluctuations in mean transverse momentum is determined to be consistent with zero. Also, no significant nonrandom fluctuations in mean transverse energy are observed. By constructing a fluctuation model with two event classes that preserve the mean and variance of the semi-inclusive p_T or e_T spectra, we exclude a region of fluctuations in $\sqrt{s_{NN}}=130$ GeV Au+Au collisions.

DOI: 10.1103/PhysRevC.66.0149XX PACS number(s): 25.75.Dw

I. INTRODUCTION

Phase instabilities near the QCD phase transition can result in nonstatistical fluctuations that are detectable in final state observables [1]. These instabilities, which may occur due to random color fluctuations [2], critical behavior at the QCD tricritical point [3], or fluctuations from the decay of a Polyakov loop condensate [4], can result in a broadening of the transverse momentum or transverse energy distributions of particles produced for different classes of events. This phenomenon is expected to be detected experimentally by searching for deviations of the distributions of the event-by-event mean transverse momentum M_{p_T} or mean transverse energy M_{e_T} of produced particles from the random distributions expected for statistically independent particle emission.

An event-by-event analysis of M_{p_T} was previously performed for 158 A GeV/c Pb+Pb collisions at the CERN SPS by Experiment NA49 [5]. In that analysis, the M_{p_T} distributions measured over the rapidity range $4<y_\pi<5.5$ and p_T range $0.005<p_T<1.5$ GeV/c were found to be consistent with random fluctuations. NA49 also performed an event-by-event analysis of the K/π ratio [6], showing only very small deviations from random fluctuations. With an increase of $\sqrt{s_{NN}}$ to 130 GeV in Relativistic Heavy-Ion Collider (RHIC) collisions, unprecedented energy densities have been observed [10]; hence conditions may be more favorable for a phase transition from hadronic matter to a quark-gluon

*Deceased.
†Author is an individual participant.

TABLE I. Statistics pertaining to the M_{p_T} analysis. The values of $\langle M_{p_T} \rangle$ are quoted for $0.2 < p_T < 1.5$ GeV/c and are not corrected for efficiency or acceptance.

Centrality	0–5 %	0–10 %	10–20 %	20–30 %
		Data		
N_{events}	72 692	149 236	149 725	150 365
$\langle N_{tracks} \rangle$	59.6	53.9	36.6	25.0
$\sigma_{N_{tracks}}$	10.8	12.2	10.2	7.8
$\langle M_{p_T} \rangle$ (MeV/c)	523	523	523	520
σ_{p_T} (MeV/c)	290	290	290	289
$\sigma_{M_{p_T}}$ (MeV/c)	38.6	41.1	49.8	61.1
		Mixed events		
$\langle M_{p_T} \rangle$ (MeV/c)	523	523	523	520
$\sigma_{M_{p_T}}$ (MeV/c)	37.8	40.3	48.8	60.0

plasma which may be indicated in nonrandom fluctuations. Presented here is an event-by-event analysis of M_{p_T} fluctuations and the first measurement of M_{e_T} fluctuations at midrapidity at the RHIC.

II. ANALYSIS

The PHENIX Experiment [7] consists of four spectrometers designed to measure simultaneously hadrons, leptons, and photons produced in nucleus-nucleus, proton-nucleus, and proton-proton collisions at RHIC. The two central arm spectrometers, which are located within a focusing magnetic field, each covering ± 0.35 in pseudorapidity and $\Delta\phi = 90°$ in azimuthal angle, are utilized in this analysis. The primary interaction trigger was defined using the Beam-Beam Counters (BBCs) [8] and Zero Degree Calorimeters (ZDCs) [9]. Events are selected with a requirement that the collision vertex along the beam axis has $|z| < 20$ cm as measured by both the BBCs and ZDCs. Event centrality is defined using correlations in the BBC and ZDC analog response as described in [10]. For the present analysis, the events are classified according to the 0–5 %, 0–10 %, 10–20 %, and 20–30 % most central events.

The drift chamber [11] is used in conjunction with the innermost pad chamber, called PC1, to measure the transverse momentum of charged particles traversing the PHENIX acceptance. A fiducial section of the drift chamber is chosen to minimize the effect of time-dependent variations in the performance of the detector during the data-taking period. The fiducial volume of the M_{p_T} analysis spans an azimuthal range of $\Delta\phi = 58.5°$ and covers the pseudorapidity range $|\eta| < 0.35$. Reconstructed tracks [12] are required to contain a match to a hit in PC1 to ensure that the tracks are well reconstructed in three dimensions for reliable momentum determination.

The M_{e_T} distribution is determined from clusters reconstructed in the two instrumented sectors of the lead-scintillator electromagnetic calorimeter [7,13,14]. The quantity e_T is defined as the transverse energy per reconstructed calorimeter cluster as described in [14], which can include clusters that have been merged. The effects of cluster merging on the M_{e_T} distribution are discussed later. The fiducial volume of the M_{e_T} analysis spans an azimuthal range of $\Delta\phi = 45°$ and covers $|\eta| < 0.35$.

There are no acceptance or efficiency corrections applied to the semi-inclusive p_T or e_T distributions prior to the calculation of M_{p_T} or M_{e_T}. Here, the term semi-inclusive refers to spectra in p_T or e_T summed over all events in a given centrality class. These corrections do not vary from event to

TABLE II. Statistics pertaining to the M_{e_T} analysis. The values of $\langle M_{e_T} \rangle$ are quoted for $0.225 < e_T < 2.0$ GeV and are not corrected for efficiency or acceptance.

Centrality	0–5 %	0–10 %	10–20 %	20–30 %
		Data		
N_{events}	69 224	138 882	140 461	137 867
$\langle N_{clus} \rangle$	68.6	62.1	41.6	28.0
$\sigma_{N_{clus}}$	11.6	13.2	10.8	8.3
$\langle M_{e_T} \rangle$ (MeV)	466	462	448	439
σ_{e_T} (MeV)	267	265	258	253
$\sigma_{M_{e_T}}$ (MeV)	34.1	36.2	43.0	51.8
		Mixed Events		
$\langle M_{e_T} \rangle$ (MeV)	466	462	448	439
$\sigma_{M_{e_T}}$ (MeV)	32.7	34.4	41.3	50.0

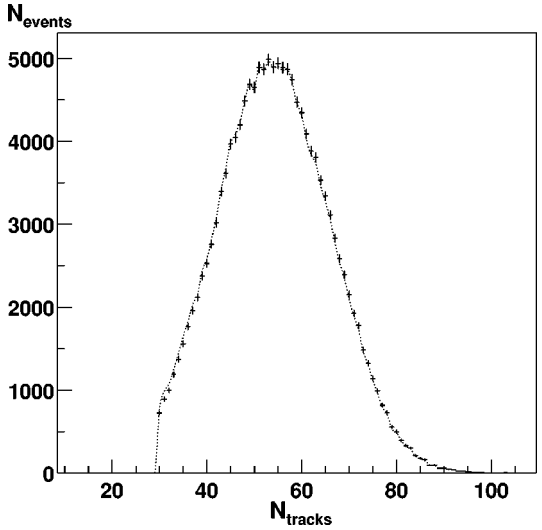

FIG. 1. The N_{tracks} distribution for the 0–10 % centrality class (data points) compared to the N_{mix} distribution from the mixed event sample (curve). Very good agreement in the data and mixed event N_{tracks} distribution is required for a precise comparison of the corresponding M_{p_T} distributions shown in Fig. 3 below.

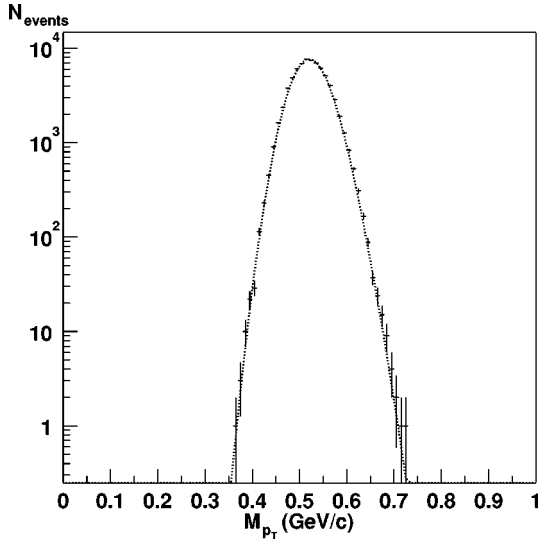

FIG. 2. The M_{p_T} distribution for the 0–5 % centrality class. The curve is the result of a Γ distribution calculation with parameters taken from the semi-inclusive p_T spectra.

event and are identical for data and mixed events (defined below); therefore they do not modify the values of the fluctuation quantities defined later. The M_{p_T} distributions are calculated using the formula

$$M_{p_T}=(1/N_{tracks})\sum_{i=1}^{N_{tracks}} p_{Ti}, \tag{2.1}$$

where N_{tracks} is the number of tracks in the event that pass the cuts outlined above and lie within the p_T range $0.2<p_T<1.5$ GeV/c. Similarly, the M_{e_T} distributions are calculated using the formula

$$M_{e_T}=(1/N_{clus})\sum_{i=1}^{N_{clus}} e_{Ti}, \tag{2.2}$$

where N_{clus} is the number of calorimeter clusters in the event that lie within the e_T range $0.225<e_T<2.0$ GeV. An event is excluded from the analysis if N_{tracks} or N_{clus} is below a minimum value to ensure that there are a sufficient number of tracks or clusters to determine a mean and to exclude background events. This minimum value for the 0–5 %, 0–10 %, 10–20 %, and 20–30 % centrality classes, respectively, is 40, 30, 20, and 10 for the M_{p_T} analysis and 30, 20, 10, and 10 for the M_{e_T} analysis. Table I lists statistics pertaining to the data samples used to determine M_{p_T} and Table II lists the statistics pertaining to the data samples used to determine M_{e_T}. The events used for the M_{p_T} and M_{e_T} analyses are considered independently of each other.

In order to compare the M_{p_T} and M_{e_T} distributions to what is expected for statistically independent particle emission, the baseline for the random distribution is defined by mixed events, which are events of multiplicity m assembled using individual tracks or clusters taken from a collection of m data events with one track or cluster taken from each data event. To obtain a precision comparison, it is important to match the number of tracks or clusters along with the mean of the semi-inclusive distribution of the mixed events to those of the data. Therefore, in both analyses, mixed events are constructed by predetermining the number of charged particle tracks or calorimeter clusters in the mixed event N_{mix} by directly sampling the corresponding data N_{tracks} or N_{clus} distributions. Figure 1 shows a comparison of the N_{tracks} distributions from the data and the normalized mixed event N_{mix} distribution for the 0–10 % centrality class. Once N_{mix} is determined, a mixed event is filled with p_T or e_T values from the data with the following criteria: (a) no two p_T or e_T values from the same data event are allowed to reside in the same mixed event, (b) only p_T or e_T values passing all cuts in the determination of M_{p_T} or M_{e_T} from the data events are placed in a mixed event, and (c) only data events from the same centrality class are used to construct a mixed event corresponding to that class. Once a mixed event is filled with N_{mix} tracks or clusters, its M_{p_T} or M_{e_T} is calculated in the same manner as for the data events.

For both analyses, the data contain a fraction of tracks or clusters within close physical proximity that have merged into a single track or cluster. This fraction is estimated by embedding simulated single-particle events that are processed through a detailed simulation of the detector response into real data events, which are then reconstructed in the same manner as the data. For the 0–5 % centrality class, we estimate that 6% of the tracks and 5% of the clusters are affected.

For the M_{p_T} analysis, tracks that are merged into a single reconstructed track typically have similar values of p_T. The result is a slightly lower value of N_{tracks} which causes a slight broadening in the width of the M_{p_T} distribution due to the reduced statistics per event. However, since the N_{tracks}

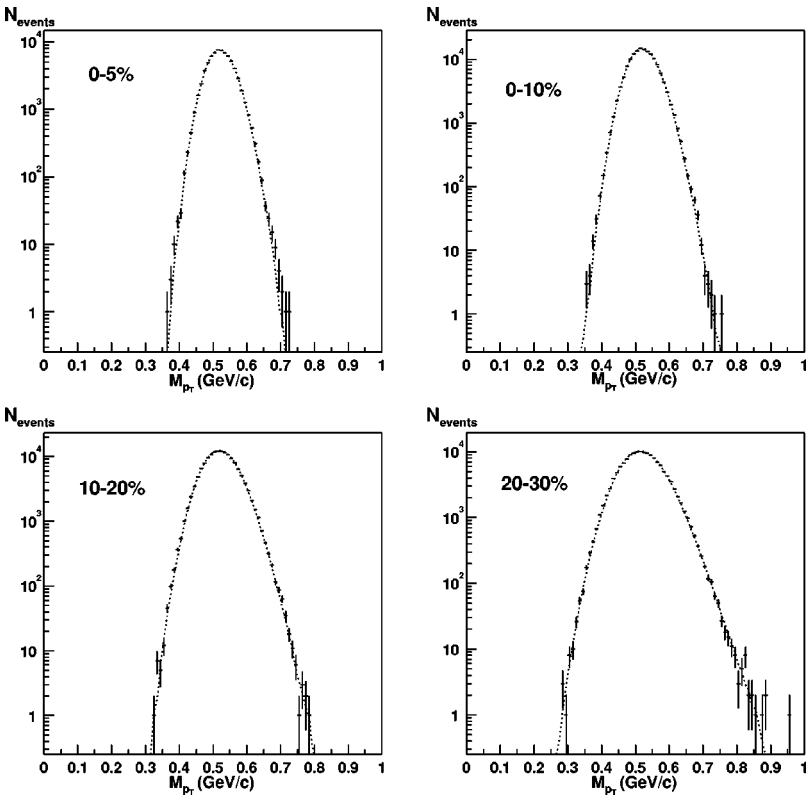

FIG. 3. The M_{p_T} distributions for all centrality classes. The curves are the random baseline mixed event distributions.

data distribution is directly sampled during the construction of mixed events, the effect of merged tracks cancels for comparisons between the data and mixed events.

For the M_{e_T} analysis, the effect of merged clusters is complicated by the fact that a single cluster is reconstructed with an e_T corresponding to the sum of the two (or more) particles contributing to the cluster. To understand this effect on the mixed events, we note that the fraction of merged clusters within a data event increases with event multiplicity. Also, many of the data events with the lowest M_{e_T} coincide with the lowest multiplicity events since they contain few, if any, merged clusters that would yield a higher M_{e_T}. When the merged clusters in the data events are randomly redistributed among the mixed events, low multiplicity mixed events can contain more merged clusters than the data events with the same multiplicity, resulting in a gross upward shift in M_{e_T} for those mixed events. This results in apparent excess nonrandom fluctuations at low M_{e_T}. Conversely, high multiplicity mixed events can contain fewer merged clusters than the data events with the same multiplicity, resulting in a gross downward shift in M_{e_T} for those mixed events. However, since the mean is taken over more clusters in this case, the effective shift in M_{e_T} is reduced at high M_{e_T}, and the apparent nonrandom fluctuations are much less pronounced. An estimate of the magnitude of this effect is presented later.

III. RESULTS

To compare directly the semi-inclusive p_T distribution to the M_{p_T} distribution assuming a statistically independent particle emission, the closed form prescription outlined in [15] is used. This prescription describes the semi-inclusive p_T distribution using a Gamma distribution,

$$f(p_T)=f_\Gamma(p_T,p,b)=\frac{b}{\Gamma(p)}(bp_T)^{p-1}e^{-bp_T}, \quad (3.1)$$

where p and b are free parameters that are related to the mean and standard deviation of the semi-inclusive distribution as

$$p=\frac{\langle p_T\rangle^2}{\sigma^2_{p_T}}, \quad b=\frac{\langle p_T\rangle}{\sigma^2_{p_T}}, \quad (3.2)$$

where

$$\sigma_{p_T}=(\langle p_T^2\rangle-\langle p_T\rangle^2)^{1/2}. \quad (3.3)$$

The reciprocal of b is the inverse slope parameter of the p_T distribution. With the track multiplicity distribution assumed to be a negative binomial distribution, $f_{NBD}(N_{tracks},1/k,\langle N_{tracks}\rangle)$, the M_{p_T} distribution can be calculated using

$$g(p_T)=\sum_{N=N_{min}}^{N_{max}} f_{NBD}(N,1/k,\langle N\rangle)f_\Gamma(p_T,Np,Nb), \quad (3.4)$$

where the sum is over N_{tracks} from N_{min} to N_{max}, which are the limits of the multiplicity. The value of the negative binomial distribution parameter k is given by

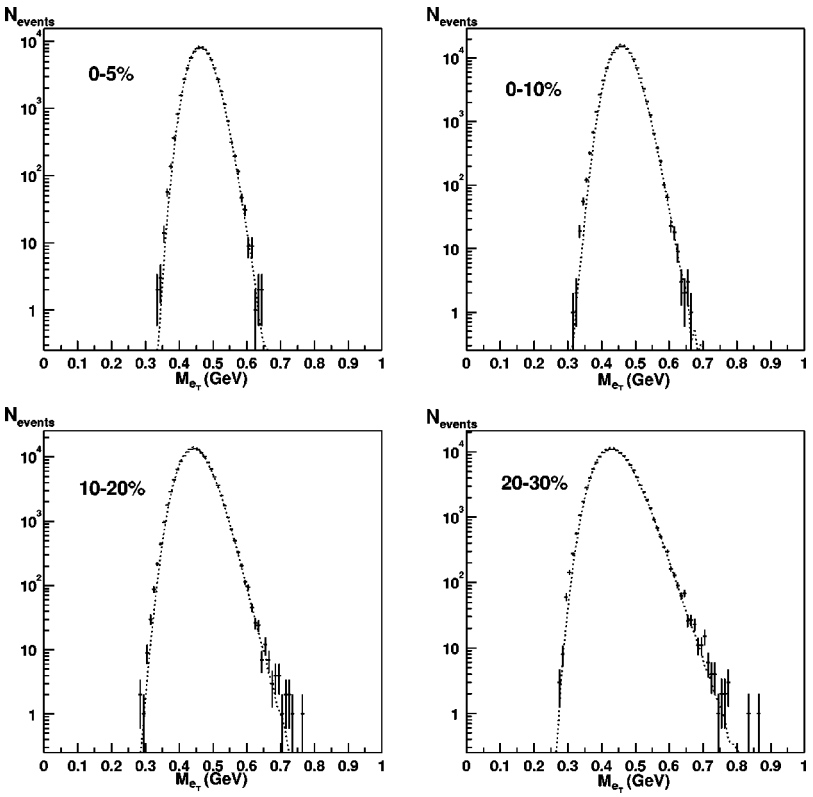

FIG. 4. The M_{e_T} distributions for all centrality classes. The curves are the random baseline mixed event distributions. The source of differences in the data and mixed event distributions are addressed in the text.

$$\frac{1}{k} = \frac{\sigma_{p_T}^2}{\langle N_{tracks} \rangle^2} - \frac{1}{\langle N_{tracks} \rangle}. \tag{3.5}$$

Therefore, given $\langle p_T \rangle$, σ_{p_T}, and $\langle N_{tracks} \rangle$ extracted from the semi-inclusive p_T distribution, the expected random M_{p_T} distribution can be calculated. Figure 2 shows the M_{p_T} distribution for the 0–5 % centrality class. Overlaid on the data as a dotted curve is the result of the calculation. The agreement between the data distribution and the calculation illustrates the absence of large nonstatistical fluctuations in the data. The remainder of this paper will quantify the amount of non-

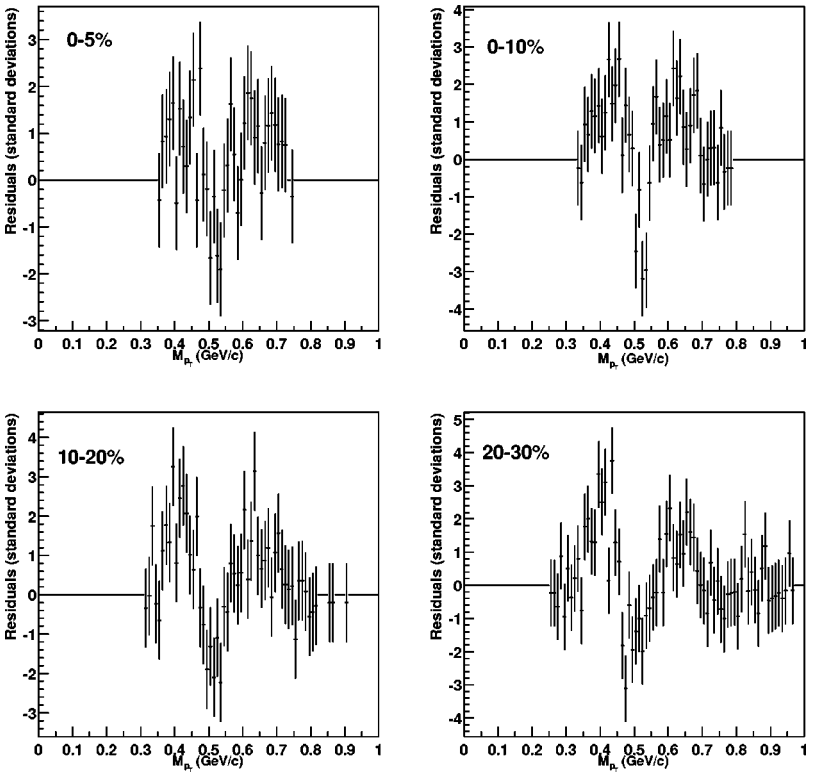

FIG. 5. The residual distribution between the data and mixed event M_{p_T} spectra as a function of M_{p_T} in units of standard deviations for all centrality classes. The total χ^2 and the number of degrees of freedom for the 0–5 %, 0–10 %, 10–20 %, and 20–30 % centrality classes are 89.0/37, 155.7/40, 163.3/47, and 218.4/61, respectively.

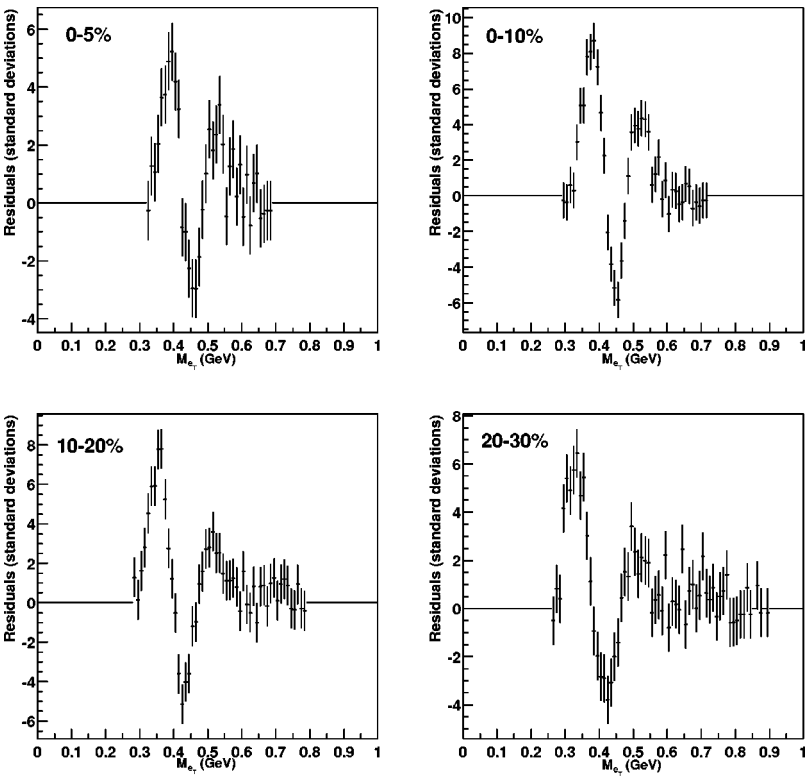

FIG. 6. The residual distribution between the data and mixed event M_{e_T} spectra as a function of M_{e_T} in units of standard deviations for all centrality classes. The total χ^2 and the number of degrees of freedom for the 0–5 %, 0–10 %, 10–20 %, and 20–30 % centrality classes are 310.0/32, 896.4/36, 678.7/47, and 553.9/53, respectively. A large fraction of the residual contributions are due to the effects of cluster merging.

statistical fluctuations observed and place limits on the level of fluctuations that can be present in central Au+Au collisions at $\sqrt{s_{NN}}=130$ GeV.

To quantify the magnitude of the deviation of fluctuations from the expectation of statistically independent particle emission, the magnitude of the fluctuation ω_T in the transverse quantity M_T, representing M_{p_T} or M_{e_T}, is defined as

$$\omega_T=\frac{(\langle M_T^2\rangle-\langle M_T\rangle^2)^{1/2}}{\langle M_T\rangle}=\frac{\sigma_{M_T}}{\langle M_T\rangle}. \tag{3.6}$$

The value of ω_T is calculated independently for the data distribution and for the baseline, or mixed event, distribution. The difference in the fluctuation from a random baseline distribution is defined as

$$d=\omega_{(T,data)}-\omega_{(T,baseline)}. \tag{3.7}$$

The sign of d is positive if the data distribution contains a correlation, such as Bose-Einstein correlations [16], when compared to the baseline distribution. The fraction of fluctuations that deviate from the expectation of statistically independent particle emission is given by

$$F_T=\frac{(\omega_{(T,data)}-\omega_{(T,baseline)})}{\omega_{(T,baseline)}}=\frac{(\sigma_{(T,data)}-\sigma_{(T,baseline)})}{\sigma_{(T,baseline)}}, \tag{3.8}$$

where $\sigma_{(T,\ data)}$ refers to the standard deviation of the event-by-event M_T data distribution and $\sigma_{(T,\ baseline)}$ is the corresponding quantity for the baseline, or mixed event, distribution. In the absence of a common language for the analysis of M_{p_T} and M_{e_T} fluctuations, the commonly used fluctuation quantity ϕ_T [17] is also presented in order to compare this measurement to previous results [5]. The quantity d is related directly to ϕ_T via

$$\phi_T=(\sigma_{(T,data)}-\sigma_{(T,baseline)})\sqrt{\langle N_T\rangle}=d\langle M_T\rangle\sqrt{\langle N_T\rangle}, \tag{3.9}$$

where N_T represents N_{tracks} or N_{clus}. The quantity ϕ_T is related to F_T by

$$\phi_T=F_T\sigma_{(T,baseline)}\sqrt{\langle N_T\rangle}. \tag{3.10}$$

TABLE III. Fluctuation quantities for the M_{p_T} analysis.

Centrality	0–5 %	0–10 %	10–20 %	20–30 %
$\omega_{(T,data)}$(%)	7.37±0.10	7.85±0.13	9.52±0.14	11.7±0.21
d(%)	0.14±0.15	0.16±0.19	0.19±0.21	0.21±0.35
F_T(%)	1.9±2.1	2.0±2.5	2.1±2.2	1.8±3.0
ϕ_{p_T} (MeV/c)	5.65±6.02	6.03±7.28	6.11±6.63	5.47±9.16

TABLE IV. Fluctuation quantities for the M_{e_T} analysis.

Centrality	0–5 %	0–10 %	10–20 %	20–30 %
$\omega_{(T,data)}$(%)	7.32±0.07	7.84±0.08	9.58±0.17	11.8±0.26
d(%)	0.30±0.09	0.37±0.12	0.38±0.20	0.40±0.32
F_T(%)	4.3±1.3	5.0±1.6	4.2±2.2	3.5±2.8
ϕ_{e_T} (MeV)	11.5±3.59	13.6±4.23	11.1±5.75	9.28±7.34

The standard deviation of the semi-inclusive spectra can be approximated by $\sigma_{(T,incl.)} \approx \sigma_{(T,baseline)} \sqrt{\langle N_T \rangle}$ [15], where $\sigma_{(T,incl.)}$ is the standard deviation of the semi-inclusive distribution as defined in Eq. (3.3). Therefore, ϕ_T is simply the fraction of nonrandom fluctuations in the event-by-event mean p_T or e_T, F_T, scaled by $\sigma_{(T,incl.)}$. An advantage of F_T over ϕ_T is that measurements expressed in F_T can be directly compared without further scaling.

The magnitudes of any nonrandom fluctuations are established by comparing the data distributions to the mixed event distributions, which serve as the random baseline distributions. For this purpose, the mixed event distributions are normalized to minimize the χ^2 value with respect to the data distributions. Figures 3 and 4 show the M_{p_T} and M_{e_T} distributions for all four centrality classes (data points) with the corresponding mixed event M_{p_T} and M_{e_T} distributions overlayed on the data as dotted curves. The broadening of the distributions for less central collisions are due to the reduction in $\langle N_{tracks} \rangle$ or $\langle N_{clus} \rangle$. Shown in Fig. 5 and Fig. 6 are the residuals between the data and mixed events, defined for each bin i as residual$_i = (M_{(T,data)_i} - M_{(T,mixed)_i})/\sigma_i$, in units of standard deviations, for each centrality class. The shapes of the residual distributions are primarily driven by the normalization procedure applied to the mixed events.

For the M_{p_T} distributions, the data and mixed event distributions are indistinguishable. However, the upper M_{e_T} edges of the data and mixed event M_{e_T} distributions show good agreement while the lower M_{e_T} edge of the data distributions are slightly wider than the mixed event distribution. If this low e_T effect were physical, it would imply fluctuations with slightly more low e_T photons since the effect is not seen in the M_{p_T} distribution for charged particle tracks. However, some of the excess fluctuations at low e_T can be attributed to the effects of cluster merging previously discussed. The magnitude of this effect has been investigated using a Monte Carlo simulation which calculates M_{e_T} after reproducing the calorimeter cluster separation distribution, the N_{clus} distribution, and the semi-inclusive e_T distributions from the data. The fluctuations in the M_{e_T} distribution with this effect included in each event are compared to a simulated mixed event M_{e_T} distribution constructed from the same generated data set using the same procedure that is applied to the data. In this manner, it is estimated that the cluster merging effect contributes an additional $F_T = 1.5\%$, 2.1%, 0.9%, and less than 0.01% to the nonrandom fluctuations for the 0–5 %, 0–10 %, 10–20 %, and 20–30 % centrality classes, respectively. The simulation confirms that the cluster merging effect significantly contributes only to the lower M_{e_T} edge of the distribution. The remainder of the excess low e_T fluctuations is likely due to correlated low energy background. GEANT [19] simulations indicate that the primary background contribution is produced by low energy electrons and muons that scatter off the pole tips of the central arm spectrometer magnet but still pass the cluster selection cuts. Because of the difficulty in quantifying the contribution of background to the excess fluctuations, the present M_{e_T} data are taken to indicate an upper limit on nonstatistical fluctuations rather than an indication of true nonstatistical fluctuations.

The values of ω_T, d, F_T, and ϕ_T for each centrality class using the mixed events as the random baseline distribution are tabulated in Table III for M_{p_T} and Table IV for M_{e_T}. The errors quoted for these quantities include statistical errors and systematic errors due to time-dependent variations over the data-taking period. The systematic errors are estimated by dividing each data set into nine subsets with each subset containing roughly equal numbers of events. For the M_{p_T} analysis, the systematic errors contribute to 81%, 88%, 76%, and 75% of the total error in ω_T and 85%, 88%, 80%, and 85% of the total error in the variables d, F_T, and ϕ_t for the 0–5 %, 0–10 %, 10–20 %, and 20–30 % centrality classes, respectively. The corresponding values for the M_{e_T} analysis are a 67%, 63%, 81%, and 82% contribution to the total errors in ω_T, and a 64%, 63%, 81%, and 82% contribution to the total errors in d, F_T, and ϕ_t for each centrality class. The cluster merging contribution estimates noted above are not applied to the values quoted in Table IV.

IV. DISCUSSION

Based upon the fluctuation measurements presented here, certain fluctuation scenarios in RHIC Au+Au collisions at $\sqrt{s_{NN}} = 130$ GeV are excluded. For this purpose, we consider two variations of a model that contains two classes of events with a difference of effective temperature, defined as $\Delta T = T_2 - T_1$, where T_2 is the inverse slope parameter of the event class with the higher effective temperature, and T_1 is the inverse slope parameter of the event class with the lower effective temperature. The first variation, model A, will consider a case where the means of the semi-inclusive p_T spectra for the two event classes are identical, but the standard deviations are different. The second variation, model B, will consider a case where the means of the semi-inclusive p_T spectra are different, but the standard deviations are identical. Since the semi-inclusive p_T distribution is an observed

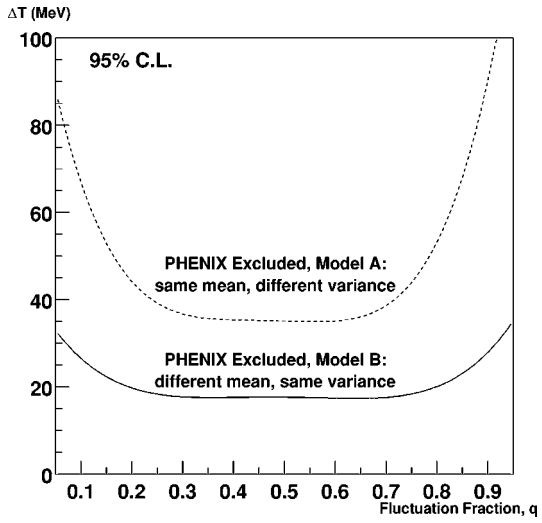

FIG. 7. The PHENIX sensitivity to nonrandom fluctuations in the two variations of the dual event class model that are excluded at the 95% confidence level by the M_{p_T} analysis in the 0–5 % centrality class. The fraction of events q in the class of events with the lower inverse slope parameter (event class 1) is plotted on the horizontal axis while the difference in inverse slope parameter between event class 1 and event class 2, ΔT, is plotted on the vertical axis. The curves represent the lower boundaries of the excluded regions.

quantity, the two event classes must be constrained in such a way that the mean and standard deviation of the final semi-inclusive p_T distribution remain constant while the effect of the fluctuation manifests itself in the M_{p_T} distribution.

The dual event class model is applied to the determination of the sensitivity to fluctuations in M_{p_T} for the 0–5 % centrality class as follows. Returning to the prescription outlined in [15], the semi-inclusive transverse p_T spectrum can be parametrized by the $f_\Gamma(p_T,p,b)$ distribution defined in Eq. (3.1). For both model variations, the fraction of events in the event class with the higher effective temperature is defined as

$$q=\frac{(N_{events})_{class\ 1}}{(N_{events})_{class\ 1}+(N_{events})_{class\ 2}}. \tag{4.1}$$

The p_T distribution of the combined sample can then be expressed as

$$f(p_T)=q\Gamma(p_T,p_1,b_1)+(1-q)\Gamma(p_T,p_2,b_2), \tag{4.2}$$

where $T_1=1/b_1$ and $T_2=1/b_2$.

For model A, the semi-inclusive p_T distributions of each event class are constrained to have the same mean, so we require

$$\mu=p/b=p_1/b_1=p_2/b_2. \tag{4.3}$$

The variance of the final semi-inclusive p_T distribution for model A is constrained by

$$\frac{\sigma^2}{\mu^2}=\frac{1}{p}=\frac{q}{p_1}+\frac{(1-q)}{p_2}. \tag{4.4}$$

With these constraints, the choice of a value for q and the effective temperature of one event class is sufficient to extract the remaining parameters from which sensitivity estimates for fluctuations in M_{p_T} are obtained.

For model B, the semi-inclusive p_T distributions of each event class are allowed to have different means, μ_1 and μ_2, so the mean of the total semi-inclusive distribution can be expressed as $\mu=q\mu_1+(1-q)\mu_2$. Defining a mean shift $\Delta\mu$ as $\Delta\mu=\mu_2-\mu_1$, we obtain

$$\mu_2=\mu+q\Delta\mu. \tag{4.5}$$

Allowing $p_1=p_2$ and applying the constraint that the variances of the two event classes are identical, yields

$$\frac{1}{p_1}=\frac{1/p-q(1-q)(\Delta\mu/\mu)^2}{1+q(1-q)(\Delta\mu/\mu)^2}. \tag{4.6}$$

With a choice of values for q and $\Delta\mu$, the remaining parameters can be calculated, including ΔT.

Both variations of the dual event class model are implemented in a Monte Carlo simulation in the following manner. The number of particles in an event is determined by sampling the N_{tracks} data distribution, approximated by a Gaussian distribution fit to the data. The p_T of each particle in an event is determined individually by sampling the appropriate $\Gamma(p_T,p,b)$ distribution fit to the semi-inclusive p_T data distribution, which yields $p=0.8$ and $b=2.46$ for 0–5 % centrality. The p_T of each particle is restricted to the p_T range of the measurement. With N_{tracks} and the p_T distribution determined, the M_{p_T} for a given number of events is calculated. The generated M_{p_T} distribution with $q=0$ for either model variation is found to be statistically consistent with the mixed event M_{p_T} distribution.

The data contain a fraction of background particles that did not originate from the collision vertex that effectively dilute the sensitivity to nonrandom fluctuations. To address this, a fraction of the particles in an event are randomly tagged as background particles, whose p_T distribution is then generated with a separate parametrization prior to calculating M_{p_T} for an event. The level of background contamination is estimated by processing HIJING [18] Au+Au events through a software chain that includes a detailed GEANT simulation [19] with the complete PHENIX detector geometry included, followed by a detailed simulation of the detector electronics response [12], whose output is then processed by track, cluster, and momentum reconstruction using the identical software and input parameters as is used for the data analysis. It is estimated that 11% of the tracks and 26% of the clusters are due to background particles, independent of centrality class over the centrality range of these measurements. The estimated p_T and e_T distributions for the background particles are well parametrized by exponential distributions. Again, the majority of the e_T background occurs at low e_T, so any correlated background would most likely contribute to the lower side of the M_{e_T} distribution.

To determine the sensitivity to fluctuations within the dual event class model, the fluctuation fraction q and the value of p_1 for model A and $\Delta\mu$ for model B are varied and the M_{p_T} distribution is generated at each step. A χ^2 test is then performed on the generated M_{p_T} distribution with respect to the mixed event data M_{p_T} distribution. For a given value of q, the χ^2 result increases as ΔT increases, which allows a fluctuation exclusion region to be defined for the single degree of freedom. The curves in Fig. 7 show the lower exclusion boundaries for the 0–5 % centrality M_{p_T} measurement at the 95% confidence level as a function of q and ΔT for both variations of the model. If the sensitivity is determined based upon the nonmixed data distribution, the lower exclusion boundary increases by less than 2 MeV for all values of q for either model. Also, for all values of q in either model, the estimated background contribution degrades the sensitivity estimates by $\Delta T = 3$ MeV for both models.

A recent model of event-by-event fluctuations where the temperature parameter $T = 1/b$ fluctuates with a standard deviation σ_T on an event-by-event basis [20] can be simply related to F_T:

$$\frac{\sigma_T^2}{\langle T\rangle^2} = \frac{2F_T}{p(\langle n\rangle - 1)}, \tag{4.7}$$

where $p = 0.8$ is the semi-inclusive parameter extracted from the present data. For the 0–5 % centrality class, the present measurement establishes a 95% confidence limit of 2.6×10^{-3} for $\sigma_T^2/\langle T\rangle^2$, or 5% for $\sigma_T/\langle T\rangle$.

V. CONCLUSIONS

The fluctuations in the M_{p_T} distributions for all centrality classes are consistent with the presence of no fluctuations in excess of the random expectation. The magnitude of F_T in all cases is positive, which may be due to the presence of Hanbury-Brown-Twiss correlations. The fluctuations in the M_{e_T} distributions do have a small nonstatistical component, much of which is attributable to the effects of merged clusters, the remainder of which are taken to indicate an upper limit on nonstatistical fluctuations in transverse energy. By defining a dual event class model, limits are set on the amount of M_{p_T} fluctuations that can be present in the angular aperture $|\eta| < 0.35$ and $\Delta\phi = 58.5°$ in $\sqrt{s_{NN}} = 130$ GeV Au+Au collisions. During the RHIC run of 2001, PHENIX has taken data for $\sqrt{s_{NN}} = 200$ GeV Au+Au collisions with about a factor of 4 increase in azimuthal angular acceptance for both the M_{p_T} and M_{e_T} analyses, which will allow the measurements to be extended toward more peripheral collisions.

ACKNOWLEDGMENTS

We thank the staff of the RHIC project, Collider-Accelerator, and Physics Departments at BNL and the staff of PHENIX participating institutions for their vital contributions. We acknowledge support from the Department of Energy and NSF (USA), Monbu-sho and STA (Japan), RAS, RMAE, and RMS (Russia), BMBF, DAAD, and AvH (Germany), FRN, NFR, and the Wallenberg Foundation (Sweden), MIST and NSERC (Canada), CNPq and FAPESP (Brazil), IN2P3/CNRS (France), DAE (India), KRF and KOSEF (Korea), and the U.S.-Israel Binational Science Foundation.

[1] H. Heiselberg, Phys. Rep. **351**, 161 (2001).
[2] S. Mrowczynski, Phys. Lett. B **314**, 118 (1993).
[3] M. Stephanov, K. Rajagopal, and E. Shuryak, Phys. Rev. Lett. **81**, 4816 (1998).
[4] A. Dumitru and R. Pisarski, Phys. Lett. B **504**, 282 (2001).
[5] H. Appelshauser *et al.*, Phys. Lett. B **459**, 679 (1999).
[6] S. V. Afanasiev *et al.*, Phys. Rev. Lett. **86**, 1965 (2001).
[7] D. P. Morrison *et al.*, PHENIX Collaboration, Nucl. Phys. **A638**, 565c (1998).
[8] K. Ikematsu *et al.*, Nucl. Instrum. Methods Phys. Res. A **411**, 238 (1998).
[9] C. Adler, A. Denisov, E. Garcia, M. Murray, H. Strobele, and S. White, Nucl. Instrum. Methods Phys. Res. A **461**, 337 (2001).
[10] K. Adcox *et al.*, PHENIX Collaboration, Phys. Rev. Lett. **86**, 3500 (2001).
[11] V. Riabov *et al.*, Nucl. Instrum. Methods Phys. Res. A **419**, 363 (1998).
[12] J. T. Mitchell *et al.*, Nucl. Instrum. Methods Phys. Res. A **482**, 491 (2002).
[13] G. David *et al.*, IEEE Trans. Nucl. Sci. **45**, 692, 705 (1998).
[14] K. Adcox *et al.*, PHENIX Collaboration, Phys. Rev. Lett. **87**, 052301 (2001).
[15] M. J. Tannenbaum, Phys. Lett. B **498**, 29 (2001).
[16] U. Wiedemann and U. Heinz, Phys. Rep. **319**, 145 (1999).
[17] M. Gazdzicki and S. Mrowczynski, Z. Phys. C **54**, 127 (1992).
[18] X-N. Wang and M. Gyulassy, Phys. Rev. D **44**, 3501 (1991).
[19] R. Brun and F. Carminati, CERN Program Library, Long Writeup W5013, 1994.
[20] R. Korus and S. Mrowczynski, Phys. Rev. C **64**, 054908 (2001).

Net Charge Fluctuations in Au + Au Interactions at $\sqrt{s_{NN}} = 130$ GeV

K. Adcox,[40] S. S. Adler,[3] N. N. Ajitanand,[27] Y. Akiba,[14] J. Alexander,[27] L. Aphecetche,[34] Y. Arai,[14] S. H. Aronson,[3] R. Averbeck,[28] T. C. Awes,[29] K. N. Barish,[5] P. D. Barnes,[19] J. Barrette,[21] B. Bassalleck,[25] S. Bathe,[22] V. Baublis,[30] A. Bazilevsky,[12,32] S. Belikov,[12,13] F. G. Bellaiche,[29] S. T. Belyaev,[16] M. J. Bennett,[19] Y. Berdnikov,[35] S. Botelho,[33] M. L. Brooks,[19] D. S. Brown,[26] N. Bruner,[25] D. Bucher,[22] H. Buesching,[22] V. Bumazhnov,[12] G. Bunce,[3,32] J. Burward-Hoy,[28] S. Butsyk,[28,30] T. A. Carey,[19] P. Chand,[2] J. Chang,[5] W. C. Chang,[1] L. L. Chavez,[25] S. Chernichenko,[12] C. Y. Chi,[8] J. Chiba,[14] M. Chiu,[8] R. K. Choudhury,[2] T. Christ,[28] T. Chujo,[3,39] M. S. Chung,[15,19] P. Chung,[27] V. Cianciolo,[29] B. A. Cole,[8] D. G. D'Enterria,[34] G. David,[3] H. Delagrange,[34] A. Denisov,[12] A. Deshpande,[32] E. J. Desmond,[3] O. Dietzsch,[33] B. V. Dinesh,[2] A. Drees,[28] A. Durum,[12] D. Dutta,[2] K. Ebisu,[24] Y. V. Efremenko,[29] K. El Chenawi,[40] H. En'yo,[17,31] S. Esumi,[39] L. Ewell,[3] T. Ferdousi,[5] D. E. Fields,[25] S. L. Fokin,[16] Z. Fraenkel,[42] A. Franz,[3] A. D. Frawley,[9] S.-Y. Fung,[5] S. Garpman,[20,*] T. K. Ghosh,[40] A. Glenn,[36] A. L. Godoi,[33] Y. Goto,[32] S. V. Greene,[40] M. Grosse Perdekamp,[32] S. K. Gupta,[2] W. Guryn,[3] H.-Å Gustafsson,[20] J. S. Haggerty,[3] H. Hamagaki,[7] A. G. Hansen,[19] H. Hara,[24] E. P. Hartouni,[18] R. Hayano,[38] N. Hayashi,[31] X. He,[10] T. K. Hemmick,[28] J. M. Heuser,[28] M. Hibino,[41] J. C. Hill,[13] D. S. Ho,[43] K. Homma,[11] B. Hong,[15] A. Hoover,[26] T. Ichihara,[31,32] K. Imai,[17,31] M. S. Ippolitov,[16] M. Ishihara,[31,32] B. V. Jacak,[28,32] W. Y. Jang,[15] J. Jia,[28] B. M. Johnson,[3] S. C. Johnson,[18,28] K. S. Joo,[23] S. Kametani,[41] J. H. Kang,[43] M. Kann,[30] S. S. Kapoor,[2] S. Kelly,[8] B. Khachaturov,[42] A. Khanzadeev,[30] J. Kikuchi,[41] D. J. Kim,[43] H. J. Kim,[43] S. Y. Kim,[43] Y. G. Kim,[43] W. W. Kinnison,[19] E. Kistenev,[3] A. Kiyomichi,[39] C. Klein-Boesing,[22] S. Klinksiek,[25] L. Kochenda,[30] V. Kochetkov,[12] D. Koehler,[25] T. Kohama,[11] D. Kotchetkov,[5] A. Kozlov,[42] P. J. Kroon,[3] K. Kurita,[31,32] M. J. Kweon,[15] Y. Kwon,[43] G. S. Kyle,[26] R. Lacey,[27] J. G. Lajoie,[13] J. Lauret,[27] A. Lebedev,[13,16] D. M. Lee,[19] M. J. Leitch,[19] X. H. Li,[5] Z. Li,[6,31] D. J. Lim,[43] M. X. Liu,[19] X. Liu,[6] Z. Liu,[6] C. F. Maguire,[40] J. Mahon,[3] Y. I. Makdisi,[3] V. I. Manko,[16] Y. Mao,[6,31] S. K. Mark,[21] S. Markacs,[8] G. Martinez,[34] M. D. Marx,[28] A. Masaike,[17] F. Matathias,[28] T. Matsumoto,[7,41] P. L. McGaughey,[19] E. Melnikov,[12] M. Merschmeyer,[22] F. Messer,[28] M. Messer,[3] Y. Miake,[39] T. E. Miller,[40] A. Milov,[42] S. Mioduszewski,[3,36] R. E. Mischke,[19] G. C. Mishra,[10] J. T. Mitchell,[3] A. K. Mohanty,[2] D. P. Morrison,[3] J. M. Moss,[19] F. Mühlbacher,[28] M. Muniruzzaman,[5] J. Murata,[31] S. Nagamiya,[14] Y. Nagasaka,[24] J. L. Nagle,[8] Y. Nakada,[17] B. K. Nandi,[5] J. Newby,[36] L. Nikkinen,[21] P. Nilsson,[20] S. Nishimura,[7] A. S. Nyanin,[16] J. Nystrand,[20] E. O'Brien,[3] C. A. Ogilvie,[13] H. Ohnishi,[3,11] I. D. Ojha,[4,40] M. Ono,[39] V. Onuchin,[12] A. Oskarsson,[20] L. Österman,[20] I. Otterlund,[20] K. Oyama,[7,38] L. Paffrath,[3,*] A. P. T. Palounek,[19] V. S. Pantuev,[28] V. Papavassiliou,[26] S. F. Pate,[26] T. Peitzmann,[22] A. N. Petridis,[13] C. Pinkenburg,[3,27] R. P. Pisani,[3] P. Pitukhin,[12] F. Plasil,[29] M. Pollack,[28,36] K. Pope,[36] M. L. Purschke,[3] I. Ravinovich,[42] K. F. Read,[29,36] K. Reygers,[22] V. Riabov,[30,35] Y. Riabov,[30] M. Rosati,[13] A. A. Rose,[40] S. S. Ryu,[43] N. Saito,[31,32] A. Sakaguchi,[11] T. Sakaguchi,[7,41] H. Sako,[39] T. Sakuma,[31,37] V. Samsonov,[30] T. C. Sangster,[18] R. Santo,[22] H. D. Sato,[17,31] S. Sato,[39] S. Sawada,[14] B. R. Schlei,[19] Y. Schutz,[34] V. Semenov,[12] R. Seto,[5] T. K. Shea,[3] I. Shein,[12] T.-A. Shibata,[31,37] K. Shigaki,[14] T. Shiina,[19] Y. H. Shin,[43] I. G. Sibiriak,[16] D. Silvermyr,[20] K. S. Sim,[15] J. Simon-Gillo,[19] C. P. Singh,[4] V. Singh,[4] M. Sivertz,[3] A. Soldatov,[12] R. A. Soltz,[18] S. Sorensen,[29,36] P. W. Stankus,[29] N. Starinsky,[21] P. Steinberg,[8] E. Stenlund,[20] A. Ster,[44] S. P. Stoll,[3] M. Sugioka,[31,37] T. Sugitate,[11] J. P. Sullivan,[19] Y. Sumi,[11] Z. Sun,[6] M. Suzuki,[39] E. M. Takagui,[33] A. Taketani,[31] M. Tamai,[41] K. H. Tanaka,[14] Y. Tanaka,[24] E. Taniguchi,[31,37] M. J. Tannenbaum,[3] J. Thomas,[28] J. H. Thomas,[18] T. L. Thomas,[25] W. Tian,[6,36] J. Tojo,[17,31] H. Torii,[17,31] R. S. Towell,[19] I. Tserruya,[42] H. Tsuruoka,[39] A. A. Tsvetkov,[16] S. K. Tuli,[4] H. Tydesjö,[20] N. Tyurin,[12] T. Ushiroda,[24] H. W. van Hecke,[19] C. Velissaris,[26] J. Velkovska,[28] M. Velkovsky,[28] A. A. Vinogradov,[16] M. A. Volkov,[16] A. Vorobyov,[30] E. Vznuzdaev,[30] H. Wang,[5] Y. Watanabe,[31,32] S. N. White,[3] C. Witzig,[3] F. K. Wohn,[13] C. L. Woody,[3] W. Xie,[5,42] K. Yagi,[39] S. Yokkaichi,[31] G. R. Young,[29] I. E. Yushmanov,[16] W. A. Zajc,[8] Z. Zhang,[28] and S. Zhou[6]

(PHENIX Collaboration)

[1]*Institute of Physics, Academia Sinica, Taipei 11529, Taiwan*
[2]*Bhabha Atomic Research Centre, Bombay 400 085 India*
[3]*Brookhaven National Laboratory, Upton, New York 11973-5000*
[4]*Department of Physics, Banaras Hindu University, Varanasi 221005, India*
[5]*University of California–Riverside, Riverside, California 92521*
[6]*China Institute of Atomic Energy (CIAE), Beijing, People's Republic of China*
[7]*Center for Nuclear Study, Graduate School of Science, University of Tokyo, 7-3-1 Hongo, Bunkyo, Tokyo 113-0033, Japan*

 0031-9007/02/89(8)/082301(6)$20.00 © 2002 The American Physical Society

[8]*Columbia University, New York, New York 10027 and Nevis Laboratories, Irvington, New York 10533*
[9]*Florida State University, Tallahassee, Florida 32306*
[10]*Georgia State University, Atlanta, Georgia 30303*
[11]*Hiroshima University, Kagamiyama, Higashi-Hiroshima, 739-8526, Japan*
[12]*Institute for High Energy Physics (IHEP), Protvino, Russia*
[13]*Iowa State University, Ames, Iowa 50011*
[14]*KEK, High Energy Accelerator Research Organization, Tsukuba-shi, Ibaraki-ken 305-0801, Japan*
[15]*Korea University, Seoul, 136-701 Korea*
[16]*Russian Research Center "Kurchatov Institute," Moscow, Russia*
[17]*Kyoto University, Kyoto 606, Japan*
[18]*Lawrence Livermore National Laboratory, Livermore, California 94550*
[19]*Los Alamos National Laboratory, Los Alamos, New Mexico 87545*
[20]*Department of Physics, Lund University, Box 118, SE-221 00 Lund, Sweden*
[21]*McGill University, Montreal, Quebec H3A 2T8, Canada*
[22]*Institut für Kernphysik, University of Münster, D-48149 Münster, Germany*
[23]*Myongji University, Yongin, Kyonggido 449-728, Korea*
[24]*Nagasaki Institute of Applied Science, Nagasaki-shi, Nagasaki 851-0193 Japan*
[25]*University of New Mexico, Albuquerque, New Mexico 87131*
[26]*New Mexico State University, Las Cruces, New Mexico 88003*
[27]*Chemistry Department, State University of New York–Stony Brook, Stony Brook, New York 11794*
[28]*Department of Physics and Astronomy, State University of New York–Stony Brook, Stony Brook, New York 11794*
[29]*Oak Ridge National Laboratory, Oak Ridge, Tennessee 37831*
[30]*PNPI, Petersburg Nuclear Physics Institute, Gatchina, Russia*
[31]*RIKEN (The Institute of Physical and Chemical Research), Wako, Saitama 351-0198, Japan*
[32]*RIKEN BNL Research Center, Brookhaven National Laboratory, Upton, New York 11973-5000*
[33]*Universidade de São Paulo, Instituto de Física, Caixa Postal 66318, São Paulo CEP05315-970, Brazil*
[34]*SUBATECH (Ecole des Mines de Nantes, IN2P3/CNRS, Universite de Nantes) BP 20722-44307, Nantes-cedex 3, France*
[35]*St. Petersburg State Technical University, St. Petersburg, Russia*
[36]*University of Tennessee, Knoxville, Tennessee 37996*
[37]*Department of Physics, Tokyo Institute of Technology, Tokyo, 152-8551 Japan*
[38]*University of Tokyo, Tokyo, Japan*
[39]*Institute of Physics, University of Tsukuba, Tsukuba, Ibaraki 305, Japan*
[40]*Vanderbilt University, Nashville, Tennessee 37235*
[41]*Waseda University, Advanced Research Institute for Science and Engineering, 17 Kikui-cho, Shinjuku-ku, Tokyo 162-0044, Japan*
[42]*Weizmann Institute, Rehovot 76100, Israel*
[43]*Yonsei University, IPAP, Seoul 120-749, Korea*
[44]*KFKI Research Institute for Particle and Nuclear Physics (RMKI), Budapest, Hungary*[†]

(Received 21 March 2002; published 5 August 2002)

Data from Au + Au interactions at $\sqrt{s_{NN}} = 130$ GeV, obtained with the PHENIX detector at the Relativistic Heavy-Ion Collider, are used to investigate local net charge fluctuations among particles produced near midrapidity. According to recent suggestions, such fluctuations may carry information from the quark-gluon plasma. This analysis shows that the fluctuations are dominated by a stochastic distribution of particles, but are also sensitive to other effects, like global charge conservation and resonance decays.

DOI: 10.1103/PhysRevLett.89.082301 PACS numbers: 25.75.Dw

The PHENIX detector [1] at the Relativistic Heavy-Ion Collider (RHIC) is a versatile detector designed to study the properties of nuclear matter at extreme temperatures and energy densities, obtained in central heavy-ion collisions at ultrarelativistic energies. A central goal of these studies is to collect evidence for the existence of the quark-gluon plasma (QGP) characterized by deconfined quarks and gluons.

There are several proposed ways to experimentally verify the existence of a QGP [2]. A general problem is that many of these signals also can be produced in a hadronic scenario, albeit special conditions of highly compressed matter have to prevail. Furthermore, it is not straightforward to determine how the various plasma signals are distorted when the deconfined matter transforms back to hadronic matter. Recent theoretical investigations [3–5] predict a drastic decrease of the event-by-event fluctuations of the net charge in local phase-space regions as a signature of the plasma state. These fluctuations are not related to the transition itself, but rather with the charge distribution in the primordial plasma state. The basic idea is that each of the charge carriers in the plasma carries less charge than

the charge carriers in ordinary hadronic matter. The charge will thus be more evenly distributed in a plasma. The main concern of the theoretical discussions is how and why the original distribution survives the transition back to ordinary matter [6,7]. Predictions, for a rapidity coverage $\Delta y \geq 1$, range up to an 80% reduction in the magnitude of the fluctuations, as measured by the variance of the net charge.

Decays of hadronic resonances influence the net charge fluctuations, whether or not deconfinement is reached. In the absence of a QGP, deviations from statistical behavior can be used to determine the abundance of, e.g., ρ and ω mesons [8]. In a hadron gas resonances are expected to decrease the fluctuations by about 25%. Globally, fluctuations will be further reduced, since charge is a conserved quantity. Although multiplicity fluctuations have been studied extensively in both hadronic and nuclear processes [9], net charge fluctuations have only recently been addressed experimentally [10,11].

In this Letter we report results from an analysis of net charge fluctuations for particles produced in Au + Au interactions at $\sqrt{s_{NN}} = 130$ GeV. The fluctuations are studied in the variables $R = n_+/n_-$, the ratio between positive and negative particles, and $Q = n_+ - n_-$, the net charge [3]. The advantages and disadvantages of these variables will also be discussed.

Information from one of the PHENIX central tracking arms (west) is used in this analysis, where events are required to have a well-defined vertex close to the center of the apparatus ($|Z| < 17$ cm), as defined by the two beam-beam counters (BBC). These cover the pseudorapidity region $3.0 < |\eta| < 3.9$. Together with the information from the two zero-degree calorimeters (ZDC), placed farther away (18 m), the BBC information is used for off-line centrality selection [12]. A total of about 5×10^5 minimum bias events has been analyzed. The PHENIX west arm spectrometer has an acceptance of 0.7 units of pseudorapidity ($-0.35 < \eta < 0.35$) and $\pi/2$ radians in azimuth φ. Charged-particle trajectories are recorded in a multiwire focusing drift chamber (DC) [13]. The combination of reconstructed DC tracks [14] with matching hits in the innermost pad-chamber plane defines the sign of the charge of the particle and also provides a high resolution measurement of the transverse momentum p_T of tracks originating from the collision vertex. Tracks with a reconstructed p_T less than 0.2 GeV/c have been excluded from the analysis due to a low reconstruction efficiency and large contributions from background sources, as revealed by simulations. No upper p_T cut has been applied.

The tracking efficiency and the charge assignment have been studied using GEANT [15] simulations. Of particular importance in this context is a realistic description of the drift chamber response, which is extracted from measured data, parametrized, and applied empirically in the simulation.

RQMD [16] simulations are used to study the detection efficiency, and the fraction of reconstructed particles that preserve their charge, as well as to evaluate the results of the analysis. The charge fluctuations in RQMD are consistent with calculations based on other hadronic models like URQMD and HIJING [3]. The overall efficiency for detecting a charged particle within the acceptance is found to be around 80% for both positive and negative particles. Correlated inefficiencies due to the limited two-track resolution and detector inhomogeneities are small enough ($<1\%$) to be safely neglected for this analysis.

Depending on p_T, between 70% and 85% of the reconstructed tracks are in one-to-one correspondence with a primarily produced particle. The remaining tracks come from secondary interactions in the detector material and from decays, where the original charge information is lost. The composition of these tracks has been studied in detail through RQMD and GEANT. The different sources are weak decays (e.g., K^0_S, Λ, $\overline{\Lambda}$ decays) (28%), γ conversion (16%), $\eta \to \pi^+\pi^-$ (6%). The remaining 50% are mainly from interactions in the detector material. Instead of trying to correct the data for effects from individual sources, we have directly compared the data with the outcome of the simulations. The predictions of RQMD have been studied both with and without experimental distortions, in order to quantify the net effect. It turns out that the experimental bias pushes the value of $\nu(Q)$ closer to the stochastic limit, as will be further discussed below.

In each event the numbers of positively charged particles n_+, negatively charged particles n_-, and their sum n_{ch} are recorded. In a stochastic scenario, with a fixed number of charged particles within the acceptance, where each particle is assigned a random charge ($+1$ or -1 with equal probability), the variance of the net charge, Q, is

$$V(Q) \equiv \langle Q^2 \rangle - \langle Q \rangle^2 = n_{ch}\,. \tag{1}$$

The normalized variance in Q is

$$\nu(Q) \equiv \frac{V(Q)}{n_{ch}} = 1\,. \tag{2}$$

For the charge ratio, in the stochastic scenario, $V(R) \equiv \langle R^2 \rangle - \langle R \rangle^2$ will approach the value $4/n_{ch}$ as n_{ch} increases and $\nu(R) \equiv n_{ch} \cdot V(R)$ asymptotically approaches 4. When an asymmetry between positive and negative particles is introduced, $\nu(R)$ is drastically affected, whereas the effect on $\nu(Q)$ is marginal. If we write the probability p_+ that a given particle has positive charge in the form $p_+ = \frac{1}{2}(1 + \varepsilon)$, and subsequently $p_- = \frac{1}{2}(1 - \varepsilon)$, we find $\nu(Q) = 1 - \varepsilon^2$, while the asymptotic value of $\nu(R)$ is $4 + 16\varepsilon + O(\varepsilon^2)$. Detector or reconstruction inefficiencies, which randomly remove particles independent of charge, do not influence those results in the stochastic scenario. The variance, $V(R)$, can be calculated from

$$\langle R\rangle = \frac{1}{A}\sum_{i=1}^{n_{ch}-1}\frac{n_{ch}-i}{i}\binom{n_{ch}}{i}p_{+}^{n_{ch}-i}p_{-}^{i};$$
$$\langle R^2\rangle = \frac{1}{A}\sum_{i=1}^{n_{ch}-1}\left(\frac{n_{ch}-i}{i}\right)^2\binom{n_{ch}}{i}p_{+}^{n_{ch}-i}p_{-}^{i}, \quad (3)$$

where $A = 1 - p_{+}^{n_{ch}} - p_{-}^{n_{ch}}$ is the new normalization due to discarding events with n_+ or n_- equal to zero. The variance of R, even for a purely stochastic charge distribution, depends on multiplicity and on the fractions of positive and negative particles.

There are other proposed measures of net charge fluctuations. Most of these are modifications of R or Q, and deal with corrections for large charge asymmetries (i.e., $\varepsilon \neq 0$) and large acceptances. Since in our case ε is close to zero, and the fraction of observed to all produced particles in an event is small, we can safely neglect those complications [17].

The data show a small excess of positive particles, growing proportionally with n_{ch}, in qualitative agreement with calculations using RQMD and GEANT. A part of this excess comes from the intrinsic isospin asymmetry and a part from secondary interactions in the detector and surrounding material.

In Fig. 1(a), $v(R)$ and $v(Q)$ are displayed as functions of n_{ch} and $v(Q)$ is multiplied by a factor of 4 to compensate for the asymptotical difference between $v(R)$ and $v(Q)$. Both $v(Q)$ and $v(R)$ are well described by the results obtained from the stochastic scenario.

Since $v(Q)$ is independent of n_{ch} one expects $v(Q)$ to be close to unity also in representations where other centrality measures are used. On the other hand, since $v(R)$ depends on multiplicity, it will have a complicated behavior as a function of centrality, making it difficult to draw any further conclusions. We will thus focus on $v(Q)$ for the rest of this analysis.

In Fig. 1(b), $v(Q)$ is displayed as a function of centrality based on the ZDC/BBC information. The full event sample, corresponding to 92% of the inelastic cross section [12], is divided into 20 centrality classes, where each class corresponds to 5% of the events. Class 20 represents the most central events. With the increased resolution on the y axis in Fig. 1(b), it is evident that $v(Q)$ is consistently below unity and deviates from stochastic behavior. The value is, however, far above the most optimistic QGP predictions $v(Q) \sim 0.2$ [3], although one should keep in mind that our coverage in rapidity is at the limit for these predictions and that we have only partial coverage in azimuth.

There may be other explanations for deviations from stochastic behavior than the one offered by the quark-gluon plasma. These include global charge conservation and neutral resonances decaying into correlated pairs of one positive and one negative particle. Both of these effects will decrease the fluctuations, and the decrease will grow in proportion to the experimental acceptance. In a stochastic scenario, taking global charge conservation into account, the normalized variance $v(Q)$ becomes $(1 - p)$, where p is the fraction of observed charged particles among all charged particles in the event. Eventually, if all charged particles are detected, $v(Q)$ will become 0.

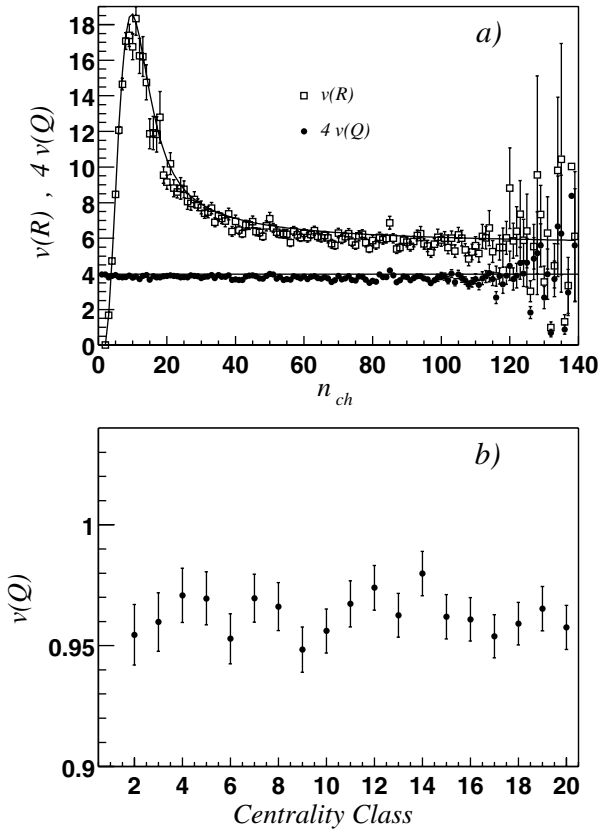

FIG. 1. (a) The normalized variances $v(Q)$ and $v(R)$ as functions of n_{ch}, together with curves for stochastic behavior. (b) The normalized variance $v(Q)$ for different centrality classes, as described in the text.

Experimentally we can change the fraction p of particles within the acceptance by using different regions of the PHENIX west arm. In Fig. 2(a), $v(Q)$, for the 10% most central events, is displayed as a function of $\Delta\varphi_d$, i.e., the chosen azimuthal interval of the spectrometer. For comparison, the results from RQMD processed through GEANT are shown. The data and the simulation show a similar trend. Note that the data points are correlated since the data in one bin is a subset of the data in the next. The error band indicates the total statistical error in each data point. The error bars represent the uncorrelated part of this statistical error. For RQMD, only the total statistical error is given. The solid line corresponds to the $(1 - p)$ dependence discussed above. The linear relationship between p and $\Delta\varphi_d$ is estimated from the phase-space distribution of particles in RQMD, including effects from reconstruction efficiency and background tracks. For larger angles, both data and the RQMD results lie consistently below the line,

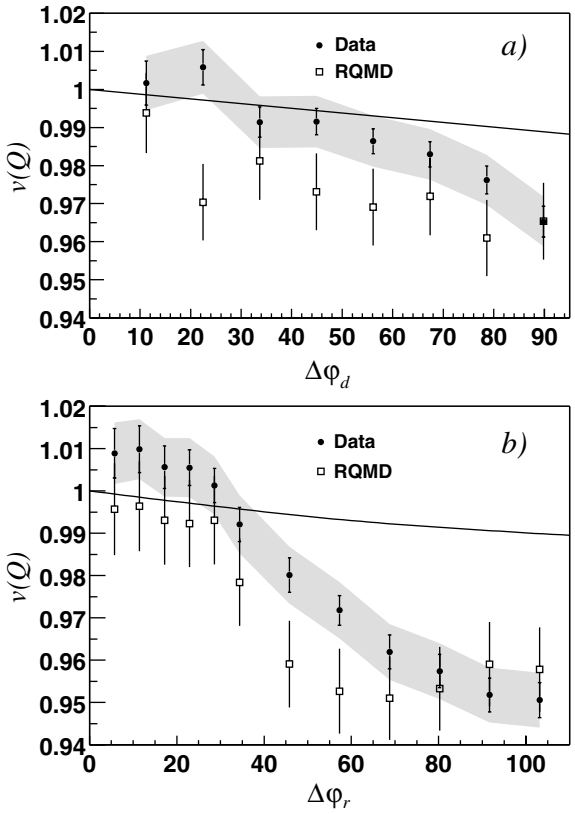

FIG. 2. $\nu(Q)$ for the 10% most central events in data and RQMD, as a function of the azimuthal coverage. For data, the error band shows the total statistical error, whereas the error bars indicate the uncorrelated part. The solid line (curve) shows the expected reduction in $\nu(Q)$ in the stochastic scenario when global charge conservation is taken into account. Azimuthal angle (in degrees) defined (a) as detector coverage, and (b) as reconstructed at the interaction vertex.

which indicates that effects from resonance decays are important.

Because of the influence of the magnetic field the positive and negative particles will have different azimuthal acceptance. On the average a charged particle (surviving the experimental cuts) will be deflected 19° in the magnetic field. The $\Delta\varphi_d$ study in Fig. 2(a) thus selects partly nonoverlapping regions of phase space for positive and negative particles. A remedy for this is to use the reconstructed φ angle for each particle φ_r, i.e., the azimuthal direction of the particle at the primary vertex, before it is deflected by the magnetic field. By choosing the azimuthal interval $\Delta\varphi_r$ symmetrically around the center of the acceptance, a better phase-space overlap is achieved for small azimuthal intervals. In Fig. 2(b), $\nu(Q)$, for the 10% most central events, is displayed as a function of $\Delta\varphi_r$. The $(1 - p)$ dependence, which is no longer linear, is given by the solid curve. Again data and the RQMD results show a similar trend, but the deviations from the curve are larger in this representation, indicating that an overlap in phase space is of importance. The errors are treated as in Fig. 2(a).

The effects of the detector inefficiency and background tracks not assigned the correct charge have been investigated in a Monte Carlo simulation. The reconstruction efficiency and the amount of background have been determined from the RQMD and GEANT simulations discussed earlier. Both the inefficiency and the background contribution have the net effect of diluting the signal and pushing the value of $\nu(Q)$ closer to 1. The dilution due to these effects can be treated as an experimental systematic error, estimated from the simulations, setting a lower limit on $\nu(Q)$. For the net charge fluctuations in the region $-0.35 < \eta < 0.35$, $p_T > 0.2$ GeV/c, and $\Delta\varphi = \pi/2$,

$$\nu(Q) = 0.965 \pm 0.007(\text{stat}) - 0.019(\text{syst}) \qquad (4)$$

is obtained for the 10% most central events. Assuming a linear behavior, an extrapolation of this value to full azimuthal coverage gives a value of $\nu(Q)$ in the range 0.78–0.86, in qualitative agreement with calculations from a hadronic gas.

Our findings are in agreement with the preliminary conclusions of NA49 [10] and STAR [11] that no indication of decreased fluctuations due to quark-gluon plasma formation is observed. STAR also attributes the deviations from a stochastic scenario to be consistent with resonance correlations.

To summarize, we have shown that the data behave in an almost stochastic manner. There are also clear indications that effects from hadronic decays are seen; the data are in good agreement with RQMD calculations, which includes the effects of global charge conservations as well as neutral hadronic resonance decays. Furthermore, the data show no centrality dependence, which is in contradiction with the expectations from a quark-gluon plasma scenario. We have clearly demonstrated that the fluctuations of the charge ratio $\nu(R)$ and of the net charge $\nu(Q)$ are well understood in a stochastic model. The R variable [3] unnecessarily complicates the evaluation of the fluctuations, and the intrinsic decrease of $\nu(R)$, as a function of centrality, can be mistaken for a "plasma fingerprint."

The measured value of $\nu(Q) = 0.965$ is far from the value predicted for a plasma. Even extrapolating the linear trend seen in the data in Fig. 2(a) to full azimuthal coverage renders values of the fluctuations, which are far above the proposed values. With the caveat of our limited acceptance in rapidity, these results clearly indicate either the absence of a plasma or a proposed signal that does not survive the transition back to hadronic matter.

We thank the staff of the Collider-Accelerator and Physics Departments at BNL for their vital contributions. We acknowledge support from the Department of Energy and NSF (U.S.A.), MEXT and JSPS (Japan), RAS, RMAE, and RMS (Russia), BMBF, DAAD, and AvH (Germany), VR and KAW (Sweden), MIST and NSERC (Canada),

CNPq and FAPESP (Brazil), IN2P3/CNRS (France), DAE and DST (India), KRF and CHEP (Korea), the U.S. CRDF for the FSU, and the U.S.-Israel BSF.

*Deceased.

†Not a participating Institution.

[1] PHENIX Collaboration, D. P. Morrison *et al.*, Nucl. Phys. **A638**, 565c (1998).
[2] For example, J.-P. Blaizot, Nucl. Phys. **A661**, 3c (1999).
[3] S. Jeon and V. Koch, Phys. Rev. Lett. **85**, 2076 (2000); M. Bleicher, S. Jeon, and V. Koch, Phys. Rev. C **62**, 061902(R) (2000).
[4] M. Asakawa, U. Heinz, and B. Müller, Phys. Rev. Lett. **85**, 2072 (2000).
[5] H. Heiselberg and A. D. Jackson, Phys. Rev. C **63**, 064904 (2001).
[6] E. V. Shuryak and M. A. Stephanov, Phys. Rev. C **63**, 064903 (2001).
[7] K. Fialkowski and R. Wit, Europhys. Lett. **55**, 184 (2001).
[8] S. Jeon and V. Koch, Phys. Rev. Lett. **83**, 5435 (1999).
[9] For example, E. A. De Wolf, I. M. Dremin, and W. Kittel, Phys. Rep. **270**, 1 (1996).
[10] NA49 Collaboration, S. V. Afanasiev *et al.*, Nucl. Phys. **A698**, 104c (2002).
[11] STAR Collaboration, J. G. Reid *et al.*, Nucl. Phys. **A698**, 611c (2002).
[12] PHENIX Collaboration, K. Adcox *et al.*, Phys. Rev. Lett. **86**, 3500 (2001).
[13] V. G. Riabov, Nucl Instrum. Methods Phys Res., Sect. A **419**, 363 (1998).
[14] J. T. Mitchell *et al.*, Nucl. Instrum. Methods Phys. Res., Sect. A **482**, 491 (2002).
[15] GEANT 3.21, CERN program library, 1993.
[16] H. Sorge, Phys. Rev. C **52**, 3291 (1995).
[17] S. Mrowczynski, nucl-th/0112007 (to be published); private communication.

Measurement of Single Electrons and Implications for Charm Production in Au + Au Collisions at $\sqrt{s_{NN}} = 130$ GeV

K. Adcox,[40] S. S. Adler,[3] N. N. Ajitanand,[27] Y. Akiba,[14] J. Alexander,[27] L. Aphecetche,[34] Y. Arai,[14] S. H. Aronson,[3] R. Averbeck,[28] T. C. Awes,[29] K. N. Barish,[5] P. D. Barnes,[19] J. Barrette,[21] B. Bassalleck,[25] S. Bathe,[22] V. Baublis,[30] A. Bazilevsky,[12,32] S. Belikov,[12,13] F. G. Bellaiche,[29] S. T. Belyaev,[16] M. J. Bennett,[19] Y. Berdnikov,[35] S. Botelho,[33] M. L. Brooks,[19] D. S. Brown,[26] N. Bruner,[25] D. Bucher,[22] H. Buesching,[22] V. Bumazhnov,[12] G. Bunce,[3,32] J. Burward-Hoy,[28] S. Butsyk,[28,30] T. A. Carey,[19] P. Chand,[2] J. Chang,[5] W. C. Chang,[1] L. L. Chavez,[25] S. Chernichenko,[12] C. Y. Chi,[8] J. Chiba,[14] M. Chiu,[8] R. K. Choudhury,[2] T. Christ,[28] T. Chujo,[3,39] M. S. Chung,[15,19] P. Chung,[27] V. Cianciolo,[29] B. A. Cole,[8] D. G. D'Enterria,[34] G. David,[3] H. Delagrange,[34] A. Denisov,[12] A. Deshpande,[32] E. J. Desmond,[3] O. Dietzsch,[33] B. V. Dinesh,[2] A. Drees,[28] A. Durum,[12] D. Dutta,[2] K. Ebisu,[24] Y. V. Efremenko,[29] K. El Chenawi,[40] H. En'yo,[17,31] S. Esumi,[39] L. Ewell,[3] T. Ferdousi,[5] D. E. Fields,[25] S. L. Fokin,[16] Z. Fraenkel,[42] A. Franz,[3] A. D. Frawley,[9] S.-Y. Fung,[5] S. Garpman,[20,*] T. K. Ghosh,[40] A. Glenn,[36] A. L. Godoi,[33] Y. Goto,[32] S. V. Greene,[40] M. Grosse Perdekamp,[32] S. K. Gupta,[2] W. Guryn,[3] H.-Å. Gustafsson,[20] T. Hachiya,[11] J. S. Haggerty,[3] H. Hamagaki,[7] A. G. Hansen,[19] H. Hara,[24] E. P. Hartouni,[18] R. Hayano,[38] N. Hayashi,[31] X. He,[10] T. K. Hemmick,[28] J. M. Heuser,[28] M. Hibino,[41] J. C. Hill,[13] D. S. Ho,[43] K. Homma,[11] B. Hong,[15] A. Hoover,[26] T. Ichihara,[31,32] K. Imai,[17,31] M. S. Ippolitov,[16] M. Ishihara,[31,32] B. V. Jacak,[28,32] W. Y. Jang,[15] J. Jia,[28] B. M. Johnson,[3] S. C. Johnson,[18,28] K. S. Joo,[23] S. Kametani,[41] J. H. Kang,[43] M. Kann,[30] S. S. Kapoor,[2] S. Kelly,[8] B. Khachaturov,[42] A. Khanzadeev,[30] J. Kikuchi,[41] D. J. Kim,[43] H. J. Kim,[43] S. Y. Kim,[43] Y. G. Kim,[43] W. W. Kinnison,[19] E. Kistenev,[3] A. Kiyomichi,[39] C. Klein-Boesing,[22] S. Klinksiek,[25] L. Kochenda,[30] V. Kochetkov,[12] D. Koehler,[25] T. Kohama,[11] D. Kotchetkov,[5] A. Kozlov,[42] P. J. Kroon,[3] K. Kurita,[31,32] M. J. Kweon,[15] Y. Kwon,[43] G. S. Kyle,[26] R. Lacey,[27] J. G. Lajoie,[13] J. Lauret,[27] A. Lebedev,[13,16] D. M. Lee,[19] M. J. Leitch,[19] X. H. Li,[5] Z. Li,[6,31] D. J. Lim,[43] M. X. Liu,[19] X. Liu,[6] Z. Liu,[6] C. F. Maguire,[40] J. Mahon,[3] Y. I. Makdisi,[3] V. I. Manko,[16] Y. Mao,[6,31] S. K. Mark,[21] S. Markacs,[8] G. Martinez,[34] M. D. Marx,[28] A. Masaike,[17] F. Matathias,[28] T. Matsumoto,[7,41] P. L. McGaughey,[19] E. Melnikov,[12] M. Merschmeyer,[22] F. Messer,[28] M. Messer,[3] Y. Miake,[39] T. E. Miller,[40] A. Milov,[42] S. Mioduszewski,[3,36] R. E. Mischke,[19] G. C. Mishra,[10] J. T. Mitchell,[3] A. K. Mohanty,[2] D. P. Morrison,[3] J. M. Moss,[19] F. Mühlbacher,[28] M. Muniruzzaman,[5] J. Murata,[31] S. Nagamiya,[14] Y. Nagasaka,[24] J. L. Nagle,[8] Y. Nakada,[17] B. K. Nandi,[5] J. Newby,[36] L. Nikkinen,[21] P. Nilsson,[20] S. Nishimura,[7] A. S. Nyanin,[16] J. Nystrand,[20] E. O'Brien,[3] C. A. Ogilvie,[13] H. Ohnishi,[3,11] I. D. Ojha,[4,40] M. Ono,[39] V. Onuchin,[12] A. Oskarsson,[20] L. Österman,[20] I. Otterlund,[20] K. Oyama,[7,38] L. Paffrath,[3,*] A. P. T. Palounek,[19] V. S. Pantuev,[28] V. Papavassiliou,[26] S. F. Pate,[26] T. Peitzmann,[22] A. N. Petridis,[13] C. Pinkenburg,[3,27] R. P. Pisani,[3] P. Pitukhin,[12] F. Plasil,[29] M. Pollack,[28,36] K. Pope,[36] M. L. Purschke,[3] I. Ravinovich,[42] K. F. Read,[29,36] K. Reygers,[22] V. Riabov,[30,35] Y. Riabov,[30] M. Rosati,[13] A. A. Rose,[40] S. S. Ryu,[43] N. Saito,[31,32] A. Sakaguchi,[11] T. Sakaguchi,[7,41] H. Sako,[39] T. Sakuma,[31,37] V. Samsonov,[30] T. C. Sangster,[18] R. Santo,[22] H. D. Sato,[17,31] S. Sato,[39] S. Sawada,[14] B. R. Schlei,[19] Y. Schutz,[34] V. Semenov,[12] R. Seto,[5] T. K. Shea,[3] I. Shein,[12] T.-A. Shibata,[31,37] K. Shigaki,[14] T. Shiina,[19] Y. H. Shin,[43] I. G. Sibiriak,[16] D. Silvermyr,[20] K. S. Sim,[15] J. Simon-Gillo,[19] C. P. Singh,[4] V. Singh,[4] M. Sivertz,[3] A. Soldatov,[12] R. A. Soltz,[18] S. Sorensen,[29,36] P. W. Stankus,[29] N. Starinsky,[21] P. Steinberg,[8] E. Stenlund,[20] A. Ster,[44] S. P. Stoll,[3] M. Sugioka,[31,37] T. Sugitate,[11] J. P. Sullivan,[19] Y. Sumi,[11] Z. Sun,[6] M. Suzuki,[39] E. M. Takagui,[33] A. Taketani,[31] M. Tamai,[41] K. H. Tanaka,[14] Y. Tanaka,[24] E. Taniguchi,[31,37] M. J. Tannenbaum,[3] J. Thomas,[28] J. H. Thomas,[18] T. L. Thomas,[25] W. Tian,[6,36] J. Tojo,[17,31] H. Torii,[17,31] R. S. Towell,[19] I. Tserruya,[42] H. Tsuruoka,[39] A. A. Tsvetkov,[16] S. K. Tuli,[4] H. Tydesjö,[20] N. Tyurin,[12] T. Ushiroda,[24] H. W. van Hecke,[19] C. Velissaris,[26] J. Velkovska,[28] M. Velkovsky,[28] A. A. Vinogradov,[16] M. A. Volkov,[16] A. Vorobyov,[30] E. Vznuzdaev,[30] H. Wang,[5] Y. Watanabe,[31,32] S. N. White,[3] C. Witzig,[3] F. K. Wohn,[13] C. L. Woody,[3] W. Xie,[5,42] K. Yagi,[39] S. Yokkaichi,[31] G. R. Young,[29] I. E. Yushmanov,[16] W. A. Zajc,[8] Z. Zhang,[28] and S. Zhou[6]

(PHENIX Collaboration)

[1]*Institute of Physics, Academia Sinica, Taipei 11529, Taiwan*
[2]*Bhabha Atomic Research Centre, Bombay 400 085, India*
[3]*Brookhaven National Laboratory, Upton, New York 11973-5000*
[4]*Department of Physics, Banaras Hindu University, Varanasi 221005, India*
[5]*University of California–Riverside, Riverside, California 92521*
[6]*China Institute of Atomic Energy (CIAE), Beijing, People's Republic of China*
[7]*Center for Nuclear Study, Graduate School of Science, University of Tokyo, 7-3-1 Hongo, Bunkyo, Tokyo 113-0033, Japan*

 0031-9007/02/88(19)/192303(6)$20.00 © 2002 The American Physical Society

[8]*Columbia University, New York, New York 10027 and Nevis Laboratories, Irvington, New York 10533*
[9]*Florida State University, Tallahassee, Florida 32306*
[10]*Georgia State University, Atlanta, Georgia 30303*
[11]*Hiroshima University, Kagamiyama, Higashi-Hiroshima 739-8526, Japan*
[12]*Institute for High Energy Physics (IHEP), Protvino, Russia*
[13]*Iowa State University, Ames, Iowa 50011*
[14]*KEK, High Energy Accelerator Research Organization, Tsukuba-shi, Ibaraki-ken 305-0801, Japan*
[15]*Korea University, Seoul, 136-701, Korea*
[16]*Russian Research Center "Kurchatov Institute," Moscow, Russia*
[17]*Kyoto University, Kyoto 606, Japan*
[18]*Lawrence Livermore National Laboratory, Livermore, California 94550*
[19]*Los Alamos National Laboratory, Los Alamos, New Mexico 87545*
[20]*Department of Physics, Lund University, Box 118, SE-221 00 Lund, Sweden*
[21]*McGill University, Montreal, Quebec, Canada H3A 2T8*
[22]*Institut für Kernphysik, University of Münster, D-48149 Münster, Germany*
[23]*Myongji University, Yongin, Kyonggido 449-728, Korea*
[24]*Nagasaki Institute of Applied Science, Nagasaki-shi, Nagasaki 851-0193, Japan*
[25]*University of New Mexico, Albuquerque, New Mexico 87131*
[26]*New Mexico State University, Las Cruces, New Mexico 88003*
[27]*Chemistry Department, State University of New York–Stony Brook, Stony Brook, New York 11794*
[28]*Department of Physics and Astronomy, State University of New York–Stony Brook, Stony Brook, New York 11794*
[29]*Oak Ridge National Laboratory, Oak Ridge, Tennessee 37831*
[30]*PNPI, Petersburg Nuclear Physics Institute, Gatchina, Russia*
[31]*RIKEN (The Institute of Physical and Chemical Research), Wako, Saitama 351-0198, Japan*
[32]*RIKEN BNL Research Center, Brookhaven National Laboratory, Upton, New York 11973-5000*
[33]*Universidade de São Paulo, Instituto de Física, Caixa Postal 66318, São Paulo CEP05315-970, Brazil*
[34]*SUBATECH (Ecole des Mines de Nantes, INP3/CNRS, Universite de Nantes), BP 20722-44307, Nantes-Cedex 3, France*
[35]*St. Petersburg State Technical University, St. Petersburg, Russia*
[36]*University of Tennessee, Knoxville, Tennessee 37996*
[37]*Department of Physics, Tokyo Institute of Technology, Tokyo, 152-8551, Japan*
[38]*University of Tokyo, Tokyo, Japan*
[39]*Institute of Physics, University of Tsukuba, Tsukuba, Ibaraki 305, Japan*
[40]*Vanderbilt University, Nashville, Tennessee 37235*
[41]*Waseda University, Advanced Research Institute for Science and Engineering, 17 Kikui-cho, Shinjuku-ku, Tokyo 162-0044, Japan*
[42]*Weizmann Institute, Rehovot 76100, Israel*
[43]*Yonsei University, IPAP, Seoul 120-749, Korea*
[44]*KFKI Research Institute for Particle and Nuclear Physics (RMKI), Budapest, Hungary*[†]

(Received 5 February 2002; published 30 April 2002)

Transverse momentum spectra of electrons from Au + Au collisions at $\sqrt{s_{NN}} = 130$ GeV have been measured at midrapidity by the PHENIX experiment at the Relativistic Heavy Ion Collider. The spectra show an excess above the background from photon conversions and light hadron decays. The electron signal is consistent with that expected from semileptonic decays of charm. The yield of the electron signal dN_e/dy for $p_T > 0.8$ GeV/c is 0.025 ± 0.004(stat) ± 0.010(syst) in central collisions, and the corresponding charm cross section is 380 ± 60(stat) ± 200(syst) μb per binary nucleon-nucleon collision.

DOI: 10.1103/PhysRevLett.88.192303 PACS numbers: 25.75.Dw

In this Letter, we report the first measurement of single electron spectra, $(e^+ + e^-)/2$, in Au + Au collisions at $\sqrt{s_{NN}} = 130$ GeV at the Relativistic Heavy Ion Collider (RHIC). The measurement of single leptons at high transverse momentum ($p_T \gtrsim 1$ GeV/c) is a useful way to study heavy-quark production, an important probe of hot and dense matter created in high energy heavy ion collisions. Charm production is sensitive to the initial state gluon density [1,2]. Nuclear and medium effects, such as shadowing and charm quark energy loss [3,4], can be studied by comparison of charm production in AA, pA, and pp collisions. Measurement of charm is important for understanding J/ψ suppression (a proposed signal of the deconfinement phase transition [5,6]) and the dilepton mass distribution in $1 < M_{l^+l^-} < 3$ GeV, where lepton pairs from charm make significant contributions [7]. In pp collisions at the CERN Intersecting Storage Rings (ISR) ($\sqrt{s} = 30$–63 GeV), production of single electrons was observed ($e/\pi \sim 10^{-4}$) for $p_T > 1$ GeV/c [8–11], and interpreted as evidence of open charm production [12]. In pp collisions at RHIC energies, the signal level is expected to be higher, since charm production increases with $\sqrt{s_{NN}}$ faster than pion production. We recently observed suppression of high p_T pion production in Au + Au collisions at

RHIC relative to binary nucleon-nucleon (NN) collision scaling [13]. If charm production scales with NN collisions, as expected in the absence of nuclear effects, the e/π ratio will be even higher in Au + Au collisions at RHIC.

Data used for this analysis were recorded by the PHENIX west-arm spectrometer [14] ($\Delta\phi = 90°$ in azimuth, $|\eta| < 0.35$ in pseudorapidity), which consisted of a drift chamber (DC), a layer of pad chambers (PC1), a ring imaging Čerenkov detector (RICH), and a lead-scintillator electromagnetic calorimeter (EMCAL). The trigger was provided by beam-beam counters (BBC) and zero-degree calorimeters (ZDC). ZDC and BBC signals were combined to select centrality: central (0%–10%), peripheral (60%–80%), and minimum bias (0%–92%) [15].

The analysis uses $1.23M$ minimum bias events with vertex position $|z| < 30$ cm. Charged particle tracks are reconstructed by the DC and the PC1 with a momentum resolution $\delta p/p \simeq 0.6\% \oplus 3.6\%\ p\ (\mathrm{GeV}/c)$. Tracks are confirmed by a matching hit in the EMCAL, which measures the energy E deposited with a resolution of $8.2\%/\sqrt{E(\mathrm{GeV})} \oplus 1.9\%$ for test beam electrons. Electron identification is performed using the RICH and the EMCAL [14]. The RICH is filled with 1 atm CO_2 and detects on average 10.8 photoelectrons per electron track, while a pion with $p < 4.7\ \mathrm{GeV}/c$ produces no signal. It is required that at least three RICH hits are associated with the track and that their hit pattern is consistent with that of an electron track. After these cuts, a clear electron signal is observed as a narrow peak centered at $E/p = 1.0$. We select tracks in the peak as electron candidates. The E/p cut reduces hadron background and removes conversion electrons created far from the vertex. A hadron deposits only a fraction of its energy in the EMCAL, and the momentum of an off-vertex conversion electron is reconstructed incorrectly. The remaining background, about 10% of the electron candidates, is caused by accidental association of RICH hits with hadron tracks. The background level is measured statistically by an event mixing method, and is subtracted from the yield.

The electron acceptance ($\sim$7.4% of dN/dy) and efficiency ($\sim$60%) are determined using a detailed GEANT [16] simulation, which satisfactorily reproduces the detector response. Additionally, a multiplicity dependent efficiency loss due to detector occupancy is evaluated by embedding simulated electrons into real events. This efficiency loss is $27 \pm 4\%$ ($4 \pm 2\%$) for central (peripheral) collisions and has no significant p_T dependence.

Figure 1 shows the p_T distributions of electrons in PHENIX for central, minimum bias, and peripheral collisions. Errors in the figure are statistical. The overall systematic uncertainty, which is the quadratic sum of several few percent effects, is about 11%. Expected sources of electrons are (1) Dalitz decays of π^0, η, η', ω, and ϕ, (2) dielectron decays of ρ, ω, and ϕ, (3) photon conversions, (4) kaon decays ($K^{0,\pm} \to \pi e \nu$),

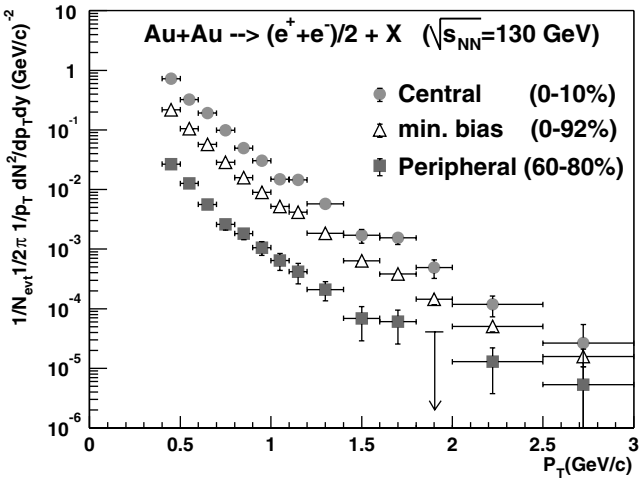

FIG. 1. Transverse momentum spectra of electrons in PHENIX from Au + Au collisions at $\sqrt{s_{NN}} = 130$ GeV.

(5) semileptonic decay of charm, and (6) other contributions such as bottom decays and thermal dileptons. In this analysis, sources (1)–(4) are considered to be background.

We have calculated the contributions from Dalitz and dielectron decays with a hadron decay generator. PHENIX has measured the p_T distributions of $\pi^{\pm}$ in $0.2 < p_T < 2.2\ \mathrm{GeV}/c$ [17] and of π^0 in $1 < p_T < 4\ \mathrm{GeV}/c$ [13]. Since the $\pi^{\pm}$ and π^0 data are consistent in the overlapping region, we fit a power law function to the combined data sets to determine the input π^0 spectrum for the decay generator. The p_T distribution of any other hadron h is obtained from the π^0 spectrum by replacing p_T with $\sqrt{p_T^2 + m_h^2 - m_{\pi^0}^2}$. The shapes of the resulting p_T spectra of $K^{\pm}$, p, and $\bar{p}$ agree with the PHENIX measurements [17] within 20%. In this parametrization h/π^0 ratios approach constants at high p_T. We assume the following asymptotic ratios to fix the relative normalizations: $\eta/\pi^0 = 0.55$, $\eta'/\pi^0 = 0.25$, $\rho/\pi^0 = \omega/\pi^0 = 1.0$, $\phi/\pi^0 = 0.40$. Except for the ϕ, these ratios are taken from proton beam data of CERN Super Proton Synchrotron (SPS), FNAL, and ISR experiments [18,19]. The η/π^0 ratio is consistent with a measurement in Pb + Pb collisions at SPS [20]. The ϕ/π^0 ratio is based on the integrated ratio $\phi/h^- \sim 0.02$ in Au + Au collisions at $\sqrt{s_{NN}} = 130$ GeV [21]. We assign to each ratio a conservative systematic uncertainty of 50%.

Photon conversions are evaluated using a combination of the GEANT simulation and the hadron decay generator. Since p_T spectra of externally converted electrons are similar to those from Dalitz decay, the conversion spectra can be approximated by scaling the Dalitz decay spectra by an experiment specific factor, $R_{\mathrm{conv}} = \mathrm{conversion/Dalitz}$. R_{conv} is evaluated using the GEANT simulation and is cross-checked by comparing the relative yield of reconstructed Dalitz and conversion pairs in the simulation and in the data. The simulation shows that R_{conv} has only a weak p_T dependence, primarily due to the energy dependence

of the pair creation cross section. $R_{\rm conv}$ is parametrized as $(1.9 \pm 0.2) \times (1 - 0.0718 \times p_T^{-0.76})$.

Background from kaon decays is also evaluated using the GEANT simulation and is found to be negligible.

The upper panel of Fig. 2 shows the ratio of the measured electrons to the calculated background versus p_T for minimum bias events. The shaded region is the quadratic sum of systematic errors in the electron measurement and in the background. The latter includes uncertainties in the normalization and the shape of the π^0 spectrum, in the h/π^0 ratios, and in $R_{\rm conv}$. A significant electron excess above the background is observed for $p_T > 0.6$ GeV/c. Central collisions show a similar excess. The peripheral collision data sample lacks sufficient statistics to reveal a signal in this analysis.

Fractional contributions to the background are shown in the lower panel of Fig. 2. More than 80% of the background is from π^0 decay, directly from the Dalitz decay or indirectly from photon conversion. The π^0 spectrum is well constrained by the PHENIX measurement. The next most important background source is η decay. Given the assigned systematic error, the upper limit of the high p_T asymptotic η/π^0 ratio is 0.83. Since this ratio, corrected for feed-down, would imply that the primary $\eta/\pi^0 \sim 1$, this provides a conservative limit on contributions from η's. Contributions from all other hadrons combined are only a few percent of the total.

Background-subtracted electron spectra are shown in Fig. 3. The error bars on the data points represent the statistical errors, while the systematic error due to the background subtraction is indicated by brackets. The integrated yield of the electron signal dN_e/dy for $p_T > 0.8$ GeV/c is 0.025 ± 0.004(stat) $\pm$ 0.010(syst) for central collisions and is 0.0079 ± 0.0006(stat) $\pm$ 0.0034(syst) for minimum bias collisions.

Semileptonic decay of charmed hadrons is an expected source of the electron signal. We use the event generator PYTHIA [22] to estimate electron spectra from charm decay. We tuned the parameters [23] of PYTHIA such that charm production data at SPS and FNAL [24] and single electron data at the ISR [9–11] are well reproduced. The charm production cross section in pp collisions from this PYTHIA calculation is $\sigma_{c\bar{c}} = 330$ μb at $\sqrt{s} = 130$ GeV. The electron spectrum in Au + Au collisions is then calculated as $EdN_e/dp^3 = T_{AA} \times Ed\sigma_e/dp^3$, where $Ed\sigma_e/dp^3$ is the electron spectrum from charm decay calculated with PYTHIA, and T_{AA} (listed in Table I) is the nuclear overlap integral calculated from a Glauber model [13]. The calculated electron spectra shown in Fig. 3 are in reasonable agreement with the data.

Before attributing the entire electron signal to open charm decays, it is necessary to quantify contributions from other possible sources. An analogous PYTHIA estimate of the bottom decay contribution is shown in Fig. 3. It becomes significant only above the measured p_T range. Expected contributions from J/Ψ and Drell-Yan are negligible. In Pb + Pb collisions at SPS, direct photons [20] and an enhanced yield of low mass dileptons [25] have been reported. If these are due to thermal radiation from hot matter, an even larger production is expected at RHIC energies and can contribute to the electron signal. Since $\rho \rightarrow e^+e^-$ contributes less than 1% to the calculated background as shown in Fig. 2, and since the dominant

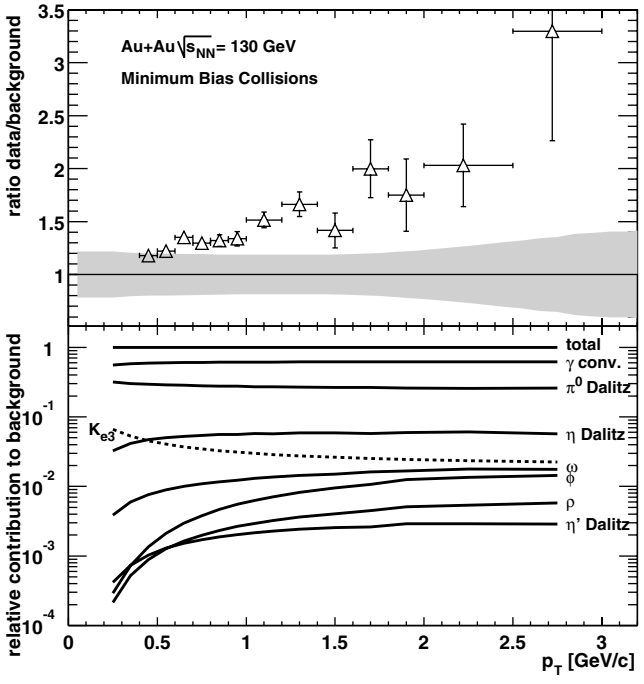

FIG. 2. Ratio of the electron data to the calculated background as a function of p_T in minimum bias collisions (upper panel) and relative contributions to the background from various sources (lower panel). The curves for ω and ϕ show the sum of the Dalitz and the dielectron decay modes.

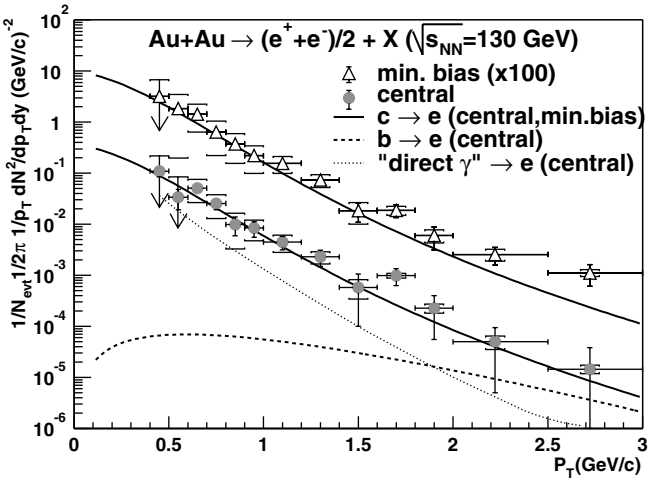

FIG. 3. The background-subtracted electron spectra for minimum bias (0%–92%) (scaled up by a factor of 100) and central (0%–10%) collisions compared with the expected contributions from open charm decays. Also shown, for central collisions only, are the expected contribution from bottom decays (dashed line) and the conversion electron spectrum from a direct photon prediction (dotted line).

TABLE I. Charm cross section per *NN* collision derived from the single electron data for central (0%–10%) and minimum bias (0%–92%) collisions. The first and second errors are statistical and systematic, respectively.

Centrality	T_{AA} (mb^{-1})	$d\sigma_{c\bar{c}}/dy\|_{y=0}$ (μb)	$\sigma_{c\bar{c}}$ (μb)
0%–10%	22.6 ± 1.6(syst)	97 ± 13 ± 49	380 ± 60 ± 200
0%–92%	6.2 ± 0.4(syst)	107 ± 8 ± 63	420 ± 33 ± 250

source of thermal dileptons is $\pi + \pi \rightarrow \rho \rightarrow e^+e^-$ [26], a significant contribution from thermal dileptons is unlikely. There are several predictions for direct photons at RHIC energies [27,28]. The conversion electron spectrum calculated from a prediction in Ref. [27] is shown in Fig. 3 for central collisions. It could explain 10%–20% of the signal, with large theoretical uncertainties.

Neglecting these other possible sources and assuming that all the electron signal is from charm, we derive the charm cross section corresponding to the electron data. We fit the charm electron spectrum from PYTHIA to the data for $p_T > 0.8$ GeV/c and obtain the rapidity density $dN_{c\bar{c}}/dy|_{y=0}$ and the total yield $N_{c\bar{c}}$ of open charm. They are then converted to cross sections per *NN* collision: $d\sigma_{c\bar{c}}/dy = (dN_{c\bar{c}}/dy)/T_{AA}$ and $\sigma_{c\bar{c}} = N_{c\bar{c}}/T_{AA}$. Results are shown in Table I. The systematic error is a quadratic sum of many sources. For central collisions, they are background subtraction (±44%), uncertainties in the PYTHIA calculation (±11% from $\langle k_T \rangle = 1.5 \pm 0.5$, ±13% from $D^+/D^0 = 0.65 \pm 0.35$, ±8% from PDFs), fit range (±18%), and T_{AA} (±7%). Note that any finite contribution from neglected sources would reduce the derived charm cross section. Without nuclear or medium effects in charm production, $\sigma_{c\bar{c}}$ per *NN* collision should be independent of centrality. Within uncertainties, our data are consistent with this expectation, in possible contrast to the attribution of increased charm production as the source of enhanced dimuon production reported in Pb + Pb collisions at SPS [29].

The single electron signal yield (divided by T_{AA} to give the cross section per *NN* collision) and the derived charm cross section are compared with single electron data of ISR experiments and charm data of fixed target experiments [24] in Fig. 4. Cross section curves calculated with PYTHIA, which has been tuned to the charm data and the ISR electron data, and a charm cross section curve from a next-to-leading order (NLO) pQCD calculation [31] are also shown in the figure. Our data are consistent with both of the calculations within large uncertainties.

In conclusion, we have observed single electrons above the expected background from decays of light hadrons and photon conversion in Au + Au collisions at $\sqrt{s_{NN}} = 130$ GeV. The observed signal is consistent with semileptonic decay of charm. The forthcoming high statistics Au + Au data and pp comparison data at full RHIC energy ($\sqrt{s_{NN}} = 200$ GeV) will be useful to clarify the nature of the single electron signal and to better determine heavy-quark production in Au + Au collisions at RHIC.

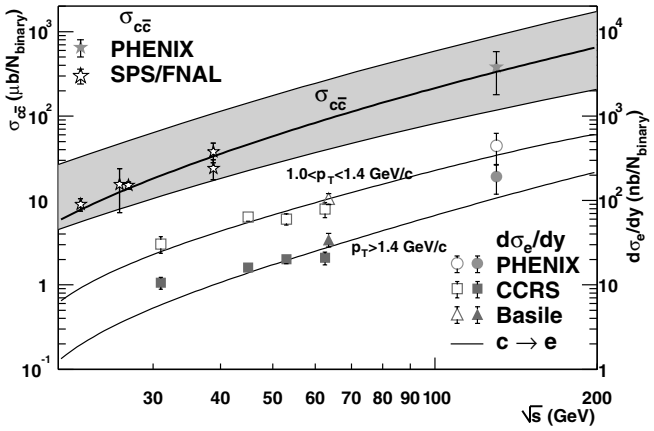

FIG. 4. Single electron cross sections $d\sigma_e/dy|_{y=0}$ of this measurement and ISR experiments [9,11,30] are displayed (bottom, right-hand scale) with charm decay contributions calculated with PYTHIA. Open and filled symbols are for $1.0 < p_T < 1.4$ GeV/c and $p_T > 1.4$ GeV/c, respectively. The derived charm cross section of this measurement is compared with charm cross sections from SPS/FNAL experiments (top, left-hand scale). The thick curve and the shaded band represent the charm cross section in the PYTHIA model and in a NLO pQCD calculation [31], respectively.

We thank the staff of the Collider-Accelerator and Physics Departments at BNL for their vital contributions. We acknowledge support from the Department of Energy and NSF (U.S.A.), MEXT and JSPS (Japan), RAS, RMAE, and RMS (Russia), BMBF, DAAD, and AvH (Germany), VR and KAW (Sweden), MIST and NSERC (Canada), CNPq and FAPESP (Brazil), IN2P3/CNRS (France), DAE and DST (India), KRF and CHEP (Korea), the U.S. CRDF for the FSU, and the U.S.–Israel BSF.

*Deceased.
†Not a participating institution.

[1] J. A. Appel, Annu. Rev. Nucl. Part. Sci. **42**, 367 (1992).
[2] B. Müller and X. N. Wang, Phys. Rev. Lett. **68**, 2437 (1992).
[3] Z. Lin and M. Gyulassy, Phys. Rev. Lett. **77**, 1222 (1996).
[4] Y. L. Dokshitzer and D. E. Kharzeev, Phys. Lett. B **519**, 199 (2001).
[5] T. Matsui and H. Satz, Phys. Lett. B **178**, 416 (1986).
[6] M. C. Abreu *et al.,* Phys. Lett. B **447**, 28 (2000).
[7] R. Vogt *et al.,* Phys. Rev. D **49**, 3345 (1994).
[8] F. W. Büsser *et al.,* Phys. Lett. **53B**, 212 (1974).
[9] F. W. Büsser *et al.,* Nucl. Phys. **B113**, 189 (1976).
[10] P. Perez *et al.,* Phys. Lett. **112B**, 260 (1982).
[11] M. Basile *et al.,* Nuovo Cimento Soc. Ital. Fis. **65A**, 421 (1981).

[12] I. Hinchliffe and C. H. Llewellyn Smith, Phys. Lett. **61B**, 472 (1976); M. Bourquin and J.-M. Gaillard, Nucl. Phys. **B114**, 334 (1976).
[13] K. Adcox *et al.,* Phys. Rev. Lett. **88**, 022301 (2002).
[14] H. Hamagaki *et al.,* Nucl. Phys. **A698**, 412 (2002).
[15] K. Adcox *et al.,* Phys. Rev. Lett. **86**, 3500 (2001).
[16] GEANT Users Guide, 3.15, CERN Program Library.
[17] K. Adcox *et al.,* nucl-ex/0112006.
[18] R. Albrecht *et al.,* Phys. Lett. B **361**, 14 (1995); G. Agakichiev *et al.,* Eur. Phys. J. C **4**, 249 (1998).
[19] M. Diakonou *et al.,* Phys. Lett. **89B**, 432 (1980).
[20] M. M. Aggarwal *et al.,* nucl-ex/0006007; M. M. Aggarwal *et al.,* Phys. Rev. Lett. **85**, 3595 (2000).
[21] C. Adler *et al.,* Phys. Rev. C **65**, R041901 (2002).
[22] T. Sjostrand, Comput. Phys. Commun. **82**, 74 (1994).
[23] We used PYTHIA 6.152 with CTEQ5L PDF [H. L. Lai *et al.,* Eur. Phys. J. C **12**, 375 (2000)]. Modified PYTHIA parameters are PARP(91) = 1.5 ($\langle k_t \rangle$), PMAS(4, 1) = 1.25 (m_c), PARP(31) = 3.5 (K factor), MSTP(33) = 1, MSTP(32) = 4 (Q^2 scale).
[24] G. A. Alves *et al.,* Phys. Rev. Lett. **77**, 2388 (1996).
[25] G. Agakichiev *et al.,* Phys. Lett. B **422**, 405 (1998).
[26] R. Rapp, Phys. Rev. C **63**, 054907 (2001).
[27] J. Alam *et al.,* Phys. Rev. C **63**, 021901 (2001).
[28] F. D. Steffen and M. H. Thoma, Phys. Lett. B **510**, 98 (2001); D. K. Srivastava, nucl-th/0103023.
[29] M. C. Abreu *et al.,* Eur. Phys. J. C **14**, 443 (2000).
[30] The 1.0–1.4 GeV/c point of CCRS is calculated from the e/π ratio in Ref. [9] and the pion cross section in B. Alper *et al.,* Nucl. Phys. **B100**, 237 (1975).
[31] M. Mangano, P. Nason, and G. Ridolfi, Nucl. Phys. **B405**, 507 (1993). Their program HVQMNR is used with CTEQ5M PDF to calculate $\sigma_{c\bar{c}}$ in Fig. 4 with $m_c = 1.5$ GeV/c^2, $\mu_F = 2m_c$, and $0.5m_c < \mu_R < 2m_c$.

Transverse-Mass Dependence of Two-Pion Correlations in Au + Au Collisions at $\sqrt{s_{NN}} = 130$ GeV

K. Adcox,[40] S. S. Adler,[3] N. N. Ajitanand,[27] Y. Akiba,[14] J. Alexander,[27] L. Aphecetche,[34] Y. Arai,[14] S. H. Aronson,[3] R. Averbeck,[28] T. C. Awes,[29] K. N. Barish,[5] P. D. Barnes,[19] J. Barrette,[21] B. Bassalleck,[25] S. Bathe,[22] V. Baublis,[30] A. Bazilevsky,[12,32] S. Belikov,[12,13] F. G. Bellaiche,[29] S. T. Belyaev,[16] M. J. Bennett,[19] Y. Berdnikov,[35] S. Botelho,[33] M. L. Brooks,[19] D. S. Brown,[26] N. Bruner,[25] D. Bucher,[22] H. Buesching,[22] V. Bumazhnov,[12] G. Bunce,[3,32] J. Burward-Hoy,[28] S. Butsyk,[28,30] T. A. Carey,[19] P. Chand,[2] J. Chang,[5] W. C. Chang,[1] L. L. Chavez,[25] S. Chernichenko,[12] C. Y. Chi,[8] J. Chiba,[14] M. Chiu,[8] R. K. Choudhury,[2] T. Christ,[28] T. Chujo,[3,39] M. S. Chung,[15,19] P. Chung,[27] V. Cianciolo,[29] B. A. Cole,[8] D. G. D'Enterria,[34] G. David,[3] H. Delagrange,[34] A. Denisov,[12] A. Deshpande,[32] E. J. Desmond,[3] O. Dietzsch,[33] B. V. Dinesh,[2] A. Drees,[28] A. Durum,[12] D. Dutta,[2] K. Ebisu,[24] Y. V. Efremenko,[29] K. El Chenawi,[40] A. Enokizono,[11] H. En'yo,[17,31] S. Esumi,[39] L. Ewell,[3] T. Ferdousi,[5] D. E. Fields,[25] S. L. Fokin,[16] Z. Fraenkel,[42] A. Franz,[3] A. D. Frawley,[9] S.-Y. Fung,[5] S. Garpman,[20,*] T. K. Ghosh,[40] A. Glenn,[36] A. L. Godoi,[33] Y. Goto,[32] S. V. Greene,[40] M. Grosse Perdekamp,[32] S. K. Gupta,[2] W. Guryn,[3] H.-Å Gustafsson,[20] J. S. Haggerty,[3] H. Hamagaki,[7] A. G. Hansen,[19] H. Hara,[24] E. P. Hartouni,[18] R. Hayano,[38] N. Hayashi,[31] X. He,[10] T. K. Hemmick,[28] J. M. Heuser,[28] M. Hibino,[41] J. C. Hill,[13] D. S. Ho,[43] K. Homma,[11] B. Hong,[15] A. Hoover,[26] T. Ichihara,[31,32] K. Imai,[17,31] M. S. Ippolitov,[16] M. Ishihara,[31,32] B. V. Jacak,[28,32] W. Y. Jang,[15] J. Jia,[28] B. M. Johnson,[3] S. C. Johnson,[18,28] K. S. Joo,[23] S. Kametani,[41] J. H. Kang,[43] M. Kann,[30] S. S. Kapoor,[2] S. Kelly,[8] B. Khachaturov,[42] A. Khanzadeev,[30] J. Kikuchi,[41] D. J. Kim,[43] H. J. Kim,[43] S. Y. Kim,[43] Y. G. Kim,[43] W. W. Kinnison,[19] E. Kistenev,[3] A. Kiyomichi,[39] C. Klein-Boesing,[22] S. Klinksiek,[25] L. Kochenda,[30] V. Kochetkov,[12] D. Koehler,[25] T. Kohama,[11] D. Kotchetkov,[5] A. Kozlov,[42] P. J. Kroon,[3] K. Kurita,[31,32] M. J. Kweon,[15] Y. Kwon,[43] G. S. Kyle,[26] R. Lacey,[27] J. G. Lajoie,[13] J. Lauret,[27] A. Lebedev,[13,16] D. M. Lee,[19] M. J. Leitch,[19] X. H. Li,[5] Z. Li,[6,31] D. J. Lim,[43] M. X. Liu,[19] X. Liu,[6] Z. Liu,[6] C. F. Maguire,[40] J. Mahon,[3] Y. I. Makdisi,[3] V. I. Manko,[16] Y. Mao,[6,31] S. K. Mark,[21] S. Markacs,[8] G. Martinez,[34] M. D. Marx,[28] A. Masaike,[17] F. Matathias,[28] T. Matsumoto,[7,41] P. L. McGaughey,[19] E. Melnikov,[12] M. Merschmeyer,[22] F. Messer,[28] M. Messer,[3] Y. Miake,[39] T. E. Miller,[40] A. Milov,[42] S. Mioduszewski,[3,36] R. E. Mischke,[19] G. C. Mishra,[10] J. T. Mitchell,[3] A. K. Mohanty,[2] D. P. Morrison,[3] J. M. Moss,[19] F. Mühlbacher,[28] M. Muniruzzaman,[5] J. Murata,[31] S. Nagamiya,[14] Y. Nagasaka,[24] J. L. Nagle,[8] Y. Nakada,[17] B. K. Nandi,[5] J. Newby,[36] L. Nikkinen,[21] P. Nilsson,[20] S. Nishimura,[7] A. S. Nyanin,[16] J. Nystrand,[20] E. O'Brien,[3] C. A. Ogilvie,[13] H. Ohnishi,[3,11] I. D. Ojha,[4,40] M. Ono,[39] V. Onuchin,[12] A. Oskarsson,[20] L. Österman,[20] I. Otterlund,[20] K. Oyama,[7,38] L. Paffrath,[3,*] A. P. T. Palounek,[19] V. S. Pantuev,[28] V. Papavassiliou,[26] S. F. Pate,[26] T. Peitzmann,[22] A. N. Petridis,[13] C. Pinkenburg,[3,27] R. P. Pisani,[3] P. Pitukhin,[12] F. Plasil,[29] M. Pollack,[28,36] K. Pope,[36] M. L. Purschke,[3] I. Ravinovich,[42] K. F. Read,[29,36] K. Reygers,[22] V. Riabov,[30,35] Y. Riabov,[30] M. Rosati,[13] A. A. Rose,[40] S. S. Ryu,[43] N. Saito,[31,32] A. Sakaguchi,[11] T. Sakaguchi,[7,41] H. Sako,[39] T. Sakuma,[31,37] V. Samsonov,[30] T. C. Sangster,[18] R. Santo,[22] H. D. Sato,[17,31] S. Sato,[39] S. Sawada,[14] B. R. Schlei,[19] Y. Schutz,[34] V. Semenov,[12] R. Seto,[5] T. K. Shea,[3] I. Shein,[12] T.-A. Shibata,[31,37] K. Shigaki,[14] T. Shiina,[19] Y. H. Shin,[43] I. G. Sibiriak,[16] D. Silvermyr,[20] K. S. Sim,[15] J. Simon-Gillo,[19] C. P. Singh,[4] V. Singh,[4] M. Sivertz,[3] A. Soldatov,[12] R. A. Soltz,[18] S. Sorensen,[29,36] P. W. Stankus,[29] N. Starinsky,[21] P. Steinberg,[8] E. Stenlund,[20] A. Ster,[44] S. P. Stoll,[3] M. Sugioka,[31,37] T. Sugitate,[11] J. P. Sullivan,[19] Y. Sumi,[11] Z. Sun,[6] M. Suzuki,[39] E. M. Takagui,[33] A. Taketani,[31] M. Tamai,[41] K. H. Tanaka,[14] Y. Tanaka,[24] E. Taniguchi,[31,37] M. J. Tannenbaum,[3] J. Thomas,[28] J. H. Thomas,[18] T. L. Thomas,[25] W. Tian,[6,36] J. Tojo,[17,31] H. Torii,[17,31] R. S. Towell,[19] I. Tserruya,[42] H. Tsuruoka,[39] A. A. Tsvetkov,[16] S. K. Tuli,[4] H. Tydesjö,[20] N. Tyurin,[12] T. Ushiroda,[24] H. W. van Hecke,[19] C. Velissaris,[26] J. Velkovska,[28] M. Velkovsky,[28] A. A. Vinogradov,[16] M. A. Volkov,[16] A. Vorobyov,[30] E. Vznuzdaev,[30] H. Wang,[5] Y. Watanabe,[31,32] S. N. White,[3] C. Witzig,[3] F. K. Wohn,[13] C. L. Woody,[3] W. Xie,[5,42] K. Yagi,[39] S. Yokkaichi,[31] G. R. Young,[29] I. E. Yushmanov,[16] W. A. Zajc,[8] Z. Zhang,[28] and S. Zhou[6]

(PHENIX Collaboration)

[1]*Institute of Physics, Academia Sinica, Taipei 11529, Taiwan*
[2]*Bhabha Atomic Research Centre, Bombay 400 085, India*
[3]*Brookhaven National Laboratory, Upton, New York 11973-5000*
[4]*Department of Physics, Banaras Hindu University, Varanasi 221005, India*
[5]*University of California–Riverside, Riverside, California 92521*
[6]*China Institute of Atomic Energy (CIAE), Beijing, People's Republic of China*
[7]*Center for Nuclear Study, Graduate School of Science, University of Tokyo, 7-3-1 Hongo, Bunkyo, Tokyo 113-0033, Japan*

 0031-9007/02/88(19)/192302(6)$20.00 © 2002 The American Physical Society

[8]*Columbia University, New York, New York 10027 and Nevis Laboratories, Irvington, New York 10533*
[9]*Florida State University, Tallahassee, Florida 32306*
[10]*Georgia State University, Atlanta, Georgia 30303*
[11]*Hiroshima University, Kagamiyama, Higashi-Hiroshima 739-8526, Japan*
[12]*Institute for High Energy Physics (IHEP), Protvino, Russia*
[13]*Iowa State University, Ames, Iowa 50011*
[14]*KEK, High Energy Accelerator Research Organization, Tsukuba-shi, Ibaraki-ken 305-0801, Japan*
[15]*Korea University, Seoul, 136-701, Korea*
[16]*Russian Research Center "Kurchatov Institute," Moscow, Russia*
[17]*Kyoto University, Kyoto 606, Japan*
[18]*Lawrence Livermore National Laboratory, Livermore, California 94550*
[19]*Los Alamos National Laboratory, Los Alamos, New Mexico 87545*
[20]*Department of Physics, Lund University, Box 118, SE-221 00 Lund, Sweden*
[21]*McGill University, Montreal, Quebec, Canada H3A 2T8*
[22]*Institut für Kernphysik, University of Münster, D-48149 Münster, Germany*
[23]*Myongji University, Yongin, Kyonggido 449-728, Korea*
[24]*Nagasaki Institute of Applied Science, Nagasaki-shi, Nagasaki, 851-0193, Japan*
[25]*University of New Mexico, Albuquerque, New Mexico 87131*
[26]*New Mexico State University, Las Cruces, New Mexico 88003*
[27]*Chemistry Department, State University of New York–Stony Brook, Stony Brook, New York 11794*
[28]*Department of Physics and Astronomy, State University of New York–Stony Brook, Stony Brook, New York 11794*
[29]*Oak Ridge National Laboratory, Oak Ridge, Tennessee 37831*
[30]*PNPI, Petersburg Nuclear Physics Institute, Gatchina, Russia*
[31]*RIKEN (The Institute of Physical and Chemical Research), Wako, Saitama 351-0198, Japan*
[32]*RIKEN BNL Research Center, Brookhaven National Laboratory, Upton, New York 11973-5000*
[33]*Universidade de São Paulo, Instituto de Física, Caixa Postal 66318, São Paulo CEP05315-970, Brazil*
[34]*SUBATECH (Ecole des Mines de Nantes, IN2P3/CNRS, Universite de Nantes), BP 20722-44307, Nantes-Cedex 3, France*
[35]*St. Petersburg State Technical University, St. Petersburg, Russia*
[36]*University of Tennessee, Knoxville, Tennessee 37996*
[37]*Department of Physics, Tokyo Institute of Technology, Tokyo, 152-8551, Japan*
[38]*University of Tokyo, Tokyo, Japan*
[39]*Institute of Physics, University of Tsukuba, Tsukuba, Ibaraki 305, Japan*
[40]*Vanderbilt University, Nashville, Tennessee 37235*
[41]*Waseda University, Advanced Research Institute for Science and Engineering, 17 Kikui-cho, Shinjuku-ku, Tokyo 162-0044, Japan*
[42]*Weizmann Institute, Rehovot 76100, Israel*
[43]*Yonsei University, IPAP, Seoul 120-749, Korea*
[44]*KFKI Research Institute for Particle and Nuclear Physics (RMKI), Budapest, Hungary*[†]

(Received 16 January 2002; published 30 April 2002)

Two-pion correlations in $\sqrt{s_{NN}} = 130$ GeV Au + Au collisions at RHIC have been measured over a broad range of pair transverse momentum k_T by the PHENIX experiment at RHIC. The k_T dependent transverse radii are similar to results from heavy-ion collisions at $\sqrt{s_{NN}} = 4.1$, 4.9, and 17.3 GeV, whereas the longitudinal radius increases monotonically with beam energy. The ratio of the outwards to sidewards transverse radii ($R_{\rm out}/R_{\rm side}$) is consistent with unity and independent of k_T.

DOI: 10.1103/PhysRevLett.88.192302 PACS numbers: 25.75.Dw

The influence of Bose-Einstein statistics on the correlation of identical charged pions at low relative momentum was first used to probe the space-time structure of pion emission in $p\bar{p}$ annihilations [1] and has subsequently been applied to relativistic heavy-ion collisions from the Bevalac to RHIC [2–7] (see [8] for recent reviews) and to a wide range of systems including e^+e^- annihilations [9]. The correlation function is defined as the ratio of the two-particle probability distribution to the product of the single-particle distributions. For a static source with no final state interactions, it is related to the Fourier transform with respect to $\mathbf{q} = \mathbf{p}_1 - \mathbf{p}_2$ of the source distribution $\rho(\mathbf{r})$, $P(\mathbf{p}_1, \mathbf{p}_2)/P(\mathbf{p}_1)P(\mathbf{p}_2) = 1 + |\tilde{\rho}(\mathbf{q})|^2$ [1]. If the source is parametrized as a multidimensional Gaussian, the enhancement in the correlation function is a Gaussian, and the Gaussian widths are each inversely proportional to the source dimensions in the canonically conjugate spatial variables. The extracted source dimensions are commonly referred to as HBT radii, after a similar technique developed by Hanbury-Brown and Twiss to measure stellar radii [10]. For dynamic sources, such as rapidly expanding sources in heavy-ion collisions, the correlation function measures "lengths of homogeneity," or the relative separations of the pions with low relative momentum. This leads to source radii which depend strongly on k_T, the mean transverse momentum of the pion pair [11–16]. If the dynamics are correctly modeled, then both the source geometry and rate of expansion can be deduced by

measuring the k_T dependence of the radii. The existence of a connection between HBT radii and heavy-ion source geometry is established by the dependence of the radii on system size [17], centrality [4,5], and reaction plane [3]. Interest in Bose-Einstein correlations in heavy-ion collisions is driven by the expectation that HBT radii are sensitive to the large and/or long-lived sources which may accompany a QCD phase transition [12,18]. Recent calculations predict that the greatest sensitivity to a long-lived source will come from measurements of the correlation function at high k_T ($\geq$0.3 GeV/c) [19,20].

We present new measurements from the PHENIX experiment on two-pion correlations in Au + Au collisions at $\sqrt{s_{NN}} = 130$ GeV in the region $|\eta| < 0.35$, $0.2 < k_T < 1.0$ GeV/c, significantly extending previous measurements by STAR [7] up to a mean-k_T 0.63 GeV/c. The data are compared to theoretical predictions for RHIC and to HBT radii from lower energy collisions at the CERN Super Proton Synchrotron and Alternating Gradient Synchrotron (at BNL). The k_T dependence of the transverse radii is used to extract a geometric transverse radius.

The PHENIX experiment has been described in detail elsewhere [21,22]. For this analysis we utilize a subset of the detectors in PHENIX. We use the hadronic particle identification capabilities present in the west arm of the PHENIX spectrometer perpendicular to the beam direction [22] with polar and azimuthal ranges of $|\eta| < 0.35$ and $\pi/4$, respectively, during its first year of running. In this analysis, the vertex is determined with a zero degree calorimeter and a pair of Čerenkov beam-beam counters (BBC). Pattern recognition and momentum reconstruction rely on a drift chamber and a pad chamber which occupy the region between 2.0 and 2.5 m from the beam axis. The momentum resolution from these detectors is $\delta p/p = 0.6\% \oplus 3.6\% p$. Particle velocity is determined from the differential time measurements of the BBC and the electromagnetic calorimeter (EMC) [23], with a combined rms resolution of 700 ps, coupled with the path length determined from pattern recognition. The momentum determination and particle identification method are similar to [24], except that the time of flight is measured by the EMC. A pion is defined as being within 1.5 standard deviations of the pion mass-squared peak but at least 2.5 standard deviations away from the kaon peak. After applying interdetector association cuts the background from misassociated EMC hits is $\sim$10% as determined by a hit randomization technique. This background does not significantly distort the extracted radius in the correlation measurements, although it reduces the measured correlation strength (λ). We did not correct for this background in our correlation analysis.

A total of 493 K events in the most central 30% of the cross section survive all off-line cuts. This sample contains 3.1 million π^+ pairs and 3.3 million π^- pairs in the analysis, and has a mean centrality of 10%.

The pion correlation function is determined from pairs of identical pions. The normalized probability of detecting two particles with relative momentum $\mathbf{q} = \mathbf{p}_1 - \mathbf{p}_2$ and average momentum $\mathbf{k} = (\mathbf{p}_1 + \mathbf{p}_2)/2$ is determined experimentally by the ratio of pairs from the same event (A) with those from different events (B): $C_2(\mathbf{q}, \mathbf{k}) = A(\mathbf{q}, \mathbf{k})/B(\mathbf{q}, \mathbf{k})$. Pairs of particles within 2 cm of each other in the drift chamber are eliminated from the analysis in both the real and background samples. Pairs that share the same EMC cluster are also removed from both samples. Finally, all pairs in the mixed background sample are required to be from events with a reconstructed BBC collision vertex within 1 cm of each other.

We correct for the Coulomb interaction of the pairs in the correlation function by parametrizing the source as a Gaussian distribution in the pair center-of-mass frame and performing an iterative procedure [25] which accounts for the finite resolution of the detector. This procedure applied to the distribution of π^+-π^- pairs is in agreement with the data, although the statistics in the Run-1 opposite-signed analysis are not sufficient to independently determine the required Coulomb correction. Systematic studies of the Coulomb correction which vary both radius and magnitude within reasonable constraints produce variations in the final radii which never exceed 0.25 fm.

The relative momenta are projected into the variables q_{long}, along the beam direction, q_{out}, parallel to the transverse momentum of the pair $\mathbf{k}_T = \frac{1}{2}(\mathbf{p}_{T_1} + \mathbf{p}_{T_2})$, and q_{side}, perpendicular to q_{long} and q_{out} [11,18]. These variables are calculated in the longitudinal comoving system (LCMS), obtained by a longitudinal boost from the lab frame to the frame in which the longitudinal pair velocity vanishes. This frame is commonly used for sources expected to be invariant under longitudinal boosts [26].

The fully corrected correlation function for π^- pairs is shown in the top panels of Fig. 1; the large q region of the correlation function has been normalized to 1 in the plots. The data are fit to a Gaussian parametrization of the source using a MINUIT based log-likelihood method [4].

$$C_2 = 1 + \lambda \exp(-R_{\text{long}}^2 q_{\text{long}}^2 - R_{\text{side}}^2 q_{\text{side}}^2 - R_{\text{out}}^2 q_{\text{out}}^2), \quad (1)$$

where R_{long}, R_{side}, and R_{out} are the conjugate variables to q_{long}, q_{side}, and q_{out}, respectively. Errors quoted in the tables and figures are statistical only. Systematic errors come mainly from the Coulomb correction and dependence of the results on the two-track distance cuts. The combined systematic error for these effects, estimated by varying the cuts and corrections within reasonable bounds, is 8% for R_{long}, and R_{side}, and 4% for R_{out}. The systematic error from residual correlations in the event-mixed background [2] is 2%, yielding a total systematic error of $\sim$8% for R_{long} and R_{side} and $\sim$4.5% for R_{out}.

The data set is subdivided into three k_T bins of equivalent statistics in order to study the momentum dependence of the correlation function. In Fig. 2, the radii for π^-

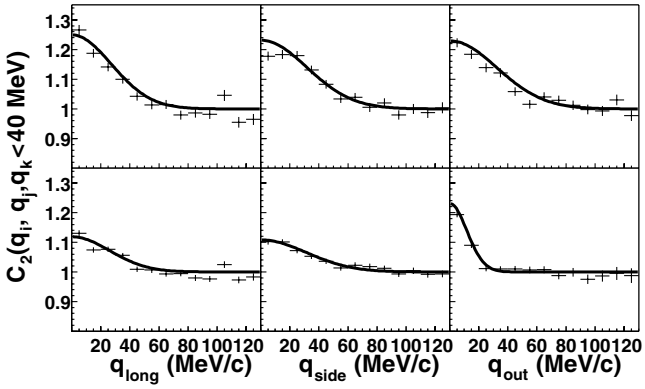

FIG. 1. The three dimensional correlation function for π^- pairs versus $q_{\rm long}$, $q_{\rm side}$, and $q_{\rm out}$ in both the LCMS frame (top) and the pair center-of-mass frame (bottom). The data are plotted versus one momentum difference variable while requiring the other two to be less than 40 MeV/c. The lines correspond to the fit to the entire distribution.

pairs are shown to agree within statistical and systematic errors with previous measurements for overlapping k_T bins at this energy for the 12% most central events. For STAR, the mean pair centrality can be approximated by the geometric mean of 8%, which is slightly more central than the mean pair centrality of 10% for the PHENIX data. This figure also shows k_T dependent radii for midrapidity pions from central collisions for $\sqrt{s_{NN}} = 17.3$ GeV Pb + Pb [6,27] and for $\sqrt{s_{NN}} = 4.9$ and 4.1 GeV Au + Au [3,4]. For the transverse radii, $R_{\rm out}$ and $R_{\rm side}$, the variation with collision energy is generally smaller than the statistical and systematic errors of the individual data points. There is no evidence for a change in the low-k_T extrapolation of $R_{\rm side}$ with increasing $\sqrt{s_{NN}}$ which would indicate a larger geometric source at higher energy. Nor is any change evident in $R_{\rm out}$ relative to $R_{\rm side}$ at high k_T, indicating a longer-lived source. This result is surprising given the factor of $\sim$3 change in the total charged particle multiplicity per unit rapidity at midrapidity [28]. Only $R_{\rm long}$ exhibits a significant variation with collision energy. To quantify this difference, we fit the $R_{\rm long}$ dependence to $A/\sqrt{m_T}$ [13,16,29] for the three sets of beam energies. The results are overlayed with the data in the bottom panel of Fig. 2 and yield $A = 3.32 \pm 0.03$, 3.05 ± 0.06, and 2.19 ± 0.05 fm GeV$^{1/2}$ for $\sqrt{s_{NN}} = 130$, 17.3, and 4.9/4.1 GeV, respectively.

Although a finite emission duration contributes to $R_{\rm out}$ but not to $R_{\rm side}$, dynamical correlations affect the two radii differently. A quantitative determination of the source lifetime can be performed only in the context of a dynamical model. The lower panel of Fig. 3 shows the k_T dependence

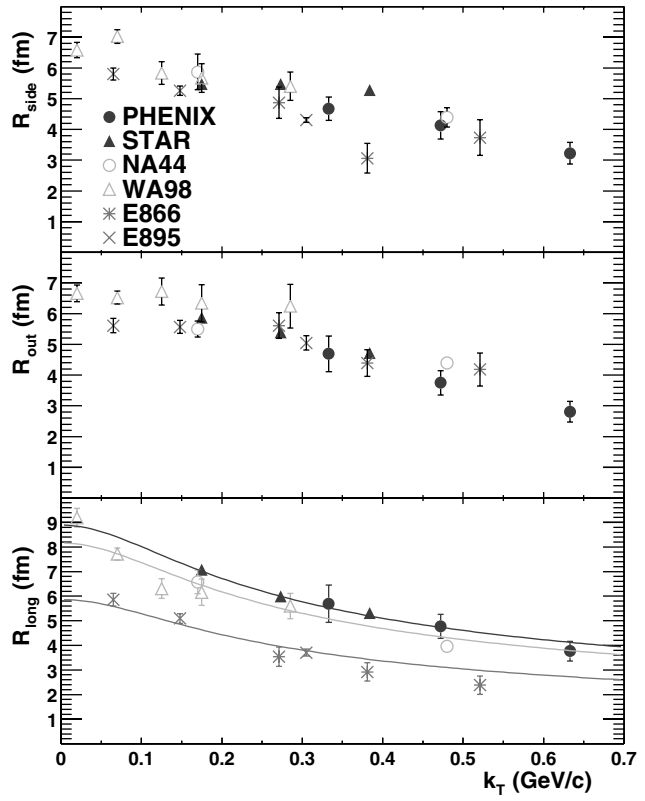

FIG. 2. HBT radii for pion pairs as a function of k_T measured at midrapidity for various energies from E895 ($\sqrt{s_{NN}} = 4.1$ GeV), E866 ($\sqrt{s_{NN}} = 4.9$ GeV), NA44, WA98 ($\sqrt{s_{NN}} = 17.3$ GeV), STAR, and PHENIX Collaborations ($\sqrt{s_{NN}} = 130$ GeV). The bottom plot includes fits to $A/\sqrt{m_T}$ for each energy region. The data are for π^- results except for the NA44 results, which are for π^+.

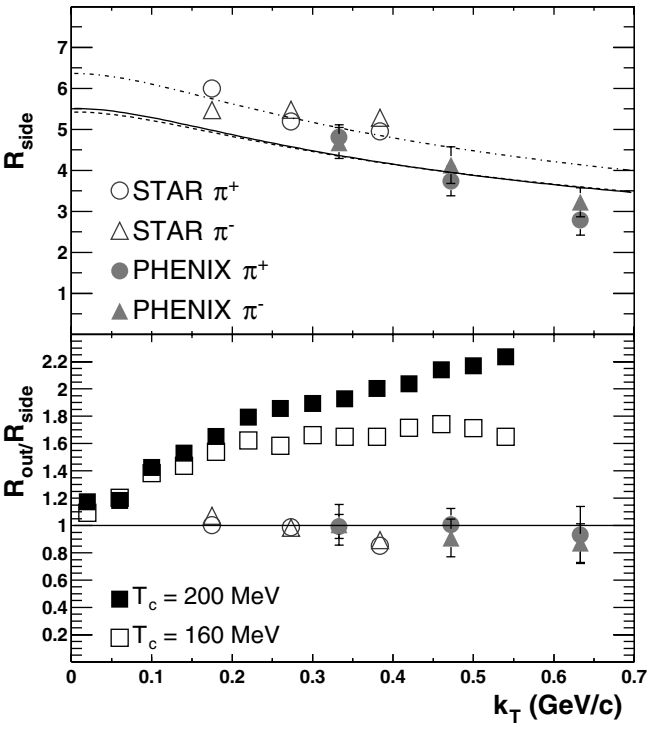

FIG. 3. The top panel shows the measured $R_{\rm side}$ from identical pions for STAR and PHENIX. The solid line is a fit of Eq. (3) to the PHENIX data, and the dashed line is the same fit for Eq. (2). The dot-dashed line is a fit of Eq. (3) to the STAR data. The bottom panel shows the ratio $R_{\rm out}/R_{\rm side}$ as a function of k_T overlayed with theoretical predictions for a phase transition for two critical temperatures.

TABLE I. The k_T dependencies of the π^+ and π^- radii in the LCMS and PCMS frames. All momenta are in MeV and all radii are in fm. The errors are statistical only.

	k_T (MeV)	200–400	400–550	550–1000
	$\langle k_T \rangle$	333	472	633
π^+	$R_{\rm inv}$	6.74 ± 0.31	6.42 ± 0.46	3.46 ± 0.46
	$\lambda_{\rm LCMS}$	0.423 ± 0.037	0.389 ± 0.039	0.287 ± 0.048
	$R_{\rm long}$	6.01 ± 0.45	4.76 ± 0.35	2.97 ± 0.38
	$R_{\rm side}$	4.81 ± 0.30	3.74 ± 0.36	2.79 ± 0.37
	$R_{\rm out}$	4.78 ± 0.30	3.76 ± 0.26	2.59 ± 0.46
	$R_{\rm out}^{\rm PCMS}$	11.35 ± 0.69	12.20 ± 1.02	8.60 ± 1.13
π^-	$R_{\rm inv}$	6.00 ± 0.30	5.96 ± 0.41	4.58 ± 0.48
	$\lambda_{\rm LCMS}$	0.431 ± 0.079	0.405 ± 0.067	0.353 ± 0.062
	$R_{\rm long}$	5.69 ± 0.76	4.77 ± 0.49	3.76 ± 0.41
	$R_{\rm side}$	4.67 ± 0.38	4.13 ± 0.45	3.22 ± 0.35
	$R_{\rm out}$	4.69 ± 0.58	3.75 ± 0.40	2.81 ± 0.34
	$R_{\rm out}^{\rm PCMS}$	11.27 ± 0.72	12.42 ± 1.18	11.89 ± 1.73

of the ratio $R_{\rm out}/R_{\rm side}$ for PHENIX and STAR along with recent calculations for a thermalized source which undergoes a first order phase transition at critical temperatures (T_c) of 160 and 200 MeV [20]. The rise in $R_{\rm out}/R_{\rm side}$ which comes predominantly from a hadronic rescattering phase is not present in the data, and the values of 1.6 ($T_c = 160$ MeV) and 2.2 ($T_c = 200$ MeV) at high k_T are excluded.

An additional consequence of strong dynamics occurs for sources in which the transverse expansion is relativistic. In this case, $R_{\rm out}$ measured in the LCMS frame is Lorentz contracted by the γ of the pion source velocity along the direction of $q_{\rm out}$ [30,31]. Current Lorentz invariant formulations of the correlation function [14,32] are insufficient to determine the source velocity due to transverse expansion; however, the pair center-of-mass system (PCMS) can be used to provide an upper limit on $R_{\rm out}$ [33]. The correlation function for π^- pairs in the PCMS frame is shown in the bottom panels of Fig. 1, and fit results for $R_{\rm out}^{\rm PCMS}$ are listed in Table I. As expected, $R_{\rm side}$ and $R_{\rm long}$ are equal to the corresponding LCMS parameters within errors.

Two analytic expressions have been used to describe $R_{\rm side}$ as a function of $m_T = \sqrt{k_T^2 + m_\pi^2}$ for a transversely expanding source,

$$R_{\rm side}^2(m_T) = \frac{R_{\rm geom}^2}{1 + \beta_f^2(\frac{m_T}{T})}, \qquad (2)$$

$$R_{\rm side}^2(m_T) = \frac{R_{\rm geom}^2}{1 + \eta_f^2(\frac{1}{2} + \frac{m_T}{T})}. \qquad (3)$$

Equation (2) is a first order approximation in $\frac{T}{m_T}$ for a longitudinally boost invariant source with finite temperature, T, and expansion velocity, $\beta_T = \beta_f \rho / R_{\rm geom}$, where $R_{\rm geom}$ is the Gaussian transverse radius [14]. Equation (3) includes an additional term in the approximation and the linear transverse expansion velocity is replaced by a transverse rapidity, $\eta_T = \eta_f \rho / R_{\rm geom}$ [16]. For a transverse surface rapidity of $\eta_f = 0.85$ ($\beta_f = 0.69$) and $T = 125$ MeV [34], a fit of Eq. (3) to the PHENIX $R_{\rm side}$ m_T dependence yields $R_{\rm geom} = 8.1 \pm 0.3$ fm with a $\chi^2/{\rm d.o.f.} = 9.6/6$. To assess systematic errors the PHENIX data are also fit to Eq. (2), yielding $R_{\rm geom} = 6.7 \pm 0.2$ fm and $\chi^2/{\rm d.o.f.} = 9.1/6$, and the STAR data are fit to Eq. (3), yielding $R_{\rm geom} = 9.4 \pm 0.1$ fm with $\chi^2/{\rm d.o.f.} = 21/6$. These fits are shown in the top panel of Fig. 3. All values of $R_{\rm geom}$ are significantly larger than the comparable 1D rms radius for a Au nucleus [35] of $\sqrt{1/3} \times \sqrt{3/5} \times 6.87 = 3.07$ fm.

In conclusion, we have extended the measurement of two particle correlations for Au + Au collisions at $\sqrt{s_{NN}} = 130$ GeV to $\langle k_T \rangle = 0.63$ GeV/c using the PHENIX detector at RHIC. Values of $R_{\rm out}^{\rm PCMS}$ are used to constrain the Lorentz effects for a relativistic transverse expansion. Fitting $R_{\rm side}(k_T)$ to two analytic expressions for an expanding source yields a transverse geometric radius that is much larger than the comparable radius for Au. We find that $R_{\rm long}(k_T)$ increases monotonically with collision energy, yet no energy dependence is discernible in the k_T dependence of $R_{\rm out}$ and $R_{\rm side}$, and the ratio, $R_{\rm out}/R_{\rm side}$, is consistent with unity and independent of k_T. The results for the transverse radii are contrary to common expectations for a first order phase transition in Au + Au collisions at these energies, as demonstrated by the comparison to a typical hydrodynamic model with hadronic rescattering. Therefore, we conclude that current concepts regarding the space-time evolution of the pion source inferred from two-pion correlations in Au + Au collisions at RHIC will need to be revised.

We thank the staff of the Collider-Accelerator and Physics Departments at BNL for their vital contributions. We acknowledge support from the Department of Energy and NSF (U.S.A.), MEXT and JSPS (Japan), RAS, RMAE, and RMS (Russia), BMBF, DAAD, and AvH (Germany), VR and KAW (Sweden), MIST and NSERC (Canada), CNPq and FAPESP (Brazil), IN2P3/CNRS

(France), DAE and DST (India), KRF and CHEP (Korea), the U.S. CRDF for the FSU, and the U.S.–Israel BSF.

*Deceased.
†Not a participating Institution.

[1] G. Goldhaber *et al.,* Phys. Rev. **120**, 300 (1960).
[2] W. A. Zajc *et al.,* Phys. Rev. C **29**, 2173 (1984).
[3] M. Lisa *et al.,* Phys. Rev. Lett. **84**, 2798 (2000).
[4] E802 Collaboration, R. Soltz *et al.,* Nucl. Phys. **A661**, 439 (1999); L. Ahle *et al.,* nucl-ex/0204001.
[5] I. G. Bearden *et al.,* Eur. J. Phys. C **18**, 317 (2000).
[6] M. M. Aggarwal *et al.,* Eur. J. Phys. C **16**, 445 (2000).
[7] STAR Collaboration, C. Adler *et al.,* Phys. Rev. Lett. **87**, 082301 (2001).
[8] U. Wiedemann and U. Heinz, Phys. Rep. **319**, 145 (1999); T. Csörgő, Heavy Ion Phys. **15**, 1 (2002).
[9] G. Abbiendi *et al.,* Eur. J. Phys. C **16**, 423 (2000).
[10] R. Hanbury-Brown and R. Twiss, Philos. Mag. **45**, 663 (1954).
[11] S. Pratt, Phys. Rev. Lett. **53**, 1219 (1984).
[12] S. Pratt, Phys. Rev. D **33**, 1314 (1986).
[13] A. N. Makhlin and Y. M. Sinyukov, Z. Phys. C **39**, 69 (1988).
[14] S. Chapman, J. R. Nix, and U. Heinz, Phys. Rev. C **52**, 2694 (1995).
[15] D. E. Fields *et al.,* Phys. Rev. C **52**, 986 (1995).
[16] U. Wiedemann, P. Scotto, and U. Heinz, Phys. Rev. C **53**, 918 (1996).
[17] J. Bartke, Phys. Lett. B **174**, 32 (1986).
[18] G. Bertsch and G. E. Brown, Phys. Rev. C **40**, 1830 (1989).
[19] D. Rischke and M. Gyulassy, Nucl. Phys. **A608**, 479 (1996).
[20] S. Soff, S. A. Bass, and A. Dumitru, Phys. Rev. Lett. **86**, 3981 (2001).
[21] D. P. Morrison, Nucl. Phys. **A638**, 565c (1998); N. Saito, *ibid.* 575c (1998).
[22] PHENIX Collaboration, H. Hamagaki *et al.,* Nucl. Phys. **A698**, 412C (2002).
[23] PHENIX Collaboration, S. White *et al.,* Nucl. Phys. **A698**, 420C (2002).
[24] K. Adcox *et al.,* nucl-ex/0112006.
[25] M. D. Baker, Nucl. Phys. **A610**, 213c (1996).
[26] J. D. Bjorken, Phys. Rev. D **27**, 140 (1983); F. Cooper, G. Frye, and E. Schonberg, Phys. Rev. D **11**, 192 (1975).
[27] NA44 Collaboration, I. G. Bearden *et al.,* Phys. Rev. C **58**, 1656 (1998).
[28] L. Ahle *et al.,* Phys. Rev. C **57**, R466 (1998); D. B. Back *et al.,* Phys. Rev. Lett. **85**, 3100 (2000).
[29] This functional form is motivated by an approximation in T/m_T in which $A = \tau_0 T$, where τ_0 is the proper time of hadronization.
[30] S. Pratt, T. Csörgo, and J. Zimanyi, Phys. Rev. C **42**, 2646 (1990).
[31] *Particle Production in Highly Excited Matter,* edited by H. H. Gutbrod and J. Rafelski (Plenum Press, New York, 1993), p. 435.
[32] F. Yano and S. Koonin, Phys. Lett. **78B**, 556 (1978).
[33] Here the radii are Lorentz *extended* by γ_s measured in the PCMS frame. For a toy model of an azimuthally symmetric source in motion but not expanding, $R_{\rm out}^{\rm PCMS} = \gamma_s\sqrt{R_{\rm side}^2 + \beta_s^2\tau^2}$.
[34] These values are taken from fits to the single particle spectra for the 5%–15% centrality bin for a linear velocity profile in a hard sphere. For a linear transverse rapidity in a Gaussian source these values vary by less than 2%.
[35] B. Hahn, D. G. Ravenhall, and R. Hofstadter, Phys. Rev. **101**, 1131 (1956).

Centrality Dependence of $\pi^{+/-}$, $K^{+/-}$, p, and $\bar{p}$ Production from $\sqrt{s_{NN}} = 130$ GeV Au + Au Collisions at RHIC

K. Adcox,[40] S. S. Adler,[3] N. N. Ajitanand,[27] Y. Akiba,[14] J. Alexander,[27] L. Aphecetche,[34] Y. Arai,[14] S. H. Aronson,[3] R. Averbeck,[28] T. C. Awes,[29] K. N. Barish,[5] P. D. Barnes,[19] J. Barrette,[21] B. Bassalleck,[25] S. Bathe,[22] V. Baublis,[30] A. Bazilevsky,[12,32] S. Belikov,[12,13] F. G. Bellaiche,[29] S. T. Belyaev,[16] M. J. Bennett,[19] Y. Berdnikov,[35] S. Botelho,[33] M. L. Brooks,[19] D. S. Brown,[26] N. Bruner,[25] D. Bucher,[22] H. Buesching,[22] V. Bumazhnov,[12] G. Bunce,[3,32] J. Burward-Hoy,[28] S. Butsyk,[28,30] T. A. Carey,[19] P. Chand,[2] J. Chang,[5] W. C. Chang,[1] L. L. Chavez,[25] S. Chernichenko,[12] C. Y. Chi,[8] J. Chiba,[14] M. Chiu,[8] R. K. Choudhury,[2] T. Christ,[28] T. Chujo,[3,39] M. S. Chung,[15,19] P. Chung,[27] V. Cianciolo,[29] B. A. Cole,[8] D. G. D'Enterria,[34] G. David,[3] H. Delagrange,[34] A. Denisov,[12] A. Deshpande,[32] E. J. Desmond,[3] O. Dietzsch,[33] B. V. Dinesh,[2] A. Drees,[28] A. Durum,[12] D. Dutta,[2] K. Ebisu,[24] Y. V. Efremenko,[29] K. El Chenawi,[40] H. En'yo,[17,31] S. Esumi,[39] L. Ewell,[3] T. Ferdousi,[5] D. E. Fields,[25] S. L. Fokin,[16] Z. Fraenkel,[42] A. Franz,[3] A. D. Frawley,[9] S.-Y. Fung,[5] S. Garpman,[20,*] T. K. Ghosh,[40] A. Glenn,[36] A. L. Godoi,[33] Y. Goto,[32] S. V. Greene,[40] M. Grosse Perdekamp,[32] S. K. Gupta,[2] W. Guryn,[3] H.-Å. Gustafsson,[20] J. S. Haggerty,[3] H. Hamagaki,[7] A. G. Hansen,[19] H. Hara,[24] E. P. Hartouni,[18] R. Hayano,[38] N. Hayashi,[31] X. He,[10] T. K. Hemmick,[28] J. M. Heuser,[28] M. Hibino,[41] J. C. Hill,[13] D. S. Ho,[43] K. Homma,[11] B. Hong,[15] A. Hoover,[26] T. Ichihara,[31,32] K. Imai,[17,31] M. S. Ippolitov,[16] M. Ishihara,[31,32] B. V. Jacak,[28,32] W. Y. Jang,[15] J. Jia,[28] B. M. Johnson,[3] S. C. Johnson,[18,28] K. S. Joo,[23] S. Kametani,[41] J. H. Kang,[43] M. Kann,[30] S. S. Kapoor,[2] S. Kelly,[8] B. Khachaturov,[42] A. Khanzadeev,[30] J. Kikuchi,[41] D. J. Kim,[43] H. J. Kim,[43] S. Y. Kim,[43] Y. G. Kim,[43] W. W. Kinnison,[19] E. Kistenev,[3] A. Kiyomichi,[39] C. Klein-Boesing,[22] S. Klinksiek,[25] L. Kochenda,[30] V. Kochetkov,[12] D. Koehler,[25] T. Kohama,[11] D. Kotchetkov,[5] A. Kozlov,[42] P. J. Kroon,[3] K. Kurita,[31,32] M. J. Kweon,[15] Y. Kwon,[43] G. S. Kyle,[26] R. Lacey,[27] J. G. Lajoie,[13] J. Lauret,[27] A. Lebedev,[13,16] D. M. Lee,[19] M. J. Leitch,[19] X. H. Li,[5] Z. Li,[6,31] D. J. Lim,[43] M. X. Liu,[19] X. Liu,[6] Z. Liu,[6] C. F. Maguire,[40] J. Mahon,[3] Y. I. Makdisi,[3] V. I. Manko,[16] Y. Mao,[6,31] S. K. Mark,[21] S. Markacs,[8] G. Martinez,[34] M. D. Marx,[28] A. Masaike,[17] F. Matathias,[28] T. Matsumoto,[7,41] P. L. McGaughey,[19] E. Melnikov,[12] M. Merschmeyer,[22] F. Messer,[28] M. Messer,[3] Y. Miake,[39] T. E. Miller,[40] A. Milov,[42] S. Mioduszewski,[3,36] R. E. Mischke,[19] G. C. Mishra,[10] J. T. Mitchell,[3] A. K. Mohanty,[2] D. P. Morrison,[3] J. M. Moss,[19] F. Mühlbacher,[28] M. Muniruzzaman,[5] J. Murata,[31] S. Nagamiya,[14] Y. Nagasaka,[24] J. L. Nagle,[8] Y. Nakada,[17] B. K. Nandi,[5] J. Newby,[36] L. Nikkinen,[21] P. Nilsson,[20] S. Nishimura,[7] A. S. Nyanin,[16] J. Nystrand,[20] E. O'Brien,[3] C. A. Ogilvie,[13] H. Ohnishi,[3,11] I. D. Ojha,[4,40] M. Ono,[39] V. Onuchin,[12] A. Oskarsson,[20] L. Österman,[20] I. Otterlund,[20] K. Oyama,[7,38] L. Paffrath,[3,*] A. P. T. Palounek,[19] V. S. Pantuev,[28] V. Papavassiliou,[26] S. F. Pate,[26] T. Peitzmann,[22] A. N. Petridis,[13] C. Pinkenburg,[3,27] R. P. Pisani,[3] P. Pitukhin,[12] F. Plasil,[29] M. Pollack,[28,36] K. Pope,[36] M. L. Purschke,[3] I. Ravinovich,[42] K. F. Read,[29,36] K. Reygers,[22] V. Riabov,[30,35] Y. Riabov,[30] M. Rosati,[13] A. A. Rose,[40] S. S. Ryu,[43] N. Saito,[31,32] A. Sakaguchi,[11] T. Sakaguchi,[7,41] H. Sako,[39] T. Sakuma,[31,37] V. Samsonov,[30] T. C. Sangster,[18] R. Santo,[22] H. D. Sato,[17,31] S. Sato,[39] S. Sawada,[14] B. R. Schlei,[19] Y. Schutz,[34] V. Semenov,[12] R. Seto,[5] T. K. Shea,[3] I. Shein,[12] T.-A. Shibata,[31,37] K. Shigaki,[14] T. Shiina,[19] Y. H. Shin,[43] I. G. Sibiriak,[16] D. Silvermyr,[20] K. S. Sim,[15] J. Simon-Gillo,[19] C. P. Singh,[4] V. Singh,[4] M. Sivertz,[3] A. Soldatov,[12] R. A. Soltz,[18] S. Sorensen,[29,36] P. W. Stankus,[29] N. Starinsky,[21] P. Steinberg,[8] E. Stenlund,[20] A. Ster,[44] S. P. Stoll,[3] M. Sugioka,[31,37] T. Sugitate,[11] J. P. Sullivan,[19] Y. Sumi,[11] Z. Sun,[6] M. Suzuki,[39] E. M. Takagui,[33] A. Taketani,[31] M. Tamai,[41] K. H. Tanaka,[14] Y. Tanaka,[24] E. Taniguchi,[31,37] M. J. Tannenbaum,[3] J. Thomas,[28] J. H. Thomas,[18] T. L. Thomas,[25] W. Tian,[6,36] J. Tojo,[17,31] H. Torii,[17,31] R. S. Towell,[19] I. Tserruya,[42] H. Tsuruoka,[39] A. A. Tsvetkov,[16] S. K. Tuli,[4] H. Tydesjö,[20] N. Tyurin,[12] T. Ushiroda,[24] H. W. van Hecke,[19] C. Velissaris,[26] J. Velkovska,[28] M. Velkovsky,[28] A. A. Vinogradov,[16] M. A. Volkov,[16] A. Vorobyov,[30] E. Vznuzdaev,[30] H. Wang,[5] Y. Watanabe,[31,32] S. N. White,[3] C. Witzig,[3] F. K. Wohn,[13] C. L. Woody,[3] W. Xie,[5,42] K. Yagi,[39] S. Yokkaichi,[31] G. R. Young,[29] I. E. Yushmanov,[16] W. A. Zajc,[8] Z. Zhang,[28] and S. Zhou[6]

(PHENIX Collaboration)

[1]*Institute of Physics, Academia Sinica, Taipei 11529, Taiwan*
[2]*Bhabha Atomic Research Centre, Bombay 400 085, India*
[3]*Brookhaven National Laboratory, Upton, New York 11973-5000*
[4]*Department of Physics, Banaras Hindu University, Varanasi 221005, India*
[5]*University of California–Riverside, Riverside, California 92521*
[6]*China Institute of Atomic Energy (CIAE), Beijing, People's Republic of China*
[7]*Center for Nuclear Study, Graduate School of Science, University of Tokyo, 7-3-1 Hongo, Bunkyo, Tokyo 113-0033, Japan*

 0031-9007/02/88(24)/242301(6)$20.00 © 2002 The American Physical Society

[8]*Columbia University, New York, New York 10027*
and Nevis Laboratories, Irvington, New York 10533
[9]*Florida State University, Tallahassee, Florida 32306*
[10]*Georgia State University, Atlanta, Georgia 30303*
[11]*Hiroshima University, Kagamiyama, Higashi-Hiroshima 739-8526, Japan*
[12]*Institute for High Energy Physics (IHEP), Protvino, Russia*
[13]*Iowa State University, Ames, Iowa 50011*
[14]*KEK, High Energy Accelerator Research Organization, Tsukuba-shi, Ibaraki-ken 305-0801, Japan*
[15]*Korea University, Seoul, 136-701 Korea*
[16]*Russian Research Center "Kurchatov Institute," Moscow, Russia*
[17]*Kyoto University, Kyoto 606, Japan*
[18]*Lawrence Livermore National Laboratory, Livermore, California 94550*
[19]*Los Alamos National Laboratory, Los Alamos, New Mexico 87545*
[20]*Department of Physics, Lund University, Box 118, SE-221 00 Lund, Sweden*
[21]*McGill University, Montreal, Quebec H3A 2T8, Canada*
[22]*Institut für Kernphysik, University of Münster, D-48149 Münster, Germany*
[23]*Myongji University, Yongin, Kyonggido 449-728, Korea*
[24]*Nagasaki Institute of Applied Science, Nagasaki-shi, Nagasaki 851-0193, Japan*
[25]*University of New Mexico, Albuquerque, New Mexico 87131*
[26]*New Mexico State University, Las Cruces, New Mexico 88003*
[27]*Chemistry Department, State University of New York–Stony Brook, Stony Brook, New York 11794*
[28]*Department of Physics and Astronomy, State University of New York–Stony Brook, Stony Brook, New York 11794*
[29]*Oak Ridge National Laboratory, Oak Ridge, Tennessee 37831*
[30]*PNPI, Petersburg Nuclear Physics Institute, Gatchina, Russia*
[31]*RIKEN (The Institute of Physical and Chemical Research), Wako, Saitama 351-0198, Japan*
[32]*RIKEN BNL Research Center, Brookhaven National Laboratory, Upton, New York 11973-5000*
[33]*Universidade de São Paulo, Instituto de Física, Caixa Postal 66318, São Paulo CEP05315-970, Brazil*
[34]*SUBATECH (Ecole des Mines de Nantes, IN2P3/CNRS, Universite de Nantes), BP 20722-44307, Nantes-cedex 3, France*
[35]*St. Petersburg State Technical University, St. Petersburg, Russia*
[36]*University of Tennessee, Knoxville, Tennessee 37996*
[37]*Department of Physics, Tokyo Institute of Technology, Tokyo, 152-8551, Japan*
[38]*University of Tokyo, Tokyo, Japan*
[39]*Institute of Physics, University of Tsukuba, Tsukuba, Ibaraki 305, Japan*
[40]*Vanderbilt University, Nashville, Tennessee 37235*
[41]*Waseda University, Advanced Research Institute for Science and Engineering, 17 Kikui-cho, Shinjuku-ku, Tokyo 162-0044 Japan*
[42]*Weizmann Institute, Rehovot 76100, Israel*
[43]*Yonsei University, IPAP, Seoul 120-749, Korea*
[44]*KFKI Research Institute for Particle and Nuclear Physics (RMKI), Budapest, Hungary*[†]

(Received 17 December 2001; published 28 May 2002)

Identified $\pi^{+/-}$, $K^{+/-}$, p, and $\overline{p}$ transverse momentum spectra at midrapidity in $\sqrt{s_{NN}} = 130$ GeV Au + Au collisions were measured by the PHENIX experiment at RHIC as a function of collision centrality. Average transverse momenta increase with the number of participating nucleons in a similar way for all particle species. Within errors, all midrapidity particle yields per participant are found to be increasing with the number of participating nucleons. There is an indication that $K^{+/-}$, p, and $\overline{p}$ yields per participant increase faster than the $\pi^{+/-}$ yields. In central collisions at high transverse momenta ($p_T \gtrsim 2$ GeV/c), $\overline{p}$ and p yields are comparable to the $\pi^{+/-}$ yields.

DOI: 10.1103/PhysRevLett.88.242301 PACS numbers: 25.75.Dw

We report first results on identified $\pi^{+/-}$, $K^{+/-}$, p, and $\overline{p}$ production as a function of collision centrality in $\sqrt{s_{NN}} = 130$ GeV Au + Au collisions, measured by the PHENIX experiment at the Relativistic Heavy Ion Collider (RHIC). The PHENIX objective is to search for signatures of deconfinement and chiral symmetry restoration and to study the transition from normal to deconfined nuclear matter by utilizing a wide variety of probes.

Early RHIC results show that the transverse energy density and particle multiplicities are considerably higher than previously observed in relativistic heavy-ion collisions [1,2]. Measured energy densities extend into the region predicted to be favorable for the formation of a quark-gluon plasma [3]. Identified hadron spectroscopy provides a tool for studying reaction dynamics beyond that of global event characterization. The yields of hadrons reflect the particle production mechanism, while spectral shapes are sensitive to the dynamical evolution of the system. The mass and centrality dependence of the spectra can help differentiate between competing theoretical descriptions such as collective hydrodynamical expansion [4,5] or transverse momentum (p_T) broadening in the partonic

stage of the reaction [6]. Additionally the relative yields of baryons and mesons at high $p_T (\simeq 2\ \mathrm{GeV}/c)$ may give insight into baryon number transport [7] and the interplay between soft and hard processes.

The PHENIX detector has diverse particle identification (PID) capabilities [8], including excellent hadron identification over a broad momentum range. This measurement was performed using a portion of the east central-arm spectrometer, covering pseudorapidity $|\eta| < 0.35$ and $\Delta\phi = \pi/4$ in azimuthal angle.

The collision z-vertex and the timing system's start signal are generated by the Beam-Beam Counters (BBC), two arrays of quartz Cherenkov radiators which surround the beam axis covering $\eta = \pm(3.0 - 3.9)$. The tracking system includes a multilayer focusing drift chamber (DC) located outside an axially symmetric magnetic field at a radial distance between 2.0 and 2.4 m followed by a multiwire proportional chamber with pixel-pad readout (PC1) [9]. Pattern recognition in the DC is based on a combinatorial Hough transform in the track bend plane [10]. The polar angle of the track is determined by PC1 and the collision z vertex. A track model based on a field-integral lookup table determines the charged particle momentum and the path length to the time-of-flight (TOF) wall. The momentum resolution is $\delta p/p \simeq 0.6\% \oplus 3.6\% p$ (GeV/c).

The timing system's stop signal for each particle is measured by the TOF scintillator wall, located at a radial distance of 5.06 m, resulting in a flight-time measurement with a resolution of $\sigma \simeq 115$ ps. Reconstructed tracks are projected to the TOF and matched with hits in the scintillator slats using a momentum-dependent search window determined by multiple scattering and the momentum resolution. A velocity dependent energy loss cut based on a Bethe-Bloch parametrization is applied to the measured TOF pulse height. Combining the momentum and flight time, we reconstruct the particle mass and select particles by applying 2σ momentum dependent cuts in mass squared.

Corrections for geometrical acceptance, decay-in-flight, momentum resolution and reconstruction efficiency are determined using a single-particle full GEANT Monte Carlo (MC) simulation. The acceptance correction assumes that the spectra are flat in azimuth and in rapidity for $|y| < 0.5$ [11]. Fiducial area cuts, energy loss, and hit-track matching cuts are applied consistently in simulation and data. In peripheral events the track reconstruction efficiency is $\approx$98%. As the centrality increases, the efficiency is reduced due to the increased detector occupancy. Multiplicity dependent corrections are obtained by embedding simulated tracks into real events. Track-by-track corrections are applied taking into account the event centrality and the particle species. The efficiency for $\pi^{+/-}$ in the most central events is $\approx(68 \pm 6)\%$, independent of momentum. In the case of overlapping hits in the TOF wall, the earliest pulse reaching each photomultiplier is recorded. This favors the faster particles; hence, in central events heavier particles suffer an additional reconstruction inefficiency of $\approx$4%. Corrections for feed-down from weak decays are not applied. A MC simulation is used to estimate the probability for reconstructing protons from Λ decays as prompt protons. Within the PHENIX acceptance this probability is $\approx$50% at $p_T = 0.5$ GeV/c, $\approx$32% at $p_T = 1$ GeV/c, and $\approx$12% at $p_T \geq 2$ GeV/c. Taking $\frac{\Lambda}{p} = 1$ as an upper limit, we estimate 33% as the upper limit of weak decay contribution to the reported p and $\overline{p}$ yields and maximal 16% change of measured $\langle p_T \rangle$.

About 140 000 minimum bias events, representing $92\% \pm 4\%$ of the total inelastic cross section of 6.8 b [1] were analyzed. This sample was subdivided into five centrality classes: 0%–5%, 5%–15%, 15%–30%, 30%–60%, and 60%–92%, using the BBC and zero-degree calorimeters for event characterization [1]. For each class, the average number of nucleons participating in the collision (N_{part}) is obtained from a Glauber model calculation [12].

Figure 1 shows the invariant yield as a function of p_T for π^+, K^+, p (left panel) and π^-, K^-, $\overline{p}$ for three centrality selections. Error bars in the figure are the combined statistical errors in the data and the corrections. Systematic uncertainties from acceptance, multiplicity-dependent efficiency corrections, and PID cuts result in an overall systematic error in the absolute normalization of $\approx$11% for all species. As a consistency check, we have added all identified charged hadron spectra in the

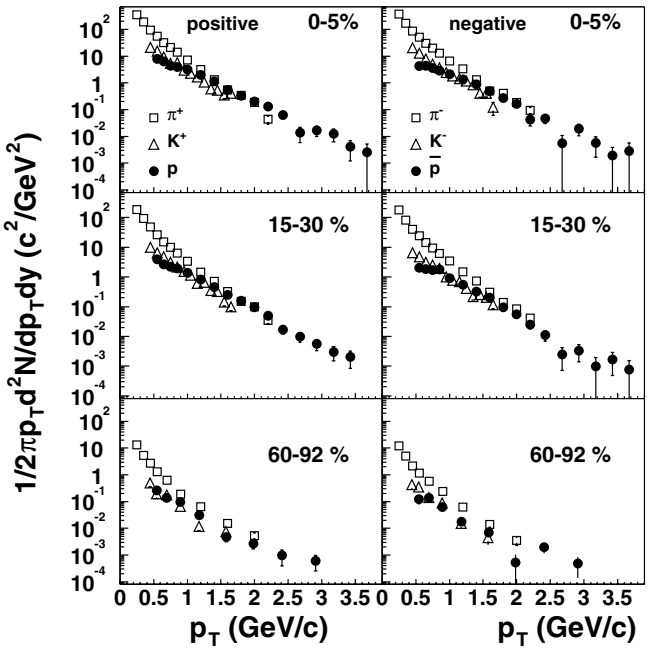

FIG. 1. Transverse momentum spectra measured at midrapidity for π^+, K^+, p (left) and π^-, K^-, $\overline{p}$ at the three different centrality selections indicated in each panel. The symbols indicated in the top panels apply for all centrality selections.

p_T region where PID is available for all species and compared to the PHENIX charged hadron measurement [12]. The results agree to better than 10% for all centralities. Additionally, the PHENIX π^0 spectra [12] and the $\pi^{+/-}$ spectra in the region of overlapping p_T are within ≈10% for the central and ≈25% for the peripheral selections, which is within the systematic errors of the two measurements. $\overline{p}$ results presented here are also in agreement (within errors) with a recent STAR publication [13].

In peripheral events the $\pi^{+/-}$ spectra exhibit a concave shape, well described by a power-law parametrization as observed in hadron-hadron collisions [14]. With increasing centrality the curvature in the spectra decreases, leading to an almost exponential dependence on p_T for the most central events. Over the measured p_T range, the $K^{+/-}$ spectra can be described by an exponential distribution either in p_T or in $m_T = \sqrt{p_T^2 + m^2}$, while the p and $\overline{p}$ spectra can be described either as a Boltzmann or an exponential distribution in m_T. The slopes of the m_T spectra flatten and the mean transverse momentum ($\langle p_T \rangle$) increases with particle mass and with centrality. This behavior has been previously observed in lower energy heavy ion collisions at the BNL-AGS [15] and at the CERN-SPS [16,17] and was attributed to collective radial motion (flow).

At lower energies, it is not uncommon for the proton yields to equal or exceed the π^+ yields, since many of the protons come from the initial state. A new feature observed for the first time at RHIC is that in central collisions at $p_T \approx 2$ GeV/c the $\overline{p}$ yields are comparable to the π^- yields. Positive and negative hadrons behave in a similar way. In central events the proton yields approach the π^+ spectra around $p_T \simeq 1.6$ GeV/c. As the centrality decreases, this happens at larger p_T. In peripheral events, p and $\overline{p}$ spectra are below the $\pi^{+/-}$ spectra over the whole measured p_T range. Since antiprotons are not as numerous as the protons, $\overline{p}$ and π^- yields become comparable only at the high end of the measured pion p_T range in the most central collisions. We note that in pp [18] and $p\overline{p}$ [19] collisions at $\sqrt{s} = 23$–63 GeV and $\sqrt{s} = 300$–1800 GeV, respectively, the $\overline{p}/\pi^-$ ratio steadily increases with p_T up to $\simeq 0.33$ at $p_T \simeq 1.5$ GeV/c nearly independent of $\sqrt{s}$. Data on baryon/meson ratios at higher p_T are available only from pp collisions at ISR energies ($\sqrt{s} = 23$–63 GeV) and show that above $p_T \simeq 1.5$ GeV/c the $\overline{p}/\pi^-$ ratio rises to $\simeq 0.4$ at $p_T \simeq 2$ GeV/c and then drops, as expected if valence quark jet fragmentation is the dominant production mechanism for high p_T hadrons. In central collisions at RHIC the high p_T (anti)proton/pion ratios are ∼1—much larger than in pp collisions.

Hydrodynamic calculations with fixed freeze-out temperature [5] or with freeze-out modeled using a hadronic cascade [4] suggest that hydrodynamic expansion is responsible for the baryon dominance at high p_T. However, protons/antiprotons produced via a baryon junction mechanism combined with jet quenching in the pion channel are shown to exhibit the same effect [7]. Intrinsic p_T broadening in the partonic phase caused by gluon saturation [6] gives yet another alternative explanation. The above models have similar predictions in the p_T range measured here, but show different behavior at higher p_T. New data with broader p_T range is needed in order to distinguish between currently available theories.

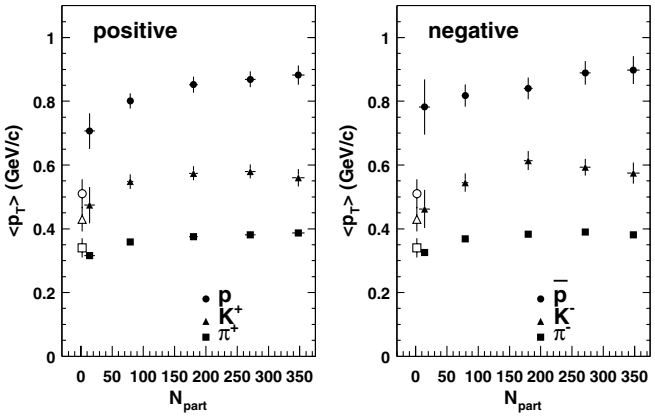

FIG. 2. Average transverse momentum for π^+, K^+, p (left) and π^-, K^-, $\overline{p}$ as a function of the number of nucleons participating in the collision $N_{\rm part}$. The error bars represent the statistical errors. The systematic errors are discussed in the text. The open points are interpolations from pp and $p\overline{p}$ data; see text for details.

To quantify the centrality and mass dependencies of hadron production, we determine the mean ($\langle p_T \rangle$ shown in Fig. 2) and the integral (dN/dy shown in Fig. 3) of the p_T distributions. Both quantities require extrapolation of the spectra below and above the measured range. For each particle species, we use at least two functional forms consistent with the data, as outlined above, and the results presented are averaged between two fits. The frac-

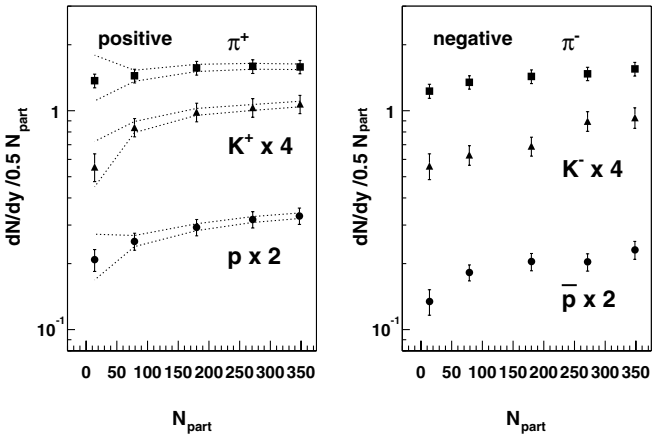

FIG. 3. $dN/dy_{|y=0}$ per participant for π^+, K^+, p (left) and π^-, K^-, $\overline{p}$ as a function of $N_{\rm part}$. The error bars include statistical and systematic errors in dN/dy. The dashed lines around the positive hadrons show the effect of the systematic error on $N_{\rm part}$ which affects all curves in the same way.

TABLE I. Integrated hadron ($\pi^{\pm}$, $K^{\pm}$, p, and $\overline{p}$) yields at midrapidity for five centrality classes (see text) identified by the indicated number of participants $N_{\rm part}$. The errors on $N_{\rm part}$ are the systematic errors. The errors listed for $\langle dN/dy_{|y=0}\rangle$ are statistical. The systematic errors are 13%, 15%, and 14% for $\pi^{\pm}$, $K^{\pm}$, p, and $\overline{p}$, respectively.

$N_{\rm part}$	348 ± 10.0	271 ± 8.4	180 ± 6.6	79 ± 4.6	14 ± 3.3
π^+	276 ± 3	216 ± 2	141 ± 1.5	57 ± 0.6	9.6 ± 0.2
π^-	270 ± 3	200 ± 2	129 ± 1.4	53.3 ± 0.6	8.6 ± 0.2
K^+	46.7 ± 1.5	35.0 ± 1.3	22.2 ± 0.8	8.3 ± 0.3	0.97 ± 0.11
K^-	40.5 ± 2.3	30.4 ± 1.4	15.5 ± 0.7	6.2 ± 0.3	0.98 ± 0.1
p	28.7 ± 0.9	21.6 ± 0.6	13.2 ± 0.4	5.0 ± 0.2	0.73 ± 0.06
$\overline{p}$	20.1 ± 1.0	13.8 ± 0.6	9.2 ± 0.4	3.6 ± 0.1	0.47 ± 0.05

tion of the yield in the extrapolated regions is estimated to be 30% ± 6% for $\pi^{+/-}$, 40% ± 8% for $K^{+/-}$, and 25% ± 7.5% for $p/\overline{p}$. Combining systematic uncertainties in the extrapolation fractions and the estimated background under mass-squared peaks (2%, 5%, and 3%) yield systematic uncertainties in the measured $\langle p_T\rangle$ of 7%, 10%, and 8% for $\pi^{+/-}$, $K^{+/-}$, and $p/\overline{p}$, respectively. Further combining the above uncertainties, which affect only the shape of the spectra, with the 11% uncertainty in the absolute normalization gives systematic uncertainties of 13%, 15%, and 14% in the measured dN/dy for $\pi^{+/-}$, $K^{+/-}$, and $p/\overline{p}$, respectively. We note that after converting to $dN/d\eta$, the sum of the identified charged hadron yields agrees with the previously published PHENIX results on total charged multiplicity $dN_{ch}/d\eta$ [1] within 5%.

Figure 2 shows the $\langle p_T\rangle$ as a function of $N_{\rm part}$ for π^+, K^+, p (left panel) and π^-, K^-, $\overline{p}$. Filled points are this measurement; open points at $N_{\rm part} = 2$ are interpolations to $\sqrt{s} = 130$ GeV obtained from pp and $p\overline{p}$ data at lower [18] and higher energies [19], respectively. In peripheral Au-Au collisions at RHIC $\pi^{+/-}$ and $K^{+/-}$ exhibit similar $\langle p_T\rangle$ to those in pp collisions, but protons and antiprotons have significantly higher $\langle p_T\rangle$, indicating that nuclear effects are important even at small $N_{\rm part}$. For all measured particle species, $\langle p_T\rangle$ increases by ≈12%–14% from the first to the second centrality bin (i.e., $N_{\rm part} = 14$ to 79). Above $N_{\rm part} = 100$ the pion and kaon average momentum appears to saturate, whereas for p and $\overline{p}$ it rises slowly. However, we note that going from peripheral to the most central event class the overall increase in $\langle p_T\rangle$ is ≈20% ± 5% independent of particle species.

Figure 3 shows the yields per participant versus $N_{\rm part}$. Error bars include statistical and multiplicity dependent systematic errors. Systematic uncertainties in $N_{\rm part}$ that can move all curves independent of mass are shown with bands around the positive hadron points. Total systematic uncertainties in $N_{\rm part}$ and the yields at each $N_{\rm part}$ are listed in Table I.

For all particle species, the yield per participant increases with $N_{\rm part}$. As for $\langle p_T\rangle$, most of the increase occurs between the two most peripheral centrality selections (i.e., $N_{\rm part} = 14$ to 79). However, in contrast with the centrality dependence of $\langle p_T\rangle$, we see an indication that the total increase in the yields per participant differs among particle species as we go from peripheral to central events. The pion yield per participant rises by 21% ± 6%(stat) ± 8%(syst). The kaon yields per participant rise faster: 94% ± 11%(stat) ± 26%(syst) and 66% ± 12%(stat) ± 20%(syst), for K^+ and K^-, respectively. Similar trends in the centrality dependence of strangeness production have been observed in lower energy heavy-ion collisions at the BNL-AGS [20] and at the CERN-SPS [17]. It is interesting to note that at RHIC p and $\overline{p}$ yields per participant behave similarly to the $K^{+/-}$ yields and also rise faster than the pions with increasing $N_{\rm part}$. The increase is 58% ± 5%(stat) ± 16%(syst) and 72% ± 9%(stat) ± 20%(syst), respectively. The similar centrality dependence in p and $\overline{p}$ yields per participant indicates that baryon/antibaryon pair production is the dominant source of protons and antiprotons alike.

In heavy-ion collisions at AGS energies [21] the $\overline{p}$ production is close to threshold, the yields per participant are lower than in pp collisions, and they decrease from peripheral to central collisions, probably due to annihilation. At the SPS, the $\overline{p}$ yield per participant is larger than the pp value and has almost no centrality dependence [22]. At RHIC, the total yield of antiprotons at midrapidity in central Au-Au collisions is a factor of ≃1000 larger than at the AGS [23] and nearly an order of magnitude above that in Pb + Pb collisions at CERN [24]. Most of the increase is due to the $\sqrt{s}$ dependence of baryon/antibaryon pair production; however, the yield per participant rises noticeably from peripheral to central collisions.

In conclusion, an intriguing new behavior in identified hadron production at RHIC is reported. In central Au-Au collisions the antiprotons yield is comparable to the π^- at high p_T—a behavior never observed before in elementary or in heavy-ion collisions. $\langle p_T\rangle$ rises with centrality similarly for all particle species, while $K^{+/-}$, p, and $\overline{p}$ yields per participant increase somewhat faster than the $\pi^{+/-}$ yields.

We thank the staff of the Collider-Accelerator and Physics Departments at BNL for their vital contributions. We acknowledge support from the Department of Energy and NSF (U.S.A.), MEXT and JSPS (Japan), RAS, RMAE, and RMS (Russia), BMBF, DAAD, and AvH (Germany), VR and KAW (Sweden), MIST and NSERC (Canada), CNPq and FAPESP (Brazil), IN2P3/CNRS

(France), DAE and DST (India), KRF and CHEP (Korea), the U.S. CRDF for the FSU, and the U.S.-Israel BSF.

*Deceased.

†Not a participating institution.

[1] K. Adcox *et al.,* Phys. Rev. Lett. **86**, 3500 (2001).

[2] K. Adcox *et al.,* Phys. Rev. Lett. **87**, 052301 (2001); B. B. Back *et al.,* Phys. Rev. Lett. **85**, 3100 (2000); C. Adler *et al.,* Phys. Rev. Lett. **87**, 112303 (2001).

[3] For example, see *Proceedings of Quark Matter 1984,* edited by K. Kajantie (Springer, Berlin, 1985); *Proceedings of Quark Matter 1987,* edited by H. Satz, H. J. Specht, and R. Stock, Z. Phys. C **38**, 1–370 (1988).

[4] D. Teaney *et al.,* Phys. Rev. Lett. **86**, 4783 (2001); nucl-th/0110037.

[5] P. Kolb *et al.,* Nucl. Phys. **A696**, 197 (2001); P. Huovinen *et al.,* Phys. Lett. B **503**, 58 (2001).

[6] J. Schaffner-Bielich *et al.,* hep-ph/0101133; nucl-th/0108048, and references therein.

[7] I. Vitev and Miklos Gyulassy nucl-th/0104066.

[8] PHENIX Collaboration, H. Hamagaki *et al.,* Nucl. Phys. **A698**, 412c (2002).

[9] J. Velkovska, in *Proceedings of Application of Accelerators in Research and Industry, 2000,* AIP Conf. Proc. 576 (AIP, New York, 2001), p. 227.

[10] J. T. Mitchell *et al.,* Nucl. Instrum. Methods Phys. Res., Sect. A **482**, 498–515 (2002).

[11] B. B. Back *et al.,* Phys. Rev. Lett. **87**, 102303 (2001).

[12] K. Adcox *et al.,* Phys. Rev. Lett. **88**, 22301 (2002).

[13] C. Adler *et al.,* Phys. Rev. Lett. **87**, 262302 (2001).

[14] C. Albajar *et al.,* Nucl. Phys. **B335**, 261 (1990).

[15] L. Ahle *et al.,* Nucl. Phys. **A610**, 139c–152c (1996).

[16] I. G. Bearden *et al.,* Phys. Rev. Lett. **78**, 2080 (1997).

[17] J. Bachler *et al.,* Nucl. Phys. **A661**, 45c–54c (1999).

[18] B. Alper *et al.,* Nucl. Phys. **B100**, 237–290 (1975).

[19] T. Alexopoulos *et al.,* Phys. Rev. D **48**, 984 (1993).

[20] L. Ahle *et al.,* Phys. Rev. C **59**, 2173 (1999); Phys. Rev. C **60**, 044904 (1999).

[21] J. Barrette *et al.,* Phys. Rev. Lett. **70**, 1763 (1993).

[22] G. I. Veres, Nucl. Phys. **A661**, 383c–386c (1999).

[23] D. Beavis *et al.,* Phys. Rev. Lett. **75**, 3633 (1995); M. Bennett *et al.,* Phys. Rev. C **56**, 1521 (1997); L. Ahle *et al.,* Phys. Rev. Lett. **81**, 2650 (1998).

[24] I. G. Bearden *et al.,* Phys. Lett. B **388** 431–436 (1996).

Suppression of Hadrons with Large Transverse Momentum in Central Au + Au Collisions at $\sqrt{s_{NN}} = 130$ GeV

K. Adcox,[40] S. S. Adler,[3] N. N. Ajitanand,[27] Y. Akiba,[14] J. Alexander,[27] L. Aphecetche,[34] Y. Arai,[14] S. H. Aronson,[3] R. Averbeck,[28] T. C. Awes,[29] K. N. Barish,[5] P. D. Barnes,[19] J. Barrette,[21] B. Bassalleck,[25] S. Bathe,[22] V. Baublis,[30] A. Bazilevsky,[12,32] S. Belikov,[12,13] F. G. Bellaiche,[29] S. T. Belyaev,[16] M. J. Bennett,[19] Y. Berdnikov,[35] S. Botelho,[33] M. L. Brooks,[19] D. S. Brown,[26] N. Bruner,[25] D. Bucher,[22] H. Buesching,[22] V. Bumazhnov,[12] G. Bunce,[3,32] J. Burward-Hoy,[28] S. Butsyk,[28,30] T. A. Carey,[19] P. Chand,[2] J. Chang,[5] W. C. Chang,[1] L. L. Chavez,[25] S. Chernichenko,[12] C. Y. Chi,[8] J. Chiba,[14] M. Chiu,[8] R. K. Choudhury,[2] T. Christ,[28] T. Chujo,[3,39] M. S. Chung,[15,19] P. Chung,[27] V. Cianciolo,[29] B. A. Cole,[8] D. G. D'Enterria,[34] G. David,[3] H. Delagrange,[34] A. Denisov,[12] A. Deshpande,[32] E. J. Desmond,[3] O. Dietzsch,[33] B. V. Dinesh,[2] A. Drees,[28] A. Durum,[12] D. Dutta,[2] K. Ebisu,[24] Y. V. Efremenko,[29] K. El Chenawi,[40] H. En'yo,[17,31] S. Esumi,[39] L. Ewell,[3] T. Ferdousi,[5] D. E. Fields,[25] S. L. Fokin,[16] Z. Fraenkel,[42] A. Franz,[3] A. D. Frawley,[9] S.-Y. Fung,[5] S. Garpman,[20] T. K. Ghosh,[40] A. Glenn,[36] A. L. Godoi,[33] Y. Goto,[32] S. V. Greene,[40] M. Grosse Perdekamp,[32] S. K. Gupta,[2] W. Guryn,[3] H.-Å. Gustafsson,[20] J. S. Haggerty,[3] H. Hamagaki,[7] A. G. Hansen,[19] H. Hara,[24] E. P. Hartouni,[18] R. Hayano,[38] N. Hayashi,[31] X. He,[10] T. K. Hemmick,[28] J. M. Heuser,[28] M. Hibino,[41] J. C. Hill,[13] D. S. Ho,[43] K. Homma,[11] B. Hong,[15] A. Hoover,[26] T. Ichihara,[31,32] K. Imai,[17,31] M. S. Ippolitov,[16] M. Ishihara,[31,32] B. V. Jacak,[28,32] W. Y. Jang,[15] J. Jia,[28] B. M. Johnson,[3] S. C. Johnson,[18,28] K. S. Joo,[23] S. Kametani,[41] J. H. Kang,[43] M. Kann,[30] S. S. Kapoor,[2] S. Kelly,[8] B. Khachaturov,[42] A. Khanzadeev,[30] J. Kikuchi,[41] D. J. Kim,[43] H. J. Kim,[43] S. Y. Kim,[43] Y. G. Kim,[43] W. W. Kinnison,[19] E. Kistenev,[3] A. Kiyomichi,[39] C. Klein-Boesing,[22] S. Klinksiek,[25] L. Kochenda,[30] V. Kochetkov,[12] D. Koehler,[25] T. Kohama,[11] D. Kotchetkov,[5] A. Kozlov,[42] P. J. Kroon,[3] K. Kurita,[31,32] M. J. Kweon,[15] Y. Kwon,[43] G. S. Kyle,[26] R. Lacey,[27] J. G. Lajoie,[13] J. Lauret,[27] A. Lebedev,[13,16] D. M. Lee,[19] M. J. Leitch,[19] X. H. Li,[5] Z. Li,[6,31] D. J. Lim,[43] M. X. Liu,[19] X. Liu,[6] Z. Liu,[6] C. F. Maguire,[40] J. Mahon,[3] Y. I. Makdisi,[3] V. I. Manko,[16] Y. Mao,[6,31] S. K. Mark,[21] S. Markacs,[8] G. Martinez,[34] M. D. Marx,[28] A. Masaike,[17] F. Matathias,[28] T. Matsumoto,[7,41] P. L. McGaughey,[19] E. Melnikov,[12] M. Merschmeyer,[22] F. Messer,[28] M. Messer,[3] Y. Miake,[39] T. E. Miller,[40] A. Milov,[42] S. Mioduszewski,[3,36] R. E. Mischke,[19] G. C. Mishra,[10] J. T. Mitchell,[3] A. K. Mohanty,[2] D. P. Morrison,[3] J. M. Moss,[19] F. Mühlbacher,[28] M. Muniruzzaman,[5] J. Murata,[31] S. Nagamiya,[14] Y. Nagasaka,[24] J. L. Nagle,[8] Y. Nakada,[17] B. K. Nandi,[5] J. Newby,[36] L. Nikkinen,[21] P. Nilsson,[20] S. Nishimura,[7] A. S. Nyanin,[16] J. Nystrand,[20] E. O'Brien,[3] C. A. Ogilvie,[13] H. Ohnishi,[3,11] I. D. Ojha,[4,40] M. Ono,[39] V. Onuchin,[12] A. Oskarsson,[20] L. Österman,[20] I. Otterlund,[20] K. Oyama,[7,38] L. Paffrath,[3,*] A. P. T. Palounek,[19] V. S. Pantuev,[28] V. Papavassiliou,[26] S. F. Pate,[26] T. Peitzmann,[22] A. N. Petridis,[13] C. Pinkenburg,[3,27] R. P. Pisani,[3] P. Pitukhin,[12] F. Plasil,[29] M. Pollack,[28,36] K. Pope,[36] M. L. Purschke,[3] I. Ravinovich,[42] K. F. Read,[29,36] K. Reygers,[22] V. Riabov,[30,35] Y. Riabov,[30] M. Rosati,[13] A. A. Rose,[40] S. S. Ryu,[43] N. Saito,[31,32] A. Sakaguchi,[11] T. Sakaguchi,[7,41] H. Sako,[39] T. Sakuma,[31,37] V. Samsonov,[30] T. C. Sangster,[18] R. Santo,[22] H. D. Sato,[17,31] S. Sato,[39] S. Sawada,[14] B. R. Schlei,[19] Y. Schutz,[34] V. Semenov,[12] R. Seto,[5] T. K. Shea,[3] I. Shein,[12] T.-A. Shibata,[31,37] K. Shigaki,[14] T. Shiina,[19] Y. H. Shin,[43] I. G. Sibiriak,[16] D. Silvermyr,[20] K. S. Sim,[15] J. Simon-Gillo,[19] C. P. Singh,[4] V. Singh,[4] M. Sivertz,[3] A. Soldatov,[12] R. A. Soltz,[18] S. Sorensen,[29,36] P. W. Stankus,[29] N. Starinsky,[21] P. Steinberg,[8] E. Stenlund,[20] A. Ster,[44] S. P. Stoll,[3] M. Sugioka,[31,37] T. Sugitate,[11] J. P. Sullivan,[19] Y. Sumi,[11] Z. Sun,[6] M. Suzuki,[39] E. M. Takagui,[33] A. Taketani,[31] M. Tamai,[41] K. H. Tanaka,[14] Y. Tanaka,[24] E. Taniguchi,[31,37] M. J. Tannenbaum,[3] J. Thomas,[28] J. H. Thomas,[18] T. L. Thomas,[25] W. Tian,[6,36] J. Tojo,[17,31] H. Torii,[17,31] R. S. Towell,[19] I. Tserruya,[42] H. Tsuruoka,[39] A. A. Tsvetkov,[16] S. K. Tuli,[4] H. Tydesjö,[20] N. Tyurin,[12] T. Ushiroda,[24] H. W. van Hecke,[19] C. Velissaris,[26] J. Velkovska,[28] M. Velkovsky,[28] A. A. Vinogradov,[16] M. A. Volkov,[16] A. Vorobyov,[30] E. Vznuzdaev,[30] H. Wang,[5] Y. Watanabe,[31,32] S. N. White,[3] C. Witzig,[3] F. K. Wohn,[13] C. L. Woody,[3] W. Xie,[5,42] K. Yagi,[39] S. Yokkaichi,[31] G. R. Young,[29] I. E. Yushmanov,[16] W. A. Zajc,[8] Z. Zhang,[28] and S. Zhou[6]

(PHENIX Collaboration)

[1]*Institute of Physics, Academia Sinica, Taipei 11529, Taiwan*
[2]*Bhabha Atomic Research Centre, Bombay 400 085, India*
[3]*Brookhaven National Laboratory, Upton, New York 11973-5000*
[4]*Department of Physics, Banaras Hindu University, Varanasi 221005, India*
[5]*University of California–Riverside, Riverside, California 92521*
[6]*China Institute of Atomic Energy (CIAE), Beijing, People's Republic of China*
[7]*Center for Nuclear Study, Graduate School of Science, University of Tokyo, 7-3-1 Hongo, Bunkyo, Tokyo 113-0033, Japan*

 0031-9007/02/88(2)/022301(6)$20.00 © 2002 The American Physical Society

[8]*Columbia University, New York, New York 10027*
and Nevis Laboratories, Irvington, New York 10533
[9]*Florida State University, Tallahassee, Florida 32306*
[10]*Georgia State University, Atlanta, Georgia 30303*
[11]*Hiroshima University, Kagamiyama, Higashi-Hiroshima 739-8526, Japan*
[12]*Institute for High Energy Physics (IHEP), Protvino, Russia*
[13]*Iowa State University, Ames, Iowa 50011*
[14]*KEK, High Energy Accelerator Research Organization, Tsukuba-shi, Ibaraki-ken 305-0801, Japan*
[15]*Korea University, Seoul 136-701, Korea*
[16]*Russian Research Center, "Kurchatov Institute," Moscow, Russia*
[17]*Kyoto University, Kyoto 606, Japan*
[18]*Lawrence Livermore National Laboratory, Livermore, California 94550*
[19]*Los Alamos National Laboratory, Los Alamos, New Mexico 87545*
[20]*Department of Physics, Lund University, Box 118, SE-221 00 Lund, Sweden*
[21]*McGill University, Montreal, Quebec H3A 2T8, Canada*
[22]*Institut für Kernphysik, University of Münster, D-48149 Münster, Germany*
[23]*Myongji University, Yongin, Kyonggido 449-728, Korea*
[24]*Nagasaki Institute of Applied Science, Nagasaki-shi, Nagasaki 851-0193, Japan*
[25]*University of New Mexico, Albuquerque, New Mexico 87131*
[26]*New Mexico State University, Las Cruces, New Mexico 88003*
[27]*Chemistry Department, State University of New York–Stony Brook, Stony Brook, New York 11794*
[28]*Department of Physics and Astronomy, State University of New York–Stony Brook, Stony Brook, New York 11794*
[29]*Oak Ridge National Laboratory, Oak Ridge, Tennessee 37831*
[30]*PNPI, Petersburg Nuclear Physics Institute, Gatchina, Russia*
[31]*RIKEN (The Institute of Physical and Chemical Research), Wako, Saitama 351-0198, Japan*
[32]*RIKEN BNL Research Center, Brookhaven National Laboratory, Upton, New York 11973-5000*
[33]*Universidade de São Paulo, Instituto de Física, Caixa Postal 66318, São Paulo CEP05315-970, Brazil*
[34]*SUBATECH (Ecole des Mines de Nantes, IN2P3/CNRS, Universite de Nantes), BP 20722-44307, Nantes-cedex 3, France*
[35]*St. Petersburg State Technical University, St. Petersburg, Russia*
[36]*University of Tennessee, Knoxville, Tennessee 37996*
[37]*Department of Physics, Tokyo Institute of Technology, Tokyo 152-8551, Japan*
[38]*University of Tokyo, Tokyo, Japan*
[39]*Institute of Physics, University of Tsukuba, Tsukuba, Ibaraki 305, Japan*
[40]*Vanderbilt University, Nashville, Tennessee 37235*
[41]*Waseda University, Advanced Research Institute for Science and Engineering, 17 Kikui-cho, Shinjuku-ku, Tokyo 162-0044 Japan*
[42]*Weizmann Institute, Rehovot 76100, Israel*
[43]*Yonsei University, IPAP, Seoul 120-749, Korea*
[44]*KFKI Research Institute for Particle and Nuclear Physics (RMKI), Budapest, Hungary*[†]

(Received 5 September 2001; published 21 December 2001)

Transverse momentum spectra for charged hadrons and for neutral pions in the range 1 GeV/c < p_T < 5 GeV/c have been measured by the PHENIX experiment at RHIC in Au + Au collisions at $\sqrt{s_{NN}}$ = 130 GeV. At high p_T the spectra from peripheral nuclear collisions are consistent with scaling the spectra from $p + p$ collisions by the average number of binary nucleon-nucleon collisions. The spectra from central collisions are significantly suppressed when compared to the binary-scaled $p + p$ expectation, and also when compared to similarly binary-scaled peripheral collisions, indicating a novel nuclear-medium effect in central nuclear collisions at RHIC energies.

DOI: 10.1103/PhysRevLett.88.022301 PACS numbers: 25.75.Dw

Ultrarelativistic heavy ion collisions provide the opportunity to study strongly interacting matter at high temperature and density. At Brookhaven National Laboratory's Relativistic Heavy Ion Collider (RHIC), nuclei as heavy as gold (Au) are accelerated to energies of $\sqrt{s_{NN}}$ = 200 GeV per nucleon-nucleon pair. In the early stages of a central collision, energy densities are expected to be sufficient to dissolve normal nuclear matter into a phase of deconfined quarks and gluons, the "quark gluon plasma" (QGP). The PHENIX experiment is designed to investigate nuclear collisions with a wide variety of probes, focusing primarily on those produced in the early stages of the collision.

Of particular interest are the products of parton scatterings with large momentum transfer ("hard scatterings"). In $p + p$ collisions hard-scattered partons fragment into jets of hadrons; these fragments are the primary source of hadrons at high transverse momentum (p_T), typically above ~2 GeV/c [1]. In a high-energy nuclear collision hard scattering will occur at the earliest time during the collision, well before the QGP is expected to form, and thus the scattered partons will subsequently experience the

strongly interacting medium created in the collision. These partons are expected to lose energy [2] in hot and dense nuclear matter through gluon bremsstrahlung, effectively quenching jet production. This would have many observable consequences, of which the most directly measurable would be a depletion in the yield of high p_T hadrons [3]. It has been suggested that the energy loss is larger in a medium of deconfined color charges than in hadronic matter [4], making "jet quenching" a potential signature for QGP formation.

To quantify such modifications we need a baseline expectation for spectra from nuclear ($A + A$) collisions in the absence of nuclear medium effects. Given that hard parton scatterings have small cross sections, one can regard the nuclei as an incoherent superposition of partons ("point-like scaling"). We approximate this by modeling the $A + A$ collision as a sum of independent nucleon-nucleon ($N + N$) collisions ("binary scaling"). For a given class of $A + A$ collisions, we can determine $\langle N_{\rm binary}\rangle$ the average number of inelastic $N + N$ collisions per event and then define the *nuclear modification factor* as the ratio,

$$R_{AA}(p_T) = \frac{(1/N_{\rm evt})d^2N^{A+A}/dp_T\,d\eta}{(\langle N_{\rm binary}\rangle/\sigma_{\rm inel}^{N+N})d^2\sigma^{N+N}/dp_T\,d\eta}. \quad (1)$$

In the absence of nuclear modifications to hard scattering, the ratio R_{AA} will be unity; thus departures from $R_{AA} = 1$ indicate nuclear medium effects. Previous measurements indicate that for p_T below 2 GeV/c, R_{AA} is smaller than one since the bulk of particle production scales with the number of nucleons participating in the reaction [5,6]. For p_T above 2 GeV/c particle production in $p + A$ collisions is enhanced compared to binary scaling, commonly referred to as the "Cronin effect" [7]. Parton shadowing as measured in lepton + A collisions [8] is also expected to modify the hadron spectra in $p + A$ and $A + A$ compared to binary scaling.

We examine high-p_T spectra of charged hadrons and neutral pions measured by the PHENIX experiment [9,10] in a central and a peripheral class of Au + Au collisions at $\sqrt{s_{NN}} = 130$ GeV. These data are obtained with the central spectrometer, which consists of two arms, "east" and "west," each covering $\Delta\phi = 90°$ and $|\eta| < 0.35$. The arms are positioned outside an axially symmetric magnetic field centered around the beam axis.

Charged particles are reconstructed using a drift chamber (DC) and two layers of multiwire proportional chambers with pad readout (PC1, PC3) in the east arm. The DC measures the particle trajectories between 2.0 and 2.4 m radius in the plane perpendicular to the beam axis. A matching hit in PC1 at ~2.5 m, together with location of the collision vertex, fixes the polar angle. Particle momenta are determined with a resolution of $\delta p/p \simeq 0.6\% \oplus 3.6\%\ p$ (GeV/c). The absolute momentum scale is known to better than 2%. Trajectories are confirmed by requiring a matching hit within a $\pm 2\sigma$ window (about 2.5 cm) in PC3 at a radius of 5 m, which eliminates nearly all secondary tracks from decays and interactions in material. The remaining background is due primarily to accidental associations. The level of background to signal is negligible below $p_T < 2$ GeV/c, rises to 1/10 at 3.5 GeV/c, and reaches 1/1 at 6 GeV/c. This background is measured statistically, by swapping the z coordinate of the PC3 hits, and subtracted from the yield.

Corrections for acceptance, reconstruction efficiency, decays in flight, momentum resolution, and dead areas are determined using a full GEANT simulation. Simulated single particles are embedded in real events to model the effect of detector occupancy. In peripheral Au + Au collisions the track reconstruction efficiency exceeds 98%, while it is reduced to 68 ± 6% for central collisions, independent of momentum. Corrections due to finite momentum resolution are negligible at low p_T and rise to the level of 30% at 5 GeV/c. The systematic errors (Table I) are dominated by the uncertainty in the Monte Carlo description of the detector, including the dead areas and the momentum resolution.

Neutral pions are measured via their $\pi^0 \to \gamma\gamma$ decay. Two separate analyses are performed, the first using a lead-scintillator (PbSc) sampling calorimeter in half ($\Delta\phi = 45°$) of the west arm aperture and the second with a lead-glass Cerenkov (PbGl) calorimeter in a quarter ($\Delta\phi = 22.5°$) of the east arm aperture. The two analyses have very different systematics, and Fig. 1 shows the agreement of their final π^0 spectra.

In both analyses, pairs of calorimeter showers are binned in pair p_T and invariant mass $m_{\gamma\gamma}$. The energy scale is verified using both the π^0 mass and E/p ratio for identified

TABLE I. Relative systematic errors on hadron yields and central-to-peripheral ratios. The errors are quoted for representative p_T and vary between the values shown. For the charged hadron (h) data the errors are highly correlated in p_T for both yields and ratios. For the π^0 data, approximately half of the error in the yield is perfectly correlated in p_T, and some correlation remains in the ratio.

Sys. error	Yield	p_T (GeV/c)	Cent/Per	p_T (GeV/c)
h data	27%	0.5	8%	all
	16%–18%	0.8-3.5		
	30%	4.7		
π^0 data	25%	1.2	24%	1.2
(PbSc)	35%	3.7	33%	3.2
π^0 data	33%	1.2	32%	1.2
(PbGl)	52%	3.7	40%	2.7
π^0 data	21%	1.2	20%	1.2
(Combined)	30%	3.7	24%	2.7
$N + N$ ref.	20%	1.0	N/A	
	35%	5.0		
$\langle N_{\rm binary}\rangle$			29%	all
Central	11%	all		
Peripheral	30%	all		

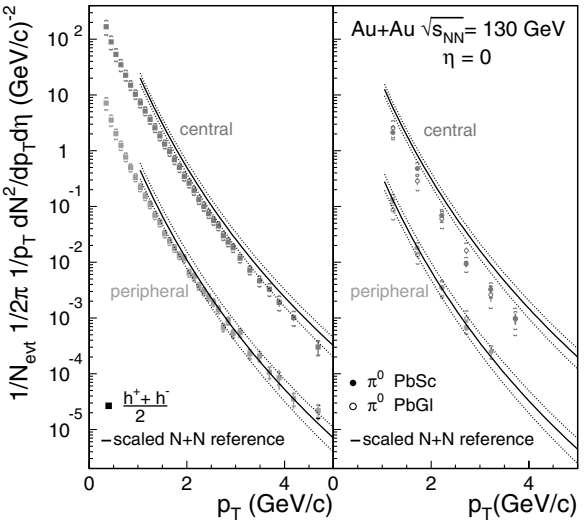

FIG. 1. The yields per event at mid-rapidity for charged hadrons (left) and neutral pions (right) are shown as a function of p_T for 60%–80% (lower) and 0%–10% (upper) event samples. The error bars indicate the statistical errors on the yield; the surrounding brackets indicate the systematic errors. Also shown are the $N + N$ references for charged hadrons and neutral pions, each scaled up by $\langle N_{\text{binary}} \rangle$ for the class. The bands indicate the uncertainty in the $N + N$ reference and in the $\langle N_{\text{binary}} \rangle$.

electrons and is known to $<1.5\%$ [11]. Hadron-induced showers are suppressed with arrival time and shower shape cuts. The combinatorial pair background is estimated by mixing showers from different events with similar centrality. The mixed $m_{\gamma\gamma}$ distribution is subtracted from the true distribution after being normalized in a region outside the π^0 mass peak. The π^0 yield in each p_T bin is determined by integrating the subtracted $m_{\gamma\gamma}$ distribution in a window determined by a Gaussian fit to the π^0 peak.

The π^0 spectra are corrected for losses due to energy resolution, cluster overlaps, analysis cuts, dead detector areas, and acceptance. Smearing of the photon energy due to resolution and cluster overlaps is used to simulate the $m_{\gamma\gamma}$ peak at each p_T, which agrees with that seen in the data. To estimate the π^0 reconstruction efficiency, the same cuts are applied to the simulated $m_{\gamma\gamma}$ distributions as applied to the real data.

Contributions to the yield from pions not originating from the vertex are estimated by GEANT simulation to be 6%–8%. The dominant sources of error are the uncertainty in the particle identification, the effect of energy smearing, and the peak extraction procedure. Their relative contributions to the total errors (see Table I) differ for the two analyses.

Event classification is provided by the combination of two beam-beam counters (BBC's) and two zero-degree calorimeters (ZDC's). We present data from two event samples, central and peripheral. The central sample covers the 0%–10% most central fraction of the geometrical Au + Au cross section, while the peripheral sample contains events in the 60%–80% selection. Using a Glauber model combined with a simulation of the BBC and ZDC responses [5], we estimate $\langle N_{\text{binary}} \rangle = 905 \pm 96$ for the central sample, $\langle N_{\text{binary}} \rangle = 20 \pm 6$ for the peripheral sample, and 45 ± 13 for the ratio between them. The errors include the uncertainties in the parameters used in the Glauber model [12], as well as in the fraction of the total geometrical cross section ($92\% \pm 4\%$) seen by the interaction trigger [13].

The p_T distributions for charged hadrons and neutral pions are shown for both centrality classes in Fig. 1. In this figure, those following, and Table I, the systematic errors shown are the quadrature sums of conservatively estimated limits on several independent errors and represent upper bounds on standard deviations. They are also substantially correlated between points.

The data are compared to the binary-scaled yield from $N + N$ collisions. Since no $N + N$ data exist at $\sqrt{s} = 130$ GeV, we parametrize the cross section $1/(2\pi p_T) d^2\sigma/d\eta\, dp_T$ for $(h^+ + h^-)/2$ as $A/(1 + p_T/p_0)^n$. We determine the parameters $A = 330$ mb/(GeV/c)^2, $p_0 = 1.72$ GeV/c, and $n = 12.4$ by interpolating between results from $p + p$ collisions at the ISR [14] and $\bar{p} + p$ collisions at the $Sp\bar{p}S$ [15] and the Tevatron [16]. The systematic error in the $N + N$ reference (Table I) is due to the error in the absolute normalization of the data used and in the interpolation technique. For neutral pions we scale the charged hadron cross section by the charged pion to charged hadron ratio π/h observed at the ISR [14]. This was found to be 0.63 ± 0.06 nearly independent of p_T above 1.5 GeV/c.

For $p_T > 2$ GeV/c the binary-scaling prediction agrees with the data from peripheral collisions for both charged and neutral particles, while for central collisions the data lie noticeably below the prediction. To examine this difference more directly, we plot the ratio R_{AA} for central collisions in Fig. 2. For the charged spectrum R_{AA} rises up to 2 GeV/c, as expected; but above 2 GeV/c, R_{AA} remains significantly below unity for both spectra.

The depletion is quite striking, since the production of high-p_T hadrons in $p + A$ collisions at fixed-target energies is known to be enhanced compared to the binary-scaling expectation for $p_T > 2$ GeV/c, i.e., the Cronin effect [7]. A similar enhancement has also been observed in heavy ion collisions at lower energies [17,18], as shown in Fig. 2. Phenomenological calculations [17] including shadowing and the Cronin effect predicted that for central Au + Au collisions at $\sqrt{s_{NN}} = 130$ GeV, $R_{AA} > 1$ for hadron spectra in the p_T range 3–9 GeV/c with a peak value of $R_{AA} \simeq 1.3$ at 4 GeV/c.

Above 2 GeV/c, R_{AA} is lower for pions than for charged hadrons, which implies that the π/h ratio is smaller in central RHIC Au + Au collisions than in ISR $p + p$ collisions. This is consistent with identified charged hadron spectra measured by PHENIX [19] for which a large yield of protons and antiprotons is observed at $p_T \sim 2$ GeV/c.

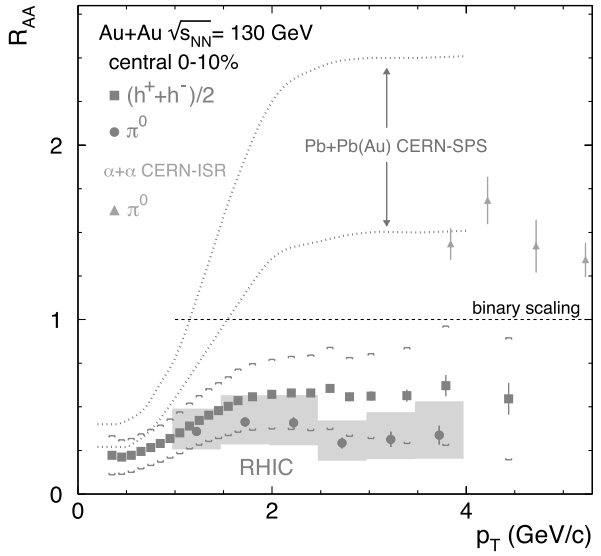

FIG. 2. The ratio R_{AA} for charged hadrons and neutral pions (weighted average of PbSc and PbGl results) in central Au + Au collisions. The error bars indicate the statistical errors on the measurement. The surrounding bands [shaded for π^0's, brackets for $(h^+ + h^-)/2$] are the quadrature sums of (i) the systematic errors on the measurement, (ii) the uncertainty in the $N + N$ reference, and (iii) the uncertainty in $\langle N_{\text{binary}} \rangle$. Also shown are the ratio of inclusive cross sections in $\alpha + \alpha$ compared to $p + p$ at $\sqrt{s_{NN}} = 31$ GeV [18], and spectra from central Pb + Pb, Pb + Au compared to $p + p$ collisions at $\sqrt{s_{NN}} = 17$ GeV [17] shown as a band indicating the range of uncertainty.

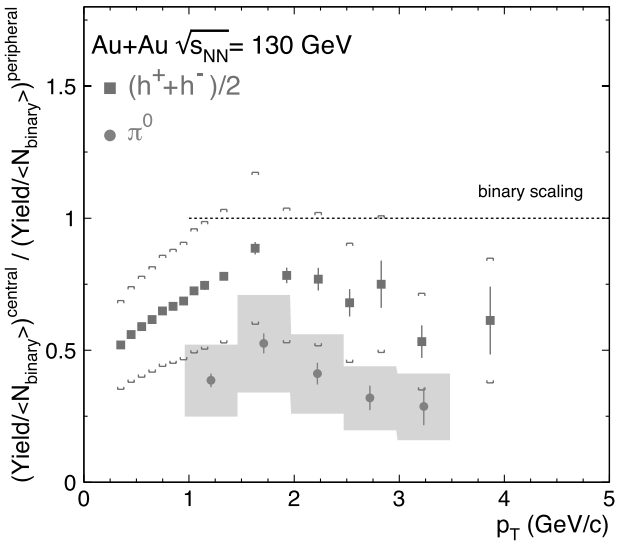

FIG. 3. Ratio of yield per event in central vs peripheral Au + Au collisions, with each divided by $\langle N_{\text{binary}} \rangle$ for that class. For π^0 the weighted average of PbSc and PbGl results is shown. The error bars indicate the statistical errors on the spectra. The surrounding bands [shaded for π^0's, brackets for $(h^+ + h^-)/2$] are the quadrature sums of (i) the parts of the systematic errors on the spectra that do not cancel in the ratio, and (ii) the uncertainty in $\langle N_{\text{binary}} \rangle$ (see Table I).

We can also examine the spectra from central collisions for modifications at high p_T by comparing them to the spectra from peripheral collisions after dividing each by the corresponding values of $\langle N_{\text{binary}} \rangle$. The central-to-peripheral ratio is a useful complement to R_{AA}, since it should be unity in the limit of point-like scaling. Many of the experimental uncertainties are reduced in this ratio (see Table I). Additionally, the uncertainty induced by the $p + p$ interpolation is eliminated, albeit at the expense of incurring that in $\langle N_{\text{binary}} \rangle$ for the peripheral class. We note that there may be effects from the centrality dependence of nuclear shadowing and/or the Cronin effect that would also be present in this comparison.

The central-to-peripheral ratios are plotted in Fig. 3. Like R_{AA} this ratio is below unity at all observed p_T for both charged hadrons and neutral pions, indicating a suppression of the yield per $N + N$ collision in central collisions relative to peripheral. The difference between the two ratios implies that the π/h ratio is smaller in central collisions than in peripheral.

We have presented spectra for charged hadrons and neutral pions measured at 90° from central and peripheral Au + Au collisions in the PHENIX experiment at RHIC. Above $p_T \sim 2$ GeV/c, the spectra from peripheral collisions appear to be consistent (albeit within a substantial systematic error) with a simple, incoherent sum of underlying $N + N$ collisions. The spectra from central collisions, in contrast, are systematically below the scaled $N + N$ expectation, when compared both to data from $p + p$ collisions and to spectra from Au + Au peripheral collisions. The suppression in central collisions is in qualitative agreement with the predictions of energy loss by scattered partons traversing a dense medium. However, other nuclear medium effects should be understood before a quantitative conclusion can be drawn. Measurements in $p + A$ at RHIC can help in this direction.

We thank the staff of the RHIC project, Collider-Accelerator, and Physics Departments at BNL and the staff of PHENIX participating institutions for their vital contributions. We acknowledge support from the Department of Energy and NSF (U.S.A.), Monbu-sho and STA (Japan), RAS, RMAE, and RMS (Russia), BMBF, DAAD, and AvH (Germany), FRN, NFR, and the Wallenberg Foundation (Sweden), MIST and NSERC (Canada), CNPq and FAPESP (Brazil), IN2P3/CNRS (France), DAE and DST (India), LG-YF, KRF, and KOSEF (Korea), and the U.S.-Israel Binational Science Foundation.

*Deceased.

†Not a participating institution.

[1] J. F. Owens *et al.,* Phys. Rev. D **18**, 1501 (1978).

[2] M. Gyulassy and M. Plümer, Phys. Lett. B **243**, 432 (1990); R. Baier *et al.,* Phys. Lett. B **345**, 277 (1995).

[3] X. N. Wang and M. Gyulassy, Phys. Rev. Lett. **68**, 1480 (1992); X. N. Wang, Phys. Rev. C **58**, 2321 (1998).

[4] R. Baier, D. Schiff, and B. G. Zakharov, Annu. Rev. Nucl. Part. Sci. **50**, 37 (2000).
[5] K. Adcox *et al.,* Phys. Rev. Lett. **86**, 3500 (2001).
[6] C. Adler *et al.,* Phys. Rev. Lett. **87**, 112303 (2001).
[7] D. Antreasyan *et al.,* Phys. Rev. D **19**, 764 (1979).
[8] J. J. Aubert *et al.,* Phys. Lett. **123B**, 275 (1983); R. G. Arnold *et al.,* Phys. Rev. Lett. **52**, 727 (1984).
[9] PHENIX Collaboration, D. Morrison *et al.,* Nucl. Phys. **A638**, 565c (1998).
[10] PHENIX Collaboration, W. Zajc *et al.,* in Proceedings of Quark Matter 2001 [Nucl. Phys. A (to be published)].
[11] K. Adcox *et al.,* Phys. Rev. Lett. **87**, 052301 (2001).
[12] We use the Woods-Saxon parameters radius $= 6.38^{+0.27}_{-0.13}$ fm, diffusivity $= 0.53 \pm 0.01$ fm [B. Hahn, D. G. Ravenhall, and R. Hofstadter, Phys. Rev. **101**, 1131 (1956)], and $\sigma^{\text{inel}}_{N+N} = 40 \pm 3$ mb.
[13] The error due to model uncertainties is 2% [5]. An additional 3.5% error results from time dependencies in the centrality selection over the large data sample.
[14] B. Alper *et al.,* Nucl. Phys. **B100**, 237 (1975).
[15] C. Albajar *et al.,* Nucl. Phys. **B335**, 261 (1990).
[16] F. Abe *et al.,* Phys. Rev. Lett. **61**, 1819 (1988).
[17] E. Wang and X. N. Wang, Phys. Rev. C **64**, 034901 (2001), and references therein.
[18] A. L. S. Angelis *et al.,* Phys. Lett. B **185**, 213 (1987).
[19] PHENIX Collaboration, J. Velkovska *et al.,* in Proceedings of Quark Matter 2001 [Nucl. Phys. A (to be published)].

Event-by-event fluctuations in particle multiplicities and transverse energy produced in 158*A* GeV Pb+Pb collisions

M. M. Aggarwal,[1] Z. Ahammed,[2] A. L. S. Angelis,[3] V. Antonenko,[4] V. Arefiev,[5] V. Astakhov,[5] V. Avdeitchikov,[5] T. C. Awes,[6] P. V. K. S. Baba,[7] S. K. Badyal,[7] S. Bathe,[8] B. Batiounia,[5] T. Bernier,[9] K. B. Bhalla,[10] V. S. Bhatia,[1] C. Blume,[8] D. Bucher,[8] H. Büsching,[8] L. Carlén,[11] S. Chattopadhyay,[2] M. P. Decowski,[12] H. Delagrange,[9] P. Donni,[3] M. R. Dutta Majumdar,[2] K. El Chenawi,[11] A. K. Dubey,[13] K. Enosawa,[14] S. Fokin,[4] V. Frolov,[5] M. S. Ganti,[2] S. Garpman,[11] O. Gavrishchuk,[5] F. J. M. Geurts,[15] T. K. Ghosh,[16] R. Glasow,[8] B. Guskov,[5] H. Å. Gustafsson,[11] H. H. Gutbrod,[17] I. Hrivnacova,[18] M. Ippolitov,[4] H. Kalechofsky,[3] K. Karadjev,[4] K. Karpio,[19] B. W. Kolb,[17] I. Kosarev,[5] I. Koutcheryaev,[4] A. Kugler,[18] P. Kulinich,[12] M. Kurata,[14] A. Lebedev,[4] H. Löhner,[16] L. Luquin,[9] D. P. Mahapatra,[13] V. Manko,[4] M. Martin,[3] G. Martínez,[9] A. Maximov,[5] Y. Miake,[14] G. C. Mishra,[13] B. Mohanty,[13,*] M.-J. Mora,[9] D. Morrison,[20] T. Mukhanova,[4] D. S. Mukhopadhyay,[2] H. Naef,[3] B. K. Nandi,[13] S. K. Nayak,[7] T. K. Nayak,[2] A. Nianine,[4] V. Nikitine,[5] S. Nikolaev,[5] P. Nilsson,[11] S. Nishimura,[14] P. Nomokonov,[5] J. Nystrand,[11] A. Oskarsson,[11] I. Otterlund,[11] T. Peitzmann,[8] D. Peressounko,[4] V. Petracek,[18] S. C. Phatak,[13] W. Pinganaud,[9] F. Plasil,[6] M. L. Purschke,[17] J. Rak,[18] R. Raniwala,[10] S. Raniwala,[10] N. K. Rao,[7] F. Retiere,[9] K. Reygers,[8] G. Roland,[12] L. Rosselet,[3] I. Roufanov,[5] C. Roy,[9] J. M. Rubio,[3] S. S. Sambyal,[7] R. Santo,[8] S. Sato,[14] H. Schlagheck,[8] H.-R. Schmidt,[17] Y. Schutz,[9] G. Shabratova,[5] T. H. Shah,[7] I. Sibiriak,[4] T. Siemiarczuk,[19] D. Silvermyr,[11] B. C. Sinha,[2] N. Slavine,[5] K. Söderström,[11] G. Sood,[1] S. P. Sørensen,[20] P. Stankus,[6] G. Stefanek,[19] P. Steinberg,[12] E. Stenlund,[11] M. Sumbera,[18] T. Svensson,[11] A. Tsvetkov,[4] L. Tykarski,[19] E. C. v. d. Pijll,[15] N. v. Eijndhoven,[15] G. J. v. Nieuwenhuizen,[12] A. Vinogradov,[4] Y. P. Viyogi,[2] A. Vodopianov,[5] S. Vörös,[3] B. Wysłouch,[12] and G. R. Young[6]

(WA98 Collaboration)

[1]*University of Punjab, Chandigarh 160 014, India*
[2]*Variable Energy Cyclotron Centre, Calcutta 700 064, India*
[3]*University of Geneva, CH-1211 Geneva 4, Switzerland*
[4]*RRC "Kurchatov Institute," RU-123182 Moscow, Russia*
[5]*Joint Institute for Nuclear Research, RU-141980 Dubna, Russia*
[6]*Oak Ridge National Laboratory, Oak Ridge, Tennessee 37831-6372*
[7]*University of Jammu, Jammu 180 001, India*
[8]*University of Münster, D-48149 Münster, Germany*
[9]*SUBATECH, Ecole des Mines, Nantes, France*
[10]*University of Rajasthan, Jaipur 302 004, Rajasthan, India*
[11]*University of Lund, SE-221 00 Lund, Sweden*
[12]*MIT, Cambridge, Massachusetts 02139*
[13]*Institute of Physics, Bhubaneswar 751 005, India*
[14]*University of Tsukuba, Ibaraki 305, Japan*
[15]*Universiteit Utrecht/NIKHEF, NL-3508 TA Utrecht, The Netherlands*
[16]*KVI, University of Groningen, NL-9747 AA Groningen, The Netherlands*
[17]*Gesellschaft für Schwerionenforschung (GSI), D-64220 Darmstadt, Germany*
[18]*Nuclear Physics Institute, CZ-250 68 Rez, Czech Republic*
[19]*Institute for Nuclear Studies, 00-681 Warsaw, Poland*
[20]*University of Tennessee, Knoxville, Tennessee 37966*

(Received 31 August 2001; published 17 May 2002)

Event-by-event fluctuations in the multiplicities of charged particles and photons, and the total transverse energy in 158*A* GeV Pb+Pb collisions are studied for a wide range of centralities. For narrow centrality bins the multiplicity and transverse energy distributions are found to be near perfect Gaussians. The effect of detector acceptance on the multiplicity fluctuations has been studied and demonstrated to follow statistical considerations. The centrality dependence of the charged particle multiplicity fluctuations in the measured data has been found to agree reasonably well with those obtained from a participant model. However, for photons the multiplicity fluctuations have been found to be lower compared to those obtained from a participant model. The multiplicity and transverse energy fluctuations have also been compared to those obtained from the VENUS event generator.

DOI: 10.1103/PhysRevC.65.054912 PACS number(s): 25.75.−q, 13.40.−f, 24.85.+p

*Corresponding author. Email address: bedanga@iopb.res.in

 ©2002 The American Physical Society

I. INTRODUCTION

Fluctuations in physical observables in heavy-ion collisions have been a topic of interest for some years as they may provide important signals regarding the formation of quark-gluon plasma (QGP) and help to address the question of thermalization [1]. With the large number of particles produced in heavy-ion collisions at Super Proton Synchrotron (SPS) and Relativistic Heavy-Ion Collider (RHIC) energies [2,3], it has now become feasible to study fluctuations on an event-by-event basis. Recently, several new methods have been proposed for the study of event-by-event fluctuations in various global observables to probe the nature of the QCD phase transition [4–7]. In a thermodynamical picture of a strongly interacting system formed in the collision, the fluctuations in particle multiplicities, mean transverse momenta ($\langle p_T \rangle$), and other global observables, are related to the fundamental properties of the system, such as the specific heat, chemical potential, and matter compressibility. These, in turn, lead towards understanding the critical fluctuations at the QCD phase boundary. The existence of a tricritical point at the QCD phase transition [4], which has lately been a topic of intense discussion, has been predicted to be associated with large event-by-event fluctuations in the above observables.

In a first-order phase transition scenario, it is believed that supercooling might lead to density fluctuations resulting in droplet formation and hot spots [8]. These might lead to rapidity fluctuations in the form of spikes and gaps in the rapidity distribution. The study of event-by-event fluctuations in the number of photons to charged particles has also been proposed as a means to search for production of disoriented chiral condensates (DCC) [9,10].

In nucleus-nucleus collisions the transverse energy E_T is an extensive global variable [11–13], which provides a direct measure of the violence of an interaction. E_T is produced by redirection of the longitudinal energy into transverse motion through interactions in which the interacting particles undergo multiple scatterings and approach thermalization. E_T is also an indicator of the energy density achieved in the collision. Since the energy density is directly related to the QGP phase transition, it is extremely important to study E_T and fluctuations in E_T. Moreover, it is interesting to compare the fluctuations of E_T to those observed in the particle multiplicities.

Much theoretical interest has been directed toward the subject of event-by-event fluctuations, motivated by the near perfect Gaussian distributions of $\langle p_T \rangle$ and particle ratios [14] measured at the SPS. For these Gaussian distributions, the variance or the width of the distributions contain information about the reaction mechanism as well as the nuclear geometry [4,15–17].

The relative fluctuation (ω_X) in an observable X can be expressed as:

$$\omega_X = \frac{\sigma_X^2}{\langle X \rangle}, \tag{1}$$

where σ_X^2 is the variance of the distribution and $\langle X \rangle$ denotes the mean value.

The value of ω_X that can be extracted from experimental data has contributions that originate both from trivial statistical effects as well as dynamical sources. To extract the dynamical part associated with new physics from the observed fluctuations, one has to understand the contributions from statistical and other known sources. Examples of known sources of fluctuations contributing to the observed experimental value of ω_X include finite particle multiplicity, effect of limited acceptance of the detectors, impact parameter fluctuations, fluctuations in the number of primary collisions, effects of rescattering of secondaries, resonance decays, and Bose-Einstein correlations. These sources of fluctuations, along with estimates of the ω_X contributions for each have been discussed by Stephanov *et al.* [4] and by Baym and Heiselberg [5].

In nucleus-nucleus (AA) collisions relative fluctuations in global observables have been found to be smaller compared to those in pp collisions. It is suggested that thermal equilibration in AA collisions makes the fluctuations small. However, the origin of fluctuations and hence the physical information content are quite different in pp and AA collisions. While in pp collisions one hopes to extract quantum mechanical information about the initial state from the event-by-event fluctuations in the final state, in heavy-ion collisions equilibration makes it difficult to achieve this goal, instead the basic aim here has been to relate the event-by-event fluctuations of the final state with the thermodynamic properties at freeze-out.

In this paper, we present fluctuations in the multiplicities of both charged particles and photons, and in the total transverse energy, over a large range of centralities as measured in the WA98 experiment at the CERN SPS. A major interest has been to search for fluctuations that have a new physical origin, such as those associated with QCD phase transition or from the formation of a DCC.

We compare the fluctuations observed in the experimental data for varying centrality conditions and rapidity intervals to those obtained from different models. In the following section the WA98 experimental setup is described. In Sec. III the criteria for the centrality selection appropriate for fluctuation studies are discussed. Multiplicity fluctuations of photons and charged particles and the effect of acceptance are presented in Sec. IV. In Sec. V, we estimate the multiplicity fluctuations in a participant model and compare to those obtained from data. Section VI deals with transverse energy fluctuations. A final discussion and summary is presented in Sec. VII.

II. EXPERIMENT AND DATA ANALYSIS

In the WA98 experiment at CERN [18], the main emphasis has been on high precision and simultaneous detection of both hadrons and photons. The experimental setup consisted of large acceptance hadron and photon spectrometers, detectors for charged particle and photon multiplicity measurements, and calorimeters for transverse and forward energy measurements. The experiment obtained data with 158A GeV Pb beams from the CERN SPS in 1994, 1995,

and 1996. The results presented here are from the Pb run in 1996 taken with the magnetic field (Goliath) turned off. The analysis makes use of the data taken with the photon multiplicity detector (PMD), the silicon pad multiplicity detector (SPMD), the midrapidity calorimeter (MIRAC), and the zero degree calorimeter (ZDC).

The circular SPMD, used for measuring charged particle multiplicity, was located 32.8 cm from the target. It had full azimuthal coverage in the region $2.35 \leqslant \eta \leqslant 3.75$. The detector had four overlapping quadrants, each fabricated from a single 300-μm-thick silicon wafer. The active area of each quadrant was divided into 1012 pads forming 46 azimuthal wedges and 22 radial bins with pad size increasing with radius to provide a uniform pseudorapidity coverage. The intrinsic efficiency of the detector was better than 99%. During the data recording, 95% of the pads worked properly. It was nearly transparent to high-energy photons, since only about 0.2% are expected to interact in the silicon. Details of the characteristics of the SPMD can be found in Refs. [19,20].

The photon multiplicity was measured using the preshower PMD placed at a distance of 21.5 m from the target. The detector consisted of 3 radiation length (X_0) thick lead converter plates placed in front of an array of square scintillator pads of four different sizes, varying from 15×15 mm^2 to 25×25 mm^2, placed in 28 box modules. Each box module had a matrix of 38×50 pads that were read out using one image intensifier and one charge-coupled device camera system. Details of the design and characteristics of the PMD may be found in Refs. [21,22]. The results presented here make use of the data from the central 22 box modules covering the pseudorapidity range $2.9 \leqslant \eta \leqslant 4.2$. The clusters of hit pads, having total analog-to-digital converter content above a hadron rejection threshold were identified as photonlike. Detailed simulations showed that the photon counting efficiencies for the central to peripheral cases varied from 68% to 73%. The purity of the photon sample, $N_{\gamma\text{-like}}$, in the two cases varied from 65% to 54%.

The transverse energy was measured with the MIRAC [23] placed 24.7 m downstream from the target. It consisted of 30 stacks, each divided vertically into six towers, each of size 20×20 cm^2, and segmented longitudinally into an electromagnetic (EM) section and a hadronic section. The depth of an EM section was $15.6X_0$ (equivalent to 51% of an interaction length), which ensured almost complete containment of the electromagnetic energy (97.4% and 91.0% containment calculated for 1 GeV and 30 GeV photons, respectively). The MIRAC was used to measure both the transverse electromagnetic (E_{T}^{em}) and hadronic (E_{T}^{had}) energies in the interval $3.5 \leqslant \eta \leqslant 5.5$ with a resolution of $17.9\%/\sqrt{E}$ and $46.1\%/\sqrt{E}$, (E in GeV), respectively. The E_{T} provides a measure of the centrality of the reaction. Events with large E_{T} correspond to very central reactions with small impact parameter and vice versa.

The ZDC measured the total forward energy E_{F} at $\theta \leqslant 0.3°$ with a resolution of $(80\%/\sqrt{E}) + 1.5\%$, with E expressed in GeV. E_{F} provides complementary information on the centrality with low E_{F} energy deposit corresponding to small impact parameter collisions.

For the results to be presented below, the following sources of errors have been included in the systematic error estimates.

A. Errors in $N_{\gamma\text{-like}}$

(a) The major source of error in $N_{\gamma\text{- like}}$ is due to the effect of clustering of the pad signals. This error is determined from the simulation by comparing the number of known tracks on the PMD with the total number of photonlike clusters. The result is that the number of clusters exceeds the number of tracks by 3% in the case of peripheral events and by 7% for high multiplicity central events [22].

(b) The uncertainty in the ADC value of the hadron rejection threshold in the PMD leads to an error in the estimation of $N_{\gamma\text{-like}}$ clusters. The hadron rejection threshold has been set at three times the minimum ionizing particle (MIP) peak. The value of MIP peak was changed by 10% of the peak value (3 ADC) in order to estimate the systematic error. The error in $N_{\gamma\text{-like}}$ value is 2.5% [22].

(c) The error due to the variation in scintillator pad-to-pad gains is found to be less than 1%.

The combined systematic error on $N_{\gamma\text{-like}}$ is asymmetric and centrality dependent. The errors are -3.2% and $+3.4\%$ for peripheral collisions and -7.1% and $+3.0\%$ for central collisions. The errors on N_{γ}, obtained after correcting for photon counting efficiency and purity of photonlike sample, will be discussed in Sec. V.

B. Errors in N_{ch}

The uncertainty in the N_{ch} obtained from SPMD has been discussed in detail in Ref. [19]. The total error has been estimated to be about 4%.

C. Errors in centrality selection through E_{T} and E_{F}

The centrality of the interaction is determined by the total transverse energy (E_{T}) measured in the MIRAC. The finite resolution in the measurement of E_{T} contributes to the systematic error. For the analysis of fluctuation in E_{T}, which uses MIRAC data directly, the centrality is determined by the forward energy E_{F}. The finite resolution in the measurement E_{F} contributes to the systematic error in E_{T} fluctuations. These errors are centrality dependent.

D. Fitting errors

The fitting errors associated with the determination of the fit parameters of the multiplicity and transverse energy distributions also contribute to the final systematic error in both the photons and charged particles and transverse energy, respectively. The maximum contribution of this error to the fluctuation was found to be 2%.

III. CENTRALITY SELECTION FOR FLUCTUATION STUDIES

The centrality of the interaction was determined by the total transverse energy measured in the MIRAC. For the part of the analysis where transverse energy data are used for the

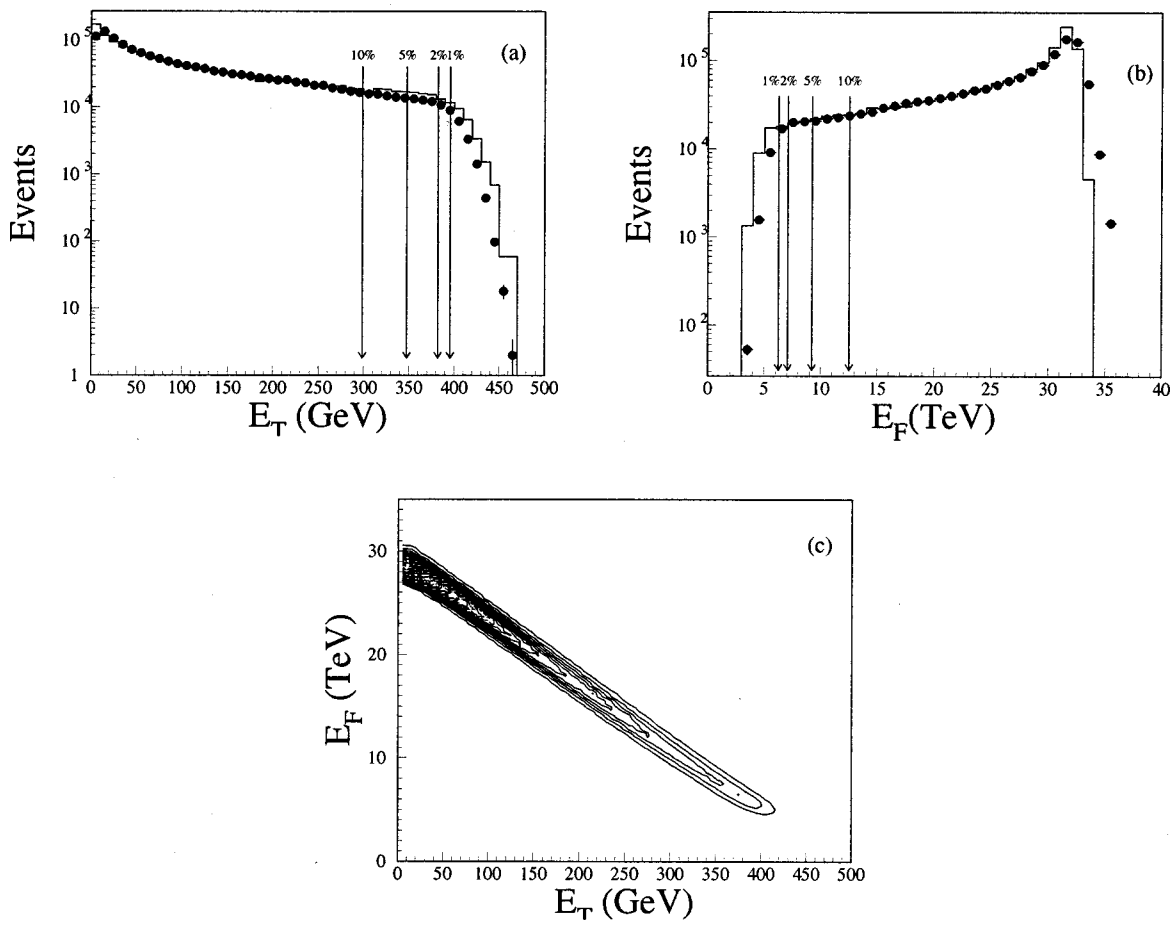

FIG. 1. Minimum bias distributions of (a) transverse energy E_T and (b) forward energy E_F produced in Pb induced reactions at 158*A* GeV on Pb. Solid histograms show the results obtained from VENUS event generator. (c) shows the anticorrelation of measured total transverse energy E_T and forward energy E_F.

fluctuation studies, the centrality was determined instead by the forward energy E_F as measured in the ZDC. The centralities are expressed as fractions of the minimum bias cross section as a function of the measured total transverse energy using MIRAC, or total forward energy using the ZDC. Figures 1(a) and 1(b) show the minimum bias distributions of E_T and E_F, respectively. The arrows in the figures indicate the values of E_T and E_F for the top (most central) 1%, 2%, 5%, and 10% of the minimum bias cross section. Predictions from VENUS 4.12 [24] are also shown as solid histograms. This will be discussed in a later section.

The anticorrelation of E_T and E_F is shown in Fig. 1(c). It illustrates that either E_T or E_F can be used nearly equivalently to define the centrality of the reaction.

Figures 2(a) and 2(b) show the minimum bias distributions for γ-like clusters and charged particles, respectively, for the full acceptances of the two detectors (PMD and SPMD). The multiplicity distributions corresponding to the centrality cuts using the total E_T for the top 1%, 2%, and 5% of the minimum bias cross section are also shown in the same figures. These distributions have been fitted to the Gaussians. The extracted fit parameters are used for the analysis of the fluctuations.

Figure 3 shows the variation of the mean (μ), standard deviation (σ), and chi square per degree of freedom (χ^2/ndf) of the photon and charged particle multiplicity distributions for different centrality bins. Here the centrality class is chosen with increasing width, as 0–1 %, 0–2 %, 0–3 %, . . . ,0–10 %. As expected, the mean value decreases and the sigma increases as we make broader centrality selection to include more of the cross section. From the χ^2/ndf values, one observes that the distributions increasingly deviate from the Gaussians with increasing width in the centrality selection. For a centrality selection width of greater than 5%, the χ^2/ndf rises above 2. The variation of μ and σ indicate that the extracted relative fluctuation (ω_χ) will grow with the increase in the width of the centrality selection interval. This indicates that the impact parameter fluctuations will dominate as the centrality selection is broadened. From this we conclude that the centrality selections should be made with as narrow bins in E_T as possible, such that the multiplicity distributions are good Gaussians and the impact parameter fluctuations are minimized. With this in mind we have used centrality selection bins of 2% widths in cross section, taken as 0–2 %, 2 − 4 %, . . . ,62–64 %.

Figure 4 shows the variation of μ, σ, and χ^2/ndf of the photon and charged particle multiplicity distributions within the full acceptance of the detectors with these narrow bins in

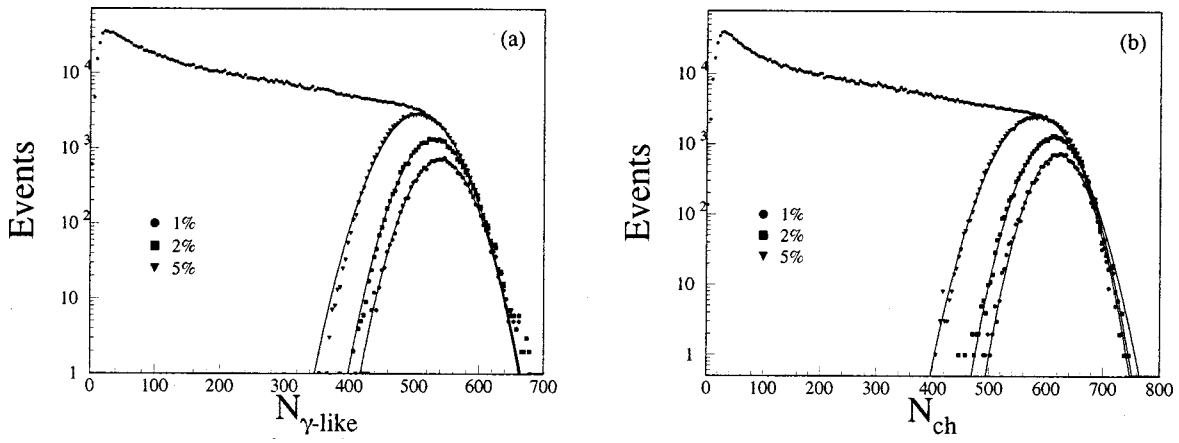

FIG. 2. Minimum bias distributions of (a) γ-like cluster multiplicity, and (b) charged particle multiplicity produced in Pb induced reactions at 158*A* GeV on Pb. The multiplicity distributions for the top 1%, 2%, and 5% most central events are also shown and fitted to the Gaussian distributions.

centrality. The data presented here cover the region from central (top 2% of the minimum bias cross sections) to peripheral collisions (up to 65% of the minimum bias cross section where the average number of participants is 26). It is seen that both the μ and σ values decrease towards peripheral collisions. The χ^2/ndf values are mostly in the region between 1.0 and 2.0 over the entire range of centralities considered. This suggests that narrow cross section slices in the E_T or E_F distributions are necessary to study the multiplicity fluctuations and minimize the influence from impact parameter fluctuations.

IV. MULTIPLICITY FLUCTUATIONS AND THE EFFECT OF ACCEPTANCE

The relative fluctuations in multiplicity for γ-like clusters and charged particles have been calculated using the μ and σ values from Fig. 4 and Eq. (1). These values are shown in Fig. 5 as functions of centrality, for full coverage of PMD ($2.9 \leqslant \eta \leqslant 4.2$) and SPMD ($2.35 \leqslant \eta \leqslant 3.75$), respectively. The errors shown in the figures are systematic errors, the sources of which have been already discussed in preceding section. For both γ-like clusters and charged particles the relative fluctuations are seen to increase in going from central to peripheral collisions. However, for charged particles the increase is much stronger.

In order to make a direct comparison of the fluctuations of photons and charged particles, the multiplicities should be studied in the region of common coverage of the detectors in terms of both pseudorapidity and azimuthal angle. In a latter section, we will compare the results obtained from data with those from model calculations for the common coverage. The region of common coverage of the two detectors in the WA98 experiment was 0.85 units in η ($2.9 \leqslant \eta \leqslant 3.75$). The general trend of the variation of the Gaussian fit parameters, with the reduced number of particles, for the common cov-

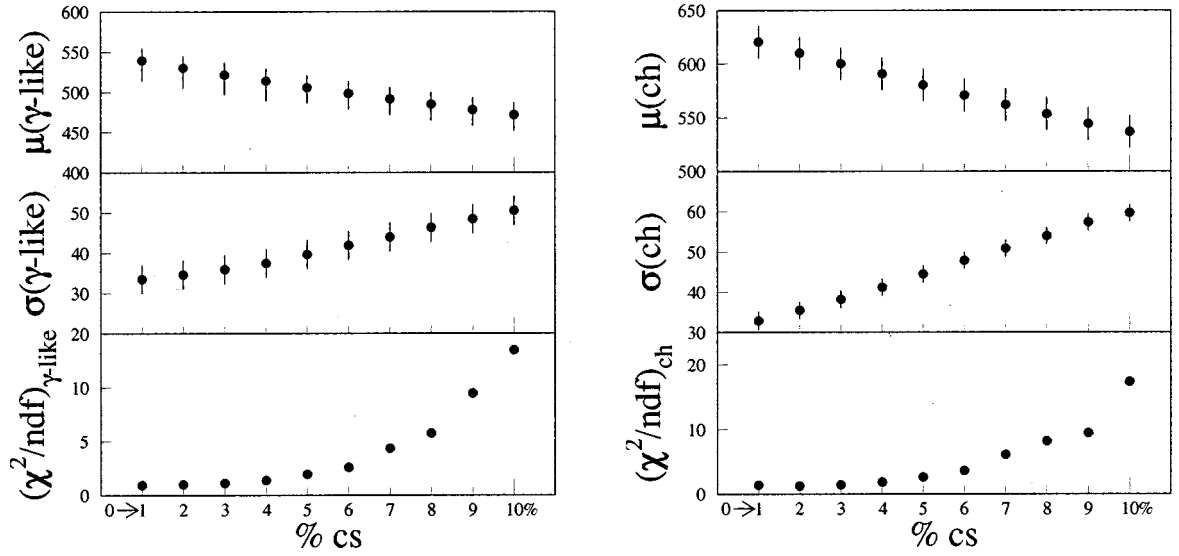

FIG. 3. The Gaussian fit parameters of the multiplicity distributions of γ-like clusters and charged particles for increasing centrality bins of increasing width. The centrality selection has been made by increasing the widths of E_T bins corresponding to $0-1\,\%, 0-2\,\%, 0-3\,\%, \ldots, 0-10\,\%$ of the minimum bias cross section.

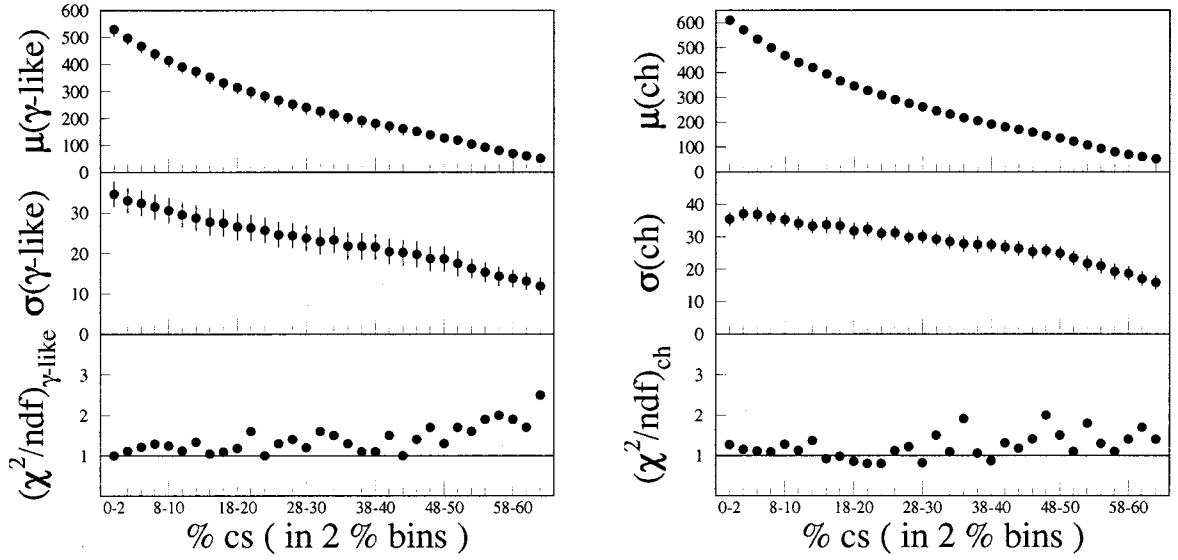

FIG. 4. The Gaussian fit parameters of the multiplicity distributions of γ-like clusters and charged particles as a function of centrality. The centrality selection has been made by selecting 2% bins in minimum bias cross section, viz., 0–2 %, 2–4 %, 4–6 %, . . . ,62–64 %. The multiplicity distributions for these centrality bins are near perfect Gaussians as can be seen from the χ^2/ndf values.

erage is found to be similar to that obtained with full coverage for each detector. Fit parameters μ, σ, and χ^2/ndf, as obtained for centrality bins of 2% in width, for the common coverage of the two detectors are shown in Fig. 6. As was the case for the larger acceptance, the μ and σ values are seen to decrease towards more peripheral event selection. The χ^2/ndf values are reasonable. Using the above values of the Gaussian parameters together with Eq. (1), the relative multiplicity fluctuations were calculated and are shown in Fig. 7. The error shown include the fit errors as well as the other systematic errors discussed earlier. The relative fluctuations for γ-like clusters is seen to be rather constant over the full centrality range with an average value of 2.2 ± 0.21. In comparison, the relative fluctuations for charged particles is 1.56 ± 0.13 at the most central bin (0–2 %) increasing to 2.8 ± 0.16 for the least central bin (62–64 %).

Following this discussion of the fluctuations in the multiplicity of photons and charged particles for the full acceptance regions and for the regions of common coverage of the photon and charged particle detectors, we now analyze the effect of detector acceptance on the observed fluctuations in more detail. For this we have taken two different η coverage regions for each detector. For the PMD the η ranges chosen are $3.0 \leqslant \eta \leqslant 4.0$ and $3.25 \leqslant \eta \leqslant 3.75$ (with full ϕ coverage). The resulting ω values for the two cases are shown in Fig. 8(a). Qualitatively, the variation of the fluctuations with centrality is similar for both coverages, but the magnitude of the relative fluctuations is lower for smaller η coverage.

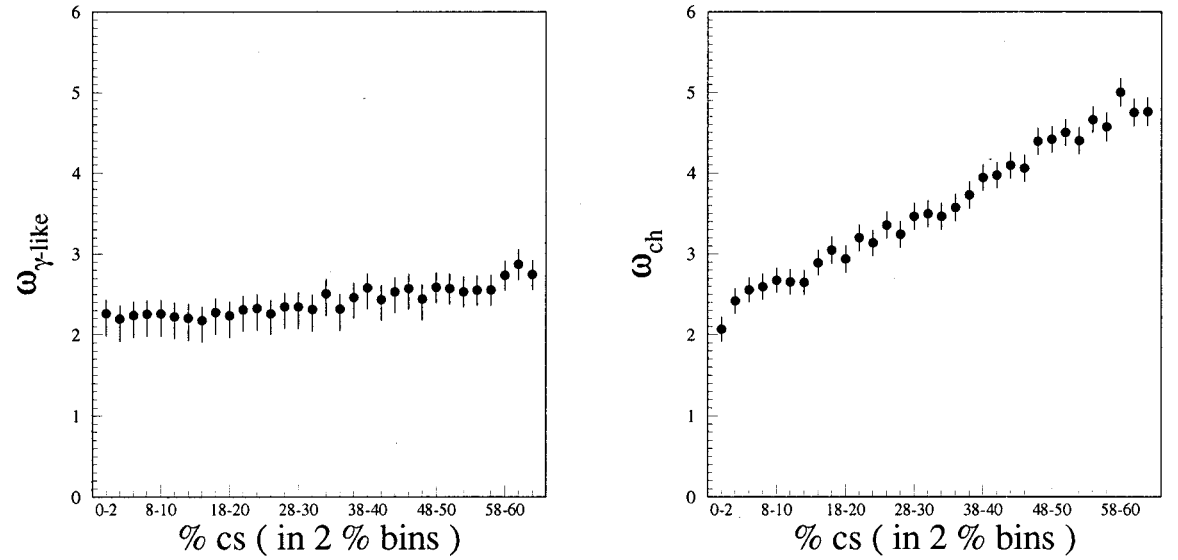

FIG. 5. Fluctuations of the multiplicity of γ-like clusters and charged particles within the full coverage of PMD and SPMD for various 2% bins of the minimum bias cross section.

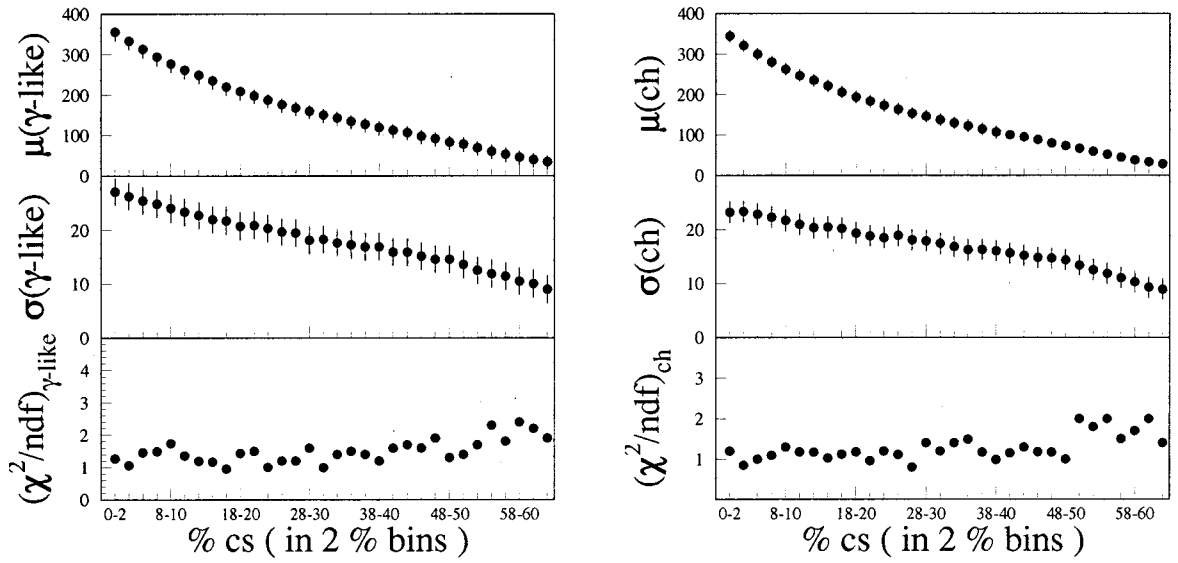

FIG. 6. Centrality dependence of the Gaussian fit parameters of the multiplicity distribution of γ-like clusters and charged particles within the common coverage of PMD and SPMD.

For the SPMD, the fluctuations were calculated for the rapidity intervals $2.35 \leqslant \eta \leqslant 3.35$ and $2.65 \leqslant \eta \leqslant 3.15$. These bins have width of one and one half units in η around midrapidity. The results are shown in Fig. 8(b). Qualitatively, the results are again similar to each other with the magnitude of the relative fluctuations decreasing as the coverage in η is decreased.

The decrease in the relative fluctuations as the acceptance is decreased can be understood in terms of a simple statistical picture [25]. Assume that there are m particles produced in the collision out of which n particles are accepted randomly into the detector acceptance. In this case, the distribution of n will follow a binomial distribution with mean mf and variance $mf(1-f)$, where f is the fraction of particles accepted. Therefore, the fluctuations in the number of particles accepted for a fixed (m) number of particles produced is $1-f$. In principle, m can have an arbitrary distribution as given by $P(m)$ with known first and second moments. The fluctuations in the n accepted particles out of the m particles produced is then given as

$$\omega_n = 1 - f + f\omega_m . \tag{2}$$

Thus considering the fluctuations in one unit of η as ω_m we can calculate the expected fluctuations for one half unit of η using the above equation. Here f corresponds to the ratio of the total number of particles accepted in one half unit of η coverage to that accepted over one unit in η. For the acceptance regions used, the average value of f for photons is about 0.52 and that of charged particles is about 0.54. Using

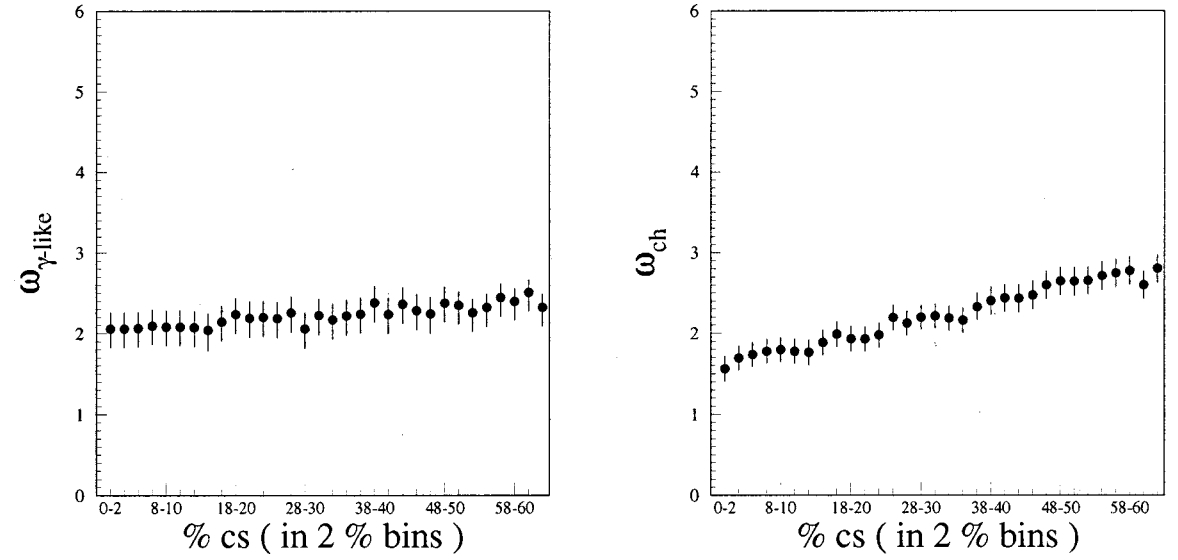

FIG. 7. Centrality dependence of the fluctuations of the multiplicity of photons and charged particles within the common coverage of the PMD and SPMD.

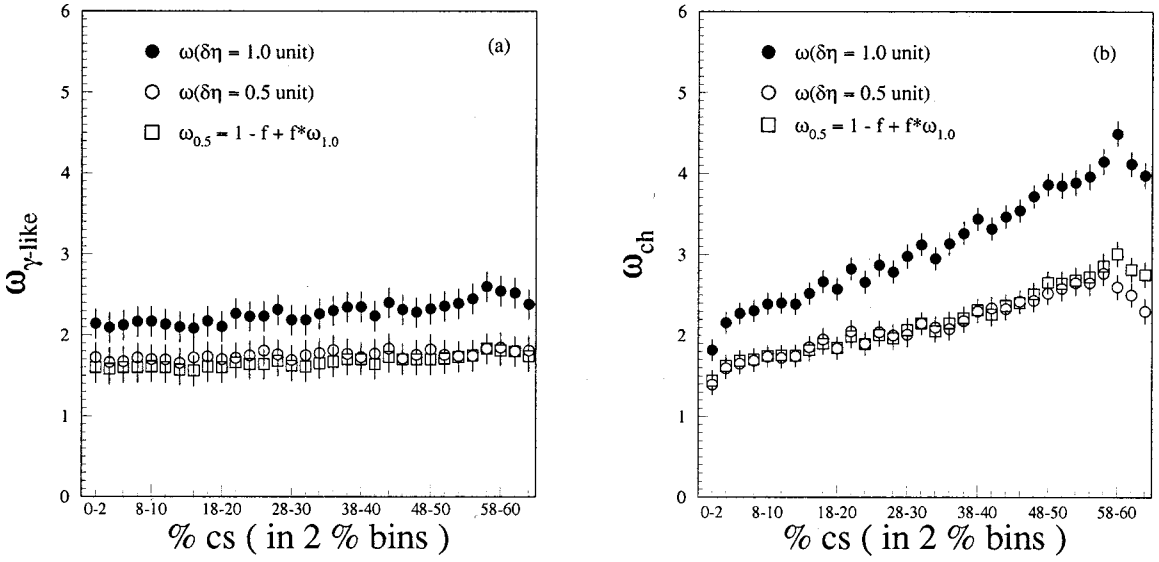

FIG. 8. Multiplicity fluctuations of photons and charged particles for two η acceptance selections. The open squares represent estimated values of fluctuations in 0.5 unit of $\delta\eta$ from the observed fluctuations in 1.0 unit of $\delta\eta$.

these values in Eq. (2) we can calculate the expected fluctuations for half unit of η coverage from the results of one unit of η coverage, under the assumption of a binomial sampling. As shown in Fig. 8 the empirical calculations almost exactly reproduce the observed result in the narrower acceptance window for charged particles and agrees reasonably well within the quoted errors for photons.

V. ESTIMATION OF FLUCTUATIONS IN A PARTICIPANT MODEL

In a picture where the nucleus-nucleus collision is thought of as the sum of contributions from many sources created in the early stage of the interaction, the variance of the distribution of any observable has contributions from (a) the fluctuations in the number of sources, largely due to different impact parameters. Even if the impact parameter window is narrowed, density fluctuations within the nucleus will make this contribution nonzero, (b) the fluctuations in the number of particles produced by each source. Quantum fluctuations in the nucleon-nucleon (*NN*) cross section can lead to such effects, (c) the fluctuations due to any dynamical process or critical behavior in the evolution of the system.

The contribution from the first two effects leads to fluctuations in the number of participant nucleons, which may be related to the initial size of the interacting system before it thermalizes. Resonance decays have also been shown to increase the multiplicity fluctuations by a large factor [4,5].

Following a simple participant model [5,15,16,26,27], the particle multiplicity (of photons or charged particles) N may be expressed as

$$N=\sum_{i=1}^{N_{\rm part}} n_i, \tag{3}$$

where $N_{\rm part}$ is the number of participants and n_i is the number of particles produced in the detector acceptance by the ith participant. On an average, the mean value of n_i is the ratio of the average multiplicity in the detector coverage to the average number of participants, i.e., $\langle n\rangle=\langle N\rangle/\langle N_{\rm part}\rangle$.

Thus the fluctuations in N will have contributions due to fluctuations in $N_{\rm part}$ ($\omega_{N_{\rm part}}$) and also due to the fluctuations in the number particles produced per participant (ω_n). Again, the fluctuations of n given as ω_n, will have a strong dependence on the acceptance of the detector. In the absence of correlations between the n_i's, the multiplicity fluctuations ω_N can be expressed as

$$\omega_N=\omega_n+\langle n\rangle\omega_{N_{\rm part}}. \tag{4}$$

Comparison of data with the results of such model calculations might reveal the extent to which the principle of superposition of nucleon-nucleon (*NN*) interactions is valid in the case of heavy-ion collisions. The participant model is expected to hold reasonably well for peripheral collisions where there are only few *NN* collisions, while for central collisions the particle production gets affected by *NN* scattering, rescatterings between produced particles, energy degradation, and other effects. Next we discuss the calculation of each of the terms in Eq. (4).

A. Calculation of $\omega_{N_{\rm part}}$

The impact parameter fluctuations are reflected in the fluctuations in the number of participants. We have estimated this contribution using the VENUS 4.12 event generator with default setting. A set of 100-K minimum bias Pb+Pb events at 158*A* GeV was generated for calculation of the number of participants. To match the centrality selection of the reaction in simulation to that in data, we have carried out a fast simulation in which $E_{\rm T}$ from VENUS was calculated within MIRAC coverage taking the resolution factors for the hadronic and electromagnetic energies of MIRAC into account.

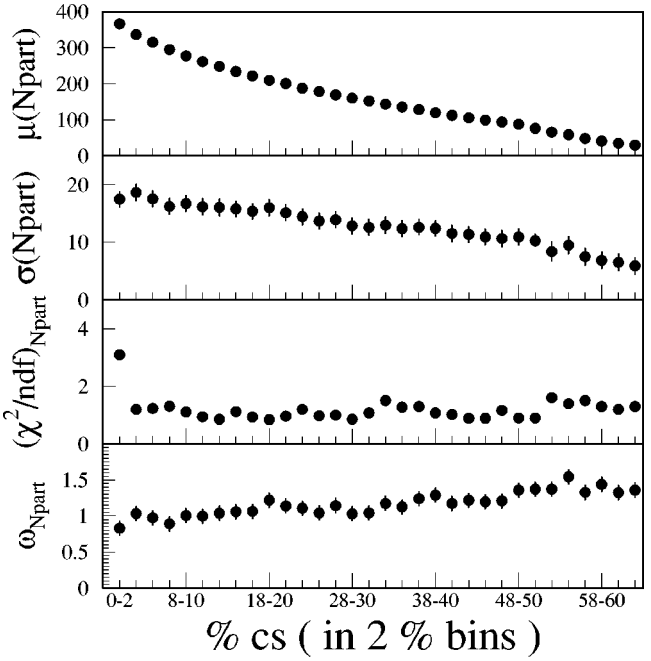

FIG. 9. Variation of μ, σ, and χ^2/ndf of the distribution of the number of participants as a function of centrality.

The corresponding E_T distributions for VENUS are shown as the solid curve in Fig. 1(a). It is seen that the agreement with data is quite reasonable.

The distributions of $N_{\rm part}$ for the same narrow (2%) bins of centrality, as discussed above for the data, are well described by the Gaussian distributions. Figure 9 shows the variation of μ, σ, χ^2/ndf, and relative fluctuation $\omega_{N_{\rm part}}$ calculated from the fit parameters with the 2% bins in centrality. One can see that the relative fluctuation in the number of participants, $\omega_{N_{\rm part}}$, is around 1. The statistical errors are small and are within the size of the symbols.

The systematic errors shown in the figures have contribution from the following sources, which have been added in quadrature.

(1) Nucleon density distribution: In order to estimate the error due to this we have calculated the number of participants from VENUS (as shown in the figure) and those from FRITIOF. The difference for each centrality bin was considered as representative of the error [28].

(2) Finite resolution of E_T: Systematic errors due to this were calculated by varying the centrality as per the MIRAC resolution [22].

(3) Fitting errors: Errors associated with the determination of the fit parameters of the Gaussian distributions also contribute to the final systematic error in the number of participants.

The quantity $\langle n\rangle$ is equal to the ratio of the mean charged particle (or photon) multiplicity for a given acceptance to the mean number of participants for the same centrality bin. Thus the contribution from the term $\langle n\rangle\omega_{N_{\rm part}}$ to the total fluctuations [Eq. (4)] can be easily obtained.

B. Calculation of ω_n

This term gives the fluctuations in the number of particles produced per participant. It has a strong dependence on acceptance as given earlier in Eq. (2) and shown in Fig. 8. To calculate ω_n as per Eq. (2) we next obtain the terms f and ω_m. The quantity f is the ratio of the number of particles per participant accepted within the acceptance of the detector ($\langle n\rangle$) to the total number of particles produced per participant ($\langle m\rangle$). The value of $\langle n\rangle$ for each centrality bin and for a given acceptance can be calculated as discussed in the preceding section. To obtain the value of $\langle m\rangle$ we make use of the data existing in the literature for *NN* collisions. As discussed in Refs. [29,30] the mean number of charged particles and photons produced in nucleon-nucleon collisions can be parametrized as a function of c.m. system energies ($\sqrt{s}$ from 2 GeV to 500 GeV) in the following manner:

$$\langle N_{\rm ch}\rangle^{NN} = -4.7(\pm 1.0) + 5.2(\pm 0.8)s^{0.145(\pm 0.01)}, \quad (5)$$

$$\langle N_{\gamma}\rangle^{NN} = -9.9(\pm 2.1) + 8.5(\pm 1.9)s^{0.113(\pm 0.015)}. \quad (6)$$

For the 158*A* GeV SPS energy discussed here this parametrization gives the average charged particle multiplicity to be 7.2 with the corresponding number for photons being 6.3. Thus the average charged particle and photon multiplicities per participant are 3.6 and 3.15, respectively.

In addition, σ for the charged particle multiplicity in nucleon-nucleon collisions shows a linear dependence with the average charged particle multiplicity as $0.576(\langle N_{\rm ch}^{NN}\rangle - 1)$, as given in Ref. [30].

This can be used to calculate ω_m, which is given as

$$\omega_m = 0.33\frac{(\langle N_{\rm ch}\rangle - 1)^2}{\langle N_{\rm ch}\rangle}. \quad (7)$$

For charged particles at SPS energies this gives a value of $\omega_m = 1.8$. However, for photons this number is not known since there is no similar parametrization. In the absence of such a parametrization of σ for photons we will also assume that $\omega_m = 1.8$ for the photon multiplicity. Fluctuations of photons, in principle, are expected to be similar to those for charged particles. This is because the majority of photons come from decay of π^0, while the majority of charged particles are charged pions ($\pi^{\pm}$).

From the values of $\langle n\rangle$, $\langle m\rangle$, and ω_m for a given acceptance and centrality, the term ω_n can then be calculated.

C. Comparison of data to model calculations

We first compare the experimental results of multiplicity fluctuations to those of the calculations using the participant model in the common coverage of PMD and SPMD. Figure 10 shows a comparison of the fluctuation in charged particles from data to that obtained from the calculations using the model described above. The results are plotted as a function of the number of participants. The horizontal errors on the number of participants are shown only on the data points. The error on ω calculated in the model is mainly due to the error on the mean number of charged particles in nucleon-

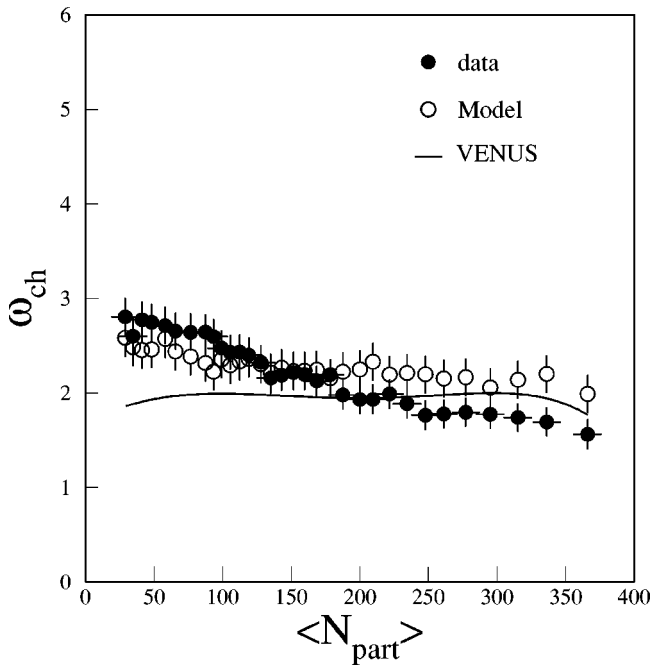

FIG. 10. The relative fluctuations ω_{ch} of the charged particle multiplicity as a function of number of participants. The experimental data are compared to calculations from a participant model and those from VENUS event generator.

nucleon interactions, the error in the number of participants calculated, and the uncertainty in the simulation of the calculated transverse energy. For clarity of presentation we have given results corresponding to alternate 2% centrality bins, i.e., 0–2 %, 2–4 %, . . . ,62–64 %. The results from VENUS are also shown in the form of a solid line in Fig. 10, and are found to remain almost constant over the entire centrality range. Charged particle fluctuations determined from data and the participant model decrease in going from peripheral to central collisions, although the dependence on centrality is weaker for the model calculation.

Figure 11 shows fluctuations in the γ-like clusters as well as N_γ after the correction. The results, plotted as a function of the number of participants, are compared to those of the participant model calculations for photons and results from VENUS. Using the estimated values of efficiency (ϵ_γ) and purity (f_p), the number of photons in an event is calculated by using the relation

$$N_\gamma = \frac{f_p}{\epsilon_\gamma}\ N_{\gamma\text{-like}}. \tag{8}$$

The photon counting efficiency in PMD varies from 68% to 73% for central to peripheral collisions. The purity of the measured photon sample varies from 65% to 54% for central to peripheral collisions.

The systematic errors associated with $N_{\gamma\text{-like}}$ have already been discussed in Sec. II. The additional errors in the conversion from $N_{\gamma\text{-like}}$ to N_γ are mainly due to errors in estimation of photon counting efficiency and purity. The sources of these errors are given below.

(1) Event-by-event variation in photon counting efficiency (ϵ_γ) and purity of photon sample (f_p). These have been found to vary from 3% to 6% for central to peripheral collisions.

(2) The purity factor depends on the ratio of the number of photons and charged particles within the PMD coverage. The systematic error associated with this ratio has been studied by using the FRITIOF [31] event generator in addition to VENUS. The average photon multiplicity estimated by using FRITIOF is found to be higher by about 4% in peripheral and by 1% in central collisions, compared to the values obtained using VENUS.

(3) The photon counting efficiency determined in the present case relies on the energy spectra of photons as given by the VENUS event generator. As the conversion probability for low-energy photons falls sharply [32] with decreasing energy below 500 MeV, the estimate of ϵ_γ may be affected if the energy spectra in the actual case is different. Photon energy spectra have been measured by the WA98 lead glass calorimeter. By extrapolating these measured spectra to the PMD acceptance we have estimated the photon counting efficiencies for different η bins and centralities. These results turn out to be lower compared to those obtained from VENUS by 2–9 % for central events and 3–13 % for peripheral events, the smaller value corresponds to larger pseudorapidity region of the PMD acceptance. The average difference in efficiencies within the PMD acceptance are 6% for central and 9% for peripheral collisions. These differences add to the systematic errors on the photon counting efficiency.

The total systematic error on the multiplicity of photons (N_γ) are -6.7% and $+12.5\%$ for peripheral collisions and -8.0% and $+9.0\%$ for central collisions.

The fluctuations in the number of photons have been estimated from the fluctuations in the number of photonlike clusters by using Eq. (8):

$$\omega_\gamma = \frac{f_p}{\epsilon_\gamma}\ \omega_{\gamma\text{-like}}. \tag{9}$$

These results are shown in Fig. 11. It is observed that the relative fluctuations of photons from the data are in reasonable agreement with those obtained from VENUS. However, the results for photons from the participant model are somewhat higher than those from the experimental data.

VI. TRANSVERSE ENERGY FLUCTUATIONS

Relativistic nuclear collisions are often described within the participant-spectator picture in which nuclei are spheres that collide with a definite impact parameter. The overlapping volumes that participate in the reaction are violently disrupted while the remaining spectator volumes shear off and suffer comparatively mild excitations. The magnitude of the E_T produced depends on the bombarding energy and the participant volume or equivalently the number of participating nucleons. The cross section for a specific value of E_T production depends to a large extent on the geometric probability of a given impact parameter. Therefore impact param-

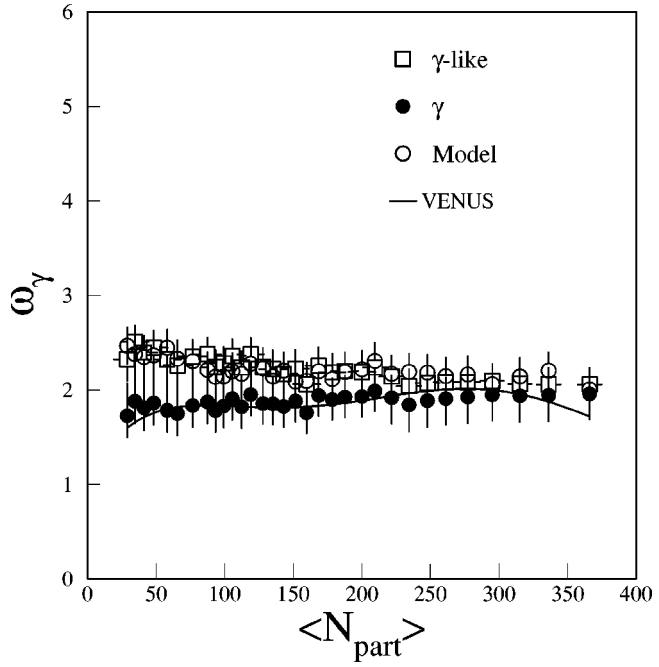

FIG. 11. The relative fluctuations ω_γ of photons as a function of number of participants. The data presented show the fluctuations in γ-like clusters and photons after correction for efficiency and purity. These are compared to calculations from a participant model and those from VENUS event generator.

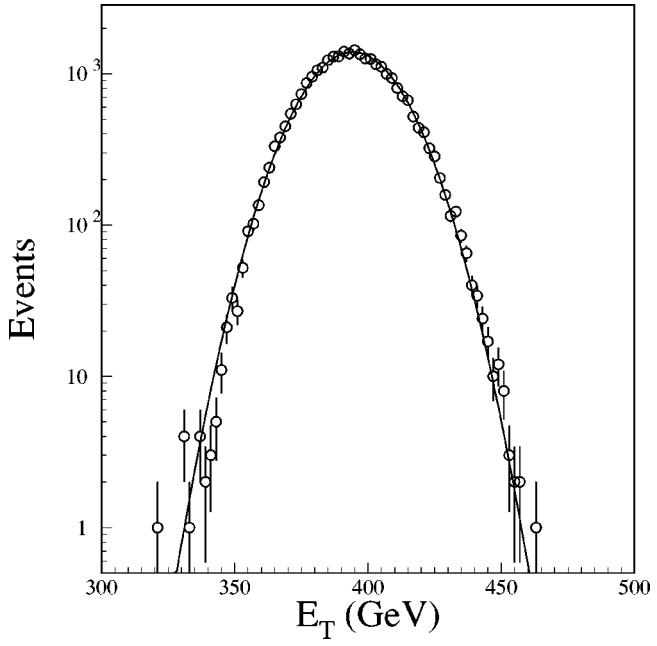

FIG. 12. The transverse energy distribution for the top 2% of the minimum bias cross section.

eter fluctuations are expected to lead to fluctuations in E_T.

Corroboration of the participant-spectator picture comes from the strong anticorrelation of E_T with the energy observed in the zero degree calorimeter, E_F as shown in the Fig. 1(b). The smaller the impact parameter, the larger is the participant volume and E_T, but the smaller is the spectator volume and E_F. E_T also correlates strongly with the produced particle multiplicity. The $d\sigma/dN_{ch}$ and $d\sigma/dN_{\gamma\text{-like}}$ spectra have virtually the same shape as $d\sigma/dE_T$ [Figs. 2(a) and 2(b)].

The study of the average total E_T as measured in the WA98 experiment and its scaling behavior with the number of participants have been discussed earlier in detail in Ref. [28]. Here we concentrate on the second moment, and study the fluctuations in E_T as was done for $N_{\gamma\text{-like}}$ and N_{ch}. For this analysis we have again taken 2% width bins in centrality using the forward energy as measured by the ZDC. Due to the poorer resolution in centrality selection of the ZDC for peripheral collisions, we present the results only up to the 50% centrality class.

The E_T distribution for the top 2% of the minimum bias cross section is shown in Fig. 12. The solid curve shows a Gasussian fit to the distribution. The μ, σ and χ^2/ndf values for such distributions at centrality bins varying from 0–2 % to 48–50 % have been extracted and are shown in Fig. 13. The χ^2/ndf values are seen to be between 1 and 2, which indicates that the distributions are well described by the Gaussians. The fluctuations in E_T have been calculated by using Eq. (1) and are shown in Fig. 14. The relative fluctuations are observed to increase in going from central to peripheral collisions. E_T, measured by the MIRAC was used in the online trigger to define the most central event sample with a threshold that occurred in the region of the top 14–18 % of the total cross section. This region is not analyzed to avoid trigger bias effects in the measured E_T distribution.

E_T has a strong correlation with the number of participant nucleons or the number of effective collisions they undergo [33]. In an attempt to understand the fluctuations in terms of

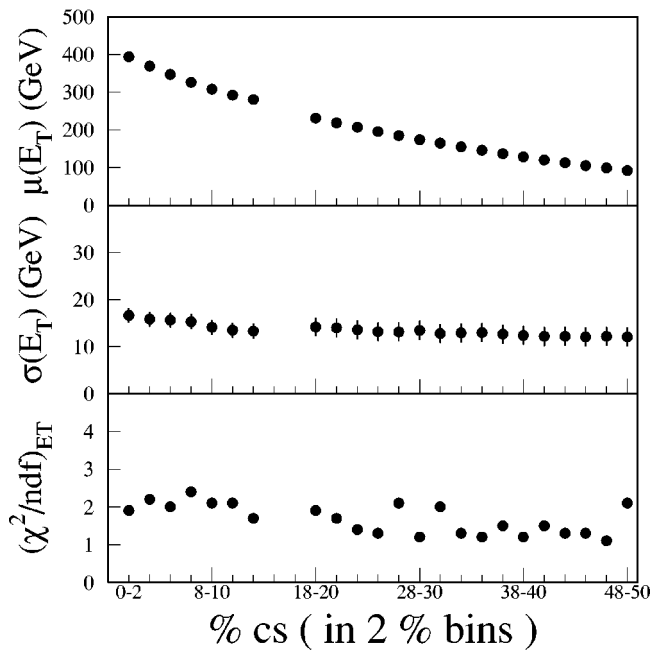

FIG. 13. Centrality dependence of μ, σ, and χ^2/ndf of the transverse energy distribution. The centrality selection is based on E_F measured with the ZDC.

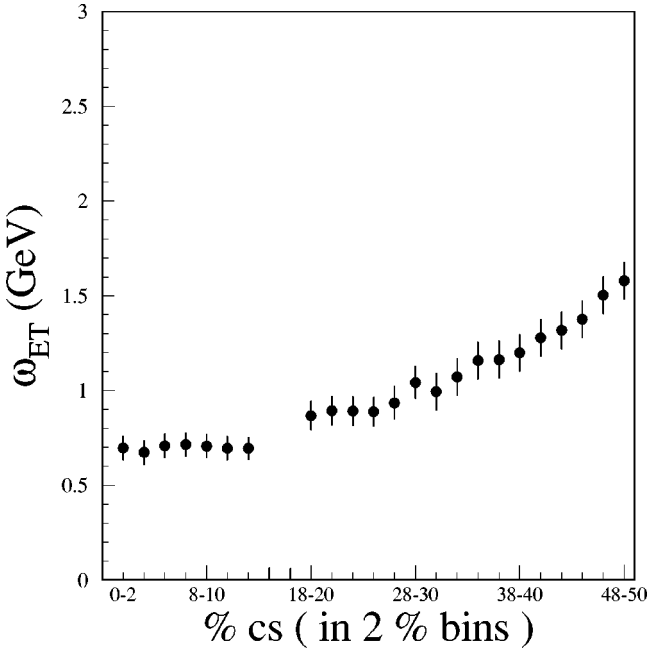

FIG. 14. Centrality dependence of the relative fluctuations in total transverse energy E_T with centrality selected by E_F.

the number of participant nucleons, the VENUS event generator has been used to determine the ratio $\mu(E_T)/\mu(N_{part})$ as a function of centrality. The $\mu(E_T)$ per participant has been found to be ~ 1.1 GeV± 0.2. This is shown in Fig. 15. The main sources of error here are due to the uncertainty in the calculation of the number of participants and the finite resolution of the calorimeters. Similar results were also obtained from WA80 and HELIOS Collaborations of Ref. [11,12].

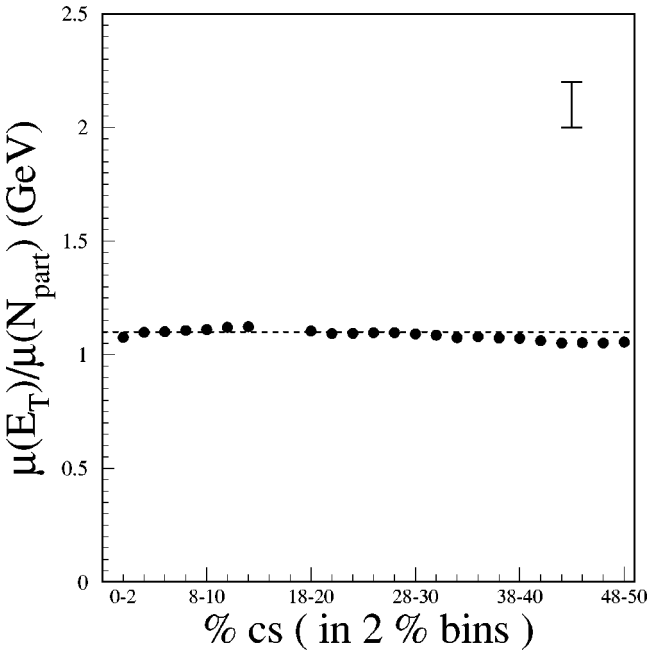

FIG. 15. E_T per participant as a function of centrality. The vertical solid line indicates the estimated systematic error in E_T per participant.

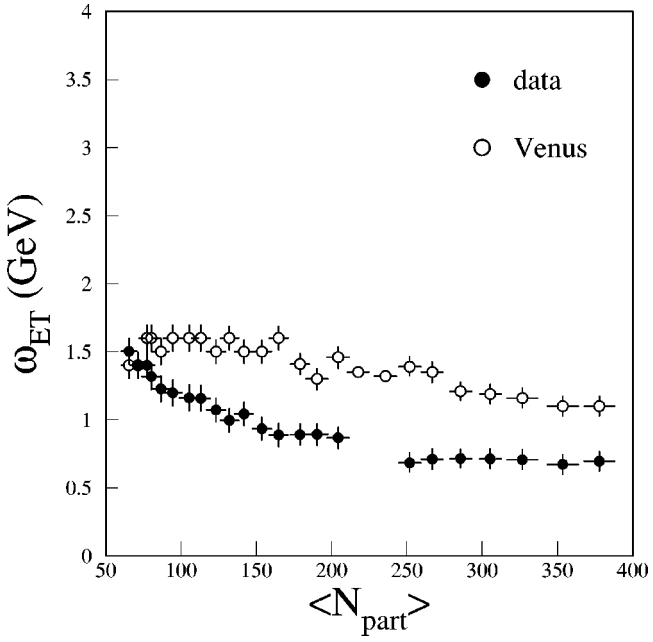

FIG. 16. Centrality dependence of the relative fluctuations in transverse energy E_T with the centrality selected from the E_F. The result is compared to VENUS using similar centrality selection criteria.

While the WA80 Collaboration has shown that E_T per participant is independent of projectile, target, and centrality but depends only on the number of wounded nucleons and the beam energy, the WA98 Collaboration has shown that transverse energy does deviate from a linear dependence on the number of participants for Pb+Pb collisions [28].

The relative fluctuations in transverse energy can be analyzed in a participant picture similar to that employed in the case of photons and charged particles [33]. An expression similar to Eq. (4) can be obtained, where the first term depends on the fluctuations in the transverse energy deposited by each particle produced per participant nucleon, with the second term coming from impact parameter fluctuations within the acceptance of the detector. Since the first term depends greatly on the detector characteristics, we compare the transverse energy fluctuations in data to those obtained from a fast simulation of the MIRAC and ZDC characteristics in VENUS in which the energy resolution for each particle was applied separately when computing the total transverse energy [23]. Figures 1(a) and 1(b) show the comparison of the simulated E_T and E_F distributions with those from data. The agreement is seen to be quite reasonable.

Figure 16 shows the comparison of E_T fluctuations from data to those obtained from simulated events using VENUS. The fluctuations are plotted as a function of the mean number of participants in various 2% bins of centrality obtained from E_F. Errors shown in the data are mainly due to uncertainties in the determination of number of participants and the finite energy resolution of the calorimeters as discussed earlier. It is seen that the fluctuation in data are systematically smaller than those obtained form VENUS. As discussed in Ref. [33] many effects like energy-momentum degradation

of nucleonic objects in successive scatterings and short-range correlations between nucleons in a nucleus may be responsible for the decrease in fluctuations in E_T of data as compared to those obtained from simulations in VENUS. The role of rescattering has also to be understood in this context.

VII. SUMMARY

A detailed event-by-event study of fluctuations in the multiplicities of charged particles and photons and transverse energy has been carried out using data from the WA98 experiment. This has been done by varying both the centrality and rapidity intervals. It is observed that the relative fluctuations increase with increase in the impact parameter interval. Hence it is important to control the impact parameter dependence by studying narrow bins in centrality. For 2% centrality bins, within which the distributions of charged particle and photon multiplicities, as well as the transverse energy, are well described by the Gaussians, the contribution from impact parameter fluctuations is around 1, as expected. The fluctuations in multiplicities and E_T are found to increase in going from central towards peripheral events. A decrease in acceptance has been found to result in decreased multiplicity fluctuations. Using a simple statistical analysis one can explain the observed decrease in a smaller acceptance knowing the fluctuations in a larger acceptance window. The observed centrality dependence of the multiplicity fluctuations of charged particles has been found to agree reasonably well with results obtained from a simple participant model that takes into account impact parameter fluctuations from VENUS and multiplicity fluctuations from *NN* data, within the quoted systematic errors. For photons the fluctuations are found to be slightly lower compared to those obtained from the participant model.

Similar calculations have been performed for the transverse energy and multiplicity distributions using VENUS. The transverse energy fluctuations from experimental data are found to be smaller than those observed in VENUS. On the other hand, after corrections for charged particle contamination in the photonlike clusters, the relative fluctuations of photons appear to be in rather good agreement with VENUS.

ACKNOWLEDGMENTS

We wish to express our gratitude to the CERN accelerator division for the excellent performance of the SPS accelerator complex. We acknowledge with appreciation the efforts of all engineers, technicians, and support staff who have participated in the construction of this experiment. This work was supported jointly by the German BMBF and DFG, the U.S. DOE, the Swedish NFR and FRN, the Dutch Stichting FOM, the Polish KBN under Contract No. 621/E-78/SPUB-M/CERN/P-03/DZ211/, the Grant Agency of the Czech Republic under Contract No. 202/95/0217, the Department of Atomic Energy, the Department of Science and Technology, the Council of Scientific and Industrial Research and the University Grants Commission of the Government of India, the Indo-FRG Exchange Program, the PPE division of CERN, the Swiss National Fund, the INTAS under Contract No. INTAS-97-0158, ORISE, Grant-in-Aid for Scientific Research (Specially Promoted Research & International Scientific Research) of the Ministry of Education, Science and Culture, the University of Tsukuba Special Research Projects, and the JSPS. ORNL is managed by UT-Battelle, LLC, for the U.S. Department of Energy under Contract No. DE-AC05-00OR22725. The MIT group has been supported by the U.S. Department of Energy under cooperative agreement No. DE-FC02-94ER40818.

[1] L. van Hove, Phys. Lett. **118B**, 138 (1982); H. Heiselberg, Phys. Rep. **351**, 161 (2001); E.V. Shuryak, Phys. Lett. B **423**, 9 (1998); M. Gazdzicki and S. Mrowczynski, Z. Phys. C **57**, 127 (1992); S. Mrowczynski, Phys. Rev. C **57**, 1518 (1998); Phys. Lett. B **430**, 9 (1998).

[2] *Proceedings of Quark Matter '99*, edited by L. Riccati, M. Masera, and E. Vercellin [Nucl. Phys **A661** (1999)].

[3] *Proceedings of Quark Matter '2001*, edited by T.J. Hallman, D.E. Kharzeev, J.T. Mitchell, and T. Ullrich [Nucl. Phys **A698** (2002)].

[4] M. Stephanov, K. Rajagopal, and E. Shuryak, Phys. Rev. Lett. **81**, 4816 (1998); Phys. Rev. D **61**, 114028 (1999).

[5] G. Baym and H. Heiselberg, Phys. Lett. B **469**, 7 (1999).

[6] M. Asakawa, U. Heinz, and B. Müller, Phys. Rev. Lett. **85**, 2072 (2000).

[7] S. Jeon and V. Koch, Phys. Rev. Lett. **83**, 5435 (1999); **85**, 2076 (2000).

[8] L. van Hove, Z. Phys. C **21**, 93 (1984); J.I. Kapusta and A.P. Vischer, Phys. Rev. C **52**, 2725 (1995).

[9] K. Rajagopal and F. Wilczek, Nucl. Phys. **B399**, 395 (1993); **B404**, 577 (1993); J.D. Bjorken, Int. J. Mod. Phys. A **7**, 4189 (1992); T.C. Brooks *et al.*, Minimax Collaboration, Phys. Rev. D **61**, 032003 (2000); J.-P. Blaizot and A. Krzywicki, *ibid.* **46**, 246 (1992).

[10] M.M. Aggarwal *et al.*, WA98 Collaboration, Phys. Rev. C **64**, 011901(R) (2001).

[11] T. Akesson *et al.*, Z. Phys. C **38**, 383 (1988).

[12] T. Akesson *et al.*, Phys. Lett. B **214**, 214 (1988).

[13] T. Alber *et al.*, NA49 Collaboration, Phys. Rev. Lett. **75**, 3814 (1995).

[14] H. Appelshauser *et al.*, NA49 Collaboration, Phys. Lett. B **459**, 679 (1999); G. Roland, Nucl. Phys. **A638**, 91c (1998).

[15] G. Baym *et al.*, Phys. Lett. B **219**, 205 (1989).

[16] F. Corriveau *et al.*, NA34 Collaboration, Z. Phys. C **38**, 15 (1988); J. Schukraft, *et al.* NA34 Collaboration, Z. Phys. C **38**, 59 (1988).

[17] R. Albrecht *et al.*, Z. Phys. C **45**, 31 (1989).

[18] H.H. Gutbrod *et al.*, Proposal for a Large Acceptance Hadron and Photon Spectrometer, Report No. CERN/SPSLC 91-17, SPSLC/P260 (unpublished).

[19] M.M. Aggarwal *et al.*, WA98 Collaboration, Phys. Lett. B **420**, 169 (1998).

[20] W.T. Lin *et al.*, Nucl. Instrum. Methods Phys. Res. A **389**, 415 (1997).
[21] M.M. Aggarwal *et al.*, Nucl. Instrum. Methods Phys. Res. A **424**, 395 (1999).
[22] M.M. Aggarwal *et al.*, WA98 Collaboration, Phys. Lett. B **458**, 422 (1999).
[23] T.C. Awes, Nucl. Instrum. Methods Phys. Res. A **279**, 497 (1989).
[24] K. Werner, Phys. Rep. **232**, 87 (1993).
[25] D.P. Mahapatra, B. Mohanty, and S.C. Phatak, Int. J. Mod. Phys. A **17**, 675 (2002).
[26] Rudolph C. Hwa, Phys. Lett. B **201**, 165 (1988).
[27] A. Giovannini and L. Van Hove, Z. Phys. C **30**, 391 (1986).
[28] M.M. Aggarwal *et al.*, WA98 Collaboration, Eur. Phys. J. C **18**, 651 (2001).
[29] G.J. Alner *et al.*, UA5 Collaboration, Phys. Rep. **154**, 247 (1987).
[30] J. Whitmore, Phys. Rep. **27**, 187 (1976); **10**, 274 (1974).
[31] B. Nilsson-Almqvist and E. Stenlund, Comput. Phys. Commun. **43**, 387 (1987).
[32] M.M. Aggarwal *et al.*, Nucl. Instrum. Methods Phys. Res. A **372**, 143 (1996).
[33] Gordon Baym *et al.*, Phys. Lett. B **190**, 29 (1987); A.D. Jackson and H. Bogglid, Nucl. Phys. **A470**, 669 (1987).

Eur. Phys. J. C 23, 225–236 (2002)
Digital Object Identifier (DOI) 10.1007/s100520100886

THE EUROPEAN PHYSICAL JOURNAL C

Transverse mass distributions of neutral pions from ^{208}Pb-induced reactions at 158·A GeV

The WA98 Collaboration

M.M. Aggarwal[4], A.L.S. Angelis[7], V. Antonenko[13], V. Arefiev[6], V. Astakhov[6], V. Avdeitchikov[6], T.C. Awes[16], P.V.K.S. Baba[10], S.K. Badyal[10], S. Bathe[14], B. Batiounia[6], T. Bernier[15], K.B. Bhalla[9], V.S. Bhatia[4], C. Blume[14], D. Bucher[14], H. Büsching[14], L. Carlén[12], S. Chattopadhyay[2], M.P. Decowski[3], H. Delagrange[15], P. Donni[7], M.R. Dutta Majumdar[2], K. El Chenawi[12], K. Enosawa[18], S. Fokin[13], V. Frolov[6], M.S. Ganti[2], S. Garpman[12], O. Gavrishchuk[6], F.J.M. Geurts[19], T.K. Ghosh[8], R. Glasow[14], B. Guskov[6], H. Å.Gustafsson[12], H. H.Gutbrod[5], I. Hrivnacova[17], M. Ippolitov[13], H. Kalechofsky[7], R. Kamermans[19], K. Karadjev[13], K. Karpio[20], B. W. Kolb[5], I. Kosarev[6], I. Koutcheryaev[13], A. Kugler[17], P. Kulinich[3], M. Kurata[18], A. Lebedev[13], H. Löhner[8], D.P. Mahapatra[1], V. Manko[13], M. Martin[7], G. Martínez[15], A. Maximov[6], Y. Miake[18], G.C. Mishra[1], B. Mohanty[1], M.-J. Mora[15], D. Morrison[11], T. Mukhanova[13], D. S. Mukhopadhyay[2], H. Naef[7], B. K. Nandi[1], S. K. Nayak[10], T. K. Nayak[2], A. Nianine[13], V. Nikitine[6], S. Nikolaev[6], P. Nilsson[12], S. Nishimura[18], P. Nomokonov[6], J. Nystrand[12], A. Oskarsson[12], I. Otterlund[12], T. Peitzmann[14], D. Peressounko[13], V. Petracek[17], F. Plasil[16], M.L. Purschke[5], J. Rak[17], R. Raniwala[9], S. Raniwala[9], N.K. Rao[10], K. Reygers[14], G. Roland[3], L. Rosselet[7], I. Roufanov[6], J.M. Rubio[7], S.S. Sambyal[10], R. Santo[14], S. Sato[18], H. Schlagheck[14], H.-R. Schmidt[5], Y. Schutz[15], G. Shabratova[6], T.H. Shah[10], I. Sibiriak[13], T. Siemiarczuk[20], D. Silvermyr[12], B.C. Sinha[2], N. Slavine[6], K. Söderström[12], G. Sood[4], S.P. Sørensen[11], P. Stankus[16], G. Stefanek[20], P. Steinberg[3], E. Stenlund[12], M. Sumbera[17], T. Svensson[12], A. Tsvetkov[13], L. Tykarski[20], E.C.v.d. Pijll[19], N.v. Eijndhoven[19], G.J.v. Nieuwenhuizen[3], A. Vinogradov[13], Y.P. Viyogi[2], A. Vodopianov[6], S. Vörös[7], B. Wysłouch[3], G.R. Young[16]

[1] Institute of Physics, 751-005 Bhubaneswar, India
[2] Variable Energy Cyclotron Centre, Calcutta 700 064, India
[3] MIT Cambridge, MA 02139, USA
[4] University of Panjab, Chandigarh 160014, India
[5] Gesellschaft für Schwerionenforschung (GSI), 64220 Darmstadt, Germany
[6] Joint Institute for Nuclear Research, 141980 Dubna, Russia
[7] University of Geneva, CH-1211 Geneva 4,Switzerland
[8] KVI, University of Groningen, 9747 AA Groningen, The Netherlands
[9] University of Rajasthan, Jaipur 302004, Rajasthan, India
[10] University of Jammu, Jammu 180001, India
[11] University of Tennessee, Knoxville, TN 37966, USA
[12] Lund University, 221 00 Lund, Sweden
[13] RRC "Kurchatov Institute", 123182 Moscow, Russia
[14] University of Münster, 48149 Münster, Germany
[15] SUBATECH, Ecole des Mines, Nantes, France
[16] Oak Ridge National Laboratory, Oak Ridge, Tennessee 37831-6372, USA
[17] Nuclear Physics Institute, 250 68 Rez, Czech Republic
[18] University of Tsukuba, Ibaraki 305, Japan
[19] Universiteit Utrecht/NIKHEF, 3508 TA Utrecht, The Netherlands
[20] Institute for Nuclear Studies, 00-681 Warsaw, Poland

Received: 3 August 2001 / Revised version: 19 November 2001 /
Published online: 8 February 2002 – © Springer-Verlag / Società Italiana di Fisica 2002

Abstract. Results on transverse mass spectra of neutral pions measured at central rapidity are presented for impact parameter selected 158·A GeV Pb + Pb, and Pb + Nb collisions. The distributions cover the range $0.5\,\mathrm{GeV}/c^2 \leq m_T - m_0 \leq 4\,\mathrm{GeV}/c^2$. The change of the spectral shape and the multiplicity with centrality is studied in detail. In going from p+p to semi-peripheral Pb+Pb collisions there is a nuclear enhancement increasing with transverse mass similar to the well known Cronin effect, while for very central collisions this enhancement appears to be weaker than expected.

1 Introduction

Heavy ion reactions at ultrarelativistic energies provide information on nuclear matter at high energy density (for reviews see e.g. [1–3]). Hadron production is generally considered to be sensitive to the late freeze-out stage of the collision, when hadrons decouple from one another. Already from the experimentally determined shape of the transverse mass spectra it is evident that heavy ion reactions are not merely a superposition of nucleon-nucleon collisions [4–6].

The broadening of the transverse mass spectra in p+A collisions compared to p+p (Cronin-effect [7]) has been attributed to *initial state* multiple scattering of partons [8, 9]. However, models which attempt to describe nucleus-nucleus reactions, like the Monte-Carlo programs VENUS [10] or RQMD [11] rely on the assumption that *final state* rescattering plays an important role in determination of the momentum distributions of the hadrons. If final state rescattering is very strong, the notion of local kinetic equilibrium may be valid, which is the basic assumption for a hydrodynamical description (see e.g. [12,13]).

It remains unclear, whether equilibration is attained. If it occurs, it will be important to isolate the contributions of thermal, pre-equilibrium, and initial state processes to the hadron yield. Since the latter are expected to dominate at large transverse momenta, it is hoped that systematic studies of hadron spectra over a large range in momentum might allow to disentangle these contributions. In the analysis of central reactions of Pb + Pb at 158·A GeV it is seen that both predictions of perturbative QCD [17,18] and hydrodynamical parameterizations [19] can describe the measured neutral pion spectra reasonably well. It is particularly surprising to observe that, on the one hand, a pQCD calculation gives a reasonable description also at relatively low momenta, while on the other hand, a hydrodynamical parameterization can provide a good description, even at very high momenta.

The understanding of the relative contributions of the various soft and hard processes in particle production is especially important in view of the recent interest in the energy loss of partons in dense matter [14,15], generally referred to as *jet quenching*, as a possible probe for the quark-gluon-plasma. One of the suggested experimental hints of jet quenching is the suppression of particle production at high transverse momenta [16]. In order to confirm such an interpretation, it is important to study other possible nuclear modifications of particle production in detail. More information in this respect may be gathered from the variation of the particle spectra for different reaction systems or different centralities. First attempts in this respect have been discussed in [17], where the neutral pion average p_T as a function of the centrality was shown to rise from p+p collisions to peripheral Pb+Pb collisions and to saturate for medium central and central Pb+Pb collisions. It was also seen that the neutral pion yield for reactions with more than about 30 participating nucleons N_{part} exhibits a scaling as N_{part}^{α} with a power $\alpha \approx 1.1$ which is approximately independent of p_T.

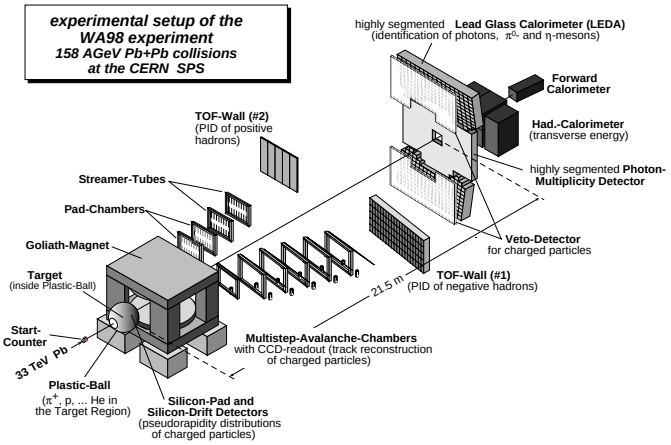

Fig. 1. The WA98 experimental setup

In the present paper we will present a detailed study of neutral pion transverse mass spectra in the range $0.5\text{GeV}/c^2 \leq m_T - m_0 \leq 4.0\text{GeV}/c^2$ and $2.3 \leq y \leq 3.0$ for collisions of Pb+Pb and Pb+Nb at 158·A GeV for different centralities.

2 Experiment

The CERN experiment WA98 [20] is a general-purpose apparatus which consists of large acceptance photon and hadron spectrometers together with several other large acceptance devices which allow to measure various global variables on an event-by-event basis. The experiment took data with the 158·A GeV ^{208}Pb beams from the SPS in 1994, 1995, and 1996. The data presented here were taken during the 1995 and 1996 beamtimes at the CERN SPS. The layout of the WA98 experiment as it existed during the final WA98 run period in 1996 is shown in Fig. 1.

Neutral pions are reconstructed on a statistical basis from their two-photon decay, using photons measured with the LEDA spectrometer in the pseudorapidity interval $2.3 < \eta < 3.0$. This detector is located 21.5 m from the target and consists of 10,080 modules. Each module is a $4 \times 4 \times 40$ cm^3 (14.3 radiation lengths) TF1 lead-glass block read out by an FEU-84 photomultiplier. The high voltage is generated on-base with custom developed [22] Cockcroft-Walton voltage-multiplier type bases which are individually controlled by a VME processor. The photomultiplier signals are digitized with a custom-built ADC system [23]. Twenty-four lead-glass modules are epoxied together in an array 6 modules wide by 4 modules high to form a super-module. Each super-module has its own calibration and gain monitoring system based on a set of 3 LEDs and a PIN-photodiode mounted inside a sealed reflecting front cover dome [24]. The photon spectrometer is separated into two nearly symmetric halves above and below the beam plane in the two regions of reduced charged-particle density which result from the sweeping action of the GOLIATH magnet. More details about the experimental setup and the photon spectrometer can be found in [25].

The acceptance of the photon spectrometer for π^0 detection in rapidity and transverse mass is shown in Fig. 2. The acceptance covers the region $2.3 < y < 3.0$, near mid-rapidity ($y_{cm} = 2.9$).

The minimum bias trigger requires a valid signal of the beam counters and a minimum amount of transverse energy $E_T \gtrsim 5\,\mathrm{GeV}$, detected by the Mid-Rapidity Calorimeter, MIRAC [21], which is located 24 m downstream of the target. MIRAC consists of a hadronic and an electromagnetic section and covers the pseudorapidity interval $3.5 < \eta < 5.5$. Data have been taken with the 158·A GeV lead beam on targets of Pb (495 and 239 mg/cm^2) and Nb (218 mg/cm^2). For the present analysis 9.7 million Pb+Pb and 0.23 million Pb+Nb minimum bias events were accumulated. The minimum bias cross sections have been calculated from the number of beam triggers and minimum bias triggers and the target thicknesses. The yields have been corrected for small non-target background contributions (typically a few percent) to obtain $\sigma_{\mathrm{mb}} \approx 6300\,\mathrm{mb}$ and 4400 mb for Pb + Pb and Pb + Nb reactions, respectively. These absolute cross sections are estimated to have an overall systematic error of less than 10%.

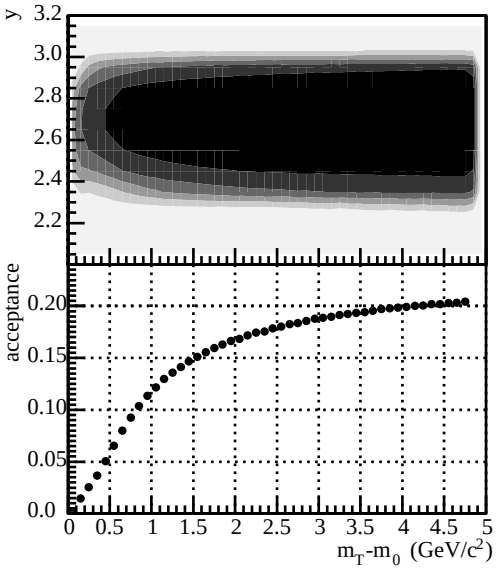

Fig. 2. Top: Geometrical acceptance for neutral pions as a function of p_T and y. Bottom: Rapidity-integrated acceptance in $2.0 < y < 3.2$ as a function of $m_T - m_0$

3 Pion reconstruction and efficiency

The method for pion reconstruction is similar to that used by the WA80 collaboration as discussed in [6]. It is also discussed at length in [25,26] so we will only briefly sketch the basics of the method.

The showers used for the extraction of the neutral pion yield via the $\gamma\gamma$ decay branch can be selected with different criteria. It has been demonstrated that the extracted yield does not depend significantly on the choice of these photon identification cuts [25]. For the present analysis, showers with a small lateral dispersion [27] have been selected as photon candidates.

Hits in LEDA are combined pairwise to provide distributions of pair mass vs. $m_T - m_0$ (where $m_T = \sqrt{p_T^2 + m_0^2}$ is the transverse mass and m_0 is the π^0 rest mass) for all possible combinations. These distributions are obtained both for real events, $R(m_{\mathrm{inv}}, m_T)$, and for so-called mixed events, $M(m_{\mathrm{inv}}, m_T)$, where a hit from one event is combined with a hit from another event with similar multiplicity. $M(m_{\mathrm{inv}}, m_T)$ provides a good description of the combinatorial background and is subtracted from $R(m_{\mathrm{inv}}, m_T)$ to obtain the mass distribution of neutral pions (see Fig. 3).

The large multiplicities, especially in central reactions of Pb + Pb, lead to a considerable probability that showers in the detector overlap and influence each other. Particles may be lost for reconstruction. In other cases the particle might be measured with an incorrect energy. These effects lead to a detector efficiency for pion reconstruction which depends on particle density. To study this detection efficiency, the GEANT [28] simulation package has been used to create artificial signals for the lead glass modules corresponding to neutral pions incident on the detector. The effects of detector noise and the digitization of the photomultiplier signals are also implemented. To obtain the π^0

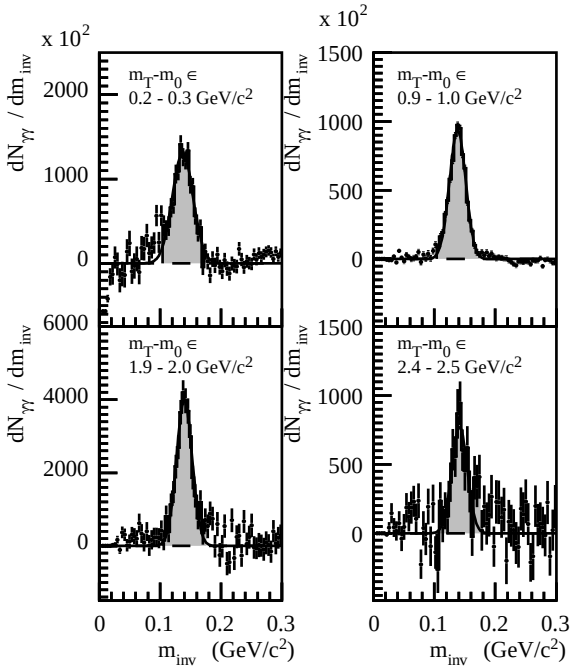

Fig. 3. Invariant mass distributions of photon pairs for minimum bias Pb + Pb collisions in different intervals of $m_T - m_0$. The combinatorial background has been calculated using mixed-event distributions and subtracted

reconstruction efficiency, these simulated photon shower pairs have been superimposed onto the measured events. The simulation provides the means to extract the probability that a pion at a given input transverse mass $m_T^{(0)}$ will be measured with $m_T^{(1)}$. These probabilities, extracted as a function of $m_T^{(0)}$, can be understood as a matrix which transforms the real physical distributions into the mea-

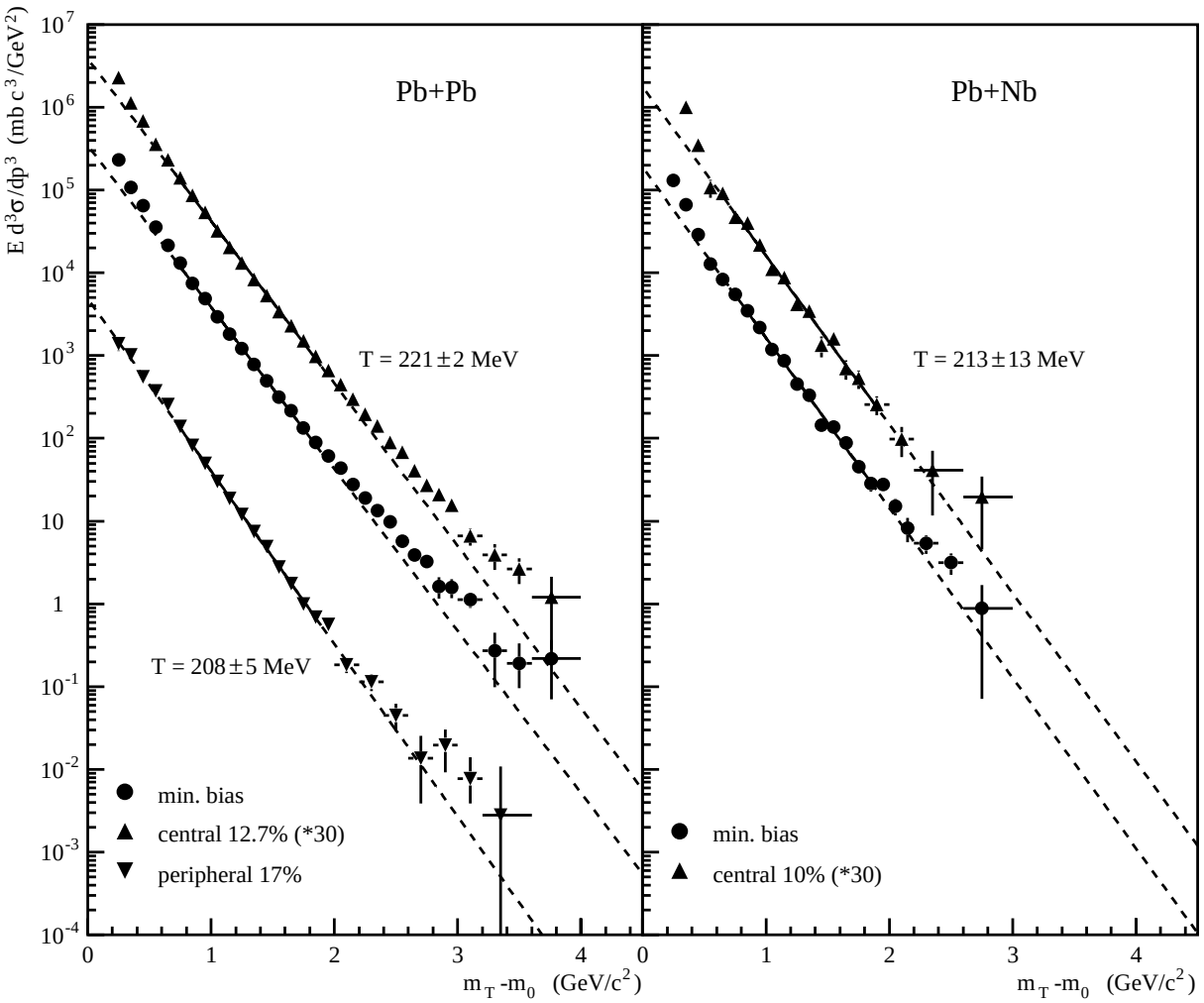

Fig. 4. Invariant cross sections of neutral pions for Pb + Pb (left) and Pb + Nb collisions (right) of different centralities as a function of $m_T - m_0$

sured ones. These correction matrices are used to correct the measured distributions. A detailed description of the efficiency correction can be found in [25].

The distributions have then been corrected for contributions from reactions of Pb projectiles with material other than the target (e.g. residual gas, exit windows, etc.). The corresponding corrections were obtained by measurements performed without target. The corrections are negligible for medium-central and central reactions.

The systematic errors on the measured transverse mass spectra are dominated by the following contributions:

- An uncertainty in the absolute calibration of the momentum scale of 1%. This may be translated into an uncertainty in the yields of a few% at low m_T rising to $\approx$ 13% at $m_T - m_0 = 3.5\,\mathrm{GeV}/c^2$, which is independent of centrality or reaction system.
- Uncertainties in the π^0 extraction which include the error in the determination of the invariant mass peak content and the propagation of the energy resolution through the acceptance and efficiency corrections. This is largest in central collisions. It leads to an error below 10% for $m_T - m_0 \geq 0.5\,\mathrm{GeV}/c^2$ for most samples.
- Uncertainties in the correction for contributions from no-target reactions, which are only relevant for peripheral reactions. This leads to an error below 10% for $m_T - m_0 \geq 0.5\,\mathrm{GeV}/c^2$.

The total centrality dependent systematic error is below 10% for $m_T - m_0 \geq 0.5\,\mathrm{GeV}/c^2$ for most centrality classes and below 20% for the most central sample.

4 Results

4.1 Neutral pion spectra

Neutral pion spectra for Pb + Pb and Pb + Nb collisions for minimum bias and selected centralities are presented in Fig. 4. On the left hand side results for Pb + Pb minimum bias as well as for the 12.7% most central and the 17% most peripheral event selections are shown. Included also are results of exponential fits:

$$f(m_T - m_0) = C \cdot \exp\left(-\frac{m_T - m_0}{T}\right) \qquad (1)$$

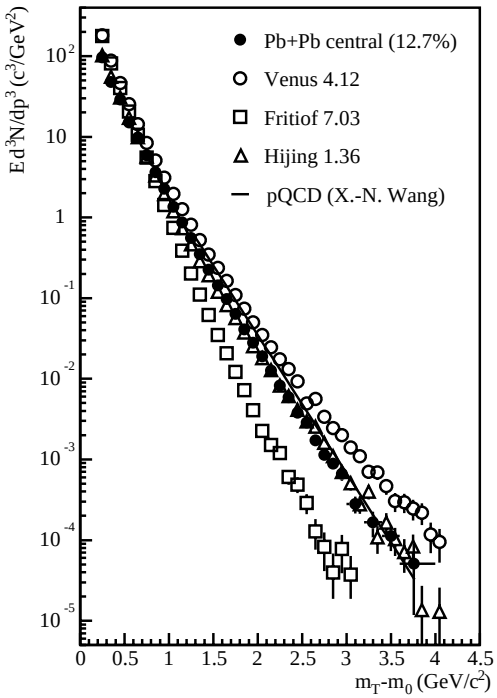

Fig. 5. Invariant multiplicities of neutral pions for central Pb + Pb collisions as a function of $m_T - m_0$ compared to predictions of Monte Carlo event generators

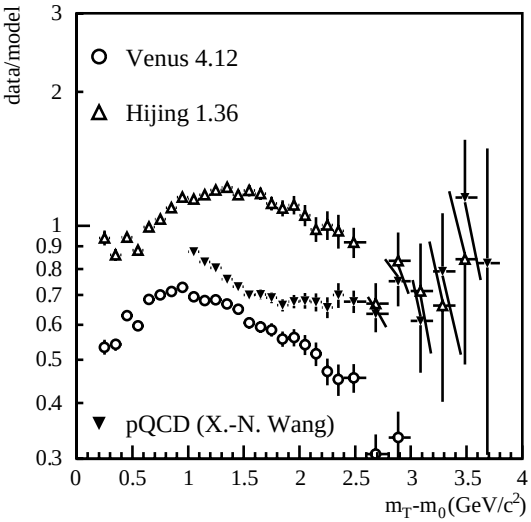

Fig. 6. Ratios of measured invariant multiplicities of neutral pions to those from Monte Carlo event generators for central Pb + Pb collisions as a function of $m_T - m_0$

fitted over the range $0.7\,\mathrm{GeV}/c^2 \leq m_T - m_0 \leq 1.9\,\mathrm{GeV}/c^2$. As noted previously [6,17], the data clearly deviate from the exponential shape when considered over the full range of transverse masses. The fit in the limited transverse mass range can, however, still be used to extract slope parameters T. For the 12.7% most central collisions one finds $T = 221 \pm 2\,\mathrm{MeV}$ which is significantly larger than the value of $T = 208 \pm 5\,\mathrm{MeV}$ for peripheral collisions. Spectra for reactions of Pb + Nb (minimum bias and 10% central) are shown on the right hand side. The spectral shapes are very similar to those for Pb + Pb collisions. For central collisions a slope parameter of $T = 213 \pm 13\,\mathrm{MeV}$ is extracted which is intermediate compared to that of peripheral and central Pb + Pb collisions. Since the statistics for the Pb + Nb dataset is limited, we will concentrate on the Pb + Pb reactions in the rest of the paper.

In Fig. 5 the multiplicity distribution for central collisions is compared to predictions of the event generators FRITIOF 7.03 [29], VENUS 4.12 [10], and HIJING 1.36 [30]. Clearly FRITIOF does not describe the data at all, while VENUS and HIJING yield a more reasonable description. The prediction of the pQCD calculation from [18] is included as a solid line, which also shows a reasonable agreement with the data. The degree of agreement of the models can be better seen in Fig. 6 where the ratio of the experimental data to the generator results is shown. FRITIOF is not included as the discrepancies are already evident from Fig. 5. VENUS overpredicts the pion production at high m_T by about a factor of two. HIJING shows the best agreement at large momenta but underpredicts the data slightly at intermediate m_T. Also the Monte Carlo models lead to a stronger concave curvature than the data. The pQCD calculation overpredicts the data by $\approx 30\%$ in the range $1.5\,\mathrm{GeV}/c \leq m_T - m_0 \leq 3.0\,\mathrm{GeV}/c$.

The momentum spectra for central collisions have been published already in [17]. As discussed in the corresponding erratum, cross section estimates had turned out to be incorrect. In the course of the present analysis it was realized that for the presentation of the results in Fig. 1 of [17], the π^0 multiplicities were incorrectly normalized. All other results and conclusions of [17] are unchanged. Unfortunately, the same improperly normalized distributions were analyzed in [18]. The correct normalization reduces the π^0 mulitiplicities by 27% with the result that the pQCD calculations presented there would overpredict the measured WA98 π^0 result, as shown in Fig. 6. Still different parameters for the p_T-broadening in these calculations might possibly enable the model to describe the central distributions better. More stringent tests of such a model can be performed when looking at the detailed centrality dependence of the pion production which has been done in the following.

The minimum bias sample has been subdivided into eight centrality samples summarized in Table 1. Measurements were performed with and without magnetic field, which does not affect the neutral pion distributions, but alters the transverse energy used to determine the centrality. The corresponding cuts have been adjusted so that always the same fractions of the minimum bias cross section were selected. The data samples with and without magnetic field agree well with each other and have been combined in the present analysis. Table 1 shows the transverse energy cuts for one particular data set as an example.

All the transverse mass distributions for Pb + Pb collisions for the different centrality classes as a function of $m_T - m_0$ have a very similar shape (see Fig. 7). The distributions are compared more closely in Fig. 8 where the spectra for given centrality classes are divided by the min-

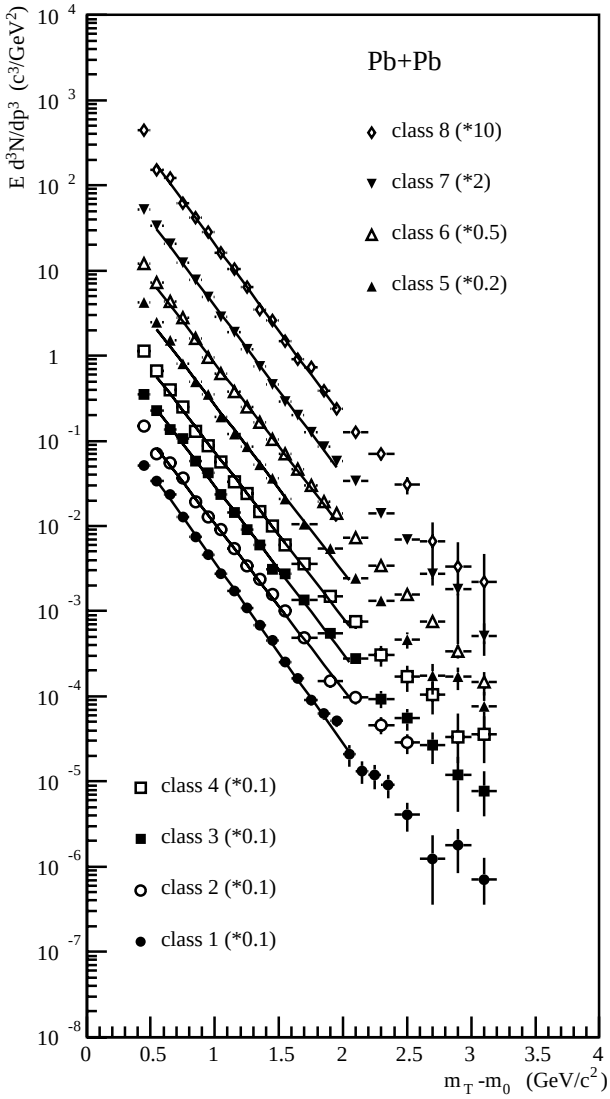

Fig. 7. Invariant multiplicities of neutral pions for Pb + Pb collisions of different centralities as a function of $m_T - m_0$. The solid lines show exponential fits to the spectra

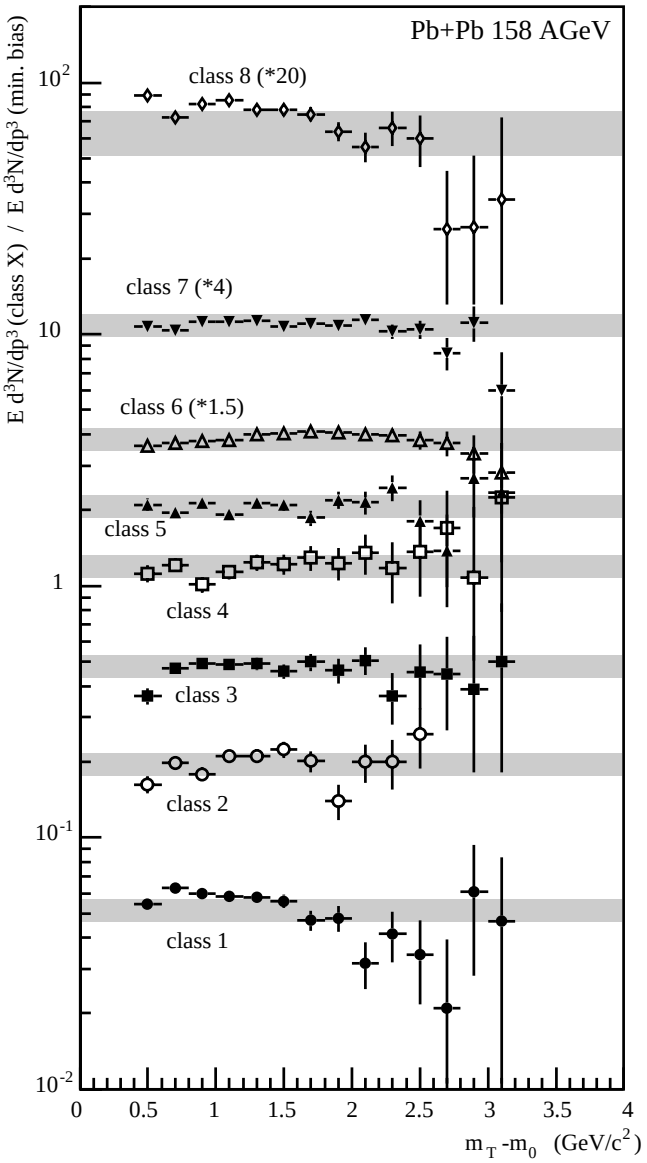

Fig. 8. Ratios of invariant multiplicities of neutral pions for Pb + Pb collisions of different centralities to minimum bias distributions as a function of $m_T - m_0$, with class 1 being the most peripheral and class 8 the most central sample. The grey bands show the estimate of the centrality dependent systematic error

imum bias spectrum. Still in these ratios no drastic variations are seen when displayed in logarithmic scale. The spectral shapes, especially for the intermediate centrality classes, are very similar. The spectra are broadened when going from peripheral reactions to semi-peripheral reactions, consistent with the nuclear enhancement seen in p + A [7] and in S + Au collisions [6]. However, the enhancement does not continue to grow for central collisions. Instead there is an indication of a stronger fall off in the most central class.

This observation is surprising, because both initial state (parton multiple scattering) and final state (hadron rescattering) mechanisms are expected to yield a further broadening of the spectra with decreasing impact parameter, i.e. increasing thickness or volume.

The change in the spectrum for the most stringent centrality selection of 1% of the minimum bias cross section appears to be relatively strong, and the question arises whether this cut is really significant enough and whether this sample should not behave similarly to the adjacent sample. We have therefore performed detailed investigations of possible backgrounds and biases with respect to this particular sample. Pile-up of multiple beam interactions is effectively suppressed by strong time and amplitude cuts on the trigger level. In addition, the total calorimeter coverage of MIRAC and the ZDC is sufficient to reject all possible pile-up events, as the measured energy would exceed the beam energy.

Also, simulations of the centrality selections including realtistic fluctuations in the detectors show that e.g. classes 7 and 8 are significantly different. This can e.g.

Table 1. Centrality classes, as selected by the amount of transverse energy measured in MIRAC, for Pb + Pb collisions. The average number of participants and binary nucleon-nucleon collisions as calculated with VENUS 4.12 with an estimate of the systematic error. Please note that the systematic error in the number of collisions is correlated for all samples

class	E_T (GeV)	$\sigma/\sigma_{\rm mb}$	$\langle N_{part}\rangle$	$\langle N_{coll}\rangle$
1	$\leq$ 24.35	17.2%	12 ± 2	9.9 ± 2.5
2	24.35 – 55.45	15.8%	30 ± 2	30 ± 5
3	55.45 –114.85	18.2%	63 ± 2	78 ± 12
4	114.85 –237.35	23.5%	132 ± 3	207 ± 21
5	237.35 –326.05	12.3%	224 ± 1	408 ± 41
6	326.05 –380.35	6.2%	290 ± 2	569 ± 57
7	380.35 –443.20	5.8%	346 ± 1	712 ± 71
8	>443.20	1.0%	380 ± 1	807 ± 81
6–8	>326.05	12.7%	323 ± 1	651 ± 65

be expressed by the mean (rms) of the distribution of the number of participating nucleons which are 346 (20) and 380 (10), respectively.

As the centrality selection is performed with the transverse energy measured slightly off midrapidity, one might suspect that midrapidity particle production could suffer a different bias, if e.g. the pseudorapidity distribution would change significantly over the small range relevant here. This is, however, not observed. The charged particle pseudorapidity density at $\eta = 0$ increases in a fashion identical to the transverse energy as can be seen in [31].

While this leads us to expect no additional bias from the event selection, the direct comparison of the spectra obtained with different analysis cuts for the most central sample (class 8) shows slightly larger variations than the other samples. We have therefore assigned a larger systematic error of 20% to this sample, as was discussed in Sect. 3.

4.2 Average p_T and inverse slopes

Another means to characterize the spectral shape is via the average transverse momentum $\langle p_T\rangle$, or via the inverse slopes T of the spectra. The truncated average transverse momentum has already been presented in [17], where it was shown that the values of $\langle p_T(p_T^{min})\rangle$, with a lower cutoff of $p_T^{min} = 0.4\,\mathrm{GeV}/c^2$, increase from peripheral to medium central collisions but seem to saturate for still smaller impact parameters. Since the $\langle p_T(p_T^{min})\rangle$ is dominated by the momentum region near the cutoff, this is not in contradiction with the dependence observed in Fig. 8. A similar analysis has been performed with inverse slope parameters which were obtained by fitting exponentials (1) to the spectra in limited regions of transverse mass. The extracted slope parameters as a function of the number of participants are shown in Fig. 9. Fits in the lowest m_T interval yield a slope of $T = 204\,\mathrm{MeV}$ for peripheral reactions. In the intermediate centrality range the slope appears to be constant at $T \approx 220\,\mathrm{MeV}$.

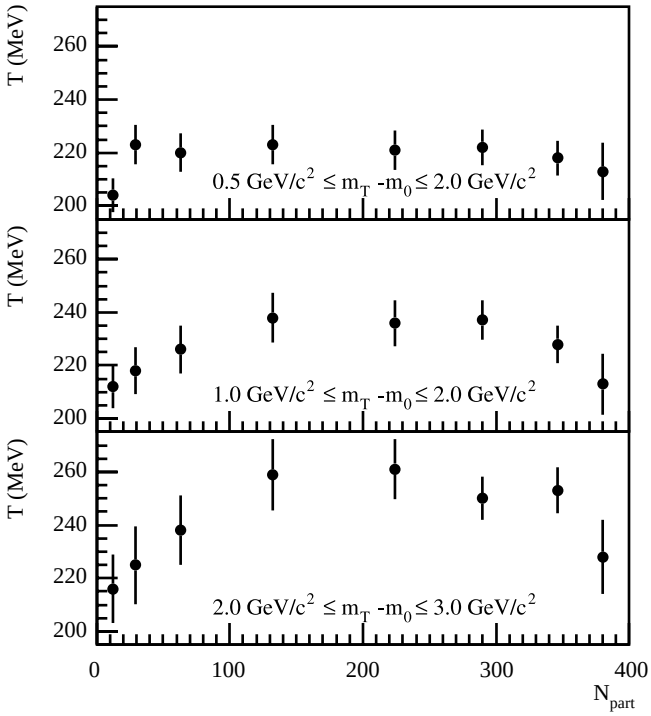

Fig. 9. Inverse slope parameters T of neutral pion transverse mass distributions as a function of the number of participants in Pb + Pb collisions. The exponential fits are performed in different regions $m_T - m_0$ as indicated. The error bars shown contain statistical and systematic errors added in quadrature

Inverse slopes have also been extracted for other intervals of transverse mass (see Fig. 9). For all centralities the slopes increase with larger transverse mass, which is another demonstration of the curvature of the spectra. The centrality dependence is more pronounced for the higher m_T regions ($1 - 2$ GeV/c^2 and $2 - 3$ GeV/c^2). There is a continuous rise in the inverse slope from very peripheral reactions up to reactions with $N_{part} \approx 130$, the highest slopes reaching $T \approx 240\,\mathrm{MeV}$ and $T \approx 260\,\mathrm{MeV}$, respectively. There is an indication of a decrease in the slope for very central collisions which is however not conclusive in view of the systematic errors.

From this analysis of the spectral shapes by looking at spectral ratios or inverse slopes one may conclude, that apart from the broadening in going from peripheral to semi-peripheral collisions, no striking features are observed. Apparently these analysis tools are not suited to extract information on possible more subtle variations.

4.3 Scaling with system size

In addition to variations of the shape of the momentum spectra it is of interest to study the variations in absolute multiplicities. Especially at high transverse momentum one naïvely expects an increase of the cross section proportional to the mass number of the nuclei and, correspondingly, an increase of the multiplicity proportional to the number of binary collisions due to the importance

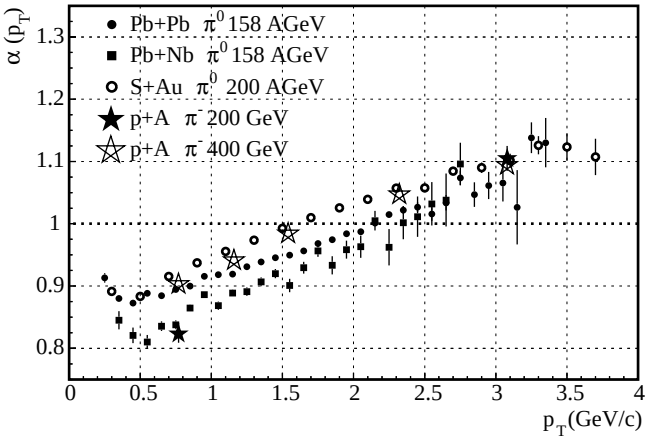

Fig. 10. Exponent α of the mass dependence of neutral pion cross sections as a function of transverse momentum. Values are obtained from ratios of minimum bias Pb + Pb and Pb + Nb collisions to a parameterization of p+p collisions. Included for comparison are results for S+Au collisions at 200·AGeV [6] and the proton induced data from [7]

of hard scattering. In fact, it was already observed in pA collisions at beam energies of $200 - 400\,\mathrm{GeV}$ [7] that the increase in cross section at high transverse momenta is even stronger than the increase in the target mass.

This behaviour can be investigated by parameterizing the data according to the phenomenological expression:

$$E\frac{d^3\sigma}{dp^3}(\mathrm{A+B}) = (A\cdot B)^{\alpha(p_T)}\, E\frac{d^3\sigma}{dp^3}(\mathrm{p+p}), \qquad (2)$$

where A and B are the mass numbers of the projectile and target nuclei. For this purpose the experimental data have been compared to a parameterization [26] of pp reactions [32–39] scaled to the same $\sqrt{s}$:

$$E\frac{d^3N}{dp^3} = C\cdot\left(\frac{p_0}{p_T+p_0}\right)^n, \qquad (3)$$

with $C = 4.125c^3/\mathrm{GeV}^2$, $p_0 = 9.02\,\mathrm{GeV}/c$ and $n = 55.77$. We have assigned a systematic error of 20% to this reference distribution. The values of the exponents α for minimum bias reactions of Pb+Pb and Pb+Nb are shown in Fig. 10. Included for comparison are results for S+Au collisions at 200·AGeV [6] and the proton induced data from [7]. All data follow the same trend, i.e. the exponent is considerably lower than one for low transverse momenta and increases monotonically with p_T finally reaching values > 1 for high p_T. However, the values differ by about 10% for the different systems and the point where they cross the line $\alpha = 1$ ranges from $p_T = 1.5\,\mathrm{GeV}/c^2$ to $2.5\,\mathrm{GeV}/c^2$. It should be noted that the different experimental trigger biases may influence these results.

This form of scaling analysis is only applicable to minimum bias reactions. To study the scaling behaviour for heavy ion reactions of different centralities the scaling with the number of participants or nucleon-nucleon collisions is more appropriate. An analysis of the scaling of the charged multiplicity with the number of participants has been performed in [40]. A more general analysis of the scaling behaviour of transverse energy and particle production in Pb + Pb collisions has been presented in [31] and the scaling of neutral pion production with the number of participants in [17]. For the present paper the number of participants and collisions have been obtained as described in [31]. The values are given in Table 1. The systematic errors of these quantities have been obtained by comparing calculations with different assumptions. In addition to VENUS and FRITIOF calculations with default parameter settings, we have investigated VENUS calculations with a modified nuclear density distribution, with a significantly worsened energy resolution of the calorimeter, with different assumptions on the size of the minimum bias cross section and ignoring the target-out contribution. These calculations are described in [31]. Moreover we have also investigated independently results of a toy model calculation of nuclear geometry and also the influence of modest variations of the nucleon-nucleon cross section entering into the calculations. The maximum deviation of any of these other calculations from the default one is within the error given in Table 1. As expected, the relative error is largest in the most peripheral sample. This is due to the uncertainty in modelling the E_T-fluctuations and the trigger threshold —effects which have been included in our error estimate.

It should be noted that the most peripheral data set in this analysis does not correspond to the most peripheral collisions theoretically possible from nuclear geometry, as they are rejected by the minimum bias trigger. Our minimum bias trigger cross section of $\approx$ 6300 mb corresponds to $\approx$ 85% of the expected total geometrical cross section. The more peripheral reactions rejected by our trigger would of course have a still larger uncertainty due to e.g. the uncertainties in the nuclear density distribution. In our samples the error is still at a reasonable level as quoted in the table.

Furthermore, the error in ratios of e.g. the number of collisions for different samples is considerably smaller, since some of the systematic effects are correlated, as is obvious e.g. for the size of the nucleon-nucleon cross section.

The scaling of the neutral pion production is analyzed both as a function of the number of collisions and as function of the number of participants. As in the earlier publications the yield is parameterized as:

$$E\frac{d^3N}{dp^3}(N_{part}) \propto (N_{part})^{\alpha_p} \qquad (4)$$

or

$$E\frac{d^3N}{dp^3}(N_{coll}) \propto (N_{coll})^{\alpha_c}. \qquad (5)$$

The results are presented in Fig. 11 where the upper panel shows the scaling with the number of participants and the lower panel with the number of collisions. The open circles represent the exponents calculated from the ratio of semi-peripheral collisions (class 2) to the parameterization of pp collisions (3). In this case a behaviour very similar

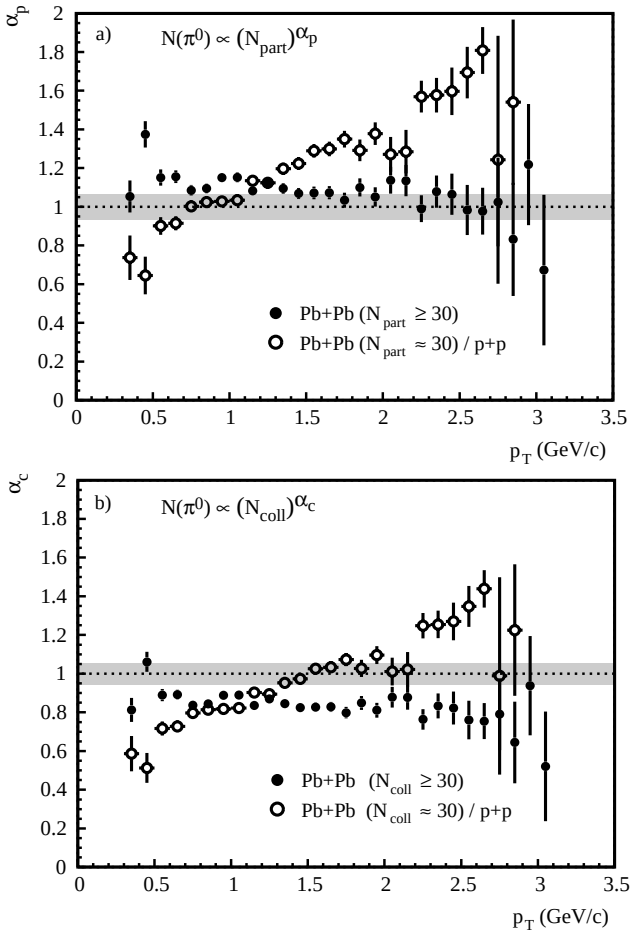

Fig. 11a,b. Exponent α of neutral pion transverse mass distributions parameterized as a function of the number of participants **a** and collisions **b** in Pb + Pb collisions. The exponents are shown as a function of p_T. The open circles are obtained from the ratio of semi-peripheral Pb+Pb data to p+p data, while for the filled circles fits of a power law to the seven most central classes are performed. The grey bands indicate the systematic error relevant for this fit from the calculation of the number of participants and collisions and from the centrality dependent systematic error of the neutral pion multiplicity. The error bars are only statistical

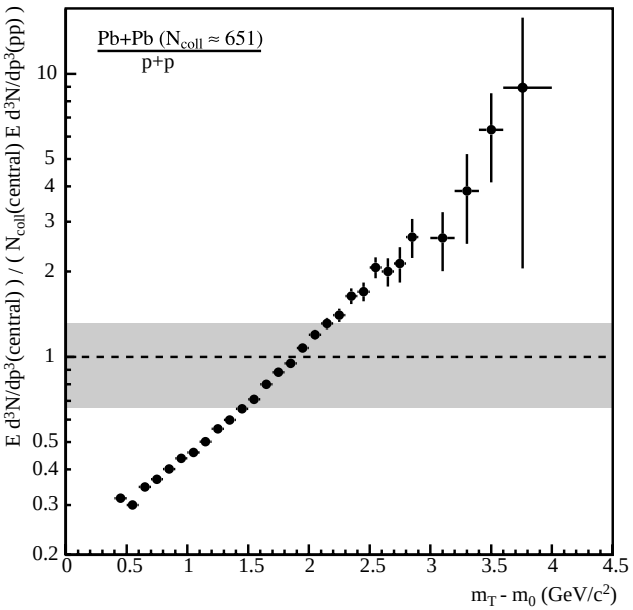

Fig. 12. Ratios of invariant multiplicity distributions of neutral pions for central Pb+Pb reactions to the parameterization of p+p reactions normalized to the number of binary collisions, also called the nuclear modification factor. The grey band shows the estimate of the systematic error due to the calculation of the number of collisions and the absolute cross section normalization relative to p+p

to the original Cronin-effect is observed: The exponents increase monotonically with increasing p_T reaching values > 1 for large p_T. A scaling of the particle yields with $(N_{coll})^{\alpha_c=1}$ is equivalent to a scaling of the minimum bias cross sections with $A^{\alpha=1}$. This value is reached in Fig. 11b at $p_T \approx 1.5\,\mathrm{GeV}/c^2$, similar to where the scaling exponents of the p+A and S+Au data in Fig. 10 reach the value of 1. However, the minimum bias Pb+Pb data in Fig. 10 show a weaker scaling exponent at intermediate and higher p_T.

Fits to the centrality classes 2-8 (displayed as filled circles in Fig. 11), i.e. up to the most central collisions, show almost constant exponents for all transverse momenta. In fact, the values even indicate a slight decrease with increasing p_T. At the highest p_T the exponents appear to be $\alpha_p \approx 1$ and $\alpha_c \approx 0.8$. They are considerably below the scaling exponents for semi-peripheral Pb+Pb relative to p+p. Noticeably the scaling exponent α_c is also significantly below the value of 1 expected as a naïve scaling for hard scatterings.

Ratios of the measured pion multiplicity distributions for two different samples (labeled X and Y) normalized to the number of collisions given in Table 1:

$$R_{XY}(m_T) \equiv \frac{\left(E\frac{d^3N}{dp^3}(m_T)/N_{coll}\right)_X}{\left(E\frac{d^3N}{dp^3}(m_T)/N_{coll}\right)_Y} \qquad (6)$$

are shown in Figs. 12, 13 and 14. In Fig. 12 the ratio of the 12.7% most central collisions to the parameterization of p+p is shown:

$$R_X(m_T) \equiv \frac{\left(E\frac{d^3N}{dp^3}(m_T)/N_{coll}\right)_X}{\left(E\frac{d^3N}{dp^3}(m_T)\right)_{pp}}. \qquad (7)$$

This special case of (6) is sometimes referred to as the *nuclear modification factor* [42]. The ratio is ≈ 0.3 at low m_T and increases exponentially towards higher m_T approaching values close to 10 [1]. This is in line with the earlier

[1] The same ratio for central Pb+Pb(Au) collisions is shown in [42]. There a curve is drawn which saturates at $R = 2$ for high p_T. It is actually dominated by data points at $p_T = 2 - 3\,\mathrm{GeV}/c$, and the WA98 data points can be seen to lie above the curve at high p_T. Remaining differences in the two figures might be due to different estimates for the pp-spectra being used in the ratios

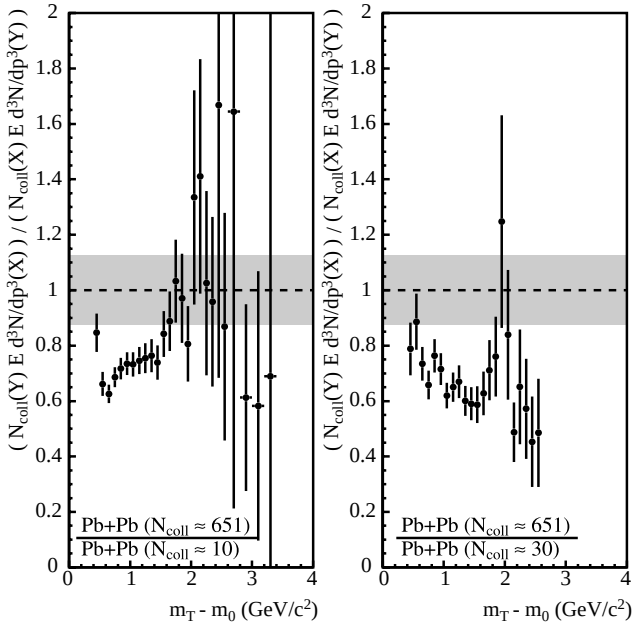

Fig. 13. Ratios of invariant multiplicity distributions of neutral pions for central to peripheral Pb+Pb collisions normalized to the number of binary collisions. The left plot shows the ratio using the most peripheral sample, the right plot a similar ratio with the second most peripheral sample. The grey bands show the estimate of the systematic error due to the calculation of the number of collisions and due to the systematic error in the π^0 distribution

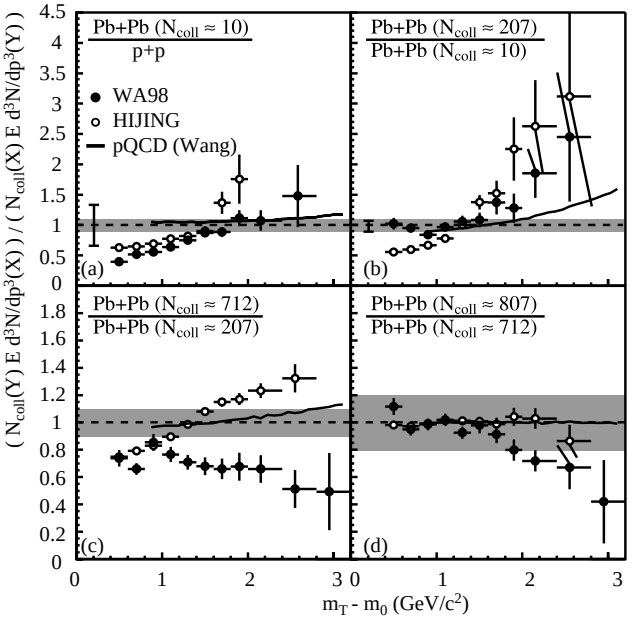

Fig. 14a–d. Ratios of invariant multiplicity distributions of neutral pions normalized to the number of binary collisions. The upper left plot **a** shows the ratio of peripheral Pb+Pb collisions to the parameterization of p+p [3]. The other plots **b**–**d** show different ratios of a more central sample to a more peripheral sample of Pb+Pb collisions. The filled circles show the experimental results, the open circles are results from the HIJING event generator and the solid lines similar ratios from pQCD calculations including p_T broadening [42]. The grey bands show the estimate of the systematic error due to the systematic error in the π^0 distribution. The additional error bar in **a** and **b** shows the normalization uncertainty due to the calculation of the number of collisions and the absolute cross section normalization relative to p+p

observations and demonstrates again that relative to p+p reactions there is a strong Cronin effect in heavy ion collisions for all centralities. However, as evident from Fig. 11b, most of the anomalous enhancement is already present in peripheral reactions, and the additional enhancement in central reactions is much weaker. In the following we will concentrate on this particular observation.

Figure 13 shows ratios of the 12.7% most central collisions to the two most peripheral samples. Both ratios are below 1 for low m_T. In comparison to the most peripheral sample (left part) the spectra are compatible with a scaling with the number of collisions in central reactions at higher m_T, while relative to the semi-peripheral class (right part) the enhancement is significantly weaker even at high m_T. Similar ratios for more detailed centrality selections are shown in Fig. 14. The ratio of peripheral Pb+Pb collisions to p+p (3) (Fig. 14a) increases strongly with increasing transverse mass – this is in line with the Cronin effect discussed above. A similar trend is observed when going from peripheral to medium-central data (Fig. 14b). In addition, the pion production is seen to increase roughly proportional to the number of collisions even at low transverse masses. Going from medium central to central (Fig. 14c) the trend is reversed: the ratio decreases with increasing transverse mass as was already seen in Fig. 8 and the pion multiplicities increase more weakly than the number of collisions. The ratio of very central to central collisions shows an indication of a similar effect although not very significant.

Included in Fig. 14 are results of HIJING calculations (open circles) for the same centralities. They show a very different trend: For all but the most central case the ratios increase with increasing transverse mass, for high transverse masses the ratio is always larger than one. HIJING does not describe p+p data well at these energies while a reasonable description of central Pb+Pb collisions is obtained by an implementation of the Cronin effect via a soft transverse momentum kick model which introduces a very strong A dependence, as was pointed out already in [41]. Thus the reasonable description of central Pb+Pb collisions by HIJING appears to be fortuitous. The authors of [41] stated that a better implementation of the Cronin effect should use an additional intrinsic p_T of the incoming partons and a likely weaker p_T broadening. Still, in any model of the Cronin effect one would expect the ratios of central to less central spectra, as shown in Fig. 14c, to be larger than one at high transverse mass. Similarly, one would expect the scaling exponent shown in Fig. 11 to be $\alpha_c > 1$ at high transverse momentum. A more refined calculation including intrinsic p_T was performed in [42] using the same model as in [18]. The results are also shown in Fig. 14 as solid lines. As expected, the ratios show a

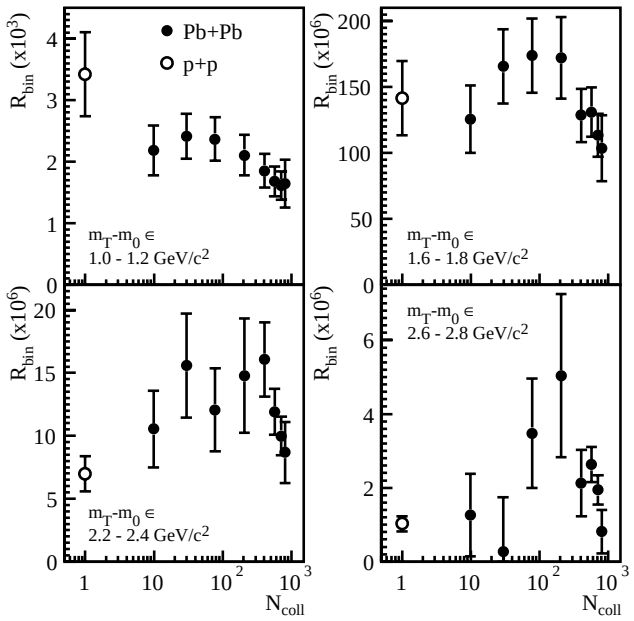

Fig. 15. Multiplicities of neutral pions normalized to the number of binary collisions $R_{bin} = (Ed^3N/dp^3)/N_{coll}$ as a function of N_{coll} for different ranges of transverse mass as indicated in the pictures. The filled circles show the experimental results for Pb+Pb reactions, the open circles the parameterization for p+p reactions (3). The error bars contain statistical and systematic errors added in quadrature

weaker increase at high m_T compared to HIJING, but are all ≥ 1 and thus do not explain the centrality dependence as seen in Fig. 14c.

With these observations in mind one can revisit the evolution of the particle yields with system size at given transverse mass. This is done in Fig. 15 where the neutral pion yield per binary collision:

$$R_{bin} \equiv E\frac{d^3N}{dp^3}/N_{coll} \tag{8}$$

is shown as a function of the number of collisions for four different transverse mass intervals. In addition to Pb+Pb reactions also the parameterization of p+p is included. At relatively low transverse mass the yield per collision decreases as expected from the scaling exponent $\alpha_c < 1$. With increasing transverse mass a rise of R_{bin} develops which is most prominent for the highest m_T. However, it is also clear that R_{bin} decreases significantly with N_{coll} for $N_{coll} > 200$. The exact point of turnover of the evolution of the pion yields could not be so easily observed in the investigation of the scaling exponents above – it is much more clearly born out when normalizing to the number of binary collisions as in R_{bin}.

5 Summary

We have presented transverse mass spectra of neutral pions in Pb+Pb reactions at 158·A GeV for different centralities. A comparison to several event generators found none of them able to adequately describe the spectra.

While there is a strong broadening of the transverse mass spectra in going from p+p to peripheral Pb+Pb reactions, and further to semi-peripheral reactions, there is an indication of a stronger fall off of the spectra when going to the most central selections. The absolute yields at high transverse momenta show an enhancement which grows stronger than with the number of collisions up to medium central Pb+Pb collisions, which is qualitatively similar to the Cronin effect observed in p+A collisions. For central collisions, however, the further increase in multiplicity at high p_T is weaker than with the number of collisions. This is in qualitative contradiction to conventional explanations of the Cronin effect (p_T-broadening) which is expected to cause a further strengthening of the nuclear enhancement with more central collisions. As a possible explanation of this behaviour one may consider that the multiple scattering mechanisms which are expected to be responsible for the apparent p_T-broadening in pA and peripheral Pb+Pb might be modified in central Pb+Pb collisions. This might be possible if both *initial* and *final* state scatterings are relevant for the enhancement, and the relative contributions are shifted more towards final state contributions in central collisions, reminiscent of a more and more thermalized system. Alternative explanations might involve suppression mechanisms independent of the nuclear enhancement in question, e.g. an onset of quenching via energy loss of produced particles (partons or hadrons) in central Pb+Pb collisions.

Acknowledgements. We wish to express our gratitude to the CERN accelerator division for excellent performance of the SPS accelerator complex. We acknowledge with appreciation the effort of all engineers, technicians and support staff who have participated in the construction of the experiment. This work was supported jointly by the German BMBF and DFG, the U.S. DOE, the Swedish NFR and FRN, the Dutch Stichting FOM, the Polish KBN under Contract No 621/E-78/SPUB-M/CERN/P-03/DZ211/, the Grant Agency of the Czech Republic under contract No. 202/95/0217, the Department of Atomic Energy, the Department of Science and Technology, the Council of Scientific and Industrial Research and the University Grants Commission of the Government of India, the Indo-FRG Exchange Program, the PPE division of CERN, the Swiss National Fund, the INTAS under Contract INTAS-97-0158, ORISE, Research-in-Aid for Scientific Research (Specially Promoted Research & International Scientific Research) of the Ministry of Education, Science and Culture, the University of Tsukuba Special Research Projects, and the JSPS Research Fellowships for Young Scientists. ORNL is managed by Lockheed Martin Energy Research Corporation under contract DE-AC05-96OR22464 with the U.S. Department of Energy. The MIT group has been supported by the US Dept. of Energy under the cooperative agreement DE-FC02-94ER40818.

References

1. Quark Matter '96 proceedings, Nucl. Phys. A **610** (1996)
2. Quark Matter '97 proceedings, Nucl. Phys. A **638** (1997)

3. Quark Matter '99 proceedings, Nucl. Phys. A **661** (1999)
4. NA49 Collaboration, P.G. Jones et al., Nucl. Phys. A **610**, 188c (1996)
5. NA44 Collaboration, I.G. Bearden et al., Phys. Rev. Lett. **78**, 2080 (1997)
6. WA80 Collaboration, R. Albrecht et al., Eur. Phys. J. C **5**, 255–267 (1998)
7. D. Antreasyan, et al. Phys. Rev. D **19**, 764 (1979)
8. A. Krzywicki et al., Phys. Lett. B **85**, 407–416 (1979)
9. M. Lev, B. Petersson, Z. Phys. C **21**, 155–161 (1983)
10. K. Werner, Phys. Rep. **232**, 87–299 (1993)
11. H. Sorge, H. Stöcker, W. Greiner, Nucl. Phys. A **498**, 567c–576c (1989)
12. K.S. Lee, U. Heinz, Z. Phys. C **43**, 425–429 (1989)
13. E. Schnedermann et al., Phys. Rev. C **48**, 2462–2475 (1993)
14. M. Gyulassy, M. Plümer, Phys. Lett. B **243**, 432 (1990); R. Baier et al., Phys. Lett. **345**, 277 (1995)
15. R. Baier, D. Schiff, B.G. Zakharov Ann.Rev.Nucl.Part.Sci. **50**, 37–69 (2000) and references therein
16. X.-N. Wang, M. Gyulassy, Phys. Rev. Lett. **68**, 1480 (1992); X.-N. Wang, Phys. Rev. C **58**, 2321 (1998)
17. WA98 Collaboration, M.M. Aggarwal et al., Phys. Rev. Lett. **81**, 4087 (1998); Phys. Rev. Lett. **84**, 578 (2000) (erratum)
18. X.-N. Wang, Phys. Rev. Lett. **81**, 2655–2658 (1998)
19. WA98 Collaboration, M.M. Aggarwal et al., Phys. Rev. Lett **83**, 926 (1999)
20. WA98 Collaboration, *Proposal for a large acceptance hadron and photon spectrometer*, 1991, Preprint CERN/SPSLC 91-17, SPSLC/P260
21. T.C. Awes et al., Nucl. Instrum. Methods Phys. Res. Section A **279**, (1989) 479
22. S. Neumaier et al., Nucl. Instrum. Methods Phys. Res. Section A **376**, 368 (1996)
23. A. L. Wintenberg et al., Proceedings of Electronics for Future Colliders Conference, May 1994, LeCroy Corp
24. T. Peitzmann et al., Nucl. Instrum. Methods Phys. Res. Section A **360**, 593 (1995)
25. WA98 Collaboration, M.M. Aggarwal et al., submitted to Phys. Rev. C, preprint nucl-ex/0006007
26. C. Blume, doctoral thesis, University of Münster, Germany (1998)
27. F. Berger et al., Nucl. Instrum. Methods Phys. Res. Section A **321**, 152–164 (1992)
28. R. Brun et al., GEANT3, CERN/DD/cc/84-1
29. B. Andersson, G. Gustafson, H. Pi, Z. Phys. C **57**, 485 (1993)
30. X.-N. Wang, M. Gyulassy, Phys. Rev. D **44**, 3501 (1991); Comput. Phys. Commun. **104**, 70 (1997)
31. WA98 Collaboration, M.M. Aggarwal et al., Eur. Phys. J. C **18**, 651–663 (2001)
32. G. Donaldson et al., Phys. Rev. Lett. **36**, 1110 (1976)
33. F.W. Büsser et al., Nucl. Phys. B **106**, 1 (1976)
34. A.L.S. Angelis et al., Phys. Lett. B **79**, 505 (1978)
35. C. Kourkoumelis et al., Z. Phys. C **5**, 95 (1980)
36. C. DeMarzo et al., Phys. Rev. D **36**, 16 (1987)
37. D.L. Adams et al., Phys. Rev. D **53**, 4747 (1996)
38. B. Alper et al., Nucl. Phys. B **100**, 237 (1975)
39. A. Breakstone et al., Z. Phys. C **69**, 55 (1995)
40. WA97/NA57 Collaborations, F. Antinori et al., Eur. Phys. J. C **18**, 57–63 (2001)
41. M. Gyulassy, P. Levai, Phys. Lett. B **442**, 1 (1998)
42. E. Wang, X.-N. Wang, *Interplay of soft and hard processes and hadron p_T spectra in pA and AA collisions*, preprint nucl-th/0104031

Measurement of the Midrapidity Transverse Energy Distribution from $\sqrt{s_{NN}} = 130$ GeV Au + Au Collisions at RHIC

K. Adcox,[40] S. S. Adler,[3] N. N. Ajitanand,[27] Y. Akiba,[14] J. Alexander,[27] L. Aphecetche,[34] Y. Arai,[14] S. H. Aronson,[3] R. Averbeck,[28] T. C. Awes,[29] K. N. Barish,[5] P. D. Barnes,[19] J. Barrette,[21] B. Bassalleck,[25] S. Bathe,[22] V. Baublis,[30] A. Bazilevsky,[12,32] S. Belikov,[12,13] F. G. Bellaiche,[29] S. T. Belyaev,[16] M. J. Bennett,[19] Y. Berdnikov,[35] S. Botelho,[33] M. L. Brooks,[19] D. S. Brown,[26] N. Bruner,[25] D. Bucher,[22] H. Buesching,[22] V. Bumazhnov,[12] G. Bunce,[3,32] J. Burward-Hoy,[28] S. Butsyk,[28,30] T. A. Carey,[19] P. Chand,[2] J. Chang,[5] W. C. Chang,[1] L. L. Chavez,[25] S. Chernichenko,[12] C. Y. Chi,[8] J. Chiba,[14] M. Chiu,[8] R. K. Choudhury,[2] T. Christ,[28] T. Chujo,[3,39] M. S. Chung,[15,19] P. Chung,[27] V. Cianciolo,[29] B. A. Cole,[8] D. G. D'Enterria,[34] G. David,[3] H. Delagrange,[34] A. Denisov,[12] A. Deshpande,[32] E. J. Desmond,[3] O. Dietzsch,[33] B. V. Dinesh,[2] A. Drees,[28] A. Durum,[12] D. Dutta,[2] K. Ebisu,[24] Y. V. Efremenko,[29] K. El Chenawi,[40] H. En'yo,[17,31] S. Esumi,[39] L. Ewell,[3] T. Ferdousi,[5] D. E. Fields,[25] S. L. Fokin,[16] Z. Fraenkel,[42] A. Franz,[3] A. D. Frawley,[9] S.-Y. Fung,[5] S. Garpman,[20] T. K. Ghosh,[40] A. Glenn,[36] A. L. Godoi,[33] Y. Goto,[32] S. V. Greene,[40] M. Grosse Perdekamp,[32] S. K. Gupta,[2] W. Guryn,[3] H.-Å. Gustafsson,[20] J. S. Haggerty,[3] H. Hamagaki,[7] A. G. Hansen,[19] H. Hara,[24] E. P. Hartouni,[18] R. Hayano,[38] N. Hayashi,[31] X. He,[10] T. K. Hemmick,[28] J. M. Heuser,[28] M. Hibino,[41] J. C. Hill,[13] D. S. Ho,[43] K. Homma,[11] B. Hong,[15] A. Hoover,[26] T. Ichihara,[31,32] K. Imai,[17,31] M. S. Ippolitov,[16] M. Ishihara,[31,32] B. V. Jacak,[28,32] W. Y. Jang,[15] J. Jia,[28] B. M. Johnson,[3] S. C. Johnson,[18,28] K. S. Joo,[23] S. Kametani,[41] J. H. Kang,[43] M. Kann,[30] S. S. Kapoor,[2] S. Kelly,[8] B. Khachaturov,[42] A. Khanzadeev,[30] J. Kikuchi,[41] D. J. Kim,[43] H. J. Kim,[43] S. Y. Kim,[43] Y. G. Kim,[43] W. W. Kinnison,[19] E. Kistenev,[3] A. Kiyomichi,[39] C. Klein-Boesing,[22] S. Klinksiek,[25] L. Kochenda,[30] D. Kochetkov,[5] V. Kochetkov,[12] D. Koehler,[25] T. Kohama,[11] A. Kozlov,[42] P. J. Kroon,[3] K. Kurita,[31,32] M. J. Kweon,[15] Y. Kwon,[43] G. S. Kyle,[26] R. Lacey,[27] J. G. Lajoie,[13] J. Lauret,[27] A. Lebedev,[13] D. M. Lee,[19] M. J. Leitch,[19] X. H. Li,[5] Z. Li,[6,31] D. J. Lim,[43] M. X. Liu,[19] X. Liu,[6] Z. Liu,[6] C. F. Maguire,[40] J. Mahon,[3] Y. I. Makdisi,[3] V. I. Manko,[16] Y. Mao,[6,31] S. K. Mark,[21] S. Markacs,[8] G. Martinez,[34] M. D. Marx,[28] A. Masaike,[17] F. Matathias,[28] T. Matsumoto,[7,41] P. L. McGaughey,[19] E. Melnikov,[12] M. Merschmeyer,[22] F. Messer,[28] M. Messer,[3] Y. Miake,[39] T. E. Miller,[40] A. Milov,[42] S. Mioduszewski,[3,36] R. E. Mischke,[19] G. C. Mishra,[10] J. T. Mitchell,[3] A. K. Mohanty,[2] D. P. Morrison,[3] J. M. Moss,[19] F. Mühlbacher,[28] M. Muniruzzaman,[5] J. Murata,[31] S. Nagamiya,[14] Y. Nagasaka,[24] J. L. Nagle,[8] Y. Nakada,[17] B. K. Nandi,[5] J. Newby,[36] L. Nikkinen,[21] P. Nilsson,[20] S. Nishimura,[7] A. S. Nyanin,[16] J. Nystrand,[20] E. O'Brien,[3] C. A. Ogilvie,[13] H. Ohnishi,[3,11] I. D. Ojha,[4,40] M. Ono,[39] V. Onuchin,[12] A. Oskarsson,[20] L. Österman,[20] I. Otterlund,[20] K. Oyama,[7,38] L. Paffrath,[3,*] A. P. T. Palounek,[19] V. S. Pantuev,[28] V. Papavassiliou,[26] S. F. Pate,[26] T. Peitzmann,[22] A. N. Petridis,[13] C. Pinkenburg,[3,27] R. P. Pisani,[3] P. Pitukhin,[12] F. Plasil,[29] M. Pollack,[28,36] K. Pope,[36] M. L. Purschke,[3] I. Ravinovich,[42] K. F. Read,[29,36] K. Reygers,[22] V. Riabov,[30,35] Y. Riabov,[30] M. Rosati,[13] A. A. Rose,[40] S. S. Ryu,[43] N. Saito,[31,32] A. Sakaguchi,[11] T. Sakaguchi,[7,41] H. Sako,[39] T. Sakuma,[31,37] V. Samsonov,[30] T. C. Sangster,[18] R. Santo,[22] H. D. Sato,[17,31] S. Sato,[39] S. Sawada,[14] B. R. Schlei,[19] Y. Schutz,[34] V. Semenov,[12] R. Seto,[5] T. K. Shea,[3] I. Shein,[12] T.-A. Shibata,[31,37] K. Shigaki,[14] T. Shiina,[19] Y. H. Shin,[43] I. G. Sibiriak,[16] D. Silvermyr,[20] K. S. Sim,[15] J. Simon-Gillo,[19] C. P. Singh,[4] V. Singh,[4] M. Sivertz,[3] A. Soldatov,[12] R. A. Soltz,[18] S. Sorensen,[29,36] P. W. Stankus,[29] N. Starinsky,[21] P. Steinberg,[8] E. Stenlund,[20] A. Ster,[44] S. P. Stoll,[3] M. Sugioka,[31,37] T. Sugitate,[11] J. P. Sullivan,[19] Y. Sumi,[11] Z. Sun,[6] M. Suzuki,[39] E. M. Takagui,[33] A. Taketani,[31] M. Tamai,[41] K. H. Tanaka,[14] Y. Tanaka,[24] E. Taniguchi,[31,37] M. J. Tannenbaum,[3] J. Thomas,[28] J. H. Thomas,[18] T. L. Thomas,[25] W. Tian,[6,36] J. Tojo,[17,31] H. Torii,[17,31] R. S. Towell,[19] I. Tserruya,[42] H. Tsuruoka,[39] A. A. Tsvetkov,[16] S. K. Tuli,[4] H. Tydesjö,[20] N. Tyurin,[12] T. Ushiroda,[24] H. W. van Hecke,[19] C. Velissaris,[26] J. Velkovska,[28] M. Velkovsky,[28] A. A. Vinogradov,[16] M. A. Volkov,[16] A. Vorobyov,[30] E. Vznuzdaev,[30] H. Wang,[5] Y. Watanabe,[31,32] S. N. White,[3] C. Witzig,[3] F. K. Wohn,[13] C. L. Woody,[3] W. Xie,[5,42] K. Yagi,[39] S. Yokkaichi,[31] G. R. Young,[29] I. E. Yushmanov,[16] W. A. Zajc,[8] Z. Zhang,[28] and S. Zhou[6]

(PHENIX Collaboration)

[1]*Institute of Physics, Academia Sinica, Taipei 11529, Taiwan*
[2]*Bhabha Atomic Research Centre, Bombay 400 085, India*
[3]*Brookhaven National Laboratory, Upton, New York 11973-5000*
[4]*Department of Physics, Banaras Hindu University, Varanasi 221005, India*
[5]*University of California–Riverside, Riverside, California 92521*
[6]*China Institute of Atomic Energy (CIAE), Beijing, People's Republic of China*
[7]*Center for Nuclear Study, Graduate School of Science, University of Tokyo, 7-3-1 Hongo, Bunkyo, Tokyo 113-0033, Japan*

 0031-9007/01/87(5)/052301(6)$15.00 © 2001 The American Physical Society

[8]*Columbia University, New York, New York 10027 and Nevis Laboratories, Irvington, New York 10533*
[9]*Florida State University, Tallahassee, Florida 32306*
[10]*Georgia State University, Atlanta, Georgia 30303*
[11]*Hiroshima University, Kagamiyama, Higashi-Hiroshima 739-8526, Japan*
[12]*Institute for High Energy Physics (IHEP), Protvino, Russia*
[13]*Iowa State University, Ames, Iowa 50011*
[14]*KEK, High Energy Accelerator Research Organization, Tsukuba-shi, Ibaraki-ken 305-0801, Japan*
[15]*Korea University, Seoul, 136-701, Korea*
[16]*Russian Research Center, "Kurchatov Institute," Moscow, Russia*
[17]*Kyoto University, Kyoto 606, Japan*
[18]*Lawrence Livermore National Laboratory, Livermore, California 94550*
[19]*Los Alamos National Laboratory, Los Alamos, New Mexico 87545*
[20]*Department of Physics, Lund University, Box 118, SE-221 00 Lund, Sweden*
[21]*McGill University, Montreal, Quebec, Canada H3A 2T8*
[22]*Institut für Kernphysik, University of Münster, D-48149 Münster, Germany*
[23]*Myongji University, Yongin, Kyonggido 449-728, Korea*
[24]*Nagasaki Institute of Applied Science, Nagasaki-shi, Nagasaki 851-0193, Japan*
[25]*University of New Mexico, Albuquerque, New Mexico 87131*
[26]*New Mexico State University, Las Cruces, New Mexico 88003*
[27]*Chemistry Department, State University of New York–Stony Brook, Stony Brook, New York 11794*
[28]*Department of Physics and Astronomy, State University of New York–Stony Brook, Stony Brook, New York 11794*
[29]*Oak Ridge National Laboratory, Oak Ridge, Tennessee 37831*
[30]*PNPI, Petersburg Nuclear Physics Institute, Gatchina, Russia*
[31]*RIKEN (The Institute of Physical and Chemical Research), Wako, Saitama 351-0198, Japan*
[32]*RIKEN BNL Research Center, Brookhaven National Laboratory, Upton, New York 11973-5000*
[33]*Universidade de São Paulo, Instituto de Física, Caixa Postal 66318, São Paulo CEP05315-970, Brazil*
[34]*SUBATECH (Ecole des Mines de Nantes, IN2P3/CNRS, Universite de Nantes) BP 20722-44307, Nantes-Cedex 3, France*
[35]*St. Petersburg State Technical University, St. Petersburg, Russia*
[36]*University of Tennessee, Knoxville, Tennessee 37996*
[37]*Department of Physics, Tokyo Institute of Technology, Tokyo, 152-8551, Japan*
[38]*University of Tokyo, Tokyo, Japan*
[39]*Institute of Physics, University of Tsukuba, Tsukuba, Ibaraki 305, Japan*
[40]*Vanderbilt University, Nashville, Tennessee 37235*
[41]*Waseda University, Advanced Research Institute for Science and Engineering, 17 Kikui-cho, Shinjuku-ku, Tokyo 162-0044, Japan*
[42]*Weizmann Institute, Rehovot 76100, Israel*
[43]*Yonsei University, IPAP, Seoul 120-749, Korea*
[44]*KFKI Research Institute for Particle and Nuclear Physics (RMKI), Budapest, Hungary*[†]

(Received 18 April 2001; published 17 July 2001)

The first measurement of energy produced transverse to the beam direction at the Relativistic Heavy-Ion Collider at Brookhaven National Laboratory is presented. The midrapidity transverse energy density per participating nucleon rises steadily with the number of participants, closely paralleling the rise in charged-particle density, such that $\langle E_T\rangle/\langle N_{ch}\rangle$ remains relatively constant as a function of centrality. The energy density calculated via Bjorken's prescription for the 2% most central Au + Au collisions at $\sqrt{s_{NN}} = 130$ GeV is at least $\epsilon_{Bj} = 4.6\ \mathrm{GeV/fm^3}$, which is a factor of 1.6 larger than found at $\sqrt{s_{NN}} = 17.2$ GeV (Pb + Pb at CERN).

DOI: 10.1103/PhysRevLett.87.052301 PACS numbers: 25.75.–q, 12.38.Mh, 13.60.Le, 13.85.Hd

The PHENIX detector [1] at RHIC, the Relativistic Heavy-Ion Collider at Brookhaven National Laboratory, is designed to measure the properties of nuclear matter at the highest temperatures and energy densities. For example, a transition to a quark-gluon plasma has been predicted for energy densities on the order of a few $\mathrm{GeV/fm^3}$ [2]. The spatial energy density (ϵ) in a relativistic collision can be estimated (following Bjorken [3]) by measuring the transverse energy density in rapidity, dE_T/dy, which is effectively the comoving energy density in a longitudinal expansion:

$$\epsilon_{Bj} = \frac{dE_T}{dy}\,\frac{1}{\tau_0 \pi R^2}\,, \tag{1}$$

where τ_0, the formation time, is usually taken as 1 fm/c, and πR^2 is the effective area of the collision. The transverse energy (E_T) is a multiparticle variable defined as

$$\begin{aligned} E_T &= \sum_i E_i \sin\theta_i\,, \\ dE_T(\eta)/d\eta &= \sin\theta(\eta)\, dE(\eta)/d\eta\,, \end{aligned} \tag{2}$$

where θ is the polar angle, $\eta = -\ln\tan\theta/2$ is the pseudorapidity, E_i is by convention taken as the kinetic energy for nucleons and the total energy for all other particles [4], and the sum is taken over all particles emitted into a fixed solid angle for each event. E_T measurements, even in limited apertures at midrapidity, provide excellent characterization of the nuclear geometry of a reaction on an event-by-event basis and are sensitive to the underlying reaction dynamics [2].

During the RHIC run in the summer of 2000, PHENIX accumulated close to 5×10^6 interaction triggers for Au + Au collisions at $\sqrt{s_{NN}} = 130$ GeV using zero degree calorimeters and beam-beam counters (BBC) as triggering devices. The events were selected with a requirement on the collision vertex position along the beam axis, $|z| \leq 20$ cm, as in the recent PHENIX publication on midrapidity multiplicity distributions [5], where further details are given.

The present measurement uses a section of the electromagnetic calorimeter (EMCal) from the PHENIX central spectrometer, with front face 5.1 m from the beam axis. This section is part of a sampling calorimeter, custom developed and built for PHENIX [6], composed of alternating Pb and scintillator tiles (PbSc) with readout of individual towers, 5.54×5.54 cm^2 in cross section, via wavelength shifting fibers in a "shashlik" geometry. The depth of the PbSc calorimeter is 18 radiation lengths (X_0) which corresponds to 0.85 interaction lengths. The PbSc calorimeter has an energy resolution of $8.2\%/\sqrt{E(\mathrm{GeV})} \oplus 1.9\%$ for test beam electrons, with measured response proportional to incident electron energy to within $\pm 2\%$ over the range $0.3 \leq E_e \leq 40.0$ GeV [6].

During construction, the calibration of the calorimeter was set by simultaneously recording the response to laser excitation and to cosmic-ray muons penetrating transversely to the tower axis. The calibration was maintained *in situ* during the run by monitoring relativistic charged particles from Au + Au collisions. The absolute energy scale was determined by test-beam measurements normalized to electrons with known energy. A final adjustment of the absolute energy scale was performed using *in situ* identified electrons ($p > 500$ MeV/c) by shifting the originally measured energy/momentum (E/p) peak from 1.02 ± 0.01 to 1.00. The accuracy of the absolute energy scale was cross-checked *in situ* against both the minimum ionizing peak (MIP) of charged particles penetrating along the tower axis and the mass of the π^0. The corrected energy distribution of EMCal clusters from 1.0 ± 0.1 GeV/c charged tracks (mostly pions) measured in the drift chamber [1] exhibits a clear MIP (Fig. 1a), as well as energy due to nuclear interactions in the material of the EMCal. The MIP position is in agreement within 2% to the value obtained in the test beam (270 MeV). The mass of the π^0, reconstructed from pairs of EMCal clusters (assumed to be photons [7]) of total energy greater than 2 GeV (Fig. 1b), is within 1.5% of the published value. This sets the systematic error of the absolute energy scale at less than 1.5%.

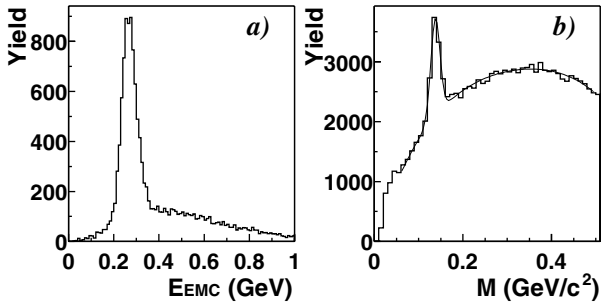

FIG. 1. (a) The distribution of EMCal clusters corresponding to 1 GeV/c charged tracks (mostly pions) from Au + Au collisions. (b) The reconstructed π^0 mass from pairs of EMCal clusters with total energy >2 GeV.

The data sample for the present E_T measurement is taken from the same runs used in our multiplicity measurement [5] (no magnetic field) and comprises about 140 000 events from the BBC trigger which detects $[92 \pm 2(\mathrm{syst})]\%$ of the nuclear interaction cross section of 7.2 b with a background contamination of $[1 \pm 1(\mathrm{syst})]\%$ [5]. The transverse energy was measured using the PbSc EMCal in a fiducial aperture $|\eta| \leq 0.38$ in pseudorapidity and $\Delta\phi = 44.4°$ in azimuth. E_T was computed for each event [Eq. (2)] using clusters of energy greater than 20 MeV, composed of adjacent towers with deposited energy of more than 3 MeV. The angle θ_i is computed from the centroid of the cluster of energy E_i assuming a particle originating from the event vertex.

The raw spectrum of measured transverse energy, $E_{T\mathrm{EMC}}$, in the fiducial aperture of the PHENIX EMCal for Au + Au collisions at $\sqrt{s_{NN}} = 130$ GeV is shown in Fig. 2, upper scale. The lower scale in Fig. 2 represents a correction of the raw $E_{T\mathrm{EMC}}$ by a factor of 12.8 to correspond to the hadronic $dE_T/d\eta|_{\eta=0}$ in the full azimuth. The 12.8 is composed of a factor of 10.6 for the fiducial acceptance, a factor of 1.03 for disabled calorimeter towers and a factor, $k = 1.17 \pm 0.01$, which is the ratio of the hadronic E_T in the fiducial aperture to the measured $E_{T\mathrm{EMC}}$. The k factor includes the response of the detector to charged and neutral particles emitted from the event vertex into the fiducial aperture, and additional corrections for energy inflow from outside the fiducial aperture and for losses [8]. These factors were calculated with a GEANT [9] based Monte Carlo (MC) simulation of the detector using HIJING as the event generator [10].

For E_T measurements at midrapidity at a collider, the EMCal acts as a thin but effective hadronic calorimeter. Charged pions with $p_T \leq 0.35$ GeV/c, kaons ($p_T \leq 0.64$ GeV/c), and protons ($p_T \leq 0.94$ GeV/c)—p_T values which are near or above the $\langle p_T \rangle$ for all three cases—stop (i.e., deposit all their kinetic energy) in the EMCal. For higher p_T hadrons, 43% leave the MIP and 57% interact, leaving an average of ~65% of their energy.

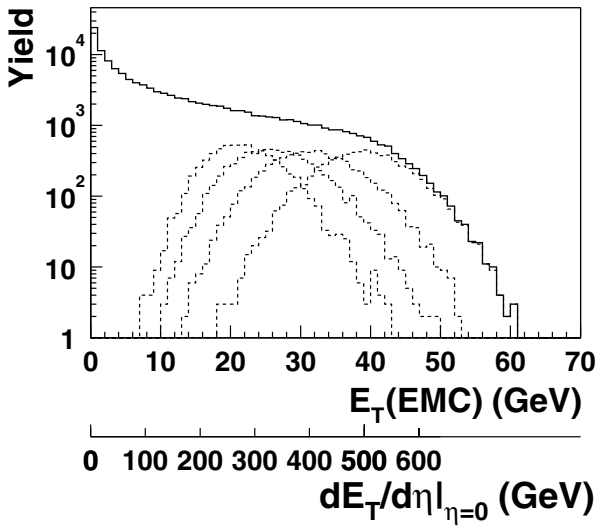

FIG. 2. The raw $E_{T\mathrm{EMC}}$ distribution measured in the $\Delta\phi = 44.4°$ azimuthal and $|\eta| \leq 0.38$ polar angle fiducial acceptance for Au + Au at $\sqrt{s_{NN}} = 130$ GeV (upper scale) and total hadronic $dE_T/d\eta|_{\eta=0}$ (lower scale); see text. The solid line is the minimum bias distribution with the BBC trigger; the dashed lines correspond to the distributions for the four most central bins in Table I.

The measured $E_{T\mathrm{EMC}}$ is 0.79 ± 0.01 of the total E_T striking the EMCal, which is composed roughly of 40% produced by charged pions, 40% by photons (from π^0 and other decays), and 20% by all other particles (including decay muons). The particle composition and $\langle p_T \rangle$ in HIJING are close to the observed values, and furthermore, the k factor is insensitive to reasonable variations (for instance, varying the momenta of all particles by $\pm 15\%$ changes the overall k by less than $\pm 2\%$), leading to an estimated systematic uncertainty in k of less than $\pm 3\%$ due to particle composition and momentum.

The main issues for the MC are the inflow contribution and losses. The losses are due to particles which originate within the aperture but whose decay products miss the EMCal (10%), or whose energy is lost due to edge effects (6%) or clustering (2%). The inflow, $(24 \pm 1)\%$ of the E_T striking the EMCal, is principally of two types: (i) albedo from the magnet poles and (ii) particles which originate outside the aperture of the calorimeter but whose decay products hit the calorimeter. The inflow component of k was checked by comparing the MC and the measurements for events with a vertex outside the normal range, just at and inside a pole face of the axial central-spectrometer magnet, $38 \leq z \leq 42$ cm, for which the calorimeter aperture is partly shadowed. The fraction of the total energy, $dE_{\mathrm{EMC}}/E_{\mathrm{EMC}}$, in bins of width 2 towers along the z coordinate of the EMCal, z_{EMC}, is shown in Fig. 3a. The HIJING MC simulation agrees with the measured data everywhere except in the range $z_{\mathrm{EMC}} > 100$ cm, which is fully shadowed by the pole, where the simulation shows $\sim 20\%$ less energy than the data. In Fig. 3b, the distributions of the cluster energy, E_{cl}, for the open aperture, $z_{\mathrm{EMC}} < -50$ cm, are shown for both HIJING and the data and are in excellent agreement. The inflow component of HIJING is also indicated as a dotted line and falls much more sharply than the total E_{cl} spectrum. The residual discrepancy of the energy in the shadowed region, which contributes roughly 10% of the total signal, results in a $\pm(2 - 3)\%$ systematic uncertainty in E_T due to the uncertainty in the inflow. Combining this with the uncertainty due to particle composition and momentum yields an overall factor $k = [1.17 \pm 0.01] \pm 4\%$ (syst), which, according to the MC, is independent of centrality.

Returning to Fig. 2, the shape of the measured transverse energy spectrum shows the characteristic form of E_T distributions in limited apertures: a peak and a sharp dropoff at low values of E_T corresponding to peripheral collisions with grazing impact; a broad, gently sloping plateau at the midrange of impact parameters, dominated by the nuclear geometry; and then at higher values of E_T, which correspond to the most central collisions where the nuclei are fully overlapped, a "knee" leading to a falloff which is very steep for large apertures and which becomes less steep, the smaller the aperture [11]. It should be emphasized that the correction of $E_{T\mathrm{EMC}}$ to $dE_T/d\eta|_{\eta=0}$

TABLE I. Average transverse energy density vs centrality. The statistical errors are negligible. Errors on $\langle dE_T/d\eta|_{\eta=0} \rangle$ are the N_{part}-dependent systematic errors from the uncertainty of the BBC cross section [5] such that all points move together. There is an additional overall (N_{part}-independent) systematic uncertainty of $\pm 4.5\%$.

Centrality	$\langle dE_T/d\eta|_{\eta=0} \rangle$ (GeV)	$\langle dN_{ch}/d\eta|_{\eta=0} \rangle$ [5]	$\langle N_{\mathrm{part}} \rangle$ [5]
0%–5%	503 ± 2	622 ± 41	347 ± 10
5%–10%	409 ± 4	498 ± 31	293 ± 9
10%–15%	340 ± 5	413 ± 25	248 ± 8
15%–20%	283 ± 7	344 ± 21	211 ± 7
20%–25%	233 ± 7	287 ± 18	177 ± 7
25%–30%	191 ± 8	235 ± 16	146 ± 6
30%–35%	154 ± 8	188 ± 14	122 ± 5
35%–40%	123 ± 7	147 ± 12	99 ± 5
40%–45%	98 ± 7	115 ± 11	82 ± 5
45%–50%	76 ± 6	89 ± 9	68 ± 4

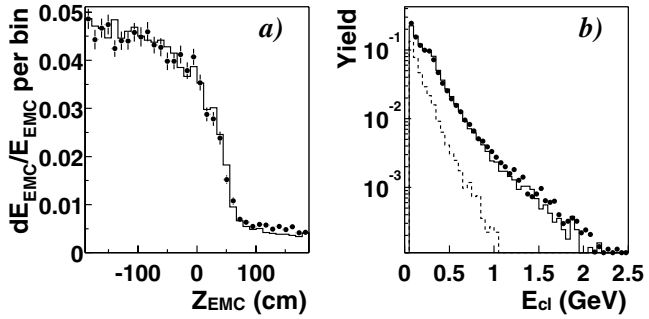

FIG. 3. (a) The fraction of $E_{T\mathrm{EMC}}$ in bins of 11.08 cm along the EMCal z_{EMC} direction for event vertex near a pole face; histogram from MC simulation and solid points from beam data. (b) EMCal cluster energy spectrum from HIJING MC (solid line), with inflow component (dotted line) compared to data (solid points).

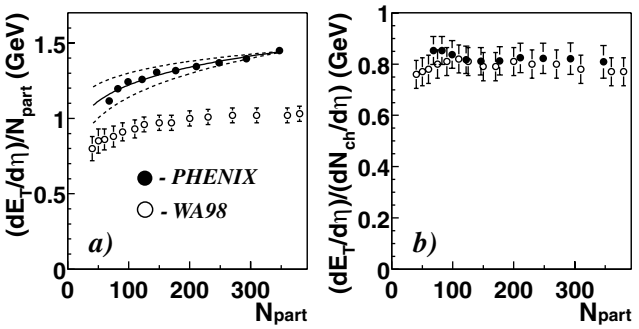

FIG. 4. (a) PHENIX transverse energy density per participant $dE_T/d\eta|_{\eta=0}/N_{\mathrm{part}}$ for Au + Au collisions at $\sqrt{s_{NN}} =$ 130 GeV as a function of N_{part}, the number of participants, compared to data from WA98 [12] for Pb + Pb collisions at $\sqrt{s_{NN}} = 17.2$ GeV. The solid line is the $N_{\mathrm{part}}^{\alpha}$ best fit and the dashed lines represent the effect of the $\pm 1\sigma$ N_{part}-dependent systematic errors for $dE_T/d\eta|_{\eta=0}$ and N_{part}. There is an additional overall (N_{part}-independent) systematic uncertainty of $\pm 4.5\%$ from $dE_T/d\eta|_{\eta=0}$ and $\pm 2.0\%$ from N_{part}. (b) PHENIX $dE_T/d\eta|_{\eta=0}/dN_{ch}/d\eta|_{\eta=0}$ versus N_{part}, including all systematic errors, compared to WA98. Note that the WA98 data in both (a) and (b) have an additional $\pm 20\%$ overall systematic error which is not shown.

by a single scale factor (predominantly acceptance) is valid up to the knee of the distribution, roughly the upper 1 percentile. Above the knee, the falloff depends on the aperture and is sensitive to detector effects as well as statistical and dynamical fluctuations. Thus an actual measurement of $dE_T/d\eta|_{\eta=0}$ for $\Delta\eta = 1.0$ and full azimuth would have a sharper falloff above the knee. With this caveat, the uncertainty in the absolute energy scale ($\pm 1.5\%$) and the uncertainty in k of $\pm 4\%$ are combined to yield an overall uncertainty in the hadronic $dE_T/d\eta|_{\eta=0}$ of $\pm 4.5\%$ (syst), independent of E_T, where the statistical error is negligible.

Midrapidity E_T distributions are a standard method of defining centrality [2,11–13]. Thus, it is important to determine for the present data the detailed relationship of transverse energy production to N_{part}, the number of nucleons participating in the collision (participants), which in earlier fixed target experiments was deduced straightforwardly by measuring the energy of spectator nucleons and fragments in a zero degree calorimeter at beam rapidity. Following a procedure used in our previous publication on the midrapidity charged multiplicity (N_{ch}) distribution, in which a clear increase of $\langle dN_{ch}/d\eta|_{\eta=0}\rangle$ per participant with the number of participants was demonstrated [5], we calculate $\langle dE_T/d\eta|_{\eta=0}\rangle$ as a function of centrality in upper percentile ranges of the 7.2 b Au + Au interaction cross section (see Table I). Figure 4a shows that $\langle dE_T/d\eta|_{\eta=0}\rangle$ per participant also increases with N_{part}, closely paralleling the rise in charged particle density (Table I). This is better illustrated in Fig. 4b where the ratio $\langle dE_T/d\eta|_{\eta=0}\rangle/\langle dN_{ch}/d\eta|_{\eta=0}\rangle$ remains constant at a value of ~ 0.8 GeV, independent of centrality. Comparison to the measurements of WA98 [12] from Pb + Pb collisions at $\sqrt{s_{NN}} = 17.2$ GeV is instructive. The WA98 data for midrapidity $\langle dE_T/d\eta|_{\mathrm{mid}}\rangle$ per participant are shown in Fig. 4a and are essentially independent of N_{part} for $N_{\mathrm{part}} > 200$ [14]. WA98 parametrizes their data as $dE_T/d\eta|_{\mathrm{mid}} \propto N_{\mathrm{part}}^{\alpha}$ with $\alpha = 1.08 \pm 0.06$ while the same parametrization for our data yields $\alpha = 1.13 \pm 0.05$. Figure 4 also shows that $\langle dE_T/d\eta|_{\eta=0}\rangle$ for central Au + Au collisions at $\sqrt{s_{NN}} = 130$ GeV is about 40% larger than found by WA98, yet, for both c.m. energies, $\langle dE_T/d\eta\rangle/\langle dN_{ch}/d\eta\rangle$ remains constant versus centrality at roughly the same value, ~ 0.8 GeV (Fig. 4b).

The Bjorken energy density for Pb + Pb collisions at $\sqrt{s_{NN}} = 17.2$ GeV was given by the NA49 Collaboration [13]. NA49 reported a value of midrapidity $dE_T/d\eta|_{\mathrm{mid}} = 405$ GeV for the most central 2% of the inelastic cross section, in agreement with WA98. This corresponds [13] to a value of $\epsilon_{Bj} = 2.9\ \mathrm{GeV/fm^3}$. A straightforward derivation of ϵ_{Bj} from our measured $dE_T/d\eta|_{\eta=0}$ of 578^{+26}_{-39} GeV for the same centrality cut, corrected to $dE_T/dy|_{y=0}$ by a factor of 1.19 ± 0.01 from our HIJING MC, and taking $\pi R^2 = 148\ \mathrm{fm^2}$ (i.e., $R = 1.18\ \mathrm{fm}\, A^{1/3}$) gives $\epsilon_{Bj} = 4.6\ \mathrm{GeV/fm^3}$, an increase of 60% over the NA49 value.

In conclusion, the midrapidity transverse energy density for central Au + Au collisions, and likely the spatial energy density, is at least 1.6 times larger at $\sqrt{s_{NN}} =$ 130 GeV (RHIC) than at $\sqrt{s_{NN}} = 17.2$ GeV (CERN). The variation of the E_T density per participant with centrality is very similar to the previously reported dependence of charged multiplicity density per participant at RHIC energies. These results, together with the observed constancy of $\langle E_T\rangle/\langle N_{ch}\rangle$ at a value ~ 0.8 GeV, indicate that the additional energy density at RHIC energies is achieved mainly by an increase in particle production rather than by an increase in transverse energy per particle.

We thank the staff of the RHIC project, Collider-Accelerator, and Physics Departments at BNL and the staff of PHENIX participating institutions for their vital

contributions. We acknowledge support from the Department of Energy and NSF (U.S.A.), Monbu-sho and STA (Japan), RAS, RMAE, and RMS (Russia), BMBF, DAAD, and AvH (Germany), FRN, NFR, and the Wallenberg Foundation (Sweden), MIST and NSERC (Canada), CNPq and FAPESP (Brazil), IN2P3/CNRS (France), DAE (India), KRF and KOSEF (Korea), and the U.S.–Israel Binational Science Foundation.

*Deceased.

†Not a participating institution (author is an individual participant).

[1] PHENIX Collaboration, D. P. Morrison *et al.,* Nucl. Phys. **A638**, 565c (1998).

[2] For example, see *Proceedings Quark Matter 1984,* edited by K. Kajantie (Springer, Berlin, 1985); *Proceedings Quark Matter 1987,* edited by H. Satz, H. J. Specht, and R. Stock [Z. Phys. C **38**, 1–370 (1988)].

[3] J. D. Bjorken, Phys. Rev. D **27**, 140 (1983).

[4] Helios Collaboration, T. Åkesson *et al.,* Z. Phys. C **38**, 383 (1988); **38**, 397 (1988).

[5] PHENIX Collaboration, K. Adcox *et al.,* Phys. Rev. Lett. **86**, 3500 (2001).

[6] E. Kistenev *et al.,* in *Proceedings of the 5th International Conference on Calorimetry in HEP* (World Scientific, Singapore, 1994), pp. 211–223; G. David *et al.,* IEEE Trans. Nucl. Sci. **45**, 692 (1998); **45**, 705 (1998).

[7] The PbSc EMCal measures ~GeV photons 2.1% higher than electrons of the same energy. This effect is corrected in Fig. 1b.

[8] $k = 1.17 = (1 - 0.24[\text{inflow}])/(0.79[\text{response}] \times \{1 - 0.18[\text{losses}]\})$

[9] GEANT 3.2.1, CERN program library.

[10] X. N. Wang and M. Gyulassy, Phys. Rev. D **44**, 3501 (1991), version 1.35.

[11] E802 Collaboration, T. Abbott *et al.,* Phys. Rev. C **63**, 064602 (2001).

[12] WA98 Collaboration, M. M. Aggarwal *et al.,* Eur. Phys. J. C **18**, 651 (2001).

[13] NA49 Collaboration, T. Alber *et al.,* Phys. Rev. Lett. **75**, 3814 (1995). (The quoted $\epsilon_{Bj} = 3.2$ GeV/fm^3 was divided by 1.10 to remove the enhancement factor applied by those authors for "head-on" collisions.)

[14] E_T is not Lorentz invariant; frame-dependent 10%–20% effects in comparing fixed target experiments to colliders are ignored in the present discussion.

Centrality Dependence of Charged Particle Multiplicity in Au-Au Collisions at $\sqrt{s_{NN}} = 130$ GeV

K. Adcox,[40] S. S. Adler,[3] N. N. Ajitanand,[27] Y. Akiba,[14] J. Alexander,[27] L. Aphecetche,[34] Y. Arai,[14] S. H. Aronson,[3] R. Averbeck,[28] T. C. Awes,[29] K. N. Barish,[5] P. D. Barnes,[19] J. Barrette,[21] B. Bassalleck,[25] S. Bathe,[22] V. Baublis,[30] A. Bazilevsky,[12,32] S. Belikov,[12,13] F. G. Bellaiche,[29] S. T. Belyaev,[16] M. J. Bennett,[19] Y. Berdnikov,[35] S. Botelho,[33] M. L. Brooks,[19] D. S. Brown,[26] N. Bruner,[25] D. Bucher,[22] H. Buesching,[22] V. Bumazhnov,[12] G. Bunce,[3,32] J. Burward-Hoy,[28] S. Butsyk,[28,30] T. A. Carey,[19] P. Chand,[2] J. Chang,[5] W. C. Chang,[1] L. L. Chavez,[25] S. Chernichenko,[12] C. Y. Chi,[8] J. Chiba,[14] M. Chiu,[8] R. K. Choudhury,[2] T. Christ,[28] T. Chujo,[3,39] M. S. Chung,[15,19] P. Chung,[27] V. Cianciolo,[29] B. A. Cole,[8] D. G. D'Enterria,[34] G. David,[3] H. Delagrange,[34] A. Denisov,[12] A. Deshpande,[32] E. J. Desmond,[3] O. Dietzsch,[33] B. V. Dinesh,[2] A. Drees,[28] A. Durum,[12] D. Dutta,[2] K. Ebisu,[24] Y. V. Efremenko,[29] K. El Chenawi,[40] H. En'yo,[17,31] S. Esumi,[39] L. Ewell,[3] T. Ferdousi,[5] D. E. Fields,[25] S. L. Fokin,[16] Z. Fraenkel,[42] A. Franz,[3] A. D. Frawley,[9] S.-Y. Fung,[5] S. Garpman,[20] T. K. Ghosh,[40] A. Glenn,[36] A. L. Godoi,[33] Y. Goto,[32] S. V. Greene,[40] M. Grosse Perdekamp,[32] S. K. Gupta,[2] W. Guryn,[3] H.-Å. Gustafsson,[20] J. S. Haggerty,[3] H. Hamagaki,[7] A. G. Hansen,[19] H. Hara,[24] E. P. Hartouni,[18] R. Hayano,[38] N. Hayashi,[31] X. He,[10] T. K. Hemmick,[28] J. Heuser,[28] M. Hibino,[41] J. C. Hill,[13] D. S. Ho,[43] K. Homma,[11] B. Hong,[15] A. Hoover,[26] T. Ichihara,[31,32] K. Imai,[17,31] M. S. Ippolitov,[16] M. Ishihara,[31,32] B. V. Jacak,[28,32] W. Y. Jang,[15] J. Jia,[28] B. M. Johnson,[3] S. C. Johnson,[18,28] K. S. Joo,[23] S. Kametani,[41] J. H. Kang,[43] M. Kann,[30] S. S. Kapoor,[2] S. Kelly,[8] B. Khachaturov,[42] A. Khanzadeev,[30] J. Kikuchi,[41] D. J. Kim,[43] H. J. Kim,[43] S. Y. Kim,[43] Y. G. Kim,[43] W. W. Kinnison,[19] E. Kistenev,[3] A. Kiyomichi,[39] C. Klein-Boesing,[22] S. Klinksiek,[25] L. Kochenda,[30] D. Kochetkov,[5] V. Kochetkov,[12] D. Koehler,[25] T. Kohama,[11] A. Kozlov,[42] P. J. Kroon,[3] K. Kurita,[31,32] M. J. Kweon,[15] Y. Kwon,[43] G. S. Kyle,[26] R. Lacey,[27] J. G. Lajoie,[13] J. Lauret,[27] A. Lebedev,[13] D. M. Lee,[19] M. J. Leitch,[19] X. H. Li,[5] Z. Li,[6,31] D. J. Lim,[43] M. X. Liu,[19] X. Liu,[6] Z. Liu,[6] C. F. Maguire,[40] J. Mahon,[3] Y. I. Makdisi,[3] V. I. Manko,[16] Y. Mao,[6,31] S. K. Mark,[21] S. Markacs,[8] G. Martinez,[34] M. D. Marx,[28] A. Masaike,[17] F. Matathias,[28] T. Matsumoto,[7,41] P. L. McGaughey,[19] E. Melnikov,[12] M. Merschmeyer,[22] F. Messer,[28] M. Messer,[3] Y. Miake,[39] T. E. Miller,[40] A. Milov,[42] S. Mioduszewski,[3,36] R. E. Mischke,[19] G. C. Mishra,[10] J. T. Mitchell,[3] A. K. Mohanty,[2] D. P. Morrison,[3] J. M. Moss,[19] F. Mühlbacher,[28] M. Muniruzzaman,[5] J. Murata,[31] S. Nagamiya,[14] Y. Nagasaka,[24] J. L. Nagle,[8] Y. Nakada,[17] B. K. Nandi,[5] J. Newby,[36] L. Nikkinen,[21] P. Nilsson,[20] S. Nishimura,[7] A. S. Nyanin,[16] J. Nystrand,[20] E. O'Brien,[3] C. A. Ogilvie,[13] H. Ohnishi,[3,11] I. D. Ojha,[4,40] M. Ono,[39] V. Onuchin,[12] A. Oskarsson,[20] L. Österman,[20] I. Otterlund,[20] K. Oyama,[7,38] L. Paffrath,[3,*] A. P. T. Palounek,[19] V. S. Pantuev,[28] V. Papavassiliou,[26] S. F. Pate,[26] T. Peitzmann,[22] A. N. Petridis,[13] C. Pinkenburg,[3,27] R. P. Pisani,[3] P. Pitukhin,[12] F. Plasil,[29] M. Pollack,[28,36] K. Pope,[36] M. L. Purschke,[3] I. Ravinovich,[42] K. F. Read,[29,36] K. Reygers,[22] V. Riabov,[30,35] Y. Riabov,[30] M. Rosati,[13] A. A. Rose,[40] S. S. Ryu,[43] N. Saito,[31,32] A. Sakaguchi,[11] T. Sakaguchi,[7,41] H. Sako,[39] T. Sakuma,[31,37] V. Samsonov,[30] T. C. Sangster,[18] R. Santo,[22] H. D. Sato,[17,31] S. Sato,[39] S. Sawada,[14] B. R. Schlei,[19] Y. Schutz,[34] V. Semenov,[12] R. Seto,[5] T. K. Shea,[3] I. Shein,[12] T.-A. Shibata,[31,37] K. Shigaki,[14] T. Shiina,[19] Y. H. Shin,[43] I. G. Sibiriak,[16] D. Silvermyr,[20] K. S. Sim,[15] J. Simon-Gillo,[19] C. P. Singh,[4] V. Singh,[4] M. Sivertz,[3] A. Soldatov,[12] R. A. Soltz,[18] S. Sorensen,[29,36] P. W. Stankus,[29] N. Starinsky,[21] P. Steinberg,[8] E. Stenlund,[20] A. Ster,[44] S. P. Stoll,[3] M. Sugioka,[31,37] T. Sugitate,[11] J. P. Sullivan,[19] Y. Sumi,[11] Z. Sun,[6] M. Suzuki,[39] E. M. Takagui,[33] A. Taketani,[31] M. Tamai,[41] K. H. Tanaka,[14] Y. Tanaka,[24] E. Taniguchi,[31,37] M. J. Tannenbaum,[3] J. Thomas,[28] J. H. Thomas,[18] T. L. Thomas,[25] W. Tian,[6,36] J. Tojo,[17,31] H. Torii,[17,31] R. S. Towell,[19] I. Tserruya,[42] H. Tsuruoka,[39] A. A. Tsvetkov,[16] S. K. Tuli,[4] H. Tydesjö,[20] N. Tyurin,[12] T. Ushiroda,[24] H. W. van Hecke,[19] C. Velissaris,[26] J. Velkovska,[28] M. Velkovsky,[28] A. A. Vinogradov,[16] M. A. Volkov,[16] A. Vorobyov,[30] E. Vznuzdaev,[30] H. Wang,[5] Y. Watanabe,[31,32] S. N. White,[3] C. Witzig,[3] F. K. Wohn,[13] C. L. Woody,[3] W. Xie,[5,42] K. Yagi,[39] S. Yokkaichi,[31] G. R. Young,[29] I. E. Yushmanov,[16] W. A. Zajc,[8] Z. Zhang,[28] and S. Zhou[6]

(PHENIX Collaboration)

[1]*Institute of Physics, Academia Sinica, Taipei 11529, Taiwan*
[2]*Bhabha Atomic Research Centre, Bombay 400 085, India*
[3]*Brookhaven National Laboratory, Upton, New York 11973-5000*
[4]*Department of Physics, Banaras Hindu University, Varanasi 221005, India*
[5]*University of California–Riverside, Riverside, California 92521*
[6]*China Institute of Atomic Energy (CIAE), Beijing, Peoples Republic of China*
[7]*Center for Nuclear Study, Graduate School of Science, University of Tokyo, 7-3-1 Hongo, Bunkyo, Tokyo 113-0033, Japan*

 0031-9007/01/86(16)/3500(6)$15.00 © 2001 The American Physical Society

[8]*Columbia University, New York, New York 10027 and Nevis Laboratories, Irvington, New York 10533*
[9]*Florida State University, Tallahassee, Florida 32306*
[10]*Georgia State University, Atlanta, Georgia 30303*
[11]*Hiroshima University, Kagamiyama, Higashi-Hiroshima 739-8526, Japan*
[12]*Institute for High Energy Physics (IHEP), Protvino, Russia*
[13]*Iowa State University, Ames, Iowa 50011*
[14]*KEK, High Energy Accelerator Research Organization, Tsukuba-shi, Ibaraki-ken 305-0801, Japan*
[15]*Korea University, Seoul, 136-701, Korea*
[16]*Russian Research Center "Kurchatov Institute," Moscow, Russia*
[17]*Kyoto University, Kyoto 606, Japan*
[18]*Lawrence Livermore National Laboratory, Livermore, California 94550*
[19]*Los Alamos National Laboratory, Los Alamos, New Mexico 87545*
[20]*Department of Physics, Lund University, Box 118, SE-221 00 Lund, Sweden*
[21]*McGill University, Montreal, Quebec H3A 2T8, Canada*
[22]*Institut für Kernphysik, University of Münster, D-48149 Münster, Germany*
[23]*Myongji University, Yongin, Kyonggido 449-728, Korea*
[24]*Nagasaki Institute of Applied Science, Nagasaki-shi, Nagasaki 851-0193, Japan*
[25]*University of New Mexico, Albuquerque, New Mexico*
[26]*New Mexico State University, Las Cruces, New Mexico 88003*
[27]*Chemistry Department, State University of New York–Stony Brook, Stony Brook, New York 11794*
[28]*Department of Physics and Astronomy, State University of New York–Stony Brook, Stony Brook, New York 11794*
[29]*Oak Ridge National Laboratory, Oak Ridge, Tennessee 37831*
[30]*PNPI, Petersburg Nuclear Physics Institute, Gatchina, Russia*
[31]*RIKEN (The Institute of Physical and Chemical Research), Wako, Saitama 351-0198, Japan*
[32]*RIKEN BNL Research Center, Brookhaven National Laboratory, Upton, New York 11973-5000*
[33]*Universidade de São Paulo, Instituto de Física, Caixa Postal 66318, Sào Paulo CEP05315-970, Brazil*
[34]*SUBATECH (Ecole des Mines de Nantes, IN2P3/CNRS, Universite de Nantes) BP 20722-44307, Nantes-cedex 3, France*
[35]*St. Petersburg State Technical University, St. Petersburg, Russia*
[36]*University of Tennessee, Knoxville, Tennessee 37996*
[37]*Department of Physics, Tokyo Institute of Technology, Tokyo, 152-8551, Japan*
[38]*University of Tokyo, Tokyo, Japan*
[39]*Institute of Physics, University of Tsukuba, Tsukuba, Ibaraki 305, Japan*
[40]*Vanderbilt University, Nashville, Tennessee 37235*
[41]*Waseda University, Advanced Research Institute for Science and Engineering, 17 Kikui-cho, Shinjuku-ku, Tokyo 162-0044, Japan*
[42]*Weizmann Institute, Rehovot 76100, Israel*
[43]*Yonsei University, IPAP, Seoul 120-749, Korea*
[44]*KFKI Research Institute for Particle and Nuclear Physics (RMKI), Budapest, Hungary*
(Received 21 December 2000)

We present results for the charged-particle multiplicity distribution at midrapidity in Au-Au collisions at $\sqrt{s_{NN}} = 130$ GeV measured with the PHENIX detector at RHIC. For the 5% most central collisions we find $dN_{ch}/d\eta_{|\eta=0} = 622 \pm 1(\text{stat}) \pm 41(\text{syst})$. The results, analyzed as a function of centrality, show a steady rise of the particle density per participating nucleon with centrality.

DOI: 10.1103/PhysRevLett.86.3500 PACS numbers: 25.75.Dw

The Relativistic Heavy-Ion Collider (RHIC) at Brookhaven National Laboratory started regular operation in June 2000, opening new frontiers in the study of hadronic matter under unprecedented conditions of temperature and energy density. The research is focused on the phase transition associated with quark deconfinement and chiral symmetry restoration expected to take place under those conditions.

In this Letter, we report results for the charged-particle multiplicity distribution at midrapidity in Au-Au collisions at $\sqrt{s_{NN}} = 130$ GeV, as measured with the PHENIX detector. These are the first RHIC results to span a broad impact parameter range.

Particle density at midrapidity is an essential global variable for the characterization of high energy nuclear collisions, providing information about the initial conditions, such as energy density. The results presented here should help to constrain the wide range of theoretical predictions [1] available at RHIC energies and to discriminate among various mechanisms of entropy and particle production. In particular, we analyze the particle density as a function of centrality, expressed by the number of participating nucleons. Such an analysis may shed light on the relative importance of soft versus hard processes of particle production and test the assumption of gluon saturation expected at RHIC energies [2,3]. Our results are compared to

different models, to similar studies obtained in Pb-Pb collisions at the CERN SPS [4–6] and to a recent measurement performed at RHIC by PHOBOS [7].

The PHENIX detector is described in Ref. [8]. The present analysis relies primarily on three PHENIX subsystems: two layers of pad chambers (PC), called PC1 and PC3, used to determine the charged particle multiplicity, the zero degree calorimeters (ZDC) and the beam-beam counters (BBC), used to derive the trigger and the off-line event selection. The PC provide three-dimensional coordinates along the charged-particle trajectories [9]. The two layers are mounted at radial distances of 2.49 m and 4.98 m, respectively, from the interaction region. Each layer has 8 wire chambers with cathode pad readout (see Fig. 1) and covers 90° in azimuth (ϕ) and ± 0.35 units of pseudorapidity (η). The ZDC are small transverse-area hadron calorimeters that measure neutron energy within a 2 mrad ($|\eta| > 6$) cone around the beam direction and are located at ± 18.25 m from the center of the interaction region [10]. The BBC comprise two arrays of 64 photomultiplier tubes, each equipped with quartz Cherenkov radiators. The BBC are located around the beam direction at ± 1.44 m from the center of the interaction region covering the full 2π azimuth and the range $\eta = \pm(3.0-3.9)$ [11].

The primary interaction trigger is generated by a coincidence between the two BBC with at least two photomultipliers fired in each of them and a requirement on the collision vertex position, usually $|z| \leq 20$ cm. Based on detailed simulations of the BBC, this trigger reflects [92 $\pm$ 2(syst)]% of the nuclear interaction cross section of 7.2 b [12]. Another trigger is generated by a coincidence between the two ZDC, each one with an energy signal larger than 10 GeV. This trigger reflects the nuclear interaction plus the mutual Coulomb dissociation cross sections. Most BBC triggers (97.8%) also satisfy the ZDC trigger requirement. The small percentage of exclusive BBC triggers is due to inefficiencies of the ZDC trigger and background interactions. These two sources are difficult to distinguish and we estimate a background event contamination of [1 $\pm$ 1(syst)]% of the total event sample.

This analysis is based on a sample of 137 784 events taken without magnetic field, satisfying the BBC trigger and with a reconstructed vertex position $|z| \leq 17$ cm.

The number of primary charged particles per event is determined on a statistical basis by correlating hits in PC1 and PC3. The analysis procedure was developed and corroborated by extensive simulations using the GEANT [13] response of the PHENIX detector to events generated with HIJING [14]. The vertex is reconstructed using the following algorithm: all hits in PC3 are combined with all hits in PC1 and the resulting lines are projected onto a plane through the beam line, perpendicular to the symmetry axis of the chambers (see Fig. 1). For events with more than $\sim$5 tracks, the distribution of these projections along the Z axis produces a distinct peak which defines the vertex position. For low multiplicity events the vertex is reconstructed from the time difference between the two BBC.

Once the vertex is known, all hits in PC3 are again combined with all hits in PC1 and the resulting tracks are projected onto the plane previously defined. The distribution of the distance R of the intersection points to the vertex position, is shown in Fig. 2. This distribution contains real tracks and tracks from the obvious combinatorial background inherent to the adopted procedure of combining all hits in PC3 with all hits in PC1. The latter can be determined by a mixed event technique; in the present analysis, each sector in PC1 was exchanged with its neighbor and the resulting combinatorial background is shown in Fig. 2 by the dotted line. The yield of this background increases quadratically with R (leading to a linear dependence in the differential dN/dR vs R presentation of Fig. 2).

The R distribution of real tracks obtained by subtracting the background (N_B) from the total number of tracks is shown in Fig. 2 by the dashed line. The sharp peak at small R is due to tracks from primary particles originating at the vertex and the long tail is due to decay products of primary particles decaying in flight. In practice, the track counting is performed up to a given R value. The fraction of counted

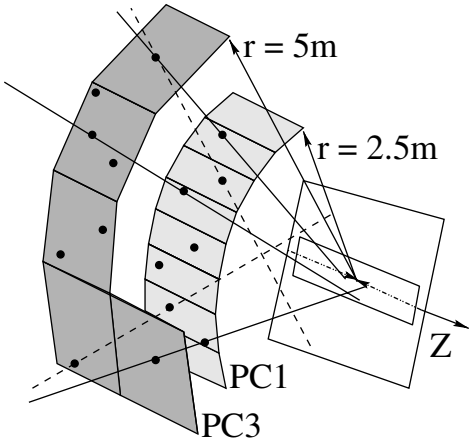

FIG. 1. Sketch of the geometry. For clarity, three PC3 sectors have been removed from the drawing.

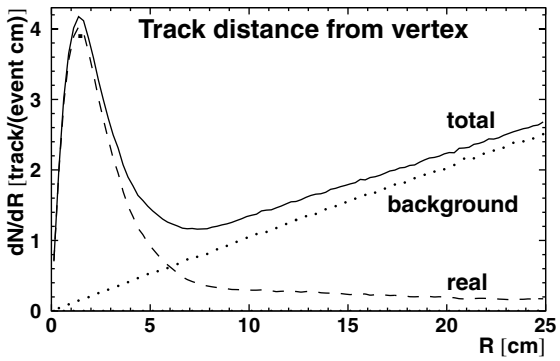

FIG. 2. Tracks per event and per cm as a function of the distance to the event vertex.

tracks as a function of R is obtained from the integral of the dashed curve normalized to the total integral up to $R = \infty$. The tail at large R values is very well described by an exponential function and therefore the extrapolation of the dashed curve to $R = \infty$ is straightforward. The larger the value of R, the smaller is the correction for the fraction of uncounted tracks, but the larger the background to be subtracted. Since the background can be reliably subtracted we performed the track counting up to $R = 25$ cm, thus including 95.9% of all tracks.

After subtracting the background, a raw multiplicity distribution is obtained to which we apply several corrections to obtain the corrected distribution of primary charged particles:

(i) A correction of 15.3% accounts for inactive gaps between the chambers, inactive electronic readout cards, and dead pads in the PC1 and PC3 detectors.

(ii) Using cosmic rays, the pad chamber hit efficiency was measured to be 99.4% for isolated single hits in agreement with an analytical study of the chamber performance [15].

(iii) The track losses due to the finite double hit resolution of the chambers depend on the event multiplicity. The losses occur in the direct counting of tracks and in the combinatorial background subtraction. The two effects were studied in great detail with Monte Carlo techniques. For the first one, the correction amounts to 13.3% for the 5% most central collisions, whereas it is only 4.9% for the 20%–25% bin. The second effect is a reduction of the combinatorial background which leads to an increase in the track multiplicity by $0.036 \times N_B$.

(iv) Finally there is a correction due to uncounted charged tracks. Two sources contribute here. First, there is a correction of 4.3% from tracks missed because the analysis is limited to $R = 25$ cm. The second source has two components. On the one hand there are primary charged particles (mainly $\pi^{\pm}$) which decay in flight. A large fraction of these decays is accounted for since, as discussed above, they produce the tail of the R distribution in Fig. 2. However, there are still a small number of decays which miss altogether PC1 and/or PC3 and those have to be added. On the other hand, there is feed down from neutral particle decays (mainly K_S^o and π^o) which lead to valid tracks. Those have to be subtracted. Both components depend on particle composition and momentum distribution. Lacking precise information about them, we performed Monte Carlo simulations, applying to the GEANT response of the pad chambers the same analysis procedure as to real data and comparing the resulting multiplicity to the original HIJING input. The result is a net correction of only $\sim$2.8%. This correction is quite robust against changes in the input. For example, a uniform 20% increase in momentum p of all pions reduces the net correction to 1%.

The systematic error in the multiplicity due to corrections (i) and (ii) is estimated at less than 2%. To these we have to add the errors associated with the background subtraction, double hit resolution (which are multiplicity dependent) and particle decays (which is multiplicity independent). We estimate the first two uncertainties to be 4.6% at the highest multiplicities, based on Monte Carlo guidance and a comparison with an identical analysis in which we imposed a 50% larger double hit resolution in PC1 and PC3. For the particle decay correction, we assign an error of 4% based on the effect of varying the momentum distribution and the particle composition in the simulations and a comparison with the results obtained with another data set measured while the detectors were retracted by 44 cm from the nominal position. Adding these errors in quadrature results in a total systematic error of 6.5% at the highest multiplicities. An additional error in $dN_{ch}/d\eta$, which enters in the analysis of the multiplicity versus centrality presented below, is the uncertainty in the total number of events due to the BBC trigger ($\pm 2\%$) and the event contamination ($\pm 1\%$).

After applying the appropriate corrections we obtain in the lower panel of Fig. 3 the minimum-bias charged-particle multiplicity distribution, in the track acceptance

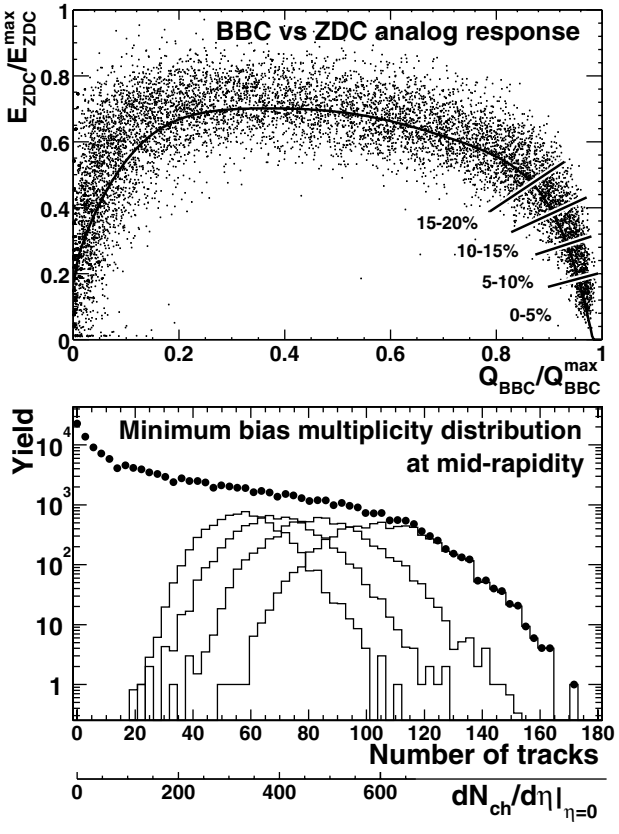

FIG. 3. BBC vs ZDC analog response (top panel) and minimum-bias multiplicity distribution in the PHENIX measurement aperture (lower panel). The lower axis converts the observed distribution to the corresponding average $dN_{ch}/d\eta$ for track multiplicities less than $\sim$120; beyond that value the shape of the distribution has a significant contribution from fluctuations into the measurement aperture.

$|\eta| < 0.35$, $\delta\phi = 88.4°$. A factor of 5.82 thus converts the observed number of tracks to $dN_{ch}/d\eta_{|\eta=0}$ in one unit of pseudorapidity and full azimuth, yielding the lower horizontal scale in Fig. 3.

Figure 3 also shows the multiplicity distributions for the four most central bins, 0%–5% to 15%–20%. The bins were defined by cuts in the space of BBC versus ZDC analog response (see Fig. 3—upper panel) and refer to percentiles of the total interaction cross section of 7.2 b. In order to avoid the ambiguities inherent in the BBC vs ZDC distribution, we selected events with increasing centrality based upon the monotonic response of another PHENIX detector. The centroids of these events projected onto the ZDC-BBC space determine the centrality contour indicated by the solid line. The cuts are made perpendicular to this contour. Simulations of the BBC and ZDC response were used to account for the effect of physics and detector fluctuations in the definition of these event classes and to relate them via a Glauber model [12] to the number of participating nucleons N_p and of binary collisions N_c. The average charged particle density scaled up to one unit of rapidity and the corresponding numbers N_p and N_c are tabulated in Table I for various centrality bins.

The PHOBOS experiment has recently reported an average $dN_{ch}/d\eta_{|\eta=0} = 555 \pm 12(\text{stat}) \pm 35(\text{syst})$ for the 6% most central collisions [7]. For the same centrality bin, we find $dN_{ch}/d\eta_{|\eta=0} = 609 \pm 1(\text{stat}) \pm 37(\text{syst})$. From the preliminary results reported by NA49 in Pb-Pb collisions at $\sqrt{s_{NN}} = 17.2$ GeV [6], we derive a particle density $dN_{ch}/dy_{|y=0} = 410$. Our result, $dN_{ch}/d\eta_{|\eta=0} = 622$ for the same centrality bin (0%–5%), represents an increase of ~80% after scaling it by 1.2 to account for the transformation from η to y.

It has recently been emphasized [2] that the centrality dependence of $dN_{ch}/d\eta$ allows one to discriminate between various models of particle production. We show in Fig. 4 our results for $dN_{ch}/d\eta$ per participant pair as a function of the number of participants N_p. Figure 4 also shows the $p\overline{p}$ value at the same $\sqrt{s}$ taken from the UA5 analysis [16]. It is interesting to note that the extrapolation of our data points to low multiplicities approaches the $p\overline{p}$ value.

TABLE I. Charged-particle density, number of participants, and collisions for various centrality bins expressed as percentiles of $\sigma_{\text{geo}} = 7.2$ b. The statistical errors are negligible and only systematic errors are quoted.

Centrality bin	$\langle dN_{ch}/d\eta_{\|\eta=0}\rangle$	$\langle N_p\rangle$	$\langle N_c\rangle$
0–5	622 ± 41	347 ± 10	946 ± 146
5–10	498 ± 31	293 ± 9	749 ± 116
10–15	413 ± 25	248 ± 8	596 ± 93
15–20	344 ± 21	211 ± 7	478 ± 75
20–25	287 ± 18	177 ± 7	377 ± 61
25–30	235 ± 16	146 ± 6	290 ± 47
30–35	188 ± 14	122 ± 5	226 ± 38
35–40	147 ± 12	99 ± 5	170 ± 30
40–45	115 ± 11	82 ± 5	130 ± 24
45–50	89 ± 9	68 ± 4	101 ± 19

Models such as HIJING predict that there is a component of particle production from soft interactions that scales linearly with N_p and a second component from hard processes (pQCD jets) that scales with N_c. Following that, we fit the data of Fig. 4 with the function $dN_{ch}/d\eta = A \times N_p + B \times N_c$ using the values of N_c and N_p tabulated in Table I. The results of the fit are shown in Fig. 4. Note that the errors in A and B are anticorrelated. In such models, the values of A and B imply a large contribution of hard processes to particle production, which increases with centrality from ~30% at $N_p = 68$ to ~50% for central collisions. HIJING predicts the same trend although the calculated values are lower than the data by ~15%. However, this is not a unique interpretation. At alternating gradient synchrotron energies, where hard processes do not occur, the particle production per participant was also observed to increase with centrality [17]. At the CERN SPS energy of $\sqrt{s_{NN}} = 17.2$ GeV, a similar behavior was observed. Using a different parametrization, $dN_{ch}/d\eta \propto N_p^{\alpha}$, WA98 finds a best fit value of $\alpha = 1.07 \pm 0.04$ [4]. Experiment WA97 quotes a value $\alpha = 1.05 \pm 0.05$, consistent with the result of WA98 but also compatible with their assumption of proportionality between multiplicity and participants [5]. A good fit to our data can also be obtained with this functional form with a higher value of $\alpha = 1.16 \pm 0.04$. One should note that the CERN results are in the lab frame, whereas ours are in the center of mass system.

Other models such as the EKRT [3] predict that at RHIC energies, the large production of semihard gluons in a small volume may saturate the gluon density. The resulting gluon fusion limits the total entropy production and thus lowers the final particle production per participant. The predictions of the EKRT model are also shown in Fig. 4.

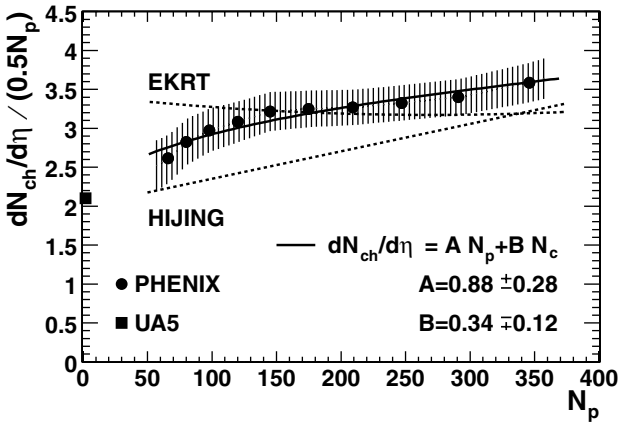

FIG. 4. Charged-particle pseudorapidity density per participant pair vs the number of participants. Predictions from HIJING [2] and EKRT [3] models, and a simple phenomenological fit are also shown. The shaded area represents the systematic errors of $dN_{ch}/d\eta$ and N_p. The errors of N_c are in Table I.

We observe no such saturation effect within our errors for Au + Au collisions at $\sqrt{s_{NN}} = 130$ GeV, but instead see a steady rise in the particle production per participant pair.

We thank the staff of the RHIC project, Collider-Accelerator, and Physics Departments at BNL and the staff of PHENIX participating institutions for their vital contributions. We acknowledge support from the U.S. Department of Energy and NSF, Monbu-sho and STA (Japan), RAS, RMAE, and RMS (Russia), BMBF and DAAD (Germany), FRN, NFR, and the Wallenberg Foundation (Sweden), MIST and NSERC (Canada), CNPq and FAPESP (Brazil), IN2P3/CNRS (France), DAE (India), KRF and KOSEF (Korea), and the U.S.-Israel Binational Science Foundation.

*Deceased.

[1] S. A. Bass *et al.,* Nucl. Phys. **A661**, 205c (1999).
[2] X. N. Wang and M. Gyulassy, preceding Letter, Phys. Rev. Lett. **86**, 3496 (2001).
[3] K. J. Eskola *et al.,* Nucl. Phys. **B570**, 379 (2000); hep-ph/0009246.
[4] WA98 Collaboration, M. M. Aggarwal *et al.,* Eur. Phys. J. **C18**, 651 (2001); nucl-ex/0008004.
[5] F. Antinori *et al.,* Report No. CERN-EP-2000-002.
[6] J. Bächler *et al.,* Nucl. Phys. **A661**, 45c (1999).
[7] B. B. Back *et al.,* Phys. Rev. Lett. **85**, 3100 (2000).
[8] D. P. Morrison, Nucl. Phys. **A638**, 565c (1998); N. Saito, *ibid.* **A638**, 575c (1998).
[9] P. Nilsson *et al.,* Nucl. Phys. **A661**, 665c (1999).
[10] C. Adler *et al.,* nucl-ex/0008005.
[11] K. Ikematsu *et al.,* Nucl. Instrum. Methods Phys. Res., Sect. A **411**, 238 (1998).
[12] We used Woods-Saxon nuclear density distribution, Au nucleus radius $R = 6.65 \pm 0.3$ fm, diffuseness $a = 0.54 \pm 0.01$ fm, and nucleon-nucleon cross section $\sigma_{nn} = 40 \pm 5$ mb.
[13] GEANT 3.2.1, CERN program library.
[14] X. N. Wang and M. Gyulassy, Phys. Rev. D **44**, 3501 (1991). We used version 1.35 with default parameters.
[15] A. Milov *et al.,* PHENIX technical note 379.
[16] G. J. Alner *et al.,* Z. Phys. C **33**, 1 (1986).
[17] L. Ahle *et al.,* Phys. Rev. C **59**, 2173 (1999).

PHYSICAL REVIEW C, VOLUME 64, 011901(R)

Localized charged-neutral fluctuations in 158*A* GeV Pb+Pb collisions

M. M. Aggarwal,[1] A. Agnihotri,[2] Z. Ahammed,[3] A. L. S. Angelis,[4] V. Antonenko,[5] V. Arefiev,[6] V. Astakhov,[6] V. Avdeitchikov,[6] T. C. Awes,[7] P. V. K. S. Baba,[8] S. K. Badyal,[8] C. Barlag,[9] S. Bathe,[9] B. Batiounia,[6] T. Bernier,[10] K. B. Bhalla,[2] V. S. Bhatia,[1] C. Blume,[9] R. Bock,[11] E.-M. Bohne,[9] Z. Böröcz,[9] D. Bucher,[9] A. Buijs,[12] H. Büsching,[9] L. Carlen,[13] V. Chalyshev,[6] S. Chattopadhyay,[3] R. Cherbatchev,[5] T. Chujo,[14] A. Claussen,[9] A. C. Das,[3] M. P. Decowski,[18] H. Delagrange,[10] V. Djordjadze,[6] P. Donni,[4] I. Doubovik,[5] A. K. Dubey,[19] S. Dutt,[8] M. R. Dutta Majumdar,[3] K. El Chenawi,[13] S. Eliseev,[15] K. Enosawa,[14] P. Foka,[4] S. Fokin,[5] M. S. Ganti,[3] S. Garpman,[13] O. Gavrishchuk,[6] F. J. M. Geurts,[12] T. K. Ghosh,[16] R. Glasow,[9] S. K. Gupta,[2] B. Guskov,[6] H. Å. Gustafsson,[13] H. H. Gutbrod,[10] R. Higuchi,[14] I. Hrivnacova,[15] M. Ippolitov,[5] H. Kalechofsky,[4] R. Kamermans,[12] K.-H. Kampert,[9] K. Karadjev,[5] K. Karpio,[17] S. Kato,[14] S. Kees,[9] C. Klein-Bösing,[9] S. Knoche,[9] B. W. Kolb,[11] I. Kosarev,[6] I. Koutcheryaev,[5] T. Krümpel,[9] A. Kugler,[15] P. Kulinich,[18] M. Kurata,[14] K. Kurita,[14] N. Kuzmin,[6] I. Langbein,[11] A. Lebedev,[5] Y. Y. Lee,[11] H. Löhner,[16] L. Luquin,[10] D. P. Mahapatra,[19] V. Manko,[5] M. Martin,[4] G. Martínez,[10] A. Maximov,[6] G. Mgebrichvili,[5] Y. Miake,[14] Md. F. Mir,[8] G. C. Mishra,[19] Y. Miyamoto,[14] B. Mohanty,[19] M.-J. Mora,[10] D. Morrison,[20] D. S. Mukhopadhyay,[3] H. Naef,[4] B. K. Nandi,[19] S. K. Nayak,[10] T. K. Nayak,[3] S. Neumaier,[11] A. Nianine,[5] V. Nikitine,[6] S. Nikolaev,[5] P. Nilsson,[13] S. Nishimura,[14] P. Nomokonov,[6] J. Nystrand,[13] F. E. Obenshain,[20] A. Oskarsson,[13] I. Otterlund,[13] M. Pachr,[15] S. Pavliouk,[6] T. Peitzmann,[9] V. Petracek,[15] W. Pinganaud,[10] F. Plasil,[7] U. v. Poblotzki,[9] M. L. Purschke,[11] J. Rak,[15] R. Raniwala,[2] S. Raniwala,[2] V. S. Ramamurthy,[19] N. K. Rao,[8] F. Retiere,[10] K. Reygers,[9] G. Roland,[18] L. Rosselet,[4] I. Roufanov,[6] C. Roy,[10] J. M. Rubio,[4] H. Sako,[14] S. S. Sambyal,[8] R. Santo,[9] S. Sato,[14] H. Schlagheck,[9] H.-R. Schmidt,[11] Y. Schutz,[10] G. Shabratova,[6] T. H. Shah,[8] I. Sibiriak,[5] T. Siemiarczuk,[17] D. Silvermyr,[13] B. C. Sinha,[3] N. Slavine,[6] K. Söderström,[13] N. Solomey,[4] G. Sood,[1] S. P. Sørensen,[7,20] P. Stankus,[7] G. Stefanek,[17] P. Steinberg,[18] E. Stenlund,[13] D. Stüken,[9] M. Sumbera,[15] T. Svensson,[13] M. D. Trivedi,[3] A. Tsvetkov,[5] L. Tykarski,[17] J. Urbahn,[11] E. C. v. d. Pijll,[12] N. v. Eijndhoven,[12] G. J. v. Nieuwenhuizen,[18] A. Vinogradov,[5] Y. P. Viyogi,[3] A. Vodopianov,[6] S. Vörös,[4] B. Wysłouch,[18] K. Yagi,[14] Y. Yokota,[14] and G. R. Young[7]

(WA98 Collaboration)

[1]*University of Panjab, Chandigarh 160 014, India*
[2]*University of Rajasthan, Jaipur 302 004, Rajasthan, India*
[3]*Variable Energy Cyclotron Centre, Calcutta 700 064, India*
[4]*University of Geneva, CH-1211 Geneva 4, Switzerland*
[5]*RRC ''Kurchatov Institute,'' RU-123182 Moscow, Russia*
[6]*Joint Institute for Nuclear Research, RU-141980 Dubna, Russia*
[7]*Oak Ridge National Laboratory, Oak Ridge, Tennessee 37831-6372*
[8]*University of Jammu, Jammu 180 001, India*
[9]*University of Münster, D-48149 Münster, Germany*
[10]*SUBATECH, Ecole des Mines, Nantes, France*
[11]*Gesellschaft für Schwerionenforschung (GSI), D-64220 Darmstadt, Germany*
[12]*Universiteit Utrecht/NIKHEF, NL-3508 TA Utrecht, The Netherlands*
[13]*University of Lund, SE-221 00 Lund, Sweden*
[14]*University of Tsukuba, Ibaraki 305, Japan*
[15]*Nuclear Physics Institute, CZ-250 68 Rez, Czech Republic*
[16]*KVI, University of Groningen, NL-9747 AA Groningen, The Netherlands*
[17]*Institute for Nuclear Studies, PL-00-681 Warsaw, Poland*
[18]*MIT, Cambridge, Massachusetts 02139*
[19]*Institute of Physics, 751 005 Bhubaneswar, India*
[20]*University of Tennessee, Knoxville, Tennessee 37966*
(Received 15 December 2000; published 31 May 2001)

Localized fluctuations in the multiplicity of charged particles and photons produced in central 158*A* GeV/*c* Pb+Pb collisions are studied. The charged versus neutral correlations in common $\eta-\phi$ phase space regions of varying azimuthal size are analyzed by two different methods. The analysis provides a model-independent demonstration of nonstatistical fluctuations in both charged particle and photon multiplicities in limited azimuthal regions. However, no correlated charge-neutral fluctuations are observed, contrary to expectations for the production of a disoriented chiral condensate. The result is not explained by the widely used VENUS model.

DOI: 10.1103/PhysRevC.64.011901 PACS number(s): 25.75.Gz, 13.40.−f, 24.90.+d

 ©2001 The American Physical Society

The formation of hot and dense matter in high energy heavy-ion collisions offers the possibility to create a new phase where matter is deconfined and chiral symmetry is restored. Indications for the formation of such a quark gluon plasma (QGP) phase are provided by several results from experiments at the CERN SPS [1]. Event-by-event fluctuations in the particle multiplicities and their ratios have recently been predicted to provide information about the nature of the QCD phase transition [2,3]. Fluctuations may also be caused by Bose-Einstein correlations, resonance decays, or more exotic phenomena such as pion lasers [4]. Enhanced fluctuations in neutral to charged pions have been predicted as a signature of the formation of disoriented chiral condensates (DCC) [5–8], which might be one of the most interesting predicted consequences of chiral symmetry restoration.

Theoretical predictions suggest that isospin fluctuations, caused by formation of a DCC, would produce clusters of coherent pions in localized phase space regions or domains. The probability distribution of the neutral pion fraction in such a domain would follow the relation $P(f)=1/2\sqrt{f}$, where $f=N_{\pi^0}/N_{\pi}$. Thus DCC formation in a given domain would be associated with large event-by-event fluctuations in the ratio of neutral to charged pions in that domain. Experimentally, such fluctuations can be deduced from the measurement of fluctuations in the number of photons to charged particles in limited $\eta-\phi$ regions. The anti-Centauro events, reported by the JACEE Collaboration [9], with large charged-neutral fluctuations are possible candidates for DCC events. The studies carried out so far in $p-\overline{p}$ [10] and heavy-ion [11,12] reactions have searched for fluctuations which extend over a large region of phase space. These measurements have provided upper limits on the presence of DCC-like fluctuations.

In this Rapid Communication we present first results on the search for nonstatistical event-by-event fluctuations in the relative number of charged particles and photons in localized $\eta-\phi$ phase space regions for central 158*A* GeV/c Pb+Pb collisions. The data presented here were taken with the 158*A* GeV Pb beam of the CERN SPS on a Pb target of 213 μm thickness during a period of WA98 operation without magnetic field. The analysis makes use of a subset of detectors of the WA98 experiment. Charged particle hits ($N_{\rm ch}$) were counted using a circular silicon pad multiplicity detector (SPMD) [11] located 32.8 cm downstream from the target. It provided uniform pseudorapidity coverage in the region $2.35<\eta<3.75$. The detector was 99% efficient for charged particle detection. The photon multiplicity was measured using a preshower photon multiplicity detector (PMD) [13] placed 21.5 m downstream of the target and covering the pseudorapidity range $2.9<\eta<4.2$. Clusters of hit scintillator pads having total energy deposit above a hadron rejection threshold are identified as photonlike ($N_{\gamma\text{-like}}$). For this analysis the pseudorapidity region of common coverage of the SPMD and PMD was selected ($2.9<\eta<3.75$). The acceptance in terms of transverse momentum (p_T) extends down to 30 MeV/c, although no explicit p_T selection is applied. Strict data selection and cleanup cuts have been applied as described in Refs. [11,14]. After cuts, a total of 85 K central events, corresponding to the top 5% of the minimum bias cross section as determined from the measured total transverse energy, have been analyzed. Average multiplicities of $\langle N_{\rm ch}\rangle=323.8$ and $\langle N_{\gamma\text{-like}}\rangle=335.7$ are obtained for this centrality selection.

The measured results are interpreted by comparison with simulated events and with several types of mixed events. Simulated events were generated using the VENUS 4.12 [15] event generator with default parameters. The output was processed through a WA98 detector simulation package in the GEANT 3.21 [16] framework. The centrality selection for the simulated data has been made in a manner identical to the experimental data by selection on the simulated total transverse energy in the WA98 acceptance ($3.2<\eta<5.4$). The simulated VENUS+GEANT events (referred as V+G) were then processed with the same analysis codes as used for the analysis of the experimental data. The photon counting efficiency and the purity of the γ-like sample were determined from these simulations to be 68% and 65%, respectively, for central events [14].

The effect of nonstatistical DCC-like charged-neutral fluctuations has been studied within the framework of a simple model in which the output of the VENUS event generator has been modified. To implement the DCC effect, the charges of the pions within a localized $\eta-\phi$ region from VENUS are interchanged pairwise ($\pi^+\pi^-\leftrightarrow\pi^0\pi^0$) according to the $P(f)=1/2\sqrt{f}$ probability distribution. The DCC-like fluctuations were generated over $\eta=3$–4 for varying intervals in $\Delta\phi$. Since the probability to produce events with DCC domains is unknown, ensembles of events, here referred to as ''nDCC events,'' were produced as a mixture of normal events with varying fractions of pure DCC-like events. The nDCC events were then tracked through GEANT.

In the search for evidence of nonstatistical charged-neutral fluctuations, two different analysis techniques have been applied. The first method employed in the present analysis is the technique of discrete wavelet transformations (DWT). DWT methods are now widely used in many applications, such as data compression and image processing, and have been shown to provide a powerful means to search for localized domains of DCC [17,18]. While there are several families of wavelet bases distinguished by the number of coefficients and the level of iteration, we have used the frequently employed $D-4$ wavelet basis [20]. The analysis has been performed with the sample function chosen to be the photon fraction, given by $f'(\phi)=N_{\gamma\text{-like}}(\phi)/(N_{\gamma\text{-like}}(\phi)+N_{\rm ch}(\phi))$ as a function of the azimuthal angle ϕ, with highest resolution scale $j_{max}=5$. The input to the DWT analysis is the spectrum of the sample function at the smallest bin size corresponding to the highest resolution scale, j_{max}, where the number of bins is $2^{j_{max}}$. The sample function is then analyzed at different scales j by being rebinned into 2^j bins. The DWT analysis yields a set of wavelets or father function coefficients (FFC) at each scale from $j=1$ to $(j_{max}-1)$. The coefficients obtained at a given scale, j, are derived from the distribution of the sample function at one higher scale, $j+1$. The FFCs quantify the deviation of the bin-to-bin fluctuations in the sample function at that higher scale relative to the average behavior. The presence of localized nonstatistical

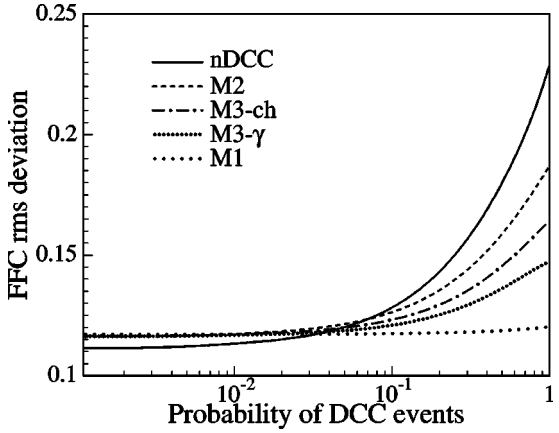

FIG. 1. The rms deviations of the FFC distributions at $j=1$ for simulated nDCC events with extent $\Delta\phi_{\mathrm{DCC}}=90°$ and for various mixed events constructed from those events, as a function of the fraction of DCC-like events present in the nDCC sample.

fluctuations will increase the root mean square (rms) deviation of the distribution of FFCs and may result in non-Gaussian tails [17,18].

The sensitivity of the DWT technique as used in this analysis is demonstrated in Fig. 1 where it has been applied to the simulated nDCC events. The rms deviation of the FFC distribution is shown as a function of the fraction of DCC-like events in the nDCC sample. The rms deviation is observed to increase strongly with increasing DCC-like fraction. Due to the inherent uncertainties in the description of ''normal'' physics and detector response in the V+G simulations, the observation of an experimental result with rms which differs from simulation with zero DCC fraction cannot be taken alone as evidence of DCC observation. For this reason four different types of mixed events have been created from the real or simulated events in order to search for nonstatistical fluctuations by removing various correlations in a controlled manner while preserving the characteristics of the measured distributions as accurately as possible. The first type of mixed events (M1) are generated by mixing hits in both the PMD and SPMD separately, with no two hits taken from the same event. Hits within a detector in the mixed events are not allowed to lie within the two track resolution of that detector. The second kind of mixed events (M2) are generated by mixing the unaltered PMD hits of one event with the unaltered SPMD hits of a different event. Intermediate between the M1 and M2 kinds of mixed events is the case where the hits within the PMD are unaltered while the SPMD hits are mixed (M3-γ), or the SPMD hits are unaltered while the PMD hits are mixed (M3-ch). In each type of mixed event the global (bin 1) $N_{\gamma\text{-like}}-N_{\mathrm{ch}}$ correlation is maintained as in the real event.

The rms deviations of the FFCs for the different kinds of mixed events produced from the nDCC events are also shown in Fig. 1. In the case of vanishing DCC-like fluctuations, the rms values of the various types of mixed events are very close to each other, and higher than the V+G rms values. This is due to the presence of additional correlations between N_{ch} and $N_{\gamma\text{-like}}$, mostly as a result of the charged particle contamination in the $N_{\gamma\text{-like}}$ sample. The rms deviations for the M1 events are found to be almost independent of probability of DCC-like events, while the rms deviations of the M2 events increase similarly, but more weakly, than those of the nDCC events. The rms deviations for the M3 sets of events are found to lie between M2 and M1. Thus, the sequence of the mixed events relative to the simulated events (or data) gives a model independent indication of the presence and source of nonstatistical fluctuations. The simple DCC model used here results in an anticorrelation between $N_{\gamma\text{-like}}$ and N_{ch}. It also results in nonstatistical fluctuations in both $N_{\gamma\text{-like}}$ and N_{ch}. It is seen that the M2 events have only the $N_{\gamma\text{-like}}$-N_{ch} anticorrelation removed while the M1 events have all nonstatistical fluctuations and correlations removed. The M3 mixed events give intermediate results because they contain only the $N_{\gamma\text{-like}}$ (M3-γ) or N_{ch} (M3-ch) nonstatistical fluctuations.

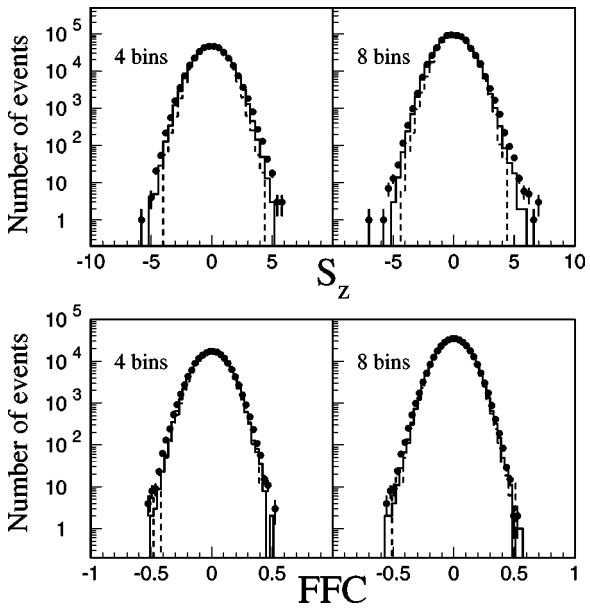

FIG. 2. The S_Z and FFC distributions for four and eight divisions in ϕ. The experimental data, M1, and V+G events are shown by solid circles, solid and dashed histograms, respectively. The number of data and mixed events is the same. The distribution for the V+G events is normalized to the data.

The FFC distributions extracted from the measured $f'(\phi)$ ratio are shown in the bottom panel of Fig. 2 for the experimental data, for M1 events (from data), and for V+G events. The results are shown for scales $j=1$ and 2, which carry information about fluctuations at 90° and 45° in ϕ. The FFC distributions of the experimental distributions are seen to be broader than the V+G and M1 results. This suggests the presence of nonstatistical fluctuations.

A more conventional method similar to that described in Ref. [11] has also been used to search for nonstatistical fluctuations. The correlation between $N_{\gamma\text{-like}}$ and N_{ch} has been studied in varying ϕ intervals, by dividing the entire ϕ space into two, four, eight, and 16 bins. The correlation plot of N_{ch} versus $N_{\gamma\text{-like}}$ [19] is obtained for each ϕ segmentation, and fitted to a second order polynomial to obtain a correlation axis (Z). The distance of separation (D_Z) between the data points and the Z axis has been calculated with the convention

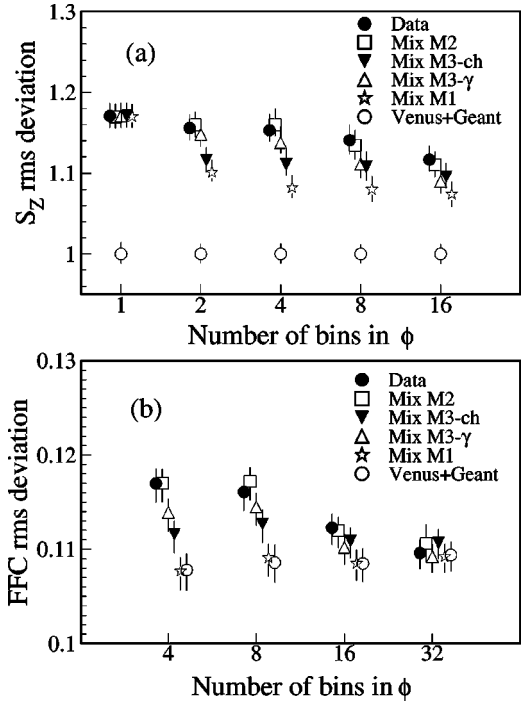

FIG. 3. The rms deviations of the S_Z and FFC distributions for various divisions in the azimuthal angle. For V+G $s(D_Z)=17.2$, 11.8, 8.12, 5.66, and 4.01 for one to 16 bins, respectively.

that D_Z is positive for points below the Z axis (increasing $N_{\gamma\text{-like}}$). In order to compare fluctuations at different bin sizes having different multiplicities we use a scaled variable, $S_Z=D_Z/s(D_Z)$, where $s(D_Z)$ is the rms deviation of the D_Z distributions for V+G events. The presence of events with localized nonstatistical fluctuations would be expected to result in a broader distribution of S_Z compared to those for normal events. The S_Z distributions calculated at four and eight bins in ϕ angle are shown in the top panel of Fig. 2 for data, M1, and V+G events. The experimental distributions are broader than the simulation and M1 results, again indicating the presence of additional fluctuations.

The rms deviations of the S_Z and FFC distributions as a function of the number of bins in azimuth is shown for experimental data, mixed events, and V+G in Fig. 3. As noted in the discussion of Fig. 1, even in the absence of DCCs there exist uninteresting correlations between $N_{\gamma\text{-like}}$ and N_{ch} which are removed by the event mixing procedure and thereby result in a difference between the real and mixed events. The mixed event rms values of Fig. 3 have therefore been rescaled by the percentage difference between the rms deviations of the V+G distributions and those of the corresponding V+G mixed events in order to better illustrate effects in the data beyond those present in V+G. The statistical errors on the values are small and lie within the size of the symbols. The error bars include both statistical and systematic errors. The systematic errors have been estimated by investigation of effects such as the uncertainties in the detection efficiencies, gain fluctuations, backgrounds, binning variations, and fitting procedures. The total systematic error was obtained as the sum in quadrature of the individual error contributions which have been determined from the variation of the final result according to the maximum estimated uncertainty for each effect.

Since the mixed events are constructed to maintain the $N_{\gamma\text{-like}}-N_{\text{ch}}$ correlations for the full azimuth (bin 1), the rms deviations of data and mixed events for this bin are identical. The difference of the S_Z rms deviations between data and V+G for this bin is the same as reported in an earlier WA98 publication [11]. The comparison of V+G and the M1 mixed events demonstrates the utility of the DWT method to normalize out the average behavior when the bin-to-bin fluctuation information is extracted. For two, four, and eight bins the values of the S_Z rms deviations of the data are 2.5σ, 3.0σ, and 2.4σ larger than those of M1 events, respectively, where $\sigma=\sqrt{(\sigma^{data}_{lower})^2+(\sigma^{\text{M1}}_{upper})^2}$ is the sum in quadrature of the total error separating the points. Similarly, the FFC rms deviations at four and eight bins for data are 3.7σ and 2.8σ larger than those of the M1 events. At 16 and 32 bins, the result for mixed events and data agree within the quoted errors. The rms deviations of the M2 events agree with those of the experimental data within error for all bins. The M3-type mixed events are found to be similar to each other within the quoted errors and lie between M1 and M2.

The observation that the rms deviations of the S_Z and FFC distributions for experimental data are larger than those of the M1 events provides model-independent evidence for the presence of localized nonstatistical fluctuations. However, the comparision of the rms deviations for data with those of M2 events implies the absence of event-by-event correlated fluctuations in $N_{\gamma\text{-like}}$ versus N_{ch}. The M3-type mixed events indicate the presence of localized independent fluctuations in $N_{\gamma\text{-like}}$ and N_{ch} of similar magnitude.

If the amount of DCC-like fluctuations in the experimental data were large, then the rms deviations shown in Fig. 3 for data would have been larger compared to those of M2 events. Since this is not the case, we compare the measured results with those obtained from the simulation as shown in Fig. 1 to extract upper limits on the probability of DCC-like fluctuations at the 90% confidence level. Within the context of this simple DCC model, upper limits on the presence of localized nonstatistical DCC-like fluctuations of 10^{-2} for $\Delta\phi$ between 45–90° and 3×10^{-3} for $\Delta\phi$ between 90–135° are extracted.

In summary, a detailed event-by-event analysis of the fluctuations in the $\eta-\phi$ phase space distributions of charged particles and photons has been performed for central Pb+Pb collisions at 158*A* GeV using two complementary analysis methods. The first analysis employed the discrete wavelet transformation technique to investigate the relative magnitude of the $N_{\gamma\text{-like}}/(N_{\text{ch}}+N_{\gamma\text{-like}})$ fluctuations in adjacent ϕ intervals of varying size. The second method studied the magnitude of the $N_{\gamma\text{-like}}$ versus N_{ch} multiplicity fluctuations in decreasing ϕ regions. Both analysis methods provide model-independent evidence for nonstatistical fluctuations at the 3σ level for ϕ intervals of greater than 45°. This is shown to be due to nonstatistical fluctuations in both $N_{\gamma\text{-like}}$ and N_{ch}. However, no significant correlated fluctuations in

$N_{\gamma\text{-like}}$ versus N_{ch} were observed, contrary to naive expectations for a DCC effect. The result is not explained by VENUS+GEANT simulations or by a simple model of DCC-like fluctuations. The interpretation of the result remains an open question.

We wish to express our gratitude to the CERN accelerator division for the excellent performance of the SPS accelerator complex. We acknowledge with appreciation the effort of all engineers, technicians, and support staff who have participated in the construction of this experiment. This work was supported jointly by the German BMBF and DFG, the U.S. DOE, the Swedish NFR and FRN, the Dutch Stichting FOM, the Polish KBN under Contract No. 621/E-78/SPUB/CERN/P-03/DZ211, the Grant Agency of the Czech Republic under Contract No. 202/95/0217, the DAE, DST, CSIR, and UGC of the Government of India, the Indo-FRG Exchange Program, the PPE division of CERN, the Swiss National Fund, the INTAS under Contract No. INTAS-97-0158, ORISE, the University of Tsukuba Special Research Projects, and the JSPS. ORNL is managed by UT-Battelle, LLC, for the U.S. Department of Energy under Contract No. DE-AC05-00OR22725. The MIT group has been supported by the U.S. Department of Energy under Cooperative Agreement No. DE-FC02-94ER40818.

[1] *Proceedings of Quark Matter '99* [Nucl. Phys. **A661** (1999)].
[2] M. Stephanov *et al.*, Phys. Rev. Lett. **81**, 4816 (1998).
[3] M. Asakawa, U. Heinz, and B. Müller, Phys. Rev. Lett. **85**, 2072 (2000); S. Jeon and V. Koch, *ibid.* **85**, 2076 (2000).
[4] S. Pratt, Phys. Lett. B **301**, 159 (1993).
[5] A. A. Anselm and M. G. Ryskin, Phys. Lett. B **266**, 482 (1991).
[6] J. D. Bjorken, Int. J. Mod. Phys. A **7**, 4189 (1992).
[7] J.-P. Blaizot and A. Krzywicki, Phys. Rev. D **46**, 246 (1992).
[8] K. Rajagopal and F. Wilczek, Nucl. Phys. **B399**, 395 (1993); **B404**, 577 (1993). S. Gavin *et al.*, Phys. Rev. Lett. **72**, 2143 (1994).
[9] JACEE Collaboration, C. M. G. Lattes *et al.*, Phys. Rep. **65**, 151 (1980).
[10] Minimax Collaboration, T. C. Brooks *et al.*, Phys. Rev. D **61**, 032003 (2000).
[11] WA98 Collaboration, M. M. Aggarwal *et al.*, Phys. Lett. B **420**, 169 (1998).
[12] NA49 Collaboration, H. Appelshauser *et al.*, Phys. Lett. B **459**, 679 (1999).
[13] M. M. Aggarwal *et al.*, Nucl. Instrum. Methods Phys. Res. A **424**, 395 (1999).
[14] WA98 Collaboration, M. M. Aggarwal *et al.*, Phys. Lett. B **458**, 422 (1999).
[15] K. Werner, Phys. Rep. **232**, 87 (1993).
[16] R. Brun *et al.*, GEANT3 guide, CERN/DD/EE/84-1, 1984.
[17] Z. Huang *et al.*, Phys. Rev. D **54**, 750 (1996).
[18] B. K. Nandi *et al.*, Phys. Lett. B **461**, 142 (1999).
[19] WA98 Collaboration, B. Mohanty *et al.*, Czech. J. Phys. **50**, 126 (2000).
[20] *Numerical Recipes* (Cambridge University Press, Cambridge, 1998).

Three-Pion Interferometry Results from Central Pb + Pb Collisions at 158A GeV/c

M. M. Aggarwal,[1] A. Agnihotri,[2] Z. Ahammed,[3] A. L. S. Angelis,[4] V. Antonenko,[5] V. Arefiev,[6] V. Astakhov,[6] V. Avdeitchikov,[6] T. C. Awes,[7] P. V. K. S. Baba,[8] S. K. Badyal,[8] C. Barlag,[9] S. Bathe,[9] B. Batiounia,[6] T. Bernier,[10] K. B. Bhalla,[2] V. S. Bhatia,[1] C. Blume,[9] R. Bock,[11] E.-M. Bohne,[9] Z. Böröcz,[9] D. Bucher,[9] A. Buijs,[12] H. Büsching,[9] L. Carlen,[13] V. Chalyshev,[6] S. Chattopadhyay,[3] R. Cherbatchev,[5] T. Chujo,[14] A. Claussen,[9] A. C. Das,[3] M. P. Decowski,[18] H. Delagrange,[10] V. Djordjadze,[6] P. Donni,[4] I. Doubovik,[5] S. Dutt,[8] M. R. Dutta Majumdar,[3] K. El Chenawi,[13] S. Eliseev,[15] K. Enosawa,[14] P. Foka,[4] S. Fokin,[5] M. S. Ganti,[3] S. Garpman,[13] O. Gavrishchuk,[6] F. J. M. Geurts,[12] T. K. Ghosh,[16] R. Glasow,[9] S. K. Gupta,[2] B. Guskov,[6] H. Å. Gustafsson,[13] H. H. Gutbrod,[10] R. Higuchi,[14] I. Hrivnacova,[15] M. Ippolitov,[5] H. Kalechofsky,[4] R. Kamermans,[12] K.-H. Kampert,[9] K. Karadjev,[5] K. Karpio,[17] S. Kato,[14] S. Kees,[9] C. Klein-Bösing,[9] S. Knoche,[9] B. W. Kolb,[11] I. Kosarev,[6] I. Koutcheryaev,[5] T. Krümpel,[9] A. Kugler,[15] P. Kulinich,[18] M. Kurata,[14] K. Kurita,[14] N. Kuzmin,[6] I. Langbein,[11] A. Lebedev,[5] Y. Y. Lee,[11] H. Löhner,[16] L. Luquin,[10] D. P. Mahapatra,[19] V. Manko,[5] M. Martin,[4] G. Martínez,[10] A. Maximov,[6] G. Mgebrichvili,[5] Y. Miake,[14] Md. F. Mir,[8] G. C. Mishra,[19] Y. Miyamoto,[14] B. Mohanty,[19] M.-J. Mora,[10] D. Morrison,[20] D. S. Mukhopadhyay,[3] H. Naef,[4] B. K. Nandi,[19] S. K. Nayak,[10] T. K. Nayak,[3] S. Neumaier,[11] A. Nianine,[5] V. Nikitine,[6] S. Nikolaev,[5] P. Nilsson,[13] S. Nishimura,[14] P. Nomokonov,[6] J. Nystrand,[13] F. E. Obenshain,[20] A. Oskarsson,[13] I. Otterlund,[13] M. Pachr,[15] S. Pavliouk,[6] T. Peitzmann,[9] V. Petracek,[15] W. Pinganaud,[10] F. Plasil,[7] U. von Poblotzki,[9] M. L. Purschke,[11] J. Rak,[15] R. Raniwala,[2] S. Raniwala,[2] V. S. Ramamurthy,[19] N. K. Rao,[8] F. Retiere,[10] K. Reygers,[9] G. Roland,[18] L. Rosselet,[4] I. Roufanov,[6] C. Roy,[10] J. M. Rubio,[4] H. Sako,[14] S. S. Sambyal,[8] R. Santo,[9] S. Sato,[14] H. Schlagheck,[9] H.-R. Schmidt,[11] Y. Schutz,[10] G. Shabratova,[6] T. H. Shah,[8] I. Sibiriak,[5] T. Siemiarczuk,[17] D. Silvermyr,[13] B. C. Sinha,[3] N. Slavine,[6] K. Söderström,[13] N. Solomey,[4] S. P. Sørensen,[7,20] P. Stankus,[7] G. Stefanek,[17] P. Steinberg,[18] E. Stenlund,[13] D. Stüken,[9] M. Sumbera,[15] T. Svensson,[13] M. D. Trivedi,[3] A. Tsvetkov,[5] L. Tykarski,[17] J. Urbahn,[11] E. C. v. d. Pijll,[12] N. v. Eijndhoven,[12] G. J. v. Nieuwenhuizen,[18] A. Vinogradov,[5] Y. P. Viyogi,[3] A. Vodopianov,[6] S. Vörös,[4] B. Wysłouch,[18] K. Yagi,[14] Y. Yokota,[14] and G. R. Young[7]

(WA98 Collaboration)

[1]*University of Panjab, Chandigarh 160014, India*
[2]*University of Rajasthan, Jaipur 302004, Rajasthan, India*
[3]*Variable Energy Cyclotron Centre, Calcutta 700 064, India*
[4]*University of Geneva, CH-1211 Geneva 4, Switzerland*
[5]*RRC Kurchatov Institute, RU-123182 Moscow, Russia*
[6]*Joint Institute for Nuclear Research, RU-141980 Dubna, Russia*
[7]*Oak Ridge National Laboratory, Oak Ridge, Tennessee 37831-6372*
[8]*University of Jammu, Jammu 180001, India*
[9]*University of Münster, D-48149 Münster, Germany*
[10]*SUBATECH, Ecole des Mines, Nantes, France*
[11]*Gesellschaft für Schwerionenforschung (GSI), D-64220 Darmstadt, Germany*
[12]*Universiteit Utrecht/NIKHEF, NL-3508 TA Utrecht, The Netherlands*
[13]*Lund University, SE-221 00 Lund, Sweden*
[14]*University of Tsukuba, Ibaraki 305, Japan*
[15]*Nuclear Physics Institute, CZ-250 68 Rez, Czech Republic*
[16]*KVI, University of Groningen, NL-9747 AA Groningen, The Netherlands*
[17]*Institute for Nuclear Studies, 00-681 Warsaw, Poland*
[18]*MIT, Cambridge, Massachusetts 02139*
[19]*Institute of Physics, 751-005 Bhubaneswar, India*
[20]*University of Tennessee, Knoxville, Tennessee 37966*
(Received 10 April 2000)

Three-particle correlations have been measured for identified π^- from central 158A GeV Pb + Pb collisions by the WA98 experiment at CERN. A substantial contribution of the genuine three-body correlation has been found as expected for a mainly chaotic and symmetric source.

PACS numbers: 25.75.Gz

 © 2000 The American Physical Society

In nuclear and particle physics, the study of Bose-Einstein correlations between identical particles is widely used. It is an essential tool to obtain information on the size and time evolution of expanding systems created in heavy ion collisions [1]. In particular, two-particle Bose-Einstein interferometry has been used for a sophisticated analysis of the dynamical evolution of the freeze-out volume via selection on the transverse momentum and rapidity of the correlated particles.

Three-particle interferometry measurements can provide additional information on the space-time emission which is not accessible by two-particle interferometry [2–5]. In particular, if the emission is fully chaotic, the three-particle interference study gives access to the phase of the source function's Fourier transform, which is affected by the emission asymmetry. These asymmetries may be induced by source geometry, flow, or resonance decays. If the source is not completely chaotic, as is likely to be the case, the interpretation is more difficult. Nevertheless, a comparison of the three-particle to the two-particle result allows one to extract the relative strength of the true three-body correlation and can in principle remove obscuring effects, such as background from misidentified tracks or long-lived decay products, and therefore provide information more directly about the degree of coherence of the emission source [4]. In this Letter we present first results from three-particle interferometry in central ^{208}Pb + ^{208}Pb collisions at the CERN SPS.

The fixed target experiment WA98 [6] combined large acceptance photon detectors with a two arm charged particle tracking spectrometer. The incident 158A GeV Pb beam impinged on a Pb target near the entrance of a large dipole magnet. The results presented here have been obtained from an analysis of the 1995 data set. These data were taken with the most central triggers corresponding to about 10% of the minimum bias cross section of 6190 mb. The π^- measurements were obtained with data from the negative particle tracking arm of the spectrometer. This tracking arm consisted of six multistep avalanche chambers with optical readout [7]. A time of flight detector with a time resolution better than 120 ps allowed for particle identification. The rapidity acceptance ranged from $y = 2.1$ to 3.1 with an average at 2.7, close to midrapidity which was 2.9. The momentum resolution of the spectrometer was $\Delta p/p = 0.005$ at $p = 1.5$ GeV/c. Severe track quality cuts were applied, resulting in a final sample of 4.2×10^6 π^-, providing 7.2×10^6 pairs and 8.2×10^6 triplets. The $\pi^-\pi^-$ correlation analysis has been reported elsewhere [8].

The most common use of hadron interferometry concerns the study of pairs of identical particles. The two-particle correlation function can be defined as

$$C_2(\mathbf{p}_1, \mathbf{p}_2) = \frac{d^2N(\mathbf{p}_1, \mathbf{p}_2)/d\mathbf{p}_1 d\mathbf{p}_2}{dN(\mathbf{p}_1)/d\mathbf{p}_1 \cdot dN(\mathbf{p}_2)/d\mathbf{p}_2},$$

where $\mathbf{p}_1$ and $\mathbf{p}_2$ are the three-momenta of the correlated particles. The product of single particle distributions in the denominator is usually obtained experimentally by a mixed event technique, whereas the pair distribution in the numerator is constructed from all pair combinations of identical particles found in each event. C_2 is normalized to unity far away from the interference region. In the plane wave approximation for chaotic sources of identical particles C_2 can be written as [9]

$$C_2(\mathbf{p}_1, \mathbf{p}_2) = 1 \pm |F_{12}|^2 \tag{1}$$

with the + (−) sign for bosons (fermions). F_{12} is the Fourier transform of the space-time source function $S(x, k_{12})$

$$|F_{12}|^2 = \frac{|\int d^4x\, S(x, k_{12}) \exp[iq_{12}x]|^2}{|\int d^4x\, S(x, k_{12})|^2} \tag{2}$$

with $q_{12} = p_1 - p_2$, the four-momentum difference of the two particles, and $k_{12} = (p_1 + p_2)/2$. F_{12} is unity as $q_{12} \to 0$. Thus the production of identical bosons is enhanced for pairs created close together in phase space with a small momentum difference $Q_{12} \equiv \sqrt{-q_{12}^2}$.

Typically $\pi\pi$ correlation data are fit with a Gaussian form for $|F_{12}|^2$,

$$C_2 = 1 + \lambda \exp[-Q_{12}^2 R^2], \tag{3}$$

or an exponential form,

$$C_2 = 1 + \lambda \exp[-2Q_{12}R], \tag{4}$$

where the parameter λ is inserted to take into account the possibility that the source may not be fully chaotic and also that any wrongly reconstructed tracks, or tracks coming from decays of long-lived resonances, will dilute the correlations in the data.

The measurement of C_2 gives access to the radius R of the source, but not to the phase ϕ_{12} contained in $F_{12} \equiv |F_{12}| \exp[i\phi_{12}]$ since C_2 is only a function of the square of the Fourier transform of the source distribution S. By contrast, the three-boson interference produced by a fully chaotic source is sensitive to the phase information of the Fourier transform of the source emission function. Indeed, for a chaotic source the three-body correlation function C_3, which is

$$C_3(\mathbf{p}_1, \mathbf{p}_2, \mathbf{p}_3) = \frac{d^3N(\mathbf{p}_1, \mathbf{p}_2, \mathbf{p}_3)/d\mathbf{p}_1 d\mathbf{p}_2 d\mathbf{p}_3}{dN(\mathbf{p}_1)/d\mathbf{p}_1 \cdot dN(\mathbf{p}_2)/d\mathbf{p}_2 \cdot dN(\mathbf{p}_3)/d\mathbf{p}_3},$$

can be written [2–5] as

$$C_3 = 1 + |F_{12}|^2 + |F_{23}|^2 + |F_{31}|^2 + 2\,\mathrm{Re}\{F_{12}F_{23}F_{31}\}, \tag{5}$$

where F_{ij} is the Fourier transform for the pair ij contained in the triplet 123. The genuine three-body correlation in C_3 is the term $2\,\mathrm{Re}\{F_{12}F_{23}F_{31}\}$.

With $F_{ij} \equiv |F_{ij}| \exp[i\phi_{ij}]$ and $W \equiv \cos(\phi_{12} + \phi_{23} + \phi_{31})$ one may rewrite

$$2\,\mathrm{Re}\{F_{12}F_{23}F_{31}\} = 2|F_{12}|\,|F_{23}|\,|F_{31}|W\,. \qquad (6)$$

Having determined $|F_{ij}|$ from the pair correlation function C_2, the measurement of C_3 gives direct access to W, the cosine of the sum of the three phases of the Fourier transforms, and hence provides complementary information on the shape of the source. Indeed, W is related to the odd space-time moments of the source which generate the phases ϕ_{ij} [4]. For example, if the source is fully chaotic and symmetric, F_{ij} are real, $\phi_{12} = \phi_{23} = \phi_{31} = 0$, and W is equal to 1. C_3 is then fully determined by C_2, and the genuine three-particle correlation is maximum. If the source is not fully chaotic, more complicated expressions should be used, mixing the effects of fully chaotic and coherent sources [4]. Nevertheless, Eq. (6) is valid in general with W interpreted as a factor expressing the relative strength of the true three-body correlation compared to that expected for a fully symmetric chaotic source. Consequently, measuring W values less than 1 does not allow one to differentiate between asymmetries or coherence in the source.

Assuming a Gaussian form of the source function, which for two bosons leads to a correlation function described by Eq. (3), one obtains

$$C_3 = 1 + \lambda \sum_{ij=12,23,31} \exp[-Q_{ij}^2 R^2] + 2\lambda^{3/2} \exp[-Q_3^2 R^2/2]W \qquad (7)$$

with $Q_3^2 \equiv Q_{12}^2 + Q_{23}^2 + Q_{31}^2$. If the exponential form of the Fourier transform is assumed instead [Eq. (4)], one obtains

$$C_3 = 1 + \lambda \sum_{ij=12,23,31} \exp[-2Q_{ij}R] + 2\lambda^{3/2} \exp[-(Q_{12} + Q_{23} + Q_{31})R]W\,. \qquad (8)$$

Inserting the values of λ and R obtained from the two-particle analysis into Eqs. (7) or (8), one can extract the three-particle strength information W.

The one-dimensional correlation function C_2, analyzed in terms of Q_{12}, is shown in Fig. 1. The two-track resolution of the spectrometer (2 cm) is dealt with by application of a proximity cut to each track pair. The data are corrected for the Coulomb and strong final state interactions in an iterative way [10], taking into account the source size obtained in the fit. The Gamow correction was abandoned as we found that it overcorrects the data for Q_{12} in the range of 0.1 to 0.3 GeV/c.

The effect of the experimental resolution, which is estimated by a full Monte Carlo, can be approximated in the interference region by a Gaussian of constant σ of 7 MeV/c both for Q_{12} and Q_3. It is taken into account

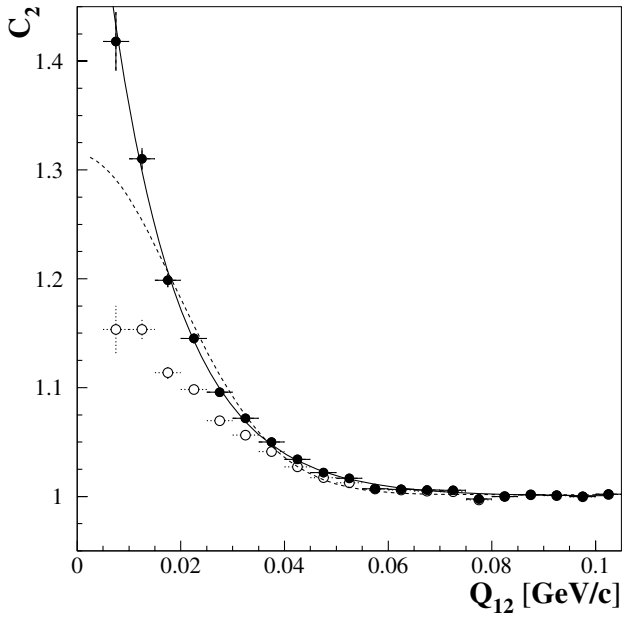

FIG. 1. The measured $\pi^-\pi^-$ correlation function C_2 (full symbols) fit with an exponential (solid curve) or Gaussian form (dashed curve) corrected for resolution. The empty symbols show the data before Coulomb and resolution corrections. Only statistical errors are shown.

by replacing the function $C_2(Q_{12})$ used to fit the noncorrected data by

$$C_2^{rc}(Q_{12}) = \int r(Q_{12}, Q'_{12}) C_2(Q'_{12})\, dQ'_{12}\,,$$

which is the convolution of $C_2(Q_{12})$ with the resolution function $r(Q_{12}, Q'_{12})$ of the spectrometer. For display purposes, Fig. 1 is obtained by multiplying each data point by $C_2^{rc}(Q_{12})/C_2(Q_{12})$. Fitting the corrected data with C_2 gives the same results as fitting the noncorrected data with C_2^{rc}. The correlation function C_2 is seen to be non-Gaussian. Instead, it is better represented by an exponential form [8]. For the C_3 analysis, an accurate description of the shape of C_2 is essential since the estimate of the W factor extracted from C_3 depends on it. The exponential fit [Eq. (4)] yielding $R = 7.29 \pm 0.11$ fm and $\lambda = 0.753 \pm 0.013$ is shown in Fig. 1.

Figure 2 shows the three-pion correlation as a function of Q_3, after correction for resolution. A very strong $\pi^-\pi^-\pi^-$ correlation is observed, which is robust under all tracking criteria. The result shown is obtained for the same sample and the same cuts applied on the three pair combinations contained in each triplet as used for the two-pion interference analysis. For the C_3 result, the Coulomb correction applied to a particular triplet is the product of the Coulomb corrections used for the three pair combinations contained in that triplet. The resolution is taken into account using the same procedure as in the two-pion analysis. The resolution has a tiny effect compared to the Coulomb correction, and it has been checked that the results are not affected by the order in which these corrections are applied to the data. The dashed line is a fit to a double exponential

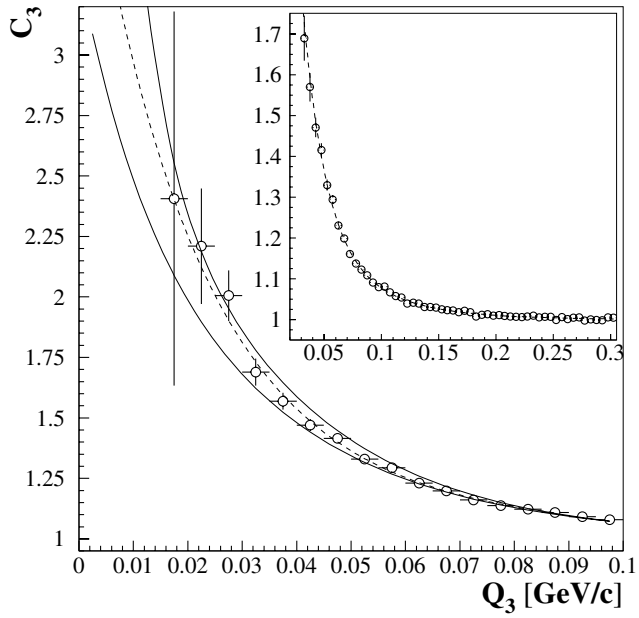

FIG. 2. The three-pion correlation function C_3 as a function of Q_3 with a fit to a double exponential form (dashed line—see text). The result is also compared to an estimate of C_3 with $W = 1$ (upper solid line) and $W = 0$ (lower solid line). The inset shows C_3 over a larger Q_3 range.

function

$$C_3 = 1 + \lambda_1 \exp[-2Q_3R_1] + \lambda_2 \exp[-2Q_3R_2] \quad (9)$$

with fitted parameters $R_1 = 5.01 \pm 0.38$ fm, $\lambda_1 = 2.79 \pm 0.32$, $R_2 = 1.72 \pm 0.12$ fm, $\lambda_2 = 0.343 \pm 0.072$, and a χ^2 per degree of freedom of 0.88. The three-pion correlation data cannot be well fitted by a Gaussian or a single exponential as a function of Q_3. Such non-Gaussian behavior has been predicted by a final-state rescattering model [11].

In Fig. 2, the three-pion correlation data are compared to an estimate using Eq. (8) with $W = 1$ (upper line) and $W = 0$ (lower line). This estimate is made using triplets from mixed events with the λ and R parameters extracted from the two-pion interferometry analysis. Although the calculated contribution to C_3 from the genuine three-pion correlation is rather small and becomes insignificant for $Q_3 > 60$–80 MeV/c, the experimental results clearly indicate a W factor which lies between 0 and 1.

As proposed in Refs. [4,12], a method to extract the experimental value of W as a function of Q_3 is to invert Eqs. (5) and (6) and rewrite $|F_{ij}|$ in terms of C_2 using Eq. (1) to obtain

$$W = \frac{\{C_3(Q_3) - 1\} - \{C_2(Q_{12}) - 1\} - \{C_2(Q_{23}) - 1\} - \{C_2(Q_{31}) - 1\}}{2\sqrt{\{C_2(Q_{12}) - 1\}\{C_2(Q_{23}) - 1\}\{C_2(Q_{31}) - 1\}}}. \quad (10)$$

In this method, the analysis must be performed in two steps. First, the λ and R parameters are determined for both the two-pion and the three-pion correlations with a fit to the data of Eqs. (4) and (9) as previously explained. Then the data are analyzed again, and, for each triplet found, characterized by the value Q_3, W is determined using Eqs. (4), (9), and (10) with the values Q_{12}, Q_{23}, and Q_{31} corresponding to the three pair combinations contained in the triplet.

For each bin in Q_3 containing N triplets, the statistical error on the mean value $\langle W \rangle$ is $\sigma/\sqrt{N}$, where σ^2 is the variance of the W distribution in this particular bin. The estimate of systematic errors is done by varying the different analysis cuts in the two- and three-pion interference studies. It includes, in particular, the cuts used to identify the pions with the time of flight system. The systematic error on the Coulomb correction due to the error on the determination of the R parameter in the two-pion fit, as well as a possible 10% systematic error on the evaluation of the Q_{12} and Q_3 resolution, is also taken into account. The effects on W of the statistical errors in the determination of C_2 and C_3 are treated as systematic errors by changing C_2 and C_3, respectively, by $\pm\sigma_{C_2}$ and $\pm\sigma_{C_3}$. All of these variations are then added in quadrature.

Figure 3 shows the W values obtained for five bins of 10 MeV/c in Q_3. The error bars are the sum of statistical and systematic errors. The statistical errors (not shown separately in Fig. 3) are nearly negligible. The slight Q_3

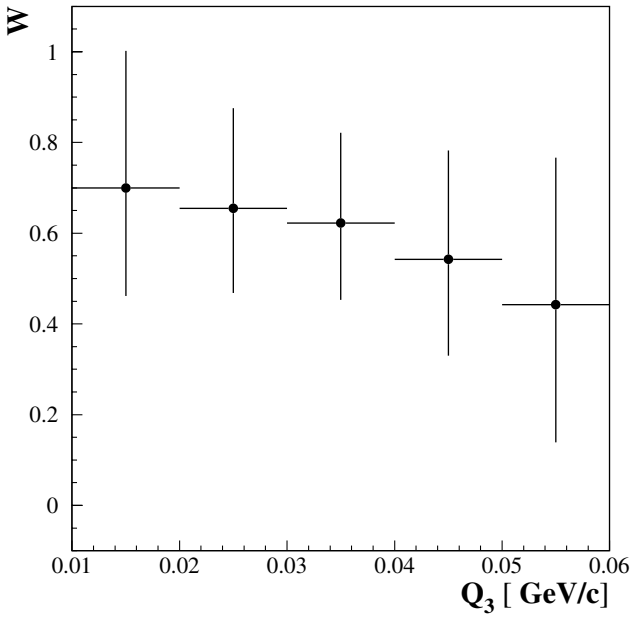

FIG. 3. The factor W as a function of Q_3. The error bars include statistical and systematic errors. The statistical errors alone (not shown) are contained within the size of the symbols except for the first bin where it amounts to twice the size of the symbol. The horizontal bars indicate the bin width.

dependence observed is not significant in view of the errors. The genuine three-body correlation is substantial with a weighted mean $\langle W \rangle = 0.606 \pm 0.005 \pm 0.179$ for $Q_3 < 60$ MeV/c. (The weighted systematic error is obtained by calculating the weighted average over the five Q_3 bins separately for each kind of systematic error. These errors are then added in quadrature. On the contrary, adding quadratically the systematic errors of the five Q_3 bins as done for weighted statistical errors, or as done in [12], would give ± 0.097 instead of ± 0.179 for the systematic uncertainty.) This result should be compared to the lower $\pi^+\pi^+\pi^+$ result of $\langle W \rangle = 0.20 \pm 0.02 \pm 0.19$ observed by the NA44 Collaboration [12] in S + Pb minimum bias collisions at 200 GeV per nucleon.

In conclusion, we have studied the $\pi^-\pi^-\pi^-$ interference of pions produced in central Pb + Pb collisions at 158 GeV per nucleon. Although its contribution is small, the genuine three-pion correlation, the portion of the correlation not trivially due to the two-pion interference, has been extracted and found to be substantial. The genuine three-pion correlation is greater than reported for S + Pb minimum bias collisions [12], but not as large as expected for a fully chaotic and symmetric source.

We thank the CERN-SPS accelerator crew for providing an excellent Pb beam. This work was supported jointly by the German BMBF and DFG, the U.S. DOE, the Swedish NFR, the Dutch Stichting FOM, the Swiss National Fund, the Humboldt Foundation, the Stiftung für deutsch-polnische Zusammenarbeit, the Department of Atomic Energy, the Department of Science and Technology and the University Grants Commission of the Government of India, the Indo-FRG Exchange Programme, the PPE division of CERN, the INTAS under Contract No. INTAS-97-0158, the Polish KBN under Grant No. 2P03B16815, the Grant-in-Aid for Scientific Research (Specially Promoted Research & International Scientific Research) of the Ministry of Education, Science, Sports and Culture, JSPS Research Fellowships for Young Scientists, the University of Tsukuba Special Research Projects, and ORISE. ORNL is managed by UT-Battelle, LLC, for the U.S. Department of Energy under Contract No. DE-AC05-00OR22725.

[1] U. A. Wiedemann and U. Heinz, Phys. Rep. **319**, 145 (1999), and references therein.
[2] I. V. Andreev, M. Plümer, and R. M. Weiner, Int. J. Mod. Phys. A **8**, 4577 (1993).
[3] B. Lörstad, Int. J. Mod. Phys. A **4**, 2861 (1989).
[4] U. Heinz and Q. H. Zhang, Phys. Rev. C **56**, 426 (1997).
[5] H. Heiselberg and A. P. Vischer, Phys. Rev. C **55**, 874 (1997).
[6] WA98 Collaboration, Proposal for a large acceptance hadron and photon spectrometer, 1991; Report No. CERN/SPSLC 91-17, SPSLC/P260.
[7] J. M. Rubio *et al.,* Nucl. Instrum. Methods Phys. Res., Sect. A **367**, 358 (1995); A. L. S. Angelis *et al.,* Nucl. Phys. **A566**, 605c (1994); M. Iżycki *et al.,* Nucl. Instrum. Methods Phys. Res., Sect. A **310**, 98 (1991).
[8] M. M. Aggarwal *et al.,* Eur. Phys. J. C **16**, 445 (2000); S. Vörös *et al.,* Nucl. Phys. **A661**, 427c (1999).
[9] G. F. Bertsch, P. Danielewicz, and M. Herrmann, Phys. Rev. C **49**, 442 (1994); E. Shuryak, Phys. Lett. **44B**, 387 (1973); Sov. J. Nucl. Phys. **18**, 667 (1974); S. Pratt, T. Csörgő, and J. Zimányi, Phys. Rev. C **42**, 2646 (1990); S. Chapman and U. Heinz, Phys. Lett. B **340**, 250 (1994).
[10] S. Pratt *et al.,* Phys. Rev. C **42**, 2646 (1990); these calculations were made with a FORTRAN program supplied by S. Pratt.
[11] T. J. Humanic, Phys. Rev. C **60**, 014901 (1999).
[12] H. Bøggild *et al.,* Phys. Lett. B **455**, 77 (1999).

Eur. Phys. J. C 18, 651–663 (2001)
Digital Object Identifier (DOI) 10.1007/s100520100578

THE EUROPEAN PHYSICAL JOURNAL C

© Società Italiana di Fisica
Springer-Verlag 2001

Scaling of particle and transverse energy production in ^{208}Pb+^{208}Pb collisions at 158·A GeV

The WA98 Collaboration

M.M. Aggarwal[1], A. Agnihotri[2], Z. Ahammed[3], A.L.S. Angelis[4], V. Antonenko[5], V. Arefiev[6], V. Astakhov[6], V. Avdeitchikov[6], T.C. Awes[7], P.V.K.S. Baba[8], S.K. Badyal[8], A. Baldine[6], L. Barabach[6], C. Barlag[9], S. Bathe[9], B. Batiounia[6], T. Bernier[10], K.B. Bhalla[2], V.S. Bhatia[1], C. Blume[9], E.-M. Bohne[9], Z.K. Böröcz[9], D. Bucher[9], A. Buijs[12], H. Büsching[9], L. Carlen[13], V. Chalyshev[6], S. Chattopadhyay[3], R. Cherbatchev[5], T. Chujo[14], A. Claussen[9], A.C. Das[3], M.P. Decowski,[18], H. Delagrange[10], V. Djordjadze[6], P. Donni[4], I. Doubovik[5], S. Dutt[8], M.R. Dutta Majumdar[3], K. El Chenawi[13], S. Eliseev[15], K. Enosawa[14], P. Foka[4], S. Fokin[5], V. Frolov[6], M.S. Ganti[3], S. Garpman[13], O. Gavrishchuk[6], F.J.M. Geurts[12], T.K. Ghosh[16], R. Glasow[9], S. K.Gupta[2], B. Guskov[6], H. Å.Gustafsson[13], H. H.Gutbrod[10], R. Higuchi[14], I. Hrivnacova[15], M. Ippolitov[5], H. Kalechofsky[4], R. Kamermans[12], K.-H. Kampert[9], K. Karadjev[5], K. Karpio[17], S. Kato[14], S. Kees[9], H. Kim[7], B. W. Kolb[11], I. Kosarev[6], I. Koutcheryaev[5], T. Krümpel[9], A. Kugler[15], P. Kulinich[18], M. Kurata[14], K. Kurita[14], N. Kuzmin[6], I. Langbein[11], A. Lebedev[5], Y.Y. Lee[11], H. Löhner[16], L. Luquin[10], D.P. Mahapatra[19], V. Manko[5], M. Martin[4], G. Martínez[10], A. Maximov[6], R. Mehdiyev[6], G. Mgebrichvili[5], Y. Miake[14], D. Mikhalev[6], Md.F. Mir[8], G.C. Mishra[19], Y. Miyamoto[14], B. Mohanty[19], M. J. Mora[10], D. Morrison[20], D. S. Mukhopadhyay[3], V. Myalkovski[6], H. Naef[4], B. K. Nandi[19], S. K. Nayak[10], T. K. Nayak[3], S. Neumaier[11], A. Nianine[5], V. Nikitine[6], S. Nikolaev[6], P. Nilsson[13], S. Nishimura[14], P. Nomokonov[6], J. Nystrand[13], F.E. Obenshain[20], A. Oskarsson[13], I. Otterlund[13], M. Pachr[15], A. Parfenov[6], S. Pavliouk[6], T. Peitzmann[9], V. Petracek[15], F. Plasil[7], W. Pinganaud[10], M.L. Purschke[11], B. Raeven[12], J. Rak[15], R. Raniwala[2], S. Raniwala[2], V.S. Ramamurthy[19], N.K. Rao[8], F. Retiere[10], K. Reygers[9], G. Roland[18], L. Rosselet[4], I. Roufanov[6], C. Roy[10], J.M. Rubio[4], H. Sako[14], S.S. Sambyal[8], R. Santo[9], S. Sato[14], H. Schlagheck[9], H.-R. Schmidt[11], Y. Schutz[10], G. Shabratova[6], T.H. Shah[8], I. Sibiriak[5], T. Siemiarczuk[17], D. Silvermyr[13], B.C. Sinha[3], N. Slavine[6], K. Söderström[13], N. Solomey[4], S.P. Sørensen[7,20], P. Stankus[7], G. Stefanek[17], P. Steinberg[18], E. Stenlund[13], D. Stüken[9], M. Sumbera[15], T. Svensson[13], M.D. Trivedi[3], A. Tsvetkov[5], L. Tykarski[17], J. Urbahn[11], E.C.v.d. Pijll[12], N.v. Eijndhoven[12], G.J.v. Nieuwenhuizen[18], A. Vinogradov[5], Y.P. Viyogi[3], A. Vodopianov[6], S. Vörös[4], B. Wysłouch[18], K. Yagi[14], Y. Yokota[14], G.R. Young[7]

[1] University of Panjab, Chandigarh 160014, India
[2] University of Rajasthan, Jaipur 302004, Rajasthan, India
[3] Variable Energy Cyclotron Centre, Calcutta 700 064, India
[4] University of Geneva, 1211 Geneva 4, Switzerland
[5] RRC "Kurchatov Institute", 123182 Moscow, Russia
[6] Joint Institute for Nuclear Research, 141980 Dubna, Russia
[7] Oak Ridge National Laboratory, Oak Ridge, TN 37831-6372, USA
[8] University of Jammu, Jammu 180001, India
[9] University of Münster, 48149 Münster, Germany
[10] SUBATECH, Ecole des Mines, Nantes, France
[11] Gesellschaft für Schwerionenforschung (GSI), 64220 Darmstadt, Germany
[12] Universiteit Utrecht/NIKHEF, 3508 TA Utrecht, The Netherlands
[13] Lund University, 221 00 Lund, Sweden
[14] University of Tsukuba, Ibaraki 305, Japan
[15] Nuclear Physics Institute, 250 68 Rez, Czech Rep.
[16] KVI, University of Groningen, 9747 AA Groningen, The Netherlands
[17] Institute for Nuclear Studies, 00-681 Warsaw, Poland
[18] MIT Cambridge, MA 02139, USA
[19] Institute of Physics, 751-005 Bhubaneswar, India
[20] University of Tennessee, Knoxville, TN 37966, USA

Received: 8 August 2000 / Revised version: 5 December 2000 /
Published online: 5 February 2001 – © Springer-Verlag 2001

Abstract. Transverse energy, charged particle pseudorapidity distributions and photon transverse momentum spectra have been studied as a function of the number of participants (N_{part}) and the number of binary nucleon-nucleon collisions (N_{coll}) in 158·A GeV Pb+Pb collisions over a wide impact parameter range. A scaling of the transverse energy pseudorapidity density at midrapidity as $\sim N_{part}^{1.08\pm0.06}$ and $\sim N_{coll}^{0.83\pm0.05}$ is observed. For the charged particle pseudorapidity density at midrapidity we find a scaling as $\sim N_{part}^{1.07\pm0.04}$ and $\sim N_{coll}^{0.82\pm0.03}$. This faster than linear scaling with N_{part} indicates a violation of the naive Wounded Nucleon Model.

1 Introduction

Heavy-ion collisions at ultrarelativistic energies probe nuclear matter at high temperatures and densities. A major goal of these studies is the search for a deconfined phase of nuclear matter. A necessary condition to reach such a phase transition is local equilibration as might be achievable through rescattering of the produced particles. Since the amount of rescattering should increase with the size of the reaction system, it is of interest to study these reactions over a wide range of centralities.

For hard processes, where cross sections are small, the naive expectation is a scaling of the particle yields with the number of binary collisions. Experimentally, the scaling of cross sections with target mass in p+A collisions was studied and the scaling was observed to be even stronger than this expectation [1]. This was later attributed to multiple parton scattering in the initial state [2,3]. From the same experiment it was also seen that particle production at intermediate p_T shows a much weaker increase with target mass.

The gross features of particle production in nucleon-nucleus collisions and reactions of light nuclei are well described in the framework of the Wounded Nucleon Model [4]. In this model the transverse energy and particle production in p+A and A+A reactions is calculated by assuming a constant contribution from each participating nucleon. This kind of scaling has also been observed by the WA80 collaboration in reactions of ^{16}O and ^{32}S projectiles with various targets where $dE_T/d\eta|_{max}$ was found to depend approximately linearly on the average total number of participants [5].

While a scaling with the number of collisions arises naturally in a picture of a superposition of nucleon-nucleon collisions, with a possible modification by initial state effects, the Wounded Nucleon Model or participant scaling is more naturally related to a system with strong final state rescattering, where the incoming particles lose their memory and every participant contributes a similar amount of energy to particle production. The scaling behavior of particle production may therefore carry important information on the reaction dynamics. Various experimental signatures in heavy ion reactions require a comparison of observables for different system sizes. Therefore it is important to have a good understanding of these basic scaling properties. The scaling behavior can also be used as a valuable test for models of particle production in heavy ion reactions (see e.g. [6]).

Furthermore, several observables in heavy ion reactions seem to show qualitative changes once a certain system size is reached. Strangeness production is enhanced in S+S reactions compared to p+p, but seems to saturate for even larger nuclei (see e.g. [7]). Recent results from the WA98 experiment [8] show a significant change of the shape of the π^0 p_T spectrum in peripheral Pb+Pb collisions compared to p+p data. The shape, however, remains unchanged in the range of semi-central Pb+Pb collisions with about 50 participating nucleons up to central reactions.

The NA50 collaboration has observed an anomalously suppressed J/ψ yield in central Pb+Pb collisions in contrast to peripheral reactions [10] where the suppression of the J/ψ yield can be explained by absorption in nuclear matter. This anomalous J/ψ suppression provides an additional incentive to study the scaling behavior of particle production with the number of participants. Most models based on J/ψ absorption by hadronic comovers assume the comover density to scale linearly with the number of participants and are then not able to fit the anomalous suppression [11,12]. Only if the hadronic comover density scales substantially faster than linearly with the number of participants it is possible to obtain reasonable fits to the anomalous suppression. It is therefore of interest to study in detail the centrality dependence of particle production and investigate its scaling properties with respect to the number of participants or collisions.

2 Experiment and data analysis

The CERN experiment WA98 is a general-purpose apparatus which consists of large acceptance photon and hadron spectrometers together with several other large acceptance devices which allow to measure various global variables on an event-by-event basis. The experiment took data with the 158·A GeV ^{208}Pb beams from the CERN SPS in 1994, 1995, and 1996. The layout of the WA98 experiment as it existed during the final WA98 run period in 1996 is shown in Fig. 1. The data presented here were taken during the 1996 lead beamtime. The transverse energy and charged particle distributions shown in this paper were measured with the magnetic field of the Goliath magnet turned off. The minimum bias cross section for this configuration was $\sigma_{mb} = (6260 \pm 280)$ mb. The error of the minimum bias cross section relates to the uncertainty of the target thickness and the uncertainty in the subtraction of the contribution from interactions outside the target. The contribution of these interactions was determined in special target-out runs. A 20% uncertainty of this contribution was assumed in the calculation of the uncertainty of the minimum bias cross section. The WA98 experiment took most of the data with the Goliath

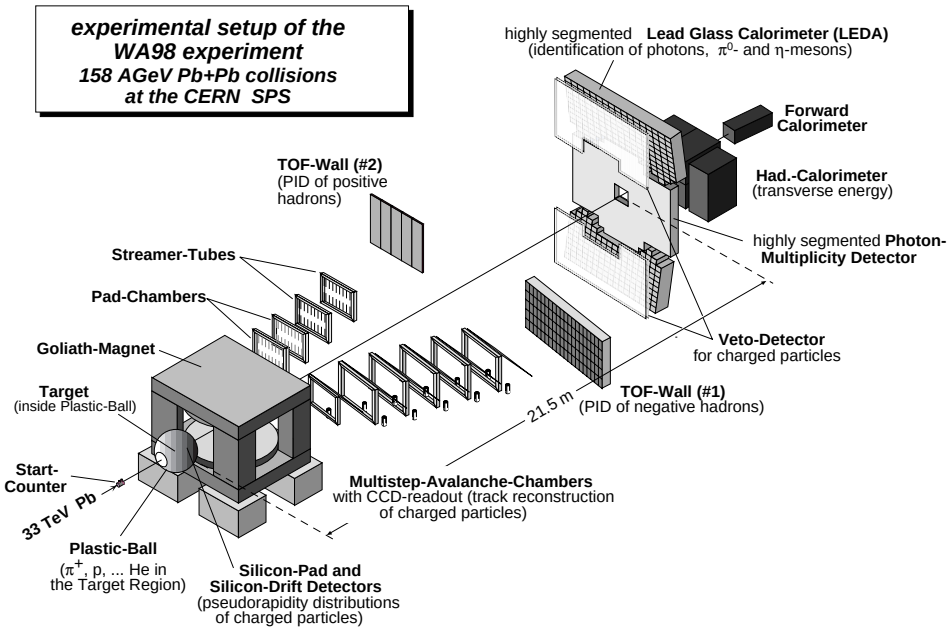

Fig. 1. The WA98 experimental setup

magnet turned on. Since the analysis of the photon and neutral pion scaling requires high statistics the respective spectra used here were measured in a field-on configuration. The minimum bias cross section for this data set was $\sigma_{mb} = (6440 \pm 300)$ mb.

The Zero Degree Calorimeter is located 30 m downstream of the target and measures the total energy of all particles within an angle $\Theta < 0.3°$ relative to the beam axis in the laboratory system. The MIRAC calorimeter is placed 24 m downstream of the target [13]. It consists of a hadronic and an electromagnetic section and covers the pseudorapidity interval $3.5 < \eta < 5.5$. MIRAC plays the central role in the WA98 minimum bias trigger where the measured E_T is required to be above a minimum threshold. The systematic errors of $dE_T/d\eta$ at midrapidity are dominated by the correction for the differences in the response of the MIRAC to hadronic and electromagnetic showers and to the extrapolation of the distribution of $dE_T/d\eta$ to midrapidity. These combine to give an overall systematic uncertainty of $\approx 20\%$ in the absolute result for $dE_T/d\eta|_{max}$. The centrality dependent part of this uncertainty is much smaller and estimated to be approximately 5% only. The correction of $dE_T/d\eta$ due to interactions outside the target for peripheral Pb+Pb reactions is less than 2%.

The charged particle multiplicity is measured with a circular Silicon Pad Multiplicity Detector (SPMD) located 32.8 cm downstream of the target [14]. It consists of four quadrants each produced from a 300 μm thick silicon wafer. This detector provides full azimuthal coverage of the pseudorapidity region $2.35 < \eta < 3.75$ with 180 Φ-bins and 22 η-bins. The pad size increases radially to provide an approximately uniform pseudorapidity coverage. In central Pb+Pb collisions the probability that a pad is hit by two or more particles is not negligible. Therefore the multiplicity in an η-ring is determined from the sum of the measured energy losses of the charged particles traversing the η-ring divided by the average energy loss per charged particle. The charged particle pseudorapidity distribution is corrected for δ-electrons produced by lead ions traversing the 213 μm thick ^{208}Pb target foil. On average these electrons give rise to roughly 11 additional hits in the SPMD. This contribution has been determined from beam triggers where no inelastic interaction took place. The systematic error of $dN_{ch}/d\eta$ relates to the uncertainty in the determination of the total energy loss of the charged particles in the SPMD and to the correction for δ-electrons. The uncertainty in the energy loss measurement is estimated to result in a 3% centrality independent systematic error. The correction for δ-electrons at midrapidity ($dN_\delta/d\eta|_{mid} \approx 9$) is assumed to be known with an accuracy of 10% and contributes significantly to the total uncertainty only for peripheral reactions. However, the $dN_{ch}/d\eta$ distributions as shown in Fig. 6 exhibit a slight asymmetry around midrapidity. We can force the $dN_{ch}/d\eta$ distribution to be symmetric by arbitrarily increasing the subtracted δ-electron contribution. For central events the δ-electron yield has to be increased by roughly 80%. This factor decreases when going to semi-central and peripheral events. It's difficult to imagine a physical reason for a much larger δ-electron production than what was measured for beam triggers. However, by making these extreme assumptions we estimate the centrality dependent error of $dN_{ch}/d\eta$ by comparing the $dN_{ch}/d\eta$ distributions with δ-electrons subtracted as measured in beam events with the $dN_{ch}/d\eta$ distributions that were forced to be symmetric. For peripheral and semi-central events this uncertainty typically is of the order of $3-4\%$ and decreases to 2% in central events. The correction of $dN_{ch}/d\eta$ measured with the SPMD in peripheral events due to interactions outside the target is typically of the order of 15%. The uncertainty of $dN_{ch}/d\eta$ due to this correction is estimated to be around 3%.

The photon distributions used in this analysis were measured with the LEDA spectrometer in the rapidity interval $2.3 < \eta < 3.0$. This detector is located 21.5 m from the target and consists of 10080 leadglass modules each read out by a photomultiplier. A streamer tube array placed directly in front of LEDA was used as a charged particle veto detector to correct for the charged hadron contamination in the leadglass. The remaining correction for neutrons and anti-neutrons has been made based on simulation results using the GEANT package [15]. The detection efficiency of photons in LEDA is based on GEANT simulations and experimental data in order to take into account the effects of overlapping showers which can result in a shift in the measured transverse momentum. These corrections require high statistics and therefore only 8 centrality classes have been used for the photon analysis here. These are the same 8 centrality classes used in the analysis of the scaling of neutral pion production presented in [8]. The systematic error on the photon and neutral pion multiplicities is estimated to be $\approx 10\%$ mainly originating from corrections for efficiency and contamination.

3 Model calculations

In the present analysis, the photon and charged particle scaling has been investigated with the centrality of the Pb+Pb collision determined from the transverse energy, E_T, measured with the MIRAC calorimeter. However, in the E_T scaling analysis, the forward energy E_F of projectile spectators measured with the Zero Degree Calorimeter has been used for the centrality selection, in order to avoid auto-correlations. Twenty-one centrality classes have been defined based on the measured E_T. Each class corresponds to 5% of the minimum bias cross section, with an additional very central class corresponding to the 1% most central events. The ZDC cannot resolve the centrality of very peripheral collisions as well as the MIRAC calorimeter and therefore the E_T scaling analysis is limited to centrality classes which correspond to more than approximately 40 participants.

The number of participants N_{part} and collisions N_{coll} for a given centrality class have been determined from a simulation based on the event generator VENUS 4.12 [16]. Control calculations were made with the FRITIOF event generator [29]. The definition of N_{part} and N_{coll} in these models is based on a geometrical picture (Glauber model) where nucleons travel on straight-line trajectories and the nucleon-nucleon cross section is independent of the number of collisions a nucleon has undergone before. The approach of using event generators allowed to take into account the energy resolution of the ZDC and MIRAC calorimeters. Furthermore, the minimum bias trigger efficiency has been included in the simulation. Figure 2 shows a comparison of the measured E_T and E_F distributions to the VENUS simulations. The overall agreement in the E_T distribution between the data and the model is good. However, the VENUS prediction extends to slightly higher transverse energy for the most central reactions. In the forward energy distribution, the strong peak for peripheral reactions is not precisely reproduced, while the general shape is quite similar. Also the event-by-event anti-correlation of E_T and E_F observed in the experimental data is in good agreement with the model calculations (see Fig. 3).

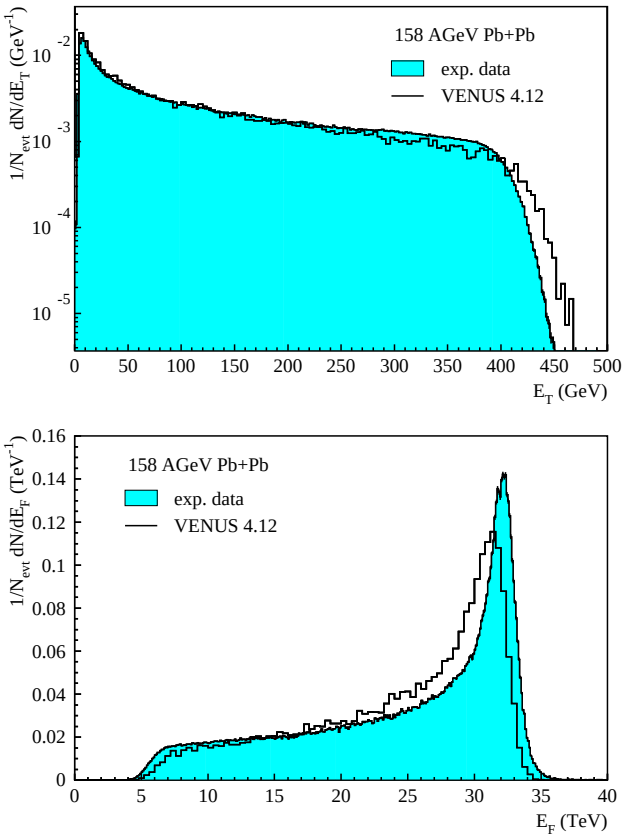

Fig. 2. Distributions of the transverse energy E_T as measured in MIRAC (upper graph) and the forward energy E_F as measured with the ZDC (lower graph) in 158·A GeV Pb+Pb collisions. Predictions of the event generator VENUS 4.12 are included

To obtain a robust estimate of N_{part} and N_{coll}, which is less sensitive to discrepancies in the energy distributions, the centrality classes in the model have been chosen to represent the same absolute cross section as the data. The effect of the centrality cuts on the distributions of the number of participants can be seen from Fig. 4, where distributions of N_{part} for centrality classes corresponding to fractions of the minimum bias cross section of 0-1%, 1-5%, 5-10%, 10-20%, 20-40%, 40-60%, 60-80% and 80-100% are shown. One can see that the limited acceptance, the detector resolution, and the fluctuations in particle production as implemented in the model lead to an overlap of the distributions of adjacent centrality classes. Nevertheless, it is observed that even a strong cut on the 1% most central reactions yields a significantly different selection than e.g. the 5% most central reactions.

Figure 5 shows a summary of the RMS-values versus the average values of the distributions of N_{part} for the centrality selections as used in the later analysis in this

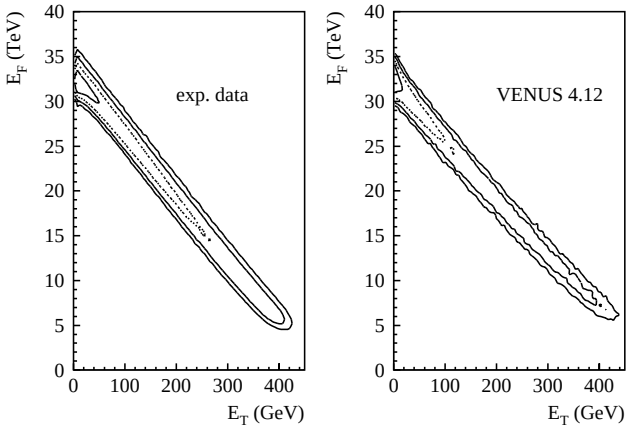

Fig. 3. Event-by-event distributions of the transverse energy E_T vs. the forward energy E_F in 158·A GeV Pb+Pb collisions. The left plot shows the experimental data and the right plot predictions of the event generator VENUS 4.12

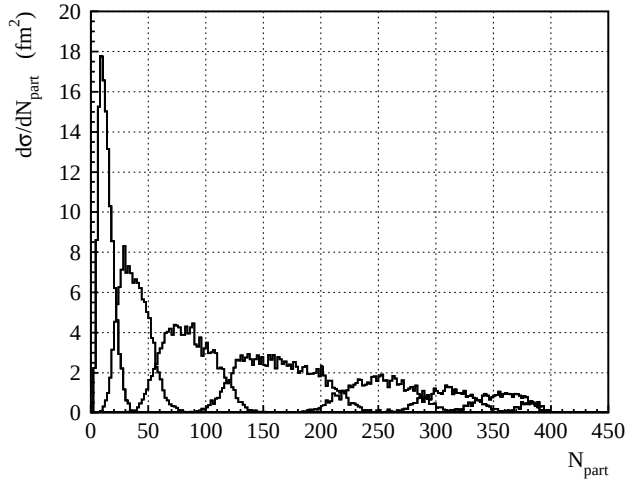

Fig. 4. Distributions of the number of participants N_{part} obtained from VENUS 4.12 for different centrality classes selected by the transverse energy E_T

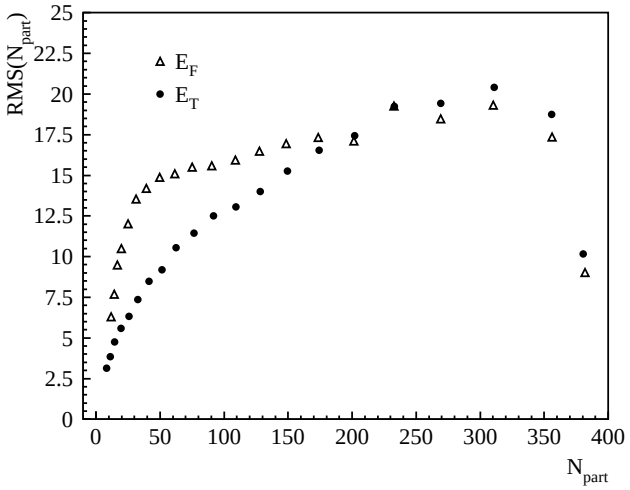

Fig. 5. RMS-values of the number of participants N_{part} obtained from VENUS 4.12 for different centrality classes selected by the transverse energy E_T and the forward energy E_F

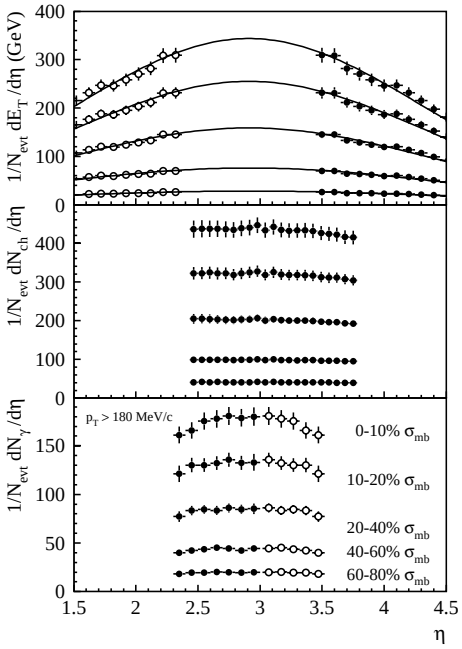

Fig. 6. Pseudorapidity distributions of transverse energy, charged particles and photons measured in 158·A GeV Pb+Pb collisions of different centrality. Photons were measured above a lower transverse momentum threshold of 180 MeV/c. The open symbols have been obtained by reflecting the measured data points at midrapidity

paper. While the classes selected with E_F have a slightly smaller width for very central reactions, for peripheral reactions the resolution of the selection is much better using E_T.

The precise number of participants or number of collisions may, however, depend on the specific model assumptions. We have therefore performed a detailed study of the influence of these assumptions and other sources of systematic errors for the analysis presented here. A summary of these studies is given in Appendix A.

4 Results

The pseudorapidity distributions for the transverse energy, the charged particle multiplicity, and the photon multiplicity are shown in Fig. 6 for five centrality classes. All distributions have been corrected for possible contributions of reactions upstream and downstream of the target and in the target frame by subtracting the respective yield determined in target-out runs, see [19] for further details. To obtain $dE_T/d\eta|_{max}$ the measured data points have been reflected at midrapidity ($\eta_{cm} = 2.91$) and fitted with a Gaussian.

A first impression of the centrality dependence of E_T and charged particle production can be obtained by normalizing the yields to the number of participants. This is shown in Fig. 7. Both for E_T and the charged multiplicity the yield per participant increases when going from peripheral to more central reactions. As described in the

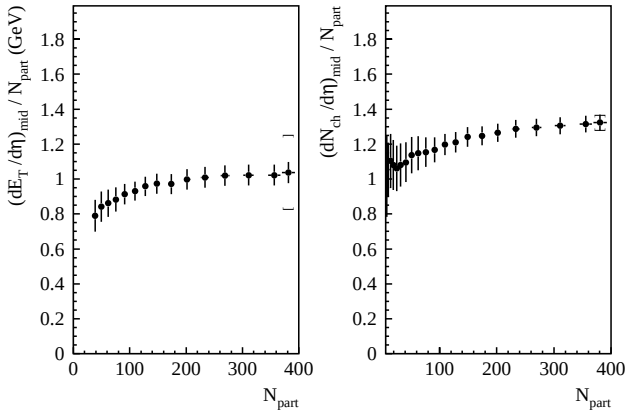

Fig. 7. Transverse energy and charged particle yields in 158·A GeV Pb+Pb reactions normalized to the number of participants as a function of the number of participants. For the number of participants an uncertainty as indicated in Fig. 16 was assumed. Furthermore, all centrality dependent errors of $dE_T/d\eta$ and $dN_{ch}/d\eta$ as described in Sect. 2 were taken into account in the calculation of the error bars. The brackets indicate the centrality independent uncertainty of the overall $dE_T/d\eta$ and $dN_{ch}/d\eta$ scale

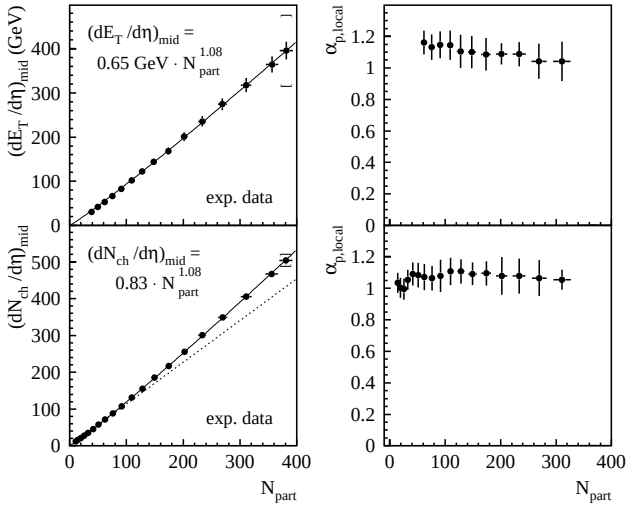

Fig. 8. Pseudorapidity density of E_T and N_{ch} at midrapidity as a function of the number of participants. The participant numbers shown here were calculated in a VENUS simulation (denoted as calculation A in the appendix). Both for E_T and N_{ch} the fit results obtained from a fit of all data points are shown. In order to demonstrate the stronger than linear increase of the data points a linear extrapolation of the charged particle multiplicity in peripheral Pb+Pb reactions ($N_{part} \approx 50$) is shown as a dotted line in the lower left plot. The scaling behavior can be verified in more detail on the right panel where the local scaling exponents are shown. The local scaling exponents have been obtained from a fit of 5 neighboring E_T and N_{ch} data points

appendix we have also used the FRITIOF model instead of VENUS to calculate the number of participants and the number of nucleon-nucleon collisions. The results of these two calculations for the number of participants are compared in the appendix (Fig. 16) and used to obtain the estimated uncertainty of the number of participants which was used in the calculation of the error bars in Fig. 7.

The scaling behavior is studied in more detail in Fig. 8 which shows the dependence of the E_T and N_{ch} pseudorapidity densities at midrapidity on the number of participants. The scaling behavior of these observables was parameterized as

$$\left.\frac{dX}{d\eta}\right|_{mid} \sim N_{part}^{\alpha_p},\ N_{coll}^{\alpha_c}, \quad X = E_T,\ N_{ch}\,. \qquad (1)$$

This functional dependence gives a reasonable description of the data for the entire centrality range. Taking the number of participants from the VENUS calculation (denoted as calculation A in the appendix) the charged particle scaling can be described by a scaling exponent $\alpha_p = 1.08$. The calculations of the number of participants using VENUS, or VENUS with an experimentally determined nucleon density distribution, or FRITIOF (denoted as calculations A, B, and F in the appendix) are all based on reasonable assumptions. These three calculations give slightly different participant numbers. We quote the average of the corresponding three scaling exponents α_p as the final result. As described in the appendix the estimated uncertainty of α_p due to the uncertainty of the number of participants is 0.036. In the fit from which we obtain the value of α_p we only take the statistical error of the data points into account. Since the statistical errors are small the fit error is negligible. In order to estimate the influence of the centrality dependent errors of $dN_{ch}/d\eta$ on α_p we systematically move the data points within the error bars and repeat the fit. From this procedure we estimate an uncertainty of 0.02 for α_p due to the centrality dependent errors of $dN_{ch}/d\eta$. Adding all errors in quadrature we finally obtain $\alpha_p = 1.07 \pm 0.04$ for the charged particle scaling.

For the E_T scaling we perform a similar error analysis. An additional uncertainty comes from the assumed centroid of the $dE_T/d\eta$ distribution. Primarily due to massive particles like protons and neutrons, the difference between pseudorapidity and rapidity could lead to an increase of the centroid relative to midrapidity ($y_{mid} = 2.91$). By varying the assumed $dE_T/d\eta$ centroid position in the η-range 2.91 ± 0.3 a corresponding error of 0.02 was estimated for the E_T scaling exponent α_p. Adding all errors in quadrature we obtain $\alpha_p = 1.08 \pm 0.06$.

In more detail, the relative scaling for different centralities can be judged from the *local scaling exponent* α_{local} shown on the right hand side of Fig. 8. These have been obtained from a fit of 5 neighboring E_T and N_{ch} data points. For the charged particles it can be seen that the scaling remains approximately constant over the whole centrality range. For E_T the local scaling exponent appears to be almost constant in the range $N_{part} > 100$. However, below $N_{part} \approx 100$ the local scaling exponent seems to increase slightly.

Considering the scaling with the number of binary nucleon-nucleon collisions and averaging the results determined with calculations A, B, and F we obtain a similarly

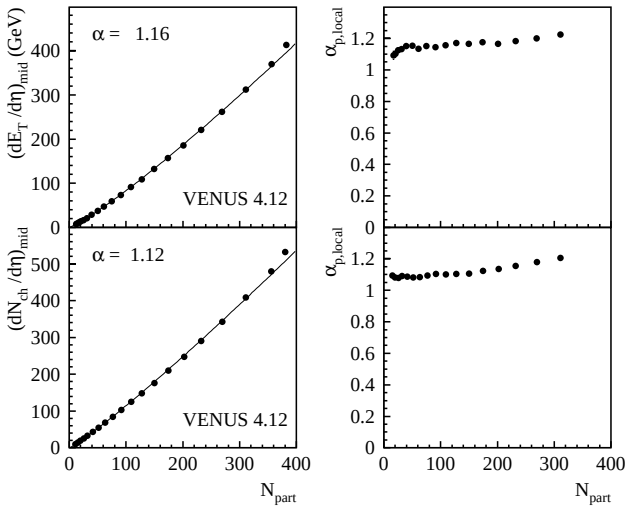

Fig. 9. Pseudorapidity density of E_T and N_{ch} at midrapidity as a function of the number of participants as in Fig. 8 from VENUS 4.12 simulations

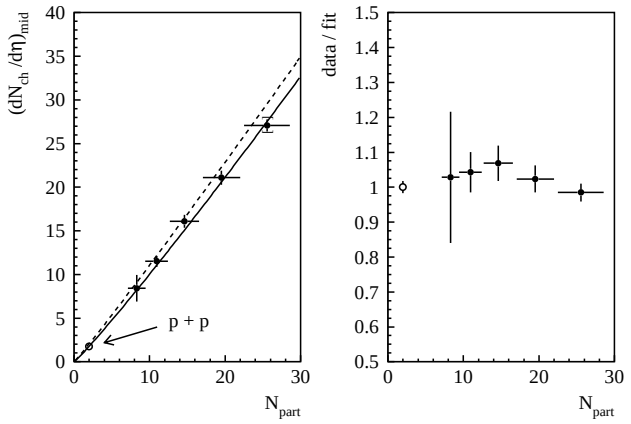

Fig. 10. Pseudorapidity density of N_{ch} at midrapidity as a function of the number of participants for p+p [22] and Pb+Pb collisions. The number of participants shown here were calculated using VENUS (calculation A in the appendix). The fit function plotted as a solid line is the same as obtained in Fig. 8. The dashed function is the fit result using the participant values from the FRITIOF calculation (calculation F). On the right hand side the ratio of the data (using participants from VENUS) to the fit function is shown

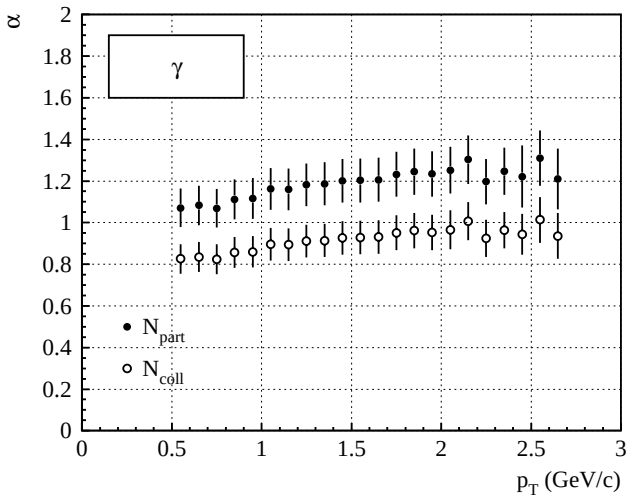

Fig. 11. Exponents for a scaling with the number of participants and nucleon-nucleon collisions for photons measured in LEDA as a function of the transverse momentum. Only reactions with $N_{part} \geq 30$ have been used. The data points shown were obtained using the number of participants from VENUS. The error bars reflect the uncertainty of the photon measurement, the uncertainty in the calculation of N_{part}/N_{coll} and the fit error

good description with $\alpha_c = 0.82 \pm 0.03$ for the charged particle scaling. For the E_T scaling we obtain $\alpha_c = 0.83 \pm 0.05$. These results are not surprising since for symmetric systems one naively expects a scaling relation to hold between the number of collisions and the number of participants:

$$N_{coll} \propto N_{part}^{\alpha_{cp}} \text{ with } \alpha_{cp} = \frac{4}{3}. \qquad (2)$$

Fits of the parameters extracted from VENUS simulations indeed yield a value of $\alpha_{cp} = 1.28$ which is close to the above value. For a scaling with $N_{part}^{1.08}$ this would lead to a behavior as $N_{coll}^{0.84}$.

A similar analysis can be performed on the data obtained from the VENUS simulation itself. The results of such an analysis are displayed in Fig. 9. It is observed that the scaling exponents are higher in the simulation, and that both for E_T and N_{ch} the exponent α shows a tendency to increase with centrality. We note here that the extraction of the number of participants and the number of binary nucleon-nucleon collisions is almost completely independent of the scaling exponent present in the underlying event generator. As described in Sect. 3 this is due to the fact that the centrality classes defined in the model calculations correspond to the same absolute cross section as the experimental centrality classes.

It is interesting to extrapolate this scaling towards smaller system sizes and compare to the expectation from pp collisions [22]. This has been done in Fig. 10. It can be seen that the scaling obtained from charged particle production in Pb+Pb collisions extrapolates nicely to pp collisions. In particular, there is no threshold effect visible in the charged particle multiplicity when going to central Pb+Pb collisions.

In a recent publication [18] we have discussed the systematics of inclusive photon production as measured with the WA98 Photon Multiplicity Detector. There it was found that the pseudorapidity density of photons at midrapidity scales with the number of participants as $N_{part}^{1.12 \pm 0.03}$. This is slightly larger, but consistent with the exponent from the present analysis of E_T and N_{ch}. Photon production can be investigated in further detail with the photon spectrometer LEDA. It can very naturally be studied as a function of the transverse momentum. The corresponding scaling exponents α extracted are shown in Fig. 11. The photon measurement in LEDA suffers from larger systematic uncertainties at low momenta, so only photons for $p_T > 500$ MeV/c have been considered. At

a transverse momentum of $p_T \approx 500$ MeV/c the inclusive photon yield shows a scaling behavior similar to that observed for E_T and N_{ch}. However, the extracted scaling exponents tend to rise with increasing p_T and at $p_T \approx 2$ GeV/c the scaling can be described as $\sim N_{part}^{1.2}$ and $\sim N_{coll}^{0.9}$.

Since a large fraction of the inclusive photons originates from the decay of neutral pions it is of interest to compare the scaling of photons to that of neutral pions which have already been discussed in [8]. These data have been reanalyzed [9] and the results of the scaling exponents with respect to the number of participants are shown in Fig. 12. The values are nearly constant at $\alpha \approx 1.1$ with a tendency to decrease towards higher transverse momenta. It should be noted that the extracted exponents are smaller compared to the values given in [8]. This is mostly due to a more sophisticated calculation of the number of participants used here.

We have recently published results on the production of direct photons in 158·A GeV Pb+Pb collisions [20,21]. A significant yield of direct photons at $p_T > 1.5$ GeV/c is observed in central collisions, while in peripheral collisions the photon production is consistent with the yield expected from the decays of neutral pions, η mesons, and other hadrons. At $p_T \approx 2$ GeV/c the direct photon yield in central collisions amounts to roughly 20% of the photons from hadronic decays. The scaling of the neutral pion yield presented in Fig. 12 appears to be consistent with the scaling of charged particles and the transverse energy, while the photon yield at higher transverse momenta seems to increase more strongly with the number of participants. We assume that for a relatively small yield of direct photons in central collisions, the centrality dependence of the inclusive photons can still be described with a scaling law as in (1). It's then obvious that the production of direct photons in central Pb+Pb collisions necessarily increases the scaling exponent α of the inclusive photons at high transverse momenta. In this respect the behavior of the extracted scaling exponents for inclusive photon and neutral pion production are consistent with the direct photon excess observed in central Pb+Pb collisions. However, due to the uncertainties of the scaling exponents for photons and neutral pions it is not possible to draw quantitative conclusions about direct photon production from Figs. 11 and 12.

In simple multiple collision models a heavy ion reaction is regarded as a sequence of independent nucleon-nucleon collisions which can be described as in free space [23,24]. After a projectile nucleon suffers an inelastic collision the assumption of local baryon number conservation assures that a baryon-like object is still present. This baryon-like object is assumed to contribute to the particle production in subsequent collisions with the same cross section as the initial nucleon. In this picture the contribution of each nucleon-nucleon collision is added incoherently which leads to a linear scaling of E_T and particle production with the number of binary collisions. If the energy degradation in each nucleon-nucleon reaction is taken into account a reasonable description of E_T and particle production can

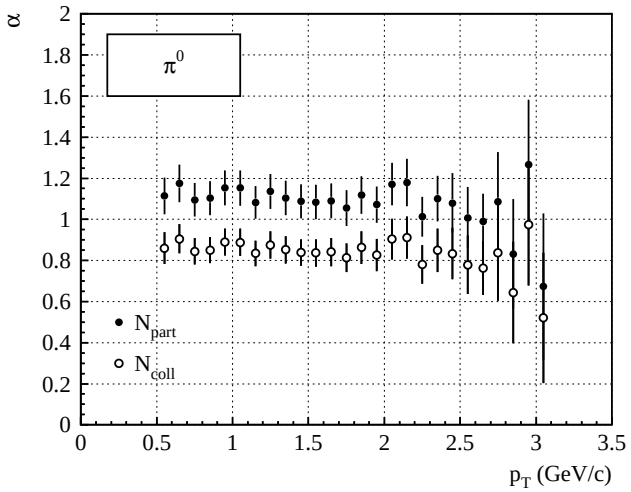

Fig. 12. Exponents for a scaling with the number of participants and nucleon-nucleon collisions for neutral pions measured in LEDA as a function of the transverse momentum. Only reactions with $N_{part} \geq 30$ have been used. The data points shown were obtained using the number of participants from VENUS. The error bars reflect the uncertainty of the π^0 measurement, the uncertainty in the calculation of N_{part}/N_{coll} and the fit error

be obtained. The approximate scaling as $N_{coll}^{0.83}$ for the transverse energy and charged particles may be used to obtain information on the average energy degradation in a nucleon-nucleon collision.

A simple way of investigating this hypothesis is to study the particle production per binary collision as a function of the effective thickness x of the two nuclei, which might be characterized in the following way [23–25]:

$$\frac{dN_{ch}}{d\eta}(AA) = N_{coll} \cdot f(x) \cdot \frac{dN_{ch}}{d\eta}(pp). \qquad (3)$$

Here $f(x)$ should describe the effect of energy degradation on particle production with x being a suitable thickness variable – we have chosen $x \equiv N_{coll}/N_{part}$. Figure 13 shows the pseudorapidity density of N_{ch} at midrapidity in Pb+Pb collisions normalized to the number of collisions and the charged particle density in pp collisions. The data show a continuous decrease of the multiplicity per collision for increasing x, i.e. the more collisions a participant suffers, the smaller is the contribution of each collision to particle production. As an example, this can be illustrated more quantitatively for the centrality classes with $N_{coll}/N_{part} \approx 1$, i.e. for the case that each participating nucleon on the average suffers two nucleon-nucleon collisions. For these reactions the actual charged particle density at midrapidity is 40% lower than one would expect from a linear scaling of the charged particle density in pp reactions with the number of binary nucleon-nucleon collisions. In a simple multiple collision picture this means that on the average the second collisions of each participant contributes only 20% of the yield of the first collision to the charged multiplicity at midrapidity.

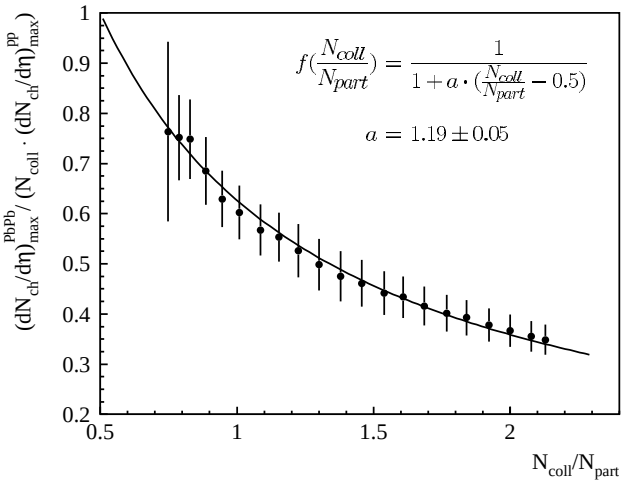

Fig. 13. Pseudorapidity density of N_{ch} at midrapidity in Pb+Pb collisions normalized to the number of collisions and the charged particle density in pp collisions. The solid line shows a fit with (4)

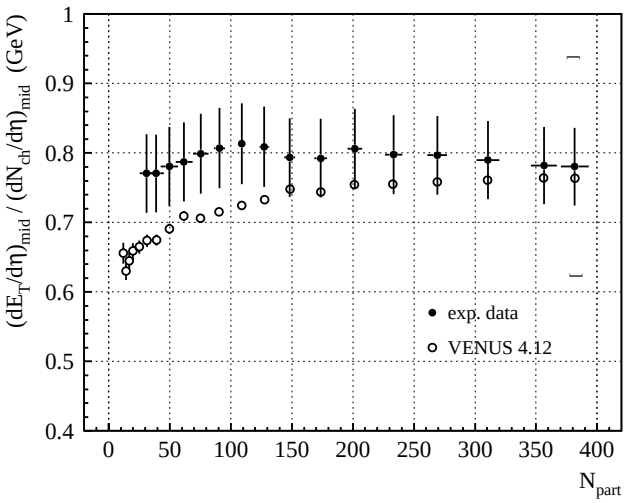

Fig. 14. $\langle E_T\rangle/\langle N_{ch}\rangle|_{mid}$ as a function of the number of participants. For comparison results of VENUS 4.12 calculations are included. The error bars indicate the centrality dependent errors of the experimental result. The overall uncertainty of $\langle E_T\rangle/\langle N_{ch}\rangle|_{mid}$ which is mainly due to the uncertainty in $(dE_T/d\eta)_{mid}$ is indicated by brackets

In proton-nucleus reactions multiplication of the charged particle multiplicity observed in pp reactions by the number of binary nucleon-nucleon collisions overestimates the measured multiplicity by $20-30\%$ [26,27]. In case of proton-nucleus reactions the target participants suffer exactly one nucleon-nucleon collision. This is of course not true in AA collisions. Nevertheless, it is interesting to apply the same recipe to heavy ion reactions. Figure 13 shows that multiplying the pp yield with the number of binary nucleon-nucleon collisions gives as much as 60% too many charged particles in central Pb+Pb reactions.

We have attempted to fit the data in Fig. 13 with the form:

$$f_{fit}\left(\frac{N_{coll}}{N_{part}}\right) = \left[1 + a\left(\frac{N_{coll}}{N_{part}} - 0.5\right)\right]^{-1}. \quad (4)$$

This function basically represents a first order Taylor approximation of the function $1/f$ in (3). A good fit is obtained with $a = 1.19 \pm 0.05$.

In the case of the Wounded Nucleon Model the eventual fragmentation of an excited nucleon after an inelastic collision is not affected by further collisions with other nucleons, no matter how many times it is successively struck. The observation of a stronger than linear increase of E_T and N_{ch} with the number of participants indicates that this model is only approximately correct. It can be clearly seen, regarding the two possible centrality variables investigated here, that the number of participants is better suited, because the scaling exponent is closer to one compared to the number of collisions.

With the present data it is possible to determine the average transverse energy per charged particle at midrapidity

$$\langle E_T\rangle/\langle N_{ch}\rangle|_{mid} \equiv \langle dE_T/d\eta|_{mid}\rangle/\langle dN_{ch}/d\eta|_{mid}\rangle, \quad (5)$$

a quantity that can be seen as a measure of the global mean transverse momentum averaged over all particle species. $\langle E_T\rangle/\langle N_{ch}\rangle|_{mid}$ is plotted in Fig. 14 as a function of centrality, represented by the number of participants. For this figure both $dE_T/d\eta$ and $dN_{ch}/d\eta$ were evaluated in identical centrality classes, defined with the forward energy E_F.

$\langle E_T\rangle/\langle N_{ch}\rangle|_{mid}$ appears to increase up to a system size of $N_{part} \approx 100$ which corresponds to an impact parameter of $b \approx 9$ fm. For more central collisions $\langle E_T\rangle/\langle N_{ch}\rangle|_{mid}$ levels off at a value of 0.80 GeV. This value is slightly higher than the maximum $\langle E_T\rangle/\langle N_{ch}\rangle|_{mid} \approx 0.66$ GeV observed in 200·A GeV S+Au and S+Al reactions [17]. VENUS 4.12 predicts a qualitatively similar behavior for $\langle E_T\rangle/\langle N_{ch}\rangle|_{mid}$, while the absolute value is approximately 100 MeV lower at $N_{part} \approx 100$. One may also note that the VENUS results continue to rise by ≈ 50 MeV when going from $N_{part} \approx 100$ to $N_{part} \approx 400$, while the experimental data appear to be completely flat in this region. A similar saturation with increasing number of participants as observed here has been seen in the (truncated) mean p_T of neutral pions with $p_T > 400$ MeV/c produced in Pb+Pb reactions [8]. A natural explanation of such a behavior would be the assumption that thermalization is reached once the system exceeds a certain minimum size.

5 Conclusions

We have analyzed the dependence of transverse energy and charged particle pseudorapidity distributions and photon transverse momentum spectra in 158·A GeV Pb+Pb collisions on the number of participants and the number of binary nucleon-nucleon collisions. A scaling behavior as $N_{part}^{1.07\pm0.04}$ and $N_{coll}^{0.82\pm0.03}$ describes the

charged particle production over the whole impact parameter range. The E_T production was studied for collisions with more than approximately 40 participants. In this centrality range the E_T production scales as $N_{part}^{1.08\pm0.06}$ and $N_{coll}^{0.83\pm0.05}$.

Photons at $p_T \approx 500$ MeV/c show a scaling behavior similar to the scaling of E_T and N_{ch}. The p_T-dependence of the photon scaling was studied and a rise of the extracted scaling exponents with increasing transverse momentum was found.

We have studied the transverse energy per charged particle as a function of centrality and found an indication of an increase from peripheral to semi-central collisions with approximately 100 participants with a subsequent saturation for larger systems.

While the global variables like E_T and charged particle multiplicity seem to scale closer to the number of participants than to the number of binary collisions, there is a clear participant scaling violation compared to a purely linear dependence. This scaling violation might e.g. have consequences for the suppression of J/ψ production from comovers, since the implied central particle densities are considerably larger than estimated based on a linear scaling.

Acknowledgements. We wish to express our gratitude to the CERN accelerator division for excellent performance of the SPS accelerator complex. We acknowledge with appreciation the effort of all engineers, technicians and support staff who have participated in the construction of the experiment. This work was supported jointly by the German BMBF and DFG, the U.S. DOE, the Swedish NFR and FRN, the Dutch Stichting FOM, Polish KBN under contract 621/E-78/SPUB/CERN/P-03/DZ211, the Grant Agency of the Czech Republic under contract No. 202/95/0217, the Department of Atomic Energy, the Department of Science and Technology, the Council of Scientific and Industrial Research and the University Grants Commission of the Government of India, the Indo-FRG Exchange Program, the PPE division of CERN, the Swiss National Fund, the INTAS under Contract INTAS-97-0158, ORISE, Research-in-Aid for Scientific Research (Specially Promoted Research & International Scientific Research) of the Ministry of Education, Science and Culture, the University of Tsukuba Special Research Projects, and the JSPS Research Fellowships for Young Scientists. ORNL is managed by Lockheed Martin Energy Research Corporation under contract DE-AC05-96OR22464 with the U.S. Department of Energy. The MIT and University of Tennessee groups have been supported by the US Dept. of Energy under the cooperative agreements DE-FC02-94ER40818 and DE-FG02-96ER40982, respectively.

Appendix A: Systematic uncertainties in model calculations

In order to obtain an estimate of the systematic uncertainties in the calculation of the number of participants and the number of nucleon-nucleon collisions we have varied several assumptions in the model calculations. The dependence of the particle and transverse energy yield on the number of participants and collisions is described with the scaling exponents α_p and α_c in this paper. In this section we investigate how the extracted scaling exponents α_p and α_c for the charged particle yield (with similar conclusions for the other observables) are affected by the different model assumptions.

In the VENUS 4.12 simulations used to obtain the number of participants and collisions we have varied

- the parameterization of the nucleon density distribution,
- the energy resolution of MIRAC and
- the minimum bias cross section.

As a cross check we have also calculated the number of participants and collisions using the event generator FRITIOF [29].

The nuclear density profile used in VENUS and FRITIOF is an effective parameterization using a Woods-Saxon shape:

$$\rho(r) = \rho_0 \cdot \frac{1}{1+\exp\left(\frac{r-R}{a}\right)}. \tag{6}$$

However, the two models make slightly different assumptions for the nuclear radius R and the diffuseness parameter a. The VENUS parameterization is

$$\begin{aligned} R_{\mathrm{VEN}} &= (1.19A^{1/3} - 1.61A^{-1/3})\ \mathrm{fm} \\ a_{\mathrm{VEN}} &= 0.54\ \mathrm{fm} \end{aligned} \tag{7}$$

which results in $R_{\mathrm{VEN}} \approx 6.78\,\mathrm{fm}$ for a lead nucleus. The radius parameter in FRITIOF for nuclei with $A > 16$ is calculated as

$$\begin{aligned} R_{\mathrm{FRI}} &= r_0 \cdot A^{1/3} \quad \text{with} \\ r_0 &= 1.16 \cdot (1 - 1.16A^{-2/3})\ \mathrm{fm}. \end{aligned} \tag{8}$$

This gives $R_{\mathrm{FRI}} \approx 6.65\,\mathrm{fm}$ for lead nuclei. The diffuseness parameter a is taken to be slightly A-dependent in FRITIOF and lies in the range $0.47\,\mathrm{fm} - 0.55\,\mathrm{fm}$. For lead nuclei FRITIOF uses

$$a_{\mathrm{FRI}} = 0.545\,\mathrm{fm}. \tag{9}$$

Electron scattering experiments have shown, however, that the density distribution has a slightly more complicated structure[1]. For a comparison we will use a parameterization fitted to electron scattering data on ^{208}Pb presented in [28]:

$$\rho_{\mathrm{exp}}(r) = \rho_0 \cdot \frac{c_1 + c_2 r + c_3 r^2}{1+\exp\left(\frac{r-R_{\mathrm{exp}}}{a_{\mathrm{exp}}}\right)} \tag{10}$$

with

$$c_1 = 0.0633,\ c_2 = -0.002045\,\mathrm{fm}^{-1}, c_3 = 0.000566\,\mathrm{fm}^{-2}$$

[1] Strictly this applies only to the charge distribution. The true nucleon distribution, especially in the inner part of the nuclei, is not experimentally accessible

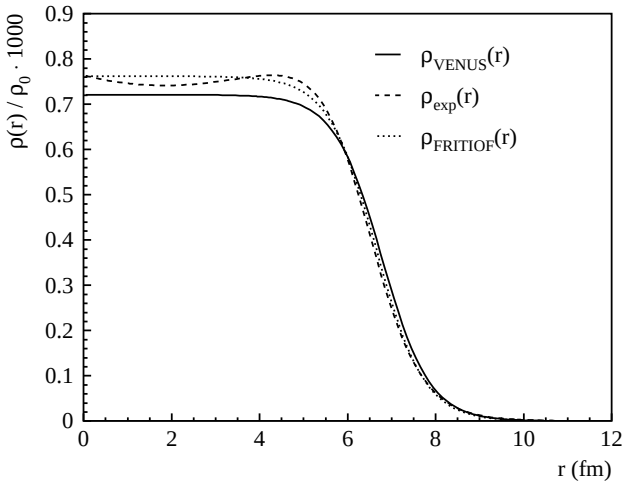

Fig. 15. Different nuclear density distributions used in the calculations of the number of participants and the number of collisions. The solid line shows the distribution implemented in the VENUS 4.12 Monte-Carlo model ((6) with the parameters (7)), the dashed line shows a parameterization of the charge distribution obtained from electron scattering (10) and the dotted line shows the density used in the FRITIOF model ((6) with the parameters (8) and (9))

and

$$R_{\rm exp} = 6.413\,{\rm fm},\ a_{\rm exp} = 0.5831\,{\rm fm}.$$

The three different distributions are shown in Fig. 15. It can be seen that the overall agreement is quite good. The default distribution of VENUS has a slightly larger radius, while the parameterization of the experimental data shows small oscillations compared to the other two distributions.

With respect to the experimental resolution we have varied the energy resolution of the MIRAC calorimeter in the simulations. The measured values of the resolution [13] are for the electromagnetic section:

$$\frac{\sigma_{\rm em}}{E} = \frac{17.9\,\%}{\sqrt{E/{\rm GeV}}} \tag{11}$$

and for the hadronic section:

$$\frac{\sigma_{\rm had}}{E} = \frac{46.1\,\%}{\sqrt{E/{\rm GeV}}}. \tag{12}$$

This has been arbitrarily worsened to

$$\frac{\sigma_{\rm em,had}}{E} = \frac{85\,\%}{\sqrt{E/{\rm GeV}}} \tag{13}$$

for both sections of the calorimeter.

For an accurate determination of the number of participants and the number of nucleon-nucleon collisions it is necessary that the experimental minimum bias threshold is reproduced in the simulation. In Sect. 2 we stated the two sources in the determination of the experimental minimum bias cross-section: the error of the target thickness and the error due to subtraction of interactions outside the target. In our approach of calculating the number of participants and nucleon-nucleon collisions we define centrality classes based on the simulated E_T (in case of the N_{ch} scaling analysis) which correspond to the same absolute cross-sections as the respective classes for the measured E_T. The uncertainty of the minimum bias cross-section due to the error of the target thickness therefore directly leads to an error of the N_{part}-values which affects the entire centrality range. However, the uncertainty in the correction for interactions outside the target affects the experimental $d\sigma/dE_T$ distribution only in the peripheral range. More precisely, since the maximum E_T measured in target-out events is around 75 GeV, according to Table 1 only the range $N_{part} < 50$ is affected.

The measured target thickness is $213 \pm 3\,\mu$m. The uncertainty of the target thickness contributes a relative error of roughly 1.5% to the error of the experimental minimum bias cross section. In order to check the influence on the extracted scaling exponent we arbitrarily increase the minimum bias threshold in the simulation by roughly 2% to $\sigma_{mb}^{sim} = 6386\,$mb. We have furthermore checked the error of α_p due to the uncertainty of the minimum bias cross section that relates to the subtraction of non-target contributions. To do this, we have used an E_T distribution without correction for reactions outside the target to translate the experimental E_T cuts into cross section

Table 1. The number of participants and binary collisions for different centrality classes obtained with the measured transverse energy in Pb+Pb collisions calculated from VENUS and FRITIOF (see text)

% of c.s.	E_T^{min} (GeV)	N_{part} VENUS	N_{coll} VENUS	N_{part} FRITIOF	N_{coll} FRITIOF
1	398.8	380.7	810.7	380.3	717.4
5	355.8	355.8	739.4	355.4	662.3
10	313.1	310.9	621.7	313.0	562.9
15	275.2	269.7	518.5	270.0	469.9
20	239.8	233.3	429.5	232.8	389.4
25	208.0	202.0	357.2	201.0	324.5
30	179.2	174.2	293.6	172.3	264.7
35	153.7	149.3	240.1	147.3	218.6
40	130.3	128.2	197.3	125.7	177.2
45	109.7	109.3	159.4	105.4	141.8
50	91.2	91.4	126.1	89.2	114.6
55	74.8	76.2	99.2	73.3	89.2
60	60.4	62.6	76.7	60.3	69.1
65	47.9	51.2	59.1	49.2	53.4
70	37.0	41.3	44.8	39.1	39.6
75	27.9	32.4	32.6	30.9	29.8
80	20.5	25.5	24.2	23.9	21.5
85	14.7	19.5	17.3	17.8	15.1
90	10.3	14.6	12.1	13.1	10.4
95	6.9	10.9	8.6	9.8	7.4
100	0.0	8.3	6.2	7.5	5.4

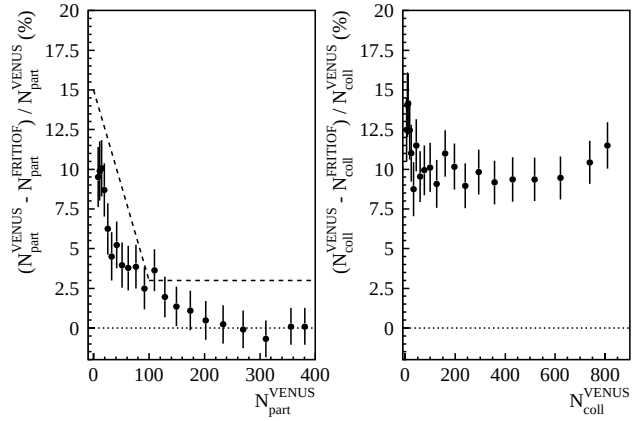

Fig. 16. Relative difference of the number of participants (left) and the number of nucleon-nucleon collisions (right) calculated with VENUS (calculation A) and FRITIOF (calculation F). The dashed line on the left plot indicates the assumed uncertainty of the participant scale that is used in the calculation of the error bars in Fig. 7

cuts. The apparent minimum bias cross section for this E_T distribution was $\sigma_{mb} = 6530$ mb.

The different calculations of the number of participants and collisions are summarized in the following list:

- A VENUS 4.12 calculations using the standard settings for the density distribution, the experimental resolution and the minimum bias cross section.
- B VENUS 4.12 calculations as in case Appendix A: with a modified density distribution according to (10).
- C VENUS 4.12 calculations as in case Appendix A: with a modified MIRAC resolution.
- D VENUS 4.12 calculations as in case Appendix A: with an a minimum bias cross section increased to $\sigma_{mb}^{sim} = 6386$ mb.
- E VENUS 4.12 calculations with cross section cuts derived from an experimental E_T-spectrum that was not corrected for interactions outside the target (apparent minimum bias cross section: $\sigma_{mb} = 6530$ mb).
- F FRITIOF calculations using standard settings as in calculation A.

As an example, the number of participants and collisions from calculation A and F are compared in Fig. 16. In peripheral Pb+Pb reactions VENUS gives up to 10% more participants than FRITIOF whereas in central reactions both simulations yield almost identical results. Almost independent of centrality the number of collisions from VENUS is roughly 10% higher than the FRITIOF result. The results of calculation A and F together with the experimental E_T intervals are given in Table 1.

For the case of the N_{ch} scaling the impact of the different model assumptions on the extracted scaling exponents α is summarized in Table 2. Considering the scaling with the number of participants we take the average of the α_p values from calculations A, B and F as our final result since all three calculations are based on reasonable assumptions. The maximum difference of 0.03 between the α_p values from these calculations is taken as one contribution to the systematic error. By adding the deviations of the results from calculations C, D and E from the mean value 1.07 in quadrature we estimate the total systematic error of α_p related to the uncertainty of the number of participants to be 0.036. The same prescription yields an uncertainty of 0.024 for the exponent α_c that described the scaling with the number of binary nucleon-nucleon collisions.

Table 2. Influence of different model assumptions on the extracted exponents α_p and α_c which describe the scaling of the charged particle yield with N_{part} and N_{coll} according to (1). In addition to the scaling exponents we quote the proportionality constants for the scaling with N_{part} (c_p) and N_{coll} (c_c) for each calculation. The full centrality range was used in the fit of (1) to the measured charged particle yields

Calculation	c_p	α_p	c_c	α_c
A	0.83	1.08	1.94	0.83
B	0.88	1.07	2.15	0.81
C	0.86	1.07	1.99	0.83
D	0.98	1.05	2.13	0.83
E	0.87	1.07	2.01	0.82
F	0.97	1.05	2.13	0.83

References

1. D. Antreasyan, et al. Phys. Rev. D **19**, (1979) 764
2. A. Krzywicki et al., Phys. Lett. **B 85**, (1979) 407
3. M. Lev, B. Petersson, Z. Phys. C **21**, (1983) 155
4. A. Bialas, A. Bleszynski, W. Czyz, Nucl. Phys. B **111**, (1976) 461
5. WA80 collaboration, R. Albrecht et al., Phys. Rev. C **44**, (1991) 2736
6. D.K. Srivastava, K. Geiger, preprint nucl-th/9808042
7. J. Sollfrank et al., Nucl. Phys. A **638**, (1997) 399c
8. WA98 collaboration, M. Aggarwal et al., Phys. Rev. Lett. **81**, (1998) 4087
9. WA98 collaboration, M. Aggarwal et al., Phys. Rev. Lett. **84**, (2000) 578 (erratum to M. Aggarwal et al., Phys. Rev. Lett. **81**, (1998) 4087)
10. NA50 collaboration, M.C. Abreu, et al., Nucl. Phys. A **638**, (1997) 261c
11. NA50 collaboration, M.C. Abreu, et al., Phys. Lett. **B 410**, (1997) 327
12. R.Vogt, Phys. Lett. **B 430**, (1998) 15
13. T.C. Awes et al., Nucl. Instr. and Meth. A **279**, (1989) 479
14. W.T Lin et al., Nucl. Instr. and. Meth. A **389**, (1997) 415
15. R. Brun et al., GEANT3, CERN/DD/cc/84-1
16. K. Werner, Phys. Rep. **232**, (1993) 87
17. WA80 collaboration, R. Albrecht et al., Z. Phys. C **55**, (1992) 539
18. WA98 collaboration, M. Aggarwal et al., Phys. Lett. B **458** (1999) 422
19. K. Reygers, doctoral thesis, University of Münster, Germany (1999)

20. WA98 collaboration, M. Aggarwal et al., Phys. Rev. Lett. **85**, (2000) 3595
21. WA98 collaboration, M. Aggarwal et al., nucl-ex/0006007, submitted to Phys. Rev. C
22. C. DeMarzo et al., Phys. Rev. D **26**, (1982), 1019
23. C.Y. Wong, Z.D Lu, Phys. Rev. D **39**, (1989) 2606
24. C.Y. Wong, Phys. Rev. D **32**, (1985) 94
25. C.Y. Wong, Introduction to High-Energy Heavy-Ion Collisions, World Scientific Co., Singapore (1994), 280–281
26. J.E Elias et al., Phys. Rev. Lett. **41**, (1978) 285
27. C.Y. Wong, Phys. Rev. D **30**, (1984) 961
28. B. Frois et al., Phys. Rev. Lett. **38**, (1977) 152
29. H. Pi, Comput. Phys. Commun. **71**, (1992) 173

Observation of Direct Photons in Central 158A GeV ^{208}Pb + ^{208}Pb Collisions

M. M. Aggarwal,[1] A. Agnihotri,[2] Z. Ahammed,[3] A. L. S. Angelis,[4] V. Antonenko,[5] V. Arefiev,[6] V. Astakhov,[6] V. Avdeitchikov,[6] T. C. Awes,[7] P. V. K. S. Baba,[8] S. K. Badyal,[8] C. Barlag,[9] S. Bathe,[9] B. Batiounia,[6] T. Bernier,[10] K. B. Bhalla,[2] V. S. Bhatia,[1] C. Blume,[9] R. Bock,[11] E.-M. Bohne,[9] Z. Böröcz,[9] D. Bucher,[9] A. Buijs,[12] H. Büsching,[9] L. Carlen,[13] V. Chalyshev,[6] S. Chattopadhyay,[3] R. Cherbatchev,[5] T. Chujo,[14] A. Claussen,[9] A. C. Das,[3] M. P. Decowski,[18] H. Delagrange,[10] V. Djordjadze,[6] P. Donni,[4] I. Doubovik,[5] S. Dutt,[8] M. R. Dutta Majumdar,[3] K. El Chenawi,[13] S. Eliseev,[15] K. Enosawa,[14] P. Foka,[4] S. Fokin,[5] M. S. Ganti,[3] S. Garpman,[13] O. Gavrishchuk,[6] F. J. M. Geurts,[12] T. K. Ghosh,[16] R. Glasow,[9] S. K. Gupta,[2] B. Guskov,[6] H. Å. Gustafsson,[13] H. H. Gutbrod,[10] R. Higuchi,[14] I. Hrivnacova,[15] M. Ippolitov,[5] H. Kalechofsky,[4] R. Kamermans,[12] K.-H. Kampert,[9] K. Karadjev,[5] K. Karpio,[17] S. Kato,[14] S. Kees,[9] C. Klein-Bösing,[9] S. Knoche,[9] B. W. Kolb,[11] I. Kosarev,[6] I. Koutcheryaev,[5] T. Krümpel,[9] A. Kugler,[15] P. Kulinich,[18] M. Kurata,[14] K. Kurita,[14] N. Kuzmin,[6] I. Langbein,[11] A. Lebedev,[5] Y. Y. Lee,[11] H. Löhner,[16] L. Luquin,[10] D. P. Mahapatra,[19] V. Manko,[5] M. Martin,[4] G. Martínez,[10] A. Maximov,[6] G. Mgebrichvili,[5] Y. Miake,[14] Md. F. Mir,[8] G. C. Mishra,[19] Y. Miyamoto,[14] B. Mohanty,[19] M.-J. Mora,[10] D. Morrison,[20] D. S. Mukhopadhyay,[3] H. Naef,[4] B. K. Nandi,[19] S. K. Nayak,[10] T. K. Nayak,[3] S. Neumaier,[11] A. Nianine,[5] V. Nikitine,[6] S. Nikolaev,[5] P. Nilsson,[13] S. Nishimura,[14] P. Nomokonov,[6] J. Nystrand,[13] F. E. Obenshain,[20] A. Oskarsson,[13] I. Otterlund,[13] M. Pachr,[15] S. Pavliouk,[6] T. Peitzmann,[9] V. Petracek,[15] W. Pinganaud,[10] F. Plasil,[7] U. v. Poblotzki,[9] M. L. Purschke,[11] J. Rak,[15] R. Raniwala,[2] S. Raniwala,[2] V. S. Ramamurthy,[19] N. K. Rao,[8] F. Retiere,[10] K. Reygers,[9] G. Roland,[18] L. Rosselet,[4] I. Roufanov,[6] C. Roy,[10] J. M. Rubio,[4] H. Sako,[14] S. S. Sambyal,[8] R. Santo,[9] S. Sato,[14] H. Schlagheck,[9] H.-R. Schmidt,[11] Y. Schutz,[10] G. Shabratova,[6] T. H. Shah,[8] I. Sibiriak,[5] T. Siemiarczuk,[17] D. Silvermyr,[13] B. C. Sinha,[3] N. Slavine,[6] K. Söderström,[13] N. Solomey,[4] G. Sood,[1] S. P. Sørensen,[7,20] P. Stankus,[7] G. Stefanek,[17] P. Steinberg,[18] E. Stenlund,[13] D. Stüken,[9] M. Sumbera,[15] T. Svensson,[13] M. D. Trivedi,[3] A. Tsvetkov,[5] L. Tykarski,[17] J. Urbahn,[11] E. C. v. d. Pijll,[12] N. v. Eijndhoven,[12] G. J. v. Nieuwenhuizen,[18] A. Vinogradov,[5] Y. P. Viyogi,[3] A. Vodopianov,[6] S. Vörös,[4] B. Wysłouch,[18] K. Yagi,[14] Y. Yokota,[14] and G. R. Young[7]

(WA98 Collaboration)

[1]*University of Panjab, Chandigarh 160014, India*
[2]*University of Rajasthan, Jaipur 302004, Rajasthan, India*
[3]*Variable Energy Cyclotron Centre, Calcutta 700 064, India*
[4]*University of Geneva, CH-1211 Geneva 4, Switzerland*
[5]*RRC "Kurchatov Institute," RU-123182 Moscow, Russia*
[6]*Joint Institute for Nuclear Research, RU-141980 Dubna, Russia*
[7]*Oak Ridge National Laboratory, Oak Ridge, Tennessee 37831-6372*
[8]*University of Jammu, Jammu 180001, India*
[9]*University of Münster, D-48149 Münster, Germany*
[10]*SUBATECH, Ecole des Mines, Nantes, France*
[11]*Gesellschaft für Schwerionenforschung (GSI), D-64220 Darmstadt, Germany*
[12]*Universiteit Utrecht/NIKHEF, NL-3508 TA Utrecht, The Netherlands*
[13]*University of Lund, SE-221 00 Lund, Sweden*
[14]*University of Tsukuba, Ibaraki 305, Japan*
[15]*Nuclear Physics Institute, CZ-250 68 Rez, Czech Republic*
[16]*KVI, University of Groningen, NL-9747 AA Groningen, The Netherlands*
[17]*Institute for Nuclear Studies, 00-681 Warsaw, Poland*
[18]*MIT, Cambridge, Massachusetts 02139*
[19]*Institute of Physics, 751-005 Bhubaneswar, India*
[20]*University of Tennessee, Knoxville, Tennessee 37966*

(Received 13 June 2000)

A measurement of direct photon production in ^{208}Pb + ^{208}Pb collisions at 158A GeV has been carried out in the CERN WA98 experiment. The invariant yield of direct photons in central collisions is extracted as a function of transverse momentum in the interval $0.5 < p_T < 4$ GeV/c. A significant direct photon signal, compared to statistical and systematical errors, is seen at $p_T > 1.5$ GeV/c. The result constitutes the first observation of direct photons in ultrarelativistic heavy-ion collisions. It could be significant for diagnosis of quark-gluon-plasma formation.

PACS numbers: 25.75.–q, 12.38.Mh, 24.85.+p

 © 2000 The American Physical Society

The observation of a new phase of strongly interacting matter, the quark-gluon plasma (QGP), is one of the most important goals of current nuclear physics research. An extensive experimental program has been undertaken at the CERN SPS accelerator with Pb-ion beams of 158*A* GeV to search for and investigate the QGP. Several observations, such as suppression of the J/ψ resonance [1] and the enhancement of strangeness [2], hint at an interesting new behavior of the matter produced in these collisions. While such observations imply a hot and dense initial phase with strong rescattering, consistent with the assumption that a quark-gluon plasma was formed, a direct signature of the plasma and its properties is missing. It is therefore of great interest to search for photons emitted directly from the early hot phase of the relativistic heavy-ion collisions.

Following early estimates of photon emission rates [3–6], Kapusta *et al.* [7] made detailed comparisons of the emissivity of the QGP and a hadron gas as two contrasting scenarios. It was demonstrated that the thermal emission rates of a hadron gas and a QGP were very similar and dependent essentially only on the temperature T. This led the authors to conclude that direct photons are a good thermometer for strongly interacting matter, but would not in themselves allow one to distinguish between the two scenarios.

Recently, it was shown by Aurenche *et al.* [8] that photon production rates in the QGP, when calculated up to two-loop diagrams, are considerably greater than the earlier lowest order estimates. A new higher order process of $q\overline{q}$ annihilation with rescattering was found to dominate the photon emission rate from quark matter at high photon energies. Following this result, Srivastava [9] reinvestigated the predicted photon production in heavy-ion collisions and showed that at sufficiently high initial temperatures the photon yield from quark matter may significantly exceed the contribution from the hadronic matter to provide a direct probe of the quark matter phase.

A large number of measurements of prompt photon production at high transverse momentum ($p_T > 3$ GeV/c) exist for proton-proton, proton-antiproton, and proton-nucleus collisions (see e.g., Ref. [10]). To a great extent, especially at higher $\sqrt{s}$, these data can be successfully described by perturbative quantum chromodynamics calculations and provide an important foundation from which to study photon production in nucleus-nucleus collisions. First attempts to observe direct photon production in ultrarelativistic heavy-ion collisions with oxygen and sulphur beams found no significant excess [11–14]. The WA80 Collaboration [14] provided the most interesting result with a p_T dependent upper limit on the direct photon production in S + Au collisions at 200*A* GeV. This result was subsequently used by several authors to rule out a simple version of the hadron gas scenario [15–18] and has been interpreted to set an upper limit on the initial temperature of $T_i = 250$ MeV [19].

In this paper we report on the first observation of direct photon production in ultrarelativistic heavy-ion collisions. The results are from the CERN experiment WA98 [20] which consists of large acceptance photon and hadron spectrometers. In addition, several other large acceptance devices allow one to measure various global variables on an event-by-event basis for event characterization. Photons are measured with the WA98 lead-glass photon detector, LEDA, which consisted of 10 080 individual modules with photomultiplier readout. The detector was located at a distance of 21.5 m from the target and covered the pseudorapidity interval $2.35 < \eta < 2.95$ ($y_{cm} = 2.9$). The particle identification was supplemented by a charged particle veto detector in front of LEDA.

The results presented here were obtained from an analysis of the data taken with Pb beams in 1995 and 1996. The 20% most peripheral and the 10% most central reactions have been selected from the minimum-bias cross section ($\sigma_{\text{min-bias}} \approx 6300$ mb) using the measured transverse energy E_T. In total, $\approx 6.7 \times 10^6$ central and $\approx 4.3 \times 10^6$ peripheral reactions have been analyzed.

The extraction of direct photons in the high multiplicity environment of heavy-ion collisions must be performed on a statistical basis by comparison of the measured inclusive photon spectra to the background expected from hadronic decays. Individual photons cannot be tagged as isolated direct photons in these reactions due to the high multiplicities. To obtain the direct photon spectrum the following steps are performed (for a detailed description of the detectors and the analysis procedure, see Ref. [21]): The raw photon spectra are accumulated after application of the photon identification criteria (such as transverse shower size) to the showers observed in the LEDA. The raw photon spectra are then corrected for contamination by charged and neutral hadrons, for conversions, for the identification efficiency, and for acceptance. The efficiency includes all effects of the detector response such as distortions by shower overlap, dead and bad modules, and energy resolution. Neutral pions are reconstructed via their $\gamma\gamma$ decay branch. Invariant mass spectra are accumulated for all photon pairs for each pair p_T bin. The photon-pair combinatorial background is estimated by event mixing and then subtracted from the real-pair spectra. The yield in the π^0 mass peak is extracted to obtain the raw neutral pion p_T spectra. These are then corrected for conversions, for the π^0 identification efficiency, and for geometrical acceptance. In addition, η mesons are extracted in a limited transverse momentum range with an analogous procedure.

The final measured inclusive photon spectra are then compared to the calculated background photon spectra to check for a possible photon excess beyond that from long-lived radiative decays. The background calculation is based on the measured π^0 and η spectra. The measured η/π^0 ratio is found to be consistent with m_T scaling [21,22] which is assumed for the spectral shapes of the η and for other unmeasured hadrons having radiative decays.

The unmeasured hadron yields relative to π^0's are taken from the literature [21]. It should be noted that the measured contribution (from π^0 and η) amounts to $\approx$97% of the expected total photon background.

Figure 1 shows the fully corrected inclusive photon spectra for peripheral and central collisions. The spectra cover the p_T range of 0.3–4.0 GeV/c (slightly less for peripheral collisions) and extend over 6 orders of magnitude. Figure 1 also shows the distributions of neutral pions which extend over a similar momentum range with slightly larger statistical errors. The calculated decay photon background is shown by the solid curves.

The ratio of measured photons to calculated background photons is displayed in Fig. 2 as a function of transverse momentum. The upper plot shows the ratio for peripheral collisions which is seen to be compatible with 1, i.e., no indication of a direct photon excess is observed. The lower plot shows the same ratio for central collisions. It rises from a value of $\approx$1 at low p_T to exhibit an excess of about 20% at high p_T.

A careful study of possible systematical errors is crucial for the direct photon analysis. The various sources of systematical errors have been investigated and are summarized in Table I. The largest contributions are from the γ and π^0 identification efficiencies and the uncertainties related to the η measurement. It should be emphasized that the inclusive photon, π^0, and η yields have been extracted with the same detector for exactly the same data sample. This decreases the sensitivity to many detector related errors and eliminates all errors associated with trigger bias or absolute yield normalization. The estimate of the systematical errors has been checked by performing the entire analysis with various photon selection criteria which change the efficiency and background corrections by factors of 2–3. The final results were verified to be consistent within the systematical errors for the different analysis cuts. Full details on the systematical error estimates are given in [21]. The total p_T dependent systematical errors are shown by the shaded regions in Fig. 2. A significant photon excess is clearly observed in central collisions for $p_T > 1.5$ GeV/c.

The final invariant direct photon yield per central collision is presented in Fig. 3. The statistical and asymmetric systematical errors of Fig. 2 are added in quadrature to obtain the total upper and lower errors shown in Fig. 3. An additional p_T dependent error is included to account for that portion of the uncertainty in the energy scale which cancels in the ratios. In the case that the lower error is less than zero, a downward arrow is shown with the tail of the arrow indicating the 90% confidence level (C.L.) upper limit ($\gamma_{\text{excess}} + 1.28\sigma_{\text{upper}}$).

No published prompt photon results exist for proton-induced reactions at the $\sqrt{s}$ of the present measurement. Instead, prompt photon yields for proton-induced reactions on fixed targets at 200 GeV are shown in Fig. 3 for comparison. Results are shown from FNAL experiment E704 [23] for proton-proton reactions, and from FNAL experiment E629 [24] and CERN SPS experiment NA3 [25] for proton-carbon reactions. These results have been divided by the total pp inelastic cross section ($\sigma_{\text{int}} = 30$ mb)

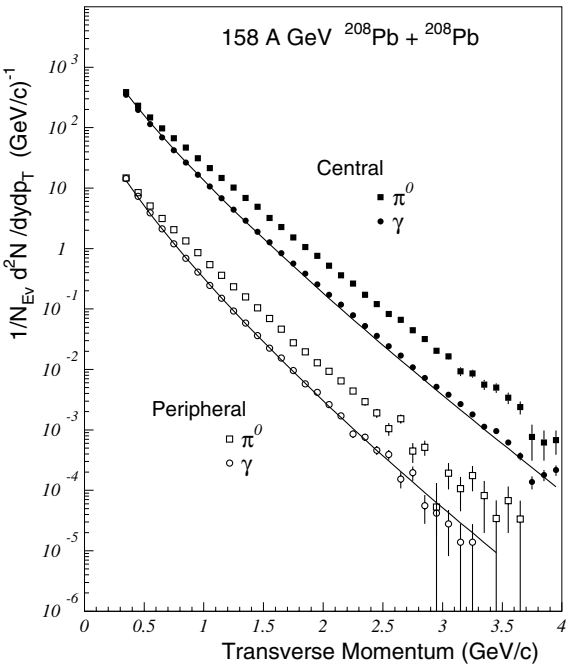

FIG. 1. The inclusive photon (circles) and π^0 (squares) transverse momentum distributions. Only statistical errors are shown.

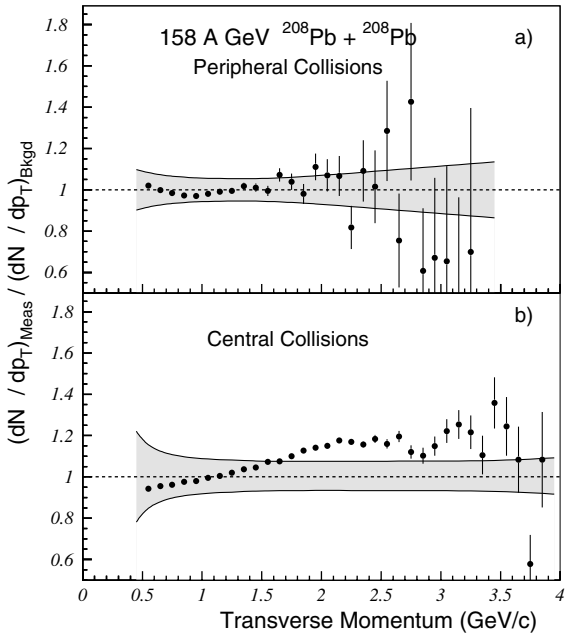

FIG. 2. The ratio of measured-to-calculated background photons as a function of transverse momentum for peripheral [part (a)] and central [part (b)] 158A GeV ^{208}Pb + ^{208}Pb collisions. The errors on the data points indicate the statistical errors only. The p_T dependent systematical errors are indicated by the shaded bands.

TABLE I. Various sources of systematical error in the WA98 158*A* GeV ^{208}Pb + ^{208}Pb direct photon analysis specified as a percentage of $(\gamma/\pi^0)_{\mathrm{meas}}$ (items *a*), $(\gamma/\pi^0)_{\mathrm{bkgd}}$ (items *b*), or $(\pi^0)_{\mathrm{meas}}/(\pi^0)_{\mathrm{bkgd}}$ (item *c*). The systematical errors are quoted at two p_T values to give an indication of the dependence on transverse momentum. See Ref. [21] for full details.

Source of Error	Peripheral Collisions (20% σ_{mb})		Central Collisions (10% σ_{mb})	
	$p_T \approx 1.0$ GeV/c	$p_T \approx 2.5$ GeV/c	$p_T \approx 1.0$ GeV/c	$p_T \approx 2.5$ GeV/c
(*a*) γ yield measurement	2.7	3.2	2.6	3.1
(*a*) π^0 yield measurement	3.1	3.0	6.5	4.2
(*a*) Nontarget background	1.5	<0.1	<0.1	<0.1
(*a*) Energy scale calibration	0.9	1.7	0.8	1.7
(*b*) Detector acceptance	0.5	0.5	0.5	0.5
(*b*) η/π ratio, m_T scaling	2.9	3.2	+3.4 (−4.8)	+3.7 (−5.2)
(*b*) Other radiative decays	1.0	1.0	1.0	1.0
(*c*) π^0 fit	1.6	6.8	2.9	0.4
Total: (quadratic sum)	5.7	8.9	+8.3 (−9.1)	+6.7 (−7.6)

and by the mass number of the target to obtain the invariant direct photon yield per nucleon-nucleon collision. They have then been multiplied by the calculated average number of nucleon-nucleon collisions (660) for the central Pb + Pb event selection for comparison with the present measurements. This scaling is estimated to have an uncertainty of less than 10%. The proton-induced results have also been scaled from $\sqrt{s} = 19.4$ GeV to the lower $\sqrt{s} = 17.3$ GeV of the present measurement under the assumption that $Ed^3\sigma_\gamma/dp^3 = f(x_T)/s^2$, where $x_T = 2p_T/\sqrt{s}$ [26]. The $\sqrt{s}$ scaling effectively reduces the 19.4 GeV proton-induced results by about a factor of 2. This comparison indicates that the observed direct photon production in central ^{208}Pb + ^{208}Pb collisions has a shape similar to that expected for proton-induced reactions at the same $\sqrt{s}$ but a yield which is enhanced.

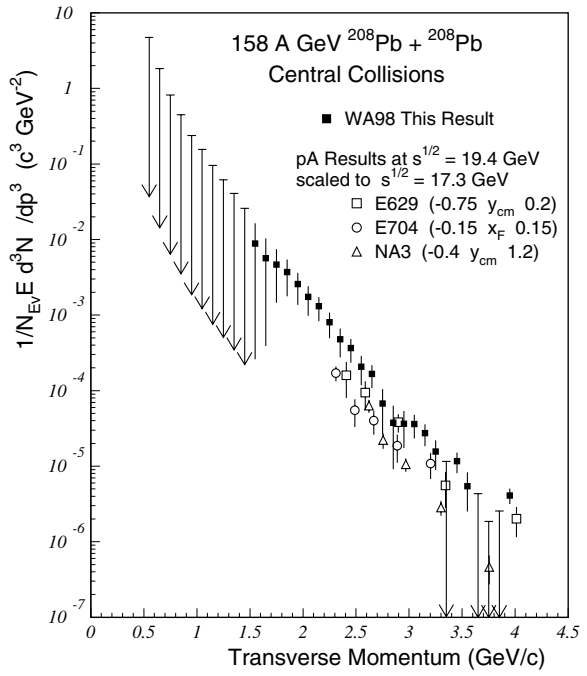

FIG. 3. The invariant direct photon multiplicity for central 158*A* GeV ^{208}Pb + ^{208}Pb collisions. The error bars indicate the combined statistical and systematical errors. Data points with downward arrows indicate unbounded 90% C.L. upper limits. Results of several direct photon measurements for proton-induced reactions have been scaled to central ^{208}Pb + ^{208}Pb collisions for comparison.

In summary, the first observation of direct photons in ultrarelativistic heavy-ion collisions has been presented. While peripheral Pb + Pb collisions exhibit no significant photon excess, the 10% most central reactions show a clear excess of direct photons in the range of p_T greater than about 1.5 GeV/c. The invariant direct photon multiplicity as a function of transverse momentum was presented for central ^{208}Pb + ^{208}Pb collisions and compared to proton-induced results at similar incident energy. The comparison suggests excess direct photon production in central ^{208}Pb + ^{208}Pb collisions beyond that expected from proton-induced reactions. The result suggests modification of the prompt photon production in nucleus-nucleus collisions, or additional contributions from preequilibrium or thermal photon emission. The result should provide a stringent test for different reaction scenarios, including those with quark-gluon-plasma formation, and may provide information on the initial temperature attained in these collisions.

We wish to express our gratitude to the CERN Accelerator Division for the excellent performance of the SPS accelerator complex. We acknowledge with appreciation the effort of all engineers, technicians, and support staff who participated in the construction of this experiment. This work was supported jointly by the German BMBF and DFG, the U.S. DOE, the Swedish NFR and FRN, the Dutch Stichting FOM, the Polish KBN under Contract No. 621/E-78/SPUB/CERN/P-03/DZ211, the Grant Agency of the Czech Republic under Contract No. 202/95/0217, the Department of Atomic Energy, the Department of Science and Technology, the Council of Scientific and Industrial Research and the University Grants Commission of the Government of India, the Indo-FRG Exchange Program, the PPE division of CERN, the Swiss National Fund, the INTAS under Contract

No. INTAS-97-0158, ORISE, Grant-in-Aid for Scientific Research (Specially Promoted Research & International Scientific Research) of the Ministry of Education, Science and Culture, the University of Tsukuba Special Research Projects, and the JSPS Research Fellowships for Young Scientists. ORNL is managed by UT-Battelle, LLC, for the U.S. Department of Energy under Contract No. DE-AC05-00OR22725. The MIT group has been supported by the U.S. Department of Energy under the cooperative agreement DE-FC02-94ER40818.

[1] M. C. Abreu *et al.,* Phys. Lett. B **410**, 337 (1997).
[2] E. Andersen *et al.,* Phys. Lett. B **449**, 401 (1999).
[3] K. Kajantie and H. I. Miettinen, Z. Phys. C **9**, 341 (1981).
[4] F. Halzen and H. C. Liu, Phys. Rev. D **25**, 1842 (1982).
[5] B. Sinha, Phys. Lett. **128B**, 91 (1983).
[6] L. D. McLerran and T. Toimela, Phys. Rev. D **31**, 545 (1985).
[7] J. Kapusta, P. Lichard, and D. Seibert, Phys. Rev. D **44**, 2774 (1991).
[8] P. Aurenche, F. Gelis, H. Zaraket, and R. Kobes, Phys. Rev. D **58**, 085003 (1998).
[9] D. K. Srivastava, Eur. Phys. J. C **10**, 487 (1999).
[10] W. Vogelsang and M. R. Whalley, J. Phys. G **23**, A1 (1997).
[11] HELIOS Collaboration, T. Åkesson *et al.,* Z. Phys. C **46**, 369 (1990).
[12] WA80 Collaboration, R. Albrecht *et al.,* Z. Phys. C **51**, 1 (1991).
[13] CERES Collaboration, R. Baur *et al.,* Z. Phys. C **71**, 571 (1996).
[14] WA80 Collaboration, R. Albrecht *et al.,* Phys. Rev. Lett. **76**, 3506 (1996).
[15] D. K. Srivastava and B. Sinha, Phys. Rev. Lett. **73**, 2421 (1994).
[16] N. Arbex, U. Ornik, M. Plümer, A. Timmermann, and R. M. Weiner, Phys. Lett. B **354**, 307 (1995).
[17] A. Dumitru, U. Katscher, J. A. Maruhn, H. Stöcker, W. Greiner, and D. H. Rischke, Phys. Rev. C **51**, 2166 (1995).
[18] J. J. Neumann, D. Seibert, and G. Fai, Phys. Rev. C **51**, 1460 (1995).
[19] J. Sollfrank *et al.,* Phys. Rev. C **55**, 392 (1997).
[20] WA98 Collaboration, CERN/SPSLC 91-17, SPSLC/P260.
[21] M. M. Aggarwal *et al.,* nucl-ex/0006007 (to be published).
[22] M. Bourquin and J.-M. Gaillard, Nucl. Phys. **B114**, 334 (1976).
[23] E704 Collaboration, D. L. Adams *et al.,* Phys. Lett. B **345**, 569 (1995).
[24] E629 Collaboration, M. McLaughlin *et al.,* Phys. Rev. Lett. **51**, 971 (1983).
[25] NA3 Collaboration, J. Badier *et al.,* Z. Phys. C **31**, 341 (1986).
[26] J. F. Owens, Rev. Mod. Phys. **59**, 465 (1987).

arXiv:nucl-ex/0006007v2 13 Jun 2000

Direct Photon Production in 158 A GeV ^{208}Pb+^{208}Pb Collisions

M.M. Aggarwal,[1] A. Agnihotri,[2] Z. Ahammed,[3] A.L.S. Angelis,[4] V. Antonenko,[5] V. Arefiev,[6] V. Astakhov,[6] V. Avdeitchikov,[6] T.C. Awes,[7] P.V.K.S. Baba,[8] S.K. Badyal,[8] C. Barlag,[9] S. Bathe,[9] B. Batiounia,[6] T. Bernier,[10] K.B. Bhalla,[2] V.S. Bhatia,[1] C. Blume,[9] R. Bock,[11] E.-M. Bohne,[9] Z. Böröcz,[9] D. Bucher,[9] A. Buijs,[12] H. Büsching,[9] L. Carlen,[13] V. Chalyshev,[6] S. Chattopadhyay,[3] R. Cherbatchev,[5] T. Chujo,[14] A. Claussen,[9] A.C. Das,[3] M.P. Decowski,[18] H. Delagrange,[10] V. Djordjadze,[6] P. Donni,[4] I. Doubovik,[5] S. Dutt,[8] M.R. Dutta Majumdar,[3] K. El Chenawi,[13] S. Eliseev,[15] K. Enosawa,[14] P. Foka,[4] S. Fokin,[5] M.S. Ganti,[3] S. Garpman,[13] O. Gavrishchuk,[6] F.J.M. Geurts,[12] T.K. Ghosh,[16] R. Glasow,[9] S. K.Gupta,[2] B. Guskov,[6] H. Å.Gustafsson,[13] H. H.Gutbrod,[10] R. Higuchi,[14] I. Hrivnacova,[15] M. Ippolitov,[5] H. Kalechofsky,[4] R. Kamermans,[12] K.-H. Kampert,[9] K. Karadjev,[5] K. Karpio,[17] S. Kato,[14] S. Kees,[9] C. Klein-Bösing,[9] S. Knoche,[9] B. W. Kolb,[11] I. Kosarev,[6] I. Koutcheryaev,[5] T. Krümpel,[9] A. Kugler,[15] P. Kulinich,[18] M. Kurata,[14] K. Kurita,[14] N. Kuzmin,[6] I. Langbein,[11] A. Lebedev,[5] Y.Y. Lee,[11] H. Löhner,[16] L. Luquin,[10] D.P. Mahapatra,[19] V. Manko,[5] M. Martin,[4] G. Martínez,[10] A. Maximov,[6] G. Mgebrichvili,[5] Y. Miake,[14] Md.F. Mir,[8] G.C. Mishra,[19] Y. Miyamoto,[14] B. Mohanty,[19] D. Morrison,[20] D. S. Mukhopadhyay,[3] H. Naef,[4] B. K. Nandi,[19] S. K. Nayak,[10] T. K. Nayak,[3] S. Neumaier,[11] A. Nianine,[5] V. Nikitine,[6] S. Nikolaev,[5] P. Nilsson,[13] S. Nishimura,[14] P. Nomokonov,[6] J. Nystrand,[13] F.E. Obenshain,[20] A. Oskarsson,[13] I. Otterlund,[13] M. Pachr,[15] S. Pavliouk,[6] T. Peitzmann,[9] V. Petracek,[15] W. Pinganaud,[10] F. Plasil,[7] U. v. Poblotzki,[9] M.L. Purschke,[11] J. Rak,[15] R. Raniwala,[2] S. Raniwala,[2] V.S. Ramamurthy,[19] N.K. Rao,[8] F. Retiere,[10] K. Reygers,[9] G. Roland,[18] L. Rosselet,[4] I. Roufanov,[6] C. Roy,[10] J.M. Rubio,[4] H. Sako,[14] S.S. Sambyal,[8] R. Santo,[9] S. Sato,[14] H. Schlagheck,[9] H.-R. Schmidt,[11] Y. Schutz,[10] G. Shabratova,[6] T.H. Shah,[8] I. Sibiriak,[5] T. Siemiarczuk,[17] D. Silvermyr,[13] B.C. Sinha,[3] N. Slavine,[6] K. Söderström,[13] N. Solomey,[4] G. Sood,[1] S.P. Sørensen,[7,20] P. Stankus,[7] G. Stefanek,[17] P. Steinberg,[18] E. Stenlund,[13] D. Stüken,[9] M. Sumbera,[15] T. Svensson,[13] M.D. Trivedi,[3] A. Tsvetkov,[5] L. Tykarski,[17] J. Urbahn,[11] E.C.v.d. Pijll,[12] N.v. Eijndhoven,[12] G.J.v. Nieuwenhuizen,[18] A. Vinogradov,[5] Y.P. Viyogi,[3] A. Vodopianov,[6] S. Vörös,[4] B. Wysłouch,[18] K. Yagi,[14] Y. Yokota,[14] G.R. Young[7]

(WA98 Collaboration)

[1] *University of Panjab, Chandigarh 160014, India*
[2] *University of Rajasthan, Jaipur 302004, Rajasthan, India*
[3] *Variable Energy Cyclotron Centre, Calcutta 700 064, India*
[4] *University of Geneva, CH-1211 Geneva 4,Switzerland*
[5] *RRC "Kurchatov Institute", RU-123182 Moscow, Russia*
[6] *Joint Institute for Nuclear Research, RU-141980 Dubna, Russia*
[7] *Oak Ridge National Laboratory, Oak Ridge, Tennessee 37831-6372, USA*
[8] *University of Jammu, Jammu 180001, India*
[9] *University of Münster, D-48149 Münster, Germany*
[10] *SUBATECH, Ecole des Mines, Nantes, France*
[11] *Gesellschaft für Schwerionenforschung (GSI), D-64220 Darmstadt, Germany*
[12] *Universiteit Utrecht/NIKHEF, NL-3508 TA Utrecht, The Netherlands*
[13] *University of Lund, SE-221 00 Lund, Sweden*
[14] *University of Tsukuba, Ibaraki 305, Japan*
[15] *Nuclear Physics Institute, CZ-250 68 Rez, Czech Rep.*
[16] *KVI, University of Groningen, NL-9747 AA Groningen, The Netherlands*
[17] *Institute for Nuclear Studies, 00-681 Warsaw, Poland*
[18] *MIT Cambridge, MA 02139, USA*
[19] *Institute of Physics, 751-005 Bhubaneswar, India*
[20] *University of Tennessee, Knoxville, Tennessee 37966, USA*

(February 8, 2008)

A measurement of direct photon production in ^{208}Pb+^{208}Pb collisions at 158 A GeV has been carried out in the CERN WA98 experiment. The invariant yield or upper limit of direct photons as a function of transverse momentum in the interval $0.5 < p_T < 4$ GeV/c is presented. A significant direct photon excess is observed at $p_T > 1.5$ GeV/c in central collisions. The results are compared to proton-induced results and to theoretical predictions. Implications for the dynamics of high-energy heavy-ion collisions are discussed.

25.75.+r,13.40.-f,24.90.+p

I. INTRODUCTION

A major current goal of the field of nuclear physics is the experimental confirmation of the existence of a new phase of strongly interacting matter, the quark gluon plasma (QGP) [1], which is predicted to exist according to lattice calculations of quantum chromodynamics. Enhanced production of strange hadrons, photons, and dileptons, and suppression of J/ψ mesons are some of the proposed consequences of QGP formation. Both J/ψ suppression [2] and strangeness enhancement [3] have been observed in relativistic heavy-ion collisions with strongly enhanced nuclear effects. While these observations naturally lead to the conclusion that the initial phase of the collision consisted of a hot and dense system with strong rescattering, which may be explained by the assumption of QGP formation, the direct experimental detection of QGP through observation of direct emission of real or virtual photons from the quark matter remains to be attained.

Historically, photons and lepton-pairs were the probes first suggested to use to search for evidence of quark-gluon plasma formation in ultrarelativistic heavy ion collisions. During the collision, real photons are produced mainly by scattering amongst the electrically charged objects while virtual (i.e. massive) photons, which later decay into pairs of oppositely charged leptons, or dileptons, are produced mainly by particle-antiparticle annihilations. Once produced, the real and virtual photons will interact with the surrounding hot dense matter through the electromagnetic interaction only. The resulting small interaction cross section implies a long mean free path in the dense matter with the consequence that the photons are likely to escape unscathed once produced. As a result, real and virtual photons carry information about the conditions of the matter from which they were produced throughout the entire history of the heavy ion collision, including especially the initial hot dense phase. Therefore, if the initial phase includes a quark-gluon plasma which radiates real and virtual photons differently than would dense hadronic matter this difference may be apparent in the photon and dilepton spectra observed by the experimentalist. This is in contrast to hadrons which, due to their extremely short mean free path in the hot dense matter, are unlikely to escape until the system has cooled and expanded to the low temperature and low density freezeout stage. As a result, quark-gluon plasma formation during the initial stage of the collision will make its presence evident via hadronic probes only if it alters the macroscopic features of the system, such as its strangeness content or collective flow, in a way which is different from dense hadronic matter *and* if these altered features are preserved until the time of freezeout. Thus the electromagnetic and hadronic probes provide complementary information. Since the real and virtual photon emission rate is greatest in hot dense matter the electromagnetic probes should carry information mostly about the dynamics (or thermodynamics) of the initial phase of the collision, while hadronic probes carry information dominantly about the late stage of the collision.

Originally, Feinberg [4] and Shuryak [5] suggested that thermal emission might be an important process in hadron-induced and even lepton-induced reactions when a large multiplicity of particles are produced in the final state. In particular they pointed out that rescattering amongst the produced particles in local thermal equilibrium during the later stages of the interaction would give rise to real and virtual photon emission. (Bjorken and Weisberg made similar suggestions at that time about the possible importance of rescattering [6]). Such a mechanism could explain the, at that time, puzzling excess dilepton yield observed at intermediate dilepton masses, $M \leq 5$ GeV/c^2 [5]. Feinberg [4] speculated upon the nature of the hot prematter remaining after the interaction and suggested that it may even be gluonic matter with embedded quarks. Shuryak [5] went on to assume formation of such a quark-gluon plasma in order to calculate the emission rates by perturbative QCD methods.

While it remains unknown whether quark-gluon plasma may be produced in hadron-induced reactions, it was suggested shortly afterwards that relativistic collisions of heavy ions provide conditions likely to result in the production of quark-gluon plasma. Initially it was suggested that such a plasma might occur at incident laboratory energies as low as a few GeV per nucleon [7] due to compression of the colliding nuclei and the resulting high baryon density. Another estimate based on extrapolations of known properties of NN and NA collisions at energies of $E_{cm} \geq 30$ GeV suggested that the fragmentation regions of AA collisions were likely to result in quark-gluon plasma formation [8]. Later calculations solving the relativistic hydrodynamic equations indicated that the highest energy densities would instead occur in the mid-rapidity region with energy densities considered sufficient for QGP formation at incident energies of around 400 GeV per nucleon [9].

Almost concurrent with the suggestions to use relativistic heavy ions as a means to produce the QGP in the laboratory were suggestions to use dilepton or photon measurements to diagnose whether QGP has been formed. First estimates considering only the lowest order elementary processes and thermal parton distributions [10,11] concluded that the thermal dilepton emission rate from the QGP should exceed that from a hadronic gas in the mass region below the ρ [10], and that real and virtual photons should provide accurate information on the temperature of the plasma [11]. A simple counting estimate indicated an expected photon enhancement relative to the number of pions in the case of QGP formation [12]. First calculations which performed the space-time integration of the lowest order production rates by solving the relativistic hydrodynamic equations confirmed [13] that the dilepton yield in the mass region

below the ρ was sensitive to the initial temperature of the QGP and to the critical temperature. Alternatively, it was suggested that the ratio of the simultaneously observed photon and dilepton pair yield might provide a signal which was sensitive to QGP formation while being insensitive to the details of the collision dynamics [14].

While these initial estimates indicated that photons and dileptons should be useful probes to diagnose the presence of QGP, the rate estimates themselves were suspect since lowest order perturbative calculations had been applied at energies, or temperatures, similar to Λ_{QCD}, the QCD scale factor. The dilepton and photon rate estimates were put on firmer ground when McLerran and Toimela [15], following the suggestion by Feinberg [4] that the photon and dilepton rates could be determined from the expectation value of the electromagnetic current correlation function, demonstrated that for each order the emission rates had an invariant form with thermal structure functions entering in a manner exactly analogous to the usual structure functions for finding a quark or gluon in a hadron. Also, it was observed that terms which contribute to the dilepton or photon emission which are problematic at the basic diagram level, are regularized in the QGP. For example, dilepton emission from quark-antiquark annihilation is infrared divergent in the limit of zero mass gluons while in the plasma gluons propagate as plasma oscillations with a plasmon mass which provides a cutoff to eliminate the divergences for small gluon momenta [15].

Later, using the resummation techniques of Braaten and Pisarski [16,17], Kapusta et al. [18] demonstrated that the photon emission rates of quark gluon matter and hadronic matter were very similar. As a consequence, it could be concluded that while photon emission was not *per se* a signature of quark gluon matter, detection of the emitted photons could provide a good measurement of the temperature of the hot and dense matter.

Recently, the situation has changed again with the demonstration by Aurenche et al. [19] that the contribution to the photon emission rate from two-loop diagrams are significantly larger than the lowest order contributions of the Compton ($q(\overline{q})g \rightarrow q(\overline{q})\gamma$) and annihilation ($q\overline{q} \rightarrow g\gamma$) processes which were previously thought to dominate the photon emission rate from the quark matter. The two-loop diagrams were shown to give a large bremsstrahlung ($qq(g) \rightarrow qq(g)\gamma$) contribution and a contribution from a previously neglected process of $q\overline{q}$ annihilation accompanied by q(g) rescattering. This annihilation with rescattering process is found to dominate the photon emission rate of the quark matter at large transverse momenta. Inclusion of these rates in hydrodynamic model calculations of heavy-ion collisions has recently shown that photon yield from the quark matter may be significantly larger than the photon yield from the hadronic matter [20]. The direct photons may therefore dominantly carry information about the quark gluon plasma.

A large body of data on prompt photon emission exists for proton-induced reactions on targets of protons, anti-protons, and light nuclei [21–35]. The prompt photon measurements have provided important input on gluon structure functions [36]. It is now possible to perform complete and fully consistent next-to-leading order (NLO) QCD calculations of the prompt photon cross sections. In general, the prompt photon data can be well described from fixed target energies up to Tevatron energies [37] which provides an important foundation for the intrepretation of direct photon production in nucleus-nucleus collisions. In the past, discrepancies with calculation have sometimes been attributed to effects of intrinsic k_T smearing arising from higher order contributions such as soft-gluon emissions [33,36,38]. While the evidence for intrinsic k_T effects remains under debate [39], the observed trend of an underestimated prompt photon yield at low transverse momentum and low incident energy is suggestive of an intrinsic k_T effect [37,39]. A thorough understanding of the source of this discrepancy will be important in the search for thermal direct photons at low transverse momentum in nucleus-nucleus collisions at the presently available low incident energies.

First attempts to observe direct photon production in ultrarelativistic heavy-ion collisions with oxygen and sulphur beams found no significant excess [40–43]. The WA80 collaboration [43] provided the most interesting result with a p_T dependent upper limit on the direct photon production in S+Au collisions at 200AGeV. This result was subsequently used by several authors to rule out a simple version of the hadron gas scenario [44–47] and to establish an upper limit on the initial temperature of $T_i = 250\,\mathrm{MeV}$ [48]. In this paper, the first observation of direct photons from ultrarelativistic heavy-ion collisions is reported for central 158 *A* GeV ^{208}Pb+^{208}Pb collisons. The implications of the result are discussed.

The organization of the paper is as follows: A description of the WA98 experimental setup including the event selection and photon spectrometer are presented in the next section. A general description of the WA98 direct photon analysis method is given in Sec. III. The details of the data analysis including a presentation of the various corrections and their associated errors for extraction of the inclusive photon, π^0, and η yields is given in Sec. IV. The final inclusive photon, π^0, and η distributions are presented in Sec. V. The direct photon result is also presented in Sec. V and the results are compared to calculation and discussed. A summary and conclusion is given in Sec. VI.

II. WA98 EXPERIMENTAL SETUP

The CERN experiment WA98 is a general-purpose apparatus which consists of large acceptance photon and hadron spectrometers together with several other large acceptance devices which allow to measure various global variables on an event-by-event basis. The experiment took data with the 158 A GeV ^{208}Pb beams from the SPS in 1994, 1995, and 1996. The results presented here were obtained from analysis of the 1995 and 1996 data sets. The layout of the WA98 experiment as it existed during the final WA98 run period in 1996 is shown in Fig. 1.

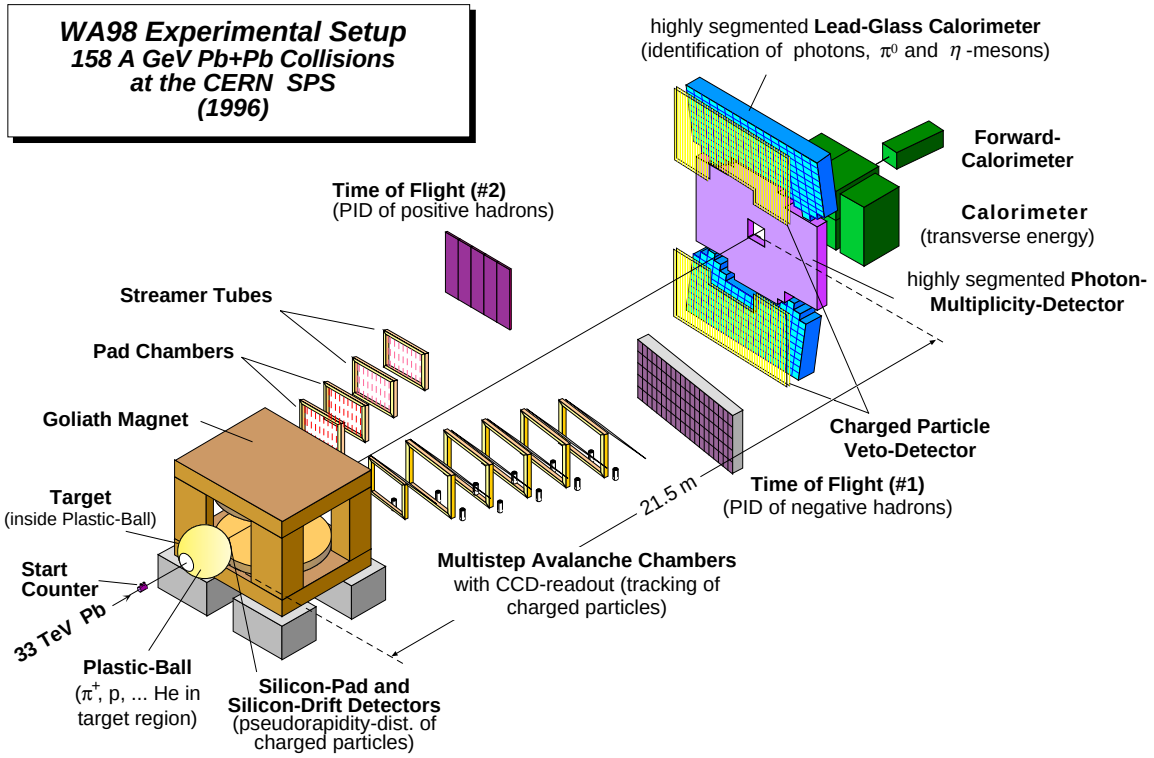

FIG. 1. The WA98 experimental setup.

A. Detector Subsytems

Each 158 A GeV ^{208}Pb beam particle is qualified in a series of trigger counters located upstream of the target. The ^{208}Pb target is mounted in a thin target wheel at the center of a 20 cm diameter spherical thin-walled aluminum vacuum chamber located within the Plastic Ball detector. The target wheel has 5 target positions, one of which was empty for non-target background measurements.

The Plastic Ball detector consists of 655 modules which provide energy measurement and particle identification of charged pions and light particles by $\Delta E - E$ measurement [49]. The Plastic Ball detector provides particle measurement over the interval $-1.7 < \eta < 1.3$. Each module comprises a slow 4 mm thick CaF_2 ΔE scintillator followed by a fast plastic scintillator readout by a common photomultiplier. The signals from the photomultipliers of the two forward-most rings of Plastic Ball modules, subtending the angular region from 30° to 50°, are split and a portion of the signals are analog summed to provide an online energy signal for trigger purposes. This signal is used to suppress interactions downstream of the target.

The target vacuum chamber is extended downstream in a 30° conical vacuum chamber which contains the Silicon Drift Detector (SDD) and the Silicon Pad Multiplicity Detector (SPMD) [50], each consisting of 300 μm thick silicon wafers. The SDD and SPMD are located 12.5 cm and 30 cm downstream from the target, respectively. These detectors

provide charged particle multiplicity measurement over the intervals of $2.5 < \eta < 3.75$ and $2.3 < \eta < 3.75$, respectively.

Charged particle momentum measurement and particle identification is accomplished using two tracking spectrometer arms. The momentum measurement is accomplished by magnetic analysis in a large (1.6 m) aperture dipole magnet called GOLIATH which provides 1.6 Tm bending power. Both tracking spectrometers use straight-line tracking outside the magnetic field. Particle identification is obtained using time-of-flight measured with scintillator slat detectors in each tracking arm. In the normal magnetic field configuration the negative tracks are deflected to the right, looking downstream, into the first tracking arm. The first tracking arm consists of six planes of multi-step avalanche chambers [51]. The active area of the first tracking chamber is 1.2×0.8 m^2 while that of the other five chambers is 1.6×1.2 m^2. The chambers produce UV photons by means of a photoemissive vapor which are then converted to visible light via wavelength shifter plates. On exiting the chamber, the visible light is reflected 45° by thin-foil mirrors to CCD cameras equipped with two-stages of image intensifiers. Each CCD pixel viewed a chamber area of about 3.1×3.1 mm^2.

The second tracking arm measures positive-charged tracks in the normal field condition. It consists of four chambers of 1.6×1.2 m^2 [52]. The first two chambers are multi-step avalanche chambers similar to those of the first tracking arm, but with the avalanche signal collected directly on an anode plane with pad readout. In total about 35000 pads per chamber are read out. The last two tracking chambers consist of streamer tubes read out with 6000 pads each. The second tracking arm was installed and operated for the 1996 run period only.

The Photon Multiplicity Detector (PMD) [53] is located at a distance of 21.5 m downstream from the target. The PMD is a large (21 m^2) preshower detector consisting of 3.3 radiation lengths of lead used to convert and count photons. The lead converter is backed by over 50000 scintillator tiles individually wrapped and readout via wavelength shifter optical fibers coupled in groups to a set of CCD cameras with image intensifiers. The PMD provides a photon multiplicity measurement over the interval $2.8 < \eta < 4.4$.

The WA98 photon spectrometer comprises the LEad-glass photon Detector Array (LEDA), and a charged particle veto detector. The photon spectrometer is divided into two halves placed above and below the beam plane to benefit from the charge-sweeping effect of the GOLIATH magnet, and is located at about the same distance as the PMD. It provides photon energy measurement over the interval $2.4 < \eta < 3.0$. The photon spectrometer is described in more detail below.

Further downstream, at a distance of 24.7 m from the target, the total transverse energy is measured in the MIRAC calorimeter [54]. The MIRAC is a sampling calorimeter with 180 calorimeter towers readout on two sides with wavelength shifter plates coupled to photomultipliers. Each tower is segmented longitudinally to provide separate measurement of the electromagnetic and hadronic energy deposit. A portion of the signal from each photomultiplier of MIRAC is split off and the analog signal is summed with appropriate weight to form a total transverse energy signal for trigger purposes. The MIRAC is deployed in a rectangular wall 3.3 m wide by 2.4 m high centered on the beam axis with a central aperture 61 cm wide by 23 cm high through which the beam passes. A portion of the MIRAC coverage overlaps with the PMD preshower detector. The MIRAC provides total transverse energy measurement with varying azimuthal coverage over the interval $3.2 < \eta < 5.4$.

Finally, the total energy of the uninteracting beam, or of the residual beam fragments and produced particles emitted near to zero degrees, is measured in the Zero Degree Calorimeter (ZDC). The ZDC consists of 35 lead/scintillator sampling calorimeter modules of 15×15 cm^2 cross sectional area each. For each module the scintillator is read out from the side with a fast wavelength shifter plate coupled to a photomultiplier with an active base. This allowed stable operation with intensities up to 1 MHz of the full 33 TeV ^{208}Pb beam. The ZDC modules were stacked in an array 7 modules wide by 5 modules high. Since it serves as the WA98 beam stop the ZDC is located in a shielded cave (not shown in Fig. 1) for radiological protection reasons. The cave is located just behind MIRAC with an entrance aperture the same size as the aperture through MIRAC.

In order to minimize backgrounds, WA98 has been designed with attention to minimize the amount of material in the beamline and in the flight paths of the detected particles. Thus, except for trigger detectors in the beamline and a small air gap in the GOLIATH magnet, the beam is transported in an evacuated beampipe (not shown in Fig. 1) from the point of extraction from the SPS through the entire experiment until just before being stopped in the ZDC. A trapezoidal chamber extends the vacuum beyond the silicon detectors to the entrance of the GOLIATH magnet. It ends with a $1.4 \times 1.$ m^2 exit window of 125 μm thick mylar suspended by a kevlar mesh of 240 μm average thickness. For the 1995 run period a 2.5 mm thick aluminum ring of 15 mm diameter with a 11 mm diameter hole was attached to the exit window at the location of the beam exit. The thick mylar and kevlar mesh was removed from the ring aperature and replaced by a thin mylar foil. While the purpose of the thin foil had been to reduce downstream interactions, the ring caused significant interactions from the beam halo and so the exit window was replaced with a homogeneous mesh and mylar foil for the 1996 run period. After a 75 cm air gap, the vacuum continues with a series of 0.5 mm thick carbon fiber beam tubes. The first beam tube is of 5 cm diameter and 1.44 m length followed by a second tube of

10 cm diameter and 4.5 m length. A third beam tube continues through the experiment with a 20 cm diameter to the front of the MIRAC calorimeter where it attaches to a rectangular vacuum pipe which defines the aperture in MIRAC and terminates the vacuum at the rear of MIRAC just before the entrance to the ZDC.

The PMD, SDD, and tracking spectrometers are not used in the present analysis and will not be discussed further. Additional details on event selection and on the photon spectrometer are given next.

B. Event Selection

The WA98 trigger detectors comprise a nitrogen gas Čerenkov counter [55] to provide a fast start signal ($\leq$ 30 ps time resolution), beam-halo veto counters, and the MIRAC calorimeter. A clean beam trigger is defined as a signal in the start counter, located 3.5 m upstream of the target, with no coincident signal in the veto scintillator counter (which had a 3 mm diameter circular hole and was located 2.7 m upstream of the target), or in beam halo scintillator counters which covered the region from the veto counter to 25 cm transverse to the beam axis. Beam fragments from upstream interactions are rejected by use of a high threshold on the start counter signal, set just below the ^{208}Pb signal. Short timescale pileup events are vetoed by an anti-coincidence requirement with a higher threshold start signal, set just above the ^{208}Pb signal. Additional background event rejection is performed offline using the amplitude and timing information from the trigger detectors. For purposes of background rejection each of the trigger logic signals is copied multiple times and recorded on TDCs with various delayed starts or delayed stops which allow to inspect the time period immediately preceeding or following the trigger event. This set of TDCs allows to reject pileup beam particles or interactions over preceeding or following time ranges of 100 ns, 500 ns, or 10 μs in the offline analysis.

The MIRAC calorimeter provides an analog total transverse energy sum for centrality selection for online trigger purposes. The WA98 minimum bias trigger requires a clean beam trigger with a MIRAC transverse energy signal which exceeds a low threshold. Two additional trigger signals are derived from the MIRAC transverse energy signal using thresholds set somewhat above and far above the minimum bias threshold. These three MIRAC thresholds define three non-overlapping event classes which are used to define the WA98 physics triggers. The thresholds were adjusted such that the so-called peripheral event class, between the lowest and next-to-lowest thresholds, corresponded to about 20% of the minimum bias event rate and the central event class, above the highest threshold, corresponded to about 10% of the minimum bias event rate. The remaining $\approx 70\%$ of the minimum bias cross section between central and peripheral event classes is referred to as the not-so-central event class. Taken together the three event classes were equivalent to the minimum bias event class. In normal run operation the central event class triggers were taken without prescale factor while the peripheral event triggers were typically downscaled by a factor of two and the not-so-central triggers were usually prescaled by a factor of 32 (after deadtime suppression) for the 1995 run period. For the 1996 run period the peripheral and not-so-central event classes were typically downscaled by a factor of 4 and 16, respectively. Downscaled beam triggers and in-spill pedestal triggers were also taken at a low rate as well as various out-of-spill calibration triggers for monitoring and calibration purposes for the various detectors. In order to obtain absolute cross section information, all trigger logic signals were counted with scalers before and after deadtime suppression, and after application of downscale factors. The scalers were recorded between spills.

In order to obtain the maximum data rate for the direct photon measurement, WA98 was operated with three different event types. The event types were distinguished by different groups of detectors with different readout deadtimes, varying up to about 5ms, 10 ms, or 15 ms for event types one, two, or three, respectively. Event type one included the trigger detectors, MIRAC, ZDC, Plastic Ball, and the photon spectrometer. Event type two also included the PMD, SPMD, and SDD. Event type three further included the tracking spectrometers. Zero-suppressed data volumes of about 50 kbyte/event were produced for central collisions. The experiment operated with a typical beam intensity of ≈ 0.5 MHz ^{208}Pb delivered to target over an effective SPS spill of about 2.5 s during the 14.4 s machine cycle. About 250 events were recorded per spill with a typical deadtime of about 80%.

C. Photon Spectrometer

The WA98 photon spectrometer consists of a large area lead-glass detector array, LEDA, supplemented with a charged particle veto (CPV) detector placed immediately in front of it (see Fig. 1). The spectrometer has an unobstructed view of the target through the vacuum chamber exit window at the entrance to the GOLIATH magnet. The photon spectrometer is separated into two nearly symmetric halves above and below the beam plane in the two regions of reduced charged particle density which result from the sweeping action of the GOLIATH magnet. The two detector halves are inclined by an angle of 8° such that photons near the center of the detector impinge with normal incidence. The maximum deviation from normal incidence to the detector surface is less than 9° at the detector corners. The

perpendicular distance to the front surface of the lead-glass is 22.1 m. This distance was chosen to allow the photon measurement near mid-rapidity while maintaining a maximum local particle hit occupancy below 3%, which is necessary to insure that overlapping shower effects remain manageable.

The acceptance of the photon spectrometer for π^0 and η detection, in rapidity and transverse momentum of the π^0 or η, is shown in Fig. 2. The acceptance is calculated for a 750 MeV photon energy threshold. The acceptance in part a) is shown for detection of a single photon from the decaying π^0. It indicates the phase space region over which π^0's contribute photons into the acceptance of the spectrometer. The acceptance for simultaneous detection of both photons from the π^0 and η two-photon decay branch is shown in parts b) and c), respectively. The acceptance covers the region $2.4 < y < 3.0$, near mid-rapidity ($y_{cm} = 2.9$).

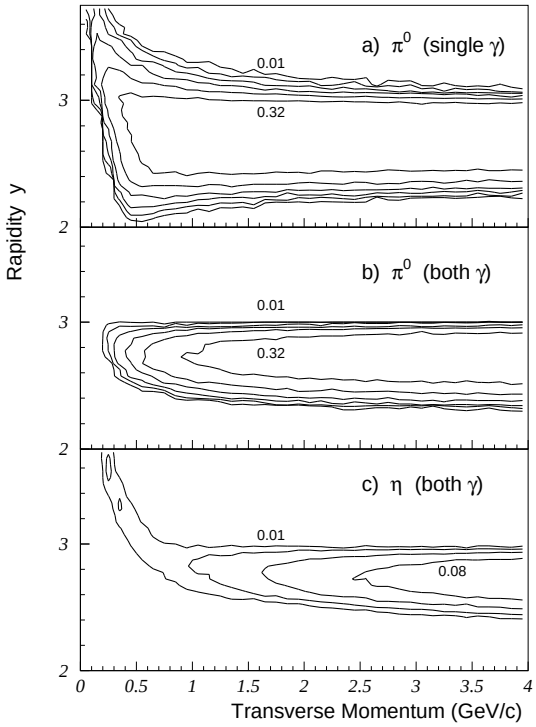

FIG. 2. The acceptance of the WA98 photon spectrometer in parent particle rapidity versus transverse momentum for a) single photons from π^0 decay and for photon-pairs from b) π^0 decay or c) η decay with a 750 MeV photon energy threshold. The contours show the fraction of full phi acceptance in steps of factors of two.

1. Lead-Glass Detector

The lead-glass detector comprises 10,080 individual lead-glass modules. Each module is a $4 \times 4 \times 40$ cm^3 (14.3 radiation lengths) TF1 lead-glass block with photomultiplier readout. The sides of each block are wrapped in an aluminized mylar reflective foil and sealed in a PVC plastic shrink tube of 0.15 mm wall thickness. Twenty-four lead-glass modules are epoxied together in an array 6 modules wide by 4 modules high to form a super-module. Each super-module has its own calibration and gain monitoring system based on a set of 3 LEDs mounted inside a sealed reflecting front cover dome [56]. Each lead-glass module views the reflected LED light through an aperture on the front surface, while the LED light is simultaneously monitored by a PIN-photodiode.

All 10,080 lead-glass modules were calibrated with 10 GeV electrons in the X1 beamline in the west area of the CERN SPS during the period of fall 1993 to spring 1994. The calibration beam was used to determine the GeV equivalent of the photodiode-normalized LED light viewed by each lead-glass module. The LED system allowed the calibration to be maintained after the lead-glass was installed in the WA98 experimental area with a new readout system. The energy and position resolution, and the non-linearity of the lead-glass detector were measured in the same test beam using electrons of incident energies from 3 GeV to 20 GeV. The measured energy resolution could be parameterized as [56]

$$\sigma/E = (5.5 \pm 0.6)\%/\sqrt{E} + (0.8 \pm 0.2)\% \tag{2.1}$$

and the measured position resolution could be parameterized as

$$\sigma_x = (8.35 \pm 0.25)\ \mathrm{mm}/\sqrt{E} + (0.15 \pm 0.07)\ \mathrm{mm} \tag{2.2}$$

with energy measured in GeV.

Each lead-glass module is read out by an FEU-84 photomultiplier with individually controlled high voltage. The high voltage is generated on-base with custom developed [57] Cockcroft-Walton voltage-multiplier type bases. The bases are controlled using a VME based processor and controllers. The photomultiplier signals are digitized with a custom-built ADC system [58] which was installed in the fall of 1994. The system features a fast shaping amplifier with dual gain ranges separated by a factor of 8 in gain. Each gain range is digitized with 10-bits resolution for 13-bits of effective dynamic range. The ADC system includes an analog memory in which the integrated signal is sampled and stored at 20 MHz in a ring buffer 16 cells deep. The analog memory provides the latency needed (≈ 400 ns) for the WA98 trigger decision without the need for cable delay of the photomultiplier signals. The readout system also includes a constant fraction discriminator with TAC for time-of-flight measurement, and overlapping module current sums for possible trigger purposes, neither of which are used for the present analysis.

After calibration and installation in WA98 with the new readout system, the high voltage of each module was adjusted to set the full-scale ADC value at 40 GeV, based on the GeV-equivalent of the calibrated LED light. During the period of datataking, the LED system was pulsed and all lead-glass modules and photodiodes were read out and recorded between spills at a frequency of a few Hz. These calibration events were used offline to provide time-dependent gain correction factors for each module. The gain correction factors were stored in a database and applied on a run-by-run basis in the offline analysis. The overall stability of the lead-glass system is indicated in Fig. 3 where the time-dependent gain correction, averaged over all lead-glass modules, is plotted as a function of time during the 1995 run period. The rms of the distribution of module gains at a given time is indicated by the vertical bars. The smallness of the rms values throughout the run period demonstrates the stability of the high voltage and readout systems while the diurnal variation of the average gain factors suggests a sensitivity of the photomultiplier gains to the temperature in the experimental hall. Fig. 3 gives a good indication of the magnitude and importance of the time-dependent gain corrections which have been applied.

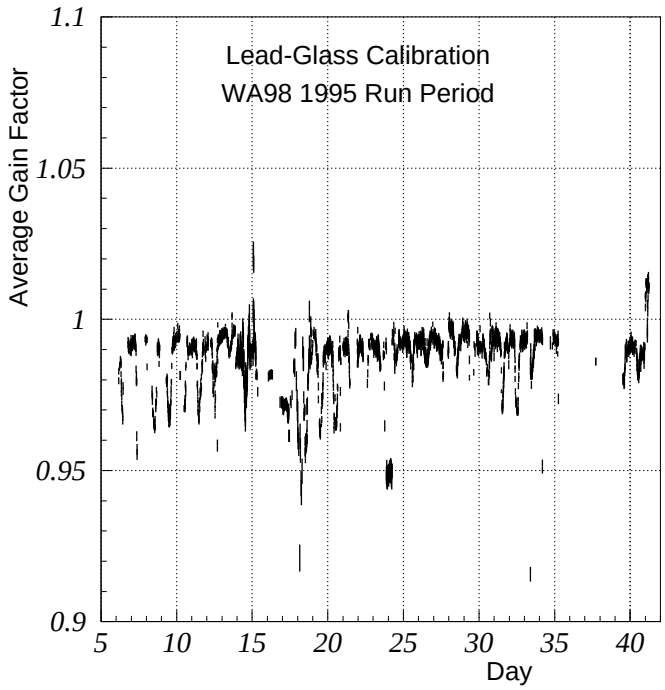

FIG. 3. The stability of the lead-glass calibration as determined with the LED monitoring system. The time-dependent gain factor, averaged over all modules, is shown as a function of time for the entire 1995 run period. The vertical size of the points indicates the rms of the distribution of time-dependent gains of all modules.

2. Charged Particle Veto Detector

In order to tag and thereby directly deduce the fraction of showers observed in the lead-glass originating from charged hadron, the photon spectrometer is supplemented by a Charged Particle Veto (CPV) detector which covers the lead-glass region of acceptance [59]. The two sections of the CPV each consist of 86 Iarocci-type plastic streamer tubes in a single layer. Each tube is tilted by 30° to avoid normal particle incidence which would result in a 7% geometrical inefficiency due to the streamer tube walls. The streamer tubes are operated with a gas mixture of 10% argon, 30% isobutane, and 60% carbon dioxide at atmospheric pressure. A streamer discharge induces a charge signal on externally mounted pads which have a size of 42 mm $\times$ 7 mm. Groups of 16 pads are connected to a charge sensitive chip which converts a charge signal into a 6 bit ADC value. In total 49120 pads and 3070 chips are necessary to read out the 19 m^2 active area of the CPV. The CPV detector is nearly transparent to high energy photons with only 2.0% of incident photons converting and producing detectable signals inside the streamer tubes. The CPV was under construction at the time of the 1995 ^{208}Pb run and was fully operational only for the 1996 run period. As a result, the CPV has been used in the analysis of the 1996 data set only.

By employing magnetic field off data, with straight-line trajectories from the target, the silicon pad multiplicity detector can be used together with the lead-glass detector to determine the average CPV efficiency *in situ*. The SPMD consists of four quadrants each divided into 1012 pads with 46 azimuthal divisions and 22 radial divisions. Each pad has roughly equal size in $\Delta\eta \times \Delta\phi$ of about $0.065 \times 2^\circ$. The efficiency for detecting a charged particle in the SPMD was measured in a test beam to be better than 99%.

III. DATA ANALYSIS METHOD

In this section we discuss the WA98 direct photon analysis method. An overview of the method is presented followed by a discussion of the details of the photon identification criteria and the photon and π^0 efficiency determination. These are the main sources of systematical error in the present direct photon analysis. Next, the method to determine the charged particle contamination in the photon yield is discussed. Then the calculation of the photon background expected from radiative decays of long-lived resonances is described. Finally, the extraction of the direct photon excess is discussed.

A. Direct Photon Analysis Overview

Due to the high photon multiplicity in central Pb+Pb collisions, and the limited photon spectrometer acceptance, it is not feasible to identify isolated single direct photons on an event-by-event basis. Instead, in the direct photon analysis presented here, the transverse momentum distribution of direct photons is determined on a statistical basis. In brief, the direct photon excess is extracted from the difference between the measured inclusive photon yield and the photon yield predicted from a calculation of the radiative decays of long-lived resonances. Among such decay photons, the π^0 and η comprise the largest source, contributing roughly 97% of the photon yield according to the expected relative abundances of produced particles (see Fig. 28). Therefore, in order to maximize the sensitivity of the measurement to a direct photon excess, it is imperative to accurately determine the π^0 and η yield.

In the WA98 measurement, the π^0 and η yield are determined via their two-photon decay branch for exactly the same event sample for which the inclusive photon yield is measured. This eliminates all systematical error sources related to absolute cross section normalization or centrality selection. In fact, this analysis method allows to determine the decay background correctly even if data sets with very different centralities or run conditions were combined arbitrarily since the averaged decay photon distribution would follow directly from the averaged π^0 and η distributions. Thus, for example, contributions from background sources such as a secondary target will not produce an apparent photon excess in this analysis, as long as their contribution to the π^0 and η yield can be extracted from the two-photon invariant mass peaks. Such background sources would distort the extracted π^0 and η transverse momentum distributions, but this distortion would also be reflected in the inclusive photon distribution. Similarly, a distortion of the photon momentum distribution due to a calibration error or non-linearity of the detector response would be reflected in the momentum (and mass) distribution of the reconstructed π^0's and η's. This means that the sensitivity of the direct photon search to detector calibration or non-linearity errors is reduced in this analysis. Furthermore, the momentum dependence of the π^0 invariant mass peak provides an *in situ* means to verify and quantify the accuracy of the detector calibration.

A major source of systematical error in the present analysis is the determination of the photon detection efficiency. Roughly speaking, since the photon detection efficiency enters quadratically in the efficiency correction of the π^0 yield extracted via its two-photon decay, but only linearly in the photon yield correction, an error in the photon

detection efficiency directly modifies the apparent photon excess. Thus a major emphasis of the present analysis is to demonstrate an accurate determination of the identification efficiencies and associated systematical errors. This is accomplished by applying different photon identification criteria having very different efficiencies and sensitivities to backgrounds, and verifying that the final corrected results are consistent in all cases.

Another source of error may be due to mis-identified non-photon backgrounds. Since the number of charged hadrons exceeds the number of photons by about a factor of three at large transverse momenta, they pose a large potential background of apparent excess photons if mis-identified as photons. Fortunately, high energy hadrons deposit only a small fraction of their incident energy in the lead-glass detector (its 40 cm length is about one interaction length). As a result, showers with large energy deposit, or large apparent transverse momentum, are predominantly photons with a hadron contamination of only about 10%. Since hadronic showers typically have large transverse dimension the hadron shower contamination can be further reduced by a factor of 2-3 by excluding showers with large width. Since the magnetic field alters the distribution and apparent transverse momenta of the charged hadrons while leaving the neutral particle distributions unchanged, a comparison of the extracted neutral shower result for magnetic field on and field off provides a consistency check of the charged hadron rejection. The Charged Particle Veto detector is used to determine the charged hadron contribution to the photon spectrum.

Another source of apparent photons is neutrons and anti-neutrons. This contribution is estimated by simulation only. Its contribution can similarly be reduced by excluding showers with large width. Consistency in the final result with different shower identification criteria and run conditions provides confirmation that the background contributions are properly eliminated.

B. Particle Identification and Yield Determination

The most critical requirement of the direct photon search is an accurate determination of the inclusive photon and π^0 yields. In general, the accuracy of the yield determination is verified by using different identification criteria with large differences in efficiency and background sensitivity, and demonstrating consistent final results. The π^0 yield is largely insensitive to background particles since the π^0's are self-identified by their mass peak in the two-photon invariant mass spectrum. The effect of background particles is mainly to increase the combinatorial background in the invariant mass spectrum which makes the problem of extraction of the peak content more difficult. On the other hand, charged hadrons and neutrons are significant backgrounds to the photon yield determination. In the present analysis, the Charged Particle Veto detector is used to identify charged hadron showers and remove the charged hadron contribution from the photon spectrum. At the same time, care must be taken not to remove converted photons from the photon or π^0 data.

The photon yield extraction involves the following steps:

Γ-1. The photon identification criteria are applied to the reconstructed showers and a photon candidate p_T spectrum is accumulated.

Γ-2. The normalized target-out background photon candidate p_T spectrum is subtracted, if necessary.

Γ-3. The CPV detector is used to determine the charged hadron contamination included in the photon candidate spectrum. The charged shower contribution is subtracted from the photon candidate distribution to produce the uncorrected neutral shower p_T spectrum.

Γ-4. The neutral shower spectrum is corrected for photon conversions and for the reconstruction efficiency.

Γ-5. The neutron and anti-neutron contamination, based on simulation, is removed to produce the raw photon p_T spectrum, within the lead-glass detector acceptance.

Γ-6. The raw photon spectrum is corrected for the geometrical acceptance to produce the final photon p_T spectrum.

The π^0 (or η) yield extraction involves the following steps:

Π-1. The photon identification criteria are applied to the reconstructed showers to produce a list of photon candidates for each event.

Π-2. The invariant mass of each photon pair within an event is calculated and sorted into invariant mass histograms according to the p_T of the photon pair. An invariant mass histogram is accumulated for each p_T bin to be used in the final π^0 p_T spectrum.

II-3. The photons are simultaneously used to construct artificial mixed events of similar multiplicity for each centrality class. The mixed events are analyzed in exactly the same manner as the real events to produce background invariant mass spectra as a function of p_T.

II-4. The final mixed event invariant mass spectra are normalized and subtracted from the the final real event invariant mass spectra to remove the combinatorial background from the real event spectra.

II-5. The normalized target-out final invariant mass spectra are subtracted from the final invariant mass spectra, if necessary.

II-6. The final invariant mass spectra are analyzed to extract the content in the π^0 (or η) peak at each p_T. The result is the uncorrected π^0 p_T spectrum.

II-7. The π^0 p_T spectrum is corrected for the π^0 reconstruction efficiency and losses due to photon conversions to produce the raw π^0 p_T spectrum within the lead-glass detector acceptance.

II-8. The raw π^0 spectrum is corrected for the geometrical acceptance and photon energy threshold to produce the final π^0 p_T spectrum.

For both the photon and π^0 analysis, the shower reconstruction itself involves the following steps [60]: First, all lead-glass detector modules with energy deposit are analyzed and contiguous modules are associated together as a cluster. The list of clusters is then analyzed to determine the number of local maxima in each cluster. Clusters with a single maximum are treated as single showers. Clusters with multiple maxima are assumed to result from overlapping showers, with one shower per maximum. The energy deposit in each module in the cluster is partitioned to the overlapping showers according to the distance of the module from the shower maxima, assuming all showers to have electromagnetic radial shower profiles. The individual showers are then analyzed to calculate the total shower energy, position, and spatial dispersion (width) [60]. The shower positions are calculated with a logarithmic weighting of the energy deposit [61] and are projected to the front surface of the lead-glass detector, correcting for the shower depth and the non-projective geometry. The distance from the shower position to the nearest hit in the CPV is also extracted. All of this information is recorded on Data Summary Tapes (DSTs) as an intermediate analysis step.

After application of the minimum energy threshold of 750 MeV used in the analysis and acceptance calculations, the showers are subject to various sets of further identification criteria. The different criteria result in varying non-photon background contaminations and photon (π^0) identification efficiencies, which must then be determined. In order to avoid shower distortions near the detector edges, or around "dead" detector modules, an edge cut is applied to require that the reconstructed shower position lies beyond a specified distance from the detector edges or dead modules. A distance cut of two module widths from the detector edge and 1.5 modules widths from the center of a dead module was used.

In the present analysis, the photon selection has been made with the following shower identification criteria:

S1. Use all reconstructed showers.

S2. Use only narrow showers which have a dispersion (width) which is less than a specified value.

S3. Use only showers which have no associated CPV hit.

S4. Use narrow showers satisfying the dispersion cut with no CPV hit.

The first condition will have the highest photon identification efficiency but largest non-photon background contribution, while the last condition will have the lowest efficiency but lowest background contributions. For the extraction of the photon yield, the criteria S1 and S2 are not entirely independent from the criteria S3 and S4 since the CPV detector is used in the first case also to determine the charged hadron contamination. The distinction is mainly in the manner in which the data is processed and in how the corrections are applied. In particular, with criteria S3 and S4 the neutral shower distribution is acquired directly, but must be corrected for photons which were rejected due to random associated hits in the CPV, or due to photon conversions, while for criteria S1 and S2 the charged shower distributions are extracted using the CPV and corrected for random associated hits and conversions and then the corrected charged shower contribution is removed from the total shower distribution to obtain the neutral shower distribution. For the π^0 yield extraction the CPV is not used at all when criteria S1 or S2 are used with the result that no corrections for random CPV hits are needed and smaller conversion corrections are required. Criteria S2 and S4 make use of the fact that the transverse size of hadronic showers, with large energy deposit, is significantly greater than that of electromagnetic showers in the lead-glass calorimeter. The cut on the shower dispersion is chosen to accept more than 99% of

the isolated photon showers while rejecting hadron showers by a factor of 2-3. However, the shower dispersion cut is more likely to lose electromagnetic showers in the case of shower overlap.

For additional consistency checks, the data has also been analyzed with the shower energy threshold increased from 750 MeV to 1.5 GeV, with the outer edge module cut increased to three module widths, and with a photon energy asymmetry cut applied in the π^0 analysis.

C. Particle Reconstruction Efficiency

The large particle multiplicities in central Pb+Pb collisions result in module occupancies in the WA98 lead-glass detector of up to 20%, which poses a special problem for the direct photon search. These large occupancies result in overlapping showers in which photons may be lost, mis-identified, or significantly altered in position or energy. This results in a significant dependence of the photon and π^0 identification efficiency on the centrality of the collision. Furthermore, the position and energy resolution, and even the energy scale, will be centrality dependent due to the effect of shower overlap. For an accurate direct photon search it is imperative to accurately determine and account for these effects. For the present analysis this has been accomplished by the method of randomly inserting test showers into real events and studying how they are altered and the efficiency with which they are recovered. This procedure has been used to determine the γ, π^0, and η reconstruction efficiency.

For this reconstruction procedure the WA98 experiment geometry was implemented in GEANT [62] with the GEANT tracking parameters for LEDA adjusted to reproduce test beam measurements of the LEDA response to electrons. The generation and transport of Čerenkov photons in GEANT was parameterized and this parameterized Čerenkov response was used in the full WA98 GEANT simulation due to the prohibitive CPU-time consumption of the full Čerenkov tracking in GEANT. Single π^0's (η's) were simulated with a uniform distribution in transverse momentum and pseudo-rapidity over the LEDA acceptance and the decay photons were tracked through GEANT. The simulated LEDA response was recorded to create a library of photon test showers in the form of digitized LEDA signals. Only simulated π^0's with both decay photons in the nominal LEDA acceptance were recorded. The reconstruction efficiency was then extracted with the procedure illustrated in Fig. 4. First the raw data were calibrated and the event was characterized by the trigger detectors and other detectors of WA98. Then three passes were made through the LEDA event analysis software. In the first pass, the calibrated LEDA data was analyzed to perform the clustering and shower characterization as described above. The position, energy, shower dispersion, and distance to nearest hit in the CPV were saved for all identified showers together with the calibrated information from the other WA98 detectors. Next, a π^0 event was read from the shower library and inserted into an empty LEDA raw event. Simulated signals in dead modules were eliminated and the event was then analyzed as a real event. The shower information reconstructed from the simulated showers in the empty LEDA was recorded together with the primary π^0 and photon information prior to the GEANT response. Finally, the real LEDA event was overlaid with the simulated LEDA event and the signals were summed. Then the superimposed event was analyzed. In this step the position, energy, shower dispersion, and distance to nearest hit in the CPV were saved only for all new showers which were not in the list of showers found in the original raw event. Also, all showers of the original event found to be missing from the reanalyzed overlap event were marked as lost. All of this information was stored for each event in a single pass through the WA98 raw data and recoded on the Data Summary Tapes. Thereafter the data analysis was performed from the DSTs since they could easily be analyzed multiple times, or simultaneously, with different shower selection criteria.

In order to determine the photon reconstruction efficiency it is necessary to determine which shower in the overlap event corresponds to the simulated photon incident on the LEDA. In the first step, the empty LEDA GEANT shower information is analyzed to determine the reconstructed position of the highest energy shower in the vicinity of the incident GEANT photon. The overlap event is then analyzed to find the shower nearest to that position. If that shower has less than twice the energy[1] of the shower in the empty LEDA event it is taken as the reconstructed photon. Otherwise the photon is considered to be lost. After the associated shower is identified, it is tested to determine whether it passes the photon energy threshold requirement and whether it passes the detector edge cut. Also, if its position falls on the location of a so-called "bad" module with questionable gain, as described below, it is eliminated. Finally, it is tested against the various shower identification criteria S1-S4 described above.

[1]The factor of two change in energy criterion determines who "eats" whom when showers overlap and is necessary to avoid double counting.

The efficiency corrections are made as a function of the measured transverse momenta. The photon reconstruction efficiency can be constructed as a two-dimensional response matrix which transforms the transverse momentum of the incident photon into the transverse momentum of the reconstructed test shower, if it passes all identification criteria (the reconstructed transverse momentum is set to zero if the criteria are not satisfied). This two-dimensional efficiency matrix must then be inverted and applied to the measured transverse momentum distribution to obtain the final efficiency corrected result [63]. Alternatively, the efficiency can be applied as an iterative one-dimensional correction. In this case, one-dimensional histograms are accumulated of the incident transverse momentum and reconstructed transverse momentum with each entry weighted according to the final transverse momentum spectrum and rapidity distribution. The reconstruction efficiency is given as the ratio of reconstructed to input distributions. This one-dimensional efficiency determination must be iterated until the weighted input distribution matches the final measured distribution.

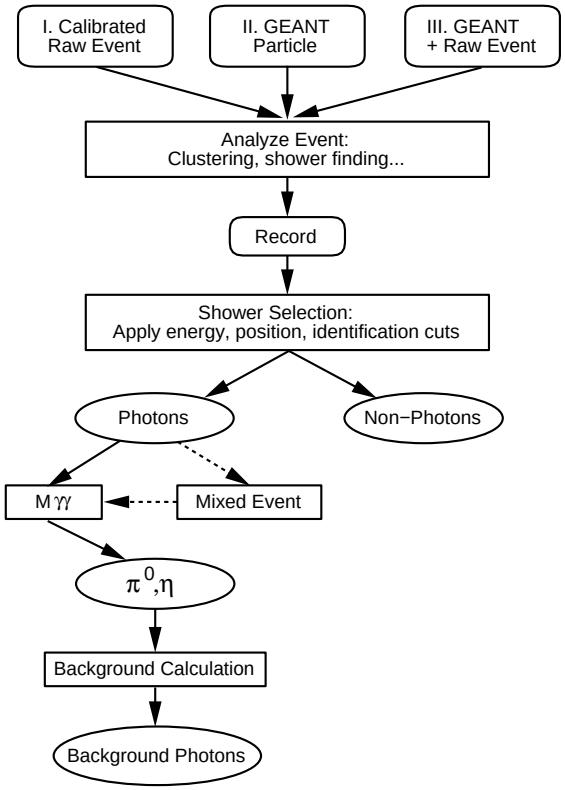

FIG. 4. An outline of the analysis procedure using the method of GEANT shower overlap used for the photon and π^0 efficiency determination. The intermediate results are recorded to DSTs after the event analysis step. The shower selection and further analysis is performed on the DSTs.

The π^0 reconstruction efficiency is similarly obtained by requiring that the showers from both of the decay photons simultaneously pass the photon identification criteria. The π^0 mass and transverse momentum is then calculated from the momenta of the two reconstructed photon showers. It is then required that the reconstructed mass fall within the π^0 peak mass integration region, and it may be additionally required that the photons pass an asymmetry ($\alpha = |E_1 - E_2|/|E_1 + E_2|$) cut on their reconstructed energies. The π^0 reconstruction efficiency is applied as a one-dimensional function of the transverse momentum. As in the photon case, the correction is determined from the ratio of reconstructed to input transverse momentum distributions. The input π^0 transverse momentum and rapidity weights must be adjusted by iteration until the assumed input transverse momentum distribution is the same as the final corrected distribution.

It should be noted that while these correction factors have been referred to as efficiency corrections, they might more properly be termed response corrections. They include essentially all detector effects other than the nominal detector acceptance. Specifically, they include the effects of detector edge cuts, dead and bad modules, energy resolution, and

distortions or loss due to shower overlap, as well as the efficiency to satisfy the specified identification criteria. In particular, the correction for smearing due to overlap and energy resolution can result in efficiency correction factors which exceed unity.

D. Background Calculation and Direct Photon Excess

As described above, the direct photon excess is obtained from the difference between the measured inclusive photon yield and the background photon yield expected from radiative decays of long-lived final state hadrons. The background photon yield in the WA98 LEDA acceptance is calculated by a Monte Carlo simulation of radiative decays of hadrons. The most important input to this calculation is the measured WA98 π^0 yield, which is extracted from the same data sample used to obtain the inclusive photon yield (see Fig. 4). Photons from π^0 decay account for about $80-90\%$ of the total expected background from radiative decays. It is important to note that the background photon yield attributed to π^0 decay includes both directly produced π^0's, as well as those from hadronic decays with π^0's in their final state. Thus, photons resulting from the $3\pi^0$ decay branch of the η are taken into account via the measured π^0 yield. On the other hand, the lifetime of the K_L^0 is sufficiently long that few of the $3\pi^0$ weak decays occur in front of the LEDA detector and therefore there is little contribution to the π^0 yield, and hence little contribution to the background photon yield. However, the weak decay of the K_S^0 to $2\pi^0$ is a special case. The K_S^0 lifetime is such that a substantial fraction of the decays are distributed over the distance between the target and the LEDA detector. As with the K_L^0 contribution, those decays which occur beyond the LEDA distance do not contribute to the π^0 or background photon yield. On the other hand, photons from a π^0 produced in a K_S^0 decay will have correctly measured energies but will be assumed to be produced at the target location and therefore will have an incorrect opening angle. This will result in a reconstructed π^0 invariant mass which is incorrect. While K_S^0 decays which occur close to the target will have a reconstructed π^0 mass which falls into the π^0 identification window, and so its decay photon contribution will be included via the measured π^0 yield, some fraction of the K_S^0 decays will occur sufficiently far from the target that their π^0 decays will not be properly identified. Only this portion of the K_S^0 decay photon contribution must be included in the calculated photon background.

The 2γ decay of the η is the second most important contribution to the photon decay background after the π^0 contribution. Together the π^0 and η photon decays constitute approximately 97% of the expected radiative decay background (see Fig. 28). Compared to the π^0 yield measurement the η measurement is more difficult due to the smaller production rate, the smaller 2γ decay branching ratio, and the resulting smaller signal to combinatorial background ratio in the 2γ invariant mass distribution. In the present analysis, the η yield is measured with modest statistical accuracy over a limited transverse momentum range due to these difficulties. In order to extrapolate the measured η transverse momentum distribution into unmeasured regions it is assumed that the η yield obeys m_T-scaling. This is the phenomenological observation [64] that the differential invariant cross sections, plotted as a function of the transverse mass $m_T = \sqrt{m_0^2 + p_T^2}$, for the various hadrons, h, have the same form, $f(m_T)$, with a normalization factor, C_h, which can vary but is found to be the same for many species:

$$E\frac{d^3\sigma_h}{dp^3} = C_h \cdot f(m_T). \tag{3.1}$$

Quite different theoretical explanations [65–67] can account for this observation. For various proton and pion-induced reactions at similar incident energies [68–75] it is observed that the η yield obeys m_T-scaling to good accuracy [76]. A scaling factor relative to π^0 production of $R_{\eta/\pi^0} = C_\eta/C_{\pi^0} = 0.55$ is obtained for the case of proton-induced reactions [76,77]. Similarly, the η yield is found to be consistent with m_T-scaling in minimum bias sulphur-induced reactions [77] at 200 *A* GeV incident energy.

Collective transverse flow will affect the spectrum of produced particles according to their mass with the result that m_T-scaling might be violated in collisions of very heavy ions. Evidence for collective transverse flow has been observed at the SPS for central ^{208}Pb+^{208}Pb collisions with estimated average transverse flow velocities as large as $\beta_T \approx 0.5$ [78–80]. For a particle of mass m and transverse momentum p_T the effective m_T inverse slope, or temperature T_{eff}, will be modified as [81]

$$T_{eff} = \frac{\sqrt{1-\beta_T^2}}{1-\beta_T\sqrt{1+m^2/p_T^2}}T \tag{3.2}$$

where β_T is the average transverse flow velocity and T is the thermal temperature. While the modification of the transverse mass spectrum is seen to decrease with increasing p_T, the effect can be significant. As an example, a

transverse flow of $\beta_T = 0.5$ would increase T_{eff} for the η by about 4% at $p_T = 2$ GeV/c which would result in an increase of about 50% in the η yield at $p_T = 2$ GeV/c.

It has been suggested that if chiral symmetry restoration occurs in the hot dense system formed in relativistic heavy ion collisions, then the masses of the η and η' mesons might decrease with an associated increase in their production rates [82,83]. These initial estimates suggested that the η and η' yields might be increased by as much as a factor of 3 and 10, respectively. Once produced, the η and η' are expected to interact relatively little in the dense matter with the result that they would survive to the final state to decay with their vacuum masses and contribute significantly to the decay background to produce excess photons and dileptons [82]. On the other hand, more recent calculations within the context of the non-linear sigma model suggest that the temperature dependence of the η and η' masses and mixing are negligible [84]. In view of these significant uncertainties in the extrapolation of the η yield from proton-induced reactions to central ^{208}Pb+^{208}Pb collisions it is important to measure the η yield directly for central collisions to provide experimental constraints on its possible contribution to the background photon yield.

Besides the π^0 and η, other hadrons with radiative decays which may contribute to the background photon yield are listed in Table I [85]. The production rates of these other hadrons are not measured in this experiment. As for the η, their production has been assumed to follow m_T-scaling with the same m_T spectrum as the measured π^0 spectrum and with relative normalizations R_{X/π^0} (equivalent to the asymptotic ratio as $p_T \rightarrow \infty$) given in Table I. Within experimental errors the ratio $R_{X/\pi^0}(p_T \rightarrow \infty) \approx 1$ independent of incident energy for the ρ and ω [64,73,75,86] and for the η' [86]. For the K^0_S a ratio of $R_{K^0_S/\pi^0} \approx 0.4$ [87–89] is observed for proton-induced reactions with indications for an increased ratio for nucleus-induced reactions [89,90].

Of the other radiative decays listed in Table I only the η' and ω are expected to contribute more than one percent of the background photons (see Fig. 28). The η' is notable in that it might be significantly enhanced due to the mechanism discussed above. While the η' production rate is not determined in the present measurement, it can be constrained by the η measurement due to its 65.5% branching ratio to $\pi\pi\eta$.

To summarize, the background photon yield in the acceptance of the WA98 lead-glass detector is calculated by a Monte Carlo simulation of radiative decays of all hadrons listed in Table I. The various hadrons are assumed to have the same transverse mass spectrum as the measured WA98 π^0 transverse mass spectrum for each event class. The yields of the other hadrons relative to the π^0 yield are given by the m_T-scaling factors listed in Table I. The one exception is the η scaling factor for central ^{208}Pb+^{208}Pb collisions where the measured η m_T-scaling factor is used. The Monte Carlo program uses the JETSET 7.3 routines [91] to implement the hadron decays with proper branching ratios and decay distributions. The hadrons are assumed to have a Gaussian rapidity distribution centered on mid-rapidity $y = 2.9$ with a width of $\sigma_y = 1.3$ according to measurements for ^{208}Pb+^{208}Pb collisions [92].

TABLE I. Dominant radiative decays which contribute to the inclusive photon background. $R_{X/\pi^0}(p_T \rightarrow \infty)$ is the assumed asymptotic ratio of yield of hadron X relative to π^0's, or equivalently the m_T-scaling factor. $\sigma(X)/\sigma(\pi^0)$ is the ratio of integrated yields which would be obtained for an exponential spectrum in m_T with a slope of 200 MeV/c^2 and the assumed R_{X/π^0} values. It is only an indication of the ratio of integrated yields since the actual value will depend on the measured π^0 m_T spectrum. The listed decays and branching ratios are taken from Ref. [85].

State	Mass	$R_{X/\pi^0}(p_T \rightarrow \infty)$	$\sigma(X)/\sigma(\pi^0)$	Decay Branch	Branching Ratio
π^0	134.98			$\gamma\gamma$	98.798%
				$e^+e^-\gamma$	1.198%
η	547.3	0.55 (0.486)	0.08	$\gamma\gamma$	39.21%
				$\pi^+\pi^-\gamma$	4.77%
				$e^+e^-\gamma$	$4.9{\cdot}10^{-3}$
				$\pi^0\gamma\gamma$	$7.1{\cdot}10^{-4}$
				$\mu^+\mu^-\gamma$	$3.1{\cdot}10^{-4}$
ρ^0	770.0	1.0	0.05	$\pi^+\pi^-\gamma$	$9.9{\cdot}10^{-3}$
				$\pi^0\gamma$	$7.9{\cdot}10^{-4}$
ω	781.9	1.0	0.05	$\pi^0\gamma$	8.5%
				$\eta\gamma$	$6.5{\cdot}10^{-4}$
η'	957.8	1.0	0.02	$\rho\gamma$	30.2%
				$\omega\gamma$	3.01%
				$\gamma\gamma$	2.11%
K^0_S	497.7	0.4	0.07	$(\pi^0\pi^0)$	(31.39%)
Σ^0	1192.6	1.0	0.007	$\Lambda\gamma$	100.%

IV. DATA ANALYSIS DETAILS

In this section, detailed results are presented for the extraction of the γ, π^0, and η yield and their error estimates, as required for the direct photon analysis. First, a description of the data sample selection is presented. This is followed by a discussion of the analysis involving the Charged Particle Veto detector. The CPV is used to determine the charged particle contamination in the photon shower sample. Next follows a description of the details of the extraction of the inclusive photon transverse momentum distributions, including a discussion of the background contributions from charged particles and neutrons, and losses due to photon conversions. The photon identification efficiency for the various methods is discussed together with a summary of the estimated systematical error on the inclusive photon measurement. Next, the π^0 yield extraction is described. This includes a discussion of the yield extraction method, efficiencies, backgrounds, and systematical error. Finally, the η yield extraction is described. The final results and the extraction of the direct photon excess are described in the following section.

A. Data Selection

The present analysis has been performed using the event samples summarized in Table II. The data have been taken over six week run periods in 1995 and in 1996 with the 158 *A* GeV ^{208}Pb beam of the SPS on ^{208}Pb targets of 495 and 239 mg/cm^2, respectively. During both run periods most data were taken with the GOLIATH magnet on, as required for the WA98 tracking spectrometer measurements. The minimum bias cross sections for the various data sets, after subtraction of the target out backgrounds, are given in Table II. Because of the change in the apparent transverse momenta of the charged particles due to the deflection in the magnetic field, the apparent transverse energy measured in MIRAC is increased with magnet on compared to the actual transverse energy. With the fixed low transverse energy trigger threshold, this resulted in larger minimum bias cross sections for the magnet on data sets. During the 1995 datataking period the vacuum exit window at the entrance to the GOLIATH magnet produced a significant background of downstream interactions which satisfied the minimum bias transverse energy threshold. These downstream interactions were eliminated by requiring an interaction at the target location by the requirement of a hit in the Plastic Ball in the angular region from 30° to 50° using the Plastic Ball trigger (described in Sec. II A) in coincidence with the minimum bias trigger. For the 1996 run period, the vacuum exit window was changed resulting in fewer downstream interactions. As a result, the Plastic Ball trigger was not required in the online trigger which resulted in less biased minimum bias cross sections. The rms variations of the minimum bias cross sections determined on a run-by-run basis are also given in Table II. The measured variation gives an indication of the uncertainty in the measured absolute cross sections due to normalization and background corrections. The background corrections were obtained from special empty target runs with no target in the target location. Due to the lower event rates, and resulting low deadtime and lack of need to be downscaled, the empty target data was taken with similar number of integrated beam triggers as obtained for the Pb data. Specifically, the 1995 and 1996 empty target data corresponded to a factor of 2.3 and 1.4 fewer beam triggers than the 1995 and 1996 Pb target data, respectively.

TABLE II. Summary of the event selection used for the present analysis. The table shows the WA98 158 *A* GeV ^{208}Pb+^{208}Pb minimum bias cross sections for the 1995 and 1996 run periods under conditions of magnetic field on and field off. The rms of the minimum bias cross section extracted run by run is indicated in parenthesis. The central event class is defined by those events falling above a high cut on the measured transverse energy where the cut is chosen to give a cross section of 635 mb above the cut. Similarly, the peripheral event class is defined by those events falling below a low transverse energy cut where the cut is chosen to give a total cross section of 4910 mb above the cut. The number of peripheral and central events used under each condition for the present analysis are listed.

Run Period	^{208}Pb Target Thickness (mg/cm^2)	Minimum Bias $\sigma_{minbias}$ (mb)	Peripheral Collisions N_{Events}	Central Collisions N_{Events}
1995 Field On	495.	6192. (56.)	2694528	2879652
1995 Field Off	495.	5971. (30.)	159291	213170
1996 Field On	239.	6451. (53.)	1203407	2937565
1996 Field Off	239.	6202. (58.)	222917	650521

The direct photon analysis has been performed for event selections corresponding approximately to the 20% most peripheral and 10% most central portions of the minimum bias cross sections. These event classes are defined by cuts on the total transverse energy, measured in MIRAC, as calculated in the offline analysis. The selections correspond closely to the online trigger event classes described in Sec. II B. More precisely, the transverse energy cut which defines the central event sample was chosen to correspond to a most central cross section of 635 mb, or impact parameters less than about 4.5 fm, for all data sets. Similarly, the transverse energy cut which defines the peripheral event sample was chosen to correspond to a cross section of 4910 mb above the transverse energy cut, or to a peripheral event sample with impact parameters greater than about 12.5 fm. Due to the variation of the minimum bias cross section for the different data sets analyzed (see Table II), the meaning of the peripheral event class (for example, as reflected in the particle multiplicity) depended on the data sample. These event class definitions are shown in Fig. 5 for the 1995 magnet on data set where the multiplicity of showers in the lead-glass fiducial region with energy above 750 MeV is plotted versus the total transverse energy. The projections onto each axis are also shown. Similar transverse energy cuts are used for the event class definitions for both the 1995 and 1996 data sets. However, quite different cuts are used for the magnet on and magnet off data sets due to the change in the apparent transverse energy scale noted above.

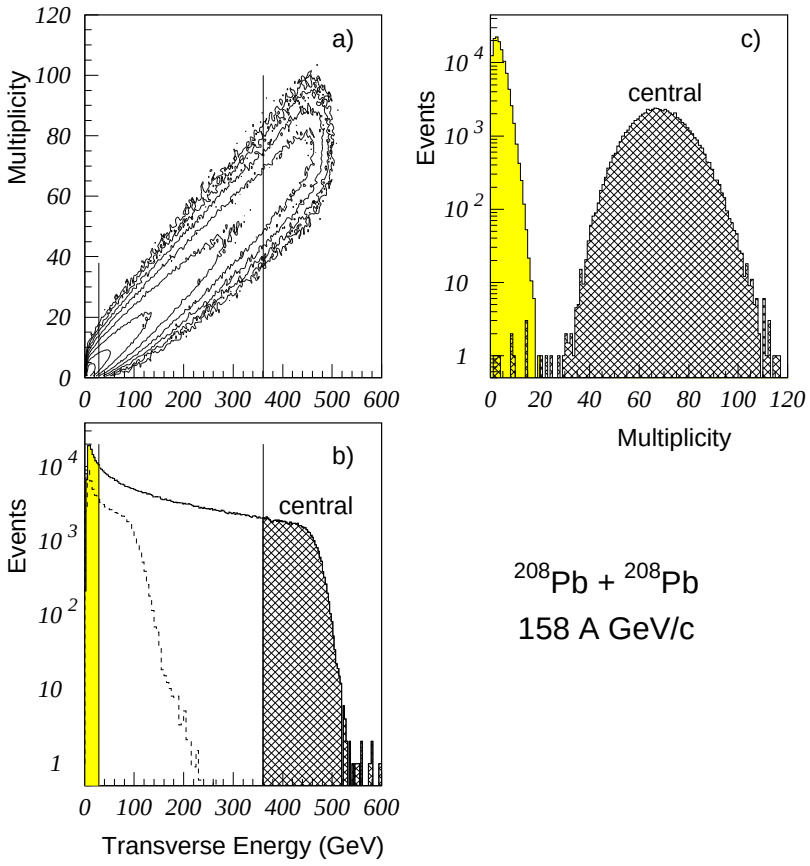

FIG. 5. The correlation between the number of showers observed in the lead-glass detector and the measured transverse energy for 158 *A* GeV ^{208}Pb+^{208}Pb collisions for a sample of the 1995 magnet on data. Part b) shows the projection onto the transverse energy axis with the shaded regions indicating the peripheral and central event class selections used for the present analysis. The distribution is uncorrected for the empty target contribution which is shown by the dashed histogram with arbitrary relative normalization. Part c) shows the projection onto the lead-glass multiplicity axis for the selected events.

We note that while the central event samples in the four data sets should be very similar in terms of the impact parameter range selection and particle multiplicity, the peripheral event samples of the different data sets are likely to be more variable. This is due to the rapid variation of the overlap geometry in the peripheral region and the variations in the minimum bias cross section and background corrections for the four data sets noted above.

In the offline analysis the various trigger signals are checked to remove events with inconsistent trigger information and to remove events with another beam particle within 100 ns or another interaction within about 300 ns of the

triggered event. These trigger cuts discard about 10% of the events. For the 1996 data set the Plastic Ball trigger was not required in the online trigger or used in the offline analysis for the final data sample. However, events which did not satisfy the Plastic Ball trigger requirement were used in the offline analysis to investigate the downstream interaction contributions in more detail. Since the downstream interactions are on light materials, such as air, mylar, and aluminum ($A < 30$) and have underestimated emission angles, they produce small measured transverse energies with the result that their contamination is almost entirely in the peripheral event sample (see Fig. 5). The peripheral data sample for the 1996 data set was smaller than that for the 1995 data set due to the factor of two larger prescale factor used in the 1996 peripheral trigger.

In addition to a selection of the data sample based on trigger cleanup cuts, the lead-glass shower data was analyzed in a preliminary scan of the data and modules with questionable gain were eliminated for the subsequent analysis. This selection was made by accumulating the shower energy spectrum for each individual module where the shower centroid was within that module. The results were compared to the average dependence across the detector surface. Modules whose spectrum deviated from the average behavior, with rather strict criteria, were flagged as bad. In the actual data analysis, showers with positions within a module which was flagged as bad were eliminated. As a result of the rejected bad modules and the modules eliminated around the edges of the detector and dead modules, the effective LEDA acceptance was reduced by about 40%.

B. Charged Particle Veto

The Charged Particle Veto detector provides essential information for the photon analysis. It allows charged showers in LEDA to be identified and associated with charged hadrons or photon conversions (see step G3 of Sec. III B). When the photon selection is made without invoking the CPV directly in the shower identification criteria (criteria S1 and S2 of Sec. III B) then the CPV is used to accumulate the transverse momentum spectrum of charged LEDA showers. This spectrum is corrected for the p_T-independent CPV efficiency and then subtracted from the total LEDA shower transverse momentum spectrum to obtain the neutral shower transverse momentum spectrum. The charge/neutral ratio is extracted and fitted as a function of the transverse momentum and used to calculate a correction factor applied to the total shower spectrum to obtain the neutral shower spectrum. The neutral shower spectrum is then corrected for neutrons and anti-neutrons, and for conversions to obtain the raw photon spectrum.

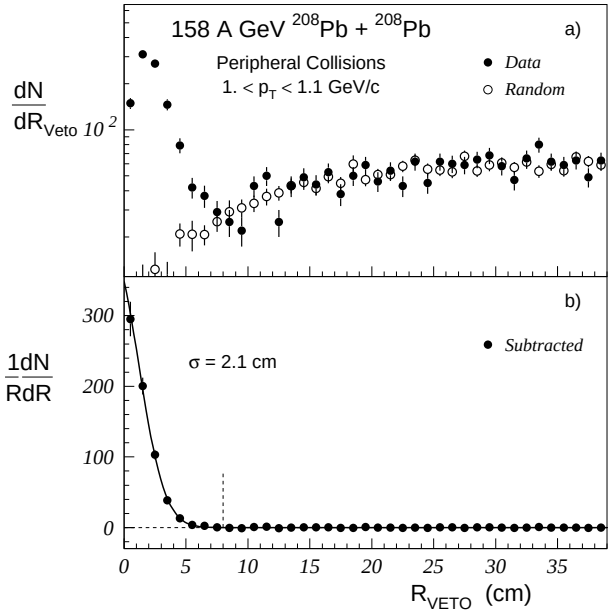

FIG. 6. The distribution of distances, R_{Veto}, to the nearest CPV hit from a shower particle in the lead-glass for peripheral events. In part a) the distribution for real events is shown by the solid circles. The distribution for randomly vetoed hits is shown by the open circles. The random veto distribution is obtained using test GEANT showers inserted into real events. The true veto radius distribution after subtraction of the random veto distribution is shown in part b).

Alternatively, the CPV can be used directly in the shower selection criteria to choose non-charged photon candidates (criteria S3 and S4 of Sec. III B). However, because the CPV detector was fully installed and operated for the 1996 run period only, it was not possible to perform the analysis with the CPV in this way for the 1995 data sample. Instead it was necessary to extract the charge/neutral correction from the 1996 data sample and apply this correction to the 1995 data. Therefore it was important to verify the consistency of the two methods in which the CPV information was used.

In the shower analysis procedure described in Sec. III C, each shower in the list of individual localized showers in LEDA is compared with the list of hits in the CPV and the distance between the LEDA shower position and the nearest CPV hit position is recorded. An example of this distance distribution is shown in Fig. 6a) for showers in peripheral collisions with transverse momenta $1 < p_T < 1.1$ GeV/c. The distribution shows a clear peak at small veto distance with a long tail extending to large veto radii. The long tail results from random associations between showers in LEDA and hits in the CPV. The veto radius distribution of these random associations is also shown in Fig. 6a). This distribution is extracted from the veto distance distribution obtained for the GEANT test photons introduced into the LEDA event, as described in Sec. III C. Since these test showers have no correlated hit in the CPV their veto distance distribution is strictly random. The random hit distribution is normalized to the distribution for real LEDA showers at large veto distance and subtracted from the distribution for real showers to obtain the distance distribution of real charged showers shown in Fig. 6b). While the random veto contribution is quite small for peripheral collisions, the detector occupancies are much greater in central collisions with the result that there is a much higher probability for a CPV hit to be randomly associated with a shower in LEDA. This is shown in Fig. 7 where the same veto distance distributions are shown for central collisions. In this case the correction for the random CPV hits is essential.

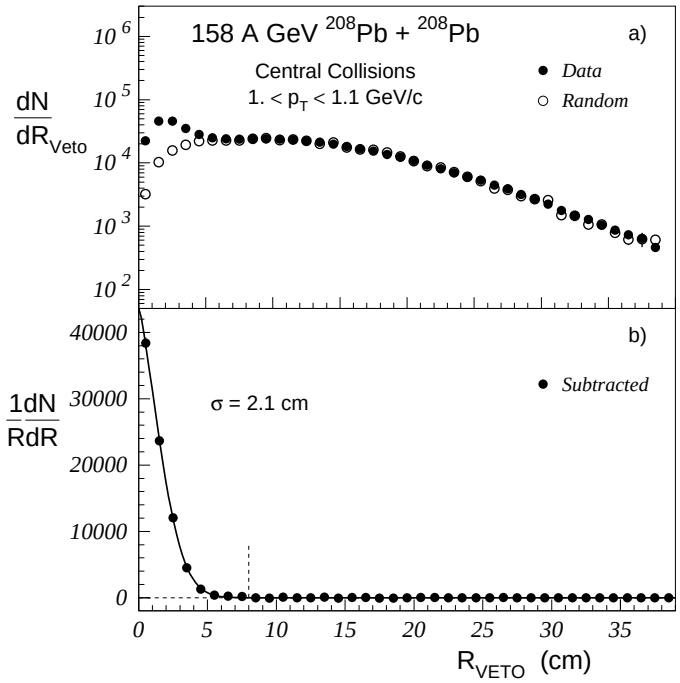

FIG. 7. The distribution of distances, R_{Veto}, to the nearest CPV hit from a shower particle in the lead-glass for central events. In part a) the distribution for real events is shown by the solid circles. The distribution for randomly vetoed hits is shown by the open circles. The random veto distribution is obtained using test GEANT showers inserted into real events. The true veto radius distribution after subtraction of the random veto distribution is shown in part b).

Based on these distributions, showers with a CPV hit within a distance cut of 8 cm are tagged as charged showers. For the analysis methods S1 and S2, in which the CPV is used to extract a charged/neutral correction factor, the charged shower yield is extracted for each p_T bin as the random subtracted yield in the veto peak within the 8 cm distance cut. The result is the charged shower p_T distribution which is then used to obtain the charged/neutral shower correction factor as a function of p_T. The charged/neutral shower ratio as a function of the shower energy is shown in Fig. 8 for peripheral collisions using a 8 cm distance cut. The peak in the spectrum at about 550 MeV is due to non-showering hadrons which pass through the lead-glass and deposit similar energy by dE/dx only. A minimum shower energy

threshold of 750 MeV has been applied in the present analysis to eliminate this minimum-ionizing particle, or MIP, peak from the photon candidates. It is seen that the charged hadron background differs for the magnet on and magnet off run conditions.

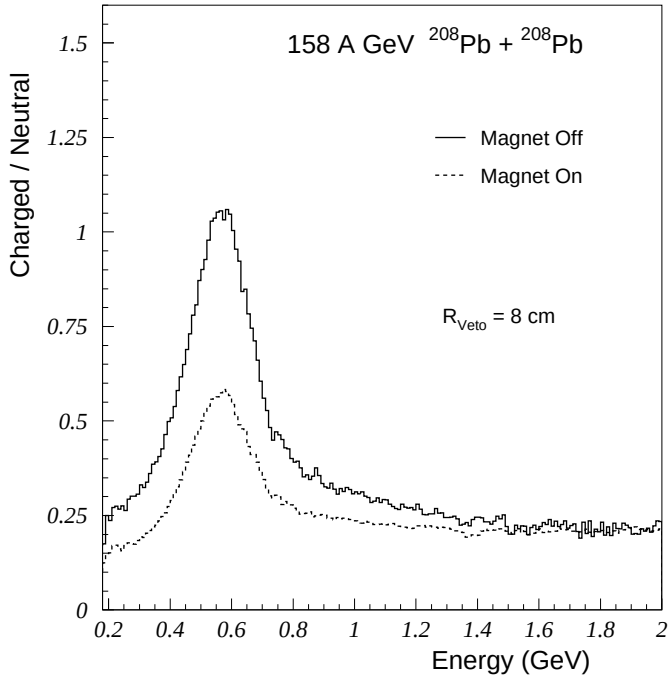

FIG. 8. The ratio of charged to neutral clusters identified in the lead-glass detector for peripheral collisions with magnet on or magnet off run conditions as a function of the total energy of the cluster in the low transverse momentum region. The solid curve shows the ratio for clusters identified as charged hits by a coincident hit in the CPV within a distance of $R_{Veto} = 8$ cm of the cluster. The peak at 550 MeV from non-showering minimum ionizing particles is clearly seen in the distributions. A minimum energy threshold of 750 MeV is used in the present analysis.

For the analysis methods S3 and S4 charged hadrons are rejected directly from photon candidate showers by an associated CPV hit within the 8 cm distance cut. In this case there is no charged/neutral correction necessary to the photon candidate spectrum. On the other hand, the loss of photon showers due to random vetos and conversions is treated as an efficiency loss which is then taken into account at a later step in the efficiency correction (see Sec. IV C 3).

The charged shower identification must be corrected for the efficiency of the Charged Particle Veto. As mentioned in Sec. II C 2, the CPV efficiency has been determined *in situ* using LEDA and the Silicon Pad Multiplicity Detector. The analysis is performed using magnet off data to allow straight line tracking between the SPMD and LEDA. Peripheral collisions are used to keep the detector occupancies low in order to minimize random hit associations. Hits in the SPMD are projected to the LEDA detector surface and associated with a hit in LEDA if they fall within the SPMD projected pad area. If a hit is found within LEDA the distance from the LEDA shower to the nearest hit in the CPV is extracted. The raw CPV efficiency, ϵ^0_{CPV}, obtained as the ratio of the number of CPV hits found to the number of SPMD-LEDA coincidence tracks, is shown in Fig. 9 as a function of the distance between the LEDA shower and the CPV hit. It is seen to increase rapidly up to a veto distance of about 15 cm and then increase very slowly for larger distances. This slow rise at large distances is due to random coincidences with hits in the CPV which artificially increase the apparent efficiency. The random CPV hit efficiency, ϵ^R_{CPV}, also shown in Fig. 9, is extracted by an event mixing technique in which the CPV data are taken from a different peripheral event than the one used for the SPMD-LEDA track. The CPV efficiency is corrected for such random CPV associations as $\epsilon_{CPV} = (\epsilon^0_{CPV} - \epsilon^R_{CPV})/(1 - \epsilon^R_{CPV})$. In addition, due to the SPMD inefficiency or interactions, there can be random coincidences between the SPMD and LEDA, for which a hit in the CPV would not be expected, which decrease the

apparent CPV efficiency. The shape of the SPMD-LEDA random coincidence distribution is also shown in Fig. 9. A small additional correction is applied to ϵ_{CPV} to account for this effect.

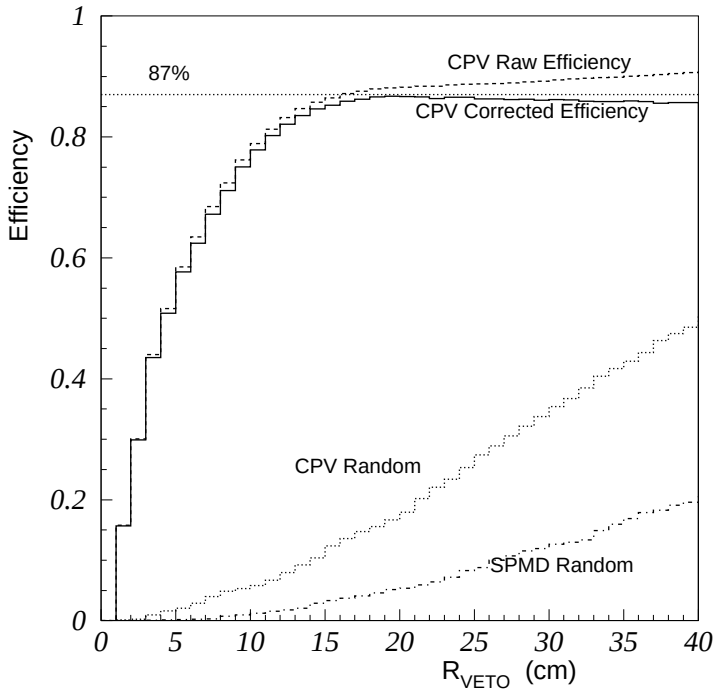

FIG. 9. The efficiency of the charged particle veto as a function of veto radius. The results are obtained from magnetic field off peripheral data. The dashed curve shows the probability that a hit in the CPV is found within a distance R_{Veto} of a charged hit in the lead-glass. The lead-glass hit has been tagged as charged by a coincident hit in the SPMD within distance R_{Veto}. The distance R_{Veto} is measured in the plane projected onto the lead-glass surface. The dashed curve includes random vetoes which artificially increase the apparent efficiency with increasing radius. The dotted curve shows the random veto efficiency of the CPV. The dot-dashed curve shows the random veto efficiency of the SPMD. The solid curve shows the final CPV efficiency result.

As shown in Fig. 9, an asymptotic corrected CPV efficiency of $\epsilon_{CPV} = 87\%$ is obtained for veto distance cuts greater than about 17 cm. It will be noted that this distance is considerably larger than indicated by the width of the veto distance distributions shown in Figs. 6 and 7. This difference is due to the fact that the CPV efficiency analysis uses all charged hits in the SPMD. Therefore it is dominated by charged hadrons which deposit very little energy in LEDA either due to poorly developed hadronic showers, or due to energy deposit by dE/dx only. These low energy showers have very poor position determination in LEDA. This effect is also evident by the observation that the width of the LEDA-CPV correlation (see Figs. 6 and 7) increases at very low transverse momentum. As a result the R_{Veto} distance cut is increased for low transverse momenta to insure that the asymptotic CPV efficiency is attained. The CPV efficiency is assumed to be 87% independent of transverse momentum.

During datataking, CPV readout errors occurred with apparently random frequency which resulted in loss of portions of the CPV data in the event. These errors were not excluded in the present analysis and account for most of the extracted CPV inefficiency. Since the readout errors resulted in loss of trailer information in the CPV data packets it was possible to identify such readout errors and determine the CPV efficiency for a data sample without readout errors. An intrinsic detector efficiency of better than 98% was obtained [59]. It was also possible to verify that the readout error rate did not vary with detector occupancy or with time during the run period. The readout errors occurred relatively frequently but affected only a small portion of the CPV data of an event when they did occur. Therefore rejection of all events in which a CPV readout error occurred would have resulted in an unacceptable reduction of the data sample.

C. Photon Analysis

The method to extract the inclusive photon transverse momentum spectra are described in Sec. III B. In summary, the procedure is to remove the charged hadron contamination from the photon candidates or candidate spectrum, remove the neutron and anti-neutron contamination, correct for photon conversions, then correct for the photon identification efficiency, and finally to correct for the detector acceptance. The details of this procedure are described in this section.

1. Charged Particle Contamination and Conversions

The CPV detector is used to select charged showers. The charged shower transverse momentum distribution is constructed from the random corrected yield in the veto peak for each p_T bin, as discussed in Sec. IV B (see Figs. 6 and 7). The random corrected charged shower p_T distribution is then corrected for the CPV efficiency to obtain the total charged shower distribution. This corrected charged shower distribution includes both charged hadrons and photon conversions. Next, the corrected charged shower p_T distribution is subtracted from the total shower distribution to obtain the raw neutral shower p_T spectrum. The neutral shower spectrum is depleted uniformly as a result of photon conversions and must be corrected by a factor $1/(1-P_C)$ where P_C is the photon conversion probability. The amount of conversion material between LEDA and the target was the same for both the 1995 and 1996 run periods. The air plus vacuum exit window contributed 5.4% to the conversion probability and the CPV material before the active volume of the CPV contributed an additional 2.0% to the conversion probability. Finally, the 1995 and 1996 target (half) thicknesses contributed an additional 3.0% and 1.45%, respectively. Thus the total photon conversion probability for the 1996 run period during which the CPV was in operation was $P_C = 8.6\%$.

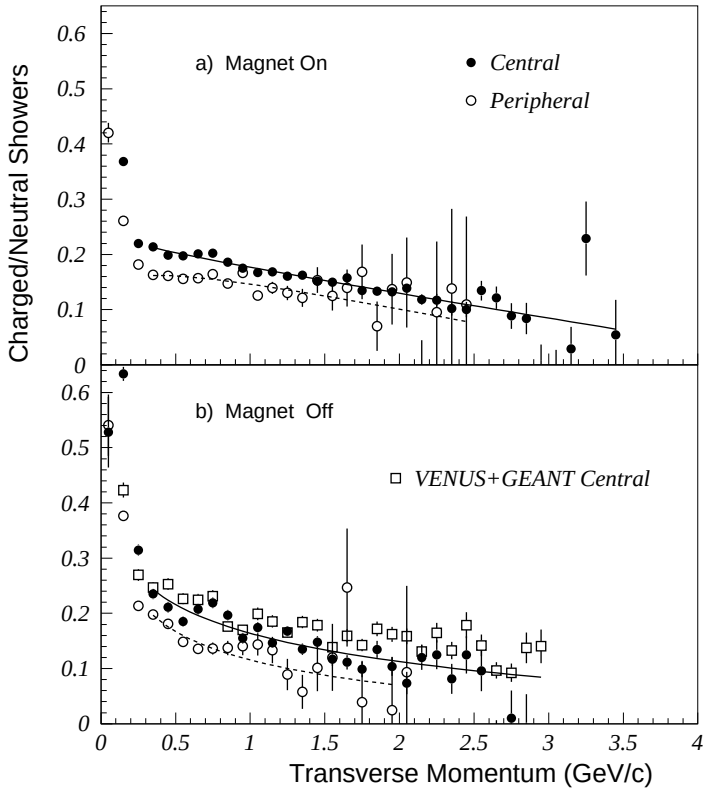

FIG. 10. The measured ratio of charged to neutral showers in the lead-glass detector for peripheral (open circles) and central (solid circles) 158 *A* GeV ^{208}Pb+^{208}Pb collisions as a function of the transverse momentum of the cluster. The results are shown for all clusters for a) magnet on and b) magnet off. The data have been corrected for photon conversions and the CPV efficiency. The lines are fitted curves.

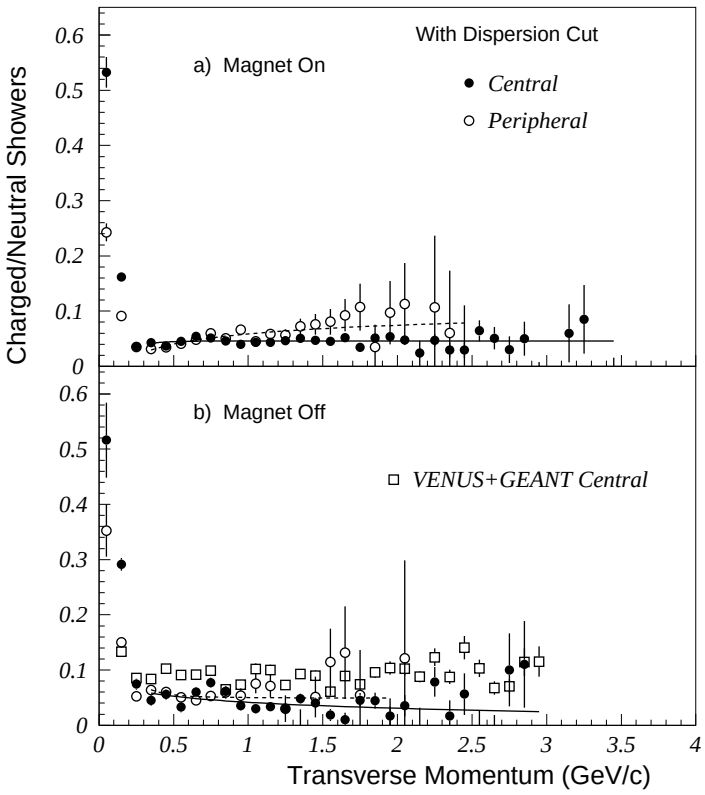

FIG. 11. The measured ratio of charged to neutral showers in the lead-glass detector for peripheral (open circles) and central (solid circles) 158 *A* GeV ^{208}Pb+^{208}Pb collisions as a function of the transverse momentum of the cluster. The results are shown for clusters which pass a photon-like dispersion cut for a) magnet on and b) magnet off. The data have been corrected for photon conversions and the CPV efficiency. The lines are fitted curves.

The neutral shower spectrum, after correction for conversions, is subtracted from the total shower spectrum to obtain the final charged hadron shower spectrum. By this procedure the amount of contamination of the selected showers due to charged hadrons is determined for each shower identification criterion and for the magnet on and magnet off run conditions. The extracted ratio of charged/neutral showers under the condition to use all showers (S1) is shown in Fig. 10 for central and peripheral collisions and for magnet on and magnet off. The charged hadrons are seen to constitute about 20% of all showers at low p_T decreasing to about 5% at the highest p_T. When the shower dispersion cut is applied in the shower selection criterion (S2) the hadron contamination is reduced to about 5% nearly independent of p_T as seen in Fig. 11. For comparison, simulation results are also shown for the case of magnet off. The simulation was performed using full VENUS 4.12 [93] events calculated for central ^{208}Pb+^{208}Pb collisions. All particles incident on LEDA were tracked with GEANT [62] with full tracking of the produced Čerenkov photons, which is the dominant component of the shower observed in the lead-glass. The results shown were obtained using the GCALOR hadronic shower package for hadrons [94]. Reasonably good agreement with measurement is observed. In addition, the GEANT calculations were performed using the GHEISHA and FLUKA hadronic shower packages. The GHEISHA results were in better agreement with measurement while the FLUKA results overpredicted the observed charged/neutral ratio with the GCALOR result intermediate between the other two results. The proper description of hadronic showers in the lead-glass is an especially severe test of the hadronic shower packages. Since only that component of the shower which produces Čerenkov light which reaches the photomultiplier contributes to the observed signal, the lead-glass response to hadrons is sensitive to details of the hadronic shower composition. For the charged/neutral corrections the measured results have been used. In contrast, the corrections for neutrons and anti-neutrons discussed below are, by necessity, based solely on the contributions calculated using GEANT.

The measured charged/neutral ratio spectra, (c/n), are fitted (as seen in Figs. 10 and 11) to remove statistical fluctuations and to extrapolate to high p_T. The lowest p_T bins are not used in the present analysis due to the sharply

increasing rise in the hadron contamination.[2] The fitted result provides the neutral/total shower ratio $1/(1+c/n)$ which is then used as a multiplicative factor to extract the neutral shower spectrum from the total shower spectrum. This charged hadron correction procedure was necessary for the analysis of the 1995 data set since there was no CPV measurement to extract the charged hadron contamination information. It also allowed to use the full 1996 data sample including periods when the CPV was not fully operational. It should be noted that the 1995 and 1996 run conditions and analysis procedures were the same, and so the amount of charged hadron contamination extracted from the 1996 data sample should be the same for the 1995 data sample. A minor difference between the two data samples is the thicker target used for the 1995 run period which resulted in an additional 1.55% conversion probability. For the magnet off data sample this is expected to have no effect since essentially all converted photons are identified as single showers, which means that the total shower spectrum is unchanged. Therefore the charged/neutral shower correction factor is the same nearly independent of the amount of conversions. For the magnet on run conditions the e^+e^- pair produced at the target will separate in the magnetic field and the total shower spectrum will depend on the amount of photon conversions. Therefore a small correction ($\approx 1\%$) for this effect has been applied to the charge/neutral ratio when used for the 1995 magnet on data. Based on the results shown in these figures, a conservative 30% uncertainty has been assumed for the charged/neutral ratio for the photon analysis.

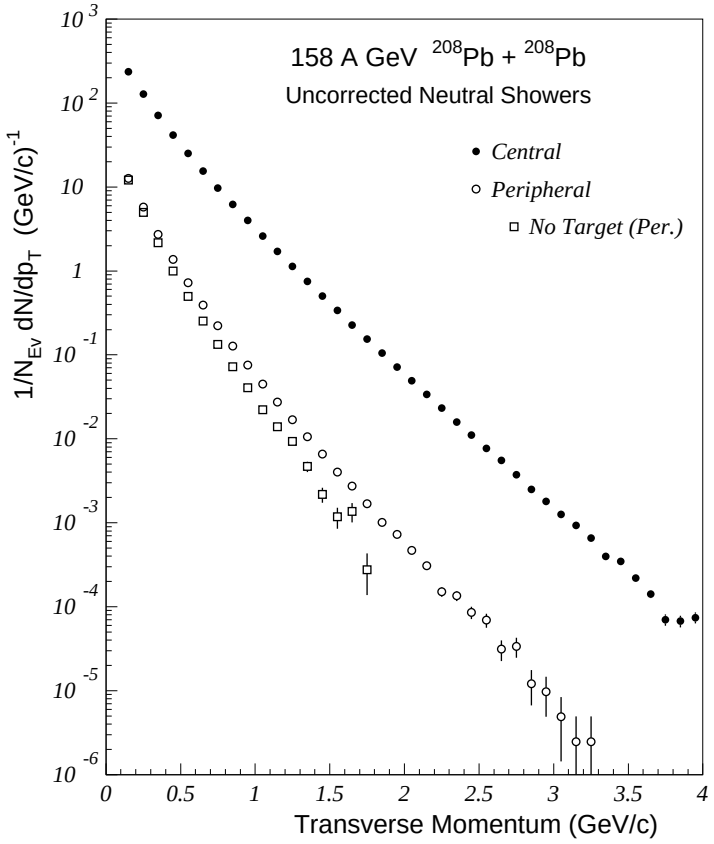

FIG. 12. The multiplicity of all neutral showers as a function of transverse momentum for peripheral (open circles) and central (solid circles) 158 *A* GeV ^{208}Pb+^{208}Pb collisions. The results are the sum of 1995 and 1996 magnet on data sets. Results are also shown (open squares) for peripheral event selection for runs with no target. The spectra have not been corrected for efficiency or acceptance. They are used as the first iteration in the iterative efficiency correction.

[2]Note that while results will be shown to low p_T for various intermediate analysis steps, the final results will be presented only for the region $p_T > 0.5$ GeV/c due to various systematical error sources which increase at low p_T.

The raw neutral shower multiplicity per event as a function of transverse momentum, uncorrected for neutrons, efficiency, or acceptance, are shown in Fig. 12. The results are shown for central and peripheral collisions for the sum of 1995 and 1996 data samples. The measured distributions extend over more than 6 orders of magnitude and extend to about 3 and 4 GeV/c for peripheral and central collisions, respectively. A flattening of the distribution is observed in going from peripheral to central collisions. Also shown is the distribution obtained for events satisfying the peripheral trigger condition for runs with no target. No events from empty target runs satisfy the central event trigger condition (see Fig. 5). The empty target data is seen to have a neutral shower multiplicity which is similar to the peripheral ^{208}Pb+^{208}Pb case but to fall more steeply with transverse momentum. The similarity is not surprising since the trigger selection on the transverse energy for peripheral Pb collisions will select events with a similar number of nucleon-nucleon collisions as for an empty target interaction. The no-target interactions most likely occur on light materials of the target wheel and vacuum system (aluminum or carbon). The steeper falling empty target spectrum results from the fact that many of those interactions occur on downstream materials and therefore have underestimated angles and correspondingly smaller apparent transverse momenta. Since the spectral shapes differ, the peripheral spectrum should be corrected for the effect of the empty target contribution. The true peripheral spectrum, S_{Per}^{True}, should be obtained from the raw peripheral spectrum, S_{Per}, and empty target spectrum S_{Empty} as

$$S_{Per}^{True} = S_{Per} + f \cdot (S_{Per} - S_{Empty}), \tag{4.1}$$

where f is the fraction of empty target events to true Pb target events in the peripheral data sample. Based on the live-beam scalers, downscale factors, and number of peripheral triggers a value of $f = 0.098$ is obtained for the results shown in Fig. 12 where the empty target results are obtained with the same trigger cleanup cuts as used for the Pb data. On the other hand, as will be discussed in regard to the π^0 result in Sec. IV D below, there are reasons to believe that the target out contribution to the peripheral data may be larger than indicated by the properly normalized empty target data. With the requirement of a coincident hit in the forward region of the Plastic Ball detector (see Sec. IV A) as for the 1995 data sample, the properly normalized fraction of empty target events in the peripheral data sample is only $f = 0.01$.

2. Neutron and Anti-neutron Corrections

The neutral shower spectra must be corrected for neutron and anti-neutron contributions to obtain the raw photon spectrum. For this correction it is necessary to rely entirely on results from simulation. The incident neutron and anti-neutron flux into the LEDA acceptance has been estimated using VENUS. In Fig. 13a) the VENUS predictions of the number of particles per decay photon are shown as a function of their incident transverse momentum for neutrons, anti-neutrons, and π^+. In the region of greatest interest at high p_T, the neutron flux is seen to exceed the π^+ flux by roughly an order of magnitude. Even the incident anti-neutron flux is similar to the π^+ flux at large p_T. Fortunately, as for the charged hadrons, the neutrons and anti-neutrons deposit only a small portion of their incident energy in the lead-glass detector which results in a much reduced apparent transverse momentum.

The response of the lead-glass detector to the neutrons and anti-neutrons, and to photons was simulated with GEANT with full tracking of the produced Čerenkov photons. The resulting ratio of neutron+anti-neutron $(n + \overline{n})$ to total neutral $(n + \overline{n} + \gamma)$ showers as a function of their apparent transverse momentum is shown in Fig. 13b). The $(n + \overline{n})$ contamination is seen to be significantly reduced in comparison to the incident flux due to the small energy deposit. The contamination is dominated by the neutron contribution. Results are shown with and without application of the shower dispersion cut. It is seen that the requirement of a narrow photon-like dispersion significantly reduces the $(n + \overline{n})$ contamination from about 5% to 1-2%.

The results shown have been calculated using the GCALOR hadronic shower package [94] of GEANT. Calculations were also performed using the GHEISHA and FLUKA hadronic shower packages. GHEISHA predicted $(n + \overline{n})$/neutral ratios which were nearly a factor of two lower than the FLUKA predictions while the GCALOR result was about 1-2% in value below the FLUKA result for the case of all showers. With the narrow shower condition applied GCALOR and FLUKA gave consistent results. While no hadronic shower package has been clearly demonstrated to be superior [95], we have chosen to use the GCALOR results, since GCALOR, as well as FLUKA, is considered to be more reliable for neutron transport.

The proton spectrum predicted by VENUS for central ^{208}Pb+^{208}Pb is considerably flatter than the measured spectrum reported by NA49 [96]. This would suggest that VENUS also overpredicts the neutron and anti-neutron yield at high transverse momentum, which would suggest a smaller contamination. On the other hand, VENUS also overpredicts the π^0 and hence inclusive photon yield at high p_T [97]. The open points in Fig. 13a) show an experimental estimate of the neutron/γ ratio based on the NA49 proton measurement and the present WA98 photon measurement.

The NA49 proton transverse mass distribution (measured over the interval $0. < m_T - m_p < 0.3$ GeV/c^2 [96]) has been fitted to an exponential with the integral yield normalized to the predicted VENUS neutron multiplicity. It is seen that the neutron/γ ratio estimated from the experimental results is quite similar to that predicted by VENUS, even in the region extrapolated beyond the NA49 measurement. Moreover, after GEANT response the final $(n + \overline{n})$/neutral ratio is very similar to the VENUS result over the entire p_T region. In view of the uncertainties inherent in comparing different experimental results with different event selections, especially for peripheral collisions, the VENUS predictions have been used for the neutron and anti-neutron corrections. Due to these uncertainties, and especially those uncertainties associated with the simulation of the neutron response, a 50% uncertainty has been assumed for the $n + \overline{n}$ contribution to the photon result.

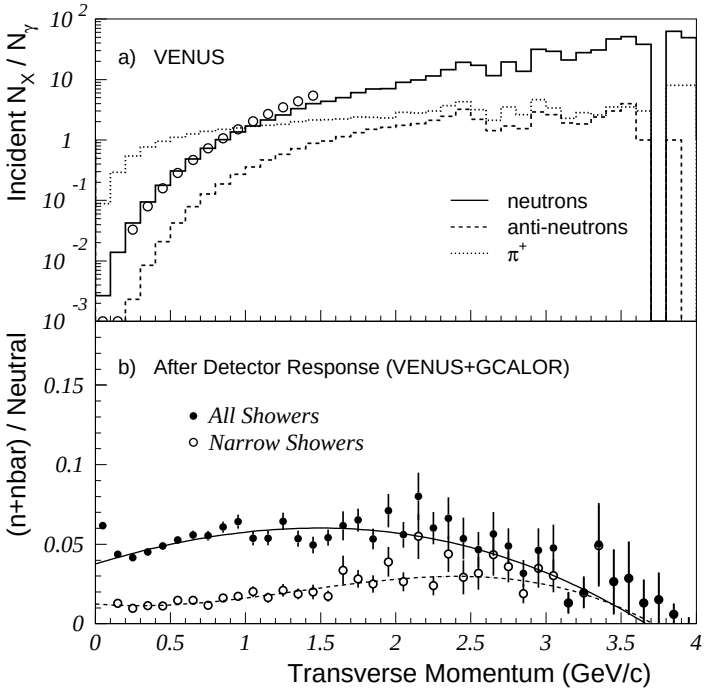

FIG. 13. In part a) the ratio of neutrons (solid line), anti-neutrons (dashed line), and π^+ (dotted line) to photons into the LEDA acceptance is shown as a function of the transverse momentum. The results are predictions of the VENUS 4.12 event generator for central 158 *A* GeV ^{208}Pb+^{208}Pb collisions. The open points are described in the text. In part b) the ratio of neutrons plus anti-neutrons to neutral $(n + \overline{n} + \gamma)$ is shown after the effects of the lead-glass detector response calculated with GEANT. Results are shown after application of shower identification criteria of using all showers (solid circles) or narrow showers (open circles). The curves are fit results.

The $(n + \overline{n})$/neutral ratio is fitted (as shown in Fig. 13b)) and the uncorrected neutral spectra (see Fig. 12) are then corrected by the factor γ/neutral$= 1 - (n + \overline{n})/(n + \overline{n} + \gamma))$ to obtain the raw photon spectrum. The anti-neutrons comprise about one third of the total neutral correction. The result is the raw inclusive photon spectra which must then be corrected for the photon reconstruction efficiency and acceptance.

3. Reconstruction Efficiency

As described in Sec. III C, the photon reconstruction efficiency is extracted by the method of inserting GEANT photon test showers into real events and determining how the test showers are modified or lost. The efficiency is extracted as the ratio of the transverse momentum spectrum of found photons divided by the transverse spectrum of input photons. The input photon and its associated found photon are weighted such that the input distribution reproduces the measured transverse momentum distribution for each event class. The input weights are taken according to the raw photon distribution (see Fig. 12) for the initial efficiency result and the weights and resulting efficiency are iterated until the input distribution agrees with the final result.

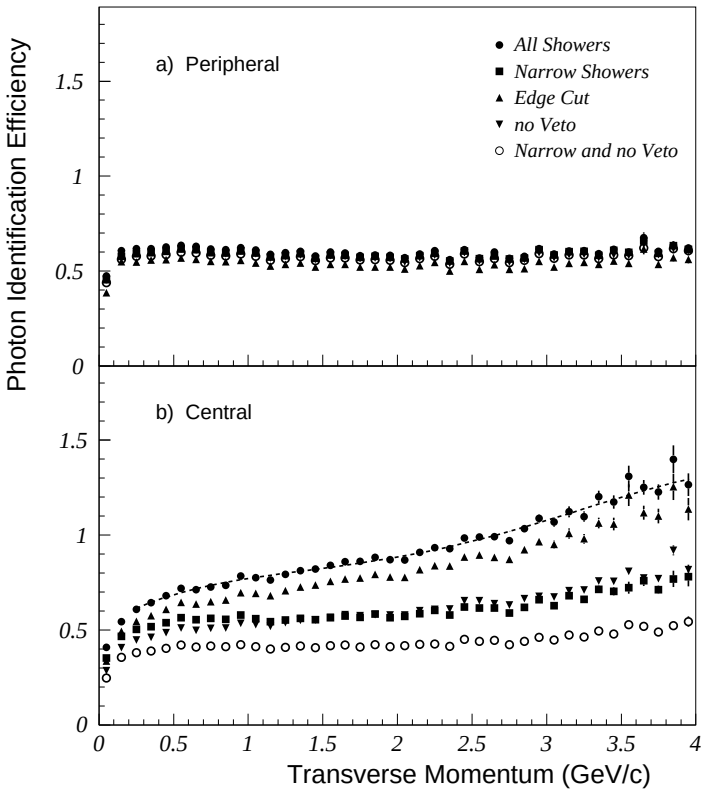

FIG. 14. The photon identification efficiency including effects of resolution, shower overlap, and excluded lead-glass modules as a function of transverse momentum for a) peripheral and b) central 158 *A* GeV ^{208}Pb+^{208}Pb collisions. The efficiencies are shown for several shower identification methods using the 1996 magnetic field on data. The efficiency is shown for the following criteria: all showers (solid circles), showers satisfying a dispersion cut (solid squares), all showers within a further restricted acceptance (solid triangles), all showers with no associated hit in the CPV (inverted solid triangles), and all showers satisfying a dispersion cut with no associated hit in the CPV (open circles). An example of the fitted parameterization of the efficiency is shown by the dashed curve in part b) for the criterion of using all showers.

The final photon identification efficiency results are shown in Fig. 14 for peripheral and central collisions in parts a) and b), respectively. The results are shown for the various photon idenification criteria (see Sec. III B): All showers (S1); Narrow showers surviving a shower dispersion cut (S2); All showers within an increased edge cut (detector edge dead region increased from 2 modules to 3 modules); All showers with no associated CPV hit (S3); and Narrow showers with no associated CPV hit (S4). As previously discussed, what is called identification efficiency should more properly be called a response correction. It includes acceptance losses resulting from the fiducial cuts to define the useable detector region as well as dead or bad modules eliminated from the analysis. The acceptance is calculated for the full geometrical area of the lead-glass detector while the identification efficiency corrects for modules removed from the acceptance in the analysis. The efficiency correction also includes resolution corrections which can increase the apparent efficiency to values greater than one.

For peripheral reactions it is seen that the photon identification efficiency is only about 60% independent of transverse momentum. This reflects the loss of acceptance due to such eliminated modules. The efficiency is seen to be slightly smaller with the increased edge cut reflecting the decreased fiducial region. Otherwise, the photon efficiency is nearly independent of the identification method for peripheral collisions. This indicates that few photons are lost by these identification criteria or by shower overlap effects.

In contrast, for central collisions a large difference in photon identification efficiency is obtained for the different identification criteria. For the case of using all recovered showers the efficiency is seen to rise strongly with transverse momentum. This is understood as a result of the increase in the shower energy, and hence its transverse momentum,

as a result of absorbing the energy of underlying showers which have been overlapped. Due to the steeply exponential transverse momentum distribution of the photons (see Fig. 12) there is a large feeddown of showers from low p_T to high p_T when the shower energy is increased due to overlap. When the shower dispersion cut is applied this rise in the efficiency is dramatically reduced, indicating that many overlapping showers are eliminated because they are found to be too broad to be single photons (recall that the clustering algorithm separates obvious shower overlap clusters with multiple maxima into multiple clusters with single maxima). The photon identification efficiency is reduced further when it is required that there be no associated hit in the CPV detector. This reduction is due to the elimination of photon showers which overlap with charged hadrons which would otherwise appear as a single photon shower. As discussed previously (see Secs. III B and IV B), all photon identification methods use the CPV information to eliminate the charged hadron contamination. The difference between methods S1, S2 and methods S3, S4 is mostly a matter of procedure. In methods S3 and S4 in which the CPV is used directly to reject charged showers no charged hadron correction of the photon candidate spectrum is necessary. On the other hand, as seen in Fig. 14 the photon losses due to random overlap with charged hits are greater, resulting in a reduced photon identification efficiency.

The photon identification efficiencies are fitted (see Fig. 14) to remove fluctuations[3] and the fitted efficiency corrections are applied to the raw photon spectra to obtain the final photon transverse momentum distributions which need only be corrected for the LEDA acceptance. The identification efficiencies obtained by iteration were compared to efficiencies obtained by the two-dimensional unfolding method III C . The systematical error on the photon identification efficiency is estimated to be 2%.

4. Systematical error

The systematical errors relevant for the direct photon analysis which contribute solely to the extraction of the inclusive photon yield are listed in Table III at two representative transverse momenta. The errors are estimated for the case of photons identified with the narrow shower criterion (S2). The 30% uncertainty in the charged/neutral measurement discussed in regard to Figs. 10 and 11 leads to the listed p_T dependent uncertainty in the photon yield due to the charged particle background correction. Based on a comparison of the magnetic field on and field off results, and a comparison with and without the CPV requirement, a 0.5% uncertainty on the photon conversion probability has been assumed. The assumed 50% uncertainty on the neutron and anti-neutron contribution discussed in regard to Fig. 13 results in the listed p_T dependent uncertainty in the photon yield. Finally a 2.0% uncertainty in the photon identification efficiency has been assumed. The systematical errors are added in quadrature to give the total systematical error on the photon yield measurement listed in Table III. Other sources of systematical error, such as the energy calibration and non-target backgrounds, which also affect the π^0 yield extraction will be discussed in Sec V D.

The total systematical error on the photon yield measurement can be investigated by comparison of the inclusive photon results obtained with the different photon identification criteria. In particular, it was shown above that the charged and neutron backgrounds are reduced by about a factor of two when the shower dispersion cut is applied. Also, the photon identification efficiencies are observed to vary by a factor of 2-3 for central collisions depending on the identification criterion (see Fig. 14). The results of such a comparison are shown in Fig. 15 for peripheral and central collisions where the photon transverse momentum spectra obtained with the various photon identification criteria are divided by the photon spectrum obtained using the criterion of all showers. Since the corrections are largest for the condition of using all showers, it is the method expected to have the largest systematical error, with errors which should be larger than those which have been estimated for the narrow shower condition. The p_T dependent upper and lower systematical errors on the photon yield measurement are indicated by the horizontal lines. In general, to the extent allowed by the statistical uncertainties, one may conclude that the various results are consistent within the systematical error estimates.

[3]Note: The fluctuations for different identification methods are correlated since the efficiencies are extracted from the same simulated shower sample for all methods

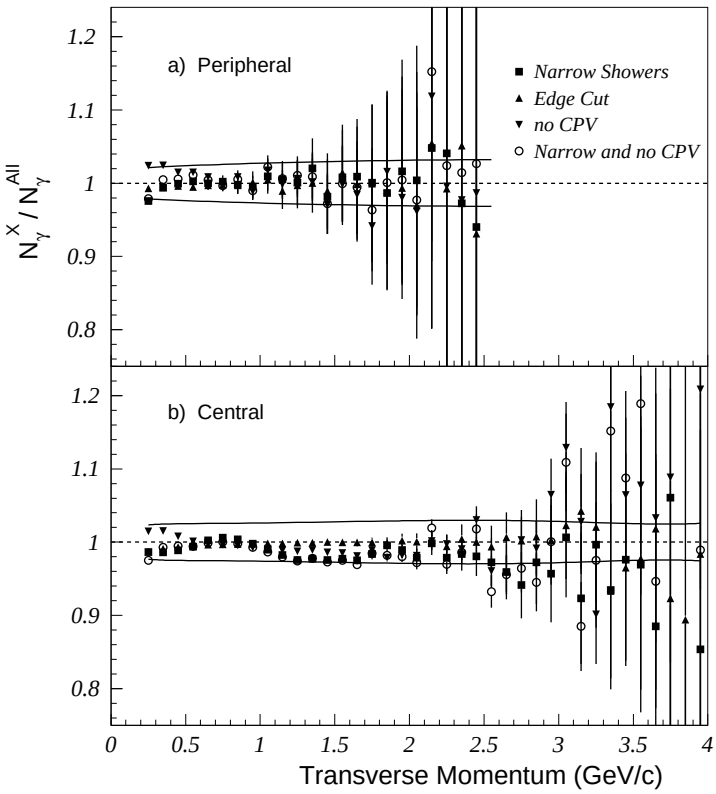

FIG. 15. The ratio of the efficiency-corrected inclusive photon yield for various methods compared to the method of using all showers (N_γ^{All}) is shown as a function of transverse momentum. The results are shown for a) peripheral and b) central 158 *A* GeV ^{208}Pb+^{208}Pb collisions for the 1996 magnet on data set. The error bars indicate statistical errors only. The deviation from unity, beyond statistical error, is indicative of the systematical error attributed to the photon identification method. The horizontal lines indicate the estimated systematical error on the photon yield determination.

D. π^0 Analysis

The method to extract the π^0 transverse momentum spectra is described in Sec. III B. In summary, the procedure is to calculate the two-gamma invariant mass spectrum for each p_T bin and extract the yield in the π^0 peak. This is done using the various photon identification criteria and run conditions and the final results are checked for consistency. While charged hadron and neutron contamination in the selected photon showers will not directly contribute to the π^0 peak and yield, they will contribute excess photon pairs in the combinatorial background which must be subtracted to obtain the yield in the peak. The large combinatorial background in the $m_{\gamma\gamma}$ invariant mass distribution, especially for central collisions, poses a special difficulty for the π^0 analysis. After the raw π^0 yield is extracted it is corrected for the π^0 identification efficiency, and finally for the lead-glass detector acceptance. The details of this procedure are described in this section.

1. π^0 Yield Extraction

The two-photon invariant mass distributions for peripheral ^{208}Pb+^{208}Pb collisions are shown in part a) of Figs. 16 and 17 for photon pair transverse momenta in the range of $0.5 < p_T < 0.6$ GeV/c and $1.5 < p_T < 1.6$ GeV/c, respectively. The distributions are obtained using all showers which pass the 750 MeV energy threshold. While it is evident that the π^0 peak content can easily be extracted at high p_T, it is seen that the peak sits on top of a rather large and broad background with a complicated shape for the case of low pair p_T. This combinatorial background arises

as a result of "random" combinations of photons within the detector acceptance where the pair of photons did not originate from the same radiative decay (e.g. different π^0's) and hence the two photons have little or no correlation. Although correlations between the photon pairs could exist, such as from a residual $\pi^0\pi^0$ Bose-Einstein correlation, or from a multi-π^0 decay final state, or from collective flow, it is expected that the shape of the photon pair combinatorial background depends mainly on the photon spectrum and on the detector acceptance. To accurately determine its shape without resort to a complicated fit procedure, an event-mixing technique has been used in which all photons of an event are paired with all photons of the next analyzed event within the same centrality selection. This procedure removes all resonance pair correlations but leaves some of the higher order correlations which might also exist in the real-pair background distribution. No attempt was made to impose cuts on the mixed event shower pairs to implement the effect of merging showers. This has the result that the mixed events are not expected to accurately reproduce the very low mass region of the real event mass spectra.

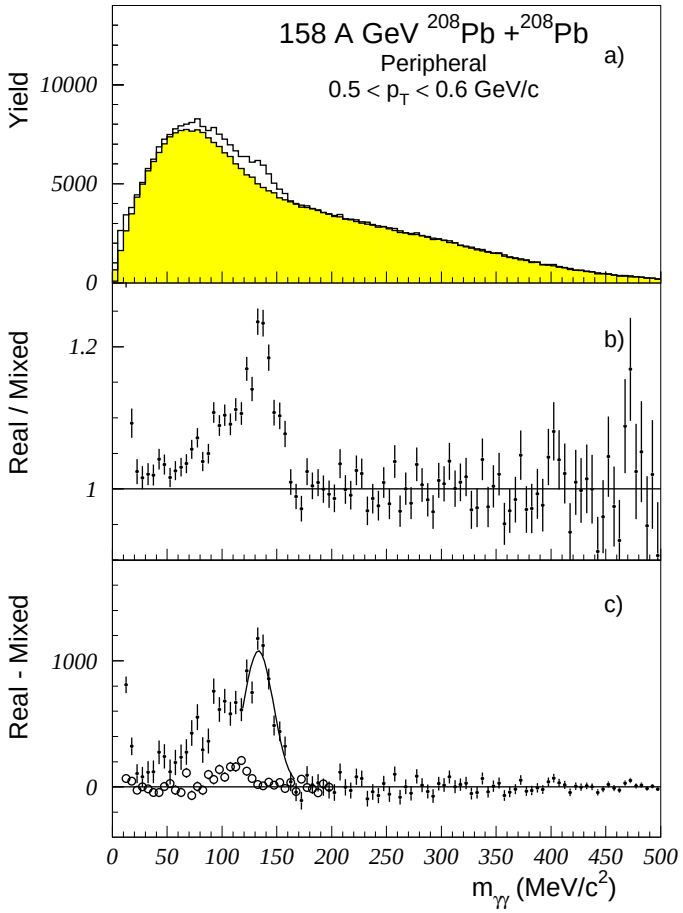

FIG. 16. The two-photon invariant mass distribution for peripheral events in the π^0 mass region with pair transverse momentum $0.5 < p_T < 0.6$ GeV/c. Results are shown for the 1996 magnet on data sample. Part a) shows the invariant mass distribution for all shower pairs for real events (solid histogram) and mixed events (filled histogram). Part b) shows the ratio of real and mixed event mass distributions. Part c) shows the real invariant mass distribution after subtracting the normalized mixed event distribution. The normalized target out background contribution is shown by the open circles in part c).

The mixed event $m_{\gamma\gamma}$ invariant mass distributions are shown as the shaded histograms in part a) of Figs. 16 and 17. The ratios of the real to mixed invariant mass distributions are shown in part b). The ratios have been normalized to unity in the region outside of the π^0 mass interval. For peripheral collisions the normalization has been calculated as the ratio of integrated yields in the mass intervals $50 - 60$ and $200 - 430$ MeV/c^2. The normalization extracted in

this way was then fit to a smooth function of p_T to determine the final mixed event background normalization. The normalized background subtracted results are shown in part c). The mixed event distribution is seen to provide a good description of the combinatorial background outside the π^0 mass region. However, a low-mass tail on the π^0 peak is observed at the lowest p_T (see Fig. 16c). Such a tail can result from π^0's produced downstream from the target, such as from K^0_S decays (see Sec. III D) or from background interactions on downstream materials. This will be further discussed below.

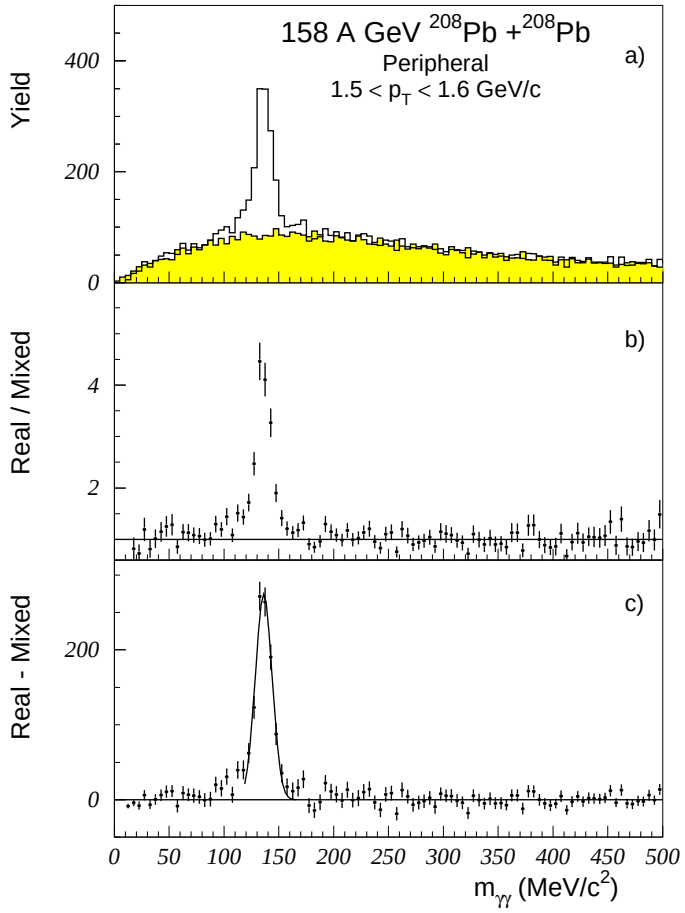

FIG. 17. The two-photon invariant mass distribution for peripheral events in the π^0 mass region with pair transverse momentum $1.5 < p_T < 1.6$ GeV/c. Results are shown for the 1995 magnet on data sample. Part a) shows the invariant mass distribution for all shower pairs for real events (solid histogram) and mixed events (filled histogram). Part b) shows the ratio of real and mixed event mass distributions. Part c) shows the real invariant mass distribution after subtracting the normalized mixed event distribution.

The $m_{\gamma\gamma}$ invariant mass distributions for central ^{208}Pb+^{208}Pb collisions are shown in part a) of Figs. 18 and 19 for photon pair transverse momenta in the range of $0.5 < p_T < 0.6$ GeV/c and $1.5 < p_T < 1.6$ GeV/c, respectively. Due to the much higher photon multiplicity in central events (see Fig.5) the combinatorial backgrounds are much greater. As a result it is seen that the π^0 peak is hardly visible at low p_T. In the same way as for peripheral events, the combinatorial background has been calculated using mixed events and normalized to the real event invariant mass distribution using the mass intervals $70 - 95$ and $220 - 430$ MeV/c^2 with the normalizations fitted to a smooth p_T dependence. The real/mixed event invariant mass distribution ratios are shown in part b) and the final normalized background subtracted invariant mass distributions are shown in part c). As for the case of peripheral collisions, the event mixed background is seen to provide a good reproduction of the combinatorial background in the region around the π^0 peak.

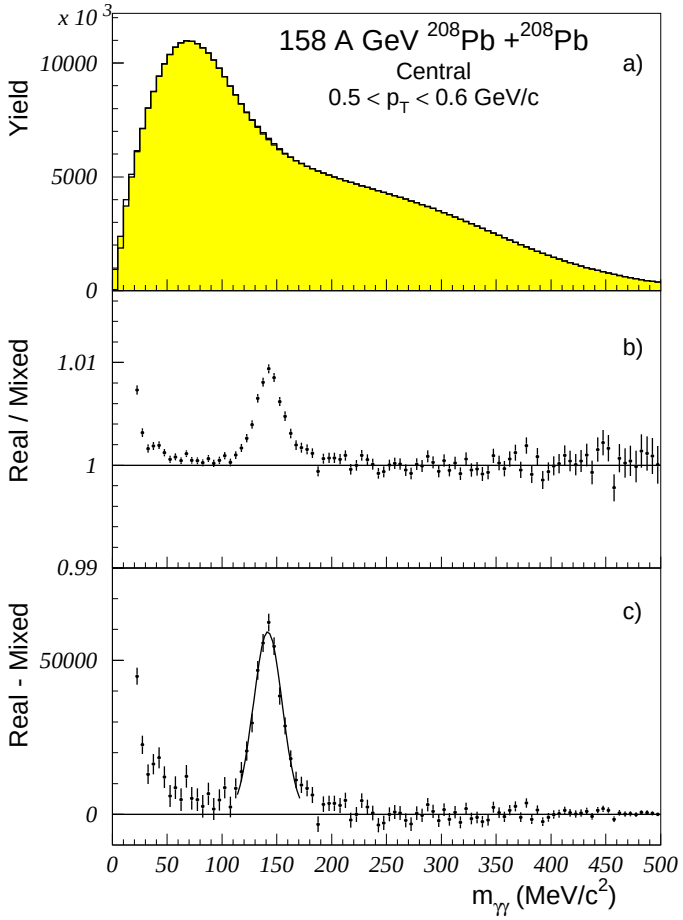

FIG. 18. The two-photon invariant mass distribution for central events in the π^0 mass region with pair transverse momentum $0.5 < p_T < 0.6$ GeV/c. Results are shown for the 1995 magnet on data sample. Part a) shows the invariant mass distribution for all shower pairs for real events (solid histogram) and mixed events (filled histogram). Part b) shows the ratio of real and mixed event mass distributions. Part c) shows the real invariant mass distribution after subtracting the normalized mixed event distribution.

Several features of the results for central collisions are notable in comparison to the results for peripheral collisions. First, it is observed that the π^0 peak is broader and shifted to higher mass as compared to the case for peripheral collisions. This is due to the effects of shower overlap and the modification of the energy and position of the original shower. Secondly, the π^0 peak is seen to exhibit a long non-gaussian tail to high mass which is also attributed to shower overlap effects. And finally, the low mass tail on the π^0 peak at low p_T is not present. The mixed event invariant mass normalization regions were chosen differently for central collisions due to these last two observations. In addition, the invariant mass distribution is observed to show structure in the very low mass region below about 50 MeV/c^2. This structure is attributed to several effects, such as splitting of overlapping showers and the above-mentioned details of the treatment of the mixed events for nearby showers. It does not affect the analysis presented here and will not be discussed further.

The π^0 transverse momentum spectra are obtained by integration of the yield in the π^0 peak region of the combinatorial background subtracted $m_{\gamma\gamma}$ invariant mass distributions for each p_T bin. The integration regions used were $110 < m_{\gamma\gamma} < 170$ MeV/c^2 for peripheral collisions and $110 < m_{\gamma\gamma} < 200$ MeV/c^2 for central collisions. The wider integration region used for central collisions is due to the previously discussed high mass tail on the π^0 peak which results from overlap effects. The uncorrected transverse momentum distributions are shown in Fig. 20 for peripheral and central collisions. The results are obtained using the full 1995 and 1996 magnet on data sample with the narrow shower identification criterion (S2) (see Sec. III B). The distributions are observed to extend over about four orders of

magnitude with similar p_T coverage but lower statistical accuracy as compared to the inclusive photon result shown in Fig. 12. The distributions are observed to be cut off at low p_T at around 0.5 GeV/c due to the acceptance limit (see Fig. 2) imposed by the 750 MeV shower energy threshold.

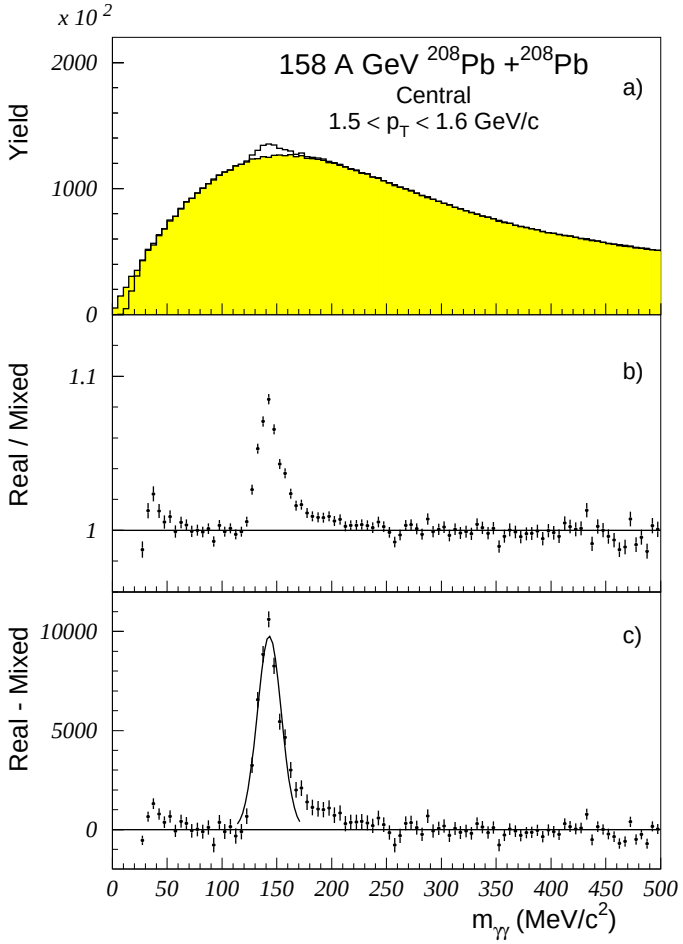

FIG. 19. The two-photon invariant mass distribution for central events in the π^0 mass region with pair transverse momentum $1.5 < p_T < 1.6$ GeV/c. Results are shown for the 1995 magnet on data sample. Part a) shows the invariant mass distribution for all shower pairs for real events (solid histogram) and mixed events (filled histogram). Part b) shows the ratio of real and mixed event mass distributions. Part c) shows the real invariant mass distribution after subtracting the normalized mixed event distribution.

As noted in the discussion of the inclusive photon result, no empty target events satisfy the central collision trigger requirement with the result that no background corrections to the photon and π^0 spectra are necessary for central collisions. On the other hand, as discussed with regard to Fig. 16, the $m_{\gamma\gamma}$ invariant mass distributions for low p_T peripheral events show a low mass tail which suggests a contribution of π^0's produced downstream of the target location. In principal, this can be verified by comparison to the $m_{\gamma\gamma}$ distribution obtained for runs taken with no target. However, when the empty target events are analyzed with the trigger requirement of a hit in the forward region of the Plastic Ball detector to eliminate downstream interactions, as used for analysis of the peripheral events, no significant peak is observed in the empty target $m_{\gamma\gamma}$ distribution. On the other hand, when the Plastic Ball hit condition is removed, a small low mass peak is observed in the empty target $m_{\gamma\gamma}$ distribution, as shown by the open symbols in Fig. 16c. With the same Plastic Ball condition as used for the Pb target the empty target contribution is reduced by a factor of more than five (see the discussion of Fig. 12). Even with the Plastic Ball condition removed, the empty target yield, appropriately normalized according to the relative number of live beam triggers, is about a factor of three lower than the observed low mass yield with the Pb target.

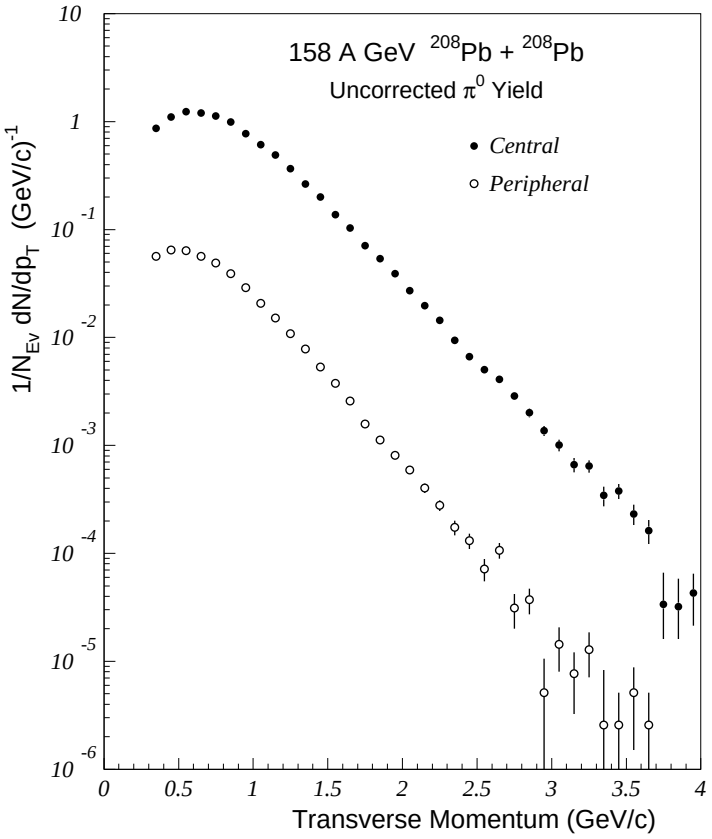

FIG. 20. The uncorrected π^0 multiplicity as a function of the transverse momentum for peripheral (open circles) and central (solid circles) 158 *A* GeV ^{208}Pb+^{208}Pb collisions. The results are for the full magnet on data sample. Narrow showers with energy above 750 MeV have been used in the invariant mass calculation. The data have not been corrected for efficiency or acceptance. These spectra are used as the first iteration in the iterative efficiency correction.

The results shown in Fig. 16 are for the 1996 magnet on data sample. A slightly larger low mass contribution with a more distinctive peak at around $m_{\gamma\gamma} \approx 100$ MeV/c^2 is observed for the 1995 data sample. As for the 1996 data, there is no such contribution seen for central collisions or for high p_T peripheral collisions (the 1995 results are shown in Figs.17,18,19). The additional 1995 low mass contribution is attributed to downstream interactions on an aluminum ring on the vacuum exit window which was removed for the 1996 run period (see Sec. II A). For the 1995 run period the Plastic Ball hit requirement was implemented directly in the online trigger. With this condition, as for the 1996 run, no significant low mass contribution was observed in the 1995 empty target data. The explanation for these observations is that the Plastic Ball condition was in fact effective to remove downstream interactions when there was no target in place. However, when the target was in place, δ-electrons produced in the target could be detected in the Plastic Ball and satisfy the Plastic Ball trigger requirement. This meant that more downstream interactions could be accepted with target in place than without target. Nevertheless, even with the Plastic Ball trigger requirement removed, the empty target result is about a factor of three below the observed low mass excess, as noted above. This observation is not understood.

For the direct photon analysis the effect of the empty target contribution has been studied under two extreme assumptions. In the first case it has been ignored completely, while in the second case the result without the Plastic Ball condition has been renormalized to be as large as possible consistent with the result for the Pb target. That is, the empty target result was increased to remove as much as possible of the low mass excess in the $m_{\gamma\gamma}$ distribution at low p_T. While these two assumptions will give different photon and π^0 p_T distributions, it might be expected that the direct photon result is not too dependent on this assumption as long as both the photon and π^0 yields from all sources are taken into account consistently. Finally, we emphasize again that this non-target background uncertainty is only relevant for the low p_T (below ~ 1 GeV/c) peripheral data sample.

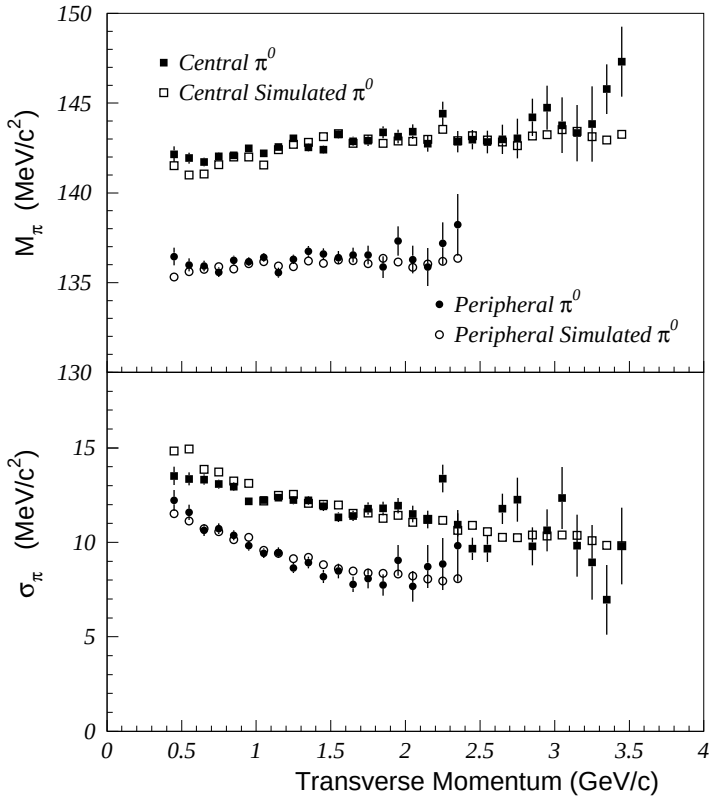

FIG. 21. The π^0 mass peak position and width, σ, resulting from a gaussian fit to the two-photon invariant mass distribution is shown as a function of the transverse momentum in the upper and lower portions of the figure, respectively. The solid symbols show results for real π^0's while the open points show the results for simulated π^0's superimposed on real events. Results are shown for peripheral (circles) and central (squares) 158 *A* GeV ^{208}Pb+^{208}Pb collisions using all shower candidates. The same fit region is used for the real and simulated data.

2. π^0 Reconstruction Efficiency

The procedure to determine the π^0 reconstruction efficiency is similar to the one for photons described in Sec. IV C 3. As described in Sec. III C, the π^0 reconstruction efficiency is extracted by inserting test π^0's into real events and determining how the test π^0's are modified or lost. The test π^0's were initially generated uniformly in transverse momentum and pseudo-rapidity. Only those π^0's which decayed to give two photons within the nominal LEDA acceptance were recorded and those photons were tracked with GEANT. The efficiency is extracted as the ratio of the transverse momentum spectrum of found π^0's divided by the transverse momentum spectrum of input π^0's. The input π^0 and its associated found π^0 are weighted such that the input distribution reproduces the measured transverse momentum distribution for each event class. The initial input weights are taken according to the raw π^0 distribution (see Fig. 20) after application of the acceptance correction and an initial estimated efficiency correction. The weights and resulting efficiency are iterated until the weighted input distribution agrees with the final result. The input π^0 distribution is weighted according to a Gaussian rapidity distribution centered on mid-rapidty with an rms width of $\sigma_y = 1.3$ [92], consistent with the final result.

After being superimposed onto real events the simulated π^0's are considered to be found if both photons are recovered and the reconstructed invariant mass of the photon pair falls within the same π^0 mass window as applied in the analysis of the real events (see Sec. IV D 1). For an accurate efficiency determination it is essential that the simulated photon showers have the same characteristics as the measured photon showers. This can be verified by comparison of the extracted π^0 mass peak for real events with that of the simulated π^0's after superposition onto real events. Such a comparison is shown in Fig. 21. The fitted mass and width of the π^0 peak are shown as a function of transverse

momentum for central and peripheral event selections for the case of using all shower candidates (S1) for the invariant mass calculation. As noted in the discussion of the invariant mass spectra, the mass and width of the π^0 peaks are observed to be significantly larger for central collisions in comparison to peripheral collisions due to the effects of shower overlap. With the narrow shower condition (S2), the π^0 peak position is about 3 MeV/c^2 lower and the π^0 peak width is about 1.5 MeV/c^2 smaller for central conditions compared to the results shown in Fig. 21. The characteristics of the reconstructed simulated π^0's are seen to be in good agreement with those of the real π^0's for both peripheral and central event selections. This indicates that the energy calibration and resolution, and their modification due to detector occupancy effects, are accurately reproduced in the simulation and therefore are properly taken into account in the efficiency determination.

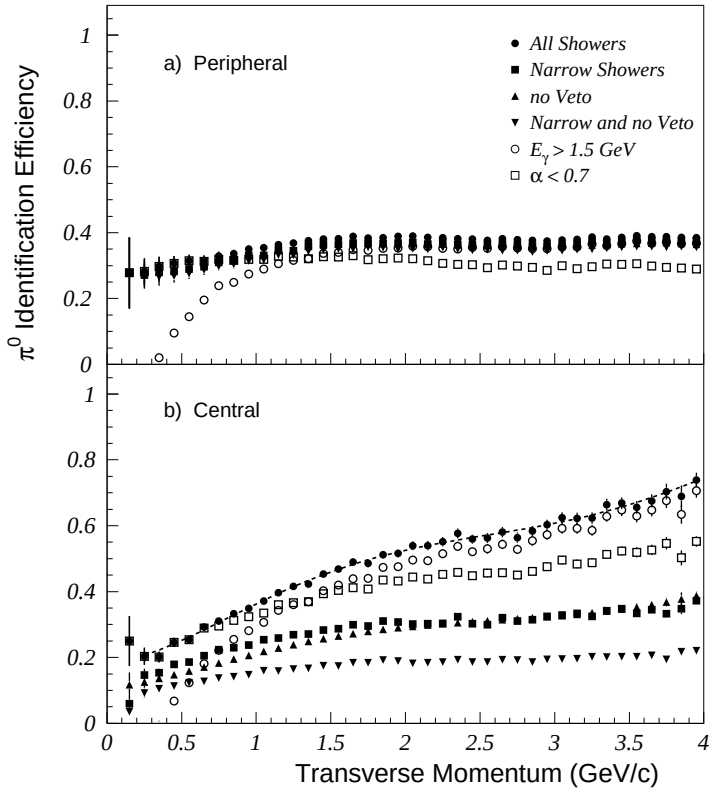

FIG. 22. The π^0 identification efficiency including effects of resolution, shower overlap, and excluded lead-glass modules. The π^0 identification efficiency is shown as a function of transverse momentum for a) peripheral and b) central 158 *A* GeV ^{208}Pb+^{208}Pb collisions. A 750 MeV shower energy threshold has been applied. The efficiency is shown for the 1996 magnet on data for the following criteria: all showers (solid circles), showers satisfying a dispersion cut (solid squares), all showers with no associated hit in the CPV (solid triangles), all showers satisfying a dispersion cut with no associated hit in the CPV (inverted solid triangles), all showers but with shower energy threshold increased to 1.5 GeV/c (open circles), and all showers with the requirement that the shower-pair energy asymmetry is less than 0.7 (open squares). An example of the fitted parameterization of the efficiency is shown by the dashed curve in part b) for the criterion of using all showers.

The final π^0 identification efficiencies are shown in Fig. 22 for peripheral and central collisions in parts a) and b), respectively. The results are shown for the various photon identification criteria (see Sec. III B): all showers (S1); narrow showers surviving a shower dispersion cut (S2); all showers with no associated CPV hit (S3); and narrow showers with no associated CPV hit (S4); all showers but with the photon energy threshold increased from 750 MeV to 1.5 GeV; shower pairs which satisfy an energy asymmetry cut $\alpha = |E_1 - E_2|/|E_1 + E_2| < 0.7$. As previously mentioned, what is called the identification efficiency should more properly be called a response correction. It includes acceptance losses resulting from the fiducial cuts to define the useable detector region as well as dead or

bad modules eliminated from the analysis. The acceptance is calculated for the full geometrical area of the LEDA while the identification efficiency corrects for modules removed from the acceptance in the analysis.

For peripheral reactions it is seen that the π^0 identification efficiency is only about 30%, nearly independent of transverse momentum, which reflects the loss of acceptance due to eliminated modules. With the 1.5 GeV shower energy threshold the efficiency is seen to drop sharply at low transverse momentum due to the loss of acceptance which results from the higher energy threshold. Similarly, the shower energy asymmetry cut results in a loss of π^0 acceptance, and hence a decreased efficiency, at large transverse momenta. Otherwise, the π^0 efficiency is nearly independent of the identification method for peripheral collisions. Again, this indicates that few photons are lost by these identification criteria or by shower overlap effects.

Similar to the photon identification efficiency, the π^0 efficiency dependence is quite different for the case of central collisions. A large difference in the π^0 identification efficiency is obtained for the different identification criteria. For the case of using all recovered showers the efficiency is seen to rise strongly with transverse momentum, exceeding the efficiency for peripheral collisions. This is understood as a shower overlap effect which results in an increase in the shower energy, and hence transverse momentum, as a result of absorbing the energy of underlying showers which get overlapped. Due to the steeply exponential transverse momentum distribution of the π^0's (see Fig. 20) there is a large feeddown of the π^0 yield from low p_T to high p_T when the shower energy is increased due to overlap. When the shower dispersion cut is applied this rise in the efficiency is dramatically reduced, and becomes more similar to the result for peripheral collisions. This indicates that many overlapping showers are eliminated because they are found to be too broad to be single photons. The π^0 identification efficiency is reduced further when it is required that there be no associated hit in the CPV detector (methods S3 and S4). This reduction is due to conversions and the elimination of photon showers which overlap with charged hadrons which would otherwise appear as a single photon shower.

The π^0 identification efficiencies are fitted (see Fig. 22) to remove fluctuations[4] and the fitted efficiency corrections are applied to the raw π^0 spectra to obtain the final π^0 transverse momentum distributions which need only be corrected for the LEDA acceptance. The systematical error on the π^0 identification efficiency is estimated to be 3% for peripheral collisions and 4% for central collisions.

3. Systematical error

The systematical errors relevant for the direct photon analysis which enter only for the inclusive π^0 yield extraction are listed in Table III at two representative transverse momenta. The errors are estimated for the case of photons identified with the narrow shower criterion (S2). Based on a comparison of the magnetic field on and field off results, and a comparison with and without the CPV requirement a 0.5% uncertainty in the π^0 yield due to photon conversions has been assumed. As mentioned above, the uncertainty in the π^0 identification efficiency has been assumed to be 3% and 4% for peripheral and central collisions, respectively. An important source of systematical error in the π^0 yield extraction at low p_T for central collisions is the error associated with the combinatorial background subtraction. The statistical error of the combinatorial background subtraction is included in the statistical error on the π^0 yield. An additional systematical error of 10^{-3} of the background yield has been assumed. This error contribution is estimated from the variability of the results at low p_T for central collisions for the different analysis methods (see Fig. 23). Besides the small peak/background ratios at low p_T for central collisions, the curvature of the background under the π^0 peak may futher complicate the extraction of the π^0 yield and increase the error beyond expectations from the magnitude of the background. The systematical errors are added in quadrature to give the total systematical error on the π^0 yield extraction listed in Table III. Other sources of systematical error, such as the energy calibration and non-target backgrounds, which affect both the photon and π^0 yield extraction will be discussed below.

As for the photon yield determination, the total systematical error estimate on the π^0 yield extraction can be investigated by comparison of the inclusive π^0 results obtained with the different identification criteria. The results of such a comparison for peripheral and central collisions are shown in Fig. 23 where the π^0 transverse momentum spectra obtained with the various conditions are divided by the π^0 spectrum obtained using the criterion of all showers (S1). Since the π^0 identification efficiencies vary by a factor of 2-3 for central collisions depending on the identification criterion (see Fig. 22) this comparison provides a sensitive indication of the accuracy of the efficiency determination. Also, the uncertainty in the π^0 peak yield extraction is probed since, for example, the application of the shower dispersion cut reduces the non-photon shower contamination and therefore improves the π^0 peak/background ratio by nearly

[4]Note: The fluctuations for different identification methods are correlated since the efficiencies are extracted from the same simulated shower sample for all methods.

a factor of two, which reduces the necessary background correction. Since the corrections are largest for the condition of using all showers, it is the method expected to have the largest systematical error, with errors which should be larger than those which have been estimated for the narrow shower condition. The p_T dependent upper and lower systematical errors on the π^0 yield measurement are indicated by the horizontal lines. In general, to the extent allowed by the statistical uncertainties, one may conclude that the various results are consistent within the given systematical error estimates. The increasing systematical deviations at low transverse momentum for central collisions are due to the above-mentioned systematical error of the combinatorial background subtraction.

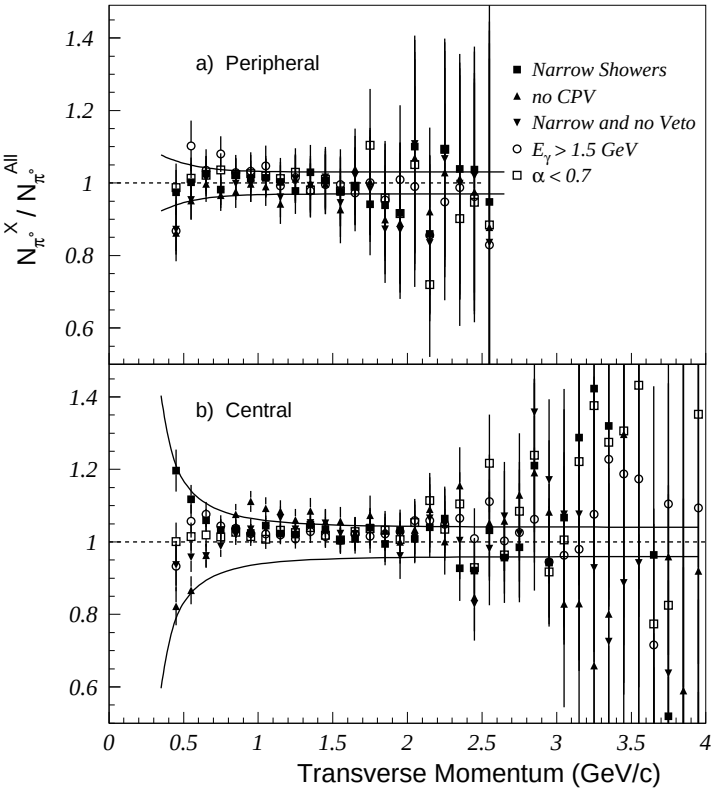

FIG. 23. The ratio of the efficiency-corrected π^0 yield for various shower identification methods compared to the method of using all showers is shown as a function of transverse momentum. The results are shown for a) peripheral and b) central 158 *A* GeV ^{208}Pb+^{208}Pb collisions for the 1996 data set. The error bars indicate statistical errors only. The horizontal lines indicate the estimated systematical errors. The deviation from unity, beyond statistical error, is indicative of the systematical error in the π^0 yield extraction.

E. η Analysis

The method to extract the η transverse momentum spectrum is similar to that used for the π^0 analysis described in Sec. III B and discussed in Sec. IV D. As for the π^0, the procedure is to calculate the $m_{\gamma\gamma}$ invariant mass spectrum for each p_T bin and extract the yield in the η peak. The extraction of the η yield is much more difficult due to the lower η production cross section and smaller branching ratio to two photons together with the very large combinatorial background in the $m_{\gamma\gamma}$ invariant mass distribution. An example of the two-photon invariant mass distributions for central ^{208}Pb+^{208}Pb collisions in the η mass region is shown in part a) of Fig. 24 for photon pair transverse momenta in the range of $1.0 < p_T < 1.2$ GeV/c. The distributions are obtained using all narrow showers which pass the 750 MeV energy threshold and include the full 1995 and 1996 magnet on data samples. The invariant mass distribution for real events is shown by the open histogram while the invariant mass distribution constructed with photons from mixed

events is shown by the shaded histogram. The difference in the two distributions is scarcely visible, even in the η peak region.

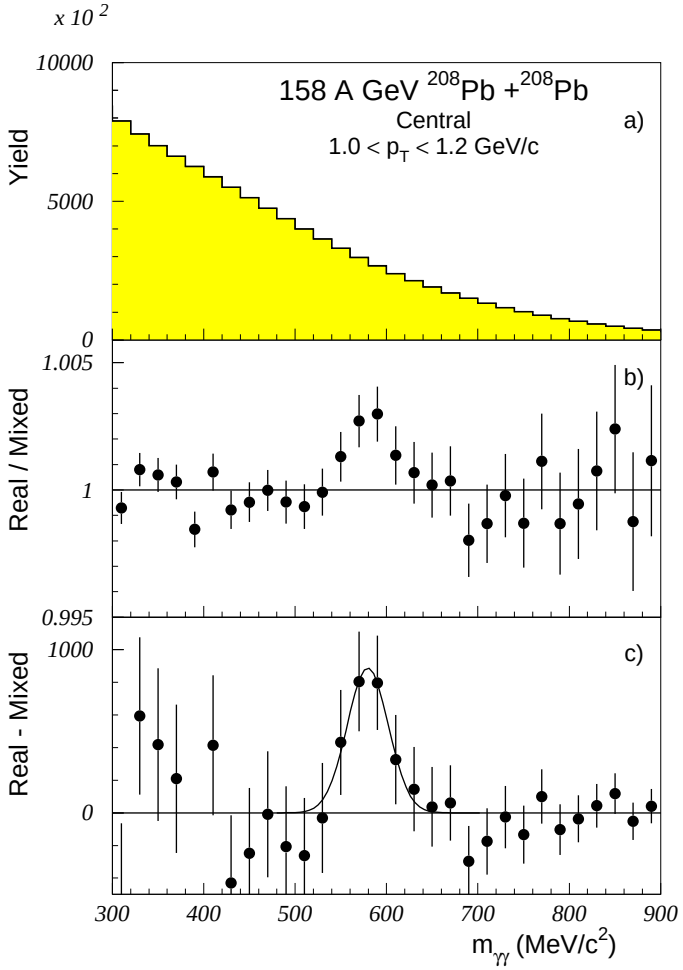

FIG. 24. The two-photon invariant mass distribution for central events in the η mass region with photon pair transverse momentum $1.0 < p_T < 1.2$ GeV/c. Part a) shows the invariant mass distribution for all shower pairs for real events (solid histogram) and mixed events (filled histogram). Part b) shows the ratio of real and mixed event mass distributions. Part c) shows the real invariant mass distribution after subtracting the normalized mixed event distribution.

The η peak yield is extracted in the same way as the π^0 yield extraction but with one additional step. To insure that the high mass tail of the π^0 peak does not affect the normalization of the background the π^0 content is first removed from the invariant mass distribution. This is done by extraction of the π^0 peak yield, as described in Sec. III B, and then subtraction of the corresponding invariant mass distribution of simulated π^0's after event overlap, normalized to the same π^0 yield, from the invariant mass distribution. This removes the π^0 peak and high mass tail from the invariant mass distribution of real photon pairs. The ratio of the π^0 subtracted real event to mixed event invariant mass distributions is shown in part b) of Fig. 24. The mixed event background normalization is given by fixing to unity the ratio of integrated yields in the mass interval $355 - 450$ and above 710 MeV/c^2. The normalized background subtracted invariant mass distribution is shown in part c). While the η peak is clearly seen to contain several thousand counts, the statistical significance of the peak is weak due the low signal to background ratio of less than 0.5%. The η peak is seen to be shifted to higher mass due to the effect of shower overlap in central collisions, similar to observation for the π^0 (see Fig. 21). The η yield is obtained by integration over the invariant mass region $500 - 640$ MeV/c^2.

The η and π^0 yields are extracted from the invariant mass distribution for each transverse momentum bin and are corrected for identification efficiency, acceptance, and the two-photon decay branching ratios. The ratio of corrected

yields, η/π^0, is shown as a function of transverse momentum in Fig. 25. While the statistical error at each point is large, due to the large combinatorial background for extraction of the η yield, there is a general tendency for a rise in the ratio with increasing p_T. This is the expected behavior if the η and π^0 yields have the same functional dependence on the transverse mass. The solid curve in Fig. 25 is the calculated ratio expected from the fit to the π^0 spectrum (see Fig. 26 and discussion below) assuming m_T-scaling. The absolute normalization is the m_T-scaling parameter which is fitted to the results of Fig. 25 to be $R_{\eta/\pi^0} = 0.486 \pm 0.077$(stat.)$\pm 0.097$(syst.). A 20% systematical error has been assumed on the absolute normalization of the η yield relative to the π^0 yield. This systematical error reflects the uncertainty due to the worse ratio of η yield to combinatorial background in the η region, and a less thorough investigation of the η efficiency corrections due to the limited statistics.

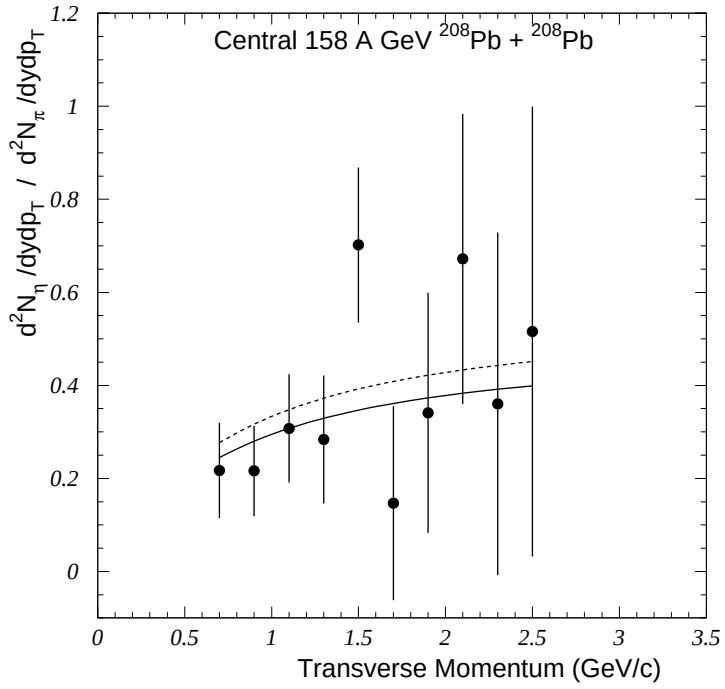

FIG. 25. The η/π^0 ratio as a function of transverse momentum for central 158 *A* GeV ^{208}Pb+^{208}Pb collisions. The solid curve is the ratio expected for m_T-scaling of the fitted π^0 result of Fig. 26 with a fitted normalization $R_{\eta/\pi^0} = 0.486$. The dashed curve is the expected result with fixed normalization$R_{\eta/\pi^0} = 0.55$.

Within errors, the fitted R_{η/π^0} ratio is in agreement with previous results. A value of $R_{\eta/\pi^0} = 0.55 \pm 0.02$ has been obtained from a compilation of previous measurements [76,77] as discussed in Sec. III C and listed in Table I. The present η measurement excludes any large enhancement of the η yield in central Pb+Pb collisions as has been suggested might occur as a consequence of chiral symmetry restoration [82,83] (see discussion of Sec. III C). The result also indicates that the m_T-scaling assumption is valid, or at least not significantly distorted by collective flow effects, for the transverse momentum range of interest for the present direct photon analysis.

Finally, we note that due to the limited data sample and lower η multiplicity it was not possible to obtain a significant η measurement for the peripheral Pb+Pb event selection. Instead, m_T-scaling has been assumed as given by the measured peripheral π^0 result with a m_T-scaling parameter of $R_{\eta/\pi^0} = 0.55$.

V. RESULTS

In this section the final inclusive π^0 and inclusive photon results are presented. The inclusive π^0 measurement is used, together with the η result of the previous section, as input to a calculation of the expected inclusive photon distribution from radiative decays. The difference between the measured and calculated photon distributions is extracted as the direct photon excess. The measured excess is presented and discussed in comparison to other measurements and model calculations.

A. π^0 and η Production

The final inclusive π^0 transverse momentum spectra for central and peripheral 158 *A* GeV ^{208}Pb+^{208}Pb collisions are shown in Fig. 26. The results presented are the sum of the 1995 and 1996 data samples with magnet on. The details of the data selection have been discussed in Sec. IV A and the characteristics of the peripheral and central data samples are summarized in Table II. The distributions have been corrected for the π^0 identification efficiency and acceptance as described in Secs. III B and IV D. The indicated errors are the total statistical errors which include also the statistical errors introduced by the combinatorial background subtraction. The systematical errors on the π^0 yield extraction have been discussed in Sec. IV D 3 and will be summarized again in Sec. V D. It should be noted that the π^0 yield per event is given rather than the absolute π^0 cross section. For the direct photon analysis the measured photon multiplicity per event will be compared to the background multiplicity calculated from the measured π^0 yield per event for the same event sample. Therefore there are no systematical errors associated with the absolute cross section determination. Also, it is recalled that the definitions of the peripheral data samples were slightly different for the 1995 and 1996 runs so that the result presented is for an averaged peripheral class. The peripheral π^0 distribution has not been corrected for target-out background (see Sec. IV D).

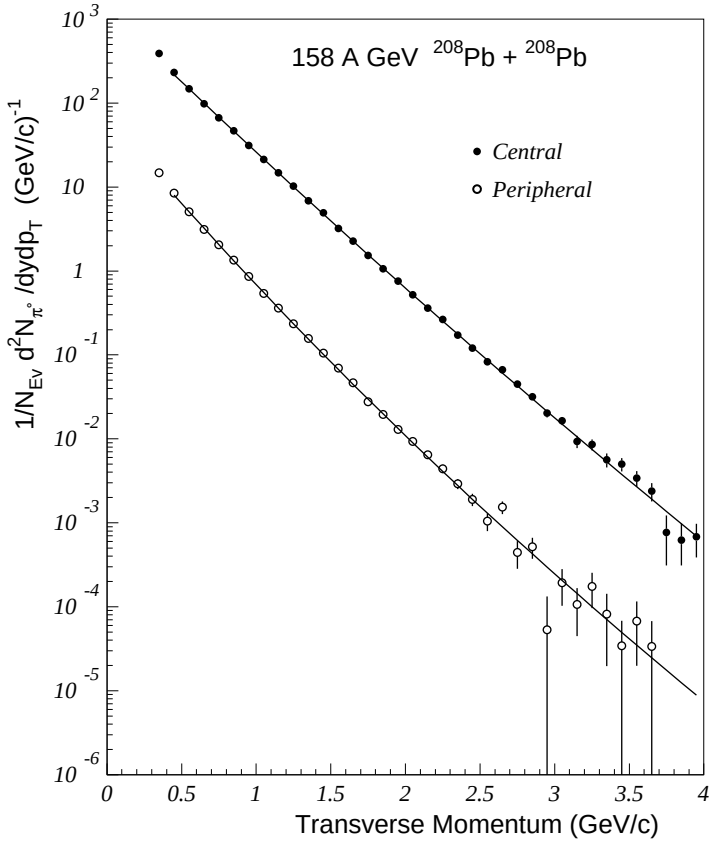

FIG. 26. The π^0 transverse momentum distribution for peripheral (open circles) and central (solid circles) 158 *A* GeV ^{208}Pb+^{208}Pb collisions for the sum of 1995 and 1996 magnet on data sets. The narrow shower photon identification criterion has been used. The data have been corrected for efficiency and acceptance. Only statistical errors are shown. The solid curves show the fit results described in the text.

The π^0 transverse mass distributions are observed to be nearly exponential over more than five orders of magnitude. On the other hand, the distributions exhibit a weak curvature which is best described by a power-law. The spectra have therefore been fitted with a QCD-inspired power-law functional form [98],

$$\frac{1}{N_{Event}}\frac{d^2N}{dydp_T} = C \cdot \left(\frac{p_0}{p_0 + p_T}\right)^n . \tag{5.1}$$

The fit region and fit results are shown by the solid curves in Fig. 26. The extracted fit parameter values are $C = 66.5 \pm 2.3, p_0 = 9.6 \pm 1.3$ GeV/c, and $n = 44.5 \pm 5.6$ with $\chi^2/33 = 1.25$ for peripheral collisions and $C = 1295 \pm 21, p_0 = 19.98 \pm 0.24$ GeV/c, and $n = 80.0 \pm 0.7$ with $\chi^2/36 = 1.06$ for central collisions.

For the power-law functional form of Eq. 5.1 the local inverse slope is calculated as

$$T = -\frac{f(p_T)}{\frac{\partial f(p_T)}{\partial p_T}} = \frac{p_0}{n} + \frac{p_T}{n}. \tag{5.2}$$

The ratio p_0/n characterizes the slope of the distribution as $p_T \rightarrow 0$, while $1/n$ characterizes the strength of the curvature. The above fit results give $p_0/n = 215.7$ and 249.8 MeV/c for peripheral and central collisions, respectively. The large fitted values of n confirm the nearly exponential spectral shapes.

More properly [98–100], the invariant π^0 yields per event can be fitted to the same functional form to provide a similarly good description.

$$\frac{1}{N_{Event}} E \frac{d^3N}{dp^3} = C' \cdot \left(\frac{p_0'}{p_0' + p_T} \right)^{n'}. \tag{5.3}$$

Fitting the invariant transverse momentum distributions in the region above 500 MeV/c gives fit parameters $C' = 46.7 \pm 2.1, p_0' = 3.64 \pm 0.06$ GeV/c, and $n' = 24.9 \pm 0.2$ with $\chi^2/32 = 1.41$ for peripheral collisions and $C' = 813. \pm 21., p_0' = 5.08 \pm 0.18$ GeV/c, and $n' = 29.3 \pm 0.8$ with $\chi^2/35 = 1.56$ for central collisions. This corresponds to $p_0'/n' = 146.0$ and 173.4 MeV/c for peripheral and central collisions, respectively. The fitted slope and curvature parameters are similar to those which have been extracted for the π^0 invariant cross sections for sulphur-induced reactions [100].

The fit results of Eq. 5.1 shown in Fig. 26 are the main experimental input to the calculation of the radiative decay background. In addition, the π^0 fit result for central collisions has been used to fit the η/π^0 ratio shown in Fig. 25 assuming m_T-scaling and to extract the m_T-scaling ratio $R_{\eta/\pi^0} = 0.486$ for central collisions, as discussed in Sec. IV E. The calculated inclusive photon distribution from radiative decays is compared to the measured inclusive photon distribution to extract the excess which may be attributed to direct photons.

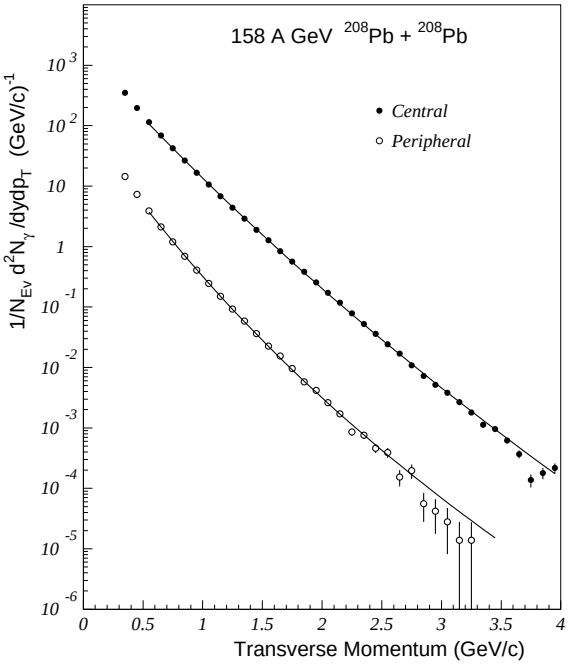

FIG. 27. The inclusive photon transverse momentum distribution for peripheral (open circles) and central (solid circles) 158 *A* GeV ^{208}Pb+^{208}Pb collisions for the sum of 1995 and 1996 magnet on data sets. The narrow shower photon identification criterion has been used. The data have been corrected for efficiency and acceptance. Only statistical errors are shown. The solid curves show the fit results described in the text.

B. Inclusive Photon Results

The final inclusive photon transverse momentum spectra for central and peripheral 158 *A* GeV ^{208}Pb+^{208}Pb collisions are shown in Fig. 27. The results presented are the sum of the 1995 and 1996 data samples with magnet on, which is exactly the same data sample as used for the final π^0 and η result. The details of the data selection have been discussed in Sec. IV A and the characteristics of the peripheral and central data samples are summarized in Table II. The distributions have been corrected for the photon identification efficiency and acceptance as described in Secs. III B and IV C. The indicated errors are statistical errors only. The systematical errors on the photon yield extraction have been discussed in Sec. IV C 4 and will be summarized again in Sec. V D. It is again noted that there are no systematical errors associated with the absolute cross section determination for the direct photon analysis. Also, it is again noted that the peripheral data sample definitions were slightly different for the 1995 and 1996 runs which means that the result represents an average peripheral class. The peripheral photon distribution has not been corrected for target-out background (see Sec. IV C 1).

Similar to the π^0 transverse mass distributions, the inclusive photon transverse momentum distributions are nearly exponential over more than six orders of magnitude. The inclusive photon distributions have been fitted with the power-law functional form of Eq. 5.1 with the fit region and results shown by the solid curves in Fig. 27. The extracted fit parameter values are $C = 115.9 \pm 3.3, p_0 = 3.2 \pm 0.4$ GeV/c, and $n = 21.8 \pm 5.6$ for peripheral collisions and $C = 1570 \pm 18, p_0 = 7.35 \pm 0.19$ GeV/c, and $n = 37.2 \pm 0.8$ for central collisions.

The measured inclusive photon distributions are to be compared to the background inclusive photon distributions calculated from radiative decays of the π^0 and other hadrons to extract the direct photon excess.

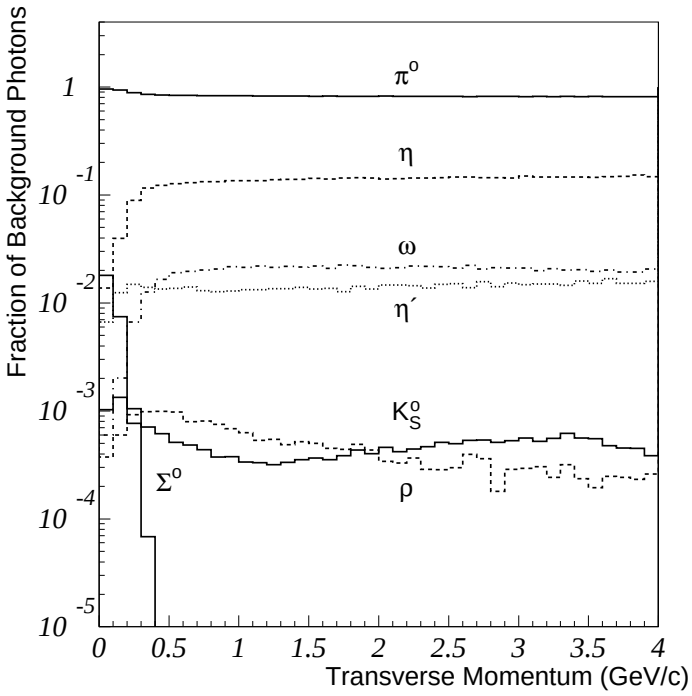

FIG. 28. The calculated fraction of all background inclusive photons from various radiative decay sources is shown as a function of the transverse momentum for central 158 *A* GeV ^{208}Pb+^{208}Pb collisions.

C. Background Photon Calculation

For each data sample or event selection in which the inclusive yield is extracted, the expected inclusive photon background from long-lived radiative decays is calculated using a Monte Carlo program which uses the JETSET 7.3 routines [91] to implement the hadron decays with proper branching ratios and decay distributions. As described in Sec. III D, the most important input to that calculation is the measured inclusive π^0 yield per event for the same

event sample. In the present analysis, the direct photon excess is to be extracted for central and for peripheral Pb+Pb collisions. The peripheral data sample is used to provide a control measurement. Therefore, the fits to the final inclusive π^0 transverse momentum distributions of Fig. 26 are the primary input to the calculations. The output of the simulation is the calculated decay photon yield per π^0 into the LEDA acceptance. This calculated γ/π^0 ratio, is to be compared to the measured ratio. Since the simulated π^0 distribution must agree with the measured π^0 distribution by construction, the difference in the measured and calculated inclusive γ yield per event gives the direct photon excess.

While photons from π^0 decay constitute the dominant source of background photons, other radiative decays are also included in the background calculation. The calculated fraction of the total background photons due to each of the various photon sources is shown in Fig. 28 for central Pb+Pb collisions. As discussed in Sec. III D, the yields of the various hadrons has been calculated with the assumption of m_T-scaling. This implies that the transverse momentum distributions of the other hadrons are determined by the measured π^0 transverse momentum distributions. The m_T-scaling normalization factors R_{X/π^0} are taken from the literature as discussed in Sec. III D and given in Table I. The quoted m_T-scaling factors are used for both peripheral and central collisions, with the exception that the measured m_T-scaling value of $R_{\eta/\pi^0} = 0.486$ extracted for the results shown in Fig. 25 and discussed in Sec. IV E is used for central collisions. As seen from Fig. 28, the η radiative decay contribution is the most significant source of background photons, beyond the π^0 contribution.[5] As will be discussed in the next section, the uncertainty on the η yield constitutes one of the largest sources of systematical error on the background photon calculation.

For the background calculations, a Gaussian rapidity distribution of particle production is assumed centered on mid-rapidity ($y = 2.9$) with an rms width of $\sigma_y = 1.3$ according to measured results for photon production in 158 *A* GeV ^{208}Pb+^{208}Pb collisions [92]. Since the LEDA is near to mid-rapidity (see Fig. 2) the rapidity distribution varies little over the detector acceptance consistent with the $\sigma = 1.3$ width. As an extreme, the background calculation has been performed with the assumption of a flat rapidity distribution. Under this assumption the calculated background photon yield would increase by about 2% for all transverse momenta above $p_T = 1$ GeV/c. The increase is greater at low p_T with an increase in the photon yield of about 5% at $p_T = 500$ MeV/c. This modest sensitivity to the assumed rapidity distribution can be understood from the limited acceptance for photons from π^0's which are emitted away from LEDA, as seen in part a) of Fig. 2. More important however, is that the calculated γ/π^0 ratio, which is the quantity relevant for the direct photon analysis, is much less sensitive to the assumed rapidity distribution. With the assumption of a flat rapidity distribution the γ/π^0 ratio is increased by only 2% at $p_T = 500$ MeV/c, 0.5% at $p_T = 1$ GeV/c, with the size of the increase rapidly decreasing at higher transverse momenta. Therefore, one may conclude that the uncertainty in the calculated γ/π^0 ratio due to extrapolation and uncertainty of the π^0 rapidity distribution is negligible.

D. Direct Photon Excess

In this section the final direct photon result is obtained and compared to results from proton-induced reactions at similar $\sqrt{s}$ and to model calculations. The direct photon yield is extracted as a function of the photon transverse momentum for central and peripheral 158 *A* GeV ^{208}Pb+^{208}Pb collisions. The results presented are the sum of the 1995 and 1996 magnet on data samples. The details of the data selection have been discussed in Sec. IV A and the characteristics of the peripheral and central data samples are summarized in Table II. As described in Sec. III A, the direct photon excess is extracted on a statistical basis as the difference between the measured inclusive photon distributions discussed in Sec. V B and the background photon distributions calculated from radiative decays of long-lived final state hadrons discussed in Sec. V C.

1. Results

Since π^0 radiative decays comprise the dominant source of background photons (see Fig. 28), it is instructive to first investigate the γ/π^0 ratio as a function of the transverse momentum. As a result of the steeply falling π^0 transverse momentum spectra (see Fig. 26), photons of a given p_T predominantly result from asymmetric π^0 decays in which the photon carries most of the momentum of the parent π^0. (Since photons from symmetric decays carry roughly half of the parent π^0 momentum they are suppressed by the lower π^0 yield at the two times higher p_T, compared to the asymmetric decay π^0's.) Therefore, the error on the predicted photon yield at a given p_T will be most strongly

[5] Note that decay photons from π^0's which are themselves decay products of other hadrons are included in the measured π^0 decay contribution, and therefore not included as decay photons from the original hadron.

correlated with the error in the measured π^0 yield at a similar, slightly higher, p_T. For the ratio γ/π^0 many sources of systematical errors partially cancel, such as errors in the energy scale calibration for the measurement, or errors in the assumed π^0 rapidity distribution for the background calculation (as discussed in Sec. V C). Therefore a comparison of the measured and calculated γ/π^0 ratios provides a sensitive indication whether a direct photon excess is observed.

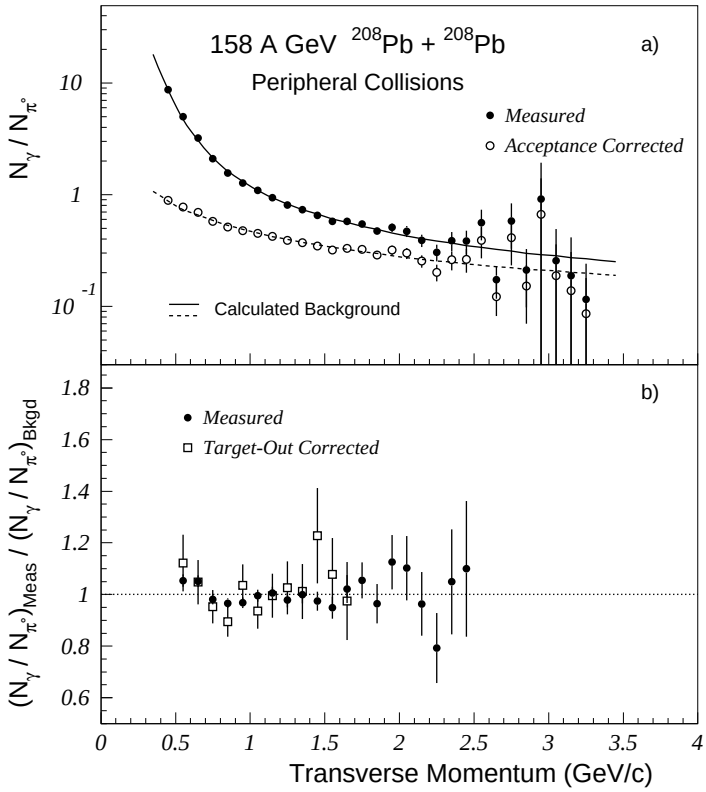

FIG. 29. The efficiency corrected (solid circles) and efficiency and acceptance corrected (open circles) γ/π^0 ratio is shown in part a) as a function of transverse momentum for peripheral 158 *A* GeV ^{208}Pb+^{208}Pb collisions. The calculated background $(\gamma/\pi^0)_{\rm Bkgd}$ ratio in the WA98 acceptance is shown by the solid curve. The dashed curve shows the calculated background with acceptance corrections. The ratio of measured $(\gamma/\pi^0)_{\rm Meas}$ ratio to calculated $(\gamma/\pi^0)_{\rm Bkgd}$ ratio for the WA98 acceptance is shown in part b). The errors on the data points indicate the statistical errors only.

The measured γ/π^0 ratio for peripheral ^{208}Pb+^{208}Pb collisions is shown as a function of transverse momentum in part a) of Fig. 29. The solid points show the measured γ yield per event divided by the measured π^0 yield per event in the LEDA acceptance, fully corrected for efficiencies and backgrounds. The errors indicate the total statistical error on the ratio from the γ and π^0 yield extraction at each p_T. The open points show the measured results additionally corrected for the γ and π^0 acceptances. The results shown are obtained using the photon identification criterion in which all showers are considered photon candidates (condition S1 of Sec. III B). This shower identification criterion provides the greatest γ and π^0 efficiency, but also requires the largest corrections and therefore has the largest expected systematical error. The measured result is compared to the predicted γ/π^0 ratio shown by the solid curve in part a). The predicted result is from the Monte Carlo calculation of the background radiative decay photons discussed in Sec. V C which is based on the measured peripheral π^0 spectrum of Fig. 26. The simulation provides the yield per event of photons and π^0's into the LEDA acceptance. The calculated result is also shown with the γ and π^0 acceptance corrections.

The predicted $(\gamma/\pi^0)_{\rm Bkgd}$ ratio from background decays is seen to be in good agreement with the measured results. This is shown more clearly in part b) of Fig. 29 where the solid points show the ratio of the measured $(\gamma/\pi^0)_{\rm Meas}$ ratio to predicted background $(\gamma/\pi^0)_{\rm Bkgd}$ ratio. Even without consideration of possible systematical errors, the rather

good agreement between the measured and calculated ratio, within statistical errors, suggests that no significant direct photon excess is observed for peripheral collisions over the transverse momentum region of measurement.

The results in part a) and solid points in part b) of Fig. 29 have not been corrected for target out backgrounds. As discussed in Sec. IV C 1 the measured target out background rate implied less than 10% of the events of the peripheral data sample were due to non-target background. The photon multiplicities per non-target background event were measured to be similar to peripheral events, but with a steeper falling p_T distribution (see Fig. 12). From the low p_T $m_{\gamma\gamma}$ invariant mass distributions for peripheral events (see Fig. 17) the non-target background events were deduced to be due to downstream interactions, as indicated by a π^0 peak shifted to lower mass, with indications for a non-target contamination larger than determined by the target out measurements, as discussed in Sec. IV D 1. The peripheral result has therefore been checked with the assumption of the maximum possible non-target correction consistent with the low mass structure observed in the low p_T invariant mass spectra. It was only possible to do this for the 1996 data sample since no low mass peak was observed in the target out data for the 1995 run due to the Plastic Ball multiplicity condition requirement in the online trigger (see Sec. IV D 1). The result is shown by the open squares in part b) of Fig. 29. Due to the smaller 1996 peripheral data sample and the maximally increased target out correction of roughly 50% of the 1996 peripheral events, the statistical errors on the corrected results are very large. Nevertheless, the corrected γ/π^0 is found to be consistent with the uncorrected ratio and confirms the lack of a significant photon excess for the case of peripheral collisions.

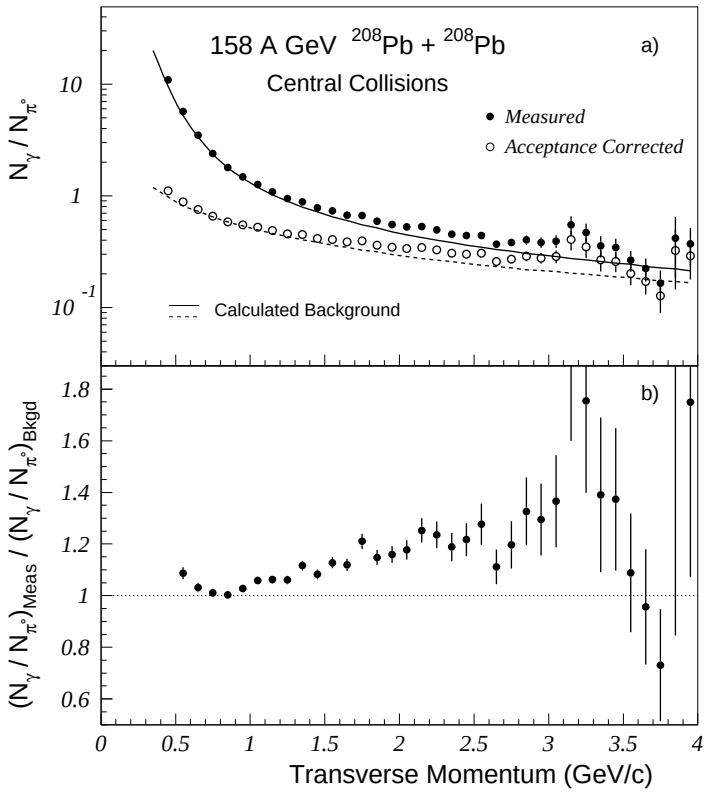

FIG. 30. The efficiency corrected (solid circles) and efficiency and acceptance corrected (open circles) γ/π^0 ratio is shown in part a) as a function of transverse momentum for central 158 *A* GeV ^{208}Pb+^{208}Pb collisions. The calculated background $(\gamma/\pi^0)_{\rm Bkgd}$ ratio in the WA98 acceptance is shown by the solid curve. The dashed curve shows the calculated background with acceptance corrections. The ratio of measured $(\gamma/\pi^0)_{\rm Meas}$ ratio to calculated $(\gamma/\pi^0)_{\rm Bkgd}$ ratio for the WA98 acceptance is shown in part b). The errors on the data points indicate the statistical errors only.

The corresponding γ/π^0 ratio results for central ^{208}Pb+^{208}Pb collisions are shown in Fig. 30. The results are obtained using the photon identification criterion in which all showers are considered photon candidates, as was used for the results of Fig. 29. The background photon calculation is based on the measured central π^0 spectrum of Fig. 26

and uses the measured R_{η/π^0} ratio for central collisions deduced from the results of Fig. 25. Compared to the result for peripheral collisions, the statistical uncertainty on the measured γ/π^0 ratio for the case of central collisions is greatly reduced due to the slightly larger event sample, and more importantly, the much higher particle multiplicities per event.

In contrast to the case for peripheral collisions, the background calculation does not account well for the measured γ/π^0 ratio for central collisions. Instead, an excess in the measured γ/π^0 ratio compared to the background calculation is clearly seen in part b) of Fig. 30. The observed excess increases with p_T up to about a 20% excess at high transverse momentum.

To determine whether the observed excess is significant, a detailed consideration of the various sources of systematical error is necessary. The final direct photon excess is to be extracted as

$$\gamma_{\rm Excess} = \gamma_{\rm Meas} - \gamma_{\rm Bkgd} = \left(1 - \frac{\gamma_{\rm Bkgd}}{\gamma_{\rm Meas}}\right) \cdot \gamma_{\rm Meas}. \tag{5.4}$$

If the ratio $\gamma_{\rm Meas}/\gamma_{\rm Bkgd}$ is equal to one within errors, then no significant photon excess is observed. The ratio $\gamma_{\rm Meas}/\gamma_{\rm Bkgd}$ and its error are determined from the measured $(\gamma/\pi^0)_{\rm Meas}$ and calculated $(\gamma/\pi^0)_{\rm Bkgd}$ ratios. Since, by construction, $(\pi^0)_{\rm Bkgd} \equiv (\pi^0)_{\rm Meas}$ within uncertainties we have

$$\frac{\gamma_{\rm Meas}}{\gamma_{\rm Bkgd}} = \frac{(\gamma/\pi^0)_{\rm Meas}}{(\gamma/\pi^0)_{\rm Bkgd}}. \tag{5.5}$$

Additional systematical errors on $\gamma_{\rm Meas}$ which partially cancel in Eq.5.5 must also be included in Eq. 5.4. Furthermore, when the absolute excess photon cross section is extracted the absolute cross section normalization errors on $\gamma_{\rm Meas}$ must be introduced.

The total systematical error on $\gamma_{\rm Meas}/\gamma_{\rm Bkgd}$ is obtained from the separate error contributions to $(\gamma/\pi^0)_{\rm Meas}$, $(\gamma/\pi^0)_{\rm Bkgd}$, and $(\pi^0)_{\rm Meas}/(\pi^0)_{\rm Bkgd}$. These various systematical error contributions to the direct photon result are summarized in Table III. The errors quoted correspond to the shower identification criterion of using narrow showers (S2), which minimizes the background corrections and therefore is expected to have the smallest systematical error. This shower identification criteria will be used to extract the final WA98 result. A comparison of the final result with the results of Figs. 29 and 30 where all showers (S1) have been used provides an additional check of the overall systematical errors. In general, many of the systematical errors are dependent on the transverse momentum and so must be estimated for each p_T. The systematical errors are listed at $p_T \approx 1$ GeV/c and 2.5 GeV/c for peripheral and central collisions to give an indication of the p_T and centrality dependence of the systematical error contributions.

TABLE III. Various sources of systematical error in the WA98 158 *A* GeV ^{208}Pb+^{208}Pb direct photon analysis specified as a percentage of $(\gamma/\pi^0)_{\rm Meas}$ (items a)), $(\gamma/\pi^0)_{\rm Bkgd}$ (items b)), or $(\pi^0)_{\rm Meas}/(\pi^0)_{\rm Bkgd}$ (item c)). The systematical errors are quoted at two p_T values to give an indication of the dependence on transverse momentum. The errors are estimated for the narrow shower identification criterion (S2). The total estimated systematical error on $\gamma_{\rm Meas}/\gamma_{\rm Bkgd}$ is given as the quadratic sum of the various contributions.

Source of Error	Peripheral Collisions ($20\%\ \sigma_{\rm mb}$)		Central Collisions ($10\%\ \sigma_{\rm mb}$)	
	$p_T \approx 1.0$ GeV/c	$p_T \approx 2.5$ GeV/c	$p_T \approx 1.0$ GeV/c	$p_T \approx 2.5$ GeV/c
Charged Particle background$^+$	1.7	2.2	1.3	1.3
γ conversion correction$^+$	0.5	0.5	0.5	0.5
Neutrons$^+$	0.6	1.0	0.9	1.9
γ reconstruction efficiency$^+$	2.0	2.0	2.0	2.0
a) γ yield measurement	2.7	3.2	2.6	3.1
γ conversion correction*	0.5	0.5	0.5	0.5
π^0 yield extraction*	0.3	<0.1	5.1	1.0
π^0 reconstruction efficiency*	3.0	3.0	4.0	4.0
a) π^0 yield measurement	3.1	3.0	6.5	4.2
a) Non-target background	1.5	<0.1	<0.1	<0.1
a) Energy scale calibration	0.9	1.7	0.8	1.7
b) Detector acceptance	0.5	0.5	0.5	0.5
b) η/π ratio, m_T-scaling	2.9	3.2	+3.4 (-4.8)	+3.7 (-5.2)
b) Other radiative decays	1.0	1.0	1.0	1.0
c) π^0 fit	1.6	6.8	2.9	0.4
Total: (quadratic sum)	5.7	8.9	+8.3 (-9.1)	+6.7 (-7.6)

$^+$ Included in γ yield measurement error. * Included in π^0 yield measurement error.

The separate systematical errors on the photon and π^0 measurement as they contribute to $(\gamma/\pi^0)_{\rm Meas}$ have been discussed previously in Secs. IV C 4 and IV D 3. As discussed in Sec. IV C 4, the photon error includes an assumed 30% uncertainty in the charged particle correction related to the results shown in Fig. 11, and an assumed 50% uncertainty in the neutron+anti-neutron correction related to the results shown in Fig. 13. A 2% uncertainty is assumed for the photon identification efficiency. The overall systematical error on the determination of the photon yield is $\sim 3\%$ which was shown to be consistent with observed systematic variations by a comparison of the γ yield determination using different shower identification methods (see Fig. 15).

The systematical errors on the π^0 yield determination listed in Table III were discussed in Sec. IV D 3. The systematical error associated with the determination of the π^0 identification efficiency was estimated to be 3% and 4% for peripheral and central collisions, respectively. An additional source of systematical error on the π^0 yield extraction is attributed to the subtraction of the combinatorial background underlying the π^0 peak in the $\gamma\gamma$ invariant mass distributions which becomes important for the case of central collisions at low p_T. This error was estimated to contribute at the level of $\sim 10^{-3}$ of the background. The overall systematical error estimate on the determination of the π^0 yield was shown by a comparison of the π^0 yield results using different shower identification methods (see Fig. 23) to be consistent with observed systematical variations.

Other systematical error contributions to the measured $(\gamma/\pi^0)_{\rm Meas}$ ratio listed in Table III are the target out background contribution and the calibration of the energy scale. Although the magnitude of the non-target correction was found to have large uncertainties, as discussed in Secs. IV C 1 and IV D 1, the peripheral $(\gamma/\pi^0)_{\rm Meas}$ ratio showed little systematic dependence on the non-target background correction, as discussed in regard to Fig. 29. No target out background correction was necessary for central collisions, as previously discussed.

Based on the observed agreement between the measured and simulated π^0 peak positions shown in Fig. 21, the calibration of the energy scale is estimated to be accurate to 0.5%. Using the measured γ and π^0 transverse momentum distributions the error on the $(\gamma/\pi^0)_{\rm Meas}$ ratio is calculated as a function of p_T assuming a 0.5% uncertainty in the p_T scale.

The uncertainty in the detector acceptance listed in Table III is relevant for the background photon calculation. As discussed in Sec. V C, the calculated $(\gamma/\pi^0)_{\rm Bkgd}$ ratio is not very sensitive to the uncertainty in the detector acceptance, or to extreme assumptions on the extrapolation of the hadron distributions outside of the detector acceptance. The quoted error estimate of 0.5% includes both effects.

One of the larger contributions to the systematical error in this analysis is attributed to the uncertainty in the η yield. While the η's constitute a relatively large source of background photons (see Fig. 25), their yield has not been measured very precisely in the present analysis (see discussion of Sec. IV E). According to the discussion of Sec. V C, m_T-scaling has been assumed in order to allow to relate the p_T spectrum of the η to the measured π^0 spectrum with only a single overall normalization factor R_{η/π^0}. For peripheral collisions the η yield has not been measured. In this case, it should be a good approximation to use the m_T-scaling factor of $R_{\eta/\pi^0} = 0.55 \pm 0.02$ [76,77] obtained from a compilation of proton and π-induced results, where the m_T-scaling assumption has also been shown to be valid. Nevertheless, we assume a larger systematical error of 20% on R_{η/π^0} since it is an unmeasured quantity and also to accommodate deviations from the m_T-scaling assumption. This results in a systematical error contribution to $(\gamma/\pi^0)_{\rm Bkgd}$ of about 3% for peripheral collisions, as shown in Table III.

For central collisions, the transverse momentum dependence of the η yield was extracted with modest precision, as discussed in Sec. IV E. The measured η/π^0 ratio was found to be consistent with the m_T-scaling assumption with a best fit overall normalization of $R_{\eta/\pi^0} = 0.486 \pm 0.077$(stat.)$\pm 0.097$(syst.). For the direct photon analysis, we have added these statistical and systematical errors in quadrature to obtain a low estimate on the η/π^0 ratio of $R_{\eta/\pi^0} = 0.36$ which is used for the lower error estimate on the γ/π^0 ratio due to the η background contribution. For the upper error estimate on the γ/π^0 ratio due to the η we have assumed a high estimate of $R_{\eta/\pi^0} = 0.66$, which is the same upper estimate used for the case of peripheral collisions. This results in a larger upper error than lower error on the $(\gamma/\pi^0)_{\rm Bkgd}$ ratio with the associated asymmetric errors listed in Table III[6].

The expected total background contribution from radiative decays other than those of the π^0 and η (predominantly the ω and η') is of the order of a few percent only (see Fig. 28). Since this contribution is unmeasured, a systematical error of $\sim 30\%$ in their yield, or 1% on the background photon contribution, has been assumed.

From the results shown in Fig. 26 it is apparent that the statistical error on the π^0 measurement limits the significance of the γ/π^0 results shown in Figs. 29 and 30, especially at high transverse momenta. This statistical error may be removed by fitting the π^0 spectra of Fig. 26, but at the cost of an additional source of systematical error. The last error listed in Table III is the estimated π^0 fit error. This error was estimated by fitting separately the π^0 spectra for the

[6]Note that an upper error estimate on the background photons contribute to the lower error estimate on the photon measurement.

1995, 1996, and sum 1995+1996 data samples and separately for the shower condition of all showers (S1) or narrow showers (S2) (*i.e.* 6 different spectra each for peripheral and central) in the high p_T region only ($p_T > 1.5$ GeV/c) and using the half-width of the maximum variation of the fit results over the full p_T region to define the fit error as a function of p_T. This error is observed to be strongly p_T dependent and increases rapidly outside of the range of measurement.

Since $(\pi^0)_{\rm Meas}/(\pi^0)_{\rm Bkgd} \equiv 1$ within uncertainties by construction, the individual systematical errors on $(\gamma/\pi^0)_{\rm Meas}$, $(\gamma/\pi^0)_{\rm Bkgd}$, and $(\pi^0)_{\rm Meas}/(\pi^0)_{\rm Bkgd}$, can be combined to give the total systematical error on $\gamma_{\rm Meas}/\gamma_{\rm Bkgd}$. The various systematical errors listed in Table III are added in quadrature to obtain the total systematical error on the $\gamma_{\rm Meas}/\gamma_{\rm Bkgd}$ ratio. While some of the errors are correlated, the correlations are such that they tend to cancel in the final ratio. Also, the π^0 fit error includes some of the errors of the π^0 yield extraction. Therefore, the assumption of independent errors is considered a conservative assumption.

The $\gamma_{\rm Meas}/\gamma_{\rm Bkgd}$ ratio as a function of transverse momentum is shown in Fig. 31 for peripheral and central 158 *A* GeV ^{208}Pb+^{208}Pb collisions. The results are shown for photons identified using the narrow shower condition (S2). As expected according to the discussion of Eq. 5.5, the $\gamma_{\rm Meas}/\gamma_{\rm Bkgd}$ ratios of Fig. 31 show the same behavior as the $(\gamma/\pi^0)_{\rm Meas}/(\gamma/\pi^0)_{\rm Bkgd}$ ratios of Figs. 29 and 30. This comparison provides an additional systematic check since the two sets of results were obtained with different shower identification criteria. As discussed previously, in addition to the larger systematical errors expected when using all showers as photon candidates, the results of Figs. 29 and 30 have larger statistical error because the π^0 measurement at each p_T is used and contributes to the statistical error, while on the other hand, the fitted π^0 results of Fig. 26 are used for the results of Fig. 31, which reduces the statistical error but increases the systematical error. The general agreement of the two sets of results again suggests that the systematical errors are not large.

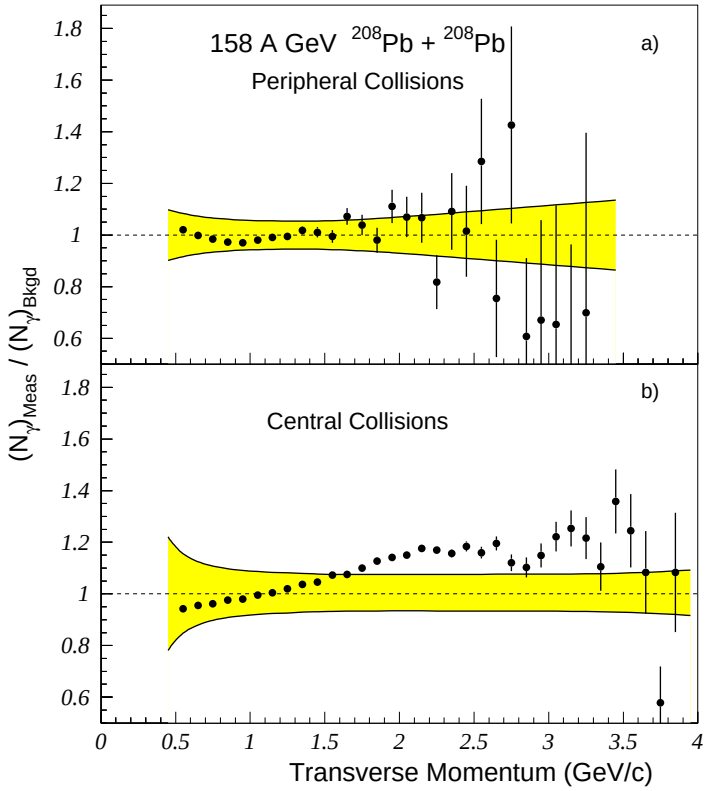

FIG. 31. The $\gamma_{\rm Meas}/\gamma_{\rm Bkgd}$ ratio as a function of transverse momentum for peripheral (part a)) and central (part b)) 158 *A* GeV ^{208}Pb+^{208}Pb collisions for the sum of 1995 and 1996 magnet on data sets. The narrow shower photon identification criterion has been used. The errors on the data points indicate the statistical errors only. The p_T-dependent systematical errors are indicated by the shaded bands ($\equiv 1^{+\sigma_L}_{-\sigma_U}$). (Note: Upper and lower errors are inverted for display purposes.)

The total p_T-dependent systematical errors listed in Table III are shown by the shaded regions in Fig. 31. The systematical errors increase strongly at low transverse momenta due the combinatorial background uncertainties in the π^0 yield extraction. They increase also at large transverse momenta due to the uncertainties in the fits to the π^0 distributions. For peripheral collisions, all measured results fall within $\sigma_{\rm stat.} + \sigma_{\rm syst.}$ of $\gamma_{\rm Meas}/\gamma_{\rm Bkgd} = 1$, which indicates that no significant photon excess is observed. On the other hand, the results for central collisions do indicate a significant photon excess in the region above about 1.5 GeV/c.

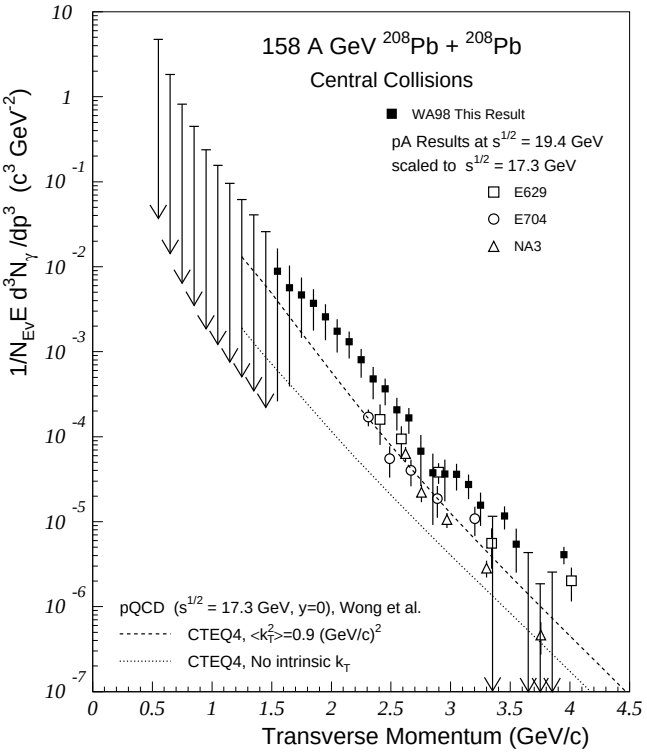

FIG. 32. The invariant direct photon multiplicity for central 158 *A* GeV ^{208}Pb+^{208}Pb collisions. The error bars indicate the combined statistical and systematical errors. Data points with downward arrows indicate unbounded 90% CL upper limits. Results of several direct photon measurements for proton-induced reactions have been scaled to central 158 *A* GeV ^{208}Pb+^{208}Pb collisions for comparison. The calculation is described in the text.

The direct photon excess for central ^{208}Pb+^{208}Pb collisions is shown in Fig. 32. The results are presented as the invariant direct photon yield per central collision. The direct photon excess is obtained according to Eq. 5.4 with the measured results of Fig. 31 and Fig. 27. The statistical and asymmetric systematical errors of Fig. 31 are added in quadrature to obtain the total upper and lower errors shown in Fig. 32. An additional p_T-dependent error is included to account for that portion of the uncertainty in the energy scale which cancels in the $(\gamma/\pi^0)_{Meas}$ ratio, but enters again with γ_{Meas} in Eq. 5.4. In the case that the lower error is less than zero a downward arrow is shown with the tail of the arrow indicating the 90% confidence level upper limit ($\gamma_{Excess} + 1.28\sigma_{Upper}$). The results are also tabulated in Table IV.

For comparion, other published fixed target prompt photon measurements for proton-induced reactions at 200 GeV are also shown in Fig. 32. Results are shown from FNAL experiment E704 [25] ($-0.15 < x_F < 0.15$) for proton-proton reactions, and from FNAL experiment E629 [21] ($-0.75 < y_{cm} < 0.2$) and CERN SPS experiment NA3 [22] ($-0.4 < y_{cm} < 1.2$) for proton-carbon reactions. These results have been divided by the total pp inelastic cross section ($\sigma_{int} = 30$ mb) and by the mass number of the target to obtain the invariant direct photon yield per nucleon-nucleon collision. They have then been multiplied by the calculated number of nucleon-nucleon collisions for the central Pb+Pb event selection for comparison with the present measurements. Based on a Glauber model calculation, the number of nucleon-nucleon collisions is calculated to be 660 for the 635 mb most central event selection used for the present analysis. This scaling of the proton-induced results is estimated to have an uncertainty of less than 10% due to uncertainties in the assumed nuclear density distribution and nucleon interaction cross section. The proton-

induced results have also been scaled from $\sqrt{s} = 19.4$ GeV to the lower $\sqrt{s} = 17.3$ GeV of the present measurement. The proton-induced results have also been scaled from $\sqrt{s} = 19.4$ GeV to the lower $\sqrt{s} = 17.3$ GeV of the present measurement under the assumption that $Ed^3\sigma_\gamma/dp^3 = f(x_T)/s^2$, where $x_T = 2p_T/\sqrt{s}$ [36]. The $\sqrt{s}$-scaling effectively reduces the 19.4 GeV proton-induced results by about a factor of two. This comparison suggests an excess direct photon production in central ^{208}Pb+^{208}Pb collisions as compared to proton-induced reactions at the same $\sqrt{s}$ of 17.3 GeV. The interpretation of the present result is further discussed in the next section.

TABLE IV. The direct photon invariant yield per event $1/N_{events} \cdot Ed^3N_\gamma/dp^3$ for central 158 *A* GeV ^{208}Pb+^{208}Pb collisions. The central event selection is defined as those events with the largest measured transverse energy with a total cross section of 635 mb for the selected central sample. The lower and upper region of uncertainty ($\pm\sigma$, including statistical and systematical errors added in quadrature) are indicated. In the case that the lower limit is less than or equal to zero, only the 90% confidence level ($+1.28\sigma$) upper limit is listed.

p_T (GeV/c)	Lower (c^3/GeV^2)	$1/N_{events} \cdot Ed^3N_\gamma/dp^3$ (c^3/GeV^2)	Upper (c^3/GeV^2)	90% C.L. Upper Limit (c^3/GeV^2)
0.55	-	-	-	4.72
0.65	-	-	-	1.83
0.75	-	-	-	0.815
0.85	-	-	-	0.450
0.95	-	-	-	0.237
1.05	-	-	-	0.156
1.15	-	-	-	0.955E-01
1.25	-	-	-	0.617E-01
1.35	-	-	-	0.409E-01
1.45	-	-	-	0.258E-01
1.55	0.259E-03	0.884E-02	0.164E-01	-
1.65	0.392E-03	0.565E-02	0.103E-01	-
1.75	0.145E-02	0.465E-02	0.748E-02	-
1.85	0.177E-02	0.371E-02	0.543E-02	-
1.95	0.136E-02	0.257E-02	0.363E-02	-
2.05	0.981E-03	0.174E-02	0.241E-02	-
2.15	0.830E-03	0.131E-02	0.173E-02	-
2.25	0.496E-03	0.806E-03	0.107E-02	-
2.35	0.274E-03	0.480E-03	0.662E-03	-
2.45	0.234E-03	0.365E-03	0.481E-03	-
2.55	0.118E-03	0.207E-03	0.286E-03	-
2.65	0.108E-03	0.166E-03	0.217E-03	-
2.75	0.262E-04	0.675E-04	0.104E-03	-
2.85	0.915E-05	0.376E-04	0.632E-04	-
2.95	0.173E-04	0.364E-04	0.537E-04	-
3.05	0.232E-04	0.360E-04	0.478E-04	-
3.15	0.183E-04	0.273E-04	0.357E-04	-
3.25	0.893E-05	0.156E-04	0.220E-04	-
3.35	-	-	-	0.116E-04
3.45	0.812E-05	0.116E-04	0.151E-04	-
3.55	0.251E-05	0.543E-05	0.826E-05	-
3.65	-	-	-	0.432E-05
3.75	-	-	-	0.186E-05
3.85	-	-	-	0.255E-05
3.95	0.314E-05	0.409E-05	0.503E-05	-

2. Comparison to Calculations

Considerable progress has been made in the theoretical description of prompt photon production in hadron-induced reactions. It is now possible to perform a complete and fully consistent next-to-leading order (NLO) QCD calculation of the prompt photon cross section and obtain a quite good description of the data at incident energies from $\sqrt{s} = 23$ GeV up to Tevatron energies ($\sqrt{s} = 1.8$ TeV) [37]. On the other hand, these same calculations which provide a

good description at high incident energy, underpredict prompt photon production at $\sqrt{s} = 19.4$ GeV. For the results shown in Fig. 32 the E704 and NA3 results are underpredicted by about a factor of two, while the E629 result is underpredicted by about a factor of five [37].

It has been proposed [36] that the intrinsic transverse momentum of the partons, as a consequence of confinement within the hadron, or of soft gluon radiation, may significantly increase the theoretical prompt photon predictions at low incident energies, or low transverse momenta. The effect of intrinsic k_T is normally neglected in state of the art perturbative QCD calculations due to the formidable technical difficulty to perform the integration over transverse degrees of freedom in the NLO calculations. Nevertheless, there has been a renewed interest to investigate intrinsic k_T effects in prompt photon production [101,102,33] largely motivated by recent high precision prompt photon measurements of FNAL experiment E706 [31,32], although the necessity for such intrinsic k_T effects remains a topic of debate [39].

Recently, Wong and Wang [101] have investigated the effects of parton intrinsic k_T on photon production under the assumption that the NLO corrections are independent of intrinsic k_T. Correction factors, or K-factors, were determined as a function of photon transverse momentum as the ratio of the NLO+LO calculation result to the leading-order (LO) result, without intrinsic k_T. The LO calculations were reevaluated with the inclusion of parton intrinsic k_T assumed to be characterized by a Gaussian distribution with $\langle k_T^2 \rangle = 4 \langle k_T \rangle / \pi$, where $\langle k_T \rangle$ is the average intrinsic k_T of a parton. The K-factors determined without intrinsic k_T were then applied to the LO result with intrinsic k_T included to obtain the final prompt photon prediction.

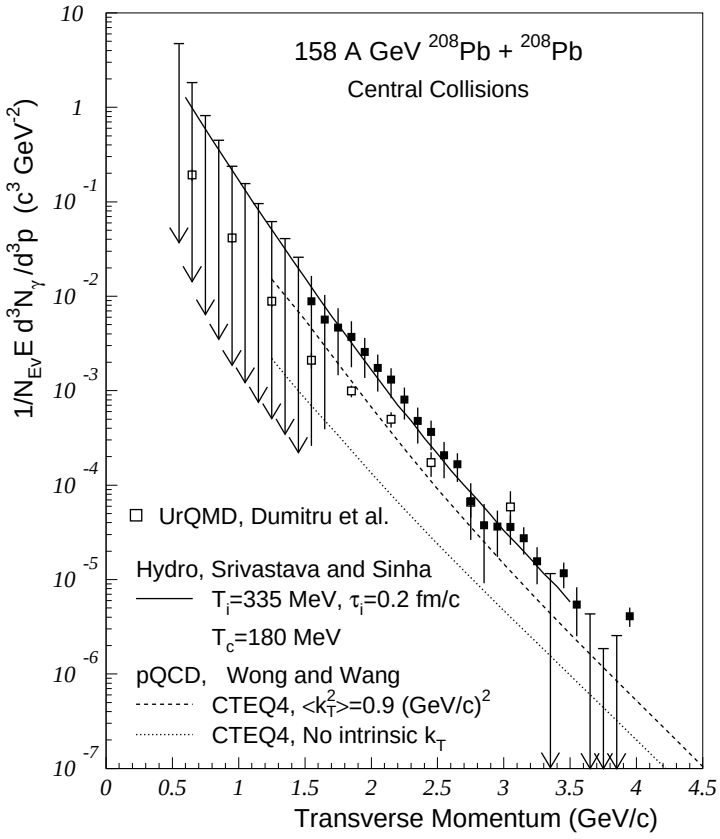

FIG. 33. The invariant direct photon multiplicity for central collisions of 158 *A* GeV ^{208}Pb+^{208}Pb compared to various predictions discussed in the text. The error bars indicate the combined statistical and systematical errors. Data points with downward arrows indicate unbounded 90% CL upper limits.

With this prescription the E704 and NA3 results shown in Fig. 32 were well described with a parton intrinsic k_T of $\langle k_T^2 \rangle = 0.9$ (GeV/c)^2 [101]. The importance of the intrinsic k_T effect decreases with increasing $\sqrt{s}$ and increasing photon p_T such that the prompt photon data at higher $\sqrt{s}$ are equally well described with or without intrinsic k_T.

Predictions of the direct photon production for $\sqrt{s} = 17.3$ GeV central ^{208}Pb+^{208}Pb collisions calculated in this manner [101] are compared to the measured results in Fig. 32 and also in Fig. 33. The calculation has been scaled to central ^{208}Pb+^{208}Pb collisions in the same way as described above for the proton-induced data. Results are shown with and without the effects of parton intrinsic k_T by the long-dashed and short-dashed curves, respectively. At this low incident energy, the parton intrinsic k_T is seen to increase the predicted photon yield by a factor which increases with decreasing p_T from about 4 to 8. The predicted direct photon yield with intrinsic k_T effects included is in good agreement with the $\sqrt{s} = 19.4$ GeV proton-induced results scaled to $\sqrt{s} = 17.3$ GeV. It is also in general agreement with the shape of the observed photon spectrum in central ^{208}Pb+^{208}Pb collisions, but underpredicts the observed yield by about a factor of 2.5. This discrepancy could be a result of further deficiencies in the prompt photon calculations when applied at low incident energy, or it may indicate new effects attributable to nuclear collisions. A possible explanation might be additional p_T broadening of the incoming partons due to soft scatterings prior to the hard scattering which produces the photon [102]. Alternatively, it may be expected that the photon production is enhanced by the additional scatterings which occur as a result of rescattering in nucleus-nucleus collisions.

It is anticipated that if a quark gluon plasma is formed in relativistic heavy ion collisions, it will evolve from the initial hard-scattering partonic stage, through a preequilibrium stage, to a finally thermalized partonic QGP phase. Therefore the Parton Cascade Model (PCM) [103] has been widely regarded as a promising tool to investigate the evolution of the initial partonic state. The VNI [104] implementation of the PCM has recently been used to predict direct photon production in central Pb+Pb collisions at the SPS [105]. Those predictions are in reasonable agreement with the present result, although they slightly overpredict the yield above $p_T = 3$ GeV/c while underpredicting the yield below 2.5 GeV/c. However, it has recently been pointed out that the method which was used to implement higher order pQCD corrections in those calculations, by rescaling Q^2 in the running coupling constant α_s, is highly questionable at SPS energies [106].

Non-equilibrium direct photon emission has also been investigated within the context of the Ultrarelativistic Quantum Molecular Dynamics model (UrQMD) [107]. The UrQMD predictions of the total direct photon production in central Pb+Pb collisions are shown by the open squares in Fig. 33 [108]. It is interesting that the UrQMD predictions are very similar to the the VNI parton cascade predictions [105]. In the UrQMD calculations, the direct photon production results strictly from meson-meson scattering, predominantly $\pi\pi \rightarrow \rho\gamma$ and $\pi\rho \rightarrow \pi\gamma$. In these calculations it was observed that the photon production in the transverse momentum region with $p_T > 1.5$ GeV/c is dominated by pre-equilibrium emission in which the scattering mesons have locally non-isotropic momentum distributions. The thermal photon emission was found to be important only in the low transverse momentum region below $p_T < 1.5$ GeV/c.

It is of particular interest to compare the observed direct photon yield to predictions of the expected yield in the event of quark gluon plasma formation. Hydrodynamic model calculations of the predicted direct photon yield are shown by the solid curve in Fig. 33 [20,109]. The hydrodynamic calculations include transverse expansion [110] with a rich hadronic equation of state including all hadrons and resonances with mass up to 2.5 GeV. The photon emission rates used for the hadronic phase are those which have been obtained from a two-loop approximation of the photon self energy using a model where the $\pi\rho$ interactions have been included [18], and also include the important contribution from the A_1 resonance [111]. The photon emission rates from the quark matter phase include the lowest order contributions from the Compton ($q(\overline{q})g \rightarrow q(\overline{q})\gamma$) and annihilation ($q\overline{q} \rightarrow g\gamma$) processes, as well as the new contributions from two-loop diagrams which have recently been shown [19] to give a large bremsstrahlung ($qq(g) \rightarrow qq(g)\gamma$) contribution and a previously neglected process of $q\overline{q}$ annihilation accompanied by q(g) rescattering which is found to dominate the photon emission rate.

As shown in Fig. 33, very good agreement with the experimental result is obtained for the case of an equation of state which includes a QGP phase transition which occurs at a critical temperature of $T_C = 180$ MeV [109] with a hadron thermal freeze-out temperature of $T_F = 100$ MeV. The calculation has been performed for the 10% most central Pb+Pb collisions for a particle density $dN/dy = 750$ with the assumption of a fast equilibration time of $\tau_0 = \frac{1}{3}T_0$ given by the uncertainty relation. This results in an initial temperature of $T_0 = 335$ MeV with a thermalization time of $\tau_0 = 0.2$ fm/c. The contribution from the quark matter in the QGP and mixed phase dominates the calculated high p_T photon yield [109]. This is attributed to the "annihilation with rescattering" process which is a special feature of dense quark matter. This calculation does not include prompt or preequilibrium contributions.

Further study will be necessary to improve the theoretical predictions of the prompt photon contribution as well as the non-equilibrium contributions. On the other hand, the hydrodynamical model calculations which provide a time integration of the emission rate with a very short initial formation time and high initial temperature may provide a reasonable approximation of the contributions from the early non-equilibrium phase of the collision [109]. Further studies will also be necessary to determine how the present direct photon results might further constrain the QGP and non-QGP scenarios. The WA80 direct photon upper limit for central S+Au collisions [43] was able to rule out thermal emission from purely hadronic matter in which the hadronic matter consisted of a simple pion gas with few degrees

of freedom [44–47] due to the constraints which the result implied on the initial temperature [48]. The S+Au direct photon limit has been shown to be consistent with the QGP transition using the new rates for quark matter, although with somewhat different parameters than presented here [112,109]. It will be important to determine whether the present result, combined with other measurements including the S+Au direct photon upper limit, can provide further constraints and provide compelling evidence for the QGP phase transition scenario.

VI. SUMMARY AND CONCLUSIONS

A search for direct photons in ^{208}Pb+^{208}Pb collisions at 158 *A* GeV has been performed using the large-area finely-segmented lead-glass calorimeter of the WA98 experiment. The analysis has been performed on nearly equal-sized event samples of the 10% most central and 20% most peripheral fractions of the total minimum bias cross section. The inclusive photon and π^0 transverse momentum distributions were measured for each event sample. Constraints were also obtained on the η transverse momentum distribution for central collisions with a modest accuracy which was limited by statistics. The systematical error sources were discussed at length with particular attention to demonstrate the accuracy of the systematical error estimates. The total systematical error for the direct photon analysis varied from about 6% to 10% over the p_T region of interest, and varied with the centrality selection. The direct photon excess was extracted on a statistical basis as the difference between the measured inclusive spectrum of photons within the detector acceptance and the calculated spectrum of photons which result from all hadrons with significant radiative decay contributions. The dominant decay contributions are those from the measured π^0's and η's.

No significant direct photon excess was observed for the peripheral event sample for transverse momenta up to about 2.5 GeV/c. This upper p_T limit of the measurement was imposed by the increasing statistical error at large p_T due to the low particle multiplicity for peripheral collisions.

In contrast, a significant direct photon excess was observed over the p_T region of about 1.5 GeV/c to 3.5 GeV/c for central ^{208}Pb+^{208}Pb collisions. At transverse momenta where the observed excess was not significant, a 90% confidence level upper limit on the direct photon excess was given. This extended the result to the full region of measurement from 0.5 GeV/c to 4 GeV/c.

The observed direct photon yield was compared to a next-to-leading order perturbative QCD calculation at the same $\sqrt{s}$ (=17.3 GeV) and scaled according to the number of nucleon-nucleon collisions calculated for the selected central event class. The measured direct photon yield was about a factor of 2-3 above the pQCD calculation which included the effects of partonic intrinsic k_T with a parameter which gave a good description of proton-induced prompt photon results at the nearest incident energy ($\sqrt{s}$=19.4 GeV). A NLO pQCD calculation without intrinsic k_T was about an order of magnitude below the measured result.

The results suggest that the additional direct photon yield in central ^{208}Pb+^{208}Pb collisions is the result of additional rescatterings in the dense matter. The measured results can be well-described by hydrodynamical model calculations which include a quark gluon plasma phase transition with an initial temperature of $T_0 = 335$ MeV and a critical temperature of $T_C = 180$ MeV [109]. The photon emission from the quark matter is found to dominate over the contribution from the hadronic matter due to the recently identified process of annihilation with rescattering [19] which is only expected to occur in dense quark matter. It will be important to determine the uniqueness of this interpretation.

ACKNOWLEDGMENTS

We wish to express our gratitude to the CERN accelerator division for the excellent performance of the SPS accelerator complex. We acknowledge with appreciation the effort of all engineers, technicians and support staff who have participated in the construction of this experiment. We acknowledge helpful discussions with D.K. Srivastava and C.-Y. Wong.

This work was supported jointly by the German BMBF and DFG, the U.S. DOE, the Swedish NFR and FRN, the Dutch Stichting FOM, the Stiftung für Deutsch-Polnische Zusammenarbeit, the Grant Agency of the Czech Republic under contract No. 202/95/0217, the Department of Atomic Energy, the Department of Science and Technology, the Council of Scientific and Industrial Research and the University Grants Commission of the Government of India, the Indo-FRG Exchange Program, the PPE division of CERN, the Swiss National Fund, the INTAS under Contract INTAS-97-0158, ORISE, Grant-in-Aid for Scientific Research (Specially Promoted Research & International Scientific Research) of the Ministry of Education, Science and Culture, the University of Tsukuba Special Research Projects, and the JSPS Research Fellowships for Young Scientists. ORNL is managed by UT-Battelle, LLC, for the U.S. Department of Energy under contract DE-AC05-00OR22725. The MIT group has been supported by the US Dept. of Energy under the cooperative agreement DE-FC02-94ER40818.

[1] See for example, Proceedings of *Quark Matter '99*, Nucl. Phys. A **661** (1999).
[2] M.C. Abreu et al., Phys. Lett. B **410**, 337 (1997).
[3] E. Andersen et al., Phys. Lett. B **449**, 401 (1999).
[4] E.L.Feinberg, Nuovo Cimento **34** A, 391 (1976).
[5] E.Shuryak, Phys. Lett. B **78**, 150 (1978).
[6] J.D.Bjorken and H.Weisberg, Phys. Rev. D **13**, 1405 (1976).
[7] S.A.Chin, Phys. Lett. B **78**, 552 (1978).
[8] R.Anishetty, P.Koehler, and L.McLerran, Phys. Rev. D **22**, 2793 (1980).
[9] K.Kajantie and R.Raitio, Phys. Lett. B **121**, 415 (1983).
[10] G.Domokos and J.I.Goldman, Phys. Rev. D **23**, 203 (1981).
[11] K.Kajantie and H.I.Miettinen, Z. Phys. C **9**, 341 (1981).
[12] F.Halzen and H.C.Liu, Phys. Rev. D **25**, 1842 (1982).
[13] S.A.Chin, Phys. Lett. B **119**, 51 (1982).
[14] B.Sinha, Phys. Lett. B **128**, 91 (1983).
[15] L.D.McLerran and T.Toimela, Phys. Rev. D **31**, 545 (1985).
[16] R.D.Pisarski, Phys. Rev. Lett. **63**, 1129 (1989).
[17] E.Braaten, R.D.Pisarski, and T.C.Yuan, Phys. Rev. Lett. **64**, 2242 (1990).
[18] J.Kapusta,P.Lichard, and D.Seibert, Phys. Rev. D **44**, 2774 (1991); Erratum, *ibid* D **47**, 4171 (1993).
[19] P. Aurenche, et al., Phys. Rev. D **58**, 085003 (1998).
[20] D. K. Srivastava, Eur. Phys. J. C **10**, 487 (1999).
[21] E629 Collaboration, M. McLaughlin et al., Phys. Rev. Lett. **51**, 971 (1983).
[22] NA3 Collaboration, J. Badier et al., Z. Phys. C **31**, 341 (1986).
[23] NA24 collaboration, C. De Marzo et al., Phys. Rev. D **36**, 8 (1987).
[24] R108 collaboration, A.L.S. Angelis et al., Nucl. Phys. B **263**, 228 (1986).
[25] E704 Collaboration, D.L. Adams et al., Phys. Lett. B **345**, 569 (1995).
[26] R806 collaboration, E. Annassontzis et al., Z. Phys. C **13**, 277 (1982).
[27] WA70 collaboration, M. Bonesini et al., Z. Phys. C **37**, 535 (1988).
[28] WA70 collaboration, M. Bonesini et al., Z. Phys. C **38**, 371(1988).
[29] R110 collaboration, A.L.S. Angelis et. al., Nucl. Phys. B **327**, 541 (1989).
[30] AFS/R807 collaboration, T. Åkesson et al., Sov. J. Nuc. Phys. **51**, 836 (1990).
[31] E706 collaboration, G. Alverson et al., Phys. Rev. D **48**, 5 (1993).
[32] E706 collaboration, L. Apanasevich et al., Phys. Rev. Lett. **81**, 2642 (1998).
[33] L. Apanasevich, et al., Phys. Rev. D **59**, 074007 (1999).
[34] UA6 collaboration, G. Ballocchi et al., Phys. Lett. B **436**, 222 (1998).
[35] CDF collaboration, F. Abe et al., Phys. Rev. Lett. **73**, 2662 (1994).
[36] J.F. Owens, Rev. Mod. Phys. **59**, 465 (1987).
[37] See for example, W. Vogelsang and M.R. Whalley, J. Phys. G: Nucl. Part. Phys. **23**, A1 (1997).
[38] J. Huston et al., Phys. Rev. D **51**, 6139 (1995).
[39] P. Aurenche et al., Eur. Phys. J. C **9**, 107 (1999).
[40] HELIOS Collaboration, T.Åkesson et al., Z. Phys. C **46**, 369 (1990).
[41] WA80 Collaboration, R. Albrecht et al., Z. Phys. C **51**, 1 (1991).
[42] CERES Collaboration, R.Baur et al., Z. Phys. C **71**, 571 (1996).
[43] R. Albrecht et al., Phys. Rev. Lett. **76**, 3506 (1996).
[44] D. K. Srivastava and B. Sinha, Phys. Rev. Lett. **73**, 2421 (1994).
[45] J. J. Neumann, D. Siebert, and G. Fai, Phys. Rev. C **51**, 1460 (1995).
[46] A. Dumitru et al., Phys. Rev. C **51**, 2166 (1995).
[47] N. Arbex et al., Phys. Lett. B **354**, 307 (1995).
[48] J. Sollfrank et al., Phys. Rev. C **55**, 392 (1997).
[49] A. Baden et al., Nucl. Instrum. Methods Phys. Res. Sect. A **203**, 189 (1982).
[50] W. T. Lin et al., Nucl. Instrum. Methods Phys. Res. Sect. A **389**, 415 (1997).
[51] J. M. Rubio et al., Nucl. Instrum. Methods Phys. Res. Sect. A **367**, 358 (1995).
[52] L. Carlén et al., Nucl. Instrum. Methods Phys. Res. Sect. A **431**, 123 (1999).
[53] M. M. Aggarwal et al., Nucl. Instrum. Methods Phys. Res. Sect. A **424**, 395 (1999).
[54] T. C. Awes et al., Nucl. Instrum. Methods Phys. Res. Sect. A **279**, 497 (1989).
[55] T.Chujo, et al., Nucl. Instr. and Meth. A **383**, 409 (1996).

[56] T. Peitzmann et al., Nucl. Instrum. Methods Phys. Res. Sect. A **376**, 368 (1996).
[57] S. Neumaier et al., Nucl. Instrum. Methods Phys. Res. Sect. A **360**, 593 (1995).
[58] A. L. Wintenberg et al., Proceedings of Electronics for Future Colliders Conference, May 1994, LeCroy Corp.
[59] K. Reygers, Doctoral thesis, University of Münster, Germany (1999).
[60] F. Berger et al., Nucl. Instrum. Methods Phys. Res. Sect. A **321**, 152 (1992).
[61] T. C. Awes et al., Nucl. Instrum. Methods Phys. Res. Sect. A **311**, 130 (1992).
[62] R. Brun and F. Carminati, *GEANT Detector Description and Simulation Tool*, CERN Program Library, Long Writeup W5013, March, 1994.
[63] D. Bucher, Doctoral thesis, University of Münster, Germany (1999).
[64] M. Bourquin and J.-M. Gaillard, Nucl. Phys. B **114** 334, (1976).
[65] R. Blankenbecler and S.J. Brodsky, Phys. Rev. D **10**, 2973 (1974).
[66] E. V. Shuryak and O. Zirhov, Phys. Lett. B **89**, 253 (1980).
[67] R. Hagedorn, Riv. Nuovo Cimento **6**, 1 (1983).
[68] F. Büsser et al., Nucl. Phys. B **106**, 1 (1976).
[69] J. Bartke et al., Nucl. Phys. B **120**, 14 (1977).
[70] G. Donaldson et al., Phys. Rev. Lett. **40**, 684 (1978).
[71] C. Kourkoumelis et al., Phys. Lett. B **84**, 277 (1979).
[72] J. Povlis et al., Phys. Rev. Lett. **51**, 967 (1983).
[73] NA27 Collaboration, M. Aguilar-Benitez et al., Z. Phys. C **50**, 405 (1991).
[74] Omega Photon Collaboration, R. Apsimon et al., Z. Phys. C **54**, 185 (1992).
[75] CERES/TAPS Collaboration, G. Agakichiev et al., Eur. Phys. J. C **4**, 231 (1998).
[76] AFS Collaboration, T. Åkesson et al., Phys. Lett. B **178**, 447 (1986).
[77] WA80 Collaboration, R. Albrecht et al., Phys. Lett. B **361**, 14 (1995).
[78] NA44 Collaboration, I.G. Bearden et al., Phys. Rev. Lett. **78**, 2080 (1997).
[79] NA49 Collaboration, H. Appelshäusser et al., Eur. Phys. J. C **2**, 661 (1998).
[80] WA98 Collaboration, M.M. Aggarwal et al., Phys. Rev. Lett. **83**, 926 (1999).
[81] J.R. Nix, Phys. Rev. C **58**, 2303 (1998).
[82] J. Kapusta et al., Phys. Rev. D **53**, 5028 (1996).
[83] Z. Huang and X.-N. Wang, Phys. Rev. D **53**, 5034 (1996).
[84] J. Jalilian-Marian and B. Tekin, Phys. Rev. D **57**, 5593 (1998).
[85] *Review of Particle Properties*, Eur. Phys. J. C **3**, 1 (1998).
[86] M. Diakonou et al., Phys. Lett. B **89**, 432 (1980).
[87] F.T. Dao et al., Phys. Rev. Lett. **30**, 1151 (1973).
[88] I. Derado et al., Z. Phys. C **50**, 31 (1991).
[89] NA35 Collaboration, T. Alber et al., Z. Phys. C **64**, 195 (1994).
[90] WA85 Collaboration, S. Abatzis et al., Phys. Lett. B **376**, 251 (1996).
[91] T. Sjöstrand and M. Bengtsson, *The Lund Monte Carlo Programs - JETSET*, CERN Program Library, W5035, March, 1994.
[92] WA98 Collaboration, M.M. Aggarwal et al., Phys. Lett. B **458**, 422 (1999).
[93] K. Werner, Phys. Rep. **232**, 87 (1993).
[94] T.A. Gabriel et al., *CALOR: A Monte Carlo Program Package for the Design and Analysis of Calorimeters*, ORNL/TM-5619, (1977).
[95] A. Ferrari and P.R. Sala, *GEANT Hadronic Event Generators: a comparison at the single interaction level*, ATLAS Internal Note, PHYS-No-086, June 1996.
[96] NA49 Collaboration, S.V. Afanasiev et al., Nucl. Phys. A **610**, 188c (1996).
[97] WA98 Collaboration, M.M. Aggarwal et al., Phys. Rev. Lett. **81**, 4087 (1998).
[98] R. Hagedorn, CERN-TH. 3684 (1983).
[99] UA1 Collaboration, G. Bocquet et al., Phys. Lett. B **366**, 434 (1996).
[100] R. Albrecht et al., Eur. Phys. J. C **5**, 255 (1998).
[101] C.-Y. Wong and H. Wang, Phys. Rev. C **58**, 376 (1998).
[102] G. Papp, P. Levai, and G. Fai, Phys. Rev. C **61**, 021902 (1999).
[103] K. Geiger and B. Müller, Nucl. Phys. B **369**, 600 (1992); K. Geiger, Phys. Rep. **258**, 237 (1995).
[104] K. Geiger, Comp. Phys. Comm. **104**, 70 (1997).
[105] D.K. Srivastava and K. Geiger, Phys. Rev. C **58**, 1734 (1998).
[106] S.A. Bass and B. Müller, Phys. Lett. B **471**, 108 (1999).
[107] S.A. Bass et al., Prog. Part. Nucl. Phys. **41**, 225 (1998).
[108] A. Dumitru et al., Phys. Rev. C **57**, 3271 (1998).
[109] D. K. Srivastava and B. Sinha, nucl-th/0000000.
[110] J. Cleymans, K. Redlich, and D.K. Srivastav, Phys. Rev. C **55**, 1431 (1997).
[111] Li Xiong, E. Shuryak, and G.E. Brown, Phys. Rev. D **46**, 3798 (1992).
[112] D. K. Srivastava and B.C. Sinha, Eur. Phys. J. C **12**, 109 (2000).

23 March 2000

PHYSICS LETTERS B

ELSEVIER

Physics Letters B 477 (2000) 37–44

Δ^{++} production in 158 A GeV ^{208}Pb + ^{208}Pb interactions at the CERN SPS

WA98 Collaboration

M.M. Aggarwal [a], A. Agnihotri [b], Z. Ahammed [c], A.L.S. Angelis [d], V. Antonenko [e], V. Arefiev [f], V. Astakhov [f], V. Avdeitchikov [f], T.C. Awes [g], P.V.K.S. Baba [h], S.K. Badyal [h], A. Baldine [f], L. Barabach [f], C. Barlag [i], S. Bathe [i], B. Batiounia [f], T. Bernier [j], K.B. Bhalla [b], V.S. Bhatia [a], C. Blume [i], R. Bock [k], E.-M. Bohne [i], Z. Böröcz [i], D. Bucher [i], A. Buijs [l], H. Büsching [i], L. Carlen [m], V. Chalyshev [f], S. Chattopadhyay [c], R. Cherbatchev [e], T. Chujo [n], A. Claussen [i], A.C. Das [c], M.P. Decowski [r], H. Delagrange [j], V. Djordjadze [f], P. Donni [d], I. Doubovik [e], S. Dutt [h], M.R. Dutta Majumdar [c], K. El Chenawi [m], S. Eliseev [o], K. Enosawa [n], P. Foka [d], S. Fokin [e], V. Frolov [f], M.S. Ganti [c], S. Garpman [m], O. Gavrishchuk [f], F.J.M. Geurts [l], T.K. Ghosh [p], R. Glasow [i], S.K. Gupta [b], B. Guskov [f], H.Å. Gustafsson [m], H.H. Gutbrod [j], R. Higuchi [n], I. Hrivnacova [o], M. Ippolitov [e], H. Kalechofsky [d], R. Kamermans [l], K.-H. Kampert [i], K. Karadjev [e], K. Karpio [q], S. Kato [n], S. Kees [i], B.W. Kolb [k], I. Kosarev [f], I. Koutcheryaev [e], T. Krümpel [i], A. Kugler [o], P. Kulinich [r], M. Kurata [n], K. Kurita [n], N. Kuzmin [f], I. Langbein [k], A. Lebedev [e], Y.Y. Lee [k], H. Löhner [p], L. Luquin [j], D.P. Mahapatra [s], V. Manko [e], M. Martin [d], G. Martínez [j], A. Maximov [f], R. Mehdiyev [f], G. Mgebrichvili [e], Y. Miake [n], D. Mikhalev [f], Md.F. Mir [h], G.C. Mishra [s], Y. Miyamoto [n], B. Mohanty [s], D. Morrison [t], D.S. Mukhopadhyay [c], V. Myalkovski [f], H. Naef [d], B.K. Nandi [s], S.K. Nayak [j], T.K. Nayak [c], S. Neumaier [k], A. Nianine [e], V. Nikitine [f], S. Nikolaev [e], P. Nilsson [m], S. Nishimura [n], P. Nomokonov [f], J. Nystrand [m], F.E. Obenshain [t], A. Oskarsson [m], I. Otterlund [m], M. Pachr [o], A. Parfenov [f], S. Pavliouk [f], T. Peitzmann [i], V. Petracek [o], F. Plasil [g], W. Pinganaud [j], M.L. Purschke [k], J. Rak [o], R. Raniwala [b], S. Raniwala [b], V.S. Ramamurthy [s], N.K. Rao [h], F. Retiere [j], K. Reygers [i], G. Roland [r], L. Rosselet [d], I. Roufanov [f], C. Roy [j], J.M. Rubio [d], H. Sako [n], S.S. Sambyal [h], R. Santo [i], S. Sato [n], H. Schlagheck [i], H.-R. Schmidt [k], Y. Schutz [j], G. Shabratova [f], T.H. Shah [h],

0370-2693/00/$ - see front matter © 2000 Elsevier Science B.V. All rights reserved.
PII: S0370-2693(00)00224-0

I. Sibiriak [e], T. Siemiarczuk [q], D. Silvermyr [m,1], B.C. Sinha [c], N. Slavine [f], K. Söderström [m], N. Solomey [d], S.P. Sørensen [g,t], P. Stankus [g], G. Stefanek [q], P. Steinberg [r], E. Stenlund [m], D. Stüken [i], M. Sumbera [o], T. Svensson [m], M.D. Trivedi [c], A. Tsvetkov [e], L. Tykarski [q], J. Urbahn [k], E.C. van der Pijll [l], N. van Eijndhoven [l], G.J. van Nieuwenhuizen [r], A. Vinogradov [e], Y.P. Viyogi [c], A. Vodopianov [f], S. Vörös [d], B. Wysłouch [r], K. Yagi [n], Y. Yokota [n], G.R. Young [g]

[a] *University of Panjab, Chandigarh 160014, India*
[b] *University of Rajasthan, Jaipur 302004, Rajasthan, India*
[c] *Variable Energy Cyclotron Centre, Calcutta 700 064, India*
[d] *University of Geneva, CH-1211 Geneva 4, Switzerland*
[e] *RRC ''Kurchatov Institute'', RU-123182 Moscow, Russia*
[f] *Joint Institute for Nuclear Research, RU-141980 Dubna, Russia*
[g] *Oak Ridge National Laboratory, Oak Ridge, Tennessee 37831-6372, USA*
[h] *University of Jammu, Jammu 180001, India*
[i] *University of Münster, D-48149 Münster, Germany*
[j] *SUBATECH, Ecole des Mines, Nantes, France*
[k] *Gesellschaft für Schwerionenforschung (GSI), D-64220 Darmstadt, Germany*
[l] *Universiteit Utrecht / NIKHEF, NL-3508 TA Utrecht, The Netherlands*
[m] *Lund University, SE-221 00 Lund, Sweden*
[n] *University of Tsukuba, Ibaraki 305, Japan*
[o] *Nuclear Physics Institute, CZ-250 68 Rez, Czech Republic*
[p] *KVI, University of Groningen, NL-9747 AA Groningen, The Netherlands*
[q] *Institute for Nuclear Studies, 00-681 Warsaw, Poland*
[r] *MIT Cambridge, MA 02139, USA*
[s] *Institute of Physics, 751-005 Bhubaneswar, India*
[t] *University of Tennessee, Knoxville, TN 37966, USA*

Received 18 January 2000; received in revised form 11 February 2000; accepted 11 February 2000
Editor: L. Montanet

Abstract

The Δ^{++}-resonance production in central 158 A GeV ^{208}Pb + ^{208}Pb collisions at the CERN SPS has been studied. The Δ^{++} production was estimated from the invariant mass spectrum of $p\pi^{+}$-pairs by subtracting a mixed event background. The measured Δ^{++} abundance is compared with the results from other experiments at lower energies, and with a model calculation assuming thermal and chemical equilibrium. © 2000 Elsevier Science B.V. All rights reserved.

PACS: 25.75.Dw
Keywords: Ultra-relativistic heavy ion collisions; Δ^{++} resonance production; Mixed event technique; Freeze-out temperature

Energetic heavy ion collisions provide the means for studies of nuclear matter under extreme conditions in the laboratory. The copious interactions between pions and nucleons in the final state of ultra-relativistic heavy ion collisions make the determination of the $\Delta(1232)$ abundance an interesting probe of the thermal conditions during the collision.

[1] E-mail: david.silvermyr@kosufy.lu.se

The Δ-resonance, apart from playing a role in particle production and interaction dynamics, may probe the conditions in heavy-ion collisions at early freeze-out times and high freeze-out densities [1]. It has been suggested that a chemical freeze-out temperature can be extracted from the $\Delta(1232)$/nucleon ratio [2]. The Δ-resonance is known to be readily produced in photon [3]- lepton [4]- and hadron [5]-induced nuclear interactions and the cross sections for production of Δ-resonances in elementary nucleon-nucleon collisions are large [6].

Recently, results on $\Delta(1232)$ production in nucleus-nucleus collisions at 95 A MeV [7], at 1 and 2 A GeV [8] and at 13.7 A GeV [9] have been reported. In this paper we present measurements on the production of Δ^{++} by means of an invariant mass analysis of $p\pi^+$-pairs in 158 A GeV central ^{208}Pb $+^{208}$Pb central collisions at the CERN SPS. The measurement utilizes the new high resolution tracking arm of WA98 [10], which consists of multi-step avalanche chambers, streamer tube detectors and a high resolution Time-Of-Flight system.

The fixed target experiment WA98 is a large-acceptance photon and hadron spectrometer designed to study ultra-relativistic heavy-ion collisions. Charged particles, produced in the interactions, traverse a large magnet and are deflected into two tracking arms, horizontally placed on both sides of the beam which allow for momentum determination and particle identification. For the Δ^{++} measurements, reported in this paper, we use the full data sample from the tracking arm for the positively charged particles [11]. This second tracking arm was installed and operated for only a portion of the final WA98 run period.

The tracking arm consists of two planes of Multi-Step Avalanche Chambers (MSACs) [12,13] and two planes of streamer tube detectors, all equipped with electronic pad readout and a highly segmented Time-Of-Flight (TOF) wall. Fig. 1a shows a schematic drawing of the second tracking arm as seen from above, with two tracks entering the acceptance. Here the *z*-axis is pointing along the beam and the *x*-axis is parallel to the bending plane of the magnet. The position resolution of the MSACs was $\sigma_x = 0.5$ mm in the horizontal direction, and $\sigma_y = 1.7$ mm in the vertical direction whereas the streamer tube detectors had an intrinsic resolution of $\sigma_x = 3.0$ mm and $\sigma_y =$ 6.5 mm. The time resolution of the TOF wall was better than 90 ps and its spatial resolution was $\sigma_x = 12.5$ mm and $\sigma_y = 26.4$ mm. Fig. 1b and 1c show p versus $t_{\mathrm{tof}} - t_{\mathrm{exp}}$ assuming pion and proton mass, respectively. Here p is the momentum, t_{tof} the measured flight time of the particle and t_{exp} the expected flight time calculated from the track length and momentum of the particle. Separation between different particle species, especially for pions and protons, is good over a wide range of momenta. Kaons and pions are no longer separable at momenta above 4 GeV/c and thus a small contamination of kaons is present among the pions at larger momenta. The momenta of the particles are first approximated assuming a uniform magnetic field and straight line fits through the tracking arm and then corrected by GEANT [14] calculations using the measured field. The momentum resolution, $\Delta p/p$, is limited by the multiple scattering, mainly in the air between the target and the detectors, the intrinsic detector resolution and by methodical uncertainties. Based on GEANT simulations we estimate $\Delta p/p$ to be about 1% at 2 GeV/c and 2% at 5 GeV/c.

The most interesting events are those where the bulk of the nuclear matter interacts, i.e. the most central events. A trigger based on the transverse energy as measured by the Mid-Rapidity Calorimeter (MIRAC) is used to enhance central collisions. The present analysis has been performed using the 8.5% most central events of the WA98 minimum bias cross section (6450 mb for the used data set) based on an offline cut on the measured transverse energy. To reject beam particles other than Pb and possible event pile-up, lower and upper cuts in the ADC and TDC values from the start-counters, placed in the beam, were performed.

During and shortly after electrical discharges, the MSACs exhibited reduced efficiencies. This has been discussed in a previous paper [12]. Thus events recorded within a short time after such a discharge, are removed from the analysis.

The tracking procedure connects hits in at least three out of the four tracking planes, by means of straight line fits, and combines a track with a valid time measurement in the TOF wall at the correct position. Due to the excellent two-track resolution and two-dimensional position resolution of the tracking planes, this procedure works almost without

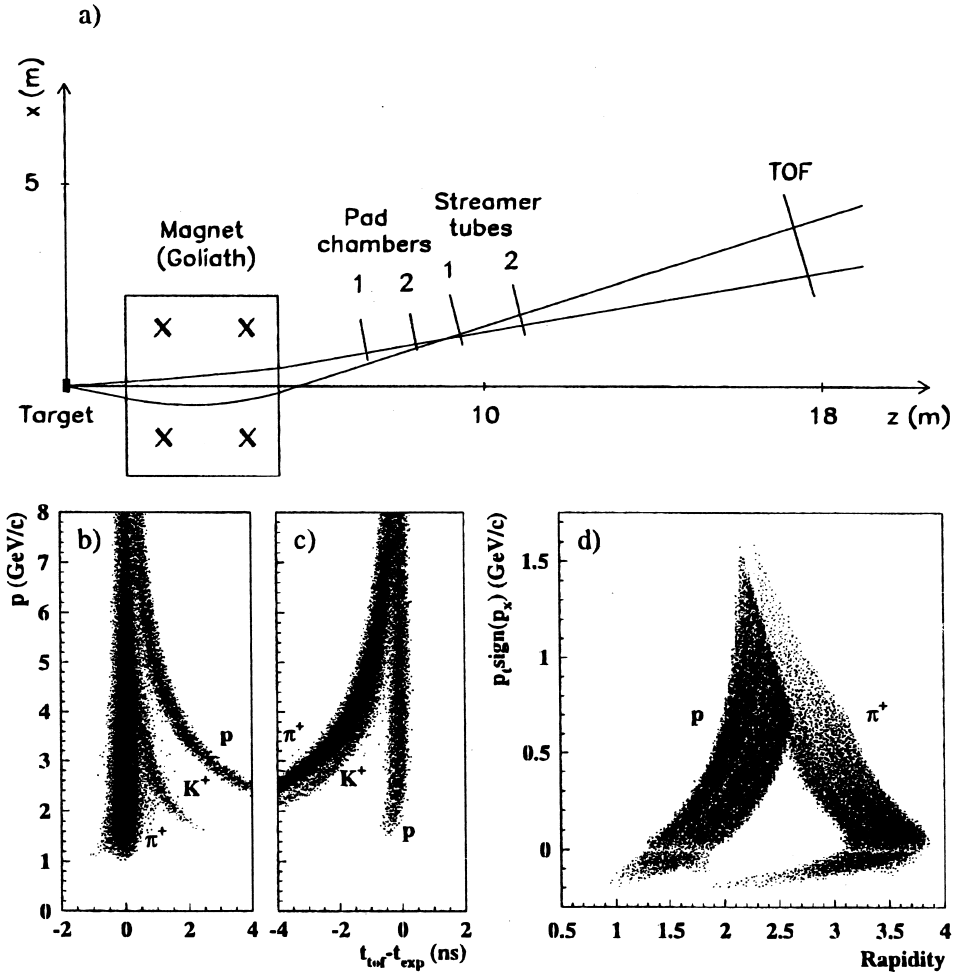

Fig. 1. (a) Overview of the tracking arm with two tracks within the acceptance. (b) Particle identification bands calculated assuming that all particles have the pion mass. (c) as in (b) assuming proton mass. (d) The distribution of accepted particles in terms of p_t and rapidity for protons and π^+.

ambiguities, in spite of the large track multiplicity within the acceptance. Cuts have been applied on the hit association in the TOF wall and on the vertical distance between the track extrapolation and the interaction point. Finally, the particle identity is obtained by cuts in $t_{\mathrm{tof}} - t_{\mathrm{exp}}$. This works up to a particle momentum of 8 GeV/c, where the separation no longer can be done unambiguously. In order not to lose any observed Δ^{++} resonances, we have chosen to use particles up to 16 GeV/c, thereby introducing a small systematic error. The small amount of contaminating kaons among pions above 4 GeV/c only gives marginal effects on the extracted Δ^{++} yield. This sort of contamination will also be present in the mixed events and its effects are to a large extent removed.

Fig. 1d shows the distributions of accepted particles for the second tracking arm in terms of transverse momentum p_t and rapidity for protons and pions. Notice the sign(p_x) factor, which unfolds the spectrum for particles with negative p_x and momentum low enough to bend across the beam line. Furthermore, a momentum cut of 8 GeV/c has been applied.

For all pairs of identified p and π^+, the invariant mass, $M_{\rm inv}$, was calculated from

$$M_{\rm inv} = \sqrt{\left(E_\pi + E_{\rm p}\right)^2 - \left(\boldsymbol{p}_\pi + \boldsymbol{p}_{\rm p}\right)^2}\,.$$

The mass resolution of the pπ^+-pair, estimated from the momentum resolution, is a few MeV. An invariant mass spectrum of such pairs (real spectrum) will consist of one part where the pion and the proton are coming from the same Δ^{++}-decay and an essentially uncorrelated combinatorial background. Due to the high multiplicity of protons and pions, the combinatorial background will be by far the dominant contribution to the invariant mass spectrum. To account for this combinatorial background, the invariant mass spectrum was calculated also with protons and pions taken from different events (mixed event). To extract the fraction ξ, of Δ^{++}, among the pπ^+-pairs, $N_{\rm pair}$, we assume that the mixed event invariant mass spectrum has the same shape as the combinatorial background in the real spectrum. This assumption has been verified by studies of ratios between real spectra and mixed event spectra. To essentially eliminate the statistical errors in the mixed event spectrum, it contains about ten times the statistics in that of the real spectrum. The real spectrum, $F(M_{\rm inv})$ can then be written as

$$F(M_{\rm inv}) = N_{\rm ev}\cdot N_{\rm pair}\big(\xi\cdot BW(M_{\rm inv},M_0,\Gamma) + (1-\xi)\,g(M_{\rm inv})\big). \qquad (1)$$

BW$(M_{\rm inv},M_0,\Gamma)$ is a modified Breit-Wigner function, filtered through our geometrical acceptance, normalized to unity. M_0 and Γ are the peak position and width respectively of the modified Breit-Wigner function. Note that neither the real spectrum nor the mixed event spectrum are corrected for acceptance. $N_{\rm ev}$ is the number of events and $g(M_{\rm inv})$ is the unit normalized mixed event spectrum. The modified Breit-Wigner function, before filtering, is given by

$$BW(M_{\rm inv},M_0,\Gamma) \propto \frac{q^3}{\left(q^3+\mu^3\right)}\,\frac{1}{\left(\left(M_{\rm inv}-M_0\right)^2+\left(\Gamma/2\right)^2\right)},$$

where q is the momentum of the proton (or pion) in the rest-frame of the pair, i.e half of the relative momentum, and $\mu = 180$ MeV/c [15]. The real spectrum can now be fitted using Eq. (1), treating ξ, M_0 and Γ as free parameters.

Fig. 2a shows the distribution of accepted Δ^{++} obtained from FRITIOF7.02 [16] events filtered through GEANT, i.e. for Δ^{++} where both decay particles fall inside the acceptance of the arm. The spectrum is unfolded in the same way as in Fig. 1d. Fig. 2b shows the invariant mass spectrum of

$$F(M_{\rm inv}) - N_{\rm ev}\cdot N_{\rm pair}\cdot(1-\xi)\,g(M_{\rm inv}),$$

i.e. the real spectrum with the background subtracted. Also shown by the solid curve is

$$N_{\rm ev}\cdot N_{\rm pair}\cdot\xi\cdot BW(M_{\rm inv},M_0,\Gamma),$$

i.e. the acceptance-filtered modified Breit-Wigner function obtained from the best fit.

The extracted number of Δ^{++} has to be corrected for acceptance and inefficiencies. Table 1 gives the values of the different correction factors with their estimated errors.

The efficiency for Δ^{++} detection is the product of the efficiencies for protons and pions. The efficiency factors given in the table are the ratio between those Δ^{++} efficiencies and the corresponding efficiencies for protons. $k_{\rm trk}$, which is about 80%, is the probability for a particle entering the arm, resulting in a track seen in at least three out of the four

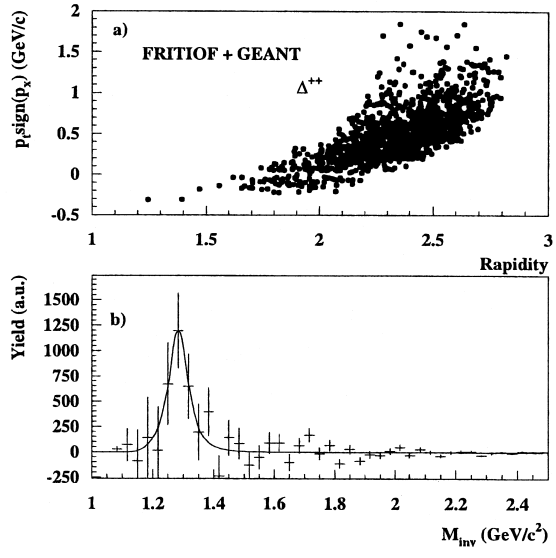

Fig. 2. (a) The distribution of accepted Δ^{++} obtained from Fritiof events. (b) The extracted Δ^{++} resonance together with the corresponding acceptance-filtered modified Breit-Wigner.

Table 1
Summary of the different correction factors and their estimated systematic errors.

Correction factors	Value
tracking efficiency, k_{trk}	0.79 ± 0.02
identification efficiency, k_{pid}	0.60 ± 0.02
geometrical acceptance, k_{geo}	0.145 ± 0.005

tracking planes and with a quality sufficient to pass the applied cuts, i.e. vertex association, χ^2 of the straight-line fit, et cetera. The k_{pid} factor corrects for the particle identification efficiency, including hardware efficiencies, effects of applied cuts on the flight times and particles decaying before reaching the TOF wall. The k_{geo} factor corrects the Δ^{++}/proton ratio for the limited azimuthal coverage of the arm estimated by GEANT simulations. The values of all the correction factors depend on the cuts we apply on the data and the systematic errors were estimated by varying these cuts within reasonable limits.

Table 2 gives the reconstructed and corrected ratio between the number of Δ^{++} and protons within the arm. Within our acceptance RQMD2.3 [17] predicts about 2.4 protons/central event and FRITIOF7.02 predicts about 5.5 protons/central event. Thus our proton multiplicity, which is about 1.83 proton per central event after efficiency corrections, seem to be in fair agreement with RQMD, whereas FRITIOF seems to overestimate.

The extraction of the Δ^{++} signal is by no means trivial as the peak is broad and the combinatorial background is large. Three different extraction methods were applied to simulated data to investigate the influence of the methods on the reconstructed number of Δ^{++} [18]. The method described above proved to be the most robust for different projectiles p, Si and Pb upon Pb target at the relevant beam energy.

Regarding the error of the extracted ratio we note that this is dominated by the statistical fluctuations in the number of combinatorial pairs under the resonance peak. Thus it is impossible to obtain the ratio with higher precision with the given statistics, independent of the extraction method. A study based on simulation results with different event generators, and variation of cuts applied to the data, indicates that the systematic error contributions resulting from the various cuts and correction factors applied to the data are considerably smaller (of the order of 10% of the obtained value) and therefore negligible in comparison to the statistical error.

However, it was observed that the chosen extraction method tended to systematically overestimate the number of Δ^{++} in simulations. A special simplified Monte Carlo event generator was constructed in order to study this effect. With this generator, several hundreds of samples of the same size as the real data sample was studied [19]. The reason for the overestimation is that although the background estimated with mixed events is almost identical to the background in the data, small differences are present. For instance, correlations between the decay products from different Δ^{++} resonances are believed to add to the systematic error of the extraction method. Pairs with the pion and proton from two different Δ^{++} decays, are almost identical to a pair originating from the same Δ^{++} due to the restricted acceptance of the tracking arm. The magnitude of the overestimation and associated error has been determined from the simulations and a correction has been applied for the ratio and error as shown in Table 2. The correction leads to an increased relative error in the ratio.

The ratio of $\Delta(1232)$/nucleons has been studied and an increase as a function of incoming beam energy has been established [8]. In a thermal model this can be interpreted as an increase of the freeze-out temperature which determines the relative population of the nucleonic resonances. The same ratio can be estimated from our data. In an isospin symmetric system, one could obtain the total number of $\Delta(1232)$ resonances, i.e. Δ^-, Δ^0, Δ^+ and Δ^{++}, by multiplying the number of Δ^{++} by an isospin factor four. In the same way, the number of nucleons, including those from resonance decays, could be estimated by multiplying the measured number of protons with a factor two. In our case, where we have an isospin

Table 2
Summary of the results.

119677 central events	Δ^{++}/proton ratio
reconstructed (uncorrected)	0.031 ± 0.015
corrected for systematic fitting error	0.021 ± 0.013
full ϕ and eff. corrected	0.309 ± 0.190

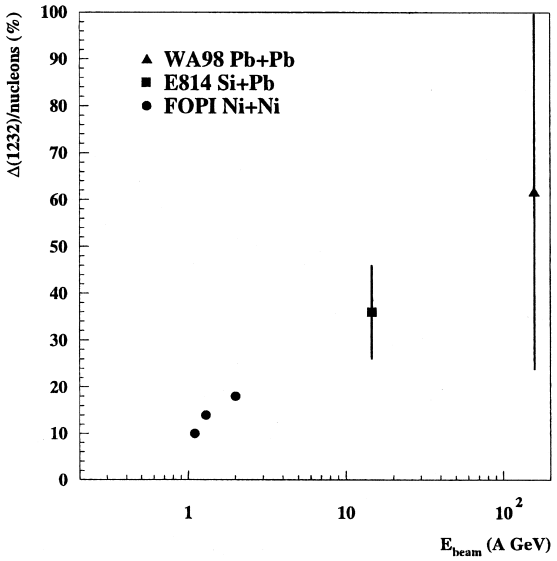

Fig. 3. The ratio $\Delta(1232)$/nucleons as a function of beam energy/nucleon.

asymmetry, in a first approximation the nucleons and the Δ-resonances are affected in the same way, and thus no correction for the isospin asymmetry is applied. Only a small contribution of baryon number is present in deuterons and weakly decaying hyperons, where the decay proton might be lost in the tracking due to the secondary vertex being far from the interaction point.

Our obtained ratio for nucleons originating from $\Delta(1232)$ resonances, is found to be quite large at central rapidities, 0.62 ± 0.38. Fig. 3 shows our results in comparison with similar results from experiments at lower beam energies. Note that the target and projectile rapidities are separated by 5.8 units at 158 A GeV. In this experiment the influence of spectator matter is thus much less than at lower beam energies.

Our obtained value of the $\Delta(1232)$/nucleon ratio can be compared to the ratio obtained from thermal model calculations, assuming chemical and thermal equilibrium. In such a calculation the maximum ratio obtained is around 0.33 [2]. Furthermore this ratio is obtained over a large range of temperatures and baryon densities, used as input to the calculations.

However, it should be pointed out that the experimental ratio also contain contributions from prior to freeze-out. For this and other reasons, e.g. the saturation of the ratio as a function of temperature, it is premature to use the experimentally extracted ratio for a precise temperature estimation and any temperature above 100 MeV seems to be in qualitative agreement with the obtained ratio.

Besides the yield, the fitting procedure also provides the width and mass of the delta peak. However the systematic errors in these values, estimated by changing cuts and extraction methods and by applying the methods to Monte Carlo samples with known parameters, are sufficiently large to preclude a meaningful discussion of a possible mass shift or changes of the width of the delta peak.

Acknowledgements

This work was supported jointly by the German BMBF and DFG, the US DOE, the Swedish NFR and FRN, the Dutch Stichting FOM, the Stiftung für Deutsch-Polnische Zusammenarbeit, the Grant Agency of the Czech Republic under contract No. 202/95/0217, the Department of Atomic Energy, the Department of Science and Technology, the Council of Scientific and Industrial Research and the University Grants Commission of the Government of India, the Indo-FRG Exchange Program, the PPE division of CERN, the Swiss National Fund, the INTAS under Contract INTAS-97-0158, ORISE, Grant-in-Aid for Scientific Research (Specially Promoted Research & International Scientific Research) of the Ministry of Education, Science and Culture, the University of Tsukuba Special Research Projects, and the JSPS Research Fellowships for Young Scientists. ORNL is managed by Lockheed Martin Energy Research Corporation under contract DE-AC05-96OR22464 with the US Department of Energy. The MIT group has been supported by the US Dept. of Energy under the cooperative agreement DE-FC02-94ER40818.

References

[1] S.A. Bass et al., Phys. Rev. C 50 (1994) 2167.
[2] G.E. Brown, J. Stachel, G.M. Welke, Phys. Lett. B 253 (1991) 19.

[3] J.M. Laget, Phys. Rep. 69 (1981) 1.
[4] J.S. O'Connell, B. Schröder, Phys. Rev. C 38 (1988) 2447.
[5] R.E. Chrien et al., Phys. Rev. C 21 (1980) 1014.
[6] J.P. DeBrion et al., Phys. Rev. Lett. 34 (1975) 910.
[7] A. Badalà et al., Phys. Rev. C 54 (1996) R2138.
[8] FOPI Collaboration, B. Hong et al., Phys. Lett. B 407 (1997) 115.
[9] E814 Collaboration, J. Barrette et al., Phys. Lett. B 351 (1995) 93.
[10] WA98 Collaboration, Proposal for a large acceptance hadron and photon spectrometer, 1991, Preprint CERN/SPSLC 91-17, SPSLC/P260.
[11] L. Carlén et al., Nucl. Instr. and Methods A 431 (1999) 123.
[12] L. Carlén et al., Nucl. Instr. and Methods A 412 (1998) 361.
[13] L. Carlén et al., Nucl. Instr. and Methods A 413 (1998) 92.
[14] R. Brun, F. Carminati, GEANT Detector Description and Simulation Tool, CERN Program Library, Long Writeup W5013, March 1994.
[15] E.L. Hjort et al., Phys. Rev. Lett. E 79 (1997) 4345.
[16] H. Pi, Comp. Phys. Comm. 71 (1992) 173.
[17] H. Sorge, Phys. Rev. C 52 (1995) 3291.
[18] K. El Chenawi, Ph.D. thesis, Lund University, 1999.
[19] D. Silvermyr, Lic. thesis, Lund University, 1999.

Eur. Phys. J. C 16, 445–451 (2000)
Digital Object Identifier (DOI) 10.1007/s100520000413

THE EUROPEAN PHYSICAL JOURNAL C

© Società Italiana di Fisica
Springer-Verlag 2000

Central Pb+Pb collisions at 158 A GeV/c studied by $\pi^-\pi^-$ interferometry

The WA98 Collaboration

M.M. Aggarwal[1], A. Agnihotri[2], Z. Ahammed[3], A.L.S. Angelis[4], V. Antonenko[5], V. Arefiev[6], V. Astakhov[6], V. Avdeitchikov[6], T.C. Awes[7], P.V.K.S. Baba[8], S.K. Badyal[8], C. Barlag[9], S. Bathe[9], B. Batiounia[6], T. Bernier[10], K.B. Bhalla[2], V.S. Bhatia[1], C. Blume[9], R. Bock[11], E.-M. Bohne[9], Z. Böröcz[9], D. Bucher[9], A. Buijs[12], H. Büsching[9], L. Carlen[13], V. Chalyshev[6], S. Chattopadhyay[3], R. Cherbatchev[5], T. Chujo[14], A. Claussen[9], A.C. Das[3], M.P. Decowski[18], H. Delagrange[10], V. Djordjadze[6], P. Donni[4], I. Doubovik[5], S. Dutt[8], M.R. Dutta Majumdar[3], K. El Chenawi[13], S. Eliseev[15], K. Enosawa[14], P. Foka[4], S. Fokin[5], M.S. Ganti[3], S. Garpman[13], O. Gavrishchuk[6], F.J.M. Geurts[12], T.K. Ghosh[16], R. Glasow[9], S. K.Gupta[2], B. Guskov[6], H. Å.Gustafsson[13], H. H.Gutbrod[10], R. Higuchi[14], I. Hrivnacova[15], M. Ippolitov[5], H. Kalechofsky[4], R. Kamermans[12], K.-H. Kampert[9], K. Karadjev[5], K. Karpio[17], S. Kato[14], S. Kees[9], C. Klein-Bösing[9], S. Knoche[9], B. W. Kolb[11], I. Kosarev[6], I. Koutcheryaev[5], T. Krümpel[9], A. Kugler[15], P. Kulinich[18], M. Kurata[14], K. Kurita[14], N. Kuzmin[6], I. Langbein[11], A. Lebedev[5], Y.Y. Lee[11], H. Löhner[16], L. Luquin[10], D.P. Mahapatra[19], V. Manko[5], M. Martin[4], G. Martínez[10], A. Maximov[6], G. Mgebrichvili[5], Y. Miake[14], Md.F. Mir[8], G.C. Mishra[19], Y. Miyamoto[14], B. Mohanty[19], D. Morrison[20], D. S. Mukhopadhyay[3], H. Naef[4], B. K. Nandi[19], S. K. Nayak[10], T. K. Nayak[3], S. Neumaier[11], A. Nianine[5], V. Nikitine[6], S. Nikolaev[5], P. Nilsson[13], S. Nishimura[14], P. Nomokonov[6], J. Nystrand[13], F.E. Obenshain[20], A. Oskarsson[13], I. Otterlund[13], M. Pachr[15], S. Pavliouk[6], T. Peitzmann[9], V. Petracek[15], W. Pinganaud[10], F. Plasil[7], U. von Poblotzki[9], M.L. Purschke[11], J. Rak[15], R. Raniwala[2], S. Raniwala[2], V.S. Ramamurthy[19], N.K. Rao[8], F. Retiere[10], K. Reygers[9], G. Roland[18], L. Rosselet[4], I. Roufanov[6], C. Roy[10], J.M. Rubio[4], H. Sako[14], S.S. Sambyal[8], R. Santo[9], S. Sato[14], H. Schlagheck[9], H.-R. Schmidt[11], Y. Schutz[10], G. Shabratova[6], T.H. Shah[8], I. Sibiriak[5], T. Siemiarczuk[17], D. Silvermyr[13], B.C. Sinha[3], N. Slavine[6], K. Söderström[13], N. Solomey[4], S.P. Sørensen[7,20], P. Stankus[7], G. Stefanek[17], P. Steinberg[18], E. Stenlund[13], D. Stüken[9], M. Sumbera[15], T. Svensson[13], M.D. Trivedi[3], A. Tsvetkov[5], L. Tykarski[17], J. Urbahn[11], E.C.v.d. Pijll[12], N.v. Eijndhoven[12], G.J.v. Nieuwenhuizen[18], A. Vinogradov[5], Y.P. Viyogi[3], A. Vodopianov[6], S. Vörös[4], B. Wysłouch[18], K. Yagi[14], Y. Yokota[14], G.R. Young[7]

[1] University of Panjab, Chandigarh 160014, India
[2] University of Rajasthan, Jaipur 302004, Rajasthan, India
[3] Variable Energy Cyclotron Centre, Calcutta 700 064, India
[4] University of Geneva, 1211 Geneva 4, Switzerland
[5] RRC Kurchatov Institute, 123182 Moscow, Russia
[6] Joint Institute for Nuclear Research, 141980 Dubna, Russia
[7] Oak Ridge National Laboratory, Oak Ridge, T 37831-6372, USA
[8] University of Jammu, Jammu 180001, India
[9] University of Münster, 48149 Münster, Germany
[10] SUBATECH, Ecole des Mines, Nantes, France
[11] Gesellschaft für Schwerionenforschung (GSI), 64220 Darmstadt, Germany
[12] Universiteit Utrecht/NIKHEF, 3508 TA Utrecht, The Netherlands
[13] Lund University, 221 00 Lund, Sweden
[14] University of Tsukuba, Ibaraki 305, Japan
[15] Nuclear Physics Institute, 250 68 Rez, Czech Republic
[16] KVI, University of Groningen, 9747 AA Groningen, The Netherlands
[17] Institute for Nuclear Studies, 00-681 Warsaw, Poland
[18] MIT, Cambridge, MA 02139, USA
[19] Institute of Physics, 751-005 Bhubaneswar, India
[20] University of Tennessee, Knoxville, T 37966, USA

Received: 3 February 2000 / Published online: 18 May 2000 – © Springer-Verlag 2000

Abstract. Two-particle correlations have been measured for identified π^- from central 158 A GeV Pb+Pb collisions and fitted radii of about 7 fm in all dimensions have been obtained. A multi-dimensional study of the radii as a function of k_T is presented, including a full correction for the resolution effects of the

apparatus. The cross term $R^2_{out-long}$ of the standard fit in the Longitudinally CoMoving System (LCMS) and the v_L parameter of the generalised Yano-Koonin fit are compatible with 0, suggesting that the source undergoes a boost invariant expansion.

The shapes of the correlation functions in Q_{inv} and $Q_{space} = \sqrt{Q_x^2 + Q_y^2 + Q_z^2}$ have been analyzed in detail. They are not Gaussian but better represented by exponentials. As a consequence, fitting Gaussians to these correlation functions may produce different radii depending on the acceptance of the experimental setup used for the measurement.

1 Introduction

The study of Bose-Einstein correlations between pairs of identical hadrons is an essential tool to obtain information on the space-time evolution of the extended hadron sources created in heavy ion collisions [1]. In particular, a strong correlation between the momenta and the space-time production points of the particles suggests expanding sources as predicted by hydrodynamic models [2]. The dynamical evolution of such systems can then be studied with interferometry via selection on the transverse momenta and rapidity of the correlated particle pairs.

In this paper, we present the analysis of two-particle correlations of identified π^- measured in the WA98 experiment for central 158 A GeV Pb+Pb collisions at the CERN SPS.

2 Experimental setup and data processing

The WA98 experiment shown in Fig. 1 combined large acceptance photon detectors with a two arm charged particle tracking spectrometer. The incident 158 A GeV Pb beam interacted with a Pb target near the entrance of a large dipole magnet. Non-interacting beam nuclei, or beam fragments were detected in a forward calorimeter located at zero degree. A mid-rapidity calorimeter measured the total transverse energy in the rapidity region $3.2 \leq \eta \leq 5.4$, which was also used in the trigger for online centrality selection. The Plastic-Ball calorimeter measured the fragmentation of the target, and silicon detectors were used to measure the charged particle multiplicity. The photon detectors consisted of a large area photon multiplicity detector and a high granularity lead-glass calorimeter for single photon, π^0, and η physics [3].

The charged particle spectrometer made use of a 1.6 Tm dipole magnet with a 2.4×1.6 m^2 air gap for magnetic deflection of the charged particles in the horizontal plane. The results presented in this paper are taken from the 1995 WA98 data set obtained with the negative particle tracking arm of the charged particle spectrometer. The second tracking arm was added to the spectrometer in 1996 to measure positive particles [4]. The first tracking arm consisted of six multistep avalanche chambers with optical readout [5] located downstream of the magnet. The active area of the first chamber was 1.2×0.8 m^2, while that of the other five was 1.6×1.2 m^2. The chambers contained a photoemissive vapour (TEA) which produced UV photons along the path of traversal of the charged particles. These were converted into visible light via wavelength shifter plates. On exit the light was reflected by mirrors at 45° to CCD cameras equipped with two image intensifiers. Each pixel of a CCD viewed a 3.1×3.1 mm^2 area of a chamber. In addition, a 4×1.9 m^2 Time of Flight wall positioned behind the chambers at a distance of 16.5 m from the target allowed for particle identification with a time resolution better than 120 ps.

Figure 2 shows the Monte Carlo generated p_T-rapidity acceptance for π^-. The acceptance ranges from y=2.1 to 3.1 with an average at 2.70. The momentum resolution of the spectrometer was $\Delta p/p$=0.005 at p=1.5 GeV/c, resulting in an average accuracy better than or equal to 10 MeV/c for all the Q variables used in the interferometry analysis and defined in section 5: $\sigma(Q_{inv})$=7 MeV/c, $\sigma(Q_{TO})$=10 MeV/c, $\sigma(Q_{TS})$=5 MeV/c, $\sigma(Q_L)$=3 MeV/c, $\sigma(Q_T)$=8 MeV/c, $\sigma(Q_0)$=5 MeV/c.

The analysis of the complete 1995 data set is presented here. These data have been taken with the most central triggers corresponding to about 10% of the minimum bias cross section of 6190 mb. Severe track quality cuts were applied at the expense of statistics resulting in final samples of 4.2×10^6 π^- for the correlation analysis and 4.6×10^5 π^- for the single particle spectrum.

3 Single particle spectra

The m_T=$\sqrt{m_\pi^2 + p_T^2}$ distribution of identified π^-, averaged over the rapidity acceptance, is shown in Fig. 3. The data were corrected for geometrical acceptance and efficiency of the chamber-camera-Time of Flight system using a full simulation of the experimental setup. The parameters of the simulation were optimized in an iterative way by comparing various distributions with the real data. The simulated data were then treated exactly like the real data. The measured $1/m_T\, dN/dm_T\, dy$ distribution was then fitted to the form $C\exp(-m_T/T)$, expected for a source in thermal equilibrium [6]. Such fits were applied to the data for different ranges of m_T, such as the one shown in Fig. 3. These fits do not reproduce the overall concave shape of the data, which is partly due to particles originating in resonance decays and could also be an indication of transverse flow [7]. The shape of the π^- m_T distribution was found to be in good agreement with that of π^0 obtained in the lead-glass calorimeter [3].

4 One-dimensional interferometry analysis

For the Bose-Einstein correlation studies, the data were Coulomb corrected in an iterative way [8]. The Gamow correction was abandoned as it overcorrects the data for

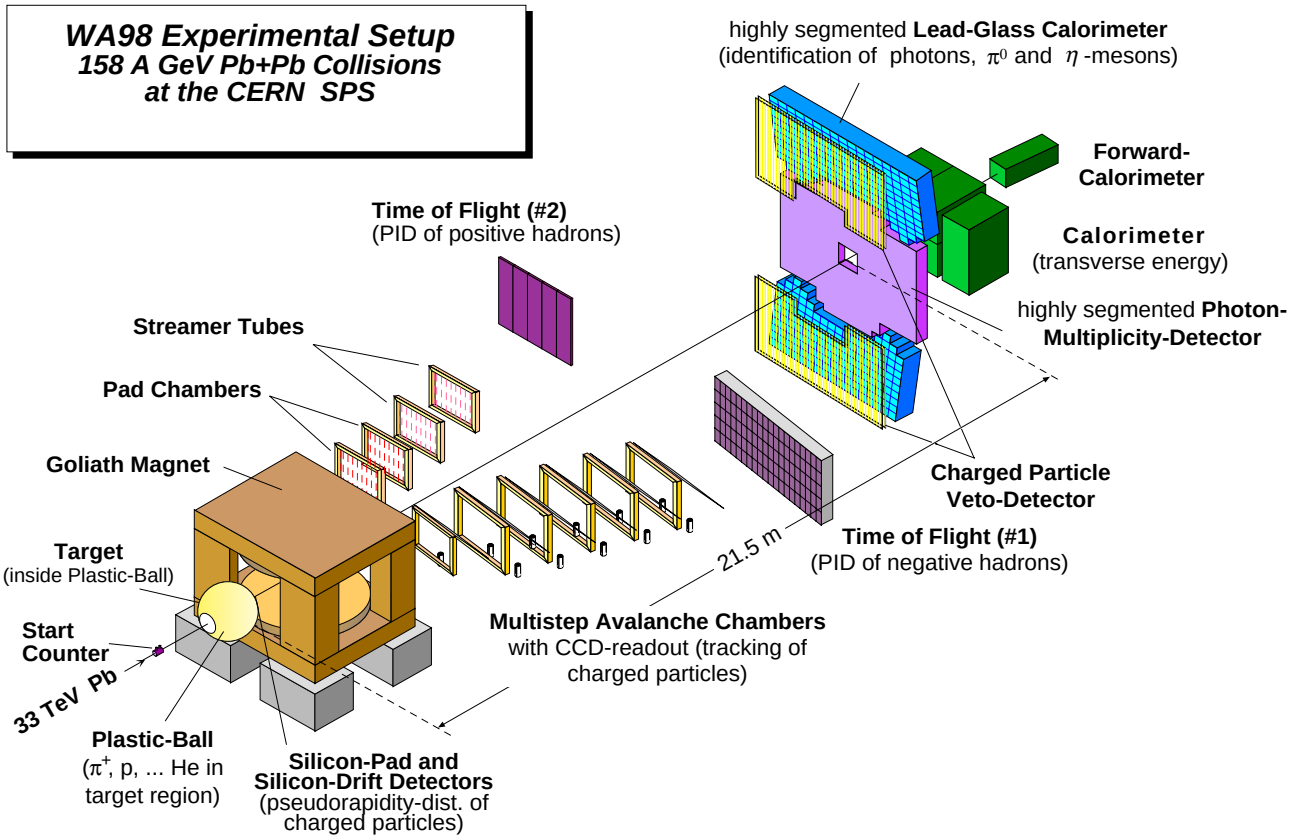

Fig. 1. Experimental setup

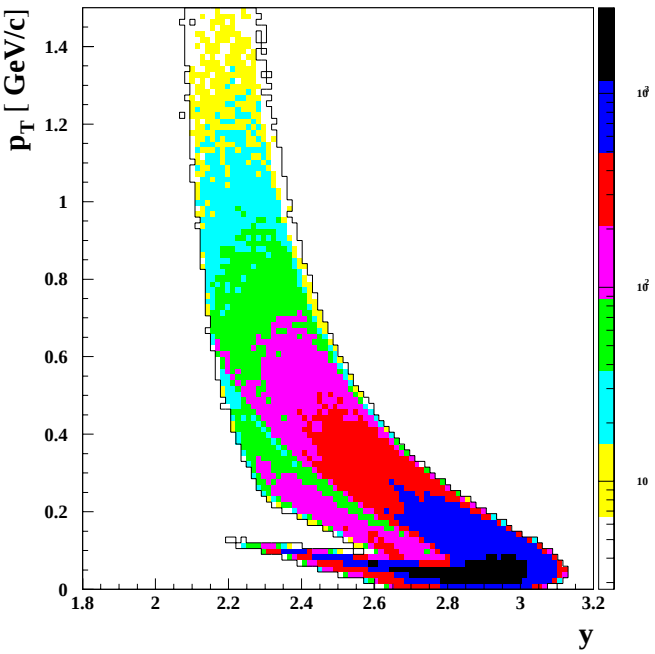

Fig. 2. p_T-rapidity acceptance

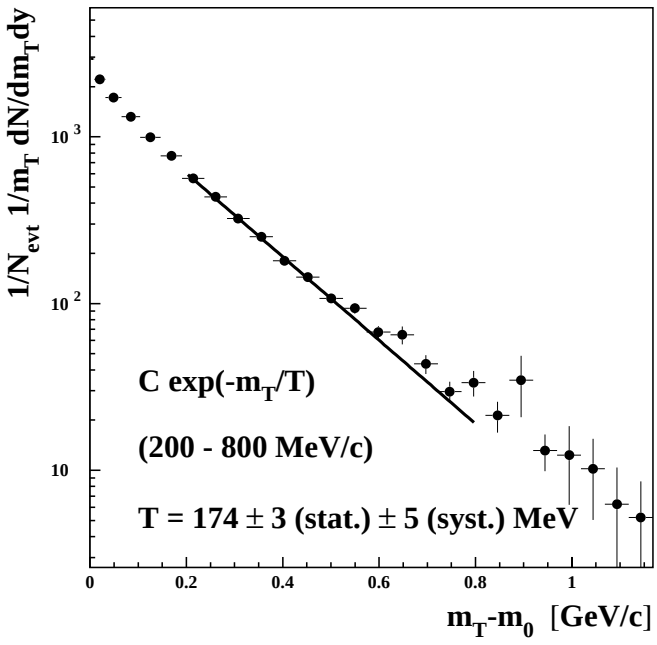

Fig. 3. m_T distribution (the fit is explained in the text)

Q_{inv} in the range of 0.1 to 0.3 GeV/c. A fit of the form $1+\lambda\exp[-Q_{inv}^2 R_{inv}^2]$ was made to the Q_{inv} correlation function yielding $R_{inv} = 6.83 \pm 0.10$ fm and $\lambda = 0.307 \pm 0.008$. An expanded view of the correlation distribution (Fig. 4) shows that the Gaussian fit used (full line) is not perfect, especially in the Q_{inv} range of 40 to 80 MeV/c where the tail of the experimental distribution shows an excess which is not well reproduced by the fit. In addition to this Gaus-

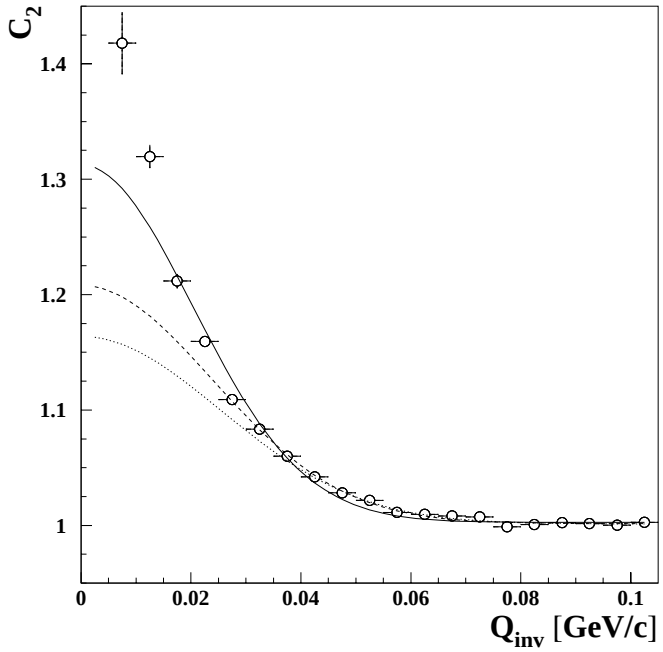

Fig. 4. Q_{inv} distribution with Gaussian fits. The full line is a fit made with all the points. The dashed line is a fit for $Q_{inv} \geq 25$ MeV/c and the dotted line is a fit for $Q_{inv} \geq 40$ MeV/c

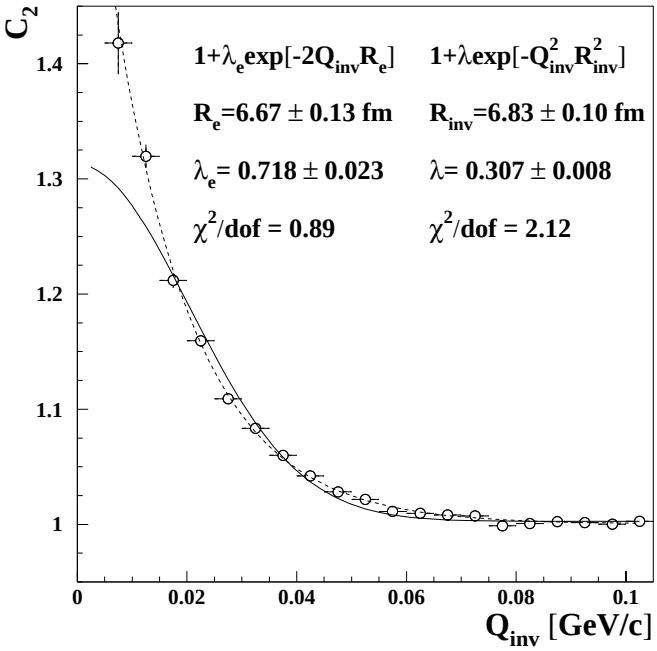

Fig. 5. Q_{inv} distribution with the Gaussian fit (full line) and the exponential fit (dashed line)

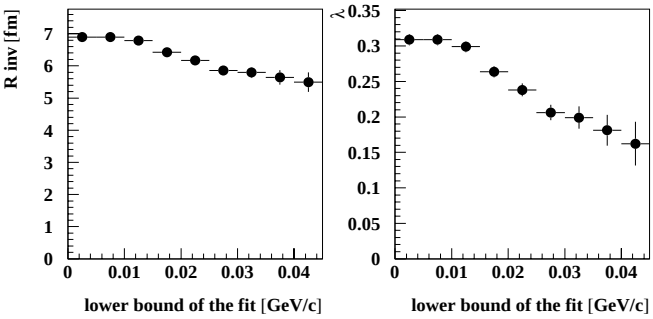

Fig. 6. Gaussian fit stability

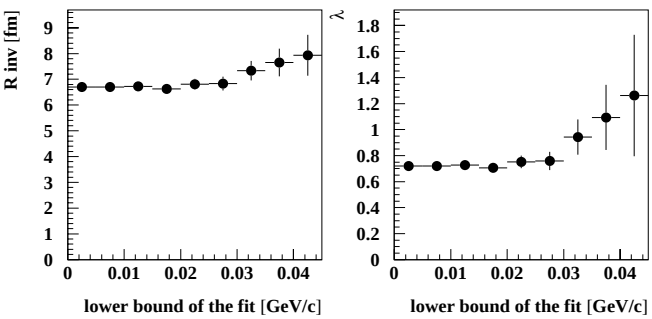

Fig. 7. Exponential fit stability

sian fit made over the whole range of Q_{inv}, Fig. 4 shows also different Gaussian fits using data in the ranges 25 MeV/c $\leq Q_{inv} \leq$ 200 MeV/c (dashed line) and 40 MeV/c $\leq Q_{inv} \leq$ 200 MeV/c (dotted line). These fits do not coincide. Different radii are then obtained for different starting points of the fit because the shape of the distribution is not Gaussian. This effect is independent of the severity of the track selection, and is therefore not due to spurious tracks. This is summarized in Fig. 6 where R_{inv} and the corresponding λ are plotted as a function of the lower bound of the fit. There is a statistically significant drop when using a Gaussian fit. A similar behaviour is observed when, instead of Q_{inv}, $Q_{space} = \sqrt{Q_x^2 + Q_y^2 + Q_z^2}$ is used, calculated in the longitudinally comoving system (LCMS) and fitted with $1+\lambda\exp[-Q_3^2R_3^2]$. This method of fitting in varying ranges has a good sensitivity to the shape. It has been repeated by replacing the Gaussian fit by an exponential fit of the form $1+\lambda_e\exp[-2Q_{inv}R_e]$ where the factor 2 is added to make the radius R_e more comparable with R_{inv}. The results (Fig. 7) show that the stability is better with the exponential fit. Figure 5 directly compares the Gaussian and exponential fits for Q_{inv}. Although the Gaussian fit still gives an acceptable χ^2/d.o.f., the exponential fit is better everywhere. A similar conclusion is reached when the first data point is excluded from the fit. This result is not based on the first bins which might be more affected by systematics due to large Coulomb correction or noise correlated with the true track signals in the chambers. It is rather based on the high statistics tail of the distribution which contributes in a different way to a Gaussian or an exponential fit. This quasi exponential behaviour is expected by different models including resonance decays [9]. As a consequence small acceptance experiments may obtain a larger radius if a Gaussian fit is used because they are less sensitive to the tail. On the contrary large acceptance experiments have higher statistics at large Q-values, and the Gaussian fit will yield lower values of the radius.

Table 1. 3-dimensional analysis

Standard fit in LCMS			Generalized Yano-Koonin fit		
R_{TS}	=	6.41±0.13 fm	R_T	=	6.54±0.11 fm
R_{TO}	=	6.60±0.16 fm	R_0	=	0.01±0.69 fm
R_L	=	7.50±0.18 fm	R_4	=	7.51±0.18 fm
λ	=	0.350±0.010	λ	=	0.325±0.009
$R^2_{out-long}$	=	-1.0±1.3 fm^2	v_L	=	0.03±0.05
χ^2/d.o.f.	=	1.06	χ^2/d.o.f.	=	1.02

5 Multi-dimensional interferometry analysis

The multi-dimensional analysis has been done with Gaussian fits to allow comparison with other experiments. Two different parameterizations have been used in the LCMS:

a) The standard fit in the 3-dimensional space of momentum differences Q_{TS} (perpendicular to the beam axis and to the transverse momentum of the pair), Q_{TO} (perpendicular to the beam axis and parallel to the transverse momentum of the pair), and Q_L (parallel to the beam axis) [10]. The fitted formula

$$C_2 = 1 + \lambda \exp[-Q^2_{TS}R^2_{TS} - Q^2_{TO}R^2_{TO} - Q^2_L R^2_L - 2Q_{TO}Q_L R^2_{out-long}]$$

includes a cross term in $Q_{TO}Q_L$ as predicted [11].

b) The generalized Yano-Koonin (GYK) fit [12] in the Q_0 (energy difference of the pair), Q_T,Q_L space according to

$$C_2 = 1+\lambda \exp[-Q^2_T R^2_T + (Q^2_0 - Q^2_L)R^2_4 - (Q\cdot U)^2(R^2_0 + R^2_4)]$$

where $U = \gamma(1, 0, 0, v_L)$, $\gamma = 1/\sqrt{1 - v^2_L}$ with v_L in units of c=1.

In the GYK approach, the radius parameters remain invariant under longitudinal Lorentz boost, the parameter v_L connecting the "arbitrary" measurement frame (LCMS) to the Yano-Koonin frame. In addition, the extraction of the duration of emission, R_0, is straightforward.

The consequence of the finite resolution in the measurement of the Q variables is an underestimate of the radii and λ parameters. Morever, as the resolution is different for each Q variable, this causes a bias which varies from parameter to parameter, leading to errors in the interpretation of the results in a multi-dimensional analysis. It is therefore essential to take into account the effect of the resolution in the fitting procedure. One way to do this is to replace the formula $C_2(\mathbf{Q})$ used to fit the data by

$$C^{rc}_2(\mathbf{Q}) = \iiint r(\mathbf{Q}, \mathbf{Q}')\, C_2(\mathbf{Q}')\, d\mathbf{Q}'$$

which is the convolution of $C_2(\mathbf{Q})$ with the resolution function $r(\mathbf{Q}, \mathbf{Q}')$. The resolution function is chosen to be Gaussian:

$r(\mathbf{Q}, \mathbf{Q}') = 1/(2\pi)^{3/2}\, 1/|V|^{1/2}$

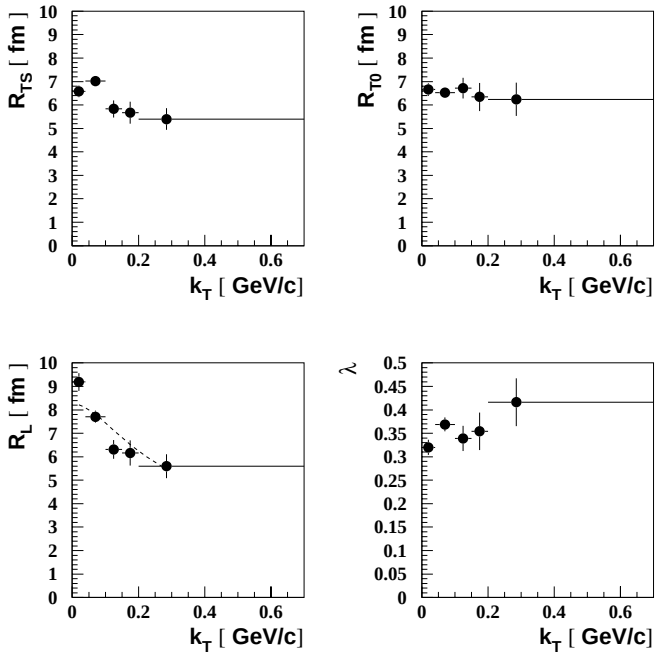

Fig. 8. 5-parameter fit as a function of k_T. The horizontal bars indicate the bin width and the points are plotted at the average k_T of the bin. The dashed line in the bottom left figure shows the result of a fit explained in the text

$$\times \exp[-1/2\, (\mathbf{Q} - \mathbf{Q}')^T\, V^{-1}\, (\mathbf{Q} - \mathbf{Q}')]$$

The diagonal elements of the covariance matrix V are equal to the square of the resolution of the different Q variables and are estimated separately as a function of $k_T = |\mathbf{p}_{T1} + \mathbf{p}_{T2}|/2$ of the pairs. The non-diagonal elements are neglected. For the one-dimensional Gaussian fit case with $\mathbf{Q} = Q_{inv}$, the resolution corrected values of the fitted parameters are $R_{inv} = 7.30 \pm 0.12$ fm and $\lambda = 0.328 \pm 0.009$.

The results of the multi-dimensional fits are presented in Table 1 for the full 1995 data sample. A multi-dimensional analysis as a function of k_T, both with the standard 5-parameter fit and with the GYK fit is shown in Figs. 8, 9, and 10.

The R_{TS} and R_L parameters from the standard fit are found to be compatible respectively with R_T and R_4 from the GYK fit. The cross term $R^2_{out-long}$ from the standard fit and v_L from the GYK fit are compatible with 0. In a source undergoing a boost invariant expansion, the lo-

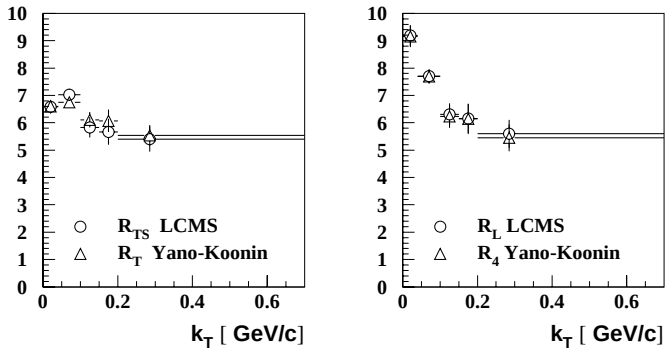

Fig. 9. Comparison of the R_{TS} and R_L parameters from the standard fit respectively with R_T and R_4 from the GYK fit as a function of k_T

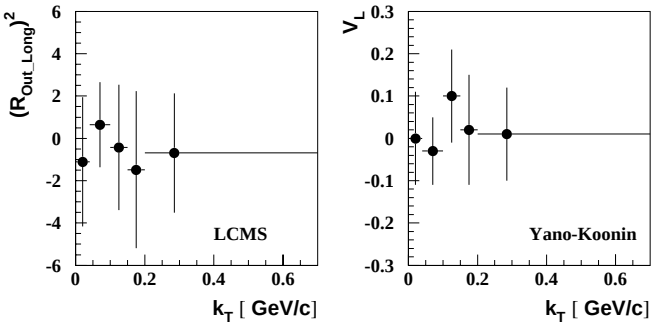

Fig. 10. The cross term $R^2_{out-long}$ from the standard fit and v_L from the GYK fit, both estimated in the LCMS, are compatible with 0 for all k_T bins

cal rest frame coincides with the LCMS. Both the cross term and v_L estimated in the LCMS are then expected to vanish [12]. As this is the case, it suggests that the source seen within the acceptance of the experiment has a strictly boost invariant expansion. The strong decrease of the longitudinal radius R_L or R_4 with k_T compared to the behaviour of the transverse radii R_T, R_{TS}, R_{TO} suggests a longitudinal expansion larger than the lateral expansion. The longitudinal radius R_L is shown with a fit of the form $1/\sqrt{m_T}$ with m_T=$\sqrt{m_\pi^2 + k_T^2}$ inspired by the hydrodynamical expansion model. Using $R_L = \tau_0\sqrt{T_0/m_T}$ with a freeze out temperature T_0 of 120-170 MeV/c, we may extract a freeze out time τ_0 in the range of 7.5-8.9 fm/c. Finally, the R_0 parameter from the GYK fit, which reflects the duration of emission, is compatible with 0 for all k_T bins, excluding a long-lived intermediate phase.

Two other experiments, NA49 and NA44, have studied charged particle interferometry in Pb+Pb collisions at CERN energies. The WA98 analysis is in good agreement with the NA49 results[13], when the comparison is made for the same mean y range of 2.70, although WA98 has used identified π^- while the NA49 analysis used unidentified negative particles. Only the R_0 parameter tends to be smaller in WA98. The direct comparison with the NA44 experiment is not possible because NA44 and WA98 do not have the same y range. The smaller radii measured by NA44[14] can be explained by the larger y range of its acceptance ($3.1< y <4.1$).

6 Conclusion

The analysis of the two-particle correlation of identified π^- from central Pb+Pb collisions at 158 A GeV gives fitted radii of about 7 fm. This should be compared to the equivalent rms radius of the initial Pb nucleus of 3.2 fm, which indicates a large final state emission volume.

The one-dimensional correlation functions analyzed in terms of Q_{inv} or Q_{space} are not Gaussian. They are better represented by exponentials. This study is based on the tail of the distributions and not on the first bins which might be subject to systematic effects. One possible explanation is that this behaviour is due to resonance effects. Fitting Gaussians to these correlation functions may produce different results depending on the acceptance of the experimental setup.

The generalized Yano-Koonin analysis gives similar results to within the error bars as the standard 3-dimensional analysis in the LCMS.

The cross term $R^2_{out-long}$ is found to be compatible with 0 in the LCMS and the same is true of v_L in the GYK fit. This suggests that the source undergoes a boost invariant expansion.

A clear dependence of the longitudinal radius parameter on k_T is observed, suggesting a larger longitudinal than transverse expansion of the source. In addition the short duration of emission disfavours any long-lived intermediate phase.

Acknowledgements. We would like to thank the CERN-SPS accelerator crew for providing an excellent lead beam and the Laboratoire National Saturne for the loan of the magnet Goliath. This work was supported jointly by the German BMBF and DFG, the U.S. DOE, the Swedish NFR, the Dutch Stichting FOM, the Swiss National Fund, the Humboldt Foundation, the Stiftung für deutsch-polnische Zusammenarbeit, the Department of Atomic Energy, the Department of Science and Technology and the University Grants Commission of the Government of India, the Indo-FRG Exchange Programme, the PPE division of CERN, the INTAS under contract INTAS-97-0158, the Polish KBN under the grant 2P03B16815, the Grant-in-Aid for Scientific Research (Specially Promoted Research & International Scientific Research) of the Ministry of Education, Science, Sports and Culture, JSPS Research Fellowships for Young Scientists, the University of Tsukuba Special Research Projects, and ORISE. ORNL is managed by Lockheed Martin Energy Research Corporation under contract DE-AC05-96OR22464 with the U.S. Department of Energy.

References

1. W. Zajc et al., Phys. Rev. **C29** (1984) 2173 and references therein.
2. T. Csörgő et al., Phys. Lett. **B347** (1995) 354; T. Csörgő et al., Phys. Lett. **B338** (1994) 134
3. T. Peitzmann et al., Nucl. Phys. **A610** (1996) 200c; M.M. Aggarwal et al., Phys. Rev. Lett. **81** (1998) 4087
4. L. Carlen et al., Nucl. Instr. and Meth. **A412** (1998) 361; L. Carlen et al., Nucl. Instr. and Meth. **A413** (1998) 92

5. J.M. Rubio et al., Nucl. Instr. and Meth. **A367** (1995) 358; A.L.S. Angelis et al., Nucl. Phys. **A566** (1994) 605c; M. Iżycki et al., Nucl. Instr. and Meth. **A310** (1991) 98
6. E. Schnedermann et al., Phys. Rev. **C48** (1993) 2462
7. M.M. Aggarwal et al., Phys. Rev. Lett. **83** (1998) 926
8. S.Pratt et al., Phys. Rev. **C42** (1990) 2646; these calculations were made with a Fortran program supplied by S. Pratt
9. S. Padula and M. Gyulassy, Nucl. Phys. **A525** (1991) 339; U.A. Wiedemann et al., Phys. Rev. **C53** (1996) 918
10. S. Pratt, Phys. Rev. **D33** (1986) 1314; G. Bertsch and G.E. Brown, Phys. Rev. **C40** (1989) 1830
11. S. Chapman et al., Phys. Rev. Lett. **74** (1995) 4400
12. S. Chapman et al., Phys. Rev. **C52** (1995) 2694 and references therein.
13. H. Appelshäuser et al., Eur. Phys. J. **C2** (1998) 661
14. I.G. Bearden et al., Phys. Rev. **C58** (1998) 1656

ELSEVIER

9 December 1999

PHYSICS LETTERS B

Physics Letters B 469 (1999) 30–36

Elliptic emission of K^+ and π^+ in 158 $A \cdot$ GeV Pb + Pb collisions

WA98 Collaboration

M.M. Aggarwal [a], A. Agnihotri [b], Z. Ahammed [c], A.L.S. Angelis [d], V. Antonenko [e], V. Arefiev [f], V. Astakhov [f], V. Avdeitchikov [f], T.C. Awes [g], P.V.K.S. Baba [h], S.K. Badyal [h], A. Baldine [f], L. Barabach [f], C. Barlag [i], S. Bathe [i], B. Batiounia [f], T. Bernier [j], K.B. Bhalla [b], V.S. Bhatia [a], C. Blume [i], R. Bock [k], E.-M. Bohne [i], Z. Böröcz [i], D. Bucher [i], A. Buijs [l], H. Büsching [i], L. Carlen [m], V. Chalyshev [f], S. Chattopadhyay [c], R. Cherbatchev [e], T. Chujo [n], A. Claussen [i], A.C. Das [c], M.P. Decowski [r], H. Delagrange [j], V. Djordjadze [f], P. Donni [d], I. Doubovik [e], S. Dutt [h], M.R. Dutta Majumdar [c], K. El Chenawi [m], S. Eliseev [o], K. Enosawa [n], P. Foka [d], S. Fokin [e], V. Frolov [f], M.S. Ganti [c], S. Garpman [m], O. Gavrishchuk [f], F.J.M. Geurts [l], T.K. Ghosh [p], R. Glasow [i], S.K. Gupta [b], B. Guskov [f], H.Å. Gustafsson [m], H.H. Gutbrod [j], R. Higuchi [n], I. Hrivnacova [o], M. Ippolitov [e], H. Kalechofsky [d], R. Kamermans [l], K.-H. Kampert [i], K. Karadjev [e], K. Karpio [q], S. Kato [n], S. Kees [i], B.W. Kolb [k], I. Kosarev [f], I. Koutcheryaev [e], T. Krümpel [i], A. Kugler [o], P. Kulinich [r], M. Kurata [n], K. Kurita [n], N. Kuzmin [f], I. Langbein [k], A. Lebedev [e], Y.Y. Lee [k], H. Löhner [p], L. Luquin [j], D.P. Mahapatra [s], V. Manko [e], M. Martin [d], G. Martínez [j], A. Maximov [f], R. Mehdiyev [f], G. Mgebrichvili [e], Y. Miake [n], D. Mikhalev [f], Md.F. Mir [h], G.C. Mishra [s], Y. Miyamoto [n], D. Morrison [t], B. Mohanty [s], D.S. Mukhopadhyay [c], V. Myalkovski [f], H. Naef [d], B.K. Nandi [s], S.K. Nayak [j], T.K. Nayak [c], S. Neumaier [k], A. Nianine [e], V. Nikitine [f], S. Nikolaev [e], P. Nilsson [m], S. Nishimura [n], P. Nomokonov [f], J. Nystrand [m], F.E. Obenshain [t], A. Oskarsson [m], I. Otterlund [m], M. Pachr [o], A. Parfenov [f], S. Pavliouk [f], T. Peitzmann [i], V. Petracek [o], F. Plasil [g], W. Pinganaud [j], M.L. Purschke [k], B. Raeven [l], J. Rak [o], R. Raniwala [b], S. Raniwala [b], V.S. Ramamurthy [s], N.K. Rao [h], F. Retiere [j], K. Reygers [i], G. Roland [r], L. Rosselet [d], I. Roufanov [f], C. Roy [j], J.M. Rubio [d], H. Sako [n], S.S. Sambyal [h], R. Santo [i], S. Sato [n], H. Schlagheck [i], H.-R. Schmidt [k], Y. Schutz [j], G. Shabratova [f], T.H. Shah [h], I. Sibiriak [e], T. Siemiarczuk [q], D. Silvermyr [m],

0370-2693/99/$ - see front matter © 1999 Published by Elsevier Science B.V. All rights reserved.
PII: S0370-2693(99)01289-7

B.C. Sinha [c], N. Slavine [f], K. Söderström [m], N. Solomey [d], S.P. Sørensen [t], P. Stankus [g], G. Stefanek [q], P. Steinberg [r], E. Stenlund [m], D. Stüken [i], M. Sumbera [o], T. Svensson [m], M.D. Trivedi [c], A. Tsvetkov [e], L. Tykarski [q], J. Urbahn [k], E.C. v.d. Pijll [l], N. v. Eijndhoven [l], G.J. v. Nieuwenhuizen [r], A. Vinogradov [e], Y.P. Viyogi [c], A. Vodopianov [f], S. Vörös [d], B. Wysłouch [r], K. Yagi [n], Y. Yokota [n], G.R. Young [g]

[a] *University of Panjab, Chandigarh 160014, India*
[b] *University of Rajasthan, Jaipur 302004, Rajasthan, India*
[c] *Variable Energy Cyclotron Centre, Calcutta 700 064, India*
[d] *University of Geneva, CH-1211 Geneva 4, Switzerland*
[e] *RRC Kurchatov Institute, RU-123182 Moscow, Russia*
[f] *Joint Institute for Nuclear Research, RU-141980 Dubna, Russia*
[g] *Oak Ridge National Laboratory, Oak Ridge, TN 37831-6372, USA*
[h] *University of Jammu, Jammu 180001, India*
[i] *University of Münster, D-48149 Münster, Germany*
[j] *SUBATECH, Ecole des Mines, Nantes, France*
[k] *Gesellschaft für Schwerionenforschung (GSI), D-64220 Darmstadt, Germany*
[l] *Universiteit Utrecht / NIKHEF, NL-3508 TA Utrecht, The Netherlands*
[m] *Lund University, SE-221 00 Lund, Sweden*
[n] *University of Tsukuba, Ibaraki 305, Japan*
[o] *Nuclear Physics Institute, CZ-250 68 Rez, Czech Republic*
[p] *KVI, University of Groningen, NL-9747 AA Groningen, The Netherlands*
[q] *Institute for Nuclear Studies, 00-681 Warsaw, Poland*
[r] *MIT, Cambridge, MA 02139, USA*
[s] *Institute of Physics, 751-005 Bhubaneswar, India*
[t] *University of Tennessee, Knoxville, TN 37966, USA*

Received 21 September 1999; received in revised form 25 October 1999; accepted 29 October 1999
Editor: L. Montanet

Abstract

An event-by-event analysis of the azimuthal angular correlation with respect to the reaction plane has been carried out for K^+ and π^+ emission near mid-rapidity in 158 $A\cdot$GeV Pb + Pb collisions. In semi-central collisions, K^+ mesons are found to be preferentially emitted out of the reaction plane, while π^+ mesons are emitted in the reaction plane. The results suggest that the kaon emission is influenced by in-medium potential effects in addition to collective flow effects. © 1999 Published by Elsevier Science B.V. All rights reserved.

1. Introduction

Relativistic heavy ion collisions provide a unique tool for the study of nuclear properties at high temperature and density. The study of collective motion in the final state of the produced hadrons is expected to provide information on both the dynamics of heavy-ion collisions and the equation of state [1]. The observation of collective behavior in the system provides a validation of a hydrodynamical description of the dynamics. Once a hydrodynamical interpretation is established the collective motion will result from pressure gradients in the matter, which will reflect the compressibility of the underlying equation of state. In the case of a phase transition from ordinary matter to quark-gluon plasma, it is expected that the compressibility should exhibit a softening due to the increased number of degrees of freedom [2].

A standard way to search for collective motion in the final state is to analyze the azimuthal distribution of particle emission with respect to the reaction

plane in terms of a Fourier expansion. The first two coefficients in the Fourier decomposition are termed the directed and elliptic flow components. The importance of collective motion measurements has been emphasized by several authors [2–5] and measurements have been reported over a range of energies; directed and elliptic flow at $0.1 \sim 1$ $A \cdot$GeV [6–9], at 10 $A \cdot$GeV [10] and also at 158 $A \cdot$GeV [11,12]. One of the striking features of these results is the change of the elliptic flow direction from out-of-plane (squeeze-out) to in-plane in the region between 1 $A \cdot$GeV and 100 $A \cdot$GeV incident energy.

The azimuthal distribution of a particular particle species in the final state is also expected to be sensitive to the in-medium potential of the particle. Namely, it is interesting to study the distributions of K^+ and K^- mesons because the kaon-nucleon potential in nuclear matter is expected to be repulsive for K^+ but attractive for K^- mesons [13–15].

Recently, the elliptic emission of nucleons, pions, and K^+ mesons has been observed in the mid-rapidity region in $0.8 \sim 1$ $A \cdot$GeV ^{197}Au + ^{197}Au and ^{209}Bi + ^{209}Bi collisions [7–9]. The observed out-of-plane emission of K^+ mesons is claimed as a consequence of the repulsive K^+-nucleon potential. On the other hand, pions and nucleons also show out-of-plane emission at this energy, which is interpreted as dominantly due to the shadowing effect of the spectator nucleons [7,16,17].

At higher incident energies, particles produced near mid-rapidity are not expected to interact with the spectator matter due to the short crossing time of the collisions. Therefore, the in-medium potential effects might be more clearly visible at SPS energies [18]. In this letter we present the azimuthal distributions, relative to the reaction plane, of K^+ and π^+ mesons near mid-rapidity in 158 $A \cdot$GeV Pb + Pb collisions. This is the first observation of the elliptic emission of K^+ mesons at SPS energies.

2. Experimental setup

The data presented here were taken with a subset of the WA98 experiment detector system using the 158 $A \cdot$GeV ^{208}Pb beams of the CERN-SPS on a Pb target of 213 μm thickness. In the WA98 setup the incident Pb beam provides a trigger by a valid signal in a gas Cherenkov start counter with a timing resolution of 30 ps and no signal in a downstream veto counter with a 3 mm diameter hole. The minimum bias trigger and centrality of the collision is determined by the total transverse energy, E_T, measured with the mid-rapidity calorimeter (MIRAC) which covers the pseudo-rapidity range of $3.5 < \eta < 5.5$. The Plastic Ball detector has full azimuthal coverage in the pseudo-rapidity range of $-1.7 < \eta < 0.5$. It identifies pions, protons, deuterons, and tritons with kinetic energies of 50 to 250 MeV by simultaneous ΔE and E measurement using the mass and energy dependence of dE/dx [11]. The measurement of identified particles near mid-rapidity is performed using two tracking spectrometer arms with a large (1.6 m) aperture dipole magnet (GOLIATH) which provides 1.6 Tm bending power. The particle identification is based on a measurement of momentum and time-of-flight.

The present analysis has been performed on the full sample of WA98 positive charged particle tracking arm data. This data sample is limited due to the fact that the positive charged particle tracking arm was installed only for the final run period of WA98. The tracking arm has a momentum resolution of $\Delta p/p \simeq 0.97\% + 0.16\% p + 0.023\% p^2$ (p in GeV/c) and a time-of-flight resolution of < 90 ps. The rapidity and transverse momentum (y, p_T) coverages of the Plastic Ball and the tracking arm are shown in Fig. 1. The (y, p_T) coverages for the

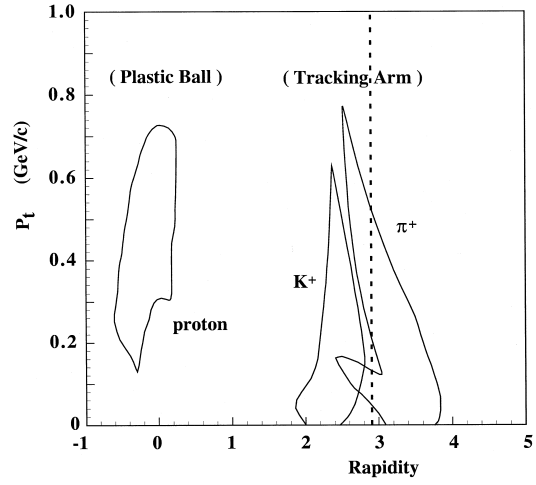

Fig. 1. The rapidity and transverse momentum (y, p_t) coverages of the Plastic Ball detector and the tracking arm. The midrapidity of the collisions is shown as dashed line.

Table 1
Results of the Fourier analysis of K^+ and π^+ mesons for semi-central 158 $A\cdot$GeV Pb + Pb collisions. The values are integrated over the indicated y and p_T ranges. Positive v_1 corresponds to an emission in the same direction as nucleons. Observed negative value of v_1 for π^+ indicates so-called anti-flow of pions. Positive and negative v_2 corresponds to an in-plane and out-of-plane elliptic emission, respectively. The values are obtained numerically by evaluating $\langle\cos(\phi-\Phi_0)\rangle$ and $\langle\cos(2(\phi-\Phi_0))\rangle$, with corrections of the reaction plane resolution at each E_T bin. The errors include the statistical errors and the errors of the experimental resolution of the reaction plane determination

Particle	y	p_T (GeV/c)	v_1	v_2
K^+	2.2–2.8	0.05–0.60	-0.004 ± 0.031	-0.24 ± 0.14
π^+	2.4–3.4	0.05–0.80	-0.010 ± 0.006	0.047 ± 0.024

present analysis are listed in Table 1. Detailed information about the positive tracking arm [20] and the experiment can be found elsewhere [11,19].

3. Experimental results

The reaction plane is determined from the azimuthal direction of the total transverse momentum vector of fragments (p, d, and t) observed by the Plastic Ball detector [11]. The azimuthal angle of the reaction plane, Φ_0 in the laboratory is determined as

$$\Phi_0 = \tan^{-1}\left(\frac{\sum_{i=1}^{N} p_{Ti}\sin(\phi_i)}{\sum_{i=1}^{N} p_{Ti}\cos(\phi_i)}\right), \qquad (1)$$

where the sum runs over all fragments. Here ϕ_i and p_{Ti} are the azimuthal angle in the laboratory and the transverse momentum of the i-th fragment, respectively. The multiplicity of protons in the Plastic Ball detector is around 8 in semi-central collisions and a minimum of three protons is required for this analysis. The Φ_0's accumulated for many events should be uniformly distributed if there is no detector bias. The observed Φ_0 distribution has a variation of less than 2% due to the detector biases such as dead channels and inefficiency. In the following analysis, we have corrected for this effect by weighting with the inverse of the yield although there is no significant difference in the results obtained with or without this correction.

The angular correlation between the azimuthal angle ϕ of K^+ and π^+ near mid-rapidity and the Φ_0 determined in the target rapidity region has been studied. Since the acceptance of π^+ crosses mid-rapidity, Φ_0 was rotated by 180° for particles in the region forward of mid-rapidity. Otherwise, the extracted value of the directed flow would be underestimated since it changes sign at mid-rapidity. Fig. 2 shows the azimuthal distributions of K^+ and π^+ mesons with respect to the reaction plane for semi-central ($50 < E_T < 250$ GeV in MIRAC) and central ($320 < E_T < 500$ GeV) Pb + Pb collisions. For π^+ mesons in semi-central collisions, the azimuthal distribution indicates weak maxima at $\phi-\Phi_0 = 0°$ and $\pm180°$, which indicates an enhanced emission in the reaction plane. On the other hand, the K^+ azimuthal distribution in semi-central collisions exhibits maxima at $\phi-\Phi_0 = \pm90°$ which demonstrates an enhanced emission out of the reaction plane. Although the statistics is limited, the results provide evidence that the K^+ emission axis is orthogonal to the in-plane emission axis of the π^+. In central collisions, as shown in Fig. 2, the azimuthal distributions for both particle types are nearly flat, as expected from the near azimuthal symmetry of the collision system at small impact parameter.

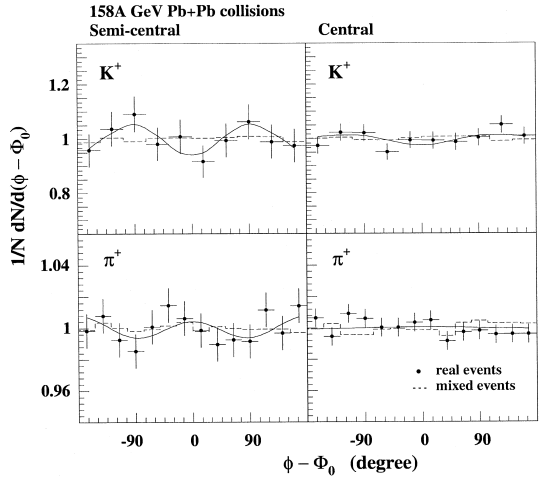

Fig. 2. The azimuthal distributions of K^+ and π^+ mesons with respect to the reaction plane for semi-central and central 158 $A\cdot$GeV Pb + Pb collisions. Solid circles with error bars show the real events and dashed histograms show the results of the mixed events. The solid curves show the fits using Eq. (2). The (y, p_T) coverages for this analysis are listed in Table 1.

To test for detector effects, such as geometrical acceptance and detector efficiency, fake events were created using a mixed-event method which were then analyzed in the same manner as the real events. The mixed-event results are shown as histograms in Fig. 2. The azimuthal distributions for the mixed-events are flat which indicates that the observed anisotropies are not due to detector effects.

The strength of the azimuthal anisotropy is evaluated by means of a Fourier expansion [21,22]. The Fourier coefficients $v_n(n=1,2)$ can be extracted from the azimuthal distribution of identified particles with respect to Φ_0;

$$\frac{1}{N}\frac{dN}{d(\phi-\Phi_0)} = 1 + 2v_1'\cos(\phi-\Phi_0) + 2v_2'\cos(2(\phi-\Phi_0)), \qquad (2)$$

where ϕ is the azimuthal angle of the particle in the laboratory frame. The Fourier coefficient v_1' quantifies the directed flow, whereas v_2' quantifies the elliptic flow. Positive v_1' corresponds to an emission in the same direction as nucleons. (Please note that this definition is opposite to our previous reports [11].) The coefficient v_2' is negative for an out-of-plane emission and positive for an in-plane emission.

The observed distributions are affected by the experimental resolution of the reaction plane determination. Since the measured Fourier coefficients are reduced by this effect, they should be corrected as [21–23]

$$v_n = \frac{v_n'}{\langle\cos(n\Delta\Phi)\rangle}, \quad (n=1,2), \qquad (3)$$

where $\Delta\Phi$ is the deviation from the true reaction plane and $\langle\ \rangle$ indicates the mean value summed over all events. The reaction plane resolution is determined by randomly subdividing the full event into two equal size subevents and extracting $\langle\cos(\Delta\Phi)\rangle \approx \sqrt{2}\cdot\sqrt{\langle\cos(\Phi_a-\Phi_b)\rangle}$, where Φ_a and Φ_b are the azimuthal angles of the reaction plane of two equal size subevents. Using the more accurate interpolation formula of Ref. [22] one obtains $\langle\cos(\Delta\Phi)\rangle = 0.360 \pm 0.018$, $\langle\cos(2\Delta\Phi)\rangle = 0.084 \pm 0.005$ for semi-central collisions.

The values of the Fourier coefficients $v_n(n=1,2)$ are obtained numerically by evaluating $\langle\cos(\phi-\Phi_0)\rangle$ and $\langle\cos(2(\phi-\Phi_0))\rangle$, respectively. The results for semi-central collisions are listed in Table 1 [1]. The values have been corrected for the reaction plane resolution according to Eq. (3) at each E_T bin. The value of v_1, indicating the strength of the directed flow, is negative for π^+, which corresponds to the direction opposite to the nucleons. This so called anti-flow of pions has been previously reported [11,12]. The value of v_1 for the K^+ meson is compatible with zero. The value of v_2 for the K^+ meson is negative with a 1.7σ separation from zero, while the value of v_2 for the π^+ mesons is positive with a 1.9σ separation from zero. Under the assumption of gaussian errors these results correspond to confidence levels of 95.7% and 97.5% for the assignment of the sign of v_2 for K^+ and π^+, respectively. Although the significance of the result is limited by statistics, one may conclude at the 93% confidence level that the elliptic emission planes for K^+ and π^+ are oriented orthogonally to one another. The systematic errors on the v_2 values due to the contamination from other particle species are estimated to be less than 8% for K^+ and 2% for π^+.

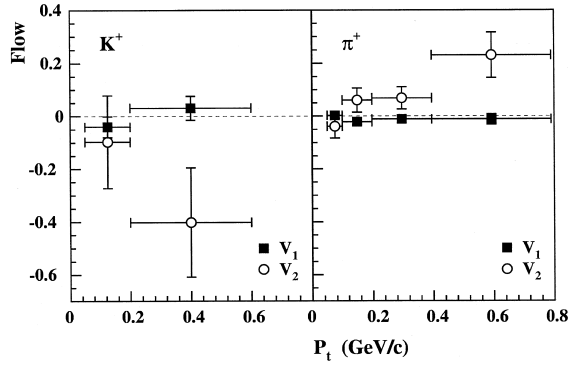

Fig. 3. The p_T dependence of the v_1 and v_2 values of K^+ and π^+ mesons for semi-central 158 $A\cdot$GeV Pb + Pb collisions. The rapidity coverages are listed in Table 1. The results are corrected for the experimental resolution of the reaction plane determination. Solid squares are used for v_1 and open circles for v_2.

Fig. 3 shows the v_1 and v_2 values as a function of the transverse momentum p_T for K^+ and π^+ mesons in semi-central collisions. For the K^+ data

[1] One can obtain the values of v_1 and v_2 from fitting the azimuthal distribution with Eq. (2). Within the errors, the fit values agree with those listed in Table 1.

only two bins are shown due to the limited statistics. The magnitude of v_2 for K^+ and π^+ mesons tends to increase with p_T, while the v_1 values remain close to zero for both particles.

4. Discussion

To compare the present results with other measurements the v_2 values for protons, pions, and kaons near mid-rapidity are plotted as a function of the beam energy in Fig. 4. For both protons and pions a transition from out-of-plane to in-plane emission occurs around 5-10 $A \cdot$GeV. At SPS energy, results from NA49 [12] have shown that protons and pions exhibit in-plane emission near mid-rapidity. Our π^+ data agree with the NA49 results within errors. Unlike the case for protons and pions, the present results indicates that K^+ mesons exhibit out-of-plane emission, which is similar to observations for 1 $A \cdot$GeV Au + Au collisions [8].

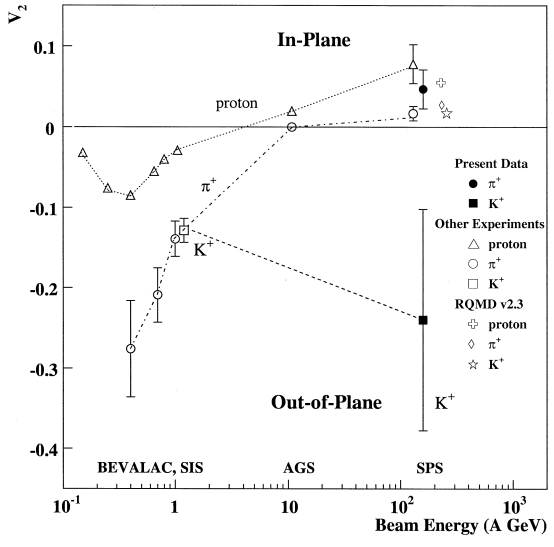

Fig. 4. Beam energy dependence of the v_2 value near mid-rapidity [6–8,10,12]. Solid symbols indicate the present data. Note that the region in (y, p_T) is different for each experiment. The RQMD (v2.3 cascade mode) calculations for proton, π^+ and K^+ in 158 $A \cdot$GeV Pb + Pb collisions are also shown for the impact parameter range $b =$ 6.5–12 fm with the filter of experimental acceptance. The data points are shifted horizontally where they overlap.

Results of RQMD model calculations (v2.3 cascade mode) [24] filtered with the experimental acceptance are also shown in Fig. 4. The RQMD results show in-plane emission for π^+, proton, and also for K^+. The RQMD calculation agrees with the measured results for π^+ and proton, but it fails to reproduce the out-of-plane elliptic emission of K^+. These results might suggest that a new ingredient to the calculation such as the in-medium potentials of the K^+ and K^- mesons is required [13–15]. A simple model calculation [25] in which K^+ mesons propagate through a static anisotropic distribution of nucleons with a repulsive K^+N potential demonstrates that a final out-of-plane elliptic emission pattern can emerge from an initially isotropic azimuthal distribution of K^+.

It is clear that if the azimuthal distribution of the pions reflects their preferential in-plane collective motion, then the out-of-plane K^+ azimuthal distribution would indicate that the kaons carry little direct information about the collective motion of the pion matter. The results therefore appear to question the assumption of a common collective flow velocity for pions and kaons.

5. Summary

In summary, we have measured the elliptic emission patterns of K^+ and π^+ mesons near mid-rapidity in 158 $A \cdot$GeV Pb + Pb collisions. In semi-central collisions, the K^+ mesons are found to be emitted preferentially perpendicular to the reaction plane, while π^+ mesons tend to be emitted in the reaction plane. The RQMD cascade calculation reproduces the v_2 values for π^+ and protons, but it fails to explain the out-of-plane emission of K^+ mesons. The results suggest that the kaon emission is influenced by in-medium potential effects in addition to collective flow effects.

Acknowledgements

We express our gratitude to the CERN accelerator division for the excellent performance of the SPS accelerator complex. We gratefully acknowledge the effort of all engineers, technicians, and support staff

who have made possible the construction and operation of this experiment. We thank Dr. T. Maruyama for useful discussions.

This work is supported by the German BMBF and DFG, the US DOE, the Swedish NFR and FRN, the Dutch Stichting FOM, the Department of Atomic Energy, the Department of Science and Technology, and the University Grants Commission of the Government of India, the Indo-FRG Exchange Programme, the Stiftung für Deutsch-Polnische Zusammenarbeit, the Grant Agency of the Czech Republic under contract No. 202/95/0217, the PPE division of CERN, the Swiss National Fund, the INTAS under contract INTAS-97-0158, the Polish KBN under contract 2P03B16815, the Ministry of Science and Technologies of the Russian Federation, the Grant-in-Aid for Scientific Research (Specially Promoted Research & International Scientific Research) of the Ministry of Education, Science, Sports and Culture, JSPS Research Fellowships for Young Scientists and also by the University of Tsukuba Special Research Projects, and ORISE. ORNL is managed by Lockheed Martin Energy Research Corporation under contract DE-AC05-96OR22462 with the US Department of Energy. MIT is supported by the US Department of Energy under the cooperative agreement DE-FC02-94ER40818.

References

[1] H. Stöcker, W. Greiner, Phys. Rep. 137 (1986) 277.
[2] D.H. Rischke, Nucl. Phys. A 610 (1996) 88c.
[3] J.-Y. Ollitrault, Phys. Rev. D 46 (1992) 229; D 48 (1993) 1132; Nucl. Phys. A 638 (1998) 195c.
[4] C.M. Hung, E.V. Shuryak, Phys. Rev. Lett. 75 (1995) 4003.
[5] H. Sorge, Phys. Rev. Lett. 78 (1997) 2309.
[6] Plastic Ball Collab., H.Å. Gustafsson et al., Phys. Rev. Lett. 52 (1984) 1590; H.H. Gutbrod et al., Phys. Lett. B 216 (1989) 267; Rep. Prog. Phys. 52 (1989) 1267; H.Å. Gustafsson et al., Phys. Rev. C 42 (1990) 640.
[7] KaoS Collab., D. Brill et al., Phys. Rev. Lett. 71 (1993) 336; Z. Phys. A 355 (1996) 61; A 357 (1996) 207.
[8] KaoS Collab., Y. Shin, Phys. Rev. Lett. 81 (1998) 1576.
[9] FOPI Collab., J.L. Ritman et al., Z. Phys. A 352 (1995) 355; N. Bastid et al., Nucl. Phys. A 622 (1997) 573.
[10] E877 Collab., J. Barrette et al., Phys. Rev. C 55 (1997) 1420; C 56 (1997) 3254; S.A. Voloshin et al., Nucl. Phys. A 638 (1998) 455c.
[11] WA98 Collab., S. Nishimura et al., in: Proc. Jaipur, ICPA-QGP, 1997; M. Kurata et al., in: Proc. Jaipur, ICPA-QGP, 1997; Prog. Theor. Phys. Suppl. 129 (1997) 179; B. Wyslouch et al., Nucl. Phys. A 638 (1998) 147c; S. Nishimura et al., Nucl. Phys. A 638 (1998) 459c; M.M. Aggarwal et al., Nucl-ex/9807004.
[12] NA49 Collab., T. Wienold et al., Nucl. Phys. A 610 (1996) 76c; H. Appelshäuser et al., Phys. Rev. Lett. 80 (1998) 4136; A.M. Poskanzer et al., Nucl. Phys. A 638 (1998) 463c.
[13] D.B. Kaplan, A.E. Nelson, Phys. Lett. B 175 (1986) 57; A.E. Nelson, D.B. Kaplan, Phys. Lett. B 192 (1987) 193.
[14] J. Schaffner, Phys. Lett. B 334 (1994) 268.
[15] G.Q. Li, C.M. Ko, Nucl. Phys. A 594 (1995) 460; G.Q. Li, C.M. Ko, B.A. Li, Phys. Rev. Lett. 74 (1995) 235.
[16] A. Jahns, Phys. Rev. Lett. 72 (1994) 3463.
[17] A. Kugler, Acta Phys. Pol. 25 (1994) 691.
[18] Z.S. Wang et al., nucl-th/9809043.
[19] WA98 Collab., Proposal for a large acceptance hadron and photon spectrometer, 1991, Preprint CERN/SPSLC 91-17, SPSLC/P260.
[20] L. Carlen, Nucl. Instrum. Methods A 431 (1999) 123.
[21] S.A. Voloshin, Y. Zhang, Z. Phys. C 70 (1996) 665.
[22] A.M. Poskanzer, S.A. Voloshin, Phys. Rev. C 58 (1998) 1671.
[23] P. Danielewicz, G. Odyniec, Phys. Lett. 157B (1985) 146.
[24] H. Sorge, Phys. Rev. C 52 (1995) 3291.
[25] K. Enosawa, T. Maruyama, private communication.

8 July 1999

PHYSICS LETTERS B

ELSEVIER

Physics Letters B 458 (1999) 422–430

Systematics of inclusive photon production in 158 · *A* GeV Pb induced reactions on Ni, Nb, and Pb targets

WA98 Collaboration

M.M. Aggarwal [a], A. Agnihotri [b], Z. Ahammed [c], A.L.S. Angelis [d], V. Antonenko [e], V. Arefiev [f], V. Astakhov [f], V. Avdeitchikov [f], T.C. Awes [g], P.V.K.S. Baba [h], S.K. Badyal [h], A. Baldine [f], L. Barabach [f], C. Barlag [i], S. Bathe [i], B. Batiounia [f], T. Bernier [j], K.B. Bhalla [b], V.S. Bhatia [a], C. Blume [i], R. Bock [k], E.-M. Bohne [i], Z. Böröcz [i], D. Bucher [i], A. Buijs [l], H. Büsching [i], L. Carlen [m], V. Chalyshev [f], S. Chattopadhyay [c], R. Cherbatchev [e], T. Chujo [n], A. Claussen [i], A.C. Das [c], M.P. Decowski [r], V. Djordjadze [f], P. Donni [d], I. Doubovik [e], S. Dutt [h], M.R. Dutta Majumdar [c], K. El Chenawi [m], S. Eliseev [o], K. Enosawa [n], P. Foka [d], S. Fokin [e], V. Frolov [f], M.S. Ganti [c], S. Garpman [m], O. Gavrishchuk [f], F.J.M. Geurts [l], T.K. Ghosh [p], R. Glasow [i], S.K. Gupta [b], B. Guskov [f], H.Å. Gustafsson [m], H.H. Gutbrod [j], R. Higuchi [n], I. Hrivnacova [o], M. Ippolitov [e], H. Kalechofsky [d], R. Kamermans [l], K.-H. Kampert [i], K. Karadjev [e], K. Karpio [q], S. Kato [n], S. Kees [i], H. Kim [g], B.W. Kolb [k], I. Kosarev [f], I. Koutcheryaev [e], T. Krümpel [i], A. Kugler [o], P. Kulinich [r], M. Kurata [n], K. Kurita [n], N. Kuzmin [f], I. Langbein [k], A. Lebedev [e], Y.Y. Lee [k], H. Löhner [p], L. Luquin [j], D.P. Mahapatra [s], V. Manko [e], M. Martin [d], A. Maximov [f], R. Mehdiyev [f], G. Mgebrichvili [e], Y. Miake [n], D. Mikhalev [f], Md.F. Mir [h], G.C. Mishra [s], Y. Miyamoto [n], D. Morrison [t], D.S. Mukhopadhyay [c], V. Myalkovski [f], H. Naef [d], B.K. Nandi [s], S.K. Nayak [j], T.K. Nayak [c], S. Neumaier [k], A. Nianine [e], V. Nikitine [f], S. Nikolaev [e], P. Nilsson [m], S. Nishimura [n], P. Nomokonov [f], J. Nystrand [m], F.E. Obenshain [t], A. Oskarsson [m], I. Otterlund [m], M. Pachr [o], A. Parfenov [f], S. Pavliouk [f], T. Peitzmann [i], V. Petracek [o], F. Plasil [g], W. Pinanaud [j], M.L. Purschke [k], B. Raeven [l], J. Rak [o], R. Raniwala [b], S. Raniwala [b], V.S. Ramamurthy [s], N.K. Rao [h], F. Retiere [j], K. Reygers [i], G. Roland [r], L. Rosselet [d], I. Roufanov [f], C. Roy [j], J.M. Rubio [d], H. Sako [n], S.S. Sambyal [h], R. Santo [i], S. Sato [n], H. Schlagheck [i], H.-R. Schmidt [k], G. Shabratova [f], T.H. Shah [h], I. Sibiriak [e], T. Siemiarczuk [q], D. Silvermyr [m], B.C. Sinha [c], N. Slavine [f],

0370-2693/99/$ - see front matter © 1999 Published by Elsevier Science B.V. All rights reserved.
PII: S0370-2693(99)00560-2

K. Söderström [m], N. Solomey [d], S.P. Sørensen [t], P. Stankus [g], G. Stefanek [q], P. Steinberg [r], E. Stenlund [m], D. Stüken [i], M. Sumbera [o], T. Svensson [m], M.D. Trivedi [c], A. Tsvetkov [e], C. Twenhöfel [l], L. Tykarski [q], J. Urbahn [k], N.v. Eijndhoven [l], G.J.v. Nieuwenhuizen [r], A. Vinogradov [e], Y.P. Viyogi [c], A. Vodopianov [f], S. Vörös [d], B. Wysłouch [r], K. Yagi [n], Y. Yokota [n], G.R. Young [g]

[a] *University of Panjab, Chandigarh 160014, India*
[b] *University of Rajasthan, Jaipur 302004, Rajasthan, India*
[c] *Variable Energy Cyclotron Centre, Calcutta 700064, India*
[d] *University of Geneva, CH-1211 Geneva 4, Switzerland*
[e] *RRC (Kurchatov Institute), RU-123182 Moscow, Russia*
[f] *Joint Institute for Nuclear Research, RU-141980 Dubna, Russia*
[g] *Oak Ridge National Laboratory, Oak Ridge, TN 37831-6372, USA*
[h] *University of Jammu, Jammu 180001, India*
[i] *University of Münster, D-48149 Münster, Germany*
[j] *SUBATECH, Ecole des Mines, Nantes, France*
[k] *Gesellschaft für Schwerionenforschung (GSI), D-64220 Darmstadt, Germany*
[l] *Universiteit Utrecht / NIKHEF, NL-3508 TA Utrecht, The Netherlands*
[m] *Lund University, SE-221 00 Lund, Sweden*
[n] *University of Tsukuba, Ibaraki 305, Japan*
[o] *Nuclear Physics Institute, CZ-250 68 Rez, Czech Republic*
[p] *KVI, University of Groningen, NL-9747 AA Groningen, The Netherlands*
[q] *Institute for Nuclear Studies, 00-681 Warsaw, Poland*
[r] *MIT Cambridge, MA 02139, USA*
[s] *Institute of Physics, 751-005 Bhubaneswar, India*
[t] *University of Tennessee, Knoxville, TN 37966, USA*

Received 9 March 1999; received in revised form 22 April 1999
Editor: L. Montanet

Abstract

The multiplicity of inclusive photons has been measured on an event-by-event basis for $158 \cdot A$ GeV Pb induced reactions on Ni, Nb, and Pb targets. The systematics of the pseudorapidity densities at midrapidity ($\rho_{\max}$) and the width of the pseudorapidity distributions have been studied for varying centralities for these collisions. A power law fit to the photon yield as a function of the number of participating nucleons gives a value of 1.12 ± 0.03 for the exponent. The mean transverse momentum, $\langle p_T \rangle$, of photons determined from the ratio of the measured electromagnetic transverse energy and photon multiplicity, remains almost constant with increasing $\rho_{\max}$. Results are compared with model predictions. © 1999 Published by Elsevier Science B.V. All rights reserved.

1. Introduction

The primary goal of ultra-relativistic heavy ion experiments is to study nuclear matter under extreme conditions, in which hadronic matter is expected to undergo a phase transition to a new state of matter, the Quark-Gluon-Plasma (QGP). For a thermalized system undergoing a phase transition, the variation of the temperature with entropy density is interesting as the temperature is expected to increase while below the transition, remain constant during the transition, and then increase again [1,2]. Temperature

fluctuations have also been proposed as a signature of the existence of a tricritical point in QCD [3]. These behaviours can be studied by two experimentally measured quantities, viz., the mean transverse momentum, $\langle p_T \rangle$, and the pseudorapidity density at midrapidity, $\rho_{\max}$, for varying impact parameter, or centrality, for a number of colliding systems. These variables also provide additional information to characterize the evolving system. $\rho_{\max}$ provides a measure of the energy density which is important to understand the reaction dynamics [4,5]. In addition, the change in shape of the pseudorapidity distribution should be investigated in detail because it may provide a clue to the formation of the QGP phase [6,7].

Except for a few measurements of photon [8–11] and neutral meson [12–15] distributions reported earlier, most studies have been restricted to charged particle measurements (a review of charged particle measurements can be found in Ref. [16,17]), due to the difficulty of precise measurements of photon distributions. The inclusive photons provide a picture of the system at freezeout since the majority of the photons emitted from the reaction are decay products of produced particles, *viz.*, π_0 and η_0, (only a small fraction is emitted directly during the initial stage of the collision [18]). The shape and width of the pseudorapidity distributions of photons may be different compared to those of the charged particles. Photon multiplicity measurements have also become increasingly important because of the recent interest in simultaneous measurements of the multiplicity of photons and charged particles in the search for Disoriented Chiral Condensates (DCC) [19,20]. The formation of a DCC is expected to give rise to large fluctuations in the relative number of emitted charged particles and photons, analogous to the Centauro and the anti-Centauro types of events observed in cosmic ray experiments [21]. Photon measurements can also be used to study flow [22] and intermittency behavior of events accompanying a possible phase transition.

In this letter, we present the first measurement of the photon multiplicity and pseudorapidity distributions, together with the $\langle p_T \rangle$ of photons produced in collisions of $158 \cdot A$ GeV Pb with Ni, Nb, and Pb targets, carried out in the WA98 experiment [23] at the CERN-SPS.

2. Experimental setup

In the WA98 experiment, the main emphasis has been on high precision, simultaneous detection of both hadrons and photons. The experimental setup consists of large acceptance hadron and photon spectrometers, detectors for charged particle and photon multiplicity measurements, and calorimeters for transverse and forward energy measurements. The present analysis makes use of the photon multiplicity detector (PMD), the midrapidity calorimeter (MIRAC) and the zero degree calorimeter (ZDC).

The PMD was placed at a distance of 21.5 meters from the target. It was a preshower detector consisting of 3 radiation length (X_0) thick lead converter plates in front of an array of square scintillator pads of four sizes, varying from 15×15 mm^2 to 25×25 mm^2, placed in 28 box modules. Each box module consisted of a matrix of 38×50 pads and was read out using one image intensifier + CCD camera system. The scintillation light was transmitted to the readout device by using a short wavelength shifting fiber spliced with a long EMA (extra-mural absorber) coated clear fiber. The total light amplification of the readout system was $\sim 40\,000$. Digitization of the CCD pixel charge was done by a set of custom built fastbus modules employing an 8 bit 20 MHz Flash ADC system. Details of the design and characteristics of the PMD may be found in Ref. [24]. The results presented here make use of the data from the central 22 box modules covering the pseudorapidity range of $2.9 \leq \eta \leq 4.2$.

The MIRAC [25] was placed behind the PMD at 24.7 meters from the target. It consisted of 30 stacks, each divided vertically into 6 towers, each of size 20×20 cm^2, and segmented longitudinally into electromagnetic (EM) and hadronic sections. The depth of an EM section is $15.6\,X_0$ (equivalent to 51% of an interaction length) which ensures essentially complete containment of the electromagnetic energy, with 97.4% and 91.0% containment calculated for 1 GeV and 30 GeV photons, respectively. Hadrons also deposit a sizable fraction of their energy in the EM section. The MIRAC measures both the transverse electromagnetic ($E_T^{\rm em}$) and hadronic ($E_T^{\rm had}$) energies in the interval $3.5 \leq \eta \leq 5.5$ with a resolution of $17.9\%/\sqrt{E}$ and $46.1\%/\sqrt{E}$, respectively, where E is expressed in GeV. The ZDC measures the total

forward energy, E_F, with a resolution of $80\%/\sqrt{E} + 1.5\%$, where E is expressed in GeV.

3. Data analysis

3.1. Event selection

The data were taken during the December 1996 Pb beam period at the CERN SPS. The thicknesses of the three targets were 250 μm, 254 μm, and 213 μm for Ni, Nb, and Pb, respectively. The fundamental ''beam'' trigger condition consisted of a signal in a gas Čerenkov start counter located 3.5 meters upstream of the target and no coincident signal in a veto counter with a 3 mm diameter circular hole located 2.7 meters upstream of the target. A beam trigger was considered to be a minimum-bias interaction if the transverse energy sum in the full MIRAC acceptance exceeded a low threshold. The data were taken using an average beam intensity of 200–300 kHz during a 3.5s spill, the number of events recorded per spill being 150–200.

Beam pile up, where a second beam trigger occurs at a time when the detectors are integrating their signals from the triggered event, was rejected by (a) using the timing information from the trigger detectors, and (b) requiring that the sum of energies in the ZDC and the MIRAC were within 3σ from the mean of the distribution. Downstream interactions were also rejected by requiring a coincident signal from the forward hemisphere of the Plastic Ball detector which surrounded the target. To correct for other sources of background, data were also taken with no target in place.

The CCD readout of the PMD was cleared every 10 μs using a clear pulse of 1 μs width generated every 10 μs. This ensured that there was no substantial noise buildup on the CCD pixels between successive event triggers. A gate of 2 μs around the clear pulse was used to veto partially or fully cleared events. The clear clock operated asynchronously and was vetoed with a 5.6 ms wide pulse when a valid trigger occurred to allow complete readout of all pixels. A further check on possible pileup in the CCD cameras was made by using a 10 μs range TDC to measure the time difference between the arrival of the last clear clock and any valid event trigger. Events with multiple interactions within the 10 μs between clear pulses were rejected in the offline analysis.

The centrality of the interaction is determined by the total transverse energy measured in the MIRAC. For the $\langle p_T \rangle$ analysis, which used the MIRAC data directly, the centrality was determined instead by the forward energy, E_F, measured in the ZDC. The centralities are expressed as fractions of the minimum bias cross section as a function of the measured total transverse energy or measured E_F. The most central selection corresponds to the top 5% of the minimum bias cross section and the peripheral selection corresponds to the lower 50–80% range. Extreme peripheral events in the 80–100% range were not analyzed.

3.2. Data reduction in the PMD

The digitized pixel charges are processed by using a pixel-to-fiber map to form fiber signals corresponding to each scintillator pad. The signals from several neighbouring scintillator pads are combined to form clusters, characterized by the total ADC content and the hit positions. On average, there is a 92% probability for photons to shower in the lead converter and produce large signals. Compared to this, hadrons give a signal mostly corresponding to minimum ionizing particles (MIP). The majority of the hadrons are rejected by applying a suitable threshold on the cluster signal. A fraction of hadrons undergoing interaction in the lead converter produce signals larger than the threshold and appear as contaminants in the photon sample. The number of clusters remaining above the hadron rejection threshold is termed as *γ-like*. The characteristics of the preshower PMD are described by the following two quantities [24]:

$$\epsilon_\gamma = N_{\rm cls}^{\gamma,{\rm th}}/N_\gamma^{\rm inc} \quad (1)$$

$$f_p = N_{\rm cls}^{\gamma,{\rm th}}/N_{\gamma\text{-like}} \quad (2)$$

where ϵ_γ is the photon counting efficiency and f_p is the fractional purity of the photon sample. $N_\gamma^{\rm inc}$ is the number of incident photons on the PMD and $N_{\rm cls}^{\gamma,{\rm th}}$ is the number of photon clusters above the threshold. Both ϵ_γ and f_p are determined by a

detailed Monte Carlo simulation using the VENUS 4.12 [27] event generator with default parameter settings and the detector simulation package, GEANT 3.21 [28]. The details of the simulation can be found in Ref. [24]. No lower threshold on the energy spectrum of photons is applied in the simulation. The photon counting efficiency decreases with increasing hadron rejection threshold. The purity improves significantly with increasing threshold only up to ~ 3 MIPs and then rather slowly at higher thresholds. For practical purposes a 3 MIP threshold appears as an optimum choice for hadron rejection. With this value the photon counting efficiencies for the central and peripheral cases are 68% and 73%, respectively. The purity of the photon sample in the two cases are 65% and 54%, respectively.

From the experimental data one determines $N_{\gamma\text{-like}}$, the number of clusters above the hadron rejection threshold. Using the estimated values of ϵ_γ and f_p, one obtains the number of photons incident on the detector in the event from the relation:

$$N_\gamma = N_{\gamma\text{-like}} \cdot f_p / \epsilon_\gamma \tag{3}$$

3.3. Extraction of $\langle p_T \rangle$ of photons

In a given event, the average transverse momentum of the produced photons may be expressed as

$$\langle p_T \rangle = \frac{E_T^{\mathrm{em}}}{N_\gamma} \tag{4}$$

where E_T^{em} is the transverse component of the electromagnetic energy, and N_γ is the number of photons in a given η-region. In the WA98 experiment, E_T^{em} and N_γ are measured with the MIRAC and the PMD, respectively, on an event-by-event basis. These detectors have complete overlap in azimuth in the pseudorapidity region $3.5 \leq \eta \leq 4.0$. Hence the data in this region are used for computing the $\langle p_T \rangle$ using the above equation.

In order to obtain the final E_T^{em} for Eq. (4), the measured electromagnetic energy in the MIRAC towers must be corrected for (1) the hadronic contribution to the EM section of the MIRAC, and (2) the energy deposited in the lead converter of the PMD because of its position in front of the MIRAC. The final expression may be written as:

$$E_T^{\mathrm{em}} = \frac{\sum_{i=1}^{N} \left[E_i^{\mathrm{em}} - f_h \cdot f_{\mathrm{bal}} \cdot \left\{ E_i^{\mathrm{had}} / (1 - f_h) \right\} \right] \sin\theta_i}{1 - f_{\mathrm{PMD}}} \tag{5}$$

where E_i^{em} and E_i^{had} are the energies measured in the electromagnetic and hadronic sections of the MIRAC towers, f_h is the fraction of the hadronic energy deposited in the EM section, f_{bal} is the balance factor taking into account the different responses for electromagnetic and hadronic particles in the EM section [25], N is the number of towers in the MIRAC within the given η range, θ_i is the polar angle of the i^{th} tower, and f_{PMD} is the fraction of the electromagnetic energy deposited in the lead converter of the PMD. By combining results from the test beam data and simulation, the value of f_{PMD} has been found to be 15%. Details of the determination of f_{PMD} and other corrections are similar to those of Ref. [9].

3.4. Systematic errors

Several different sources contribute to the final systematic error in the determination of the number of photons, N_γ. The error due to the effect of clustering of the pad signals is the dominant one. This error is determined from the simulation by comparing the number of known tracks on the PMD with the total number of clusters obtained after clustering. Apart from the effect of multiplicity as discussed in Ref. [10], the arrangement of box modules in the present setup leads to splitting of clusters at the box boundaries. The net result is that the number of clusters exceeds the number of tracks with a deviation of 3% in the case of peripheral events and 7% for high multiplicity central events.

The number of γ-like clusters depends on the ADC value of the MIP peak as determined from Pb + Pb data. It has been estimated [24] that because of an admixture of $\sim 20\%$ photons in the MIP data sample, the extracted MIP ADC value is higher by 2 ADC channels. This causes the extracted photon multiplicity to be lower by 2.5%. We have included

this as a source of systematic error. The error on ϵ_γ because of the variation in pad-to-pad gains is found to be less than 1%.

The purity factor, f_p, depends on the ratio between the number of photons and charged particles within the PMD coverage. The systematic error associated with this ratio has been studied by using the FRITIOF [29] event generator in addition to VENUS. The average photon multiplicity estimated using FRITIOF is found to be higher by about 4% in peripheral and by 1% in central collisions, relative to the values obtained with VENUS.

The combined systematic error on the final photon multiplicity is asymmetric and varies with the centrality of the reaction. The total systematic errors are -3.4% and $+7.5\%$ for peripheral collisions and -7.1% and $+3.4\%$ for central collisions, varying little throughout the PMD acceptance. The negative error implies overestimation of the number of photons.

The photon counting efficiency determined in the present case relies on the energy spectra of photons as given by the VENUS event generator. As the conversion probability for low energy photons falls sharply [26] with decreasing energy below 500 MeV, the estimate of ϵ_γ may be affected if the energy spectra in the actual case is different. Preliminary measurements of the photon energy spectra with the WA98 lead glass spectrometer indicate that there is an enhancement of photons below $p_T = 250$ MeV/c over that given by VENUS. Taking into account this excess of low energy photons in the PMD acceptance, the photon counting efficiency would be overestimated by 2–9% for central events and 3–13% for peripheral events, the smaller value being for large pseudorapidity and the larger value being for the smaller pseudorapidity region of the PMD acceptance. This effect would increase the quoted PMD photon multiplicities. However, this uncertainty in the photon counting efficiency due to the uncertainty in the photon spectrum has not been included in the final errors presented in this letter. The WA98 low energy photon measurements will be described in a separate publication.

The systematic error on the determination of $\langle p_T \rangle$ depends on the error in both $E_T^{\rm em}$ and N_γ. The major source of errors in $E_T^{\rm em}$ are the contributions of hadronic energy deposited in the electromagnetic section of the MIRAC and the fraction of the electromagnetic energy deposited in the lead converter of the PMD. This is estimated to vary from 8.8% to 10.5% from peripheral to central events. Thus the combined systematic error on $\langle p_T \rangle$ has been estimated to vary from 11.5% to 12.7%.

4. Results and discussions

The photon multiplicity is determined using Eq. (3) on an event-by-event basis from the total number of γ-like clusters within the PMD coverage. The target out contribution to N_γ is almost absent because of the 3 MIP threshold for hadron rejection. The resulting minimum bias distributions of N_γ are shown in Fig. 1 for Pb + Ni, Pb + Nb, and Pb + Pb reactions at $158 \cdot A$ GeV. For comparison, the corresponding photon multiplicity distributions from the VENUS 4.12 event generator with default parameter settings, are superimposed in the same figure. The shape of these three distributions is governed by the collision geometry. For asymmetric collisions of Nb and Ni targets, small shoulders are present around N_γ of 300 and 200, respectively. This shoulder is produced when a decrease in the impact parameter leads to little increase in particle production and the cross sections for these small impact parameters pile up at

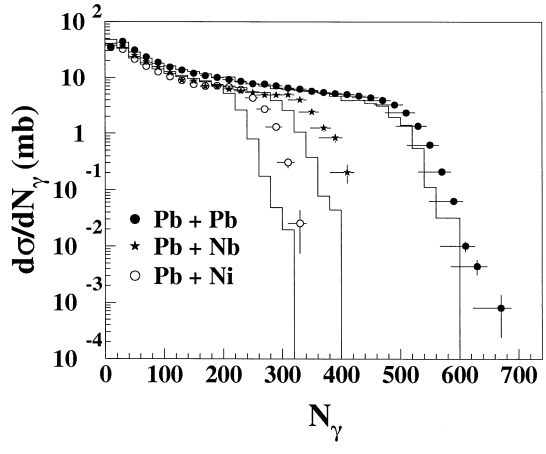

Fig. 1. Minimum bias inclusive photon cross sections for Pb + Ni, Pb + Nb, and Pb + Pb reactions at $158 \cdot A$ GeV. Solid histograms are the corresponding distributions obtained from the VENUS event generator.

a fixed N_γ. The VENUS event generator does not reproduce this shoulder well. The N_γ values are higher for the data compared to those of VENUS.

The pseudorapidity distribution of photons at different centralities are shown in Fig. 2 (a) for Pb + Pb collisions. The data have been corrected for geometry, efficiency, and purity factors. The filled symbols represent the measured data, and the open symbols are reflections of the filled symbols at $\eta_{\rm c.m.}(=2.92)$. The histograms show the corresponding distributions obtained from the VENUS event generator. The discrepancy between the VENUS results and the data is about 10% for central collisions at midrapidity. The pseudorapidity distribution of photons at different centralities for Pb + Nb and Pb + Ni are shown in Fig. 2 (b) and (c), respectively. The discrepancies between the data and VENUS are larger for these reactions compared to that of Pb + Pb.

The pseudorapidity distributions have been fitted with Gaussian functions to extract the peak position of the distribution ($\eta_{\rm peak}$), the pseudorapidity density ($\rho_{\rm max}$), and the width (σ). The fits are good in all cases, χ^2 per degree of freedom being in the range of 2–4. Typical fits for the top centrality class for all the three targets are shown in Fig. 2. The $\eta_{\rm peak}$ values for Pb + Pb distributions remain constant at 2.92 for all centralities. For Pb + Nb, $\eta_{\rm peak}$ decreases from 3.03 ± 0.15 for central collisions to 2.95 ± 0.32 in the case of peripheral collisions. The corresponding values for the Pb + Ni reaction are 3.10 ± 0.16 and 2.99 ± 0.31. Fig. 3(a) and (b) show $\rho_{\rm max}$ and σ for the three reactions as functions of the number of participant nucleons, $N_{\rm part}$, at different centralities. The $N_{\rm part}$ values are determined from the VENUS event generator. $\rho_{\rm max}$ increases with $N_{\rm part}$ while σ doesn't change with increase of $N_{\rm part}$.

More insight into the systematics of the particle production can be obtained by computing the integrated number of photons ($N_\gamma^{\rm tot}$) over the full phase space. This has been obtained from the Gaussian fit parameters to the pseudorapidity distributions.

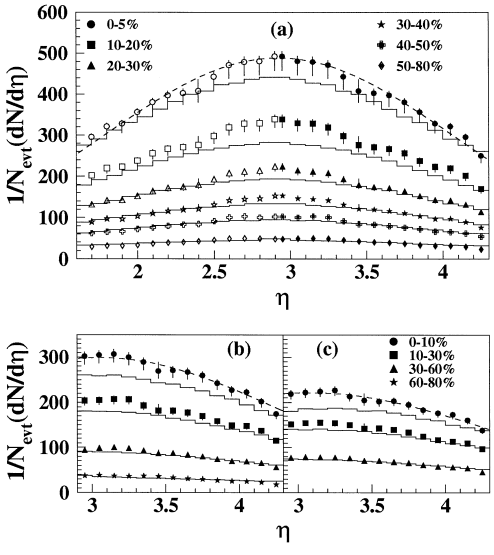

Fig. 2. Pseudorapidity distributions of photons in Pb induced reactions at $158 \cdot A$ GeV on (a) Pb, (b) Nb, and (c) Ni targets. The solid histograms are the corresponding distributions obtained from the VENUS event generator. In the Pb + Pb system, open symbols are the reflections of the measured data points around $\eta = 2.92$. The dashed curves represent gaussian fits to the data points corresponding to the case of 0–5% centrality for Pb + Pb and 0–10% centrality for Pb + Nb and Pb + Ni.

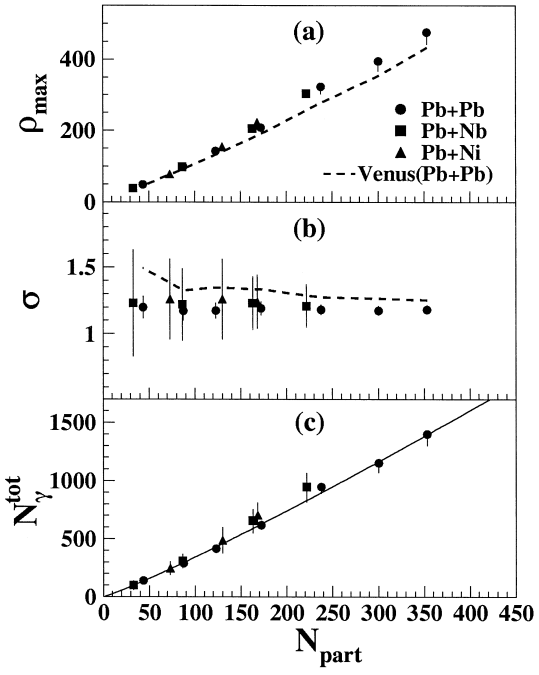

Fig. 3. (a) Pseudorapidity density ($\rho_{\rm max}$), (b) width of the pseudorapidity distributions (σ), and (c) integrated values of number of photons ($N_\gamma^{\rm tot}$), as functions of the number of participant nucleons at different centrality bins for Pb induced reactions on Ni, Nb, and Pb targets at $158 \cdot A$ GeV. The solid line in (c) is a power-law fit to the data, which yields the value of the exponent, $\alpha = 1.12 \pm 0.03$.

Fig. 3(c) shows the extracted values of $N_\gamma^{\rm tot}$ for Pb + Pb as a function of $N_{\rm part}$. The solid line shows a fit to the data using the function:

$$N_\gamma^{\rm tot} = C \cdot \left(N_{\rm part}\right)^{\alpha} \quad (6)$$

where C is a proportionality constant. The value of the exponent, α, is extracted to be 1.12 ± 0.03. To further explore the systematics, we have divided the full η region (0–6) into two parts, one corresponding to the central rapidity region, $2.4 \le \eta \le 3.4$, and the other beyond this. For both of these cases, the Pb + Pb data yields a value of $\alpha = 1.12$. In comparison, fitting the photon distribution from the VENUS event generator in the same two regions yield different exponents, with 1.10 ± 0.07 at mid-rapidity and only 1.0 ± 0.05 for the outer region.

The mean transverse momentum, $\langle p_T \rangle$, as a function of $\rho_{\rm max}$, the pseudorapidity density of photons at midrapidity, is shown in Fig. 4 for Pb + Pb collisions. For the data set considered, the target-out contributions were less than 1% for peripheral collisions and there was no effect for other centralities. The point at $\rho_{\rm max} \simeq 525$ corresponds to the highest centrality bin, 0–1% of the minimum bias cross section for Pb + Pb. The systematic errors on the absolute values are indicated by the upper and lower brackets on the figure. The $\langle p_T \rangle$ values are constant within the quoted error. For comparison, the results obtained from the VENUS event generator are superimposed in the figure. The $\langle p_T \rangle$ values obtained from VENUS are systematically higher compared to data, and show very little change with centrality. The indication of a small rise and saturation of $\langle p_T \rangle$ seen in the data is similar to what has been reported for neutral pions [15].

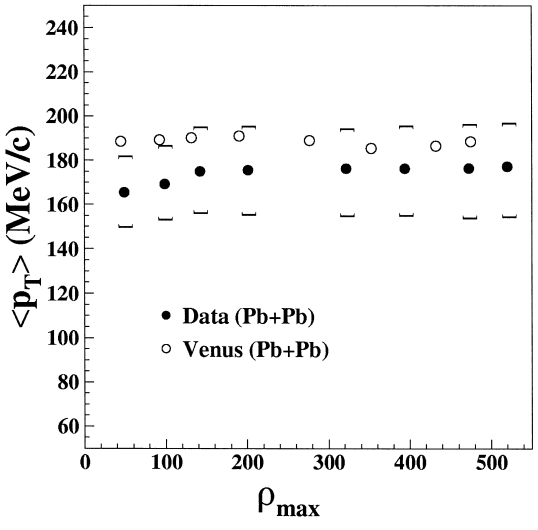

Fig. 4. The mean transverse momentum, $\langle p_T \rangle$, of photons as a function of the pseudorapidity density of photons at midrapidity, $\rho_{\rm max}$, corresponding to different centralities. The $\langle p_T \rangle$ values obtained from the VENUS event generator for Pb + Pb are superimposed for comparison. Statistical errors on the data are within the size of the symbols and systematic errors are shown by the brackets.

5. Summary

Photon multiplicities have been measured, on an event-by-event basis, in the forward region for $158 \cdot A$ GeV Pb induced reactions on Ni, Nb, and Pb targets. The peak positions of the photon pseudorapidity distributions are found to shift forward in going from the Pb target to Nb and Ni, as expected. The photon pseudorapidity densities increase with the number of participant nucleons, while the widths of the pseudorapidity distributions remain constant with centrality. The integrated number of photons scales like $N_{\rm part}^{1.12}$, almost independent of the rapidity range over which the integration is performed. This is similar to the predictions of the VENUS event generator, except that VENUS shows a smaller power for forward rapidities. The photon mean transverse momentum has been determined from the event-by-event ratio of the electromagnetic transverse energy to the number of photons. After an initial rise with increasing $\rho_{\rm max}$, the value of $\langle p_T \rangle$ is observed to remain constant.

Acknowledgements

We wish to express our gratitude to the CERN accelerator division for the excellent performance of the SPS accelerator complex. We acknowledge with appreciation the effort of all engineers, technicians, and support staff who have participated in the construction of this experiment.

This work was supported jointly by the German BMBF and DFG, the US DOE, the Swedish NFR,

the Dutch Stichting FOM, the Stiftung fuer Deutsch-Polnische Zusammenarbeit, the Grant Agency of the Czech Republic under contract No. 202/95/0217, the Department of Atomic Energy, the Department of Science and Technology, the Council of Scientific and Industrial Research and the University Grants Commission of the Government of India, the Indo-FRG Exchange Programme, the PPE division of CERN, the Swiss National Fund, the INTAS under Contract INTAS-97-0158, ORISE, Research-in-Aid for Scientific Research (Specially Promoted Research & International Scientific Research) of the Ministry of Education, Science and Culture, the University of Tsukuba Special Research Projects, and the JSPS Research Fellowships for Young Scientists. ORNL is managed by Lockheed Martin Energy Research Corporation under contract DE-AC05-96OR22464 with the US Department of Energy. The MIT group has been supported by the US Dept. of Energy under the cooperative agreement DE-FC02-94ER40818.

References

[1] E.V. Shuryak, O. Zhirov, Phys. Lett. B 89 (1980) 253.
[2] L. van Hove, Phys. Lett. B 118 (1982) 138.
[3] M. Stephanov, K. Rajagopal, E. Shuryak, Phys. Rev. Lett. 81 (1998) 4816.
[4] J.D. Bjorken, Phys. Rev. D 27 (1983) 140.
[5] M. Kataja, P.V. Ruuskanen, L. McLerran, H. von Gersdorff, Phys. Rev. D 34 (1986) 2755.
[6] S. Sarkar, D.K. Srivastava, B. Sinha, Phys. Rev. C 51 (1995) 318; C 51 (1995) 2845 (E).
[7] A. Dumitru, U. Katscher, J.A. Maruhn, H. Stocker, W. Greiner, D.H. Rischke, Z. Phys. A 353 (1995) 187.
[8] WA93 Collaboration, M.M. Aggarwal, Phys. Rev. C 56 (1997) 1160.
[9] WA93 Collaboration, M.M. Aggarwal, Phys. Lett. B 404 (1997) 207.
[10] WA93 Collaboration, M.M. Aggarwal, Phys. Rev. C 58 (1998) 1146.
[11] WA80 Collaboration, R. Albrecht, Phys. Lett. B 201 (1987) 390.
[12] WA80 Collaboration, R. Albrecht, Nucl. Phys. A 488 (1988) 651.
[13] WA80 Collaboration, R. Albrecht, Phys. Lett. B 361 (1995) 14.
[14] WA80 Collaboration, R. Albrecht, Eur. Phys. J. C 5 (1998) 255.
[15] WA98 Collaboration, M.M. Aggarwal, Phys. Rev. Lett. 81 (1998) 4087.
[16] J. Stachel, G.R. Young, Ann. Rev. Nucl. Part. Sc. 44 (1994) 537.
[17] M.M. Aggarwal, S.I.A. Garpman, Int. J. Mod. Phys. E 4 (1995) 477.
[18] E.L. Feinberg, Nuovo Cimento A 34 (1976) 391; E.V. Shuryak, Phys. Lett. B 79 (1978) 135; B. Sinha, Phys. Lett. B 197 (1987) 263; D.K. Srivastava, B. Sinha, Phys. Rev. Lett. 73 (1994) 2421.
[19] J.D. Bjorken, K.L. Kowalski, C.C. Taylor, Baked Alaska, SLAC-PUB-6109, 1993 and hep-ph/9309235; K. Rajagopal, F. Wilczek, Nucl. Phys. B 399 (1993) 395.
[20] M.M. Aggarwal et al., WA98 Collaboration, Phys. Lett. B 420 (1998) 169; T.K. Nayak et al., WA98 Collaboration, Nucl. Phys. A 638 (1998) 249c.
[21] C.M.G. Lattes, Y. Fujimoto, S. Hasegawa, Phys. Rep. 65 (1980) 151; Y. Takahasi et al., JACEE Collaboration, in: L. Jones (Ed.), Proc. 7th Int'l. Symp. on Very High Energy Cosmic Ray Interactions, 1992, Ann Arbor, Michigan.
[22] WA93 Collaboration, M.M. Aggarwal, Phys. Lett. B 403 (1997) 390.
[23] Proposal for a Large Acceptance Hadron and Photon Spectrometer, CERN/SPSLC 91-17, SPSLC/P260.
[24] M.M. Aggarwal, Nucl. Instr. and Meth. A 424 (1999) 395.
[25] T.C. Awes, Nucl. Instr. and Meth. A 279 (1989) 479.
[26] M.M. Aggarwal, Nucl. Instr. and Meth. A 372 (1996) 143.
[27] K. Werner, Phys. Rep. C 232 (1993) 87.
[28] R. Brun et al., GEANT3 user's guide, CERN/DD/EE/84-1, 1984.
[29] B. Nilsson-Almqvist, E. Stenlund, Comp. Phys. Comm. 43 (1987) 387.

Freeze-Out Parameters in Central 158*A* GeV ^{208}Pb + Pb Collisions

M. M. Aggarwal,[1] A. Agnihotri,[2] Z. Ahammed,[3] A. L. S. Angelis,[4] V. Antonenko,[5] V. Arefiev,[6] V. Astakhov,[6] V. Avdeitchikov,[6] T. C. Awes,[7] P. V. K. S. Baba,[8] S. K. Badyal,[8] A. Baldine,[6] L. Barabach,[6] C. Barlag,[9] S. Bathe,[9] B. Batiounia,[6] T. Bernier,[10] K. B. Bhalla,[2] V. S. Bhatia,[1] C. Blume,[9] R. Bock,[11] E.-M. Bohne,[9] Z. K. Böröcz,[9] D. Bucher,[9] A. Buijs,[12] H. Büsching,[9] L. Carlen,[13] V. Chalyshev,[6] S. Chattopadhyay,[3] R. Cherbatchev,[5] T. Chujo,[14] A. Claussen,[9] A. C. Das,[3] M. P. Decowski,[18] H. Delagrange,[10] V. Djordjadze,[6] P. Donni,[4] I. Doubovik,[5] S. Dutt,[8] M. R. Dutta Majumdar,[3] K. El Chenawi,[13] S. Eliseev,[15] K. Enosawa,[14] P. Foka,[4] S. Fokin,[5] V. Frolov,[6] M. S. Ganti,[3] S. Garpman,[13] O. Gavrishchuk,[6] F. J. M. Geurts,[12] T. K. Ghosh,[16] R. Glasow,[9] S. K. Gupta,[2] B. Guskov,[6] H. Å. Gustafsson,[13] H. H. Gutbrod,[10] R. Higuchi,[14] I. Hrivnacova,[15] M. Ippolitov,[5] H. Kalechofsky,[4] R. Kamermans,[12] K.-H. Kampert,[9] K. Karadjev,[5] K. Karpio,[17] S. Kato,[14] S. Kees,[9] H. Kim,[7] B. W. Kolb,[11] I. Kosarev,[6] I. Koutcheryaev,[5] T. Krümpel,[9] A. Kugler,[15] P. Kulinich,[18] M. Kurata,[14] K. Kurita,[14] N. Kuzmin,[6] I. Langbein,[11] A. Lebedev,[5] Y. Y. Lee,[11] H. Löhner,[16] L. Luquin,[10] D. P. Mahapatra,[19] V. Manko,[5] M. Martin,[4] G. Martínez,[10] A. Maximov,[6] R. Mehdiyev,[6] G. Mgebrichvili,[5] Y. Miake,[14] D. Mikhalev,[6] Md. F. Mir,[8] G. C. Mishra,[19] Y. Miyamoto,[14] D. Morrison,[20] D. S. Mukhopadhyay,[3] V. Myalkovski,[6] H. Naef,[4] B. K. Nandi,[19] S. K. Nayak,[10] T. K. Nayak,[3] S. Neumaier,[11] A. Nianine,[5] V. Nikitine,[6] S. Nikolaev,[6] P. Nilsson,[13] S. Nishimura,[14] P. Nomokonov,[6] J. Nystrand,[13] F. E. Obenshain,[20] A. Oskarsson,[13] I. Otterlund,[13] M. Pachr,[15] A. Parfenov,[6] S. Pavliouk,[6] T. Peitzmann,[9] V. Petracek,[15] F. Plasil,[7] W. Pinganaud,[10] M. L. Purschke,[11] B. Raeven,[12] J. Rak,[15] R. Raniwala,[2] S. Raniwala,[2] V. S. Ramamurthy,[19] N. K. Rao,[8] F. Retiere,[10] K. Reygers,[9] G. Roland,[18] L. Rosselet,[4] I. Roufanov,[6] C. Roy,[10] J. M. Rubio,[4] H. Sako,[14] S. S. Sambyal,[8] R. Santo,[9] S. Sato,[14] H. Schlagheck,[9] H.-R. Schmidt,[11] Y. Schutz,[10] G. Shabratova,[6] T. H. Shah,[8] I. Sibiriak,[5] T. Siemiarczuk,[17] D. Silvermyr,[13] B. C. Sinha,[3] N. Slavine,[6] K. Söderström,[13] N. Solomey,[4] S. P. Sørensen,[20] P. Stankus,[7] G. Stefanek,[17] P. Steinberg,[18] E. Stenlund,[13] D. Stüken,[9] M. Sumbera,[15] T. Svensson,[13] M. D. Trivedi,[3] A. Tsvetkov,[5] L. Tykarski,[17] J. Urbahn,[11] E. C. v. d. Pijll,[12] N. v. Eijndhoven,[12] G. J. v. Nieuwenhuizen,[18] A. Vinogradov,[5] Y. P. Viyogi,[3] A. Vodopianov,[6] S. Vörös,[4] B. Wysłouch,[18] K. Yagi,[14] Y. Yokota,[14] and G. R. Young[7]

(WA98 Collaboration)

[1]*University of Panjab, Chandigarh 160014, India*
[2]*University of Rajasthan, Jaipur 302004, Rajasthan, India*
[3]*Variable Energy Cyclotron Centre, Calcutta 700 064, India*
[4]*University of Geneva, CH-1211 Geneva 4, Switzerland*
[5]*RRC "Kurchatov Institute," RU-123182 Moscow, Russia*
[6]*Joint Institute for Nuclear Research, RU-141980 Dubna, Russia*
[7]*Oak Ridge National Laboratory, Oak Ridge, Tennessee 37831-6372*
[8]*University of Jammu, Jammu 180001, India*
[9]*University of Münster, D-48149 Münster, Germany*
[10]*SUBATECH, Ecole des Mines, Nantes, France*
[11]*Gesellschaft für Schwerionenforschung (GSI), D-64220 Darmstadt, Germany*
[12]*Universiteit Utrecht/NIKHEF, NL-3508 TA Utrecht, The Netherlands*
[13]*Lund University, SE-221 00 Lund, Sweden*
[14]*University of Tsukuba, Ibaraki 305, Japan*
[15]*Nuclear Physics Institute, CZ-250 68 Rez, Czech Republic*
[16]*KVI, University of Groningen, NL-9747 AA Groningen, The Netherlands*
[17]*Institute for Nuclear Studies, 00-681 Warsaw, Poland*
[18]*MIT, Cambridge, Massachusetts 02139*
[19]*Institute of Physics, 751-005 Bhubaneswar, India*
[20]*University of Tennessee, Knoxville, Tennessee 37966*

(Received 29 January 1999)

Neutral pion production in central 158*A* GeV ^{208}Pb + ^{208}Pb collisions has been studied in the WA98 experiment at the CERN Super Proton Synchrotron. The π^0 transverse mass spectrum has been analyzed in terms of a thermal model with hydrodynamic expansion. The high accuracy and large kinematic coverage of the measurement allow one to limit previously noted ambiguities in the extracted freeze-out parameters. The results are shown to be sensitive to the shape of the velocity distribution at freeze-out.

PACS numbers: 25.75.Dw, 24.10.Pa

 0031-9007/99/83(5)/926(5)$15.00 © 1999 The American Physical Society

Heavy ion reactions at sufficiently high energies produce dense matter which may provide the necessary conditions for the transition from a hadronic state to a deconfined phase, the quark-gluon plasma. Since a finite thermalized system without external containment pressure will necessarily expand, part of the thermal excitation energy will be converted into collective motion which will be reflected in the momentum spectra of the final hadrons. The dynamics of the expansion may depend on the presence or absence of a plasma phase. The strongly interacting hadrons are expected to decouple in the late stages of the collision. Their transverse momentum spectra should therefore provide information about the conditions of the system at freeze-out, in particular about the temperature and collective velocity of the system, if the thermal assumption is valid.

The application of a thermal description is nontrivial. There is no reason to believe that chemical and kinetic freeze-out should be identical nor that there should be unique thermal freeze-out temperatures for all hadrons or unique chemical freeze-out temperatures for all flavor changing reactions. It is likely that chemical equilibrium is not fully attained (see, e.g., [1]), implying that chemical parameters will also influence momentum spectra through contributions from decays of heavier resonances. Furthermore, it is not obvious that this problem should have a stationary solution since particle emission will occur throughout the full time evolution of the collision and so, in principle, would require a full space-time integration with varying parameters.

Most attempts to extract freeze-out parameters from experiment assume local thermal equilibrium and fit parametrizations of hydrodynamical models to the experimental distributions [2–7]. Already the earliest analyses [2] noted ambiguities in fitting the hadron transverse mass spectra due to an anticorrelation between the fitted temperature T and transverse flow velocity β_T.

Two-particle interferometric (HBT) measurements provide information on the spatial and temporal extent of the emission volume, but are also sensitive to the collective motion of the source (see, e.g., [3,8,9]). Within a hydrodynamical parametrization of the source at freeze-out, the transverse two-particle correlations have been shown to be sensitive only to the ratio β_T^2/T [3]. Hence HBT analyses have a $\beta_T - T$ ambiguity which is roughly orthogonal to that resulting from fits to the single particle spectra. This fact has recently been used by the NA49 Collaboration to constrain the freeze-out parameters to lie within the region $\langle\beta_T\rangle = 0.55 \pm 0.12$ and $T = 120 \pm 12$ MeV for central Pb + Pb collisions [6]. Alternatively, a recent analysis of π^+, K^+, and K^- distributions and π^+ and π^- two-particle correlations measured by the NA44 Collaboration for central Pb + Pb collisions using a nine-parameter hydrodynamical model fit [10] gave freeze-out parameters of $\langle\beta_T\rangle = 0.443 \pm 0.023$ and $T = 95.8 \pm 3.5$ MeV. These analyses suggest that a single set of freeze-out parameters can describe the hadron single particle distributions and two-particle correlations, with moderate temperature and large transverse flow velocity.

On the other hand, various thermal model analyses of particle production ratios, especially strangeness production (see, e.g., Ref. [11] for a recent summary), have indicated rather high chemical freeze-out temperatures. Use of integrated yields in these analyses allows one to obtain conclusions on the temperature which are insensitive to the amount of transverse flow. In a recent analysis of results at SPS energies, including Pb + Pb collisions, good agreement is obtained if partial strangeness saturation is assumed with a chemical freeze-out temperature of about 180 MeV [12].

A successful thermal interpretation of relativistic heavy ion collisions must provide an accurate description of the pion spectra since pions provide the "thermal bath" of the late stages of the collision. In this Letter we discuss the extraction of thermal freeze-out parameters from the neutral pion transverse mass distribution for central 158A GeV ^{208}Pb + ^{208}Pb collisions. These data provide important constraints due to their accuracy and coverage in transverse mass. The analysis of the π^0 spectrum, within a particular hydrodynamical model, reveals the importance of the shape of the velocity distribution at freeze-out. The default shape, derived from a Gaussian spatial distribution, favors a large thermal freeze-out temperature, similar to temperatures extracted for chemical freeze-out, but in contradiction to conclusions obtained based on analyses of limited coverage particle spectra and HBT results [6,10,13].

The CERN experiment WA98 [14–16] consists of large acceptance photon and hadron spectrometers together with several other large acceptance devices which allow one to measure various global variables on an event-by-event basis. The results presented here were obtained from an analysis of the data taken with Pb beams in 1995 and 1996. The 10% most central reactions ($\sigma_{\text{central}} \approx$ 630 mb) have been selected using the transverse energy E_T measured in the MIRAC calorimeter.

Neutral pions are reconstructed via their $\gamma\gamma$ decay branch using the WA98 lead-glass photon detector, LEDA, which consisted of 10 080 individual modules with photomultiplier readout. The detector was located at a distance of 21.5 m from the target and covered the pseudorapidity interval $2.35 < \eta < 2.95$. The general analysis procedure, described in [16], is similar to that used in the WA80 experiment [7]. The momentum distributions are fully corrected for geometrical acceptance and reconstruction efficiency. The systematic error on the absolute yield is $\approx$10% and increases sharply below $p_T = 0.4$ GeV/c. An additional systematic error originates from the uncertainty on the momentum scale of 1%. The influence of this rises slowly for large p_T and leads to an uncertainty on the yield of 15% at $p_T = 4$ GeV/c.

The measured neutral pion cross section from central Pb + Pb reactions as a function of $m_T - m_0$ is shown in Fig. 1. Included is a fit with a hydrodynamical model

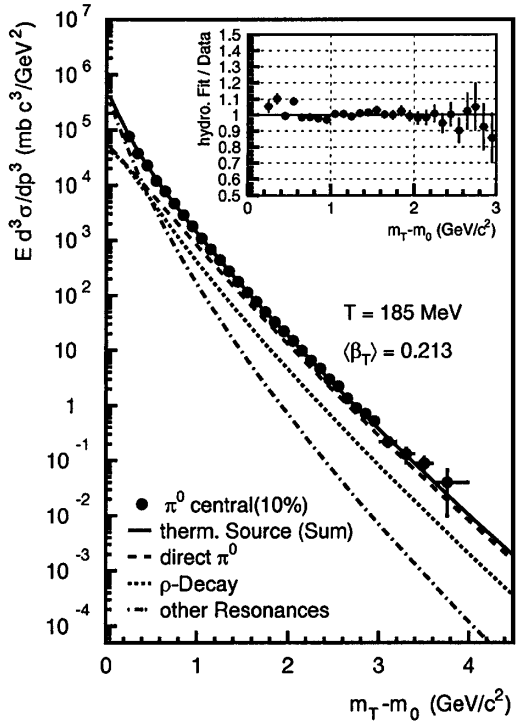

FIG. 1. Transverse mass spectra of neutral pions in central collisions (10% of minimum bias cross section) of 158*A* GeV Pb + Pb. The invariant cross section of neutral pions is compared to a fit using a hydrodynamical model [5] including transverse flow and resonance decays, with the direct production and the contribution of ρ decays and all other resonances shown separately. The ratio of the fit to the data is shown in the inset. m_0 is the π^0 mass.

[5] including transverse flow and resonance decays. This computer program calculates the direct production and the contributions from the most important resonances having two- or three-body decays including pions (ρ, K^0_S, $K^\star$, Δ, $\Sigma + \Lambda$, η, ω, η'). The code, originally intended for charged pions, has been adapted to predict neutral pion production. The model uses a Gaussian transverse spatial density profile truncated at 4σ. The transverse flow rapidity is assumed to be a linear function of the radius. For all results presented here, a baryonic chemical potential of $\mu_B = 200$ MeV has been used. The results are not very sensitive, however, to the choice of μ_B for the $m_T - m_0$ region considered here.

This model provides an excellent description of the neutral pion spectra with a temperature $T = 185$ MeV and an average flow velocity of $\langle\beta_T\rangle = 0.213$. These values are very similar to the parameters obtained with similar fits to neutral pion spectra in central reactions of ^{32}S + Au [7]. The 2σ lower limit on the temperature is $T^{\text{low}} = 171$ MeV, and the corresponding upper limit on the flow velocity is $\langle\beta_T^{\text{upp}}\rangle = 0.253$. (All limits given use the data for $m_T - m_0 > 2$ GeV/c^2 as upper limits only to allow for additional hard-scattering contributions.)

The observed curvature at low m_T is largely a result of resonance decay contributions. Performing a fit with only the direct contribution leads to $T = 142$ MeV and $\langle\beta_T\rangle = 0.301$, with corresponding 2σ limits of $T^{\text{low}} = 135$ MeV and $\langle\beta_T^{\text{upp}}\rangle = 0.318$, similar to other analyses which have neglected decay contributions [6,17]. The larger average velocity which results in this case is due to the fact that all of the observed curvature must now be accounted for by transverse flow.

The high statistical accuracy and large transverse mass coverage of the present π^0 measurement reveals the concave curvature of the π^0 spectrum over a large m_T range, which constrains the parameters significantly. This is further demonstrated by studying the local slope at each m_T. The local (inverse) slope is given by

$$T^{-1}_{\text{local}} = -\left(E\,\frac{d^3\sigma}{dp^3}\right)^{-1} \frac{d}{dm_T}\left(E\,\frac{d^3\sigma}{dp^3}\right). \qquad (1)$$

The local slope results are plotted in Fig. 2. Each individual value of T_{local} has been extracted from 3 adjacent data points of Fig. 1. The data are compared to the hydrodynamical model best fit results of Fig. 1, as well as fits in which the transverse flow velocities have been fixed to larger values comparable to those obtained by Refs. [10] and NA49 [6] (sets 2 and 3). The corresponding fit parameters are given in Table I. The comparison demonstrates that while the large transverse flow velocity fits can provide a reasonable description of the data up to transverse masses of about 1 GeV, they significantly overpredict the local slopes at large transverse mass. While application of the hydrodynamical model at large transverse mass is questionable, the model cannot overpredict the measured yield. The observed overprediction therefore rules out the assumption of large transverse flow velocities, or points to a deficiency in the model assumptions used in these fits.

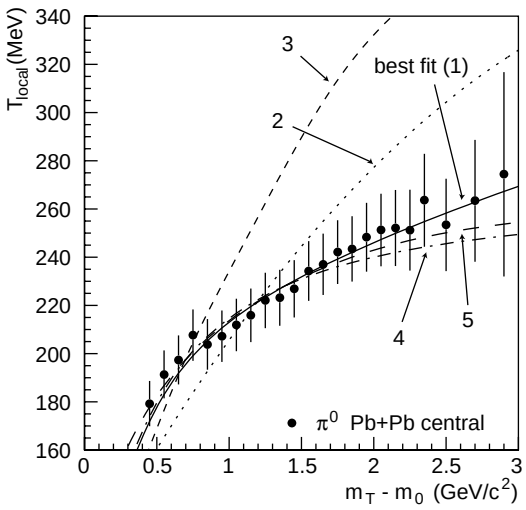

FIG. 2. The local inverse slope of the transverse mass spectrum of neutral pions in central collisions of 158*A* GeV Pb + Pb. The measured results (solid points) are compared to the hydrodynamical model best fit result (solid line; $T = 185$ MeV and $\langle\beta_T\rangle = 0.213$, also shown in Fig. 1) and to the other results given in Table I.

TABLE I. Parameters for different hydrodynamical model fits to the neutral pion spectrum shown in Figs. 2 and 3. The temperature T and average and rms transverse flow velocities $\langle\beta_T\rangle$ and $\beta_{\rm rms}$ are given together with the effective temperature $T_{\rm eff} = T/\sqrt{(1 - \langle\beta_T\rangle)/(1 + \langle\beta_T\rangle)}$.

Set	Spatial profile	T (MeV)	$\langle\beta_T\rangle$	$\beta_{\rm rms}$	$T_{\rm eff}$ (MeV)	χ^2/d.o.f.
1	Gauss	185 ± 4	0.213 ± 0.020	0.107	230	25.9/18
2	Gauss	75 ± 1	0.469	0.199	125	386/19
3	Gauss	49 ± 1	0.527	0.213	88	578/19
4	uniform	178 ± 13	0.274 ± 0.046	0.093	235	33.3/18
5	Woods-Saxon	$146\ ^{+21}_{-16}$	$0.365\ ^{+0.056}_{-0.069}$	0.137	214	26.7/18

The curvature in the π^0 spectrum at large transverse mass is a result of the distribution of transverse velocities. Although the spectrum is not directly sensitive to the spatial distribution of particle emission, within this model it is dependent indirectly on the spatial distribution due to the assumption that the transverse rapidity increases linearly with radius. The large curvature at large transverse mass is due to high velocity contributions which result from the tail of the assumed Gaussian density profile [18]. Figure 3 shows the transverse source velocity distributions $dN/d\beta_T$ for the different parameter sets. (More precisely these are source emission functions integrated over all variables except the transverse velocity and the rapidity; i.e., they are weighted with the produced particle multiplicity.) The curves labeled 1–3 correspond to the calculations in Fig. 2 using a Gaussian spatial profile. In addition, velocity profiles are shown for a uniform density profile (set 4) and for a Woods-Saxon distribution:

$$\rho(r) = \frac{1}{1 + \exp[(r - r_0)/\Delta]} \qquad (2)$$

with $\Delta/r_0 = 0.02$ (set 5). These are included in Figs. 2 and 3. It is seen that the uniform density assumption truncates the high velocity tail resulting in less curvature in the pion spectrum, while the Woods-Saxon has a more diffuse edge at high β_T.

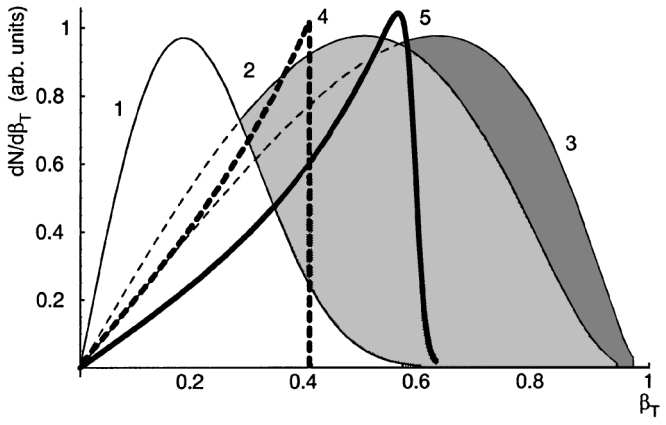

FIG. 3. Unnormalized multiplicity distributions as a function of the transverse source velocity for the parameter sets given in Table I.

While the Gaussian and uniform density assumptions have very different velocity profiles, it is interesting that both can provide acceptable fits to the pion spectrum with best fit results with similar $\langle\beta_T\rangle$ and T parameters, which give similar effective temperatures, and which have similar velocity widths, $\beta_{\rm rms}$, as shown in Table I. Compared to the Gaussian profile result, the best fit result using the uniform profile gives a lower temperature of 178 MeV and would lead to weaker limits of $\langle\beta_T^{\rm upp}\rangle = 0.42$ and $T^{\rm low} = 134$ MeV. Limits cannot be set using the Woods-Saxon profile due to increased fit ambiguity. If the data for $m_T - m_0 > 2$ GeV/c^2 are used only as upper limits, as explained above, a best fit result with $T = 129$ MeV and $\langle\beta_T\rangle = 0.42$ is obtained.

The data presented here can be well described with high thermal freeze-out temperatures, similar to temperatures which have been extracted for chemical freeze-out [12], and small transverse flow velocities. (Note again that chemical and thermal freeze-out are not necessarily expected to be the same.) On the other hand, if the larger velocities obtained in other analyses which have considered limited particle spectra together with HBT results [6,10,13] persist, then the present analysis suggests much lower thermal freeze-out temperatures. For example, none of the different velocity profile assumptions used in this analysis allowed us to reproduce the results of Ref. [6]—all profiles studied require a temperature of 90 MeV or less, if $\langle\beta_T\rangle = 0.55$ is assumed. The present data obviously provide important information on the shape of the freeze-out velocity distribution. A more extensive systematic study would require further guidance from full hydrodynamical calculations, which is beyond the scope of this paper. Recent hydrodynamical model calculations [19,20] have found reasonable agreement with transverse mass spectra within a broad range of assumptions. However, in these studies it was not attempted to limit the model parameters or assumptions by a rigorous comparison to the data.

In summary, we have argued that hydrodynamical models which attempt to extract the thermal freeze-out parameters of relativistic heavy ion collisions must provide an accurate description of the pion spectra, since pions most directly reflect the thermal evironment in the late stage of the collision. In particular, models, or parameter

sets, which overpredict the observed pion yields, even at large transverse mass, can immediately be ruled out. We have demonstrated that the high accuracy neutral pion spectra with large transverse mass coverage can constrain the thermal freeze-out parameters and model assumptions. Within the context of the hydrodynamical model of Ref. [5], the default velocity profile favors large thermal freeze-out temperatures similar to the chemical freeze-out temperature determined for the same system [12]. Only special choices of the velocity profile allow large average freeze-out velocities similar to those extracted from other recent analyses which consider also HBT results [6,10,13]. On the other hand, the corresponding freeze-out temperatures are then ≈ 90 MeV, significantly lower than other estimates. The present results indicate that the determination of the freeze-out parameters remains an open question. It will be important to determine whether full hydrodynamical models can reproduce the high precision pion data and thereby constrain the assumed freeze-out hypersurface.

We thank Urs Wiedemann for assistance with the model calculations and valuable discussions. This work was supported jointly by the German BMBF and DFG, the U.S. DOE, the Swedish NFR and FRN, the Dutch Stichting FOM, the Stiftung für Deutsch-Polnische Zusammenarbeit, the Grant Agency of the Czech Republic under Contract No. 202/95/0217, the Department of Atomic Energy, the Department of Science and Technology, the Council of Scientific and Industrial Research and the University Grants Commission of the Government of India, the Indo-FRG Exchange Program, the PPE division of CERN, the Swiss National Fund, the INTAS under Contract No. INTAS-97-0158, ORISE, Grant-in-Aid for Scientific Research (Specially Promoted Research and International Scientific Research) of the Ministry of Education, Science and Culture, the University of Tsukuba Special Research Projects, and JSPS. ORNL is managed by Lockheed Martin Energy Research Corporation under Contract No. DE-AC05-96OR22464 with the U.S. Department of Energy. The MIT group has been supported by the U.S. Department of Energy under the cooperative agreement DE-FC02-94ER40818.

[1] F. Becattini, Z. Phys. C **69**, 485–492 (1996).
[2] E. Schnedermann, J. Sollfrank, and U. Heinz, Phys. Rev. C **48**, 2462 (1993).
[3] S. Chapman, J. R. Nix, and U. Heinz, Phys. Rev. C **52**, 2694 (1995).
[4] P. Braun-Munzinger *et al.*, Phys. Lett. B **344**, 43 (1995).
[5] U. A. Wiedemann and U. Heinz, Phys. Rev. C **56**, 3265 (1997).
[6] NA49 Collaboration, H. Appelshäuser *et al.*, Eur. Phys. J. C **2**, 661–670 (1998).
[7] WA80 Collaboration, R. Albrecht *et al.*, Eur. Phys. J. C **5**, 255 (1998).
[8] S. Pratt, Phys. Rev. D **33**, 1314 (1986).
[9] U. Heinz *et al.*, Phys. Lett. B **382**, 181 (1996).
[10] J. R. Nix *et al.*, nucl-th/9801045.
[11] J. Sollfrank, J. Phys. G **23**, 1903 (1997).
[12] F. Becattini, M. Gaździcki, and J. Sollfrank, Eur. Phys. J. C **5**, 143 (1998).
[13] J. R. Nix, Phys. Rev. C **58**, 2303 (1998).
[14] WA98 Collaboration, P. Dönni *et al.*, CERN/SPSLC 91-17, SPSLC/P260, 1991.
[15] WA98 Collaboration, M. Aggarwal *et al.*, Nucl. Phys. **A610**, 200c (1996).
[16] WA98 Collaboration, M. M. Aggarwal *et al.*, Phys. Rev. Lett. **81**, 4087 (1998).
[17] NA44 Collaboration, I. G. Bearden *et al.*, Phys. Rev. Lett. **78**, 2080 (1997).
[18] U. Heinz and U. A. Wiedemann (private communication).
[19] A. Dimitru and D. H. Rischke, Phys. Rev. C **59**, 354–363 (1999).
[20] P. Huovinen, P. V. Ruuskanen, and J. Sollfrank, Nucl. Phys. **A650**, 227–244 (1999).

Centrality Dependence of Neutral Pion Production in 158A GeV ^{208}Pb + ^{208}Pb Collisions

M. M. Aggarwal,[1] A. Agnihotri,[2] Z. Ahammed,[3] A. L. S. Angelis,[4] V. Antonenko,[5] V. Arefiev,[6] V. Astakhov,[6] V. Avdeitchikov,[6] T. C. Awes,[7] P. V. K. S. Baba,[8] S. K. Badyal,[8] A. Baldine,[6] L. Barabach,[6] C. Barlag,[9] S. Bathe,[9] B. Batiounia,[6] T. Bernier,[10] K. B. Bhalla,[2] V. S. Bhatia,[1] C. Blume,[9] R. Bock,[11] E.-M. Bohne,[9] Z. K. Böröcz,[9] D. Bucher,[9] A. Buijs,[12] H. Büsching,[9] L. Carlen,[13] V. Chalyshev,[6] S. Chattopadhyay,[3] R. Cherbatchev,[5] T. Chujo,[14] A. Claussen,[9] A. C. Das,[3] M. P. Decowski,[18] V. Djordjadze,[6] P. Donni,[4] I. Doubovik,[5] M. R. Dutta Majumdar,[3] K. El Chenawi,[13] S. Eliseev,[15] K. Enosawa,[14] P. Foka,[4] S. Fokin,[5] V. Frolov,[6] M. S. Ganti,[3] S. Garpman,[13] O. Gavrishchuk,[6] F. J. M. Geurts,[12] T. K. Ghosh,[16] R. Glasow,[9] S. K. Gupta,[2] B. Guskov,[6] H. A. Gustafsson,[13] H. H. Gutbrod,[10] R. Higuchi,[14] I. Hrivnacova,[15] M. Ippolitov,[5] H. Kalechofsky,[4] R. Kamermans,[12] K.-H. Kampert,[9] K. Karadjev,[5] K. Karpio,[17] S. Kato,[14] S. Kees,[9] H. Kim,[7] B. W. Kolb,[11] I. Kosarev,[6] I. Koutcheryaev,[5] T. Krümpel,[9] A. Kugler,[15] P. Kulinich,[18] M. Kurata,[14] K. Kurita,[14] N. Kuzmin,[6] I. Langbein,[11] A. Lebedev,[5] Y. Y. Lee,[11] H. Löhner,[16] L. Luquin,[10] D. P. Mahapatra,[19] V. Manko,[5] M. Martin,[4] A. Maximov,[6] R. Mehdiyev,[6] G. Mgebrichvili,[5] Y. Miake,[14] D. Mikhalev,[6] G. C. Mishra,[19] Y. Miyamoto,[14] D. Morrison,[20] D. S. Mukhopadhyay,[3] V. Myalkovski,[6] H. Naef,[4] B. K. Nandi,[19] S. K. Nayak,[10] T. K. Nayak,[3] S. Neumaier,[11] A. Nianine,[5] V. Nikitine,[6] S. Nikolaev,[6] P. Nilsson,[13] S. Nishimura,[14] P. Nomokonov,[6] J. Nystrand,[13] F. E. Obenshain,[20] A. Oskarsson,[13] I. Otterlund,[13] M. Pachr,[15] A. Parfenov,[6] S. Pavliouk,[6] T. Pietzmann,[9] V. Patracek,[15] W. Pinanaud,[10] F. Plasil,[7] M. L. Purschke,[11] B. Raeven,[12] J. Rak,[15] R. Raniwala,[2] S. Raniwala,[2] V. S. Ramamurthy,[19] N. K. Rao,[8] F. Retiere,[10] K. Reygers,[9] G. Roland,[18] L. Rosselet,[4] I. Roufanov,[6] C. Roy,[10] J. M. Rubio,[4] H. Sako,[14] S. S. Sambyal,[8] R. Santo,[9] S. Sato,[14] H. Schlagheck,[9] H.-R. Schmidt,[11] G. Shabratova,[6] I. Sibiriak,[5] T. Siemiarczuk,[17] D. Silvermyr,[13] B. C. Sinha,[3] N. Slavine,[6] K. Söderström,[13] N. Solomey,[4] S. P. Sørensen,[20] P. Stankus,[7] G. Stefanek,[17] P. Steinberg,[18] E. Stenlund,[13] D. Stüken,[9] M. Sumbera,[15] T. Svensson,[13] M. D. Trivedi,[3] A. Tsvetkov,[5] C. Twenhöfel,[12] L. Tykarski,[17] J. Urbahn,[11] N. v. Eijndhoven,[12] G. J. v. Nieuwenhuizen,[18] A. Vinogradov,[5] Y. P. Viyogi,[3] A. Vodopianov,[6] S. Vörös,[4] B. Wysłouch,[18] K. Yagi,[14] Y. Yokota,[14] and G. R. Young[7]

(WA98 Collaboration)

[1]*University of Panjab, Chandigarh 160014, India*
[2]*University of Rajasthan, Jaipur 302004, India*
[3]*Variable Energy Cyclotron Centre, Calcutta 700 064, India*
[4]*University of Geneva, CH-1211 Geneva 4, Switzerland*
[5]*RRC (Kurchatov), RU-123182 Moscow, Russia*
[6]*Joint Institute for Nuclear Research, RU-141980 Dubna, Russia*
[7]*Oak Ridge National Laboratory, Oak Ridge, Tennessee 37831-6372*
[8]*University of Jammu, Jammu 180001, India*
[9]*University of Münster, D-48149 Münster, Germany*
[10]*SUBATECH, Ecole des Mines, Nantes, France*
[11]*Gesellschaft für Schwerionenforschung (GSI), D-64220 Darmstadt, Germany*
[12]*Universiteit Utrecht/NIKHEF, NL-3508 TA Utrecht, The Netherlands*
[13]*University of Lund, SE-221 00 Lund, Sweden*
[14]*University of Tsukuba, Ibaraki 305, Japan*
[15]*Nuclear Physics Institute, CZ-250 68 Rez, Czech Republic*
[16]*KVI, University of Groningen, NL-9747 AA Groningen, The Netherlands*
[17]*Institute for Nuclear Studies, 00-681 Warsaw, Poland*
[18]*MIT, Cambridge, Massachusetts 02139*
[19]*Institute of Physics, 751-005 Bhubaneswar, India*
[20]*University of Tennessee, Knoxville, Tennessee 37966*

(Received 26 June 1998)

The production of neutral pions in 158A GeV ^{208}Pb + ^{208}Pb collisions has been studied in the WA98 experiment at the CERN Super Proton Synchrotron (SPS). Transverse momentum spectra are studied for the range $0.3 \leq m_T - m_0 \leq 4.0$ GeV/c. The results for central collisions are compared to various models. The centrality dependence of the neutral pion spectral shape and yield is investigated. An invariance of the spectral shape and a simple scaling of the yield with the number of participating nucleons is observed for centralities with greater than about 30 participating nucleons. This is most naturally explained by assuming an equilibrated system. [S0031-9007(98)07532-2]

PACS numbers: 25.75.Dw

 © 1998 The American Physical Society

Ultrarelativistic heavy-ion collisions produce dense matter which is expected to be in the form of a deconfined phase of quarks and gluons, or quark gluon plasma (QGP), at sufficiently high energy densities. The transverse momentum spectra of produced pions can provide information on both the initial and the final state properties of the hot hadronic matter. The low p_T pion production would dominantly reflect the temperature of the hadronic system at the freeze-out stage occurring late in the reaction. It is strongly influenced by rescattering among the final state hadrons. The high p_T pion production is expected to be dominated by hard scattering of the partons. In pA collisions the high p_T region is known to be enhanced (Cronin effect [1]) due to initial state scattering of the incident partons leading to a broadening of their incoming p_T. In AA collisions, many of the scattered partons must traverse the excited matter to escape and therefore may undergo additional rescatterings and energy loss [2]. In the case of significant parton rescattering, the parton distributions may approach thermal distributions with a temperature reflecting the initial state of the excited matter. The intermediate p_T region of the pion spectrum might then reflect this initial temperature. Indeed, one of the earliest signatures of QGP formation, proposed by Van Hove [3], was the observation of a saturation of the average transverse momentum with increasing energy (or entropy) density for systems excited just above the critical energy density. With increasing energy density, the initial temperature would not rise above the critical temperature until all of the latent heat of the QQP phase transition had been extracted.

For these reasons it is of interest to study the centrality dependence of the pion production. It is generally believed that the initial energy density increases with increasing centrality, due to the many overlapping interactions. Also, the volume of the excited matter increases with centrality, as well as the amount of rescattering. Since rescattering is the feature which distinguishes AA collisions nontrivially from pp collisions, and since significant rescattering is a prerequisite for thermalization, it is imperative to demonstrate an understanding of the centrality dependence of the AA results in order to understand the effects of rescattering. While those effects may be minor on extensive observables, like the particle multiplicity or transverse energy, they should be most evident on the momentum distribution of the produced particles. Recently it has been argued that a parton cascade description could successfully describe many of the features of central Pb + Pb collisions at the CERN Super Proton Synchrotron (SPS) energies [4]. Surprisingly, low momentum transfer soft parton collisions were found to have little influence on the final observables. Similarly, recent perturbative QCD calculations were able to reproduce the preliminary WA98 neutral pion result for central collisions [5,6] without need for the effects of parton energy loss or rescattering [7]. In this Letter we present neutral pion spectra for 158A GeV ^{208}Pb + ^{208}Pb collisions and investigate in detail the centrality dependence of the spectral shape and yield.

The CERN experiment WA98 [5,8] consists of large acceptance photon and hadron spectrometers together with several other large acceptance devices which allow one to measure various global variables on an event-by-event basis. The results presented here were obtained from an analysis of the data taken with Pb beams in 1995 and 1996. The minimum bias (min-bias) reactions ($\sigma_{\text{min-bias}} \approx 6300$ mb) are divided into eight centrality classes using the transverse energy E_T measured in the MIRAC calorimeter. In total, $\approx 9.6 \times 10^6$ reactions have been analyzed.

Neutral pions are reconstructed via their $\gamma\gamma$ decay branch using the WA98 lead-glass photon detector, LEDA, which consisted of 10 080 individual modules with photomultiplier readout. The detector was located at a distance of 21.5 m from the target and covered the pseudorapidity interval $2.35 < \eta < 2.95$. The measurement of neutral pions, though difficult at low transverse momenta, is superior to those of charged pions at high momenta because of the improving energy resolution of the calorimetric measurement.

The general analysis procedure is similar to that used in the WA80 experiment and described in [9]. Hits in the lead-glass detector are combined in pairs to provide distributions of pair mass vs pair transverse momentum (or transverse mass) for all possible combinations. Subtraction of the combinatorial background is performed using mixed event distributions. The resulting momentum distributions are corrected for geometrical acceptance and reconstruction efficiency. The efficiency depends on the particle occupancy in the detector and therefore has been calculated independently for each centrality bin. The systematic error of the pion yields is mainly due to errors in the reconstruction efficiency for central collisions and to corrections for nontarget interactions for peripheral collisions. The systematic error on the absolute yield is $\approx 10\%$ and increases sharply below $p_T = 0.4$ GeV/c. An additional systematic error originates from the uncertainty of the momentum scale of 1%. The influence of this rises slowly for higher p_T and leads to an error of 15% at $p_T = 4$ GeV/c. A detailed discussion of the analysis procedure and the error contributions will be given in a forthcoming publication.

The measured neutral pion spectrum from central Pb + Pb reactions (10% of min-bias cross section) as a function of $m_T - m_0$ is shown in Fig. 1. The data are compared to predictions of the string model Monte Carlo generators FRITIOF 7.02 [10] and VENUS 4.12 [11]. As already observed in S + Au reactions [9], both generators fail to describe the data well at large m_T. The FRITIOF prediction is more than an order of magnitude lower at high m_T while VENUS significantly overpredicts the data. Alternatively, it has recently been shown that

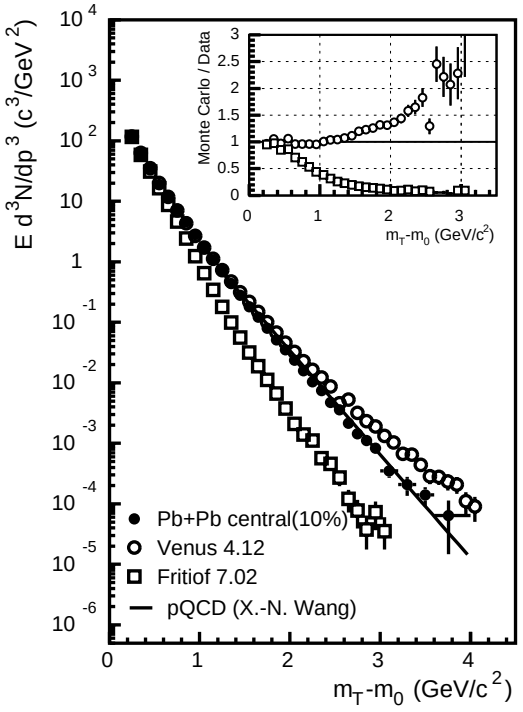

FIG. 1. Transverse mass spectra of neutral pions in central collisions of 158*A* GeV Pb + Pb. Invariant yields per event are compared to calculations using the FRITIOF 7.02 [10] and VENUS 4.12 [11] Monte Carlo programs. Predictions of a pQCD calculation [7] are included as a solid line. The inset shows the ratios of the results of the Monte Carlo codes to the experimental data.

perturbative QCD (pQCD) calculations, including initial state multiple scattering and intrinsic p_T [7], are able to describe the preliminary WA98 data at intermediate and high p_T. This prediction is included in Fig. 1 as a solid line. (The results shown have been corrected for a small numerical error by the author of [7] and have changed by $\approx 10\%-30\%$ compared to the publication.) The pQCD calculation shows a very good agreement in the high m_T region. This surprising agreement has been interpreted as an indication for unexpectedly small effects of parton energy loss [7]. On the other hand, the parton cascade Monte Carlo code, VNI, which provides a more detailed pQCD description, overpredicts the measured WA98 result by more than a factor of 10 at large p_T [4]. In an alternative picture, hydrodynamical descriptions (see, e.g., [12]) with properly adjusted parameters can describe the momentum spectra reasonably well.

In view of the above discussion and the difficulty to describe the details of the neutral pion spectrum, it is apparent that the theoretical description of ultrarelativistic nucleus-nucleus collisons remains uncertain. In order to demonstrate a consistent description of nuclear effects it is important to investigate the details of the pion production as a function of the system size. To study the centrality dependence of the spectral shape in a manner which is independent of model or fit function we have used the truncated mean transverse momentum $\langle p_T(p_T^{\min})\rangle$, where

$$\langle p_T(p_T^{\min})\rangle = \left(\int_{p_T^{\min}}^{\infty} p_T \frac{dN}{dp_T}\, dp_T \Big/ \int_{p_T^{\min}}^{\infty} \frac{dN}{dp_T}\, dp_T\right) - p_T^{\min}. \quad (1)$$

The lower cutoff $p_T^{\min} = 0.4$ GeV/c is introduced to avoid systematic errors from extrapolation to low p_T and has been chosen according to the lowest p_T of the present data where systematic uncertainties imposed by the necessary corrections are still small. In general, the value of $\langle p_T(p_T^{\min})\rangle$ differs from the true average p_T, except in the case of a purely exponential distribution $d\sigma/dp_T$. For a purely exponential invariant cross section, $d^2\sigma/dp_T^2$, $\langle p_T(p_T^{\min})\rangle$ decreases with increasing $p_T^{\min}$.

Figure 2 shows $\langle p_T(p_T^{\min})\rangle$ as a function of the average number of participants N_{part} for 158*A* GeV ^{208}Pb + Pb collisions. For comparison, $\langle p_T(p_T^{\min})\rangle$ values for 200*A* GeV S + Au [9] and from a parametrization of pp data [13] are also included. N_{part} is extracted by the assumption of a monotonic relation between impact parameter and transverse energy and using the resulting correspondence between measured cross section and impact parameter. The average number of participants is calculated from nuclear geometry using the extracted impact parameter. Together these data show the general trend of a rapid increase of $\langle p_T(p_T^{\min})\rangle$ compared to pp results for small system sizes. For N_{part} greater than about 30 the

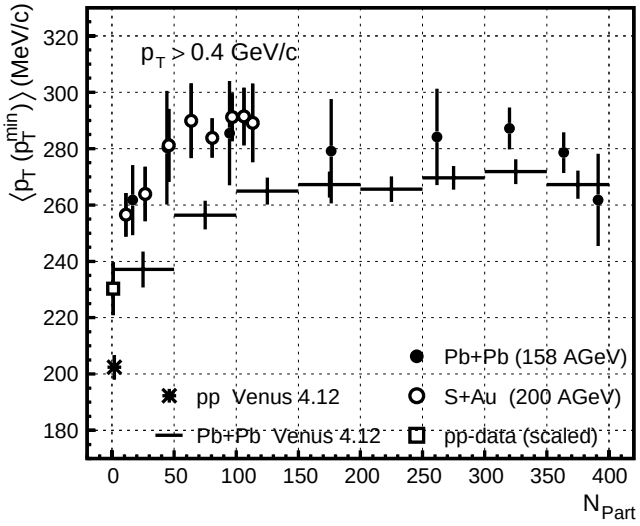

FIG. 2. Truncated mean transverse momentum $\langle p_T(p_T^{\min})\rangle$ of π^0 mesons as defined by Eq. (1) plotted as a function of the average number of participants N_{part}. The solid circles correspond to the 8 E_T based centrality selections for Pb + Pb. The open square shows $\langle p_T(p_T^{\min})\rangle$ extracted from a parametrization of pp data scaled to the same c.m. energy [13], the open circles the results for S + Au collisions at 200*A* GeV [9]. For comparison, results from VENUS 4.12 [11] are included as histograms for Pb + Pb collisions and as a star for pp. A cut parameter $p_T^{\min} = 0.4$ GeV/c was used.

mean transverse momentum appears to attain a limiting value of ≈ 280 MeV$/c^2$. [The variation of $\langle p_T(p_T^{\min})\rangle$ has been studied for values of $p_T^{\min} = 0.2$–1.0 GeV$/c$. The saturation is always observed; the statistical significance, however, decreases with increasing threshold.] VENUS 4.12 [11] calculations show a qualitatively similar behavior, but underpredict the present data, as well as the pp data. The simple implementation of rescattering which is used in this model seems to be strong enough to lead to a saturation for semiperipheral collisions as in the experimental data. One should, however, keep in mind that VENUS 4.12 does not correctly describe pion production at high p_T (see Fig. 1).

Earlier investigations of the dependence of $\langle p_T\rangle$ of pions on system size [9,14,15] at SPS energies have suggested such a saturation for large systems. The present study is the first investigation of the dependence with Pb ions at the SPS. Preliminary results from the AGS have indicated a weak increase in the average m_T of pions with the number of participants for Au + Au collisions [16].

It is important to note that the observed limiting behavior is very different from the observations in pp or $p\overline{p}$ collisions. For very high energies $\langle p_T\rangle$ rises with the pseudorapidity density of charged particles [17–20]. In that case, more violent parton scatterings presumably result in a harder spectrum of leading particles together with a greater multiplicity of fragmentation products. This would lead to the observed correlation between $\langle p_T\rangle$ and multiplicity. At lower $\sqrt{s}$, comparable to the data presented here, $\langle p_T\rangle$ decreases for increasing multiplicity [21], most likely due to energy conservation. In the case of nuclear reactions, this anticorrelation is lost due to the large number of binary collisions. Instead, the initial increase of $\langle p_T(p_T^{\min})\rangle$ with N_{part} is interpreted as a result of multiple scattering. Initial state multiple scattering, as suggested as an explanation for the Cronin effect [1], would imply a continuing increase of $\langle p_T(p_T^{\min})\rangle$ for more central collisions. Here, however, the surprising observation is that additional multiple scattering, implied by increasing N_{part}, does not alter the pion distributions. This is most easily understood as a consequence of final state rescattering and is, of course, the behavior expected for a thermalized system.

More detailed information about the centrality dependence of the pion spectral shape and yield is shown in Fig. 3 where the neutral pion yield per event has been parametrized as $Ed^3N/dp^3 \propto N_{\text{part}}^{\alpha(p_T)}\sigma_0(p_T)$. The results for $N_{\text{part}} > 30$ are well described by this scaling with an exponent $\alpha(p_T) \approx 1.3$, independent of p_T. Consistent with the previous discussion, the results indicate a constant spectral shape over the entire interval of measurement from $0.5 < p_T < 3$ GeV$/c$. The observed $N_{\text{part}}^{4/3}$ scaling for symmetric systems implies a scaling with the number of nucleon collisions, as confirmed by a similar analysis. However, this scaling does not extrapolate from the pp results. On the contrary, when comparing semiperipheral Pb + Pb collisions with pp the exponent

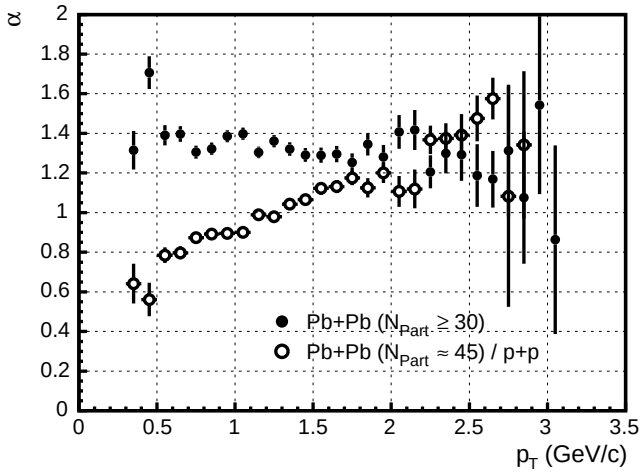

FIG. 3. The exponent $\alpha(p_T)$ of the dependence of the π^0 yield on the average number of participants N_{part} plotted as a function of the transverse momentum for 158A GeV Pb + Pb. The solid circles are calculated based on a fit to the centrality selections with $N_{\text{part}} \geq 30$. The open circles are calculated based on the ratio of the semiperipheral data ($N_{\text{part}} \approx 45$) to a parametrization of pp data.

α varies over the entire p_T interval, confirming the very different spectral shapes.

In summary, we have analyzed the centrality dependence of high precision transverse momentum spectra of neutral pions from 158A GeV Pb + Pb collisions. The neutral pion spectra are observed to show increasing deviation from pp results with increasing centrality, indicating the importance of multiple scattering effects. However, for centralities with more than about 30 participating nucleons, the shape of the transverse momentum spectrum becomes invariant over the interval $0.5 < p_T < 3$ GeV$/c$. In this interval the pion yield scales like $N_{\text{part}}^{1.3}$, or like the number of nucleon collisions, for this range of centralities. Since the amount of rescattering increases with centrality, the invariance of the spectral shape with respect to the number of rescatterings, most naturally suggests a dominantly thermal emission process. It will be important to determine whether cascade models which reproduce the observed invariant spectral shape will support the interpretation as an "effective" thermalization due to significant rescattering.

We wish to express our gratitude to the CERN accelerator division for excellent performance of the SPS accelerator complex. We acknowledge with appreciation the effort of all engineers, technicians, and support staff who have participated in the construction of the experiment. This work was supported jointly by the German BMBF and DFG, the U.S. DOE, the Swedish NFR and FRN, the Dutch Stichting FOM, the Stiftung für Deutsch-Polnische Zusammenarbeit, the Grant Agency of the Czech Republic under Contract No. 202/95/0217, the Department of Atomic Energy, the Department of Science and

Technology, the Council of Scientific and Industrial Research and the University Grants Commission of the Government of India, the Indo-FRG Exchange Program, the PPE division of CERN, the Swiss National Fund, the International Science Foundation under Contract No. N8Y000, the INTAS under Contract No. INTAS-93-2773, ORISE, Research-in-Aid for Scientific Research (Specially Promoted Research & International Scientific Research) of the Ministry of Education, Science and Culture, the University of Tsukuba Special Research Projects, and the JSPS Research Fellowships for Young Scientists. ORNL is managed by Lockheed Martin Energy Research Corporation under Contract No. DE-AC05-96OR22464 with the U.S. Department of Energy. The MIT group has been supported by the U.S. Department of Energy under the cooperative agreement DE-FC02-94ER40818.

[1] D. Antreasyan *et al.*, Phys. Rev. D **19**, 764 (1979).
[2] X.-N. Wang and M. Gyulassy, Phys. Rev. Lett. **68**, 1480 (1992).
[3] L. Van Hove, Phys. Lett. **118B**, 138 (1982).
[4] D. K. Srivastava and K. Geiger, Phys. Rev. C **56**, 2718 (1997).
[5] WA98 Collaboration, M. Aggarwal *et al.*, Nucl. Phys. **A610**, 200c (1996).
[6] WA98 Collaboration, T. Peitzmann *et al.*, in *Quark Matter '97, Proceedings of the 13th International Conference on Ultrarelativistic Nucleus-Nucleus Collisions, Tsukuba, Japan* (to be published).
[7] X.-N. Wang, e-print hep-ph/9804384, 1998; (private communication).
[8] WA98 Collaboration, Report No. CERN/SPSLC 91-17, SPSLC/P260, 1991.
[9] WA80 Collaboration, R. Albrecht *et al.*, Eur. Phys. J. C **5**, 255–267 (1998).
[10] B. Andersson, G. Gustafson, and H. Pi, Z. Phys. C **57**, 485 (1993).
[11] K. Werner, Phys. Rep. **232**, 87 (1993).
[12] U. A. Wiedemann and U. Heinz, Phys. Rev. C **56**, 3265 (1997).
[13] C. Blume, Doctoral thesis, University of Münster, Germany, 1998.
[14] WA80 Collaboration, R. Albrecht *et al.*, Phys. Lett. B **201**, 390 (1987).
[15] HELIOS Collaboration, T. Åkesson *et al.*, Z. Phys. C **46**, 361 (1990).
[16] E866 Collaboration, L. Ahle *et al.*, Nucl. Phys. **A610**, 139c (1996).
[17] SFM Collaboration, A. Breakstone *et al.*, Phys. Lett. B **183**, 227 (1987).
[18] UA1 Collaboration, G. Arnison *et al.*, Phys. Lett. **118B**, 167 (1982).
[19] CDF Collaboration, F. Abe *et al.*, Phys. Rev. Lett. **61**, 1819 (1988).
[20] E735 Collaboration, T. Alexopoulos *et al.*, Phys. Lett. B **336**, 599 (1987).
[21] T. Kafka *et al.*, Phys. Rev. D **16**, 1261 (1977).

Erratum: Centrality Dependence of Neutral Pion Production in 158*A* GeV ^{208}Pb + ^{208}Pb Collisions [Phys. Rev. Lett. 81, 4087 (1998)]

M. M. Aggarwal, A. Agnihotri, Z. Ahammed, A. L. S. Angelis, V. Antonenko, V. Arefiev, V. Astakhov, V. Avdeitchikov, T. C. Awes, P. V. K. S. Baba, S. K. Badyal, A. Baldine, L. Barabach, C. Barlag, S. Bathe, B. Batiounia, T. Bernier, K. B. Bhalla, V. S. Bhatia, C. Blume, R. Bock, E.-M. Bohne, Z. K. Böröcz, D. Bucher, A. Buijs, H. Büsching, L. Carlen, V. Chalyshev, S. Chattopadhyay, R. Cherbatchev, T. Chujo, A. Claussen, A. C. Das, M. P. Decowski, V. Djordjadze, P. Donni, I. Doubovik, M. R. Dutta Majumdar, K. El Chenawi, S. Eliseev, K. Enosawa, P. Foka, S. Fokin, V. Frolov, M. S. Ganti, S. Garpman, O. Gavrishchuk, F. J. M. Geurts, T. K. Ghosh, R. Glasow, S. K. Gupta, B. Guskov, H. A. Gustafsson, H. H. Gutbrod, R. Higuchi, I. Hrivnacova, M. Ippolitov, H. Kalechofsky, R. Kamermans, K.-H. Kampert, K. Karadjev, K. Karpio, S. Kato, S. Kees, H. Kim, B. W. Kolb, I. Kosarev, I. Koutcheryaev, T. Krümpel, A. Kugler, P. Kulinich, M. Kurata, K. Kurita, N. Kuzmin, I. Langbein, A. Lebedev, Y. Y. Lee, H. Löhner, L. Luquin, D. P. Mahapatra, V. Manko, M. Martin, A. Maximov, R. Mehdiyev, G. Mgebrichvili, Y. Miake, D. Mikhalev, G. C. Mishra, Y. Miyamoto, D. Morrison, D. S. Mukhopadhyay, V. Myalkovski, H. Naef, B. K. Nandi, S. K. Nayak, T. K. Nayak, S. Neumaier, A. Nianine, V. Nikitine, S. Nikolaev, P. Nilsson, S. Nishimura, P. Nomokonov, J. Nystrand, F. E. Obenshain, A. Oskarsson, I. Otterlund, M. Pachr, A. Parfenov, S. Pavliouk, T. Peitzmann,* V. Petracek,* W. Pinanaud, F. Plasil, M. L. Purschke, B. Raeven, J. Rak, R. Raniwala, S. Raniwala, V. S. Ramamurthy, N. K. Rao, F. Retiere, K. Reygers, G. Roland, L. Rosselet, I. Roufanov, C. Roy, J. M. Rubio, H. Sako, S. S. Sambyal, R. Santo, S. Sato, H. Schlagheck, H.-R. Schmidt, G. Shabratova, I. Sibiriak, T. Siemiarczuk, D. Silvermyr, B. C. Sinha, N. Slavine, K. Söderström, N. Solomey, S. P. Sørensen, P. Stankus, G. Stefanek, P. Steinberg, E. Stenlund, D. Stüken, M. Sumbera, T. Svensson, M. D. Trivedi, A. Tsvetkov, C. Twenhöfel, L. Tykarski, J. Urbahn, N. v. Eijndhoven, G. J. v. Nieuwenhuizen, A. Vinogradov, Y. P. Viyogi, A. Vodopianov, S. Vörös, B. Wysłouch, K. Yagi, Y. Yokota, and G. R. Young

(WA98 Collaboration)

In this paper, the absolute cross section determination associated with the different centrality selections was made with a limited data set which was not representative of the full analysis. This resulted in a systematic overestimate of the number of participants N_{part} (or the number of collisions). The relative magnitude of this correction is significant for the most peripheral centrality class and nearly negligible for the most central event class. The neutral pion transverse momentum spectra are unchanged. As a result of this correction, the data points of Fig. 2 should be shifted by varying degrees towards the origin on the number of participants scale. However, the conclusion of a saturation of the average transverse momentum with increasing centrality drawn from this figure remains unchanged.

Similarly, the major conclusion of Fig. 3 remains unchanged: In the region of centralities where the saturation of the average transverse momentum is observed, the scaling of the pion yield is independent of the transverse momentum; i.e.,

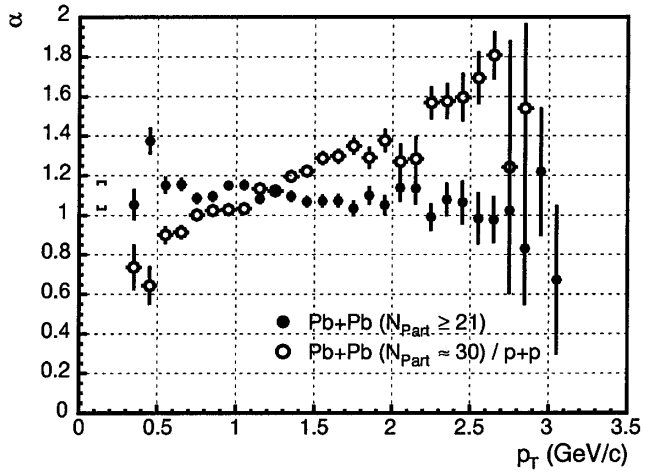

FIG. 1. The exponent $\alpha(p_T)$ of the dependence of the π^0 yield on the average number of participants N_{part} plotted as a function of the transverse momentum for 158*A* GeV Pb + Pb. The solid circles are calculated based on the centrality selections with $N_{\text{part}} \geq 21$. The open circles are calculated based on the ratio of the semiperipheral data ($N_{\text{part}} \approx 30$) to a parametrization of *pp* data. The brackets indicate the estimated systematic error on the exponent α.

 0031-9007/00/84(3)/578(2)$15.00 © 2000 The American Physical Society

the spectral shape does not change. However, with the corrected assignment of the number of participants the scaling exponent is reduced to $\alpha \approx 1.1$ from the value of $\alpha \approx 1.3$ given previously. The corrected version of Fig. 3 is displayed in Fig. 1. In addition to the correction of the cross section determination, the event generator VENUS 4.12 [1] has been used to relate the measured cross section to the number of participants N_{part}. The differences in N_{part} from this calculation compared to various Glauber calculations are used to estimate the systematic error on the exponent α shown in Fig. 1. The values for the exponents α of the scaling from pp data compared to semiperipheral Pb + Pb data are slightly higher than before, while the fit using semiperipheral up to very central Pb + Pb data yields a significantly smaller value. A further conclusion can be drawn from this corrected analysis: At high transverse momentum the increase in pion production going from pp to peripheral heavy ion reactions is much stronger than in going from semiperipheral to central heavy ion reactions.

*The names of these authors were misspelled in the original publication.

[1] K. Werner, Phys. Rep. **232**, 87 (1993).

ELSEVIER

19 February 1998

PHYSICS LETTERS B

Physics Letters B 420 (1998) 169–179

Search for disoriented chiral condensates in 158 AGeV Pb + Pb collisions

WA98 Collaboration

M.M. Aggarwal [a], A. Agnihotri [b], Z. Ahammed [c], A.L.S. Angelis [d], V. Antonenko [e], V. Arefiev [f], V. Astakhov [f], V. Avdeitchikov [f], T.C. Awes [g], P.V.K.S. Baba [h], S.K. Badyal [h], A. Baldine [f], L. Barabach [f], C. Barlag [i], S. Bathe [i], B. Batiounia [f], T. Bernier [j], K.B. Bhalla [b], V.S. Bhatia [a], C. Blume [i], R. Bock [k], E.-M. Bohne [i], D. Bucher [i], A. Buijs [l], E.-J. Buis [l], H. Büsching [i], L. Carlen [m], V. Chalyshev [f], S. Chattopadhyay [c], R. Cherbatchev [e], T. Chujo [n], A. Claussen [i], A.C. Das [c], M.P. Decowski [r], V. Djordjadze [f], P. Donni [d], I. Doubovik [e], M.R. Dutta Majumdar [c], K. El Chenawi [m], S. Eliseev [o], K. Enosawa [n], P. Foka [d], S. Fokin [e], V. Frolov [f], M.S. Ganti [c], S. Garpman [m], O. Gavrishchuk [f], F.J.M. Geurts [l], T.K. Ghosh [p], R. Glasow [i], S.K. Gupta [b], B. Guskov [f], H.A. Gustafsson [m], H.H. Gutbrod [j], R. Higuchi [n], I. Hrivnacova [o], M. Ippolitov [e], H. Kalechofsky [d], R. Kamermans [l], K.-H. Kampert [i], K. Karadjev [e], K. Karpio [q], S. Kato [n], S. Kees [i], H. Kim [g], i B.W. Kolb [k], I. Kosarev [f], I. Koutcheryaev [e], A. Kugler [o], P. Kulinich [r], V. Kumar [b], M. Kurata [n], K. Kurita [n], N. Kuzmin [f], I. Langbein [k], A. Lebedev [e], Y.Y. Lee [k], H. Löhner [p], L. Luquin [j], D.P. Mahapatra [s], V. Manko [e], M. Martin [d], A. Maximov [f], R. Mehdiyev [f], G. Mgebrichvili [e], Y. Miake [n], D. Mikhalev [f], G.C. Mishra [s], Y. Miyamoto [n], D. Morrison [t], D.S. Mukhopadhyay [c], V. Myalkovski [f], H. Naef [d], B.K. Nandi [s], S.K. Nayak [j], T.K. Nayak [c], S. Neumaier [k], A. Nianine [e], V. Nikitine [f], S. Nikolaev [e], S. Nishimura [n], P. Nomokonov [f], J. Nystrand [m], F.E. Obenshain [t], A. Oskarsson [m], I Otterlund [m], M. Pachr [o], A. Parfenov [f], S. Pavliouk [f], T. Peitzmann [i], V. Petracek [o], F. Plasil [g], M.L. Purschke [k], B. Raeven [l], J. Rak [o], S. Raniwala [b], V.S. Ramamurthy [s], N.K. Rao [h], F. Retiere [j], K. Reygers [i], G. Roland [r], L. Rosselet [d], I. Roufanov [f], C. Roy [j], J.M. Rubio [d], H. Sako [n], S.S. Sambyal [h], R. Santo [i], S. Sato [n], H. Schlagheck [i], H.-R. Schmidt [k], G. Shabratova [f], I. Sibiriak [e], T. Siemiarczuk [q], B.C. Sinha [c], N. Slavine [f], K. Söderström [m], N. Solomey [d], S.P. Sørensen [t],

0370-2693/98/$19.00 © 1998 Elsevier Science B.V. All rights reserved.
PII S0370-2693(97)01528-1

P. Stankus [g], G. Stefanek [q], P. Steinberg [r], E. Stenlund [m], D. Stüken [i], M. Sumbera [o], T. Svensson [m], M.D. Trivedi [c], A. Tsvetkov [e], C. Twenhöfel [l], L. Tykarski [q], J. Urbahn [k], N. v. Eijndhoven [l], W.H. v. Heeringen [l], G.J. v. Nieuwenhuizen [r], A. Vinogradov [e], Y.P. Viyogi [c], A. Vodopianov [f], S. Vörös [d], M.A. Vos [l], B. Wysłouch [r], K. Yagi [n], Y. Yokota [n], G.R. Young [g]

[a] *University of Panjab, Chandigarh 160014, India*
[b] *University of Rajasthan, Jaipur 302004, Rajasthan, India*
[c] *Variable Energy Cyclotron Centre, Calcutta 700 064, India*
[d] *University of Geneva, CH-1211 Geneva 4, Switzerland*
[e] *RRC (Kurchatov), RU-123182 Moscow, Russia*
[f] *Joint Institute for Nuclear Research, RU-141980 Dubna, Russia*
[g] *Oak Ridge National Laboratory, Oak Ridge, TN 37831-6372, USA*
[h] *University of Jammu, Jammu 180001, India*
[i] *University of Münster, D-48149 Münster, Germany*
[j] *SUBATECH, Ecole des Mines, Nantes, France*
[k] *Gesellschaft für Schwerionenforschung (GSI), D-64220 Darmstadt, Germany*
[l] *Universiteit Utrecht / NIKHEF, NL-3508 TA Utrecht, The Netherlands*
[m] *University of Lund, SE-221 00 Lund, Sweden*
[n] *University of Tsukuba, Ibaraki 305, Japan*
[o] *Nuclear Physics Institute, CZ-250 68 Rez, Czech Republic*
[p] *KVI, University of Groningen, NL-9747 AA Groningen, The Netherlands*
[q] *Institute for Nuclear Studies, 00-681 Warsaw, Poland*
[r] *MIT Cambridge, MA 02139, USA*
[s] *Institute of Physics, 751-005 Bhubaneswar, India*
[t] *University of Tennessee, Knoxville, TN 37966, USA*

Received 1 October 1997; revised 23 November 1997
Editor: L. Montanet

Abstract

The restoration of chiral symmetry and its subsequent breaking through a phase transition has been predicted to create regions of Disoriented Chiral Condensates (DCC). This phenomenon has been predicted to cause anomalous fluctuations in the relative production of charged and neutral pions in high-energy hadronic and nuclear collisions. The WA98 experiment has been used to measure charged and photon multiplicities in the central region of 158 AGeV Pb + Pb collisions at the CERN SPS. In a sample of 212646 events, no clear DCC signal can be distinguished. Using a simple DCC model, we have set a 90% C.L. upper limit on the maximum DCC production allowed by the data. © 1998 Elsevier Science B.V.

1. Introduction

The approximate chiral symmetry of the QCD vacuum is believed to be spontaneously broken in nature by the formation of an isoscalar quark condensate. Disoriented Chiral Condensates (DCC) may form in large, hot regions of hadronic matter where this symmetry has been briefly restored [1]. A DCC has an equal probability to be in any state related to the normal vacuum by a chiral rotation. By projecting the space of these available states onto a basis of definite isospin, it has been found that the charge distribution of pions emitted from a single, large DCC domain has a characteristic form [2,3]:

$$P(f) = \frac{1}{2\sqrt{f}} \tag{1}$$

where f is the neutral fraction,

$$f = \frac{N_{\pi^0}}{N_{\pi^0} + N_{\pi^+} + N_{\pi^-}} \quad (2)$$

where N_{π^0}, N_{π^+} and N_{π^-} are respectively the numbers of neutral, positive and negative pions produced. This allows the possibility of hadronic interactions with anomalous fluctuations between charged pions and neutral pions, as seen through their two-photon decay channel.

The phenomenology of DCCs was first introduced in the context of hadronic collisions by Bjorken et al., whose "Baked Alaska" model [4] postulated that a hot shell, expanding at the speed of light, could shield the cool interior from the influence of the normal vacuum outside, allowing a large region of DCC to form. Rajagopal and Wilczek [5,6] studied the production of DCCs in nuclear collisions by studying the chiral phase transition in QCD, via its similarity to the O(4) Heisenberg magnet [7]. Through numerical simulations, they found that as the system rapidly expands and cools through the phase transition, the equations of motion induce a non-equilibrium relaxation of the chiral fields which amplifies the production of soft pion modes in a well-defined chiral direction. This effectively creates clusters of low-p_T pions, with the cluster charge distribution following Eq. (1). It should be noted that, in both studies, the strongest influence on the final state composition is the symmetry itself rather than the exact physics scenario studied. Further work confirmed these initial results, even after accounting for quantum fluctuations, and proposed other mechanisms which might allow for large, long-lived DCCs [1].

By allowing the possibility of events with almost no electromagnetic energy, DCCs are an attractive hypothesis to explain the "Centauro" events seen in cosmic rays [8]. These events have already motivated searches for unusual charge fluctuations at the $S\bar{p}pS$ (by UA1 [9] and UA5 [10]) and at the Tevatron (by Minimax [11] and CDF [12]). And yet, there have been no systematic studies utilizing the simultaneous measurement of charged and neutral multiplicities in heavy ion collisions at any energy. It has been argued [1] that heavy ion collisions at SPS energies, the highest currently available, might create the large volumes which favor the development of long-wavelength oscillations within the reaction zone. It is true that large baryon number in the central region complicates theoretical calculations and may obscure the initial signal via the rescattering of secondaries. It is also possible that most of the pions measured in pp collisions at comparable energies are produced resonantly [13], leaving few "direct" pions which may be influenced by a DCC. We must keep in mind, however, that these are extrapolations from lower energies and smaller systems. Their cumulative effect is uncertain, especially at higher energies where the formation of a quark-gluon plasma would render previous measurements inapplicable. In any case, in the absence of any substantial experimental evidence for or against DCCs in heavy ion collisions at SPS energies, and a great deal of theoretical evidence in their favor, it is imperative to simultaneously measure charged and neutral particles at the SPS and analyze their fluctuations to perhaps isolate a DCC signal. Observing such a signal might be an indication of the chiral phase transition in hot nuclear matter.

2. Experimental setup

The WA98 experiment [14] is a general-purpose, large-acceptance photon and hadron spectrometer with the ability to measure several different global observables event-by-event. For this search, we use a subset of the full apparatus, shown schematically in Fig. 1. We measure charged particles with a Silicon Pad Multiplicity Detector (SPMD) and photons with a Photon Multiplicity Detector (PMD). Using these, we are able to count charged particles and photons in the central pseudorapidity region on an event-by-event basis. For a determination of the centrality of each collision, we use the transverse energy (E_T) measured in the Midrapidity Calorimeter (MIRAC [15]). For removal of background events, we also use the Zero-Degree Calorimeter (ZDC) and the Plastic Ball detector [16].

2.1. Charged particle multiplicity

We count charged particles using a circular Silicon Pad Multiplicity Detector (SPMD) [17] located

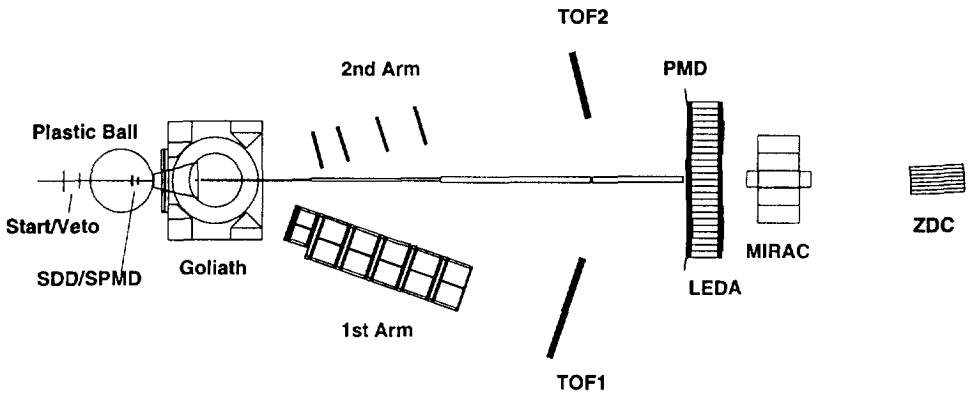

Fig. 1. The WA98 Experiment at the CERN SPS. This analysis uses the Silicon Pad Multiplicity Detector (SPMD) and the Photon Multiplicity Detector (PMD) to measure the charged and neutral multiplicity for each event, and the Mid-Rapidity Calorimeter (MIRAC) for the measurement of event centrality.

32.8 cm from the target covering $2.35 < \eta < 3.75$, the central rapidity region at SPS energies (where $\eta_{\rm CMS} = 2.9$), and full azimuth. The detector consists of four overlapping quadrants, each fabricated from a single 300 μm thick silicon wafer. The active area of each quadrant is divided into 1012 pads forming 46 azimuthal wedges and 22 radial bins with a pad size increasing with radius to provide uniform pseudorapidity coverage. The efficiency of detecting a charged particle in the active area has been determined in a test beam to be better than 99%. Conversely, the detector is transparent to high energy photons, since only about 0.2% are expected to interact in the silicon. During the data taking, 95% of the pads worked properly and are used in this analysis.

In a central Pb + Pb collision, the occupancy can be as high as 20%, implying that $\approx 20\%$ of the hit pads contain two or more particles, a "hit" being defined as a pad with a deposited energy exceeding 1/2 of the most probable energy loss. An unbiased way to estimate the total number of charged particles in a given event under such conditions is to use the sum of the energy deposited in hit pads divided by the mean energy loss per particle as determined in low-multiplicity events:

$$N_{\rm ch} = \sum_{i=\rm hits} \frac{dE/dx_i}{\langle dE/dx \rangle}.$$

Because of the fluctuations in the energy loss, described by a Landau distribution, the uncertainty on $N_{\rm ch}$ can be estimated to be $\Delta N_{\rm ch}/N_{\rm ch} = 60\%/\sqrt{N_{\rm ch}}$, the numerator being the width of the Landau distribution with the peak normalized to 1. For typical central events with a multiplicity of ≈ 600, this gives an uncertainty of about 2%. To check the overall scale, we compare the results with the multiplicity obtained by assuming that the particles are distributed uniformly so the multi-hit probability is given by Poisson statistics. A simple calculation gives $N'_{\rm ch} = -N_{\rm pads}\log(1 - N_{\rm hits}/N_{\rm pads})$, where $N_{\rm pads}$ is the total number of pads, and $N_{\rm hits}$ is the total number of hits. Using this as a check, we estimate the systematic error on $N_{\rm ch}$, due to uncertainties in the gains and backgrounds, to be about 4%.

2.2. Photon multiplicity

We count photons in the preshower Photon Multiplicity Detector (PMD) situated 21.5 m from the target, covering the region $2.8 < \eta < 4.4$. The photons impinging on the detector are converted in 3.34 X_0 thick lead and iron and the secondaries are detected in 3mm-thick square plastic scintillator pads of varying sizes (15mm, 20mm and 23mm). A matrix of 50 × 38 pads is placed in one light-tight box module and read out individually via wavelength shifting optical fibers coupled to an image intensifier and CCD camera system similar to that described in [18]. The modules with smaller pads were mounted in the forward angle region to minimize cluster overlap at large multiplicities and to provide reason-

ably uniform occupancy. Out of a total of 28 box modules implemented in the PMD, the data presented here correspond to 19 box modules having 35524 pads. The average occupancy for the part of the detector considered in the present case is around 15% for central events.

The principle of photon identification makes use of the fact that photons are more likely to shower in the lead converter and produce a large signal in the scintillator pads, while non-showering hadrons will produce a signal corresponding to a single minimum ionizing particle (MIP). Signals from several neighbouring pads are combined to form clusters and those with energy deposition larger than that corresponding to 3 MIPs are considered to be "γ-like" clusters. We denote the number of γ-like clusters in each event as "$N_{\gamma\text{-like}}$". This selection criteria gives an average photon counting efficiency of about 70% which is almost uniform over the range of centrality and pseudorapidity considered. It also creates an effective lower p_T cutoff of 30 MeV/c, at which point the efficiency falls below 35%. About 15% of the produced hadrons impinging on the PMD interact in the converter, generating secondaries which also deposit large energy on the detector. This contamination constitutes a background to photon counting. In order to minimize effects due to variations in the angular distributions of charged particles, we only use data with the Goliath magnet turned off.

The lead target, the exit window of the vacuum chamber (extending to the edge of the magnet), and the air gap between the magnet and the PMD constitute about $10\% X_o$ of material upstream of the PMD. Although some low-energy photons tend to convert in the material and escape detection, higher-energy photons tend to be detected via a high-energy conversion electron or positron.

The photon counting efficiency, hadron contamination and the associated errors are derived using test beam data and GEANT simulation using a method similar to the ones described in [18,19]. The level of hadron contamination in the PMD was verified by comparing the azimuthal distribution of hits for magnet-on and magnet-off data [20]. The azimuthal distribution of charged tracks becomes very non-uniform in the presence of the magnetic field, the amount of non-uniformity indicating the magnitude of the hadron contamination.

It should be emphasized that in this analysis, we do not correct the data using the abovementioned parameters. Instead we account for all of the detector effects by fully simulating the conversion of particles in the detector, as described below.

2.3. Data and event selection

In this analysis, we study reactions induced by a 158 AGeV Pb beam incident upon a 213 μm thick ^{208}Pb target. The fundamental "beam" trigger condition consists of a signal in a gas Čerenkov start counter [21] located 3.5 meters upstream of the target and no coincident signal in a veto counter with a 3mm circular hole located 2.7 meters upstream from the target. A beam trigger is considered to be a minimum-bias interaction if the transverse energy sum in the full MIRAC acceptance exceeds a lower threshold.

Pileup events are eliminated by a combination of the start counter ADC, which measures the number of beam particles passing through the counter, and a system of TDCs each started by a particular trigger counter and stopped by a second trigger. Using these, we remove events where a second interaction trigger occurred within a $\pm 10\mu$s window before and after the recorded event. After these cuts, we estimate that .02% of the remaining events are due to pileup. In addition pileup events are eliminated by requiring the sum of energy deposited in the MIRAC ($3.5 < \eta < 5.5$) and ZDC ($\eta > 6$) to be consistent with a single event. This leaves us with .01% of the event sample which may contain pileup events with less than 70 additional particles at mid-rapidity. After applying all cuts, 70% of the data sample remains.

3. General features of data and comparison with VENUS 4.12

To describe the bulk of the data, we use the VENUS 4.12 [22] event generator with its default settings. To compare VENUS with our data, we propagate the raw generator output through a full simulation of our experimental setup using the GEANT 3.21 [23] package from CERN. The simulation incorporates the detector physics effects and

folds them into the generated data, which is then analyzed using the same code used for the raw experimental data. In the rest of this paper, the term "VENUS" refers to the combination of VENUS 4.12 and the full GEANT 3.21 detector simulation, not to the raw generator output, unless otherwise specified.

The SPMD simulation includes the effect of Landau fluctuations in the energy loss of charged particles in the silicon and the pad geometry of the detector. In addition to the secondaries from the ion-ion collision itself, the SPMD is also sensitive to the beam halo as well as the δ-rays generated by the $^{82+}$Pb ion passing through the lead target. Since we have no means by which to distinguish the two components, we refer to all of the particles produced in beam events as "δ-rays". We can get a conservative estimate of the δ-ray multiplicity in physics events by studying events that satisfy the conditions for a beam trigger but not the interaction trigger. These "beam" events have a mean multiplicity in the SPMD of $11.4 \pm .5$ and a width of $5.9 \pm .3$. The angular distribution is consistent with a spatially uniform illumination of the detector surface. To include these ion-induced δ-rays in the simulation, we sample the measured charged multiplicity distribution for beam events and add it to the charged particle multiplicity for each simulated event. We estimate the uncertainty in the absolute scale of $N_{\rm ch}$ from the simulation to be less than 3% and the relative uncertainty between data and VENUS to be less than 2%.

The PMD simulation also incorporates the effects of additional fluctuations to the energy loss arising due to the statistical nature of the scintillation process; light transport through the wavelength shifting fibres and the image intensifier chains; and imperfections in the electro-optical imaging. The widths due to this extra fluctuation were obtained by a comparison of the GEANT and test beam results using single pions and electrons at various energies. As all of the readout chains were not used in the test beam experiment, a method of detailed intercomparison of the various features of data and simulation was used to obtain the gains of the individual readout units. We estimate the uncertainty on the absolute multiplicity scale of simulated γ-like clusters, due to uncertainties in various parameters of the simulation and data analysis, to be 15%, and that the relative uncertainty between data and VENUS is 5%.

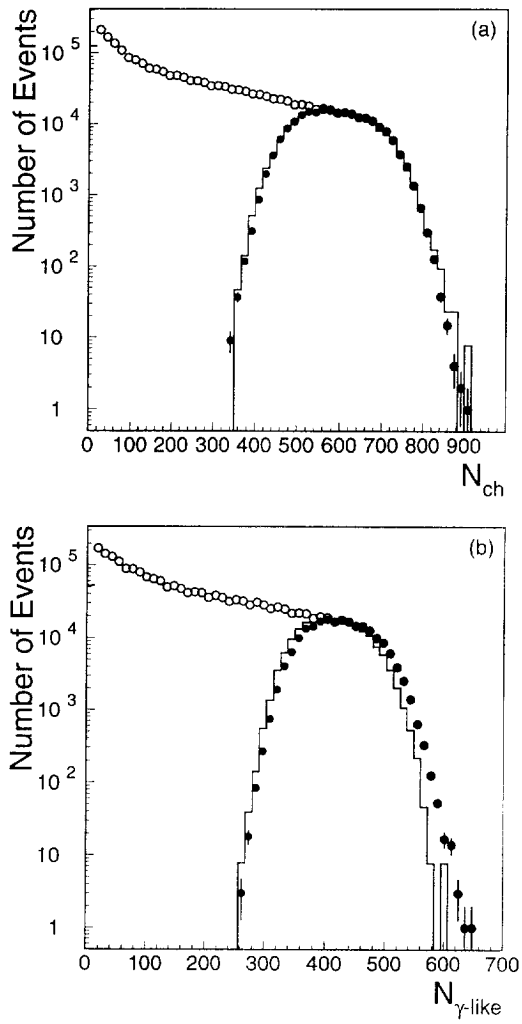

Fig. 2. The charged and neutral multiplicity distributions are shown in a) and b). The open circles represent the minimum-bias distribution. The "central" sample ($E_T > 300$ GeV) is represented by closed circles for the data and by histograms for VENUS.

In Figs. 2a and 2b we present the minimum-bias multiplicity distribution for charged particles and γ-like clusters. For the DCC search, we will concentrate on the most central events, defined by a measured transverse energy of at least 300 GeV in $3.5 < \eta < 5.5$. These correspond roughly to 10% of the measured Pb + Pb minimum bias cross section $\sigma_{\rm mb} = 6200 \pm 620$ mb. After all cuts are applied,

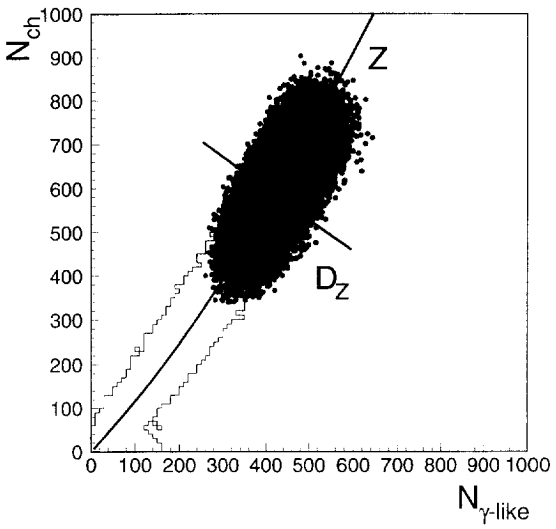

Fig. 3. The scatter plot showing the correlation between N_{ch} and $N_{\gamma\text{-like}}$. The solid outline shows the trend of the minimum bias data. The central sample (with $E_T > 300$ GeV) is shown as points for the data and as a hatched region for VENUS (with much lower statistics). Overlaid on the plot are the Z axis and the D_Z axis at a particular value of Z as explained in the text.

there are 212646 events in this sample, which we will refer to as the "central" sample in the rest of this paper. The central data sample is shown by closed circles in Figs. 2a and 2b and a comparison with VENUS events chosen by identical cuts is shown by the histogram. The correlation between the charged and neutral multiplicities is presented in Fig. 3 with the minimum bias distribution outlined, the central VENUS events hatched, and the central data events shown as scattered points, each point corresponding to a single event.

The most distinctive feature of the scatter plot is the strong correlation between the charged and neutral multiplicities. A reasonable explanation of this would be if most of the produced particles are pions with their charge states partitioned binomially, as measured in pp experiments at similar energies [24,25]. A binomial distribution leads to a correlation width $\sigma(N_{ch} - N_\gamma) \propto \sqrt{N_{ch} + N_\gamma}$, which would explain the very tight correlation, since the relative fluctuations are proportional to $1/\sqrt{N_{ch} + N_\gamma}$ and $N_\gamma \propto N_{\gamma\text{-like}}$. As this is seen in both data and VENUS, we can study the contributions to the different multiplicities to verify this hypothesis. In fact, about 80% of the charged particles produced in VENUS and detected in the SPMD are pions, the rest being protons and kaons. Most of the particles are produced at the interaction vertex, the rest being from η and strange decays, 12% coming from V_o's alone. About 85% of produced photons come from π^0 decays. Thus, by simply counting the charged particles and photons produced in a heavy ion collision, we have a reasonable estimate of the number of charged and neutral pions created.

We verify the binomial nature of the charge fluctuations in VENUS by studying its "binomiality":

$$B = \frac{N_{\pi_{ch}} - p_{ch} N_\pi}{\sqrt{p_{ch}(1 - p_{ch}) N_\pi}} \tag{3}$$

where $N_{\pi_{ch}}$ and N_π are number of charged pions and the total number of pions for each event, and $p_{ch} = N_{\pi_{ch}}/N_\pi$ is the probability that a pion is charged. For a pure binomial distribution, $p_{ch} = 2/3$ and B has a Gaussian distribution with a mean at zero and an RMS of one. For VENUS without GEANT, we find an RMS of approximately .95 for pions produced in the central rapidity region in events with an impact parameter less than 6 fm. This is consistent with the hypothesis that the correlation arises mainly from the binomial partition of N_π, the total pion multiplicity.

4. Event-by-event search for DCCs

DCCs should modify the binomial partitioning of N_π into charged and neutral pions. Events in which a DCC is produced (henceforth referred to as "DCC events") will show up as deviations from the binomial behavior and appear as outliers with respect to the bulk of the data. We have already discussed that the charged and neutral multiplicities are directly sensitive to the charged and neutral pion multiplicities in each event. Thus, DCC events should appear in the correlation of charged and neutral multiplicities, while the individual distributions will be mainly unaffected.

4.1. Data analysis

The strong correlation between charged and neutral multiplicities described above suggests a more

appropriate coordinate system with one axis being the measured correlation axis and the other perpendicular to it. If all detected particles were pions and the detectors were perfect and had identical pseudorapidity acceptance, then the correlation axis would be a straight line. Instead, we must account for the fact that at high multiplicities, the pseudorapidity distributions tend to narrow, changing the relative acceptance of charged and neutral particles due to the non-identical apertures of the SPMD and PMD. Moreover, the large occupancies in the PMD lead to a slight saturation effect. It is then useful to define a coordinate system consisting of a correlation axis (Z) described by a second-order polynomial, and the perpendicular distance (D_Z) from it, which is defined to be positive for points below this Z axis. These axes are shown superimposed on Fig. 3 and the projection along the Z-axis is shown in Fig. 4a. The full projection along the D_Z-axis is shown in Fig. 4b. To a very good approximation, the data are Gaussian distributed, which is consistent with binomial partition. The VENUS results, shown by the histogram, are also Gaussian, but with a slightly smaller width.

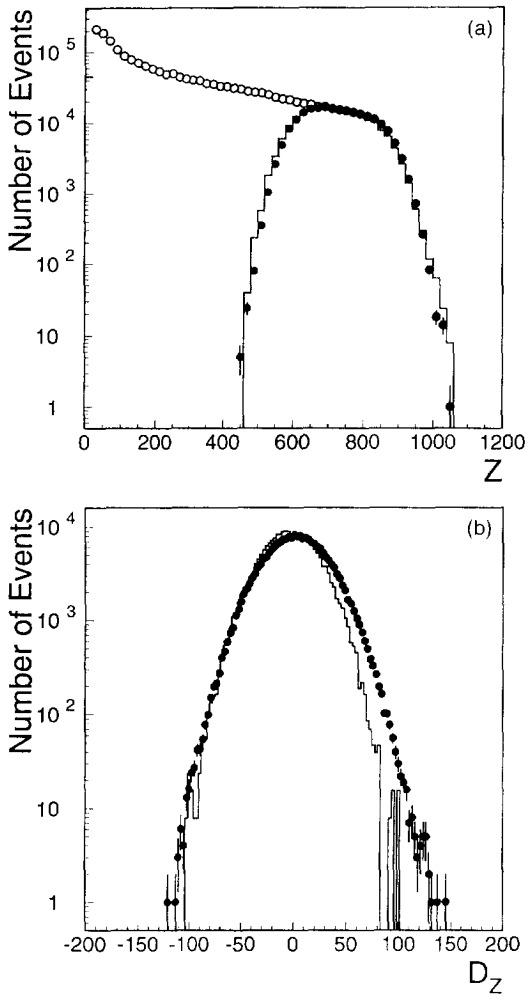

Fig. 4. a.) The distribution of Z, with the same conventions as in Fig. 2. b.) The distribution of D_Z in the "central" sample for the data (closed circles) and for VENUS (histogram). The difference in the mean between the two distributions arises due to the overall scale differences discussed in Section 3.

In both cases, σ_{D_Z}, the standard deviation of a gaussian fit in the D_Z direction, increases with increasing Z. We have chosen to work with the scaled variable $S_Z \equiv D_Z/\sigma_{D_Z}$ in order to compare relative fluctuations at different multiplicities. While binomial partition leads to fluctuations that grow as $\sqrt{N_\pi}$, the data as well as VENUS follow a slightly different power law, due to the presence of contaminating particles, like nucleons kaons, and etas. A reasonable parametrization of σ_{D_Z} for $Z > 200$ has been found to be $\sigma_{D_Z} = C + Z^\beta$ where $C = 7.5 \pm .1$ for the data, and $C = 4.8 \pm .1$ for the simulated events, the exponent being fixed to $\beta = .46$ in both cases. The discrepancy between VENUS and the data can be seen more clearly by measuring the width of the S_Z distribution with the σ_{D_Z} in the denominator taken from the simulation. The VENUS distribution is a gaussian of width $.998 \pm .002$ (fit error only) and the data is also gaussian, of width $1.13 \pm .07$ (error from relative scale uncertainties included). Henceforth, S_Z will refer to D_Z/σ_{D_Z}(VENUS) unless otherwise specified.

4.2. Model of DCC production

To estimate the effect of DCC production we have modified the VENUS events to include characteristic fluctuations in the relative production of charged and neutral pions. We assume that only a single domain of DCC is formed in each central collision. A certain fraction $\zeta = N_\pi^{\mathrm{DCC}}/N_\pi$ of the VENUS pions is associated with this domain (where N_π^{DCC} is the number of DCC pions) and a value of f

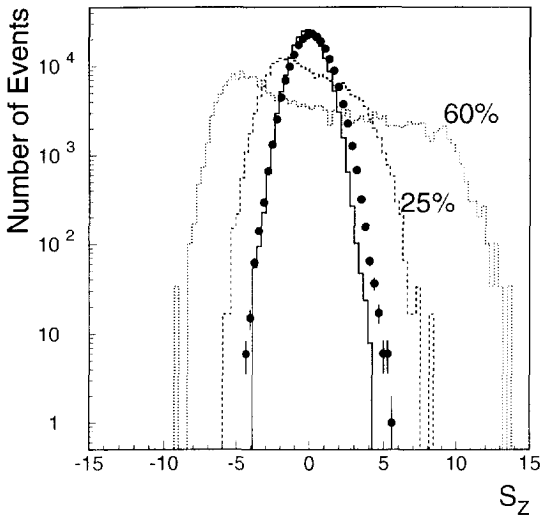

Fig. 5. S_Z distribution for the experimental data is shown, overlaid with VENUS simulations incorporating 0%, 25% and 60% DCC in every event. All of the distributions are normalized to the total number of real events.

is chosen randomly according to the distribution shown in Eq. (1). Then the charges of the pions are interchanged pairwise ($\pi^+\pi^-$ or $\pi^0\pi^0$) until the charge distribution matches the chosen value of f. We do not modify the momentum of the chosen pions, therefore the momentum spectrum of pions produced by a DCC is the same as for the non-DCC pions. This simulates a DCC accompanied by the normal hadronic background in a way that conserves energy, momentum, and charge. The S_Z distribution for the $\zeta = 0\%$, 25% and 60% DCC hypotheses are shown in Fig. 5 with the data overlaid as closed circles. It is clear that the distributions get wider as ζ is increased.

4.3. Upper limit calculation

As seen in the previous section, DCC events will show up as non-statistical tails on the D_Z axis. We see no such events in our data sample. Thus, we are faced with the possibilities that single-domain DCCs are very rare, very small, or both. To check which hypotheses are consistent with our data, we determine upper limits on the frequency of DCC production as a function of its size, as represented by ζ.

We have computed S_Z distributions for several values of ζ, ranging from 15% to 90%. To define an efficiency for detecting DCCs, we start from the observation that the distribution assuming the null hypothesis is Gaussian. With our statistics, we expect few events farther than 5 to 6 σ from the mean. An event containing a DCC, however, has an enhanced probability of being found in this region. The cut $|S_Z| > S_{\rm cut}$ then defines a two-dimensional region in the scatter plot in which all events are considered to be "DCC candidates". Once the cut is set, the DCC efficiency is defined, for $N_{\rm MC}$ VENUS events, as

$$\epsilon(S_{\rm cut},\zeta) = \frac{N(|S_Z| > S_{\rm cut},\zeta)}{N_{\rm MC}} \tag{4}$$

which is a function of both the DCC fraction and the cut position.

The expected non-DCC background is determined by a Gaussian fit to the VENUS distribution assuming $\zeta = 0$, in order to extrapolate beyond the Monte Carlo statistics. With the efficiency and background determined, we calculate the Poisson upper limit $N_{\rm U.L.}$ for a 90% confidence level, which is ≈ 2.3 if there are no measured events over the cut and no background events are expected. These three numbers are combined into an upper limit, for $N_{\rm Data}$ central events, via the formula:

$$\frac{N_{\rm DCC}}{N_{\rm Data}}(S_{\rm cut},\zeta) \le \frac{N_{\rm U.L.}}{\epsilon(S_{\rm cut},\zeta)}\frac{1}{N_{\rm Data}} \tag{5}$$

where $N_{\rm DCC}$ is the number of DCC events.

We have calculated limits for two scenarios. The first is based upon the conservative assumption that VENUS should describe the data perfectly in the absence of a DCC signal. Under these assumptions, $S_Z = D_Z/\sigma_{D_Z}$(VENUS) as obtained from VENUS (the default procedure) and $S_{\rm cut} = 6.$, which is well away from the data point with the largest S_Z. The 90% C.L. limit is presented in Fig. 6 as a solid line. The other scenario assumes that the difference between the data and VENUS is due to detector effects and that the widths should be the same. In this case, $S_Z = D_Z/\sigma_{D_Z}$(data), with σ_{D_Z} taken from the data, and we choose a tighter cut $S_{\rm cut} = 5$. This limit is presented in the same figure as a dashed line. The two limits are quite different at $\zeta = 15\%$ but get closer at $\zeta > 30\%$. In both cases, the uncertainty in the absolute comparisons between the data and

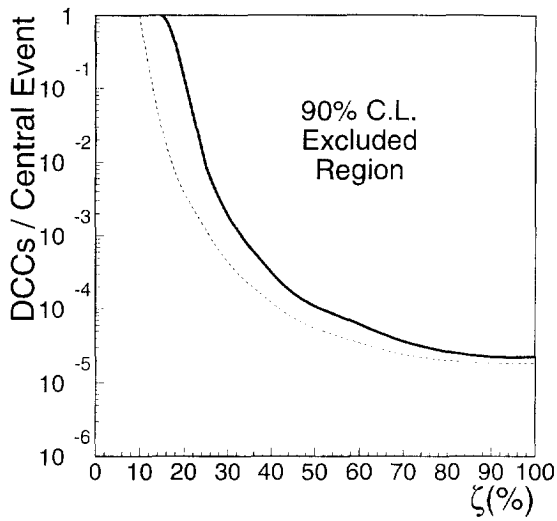

Fig. 6. 90% C.L upper limit on DCC production per central event as a function of the fraction of DCC pions under two assumptions. The thick line gives the upper limit obtained by assuming the σ_{D_Z} in S_Z is completely given by the VENUS calculation requiring to make a cut at 6σ. The dashed line shows a less conservative limit obtained by using the σ_{D_Z} measured in the data itself. This allows us to make a tighter cut at 5σ, increasing the DCC detection efficiency.

VENUS have not been included in the upper limit estimate.

5. Discussion

Earlier studies estimated the DCC radius to be around $R \approx 3$–4 fm. Coupled with a vacuum energy density u given by the chiral effective potential to be 60–120 MeV/fm^3, and an assumed Gaussian p_T distribution of width $\approx 1/R$, an average DCC was thought to generate $\frac{4}{3}\pi R^3(u/m_\pi) \approx 50$–230 pions [26]. The SPMD sees all of the charged particles produced in the central rapidity region, 80% of which are pions, letting us estimate the total number of centrally produced pions in an average event to be about 720. Thus, we would expect a DCC to correspond to $\zeta \approx$ 5–30%. Our analysis clearly rules out anything larger than about 25% within the scope of the assumed model, but cannot say much about anything smaller. However, if the pions tend to cluster in phase space, there are methods that should be able to find DCC events, and these are currently under study [27,28].

A small and frequent DCC might also appear as a slightly enhanced width, similar to what we observe in our data when compared to VENUS. However, this enhancement could also result from uncertainties in the detector modelling or the underlying physics model itself. For instance, theoretical uncertainties might arise because no model has ever been used to study charge correlations in heavy ion collisions. Rescattering phenomena, resonances, or Bose-Einstein effects may have predictable effects on the expected binomial distribution. These issues will be addressed in future studies.

6. Conclusions

We have used the WA98 apparatus to perform the first search for the production of Disoriented Chiral Condensates in 158 AGeV Pb + Pb collisions. No events with large charged-neutral fluctuations have been observed. By comparing the correlations of the charged and neutral multiplicity, measured on an event-by-event basis, to a simple model incorporating a DCC signal into VENUS 4.12 events, we have set a 90% CL upper limit on the frequency of DCC production as a function of its size.

Acknowledgements

We wish to express our gratitude to the CERN accelerator division for excellent performance of the SPS accelerator complex. We acknowledge with appreciation the effort of all engineers, technicians and support staff who have participated in the construction of the this experiment. This work was supported jointly by the German BMBF and DFG, the US DOE, ORISE, the Swedish NFR, the Dutch Stichting FOM, the Stiftung fuer Deutsch-Polnische Zusammenarbeit, the Grant Agency of the Czech Republic under contract No. 202/95/0217, the Department of Atomic Energy, the Department of Science and Technology, the Council of Scientific and Industrial Research and the University Grants Commission of the Government of India, the Indo-FRG Exchange Programme, the PPE division of CERN, the Swiss National Fund, the International Science Foundation under Contract N8Y000, the INTAS under Contract

INTAS-93-2773, Research-in-Aid for Scientific Research (Specially Promoted Research & International Scientific Research) of the Ministry of Education, Science and Culture, the University of Tsukuba Special Research Projects, and the JSPS Research Fellowships for Young Scientists. ORNL is managed by Lockheed Martin Energy Research Corporation under contract DE-AC05-96OR22464 with the US Department of Energy. The MIT group has been supported by the US Dept. of Energy under the cooperative agreement DE-FC02-94ER40818. In addition we would like to thank R. Birgeneau, H.Y. Chang, A.E. Chen, W.S. Edgerly, W.T. Lin, O. Runolfsson and B. Wadsworth.

References

[1] K. Rajagopal, in: Hwa (Ed.), Quark-Gluon Plasma 2, World Scientific, 1995.
[2] A. Anselm, M.G. Ryskin, Phys. Lett. B 266 (1991) 482.
[3] J.P. Blaizot, A. Krzywicki, Phys. Rev. D 46 (1992) 246.
[4] J.D. Bjorken, K.L. Kowalski, C.C. Taylor, SLAC-PUB-6109 1993.
[5] K. Rajagopal, F. Wilczek, Nucl. Phys. B 399 (1993) 395.
[6] K. Rajagopal, F. Wilczek, Nucl. Phys. B 404 (1993) 577.
[7] R.D. Pisarski, F. Wilczek, Phys. Rev. D 29 (1984) 338.
[8] Y. Fujimoto, S. Hasegawa, C.M.G. Lattes, Phys. Rep. 65 (1980) 151.
[9] G. Arnison et al., Phys. Lett. B 122 (1983) 189.
[10] G.J. Alner et al., Phys. Lett. B 180 (1986) 415.
[11] T.C. Brooks et al., Phys. Rev. D 55 (1997) 5667.
[12] P. Melese for the CDF Collaboration, in: Proceedings XI Topical Workshop on $\bar{p}p$ Collider Physics, Padova, Italy, May 27–June 1, 1996.
[13] F. Becattini, U. Heinz, Z. Phys. C 76 (1997) 269.
[14] P. Dönni et al., CERN/SPSLC 91-17 and CERN/SPSLC 95-35.
[15] T.C. Awes et al., Nucl. Instr. and Meth. A 279 (1989) 479.
[16] A. Baden et al., Nucl. Instr. and Meth. A 203 (1982) 189.
[17] W.T. Lin et al., Nucl. Inst. and Meth. A 389 (1997) 415.
[18] M.M. Aggarwal et al., Nucl. Inst. and Meth. A 372 (1996) 143.
[19] M.M. Aggarwal et al., submitted to Phys. Rev. C. (1997).
[20] W.H. van Heeringen, Ph.D. thesis University of Utrecht, 1996.
[21] T. Chujo et al., Nucl. Instr. and Meth. A 383 (1996) 409.
[22] K. Werner, Phys. Rept. 232 (1993) 87.
[23] CERN, GEANT 3.21 Manual.
[24] P. Grassberger, H.I. Miettinen, Nucl. Phys. B 89 (1975) 109.
[25] J. Whitmore, Phys. Rep. C 10 (1974) 273.
[26] S. Gavin, Nucl. Phys. A 590 (1995) 163.
[27] Z. Huang, I. Sarcevic, R. Thews, X.N. Wang, Phys. Rev. D 54 (1996) 750.
[28] T.K. Nayak, in: B.C. Sinha, D.K. Srivastava, Y.P. Viyogi (Eds.), Proc. of International Conf. on Physics and Astrophysics of the Quark-Gluon Plasma (ICPA-QGP'97 New Delhi, 1997), Narosa Publishing House, in press.